

An aerial, black and white photograph of a coastal city, likely San Francisco, showing a large harbor with several ships, a complex network of roads and bridges, and industrial areas. The image is the background for the book cover.

VOLUME I

Coastal Engineering

1978 PROCEEDINGS

PROCEEDINGS
OF THE

Sixteenth Coastal Engineering Conference

August 27 to September 3, 1978
Hamburg, Germany

Volume I

Sponsored by
ASCE Coastal Engineering Research Council
ASCE Waterway, Port, Coastal and Ocean Division
Ministry for Research and Technology
of the Federal Republic of Germany
Free and Hanseatic City of Hamburg,
Association for Port and Coastal Engineering
and
International Association of the
Physical Sciences of the Oceans



Published by the American Society of Civil Engineers
345 East 47th Street, New York, N.Y. 10017
Net Price: \$50.00

ACKNOWLEDGMENTS

The following engineers served as the Organizing Committee for the Sixteenth International Conference on Coastal Engineering:

KARL-EDUARD NAUMANN, Chairman
Association for Port and Coastal Engineering (Hamburg)

HANS-WERNER PARTENSCKY, Co-Chairman
Technical University of Hannover

WINFRIED SIEFERT, Secretary
Port and River Authority, Cuxhaven

ALFRED FÜHRBÖTER
Technical University of Braunschweig

HARALD GÖHREN
Port and River Authority, Hamburg

JOHANN KRAMER
Board of Maritime Works, Aurich

HANS ROHDE
Federal Institute for Waterways Engineering, Hamburg

JOSEF SINDERN
Waterways and Navigation Board North, Kiel

HANS VOLLMERS
University of Federal German Armed Forces, München

The use of photographs by U. Muuss, N. Rüpke, and H. Engler for use on the Parts title pages is gratefully acknowledged.

CONTENTS

ACKNOWLEDGMENTS	iii
-----------------------	-----

WELCOMING ADDRESSES

Dr. -Ing. Karl-Eduard Naumann	1
Burgomaster Mrs. Helga Elstner	4
Minister Dr. Volker Hauff	7
Dr. Hans-Werner Partenscky	10

INVITED LECTURES

STRUGGLE OF PHYSICS AND MATHEMATICS IN COASTAL ENGINEERING H. Lundgren	13
THEME SPEECH: MODELS, CAN WE LEARN FROM THE PAST AND SOME THOUGHTS ON THE DESIGN OF BREAKWATERS W. A. Price	25

PART I THEORETICAL AND OBSERVED WAVE CHARACTERISTICS

Chapter 1 A WORLD WAVE DATA CENTRE Laurence Draper	51
Chapter 2 ON LONG-TERM STATISTICS FOR OCEAN AND COASTAL WAVES Michel K. Ochi	59
Chapter 3 WIND WAVE FREQUENCIES IN A TROPICAL CYCLONE REGION Rodney J. Sobey	76
Chapter 4 COMPARISON OF SHIPBORNE WAVE RECORDER AND WAVERIDER BUOY DATA USED TO GENERATE DESIGN AND OPERATIONAL PLANNING CRITERIA C. G. Graham, G. Verboom and C. J. Shaw	97
Chapter 5 WAVE CLIMATE IN SOME ZONES OFF THE BRAZILIAN COAST Alberto Homsí	114

Chapter 6	
WAVE CLIMATE STUDY IN THE REGION OF THE EAST FRISIAN ISLANDS AND COAST	
Hanz Dieter Niemeier	134
Chapter 7	
AN EVALUATION OF EXTREME WAVE CLIMATE AT KEAHOLE POINT, HAWAII	
Charles L. Bretschneider and Richard E. Rocheleau	152
Chapter 8	
THE USE OF IMAGING RADAR IN STUDYING OCEAN WAVES	
M. G. Mattie and D. Lee Harris	174
Chapter 9	
H F SKYWAVE RADAR MEASUREMENT OF HURRICANE WINDS AND WAVES	
Joseph W. Maresca, Jr., and Christopher T. Carlson	190
Chapter 10	
RADAR OBSERVATION OF HURRICANE WAVE DIRECTIONS	
D. B. King and O. H. Shemdin	209
Chapter 11	
THE OBSERVED JOINT DISTRIBUTION OF PERIODS AND HEIGHTS OF SEA WAVES	
Yoshimi Goda	227
Chapter 12	
ANOMALOUS DISPERSION OF FOURIER COMPONENTS OF SURFACE GRAVITY WAVES IN THE NEAR SHORE AREA	
Fritz Büsching	247
Chapter 13	
INFRAGRAVITY WAVES IN STORM CONDITIONS	
R. A. Holman, D. A. Huntley and A. J. Bowen	268
Chapter 14	
EXTREMAL PREDICTION OF SIGNIFICANT WAVE HEIGHT	
Enrique Copeiro	285
Chapter 15	
DEEPWATER DIRECTION FROM AN INTENSITY ARRAY	
Alan L. Higgins and Richard J. Seymour	305
Chapter 16	
NATURAL WAVE TRAINS: DESCRIPTION AND REPRODUCTION	
H. Lundgren and S. E. Sand	312

Chapter 17		
WAVE LENGTH, WAVE VELOCITY AND SHOALING CHARACTERISTICS OF RANDOM WAVES		
Akira Kimura and Yuichi Iwagaki		320
Chapter 18		
PERIODIC THEORY VELOCITY PREDICTION IN RANDOM WAVE		
John H. Nath and Koji Kobune		340
Chapter 19		
HIGHER ORDER WAVE SPECTRA		
Paul C. Liu and Albert W. Green		360
Chapter 20		
ANALYSES OF HINGED WAVEMAKERS FOR RANDOM WAVES		
Robert T. Hudspeth, Douglas F. Jones and John H. Nath		372
Chapter 21		
AN INCLINED-PLATE WAVE GENERATOR		
Fredric Raichlen and Jiin-Jen Lee		388
Chapter 22		
CHANGES IN HEIGHT OF SHORT WAVES ON LONG WAVES		
Michio Sato and Kazuo Nakamura		400
Chapter 23		
COMPUTATIONS OF SHORT WAVES IN SHALLOW WATER		
M. B. Abbott, H. M. Petersen and O. Skovgaard		414
Chapter 24		
BOTTOM DISSIPATION IN FINITE-DEPTH WATER WAVES		
S. V. Hsiao and O. H. Shemdin		434
Chapter 25		
EXCITATION OF LOW FREQUENCY TRAPPED WAVES		
Robert King and Ronald Smith		449
Chapter 26		
VOCOIDAL THEORY FOR ALL NON-BREAKING WAVES		
D. H. Swart and C. C. Loubser		467
Chapter 27		
FIELD STUDY OF BREAKING WAVE CHARACTERISTICS		
Lee L. Weishar and Robert J. Byrne		487
Chapter 28		
PROBABILITY DENSITY FUNCTIONS OF BREAKING WAVES		
Edward B. Thornton and George Schaeffer		507

Chapter 29	
WAVE CHARACTERISTICS IN THE SURF ZONE	
I. A. Svendsen, P. A. Madsen and J. Buhr Hansen	520
Chapter 30	
SPILLING BREAKERS, BORES, AND HYDRAULIC JUMPS	
D. H. Peregrine and I. A. Svendsen	540
Chapter 31	
ESTIMATION OF WATER PARTICLE VELOCITY OF BREAKING WAVE	
Tetsuo Sakai and Yuichi Iwagaki	551
Chapter 32	
ENERGY LOSS AND SET-UP DUE TO BREAKING OF RANDOM WAVES	
J. A. Battjes and J. P. F. M. Janssen	569
Chapter 33	
THE ENERGY SPECTRA OF SURF WAVES ON A CORAL REEF	
Theodore T. Lee and Kerry P. Black	588
Chapter 34	
WIND-GENERATED WAVE DIFFRACTION BY BREAKWATER GAP	
Hooshang Raissi and R. L. Wiegel	609
Chapter 35	
DIFFRACTION DIAGRAMS FOR DIRECTIONAL RANDOM WAVES	
Yoshimi Goda, Tomotsuka Takayama and Yasumasa Suzuki	628
Chapter 36	
INFLUENCE OF BREAKWATER-REFLECTION ON DIFFRACTION	
Karl-Friedrich Daemrich and Sören Kohlhase	651
Chapter 37	
A NUMERICAL APPROACH FOR THE DETERMINATION OF THE WAVE HEIGHT DISTRIBUTION IN A HARBOUR	
S. Kohlhase, K.-F. Daemrich, U. Berger, E. Tautenhain and O. Burkhardt	664
Chapter 38	
A COMPARISON BETWEEN MODEL AND PROTOTYPE WAVES IN HARBOURS	
Sverre Bjørndal and Alf Tjørnum	677
Chapter 39	
WAVE HEIGHT DISTRIBUTION AROUND PERMEABLE BREAKWATERS	
Shintaro Hotta	695
Chapter 40	
A COMBINED FE-BIE METHOD FOR WATER WAVES	
A. Hauguel	715

Chapter 41	
WAVE REFRACTION ACROSS A SHEARING CURRENT	
Ivar G. Jonsson and Ove Skovgaard	722
Chapter 42	
EXPERIMENTAL STUDY OF WIND WAVES GENERATED ON CURRENTS	
Hajime Kato and Hiroichi Tsuruya	742
Chapter 43	
VARIABILITY OF LONGSHORE CURRENTS	
R. T. Guza and E. B. Thornton	756
Chapter 44	
LONGSHORE CURRENTS DUE TO SURF ZONE BARRIER	
P. Bettess, C. A. Fleming, J. C. Heinrich, O. C. Zienkiewicz and D. I. Austin	776
Chapter 45	
OBSERVATION OF NEARSHORE CURRENT AND EDGE WAVES	
Tamio O. Sasaki and Kiyoshi Horikawa	791
Chapter 46	
COMPARISON OF MODEL AND OBSERVED NEARSHORE CIRCULATION	
James H. Allender, John D. Ditmars, Wyman Harrison and Robert A Paddock	810
Chapter 47	
RIP CURRENT SPACING AS AN EIGENVALUE	
Noriyuki Iwata	828
Chapter 48	
WIND-INDUCED WATER SURFACE SET-UP AND DRIFT CURRENTS	
Frederick L. W. Tang, Jin Wu, Charles C. C. Chang and Shan-Hwei Ou	841
Chapter 49	
DRIFT SPEED OF BUOYS IN WAVES, WITH APPENDIX BY M. S. LONGUET- HIGGINS	
John H. Nath	859
Chapter 50	
NEAR-BOTTOM CURRENT MEASURED BY ACOUSTIC SENSORS	
K. A. Selanger and T. Carstens	878
Chapter 51	
OSCILLATORY LAMINAR FLOW ABOVE A ROUGH BED	
C. B. George and J. F. A. Sleath	898
Chapter 52	
EXTREME SEA LEVELS FROM TIDE AND SURGE PROBABILITY	
D. T. Pugh and J. M. Vassie	911

Chapter 53		
ANALYSIS OF MAXIMUM SEA LEVELS IN SOUTHERN ENGLAND		
J. Graff and D. L. Blackman		931
Chapter 54		
FREQUENCIES AND PROBABILITIES OF EXTREME STORM SURGES		
Alfred Führbötter		949
Chapter 55		
STORM SURGE PREDICTION BY COMBINED WIND AND TIDE DATA		
Hermann Christiansen and Winfried Siefert		965
Chapter 56		
NUMERICAL STORM SURGE FORECASTING		
Manfred Engel		975
Chapter 57		
STORM SURGE PREDICTION IN TIDAL RIVERS: A NEW CONCEPTION		
Winfried Siefert		986
Chapter 58		
STORM SURGE FORECASTING METHODS IN ENCLOSED SEAS		
P. F. Hamblin		998
Chapter 59		
ANALYSIS OF STORM TIDE WAVES		
Volker Barthel		1016
Chapter 60		
COASTAL FLOOD SIMULATION IN STRETCHED COORDINATES		
H. Lee Butler		1030
Chapter 61		
ADJUSTMENT AND VERIFICATION OF THE RANDDELTA II MODEL		
A. Langerak, M. A. M. de Ras and J. J. Leendertse		1049
Chapter 62		
WAVE SET-UP IN THE SURF ZONE		
Uwe A. Hansen		1071
Chapter 63		
ROLE OF 2D AND 3D MODELS IN JONSDAP '76		
A. M. Davies		1085
Chapter 64		
A NEW APPROACH FOR TIDAL COMPUTATIONS		
C. Le Provost		1104
Chapter 65		
HYDRODYNAMIC MODELING OF THE SOUTHERN NORTH SEA		
David Prandle		1122

PROCEEDINGS
OF THE

Sixteenth Coastal Engineering Conference

August 27 to September 3, 1978
Hamburg, Germany

Volume I

Sponsored by
ASCE Coastal Engineering Research Council
ASCE Waterway, Port, Coastal and Ocean Division
Ministry for Research and Technology
of the Federal Republic of Germany
Free and Hanseatic City of Hamburg,
Association for Port and Coastal Engineering
and
International Association of the
Physical Sciences of the Oceans



Published by the American Society of Civil Engineers
345 East 47th Street, New York, N.Y. 10017
Net Price: \$50.00

ACKNOWLEDGMENTS

The following engineers served as the Organizing Committee for the Sixteenth International Conference on Coastal Engineering:

KARL-EDUARD NAUMANN, Chairman
Association for Port and Coastal Engineering (Hamburg)

HANS-WERNER PARTENSCKY, Co-Chairman
Technical University of Hannover

WINFRIED SIEFERT, Secretary
Port and River Authority, Cuxhaven

ALFRED FÜHRBÖTER
Technical University of Braunschweig

HARALD GÖHREN
Port and River Authority, Hamburg

JOHANN KRAMER
Board of Maritime Works, Aurich

HANS ROHDE
Federal Institute for Waterways Engineering, Hamburg

JOSEF SINDERN
Waterways and Navigation Board North, Kiel

HANS VOLLMERS
University of Federal German Armed Forces, München

The use of photographs by U. Muuss, N. Rüpke, and H. Engler for use on the Parts title pages is gratefully acknowledged.

CONTENTS

ACKNOWLEDGMENTS	iii
-----------------------	-----

WELCOMING ADDRESSES

Dr. -Ing. Karl-Eduard Naumann	1
Burgomaster Mrs. Helga Elstner	4
Minister Dr. Volker Hauff	7
Dr. Hans-Werner Partenscky	10

INVITED LECTURES

STRUGGLE OF PHYSICS AND MATHEMATICS IN COASTAL ENGINEERING H. Lundgren	13
THEME SPEECH: MODELS, CAN WE LEARN FROM THE PAST AND SOME THOUGHTS ON THE DESIGN OF BREAKWATERS W. A. Price	25

PART I THEORETICAL AND OBSERVED WAVE CHARACTERISTICS

Chapter 1 A WORLD WAVE DATA CENTRE Laurence Draper	51
Chapter 2 ON LONG-TERM STATISTICS FOR OCEAN AND COASTAL WAVES Michel K. Ochi	59
Chapter 3 WIND WAVE FREQUENCIES IN A TROPICAL CYCLONE REGION Rodney J. Sobey	76
Chapter 4 COMPARISON OF SHIPBORNE WAVE RECORDER AND WAVERIDER BUOY DATA USED TO GENERATE DESIGN AND OPERATIONAL PLANNING CRITERIA C. G. Graham, G. Verboom and C. J. Shaw	97
Chapter 5 WAVE CLIMATE IN SOME ZONES OFF THE BRAZILIAN COAST Alberto Homsí	114

Chapter 6		
WAVE CLIMATE STUDY IN THE REGION OF THE EAST FRISIAN ISLANDS AND COAST		
Hanz Dieter Niemeier		134
Chapter 7		
AN EVALUATION OF EXTREME WAVE CLIMATE AT KEAHOLE POINT, HAWAII		
Charles L. Bretschneider and Richard E. Rocheleau		152
Chapter 8		
THE USE OF IMAGING RADAR IN STUDYING OCEAN WAVES		
M. G. Mattie and D. Lee Harris		174
Chapter 9		
H F SKYWAVE RADAR MEASUREMENT OF HURRICANE WINDS AND WAVES		
Joseph W. Maresca, Jr., and Christopher T. Carlson		190
Chapter 10		
RADAR OBSERVATION OF HURRICANE WAVE DIRECTIONS		
D. B. King and O. H. Shemdin		209
Chapter 11		
THE OBSERVED JOINT DISTRIBUTION OF PERIODS AND HEIGHTS OF SEA WAVES		
Yoshimi Goda		227
Chapter 12		
ANOMALOUS DISPERSION OF FOURIER COMPONENTS OF SURFACE GRAVITY WAVES IN THE NEAR SHORE AREA		
Fritz Büsching		247
Chapter 13		
INFRAGRAVITY WAVES IN STORM CONDITIONS		
R. A. Holman, D. A. Huntley and A. J. Bowen		268
Chapter 14		
EXTREMAL PREDICTION OF SIGNIFICANT WAVE HEIGHT		
Enrique Copeiro		285
Chapter 15		
DEEPWATER DIRECTION FROM AN INTENSITY ARRAY		
Alan L. Higgins and Richard J. Seymour		305
Chapter 16		
NATURAL WAVE TRAINS: DESCRIPTION AND REPRODUCTION		
H. Lundgren and S. E. Sand		312

Chapter 17		
WAVE LENGTH, WAVE VELOCITY AND SHOALING CHARACTERISTICS OF RANDOM WAVES		
Akira Kimura and Yuichi Iwagaki		320
Chapter 18		
PERIODIC THEORY VELOCITY PREDICTION IN RANDOM WAVE		
John H. Nath and Koji Kobune		340
Chapter 19		
HIGHER ORDER WAVE SPECTRA		
Paul C. Liu and Albert W. Green		360
Chapter 20		
ANALYSES OF HINGED WAVEMAKERS FOR RANDOM WAVES		
Robert T. Hudspeth, Douglas F. Jones and John H. Nath		372
Chapter 21		
AN INCLINED-PLATE WAVE GENERATOR		
Fredric Raichlen and Jiin-Jen Lee		388
Chapter 22		
CHANGES IN HEIGHT OF SHORT WAVES ON LONG WAVES		
Michio Sato and Kazuo Nakamura		400
Chapter 23		
COMPUTATIONS OF SHORT WAVES IN SHALLOW WATER		
M. B. Abbott, H. M. Petersen and O. Skovgaard		414
Chapter 24		
BOTTOM DISSIPATION IN FINITE-DEPTH WATER WAVES		
S. V. Hsiao and O. H. Shemdin		434
Chapter 25		
EXCITATION OF LOW FREQUENCY TRAPPED WAVES		
Robert King and Ronald Smith		449
Chapter 26		
VOCOIDAL THEORY FOR ALL NON-BREAKING WAVES		
D. H. Swart and C. C. Loubser		467
Chapter 27		
FIELD STUDY OF BREAKING WAVE CHARACTERISTICS		
Lee L. Weishar and Robert J. Byrne		487
Chapter 28		
PROBABILITY DENSITY FUNCTIONS OF BREAKING WAVES		
Edward B. Thornton and George Schaeffer		507

Chapter 29	
WAVE CHARACTERISTICS IN THE SURF ZONE	
I. A. Svendsen, P. A. Madsen and J. Buhr Hansen	520
Chapter 30	
SPILLING BREAKERS, BORES, AND HYDRAULIC JUMPS	
D. H. Peregrine and I. A. Svendsen	540
Chapter 31	
ESTIMATION OF WATER PARTICLE VELOCITY OF BREAKING WAVE	
Tetsuo Sakai and Yuichi Iwagaki	551
Chapter 32	
ENERGY LOSS AND SET-UP DUE TO BREAKING OF RANDOM WAVES	
J. A. Battjes and J. P. F. M. Janssen	569
Chapter 33	
THE ENERGY SPECTRA OF SURF WAVES ON A CORAL REEF	
Theodore T. Lee and Kerry P. Black	588
Chapter 34	
WIND-GENERATED WAVE DIFFRACTION BY BREAKWATER GAP	
Hooshang Raissi and R. L. Wiegel	609
Chapter 35	
DIFFRACTION DIAGRAMS FOR DIRECTIONAL RANDOM WAVES	
Yoshimi Goda, Tomotsuka Takayama and Yasumasa Suzuki	628
Chapter 36	
INFLUENCE OF BREAKWATER-REFLECTION ON DIFFRACTION	
Karl-Friedrich Daemrich and Sören Kohlhase	651
Chapter 37	
A NUMERICAL APPROACH FOR THE DETERMINATION OF THE WAVE HEIGHT DISTRIBUTION IN A HARBOUR	
S. Kohlhase, K.-F. Daemrich, U. Berger, E. Tautenhain and O. Burkhardt	664
Chapter 38	
A COMPARISON BETWEEN MODEL AND PROTOTYPE WAVES IN HARBOURS	
Sverre Bjørndal and Alf Tjørnum	677
Chapter 39	
WAVE HEIGHT DISTRIBUTION AROUND PERMEABLE BREAKWATERS	
Shintaro Hotta	695
Chapter 40	
A COMBINED FE-BIE METHOD FOR WATER WAVES	
A. Hauguel	715

Chapter 41	
WAVE REFRACTION ACROSS A SHEARING CURRENT	
Ivar G. Jonsson and Ove Skovgaard	722
Chapter 42	
EXPERIMENTAL STUDY OF WIND WAVES GENERATED ON CURRENTS	
Hajime Kato and Hiroichi Tsuruya	742
Chapter 43	
VARIABILITY OF LONGSHORE CURRENTS	
R. T. Guza and E. B. Thornton	756
Chapter 44	
LONGSHORE CURRENTS DUE TO SURF ZONE BARRIER	
P. Bettess, C. A. Fleming, J. C. Heinrich, O. C. Zienkiewicz and D. I. Austin	776
Chapter 45	
OBSERVATION OF NEARSHORE CURRENT AND EDGE WAVES	
Tamio O. Sasaki and Kiyoshi Horikawa	791
Chapter 46	
COMPARISON OF MODEL AND OBSERVED NEARSHORE CIRCULATION	
James H. Allender, John D. Ditmars, Wyman Harrison and Robert A Paddock	810
Chapter 47	
RIP CURRENT SPACING AS AN EIGENVALUE	
Noriyuki Iwata	828
Chapter 48	
WIND-INDUCED WATER SURFACE SET-UP AND DRIFT CURRENTS	
Frederick L. W. Tang, Jin Wu, Charles C. C. Chang and Shan-Hwei Ou	841
Chapter 49	
DRIFT SPEED OF BUOYS IN WAVES, WITH APPENDIX BY M. S. LONGUET- HIGGINS	
John H. Nath	859
Chapter 50	
NEAR-BOTTOM CURRENT MEASURED BY ACOUSTIC SENSORS	
K. A. Selanger and T. Carstens	878
Chapter 51	
OSCILLATORY LAMINAR FLOW ABOVE A ROUGH BED	
C. B. George and J. F. A. Sleath	898
Chapter 52	
EXTREME SEA LEVELS FROM TIDE AND SURGE PROBABILITY	
D. T. Pugh and J. M. Vassie	911

Chapter 53	
ANALYSIS OF MAXIMUM SEA LEVELS IN SOUTHERN ENGLAND	
J. Graff and D. L. Blackman	931
Chapter 54	
FREQUENCIES AND PROBABILITIES OF EXTREME STORM SURGES	
Alfred Führbötter	949
Chapter 55	
STORM SURGE PREDICTION BY COMBINED WIND AND TIDE DATA	
Hermann Christiansen and Winfried Siefert	965
Chapter 56	
NUMERICAL STORM SURGE FORECASTING	
Manfred Engel	975
Chapter 57	
STORM SURGE PREDICTION IN TIDAL RIVERS: A NEW CONCEPTION	
Winfried Siefert	986
Chapter 58	
STORM SURGE FORECASTING METHODS IN ENCLOSED SEAS	
P. F. Hamblin	998
Chapter 59	
ANALYSIS OF STORM TIDE WAVES	
Volker Barthel	1016
Chapter 60	
COASTAL FLOOD SIMULATION IN STRETCHED COORDINATES	
H. Lee Butler	1030
Chapter 61	
ADJUSTMENT AND VERIFICATION OF THE RANDDELTA II MODEL	
A. Langerak, M. A. M. de Ras and J. J. Leendertse	1049
Chapter 62	
WAVE SET-UP IN THE SURF ZONE	
Uwe A. Hansen	1071
Chapter 63	
ROLE OF 2D AND 3D MODELS IN JONSDAP '76	
A. M. Davies	1085
Chapter 64	
A NEW APPROACH FOR TIDAL COMPUTATIONS	
C. Le Provost	1104
Chapter 65	
HYDRODYNAMIC MODELING OF THE SOUTHERN NORTH SEA	
David Prandle	1122

WELCOMING ADDRESS

Dr.-Ing. Karl-Eduard Naumann
President of the Hafenbautechnische Gesellschaft
and
Chairman, Organizing Committee, 16th ICCE

Excellencies, distinguished guests, dear colleagues and friends,
ladies and gentlemen:

On behalf of the Organizing Committee for this 16th International Conference on Coastal Engineering, it is my special privilege as its Chairman to welcome you all very heartily here in the Congress-Center Hamburg to inaugurate a week of lectures and discussions on the manifold problems of Coastal Engineering. The Organizing Committee is very happy about the large number of participants being 621 up to now coming from 41 countries all over the world.

Especially I should like to welcome Mrs. Helga Elstner, second Burgomaster, who is representing the Senate of this Free and Hanseatic City of Hamburg, the host-city for our conference this week. Thank you, Mrs. Burgomaster, for coming here and for your kind readiness to speak to us. In addition, we must give our respectful thanks for the generous sponsorship which the Senate has provided for organizing this conference.

Another special welcome is to Dr. Volker Hauff, Federal Minister for Research and Technology, who has come from Bonn to join this opening ceremony and to speak to us about the viewpoints of the German Federal Government concerning Coastal Engineering, especially the efforts made to defend the low German coast, which, because of its nature is very sensitive to the attacks of the sea. Thank you, Dr. Hauff, for coming and for the assistance and sponsoring your Ministry gave us when we were preparing this conference.

In addition to the Senate of Hamburg and the Federal Ministry for Research and Technology, there are three other sponsors of our conference. First the "Kuratorium für Forschung im Küsteningenieurwesen" which could be translated as the "Committee for Coastal Engineering Research". It is a coordinating and collaboration body of the Federal Republic and four coastal states. The KFKI is supporting our conference by publishing a special issue of the periodical "Die Küste" (the coast), which you all have in your conference-portfolio; it is written both in English and German and gives extensive information about the history and present problem of the German coast as well as pinpointing some features of the relevant research in this country. We are very grateful to the KFKI for this assistance.

The second sponsor is the "Hafenbautechnische Gesellschaft" (HTG), which may be translated as the "Association for Port and Coastal Engineering". This is a scientific association with the aim of studying scientific and practical problems of a technical and economical nature in the following fields:

- planning and constructing ports, port installations and traffic ways within ports;
- operating ports and port installations;
- planning, constructing and operating waterways;
- coastal research and coastal engineering.

This association is the local organizer of our Conference and bears the financial responsibility for it. The Organizing Committee is composed only of members of the HTG.

Last but not least I should gratefully mention the Coastal Engineering Research Council (CERC), borne by the American Society of Civil Engineers under the leadership of our "Grand Old Man" Dean O'Brien and his "Right Hand" Professor Johnson. Since the ICCEs came into existence in 1950, they all have been sponsored by the CERC at least by publishing the proceedings and thus providing the continuity of the respective literature as well as the exchange of the research results.

And now, ladies and gentlemen, let me welcome you all, the participants of this 16th ICCE in Hamburg. After a remarkably long row of conferences held in the past in different countries with different local conditions, the 16th ICCE has been convened to Hamburg, the biggest city of the Federal Republic of Germany, its most important seaport and industrial center. But we hope you will find that Hamburg is also a very beautiful city, worth visiting to enjoy its beautiful features, art treasures, opera and theaters, museums and other attractions. However, it is very difficult for Hamburg to compete with such wonderful settings as Vancouver, Copenhagen and Honolulu, to mention only the sites of the last three Conferences, which, moreover, were all favoured by excellent weather conditions. The Organizing Committee cross their fingers that similar favourable weather conditions will also be granted for this year's conference. After several summer-months spoiled by rain and terrible weather, we hope that now the celestial water reservoirs are empty and you will enjoy Hamburg generally in sunshine.

People in this country are disquieted by the increasing height and frequency of storm surges at our coast. Up to 1961 coastal and harbour engineers worked with a highest high water level, which dated back to 1825. No higher water levels had occurred up to February 1962, when the extreme water level of 1825 was exceeded by about half a meter. Then dikes were damaged heavily at many spots. But the frequency of storm surges continued to grow, and in January 1976 a new alarming water level was measured, which exceeds the peak of 1825 by

nearly one and a half meters. The reasons for this remarkable and disturbing development are contested up to now, as no scientifically founded answer is available on the question of why frequency and peak levels of storm surges at our coast have been growing so vehemently for about 25 years. We see a field of problems here, which will still take much effort to solve. Anyhow, you will understand that due to these facts the public interest in coastal engineering is very lively and widespread in this country. We hope that this conference will make a noteworthy contribution towards solving the problems.

Ladies and gentlemen, I should like to finish my welcoming speech by expressing our sincere thanks for the broad participation in this conference and wishing you all an agreeable and successful time in our country and in this Free and Hanseatic City of Hamburg.

I leave the desk first to Mrs. Burgomaster Helga Elstner, representing the Senate of Hamburg and then to Dr. Volker Hauff, Federal Minister for Research and Technology, representing the Federal Government. Thank you.

WELCOMING ADDRESS

Burgomaster Mrs. Helga Elstner
Senate of the Free and Hanseatic City of Hamburg

Ladies and Gentlemen. In the name of the Senate of the Free and Hanseatic City of Hamburg, and also personally, I welcome you most cordially here in our Congress Centre. We in Hamburg are happy that the International Conference on Coastal Engineering is being held in our city for the first time and that the "Hafenbautechnische Gesellschaft" has been entrusted with its organization.

We are pleased not only because this scientific event animates the diversity of the conference scene here in Hamburg, but also because the people and their representatives in this great seaport have an interest in the topic of coastal engineering which stems quite naturally from its geographical location. This interest in subjects of coastal research is as old as Hamburg itself and goes back almost a thousand years to Hamburg's beginnings as a centre of shipping and trade. Down the centuries they improved and enlarged the port, while the river Elbe, as its link with the sea, was regulated, deepened and protected. In the 14th century, our ancestors built an imposing defensive tower on a small island in the Elbe estuary to protect their shipping. Later on, upon the insecure ground of the shallow and hazardous coastal waters of the rough North Sea, they constructed sea marks, wooden beacons and flares, which had to be well secured against sea attack.

The construction of marks, regulating works along the Elbe as far as the estuary, dike building since the 16th century on the island of Neuwerk and on the coast at Cuxhaven--which belonged to Hamburg from the 14th century until 1937--also the experience and observations of tidal movement, currents, changes in the coastline and other natural phenomena which Hamburg seafarers and pilots collected and evaluated, are part of the knowledge which is now understood worldwide in research and teaching as "coastal engineering".

Stemming from its port interests, Hamburg has in the past made important contributions in this field. I will mention just two examples here. More than a century ago, Heinrich Hübbe, a hydraulics engineer with the authority responsible for the port and the Elbe waterway, and who later became its director, investigated the processes of sand movement in the tidal mudflats of the Elbe estuary and published the results in 1861 in a then epoch-making work. At about the same time Hugo Lentz, another engineer with the same authority, studied the tidal movements in the German Bight. After many years of careful gauge observations, he published the first tide tables for the southern and eastern North Sea coast. Even by our present state of knowledge these show a remarkably high standard of reliability.

But whatever Hamburg's pride in its long history, our attention is focussed very much on the needs of the present. In the field of coastal engineering we are engaged in two tasks which are of the greatest importance:

1. As a tidal harbour and as a city whose limits extend well into the Elbe marshland area, Hamburg is directly affected by the natural phenomena occurring in the North Sea and in the Elbe estuary. Our particular concern here is, of course, the storm tides, which advance in the tidal rivers far into the hinterland. After a long period of relative calm, a great storm tide occurred in 1962 and claimed the lives of many people as well as causing heavy material damage. Steps were immediately taken to make Hamburg safe against future storm tides, but hardly had work been completed before an even higher surge threatened us in 1976. Once again great flood damage was caused, this time particularly in the actual dockland area. These parts now are being well protected. This is a programme which includes not only the building of dikes, flood protection walls, storm barriers, etc., but also research into the problem of storm tides so as to be prepared for possible future developments and, especially, to develop reliable forecasting procedures by which precautions are possible for a good time in advance.
2. A further aspect of our coastal engineering activities is exemplified by a project directly on the North Sea coast. In 1962, following negotiations with the Land of Lower Saxony, Hamburg acquired an area of about 100 km² in the Wadden Sea of the Elbe estuary so as to prepare plans for a so-called outer port and to put these plans into effect when the time came. The location is unique on Germany's North Sea coast. The natural channel there is more than 20 m deep, so that--quite apart from the outer-port function--a harbour could be built for the largest bulk freighters which--because of the tidal conditions in the Elbe--could no longer reach Hamburg. This off-shore location is an area of complicated hydrodynamic and coastal morphologic processes and interrelations which called for extensive investigations, and a research unit was set up especially for this purpose in 1963. The concentrated and now largely completed research programme has, in addition to the immediate planning objectives, yielded valuable scientific information in the field of coastal engineering. These findings were published in the relevant technical literature and also featured in part at the coastal engineering conferences of recent years. But no doubt you all know this better than I do. My intention is merely to underline the fact that the interests of the seaport of Hamburg and your concern with coastal engineering are closely linked. Your field of interest has always been of particular importance for Hamburg as one of the world's leading ports, and it will continue to be so in the future. That is the reason for our particular pleasure in having you here as our guests.

I hope that, in spite of the demands of the Conference, you will find sufficient time to make the acquaintance of Hamburg, to enjoy its atmosphere, and to gain impressions which will remain with you when

you are back home in your own countries with which Hamburg maintains particular ties in peaceful international trade.

WELCOMING ADDRESS

Dr. Volker Hauff
Federal Minister for Research and Technology
Bonn

Ladies and Gentlemen. On behalf of the Government of the Federal Republic of Germany I would like to extend a cordial welcome to you, the participants of the 16th International Congress on Coastal Engineering in Hamburg.

We are especially pleased that you decided to hold your Congress this year near the North Sea after your last one took place on a very beautiful island in the Pacific. In general, these two places have very little in common. But for coastal engineers, both places--apart from providing a nice environment for meetings--have something to offer which is of professional interest to them: the problems of protection against extremely high water levels.

As you all know, the Federal Republic of Germany is a country with a relatively short coastline. Nevertheless, this shore line has always posed many problems to the population living near to it. Dikes have been constructed in Germany along the sea for roughly 1000 years because the coasts are generally flat, and they have to be protected against the impact of storm floods. One of the last most spectacular ones, the storm tide of 1962, caused heavy damage. The surges of 1973 and 1976 showed that the exceptional storm tide of 1962 was not an isolated incident and that even higher water levels may occur in the future--a prospect which leads to many lively discussions among experts and politicians as well as among the population. Of course, nobody knows exactly what the future has in store for us. But this problem must be regarded, as you will do during this Conference, from a scientific, an engineering and from an economic point of view.

Referring to the economic--and that means financial--aspect of coastal protection, I should like to give you a figure indicative of what the Federal Government is spending on improvements in coastal protection. In 1977 alone grants exceeding DM 120 million were provided and another DM 50 million were spent for this purpose by the Länder. But this is only one year under a long-range programme which is to secure the necessary construction work needed to protect the flat 10,000 square-kilometer near-coast areas. This figure gives you, I think, a good idea of the great importance which the government attaches to coastal protection.

There are also other coastal engineering aspects of concern to the Federal Government. In my country the extension and improvement of the navigable waterways is the task of the Federal Government. Shipping is very important for us: the importation of raw materials

and the exportation of industrial products call for safe and efficient ports. The traditional ports like Hamburg are situated on the large tidal rivers and at a distance of up to 100 km from the coast. The navigation channels from and to the harbours have to be developed for very large ships, and they have to be maintained in good condition in spite of the eternal problems of sediment transportation. Moreover, the development of new port facilities closer to the coast is under consideration by the competent authorities requiring careful planning based on a great number of environmental data.

It is obvious that all these practical aspects of coastal engineering must be supported by extensive research projects. Therefore, both the Federal and the Länder governments operate their own laboratories dealing mainly with project-oriented research, while the universities and their institutions primarily carry out basic engineering research. Cooperation between the various laboratories is of great importance because many of them are too small to handle complex projects which often require huge technical facilities and a substantial amount of support. This cooperation is ensured by the Coordinating Committee for Coastal Engineering (Kuratorium für Forschung im Küsteningenieurwesen).

As the Federal Minister responsible for research and technology, I deem it very important that there is always a continuous exchange and transfer of know-how among the institutions and disciplines involved in order to optimize the process of innovation which, in turn, is a prerequisite for progress in science and engineering. One example which illustrates these needs but also shows the possibilities in coastal engineering is the application of remote sensing techniques which permit collection of environmental data in coastal areas. Aircraft and satellites used as data collection platforms can be of considerable benefit to broaden the knowledge of actual coastal processes.

Furthermore, I should like to emphasize the role which coastal engineers can play in advising the developing countries in their needs to develop and manage their coastal areas. The advice in coastal engineering can be of considerable importance to those countries which want to make use of their natural resources, construct ports, control shore erosion or conserve the natural environment. Coastal engineers may also render advice with regard to problems related to the use of the renewable and unrenewable resources of the coastal area and problems of coastal urbanization. Many countries providing good training programmes in coastal engineering should consider the possibility of initiating training programmes for scientific and technical staff of developing countries in order to help them achieve a professional standard enabling them to manage their own coastal problems.

This International Congress provides--I trust--a good opportunity for advancement, continuation and expansion of international cooperation by the exchange of both theoretical results and experience gained in practical field work. Your programme which covers so wide a range of subjects and envisages papers by experts from so many countries will certainly stimulate discussions and will give new impulses to future research work. I therefore trust that you all will benefit

from your participation in this Congress, and I do hope that you will also enjoy your stay in this city and in this country.

Ladies and Gentlemen, I declare the 16th International Congress on Coastal Engineering open, and I sincerely wish you every success in your task.

WELCOMING ADDRESS

Dr. Hans-Werner Partenscky
Technical University of Hannover

Distinguished guests, dear colleagues and friends, ladies and gentlemen,

Dinner speeches are not very popular, neither for the speaker nor for the listeners. I nevertheless feel obliged to say a few words on this occasion.

First, I should like to extend our sincerest thanks to the American Society of Civil Engineers as well as to the Coastal Engineering Research Council, for the honour shown us in permitting the 16th International Conference on Coastal Engineering to be held in the Federal Republic of Germany here in Hamburg. Also, I should like to thank our guest speakers, Prof. Helge Lundgren from Denmark and Mr. Allan Price from the United Kingdom, for their excellent and stimulating speeches which they delivered to the audience during the Conference. Our thanks are equally extended to all authors for their presentations as well as to all those who participated actively in the scientific discussions. They all contributed in a very fine way to scientific progress in our field of Coastal Engineering.

Ladies and Gentlemen, all of you are certainly aware of the fact that Conferences of this kind are not possible without the moral and financial support of potential sponsors. I would therefore like to take this opportunity to address our sincere thanks to the Free and Hanseatic City of Hamburg and to the Federal Ministry for Research and Technology as well as to the numerous private associations, construction companies and consulting engineering firms--the list of all of them is too long to name them individually--for their generous support which helped us considerably to make possible this congress with its social events.

Ladies and Gentlemen, there is an old French saying which I have cited already on other occasions. It says:

"On ne peut pas aimer toutes les femmes du monde, mais on peut au moins essayer."

If I translate this into English, it goes like this:

"You can't be in love with all the women in the world, but you could at least try."

This is the way we felt in the German Organising Committee when we started with the first preparations for this Conference: "We

thought, we could at least try!" We did not know then what was ahead of us. It was only when we found out, that a considerable burden of our task could be delegated to the "German Convention Service", that we felt we would manage. I should therefore like to extend our sincere thanks at this occasion to Mrs. Lau-Thurner and her charming and effective young assistants for their help in preparing this conference. I should also like to mention the Secretary of our Organising Committee, Dr. Siefert, who was involved in many details of our preparations for almost two years. Thank you, Dr. Siefert, for all your efforts.

Gentlemen, there is one last, but very important thank-you, I have the privilege to extend in your name tonight. I would like to thank all ladies who have accompanied their husbands to this Conference and to this Banquet for being here with us and for being so especially beautiful tonight.

Our field of Coastal Engineering is still a relatively young science and more systematic research work is needed to cope with the impact of waves and storm surges against our coasts, and to develop better and more economical design criteria for coastal works. This is clear to us,--but not necessarily so evident to others. Therefore, when preparing this conference, I was often asked by "outsiders": "Why do we need Coastal Engineering?" The answer was of course easy for me. But being a professional, I felt that some more facts and data were needed to support my opinion on the importance of our field. So, I went deeper into the subject. I first investigated our situation in the Federal Republic of Germany by measuring the length of our coastline, the islands included. I then divided this figure by the population. The result was surprising: only a length of 1.9 m was available per person during the summer season.

Being a serious scientist, I assumed that only 30 percent of our population would be at our German beaches at the same time. The result was still unbelievable: only 6 cm of coastline per capita would then be available during the three summer months. No wonder, that it is so crowded at our German Beaches! To find out if this could have an effect on the stability of our shorelines, I consulted some experts of our German Coast Guard. The answer was astonishing: "The damage caused during the 3 month summer season by the tourists,--and especially by the nudists in the dunes,--is comparable to the damage of two average storm floods!

Now, everyone will understand why we need Coastal Engineering and Shore Protection in Germany. Going further into the subject, I found out that the situation with respect to the available length of shoreline per capita in other countries is not quite as critical as in the Federal Republic of Germany. For example, in the Netherlands we have 5 cm of shoreline per capita, in Japan 8 cm, in England 13 cm, in the USA 66 cm, Denmark 150 cm and Australia 180 cm per capita,--to name a few. However, I was informed that swimming at beaches is only allowed in restricted areas in most of these countries, i.e., the tourists are concentrated at certain spots, which certainly means that other countries need coastal engineering and "people management" too! We can be convinced, therefore, that our efforts of these last days

were not in vain and will certainly help to develop, maintain and protect our coasts all over the world.

Ladies and Gentlemen, our Conference comes to an end. We hope that the scientific program with its presentation of more than 200 contributions from 41 different countries will stimulate and help you in your own further research work and that we will all meet again in good health two years from now to the 17th International Conference on Coastal Engineering to be held in Sidney, Australia.

Let me thank all of you for coming to Hamburg. We all wish to those of you who will participate in one of the after-congress excursions much fun and good weather,—and to all of you a happy return to your home countries.

STRUGGLE OF PHYSICS AND MATHEMATICS
IN COASTAL ENGINEERING

H. Lundgren
Technical University of Denmark

ABSTRACT

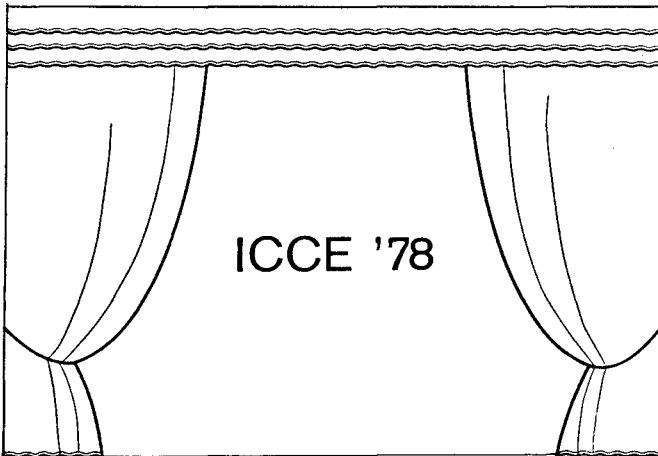
This paper gives examples of the separate and combined efforts of Physics and Mathematics in coastal engineering with particular reference to the possibilities in the future. It points to the fact that physical thinking is necessary as an inspiration to mathematical and numerical work.

While there is relatively little duplication of work (among the various institutions) of a purely theoretical character, the same statement does not apply to numerical models. One may hope that the future will produce more coordination in this respect.

There are two disciplines where the establishment of high quality numerical models will require a particularly strong combination of basic research, numerical expertise and field work: three-dimensional mixing processes and sediment problems. It would seem that no single institution has available both the integrated expertise and the capital investment required. Hence, a close cooperation among several institutions is almost mandatory.

1. INTRODUCTION

A perfect Opening Ceremony has set the stage for

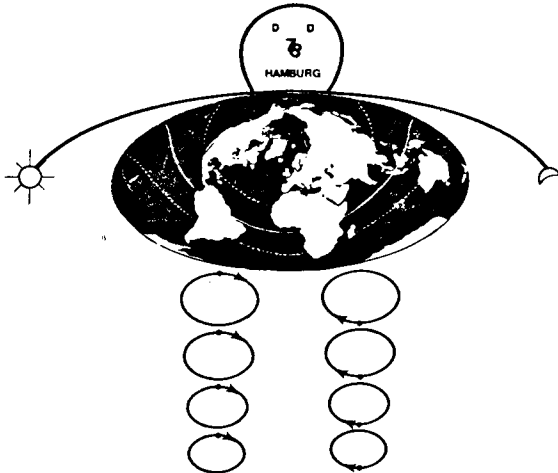


It is indeed a great honour to have been selected by the Organizing Committee to give an invited lecture at such occasion. In addition, it is a very difficult task: Let alone that more than 600 conference participants represent widespread scientific and practical interests within the various fields of coastal engineering; the lecture is also attended by the accompanying ladies.

The first play on this stage has THE CAST:

Mr. PHYSICUS, Master of the play
 Mrs. MATHEMATICA, Mr. Physicus' wife
 Miss NUMERICA, their daughter
 Mr. HARDWARE, Miss Numerica's boyfriend
 Miss SOFTWARE, young girl, often in troubles

Mathematica was married to Physicus at a quite mature age of his. As in all marriages there are both hours of happiness and hours of distress. The serious question about Numerica is: 'Is Physicus her true father or?' If not, very few coastal engineers will respect her. Miss Software is very interested in Mr. Hardware, always trying to get control of him but rarely succeeding!



Mr. PHYSICUS

Physicus was the first figure that entered the stage of Coastal Engineering, both in the sense that harbours and coasts were physical problems, and in the sense that scientific studies normally started with physical models.

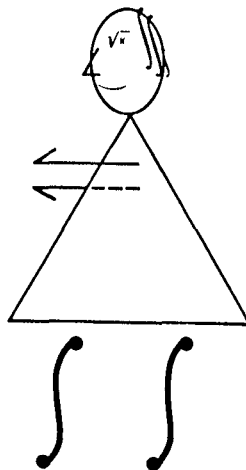
Physicus' main disciplines are:

- a. Wave phenomena
- b. Tides, surges and currents
- c. Mixing phenomena
- d. Sediment problems
- e. Structures

2. WAVE PHENOMENA

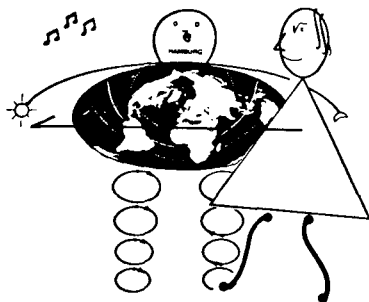
Regular waves is one of the fields where Mathematica has had her greatest triumphs. She has always been very fond of closed (boundary) problems associated with Laplace' equation.

Before Physicus met her, he had made good progress with propagation considerations in shoaling and refraction by assuming that none of the energy flux was reflected from a gently sloping bed. Without improper interference from Mathematica, he should continue his propagation line of research, basing the description in each vertical of the slope on the time profile, i.e. the variation over the period T . Such approach should offer possibilities of treating the deformation of regular waves towards breaking, as well as broken waves (surf).



Mrs. MATHEMATICA

Naturally, when it comes to basic concepts, there is complete harmony between Physicus and Mathematica. For example, the latter originally derived the radiation stress for small sinusoidal waves in combination with a constant current. Physicus, on the other hand, is inclined to think of it as the wave thrust, $F_w = \bar{F}_m + \bar{F}_p$, where \bar{F}_m is the mean value over the wave period of the momentum force, and \bar{F}_p is the mean value of the pressure force. In establishing the equation of mean momentum, he considers the wave thrust as an analogy to the German 'reaction force' (Reaktionskraft), which was used around 1930 in the theory of steady state flow in hydraulic engineering (Wasserbau).



The wave thrust can be determined for any periodic flow, including breakers and surf. Physicus realizes, however, that the mean values, \bar{F}_m and \bar{F}_p , do not give any information about the variation of the momentum and pressure forces over the period. He knows that the equation of momentum is something much more universal than just its 'mean value over the period'. He likes to dream that the general equation of momentum may be used for studying important problems, such as wave deformation and breaking. Of course, the fact that F_p contains a first order term, where \bar{F}_p is of second order, presumably presents a serious difficulty.

In addition, Physicus recalls that the equation of moment of momentum has been used, in a qualitative manner, to explain the formation of sand bars on a coast as the result of water flowing along the sea bed towards the breaker line, where there is a particularly large part of the momentum force near the wave crest. Could it be that the moment of momentum could also be used to explain the skewness of waves on a slope because of the moment of the pressures exerted on the bed by a wave, the height of which increases as the depth decreases?

There is also complete agreement between Physicus and Mathematica with respect to the mean energy level, which is defined for any periodic potential flow. Physicus has difficulties, however, in seeing how the energy concept could be effectively used for the solution of general problems.

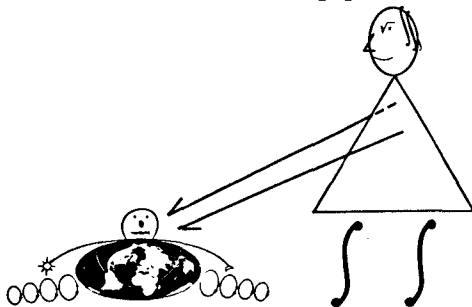
Attention should definitely be drawn to the fairly new concept, wave action, defined as E/ω_r , where E is the total energy of a periodic wave and ω_r its frequency relative to a current. For problems where regular waves are combined with currents it has been proved that the wave action flux and the conservation of wave action are concepts of a fundamental nature, analogous to the energy flux and the conservation of energy in the case of waves without currents.

Relative to the current the wave energy is propagated with the relative wave group velocity, c_{gr} , along the orthogonals. If c_{gr} is vectorially added to the current velocity, the absolute wave group velocity, c_{ga} , results. The direction of c_{ga} is called the wave ray.

For irregular waves the energy is distributed over the frequencies. Hence, it should be possible to apply the wave action concept also to the combination of currents and irregular waves, even with inclusion of the phase and direction information from the waves.

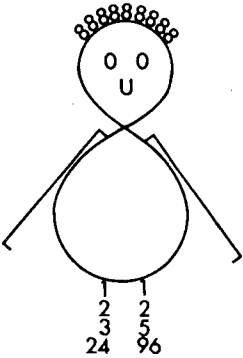
Wave description represents a field where Mathematica has long played a dominant rôle. Firstly, coastal engineers had to work with regular sinusoidal waves. Secondly, cnoidal waves came into the picture; because of the simplifying assumptions necessary, there is not one cnoidal theory but several with some secondary differences. Thirdly, Stokes waves of higher order, up to the fifth, appeared on the stage. In all these cases the waves were periodic and symmetric, even over sloping bed.

Simultaneously with this development, Mathematica transferred the concept 'energy spectrum' from a number of other physical sciences where it had served well since it was introduced in 1923 by Wiener in his 'generalized harmonic analysis'. She has used this tool unscrupulously - with a lot of success too - along our coasts for several decades in spite of two objections: (1) The spectrum is well fit only to a linear Gaussian stochastic process, i.e. a process consisting of



small sinusoidal components. (2) The spectrum throws away half the information (the phase relationships) available in a wave record.

Naturally, Physicus did not like being suppressed by his wife and, indeed, the consequences came about a decade ago when it was discovered that a model wave train with the correct spectrum did not produce one single shock force on a vertical face breakwater. Later on it was realized that the response of moored ships in models could differ much for two wave trains with the same spectrum. And, still worse, the stability of rubble mound breakwaters could be extremely different for two such wave trains.



Miss NUMERICA

Therefore, around 1970 Physicus went into action asking for natural wave trains in his models, also expressed as his desire for the correct wave grouping. The first successes of his action appeared immediately; however, he will have to work very hard together with Mathematica and Numerica before a really satisfactory result will be obtained.

To ask for natural wave trains in physical and numerical models is almost identical to a desire for a deterministic description of natural waves. In two dimensions (wave flumes) it is easy to give such a description under the (quite restrictive) assumption of linear superposition.

In three dimensions the matter is considerably more complicated. For more than a decade rough approximations to directional spectra have been determined by means of arrays of, say, three to five wave recorders. In this context, Mathematica has confined the data analysis to the determination of all the correlation coefficients that could be produced from the records.

Physicus is inclined to prefer a set of three recorders in one vertical (called Point 1): one recording the water surface elevation, η_1 , and two that record the horizontal orbital velocities, u_1 and v_1 . From

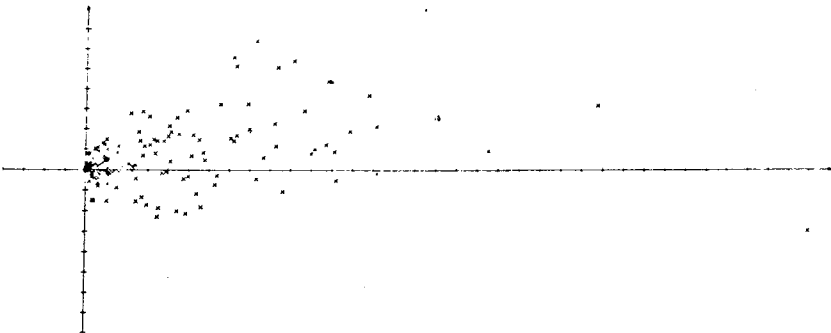


Fig. 1 Energy distribution between 0.2265 hz and 0.2535 hz

these three records it is possible, for each frequency interval, and under the assumption of linear superposition, to determine the directions, the amplitudes and the phases of the components.

From such a recording for a storm situation the components of energy in an interval centered around 0.240 hz have been plotted as the individual points shown in Fig. 1. The frequency interval chosen is the one with most energy. Each point represents a vector from the origin of the coordinate system.

With the knowledge of directions, amplitudes and phases at Point 1, the wave motion may be calculated at some other point, called Point 2. An example of this is illustrated by Fig. 2, where the calculated horizontal u_2 -component has been compared with the recorded one. As a first

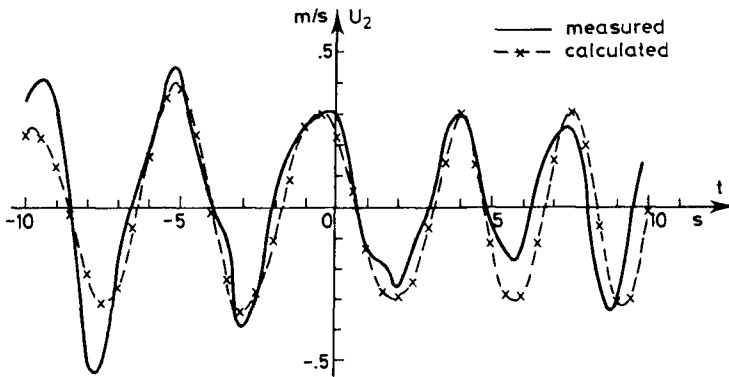


Fig. 2 Horizontal velocity u_2 at point P_2

attempt the agreement is reasonably good. The discrepancies are probably mainly due to two circumstances: (1) The velocity meters were placed rather low, so their response to higher frequencies was strongly damped. (2) The nonlinear interaction of the wave components has not been taken into account. — In this connection it should be mentioned that the vector from Point 1 to Point 2 has a length of about $1.3 \bar{L}$, where \bar{L} is the mean wave length. The vector forms an angle of 22° with the mean direction of wave energy propagation.

With an embryo of a deterministic description available, Physicus suggests that F_m and F_p be investigated as stochastic processes with a view to a deterministic description of the long waves generated in harbours by the groups of short waves.

Recently this connection between long waves and the short wave groups has been demonstrated by two physical model tests with a moored ship in a harbour, as illustrated by Fig. 3. In the upper part of the figure the surge and sway of the ship, as well as the waves in the harbour, are shown with the irregular wave train $\eta(t)$ as input to the model. In the lower part the same quantities appear when the input is $\eta^2(t)$, smoothed as moving average over 30 s.

Until now the investigation of short wave disturbances in harbours, including motion of moored ships, has been a matter for

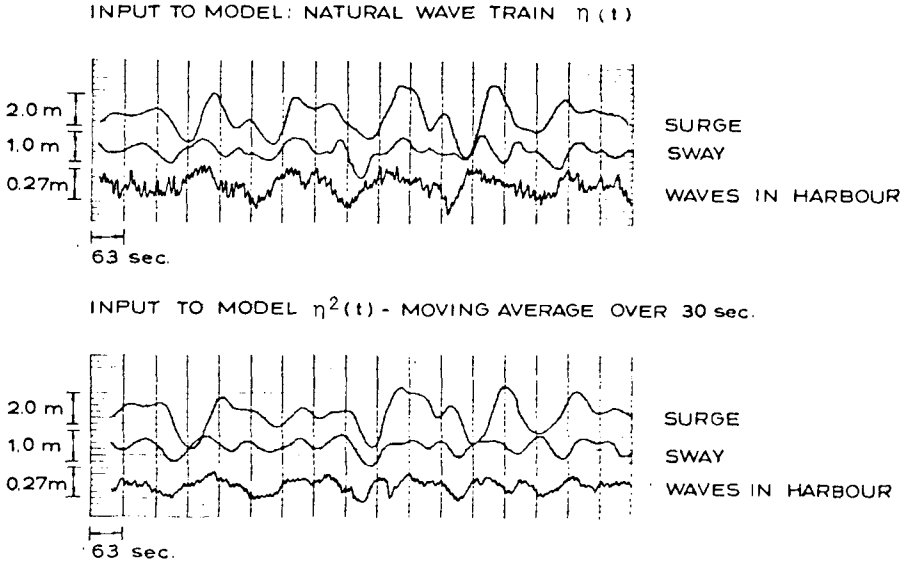
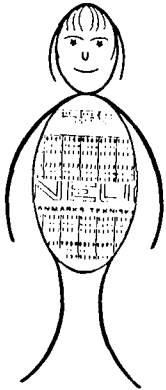


Fig. 3 Ship motions generated by irregular waves and by a simulation of drift forces

physical models exclusively. With Numerica's maturing, however, this field is now within her reach.



Miss SOFTWARE

Provided that the water depth is not too large compared with the essential wave lengths involved, the ordinary shallow water theory may be taken as the starting point. In this theory there are three dependent variables: the surface elevation η and the two horizontal fluxes (p, q) , all of them functions of $(x, y; t)$. Since the vertical accelerations must not be neglected in short waves, four Boussinesq-type terms have to be added to each of the two momentum equations. These terms are mixed derivatives of the third order, which have required special manipulations in order to make Numerica's difference schemes algorithmically efficient. Indeed, in order to handle problems of such complicated nature, Software needed many years of university education.

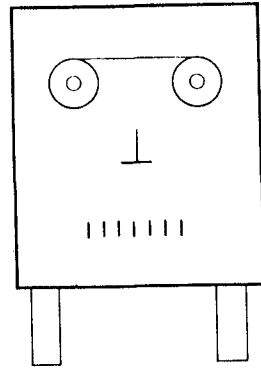
Fig. 4 shows a perspective plot of regular waves in a Danish harbour, as viewed from the harbour entrance.

Since Numerica handles the three difference equations by a time-step method, Software does not notice any difference whether the waves are regular or irregular. For irregular waves Fig. 5 shows the disturbance coefficients K along two wharfs in the same harbour as above, defined by $K = \bar{H}/\bar{H}_1$, where \bar{H} is the mean wave height at the wharf and \bar{H}_1 the mean height of the incoming wave at the entrance. The full curves present the results from a physical model, whereas the dotted curves are produced by Numerica.

If an essential part of the energy pertains to wavelengths that are rather short in comparison with the depth, as is the case in ocean engineering, the Boussinesq-type equations are not sufficiently accurate. Then Numerica will probably have to handle computations in several layers. This may become economical some time in the future when Hardware is willing to work for a lower salary.

Hindcasting and forecasting of the wave weather is already an important field for Numerica's activity and, without any doubt, the future will show greatly increased activity of higher and higher quality.

As illustrated in Fig. 6, the input to a wind wave model may consist of a series of barometric pressure charts. Conveniently, the output may be a series of charts of significant wave heights.



Mr. HARDWARE

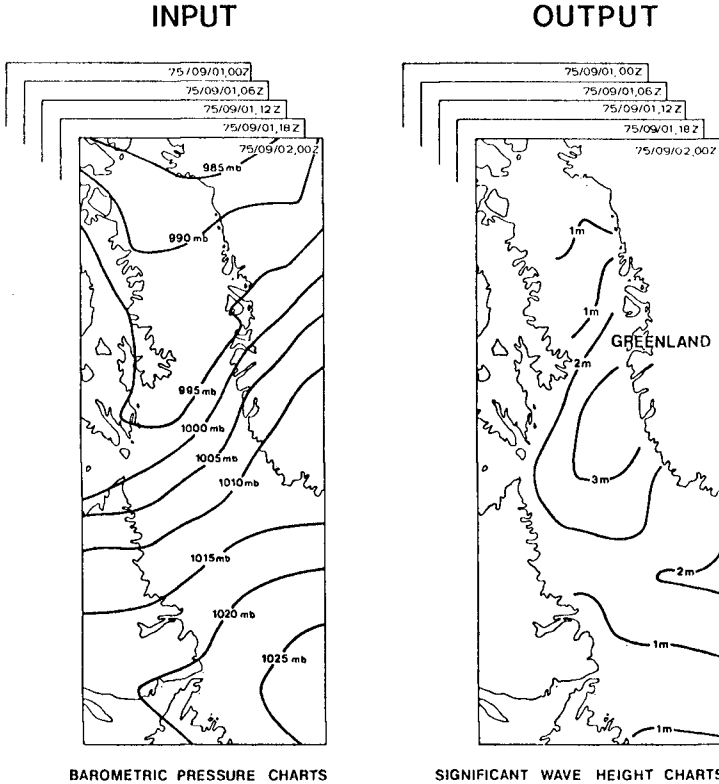


Fig. 6 Input to and output from wind wave model

In order to produce Fig. 6, Numerica discretized the sea surface in $10 \cdot 23 = 230$ grid points with a mesh of 150 km. At each grid point the wave energy was distributed over 12 directions and 10 frequencies, i.e. 120 values. The time step was 3 hours. In the energy transport equation she included both growth and decay terms.

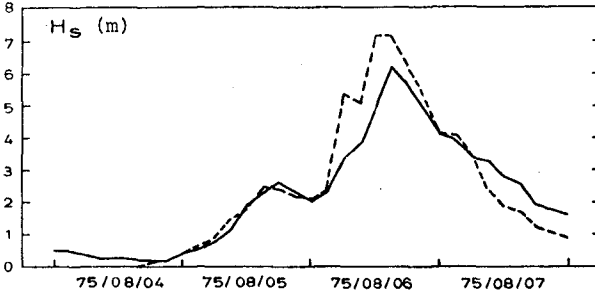


Fig. 7 Variation of wave heights

For a check point near the centre of the area shown in Fig. 6, Fig. 7 gives the variation of the significant wave height during a storm, the full curve indicating the recorded values and the dotted curve the computed ones.

The recorded and computed spectra are compared in Fig. 8. At present the model has a tendency to give peak frequencies that are slightly on the low side. Numerica may remedy this tendency in the future.

Wave breaking has always been, and is still, the wave phenomenon in greatest need of rational treatment, particularly because of its paramount importance for most coastal sediment problems. Qualitative descriptions as spilling, plunging etc. are unsatisfactory. It is hoped that Physicus will soon come up with the combination of quantitative parameters that will characterize the initiation and development of the various breaking processes. Will his thoughts first of all go in the direction of momentum and moment of momentum?

3. TIDES, SURGES AND CURRENTS

In the field of tides and surges, Numerica has been very active in many institutions all over the world, producing a large number of two-dimensional, vertically integrated models. More international coordination at an early stage might have increased the efficiency of intellectual efforts.

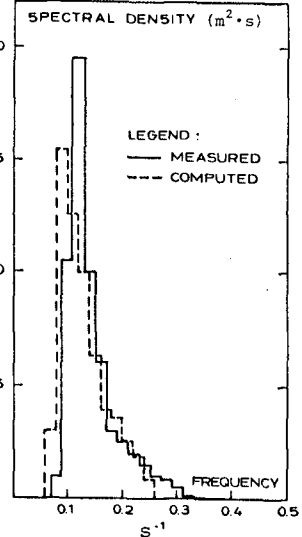
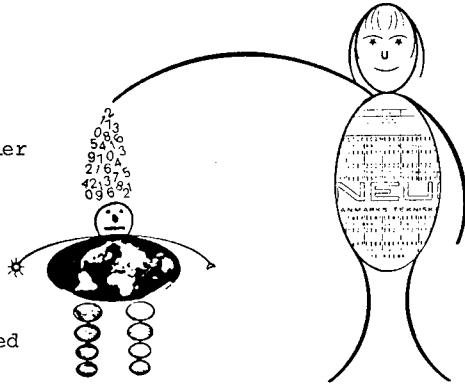


Fig. 8 Spectra

In two different ways Numerica may assist Physicus:

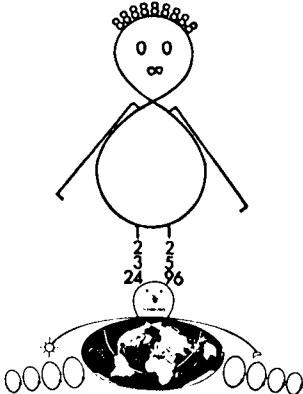
(a) Numerica may treat a larger geographic area with Software designed to deliver data for boundary conditions as input to a smaller area physical model and, perhaps, also data for calibration of the physical model. This combination has been termed a 'hybrid model'.

(b) Numerica may study a larger number of alternatives, prior to the selection of a few for detailed studies in a physical model.



4. MIXING PHENOMENA

Numerica has initiated a large number of two-dimensional and some three-dimensional models of stratified flows of different types.



As she has grown up, one is sometimes inclined to think that she has become a member of Women's Lib, trampling upon Physicus, and believing that she could perpetuate life on this globe all by herself, for example by cloning. She could easily get into troubles, however; for example, in the following ways:

(a) By shipping Software as a package with deficiency in physical basis.

(b) By not observing that discretization can lead to scale effects, for instance, in the transport-dispersion equation where the diffusion coefficient D is dependent upon both its physical value and the grid size.

(c) By not noticing that an Eulerian solution of a Lagrangian process, e.g. transport, without special precautions will lead to a non-physical, numerical increase of the dispersion.

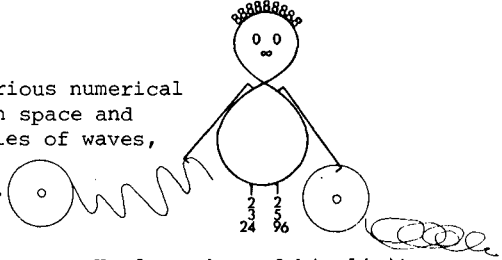
A large and important area for Numerica's future activity lies in the continued development of integrated hydrodynamic/water quality models.

5. SEDIMENT PROBLEMS

Because of all the scale effects inherent in physical sediment models, it has long been known that sediment problems will offer a particularly fertile ground for Numerica's activity.

In order to establish a high quality model, the cooperation of many scientists will be required, as illustrated by the following list:

- (a) Basic research on wave breaking.
- (b) Combination of waves and currents.
- (c) Basic research on sediment transport in waves and currents.
- (d) Expertise in constructing fast numerical algorithms.
- (e) Experience in organizing the various numerical modules with different scales in space and time, as illustrated by the scales of waves, currents and sedimentation.
- (f) Good field data for calibration.



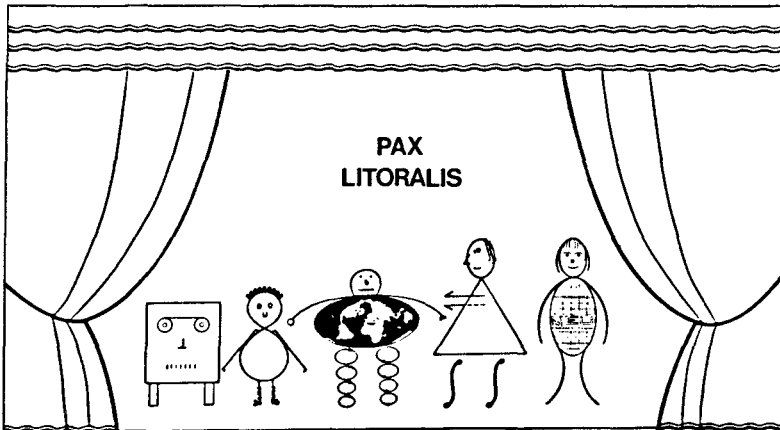
The computer capacity required is so large that Numerica might easily stress Hardware beyond his limits.

6. STRUCTURES

In many cases structures are entirely under Physicus' rule. An important exception is Morison's formula for cylinders. Here C_d has been assumed to be constant over the wave period, whereas Physicus would think that the separation points move and C_d changes with the pressure gradient. On the other hand, it is likely that the pressure gradient always imposes the value $C_m = 2$.

7. END

While the actors of this play thank the audience for their attention, they promise that they will cooperate in harmony in the future. They also express the hope that there will be extended coordination among the Coastal Engineering institutions around the world, and that there will be peace along our coasts.



ACKNOWLEDGEMENT: The author of this paper expresses his best thanks to the German Organizing Committee, as well as his sincere gratitude to all the colleagues who have contributed directly to parts of this paper or indirectly to its philosophy. He has chosen to give no reference, in accordance with the principle: Nobody named, nobody forgotten.

THEME SPEECH by W A PRICE

Senior Principal Scientific Officer
Head of Coastal and Port Engineering Division
Hydraulics Research Station, Wallingford, England

- (i) MODELS - CAN WE LEARN FROM THE PAST?
- (ii) SOME THOUGHTS ON THE DESIGN OF BREAKWATERS

I would like to deal with two quite different subjects. Firstly, the Hydraulic Modelling of Estuaries and Coasts and, secondly, Breakwaters.

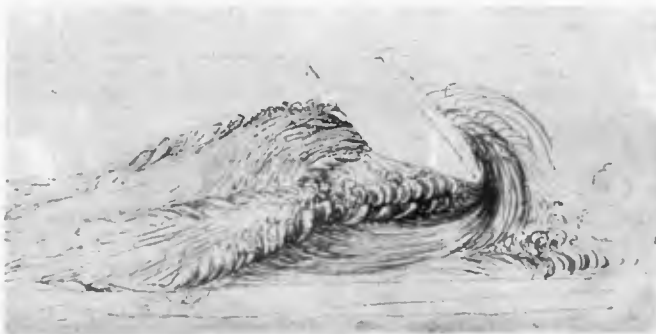
MODELS - CAN WE LEARN FROM THE PAST?

Flow visualization

Leonardo da Vinci who lived some 500 years ago gave our profession a fitting motto which is especially applicable to those of us who deal with models. He is reported to have said "When dealing with water first experiment then use judgement". It is appropriate that his name be mentioned at one of our Conferences because he was one of the leading coastal engineers of his day and for part of his life planned and supervised the construction of canal and harbour works over a large part of Middle Italy. He was the first to describe a multiplicity of hydraulic phenomena - the velocity distribution in a vortex, the profiles of free jets, the formation of eddies at abrupt expansions, the propagation, interference and reflection of waves and the hydraulic jump. He was also an experimenter and suggested the technique often used today that internal currents could be observed by means of suspended particles in a glass walled tank, Ref.1. He thus spoke from experience.

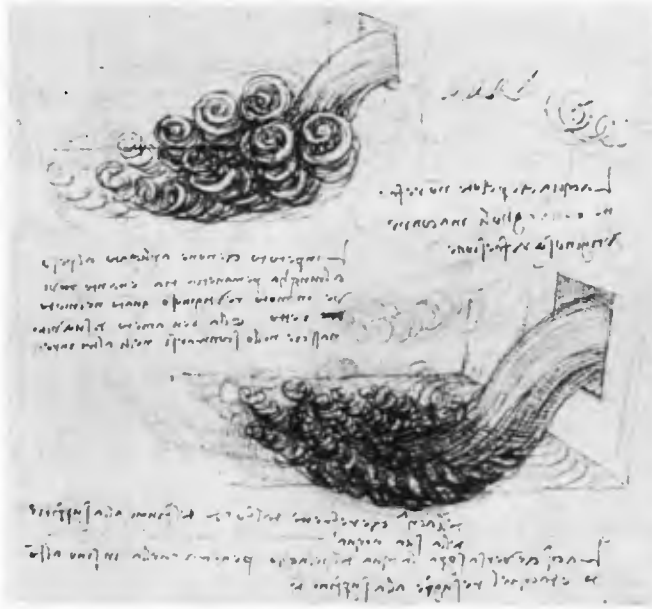
One of his drawings showing water flowing past an obstruction is shown in Fig.1a. It records what he observed. However, as a working drawing he realized that it could be improved so that when he sketched

Fig.1 DRAWINGS BY LEONARDO DA VINCI



(a) Flow past an obstruction

water issuing from a rectangular hole in a dam (Fig.1b), he drew the flow like human hair; this was probably the first expression of the concept of flow in stream tubes. There are many other drawings like these which were used in connection with a project to canalise the River Arno in Italy, Ref.2.



(b) Flow from a hole in a dam

I have used these drawings to introduce and underline an important property of physical models - one that is sometimes neglected and played down - the ability to help us visualize the flow. One method of gaining this insight from models is to use floats as in Fig.2.

We have come a long way since Leonardo da Vinci. We now have good instrumentation, sophisticated control equipment, data can be acquired, logged and plotted by mini computer. These are all welcome developments so long as we remember that instruments cannot improve the quality of the processes we are trying to scale and are not a substitute for our eyes.

History of Estuary Models

River models appear to have been first used in France in 1875 when a model was constructed to investigate the suitability of certain river training schemes that had been proposed by a Monsieur Fague. It was Reynolds working about the same time in Manchester, England, who built a model of the estuary of the Mersey and introduced for the first time the general idea of dynamical similarity, Refs. 3, 4 & 5.

Broadly speaking during the history of the development of coastal and estuary models three very distinct ranges of scales have been used.



Fig.2 FLOAT TRACKS IN A MODEL

Reynolds and Vernon Harcourt at the end of the last century built to scales of about 1/30 000 to 1/40 000 although they did use others. Gibson and Allen in the 1920's, Ref.6, built to scales of about 1/3000 to 1/6000, Fig.3, and these days the major laboratories to scales of about 1/500 to 1/1000. Fig.4 shows the comparative sizes of a hypothetical estuary to these scales.

I would discard the 1/30 000 variety as being of little practical use but there are some who would disagree. I am particularly interested in the shift in scale by a factor of, say 6, that has taken place since the 1920's. Has this been entirely justified? Are we sure that it has



Fig.3 MERSEY, DEE AND LIVERPOOL BAY MODEL
Horizontal Scale 1:7040 Vertical Scale 1:190

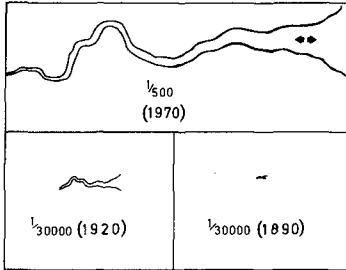


Fig.4 AN ESTUARY TO DIFFERENT SCALES



Fig.5 SCALE OR SIZE ?

not come about partly because of larger resources and more space being available to the major laboratories?

Scale or size

I would like to pose three more questions. Have certain scales become fashionable? Do we confuse scale with size? Would the person on the right of Fig.5 build models many times larger than the person on the left? I think he might, but this would not be necessary. His house would have to be bigger because that is a question of size but not necessarily his models - that is a question of scale and the problems associated with the reproduction of physical processes. I stress that I would not deny that larger models are better than smaller ones but I would question whether we have the tools to help us decide with any confidence how much better one scale is than another.

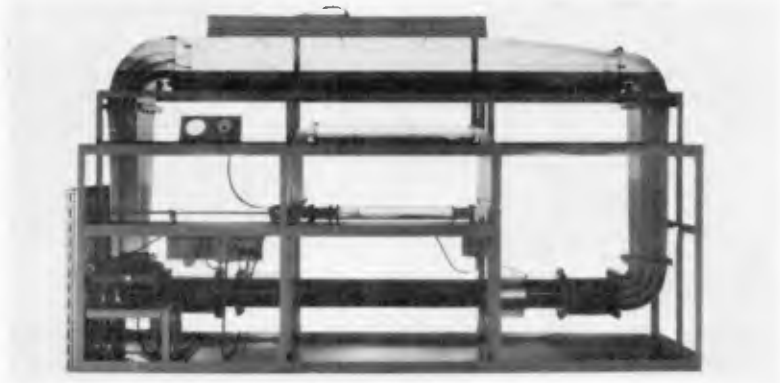
I once took a visitor around a model I had built and he was so impressed that on leaving he asked me whether I thought the model was more accurate than the prototype. I thought for a moment and not to disappoint him I said "Yes"! Perhaps we all tend to believe that models are better than we think. What we need to know is how much does the situation improve if we move from one scale to another? My feeling is less than we think. How can we judge? There are methods.

Dimensional Analysis

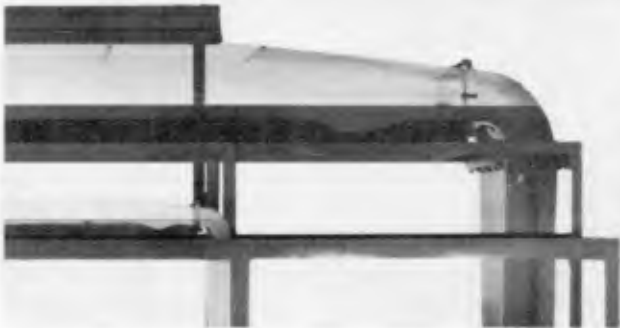
Yalin has tried to provide a yardstick through the use of dimensionless analysis. The method has been the subject of considerable controversy but it is like any other mathematical tool - used correctly it is a useful device - used incorrectly it can be misleading. He has demonstrated that the theory works by building a model which for practical purposes is close to perfection, Refs. 7 & 8.

Fig.6a shows two flumes, one a 1/3 scale model of the other. From the identity of his dimensionless numbers he was able to choose the properties of the fluids and the bed materials almost exactly. By driving two pumps from a common variable speed drive he was able to obtain the necessary ratio between the model and prototype values of the flow. The bed forms were reproduced perfectly to scale, Fig.6b.

Fig. 6 YALIN'S SIMILARITY FLUMES



(a) General arrangement of flumes



(b) Enlargement of bed features

Again, while working at Wallingford, Yalin made further model/prototype comparisons in a tilting flume. Once more he had control of the variables but because it was a larger facility he was able to make more measurements. He calculated that the wave length of the "prototype" bed features should be 3.6 times greater than those in the model and Fig.7 shows that they were. The ratio of solids discharge should be 47 and that this was the case is illustrated in Fig.8.

Practical Difficulties

Yalin is the first to admit, however, that practical considerations make the criteria of similarity difficult to apply. The model and the prototype are on the same planet and hence subject to the same gravity and there are other physical reasons which make perfect similarity impossible. So of what use is the dimensional method? In the foreword to his book Yalin says "Whether applicable or not the exact solution should be determined and then when it proves impracticable used as a frame of reference to judge the degree of correctness of the adopted solution". That is, we have to compromise but in most cases we do not understand the rules.

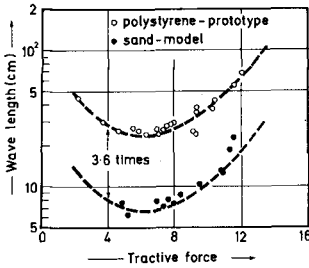


Fig. 7 COMPARISON OF WAVE LENGTHS - MODEL AND PROTOTYPE

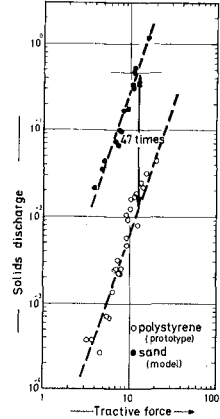


Fig. 8 COMPARISON OF SOLIDS DISCHARGE - MODEL AND PROTOTYPE

If we knew that the error involved in scaling a particular process was of the form shown in Fig.9 then we could choose an error which was acceptable in making our choice of scales. This hypothetical curve sums up what we need to find out and where some of our fundamental research should be directed. For example, when we relax certain parameters, like the dimensionless ones used by Yalin, what errors are involved?

It is interesting that when Reynolds had finished his studies on the Mersey estuary he set himself the task of learning more about scale by building movable bed models of hypothetical V-shaped estuaries to different scales. We could copy this example to advantage.

Until more fundamental work is carried out the choice of scales for estuary and coastal models will be based too much on practical arguments like these. (i) We need measurable tides and currents to make good measurements. (ii) To keep distortion to a minimum we need a large horizontal scale. There are other practical considerations and they are important but they should only be used as part of a total argument. The scaling of the physical processes and a greater knowledge of them is of fundamental importance.

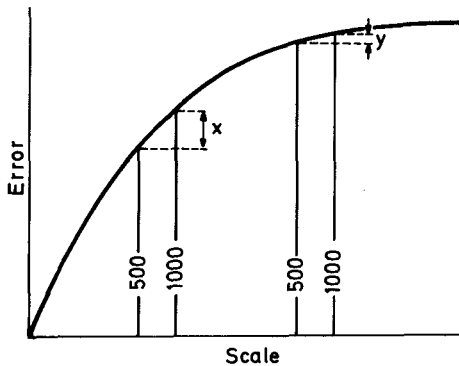


Fig. 9 HYPOTHETICAL ERROR FUNCTION FOR A PARTICULAR PROCESS TO BE SCALED

Reynolds and Froude Numbers

Until we know more of the rules we must make the most of those we have. I sometimes think that we restrict ourselves unduly by interpreting some of them too rigidly. Take Reynold's Number as an example. The flow in the model needs to be turbulent for no other reason perhaps than that the head loss should be proportional to v^2 rather than v in the laminar case. To avoid laminar flow a limit is put on the Reynold's Number say of 1500. But is the size of this number an even approximate indicator of the level of turbulence in a tidal model? I would suggest that it is not. In this case the flow accelerates and decelerates, there are changes in geometry, there are the turns of the tide - all of which tend to induce and enhance turbulence. One could happily work at much lower Reynolds Numbers and if this is the case one argument that is used against smaller models would partly disappear. Reynolds said "For flow other than in parallel pipes the Reynold's Number at the critical velocity is of course different".

I do not think that we allow ourselves sufficient freedom with the Froude relationship either. Obviously there is little latitude if we are dealing with tidal propagation in a long estuary because the speed of propagation is proportional to $\sqrt{\text{depth}}$ or thereabouts. But there are cases where some relaxation is possible. HRS once built a model of Aberdeen Harbour, Hong Kong, Fig.10 in which we had the ability of increasing the discharges by a factor of 4 over what they would be on a Froude basis, Ref.9. You will see, Fig.11, that allowing for the change in the velocity scale the current velocities at Y, a critical



Fig.10 MODEL OF ABERDEEN HARBOUR
- HONG KONG

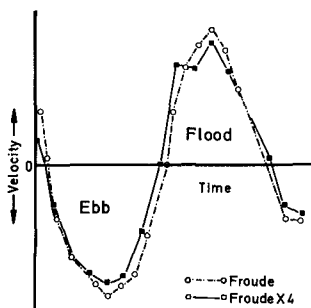


Fig.11 CURRENT VELOCITIES AT Y -
(FROUDE AND 4 X FROUDE)

A relaxation of both the Reynold's and Froude criteria allows greater freedom. The model is a tool or an analogue that we can manipulate by making sensible departures but the answer must be right for approximately the right reason. If it isn't then the results we obtain for any changes we make will be wrong. On the fly leaf of some works of fiction they put this phrase - "Any similarity between the characters in this book with those living or dead is purely imaginary". We want to avoid having to put at the beginning of our reports this transcription - "Any similarity between the model and prototype is purely coincidental".

position, are almost identical. I would suggest that this "distortion" in the Froudian velocity scales could be used to advantage in many studies. In sediment transport models it might be a valid way of getting over the problem of the initiation of movement of the sediment.

Instrumentation

What effect does the development of better instruments have on our attitude to model scales? With lasers we can now measure down to a velocity of zero and at a point and with no interference with the flow. This fact alone should encourage us to consider whether we dare go smaller or perhaps what is more important consider reducing vertical exaggeration.

Movable bed models

I would like to say a little more about mobile bed models because it is in this area that physical models of coasts and estuaries can border on the inadequate and where a great deal of interpretation is necessary.

We normally test the validity of a movable bed by running it for some time and then surveying it and making a comparison with nature or with changes that have taken place in nature over a given time. Provided the whole bed is mobile and the surveys agree we say that the sediment transport scale at all points over the mobile area is the same. However, we know even without measurement, that in many of our estuary models the distribution of sediment with depth is quite wrong as illustrated in Fig.12.

What we have at best is a 2 layer model and what we are assuming is that in nature a large proportion of the material is travelling in the bottom layers. It is only in exceptional circumstances, approaching the kind described earlier, that it is a true sediment transport model.

Neither is there any way around the problem of ripple formation which to scale bears no relation to features found in the prototype. In the 1950's claims were made that a material had been found which

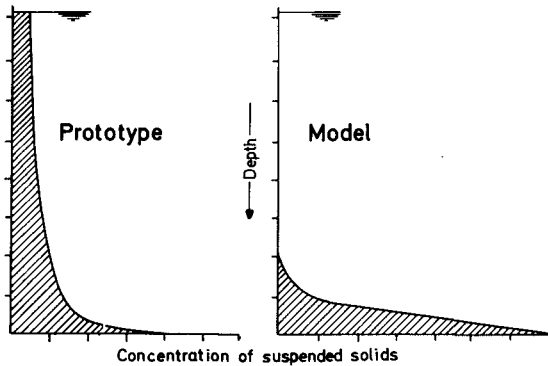


Fig. 12 SKETCH OF SOLIDS CONCENTRATION

would move without rippling. The competition reached something of the intensity that in other periods of our history alchemists tried to turn base metals into gold. At least we know for ripples that the problem is insoluble.

Nevertheless provided we use the technique with care I feel that movable bed models are useful but I would prefer to look on the loose material as an indicator or as a tracer. When used to study changes in small areas they are invaluable, as for example in the study of the improvement that might be achieved over a bar at the entrance to a tidal inlet by a training wall. Here it is justified, in my view, to mould a small area of the model in mobile material as illustrated in Fig.13. In this way the approach flows to the area of interest are maintained by the solid bed - having made the assumption that the depths at the boundaries of the mobile material will remain relatively unaffected by any works that are introduced. Wave-cum-tidal models of this type are quite reliable and relatively easy to manipulate. Littoral drift is promoted by running waves from say two predominant directions. A feature like a bar will form in the right place when the scale of sediment transport under waves equals the scale of sediment transport under tidal currents. Returning to the point made about Froude scales this is under the operator's control to some extent. For example, suppose the bar is forming too close inshore then, in my view, one is justified in dispensing with Froude tidal velocity scales by shortening the tidal period to push the bar out to sea or vice versa.

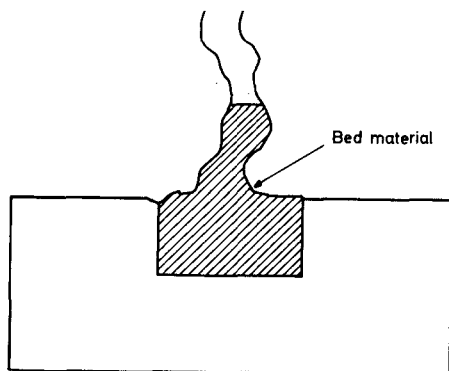


Fig. 13' TIDAL INLET MODEL

If the flow is canalised between banks as in the upper reaches of our major estuaries then loose material used as an indicator of bed deposition and erosion is a powerful technique.

I would not want to give the impression that the movable bed studies discussed so far are easy to carry out or to interpret but in my view they represent a realistic approach to these sorts of problems. Where we do strike extreme difficulty, however, is in the modelling of the wide approaches to our major estuaries with their multiplicity of banks and channels. Our inadequacies to scale sediment transport in this situation shows up most markedly.

If as I am suggesting we can model sediment transport only approximately, and at certain times hardly at all, then a small increase in the inaccuracy would be neither here nor there. In the 1920's there were movable bed models at scales of 1/3000 but their operators had one important practical advantage over us. If they didn't like the bed material they could change it overnight whereas we are reluctant to dig out 50m³ of expensive material. We tend to make the best of it.

I was in touch with Professor Jack Allen recently. He is a direct link with Reynolds through Gibson. In a letter to me he said this:-

"The reluctance of some researchers to use mobile beds or to experiment with different bed materials is partly their commitment to very large models in which the time required and the expense incurred in moulding, surveying and "proving" have encouraged them to be content in inferring, from observations of water movements alone over a fixed bed, what will happen to sand and silt in a natural estuary as a result of the construction of the proposed works. They, therefore, possibly fail to take sufficient account of the effect on the water movements of alterations to the bed created by the works themselves".

I will develop the theme later that mathematical models or computation are the eventual answers but I would not neglect the possibility that a small physical model and a mathematical model might be a good way to solve some of these problems in the future.

Sediment transport - fixed bed models

Another approach to the sediment transport problem is to build a fixed bed model, observe current velocities and integrate these with field observations of sediment flux, Fig.14.

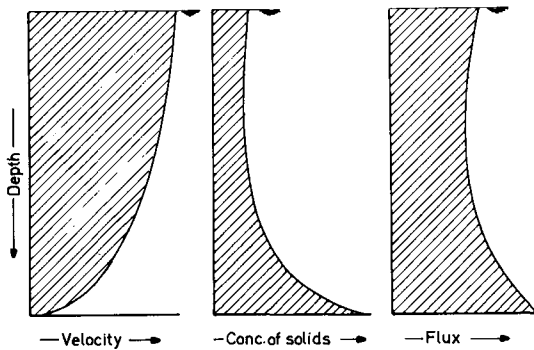


Fig. 14 SEDIMENT FLUX FROM FIXED BED MODELS

We have tried this method at the Hydraulics Research Station but have certainly not exhausted its possibilities. For studies of large areas the difficulties at the moment certainly outweigh the advantages but for studies of small areas it has its merits. The crux of the problem is that the laws of continuity so far as water movements are concerned are certainly satisfied in a physical model but the difficulty is that they cannot be established by measurement with the accuracy required using conventional instruments. I can illustrate the problem as follows. The laws of sediment transport are a high power of the velocity - let us say V^5 for the sake of argument which means that if current velocities are in error by 5% the sediment flux will be out by approximately 25%. The consequences of such an error are obvious. Better current meters of the kind mentioned earlier make this method well worth pursuing.

Mathematical Models

When we talk about problems associated with tidal propagation, current velocities, salinity intrusion, there is a case for using either a physical or a mathematical approach. When it comes to sediment transport the solutions must lie eventually with mathematics, physics and computation. Considerable advances have been made in recent years but our knowledge is still so inadequate we are well advised, as far as possible, to use both techniques together.

The term Mathematical Model, is a misnomer because it belies the important characteristic of this technique - the ability to deal with physics processes full size. Provided we know the laws everything is possible but the problems involved in discovering these laws are formidable. For example, considerable effort has been expended to establish the laws of sediment transport and yet when faced with the problem of estimating maintenance dredging in a tidal cum wave environment we would be glad to get an answer which was accurate to a factor of less than 2.

To describe the way in which topographical features like banks and channels are formed and maintained means reproducing some very complicated secondary processes. The change in velocity, suspended solids, salinity with depth can be accommodated with a multi-layer approach - water and solids being exchanged between layers, but the flow round bends can only be described adequately by building in lateral influences.

I list these difficulties not to detract from the value of Mathematical Models but to remind ourselves that more sophistication means greater costs. What we are creating in building models, both in the physical and mathematical sense, are engineering tools not basic research facilities. A certain scheme to be constructed will only warrant a certain amount of money spent on investigation. The cost of physical model studies has increased considerably over the last 10 years in real terms. In the case of Mathematical Models - new developments hardly ever increase computing time by a factor of 2 - more often a factor of 8 or more. Unless the unit cost of computing comes down to match the extra sophistication they might become too expensive to use, except on some of the larger jobs.

Although I have dealt with the subject of Mathematical modelling rather "en passant" I believe there is a need to keep the advances in this technique and that of physical modelling constantly under review. This should be done in a way that illustrates the strengths and weaknesses of both techniques and where they can be used to advantage together. More contact should be encouraged between mathematical and physical modellers because the two subjects must go hand in hand. Hybrid models will go some way to bringing about a stronger link than exists at present. The possibility of interacting physical and mathematical models in real time has considerable potential for the future.

Summary

- (1) We should not undervalue physical models as visual aids. They give us a view of a situation that we can never get from the prototype.
- (2) We should work towards solving our problems by the smallest model for the job in hand but we do not yet have all the information to make the ultimate choice of scale.
- (3) We should question the way we use the Reynolds and Froude criteria.
- (4) Mathematical and physical models are powerful techniques which should not be seen to be in competition. They should be looked on as complementary to one another. We need both methods to improve the confidence we place on our advice.

REFERENCES:

1. ROUSE H, INCE S: History of Hydraulics. Supplement to La Houille Blanche (1954) 5.
2. CLARKE K, PEDRETTI C: The Drawings of Leonardo da Vinci in Windsor Castle. 3 Vols. London: Phaidon Press.
3. REYNOLDS O: On Certain Laws Relating to the Regime of Rivers and on the Possibility of Experiments at Small Scale. British Association Report, 1887.
4. Report of the Committee Appointed to Investigate the Action of Waves and Currents on the Beds and Foreshores of Estuaries by Means of Working Models. British Association Report, 1889.
5. 4th International Congress on Inland Navigation, 1890.
6. ALLEN J: Scale Models in Hydraulic Engineering. London: Longmans, Green & Co. 1947.
7. YALIN M S: Similarity in Sediment Transport by Currents. London: Her Majesty's Stationery Office, 1965. (Hydraulics Research Paper No.6, Hydraulics Research Station, Wallingford).
8. YALIN M S: Theory of Hydraulic Models. London: Macmillan, 1971.
9. Aberdeen Harbour, Hong Kong. Wallingford, Hydraulics Research Station, 1966. (Report EX 333).

SOME IDEAS ON BREAKWATERS

(Continuation of theme speech by W A Price)

Introduction

Many of us I am sure have realized that the science of the design of breakwaters has reached a crucial point in their development. A great deal of work is being done in many parts of the world on many important aspects of the problem and if I do no more than review some of the present day thinking and suggest some lines for further research, I will be well pleased. After producing the first draft of this lecture I read a paper by Magoon & Baird (not published at the time of writing) presented at a Symposium held at the British Hovercraft Corporation on the Isle of Wight, England, which expresses the need to put more science into the subject which is very much the theme of my lecture, Ref.10.



Fig. 15 ALDERNEY BREAKWATER - CHANNEL ISLANDS

History

It would be impossible to say who built the first breakwater. Ever since man realized that he could gain protection from the waves behind a headland he used this principle to protect his boats with stone breakwaters. Hence the beginning is in antiquity. Quite recently Jacques Cousteau in searching for the lost city of Atlantis discovered underwater remains of a Minoan breakwater 4000 years old, Ref.11. However, the first empirical formula for breakwater design did not appear until 1933.

Well known names are attached to the later chapters of the story - Carvalho, Vera Cruz, Irribarren, Epstein, Tyrell, Jackson, Hudson, Davidson and no review of the subject would be complete without acknowledging the excellent pioneering work carried out by the US Army Engineer Waterways Experimental Station, Vicksburg, Refs.12 - 21.

The Hudson Equation

I would like to start by looking at the form and basis of the now famous Hudson equation.

$$W = \frac{\rho_r H^3}{K_D (\rho_r / \rho_w - 1)^3 \cot \alpha}$$

H = Wave height

ρ_r = Specific weight of armouring

ρ_w = Specific weight of water

W = Height of armour unit

α = Slope of breakwater face

K_D = Coefficient of Stability

This is a surprisingly simple equation when you think about the complexity of the phenomena involved - wave breaking, penetration of flow into the bank, run up, interblock friction, hydraulic drag, interlocking and others. It is based on the assumption that regardless of the way in which the waves break the disturbing forces due to drag or lift from plunging or collapsing breakers are proportional to the square of the wave height and displacements will be resisted by the immersed weight of the blocks alone. This theoretical analysis was supported by a series of classical experiments.

Armour Units

Subsequent to the development of this equation there was a dramatic increase in the size of ships which meant that harbours had to be built in deeper water and usually at more exposed sites. Larger stones were required and at some sites these were not available in the necessary sizes or not available at all. It was these factors that led to the development of the multiplicity of armour units we know today.

Perhaps after cubes and other rectangular blocks the Tetrapod, designed by Pierre Danel was the first of these, Fig.16. It is half the weight of an equivalent stone to resist the same wave height. Whether to escape the patent on this block or to satisfy the basic need of engineers to innovate, many other designs have followed, Fig.19.

The designers of these blocks, to a larger or lesser degree, tried to achieve an open structure to provide a permeable assembly, a low centre of gravity and projections to form interlocks with neighbouring units and thus increase their resistance to removal by waves. A saving in the amount of concrete required to make the unit was of primary



Fig. 16 TETRAPOD



Fig. 17 TRIBAR



Fig. 18 DOLOSSE

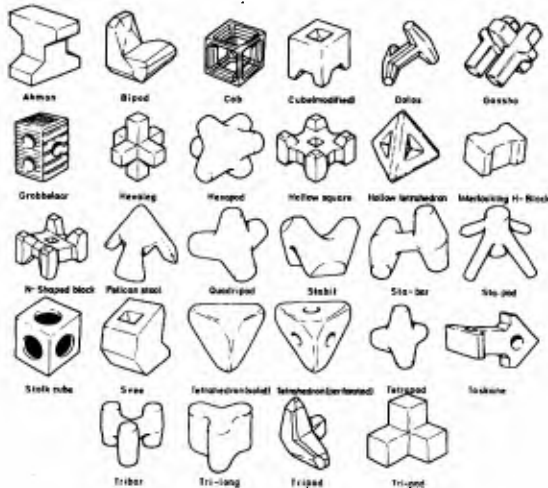


Fig. 19 ARMOUR UNITS

importance. Interblock friction was brought into play as in the regularly placed Tribar, Fig.17

Merrifield and Zwanborn exploited interlocking in designing the Dolosse which are one fifth to one sixth the weight of a stone to resist the same wave height: a considerable achievement, Ref.22, Fig.18.

One of the simplest and most effective blocks, in my view, is the Tripod designed by Muir-Wood. It is half a cube. The neat thing about it is that being half a cube once you have built one you can reproduce others with very simple form work, Fig.20. The K_D value is about 7.

Need for new approach

Through all these developments the Hudson equation appeared to stand firm and has been used to describe the stability of all blocks. Hudson never claimed that it should, but perhaps he is paying the price of all philosophers in that they are often quoted but never read. He has in fact cautioned that his equation was applicable to quarry stone only. Subsequently, however, and in my view quite rightly, he used his theoretical approach to describe the stability of Tetrapods.

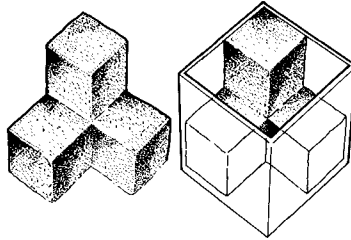


Fig. 20 TRIPOD - METHOD OF CONSTRUCTION

I will develop the thesis that all blocks are not alike - they exploit different qualities to achieve stability and these individual characteristics should be recognised more so than they are at present in any equation that describes their stability. Unless we do then we will not fully understand the behaviour of complicated blocks.

Let me use an analogy. Man has always been faced with the problem of spanning gaps. Through history he has tried to span larger and larger gaps and he has had to employ new methods from beams to arches, cantilevers and catenaries.

I want to use the analogy in two ways. The first is not in the mainstream of the argument but is important and it is this. In the early stages of design do we give enough attention to methods of construction other than rubble mound breakwaters like, for example, Lundgren's caissons? I suspect that we do not but this is a whole debate in itself so I will return to using the analogy in another way.

Bridges exploit the various properties of different materials like stone, concrete, steel, for their stability and this is analysed in different ways. Armour blocks too have various qualities that contribute to their stability. Some of the important ones are weight, interlocking, interblock friction, hydraulic drag, permeability of assembly etc. Qualitatively we can assess the blocks shown in Fig.21 like this

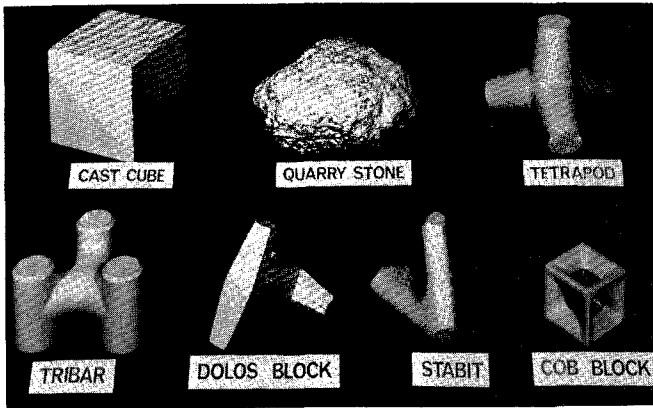


Fig. 21 ARMOUR UNITS - SCALED TO RESIST EQUAL WAVE HEIGHTS

- the stone and the cube rely on weight for their stability, the Tetrapod on weight and a small amount of interlocking, the Tribar on interblock friction and weight and the Dolos on a small amount of weight and a great deal of interlocking. They are certainly not different shaped bits of stone. Any advance on the Hudson equation must, therefore, recognise this and describe a block's stability in terms of these parameters.

[To digress slightly - interlocking is probably difficult to quantify although I would suggest it could perhaps be determined like this. Lay cover layers in the laboratory and determine the force required to remove units from the pack. Forces will vary from those equivalent to the weight of the unit to a force required to remove a block that is fully interlocked. We could express this variation in a dimensionless number of the form say -

$$I = \frac{\text{"Average" force required to remove block}}{\text{Weight of Armour Unit}}$$

This parameter expresses the way a particular block relies on the weight of neighbouring units for its stability.]

Types of failure

Another case for reappraisal is the very different way damage occurs for compact and open forms of block. With compact forms, like stones and Tetrapods, for which no friction or little interlocking is assumed a steady increase of damage is to be expected as the wave attack is extended in time, Fig.22, Ref.23. This pattern of damage is quite different for the blocks of open form with their properties of high interblock friction and interlocking. They exhibit a stiffness which resists damage over an initially large range of wave heights but once the applied forces are high enough to disturb the cover layer a rapid removal of units results and the margin of safety between acceptable damage and failure for closed forms becomes very small and could be well within the range of uncertainty of prediction of the design wave height. We need to take this fact into account in the design. The use of blocks that interlock puts a considerable premium on a good knowledge of the wave climate. I have heard Dean O'Brien call many times for more wave recording. I wholeheartedly agree with him. Highway engineers would not be prepared to design motorways with the lack of information Coastal Engineers are sometimes asked to design breakwaters.

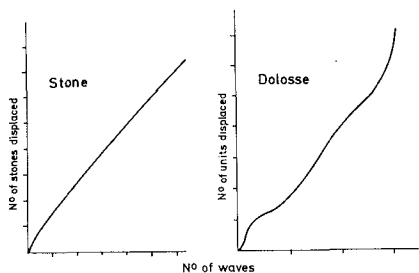


Fig 22 HISTORY OF DAMAGE - STONES AND DOLOSSE

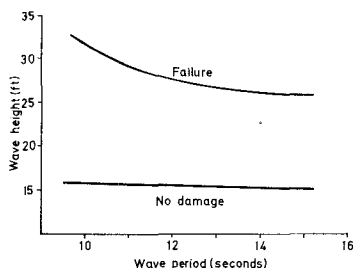


Fig.23 DOLOSSE - EFFECT OF WAVE PERIOD

The influence of wave period

Let me turn to the other side of the equation - the disturbing influence of the waves. Hudson found it quite sufficient to describe the sea in terms of a wave height. Whillock, working with Dolosse and the results have been confirmed by Burcharth, Zwamborn, & Bruun, Ref.26, showed that wave period was also important so far as this armour unit was concerned, Fig.23, Ref.24. Is there a discrepancy with the early Hudson results? I do not think there is. Within the scatter of his results for stone breakwaters there was probably a small period dependence but it was so small that he was justified in ignoring it.

The explanation probably lies partly in the fact that Dolosse with their limbs projecting through the cover layer are subject to much greater drag forces than stones which tend to protect one another in times of high surface currents. These currents are likely to be at their maximum when long period waves surge rather than break on the slope. Brebner shows that the Drag to Weight ratio for stones and Dolosse are almost the same, Ref.25. Quite recently experiments carried out at HRS confirms this fact. However, this does not mean that when they are in a pack that the effective drag to weight ratios are the same. Per Bruun has pointed out the importance of wave resonance and says that "elements that protrude should be avoided", Ref. 26. How dependent on wave period are other units? I do not know but I think we should find out.

Effect of angle of attack

Tests with stone breakwaters and tests done by SOTRAMER with Tetrapods show that their stability increases with angle of attack. This behaviour is quite different for Dolosse, Fig.24. The reason is again the production of high surface currents this time caused by waves running along the breakwater and setting up high drag forces on projecting limbs. The amplification of the wave height due to the Mach-Stem effect further complicates the issue.

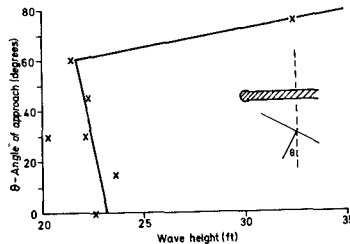


Fig. 24 DOLOSSE - EFFECT OF ANGLE OF ATTACK

Every now and again one reads a paper containing an idea which one would have liked to have had oneself. Such a paper was presented at the Hamburg Conference by Brebner, Ref.25. He filled shallow boxes with stones and Dolosse and gradually tipped them about their bottom edge. The failure of the rock occurred at about 50° whereas the Dolosse had an

angle of repose of at least 80° and in one remarkable test 91° . He carried out tests where he layered Dolosse and stone in a tilting flume and ran water over them. The "wipe out" velocity was essentially the same for both the quarystone bed and the one constructed of Dolos. He concluded that "the effectiveness of the Dolos unit is not materially affected by the drag to weight ratio but to its high angle of repose". Interlocking can only be brought fully into play by using Dolosse on steep slopes. Brebner puts it this way - "one can also suggest that the steeper the breakwater slope ... when attacked by normal waves the better the Dolos unit appears to be". He points out that "this is the reason why the stability of Dolosse are affected by the angle of attack whereas stones are not", Ref.24.

Random Sea Testing

Random sea testing has become fairly commonplace in our laboratories although we still continue to argue how best they should be synthesised.

Johnson and Ploeg have questioned whether seas are necessarily random - the implication being that if they are not then the wave groupings will be different, Refs.27 & 28. Shuttler at HRS has measured the frequency of wave groups for a number of wave spectra (Moskowitz, Jonswap and a bimodal spectrum generated using the HRS synthesiser). These compare very favourably with published field data. I still think, however, there is still some debate about this question and more work needs to be done because it is an important one.

Burcharth and Ploeg have shown that coastal structures respond differently when exposed to various wave patterns that contain the same maximum waves: there is a significant influence of succession, Refs.29 & 30. They stress the importance of research into the occurrence and frequency of characteristic wave patterns in wave records so that the results can be incorporated in sea conditions used in model tests. Incidentally Boucherth proposes a new form of the Hudson equation for Dolosse pointing out that it would be appropriate to plot a Stability Number defined as

$$\frac{H}{\left(\frac{W}{\rho_r}\right)^{\frac{1}{3}} \left(\frac{\rho_r}{\rho_w} - 1\right)}$$

against a Surf Similarity parameter (Batjes), Ref.31.

This dimensionless parameter was designed by Batjes and its importance has probably not as yet been fully recognised. It is a convenient way of describing the way in which the wave breaks.

$$\zeta = T \left(\frac{g}{2\pi H}\right) \tan \alpha$$

where H = Wave height

W = Weight of Dolos

- ρ_r = Specific weight of blocks
 ρ_w = Specific weight of water
 T = Zero crossing wave period
 g = acceleration due to gravity
 α = angle of slope

Summary of the Important Parameters

Abernethy, as early as 1970, Ref.32, when carrying out an investigation to provide information for the design of Tribar armouring for a large reclamation project in Botany Bay, New South Wales, developed a similar theme to the one in this lecture when he suggested that any analysis of Tribars, and he could have included other armour units, based upon the Hudson formula must be considered suspect for many reasons. He suggested that the damage function Δ is dependent upon eleven dimensionless parameters. Taking these and adding others we could write a list of some of the more important variables affecting the damage function as follows:-

- | | | |
|--|---|-----------------------|
| (1) Weight of unit | } | Block Characteristics |
| (2) Density of material | | |
| (3) Interblock friction | | |
| (4) Packing Density | | |
| (5) Permeability of Assembly | | |
| (6) Height of Bank | | |
| (7) Hydraulic drag | | |
| (8) Wave Spectrum | } | Disturbing Influences |
| (9) Wave grouping | | |
| (10) Angle of attack | | |
| (11) Water depth | | |
| (12) Number of waves impinging
on slope | | |

The list is formidable and is not complete but it indicates the size of the problem.

Structural Damage

Vasco Costa, Baird, Lalevang, Magoon and Stickland have made major contributions to the subject and have highlighted among other things the problem of wear and the structural stability of the individual units. These are subjects which are worthy of further study. It occurs to me to wonder whether with blocks that interlock there is the possibility that impact loads could be transferred from block to block, and perhaps by chance the combination of forces caused by waves breaking out of phase with loads transferred from unit to unit could be one of the reasons blocks break, Fig.25.

Dolosse

To clear up any misinterpretation of what I might have said I need to say a word about Dolos in particular. There is no doubt that it is a good armour unit and perhaps because it is superior in many respects to others in using the properties of a solid almost to the limit that we must use it with care. Until we understand all its properties we should

not exploit them to the full. I have used Dolosse in this lecture because more work has been done on this unit than any other and believing that they typify the family of blocks that interlock at least qualitatively.

Need for co-operation and further research

Apart from the few painstaking and excellent pieces of work that I have already referred to good designs have been produced based on careful tests but for one reason or another they are not consistent with others in the field and the results are then more or less lost to the science. We must do more experiments where we keep some of the variables constant while varying others.

It seems to be opportune that we should get down to some fundamental research preferably organised on a world wide basis and not rely

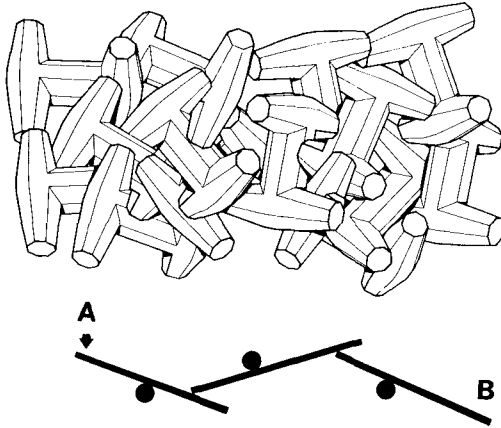


Fig.25 TRANSFER OF LOADS - INTERLOCKING BLOCKS

almost entirely on laboratory testing of specific schemes for insight to the problem. I was glad to hear at the Conference Professor Edge describe plans that ASCE have in this direction.

When writing about armour blocks nearly 30 years ago Pierre Danel, the inventor of the Tetrapod, said this -

"Engineers have too few opportunities for examining an overall problem in a sufficiently disinterested way and for a sufficient length of time. Each one is bound by his specialized field and naturally has a tendency to only consider solutions which entirely satisfy his own particular requirement".

It might sound a small point but if we could only agree about what we mean by certain percentages of damage and failure this would be a considerable step forward.

If we continue to test with the object of getting a stability factor alone we will lose the feel for the subject and our designs will suffer. The improvement of armour blocks has meant that their behaviour has become more and more detached from the supporting theory. One serious consequence is that data obtained from one situation cannot be applied to others. In my view we need to make advances quickly.

ACKNOWLEDGEMENTS

This lecture was given with the permission of the Director of the Hydraulics Research Station, Wallingford. I would particularly like to thank Mr A F Whillock whose ideas are incorporated in the section on breakwaters, Professor Emeritus Jack Allen for his comments and the loan of early slides and many of the staff at HRS for their instructive remarks. To others too numerous to mention I would like to say "Thank You".

The drawings by Leonardo da Vinci are published by permission of the Royal Library, Windsor Castle.

REFERENCES:

- 1 MAGOON O, BAIRD W F: Breakage of Breakwater Armour Units. Symposium on Design of Rubble Mound Breakwaters, 1977. (Paper No.6). Shanklin, Isle of Wight, British Hovercraft Corporation.
- 2 The world of Jacques Cousteau - Calypso's search for Atlantis. Television programme on BBC1. British Broadcasting Corporation, 1978.
- 3 JACKSON R A: Design of Cover Layers for Rubble-Mound Breakwaters Subjected to Non-breaking Waves. Vicksburg: United States Army Engineer Waterways Experiment Station, 1968. (Research Report No.2-11).
- 4 IRRIBARREN R: A Formula for the Calculation of Rock-Fill Dikes. Translation from Revista de Obras Publicas, 1938. Berkeley: University of California Fluid Mechanics Laboratory, 1948. (Technical Report HE-116-295).
- 5 IRRIBARREN R, NOGALES C: Generalization of the Formula for Calculation of Rock-Fill Dikes and Verifications of its Coefficients. Translation from Revista de Obras Publicas May 1950. Vicksburg, Miss: United States Army Engineer Waterways Experiment Station, 1951. (Translation No.51-4).
- 6 HUDSON R Y, JACKSON R A: Stability of Rubble-Mound Breakwaters. Vicksburg, Miss: United States Army Engineer Waterways Experiment Station, 1953. (Technical Memorandum No.2-365).

- 7 HUDSON R Y: Design of Quarry-Stone Cover Layers for Rubble-Mound Breakwaters. Vicksburg, Miss: United States Army Engineer Waterways Experiment Station, 1958. (Research Report No.2-2).
- 8 HUDSON R Y, JACKSON R A: Design of Tetrapod Cover Layer for Rubble-Mound Breakwater, Crescent City Harbor, Crescent City, California. Vicksburg, Miss: United States Army Engineer Waterways Experiment Station, 1955. (Technical Memorandum No.2-413)
- 9 HUDSON R Y: Protective Cover Layers for Rubble-Mound Breakwaters, Studies Completed Through March 1957. Vicksburg, Miss: United States Army Engineer Waterways Experiment Station, 1958. (Miscellaneous Paper No.2-276).
- 10 HUDSON R Y, JACKSON R A: Design of Tribar and Tetrapod Cover Layers for Rubble-Mound Breakwaters. Vicksburg, Miss: United States Army Engineer Waterways Experiment Station, 1959. (Miscellaneous Paper No.2-296).
- 11 HUDSON R Y: Wave Forces on Rubble-Mound Breakwaters and Jetties. Vicksburg, Miss: United States Army Engineer Waterways Experiment Station, 1961. (Miscellaneous Paper No.2-453).
- 12 SAVILLE T: Wave Run-up on Shore Structure. Proc. Amer. Soc. Civ. Engrs 82 (1956) WW2 Paper 925.
- 13 MERRIFIELD R M, ZWAMBORN J A: The Economic Value of a New Breakwater Armor Unit 'Dolos'. Proc. 10th Conf. Coastal Engng, Tokyo, 1966 Vol.2 p.885-912.
- 14 Riprap Design for Wind Wave Attack - A Laboratory Study in Random Seas. Wallingford: Hydraulics Research Station, 1975. (Report EX 707).
- 15 WHILLOCK A F, PRICE W A: Dolosse Blocks as Breakwater Armouring. HRS Notes 19 (1977) June p.5-6.
- 16 BREBNER A: Performance of Dolos Blocks in an Open Channel Situation. Summaries, 16th Int. Conf. Coastal Engng, Hamburg 1978 Paper No.203.
- 17 BRUUN P, GUNBAK A R: New Design Principles for Rubble Mound Structures. Trondheim, Norwegian Institute of Technology, 1976.
- 18 JOHNSON R R, PLOEG F: The Problem of Defining Design Wave Conditions. Ottawa, National Research Council of Canada, Hydraulic Laboratory.
- 19 JOHNSON R R, PLOEG F: The Problem of Defining Design Wave Conditions. Ottawa, National Research Council of Canada, Hydraulic Laboratory.

- 20 BURCHARTH H F: The Effect of Waves with Different Patterns on On-Shore Structures. Aalborg University Centre, 1978. (Bulletin No.12).
- 21 BURCHARTH H F: Effect of Waves on On-Shore Structures. Ann.Rept Hydraulics Research Station, Wallingford 1977 p.8-12.
- 22 BATTJES F A: Surf Similarity. Proc. 14th Conf. Coastal Engng, Copenhagen, 1974 Vol 1 p.466-480.
- 23 ABERNETHY C L: Stability of Tribar Armouring. Ann.Rept Hydraulics Research Station, Wallingford 1971. p.57-60.

WELCOMING ADDRESS

Dr.-Ing. Karl-Eduard Naumann
President of the Hafenbautechnische Gesellschaft
and
Chairman, Organizing Committee, 16th ICCE

Excellencies, distinguished guests, dear colleagues and friends,
ladies and gentlemen:

On behalf of the Organizing Committee for this 16th International Conference on Coastal Engineering, it is my special privilege as its Chairman to welcome you all very heartily here in the Congress-Center Hamburg to inaugurate a week of lectures and discussions on the manifold problems of Coastal Engineering. The Organizing Committee is very happy about the large number of participants being 621 up to now coming from 41 countries all over the world.

Especially I should like to welcome Mrs. Helga Elstner, second Burgomaster, who is representing the Senate of this Free and Hanseatic City of Hamburg, the host-city for our conference this week. Thank you, Mrs. Burgomaster, for coming here and for your kind readiness to speak to us. In addition, we must give our respectful thanks for the generous sponsorship which the Senate has provided for organizing this conference.

Another special welcome is to Dr. Volker Hauff, Federal Minister for Research and Technology, who has come from Bonn to join this opening ceremony and to speak to us about the viewpoints of the German Federal Government concerning Coastal Engineering, especially the efforts made to defend the low German coast, which, because of its nature is very sensitive to the attacks of the sea. Thank you, Dr. Hauff, for coming and for the assistance and sponsoring your Ministry gave us when we were preparing this conference.

In addition to the Senate of Hamburg and the Federal Ministry for Research and Technology, there are three other sponsors of our conference. First the "Kuratorium für Forschung im Küsteningenieurwesen" which could be translated as the "Committee for Coastal Engineering Research". It is a coordinating and collaboration body of the Federal Republic and four coastal states. The KFKI is supporting our conference by publishing a special issue of the periodical "Die Küste" (the coast), which you all have in your conference-portfolio; it is written both in English and German and gives extensive information about the history and present problem of the German coast as well as pinpointing some features of the relevant research in this country. We are very grateful to the KFKI for this assistance.

The second sponsor is the "Hafenbautechnische Gesellschaft" (HTG), which may be translated as the "Association for Port and Coastal Engineering". This is a scientific association with the aim of studying scientific and practical problems of a technical and economical nature in the following fields:

- planning and constructing ports, port installations and traffic ways within ports;
- operating ports and port installations;
- planning, constructing and operating waterways;
- coastal research and coastal engineering.

This association is the local organizer of our Conference and bears the financial responsibility for it. The Organizing Committee is composed only of members of the HTG.

Last but not least I should gratefully mention the Coastal Engineering Research Council (CERC), borne by the American Society of Civil Engineers under the leadership of our "Grand Old Man" Dean O'Brien and his "Right Hand" Professor Johnson. Since the ICCEs came into existence in 1950, they all have been sponsored by the CERC at least by publishing the proceedings and thus providing the continuity of the respective literature as well as the exchange of the research results.

And now, ladies and gentlemen, let me welcome you all, the participants of this 16th ICCE in Hamburg. After a remarkably long row of conferences held in the past in different countries with different local conditions, the 16th ICCE has been convened to Hamburg, the biggest city of the Federal Republic of Germany, its most important seaport and industrial center. But we hope you will find that Hamburg is also a very beautiful city, worth visiting to enjoy its beautiful features, art treasures, opera and theaters, museums and other attractions. However, it is very difficult for Hamburg to compete with such wonderful settings as Vancouver, Copenhagen and Honolulu, to mention only the sites of the last three Conferences, which, moreover, were all favoured by excellent weather conditions. The Organizing Committee cross their fingers that similar favourable weather conditions will also be granted for this year's conference. After several summer-months spoiled by rain and terrible weather, we hope that now the celestial water reservoirs are empty and you will enjoy Hamburg generally in sunshine.

People in this country are disquieted by the increasing height and frequency of storm surges at our coast. Up to 1961 coastal and harbour engineers worked with a highest high water level, which dated back to 1825. No higher water levels had occurred up to February 1962, when the extreme water level of 1825 was exceeded by about half a meter. Then dikes were damaged heavily at many spots. But the frequency of storm surges continued to grow, and in January 1976 a new alarming water level was measured, which exceeds the peak of 1825 by

nearly one and a half meters. The reasons for this remarkable and disturbing development are contested up to now, as no scientifically founded answer is available on the question of why frequency and peak levels of storm surges at our coast have been growing so vehemently for about 25 years. We see a field of problems here, which will still take much effort to solve. Anyhow, you will understand that due to these facts the public interest in coastal engineering is very lively and widespread in this country. We hope that this conference will make a noteworthy contribution towards solving the problems.

Ladies and gentlemen, I should like to finish my welcoming speech by expressing our sincere thanks for the broad participation in this conference and wishing you all an agreeable and successful time in our country and in this Free and Hanseatic City of Hamburg.

I leave the desk first to Mrs. Burgomaster Helga Elstner, representing the Senate of Hamburg and then to Dr. Volker Hauff, Federal Minister for Research and Technology, representing the Federal Government. Thank you.

WELCOMING ADDRESS

Burgomaster Mrs. Helga Elstner
Senate of the Free and Hanseatic City of Hamburg

Ladies and Gentlemen. In the name of the Senate of the Free and Hanseatic City of Hamburg, and also personally, I welcome you most cordially here in our Congress Centre. We in Hamburg are happy that the International Conference on Coastal Engineering is being held in our city for the first time and that the "Hafenbautechnische Gesellschaft" has been entrusted with its organization.

We are pleased not only because this scientific event animates the diversity of the conference scene here in Hamburg, but also because the people and their representatives in this great seaport have an interest in the topic of coastal engineering which stems quite naturally from its geographical location. This interest in subjects of coastal research is as old as Hamburg itself and goes back almost a thousand years to Hamburg's beginnings as a centre of shipping and trade. Down the centuries they improved and enlarged the port, while the river Elbe, as its link with the sea, was regulated, deepened and protected. In the 14th century, our ancestors built an imposing defensive tower on a small island in the Elbe estuary to protect their shipping. Later on, upon the insecure ground of the shallow and hazardous coastal waters of the rough North Sea, they constructed sea marks, wooden beacons and flares, which had to be well secured against sea attack.

The construction of marks, regulating works along the Elbe as far as the estuary, dike building since the 16th century on the island of Neuwerk and on the coast at Cuxhaven--which belonged to Hamburg from the 14th century until 1937--also the experience and observations of tidal movement, currents, changes in the coastline and other natural phenomena which Hamburg seafarers and pilots collected and evaluated, are part of the knowledge which is now understood worldwide in research and teaching as "coastal engineering".

Stemming from its port interests, Hamburg has in the past made important contributions in this field. I will mention just two examples here. More than a century ago, Heinrich Hübbe, a hydraulics engineer with the authority responsible for the port and the Elbe waterway, and who later became its director, investigated the processes of sand movement in the tidal mudflats of the Elbe estuary and published the results in 1861 in a then epoch-making work. At about the same time Hugo Lentz, another engineer with the same authority, studied the tidal movements in the German Bight. After many years of careful gauge observations, he published the first tide tables for the southern and eastern North Sea coast. Even by our present state of knowledge these show a remarkably high standard of reliability.

But whatever Hamburg's pride in its long history, our attention is focussed very much on the needs of the present. In the field of coastal engineering we are engaged in two tasks which are of the greatest importance:

1. As a tidal harbour and as a city whose limits extend well into the Elbe marshland area, Hamburg is directly affected by the natural phenomena occurring in the North Sea and in the Elbe estuary. Our particular concern here is, of course, the storm tides, which advance in the tidal rivers far into the hinterland. After a long period of relative calm, a great storm tide occurred in 1962 and claimed the lives of many people as well as causing heavy material damage. Steps were immediately taken to make Hamburg safe against future storm tides, but hardly had work been completed before an even higher surge threatened us in 1976. Once again great flood damage was caused, this time particularly in the actual dockland area. These parts now are being well protected. This is a programme which includes not only the building of dikes, flood protection walls, storm barriers, etc., but also research into the problem of storm tides so as to be prepared for possible future developments and, especially, to develop reliable forecasting procedures by which precautions are possible for a good time in advance.
2. A further aspect of our coastal engineering activities is exemplified by a project directly on the North Sea coast. In 1962, following negotiations with the Land of Lower Saxony, Hamburg acquired an area of about 100 km² in the Wadden Sea of the Elbe estuary so as to prepare plans for a so-called outer port and to put these plans into effect when the time came. The location is unique on Germany's North Sea coast. The natural channel there is more than 20 m deep, so that--quite apart from the outer-port function--a harbour could be built for the largest bulk freighters which--because of the tidal conditions in the Elbe--could no longer reach Hamburg. This off-shore location is an area of complicated hydrodynamic and coastal morphologic processes and interrelations which called for extensive investigations, and a research unit was set up especially for this purpose in 1963. The concentrated and now largely completed research programme has, in addition to the immediate planning objectives, yielded valuable scientific information in the field of coastal engineering. These findings were published in the relevant technical literature and also featured in part at the coastal engineering conferences of recent years. But no doubt you all know this better than I do. My intention is merely to underline the fact that the interests of the seaport of Hamburg and your concern with coastal engineering are closely linked. Your field of interest has always been of particular importance for Hamburg as one of the world's leading ports, and it will continue to be so in the future. That is the reason for our particular pleasure in having you here as our guests.

I hope that, in spite of the demands of the Conference, you will find sufficient time to make the acquaintance of Hamburg, to enjoy its atmosphere, and to gain impressions which will remain with you when

you are back home in your own countries with which Hamburg maintains particular ties in peaceful international trade.

WELCOMING ADDRESS

Dr. Volker Hauff
Federal Minister for Research and Technology
Bonn

Ladies and Gentlemen. On behalf of the Government of the Federal Republic of Germany I would like to extend a cordial welcome to you, the participants of the 16th International Congress on Coastal Engineering in Hamburg.

We are especially pleased that you decided to hold your Congress this year near the North Sea after your last one took place on a very beautiful island in the Pacific. In general, these two places have very little in common. But for coastal engineers, both places--apart from providing a nice environment for meetings--have something to offer which is of professional interest to them: the problems of protection against extremely high water levels.

As you all know, the Federal Republic of Germany is a country with a relatively short coastline. Nevertheless, this shore line has always posed many problems to the population living near to it. Dikes have been constructed in Germany along the sea for roughly 1000 years because the coasts are generally flat, and they have to be protected against the impact of storm floods. One of the last most spectacular ones, the storm tide of 1962, caused heavy damage. The surges of 1973 and 1976 showed that the exceptional storm tide of 1962 was not an isolated incident and that even higher water levels may occur in the future--a prospect which leads to many lively discussions among experts and politicians as well as among the population. Of course, nobody knows exactly what the future has in store for us. But this problem must be regarded, as you will do during this Conference, from a scientific, an engineering and from an economic point of view.

Referring to the economic--and that means financial--aspect of coastal protection, I should like to give you a figure indicative of what the Federal Government is spending on improvements in coastal protection. In 1977 alone grants exceeding DM 120 million were provided and another DM 50 million were spent for this purpose by the Länder. But this is only one year under a long-range programme which is to secure the necessary construction work needed to protect the flat 10,000 square-kilometer near-coast areas. This figure gives you, I think, a good idea of the great importance which the government attaches to coastal protection.

There are also other coastal engineering aspects of concern to the Federal Government. In my country the extension and improvement of the navigable waterways is the task of the Federal Government. Shipping is very important for us: the importation of raw materials

and the exportation of industrial products call for safe and efficient ports. The traditional ports like Hamburg are situated on the large tidal rivers and at a distance of up to 100 km from the coast. The navigation channels from and to the harbours have to be developed for very large ships, and they have to be maintained in good condition in spite of the eternal problems of sediment transportation. Moreover, the development of new port facilities closer to the coast is under consideration by the competent authorities requiring careful planning based on a great number of environmental data.

It is obvious that all these practical aspects of coastal engineering must be supported by extensive research projects. Therefore, both the Federal and the Länder governments operate their own laboratories dealing mainly with project-oriented research, while the universities and their institutions primarily carry out basic engineering research. Cooperation between the various laboratories is of great importance because many of them are too small to handle complex projects which often require huge technical facilities and a substantial amount of support. This cooperation is ensured by the Coordinating Committee for Coastal Engineering (Kuratorium für Forschung im Küsteningenieurwesen).

As the Federal Minister responsible for research and technology, I deem it very important that there is always a continuous exchange and transfer of know-how among the institutions and disciplines involved in order to optimize the process of innovation which, in turn, is a prerequisite for progress in science and engineering. One example which illustrates these needs but also shows the possibilities in coastal engineering is the application of remote sensing techniques which permit collection of environmental data in coastal areas. Aircraft and satellites used as data collection platforms can be of considerable benefit to broaden the knowledge of actual coastal processes.

Furthermore, I should like to emphasize the role which coastal engineers can play in advising the developing countries in their needs to develop and manage their coastal areas. The advice in coastal engineering can be of considerable importance to those countries which want to make use of their natural resources, construct ports, control shore erosion or conserve the natural environment. Coastal engineers may also render advice with regard to problems related to the use of the renewable and unrenewable resources of the coastal area and problems of coastal urbanization. Many countries providing good training programmes in coastal engineering should consider the possibility of initiating training programmes for scientific and technical staff of developing countries in order to help them achieve a professional standard enabling them to manage their own coastal problems.

This International Congress provides--I trust--a good opportunity for advancement, continuation and expansion of international cooperation by the exchange of both theoretical results and experience gained in practical field work. Your programme which covers so wide a range of subjects and envisages papers by experts from so many countries will certainly stimulate discussions and will give new impulses to future research work. I therefore trust that you all will benefit

from your participation in this Congress, and I do hope that you will also enjoy your stay in this city and in this country.

Ladies and Gentlemen, I declare the 16th International Congress on Coastal Engineering open, and I sincerely wish you every success in your task.

WELCOMING ADDRESS

Dr. Hans-Werner Partenscky
Technical University of Hannover

Distinguished guests, dear colleagues and friends, ladies and gentlemen,

Dinner speeches are not very popular, neither for the speaker nor for the listeners. I nevertheless feel obliged to say a few words on this occasion.

First, I should like to extend our sincerest thanks to the American Society of Civil Engineers as well as to the Coastal Engineering Research Council, for the honour shown us in permitting the 16th International Conference on Coastal Engineering to be held in the Federal Republic of Germany here in Hamburg. Also, I should like to thank our guest speakers, Prof. Helge Lundgren from Denmark and Mr. Allan Price from the United Kingdom, for their excellent and stimulating speeches which they delivered to the audience during the Conference. Our thanks are equally extended to all authors for their presentations as well as to all those who participated actively in the scientific discussions. They all contributed in a very fine way to scientific progress in our field of Coastal Engineering.

Ladies and Gentlemen, all of you are certainly aware of the fact that Conferences of this kind are not possible without the moral and financial support of potential sponsors. I would therefore like to take this opportunity to address our sincere thanks to the Free and Hanseatic City of Hamburg and to the Federal Ministry for Research and Technology as well as to the numerous private associations, construction companies and consulting engineering firms--the list of all of them is too long to name them individually--for their generous support which helped us considerably to make possible this congress with its social events.

Ladies and Gentlemen, there is an old French saying which I have cited already on other occasions. It says:

"On ne peut pas aimer toutes les femmes du monde, mais on peut au moins essayer."

If I translate this into English, it goes like this:

"You can't be in love with all the women in the world, but you could at least try."

This is the way we felt in the German Organising Committee when we started with the first preparations for this Conference: "We

thought, we could at least try!" We did not know then what was ahead of us. It was only when we found out, that a considerable burden of our task could be delegated to the "German Convention Service", that we felt we would manage. I should therefore like to extend our sincere thanks at this occasion to Mrs. Lau-Thurner and her charming and effective young assistants for their help in preparing this conference. I should also like to mention the Secretary of our Organising Committee, Dr. Siefert, who was involved in many details of our preparations for almost two years. Thank you, Dr. Siefert, for all your efforts.

Gentlemen, there is one last, but very important thank-you, I have the privilege to extend in your name tonight. I would like to thank all ladies who have accompanied their husbands to this Conference and to this Banquet for being here with us and for being so especially beautiful tonight.

Our field of Coastal Engineering is still a relatively young science and more systematic research work is needed to cope with the impact of waves and storm surges against our coasts, and to develop better and more economical design criteria for coastal works. This is clear to us,--but not necessarily so evident to others. Therefore, when preparing this conference, I was often asked by "outsiders": "Why do we need Coastal Engineering?" The answer was of course easy for me. But being a professional, I felt that some more facts and data were needed to support my opinion on the importance of our field. So, I went deeper into the subject. I first investigated our situation in the Federal Republic of Germany by measuring the length of our coastline, the islands included. I then divided this figure by the population. The result was surprising: only a length of 1.9 m was available per person during the summer season.

Being a serious scientist, I assumed that only 30 percent of our population would be at our German beaches at the same time. The result was still unbelievable: only 6 cm of coastline per capita would then be available during the three summer months. No wonder, that it is so crowded at our German Beaches! To find out if this could have an effect on the stability of our shorelines, I consulted some experts of our German Coast Guard. The answer was astonishing: "The damage caused during the 3 month summer season by the tourists,--and especially by the nudists in the dunes,--is comparable to the damage of two average storm floods!

Now, everyone will understand why we need Coastal Engineering and Shore Protection in Germany. Going further into the subject, I found out that the situation with respect to the available length of shoreline per capita in other countries is not quite as critical as in the Federal Republic of Germany. For example, in the Netherlands we have 5 cm of shoreline per capita, in Japan 8 cm, in England 13 cm, in the USA 66 cm, Denmark 150 cm and Australia 180 cm per capita,--to name a few. However, I was informed that swimming at beaches is only allowed in restricted areas in most of these countries, i.e., the tourists are concentrated at certain spots, which certainly means that other countries need coastal engineering and "people management" too! We can be convinced, therefore, that our efforts of these last days

were not in vain and will certainly help to develop, maintain and protect our coasts all over the world.

Ladies and Gentlemen, our Conference comes to an end. We hope that the scientific program with its presentation of more than 200 contributions from 41 different countries will stimulate and help you in your own further research work and that we will all meet again in good health two years from now to the 17th International Conference on Coastal Engineering to be held in Sidney, Australia.

Let me thank all of you for coming to Hamburg. We all wish to those of you who will participate in one of the after-congress excursions much fun and good weather,—and to all of you a happy return to your home countries.

STRUGGLE OF PHYSICS AND MATHEMATICS
IN COASTAL ENGINEERING

H. Lundgren
Technical University of Denmark

ABSTRACT

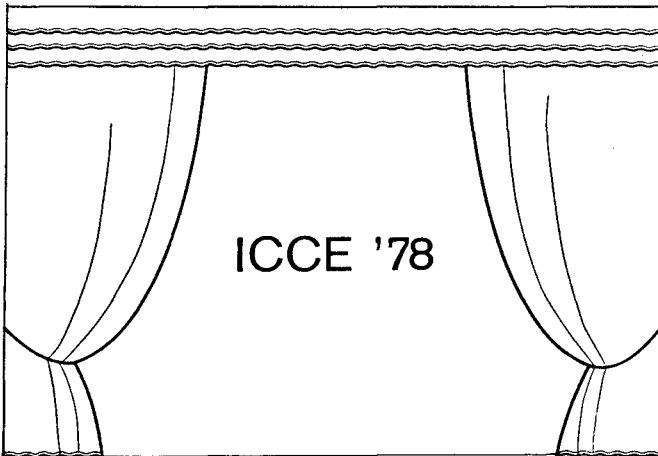
This paper gives examples of the separate and combined efforts of Physics and Mathematics in coastal engineering with particular reference to the possibilities in the future. It points to the fact that physical thinking is necessary as an inspiration to mathematical and numerical work.

While there is relatively little duplication of work (among the various institutions) of a purely theoretical character, the same statement does not apply to numerical models. One may hope that the future will produce more coordination in this respect.

There are two disciplines where the establishment of high quality numerical models will require a particularly strong combination of basic research, numerical expertise and field work: three-dimensional mixing processes and sediment problems. It would seem that no single institution has available both the integrated expertise and the capital investment required. Hence, a close cooperation among several institutions is almost mandatory.

1. INTRODUCTION

A perfect Opening Ceremony has set the stage for

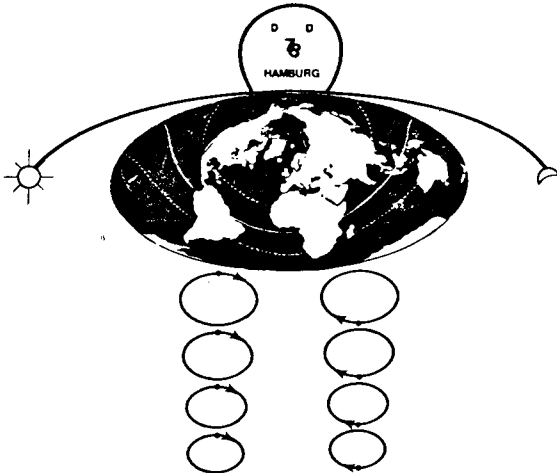


It is indeed a great honour to have been selected by the Organizing Committee to give an invited lecture at such occasion. In addition, it is a very difficult task: Let alone that more than 600 conference participants represent widespread scientific and practical interests within the various fields of coastal engineering; the lecture is also attended by the accompanying ladies.

The first play on this stage has THE CAST:

Mr. PHYSICUS, Master of the play
 Mrs. MATHEMATICA, Mr. Physicus' wife
 Miss NUMERICA, their daughter
 Mr. HARDWARE, Miss Numerica's boyfriend
 Miss SOFTWARE, young girl, often in troubles

Mathematica was married to Physicus at a quite mature age of his. As in all marriages there are both hours of happiness and hours of distress. The serious question about Numerica is: 'Is Physicus her true father or?' If not, very few coastal engineers will respect her. Miss Software is very interested in Mr. Hardware, always trying to get control of him but rarely succeeding!



Mr. PHYSICUS

Physicus was the first figure that entered the stage of Coastal Engineering, both in the sense that harbours and coasts were physical problems, and in the sense that scientific studies normally started with physical models.

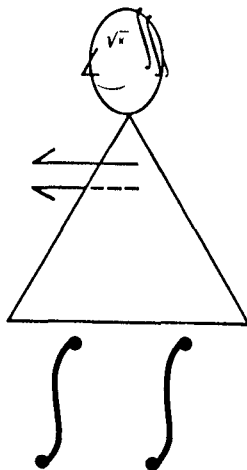
Physicus' main disciplines are:

- a. Wave phenomena
- b. Tides, surges and currents
- c. Mixing phenomena
- d. Sediment problems
- e. Structures

2. WAVE PHENOMENA

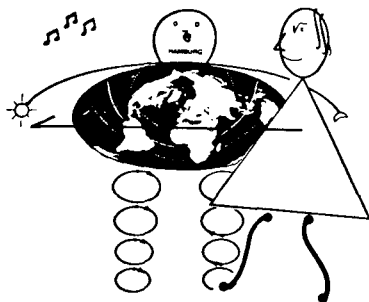
Regular waves is one of the fields where Mathematica has had her greatest triumphs. She has always been very fond of closed (boundary) problems associated with Laplace' equation.

Before Physicus met her, he had made good progress with propagation considerations in shoaling and refraction by assuming that none of the energy flux was reflected from a gently sloping bed. Without improper interference from Mathematica, he should continue his propagation line of research, basing the description in each vertical of the slope on the time profile, i.e. the variation over the period T . Such approach should offer possibilities of treating the deformation of regular waves towards breaking, as well as broken waves (surf).



Mrs. MATHEMATICA

Naturally, when it comes to basic concepts, there is complete harmony between Physicus and Mathematica. For example, the latter originally derived the radiation stress for small sinusoidal waves in combination with a constant current. Physicus, on the other hand, is inclined to think of it as the wave thrust, $F_w = \bar{F}_m + \bar{F}_p$, where \bar{F}_m is the mean value over the wave period of the momentum force, and \bar{F}_p is the mean value of the pressure force. In establishing the equation of mean momentum, he considers the wave thrust as an analogy to the German 'reaction force' (Reaktionskraft), which was used around 1930 in the theory of steady state flow in hydraulic engineering (Wasserbau).



The wave thrust can be determined for any periodic flow, including breakers and surf. Physicus realizes, however, that the mean values, \bar{F}_m and \bar{F}_p , do not give any information about the variation of the momentum and pressure forces over the period. He knows that the equation of momentum is something much more universal than just its 'mean value over the period'. He likes to dream that the general equation of momentum may be used for studying important problems, such as wave deformation and breaking. Of course, the fact that F_p contains a first order term, where \bar{F}_p is of second order, presumably presents a serious difficulty.

In addition, Physicus recalls that the equation of moment of momentum has been used, in a qualitative manner, to explain the formation of sand bars on a coast as the result of water flowing along the sea bed towards the breaker line, where there is a particularly large part of the momentum force near the wave crest. Could it be that the moment of momentum could also be used to explain the skewness of waves on a slope because of the moment of the pressures exerted on the bed by a wave, the height of which increases as the depth decreases?

There is also complete agreement between Physicus and Mathematica with respect to the mean energy level, which is defined for any periodic potential flow. Physicus has difficulties, however, in seeing how the energy concept could be effectively used for the solution of general problems.

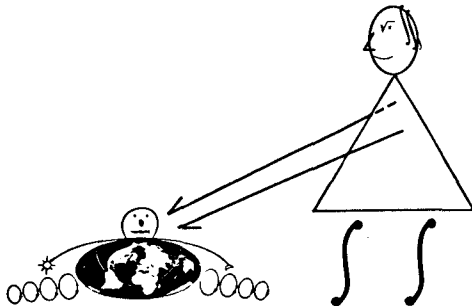
Attention should definitely be drawn to the fairly new concept, wave action, defined as E/ω_r , where E is the total energy of a periodic wave and ω_r its frequency relative to a current. For problems where regular waves are combined with currents it has been proved that the wave action flux and the conservation of wave action are concepts of a fundamental nature, analogous to the energy flux and the conservation of energy in the case of waves without currents.

Relative to the current the wave energy is propagated with the relative wave group velocity, c_{gr} , along the orthogonals. If c_{gr} is vectorially added to the current velocity, the absolute wave group velocity, c_{ga} , results. The direction of c_{ga} is called the wave ray.

For irregular waves the energy is distributed over the frequencies. Hence, it should be possible to apply the wave action concept also to the combination of currents and irregular waves, even with inclusion of the phase and direction information from the waves.

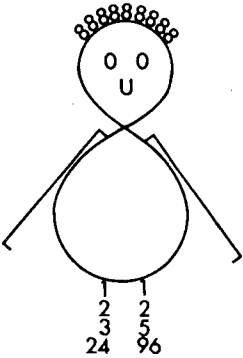
Wave description represents a field where Mathematica has long played a dominant rôle. Firstly, coastal engineers had to work with regular sinusoidal waves. Secondly, cnoidal waves came into the picture; because of the simplifying assumptions necessary, there is not one cnoidal theory but several with some secondary differences. Thirdly, Stokes waves of higher order, up to the fifth, appeared on the stage. In all these cases the waves were periodic and symmetric, even over sloping bed.

Simultaneously with this development, Mathematica transferred the concept 'energy spectrum' from a number of other physical sciences where it had served well since it was introduced in 1923 by Wiener in his 'generalized harmonic analysis'. She has used this tool unscrupulously - with a lot of success too - along our coasts for several decades in spite of two objections: (1) The spectrum is well fit only to a linear Gaussian stochastic process, i.e. a process consisting of



small sinusoidal components. (2) The spectrum throws away half the information (the phase relationships) available in a wave record.

Naturally, Physicus did not like being suppressed by his wife and, indeed, the consequences came about a decade ago when it was discovered that a model wave train with the correct spectrum did not produce one single shock force on a vertical face breakwater. Later on it was realized that the response of moored ships in models could differ much for two wave trains with the same spectrum. And, still worse, the stability of rubble mound breakwaters could be extremely different for two such wave trains.



Therefore, around 1970 Physicus went into action asking for natural wave trains in his models, also expressed as his desire for the correct wave grouping. The first successes of his action appeared immediately; however, he will have to work very hard together with Mathematica and Numerica before a really satisfactory result will be obtained.

To ask for natural wave trains in physical and numerical models is almost identical to a desire for a deterministic description of natural waves. In two dimensions (wave flumes) it is easy to give such a description under the (quite restrictive) assumption of linear superposition.

In three dimensions the matter is considerably more complicated. For more than a decade rough approximations to directional spectra have been determined by means of arrays of, say, three to five wave recorders. In this context, Mathematica has confined the data analysis to the determination of all the correlation coefficients that could be produced from the records.

Physicus is inclined to prefer a set of three recorders in one vertical (called Point 1): one recording the water surface elevation, η_1 , and two that record the horizontal orbital velocities, u_1 and v_1 . From

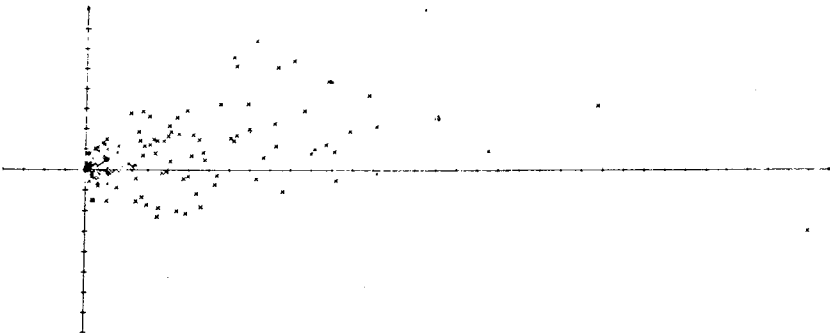


Fig. 1 Energy distribution between 0.2265 hz and 0.2535 hz

these three records it is possible, for each frequency interval, and under the assumption of linear superposition, to determine the directions, the amplitudes and the phases of the components.

From such a recording for a storm situation the components of energy in an interval centered around 0.240 hz have been plotted as the individual points shown in Fig. 1. The frequency interval chosen is the one with most energy. Each point represents a vector from the origin of the coordinate system.

With the knowledge of directions, amplitudes and phases at Point 1, the wave motion may be calculated at some other point, called Point 2. An example of this is illustrated by Fig. 2, where the calculated horizontal u_2 -component has been compared with the recorded one. As a first

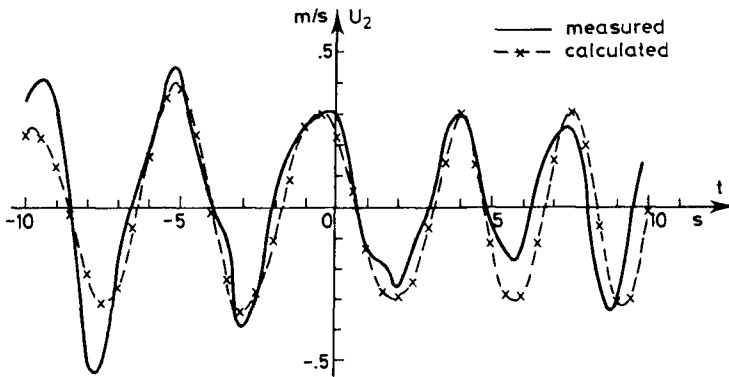


Fig. 2 Horizontal velocity u_2 at point P_2

attempt the agreement is reasonably good. The discrepancies are probably mainly due to two circumstances: (1) The velocity meters were placed rather low, so their response to higher frequencies was strongly damped. (2) The nonlinear interaction of the wave components has not been taken into account. — In this connection it should be mentioned that the vector from Point 1 to Point 2 has a length of about $1.3 \bar{L}$, where \bar{L} is the mean wave length. The vector forms an angle of 22° with the mean direction of wave energy propagation.

With an embryo of a deterministic description available, Physicus suggests that F_m and F_p be investigated as stochastic processes with a view to a deterministic description of the long waves generated in harbours by the groups of short waves.

Recently this connection between long waves and the short wave groups has been demonstrated by two physical model tests with a moored ship in a harbour, as illustrated by Fig. 3. In the upper part of the figure the surge and sway of the ship, as well as the waves in the harbour, are shown with the irregular wave train $\eta(t)$ as input to the model. In the lower part the same quantities appear when the input is $\eta^2(t)$, smoothed as moving average over 30 s.

Until now the investigation of short wave disturbances in harbours, including motion of moored ships, has been a matter for

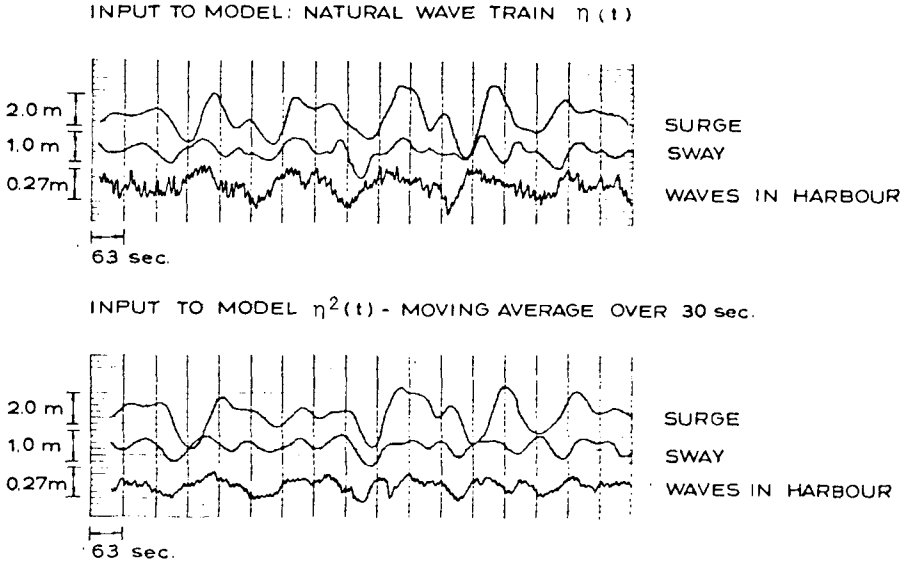
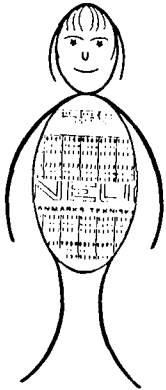


Fig. 3 Ship motions generated by irregular waves and by a simulation of drift forces

physical models exclusively. With Numerica's maturing, however, this field is now within her reach.



Miss SOFTWARE

Provided that the water depth is not too large compared with the essential wave lengths involved, the ordinary shallow water theory may be taken as the starting point. In this theory there are three dependent variables: the surface elevation η and the two horizontal fluxes (p, q) , all of them functions of $(x, y; t)$. Since the vertical accelerations must not be neglected in short waves, four Boussinesq-type terms have to be added to each of the two momentum equations. These terms are mixed derivatives of the third order, which have required special manipulations in order to make Numerica's difference schemes algorithmically efficient. Indeed, in order to handle problems of such complicated nature, Software needed many years of university education.

Fig. 4 shows a perspective plot of regular waves in a Danish harbour, as viewed from the harbour entrance.

Since Numerica handles the three difference equations by a time-step method, Software does not notice any difference whether the waves are regular or irregular. For irregular waves Fig. 5 shows the disturbance coefficients K along two wharfs in the same harbour as above, defined by $K = \bar{H}/\bar{H}_1$, where \bar{H} is the mean wave height at the wharf and \bar{H}_1 the mean height of the incoming wave at the entrance. The full curves present the results from a physical model, whereas the dotted curves are produced by Numerica.

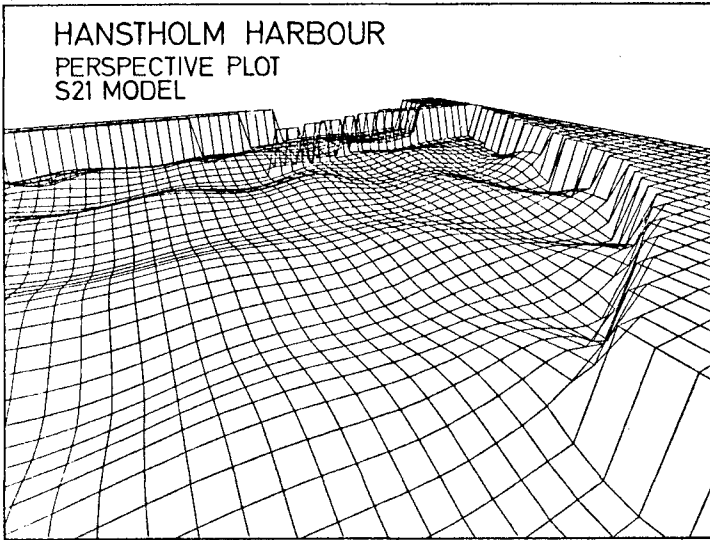


Fig. 4 Regular waves in the outer harbour

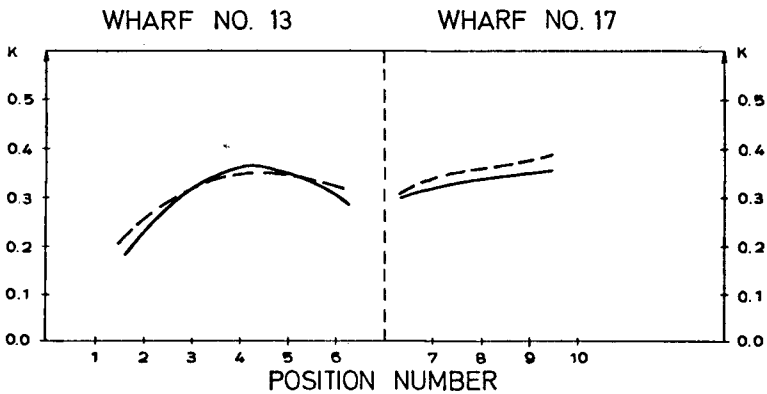


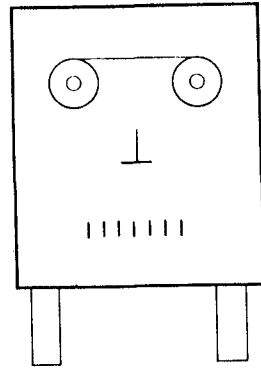
Fig. 5 Mean wave height coefficients in the inner harbour

The above results provide convincing evidence that, on the whole, time-step methods are superior over other methods, particularly because of their ability to deal with nonlinear terms and their capacity for being extended to more general problems.

If an essential part of the energy pertains to wavelengths that are rather short in comparison with the depth, as is the case in ocean engineering, the Boussinesq-type equations are not sufficiently accurate. Then Numerica will probably have to handle computations in several layers. This may become economical some time in the future when Hardware is willing to work for a lower salary.

Hindcasting and forecasting of the wave weather is already an important field for Numerica's activity and, without any doubt, the future will show greatly increased activity of higher and higher quality.

As illustrated in Fig. 6, the input to a wind wave model may consist of a series of barometric pressure charts. Conveniently, the output may be a series of charts of significant wave heights.



Mr. HARDWARE

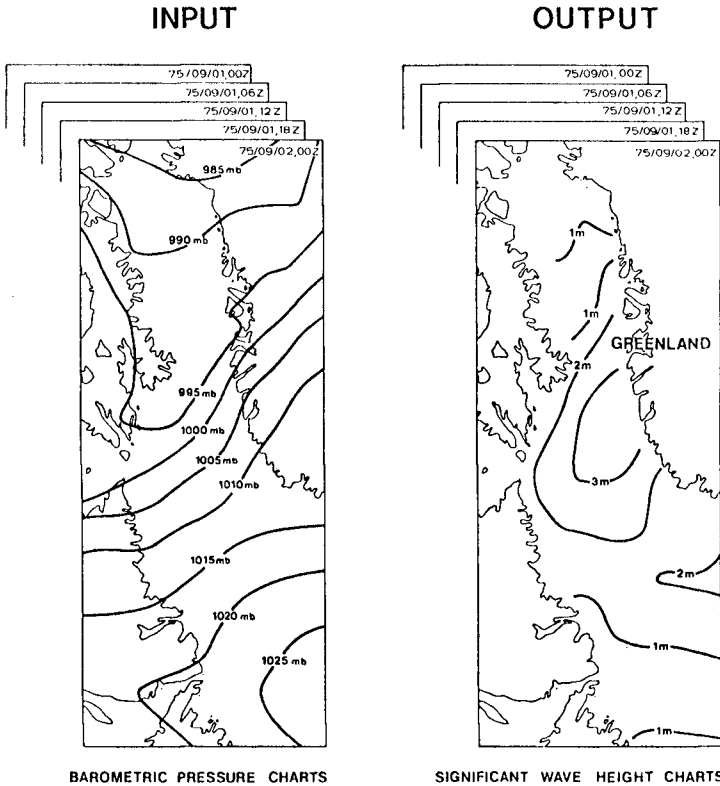


Fig. 6 Input to and output from wind wave model

In order to produce Fig. 6, Numerica discretized the sea surface in $10 \cdot 23 = 230$ grid points with a mesh of 150 km. At each grid point the wave energy was distributed over 12 directions and 10 frequencies, i.e. 120 values. The time step was 3 hours. In the energy transport equation she included both growth and decay terms.

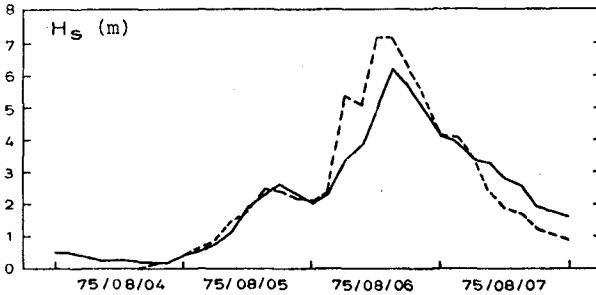


Fig. 7 Variation of wave heights

For a check point near the centre of the area shown in Fig. 6, Fig. 7 gives the variation of the significant wave height during a storm, the full curve indicating the recorded values and the dotted curve the computed ones.

The recorded and computed spectra are compared in Fig. 8. At present the model has a tendency to give peak frequencies that are slightly on the low side. Numerica may remedy this tendency in the future.

Wave breaking has always been, and is still, the wave phenomenon in greatest need of rational treatment, particularly because of its paramount importance for most coastal sediment problems. Qualitative descriptions as spilling, plunging etc. are unsatisfactory. It is hoped that Physicus will soon come up with the combination of quantitative parameters that will characterize the initiation and development of the various breaking processes. Will his thoughts first of all go in the direction of momentum and moment of momentum?

3. TIDES, SURGES AND CURRENTS

In the field of tides and surges, Numerica has been very active in many institutions all over the world, producing a large number of two-dimensional, vertically integrated models. More international coordination at an early stage might have increased the efficiency of intellectual efforts.

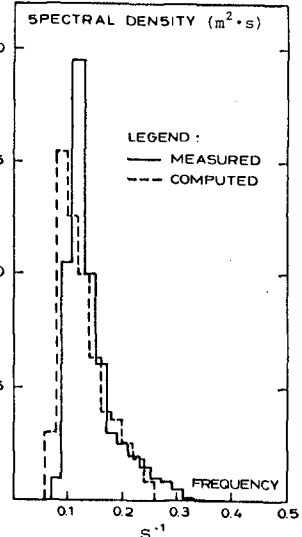
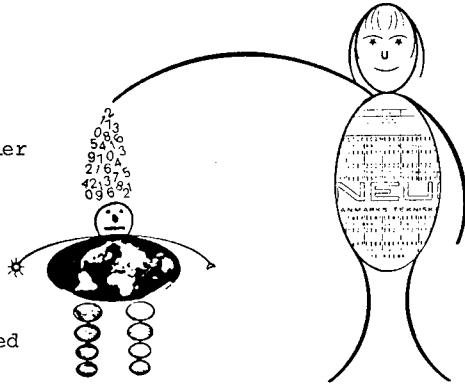


Fig. 8 Spectra

In two different ways Numerica may assist Physicus:

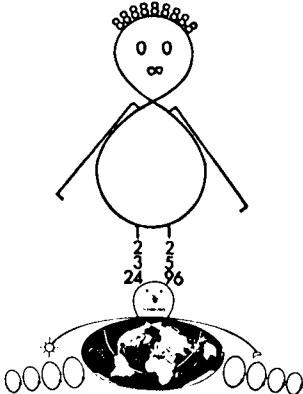
(a) Numerica may treat a larger geographic area with Software designed to deliver data for boundary conditions as input to a smaller area physical model and, perhaps, also data for calibration of the physical model. This combination has been termed a 'hybrid model'.

(b) Numerica may study a larger number of alternatives, prior to the selection of a few for detailed studies in a physical model.



4. MIXING PHENOMENA

Numerica has initiated a large number of two-dimensional and some three-dimensional models of stratified flows of different types.



As she has grown up, one is sometimes inclined to think that she has become a member of Women's Lib, trampling upon Physicus, and believing that she could perpetuate life on this globe all by herself, for example by cloning. She could easily get into troubles, however; for example, in the following ways:

(a) By shipping Software as a package with deficiency in physical basis.

(b) By not observing that discretization can lead to scale effects, for instance, in the transport-dispersion equation where the diffusion coefficient D is dependent upon both its physical value and the grid size.

(c) By not noticing that an Eulerian solution of a Lagrangian process, e.g. transport, without special precautions will lead to a non-physical, numerical increase of the dispersion.

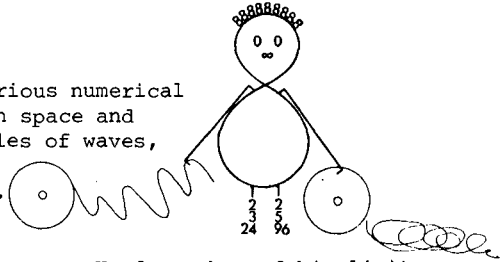
A large and important area for Numerica's future activity lies in the continued development of integrated hydrodynamic/water quality models.

5. SEDIMENT PROBLEMS

Because of all the scale effects inherent in physical sediment models, it has long been known that sediment problems will offer a particularly fertile ground for Numerica's activity.

In order to establish a high quality model, the cooperation of many scientists will be required, as illustrated by the following list:

- (a) Basic research on wave breaking.
- (b) Combination of waves and currents.
- (c) Basic research on sediment transport in waves and currents.
- (d) Expertise in constructing fast numerical algorithms.
- (e) Experience in organizing the various numerical modules with different scales in space and time, as illustrated by the scales of waves, currents and sedimentation.
- (f) Good field data for calibration.



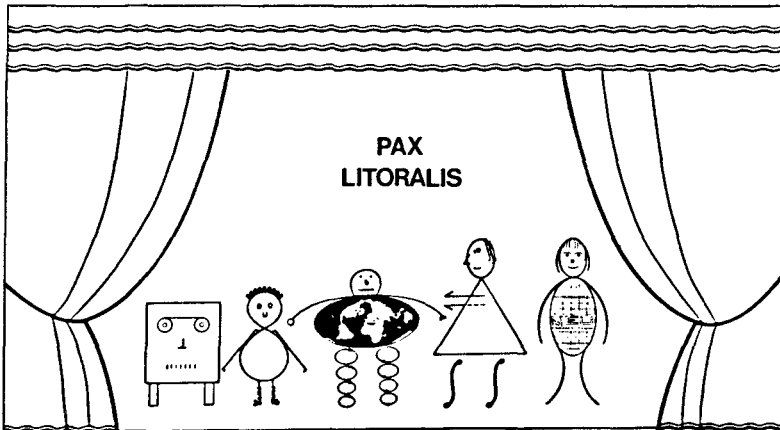
The computer capacity required is so large that Numerica might easily stress Hardware beyond his limits.

6. STRUCTURES

In many cases structures are entirely under Physicus' rule. An important exception is Morison's formula for cylinders. Here C_d has been assumed to be constant over the wave period, whereas Physicus would think that the separation points move and C_d changes with the pressure gradient. On the other hand, it is likely that the pressure gradient always imposes the value $C_m = 2$.

7. END

While the actors of this play thank the audience for their attention, they promise that they will cooperate in harmony in the future. They also express the hope that there will be extended coordination among the Coastal Engineering institutions around the world, and that there will be peace along our coasts.



ACKNOWLEDGEMENT: The author of this paper expresses his best thanks to the German Organizing Committee, as well as his sincere gratitude to all the colleagues who have contributed directly to parts of this paper or indirectly to its philosophy. He has chosen to give no reference, in accordance with the principle: Nobody named, nobody forgotten.

THEME SPEECH by W A PRICE

Senior Principal Scientific Officer
Head of Coastal and Port Engineering Division
Hydraulics Research Station, Wallingford, England

- (i) MODELS - CAN WE LEARN FROM THE PAST?
- (ii) SOME THOUGHTS ON THE DESIGN OF BREAKWATERS

I would like to deal with two quite different subjects. Firstly, the Hydraulic Modelling of Estuaries and Coasts and, secondly, Breakwaters.

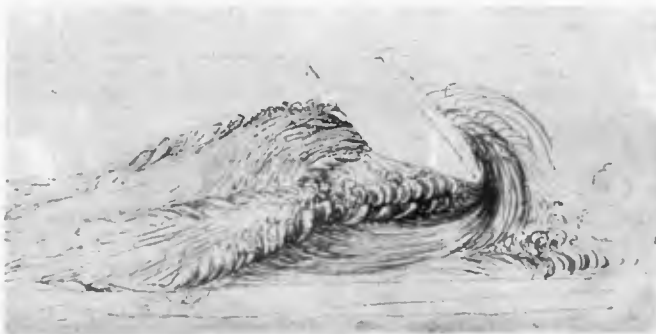
MODELS - CAN WE LEARN FROM THE PAST?

Flow visualization

Leonardo da Vinci who lived some 500 years ago gave our profession a fitting motto which is especially applicable to those of us who deal with models. He is reported to have said "When dealing with water first experiment then use judgement". It is appropriate that his name be mentioned at one of our Conferences because he was one of the leading coastal engineers of his day and for part of his life planned and supervised the construction of canal and harbour works over a large part of Middle Italy. He was the first to describe a multiplicity of hydraulic phenomena - the velocity distribution in a vortex, the profiles of free jets, the formation of eddies at abrupt expansions, the propagation, interference and reflection of waves and the hydraulic jump. He was also an experimenter and suggested the technique often used today that internal currents could be observed by means of suspended particles in a glass walled tank, Ref.1. He thus spoke from experience.

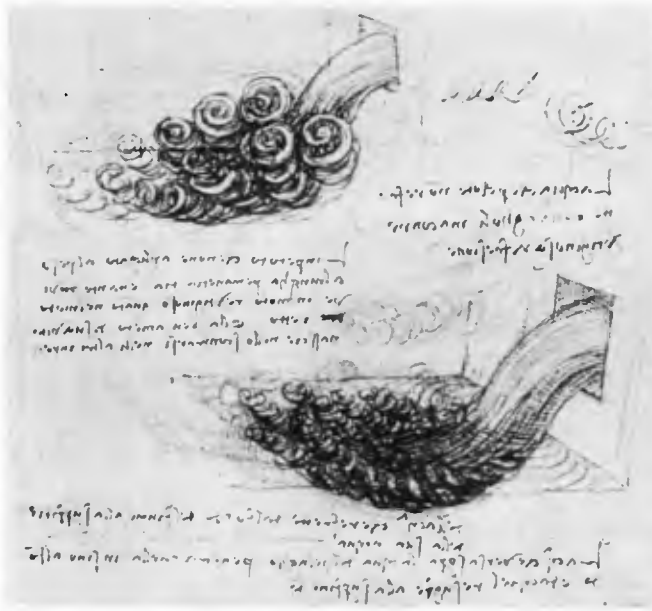
One of his drawings showing water flowing past an obstruction is shown in Fig.1a. It records what he observed. However, as a working drawing he realized that it could be improved so that when he sketched

Fig.1 DRAWINGS BY LEONARDO DA VINCI



(a) Flow past an obstruction

water issuing from a rectangular hole in a dam (Fig.1b), he drew the flow like human hair; this was probably the first expression of the concept of flow in stream tubes. There are many other drawings like these which were used in connection with a project to canalise the River Arno in Italy, Ref.2.



(b) Flow from a hole in a dam

I have used these drawings to introduce and underline an important property of physical models - one that is sometimes neglected and played down - the ability to help us visualize the flow. One method of gaining this insight from models is to use floats as in Fig.2.

We have come a long way since Leonardo da Vinci. We now have good instrumentation, sophisticated control equipment, data can be acquired, logged and plotted by mini computer. These are all welcome developments so long as we remember that instruments cannot improve the quality of the processes we are trying to scale and are not a substitute for our eyes.

History of Estuary Models

River models appear to have been first used in France in 1875 when a model was constructed to investigate the suitability of certain river training schemes that had been proposed by a Monsieur Fague. It was Reynolds working about the same time in Manchester, England, who built a model of the estuary of the Mersey and introduced for the first time the general idea of dynamical similarity, Refs. 3, 4 & 5.

Broadly speaking during the history of the development of coastal and estuary models three very distinct ranges of scales have been used.



Fig.2 FLOAT TRACKS IN A MODEL

Reynolds and Vernon Harcourt at the end of the last century built to scales of about 1/30 000 to 1/40 000 although they did use others. Gibson and Allen in the 1920's, Ref.6, built to scales of about 1/3000 to 1/6000, Fig.3, and these days the major laboratories to scales of about 1/500 to 1/1000. Fig.4 shows the comparative sizes of a hypothetical estuary to these scales.

I would discard the 1/30 000 variety as being of little practical use but there are some who would disagree. I am particularly interested in the shift in scale by a factor of, say 6, that has taken place since the 1920's. Has this been entirely justified? Are we sure that it has



Fig.3 MERSEY, DEE AND LIVERPOOL BAY MODEL
Horizontal Scale 1:7040 Vertical Scale 1:190

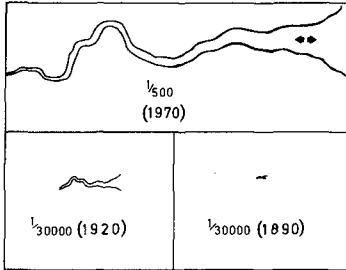


Fig.4 AN ESTUARY TO DIFFERENT SCALES



Fig.5 SCALE OR SIZE ?

not come about partly because of larger resources and more space being available to the major laboratories?

Scale or size

I would like to pose three more questions. Have certain scales become fashionable? Do we confuse scale with size? Would the person on the right of Fig.5 build models many times larger than the person on the left? I think he might, but this would not be necessary. His house would have to be bigger because that is a question of size but not necessarily his models - that is a question of scale and the problems associated with the reproduction of physical processes. I stress that I would not deny that larger models are better than smaller ones but I would question whether we have the tools to help us decide with any confidence how much better one scale is than another.

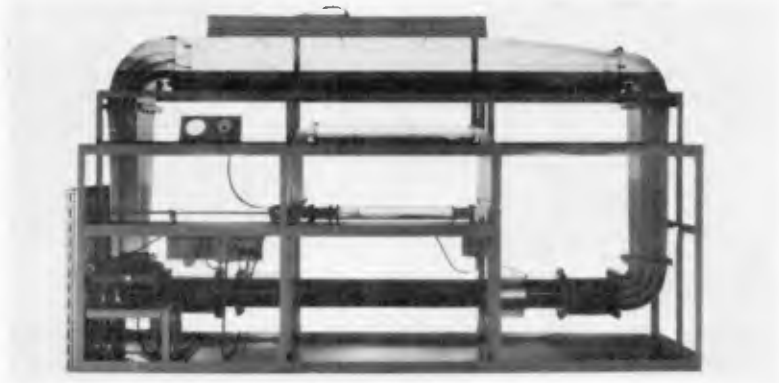
I once took a visitor around a model I had built and he was so impressed that on leaving he asked me whether I thought the model was more accurate than the prototype. I thought for a moment and not to disappoint him I said "Yes"! Perhaps we all tend to believe that models are better than we think. What we need to know is how much does the situation improve if we move from one scale to another? My feeling is less than we think. How can we judge? There are methods.

Dimensional Analysis

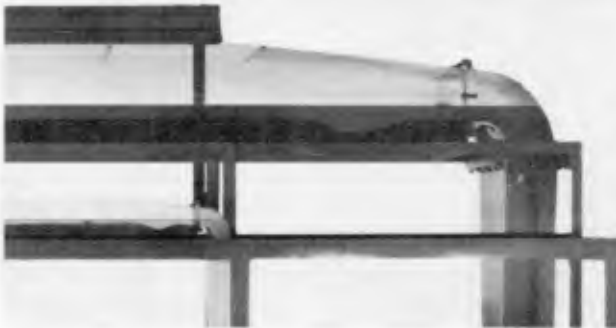
Yalin has tried to provide a yardstick through the use of dimensionless analysis. The method has been the subject of considerable controversy but it is like any other mathematical tool - used correctly it is a useful device - used incorrectly it can be misleading. He has demonstrated that the theory works by building a model which for practical purposes is close to perfection, Refs. 7 & 8.

Fig.6a shows two flumes, one a 1/3 scale model of the other. From the identity of his dimensionless numbers he was able to choose the properties of the fluids and the bed materials almost exactly. By driving two pumps from a common variable speed drive he was able to obtain the necessary ratio between the model and prototype values of the flow. The bed forms were reproduced perfectly to scale, Fig.6b.

Fig. 6 YALIN'S SIMILARITY FLUMES



(a) General arrangement of flumes



(b) Enlargement of bed features

Again, while working at Wallingford, Yalin made further model/prototype comparisons in a tilting flume. Once more he had control of the variables but because it was a larger facility he was able to make more measurements. He calculated that the wave length of the "prototype" bed features should be 3.6 times greater than those in the model and Fig.7 shows that they were. The ratio of solids discharge should be 47 and that this was the case is illustrated in Fig.8.

Practical Difficulties

Yalin is the first to admit, however, that practical considerations make the criteria of similarity difficult to apply. The model and the prototype are on the same planet and hence subject to the same gravity and there are other physical reasons which make perfect similarity impossible. So of what use is the dimensional method? In the foreword to his book Yalin says "Whether applicable or not the exact solution should be determined and then when it proves impracticable used as a frame of reference to judge the degree of correctness of the adopted solution". That is, we have to compromise but in most cases we do not understand the rules.

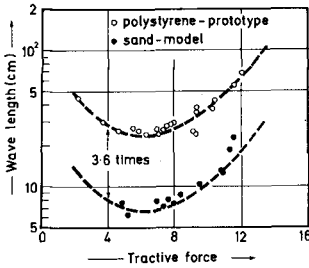


Fig. 7 COMPARISON OF WAVE LENGTHS - MODEL AND PROTOTYPE

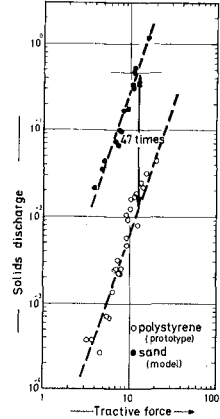


Fig. 8 COMPARISON OF SOLIDS DISCHARGE - MODEL AND PROTOTYPE

If we knew that the error involved in scaling a particular process was of the form shown in Fig.9 then we could choose an error which was acceptable in making our choice of scales. This hypothetical curve sums up what we need to find out and where some of our fundamental research should be directed. For example, when we relax certain parameters, like the dimensionless ones used by Yalin, what errors are involved?

It is interesting that when Reynolds had finished his studies on the Mersey estuary he set himself the task of learning more about scale by building movable bed models of hypothetical V-shaped estuaries to different scales. We could copy this example to advantage.

Until more fundamental work is carried out the choice of scales for estuary and coastal models will be based too much on practical arguments like these. (i) We need measurable tides and currents to make good measurements. (ii) To keep distortion to a minimum we need a large horizontal scale. There are other practical considerations and they are important but they should only be used as part of a total argument. The scaling of the physical processes and a greater knowledge of them is of fundamental importance.

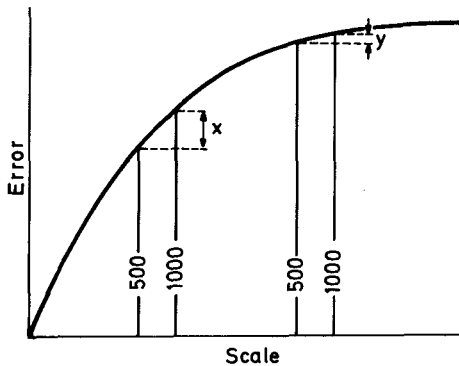


Fig. 9 HYPOTHETICAL ERROR FUNCTION FOR A PARTICULAR PROCESS TO BE SCALED

Reynolds and Froude Numbers

Until we know more of the rules we must make the most of those we have. I sometimes think that we restrict ourselves unduly by interpreting some of them too rigidly. Take Reynold's Number as an example. The flow in the model needs to be turbulent for no other reason perhaps than that the head loss should be proportional to v^2 rather than v in the laminar case. To avoid laminar flow a limit is put on the Reynold's Number say of 1500. But is the size of this number an even approximate indicator of the level of turbulence in a tidal model? I would suggest that it is not. In this case the flow accelerates and decelerates, there are changes in geometry, there are the turns of the tide - all of which tend to induce and enhance turbulence. One could happily work at much lower Reynolds Numbers and if this is the case one argument that is used against smaller models would partly disappear. Reynolds said "For flow other than in parallel pipes the Reynold's Number at the critical velocity is of course different".

I do not think that we allow ourselves sufficient freedom with the Froude relationship either. Obviously there is little latitude if we are dealing with tidal propagation in a long estuary because the speed of propagation is proportional to $\sqrt{\text{depth}}$ or thereabouts. But there are cases where some relaxation is possible. HRS once built a model of Aberdeen Harbour, Hong Kong, Fig.10 in which we had the ability of increasing the discharges by a factor of 4 over what they would be on a Froude basis, Ref.9. You will see, Fig.11, that allowing for the change in the velocity scale the current velocities at Y, a critical



Fig. 10 MODEL OF ABERDEEN HARBOUR
- HONG KONG

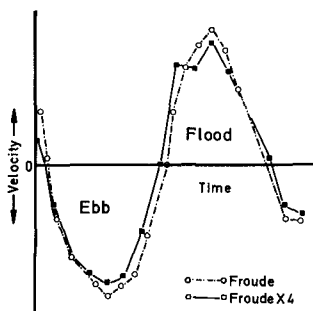


Fig. 11 CURRENT VELOCITIES AT Y -
(FROUDE AND 4 X FROUDE)

A relaxation of both the Reynold's and Froude criteria allows greater freedom. The model is a tool or an analogue that we can manipulate by making sensible departures but the answer must be right for approximately the right reason. If it isn't then the results we obtain for any changes we make will be wrong. On the fly leaf of some works of fiction they put this phrase - "Any similarity between the characters in this book with those living or dead is purely imaginary". We want to avoid having to put at the beginning of our reports this transcription - "Any similarity between the model and prototype is purely coincidental".

position, are almost identical. I would suggest that this "distortion" in the Froudian velocity scales could be used to advantage in many studies. In sediment transport models it might be a valid way of getting over the problem of the initiation of movement of the sediment.

Instrumentation

What effect does the development of better instruments have on our attitude to model scales? With lasers we can now measure down to a velocity of zero and at a point and with no interference with the flow. This fact alone should encourage us to consider whether we dare go smaller or perhaps what is more important consider reducing vertical exaggeration.

Movable bed models

I would like to say a little more about mobile bed models because it is in this area that physical models of coasts and estuaries can border on the inadequate and where a great deal of interpretation is necessary.

We normally test the validity of a movable bed by running it for some time and then surveying it and making a comparison with nature or with changes that have taken place in nature over a given time. Provided the whole bed is mobile and the surveys agree we say that the sediment transport scale at all points over the mobile area is the same. However, we know even without measurement, that in many of our estuary models the distribution of sediment with depth is quite wrong as illustrated in Fig.12.

What we have at best is a 2 layer model and what we are assuming is that in nature a large proportion of the material is travelling in the bottom layers. It is only in exceptional circumstances, approaching the kind described earlier, that it is a true sediment transport model.

Neither is there any way around the problem of ripple formation which to scale bears no relation to features found in the prototype. In the 1950's claims were made that a material had been found which

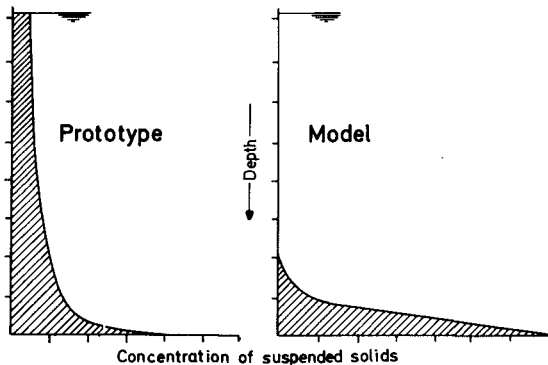


Fig. 12 SKETCH OF SOLIDS CONCENTRATION

would move without rippling. The competition reached something of the intensity that in other periods of our history alchemists tried to turn base metals into gold. At least we know for ripples that the problem is insoluble.

Nevertheless provided we use the technique with care I feel that movable bed models are useful but I would prefer to look on the loose material as an indicator or as a tracer. When used to study changes in small areas they are invaluable, as for example in the study of the improvement that might be achieved over a bar at the entrance to a tidal inlet by a training wall. Here it is justified, in my view, to mould a small area of the model in mobile material as illustrated in Fig.13. In this way the approach flows to the area of interest are maintained by the solid bed - having made the assumption that the depths at the boundaries of the mobile material will remain relatively unaffected by any works that are introduced. Wave-cum-tidal models of this type are quite reliable and relatively easy to manipulate. Littoral drift is promoted by running waves from say two predominant directions. A feature like a bar will form in the right place when the scale of sediment transport under waves equals the scale of sediment transport under tidal currents. Returning to the point made about Froude scales this is under the operator's control to some extent. For example, suppose the bar is forming too close inshore then, in my view, one is justified in dispensing with Froudian tidal velocity scales by shortening the tidal period to push the bar out to sea or vice versa.

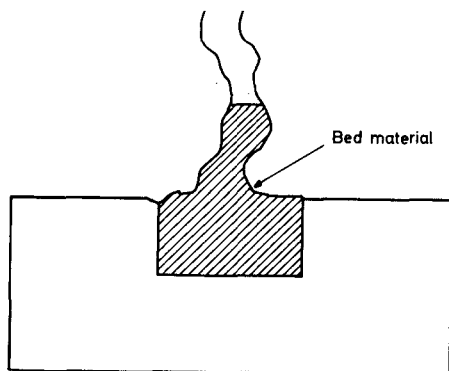


Fig. 13' TIDAL INLET MODEL

If the flow is canalised between banks as in the upper reaches of our major estuaries then loose material used as an indicator of bed deposition and erosion is a powerful technique.

I would not want to give the impression that the movable bed studies discussed so far are easy to carry out or to interpret but in my view they represent a realistic approach to these sorts of problems. Where we do strike extreme difficulty, however, is in the modelling of the wide approaches to our major estuaries with their multiplicity of banks and channels. Our inadequacies to scale sediment transport in this situation shows up most markedly.

If as I am suggesting we can model sediment transport only approximately, and at certain times hardly at all, then a small increase in the inaccuracy would be neither here nor there. In the 1920's there were movable bed models at scales of 1/3000 but their operators had one important practical advantage over us. If they didn't like the bed material they could change it overnight whereas we are reluctant to dig out 50m³ of expensive material. We tend to make the best of it.

I was in touch with Professor Jack Allen recently. He is a direct link with Reynolds through Gibson. In a letter to me he said this:-

"The reluctance of some researchers to use mobile beds or to experiment with different bed materials is partly their commitment to very large models in which the time required and the expense incurred in moulding, surveying and "proving" have encouraged them to be content in inferring, from observations of water movements alone over a fixed bed, what will happen to sand and silt in a natural estuary as a result of the construction of the proposed works. They, therefore, possibly fail to take sufficient account of the effect on the water movements of alterations to the bed created by the works themselves".

I will develop the theme later that mathematical models or computation are the eventual answers but I would not neglect the possibility that a small physical model and a mathematical model might be a good way to solve some of these problems in the future.

Sediment transport - fixed bed models

Another approach to the sediment transport problem is to build a fixed bed model, observe current velocities and integrate these with field observations of sediment flux, Fig.14.

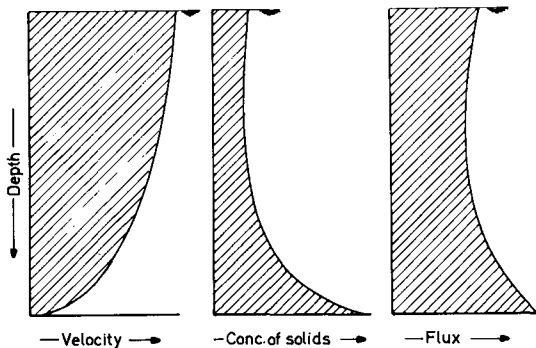


Fig. 14 SEDIMENT FLUX FROM FIXED BED MODELS

We have tried this method at the Hydraulics Research Station but have certainly not exhausted its possibilities. For studies of large areas the difficulties at the moment certainly outweigh the advantages but for studies of small areas it has its merits. The crux of the problem is that the laws of continuity so far as water movements are concerned are certainly satisfied in a physical model but the difficulty is that they cannot be established by measurement with the accuracy required using conventional instruments. I can illustrate the problem as follows. The laws of sediment transport are a high power of the velocity - let us say V^5 for the sake of argument which means that if current velocities are in error by 5% the sediment flux will be out by approximately 25%. The consequences of such an error are obvious. Better current meters of the kind mentioned earlier make this method well worth pursuing.

Mathematical Models

When we talk about problems associated with tidal propagation, current velocities, salinity intrusion, there is a case for using either a physical or a mathematical approach. When it comes to sediment transport the solutions must lie eventually with mathematics, physics and computation. Considerable advances have been made in recent years but our knowledge is still so inadequate we are well advised, as far as possible, to use both techniques together.

The term Mathematical Model, is a misnomer because it belies the important characteristic of this technique - the ability to deal with physics processes full size. Provided we know the laws everything is possible but the problems involved in discovering these laws are formidable. For example, considerable effort has been expended to establish the laws of sediment transport and yet when faced with the problem of estimating maintenance dredging in a tidal cum wave environment we would be glad to get an answer which was accurate to a factor of less than 2.

To describe the way in which topographical features like banks and channels are formed and maintained means reproducing some very complicated secondary processes. The change in velocity, suspended solids, salinity with depth can be accommodated with a multi-layer approach - water and solids being exchanged between layers, but the flow round bends can only be described adequately by building in lateral influences.

I list these difficulties not to detract from the value of Mathematical Models but to remind ourselves that more sophistication means greater costs. What we are creating in building models, both in the physical and mathematical sense, are engineering tools not basic research facilities. A certain scheme to be constructed will only warrant a certain amount of money spent on investigation. The cost of physical model studies has increased considerably over the last 10 years in real terms. In the case of Mathematical Models - new developments hardly ever increase computing time by a factor of 2 - more often a factor of 8 or more. Unless the unit cost of computing comes down to match the extra sophistication they might become too expensive to use, except on some of the larger jobs.

Although I have dealt with the subject of Mathematical modelling rather "en passant" I believe there is a need to keep the advances in this technique and that of physical modelling constantly under review. This should be done in a way that illustrates the strengths and weaknesses of both techniques and where they can be used to advantage together. More contact should be encouraged between mathematical and physical modellers because the two subjects must go hand in hand. Hybrid models will go some way to bringing about a stronger link than exists at present. The possibility of interacting physical and mathematical models in real time has considerable potential for the future.

Summary

- (1) We should not undervalue physical models as visual aids. They give us a view of a situation that we can never get from the prototype.
- (2) We should work towards solving our problems by the smallest model for the job in hand but we do not yet have all the information to make the ultimate choice of scale.
- (3) We should question the way we use the Reynolds and Froude criteria.
- (4) Mathematical and physical models are powerful techniques which should not be seen to be in competition. They should be looked on as complementary to one another. We need both methods to improve the confidence we place on our advice.

REFERENCES:

1. ROUSE H, INCE S: History of Hydraulics. Supplement to La Houille Blanche (1954) 5.
2. CLARKE K, PEDRETTI C: The Drawings of Leonardo da Vinci in Windsor Castle. 3 Vols. London: Phaidon Press.
3. REYNOLDS O: On Certain Laws Relating to the Regime of Rivers and on the Possibility of Experiments at Small Scale. British Association Report, 1887.
4. Report of the Committee Appointed to Investigate the Action of Waves and Currents on the Beds and Foreshores of Estuaries by Means of Working Models. British Association Report, 1889.
5. 4th International Congress on Inland Navigation, 1890.
6. ALLEN J: Scale Models in Hydraulic Engineering. London: Longmans, Green & Co. 1947.
7. YALIN M S: Similarity in Sediment Transport by Currents. London: Her Majesty's Stationery Office, 1965. (Hydraulics Research Paper No.6, Hydraulics Research Station, Wallingford).
8. YALIN M S: Theory of Hydraulic Models. London: Macmillan, 1971.
9. Aberdeen Harbour, Hong Kong. Wallingford, Hydraulics Research Station, 1966. (Report EX 333).

SOME IDEAS ON BREAKWATERS

(Continuation of theme speech by W A Price)

Introduction

Many of us I am sure have realized that the science of the design of breakwaters has reached a crucial point in their development. A great deal of work is being done in many parts of the world on many important aspects of the problem and if I do no more than review some of the present day thinking and suggest some lines for further research, I will be well pleased. After producing the first draft of this lecture I read a paper by Magoon & Baird (not published at the time of writing) presented at a Symposium held at the British Hovercraft Corporation on the Isle of Wight, England, which expresses the need to put more science into the subject which is very much the theme of my lecture, Ref.10.



Fig. 15 ALDERNEY BREAKWATER - CHANNEL ISLANDS

History

It would be impossible to say who built the first breakwater. Ever since man realized that he could gain protection from the waves behind a headland he used this principle to protect his boats with stone breakwaters. Hence the beginning is in antiquity. Quite recently Jacques Cousteau in searching for the lost city of Atlantis discovered underwater remains of a Minoan breakwater 4000 years old, Ref.11. However, the first empirical formula for breakwater design did not appear until 1933.

Well known names are attached to the later chapters of the story - Carvalho, Vera Cruz, Irribarren, Epstein, Tyrell, Jackson, Hudson, Davidson and no review of the subject would be complete without acknowledging the excellent pioneering work carried out by the US Army Engineer Waterways Experimental Station, Vicksburg, Refs.12 - 21.

The Hudson Equation

I would like to start by looking at the form and basis of the now famous Hudson equation.

$$W = \frac{\rho_r H^3}{K_D (\rho_r / \rho_w - 1)^3 \cot \alpha}$$

H = Wave height

ρ_r = Specific weight of armouring

ρ_w = Specific weight of water

W = Height of armour unit

α = Slope of breakwater face

K_D = Coefficient of Stability

This is a surprisingly simple equation when you think about the complexity of the phenomena involved - wave breaking, penetration of flow into the bank, run up, interblock friction, hydraulic drag, interlocking and others. It is based on the assumption that regardless of the way in which the waves break the disturbing forces due to drag or lift from plunging or collapsing breakers are proportional to the square of the wave height and displacements will be resisted by the immersed weight of the blocks alone. This theoretical analysis was supported by a series of classical experiments.

Armour Units

Subsequent to the development of this equation there was a dramatic increase in the size of ships which meant that harbours had to be built in deeper water and usually at more exposed sites. Larger stones were required and at some sites these were not available in the necessary sizes or not available at all. It was these factors that led to the development of the multiplicity of armour units we know today.

Perhaps after cubes and other rectangular blocks the Tetrapod, designed by Pierre Danel was the first of these, Fig.16. It is half the weight of an equivalent stone to resist the same wave height. Whether to escape the patent on this block or to satisfy the basic need of engineers to innovate, many other designs have followed, Fig.19.

The designers of these blocks, to a larger or lesser degree, tried to achieve an open structure to provide a permeable assembly, a low centre of gravity and projections to form interlocks with neighbouring units and thus increase their resistance to removal by waves. A saving in the amount of concrete required to make the unit was of primary



Fig. 16 TETRAPOD



Fig. 17 TRIBAR



Fig. 18 DOLOS

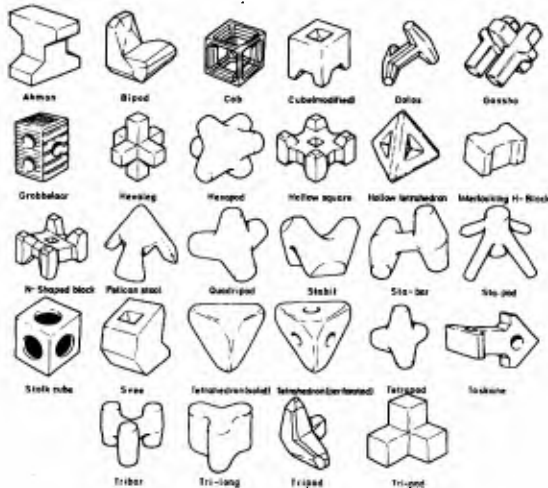


Fig. 19 ARMOUR UNITS

importance. Interblock friction was brought into play as in the regularly placed Tribar, Fig.17

Merrifield and Zwanborn exploited interlocking in designing the Dolosse which are one fifth to one sixth the weight of a stone to resist the same wave height: a considerable achievement, Ref.22, Fig.18.

One of the simplest and most effective blocks, in my view, is the Tripod designed by Muir-Wood. It is half a cube. The neat thing about it is that being half a cube once you have built one you can reproduce others with very simple form work, Fig.20. The K_D value is about 7.

Need for new approach

Through all these developments the Hudson equation appeared to stand firm and has been used to describe the stability of all blocks. Hudson never claimed that it should, but perhaps he is paying the price of all philosophers in that they are often quoted but never read. He has in fact cautioned that his equation was applicable to quarry stone only. Subsequently, however, and in my view quite rightly, he used his theoretical approach to describe the stability of Tetrapods.

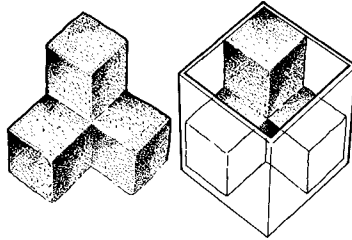


Fig. 20 TRIPOD - METHOD OF CONSTRUCTION

I will develop the thesis that all blocks are not alike - they exploit different qualities to achieve stability and these individual characteristics should be recognised more so than they are at present in any equation that describes their stability. Unless we do then we will not fully understand the behaviour of complicated blocks.

Let me use an analogy. Man has always been faced with the problem of spanning gaps. Through history he has tried to span larger and larger gaps and he has had to employ new methods from beams to arches, cantilevers and catenaries.

I want to use the analogy in two ways. The first is not in the mainstream of the argument but is important and it is this. In the early stages of design do we give enough attention to methods of construction other than rubble mound breakwaters like, for example, Lundgren's caissons? I suspect that we do not but this is a whole debate in itself so I will return to using the analogy in another way.

Bridges exploit the various properties of different materials like stone, concrete, steel, for their stability and this is analysed in different ways. Armour blocks too have various qualities that contribute to their stability. Some of the important ones are weight, interlocking, interblock friction, hydraulic drag, permeability of assembly etc. Qualitatively we can assess the blocks shown in Fig.21 like this

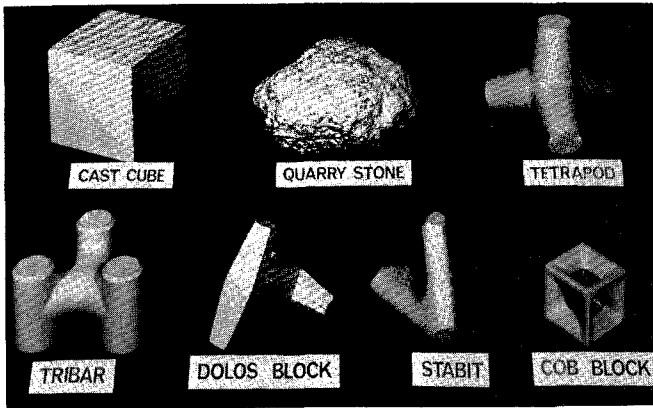


Fig. 21 ARMOUR UNITS - SCALED TO RESIST EQUAL WAVE HEIGHTS

- the stone and the cube rely on weight for their stability, the Tetrapod on weight and a small amount of interlocking, the Tribar on interblock friction and weight and the Dolos on a small amount of weight and a great deal of interlocking. They are certainly not different shaped bits of stone. Any advance on the Hudson equation must, therefore, recognise this and describe a block's stability in terms of these parameters.

[To digress slightly - interlocking is probably difficult to quantify although I would suggest it could perhaps be determined like this. Lay cover layers in the laboratory and determine the force required to remove units from the pack. Forces will vary from those equivalent to the weight of the unit to a force required to remove a block that is fully interlocked. We could express this variation in a dimensionless number of the form say -

$$I = \frac{\text{"Average" force required to remove block}}{\text{Weight of Armour Unit}}$$

This parameter expresses the way a particular block relies on the weight of neighbouring units for its stability.]

Types of failure

Another case for reappraisal is the very different way damage occurs for compact and open forms of block. With compact forms, like stones and Tetrapods, for which no friction or little interlocking is assumed a steady increase of damage is to be expected as the wave attack is extended in time, Fig.22, Ref.23. This pattern of damage is quite different for the blocks of open form with their properties of high interblock friction and interlocking. They exhibit a stiffness which resists damage over an initially large range of wave heights but once the applied forces are high enough to disturb the cover layer a rapid removal of units results and the margin of safety between acceptable damage and failure for closed forms becomes very small and could be well within the range of uncertainty of prediction of the design wave height. We need to take this fact into account in the design. The use of blocks that interlock puts a considerable premium on a good knowledge of the wave climate. I have heard Dean O'Brien call many times for more wave recording. I wholeheartedly agree with him. Highway engineers would not be prepared to design motorways with the lack of information Coastal Engineers are sometimes asked to design breakwaters.

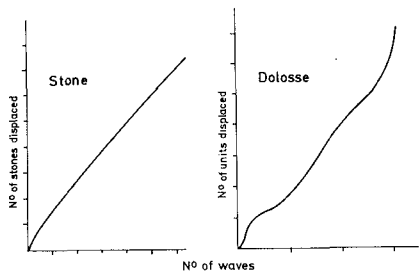


Fig 22 HISTORY OF DAMAGE - STONES AND DOLOSSE

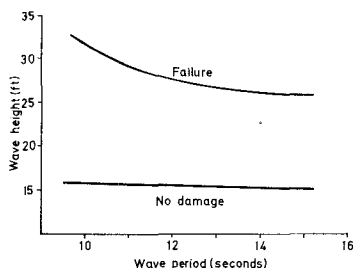


Fig.23 DOLOSSE - EFFECT OF WAVE PERIOD

The influence of wave period

Let me turn to the other side of the equation - the disturbing influence of the waves. Hudson found it quite sufficient to describe the sea in terms of a wave height. Whillock, working with Dolosse and the results have been confirmed by Burcharth, Zwamborn, & Bruun, Ref.26, showed that wave period was also important so far as this armour unit was concerned, Fig.23, Ref.24. Is there a discrepancy with the early Hudson results? I do not think there is. Within the scatter of his results for stone breakwaters there was probably a small period dependence but it was so small that he was justified in ignoring it.

The explanation probably lies partly in the fact that Dolosse with their limbs projecting through the cover layer are subject to much greater drag forces than stones which tend to protect one another in times of high surface currents. These currents are likely to be at their maximum when long period waves surge rather than break on the slope. Brebner shows that the Drag to Weight ratio for stones and Dolosse are almost the same, Ref.25. Quite recently experiments carried out at HRS confirms this fact. However, this does not mean that when they are in a pack that the effective drag to weight ratios are the same. Per Bruun has pointed out the importance of wave resonance and says that "elements that protrude should be avoided", Ref. 26. How dependent on wave period are other units? I do not know but I think we should find out.

Effect of angle of attack

Tests with stone breakwaters and tests done by SOTRAMER with Tetrapods show that their stability increases with angle of attack. This behaviour is quite different for Dolosse, Fig.24. The reason is again the production of high surface currents this time caused by waves running along the breakwater and setting up high drag forces on projecting limbs. The amplification of the wave height due to the Mach-Stem effect further complicates the issue.

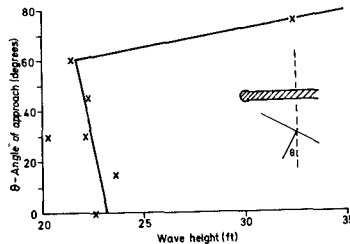


Fig. 24 DOLOSSE - EFFECT OF ANGLE OF ATTACK

Every now and again one reads a paper containing an idea which one would have liked to have had oneself. Such a paper was presented at the Hamburg Conference by Brebner, Ref.25. He filled shallow boxes with stones and Dolosse and gradually tipped them about their bottom edge. The failure of the rock occurred at about 50° whereas the Dolosse had an

angle of repose of at least 80° and in one remarkable test 91° . He carried out tests where he layered Dolosse and stone in a tilting flume and ran water over them. The "wipe out" velocity was essentially the same for both the quarystone bed and the one constructed of Dolos. He concluded that "the effectiveness of the Dolos unit is not materially affected by the drag to weight ratio but to its high angle of repose". Interlocking can only be brought fully into play by using Dolosse on steep slopes. Brebner puts it this way - "one can also suggest that the steeper the breakwater slope ... when attacked by normal waves the better the Dolos unit appears to be". He points out that "this is the reason why the stability of Dolosse are affected by the angle of attack whereas stones are not", Ref.24.

Random Sea Testing

Random sea testing has become fairly commonplace in our laboratories although we still continue to argue how best they should be synthesised.

Johnson and Ploeg have questioned whether seas are necessarily random - the implication being that if they are not then the wave groupings will be different, Refs.27 & 28. Shuttler at HRS has measured the frequency of wave groups for a number of wave spectra (Moskowitz, Jonswap and a bimodal spectrum generated using the HRS synthesiser). These compare very favourably with published field data. I still think, however, there is still some debate about this question and more work needs to be done because it is an important one.

Burcharth and Ploeg have shown that coastal structures respond differently when exposed to various wave patterns that contain the same maximum waves: there is a significant influence of succession, Refs.29 & 30. They stress the importance of research into the occurrence and frequency of characteristic wave patterns in wave records so that the results can be incorporated in sea conditions used in model tests. Incidentally Boucherth proposes a new form of the Hudson equation for Dolosse pointing out that it would be appropriate to plot a Stability Number defined as

$$\frac{H}{\left(\frac{W}{\rho_r}\right)^{\frac{1}{3}} \left(\frac{\rho_r}{\rho_w} - 1\right)}$$

against a Surf Similarity parameter (Batjes), Ref.31.

This dimensionless parameter was designed by Batjes and its importance has probably not as yet been fully recognised. It is a convenient way of describing the way in which the wave breaks.

$$\zeta = T \left(\frac{g}{2\pi H}\right) \tan \alpha$$

where H = Wave height

W = Weight of Dolos

- ρ_r = Specific weight of blocks
 ρ_w = Specific weight of water
 T = Zero crossing wave period
 g = acceleration due to gravity
 α = angle of slope

Summary of the Important Parameters

Abernethy, as early as 1970, Ref.32, when carrying out an investigation to provide information for the design of Tribar armouring for a large reclamation project in Botany Bay, New South Wales, developed a similar theme to the one in this lecture when he suggested that any analysis of Tribars, and he could have included other armour units, based upon the Hudson formula must be considered suspect for many reasons. He suggested that the damage function Δ is dependent upon eleven dimensionless parameters. Taking these and adding others we could write a list of some of the more important variables affecting the damage function as follows:-

- | | | |
|--|---|-----------------------|
| (1) Weight of unit | } | Block Characteristics |
| (2) Density of material | | |
| (3) Interblock friction | | |
| (4) Packing Density | | |
| (5) Permeability of Assembly | | |
| (6) Height of Bank | | |
| (7) Hydraulic drag | | |
| (8) Wave Spectrum | } | Disturbing Influences |
| (9) Wave grouping | | |
| (10) Angle of attack | | |
| (11) Water depth | | |
| (12) Number of waves impinging
on slope | | |

The list is formidable and is not complete but it indicates the size of the problem.

Structural Damage

Vasco Costa, Baird, Lalevang, Magoon and Stickland have made major contributions to the subject and have highlighted among other things the problem of wear and the structural stability of the individual units. These are subjects which are worthy of further study. It occurs to me to wonder whether with blocks that interlock there is the possibility that impact loads could be transferred from block to block, and perhaps by chance the combination of forces caused by waves breaking out of phase with loads transferred from unit to unit could be one of the reasons blocks break, Fig.25.

Dolosse

To clear up any misinterpretation of what I might have said I need to say a word about Dolos in particular. There is no doubt that it is a good armour unit and perhaps because it is superior in many respects to others in using the properties of a solid almost to the limit that we must use it with care. Until we understand all its properties we should

not exploit them to the full. I have used Dolosse in this lecture because more work has been done on this unit than any other and believing that they typify the family of blocks that interlock at least qualitatively.

Need for co-operation and further research

Apart from the few painstaking and excellent pieces of work that I have already referred to good designs have been produced based on careful tests but for one reason or another they are not consistent with others in the field and the results are then more or less lost to the science. We must do more experiments where we keep some of the variables constant while varying others.

It seems to be opportune that we should get down to some fundamental research preferably organised on a world wide basis and not rely

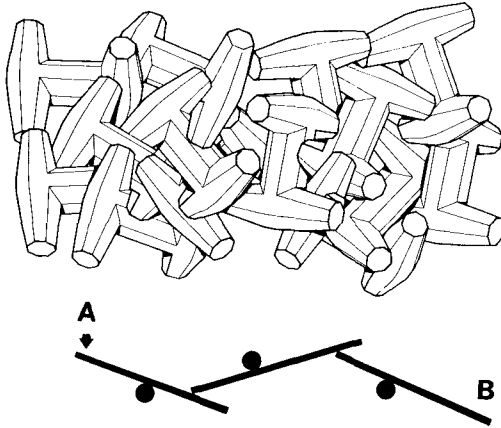


Fig.25 TRANSFER OF LOADS - INTERLOCKING BLOCKS

almost entirely on laboratory testing of specific schemes for insight to the problem. I was glad to hear at the Conference Professor Edge describe plans that ASCE have in this direction.

When writing about armour blocks nearly 30 years ago Pierre Danel, the inventor of the Tetrapod, said this -

"Engineers have too few opportunities for examining an overall problem in a sufficiently disinterested way and for a sufficient length of time. Each one is bound by his specialized field and naturally has a tendency to only consider solutions which entirely satisfy his own particular requirement".

It might sound a small point but if we could only agree about what we mean by certain percentages of damage and failure this would be a considerable step forward.

If we continue to test with the object of getting a stability factor alone we will lose the feel for the subject and our designs will suffer. The improvement of armour blocks has meant that their behaviour has become more and more detached from the supporting theory. One serious consequence is that data obtained from one situation cannot be applied to others. In my view we need to make advances quickly.

ACKNOWLEDGEMENTS

This lecture was given with the permission of the Director of the Hydraulics Research Station, Wallingford. I would particularly like to thank Mr A F Whillock whose ideas are incorporated in the section on breakwaters, Professor Emeritus Jack Allen for his comments and the loan of early slides and many of the staff at HRS for their instructive remarks. To others too numerous to mention I would like to say "Thank You".

The drawings by Leonardo da Vinci are published by permission of the Royal Library, Windsor Castle.

REFERENCES:

- 1 MAGOON O, BAIRD W F: Breakage of Breakwater Armour Units. Symposium on Design of Rubble Mound Breakwaters, 1977. (Paper No.6). Shanklin, Isle of Wight, British Hovercraft Corporation.
- 2 The world of Jacques Cousteau - Calypso's search for Atlantis. Television programme on BBC1. British Broadcasting Corporation, 1978.
- 3 JACKSON R A: Design of Cover Layers for Rubble-Mound Breakwaters Subjected to Non-breaking Waves. Vicksburg: United States Army Engineer Waterways Experiment Station, 1968. (Research Report No.2-11).
- 4 IRRIBARREN R: A Formula for the Calculation of Rock-Fill Dikes. Translation from Revista de Obras Publicas, 1938. Berkeley: University of California Fluid Mechanics Laboratory, 1948. (Technical Report HE-116-295).
- 5 IRRIBARREN R, NOGALES C: Generalization of the Formula for Calculation of Rock-Fill Dikes and Verifications of its Coefficients. Translation from Revista de Obras Publicas May 1950. Vicksburg, Miss: United States Army Engineer Waterways Experiment Station, 1951. (Translation No.51-4).
- 6 HUDSON R Y, JACKSON R A: Stability of Rubble-Mound Breakwaters. Vicksburg, Miss: United States Army Engineer Waterways Experiment Station, 1953. (Technical Memorandum No.2-365).

- 7 HUDSON R Y: Design of Quarry-Stone Cover Layers for Rubble-Mound Breakwaters. Vicksburg, Miss: United States Army Engineer Waterways Experiment Station, 1958. (Research Report No.2-2).
- 8 HUDSON R Y, JACKSON R A: Design of Tetrapod Cover Layer for Rubble-Mound Breakwater, Crescent City Harbor, Crescent City, California. Vicksburg, Miss: United States Army Engineer Waterways Experiment Station, 1955. (Technical Memorandum No.2-413)
- 9 HUDSON R Y: Protective Cover Layers for Rubble-Mound Breakwaters, Studies Completed Through March 1957. Vicksburg, Miss: United States Army Engineer Waterways Experiment Station, 1958. (Miscellaneous Paper No.2-276).
- 10 HUDSON R Y, JACKSON R A: Design of Tribar and Tetrapod Cover Layers for Rubble-Mound Breakwaters. Vicksburg, Miss: United States Army Engineer Waterways Experiment Station, 1959. (Miscellaneous Paper No.2-296).
- 11 HUDSON R Y: Wave Forces on Rubble-Mound Breakwaters and Jetties. Vicksburg, Miss: United States Army Engineer Waterways Experiment Station, 1961. (Miscellaneous Paper No.2-453).
- 12 SAVILLE T: Wave Run-up on Shore Structure. Proc. Amer. Soc. Civ. Engrs 82 (1956) WW2 Paper 925.
- 13 MERRIFIELD R M, ZWAMBORN J A: The Economic Value of a New Breakwater Armor Unit 'Dolos'. Proc. 10th Conf. Coastal Engng, Tokyo, 1966 Vol.2 p.885-912.
- 14 Riprap Design for Wind Wave Attack - A Laboratory Study in Random Seas. Wallingford: Hydraulics Research Station, 1975. (Report EX 707).
- 15 WHILLOCK A F, PRICE W A: Dolosse Blocks as Breakwater Armouring. HRS Notes 19 (1977) June p.5-6.
- 16 BREBNER A: Performance of Dolos Blocks in an Open Channel Situation. Summaries, 16th Int. Conf. Coastal Engng, Hamburg 1978 Paper No.203.
- 17 BRUUN P, GUNBAK A R: New Design Principles for Rubble Mound Structures. Trondheim, Norwegian Institute of Technology, 1976.
- 18 JOHNSON R R, PLOEG F: The Problem of Defining Design Wave Conditions. Ottawa, National Research Council of Canada, Hydraulic Laboratory.
- 19 JOHNSON R R, PLOEG F: The Problem of Defining Design Wave Conditions. Ottawa, National Research Council of Canada, Hydraulic Laboratory.

- 20 BURCHARTH H F: The Effect of Waves with Different Patterns on On-Shore Structures. Aalborg University Centre, 1978. (Bulletin No.12).
- 21 BURCHARTH H F: Effect of Waves on On-Shore Structures. Ann.Rept Hydraulics Research Station, Wallingford 1977 p.8-12.
- 22 BATTJES F A: Surf Similarity. Proc. 14th Conf. Coastal Engng, Copenhagen, 1974 Vol 1 p.466-480.
- 23 ABERNETHY C L: Stability of Tribar Armouring. Ann.Rept Hydraulics Research Station, Wallingford 1971. p.57-60.



Port of Emden

PART I

THEORETICAL AND OBSERVED WAVE CHARACTERISTICS

Small Island during Storm Tide



CHAPTER 1

A WORLD WAVE DATA CENTRE

by

Laurence Draper
Institute of Oceanographic Sciences
Wormley, Godalming, Surrey GU8 5UB, U.K.

ABSTRACT

There is a growing need for instrumentally-measured wave data, but it is not easy to discover what measurements, if any, may have been made in any particular area. To try to alleviate the situation the Institute of Oceanographic Sciences is establishing an international reference centre which will create and maintain an inventory of such data. It is appealing for volunteers world-wide to help in identifying locations where waves have been measured.

It will be operated through the U.K. Marine Information and Advisory Service at the Wormley Laboratory of the Institute.

The birth of wave recording can be assumed to have occurred during the Second World War, prompted by the need to land through surf on unfamiliar beaches and assisted by the developments in electronics which allowed the complexities of wave motion to be monitored at a distance. After peace returned, the applications of the new capability to coastal engineering were soon appreciated and instruments began to be deployed on many coasts of the world. The demand for data far exceeded the supply, and research laboratories, both engineering and oceanographic, found themselves being asked to advise on wave conditions, provide and interpret measured data and, where none existed, to predict wave conditions for both design and operational needs. Amongst the laboratories which responded to the need was the UK Institute of Oceanographic Sciences (known previously as the National Institute of Oceanography) which designed and built wave recording instruments, installed them around the UK and elsewhere, developed methods of analysis and data presentation and built up an index of sources of instrumentally-measured wave data. This index, along with the expertise built up within the Institute and elsewhere, meant that the Institute became a focus for questions on data

sources and advice on all aspects of waves, a large proportion of the questions coming from engineers working on coastal and also on offshore installations.

About ten years ago the Permanent International Association of Navigation Congresses (PIANC) established its International Waves Commission on which the author sat for a time as the UK Representative, under the Chairmanship of Professor J. Larras. It compiled a list containing brief but relevant details supplied by its members of instrumentally-measured wave data, and developed a system whereby the owners of such data could be identified through a network of area representatives. Each representative, on identifying a source of wave data, would obtain answers to a set of standard questions so that any potential additional user could quickly ascertain whether or not the measured wave data would be likely to be of value to him. It would also be possible to compare the characteristics of different data sources. It was originally intended that these completed questionnaire forms would then be sent to the Commission to allow the central inventory to be established and continually updated. Unfortunately, after devising the scheme, PIANC was unable to establish an on-going unit to operate it. Meanwhile, the amount of data being measured continued to increase as did the demand, but the potential value of wave data was being lost because the measurements were not known to later potential users, simply because there was no organization responsible for cataloguing even their existence, and wave conditions were needing to be re-measured unnecessarily.

The questionnaire form was developed further, under the chairmanship of Dr. J.R. Wilson, by the Task Team on Wave Data Management of the Intergovernmental Oceanographic Commission (IOC). The Institute of Oceanographic Sciences then made an offer to IOC to become a Responsible National Oceanographic Centre for Waves (RNODC(Waves)). The intention is that the Marine Information and Advisory Service will operate the PIANC scheme, and establish the RNODC(Waves) as an operational centre which will attempt to identify all sources of instrumentally-measured wave data through an international network of area representatives. The wave data questionnaire has evolved as a consequence of limited experimental use so far. It can form the basis of an Inventory to be used in satisfying the needs of a potential wave data user to identify suitable sources.

There is a demand for copies of this Wave Data Inventory but in its present form it is not practical to distribute it on account of its bulk. However, it is proposed to compile a Wave Data Catalogue in which the essential minimum information from the Inventory is condensed. This will constitute the working document within the RNODC (Waves). A number of people around the world, active in

RESPONSIBLE NATIONAL OCEANOGRAPHIC DATA CENTRE (WAVES)

Marine Information and Advisory Service of the Institute of Oceanographic Sciences of U.K. in association with the Permanent International Association of Navigation Congresses (PIANC), I.O.C. Working Committee on International Oceanographic Data Exchange

INSTRUMENTAL WAVE DATA INFORMATION

for inventory purposes or to accompany submission of data.

PART I : IDENTIFICATION OF DATA			
1.1 Source responsible for the data and from whom the data or further information may be obtained.			
Name			
Organization			
Address			
1.2 Name and Position of wave measurement site (or cruise/flight identifiers including start/end dates).			
1.3 Start and End dates of Wave Measurements (ignore temporary breakdowns).			
Start	d	/m	/y
End	d	/m	/y
1.4 Other information which may be necessary to identify this data.			

PART I should always be completed and, where no data is transmitted, PART II represents the essential minimum of additional information required for INVENTORY PURPOSES. When the form accompanies data, it is essential that sufficient information is provided to fully qualify the data for future users. Where convenient, entries may be replaced by references to other documents forwarded either with this form or previous forms. Metric units are preferred. If the space allowed is not adequate please use additional pages.

Return this completed form to :

(1) (name)

Address :

or (2) If (1) has not been completed, to :

RNODC(Waves)
 MLAS, IOS, WORMLEY, GODALMING, SURREY, GU8 5UB, U.K.

(Jan. 78)

Inventory form, first page.

the engineering aspects of waves and who have a direct interest in knowing of the existence, and quality, of instrumentally-measured wave data, have expressed a willingness to participate in the scheme as Area Representatives. The response to informal approaches has been encouraging, but more offers will be welcomed. It is proposed to leave the appointment of Area Representatives until after this conference, when a list of appointees will be compiled and published. An area representative will be a person active in this field who could obtain the backing of his establishment to run an effective search and identify mission, or even the establishment itself, provided that a dedicated individual would take responsibility for operations. It is a responsible and rewarding task, hopefully not too onerous, which will contribute significantly to engineering operations in the world. It does not seem that either the RNODC(Waves) or UNESCO will be able to provide funds externally for the running of the scheme, but it is planned that RNODC(Waves) will supply each Area Representative with questionnaire forms, a copy of the Catalogue and occasional up-date material. He will also maintain his own inventory of completed questionnaire forms relevant to his area. The four-page questionnaire form is illustrated in the figure. It consists of one sheet of paper folded to A4 size. The questions are arranged so that answers can be stored for computer retrieval. The RNODC(Waves) will provide anyone with advice on wave data measurements, analysis, interpretation and presentation, as well as reports on the data themselves if copies are available to the RNODC(Waves).

Although the early response to the appeal for Area Representatives has been excellent and the scheme is starting with good coverage, offers of participation will be welcomed at any time. In any one country it is likely that there will be a primary representative person or organization, so that additional participants will be asked to channel their completed forms through the primary representative for their areas. For example, it is likely that all U.S. participants will be asked to forward their forms to Mr. Wellington Waters of the USNODC in Washington for onward transmission to the RNODC(Waves).

It is hoped that the establishment of an effective RNODC(Waves) will be of appreciable communal benefit and will tidy up what is at present an active but only partially effective operation. It seems likely that it will be an on-going scheme dedicated to helping anyone working in an area affected by waves, whether in the building of structures intended to provide protection from them, the operation of vehicles through them, the abstraction of energy from them or in many other activities where waves have to be taken into account.

PART II : INVENTORY	
2.1 Report Title (if published).	
2.2 Description of Measurement Site.	2.3 Description of Measurements.
a) Sea Area	a) Type of instrument (e.g. waverider, resistance staff, pressure gauge, altimeter, etc.)
b) Latitude and Longitude (express as range if necessary)	b) Type of instrument mounting (e.g. ship, aircraft, tripod on sea bed, midwater mooring, etc.)
c) Mean Water depth	c) Digital sampling frequency (If applicable).
d) Mean Tidal Range Spring Neap	d) Duration of individual records.
e) Approximate maximum currents (if known).	e) Interval between starts of successive records.
2.4 Comment on presence of offshore bars, structures or obstructions, and whether or not their presence would make the data untypical of the area.	
2.5 Primary reason for measurements (brief statement)	
2.6 List any other observations made with the wave measurements	
2.7 Data available - state form and medium in which available (state NONE where none available) to other users.	
a) Original Data (e.g. chart records, analogue mag. tape records etc.)	
b) Processed Data (e.g. listings of Tucker-Draper statistics, spectral estimates on mag. tape, etc.)	
c) Analysis Presentations (e.g. exceedance diagrams, period histograms etc.)	

Inventory form, second page.

PART III : DATA DOCUMENTATION IIIA - INSTRUMENTATION	
3.1	Have you previously forwarded an inventory for this set of data? YES/NO.
3.2	Description of Instrument. <ul style="list-style-type: none"> a) Name of Instrument including Manufacturer and Model No. b) Pertinent physical characteristics (including modifications). c) Depth of sensors below, or height above, mean water level. <ul style="list-style-type: none"> Height of sensors above sea floor (if more appropriate). d) Recording Medium (e.g. strip chart, digital magnetic tape, analogue magnetic tape, etc.) e) Date and Method of calibrations (please state if not calibrated) and comment on stability of calibration. f) Steps taken to control biological fouling (if applicable).
3.3	Instrument Remarks (Specify operation failures during data collection, instrumental response characteristics, e.g. bandwidth and range, chart speed or other comments helpful in data interpretation).

Inventory form, third page.

PART III - continued. IIIB - DATA PROCESSING
3.4 a) Type of processing performed on data (e.g. spectral, Tucker-Draper, etc.) b) Main start and end dates of processed data.
3.5 Remarks on Data Reduction and Processing. (Include any comments pertinent to the interpretation of the data, e.g. description of methods used in deriving parameters, corrections applied to the data, filtering performed on the data, etc.)
3.6 a) Are the data checked and edited? Y/N. b) What criteria were used for the editing and quality assessment of the data?
3.7 General Remarks (Enter any other comments useful in interpretation and use of data reported).
3.8 If transmitting data for the first time in computer compatible form please append a detailed description of its format and a detailed definition of each data field including units.

Inventory form, fourth page

ACKNOWLEDGEMENT

This work is supported by the U.K. Departments of Energy and Industry.

REFERENCE

1973 Final Report of the International Commission for the study of Waves. Annexe No. 4 PIANC Bulletin No. 15, Vol. II.

CHAPTER 2

ON LONG-TERM STATISTICS FOR OCEAN AND COASTAL WAVES

Michel K. Ochi*

ABSTRACT

This paper discusses the statistical properties of long-term ocean and coastal waves derived from analysis of available data. It was found from the results of the analysis that the statistical properties of wave height and period obey the bi-variate log-normal probability law. The method to determine the confidence domain for a specified confidence coefficient is presented so that reliable information in severe seas where data are always sparse can be obtained from a contingency table. Estimation of the extreme significant wave height expected in the long-term is also discussed.

INTRODUCTION

For the design of ocean and coastal structures, it is very important to obtain information on wave characteristics over a period of time sufficiently long to cover the lifetime of the structures. Collection of data on wave height and period has been made by several researchers through either visual observations or measurements, and their results are usually presented in tabular form [1][2][3][4][5]. Although considerable attention has been given to statistical information of long-term wave height, we have as yet little information on the combined properties of wave height and period for the long-term.

A statistical contingency table on wave height and period provides valuable information for the design of ocean and coastal structures. However, data for severe seas, which are indeed necessary for design, are unreliable since such data are, without exception, sparse. One way to solve this problem is to represent wave statistical data by a certain probability law which governs the data, and then obtain necessary information for design from the probability function.

The purpose of this paper is to provide solutions to the problems cited in the foregoing discussion. For this, the joint probability

*David W. Taylor Naval Ship Research and Development Center, Washington, D.C., U.S.A.

distribution of wave height and period for data accumulated over many years is derived, and a method to establish the confidence domain for a specified confidence coefficient is presented. A method for predicting the extreme value of significant wave height from the long-term accumulation of data is also discussed.

LONG-TERM WAVE STATISTICS

Long-term wave statistics as defined in this study is the statistical information of wave characteristics such as wave height and period accumulated over a sufficiently long period of time. In accumulating data for long-term wave statistics, wave observations are usually made for 20-30 minute intervals. Wave height and period are expressed in terms of significant wave height (or average wave height) and zero-crossing period (or average wave period), respectively, and the accumulated data are usually presented in tabular form known as a contingency table.

Examples of a contingency table for long-term wave statistics are shown in Tables 1 through 3. Table 1, taken from Reference [1], shows the tabulation of significant wave height and zero-crossing period, both analyzed from records obtained at Weather Station 1 (59°N, 19°W) in the North Atlantic. The numbers given in the contingency table are those per 1,000 observations. Table 2 shows an example of data on significant wave height and period observed during 20 months (from November 1961 to March 1964) at Port Hueneme, California, presented in Reference [2]. Table 3, taken from Reference [3], shows an example of a contingency table on significant wave height and modal period where the wave spectrum has a peak value. The table provides information based on a total of 2,304 measurements in one year (from March 1972 to February 1973) at Tiner Point, New Brunswick, Canada. There are many other examples of contingency tables similar to those shown in these tables, Reference [4] and [5] for example.

Needless to say all of these long-term wave statistics are extremely valuable in providing information for the design of ocean and coastal structures. However, a problem always exists in the use of this information for design. That is, data in severe seas are unreliable, since they are, without exception, sparse. For instance, information above 10 ft (3.05 m) significant wave height in the example shown in Table 3 are few; only 15 cases are observed in a total of 2,304 observations which is equivalent to about 0.7 percent. This implies that it is not appropriate to use the numbers given in this sort of table in practice.

One way to solve this problem is to apply the statistical inference concept and establish the confidence domains from the data, taking into account the correlation between significant wave height and period. For this, it is necessary to find the joint probability distribution which is applicable to significant wave height and period.

PROBABILITY DISTRIBUTION FOR LONG-TERM WAVE STATISTICS

In order to derive the combined statistical characteristics of the two random variables, significant wave height, H_s , and zero-crossing period, T_0 , we may first consider the marginal probability distribution of significant wave height. It is noted here that, although considerable attention has been given to statistical information of significant wave height, the probability function which is applicable to significant wave height is the focus of much criticism. Some claim that the log-normal distribution is appropriate [6][7][8], while others believe the data can be better fitted by the Weibull distribution [9][10]. The results of the present analysis, however, illustrate that significant wave height appears to follow the log-normal probability law over the range for the cumulative distribution up to 0.99. This conclusion appears to be valid for both ocean and coastal waves. To support this statement, the following discussion will be given:

Figure 1 shows the cumulative distribution function of significant wave height of ocean waves. The data are taken from the contingency table given in Table 1, and are plotted on log-normal probability paper. As can be seen in the figure, the data follow the log-normal distribution for the cumulative distribution up to 0.99. On the other hand, Figure 2 shows the same data plotted on Weibull probability paper. This figure shows that the data may also be represented by the Weibull probability distribution except for small significant wave height. Thus, one may have the impression that there is no significant difference in representing the statistical characteristics of significant wave height by the log-normal or Weibull probability law. However, if comparison is made between these two probability density functions and histograms, then the difference becomes pronounced.

Figure 3 shows a comparison between the histogram, log-normal and Weibull probability density functions. As can be seen in the figure, the log-normal probability density function agrees reasonably well with the histogram over the entire range of significant wave heights. On the other hand, the Weibull probability density function agrees well with the histogram for large significant wave height, but the agreement is rather poor for small significant wave height. This is the general trend observed in the analysis of the significant wave height data.

Examples of statistical analysis of significant wave height for coastal waves are shown in Figures 4 through 7. The cumulative distribution function of the significant wave height measured at Tiner Point, Canada [3] is plotted on log-normal probability paper (Figure 4) as well as on Weibull probability paper (Figure 5). On the other hand, comparison between the two probability density functions and the histogram is shown in Figure 6. As can be seen in these figures, the same conclusion derived from analysis of the significant wave height for ocean waves may also be applicable to the significant wave height for coastal waves.

As another example for coastal waves, Figure 7 shows a comparison between the histogram and the log-normal distribution of the significant wave height obtained at Port Hueneme, California [2]. Thus, it may safely be concluded that the log-normal probability distribution represents reasonably well the histogram over the entire range of significant wave height for ocean as well as coastal waves.

In regard to the marginal probability distribution of zero-crossing wave period (or modal wave period), it was found through the present study that the wave period appears to follow the log-normal probability law for both ocean and coastal waves. Although an attempt was made to represent the wave period data by the Weibull probability distribution, the representation was extremely poor for all examples. Figures 8 through 10 show examples of a comparison between histograms and the log-normal probability density functions. The figures pertain to comparisons made for data observed at Station 1 in the North Atlantic (Figure 8), at Tiner Point, Canada (Figure 9), and at Port Hueneme, California (Figure 10), respectively. As can be seen in these comparisons, wave period appears to be represented by the log-normal probability law.

From the foregoing discussion, it has been concluded that significant wave height follows the probability distribution given by,

$$f(H_s) \sim \Lambda(\mu_{HS}, \sigma_{HS}) \quad (1)$$

where, $\Lambda(\mu_{HS}, \sigma_{HS})$ is the log-normal probability density function with parameters μ_{HS} and σ_{HS} . Similarly, the zero-crossing wave period follows the probability distribution given by,

$$f(T_0) \sim \Lambda(\mu_{T_0}, \sigma_{T_0}) \quad (2)$$

The modal period also obeys the same distribution law as given in Equation (2) but with different parameters.

Then, from the properties of the log-normal probability distribution, it can be derived that the combined statistical properties of significant wave height and period follow the bi-variate log-normal probability law which may be written as,

$$f(H_s, T_0) \sim \Lambda(\mu_{HS}, \sigma_{HS}, \mu_{T_0}, \sigma_{T_0}, \rho) \quad (3)$$

where, ρ is a correlation coefficient between two random variables, H_s and T_0 , and its value can be determined from the data.

Various statistical properties of significant wave height and period can be derived based on Equation (3). First, it is possible

from Equation (3) to evaluate the confidence domain for a specified confidence coefficient which will provide reliable information for severe seas where data are always sparse in the contingency tables. Also, the statistical properties of the zero-crossing period (or modal period) for a specified significant wave height can be obtained as the conditional log-normal probability distribution given by,

$$f(T_s | H_s) \sim \Lambda \left(\mu_{T0} + \rho \frac{\sigma_{T0}}{\sigma_{HS}} (\ln H_s - \mu_{HS}), \sqrt{1-\rho^2} \sigma_{T0} \right) \quad (4)$$

DERIVATION OF CONFIDENCE DOMAIN

Derivation of the confidence domain for a specified confidence coefficient may be made around the modal value which represents that combination of significant wave height and zero-crossing (or modal) period most likely to occur. For the log-normal distributions given in Equations (1) and (2), the modal value (H_*, T_*) is given by,

$$(H_*, T_*) \sim (e^{\mu_H - \sigma_H^2}, e^{\mu_T - \sigma_T^2}) \quad (5)$$

Next, let us transform the joint probability density function given by Equation (3) into the following two new random variables, r and θ , shown in Figure 11.

$$\begin{cases} H_s = H_* + r \cos \theta \\ T_o = T_* + r \sin \theta \end{cases} \quad (6)$$

By carrying out the transformation of random variables given in Equation (6), the joint probability density function of r and θ , $f(r, \theta)$ becomes,

$$f(r, \theta) = \frac{r}{\sigma_1 \sigma_2 (2\pi) \sqrt{1-\rho^2} (H_o + r \cos \theta) (T_o + r \sin \theta)} \\ \times \exp \left\{ -\frac{1}{2(1-\rho^2)} \left[\left(\frac{\ln(H_o + r \cos \theta) - \mu_H}{\sigma_H} \right)^2 - 2\rho \left(\frac{\ln(H_o + r \cos \theta) - \mu_H}{\sigma_H} \right) \right] \right\}$$

$$x \left(\frac{\ln(T_o + r \sin \theta) - \mu_T}{\sigma_T} \right) + \left(\frac{\ln(T_o + r \sin \theta) - \mu_T}{\sigma_T} \right)^2 \quad (7)$$

In order to determine the confidence domain around the modal value (H_*, T_*), consider the conditional probability density function of r for a given θ . That is,

$$f(r|\theta) = \frac{f(r, \theta)}{\int_0^{\infty} f(r, \theta) dr} \quad (8)$$

Then, a point r , which yields a contour curve whose enclosed area is equal to a specified confidence coefficient, γ , can be determined from the following relationship:

$$\int_0^{r_i} f(r|\theta) dr = \gamma \quad (9)$$

Figure 12 shows an example of a thus derived confidence domain using Draper's data obtained in the North Atlantic [1]. The black circle in the figure represents the combination of significant wave height and zero-crossing period which is most likely to occur. The closed curves given in the figure outline the statistical confidence domains inside of which the probabilities of occurrence of the wave conditions are the specified values. The numbers in the figure refer to the number of observations given in Table 1. These numbers, however, for convenience sake, are regrouped and are divided by 1,000 so that the total number is equal to 1.

Figures 13 and 14 show two examples of such confidence domains derived using data on coastal waves. Confidence domains using the data obtained at Tiner Point, Canada, are given in Figure 13, while those using the data obtained at Port Hueneme, California, are given in Figure 14. The numbers in these figures refer to the frequencies of observations given in Tables 2 and 3, respectively. As can be seen in Figures 12 through 14, the domain for a confidence coefficient of 0.99 sufficiently covers the measured data. The significant benefit of drawing the confidence domains is that information in severe seas where data are always sparse can be clearly estimated from the overall data given in the contingency tables.

ESTIMATION OF EXTREME SIGNIFICANT WAVE HEIGHT

One of the most important pieces of information concerning long-term wave statistics is the largest value (extreme value) of significant wave height. The information is of particular importance for the design of ocean and coastal structures.

Although the significant wave height follows the log-normal probability law, this holds only for the cumulative probability distribution up to 0.99 as was discussed in the previous section. Therefore, it is not appropriate to estimate the extreme significant wave height based on the log-normal distribution, since the value of the cumulative probability distribution will be greater than 0.99 for the extreme value. Instead, it may be evaluated by applying the concept of asymptotic distribution of extreme values which is applicable for any probability distribution if certain conditions are met. For this purpose, let us assume that the cumulative distribution function can be expressed asymptotically in the following form:

$$F(x) = 1 - e^{-q(x)} \quad (10)$$

Then, it can be derived that the probable extreme value in n number of observations, denoted by \bar{Y}_n , satisfies the following condition when n is large:

$$e^{-q(\bar{Y}_n)} = \frac{1}{n} \quad (11)$$

This in turn, implies that the probable extreme value can be evaluated from,

$$\frac{1}{1 - F(\bar{Y}_n)} = n \quad (12)$$

As an example, Figure 15 shows the left-hand side of Equation (12) (often called the return period) in logarithmic form using the significant wave height data obtained at Tiner Point, Canada. Since a total of 2,300 observations of significant wave height were made in one year, the probable extreme significant wave height expected to occur in 20 years, for example, can be estimated from the figure as the wave height for which the ordinate is $\ln(2,300 \times 20) = 10.74$; namely, 18.0 ft (5.5 m).

Figure 16 shows the results of a similar analysis to that shown in Figure 15 but using data obtained at Port Hueneme, California. A

total of 3,400 observations of significant wave height were made in 20 months for this example; hence the probable extreme significant wave height expected to occur in 20 years can be estimated from the figure as the wave height for which the ordinate is 10.62; namely, 9.7 ft (2.96 m).

CONCLUSIONS

This paper discusses statistical properties of the long-term ocean and coastal waves derived from analysis of available data. In the analysis, correlation between wave height and period is taken into consideration, and data on ocean waves accumulated in the North Atlantic as well as data on coastal waves obtained at Tiner Point, Canada, and Port Hueneme, California, are analyzed.

It is found from the results of analysis that statistical properties of both wave height and period are approximately represented by the log-normal probability law, and that the joint probability of wave height and period obeys the bi-variate log-normal probability law. This conclusion appears to be valid for both ocean and coastal waves.

The confidence domain of wave height and period for a confidence coefficient of 0.99 sufficiently covers the measured data. A significant benefit of drawing the confidence domains lies in obtaining information in severe seas where the data are always sparse in the contingency table.

The estimation of the largest significant wave height (extreme value) expected to occur in a specified long period of time is discussed by applying the concept of asymptotic statistical distribution of extreme values.

REFERENCES

1. Draper, L. and Squire, E.M., "Waves at Ocean Weather Ship Station INDIA," Trans. Roy. Inst. Nav. Arch., Vol 109, 1967.
2. Thompson, E.F., "Wave Climate at Selected Locations Along U.S. Coasts," Coastal Eng. Res. Center, Tech. Rep. 77-1, 1977.
3. Khanna, J. and Andru, P., "Lifetime Wave Height Curve for Saint John Deep Canada," Proc. Symp. on Ocean Wave Measure. and Analysis, Vol 1, 1974.
4. Hogben, N. and Lumb, F.E., Ocean Wave Statistics, National Physical Laboratory, H.M. Stationery Office, London, 1967.
5. Walden, H., "Die Eigenschaften der Meerswellen in Nordatlantischen Ozean," Deutscher Wetterdienst, Einzelveröffentlichungen, Nr 41, 1964 (in German).

6. Jasper, N.H., "Statistical Distribution Patterns of Ocean Waves and of Wave-Induced Ship Stresses and Motions, with Engineering Applications," Trans. Soc. Nav. Arch. & Mar. Eng., Vol 64, 1956.

7. Davidan, I.N. et al., "The Results of Experimental Studies on the Probabilistic Characteristics of Wind Waves," Proc. Dynamics of Marine Vehicles and Structures in Waves, 1974.

8. Ward, E.G., Evans, D.J., and Pompa, J.A., "Extreme Wave Heights Along the Atlantic Coast of the United States," Proc. Offshore Tech. Conference, OTC 2846, 1977.

9. Houmb, O.G., and Overvik, T., "Parameterization of Wave Spectra and Long Term Joint Distribution of Wave Height and Period," Proc. Behavior of Offshore Structures, 1976.

10. Nordenstrom, N., "Method for Predicting Long Term Distribution of Wave Loads and Probability of Failure for Ships," Appendix I, Long-Term Distribution of Wave Height and Period, Det Norske Veritas Report No. 69-21-S, 1969.

Table 1: Statistical data on wave height and period obtained at Weather Station I in the North Atlantic [1]

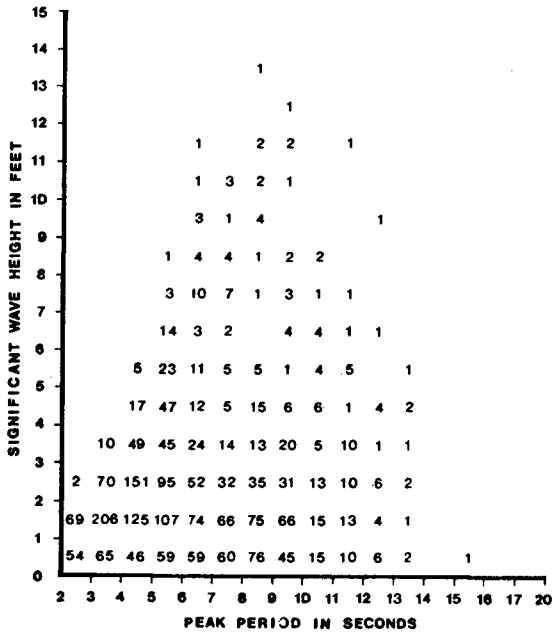
		ZERO-CROSSING WAVE PERIOD																	
		6.0	6.5	7.0	7.5	8.0	8.5	9.0	9.5	10.0	10.5	11.0	11.5	12.0	12.5	13.0		13.5	14.0
48 FT	14.6 M																	1	1
46	14.0																		0
44	13.4																		0
42	12.8																		1
40	12.2																1	2	
38	11.6																	2	
36	11.0																	6	
34	10.4																	4	
32	9.8																	5	
30	9.2																	11	
28	8.5																	8	
26	7.9																	17	
24	7.3																	18	
22	6.7																	19	
20	6.1																	36	
18	5.5																	55	
16	4.9																	68	
14	4.3																	87	
12	3.7																	118	
10	3.1																	151	
8	2.4																	167	
6	1.8																	142	
4	1.2																	73	
2	0.6																	9	
0	0																	1000	
		4	5	20	71	147	125	196	126	106	68	57	25	22	9	3	6	1000	

Table 2: Statistical data on wave height and period obtained at Port Hueneme, California [2]

PERIOD (SECS)	HEIGHT (FT)															EU- TOT.	NO- OBS.			
	0.2	0.5	1.0	1.5	2.0	2.5	3.0	3.5	4.0	4.5	5.0	5.5	6.0	6.5	7.0					
0.5 - 1.0	85																			
1.0 - 1.5																				
1.5 - 2.0																				
2.0 - 2.5																				
2.5 - 3.0																				
3.0 - 3.5																				
3.5 - 4.0																				
4.0 - 4.5																				
4.5 - 5.0																				
5.0 - 5.5																				
5.5 - 6.0																				
6.0 - 6.5																				
6.5 - 7.0																				
7.0 - 7.5																				
7.5 - 8.0																				
8.0 - 8.5																				
8.5 - 9.0																				
9.0 - 9.5																				
9.5 - 10.0																				
10.0 - 10.5																				
10.5 - 11.0																				
11.0 - 11.5																				
11.5 - 12.0																				
12.0 - 12.5																				
12.5 - 13.0																				
13.0 - 13.5																				
13.5 - 14.0																				
14.0 - 14.5																				
14.5 - 15.0																				
15.0 - 15.5																				
15.5 - 16.0																				
16.0 - 16.5																				
16.5 - 17.0																				
17.0 - 17.5																				
17.5 - 18.0																				
18.0 - 18.5																				
18.5 - 19.0																				
TOTAL	133	330	221	162	83	44	26	16	10	6	2	2	1	1	1	1	1	1	1	1
CUM. TOTAL	1000	847	526	367	285	222	186	160	150	140	130	120	110	100	90	80	70	60	50	40
COL. NO.	9.764	9.770	10.000	10.333	10.677	11.021	11.365	11.709	12.053	12.397	12.741	13.085	13.429	13.773	14.117	14.461	14.805	15.149	15.493	15.837

MEAN OF HGT. HEIGHT = 2.13 FT OVERALL WAVE PERIOD = 10.46 SECS
 VARIANCE OF HGT. HEIGHT = 1.86 FT² VARIANCE OF WAVE PERIOD = 0.40 SEC²
 STANDARD DEVIATION OF HEIGHT = 1.36 FT STANDARD DEVIATION OF PERIOD = 0.69 SEC

Table 3: Statistical data on wave height and period obtained at Tiner Point, Canada [3]



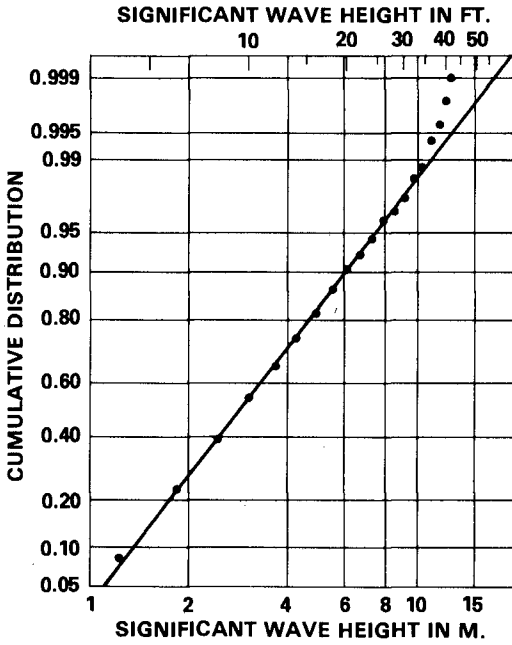


Figure 1: Cumulative distribution function of significant wave height plotted on log-normal probability paper (Data from Reference 1)

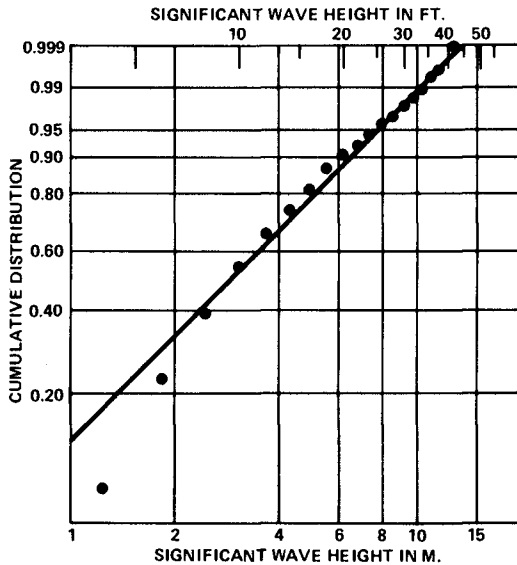


Figure 2: Cumulative distribution function of significant wave height plotted on Weibull probability paper (Data from Reference 1)

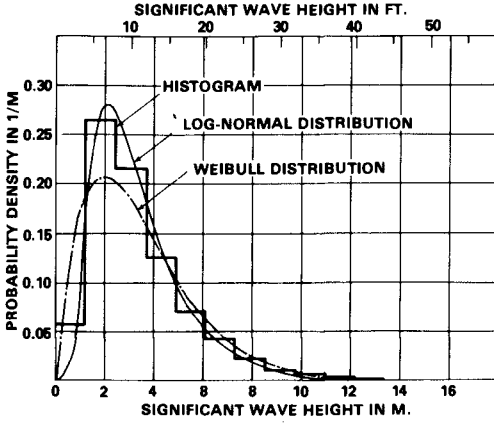


Figure 3: Comparison between histograms of significant wave height and log-normal and Weibull probability density functions (Data from Reference 1)

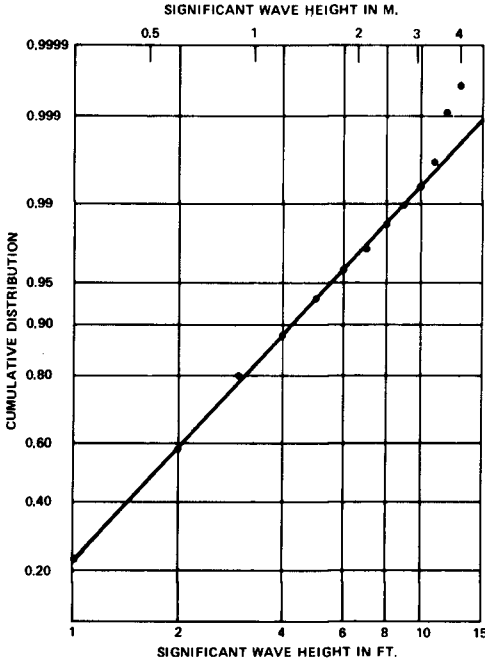


Figure 4: Cumulative distribution function of significant wave height plotted on log-normal probability paper (Data from Reference 3)

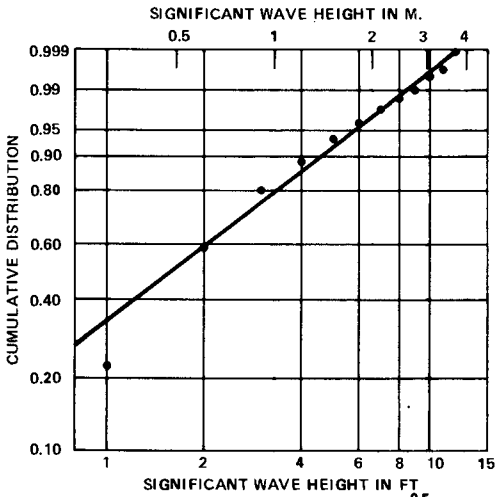


Figure 5: Cumulative distribution function of significant wave height plotted on Weibull probability paper (Data from Reference 3)

Figure 6: Comparison between histogram of significant wave height and log-normal and Weibull probability density functions (Data from Reference 3)

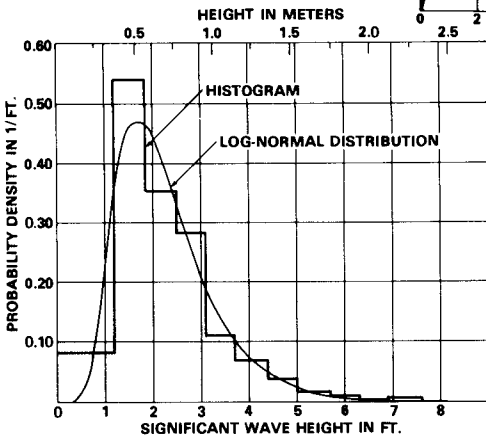
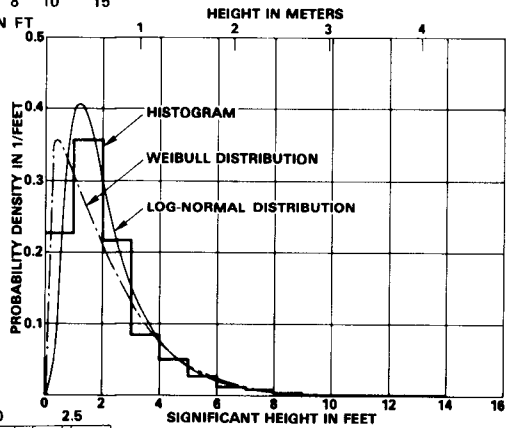


Figure 7: Comparison between histogram of significant wave height and log-normal probability density function (Data from Reference 2)

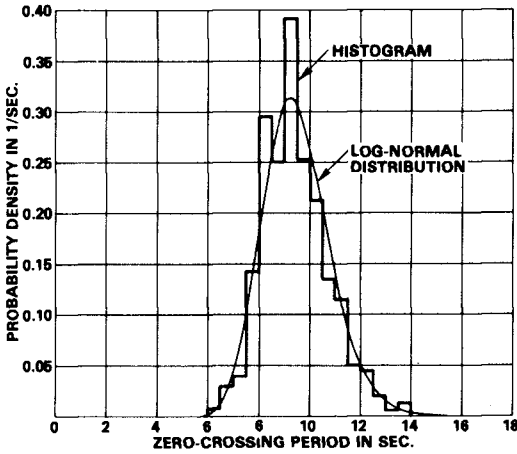


Figure 8: Comparison between histogram of zero-crossing period and log-normal probability density function (Data from Reference 1)

Figure 9: Comparison between histogram of modal period and log-normal probability density function (Data from Reference 3)

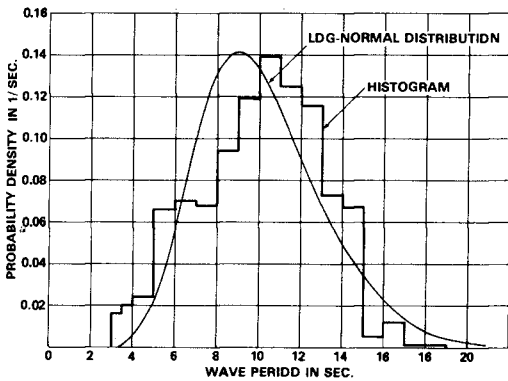
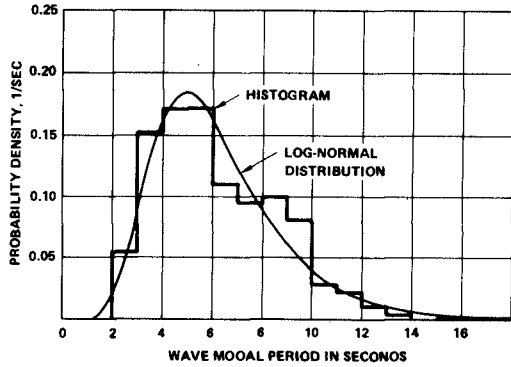


Figure 10: Comparison between histogram of wave period and log-normal probability density function (Data from Reference 2)

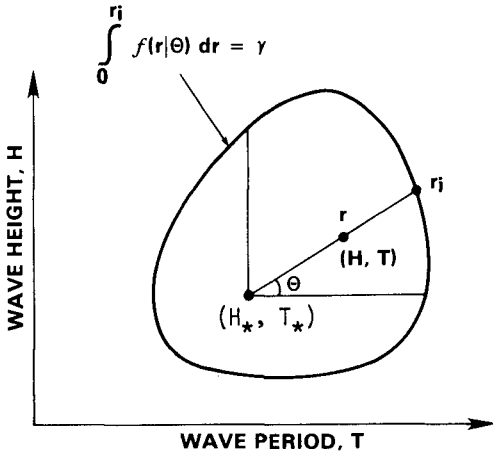


Figure 11: Pictorial sketch illustrating transformation of random variables

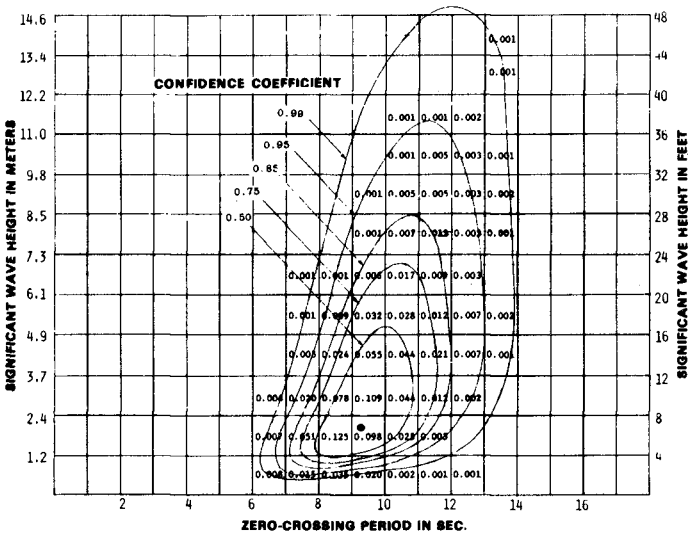


Figure 12: Comparison of domains of significant wave height and zero-crossing period for various confidence coefficients (Data from Reference 1)

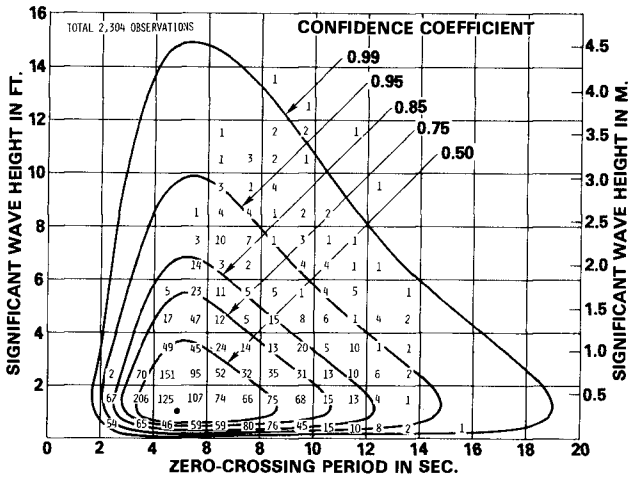


Figure 13: Comparison of domains of significant wave height and modal period for various confidence coefficients (Data from Reference 3)

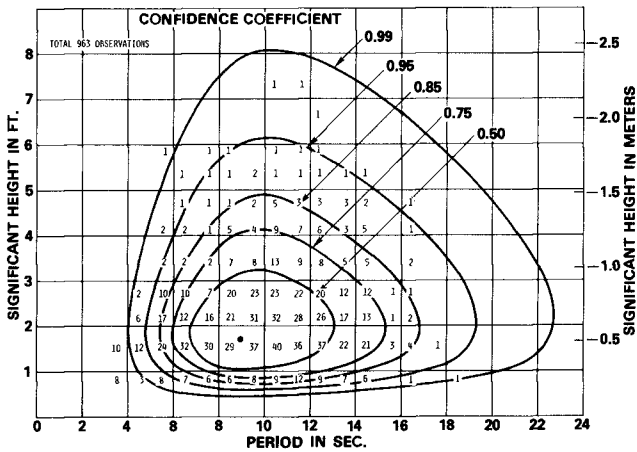


Figure 14: Comparison of domains of significant wave height and period for various confidence coefficients (Data from Reference 2)

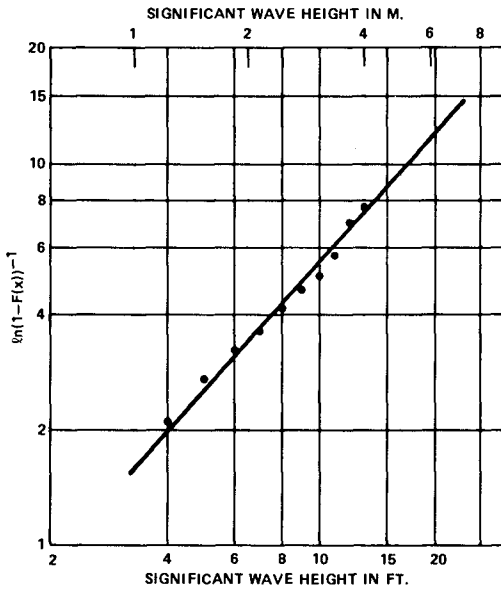
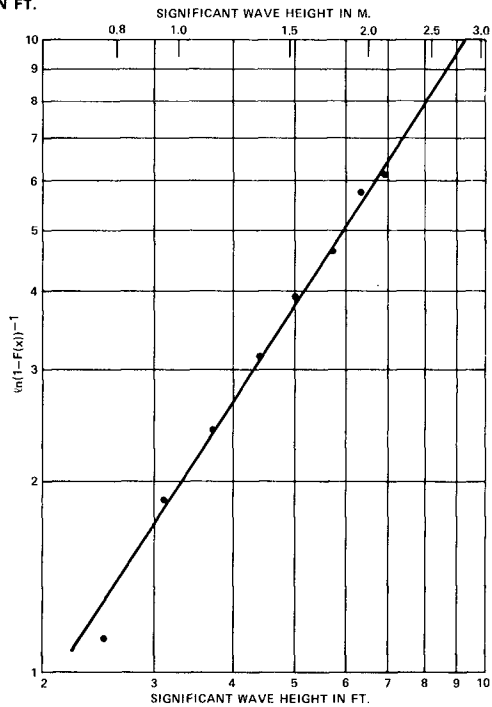


Figure 15: Probable extreme significant wave height at Tiner Point, Canada (Data from Reference 3)

Figure 16: Probable extreme significant wave height at Port Hueneme, California (Data from Reference 2)



CHAPTER 3

WIND WAVE FREQUENCIES IN A TROPICAL CYCLONE REGION

Rodney J. Sobey #

INTRODUCTION

Australia's Coral Sea coast from Bundaberg north to Cape York has a wind wave climate that is almost unique. The coastline is afforded unparalleled protection from the 1900 km Great Barrier Reef, yet it lies in a tropical cyclone region and must expect recurrent intense wind and wave conditions.

The Great Barrier Reef is a continuous chain of quite separate coral reef clusters located near the edge of the continental shelf. The separate reefs are often exposed at low tide, the inner fringe of the clusters ranges from 10 km offshore north of Cairns to 200 km offshore south of Rockhampton and the outer fringe is typically some 50 km further offshore, beyond which the ocean bed drops rapidly away. Incident wave energy from the Coral Sea is invariably dissipated on the outer edge of the Reef and wave conditions on the continental shelf can reasonably be considered due to local wind conditions. The Reef imposes an effective fetch limitations on wave generation over the continental shelf and there is, as a consequence, a moderately rapid response of wave conditions to changes in local wind conditions. A pronounced diurnal variation in the wind climate is reflected also in the wave climate and the stability of the region's tropical climate leads to frequent calm to slight sea conditions. This stability however is occasionally exploded by the generation and passage of a tropical cyclone in mid to late summer. Large waves can be generated by the intense winds of the tropical cyclone (hurricane or typhoon), often an order of magnitude greater than those in response to non-cyclonic events.

The rational design of coastal structures and the rational pursuit of coastal zone management requires appropriate estimates of the frequency of occurrence of waves of various heights. Ideally such information is obtained from an extreme value analysis of long term wave records at the particular site in question. Permanent wave recording programs unfortunately have only become common practice in the present decade and wave records, if they exist at all for a particular site, are rarely long enough to allow a satisfactory extreme value analysis. It is clear, in the Australian context at least, that historical wave data alone is not yet sufficient to derive satisfactory estimates of long term wave frequencies. The alternative is system modelling.

Wind is a major meteorological variable and its long term recording has been a standard meteorological practice now for over half a century.

Senior Lecturer, Department of Civil and Systems Engineering,
James Cook University, Townsville 4811, Australia.

Suitable data is normally available to estimate the statistical characteristics of a local wind climate. There is also now a developing confidence in wind wave forecasting techniques. Used together, it is possible to simulate several thousand years of statistically likely wind wave observations. A summary of these simulated observations will provide a reasonable estimate of long term wind wave frequencies for a particular site.

METHODOLOGY

Statistical simulation is now established as a basic technique in the study of a wide range of geophysical phenomena; earthquakes, precipitation, floods, wind, storm tides and wind waves have all been considered in this manner. The need for a stochastic approach stems from the recognised inadequacy of current deterministic models to make predictions beyond a few days. The present approach can be described as stochastic - deterministic; long term prediction of winds is essentially stochastic whereas the short term forecasting of the waves generated by a predicted wind field is deterministic. The approach involves a largely stochastic input (wind) to a deterministic system (wind-wave generation) yielding of course a stochastic output (wind waves). As pointed out by Nolte (7), the determination of wind wave statistics involves three important considerations: (i) desired end use, (ii) existing data base, and (iii) mathematical system model. All three should be defined and their compatibility established.

Desired End Use. - Essentially the objective is the estimation of the significant wave height - frequency relationship for a typical coastal site behind the Great Barrier Reef along Australia's Coral Sea coast. Reliable estimates of waves with average recurrence intervals in excess of 100 years are sought. It is recognised however that it is not always the maximum wave in any one year that causes the most damage. It may be that sustained attack from a more modest wave can be just as significant. The technique adopted should potentially allow the estimation of a wave height - duration - frequency relationship as well as the more common wave height - frequency relationship.

Existing Data Base. - Available data held by the (Australian) Bureau of Meteorology is far from perfect and the final result can be of course no better than the basic data. The adopted data base was drawn from Bureau records held in computer compatible form (1), specifically Card 7 "Hourly Surface Observations" and Card 13 "Tropical Cyclones and Tropical Disturbances". The Card 7 data includes three-hourly observations of mean wind speed and direction at coastal city airports. These sites are removed somewhat from the continental shelf but the quality of the data is good and the records are comprehensive. The wind speed observations are taken as wind speeds at the standard height of 10 m in the boundary layer. Card 13 data, while clearly the more important data source, is disappointing in terms of data quality. Notwithstanding some reservations they constitute the only historical data available for the estimation of long term wind fields, cyclonic and non-cyclonic, in the region.

SYSTEM MODEL

Even a brief consideration of the wind wave climate behind the Great Barrier Reef establishes the need to consider non-cyclonic as well as cyclonic conditions. While extreme wave conditions are invariably associated with a tropical cyclone, years pass without such an event in the immediate region. Even when a cyclone does influence the region it may not pass sufficiently close to affect the long term frequency of wind waves at the site. More often than not non-cyclonic winds will be responsible for the maximum wave conditions during any year and this fact must be included in the mathematical model.

Geophysical and especially hydrological time series $Z(t)$ are frequently postulated (5,8) as the summation of three separate components (see Fig. 1), such that

$$Z(t) = P(t) + C(t) + R(t). \quad (1)$$

$P(t)$ is a periodic component that is often possible to reconcile with known physical effects. Astronomical tide and, in the present context, diurnal and annual weather cycles are obvious examples. $C(t)$ is an infrequent catastrophic event such as an earthquake, a landslide and, in the present context again, a tropical cyclone. The residue $R(t)$ is a non-pure random series with a clear element of persistence. The component P is represented as a deterministic function of time whereas C and R are stochastic functions of time. Eq. 1 has been adopted as the basis of the mathematical system model.

The simulation methodology adopted is illustrated in Fig. 2. The cycle is initiated by determining the existence or otherwise of a tropical cyclone. Should one exist it must then be decided if it passes sufficiently close to the nominated site to influence the local wave climate. If it does not, this fact is recorded and the cycle is repeated. Should it influence the site the storm intensity and track are chosen and an estimate made of the maximum significant wave height at the site during the passage of the storm. This information is also recorded and the cycle repeated. When a tropical cyclone does not exist, and this is most of the time, non-cyclonic wind conditions are appropriate and the significant wave height at the site is predicted. Again this information is recorded and the cycle repeated. Details of this simulation cycle follow, firstly for non-cyclonic wind waves and then tropical cyclone wind waves.

Wave conditions throughout are represented solely in terms of significant wave height, with no consideration of directional spectra or even one-dimensional spectra. Further the Sverdrup-Munk-Bretschneider forecasting technique (13), deterministic and empirical, is adopted in the estimation of wind-generated waves under both cyclonic and non-cyclonic conditions.

CHARACTERISTICS OF NON-CYCLONIC WIND RECORDS

Following the adopted simulation methodology for non-cyclonic winds, the first step is the generation of a statistically equivalent wind record (magnitude and direction). A necessary preliminary step is an evaluation of the statistical characteristics of the wind climate, as represented by the Card 7 data, to assist in the selection of an appropriate synthetic

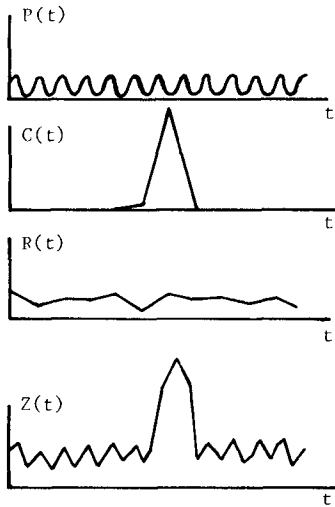


Fig. 1 GEOPHYSICAL TIME SERIES DECOMPOSITION

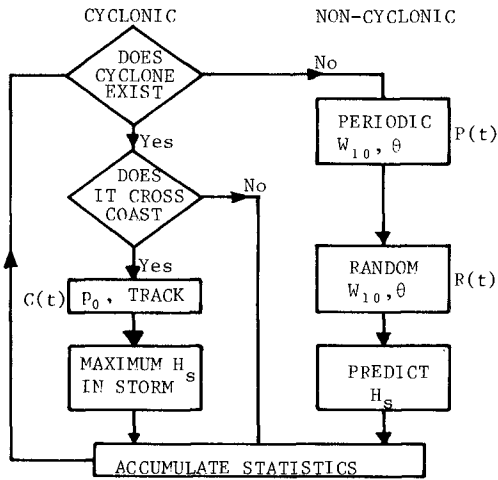


Fig. 2 WIND WAVE SIMULATION METHODOLOGY

generation technique. The available three-hourly wind records for two typical sites, Townsville and Rockhampton airports, were subjected to standard time series analysis techniques, namely spectral, correlation and probability analyses.

Spectral Analyses. - It was anticipated that the wind spectrum would cover a wide range of frequencies from seasonal effects around 0.003 cpd (cycles per day) to diurnal variations at 1 cpd to turbulence and gusts above 1000 cpd. Spectral resolution is bounded at the lower end by the time step Δt of the data series and at the upper end by the length of the data series, which is of course limited by computer storage. Using the FFT technique and a second data series formed from daily averages of the three-hourly records, a reasonable estimate of the wind magnitude and wind direction spectra can be obtained over the frequency range 0.000122 cpd to 4 cpd. The maximum frequency available is well below the range for gusts and turbulence which can not be discerned from the data available. This is no handicap however as such information is not required for the SMB wave forecasting technique.

Composite wind speed and wind direction power spectra for Townsville and Rockhampton airports are given elsewhere by Sobey, Rossow and McMonagle (11). All four spectra show the same trend, namely clear spectral peaks at frequencies of 1 cpd and around 0.0027 cpd, representing observable weather periodicities at periods of 1 day (diurnal) and 1 year (seasonal), together with a significant residual of essentially random noise throughout the spectrum.

Correlation Analyses. - Time domain analyses of the wind data in the form of auto and cross-correlation computations were undertaken in addition to the frequency domain analyses above. The base data only ($\Delta t = 3$ hr) was subjected to this analysis and a typical result (wind magnitude at Rockhampton airport) is shown in Fig. 3.

These results confirm the indications of the spectra. The diurnal periodicity is particularly clear and extension of the time-lag scale would also show the seasonal periodicity. The randomness of the residue is represented by the decay of the mean position to zero as the time-lag increases. The gradual exponential-like decay exhibits the characteristics of a Markov process in that substantial "memory" of preceding conditions is retained.

Probability Analyses. - Finally consideration was given to the amplitude domain characteristics. Figs. 4(a) and (b) show frequency histograms of wind magnitude and direction for Rockhampton airport. Davenport (3) considered the statistics of the total population of mean wind speeds and, assuming initially that the wind is isotropic and that there is no "prevailing" wind, showed that the mean wind followed the Rayleigh distribution. However prevailing wind conditions are normally experienced and Davenport has indicated that directional characteristics can reasonably be accommodated by the Weibull distribution, whose cumulative distribution function (CDF) is

$$F(W_{10}) = 1 - \exp\left[-\left(\frac{W_{10}}{c}\right)^k\right] \quad (2)$$

Additional flexibility is introduced by this two parameter distribution

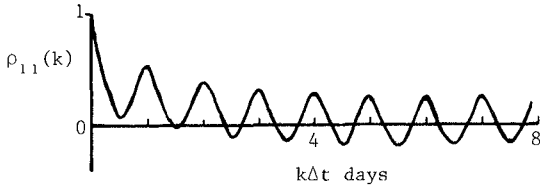


Fig. 3 WIND SPEED CORRELOGRAM AT ROCKHAMPTON

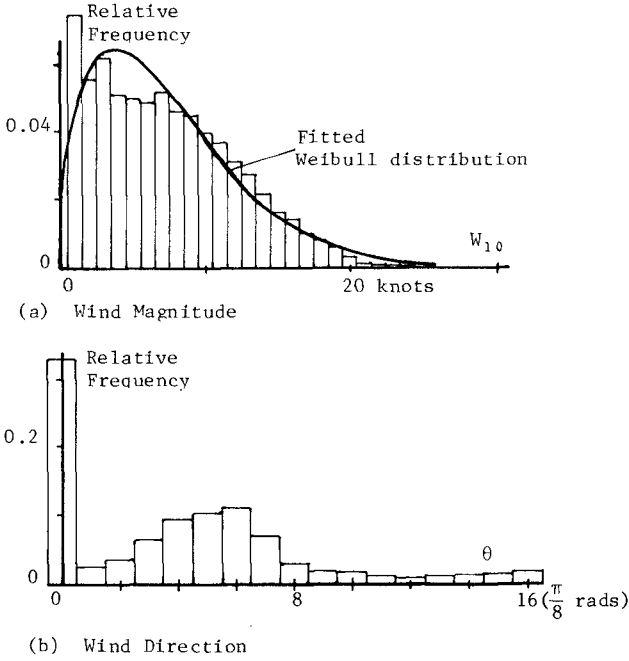


Fig. 4 WIND FREQUENCY HISTOGRAMS AT ROCKHAMPTON

compared with the single parameter Rayleigh distribution (The Weibull distribution reduces to the Rayleigh distribution when $c = (2)^{1/2}\sigma$ and $k = 2$). It is apparent from the histogram in Fig. 4(a) that a Weibull distribution would be appropriate.

Calm Observations. - The wind records for both Townsville and Rockhampton contain a significant number of calm observations (approximately 30% of the record); this is a common characteristic of normally stable tropical conditions and appropriate consideration must be given to this situation. For analysis purposes it may be considered in terms of conditional probability - a Bernoulli distribution for calm or non-calm conditions and appropriate distributions for magnitude (Weibull) and direction (discrete), given that a wind exists.

This aim was implicitly achieved in the following manner. Calm observations were retained only in the wind direction records where they were entered as zeros, whereas the sixteen compass points from NNE through S to N were entered as integers 1 to 16. The left hand block of the histogram in Fig. 4(b) represents the calm observations. If zero is retained as a "direction", a simulated direction of zero represents a calm day.

WEATHER PERIODICITIES

A major feature of the non-cyclonic wind records is the diurnal weather cycle. An annual weather cycle is also apparent but less pronounced. On this evidence the periodic component $P(t)$ of Eq. 1 has been assumed to comprise only two Fourier components having angular speeds of $\omega = 2\pi$ rad/day and $\Omega = 2\pi/365.25$ rad/day respectively. The periodic component can be written as

$$P(t) = a \sin(\omega t + \phi) + A \sin(\Omega t + \Phi). \quad (3)$$

It is necessary however to consider both magnitude and direction of the wind; magnitude can be represented at $P_1(t)$, direction as $P_2(t)$ and Eq. 3 rewritten as

$$P_{1,i} = a_1 \sin(\omega t_i + \phi_1) + A_1 \sin(\Omega t_i + \Phi_1) \quad (4a)$$

$$P_{2,i} = a_2 \sin(\omega t_i + \phi_2) + A_2 \sin(\Omega t_i + \Phi_2). \quad (4b)$$

Separation of the periodicities (i.e. determination of $a_1, \phi_1 \dots A_2, \Phi_2$) is somewhat subjective. The initial approach was classical harmonic analysis, fitting Eq. 4 to the data by the method of least squares. Typically however the random component $R(t)$ is at least the same order of magnitude as the periodic component and, while harmonic analysis was numerically successful, the computed amplitudes did not match in magnitude the measured spectral peaks. As an alternative the spectral peaks themselves can be used in the estimation of $a_1, \phi_1 \dots$ etc.

From Parseval's theorem the amplitude of a single periodic component is related to the single-sided power spectrum $P(f)$ as

$$a^2 = 2 \int_0^N P(f) df, \quad (5)$$

from which it is possible to directly evaluate the amplitudes a_1, a_2, A_1, A_2 in Eq. 4 from the measured spectra. Estimation of the phase angles $\phi_1, \phi_2, \Phi_1, \Phi_2$ was much more subjective; it was based on visual estimates

from a number of sample records, three-hourly observations for ϕ_1 and ϕ_2 and monthly averaged observations for Φ_1 and Φ_2 . No doubt it is possible to improve this estimation but time did not permit pursuance of this point. The time datum throughout was taken as 00⁰⁰ hours 1 July 1950.

With the periodic signal $P(t)$ thus defined deterministically it may be subtracted from the complete record $Z(t)$ leaving theoretically (see Eq. 1) the components $C(t)$ and $R(t)$. Strictly it would be further possible to separate tropical cyclone winds $C(t)$ from this record. However the deletions from the record would be small in number and their retention would not unduly influence the population statistics of $R(t)$. They would of course have a significant influence on the extreme value statistics of $R(t)$ but the wind data has not been used for such a purpose.

RANDOM WIND COMPONENT

The auto-spectra for Townsville and Rockhampton indicate a substantial random-like residue that would remain after extraction of the ω and Ω periodicities; this is the component $R(t)$ of Eq. 1. The associated correlograms (Fig. 3 is typical) support this observation to some extent but also show a high level of persistence or memory. Physically this represents the observable tendency of high winds from a particular direction to follow high winds from much the same direction and alternatively for calm conditions to follow calm conditions. In time series analysis this persistence is measured by the auto-correlation function ρ_k which is a measure of the degree of linear dependence between observations separated by time $k\Delta t$, Δt being the time interval (3 hrs) of the observations.

Again both components of the residue must be considered, $R_1(t)$ representing wind speed magnitude and $R_2(t)$ representing wind direction, the two series being of course related. A multivariate Markovian generating process proposed by Matalas (6) for the synthetic generation of streamflow at two sites in the same river basin would appear to be an appropriate and relatively straightforward generating process in the present context. For two related series $x_1(t)$ and $x_2(t)$ that are Normally distributed, the Matalas algorithm preserves the sample estimates of:

μ_1, μ_2	- the means of x_1 and x_2
σ_1, σ_2	- the variances of x_1 and x_2
$\rho_{11}(1), \rho_{22}(1)$	- the lag-one auto-correlations
$\rho_{12}(0), \rho_{21}(0)$	- the lag-zero cross-correlations, and
$\rho_{12}(1), \rho_{21}(1)$	- the lag-one cross-correlations.

The multivariate generating process is

$$X_{i+1} = A X_i + B \epsilon_{i+1} \quad (6)$$

where

$$X_i = \begin{bmatrix} x_{1,i} - \hat{\mu}_1 \\ x_{2,i} - \hat{\mu}_2 \end{bmatrix}$$

ϵ_{i+1} is a vector of independent $N(0,1)$ distributed sampling deviates and the matrices A and B are defined as

$$A = M_1 M_0^{-1} \quad (7)$$

$$\text{and } BB^T = M_0 - M_1 M_0^{-1} M_1^T$$

$$\text{where } M_1 = \begin{bmatrix} \hat{\beta}_{11}(1)\delta_1^2 & \hat{\beta}_{12}(1)\delta_1\delta_2 \\ \hat{\beta}_{21}(1)\delta_1\delta_2 & \hat{\beta}_{22}(1)\delta_2^2 \end{bmatrix}$$

$$\text{and } M_0 = \begin{bmatrix} \delta_1^2 & \hat{\beta}_{12}(0)\delta_1\delta_2 \\ \hat{\beta}_{21}(0)\delta_1\delta_2 & \delta_2^2 \end{bmatrix}$$

Young and Pisano (15) have shown that B is not unique and, with $C = BB^T$, suggest using the lower triangular form

$$B = \begin{bmatrix} \sqrt{C_{11}} & 0 \\ \frac{C_{12}}{\sqrt{C_{11}}} & \sqrt{C_{22} - \frac{C_{12}^2}{C_{11}}} \end{bmatrix} \quad (8)$$

There remains a problem in that the $x_1(t)$ and $x_2(t)$ series must be Normally distributed. As seen in Fig. 4 the distributions of the R_1 and R_2 series are clearly not Normal.

A preliminary step is the adoption of suitable distributions to describe the R_1 and R_2 series respectively. R_1 has been fitted to a Weibull distribution by the method of maximum likelihood. No attempt was made to fit any distribution to the R_2 series and it was retained in a discrete histogram form.

Young and Pisano discuss "minimum skewness" transformations of the base data series to yield series that more closely follow a Normal distribution, the minimum skewness referring to the fact that the Normal distribution has zero skewness. They mention logarithmic and square-root transformations in the context of streamflow simulation and adopt the former. In the present context the two related series are not physically the same, as for example in the dual site streamflow case, and it would seem unlikely that the same transformation would be equally satisfactory for both wind magnitude R_1 and wind direction R_2 .

The adopted approach is rather direct; each residual is transformed to another having the same mean and variance but nominally zero skewness by matching the cumulative probabilities of the residual and normal distributions. The residual distribution was chosen as Weibull for the R_1 series and discrete for R_2 . The $R_2 \rightarrow x_2$ transformation contains an additional step, the rotation of the direction datum so that the peak region is central to the record and the relocation of the calm observations (direction zero) to harmonise with this distribution. In both cases it was necessary to adopt truncated Normal distributions, omitting wind speeds less than zero and directions less than zero and greater than sixteen. This CDF transformation has proved moderately successful. The reverse transformation in both cases is equally straightforward.

The steps involved in preparation for the synthetic generation are -

1. Separate $R(t)$ from data files $Z(t)$
2. Calculate $\hat{\mu}_1, \hat{\sigma}_1$ from $R_{1,i}$ and $\hat{\mu}_2, \hat{\sigma}_2$ from $R_{2,i}$
3. Fit Weibull distribution to $R_{1,i}$
4. CDF transformations on residual series
 $R_{1,i} \rightarrow x_{1,i}$ and $R_{2,i} \rightarrow x_{2,i}$
5. Calculate $\hat{\rho}_{11}(1), \hat{\rho}_{22}(1), \hat{\rho}_{12}(0), \hat{\rho}_{21}(0), \hat{\rho}_{12}(1)$ and $\hat{\rho}_{21}(1)$ from $x_{1,i}$ and $x_{2,i}$

The steps involved in the actual synthetic generation are -

1. Generate synthetic $x_{1,i}$ and $x_{2,i}$ series from Matalas algorithm
2. Inverse CDF transformation to synthetic $R_{1,i}$ and $R_{2,i}$ series:
 $x_{1,i} \rightarrow R_{1,i}$ and $x_{2,i} \rightarrow R_{2,i}$

Questions remain concerning the adequacy of the first-order Markov generating process in modelling long term persistence, for example the Hurst phenomenon. According to O'Connell (8), the retention of only lag-zero and lag-one correlations leads to the reproduction of only high frequency behaviour and cannot capture long term persistence. Several alternate generating processes have been proposed in the hydrology literature but there does not seem as yet to be any general agreement even in the case of streamflow. The Matalas algorithm certainly reproduces many of the observable features of geophysical time series and is just as certainly not the weak link in the present methodology.

NON-CYCLONIC WIND WAVE PREDICTION

At time t_i during non-cyclonic wind simulation the wind speed is

$$W_{10} = P_{1,i} + R_{1,i} \quad (9)$$

and the wind direction is

$$\theta = P_{2,i} + R_{2,i} \quad (10)$$

Wind conditions are simulated every 3 hours. This wind is assumed active in direction θ for sufficient time that the generated sea condition is fetch-limited. This would certainly not always be true but becomes an increasingly better assumption for higher wind speeds where interest is of course centred; it will always be conservative. Adopted fetches along radiating lines, corresponding to the sixteen compass points, from the nominated site to the coast or the inner edge of the Great Barrier Reef are taken direct from appropriate navigation charts.

Assuming deep water conditions wind waves have been predicted directly from the empirical equations (13) to the Sverdrup-Munk-Bretschneider forecasting method:

$$\frac{gH}{W_{10}^2} = 0.283 \tanh\left[0.0125 \left(\frac{gF}{W_{10}^2}\right)^{0.42}\right] \quad (11)$$

$$\frac{C}{W_{10}} = 1.20 \tanh\left[0.077 \left(\frac{gF}{W_{10}^2}\right)^{0.25}\right] \quad (12)$$

$$\frac{gt_D}{W_{10}} = K \exp \sqrt{A \ln^2 \frac{gF}{W_{10}^2} - B \ln \frac{gF}{W_{10}} + C_* + D \ln \frac{gF}{W_{10}}} \quad (13)$$

where K, A, B, C_* and D are constants, H is the significant wave height, C the wave celerity, F the fetch length and t_D the wind duration. Again the assumption of deep water conditions is conservative. Eq. 11 has been used directly to estimate wave height at time t_i corresponding to the wind magnitude and direction indicated by Eqs. 9 and 10.

TROPICAL CYCLONE OCCURRENCES

The advent of a tropical cyclone is an infrequent event and has been considered as a completely separate influence on the local wind and wave climates. The basic steps of the non-cyclonic wind wave simulation described above, namely simulate the wind field, then predict the resulting wave field, are repeated in principle for tropical cyclone wind waves with the details of course much altered. These steps however must be preceded by the simulation of the existence of a tropical cyclone, a step that has no parallel in the previous section. Given that a cyclone occurs, the methodology proceeds implicitly to the simulation of a moving wind field system and thence to the prediction of wind waves that would be generated at the nominated site by the moving wind field.

The stochastic modelling of tropical cyclone or hurricane occurrences in a particular region has been considered in detail by Russell (9), the approach adopted herein differing in detail but not in spirit. A suitable stochastic model should permit predicting multiple occurrence or none at all during the cyclone season. Within each southern hemisphere season, taken as mid-December to mid-April (a total of 121 days or 122 in a leap year), it should permit prediction of the time of occurrence of any events. Storm occurrences are assumed to follow a uniform Poisson process, which describes independent incidents occurring along a continuous time axis with a constant average rate of occurrence of λ per season. The distribution of storm occurrence time at particular time t_i then follows a Poisson distribution with parameter λt_i . The distribution of inter-arrival time τ between separate storms is more relevant in the present context however and, for a Poisson process, τ has an exponential distribution with parameter λ :

$$f(\tau) = \lambda e^{-\lambda\tau} \quad \text{for } \tau > 0. \quad (14)$$

No detailed analysis of the appropriateness of the Poisson process assumption has been undertaken, there being no reason to doubt its applicability in these circumstances.

TROPICAL CYCLONE WIND FIELD

The meteorological characteristics of a tropical cyclone and Australian data on the statistics of the various cyclone parameters are discussed in detail in Ref. 10. The tropical cyclone is essentially an atmospheric phenomenon, developing over tropical seas in mid to late summer. Extremely low central pressures (< 960 mb at M.S.L.), high vortex winds (> 40 m/s) and the presence of an eye are the dominant features of the atmospheric flow structure. The aerodynamics of the

tropical cyclone and the hydrodynamics of the underlying water body are coupled at the water surface by the atmospheric pressure and wind shear stress. The M.S.L. pressure and sustained wind both change significantly with distance from the eye, which itself moves forward, typically in a south-westerly direction in the Coral Sea. The hydrodynamic response is complex and transient and comprises both long waves (surge) and the short waves (wind waves), the latter being of interest in the present context.

According to current wind wave generation theories it is the near surface spectrum of the turbulent pressure fluctuations that is directly responsible for wind wave generation. Information on this aspect of tropical cyclones is just not available although the mean flow pressure structure can be predicted with some confidence. Existing tropical cyclone wind wave theories tend to relate wave generation to the near surface mean flow wind structure, specifically in the SMB approach to W_{10} . The spatial distribution of W_{10} within a moving storm is still the matter of some debate and the parameterised wind field adopted in Ref. 10 will also be adopted here. This is basically the N.H.R.P. tropical cyclone model (4); in Ref. 10 this model has been mathematically formalised and suitably modified to describe a Coral Sea tropical cyclone. The basic storm parameters number four:

- (1) Central pressure p_0 at Mean Sea Level
 - (2) Maximum sustained wind W_{10} at a height of 10 m above M.S.L.
 - (3) Radius to maximum wind R
 - (4) Speed V_E and direction of eye (i.e. track or path)
- and moving wind fields are built up in terms of these parameters. A sample wind field is given in Ref. 11.

Following Russell, the next step is to assign, from the historical data or otherwise, suitable probability distributions to these four parameters. The adopted procedure to some extent follows Sobey, Harper and Stark (10) and Stark (12) and is closely related to the available historical data.

Central Pressure. - The Card 13 meteorological data was searched by computer to extract all tropical cyclones passing within 200 n miles of the nominated site. As the Card 13 data does not distinguish between tropical cyclones and tropical disturbances only those "hits" less than or equal to 990 mb have been retained and termed tropical cyclones for the purpose of this study, the less intense disturbances being implicitly considered as non-cyclonic events. It was assumed that the partial duration series so formed followed a Gumbel or Extreme Value Type I distribution, using smallest value criteria: the probability density function (PDF) is

$$f(p_0) = \alpha \exp[\alpha(p_0 - u) - e^{\alpha(p_0 - u)}], \quad (15)$$

where α is the dispersion and u the mode of the Gumbel distribution. These distribution parameters are estimated from the partial duration series by the method of maximum likelihood. Also calculated was the Kolmogorov-Smirnov goodness-of-fit statistic, which measures the suitability of the assumed CDF in describing the observed cumulative frequency histogram. The K-S statistics indicate that the Gumbel distribution is by no means a perfect representation of the historical data. This however

is considered more as a measure of the unsatisfactory nature of the data than a condemnation of the Gumbel distribution. Certainly other extreme value distributions could have been adopted but this would not improve the quality of the data.

Maximum Sustained Wind. - The modified N.H.R.P. model relates V_{10} directly to the central pressure as:

$$V_{10} = K \sqrt{\frac{P_{\infty} - P_0}{\rho_a e}} \quad (16)$$

No probabilistic interpretation is introduced into this choice. The M.S.L. ambient pressure p_{∞} has been taken as 1013 mb, the wind coefficient K has been set at unity (Ref. 10) and ρ_a is the mass density of air.

Radius to Maximum Wind. - Russell adopts a log-normal distribution for R from U.S. data for the Gulf of Mexico but equivalent Australian data is not available. Card 13 data has an entry for distance from storm centre to position of maximum *reported* mean wind in the area influenced by the tropical cyclone. This is of course unlikely to be the radius of maximum winds, as the data recording network together with additional ship reports provide only a very sparse coverage in northern Australia. In many cases also this entry has been left blank, in implicit recognition of this problem. The feasibility of relating R to central pressure and latitude is discussed in Ref. 10, but not adopted. It was concluded that a subjective decision on R must be made, which was to set it at 30 km for all Coral Sea tropical cyclones with no regional variation. This approach was also adopted herein.

Storm Track. - The Card 13 data is somewhat more helpful on this aspect although it is still not entirely adequate. Russell, for the Gulf of Mexico, adopted a Normal distribution for storm speed V_g , a uniform distribution for coast crossing position and a linear relationship between coast crossing heading and position; the Australian data is insufficient to allow such a detailed description of storm movements but it is possible to make some reasonable assumptions.

The data is entered as position co-ordinates (latitude and longitude) at various times throughout the life of the tropical cyclone, one such entry per card. The time spacing between cards is a minimum of 3 hrs but is often much longer. In the case of storm speed the data that can be extracted is rather scattered but an average value of 28 km/hr was established in Ref. 10 and is also adopted here. The data was considered too scattered to attempt the adoption of a distribution about this mean.

Data on coast crossings was also too sparse and too scattered to draw any conclusions. Russell's data was apparently not too much better and he found it necessary to assume a uniform distribution for coast crossing position for landfalling storms. This assumption is quite reasonable and is adopted for landfalling storms herein.

In formal terms the probability of a landfalling tropical cyclone crossing the coast a distance y from a nominated coastal site with

equal probability over a length of coast extending a distance L both sides of the site is described by the PDF

$$f(y) = \begin{cases} \frac{1}{2L} & \text{for } -L \leq y \leq L \\ 0 & \text{elsewhere.} \end{cases} \quad (17)$$

The remaining decision concerns storm direction and here some very subjective assumptions are necessary as the Card 13 data is very inconclusive (10). It has been assumed that only one-half of all tropical cyclones passing within 200 n miles of the site actually cross the coast in this region and that these storms cross essentially at right angles to the general line of coastline; the remaining storms are assumed to move away from the site and not to unduly influence the coastal wave climate. In formal terms again the probability of a land-falling tropical cyclone, given that the storm exists, is described by the Bernoulli distribution: the probability mass function (PMF) is

$$p = \begin{cases} 0.5 & \text{for a landfalling storm} \\ 0.5 & \text{for a non-landfalling storm,} \end{cases} \quad (18)$$

TROPICAL CYCLONE WIND WAVES

Existing wind wave generation theories attempt to describe a process of gradual energy transfer to the sea across the air-sea interface, in which both wave height and wave celerity gradually increase under a steady wind towards some plateau level determined by the physical characteristics of the atmospheric boundary layer (represented by W_{10} alone in the SMB approach). The time scale of the energy transfer process is measured in hours and the atmospheric forcing must be maintained for the wave to continue to grow as it propagates across the sea. Should the wave impinge on a shoreline (a fetch limitation) or should the atmospheric forcing not be sustained (a duration limitation), then the wave may cease to grow before it reaches the plateau level, termed a fully arisen sea. Sustained forcing beyond the stage where there is sufficient time and sufficient fetch to attain the plateau level will not further increase the height or celerity of the wave. In physical terms the waves have been built up to a limiting steepness beyond which further energy transfer is dissipated in wave breaking.

Wave decay in deep water however is an even more gradual process. Swell waves behave almost as an ideal fluid and may propagate over hundreds of kilometres of ocean without appreciable decay. An opposing wind would of course hasten decay.

Wave generation within a tropical cyclone is clearly a very complicated process. Field observations are very sparse and rarely amount to more than water level versus time traces at a handful of sites. The spatial structure of the storm largely determines the distribution of wind waves and although peak waves do not necessarily coincide with peak wind velocities, it is implicit that there is a gradual decay away from the region of maximum waves. In deep water well beyond the edge of the continental shelf the spatial distribution of wind waves about the storm eye is thought to be broadly axi-symmetric, except for the forward motion of the storm, in a similar manner to the spatial

distribution of sustained wind within the tropical cyclone. Fetch limitations imposed by the coastline as the storm crosses the continental shelf would have a substantial influence on this structure; the Great Barrier Reef introduces further fetch limitations and further complications. The spatial distribution of wind waves over the continental shelf will certainly be different from the offshore situation. A numerical model developed by Cardone, Pierson and Ward (2) to predict the directional spectra of hurricane-generated waves largely confirms this general description.

MODIFIED WILSON MODEL

The Cardone et al model is based on the numerical integration of the wave energy balance or radiative transfer equation. A much less time consuming though certainly less satisfactory approach is to represent the developing sea conditions in terms of just significant wave height rather than directional spectra. Such an approach can be based on the SMB empirical forecasting equations, rather than wind wave generation theories. This was in essence the approach adopted for non-cyclonic conditions.

Wilson (14) has proposed a numerical technique, based on the SMB equations, for estimating deep water wave generation by a wind system that varies in both space and time. Waves are implicitly assumed to propagate along a *straight line* path in co-ordinate direction s , along which the wind W_{10} varies with both position s and time t . The method also assumes that local wave conditions are uniquely described by the significant wave height H . The method adopted herein is essentially Wilson's except that due consideration has been given to the mathematical formulation of the problem and the consequent numerical integration.

In mathematical terms the wave generation process is assumed to be described in deep water by two simultaneous functional relationship of the form

$$H = H(t, W_{10}) \quad (19a)$$

and

$$C = C(t, W_{10}) \quad (19b)$$

where $W_{10} = W_{10}(s, t)$. When W_{10} is a constant, Eqs. 19 are identical to the SMB Eqs. 11 to 13. When W_{10} is not a constant the rate of change of H and C with time is

$$\frac{dH}{dt} = \frac{\partial H}{\partial t} + \frac{\partial H}{\partial W_{10}} \cdot \frac{dW_{10}}{dt} \quad (20)$$

and

$$\frac{dC}{dt} = \frac{\partial C}{\partial t} + \frac{\partial C}{\partial W_{10}} \cdot \frac{dW_{10}}{dt} \quad (21)$$

At a particular position s , W_{10} is a function of t only:

$$\frac{dW_{10}}{dt} = f(s, t) \quad (22)$$

where the function $f(s, t)$ is specified uniquely by the adopted moving wind system. The wave being generated travels at the instantaneous group velocity C_g ($=\frac{1}{2} C$ in deep water):

$$\frac{ds}{dt} = C_g \quad (23)$$

Eqs. 20 to 23 form a system of four simultaneous ordinary differential equations that can be integrated numerically in time by the Runge-Kutta method. Following Wilson in spirit but not in detail the partial derivatives on the right hand sides of Eqs. 20 and 21 can be estimated from the deep water SMB equations. The details can be found in Ref. 11.

There is some difficulty with the SMB equations when the wind opposes the direction of wave propagation for a period of time. The SMB equations themselves are strictly inapplicable but numerical integration remains continuous - $\frac{dH}{dt}$ and $\frac{dC}{dt}$ become negative, H and C both decrease and eventually a negative wave height is predicted. Physically of course this would not happen but there would be some attenuation. A conservative approach to this difficulty is adopted by setting the right hand sides of Eqs. 20 and 21 to zero whenever a negative value is computed.

The remaining problem in the mathematical formulation is the specification of suitable initial conditions at $t = 0$. It is assumed in general that the wave is initiated in still water, i.e.

$$H = C = s = 0 \text{ and } W_{10}(0,0) \text{ at } t = 0.$$

MAXIMUM SIGNIFICANT WAVE AT NOMINATED SITE IN A TROPICAL CYCLONE

The application of the above mathematical model to the estimation of tropical cyclone wind waves on the continental shelf is relatively straight-forward. Given the storm central pressure and track, a moving wind system is predicted. According to the Wilson model any straight line drawn across the continental shelf will represent a fetch along which a wave will propagate. It is a simple exercise in trigonometry to determine at any time from the moving wind field the wind speed component directed along the adopted fetch line; this becomes the local $W_{10}(s,t)$. Interest is largely centred on coastal sites and all waves arriving at such sites are assumed to have been initiated at the inner fringe of the Great Barrier Reef; no wave energy is assumed to penetrate beyond the Reef from the Coral Sea. To avoid the necessity to consider shoaling and refraction in the wave model the nominated coastal site is assumed to be a near shore deep water site typically 10 km offshore such that shallow water effects need not be considered; wave routing shoreward from this point would need to consider shoaling, refraction and wave breaking to arrive at a site design wave.

For a particular near shore site a number of radiating straight-line "fetches" can be drawn towards the Reef and waves can be computed along each of these fetches in turn. Under the complicated forcing resulting from the passage of a tropical cyclone, wave energy can reach a site from potentially all points of the compass, contributing to the local directional spectrum at that time. The significant wave height at that particular time is an integral measure of the directional spectrum. The wave model predicts significant waves arriving at the coastal site at a number of different times from a number of different

directions; what to take as *the* maximum significant wave at the site is not particularly clear. The adopted procedure outlined below attempts to take some account of the development of the directional spectrum in the adoption of the maximum significant wave:

1. Radiating fetch lines are drawn from the coastal site towards the Great Barrier Reef at 15° spacings.
2. Waves are initiated at the Reef end of these fetch lines every half-hour during the passage of a tropical cyclone.
3. The two waves reaching the coastal site respectively before and after each integral hour along each fetch are interpolated to estimate the wave height for that fetch at that hour. Interpreting the radiating fetches as the contributions to the directional spectrum at the site at that time, an appropriate estimate of the wave height at the site at that integral hour is the root mean square value of the respective fetch contributions.
4. The maximum significant wave height for the particular site and storm track is taken as the highest value computed in 3 above; it typically occurs at one hour before storm landfall.

A computer program was developed for this purpose and could be used in the wave simulation procedure. However it was rather time consuming and it was decided instead to develop a somewhat simplified model of the situation in the form of a "universal" maximum significant wave profile that would obviate the need for such an extreme computational exercise.

COASTAL PROFILE OF MAXIMUM SIGNIFICANT WAVE

The steps adopted in the construction of a coastal profile of maximum significant wave height during the passage of a landfalling tropical cyclone were as follows:

1. The appropriate region of continental shelf between the Queensland coast and the Great Barrier Reef is idealised to a straightline coast and a straightline Reef perhaps angled to the coast and at a distance offshore from the site. The water over the continental shelf is assumed deep in the sense of the SMB forecasting equations.
2. Passage of a landfalling tropical cyclone across the continental shelf is assumed to be satisfactorily represented by storm movement at right angles to the straightline coast from sea to land.
3. A number of nearshore deep water coastal sites 10 km offshore are considered at 25 km spacings for distances N and S of landfall.
4. The maximum significant wave height was estimated at each of these coastal sites for storms with central pressures of 990 mb, 960 mb and 930 mb respectively. A typical result, for Cleveland Bay at Townsville, is shown in Fig. 5. The shape of these profiles was physically expected and is somewhat analogous to the storm surge profile that is forced by the same tropical cyclone. The waves peak approximately a radius of maximum winds to the south of the landfall position. In the range of central pressure considered there appeared to be an approximate linear relationship between increase in wave height at a particular position and decrease in central pressure.

TROPICAL CYCLONE WAVE SIMULATION

The steps involved in the tropical cyclone wind wave simulation can be summarised as follows:

1. Simulate the occurrence of the next tropical cyclone from the exponential distribution (Eq. 14) by the Monte Carlo procedure.
2. Simulate storm central pressure from the Cumbel distribution (Eq. 15) below 990 mb by the Monte Carlo procedure.
3. Simulate the storm track from the Bernoulli distribution (Eq. 18) by the Monte Carlo procedure. If not a landfalling storm return to the simulation of non-cyclonic conditions. If a landfalling storm simulate the coast crossing position from the uniform distribution (Eq. 17) by the Monte Carlo procedure.
4. For a landfalling storm predict the maximum significant wave height at the site from Fig. 5 or its equivalent for another site.

TYPICAL RESULTS

Some 5000 years of statistically likely wind wave records, nominally from 2001 AD to 7000 AD, can be simulated following the methodology described above. Typical results can be found in Ref. 11. While tropical cyclones are clearly responsible for the majority of the very high waves, non-cyclonic conditions make a dominant contribution to the long term statistics in the moderate wave height range.

The resulting significant wave height - average recurrence interval curve for Cleveland Bay at Townsville is shown in Fig. 6. The tendency towards a bi-modal character again illustrates the separate contributions to the long term statistics from cyclonic and non-cyclonic conditions. Such a curve would be appropriate for design purposes.

The procedures adopted for the wind wave simulation methodology will nominally estimate also the wave period associated with the predicted wave height at any given time. This would considerably increase the computational effort and was not attempted. However if the assumption is made that a fully arisen sea condition exists then a wave period appropriate to a nominated wave height may be estimated from the universal one-dimensional wave spectrum of Pierson and Moskowitz (13). Assuming the distribution of wave heights within the particular storm follows the accepted Rayleigh distribution, the significant wave height can be related to the total spectral energy and hence to the peak frequency or wave period of the Pierson-Moskowitz spectrum as

$$T_p = \pi \left(\frac{5}{\alpha}\right)^{1/4} \left(\frac{H}{g}\right)^{1/2} \quad (24a)$$

where the Phillips constant α is 0.0081. Evaluating the constant term, Eq. 24a becomes

$$T_p = 15.66 \left(\frac{H}{g}\right)^{1/2} \quad (24b)$$

The assumption of a fully arisen sea will not always be valid, in which case Eq. 24 will overestimate the wave period.

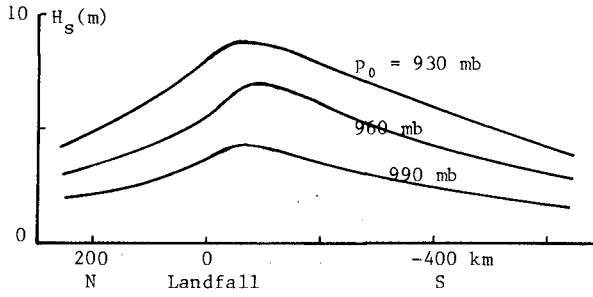


Fig. 5 COASTAL PROFILE OF TROPICAL CYCLONE WIND WAVES NEAR TOWNSVILLE

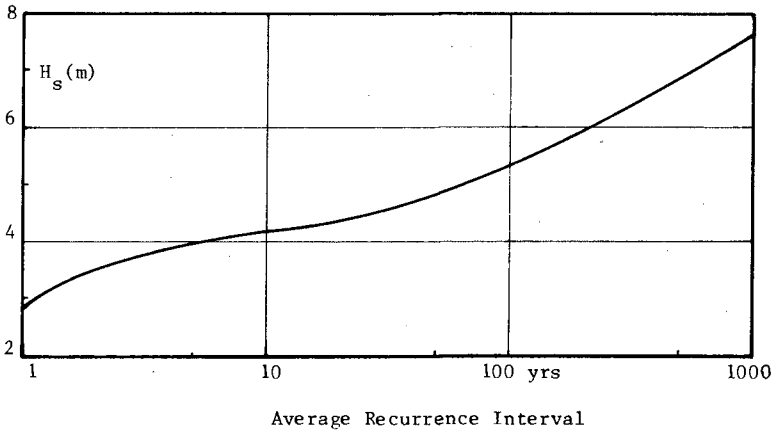


Fig. 6 WIND WAVE RETURN PERIODS FOR CLEVELAND BAY, TOWNSVILLE

CONCLUSIONS

In a general sense mathematical system modelling has been confirmed as a realistic alternative to historical wave data in the prediction of long term wind wave frequencies in a tropical cyclone region. In the vast majority of cases where historical wave data is either not available or covers only a few years, system modelling is clearly a superior approach when maximum advantage is taken of historical wind and tropical cyclone records, as in the present model.

In a tropical cyclone region the importance of non-cyclonic conditions for short and medium term recurrence intervals has been established. The resulting frequency distribution is clearly bi-modal representing the separate influences of cyclonic and non-cyclonic conditions.

More specifically for Australia's Coral Sea coast, the Great Barrier Reef effectively prevents wave penetration on to the continental shelf from further offshore and provides a significant fetch limitations on locally generated wind waves.

ACKNOWLEDGEMENTS

The financial support and active participation of Blain, Bremner and Williams Pty. Ltd., Consulting Civil and Structural Engineers, Brisbane and of the Townsville Harbour Board is sincerely acknowledged.

REFERENCES

1. Bureau of Meteorology, "Data Held in Computer Compatible Form", Melbourne, undated.
2. Cardone, V.J., Pierson, W.J. and Ward, E.G., "Hindcasting the Directional Spectra of Hurricane-Generated Waves", *Jnl. Petroleum Technology*, AIME, 261, 1976, pp. 385-394.
3. Davenport, A.G., "The Dependence of Wind Loads on Meteorological Parameters", *Proc., Seminar Wind Effects on Buildings and Structures*, Ottawa, Sept. 1967, pp. 19-82.
4. Graham, H.E. and Nunn, D.E., "Meteorological Considerations Pertinent to Standard Project Hurricane, Atlantic and Gulf Coast of the United States", U.S. Weather Bureau, National Hurricane Research Project, Report 33, 1959.
5. Kisiel, C.C., "Time Series Analysis of Hydrologic Data", *Advances in Hydroscience*, 5, 1969, pp. 1-119.
6. Matalas, N.C., "Mathematical Assessment of Synthetic Hydrology", *Water Resources Research*, 3, 1967, pp. 937-945.
7. Nolte, K.G., "Statistical Methods for Determining Extreme Sea States", *Procs.*, 2nd Int. Conf. Port and Ocean Engineering under Arctic Conditions, University of Iceland, 1973, pp. 1-38.

8. O'Connell, P.E., "General Report-Stochastic and Statistical Models", Procs., Int. Symp. Uncertainties in Hydrologic and Water Resources Systems, Tuscon, 1972, pp. 1363-1403.
9. Russell, L.R., "Probability Distributions for Hurricane Effects", Jnl. Waterways, Harbors and Coastal Engineering Div., ASCE, 97, 1971, pp. 139-154.
10. Sobey, R.J., Harper, B.A. and Stark, K.P., "Numerical Simulation of Tropical Cyclone Storm Surge", Dept. of Civil and Systems Engineering, James Cook University, Research Bulletin No. CS14, May 1977.
11. Sobey, R.J., Rossow, D.J. and McMonagle, C.J. "Long Term Wind Wave Frequencies at Cleveland Bay and Rosslyn Bay", Dept. of Civil and Systems Engineering, James Cook University, Research Bulletin No. CS16, July 1978.
12. Stark, K.P. "Simulation and Probabilities of Tide and Cyclonic Storm Surges", Procs., 4th Australian Conf. Coastal and Ocean Engineering, Institution of Engineers Australia, Adelaide, November 1978, pp 44-48.
13. U.S. Army Coastal Engineering Research Center, "Shore Protection Manual", 1, U.S. Govt. Printing Office, 1973.
14. Wilson, B.W., "Deep Water Wave Generation by Moving Wind Systems", Jnl. Waterways and Harbors Div., ASCE, 87, 1961, pp. 113-141.
15. Young, G.K. and Pisano, W.C., "Operational Hydrology using Residuals", Jnl. Hydraulics Div., ASCE, 94, 1968, pp. 909-923.

COMPARISON OF SHIPBORNE WAVE RECORDER AND WAVERIDER BUOY DATA
USED TO GENERATE DESIGN AND OPERATIONAL PLANNING CRITERIA

by

C.G. Graham¹, G.Verboom² and C.J.Shaw²

ABSTRACT

This paper presents the results of recent investigations at three sites where waves have been monitored simultaneously by two commonly used deep-water wave recorders, over a total period of 16 sensor-years. The study confirms earlier statements that there are relative differences between the wave parameters and statistical values calculated from the measurements of the two instruments. However, the large amount of data has enabled the authors to quantify the results in engineering terms and to assess the implications for extreme value analysis, spectral analysis and wave climate operational planning.

INTRODUCTION

A considerable proportion of the instrumental wave recordings collected in Northwest European Waters has been obtained using either shipborne wave recorders (SBWR) or wave-rider buoys (WRB). The offshore engineer, who needs to establish operational and design wave criteria for a particular site, will draw upon the nearest reliable set of wave data, which may have been collected by either or both instruments.

Where a relative accuracy (in terms of gain and offset) of $\pm 10\%$ is acceptable, then the sensor used to collect the measurements is probably immaterial (provided of course it has been properly maintained and calibrated). However, in the situation where a higher degree of accuracy is required then the 'absolute' accuracy of the instrument(s) used becomes a prime consideration.

A number of workers, for example Draper (*ref. 9*) and Van Aken (*ref. 18*) have reported the results of field and laboratory investigations into both the 'absolute' and relative accuracies of the SBWR and WRB. This paper is intended to complement this work, not by comparing a small sample of data, but by presenting the results of an overall examination of simultaneous measurements collected over a total period of 16 sensor-years. It is hoped that these results will provide a useful guide to interpreting SBWR and WRB data, especially where they both appear in the same data set.

PURPOSE OF THE INVESTIGATION

The last 10 years have seen a rapid expansion in hydrocarbon exploration and production activities in the waters of the Northwest European Continental Shelf. In order to carry out these activities as safely, efficiently and economically as possible, a considerable amount of information about the environment is needed. Ten years ago very little measured data were available for the Continental Shelf areas away from the coast (water depths 50m to 200m).

Today, with five to eight years of data from particular sites (though the data return has often only been in the order of 60 to 70%), our knowledge has increased significantly, but it must be realised that the amount of data is, statistically speaking, still limited. To provide the environmental operational and design criteria statistics required by the offshore oil and gas industries to the accuracy and confidence levels often quoted would, from a mathematical point of view, need many more years of data. Since it is totally unrealistic to wait such a length of time, theoretical methods (such as hindcasting and correcting for relative severity) have been developed which compensate for the limited amount of data. It is essential that the accuracy of the measurements themselves should be considered if these methods are to have any significant meaning.

What accuracy levels are required? For most offshore operations carried out by the oil industry a wave height accuracy, in the field and at the planning stage, in the order of $\pm 4\%$ is probably acceptable. However, what is unlikely to be acceptable is an offset or difference in gain between two measuring instruments — particularly at low wave heights — which would create an unwelcome bias to the results of any analysis work. For this situation, it is important to quantify the relative difference between the two instruments.

¹ Environmental Consultancy Section, Marex, Cowes, England. (also Dept. of Civil Eng., University of Southampton, England.)

² Oceanographic Dept., Shell Internationale Petroleum Maatschappij B.V., Den Haag, Netherlands.

The 'absolute' accuracy of wave heights is important for structural design, however, in particular for extreme value analysis. In the formulation of extreme wave height criteria, an accuracy of $\pm 2\%$ is sometimes quoted (e.g. Draper, *ref. 9*). While this degree of accuracy is certainly attainable with individual components in the measurement system, it is doubtful if the system itself is capable of such 'absolute' accuracy. Indeed in high sea states the problem is compounded since the sea surface itself becomes difficult to define.

This apparent need for such high degrees of accuracy is understandable when it is realised that an extra 0.3 metre on the design wave height for an offshore structure (approximately +1% in the Northern North Sea) could increase the cost of the project by as much as \$2 million. While the industry certainly has no wish to under-design, neither does it wish to over-build since this is a waste of both money and scarce resources.

In some respects, all design work is empirical, so that the 'absolute' accuracy of an instrument might be regarded as academic if the data measured by one particular instrument (when fully calibrated) are generally accepted as the standard and are used as a basis for all design work. Measurements from the WRB (manufactured by Datawell) tend to be viewed in this light by some engineers.

When a relative difference appears consistently between two instruments — such as seen between the SBWR and WRB — then there is a real need to quantify the difference and this is the purpose of this paper.

BASIC DESCRIPTION OF THE SBWR AND WRB

The shipborne wave recorder was developed by the UK Institute of Oceanographic Sciences and has been described in detail by Tucker (*ref. 16*). It comprises two pairs of accelerometer and pressure units, one each side of the ship, approximately on the pitch axis. The accelerometers sense the heave of the ship which is itself a measure of the ship's response to waves of wavelength rather longer than the vessel's length, whilst the pressure units sense the short wavelength waves within the length of the ship. The output from the four sensors is combined to produce a wave signal which needs to be corrected for depth attenuation and instrumental response. As described by Van Aken (*ref. 18*), the SBWR has an advantage over the other wave measuring systems in that it is relatively easy to install (although dry-docking is usually necessary). It does have a drawback in terms of accurate calibration, originating from the fact that the wave signal is obtained synthetically from the ship's movement and the water pressure on the vessel's hull.

Details on calibrating and establishing the frequency response of the SBWR may be found in papers by Cartwright (*ref. 1*), Ewing (*ref. 10*), Darbyshire (*ref. 2*) and Van Aken (*ref. 18*).

A new integrated circuit version of the SBWR has recently been designed by I.O.S. and has been tested in service.

In 1965, the Datawell accelerometer Waverider buoy became available. This buoy is spherical, has a diameter of 0.7m (standard size) and produces a wave displacement signal by integrating twice the vertical accelerations of the buoy under the influence of wave action. This signal is then used to modulate a radio transmitter whose transmission can be received up to about 25 km away. The buoy accelerometer is kept in a vertical position by means of a cardanic suspension in a glass sphere filled with fluid.

The buoy itself can be moored in a number of different ways but the most common utilises 15 metres of rubber cord beneath the buoy, connected to a weighted mooring line leading to an anchor weight on the sea bed.

The response characteristics of the WRB are almost constant for wave frequencies between 0.065 Hz (15.4 sec) and 0.50 Hz (2 sec) being within 3% amplitude error, but for higher frequencies this response first increases due to resonance then tails off rapidly (*ref. 3*).

The WRB is not truly 'wave following' since it is not a fixed point reference. It tends to rotate in the horizontal plane with the passing of each wave and in short-crested seas may have a tendency to 'roll off' the wave crests.

DATA SOURCES

The input wave data for this comparison study were collected by the UKOOA Oceanographic Committee over a total period of nearly 16 wave sensor-years using weatherships at three stations on the UK Continental Shelf, as shown in *Figure 1*.

	Position	Water Depth	Data Measured	
			from	to
Stevenson Station	61°20'N., 0°00'E East of Shetlands	159 metres	Feb. '73	Feb. '76
Fitzroy Station	60°00'N., 4°00'W West of Shetlands	122	Dec. '73	May '76
Boyle Station	50°40'N., 7°30'W Celtic Sea	107	May '74	May '77

The following weatherships were used:

Vessel	Length Overall
	<i>metres</i>
m/v Edelstein (<i>later renamed Silver Pit</i>)	41.9
m/v Famita	41.9
m/v Ami	41.8
m/v Jomi	40.9
m/v Skagerak	46.9

Each ship used was fitted with a SBWR and maintained station within 2 miles of a moored WRB. The output from both instruments was recorded simultaneously on paper chart rolls as 15 minute samples every three hours. As an additional data recording method, the wave traces were also recorded continuously on FM analogue magnetic tape.

Both SBWR and WRB instrument sets were subject to regular maintenance and calibration checks. The SBWR transducer depths on the five ships ranged from 1.0 to 1.9 metres below the water line.

DATA PROCESSING

The SBWR and WRB chart roll records were processed on-shore according to the standard Tucker-Draper H₁, H₂ method of hand chart analysis.

A full description of this method is described in Tucker (*ref. 17*) and Draper (*ref. 6*).

From each 15-minute sample, the following wave parameters were computed:—

- H_s Significant Wave Height, the average height of the highest one third of the waves in the sample. H_s is related to the root mean square wave height and the square root of the sea surface energy. In more simple terms, it is approximately the same as the average wave height reported by an experienced observer through visual estimation.
- H_{max} (3 hrs) The highest wave height computed to occur within the 3-hour recording interval by the Tucker-Draper method.
- T_z The Mean Zero Up-crossing Period. This is obtained by dividing the duration of the record (in seconds) by the number of times the wave trace passes through the mean water level in an upward direction.

For the SBWR, a correction is required in the calculations to compensate for depth attenuation and instrumental response. This correction is defined by the equation (*ref. 14*):—

$$K_{SBWR} = 0.83 [1 + (8.8\mu)^{-2}]^{3/2} \exp (\beta\mu^2 d/g) \dots \dots \dots (1)$$

where $\mu = \frac{2\pi}{T_z}$ radians/sec

$\beta = 2.5$ (a dimensionless constant)

$g = 9.81$ m/sec²

$d =$ depth of pressure unit below waterline in metres.



Figure 1 – U.K.O.O.A. Weather Ship Stations

For the WRB, K usually equals 1.0 depending upon the instrument calibration, since the instrument response is generally regarded as constant for the majority of wave frequencies (*ref. 3*).

The following points are worth noting about the data processing method:--

1. If an H_s value is computed using the Tucker-Draper method from each of a series of wave records taken under the same stationary wave conditions, then the H_s values obtained will be found to vary from record to record in a random manner. The value required is the average of the large number of records measured at the same time in the same sea state but since only one reading is usually available in practice, it is important to realise that there is random error associated with each data value computed. The error has been quoted by Draper (*ref. 6*) to be in the order of $\pm 10\%$ (one standard error). The overall effect of this random error, when dealing with many data samples, is smoothed out, so that the long-term wave height distribution of H_s is unlikely to be affected except at the tail of the distribution containing values for the single event samples at the peak of the largest storm.

The implication of this for comparing WRB and SBWR H_s values, computed by the Tucker-Draper method, is that the comparison is 'clouded' by the random error effects which produce appreciable scatter in the H_s data points derived from the two instruments. However, it is expected that a realistic smoothed out relationship between the two instruments can be derived.

2. In the Tucker-Draper method, the computation of H_s is related to the T_z value. Thus any differences in the T_z values computed from the records of the two instruments will also be reflected in the H_s values computed. However, by examining Table 1 of Draper (*ref. 6*) it will be seen that differences in T_z would need to be quite large to affect the value of H_s , so this factor will have only minor influence.
3. In equation (1) above a single coefficient 'K' is derived to correct the SBWR records for the effects of depth attenuation and instrumental response. It can be seen that K is dependent upon values input for β (a constant), d (the transducer depth) and T_z . Their relative influence on 'K' — and hence on the SBWR H_s values computed — is clearly demonstrated in *Figures 2 and 3*.

Figure 2 is for a transducer depth of 1.0 metre below the water line, while *Figure 3* is for 1.75 metre depth. Obviously at the greater depth a larger correction is needed and therefore the value of 'K' used is greater. Curves are also presented in the figures for the range of β values sometimes applied (for these data $\beta = 2.5$ was used). Finally on each graph has been presented a curve for $\beta = 2.5$ and T_z multiplied by 1.25. This curve has been presented to demonstrate that for mean wave periods below about 9.0 seconds, the value of 'K' is very dependent upon any changes in T_z . For example, for $d = 1.0\text{m}$, $\beta = 2.5$ and a T_z of 5 seconds, 'K' = 1.26. However, if a period of 6.25 seconds had been used, then 'K' would only equal 1.09.

4. Since both the Tucker-Draper H_s and SBWR K values are related to T_z , it should be emphasised that the SBWR/WRB comparison study results presented here are generally only true for the particular size of weathership used, the depths of SBWR pressure sensors and the particular wave climatic conditions experienced at the three weather-station locations.

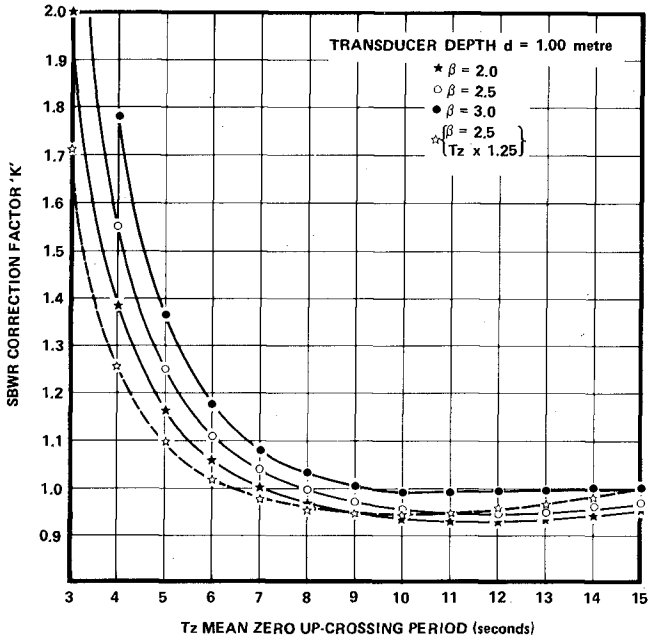


Figure 2 — SBWR Correction Curve — Transducer Depth 1.00m

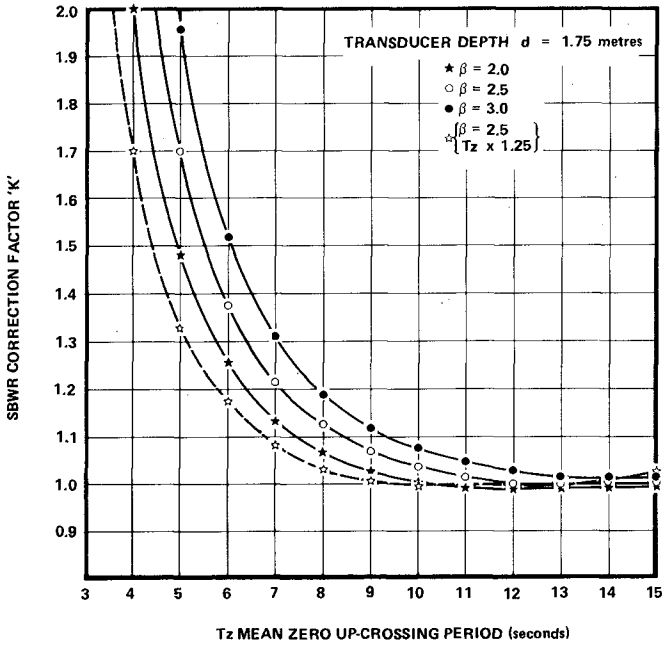


Figure 3 — SBWR Correction Curve — Transducer Depth 1.75m

STATISTICAL METHODS USED TO COMPARE THE SBWR AND WRB PROCESSED DATA

The following statistical procedures were employed to compare the SBWR and WRB simultaneous H_s and T_z values:—

1. STANDARD LINEAR REGRESSION ANALYSIS

This analysis establishes how well a straight line defines the relationship between the two variables 'Y' and 'X'. The 'Y' on 'X' regression analysis computes the equation for a straight line by a least-squares fit parallel to the 'Y' axis, through the data points. The 'X' on 'Y' regression analysis, on the other hand, computes a similar straight line but by a least-squares fit parallel to the 'X' axis.

The degree of scatter and 'goodness of fit' of a linear relationship between 'Y' and 'X' can be defined in terms of the dimensionless linear correlation coefficient, r . When $r = 1$, this indicates a perfect correlation, while $r = 0$ signifies no correlation at all.

Also computed in this analysis is the 'standard error of estimate' which has properties analogous to the standard deviation. For example, in the 'Y' on 'X' regression analysis, the standard error of estimate, S_{yx} , is computed. If we were to construct lines parallel to the regression line of 'Y' on 'X' at respective vertical distances S_{yx} , $2S_{yx}$ and $3S_{yx}$ from it, we should find with sufficient data samples, that there would be included between these lines about 68%, 95% and 99.7% of the sample points.

In the 'X' on 'Y' regression, a similar standard error of estimate is computed parallel to the horizontal axis.

2. MAJOR AXIS LEAST-SQUARES REGRESSION ANALYSIS

In the standard linear regression analysis, two 'best lines' are fitted to the data, the first by minimising the error parallel to the vertical axis and the second by minimising parallel to the horizontal axis. However, in most cases, and in particular for this study, the co-ordinates of the sample data points are in error parallel to both axes together. Therefore, neither of the standard regression analysis 'best lines' is appropriate by itself and even if an arithmetic mean line is computed between them, the result is rather unsatisfactory.

An improved method is to find a line such that the sum of the squares of the perpendicular distances of the points from this line is a minimum. This line is termed the Major Axis line and is described by York (*ref. 20*).

3. MAJOR AXIS ANALYSIS, LINE CONSTRAINED TO PASS THROUGH ORIGIN

For this, the major axis computations are adapted to produce a line constrained to pass through the origin. In this way the relationship between the 'Y' and 'X' data points can be simply defined in terms of the slope of this line. Such an analysis becomes particularly appropriate when more than two variables are compared together, as illustrated by the comparison of three wave sensors in Pitt *et al.* (*ref. 15*).

4. GROUPED CLASS INTERVAL ANALYSIS

The fourth method employed is described as 'Grouped Class Interval Analysis' and was applied in an attempt to see how any differences between 'Y' and 'X' varied from class interval to class interval.

The 'X'-axis is split up into equal intervals. For each of these intervals the mean 'X' and mean 'Y' are calculated together with the standard deviation of 'Y'. Unfortunately this analysis method suffers from the same limitations as the standard 'Y' on 'X' linear regression analysis method in that only scatter parallel to the vertical axis is examined, while the scatter parallel to the horizontal axis is ignored.

5. EQUI-PROBABILITY ANALYSIS

If there are a series of N values of 'X' and N values of 'Y', then these two data sets may be arranged in ascending order:—

$$X_1, X_2 \dots\dots\dots X_m \dots\dots\dots X_n \quad \text{and}$$

$$Y_1, Y_2 \dots\dots\dots Y_m \dots\dots\dots Y_n$$

such that $Q(X_m)$ and $Q(Y_m)$ are the respective cumulative probabilities of X and Y exceeding X_m and Y_m .

If $Q(X)$ is set equal to $Q(Y)$ then an equi-probability analysis can be carried out to determine the relationship between Y and X over the whole of the cumulative probability distribution.

This form of analysis is particularly appropriate since the H_s wave height cumulative probability distribution is often used directly by the offshore engineer in both the planning and design function.

6. EXTREME VALUE ANALYSIS

One method of extreme value analysis is to extrapolate cumulative probability distributions (all data points included) in order to estimate the values for extreme events with return periods of 1, 10, 50 or 100 years. (N.B. by themselves, 5 years or so of wave data are inadequate for this process without some form of mathematical correction for the relative severity of the particular 5 years covered by the measurements.)

For a comparison of SBWR and WRB data it is therefore important to assess the effect of any differences on the results of the extreme value analysis.

The extreme value analysis itself is based on the best fit of the cumulative probability distribution to a particular mathematical equation. In graphical terms, this best fit is reflected in how well the data points making up the distribution plot out as a straight line on the relevant cumulative probability graph paper.

For wave height data a number of different distribution equations are commonly applied. These include the Weibull, log-normal, Gumbel's Third Asymptote and Gumbel's First Asymptote. For this study, the Weibull scale distribution (*ref. 17*) was chosen on the basis of Jenkinson (*ref. 14*).

The SBWR and WRB H_s cumulative probability distribution data points were plotted out on the Weibull scale and a least-squares criterion was used to establish the two 'best fit' lines. These lines were then extrapolated up to the probability levels associated with return periods of 1, 10, 50 and 100 years, making it possible to compare the extreme event H_s values predicted by the SBWR and WRB distributions.

Out of these six comparison methods it was found that the Major Axis Line Through the Origin and the Equi-probability Analyses produced the most meaningful results.

PRESENTATION AND DISCUSSION OF STUDY RESULTS

The statistical methods described were applied in turn to the SBWR and WRB processed H_s and T_z values. Initially each monthly set of data was examined, before carrying out an overall analysis for each of three weathering stations and all three stations combined. The characteristics displayed in the overall analyses were reflected in the monthly data. Though fluctuations were noted from month to month, no significant trend was evident — except of course for a natural bias in the summer months towards lower wave heights compared with the winter months. A sample month of simultaneous H_s and T_z data is presented in *Figures 4 and 5*.

Co-ordinates: Y axis — SBWR (H_s or T_z values)
 X axis — WRB (H_s or T_z values)

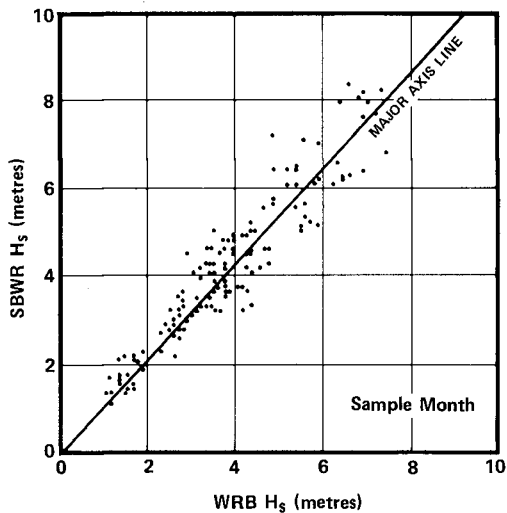


Figure 4 – Comparison of SBWR and WRB – Significant Wave Height

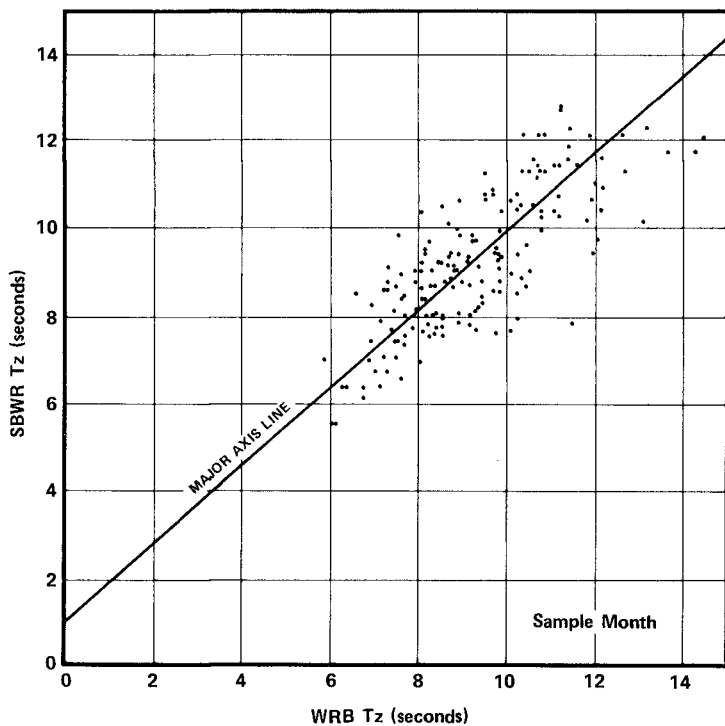


Figure 5 – Comparison of SBWR and WRB – Mean Zero Up-crossing Wave Period

COMPARISON OF SBWR AND WRB SIGNIFICANT WAVE HEIGHTS

Table 1 below presents the results of the linear regression and major axis analyses:

Statistic	Station A	Station B	Station C	All Stations
No. of data point pairs	4273	3350	3860	11,483
Linear correlation coefficient 'r'	0.952	0.942	0.943	0.949
Y on X Linear Regression Analysis				
Slope (M_{YX})	0.975	1.016	1.013	1.002
Intercept (C_{YX})	+0.334m	+0.206m	+0.145m	+0.225m
Standard Error of Estimate (S_{YX})	0.507m	0.539m	0.403m	0.487m
X on Y Linear Regression Analysis				
Slope (M_{XY})	0.929	0.874	0.878	0.899
Intercept (C_{XY})	-0.042m	+0.146m	+0.123m	+0.063m
Standard Error of Estimate (S_{XY})	0.495m	0.500m	0.375m	0.461m
Major Axis Line (Y on X)				
Slope (b)	1.025	1.084	1.079	1.059
Intercept (a)	+0.190m	+0.010m	-0.004m	+0.073m
Standard Deviation of Slope σ_b	0.005	0.007	0.006	0.003
Standard Deviation of Intercept σ_a	0.758m	0.855m	0.703m	0.759m
Major Axis constrained to pass through origin				
Slope (b)	1.077	1.086	1.078	1.080
Standard Error of Estimate	0.364m	0.372m	0.279m	0.340m

Table 1 — Results of Linear Regression and Major Axis Analysis — SBWR/WRB H_s Comparison

The linear regression analysis results presented above reflect the scatter associated with the Tucker-Draper method, quoted earlier at $\pm 10\%$ for the computation of H_s . Some variations in the results from the three stations are noted, in particular with the 'Station A' ordinary major axis analysis. However, the final analysis of the major axis line constrained to pass through the origin produced virtually identical results for all three weather ship locations in that *on average*:

$$H_s\text{SBWR} = 1.08 H_s\text{WRB}$$

Further analyses were applied to see if this relationship varied with wave height; the most meaningful results were obtained from the equi-probability and extreme value analyses. The results for each threshold wave height are set out for each station in Table 2 below:

WRB H _s Threshold Wave Height	Percentage Increase H _s SBWR over WRB			
	Station A	Station B	Station C	All Stations
<i>metres</i>	%	%	%	%
1.0	+18.0	+17.0	+10.0	+14.0
1.5	+17.3	+11.3	+4.7	+10.0
2.0	+11.0	+10.5	+7.5	+10.0
2.5	+11.2	+8.0	+6.8	+8.0
3.0	+9.3	+8.3	+9.0	+7.3
3.5	+8.6	+7.1	+8.6	+7.1
4.0	+7.5	+8.0	+7.5	+8.3
4.5	+6.9	+7.1	+11.3	+8.9
5.0	+6.2	+6.0	+10.0	+6.0
5.5	+5.6	+7.3	+9.1	+5.5
6.0	+3.5	+8.3	+8.3	+8.3
6.5	+4.6	+9.2	+4.6	+6.2
7.0	+6.3	+7.1	+1.4	+7.1
7.5	+3.7	+5.3	-1.3	+5.3
8.0	+6.3	+6.3	-3.8	+5.0
8.5	+7.9	+2.9	0.0	+5.9
9.0	+8.9	+7.8	0.0	+5.6
9.5	+7.9	+6.3	*	+5.3
10.0	*	+5.0	*	+3.0
Return Period				
1 Year	+3.4	+4.4	+1.7	+5.1
10 Years	+3.2	+3.7	+0.8	+4.6
50 Years	+3.6	+3.2	+0.2	+4.3
100 Years	+2.8	+2.9	-0.1	+4.2

*Insufficient data points for computation

Table 2 — Results of Equi-probability and Extreme Value Analyses

The results for all stations combined are presented in *Figure 6*, the left-hand ordinate is scaled in terms of the SBWR threshold wave heights, while the right-hand ordinate is scaled in terms of the percentage increase of the SBWR H_s over the WRB.

The equi-probability analyses do exhibit a fairly constant percentage increase of the SBWR H_s over the WRB for the central band of wave heights. However, at higher wave heights this percentage appears to reduce, particularly at Station C, though the effect is less at Station A and B. The extreme value analysis goes on to confirm the tendency but it must be borne in mind that this latter exercise is bound by two limitations:

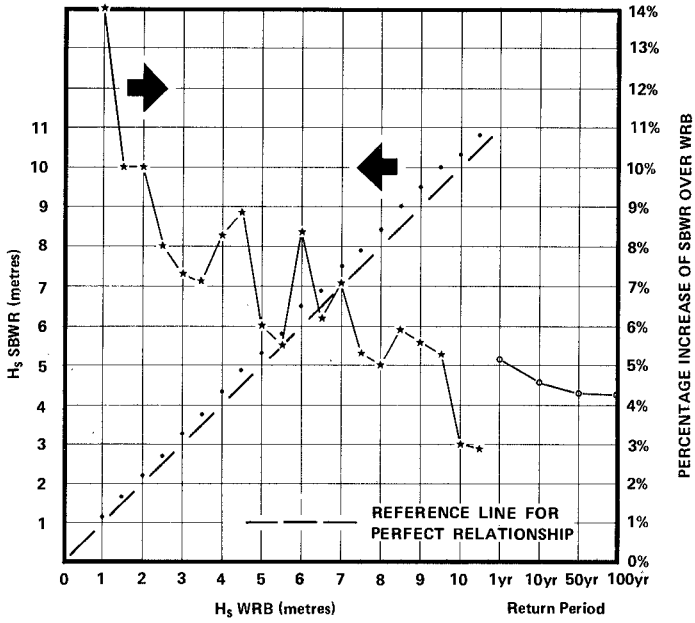


Figure 6 — Results of H₅ Equi-probability and Extreme Value Analyses — All Stations

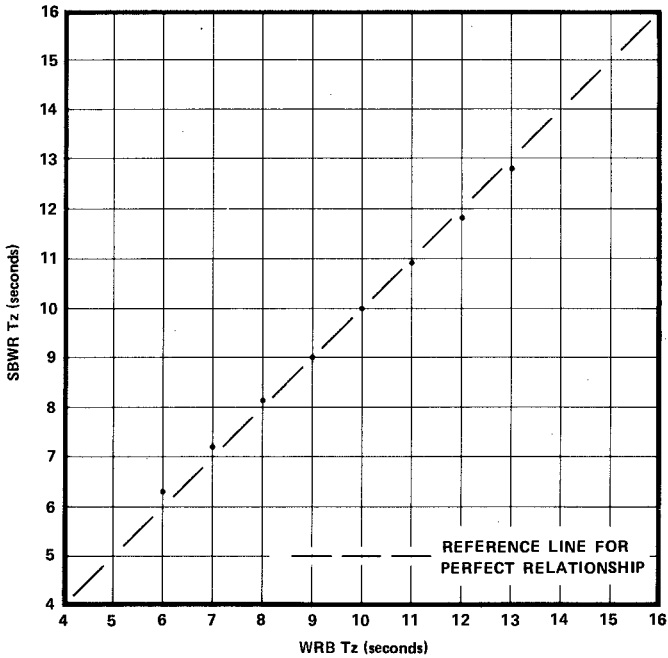


Figure 7 — Results of Tz Equi-probability Analysis — All Stations

1. The data have been constrained to follow the equation of the Weibull cumulative probability distribution
2. The extrapolation process is very dependent upon the scatter in the data points and the 'best fit' line computed.

It would therefore be dangerous to conclude too much from these results but they do, nevertheless, demonstrate the practical implications when interpreting or extrapolating data sets from the two sensors.

The apparent convergence between the SBWR and WRB H_s values as the wave height increases is probably explained by the operation of the SBWR instrument itself. At wavelengths longer than the length of the weathership (which are usually associated with high wave heights), the SBWR accelerometer components predominate (the ship effectively becomes a waverider) while the pressure transducers contribute very little. For seas shorter than the length of the ship (and therefore lower wave heights) the situation is reversed. In other words, from the analysis viewpoint, at high wave heights, the value of 'K' in equation (1), used to correct the SBWR data for instrument response, is approximately equal to 1.0. At lower wave heights, when the wave periods tend to be shorter, the value of 'K' needs to be greater than 1.0 to correct for the now influential pressure transducers.

Further analyses such as comparing wave heights in particular wave period bands were considered but are outside the scope of this particular study.

COMPARISON OF SBWR AND WRB MEAN ZERO UP-CROSSING PERIODS

Table 3 below presents the results of the linear regression and major axis analyses:

Statistic	Station A	Station B	Station C	All Stations
No. of data point pairs	4273	3350	3860	11,483
Linear Correlation Coefficient — 'r'	0.753	0.755	0.814	0.780
Y on X Regression Analysis				
Slope (M_{yx})	0.713	0.706	0.691	0.710
Intercept (C_{yx})	+2.324 sec	+2.630 sec	+2.656 sec	+2.471 sec
Standard Error of Estimate (S_{yx})	0.926 sec	0.889 sec	0.794 sec	0.879 sec
X on Y Regression Analysis				
Slope (M_{xy})	1.611	0.807	0.959	0.856
Intercept (C_{xy})	+0.796 sec	+1.530 sec	+0.112 sec	+1.063 sec
Standard Error of Estimate (S_{xy})	0.978 sec	0.951 sec	0.936 sec	0.965 sec
Major Axis Line (Y on x)				
Slope (b)	0.930	0.915	0.818	0.888
Intercept (a)	+0.591	+0.853	+1.656	+1.035
Standard Deviation of Slope (σb)	0.012 sec	0.014 sec	0.009 sec	0.007 sec
Standard Deviation of Intercept (σa)	2.496 sec	2.500 sec	1.832 sec	2.228 sec
Major Axis constrained to pass through origin				
Slope	1.002	1.014	1.022	1.012
Standard Error of Estimate	0.721 sec	0.699 sec	0.670 sec	0.699 sec.

Table 3 — Results of Linear Regression and Major Axis Analysis — SBWR/WRB T_z Comparison

The linear regression analysis results — in particular the correlation coefficients in the order of only 0.75 — reflect a considerable scatter in the T_z calculated from the records of the two instruments. Significantly, for all three stations, each major axis line constrained to pass through the origin has a slope of approximately 1.0, thus indicating that *on average* the mean zero up-crossing periods from the two instruments are equal. This apparent equality should be judged only in the context of the associated scatter.

The relatively larger intercept values and slopes less than 1.0 in the equations of the ordinary major axis lines might suggest that the SBWR tends to give longer wave periods. This aspect was investigated further and the most realistic results were produced by the equi-probability analysis. It was found that for all three weatherships, the SBWR and WRB Tz cumulative probability distributions were virtually the same. However, a slight tendency was noted for the SBWR wave periods to be longer than the WRB at low periods, while at high periods the opposite was found. This tendency can be seen in the Tz equi-probability results presented in *Figure 7*.

In effect, all the analyses showed that, *on average*, the SBWR and WRB Tz's are nearly the same, while for individual wave samples, considerable scatter can be expected. This scatter is probably caused by one or more of the following factors acting together:—

1. The SBWR and WRB are not measuring the same waves. Though sample times are simultaneous, the two instruments are separated by anything up to 2 miles.
2. The response characteristics of the weathership in different sea states and combinations of wind-waves and swell will vary and thus might affect the recordings.
3. Ship's heading relative to the sea.
4. The inherently different noise characteristics of the two instruments.

SUPPLEMENTARY ANALYSIS – WAVE SPECTRA

A comparison of simultaneous SBWR and WRB data in the frequency domain is presently under study and has yet to be completed.

It is expected that this work will produce different comparison results from those presented above. It is felt that the prime reason for this will be that in the frequency domain, it is possible to correct for the SBWR instrument response at each frequency component, while in the time domain analysis, the correction is dictated solely by the Tz count.

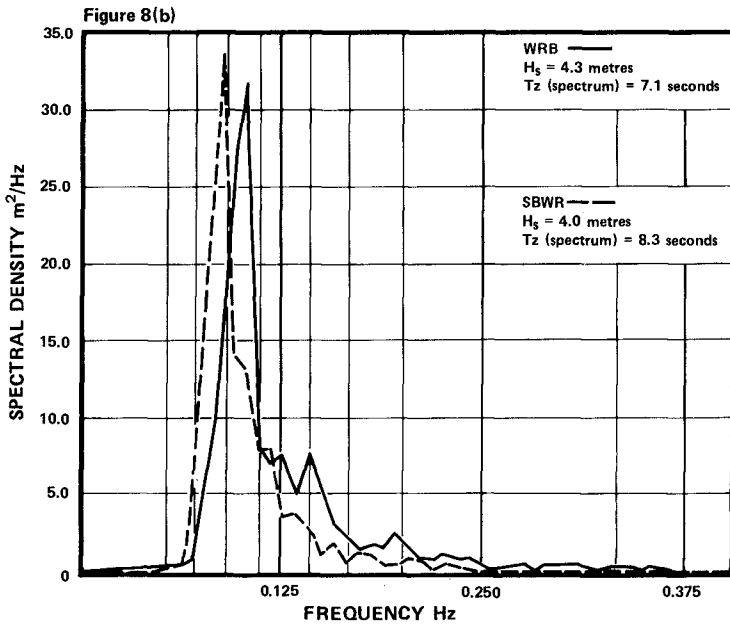
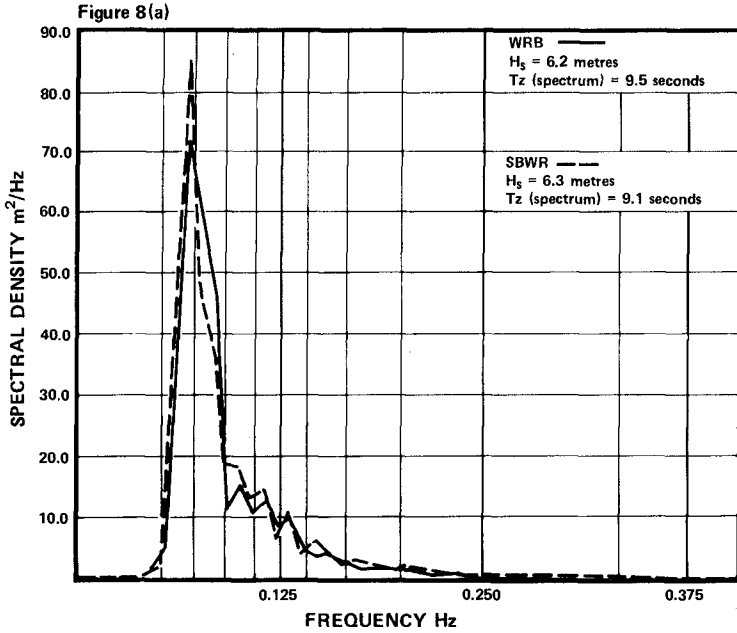
Figure 8(a) shows an example of simultaneous SBWR and WRB spectra which happen to compare rather favourably while *Figure 8(b)* is an example of a not so favourable comparison.

SUMMARY OF CONCLUSIONS

1. On average, the SBWR was found to record significant wave heights 8% higher than the WRB. This percentage difference was greater at low wave heights and less at high wave heights.
2. For most planning and design work it is recommended that this relative difference should be taken into account, especially in the situation where a data set contains a mixture of H_s values from the two instruments.
3. The convergence of the SBWR and WRB data as the wave height increases has important implications for extreme value analysis. The convergence is carried through into the extrapolations and into any extreme values thereby derived. This effect should be considered in the evaluation process to establish design wave height values.
4. On average, it was found that mean zero up-crossing periods from the two instruments were the same. However, appreciable scatter about the average was noted in the results.
5. Care should be exercised in applying the results of this study to significantly different SBWR systems (in terms of vessel length and transducer depth).
6. This study has highlighted the obvious benefit of having two sensors measuring the same parameter. Equipment faults and sensor drifts which did not show up initially often become very apparent when data from the SBWR and WRB were processed and then compared.

ACKNOWLEDGEMENTS

The authors wish to thank the Oceanographic Committee of the United Kingdom Offshore Operators Association for permission to utilize their proprietary wave records in the preparation of this study.



Figures 8(a) and 8(b) — Comparison of Simultaneous Shipborne Wave Recorder and Waverider Buoy Spectra.

REFERENCES

1. Cartwright D.E., 1961
"The Use of Directional Spectra in Studying the Output of a Wave Recorder on a Moving Ship"
Ocean Wave Spectra. Englewood Cliffs N.J. Prentice Hall, 203-218.
2. Darbyshire M., 1961
"A Method of Calibration of Shipborne Wave Recorders"
Deutsche Hydrographische Zeitschrift, 14, Part 2, 56-63
3. Datawell, 1970
"Operation and Service Manual for the Waverider Buoy"
Haarlem Netherlands:- Datawell bv. 1-55
4. Draper L., 1963
"Derivation of a 'Design Wave' from Instrumental Records of Sea Waves"
Proceedings of the Institute of Civil Engineers, 26, 291-304
5. Draper L., 1966
"The problems of Sea Wave Recording"
Proceedings of the I.E.R.E. Conference on Electronic Engineering in Oceanography, Paper No. 3, 1-3.
6. Draper L., 1967
"The Analysis and Presentation of Wave Data - A Plea for Uniformity"
Proceedings 10th Conference on Coastal Engineering, 1, 1-11. New York :- American Society of Civil Engineers
7. Draper L., 1970
"Routine Sea Wave Measurement - A Survey"
Underwater Science and Technology Journal, 2, 81-86.
8. Draper L. and Fortnum B.C.H., 1974
"Wave Recording Instruments for Civil Engineering Use"
Wormley:- U.K. Institute of Oceanographic Sciences.
9. Draper L., Humphery J.D. and Pitt E.G., 1974
"The Large Height Response of Two Wave Recorders"
Proceedings of 14th Coastal Engineering Conference.1, 184-192.
New York:- American Society of Civil Engineers.
10. Ewing J.A. and Hogben N., 1971
"Wave Spectra from Two British Research Trawlers"
National Physical Laboratory Ship, Report No. 150, 1-95.
11. Harris M.J. and Tucker M.J., 1963
"A Pressure Recorder for Measuring Sea Waves"
Instrument Practice, 1055-1059.
12. Institute of Oceanographic Sciences (UK) 1967
"Handbook for the Shipborne Wave Recorder"
National Institute of Oceanography,
Report No. H11, 1-18,
13. Jenkinson A.F., 1955
"The Frequency Distribution of the Annual Maximum (or Minimum) Values of Meteorological Elements"
Quarterly Journal of the Meteorological Society, 81, 158-171.
14. Page E.M. 1970
"The Analysis of Shipborne Wave Records Using an IBM 1800 Computer"
N.I.O. Internal Report No. N24, 1-157
Wormley UK:- National Institute of Oceanography.
15. Pitt E.G., Driver J.S. and Ewing J.A., 1978
"Some Intercomparisons between Wave Recorders"
I.O.S. Report No. 43, 1-63.
Taunton UK:- Institute of Oceanographic Sciences.
UNPUBLISHED MANUSCRIPT
16. Tucker M.J., 1956
"A Shipborne Wave Recorder"
Transactions of Royal Institute of Naval Architects, 98, 236-250.
17. Tucker M.J., 1963
"Analysis of Records of Sea Waves"
Proceedings of the Institution of Civil Engineers, 26, 305-316.
18. Van Aken H.M. and Bouws E., 1974
"Frequency Response of the Shipborne Wave Recorder"
Symposium on Ocean Waves, New Orleans 1974, 1, 281-300
New York:- American Society of Civil Engineers.
19. Weibull W., 1951
"A Statistical Distribution of wide applicability"
Journal of Applied Mechanics, 18, 293-297
20. York D., 1966
"Least Squares Fitting of a Straight Line"
Canadian Journal of Physics, 44, 1079-1086.

CHAPTER 5

WAVE CLIMATE IN SOME ZONES OFF THE BRAZILIAN COAST

Alberto Homsí¹

INTRODUCTION

METEOROLOGICAL FEATURES - The Brazilian coast could be considered a calm area not affected by violent tropical storms. The major meteorological factor in Brazil is the South Atlantic anticyclone, almost permanent, which causes periodical northward heading of cold fronts. A slightly reduced energy and frequency of storms could be observed going up from South coast toward North and could reach the major part of Northeast region.

As a general condition the average monthly frequency of cold fronts passing along the Brazilian coast is higher during the winter - five per month with an average duration of 3 days, decreasing to 2 per month during summer with an average duration of 5 days. During winter high waves could occur between Santos and Macaé caused by a depression near the Rio de Janeiro as the cold front stays at North, before the cold front goes down to South. Fig.1 shows the average flow pattern across Brazil for summer and winter periods and a six days cold front advancing toward North, going into as far as to tropical latitudes during winter time. The daily tracks of the winter cyclones appear on this figure; they do not get beyond latitudes of 40° South.

WAVE MEASUREMENTS - CHARACTERISTICS AND CHRONOLOGY - Instrumental observations of waves in Brazil were initiated in 1962 with one year wave measurements and direction observations in Tramandaí, at the very South of the Brazilian coast. After the occasion thirteen other wave recording stations have seldom been installed simultaneously along the near-shore coastline (See Fig. 2), to collect wave data for some limited period on an ad-hoc basis. These limitations unfortunately occur because wave measurements are intrinsically difficult and normally expensive, restricting in quality the required data. As it could be observed from Fig. 4, only from 1973 the wave measurements have occasionally been taken on a simultaneous basis for two or few more locations. The information so obtained (See Fig. 3), could generally have application for the planning, design, construction and operation of local coastal engineering structures, but could not provide a reliable picture covering all the coast, and could not be used for the research of wave generation.

A NEED FOR A COMPREHENSIVE WAVE MEASUREMENT PROGRAM - Reliable information on waves along the Brazilian coast can only be obtained by installing, at suitable locations, and for sufficient time length (from three to five years, for example), wave recording stations being part of a system to carry out a comprehensive program of obser-

¹Head of Scientific and Technical Support Division-INPH-PORTOBRÁS-MT

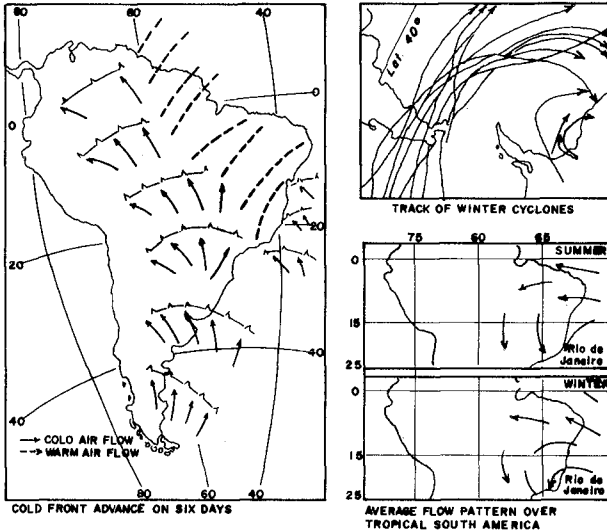


Fig. 1

REF. DHI ARACRUZ REPORT Nº 4



Fig. 2 ○ Wave Measurement Stations in This Paper
⊕ Planned Wave Measurement Stations (BRAZ WAVE)

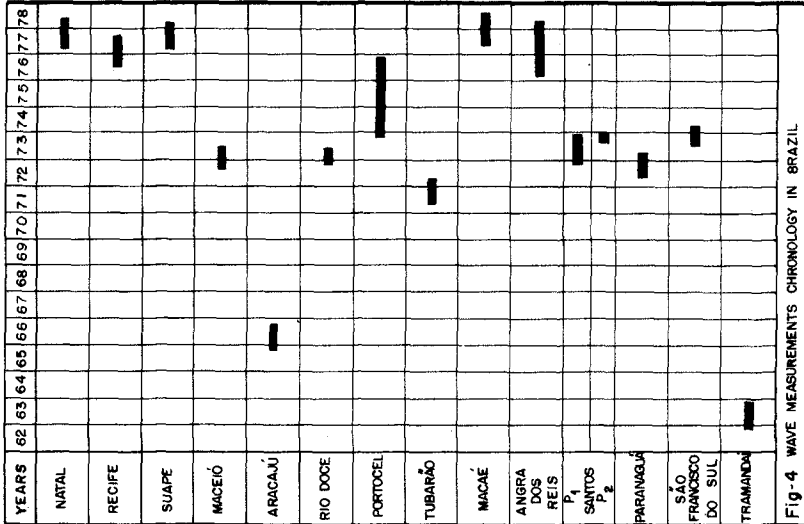


Fig-4 WAVE MEASUREMENTS CHRONOLOGY IN BRAZIL

Fig - 3	MEASURE- MENT PERIOD	NUMBERS OF RECORDS	LOCAL DEPTH	ISEN- CONTOUR DIRECTION	DAILY RECORDS	MEASURE- MENT EFFICIENCY	TYPE OF WAVE RECORDS
NATAL	4/4/77 to 1/4/78 (Mess) 1182 (Proc)	2288	-14	340°N	8	79 %	Pressure
RECIFE	22/7/76 to 19/10/77	585	-10	4°N	2	65%	Ultrasonic
SUAPE	2/3/77 to 2/3/78	2628	-17	12°N	8	90 %	Accelero- meter Buoy
MACEIO	29/8/72 to 31/6/73	—	-10	4°N	8	—	Pressure
ARACAU	9/65 to 8/66	388	-20	35°N	2	33 %	Ultrasonic
RIO DOCE	13/10/72 to 31/5/73	189	P ₁ -22 P ₂ -53	60°N	2	40 %	Ultrasonic
PORTOCEL	10/9/73 to 30/12/74 (Mess) 876 (Proc)	3080	-16	36°N	8	85 % 55 %	Pressure
TUBARAO	1/6/71 to 28/4/72 (Mess) 385 (Proc)	800	-9	40°N	4	65%	Pressure
MACAE	1/6/77 to 31/7/78	499	-17	84°N	2	68 %	Ultrasonic
ANGRA DOS REIS	14/4/76 to 17/3/78	3943	-14,5	90°N	8	75 %	Pressure
SANTOS	17/72 to 7/73	540	-10	65°N	3	49 %	Ultrasonic
P ₁	11/73	108	-15	65°N	3	37 %	Ultrasonic
P ₂	11/73	108	-15	65°N	3	37 %	Ultrasonic
PARANGA	4/72 to 3/73	553	-10	38°N	3	50.5 %	Ultrasonic
SAO FRANCISCO DO SUL	6/73 to 3/74	109	-22	28°N	2	20 %	Pressure
TRAMANDA	10/62 to 9/63	335	-17,50	18°N	2	46 %	Ultrasonic

vations of wave direction and also instrumental measurement of wave heights and periods, to detect annual and seasonal changes taking place in the characteristics parameters of the wave conditions. The more reliable the resulting information on waves, the better a coastal or an offshore structure could be properly and economically designed.

The increasing demand from 1975, for studies of coastal and offshore engineering problems, has led the INPH to undertake an evaluation of how the available wave record observations, specifically made for the design of a coastal engineering work, could be of a possible and reasonable use in adjacent areas; and what kind of overall wave measurement and analysis program would be needed for the entire Brazilian coast, in order to get more accurate wave data to be mainly used in studies with simulation of random sea states, and in the research of wave generation (four random wave generators are going to be installed in the INPH in the beginning of 79, with the cooperation of the Danish Hydraulic Institute).

With this evaluation it was possible to reach a diagnosis of the present state of understanding of the wave climate for the various wave recording locations, as well as an assessment of its usefulness. Experience gained with this evaluation formed the basis for the laying down of basic criteria, methodology and specifications (See Fig. 2) for the Brazilian Wave Measurement Project (BRAZWAVE) in order to derive the wave climatology by means of measurements and calculations. As waves information heavily affect the ultimate cost of a coastal or an offshore project, the cost of the wave information to be obtained with the BRAZWAVE are warranted by: the economy in capital cost of overdesigned structures, the economy in operational costs, major repair costs and costs of total reconstruction of underdesigned structures.

WAVE STATISTICS AND ANALYSIS METHODOLOGY

The wave statistics results presented in this paper are based in the analysis results of about seventeen thousands stripchart wave records of about fifteen minutes, obtained by means of fifteen wave record stations. With the exception of two or three stations where the significant wave heights were calculated by the average of the highest one-third wave, all records were processed according to Tucker-Draper's simplified method. In the case of Natal, the wave records have been processed also by spectral analysis.

WAVE CONDITIONS ALONG THE COAST

SHALLOW WATER WAVE HEIGHT TRENDS - Fig. 5 shows the general wave height trends along the Brazilian coast for H_s max - the maximum significant wave height recorded during the observation period, for NE, E, SE and S directions, for the various seasons and for all seasons - all directions. The highest H_s max being 4,90m, occurred off Tramandaí for E and SE direction during the autumn. In Macaé the highest H_s max, also higher than 4,00m, occurred for S direction du

ring the spring.

As a general feature, from Rio Doce to Natal and for NE direction, the wave heights are less than 2,00m. For the other places, NE waves were not observed as a result of local shore configurations.

Because of the heavy local refraction the waves undergo (caused by the sea bottom topography) no E direction waves were recorded at Santos, Angra dos Reis, Macaé and Tubarão; for the other places, with the exception of Tramandaí and Natal where the waves are higher, the Hs max trend assumes values around 2,00m. SE direction waves have been observed all along the coast. At Tramandaí they range from 4,00 to 5,00m; at Tubarão and Maceió, they stay less than 2,00m, and for all the other places between 2,00 and 4,00m.

Only for Natal and Recife, S direction waves were not observed. For Tramandaí, S.F. Sul, Paranaguá, Portocel, Maceió and Suape the wave heights lie between 1,00 and 2,00m; for Aracaju, Rio Doce, Angra dos Reis and Santos between 3,00 and 4,00m; and for Macaé they stay, between 4,00 and 5,00m.

During the spring at Macaé and Natal, the trends stays around 3,00 and 4,00m; for the other places around 2,00 and 3,00m.

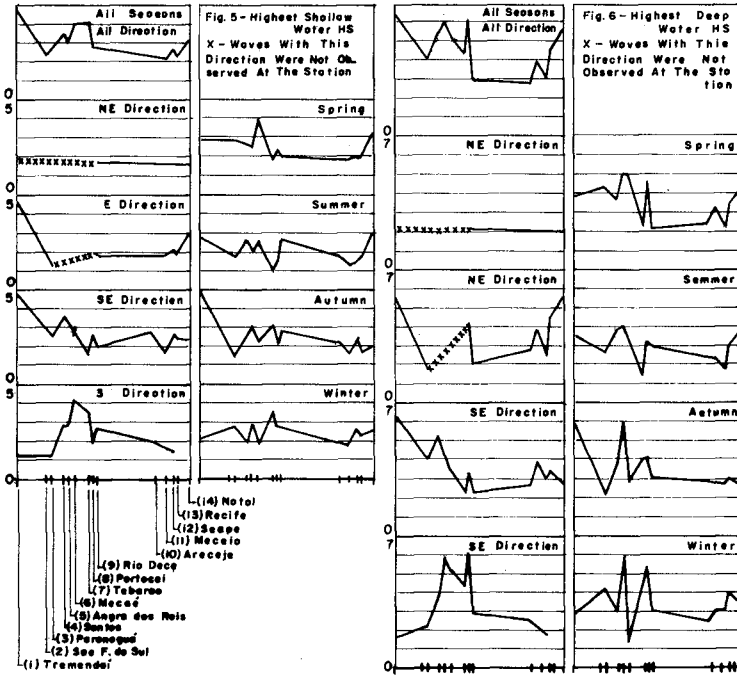
During summer Hs max assumes values between 1,00 and 3,00m. In the autumn for all the places, exception made for Tramandaí, Hs max lies between 1,50 and 3,00m. In winter season all along the coast, the trend lies between 2,00 and 3,00m with the exception of Tubarão where it is about 3,50m. Considering all seasons all directions trend, Hs max values smaller than 2,00 were not observed.

DEEP WATER WAVE HEIGHT TRENDS - Fig. 6 shows the equivalent deep water wave height trends derived after the wave rays have been back tracked from shallow water waves directions. The trends show themselves more irregular than in shallow water. The highest Hs max deep water wave is found off Tramandaí with about 6,50m for E and SE direction during the autumn. Offshore Santos an Hs max of about 5,40m was found for SE direction. In the case of S direction, waves of about 5,50 to 6,00m could be found off Angra dos Reis, Macaé and Portocel, during winter and spring seasons.

As a general feature the Hs max waves become smaller the more northern the place is. An exception is made to S direction waves which pass through a maximum at about Angra dos Reis and Portocel, to decrease towards the north. The shallow water wave trends and mainly the deep water wave trends results should be taken with precaution due to the restrictions imposed by the near-shore method of observation of wave directions. (Visual).

WAVE CLIMATE ALONG THE COAST

The wave statistics presented herein for each location represent a seasonal and or annual reduction for publication, of the monthly results obtained in the whole analysis involved in this paper for the wave parameters: Hs, Hm (maximum wave height of the wave records), Tz, Tc, E (spectral width) and D (wave direction), of the joint-distribution of Tz x Hs, Hs x Tz and Hs x D, the Life-Time-Wave-Distri



bution of H_s and H_m and the exceedance distributions of H_s .

TRAMANDAÍ - Fig. 7 presents some statistics information about the wave climate off Tramandaí coast. The field observations and a first simplified analysis were done by the "Instituto de Pesquisas Hidráulicas" of the Federal University of Rio Grande do Sul for PETROBRÁS (the Brazilian State Oil Company) for the purposes of the hydraulic model studies of the Tramandaí bar.

A range of T_z periods from 5 to 13,5 seconds, not varying for the various seasons were recorded, presenting a slightly asymmetric distribution, with a maximum at about 7,5 seconds. The maximum occurrence for $T_z \times D$ joint distribution is for 7,5 seconds and 105° N. For $T_z \times H_s$ it is 8,5 seconds and 1,5m. The H_s wave heights do show significant variations, tending to be higher in the autumn. Larger H_s wave heights of about 4 to 5m are associated with periods of about 13,5 seconds and larger, and with the SE direction. The H_s wave for a 30 year return period is 6,0m.

PARANAGUÁ - The wave measurements were done by the INPH to give support to the studies of disposal areas for the dredging materials of the new channel entrance of Paranaguá Port.

Fig. 8 shows information about the Paranaguá wave climate. The $H_s \times T_z$ distribution has a maximum percentage of occurrence - 20%, for 1,00m and 5,5 seconds. For $H_s \times D$ the maximum is also 20% for 1,0m and 135° N. From Life-Time-Wave Log-Normal Distribution an H_s of 4,20m was predicted for a return period of 30 years. T_z periods do show a significant variation being longer in autumn with periods up to about 12 seconds.

SANTOS - For Santos the INPH made recordings of sea waves at two points simultaneously. P_2 point at -15,00m and P_1 Point at -10,00m, as a part of a large coastal measurements project for the hydraulic studies of the Port of Santos Expansion Program. The P_2 record station had been in operation only during the winter and spring, what restricts the comparisons which could be made between the wave characteristic parameters distributions of P_2 and P_1 . During the winter the H_s distribution for P_1 and P_2 shows the same range while a larger frequency of occurrence of low H_s could be noted in the case of P_1 . In the case of spring the range of H_s for P_2 station is wider and with larger H_s wave heights.

A comparison between the Life-Time-Wave Log-Normal Distribution of H_m for P_1 and of H_s for P_2 shows that they are almost coincident; anyway, one must be aware that for P_2 point the measurements of summer and autumn were not included and in the case they were, this coincidence should not occur.

The maximum value for H_s was 3,5m at P_2 and 2,40m at P_1 .

The T_z period distribution ranges are about the same, at P_1 and P_2 , during winter, spring and for all seasons.

In the case of P_1 , the most common situation for $T_z \times D$ joint distribution is 12 seconds and 170° N; for $H_s \times T_z$ it is 1,0m and 12 seconds, and for $H_s \times D$, 1,0m and 170° N. At P_2 there is a tendency to associate larger T_z period with 165° wave direction, and larger H_s

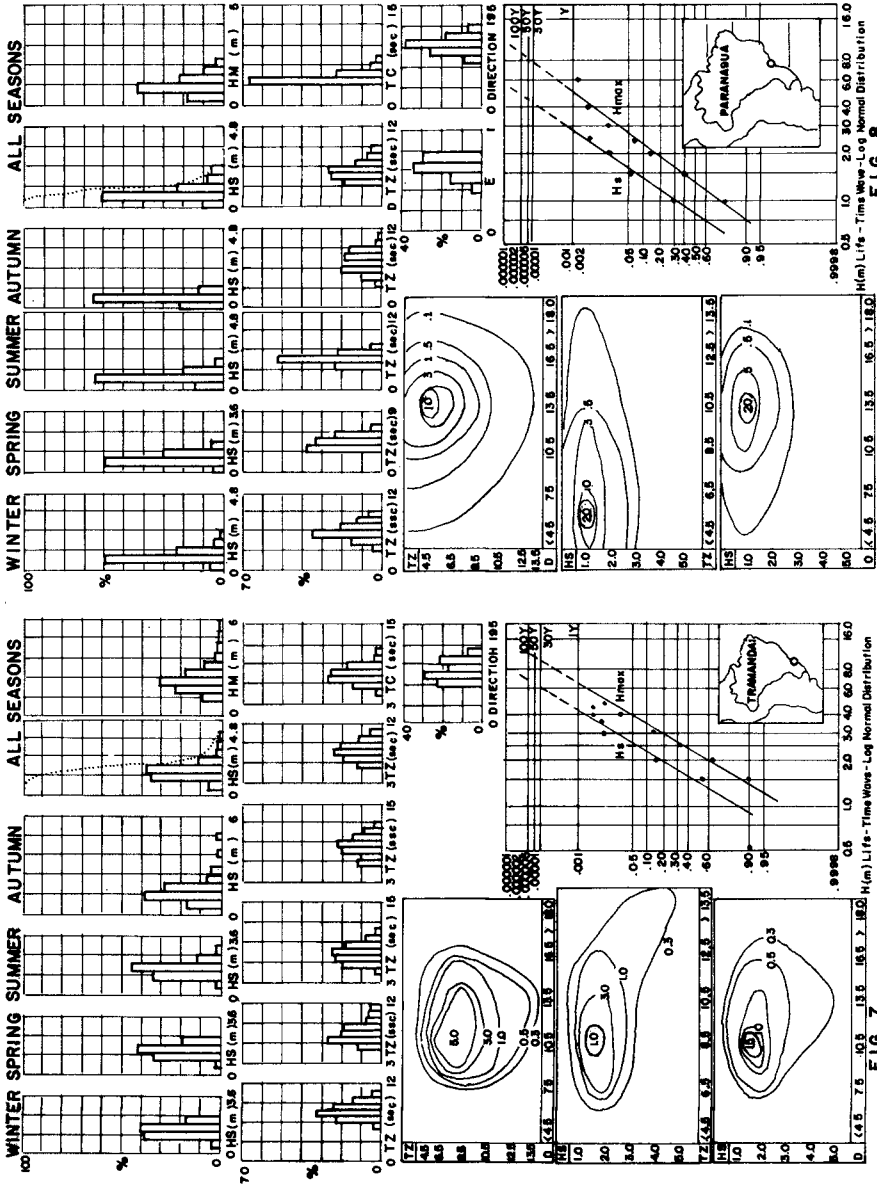


FIG. 7

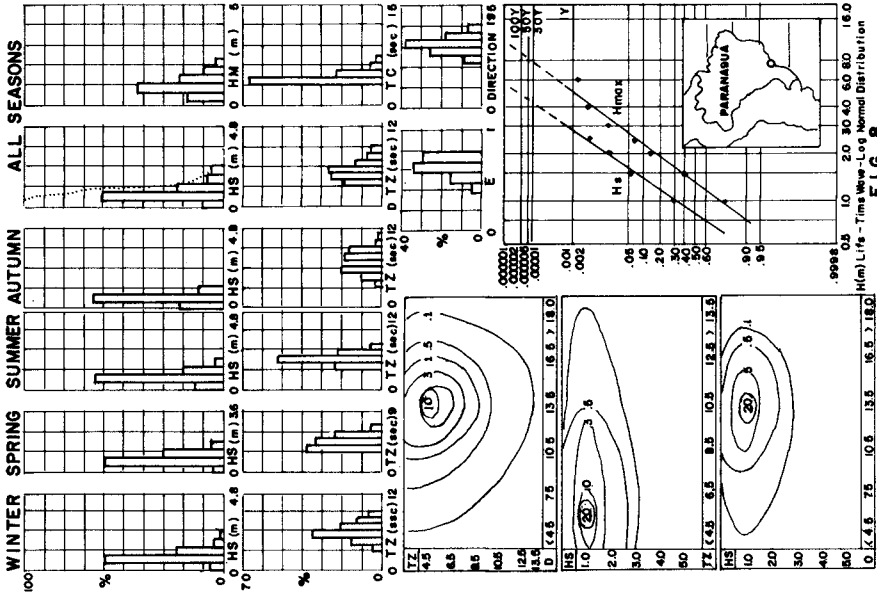


FIG. 8

with southern wave direction and with 12 to 13 seconds T_z periods.

ANGRA DOS REIS - Two years of wave measurements have been made and processed by "FURNAS - Centrais Elétricas S/A" for the purposes of the hydraulics studies of the water intake protection works for the Angra dos Reis Nuclear Power Station. Fig. 10 presents the wave climate based on the first year of measurements.

During the winter and summer no H_s waves higher than 2,00 were observed, while in spring and autumn the waves respectively go up to 2,5 and 3,00m. A prediction of $H_s = 4,00$ m could be observed for 30 years return period.

The range of the T_z distributions become wider going from spring to winter. The most common situation for $H_s \times D$ distribution is a frequency of 45% for the binary 0.5/1,0m and 165° N.

MACAÉ - The INPH was charged by PETROBRÁS (The Brazilian Oil State Company) to develop the hydraulics studies of the Maritime Terminal of Macaé. This terminal, now under construction, should provide 12 sheltered berths for the supply boats of the Campos Oil Field. As a part of the field measurements, wave have been recorded since June 1977. The first year of measurements has been analysed (See Fig. 11). The H_s distribution do show larger waves in the spring with heights of more than 4,00m. During the winter the H_s highest wave is less than 2,00m. Summer and autumn seasons show maximum H_s waves of about 3,00m. With the exception of the spring, when the T_z period distributions range from 4 to 10 seconds, for the other seasons the range is wider, going from 4 to about 14 seconds.

Due mainly to diffractions around nearby islands, the range of wave directions distribution obtained at the site is narrow going from 135° N to 170° N. Because of this, a second wave measurement station is now in operation to get information of waves coming from NE and E direction. The most common situation of the $T_z \times D$ joint distribution was for 8 seconds and 150° N; for the $H_s \times T_z$ it was 1,50m and 8 seconds, and for the $H_s \times D$, 1,5m and 150° N. There is a strong association with higher waves heights and the direction 150° N.

TUBARÃO - CVRD (Tubarão Iron Ore Terminal) made a wave survey during 71/72 and the data were analysed by the CTH (Centro Tecnológico de Hidráulica). Fig. 12 shows the statistics obtained based on the processed CTH data. It is during winter and spring that occur the highest H_s waves being more severe during winter ranging from 0,0 to 4,00m and from 0,5 to less than 4,00m for the spring. Summer is the most calm season. The T_z period distributions range for the various seasons from 6 to 15 seconds. Higher wave heights are associated with 180° N direction and with 10,5 seconds periods.

PORTOCEL - The specialized Terminal of Portocel situated at about 65 Km north of CVRD Tubarão Iron Ore Terminal is now in operation. The wave observations carried out during the period 73/74 were analysed by the Danish Hydraulic Institute (DHI) and those of the period 76/77 by the INPH. Fig. 13 shows some statistics results obtain

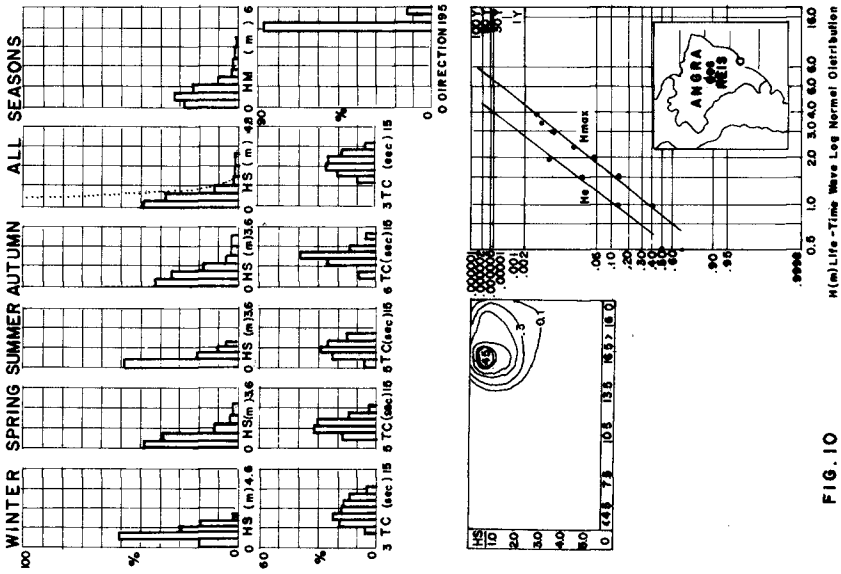


FIG. 9

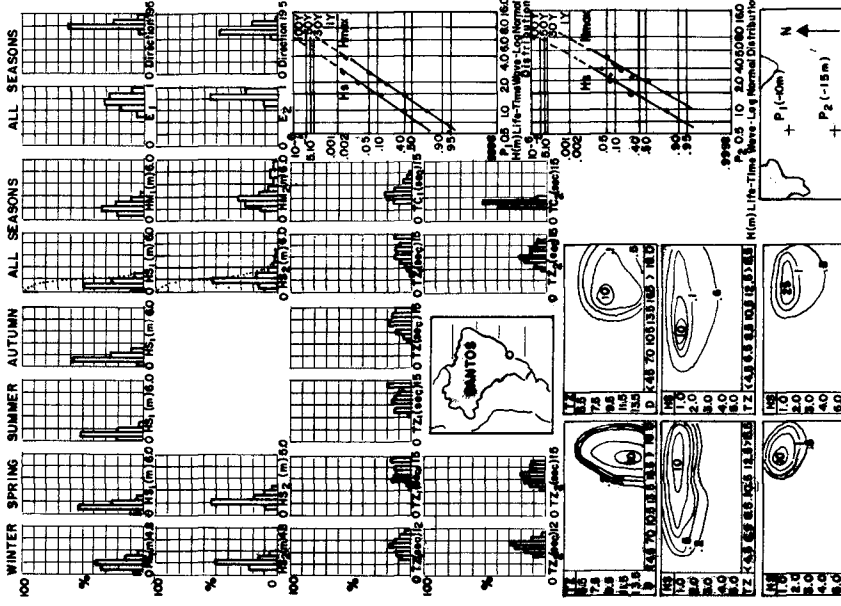


FIG. 10

FIG. 9

FIG. 10

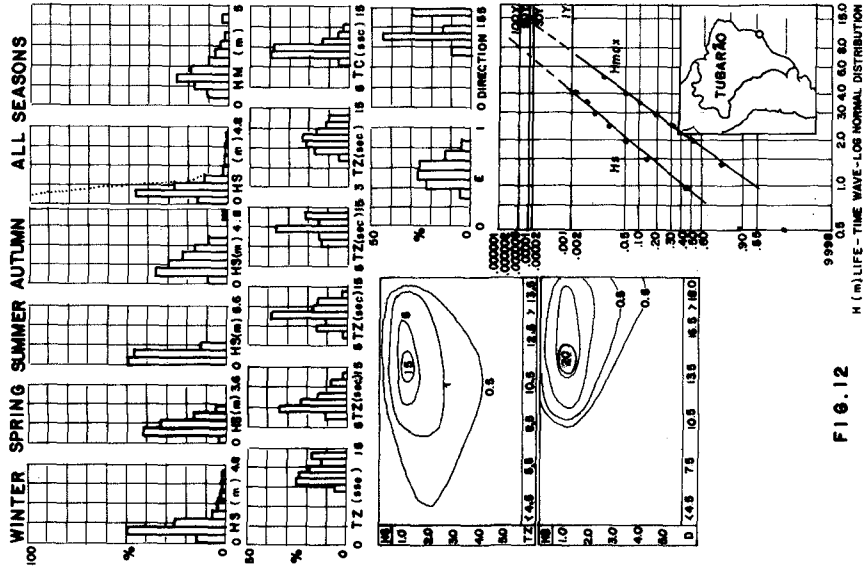


FIG. 11

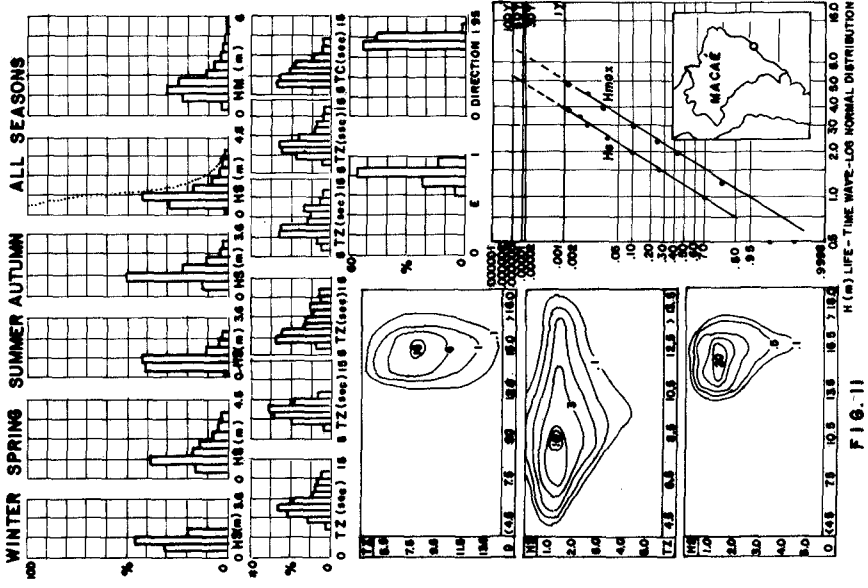


FIG. 12

ed for the period of 76/77, which did not include observation of wave directions.

During the spring and autumn the Hs wave distribution ranges from 0,00 to 2,50m. During the winter the conditions are a little more severe, ranging from 0,00 to 3,00m. In the summer, from 0,0 to 1,20m. With the exception of autumn when the Tz period distribution ranges from 5,5 to 10 seconds, for all the seasons it varies from 4,5 to about 12 seconds. The highest frequency (25%) is associated with the binary 1,0m and 7,5 seconds for the joint distribution Hs x Tz. According to Time-Life Log-Normal Distribution, a significant wave of about 4,40m is predicted for a return period of 50 years.

RIO DOCE - The CTH (Centro Tecnológico de Hidráulica) made wave recordings off Rio Doce at PETROBRÁS P₁ and P₃ oil survey platforms, in the period 72/73, and processed the resulted 189 strip-charts records. Fig. 14 presents some wave statistics information based on the CTH calculations. It is important to note that the observation period was less than one year and it did not include the winter. The most severe conditions were found in the autumn with Hs waves going as high as 3,00m and HM as high as 4,50m. The Tz period distributions ranges from 3 to 8 seconds for the spring, 5 to 13 seconds for the summer, and 5 to 11 seconds for the autumn. The most common situation for the Hs x Tz joint distribution is 1,50m and 6,5 seconds with a frequency of 15%. The direction distribution show gaps due probably to an exaggerated simplification on the wave direction method of observation.

ARACAJU - The wave measurements off Aracaju were made by the IPH of the Federal University of Rio Grande do Sul (Motta, V. F-1966), for the studies of the Off-Shore Terminal (TECARMO) of PETROBRÁS. During the autumn (See Fig. 15) the significant waves went up to 2,50m while during spring, summer and winter less than 2,00m. A maximum wave height of 4,00m were observed during the autumn.

As regard of Ts (Significant Period) the range of the respective distributions become wider going from spring to summer and autumn, narrowing in the winter. Only during the autumn Ts values of about 14 seconds were found. A high frequency of 15% was found for the binary 8 seconds and 120° N; for Hs x Ts the most common binary was 1,50m and 7 seconds with a frequency of 20%. The 30 year return period Hs wave assume a value of about 3,50m.

MACEIÓ - The Danish Hydraulic Institute has carried out the hydraulic studies of the SALGEMA Terminal at Maceió. Fig. 16 presents some wave statistics based on the results of those studies.

The most severe conditions occur during the spring when Hs waves go up to about 2,20m. During autumn and winter the significant waves do not get nearer than 2,00m. In the summer the maximum waves lie at about 1,50m.

The most common situation for the joint distribution of Hs x D is 1,00m and 120° N, with a frequency of 20%.

The Life-TimeWave Log-Normal Distribution of Hs was constructed by

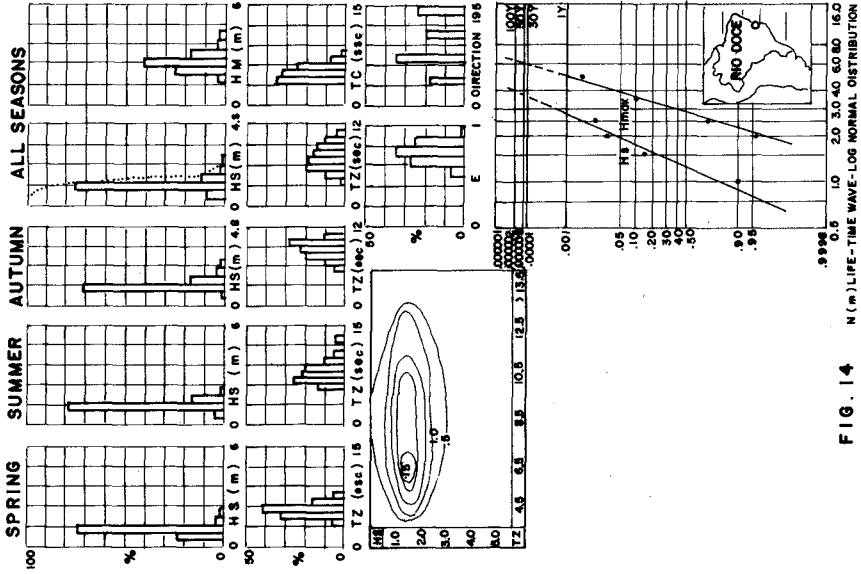


FIG. 13 H (m) Life-Time Wave - Log Normal Distribution

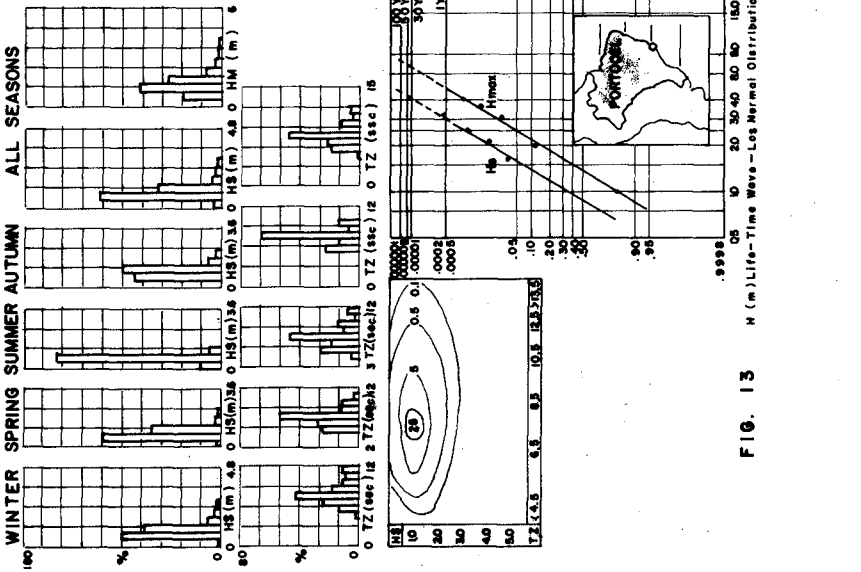


FIG. 14 H (m) Life-Time Wave - Log Normal Distribution

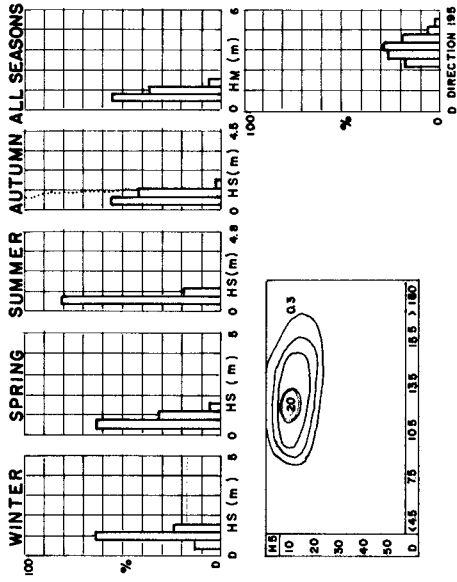


FIG. 15

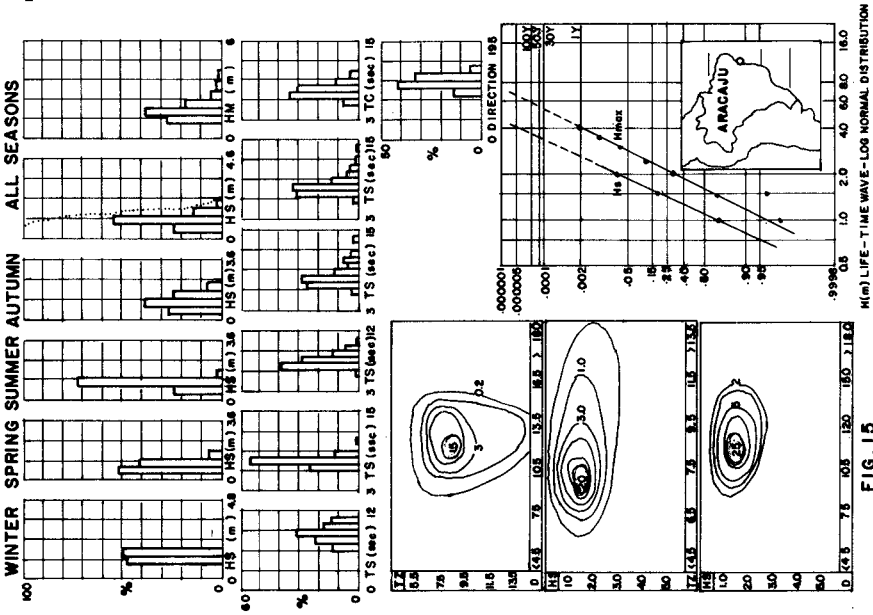


FIG. 16

using the daily H_s highest waves observed. For a return period of 30 years a prediction is made for an $H_s = 2,40m$. For 100 years, $H_s = 2,70m$.

SUAPE - The INPH was charged by the Government of the State of Pernambuco to develop extensive hydraulic studies comprising field measurements, stability and agitation models including mooring forces, by using irregular waves generators, and movable bed model including the coast and the estuary at Suape.

The wave measurements were made by the IPR (Radioactive Research Institute of NUCLEBRÁS) by means of an accelerometer buoy of Datawell. Fig. 167 shows the wave statistics analysis made by the INPH for the first year of measurements. During the autumn and winter the wave conditions are slightly more severe than during summer and spring. The highest H_s wave was about 3,00m and the highest maximum recorded wave about 4,50m.

A maximum T_z period of 10 seconds with a high concentration around 6,5 seconds was observed. The joint distribution show a concentration of 14% for the binary 6,5 seconds and $105^\circ N$; a slight tendency to associate large periods with northern wave directions could be observed. A high concentration of 35% for the binary 1,50m and 6,50 seconds occur, in the case of the $H_s \times T_z$ joint distribution. For the $H_s \times D$ distribution the most common frequency was for the binary 1,50m and $105^\circ N$. A slight association is observed between the highest waves and $135^\circ/150^\circ N$ wave direction. The Life-Time-wave Distribution provides a prediction of a significant wave of 3,90m which might occur over a return period of 30 years.

RECIFE - The INPH made recordings of sea waves at a point off Recife Port and used the Tucker-Draper's method of analysis. In Fig. 18 some wave statistics results obtained may be observed. The significant wave height exceeded 1,00m for 81% of the year. The variation in height for spring, summer and autumn is not significant; only during the winter the conditions are more severe with H_s waves up to 2,50m.

The scatter diagram $T_z \times D$ shows a tendency of wave with NE direction to be associated with periods of 6,5 seconds and waves of SE direction to be associated with periods from 10 to 12 seconds; the most frequent combination was when T_z period was about 6,5 seconds and the wave direction $120^\circ N$. For the $H_s \times T_z$ and $H_s \times D$ distributions the most frequent situations were respectively 1,5m and 6,5 seconds, and 1,50m $110^\circ N$.

The Life-Time-Wave Distribution predicts a significant wave of 3,40m which might occur over a period of time of 30 years.

NATAL - The INPH is developing a comprehensive hydraulic study of the coast of Rio Grande do Norte around Natal and of the estuary of the Potengi river where the port of Natal is situated. The expansion plans include the increasing of the depth of the entrance channel to -12,00m. The wave measurements started at April/77 and is going to continue until April/79.

Fig. 19 include the statistic analysis made by the INPH by using the

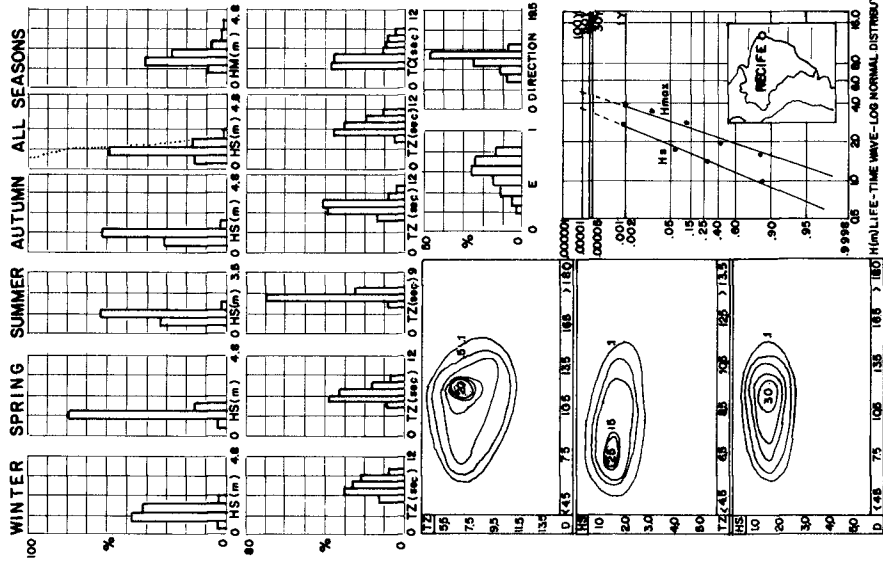


FIG. 17

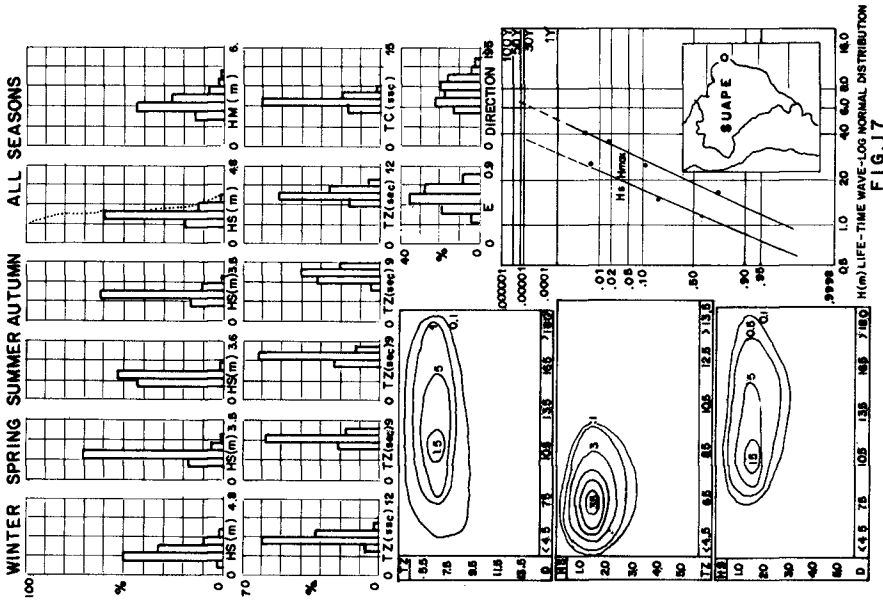


FIG. 18

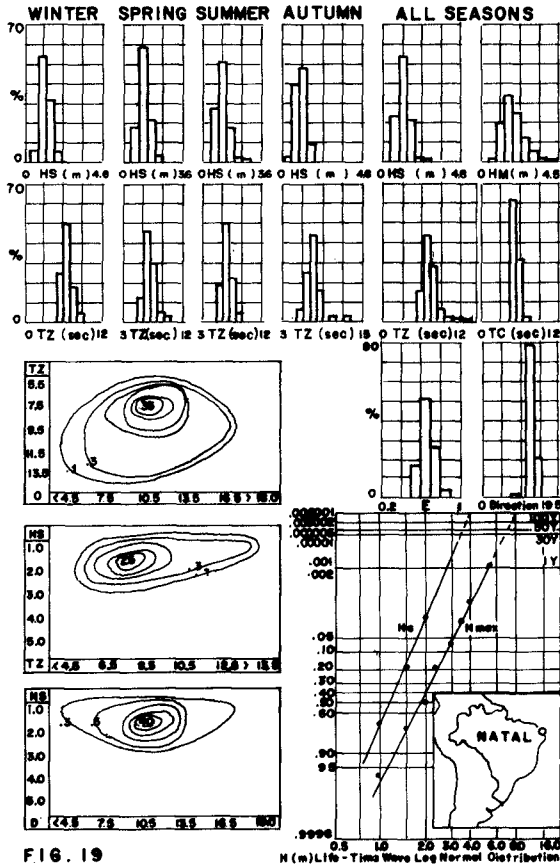
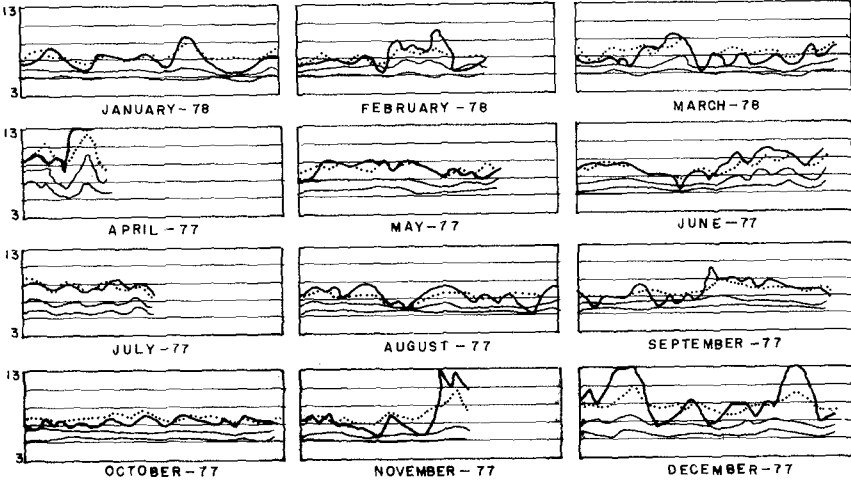


FIG. 19

H (m) Life-Time Wave Log Normal Distribution

NATAL

FIG. 20



TP: —; TZ, TC (SPEC. ANAL): —; TZ (TUCKER - DRAPER):
 COMPARISON OF PEAK PERIOD, ZERO CROSSING AND CREST PERIODS

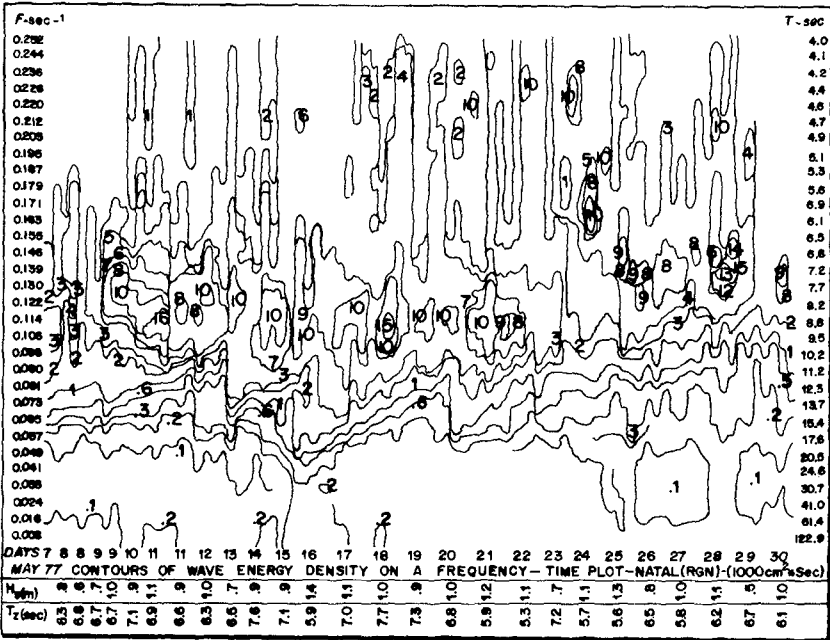


FIG. 21

Tucker-Draper's simplified method. The highest Hs wave was 3,00m and the highest maximum measured wave, 5,00m. During the autumn occur Tz periods of more than 13 seconds while in the other seasons the maximum is 9 seconds. The Hs x Tz distribution shows that there is a tendency to associate small wave heights with high periods; the highest frequency of occurrence is 25% for the binary 1,50m and 7,5 seconds. In the case of Tz x D distribution the most common frequency (35%) is for 7,5 seconds and 105° N. For Hs x D the most common frequency has a very high percentage (40%) for the binary 1,50m and 105° N. An Hs wave of about 3,40m is probable to occur in a return period of 30 years. Fig. 20 presents a comparison of the periods obtained from the analysis of four daily strip-chart records by applying Spectral Analysis: Tp and Tc; and the Tz(.....) periods obtained by the Tucker-Draper method. In this figure the average of the four daily results were plotted. It could be observed that the zero-crossing period obtained by the simplified method has higher values than the obtained by spectral analysis. The trends of the peak period and the zero-crossing (Tucker-Draper) period compare well for the months of January, May, June, July and October, and reasonable well for August, September and November. The relation Tz/Tc for all seasons show values between 1,00 and 2,00 for the case of Tucker-Draper's analysis method, there being about 1% between 1,00/1,20 and 71% between 1,20/1,40. For the case of spectral analysis the relation Tz/Tc shows a range between 1,00/1,60 with 88% between 1,0/1,20 and 11% between 1,20/1,40m.

In the case of Tp/Tz (Tz of the S-A method) relation the values range from a little less than one (6.5%) to a little more than 2,00m (2%). The maximum occurrence is for 1,0/1,20 (45%) and 1,20/1,40 (40%). It is for the lowest value of the periods Tz and Tc that the relation Tz/Tc nearest to 1,00 are observed (due to filter effect of the pressure recorder). This characteristic is more accentuated in the case of the Tz/Tc Tucker-Draper's relation.

Fig. 21 shows the actual spectra for 24 days with significant wave height and zero-crossing period obtained from each strip-chart spectrum. The peak periods generally vary between 7,5 and 9,0 seconds.

THE PROBABLE WAVE INCOMING ENERGY

The wave action and the correspondent total energy at a location vary from season to season and, for each season from year to year. The actual situation is an irregular seasonal and yearly wave action. The information on this variability is important mainly for the cases of littoral process studies and work construction programs. The monthly, seasonal and annual wave energy could be obtained by considering the frequencies f_i of the distribution of the significant waves (Hs), calculating $\sum_i H_s^2 \times f_i$ for each month, each season, each year and for each location.

Fig. 22 shows the relative energy loads for the seasons, and for the year by taking as denominator the average of the annual expected wave energy of each location. The highest annual wave energy load occurred for Tramandaí (1.94) followed by Santos (1.53 for P₂ point) and Macaé (1.36).

In the case of the seasons, the highest seasonal wave energy load for each location occurred, for Tramandaí, in the spring (2.13) followed by Macaé also in the spring (1.98), Tubarão in the autumn (1.72); Suape in the winter (1.67) and Santos in the spring (1.60 for P₂ point).

	NATAL	RECIFE	SUAPE	MACEIO	ARACAJU	RIO DOCE	PORTOCEL	TUBARAO	MACAÉ	ADOS REIS	SANTOS P 1	SANTOS P 2	PARANAGUA	TRAMANDAI
YEAR	1.15	1.14	1.13	0.73	1.09	1.17	0.68	0.91	1.36	0.40	0.73	1.53	0.66	1.94
SPRING	1.15	1.16	0.99	0.67	0.74	0.94	0.68	1.02	1.98	0.43	0.64	1.60	0.74	2.13
WINTER	1.46	1.52	1.67	1.20	1.54	—	0.84	0.93	1.05	0.48	0.98	1.42	0.74	1.81
AUTUMN	0.85	0.86	1.10	0.69	1.28	1.41	0.84	1.72	1.59	0.54	0.76	—	0.42	1.94
SUMMER	1.09	0.84	0.80	0.50	0.90	1.20	0.39	0.38	1.00	0.27	0.59	—	0.53	1.89

ACKNOWLEDGEMENTS

The author would like to express his appreciation to the Management of PORTOBRÁS - Empresa de Portos do Brasil S/A, for making this study possible and to the various organizations involved in the wave measurements in Brazil.

Processing and organization of the data were possible with the help of : Miss B.M. Vargas, J. R. Cerdeira, M.F.C. Dourado, D. Accetta, L.C. Pucci and W.C. Scisinio. Thank for Mrs N.R. Veloso for the drawing and for Miss E.H. Jorge for the typing.

REFERENCES

Barceló , J. L. 1974 On the Portuguese Wave Regimen
Proc. 14th Conference Coastal Engineering, Copenhagen.

Draper, L 1966 The Analysis and Presentation of wave Data a Plea for Uniformity.
Proc. 10th Conference Coastal Engineering, Tokyo.

Draper, L. 1976 Revisions in Wave Data Presentation. ·
Proc. 15th Conference Coastal Engineering, Hawaii

Detle, H. and Führbuter, A.1976 Wave Climate Analysis for Engineering Purpose.
Proc. 15th Conference Coastal Engineering, Hawaii

CHAPTER 6

WAVE CLIMATE STUDY In THE REGION OF THE EAST FRISIAN ISLANDS AND COAST

by Hanz Dieter Niemeyer ¹⁾

1. The investigation area and research aims

The East Frisian Islands and Coast - located at the southern border of the North-Sea - are significantly characterized by a chain of off-shore islands which are separated from the mainland by wide spread tidal flats (FIG.1). Between the islands there are small and deep tidal inlets with strong currents, through which the tidal volume covering the flats is streaming in and out, with a tidal range of about 2,5 m.

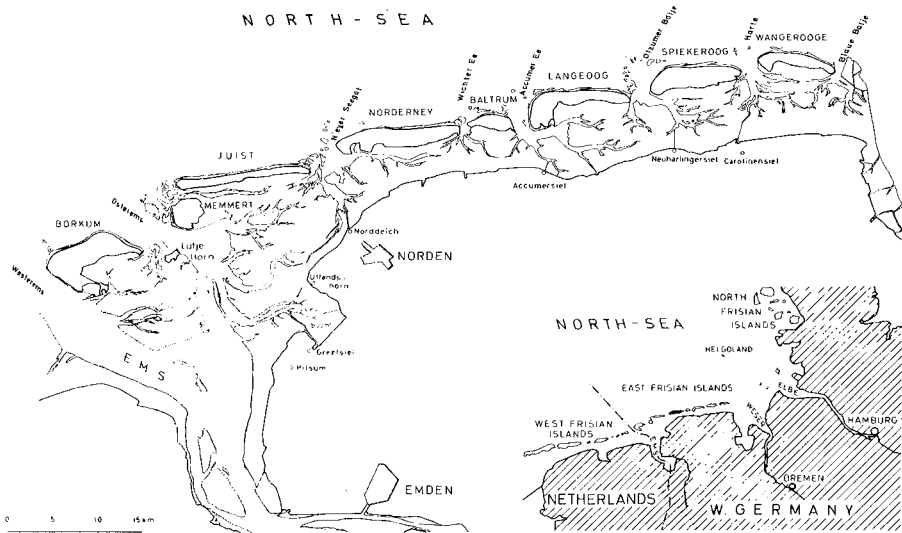


Fig. 1: The East Frisian Islands and Coast

Seaward the tidal inlets are enclosed by an arched chain of separated shoals ranging from the eastern part of one island to the northwestern one of the other island. During the occurrence of high wave conditions these chains have the effect of closed bars where an intensive wave energy dissipation is forced by limited water depth.

Compelled by economic reasons the special research area was restricted to the zone around the tidal inlet Norderneyer Seegat (FIG.2) which significantly represents the

¹⁾ Dipl.-Ing., Head of Hydrographic Branch, Forschungsstelle für Insel- und Küstenschutz (Research Station for Island and Coast Protection), D 2982 Norderney, Germany F.R.

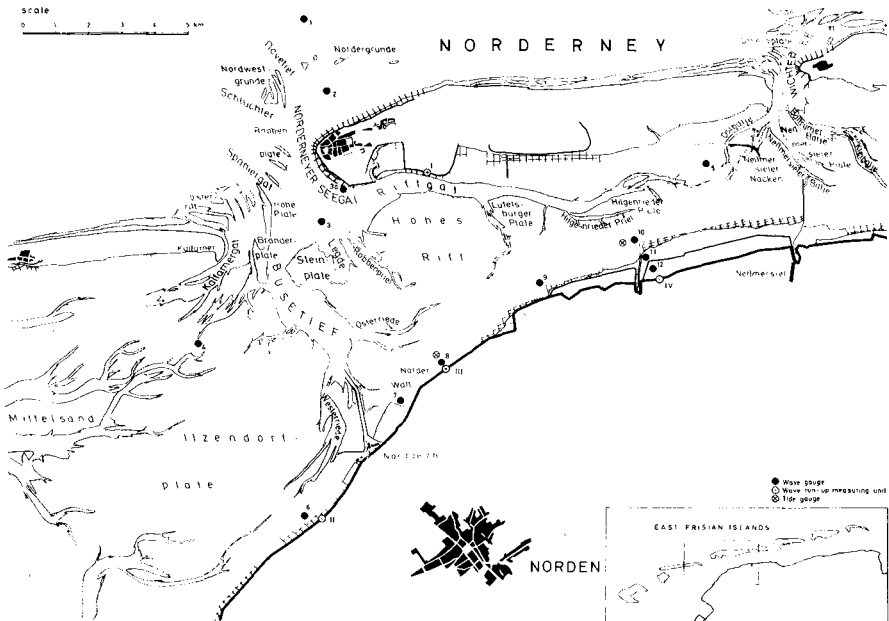


Fig. 2: Research Area and Measuring Net

main hydrographic and morphological features of the whole region of the East Frisian Islands and Coast.

There a measuring net of 13 wave measurement stations and also four wave run-up gauges inserted on sea dykes was erected (FIG.2). The spatial distribution of the wave measurement stations allows to record the changes in wave climate from the open sea to the mainland coast. The conception of the measuring net has therefore been orientated at the morphological features of the region in order to obtain data of their influences on waves propagating from the open sea to the mainland coast (LUCK + NIEMEYER 1977).

The main research aims of the wave measurement program are:

1. Derivation of a computable relationship, allowing the estimation of wave action in the seaward region of the East Frisian Islands and Coast as a function of wind conditions
2. Analysis of wave energy dissipation due to wave breaking on the bar
3. Determination of wave damping on the tidal flats
4. Establishment of design parameters for protection structures in function of wave action and wave loads in respect of the morphological and structural boundary conditions

In the on hand paper the first results of the study are presented, mainly referring to the changes of the heights of waves travelling from the open sea to the mainland coast.

2. Wave generation factors

The range of wind directions being most important for wave generation with respect to the research area extends from W to NNE (FIG.3). The length of fetch is great enough in consideration of the restricted water depth to establish a fully arisen sea within a few hours. Waves generated by winds from these directions are the only important for design conditions.

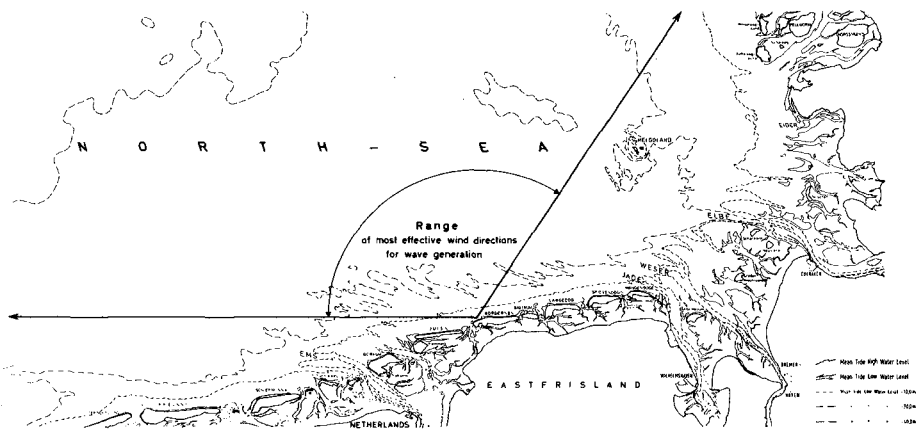


Fig. 3: Wave Generating Area

The hydrographical features of the generation area led to the conclusion that waves generated by normal high wind speeds within this range of directions should not differ in their order of magnitude.

The first investigations therefore were carried out in order to get a quantitative description of the interaction between wind velocity and wave height.

Linear regression analysis clearly shows that there is a rather high correlation between the significant wave height and the mean wind speed prevailing the last six hours before starting the wave measurements (FIG.4). In order to get dimensionally correct equations the significant wave height is plotted versus the ratio of chosen wind speed squared and gravitational acceleration.

But field data better meet a power curve fit for the same parameters than linear regression (FIG.5). The best accom-

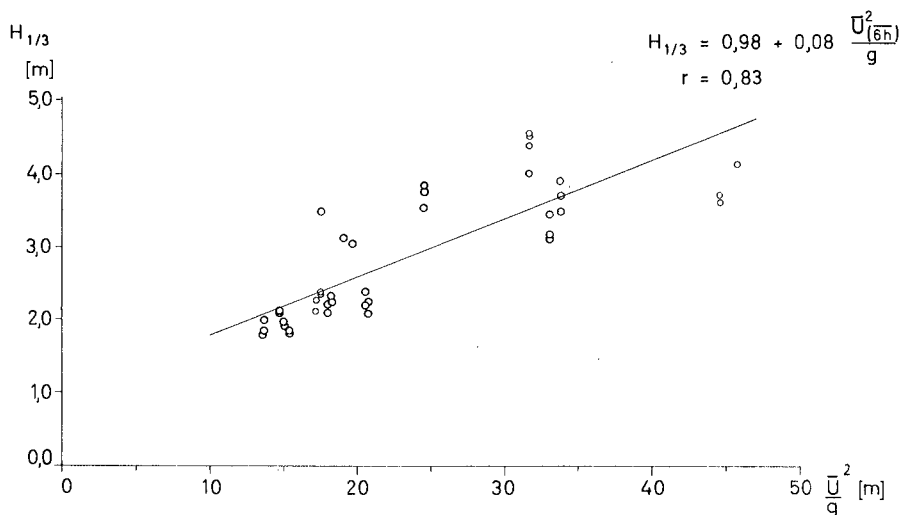


Fig. 4: Linear Regression of $H_{1/3}$ and $\frac{\bar{U}^2(\bar{6h})}{g}$

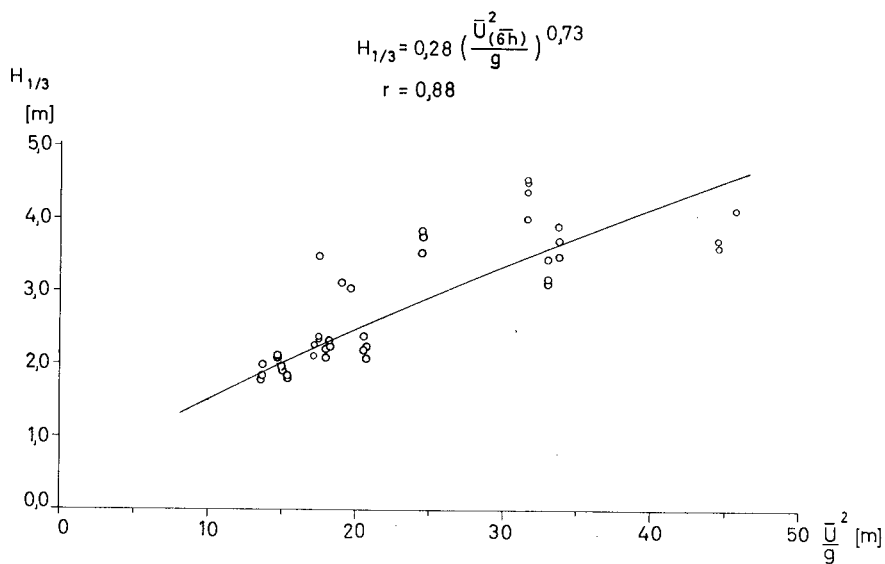


Fig. 5: Power Curve Fit for $H_{1/3}$ and $\frac{\bar{U}^2(\bar{6h})}{g}$

odation of data and the computed equation could be reached for a power curve fit using the mean wind velocity for the last three hours before starting the wave measurements (FIG.6). Exactly as for the significant wave height there is a high correlation between maximum wave height and mean wind speed on the same boundary conditions (FIG.7).

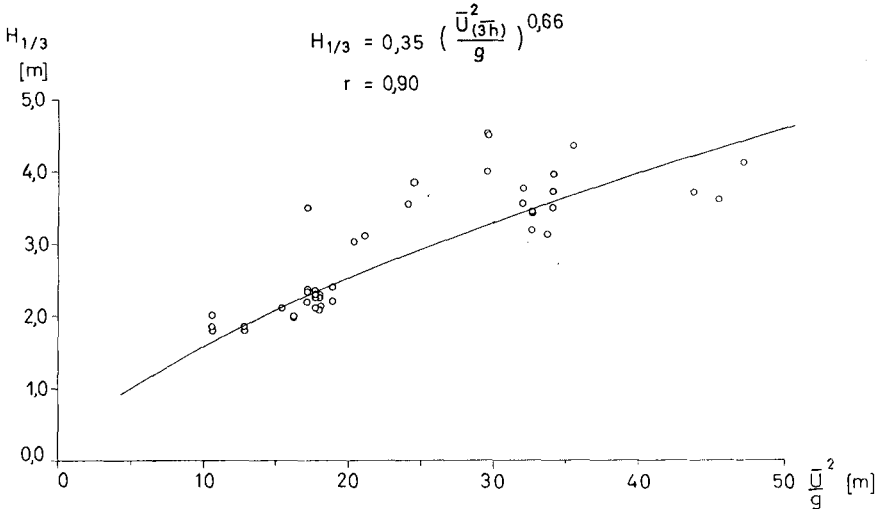


Fig. 6: Power Curve Fit for $H_{1/3}$ and $\frac{\bar{U}^2}{g}$

These results show that the last three hours of the prevailing wind speed are the most important for the height of the occurring waves in the investigation area.

When comparing these results with the investigations of SCHÜTTRUMPF (1973) for the southern North Sea which are based on the hindcasting method of BRETSCHNEIDER (1954, 1957) it seems to be that for higher wind speeds than those measured during this research period a longer wind duration must be taken into consideration. Equally the influence of the distinct wind directions from W to NNE could increase on those conditions because then with the growing fetch length needed for the occurrence of a fully arisen sea even small differences in the hydrographical features become more important for wave generation.

But the obtained results meet well enough the requirements for the estimation of wave conditions in the seaward region of the research area by forecasting or hindcasting techniques.

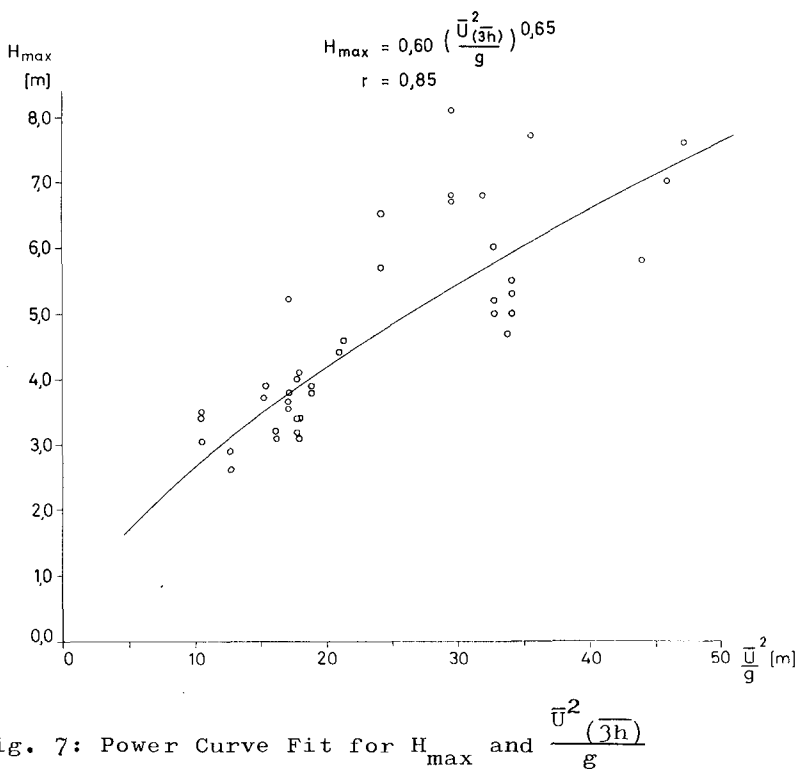


Fig. 7: Power Curve Fit for H_{\max} and $\frac{\bar{U}^2}{g}$

3. Wave energy dissipation due to wave breaking on the bar

The incoming waves reach the bar seaward of the tidal inlet Norderneyer Seegat and the northwestern shore of the island of Norderney. There the limited water depth induces the breaking of the higher waves. During high wave conditions the bar could be distinguished as a ring of white foam on which nearly all waves are broken ranging from the eastern end of the island of Juist around the tidal inlet Norderneyer Seegat and the northwestern shore of the island of Norderney.

It can be seen on aerial photographs that there is a significant difference between the western and the eastern part of the bar in respect of the height and areal extension of the shoals (FIG.8).

The analysis of data verifies that these different morphological features condition a distinct form of surf processes leading to a locally diverse form of wave energy dissipation in a quantitative und qualitative manner: The



Fig. 8: Aerial Photograph of the Bar Enclosing the Tidal Inlet Norderneyer Seegat and the Northwestern Shore of the Island of Norderney

waves which pass the bar in front of the northwestern shore of the island of Norderney are higher than those passing the part in front of the tidal inlet Norderneyer Seegat.

In the eastern part the water depth of the bar has a great influence on the height of waves recorded landward of the bar. There is a rather satisfactory correlation between significant wave height measured at station 2 and water depth (FIG.9). But the correlation coefficient is not high enough to believe that there is not any other important influence, because the graph indicates that waves of a different height can occur in the same water depth.

In order to describe wave energy dissipation on the bar it is useful to take into account not only the wave heights recorded seaward of the bar but also the water depth on the bar itself. As it is very difficult to define a concrete water depth on the bar it is replaced by the actual mean height of tide water level occurring during a measuring period.

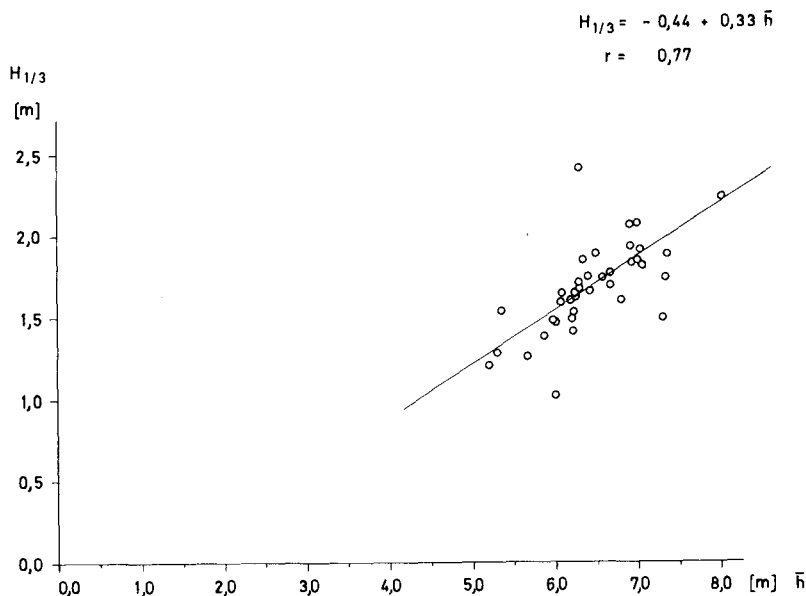


Fig. 9: Relation of Significant Wave Height and Water Depth at Station 2

In the eastern part of the bar in front of the north-western shore of the island of Norderney wave energy dissipation can be described by the ratio of wave heights landward and seaward of the bar. It is dependent on the wave heights seawardly recorded in relation to the height of the tide water level:

$$\frac{H_{II}}{H_I} = f \left(\frac{H_I}{W_{PN}} \right) \quad (1)$$

Explanatory in figures 10 and 11 wave energy dissipation is shown for the significant and maximum wave height. Data are best met by an exponential curve fit which is well proved by the high correlation coefficients (FIG.10 and 11).

This result allows the determination of wave heights in front of the northwestern shore of the island of Norderney for a certain tide water level and wave heights seaward of the bar which can be easily estimated by the developed forecasting formulas.

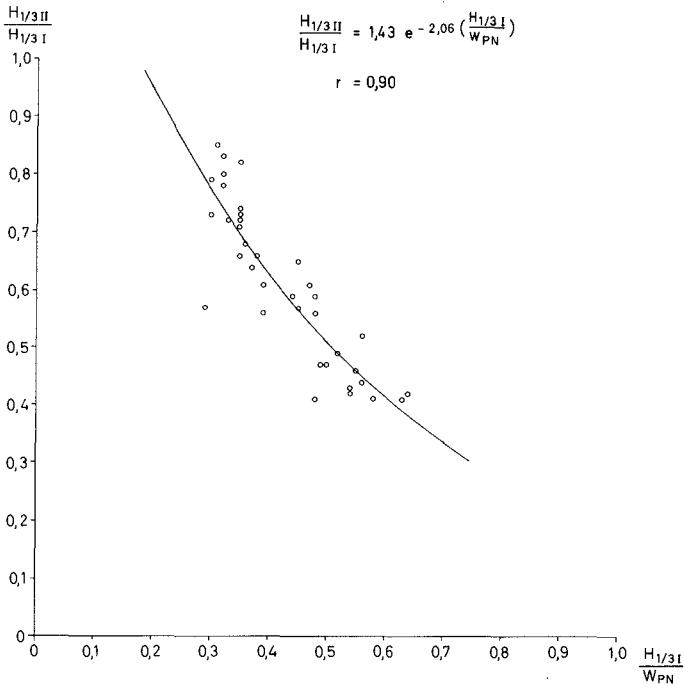


Fig. 10: Damping of Significant Wave Height on the Eastern Part of the Bar

These findings furthermore indicate the important protective function of the bar for the northwestern shore of the island. As the wave heights increase more considerably than the tide water levels during the occurrence of storm tides, wave energy dissipation increases as well.

On the western part of the bar seawardly enclosing the tidal inlet Norderneyer Seegat the water depth in respect of incoming wave heights is much smaller than in the eastern part. As additionally the areal extension of the shoals is much larger than in the eastern part the important influences for surf processes and the connected wave energy dissipation differ as well.

Wave height damping on this part of the bar is only dependent on the incoming wave heights but not on the changing water depths on the bar.

There is a linear relationship between the wave heights seaward of the bar and the difference to those landward of the bar which could be proved by regression analysis for the significant and maximum wave height. The data fit the

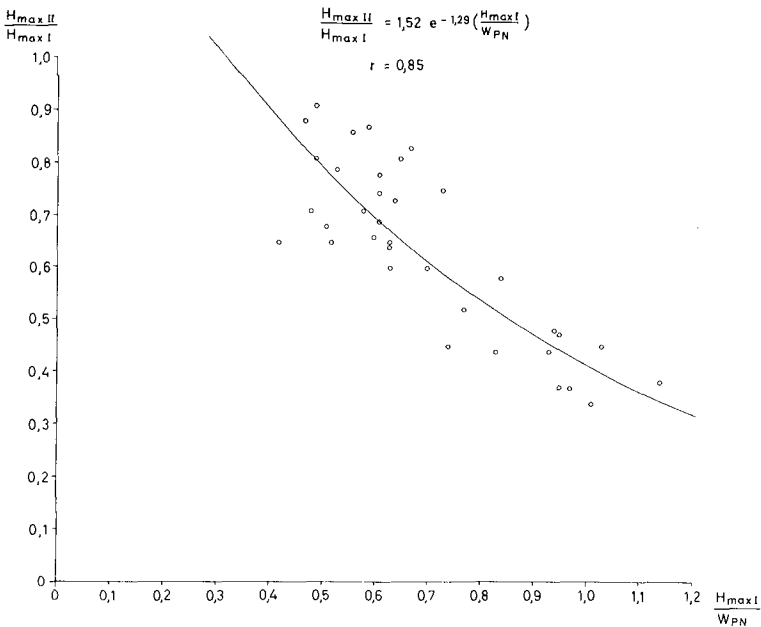


Fig. 11: Damping of Maximum Wave Height on the Eastern Part of the Bar

computed equation nearly precisely which is as well proved by the very high correlation coefficients (FIG.12 and 13).

The decrease of wave energy in front of the tidal inlet is of great importance for the wave conditions on the tidal flats and the wave loads on the dykes on the mainland coast. In this respect the part of the bar enclosing the tidal inlet has an essential protective function for the mainland coast.

The intensive wave energy dissipation on the bar is easily demonstrated by the ratio of maximum wave height to water depth recordered at the two stations landward of the bar. Its value is always much smaller than that necessary for shallow water wave breaking

$$H_b = h_b \quad (2)$$

which has been established by FÜHRBÖTER (1974) and SIEFERT (1974) by field measurements in shallow water regions. In this case the orders of magnitude are as follows:

$$H_{\max II} \leq 0,57 h \quad (3)$$

$$H_{\max III} \leq 0,39 h \quad (4)$$

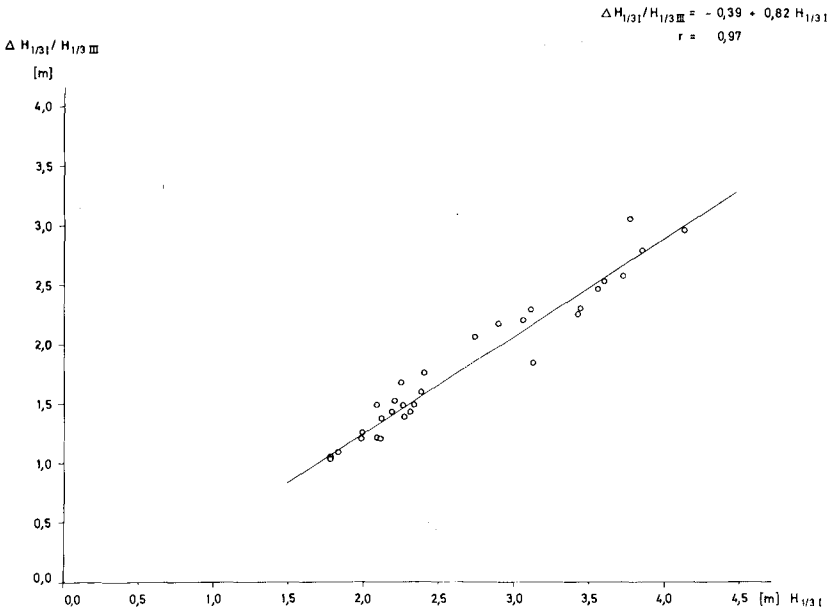


Fig. 12: Damping of Significant Wave Height on the Western Part of the Bar

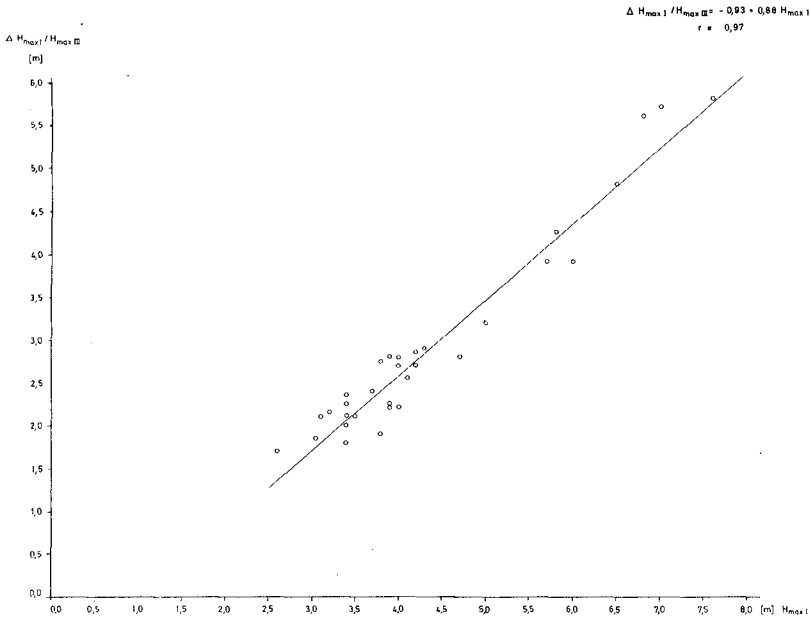


Fig. 13: Damping of Maximum Wave Height on the Western Part of the Bar

Landward of the bar wave breaking due to limited water depth cannot therefore occur before the new generated waves reach the shore of the island or the dykes on the mainland coast (FIG.14).



Fig. 14: Wave Breaking on the Bar in front of the Northwestern Shore of the Island of Norderney

4. Wave height damping on the tidal flats

While the waves passing the eastern part of the bar attack the northwestern shore of the island of Norderney, those which are generated after breaking on the eastern part spread out over the tidal flats. Though they are not high enough to be broken because of the limited water depth a certain wave damping on the tidal flats could be observed. It must be explained as a combined superposing effect of bottom friction, refraction, diffraction and shoaling.

The damping of maximum wave height from the inner part of the tidal inlet can be described as a function of itself in relation to the water depth at the end of the travel distance (FIG.15). One gets a more complicated expression for the damping of the significant wave height (FIG.15), but the influence of water depth can be distinguished too.

The intensity of wave height damping on the tidal flats can be described by another example:

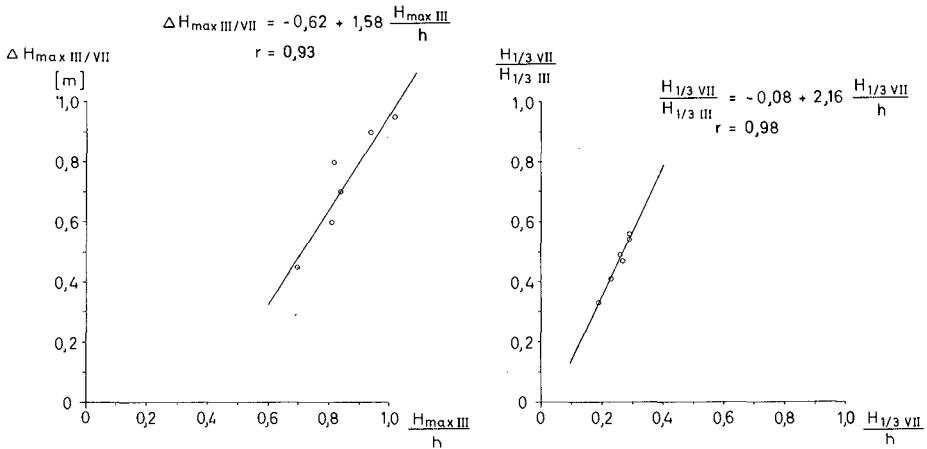


Fig. 15: Wave Height Damping on the Tidal Flats

The comparison between the ratio of maximum wave height and water depth at the two stations with a different distance to the tidal inlet shows that there is a nearly continuous damping of maximum wave height with respect to water depth and travel distance (FIG.16). Considering the growing heights of flats with increasing distance from the tidal inlet in connection with the constant ratio of wave height and water depth it is possible to come to the conclusion that there is a well-balanced dynamic equilibrium between the morphological configuration of the flats and the local wave climate.

But this result includes another important fact, because one wave measuring station is situated in front of a dyke without foreland the other on a dyke foreland. The obtained ratio of wave height and water depth is significant for flats without any wave breaking according to the investigation of SIEFERT (1974) in the southwestern region of the Elbe estuary. Regarding both results the up to now generally accepted theory of an intensive wave damping due to wave breaking on dyke forelands must be abandoned.

Regarding the topography of the research area it seems to be that the existence of dyke forelands is even a consequence of the local low wave energy.

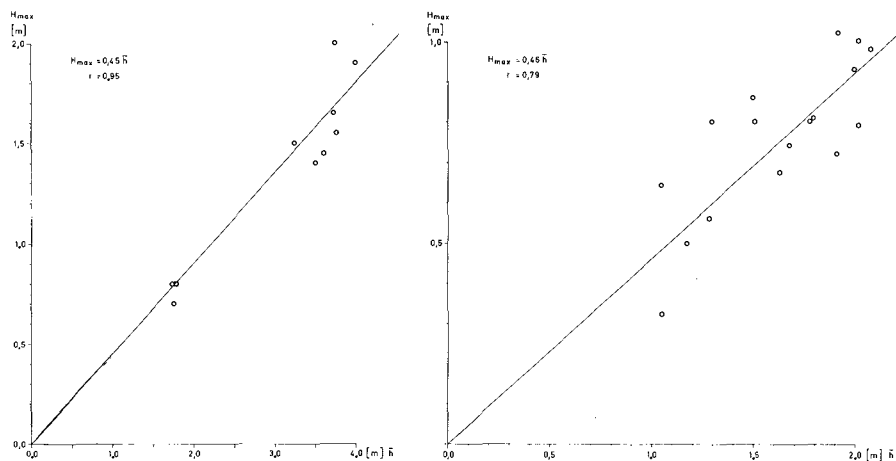


Fig. 16: Relation of Maximum Wave Height and Water Depth at the two Stations (8 + 12) on the Mainland Coast

5. Investigations on wave run-up

These investigations on wave climate are combined with those on wave run-up on sea dykes. Therefore four wave run-up gauges were meanwhile placed on sea dykes. But undisturbed wave run-up measurements can only be carried out at the occurrence of very high storm tide water levels. As such an event has not yet happened since the start of the measurements with the run-up gauges, there are not until now any measurements leading to new results.

But the influence of wave parameters on wave run-up has already been analysed by the investigations of HUNT (1959) on monochromatic waves as well as by those of VAN OORSCHOT and D'ANGREMOND (1968) on wave spectra.

Their commonly accepted results show that the height of wave run-up in respect of the occurring spectrum is dependent on the wave period and the square root of wave height. Accordingly wave run-up is here described as wave run-up potential only considering wave parameters and neglecting all other influences (NIEMEYER 1977b).

The data of 17 wave records of field measurements which include about 1800 waves are used for computing wave run-up potential with respect to the higher and longer waves of the spectrum. Important for the highest five per cent of wave run-up potential are the highest and longest ten per cent of waves. But the maximum wave run-up potential for every record is caused by its highest and longest waves. In figure 17 computations of wave run-up potential for all 17 records are shown for comparison (FIG.17):

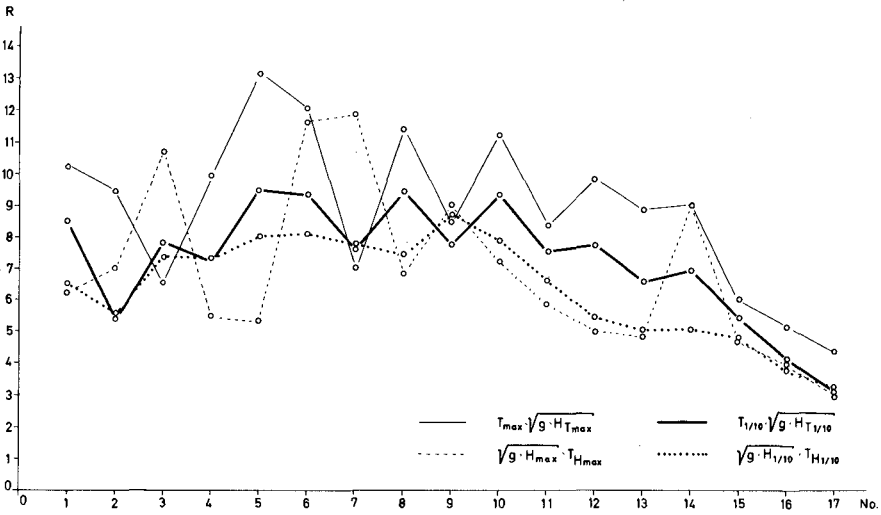


Fig. 17: Comparison of Several Computed Wave Run-Up Potentials by Using Wave Data of Field Measurements

1. wave run-up potential R_{Tmax} of the longest wave with period T_{max} and height H_{Tmax}
2. wave run-up potential R_{Hmax} of the highest wave with height H_{max} and period T_{Hmax}
3. wave run-up potential $R_{T1/10}$ of a wave with the mean period $T_{1/10}$ and the mean height $H_{T1/10}$ of the longest ten per cent of waves
4. wave run-up potential $R_{H1/10}$ of a wave with the mean height $H_{1/10}$ and the mean period $T_{H1/10}$ of the highest ten per cent of waves

Mostly the highest computed wave run-up potential is caused by the longest wave of the considered records. Comparing all computed wave run-up potentials the following relations are gained:

$$R_{T1/10} = 0,82 R_{Tmax} \quad (5)$$

$$R_{Hmax} = 0,78 R_{Tmax} \quad (6)$$

$$R_{H1/10} = 0,72 R_{Tmax} \quad (7)$$

$$R_{H1/10} = 0,92 R_{Hmax} \quad (8)$$

6. Summary

The Research Station for Island and Coast Protection Nordeney has been operating the wave measurement program East Frisian Island and Coast for two years. The first results of this study can be summarized in the following manner:

1. There is a high correlation between the wind speed prevailing the last three hours and the heights of local waves subsequently occurring.
2. Wave energy dissipation on the bar enclosing the tidal inlet and the northwestern shore of the island situated westward of the inlet can be described in a quantitative manner in respect of the different morphological features of the bar.
3. The intensive wave energy dissipation on the bar prevents the breaking of waves spreading out over the tidal flats due to limited water depth, which indicates in spite of that a wave height damping in a certain order of magnitude.
4. The continuous wave damping on the tidal flats leads to such a decrease of heights that there cannot occur any wave breaking due to restricted water depth during the duration of high storm tide water levels.
5. It seemed to be that not the highest, but mainly the longer waves induce the highest wave run-up on sea dykes.

7. Acknowledgements

The wave measurement program East Frisian Islands and Coast is supported by the German Federal Ministry for Research and Technology (BMFT) through the German Committee on Coastal Engineering Research (KFKI).

8. References

- BRETSCHNEIDER, C.L.: Generation of Wind Waves over a Shallow Bottom. Beach Erosion Board, T. M. 51. 1954
- BRETSCHNEIDER, C.L.: Hurricane Design Wave Practise. Proc. ASCE, Vol. 83, WW 2. 1957
- FÜHRBÖTER, A.: Einige Ergebnisse aus Naturuntersuchungen in Brandungszonen, Mitt. d. Leichtweiß-Inst. 40, 1974
- HUNT, I.A.: Design of Seawalls and Breakers. Proc. ASCE, Vol. 85, WW 3. 1959
- LUCK, G. + NIEMEYER, H.D.: Das Seegangsmessprogramm Ostfriesische Inseln und Küste. Dt. Gewässerkdl. Mitt., H. 6, 1977
- NIEMEYER, H.D.: Seegangsmessungen auf Deichvorländern. Jber. 1976 Forsch.-Stelle f. Insel- u. Küstenschutz Norderney, Bd. XXVIII. 1977a
- NIEMEYER, H.D.: The Estimation of Design Wave Run-up on Sea Dykes in Consideration of Overtopping Security. Proc. 17th IAHR-Congress, Baden-Baden. 1977b
- SCHÜTTRUMPF, R.: Über die Bestimmung von Bemessungswellen für den Seebau am Beispiel der südlichen Nordsee. Mitt. Franzius-Inst., H. 39, 1973
- SIEFERT, W.: Über den Seegang in Flachwassergebieten. Mitt. Leichtweiß-Inst. 40, 1974
- VAN OORSCHOT, J.N. + D'ANGREMOND, K.: The Effect of Wave Energy Spectra on Wave Run-up. Proc. 11th Intern. Confer. on Coastal Engineering. 1968

9. List of symbols

g	gravitational acceleration
h	water depth
h_b	depth of water at breaking wave
H_b	wave height at breaking
$H_{1/3}$	significant wave height
$H_{1/10}$	average height of highest ten per cent of waves for given rime period
H_{\max}	maximum wave height for specified period of time
$H_{T1/10}$	average height of longest ten per cent of waves for given time period
$H_{T\max}$	height of the longest wave for specified period of time

$H_I, H_{II}, \dots, H_{XII}$	wave height measured at stations 1, 2, 12
$R_{H1/10}$	wave run-up potential of a wave with average height and period of highest ten per cent of waves for given period of time
R_{Hmax}	wave run-up potential of the highest wave for specified period of time
$R_{T1/10}$	wave run-up potential of a wave with average height and period of the longest ten per cent of waves for given period of time
R_{Tmax}	wave run-up potential of the longest wave for specified period of time
$T_{1/10}$	average period of longest ten per cent of waves for given period of time
T_{max}	maximum wave period for specified period of time
\bar{U}	wind speed
$\bar{U}(\overline{3h})$	mean wind speed prevailing the last three hours before starting wave measurements
$\bar{U}(\overline{6h})$	mean wind speed prevailing the last six hours before starting wave measurements
W_{PN}	height of tide water level
$\Delta H_I/H_{III}$	difference of wave heights measured at station 1 and 3
r	correlation coefficient

CHAPTER 7

AN EVALUATION OF EXTREME WAVE CLIMATE AT KEAHOLE POINT, HAWAII

by

Charles L. Bretschneider¹ and Richard E. Rocheleau²

INTRODUCTION AND SUMMARY

An evaluation of extreme wave climate was made for Keahole Point, Hawaii. This evaluation was based on three separate sources of wave data and five methods of statistical evaluations. The three sources of data include (1) wave hindcasts data of 10 severe storms between 1947-1961 by Marine Advisors (1963), (2) wave hindcast data of 11 severe storms between 1947-1965 by U.S. Army Corps of Engineers, Honolulu District, and (3) shipboard wave observations of the U.S. Navy reports. Figure 5 shows SSMO area No. 1 for south and southwest of the islands and SSMO areas Nos. 2 and 3 for north of the islands.

The five methods of statistical extrapolations for extreme events include: (1) Gumbel's (1958) first asymptotic distribution, (2) Weibull distribution (1961), and (3,4,&5) semilog, log normal and normal distributions. The three most widely used distribution functions are: (1) Gumbel's (1958), (2) log normal (see Jasper, 1956), and (3) Weibull (1961), given in order as to the author's preference. The statistical extrapolations for Keahole Point, Hawaii, are given in Table 9 and Figure 9. Only Gumbel's (1958) distribution was applied to the north shore as shown in Table 8.

Based on Gumbel's distribution function, the results of the wave hindcasts statistics on the average (50 year recurrence interval) indicate that (1) the Marine Advisors (1963) wave hindcasts are about 25 percent higher than the U.S. Army Corps of Engineers wave hindcasts and (2) the U.S. Navy SSMO observations and the U.S. Army Corps of Engineers wave hindcasts are in closest agreement.

Shipboard wave observations have always been subjected to questions. However, various authors have correlated instrumentally measured and observed wave observations. A summary of these correlations are given in Table 6. No correction was made to the statistical analysis of the SSMO data.

Explanations are in order for the discrepancies between the three sources of data: (1) Both the U.S. Army Corps of Engineers and Marine Advisors have many years of experience in wave forecasting and hence their data should be reliable, (2) ship captains tend to avoid the worst of any storm, and also they are usually too occupied to make accurate observations

¹ Chairman and Professor, Department of Ocean Engineering, University of Hawaii

² Ph.D. Graduate Student at University of Delaware, formerly M.S. Graduate Student, University of Hawaii.

during heavy seas, and thus the extreme wave conditions are never experienced in the summaries of SSMO data, (3) it might be assumed that the Corps of Engineers hindcasts are somewhat low because they are in near agreement with the SSMO data which are assumed to be low. Perhaps one might use an average of the two sets of hindcast data, and (4) wave forecasting (and wave hindcasting) by experienced oceanographers is more accurate than visual wave observations. There are a number of experienced oceanographers who can make very accurate wave forecasts. The U.S. Navy Fleet Numerical Weather Central at Monterey, California, has a very excellent computer program that can produce wave forecasts more accurately than shipboard wave observations. There are other commercial computer programs equally calibrated to give the same accuracy.

The usefulness of the wave statistics of Hogben and Lumb (1966) and the U.S. Navy SSMO data should be limited to the similar conditions of ship routes under which the wave observations were taken. These data should never be used for the determination of extremes, since the extreme conditions have been absent. A very good case for the above statement can be made for Cape Horn, South America. Cape Horn is one of the most severe storm areas of the world, and yet the wave statistics of Hogben and Lumb (1966) would indicate the area to be relatively calm when we know from history that this is not true. The point here is that the ships avoid going around the Horn, and instead go either through the Magellan Straits or the Panama Canal. Perhaps an exception to the above is the area in the North Sea, where there is heavy ship traffic and many ships can hardly avoid extreme storm wave conditions in the North Sea.

The problem, of course, is how one can use the visual wave observations since these are very plentiful. First, the visual wave observations are excellent for ships avoiding extreme storm wave conditions. Insofar as obtaining reliable wave statistics from visual wave observations, somebody should determine a correlation between regular enroute shipboard wave observations and the extreme wave conditions that were avoided by the ships captain. Such a correlation is far more important than the correlation equations given in Table 6.

In view of the above discussions, it is concluded that: (1) at present wave hindcasting (now very accurate) is the best method for obtaining extreme wave statistics, since one can go back to 50 or more years of weather maps, and it is the only method that gives both the duration of the storms and simultaneous occurrences of swell from distant storms; (2) presently offshore and coastal engineering structures at Keahole Point should be designed on the basis of Marine Advisors' wave statistics as summarized in Figure 9 and Table 9; (3) a refinement of wave statistics for extremes at Keahole Point can only be obtained by wave hindcasts of severe storms prior to 1947 and after 1965; and, (4) there are available a number of calibrated computer programs for wave forecasting and hindcasting. The University of Hawaii does not yet have a computer program for wave hindcasting, but instead should use one of those already available.

WAVE CLIMATE IN HAWAIIAN WATERS

Waves affecting waters around the Hawaiian islands result from storms in all parts of the Pacific Basin and even in parts of the Indian Ocean. The superposition of distant and locally generated waves together with the influence of the islands result in a complex wave climate. The wave climate for the islands has been classified into four general types characterized by wave height, wave period, and direction of approach. Figure 1, from Moberly and Chamberlain (1964), shows the direction of approach of the four main wave types. Figure 2 shows the generating areas from which waves may approach Keahole Point, Hawaii. A fifth type of waves are those associated with hurricanes. Although hurricanes are less frequent than ordinary storms, hurricane generated waves must be considered for design purposes.

The above types of wave climate are discussed briefly:

- (1) Northeast tradewind waves. Northeast tradewind waves are present a large percentage of the time, but dominate from April to November when the tradewinds are present 90 to 95 percent of the time. The tradewinds blow 12 to 15 knots per hour about 50 percent of the time generating waves from 4 to 11 feet in height with periods of 5 to 9 seconds due to the long uninterrupted fetches. These waves approach the island between the north and northeast.
- (2) Southern swell. Southern swell approaches from between the southeast and the southwest. It is most frequent from April through October, resulting from severe winter storms in the southern hemisphere. Due to the decay over the distances, these waves usually arrive as low, long-period swell, typically 1 to 6 feet high with periods of 14 to 22 seconds. However, swell substantially larger than 6 feet has been observed along the southern boundary of the islands.
- (3) Kona storm waves. These waves approach the islands infrequently with the passage of kona storms which are generally cold-core, low-pressure systems of large radius. During the passage of such systems the tradewinds are replaced by south or southwesterly winds generating waves which arrive from the southeast to west. Although infrequent, the severity of kona storms varies from a light breeze to gale strength. The associated wave climate varies over a wide range. Waves of 10 to 15 feet with periods of 8 to 10 seconds are not uncommon.
- (4) North Pacific swell. North Pacific swells, having been generated by severe storms near the Western Aleutians or from mid-latitude low pressure systems, approach the islands from the north. These waves are most frequent from October through May and are responsible for the large surf observed in many areas.
- (5) Hurricane waves. Although not included in many discussions of Hawaiian waves, a fifth type of wave is important for design considerations. Large waves produced by passing hurricanes may affect many island locations. These tropical cyclones are characterized by a warm low-pressure core with sustained wind speeds substantially higher than those

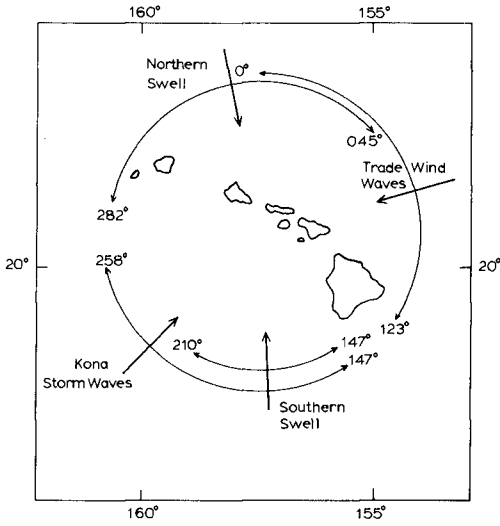


FIG. 1 APPROACH DIRECTION OF FREQUENTLY OCCURRING WAVES IN HAWAIIAN WATERS
After Moberly and Chamberlain (1964)

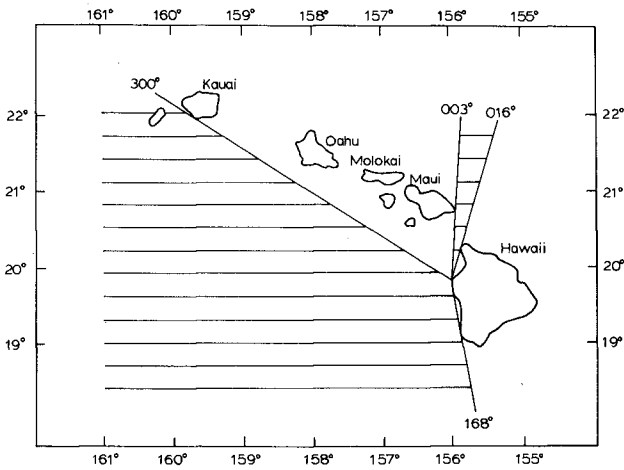


FIG. 2 GENERATION AREAS FROM WHICH WAVES MAY APPROACH KEAHOLE POINT

associated with tropical (kona) storms. Hurricane waves are important for design considerations and are based on the model hurricane for Hawaii as determined by Bretschneider and Tamaye (1976).

SOURCES OF WAVE DATA

Three sources of data have been analyzed to determine long-term wave heights. These are described below.

(1) Marine Advisers: Severe Storm Wave Characteristics in the Hawaiian Islands (1963). The report presents the results of a hindcasting program to determine the wave conditions produced by the 10 most severe storms of the 15-year period from 1947 through 1961 for all Hawaiian waters. These hindcasts were specific for waves approaching either the west coast of Lanai or the west coast of Molokai. Certainly not all the storms analyzed would have affected Keahole Point and even those which did may have had considerably altered wave characteristics at that location. However, these 10 most severe storms, without regard to sheltering effects or direction, were analyzed to provide an upper limit on the severity of the deepwater wave climate expected to occur. The direction of wave approach to the islands is shown in Figure 3. A complete discussion of the storm systems involved may be found in the Marine Advisers' (1963) report. Table 1 gives a summary of these wave hindcasts.

(2) Corps of Engineers: Hindcasts for Harbor Planning (1968). The U.S. Army Corps of Engineers, Honolulu District made hindcasts of 17 storms affecting the Hawaiian Islands from 1947 through 1965. Seven of these which resulted in severe waves at Honokohau Bay are applicable to Keahole Point. In addition, four storms north of the islands which generated large swell from a direction possibly affecting Keahole Point have been included. The inclusion of these storms is based on the location of the generation area relative to the window between Maui and Hawaii rather than on actual observations. Table 2 summarizes these hindcast results specific to Keahole Point. The approach directions of the waves from the 11 storms are presented in Figure 4. Six of the storms shown in Table 2 are also given in Table 1.

(3) U.S. Navy Hydrographic Office: Summary Synoptic Meteorological Observations (SSMO). Figure 5 shows 3 SSMO areas. Area No. 1 is for the windward or north and east areas of the Hawaiian Islands; Area 2 is for the leeward or south and west areas of the Hawaiian Islands; and Area 3 is for the north and west areas of the island of Kauai. SSMO provide monthly and annual summaries of many individual shipboard wave observations over the 8-year period from 1963 to 1971. The waves are classified by observed wave height and wave period, but not by direction. Table 19 of the SSMO reports for the annual summaries are reproduced in Tables 3, 4 and 5 for SSMO areas 1, 2 and 3, respectively. Table 6 represents various equations or relations between measured significant wave heights and shipboard wave observations. It appears that the overall best equation would be equation (d) of Table 6 to convert shipboard wave observations to significant wave height. The observed wave period is essentially the significant wave period, but the relationships given in Table 7 are used to determine f_0^{-1} and \bar{T} of the wave spectrum where

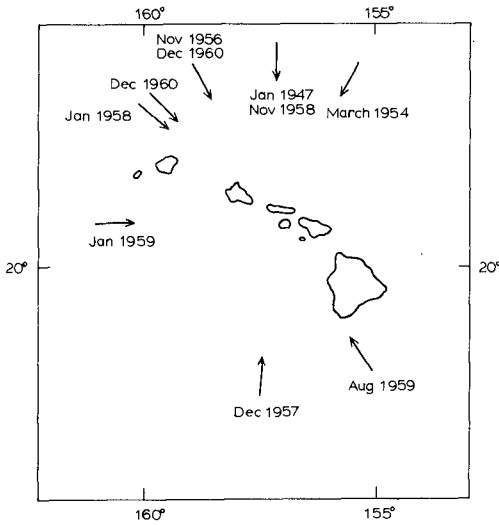


FIG. 3 DIRECTION OF WAVE APPROACH TO THE HAWAIIAN ISLANDS FROM 10 STORMS HINDCAST BY MARINE ADVISERS FROM 1947 THROUGH 1961

TABLE 1
HINDCAST WAVE CHARACTERISTICS FOR TEN STORMS
FROM 1947-1961. (FROM MARINE ADVISERS, 1963)

Storm Date	Significant Wave Height (ft.)	Significant Wave Period (seconds)	Direction (°True)
January 3, 1947	15.7	16.4	0
March 6, 1954	25.0	17.2	027
November 27, 1956	12.8	16.8	332
December 2, 1957	32.5	14.5	185
January 12, 1958	27.1	23.5	310
November 22, 1958	12.5	14.6	0
January 18, 1959	7.0	13.5	268
August 6, 1959	16.8	15.9	148
December 11, 1960	18.0	19.6	315
December 20, 1960	13.8	18.0	332

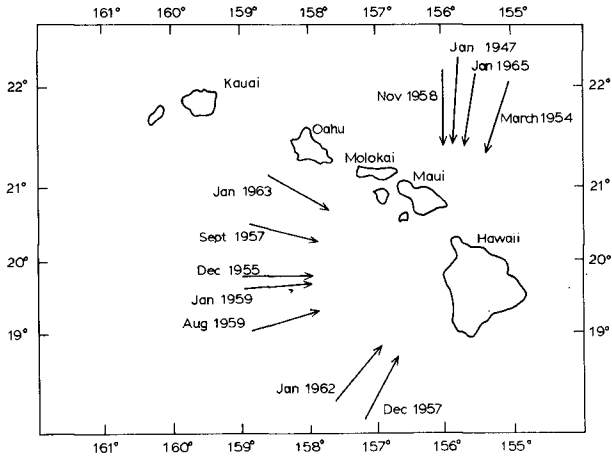


FIG. 4 DIRECTION OF WAVE APPROACH TO KEAHOLE POINT FROM 11 STORMS HINCAST BY THE CORPS OF ENGINEERS FROM 1947 THROUGH 1965

TABLE 2
HINCAST WAVE CHARACTERISTICS FOR ELEVEN STORMS
EFFECTING KEAHOLE POINT FROM 1947-1965

(Based on hindcasts from the Corps of Engineers, 1968)

Storm Date	Significant Wave Height (ft.)	Significant Wave Period (seconds)	Direction (°True)
January 3, 1947	14.5	17.3	005
March 6, 1954	22.9	17.2	020
December 20, 1955	14.8	11.2	270
September 5, 1957	18.9	21.1	286
December 2, 1957	25.5	13.4	210
November 22, 1958	14.6	14.3	357
January 18, 1959	14.0	9.6	267
August 6, 1959	22.5	12.0	255
January 7, 1962	13.6	11.1	222
January 16, 1963	23.0	14.5	300
February 2, 1965	27.0	17.2	010

TABLE 3
SUMMARY OF EIGHT YEARS OF SHIPBOARD OBSERVATIONS WINDWARD OF THE
HAWAIIAN ISLANDS (FROM SUMMARY OF SYNOPTIC METEOROLOGICAL OBSERVATIONS)
TABULATED AS PERCENT FREQUENCY OF OCCURRENCE (SSMO AREA 1)

Wave Height (feet)													TOTAL	
Period (sec)	<1	1-2	3-4	5-6	7	8-9	10-11	12	13-16	17-19	20-22	23-25		26-32
<6	1.0	8.7	17.9	9.4	3.3	1.3	.3	.1	.1	*	.0	.0	.0	4215
6-7	*	1.3	6.9	10.8	6.0	2.6	1.1	.6	.2	*	*	*	.0	2949
8-9	*	.3	1.6	3.8	4.5	2.3	1.1	.5	.4	.1	*	*	.0	1447
10-11	.0	.1	.4	.9	1.5	1.1	.7	.4	.4	.1	*	*	*	549
12-13	.0	*	.1	.3	.4	.4	.3	.2	.1	*	*	.0	.0	189
>13	.0	*	.0	.1	.1	.1	.1	.1	.1	*	*	*	*	70
INDET	2.4	.8	.8	.7	.3	.2	.1	*	*	.0	.0	.0	.0	528
TOTAL	349	1121	2780	2595	1609	792	354	175	125	26	13	6	2	9947
PCT	3.5	11.3	27.6	26.0	16.2	8.1	3.6	1.8	1.3	.3	.1	.1	*	100.0

TABLE 4
SUMMARY OF EIGHT YEARS OF SHIPBOARD OBSERVATIONS LEEWARD OF THE
HAWAIIAN ISLANDS (FROM SUMMARY OF SYNOPTIC METEOROLOGICAL OBSERVATIONS)
TABULATED AS PERCENT FREQUENCY OF OCCURRENCE (SSMO AREA 2)

Wave Height (feet)													TOTAL	
Period (sec)	1	1-2	3-4	5-6	7	8-9	10-11	12	13-16	17-19	20-22	23-25		26-32
6	1.5	12.5	21.2	8.3	3.2	1.0	.3	.1	.1	.0	.0	.0	.0	7978
6-7	.1	2.1	8.1	8.6	6.2	2.2	.9	.3	.2	*	*	*	.0	4707
8-9	*	.4	2.2	2.8	2.8	1.6	1.0	.4	.2	*	*	*	.0	1884
10-11	.0	.1	.5	.7	.7	.6	.4	.2	.2	*	*	*	.0	548
12-13	.0	*	*	.2	.3	.2	.1	*	.1	.0	.0	*	*	163
13	.0	.0	.0	.1	.1	.1	*	*	*	*	*	.0	.0	64
INDET	3.6	1.1	1.1	.6	.2	.1	.1	*	*	.0	.0	.0	.0	1102
TOTAL	852	2696	5501	3476	2218	956	485	152	106	14	9	10	1	16446
PCT	5.3	16.2	33.1	21.2	13.6	5.9	2.8	.9	.7	.1	.1	.1	*	100.0

TABLE 5
SUMMARY OF EIGHT YEARS OF SHIPBOARD OBSERVATIONS FROM
HAWAIIAN ISLANDS (FROM SUMMARY OF SYNOPTIC METEOROLOGICAL OBSERVATIONS - AREA 3)
TABULATED AS PERCENT FREQUENCY OF OCCURRENCE

Period (sec)	Wave Height (feet)													TOTAL
	<1	1-2	3-4	5-6	7	8-9	10-11	12	13-16	17-19	20-22	23-25	26-32	
<6	.7	8.1	13.7	7.8	3.3	1.3	.7	.2	.2	.1	.0	.0	.0	2055
6-7	*	1.2	6.9	9.0	8.5	3.5	1.6	.6	.3	.1	.0	.0	.0	1796
8-9	*	.3	2.1	3.6	4.6	3.2	2.7	.5	.5	.1	.1	*	*	1004
10-11	.0	.1	.7	1.1	1.5	1.5	.9	.4	.6	.1	*	*	.0	389
12-13	.0	*	.1	.2	.5	.3	.3	.2	.3	*	.1	.0	.0	106
>13	.0	.0	.0	.1	.1	.1	.2	.0	.1	*	*	.0	.0	35
INDET	1.8	.3	.9	.6	.5	.2	.1	*	*	.0	.0	.0	.0	255
TOTAL	149	585	1399	1269	1057	570	355	106	106	28	10	3	2	5640
PCT	2.6	10.1	24.5	22.3	18.9	10.3	6.5	2.0	2.0	.5	.2	.1	*	100.0

TABLE 6
CORRELATION BETWEEN INSTRUMENTALLY MEASURED AND OBSERVED WAVE HEIGHTS
(Compiled by Rocheleau, 1977)

Reference	Wave Height (meters)	Correlation Coefficient
Brooks & Jasper (1957)	(a) $H_s = 1.088H_{ob}$	0.86
Cartwright (1964)	(b) $H_s = 1.17H_{ob}$	
(stations I & J)	(c) $H_s = 1.28 + .88H_{ob}$	
Hogben & Lumb (1967)	(d) $H_s = 1.05H_{ob}$	
(stations A, I, J, K)	(e) $H_s = 1.23 + .89H_{ob}$	
Nordenstrom (fit to Hogben & Lumb data)	(f) $H_s = 1.51 + .848H_{ob}$	
Nordenstrom (fit to Cartwright data)	(g) $H_s = 1.78_{ob}^{0.72}$	

* NOTE: Hogben & Lumb use the notation H_{ows} and we use H_{ob}

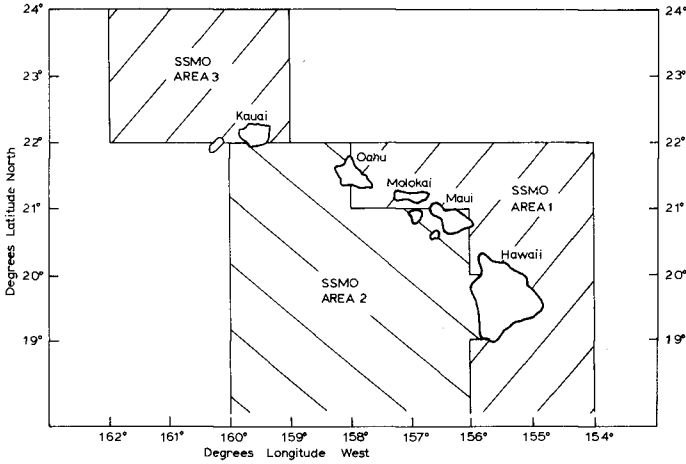


FIG. 5 BOUNDARIES OF THE SYNOPTIC METEOROLOGICAL OBSERVATION AREAS
HAWAIIAN SSMO AREAS 1, 2 & 3

TABLE 7
CORRELATION BETWEEN INSTRUMENTALLY MEASURED AND OBSERVED WAVE PERIODS
(After Hogben and Lumb, 1967)*

BEST STRAIGHT LINE (In Seconds)	Root mean square deviation, sec	Correlation Coefficient
(a) $\bar{T} = 4.7 + 0.32 T_{ob}$	0.88	
(b) $\bar{T} = 5.19 + 0.37 T_{ob}$	1.12	
(c) $\bar{T} = 4.945 + 0.345 T_{ob}^{**}$	--	
$f_0^{-1} = 4.1 + 0.76 T_{ob}$	2.15	
BEST LINE THRU ORIGIN		
(a) $\bar{T} = 0.73 T_{ob}$	1.20	0.50
(b) $\bar{T} = 0.86 T_{ob}$	1.40	0.48
(c) $\bar{T} = 0.795 T_{ob}^{**}$	--	
$f_0^{-1} = 1.12 T_{ob}$	2.23	0.50

* Hogben and Lumb use the notation \bar{T} for our \bar{T} and T_0 for our f_0^{-1} .
We use T_{ob} for T_{oms} .

** Equations (c) are the corresponding averages of (a) and (b).

f_0^{-1} is the model period or period of maximum energy density of the frequency spectrum and T is the zero crossing wave period. Figure 2 shows the possible approach directions for Keahole Point. The direction of wave approach is normally essential to determine the affected locations. Figure 5 shows the boundaries of SSMO Area 2, and it has been assumed that any sea state observed in the area could have affected Keahole Point. Similarly, all waves which affect the Point would propagate through the observation area. Unfortunately, there are no data which actually show the observations in SSMO Area 2 to be representative of Keahole Point. However, the SSMO data does give a means by which to make relative comparisons between the various SSMO areas.

STATISTICAL METHODS FOR EXTRAPOLATION TO FUTURE EVENTS

Except for data tabulated as a maximum series there is no widely applicable theoretical basis for determining the underlying probability distribution function or a suitable method of plotting the probabilities of exceedance calculated from the data. The criteria generally used is that data accurately fit by the chosen curve may be extrapolated. It is obviously best if the data are fit by a straight line. Several methods which have yielded such results in the past for wind and wave data and their application are discussed below.

(1) Gumbel's First Asymptotic Distribution. The first asymptote is described by the distribution function

$$F(x) = \exp \{-\exp[-\alpha(x-\mu)]\} \quad (1)$$

where

x = the variable of interest

α, μ = parameters of the extreme distribution.

A linear reduction is made by introducing the reduced variate

$$y = \alpha(x-\mu) \quad (2)$$

Substitution of y into equation 1 yields

$$y = -\ln \{-\ln F(x)\} \quad (3)$$

Gumbel has shown that the reduced variate (y) and return period (T) are related by

$$y = -\ln \ln \left(\frac{T}{T-1} \right) \quad (4)$$

where

T = the return period in same time interval as the maximum series. For large T , this reduces to

$$y = \ln T - 1/2 T \quad (5)$$

which has an error of only $\pm .7\%$ for $T \geq 7$.

Solving equation 5 for T

$$T = \exp(y) + 1/2 \quad (6)$$

$$\approx \exp(y) \text{ for large } T. \quad (7)$$

Substituting $y = \ln T$ into equation 2 yields $x = \ln T/\alpha + \mu$ which lends validity to the use of the semi-logarithmic plot for extreme data with an underlying exponential distribution for return periods greater than seven. Conversely, if the data were fit well by the logarithm of the return period vs x , it should be possible to use Gumbel's first asymptotic distribution for the analysis of these data.

Many techniques have been proposed for the proper selection of the parameters α , μ of the extreme distribution. These often were proposed for calculational convenience. With the proliferation of computers, one of the simplest methods is the use of least squares analysis. The line so determined represents the expected maxima at each return period. The actual values will be dispersed around these expected values.

One significant advantage of the extreme value model is the applicability of confidence bands around the line of expected values. Two sets of confidence bands may be calculated. The first is a function of the reduced variate and slope and is used to determine the goodness of fit of the assumed distribution. The second is a function of the slope only and is used to predict confidence levels of the extreme values.

(2) Weibull Distribution. Weibull in 1961 proposed a simple distribution which has been used for various civil engineering problems. The application of this distribution to the description of wind wave short-term statistics was suggested by Bretschneider (1965). Several sets of wave data, for example, Flatseth and Pederson (1970) and Battjes (1972), have been found to be described by the Weibull distribution. The Weibull distribution function is given by

$$F(x) = 1 - \exp \left\{ - \left[\frac{x-A}{B} \right]^C \right\} \quad (8)$$

where

A = the lower limit of the variable x

B = the scale factor

C = the shape factor

When the lower limit A is zero, this is known as a Frechet distribution. Rearranging the terms in equation 8 and taking the logarithm twice yields

$$\ln \ln(1-F(x))^{-1} = C \ln x - C \ln B \quad (9)$$

The appropriate values of B and C are determined from the slope and intercept of the straight line, using the statistical least squares technique.

(3) Semi-log Plot. Another technique which has been used by many authors involves plotting $\log \{1-F(X)\}^{-1}$ versus x . If a linear relationship is obtained, extrapolation beyond the observed data should yield an acceptable estimate of the expected wave height for the design return period.

(4) Log Normal Distribution. Following the work of Jasper (1956) and Darbyshire (1956), Draper (1963) concluded that the height and period of the design wave can best be estimated from a Gaussian distribution of the logarithm of the height or period. This technique may be applied to whichever wave height parameter is required (i.e. mean wave height, significant wave height, etc.) However, the data does curve off at the upper limits in some cases.

(5) Normal Distribution. One of the simplest methods of analysis first used in hydraulic studies and later extended for design hurricanes and waves is the method of Beard (1952), which assumes a Gaussian distribution. In this analysis, the cumulative probability and recurrence interval are defined by:

$$P(X \leq x_m) = F(x_m) = 1 - \frac{m+a}{M+B} \quad (10)$$

$$T_m = [1 - F(x_m)]^{-1}/n \quad (11)$$

where $F(x_m)$ = the assigned value of the probability distribution function of event m

m = rank of the observed value when ordered by increasing magnitude

M = total number of observed events

T_m = return period in years of event x_m

a, b = arbitrary constants to assure $0 < F(x) < 1$

n = number of observations/year

The method of Beard (1952) is to plot $F(x_m)$ versus x_m on normal probability paper. The points are then connected by a smooth curve which is extrapolated beyond the region of the observed data. For any return period of interest, the value of the probability distribution function is calculated and the expected value read from the plot.

Design Life and Risk Factors. In the design of an ocean structure the engineer needs to determine the risks involved in using a chosen design wave. The calculated return period is the average expected duration between events of a given magnitude, however, this value provides no indication of when the event may occur. Court (1952) and others have related design life, design return period, and risk in simple probabilistic terms to aid the design engineer. The argument presented is summarized here.

Assuming the annual maxima to be independent, the probability that x_m will not be exceeded in N years is given by

$$[P'(x \leq x_m)]^N \tag{12}$$

The probability of at least one more exceedance in N years is

$$P(X_{\max} > x_m) = 1 - [P'(X \leq x_m)]^N \tag{13}$$

The return period based on the work of Langbein (1949) and used by Rocheleau (1977) is given by

$$T_y = \{1 - [F(x_m)]^n\}^{-1} \tag{14}$$

Substituting T_y from equation 14 yields

$$P(X_{\max} > x_m) = 1 - (1 - 1/T_y)^N \tag{15}$$

N may be considered as the design life with a probability of failure given by $P(X_{\max} > x_m)$ for the event with a return period T_y . For convenience the design life is defined in terms of return period by

$$N = T_y/U \tag{16}$$

where

$U =$ a positive value ≥ 1 .

For design calculations, the value $P(X_{\max} > x_m)$ is considered as the risk (R). Substituting into equation 15 yields

$$R = 1 - (1 - 1/T_y)^{T_y/U} \tag{17}$$

For large T_y this becomes

$$R = 1 - e^{-1/U} \tag{18}$$

Solving for the factor U in equation 18,

$$U = -1/\ln(1-R) \tag{19}$$

Substituting equation 19 into equation 16, yields

$$N = -T_y (\ln(1-R)) \tag{20}$$

Thus for a chosen design life and risk factor, the necessary design return period may be calculated.

SUMMARY OF ANALYSIS

1. Keahole Point, South Shore and SSMO Area 2: Figure 5 will be discussed first, inasmuch as we have available two sets of wave hindcast data for locations around Keahole Point, and also the SSMO data for Area 2. Figures 6 and 7, based on Gumbel's distribution, show the results using the Marine Advisers (1963) wave hindcasts and the U.S. Corps of Engineers (1964) wave hindcast data, respectively. Figure 8 is based on the SSMO data for Area 2, where H, shipboard wave observations, have not been corrected to significant wave height.

Figure 9 shows the comparisons of expected wave heights from various methods of statistical extrapolations for the above three sources of data used in Figures 6, 7 and 8. It is seen that the various methods of statistical analysis give quite a wide variation in results based on the three sources (Figures 9a, 9b, and 9c). Figure 9d shows the variations of the three sets of data for the Gumbel distribution of wave heights.

Table 9 gives the results of statistical evaluations of wave height data (based on Figure 9) for Keahole Point, Hawaii.

2. North Shore of Oahu and SSMO Areas 1 and 3: Wave hindcast data of severe storms (similar to Tables 1 and 2) are not available for the north shores of Hawaii and hence we consider only shipboard wave observations for SSMO Areas 1 and 3. Figures 10 and 11 are the corresponding results based on the Gumbel distribution. We are also interested in the statistics for extreme waves for the north shore of the island of Oahu. SSMO Area 1 is mostly for the island of Hawaii and SSMO Area 3 is mostly for the island of Kauai. Therefore, we have averaged to two sets of data and assumed that this would be generally applicable halfway between Areas 1 and 3, or the north shore of the island of Oahu. Figure 12 shows the results of this averaging.

Table 8 gives a summary of the statistical analysis of the three SSMO areas. Based on shipboard wave observations, it is surprisingly interesting that the statistical analysis results give essentially the same extreme wave heights for all three SSMO areas for corresponding recurrence intervals. The explanation for this can be made, in view of the large SSMO areas surrounding Hawaii (see Figure 5). It would appear that the islands have little effect on the waves over large sections of the SSMO areas where the ship observations are made, because there can be large fetch lengths in any direction away from the islands. Evidently, the southern swells off the south shore of Hawaii either pass around or through the islands from SSMO Area 2 to SSMO Areas 1 and 3. This is probably not completely true, as it is also likely that the southern swell is not important in determining the extremes, and in some cases may even be absent from SSMO reports, particularly when tradewind waves are predominant.

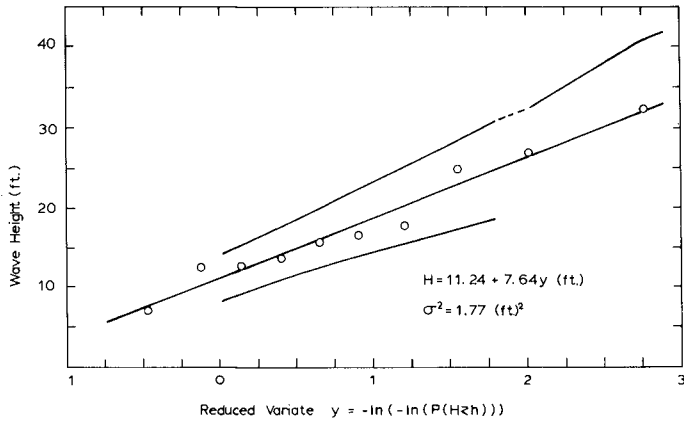


FIG. 6 LINE OF BEST FIT USING GUMBEL'S DISTRIBUTION FOR SIGNIFICANT WAVE HEIGHTS FROM 10 STORMS AFFECTING THE HAWAIIAN ISLANDS FROM 1947 THROUGH 1961 HINDCASTS BY MARINE ADVISORS (1964)

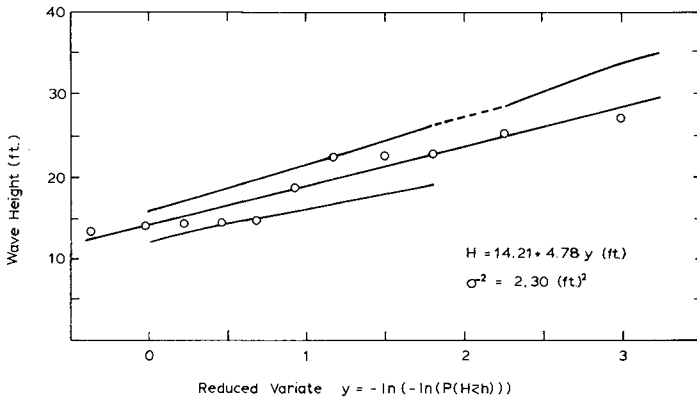


FIG. 7 LINE OF BEST FIT USING GUMBEL'S DISTRIBUTION FOR SIGNIFICANT WAVE HEIGHTS FROM 11 STORMS AFFECTING KEAHOLE POINT FROM 1947 THROUGH 1965 HINDCASTS BY U.S. CORPS ENGINEERS (1968)

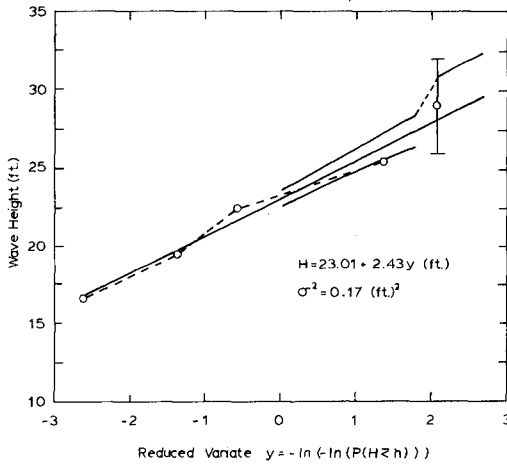


FIG. B LINE OF BEST FIT USING GUMBEL'S DISTRIBUTION FOR EIGHT YEARS OF SHIPBOARD OBSERVATIONS IN SSMO AREA 2

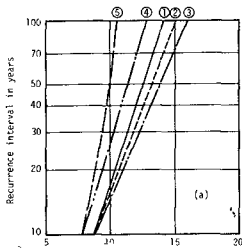


Fig. 9a Significant Wave Height in Meters

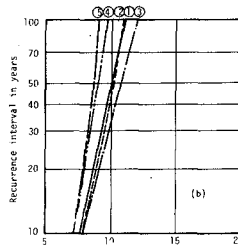


Fig. 9b Significant Wave Height in Meters

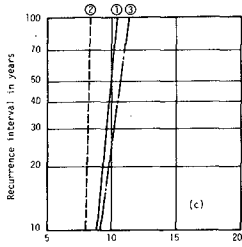


Fig. 9c Observed Wave Height in Meters

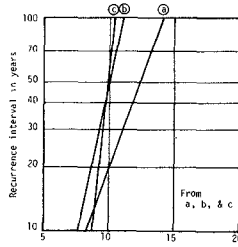


Fig. 9d Gumbel Distribution of Wave Heights

Fig. 9 Comparisons of Expected Wave Heights from Various Methods of Statistical Extrapolations for Three Sources of Data

- 1 ————— Gumbel's First Distribution
- 2 - - - - - Weibull Distribution
- 3 ———— Semi-log Distribution
- 4 ———— Log Normal Distribution
- 5 ———— Normal Distribution

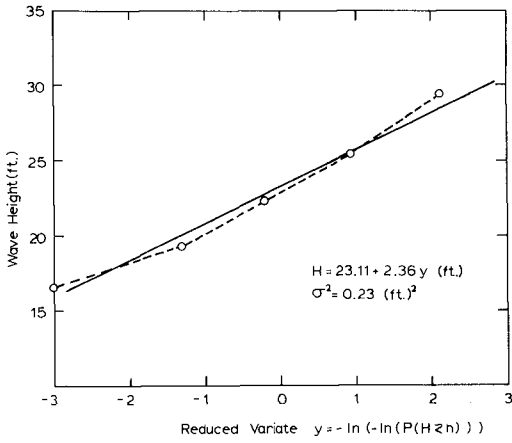


FIG.10 GUMBEL'S FIRST ASYMPTOTIC DISTRIBUTION
 SSMO: AREA #1

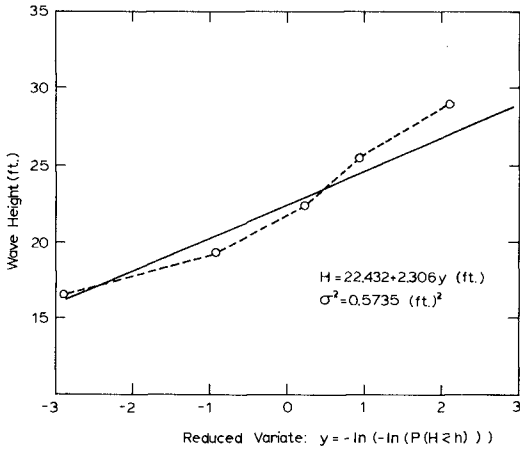


FIG.11 GUMBEL'S FIRST ASYMPTOTIC DISTRIBUTION
 SSMO: AREA #3

TABLE 8

RESULTS OF STATISTICAL EVALUATIONS OF SSMO WAVE HEIGHT DATA FOR SOUTH SHORE AND NORTH HAWAII BASED ON GUMBEL'S DISTRIBUTION

Wave Heights in Meters

SSMO Area No.	Recurrence Interval in Years				
	10	25	50	75	100
1	8.7	9.4	9.9	10.2	10.4
2	8.7	9.4	9.9	10.2	10.4
3	8.4	9.1	9.6	9.9	10.1
average 1 and 3	8.8	9.4	9.9	10.1	10.3

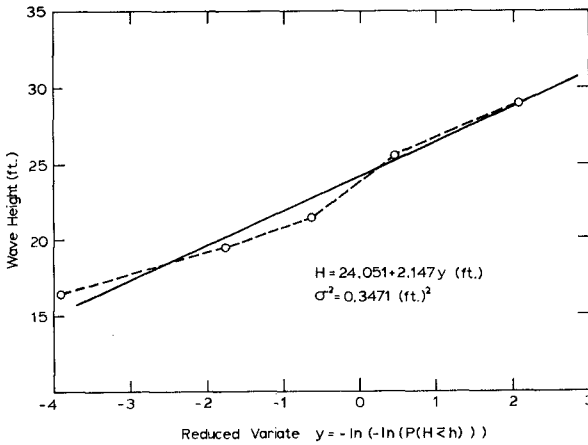


FIG.12 GUMBEL'S FIRST ASYMPTOTIC DISTRIBUTION
SSMO: AREAS #1 & #2

TABLE 9 RESULTS OF STATISTICAL EVALUATIONS OF WAVE HEIGHT DATA FOR KEAHOLE POINT, HAWAII					
(a) Based on Significant Wave Hindcasts of 10 Storms (1947-1961) by Marine Advisors (1963)					
STATISTICAL METHOD	RECURRENCE INTERVAL IN YEARS				
	10	25	50	75	100
1	8.7	10.9	12.5	13.5	14.1
2	8.8	11.5	13.4	14.4	15.0
3	8.8	11.6	13.8	15.1	16.0
4	7.8	9.8	11.2	12.0	12.7
5	7.8	9.0	9.8	10.2	10.5
(b) Based on Significant Wave Hindcasts of 11 Storms (1947-1965) by U.S. Army Corps of Engineers (1968)					
STATISTICAL METHOD	RECURRENCE INTERVAL IN YEARS				
	10	25	50	75	100
1	7.6	8.9	10.0	10.6	11.0
2	7.8	9.1	10.1	10.4	10.7
3	7.8	9.3	10.7	11.5	12.0
4	7.2	8.3	9.0	9.5	9.8
5	7.2	8.1	8.6	8.8	9.0
(c) Based on Shipboard wave observations from U.S. Navy Oceanographic Office SSMO Report for Area 2 (Southern routes of Hawaii, 1963-1971)					
STATISTICAL METHOD	RECURRENCE INTERVAL IN YEARS				
	10	25	50	75	100
1	8.7	9.4	9.9	10.2	10.4
2	7.8	8.0	8.1	8.2	8.3
3	9.1	9.9	10.6	11.0	11.3
NOTES: Wave Heights are given in meters.					
IN TABLES	NOTATIONS IN FIGURES	TYPE OF DISTRIBUTION			
1	-----	Gumbel's First			
2	- - - - -	Weibull			
3	- - - - -	Semilog			
4	- - - - -	Log Normal			
5	-----	Normal			

ACKNOWLEDGEMENTS

The material given here represents partial results of research supported by the Sea Grant Office of the National Oceanographic Administration (NOAA) under Sea Grant Contract Nos. 04-6-158-44026 and 04-6-158-44114. Much of the material presented here was taken from the M.S. Plan B paper of Richard Rocheleau (1977) for Keahole Point and SSMO Area 2. Mr. Michael Miller did the analysis of the SSMO data for Areas 1 and 3 and the north shore of Oahu.

REFERENCES

- Battjes, J.A. (1972) "Long Term Wave Height Distributions at Seven Stations around the British Isles," Deutsche Hydrographische Zeitschrift.
- Beard, R.L. (1952) "Statistical Methods in Hydrology," U.S. Army Office of Chief of Engineers.
- Bretschneider, C.L. and E.E. Tamaye (1976) "Hurricane Wind and Wave Forecasting Techniques," Proc. 1976 Coastal Engineering Conference, Honolulu, Ch. 13, pp. 202-237, ASCE, New York.
- Court, Arnold (1952) "Some New Statistical Techniques in Geophysics," Advances in Geophysics, Vol. 1.
- Darbyshire, J. (1961) "Prediction of Wave Characteristics over the North Atlantic," Journal of the Institute of Navigation, Vol. 14.
- Draper, L. (1963) "Derivation of a 'Design Wave' from Instrumental Records of Sea Waves," Proc. of the Institute of Civil Engineers, London, England.
- Flatseth, J. and B. Pederson (1970) "Distribution of Wave Height in Different Ocean Areas of the World," Report No. 70-7-S for Research Dept., Det Norske Veritas, Oslo, Norway.
- Gumbel, E.J. (1958) Statistics of Extremes, Columbia University Press, New York.
- Hogben, N. and F.E. Lumb (1966) Ocean Wave Statistics, Ministry of Technology, National Physical Laboratory, London.
- Jasper, N.H. (1956) "Statistical Distribution Patterns of Ocean Waves and Wave Induced Ship Stresses and Motions with Engineering Applications," Transactions, Society of Naval Architects and Marine Engineers, November.
- Langbein, W.B. (1949) "Annual Floods and the Partial Duration Series," Transactions, American Geophysical Union, Vol. 30.
- Marine Advisers (1964) "Characteristics of Deep-Water Waves in the Oahu Area for a Typical Year," La Jolla, California.

Marine Advisers (1963) "Severe Storm Wave Characteristics in the Hawaiian Islands," La Jolla, California.

Moberly, R. and T. Chamberlain (1964) "Hawaii Beach Systems," Hawaii Institute of Geophysics, Report HIG 64-2.

Munchmeyer, F. and C.L. Bretschneider (1978) "Some Design Criteria for OTEC Installations for Keahole Point, Hawaii," Proc. 16th International Coastal Engineering Conference, Hamburg, Germany.

Rocheleau, R.E. (1977) "Evaluation of Extreme Wind and Wave Climate in Hawaii with Special Application to Keahole Point and the North Shore of Hawaii," M.S. Plan B Paper, Look Lab of Oceanographic Engineering, Department of Ocean Engineering, Technical Report No. 77-41, U. of Hawaii.

U.S. Army Engineer District (1968) "General Design Memorandum-Honokahau Harbor for Light Draft Vessels," Honolulu, Hawaii, January 1968.

U.S. Naval Oceanographic Office, Summary of Synoptic Meteorological Observations, U.S. National Technical Information Service, Springfield, Virginia.

Weibull, W. (1961) "A Statistical Distribution Function of Wide Applicability," Journal of Applied Mechanics.

CHAPTER 8

THE USE OF IMAGING RADAR IN STUDYING OCEAN WAVES

by

M. G. Mattie¹ and D. Lee Harris²

INTRODUCTION

Imaging radar can be used to provide information about the two-dimensional character of the wave field. This is especially important near shore where the effects of refraction and shoaling interfere with the simple interpretation of a directional spectrum based on records from a network of gages.

Imaging radar has the advantages of providing full two-dimensional information of the type provided by aerial photography and of being available continuously, including night time and during storms.

Imaging radar, of course, also has some disadvantages when compared to other data gathering systems. Specifically, the imaging radar does not provide a measure of wave height. It does not provide as much resolution as aerial photography and the shorter waves of interest may be missed. The most important disadvantage is that short ripples are essential to the detection of long waves, hence swell is not detected outside the breaker zone when the wind is calm or the high frequency waves are inhibited by oil slicks.

Several characteristics of the radar images of waves, as compared to aerial photography, are illustrated in Figure 1. Note the similarity of the wave patterns in the radar image and the aerial photograph. The image does not show any features of the land. The location of the radar is shown on the aerial photography by an "X".

Ijima et al (1964) and Wright (1965) appear to have been among the first to report the use of radar for imaging ocean waves. Oudshoorn (1960), Wills and Beaumont (1971), Evmenov et al (1973) and others have published photographs of a radar scope showing waves. This report differs from earlier papers on this topic by providing a discussion of practical procedures for overcoming some of the more mundane technical difficulties associated with routine data collection.

¹Physicist, Coastal Oceanography Branch, U.S. Army Coastal Engineering Research Center, Kingman Building, Fort Belvoir, VA 22060

²Oceanographer, Research Division, U.S. Army Coastal Engineering Research Center, Kingman Building, Fort Belvoir, VA 22060

Landward of the bar wave breaking due to limited water depth cannot therefore occur before the new generated waves reach the shore of the island or the dykes on the mainland coast (FIG.14).



Fig. 14: Wave Breaking on the Bar in front of the Northwestern Shore of the Island of Norderney

4. Wave height damping on the tidal flats

While the waves passing the eastern part of the bar attack the northwestern shore of the island of Norderney, those which are generated after breaking on the eastern part spread out over the tidal flats. Though they are not high enough to be broken because of the limited water depth a certain wave damping on the tidal flats could be observed. It must be explained as a combined superposing effect of bottom friction, refraction, diffraction and shoaling.

The damping of maximum wave height from the inner part of the tidal inlet can be described as a function of itself in relation to the water depth at the end of the travel distance (FIG.15). One gets a more complicated expression for the damping of the significant wave height (FIG.15), but the influence of water depth can be distinguished too.

The intensity of wave height damping on the tidal flats can be described by another example:

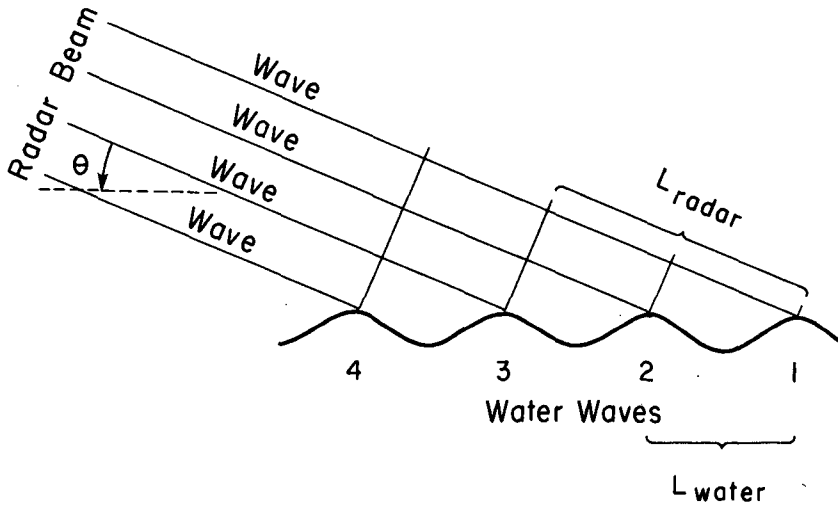


Figure 2. Illustration of first order Bragg Scattering. Each wave acts as a reflector. Reflection from several waves must be in phase for a significant return signal.

are nearly always in equilibrium with the wind. Thus if the wind is calm and the water surface glassy, the swell waves which may exist will not be detected seaward of the surf zone.

At least three processes have been recognized by which the long waves modulate the radar return from the short waves (Lynch and Wagner, 1970 Valenzuela, 1978). It has been known for many years that the convergence zone on the front face of the traveling waves tends to increase the height and decrease the length of the capillary waves and that the divergence zone on the back face of the waves has the opposite effect (Phillips, 1966). This process has been investigated in greater detail and with specific reference to the radar cross section by Keller and Wright (1975), Valenzuela and Wright (1976), Wright (1978), Reece (1978) and many others. This process is illustrated in Figure 3.

The strength of the radar return (generally called the radar cross section) from the sea is a function of the grazing angles, as shown by Skolnik (1970). The slope of the water surface for a distance of many radar wavelengths, varies with the phase of the long waves as shown in Figure 4. The angle is greater for the face of the wave facing the radar than for the opposite face. This process has been investigated extensively by Valenzuela (1970).

When the grazing angle is low the crest of one wave may prevent irradiation of the following trough, producing a shadow zone between successive wave crests as illustrated in Figure 5. This situation produces a maximum contrast in the return from different phases of the

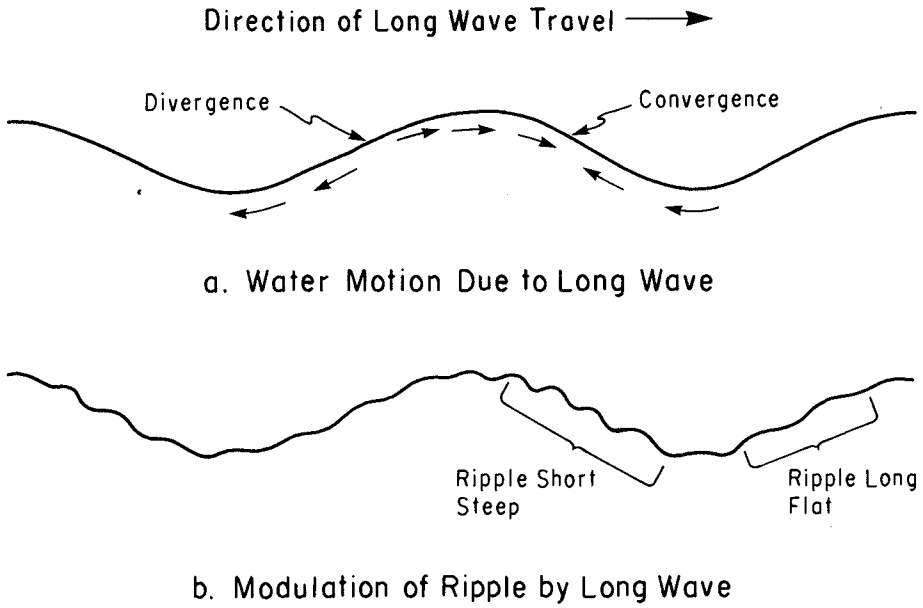


Figure 3. Modulation of short waves by long waves

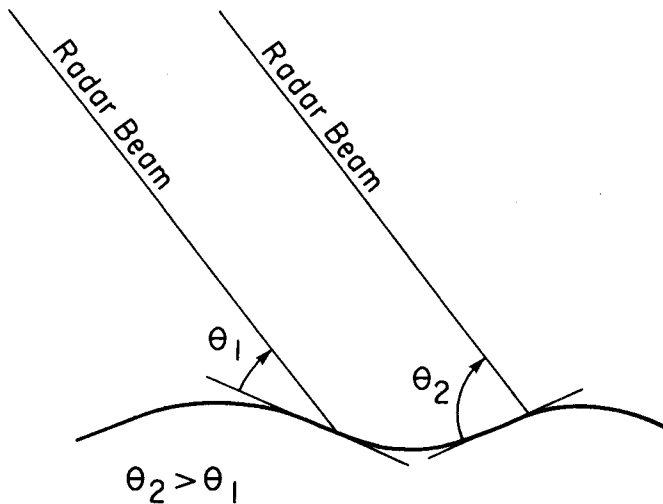


Figure 4. Modulation of the incident angle of the radar beam by the long waves.

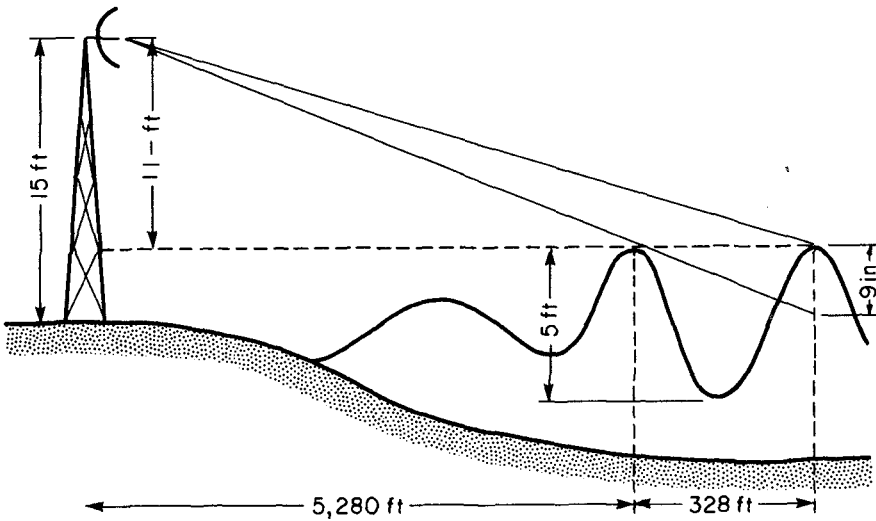


Figure 5. Illustration of the shadowing of a portion of one wave, by a wave nearer to the radar.

wave. When the wave heights are variable, as they usually are, and the grazing angle is small, the crest of a large wave may shadow at least part of the crest of a following lower wave, so that at least parts of some wave crests are missing in the return signals from the longer useable ranges.

The smallest spot which can be distinguished on the radar scope is determined by the duration of the transmitted energy pulse and the ratio of the radar wavelength to the effective length of the radar antenna as shown in Figure 6. The factor of $1/2$ in the equation for ΔR occurs because the radar beam must travel across the spot once in each direction to permit detection. The smallest available pulse length in many radar systems is too long to permit the recognition of water waves. Some commercial marine navigation radars, however, do provide pulse lengths as short as 50 nanoseconds, (50×10^{-9} seconds) for ranges of 5.5 kilometers or less. This pulse length is short enough for the detection of 4-second waves in deep water. Shorter pulses could be used to permit the detection of shorter waves. This would involve a reduction in power and maximum range. Shorter pulses are not generally available in commercial radar systems.

The angular resolution is proportional to the ratio of the radar wavelength to the effective length of the radar antenna. Commercial marine radar manufacturers often provide several optional antenna systems. The shortest, and most widely used, provides an angular resolution of about 2.0 degrees. The longest gives a resolution of about 0.6 degrees. Obviously the longest antenna is preferable for imaging waves.

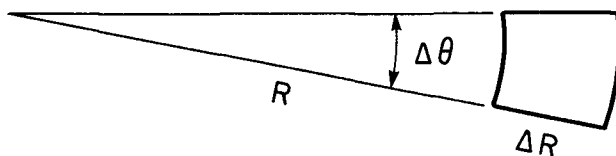


Figure 6. Resolution cell for the radar image. R is the range, ΔR resolution along the radar beam. $\Delta R = c\Delta T/2$, where c is the speed of light and Δt is the duration of a radar pulse. $\Delta\theta$ is the azimuthal resolution.

The intensity of the radiated energy decreases with the square of the distance from the antenna. The intensity of the back scattered energy likewise decreases with the square of the distance from the target. Thus the power returned to the antenna, decreases with the fourth power of the distance between antenna and the reflecting surface.

If the signal is strong enough to reveal distant targets, the scope may be saturated by nearby targets, so that no details are revealed. When the signal level is low enough to reveal details near the center of the scope, distant targets may escape detection. Some improvement may be made by using circuits which provide increased amplification at increased distances.

PRACTICAL CONSIDERATIONS

The optimum settings of the controls on the radar, for imaging waves, depend on ambient conditions and can be found for any given conditions by a little experimentation with the controls. Most wave data collection systems, however, are unattended and the need for frequent adjustment to the radar controls to obtain optimum performance has been a handicap in the exploitation of microwave, ground based radar for the collection of wave data.

A solution to this problem may be obtained by combining a control system which will vary the controls during each observation according to a preset schedule. An off-the-shelf 3 cm (X-band) marine radar has been combined with a control system which turns the radar on at preset times. After a brief warm up period, a series of 1-9 sweeps of the radar over the sea at each of several console settings is photographed. Photographs of the radar scope displaying sea conditions as shown for four range settings are presented in Figure 7. Note that the clearest image of this wave field is found at a range of 1.2 kilometers with 14-15 individual waves being discernable. We find that the clearest images are generally obtained with a range setting between ten and twenty wavelengths. Note also that the radar scope tends to be saturated near the center with faint images near the maximum range.

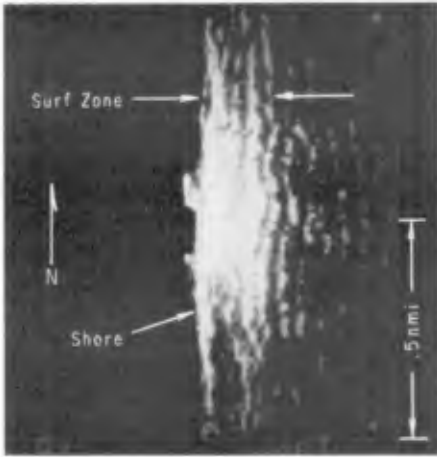
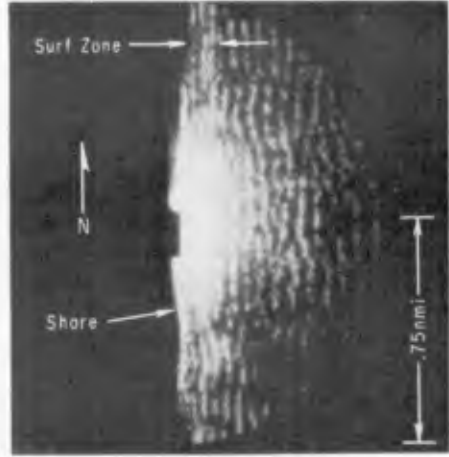
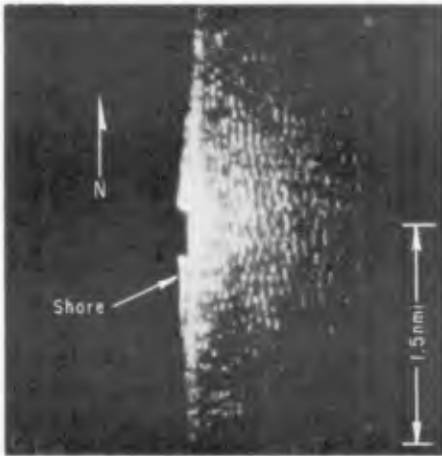
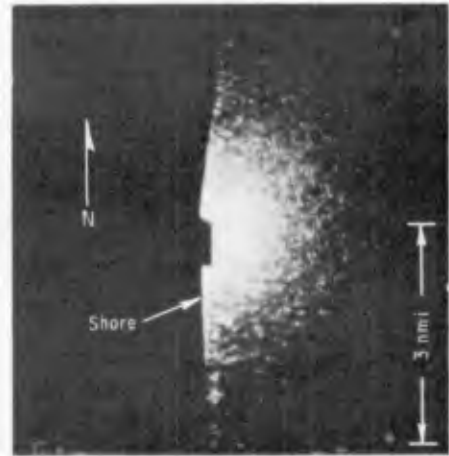
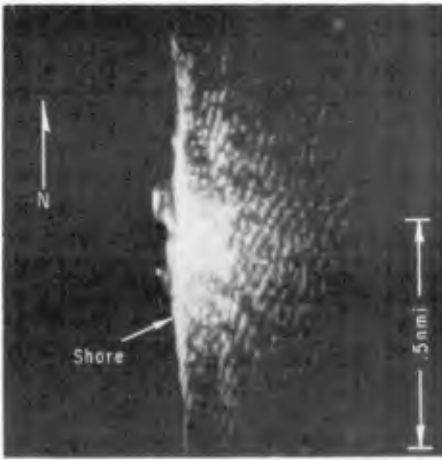
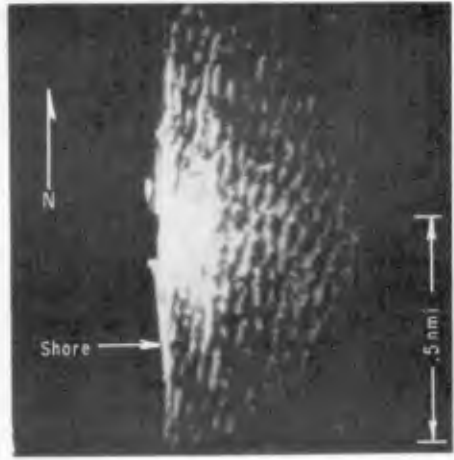
Range \sim .8 kmRange \sim 1.2 kmRange \sim 2.5 kmRange \sim 5. km

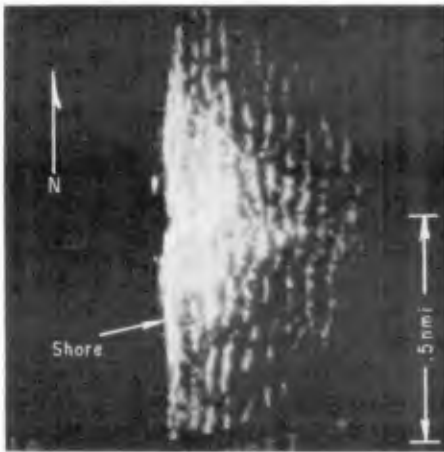
Figure 7. View of the radar images of waves at four ranges.
Coast Guard Radar on Naussett Beach, Cape Cod, Mass.



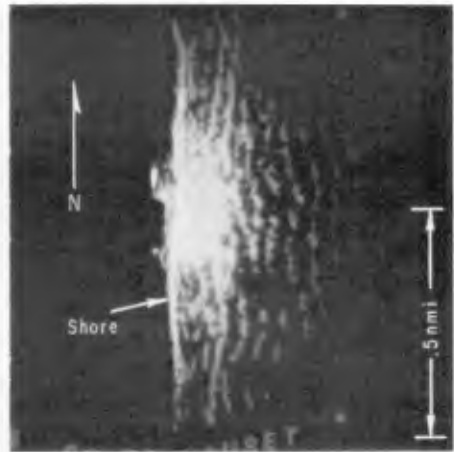
0026



0500



0924



1324

Figure 8. Development of the wave field as revealed by radar

Because of the effects of modulation of the ripples and surface slope on the radar return, it has been seen that longer and steeper waves can be detected at a greater range than short or flat waves. Thus the optimum range setting is seen to be a function of wavelength and wave steepness. This cannot be known in advance. Therefore the system is programmed to take a sequence of pictures at several ranges at a pulse length near 50 nanoseconds as a part of each observation. At present only one level of intensity is provided, but it appears that the addition of two intensity levels to the system would be an improvement. Only the most satisfactory photograph of the set is routinely analyzed.

One might expect the curvature of the earth to be a factor in determining the optimum antenna elevation, but this does not turn out to be the case. When commercial radar is used, the range is restricted to the order of 5.5 kilometers by the weak power return for longer ranges.

At this range an elevation of two meters is sufficient for the radar signal to illuminate the surface at maximum range, even in a vacuum. Refraction by the atmosphere causes radar beams to bend in the direction of the earth. On the average the radar waves propagate along a spherical surface whose radius is $4/3$ the radius of the earth. Refraction of the radar beam is greatest when the temperature of the air increases and the humidity decreases with elevation. Propagation parallel to the earth's surface is occasionally observed. The optimum elevation of the radar antenna is a function of the ambient wave conditions. As previously stated, the greatest contrast between wave crest and trough is obtained when the crest of one wave shadows the following trough but does not shadow the following crest. Variation of the antenna elevation to satisfy ambient conditions, however, cannot be accomplished very easily and it is not always possible to obtain an optimum value. Our most successful operations have been obtained with elevations between 20 and 40 meters.

ADDITIONAL EXAMPLES OF RADAR WAVE DATA

Figure 8 shows the development of a wave field near Cape Cod, Massachusetts. All views were obtained with a maximum range of 925 meters. One can easily follow the gradual change in wave direction from SE to E and the increase in wavelength from midnight to 0900. The wind had been blowing from the SE at 15 m/sec for three hours before the first photographs and varied between 14 and 17 m/sec until noon. The wind had shifted to NE by 1324. Wave refraction near shore can be seen in the first two photographs.

Figure 9 shows even stronger evidence of refraction and the presence of at least two distinct wave trains. Two or more distinct wave trains can be identified in a large fraction of our radar photographs of the wave field.

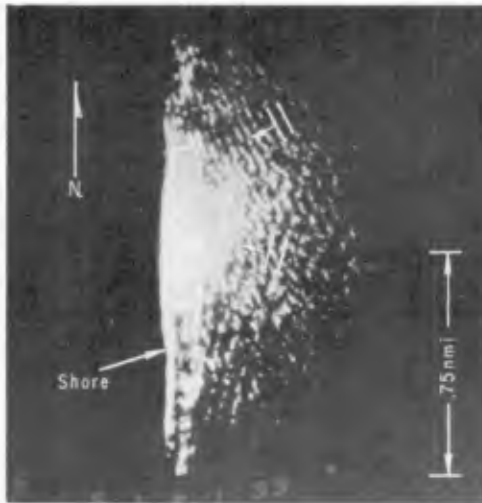


Figure 9. Two wave trains and refraction shown on the Radar Scope.
Coast Guard Radar, Cape Cod, Mass., Jan. 8, 1976.

It is obvious that wavelength could be measured in many of the radar pictures and that the wavelength decreases as the shore is approached. By following a single wave train such as that indicated by the arrow in the two pictures shown in Figure 10, it is also possible to measure the phase speed of a wave. The straight vertical line on the image is an offshore breakwater. The elapsed time between these two pictures is 5.46 seconds. Two intermediate frames have been omitted.

One of the remarkable features noted in many of the radar photographs is the persistence of individual waves. It is often possible to identify a single wave crest from the time it appears at the edge of the scope until it breaks against the shore. The wave patterns are very consistent from frame to frame. There appear to be perturbations in intensity and direction along many wave fronts, but the wave pattern, taken as a whole, gives the appearance of continuity for the full distance over which the waves can be followed.

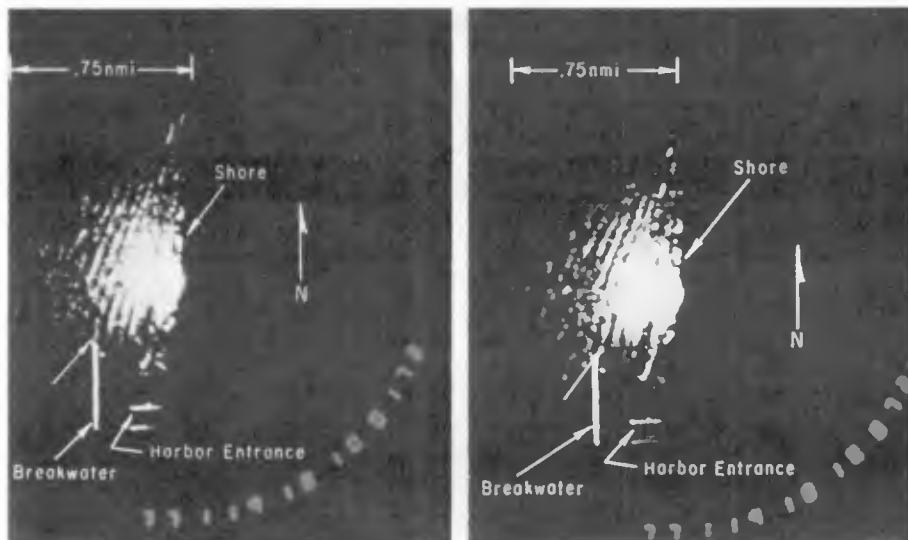


Figure 10. Two views of the radar scope separated by 5.46 seconds illustrating technique for measuring the phase speed of water waves from photographs of the radar scope. CERC radar Channel Islands Harbor, CA, April 29, 1977.

ANALYSES OF THE PHOTOGRAPHS

The device which we have found to be most convenient for analyzing small quantities of radar film is shown in Figure 11. A 16 mm analytical projector is mounted to the left of the viewing screen. This projector can advance the film frame by frame, or automatically, at various speeds between 1 and 24 frames per second. A mirror is used to extend the light path and to form the image by rear projection on a ground glass screen. This arrangement permits the operator to review the film rapidly and select the best frame from each observation for evaluation. The protractor and ruler mounted over the display screen permits rapid determination of the direction of selected waves. When the only information wanted is the direction of the prominent wave trains at a selected point, evaluation of each observation requires only about a minute. In general, however, the radar record shows systematic variation of wave direction with location. A few frames may be selected for enlargement to reveal perspective about the wave field that is not provided by a network of wave sensors within a small area.



Figure 11. Device used for the analysis of radar film.

VALIDATION

In order to illustrate the agreement between data obtained with this radar and by other techniques, a few samples of radar images coincident with other independent wave measurements are presented in Table 1. The data were obtained during the West Coast Experiment which was a preflight test in preparation for SEASAT. The aerial photographs were obtained by NASA. Copies are available from U. S. Geological Survey EROS Data Center, Sioux Falls, South Dakota. The SAR images were provided by JPL. The procedure employed for analysis of SAR data has been described by Elachi (1978).

In interpreting the data in Table 1, it should be noted that the observations are not exactly synoptic and that the data appearing in any of the aerial photographs were collected within a few milliseconds.

A more extensive comparison of wave direction as determined by the CERC radar and a pressure gage array is in preparation. Publication by Mattie, Hsiao and Evans in the Journal of Geophysical Research sometime in 1979 is planned.

Table 1. Comparison of Information From CERC Radar Images With That Obtained With Other Direction Measuring Devices.

Date (1977)	Time	Wave Direction at NUC	Wave Length	Wave Period (Sec)	Wave Direction	Wave Length	Wave Period (Sec)			
CERC RADAR										
March 14	11:30	$283^\circ \pm 4^\circ$	$84 \pm 11m$	$8.6 \pm .9$	$284^\circ \pm 2^\circ$	$80 \pm 16m$	$7.6 \pm .9$			
		$261^\circ \pm 4^\circ$	$168 \pm 22m$	15.5 ± 2	$264^\circ \pm 3^\circ$	$120 \pm 16m$	10.2 ± 1			
March 29	11:00	$282^\circ \pm 4^\circ$	$107 \pm 21m$	9.2 ± 1.4	$288^\circ \pm 2^\circ$	$89 \pm 16m$	$8.1 \pm .9$			
		$256^\circ \pm 4^\circ$	$160 \pm 22m$	14.7 ± 2.2	$257^\circ \pm 3^\circ$	$109 \pm 16m$	9.4 ± 1			
U2 AERIAL PHOTO										
					$316^\circ \pm 2^\circ$	$40 \pm 16m$	$5.1 \pm .5$			
					$320^\circ \pm 2^\circ$	$30 \pm 16m$	4.4 ± 1			
SAR										
March 28	18:00	$285^\circ \pm 4^\circ$	$136 \pm 22m$	10.8 ± 1.5	286	Direction Refracted to NUC	Wave Length			
		$261^\circ \pm 4^\circ$	$105 \pm 22m$	9.9 ± 1.4				283°	138m	$9.4 \pm .1$
		$242^\circ \pm 4^\circ$	$182 \pm 22m$	15.2 ± 1.5				262°	208m	$11.5 \pm .2$

1. Photographs of the radar scope and the corresponding portion of the aerial photograph are shown in Figure 1.
2. The CERC radar images and the U2 photos for March 14 and 29 were taken within a 10 minute period on each day. The CERC radar measurement at 18:00 hours on March 28 is an average of three images taken within \pm 30 minutes of the SAR data. The 285° direction wave train appeared on all three images. The 261° and 242 direction trains each appear on only two of the three images used in the average.
3. Wave direction and period for SAR data were obtained from direction plots generated from the fourier transform. These were provided by JPL.
4. Periods estimates were obtained from wave length and depth through airy wave theory.
5. Wave length measurements were not all made at the same depth.

SUMMARY AND RECOMMENDATIONS

It has been shown by means of examples that it is often possible to obtain useful images of the nearshore ocean wave field with X-band based radar. The physical principles involved in the use of radar to image the wave field have been simply described. A comparison of wave direction, wavelength and period estimates obtained with the surface based radar and similar data obtained by other more expensive means shows that the information obtained with radar is comparable in quality with similar data obtained by other means. The surface based radar does not provide wave height information. This paper is a summary of a longer report on this topic by Mattie and Harris (1979).

It is recommended that if only a single wave sensor is to be used at any location, a good gage whose record permits the computation of one dimensional energy spectra should be used. If two or more sensors can be utilized, the second should be an imaging radar which can provide direct information about the two-dimensional nature of the wave field most of the time.

ACKNOWLEDGEMENTS

Data presented in this paper, unless otherwise noted, were obtained from research conducted by the United States Army Coastal Engineering Research Center under the Civil Works research and development program of the United States Army Corps of Engineers. Permission to publish this information is appreciated. The findings of this paper are not to be construed as official Department of the Army position unless so designated by other authorized documents.

REFERENCES

- Elachi, C., "Radar Imaging of the Ocean Surface", *Boundary-Layer Meteorology*, Vol. 13, Nos. 1, 2, 3 and 4, January 1978, pp. 165-179.
- Eymenov, V. F., Kozhukhov, I. V., Nichiporenko, N. T., and Khulop, G. D. "Test of the Radar Method of Defining Ocean Wave Elements", *Fluid Mechanics - Soviet Research*, Volume 2, No. 5, September - October 1973, pp. 141-145.
- Ijima, T., Takahashi, T., Sasaki, H., "Application of Radars to Wave Observations", *Proceedings of 11th Japanese Conference of Coastal Engineering*, 1964, pp. 81-88.
- Keller, W. C., and Wright, J. W., "Modulation of Microwave Backscatter by Gravity Waves in a Wave Tank", *NRL Report 7968*, Naval Research Laboratory, Washington, D.C., March 1976.

- Valenzuela, G. R., "Theories for the Interaction of Electromagnetic and Oceanic Waves - A Review", *Boundary-Layer Meteorology*, Vol. 13, Nos. 1, 2, 3, and 4, January 1978, pp. 61-85.
- Wills, T. G., and Beaumont, H., "Wave Direction Measurement Using Sea Surveillance Radars", Technical Memorandum IR 118, Royal Aircraft Establishment, April 1971.
- Wright, F. F., "Wave Observation by Shipboard Radra", *Ocean Science and Ocean Engineering* 1965, Vol. 1, pp. 506-514.
- Wright, J. W., "Detection of Ocean Waves by Microwave Radra: The Modulation of Short Gravity - Capillary Waves", *Boundary-Layer Meteorology*, Vol. 13, 1978, pp. 87-105.
- Lynch, P. J. and Wagner, R. J., "Rough-Surface Scattering: Shadowing Multiple Scatter and Energy Conservation", *Journal of Mathematical Physics*, Vol. II, 1970, 3032-3042.
- Mattie, M. G. and Harris, D. L., "A System for Using Radar to Record Wave Direction", to be published by the Coastal Engineering Research Center, Fort Belvoir, VA, 22060, 1979.
- Oudshoorn, H. M., "The Use of Radar in Hydrodynamic Surveying", *Proceedings of the 7th Conference on Coastal Engineering*, The Hague, Netherlands, Vol. 1, August 1960, pp. 59-76.
- Pawka, Steven S., Inman, Douglas L., Lowe, Robert L. and Holmes, Linda, "Wave Climate at Torrey Pines Beach, California", Technical Paper No. 76-5, U.S. Army Corps of Engineers, Coastal Engineering Research Center, Fort Belvoir, VA 22060, 1976.
- Phillips, O. M., "The Dynamics of the Upper Ocean", Cambridge University Press, London, 1966, Second Edition 1977, pp. 56-63.
- Reece, A. M., "Modulation of Short Wave by Long Waves", *Boundary-Layer Meteorology*, Vol. 13, Nos. 1, 2, 3 and 4, January 1978, pp. 203-214.
- Skolnik, M. I., *Radar Handbook*, McGraw-Hill, New York, NY, 1970.
- Valenzuela, G. R., 1970, "The Effective Reflection Coefficients in Forward Scatter from a Dielectric Slightly Rough Surface", *Proc. IEEE* 58, 1279.
- Valenzuela, G. R., "The Growth of Gravity-Capillary Waves in a Coupled-Shear Flow", *J. Fluid Mech.* 76, pp. 229-250, 1976.

CHAPTER 9

HF SKYWAVE RADAR MEASUREMENT OF HURRICANE WINDS AND WAVES

Joseph W. Maresca, Jr. and Christopher T. Carlson*

I. INTRODUCTION

We measured significant wave height, and surface wind speed and direction for the first two Gulf of Mexico hurricanes of the 1977 season using a high frequency (HF) skywave radar. The radar measurements were made from California by using the SRI-operated Wide Aperture Research Facility (WARF). We recorded sea backscatter for hurricanes Anita and Babe, at distances more than 3000 km from the WARF, by means of single F-layer ionospheric reflection. We compiled real-time maps of the surface wind direction field within a radial distance of 200 km of the storm center, then estimated the hurricane position from these radar wind maps, and developed a track for Anita over a 4 day period between 30 August and 2 September 1977 as the storm moved westward across the Gulf of Mexico. The radar track was computed from 17 independent position estimates made before Anita crossed the Mexican coast, and was subsequently compared to the official track produced by National Hurricane Center (NHC). Agreement between the WARF position estimates and coincident temporal positions on the NHC smooth track was ± 19 km. At approximately 0000Z on 1 September 1977, Anita passed within 50 km of the National Data Buoy Office (NDBO) open ocean moored buoy EB-71, and provided us with the opportunity to compare WARF estimates of the significant wave height, and surface wind speed and direction in all four quadrants of the storm with those made at the buoy. Agreement between the WARF and EB-71 measurements was within 10%.

Two days after Anita crossed land, tropical storm Babe--a weaker, short-lived storm--developed. WARF estimates of the significant wave height, and surface wind speed and direction were made for selected regions of the storm.¹ No in situ wave measurements were available for comparison to the WARF measurements. WARF estimates of the wind speed were compared to wind speed measurements made at nearby oil platforms, and surface wind speeds computed from flight level winds (305 m) measured by a NOAA reconnaissance aircraft. Agreement was again within 10%. The purpose of this paper is to describe the capability of remotely monitoring hurricanes and other open ocean storms by using an HF skywave radar. We will describe the important aspects of the WARF skywave radar, the sea echo Doppler spectra, the method of analysis used to estimate the wave and wind parameters, and the accuracy of these radar-derived quantities.

* SRI International, Menlo Park, California 94025.

II. WARF SKYWAVE RADAR

The Wide Aperture Research Facility (WARF)² is a high-resolution experimental high frequency skywave radar located in central California. The radar is bistatic and operates in the HF band between 6 and 30 MHz. Ocean areas are illuminated by a 20-kW swept-frequency continuous-wave (SFCW) signal from a transmitter site located at Lost Hills, California. The energy reflected from the surface beam is received 185 km to the north at Los Banos, California. The receiving antenna array is 2.5-km long and consists of a double linear array of 256 whip antennas producing a nominal $1/2^\circ$ azimuthal beamwidth at 15 MHz. The signal propagates to and from remote ocean patches by means of one or more ionospheric "reflections."

The coverage area is shown in Figure 1. The radar can be directed either east or west, and can be electronically steered in azimuth $\pm 32^\circ$ from boresight anywhere within the coverage area in $1/4^\circ$ increments. Position accuracy is a function of midpath ionospheric height estimates where uncertainty in the midpath height results in a nominal position accuracy of approximately 20 km. At any one location, the accuracy between consecutive measurements in range and azimuth is an order of magnitude better. WARF has multiple-beam capability, and sea backscatter is usually received simultaneously at four adjacent ocean areas from four different beams separated by $1/4^\circ$. The size of the ocean scattering patch is a function of the beamwidth, the range, the range cell separation, and the number of range cells averaged together. The size of the minimum scattering patch at a range of approximately 2000 km is 3 km in range by 15 km in cross range.

III. IONOSPHERIC PROPAGATION

The ionosphere consists of ions produced in the earth's atmosphere, primarily by solar radiation. Radio-wave propagation by means of ionospheric reflection occurs primarily between elevations of 100 km and 500 km. A graph of electron density as a function of height may show peaks in the ionospheric profile. These peaks are defined as layers and are designated by E_s (sporadic-E), E, F1, and F2. They correspond to peak electron densities located at about 110, 120, 200, and 300 km above the earth, respectively. Ionospheric conditions are transient in time and space and depend on the stability and strength of the electron density profile.³

The minimum radar range for one hop ionospheric propagation is approximately 1000 km; the maximum radar range is approximately 3000 km. The ionosphere will support propagation to a specific range over a limited frequency band. The achievable range is dependent on time of day, geographical region, and ionospheric height. We use two different types of real-time ionospheric soundings at WARF to manage the ionospheric propagation. An oblique-incidence sounding shown in Figure 2 is primarily used to determine: the relative signal strength; the radio

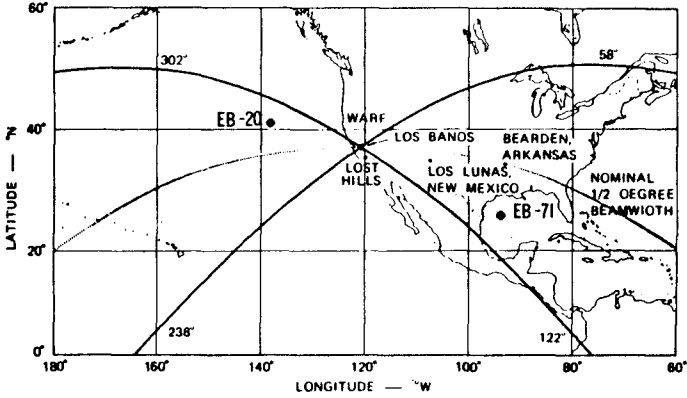


FIGURE 1 COVERAGE AREA OF THE WARF HF SKYWAVE RADAR. All Anita measurements were made west of 88° W in the Gulf of Mexico.

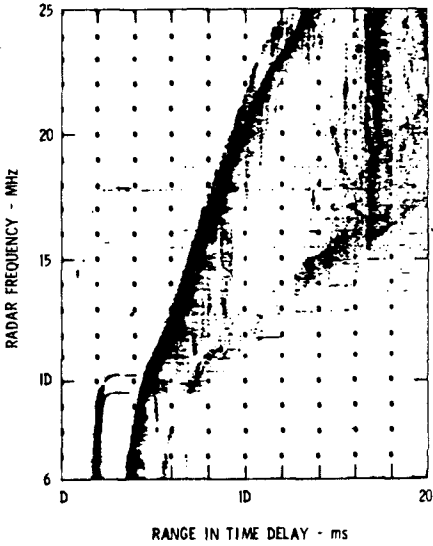


FIGURE 2 OBLIQUE-INCIDENCE SOUNDING TAKEN AT WARF. The oblique-incidence sounding is a plot of energy received for a given frequency at a given range.

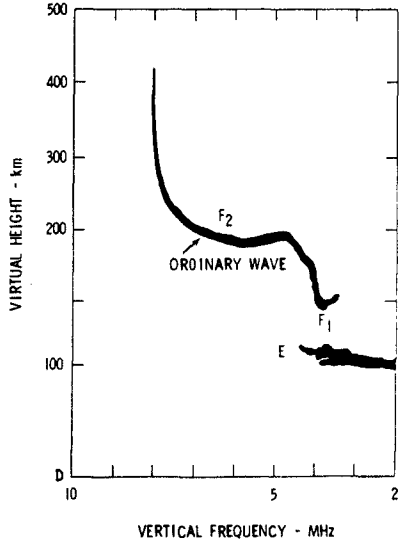


FIGURE 3 VERTICAL-INCIDENCE IONOSPHERIC SOUNDING TAKEN AT WARF. The vertical-incidence sounding is a plot of overhead energy for different frequencies.

frequencies that will propagate to a particular range; and certain types of ionospheric disturbances such as traveling waves, and focusing or defocusing of energy. A vertical-incidence sounding shown in Figure 3 taken between the WARF transmitting and receiving arrays is primarily used to measure the overhead ionospheric mode structure and height of each ionospheric layer. A frequency surveillance spectrum analyzer is used to select interference-free frequency bands.

IV. SEA ECHO DOPPLER SPECTRUM

The sea backscatter received at the WARF is coherently processed in range and Doppler to produce a sea echo Doppler spectrum. We usually process 21 independent Doppler spectra spaced at 3-km range intervals. These spectra are obtained simultaneously at each of four adjacent radar beams. A total of 84 independent Doppler spectra are obtained for each coherent time period. We compute an average spectrum from a subset of these Doppler spectra, depending on the type of measurement and the time and space scales associated with the ocean surface features. An example of a mean sea echo Doppler spectrum produced by averaging 112 spectra obtained from four consecutive 102.4 s coherent time periods, over a scattering patch consisting of 21 range cells and 3 adjacent beams is shown in Figure 4.

The sea echo Doppler spectrum shown in Figure 4 is characterized by two dominant first-order echoes surrounded by a second-order continuum. Crombie⁴ interpreted the first-order echoes in terms of simple Bragg scattering that represented a resonant response between radio waves of wave number k_0 and ocean waves of wave number $k = 2 k_0$. The radar measures the relative power and Doppler of the ocean waves traveling radially toward or away from the radar. The power ratio of the two first-order echoes are indicative of the wave direction of the waves of wave number k . Because k is usually large ($k > 0.5$), it is assumed that the wind direction is identical to the direction of these waves.

The wave height spectrum is derived from the second-order structure surrounding the first-order echoes. For hurricanes, the power in the second-order echoes is large. As the total wave energy increases, the amplitude of the second-order echoes increases as illustrated in Figure 5. Barrick^{5,6} derived theoretical expressions that accurately model the HF scattering process to second order. For a specific directional wave spectrum, the model computes the Doppler spectrum. The effects of the wind direction, wave directionality and the wave frequency spectrum on the modeled Doppler spectrum have been extensively studied by the use of this model.

V. HURRICANE DATA SAMPLING

Data sampling during a hurricane is divided into two tasks to optimize the sampling time and the data quality. The spectral resolution,

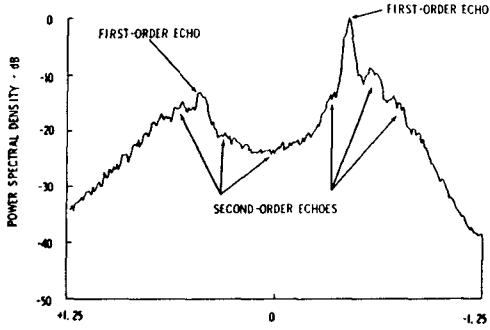


FIGURE 4 AVERAGE SEA ECHO DOPPLER SPECTRUM RECORDED WITHIN 35 km OF THE CENTER OF HURRICANE ANITA AT 2343Z ON 31 AUGUST 1977.

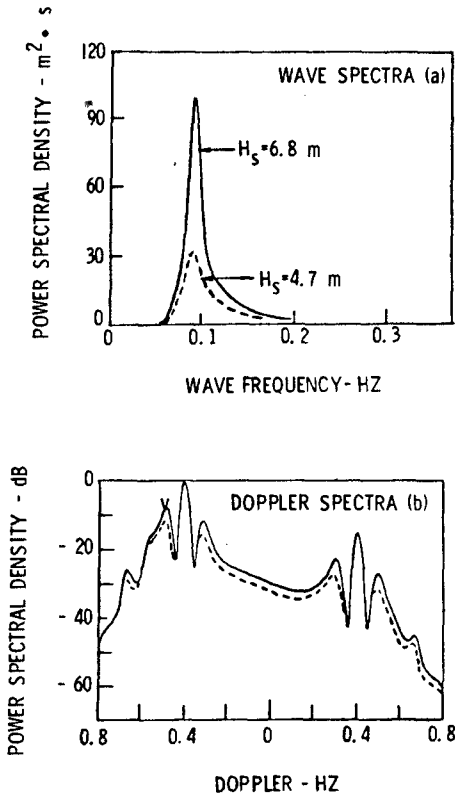


FIGURE 5 Example of Two Synthetic Doppler Spectra (b) Produced from Two Input Wave Spectra (a) With the same Directional Distribution and Radar-to-Wind Direction, but Different Total Wave Energy (0.02 Hz Resolution).

directly related to the coherent integration time, can be much coarser for first-order measurements than for second-order measurements. Wind direction estimates are computed from the first-order echoes, and can be computed considerably more rapidly than wave height and wind speed estimates, which are computed from the second-order echoes. Usually, the longer the coherent integration time, the greater the influence the ionosphere has on the quality of the data.

The quality of the recorded sea backscatter depends on the ionospheric conditions over short periods on the order of minutes. High-quality sea backscatter is obtained if the radio waves propagate by means of a strong, single, stable, coherent ionospheric layer. Sometimes the signals may be received at the same time from two or more different paths (multipath). In this case, the second or succeeding signals will be reflected from different parts of the ocean and different parts of the ionosphere, and will contaminate the sea echo received from the first path. If the ionosphere is changing in time or space during the coherent radar dwell (time period), further degradation of the data will occur. The ability to predict the ionospheric conditions would enable the radar operator to minimize the contaminating effects of the ionosphere, improve the quality of sea backscatter, and reduce the sampling time. The ionospheric soundings provide some data quality information. The vertical and oblique incidence soundings are taken every 10 minutes; a complete sounding requires approximately 3 minutes. The coherent radar measurements made at WARF require between 10 and 100 seconds to complete. Because the time it takes to complete a sounding is greater than the time required to record the sea backscatter data, assessment of the data quality is difficult for rapidly changing ionospheres. Therefore, real-time output of the data from the WARF site minicomputer is used to verify data quality.

The wind direction measurement is not extremely sensitive to ionospheric contamination caused by multipath or smearing because only the amplitude of the two strong first-order echoes must be measured. Coherent integration times of 12.8 seconds (0.078-Hz resolution) are sufficient to resolve the peaks of the first-order echoes. We can map the wind-direction field in a hurricane by scanning in range and azimuth. It is possible to routinely map the surface-wind-direction field of a hurricane and this can be accomplished in about 10 minutes. Once the surface-wind-direction map is made, the storm center can be identified for tracking purposes, and regions of interest can be selected for more extensive monitoring of wind speed and wave height anywhere within the storm.

The significant wave height and wind speed measurements are sensitive to ionospheric contamination. This contamination is the largest source of error in these measurements. A coherent integration time of 102.4 seconds (0.01-Hz resolution) is required to resolve the second-order echoes. The ionosphere does not generally support coherent integration time periods of this length. Multipath and ionospheric smearing can seriously degrade the weaker second-order echoes. Because of this

contamination, we are not able to routinely estimate wave height for each 102.4-second time period as we were able to calculate wind direction for each 12.8-second time period. A sampling strategy that combines careful propagation management through selection of frequencies, which result in a stable, coherent, single propagation path, and signal processing that minimizes the contaminating effects of the ionosphere are used to obtain a data set suitable for analysis. Recent work by SRI and NOAA⁷ has resulted in improved methods of collecting high quality data by sorting the data according to a spectral sharpness index. The effect of ionospheric contamination, however, is less severe for data recorded during large waves generated during a hurricane. The amplitude of the second-order echoes containing the wave height information may be stronger than the contamination effects, and thus, wave height can be calculated despite the contamination.

For the Anita and Babe wind direction measurements, we divided the data into 16 groups and analyzed three consecutive 12.8-second coherent radar dwells. Each wind direction estimate was calculated from a minimum of 15 Doppler spectra. At a range of 3000 km, the size of each scattering patch is 15 km × 25 km. It would be desirable to compute wave height and wind speed from a similar data set, but this is not generally possible. Longer coherent time periods and more independent samples of the spectra are required to obtain a high quality sample. We could collect the data over a small scattering patch by averaging over a long time, or we could increase the scattering patch size and average in space. Averaging in space is preferable because it reduces the total time required to obtain a mean Doppler spectrum. For the Anita and Babe wave height and wind speed measurements, we analyzed the data from three of the adjacent azimuth cells and 21 contiguous range cells. The total scattering patch is 63 km × 50 km. Several consecutive integration periods are required to record the data.

VI. WIND DIRECTION MEASUREMENT

HF skywave radar has been used to map the surface-wind fields associated with large weather systems⁸ and tropical storms.⁹ The radar measured surface-wind directions are derived from the predominant direction of ocean gravity waves, approximately 10-m long. The waves satisfying the first-order Bragg scattering condition, $k = 2k_0$, are assumed to be tightly coupled to the wind for time scales on the order of tens of minutes. This assumption is reasonable for the high wind speed conditions associated with hurricanes. Available directional wave spectra measurements¹⁰⁻¹² indicate that the dominant wave direction is representative of the predominant wind direction. For open ocean conditions, agreement between the WARF radar and shipboard anemometer measurements of wind direction is $\pm 16^\circ$ ¹³. For hurricane winds, the agreement between coincident wind direction measurements made by the NOAA National Data Buoy Office (NDBO) data buoys and the WARF radar is better than 10° ^{1,9}.

The radar measures the relative power between the approaching and receding waves that satisfies the Bragg scattering condition. If a cosine directional distribution¹⁰

$$G(\theta) = \cos^s \theta / 2 \quad (1)$$

is assumed, then the relative power of the approaching and receding waves measured by the radar is sufficient to estimate θ with an ambiguity about the beam direction. This left-right ambiguity is resolved by the predictable cyclonic surface circulation within the hurricane. The shape of $G(\theta)$ is controlled by the spreading parameter, s , where θ is the angle between the radar beam and the wind direction. For open ocean conditions, we have estimated s from several models.^{11,13} For the maximum hurricane winds, the values of s estimated from these models are too low. Based upon previous hurricane analyses and spot measurements of wind direction at NDBO data buoys, we used values of s between 1.0 and 2.0. No attempts were made to account for variations in s as a function of location within the hurricane.

VII. SIGNIFICANT WAVE HEIGHT

Barrick⁶ derived an integral expression that predicts the Doppler spectrum for a specific directional wave spectrum input. Recent efforts have succeeded in inverting this integral expression to compute the input rms wave height,^{14,15} one-dimensional wave frequency spectrum,¹⁶⁻¹⁹ and the directional distribution.¹⁷⁻¹⁹ Barrick's^{14,16} expressions have been used to analyze skywave radar data recorded for a Pacific Ocean storm¹⁵ and tropical storms.^{1,20}

We used a power law derived from simulated data by Maresca and Georges¹⁵ to compute rms wave height by relating the ratio of the total second-order and first-order power to the rms wave height:

$$k_0 h = a R_2^b \quad (2)$$

where $0.2 \leq k_0 h \leq 1.0$, h is the rms wave height; k_0 is the radar wave number; R_2 is the ratio of the total second- to total first-order power; and $a = 0.8$ and $b = 0.6$ are constants. This average expression was derived from theoretical simulations of the Doppler spectra for different radar-to-wind directions, directional distributions, functional forms of the wave frequency spectrum, and operating radar frequencies. Equation (2) is accurate to within 10%. Discussion of the errors can be found in Maresca and Carlson,¹ and Maresca and Georges.¹⁵

VIII. WIND SPEED

Historically, wave models have been developed to predict wave height and the wave spectrum from an input wind field. The accuracy of these models is dependent upon the accuracy of the input winds. Hasselmann et al.²¹ proposed a one-dimensional parametric wind-wave model for fetch limited growing wind-sea conditions. Ross and Cardone²²⁻²⁵ empirically derived a power law expression for hurricanes based on the form proposed by Hasselmann that relates the nondimensional wave energy, \tilde{E} , by using wind, wave and fetch measured during hurricanes Ava, Camille, and Eloise. For hurricanes,

$$\tilde{E} = 2.5 \times 10^{-5} \tilde{R}^{0.45} \quad (3)$$

where $\tilde{E} = E g^2 / W^4$; $\tilde{R} = r g / W^2$; $E = h^2$; and $H_s = 4h$. In \tilde{E} and \tilde{R} , E is the total wave energy; h is the rms wave height; H_s is the significant wave height; r is the radial distance from the eye to the measurement point that accounts for fetch; g is the gravitational acceleration; and W is the wind speed. Solving for wind speed in Eq. (3), we obtain

$$W = \left(\frac{h^2 g^2}{2.5 \times 10^{-5} (r g)^{.45}} \right)^{0.323} \quad (4)$$

The wind-wave model used to derive Eq. (4) is applicable for slow moving storms in which $W > 15$ m/s and $\tilde{R} < 3 \times 10^4$. For the unusual cases where the storms move very fast or very slow, Ross and Cardone²⁴ showed that significant differences in the modeled and measured wave heights occur.

We used Eq. (4) to calculate wind speed for both Anita and Babe and compared our results with the wind speeds measured at NDBO buoys, oil platforms, and by reconnaissance aircraft. The radial fetch (r) was measured from the WARF-derived wind maps, and the wave height (h) was computed using Eq. (2). The radar-derived W is not an instantaneous wind speed estimate; it is a smooth temporal and spatial average of the winds. Our radar-derived W was compared to the 15-minute wind speed averages made at NDBO moored data buoys.

IX. ANITA MEASUREMENTS

Hurricane Anita formed as a tropical depression in the Gulf of Mexico at about 1200Z on 29 August 1977. Anita developed into a tropical storm at approximately 0600Z on 30 August 1977, and about 12 hours later intensified into the first Gulf of Mexico hurricane of the 1977 season. As Anita moved west across the Gulf, winds in excess of 75 m/s were recorded. Five days of skywave data beginning on 29 August 1977 were recorded prior to Anita's landfall on 2 September 1977 approximately 48 km south of Brownsville, Texas. Twenty-one radar wind maps were compiled at WARF. The first 4 wind maps were not used in the

radar-derived track presented here because the radar showed two distinct centers during this early period. On 30 August 1977, the storm intensified and developed one center. The wind maps were updated 3 to 5 times per day during both daytime and nighttime periods and were used to develop the WARF-derived track. Figure 6 shows the radar-derived positions in relation to the official NHC smooth track produced from reconnaissance aircraft measurements, visible and infrared satellite cloud photographs, and shore-based microwave Doppler radar. The relative agreement between the WARF position estimates and the interpolated temporal position estimates along the smooth track is ± 19 km.

There are two principal errors associated with the WARF hurricane position fixes: the absolute position error of the radar and the errors associated with locating the storm center from the radar wind direction measurements. We estimate the range errors of the radar caused by errors in determining the ionospheric height at midpath to be 20 km. If a coastal scan is included as part of collecting the wind map data, the land echo can be used as a reference to more accurately determine the ionospheric height, and therefore, reduce this error. We estimate the error in azimuth caused by ionospheric tilting to be 20 km. These range and azimuth errors can be reduced significantly by installing an HF repeater along the coast which receives our signal and transmits it back with a known frequency shift. Assuming similar mean ionospheric conditions within 200 km of the storm center, the entire wind map can be translated in azimuth and range to correct for the absolute position error. The location of the wind direction measurement with respect to the storm center is generally not affected by these position errors. We estimate the error associated with determining the storm center from the radar maps to be 20 km. The error is caused by the left/right ambiguity in the wind direction measurement. We can expect a maximum error of about 40 km from these two sources of error. In comparing the WARF position fixes to the NHC track we found relative differences of between 5 and 50 km. We attribute these relative differences to the above sources of error.

Anita passed 50 km south of NDBO buoy EB-71 at about 0000Z on 1 September 1977. Two WARF-derived wind maps were made at 2140Z on 30 August 1977 and 0120Z on 1 September 1977 that bracket this time period. One of these wind maps is shown in Figure 7. Also shown on Figure 7 are surface wind direction fields derived from data recorded by NDBO buoy EB-71. These buoy-measured wind directions were recorded at 2-hour intervals during the period ± 18 hours of Anita's passing EB-71. The buoy-derived wind field was computed by a time-space conversion that assumed uniform wind direction and lateral storm motion during this period. We compared the buoy-derived wind directions to the WARF-derived wind directions; agreement was within 19° . Agreement between the WARF-derived wind direction estimate coincident in time and space with the buoy wind direction estimate was 1° .

Between 2314Z on 31 August 1977 and 0020Z on 1 September 1977, WARF measurements were made at five locations surrounding the center of the

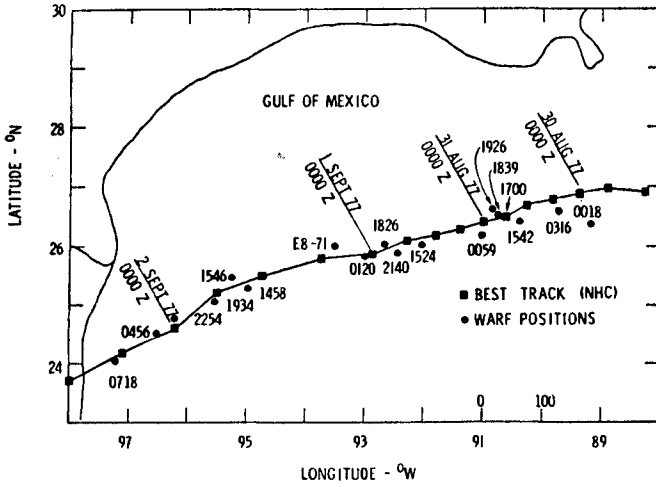


FIGURE 6 WARF-Measured Track of Hurricane Anita produced from the Radar Wind Maps

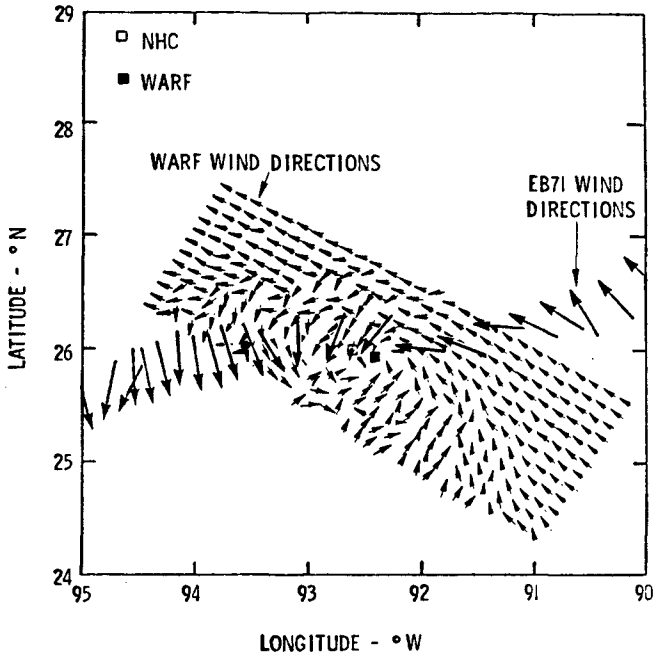


FIGURE 7 WARF-Derived Wind Direction Map made for Anita at 2140Z on 31 August 1977.

storm. The location of each measurement relative to the storm center was interpolated from the two wind maps. We computed the wind direction by using Eq. (1), wind speed by using Eq. (4), and wave height by using Eq. (2) at each location (see Table 1), and compared these measurements to a buoy-derived wind and wave field. The maps of the spatial distribution of the wind direction, wind speed, and wave height were compiled from NDBO EB-71 data buoy measurements. Each parameter was plotted in relation to the storm center and is shown in Figures 8, 9, and 10. We assumed that Anita moved uniformly with no change in the meteorological conditions during the period 18 hours before and 18 hours after passing the buoy.

Table 1
WARF ESTIMATES OF SIGNIFICANT WAVE HEIGHT,
WIND SPEED, AND WIND DIRECTION

Point	Lat (°N)	Long (°W)	Time (GMT)	r* (km)	N*	H _s * (m)	W* (m/s)	φ* (°N)
A	25.7	92.9	2314	35	80	5.8	26.7	277.5
A	25.7	92.9	2343	35	112	5.2	22.8	-
B	26.3	92.1	2324	75	80	6.0	24.4	95.1
C	26.3	93.1	2358	65	35	5.8	24.4	70.2
D	25.7	92.1	0003	65	134	5.1	22.5	168.8
E	25.2	91.1	0020	180	49	4.6	18.1	137.2

*
r = Radial Distance
N = Number of Spectra Averaged
H_s = Significant Wave Height
W = Wind Speed
φ = Wind Direction

The significant wave height shown in Figure 8 was measured at the buoy every 3 hours; the wind direction and wind speed shown in Figures 9 and 10, were measured at the buoy every 2 hours. During this 36-hour period, Anita began to intensify, and the validity of the buoy-derived wind and wave fields are suspect. Exact comparison of the EB-71 and WARF measurements are difficult because of the differences in the time, location, and area of ocean monitored. On Figure 8 we also included the wave hindcast for significant wave height computed by Cardone et al.²⁵ for comparison.

The WARF estimates made at Point B (26.3°N, 92.1°W) are in close proximity to the buoy-derived estimates located at (26.2°N, 92.1°W). The remaining WARF wind and wave height estimates are too far away from the buoy-derived quantities for direct comparison, but the agreement between the WARF- and buoy-derived wind and wave fields is reasonable.

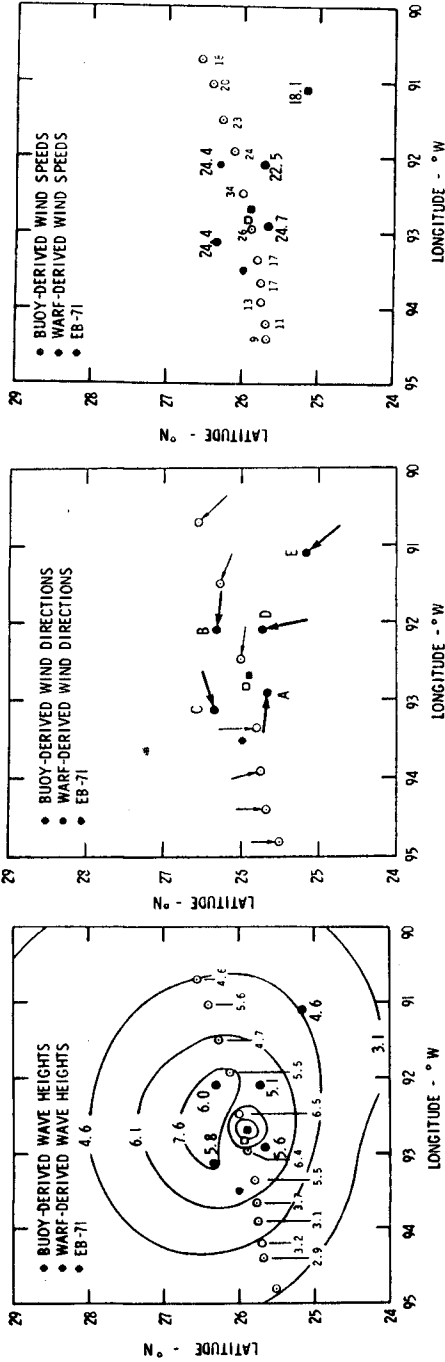


FIGURE 8 Comparison of the WARP-Derived Significant Wave Height (m) measured between 2342Z on 31 August 1977 and 0020Z on 1 September 1977. The wave height contours are reproduced from Figure 9 of Reference 25. The letter designations are given on Figure 9.

FIGURE 9 Comparison of the WARP-Derived Wind Directions (→) made between 2342Z on 31 August 1977 and 0020Z on 1 September 1977 and the EB-71-Derived Wind Directions (→) made between 0600Z on 31 August 1977 and 1800Z on 1 September 1977.

FIGURE 10 Comparison of the WARP-Derived Wind Speed (m/s) measured between 2342Z on 31 August 1977 and 0020Z on 1 September 1977 and the EB-71-Derived Wind Speeds (m/s) measured between 0600Z on 31 August 1977 and 1800Z on 1 September 1977.

The wave hindcast was compared to both the buoy- and WARF-derived wave heights. We find good agreement between the hindcast, buoy and WARF estimates of wave height along the 4.6-m contour east of the hurricane. The buoy estimate west of the hurricane along the 4.6-m contour line suggests the radius of this contour line is too large. WARF estimates of wave height at Points B and C, located at the extremes of the hindcast region of highest waves, are lower than the hindcast. The good agreement of Point B with the nearby buoy estimate, and the consistency of the WARF estimates at Point B and C suggest that the 7.6-m contour should be smaller. The WARF estimates of wave height at Points A and D are located between the 6.1-m contours. Again the buoy- and WARF-derived wave heights suggest that the 6.1-m contour line is too large. We should also note that any contamination of the sea echo Doppler spectra by the ionosphere would result in radar wave-height estimates that would be too high. The composite of wave height data obtained from the hindcast and EB-71 buoy indicate the validity of the WARF wave height estimates.

The agreement between the WARF-derived estimates of wind speed and the buoy-derived estimates of wind speed is good. There are three principal errors associated with the WARF wind speed estimate: error in estimating the radial fetch, error in estimating the rms wave height and error in the parametrics model. We computed the error in calculating wind speed for a ± 0.5 m error in estimating wave height for a significant wave height of 5.5 m (9.1% error) for radial fetches of 30, 50, 70 and 100 km. The errors were less than 1.6 m/s. We also computed the error in calculating wind speed for a ± 20 km error in estimating the radial fetch for a significant wave height of 5.5 m and radial fetches of 30, 50, 70, and 100 km. For radial fetches greater than 30 km, a +20 km error causes an error of less than 2 m/s in wind speed. For radial fetches greater than 50 km, a -20 km error causes an error of less than 2 m/s in wind speed. This represents less than an 8% error. These errors are typical of the WARF estimates of the significant wave height and radial fetch measurements. The errors associated with the model are discussed in Ross and Cardone.²⁴ For Anita, the mean and rms differences between the Cardone et al.²⁵ parametric model forecast and measured wave heights at EB-71 is 0.21 ± 0.83 m. This includes errors in measuring wave height at the buoy and radial fetch from the conventional position fixes. We also calculated the wind speed using Eq. (4) for some of the buoy-measured wave heights shown in Figure 8, and compared the calculated wind speed measurements to wind speeds measured at the buoy (Table 2). The data is indicative of the accuracy we could expect from the WARF estimates of wind speed using Eq. (4). For these data, we believe the largest sources of error in the comparison are the uncertainty in the radial distance to each point caused by compiling the map over a 36-hour period, and the assumption of a symmetrical distribution of the winds.

Table 2

COMPARISON OF WIND SPEED VALUES CALCULATED
FROM EQ. (4) DERIVED FROM EB-71 SIGNIFICANT
WAVE HEIGHT MEASUREMENTS

Lat (°N)	Long (°W)	H_S^* (m)	r^* (km)	W_C^* (m/s)	W_m^* (m/s)	Difference (m/s)
25.5	94.8	2.5	217	11.9	7.6	+4.3
25.7	94.4	2.9	174	13.5	9.0	+4.5
25.7	93.9	3.1	124	14.9	13.3	+1.6
25.8	93.4	5.5	69	23.4	17.4	+6.0
26.0	92.5	6.5	24	30.4	34.1	-3.7
26.3	91.5	4.7	126	19.4	23.1	-3.7
26.6	90.7	4.6	212	17.7	18.1	-0.4

* H_S = Significant Wave Height

r = Radial Distance

W_C = Computed Wind Speed

W_m = Measured Wind Speed

X. BABE DATA

We recorded skywave data for Babe from 2000Z on 4 September 1977 until landfall on 5 September 1977. Wind direction maps were made at 2253Z on 4 September 1977 and 1507Z on 5 September 1977. Babe was already onshore before the second map was made. We analyzed a sea echo Doppler spectrum near the peak winds for wind speed. This spectrum was recorded at a radius of 50 km from the hurricane center (27.9°N, 91.6°W). The WARF estimate of significant wave height was 3.6 m. The wind speed was computed by using Eq. (4) and was compared to wind speeds measured at several offshore oil platforms at 2100Z and from aircraft reconnaissance at 1800Z. Winds measured from aircraft at an altitude of 305 m were reduced to the equivalent 10 m wind for comparison to the radar data. We reduced the aircraft winds to the surface using a simple ratio relating upper level gradient wind to the surface wind, indicated by Elsberry et al.²⁶ calculations. Using the two layer Cardone²⁷ marine boundary layer model, Elsberry et al.²⁶ computed the ratio of the wind at the top of the upper layer to the wind at the top of the surface layer for different regions of the hurricane, different surface roughness and different ratios of heat conductivity to eddy viscosity. For moderate to high wind speeds, the top of the surface layer is approximately 20 m. This wind ratio ranges from about 0.5 to 0.85. The lower value represents regions near the peak winds. We assumed the 305 m aircraft wind was representative of the wind at the top of the upper layer and reduced it to 20 m using a ratio of 0.6. The corrected 20 m wind is 18.5 m/s. We realize the error associated with this calculation can

be large. We computed the 19.5 m WARF wind speed for comparison by assuming a logarithmic profile in the surface boundary layer of the form

$$W(z) = \frac{W_*}{k} \ln \left(\frac{z}{z_0} \right) \quad (5)$$

where $W(z)$ is the wind speed at a height of z , $W_* = C_D W^2$ is the friction velocity, C_D is the drag coefficient, $k \approx 0.4$ is Von Karman's constant, and z_0 is the surface roughness. We estimated $z_0 = 0.00392$ m for hurricane conditions using the wind speeds measured during Eloise²⁸ at NDBO buoy EB-10 at 10 m, and a constant drag coefficient of 0.0026 proposed by Wu²⁹ for high wind speeds to calculate W_* . We found good agreement between our 19.5 m computed wind speed using Eq. (5) for Eloise and the 19.5 m Eloise wind speed computed by Ross and Cardone.²⁴ Using $z_0 = 0.00392$ m and $C_D = 0.0026$ m we computed the 19.5 m WARF Babe wind speed to be 18.3 m/s. We also computed the maximum wind speed, W_{\max} , and the maximum sustained wind speed, W_s , for a storm moving at 5.1 m/s from the following expressions³⁰ relating the central pressure and radius of the storm to wind speed at 10 m:

$$W_{\max} = 0.868 [6.45(P_n - P_o)^{1/2} - 0.296 \text{ rf}] \quad (6)$$

and

$$W_s = 0.865 W_{\max} + 0.5 V_F \quad (7)$$

where W_{\max} and W_s are in m/s, P_n is the normal pressure of 1013 mb, P_o is the central pressure in mb, r is the radius in km, f is the coriolis parameter in radians/hour, and V_F is the forward motion of the storm in m/s. The maximum wind recorded from the aircraft at 1800Z were located approximately 60 km from the center and the central pressure was reported as 1000 mb. We calculated $W_{\max} = 16.4$ m/s and $W_s = 16.8$ m/s. We summarize these wind speed estimates in Table 3. Because none of the wind speed estimates are coincident in time or space with the WARF estimate and the assumptions inherent in deriving these quantities we can only compare the results qualitatively. The WARF wind speed estimate is reasonable.

XI. SUMMARY

Spatially-averaged hurricane wind speed, wind direction, and wave height estimates made at the WARF for Anita and Babe were compared to point measurements made at NDBO buoys and oil platforms and by reconnaissance aircraft. Agreement was within the nominal measurement accuracy of all the sensors. The WARF data set is not limited to the results presented in this paper. Other analyses of the radar data that were not obtained in the vicinity of the buoy are also available. These

experiments indicate that during a hurricane, HF skywave radar can provide operational surface data that are as accurate as the more recognized in situ measurements. The supportive surface data supplied by the WARF radar would prove particularly useful for tracking during early formative stages of hurricanes when multiple centers may be observed or when cirrus shielding may obscure visual location by satellite cloud photography. The high resolution, large coverage area, real-time steering and continuous monitoring capabilities are unique to skywave radar. The hurricane data obtained from skywave radar complements data obtained from satellites, aircraft, and buoys.

Table 3
BABE WIND SPEED ESTIMATES MADE ON 4 SEPTEMBER 1977

Sensor	Observation (GMT)	Bearing From Hurricane Center (°N)	Radial Distance From Hurricane Center (km)	Wind Speed (m/s)
WARF (10 m)	2253	340	60	18.2
WARF (19.5 m)	2253	340	60	18.3
Aircraft (305 m)	1800	25	60	30.8
Aircraft (19.5 m)	1800	25	60	18.5
Oil Platform (19.5 m)	2100	320	100	15.4
Oil Platform (19.5 m)	2100	0	35	11.3
W _{CM} ¹ (9.1 m)	-	-	60	16.4
W _{CS} ² (9.1 m)	-	-	60	16.8

¹Computed maximum wind speed from Eq. (3-35) in Reference 30.

²Computed maximum sustained wind speed from Eq. (3-34) in Reference 30.

Acknowledgments. This work was supported by the Air Force of Scientific Research (AFOSR) under Contract No. F49620-76-C-0023. We gratefully acknowledge the help of G. Glassmeyer, W. Preuss, G. Tomlin, and C. Powell of SRI in collecting data at WARF; D. Westover for writing the real-time sampling software; and B. Richards and J. King for typing the manuscript.

REFERENCES

1. J. W. Maresca, Jr. and C. T. Carlson, "Tracking and Monitoring Hurricanes by HF Skywave Radar over the Gulf of Mexico," Technical Report 1, SRI International, Menlo Park, California (1977).
2. "SRI Remote Measurements Laboratory Research Capabilities," brochure, Stanford Research Institute, Menlo Park, California (1977).
3. K. Davies, Ionospheric Radio Propagation, NBS Monograph 80, U.S. Government Printing Office, Washington, D.C. (1965).
4. D. D. Crombie, "Doppler Spectrum of Sea Echo at 13.56 mc/s," Nature, Vol. 175, pp. 681-682 (1955).
5. D. E. Barrick, "First-order Theory and Analysis of MF/HF/VHF Scatter From the Sea," IEEE Trans. Antennas and Propagation, AP-20, pp. 2-10 (1972).
6. D. E. Barrick, "Remote Sensing of Sea State by Radar," Remote Sensing of the Troposphere, V. E. Derr, ed., U.S. Government Printing Office, Washington, D.C. (1972).
7. T. M. Georges and J. W. Maresca, Jr., "The Effect of Radar Beamwidth on the Quality of Sea Echo Doppler Spectra Measured with HF Skywave Radar," accepted by Radio Science.
8. J. R. Barnum, J. W. Maresca, Jr., and S. M. Serebreny, "High-Resolution Mapping of Oceanic Wind Fields with Skywave Radar," IEEE Trans. on Antennas and Propagation, AP-25, pp. 128-132 (1977).
9. J. W. Maresca, Jr. and J. R. Barnum, "Remote Measurements of the Position and Surface Circulation of Hurricane Eloise by Skywave Radar," accepted by Monthly Weather Review.
10. M. S. Longuet-Higgins, D. E. Cartwright, and N. D. Smith, "Observations of the Directional Spectrum of Sea Waves Using Motions of a Floating Buoy," Ocean Wave Spectra, pp. 111-136, Prentice-Hall: Englewood Cliffs, New Jersey (1963).
11. H. Mitsuyasu, F. Tasai, T. Suhara, S. Mizuno, M. Ohkusu, T. Honda, and K. Rikiishi, "Observations of the Directional Spectrum of Ocean Waves Using a Clover Leaf Buoy," J. Phys. Oceanog., Vol. 5, No. 4, pp. 750-760 (1975).
12. J. A. Ewing, "Some Measurements of the Directional Wave Spectrum," J. Marine Research, Vol. 27, pp. 163-171 (1969).
13. R. H. Stewart and J. R. Barnum, "Radio Measurements of Oceanic Winds at Long Ranges: An Evaluation," Radio Science, Vol. 10, pp. 853-857 (1975).
14. D. E. Barrick, "Extraction of Wave Parameters from Measured HF Sea-Echo Doppler Spectra," Radio Science, Vol. 12, pp. 415-424 (1977).
15. J. W. Maresca, Jr. and T. M. Georges, "HF Skywave Radar Measurement of the Ocean Wave Spectrum," submitted to J. Geophys. Research.
16. D. E. Barrick, "The Ocean Waveheight Nondirectional Spectrum from Inversion of the HF Sea-echo Doppler Spectrum," Remote Sensing of Environment, Vol. 6, pp. 201-277 (1977).
17. B. J. Lipa, "Derivation of Directional Ocean-wave Spectra by Integral Inversion of Second-order Radar Echoes," Radio Science, Vol. 12, pp. 425-434 (1977).
18. B. J. Lipa, "Inversion of Second-order Radar Echoes from the Sea," J. Geophys. Research, Vol. 83, pp. 959-962 (1977).

19. D. E. Barrick and B. J. Lipa, "Ocean Surface Features Observed by HF Coastal Ground-wave Radars: A Progress Review," Ocean Wave Climate, eds. M. D. Earle and A. Malahoff, Plenum Publishing Company (1978).
20. J. W. Maresca, Jr., "High Frequency Skywave Radar Measurements of Waves and Currents Associated with Tropical and Extra-Tropical Storms," Ocean Wave Climate, eds. M. D. Earle and A. Malahoff, Plenum Publishing Company (1978).
21. K. Hasselmann, D. B. Ross, P. Muller, and W. Sell, "A Parametric Wave Prediction Model," J. Phys. Oceanog., Vol. 6, pp. 200-228 (1976).
22. D. B. Ross, "A Simplified Model for Forecasting Hurricane Generated Waves" (Abstract), Bull. Am. Meteorol. Soc., presented at Conference on Atmospheric and Oceanic Waves, Seattle, Washington, March 29-April 2, 1976 American Meteorological Society (1976).
23. V. J. Cardone and D. B. Ross, "State of Art Wave Predictions and Data Requirements," Ocean Wave Climate, eds. M. D. Earle and A. Malahoff, Plenum Publishing Company (1978).
24. D. B. Ross and V. J. Cardone, "A Comparison of Parametric and Spectral Hurricane Wave Prediction Products," to be published in the Proceedings of "NATO Symposium on Turbulent Fluxes Through the Sea Surface, Wave Dynamics and Prediction," Marseille, France, September 12-16, 1977, Plenum Publishing Company (1978).
25. V. J. Cardone, D. B. Ross, and M. R. Ahrens, "An Experiment in Forecasting Hurricane Generated Sea States," Proceedings of the 11th Technical Conference on Hurricanes and Tropical Meteorology, Miami, Florida (December 13-16, 1977).
26. R. L. Elsberry, N. A. S. Pearson, L. B. Corngati, Jr., "A Quasi-Empirical Model of the Hurricane Boundary Layer," J. Geophys. Research, Vol. 79, pp. 3033-3040 (1974).
27. V. J. Cardone, "Specification of the Wind Distribution in the Marine Boundary Layer for Wave Forecasting," Rept. TR 69-1 Geophys. Sci. Lab., New York University NTIS No. AD702490 (1969).
28. G. W. Whithee and A. Johnson, Jr., "Data Report: Buoy Observations During Hurricane Eloise, September 19-October 11, 1975," Environmental Sciences Division, Data Buoy Office, National Oceanic and Atmospheric Administration, Bay St. Louis, Mississippi (1975).
29. J. Wu, "Wind Stress and Surface Roughness at Air-Sea Interface," J. Geophys. Research, Vol. 74, pp. 444-455 (1969).
30. U.S. Army Coastal Engineering Research Center, Shore Protection Manual, Vol. 1, U.S. Government Printing Office, Washington, D.C. (1973).

CHAPTER 10

RADAR OBSERVATIONS OF HURRICANE WAVE DIRECTIONS

by

D. B. King¹ and O. H. Shemdin²

ABSTRACT

This paper presents an analysis of data collected in a hurricane wave research program. The data were collected with a synthetic aperture radar (SAR) during five aircraft flights into hurricanes in August and September, 1976. These data are the first collected on the directional distributions of waves throughout the region of active generation.

The wave patterns in all of the storms are similar and show a marked radially asymmetry. The dominant waves propagate ahead of the storm in a broad arc that has an apparent center in a region of confused sea to the right and rear of the hurricane eye. The asymmetry in the wave patterns is attributed to the forward motion of the storms. The wave directions throughout the storms do not show a sensitive dependence on the forward speed of the storms or on their maximum wavespeeds. However, there is an increase in peak wavelength with increasing windspeed and forward velocity.

Introduction

Hurricane waves play a controlling factor in the design of permanent structures along the Gulf and East Coasts of the United States and in other parts of the world. In spite of their importance, they are poorly understood and often not adequately predicted. This lack of understanding is due partially to the difficulty of data collection and partially to the fact that the wave generation process is not completely understood, even for the case of simple windfields.

Some of the first research on hurricane waves was conducted by Tannehill (1936). He, along with Arakawa (1954) and Pore (1957) compiled information on hurricane wave heights and directions collected from shipboard observations. This technique has not been followed up by other researchers because the frequency and the nature of the observations rendered them inadequate for an understanding of the processes involved.

-
1. Scientist, Oceanography and Climate Group, Jet Propulsion Laboratory, Pasadena, California.
 2. Head, Oceanography and Climate Group, Jet Propulsion Laboratory, Pasadena, California and Professor of Coastal and Oceanographic Engineering, University of Florida, Gainesville, Florida.

Few other measurements were collected until recently, when two large programs were initiated. The first, in the late 60's and early 70's, involved the instrumentation of offshore oil platforms in the Gulf of Mexico (See Ward (1974)). The second is a continuing project by the NOAA Data Buoy Office in which deep water environmental buoys have been moored at various offshore locations along the U.S. coasts. These buoys have recently encountered several hurricanes (See Withee and Johnson (1975), Johnson and Speer (1978) and Johnson and Renwick (1978)). Most of the reported wave height measurements are in the form of time histories of significant wave heights and dominant periods showing variations during periods when storms pass by or over the measurement sites. More recently, data revealing the directional nature of waves were analyzed and directional wave height spectra were reported (See Forristall et al (1978)). However, these results are restricted to only one site. The data do not reveal the directional distributions of wave fields over the entire region of hurricane influence.

The Aircraft Hurricane Program

In August and September 1976, and again in October 1977, the Jet Propulsion Laboratory (JPL) participated in a hurricane research program with a number of other NASA research centers and with the NOAA — National Hurricane and Environmental Meteorological Laboratory. JPL collected information on the directional properties of hurricane waves using a Synthetic Aperture Radar (SAR) onboard a NASA CV-990 research aircraft. The 1976 flights were made into Tropical Storm Emmy on August 24 (designated as Emmy 1 in this paper), Hurricane Emmy on August 25 (Emmy 2), Hurricane Frances on August 31 (Frances), Tropical Storm Gloria on September 28 (Gloria 1), and Hurricane Gloria on September 30 (Gloria 2). These storms were all in the western Atlantic. The flight tracks and storm paths are shown in Figure 1. Approximately 700 minutes of data was collected in these five storms. Table 1 lists the important parameters associated with each storm.

On October 5, 1977, the JPL-SAR collected data in Typhoon Heather in the eastern Pacific. Images have also been obtained with the Seasat-1 SAR from Typhoon Fico on July 15, 1978. Data from these two storms are not included in this paper but preliminary analysis shows that their wave patterns are in good agreement with the data presented here.

The Synthetic Aperture Radar (SAR)

The data presented in this paper represent the first extensive collection of directional wave data throughout the region of hurricane influence. The data were obtained with the SAR, a sensor that provides all weather images of the sea surface topography during day or night. The images are similar in appearance to photographs of the sea surface. The SAR transmits a microwave pulse in the L-band region (23.0 cm wavelength) and records the intensity and phase history of the signal returned from the sea surface. This information is then converted

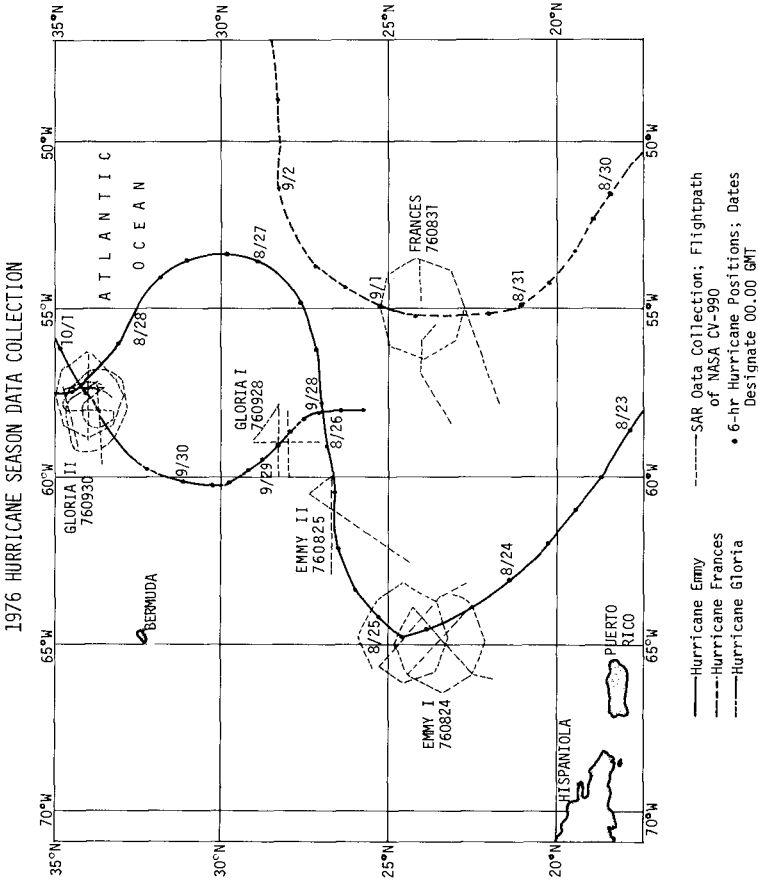


Figure 1. Flight paths of hurricanes Emmy, Frances and Gloria in 1976. The flight patterns and locations of hurricane interceptions are also shown.

Table 1. Important hurricane parameters associated with hurricanes Emmy 1 and 2, Frances and Gloria 1 and 2. The parameters are representative for the periods from 18 hours before SAR data collection to 6 hours after SAR data collection.

Hurricane	Emmy 1	Emmy 2	Frances	Gloria 1	Gloria 2
Date	Aug. 24	Aug. 25	Aug. 31	Sept. 28	Sept. 30
Time of Collection (GMT)	15:34-19:23	15:20-16:48	15:13-18:24	16:46-17:45	15:58-20:14
Max Winds (kn)	60	65-70	75-85	60-65	85-95
Min Pressure (mb)	995	990	975-963	992-988	980
Forward Speed (kph)	14-20	24-27	20-22	10-12	27-28
Heading	Turn NW-NE	E	N	NW	NE
Radius of Gale Force Winds (nm)	225	225	225	175	250

through the use of an optical correlator to an image of the sea surface. Figure 2(a) is an example of an image showing surface waves.

The SAR has many advantages over optical photography. Operating at L-Band it can penetrate cloud cover and, being an active system, it is independent of solar illumination. The image can be further processed to yield the wave phase-speed and to resolve the 180° ambiguity in the direction of wave propagation. The imaging characteristics of the SAR and its application to oceanography has been the subject of intensive investigations recently (See for example Shemdin et al (1978)).

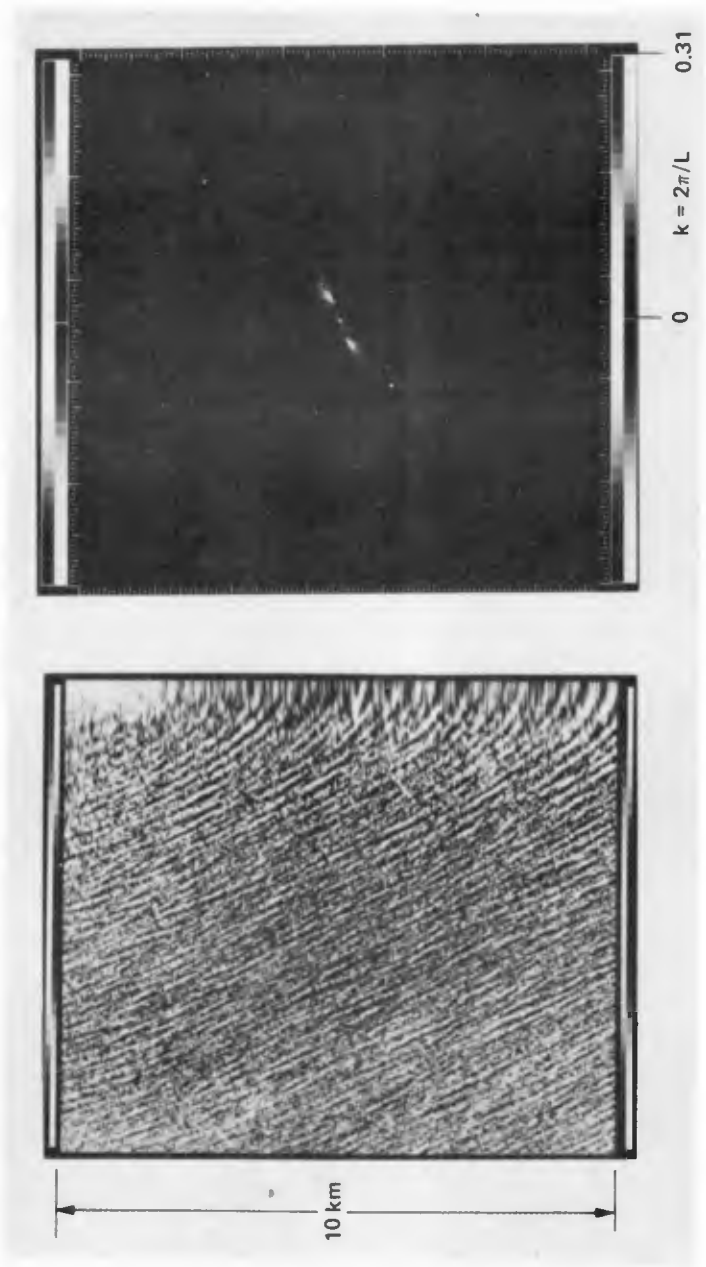
A two-dimensional spectral transform of the SAR image provides a convenient representation of the wavelengths and corresponding directions that appear in a wave image. The Fourier transform of the image shown in Figure 2(a) is given in Figure 2(b). The center of the transform represents an infinite wave length (or zero wave number). The wave direction is determined by the azimuthal angle of the two spectral peaks which are symmetrically aligned with respect to the origin.

Observed Directional Wave Patterns in Hurricanes

Figure 3 shows processed SAR wave imagery at selected locations throughout Gloria 2. Each wave image is enlarged ten times relative to the hurricane scale. The direction of hurricane forward motion is to the top of the figure. For comparison, all the hurricane flights were oriented in this manner, regardless of the direction of true north. These images are placed in their proper location relative to the moving eye of the hurricane. Fourier transforms of each of the wave images in Figure 3 are shown in Figure 4. The transform scale is shown in the lower right hand corner of Figure 4. The innermost circle designates 300 meter waves, the next innermost designates 250 meter waves, then 200, 150, and 100 meter waves. The outside edges of the transforms are at 75 meter waves.

The striking feature of Figures 3 and 4 is the pronounced asymmetry in the wave field. There is an arc of waves which extends from the right front quadrant through the left front and into the left rear quadrant. The waves along the arc are propagating outward from the storm center. The hurricane winds are blowing in a counterclockwise spiral and thus the dominant waves in much of the storm are traveling at 90° or more with respect to the local wind direction. This is shown in Figure 5. The arc appears to have its center in the right rear quadrant but there is no distinct origin. Instead, the wave patterns in this area suggest a confused sea. The Fourier transforms show multiple dominant peaks which are traveling in different directions.

The pronounced asymmetry in the wave field is caused primarily by the forward motion of the hurricane. The counter-clockwise winds (for northern hemisphere storms) blow faster on the right hand side of a



(a)

(b)

Figure 2. Aircraft flight into hurricane Gloria on 30 September 1976 at 9.15 km altitude. Image location is 94 km ahead of eye in direction of hurricane travel.

(a) L-band SAR image of ocean waves. Dominant wave length is 225 m.

(b) 2-D Fourier transform of image.

DIGITALLY CORRECTED SAR WAVE IMAGERY

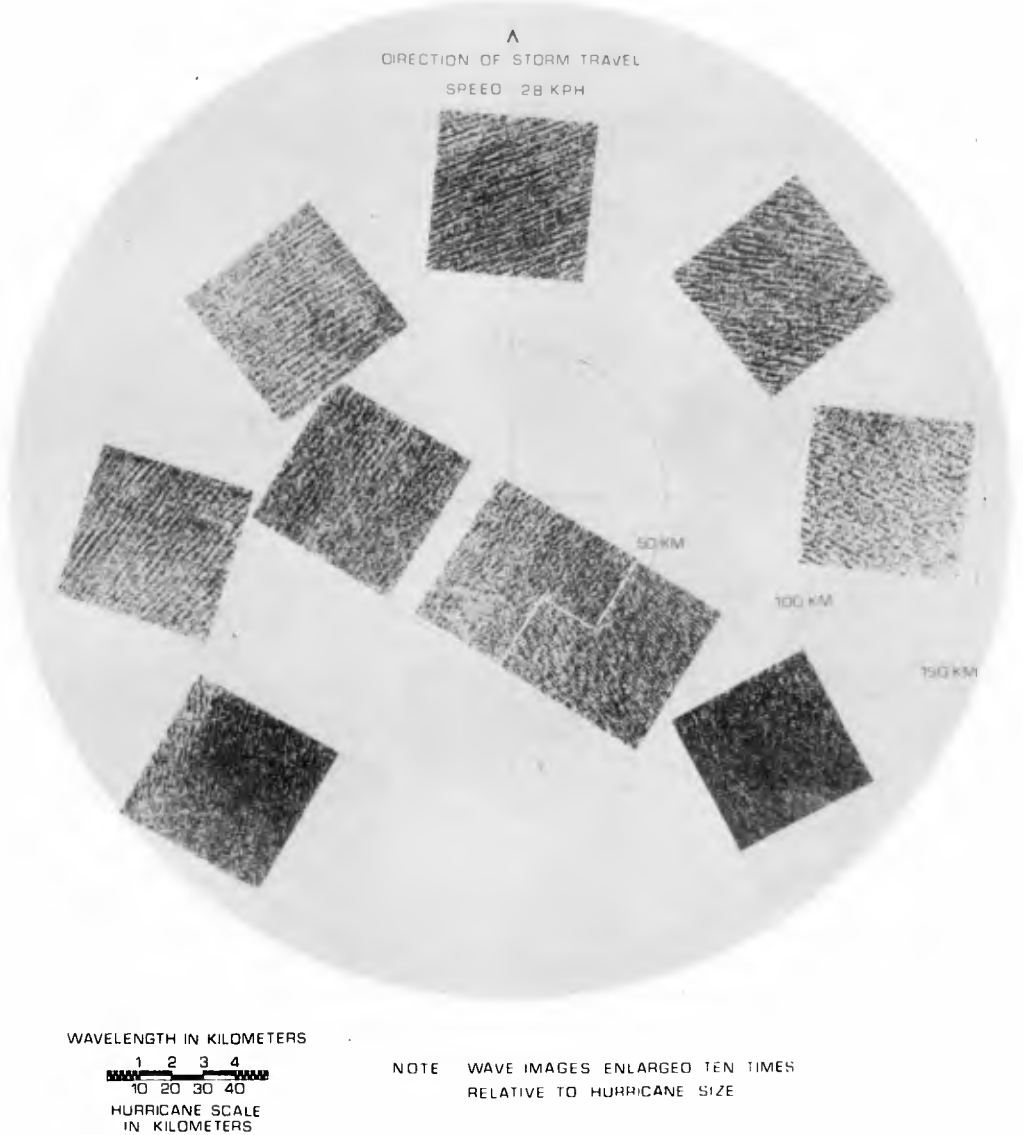


Figure 3. SAR wave patterns in hurricane Gloria 2.

HURRICANE GLORIA 30 September 1976
DIRECTIONAL SPECTRAL WAVE TRANSFORMATIONS

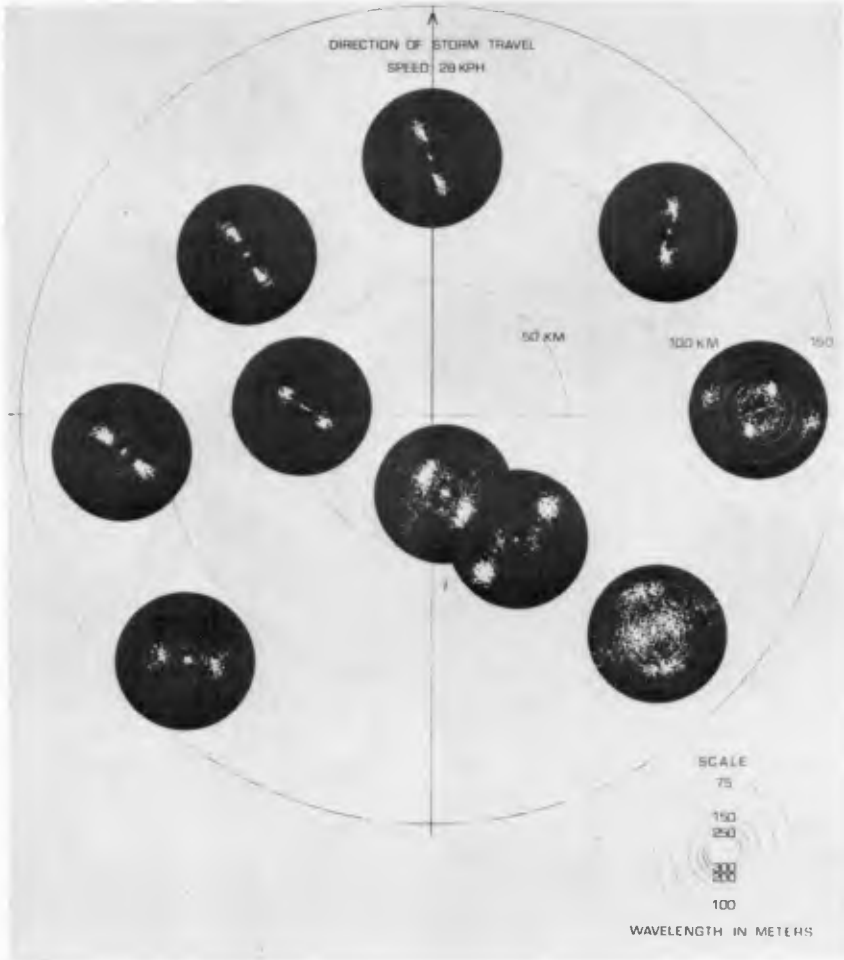


Figure 4. Fourier transforms of Gloria 2 wave images shown in Figure 3.

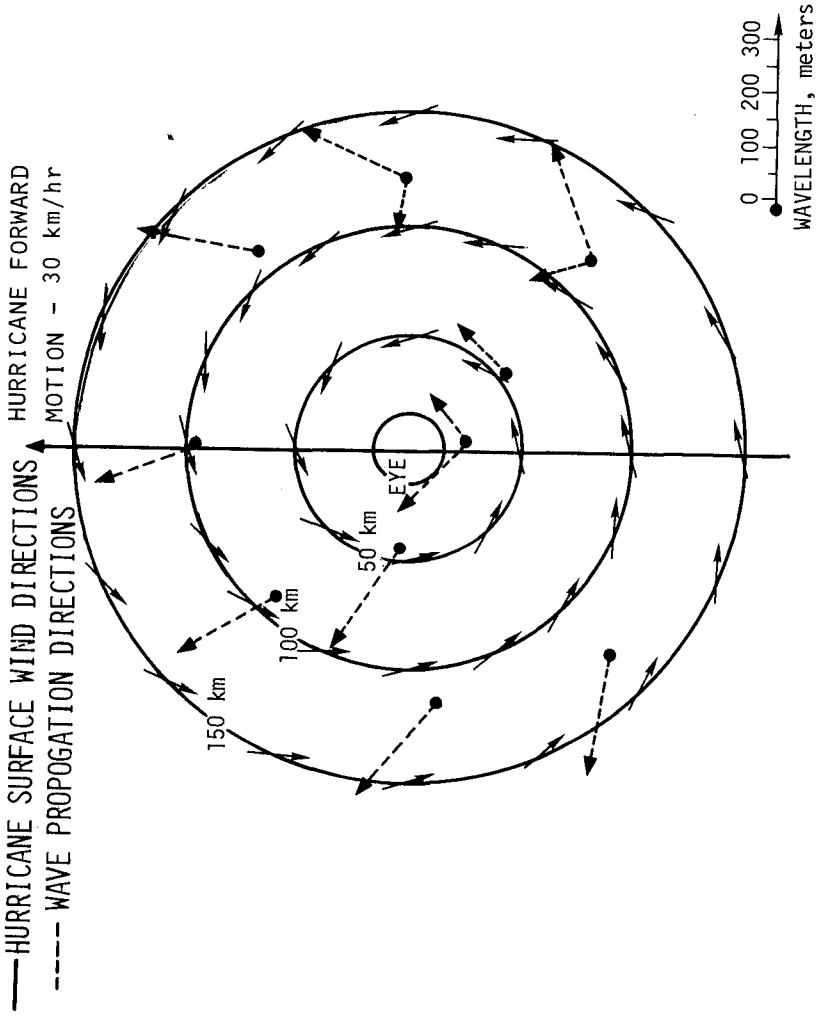


Figure 5. Dominant wave number vectors compared to wind directions in hurricane Gloria 2.

moving hurricane than on the left due to the added speed of the storm. This causes larger waves to be generated in this area. However, more importantly, these waves tend to travel with the storm and so stay in the generation region much longer. These dominant waves then propagate throughout most of the storm depending on the group velocities and directions of propagation.

In comparing the wave patterns in different storms, it is necessary to know how the meteorological parameters vary in different storms. A comparison of wind speeds, central pressures, forward speeds, headings and radii of gale force winds are given in Table 1 for the five 1976 flights. The maximum wind speeds and hurricane forward speeds are likely to play important roles in the wave generation processes. A spread in these two parameters for the hurricanes shown would have been desirable. Unfortunately, this was not the case. All of the storms were of weak to moderate intensity (max winds of 60 to 90 knots) and of a moderate to medium forward speed (11 to 28 kph). Also, the slower storms had lower windspeeds and the faster storms had higher windspeeds, making it impossible to determine the relative importance of these two parameters. However, the wavefields show variations which can be related to these two parameters. Gloria 1 was the slowest moving storm. The next slowest was Emmy 1 whose wave pattern was complicated by the fact that she was in a 90° right turn during the time of data collection. Then in ascending order were Frances, Emmy 2 and Gloria 2. The maximum wind speed follows the same ascending order with the exception of Frances and Emmy 1 which are reversed.

Figures 6, 7, and 8 show spectral transforms from the five flights taken in the left-front, the right-front, and the right-rear quadrants, respectively. The transforms were taken in areas that appeared interesting and in which data from most of the storms were in close proximity. Table 2 summarizes the information in Figures 6, 7 and 8.

The left-front quadrant (Figure 6 and Table 2) is a typical example of the waves that propagate outward ahead of the storms. The directions of wave propagation in all of the transforms are in close agreement and within the uncertainty limit of determining the true heading of each storm. The peak wavelengths vary in close agreement with variations in intensity and forward speed of storms, the more intense and faster moving storms have longer wavelengths. The one anomalous point is Emmy 1, which may be due to the fact that Emmy 1 was in a turn.

The transforms in the right-front quadrant (Figure 7 and Table 2) exhibit the longest dominant waves compared to other regions of the storm. In this quadrant the wave propagation directions are in good agreement. Some variation is observed but is attributed to the spatial separations of the areas analyzed. As in the left front quadrant, the peak wavelengths again vary with the forward speed of the hurricane and its maximum wind speed.

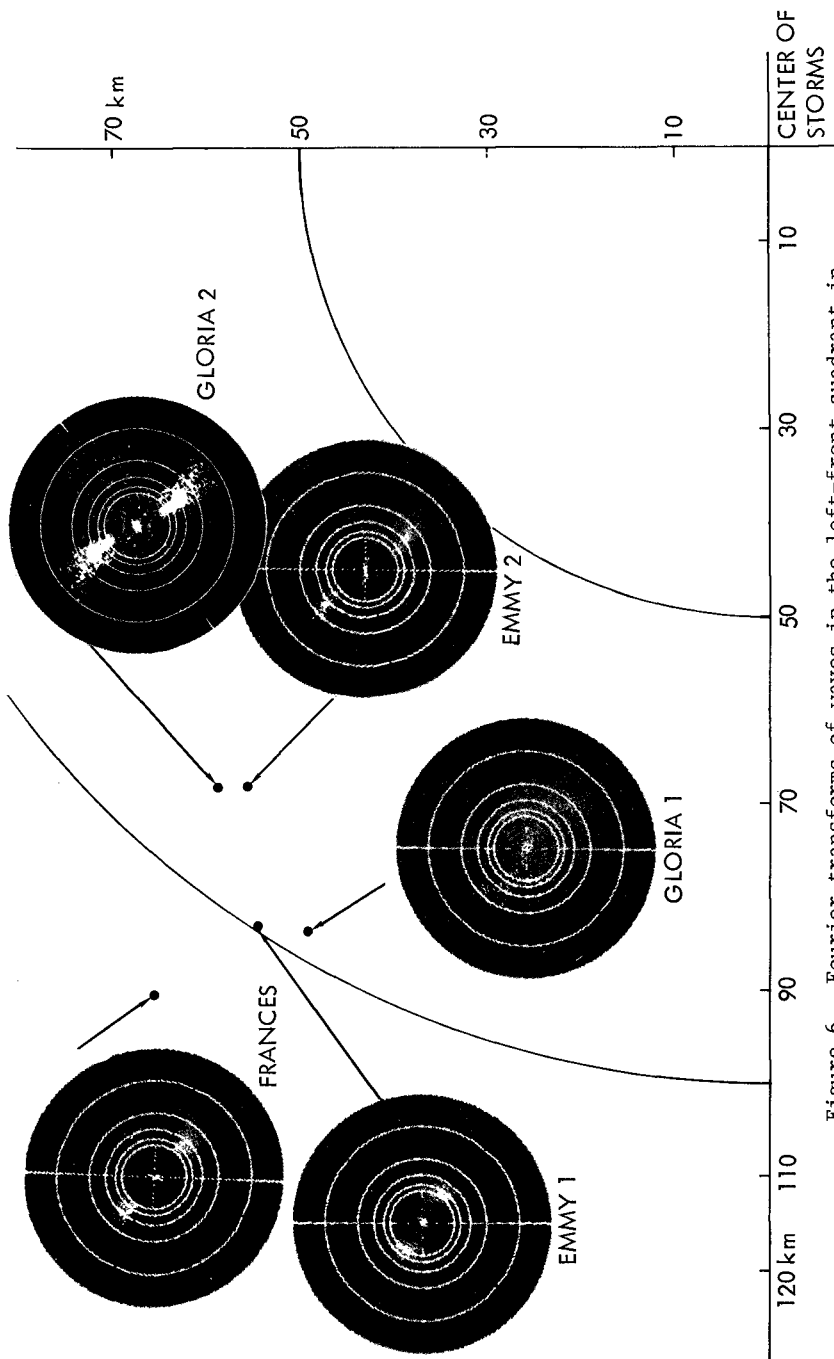


Figure 6. Fourier transforms of waves in the left-front quadrant in five hurricanes.

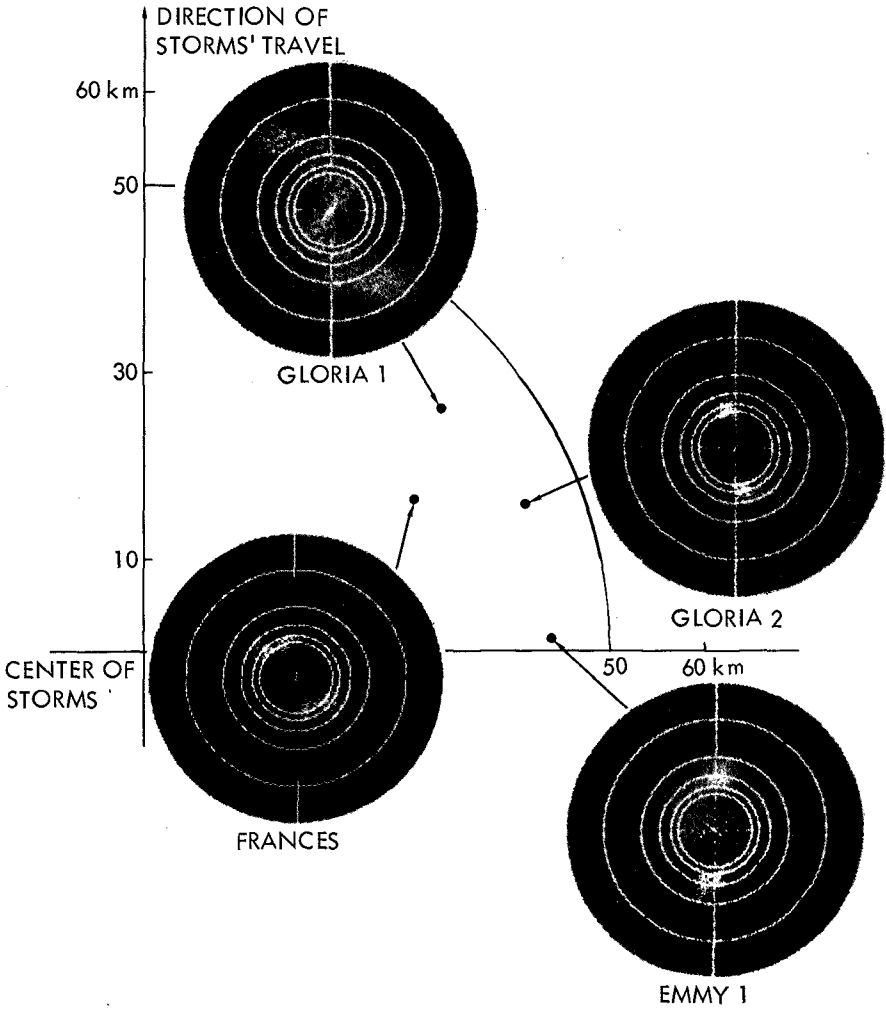


Figure 7. Fourier transforms of waves in the right-front quadrant in five hurricanes.

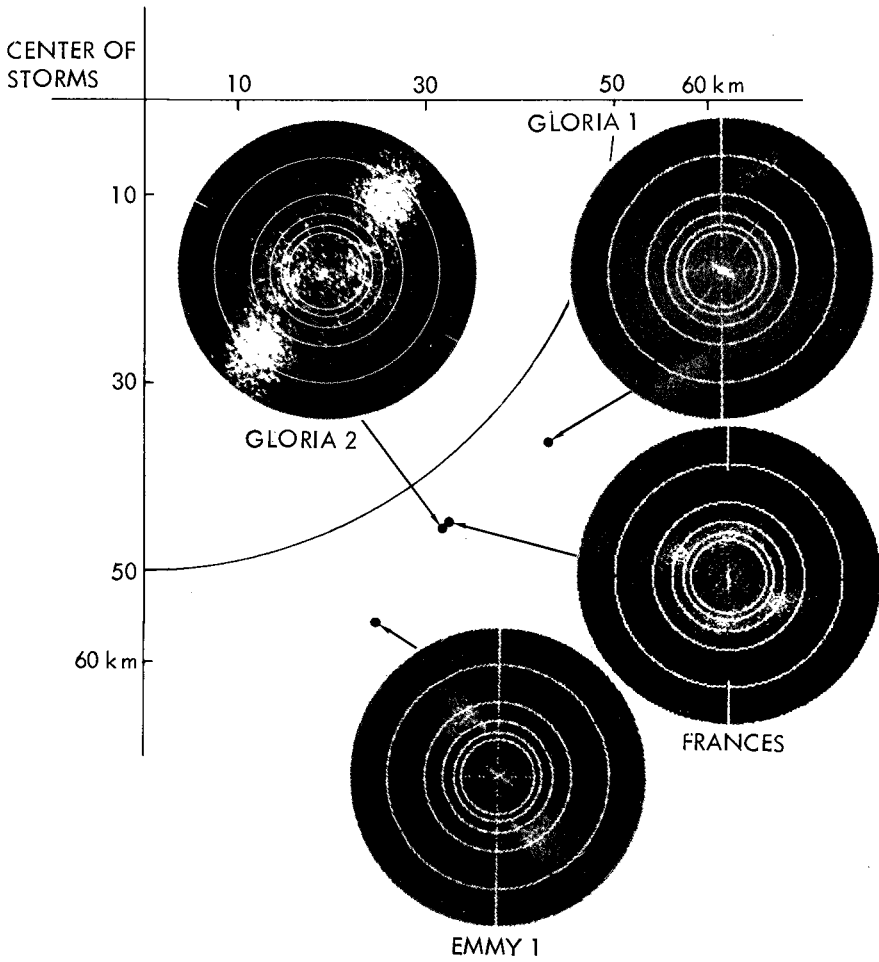


Figure 8. Fourier transforms of waves in the right-rear quadrant in five hurricanes.

Table 2. Dominant wave lengths and wave directions measured for five hurricanes in left-front, right-front, and right-rear quadrants.

	<u>Peak Wavelength (in meters)</u>	<u>Direction (+20°)</u>
LEFT FRONT QUADRANT		
Near 100 km, 315° from storm center		
Emmy 1	275	300°
Emmy 2	190	320°
Frances	230	310°
Gloria 1	160*	315°
Gloria 2	275	320°
RIGHT FRONT QUADRANT		
Near 40 km, 80° from storm center		
Emmy 1	250	5°
Frances	300 275	345° 320°
Gloria 1	125*	325°
Gloria 2	275	350°
RIGHT REAR QUADRANT		
Near 60 km, 140° from storm center		
Emmy 1	160	335°
Frances	250 210	5° 120°
Gloria 1	100	10°
Gloria 2	280 120	80° 30°

*Poor quality images; wave lengths inferred.

The right-rear quadrant (Figure 8 and Table 2) has different properties because it shows little agreement among different hurricanes in wave direction, in contrast to the other two regions examined. It is difficult to determine the causes of the diversity observed. However, it is reasonable to conclude that this region deserves special attention in future modeling efforts and in future data collection missions. Nevertheless, in spite of the apparent confusion in the wave directions in this quadrant, the dominant wavelengths tend to vary with the maximum wind speed and forward speed parameters.

Thus based on dominant wavelengths in three different quadrants the hurricanes under study fall into the following ascending order: Gloria 1, Emmy 1, Frances, Emmy 2, and Gloria 2. There are two exceptions. Emmy 1 is out of this order in the left-front quadrant and Frances and Gloria 2 are reversed in the right-front quadrant.

The correlation between increasing wind speed and dominant wavelength is straightforward and in agreement with known wave generation theories. The argument for an observed correlation between increasing forward storm speed and wave length is more subtle. As waves are generated in the right-hand side of the storm, those that are correctly aligned will travel in the same direction as the storm. These waves are generated over a spectrum of wavelengths and, as such, have a spectrum of group velocities, some slower and some faster than the storm. The generated waves will either lag the storm forward motion and increase in height to saturation through breaking or travel faster than the storm and appear as waves ahead of the storm. The dominant waves, however, are likely to be those waves which extract maximum energy from the wind through elongated residency in the region of intense wave generation. The latter is determined by the difference between the wave group velocity and forward speed of the hurricane. Also, nonlinear interaction plays an important role in affecting energy transfers across a wave spectrum. In an active generation region the frequency of the spectral peak shifts continuously to lower frequencies. The processes of atmospheric transfer, dissipation and nonlinear transfer must all be correctly simulated in a moving circular storm pattern in order to predict the observed directional wave patterns. It is clear that this type of analysis must now follow. However, it is possible to infer that the dominant waves are likely to have wave lengths longer than those which are resonant with the hurricane forward speed. Such inference is consistent with Figure 9 and Table 2 which indicate that the dominant waves are considerably longer than those which are resonant with the hurricane forward motion.

Summary and Conclusions

In summary, this paper presents a unique data set on the directional distribution of wave fields in hurricanes, and as such it provides an insight into the configurations associated with such wind fields. However, it also opens the question of why these wave fields are as they appear. The paper introduces in a qualitative manner certain hypotheses on the generation processes in hurricanes. It also

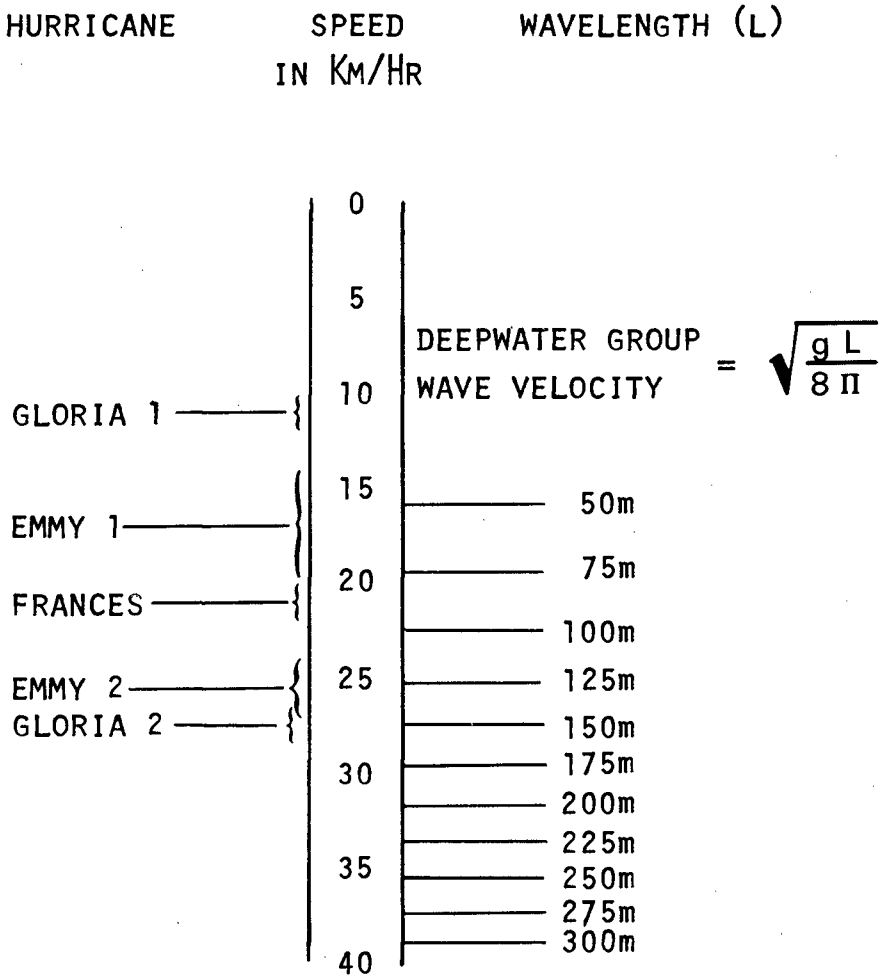


Figure 9. Comparison of hurricane forward speeds and equivalent wave lengths having equal group velocities.

lay the ground for a logical follow-on analytical effort, namely that of modeling the generation processes through the use of numerical techniques.

ACKNOWLEDGEMENT

This research was supported by the Severe Weather Program of the NASA-Office of Applications. The authors acknowledge the valuable support of Dr. R. Sheets of the NOAA-National Hurricane and Environmental Meteorological Laboratory. Mr. W. Stromberg assisted in digitizing the images and calculating the Fourier transforms. Mr. E. McMillan participated in collecting the data with the SAR.

REFERENCES

- Arakawa, H. (1954), "On the Pyramidal, Mountainous, and Confused Sea in the Right or Dangerous Semi-circle of Typhoon," Meteorology and Geophysics Papers, Vol. V, No. 2, pp. 114-123, Tokyo.
- Forristall, C. Z., Ward, E. C., Cardone, V.J., and Borgman, L.E. (1978), "The Directional Spectra and Kinematics of Surface Gravity Waves in Tropical Storm Delia," J. Phys. Oceanogr., Vol. 8, pp. 888-909.
- Johnson, Andrew, Jr., and George A. Speer, (1978), "Data Report: Buoy Observations During Hurricane Belle, August 1976," National Space Technologies Laboratories, NSTL Station, Miss., February 13.
- Johnson, Andrew, Jr., and Stephen M. Reniwick (1978), "Data Report: Buoy Observations During Hurricanes Anita and Babe, 1977," NOAA Data Buoy Office, National Space Technology Laboratories, NSTL Station, Miss., August 14.
- Pore, Arthur (1957), "Ocean Surface Waves Produced by Some Recent Hurricanes," Monthly Weather Review, Dept. of Commerce, Vol. 85, No. 12, pp. 385-392.
- Shemdin, O. H., Brown, W. E., Standhammer, F. C., Shuchman, R., Rawson, R., Zelenka, J., Ross, D. B., McLeish, W. and Berles, R. A. (1978), "Comparison of In-Situ and Remotely Sensed Ocean Waves Off Marineland, Florida," J. Bound. Layer Meteo., Vol. 13, pp. 193-202.
- Tannehill, I. R. (1936), "Sea Swells in Relation to Movement and Intensity of Tropical Storms," Monthly Weather Review, Dept. of Commerce, Vol. 64, No. 7, pp. 231-238.

Ward, E. G. (1974), "Ocean Data Gathering Program - An Overview,"
Paper OTC 2108-B Six Offshore Techn. Conf., Houston, May 6-8.

Withee, G. W., and Johnson, A., (1975), "Data Report: Buoy Observations
During Hurrican Eloise (September 19 to October 11, 1975), "Environ-
mental Science Div., Data Buoy Office, NOAA, U.S. Dept. of Commerce.

CHAPTER 11

THE OBSERVED JOINT DISTRIBUTION OF PERIODS AND HEIGHTS OF SEA WAVES

Yoshimi Goda

Marine Hydrodynamics Division, Port and Harbour Research Institute
Ministry of Transport, Nagase, Yokosuka, Japan

ABSTRACT

Analysis is made of 89 records of surface waves for the joint distribution of the heights and periods of zero up-crossing waves. Records are classified into five groups according to the rank of the correlation coefficient between individual wave heights and periods, and the data of the joint distribution are presented for five groups separately. In comparison with the present data, the theory of Longuet-Higgins for a narrow band spectrum can describe the joint distribution in its upper portion with high waves when the spectral width parameter is fitted to the marginal distribution for wave periods, although the joint distribution in the lower portion with low waves shows deviation from the theory. Another theory by a group of C.N.E.X.O. based on the distribution of positive maxima can describe the general pattern of observed distribution better than the former theory, but the agreement remains qualitative. The present data also suggests that the joint distribution of wave periods and heights may be parameterized with the correlation coefficient between wave heights and periods.

INTRODUCTION

In the analysis of sea waves, the relationships between characteristic wave periods such as the highest, significant, and mean wave periods are often discussed, as there exists a growing demand for such information in the design of coastal and offshore structures. The problem is one aspect of the joint distribution of wave heights and periods. When the problems of irregular wave runups, overtopping, and wave forces are analyzed by the wave-by-wave method, the information of the joint distribution becomes vital for solving these problems.

The theory of the joint distribution of wave heights and periods was given by Longuet-Higgins [1] in 1975 in a closed form under the assumption of a narrow band spectrum. It was recapitulation of his previous work [2] on the statistical properties of random, moving surface. The theoretical distribution is characterized by having the axis of symmetry at $T = \bar{T}$ as demonstrated in Fig. 1, while sea waves generally demonstrate asymmetric distribution with respect to wave periods as exhibited by Chakrabarti and Cooley [3]. A measure of asymmetry is the correlation coefficient between wave heights and periods, which sometimes amounts to more than 0.7 among sea waves, while the theoretical distribution of Longuet-Higgins yields zero correlation.

The asymmetric pattern of the joint distribution of wave heights and periods was incorporated in the theory by Ahran, Cavanié, Ezraty,

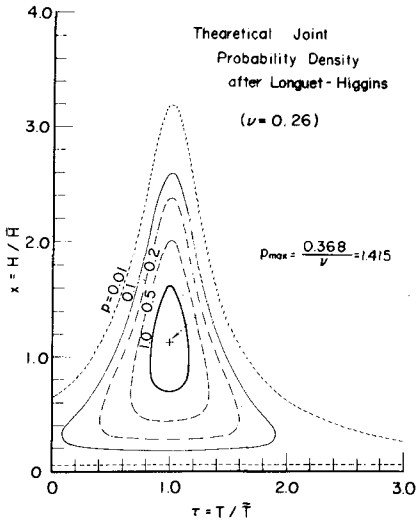


Fig. 1 Joint Probability Density by Longuet-Higgins' Theory ($\nu = 0.26$)

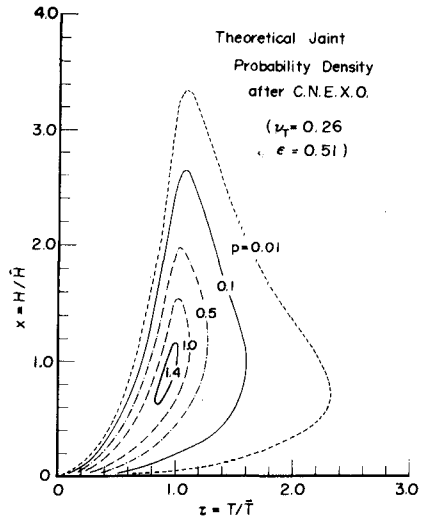


Fig. 2 Joint Probability Density by the Theory of C.N.E.X.O. ($\epsilon = 0.51$ and $\nu = 0.26$)

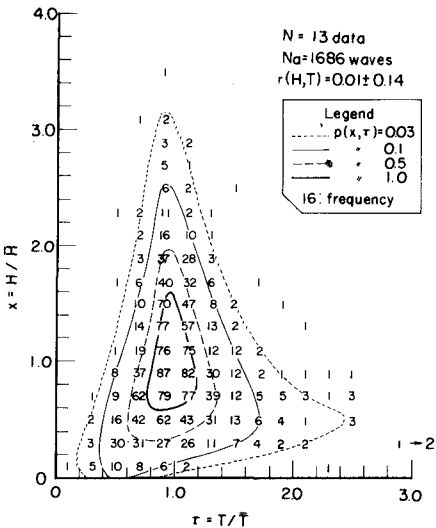


Fig. 3 Example of Observed Joint Probability Density for a Group of Wave Data with $r(H,T) = -0.25 \sim 0.19$

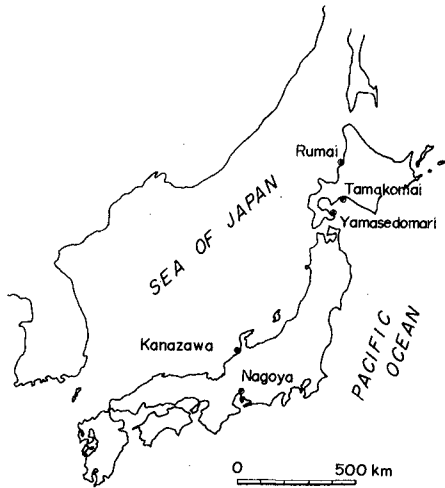


Fig. 4 Location Map of Wave Observation Stations

and Laurent, i.e., a group of C.N.E.X.O. [4,5,6]. They formulated the joint distribution of the amplitudes and quasi-periods of positive maxima on the basis of Cartwright and Longuet-Higgins [7]. The quasi-periods of positive maxima were estimated from the second derivatives of surface elevations at the maxima by fitting a sinusoidal wave profile. They further presumed that it could be applicable to the joint distribution of the heights and periods of zero up-crossing waves by replacing the amplitude of positive maximum with one-half wave height and the quasi-period of positive maximum with the zero crossing wave period. The theory was found to agree with the ocean wave data except for the region of large nondimensional wave periods where the theory tends to overestimate the probability density.

Sea waves are known to exhibit large variability in their statistical parameters such as the correlation coefficient and spectral width parameters. It is readily conceived that the characteristics of the joint distribution of wave heights and periods could be examined in detail by making a rankwise analysis according to the magnitude of statistical parameters. Following this concept, reanalysis of the available surface wave records was made for the joint distribution of wave heights and periods after classifying the data according to the rank of the correlation coefficient of individual wave heights and periods. The analysis has yielded several findings on the characteristics of the joint distribution as it will be seen in the subsequent chapters.

Note: Throughout the present paper a wave is defined by the zero up-crossing method, and no reference is made of a wave defined by the crest-to-trough method except for the number of maxima in a wave record.

FORMULAE OF JOINT PROBABILITY DENSITY

The joint probability density of wave heights and periods by the theory of Longuet-Higgins can be written as in the following form after normalizing wave heights and periods with their mean values, or \bar{H} and \bar{T} , respectively:

$$p(x, \tau) = \frac{\pi x^2}{4\nu} \exp\left\{-\frac{\pi}{4}x^2\left[1 + \frac{(\tau-1)^2}{\nu^2}\right]\right\}, \quad (1)$$

where,

$$x = H/\bar{H} \quad \text{and} \quad \tau = T/\bar{T}.$$

The parameter ν is a measure of spectral bandwidth defined by

$$\nu = [m_0 m_2 / m_1^2 - 1]^{1/2} \equiv \nu_S, \quad (2)$$

where,

$$m_n = \int_0^\infty f^n S(f) df. \quad (3)$$

An example of the joint probability density is shown in Fig. 1 for the case of $\nu = 0.26$.

The marginal distribution of wave heights is shown to be the Rayleigh, by integrating Eq. 1 with respect to τ from $-\infty$ to ∞ .

The marginal distribution of wave periods is similarly derived as

$$p(\tau) = \int_0^{\infty} p(x, \tau) dx = \frac{v^2}{2[v^2 + (\tau-1)^2]^{3/2}} \quad (4)$$

The distribution has a tail in the region of $\tau < 0$ which is unrealistic, but the assumption of narrow band spectrum with the condition $v \ll 1$ yields the probability of $\tau < 0$ practically nil.

As the distribution is symmetric with respect to $\tau = 1$, the mean of heightwise ranked period remains at $\bar{\tau}_H = 1$. The standard deviation of heightwise ranked period is calculated from the conditional joint probability density as

$$\sigma_H(\tau) = \frac{v}{\sqrt{\pi/2} x} \quad (5)$$

Because this diverges as x goes to zero, the overall standard deviation of wave periods cannot be defined. As an alternative measure of the dispersion of wave periods, Longuet-Higgins [1] introduced the interquartile range of the marginal distribution of nondimensional wave periods and correlated it with the spectral width parameter v . Alternatively, v can be estimated from the interquartile range of nondimensional wave period as

$$v = \frac{\sqrt{3}}{2} \text{IQR}(\tau) \equiv v_T \quad (6)$$

In order to avoid confusion, v_T estimated by Eq. 6 is henceforth called the period bandwidth parameter.

The applicability of Longuet-Higgins' theory to waves with a narrow band spectrum can be proved, for example, with the data of numerically simulated random wave profiles [8]. The upper limit of v may be taken at about 0.1 if it is to be estimated from the spectrum [9]. It will be later shown however that the theory can be partially applied to sea waves with broad band spectra as well if v is estimated from the bandwidth of period distribution by Eq. 6.

The joint probability density of wave heights and periods by the group of C.N.E.X.O. has the following form:

$$p(\xi, \zeta) = \frac{\alpha^3 \xi^2}{4\sqrt{2\pi}\epsilon(1-\epsilon^2)\zeta^5} \exp\left\{-\frac{\xi^2}{8\epsilon^2\zeta^4}[(\zeta^2-\alpha^2)^2 + \alpha^4 a^2]\right\}, \quad (7)$$

where,

$$\xi = H/\sqrt{m_0}, \quad \zeta = \bar{\zeta}\tau = \bar{\zeta}T/\bar{T}, \quad \alpha = \frac{1}{2}(1 + \sqrt{1-\epsilon^2}), \quad \text{and} \quad a = \epsilon/\sqrt{1-\epsilon^2}. \quad (8)$$

Though Battjes [10] recommends to introduce the relationship between the mean interval of positive maxima and that of zero up-crossings into the term of ζ so as to have theoretical consistency, the original form is employed in the subsequent calculation as it produces fairer agreement with observation data.

The parameter ϵ is a measure of spectral bandwidth introduced by Cartwright and Longuet-Higgins [7] as

$$\epsilon = [1 - m_2^2/m_0m_4]^{1/2} \equiv \epsilon_S \quad (9)$$

This parameter is very sensitive to the Nyquist frequency of spectral

analysis relative to the frequency of spectral peak when applied to sea waves [11,12]. The group of C.N.E.X.O. recommends the use of the following parameter for ϵ :

$$\epsilon = [1 - N_0^2/N_c^2]^{1/2} \equiv \epsilon_T, \quad (10)$$

in which N_0 and N_c denote the numbers of zero up-crossings and maxima within a wave record, respectively. Though ϵ_S and ϵ_T should give the same value from theoretical point of view, sea waves usually produce ϵ_T less than ϵ_S without a definite interrelation. In this sense, ϵ_T estimated by Eq. 10 should be treated separately from ϵ_S estimated by Eq. 9, and it is henceforth called the apparent spectral width parameter.

The marginal distribution of wave heights derived from Eq. 7 is nearly the Rayleighian when ϵ is not large. The marginal distribution of wave periods is obtained as

$$p(\zeta) = \frac{\alpha^3 a^2 \zeta}{[(\zeta^2 - \alpha^2)^2 + \alpha^4 a^2]^{3/2}}. \quad (11)$$

The mean value of ζ which is estimated by numerically integrating Eq. 11 remains close to 1.0 for the range of $0 < \epsilon < 0.95$. The period bandwidth parameter ν_T can also be estimated numerically from Eq. 11. It is interesting to note that there exists an approximate relation of

$$\nu_T \approx 0.5\epsilon_T + 0.023\epsilon_T^2 \quad ; \quad 0 < \epsilon_T < 0.85, \quad (12)$$

which nearly coincides the relation of $\nu = \frac{1}{2}\epsilon$ derived by Longuet-Higgins [1] for a very narrow band spectrum.

After evaluating $\bar{\xi}$ and $\bar{\zeta}$, the joint probability density can be expressed in terms of the mean wave height and period, \bar{H} and \bar{T} . An example of the joint probability density is shown in Fig. 2, which corresponds to the parameter of $\epsilon_T = 0.51$ and $\nu_T = 0.26$. Asymmetric pattern of the probability density curves is observable even at this level of apparent spectral width parameter.

For comparison with these theoretical joint probability density, a result of compilation of correlation tables of observed sea waves is exhibited in Fig. 3, which represents the data of a group of sea waves with the correlation coefficient $r(H,T)$ between individual wave heights and periods being in the rank of -0.25 to 0.19; the definition of $r(H,T)$ is as follows:

$$r(H,T) = \frac{1}{\sigma_H \sigma_T N_0} \sum_{i=1}^{N_0} (H_i - \bar{H})(T_i - \bar{T}) \quad (13)$$

where σ_H and σ_T denotes the standard deviations of wave heights and periods, respectively, and N_0 is the number of zero up-crossing waves. The groups of 13 wave records in this rank of correlation coefficient had the mean of $\nu_T = 0.26$ for the period bandwidth parameter. The observed density is close to the theory of Longuet-Higgins rather than that of C.N.E.X.O. except for the range of $x = H/\bar{H} < 0.4$.

PRESENTATION OF SEA WAVE DATA

In order to investigate the applicability of the above theories to sea waves, an examination of various wave records was undertaken. The data were taken from the same source with the author's previous analysis of statistical properties [11,12]. Among 171 records analyzed, 89 records were selected under the conditions that each record exhibits a clearly defined single spectral peak and the significant wave height does not exceed about 0.4 times the water depth. The latter condition was introduced to exclude the influence of random wave breaking upon the statistical properties of observed wave records [13]. In total, 10,584 zero up-crossing waves were counted in 89 records.

The stations of wave observations and other data are listed in Table 1 and their locations are shown in Fig. 4. The data at Nagoya were recorded inside and outside a long mole, and they represent deep-water wind waves generated in a short fetch. The other data were recorded at coastal stations, and they mostly represent shallow water waves generated in medium to long fetches; some of them are wind waves and others are young swell.

All the data were recorded on the charts of servo-balanced type pen-writing recorders and were digitized with the aid of a manually operating X-Y digitizer with a magnifier. The digitized wave records were analyzed for their statistical properties as well as spectral characteristics by a computer program. Examples of wave spectra are shown in Fig. 5, where the spectrum is normalized by means of the frequency at the spectral peak, f_p , and the zeroth moment of spectrum, m_0 . The waves observed at Nagoya Port usually show sharp peaks and a few humps at high frequency range, while most of coastal waves have the spectral slope at high frequency range milder than -5. In general, however, the Pierson-Moskowitz type or the Bretschneider-Mitsuyasu type spectral form provides a fair approximation to the spectra of observed waves.

The analysis of the joint distribution of observed wave heights and periods was proceeded first by classifying 89 records into five groups according to the magnitudes of the correlation coefficient $r(H,T)$, because $r(H,T)$ is considered to represent the pattern of joint distribution best. Table 2 lists the numbers of wave data in five groups of $r(H,T)$ as well as the numbers of wave data in ranked groups of v_T . The data of Nagoya Port is characterized with low values of $r(H,T)$ and v_T though its cause is not clarified. There is a possibility that short fetched wind waves may exhibit such characteristics as there is such indication in the data compiled by Bretschneider [13]. The parameters of v_S and ϵ_T as listed in Table 1 do not show marked difference between Nagoya data and coastal wave data. Various statistical properties of the data analyzed are listed in groupwise in Table 3 with the mean values and the standard deviations. The correlation coefficient $r_{1/3}(H,T)$ is the one calculated for the highest one-third waves, which is a measure of correlation among high waves, and Q_p is the spectral peakedness parameter defined as [8]

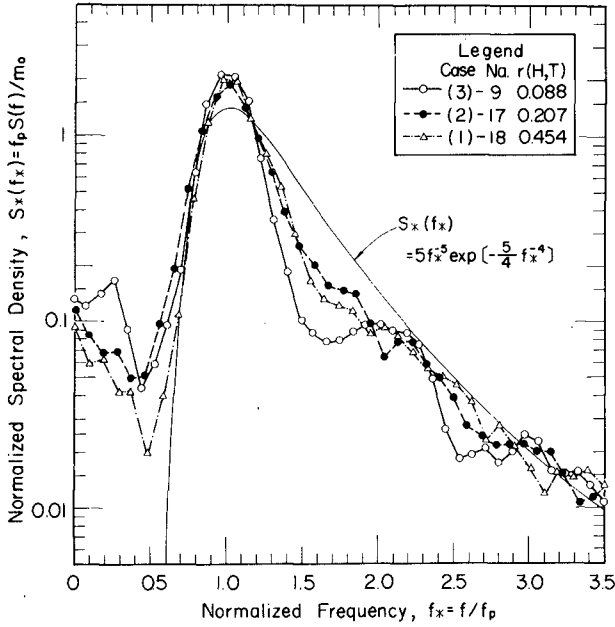
$$Q_p = \frac{2}{m_0} \int_0^{\infty} f S^2(f) df \quad (14)$$

Table 1 Description of Wave Data

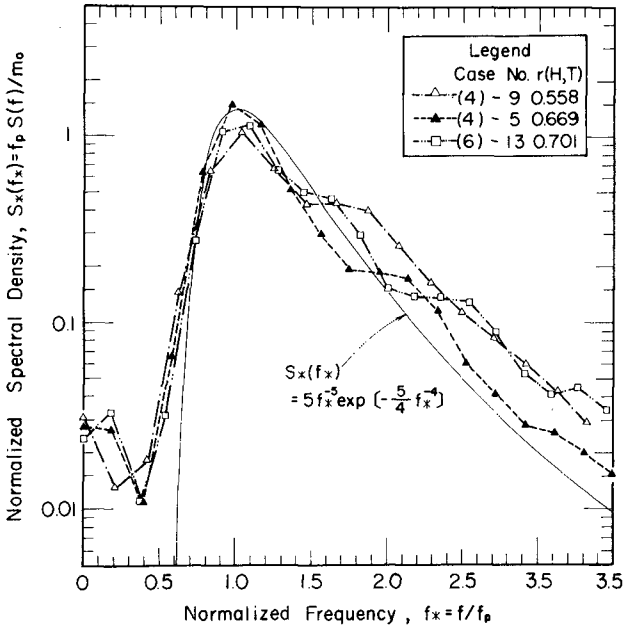
Station	Nos. of Data	Water Depth (m)	Fetch	Range of $H_{1/3}$ (m)	Range of $T_{1/3}$ (s)	v_s	ϵ_T	Wave Recorder	Sampling Time, Δt (s)
Nagoya	42	10	short	0.20~1.22	2.1 ~ 3.7	0.22 ~ 0.63	0.47 ~ 0.77	capacitance gage	0.25
Rumoi	24	11	long	2.2 ~ 4.5	5.9 ~ 9.6	0.28 ~ 0.66	0.65 ~ 0.90	step-resist. gage	0.5
Yamasedomari	6	13	long	1.9 ~ 4.9	7.0 ~ 13.7	0.54 ~ 0.89	0.79 ~ 0.95	step-resist. gage	0.5
Tomakomai	3	11	long	2.9 ~ 4.1	6.9 ~ 8.0	0.46 ~ 0.53	0.64 ~ 0.65	step-resist. gage	1.0
	5	14	long	2.4 ~ 2.8	6.7 ~ 7.5	0.34 ~ 0.69	0.63 ~ 0.77	step-resist. gage	0.5
Kanazawa	9	20	long	1.0 ~ 6.8	4.7 ~ 12.4	0.34 ~ 0.60	0.47 ~ 0.82	inv. echo-sounder	1.0

Table 2 Numbers of Wave Data in Respective Ranks of $r(H,T)$ and v_T

Station	Rank of $r(H,T)$				Total	Rank of v_T				Total
	-0.25 ~ 0.19	0.20 ~ 0.39	0.40 ~ 0.59	0.60 ~ 0.81		0.19 ~ 0.29	0.30 ~ 0.39	0.40 ~ 0.49	0.50 ~ 0.67	
Nagoya	13	17	12	-	42	25	14	2	-	42
Rumoi	-	-	7	15	24	-	2	11	9	24
Yamasedomari	-	-	2	2	6	-	1	1	2	6
Tomakomai	-	-	1	6	8	-	1	5	1	8
Kanazawa	-	1	1	4	9	2	1	2	3	9
Total	13	18	23	27	89	27	19	21	15	89



(1) Wave data of Nagayo Port



(2) Wave data of coastal stations

Fig. 5 Examples of Spectra of Observed Waves

Table 3 Compilation of Statistical Data in Five Ranks of $r(H,T)$

Items	Rank of $r(H,T)$					Whole Data
	-0.25 ~ 0.19 13	0.20 ~ 0.39 18	0.40 ~ 0.59 23	0.60 ~ 0.69 27	0.70 ~ 0.81 8	
Nos. of Records	129.7(21.1)	148.6(14.6)	112.7(31.6)	105.5(39.4)	97.6(31.7)	89 118.9(35.0)
[Wave Height Ratio]						
$H_{max}/H_1/3$	1.702(0.210)	1.752(0.272)	1.693(0.256)	1.597(0.164)	1.536(0.148)	1.663(0.231)
$H_1/10/H_1/3$	1.281(0.063)	1.276(0.037)	1.285(0.039)	1.284(0.051)	1.267(0.039)	1.281(0.046)
$H_1/3/H$	1.610(0.058)	1.570(0.042)	1.594(0.074)	1.619(0.053)	1.614(0.057)	1.601(0.061)
[Wave Period Ratio]						
$T_{max}/T_1/3$	0.943(0.131)	0.963(0.083)	1.025(0.112)	1.018(0.105)	1.060(0.105)	1.002(0.113)
$T_1/10/T_1/3$	0.994(0.022)	0.999(0.028)	1.012(0.043)	1.023(0.041)	1.029(0.030)	1.012(0.038)
$T_1/3/\bar{T}$	0.983(0.047)	1.061(0.025)	1.156(0.047)	1.252(0.041)	1.331(0.042)	1.156(0.116)
$T_1/3/T_p$	0.966(0.035)	0.950(0.020)	0.915(0.062)	0.901(0.046)	0.890(0.045)	0.923(0.053)
\bar{T}/T_p	0.983(0.061)	0.895(0.030)	0.794(0.070)	0.720(0.044)	0.669(0.035)	0.808(0.116)
[Correl. Coef.]						
$r(H,T)$	0.014(0.137)	0.295(0.064)	0.511(0.048)	0.650(0.034)	0.730(0.033)	0.457(0.239)
$r_{13}(H,T)$	-0.068(0.134)	-0.032(0.104)	0.010(0.163)	0.078(0.160)	0.179(0.098)	0.026(0.159)
[Spectr. Parameter]						
ϵ_S	0.832(0.035)	0.803(0.059)	0.865(0.044)	0.878(0.042)	0.880(0.042)	0.853(0.054)
ϵ_T	0.584(0.074)	0.570(0.054)	0.716(0.100)	0.747(0.075)	0.781(0.078)	0.683(0.113)
ν_S	0.515(0.061)	0.487(0.059)	0.489(0.108)	0.562(0.081)	0.657(0.109)	0.526(0.102)
ν_T	0.268(0.048)	0.287(0.028)	0.384(0.086)	0.500(0.062)	0.582(0.054)	0.400(0.123)
Q_p	2.412(0.698)	2.369(0.356)	2.116(0.566)	1.740(0.228)	1.758(0.210)	2.064(0.526)
$\Delta t/T_p$	0.092(0.014)	0.105(0.026)	0.069(0.019)	0.060(0.015)	0.063(0.015)	0.076(0.026)

RESULTS OF DATA ANALYSIS

Marginal Distribution of Wave Heights

As reported by many researchers, the marginal distribution of wave heights does not show any significant deviation from the Rayleigh. An indication is the mean values of three height ratios listed in Table 3, which are close to the theoretical values of the Rayleigh distribution. The chi-square test for the goodness-of-fitness to the Rayleigh was made for the present data with 14 classes of wave heights. The probability that the total data has come from the population of the Rayleigh distribution is calculated as about 0.30, and the probability that the data in the rank of $r(H,T) = 0.70 \sim 0.81$ has come from the Rayleigh distribution is about 0.10. Thus the hypothesis of the Rayleigh distribution cannot be discarded for the present data.

Marginal Distribution of Wave Periods

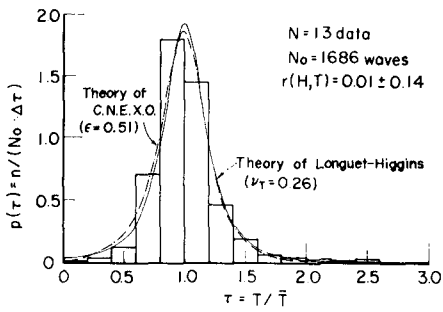
Figure 6 shows the marginal distribution of observed wave periods normalized by the mean wave period of respective wave records. For the data with $r(H,T)$ less than 0.4, both of the theoretical distributions of Eqs. 4 and 7 provide good approximation so long as the period bandwidth parameter obtained from the data is employed in theoretical estimation. The two theories do not yield much difference for small values of v_T . As v_T increases, the observed marginal distribution deviates gradually from the theoretical ones, which become unapplicable for $r(H,T) \gtrsim 0.6$. It should be noted that the maximum value of $r(H,T)$ and v_T predicted by the theory of C.N.E.X.O. is about 0.69 and 0.55, respectively, both of which correspond to the case of $\epsilon = 0.99$.

Joint Distribution of Wave Heights and Periods

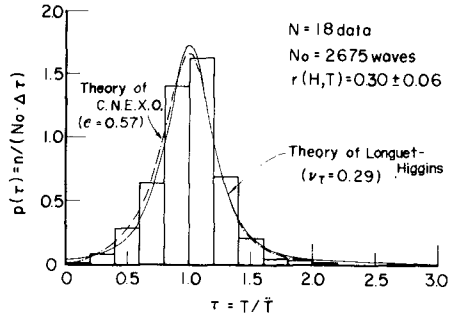
The joint distribution of wave heights and periods were analyzed with the rank of $\Delta H/\bar{H} = \Delta T/\bar{T} = 0.2$ after having been normalized with \bar{H} and \bar{T} . The correlation table with the curves of probability density for the group of $r(H,T) = -0.25$ to 0.19 has been presented as Fig. 3 for comparison with theoretical ones. The correlation tables for the other four groups of $r(H,T)$ are shown in Fig. 7. As $r(H,T)$ increases, the asymmetry of joint distribution becomes conspicuous and the position of maximum probability density moves toward the origin. The change of the pattern is qualitatively in accordance with the theory of C.N.E.X.O.

Characteristics of Heightwise Ranked Wave Periods

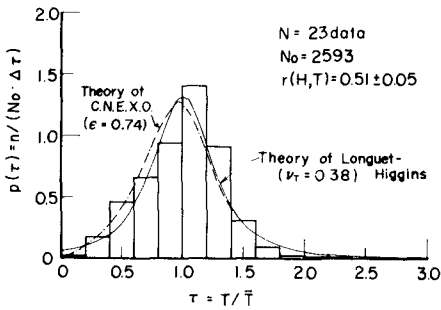
One feature of Fig. 3 and Fig. 7 is that the center of wave periods at each level of wave height does not vary in the upper portion of correlation table and the distribution is symmetric there. This feature is clearly shown in Fig. 8, where the mean of heightwise ranked wave periods is plotted against the wave height level. The ranked mean \bar{T}_H of high waves relative \bar{T} shifts toward large values as $r(H,T)$ increases, but it holds a common value among high waves as seen in Fig. 8(a). The shift of \bar{T}_H is an apparent phenomenon, however, as demonstrated in Fig. 8(b), where the ranked mean of wave period is normalized with the period corresponding to the spectral peak, T_p . Figure 8(b) shows that \bar{T}_H of high waves remains in the range of $(0.87 \sim 0.98)T_p$ irrespective of $r(H,T)$. The mean of wave periods with $H > 1.4\bar{H}$, for example, is calculated to be $(0.91 \sim 0.97)T_p$. The figure also indicates that the increase



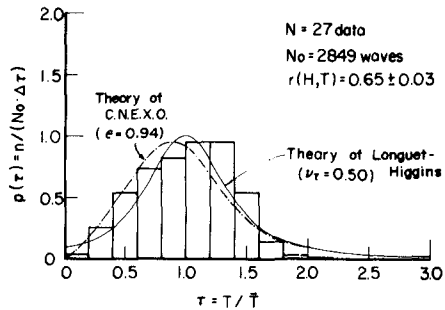
$$(1) r(H, T) = -0.25 \sim 0.19$$



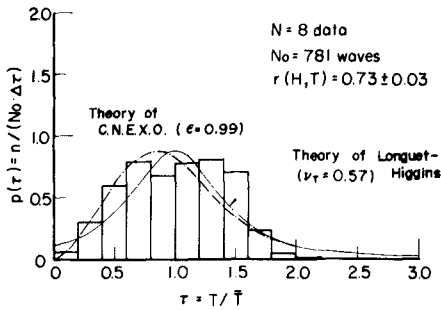
$$(2) r(H, T) = 0.20 \sim 0.39$$



$$(3) r(H, T) = 0.40 \sim 0.59$$

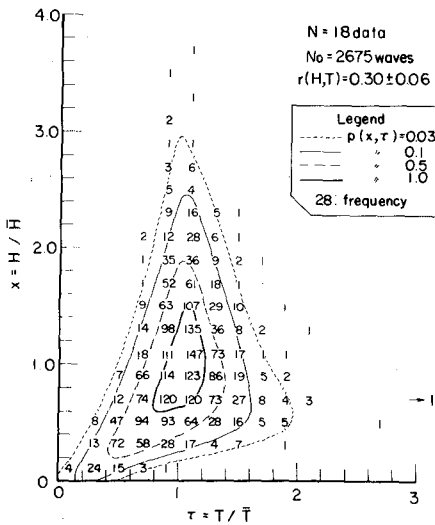


$$(4) r(H, T) = 0.60 \sim 0.69$$

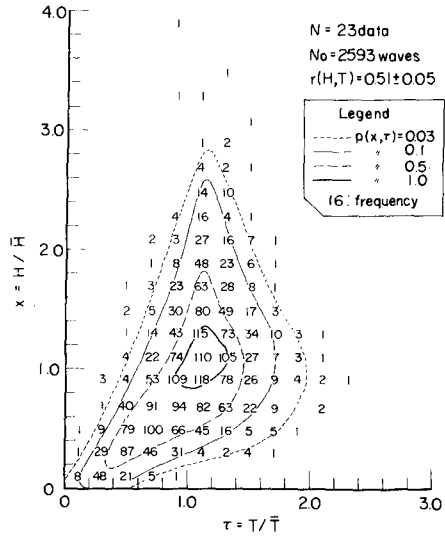


$$(5) r(H, T) = 0.70 \sim 0.81$$

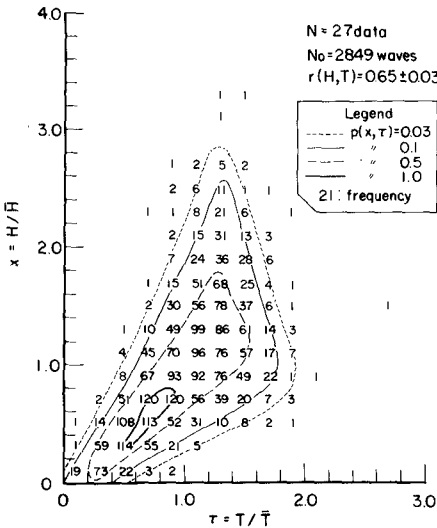
Fig. 6 Marginal Distribution of Wave Periods Ranked in Five Groups of Correlation Coefficient, $r(H, T)$



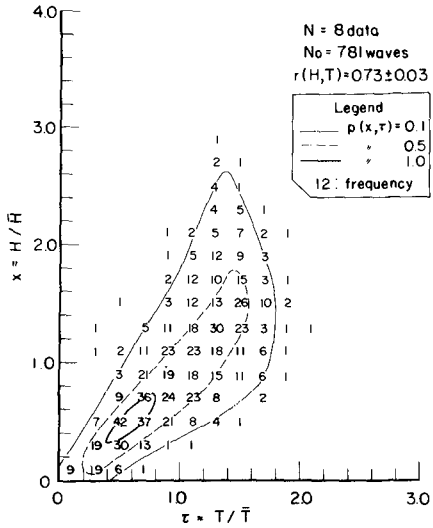
(1) $r(H,T) = 0.20 \sim 0.39$



(2) $r(H,T) = 0.40 \sim 0.59$

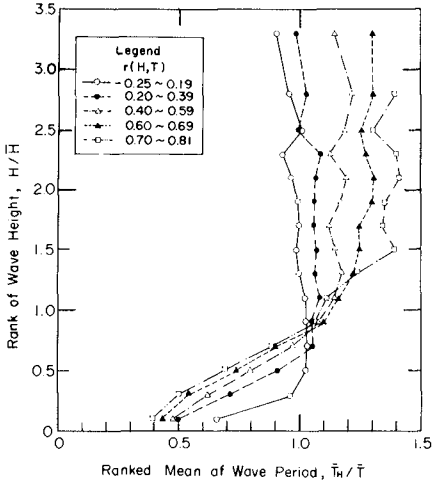


(3) $r(H,T) = 0.60 \sim 0.69$

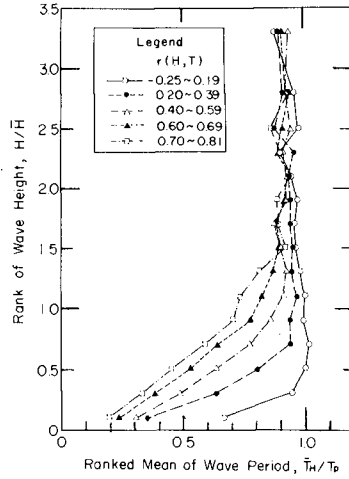


(4) $r(H,T) = 0.70 \sim 0.71$

Fig. 7 Joint Distribution of Observed Wave Heights and Periods Grouped in the Rank of Correlation Coefficient, $r(H,T)$



(a) reference period of \bar{T}



(b) reference period of T_p

Fig. 8 Mean Period of Heightwise Ranked Waves

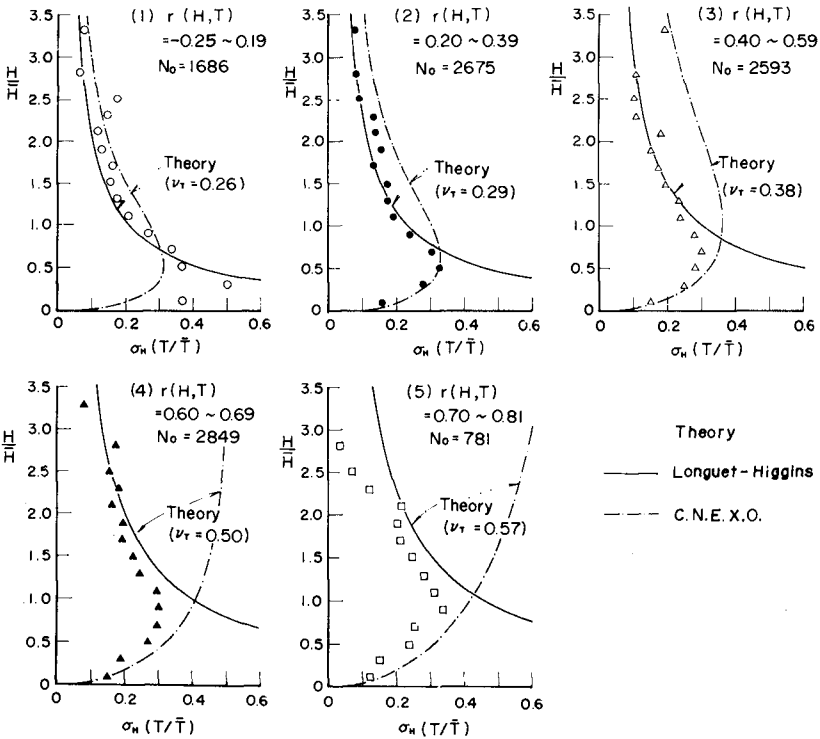


Fig. 9 Standard Deviation of Heightwise Ranked Wave Periods

of $r(H,T)$ is owing to the appearance of small waves with very short periods.

The constancy of mean ranked wave periods is inherent in the theory of Longuet-Higgins although its shift with respect to \bar{T} cannot be dealt with. The theory of C.N.E.X.O., on the other hand, can yield the increase of mean wave periods of high waves with the increase of ϵ , but the mean wave period steadily elongates itself as the level of wave height rises.

The spread of wave periods in a particular rank of wave height can be represented with their standard deviation. Figure 9 shows the results of the calculation of standard deviations of heightwise ranked wave periods for five groups of wave data classified by the rank of $r(H,T)$. The theory of Longuet-Higgins is seen to predict the spread of wave periods of high waves when the mean period bandwidth parameter of respective wave group is employed in calculation of Eq. 5, although the decrease of standard deviations in the region of small waves cannot be predicted. The theory of C.N.E.X.O., on the other hand, can present the standard deviation decreasing in the lower portion of wave heights, but it yields the deviation much larger than the observed ones in the upper portion of wave heights especially for groups with high correlation coefficients.

DISCUSSIONS ON THE GOVERNING PARAMETERS OF JOINT DISTRIBUTION

It has been demonstrated that the joint distribution of the heights and periods of sea waves exhibit quite large variations. One of the questions may be what the parameter is governing the joint distribution. There are two spectral width parameters of ν_S and ϵ_S defined by Eqs. 2 and 9, respectively. Statistical analysis of wave records yields the apparent spectral width parameter of ϵ_T by Eq. 10, the period bandwidth parameter of ν_T by Eq. 6, and the correlation coefficient between individual wave heights and periods by Eq. 13. Among these parameters, ϵ_S is not qualified for describing the statistical properties of sea waves, because ϵ_S is essentially 1.0 for wind-generated water waves and becomes less than 1.0 owing to incompetence in the high frequency response of a wave recorder [11,12]. The parameter ν_S may need further examination, but the present data at least reject the effectiveness of ν_S because of large scatter of ν_S without associating itself with the statistical properties of waves analyzed.

The question is thus focussed on the selection among three parameters of ϵ_T , ν_T , and $r(H,T)$. The relationships among them are first examined as shown in Figs. 10 to 12. The relationship between ν_T and $r(H,T)$ is most conspicuous with the correlation coefficient between them amounting to 0.80. If one makes a polynomial regression analysis instead of linear regression, a much higher correlation will be obtained. Among the whole data, those in the range of $r(H,T) \gtrsim 0.4$ closely follow the trend of the theory of C.N.E.X.O. as well as the result of numerically simulated wave analysis [8], even though both the theory and the simulation data cannot explain the existence of data with $r(H,T) > 0.7$ or $\nu_T > 0.55$. The relationship between ν_T and ϵ_T is obscure although the means of rankwise data indicate the existence of interrelation, which is close to the data of simulation study. The correlation coef-

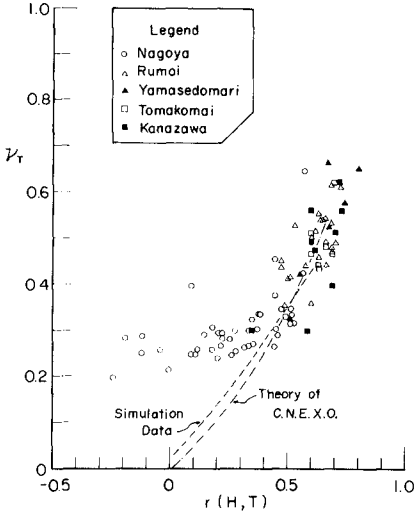


Fig. 10 Correlation between v_T and $R(H,T)$

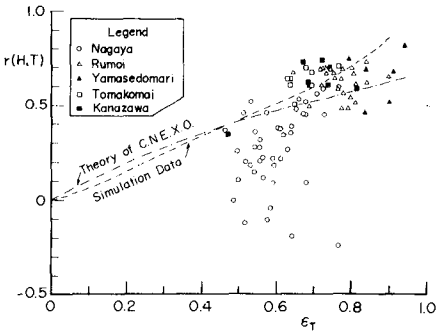


Fig. 11 Correlation between $r(H,T)$ and ϵ_T

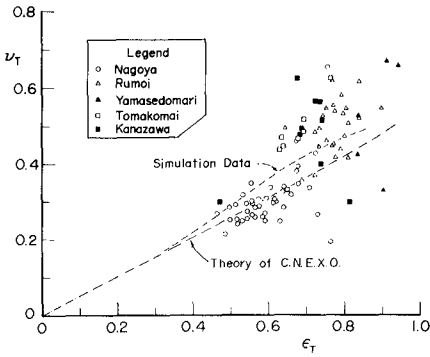


Fig. 12 Correlation between v_T and ϵ_T

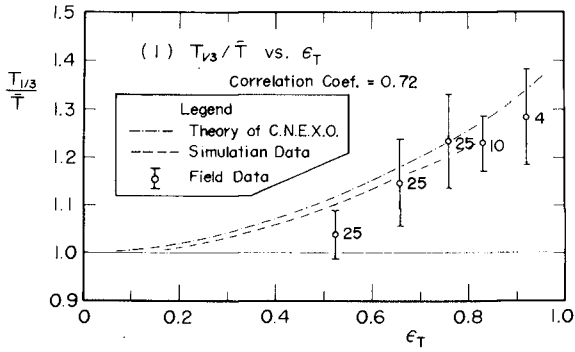
ficient between v_T and ϵ_T is calculated as 0.72. The third set of relationship, that is the one between $r(H,T)$ and ϵ_T , is clouded with the presence of the data with $r(H,T) \lesssim 0.3$, which come from the Nagoya Port data. The correlation coefficient between $r(H,T)$ and ϵ_T nevertheless has the value of 0.66 for the present data.

A criterion for the selection of governing parameter will be a high level of correlation with statistical properties of the joint distribution of wave heights and periods. One of the appropriate properties is the ratio of significant to mean wave period, $T_{1/3}/\bar{T}$, as employed by the group of C.N.E.X.O. for demonstration of the influence of ϵ_T . Figure 13 is the result of comparison of the influence of three parameters upon $T_{1/3}/\bar{T}$. Data are shown in the form of ranked mean and standard deviations with the number of records in respective ranks. The wave period ratio, $T_{1/3}/\bar{T}$, is seen to be closely related with the three parameters. The relationships are also close to those derived by the theory of C.N.E.X.O. and the simulation data. Among three parameters, their correlations with $T_{1/3}/\bar{T}$ is lowest for ϵ_T with the correlation coefficient of 0.72, while v_T and $r(H,T)$ show the coefficient of 0.92 and 0.94, respectively.

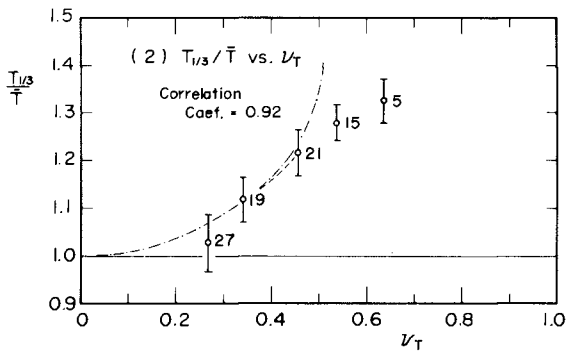
The degree of correlation between $T_{1/3}/\bar{T}$ and ϵ_T of the present data is about the same with the data presented by the group of C.N.E.X.O., as judged from the magnitude of standard deviations of $T_{1/3}/\bar{T}$. In this sense, ϵ_T seems inferior to the other two parameters. Between the remaining two, $r(H,T)$ is slightly superior to v_T on the basis of the former's high correlation coefficient. In the application of the theory of Longuet-Higgins, however, the information of period bandwidth parameter is required, and from this point of view v_T may be more convenient than $r(H,T)$. The final selection between $r(H,T)$ and v_T cannot be made at this stage yet, and it will necessitate the analysis of many more data of sea waves.

A remaining question is the correlation of these parameters with spectral characteristics. Though v and ϵ have originally been derived from spectral moments, v_T and ϵ_T are the parameters estimated from the statistical analysis of wave profiles; their relationships with v_S and ϵ_S cannot be well established at least for the present data. The definition of correlation coefficient $r(H,T)$ is independent of wave spectrum and it has not been related to a wave spectrum (variance) except for a numerical simulation study [8]: the spectrum proposed by Bretschneider [13] with $r(H,T)$ as a parameter is an apparent one and not the variance spectrum analyzed by the spectral theory. As indicated in Figs. 10 to 12, these parameters vary over quite large ranges. A spectral characteristics which seems to be related to these parameters to some extent is the spectral peakedness parameter defined by Eq. 14. As shown in Fig. 14, the period bandwidth parameter v_T of the present data does indicate an interrelation with Q_p ; the correlation coefficient between them is -0.65. The correlations of other two parameters ϵ_T and $r(H,T)$ with Q_p are not so prominent, however.

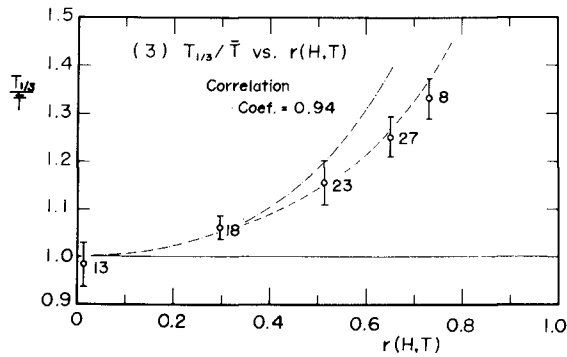
Another factor which may affect the parameter of the joint distribution of wave heights and periods is the sampling interval of wave profile relative to the spectral peak period, or $\Delta t/T_p$. The present data shows the relationship between v_T and $\Delta t/T_p$ as in Fig. 15.



(1) influence of ϵ_T on $T_{1/3}/\bar{T}$



(2) influence of ν_T on $T_{1/3}/\bar{T}$



(3) influence of $r(H,T)$ on $T_{1/3}/\bar{T}$

Fig. 13 Comparison of the Parameters of ϵ_T , ν_T , and $r(H,T)$ for Their Influences upon the Wave Period Ratio of $T_{1/3}/\bar{T}$

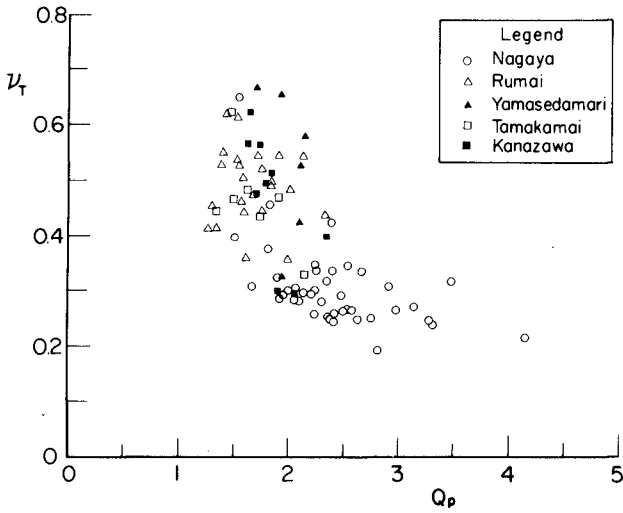


Fig. 14 Correlation between ν_T and Q_p

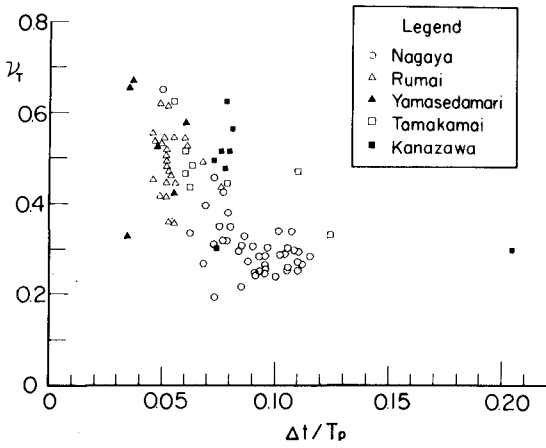


Fig. 15 Correlation between ν_T and $\Delta t / T_p$

A negative correlation between them is somewhat expected, though the quantitative analysis should await the accumulation of a greater number of sea wave data.

SUMMARY

The joint distribution of wave heights and periods exhibits statistical variability greater than the marginal distributions of wave heights and periods. Any analysis of the joint distribution should have a sufficiently large number of wave records as the data base. The present analysis based on 89 records cannot be claimed to be very reliable, it nevertheless covers a variety of wave conditions from short-fetched wind waves to young swell in shallow water. Findings made in this analysis can be summarized as follows:

1. The joint distribution of wave heights and periods of sea waves is characterized with no correlation among high waves and a strong correlation among low waves.
2. The mean period of waves higher than a certain level is independent of the wave height, and it remains at a value slightly less than the period corresponding to the spectral peak.
3. The theory of Longuet-Higgins can explain the characteristics of the joint distribution in its upper portion with high waves if the spectral width parameter is so selected to fit the marginal distribution of wave periods, even though the theory disagrees with the observed joint distribution in its lower portion with low waves.
4. The theory by the group of C.N.E.X.O. can qualitatively predict the change of the joint distribution with the increase of spectral width parameter, but the quantitative agreement is only partial.
5. The parameter governing the joint distribution seems to be the correlation coefficient between individual wave heights and periods and/or the period bandwidth parameter. The apparent spectral width parameter is less influential than the formers.

REFERENCES

- [1] Longuet-Higgins, M. S.: On the joint distribution of the periods and amplitudes of sea waves, *J. Geophy. Res.*, Vol. 80, No. 18, June 1975, pp.2688-2693.
- [2] Longuet-Higgins, M. S.: The statistical analysis of a random, moving surface, *Phil. Trans. Roy. Soc. London, Ser. A*(966), Vol. 249, 1957, pp.321-387.
- [3] Chakrabarti, S. K. and Cooley, R. P.: Statistical distribution of periods and heights of ocean waves, *J. Geophy. Res.*, Vol. 82, No. 9, March 1977, pp.1363-1368.
- [4] Arhan, M., Cavanié, A., and Ezraty, R.: Etude théoretique et expérimentale de la relation hauteur-période des vages de tempête, *Internal Rept.*, A.R.A.E., IFP 24 191, 1976, 28p.

- [5] Cavanié, A., Arhan, M., and Ezraty, R.: A statistical relationship between individual heights and periods of storm waves, Proc. BOSS '76, Vol. II, Trondheim, 1976, pp.354-360.
- [6] Ezraty, R., Laurent, M., and Arhan, M.: Comparison with observation at sea of period or height dependent sea state parameters from a theoretical model, OTC 2744, 9th Offshore Tech. Conf., 1977.
- [7] Cartwright, D. E. and Longuet-Higgins, M. S.: The statistical distributions of the maxima of a random function, Proc. Roy. Soc., Ser. A., Vol. 237, 1956, pp.212-232.
- [8] Goda, Y.: Numerical experiments on wave statistics with spectral simulation, Rept. Port and Harbour Res. Inst., Vol. 9, No. 3, 1970, pp.3-57.
- [9] Goda, Y.: Analysis of the joint distribution of the periods and heights of sea waves with observed records, Tech. Note of Port and Harbour Res. Inst., No. 272, 1977, 19p. (in Japanese).
- [10] Battjes, J. A.: Probabilistic aspects of ocean waves, Report No. 77-2, Communications on Hydraulics, Dept. Civil Engg., Delft Univ. of Tech., 1977, 52p.
- [11] Goda, Y. and Nagai, K.: Investigation of the statistical properties of sea waves with field and simulation data, Rept. Port and Harbour Res. Inst., Vol. 13, No. 1, 1974, pp.3-37. (in Japanese)
- [12] Goda, Y.: Estimation of wave statistics from spectral information, Proc. Int. Symp. on Ocean Wave Measurement and Analysis (WAVES 74), Vol. I, 1974, pp.320-337.
- [13] Bretschneider, C. L.: Wave variability and wave spectra for wind-generated gravity waves, U.S. Army Corps of Engrs., Beach Erosion Board, Tech. Memo, No. 113, 1959, 192p.

LIST OF MAJOR SYMBOLS

H_{\max}	: height of highest wave
$H_{1/10}$: mean height of highest one-tenth waves
$H_{1/3}$: mean height of highest one-third waves
\bar{H}	: mean wave height
Q_p	: spectral peakedness parameter defined by Eq. 14
$r(H, T)$: correlation coefficient between individual wave heights and periods
$r_{13}(H, T)$: correlation coefficient among highest one-third waves
T_p	: wave period corresponding to spectral peak frequency
T_{\max}	: period of highest wave
$T_{1/10}$: mean period of highest one-tenth waves
$T_{1/3}$: mean period of highest one-third waves
\bar{T}	: mean wave period
$x = H/\bar{H}$: nondimensional wave height
Δt	: time interval between successive sampling of surface elevation
ϵ_S	: spectral width parameter defined by Eq. 9
ϵ_T	: apparent spectral width parameter defined by Eq. 10
$\zeta = \bar{\zeta}\tau$: nondimensional wave period
ν_S	: spectral width parameter defined by Eq. 2
ν_T	: period bandwidth parameter defined by Eq. 6
$\xi = H/\sqrt{m_0}$: nondimensional wave height
$\tau = T/\bar{T}$: nondimensional wave period

ANOMALOUS DISPERSION OF FOURIER COMPONENTS OF SURFACE GRAVITY WAVES IN THE NEAR SHORE AREA

by

Fritz Büsching ¹⁾

ABSTRACT

Water level deflections $\eta(t)$ have been measured synchronously at some positions in a beach profile on the isle of SYLT / North Sea during severe storm surge conditions as well as at attenuating wave action.

A steadily increasing wave period \bar{T}_z in the upbeach direction, turning out from strip chart evaluations, is in accordance with the result of FOURIER syntheses. Near shore wave deformation is explained by ANOMALOUS dispersion of the frequency components.

1. INTRODUCTION

Because of the well known restrictions of model investigations on surf zone processes (FÜHRBÖTER 1970 and 1971) since 1971 comprehensive field investigations have been performed by members of the LEICHTWEISS-INSTITUT on the west coast of the isle of SYLT / North Sea.

Especially the energy transformation on the beach was considered by FÜHRBÖTER (1974) based on strip chart evaluations and on a linear analysis.

Later on in this respect the spectrum analysis was used by the author (BÜSCHING, 1974, 1975, 1976).

The present study refers to both partly previously presented data sets analyzed by means of the zero-up-crossing evaluation method and by spectral functions respectively. In the first part of this study the description of the wave deformation in the upbeach direction is based on strip chart evaluations, whereas the second part consists of an attempt to explain these deformation processes by spectral methods.

1) Chief-Engineer, Dr.-Ing. Div. of Hydrodyn. and Coastal Engineering
Techn. Univ. Braunschweig, Federal Republik Germany

2. WAVE PARAMETERS IN THE NEAR SHORE ZONE

In a conservative treatment of the transformation of shoaling waves into breaking and finally into broken waves the wave period is assumed to be a constant, whereas wave heights, lengths and celerities change. In addition to this it is well known that real gravity waves continuously change form as they proceed into shallower water.

This, however, is not only represented by the different asymmetries previously defined (BIESEL, 1951 ; PATRICK and WIEGEL, 1956 ; ABEYMO, 1968 ; IWAGAKI, SAKAI and KAWASHIMA, 1973 ; FÜHRBÖTER, 1974) but also by the so-called decomposition of the initial wave into two or more waves (solitons) (MULTER and GALVIN, 1967 ; MADSEN and MEI, 1969 ; ZABUSKY and GALVIN, 1971 ; GALVIN, 1972).

Applying the zero-up-crossing evaluation method on strip chart records of water level deflexions which are deformed in such a way, this method turns out to be somewhat questionable, as in the present case the result is a steadily increasing mean wave period \bar{T}_z in the upbeach direction.

This can be seen from Fig. 1 containing the variation of some wave parameters in the coast perpendicular measuring profile on the isle of SYLT for synchronous measurements at fixed positions on March 18th and April 3rd, 1973 respectively.

The shown parameters (mean wave heights \bar{H}_z and mean wave periods \bar{T}_z) refer to synchronously measured water level deflexions taken by echo sounders at the offshore positions at 225 m, 570 m, 940 m and 1280 m and by pressure type wave meters at the beach positions 40,50, 60, 70, 80, 90 and 100 m.

The details of the wave measuring instrumentation used are given by FÜHRBÖTER and BÜSCHING (1974). Because of the lack of space in the following it shall only be considered here the measurements on the beach face, where in addition to the above mentioned parameters the wave propagation velocities could be determined from the phase differences between the respective synchronously taken wave traces.

Additional interpretation of the more offshore measurements and the influence of the long shore bar (ridge) on the wave deformation will be given in

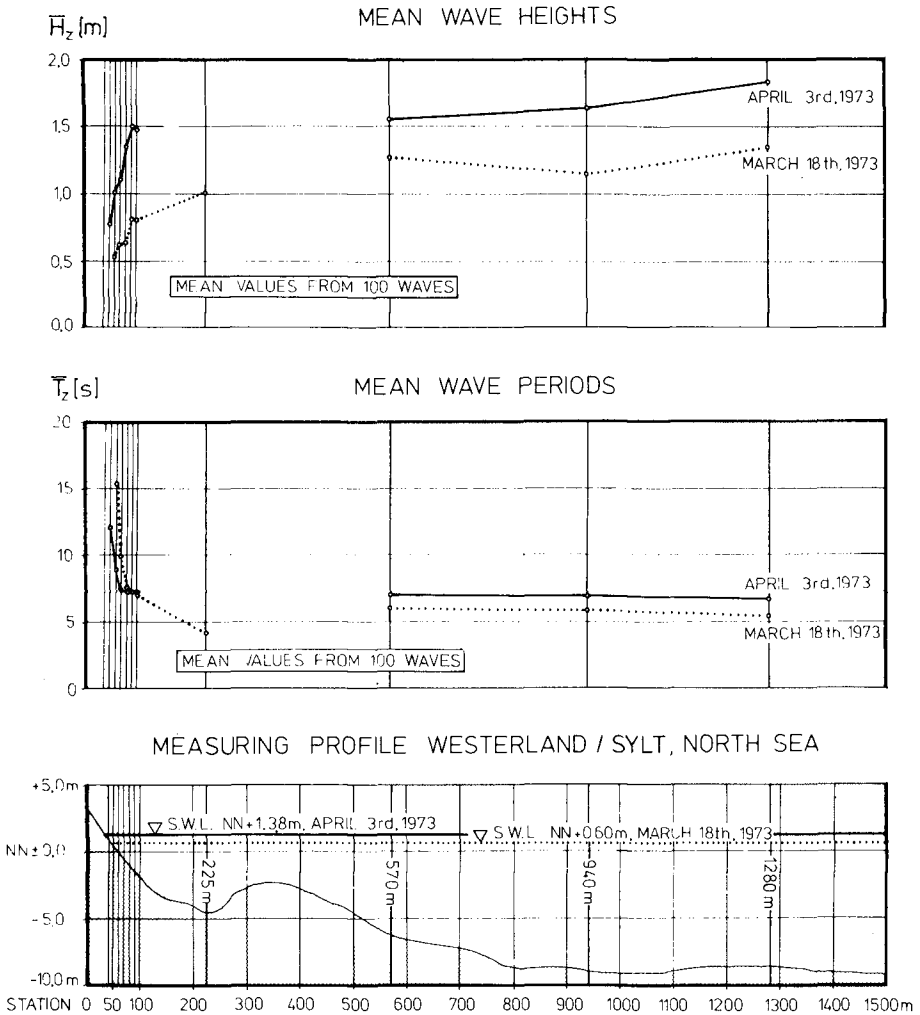


Fig. 1 : Mean wave heights and periods in the measuring profile on the isle of SYLT / North Sea

another paper (BÜSCHING, 1978) with reference to the measurements of RAMAN (1976) and WANG and YANG (1976) in the same area.

As regards energy dissipation treatments based on the present measurements, they are contained in FÜHRBÖTER (1974).

The complete strip chart data are plotted in Fig. 2 with reference to the beach measuring positions. With the known wave propagation velocity the mean wave

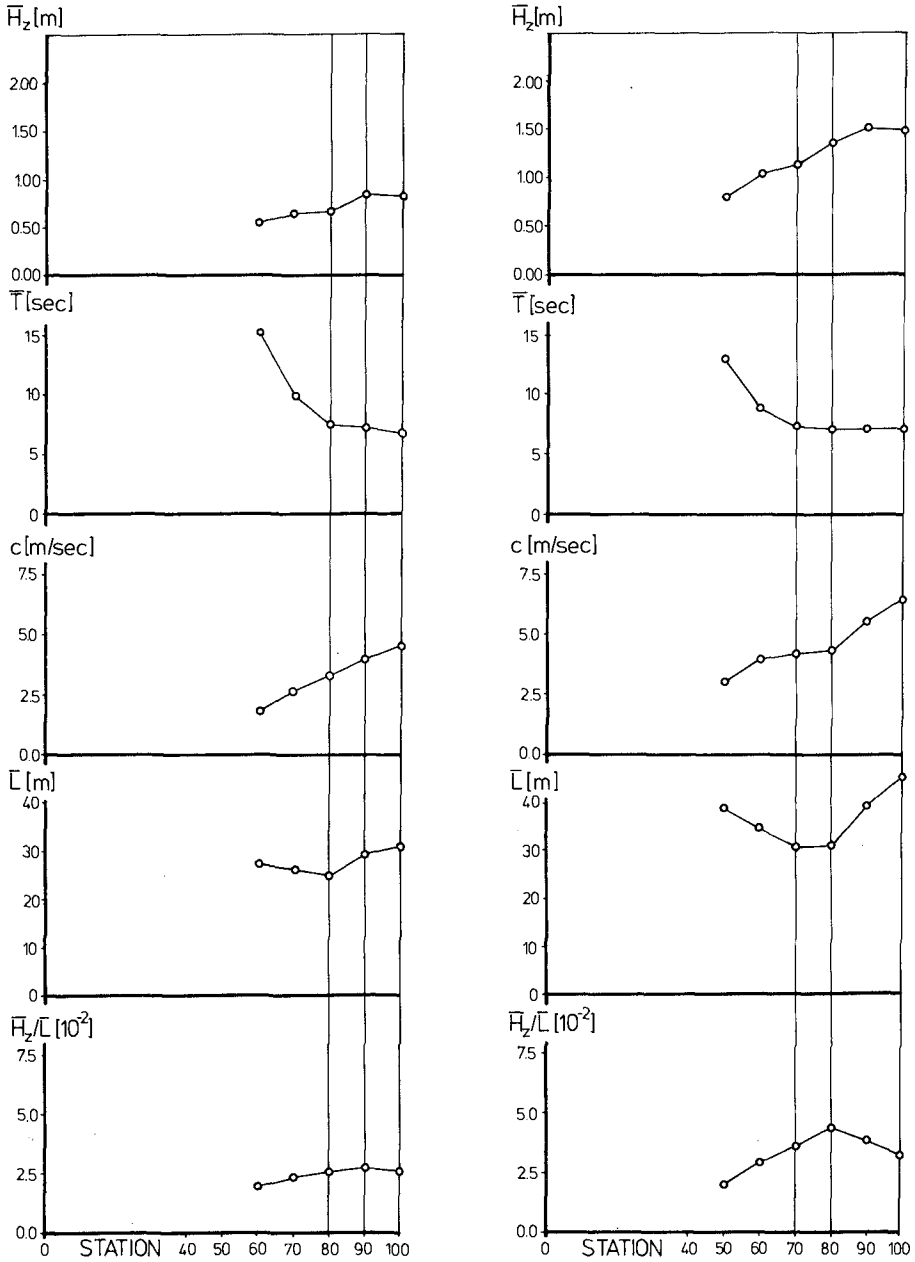


Fig. 2 : Variation of wave parameters on the beach during measurements on March 18th and April 3rd, 1973 respectively

length \bar{L}_z and mean steepness \bar{H}_z/\bar{L}_z can be calculated.

As to be seen from Fig. 2 the overall impression is that mean wave lengths decrease until the maximum steepness is reached and from that moment on the wave length again increases along with decreasing wave steepness.

It is worth mentioning here that the maximum steepness values $\bar{H}_z/\bar{L}_z = 0.028$ and $\bar{H}_z/\bar{L}_z = 0.044$ respectively are both in reasonable agreement with MICHE's formula for the breaker steepness

$$H_b/L_b = 0.140 \tanh [2 \pi d_b / L_b]$$

The magnitude of underprediction by this formula is minimal and can as well be interpreted as errors in the local water depth measurements of the order of only 5 and 10 cm respectively.

In order to demonstrate the variation of wave heights (\bar{H}_z), wave lengths (\bar{L}_z) and horizontal wave asymmetries ($\alpha = \Delta L/L$ as defined by FÜHRBÖTER (1974)) in an overall view the average wave deformation is plotted for both measurements in Fig. 3.

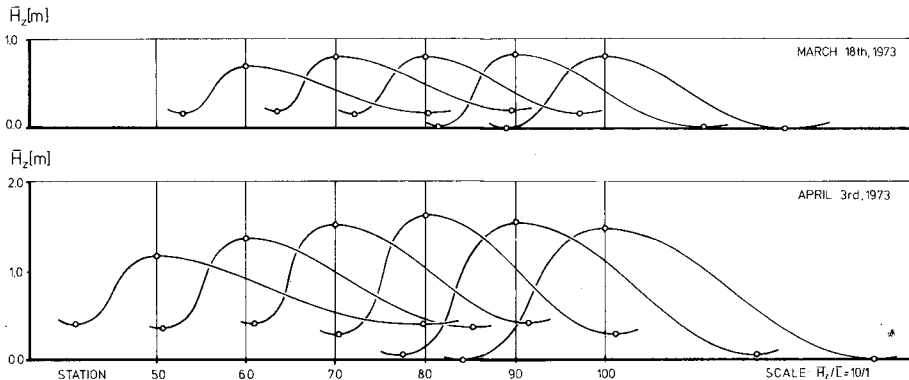


Fig. 3: Average wave deformation based on the variation of wave height \bar{H}_z , wave length \bar{L}_z and horizontal wave asymmetry α only

Constructing these sets of curves mass conservation. In both cases is preserved in such a way that the initial volumes of the water mass under the waves at position 100 m were placed beneath each deformed wave contour. Thus with the wave shapes changing in the upbeach direction the water level increases.

As the construction of each wave contour is based on three points only, this procedure, however, can only deliver a crude estimate of the wave set up, which is obviously underpredicted because especially the indicated convex front faces significantly deviate from the real shapes of steep, breaking and broken waves. Further interpretation of these measurements will be given in the above mentioned additional paper.

3. SPECTRAL FUNCTIONS

As mentioned before analyses based on the zero-up-crossing or similar methods applied to strip chart records of near shore water level deflexions are valuable only to a certain extent, because deformations like the decomposition into solitons are not considered herein.

This is supposed to be the reason why the author previously was not able to establish a correlation of some quality between the significant wave period $T_z^{1/3}$ (of the zero-up-crossing-method) and the spectral peak period determined in different ways. (BÜSCHING, 1974 ; also HARRIS, 1972).

As the above demonstrated variation of wave parameters in the upbeach direction is difficult to explain in the time domain, in the following an attempt of explanation in the frequency domain is presented by means of the storm surge data of December 13th to 14th, 1973 and measurements at attenuating wave action.

This was formerly started with the investigation of synchronously measured energy spectra taken in the beach profile of Fig. 1 at positions 100 m and 85 m distant from the shoreline respectively.

The present study consists, however, in an analysis of the TRANSFER FUNCTIONS and COHERENCE FUNCTIONS based on cross power spectrum analysis. Because of the lack of space here it is not possible to go into the details of the spectrum analysis. The basic parameters, however, in this respect are equal to those mentioned in the author's previous work (BÜSCHING, 1975 and 1976).

As is well known the complex transfer function measures the relationship between any two signals at specific frequencies by relative PHASE and MAGNITUDE. In the present case the signals represent the water level deflexions $\eta_{100}(t)$ and $\eta_{85}(t)$ at positions 100 m and 85 m respectively. Hence the transfer function is defined as

$$H_{\eta_{85} \eta_{100}}(f) = \frac{S_{\eta_{100}, \eta_{85}}}{S_{\eta_{85}, \eta_{85}}}$$

with

$S_{\eta_{100} \eta_{85}}(f)$ = CROSS POWER SPECTRUM from the water level deflexions at positions 100 and 85 m.

and

$S_{\eta_{85} \eta_{85}}(f)$ = AUTO POWER SPECTRUM at position 85 m.

The coherence function is constructed to detect the presence of noise (or nonlinear distortion) in the transfer functions. If the transfer system is linear (and noise-free) the input to output coherence must be 1 (BENDAT and PIER-SOL, 1968).

Because of the shape of the coherence functions in the present case the frequency range 0 to 0.36 Hz was selected for evaluation only.

As an example in Fig. 4 the total set of interesting spectral functions is plotted belonging to the measuring interval at the highest storm tide water level (mean record water depth $z_3 = 3.1$ m).

In the upper part of the graph the respective energy spectra are shown, whereas the coherence function and the transfer function subdivided into magnitude and phase are plotted below.

For instance at the spectral peak at a frequency $f = 0.073$ Hz the coherence is a maximum and the magnitude of the transfer function is greater than 1. This means in the present case that - as expected - at this frequency the amplitude of the respective FOURIER COMPONENT at position 100 m is greater than that at position 85 m and on the other hand the phase difference is about 80 degrees, which can be seen from the $\vartheta(f)$ -curve plotted below.

As the distance of the measuring devices x [m] is known, the phase information $\vartheta(f)$ [degrees] of the transfer function can easily be converted into a PHASE VELOCITY plot $c(f)$ [m/sec]:

$$\left. \begin{aligned} \frac{\vartheta}{360^\circ} &= \frac{x}{L} \\ c &= \frac{L}{T} = L \cdot f \end{aligned} \right\} c = \frac{x \cdot 360^\circ}{\vartheta} \cdot f \text{ [m / sec]}$$

$f = \frac{1}{T}$ = frequency of FOURIER component

L = length of the component wave

T = period of the component wave

This curve is also shown in the lower part of Fig. 4.

In this connexion it has to be mentioned here that the transformation of the phase information $\vartheta(f)$ - presented in the range $-180^\circ \leq \vartheta \leq +180^\circ$ only - is based on the assumption that the magnitude of the phase velocity of dominant

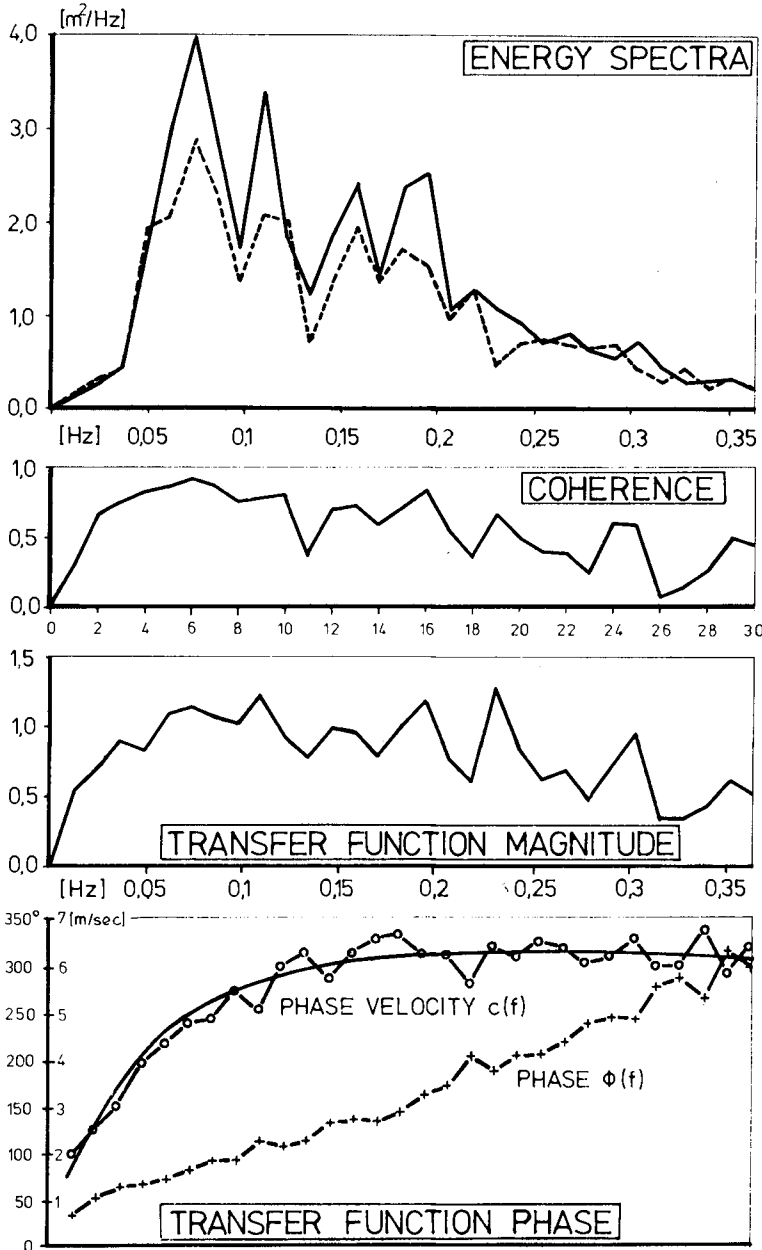


Fig. 4 : Spectral functions from water-level-deflection-measurements on December 12th, 1973, 3.46 a.m.

FOURIER components (near the spectral peak) roughly corresponds to that predicted by the dispersion formula or the shallow water relation. If alternatively phase angles $\theta \pm 360^\circ$ were considered for the transformation quite unrealistic phase velocities would turn out in the present case.

During the storm surge period of about 30 hours in total at 16 measuring intervals samples were analyzed as illustrated in Fig. 4.

The results of these measurements in the form of MEAN VALUES of coherence, transfer function magnitude and phase velocity are plotted in Fig. 5 along with the storm tide curve.

The mean values are related to the frequency ranges as listed in the inset. In case the smallest frequency range only containing the lowest frequency FOURIER components

$$(7) \quad 0 < f \leq 0.06 \text{ Hz}$$

is disregarded, because the confidence of the FOURIER ANALYSIS is not sufficient at low frequencies, the overall impression is that mean values of coherence $\bar{\gamma}^2$ and transfer function magnitude decrease with an increasing number of contributing frequency components (say from curves (6) to curves (2')), whereas the mean values of the phase velocities increase from curve (6) to curve (2').

This means that a linear relationship would rather exist at lower frequency FOURIER components and especially at high water levels, which should be expected.

By contrast an average the higher frequency components are faster than the longer ones.

The later phenomenon is analyzed more detailed in the following, whereas some remarks regarding the transfer function magnitude are contained in BÜSCHING (1978).

Fig. 6 contains two different sets of curves in the respective frequency band up to 0.36 Hz :

1. A more regular set of curves representing a presentation of the well known DISPERSION FORMULA for the wave propagation

$$c = \frac{L}{T} = L \cdot f = \left(\frac{g \cdot L}{2 \pi} \tanh \frac{2 \pi d}{L} \right)^{1/2}$$

The respective phase velocity curves $c(f)$ are marked by the parameter of the water depth d [m] at the left hand side ; and

2. The set of phase velocity curves $c(f)$, resulting from the storm surge measurements smoothed by non-linear regressions.

As is well known the above dispersion relationship describes a so-called NORMAL DISPERSION : Lower frequency components travel faster than the higher ones ; only in very shallow water all components travel with nearly the same speed. By contrast this does not come out of the storm surge measurements in the near shore area. Here a so-called ANOMALOUS DISPERSION turns out

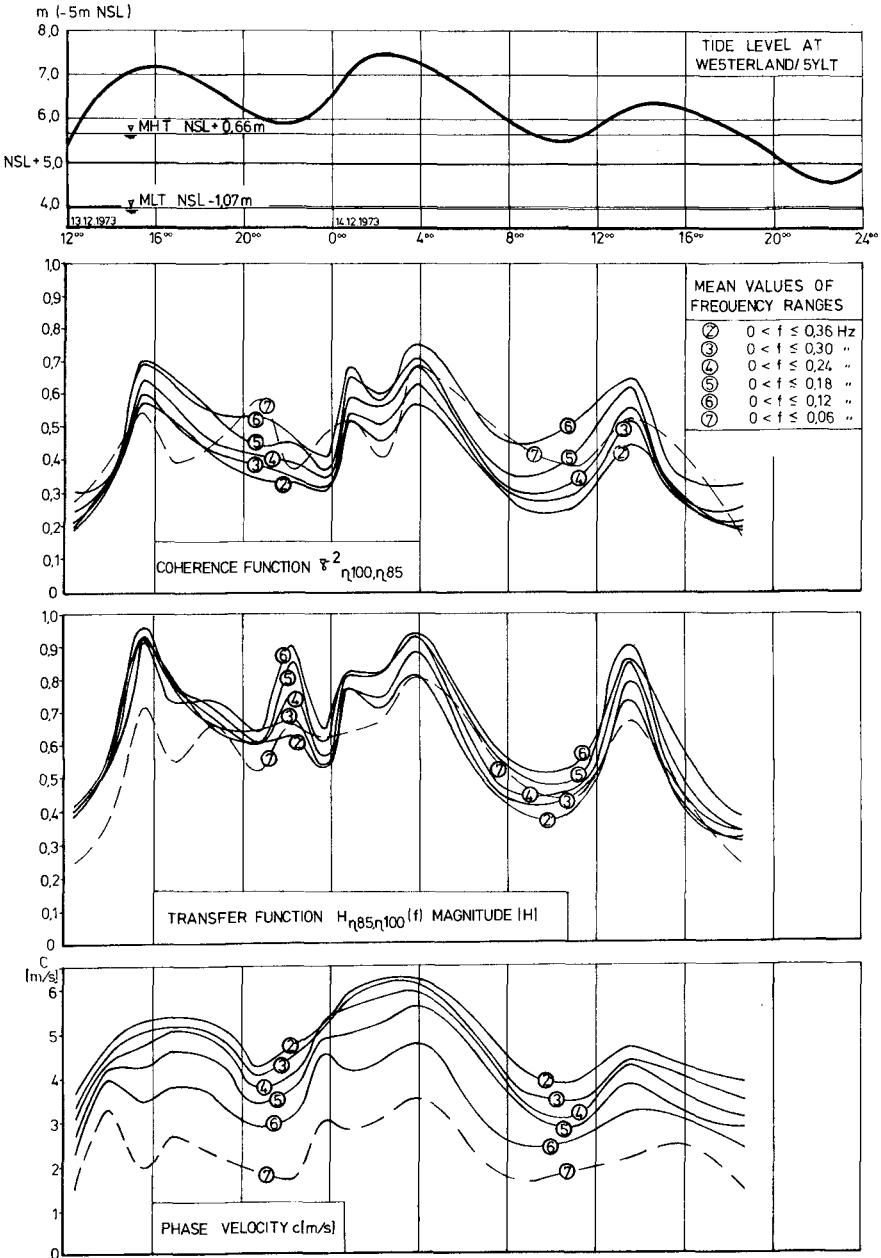


Fig. 5 : Mean values of COHERENCE, TRANSFER FUNCTION MAGNITUDE and PHASE VELOCITY of the measurements on December 13th and 14th, 1973

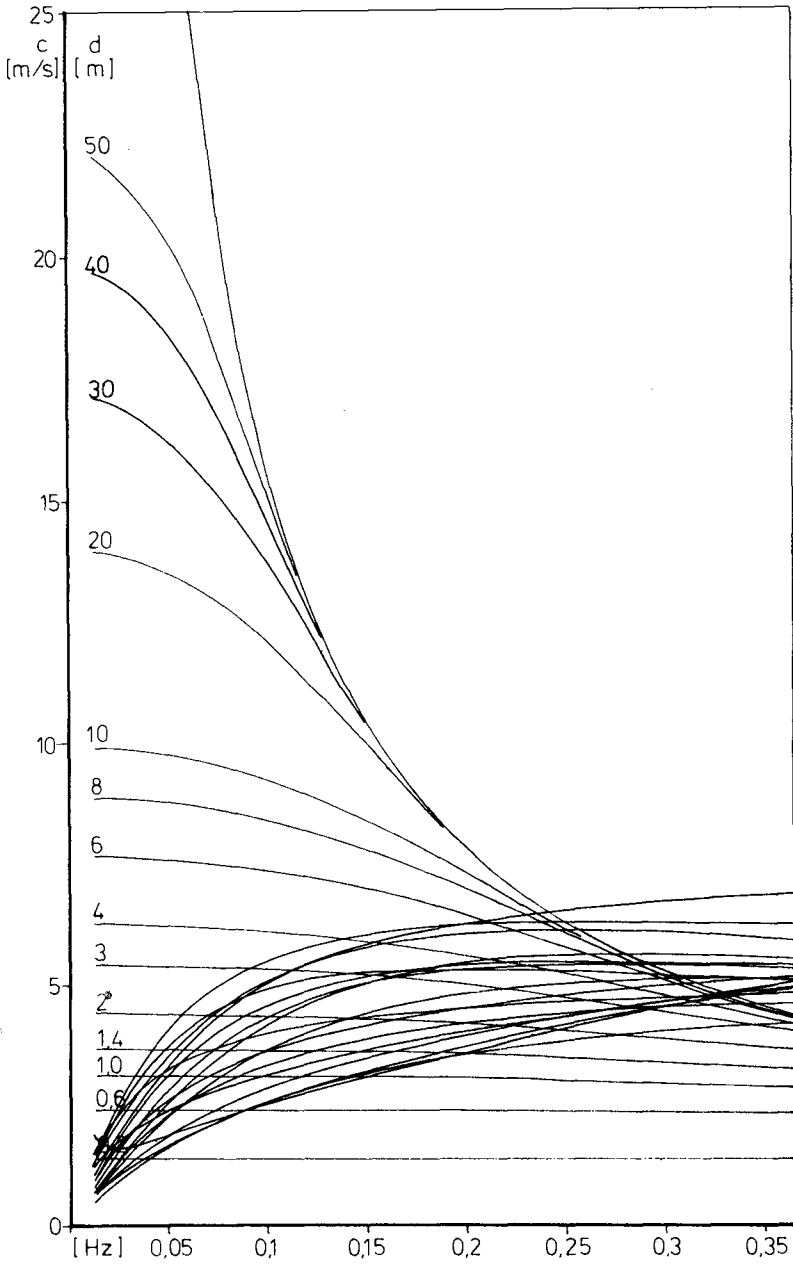


Fig. 6 : Predicted and measured dispersion of phase velocities

in the shown frequency band. Even if in the example of Fig. 4 the range of highest coherence, say greater than $\bar{\gamma}^2 \geq 0,8$ in between 0.05 and 0.08 Hz is regarded as reliable only, the statement remains true: In very shallow water the higher frequency components travel faster than the longer ones (in the shown frequency band). In addition it is remarkable that the frequency points of the phase-velocity-plots $c(f)$ form smooth curves wherever the coherence shows appreciable values.

Hence, those components can possibly be regarded as anyhow coupled components of predominating wave systems approaching the beach more or less perpendicularly, whereas especially at very low frequencies (right next to $f = 0$) and at higher frequencies the rate of scatter in the frequency points of the phase information gradually increases with the water depth decreasing. Because of the low coherence in those frequency ranges it is, however, not worthwhile to try an analysis.

According to similar measurements on a platform, standing in a water depth of about $d = 30$ m even at that position about 100 km offshore exists a distinct deviation from the conventional dispersion relationship. As to be seen from Fig. 7 representing a swell measurement on November 22nd, 1975 ($2,0 \leq H \leq 2,5$ m) a distinct normal dispersion exists only on the right hand side of the spectral peak at a frequency $f = 0.12$ Hz, which corresponds to a coherence of $\bar{\gamma}^2 > 0.94$. On the left hand side, however, the tendency for an ANOMALOUS DISPERSION exists, which is at least reliable at high coherence values as indicated in the graph. At lower frequencies again there is a remarkable scatter in the frequency points accompanied by decreasing coherence and phase angles uncertain to determine from the respective plot. In the case of very large phase velocities resulting from very small phase angles at low frequencies it can, however, be supposed that here the phase angle must be changed to $\vartheta + 360^\circ$, see dotted line in Fig. 7.

Comparing this plot to the dispersion formula it turns out that only the phase velocity very near to the spectral peak roughly corresponds to that predicted by the formula. On the right hand side there are higher values to be seen, whereas phase velocities are less on the left hand side.

If high enough frequency components can be regarded as deep water components, which are unaffected by the bottom and the influence of the water depth is regarded to be the dominant parameter for a certain critical frequency $f_{crit.}$ at which NORMAL dispersion changes into ANOMALOUS dispersion, it can be stated from this graph that this critical frequency is considerably less than that determined by the condition $d = L/2$ according to linear theory. In the present case

$$f_{crit.} = 0.11 < f_{(d = L/2)} = 0.16 \text{ Hz}$$

With the above findings in mind in the following the behaviour of the FOURIER components in the near shore area are considered again. In order to simplify in the lower part of Fig. 8 the storm surge measurements are represented by 3 smoothed curves only, belonging to water depth $Z_3 = 3.1$ m, $Z_3 = 1.65$ m, $Z_3 = 1.40$ m respectively. As concerns the nearly horizontal portion of the phase velocity curve, corresponding to the maximum water depth $Z_3 = 3.1$ m, this indicates nearly complete non-dispersiveness at frequencies $f \geq 0.2$ Hz.

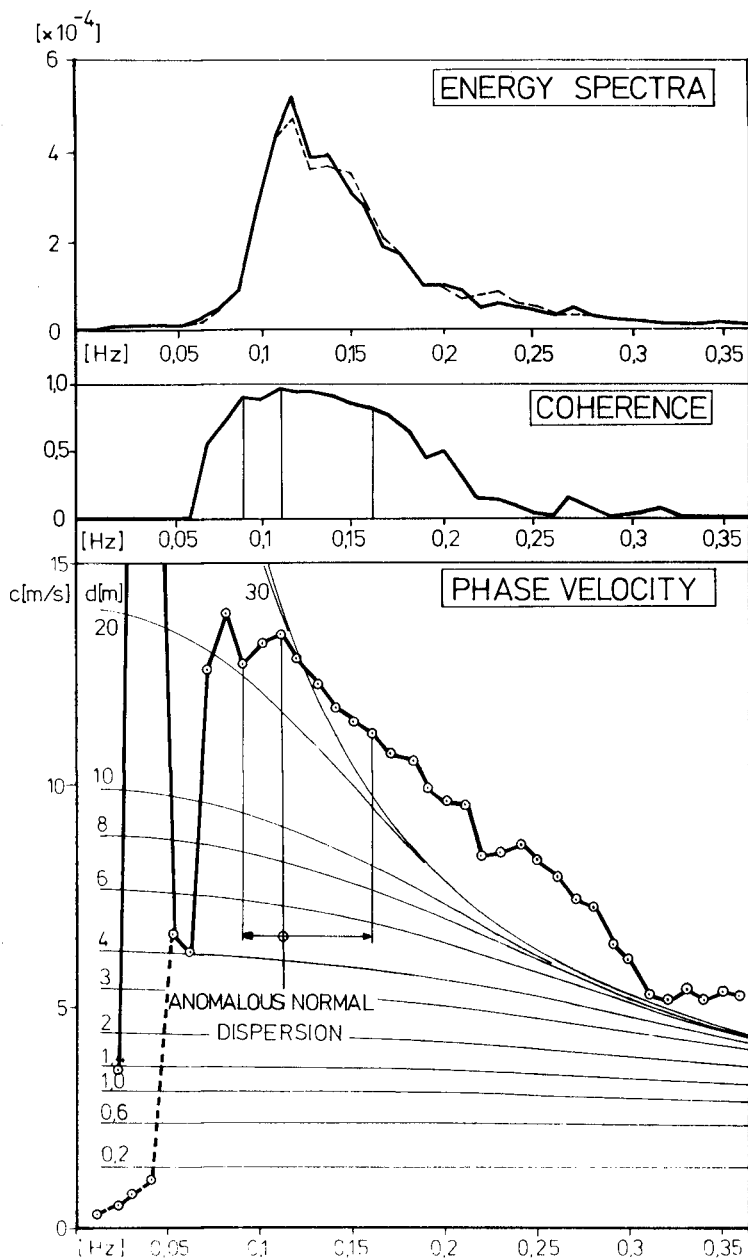


Fig. 7 : Spectral functions of a swell-measurement in a water depth $d \approx 30$ m on November 22nd, 1975

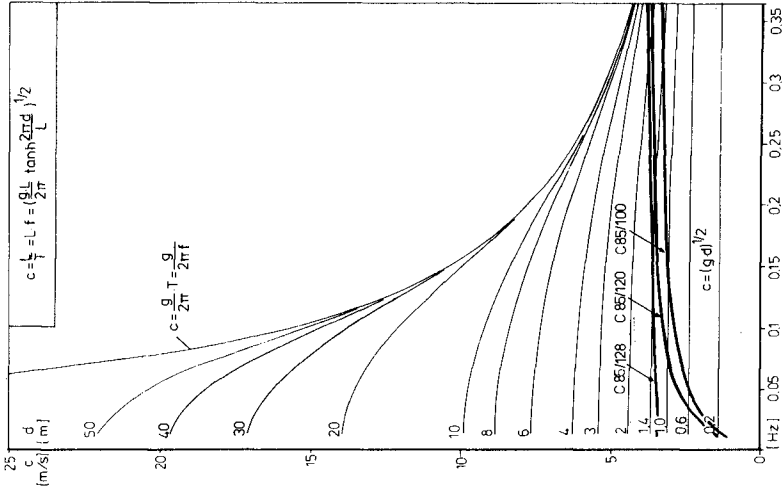


Fig. 9 : Weak anomalous dispersion of phase velocities at attenuating wave action, January 20th, 1974

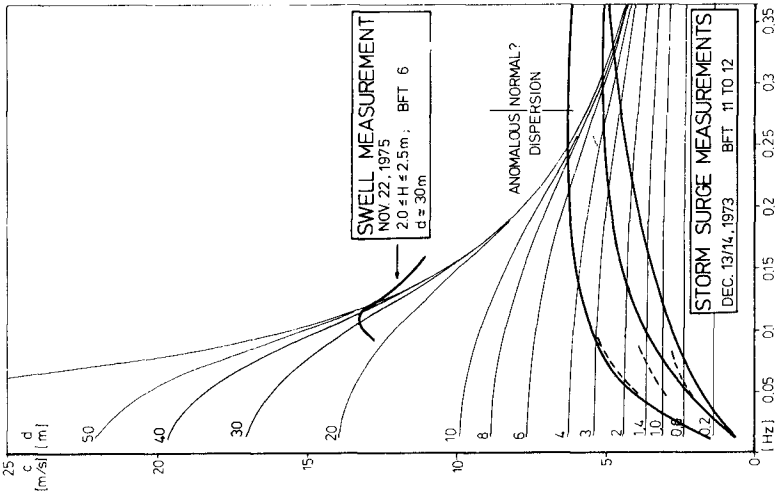


Fig. 8 : Normal and anomalous dispersion of phase velocities

This, however, can also be interpreted as the frequency range where normal dispersion changes to anomalous dispersion. The respective critical frequency f_{crit} is still to be found in the shown frequency band, whereas that of the condition $d = L/2$ according to linear theory is not :

$$0.25 < f_{crit} < 0.30 \text{ Hz} < f_{(d = L/2)} = 0.5 \text{ Hz}$$

In accordance with the even higher critical frequencies ($f_{(d = L/2)} = 0.69 \text{ Hz}$ and $f_{(d = L/2)} = 0.75 \text{ Hz}$ for deep water components at the lower water depth $Z_2 = 1.65 \text{ m}$ and $Z_3 = 1.40 \text{ m}$ respectively, the curves are steeper in the shown frequency band. Hence, the ANOMALOUS DISPERSION in this frequency band gets even more distinct with the water depth decreasing.

This tendency also turns out from the dotted lines representing the respective ranges of maximum coherence values only.

On the other hand it can as well be presumed from this plot a position just seaward of the breakers where the non-dispersive property is even more distinct than at the water depth $Z_3 = 3.1 \text{ m}$. Presumably such a position depends on the actual ratio H/d .

Actually this kind of PHASE COUPLING comes out of the measurements of THORNTON, GALVIN, BUB and RICHARDSON (1976) and this condition is almost included in the profile measurement on January 20th, 1974 carried out at attenuating wave action, see Fig. 9.

The three curves shown result from synchronous measurements at positions 128 m, 120 m, and 100 m with reference to position 85 m. Hence, the curves can be attributed to positions 106.5 m, 102.5 m and 92.5 m respectively.

Compared to the storm surge measurements the dispersion in this case is minimal in the total frequency range at position 106.5 m and with the water depth decreasing the weak dispersive property is preserved at frequencies $f > 0.1 \text{ Hz}$, where in the present case appreciable values of energy density are to be found in the respective energy spectra, see BÜSCHING, 1976.

In order to demonstrate the so-called ANOMALOUS DISPERSION with its effect on the deformation of the waves, Fig. 10 refers to the above mentioned profile measurement of January 20th, 1974 with the weak anomalous dispersive property only.

Assumed that at a certain position outside the shown profile all components are in phase and from that moment on propagate with their own singular phase speeds, one can perform a FOURIER SYNTHESIS after a certain time of propagation, which is 10 sec in the present case. In order to clarify this in Fig. 10 the 0.1 Hz-FOURIER-component is to be seen fixed at the three positions mentioned above.

Additionally only the 0.3 Hz-component is plotted. It is obvious that already at the position 106.5 m the 0.3 Hz-component leads the 0.1 Hz-component and the relative position of the 0.3 Hz-component is shifted in the upbeach direction (with the water depth decreasing). The total FOURIER synthesis consisting of the superimposition of 30 components representing the frequency range

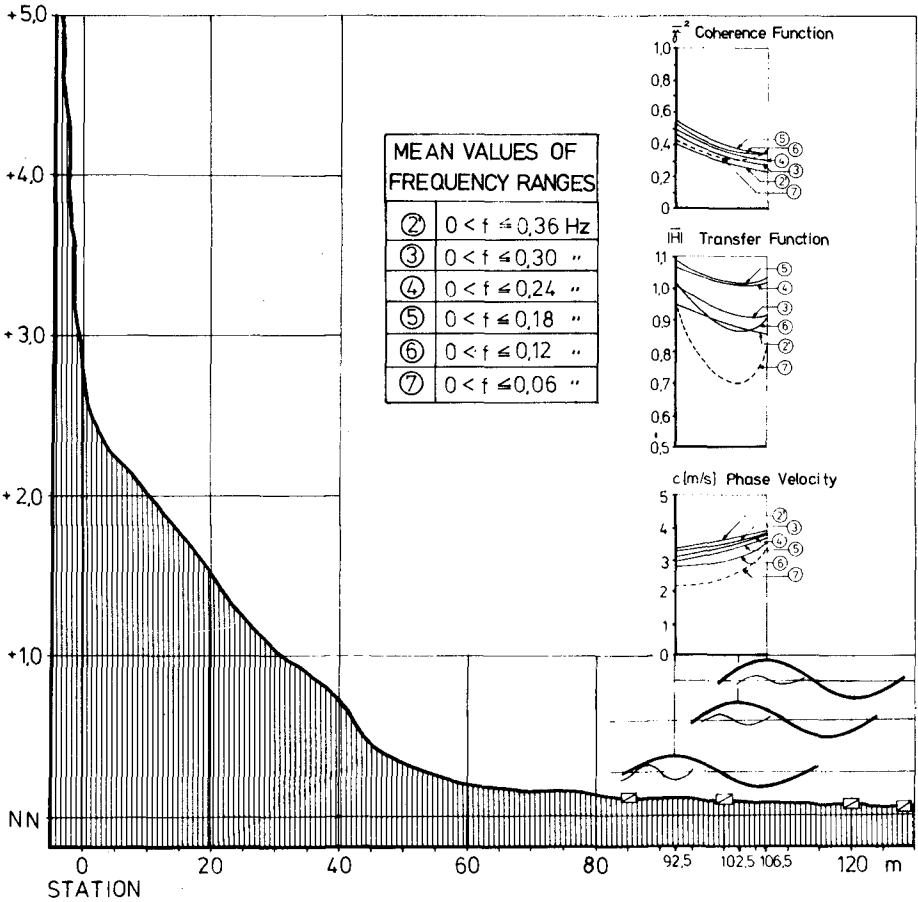


Fig. 10 : Relative behaviour of the frequency components 0.1 Hz and 0.3 Hz at decreasing water depth on January 20th, 1974

$0 < f \leq 0.36$ Hz delivers the average wave deformation in the time domain, see middle part of Fig. 11.

The total set of varying wave parameters is to be seen on the right and left hand side of this figure respectively.

Wave heights and periods are taken from the graph as indicated, whereas the variation of the average wave propagation velocity is assumed to be equal to the phase velocity of the peak frequency component.

Hence, the wave length and steepness could also be calculated.

JANUARY 20, 1974

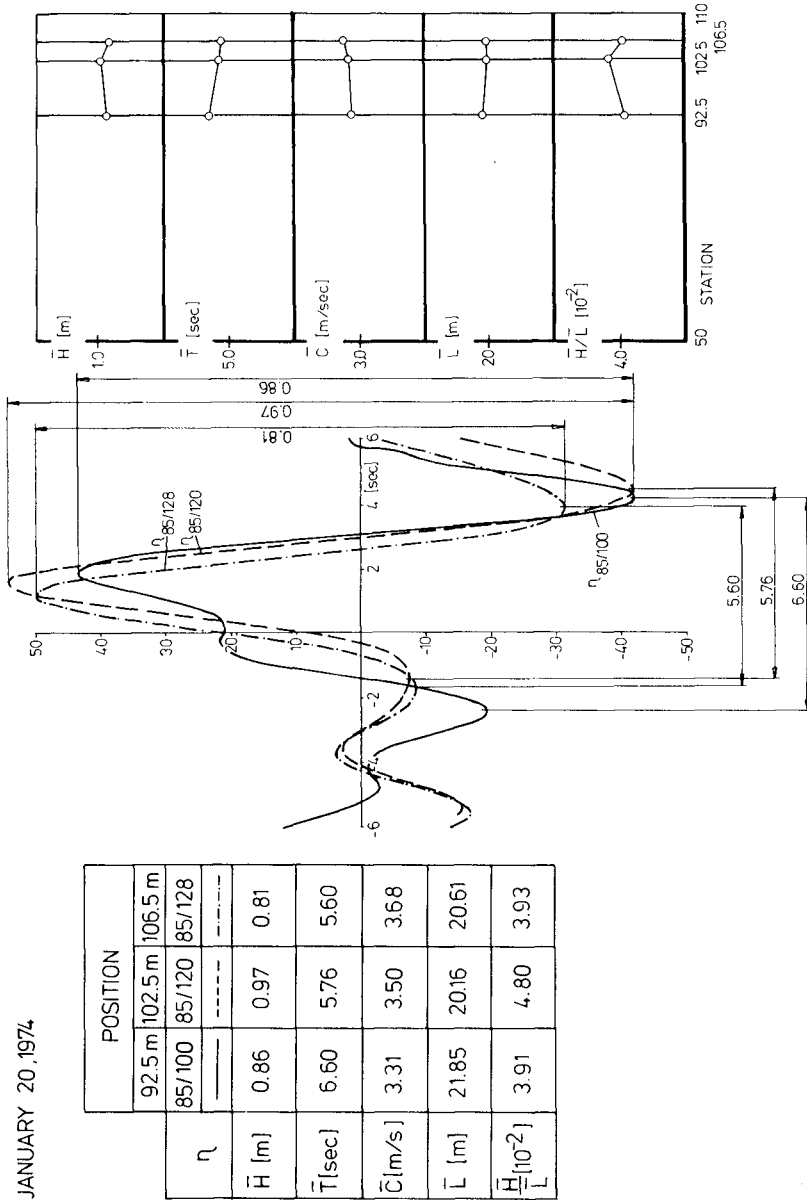


Fig. 11 : Average wave deformation resulting from a FOURIER synthesis considering anomalous dispersion of frequency components

4. CONCLUSION

Comparing the results from the time domain wave analysis of the measurements on March 18th and April 3rd, 1973 (Figure 2 and 3) with the results from the FOURIER synthesis considering anomalous dispersion (from the measurements of January 20th, 1974, see Fig. 11) it can be stated that both treatments qualitatively deliver similar variations of the wave parameters.

With the water depth decreasing in the upbeach direction

- a) the wave height \bar{H} at first increases and then continuously decreases,
- b) the wave period \bar{T} increases,
- c) the wave velocity \bar{c} decreases,
- d) the wave length \bar{L} at first decreases and after wave breaking increases and as a result of a) and d)
- e) the steepness \bar{H} / \bar{L} at first increases and then decreases.

The findings according to a), c) and e) are in agreement with the conservative treatment of near shore processes, whereas the increase of the wave period with the consequence of the shown behaviour of the wave length is not. In the following this discrepancy is tried to be explained in terms of a spectral treatment :

Assumed that at idealized conditions there exists a swell in deep water propagating towards the shore (with a normal dispersion), its content of higher order harmonics decreases the more it travels away from its origin.

With the water depth decreasing the swell is increasingly affected by the bottom in such a way that at first only the longer components decrease in phase velocity. As the higher frequency components, being deep water components, keep their phase velocities they recover the more the longer components slow down. At a certain position possibly more or less all of the components travel with approximately the same speed, which means nondispersiveness.

The above described behaviour, which is qualitatively in accordance with the conventional dispersion relationship, at first represents increasingly shortening waves and finally the non-dispersive property leads to high and steep (shoaling) waves, which would not change form very much, if the bottom would be plane at this position.

With the water depth, however, further decreasing the higher frequency components pass the longer ones and thus in a superimposition once again longer waves are produced.

As regards the breaking process the differences between the phase velocities of higher and longer components are such that a regular wave shape can no longer be preserved. The kinetic energy of the continuously slowed down longer components possibly is gradually transferred into potential energy causing a water level increase (wave set up), whereas at breaking that part of kinetic energy associated with the unaffected higher frequencies leaves the former wave shape producing foamlines.

An explanation like this would be in accordance with the author's previous finding of increasing energy densities at higher frequencies at the expense of the energy densities associated with lower frequencies (BÜSCHING, 1976).

In addition, with respect to Fig. 11 it is obvious that the FOURIER synthesis can better describe the deformation of shoaling waves than at least by means of parameters derived from the zero-up-crossing method as to be seen from Fig. 3.

It clearly turns out that the maximum steepness does not occur together with the maximum asymmetry, which is indicated (in this case) by a continuously steepening front face (Fig. 11). Furthermore finally there exists a saddle on the rear face of the wave, which can be compared very well to the formation of solitons.

In this connection it shall be mentioned here that an anomalous dispersion does not necessarily contradict GALVIN's (1972) wave tank observations stating that in shallow water initially sinusoidal waves decompose into two or more waves (solitons) which travel at different speeds in such a way that the bigger travel faster than the smaller and the crest elevation and the height of the bigger increases.

In this respect a definition is needed between "bigger" and "smaller" waves in terms of a spectral treatment, as it can very well be possible that the longer frequency components are associated with the smaller resultant water level deflection if the respective energy densities are less at those frequencies.

Hence, being able to reconstruct significant features of the input water level deflections, this may be an indication that the respective result (ANOMALOUS DISPERSION) obtained by a linear analysis might not be that bad.

Finally some important consequences of an anomalous dispersion associated with energy dissipation, being a very common phenomenon in physics, shall be pointed out :

- 1) As is well known from capillary waves the group velocity of anomalously propagating waves exceeds the phase velocity and thus the energy propagates faster than the singular FOURIER components of a wave system. As concerns gravity waves this may be an indication why the wave energy is transmitted so rapidly, - especially in plunging breakers. Possibly this process can be compared on the one hand with the strong attenuation of capillary waves and on the other hand with the absorption of electromagnetic waves, although the mechanisms - except anomalous dispersion - are completely different.
- 2) In a dispersive system small nonlinear disturbances travel with different velocities and thus an accumulation is more or less prevented. (LIGHT-HILL, 1978). So, at least, the question is open about the rates of contribution on wave deformation by nonlinear and dispersive properties.

5. ACKNOWLEDGEMENTS

This paper is still an outcome of the research program "ENERGIEUMWANDLUNG IN BRANDUNGSZONEN" sponsored by the DEUTSCHE FORSCHUNGSGEMEINSCHAFT (GERMAN RESEARCH FOUNDATION).

The author is indebted to a. Prof. Dr.-Ing. A. Führbäter, Head of the LEICHTWEISS-INSTITUT, for making this work possible, to Prof. K. Harikawa, University of Tokyo, for fruitful discussions and to Dipl. math. F. Wolpers for performing comprehensive computations.

6. REFERENCES

- ADEYMO, M.D., Effect of beach slope and shoaling on Wave Asymmetry
 Proc. Eleventh Conf. Coastal Engineering, London 1968
- BENDAT, J.S. and PIERSOL, A. G., Measurement and Analysis of Random Data, John Wiley and Sons, 1966
- BIESEL, F., Study of Wave Propagation in water of gradually varying depth. Gravity waves circular No. 521, Nat. Bureau of Standards, Washington D.C. 1951
- BÜSCHING, F., Über Orbitalgeschwindigkeiten irregulärer Brandungswellen
 Mitt. Leichtweiss-Institut der Techn. Universität Braunschweig, H. 42, 1974
- BÜSCHING, F., Über die Änderungen von Wellenperioden im Brandungsbereich
 Mitt. Leichtweiss-Institut der Techn. Universität Braunschweig, H. 47, 1975
- BÜSCHING, F., On Energy Spectra of Irregular Surf Waves
 Proc. 15th Int. Conf. Coastal Engineering Honolulu, Hawaii, 1976
- BÜSCHING, F., Wave Deformation due to Decreasing Water Depth
 Mitt. Leichtweiss-Institut der Techn. Universität Braunschweig, H. 63, 1978
 in printing
- FÜHRBÖTER, A., Air Entrainment and Energy Dissipation in Breakers
 Proc. XIIth Coastal Engineering Conference Washington, 1970
- FÜHRBÖTER, A., Über die Bedeutung des Lufteinschlages für die Energieumwandlung in Brecherzonen a) Mitt. Franzius-Institut TU Hannover; H.35, 1971
 b) Die Küste, H. 21, 1971
- FÜHRBÖTER, A., Einige Ergebnisse aus Naturuntersuchungen in Brandungszonen
 Mitt. Leichtweiss-Institut der Techn. Universität Braunschweig, H. 40, 1974
- FÜHRBÖTER, A., BÜSCHING, F., Wave Measuring Instrumentation for Field Investigations on Breakers; Ocean Wave Measuring and Analysis, Vol. 1, New Orleans; USA 1974, published by ASCE New York

- GALVIN, C. J., Wave Breaking in Shallow Water in "Waves on Beaches", edited by R. E. Meyer, Academic Press, Inc. New York and London, 1972
- HARRIS, D. L., Characteristics of Wave Records in the Coastal Zone, in "Waves on Beaches", edited by R.E. Meyer, Academic Press, Inc. New York and London, 1972
- IWAGAKI, Y., SAKAI, T., and KAWASHIMA, I., 1973, On the Vertical Distribution of Water Particle Velocity Induced by Waves on Beach Coastal Engineering in Japan 1973
- LIGHTHILL, J., Waves in Fluids, Cambridge University Press, Cambridge, London, New York, Melbourne 1978
- MADSEN, O. S., and MEI, C.C., The transformation of a Solitary Wave Over an Uneven Bottom, J. Fluid Mech. 39, 1969, 781-791.
- MULTER, R. H. and GALVIN, C. J., Secondary Waves : Periodic Waves of Non-permanent Form (abstract), Trans. Am. Geophys. Union, 48, 1967, 139-140.
- PATRICK, D. A. and WIEGEL, R. L., Amphibian Tractors in the Surf, Proc. First Conf. on Ships and Waves, The Engineering Foundation Council on Wave Research and the American Society of Naval Architects and Marine Engineers, 1955
- RAMAN, H., On the Spectral Analysis and Directionality of Wave Spectra with Reference to the German North Sea Coast Mitt. Leichtweiss-Institut der Techn. Universität Braunschweig, H. 51/1976
- THORNTON, E. B., GALVIN, J.J., BUB, F. L., RICHARDSON, D.P., Kinematics of Breaking Waves, Proc. 15th Int. Conf. Coastal Engineering Honolulu, Hawaii, 1976
- WANG, H., YANG, W.-C., Measurements and Computation of Wave Spectral Transformation at Island of SYLT, North Sea, Mitt. Leichtweiss-Institut der Techn. Universität Braunschweig, H. 52, 1976
- ZABUSKY, N. J. and GALVIN, C. J., Shallow Water Waves, The Korteweg-De Vries Equations and Solitons, J. Fluid Mech. 47, 1971, 811-824

CHAPTER 13

Infragravity Waves in Storm Conditions

R. A. Holman, D. A. Huntley, and A. J. Bowen*

ABSTRACT

Nearshore sediment is actively reworked during major storms, often significantly altering the nearshore morphology. It has been suggested that infragravity waves with wave periods 30-300 seconds are very important in the formation of major nearshore features.

A field study to further understand the nature of infragravity waves was carried out in Martinique Beach, Nova Scotia. Velocity measurements were taken using three electromagnetic flowmeters. Incident conditions varied from calm to swell and wind waves generated by hurricane Belle. Spectral analysis of the low tides revealed a sharp increase in the infragravity band energy associated with the storm. Throughout the storm the spectra of all three instruments were dominated by a strong 100 second peak which remained constant in frequency despite significant changes in the incident wave field. This peak is found to satisfy edge wave theory. A frequency selection mechanism based on longshore topographic trapping of edge waves is suggested.

INTRODUCTION

Surf beat, low frequency motion with wave periods of 30 to 300 seconds usually associated with shoaling waves, was first observed and christened by Munk (1949) and Tucker (1950). Their observations were relatively low amplitude (approximately 1/10 of the incident swell), which they explained as a modulation of a beating incident wave field with no longshore variability.

Gallagher (1971) modelled surf beat as edge waves with energy transfer from the incident waves through a non-linear mechanism. Huntley (1976) showed field evidence of a series of discrete, energetic infragravity (surf beat) peaks which he proved were edge waves.

Bowen and Inman (1971) suggest that natural, crescentic bars could theoretically be caused by edge waves. Reversing the logic, they then use the existence of crescentic bars to predict that narrow low frequency peaks of significant edge wave energy should exist on natural beaches. Suhayda (1974a, 1974b) presents field evidence which appears to confirm that standing infragravity waves generated perpendicular to the beach can lead to the formation of straight longshore bars.

* Department of Oceanography
Dalhousie University
Halifax, Nova Scotia, Canada

Coupling this latter hypothesis that low frequency waves are closely related to major features with the common observation that these features undergo significant change under storm conditions (Schalk, 1963, Short, 1975) leads to the conclusion that surf beat probably forms an important part of the nearshore wave climate, especially during storms when one would expect to see narrow, strong peaks of low frequency energy. It is the purpose of this paper to present a field study of surf beat activity during incident conditions varying from calm to hurricane generated swell. Interestingly, a narrow 100 second peak is found to dominate the spectrum during storm conditions.

EDGE WAVES

Edge waves are normal modes of oscillation on a sloping beach. Eckart (1951) solved the shallow water equations for a plane beach of slope $\tan \beta$ to find the velocity potential ϕ , where

$$\phi = \frac{a_n g}{\sigma} f_n(x) \cos(ky - \sigma t) \quad \text{for a progressive edge wave} \tag{1}$$

and $\phi = \frac{a_n g}{\sigma} f_n(x) \cos ky \cos \sigma t$ for a standing edge wave.

Here a_n is the shoreline amplitude of the edge wave of modal number n , g is the gravitational acceleration, σ is the angular frequency, k the longshore wavenumber and t is time. x , y , and z are a right-handed Cartesian co-ordinate set with x positive to seaward from the still water shoreline and z positive upwards from mean sea level. The off-shore behaviour is given by

$$f_n(x) = e^{-kx} L_n(2kx) \tag{2}$$

where L_n is the Laquerre polynomial of order n , having n zero crossings. Figure 1 is a plot of $f_n(x)$ against the non-dimensional offshore distance $\chi = \sigma^2 x / (g\beta)$ for the first four modes. The offshore profile of a standing incident wave is included for comparison. Edge waves must satisfy the dispersion relation

$$\sigma^2 = gk (2n+1) \tan \beta. \tag{3}$$

The onshore velocity u , longshore velocity v , and edge wave elevation η are given by

$$u = \frac{\partial}{\partial x} \phi, \quad v = \frac{\partial}{\partial y} \phi, \quad \eta = -\frac{1}{g} \frac{\partial}{\partial t} \phi \tag{4}$$

For a progressive wave at the shoreline, the ratio of u and v is simply

$$\frac{u}{v} = 2n+1$$

showing the dominance of u for higher modes.

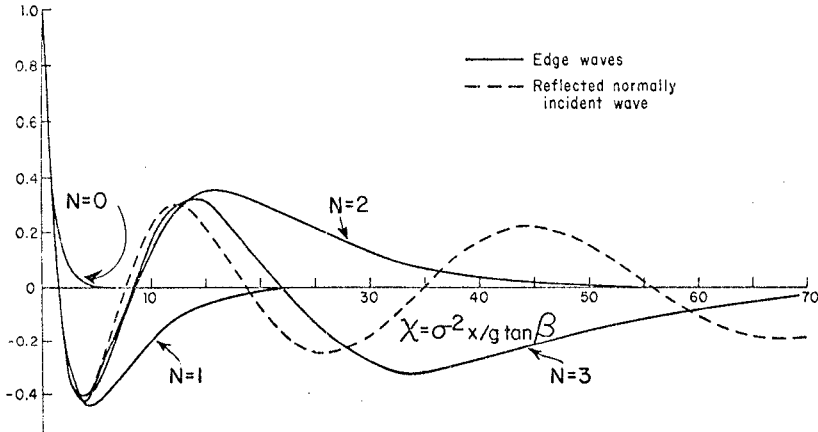


Fig. 1 Offshore dependence $f_n(x)$ for edge wave modes 0, 1, 2, and 3, and or normally incident reflected wave.

EXPERIMENTAL

The site chosen for the field experiment was Martinique Beach, about eighty kilometers east of Halifax, Nova Scotia. Martinique has a fairly simple topography with an almost linear offshore profile of beach slope $\beta = 0.02$. The slightly concave shoreline is terminated at one end by a headland and at the other by a reef which extends 250 m offshore (figure 2). A second reef divides the length of the beach in the ratio 2:1. The beach has an open exposure to the Atlantic.

An array of sensors was set up along two ranges approximately 700 m from the west end of the beach (figure 3). The west range consisted of two Marsh-McBirney electromagnetic flowmeters labelled MMB1 and MMB2. One hundred meters to the east was a Cushing, spartype electromagnetic flowmeter labelled Cush. Sensors were mounted 50 cm above the sea bed.

All data was digitized at a 1/3 second interval prior to spectral analysis. Spectra presented will have two degrees of smoothing. A half filter width of 30 (HF=30), with a bandwidth of .0142 hz, was used to give a broad spectral picture (95% confidence limits are 0.75 and 1.4). For higher resolution a half width of 10 (HF=10), with a bandwidth of .0044 hz and confidence limits of 0.6 and 1.9, was used.

Four fifty minute data runs, centered at high, low, and both mid-tides, were usually taken per tidal cycle. Data was collected from the 6th to the 12th of August, 1976.

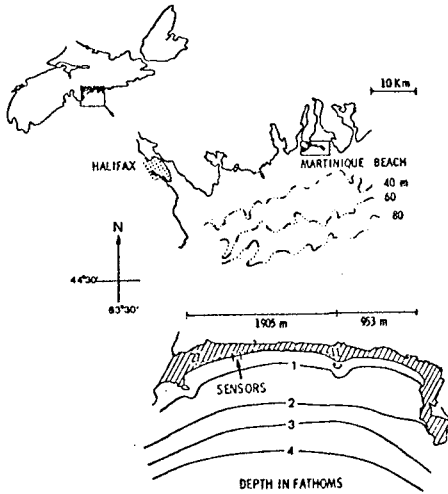


Fig. 2
Location and plan view of
Martinique beach.

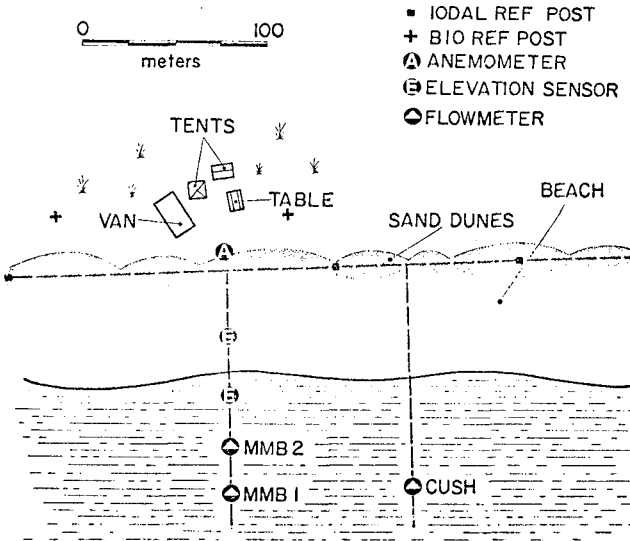


Fig. 3 Placement of sensors.

An overall summary of the visually observed wind and wave climate is shown in figure 4. Individual runs are indicated by stars with every fifth one numbered. Weather conditions changed through the week from four days of relative calm with low regular swell to winds of over 20 m/sec and accompanying high wave activity associated with the tail end of hurricane Belle which passed to the west (figure 5). Local winds were almost directly onshore at the height of the storm, shifting to the west during the decay. Rough visual estimates of significant wave height and significant wave period (figure 4) also reflect the presence of the storm, although the latter tends to underestimate the period of the spectral swell peak.

Figure 6 shows the mean run-up and visually estimated breakpoint for each run. Randomness of the incident waves and lack of an offshore length scale made breakpoint estimation difficult and introduced some scatter.

Beach profiles, taken at the beginning and end of the week, show a significant movement of sand during the storm (figure 7). This was also demonstrated by the partial burial of the two flowmeters in the west range.

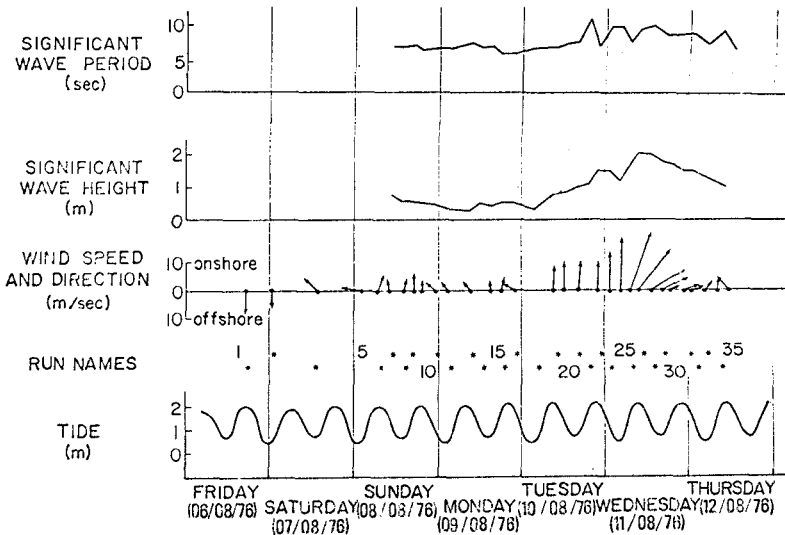


Fig. 4 Summary of the week of the experiment. Runs are indicated by stars with every fifth one numbered. The storm started in run 21, and peaked in run 26.

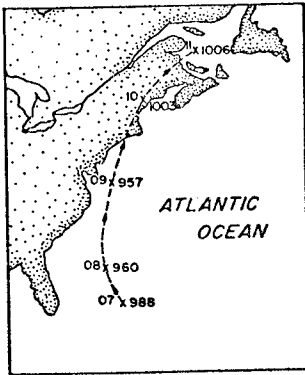


Fig. 5 Path of hurricane Belle. Numbers to left of x's indicate the day of the month, those of the right are barometric pressure.

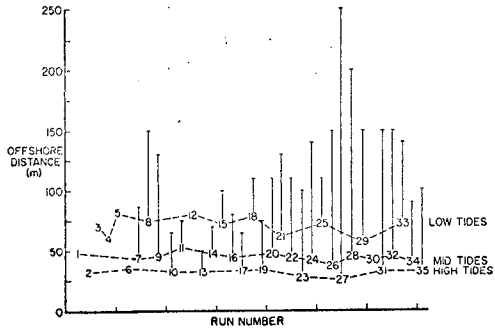


Fig. 6 Mean runup (numbers) and break point (short horizontal lines) for each run. Long vertical lines are then the surf zone width. There is no data for runs 1-6.

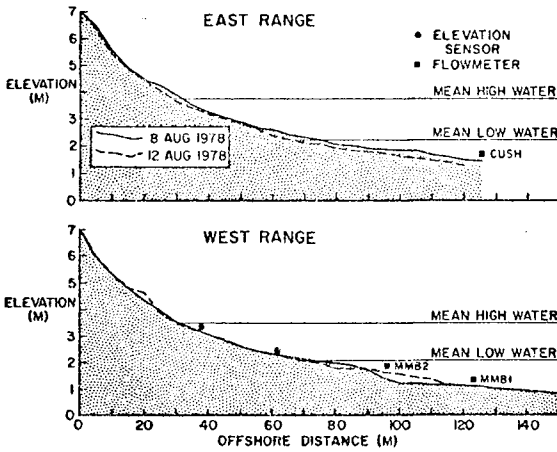


Fig. 7 Beach profiles before and after storm for both ranges. MMB2 was buried by the storm.

RESULTS AND DATA ANALYSIS

Edge wave amplitudes dies away relatively rapidly offshore. Therefore, only the low tide runs, when the instruments are closest to the shore, will be considered in this paper.

Figure 8 shows the mean currents for each run. On/offshore currents are generally weak until run 21. MMB1 and MMB2 then jump to approximately 20 cm/sec offshore drift, staying offshore until the end of the experiment. The longshore currents change from a general westward drift during calm conditions to an eastward drift, the direction of travel of the storm waves, during the storm. Run 21 shows a longshore current divergence, with eastward flow at the east flowmeter and westward flow at the west range. This is consistent with a rip cell with rip heads slightly west of the west range and a larger distance east of the east flowmeter. Visual observations made by a diver during the run confirm this, reporting a rip current of approximately 50 cm/sec 15 m to the west of the west range.

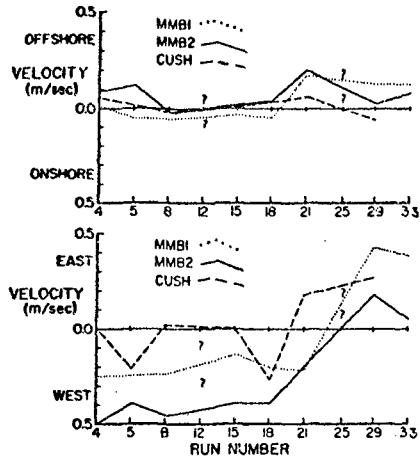


Fig. 8. Mean currents for the three instruments. Question marks indicate missing data.

Figure 9 shows a partial time series from run 29 just after the height of the storm. The longshore currents show substantial low frequency energy at a variety of time scales. The onshore currents show 100 second period activity particularly between 36 and 42 minutes. Evidence of shoaling can be seen from comparison of the on/offshore components of MMB1 and MMB2. MMB1 shows more of the variance contained in the higher frequencies (wind waves and swell), while the MMB2 shows relatively more variance in low frequencies. There is also some evidence of bore-bore capture, for instance at 42 minutes.

Figure 10 shows two spectra from the onshore channel of MMB2; run 12 is typical of calm conditions, while run 25 is at the height of the storm. The instrument is in the surf zone in both cases. Both spectra are fairly featureless with run 12 much flatter and of lower energy. The spectrum from run 25 is red up to a well-defined 100 second peak. Huntley and Bowen (1975) remark on the flatness of surf zone spectra when plotted on a log-linear scale. They are able to empirically parameterize the exponential decay coefficient, p , as a function of

local water depth h and wave amplitude at breaking a_b , as

$$p \propto h^{5/2} a_b^{-2}$$

Contrary to their result, this data shows p to vary as a positive exponent of a_b and a possibly negative component of h .

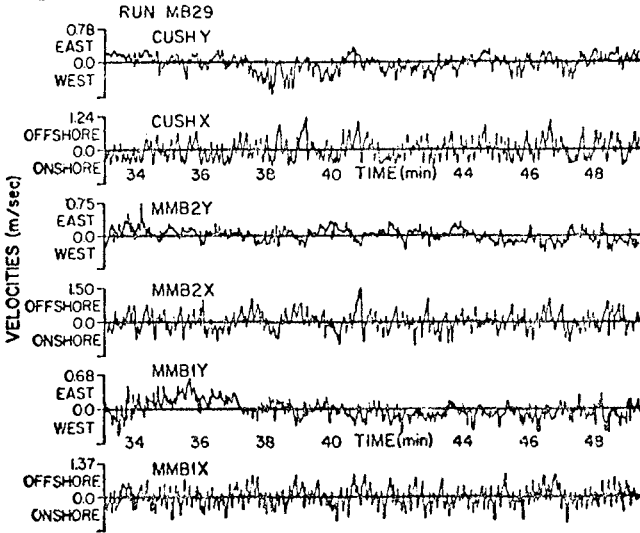


Fig. 9 Example time series for the three instruments. Run 29 is near the height of the storm.

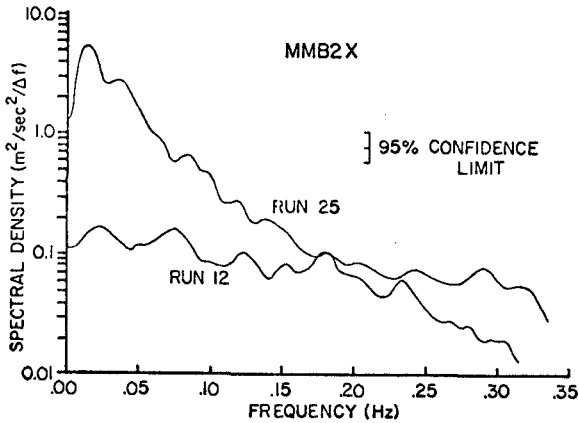


Fig. 10 Example onshore velocity spectra from calm conditions (run 12) and from storm conditions (run 25).

An estimate of the importance of the low frequency energy can be made by splitting the spectrum into a high frequency part consisting of swell, wind waves and higher frequencies, and a second part containing the lower frequencies. For run 29, the small dip in the spectrum at 0.075 hz is consistent with the low frequency side of the swell peak from the deeper MMB1 and is used as the division point. The low frequencies are found to account for 84% of the total energy for this run.

Picking a division point for run 12 is more difficult. Even using a relatively high value of .09 hz, the low frequencies account for only 41% of the total energy. Table 1 shows numerical comparisons between the calm run 12 and the stormy run 25. The mean square velocities were taken from the spectra in figure 10.

Table I. Comparison between calm and storm conditions.

Run ID	12 (calm)	25 (storm)
wind speed (m/sec)	1.5	21.2
significant wave height (m)	0.3	1.0+1.5
significant wave period (sec)	7.0	11.0
mean longshore current (m/sec)	-0.45	no data
Mean Square Velocities - MMB2X (all in m^2/sec^2)		
low frequency	$1.2. \times 10^{-2}$	1.86×10^{-1}
high frequency	1.77×10^{-2}	0.349×10^{-1}
total	2.98×10^{-2}	2.195×10^{-1}
% low frequency of total	41%	84%

Figure 11 shows time series of the spectra for the onshore and longshore components of the three flowmeters. Each heavy line represents an individual spectrum, from the first low tide, run 3, on the lower left of each plot, through to the last low tide, run 33, on the upper right. Each run is labelled above its y axis.

An obvious feature in the spectra is the presence of very low frequency energy in all longshore and many onshore spectra. Reduced smoothing fails to improve the detail of the energy. Because resolution is limited by run length, it can only be said that the low frequency hills are made up of energy from wave periods between about 3 and 200 minutes. Detrending largely removes periods longer than 200 minutes. Cross-spectral analysis between different channels of the

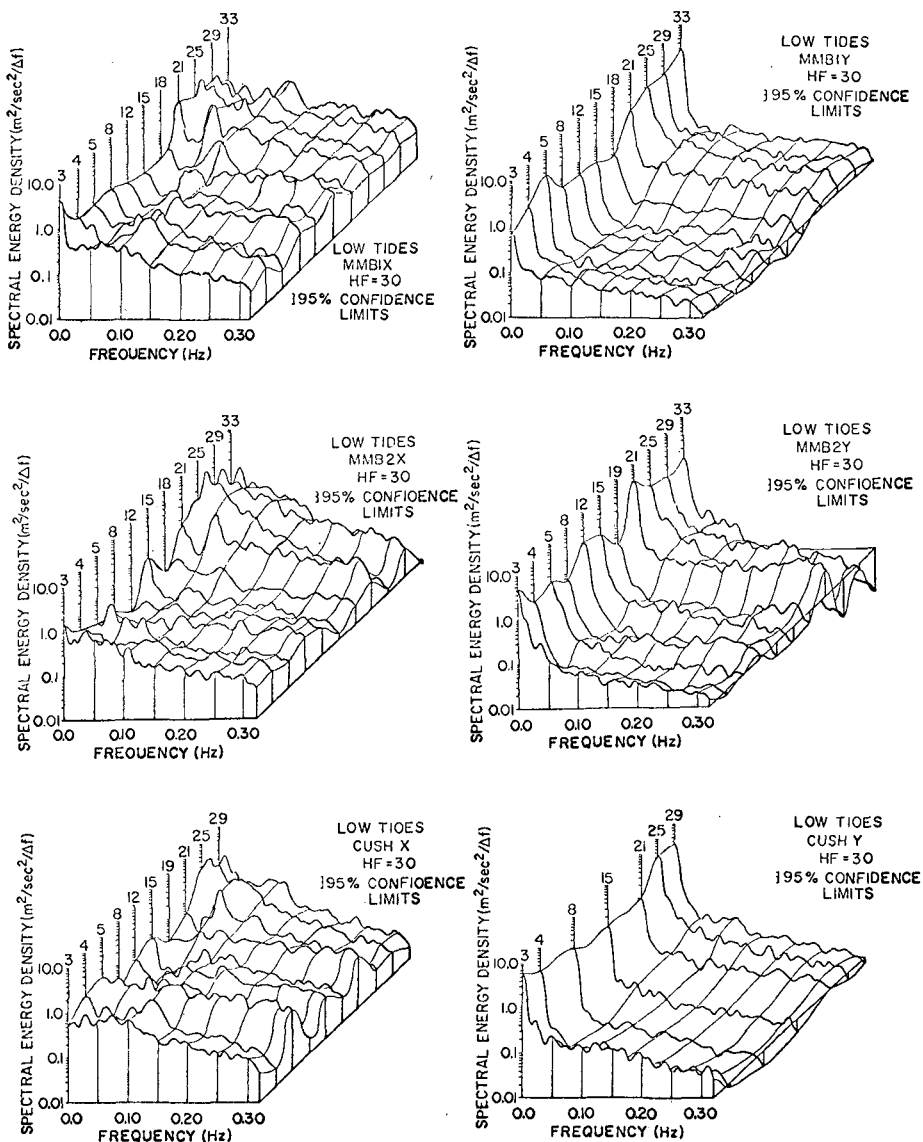


Fig. 11 Spectral time series for onshore and longshore velocities of all instruments. Each bold line is an individual spectrum with run numbers above the y-axis.

same instrument and between the same channels of different instruments reveals no pattern; coherences are usually insignificant. This implies a forced flow, not a free wave. One possibility is that the very low frequency energy may represent movements of the longshore current relative to the instrument.

The general trend of the week can be seen clearly from the spectral time series. The long calm period for the first half of the week is reflected by the low energies of the first seven spectra. The onshore component of MMB2, the shallowest instrument is, on average, featureless, while for MMB1 and Cush, a weak, unsteady wind wave peak is seen.

The forerunners of hurricane Belle appear in the onshore spectra of all three instruments on run 21 as an energetic swell peak of period 16 seconds and RMS velocity 14 cm/sec. This peak is then lost in the overall high energies of the shallow MMB2, but is seen to slowly shift to higher frequencies for MMB1 and Cush in agreement with expected wave dispersion.

Following the appearance of the storm forerunners in run 21 is a sudden, order of magnitude, increase in low frequency energy in the onshore velocity components of all instruments. In particular, for run 25, the spectra from all three instruments is dominated by a narrow, strong, 100 second peak. Throughout the rest of the storm, this peak continued to dominate the MMB2x and Cushx and stayed constant in frequency for all three instruments even though incident conditions changed significantly. (The peak seems to disappear for MMB1x. However, rerunning the spectra with decreased smoothing shows it to be present). For the MMB2x on run 25, the 100 second peak has a corresponding RMS velocity of 30 cm/sec.

Edge wave energy shows an offshore decay described by $[\frac{\partial}{\partial x} f_n(\lambda x)]^2$ for the onshore velocity component. Since the instruments MMB1 and MMB2 were at different offshore distances on the same range, the ratio of the energies of the 100 second peaks could be compared to the theoretical ratio for edge waves of various modes. The observed ratios of 0.56 for run 25 and 0.36 for run 29 compare reasonably with the theoretical values for a mode 1 edge wave of 0.61 and 0.53 respectively, considering the difficulty involved in estimating a velocity from a spectrum. As can be seen from figure 1, the offshore energy decay for higher mode edge waves is quite similar to that of mode 1 for the small values of χ involved ($\chi \approx 1.5$).

Cross spectra between the onshore components of the different instruments were run with reduced smoothing. A peak which is highly coherent over the distance between instruments usually indicates a wave motion, while a peak which has only a low coherence is probably just a forced flow. Figure 12a shows spectra from the three instruments for run 29. The peaks at 100 seconds are quite narrow and consist in frequency from instrument to instrument. Figure 12b shows the

coherence and phase between the onshore velocity components of MMB2 and Cush. The 100 second peak shows up clearly with a coherence of 0.88 and a phase of 0±11 degrees. Cross spectra between other parts of onshore velocity components give similar results.

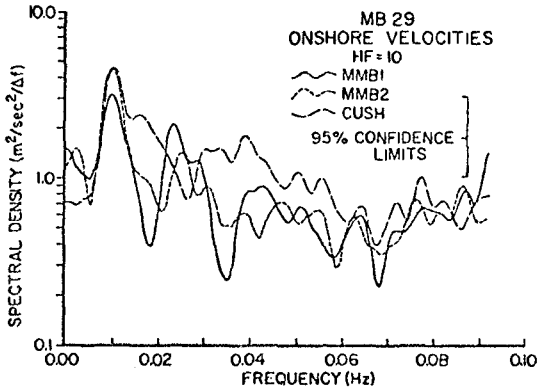


Fig. 12a Onshore velocity spectra for run 29 for the three instruments. Higher resolution is achieved by reducing the smoothing. The 100 second peaks stand out clearly in all three spectra.

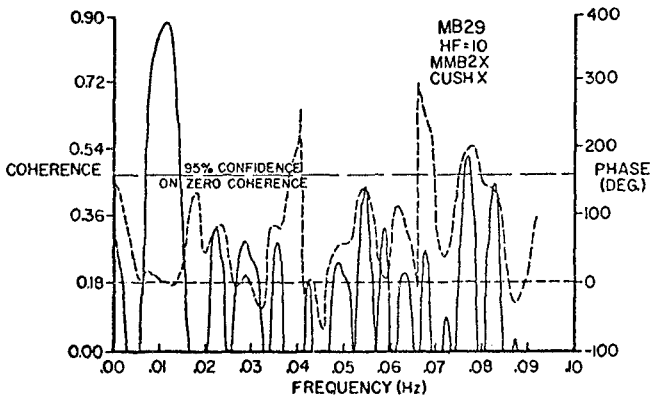


Fig. 12b Coherence and phase between the onshore velocities of the MMB2 and Cush for run 29. The 100 second peaks in figure 12a are seen to be highly coherent with a phase of 0°.

The corresponding 100 second peak is not present in the longshore spectra of MMB1 and Cush (figure 11) and only weakly present in that of MMB2, even with reduced smoothing to eliminate contamination from the very low frequency redness. Similarly, u-v cross-spectra fail to show significant coherence at 100 seconds. A possible explanation for this is shown in figure 13 which plots the offshore profile of the longshore velocity for 100 second mode 0, 1, and 2 edge waves (higher mode edge waves and standing incident waves are similar to mode 2). The positions of the flowmeters for runs 25 and 29 are superimposed on the figure. It is unfortunate that the zero crossing of longshore current for modes greater than 0 lies so close to the position of MMB1 and Cush. Even for run 25, a lower low tide, the longshore velocity at Cush is only 25% of the shoreline value, hence only 6% of the shoreline energy would be seen. The shallower MMB2 would see somewhat more energy, about 30% for run 25 and 10% for run 29. This may explain why MMB2 is the only channel on which the 100 second peak is seen.

For comparison, the onshore velocity component for a mode 1 edge wave is also plotted figure 13. The first zero crossing for this mode is well away from the instrument position. Coupled with this is the fact that the ratio of onshore velocity to longshore velocity at the shoreline goes as $(2n+1)$ for progressive edge waves and $(2n+1) \tan ky$ for standing edge waves. Thus, even for the worst case, MMB2 on run 25, the ratio of the onshore to longshore velocities for a mode 1 edge wave, as seen by the instrument, should be about 4:1 and the ratio of the spectral energies 16:1. For higher modes the ratio would be higher. This explains why the onshore peak can be so strong and the longshore peak so weak, and still be consistent with edge wave motion.

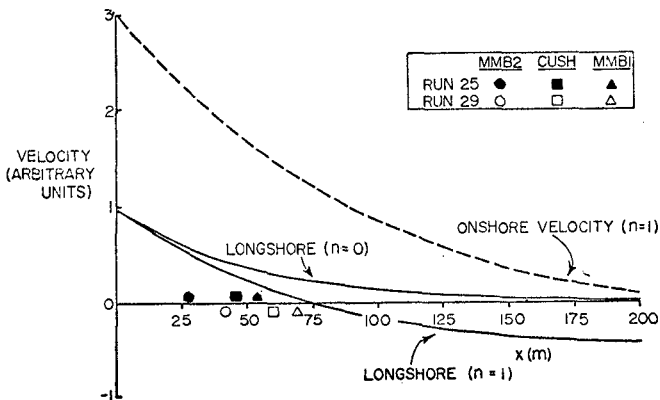


Fig. 13 Offshore behaviour of longshore current for a 100 second edge wave of mode 0, 1 and 2. The instrument positions for runs 25, 29 are included and are very close to the first node. This is not true for onshore velocity as seen from the mode 1 profile.

FREQUENCY SELECTION

The presence of energetic, low frequency waves, steady in frequency through a variety of hurricane-generated incident conditions, is important to the coastal engineer for the understanding of the growth of large beach features. However, there must be some underlying mechanism which provides the frequency selection either through forcing, damping, topographic constraints, or a combination of these.

The forcing mechanisms proposed by Longuett-Higgins and Stewart (1964) and Gallagher (1971) depend on beating in the incident wave field. This was tested directly by comparing the time series of the low-passed velocity and the incident envelope (the square of the high-pass record which is then smoothed). The correlation was not significant for the several time series tested, suggesting a broad banded forcing. However, it should be remembered that the time series tested were from within the surf zone where the strong non-linearities associated with breaking could have easily obscured the low frequency forcing.

If surf zone sampling is assumed to be dominant, then Guza and Bowen (1976) suggest that edge waves are most likely to survive if their offshore length scales are large compared to the width of the surf zone. This simply favours low frequencies and high mode numbers but does not provide a selection mechanism for a particular frequency.

Ball (1967) suggested that particular offshore beach topographies can select favoured edge wave modes, the cut-off modes. Huntley (1976) finds field evidence for cut-off modes from Hell's Mouth Bay. However, this cut-off requires the beach profile to flatten in water which is not "deep" for the edge wave, a requirement not met by Martinique with its approximately plane profile. For the large longshore wavelengths inferred for these low frequencies, the longshore beach topography provides the most significant constraint on possible length scales and hence edge wave frequencies. The headland and reef at the beach ends, and the second reef two thirds of the distance along the beach suggests $b=953m$ as a fundamental longshore length scale for the beach (figure 2). As free waves reflected between end walls on a sloping beach are necessarily edge waves, an obvious model to consider is one based on the superposition of standing edge waves. Requiring that an integral number m of half-wavelengths fit into b , and using equation 3, we find

$$f = \left(\frac{g \tan \beta}{4\pi b} \right)^{\frac{1}{2}} (m(2n+1))^{\frac{1}{2}}$$

$$= 4.04 \times 10^{-3} (m(2n+1))^{\frac{1}{2}}$$

The combination of $m=2$, $n=1$ provides an excellent fit, predicting a frequency of .0099 hz compared to the observed frequency of .01 hz. However, it should be noted that equation (5) describes a whole suite of possible edge waves which could fit the beach. Addition of surf zone damping constraints as described previously and forcing as discussed by Gallagher (1971) and extended by Bowen and Guza (1978) does not alter the picture significantly enough to produce the narrow 100 second peak observed. So the present theoretical picture is one of a fairly broad-banded spectrum with the only features being "valleys" at frequencies where the non-dimensional offshore distance of the instrument $\chi_1 = \sigma^2 x_1 / g\beta$ corresponds to an edge node (see figure 1).

Further evidence that topographic constraints are basic to the frequency selection is provided by data taken at approximately the same location on Martinique Beach in July of the previous year when the beach was steeper, with $\beta=0.05$. On that day, a narrow, energetic peak centered at 62 seconds was observed (figure 14). If the same length scale is responsible for both the 62 and the 100 second peaks, then, using equation (3), the ratio of edge wave periods for a change in beach slope should be

$$\frac{T_1}{T_2} = \left(\frac{\beta_2}{\beta_1} \right)^{\frac{1}{2}} = 0.63$$

This ratio is almost exactly satisfied for the two peaks indicating that in the face of different incident conditions and a different offshore profile, the edge wave adjusts to give the same wavelength, presumably because of longshore topographic trapping.

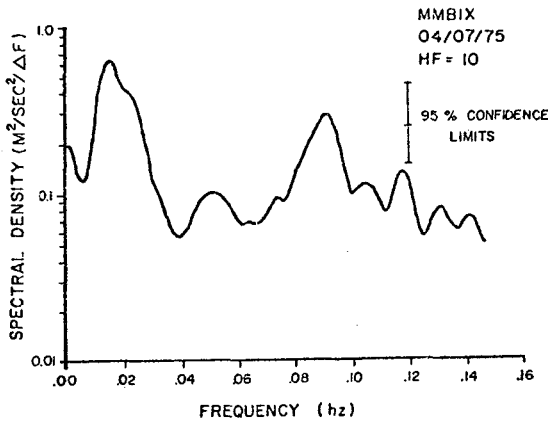


Fig. 14

Onshore velocity spectrum taken from the same location on 4 July 1975. Note the strong 62 second peak.

CONCLUSIONS:

A field experiment recording wave velocities during both calm and storm conditions showed a dramatic jump in infragravity (0.003-0.03 Hz) energy during the storm. At the height of the storm, infragravity waves accounted for 84% of all spectral energy. This low frequency dominance sheds doubt on the relevance of the simple, visually-observed, wave statistics in understanding surf zone dynamics.

A strong 100 second peak appeared in the onshore velocity spectra of all flowmeters near the beginning of the storm. This peak remained dominant and consistent in frequency through two further tides despite significant changes in the incident wave climate. Longshore topographic constraints are probably important in providing the lengthscale necessary for frequency selection, although the addition of forcing and damping constraints to the topographic model produces a fairly broad-banded theoretical spectrum, not the narrow 100 second peak observed.

REFERENCES

- Ball, F. K., Edge waves in a ocean of finite depth. *Deep Sea Res. Oceanogr. Abstr.*, 14, 79-88, 1967.
- Bowen, A. J. and R. T. Guza, Edge waves and surf beat. *J. Geophys. Res.*, 83, 1913-1920, 1978.
- Bowen, A. J., and D. L. Inman, Edge waves and crescentic bars. *J. Geophys. Res.*, 76, 8662-8671, 1971.
- Gallagher, B., Generation of surf beat by non-linear wave interactions. *J. Fluid Mech.*, 49, 1-20, 1971.
- Guza, R. T. and A. J. Bowen, Resonant interactions for waves breaking on a beach. *in* Proceedings of the 15th International Conference on Coastal Engineering, pp. 560-579, American Society of Civil Engineers, New York, 1976.
- Huntley, D. A., Long-period waves on a natural beach. *J. Geophys. Res.* 81, 6441-6449, 1976.
- Huntley, D. A. and A. J. Bowen, Comparison of the hydrodynamics of steep and shallow beaches. *in* Nearshore Sediment Dynamics and Sedimentation, edited by J. Hails and A. Carr, Wiley Interscience, London, pp. 69-110, 1975.
- Longuet-Higgins, M. S. and R. W. Stewart, Radiation stress in water waves: a physical discussion, with applications. *Deep Sea Res. Oceanogr. Abstr.*, 11, 529-562, 1964.
- Munk, W. H., Surf beats. *Eos Trans. AGU*, 30, 849-854, 1949.
- Schalk, M., Study of nearshore bottom profiles east and southwest of Point Barrow, Alaska; comparison of profiles and the barrier islands in the Point bay and Plover Island areas. *Arctic Inst. North America, Projects ONR 217, 241, Final Rept.*, 16 pp, unpub. manuscript.

- Short, A. D., Multiple offshore bars and standing waves. *J. Geophys. Res.*, 80, 3838-3840, 1975.
- Suhayda, J. N., Standing waves on beaches. *J. Geophys. Res.*, 72 (21), 3065-3071, 1974a.
- Suhayda, J. N., Determining infragravity wave spectra. in International Symposium on Ocean Wave Measurements and Analysis, v. 1, 54-63, 1974b.
- Tucker, M. J., Surf beats: Sea waves of 1 to 5 minute period. *Proc. Roy. Soc., Ser. A*, 202, 565-573, 1950.

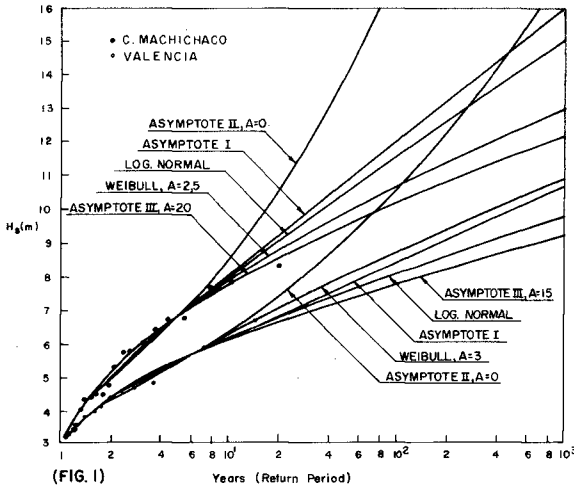
CHAPTER 14

EXTREMAL PREDICTION OF SIGNIFICANT WAVE HEIGHT Enrique Copeiro*

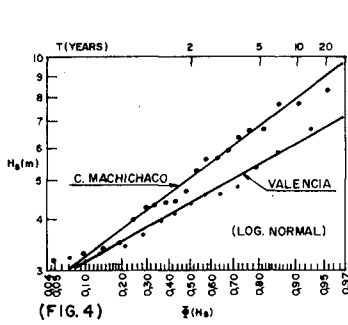
The most generally used procedure for estimating the extremal distribution of geophysical variates consists in obtaining a sample of extreme values (for instance a number of annual maxima) and fitting to them a distribution function. One of the main problems involved in this procedure is the choice of the type of distribution adequate in each case. No general agreement exists, to date, for any geophysical variate. This means a serious trouble because of the wide range of extrapolations which can usually be obtained by using different functions. Some of the authors who have tackled this problem have adopted a strictly empirical point of view, going as far in it as to advise to make a choice for each particular case, according to the goodness-of-fit obtained when several types of distribution functions are fitted to the sample. Others have instead tried to base the choices on some theoretical foundation, placing less emphasis in the goodness of the fits and generally suggesting the use of one or other of the three well known Asymptotic Extremal Distributions.

In actual practice, the casuistic choice of function from each extremal sample -- does not provide a reliable solution to this problem as a general criterion. The methodology in use today for estimating distributions from extremal samples (or, in general, from samples of independent values) of a random variate suffers from ambiguity in several respects (1). Because of that, it is often uncertain to determine how much of the differences observed between goodness of fits is due to the methodology itself or to the different degree of adequacy of the functions which are being tried. This reduces the meaning of the differences between fits, particularly when they are small. Minor differences between fits can not be considered relevant in the choices. This is unfortunate because in most real cases the extremal sample available is not too large and usually some different functions can be used which give only minor differences between its goodness-of-fits but which diverge considerably in extrapolations. The variate significant wave height (H_s) is a good example, its extremal samples being obtained by hindcasting (or visual estimates) and resulting not only of small size generally but also of moderate (or low) accuracy. In Figs.(2) to (6) two published extremal samples of H_s (2) hindcasted for Cabo Machichaco (Bay of Biscay, Spain) and Valencia (Spain) have been fitted, with minor differences between fits, by distribution functions Asymptote-I, Asymptote-II, Asymptote-III, Weibull and Log-Normal. All of these functions have been recommended for general use (Asymptote-I, (2); Asymptote-II, (3); Asymptote-III, (4), or used in some published cases, for the variate H_s . The dispersion of extrapolations is broad (Fig.(1)): For T=100 years the maximum difference between results is 3 m. at Valencia and 7 m. at Cabo Machichaco. These differences would have large repercussions in the design of maritime structures, and the differences between goodness-of-fits could not provide a reliable choice criterion in both cases. It can be proved (1) that the reliability of every extremal sample (or any set of observed probabilities obtained by random sampling) is not constant but varies along the values of the variate. The approximation to the true (population) probabilities is best at the center of the distribution function $F(x)=0,5$, and diminishes towards both tails. From this point of view, a non-ambiguous fitting criterion was developed (1). When using it, the upper and lower tails of the sample points are excluded from the fits because of their low reliability. Therefore it must be realized that the effective or useful size of the samples is quite smaller than their total size. The need for very long samples is thus emphasized, the others not being capable to yield reliable extrapolations in individual analysis.

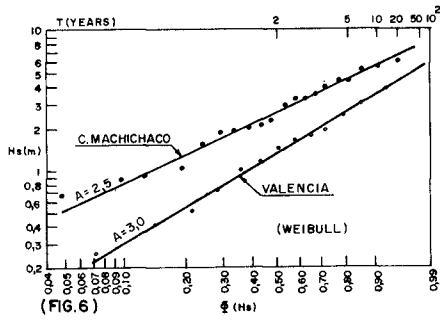
The theoretical justifications stem from the basic extremal equation for a random variate X : $\Phi(x)=(F(x))^n$, where $\Phi(x)$ is the probability of x not to be exceeded in any of n random trials, and $F(x)$ is the distribution function of the variate or probability of x not being exceeded in a single trial. For x approaching 1 and n large enough, the extremal distribution converges asymptotically towards one of the so-called First, Second and Third Asymptotic Extremal distribution functions, when one of three types of conditions is fulfilled by the tail of interest of $F(x)$. Because these conditions are quite broad, covering a very wide spectrum of distribution functions, and n is supposed to be large for -- most geophysical variates along one year (the basic geophysical cycle), a great number of authors have assumed (notably after the fundamental work of E.Gumbel (5)) that the extremal distribution of any geophysical variate could be closely approximated by one or other of the three Asymptotes. References (5) and (1) mention a good number of published applications of the Asymptotes in extremal analysis of variates like temperature, wind speed, -- rainfall, river discharge, significant wave height, etc. In the justifications for the -- use of the Asymptotes it has generally been assumed that, for instance, a variate like -- the average discharge in 24 hours has in a year a value of $n=365$, a number which is fairly high and supposed to yield statistical independence at high levels of the variate (E.Gum-
* Head, Coastal Engineering Dept., Laboratorio de Puertos "Ramón Iribarren", Madrid.



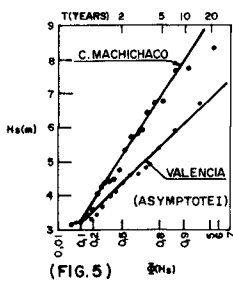
(FIG. 1)



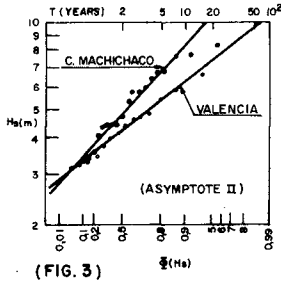
(FIG. 4)



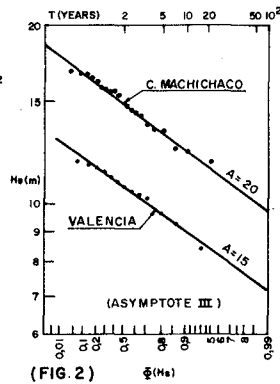
(FIG. 6)



(FIG. 5)



(FIG. 3)



(FIG. 2)

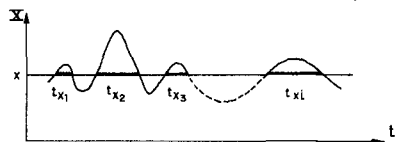
bel, (5)). This interpretation of the parameter \underline{n} is erroneous. Variates like temperature, whose evolution is not discrete but continuous with time, can not be said to "occur" a certain "number of times" along a year. The variate takes an infinitude of values within a finite time interval. Therefore, it is not possible to assign directly a value to \underline{n} . This, -- which is self-evident for an instantaneous variate like temperature, can be shown to be al so true for other variates. J.Battjes (6), commenting on an extremal analysis of H_s , showed that when parameter \underline{n} is given a value equal to the duration of the year divided by the duration of each H_s record, an absurd result is obtained. This author was the first, to the knowledge of the writer, to realize for a particular variate that such an assumption for \underline{n} is not correct (in spite of what, some further extremal analysis of H_s with the same erroneous criterion for \underline{n} have been published later). Actually the same \underline{s} applies to all geophysical variates which consist in averages or totals within a fixed time interval. These variates belong to a group whose evolution with time is continuous, to which most of the -- variates relevant in civil engineering belong: Rainfall in a time interval; Discharge in a time interval; Average wind speed in a time interval; Significant wave height; etc. The average discharge in 24 hours does not take on 365 values in a year, but an infinitude. -- The fact that just 365 of them are juxtaposed in time is not particularly relevant. It can be shown (1) that an assumption like $n=365$ leads to an absurd result in the extremal analysis of this variate too, and so for all the variates of the same type. It will be shown later on that, for that type of variates, \underline{n} is not a constant value but a function of the variate. From this follows that the derivation of the Asymptotes, which was done with the implicit assumption $\underline{n=constant}$ (see, for instance, (5)), is not valid for the continuous-evolution variates. Therefore the extensive use which has been done of the Asymptotes for -- those variates does not have any theoretical justification as yet. The writer (7) presented a model by which the extremal equation can be applied to continuous variates:

1.- EXTREMAL EQUATION FOR CONTINUOUS EVOLUTION VARIATES

The extremal equation $\Phi(x)=(F(x))^{\underline{n}}$ was stated on a discrete basis for the occurrence of the variate. In order to apply this equation to a continuous-evolution variate, the variate itself must be prepared for a discrete analysis. This can be done when, instead of the individual values taken by the variate, the undulations described by the variate in -- its evolution along time are taken into consideration. The undulations can be said to have individual physical entity with finite dimensions and can therefore give support to a discrete analysis. Each entire undulation can not be assigned a certain duration. Instead, only a fixed level \underline{x} of the variate will be considered. Cutting the continuous curve at -- the level \underline{x} , a number of isolated undulations (what will be called "curves of exceedance of \underline{x} " or more simply "x-exceedances") remain above the cut. Now a dichotomy can be established at each level \underline{x} : The probability of occurrence of a x-exceedance, or of its non occurrence. This entails to change the continuous axis "time" into a discrete "number of times" (or statistical trials) in which an event (x-exceedance) might happen or not. For that, -- the "duration" of each statistical trial is taken as the average duration $t(x)$ of the x-exceedances. The "number of trials" at the level \underline{x} is, in an average year of duration T_y :

$$n(x) = \frac{T_y}{t(x)} . \text{ Being } n_x \text{ the average number of x-exceedances in a year or } n_x = \frac{\sum t x_i}{t(x)}$$

the probability that in a single "trial" a x-exceedance does not occur is $1 - \frac{n_x}{n(x)} = 1 - \frac{\sum t x_i}{T_y}$.



This is the expression for the distribution function $F(x)$ of the former continuous-evolution variate X. Therefore, the probability that in the $n(x)$ trials of the average year no x-exceedance will appear, or extremal distribution function, is:

$$\Phi(x) = [F(x)]^{n(x)}$$

The resulting expression is similar to the extremal equation for a discrete evolution variate except for the exponent, which now is not constant but a function of the variate. The type of function corresponding to $\Phi(x)$ will be determined once the types of functions $F(x)$ and $n(x)$ are found. This will be done in the following for some variates, chiefly H_s . An empirical determination of the form of $F(x)$ and $n(x)$ from several samples is far more reliable than the same direct estimate for $\Phi(x)$, due to the incomparably higher number, length and accuracy of the samples of $F(x)$ and $n(x)$ than of $\Phi(x)$. The extremal samples can best be used as control checks for the predictions made with the extremal equation. This was done in (1) for a few cases.

2.- FUNCTION $n(x)$

It will be first indicated which is the kind of relationship existing between the values of $n(x)$ corresponding to the whole population and the estimates of this parameter - obtained from a limited sample or observation period. For each sample, estimates of $n(x)$ are obtained from the observed average durations $t(x)$ of the exceedances.

- The higher the number of exceedances, the more reliable (close to the population) the estimate of $t(x)$ and thus of $n(x)$. In every single observation period that number varies along the range of values of X (Fig. 48), having a sharp maximum at a certain level - (very close to the center of the distribution function, $F(x)=0,5$, (1), and steadily diminishing towards both tails. The reliability varies in the same way too.

- Assuming that along a certain "central" stretch of values of X the $n(x)$ estimates are correct or acceptable, the estimates belonging to the adjacent zones in both directions will show a random deviation from the population values due to their low reliability.

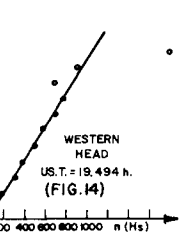
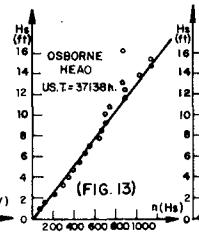
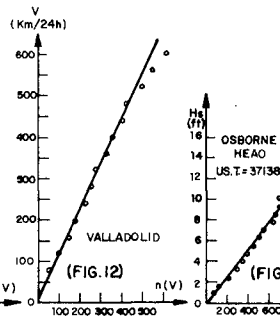
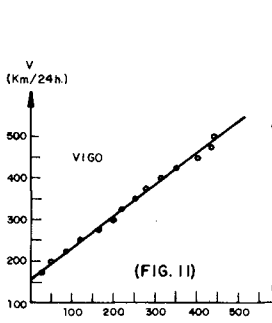
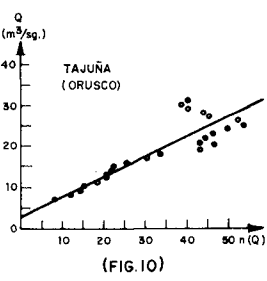
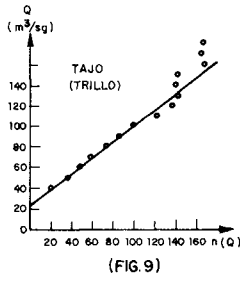
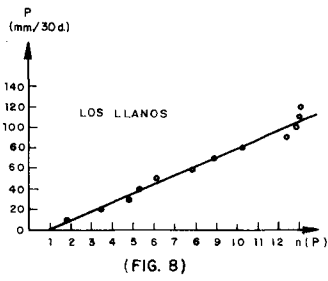
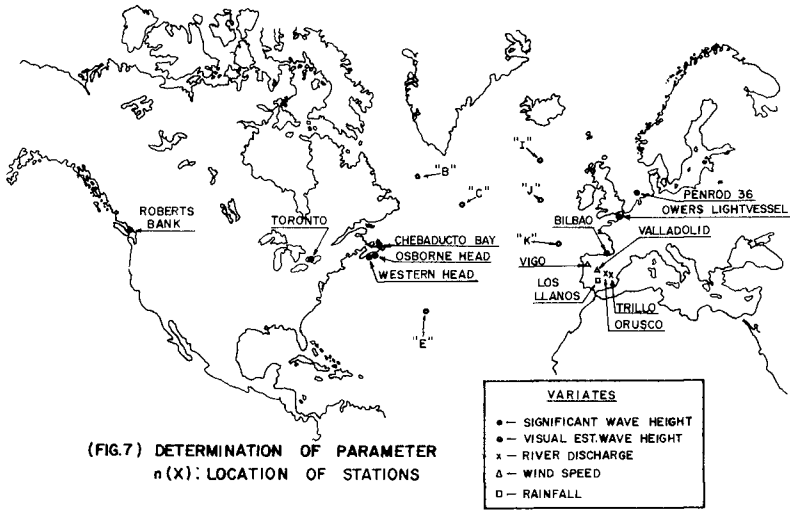
- The variate may be in general unlimited in both directions, but each sample will instead be necessarily limited by a maximum and a minimum values. The observed values of $n(x)$ will show, at both ends, systematic deviations: Towards $n(x)=0$ at the minimum observed value of X , and towards $n(x)=\infty$ at the maximum. Most geophysical variates, such as H_s , have a natural lower limit at $x=0$, and then only the upper systematic deviation exists.

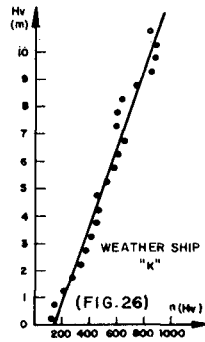
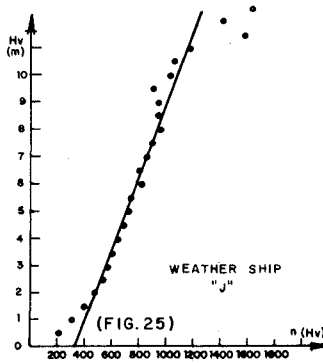
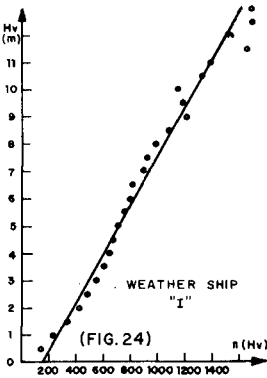
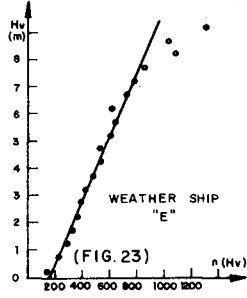
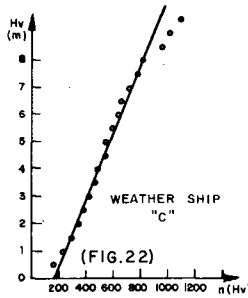
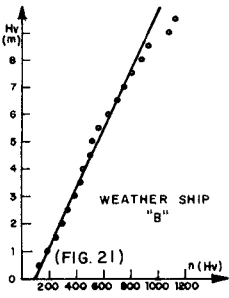
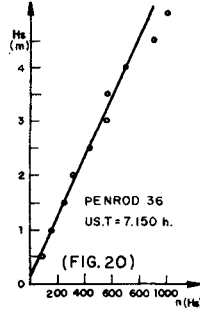
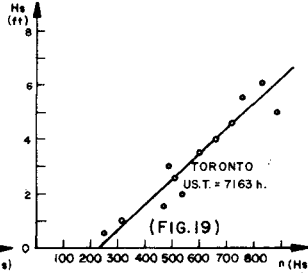
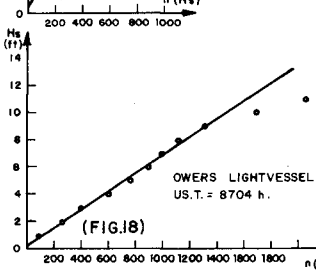
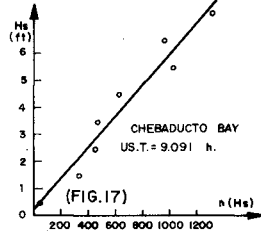
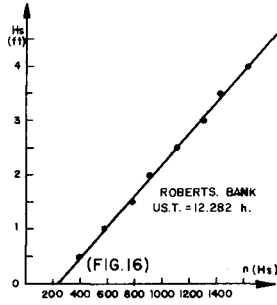
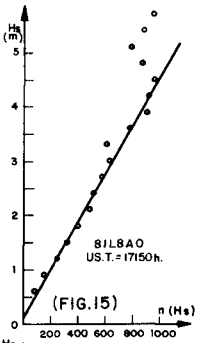
STATION	SITUATION	VARIABLE	OBSERVATION PER.	USEFUL TIME	INTERVAL NET. OBSERV.	DEPTH (m.)	SOURCE		
LOS LLLANDS	CUENCA (SPAIN)	RAINFALL IN 30 DAYS	1-X-1940-1-X-1970		30 DAYS		INTECSA (MADRID)		
VALLADOLID	VALLAOLID (SPAIN)	AVERAGE WIND	1-X-1970-1-X-1979		12-24 HOURS		INSTITUTO METEOROLOGICO NACIONAL (MADRID)		
PEÑADOR	VIGO (SPAIN)	SPEED IN 24 HOURS	1-11-1970-1-X-1972						
TRILLO	RIVER TAJO (SPAIN)	AVERAGE DISCHARGE	1-X-1963-1-X-1973		24 HOURS		J. GRIJEDA (CENTRO DE ESTUDIOS HIDROGRAFICOS)		
ORUSCO	RIVER TAJUÑA (SPAIN)	IN 24 HOURS	1-X-1962-1-X-1963						
OSBORNE HEAD	NORTH ATLANTIC (W.)	SIGNIFICANT WAVE HEIGHT (INSTRUMENTALLY RECORDED)	18-11-1970-1-X-1976	37.138 H. (701%)	3 HOURS	30.3	DON SIRRELL (MARINE INFORMATION DIRECTORATE, CANADA)		
WESTERN HEAD	NORTH ATLANTIC (W.)		15-IV-1970-9-V-1973	18.494 H. (74.2%)		40-43			
CNEBADUCTO BAY	NORTH ATLANTIC (W.)		24-X-1974-4-11-1976	9.091 H. (81.3%)		26.7			
ROBERTS BANK	STRAITS OF GEORGIA		7-11-1974-3-IV-1976	12.282 H. (70.0%)		139			
TORONTO	LAKE ONTARIO		15-IV-1972-18-VI-1973	7.165 H. (81.2%)		108			
OWERS LIGHTYESSSEL	ENGLISH CHANNEL		1-X-1978-1-X-1979	8.704 H. (99.4%)		13-15		L. DRAPER (LOS, UK)	
PENROO 36	NORTH SEA		1-11-1973-1-11-1974	7.150 H. (81.9%)		26		E. BOUWENKAMP, METRO	
BILBAO, P. LUCERO	BAY OF BISCAY		2-IV-1976-2-IV-1978	17.335 H. (98.6%)		3-4 HOURS		40	L. TEJEDOR (THAM-PSA, MADRID)
WEATHER SHIP "B"	NORTH ATLANTIC (W.)		VISUALLY ESTIMATED WAVE HEIGHT	1949-1972		91%		1-3 HOURS	ENVIRONMENTAL DATA SERVICE (U.S.A.)
WEATHER SHIP "C"				1952-1972		92%			
WEATHER SHIP "E"		1932-1972		89%					
WEATHER SHIP "J"		1949-1971		88%					
WEATHER SHIP "K"		1949-1971		88%					
WEATHER SHIP "X"	NORTH ATLANTIC (E.)		1949-1969	93%					

TABLE-7

These conditions were satisfied by the linear relationship $n(x)=A(x-B)$, in the analysis of 13 sets of data (see Table 1) belonging to the following continuous evolution variates: Instrumentally recorded significant wave height (8 cases); average wind speed in - 24 hours (2 cases); average river discharge in 24 hours (2 cases); and total rainfall in - 30 days (1 case). In Fig. 7 the location of all observation stations is shown. Figs. 8 to 20 show the linear fits. In this figures, the points for whose computation less than 10 exceedances were available have been excluded. That has limited considerably the deviations which could be seen. The fact that in the cases analyzed the upper deviation next to the central stretch starts more often towards large $n(x)$ values than towards small ones, goes in well with the skewness which was appreciated in the distributions of the durations at each level of X . The skewness indicates a higher frequency of durations below the average than above it. The proper fit of the function $n(x)$ to the data calls for the use of "accuracy intervals" as defined in (1). However, visual fits are acceptable for extremal analysis provided that the "central" stretch of reliable estimate is long enough. Later on some interesting results concerning H_s are obtained.

In Figs. 21 to 26 six long duration sets of visually estimated wave height are analyzed. These are not intended to be a check of the linear function, since the reliability of the visual estimates is as yet less clear than should be. However, they have been included here because of the practical importance of visual wave observations. The central and lower points lie in a peculiar sinuous pattern, which only becomes straight on a log-log paper (1). This seem to give support to the power relationship between H_s and H_v sugges-





ted by Nordstrom (9). But the log-log plots yield a quick systematic deviation of the upper tail, which might indicate that the power relationship is not applicable to the higher waves. It is possible that no single simple relationship is valid for the whole range of wave heights. This point still needs clarification, and in the mean time the linear fits of Figs. 21 to 26 will be used (in following sections) as an approximation which probably (in view of the acceptable behaviour of the upper points) is reasonably accurate for extrapolations.

3.- FUNCTION F(x)

Only the variate significant wave height will be tackled in this section. The 8 sets of instrumental data used in the preceding section (Table 1) will be analyzed, together with other 12 sets selected from the technical literature (Table 2). The aim of the selection was to choose the longest possible durations (and complete annual series when duration consists in a small number of years) and waters not too shallow at the site. The result is a compromise which seems acceptable as a whole. Fig. 28 shows the location of the 20 stations.

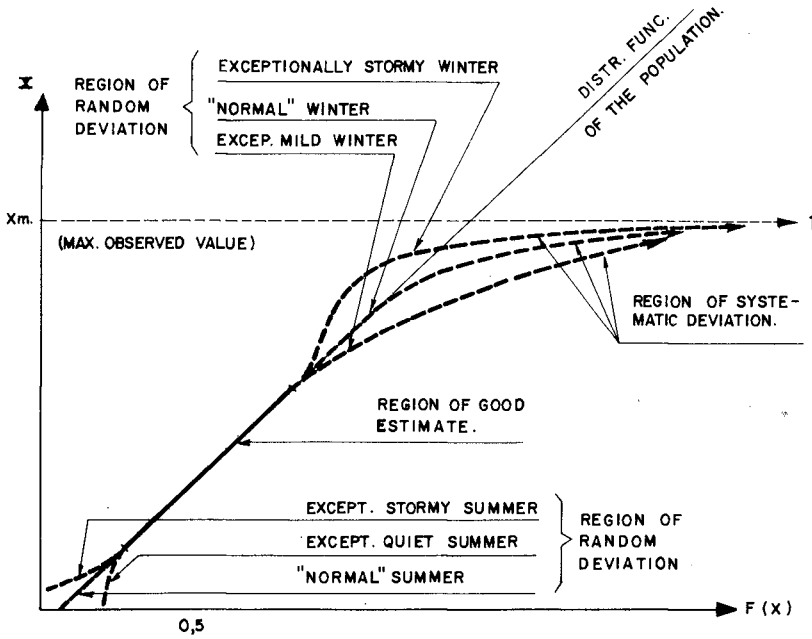
A comparison has been done between the distribution functions Exponential, Log-Normal, Weibull and Double Exponential (Asymptote-I) which are the most widely used today for H_s . No general agreement exists today in this respect, what is unfortunate because of the large differences which can be obtained in the extrapolations when one or another of those functions are used. The comparative study is set up under the initial hypothesis that for any geophysical variate a single type of distribution is valid, at least within each type of homogeneous climate which can be discriminated in the behaviour of that variate. The results obtained prove that the hypothesis works in the case of H_s . The relative amount of swell existing within the waves recorded at each site has been chosen as an operative criterion to discriminate between different "wave climates". The situation of the stations relative to prevailing winds, size and limitations of available fetches and local shelters, and tables of coincidence wave height-wave period, have been evaluated in order to assign each station to a certain group. According to this, four different groups have been defined: In both extremes are the groups denominated "Very low swell" (Toronto, Roberts Bay, Morecambe Bay, Mersey Bar, Nice, Benghazi, Chausey Sud, Dunkerque), and "Heavy swell" (important relative weight of swell reaching relatively high values of the variate: Sevenstones, Bilbao, Cattlewash, Camp Pendleton). As intermediate groups, "Low swell" (Chebaducto Bay, St. John-Deep, Smith's Knoll) and "Moderate swell" (Osborne Head, Western Head, Penrod 36, Varne, Owers Lightvessel). It must be admitted that the border between the two intermediate groups is not altogether clear, but that is not a serious trouble in the comparative study.

STATION	SITUATION	DEPTH (m.)	OBSERVATION PER.	USEFUL TIME	INTERVAL BET. OBSER.	SOURCE
DUNKERQUE	NORTH SEA (S)		12-IV-1960-17-VIII-1966	708 DAYS		R. BONNEFILLE ET AL. (1967) ($H_{max} \sim H_s$)
CHAUSEY SUD	ENGLISH CHANNEL	19.5	27-VI-1956-4-IV-1961	1204 DAYS		H ALLEN (1970)
NICE	MEDIT. SEA (N)	9-14	17-IX-1964-27-V-1962	606 DAYS		
CAMP PENDLETON	NORTH PACIFIC (W)	9.8	1954 AND 1958		6 H.	H. POWERS ET AL. (1968)
BENGHAZI	MEDIT SEA (S)	12.8-14.6	1961-1969 (IRREGULAR)			H. SINGH ET AL. (1968)
ST. JOHN DEEP	NORTH ATLANT. (W)	36.6	I-III-1972-29-II-1973			J. KHARNA ET AL. (1974)
CATTLEWASH	CARIB. SEA (E)		XII-1972-XI-1973			C. DEANE (1974)
MORECAMBE BAY	IRISH SEA	21.9	XI-1966-X-1967	8760 HOURS	3 H.	
MERSEY BAR	IRISH SEA	17.6	IX-1968-VIII-1968	8760 HOURS	3 H.	
SEVENSTONES	NORTH ATLANT. (W)	60.4	I-1962-XI-1962	8760 HOURS	3 H.	J. BATTJES (1970)
VARNE	ENGLISH CHANNEL	27.5	II-1968-I-1968	8760 HOURS	3 H.	
SMITHS KNOLL	NORTH SEA	49.4	III-1968-II-1968	8760 HOURS	3 H.	

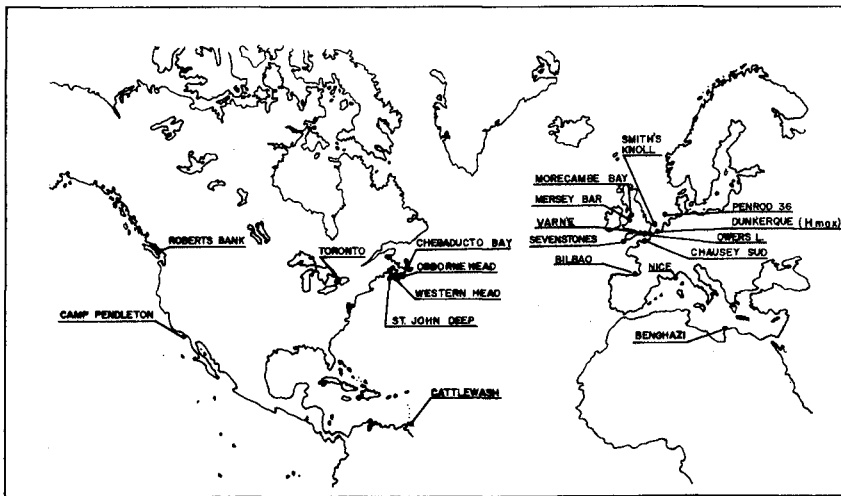
TABLE-2

Similarly to what was done for parameter $n(x)$, it will be indicated which kind of relationship exists between the values of $F(x)$ corresponding to the population of the variate and the values observed in a sample of limited size (observed distribution):

SAMPLE OF INDEPENDENT OBSERVATIONS: In a sample of N independent observations of a random event, the probability of the observed probability of success being $\frac{m}{N}$ can be computed from the binomial distribution, $P(m)_N = \binom{N}{m} p^m (1-p)^{N-m}$ where p is the true (population) probability of success in a single trial. Now, the event "success" is the occurrence of a value higher than x in each observation of a random variate X with a distribution function $F(x)$. The probability that in N independent observations the observed probability at the level x (the observed frequency of x being exceeded) is $\frac{m}{N}$, can be computed as: $P(x, m)_N = \binom{N}{m} q(x)^m (1-q(x))^{N-m}$ where $q(x) = (1-F(x))$. The reliability of a sample estimate of $q(x)$ can be measured as the probability of the observed probability $\frac{m}{N}$ to fall inside a certain (arbitrary) interval around the true probability $q(x)$: $((1-k)q(x) < \frac{m}{N} < (1+k)q(x))$. It can be shown (1) that: a) The convenient intervals ("accuracy intervals") should be defined in relative terms with respect to $q(x)$, so that k is a certain percentage of $q(x)$ to be deter-



(FIG. 27).— OBSERVED DISTRIBUTION CURVES: CHARACTERISTIC REGIONS.



(FIG. 28).— DETERMINATION OF $F(H_0)$: LOCATION OF STATIONS

mined accordingly to the accuracy required by the user; b) the appropriate "true" probability to be used as reference for these intervals is $q(x)$ for the upper half of the distribution function ($q(x) < 0,5$) and $F(x)$ for its lower half ($F(x) < 0,5$). The use of the binomial distribution as indicated above shows that, for any fixed width of the accuracy intervals (any constant value of k), the reliability of the observed probability (probability of that probability to fall inside the intervals) is maximum at the center of the distribution function $F(x)=q(x)=0,5$, and diminishes towards both tails of the distribution. Thus, for any sample of independent values of a random variate X , provided it is large enough, two characteristic regions can be discriminated in the set of observed probability points:

- A central region of good estimate, where the observed probabilities are close to the true (population) probabilities.

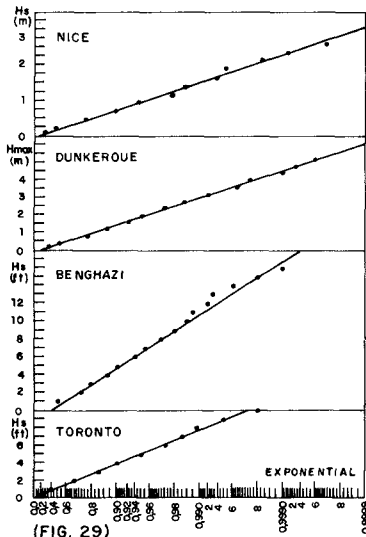
- Regions of poor estimates at both tails, where the observed probabilities are expected to show wide random deviations from the population probabilities. Limits between both regions can be set by use of accuracy intervals, as discussed in (1) (Accuracy intervals can be defined in terms of the probability or of the value of the variate, and different procedures for estimating their values from the sample itself can be used).

SAMPLE OF CONTINUOUS OBSERVATIONS: If a continuous-evolution variate is observed systematically with short time intervals between records (for instance H_s , with typical observation intervals of 2-3-4 hours), statistical independence between observations can not be assumed. The high density of observations allows the whole curve of evolution of the variate to be drawn, and from it a complete observed distribution (with probabilities from 0 to 1) can be obtained. It can be shown (1) that also for these samples the observed probabilities have a maximum reliability at the center of the distribution function and lower reliability towards both tails. For a sampling period long enough, three characteristic regions can be distinguished in the observed distribution curve: Two of them are the same as indicated above for independent observations, and the third is a final systematic deviation of the uppermost and lowermost tails, which converge asymptotically towards cumulative probabilities $\underline{1}$ and $\underline{0}$ at the maximum and minimum values of the variate observed in the sampling period. This is a natural consequence of any finite sample having a maximum and a minimum observed values, in contrast with the population whose values are in general unlimited. In Fig. (27) the three characteristic regions of an observed distribution of H_s are shown. The lower systematic deviation does not appear, since this variate has a natural lower bound at $H_s=0$. When estimating the distribution function of the population from one of such observed distributions, only the central region of expected good estimate should be considered for the fit.

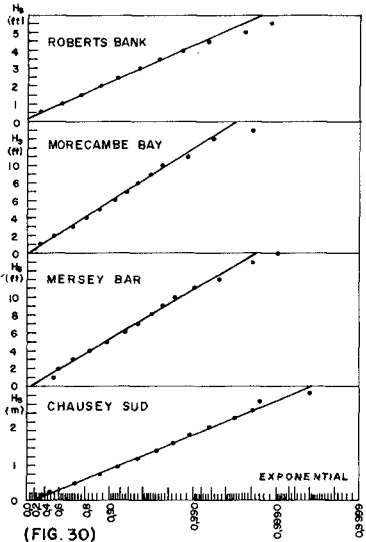
Comparative studies published in previous years have adopted the criterion of choosing the function which would give the best fit to the whole set of sample points, and specially to its upper tail if extrapolation is the final goal. Such a criterion is erroneous, particularly for continuous or almost-continuous observations, as Fig. 27 makes it evident. The aim of fitting the complete observed distribution and the aim of estimating from it the distribution of the population are not only two different purposes but in fact incompatible. In particular, to place the emphasis of the fit in following the uppermost tail of the observed distributions means to follow the points with the poorest reliability, belonging to the region of expected random deviation or, worse, to the final systematic deviation. This can only lead us away from the expected behaviour of the population, in extrapolations.

In order to compare the behaviour of the 4 functions, it will be checked whether the deviations of the observed values in the regions of "random deviation" are actually random in the set of fits, or whether they are systematic. This criterion suffices to solve satisfactorily the comparison. Although the strictly correct method would be a simultaneous use of accuracy intervals to make the fits and confidence intervals to evaluate the deviations quantitatively, such laborious procedure does not prove necessary in this case. The Exponential and Log-Normal functions will be compared first and later on the Weibull and Double Exponential which are closely related to the Exponential.

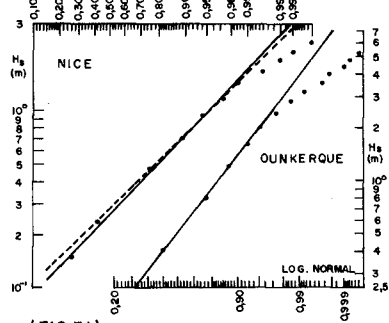
EXPONENTIAL - LOG-NORMAL. - In Figs. 29, 30, 31, 32, the fits corresponding to the group "very low swell" can be seen. The Exponential fits are uniformly satisfactory, with deviations which are not systematic and start at reasonable levels of the probability. -- The longer the observation period, the longer is the central region of good fit (Nice, Dunkerque, Chausey Sud). Instead, the Log-Normal fits are uniformly poor. The upper tails show systematic deviation towards low values of the variate, deviation which begins to show very quickly. In Figs. 33, 35, the group "heavy swell" is fitted, showing quite a different behaviour. The Log-Normal fits are good from the lower region to high levels of --



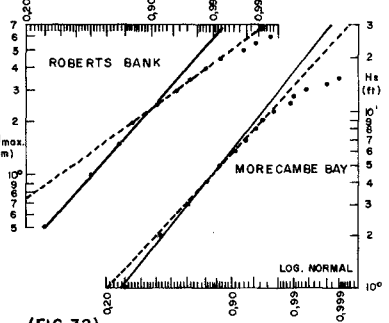
(FIG. 29)



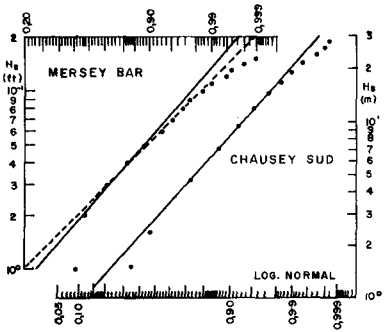
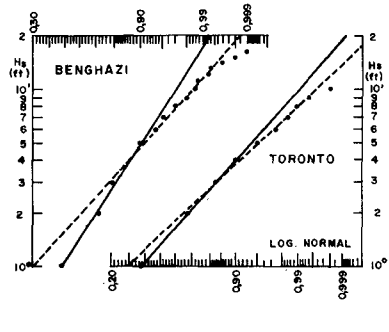
(FIG. 30)

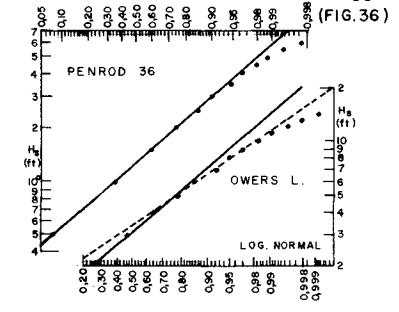
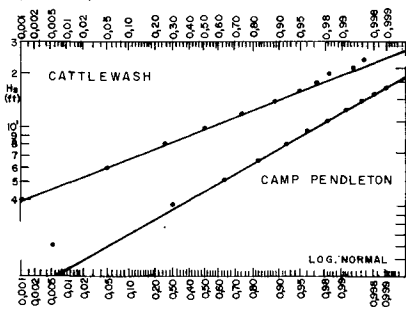
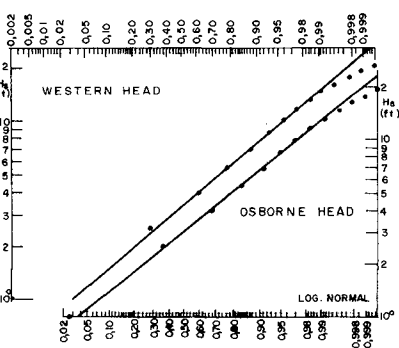
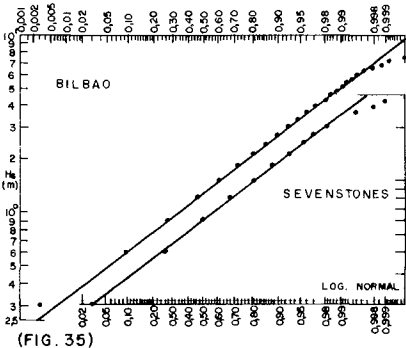
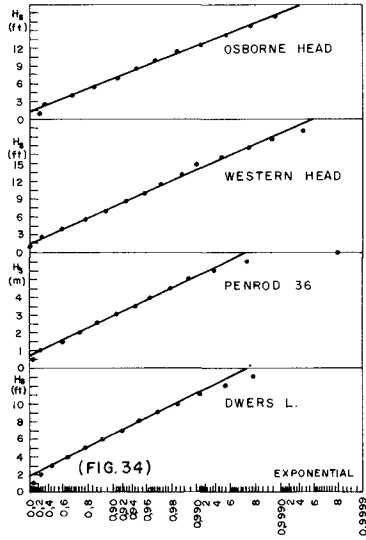
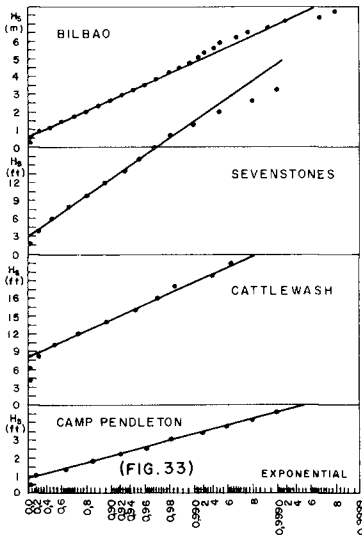


(FIG. 31)



(FIG. 32)





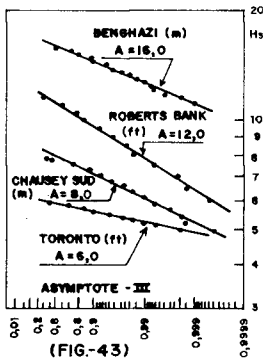
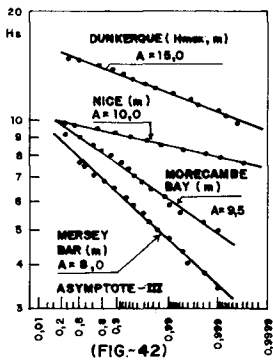
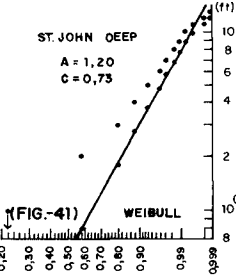
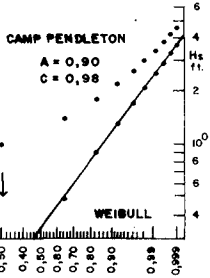
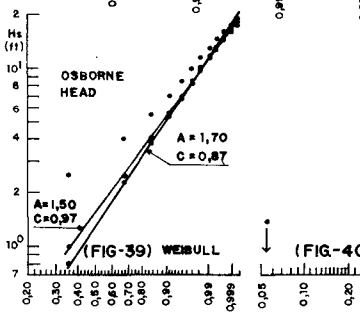
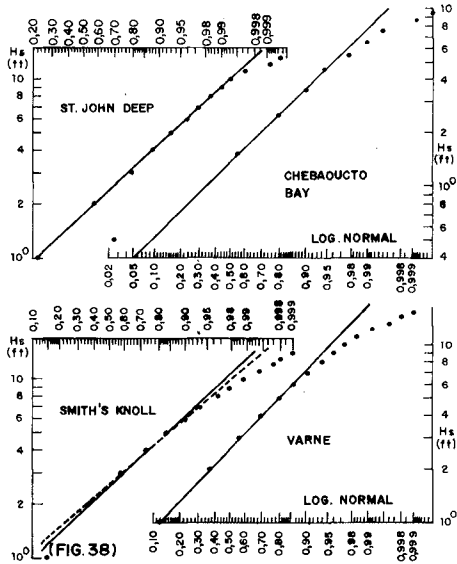
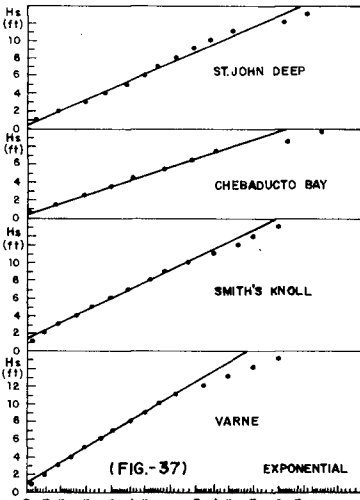
the probability. The Exponential function behaves well in the upper region, but shows a -- sharp systematic deviation in the lower tail. The number of stations included in this group is small, but the inspection of the two remaining groups will clarify the behaviour of both functions. In Figs. 34, 36, 37, 38, the "low swell" and "moderate swell" groups are plotted. The fits show characteristics which are intermediate between those seen in the former groups. As a rule the Log-Normal behaves better in the lower part of the central region, but in the upper zone shows a quick, systematic deviation. At Penrod 36, Owers L., Varne and - Smith's Knoll, the deviations start at probabilities from 0,8 to 0,9, which means a total exceedance time of 73 to 36 days (their observation period is 1 year). This is certainly - excessive, since a good number of exceedances are included in that time for those levels - of H. Even if only the upper part of the central region is fitted, neglecting the lower - part^s (discontinuous lines in the figures), the Log-Normal still deviates systematically in its upper tail. Therefore this function should be rejected for extrapolations. The Exponen - tial law shows for this two groups a systematic deviation at its lower tail. This deviation starts at low values of H_s for low levels of swell, and at higher points for high levels - of swell. At the upper half of the distributions, the Exponential function behaves uniform - ly well for both groups and hence for all the 4 groups. Therefore this function appears - to be in principle acceptable for extrapolations and, thus, for extremal analysis, although its lower tail can not be used when swell has any relative importance.

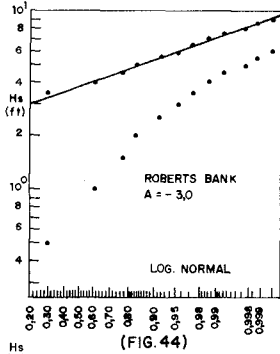
EXPONENTIAL - WEIBULL.- Exponential: $F(x)=1-e^{-\frac{x-A}{B}}$; Weibull: $F(x)=1-e^{-\frac{(x-A)^C}{B}}$

The difference between both expressions is only the exponent C which appears in the Weibull function. The aim of this comparison is thus to investigate whether the inclusion of that third parameter in the Exponential function leads to better fits. The individual fits of - the 20 stations are not shown here because of space limitations (they can be seen in (1)), but in the following table the values obtained for A and C in the fits are listed. Its -- three parameters give to the Weibull function a higher flexibility, but also a higher degree of indetermination for estimating the values of the parameters themselves. This is -- specially true for observations of not long duration, whose central region of good estimate is short. As an example, in Fig. 39 the fit corresponding to Osborne Head is shown: -- When parameter A is increased in 0,2 feet (\approx 6 cms.), parameter C (which is a certain measure of the slope of the line) changes from 0,97 to 0,87. Should the data of this station belong to a short observation period, there would be no clear way to make a choice between both fits. Due to its high sensitivity to small changes in A (parameter which arranges the points for the fit), the parti - cular values obtained for C must be understood with some am - plitude. In the evaluation of the table, the really meaning - ful values are those corresponding to the stations with rela - tively long observation periods (Osborne Head, Chausey Sud , Nice, Bilbao, Camp Pendleton, Western Head, Dunkerque, Roberts Bank). Their central region of good estimate is the longest, and thus the influence of the upper and lower sample peculiarities in the fit is reduced. In all these stations the C va - lues are very close to 1. According to what was indicated -- above about the accuracy of C estimates, it can be assumed - $C=1$ for all, in practice. Therefore it has not been found jus - tified to include this third parameter and the choice is -- still the 2-parameters Exponential function. In the table, - the cases in which C takes on values not close to 1 belong to samples with the shortest durations (1 year), where it can be supposed that the peculiar flexibility of the Weibull function leads the one who performs the fit to follow to some extent - the deviations of the tails since the central region of good estimate is too short for an unequivocal choice of A. The Wei - bull function has, in Exponential paper, a curvature concave upwards for $C<1$ and concave downwards for $C>1$, but not always that flexibility allows it to fit the deviations of both tails simultaneously in short samples: In Figs. 49, 50, 51 three cases are shown where the fit of the lower tail leads to an ill behaviour of the rest of - the distribution (compare with Figs. 39, 40, 41, where the lower tail was not fitted. In - these kind of fits, the values given to A makes the lower points "disappear" from the probability paper, giving an outward look of perfect fit throughout).

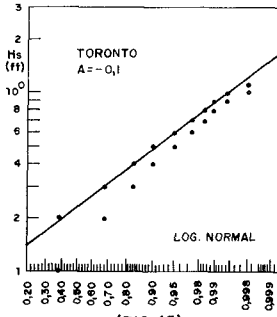
	(m.)	C
Camp Pend.	0,27	0,98
Bilbao	0,60	1,02
Cattlew.	1,52	1,24
Sevens.	0,61	1,20
Osborne H.	0,46	0,97
Western H.	0,52	0,93
Penrod 36	0,50	1,05
Owers L.	0,12	1,41
Varne	0,15	1,11
Smith's K.	0,06	1,31
St.John D.	0,37	0,73
Cheb.Bay	0,15	0,99
Dunker.	0	0,97
Chausey S.	0	0,96
Nice	0	1,02
Rob. Bay	0	1,09
Benghazi	0	0,81
Morc.Bay	0	1,05
Mers. Bar	0	1,02
Toronto	0	1,03

Other 3-parameter functions do also have a high flexibility. For instance, in Figs. 42, 43 the group of stations "very low swell" has been fitted with Asymptote-III functions. The Log-Normal function may include a third parameter too (change $H_s = H_s' \cdot A$): see in Figs. 44, 45, how in this way the fits obtained in Figs. 29, 30 with two parameters are improved with 3.

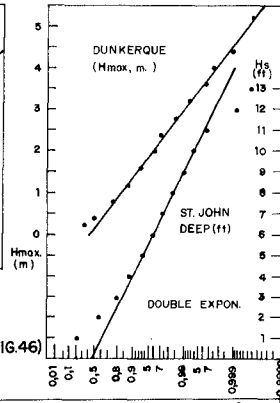




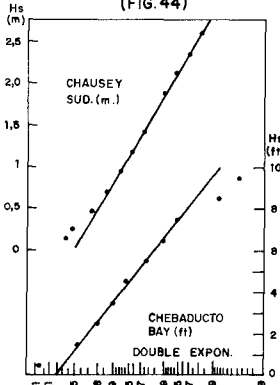
(FIG. 44)



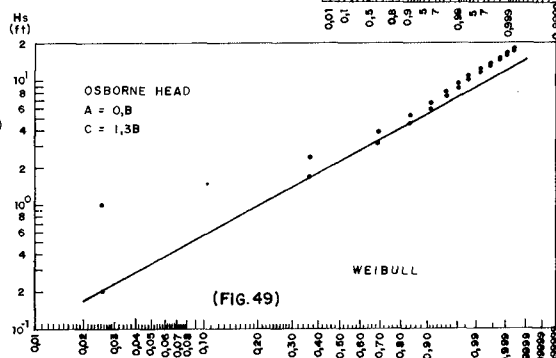
(FIG. 45)



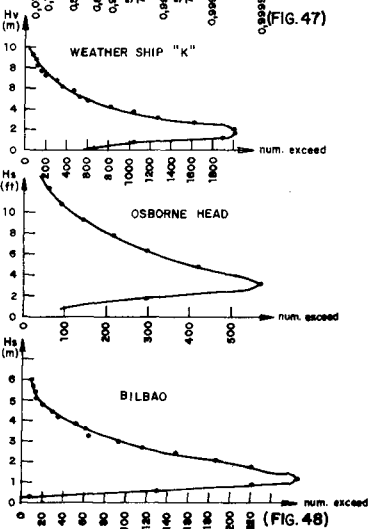
(FIG. 46)



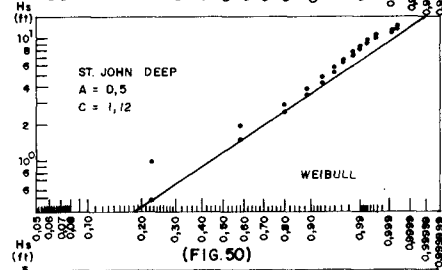
(FIG. 47)



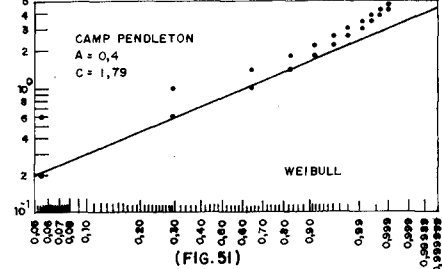
(FIG. 49)



(FIG. 48)



(FIG. 50)



(FIG. 51)

Even more flexibility would be attained with 4 parameters (Log-Normal with the change $H_s = \frac{H_s - A}{B - H_s}$), and so on. But, as it has been shown, the proper use of functions with a high number parameters would only be feasible had we a better knowledge of the statistical properties - of geophysical variates, than is available today. Otherwise their flexibility is more of a trouble than an advantage. More detailed statistical studies including large numbers of samples are needed. In the mean time we have to be content with the usual simple functions which, if proved well-behaved (like the Exponential herein), are able to give reasonable approximations.

EXPONENTIAL - DOUBLE EXPONENTIAL.- Both functions converge quite quickly for large probabilities:

$$\text{Exponential: } F(x) = 1 - e^{-\frac{x-A}{B}} \quad \text{Convergence: } F(x) \xrightarrow{F(x) \rightarrow 1} e^{-(F(x)-1) \frac{x-A}{B}} = e^{-\frac{x-A}{B}} \quad (\text{Double Exponential}).$$

The speed of the convergence can be visually appreciated by comparing both probability papers. The difference between their probability scales is that, for the lower probabilities, the Double Exponential scale is "stretched" with respect to the other. However this feature is not able to improve, in general, the fits in the lower part of the distributions (which were found to be unsatisfactory with the Exponential). Some of the fits can be seen in Figs. 46, 47 (the rest can be seen in (1)) showing a systematic deviation, this time upwards instead of downwards: The "stretching" of the scale was excessive. Therefore the use of this function is not advisable.

CONCLUSIONS.- None of the 4 functions tried is adequate for the whole extent of the distributions in all the stations studied. The Exponential function has been found to behave satisfactorily in the upper part of the distributions, and thus apt for extrapolations. In the lower part its fits are good when swell is negligible, but as the importance of swell reaches higher levels of H_s so grows a lower region with a systematic deviation. Log-Normal function behaves reciprocally: its fits are good in the lower region, reaching higher levels of H_s as the importance of swell also reaches higher H_s values. In the upper region, the fits show a systematic deviation. This result suggests that the statistical heterogeneity found in each station corresponds with different physical properties of swell -- and sea, each of which is predominant within a certain range of H_s values (with a region of overlapping). The Exponential function could then describe statistically the growth of the sea caused by wind fields reaching the observation site, originated by differential pressure centers (typically low pressure centers). The highest waves are almost everywhere -- formed in this way; thus the adequacy of the Exponential law for extrapolations. On the other hand, the Log-Normal law seems to fit correctly the region where waves are a mixture, in space and time, of a good proportion of swell, low waves formed by the local microclimate, and sea that is being generated by larger wind fields. It is curious to notice that -- the Log-Normal distribution is theoretically correct for natural variates formed by a high number of random factors which join their individual effects in a multiplicative way (V. - Chow, 1955). In (1) further speculations along the same line are indicated to reason this hypothesis, which is able to explain why the deviation of the observed points in the lower tail of the Exponential fits takes place in the form of a quite sudden drop. Summing up, at every single station a discrimination between different wave "climates" can be made, according to the different relative importance of swell along the H_s levels. This discrimination has proved effective in selecting distribution functions with general applicability.

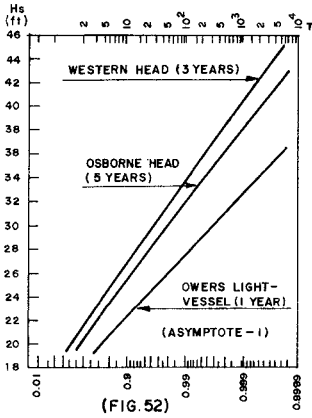
EXTREMAL DISTRIBUTION $\Phi(H_s)$

From the results obtained before for $n(H_s)$ and $F(H_s)$, the following expression is reached for $\Phi(H_s)$:

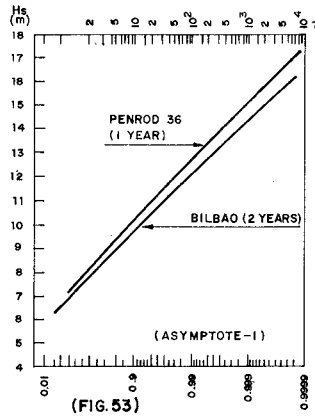
$$\text{Convergence: } \Phi(H_s) = (F(H_s))^{n(H_s)} \xrightarrow{F(H_s) \rightarrow 1} e^{-(1-F(H_s))n(H_s)}; \quad F(H_s) = 1 - e^{-\frac{H_s - k_1}{k_2}};$$

$$n(H_s) = k_3(H_s - k_4); \quad \Phi(H_s) \rightarrow e^{-(H_s - C)e^{-\left(\frac{H_s - A}{B}\right)}}$$

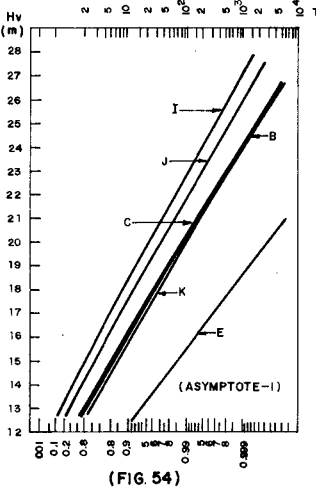
It is a 3-parameters distribution function. Should $n(H_s)$ have an exponential form, the expression for $\Phi(H_s)$ would be the double exponential or Asymptote-I. With a linear growth for $n(H_s)$, $\Phi(H_s)$ has a quicker growth than the Asymptote-I has. In Figs. 52, 53, 54, - 55, the extremal distributions computed for the 14 wave observation stations listed in Table 1 have been plotted in Asymptote-I paper. From the curvature of the distributions it turns out that the use of Asymptote-I for fitting extremal samples of H_s consistently overestimates the real values in the extrapolations. However the overestimations are small, -



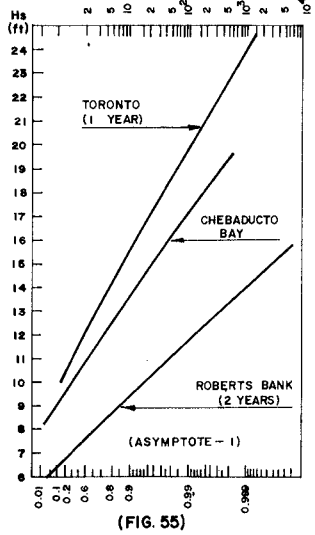
(FIG. 52)



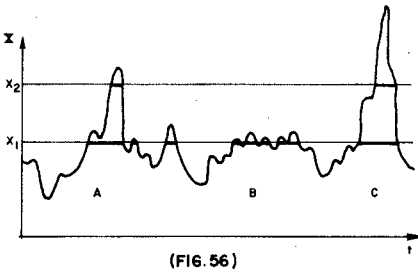
(FIG. 53)



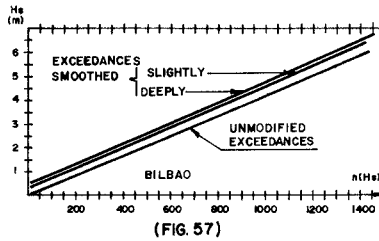
(FIG. 54)



(FIG. 55)



(FIG. 56)



(FIG. 57)

and acceptable for most applications, within the range of return periods usual in practice. Instead, the Asymptote-II would cause large (unacceptable) overestimates.

The good performance showed by the linear and exponential functions with the sets of data analyzed in the two previous sections makes one confident that this simple laws will yield sufficiently accurate results for the extremal analysis of H_s . In some meaningful cases, a good correspondence between both functions has been noticed. In station Bilbao, for instance, where exceptionally rough winters took place within the observation period, the sharp deviation of the sample points above the exponential fit for $F(H_s)$ (Fig. 33) starts almost exactly at the same point where the (also sharp) deviation appears above the linear fit for $n(H_s)$ (Fig. 15). This kind of correspondence is to be expected only in case of very exceptional winter seasons (abnormally rough or mild), since not only the durations but also the number of exceedances play a role in $F(H_s)$.

Some aspects of the use of the extremal equation for significant wave height predictions will be commented in the following sections.

5.- STATISTICAL INDEPENDENCE

One of the basic hypothesis on which the extremal model that is being used here was built, is the independence between "statistical trials". This means randomness in the presentation of exceedances. The practical adequacy of this hypothesis must be inquired.

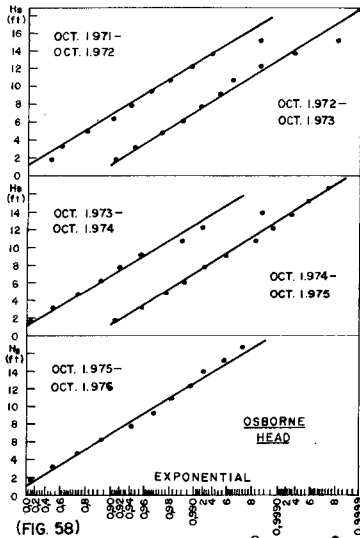
When the crest of an exceedance is long, it usually follows a sinuous pattern rather than a smooth curve (Fig. 56, case B). These secondary peaks are obviously interdependent. Should this feature be dominant along the entire range of values of the variate, the use of the model would become rather difficult. Fortunately the crests of the exceedances which reach high levels of the variate are typically pointed, leaving little room for secondary oscillations. In order to check in a real case the quantitative influence of this effect, one year of H_s observations in Bilbao (April 1976-April 1977) has been used to compute 3 different estimates of $n(H_s)$: a) using the entire H_s -course unmodified (analyzed by computer); b) using the H_s -course where secondary peaks have been suppressed by a slight smoothing (hand made) of the exceedances; c) deep smoothing of the exceedances. The result (Fig. 57) are three straight lines which run quite parallel. Thus the relative difference between the three estimates steadily diminishes with increasing levels of the variate. At H_s levels relevant for extremal predictions, the predictions calculated with any of these $n(H_s)$ estimates are practically identical.

The distinction between these secondary peaks and proper exceedance curves is not always neat. Sometimes (Fig. 56, case A) crests with good sizes lie close to each other in a way that suggests some kind of inter-dependence. In this respect, it can be remembered that P. Rijkooort and J. Hemelrijk (1957) found proof of statistical dependence between storms in the North Sea. Again it can be argued that this dependence loses importance with increasing levels of the variate. At medium and long return periods the exceedances appear typically as isolated, well-spaced peaks. This seems to be the general behaviour of geophysical variates. In (1) some real records are shown which illustrate his statement, and two comparisons between extremal predictions and extremal samples for the variates average wind speed and total rainfall in an interval show good agreement even for low return periods. It is unfortunate that accurate (instrumental) extremal samples of H_s are not available with enough length to make similar checks, but in principle there are no reasons to assume a too different behaviour for this variate.

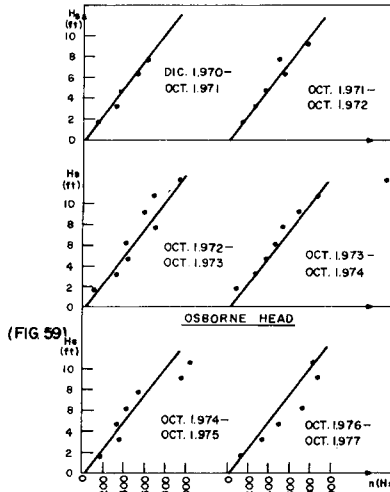
6.- HYPERANNUAL CYCLICITY

The extremal distribution has been stated here on a yearly basis (probability of not-exceedance in the average year). The use of this probability in terms of return periods implies the assumption of randomness in the intensity of the variate in different years. The adequacy of this hypothesis should be questioned.

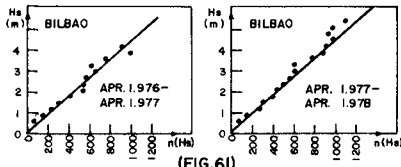
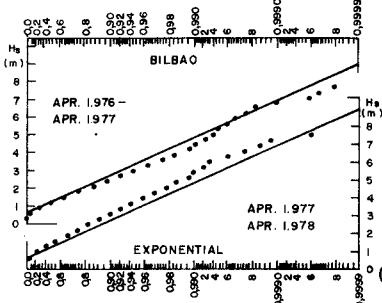
Numerous authors have found significant evidences of some kind of periodicity (more properly called "pulsations") in several geophysical variates. These pulsations are generally thought of as being connected with the 11-years cycles found in the solar activity. Pulsations of about 11 (or 22) years in the maxima of the variate should not appreciably influence the practical use of predictions made on an average-year basis, since usual design return periods have an order of magnitude of hundreds of years. However, it can still be questioned whether the estimates of $n(x)$ and $F(x)$ (with which the extremal prediction is calculated) are random from year to year. Should they be subject to pulsations, a minimum



(FIG. 58)

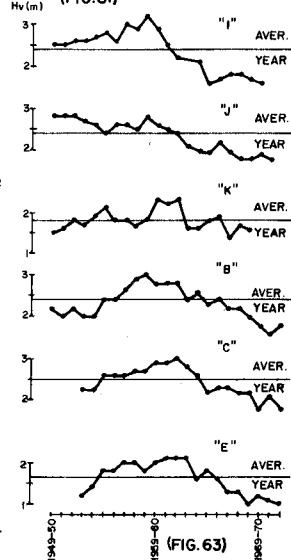


(FIG. 59)

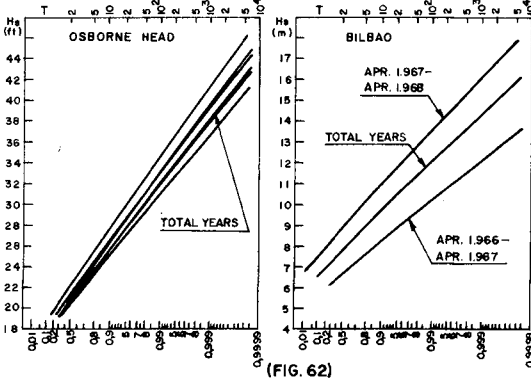


(FIG. 61)

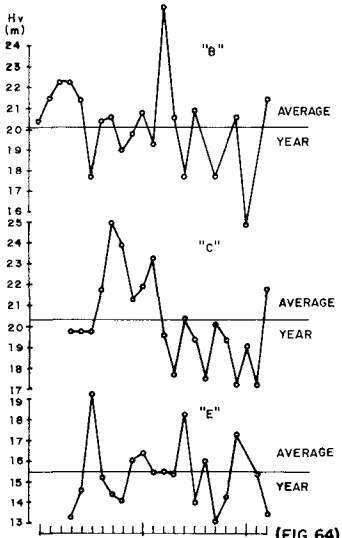
(FIG. 60)



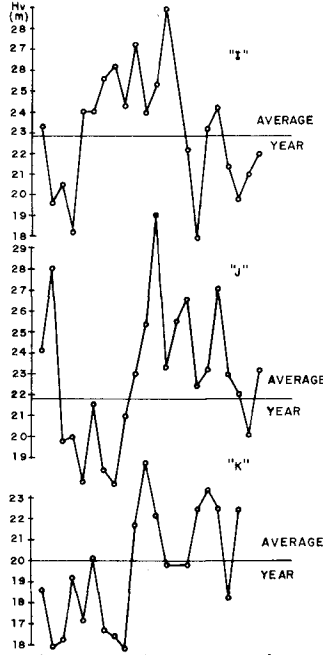
(FIG. 63)



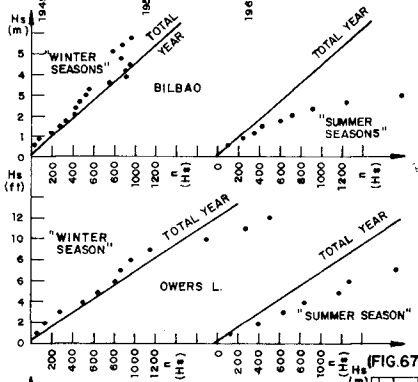
(FIG. 62)



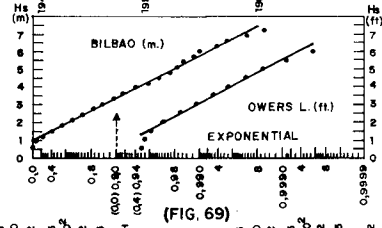
(FIG. 64)



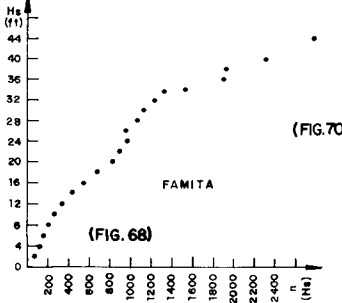
(FIG. 65)



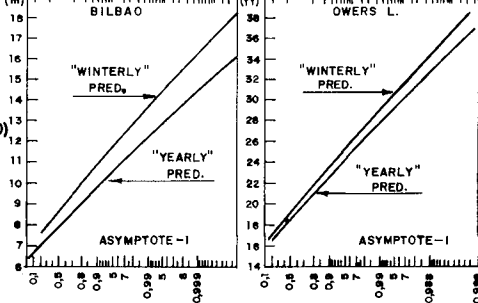
(FIG. 67)



(FIG. 69)



(FIG. 68)



(FIG. 70)

observation period of those 11 or 22 years would be needed for a proper characterization of the "average year". Long duration instrumental records are still missing, but the visual observations of wave height in the Weather Ships (more than 20 years) will be used to get some information. In Fig. 63, the wave height corresponding to probability $F(H_s) = 0,5$ in the distribution observed each year (October-October) are plotted for six Weather -- Ships. Clear grouping of higher and lower heights appears in most of them, with semi-periods curiously near -- to the 11 years above mentioned. Extremal distributions were computed for the six W.S. with each yearly estimate of $F(H_s)$, $n(H_s)$ (1). In Figs. 64, 65, the points corresponding to $T=100$ years in each prediction are -- plotted, showing that in some Ships there is no trace of grouping and where grouping may seem to be detected it does not keep in correspondence with the groupings observed in Fig. 63. Although the quantitative value of -- these estimates does not seem to be high (next section), the qualitative pattern obtained suggests that cycli city does not have a significant influence in the extremal predictions of H_s .

7.- SUFFICIENT ESTIMATES OF $n(H_s)$ AND $F(H_s)$

Even assuming that the hypothesis of annual randomness is reasonable in practice, still remains the problem of determining which is the minimum observation time necessary to obtain acceptably accurate estimates of the extremal distribution, i.e. how many years are enough to get a good estimate of $n(H_s)$. Recent works assume that one single year of observation is enough to yield the average year in terms of $F(H_s)$. However this -- hypothesis has never been sufficiently checked, and the main reason to keep it is probably the tight time li mits which are customary in actual projects. In Figs. 58, 60, the observed distributions for each year in Osborne Head (5 years) and Bilbao (2 years) are compared with the distributions fitted to the complete sets of observations. In Figs. 59 and 61 the same comparison is carried out with the parameter $n(H_s)$. In Fig. 62 the extremal predictions computed from each 1-year estimates are plotted. For $T=500$ years (10% risk of exceedance in 50 years), the difference between the higher and lower predictions is 1,3 m. at Osborne Head ($\pm 5,72$ of the intermediate value), and 3,7 m. at Bilbao ($\pm 13,62$). Although the number of years worked out is too small for stating general conclusions, the results might be indicative of two wave climates with different degrees of -- homogeneity. Anyway the dispersion of results obtained for Bilbao represents a heavy influence on the design of maritime structures and shows the need for wider comparative studies of this kind in various ocean areas.

The comparisons made for Bilbao and Osborne Head show reasonable agreement between the yearly estima tes of $n(H_s)$. The differences obtained in the extremal predictions are almost exclusively due to the different yearly estimates of $F(H_s)$. Furthermore, it can be easily showed (1) that $\Phi(x)$ is far more sensitive to varia tions of $F(x)$ than of $n(x)$.

Figs. 64, 65 show a large variability of the yearly estimates of $\Phi(H_s)$, much in excess than what was observed in Fig. 62. Moreover the yearly estimates of $n(H_s)$ (showed in (1)) also show a high dispersion, in -- contrast with the behaviour of Figs. 59, 61. This suggests a deficiency in the visual observations of wave -- height. It seems that a higher number of $n(H_s)$ values than a year includes is necessary to get an acceptable approximation of $n(H_s)$, and that a higher number of observations of H_s is needed than what is usually performed in a year, in order to get an acceptable estimate of $F(H_s)$, in that year (aside from the variability of -- both parameters from year to year). It can be concluded that 1-year of visual observations do not suffice to obtain useful extremal predictions of wave height.

With the aim of reducing as much as possible the time of observation, some published works use only a "winter season" (often the roughest 6 months of the year) of measurements in order to estimate the upper ta il of $F(H_s)$. In Figs. 66, 67, 69, estimates of $F(H_s)$ and $n(H_s)$ in the "winter season" (October-March) and "sum mer season" (April-September) during one year in Owers Lightvessel and 2 years in Bilbao, are compared with -- the estimates obtained with complete years. Both stations were selected for the completeness of their observa tions. The resulting extremal predictions are compared in Fig. 70: The "winterly" predictions are higher (for $T=500+1,8$ m. at Bilbao and 0,5 m. at Owers L.). This is a natural consequence of having used the same distribu tion (Exponential) for the "winterly" and "yearly" estimates: since not all the H_s values of the "winter sea son" are higher than the values of the "summer season", the slope of the exponential line for the winterly es timate is steeper than for the whole year estimate. "Winterly" predictions are bound to stay systematically -- higher than yearly ones, unless distribution functions are used which can be made to converge in their upper tails (different functions, or maybe variable-parameters functions). This possibility is above our present kno wledge of the behaviour of geophysical variates. It must be indicated that the use of more flexible functions may worsen the situation: when the Weibull distribution was used instead of the Exponential, the difference be tween predictions was 2,0 m. for Owers Lightvessel.

The different $n(H_s)$ estimates did not appreciably account for the variability in extremal predictions. However, the "winterly" points form a peculiar double arch above (higher durations) the complete-year line. The same pattern can be seen in Fig. 68 corresponding to 6 "winterly seasons" recorded by rescue ship "Famita" -- (North Sea). These points do not show the linear trend which was clear in the complete-year estimates.

ACKNOWLEDGEMENTS

This paper is a resume of a part of the Doctoral Thesis presented by the author to the Faculty of Civil Engineering at Santander (Spain). The study, published in (1), was carried out at the Laboratorio de Puertos -- "Ramón Iribarren" within a research program on wave climate. The author wishes to thank the kind help of W. Bar ird and D. Birrell (Mar. Direct., (Canada), L. Draper (I.O.S., U.K.), L. Bows (K.N.M.I., Netherlands), E. Cirujeda (C.E.H., Spain), H. Allen (L.N.H.C., France) and L. Tejedor (Thalassa, Spain) in the acquisition of data; V. Fernán dez Dupuy for providing free use of the excellent computer facilities of Intessa (Madrid); J. Conde and A. Arcilla (Lab. de Puertos) for their critical reading of the manuscript. The necessary computer programs were com pletely done by staff of Intessa.

REFERENCES: (1) E. Copeiro (1978): "Análisis extremal de variables geofísicas" Publ. 14-B Laboratorio de Puertos "Ramón Iribarren", Madrid (in press) - (2) P. Suárez Bores (1974): "Sea observation in coastal areas: the spanish offshore network". Int. Symp. Wave Measur. and Analysis, New Orleans - (3) H. Thom (1973): "Asymptotic Extreme-Value Distributions of Wave Heights in the Open Ocean" Proc. ASCE vol. 99 No. MW3, Aug. - (4) M. St. Denis (1973): "Some Cautions on the Employment of the Spectral Technique to Describe the Waves of the Sea and the Response The reto of Oceanic Systems". Preprints, Offsh. Tech. Conf., Houston. - (5) E. Gumbel (1958): "Statistics of Extremes" New York, Columbia Un. Press. - (6) J. Battjes (1970): "Long term wave height distribution at seven stations around the British Isles" N.I.O. Internal Rep. n.º A.44 - (7) E. Copeiro (1976): "Un método práctico de estimar oleaje extremal para el cálculo de estructuras marítimas" Revista de Obras Públicas, Junio, Madrid.

CHAPTER 15

DEEPWATER DIRECTION FROM AN INTENSITY ARRAY

Alan L. Higgins*
Richard J. Seymour**

I. INTRODUCTION

Knowledge of the distribution of wave intensity along a shoreline can be used to infer deepwater directional information for non-locally generated waves. Measurement of this energy distribution may be accomplished using a network of widely spaced nearshore wave gages known as an intensity array. Analysis for intensity array data uses the principle that deepwater swell of a given frequency produces varying patterns of nearshore wave intensity, which depend on the unrefracted directional energy distribution for that frequency. Assuming linear wave propagation to the measurement sites, this dependence may be inverted and applies at all frequencies. Energy spectra measured at the intensity array may be used in this manner to estimate the deepwater directional spectrum. In Part II, details of the relationship between deepwater directional spectrum and nearshore energy spectra are discussed. In Part III, intensity array data are applied to detection of waves incident within a narrow directional interval. Part IV describes the application of an intensity array to detection of long period southern swell in San Diego, California. Comments regarding the relative merits of the method follow in Part V.

II. THEORY

From measured bathymetry offshore of the array, refraction diagrams may be prepared for all frequencies and directions of interest, using linear wave theory. For each such diagram and at each gage site, the ratio of energy at the gage site to deepwater energy is determined. These amplification factors may be calculated from ray spacings or by analytic means.

Consider an intensity array whose gages are located at x_i ($i = 1, 2, \dots, N$). For each frequency f , a directional distribution will be calculated at a discrete set of directions, θ_j ($j = 1, 2, \dots, M$). Denote the amplification factors $a_{ij}(f)$ and suppose a deepwater directional spectrum $d_j(f)$ produces measured nearshore energy spectra $e_i(f)$, where i and j are position and direction indices, respectively. Since the propagation is linear,

$$e_i(f) = \sum_j a_{ij}(f) d_j(f)$$

In matrix form,

*Scripps Institution of Oceanography, UCSD, La Jolla, California

**California Dept. of Navigation and Ocean Development, Scripps
Institution of Oceanography, UCSD, La Jolla, California

$$\begin{bmatrix} e_1(f) \\ e_2(f) \\ \vdots \\ e_N(f) \end{bmatrix} = \begin{bmatrix} a_{11}(f) & a_{1M}(f) \\ \vdots & \vdots \\ a_{N1}(f) & a_{NM}(f) \end{bmatrix} \begin{bmatrix} d_1(f) \\ d_2(f) \\ \vdots \\ d_M(f) \end{bmatrix} \quad \text{or } \underline{e} = \underline{A} \underline{d}$$

For an array of fixed size ($N = \text{const}$), the choice of M is a compromise between angular resolution and smoothing which may be required for stability of the directional distributions. For the case $N = M$, no smoothing is employed. The matrix $\underline{A} = \{a_{ij}\}$ may be inverted to solve for \underline{d} ,

$$\underline{d} = \underline{A}^{-1} \underline{e}. \quad \text{equ. 1}$$

For $N > M$, the linear equations $\underline{e} = \underline{A} \underline{d}$ are overdetermined. One must then seek a solution \underline{d} which approximately satisfies all equations. Define an error vector $\underline{\epsilon}$ by

$$\underline{\epsilon} = \underline{A} \underline{d} - \underline{e}.$$

Minimization of the sum squared error $\underline{\epsilon}^T \underline{\epsilon}$ (see Claerbout, 1976) results in the least squares estimate

$$\underline{d} = (\underline{A}^T \underline{A})^{-1} \underline{A}^T \underline{e}. \quad \text{equ. 2}$$

For each frequency at which this computation is repeated, goodness-of-fit is measured by

$$\underline{\epsilon}^T \underline{\epsilon} = \underline{e}^T \underline{e} - \underline{e}^T \underline{A} \underline{d}.$$

III. UNIDIRECTIONAL WAVES

The assumption that directional distributions are unimodal and narrow makes it possible to estimate incidence angles with an intensity array containing only a few gages. Theoretical proportions of energy at the set of measurement sites are calculated from refraction diagrams as described in Section II. For a given frequency, these proportions vary as a function of the assumed deepwater direction. An estimated direction is chosen for which the theoretical proportions are in closest agreement with measured proportions.

As a measure of agreement, various correlation coefficients are available. The standard product moment coefficient is given by

$$\phi^2 = \frac{\sum_{i=1}^N (m_i - \bar{m})(t_i - \bar{t})^2}{\sum_{i=1}^N (m_i - \bar{m})^2 \cdot \sum_{i=1}^N (t_i - \bar{t})^2}$$

where m and t denote measured and theoretical energies, respectively, and overscoring indicates quantities averaged over all gages. The use of this coefficient emphasizes the relationship of energy proportions which differ greatly from the mean.

When the amplification factors provided by linear refraction theory are of questionable quality, it is desirable to employ a correlation measure which is relatively insensitive to parameter errors. One nonparametric measure having this robust property is Spearman's rank-difference coefficient. For its application, the gage sites are ranked both in order of measured energies and theoretical energies. Spearman's coefficient is based entirely on the difference in ranking and is not severely effected by wild observations or erroneous parameters.

IV. APPLICATION

A four-gage intensity array presently exists in the county of San Diego, California under the operation of the California Coastal Engineering Data Network (Seymour and Sessions, 1976). Data from this array were applied to detection of swell produced by equatorial storms or by storms in the South Pacific. Ships observations of meteorological data for these areas are sparse and as a result, hindcasts are not available. This study was supported by the California Coastal Commission to provide wave climate data for development of engineering structures on south-facing coastline segments.

The array spans 37 miles, with gages at Imperial Beach, Ocean Beach, La Jolla and Oceanside. Bathymetric charts for this region were used by the Los Angeles District of the Army Corps of Engineers to prepare refraction diagrams. Approach azimuths were considered from 180° to 230° in 10° increments. Periods mapped were 14, 16, 18 and 20 seconds. From these diagrams, 96 ($4 \times 4 \times 6$) amplification factors were estimated by graphical means. In this process, a weighted average of ray separations around the gage sites was used, discarding those rays which produce crossings.

The diagrams were generated by the Delaware-Dobson method and do not take account of such non-linear effects as dissipation and diffraction. Therefore, behavior of waves travelling near islands or other types of aberrant bathymetry or over long shallow shelves is not accurately described.

The technique of Section III was applied to obtain product-moment and rank-difference correlation coefficients for long period swell from the southwestern quadrant. An event was defined as exceedance of an arbitrary threshold of 0.90 by both coefficients. Given an event, the amplification factors are assumed to be known and the deepwater energy can be estimated. For each gage,

$$a_i d = e_i, \quad i = 1, N.$$

Minimization of the sum squared error

$$\sum_i (e_i - a_i d)^2$$

gives the least squares estimate of d as a weighted average.

$$d = \frac{\sum_i a_i e_i}{\sum_i a_i^2}$$

Evaluation of the array performance is difficult in the absence of ground truth measurements. Some concurrent data do exist from a five-element linear array operated by the Shore Processes Laboratory at Scripps Institution of Oceanography (Pawka, et al., 1976). The location of this array is not ideal since it is sheltered from southern swell by Point La Jolla. Also, spectral instability associated with limited record length produces large directional ambiguity, particularly in the southwestern quadrant. Comparison for one simultaneous run is shown in Figure 1. Southern swell is refracted offshore of Point La Jolla and again enters deep water over La Jolla Canyon before reaching the linear array. Directions on the abscissa of Figure 1 account for only the latter refraction and should not be compared directly with azimuths listed for the intensity array. However, the general trend can be seen.

Directional spectra for the entire year of 1973 is available from a similar four-element linear array. Peaks of these spectra corresponding to southern swell were picked out. The number of these peaks is compared month-by-month in Figure 2 with events detected in 1977 by the intensity array. Entries on this graph are total events per month divided by the number of days per month in which equipment was operational.

V. CONCLUSION

Records from the individual gages of an intensity array have the intrinsic value of providing local wave climate data at a number of locations. Data processing for the array, as described in Section III, is much simpler and results directly in a deepwater directional spectrum. An additional advantage over coherent arrays is that intensity array estimates appear to exhibit greater directional stability for short periods.

The intensity array method is ad hoc in the sense that confidence intervals are not available. Erroneous amplification factors bias the directional estimates in a data dependent manner. Computation by the method of Section III suffers the obvious difficulty of being invalid for non-narrow directional distributions.

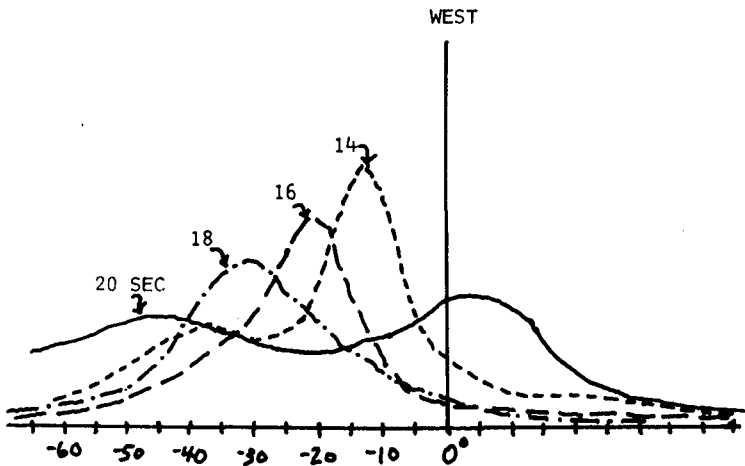
Site selection for intensity array gages is both important and difficult. One objective is to choose a set of unique locations for which the matrices of amplification factors, A in Equation 1 or $A^T A$ in Equation 2, are non-singular and well-conditioned. On the other hand, restriction must be made to sites at which wave propagation is practically linear.

7 JUNE 0355

Fit Parameters

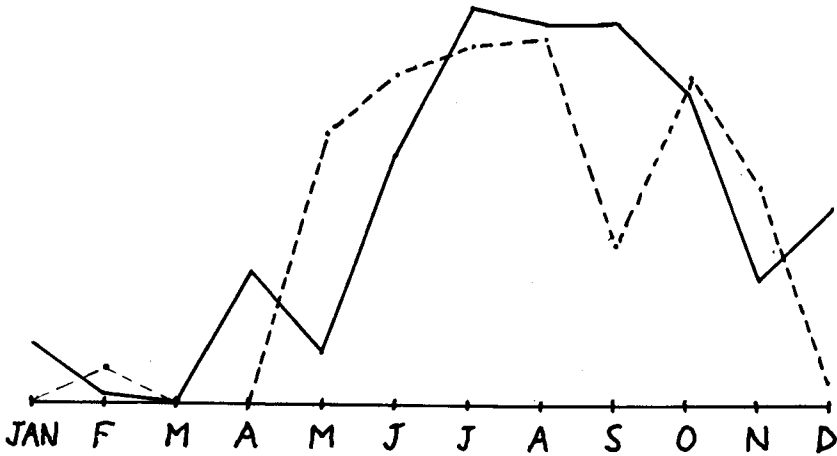
Azi	14 sec	16 sec	18 sec	20 sec
180	.65	-.40	.40	1.00
190	0	-.80	.40	.80
200	.40	.40	.20	.80
210	.40	.40	.40	.40
220	.80	.40	.80	.40
230	.80	1.00	.40	.40

Directional spectra refracted to deep water north of Point La Jolla



Total monthly occurrences of southern swell as determined from:

- Intensity array, 1977
----- Linear (coherent) array, 1973



REFERENCES

Claerbout, J. F.: 1976. Fundamentals of Geophysical Data Processing with Applications to Petroleum Prospecting, McGraw-Hill, 1976.

Pawka, S. S., D. L. Inman, R. L. Lowe, and L. Holmes: 1976. "Wave Climate at Torrey Pines Beach, California." Tech. Paper 76-5, Coastal Engr. Research Center, Ft. Belvoir, Va., May 1976.

Seymour, R. J., and M. H. Sessions: 1976. "A Regional Network for Coastal Engineering Data." Proc., Fifteenth Int. Conf. on Coastal Engineering, Honolulu, Hawaii, July 1976.

CHAPTER 16

NATURAL WAVE TRAINS: DESCRIPTION AND REPRODUCTION

H. Lundgren¹ and S. E. Sand²

ABSTRACT

In many applications there is a great need for a correct description of the natural, irregular three-dimensional sea and its reproduction in physical and numerical models. Because of the tremendous difficulties inherent in the nonlinearities, the science of coastal engineering is still very far from this ultimate goal.

Indeed, the scope of this paper is comparatively very modest: To describe and reproduce natural, irregular two-dimensional waves, i.e. waves propagating in one direction in a flume. In addition, this scope is fulfilled only by assuming linear superposition of Fourier terms.

As opposed to the usual spectral description, the deterministic description presented here does not eliminate the phase information in the wave train recorded. Because of the nonlinearities, however, the linear deterministic description invariably degenerates with the distance travelled by the waves. It appears though from the present paper that the degeneration is fairly slow even for rather steep waves.

1. INTRODUCTION

Traditionally, irregular waves are represented by their spectra. For a number of applications, however, the main interest lies in the lengths of groups of higher waves and in the wave shapes. This is certainly true for the stability of rubble mounds, shock forces, rolling and pitching of ships, wave drift forces, and generation of long waves. Hence, for the last decade the Danish Hydraulic Institute has emphasized the reproduction of natural wave trains (Ref. 4).

As a consequence of this philosophy, it is desirable in some cases to use a deterministic description instead of the stochastic one, with a view also to a deterministic reproduction.

2. DETERMINISTIC DESCRIPTION

In principle, when progressive waves in a flume are recorded at one point, the time series of all other quantities (such as eleva-

¹Professor of Marine Civil Engineering, Institute of Hydrodynamics and Hydraulic Engineering (ISVA), Technical University of Denmark, DK-2800 Lyngby. - Consultant, Danish Hydraulic Institute.

²Ph.D.-student, ISVA, Technical University of Denmark.

tions, orbital velocities and pressures) are defined down along the flume. The present theory is based upon a linearized decomposition in a Fourier series, so that each component propagates independently.

Let the waves $\eta(x,t)$ be recorded at $x = 0$ as the wave train $\eta(0,t)$. It is desired, for example, to calculate the time series $p_b^+(x,t)$ of the bed pressure (in excess of hydrostatic pressure) at a fixed distance x from the wave recorder. p_b^+ may be expressed as

$$p_b^+(x,t) = \gamma \sum_{n=1}^{\infty} \frac{a_n \cos(nft - k_n x) + b_n \sin(nft - k_n x)}{\cosh k_n h} \quad (1)$$

where a_n, b_n are the Fourier coefficients belonging to a finite interval, $|t| < t_0$, of the recorded wave $\eta(0,t)$, $f = \pi/t_0$, h is the water depth, and k_n is the wave number corresponding to the circular frequency nf .

a_n, b_n may be found from the usual integral expressions

$$a_n = \frac{1}{t_0} \int_{-t_0}^{t_0} \eta(0,\tau) \cos n f \tau \, d\tau \quad (2a)$$

$$b_n = \frac{1}{t_0} \int_{-t_0}^{t_0} \eta(0,\tau) \sin n f \tau \, d\tau \quad (2b)$$

which, inserted in Eq. (1), give

$$p_b^+(x,t) = \gamma \sum_{n=1}^{\infty} \frac{f}{\pi} \int_{-t_0}^{t_0} \frac{\eta(0,\tau) \cos(nf\tau - nft + k_n x)}{\cosh k_n h} \, d\tau \quad (3)$$

Here, the order of integration and summation is inverted. If, in addition, $t_0 \rightarrow \infty$, the basic frequency f may be replaced by $d\omega$ and nf may be written $nf = \omega$, leading to the convolution integral

$$p_b^+(x,t) = \gamma \sqrt{g/h} \int_{-\infty}^{+\infty} P(\tau-t, x) \eta(0,\tau) \, d\tau \quad (4)$$

where

$$P(\tau-t, x) = \frac{1}{\pi} \sqrt{h/g} \int_0^{+\infty} \frac{\cos[(\tau-t)\omega + k_\omega x]}{\cosh k_\omega h} \, d\omega \quad (5)$$

and k_ω is the wave number corresponding to ω and h .

For $x = 0$ Eqs. (4+5) give the bed pressures at the point, where η is recorded. $P(\tau-t, 0)$ is shown as a function of $(t-\tau)\sqrt{g/h}$ in Fig. 1.

The curve gives a clear impression of how the bed pressures $p_b^+(0,t)$ are influenced by the elevations $\eta(0,\tau)$, and, as could be expected, the weighting of $\eta(0,\tau)$ is such that $\tau = t$ has the maximum influence on the bed pressure at time t .

Using the same procedure as above, formulae for all other quantities along the flume, such as elevations, orbital velocities etc., may be derived. Each quantity can be expressed as an integral

$$\left(\frac{g}{h}\right)^\alpha \int_{-\infty}^{+\infty} (\text{influence function}) \cdot \eta(0,\tau) \, d\tau \quad (6)$$

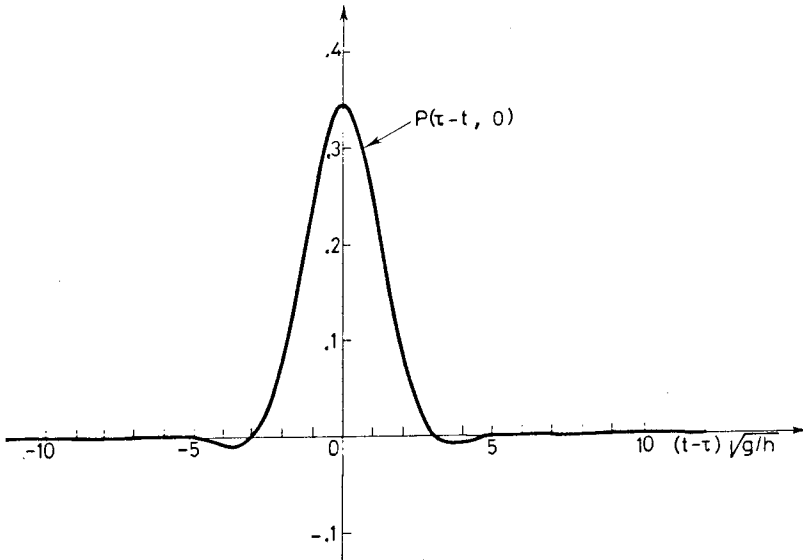


Fig. 1. Dimensionless influence function $P(\tau-t, 0)$

Some dimensionless influence functions are given below:

For water surface elevations:

$$E(\tau-t, x) = \frac{1}{\pi} \sqrt{h/g} \int_0^{\infty} \cos [(\tau-t)\omega + k_{\omega}x] d\omega \quad \alpha = \frac{1}{2} \quad (7)$$

For bed velocities:

$$U(\tau-t, x) = \frac{1}{\pi} \frac{h}{g} \int_0^{\infty} \frac{\omega \cos [(\tau-t)\omega + k_{\omega}x]}{\sinh k_{\omega}h} d\omega \quad \alpha = 1 \quad (8)$$

For bed pressures:

See Eq. (5).

$P(\tau-t, x)$ is shown as a function of $(t-\tau)\sqrt{g/h}$ in Fig. 2 for two values of x/h .

Fig. 2 shows that the main loop of P is shifted to the right when x is increased. Hence it follows from Eq. (4) that the main influence of $\eta(0, \tau)$ on the pressure $p_b^+(x, 0)$ for $t = 0$ originates from increasing negative values of τ when x increases, i.e. for increasing x the useful information is found earlier in the time series $\eta(0, \tau)$.

Fig. 2 also illustrates how far back in time it is needed to know η in order to obtain a certain accuracy. For larger values of x the oscillations of P have longer 'wave lengths' and decrease more slowly, due to the influence of the higher frequencies.

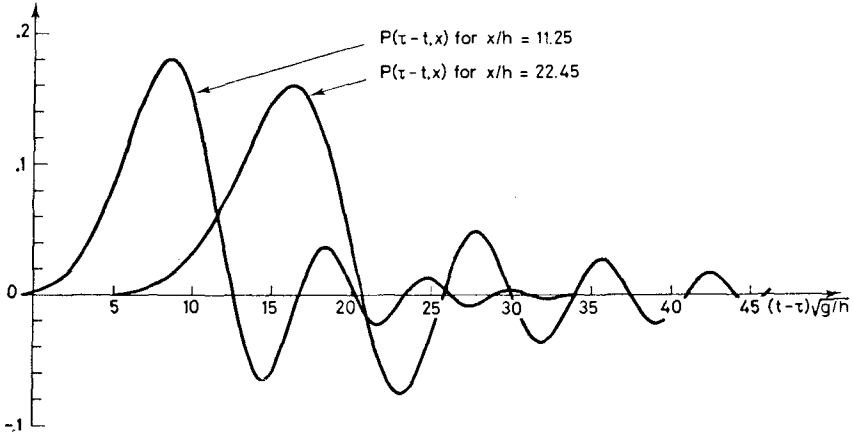


Fig. 2 Dimensionless influence function $P(\tau-t, x)$

In Fig. 3 the influence function, $E(\tau-t, x)$, for surface elevations will be seen as a function of $(t-\tau)\sqrt{g/h}$ for two values of x/h . As compared with the P-function in Fig. 2, the E-function decreases much more slowly with large values of $t-\tau$. This slow decrease is due to the higher frequencies (for which the bed pressures are strongly damped). At the same time the 'wave lengths' of the E-function decrease so rapidly that it is not too essential to extend the integration in the convolution integral for $\eta(x,t)$ very far in the direction of negative τ .

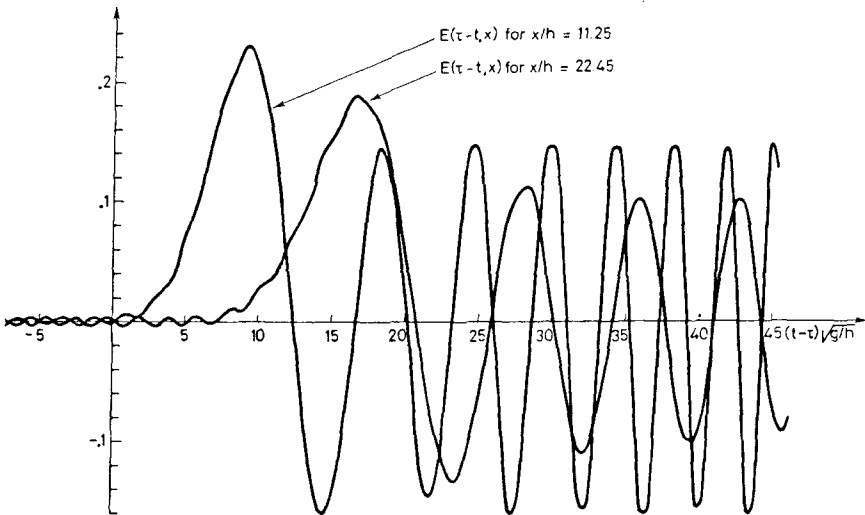


Fig. 3 Dimensionless influence function $E(\tau-t, x)$

3. TESTS ON DETERMINISTIC DESCRIPTION

The theory of deterministic description was tested in a flume ($h = 0.40$ m) with the input wave gauge at $x = 0$ and pressure cells mounted in the bottom of the flume at $x = 0$, $x = 4.5$ m and $x = 8.98$ m. The wave trains used for the tests had mean periods of 0.84 s, 1.02 s and 1.72 s, respectively, i.e. mean wave lengths of 1.09 m, 1.58 m and 3.4 m. The maximum steepness ranged from 2% to 8%.

The record $\eta(0, \tau)$ was used as input in Eq. (4) together with one of the influence functions in Fig. 2. Fig. 4 demonstrates that the calculated output $p_b^+(x, t)$ agreed reasonably well with the recorded one for $x = 8.98$ m.

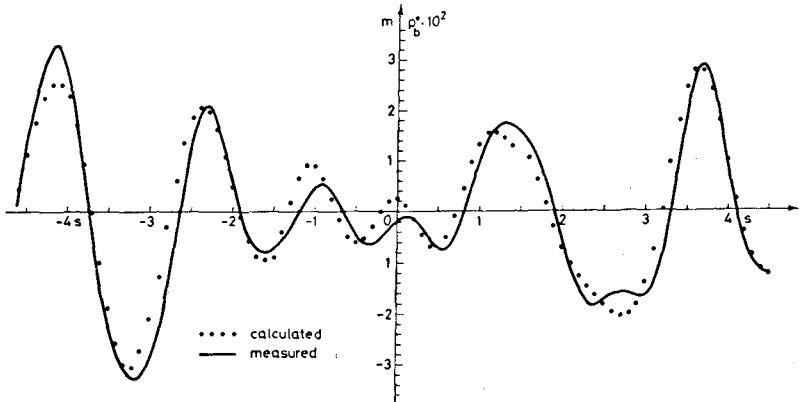


Fig. 4 Calculated and measured bed pressures at $x = 8.98$ m

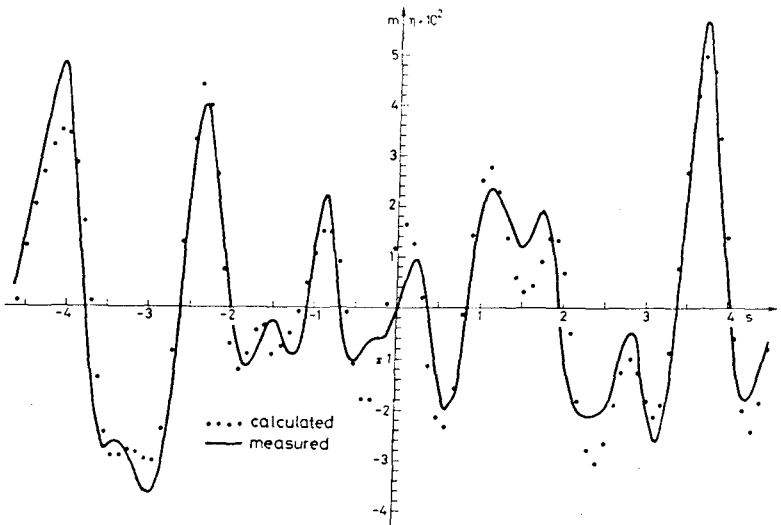


Fig. 5 Calculated and measured elevations at $x = 8.98$ m

Also the elevations along the flume were tested at $x = 4.5$ m and $x = 8.98$ m. Again, the record $\eta(0, \tau)$ was used as input in Eq. (6) which, together with one of the influence functions in Fig. 3 gave $\eta(x, t)$. Fig. 5 shows the elevations for $x = 8.98$ m.

At a given position the agreement between measured and calculated elevations was the same for all tests. It was found, however, that the deviations increased with x , due to nonlinear interactions.

4. DETERMINISTIC REPRODUCTION

For the generation of small, regular waves the exact transfer function was in essence derived in 1929 by Havelock (Ref. 5) and presented to the engineering world in 1951 by Biésel (Ref. 1) in the following form

$$H = \frac{2 \sinh^2 kh}{\sinh kh \cdot \cosh kh + kh} \cdot 2e = \frac{2 \tanh kh}{1 + G} \cdot 2e \tag{9}$$

where $2e$ is the stroke of the piston.

For the generation of waves with a given spectrum Eq. (9) has been directly applied (Refs. 2-3).

For the generation of natural waves in fairly shallow water an approximate transfer function was applied by the senior author (cf. Ref. 4) with the specific purpose of reproducing, in a short flume, shock forces on vertical face breakwaters.

The scope of the deterministic reproduction has been to generate a given natural wave train in arbitrary depth in a flume at a distance x_0 from the piston. This has been achieved by means of Eq. (9) in combination with the theory of deterministic description presented above, x being equal to $-x_0$ for calculation backwards to the paddle.

From the Fourier series of the recorded natural wave train $\eta(x_0, t)$, the amplitude and phase for each frequency is, by means of Eq. (9), transformed into a contribution to the piston position.

Thereafter, the procedure is completely analogous to the one described in Sec. 2, resulting in the following convolution integral for the piston position

$$x_p(t) = \sqrt{g/h} \int_{-\infty}^{+\infty} X(t-\tau, x_0) \eta(x_0, \tau) d\tau \tag{10}$$

where the influence function is

$$X(t-\tau, x_0) = \frac{1}{2\pi} \sqrt{h/g} \int_0^{\infty} \frac{1 + G}{\tanh kh} \sin [(t-\tau) \omega + k x_0] d\omega \tag{11}$$

with $k = k(\omega)$. The X -function is shown in Fig. 6 for $x_0/h = 5.56$ and may be interpreted in a way similar to Fig. 3.

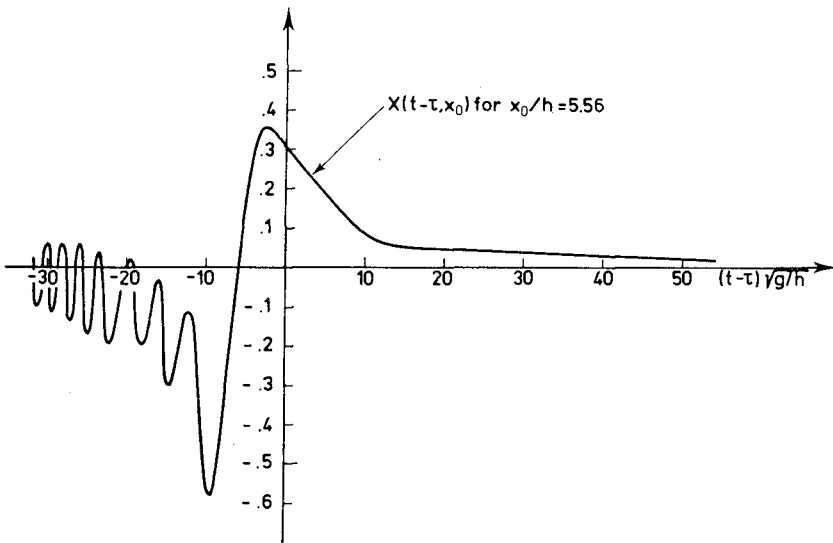


Fig. 6 Dimensionless influence function $X(t-\tau, x_0)$

5. TESTS ON DETERMINISTIC REPRODUCTION

The theory of deterministic reproduction was tested in a flume ($h = 0.36$ m) with a wave gauge mounted $x_0 = 2$ m from the piston. At this position it was attempted to reproduce various wave trains from Hanstholm, Denmark.

In addition, the piston positions were recorded as a feed back signal to be used as the basis for a calculation of expected elevations at point x_0 in the flume. For the latter purpose Eqs. (10) - (11) are easily inverted, yielding the surface elevations with the piston motion as input. As stated by Biéssel (Ref. 1) one must be aware of the local disturbances at the generator. The local oscillations at the piston are, however, already reduced to one percent at a distance of three water depths from the piston.

Hence, the test procedure was:

- (a) calculate the piston positions x_p on the basis of a natural wave record,
- (b) by means of the feed back signal calculate the expected elevations at x_0 .

Fig. 7 illustrates the close agreement between the values $\eta(x_0, t)$ actually reproduced in the flume and the values calculated from the actual piston motion x_p . (The latter deviated slightly from the desired piston motion because of the imperfect control of the hydraulic power system.)

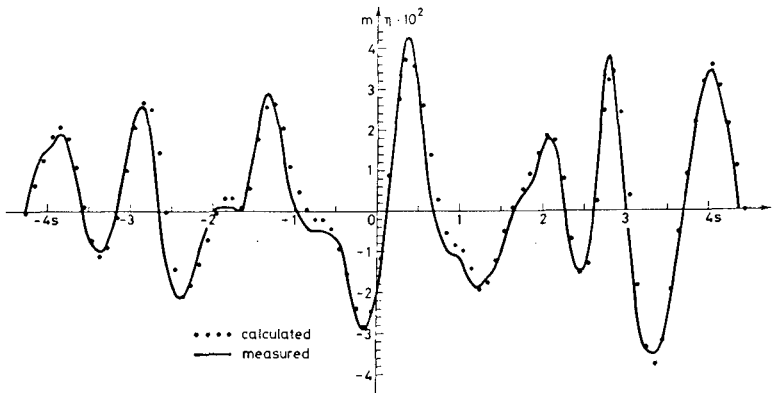


Fig. 7 Calculated and measured elevations at $x_0 = 2$ m

6. FUTURE DEVELOPMENTS

The encouraging results obtained with the linear two-dimensional theory makes it attractive to extend the theory to nonlinear terms and to three dimensions.

References

1. Biésel, F.: Étude théorique d'un certain type d'appareil à houle. *La Houille Blanche*, 6^e Ann., N^o 2, pp. 156-165, Mars-Avril 1951.
2. Fryer, D.K., G. Gilbert and M.J. Wilkie: A wave spectrum synthesizer. *J. Hydr. Res.*, Vol. 11, No. 3, pp. 193-204, 1973.
3. Gilbert, G., D.M. Thompson and A.J. Brewer: Design curves for regular and random wave generators. *J. Hydr. Res.*, Vol. 9, No. 2, pp. 163-196, 1971.
4. Gravesen, H., E. Frederiksen and J. Kirkegaard: Model tests with directly reproduced nature wave trains. 14th Coastal Engrg. Conf., Copenhagen 1974, Vol. I, pp. 372-385, Am. Soc. Civ. Engrs. (1975).
5. Havelock, T.H.: Forced surface-waves on water. *Phil. Mag. and J. of Sci.*, S. 7, Vol. 8, No. 51, pp. 569-576, Oct. 1929.

CHAPTER 17

WAVE LENGTH, WAVE VELOCITY AND SHOALING CHARACTERISTICS OF RANDOM WAVES

Akira Kimura* and Yuichi Iwagaki**

ABSTRACT

Fundamental properties of random waves determined by the zero-up-cross method are discussed. Firstly, the wave length and the wave velocity are treated. Experiments are carried out with some supplemental definitions such as the spatial zero-up-cross method in a laboratory wave tank. Average values of K (= a ratio of measured wave length to theoretical one L_e/L_{th}) and R (= a ratio of measured wave velocity to theoretical one C_e/C_{th}) are very close to unity though data are considerably scattered. But the relations between $L_e \sim T_e$ and $C_e \sim T_e$ are slightly different from the theoretical ones where T_e is the measured wave period. Secondaly, breaking characteristics on sloping beaches are treated. The wave height H_b , the wave length L_b and the water depth h_b are measured at a breaking point. Breaking characteristics of random waves are considerably different from those of periodic waves. The measured wave height-water depth ratio H_b/h_b is plotted against the water depth-wave length ratio h_b/L_0 about 30 ~ 40% below the breaker inception curve for periodic waves.

INTRODUCTION

There are two method of analysis for random sea waves. One is a wave spectrum analysis and the other is an analysis by the wave statistics. The zero-up-cross method is the most general one to treat the wave statistics. It has been considered that the method of wave spectrum analysis is supported by the small amplitude wave theory, but analysis by the zero-up-cross method are convenient to some extent. But recently the authers showed that the spectrum analysis method is not theoretically supported for random waves in a shallow-water region [Iwagaki and Kimura (1977)]. And the spectrum analysis method is not applicable also for discontinuous phenomena such as wave breaking, overtopping and etc. On the other hand, the analysis by the zero-up-cross method seems to be empirically usefull for treating these discontinuous phenomena. But this method does not have analytical bases and very few studies have examined the validity of this method. Then fundamental studies on properties of zero-up-crossing waves are desired to know the effectiveness of this method of analysis

* Research Assistant, ** Professor of Department of Civil Engineering Faculty of Engineering, Kyoto University, Kyoto, Japan

WAVE LENGTH

It is very difficult to measure the random wave length because no apparent scale or level line for measurement is available in the real sea condition. Some times oceanographers measured intervals of successive wave crests on ship sides. This definition of wave length is intuitive and uncertain. Pierson(1954) studied the following theoretical relation between the mean wave length and the mean wave period which are determined by the crest-to-crest method:

$$L_m = K \frac{gT_m^2}{2\pi} \quad (1)$$

and concluded that $K=2/3$ for a uni-directional Neumann spectrum, where g is the acceleration of gravity, L_m and T_m are the mean wave length and the mean wave period of crest-to-crest wave. He assumed that wave length of component waves are equal to those by the small amplitude wave theory. Ewing(1969) studied the theoretical relation between the mean wave length and the mean wave period of crest-to-crest waves for Pierson-Moskowitz spectrum. He introduced directional spectra and concluded that K in Eq.(1) changes from $1/3$ to $3/4$ according to an increase of truncation frequencies in a high frequency region of the power spectrum. But the crest-to-crest method is not natural to determine the wave length, because there are many maxima on the surface of random waves as seen in Fig.1 if the spectrum width is not narrow [Longuet-Higgins(1957)]. The zero-up-cross method seems preferable for a definition of the wave length. In this section, wave lengths determined by the zero-up-cross method are treated.

DEFINITION OF WAVE LENGTH

Generally the wave period is determined from a record measured with a wave gauge at a fixed point. On the other hand, the wave length is usually determined from a photograph. Then it is difficult to treat the wave length and the wave period as properties of the same wave by the difference of definitions, because the random wave profile changes gradually with propagation. Changes of the wave profile is very slight and wave propagation can be easily followed if the distance of propagation is short. Fig.2 shows wave records measured by three wave gauges installed 1m apart in the wave tank. It can be seen that changes of wave records are very small. Then the wave length and wave period of random waves can be determined as those for periodic waves in case when the travelling interval is very short. But as a nature of random waves, wave profiles change gradually. Then following two supplemental definitions are made to determine the wave length and the wave period.

- (1) The wave period is determined from a record measured with the No.2 wave gauge shown in Fig.2 by the zero-up-cross method.
- (2) The wave length is determined from a photograph taken at an instance when the water surface crosses the still water level downward at the No.2 wave gauge.

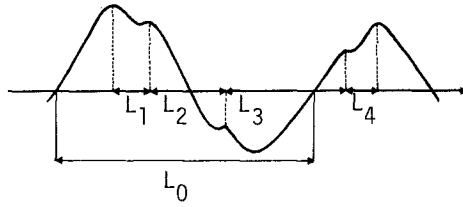


Fig.1 Definition of wave length

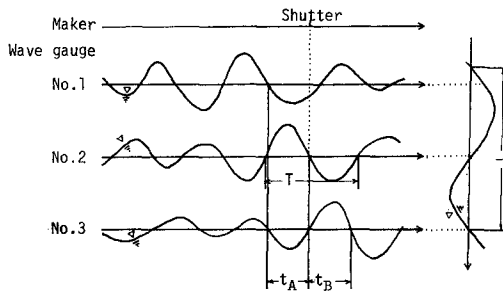


Fig.2 Definition of wave period and wave velocity

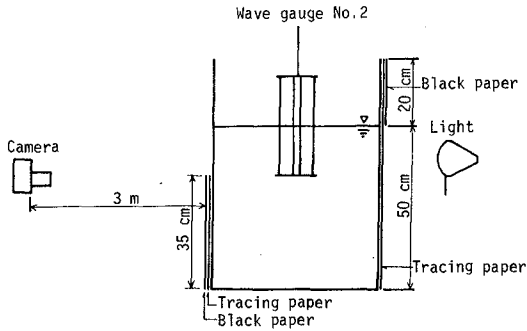


Fig.3 Equipments for photographing

EXPERIMENTS

A random wave generator of electro-hydraulic type is installed at one end of a 27m long, 50cm wide and 75cm deep glass sided wave tank. Measurements were carried out in a 4m long interval apart 12m from the wave generator. On the surface of fore-side glass, a 3mm wide black tape was marked to show a still water level and scale marks were placed with the same black tape. Fig.3 shows illustration of the equipment for photographing. Tracing papers were used to make scattered light. Rest part of the glass was covered with black papers to prevent a camera from direct light of lamps. Random waves were generated with a random wave simulation system [Kimura and Iwagaki(1976)]. Fig.4 shows power spectra of random waves used in this study. A photograph was taken at the instant when the water surface crossed the black tape downward at the No. 2 wave gauge. This instant was automatically marked on a chart of the pen-oscillograph which was connected with a flash terminal socket of the camera. Photo-1 shows an example of the wave profile. Wave lengths were analyzed from these photographs by using a film motion analyzer.

EXPERIMENTAL RESULTS

Typical values of the mean wave height H_m , the mean wave period T_m , the significant wave height $H_{1/3}$ and the significant wave period $T_{1/3}$ are shown in Table 1. f_p is the peak frequency of the power spectrum. Measured wave lengths are plotted in Fig.5 (a) ~ (d). Chain lines in these figures mean the theoretical relation between the wave length and the waveperiod by the small amplitude wave theory. About 250 data are plotted in each figure. Data are considerably scattered but tendencies of data seem in average to agree fairly well with the theoretical curves in every cases. And the value of \bar{K} which makes D minimum in the following equation is very close to unity as shown in Table 1:

$$D = \sum [L_e - \bar{K} L_{th}]^2 \quad (2)$$

in which L_{th} is the theoretical wave length by the small amplitude wave theory under the condition that the water depth is 50cm. Then it is known that the wave length and the wave period satisfy the theoretical relation approximately if the discussion is confined only on the mean value. But it can be seen from these four figures that there are little difference between the mean tendency and the theoretical curve if data are examined carefully in detail. The mean tendency of data has slightly mild inclination compared with the theoretical curve. In fig.6 (a) ~ (d), relations of L_e/L_{th} versus T_e of measured data are plotted in each case. Values of L_e/L_{th} decrease gently with increase of T_e in every figures. Fig.7 shows a results of best fit curves with the 3rd order polynomial expression. The approximated curve in each case has slightly mild inclination compared with the theoretical curve. And it is very interesting that each curve does not coincide but shifts upward as f_p decreases.

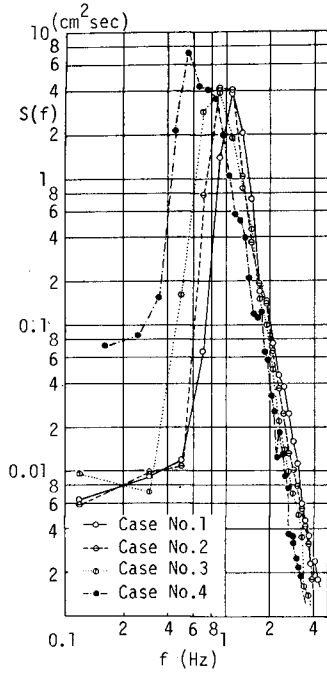


Fig.4 Power spectra of experimental waves



Photo 1 Wave profile of random wave

Table-1 Statistical properties of random waves

Case No.	f_p (Hz)	T_m (sec)	H_m (cm)	$T_{1/3}$ (sec)	$H_{1/3}$ (cm)	\bar{K}	T_c (sec)	\bar{R}
1	1.2	0.88	5.21	0.89	8.15	0.99	0.92	1.02
2	1.0	0.94	5.28	0.99	8.36	0.98	1.21	1.02
3	0.8	1.00	4.98	1.11	7.82	0.95	1.15	1.00
4	0.6	1.30	5.83	1.50	9.04	0.96	1.32	1.02

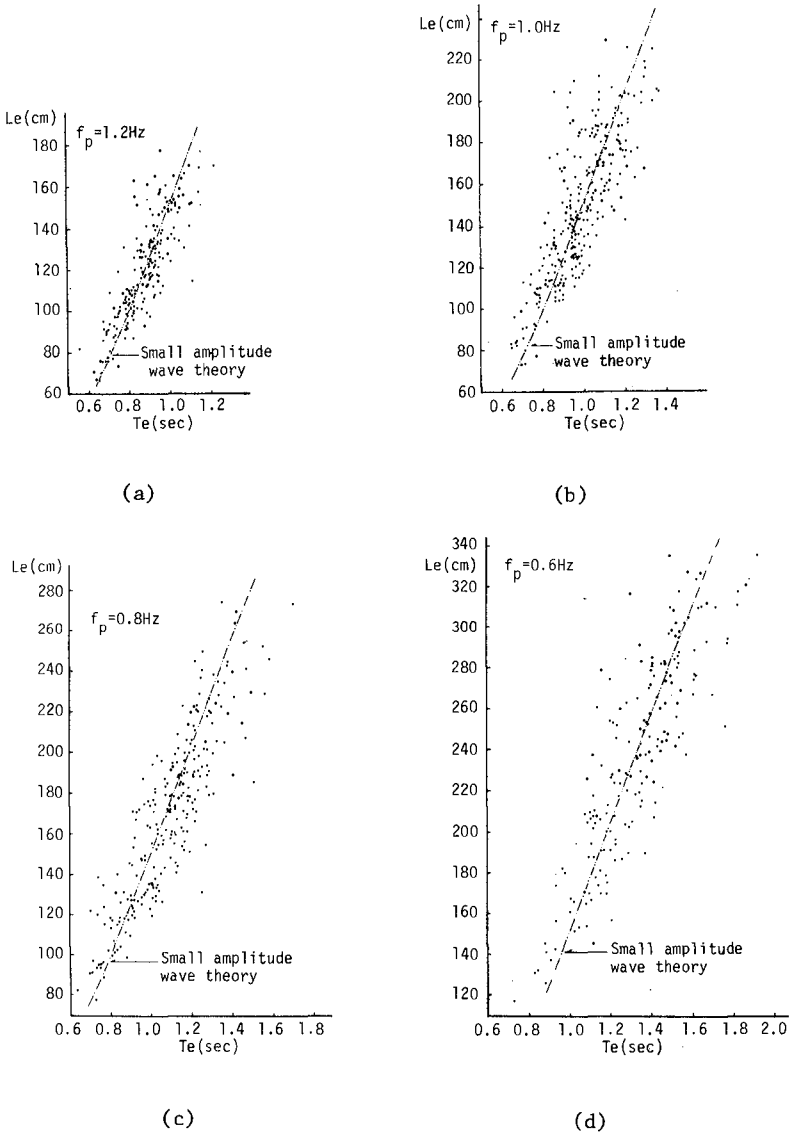
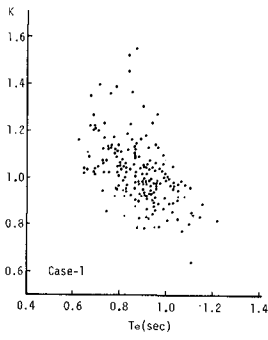
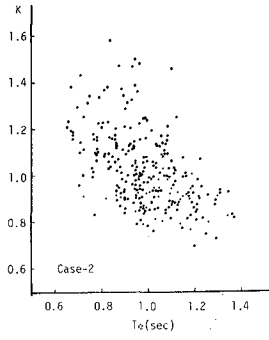


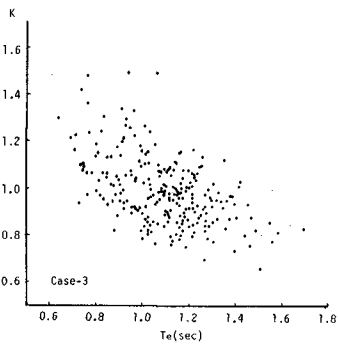
Fig.5 Relations between wave length and wave period for random waves



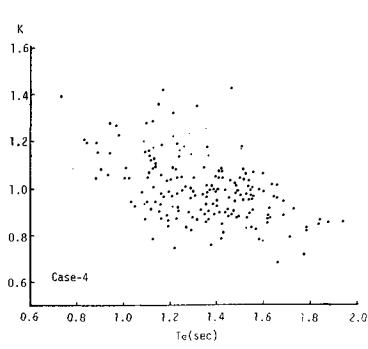
(a)



(b)



(c)



(d)

Fig.6 Relations between $K (= L_e/L_{th})$ and T_e

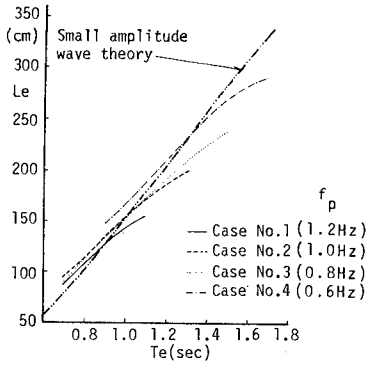


Fig.7 Best fit curves of wave length \sim wave period relations for measured data

Table-2 Water depth at each wave gauge

Case No.	i	h(cm)											
		W-1	W-2	W-3	W-4	W-5	W-6	W-7	W-8	W-9	W-10	W-11	W-12
I	1/10	50	50	40	30	20	10	-	-	-	-	-	-
II	1/20	50	50	50	50	45	40	35	30	25	20	15	10

Table-3 The mean water depth of measured breaking waves

Case No.	i	f_p (Hz)	h_b (cm)
I-1	1/10	0.8	14
I-2	1/10	1.0	12
I-3	1/10	1.2	13
II-1	1/20	0.8	21
II-2	1/20	1.0	21
II-3	1/20	1/2	19

Then the wave length of random waves cannot be determined only by the water depth, but f_p or the mean wave period is needed in addition to them. T_c in Table 1 shows the period of intersection between the best fit curve and the theoretical curve.

WAVE VELOCITY

It has already explained that the profile of a random wave is conserved with very small change if the distance of propagation is very short. Then the wave velocity can also be determined by measuring the time spent for a wave crest or a zero-crossing point to propagate a fixed interval. In this section, the velocity of zero-down-crossing point is determined as the wave velocity C_e . The wave gauge interval from the No.1 wave gauge to the No.3 wave gauge divided by $t_A + t_B$ is determined as the wave velocity in this study, in which t_A and t_B are the times spent for the zero-down-cross point to propagate the wave gauge No.1 to No.2 and No.2 to No.3 respectively. The wave period T_e was determined by the zero-up-cross method with the No.2 wave gauge record as before. Same waves as used to measure the wave length were selected to determine the wave velocities. Experimental data are plotted in Fig.8 (a) ~ (d). Data are considerably scattered, but agree fairly well with theoretical curve shown by the chaine line. And R which makes E in the following equation minimum is very close to unity as shown in Table 1:

$$E = \sum [C_e - \bar{R} C_{th}]^2 \quad (3)$$

where C_{th} is the theoretical wave velocity calculated with the wave period T_e by the small amplitude wave theory. Then if discussions are confined only on the mean value, the relation between the wave velocity and the wave period satisfies approximately the theoretical relation by the small amplitude wave theory. But it can be seen from these figures that many of the data are plotted above the theoretical curve in the region where the wave period is small. Fig.9 shows the best fit curves for the plotted data with the 3rd order polynomial expression. The best fit curve is plotted above the theoretical curve in the region where the wave period is small and gradually approaches to the theoretical curve as T_e increases. It is interesting that each curve does not coincide when T_e is small, but shifts slightly upward with increase of f_p . f_p or the mean wave period is needed in addition to the wave period and the water depth to calculate the wave velocity when T_e is small. But when T_e is greater than $1.1T_m$, the wave velocity can be calculated approximately by the water depth and the wave period.

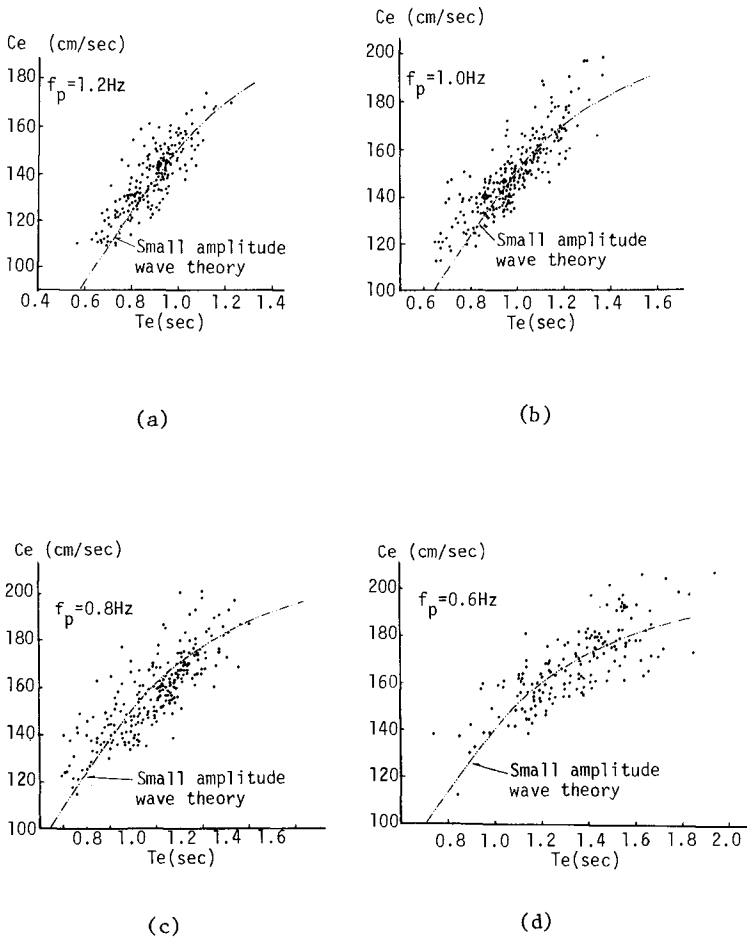


Fig.8 Relations between wave velocity and wave period for random waves

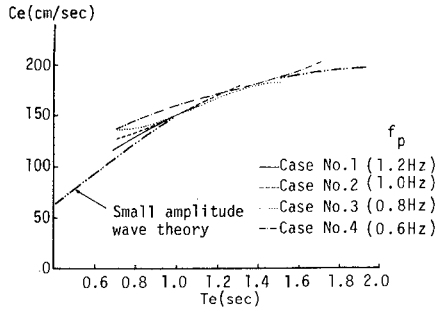


Fig.9 Best fit curves of wave velocity \sim wave period relations for measured data

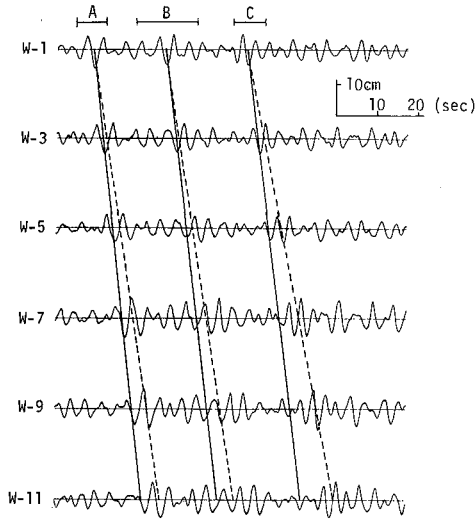


Fig.10 Wave velocity and group velocity over long distance

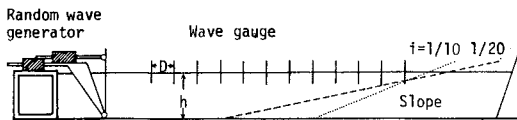


Fig.11 Experimental equipments for wave breaking

The results so far are for the wave velocities which are measured in the short distance. Fig.10 shows the records measured with 6 wave gauges installed 2m apart in the wave tank. It can be seen that wave profiles change gradually with propagation, but clear crests are easily followable. Then mean velocities of random waves over a long distance can be also determined. The solid lines show the theoretical wave velocities which are calculated with the mean periods of the wave groups marked as A,B and C above the W-1 wave gauge record. Each line starts from a clear trough at the middle part of the wave group in the W-1 wave gauge record. The solid lines connect the same wave troughs, then wave velocities over the short distance are very close to the theoretical wave velocities. But each line go over gradually the wave group among propagation. The theoretical wave velocities are a little faster than the velocities of wave groups. Broken lines show the group velocities calculated with the same wave periods as those of the solid lines. These broken lines always pass through middle part of the wave groups. Then over the long distance the wave velocity seems to be equal to the group velocity.

BREAKING CHARACTERISTICS OF RANDOM WAVES

Breaking characteristics of periodic waves have been studied theoretically and experimentally for many years. Many significant results were obtained from these studies. And breaking characteristics of random waves have been treated by Collins(1970), Battjes(1972), Kuo et al(1972), Nath et al(1974) and Goda(1975). They discussed changes of mean and significant wave heights or deformation of probability distribution of the wave height by wave breaking under the assumption that breaking characteristics of the zero-up-crossing waves are equal to those of regular waves. Collins used the breaking criterion by Le Méhauté and Koh.

$$H_b/H_0 = 0.76 \lambda^{1/7} (H_0/L_0)^{-1/4} \quad (4)$$

where H is the wave height, L the wave length and λ the slope of the beach, suffix b means the value at the breaking point and suffix 0 in deep water. Battjes used the following theoretical relation by Miche and Hamada:

$$H_b/L_b = 0.142 \tanh(2\pi h_b/L_b) \quad (5)$$

where h_b is the water depth at the breaking point. Kuo et al recommended the following criterion obtained from field observations:

$$H_b/h_b = 0.63 \quad (6)$$

Nath et al used the following equation proposed by Dean:

$$H_b = 0.278 T_b^2 \quad (\text{m-sec}) \quad (7)$$

Goda used the approximate expression of breaker inception proposed by himself for regular waves:

$$H_b/L_0 = A [1.0 - \exp\{-1.5\pi(h_b/L_0)(1.0 - 1.5\epsilon^{4/3})\}] \quad (8)$$

where $A=0.17$.

But the common problem to these studies is the fundamental assumption that breaking characteristics of zero-up-crossing waves are same as those of regular waves. In this section, breaking characteristics of zero-up-crossing waves on a sloping beach are examined experimentally to make clear the above assumption.

EXPERIMENTS

The same wave tank and the random wave generator were used in the experiments. Sloping beaches of 1/10(Case-I) and 1/20(Case-II) were installed in the wave tank and 6 wave gauges(Case-I) or 12 wave gauges(Case-II) were provided with 1m interval on the slope as shown in Fig.11. The water depth at each wave gauge point is shown in Table 2. Measurements were carried out in the interval of 3m long around the breaking point. The water depth changes from 40cm to 10cm in Case-I and from 25cm to 10cm in Case-II in this interval. Same equipments for photographing are provided as shown in Fig.3. A camera and a 16mm movie camera were set 3m apart from the wave tank. Photographs were analyzed and several properties of breaking waves were determined by the following definitions:

- (1) The wave height H_b and the wave length L_b at the breaking point are determined from the photograph taken at the instance of breaking as shown in Fig.12. But the water depth h_b at the breaking instant is determined from the 16mm movie film.
- (2) The period of breaking wave is determined from a record measured by the nearest offshore wave gauge.

These definitions are different somewhat from those for regular waves, but very close values to those by the usual method were obtained at the preliminary experiments. Fig.13 shows the power spectra used in the experiments of which f_p are (1) 0.8Hz, (2) 1.0Hz and (3) 1.2Hz. Hereafter the case number will be expressed as I-1, which means that the experiment was carried with 1/10 slope and random waves of the peak frequency 0.8Hz.

REPRESENTATION OF EXPERIMENTAL RESULTS

The mean water depth of wave breaking measured in each case is

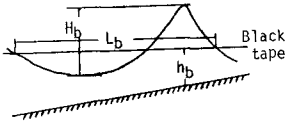


Fig.12 Definition sketch of breaking wave height H_b , wave length L_b and water depth h_b

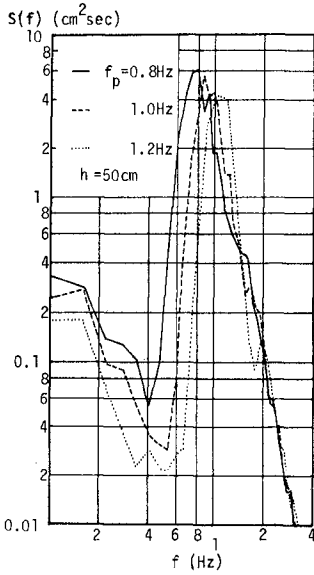


Fig.13 Power spectra of experimental waves for wave breaking and shoaling

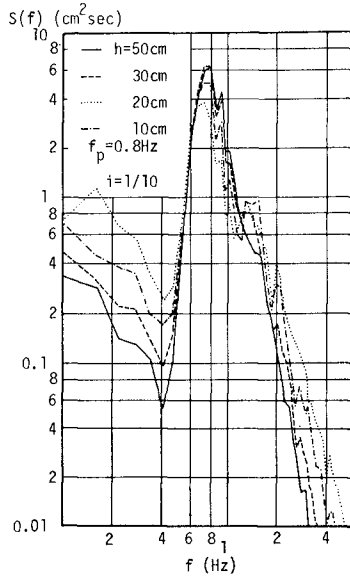


Fig.14 Transformation of power spectrum on 1/10 slope

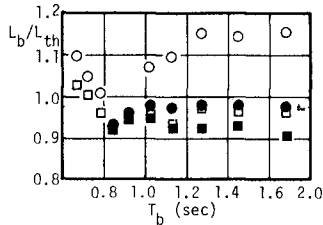


Fig.15 L_b/L_{th} of regular waves

shown in Table-3. There were very few waves which break in the region where $h > 25\text{cm}$ in Case-I. Most of waves break in the region between the water depth of 25cm and 15cm in Case-II. In both cases very small waves and reproduced waves after breaking break generally in the region where the water depth is less than 5cm. These waves in such shallow region were excluded because they seem to be affected by surf beat phenomena. Breaking type of most waves was of plunging breaker. Spilling type breaking was observed sometimes in the region where $h > 30\text{cm}$. Fig.14 shows an example of transformation of the power spectrum. The water depth changes from 50cm to 10cm in this figure. Where the water depth is larger than 30cm there is no apparent change in the shape of power spectrum. But in the region where h is less than 20cm, the energy of power spectrum around the peak frequency decreases and increases in the regions where $f < 0.4\text{Hz}$ and $f > 1.0\text{Hz}$. This means that sudden changes happened on the water surface in this shallow region.

WAVE LENGTH AT BREAKING POINT

Breaking characteristics of regular waves on 1/10 and 1/20 slopes were examined in the experiments. The breaking wave length L_b is compared with the theoretical one L_{th} in Fig.15. White circles show experimental data on 1/10 slope and black circles show those on 1/20 slope. It can be seen in this figure that the ratio of measured wave length to theoretical one L_b/L_{th} on 1/20 slope are very close to unity but the data on 1/10 slope are plotted considerably above unity. This is because the water depth to calculate the theoretical wave length is determined at the crest phase of the wave as shown in Fig.12. White squares (1/10) and black squares (1/20) show the modified values of L_b/L_{th} , where L_{th} is calculated with the water depth at the center of the wave profile. The data are corrected to some extent. Figs.16(a) and (b) show the experimental results of L_b/L_{th} for random waves in Cases I and II respectively. L_{th} in these figures were calculated with the water depth at the wave crest phase. Many data in Case-I are plotted above the line of unity L_b/L_{th} , but in Case-II many data are plotted below this line as seen in Fig.15. And with respect to the mean tendency of plotted data, L_b/L_{th} decreases as T_b increases in both cases and mean line for each case shifts rightward as f_p decreases. Such tendencies have been observed in Fig.5.

BREAKING CHARACTERISTICS OF RANDOM WAVES

Miche and Hamada gave the breaking criterion for periodic waves shown by Eq.(5). Experimental results of regular waves on 1/10 and 1/20 slopes are compared with Eq.(5) which is shown by the solid line in Fig. 17. The data on 1/20 slope are plotted below the theoretical curve, but the data on 1/10 slope agree fairly well with this equation. The relation between H_b/L_b and h_b/L_b for random waves is plotted in Figs.18(a) for

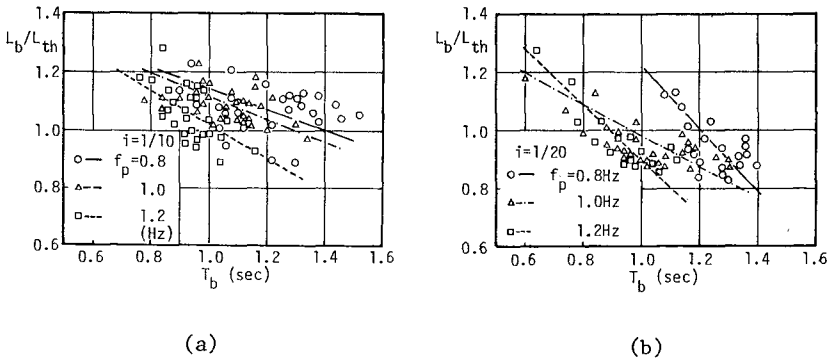


Fig.16 L_b/L_{th} of random waves

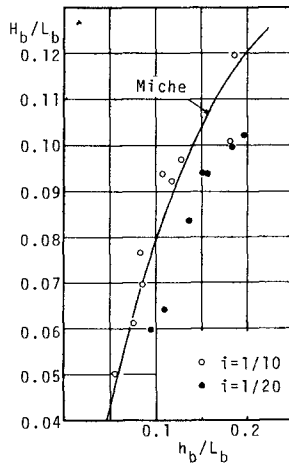


Fig.17 Relations between H_b/L_b and h_b/L_b for regular waves

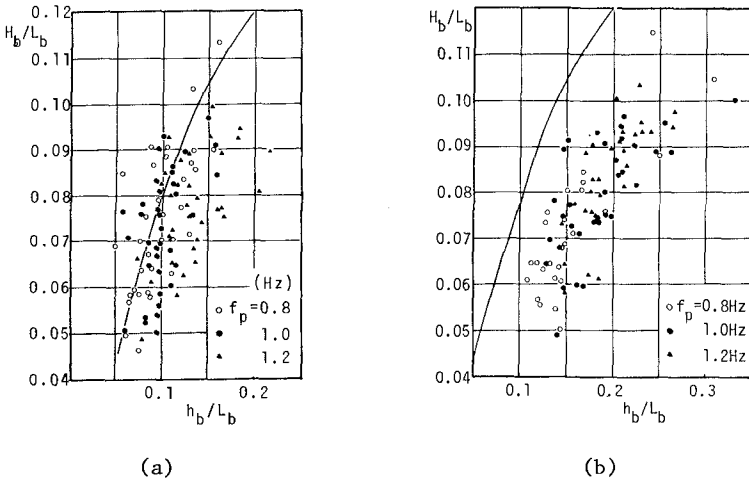


Fig.18 Relations between H_b/L_b and h_b/L_b for random waves

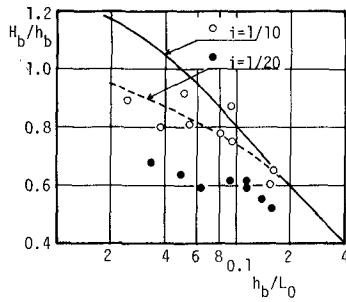


Fig.19 Relations between H_b/h_b and h_b/L_0 for regular waves

1/10 slope, and (b) for 1/20 slope respectively. Mean tendency of data agrees fairly well with the theoretical curve in Case-I, but in Case-II the data are plotted about 30% below the theoretical curve. Then the difference of slope affects largely breaking characteristics of random waves. To estimate the influence of slope, these data are compared with the breaker inception curve by Goda [Eq.(8)]. Firstly, experimental data of regular waves are compared with the breaker inception in Fig.19, in which solid line is for 1/10 slope and the break line is for 1/20 slope. Data are plotted below the lines in both cases. Then experimental results for random waves are plotted in Figs.20(a) and (b). In these figures L_0 is the wave length in deep water calculated with the measured wave period T_b . It is found from both figures that H_b/h_b decreases as h_b/L_0 increases, so that the breaking criterion such that $H_b/h_b = \text{constant}$ for cnoidal waves or solitary wave is not available in this region ($0.03 < h_b/L_b < 0.4$).

Then the effect of slope must be considered for breaking characteristics of random waves as seen in Eq.(8) or Eq.(4). The data are compared with Eq.(8) in Fig.20, in which the data are plotted about 30~40% below the curves in both cases of 1/10 and 1/20 slopes. Then it can be concluded that random wave break easily compared with regular waves. Dotted lines in these figures are modified breaker inception curves with changing A in Eq.(8) from 0.11 to 0.13. It is known that $A=0.12$ for Case-I and $A=0.11$ for Case-II are adequate.

Goda pointed out that changes of the water depth by surf beat affect largely breaking characteristics of random waves. Fig.21 shows the wave records obtained in Case II-1, in which dotted lines express what is called surf beat obtained by cutting off the higher frequency components than 0.35Hz. The mean amplitude decreases as the water depth increases. Apparent surf beat phenomenon cannot be observed at $h=25\text{cm}$. The mean breaking depth of water measured in Case II-1 is 21cm as shown in Table 3, so that the change of water depth by surf beat phenomenon seems to be negligible in this case and also in other cases.

Some other factors will be considered which affect the phenomena of random wave breakings such as unsteady back wash, variation of mean water level due to non-stationary radiation stress and etc. But it is very difficult to estimate the influence of these phenomena because they have not been made clear yet.

CONCLUSION

Fundamental properties of random waves defined by the zero-up-cross method are examined experimentally in a laboratory wave tank, and the following conclusions could be obtained:

The properties such as the wave length and the wave velocity are very close to those of regular waves, but certain properties in wave breaking are considerably different though random waves have their own inherent characteristics. Then it can be finally concluded that the analysis by using the zero-up-cross method is not a conventional method for random waves but an effective method to analyze dynamic properties of random waves. However it is worth mentioning that certain dynamic

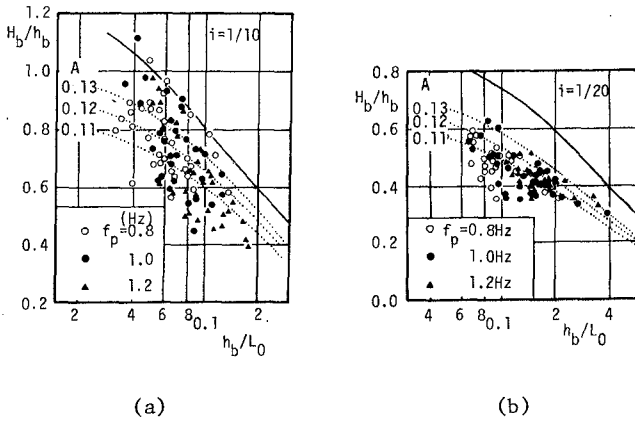


Fig.20 Relations between H_b/h_b and h_b/L_0 for random waves

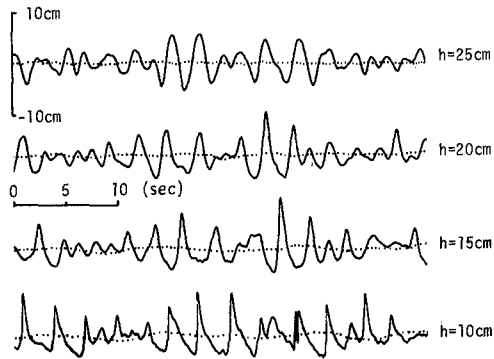


Fig.21 Surf beats at various water depth

properties of zero-up-crossing waves are considerably different from those of regular waves.

ACKNOWLEDGEMENT

The authors wish to acknowledge to Mr. N.Kishida for his assistant throughout the experiments.

REFERENCES

- Battjes, J. A. : Set-up due to irregular waves, Proc. 13th Coast. Engg. Conf., 1972, pp.1993-2004.
- Collins, J. I. : Probabilities of breaking wave characteristics, Proc. 12th Coast. Engg. Conf., 1970, pp.399-414.
- Ewing, J. A. : A note on wave length and period in Confused seas, Jour. of Geoph. Res., Vol.74, No.6, 1969, pp.1406-1408.
- Goda, Y. : Irregular wave deformation in the surf zone, Coastal Engg. in Japan, Vol. XVIII, 1975, pp.13-26.
- Kimura, A. and Y. Iwagaki : Random wave simulation in a laboratory wave tank, Proc. 15th Coast. Engg. Conf., 1976, pp.368-387.
- Longuet-Higgins, M, S. : The statistical analysis of a random, moving surface, Jour. Fluid Mech., Vol.249, A. 966, 1957, pp.321-387.
- Nath, J. H. and F. L. Ramsey : Probability distributions of breaking wave heights, Waves'74, 1974, pp.379-395.
- Kuo, C. T. and S. G. Kuo : The change of the wave height distribution of wind waves by the breakings, Proc. 19th Coast. Engg. in Japan, 1977, pp.137-142. (in Japanese)
- Pierson, W. J. Jr : An interpretation of the observable properties of sea waves in terms of the energy spectrum of the gaussian record, Trans. American Geophysical Union, Vol.35, No.5, 1954, pp.747-757.

CHAPTER 18

PERIODIC THEORY VELOCITY PREDICTION IN RANDOM WAVE

by John H. Nath¹, F. ASCE and Koji Kobune²

Abstract

Large waves in a series of random ocean waves are considered in the design of ocean structures. When random structural vibrations can be ignored, periodic wave theories are used to predict the water particle kinematics for a design wave even though the real wave is irregular. This paper presents the authors' first attempt to quantify the validity of using periodic wave theory for random waves. Measurements of maximum horizontal and vertical velocities were made in laboratory generated periodic and random waves. They compared favorably with predictions from periodic wave theories (even with Airy theory) particularly for the large waves in a series. Since the design wave concept is applied to the largest waves, the conclusion is that periodic wave theory may be adequate, providing an appropriate factor of safety is used to account for the differences between the actual maximum wave kinematics in nature and those in the predictive theory.

1.0 INTRODUCTION

Presented herein is a part of a continuing program of study at Oregon State University to determine the wave kinematics and dynamics in a closed system wave flume with experimentation and theory. Mass transport is also being studied and a first report on that subject is included in (8). For example, it is known that in wave flumes circulation patterns of mass transport must occur, the configurations of which are time dependent. How much these circulations affect the waves, and thus the experiments which depend on them, is not yet known. However, in the region in which measurements were made for this study, it is felt that the influence of circulation within the flume was small. Therefore, it was assumed to be negligible.

1.1 Purpose and Scope

The purpose of the work was to make measurements of water particle kinematics in individual random waves and to compare the results with predictions from periodic wave theory. The scope of the work included measurements of the maximum horizontal velocities under the crests and troughs of periodic and random waves and the vertical velocities at approximately the nodes. These measurements are compared with theoretical predictions and the errors are examined statistically. We estimate that the random waves in the laboratory have characteristics that are close enough to real ocean waves that the results can be applied to design conditions.

At least two methods have been developed to represent random ocean waves for the prediction of wave forces on marine structures. One is the conventional method which uses the design wave concept designated by

¹Professor and Director of Environmental Fluid Dynamics Laboratory, Oregon State University, Corvallis, Oregon 97331, USA.

²Chief, Storm Surge and Tsunami Laboratory, Hydraulic Eng. Division, Port and Harbour Research Institute, Japan.

height (H_D) and period (T_D) and direction. The other utilizes the mean square spectral density of the water surface fluctuation which is herein called the wave spectrum. The latter method is important for the dynamic analysis of marine structures, such as relatively flexible offshore oil facilities. Short, stiff offshore oil facilities and massive structures, such as sea walls and breakwaters, are not very dynamically responsive to the waves and can, therefore, be treated with the design wave approach. The dynamic stability and fatigue characteristics of relatively flexible structures should be examined against the continuous random wave action. However, stiff structures can be designed as if the maximum wave loads are applied in a static manner.

The design wave technique includes considerations for the water depth, h , the wave height, H , and the period, T , which are determined on the basis of a statistical study. Wave records, hindcasting, experience and judgment are utilized. The design wave height is usually a large, rare value, and is sometimes specified as the "one hundred year wave" or something analogous thereto. The design wave should be defined as the largest wave to which the structure is likely to be subjected in its lifetime. On the other hand, the probability distribution of wave magnitudes can be estimated for a site for the lifetime of the structure and the design decision is focused on selecting a probability level beyond which the chances of having a higher wave are very small. The wave size at this probability level then becomes the design wave.

The water kinematics within such a wave are estimated by fitting a periodic wave to the profile and using an appropriate periodic wave theory. However, the design wave in nature will have an irregular profile and the kinematics may be different from those for a periodic wave.

Thus, the purpose of this study can be restated to be to examine the validity of using periodic wave theory for the design wave method, by estimating the error to be expected when a periodic wave theory is used to predict the water kinematics within a particular random wave.

1.2 Literature Review

Because of the difficulty of making Eulerian measurements of water particle velocities, few experimental studies on water kinematics of *random* waves have been reported.

Iwagaki, et. al., (4) measured water particle velocities of random waves utilizing a sonic doppler current meter. They found that Reid's numerical filter (9), i.e. superposition of many sinusoidal component waves, provided a fairly good estimate of the time series of water kinematics for a given time series of water surface elevation. Their velocity measurements showed that the horizontal velocity variation closely followed the water surface elevation, where the maxima and minima appeared at the wave crests and troughs, respectively, even in random waves. The vertical velocity was related to the slope of the water surface, and the peak vertical velocity occurred when the water surface crossed the still water level. The frequency response function for velocities was computed. The measured response functions turned out to be larger than the predicted response function for the high frequency range. They commented that such a difference was partly caused by the noise from the sonic doppler current meter.

Tsuchiya and Yamaguchi (10) measured the velocity of wind generated waves in a recirculation wave tank utilizing the sonic doppler current meter. They also noted the contamination of their record by the noise from the current meter.

The discussion about the water particle velocities of discrete waves in random waves is seen in the study by Grace and Rocheleu (2). They measured the near bottom velocities with a propeller meter beneath the wave crests and troughs of long period waves (from 14 to 20 seconds) simultaneously with the dynamic pressure at Waikiki Shore, Hawaii. For this wave period range and water depth (10.6 m), there was almost a constant ratio of the horizontal velocity beneath a wave crest, u_+ , to the wave height deduced from Airy theory, H_p . The wave heights were defined as the average of the trough to crest height fore and aft the crest. Thus, their definition is different from the zero upcrossing wave height. The residuals between measured and predicted velocities were examined. The distribution turned out to be normal with a mean of -0.18 cm/sec and the standard deviation of 7.25 cm/sec. From the above discussion, they concluded that Airy theory provided an excellent prediction of the velocity beneath the wave crests.

Lee, et. al., (7) recently tested laser doppler anemometers in random wave action and they reported that it was a highly suitable instrument for laboratory study of waves. A full discussion about the kinematics, however, was not given in the paper.

2.0 METHOD

The methods used to meet the objectives are briefly presented, beginning with a condensed review of error sources.

2.1 Errors

In an experimental study of this kind, there are many sources of error between predictions and actual forces experienced by the structure. Some very important sources are:

1. Antiseptic conditions in the laboratory are considerably different than the conditions in the ocean. Wind driven ocean waves can be short crested and generally variable in many respects. The waves in this study were strictly two-dimensional. Wave theories assumed the waves are long crested and it is helpful to have laboratory waves modeling such conditions in order to corroborate the predictions.

2. Experimental errors can be minimized with proper calibration procedures. The natural frequencies of the measurement systems should be much higher than the frequencies of the items being measured. This study increased the reliability of the measurements by using two different instruments, a hot film anemometer and a small propeller meter. In addition, the signal to noise ratio should be on the order of 10:1 for precise measurements.

3. Innate errors in the wave theories contribute to overall errors. Since perfect measurements are not possible, it can only be said that results from the laboratory reflect the differences between theory and measurements as determined within the accuracy limits of the measurements. Often errors in theory are increased because theories are used in regions between the wave trough and wave crest even though boundary conditions

are established at the still water surface. It is not possible to find absolute errors in such cases.

4. Reflections from the beach can modify results, particularly for random waves. In order to get representative samples of waves, long periods of time are used. For this study the wave absorber was a concrete beach with a 1:12 slope which fairly well dissipated the wave energy. From previous experience, reflection coefficients range from 3% to 12% for wave periods of 1 to 5 secs. In addition, for long periods of testing, certain mass transport circulations must be established in the flume as previously mentioned. Such mass transport circulations cannot be adequately evaluated at this time.

2.2 Wave Theories

Three wave theories are employed to predict the maximum and minimum velocities -- Airy theory, which is simple and widely used for design of marine facilities; Stokes' fifth order theory; and Dean's Stream Function theory. Dean (1) showed that Stokes' fifth order theory is accurate for deep and near deep water wave conditions, and that Dean's Stream Function theory covers deep, intermediate and near shallow water wave conditions. The comparison was based on how well the theory predicted the kinematic and dynamic free surface boundary conditions. Mostly, deep water waves were tested for this work and there is no real difference between the predictions from Stokes' fifth order theory and those from Dean's Stream Function theory.

2.3 Laboratory Arrangement and Procedures

2.3.1 Facilities and instruments

The experiments were conducted in the Wave Research Facility at Oregon State University which is shown in Fig. 1. The wave tank is 104 m long, 3.7 m wide and 4.6 m deep. The wave absorber is a concrete beach with a slope of one on twelve. The wave generator has a flap-type wave board. The wave board is driven by a hydraulic piston which is controlled by an electric input, which can be either a sinusoidal or random signal. Additional information can be found in (3,8).



Fig. 1 Elevated View of OSU Wave Research Facility

The water surface elevation was measured with a Sonic System Model 86 sonic wave profiler. The velocities were measured with a Nover Nixon Streamflo Probe 403 propeller current meter and a Thermo Systems, Inc. (TSI) 1240-60W X-type cylindrical hot film anemometer, which are shown in Figs. 2 and 3.

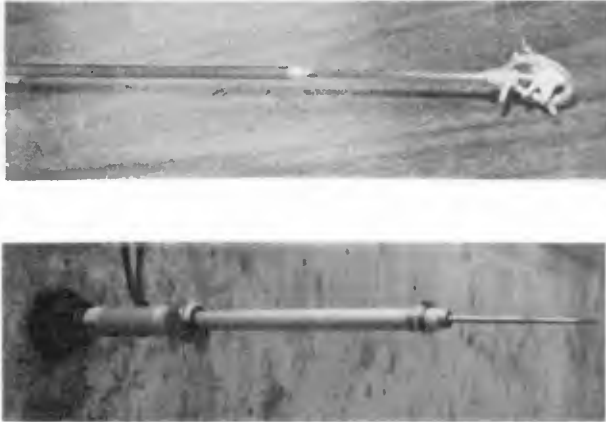


Fig. 3 Hot Film Anemometer Probe

The hot film probe was coupled with TSI model 1050 constant temperature anemometer and model 1052 linearizers. These probes were installed on the side walls of the wave tank as shown in Fig. 4.

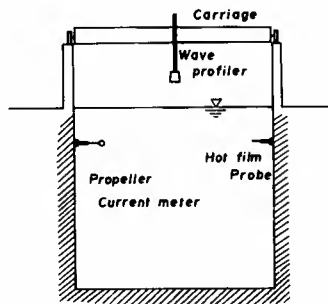


Fig. 4 Probe Set-up Looking North

The propeller probe has a diameter of 1.2 cm and is composed of five blades. When the propeller revolves, the passage of a blade past a gold wire tip, contained in the head of the slim support of the propeller, generates an electric pulse. The hot film probe has an orthogonal pair of quartz coated cylindrical hot film sensors with diameter of 0.15 mm and sensing length of 2.0 mm. The sensors were operated at a low overheating ratio of 1.03 throughout the measurements, in order to avoid the generation of air bubbles on the sensor surface, which reduces the sensitivity. It was oriented in the waves as shown in Fig. 5.

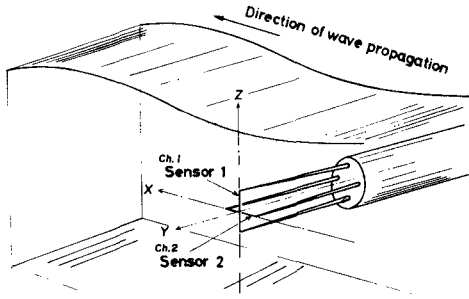


Fig. 5 Hot Film Anemometer Orientation

The hot film output voltage was linearized with a device which approximates the relation between the nonlinear output voltage, E_B , and the flow speed, V , by a fourth order polynomial. Thus, the relation of the linearized output voltage, E , to the flow speed, V , is expressed by the following equation:

$$E = A(\theta) V \quad (1)$$

where $A(\theta)$ is the directional function for the linearized output voltage, which is determined through calibration; and it takes a maximum when the yaw angle θ is zero, i.e., when the flow direction is perpendicular to the sensor axis and decreases according to the increase of θ , up to 90° . As shown in Fig. 5, Sensor 1 was most sensitive to the horizontal velocity component, while Sensor 2 was most sensitive to the vertical velocity component. For data reduction, the maximum value in the time variation of the linearized output was processed using the calibration coefficient $A(0)$.

2.3.2 Calibration procedure

Calibration procedures are described in detail in (6) and reviewed briefly here. The primary calibration was conducted by swinging each probe in still water at the bottom of a long pendulum, which generated a damped free oscillation. Figure 6 illustrates the pendulum and Fig. 7 shows a typical output from the propeller meter. The hot film output was equally accurate, but continuous. The pendulum motion was monitored with a sonic sensor turned sideways and beamed to the reflector shown in Fig. 6. The range of the period of the pendulum motion was set from two to three seconds. The significant wave periods of the test random waves fall into this range.

The number of impulses per second from the propeller meter was calibrated from the pendulum motion for what is herein termed the low speed range. For speeds greater than about 9 cm/sec. the calibration curve fell on a straight line as shown in Fig. 8, where V_{max} is taken from the maxima of the pendulum velocities. It was also calibrated from a hand oscillated carriage, the motion of which was carefully monitored with the sonic sensor. The results are shown in Fig. 9 with the best fit straight line from Fig. 8 superimposed. The effects from non-alignment of the axis with the water flow direction was also examined

and found to be appreciable (6). Thus, only the horizontal wave velocities at the crests and troughs were considered with the propeller meter, as well as vertical velocities at the zero crossings.

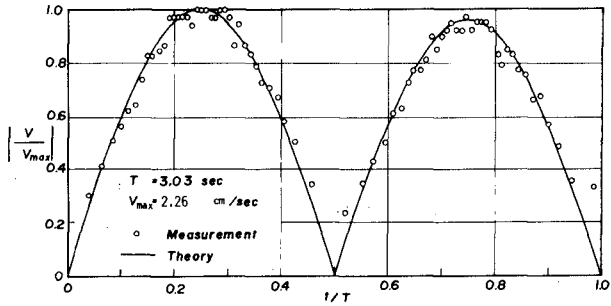
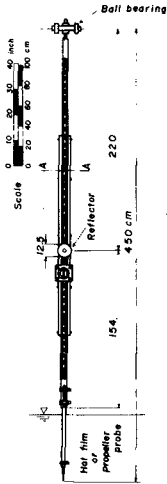


Fig. 7 Response of Propeller Current Meter

Fig. 6 Pendulum Calibration for Hot Film Anemometer

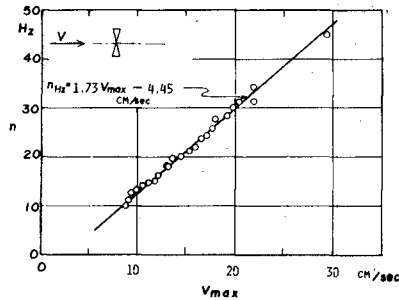


Fig. 8 Calibration of Propeller Current Meter for Low Speed Range

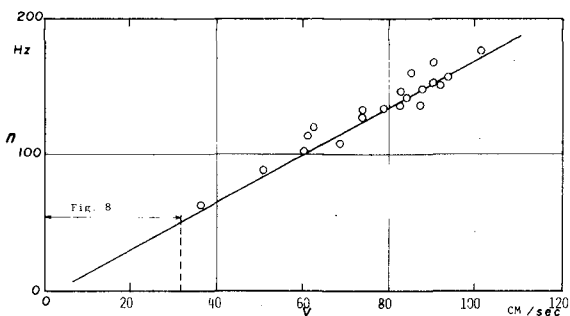


Fig. 9 Calibration of Propeller Current Meter for High Speed Range

The sensitivity of the hot film sensor is easily affected by dirt and fluid temperature. Therefore, the hot film anemometer was calibrated at the beginning and the end of each series of runs. In the case that these two calibrations were different, but not too different, the first half of the run was processed using the result of the calibration at the beginning, while the latter half was processed using the result at the end. A calibration example is shown in Fig. 10 where the plotted gage readings are for the velocity maxima, as with the propeller gage.

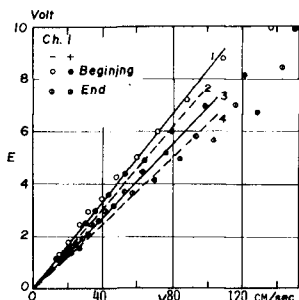


Fig. 10 Calibration for Periodic Wave Tests (Series I)

2.4 Test Schedule

Testing was first performed on periodic waves in order to compare laboratory measurement with the theories that are felt to be most applicable. Measurements were made simultaneously with the propeller meter and the hot film anemometer in order to also compare results between these two measurement methods. The test schedule was then organized into the topics of instrument calibration, comparison between instruments, comparison between measurements and periodic wave mathematical predictions, and comparisons between measurements in random waves and predictions from periodic wave theory. The tests were intended to sample a wide range of wave height and period as indicated in Table 1. Some measurements were made by Jensen (5) using the propeller meter only. These measurements concentrated in the area between the wave trough and the wave crest.

Table 1 Wave Conditions for Periodic Waves Tested

Wave height H (cm)	Wave period T (sec)	Ursell number U	Index in ref. (1)	Probe Position z (cm)		
				Series I	Series II	Series III
110.0	2.50	1.89		-122.0	-61.0	-30.5
83.5	2.50	0.72		--	--	-30.5
38.4	2.50	0.65		-122.0	-61.0	--
82.6	2.07	0.78	8-C	-122.0	-61.0	-30.5
28.7	2.07	0.18	8-A	-122.0	-61.0	--
40.5	1.47	0.10	9-C	-122.0	-61.0	--
14.3	1.47	0.024	9-A	-122.0	-61.0	--
61.3	4.61	5.4	6-A	-122.0	-61.0	--
52.4	3.28	1.72	7-A	-122.0	-61.0	--
104.9	3.28	4.02	7-B	-122.0	-61.0	--

*Note Series I and II were repeated twice for two propeller orientations: horizontal and vertical. In Series III, hot film only was operated. Another series was tested by Jensen with the propeller meter at several vertical positions between the wave trough and crest.

Two wave spectra were used for the random wave tests, wherein the water velocity measurements were made primarily with the hot film anemometer. The spectra are shown in Figs. 11 and 12.

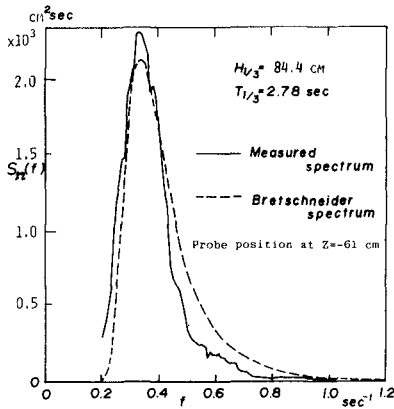


Fig. 11 Experimental Wave Spectrum I

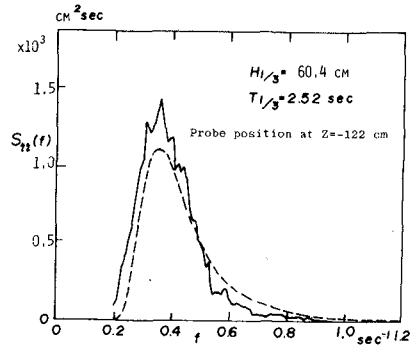


Fig. 12 Experimental Wave Spectrum II

On the figures the random wave parameters were obtained from the direct reduction of zero upcrossing wave heights and periods. The wave trains were approximately 160 secs. long and they contained approximately 60 zero upcrossing waves each. The range of parameters for the individual waves in spectrum I are shown in Fig. 13. The periodic wave conditions are shown with triangles on Fig. 13 and the random waves are solid dots. Figure 14 gives the parametric variations for spectrum II.

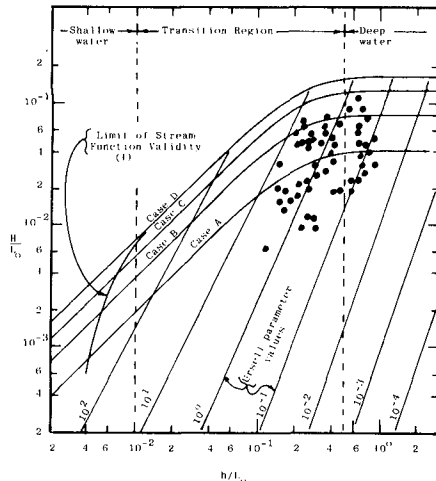
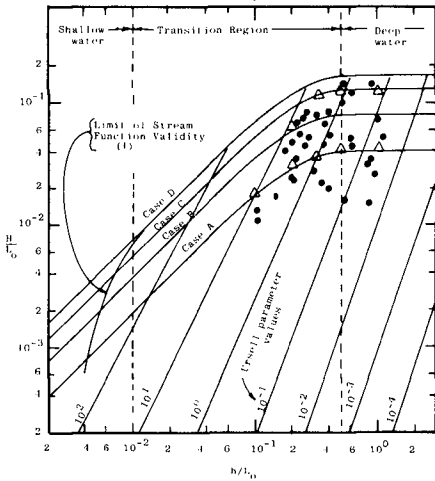


Fig. 13 Range of Periodic Waves, Δ , Individual Random waves, \bullet , for Spectrum I.

Fig. 14 Range of Individual Random Waves for Spectrum II.

2.5 Data Analysis

The accuracies of all experimental studies are particularly dependent on the care taken and the methods used to analyze the data. The intent of this section is to explain the methods used herein and to point out problem features.

The hot film anemometer turned out to be a versatile and excellent instrument for this study. However, we did not realize until after the study that the entire velocity vector, as a function of time, at a point, can be measured with it as reviewed in (12) and clarified in (6). It is suggested that for future experimental studies dealing with wave theory verification that the entire vector be thus determined. However, wake problems are still bothersome wherein one sensor can shield the other, or the mounting itself might shield both sensors, as seems to have been the case in (12) for some flow directions. Anyway, the maximum horizontal and vertical velocities are very important in design and they are featured in this study.

The propeller meter output is sometimes difficult to read if the impulses are too close. The recording media must be run at sufficient

speed for adequate resolution. As previously stated, the propeller meter is very sensitive to flow direction and for this study only, the data were utilized where it was felt the flow direction was parallel with the propeller axis.

2.5.1 Periodic waves

A sample record for periodic waves is shown in Fig. 15, which is a photocopy of the actual visicorder recording. The record shows, from the top, water surface elevation, nonlinear outputs from Sensors 1 and 2, linearized outputs from Sensors 1 and 2, and the output from the propeller, the orientation of which is horizontal for this record.

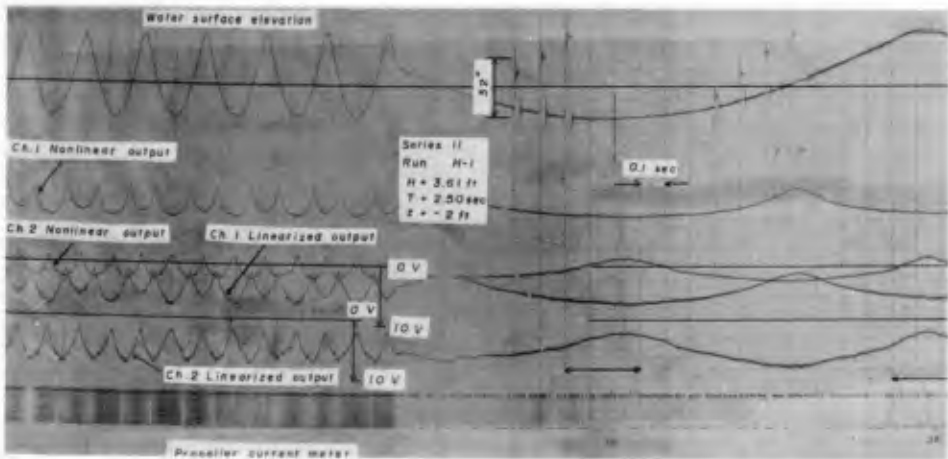


Fig. 15 Sample Record of Periodic Wave

It is seen that the pulses from the propeller are dense at a wave crest and trough. The maximum frequency, n , of the pulses was determined as the mean frequency over a period of from 0.3 to 0.2 seconds under the wave crests and troughs. The maximum velocities were reduced with the conversion relation given on Fig. 8. The linearized output from Sensor 1 shows maxima at wave crests and troughs, while that from Sensor 2 shows minima. In the same way, the output from Sensor 2 shows maxima at wave nodes approximately, while that from the other sensor shows minima. Thus, variations of the output from Sensors 1 and 2 correspond to those of the magnitude of the theoretical horizontal and vertical velocity component, respectively. However, it should be noted that the minimum voltage is not zero, while wave theories predict that the minimum magnitude of each velocity component is zero. This is caused by the effect of the parallel velocity component. Each cylindrical film sensor output voltage is due to both the normal and transverse velocity components with respect to the sensor axis. When the normal velocity component is a minimum there can still be a sizable parallel component that will create a voltage reading. From the records, the following maximum velocities were reduced from the maximum output voltage using the corresponding calibration curves for each sensor.

- u_+ : the horizontal velocity beneath a wave crest
 u_- : the horizontal velocity beneath a wave trough
 w_+ : the vertical velocity when the water surface crosses the still water level upward
 w_- : the vertical velocity when the water surface crosses the still water level downward

2.5.2 Random waves

A typical record for the random wave tests is shown in Fig. 16. Generally, the maxima of the output voltage from Sensor 1 appear beneath the wave crests and troughs where the output from Sensor 2 shows its minima. The maxima of Sensor 2 appear at the wave nodes while the output from Sensor 1 shows the minima. These aspects are clearly seen for large waves and have the same general characteristics as observed in the periodic wave tests. Hence, the maximum values of horizontal and vertical velocity components in a random wave train were processed in the same way that was used for the periodic wave tests.

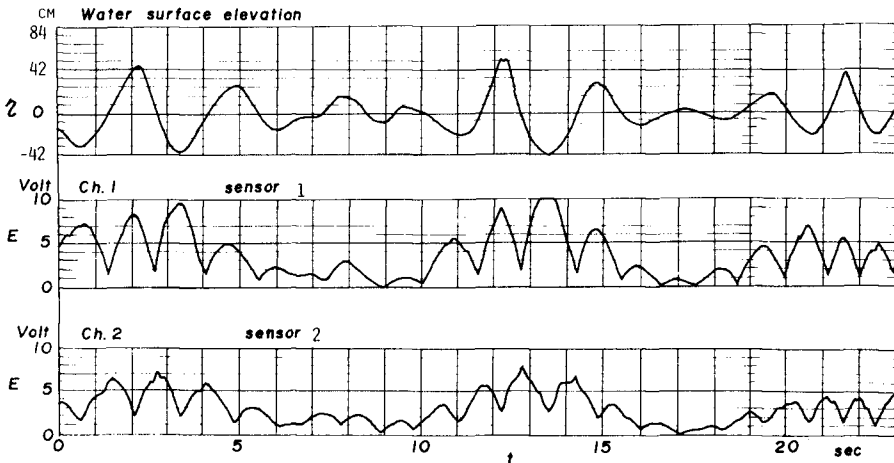


Fig. 16 Sample Record of Random Wave Test (Spectrum II, $Z = -61$ cm)

3.0 RESULTS

This section will first compare the results from the hot film anemometer to those from the propeller meter. Periodic wave theory predictions will then be compared to measurements in periodic waves, followed by measurements in random waves.

The measurements made with the hot film anemometer compared very favorably with the propeller meter. Correlation curves were obtained and the coefficients calculated for various wave conditions. The results are displayed in Table 2.

Table 2 Correlation Coefficients between propeller meter and hot film anemometer for various conditions

Wave Type	Probe Position (cm)	Velocity Measured	Correlation Coefficient
Periodic	-61	$u_{+,-}$	0.993
"	-61	$w_{+,-}$	0.974
"	-122	$u_{+,-}$	0.991
"	-122	$w_{+,-}$	0.947
Spectrum I	-61	$u_{+,-}$	0.983
"	-61	$w_{+,-}$	0.976
Spectrum II	-61	$u_{+,-}$	0.952
"	-61	$w_{+,-}$	0.970

For comparing predictions vs. measurements for velocities, the error is defined as

$$r = \frac{(u)_{\text{measured}} - (u)_{\text{predicted}}}{(u)_{\text{predicted}}} \quad (2)$$

where u stands for $u_{+,-}$ or $w_{+,-}$.

In order to compare linear theory to measurements of fairly high finite amplitude waves, it is necessary to use a fictitious water depth so that the wave crests and troughs for linear theory will occur at the same elevations as the measurements. This condition is shown in Fig. 17. An example of a few measurements vs. theory, for an intermediate water depth wave, is shown in the usually accepted way in Fig. 18. All of the errors for the periodic wave tests were calculated according to Eq. 2 for each of the theories and they are summarized in Table 3. Wave steepness A, B and C refer to the Dean classification with $H_A = 1/4 H_b$ and $H_c = 3/4 H_b$, etc.

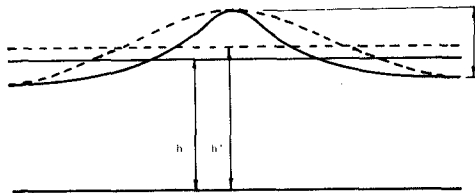


Fig. 17 Finite Amplitude vs. Airy Wave

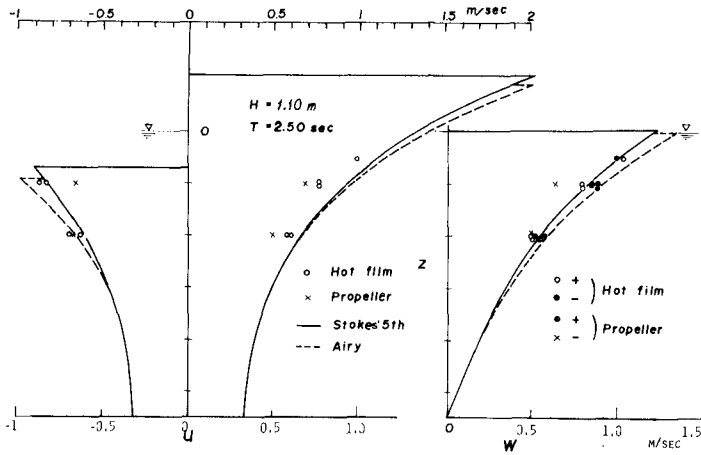


Fig. 18 Comparison with Theory (run 1)

Table 3 Error Mean and Standard Deviation for Periodic Waves

Item	Elevation	Wave Steepness	Theory	u_+	u_-	w_+	w_-
Mean	Above Trough	A	Dean's ψ	-.094			
			Airy	-.075			
		B	Dean's ψ	-.040			
			Airy	-.040			
	C	Dean's ψ	-.072				
		Airy	-.077				
	ALL	Dean's ψ	-.061				
Airy		-.063					
-61 cm		Stokes 5th	-.043	+.196	+.056	-.031	
		Airy	-.040	+.112	+.016	-.070	
-122 cm		Stokes 5th	-.032	+.110	-.101	-.071	
		Airy	-.025	+.059	-.126	-.098	
Standard Deviation	Above Trough	A	Dean's ψ	.097			
			Airy	.106			
		B	Dean's ψ	.083			
			Airy	.071			
	C	Dean's ψ	.063				
		Airy	.069				
	ALL	Dean's ψ	.084				
Airy		.079					
-61 cm		Stokes 5th	.106	.089	.115	.111	
		Airy	.116	.120	.117	.095	
-122 cm		Stokes 5th	.201	.123	.211	.122	
		Airy	.209	.133	.213	.110	

The means of the relative error show that the horizontal velocity beneath the wave crests are three to four percent smaller and those beneath the wave troughs are 10 to 20 percent larger than those predicted from the theories. On the other hand, the measured vertical velocities, in general, are smaller than the theoretical predictions for both w_+ and w_- . The standard deviations vary from 0.1 to 0.2 at the level of -122 cm and they are about 0.1 at the level of -61 cm. According to the mean and standard deviations listed, there was no significant difference for the wave theory used; higher order wave theories or Airy theory. Hence, for the convenience of the remainder of the computation herein, Airy theory is used to predict the velocities of each discrete wave in a random wave train. This conclusion was also reached in (4).

The results from measurements vs. predictions for the two random waves were quite encouraging for the continued use of the Airy theory, even above the wave troughs. For both spectra tested, the individual zero upcrossing wave height distributions were closely approximated by the Rayleigh distribution as shown in Fig. 19. In addition, the maximum horizontal velocities under the wave crests were closely approximated by the Rayleigh distribution as shown in Fig. 20.

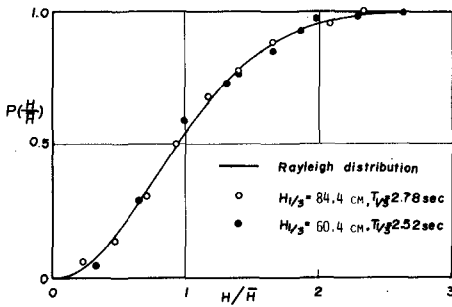


Fig. 19 Random Wave Height Distribution

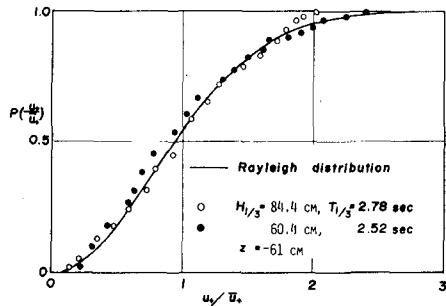


Fig. 20 Probability Distribution of Horizontal Velocities Beneath the Wave Crests.

The comparison between Airy theory and measurements for the horizontal velocities is shown in Fig. 21 for the vertical velocities, for $z = -61 \text{ cm}$. The scatter appears to be reasonable and was treated statistically as will be explained. For vertical velocities, the correlation was 0.934 for w_- and 0.638 for w_+ , with the plots looking much like Fig. 21.

Samples of how the errors were plotted on normal probability paper are shown in Figs. 22 and 23. The figures show that as the sample size is reduced by focusing on the smaller number of larger waves (i.e. $H_{1/10}$ vs. $H_{1/3}$) the standard deviation of the errors is reduced! This means that the factor of safety can be made smaller for calculating the kinematics for the larger waves, as will be shown. The total sample sizes were from 60 to 70 waves.

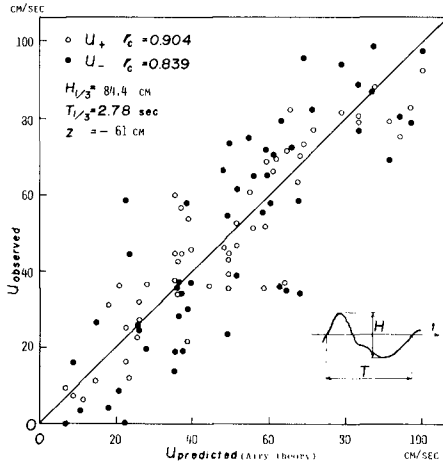


Fig. 21 Comparison Between Predicted and Observed Horizontal Velocities for Random Waves

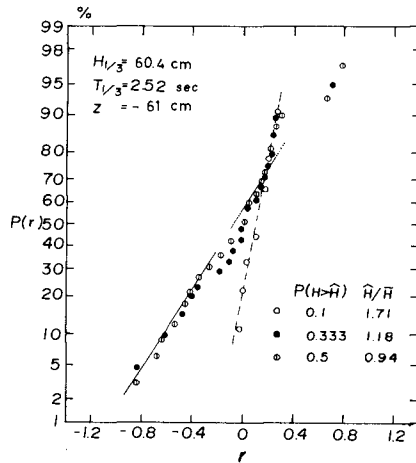
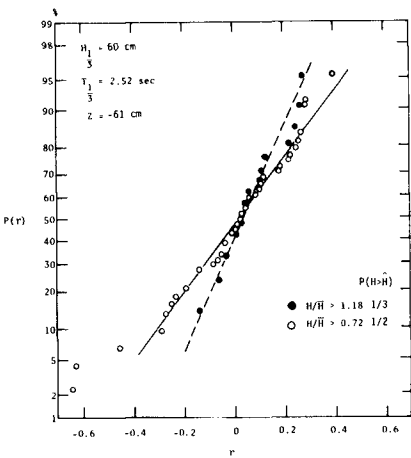


Fig. 22 Probability Distribution of Relative Errors for Horizontal Velocities Under Wave Crests

Fig. 23 Probability Distribution of Relative Errors for Vertical Velocities

The normal distribution hypothesis was checked with the chi square test and it was found that almost all populations passed the test at a significance level of 95%. The populations of $H_{1/10}$ were not checked because they were quite small. In this manner, the mean and standard deviations of the errors between the measurements and Airy theory were compared for various fractions of the wave height populations for sensor position below the wave troughs. The results are shown in Table 4. It is seen that the standard deviations of the errors clearly reduced markedly as the height of the samples were restricted to ever increasing wave heights. The data between wave troughs and crests were treated similarly, with similar trends resulting. However, the means were closer to zero and the standard deviations were even smaller, as reviewed in the next section.

Table 4 Errors as Functions of Wave Height Fraction

Spectrum	Sensor Position (Z)	Wave Height Fraction $P(H > \hat{H})$	error mean (r)				error standard deviation (σ_r)			
			u_+	u_-	w_+	w_-	u_+	u_-	w_+	w_-
I	-61 cm	.10	-.05	-.01	-.17	.06	.09	.14	.33	.11
		.33	.00	.04	-.02	.04	.15	.23	.36	.12
		.50	-.03	.03	.04	-.01	.22	.29	.39	.18
		.67	.00	.03	.08	-.01	.26	.29	.48	.17
		.90	.02	.04	.09	-.02	.34	.45	.53	.17
	-122 cm	.10	-.17	.08	-.24	-.10	.09	.12	.28	.09
		.33	-.17	.07	-.06	-.10	.26	.37	.32	.09
		.50	-.09	.13	-.05	-.13	.28	.38	.39	.16
		.67	-.06	.11	.02	-.06	.33	.39	.46	.16
		.90	-.04	.12	.09	-.07	.46	.51	.65	.20
II	-61 cm	.10	.10	-.03	.01	-.09	.14	.19	.31	.17
		.33	.06	.04	.00	-.08	.13	.30	.42	.17
		.50	.01	.08	-.03	-.09	.21	.37	.41	.17
		.67	.05	.15	-.01	-.03	.34	.51	.49	.33
		.90	.07	.16	.06	-.04	.37	.55	.51	.33
	-122 cm	.10	-.04	.01	-.02	-.20	.09	.22	.14	.11
		.33	-.03	.05	.08	-.13	.15	.29	.36	.12
		.50	-.07	.16	-.15	-.15	.19	.31	.34	.21
		.67	-.03	.17	-.09	-.14	.36	.53	.39	.18
		.90	-.01	.22	-.06	-.18	.43	.70	.48	.29

4.0 DISCUSSION

The comparisons between the measurements made with the hot film anemometer and the propeller meter were very good. From this it can be concluded that the laboratory and experimental techniques concerning the instruments were excellent. Experimentation in periodic waves showed fairly good agreement between measurements and periodic wave theory. This was done in order to compare with the work of others and as another

step in verifying the laboratory method for measuring wave velocities. Since the agreement between measurements and predictions was quite good it is felt that the measurements then made within random waves would be quite reliable.

The laboratory data indicate that the large random waves have the smaller standard deviations of errors between theoretical predictions and measurements. In addition, the variation of the means and the standard deviations are about the same whether one utilizes finite amplitude wave theories or the Airy wave theory. The hot film anemometer is reliable and relatively handy to use *providing* proper calibration techniques are utilized. There is still a wake problem which can be minimized with the proper orientation of the hot film anemometer.

Thus, according to the measurements made for this study, it is reasonable to use periodic wave theory to predict the particle kinematics in large waves, given that a complete dynamic analysis of the structure is not necessary. Thus, the designer may be interested in predicting *maximum* values (e.g. maximum horizontal velocity) *given* the design wave. The errors in this work were distributed normally so that two standard deviations added to the mean will include 97.7% of the population and three standard deviations will include 99.9%. Considering the errors between laboratory random waves and actual storm waves, it would seem to be prudent to use the 3σ level.

Now consider Eq. 2 for error definition and let r_{u+} be the error under the crest for the maximum horizontal velocity. In the field, the actual maximum horizontal velocity under the crest for the *design* wave (given that it occurs) will also be in error with design predictions. Let this occurrence be designated as

$$\epsilon_{u+} = \frac{u_a - u_p}{u_p} \quad (3)$$

where u_a is the actual maximum horizontal velocity. Now, let $u_a = u_d$, the design value for the maximum horizontal velocity, and solve for it from Eq. 2

$$u_d = u_p (1 + \epsilon_{u+}) \quad \text{or} \quad (4)$$

$$u_d = u_p \cdot FS \quad (5)$$

where u_p , again, is the value predicted from Airy theory and FS is the factor of safety. The error value must now be estimated. We propose

$$\epsilon_{u+} = \overline{r_{u+}} + 3\sigma \quad (6)$$

where the overbar indicates the average value, and the values of FS determined therefrom are displayed in Fig. 24. The factors of safety for the spectrum conditions were calculated for the $H_{1/10}$ conditions.

Since the larger waves in the random series have the smallest standard deviation for the errors and a relatively small variation in the means, it is concluded that it is reasonable to use periodic theory (in

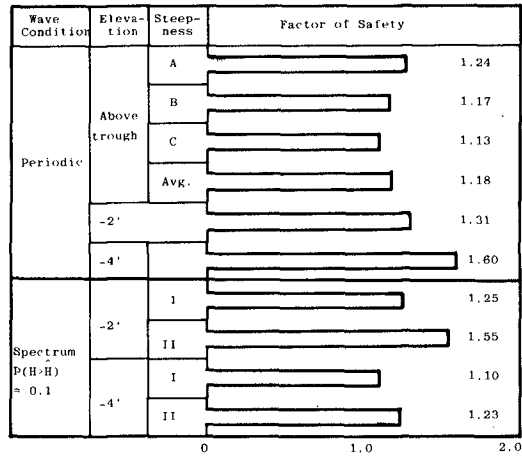


Fig. 24 Factor of Safety for u_+ for Airy Theory

fact Airy wave theory) to predict the conditions in large waves at sea providing an appropriate factor of safety is used. An example is shown here for u_+ . Similar safety factors can be developed for other wave parameters at the discretion of the designer.

5.0 ACKNOWLEDGEMENTS

Some of the work in this research was supported by the National Science Foundation Grant No. ENG76-16423, on the section regarding wave kinematics and circulation in a closed system wave flume. Dr. Tokuo Yamamoto provided valuable comments at the beginning of the work. The authors are indebted to Prof. C. K. Sollitt and Mr. Robert Jensen for use of the data on horizontal velocity measurements above the trough, which were collected from Mr. Jensen's M. S. Thesis.

REFERENCES

1. Dean, R.G., "Evaluation and Development of Water Wave Theories for Engineering Application," Special Report No. 1, U.S. Army, Coastal Engineering Research Center, Vol. ii, 1974, p. 534.
2. Grace, R.A. and R.T. Rocheleu, "Near-Bottom Velocities Under Waikiki Swells," James K.K. Look Laboratory of Oceanographic Engineering, University of Hawaii, Technical Report No. 31, 1973, p. 55.
3. Hudspeth, R.T., D.F. Jones and J.H. Nath, "Design of Hinged Wave-makers for Random Waves," 16th International Conference on Coastal Engineering, Hamburg, September 1978.
4. Iwagaki, Y., T. Sakai and H. Ishida, "Correlation of Water Particle Velocity with Water Level Variation for Irregular Waves," Coastal Engineering in Japan, Vol. 16, 1973, pp. 19-28.

4. Iwagaki, Y., T. Sakai and H. Ishida, "Correlation of Water Particle Velocity with Water Level Variation for Irregular Waves," Coastal Engineering in Japan, Vol. 16, 1973, pp. 19-28.
5. Jensen, R., "Finite Amplitude Deep Water Wave: a comparison of theoretical and experimental kinematics and dynamics," Thesis for Master of Ocean Engineering Degree, Oregon State University, June 1979.
6. Kobune, K., "Random Wave Velocity Field from Periodic Theory," Thesis for the Degree of Civil Engineer, Oregon State University, June 1978, presented December 1977.
7. Lee, A., C. A. Grated and T.S. Durrani, "Velocities Under Periodic and Random Waves," Proceedings of 14th Conference on Coastal Engineering, 1974, pp. 558-574.
8. Nath, J. H., "Drift Speed of Buoys in Waves," Proceedings of 16th International Conference on Coastal Engineering, Hamburg, 1978.
9. Reid, R.O., "Correlation of Water Level Variation with Wave Forces on a Vertical Pile for Nonperiodic Waves," Proceedings of 4th International Conference on Coastal Engineering, 1958, pp.749-786.
10. Tsuchiya, Y. and M. Yamaguchi, "Horizontal and Vertical Water Particle Velocities Induced by Waves," Proceedings of 14th International Conference on Coastal Engineering, 1974, pp. 555-568.
11. Ursell, F., "The Long-Wave Paradox in the Theory of Gravity Waves," Proceedings of the Cambridge Philosophical Society, Vol. 49, 1963, pp. 685-694.
12. Van Dorn, W. G. and S. E. Pazan, "Laboratory Investigation of Wave Breaking, Part III: deep water waves," Advanced Ocean Engineering Laboratory Report No. 71, Scripps Institution of Oceanography, University of California, San Diego, 1975, p. 105.

CHAPTER 19

HIGHER ORDER WAVE SPECTRA¹

By Paul C. Liu², M. ASCE and Albert W. Green³

1. INTRODUCTION

As part of an effort aimed at examining the empirical aspects of nonlinear processes of wind-generated waves, this paper presents calculations and examples of bispectra and trispectra and indicates applications of these results to the study of wave growth processes.

Recent publications on wave studies have indicated that the growth process of wind waves is primarily associated with the nonlinear energy flux due to wave-wave interactions. While most of these studies are conjectures from theoretical considerations, it is of interest to explore the nonlinear studies empirically. From available wave data largely recorded at a single station, a first step is to perform bispectral and trispectral analyses of the data. Since the unispectrum provides information on the energy content of the frequency components, the bispectrum and trispectrum generally provide information on the interactive relations between two and three frequency components, respectively. These higher order interactive relations can thus be considered as estimates or characterizations of nonlinear interactions.

Hasselmann, Munk, and McDonald (1962), perhaps the first to use bispectral analysis, demonstrated that calculations of observed bispectra of ocean waves correlate reasonably well with theoretically derived bispectra. Other ocean wave bispectra were presented by Garrett (1970) and Houmb (1974). Trispectral analysis has not yet been attempted in practical problems.

2. CALCULATION PROCEDURES

By definition, a bispectrum is the two-dimensional Fourier transform of the third-order covariance function of the data; a trispectrum is the three-dimensional Fourier transform of the fourth-order covariance function of the data. A two- or three-dimensional Fourier transform of the corresponding covariance function is generally cumbersome

¹GLERL Contribution No. 160.

²Physical Scientist, Physical Limnology and Meteorology Group, Great Lakes Environmental Research Laboratory, National Oceanic and Atmospheric Administration, 2300 Washtenaw Avenue, Ann Arbor, Michigan 48104.

³Chief, Physical Oceanography Branch, Oceanography Division, Naval Oceanographic Research and Development Activity, Code 331, NSTL Station, Mississippi 39529.

to calculate. However, following procedures discussed by Haubrich (1965) and Hinch and Clay (1968), which use fast Fourier transform directly on the data, the bispectrum and trispectrum can be feasibly calculated.

For a given discrete series of ℓ data points at a sampling interval Δt , $\zeta(\ell\Delta t)$, with $\ell = 1, 2, \dots, L$, subdividing the series into P non-overlapping subseries, each of length K , such that $p = 0, 1, \dots, p - 1$ and $k = 1, 2, \dots, K$ yield

$$\zeta_p(k\Delta t) = \zeta[(pK + k)\Delta t],$$

and the K complex Fourier coefficients for each group are given by

$$X_p(\omega) = \left(\frac{\Delta t}{2\pi K}\right)^{1/2} \sum_{j=1}^K \zeta_p(j\Delta t) e^{i2\pi kj/K}, \quad k = 1, 2, \dots, K. \quad (1)$$

Then the unispectrum, the bispectrum, and the trispectrum can be estimated by

$$S_2(\omega) = \frac{1}{P} \sum_{p=1}^P X_p(\omega) X_p^*(\omega), \quad (2)$$

$$S_3(\omega_1, \omega_2) = \frac{1}{P} \sum_{p=1}^P X_p(\omega_1) X_p(\omega_2) X_p^*(\omega_1 + \omega_2), \quad (3)$$

and

$$S_4(\omega_1, \omega_2, \omega_3) = \frac{1}{P} \sum_{p=1}^P X_p(\omega_1) X_p(\omega_2) X_p(\omega_3) X_p^*(\omega_1 + \omega_2 + \omega_3), \quad (4)$$

respectively. The asterisks in equations (2)-(4) indicate complex conjugates. In the actual computations $P = 30$ is used for each 20-min data segment of $L = 1800$ and $\Delta t = 2/3$ s to obtain smoothed spectral estimates with 60 degrees of freedom.

Because of the symmetric relations in the definitions of higher order spectra, spectral estimates are needed only within a fundamental region. The fundamental region for $S_2(\omega)$ is the line segment $0 \leq \omega \leq \omega_N$; for $S_3(\omega, \omega_1)$ the triangle defined by $0 \leq \omega \leq \omega_1$ and $0 \leq \omega_1 \leq \omega_N$; and for $S_4(\omega, \omega_1, \omega_2)$ the tetrahedron defined by $0 \leq \omega \leq \omega_1$, $0 \leq \omega_1 \leq \omega_2$, and $0 \leq \omega_2 \leq \omega_N$, with $\omega_N = 2\pi/(2\Delta t)$ representing the Nyquist frequency. A detailed discussion of these procedures and their theoretical backgrounds is given in Liu (1977a).

3. HIGHER ORDER SPECTRA OF KNOWN FUNCTIONS

In order to understand and interpret the higher order spectral behavior of actual wave data, unispectra, bispectra, and trispectra of three known functions are first calculated as examples. Figures 1, 2,

and 3 show the results for a synthesized sinusoidal record with three frequency components, a Gaussian white noise, and a second-order autoregressive process, respectively. All calculations are based on 1800 generated data points at 2/3-s sampling intervals.

In the figures, logarithms of unispectral density are plotted versus frequency; the bispectra show the contours of the logarithms of bispectral amplitude plotted in the triangular fundamental region. The increasing contour levels are represented by the increasing darkness in the shaded areas. For the trispectra, a tetrahedral fundamental region is represented by cutting discrete layers along one frequency axis parallel to the plane formed by the other two frequency axes. In each trispectral layer, the number on the corner represents the third frequency. The logarithms of trispectral amplitude are again contoured, with increasing level represented by increasing darkness in the shaded areas.

Figure 1 shows the sinusoidal wave with three frequency components of 0.1 Hz, 0.2 Hz, and 0.3 Hz. There are three delta functions at the three components in the unispectrum. Its bispectrum has strong interactions at components (0.1, 0.1), (0.2, 0.2), (0.3, 0.3), as well as (0.1, 0.2), (0.1, 0.3), and (0.2, 0.3). Its trispectrum is characterized by the strong interactions between the various second-order interactions shown in the bispectrum and other frequency components, with the strongest interaction at (0.1, 0.1, 0.1), (0.2, 0.2, 0.2), and (0.3, 0.3, 0.3).

Figure 2 shows the results for the computer-generated Gaussian white noise. Its bispectrum is practically zero and its trispectrum is characterized by random patterns without specifically stronger interactions. Figure 3 shows the second-order autoregressive process X_t defined by

$$X_t = X_{t-1} - 0.5X_{t-2} + Z_t ,$$

where Z_t is the Gaussian white noise generated for Figure 2. Its unispectrum, bispectrum, and trispectrum are all characterized by higher interactions at the low frequency range and a gradual decrease in magnitude toward the higher frequencies.

It is clearly shown by these results that bispectral and trispectral densities are directly related to and dependent on unispectral characteristics, which is what would be expected from theoretical analysis (Hasselmann, 1962). It seems reasonable to infer that the higher order interactions presented in this paper are estimates of nonlinear interactions.

As the basic assumption for higher order spectral analysis is stationarity while the growth process of surface waves is clearly nonstationary, a modified assumption of local stationarity in which the

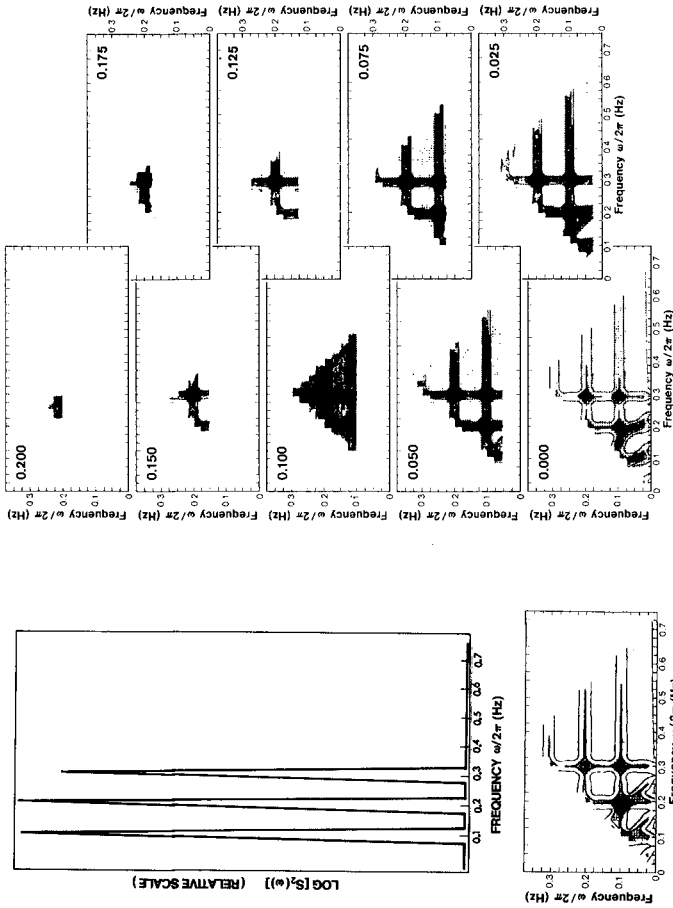


Figure 1 Spectra for a sinusoidal wave with three frequency components.

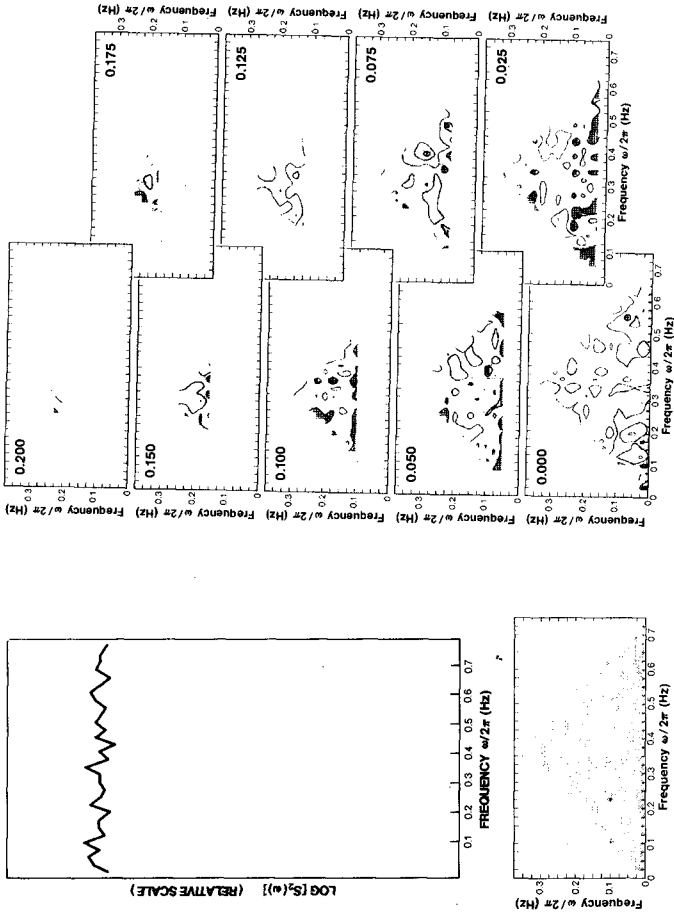


Figure 2 Spectra for a Gaussian white noise.

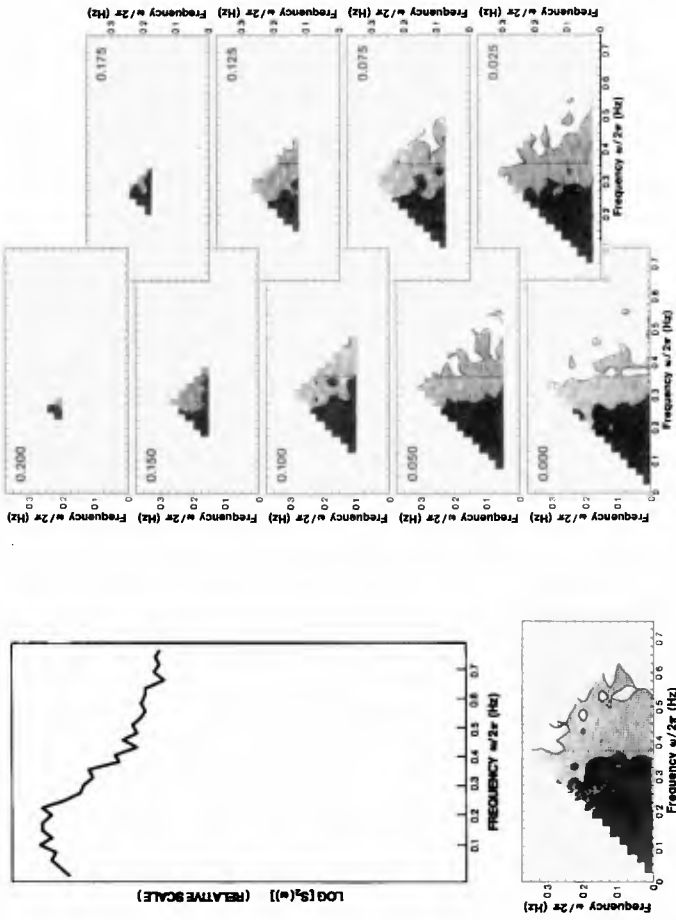


Figure 3 Spectra for a second-order autoregressive process.

process is considered to be stationary only within a local time interval can be used. A previous study (Liu, 1977b) indicated that the local stationarity assumption is statistically acceptable in actual applications.

4. HIGHER ORDER SPECTRA OF WAVE DATA

The calculations using equations (1)-(4) have been applied to an episode of recorded wave data. The episode was recorded continuously on 9 August 1972 in Lake Ontario approximately 35-km offshore of Oswego, New York, with a Waverider deployed in 150 m of water. Figure 4 shows the wind conditions during the episode, which started at a wind speed of 8 m s^{-1} and increased to over 11 m s^{-1} in 3 hours. The westerly wind direction provided fairly constant and long fetches during the episode. The group of short straight lines plotted on the figure indicates the locations in time of 64 overlapping segments of wave data analyzed for the episode. Each segment is 20-min long and has a 17.5-min overlap with the next segment. Figure 5 shows the computed unispectral density versus frequency versus time. The three-dimensional perspective figure presents a clear overview of spectral growth during the episode. Figure 6 presents six bispectra from the episode at 30-min intervals as representative of the whole process. As the temporal variations are gradual, the figures clearly show that the magnitude of the bispectral amplitude increases and the hills and ridges migrate toward lower frequencies during wave growth. Figure 7 presents three representative trispectra at 1-hour intervals. The trispectrum on the left is 2.5 min from the beginning of the episode; the one in the middle is 1-hour later, with the trispectral interactions increasing and migrating toward lower frequencies; the one on the right is 2 hours from the first during the intensive wave growth stage. The intensity of trispectral density has increased significantly as shown by the very dark contour areas.

These results give only qualitative features of the higher order spectra during wave growth. In order to use these results for quantitative study, efforts must be made to examine the relative growth behavior of the individual higher order spectral components. Liu (1977a) has pursued this approach and found that, during the intensive stage of wave growth, the interaction between the components of peak-energy frequency and the next lower frequency grows consistently stronger than its interaction with the next higher frequency. Thus, the peak-energy frequency transfers more energy to the lower frequency components than to the higher ones, confirming the well-known fact that unispectral peaks shift progressively toward lower frequencies during wave growth.

5. CONCLUDING REMARKS

This paper has presented results of higher order wave spectra calculations with an intent to study nonlinear processes of wave growth by examining these higher order interactions. While the higher order spectra can be feasibly calculated from given wave data, it is only

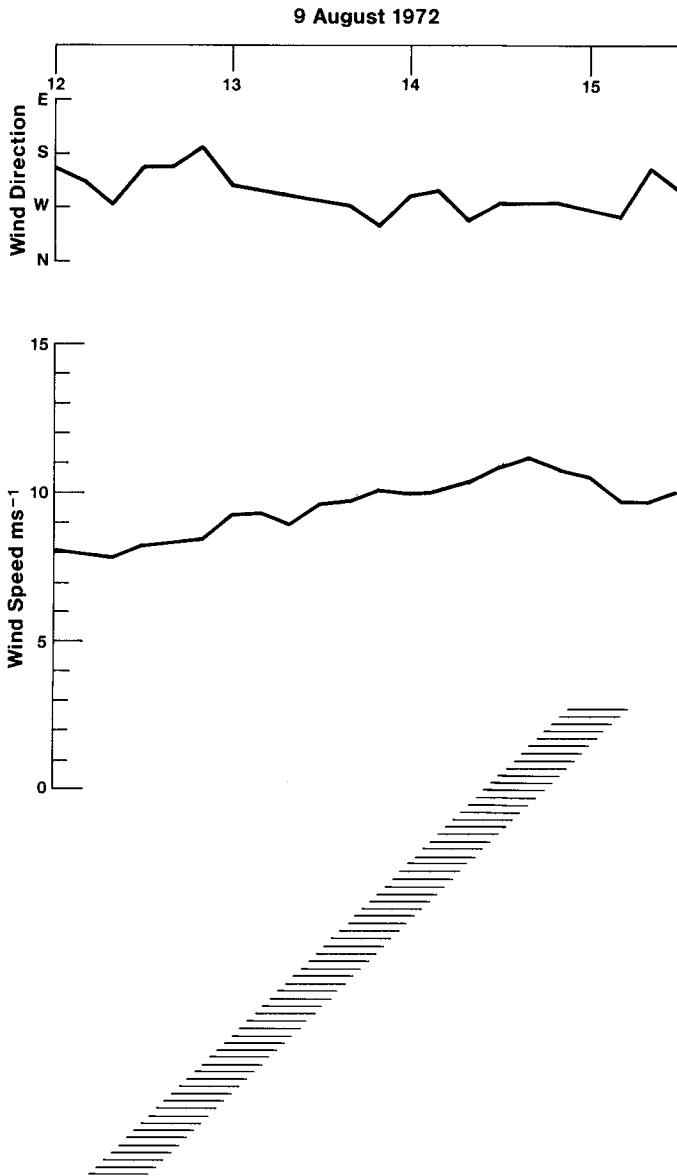


Figure 4 Wind conditions for the 9 August 1972 episode in eastern Lake Ontario.

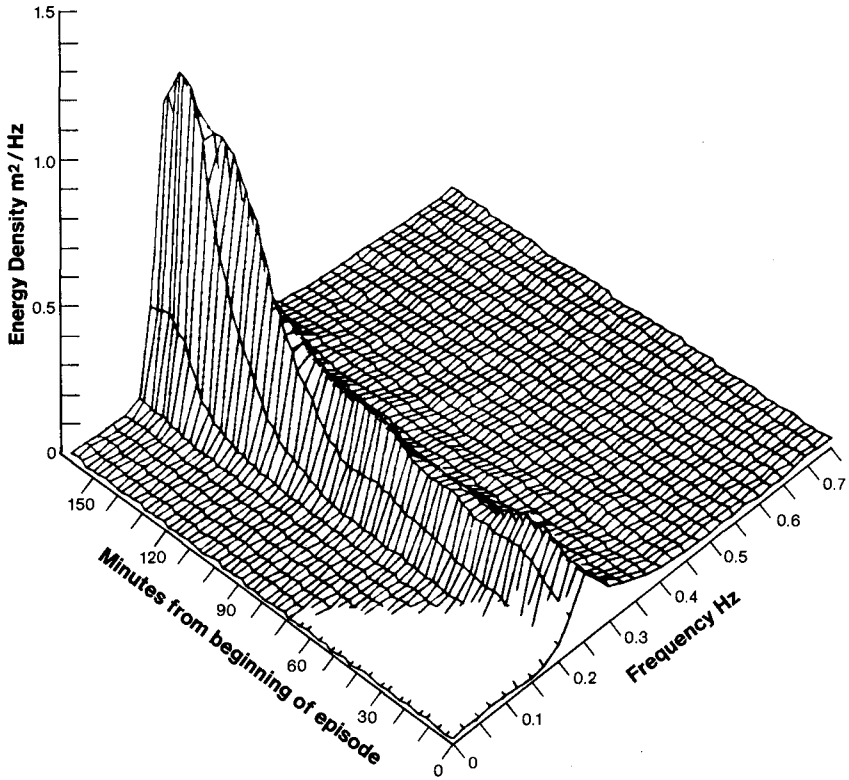


Figure 5 Perspective view of unispectra versus time during the 9 August 1972 episode.

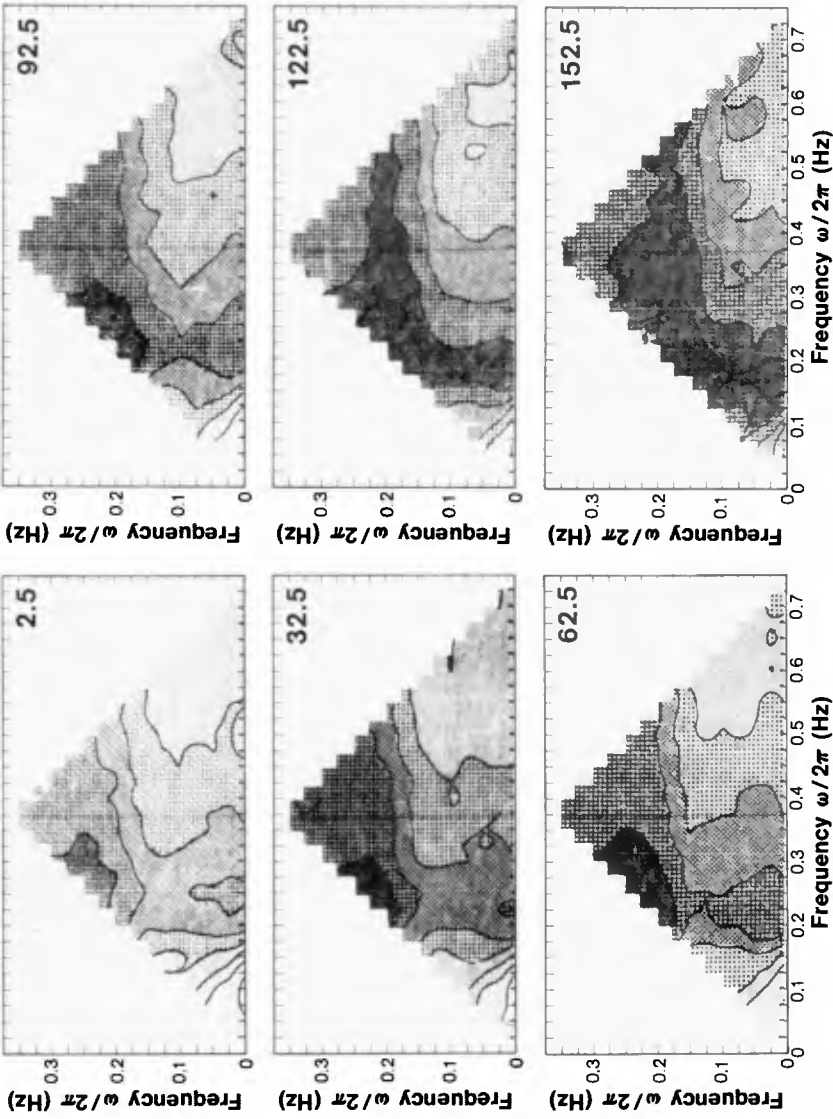


Figure 6 Bispectra during the 9 August 1972 episode. The numbers 2.5, 32.5, . . . , and 152.5 represent minutes from beginning of the episode.

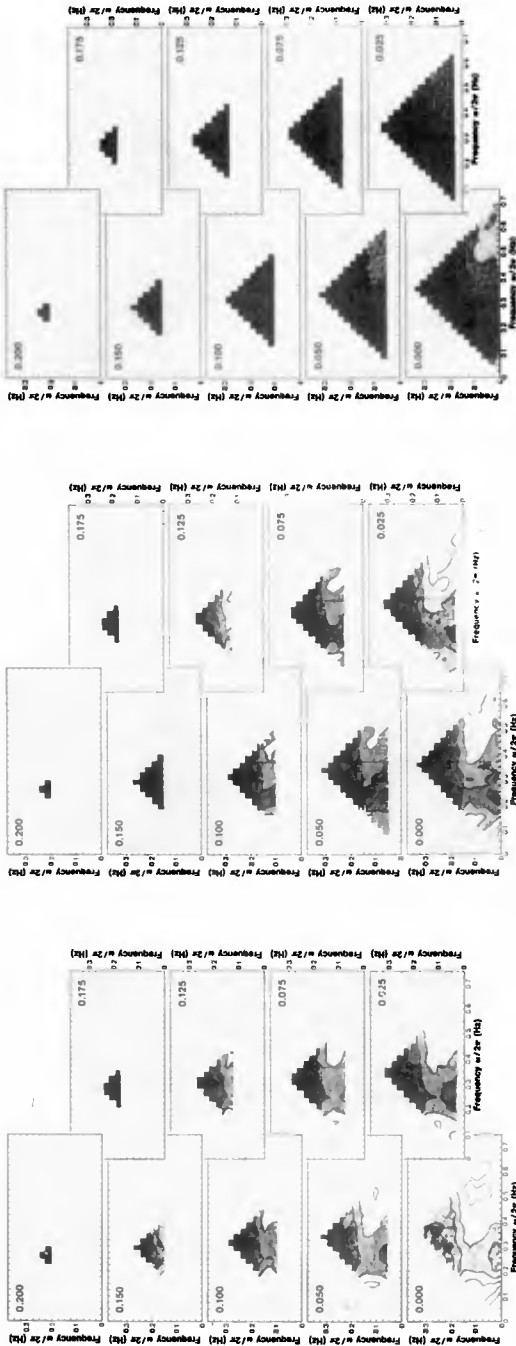


Figure 7 Trispectra during the 9 August 1972 episode at 1 hour interval from left.

inferred that these spectra are estimates of nonlinear interactions. At present, nonlinear processes have only been studied theoretically; it is hoped that an empirical effort presented in this paper will serve to indicate another approach to greater understanding of the processes. Efforts to further interpret and use these results will be continued.

6. REFERENCES

- Garrett, J. F. (1970): Field observations of frequency domain statistics and nonlinear effects in wind-generated ocean waves. Ph.D. Thesis, the University of British Columbia.
- Hasselmann, K. (1962): On the nonlinear energy transfer in a gravity-wave spectrum. Part 1: General theory. *J. Fluid Mech.*, 12:481-500.
- Hasselmann, K., W. Munk, and G. McDonald (1962): Bispectra of ocean waves. In: *Time Series Analysis*, Ed. M. Rosenblatt, Wiley, New York, 125-139.
- Haubrich, R. A. (1965): Earth noise, 5 to 500 millicycles per second. Part 1, Spectral stationarity, normality, and nonlinearity. *J. Geophys. Res.*, 70:1415-1427.
- Hinch, M. J., and C. S. Clay (1968): The application of the discrete Fourier transform in the estimation of power spectra, coherence, and bispectra of geophysical data. *Rev. Geophys. Space Phys.*, 6:347-363.
- Houmb, O. G. (1974): Spectra and bispectra of ocean waves. In: *Proc. 14th Coastal Engineering Conf.*, Vol. 1, American Society of Civil Engineers, Copenhagen, Denmark, 301-320.
- Liu, P. C. (1977a): Temporal spectral growth and nonlinear characteristics of wind waves in Lake Ontario. Ph.D. Thesis, the University of Michigan.
- Liu, P. C. (1977b): Higher order spectra and stationarity of wind waves. In: *Preprint Proceedings of the Fifth Conference on Probability and Statistics*, American Meteorological Society, Las Vegas, Nevada, 254-259.

CHAPTER 20

ANALYSES OF HINGED WAVEMAKERS FOR RANDOM WAVES

Robert T. Hudspeth
Oregon State University
Corvallis, Oregon 97331

Douglas F. Jones
CONOCO, Ponca City, OK
present address: Dames & Moore, Anchorage, AK 99501

John H. Nath
Oregon State University
Corvallis, Oregon 97331

ABSTRACT

The theoretical dimensionless frequency response functions for the wavemaker stroke spectrum, $Q_S(\omega)$, and for the wavemaker dynamic pressure moment spectrum, $Q_M(\omega)$, were verified experimentally in the Oregon State University-Wave Research Facility (OSU-WRF) from random waves which were simulated from two types of two-parameter theoretical design wave spectra. The random motions of the wavemaker were first digitally simulated by a unique inverse stacked FFT algorithm which were then used to drive the wavemaker through digital-to-analog converters (DAC). The dimensionless frequency response function for the hydrodynamic pressure moment spectrum was not measured directly but was computed from the dynamic covariance equations for a hinged wavemaker of variable-draft by linear combinations of related dimensionless frequency response functions and cross-spectral estimates. The measured estimates were found to agree reasonably well with the analytical approximations, and these measured stochastic hydrodynamic pressure moment estimates on a hinged wavemaker of variable-draft are believed to be unique.

INTRODUCTION

The elaborate design curves for hinged wavemakers presented by Gilbert, *et al* (1971) have been extended in a minor way (for the case of deterministic waves only) to variable-draft hinged wavemakers by Hudspeth and Chen (1978). Experimental comparisons of these theoretical design curves with deterministic waves which were approximately 25% of the theoretical breaking limit were reported by Hudspeth and Leonard (1978a) for measured data which span one decade of dimensionless relative wave frequency. The squared modulus of the dimensionless wavemaker gain function, S/H , in which S = the wavemaker stroke and H = the wave height, for deterministic waves may be shown to be equivalent to the squared modulus of the dimensionless frequency response function for the wavemaker stroke spectrum; *viz*,

$$\left| \frac{S}{H} \right|^2 = |Q_S(\omega)|^2 = \frac{S(\omega)}{S(\omega)} \frac{SS}{\eta\eta} \quad (1)$$

and the squared modulus of the dimensionless wavemaker hydrodynamic pressure moment about the wavemaker hinge, M , may be shown to be equivalent to the squared modulus of the dimensionless frequency response function for the wavemaker hydrodynamic pressure moment spectrum; *viz*,

$$|Q_M(\omega)|^2 = \frac{S(\omega)}{W^2 S(\omega)} \frac{MM}{\eta\eta} \quad (2a)$$

in which

$$W = \rho g B h (h - \Delta) \quad (2b)$$

in which ρ = density of fluid; g = gravitational constant; B = width of waveboard; and the dimensions h and Δ are defined in Fig. 1. These theoretical dimensionless frequency response functions for the stochastic design of hinged wavemakers of variable-draft were verified experimentally in the Oregon State University-Wave Research Facility (OSU-WRF) for two types of two-parameter theoretical spectra; *viz*, the relatively narrow-banded Scott spectrum and the relatively broad-banded Bretschneider-Pierson-Moskowitz spectrum.

We shall first give the analytical expressions for the dimensionless frequency response functions required for the stochastic design of hinged wavemakers which were experimentally verified in the OSU-WRF. A brief description will be presented next. Finally, graphical comparisons will be given between the theoretical and experimental dimensionless frequency response functions. The experimental values were computed from measured time series that were synthesized from the two-parameter theoretical design wave spectra. These theoretical dimensionless frequency response functions should be useful for the stochastic design of hinged wavemakers of variable-draft in wave flumes which have water on one side only of the wavemaker.

FREQUENCY RESPONSE FUNCTIONS

From the dynamic covariance equations for a hinged wavemaker of variable-draft in the wave flume shown in Figure 1, it may be shown [cf. Hudspeth and Leonard (1978b)] that the real-valued dimensionless theoretical frequency response function for radial frequency $\omega = 2\pi f$ is given by

$$Q_S(\omega) = \frac{KH}{4 \sinh Kh} \Gamma(\kappa, K) \left[\frac{2Kh + \sinh 2Kh}{K(h-\delta) \sinh Kh - \cosh Kh + \cosh K\delta} \right] \quad (3a)$$

in which

$$\Gamma^2(\kappa, K) = \left[\frac{K}{\kappa} \right] \left\{ \frac{1 + \frac{2\kappa(h-\Delta)}{\sinh 2\kappa(h-\Delta)}}{1 + \frac{2Kh}{\sinh 2Kh}} \right\} \quad (3b)$$

provided that the propagating wave number in the constant depth domain immediately adjacent to the wavemaker of depth, h , is determined from

$$\omega^2 = gK \tanh Kh \quad (3c)$$

and provided that the wave number in the constant depth test section domain of depth, $h-\Delta$, is determined from

$$\omega^2 = g\kappa \tanh \kappa(h-\Delta) \quad (3d)$$

The dimensionless complex-valued frequency response function for the hydrodynamic pressure moment on the wavemaker may be computed from the dimensionless complex-valued moment amplitude given by Hudspeth and Chen (1978) according to

$$Q_M(\omega) = M_p'(\omega) + i M_e'(\omega) \quad (4)$$

in which the dimensionless moment due to the *propagating* mode is given by

$$M_p'(\omega) = \Omega \frac{\{K(h-\delta) \sinh Kh - \cosh Kh + \cosh K\delta\}}{Kh \cdot K(h-\Delta) \cdot K(h-\delta) \sinh Kh} \Gamma(\kappa, K) \quad (5a)$$

and the dimensionless moment due to the *evanescent* modes is given by

$$M_e'(\omega) = \Omega \frac{(Kh)^3 \{2Kh + \sinh 2Kh\}}{K(h-\Delta) \cdot K(h-\delta) \sinh Kh \{K(h-\delta) \sinh Kh - \cosh Kh + \cosh K\delta\}} \Gamma(\kappa, K) \sum_{n=2}^{\infty} \frac{\{K_n(h-\delta) \sin K_n h + \cos K_n h - \cos K_n \delta\}^2}{(K_n h)^4 \{2K_n h + \sin 2K_n h\}} \quad (5b)$$

in which

$$\Omega = (h-\Delta) \frac{\omega^2}{g} \quad (5c)$$

and the evanescent eigenvalues, K_n , are computed from

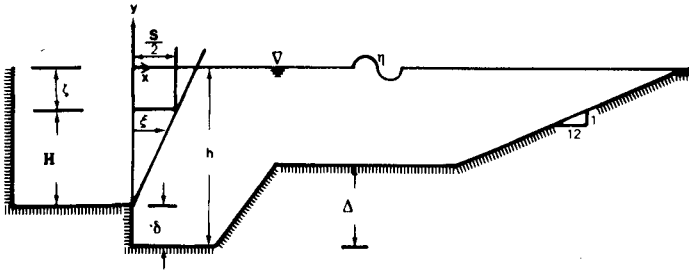


Fig. 1 Definition sketch for wave flume geometry with a hinged wavemaker of variable draft

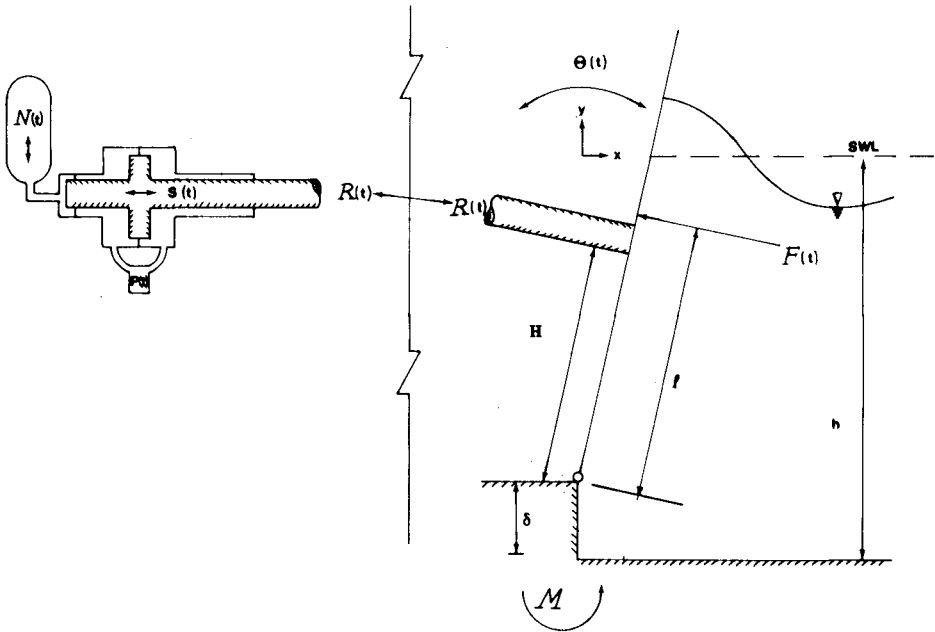
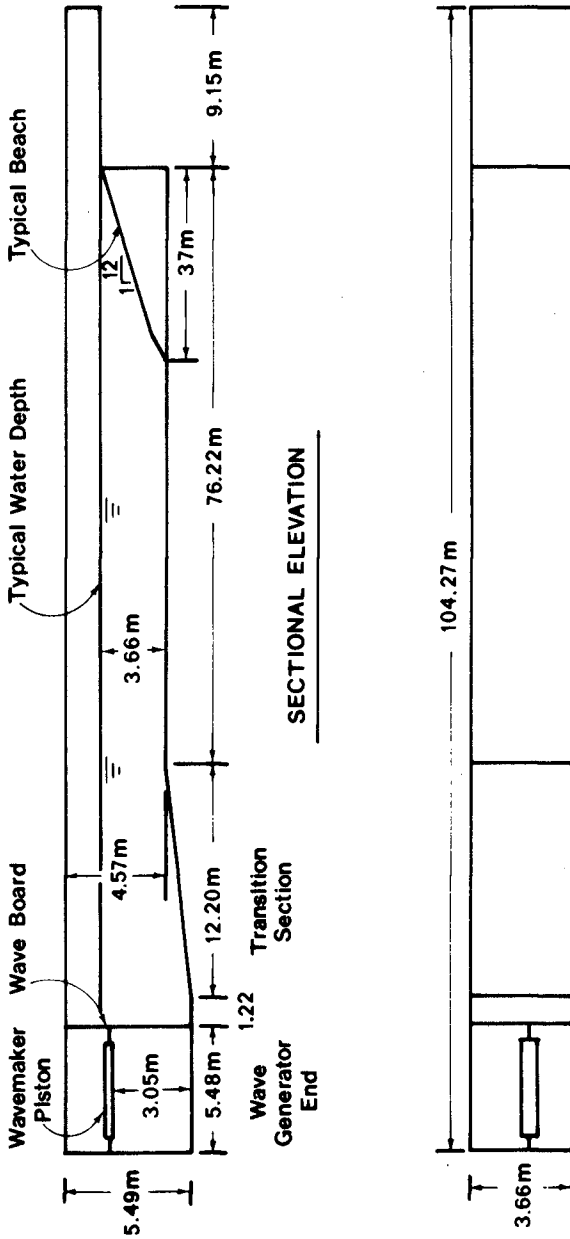


Fig. 2 Schematic representation of hydraulic piston and hinged wavemaker dynamic system in OSU-WRF



NOT TO SCALE

PLAN

Fig. 3 Schematic representation of OSU-WRF geometry

$$\omega^2 = -g K_n \tan K_n h; n > 1 \quad (5d)$$

The dynamic equation of motion for the translational motion of the wavemaker hydraulic piston displacement, $S(t)$, shown schematically in Figure 2, is given by [cf. Hudspeth and Leonard (1978a)]

$$P(t) = \frac{M(t)}{H} - N(t) + A\ddot{S}(t) + B\dot{S}(t) \quad (6)$$

in which $P(t)$ = hydraulic piston pressure force; $M(t)$ = hydrodynamic pressure moment on the waveboard about the wavemaker hinge; H = hydrodynamic pressure force moment arm about the wavemaker hinge; $N(t)$ = dynamic nitrogen gas pressure force and the coupled translational mass of the hydraulic piston, m , and the rotational inertia of the hinged wavemaker, I/H^2 , is given by

$$A = m + \frac{I}{H^2} \quad (7a)$$

and the coupled translational viscous resistance of the hydraulic piston, μ , and the rotational viscous resistance of the hinged wavemaker, ν/H^2 , is given by

$$B = \mu + \frac{\nu}{H^2} \quad (7b)$$

The time dependent nitrogen gas pressure term, $N(t)$, was not recorded directly in the OSU-WRF and had to be estimated from the measured piston displacement, $S(t)$. The nitrogen gas system in the MTS designed OSU-WRF is used to backpressure the wavemaker piston in order to compensate for the static column of fluid on the wave flume side only of the hinged wavemaker [*vide* Fig. 2]. The time varying nitrogen gas pressure is a result of the small volume changes induced by the motion of the wavemaker piston. The total nitrogen gas pressure on the wavemaker piston may, therefore, be approximated by a static plus a time varying component according to the real gas equation:

$$N = N_s + N(t) = \frac{nZRTA_N}{V_N + A_N S(t)} \quad (8)$$

in which n = mass of the nitrogen gas; Z = the compressibility coefficient for a real gas; R = gas constant for nitrogen; T = temperature; V_N = static volume of nitrogen gas; and A_N = surface area of the terminal end of the wavemaker ram normal to the wavemaker stroke. For the experimental verifications in the OSU-WRF, the ratio of $A_N S(t)/V_N \ll 1.0$; and we may expand Eq. 8 by the binomial theorem to obtain, approximately,

$$N_s + N(t) = \frac{nZR^T A_N}{V_N} \left\{ 1 - \frac{A_N S(t)}{V_N} + 0 \left(\frac{A_N S(t)}{V_N} \right)^2 \right\} \quad (9)$$

in which the static nitrogen gas pressure component exactly balances the hydrostatic moment on the wavemaker flap while the dynamic nitrogen gas pressure component acts like a stiffness element in opposing positive displacements of the piston.

Consequently, the experimental dimensionless frequency response functions were estimated by replacing the exact dynamic nitrogen gas pressure force in Eq. 6 with an equivalent linear spring element approximated by

$$N(t) = -KS(t) \quad (10)$$

in which the equivalent spring constant, K , is determined from a static moment balance between the hydrostatic pressure moment on the wavemaker flap and the static nitrogen gas pressure force according to

$$K = nZR^T \left(\frac{A_N}{V_N} \right)^2 = \frac{\rho g h^3 B A_N}{6H V_N} \quad (11)$$

in which B = width of the hinged wavemaker flap in Fig. 2. Substituting Eq. 10 into Eq. 6 and evaluating the equivalent nitrogen gas spring constant, K , from the static water depth in the wave flume at the time of experimental testing according to Eq. 11, the coupled dynamic equation of motion for the hinged wavemaker system becomes

$$P(t) = \frac{M(t)}{H} + KS(t) + A\ddot{S}(t) + B\dot{S}(t) \quad (12)$$

The covariance function for a stationary stochastic process such as that described by Eq. 12 may be defined by [cf. Papoulis (1965)]

$$C(\tau) = E\{X(t) \cdot X^*(t+\tau)\} \quad (13)$$

in which $E\{\cdot\}$ = expectation operator and the superscript asterisk $*$ = the complex conjugate value for a stochastic process $X(t)$. The Fourier transform of the covariance function yields the frequency spectrum [cf. Papoulis (1965)]. Solving Eq. 12 for the hydrodynamic pressure moment on the wavemaker, $M(t)$, and forming the covariance function according to Eq. 13, the following dynamic covariance equation is obtained for a variable draft hinged wavemaker [cf. Hudspeth and Leonard (1978b)]:

$$C_{MM}(\tau) = H^2 \{ C_{PP}(\tau) + |Q(\omega)|^2 C_{SS}(\tau) - Q(\omega) C_{PS}(\tau) - Q^*(\omega) C_{SP}(\tau) \} \quad (14)$$

in which the complex-valued frequency response function for the wavemaker is given by

$$Q(\omega) = \frac{Q(\omega)}{I} + i \frac{Q(\omega)}{V} \quad (15a)$$

$$= (K - \omega^2 A) + i(\omega B) \quad (15b)$$

and $C_{PS}(\tau)$ = cross-covariance function between the hydraulic oil piston pressure, $P(t)$, and the wavemaker stroke, $S(t)$. We note that our definition for the complex-valued frequency response function is the reciprocal of the usual structural definition for the response receptance of a single-degree-of-freedom oscillator [cf. Robson (1963)]. Dividing the Fourier transform of Eq. 14 by the spectrum of the water surface elevation, $S_{nn}(\omega)$, and a non-dimensional factor defined by Eq. 2b, we obtain the following dimensionless frequency response function for the hydrodynamic pressure moment on the hinged wavemaker:

$$|Q_M(\omega)|^2 = \frac{S(\omega)}{W^2 S_{nn}(\omega)} \quad (16a)$$

$$= \left\{ \frac{H}{W} \right\}^2 \left\{ Q_P^2(\omega) + |Q_W(\omega)|^2 Q_S^2(\omega) - 2Q(\omega) \frac{PS}{I S(\omega)} - 2Q(\omega) \frac{PS}{V S(\omega)} \right\} \quad (16b)$$

in which $C_{PS}(\omega)$ and $Q_{PS}(\omega)$ = the co- and quad- spectrum, respectively, for the cross-spectrum between the hydraulic piston pressure and the wavemaker stroke. Graphically, we may now compute the dimensionless frequency response function for the hydrodynamic pressure moment on a hinged wavemaker of variable draft from a linear combination of individual frequency response functions with cross-spectral components. We remark that this method for verifying the dimensionless frequency response functions for the stochastic design of variable-draft hinged wavemakers from the dynamic covariance equations using measured realizations of the hydraulic piston pressure and the piston motion must be considered as an approximation in contrast to the direct measurement of the hydrodynamic pressure moment on the wavemaker. However, for the purpose of verifying the stochastic design method via the dynamic covariance equation, this approximation should be adequate.

OSU-WRF DESCRIPTION

The experimental verification of the theoretical dimensionless frequency response function for the wavemaker gain function, $Q_S(\omega)$, and for the hydrodynamic pressure moment on the wavemaker, $Q_M(\omega)$, were conducted in the Oregon State University-Wave Research Facility (OSU-WRF) shown schematically in Fig. 3. The wave flume is 104.27 m long, 3.66 m wide,

and has a relocatable bottom in the test section. Experimental data were obtained for a test section depth of $h-\Delta = 3.51$ m.

The hinged wavemaker in the OSU-WRF is sealed under pressure along both vertical sides and the horizontal hinged bottom so that water is not allowed in the dry well behind the wavemaker. This dry well reduces the power requirements for the wavemaker and also eliminates the need to place any wave dissipating material behind the wavemaker. The hinged wavemaker is controlled by a 112 kW, 24 MPa hydraulic pump through a hydraulic servo-mechanism mounted 3.05 m above the wavemaker hinge. The forced motion of the wavemaker may be either periodic or random and may be activated by either an electronic function generator or a digital time sequence synthesized on a PDP 11 E10 digital minicomputer through digital-to-analog converters (DAC). A description of a unique inverse finite Fourier transform algorithm (FFT) developed at the OSU-WRF to generate either periodic or random waves of the periodic-random type through a minicomputer is described by Hudspeth and Borgman (1978). The random motions of the hinged wavemaker in the OSU-WRF which were used to verify the linear wave theory dimensionless wavemaker frequency response functions for random waves were synthesized from a stacked FFT digital computer algorithm using the theoretical dimensionless wavemaker frequency response function, $Q_S(\omega)$, and two types of theoretical two-parameter wave spectra. A comparison of two methods used to digitally filter Gaussian white noise to generate random wave spectra in the OSU-WRF is described by Hudspeth and Nath (1978). Similar digital random wave simulations have been described by Weber and Christian (1974), Funke (1974), van Oorschot and Koopmans (1976), and Kimura and Iwagaki (1976). Additional information on the OSU-WRF is presented in Nath (1978) and in Nath and Kobune (1978).

The two types of two-parameter theoretical wave spectra selected to synthesize the random waves used to verify the dimensionless frequency response functions are listed in Table 1. The Pierson-Moskowitz spectrum may be seen from Table 1 to be equivalent to the Bretschneider spectrum when the two parameters of m_0 and ω_0 are employed. The two parameters required to synthesize the wavemaker motion from these spectra are: 1) the peak spectral frequency, ω_0 , and 2) the total area under the spectrum which may be computed from

$$m_0 = \int_0^{\infty} \frac{S(\omega)}{\eta} d\omega \quad (17)$$

for one-sided spectral density functions.

Table 1. Theoretical Two-Parameter Wave Spectra

SPECTRUM	$S_{\eta\eta}(\omega)$
SCOTT	$3.424 m_o \exp - \left\{ \frac{(\omega - \omega_o)^2}{0.065(\omega - \omega_o + 0.265)} \right\}^{\frac{1}{2}}$ $0; 1.65 < \omega - \omega_o < -0.265$
BRETSCHNEIDER	$5 \frac{m_o}{\omega_o} \left(\frac{\omega_o}{\omega} \right)^5 \exp - \left[1.25 \left(\frac{\omega_o}{\omega} \right)^4 \right]$
PIERSON-MOSKOWITZ	$5 \frac{m_o}{\omega_o} \left(\frac{\omega_o}{\omega} \right)^5 \exp - \left[1.25 \left(\frac{\omega_o}{\omega} \right)^4 \right]$

SPECTRAL RESPONSE FUNCTIONS FOR HINGED WAVEMAKERS

The dimensionless frequency response function for the wavemaker stroke spectrum, $Q_S(\omega)$, was estimated from measurements of the wavemaker stroke, $S(t)$, and the instantaneous water surface elevation, $\eta(t)$. The measured wavemaker stroke was recorded through an LVDT mounted just above the wavemaker hinge in the dry well behind the wavemaker [*vide*, Fig. 3]. This LVDT signal was calibrated by rotating the wavemaker through a discrete set of arcs measured at the height of the wavemaker piston and by then correlating the LVDT signal with these measured rotations. The instantaneous water surface elevation was recorded in the test section of the wave flume by a Sonic System Model 86 sonic wave profiler. The sonic wave profiler was calibrated by displacing the sonic transducer through a discrete sequence of vertical distances measured above the still water level in the absence of waves and by correlating the sonic transducer output with these measured displacements.

The two-sided spectral densities for the two data records which are required in order to estimate the dimensionless frequency response function by Eq. 1 were estimated from an integer Finite Fourier Transform (FFT) algorithm which is intrinsic to the SPARTA function library of the Laboratory Peripheral System written by DEC for the OSU-WRF PDP 11 E10 mini-computer. A total of 8192 discrete time values were digitized at even

time intervals $\Delta t = 0.06$ seconds for each of the three realizations synthesized from each of the two theoretical design wave spectra listed in Table 1. The measured data signals were digitized through analog-to-digital converters (ADC) simultaneously with the activation of the motion of the wavemaker piston by the FFT-synthesized wavemaker signal through digital-to-analog converters (DAC). This digital activation of the wavemaker piston motion through a digital signal required a small sending rate time interval, Δt , in order to avoid overdriving the servo-mechanism and results in the small sampling rate for the simultaneous digital recording of the multichannel data signals. The two-sided spectral densities required in the analyses were computed from the discrete complex-valued FFT coefficients, $X(m)$, by the following:

$$S(\omega) = \frac{X(m) \cdot X^*(m)}{d\omega} \quad (18a)$$

in which

$$d\omega = 2\pi df = \frac{2\pi}{(LX) \cdot \Delta t} = \frac{2\pi}{(8192)(0.06)} \quad (18b)$$

Figures 4 and 5 compare the theoretical target wave spectra with a typical smoothed measured wave spectra for the Scott spectra and for the Bretschneider-Pierson-Moskowitz spectra, respectively, which were used in the experimental verifications. Each measured spectrum was smoothed by a box-car filter using 13 discrete spectral estimates which give 26 degrees-of-freedom for discrete spectral estimates computed from FFT coefficients.

Figure 6 compares the squared modulus of the theoretical dimensionless frequency response function for the wavemaker stroke spectrum computed from Eq. 3a with the measured dimensionless frequency response function estimated from the spectral estimates according to Eq. 1.

Figure 7 compares the square modulus of the theoretical dimensionless frequency response function for the wavemaker hydrodynamic pressure moment computed from Eq. 4 with measured frequency response functions which were approximated from spectral estimates of the measured data according to Eq. 16b.

CONCLUSIONS

A minor extension of the elaborate stochastic design curves for hinged wavemakers developed by Gilbert, *et al* (1971) were experimentally verified in the Oregon State University-Wave Research Facility (OSU-WRF) using two types of theoretical two-parameter design wave spectra. The analytical expressions for the dimensionless frequency response functions for the wavemaker stroke spectrum, $Q_S(\omega)$, and for the hydrodynamic pressure moment spectrum, $Q_M(\omega)$, were shown to give quite good agreement with

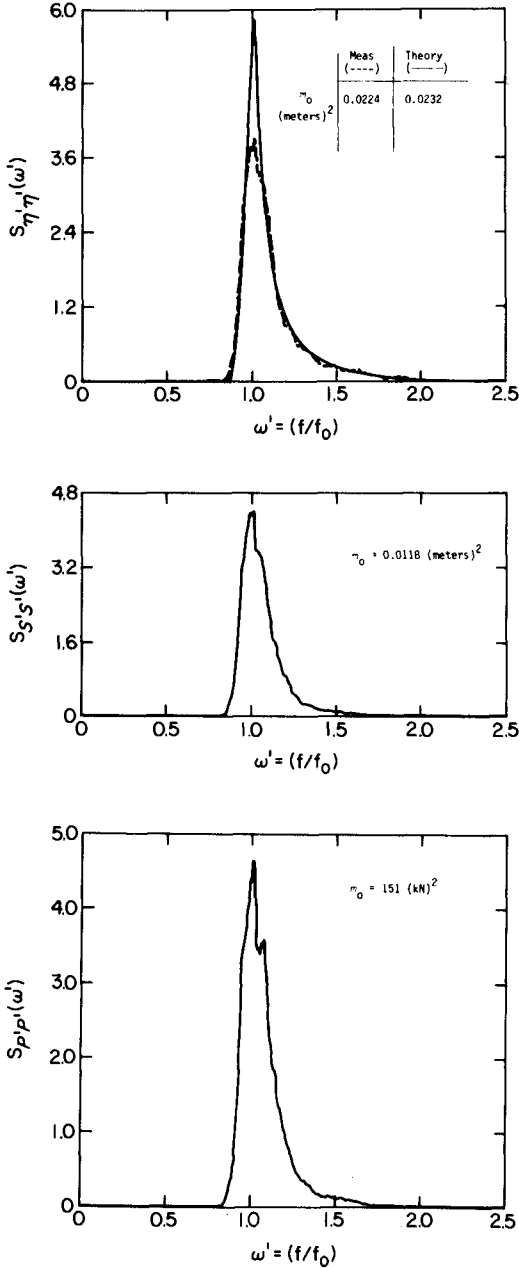


FIG. 4 TYPICAL SCOTT SPECTRA FOR WATER SURFACE ELEVATION, η WAVEMAKER STROKE, S , AND HYDRAULIC OIL PRESSURE, P [$f_0 = 0.2857 \text{ sec}^{-1}$ AND SUPERSCRIPIT PRIMES ' INDICATE NONDIMENSIONAL QUANTITIES]

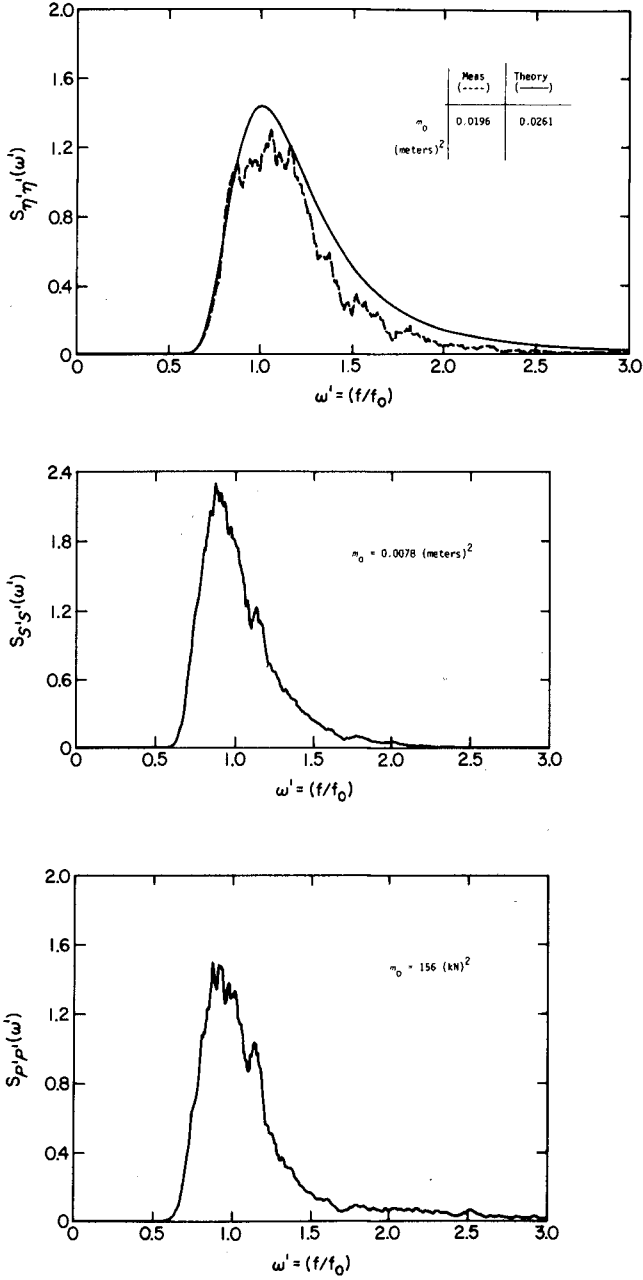


FIG. 5 TYPICAL BRETSCHNEIDER-PIERSON-MOSKOWITZ SPECTRA FOR WATER SURFACE ELEVATION, η , WAVEMAKER STROKE, S , AND HYDRAULIC OIL PRESSURE, P . [$f_0 = 0.3333 \text{ sec}^{-1}$ AND SUPERSCRIPIT PRIMES INDICATE NONDIMENSIONAL QUANTITIES]

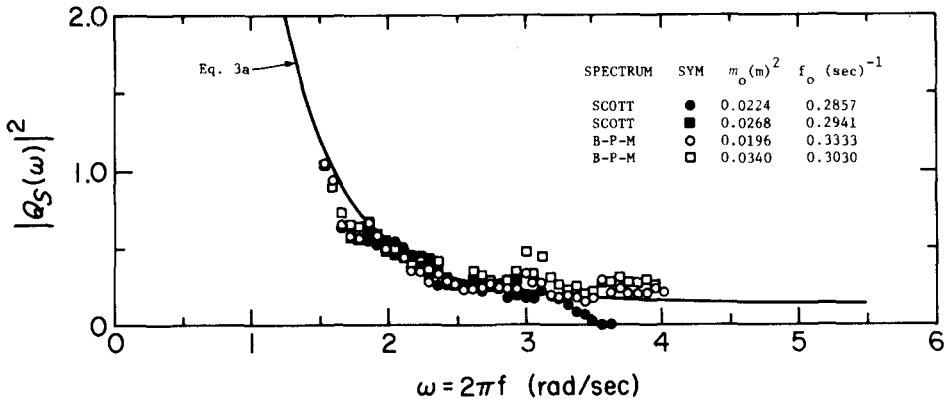


FIG. 6 COMPARISON BETWEEN THEORETICAL AND MEASURED DIMENSIONLESS FREQUENCY RESPONSE FUNCTIONS FOR THE WAVEMAKER STROKE

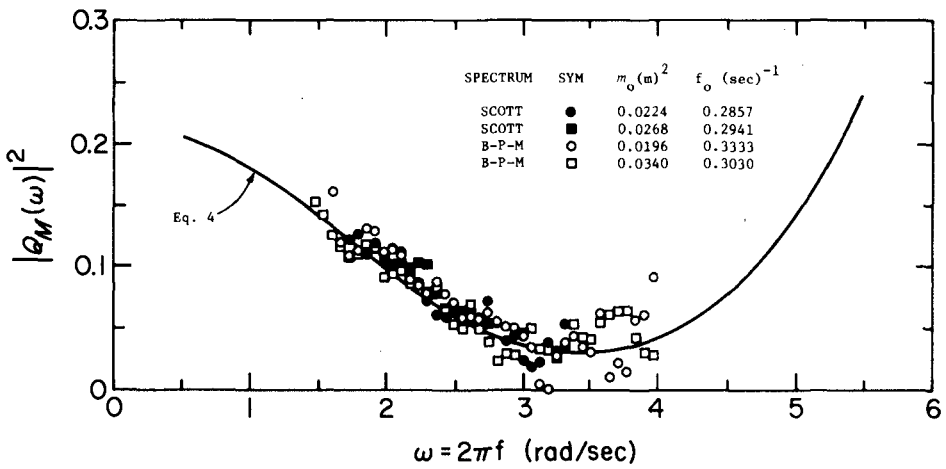


FIG. 7 COMPARISON BETWEEN THEORETICAL AND MEASURED DIMENSIONLESS FREQUENCY RESPONSE FUNCTIONS FOR THE HYDRODYNAMIC PRESSURE MOMENT ON A HINGED WAVEMAKER

the spectral estimates from the measured data. The dimensionless frequency response function for the hydrodynamic pressure moment spectrum was not measured directly but was estimated from the dynamic covariance equation for a hinged wavemaker using a linear combination of related dimensionless frequency response functions and cross-spectral estimates. The dynamic component of the nitrogen gas pressure force in the MTS designed wavemaker was found to be well approximated by an equivalent linear spring in which the spring constant was estimated by a static moment balance between the static nitrogen gas pressure force on the wavemaker flap and the static column of water in the wave flume. The use of the analytical expressions for these dimensionless frequency response functions in the stochastic design of large scale hinged wavemakers of variable-draft appears to be experimentally justified by these stochastic hydrodynamic pressure moment measurements which are believed to be unique.

ACKNOWLEDGMENTS

We gratefully acknowledge the financial and technical support provided by the Continental Oil Corporation (CONOCO) for the experimental verifications. Additional financial support was provided through the Oregon State University Sea Grant College Program, Department of Commerce, under Grant No. 04-7-158-44085.

REFERENCES

- Funke, E.R. (1974), "Random Wave Signal Generator by Minicomputer," Proceedings Fourteenth Coastal Engineering Conference, Chap. 19, Vol. I, Copenhagen, Denmark, pp.353-371.
- Gilbert, G., Thompson, D.M. and Brewer, A.J., (1971), "Design Curves for Regular and Random Wave Generators," Journal of Hydraulic Research, Vol. 9, No. 2, pp. 163-196.
- Hudspeth, R.T. and Chen, M.C., (1978), "Design Curves for Hinged Wavemakers: I - Theory," ASCE, Journ. Hyd. Div., (in review).
- Hudspeth, R.T. and Leonard, J.W., (1978a), "Design Curves for Hinged Wavemakers: II - Experiments," ASCE, Journal Hyd. Div., (in review).
- Hudspeth, R.T. and Leonard, J.W., (1978b), "Dynamic Covariance Equations for Hinged Wavemakers," Engineering Structures, (in review).
- Hudspeth, R.T. and Borgman, L.E., (1978), "Efficient FFT Simulation of Digital Time Sequences," ASCE, Journal Engineering Mechanics Division, (in press).
- Hudspeth, R.T. and Nath, J.H., (1978), "Comparisons of Digital Random Wave Simulations," ASCE, Journal Waterways, Port, Coastal and Ocean Engineering Div., (in review).
- Kimura, A. and Y. Iwagaki, (1976), "Random Wave Simulation in a Laboratory Wave Tank," Proceedings Fifteenth Coastal Engineering Conference, Chapter 21, Vol. 1, Honolulu, Hawaii, pp. 368-387.
- Nath, J.H., (1978), "Drift Speeds of Buoys in Waves," Proceedings of 16th International Conference on Coastal Engineering, Hamburg, Germany.
- Nath, J.H. and Kobune, K., (1978), "Periodic Theory Velocity Prediction in Random Wave," Proceedings of 16th International Conference on Coastal Engineering, Hamburg, Germany.
- Papoulis, A., (1965), Probability, Random Variables, and Stochastic Processes, McGraw-Hill Book Co., New York, pp. 336-352.
- Robson, J.D., (1963), An Introduction to Random Vibrations, Edinburgh University Press, Edinburgh, Eng., pp. 52-57.
- van Oorschot, J.H. and Koopmans, F., (1976), "Random Wave Generation for Research on Immersed Marine Vehicles," Eleventh Symposium on Naval Hydrodynamics, London, England.
- Weber, N.B. and Christian, C.D., (1974), "A Programmable Irregular Wave Generator," Proceedings Fourteenth Coastal Engineering Conference, Chapter 18, Vol. 1, Copenhagen, Denmark, pp. 340-351.

CHAPTER 21

AN INCLINED-PLATE WAVE GENERATOR

by Fredric Raichlen¹ and Jiin-Jen Lee²

ABSTRACT

A numerical method for determining the characteristics of waves generated by a hinged inclined-plate wave generator operating in a constant depth channel is discussed. The analysis is in reasonably good agreement with experimental results. The results indicate the sloping generator operating under certain conditions is completely inefficient, i.e., for a given stroke and depth-to-wave-length ratio, very small waves are produced; for other wave periods for the same conditions significantly larger waves are generated.

INTRODUCTION

The inclined-plate wave generator discussed herein consists of a plate with one edge hinged and attached to the bottom and mounted, in its at-rest position, at a given angle in a constant depth wave tank; the plate is moved about this position with a periodic motion. The purpose of this investigation was to determine, theoretically and experimentally, the characteristics of such a wave-maker.

Two different problems served as incentives for this study. An understanding of the characteristics of such a generator may be important in predicting waves which could arise from the impulsive movement of a sloping nearshore region due to an earthquake. This is a transient problem, but an understanding of the characteristics of an inclined wave generator, i.e., the transfer function, would assist in the solution of this type of problem. (Linear aspects of the generation of impulsive waves have been explored and presented by Hammack (1973) and the interested reader is referred to that publication.) The steady state problem is related to a proposed offshore mobile breakwater constructed from a group of moored partly sunk barges. By mooring each barge in an inclined position with one end resting on the bottom and the other end near the free surface pointing in the direction of wave incidence, a temporarily protected site may be created. An understanding of the waves generated by an inclined wave-generator is important to the understanding of the transmission characteristics associated with this type of breakwater.

Numerous investigators have studied analytically the wave generating characteristics of vertical wave generators, among these are Havelock (1929), Biesel and Suquet (1951), Ursell *et al.* (1960), Madsen (1970), and Gilbert *et al.* (1971). Several of these investigators have conducted experiments or used experimental data of others to compare to

¹Prof. of Civil Engrng., W. M. Keck Lab. of Hydr. & Water Res., Calif. Inst. of Tech., Pasadena, CA, USA.

²Assoc. Prof. of Civil Engrng., Univ. of So. Calif., Los Angeles, CA, USA.

their theory. Gilbert *et al.* (1971) and Hammack (1973) studied the behavior of more unusual generators; the former investigating the characteristics of a moving wedge and the latter studying the waves generated by the motion of a section of the bottom of a constant depth tank. In addition to these, theoretical studies have been conducted by Tuck and Hwang (1972) relating to the impulsive generation of long waves by the movement of a continuously sloping beach. These studies provide insight into the general problem of wave generation, and suggest certain differences which might be realized for the inclined-plate generator.

THEORETICAL CONSIDERATIONS

For the analysis of waves generated by the periodic oscillations of an inclined plate hinged at the bottom, the fluid is assumed inviscid and the flow irrotational. The velocity potential, ϕ , is expressed in a separable manner as:

$$\phi(x,y;t) = \phi(x,y)e^{-i\sigma t} \quad (1)$$

where x is in the horizontal direction and y represents the depthwise direction as shown in the definition sketch, Fig. 1, $i = \sqrt{-1}$, and σ is the circular wave frequency defined as $2\pi/T$ where T is the wave period. The spatial variation of the velocity potential, $\phi(x,y)$, must satisfy the two-dimensional Laplace's equation:

$$\frac{\partial^2 \phi}{\partial x^2} + \frac{\partial^2 \phi}{\partial y^2} = 0 \quad (2)$$

with the following boundary conditions:

$$(i) \quad \frac{\partial \phi}{\partial y} = 0 \quad \text{at the bottom, } y = 0 \quad (3a)$$

$$(ii) \quad \frac{\partial \phi}{\partial n} = -i\sigma\xi\varepsilon \quad \text{on the surface of the inclined plate (The } n\text{-direction is normal to the boundary, } \xi \text{ is the distance from the hinge point to the position } (x,y) \text{ at the plate surface, and } \varepsilon \text{ is the maximum angular displacement of the plate.)} \quad (3b)$$

$$(iii) \quad \frac{\partial \phi}{\partial n} = \frac{\sigma^2}{g} \phi \quad \text{on the free surface, } y = h \quad (3c)$$

(This is a linearized free surface condition; thus, small amplitude wave motion is assumed.)

$$(iv) \quad \frac{\partial \phi}{\partial n} = ik\phi \quad \text{at } x = x_{01}, \text{ to approximately represent the radiation condition. (This condition for Region II at } x = x_{02} \text{ is shown also in Fig. 1.)} \quad (3d)$$

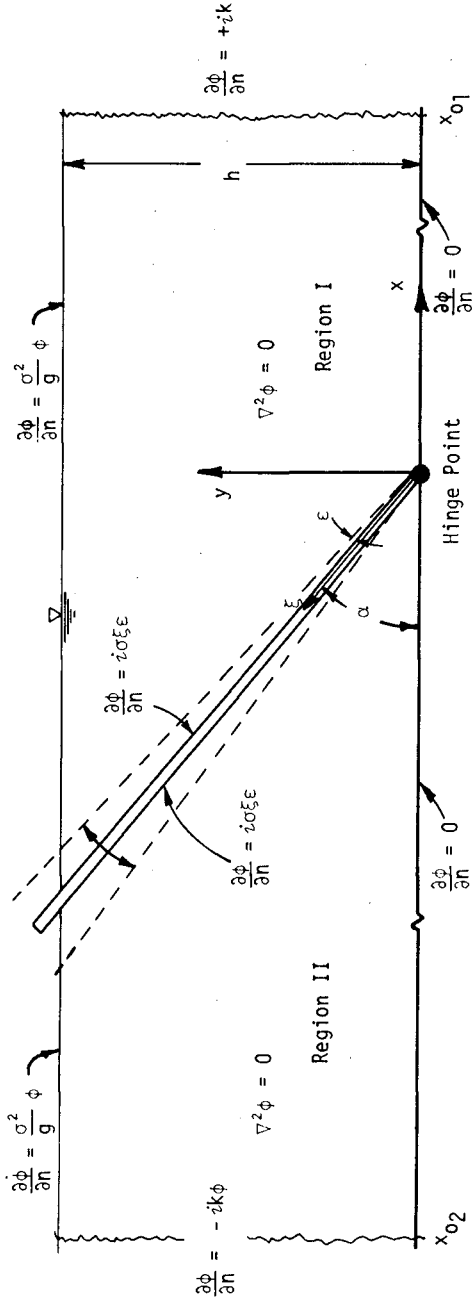


Figure 1 Definition Sketch for Theoretical Analysis.

Since the two regions cannot be represented by a separable coordinate system, it is advantageous to seek the solution of Eq. 2 by the boundary integral method. (A description of this method can be found in a number of texts on partial differential equations, e.g. Carrier and Pearson (1976).) Thus, the velocity potential can be expressed as:

$$\phi(\vec{x}) = \frac{1}{2\pi} \int_C \left[\ln\left(\frac{1}{r}\right) \frac{\partial\phi}{\partial n} - \phi \frac{\partial}{\partial n} \ln\left(\frac{1}{r}\right) \right] ds \quad (4)$$

where r represents the distance between the field point \vec{x} and the boundary points, and ds is a differential length along the boundary. The boundary integration is to be performed in a counter-clockwise direction, and the position vector \vec{x} of a field point is in the interior of the region to be considered. Eq. 4 implies that if one knows both ϕ and $\frac{\partial\phi}{\partial n}$ at the boundary of the region, the solution ϕ at the interior can be found readily. However, as indicated in the boundary conditions (Eqs. 3), the value of ϕ along the boundary needs to be determined before the value of the velocity potential in the interior of the fluid can be obtained. For this purpose, the following integral equation is obtained from Eq. 4 by allowing the field point \vec{x} to approach the boundary point \vec{x}_j :

$$\phi(\vec{x}_j) = \frac{1}{\pi} \int \left[\phi \frac{\partial}{\partial n} (\ln r) - \ln(r) \frac{\partial\phi}{\partial n} \right] ds \quad (5)$$

An approximate solution of ϕ in Eq. 5 is obtained numerically by dividing the boundary into a finite number of segments, N . In this manner Eq. 5 can be written in the following discrete form:

$$\phi(\vec{x}_j) = \frac{1}{\pi} \sum_{i=1}^N \left[\phi(\vec{x}_i) \frac{\partial}{\partial n} \ln(r_{ij}) - \ln(r_{ij}) \frac{\partial\phi}{\partial n}(\vec{x}_i) \right] \Delta s_i \quad (6)$$

where Δs_i represents the boundary segment length and r_{ij} is the distance between the i^{th} and the j^{th} segment. Eq. (6) can be expressed as a matrix equation as:

$$\begin{bmatrix} \phi(\vec{x}_1) \\ \vdots \\ \phi(\vec{x}_N) \end{bmatrix} = \frac{1}{\pi} \begin{bmatrix} (G_n)_{ij} \end{bmatrix} \begin{bmatrix} \phi(\vec{x}_1) \\ \vdots \\ \phi(\vec{x}_N) \end{bmatrix} - \frac{1}{\pi} \begin{bmatrix} (G)_{ij} \end{bmatrix} \begin{bmatrix} \frac{\partial\phi}{\partial n}(\vec{x}_1) \\ \vdots \\ \frac{\partial\phi}{\partial n}(\vec{x}_N) \end{bmatrix} \quad (7)$$

The elements in matrices G_n and G are defined as:

$$(G_n)_{ij} = \frac{1}{r_{ij}} \left[-\frac{(x_i - x_j)}{r_{ij}} \left(\frac{\Delta y}{\Delta s} \right)_j + \frac{(y_i - y_j)}{r_{ij}} \left(\frac{\Delta x}{\Delta s} \right)_j \right] \Delta s_j \quad (i \neq j)$$

$$(G_n)_{ij} = \left[\frac{(-x_{ss}y_s + x_s y_{ss})_i}{2} \right] \Delta s_i$$

$$(G)_{ij} = \left[\ln(r_{ij}) \right] \Delta s_j$$

(i ≠ j)

$$(G)_{ii} = \left[\ln\left(\frac{1}{2} \Delta s_i\right) - 1 \right] \Delta s_i$$

The vector $\frac{\partial \phi}{\partial n}(\vec{x}_i)$ in Eq. 7 involves the plate velocity, the bottom boundary condition, the radiation condition at either x_{01} or x_{02} and the free surface boundary condition and is given by:

$$\frac{\partial \phi}{\partial n}(\vec{x}_i) = \left[\underbrace{\frac{\partial \phi}{\partial n}(\vec{x}_1) \dots \frac{\partial \phi}{\partial n}(\vec{x}_p)}_{\text{"p" elements on the plate}}, \underbrace{0 \dots 0}_{\text{elements at bottom}}, \underbrace{ik\phi(\vec{x}_\ell) \dots ik\phi(\vec{x}_m)}_{\text{elements at the radiation boundary}}, \underbrace{\frac{\sigma^2}{g} \phi(\vec{x}_n) \dots \frac{\sigma^2}{g} \phi(\vec{x}_q)}_{\text{elements at the free surface}} \right]$$

It is clear that the vector $\frac{\partial \phi}{\partial n}(\vec{x}_i)$ contains values of the velocity potential along both the radiation boundary and the free surface which are to be evaluated in the solution. Therefore, to obtain a solution, the vector $\frac{\partial \phi}{\partial n}(\vec{x}_i)$ is represented by the linear superposition of vectors involving the known values of the velocity of the plate and the unknown velocity potentials on the boundaries. After some manipulation Eq. 7 can be rearranged into a form which can be solved readily:

$$\left\{ \begin{matrix} \left[\frac{1}{\pi} (G_n)_{ij} - I \right] \\ - \frac{1}{\pi} \begin{bmatrix} 0 \cdot (G_{ij}) \\ \dots \\ ik(G_{ij}) \\ \dots \\ \frac{\sigma^2}{g} (G)_{ij} \end{bmatrix} \end{matrix} \right\} \begin{bmatrix} \phi(\vec{x}_1) \\ \phi(\vec{x}_2) \\ \vdots \\ \vdots \\ \phi(\vec{x}_N) \end{bmatrix} = \frac{1}{\pi} G_{ij} \begin{bmatrix} \frac{\partial \phi}{\partial n}(\vec{x}_1) \\ \vdots \\ \frac{\partial \phi}{\partial n}(\vec{x}_p) \\ 0 \\ \vdots \\ 0 \end{bmatrix} \quad (8)$$

(A)
(B)
(D)
(E)

and from Eq. 8 one can obtain the following matrix expression for the velocity potential at the boundary $\phi(\vec{x}_i)$:

$$\begin{aligned}\phi(\vec{x}_t) &= (A - B)^{-1} \cdot D \cdot \underline{f} \\ &= M\underline{f}\end{aligned}\quad (9)$$

From the linearized dynamic free surface condition the wave amplitude at the free surface is given as:

$$\eta = -\frac{1}{g} \frac{\partial \phi}{\partial t} \Big|_{y=h} \quad (10)$$

In obtaining the numerical solutions described by Eqs. 6, 7, 8, two aspects of the problem should be mentioned. The first deals with the distribution of the elements on the boundary. The basic requirement is that the length of a boundary-element must be small compared to the wave length. Such requirement is particularly important in regions near the plate where the water depth is changing.

For the experimental conditions of $h = 15.24$ cm and $\alpha = 21.8^\circ$ the entire boundary of Region I was divided into 85 segments which include 20 segments on the wave-generating plate and 20 segments for the portion of the free surface which is located directly above the inclined plate; the remaining segments were distributed around the rest of the boundary. It should be noted the segments are not of equal length but are considerably smaller in the region over the plate on the free surface compared to the free surface in the constant depth region. The segment length was determined from numerical experiments. Numerical experiments were also conducted with the "radiative" boundary (at $x_{01} = 1.22$ m for the experimental arrangement) extended to $1.5 x_{01}$ and $2.0 x_{01}$. It was found that the results from these extended regions were nearly identical to those when the "radiative" boundary was set at 1.22 m. In other words, progressive waves of the same amplitude were found at $x_{01} = 1.22$ m, 1.83 m, or even at 2.44 m, i.e., for 8, 12, or 16 depths from the toe, respectively.

The second aspect of the numerical solution which must be given special attention is the treatment of the "corner point" above the plate where the water depth goes to zero. To avoid difficulty in this region the "corner" point was eliminated in the computation and it was replaced with a very small vertical segment. The numerical solution indicated that without such an approximation the results would be very sensitive to the distribution of the boundary elements. However, if a small portion of the "tip" of the fluid volume above the plate was eliminated, the solution was quite stable and the results tended to converge. The ratio of the length of the portion which was eliminated to the length of the inclined plate varied from 0.5% to 4%. The numerical results presented in the following section are obtained by eliminating a portion which is approximately 1% of the length of the plate. (Of course, a more sophisticated treatment of the region where the water depth tends to zero would be a welcome addition to the theoretical treatment of the problem.)

EXPERIMENTAL EQUIPMENT AND PROCEDURES

The experiments were conducted in a wave tank which is 18.3 m long, 84 cm wide, and 30 cm deep. The wave machine is located at one end of the tank and a rock-covered beach was placed at the opposite end for purposes of wave dissipation thereby substantially reducing the amplitude of reflected waves.

The wave generator could be inclined in the at-rest position at a specified angle and consisted of an inclined plate with a hinge at one end which was attached to the bottom of the wave tank. The top of the plate was restrained to be in contact with two horizontal arms which were connected at their opposite ends to a carriage which was mounted to horizontal rails by linear ball bushings. Ball bearings were attached to the end of each arm at the point of contact between the arm and the wave plate. Thus, as the carriage moved the hinged plate was forced to undergo a periodic motion with a maximum angular excursion, ϵ . A rod approximately 1.8 m long connected the carriage to an eccentric mounted to the output shaft of a variable speed motor; hence, varying the eccentricity varied the stroke. In this manner the inclined plate was forced to move with minimum modification to existing wave generating equipment.

The wave plate was constructed of plywood with a very small clearance (less than 1 mm) where it was hinged at the bottom. Along each sidewall of the wave tank the clearance was approximately 1.5 mm. Only waves were measured for the region for which the included angle between the wave machine and the bottom was an obtuse angle (Region I in Fig. 1). Various methods were used to measure both the angle of the plate and the stroke of the wave machine to ensure accuracy; both of these measurements were important in the comparison of the experimental results to the theory.

Mounted directly to the output shaft of the motor was a circular disk with 150 holes uniformly spaced near its circumference. A photocell and a light source were independently mounted on either side of the disk and aligned with the holes so as it rotated the interrupted light generated a pulsed voltage output. The frequency of these pulses was determined using an electronic counter; hence, the rotational speed of the motor could be accurately set and measured. In this manner the wave period could be determined to within less than 0.1 per cent.

The waves were measured approximately 6 m from the toe of the inclined-plate ($x = 6$ m); for the experiments conducted, this corresponds to 24 to 38 depths away from the generation region. All measurements were made using conventional parallel-wire-resistance wave gages which were calibrated before and after each experiment. The wave heights were measured before any reflections from the beach could return to the wave gage. Thus, a reasonably accurate determination of the incident wave could be obtained.

RESULTS AND DISCUSSION OF RESULTS

In this section the results that have been obtained from the theory and the experiments are presented and discussed. In Figure 2 the

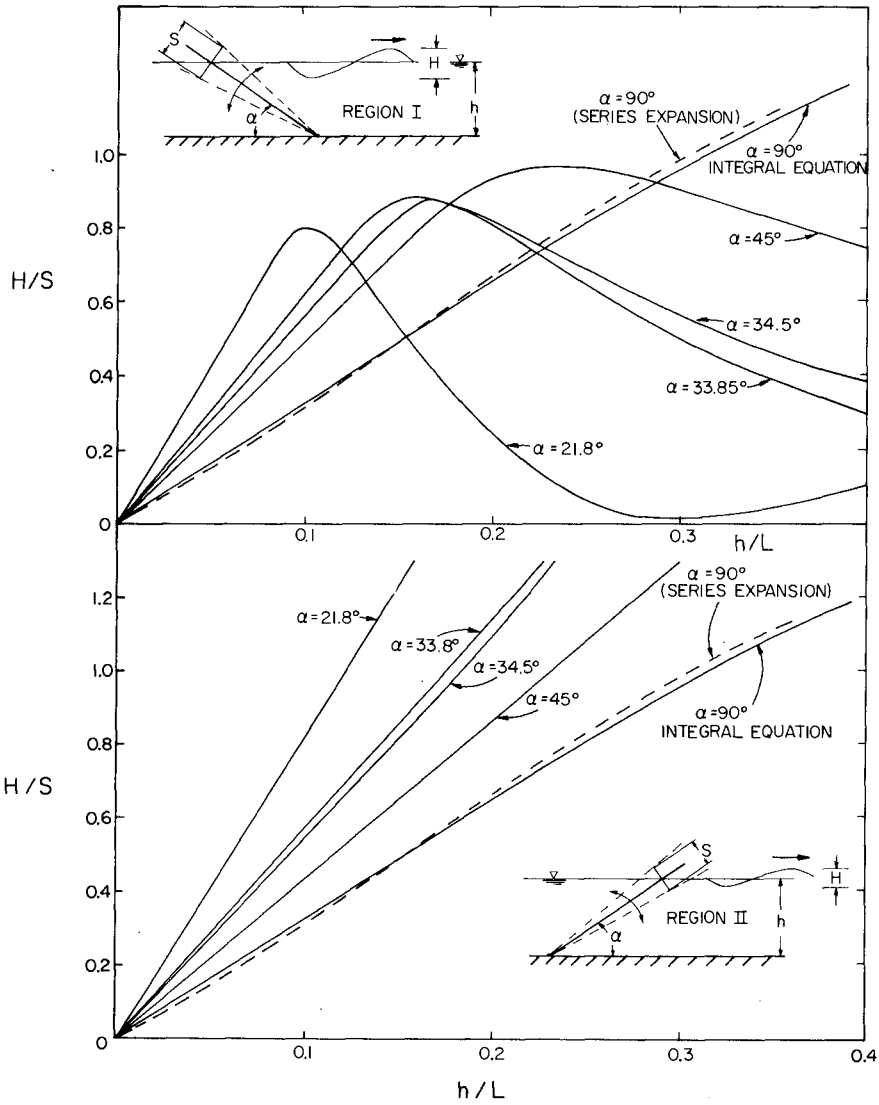


Figure 2 Theoretical Results for the Waves Generated by an Oscillating Inclined-Plate.

theoretical results are presented for the wave-maker theory described previously in the two regions: Region I where the region is bounded by the wave machine making an obtuse angle with the bottom, and Region II whose upstream limit is where the wave machine makes an acute angle with the bottom. (These two regions are shown in the insets in Figure 2.) The ordinate is the ratio of the wave height to the total stroke of the wave machine and the abscissa is the ratio of the depth to the wave length in the constant depth region. The stroke is the maximum excursion of the plate measured perpendicular to the plate at the plate-water-surface intersection with the generator in its at-rest-position. The wave length used is determined from small amplitude water wave theory for the given depth in the constant depth region and the measured wave period.

Attention is first directed to the lower portion of Figure 2 where the generation curves are shown for Region II for five different angles of inclination of the wave machine. A comparison is shown between the results using a series expansion for a perpendicular wave machine, i.e., $\alpha = 90^\circ$, and the results from the integral equation technique developed in this study. (The results of the analysis using a series expansion can be found in several references, e.g., Biesel and Suquet (1951)). Reasonable agreement between the two theories is seen with the disagreement attributed to certain approximations which are inherent in the present numerical approach.

It is noted that only a limited portion of the theoretical curves are shown, although the range in the ratio of depth to wave length extends from shallow water wave to nearly deep water wave conditions. Figure 2 shows, for a given ratio of depth to wave length, as the angle α decreases, the ratio of wave height to stroke increases, and the increase is approximately proportional to $(1/\sin\alpha)$. This is because the wetted length of the wave maker relative to the perpendicular plate increases in that ratio. It is recalled, the value of H/S for a perpendicular generator for large h/L is two; hence, for the inclined cases one would expect the height-to-stroke ratio to approach a limit of $(2/\sin\alpha)$.

The wave generation characteristics of the inclined plate in Region I are quite different from those just shown in Region II. Theoretical curves of the variation of the ratio of wave height to wave machine stroke with the ratio of depth-to-wave-length are shown in the upper portion of Figure 2 for plates with five angles of inclination. Again, for reference, the theoretical curves are presented for the hinged wave generator which is perpendicular to the water surface in its at-rest position ($\alpha = 90^\circ$) for both theories mentioned. The appearance of the other curves is interesting in that for a given wave stroke as the ratio of the depth to the wave length increases the wave height reaches a maximum and then decreases. (For small values of h/L the curves shown are nearly the same as the corresponding curves in Region II.) For the smallest angle investigated ($\alpha = 21.8^\circ$) the maximum wave height generated for a given stroke is about 0.8 and occurs at a ratio of depth-to-wave length of approximately 0.1; a minimum of nearly zero is realized for a depth-to-wave length ratio of about 0.3.

The reason for this variation is that waves are generated along this sloping face and propagate to the constant depth region. As waves

propagate past the hinge point into Region I, a portion is reflected back into the triangular region above the wave plate. For certain ranges of h/L the reflection is more than for others. This action essentially describes a resonant condition which can lead to maximum and minimum efficiencies of wave generation. This does not take place when waves are generated in Region II, since there is not a free surface above the wave generator for that case.

In Figure 3 experimental results are presented in addition to the theory for wave generators with four different angles: $\alpha = 21.8^\circ$, 33.85° , 45° , and 90° . In general, it appears that the theory agrees reasonably well with the experimental results. There is some disagreement which can be noted, and the reasons for this are: the effect of dissipation on the wave heights measured 24 to 38 depths from the wave generator, energy leakage around the sides of the wave generator, and, of course, the approximate nature of numerical theories. With the leakage less than 1% of the wetted area one would not expect as large a difference as observed for the case of $\alpha = 45^\circ$ (see Madsen, 1970).

CONCLUSIONS

In general, it can be concluded the numerical method developed provides a reasonable means of predicting the characteristics of the inclined plate wave generator. Two regions of generation are apparent with the response of the generator in these two regions distinctly different except for small ratios of depth-to-wave length. For certain at-rest angles of inclination and ratios of depth-to-wave length the generator could be described as being totally inefficient.

ACKNOWLEDGMENT

This study was supported in part by Grants ENV77-20499 and ENV77-01599 of the National Science Foundation and from support of the U.S. Navy Civil Engineering Laboratory. Certain of the experiments were conducted by Ella Wong.

REFERENCES

- Biesel, F. and Suquet, F., "Etude Theorique d'un Certain Type d'Appareil à Houle," La Houille Blanche, Vol. 6, 1951 (for English translation see Project Report 39, St. Anthony Falls Hydraulic Laboratory, University of Minnesota).
- Carrier, G. F. and Pearson, C. E., "Partial Differential Equations," Academic Press, 1976.
- Gilbert, G., Thompson, D. M., and Brewer, A. J., "Design Curves for Regular and Random Wave Generators," Journal of Hydraulic Research, Vol. 9, No. 2, 1971.
- Hammack, J. L. Jr., "A Note on Tsunamis - Their Generation and Propagation in an Ocean of Uniform Depth," Journal of Fluid Mechanics, Vol. 60, Part 4, Oct. 1973.
- Havelock, T. H., "Forced Surface-Waves on Water," Philosophical Magazine, Vol. VIII, Oct. 1929.

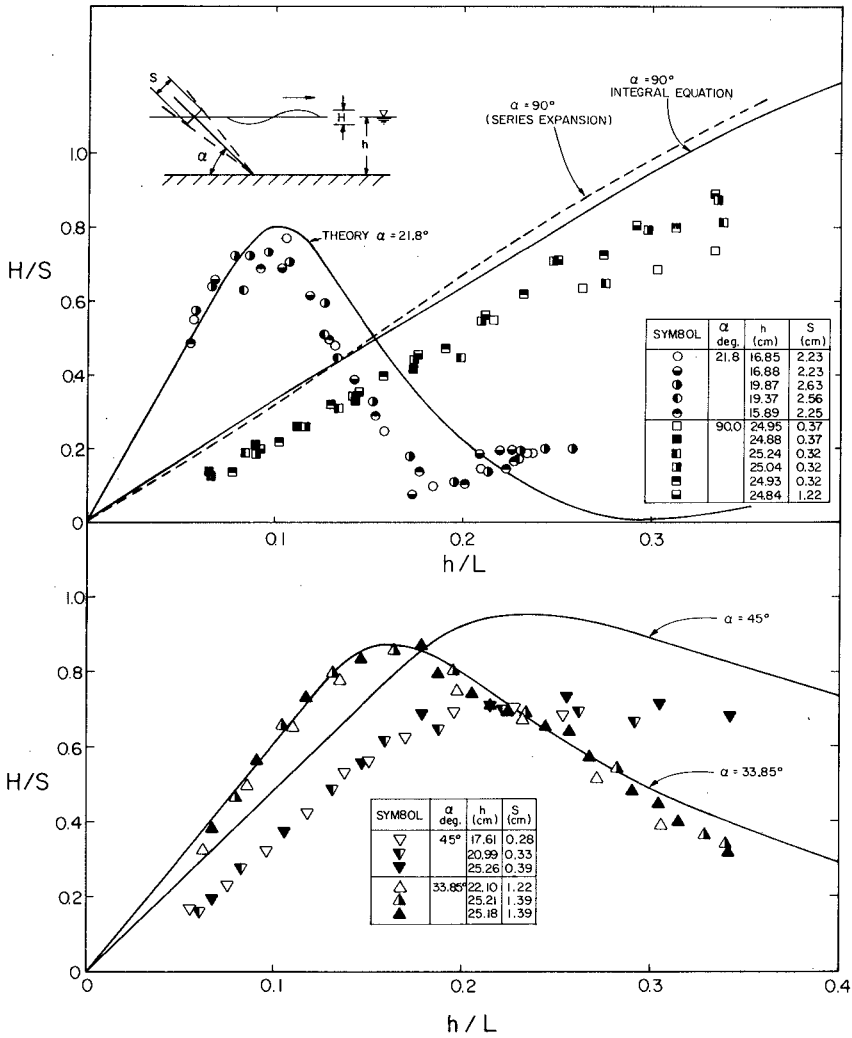


Figure 3 A Comparison of Experimental and Theoretical Results for the Waves Generated by an Oscillating Inclined-Plate.

- Madsen, O. S., "Waves Generated by a Piston-Type Wavemaker," Proceedings of the 12th Coastal Engineering Conference, Washington, D.C., 1970.
- Tuck, E. O. and Hwang, L.-S., "Long Wave Generation on a Sloping Beach," Journal of Fluid Mechanics, Vol. 51, Part 3, Feb. 1972.
- Ursell, F., Dean, R. G., and Yu, Y. S., "Forced Small-Amplitude Water Waves - a Comparison of Theory and Experiment," Journal of Fluid Mechanics, No. 7, Part 1, 1960.

CHAPTER 22

CHANGES IN HEIGHT OF SHORT WAVES ON LONG WAVES

by Michio Sato* and Kazuo Nakamura**

ABSTRACT

In this paper we describe an experimental study on changes in height of short gravity waves on long waves.

Experiments were conducted by making mechanically generated long waves superpose on mechanically generated short waves in a wave flume of 30m long and 1m wide.

Exact solution by Longuet-Higgins and Stewart explained our experimental results, but approximate expression $a' = a_1(1+P)$ which is widely accepted seemed to be inadequate to explain our results.

INTRODUCTION

It has been considered that, when gravity waves of short wavelength ride upon the surface of longer waves, the short waves become shorter and higher at the crests of longer waves, and they become longer and lower in the troughs. Unna(1) estimated the changes in amplitude and wavelength of short waves. Later his estimation on the change in amplitude was corrected by Longuet-Higgins and Stewart(2). They calculated it by taking into account the non-linear interactions between the two wave trains. According to their theory by using the perturbation method, the surface elevation of short waves is given by

$$\zeta = a_1(1+P)\sin \psi_1 + a_1 Q \cos \psi_2 \quad (1)$$

where a is amplitude, ψ is phase and subscript 1 denotes quantities of short waves. P and Q are expressed by somewhat complicated expressions when waves are in water of finite depth, but in the case of deep water, they are given by

$$P = a_2 k_2 \sin \psi_2 \quad Q = - a_2 k_1 \cos \psi_2 \quad (2)$$

where k is wave number and subscript 2 denotes quantities of the longer waves. Longuet-Higgins and Stewart described that, if P and Q are any small quantities, the expression (1) represents a wave of slightly modified amplitude

$$a' = a_1(1+P) \quad (3)$$

* Assistant Professor of Marine Civil Engineering, Kagoshima University, Kagoshima, Japan

** Technical Official of Marine Civil Engineering, Kagoshima University, Kagoshima, Japan

They also showed that equation (3) could be obtained in some cases from the physical point of view in terms of a radiation stress. From equation (3), the amplitude of short waves is predicted to become larger at the crests of longer waves and smaller in the troughs. Longuet-Higgins (3) discussed a mechanism in the generation of sea waves on the basis of equation (3). Phillips (4) obtained expressions for the change of short waves similar to equations (1) and (3) under the influence of wind, and discussed the attenuation of long waves passing through a local wind-generated sea. In equation (1), it is true that P is small. But Q is not always small, because $a_2 k_1$ is equal to $a_2 k_2 (k_1/k_2)$ and k_1/k_2 is able to become large. Therefore, $a_2 k_1$ is much larger than $a_2 k_2$. For example, if waves with period of 1 second ride on longer waves with period of 10 seconds and a_2 is 2.48m in deep water, then ζ is given by

$$\zeta = a_1(1+0.1\sin\Psi_2)\sin\Psi_1 - a_1(10\cos\Psi_2)\cos\Psi_1$$

This indicates that the change of ζ is dominated by Q rather than $(1+P)$. The change of ζ is shown in figure 1. The short waves become higher not at crests of longer waves, but at phases where surface elevation of longer waves is near the still water level.

Can we analyse the actual phenomena on the basis of equation (1)? Can equation (3) explain the actual phenomena? This is the reason why we made the present experiments on this phenomena.

EXPERIMENTAL EQUIPMENT AND PROCEDURE

Experimental studies on the interaction between wind generated short waves and mechanically generated long waves were performed by Mitsuyasu(5), Phillips & Banner(6) and Lee(7). But these were not designed to test directly the validity of the results of Longuet-Higgins and Stewart.

The presence of wind would probably prevent such experiments or field measurements testing the validity of the theory through problems such as interaction among waves, wind and a wind-induced current field which are not completely understood. So we attempted to superimpose mechanically generated long waves on mechanically generated short waves. The experiments were carried out in a wave flume, 30 m long and 1 m wide (Figure 2). A flap type wave generator driven by a servo-controlled DC motor was installed at one end of the flume. The long waves were superposed on the short waves in the following way.

We generated short waves first, and long waves subsequently to make the long waves run after the short waves and catch up with them. Capacitance type wave gauges were used to measure the water surface elevation. The experimental procedures

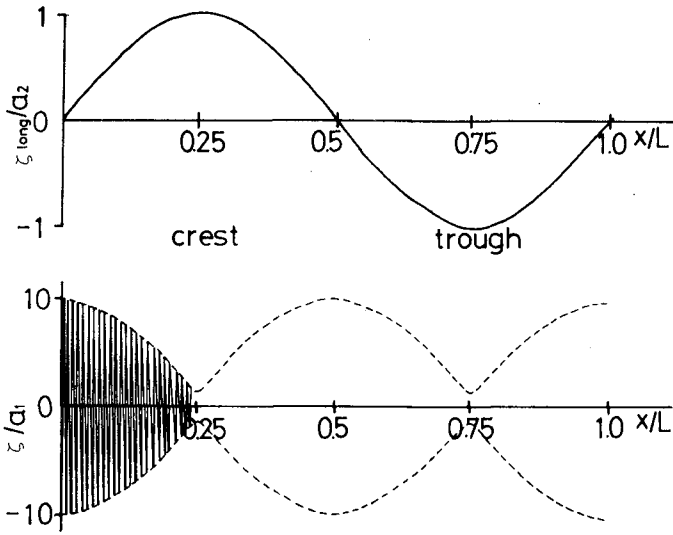


Figure 1. Change in amplitude of short waves calculated on the basis of equation (1)

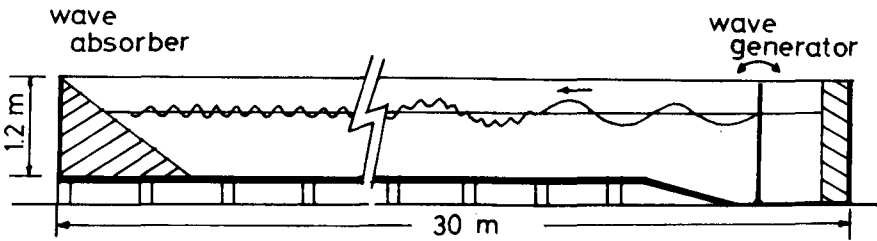


Figure 2. Experimental apparatus

Table 1. Wave characteristics used in experiment

h (water depth)	40,60,80 cm
T (wave period)	3~7 sec (long waves) 0.5~0.9 sec (short waves)
H (wave height)	1~13 cm (long waves) 0.6~4 cm (short waves)
Reflection coefficient	5~10 % (short waves) 10~20 % (long waves)

are summarized in figure 3.

In the early stage of our experiments, we used an electric highpass filter to pick up only the surface elevations due to the short waves. But the highpass filter was inadequate to be used in our experiments, because the error caused by phase shift due to the highpass filter lead us to wrong conclusions. Therefore, instead of the filter, we selected a frequency analyser with stored program system to process the measured signals. Wave characteristics used in our experiments are shown in table 1.

EXPERIMENTAL RESULTS AND DISCUSSIONS

On the basis of the records measured in the way as described above, we calculated power spectra of surface elevation by using the analyser through the fast Fourier transform method. One of examples of calculated spectra is shown in figure 4. In this figure, (a) shows the power when short waves and long waves were superposed, (c) and (d) are the power of the long waves only, and that of the short waves only, respectively, when they were generated solely. A quadruple enlarged scales are used as the axis of the ordinates in (b) and (d). f_1 and f_2 mean the frequency of the short waves and that of the long waves respectively. Only the relative values of powers among the components included in the records could be obtained by the reason of the program which was provided in the analyser.

Two components with frequencies f_1-f_2 and f_1+f_2 are produced by the second order nonlinear interaction between the long waves and the short waves, and they do not appear in (c) and (d). When both of the two wave trains are superposed, the f_1 component decreases its power comparing with the power of short waves contained before both waves were superposed. In our experiments waves of rather small steepness (especially in long waves) were used because of capacity of the wave generator. Therefore, components produced by the third order interaction were very small. This seems to be convenient to examine the theory based on second order interaction.

It has been shown that the components with frequency $f_1 \pm f_2$ will be produced through the second order interaction in the exact solution obtained by Longuet-Higgins and Stewart by using the perturbation method. contribution of the second order interaction to the elevation of free surface is given by

$$\zeta^{(2)} = \frac{1}{2g} a_1 a_2 [C \cos(\Psi_1 - \Psi_2) - D \cos(\Psi_1 + \Psi_2)] \quad (4)$$

where

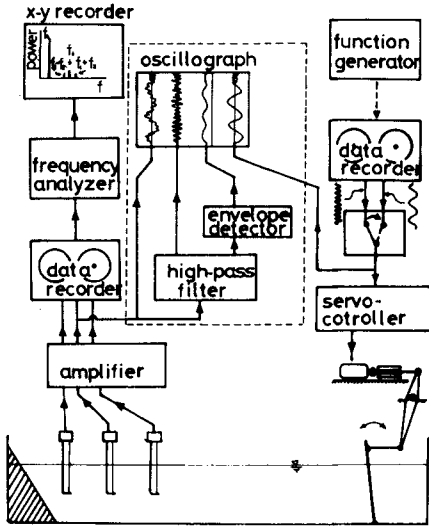


Figure 3. Experimental procedure

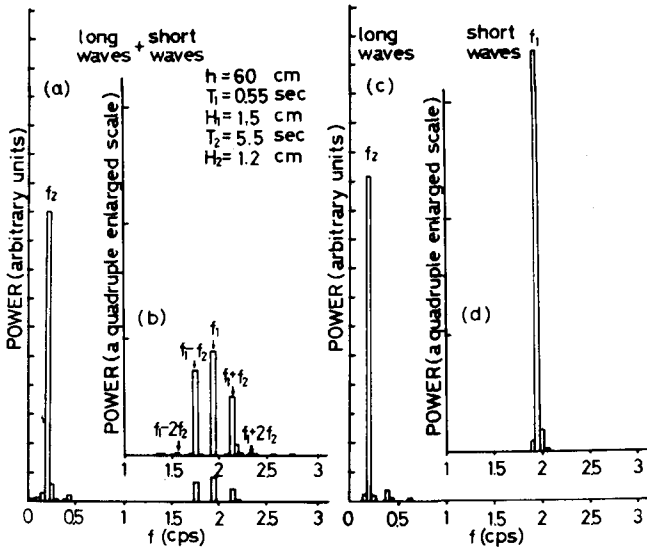


Figure 4. Example of power spectrum

$$C = \frac{[2\sigma_1\sigma_2(\sigma_1 - \sigma_2)(1 + \alpha_1\alpha_2) + \sigma_1^3(\alpha_1^2 - 1) - \sigma_2^3(\alpha_1^2 - 1)](\sigma_1 - \sigma_2)(\alpha_1\alpha_2 - 1)}{\sigma_1^2(\alpha_1^2 - 1) - 2\sigma_1\sigma_2(\alpha_1\alpha_2 - 1) + \sigma_1^2(\alpha_1^2 - 1) + (\sigma_1^2 + \sigma_2^2) - \sigma_1\sigma_2(\alpha_1\alpha_2 + 1)} \quad (5)$$

and D is given by a similar expression with the signs of α_2 , σ_2 reversed. σ denotes angular frequency, α is equal to $\coth kh$. Equation (1) is derived by combining the first approximation for the surface elevation of short waves, i.e. $a_1 \sin \psi_1$, with equation (4). Now, we put $a_1 a_2 C / 2g$ as $a_{f_1 - f_2}$, $a_1 a_2 D / 2g$ as $a_{f_1 + f_2}$ and a_1 as a_{f_1} . Then, we compare the experimental values of ratios $a_{f_1 - f_2}$ and $a_{f_1 + f_2}$ to a_{f_1} with theoretical values. Figure 5-(1)~(3) show the results. A full line and a broken line represent theoretical values of $|a_{f_1 - f_2} / a_{f_1}|$ and that of $|a_{f_1 + f_2} / a_{f_1}|$, respectively. In figure 5-(1), the wave steepness and the relative depth of long waves were kept constant and the ratio of frequency of short waves to that of long waves was changed. In figure 5-(2), the steepness of long waves was changed, and in figure 5-(3), the relative depth was changed. Experimental values agree with the theoretical curves. In figure 6, the wave profile ① within the part enclosed by solid line is one of examples of surface elevation when the short waves ride on the long waves. Powers of components included in this wave profile are given in the same figure, too. The wave profile ② was obtained by the following way. We calculated the Fourier transform of wave profile ① first and made the Fourier coefficients of components with frequencies in the range ② equal to zeros. Then, we calculated the inverse Fourier transform of the results. The wave profile ① can be regarded as the profile of the long waves. By the same procedure, we obtained the wave profile ② from the components with frequencies in the range ②. This can be regarded as the short waves on the long waves and this should correspond to ζ given by equation (1). Figure 7 is another examples whose power is shown in figure 4. Figure 7-(a) is the profile of long waves and (b), (c) and (d) are that of component with frequency $f_1 + f_2$, f_1 and $f_1 - f_2$, respectively. Adding up these three wave profiles, we get the wave profile (e). In these examples, the short waves become higher twice in one cycle of the long waves and not at the crests of long waves but at the phases that the surface elevation of long waves is near the still water level. Other results with frequency ratio σ_1 / σ_2 greater than 7 of our experiments show a similar tendency. As the frequency ratio σ_1 / σ_2 becomes small, the changes of amplitude of short waves become to correspond with the surface elevation due to the long waves. An example of such cases is shown in figure 9. In this case, the amplitude of short waves becomes large not at the crest of the long waves at the back faces.

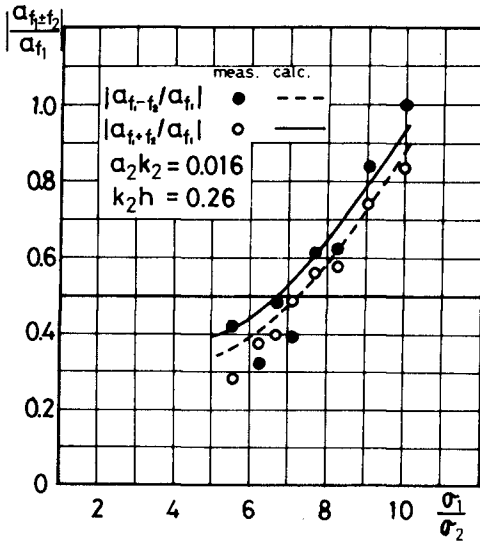


Figure 5. Comparison of calculated amplitudes of waves produced by second order interaction and experimental results (1)

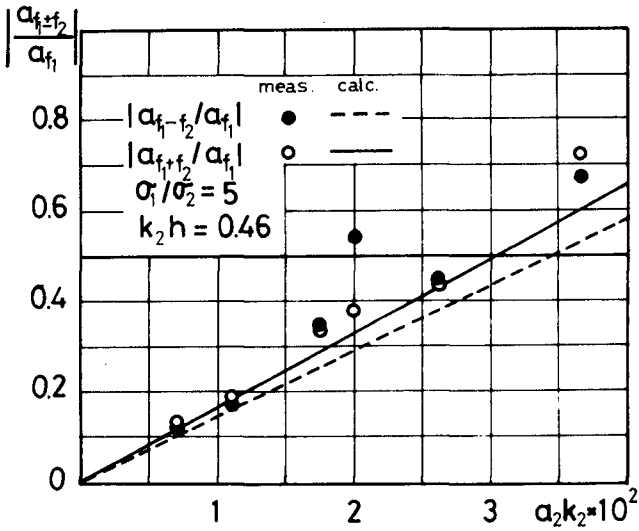


Figure 5-(2). Comparison of calculated amplitudes of waves produced by second order interaction and experimental results (2)

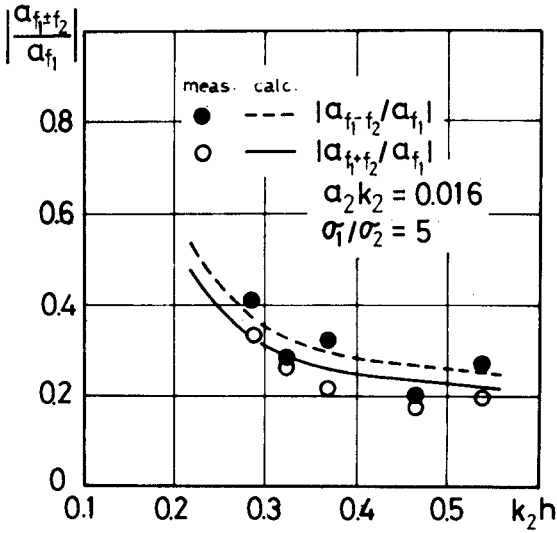


Figure 5-(3). Comparison of calculated amplitudes of waves produced by second order interaction and experimental results (3)

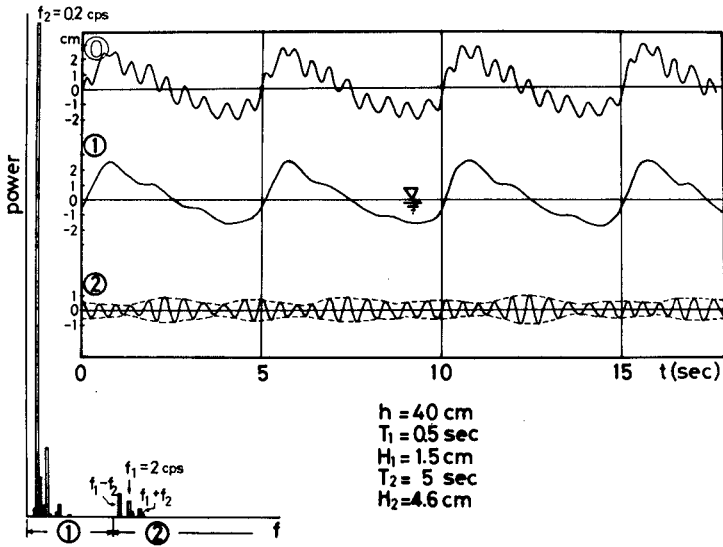


Figure 6. Separation of wave profile into long wave and short wave

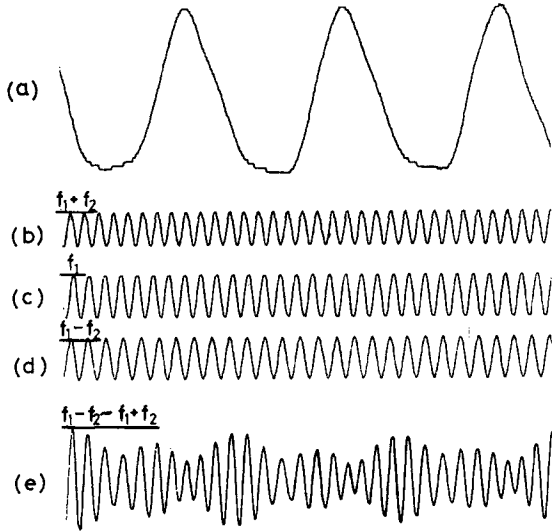


Figure 7. Wave profiles of components which compose short wave, and modulation of short wave

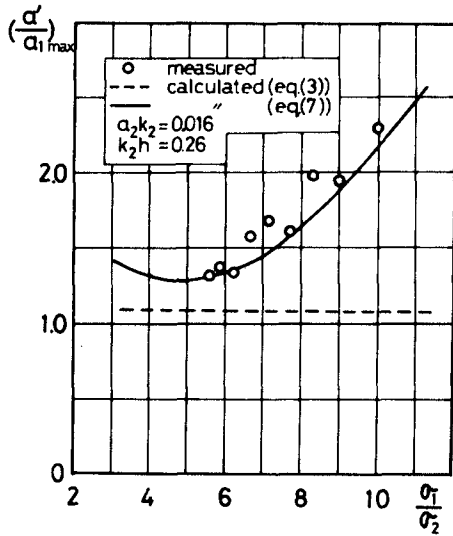


Figure 8-(1). Ratio of maximum amplitude of modulated short wave to amplitude of f_1 component, (1)

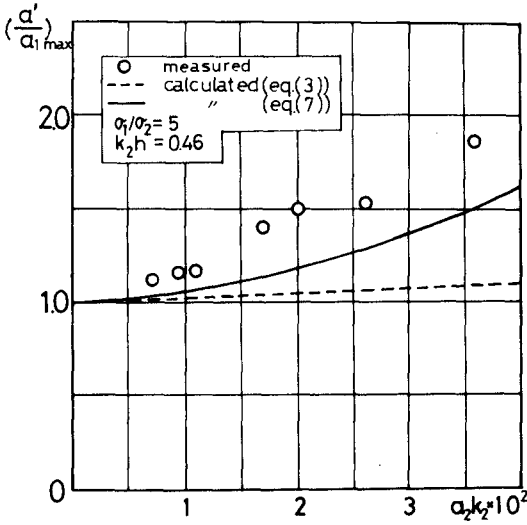


Figure 8-(2), Ratio of maximum amplitude of modulated short wave to amplitude of f_1 component, (2)

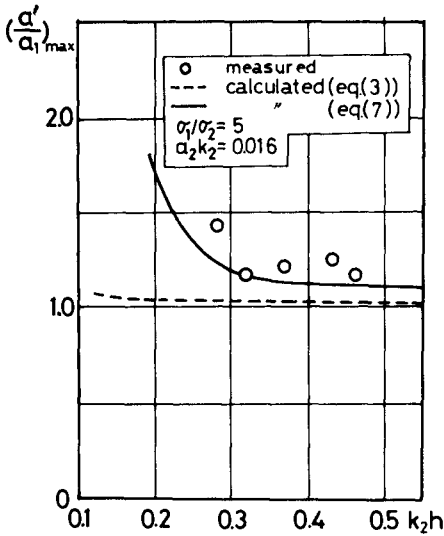


Figure 8-(3), Ratio of maximum amplitude of modulated short wave to amplitude of f_1 component, (3)

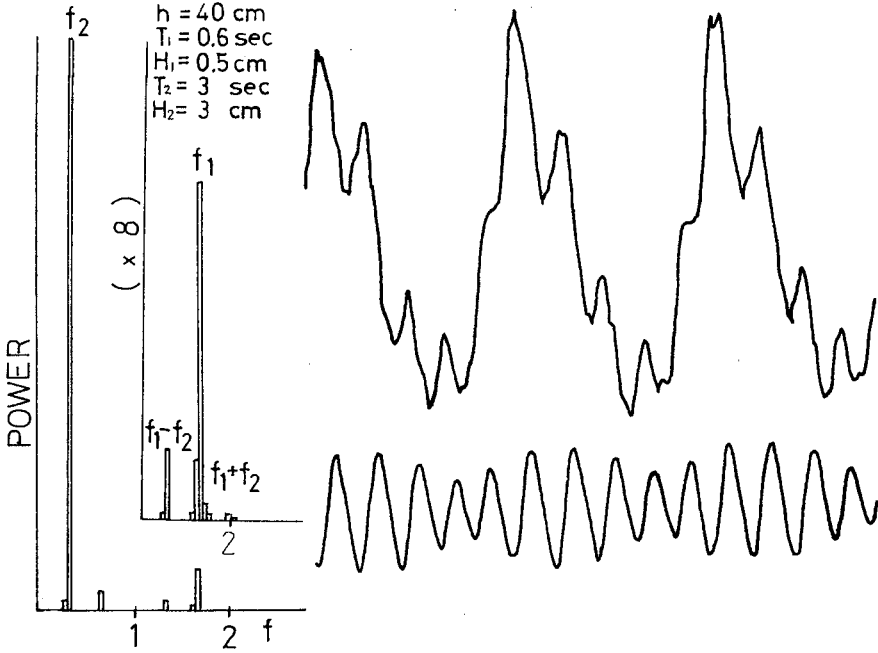


Figure 9. Profile of short waves when σ_1/σ_2 is small

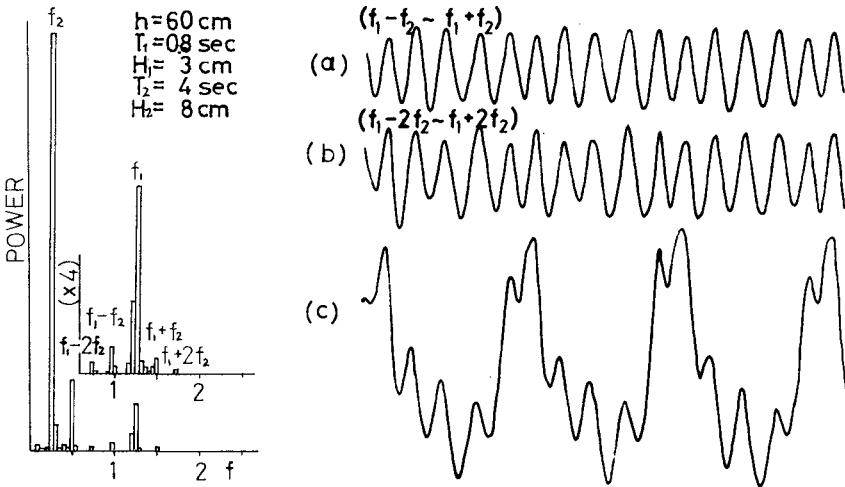


Figure 10. Effect of components with frequency $f_1 \pm 2f_2$ on modulation of short wave

Figure 8-(1)~(3) show how much the amplitude of short waves become larger relative to the amplitude of component with frequency f . Equation (1) can be written as follows

$$\zeta = a' \sin[\Psi_1 + \tan^{-1}(Q/(1+P))] \quad (6)$$

Then, modulated amplitude a' is given by

$$a' = a_1 \sqrt{(1+P)^2 + Q^2} \quad (7)$$

In figure 8, experimental results are compared with the predicted values by equation (3) and equation (7).

White circles show the experimental results, a full line shows the calculated one on the basis of equation (7), and a broken line shows calculated one on the basis of equation (3). Experimental results agree approximately with the predicted values by equation (7).

From the results above mentioned, we may conclude that the exact solution on the changes in height of short gravity waves on long waves by Longuet-Higgins and Stewart can sufficiently explain our experimental results.

But the approximate expression (3) which is widely accepted seems to be inadequate to explain the actual phenomena.

In our experiments long waves were restricted to small steepness. However, as the steepness become large, higher order interaction will become to play the important part of the change. This is suggested in some of our experimental results. In figure 10, (a) shows the wave profile with frequency of $f_1 - f_2 \sim f_1 + f_2$, and (b) shows that with frequency of $f_1 - 2f_2 \sim f_1 + 2f_2$. Components with frequency $f_1 \pm 2f_2$ modify the aspect of change in amplitude of short waves.

In figure 11, (a) is the wave profile with frequency of $f_1 - 2f_2 \sim f_1 + 2f_2$, and, in this example, not only amplitude of short waves but also frequency is modulated.

Though we didn't investigate systematically about these problems, these examples seem to suggest that the actual phenomena in nature is more complicated than the second order theory will predict.

CONCLUSION

Changes in height of short gravity waves on long waves were investigated experimentally by making mechanically generated long waves superimpose on mechanically generated short waves. The experimental results were compared with theoretical results by Longuet-Higgins and Stewart.

It becomes clear that the exact solution by them can sufficiently explain our experimental results. But approximate expression (3) seems to be inadequate to explain our results.

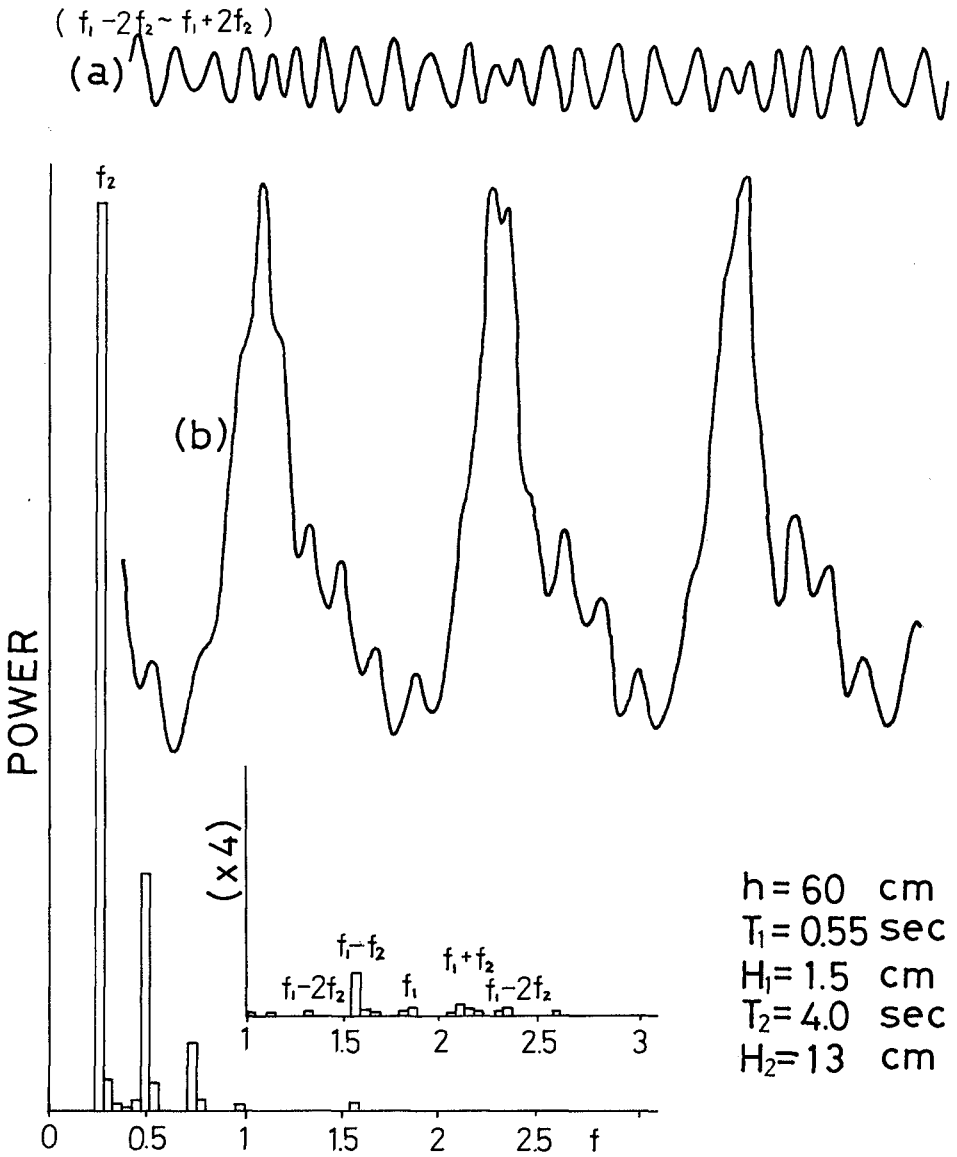


Figure 11. Example of experimental results in which not only amplitude but also frequency of short wave is modulated

REFERENCE

- (1) Unna, P. J. 1947. Sea waves. *Nature* 159, 239-242.
- (2) Longuet-Higgins, M. S. and Stewart, R. W. 1960. Changes in the form of short gravity waves on long waves and tidal currents. *J. Fluid Mech.* 8, 565-583.
- (3) Longuet-Higgins, M. S. 1969. A nonlinear mechanism for the generation of sea waves. *Proc. Roy. A.* 311, 371-389.
- (4) Phillips, O.M. 1963. On the attenuation of long gravity waves by short breaking waves. *J. Fluid Mech.* 16, 321-332.
- (5) Mitsuyasu, H. 1966. Interactions between water waves and wind (I). *Rep. Res. Inst. Appl. Mech., Kyushu University*, 14, 67-88.
- (6) Phillips, O. M. and Banner, M. L. 1974. Wave breaking in the presence of wind drift and swell. *J. Fluid Mech.* 66, 625-640.
- (7) Peter, H. Y. Lee. 1977. Doppler measurements of the effects of gravity waves on wind-generated ripples. *J. Fluid Mech.* 81, 225-240.

CHAPTER 23

COMPUTATIONS OF SHORT WAVES IN SHALLOW WATER

M.B. Abbott¹, H.M. Petersen² and O. Skovgaard³

ABSTRACT

The simulation of short wave propagation, including refraction, diffraction, partial reflection and all other such features, is made possible by a new version of the System 21, Jupiter. The System-generated models can describe any bathymetry and topography with any time-varying mean flow, correctly accounting for wave and current interactions, wave-thrusts or radiation stresses, longshore currents and other "second order" effects. The models work with irregular waves just as well as with regular waves. Radiation boundary modules are also provided so that models can be cut-out in any desired region and new features introduced without invalidating the field-study-determined boundary data. As models are system-generated, they can be constructed and run in a few hours, starting from charts, a lay-out of the proposed engineering works and the available boundary data. The development and testing of the System is briefly described, followed by an account of its applications in coastal engineering practice.

1. INTRODUCTION AND BACKGROUND

The modelling system used to compute short waves in shallow water that is the subject of this work constitutes the eight version of the System 21 "Jupiter" (Abbott, Damsgaard and Rodenhuis, 1973). This system was originally conceived for nearly-horizontal flow (negligible vertical acceleration) computations in two dimensions in plane and for vertically homogeneous (unstratified) waters. It was constructed in a system form capable of generating and running models when provided with only an elementary description of the area to be modelled, the boundary and other auxiliary conditions (e.g. barometric pressure fields or geostrophic wind fields) and resistance and similar parameters. (The difference between a model and a modelling system can be compared with the difference between a product and a factory to build products. Each

¹ Reader, International Institute for Hydraulic and Environmental Engineering, Delft, Netherlands, and Head, Computational Hydraulics Centre, Danish Hydraulic Institute, DK-2970 Horsholm, Denmark.

² Engineer, Computational Hydraulics Centre, Danish Hydraulic Institute.

³ Assoc. Prof., Laboratory of Applied Mathematical Physics, Bldg. 303B, Technical University of Denmark, DK-2800 Lyngby, Denmark; formerly Engineer, Computational Hydraulics Centre, Danish Hydraulic Institute.

product can be made individually more cheaply than the factory, but once the investment in the factory is made, the factory-produced products can be made more cheaply than the individually-made or "one-off" products. Thus although a modelling system costs roughly an order of magnitude more in money and time, as compared with a single one-off model, once built it can produce models at a fraction of the cost and in a fraction of the time required for one-off models). The System 21 was based upon various one-off models developed between 1960 and 1968 (e.g. Abbott, 1963; Sobey, 1970). It was started in 1969 but was only strongly backed from mid 1970. The first prototype was field tested in late 1971, pre-production versions ran in 1972 on two engineering contracts (Karachi harbour seiche analysis and Penang causeway connection) and the first production version, the Mark 5, came into use in 1973. This version used a four-stage difference scheme and was stable over a sufficiently wide range of Courant numbers and bathymetric configurations to provide a practical engineering instrument. On the basis of the success of this version, it was possible, from 1974 onwards, to design and develop an improved version, the Mark 6. This was field tested in 1975 and took-over as the main production version from 1976 onwards. These two versions have been the most widely used of all modelling systems in hydraulic and coastal engineering practice, accounting for 44 contracts in 13 countries, providing modelling services for engineering works the construction cost of which exceeds U.S.\$ 10,000,000,000.

This work on nearly-horizontal flow modelling took place in the environment of institutes well known for their pioneering work in short wave theory and practice. The Danish Hydraulic Institute had pioneered the use of irregular wave generators, essential for wave disturbance testing with ships, and together with the Technical University of Denmark had engaged in much basic research on short wave phenomena. On the other hand, the numerical tools available for short wave modelling were, more or less, the usual ones of linear-harmonic analysis and geometric-optical analogy, and these appeared increasingly incongruous in this environment.

Accordingly, it was decided to produce an instrument compatible with physical modelling over the widest possible range of applications and one that would be more satisfactory from the standpoint of modern wave theory. This instrument would be a logical development of the System 21, extending it to provide the simplest description of vertical accelerations with a sufficient range of validity, corresponding to the theory and equation formulations of Boussinesq (1877).

Now it was well known from earlier work (e.g. Abbott and Rodenhuis, 1972) that solutions of the equations of Boussinesq were exceedingly sensitive to errors. On the other hand, if any such instrument were to be of practical value, it would have to work with only a small number of descriptive points per wave length (as little as 6) in order that computing costs should remain acceptable. The main problem was then to produce a numerical scheme that was of such a high accuracy that worthwhile results could be obtained with very coarse descriptions.

At first sight, the task of designing a scheme of sufficient accuracy appeared quite overwhelming, apparently involving the

balancing-out of well over 100 terms in the truncation error, one against the other, each balancing necessitating the use of substitutions of formidable complexity. However, earlier work (Peregrine 1974; Abbott and Rodenhuis, 1972) had already indicated a possible simplification and on this basis of this work and its later elaborations (e.g. Bona & Smith, 1976) it was possible to develop satisfactory methodology of error elimination.

2. CONTINUUM AND DISCRETE DESCRIPTION

The present system solves difference equations that are consistent with the following differential equations

$$n \frac{\partial \zeta}{\partial t} + \frac{\partial p}{\partial x} + \frac{\partial q}{\partial y} = 0 \quad (1)$$

$$\begin{aligned} n \frac{\partial p}{\partial t} + \frac{\partial}{\partial x} \left(\frac{p^2}{h} \right) + \frac{\partial}{\partial y} \left(\frac{pq}{h} \right) + n^2 gh \frac{\partial \zeta}{\partial x} \\ = n \frac{Dh}{2} \left[\frac{\partial^3}{\partial x^2 \partial t} \left(\frac{Dp}{h} \right) + \frac{\partial^3}{\partial x \partial y \partial t} \left(\frac{Dq}{h} \right) \right] \\ - n \frac{D^2 h}{6} \left[\frac{\partial^3}{\partial x^2 \partial t} \left(\frac{p}{h} \right) + \frac{\partial^3}{\partial x \partial y \partial t} \left(\frac{q}{h} \right) \right] \\ - (1-n)^3 \frac{\alpha v}{d^2} p - \frac{(1-n)}{n} \frac{\beta}{d} p \sqrt{\left(\frac{p}{h} \right)^2 + \left(\frac{q}{h} \right)^2} \end{aligned} \quad (2)$$

$$\begin{aligned} n \frac{\partial q}{\partial t} + \frac{\partial}{\partial y} \left(\frac{q^2}{h} \right) + \frac{\partial}{\partial x} \left(\frac{pq}{h} \right) + n^2 gh \frac{\partial \zeta}{\partial y} \\ = n \frac{Dh}{2} \left[\frac{\partial^3}{\partial y^2 \partial t} \left(\frac{Dq}{h} \right) + \frac{\partial^3}{\partial x \partial y \partial t} \left(\frac{Dp}{h} \right) \right] \\ - n \frac{D^2 h}{6} \left[\frac{\partial^3}{\partial y^2 \partial t} \left(\frac{q}{h} \right) + \frac{\partial^3}{\partial x \partial y \partial t} \left(\frac{p}{h} \right) \right] \\ - (1-n)^3 \frac{\alpha v}{d^2} q - \frac{(1-n)}{n} \frac{\beta}{d} q \sqrt{\left(\frac{p}{h} \right)^2 + \left(\frac{q}{h} \right)^2} \end{aligned} \quad (3)$$

In open water the pore volume n is set to 1 while in permeable breakwater and similar porous structures is it set to the prevolume.

The equations are solved using a difference scheme that is brought to third order accuracy in all its essential terms, by use of the elimination method described by Abbott, Petersen and Skovgaard (1978). The range of application of the equation system (1, 2, 3) is also given in that work, together with experimentally derived phase portraits and other more theoretical information.

3. FIELD TESTS AND APPLICATIONS

In order to prove the System, simulations were first made of one-dimensional situations. Fig. 1 shows results of a simulation of shoaling cnoidal waves, the computed results being compared with the experiments of Madsen and Mei (1969). The agreement is seen to be very satisfactory. Another simulation is that of wave reflection and transmission at a permeable breakwater. In this case, illustrated in fig. 2, comparisons were made with experimental results reported with Keulegan (1973). In this case it is shown that by setting n to its physical value, values of the laminar and turbulent resistance parameters α and β can be found such that the experimental results are recovered to an acceptable accuracy. It should be added that the α and β values so found were entirely reasonable on physical grounds.

Results of a two dimensional simulation with small-amplitude periodic waves is shown in fig. 3 together with the results of the corresponding classical Sommerfeld diffraction theory. The agreement is again striking. Fig. 4 shows a perspective plot of the wave pattern of fig. 3, providing a more visually familiar picture.

Field testing of the Mark 8 was rounded-off by simulations of regular and irregular wave behaviour in Hanstholm harbour, Denmark. The prototype is illustrated in fig. 5 while fig. 6 shows the physical model that provided the results used for the comparison. Fig. 7 shows the Hanstholm physical model bathymetry(a) and how well this bathymetry is resolved in the numerical model(b). A perspective plot of fig. 7b is provided in fig. 8, for comparison with the photographs.

The first stages in a simulation, when a model is "cold started", are pictured by contours in fig. 9 for periodic waves. The first diffractions and refractions are clearly seen. Fig. 10 shows how steady a state can be attained with periodic waves after a suitable number of time steps have been run (here about 300-400 are necessary). The corresponding comparison between physical model and numerical model results for periodic waves is shown in fig. 11. The agreement is satisfactory taking account of the over-sensitivity of periodic wave amplification factors to measuring station positions and periods (Sørensen, 1973; Abbott, Petersen and Skovgaard, 1978). The reproducibility of phenomena with irregular waves, exemplified in plan in fig. 12, is generally more satisfactory and the comparison between physical model and numerical model results (fig. 13) is correspondingly much better. By way of visual verification, fig. 14 shows a perspective plot of waves in the outer harbour of Hanstholm.

When preparing a system model it is usual to set the charts of the region on a plotting table and follow contours with the plotter follower. The sequence of positions of the follower are translated by

SIMULATION OF CERC EXPERIMENTS ON SHOALING

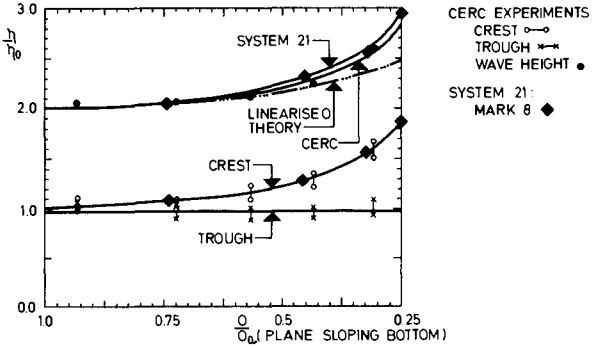


Fig. 1.

Comparison of numerical computations of shoaling waves obtained using the System in one-dimensional mode, as compared with the experimental results of Madsen and Mei (1969).

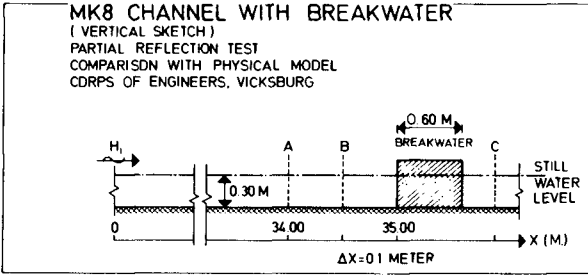


Fig. 2.

Water elevation for wave transmission through a permeable breakwater, with partial reflection, obtained using the System in one-dimensional mode.

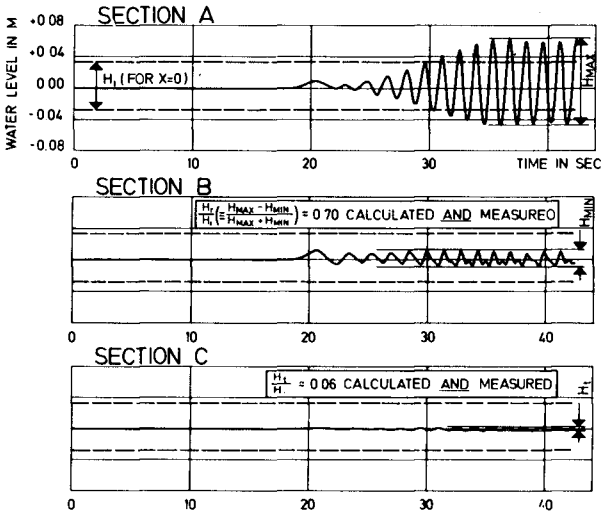


Fig. 3. Comparison of two-dimensional computations of pure diffraction with the analytical results of Sommerfeld. Plan view of contours.

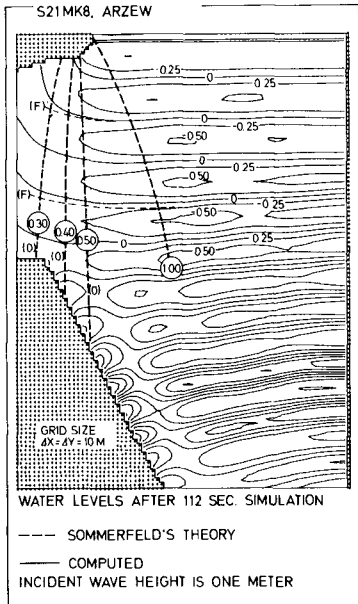


Fig. 4.

Perspective plot of the situation shown in fig. 3

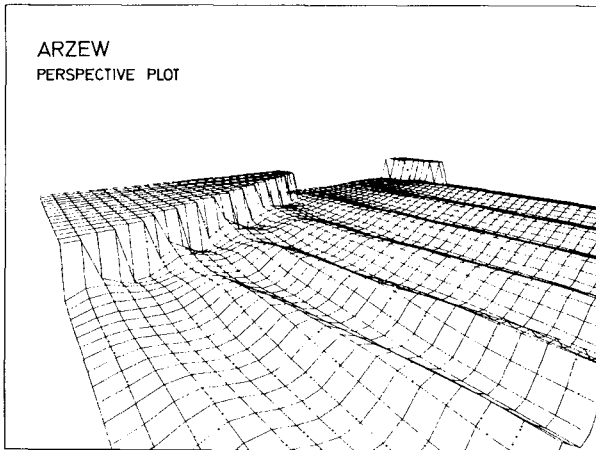




Fig. 5. Aerial photograph of harbour at Hansthalm.



Fig. 6. Photograph of physical model of harbour at Hansthalm.

HANSTHOLM HARBOUR

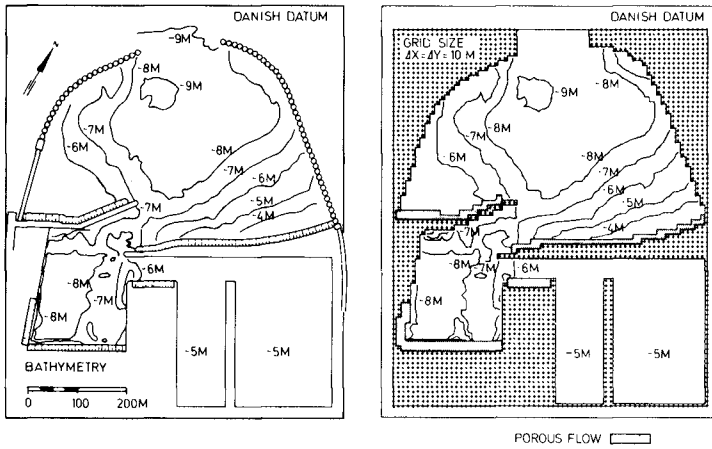


Fig. 7. Contours of the Hanstholm harbour as
 a. (left) used in the physical model tests, and
 b. (right) used in the numerical model tests.
 The porous areas are shown in both a and b.

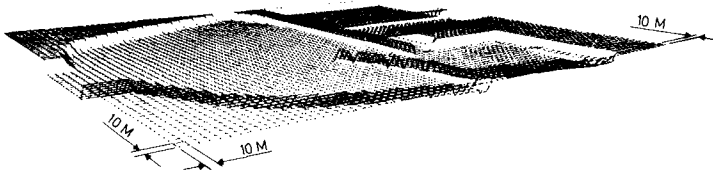


Fig. 8. Perspective plot of the numerical model bathymetry
 (Hanstholm harbour).

PERIODIC WAVES: STARTING OF MODEL FROM COLD

S21MK8, HANSTHOLM HARBOUR

S21MK8, HANSTHOLM HARBOUR

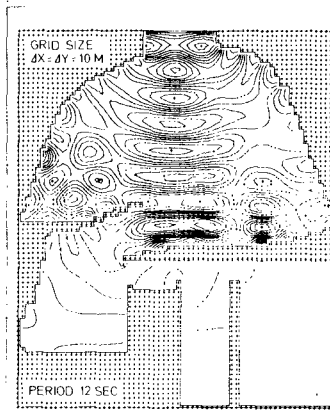
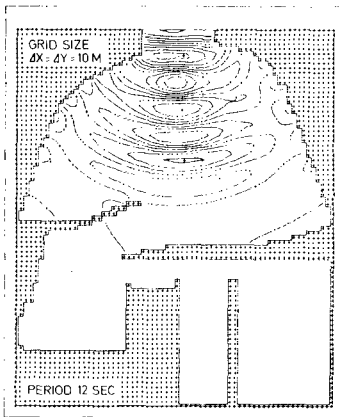


Fig. 9. Surface elevation contours with regular waves.
Left: After 44 sec. simulation.
Right: After 88 sec. simulation.

PERIODIC WAVES: STEADY STATE

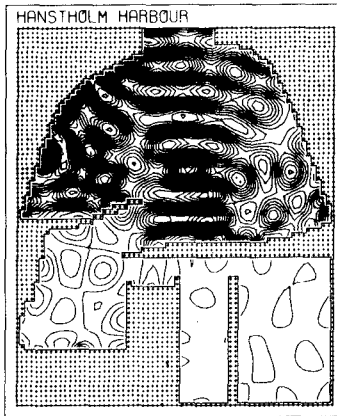
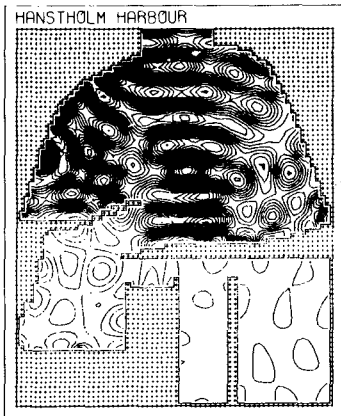
WAVE PERIOD $T=12$ SEC

Fig. 10. Surface elevation contours with regular waves compared for one wave period time difference to illustrate the steady state attained.
Left: After 468 sec. simulation.
Right: After 480 sec. simulation.

PERIODIC WAVES: COMPARISON WITH PHYSICAL MODEL
HANSTHOLM INNER HARBOUR

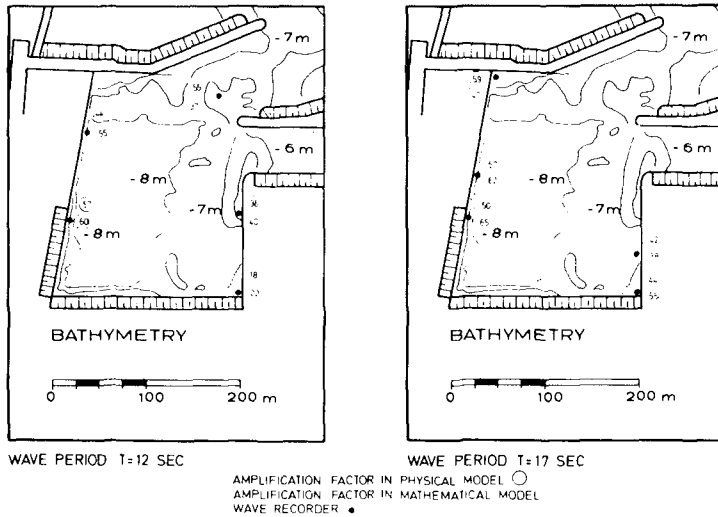


Fig. 11. Comparisons between amplification factors obtained in the first inner harbour in the physical model with those computed using the System, for 12s and 17s periodic waves of 10 cm amplitude applied at the harbour entrance.

suitable software into a digital description of the region and from this the grid points of a model of any size, orientation and degree of resolution can be generated. The results usually contain a considerable amount of 'noise' (2-4 points per resolved wave length), as illustrated by the bathymetry contours of a model resulting from this process, shown in Fig. 15a. Since this 'noise' is irrelevant to the essential behaviour of the model and it is improperly resolved in the model, it is usual to filter the bathymetry during the grid-generating process. By way of contrast with Fig. 15a, a very heavily smoothed model bathymetry is shown in Fig. 15b. Considerably less smoothing is used in System 21 models.

This process of automatic model generation and model operation allows the use of many different model areas in a single job. Fig. 16 illustrate the use of this facility in a study of a large harbour in the Persian Gulf. The objective here was to determine wave agitation in the area at different stages of the harbour construction. Fig. 17 shows the irregular wave train used as input while Fig. 18 shows (with a greatly exaggerated vertical-horizontal scale) a perspective plot of wave action around a 200 m long obstruction placed in the area. Fig. 19 shows the corresponding isolines of significant wave heights. (Figs. 16-19 courtesy Stevin Dredging B.V.).

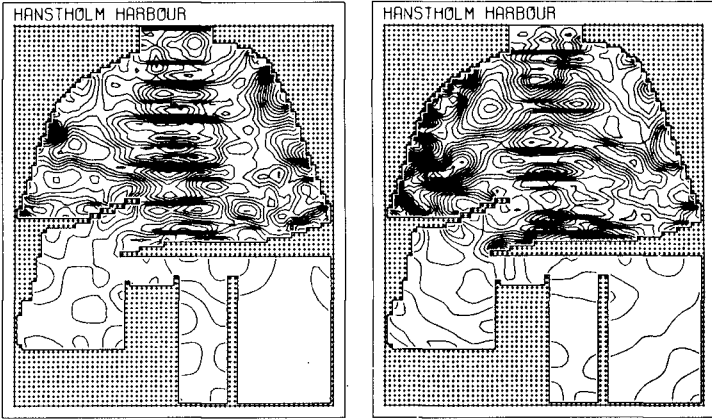


Fig. 12. Surface elevation contours with irregular waves (Significant wave height ≈ 1.5 m). Left: After 400 sec. simulation. Right: After 500 sec. simulation.

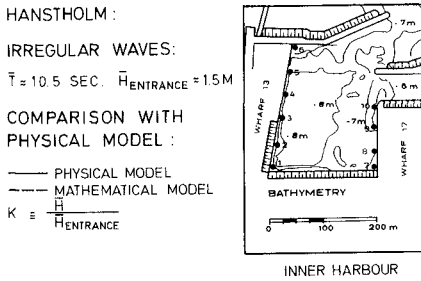
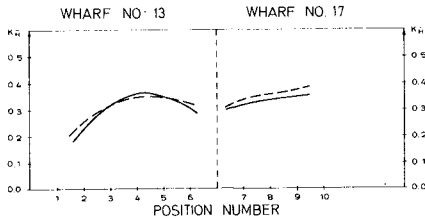


Fig. 13. Comparison between amplification factors obtained in the first inner harbour in the physical model with those computed using the System model, for tests with irregular, field-measured waves, applied at the harbour entrance.



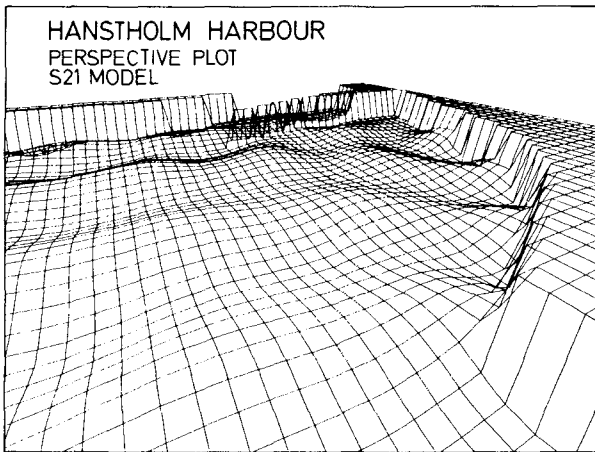


Fig. 14. A perspective plot of regular waves in the outer harbour (view from the harbour entrance).

Another application is illustrated by the contours of a Mediterranean harbour in Fig. 20. Fig. 21 shows 10s waves penetrating the harbour as viewed from two different elevations. Fig. 22 shows 14s waves, the upper picture corresponding to 143 time steps (200 sec simulation), and the bottom picture to 200 time steps (280 sec simulation) after starting from cold. The time step here was 1.4s. A corresponding chart of amplification factors is shown in Fig. 23.

It is possible to include ship motions simultaneously with wave motions in a new version of the system. At each time step the pressure field around the ship is computed simultaneously with the wave field, the resultant force and thence motion of the ship is determined, the ship moved into the corresponding new position. Then at the next time step this process is repeated.

A typical resulting movement in pure (heave) of a dredger is illustrated in Fig. 24.

4. ECONOMIC FEASIBILITY

The results obtained with this latest version of the System 21 show that it is capable of solving a wide range of short wave problems of engineering interest. Models can be constructed from charts and run under

BATHYMETRY : BINTULU

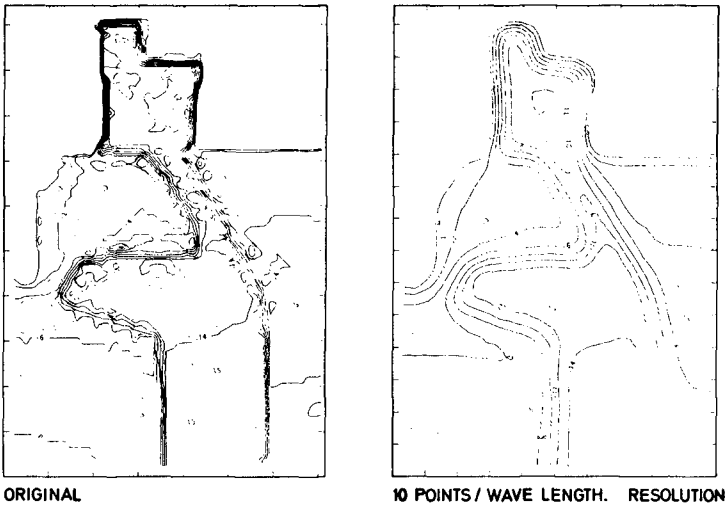


Fig. 15. Contours of the Bintulu Deep water harbour (Borneo) as
 a. (left) generated by the grid process (no smoothing)
 b. (right) generated by the grid process, when great
 smoothing are requested.

a wide range of incident wave climates in a few hours, or at most days and a large number of alternative engineering solutions can be investigated. The results are compatible with the input data used to steer irregular wave generators for physical model tests, so that a working interaction between numerical and physical models is practical.

However, it must be accepted that short wave modelling is more demanding in the level of resolution required, as compared with the now established nearly-horizontal flow modelling of tides, storm surges, seiches and similar "long-period" phenomena. This need for a much finer resolution implies the use of many more grid points in both space and time in a model and although the operational speed of the code is but little reduced by the higher accuracy and vertical acceleration resolving capacity, the cost of running a model for a given physical time becomes important. This cost must, of course, be acceptable to engineering practice if the work is to have any other than an academic interest. For example, the cost of running the simulation shown in Fig. 22 is about U.S. \$ 24 per physical minute simulation of the 3 km² harbour. It is considered necessary, however, that this price be reduced to U.S. \$ 6

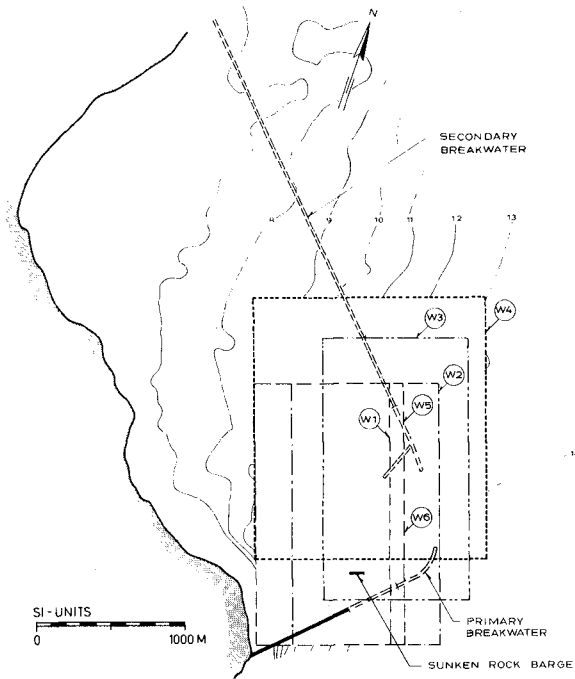


Fig. 16. Mathematical model grids used in a large harbour in the Persian Gulf.

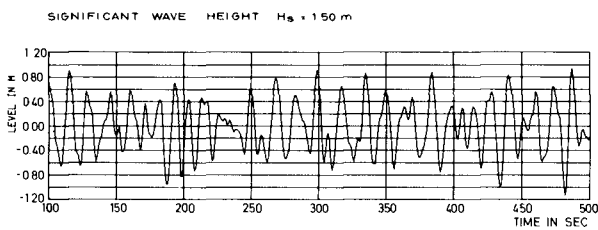


Fig. 17. The irregular wave train which was used as input to the S21 models in Fig. 16.

PERSPECTIVE PLOT

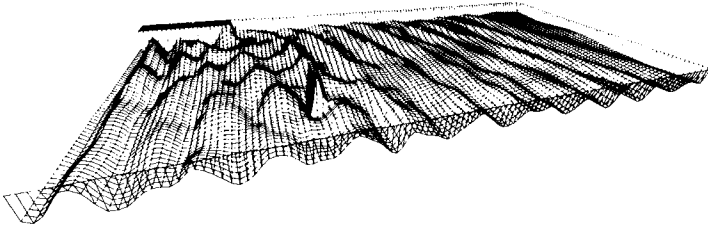


Fig. 18. A perspective plot of the wave action around the sunken rock barge in fig. 16.

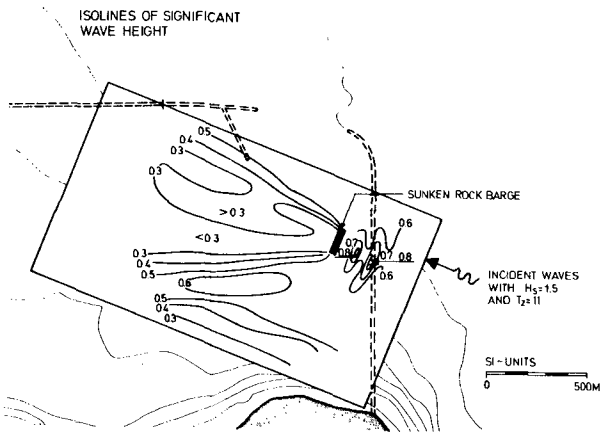


Fig. 19. Isolines of significant wave height H_s around the sunken rock barge in fig. 16.

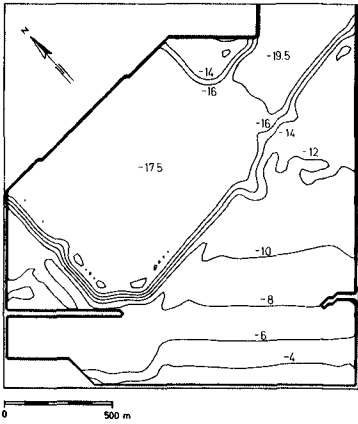
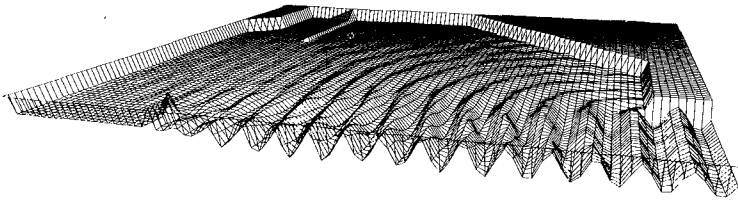
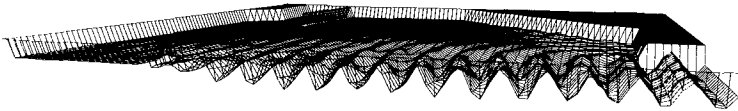


Fig. 20. Bathymetry (depths in meters) of the planned Misurata Harbour, used in the numerical model tests in figs. 21-23.

MISURATA: S21 MODEL, (WAVE PERIOD = 10 SEC.)



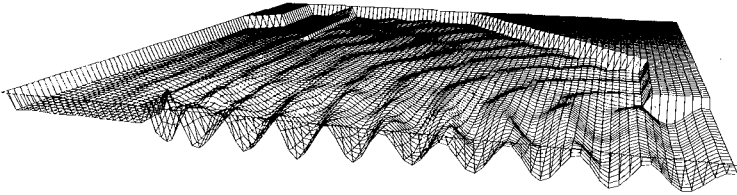
HIGHER LEVEL VIEW



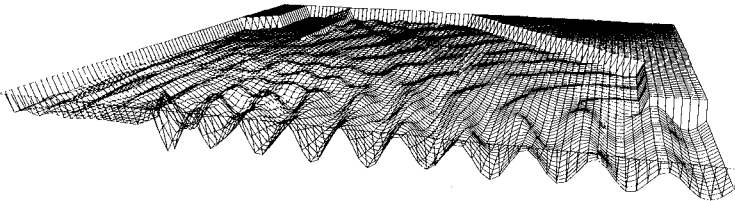
LOWER LEVEL VIEW

Fig. 21. Perspective plots of a regular wave field in the planned Misurata Harbour (wave period $T = 10$ sec.).

MISURATA: S21 MODEL, (WAVE PERIOD = 14 SEC.)



200 SEC. AFTER STARTING



280 SEC. AFTER STARTING

Fig. 22. Perspective plots of a regular wave field in the planned Misurata Harbour (wave period $T = 14$ sec.).

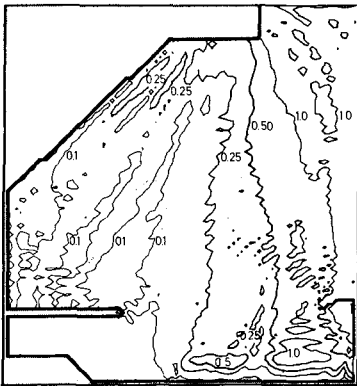


Fig. 23. Amplification factors for a regular wave field in the planned Misurata Harbour (wave period $T = 10$ sec.).

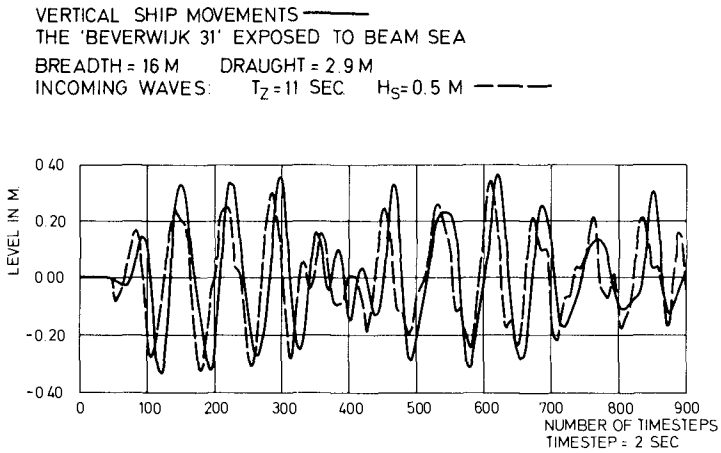


Fig. 24. Simulation of heave motion of a dredger exposed to beam sea.

per physical minute by mid 1979 in order that the system may have a satisfactory range of practical applications. It is expected that this objective will be met. This new System 21 version obviously has a wide range of applications, to ship motions, sediment transport and other problems, as outlined by Abbott, Petersen and Skovgaard (1978).

ACKNOWLEDGEMENT

This work was carried out with the partial support of the Danish Technological Research Council.

Notation

d	Rubble diameter (m)
D	Mean water depth (m)
h	Water depth, $\cong D + \xi$ (m)
n	Pore volume
p	x-volume flux, or alternatively x-horizontal momentum level per unit density, ($m^2 s^{-1}$)
q	y-volume flux, or alternatively y-horizontal momentum level per unit density, ($m^2 s^{-1}$)
t	Time (s)
x	Horizontal coordinate (m)
y	Horizontal coordinate, direction orthogonal to that of x (m)
z	Bed elevation (m)
α	Laminar flow resistance coefficient for a permeable breakwater
β	Turbulent flow resistance coefficient for a permeable breakwater
ξ	Water surface elevation (m)
ν	Kinematic viscosity ($m^2 s^{-1}$)

REFERENCES

- ABBOTT, M.B. and G.S. RODENHUIS (1972), A Numerical Simulation of the Undular Hydraulic Jump, *Journ.Hyd.Res.*, Vol. 10, No. 3, pp. 239-257.
- ABBOTT, M.B., A. DAMSGAARD and G.S. RODENHUIS (1973), System 21, "Jupiter" (A Design System for Two-Dimensional Nearly Horizontal Flows), *Journ.Hyd.Res.*, Vol. 11, No. 1, pp. 1-28.
- ABBOTT, M.B., H.M. PETERSEN and O. SKOVGAARD (1978), On the Numerical Modelling of Short Waves in Shallow Water, *Journ.Hyd.Rev.*, Vol. 16, No. 3, pp. 173-204.
- BONA, J.L. and R. SMITH (1976), A Model for the Two-Way Propagation of Water Waves in a Channel, *Math.Proc.Camb.Phil.Soc.*, Vol. 79, pp. 167-182.
- BOUSSINESQ, J. (1877), *Essai sur la Théorie des Eaux Courantes*. Institut de France, Académie des Sciences, *Memoires Présentés par Divers Savants*, Vol. 23, No. 1, 680 pp.
- KEULEGAN, G.H. (1973), *Wave Transmission Through Rock Structures, Hydraulic Model Investigation*, U.S. Army Engineer Waterways Experiment Station, Hydraulics Laboratory, Vicksburg, Mississippi, Res.Rep. H-73-1, 75 pp.
- MADSEN, O.S. and C.C. MEI (1969), The Transformation of a Solitary Wave Over an Uneven Bottom, *Journ.Fluid Mech.*, Vol. 39, Part 4, pp. 781-797.
- PEREGRINE, D.H. (1974), Discussion of: A Numerical Simulation of the Undular Hydraulic Jump, by M.B. ABBOTT and G.S. RODENHUIS, *Journ. Hyd.Res.*, Vol. 12, No. 1, pp. 141-157.
- SORENSEN, T. (1973), Model Testing with Irregular Waves, Dock and Harbour, Authority 5, Vol. 54, No. 631, pp. 2-5.

BOTTOM DISSIPATION IN FINITE-DEPTH WATER WAVES

By

S. V. Hsiao¹ and O. H. Shemdin²

ABSTRACT

The dissipation of wave energy by various bottom mechanisms plays an important role in the spectral transformation of waves as they propagate from deep to shallow water. Three bottom dissipation mechanisms are discussed. The bottom friction mechanism is investigated in detail and a method for calculating the friction coefficient is proposed. The method is tested by comparison with field measurements. Dissipation due to percolation and bottom motion are also discussed. The magnitude of dissipation rates induced by the different mechanisms are compared under various wave and bottom conditions.

1. Introduction

The dissipation due to bottom friction is the work done by the wave orbital velocity against the bottom turbulent shear stress. The latter is usually expressed as

$$\vec{\tau} = \rho C_f |\vec{u}| \vec{u} \quad , \quad (1)$$

where $\vec{\tau}$ is the turbulent shear stress, ρ is the density of water, C_f is the friction coefficient, and \vec{u} is the velocity immediately outside the bottom boundary layer. Previous studies by Bretschneider and Reid (1954) and Hasselmann and Collins (1968) had indicated that the friction coefficient is of order 10^{-2} . Consequently, this value has been widely used. More recently, the friction coefficient has been observed to vary significantly above and below this value depending on the sand grain diameter and whether bottom ripples are present. This paper reviews the mechanisms responsible for generating bottom ripples and a method is proposed for estimating bottom friction coefficients under various bottom configurations.

The dissipation due to percolation is caused by viscous damping of energy induced by water seeping through the pores of the sandy bottom. Waves propagating above soft muddy bottoms can have their energy transferred at a rapid rate to the bottom mud layer where it is dissipated by the viscous motion induced in the bottom mud. The magnitude of such energy dissipation can be one to two orders of magnitude greater than that due to bottom friction or percolation. The rates of energy dissipation due to these three mechanisms are compared at corresponding water depths

¹Scientist, Oceanography and Climate Group, Jet Propulsion Laboratory, California Institute of Technology, Pasadena, California.

²Head of Oceanography and Climate Group, Jet Propulsion Laboratory, California Institute of Technology, Pasadena, California and Professor, Department of Coastal and Oceanographic Engineering, Univ. of Fla., Gainesville, Florida.

in the last section of this paper.

II. Review of Bottom Friction Studies

Bottom friction was first investigated by Putnam and Johnson (1949). They used the quadratic friction law, $\vec{\tau} = \rho C_f |\vec{u}| \vec{u}$, and found the dissipation rate for sinusoidal waves to be

$$\frac{1}{E} \frac{dE}{dt} = -\frac{4}{3} \frac{C_f \omega^3 H}{g \sinh^3 kh}, \quad (2)$$

where E is wave energy, t is time, ω is wave frequency, H is wave height, k is wave number, and h is water depth. Bretschneider and Reid (1954) applied Putnam and Johnson's equation and found $C_f = 0.01$ for the sandy bottoms of the Gulf of Mexico. Hasselmann and Collins (1968) assumed the wave field to be Gaussian. They derived the following equation to compute the rate of energy dissipation in a random sea

$$\frac{1}{F(\vec{k})} \frac{dF(\vec{k})}{dt} = -\frac{g C_f k_i k_j}{\omega^2 \cosh^2 kh} (\delta_{ij} \langle |\vec{u}| \rangle + \langle \frac{u_i u_j}{|\vec{u}|} \rangle), \quad (3)$$

where $F(\vec{k})$ is the wave energy density at wave number \vec{k} , $\langle \rangle$ denotes the ensemble average, $i, j = 1, 2$, u_1 and u_2 are the two orthogonal components of \vec{u} , k_1 and k_2 are the two corresponding wave number components of \vec{k} . They found C_f to be 0.015 using the wave spectra measured offshore of Panama City, Florida. Based on these two studies C_f values of the order 10^{-2} have been widely used (see for example Collins (1972) and U.S. Army Coastal Engineering Research Center (1973)). More recently, much higher values have been reported. Van Ieperen (1975) computed the friction coefficients for wave data obtained offshore of Melkbosstrand, South Africa to be in the range 0.06 - 0.10.

Laboratory and semi-theoretical studies by Jonsson (1965) indicate that C_f is a function of both the wave Reynolds number defined, $R = a U_m / \nu$, and the relative roughness defined, a/k_s , where a is one half of the horizontal orbital excursion above the bed, U_m is the maximum wave orbital velocity outside the bottom boundary layer, ν is the kinematic viscosity of water, and k_s is the bottom roughness. A friction factor diagram showing the relationship between the friction coefficient, the wave Reynolds number, and the relative roughness was first proposed by Jonsson (1965) based on very little data. Expanding the data base through a series of laboratory tests, Kamphuis (1975) presented his friction coefficient diagram shown in Figure 1 which shows that the friction coefficient can easily vary by one order of magnitude either above or below the widely used value of 10^{-2} depending on bottom roughness.

When sand ripples are formed on a sandy bottom, the bottom dissipation is enhanced due to form drag. Additional energy dissipation occurs in the vortices formed above the ripple troughs. The formation

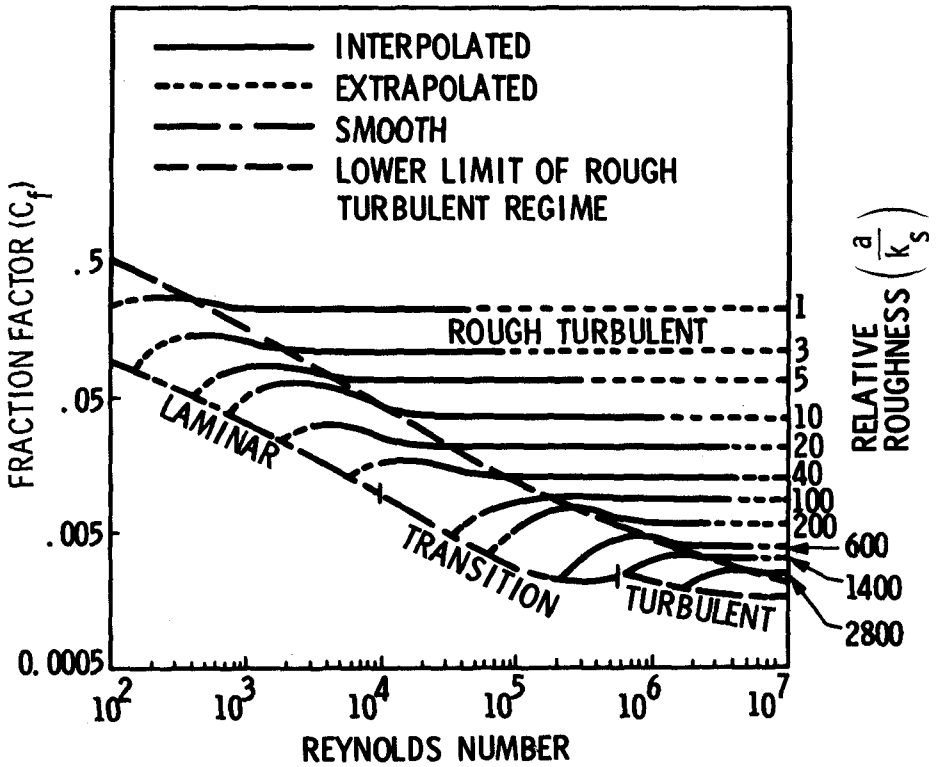


Figure 1. Friction factor diagrams (after Kamphuis, 1975).

of ripples has been investigated extensively in the laboratory, and to a lesser extent in the field. A review of these studies was reported by Dingler (1975) who also formulated a relationship for the prediction of bottom sand movement under wave action. The condition for the onset of sand motion suggested by Dingler (1975) has the form

$$\frac{\gamma_s T^2}{\rho D_s} = 240 \left(\frac{2a}{D_s} \right)^{4/3} \left(\frac{\rho \gamma_s D_s^3}{\mu^2} \right)^{-1/9} \quad (4)$$

where $\gamma_s = (\rho_s - \rho) g$, ρ_s is the density of sand, T is wave period, D_s is the mean sand diameter, and μ is the viscosity of water. If this condition is satisfied, bottom ripples can be expected. The ripple slopes, ζ/λ_s , were found to have a functional dependence on a dimensionless stress parameter, θ_s , defined in terms of wave orbital velocity and bottom sediment properties as follows:

$$\theta_s = \rho \frac{U_m^2}{\gamma_s D_s} \quad (5)$$

(see Figure 2). The ripples were found to vanish for $\theta \geq 2.5 \times 10^2$.

A different characterization of ripple properties was reported by Nielsen (1977) who found the dimensionless ratio, λ_s/a , to be functionally dependent on U_m/w , where w is the fall velocity of sand. The experimental results supporting such a relationship are shown in Figure 3. From the results of Dingler and Nielsen, it is possible to determine whether ripples are present, and then to predict the lengths and heights of such ripples. The only necessary inputs are the properties of prevailing waves and bottom sediment. As will be shown in the following sections, the ripple heights determine the bottom roughness and consequently the magnitude of the friction coefficient.

III. A Proposed Method for Estimating the Bottom Friction Coefficient

From the discussion in section II, it is clear that a constant C_f value of 10^{-2} cannot be expected to be universally valid. In this section, a method for determining C_f is proposed.

In analogy with friction losses over rigid boundaries, the use of a friction diagram such as shown in Figure 1 is necessary to estimate C_f . For given wave and depth conditions, it is possible to determine the Reynolds number $R = U_m a/\nu$ and the orbital amplitude, a . Still, the roughness height, k_s , must be estimated before C_f is determined.

For a flat bottom, the roughness height, k_s , is assumed to be equal to the sediment diameter, D_s . Therefore, under conditions when Equation (4) can not be satisfied or $\theta \geq 2.5 \times 10^2$ the value of k_s is determined directly from D_s . Then C_f is defined from known value of (a/k_s) and R using Figure 1.

When the wave and bottom sediment conditions satisfy Equation (4), bottom ripples form. Their heights, ζ , and lengths, λ_s , are then determined in the manner discussed in section II. In the presence of ripples Tunstall and Inman (1975) found that the experimental results of Bagnold (1946), Inman and Bowen (1963), Jonsson (1966), Carstens et al (1969), and Reidel et al (1972) all supported an inverse dependence of

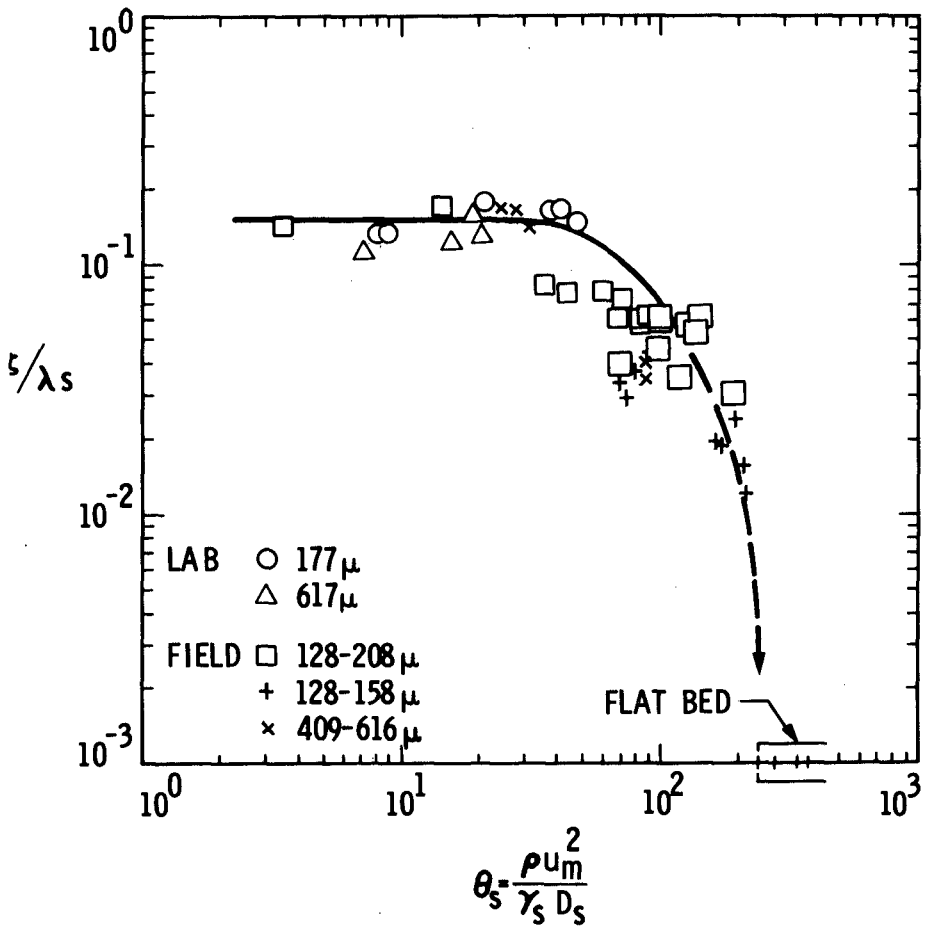


Figure 2. Ripple steepness vs. relative stress (after Dingler, 1975).

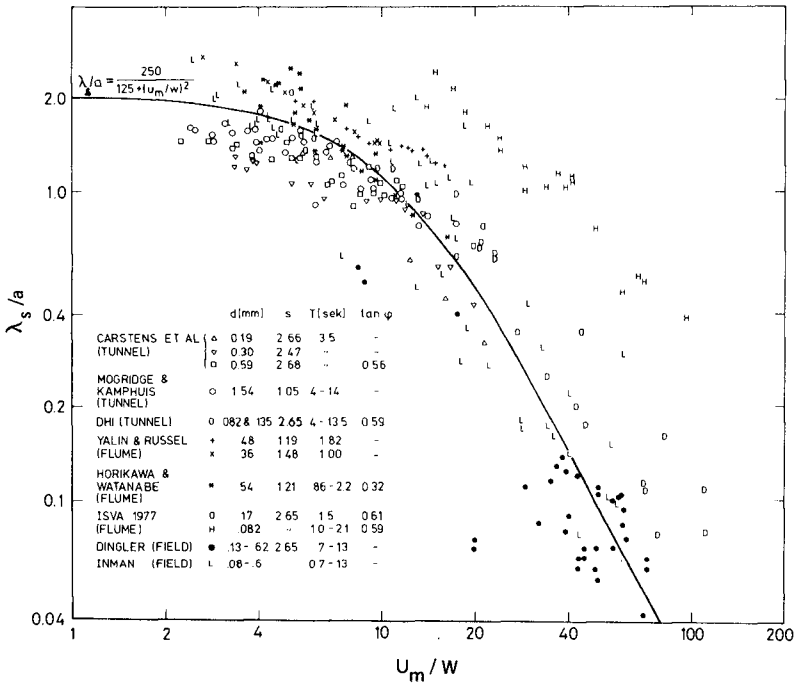


Figure 3. λ_s/a vs. U_m/w (after Nielsen, 1977).

C_f on (a/k_s) provided that $k_s = 4\zeta$. The friction coefficient diagram shown in Figure 1 is in fact constructed to provide the correct C_f value for a given R value. As ripples form, the k_s value increases in proportion to the ripple height, ζ , so that the ratio of (a/k_s) decreases. The latter increases C_f . In the following section the validity of this procedure is tested against new field data not used in deriving the friction diagram.

IV. Friction Coefficients Computed from Field Measurements

Two sets of wave data were available to compute the friction coefficients in order to verify the method described in section III. One is the wave spectra obtained offshore of Panama City, Florida on September 9, 1965 (Breeding, 1972). The waves were measured by two pressure sensor arrays located at 31.7 m and 19.2 m water depths. The other is the spectra obtained offshore of Marineland, Florida on December 14, 1975 (Shemdin et al, 1975). A Geodolite laser sensor was used to measure the waves at 31 m water depth and a pitch-and-roll buoy was used at 8.5 m water depth.

The C_f values were computed from spectra at two different depths using a method similar to that of Hasselmann and Collins (1968). For the Panama City case the C_f values were found to be in the range 0.035-0.05. A sample predicted shallow water spectrum is compared with the measured shallow water spectrum in Figure 4. The C_f value in this particular calculation is 0.04.

Using the method described in section III, the estimated C_f value is 0.03. It is also found to be approximately a constant between the two measuring stations based on wave and sediment conditions at both stations. A summary of wave and sediment conditions needed to calculate C_f is shown in Table 1. The agreement between the proposed procedure for calculating C_f and the values obtained from shoaling spectra is of order 25%. The agreement is considered reasonable.

For the Marineland data the computations are somewhat more complicated by the fact that conditions vary sufficiently between the two stations to warrant different bed forms and C_f values. From the measured wave spectra, a constant C_f value of 0.008 is computed. The procedure outlined in section III provide C_f estimates which vary from 0.05 at 30 m water depth to 0.002 at 8.5 m water depth. A summary of wave and sediment parameters is shown in Table 1. In order to test the validity of the procedure outlined in section III, predicted shallow water spectra are compared with measured shallow water spectra in Figure 5. The predicted spectra are based on (a) fixed $C_f = 0.008$, and (b) variable C_f from 0.05 in deep water to 0.002 in shallow water. At high frequencies the fixed and variable C_f values give similar results. At low frequencies the variable C_f value procedure gives better agreement with the measured values in shallow water. The Marineland data set serves to demonstrate that predicting shallow water waves may not be as simple as defining a representative value for the entire shoaling region and that more detailed measurements are needed to verify the procedure outlined in section III.

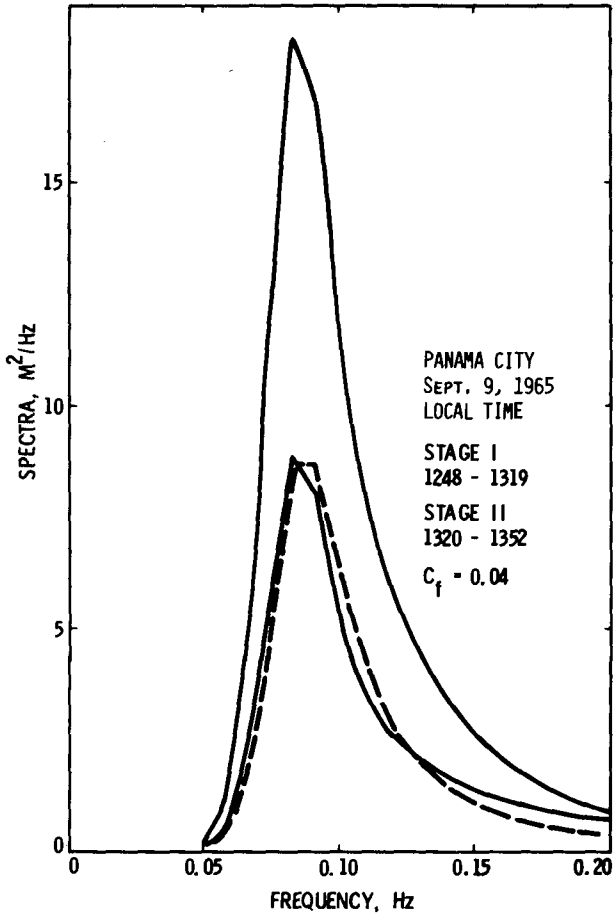


Figure 4. Comparison between measured and computed Panama City spectra. — measured, -- computed at Stage II.

Table 1. Estimation of Friction Coefficients from Wave and Sand Parameters

Variable	Marineland		Panama City	South Africa (TBO 37)
h	30	8,5	19,2 - 31.7	10.6 - 32
T_m	8	8	12	13.7
$H_{1/3}$	1.7	1.5	1,9 - 3,7	2.3 - 2,8
d_o	0,49	1,68	1.9 - 2.9	2.6 - 4.5
D_s	$(0,1 \times 10^{-3})$		$(0,4 \times 10^{-3})$	$(1,5 \times 10^{-3})$
λ	0.070	0.032	0.24	0.9
θ	24 - 290		33 - 82	15 - 45
ζ	0.012	0	0.024	0.15
k_s	0.048	0.0001	0,096	0.60
C_f	0.05	0.002	0.03	0.10

h	= water depth (m)	λ_s	= ripple wave length (m)
T_m	= peak period (sec)	θ_s	= nondimensional relative stress
$H_{1/3}$	= significant wave height (m)	ζ	= ripple wave height (m)
d_o	= horizontal excursion (m)	k_s	= roughness height (m) (4ζ as was suggested by Jonsson, 1966)
D_s	= median sand diameter (m)	C_f	= friction coefficient

Finally, the procedure proposed in section III is tested by using it to estimate a C_f value for the waves measured offshore of Melkbosstrand, South Africa. The bottom sediment properties in that region were not reported. A value of $C_f = 0.1$, in agreement with that calculated from shoaling spectra, could only be predicted if the bottom material was composed of coarse sand with $D_s = 1.5$ mm. Under such conditions bottom ripples can form and the high reported C_f values can be explained. A summary of wave and assumed sediment conditions for Melkbosstrand is also included in Table 1.

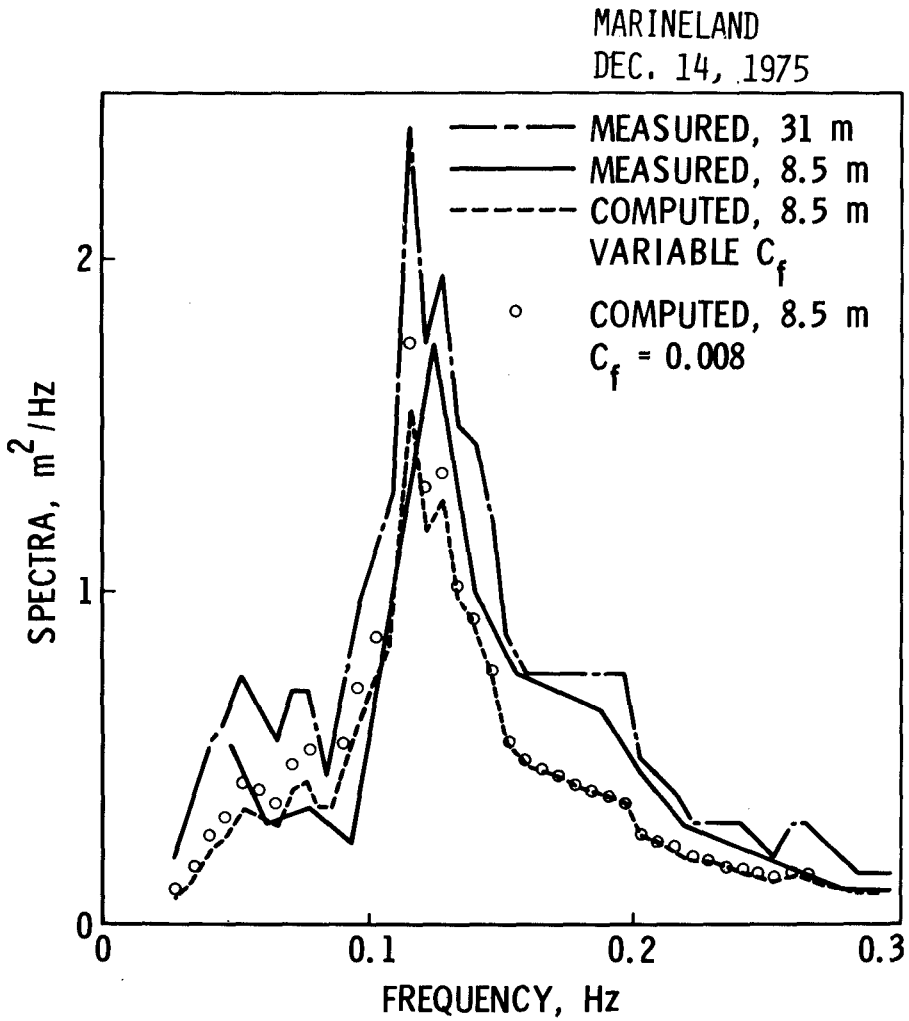


Figure 5. Comparison between measured and computed Marineland wave spectra.

V. Percolation Dissipation

Putnam (1949) was the first to compute the wave energy dissipation rate due to percolation in an isotropic permeable sandy bottom. However, he overestimated the dissipation rate by a factor of four due to an arithmetic error. Later, Bretschneider and Reid (1954) applied Putman's equation to study the wave height modification and consequently overestimated the percolation damping. A more general equation to compute the percolation dissipation rate was given by Shemdin et al (1977) as

$$\frac{1}{E} \frac{dE}{dt} = -k \sqrt{\alpha\beta} \frac{\tanh \sqrt{\frac{\alpha}{\beta}} kd}{\cosh^2 kh}, \quad (5)$$

where α and β are the horizontal and vertical coefficients of permeability, respectively, and d is the thickness of the sand layer. Using this equation and the magnitude of permeability coefficients determined by Sleath (1970) they computed the dissipation rates at different water depths. The results are compared with corresponding friction dissipations in Figure 6. These results demonstrate that percolation dissipation can be more important than friction dissipation for coarse sand in deeper water.

VI. Bottom Motion Dissipation

Excessive attenuation of wave energy in the Mississippi Delta area was reported by Bea (1974) and Tubman and Suhayda (1976). The attenuation cannot be reasonably explained by refraction, shoaling, bottom friction, nor bottom percolation. It is believed that the excessive attenuation is due to the effect of the wave-induced motion in the soft muddy bottom. Gade (1958, 1959) studied the wave energy dissipation effects of a non-rigid bottom in shallow water. His results are restricted to only shallow water waves. (i.e., $kh < 0.1\pi$) and cannot be applied to intermediate waver waves. Mallard and Dalrymple (1977) studied the effects of an ideal elastic bottom on water waves. Their computations, which neglected viscosity in the mud, show no wave energy loss. Hsiao and Shemdin (1978) assumed a viscoelastic bottom and obtained the following dispersion equation

$$k = \frac{\omega^2}{g} \frac{1 + \tanh kh \Omega}{\tanh kh + \Omega} \quad (6)$$

where Ω is a function of wave and bottom properties and k is the complex wave number in which the imaginary part is a measure of energy dissipation. The dissipation rates predicted by Equation (6) can explain the wave decay rates reported by Tubman and Suhayda (1976). Some computed dissipation rates using Equation (6) are shown in Figure 6 for comparison with dissipation rates due to friction and percolation. It can be clearly seen that the dissipation rate due to bottom motion can be one to two orders of magnitude greater than those due to friction and/or percolation.

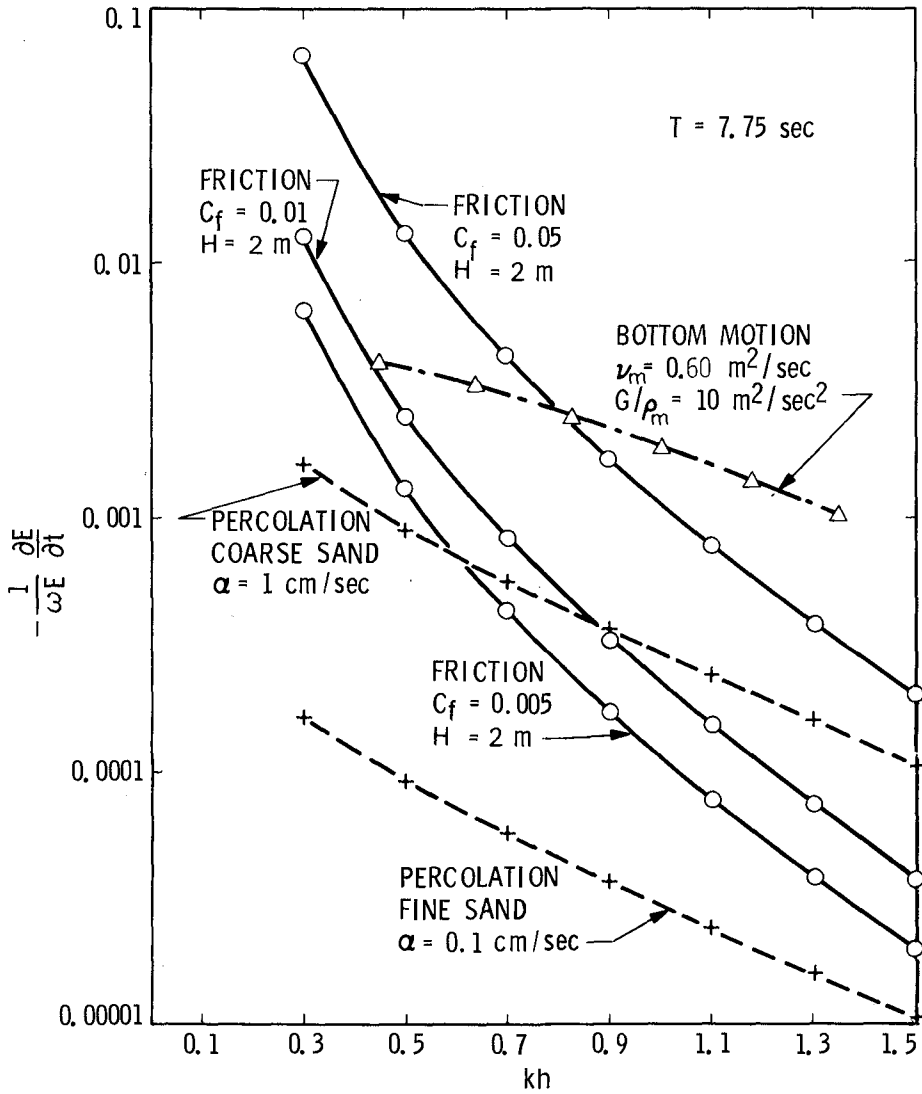


Figure 6. Comparison between dissipation mechanisms. ν_m = kinematic viscosity of mud, G = shear modulus of mud, ρ_m = density of mud (after Shemdin et al, 1977).

VII. Conclusions

It is shown that any of the three dissipation mechanisms discussed in this paper, namely friction, percolation, and bottom motion can be dominant in dissipating wave energy in shallow water depending on wave properties and bottom sediment properties. None can be arbitrarily neglected. Information on bottom sediment is considered of critical importance to properly identify the prevailing mechanism. Such information is not routinely obtained when measuring shoaling waves.

The friction coefficient is found to vary considerably above or below the widely used 10^{-2} value. A method for estimating the friction coefficient is suggested and found to give acceptable values over a broad range of conditions.

ACKNOWLEDGEMENT

Financial support for this study was provided by ONR-Geography Program, Contract No. N00014-76-MP60029, and by NATO Special Grant No. SRG 14. The Marineland data were gathered under NASA-Office of Applications. The wave spectra at Marineland were provided by W. McLeish of NOAA-AOML. The Panama City data were provided by J.E. Breeding, Jr. of Naval Coastal Systems Laboratory.

REFERENCES

1. Bagnold, R. A., (1946) Motion of waves in shallow water: Interaction between waves and sand bottoms. Proc. R. Soc. London, A187, 1-15.
2. Bea, R. G., (1974) Gulf of Mexico hurricane wave heights. Proc. 6th Offshore Tech. Conf., OTC 2110, Dallas, Texas.
3. Breeding, J. E., Jr., (1972) Refraction of gravity water waves. Naval Coastal Systems Lab., Rep. NCSL 124-72, 161 pp.
4. Bretschneider, C. L. and R. O. Reid, (1954) Changes in wave height due to bottom friction, percolation, and refraction. Tech. memo., Beach Erosion Board, U.S. Army Corps of Engineers, No. 45, 36 pp.
5. Carstens, M. R., F. M. Neilson, and H. D. Altinbilek, (1969) Bed forms generated in the laboratory under an oscillatory flow: analytical and experimental study. Tech. memo., Coastal Eng. Res. Center, U.S. Army Corps of Engineers, 28, 105 pp.
6. Collins, J. I., (1972) Prediction of shallow-water spectra. J. Geophys. Res., 77, 2693-2707.
7. Dingler, J. R. (1975) Wave-formed ripples in near shore sands. Ph.D. Dissertation, U.C. San Diego.
8. Gade, H. G., (1958) Effects of a nonrigid, impermeable bottom on plane surface waves in shallow water. J. Marine Res., 16, 61-82.
9. Gade, H. G., (1959) Notes on the effect of elasticity of bottom sediments to the energy dissipation of surface waves in shallow water. Archiv for Matematik og Naturvidenskab, B. LV., Nr. 3, 69-80.
10. Hasselmann, K. and J. I. Collins, (1968) Spectral dissipation of finite-depth gravity waves due to turbulent bottom friction. J. Marine Res., 26, 1-12.
11. Hsiao, S. V. and O. H. Shemdin, (1978) Interaction of ocean waves with a soft bottom. Submitted to J. Geophys. Res.
12. Inman, D. L. and A. J. Bowen, (1963) Flume experiments on sand transport by waves and currents. Proc. 8th Coastal Eng. Conf. ASCE. 137-150.
13. Jonsson, I. G., (1965) Friction factor diagram for oscillatory boundary layers. Prog. Rep., Coastal Eng. Lab., Tech. Univ. Denm., No. 10, 10-21.
14. Jonsson, I. G., (1966) Wave boundary layers and friction factors. Proc. 10th Coastal Eng. Conf., ASCE. 127-148.

15. Kamphuis, J. W., (1975) Friction factor under oscillatory waves. Proc. ASCE, 101, WW 2, 135-144.
16. Mallard, W. W. and R. A. Dalrymple, (1977) Water waves propagating over a deformable bottom. Proc. 9th Offshore Tech. Conf., OTC 2895, Houston, Texas.
17. Nielsen, P., (1977) A note on wave ripple geometry. Prog. Rep., Inst. Hydrodyn. and Hydraulic Eng., Tech. Univ. Denm., No. 43, 17-22.
18. Putnam, J. A., (1949) Loss of wave energy due to percolation in a permeable sea bottom. Trans. Amer. Geophys. Un., 30, 349-356.
19. Putnam, J. A., and J. W. Johnson, (1949) The dissipation of wave energy by bottom friction. Trans. Amer. Geophys. Un., 30, 67-74.
20. Riedel, H. P., J. W. Kamphuis, and A. Brebner, (1972) Measurement of bed shear stress under waves. Proc. 13th Coastal Eng., Conf., ASCE, 587-604.
21. Shemdin, O. H., J. E. Blue, and J. A. Dunne, (1975) SEASAT-A surface truth program, Marineland test plan. Jet Propulsion Lab., 622-5.
22. Shemdin, O. H., K. Hasselmann, S. V. Hsiao, and K. Herterich, (1977) Nonlinear and linear bottom interaction effects in shallow water. NATO Symp. on Turb. Fluxes through the Sea Surface, Wave Dyn. and Prediction, Marseille, France.
23. Sleath, J. F. A., (1970) Wave-induced pressures in beds of sand. Proc. ASCE, 96, HY 2, 367-378.
24. Tubman, M. W. and J. N. Suhayda, (1976) Wave action and bottom movements in fine sediments. Proc. 15th Coastal Eng. Conf., ASCE. 1168-1183.
25. U. S. Army Coastal Engineering Research Center, (1973) Shroe protection manual. Dept. of the Army, Corps of Engineers.
26. Van Ieperen, M. P., (1975) The bottom friction of the sea-bed off Melkbosstrand, South Africa: a comparison of a quadratic with a linear friction model. Dtsch. Hydrogr. Zr., 28, 72-88.

CHAPTER 25

EXCITATION OF LOW FREQUENCY TRAPPED WAVES

by

ROBERT KING* & RONALD SMITH**

Weak nonlinear interactions in water of non-constant depth between an incident wave, a side-band incident wave and a relatively low frequency trapped wave are shown to lead to the generation of the trapped wave. Three situations are considered in detail: edge waves in a wide rectangular basin, progressive edge waves on a straight beach, and standing waves in a narrow wave tank.

1. Introduction

The formation of crescent-shaped sand-bars along laboratory beaches was shown by Bowen and Inman (1971) to be due to the presence of standing edge waves. For their explanation to be relevant to naturally occurring crescentic bars it would be necessary for the edge waves to have periods of between 30 and 60 seconds. It is thus of interest to consider how such standing edge waves are generated. A possible mechanism would be via resonant interactions between two edge waves and an incident untrapped wave (Guza and Davis, 1974). However, for this to produce edge waves of the required period the necessary periods of the incident waves would be between 15 and 30 seconds, but, typically, there is not much surface wave energy at such long periods (Sonu, 1972).

In this paper we consider a wavefield consisting of a relatively short scale incident wave, the dominant Fourier component of which is characterised by (ω, k) , and a long scale trapped wave characterised by (σ, κ) . The wavelength of the long scale motion is taken to be much greater than that of the short scale motion, i.e. $|k| \gg |\kappa|$. This means that, except in the immediate vicinity of the shoreline, we can assume the water to be "deep" with respect to (ω, k) and "shallow" with respect to (σ, κ) . Since the system is non-linear, weakly non-linear interactions give rise to the harmonics $(\omega \pm \sigma, k \pm \kappa)$ being present.

* Irrigation and Drainage Consultant, Brick Kiln Lane, Thorrington N.E. Essex.

** C.E.G.B. Research Fellow, Department of Applied Mathematics and Theoretical Physics, University of Cambridge.

Now, if $\omega \gg \sigma$, then the harmonics $(\omega + \sigma, k + \kappa)$ are very close to (ω, k) and therefore almost satisfy the dispersion relation for incident waves. Thus, there is an almost-resonant triad consisting of the short scale wave (ω, k) , one of the side-band waves $(\omega + \sigma, k + \kappa)$ and the long scale wave (σ, κ) . Indeed, if the strong inequalities are relaxed then there can be exact resonance between two incident and one trapped wave (Gallagher, 1971). The existence of such a triad of waves makes it feasible for there to be a significant energy transfer from (ω, k) to (σ, κ) (Phillips, 1974). Numerical estimates made in §2.4 suggests that edge waves in the sea can be generated by the side-band mechanism.

As has been pointed out by Phillips (1974), resonant interactions between waves of different length scales can be interpreted as short waves propagating on a non-uniform current. It was shown by Longuet-Higgins and Stewart (1961) that there is not a partition between wave energy and stream energy. However, in the absence of dissipation there is a conserved property of the short waves - wave action - which can be identified with wave energy when there is no current (Bretherton and Garrett, 1968). In the present problem the current is of limited extent and from wave action considerations it can be concluded that, in the absence of dissipation, there is no net energy transfer from the short waves to the trapped waves. Specifically, the energy feed from the incident wavetrain is exactly negated by the energy extracted by the reflected waves. Through ignoring the presence of any reflected waves, the mechanism being studied in this paper relies crucially upon there being dissipation, particularly near the shoreline.

Although the generation of standing edge waves is the primary concern of this paper, the side-band mechanism need not be restricted to standing waves nor to edge waves. In §§3 and 4 respectively, we briefly consider the generation of progressive edge waves on an open beach and the generation of longitudinal standing waves in a narrow wave tank. It is hoped that this latter situation might permit laboratory testing of the side-band mechanism using apparatus of modest dimensions.

2. The generation of standing edge waves

2.1 Equations of motion

Consider a body of water, the free surface of which is at rest, $z=0$, where z is measured vertically upwards. The equations for small amplitude oscillations of an ideal fluid can be written in the form

$$\nabla^2 \phi + \phi_{zz} = 0,$$

$$\phi_{tt} + g\phi_z = R \quad \text{at } z = 0,$$

$$\phi_z + \nabla h \cdot \nabla \phi = 0 \quad \text{at } z = -h(\underline{x}),$$

where ϕ denotes the velocity potential, $h(\underline{x})$ the depth, ∇ the horizontal gradient operator and R represents complicated nonlinear terms which are, correct to second order in the wave amplitude,

$$R = -\nabla \cdot (\phi_t \nabla \phi) - \partial_t \left[\frac{1}{2} (\nabla \phi)^2 + \frac{1}{2} \phi_z^2 + g^{-2} \phi_t \phi_{ttt} \right].$$

If $W(\underline{x}, z; \sigma)$ represents a free standing wave mode of the undamped linear system with frequency σ , then W satisfies the equations

$$\nabla^2 W + W_{zz} = 0, \quad -\sigma^2 W + g W_z = 0 \text{ at } z = 0, \quad W_z + \nabla h \cdot \nabla W = 0 \text{ at } z = -h(\underline{x}).$$

For each eigenfunction W an application of Green's Theorem leads to the evolution equation

$$\left(\frac{d^2}{dt^2} + \sigma^2 \right) \int_{\Omega} [W\phi]_{z=0} + g \int_{\partial\Omega} \int_{-h}^0 \left(\phi \frac{\partial W}{\partial n} - W \frac{\partial \phi}{\partial n} \right) = \int_{\Omega} [RW]_{z=0} \quad (2.1)$$

where Ω denotes the water surface, $\partial\Omega$ the boundary of Ω and $\partial/\partial n$ denotes differentiation along the outward normal to $\partial\Omega$. If Ω is of infinite extent, then, to assure the convergence of the integrals, it may be necessary to take W to be that leaky trapped wave which decays exponentially at infinity (Longuet-Higgins, 1967). Equation (2.1) enables us to determine the effect of the nonlinearity upon the evolution of the standing waves without the necessity of explicitly evaluating the correction terms due to the nonlinearity. It corresponds to the non-secularity or integrability condition which arises in a direct solution of the governing differential equations (Bretherton and Garrett, 1968).

Let $w(z; \omega, h)$ be a local solution to the progressive wave eigenvalue problem for waves of frequency ω :

$$-(\nabla\theta)^2 w + w_{zz} = 0,$$

$$w = 1 \text{ and } w_z = \omega^2/g \text{ at } z = 0,$$

$$w_z = 0 \text{ at } z = -h(x),$$

where $|\nabla\theta|$ is the local wave-number (eigenvalue). The equation which enables us to focus our attention on the effect of nonlinearity on the ω -component of the wavefield is

$$(\partial_t^2 + \omega^2)\phi_{z=0} - g \int_{-h}^0 w(\nabla^2 + (\nabla\theta)^2)\phi dz - g\nabla h \cdot [\nabla w \nabla \phi]_{z=-h} = R. \quad (2.2)$$

Just as it is not essential to explicitly evaluate the nonlinear

corrections to Φ , in both equations (2.1) and (2.2) the vertical structure of Φ need not be represented exactly. This fact will be used subsequently when $w(z; \omega \pm \sigma, h)$ are approximated firstly by $w(z; \omega, h)$ and then by $w(z; \omega, \infty)$.

The model equations presented above are inadequate to describe the complicated structure of the surf zone. This problem is most easily overcome by making the following assumptions: (a) The incident short waves are not reflected at the beach, yet the trapped waves are totally reflected. (b) The wavelength of the incident waves does not change as they shoal. The consequence of these assumptions is that our approximation for Φ , and more particularly R , is grossly in error in the immediate vicinity of the shoreline. As can be seen from equation (2.1), a local error in R need not greatly effect our estimate of the growth rate of the standing wave. In the calculations given below, assumption (a) is made at the onset but the use of assumption (b) is delayed.

The assumptions (a) and (b) were also made by Gallagher (1971). For his analysis it is extremely difficult to provide a justification because there is not a marked disparity in length scales between the incident and trapped waves. Guza and Davis (1974) chose the opposite extreme of perfect reflection of the incident waves. The no-reflection boundary condition is also appropriate to situations where there is no coastal boundary, such as in the excitation of ducted waves on an under-sea ridge (Buchwald, 1969).

On vertical sections of the boundary we impose the normal velocity conditions

$$\partial W / \partial n = 0, \quad \partial \Phi / \partial n = Q,$$

where Q is non-zero on those sections of the boundary which are being used (or interpreted) as being wavemakers for the generation of the incident waves.

2.2 Side-band representation

For the interaction mechanism under consideration, the wavefield is dominated by the incident wave of frequency ω and the standing trapped wave of frequency σ . A vitally important role is also played by the side-band incident waves of frequencies $\omega \pm \sigma$. Accordingly, we write the velocity potential as

$$\begin{aligned} \Phi = \exp(i\omega t - i\theta(\underline{x})) & \left[\Phi_0(\underline{x}, t)w(z; \omega, h) + \Phi_+(\underline{x}, t)w(z; \omega + \sigma, h)e^{i\sigma t} \right. \\ & \left. + \Phi_-(\underline{x}, t)w(z; \omega - \sigma, h)e^{-i\sigma t} \right] + W(\underline{x}, z; \sigma)\eta(t)e^{i\sigma t} + * + \Phi'. \end{aligned} \quad (2.3)$$

Here Φ_0 , Φ_+ and η are the slowly-varying amplitudes of the incident, side-band and the trapped waves respectively. All other contributions to the wavefield are assumed to play no significant role in the generation of the trapped waves, and are collectively represented by Φ' . The

formally largest of such neglected terms are virtual modes with frequencies 2ω , 2σ and the wave set-up which has zero frequency. Reflections on the vertical sections of the boundary $\partial\Omega$ could be represented by permitting ϕ_0 , ϕ_{\pm} and θ to be multiple-valued.

Substituting for ϕ in (2.2) and equating $\exp(i\omega t - i\theta)$ terms gives

$$2i\omega\phi_{0t} + \phi_{0tt} + ig \int_{-h}^0 w\{2\nabla\theta \cdot \nabla(w\phi_0) + W\phi_0 \nabla^2\theta\} dz - \int_{-h}^0 w\nabla^2(w\phi_0) dz - g\nabla h \cdot [\nabla w(\phi_0 w)]_{z=-h} = R_0,$$

where w stands for $w(z; \omega, h)$ and R_0 is the $\exp(i\omega t - i\theta)$ term in the side-band representation for the nonlinear terms. For the side-band amplitudes ϕ_{\pm} similar equations involving $w(z; \omega, \sigma, h)$ are obtained. We

note that even though we shall only represent R correct to quadratic terms, the explicit representation for R_0 in terms of ϕ_{\pm} , η is quite unwieldy.

We now make the following simplifying assumptions

$$\omega \gg \sigma, \quad |\nabla\theta|L \gg 1, \quad \omega/(L|\nabla\theta|) \gg \eta_L/\eta,$$

where L is a length scale appropriate to either the topographic variations or to the trapped waves. Physically the assumptions mean that the incident wave is very short and that an individual wave packet is "unaware" that the standing wave is growing in amplitude. Mathematically the assumptions mean that in the expression for R_0 , and the corresponding expressions in the equation for the side-bands, derivatives of the short wave exponent $(\omega t - \theta(x))$ dominate derivatives either of the wave amplitude ϕ_0 , ϕ_{\pm} , η or of the mode shapes w , W . Also, we can justify approximating $w(\bar{z}; \omega \pm \sigma, h)$ by $w(z; \omega, h)$. Retaining only the largest real and imaginary terms, we can simplify the equations for the progressive waves to

$$\begin{aligned} \zeta \cdot \nabla \phi_0 + (\nu + \frac{1}{2} \nabla \cdot \zeta) \phi_0 &= \left[W \frac{\omega^2 \sigma^2}{g^2} + i \nabla \theta \cdot \nabla W \right] (\eta^* \phi_+ + \eta \phi_-) \\ &+ \left[\frac{\omega^4}{g^2} - (\nabla \theta)^2 \right] \frac{\sigma W}{2\omega} (\eta^* \phi_+ - \eta \phi_-), \end{aligned} \tag{2.4a}$$

$$\begin{aligned} \underline{c} \cdot \nabla \phi_+ + i\sigma \phi_+ + (v + \frac{1}{2} \nabla \cdot \underline{c}) \phi_+ &= \left[W \frac{\omega^2 \sigma^2}{g^2} + i\nabla \theta \cdot \nabla W \right] \eta \phi_0 \\ &- \left[\frac{\omega^4}{g^2} - (\nabla \theta)^2 \right] \frac{\sigma W}{2\omega} \eta \phi, \end{aligned} \quad (2.4b)$$

$$\begin{aligned} \underline{c} \cdot \nabla \phi_- - i\sigma \phi_- + (v + \frac{1}{2} \nabla \cdot \underline{c}) \phi_- &= \left[W \frac{\omega^2 \sigma^2}{g^2} + i\nabla \theta \cdot \nabla W \right] \eta^* \phi_0 \\ &+ \left[\frac{\omega^4}{g^2} - (\nabla \theta)^2 \right] \frac{\sigma W}{2\omega} \eta^* \phi_0, \end{aligned} \quad (2.4c)$$

where \underline{c} is the group velocity of the incident waves of frequency ω , and the v terms are an empirical representation of the damping. The left-hand side terms could have been anticipated from the fact that in the absence of currents and damping, the wave energy of the short waves propagates at the group velocity.

If the low frequency component of the wavemaker motion is neglected and if W is normalised:

$$\int_{\Omega} [W^2]_{z=0} = \ell^{-2},$$

then substituting (2.3) into (2.1), and equating coefficients of $e^{i\sigma t}$, we obtain the following simplification of the standing wave equation

$$\begin{aligned} \eta_L + v' \eta &= \int_{\Omega_1} (\phi_0^* \phi_+ + \phi_0 \phi_-^*) \left[\frac{1}{2} W \left(\frac{\omega^4}{g^2} - (\nabla \theta)^2 \right) + \frac{i\omega}{\sigma} \nabla \theta \cdot \nabla W \right] \ell^2 \\ &- \frac{i\omega \ell^2}{\sigma} \int_{\partial \Omega_1} (\phi_0^* \phi_+ + \phi_0 \phi_-^*) \frac{\partial \theta}{\partial n} W \Big|_{z=0} \end{aligned}$$

$$+ \int_{\Omega_1} (\Phi_0^* \Phi_+ - \Phi_0 \Phi_+^*) 2 \frac{\omega^3 \sigma}{g^2} W \Big|_{z=0} \lambda^2 - \frac{i \lambda^2}{2\sigma} \int_{\Omega - \Omega_1} |RW|_{z=0} \quad (2.5)$$

Here, ν' is an empirical representation of damping, Ω_1 denotes that region of the water surface in which (2.3) is thought to be an adequate description of the waves, and in Ω_1 we have only retained the largest real and largest imaginary contributions to R . If θ were multiple-valued (due to there being reflections off vertical portions of $\partial\Omega$) then different branches of θ would contribute separately to the nonlinear terms.

To make further progress we must either give a description of the waves which is valid in the surf zone $\Omega - \Omega_1$ or we must be able to neglect the $\Omega - \Omega_1$ term in (2.5). Here we choose the latter alternative. It is reasonable to assume that the effects of both reflection and strong nonlinearities is to keep the interaction term R bounded. Thus to ignore the effect of the $\Omega - \Omega_1$ region it suffices that it has small extent relative to the interaction region. The previously assumed disparity of length scales between the incident and trapped waves adds credence to this further assumption.

We observe that all the retained quadratic terms in equations (2.4) and (2.5) involve derivatives of the short wave exponent $(\omega t - \theta)$. Thus of the formally largest neglected terms in (2.3) it is only the $2(\omega t - \theta)$ virtual modes which would lead to any change in equations (2.4) or (2.5). A calculation akin to that of Stokes (1849) leads to the extra terms

$$i\lambda\phi_0^2\phi_0^*, \quad i\lambda\phi_0^2\phi_-^*, \quad i\lambda\phi_0^2\phi_+^*$$

on the right-hand sides of equations (2.4a,b,c), where

$$\lambda = \frac{1}{8}\omega^3 k^2 g^{-2} (1 + \frac{1}{8} \text{Coth } 4 kh).$$

These terms play a very minor role in the energy transfer mechanism and for simplicity we continue to ignore them.

2.3 Onset of instability

To explain the onset of the instability we assume that the system is started from a state of near rest and we can thus regard the sidebands ϕ_{\pm} and the standing wave η as being of very small amplitude. Thus the incident wave amplitude ϕ_0 approximately satisfies the linear equation

$$\zeta \cdot \nabla \Phi_0 + (\nu + \frac{1}{2} \nabla \cdot \zeta) \Phi_0 = 0, \quad (2.6)$$

and the perturbation quantities Φ_+ , Φ_- , η satisfy couple linear equations. The form of equations (2.5) leads us to define the sum and difference terms:

$$\eta |\Phi_0|^2 S = \Phi_0^* \Phi_+ + \Phi_0 \Phi_-^*, \quad \eta |\Phi_0|^2 D = \Phi_0^* \Phi_+ - \Phi_0 \Phi_-^*,$$

where during the initial stages of the instability S and D satisfy the first order differential equations

$$\zeta \cdot \nabla S + i\sigma S = 2 \omega^2 \sigma^2 W|_{z=0}, \quad (2.7)$$

$$\zeta \cdot \nabla D + i\sigma D = 2i\nabla\theta \cdot \nabla W|_{z=0} - \left(\frac{\omega^4}{g^2} - (\nabla\theta)^2\right) \frac{\sigma}{\omega} W|_{z=0}$$

The boundary conditions for these equations are that $S = D = 0$ far away from the interaction region. It now follows from equation (2.5), with the $\Omega - \Omega_1$ term neglected, that η grows exponentially with time, the exponent being

$$-\nu' + \int_{\Omega_1} |\Phi_0|^2 S \left[\frac{1}{2} W \left(\frac{\omega^4}{g^2} - (\nabla\theta)^2 \right) + i \frac{\omega}{\sigma} \nabla\theta \cdot \nabla W \right]_{z=0} \ell^2 \quad (2.8)$$

$$+ \int_{\Omega_1} |\Phi_0|^2 D \left[2 \frac{\omega^3 \sigma}{g^2} W \right]_{z=0} \ell^2 - \int_{\partial\Omega_1} |\Phi_0|^2 \frac{i\omega}{\sigma} SW|_{z=0} \frac{\partial\theta}{\partial n} \ell^2.$$

The condition for there to be an instability is that the time exponent (2.8) should have a positive real part.

2.4 Uniformly sloping beach

In the representation (2.3) no account is taken of any reflection of the short waves. As a consequence, even if there is no wave-breaking the description is inappropriate near the shoreline and predicts spurious singularities. For our present purposes these singularities are particularly unfortunate in that the expression (2.8) is sensitive to our choice of Ω_1 . It is to avoid this dilemma that we invoke the assumption (b) referred to in §2.1. Thus we assume that the

beach angle is so steep that the deep water description for the incident waves is appropriate in a region Ω_1 which extends to within the order of one wavelength of the shoreline. Since the modified representation for Φ is free from singularities (though still not valid in $\Omega - \Omega_1$) we can also approximate Ω_1 by the entire water region Ω in the integrals (2.8).

The only geometry for which an exact solution for a linear trapped wave is known is a beach of constant slope in a channel with parallel vertical walls which are orthogonal to the beach. The exact solutions involve a superposition of exponentials (Ursell, 1952), the normalised solution for the lowest mode being

$$W = \left[2(\cos \alpha)^{\frac{1}{2}} \pi^{\frac{1}{2}} \right] \cos ly \exp(-lx \cos \alpha + lz \sin \alpha), \quad \sigma^2 = g l \sin \alpha,$$

where α is the beach angle and π/l is the distance between the vertical walls. If we are to retain the convenience of working only with exponential functions, then it is necessary that the coefficients c, v in equations (2.6-2.7) are constant. Fortunately, this is indeed the case when the beach angle is sufficiently steep (i.e. $(\sigma/\omega)^2 \ll \tan^2 \alpha$) that the deep water approximation (b) can be used. For incident waves normal to the beach the appropriate solutions to equations (2.6-2.8) for the lowest mode edge waves are

$$\Phi_0 = A \exp(vx/c) \quad \text{with} \quad \underline{c} = (-c, 0, 0),$$

$$S = \frac{2 \omega^2 l \sin \alpha W|_{z=0}}{g(c l \cos \alpha + i \sigma)} \quad D = \frac{i 2 \omega^2 l \cos \alpha W|_{z=0}}{g(c l \cos \alpha + i \sigma)}$$

$$\text{exponent} \doteq v' + |A|^2 \frac{2 \omega^5 l \cos \alpha}{g^3} \left[1 + i(c l \cos \alpha / \sigma) \right] \left[\frac{l \cos \alpha + 2(v/c)}{l \cos \alpha - (v/c)} \right]$$

Thus, if the wave steepness $\omega^3 |A| g^{-2}$ exceeds the critical value

$$\left[\frac{v' \omega}{2 g l \cos \alpha} \left\{ \frac{l \cos \alpha - (v/c)}{l \cos \alpha + 2(v/c)} \right\} \right]^{\frac{1}{2}} \quad (2.9)$$

then the edge wave will grow in amplitude.

As a numerical example of the estimate (2.9), to a moderately large laboratory size situation we specify the values

$$\alpha = \pi/6, \quad \ell = \pi m^{-1}, \quad \sigma \sim 4s^{-1}, \quad \omega \sim 20 s^{-1}, \quad \nu/c \sim 10^{-1} m^{-1}.$$

Although the value of ν/c corresponds to a dirty surface, we note that $(\nu c/\ell)$ is essentially negligible. Guza and Davis (1974) show that a laminar model of edge wave damping gives

$$\nu' = \bar{\nu}^{\frac{1}{2}} \ell \sigma^{\frac{1}{2}} \cot \alpha \quad 2^{-\frac{1}{2}},$$

where $\bar{\nu}$ is the kinematic viscosity. Thus we can estimate that $\nu' \sim 7 \times 10^{-3} s^{-1}$, critical steepness ~ 0.05 .

Hence the instability would appear to be realisable in a laboratory situation.

If we regard σ/ω , $\bar{\nu}$ as being fixed, then we can use the above results to determine the dependence of the critical steepness upon the beach angle α and wavenumber ℓ :

$$\text{critical steepness} \sim \ell^{\frac{3}{8}} \alpha^{\frac{1}{8}}.$$

Thus an increase of the length scale, i.e. a decrease of ℓ , lowers the critical steepness. Regrettably, the deep water approximation is not applicable to naturally occurring beaches where $(\tan \alpha)^2$ is typically 10^{-3} or less. In such cases there seems no alternative but to allow for shoaling. Within the framework of the present calculations, this would entail choosing Ω_1 as to avoid the spurious singularities. (The authors hope to present at a later date a more complicated calculation procedure which avoids the singularities).

3. Progressive edge waves.

For progressive trapped waves the longshore direction plays the role of a second time-coordinate. Although the mathematical consequences of this change of role are numerous, they are individually quite minor and we can follow the pattern of calculations developed in §2.

On the assumptions that the coastal curvature is small relative to the wavenumber of the trapped waves and that the seaward depth topography varies very slowly in the longshore y -direction, the local eigenvalue problem for trapped waves of frequency σ and longshore wavenumber ψ_y is

$$W_{xx} + W_{zz} - \psi_y^2 W = 0, \quad -\sigma^2 W + gW_z = 0 \text{ at } z = 0,$$

$$W_z + h \frac{W}{x} = 0 \text{ at } z = -h.$$

The corresponding integral form of the equations of motion is

$$(\partial_t^2 + \sigma^2) \int_0^\infty [W\Phi]_{z=0} dx - g \int_0^\infty \int_{-h}^\infty W(\partial_y^2 + \psi_y^2) \Phi dz dx + g \int_0^\infty h_y [W\Phi]_{z=-h} dx \tag{3.1}$$

$$+ \left[\int_{-h}^0 \left(\Phi \frac{\partial W}{\partial x} - W \frac{\partial \Phi}{\partial x} \right) dz \right]_0^\infty = \int_0^\infty [RW]_{z=0} dx.$$

For the progressive waves the eigenvalue problem and integral version of the nonlinear equations remain as in §2.1, but it is natural to regard the longshore dependence of the phase measurement θ as being imposed by conditions far from the shore.

The time-like character of the y-coordinate leads us to modify the side-band representation of the wavefield:

$$\begin{aligned} \Phi = e^{i(\omega t - \theta)} & \left[\Phi_0(x, y, t) w(z; \omega, h) + \Phi_+(x, y, t) w(z; \omega + \sigma, h) e^{i(\sigma t - \psi)} \right. \\ & \left. + \Phi_-(x, y, t) w(z; \omega - \sigma, h) e^{-i(\sigma t - \psi)} \right] + W(x, z; \sigma, y) \eta(y, t) e^{i(\sigma t - \psi)} \tag{3.2} \end{aligned}$$

Thus, the y-dependence on the length scale of ψ_y^{-1} is represented

explicitly by the ψ exponents, and possible very slow y-dependence associated with any instability is represented via the amplitude factors Φ_0, Φ_\pm, η . This representation is assumed to be accurate in a region $(a, \infty)^t$ which excludes the shoreline.

Making the same simplifying assumptions as in §2.2, i.e.

$$\omega \gg \sigma, \quad |\nabla\theta|L \gg 1, \quad \omega/(L|\nabla\theta|) \gg \eta_t/\eta,$$

we can simplify the equations for the incident waves to

$$c_1 \Phi_{0,x} + (\nu + \frac{1}{2} c_1) \Phi_0 = \left[W \frac{\omega^2 \sigma^2}{g^2} + i\theta \frac{W}{x} \right] (\eta^* \Phi_+ + \eta \Phi_-)$$

$$+ \left[\frac{\omega^4}{g^2} - (\nabla\theta)^2 \right] \frac{\sigma W}{2\omega} - \theta_y \psi_y W \left[\eta^* \phi_+ - \eta \phi_- \right], \quad (3.3a)$$

$$c_1 \phi_{+x} + i(\sigma - c_2 \psi_y) \phi_+ + (\nu + \frac{1}{2} c_1)_x \phi_+ = \left[W \frac{\omega^2 \sigma^2}{g^2} + i \theta_x W_x \right] \eta \phi_0 - \left[\left(\frac{\omega^4}{g^2} - (\nabla\theta)^2 \right) \frac{\sigma W}{2\omega} - \theta_y \psi_y W \right] \eta \phi_0, \quad (3.3b)$$

$$c_1 \phi_{-x} - i(\sigma - c_2 \psi_y) \phi_- + (\nu + \frac{1}{2} c_1)_x \phi_- = \left[W \frac{\omega^2 \sigma^2}{g^2} + i \theta_x W_x \right] \eta^* \phi_0 + \left[\left(\frac{\omega^4}{g^2} - (\nabla\theta)^2 \right) \frac{\sigma W}{2\omega} - \theta_y \psi_y W \right] \eta^* \phi_0, \quad (3.3c)$$

where $(c_1, c_2, 0)$ is the group velocity of the incident waves of frequency ω and the ν terms are an empirical allowance for the damping. The corresponding equation for the trapped wave is

$$\begin{aligned} \eta_t + c' \eta_y + (\nu' + \frac{1}{2} c'_y) \eta &= \frac{\sigma^2}{g} \int_a^\infty (\phi_0^* \phi_+ + \phi_0 \phi_-^*) \left[\frac{1}{2} W \left(\frac{\omega^4}{g^2} - (\nabla\theta)^2 \right) \right. \\ &+ i \frac{\omega \theta}{\sigma} \frac{W_x}{x} - \frac{\omega \theta}{\sigma} \frac{W \psi_y}{y} \left. \right] dx + \frac{\sigma^2}{g} \int_a^\infty (\phi_0^* \phi_+ - \phi_0 \phi_-^*) \frac{2\omega^3 \sigma}{g^2} \frac{W}{z=0} dx \\ &+ \frac{i\sigma\omega}{g} \left[(\phi_0^* \phi_+ + \phi_0 \phi_-^*) W \right]_{z=0} \theta_x - \frac{i\sigma}{g} \int_0^a [RW]_{z=0} dx. \end{aligned} \quad (3.4)$$

where c' is the longshore group velocity of the trapped waves and W is normalised:

$$\int_0^\infty |W^2|_{z=0} dx = g\sigma^{-2}$$

We shall assume that the representation (3.2) applies sufficiently close to the shore that the $(0,a)$ term in equation (3.4) can be neglected. As noted in §2.2 the particularly simple form of the left-hand-side terms is related to the fact that in the absence of interactions or damping the wave energy of the incident and trapped waves propagate at their respective group velocities.

In considering the onset of instability it is again convenient to introduce the sum and difference terms S and D . To determine the development of η it is convenient to use axes moving with the local group velocity c' . The evolution can be assumed to be exponential only if the topography and the incident wave amplitude Φ_0 are both independent of y . For the special case of edge waves on a uniformly sloping beach of large angle (i.e. $\tan^2\alpha \gg (\alpha/\omega)^2$) it is possible to obtain an analytic description of the onset condition

$$\text{critical steepness} = \left(1 - \frac{\ell c_2}{\sigma}\right)^{\frac{1}{2}} \left[\frac{v'\omega}{2g\ell\cos\alpha} \left\{ \frac{\ell\cos\alpha - v/c_1}{\ell\cos\alpha + 2v/c_1} \right\} \right]^{\frac{1}{2}} \quad (3.5)$$

The group velocity c_2 of the incident waves is less than the phase velocity σ/ℓ of the trapped wave. Thus, the extra factor in (3.5) as opposed to (2.9) does not make a substantial reduction in the numerical estimates.

4. Standing waves in a narrow tank

Laboratory experiments permit much more stringent testing of theories than field measurements, but edge wave experiments can make severe demands upon facilities due to the large area of water involved (Bowen and Inman, 1969). With this in mind, we now show the side-band theory can be used to predict the growth of a standing wave in a narrow channel. Numerical estimates of the onset conditions are obtained for the particular case of a tank with a sloping bottom and a plane wave-maker positioned at one end. As with §3, the pattern of calculations developed in §2 can again be followed with only a few minor alterations.

We consider here a tank of length L and breadth B such that $L \gg B$. Axes are chosen so that x is measured along the tank, y across the tank and z vertically upwards. In this case we have $w(y,z;\omega,h)$ as a local solution to the progressive wave eigenvalue problem:

$$-\theta^2 \frac{\partial^2 w}{\partial x^2} + w_{yy} + w_{zz} = 0, \quad w_z = \frac{\omega^2 w}{g} \quad \text{at } z = 0,$$

$$w_z = 0 \quad \text{at } z = -h(x), \quad w_y = 0 \quad \text{at } y = 0, B,$$

with the normalisation

$$\int_0^B [w^2]_{z=0} dz = B.$$

For each position x , the local energy transport equation for the progressive waves is

$$\begin{aligned} (\partial_t^2 + \omega^2) \int_0^B [w\Phi]_{z=0} dy - \int_{-h}^0 w(\partial_x^2 + \theta_x^2)\Phi dz dy - g \int_0^B [wh_x \Phi_x]_{z=-h} dy \\ = \int_0^B [wR]_{z=0} dy. \end{aligned} \tag{4.1}$$

Following §2.2, the side-band representation of the wavefield is written as

$$\begin{aligned} \Phi = \exp(i\omega t - i\theta(x)) \left[\Phi_0(x,t)w(y,z;\omega,h) + \Phi_+(x,t)w(y,z;\omega+\sigma,h) e^{i\sigma t} \right. \\ \left. + \Phi_-(x,t)w(y,z;\omega-\sigma,h) e^{-i\sigma t} \right] + W(x,z;\sigma)\eta(t) e^{i\sigma t + i\theta(x)}. \end{aligned} \tag{4.2}$$

We again make the assumptions

$$\omega \gg \sigma \quad |\theta_x|L \gg 1, \quad \omega \gg L|\theta_x|\eta_t/\eta.$$

The resulting equations for the progressive waves are

$$\begin{aligned} c\Phi_0 + (\nu + \frac{1}{2}c_x)\Phi_0 &= R_0, \\ c\Phi_+ + i\sigma\Phi_+ + (\nu + \frac{1}{2}c_x)\Phi_+ &= R_+, \\ c\Phi_- - i\sigma\Phi_- + (\nu + \frac{1}{2}c_x)\Phi_- &= R_-, \end{aligned}$$

where

$$\begin{aligned} R_0 = B^{-1} \int_0^B w \left[w \left(W \frac{\omega^2 \sigma^2}{g^2} + i\theta_{xx} W \right) (\eta^* \Phi_+ + \eta \Phi_-) \right. \\ \left. + \frac{\sigma W}{2\omega} \left(\frac{\omega^4 w}{g^2} - \theta_x^2 w + w_{yy} \right) (\eta^* \Phi_+ - \eta \Phi_-) \right]_{z=0} dy, \end{aligned}$$

$$R_+ = B^{-1} \int_0^B w \left[w \left(W \frac{\omega^2 \sigma^2}{g^2} + i \theta \frac{W}{x} \right) \eta \phi_0 - \frac{\sigma W}{2\omega} \left(\frac{\omega^4 w}{g^2} - \theta^2 w + w_{yy} \right) \right. \\ \left. \eta \phi_0 \right]_{z=0} dy,$$

$$R_- = B^{-1} \int_0^B w \left[w \left(W \frac{\omega^2 \sigma^2}{g^2} + i \theta \frac{W}{x} \right) \eta^* \phi_0 + \frac{\sigma W}{2\omega} \left(\frac{\omega^4 w}{g^2} - \theta^2 w + w_{yy} \right) \right. \\ \left. \eta^* \phi_0 \right]_{z=0} dy.$$

The corresponding equation for the standing wave is

$$\eta_t + \nu \eta = \ell B^{-1} \int_0^B \int_a^L \left[\frac{1}{2} W \left(\frac{\omega^4 w^2}{g^2} - \theta^2 w^2 + w^2 \right) \right. \\ \left. + \frac{i\omega}{\sigma} \theta \frac{W}{x} \right]_{z=0} (\phi_0^* \phi_+ + \phi_0 \phi_-^*) dx dy \\ + \ell B^{-1} \int_0^B \int_a^L \frac{2\omega^3 \sigma}{g^2} w^2 W \Big|_{z=0} (\phi_0^* \phi_+ - \phi_0 \phi_-^*) dx dy \\ + \ell B^{-1} \int_0^B \left[\frac{i\omega}{\sigma} \theta \frac{W}{x} \Big|_{z=0} w^2 (\phi_0^* \phi_+ + \phi_0 \phi_-^*) \right]_{x=a} dy - \frac{iB^{-1}}{2\sigma} \int_0^a [RW]_{z=0} dy,$$

where we have assumed the normalisation

$$\int_0^B \int_0^L [W^2]_{z=0} dx dy = B\ell^{-1}.$$

If the progressive and the standing waves are plane, i.e. w and W are independent of y , then the above equations reduce to a one-dimensional form of equations (2.4) and (2.5). Thus, provided we can neglect the effect of the nearshore region $(0,a)$, we can directly apply the analysis of §2.3.

For a shallow tank of depth αx an approximate normalised solution for the standing wave is

$$W = KJ_0(2\sqrt{\ell x}),$$

where

$$J'_0(2\sqrt{\ell L}) = 0, \quad \sigma^2 = \alpha g \ell, \quad K^2 = \frac{1}{\ell \int_a^L J_0^2(2\sqrt{\ell x}) dx}$$

Following the onset-of-instability calculation of §§2.3,2.4 we make the deep water assumption i.e. $(\sigma/\omega)^2 \ll \tan^2 \alpha$, and define the sum and difference terms to be

$$S = \frac{2\omega^2 \sigma^2}{cg^2} K e^{i\sigma x/c} \int_x^L J_0(2\sqrt{\ell x}) e^{-i\sigma x/c} dx,$$

$$D = -2i\frac{\theta_x}{c} K e^{i\sigma x/c} \int_x^L \ell^{\frac{1}{2}} x^{-\frac{1}{2}} J_1(2\sqrt{\ell x}) e^{-i\sigma x/c} dx,$$

where $\underline{c} = (-c, 0, 0)$. Hence an expression for the onset condition can be found, and the standing wave will grow if the steepness at the wavemaker exceeds the critical value

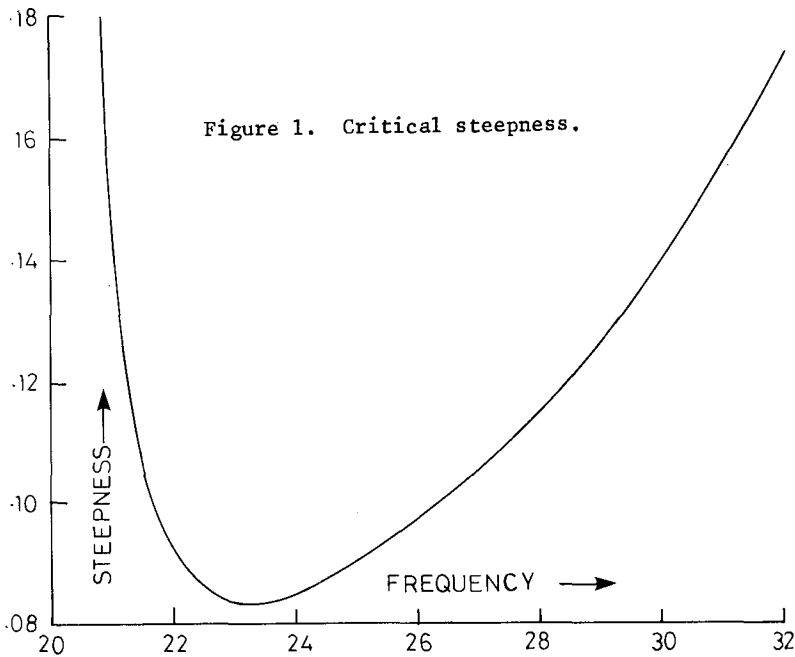
$$\left[\frac{\omega v' c \int_0^L J_0^2(2\sqrt{\ell x}) dx}{2\sigma g [I_1 + 2I_2 + I_3]} \right]^{\frac{1}{2}},$$

where the real integrals I_1, I_2, I_3 are defined:

$$I_1 = - \int_0^L \int_x^L \ell^{\frac{1}{2}} x^{-\frac{1}{2}} e^{-2\nu(L-x)/c} J_1(2\sqrt{\ell x}) J_0(2\sqrt{\ell x}) \sin(\sigma(\bar{x}-x)/c) d\bar{x} dx,$$

$$I_2 = - \int_0^L \int_x^L \ell^{\frac{1}{2}} x^{-\frac{1}{2}} e^{-2\nu(L-x)/c} J_1(2\sqrt{\ell x}) J_0(2\sqrt{\ell x}) \sin(\sigma(\bar{x}-x)/c) d\bar{x} dx,$$

$$I_3 = \int_0^L e^{-2\nu L/c} J_0(2\sqrt{\ell x}) \sin(\sigma x/c) dx.$$



If we consider a particular situation of a narrow tank of length 4m, with a beach of slope $\alpha = 0.1$, the numerical integration of the above expression leads to the graph (fig. 1) of the wave steepness at the wavemaker. The damping for the standing wave was taken to be constant $\nu = 0.01s^{-1}$, and the damping for the progressive waves was calculated using the formula

$$\nu = \frac{1}{2} \frac{\omega^2}{g^2} \left(\frac{\omega \times \text{viscosity}}{2} \right)^{\frac{1}{2}}, \text{ with viscosity} = 1.3 \times 10^{-6} m^2 s^{-1}.$$

This expression for ν corresponds to the "dirty water" limit of an inextensible surface film. Results for frequencies below $\omega = 20$ have not been presented because the results are dominated by the beach contribution I_3 , and it may not be justifiable to neglect the effects of shoaling and wave reflection. For example, at $\omega = 20.5$ the other two contributions are exactly cancelled out. However, by $\omega = 28$ the beach contribution is less than one percent. The narrowness of the frequency band in which the low frequency mode can be generated is due to the difficulties in simultaneously satisfying the requirements that the short waves penetrate far enough to be "aware" of the nonuniformity of the low frequency mode, and yet do not penetrate so far that there is significant cancelling of contributions from successive crests of the standing wave.

Acknowledgement

This work is the implementation by RK of detailed research proposals made by RS in Fluid Mechanics Research Institute Rep. No. 43 (1973), Univ. Essex. RK and RS are indebted to the SRC and CEGB respectively for financial support.

References

- Bowen, A.J. and Inman, D.L. 1969 Rip currents 2. J. Geophys. Res. 74, No.23, 5479-5490.
- Bowen, A.J. and Inman, D.L. 1971 Edge waves and crescentic bars. J. Geophys. Res. 76, No.36, 8662-8671.
- Bretherton, F.P. and Garrett, C.J.R. 1969 Wavetrains in inhomogeneous moving media. Proc. Roy. Soc. A. 302, 529-554.
- Buchwald, V.T. 1969 Long waves on oceanic ridges. Proc. Roy. Soc. A. 308, 343-354.
- Gallagher, B. 1971 Generation of surf beat by non-linear wave interactions. J. Fluid Mech. 49, Pt.1, 1-20.
- Guza, R.T. and Davis, R.E. 1974 Excitation of edge waves by waves incident on a beach. J. Geophys. Res. 79, No.9, 1285-1291.
- Longuet-Higgins, M.S. and Stewart, R.W. 1961 The changes in amplitude of short gravity waves on steady nonuniform currents. J. Fluid Mech. 10, 529-549.
- Longuet-Higgins, M.S. 1967 The trapping of wave energy round islands. J. Fluid Mech. 29, 781-821.
- Phillips, O.M. 1974 Non-linear dispersive waves. Ann. Rev. of Fluid Mech. 6, 93-100.
- Sonu, C.J. 1972 Comment on paper by A.J. Bowen and D.L. Inman, Edge waves and crescentic bars. J. Geophys. Res. 77, No.33, 6629-6633.
- Stokes, Sir G.G. 1849 On the theory of oscillatory waves. Trans. Camb. Phil. Soc. 8, 441-455.
- Ursell, F. 1952 Edge waves on a sloping beach. Proc. Roy. Soc. A. 214, 79-97.

CHAPTER 26

VOCOIDAL THEORY FOR ALL NON-BREAKING WAVES

by D.H. Swart and C.C. Loubser¹⁾

ABSTRACT

The ideal theory for the prediction of wave-induced phenomena should be sufficiently accurate in all relative water depths, easy to apply and extensively tabulated. No available theory meets all these requirements. Vocoidal theory has been developed for application in all water depths. An extensive evaluation against experimental data proves that this theory meets the above requirements.

1. INTRODUCTION

During the past two decades great progress has been made in the development of new techniques for the prediction of wave-induced phenomena, such as the flow field in the vicinity of a coastal structure, longshore currents, forces on marine structures, ship motions, coastal sediment transport and combined wave diffraction and refraction. With the development of these more sophisticated techniques came the need for more accurate wave theories. Coastal sediment transport is an example of such a need.

Until about 10 years ago, the only way of predicting longshore sediment transport was to use an overall predictor [26], i.e. a formula yielding the total longshore sediment transport across the breaker zone. An example of such a theory is the well-known CERC-formula [22]. In 1967, Bijker published the first detail predictor [2], based on a uniform flow sediment transport formula. This method predicts the local longshore sediment transport rate. Subsequently, various researchers refined the Bijker technique, although the basic principle has remained the same. As the predictors become more sophisticated, the input required gets more extensive and it becomes more important to have accurate values for these input parameters. For example, because the transport is proportional to the longshore current raised to some power (between 3 and 6 [32]), a wrong prediction of the current by 10% will result in an error of 33% to 77% in the estimate of the transport. The longshore current, in turn, is determined from the balance between wave thrust (radiation stress) and dissipative forces (bed friction and lateral mixing). The Airy wave theory, which is the theory most frequently applied to water wave problems, can result in a radiation stress estimate at the breaker line up to 300% higher than the actual radiation stress. However, this does not imply that the longshore current will be overpredicted by the same amount, because the current velocity is linked to the radiation stress via an empirical roughness coefficient. It does, however, underline the importance of finding a more accurate description of the wave characteristics in shallow water.

Both for the prediction of erosional/depositional patterns in the vicinity of a coastal structure, by making use of a composite mathematical model, and for

1) National Research Institute for Oceanology, Stellenbosch, South Africa.

the computation of longshore sediment transport on a straight coast, accurate wave characteristics are required over the whole area of active transport. This zone can extend to depths of more than 50m [26], depending on the wave and sediment characteristics. For the prediction of erosional/depositional patterns wave characteristics and sediment transport computations are needed at numerous grid points. This requires large computer storage [8]. Both for this application and for the hand-computation of sediment transport rates, it must be possible to calculate the required wave characteristics easily. This can be done only if the wave theory under consideration either has simple algebraic expressions or is extensively tabulated.

A review was made of the available water wave theories [27] and the conclusion drawn that no existing theory meets all the above requirements. Vocoidal theory has therefore been developed in answer to these needs. The analytical and experimental validity of this theory is compared in Section 4 with that of other theories.

2. DERIVATION OF EXISTING WATER WAVE THEORIES

An insight into the techniques used for the derivation of the various existing theories is crucial for the understanding of the key differences between the results obtained. It is also the determining factor for the choice of a technique for the derivation of the new wave theory in Section 3.

2.1 Assumptions

The following well-known assumptions are common to all existing water wave theories and are therefore given below without any discussion, namely : (1) only non-breaking waves are considered; (2) the water movement is two-dimensional; (3) the water depth is constant, i.e. the bed is horizontal; (4) the flow is frictionless; (5) the fluid density is invariant; (6) surface tension effects are neglected; and (7) the wave motion is periodic and the waves propagate with constant velocity in water of constant depth.

2.2 Basic governing equations

The basic governing equations for the wave boundary value problem can be derived by making use of the above-mentioned assumptions. These governing equations are : (1) equation for the conservation of fluid mass, (2) equations of motion and (3) expression for the rotation of a fluid particle. These equations are given below without further explanation, as they can be found in numerous text books (e.g. [11] and [20]).

Conservation of mass (CM)

$$\frac{\partial u}{\partial x} + \frac{\partial w}{\partial z} = 0 \quad \dots (1)$$

where x and z are the horizontal and vertical coordinates and u and w are the horizontal and vertical orbital velocity components.

Equations of motion (EM)

In the x -direction :

$$\frac{1}{\rho} \frac{\partial p}{\partial x} + \frac{\partial u}{\partial t} + u \frac{\partial u}{\partial x} + w \frac{\partial u}{\partial z} = 0 \quad \dots (2)$$

In the z-direction :

$$g + \frac{1}{\rho} \frac{\partial p}{\partial z} + \frac{\partial w}{\partial t} + u \frac{\partial w}{\partial x} + w \frac{\partial w}{\partial z} = 0 \quad \dots (3)$$

where p is the pressure, g the gravitational acceleration, ρ the fluid density and t time.

Rotation of a fluid particle (RF)

The mean angular velocity R of an element of water is :

$$R = \frac{1}{2} \left(\frac{\partial w}{\partial x} - \frac{\partial u}{\partial z} \right) \quad \dots (4)$$

If R = 0 the flow is irrotational, otherwise it is rotational. For cases where R ≠ 0 Van Hijum [29] shows, by using the equations of motion, that

$$\frac{DR}{Dt} = \frac{\partial R}{\partial t} + u \frac{\partial R}{\partial x} + w \frac{\partial R}{\partial z} = 0 \quad \dots (5)$$

Equations (1) to (4) are the basic governing equations common to all solutions of the water wave problem.

2.3 Boundary conditions

All solutions to the system of equations (1) to (4) above should satisfy a number of boundary conditions, namely : (1) a *kinematic boundary condition* at both (a) the bed and (b) free surface, stating that no particle can pass through these boundaries (i.e. both bed and free surface are stream lines) and (2) a *dynamic boundary condition* which specifies that the pressure just inside the water mass should equal the atmospheric pressure.

re (1a) The *kinematic bed boundary condition (KBBC)* implies that

$$w = 0 \quad \text{at} \quad z = 0 \quad \dots (6)$$

re (1b) The *kinematic free surface boundary condition (KFSBC)* can be transformed to :

$$w = (u - c) \frac{\partial \eta}{\partial x} \quad \text{at} \quad z = d + \eta \quad \dots (7)$$

where η denotes the free surface wave profile, d the mean water depth and c the wave celerity

re (2) The *dynamic free surface boundary condition (DFSBC)* states simply that

$$p = 0 \quad \text{at} \quad z = d + \eta \quad \dots (8)$$

where p is the amount by which the pressure exceeds atmospheric pressure.

2.4 Solutions to the problem

The solutions found to date for the wave boundary value problem can be classified as follows : (1) irrotational theories, (2) rotational theories and (3) modified theories, which are discussed under these headings below. Discussions of these classes of theories can be found in numerous text books and original papers so that only those characteristics of the theories which are relevant to the present study are given in the following discussion. Table 5, in turn, is a summary of the discussion below.

Irrotational wave theories

When $R = 0$ in equation (5) it is possible to define a velocity potential ϕ (or stream function Ψ) which, in a reference system moving along with a celerity the same as that of the wave, is given by

$$u - c = - \frac{\partial \phi}{\partial x} = - \frac{\partial \Psi}{\partial z} \quad \dots (9)$$

$$w = - \frac{\partial \phi}{\partial z} = + \frac{\partial \Psi}{\partial x} \quad \dots (10)$$

With the aid of the above definition for ϕ , the equation for conservation of mass (equation (1)) is transformed into the well-known Laplace equation ($\nabla^2 \phi = 0$) and in addition the rotation is identically zero when equations (9) and (10) are substituted into equation (5). Similarly, when the stream function Ψ is used, the rotation R in equation (5) is transformed into the Laplace equation ($\nabla^2 \Psi = 0$) and the conservation of mass equation (equation (1)) is exactly satisfied when equations (9) and (10) are substituted into it. Therefore

$$\begin{aligned} \nabla^2 \phi &= 0 \\ \text{or} \quad \nabla^2 \Psi &= 0 \end{aligned} \quad \dots (11)$$

In all irrotational theories, the Laplace equation is used instead of equation (1) when solving the governing equations. The velocity potential ϕ (or stream function Ψ) is determined by the domain in which it exists, i.e. it is a function of η , which in turn specifies the free surface. It is, consequently, not possible to find a unique solution to equations (6), (7), (8) and (11) above. These equations must be simplified by means of approximations to linearize the problem in such a manner that the non-linear terms in the defining equations become small when compared with the linear terms. These approximations determine the specific form of the irrotational theory. Three main methods of solution are used, namely: (i) analytical perturbation of ϕ , η and c , as is performed in the Stokesian wave theories, which are valid for deep water, (ii) analytical perturbation of ϕ , leading to the cnoidal wave theories, which are valid for shallow water and (iii) numerical perturbation of ϕ or Ψ , which leads to the so-called numerical theories, valid for $H/d \leq 0.78$.

re (i) Stokesian wave theories

Taylor series expansions are assumed for ϕ , η and c . By assuming that $H/d \ll 1$ (where H is the wave height) and thus that the free surface boundary conditions (7) and (8) can be applied at the mean water level, i.e. at $z = d$, a first-order solution, called Stokes I, is found. A second-order solution is obtained by making use of the first-order solution, etc. The higher the order of the expansion, the greater the mathematical effort required to obtain a solution. Although higher-order Stokesian theories do exist, only Stokes I (Airy), II and V are used frequently. The first-order Stokes theory is valid for deep water only because of the assumption that $H/d \ll 1$. In addition, higher-order Stokesian theories become unstable in shallow water because of the magnitude of the expansion parameter.

Earlier comparisons with experimental data show that predictions given by Stokes I are good for deep water but get progressively poorer as the water depth decreases.

re (ii) Cnoidal wave theories

The assumption is made that both d/λ and H/d are $\ll 1$ where λ is the wave length, i.e. small-amplitude waves in shallow water are considered. The choice of an appropriate expansion parameter allows the expansion of ϕ into a Taylor series. The Laplace equation and kinematic bed boundary condition (equation (6)) are used to simplify this Taylor expansion to an equation in terms of the first-order term in ϕ . Only the terms necessary to obtain the first-order cnoidal theory are retained. Substitution of this expression for ϕ into the free-surface boundary conditions (equations (7) and (8)) yields the well-known long-wave equations, which are simplified to the Korteweg-de Vries equation and solved for η and c . Cnoidal theories can only be applied in shallow water, because of the assumptions made regarding the expansion parameter which yields imaginary wave celerities for $\lambda/d \lesssim 10$. However, comparison with measurements show that, provided the wave length is known, the cnoidal theory offers a good representation of the wave profile for deep to shallow water. This is not surprising since the cnoidal wave profile has as limiting cases a sinusoidal profile in deep water and a solitary wave profile in shallow water.

re (iii) Numerical wave theories

The rapid development of digital computers over the last three decades has opened up a new way of solving the defining equations (6) to (8) and (11) above by finding a solution, using direct numerical calculation. The best known numerical irrotational theories published to date are those of Chappellear [3], Dean [6], Von Schwind and Reid [31] and Cokelet [4]. The principle used is straightforward, namely: (1) find a Fourier series solution to the Laplace equation, and (2) optimize iteratively the coefficients in the Fourier series by means of the free-surface boundary conditions. The order of the Fourier series determines the accuracy to which the boundary conditions can be approximated. Each additional term of the Fourier series expansion added reduces the error in the free-surface boundary conditions. Dean used a variable number of terms in the Fourier expansion, and terminated the iterative procedure as soon as consecutive iterations (additions of further terms) resulted in small improvements in the error in the free-surface boundary conditions. The number of Fourier terms in Dean's solution varies between 2 (for deep water) and 19 (for shallow water). Dean showed that his stream function solution corresponds more closely to the free-surface boundary conditions than the theories of Chappellear and Von Schwind/Reid do. Cokelet raised the level of accuracy by using 110 Fourier terms. As a result, his solution to Laplace is more accurate than any other to date. However, the advantage of Dean's method over that of Cokelet is that Dean's results are tabulated more conveniently for engineering use. Furthermore, the resulting celerities for 24 arbitrarily chosen sets of initial conditions (T , d , H) as computed by using Dean's and Cokelet's theories differed by a maximum of 2.8%; the mean difference being 1.4%. In all cases Cokelet's theory yielded larger celerities. The conclusion is that the improvement obtained in the celerity by extending the Fourier series to the 110th order is not significant for engineering purposes. Furthermore, Cokelet's theory has not yet been tabulated to permit the prediction of time-dependent wave properties, such as the wave profile and orbital velocities.

Earlier comparisons with measurements have shown Dean's stream function theory to be in good agreement with data for all water depths within its tabulated range.

Rotational wave theories

The assumption of frictionless flow can normally be regarded as a good approximation over the greater portion of the water column. Frictionless flow implies irrotationality. It is possible to obtain an easy solution for the horizontal orbital velocity by making use of the conservation of mass equation (1). Because frictionless flow is also assumed for this approach, the resulting theory should be an irrotational theory. However, it is possible that due to approximations made in finding a solution, a finite value of R , as given by equation (4), remains. Such theories will be called rotational theories. The equation for conservation of mass (equation (1)) is integrated over the depth. After substitution of the kinematic boundary conditions (equations (6) and (7)) and assuming no net mass transport (which is valid as long as no set-up occurs) an equation is found for the mean horizontal orbital velocity u , namely :

$$\bar{u} = \frac{c\eta}{d+\eta} \quad \dots (12)$$

As no assumptions are made regarding rotationality, equation (12) is equally valid for irrotational wave theories and can, in fact, be used to check whether any given theory adheres to the original continuity equation (1) (see Table 5). Any expression for the instantaneous horizontal orbital velocity u which satisfies equation (12) therefore also satisfies equation (1). Expressions for the wave celerity c and wave profile η are found from the equations of motion, by making use of an assumed form of the orbital velocity u . Two recent examples of this approach are the rotational wave theories of Van Hijum [30] and Mejlhede [19].

To date no comparison has been made between actual measurements and predictions given by rotational theories.

Modified wave theories

As stated above, the simple-to-apply Airy wave theory yields predictions which become poorer as the water depth decreases. Various modifications have therefore been suggested to improve Airy theory's correspondence to wave characteristics in shallow water. The two most successful modifications are (1) Goda's empirical modification [9] of the Airy horizontal orbital velocity and (2) Hedges' theoretical modification [10][18] of the Airy wave celerity. Rather than modify Airy, another approach is to simplify the cnoidal solution, which is in any case applicable to shallow water conditions. In this manner, a good theory is obtained for shallow water which at the same time is easy to apply. The best example of such a simplified theory is Van Hijum's simplification [30] of the cnoidal wave profile, in which the cnoidal function is approximated by a cosine function raised to a variable power (depending on T , d , H).

Earlier comparisons with measured horizontal orbital velocities showed that Goda's approximation for the orbital velocity under the wave crest is superior to that predicted by Airy theory and is surpassed only by predictions for horizontal orbital velocity made with Dean's stream function theory.

2.5 Summary

The discussion above indicates that :

- (1) Numerical theories show the greatest overall adherence to boundary conditions.

- (2) None of the available theories agrees well with data for all water depths. The best theory which is still applicable in practice is Dean's numerical stream function theory.
- (3) No one analytical theory is clearly superior to any of the other analytical theories as far as experimental validity is concerned.

The derivation of a new theory is described in the next section. This theory incorporates the properties of the best contemporary theories and is easy to apply.

3. VOCOIDAL WATER WAVE THEORY

3.1 General

As indicated in Section 2 above, the theoretical derivation of a water wave theory involves the approximation of the free-surface boundary conditions. Depending upon these approximations, various classes of solutions are found. A different approach is used below, namely, (1) qualitative assumptions are made regarding the expressions for η , c and u in terms of unknown parameters (Section 3.2), (2) by substituting these qualitative expressions into the free-surface boundary conditions, three equations are found from which the above-mentioned parameters can be solved numerically (Sections 3.3 and 3.4) and (3) algebraic formulae for the parameters are determined by means of curve-fitting techniques (Section 3.5).

3.2 Qualitative assumptions

Wave profile η

A wave profile of the type given by the cnoidal theory provides the best fit to data, mainly because it has as theoretical limiting forms a sinusoidal wave in deep water and a solitary wave in extreme shallow water. Van Hijum [30] showed that the following expression has the same characteristics :

$$\frac{\eta}{H} = (\cos^2 \pi X)^P - \eta_{*t} \quad \dots (13)$$

where $X = x/\lambda$, η_{*t} is the dimensionless ($\pm H$) trough elevation and P is a parameter which depends on the wave conditions (H/d , λ/d). By expressing $(\cos^2 \pi X)^P$ as an infinite series, η_{*t} is found, after integration, to be :

$$\eta_{*t} = (\pi P)^{-\frac{1}{2}} \{ 1 - (8P)^{-1} + \frac{1}{2}(8P)^{-2} \} \quad \dots (14)$$

When $P = 1$ equation (13) represents a sinusoidal profile and when $P \gg 1$ the profile given by equation (13) tends towards a solitary profile. Equation (13) is used here to define the wave profile η .

A new function, which simplifies the representation of formulae in the new wave theory, namely the variable order cosine function, or *voc*-oidal function, is defined :

$$\text{voc}(P, X) = (\cos^2 \pi X)^P \quad \dots (15)$$

where P is the order of the function.

Wave celerity c

Hedges [10] has shown that when applying the free-surface boundary conditions

at some fixed "effective" level d_e the wave celerity is given by :

$$\frac{c^2}{gd} = \frac{1}{kd} \tanh Nkd \quad \dots (16)$$

where $N = d_e/d$. He shows that N tends to unity in deep water (same result as given by Stokes I) and to $1 + \eta_c/d$ in very shallow water ($\eta_c =$ crest elevation of wave - same result as given by solitary theory). Equation (16) is used here to define the wave celerity c . N remains to be determined in terms of the wave conditions (H/d , λ/d).

Orbital velocity u

The approach leading to equation (12) is used to define the horizontal orbital velocity u . Mejlhede [19] shows that the following expression for u satisfies equation (12) :

$$u = \frac{c\eta M(X)k \cosh [M(X)kz]}{\sinh [M(X)k(d+\eta)]} \quad \dots (17)$$

where $M(X)$ is a function of the wave conditions (H/d , λ/d) and also of X . Equation (17) is used to define the orbital velocity u in the new wave theory. Thus the new theory is not derived from the Laplace equation. It does not, however, necessarily imply that the theory is rotational, as will be seen in Section 3.3.1. Equation (17) represents an exact solution to the continuity equation which satisfies both kinematic boundary conditions.

3.3 Formulation of the governing equations

The wave boundary-value problem has now been reduced to a set of equations in which the unknowns are not η , c and u but the wave profile parameter P , the wave celerity parameter N and the orbital velocity parameter $M(X)$. An expression for $M(X)$ in terms of P is found below by using equation (4), after which optimum values of P and N are found by evaluating the pressure p from the equations of motion and equating it to the pressure in Bernoulli's equation.

3.3.1 A value for $M(X)$ in terms of P

Equation (5) specifies that any particle retains its rotation. For the free surface, which is a stream line, it is possible to write $R[z=d+\eta] =$ constant. An expression for R at the free surface is found by combining equations (4), (7) and (17) :

$$[R]_{z=d+\eta} = \frac{1}{2} \left[\frac{\partial}{\partial x} \left\{ (u-c) \frac{\partial \eta}{\partial x} \right\} - c\eta(M(X)k)^2 \right]_{z=d+\eta} \quad \dots (18)$$

which can be rewritten as

$$M(X)^2 = \left[\frac{\frac{\partial u}{\partial x} \frac{\partial \eta}{\partial x} + (u-c) \frac{\partial^2 \eta}{\partial x^2} - 2R}{c\eta k^2} \right]_{z=d+\eta} \quad \dots (19)$$

At the wave trough, that is at $X = 0.5$, equation (19) reduces to

$$M(0.5)^2 = \left[\frac{-2R}{c\eta_t k^2} \right]_{z=d+\eta} \quad \dots (20)$$

where subscript t denotes the wave trough.

$R [z=d+\eta] = 0$ (and consequently $M(0.5) = 0$) is a solution to equation (20). Therefore $R[z=d+\eta] = 0$ is used. At the wave trough, where $M(0.5) = 0$, equation (17) reduces to equation (12). Substitution of this equation (12) into equation (4) indicates that $R [X=0.5] = 0$ for all $0 \leq z \leq d + \eta$. As all stream lines in the flow field pass through $X = 0.5$, this implies that the flow will be irrotational, provided that $M(X)$ is determined exactly from equation (18). However, since small approximations have to be made to obtain a usable solution (see below) the flow will not be completely irrotational but will retain a small rotation, which can be neglected when secondary wave properties are derived.

Substitution of zero rotation into equation (19) and rearrangement yields :

$$M(X)^2 = \left[\frac{\frac{\partial(u/c)}{\partial X} \frac{\partial(\eta/H)}{\partial X} + (u/c - 1) \frac{\partial^2(\eta/H)}{\partial X^2}}{4\pi^2(\eta/H)} \right]_{z=d+\eta} \dots (21)$$

Equation (21) provides an implicit equation for $M(X)$ in terms of P and X .

3.3.2 Optimum values of P and N

Integration of equation (3) to z and substitution into the resulting equation of the dynamic free-surface boundary condition results in an expression for the pressure p , which at the bed ($z=0$) becomes :

$$\left[\frac{p}{\rho} \right]_{z=0} = g(d+\eta) + \left[\frac{u^2 + w^2}{2} - uc \right]_0^{d+\eta} \dots (22)$$

Since the bed is a stream line, the pressure at the bed should also satisfy Bernoulli's equation, that is

$$\left[\frac{p}{\rho} \right]_{z=0} = \left[gd - \frac{(u-c)^2}{2} \right]_{z=0} + k_1 \dots (23)$$

where k_1 is a constant.

The pressure can be eliminated from equations (22) and (23) to yield, after substituting the kinematic bed boundary condition into the resulting equation, an expression for c^2/gd :

$$\frac{c^2}{gd} = \left[\frac{\eta/d}{(u/c) - \frac{1}{2} \{ (u/c)^2 + (w/c)^2 - (w_0/c)^2 \}} \right]_{z=d+\eta} \dots (24)$$

where $w_0 = -c \frac{\partial \eta}{\partial x} \Big|_{\eta=0, z=d+\eta}$, that is, w_0 is the value of w at the free surface when $\eta=0$.

Because of assumption (7) in Section 2.1 above, the wave celerity defined by equation (24) must be a constant, that is

$$\frac{\partial}{\partial X} \left[\frac{c^2}{gd} \right] = 0 \quad \text{for } 0 \leq X \leq 0.5 \dots (25)$$

Equations (21), (24) and (25) are the governing equations used to find solutions for P , N and $M(X)$.

3.4 Solving the governing equations

The solution is determined in two phases, namely (1) a first-order solution is found by assuming $u/c \ll 1$, and (2) a second-order correction is applied to compensate for the fact that u/c is not negligible with respect to unity. This two-phase approach is necessary because $M(X)$ cannot be determined at wave breaking.

The exact solution to equations (21), (24) and (25) above can only be obtained numerically for $u/c < 1$. The following wave conditions (H/d , λ/d) are used :

$$\begin{array}{ll} 0.01 \leq H/d \leq 0.8 & 1 \leq \lambda/d \leq 75 \\ 0.01, 0.02, 0.05, 0.1(0.1)0.8 & 1, 2, 5, 8(2) 20, 20(10) 50, 75 \end{array}$$

Equation (25) is satisfied by computing c^2/gd from equation (24) at 1000 discrete intervals in the area $0 \leq X \leq 0.5$ and choosing that combination of P and N for which the relative standard deviation of the computed c^2/gd -values is the least.

Although the maximum theoretical breaker index H/d is about 0.78, experimental data indicate that H/d -values as high as 1.3 can occur. To ensure that the theory developed herein is applicable in this area the numerical solution of equations (21), (24) and (25) is repeated with the assumption that $u/c \ll 1$ for an extended H/d range $0.01 \leq H/d \leq 1.3$. The following ratios are computed for those wave conditions at which an exact solution was found above.

$$\begin{aligned} R_P &= P/P_1 \\ R_N &= N/N_1 \end{aligned} \quad \dots (26)$$

$$\text{and } R_M = M(0)/M_1(0)$$

where subscript 1 denotes the solution with the small-amplitude assumption (that is $u/c \ll 1$) and P , N and $M(0)$ denote the "exact" solution, that is the solution in which no assumption is made regarding the value of u/c .

The results obtained for the above-mentioned wave conditions indicate the following :

- (1) It is possible to find solutions for P_1 , N_1 and $M_1(0)$ for all wave conditions listed ($H/d \leq 1.3$).
- (2) The values of R_M and R_N vary systematically with H/d for all λ/d -values.
- (3) For any given λ/d -value N tends to $1 + \eta_c/d$ for large H/d .
- (4) For any given λ/d -value $M(0)$ tends asymptotically towards a constant value with varying H/d . For all practical purposes $M(0)$ is constant for $H/d \geq 0.7$.
- (5) R_P varies systematically with λ/d for all H/d -values. The variation of R_P with H/d is analogous to the variation of P_1 with H/d at large λ/d -values (say $\lambda/d = 50$).

The above observations imply that it is possible to use the small-amplitude solution to extend the range of the "exact" solution.

3.5 Algebraic expressions for P, N and M(X)

The values determined as described above for P, N, M₁(0), R_P, R_N and R_M are correlated to the wave conditions (H/d, λ/d) and algebraic expressions are determined by curve-fitting. The resulting algebraic expressions are listed below.

Wave profile parameter P

$$(1) \quad P_1 = \begin{cases} 1.03 F_s + 9 + 3.33 \exp(-0.109(11 + F_s)) & \text{for } F_s > -11 \\ 1 & \text{for } F_s \leq -11 \end{cases} \quad \dots (27)$$

where $F_s = \frac{U_r - U_{r0}}{\theta} \quad \dots (28)$

$$U_r = (H/d)(\lambda/d)^2 = \text{Ursell parameter}$$

$$U_{r0} = 63 + 90 (H/d)^{1.48} \quad \dots (29)$$

$$\theta = \begin{cases} 1.01 \exp(3.31(H/d)) & \text{for } H/d \geq 0.505 \\ 5.38 & \text{for } H/d < 0.505 \end{cases} \quad \dots (30)$$

$$(2) \quad R_P = R_{P1} - (R_{P1} - 1) \exp(b \lambda/d) \quad \dots (31)$$

where $R_{P1} = 1 + 0.0021 (P_{1i} - 1) + 6.09 \times 10^{-7} (P_{1i} - 1)^{2.56} \quad \dots (32)$

$$b = -0.0916 + 2.718 \times 10^{-4} P_{1i} \quad \dots (33)$$

$$P_{1i} = P_1\text{-value for } \lambda/d = 50$$

$$(3) \quad P = R_P P_1 \quad \dots (34)$$

Wave celerity parameter N

$$(4) \quad N_1 = \begin{cases} 1 + 0.19 F_N^{1.5} & \text{for } F_N < 0.72 \\ 0.6 + 0.72 F_N & \text{for } F_N \geq 0.72 \end{cases} \quad \dots (35)$$

$$\text{where } F_{RN} = (H/d)(\lambda/d)^{0.1} \quad \dots (36)$$

$$(5) \quad R_N = \begin{cases} 1 & \text{for } F_{RN} < 0.093 \\ 0.67 F_{RN} + 0.938 & \text{for } F_{RN} \geq 0.093 \end{cases} \quad \dots (37)$$

$$\text{where } F_{RN} = (H/d)(\lambda/d)^{-1} \quad \dots (38)$$

$$(6) \quad N = R_N N_1 \quad \dots (39)$$

Orbital velocity parameter M(X)

(7) For any given wave condition (H/d, λ/d) equation (19) can be used to obtain numerical values of M(X) for $0 \leq X \leq 0.5$. These M(X)-values vary systematically from M_p at X = 0 to zero at X = 0.5. It is shown in [27] that M(X) can be closely approximated by

$$M(X) = \begin{cases} (M_p - M_t) \cos \pi X + M_t & \text{for } r_1 P_1 < 0.5 \\ M_p \text{ voc}(r_1 P_1, X) & \text{for } r_1 P_1 \geq 0.5 \end{cases} \quad \dots (40)$$

M_t is defined in (8) to (10) below and M_p in (11) below and where r_1 as determined by curve-fitting equals :

$$r_1 = 0.4 \{1 - P_1^{-0.9}\} \quad \dots (41)$$

Maximum value M_p of orbital velocity parameter M(X)

(8) The maximum value M_t of M(X) as determined by equation (19) is always found at X = 0. An expression^p for $M_t(0)$ is determined analytically from equation (19) by setting X = 0 and rearrangement :

$$M_t(0) = \left(\frac{P_1}{2\eta_{*c1}} \right)^{\frac{1}{2}} \quad \dots (42)$$

where $\eta_{*c1} = 1 - \eta_{*t1}$ and subscript 1 refers to the first-order approximation.

$$(9) \quad R_M = \begin{cases} \frac{0.54}{1+6.7(H/d)^4} + 0.46 & \text{for } H/d \leq 0.7 \\ 0.667 & \text{for } H/d > 0.7 \end{cases} \quad \dots (43)$$

$$(10) \quad M_p = M(0) = \begin{cases} R_M M_{p1} & \text{for } H/d \leq 0.7 \\ (R_M M_{p1})_{H/d=0.7} & \text{for } H/d > 0.7 \end{cases} \quad \dots (44)$$

Minimum value M_t of orbital velocity parameter $M(X)$

(11) The solution to equation (20) indicates that $M_t = M(0.5) = 0$. However, when $P_1=1$, that is, for very deep water, $r_1 = 0$, thereby indicating a constant $M(X)$ -value for $0 \leq X < 0.5$. The resulting discontinuity at $X = 0.5$ is unrealistic. To a lesser extent the same phenomenon occurs for $1 \leq P_1 \leq 2$. To prevent the discontinuity from occurring, the following approximations are made: (i) $M(X)$ -values in the area $0.45 \leq X \leq 0.49$ are extrapolated to $X = 0.5$ and the value thus found is used as a minimum value M_t for $M(X)$ where

$$M_t = R_M \exp \{ - 4.2 (P_1 - 1) \} \quad \dots (45)$$

and (ii) the X -variation of $M(X)$ is determined by equation (40a) rather than by equation (40b). It is shown in [27] that the effect of the approximations on the predicted horizontal orbital velocity amounts to less than 2% of the actual velocity for any location within the fluid.

Because $M(X)$ as determined from equation (40) is an approximate solution to equation (19), the flow will not be irrotational. However, computations covering the same wave conditions used in Section 3.4 above indicate that \bar{K} never exceeds a few per cent of $(2\pi/T)$ and can for practical purposes be assumed equal to zero. This implies that although the flow is, as a result of the approximation of $M(X)$, rotational, the rotation is negligible.

3.6 Presentation of other wave properties

As stated in Section 1, the aim of the study is the derivation of a simple-to-apply wave theory in which wave characteristics can be computed from algebraic expressions. For this reason, algebraic expressions were also derived in [27] for the following primary wave characteristics, namely, vertical orbital velocity, horizontal and vertical orbital excursions, mass transport velocity, group velocity, wave energy/unit surface area and the pressure within the wave. Where necessary, further parameters were introduced and expressions determined for them by curve-fitting techniques, in a similar manner as in Section 3.5 above.

A quantitative knowledge of secondary wave-induced phenomena, such as shoaling of water waves, wave refraction, diffraction and breaking, principal radiation stresses, wave set-up, generation of longshore breaker-zone currents, shear stresses exerted on the bed due to combined current and wave action, wave-induced bed-form generation, sediment entrainment and sediment suspension, is essential for the prediction of the effect of waves on the coastal environment. These aspects will be studied in follow-up reports to [27].

3.7 Tabulation of parameters

To facilitate the easy use of the theory, it is essential to tabulate the main parameters in terms of the wave conditions (H/d , λ/d), in a way similar to that for linear wave theory. It is intended to publish such a book of tables in 1979. However, abridged tables are included here as Tables 1 to 4.

4. VERIFICATION OF WATER WAVE THEORIES

4.1 Evaluation

The various theories mentioned in Section 2 are evaluated in this section (see Table 6). The data sets used in the evaluation are summarized in Table 7. There are various methods for the verification of wave theories. Dean [7] mentions two methods, namely (1) an analytical verification, that is, the adherence of each

TABLE 1 : λ/L AS A FUNCTION OF H/L AND T/\sqrt{L}

T/\sqrt{L} \ H/L	.01	.02	.05	.10	.20	.30	.40	.50	.60	.70	.80	.90	1.00
1	.16	.16	.16	.16	.16								
2	.64	.64	.64	.64	.64	.64							
4	2.51	2.51	2.51	2.51	2.52	2.53	2.53	2.54	2.54				
6	4.91	4.91	4.91	4.92	4.97	5.03	5.13	5.21	5.28	5.39			
8	7.17	7.18	7.18	7.20	7.29	7.45	7.61	7.78	7.97	8.26	8.53	8.77	
10	9.24	9.24	9.25	9.27	9.38	9.58	9.72	9.95	10.20	10.52	10.98	11.42	11.84
12	11.45	11.45	11.47	11.49	11.63	11.92	12.22	12.54	13.00	13.42	13.92	14.48	15.13
14	13.53	13.53	13.55	13.59	13.73	14.08	14.45	14.83	15.44	16.20	16.94	17.64	18.35
16	15.59	15.59	15.61	15.66	15.81	16.22	16.65	17.09	17.84	18.75	19.63	20.49	21.33
18	17.64	17.64	17.66	17.71	17.88	18.36	18.82	19.34	20.23	21.27	22.29	23.29	24.26
20	19.67	19.68	19.70	19.76	19.93	20.45	20.99	21.57	22.60	23.78	24.94	26.07	27.17
25	24.74	24.75	24.78	24.86	25.06	25.68	26.37	27.09	28.52	30.03	31.51	32.96	34.39
30	29.78	29.79	29.83	29.93	30.19	30.89	31.71	32.58	34.41	36.24	38.05	39.82	41.58
35	34.82	34.83	34.88	34.99	35.30	36.08	37.04	38.05	40.29	42.45	44.57	46.68	48.78
40	39.84	39.85	39.91	40.05	40.41	41.25	42.24	43.43	46.17	48.65	51.11	53.51	55.88
45	44.86	44.87	44.94	45.10	45.53	46.42	47.54	48.19	52.05	54.86	57.64	60.35	63.02
50	49.88	49.89	49.97	50.24	50.61	51.59	52.94	54.75	57.94	61.07	64.16	67.19	70.17
75	74.93	74.95	75.07	75.36	76.10	77.35	79.37	82.60	87.44	92.18	96.87	101.44	105.95
100	99.95	99.99	100.15	100.53	101.60	103.08	105.76	110.57	117.07	123.43	129.70	135.83	141.86

TABLE 2 : WAVE PROFILE PARAMETER (β) AS A FUNCTION OF H/L AND λ/L

H/L \ λ/L	.01	.02	.05	.10	.20	.30	.40	.50	.60	.70	.80	.90	1.00
1	1.00	1.00	1.00	1.01	1.02								
2	1.00	1.00	1.01	1.01	1.03	1.05							
4	1.00	1.00	1.01	1.03	1.06	1.09	1.12	1.13	1.12				
6	1.00	1.01	1.02	1.04	1.08	1.13	1.17	1.18	1.18	2.91			
8	1.00	1.01	1.02	1.05	1.20	1.20	1.22	1.24	2.89	4.79	6.19	7.18	
10	1.00	1.01	1.04	1.48	2.26	2.92	3.42	3.67	5.92	7.48	8.44	9.00	9.34
12	1.00	1.01	1.33	2.10	3.68	5.31	6.91	8.24	10.17	11.99	13.76	15.31	16.14
14	1.00	1.01	1.47	2.87	5.50	8.44	11.60	14.50	15.78	15.71	15.01	14.14	13.31
16	1.00	1.14	2.09	3.80	7.75	12.41	17.57	22.54	22.82	21.39	19.42	17.52	15.88
18	1.00	1.31	2.57	4.90	10.46	17.19	24.84	32.37	31.30	28.15	24.64	21.47	18.86
20	1.02	1.51	3.12	6.18	13.63	22.81	33.40	43.98	41.24	36.00	30.65	26.00	22.26
25	1.30	2.11	4.85	10.23	23.51	40.41	60.28	80.69	72.35	60.34	49.11	39.82	32.58
30	1.66	2.88	7.10	15.51	36.41	62.85	94.75	128.44	112.34	91.27	72.36	57.15	45.47
35	2.09	3.83	9.51	22.03	51.84	89.87	136.68	187.42	161.23	128.67	100.28	77.86	60.87
40	2.61	4.97	13.31	29.76	69.83	121.35	185.99	257.80	219.03	172.48	132.77	101.89	78.72
45	3.21	6.32	17.29	38.63	90.25	157.22	242.61	339.66	285.69	222.63	169.78	129.18	98.96
50	3.90	7.88	21.85	48.41	113.09	197.51	306.44	433.01	361.15	279.04	211.26	159.70	121.58
75	8.90	19.06	52.77	114.45	263.18	482.16	731.16	1059.56	867.24	652.74	484.39	346.24	270.11
100	16.64	35.74	96.43	206.64	472.91	831.74	1326.40	1979.69	1580.47	1173.31	865.54	640.13	477.55

TABLE 3 : DIMENSIONLESS TROUGH DEPTH (η_{tr}) AS A FUNCTION OF H/L AND λ/L

H/L \ λ/L	.01	.02	.05	.10	.20	.30	.40	.50	.60	.70	.80	.90	1.00
1	.4980	.4978	.4974	.4966	.4951								
2	.4979	.4976	.4966	.4953	.4923	.4893							
4	.4977	.4973	.4957	.4930	.4874	.4819	.4775	.4759	.4763				
6	.4976	.4970	.4948	.4911	.4832	.4754	.4691	.4666	.4674				
8	.4975	.4967	.4941	.4891	.4849	.4846	.4818	.4853	.4880	.3170	.2323	.2069	
10	.4974	.4965	.4909	.4852	.4850	.4863	.4941	.4846	.4871	.2078	.1914	.1855	.1621
12	.4973	.4963	.4859	.4867	.4841	.4890	.4936	.4947	.4873	.1658	.1658	.1659	.1672
14	.4973	.4962	.4847	.4888	.4831	.4911	.4839	.4859	.4842	.1444	.1444	.1487	.1532
16	.4972	.4956	.4879	.4861	.4904	.4885	.4836	.4882	.4873	.1213	.1272	.1338	.1403
18	.4972	.4945	.4853	.4844	.4873	.4851	.4836	.4846	.4804	.1059	.1131	.1210	.1290
20	.4952	.4925	.4868	.4824	.4814	.4875	.4893	.4848	.4876	.0937	.1015	.1101	.1189
25	.4896	.4857	.4817	.4743	.4855	.4885	.4925	.4827	.4862	.0723	.0803	.0891	.0985
30	.4865	.4812	.4781	.4721	.4832	.4870	.4879	.4827	.4852	.0590	.0662	.0745	.0834
35	.4876	.4790	.4769	.4719	.4828	.4862	.4812	.4844	.4827	.0464	.0527	.0603	.0722
40	.4832	.4847	.4832	.4830	.4874	.4812	.4813	.4851	.4881	.0429	.0489	.0558	.0653
45	.4830	.4820	.4847	.4895	.4893	.4840	.4862	.4838	.4878	.0413	.0453	.0496	.0566
50	.4766	.4978	.4920	.4807	.4810	.4801	.4822	.4871	.4897	.0338	.0388	.0444	.0511
75	.4865	.4884	.4873	.4857	.4848	.4862	.4808	.4872	.4892	.0221	.0256	.0297	.0343
100	.4873	.4840	.4874	.4892	.4859	.4896	.4855	.4827	.4842	.0163	.0192	.0223	.0258

The dotted line indicates the approximate theoretical wave breaking limit

TABLE 4 : MAXIMUM ORBITAL VELOCITY PARAMETER (u_m) AS A FUNCTION OF H/d AND λ/d

H/d λ/d	.01	.02	.05	.10	.20	.30	.40	.50	.60	.70	.80	.90	1.00
1	1.000	1.000	1.000	1.000	1.000								
2	1.000	1.000	1.000	1.000	1.000	1.000							
4	1.000	1.000	1.000	1.000	1.000	1.000	1.000						
6	1.000	1.000	1.000	1.000	1.000	1.000	1.000	1.000					
8	1.000	1.000	1.000	1.000	1.018	1.000	1.000	1.005	1.104				
10	1.000	1.000	1.002	1.115	1.261	1.326	1.308	1.216	1.320	1.313	1.104	1.104	1.313
12	1.000	1.000	1.084	1.260	1.514	1.670	1.721	1.673	1.642	1.340	1.540	1.540	1.540
14	1.000	1.000	1.173	1.415	1.776	2.018	2.131	2.114	1.970	1.779	1.779	1.779	1.779
16	1.000	1.037	1.270	1.579	2.047	2.371	2.539	2.548	2.301	2.026	2.026	2.026	2.026
18	1.000	1.087	1.372	1.750	2.325	2.727	2.945	2.974	2.633	2.278	2.278	2.278	2.278
20	1.001	1.139	1.480	1.928	2.609	3.085	3.347	3.392	2.964	2.533	2.533	2.533	2.533
25	1.085	1.285	1.769	2.397	3.332	3.977	4.335	4.406	3.781	3.175	3.175	3.175	3.175
30	1.179	1.446	2.081	2.888	4.060	4.856	5.298	5.389	4.584	3.814	3.814	3.814	3.814
35	1.283	1.621	2.410	3.391	4.783	5.721	6.242	6.353	5.376	4.450	4.450	4.450	4.450
40	1.394	1.806	2.752	3.899	5.500	6.576	7.175	7.305	6.162	5.083	5.083	5.083	5.083
45	1.513	2.001	3.101	4.408	6.211	7.423	8.101	8.249	6.944	5.715	5.715	5.715	5.715
50	1.638	2.203	3.456	4.915	6.917	8.266	9.022	9.188	7.723	6.345	6.345	6.345	6.345
75	2.332	3.285	5.241	7.418	10.410	12.440	13.585	13.845	11.594	9.487	9.487	9.487	9.487
100	3.097	4.412	7.007	9.893	13.876	16.587	18.119	18.472	15.448	12.622	12.622	12.622	12.622

TABLE 5 : REVIEW OF AVAILABLE PERIODIC WATER WAVE THEORIES

NAMES OF THEORIES	GOVERNING EQUATIONS	IRROTATIONAL FLOW	ANALYTICAL VALIDITY ADHERENCE TO				ADVANTAGEOUS PROPERTIES	REFERENCE TO LITERATURE
			CONTINUITY	KSBC	KFSBC	DFSBC		
Stokes I, II, V, gravity cnoidal	La Place La Place	✓ ✓	✓ ✓	✓ ✓	x x	x x	c, η , u in deep water η in all water depths for known λ	[1], [5], [11], [23], [24], [15], [19], [25]
Dean's numerical ψ	La Place	✓	✓	✓	✓	x	c, η in tabulated range	[6], [7]
Hedgcs modified c Goda's empirical u	La Place N/A	✓ -	x -	✓ -	x -	x -	c in all water depths u at wave crest in all depths	[10], [18] [9]
Van Hijum's simplified cnoidal (P-wave)	Conservation of mass and eq. of motion	x	✓	✓	✓	x	useful simplification of cnoidal η	[30]
Mejlhede's cnoidal	Conservation of mass and eq. of motion	x	✓	✓	✓	✓	useful higher order expression of u	[19]
Van Hijum's numerical	rotational flow	x	✓	✓	✓	✓	all boundary conditions exactly satisfied for both [13] and [29]	[29]

TABLE 6 : THEORIES EVALUATED

NAME OF THEORY	THEORY NUMBER	REFERENCE TO LITERATURE
Stokes I (Airy)	1	Airy [1], Ippen [11]
Stokes II	3	Stokes [24], Ippen [11]
Stokes V	10	De [5], Skjelbreia [23]
Dean	11	Dean [6], [7]
Svendsen's cnoidal	4	Svendsen [25]
Keulegan et al's cnoidal	12	Keulegan et al [15]
Mejlhede's cnoidal	13	Mejlhede [19]
Mejlhede 1; $\beta=0$	6	Mejlhede [19]
Mejlhede 2; $\beta \neq 0$	7	Mejlhede [19]
Hedgcs	9	Hedgcs [10], Lewis [18]
Goda	2	Goda [9]
P-wave	8	Van Hijum [30]
Vocoidal	5	Swart [27]

TABLE 7 : NUMBER OF DATA SETS FOR EACH DATA ORIGIN

DATA ORIGIN	ORBITAL VELOCITY u	WAVE PROFILE η	WAVE LENGTH λ/d
Le Mehaut et al (1978)[17]	8	1	
Iwagaki and Sakai (1970)[12]	12	21	
Horison and Crooke (1953)[21]	5		
Goda (1964)[9]	18		
Van Hijum (1972)[30]	25		
Touckiya & Yamaguchi (1972)[28]		2	75
Kneesen (1976)[16]		36	
Wiegel (1960) [33]		2	
Dean (1965) [6]		1	
Iwagaki & Yamaguchi (1972)[13]			67
Karpul (1968)[14]	29		
NRIO (1977)	27	217	217
TOTAL	124	280	359

theory to the free-surface boundary conditions, and (2) an experimental verification, based on the adherence of each theory to observed data. Another possibility exists, namely, (3) a comparison of each theory with an exact solution to the governing equations, such as Cokelet's numerical theory. Possibilities (1) and (3) test the extent to which any given theory adheres to the governing equations and boundary conditions, but do not necessarily indicate the correlation with observed data. The reason for this is that the governing equations are in themselves approximations; they do not include the effects of, for example, surface tension and the bed slope, both of which are important near wave breaking. Provided that observations can be made with sufficient accuracy under controlled conditions, i.e. when errors due to both measuring equipment (techniques) and the generation of waves in too shallow water are minimized, experimental verification is the most reliable of the above methods. However, the available data are frequently contaminated, especially by secondary waves because of the method of generation used. Because of the large number of data sets used (see Table 7) errors due to both generation and measuring techniques are to some degree averaged out.

Dean's computations [7] regarding the adherence of various theories to the free-surface boundary conditions indicate that this measure (analytical verification) is not always a true reflection of the relative validity of the various theories. For example, the Stokes I (Airy) theory (derived for deep water) has a smaller dynamic free surface boundary condition error than the cnoidal theory (derived for shallow water) under shallow water conditions ($H/H_b = 1$ where b denotes breaking waves, $d/\lambda_0 < 0.195$) (Dean [7]). Therefore, the analytical verification, in the way defined by Dean [7], is not discussed further in this paper. However, an extensive analysis of the analytical verification of the above 13 theories will be contained in a follow-up to [27], which is being prepared at present.

A practical comparison with Cokelet's theory is not yet possible, because the tabulation of parameters in Cokelet's theory permits only the calculation of wave characteristics which are independent of time. However, the comparison between the theories of Dean and Cokelet, mentioned in Section 2.4 above, indicates that Dean's theory can, for engineering purposes, be assumed to be an "exact" solution to the "approximate" governing equations.

The following procedure has been adopted to establish experimental validity :

- (1) The relative error E_r for each wave characteristic W is given by :

$$E_r = \left| \frac{W_p - W_m}{W_m} \right| \quad \dots (46)$$

where subscripts p and m denote predicted and measured values, respectively.

- (2) Relative errors for the orbital velocity u under the wave crest, wave length λ and wave profile η are computed by applying each theory to all data sets for which relevant data are available.
- (3) To assist the evaluation of the application range of the various wave theories, an Ursell-like parameter which depends solely on the wave conditions T , d and H , is defined, namely,

$$F_c = (H/d)^{\frac{1}{2}} T_c^{2\frac{1}{2}} \quad \dots (47)$$

$$\text{where } T_c = T (g/d)^{\frac{1}{2}} = (2\pi)^{\frac{1}{2}} (\lambda_0/d)^{\frac{1}{2}} \quad \dots (48)$$

A wave with a height $H = 1\text{m}$ and period $T = 8\text{s}$ has F_c -values of 0.3, 17, 934 and 3143 in water depths of 200m, 20m, 2m and 1m respectively, that

is, F_c varies from zero in very deep water to a few thousand in very shallow water. The values of F_c for shallow water are limited by wave breaking.

- (4) For each wave characteristic and wave theory the mean and standard deviation of the absolute values of all relative errors are computed for each of the following F_c -groups (0-50, 50-100, 100-200, 200-500, 500-1000 and > 1000). Those theories which do not differ at a 5% significance level from the theory with the smallest mean relative error in each of the above-mentioned F_c -groups are singled out as being the best theories for the prediction of the specific wave characteristic in that F_c -group. A theory is considered to fall within its validity area if it passes this statistical test.
- (5) The resulting validity areas of the various theories for the prediction of u , λ and η are shown in Figures 1 to 3. Also shown in each F_c -group is the average of the mean relative errors of the equivalent good theories.
- (6) Figure 4 indicates the overall validity areas of the evaluated theories and, as such represents a generalized experimental validity, which is not bound to a specific wave characteristic. The theories listed in this figure are those with a higher than average occurrence in any given F_c -group (that is those appearing two or three times in the specific F_c -group on Figures 1 to 3).

4.2 Results

- (1) According to Figure 4 only two wave theories are valid for all F_c -groups, namely, Dean's stream function theory and Vocoidal theory, that is, only these two theories are suggested for application in all relative water depths (theory numbers are listed in Table 6).
- (2) However, Dean's tabulated range restricts the application of his theory at both high and low H/d values.
- (3) In the restricted range of Dean's tables there is no significant difference between Dean's results and those obtained by Vocoidal theory. It can therefore be concluded that Vocoidal theory is equivalent at a 5% significance level to Dean's theory, which in turn was shown, for engineering purposes, to be an "exact" solution to the governing equations.
- (4) The wave profile predicted by Vocoidal theory for $F_c < 200$ is not statistically equivalent to the best theories in this range. The relative errors in the 0-50, 50-100 and 100-200 F_c -groups for Vocoidal theory are 6%, 7% and 8% respectively, as compared to 5%, 5% and 7% for the best theories.
- (5) Within its application range, i.e. for $(T\sqrt{g/d})^{-1} < 0.126$, Mejlhede's gravity cnoidal theory is statistically equivalent to Dean's stream function theory and Vocoidal theory. The same does not apply to the Keulegan/Patterson and Svendsen cnoidal theories [15], [25].
- (6) Stokes I, II and V are statistically equivalent to the better theories for $F_c \leq 200$, 100 and 200 respectively, which indicates that the use of Stokes II theory for anything but deep water is normally not advisable and that Stokes I is, generally speaking, equivalent to Stokes V.
- (7) Goda's theory is listed in the $500 \leq F_c \leq 1000$ column only because of its good adherence to orbital velocity data.
- (8) Mejlhede's rotational cnoidal theory is statistically equivalent to the better theories for $F_c \leq 200$. Beyond this range, it yields unrealistic horizontal orbital velocities under the wave crest, which tend to zero at the bed and to some extremely high value (far greater than the wave celerity) at the free surface.

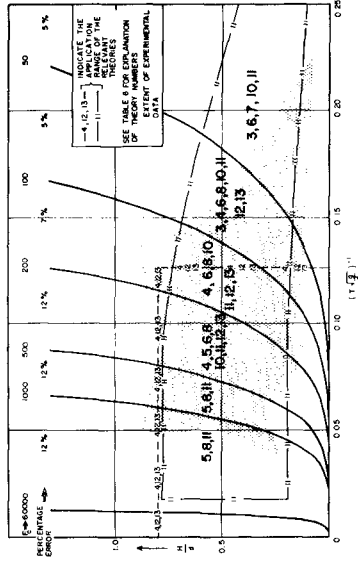


FIGURE 1 BEST THEORIES FOR THE PREDICTION OF THE ORBITAL VELOCITY UNDER THE WAVE CREST

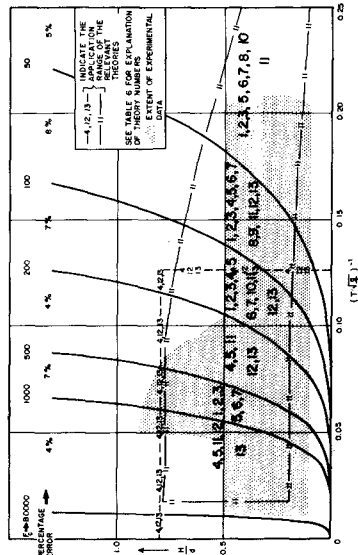


FIGURE 2 BEST THEORIES FOR THE PREDICTION OF THE WAVE LENGTH

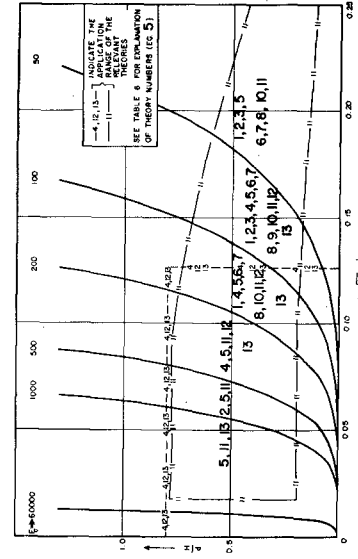


FIGURE 3 BEST THEORIES FOR THE PREDICTION OF THE WAVE PROFILE

FIGURE 4 REGIONS OF OVERALL VALIDITY: VARIOUS WAVE THEORIES

- (9) The simple-to-apply Van Hijum-approximation to cnoidal theory is statistically equivalent to the better theories for $F_c \leq 200$. It should preferably not be used beyond this range because the predicted horizontal orbital velocity tends to a constant value over the full depth from bed to free surface.

5. SUMMARY AND CONCLUSIONS

1. There is a need for a water wave theory which is (i) sufficiently accurate in all relative water depths, (ii) expressed in terms of algebraic expressions, (iii) relatively easy to apply/require little computer time and (iv) well-tabulated. None of the available theories meets all these requirements.
2. Vocoidal theory has therefore been developed from first principles in answer to these needs. The theory is simple to apply and is expressed algebraically (see equations (13), (16) and (17)).
3. Frictionless flow was assumed in the derivation of Vocoidal theory, but because of an approximation made in the representation of the time-variation of the horizontal orbital velocity, the theory contains a small rotation, which can, for practical purposes, be neglected.
4. An extensive analysis of the experimental validity of thirteen different theories indicates that only two of the evaluated theories consistently yield good results in all relative water depths, namely, Vocoidal theory and Dean's stream function theory.
5. Dean's theory is only applicable in a restricted H/d-range (see - 11 - line in Figure 4), which can never be extended beyond $H/d = 0.78$.
6. Vocoidal theory is therefore recommended for general application for all relative water depths.

LIST OF REFERENCES

1. AIRY C.B. Tides and waves; Encyc. Metrop. Art. No 192, 1845.
2. BIJKER E.W. Some considerations about scales for coastal models with movable bed; Delft Hydraulics Laboratory, Publ. No 50, 1967.
3. CHAPPELEAR J.E. Direct numerical calculation of wave properties; Journal of Geophysical Research, Vol. 66, No 2., 1961.
4. COKELET E.D. Steep gravity waves in water or arbitrary uniform depth; Phil. Trans. of the Royal Society of London, Series A, Vol 286, 1977.
5. DE S.C. Contributions to the theory of Stokes; Proc. Cambridge Phil. Soc., No 51, 1955.
6. DEAN R.G. Stream function representation of nonlinear ocean waves; Journal of Geophysical Research Vol 70 No 18, 1965.
7. DEAN R.G. Evaluation and development of water wave theories for engineering application; Vol 1 & 2, Special report No 1, prepared for U.S. Army, Corps of Engineers, CERC, 1974.
8. FLEMING C.A. The development and application of a mathematical sediment transport model; Ph. D. Thesis, University of Reading, 1977.
9. GODA Y. Wave forces on a vertical circular cylinder : Experiments and a proposed method of wave force computation; Report of Port and Harbour Technical Research Institute No 8, 1964.
10. HEDGES T.S. An empirical modification to linear wave theory; Proc. Instn. Civ. Engrs. Part 2 No 61, 1976.
11. IPPEN A.T. Estuary and coastline hydrodynamics; McGraw-Hill, New York 1966.
12. IWACAKI Y. and SAKAI T. Horizontal water particle velocity of finite amplitude waves; 12th Conf. Coast. Eng. Vol 1, 1970.
13. IWACAKI Y. and YAMACUCHI M. Studies on cnoidal waves (sixth report) - Limiting condition for application of cnoidal wave theory; Annuals, D.P.R.I., Kyoto University, No 11B, 1968.

14. KARPUL M. Investigation into aspects of orbital velocity of waves in shoaling water; M.Sc. Thesis, University of Cape Town, 1978.
15. KEULEGAN G.H. and PATTERSON G.W. Mathematical theory of irrotational translation waves; J. Res. Mat. Bur. Stand., No 24, 1940.
16. KNOESEN J.S. 'n Sistematiese ondersoek van golwe in 'n kanaal ten opsigte van die vorm daarvan, die orbitaalbeweging daaronder en die vergelyk van bogenoemde met die eerste orde teorie; Final year thesis, University of Stellenbosch, R.S.A., 1976.
17. LE MEHAUTE B., DIVOKY D. and LIN A. Shallow water waves : a comparison of theories and experiments; 11th Conf. Coast. Eng. Vol 1, 1968.
18. LEWIS A.W. Discussion on an empirical modification to linear wave theory by T.S. Hedges; Proc. Instn. Civ. Engrs. Part 2, 1977.
19. MEJLHEDE N. Cnoidal waves on arbitrary depth; Prog. Rep 36, Inst. Hydrodyn. and Hydraulic Engrg. Tech. Univ. Denmark, 1975.
20. MILNE-THOMSON L.M. Theoretical hydrodynamics; Chapter XIV, 2nd Ed. 1949.
21. MORISON J.R. and CROOKE R.C. The mechanics of deep water, shallow water, and breaking waves; U.S. Army, Corps of Engineers, Beach Erosion Board, TM. No 40, 1953.
22. SHORE PROTECTION MANUAL Vol 1, U.S. Army CERC, 1973.
23. SKJELBREIA L. and HENDRICKSON J.A. Fifth order gravity wave theory; Proc. 7th Conf. Coast. Eng., 1961.
24. STOKES G.G. On the theory of oscillatory waves; Trans. Cambridge Phil. Soc. Vol 8, and supplement, Sci. Papers Vol 1, 1847.
25. SVENDSEN I.A. Cnoidal waves over a gently sloping bottom; Series Paper 6, ISVA, Technical University of Denmark, 1974.
26. SWART D.H. Predictive equations regarding coastal transports; 15th Conf. Coast. Eng. Vol 2, 1976.
27. SWART D.H. Vocooidal water wave theory, Vol 1 : Derivation ; Coastal Engineering and Hydraulics Division, NRIO, CSIR, 1978.
28. TSUCHIYA Y. and YAMAGUCHI M. Some considerations on water particle velocities of finite amplitude wave theories; Coast. Eng. in Japan, Vol 15, 1972.
29. VAN HIJUM E. Niet-rotatie vrije benadering van de waterbeweging bij regelmatige korte golven in water met een konstante diepte; Spuurwerkverslag S171 deel II, 1975.
30. VAN HIJUM E. P-golf; Unpublished note, 1972.
31. VON SCHWIND J.J. and REID R.O. Characteristics of gravity waves of permanent form; Journal of Geophysical Research, 1972.
32. WHITE W.R., MILLI H. and CRABBE A.D. Sediment transport : an appraisal of available methods; HRS, Wallingford, Report INT 119, Vols 1 and 2, 1973.
33. WIEGEL R.L. A presentation of cnoidal wave theory for practical application; Jour. Fluid. Mech. 7, Part 2, 1960.

CHAPTER 27

FIELD STUDY OF BREAKING WAVE CHARACTERISTICS

LEE L. WEISHAR*
ROBERT J. BYRNE[†]

ABSTRACT

This study focuses upon four elements of breaking wave behavior:

- 1) Relative breaking depth criteria
- 2) Breaking wave classification
- 3) Evaluation of the plunge distance
- 4) Breaking wave height prediction

The data set is 116 waves filmed at Virginia Beach, Va., on the Atlantic U.S. coast. The cine-photographic observation technique permitted the viewer to freeze the free surface profile at successive time steps as the waves passed an upright plane grid placed perpendicular to the beach. The results indicate that:

- 1) While the average value of $H_b/d_b \approx 0.78$, there was a significant difference between plunging and non-plunging waves.
- 2) Neither the breaker classification of Galvin nor that of Battjes successfully discriminated between plunging and spilling breakers.
- 3) The distance travelled by the foreface of a plunging wave was found to be underestimated by the free fall trajectory model advanced by Galvin. The field observations show the weakness to be in the plunge time arising from neglect of the vertical velocity component.
- 4) The breaking wave height prediction formulation advanced by Komar and Gaughan adequately predicts the breaking wave height within the constraints of calculating deep water wave characteristics, neglecting wave refraction and frictional effects. The combined data set covers the breaker wave height between laboratory scale observations to greater than 3 m.

*Geosciences Department, Purdue University, West Lafayette, Indiana, 47907, USA.

[†]Virginia Institute of Marine Science, Gloucester Point, Virginia, 23062, USA, and School of Marine Science, William and Mary College, Williamsburg, Va.

INTRODUCTION

The purpose of the study was to compare field observations of breaking wave characteristics with existing formulations, which for the most part have been derived from wave tank observations. Four elements of breaking wave behavior are addressed:

- 1) Relative breaking depth criteria
- 2) Breaking wave classification
- 3) Evaluation of the plunge distance
- 4) Breaking wave height prediction

METHODS. The field measurements were obtained from cine-photography of waves as they passed through an upright plane grid installed perpendicular to the beach. The field site was at Virginia Beach, Va. (Fig. 1), an ocean beach receiving waves generated in the North Atlantic Ocean. The observations were made in the summer when the wave climate is dominated by swell with characteristic average wave period of about 8 seconds generated by the Bermuda "high". Levelled rectangular grid sections, 3.3 m in length, were fixed to pipes jettied into the substrate. The square unit cell of the pipe grid was 61 cm (2 ft) on a side with each side further indexed to 30.5 cm (1 ft), (Fig. 2). The grids extended from the top of the foreshore to about 40 m offshore (Fig. 3).

Cine photography was achieved by mounting a motor-driven 16 mm Bolex camera with wide angle lens on the existing pier some 50 m from the grid (Fig. 4). Film advance rate was 12.53 frames/sec. Three film runs, obtained over a one hour period on 26 September 1968 constitute the data base for this report. The semi-diurnal tide has a mean range of 1.04 m. The observations were made about 2 hours after high water.

After each run the sediment surface was profiled relative to the grid. As no significant changes were observed between runs, a single profile was used in the analysis (Fig. 3). Mean water level relative to the grid was determined from a series of graduated transparent pipes (5 cm diameter) with constricted orifice (0.32 cm) which acted to filter high frequency fluctuations. The internal water level within the tubes was visually monitored.

The observation method allowed the viewer to freeze the free surface profile at successive time steps so the complete transformation of individual waves could be traced. Basic film data reduction was achieved using a Lafayette Analyst Time-Motion Projector with the image projected on a wide rear surface screen. Water surface elevation was estimated to 3 cm (0.1 ft) on the grid cell.

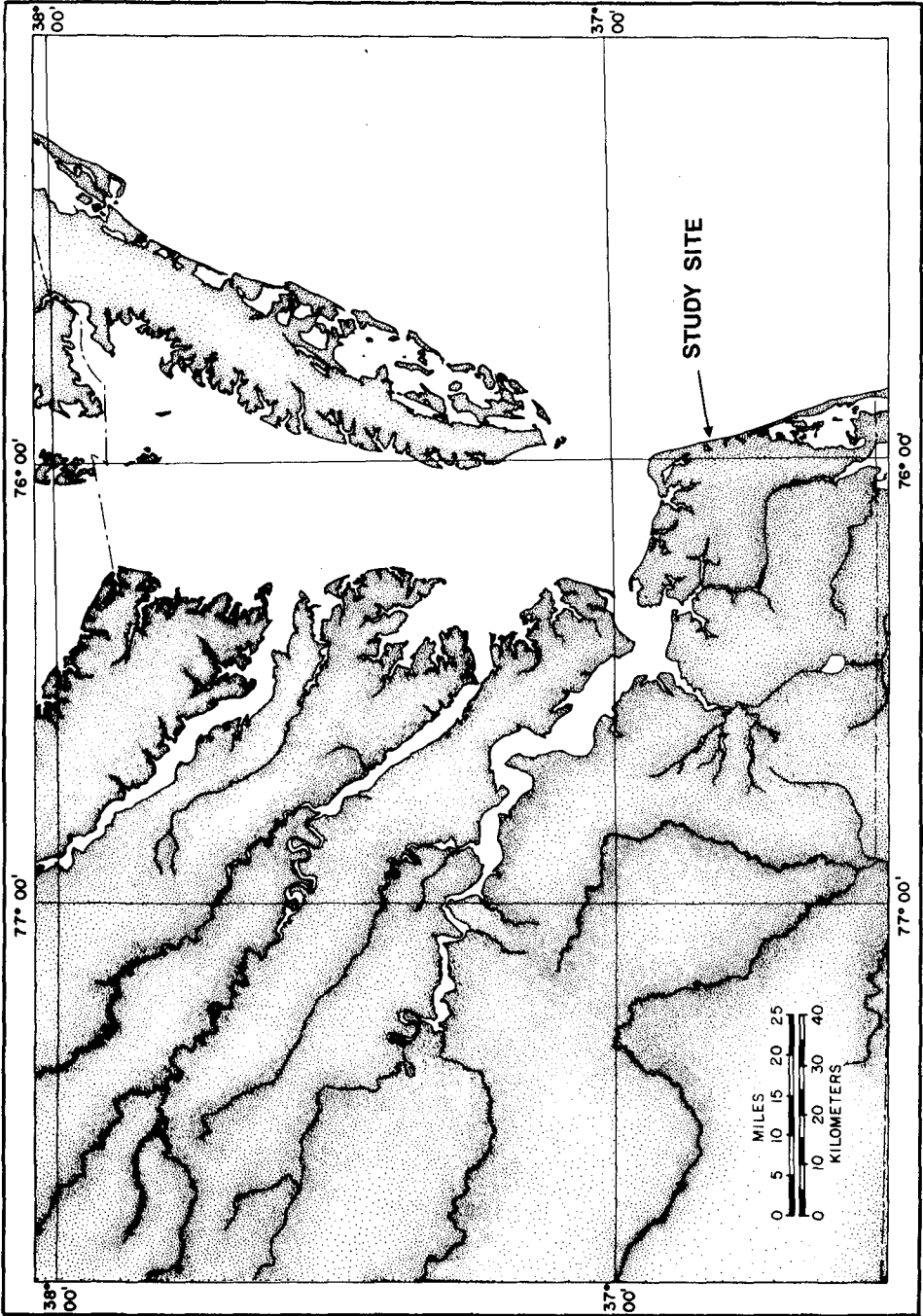


FIGURE 1. LOCATION MAP.



FIGURE 2. GRID IN PLACE.

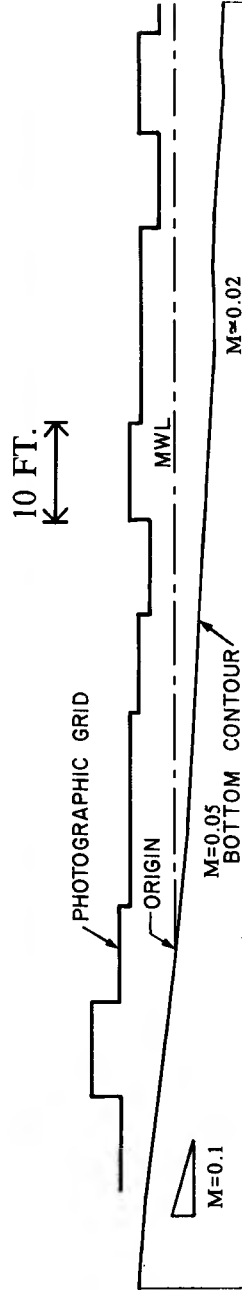


FIGURE 3. GRID LAYOUT DURING EXPERIMENT.



FIGURE 4. AERIAL VIEW OF PIER USED AS CAMERA PLATFORM.

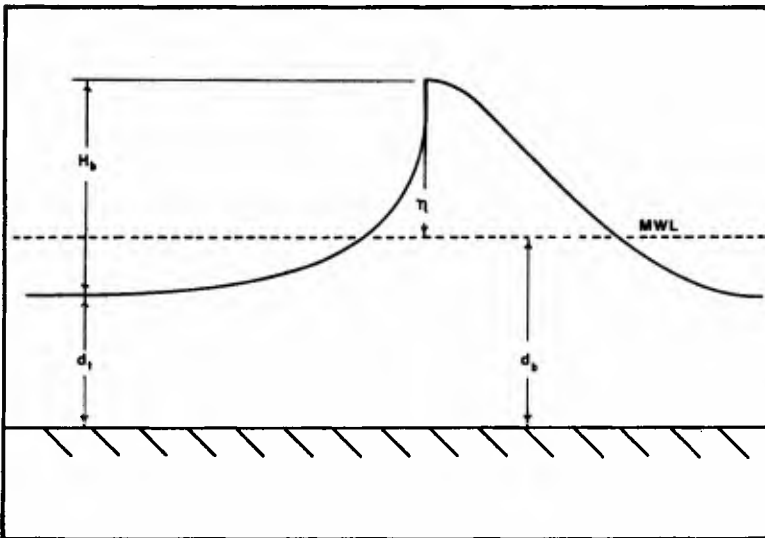


FIGURE 5. DEFINITION SKETCH FOR RELATIVE BREAKING DEPTH.

The observed waves were categorized according to breaker type. The criterion for breaking of "spilling" waves was the first appearance of foam cascading down the foreface. In the case of "plunging" waves, the criterion used was the position when initial overturning appeared with the formulation of a protruding lip or jet at the top of the near vertical foreface. While well-developed plunging waves and well-developed continuously spilling waves were distinct and easily separable, some breaker events were less clear. In some cases there was obvious interference between an incoming plunging wave and a strong backwash or cases when a wave was overtaking another while breaking. In a few cases the spilling crest would transform to a plunging crest. The 116 waves were distributed as follows: 70 well-developed plunging; 18 interference plunging; 21 well-developed spilling; and 7 spilling transformed to plunge.

For calculations involving breaker wave period, T_b , the observed period at a distance of 21 m from the mean water line was used. The period was considered to be the elapsed time between the passing of the wave in question and the passing of the prior wave. Wave celerity was considered to be the speed of travel over the 2 m distance prior to the inception of breaking. A data listing is given in Weishar (1976).

RELATIVE BREAKING DEPTH

The limiting wave height to depth ratio has been the subject of considerable study since the work of McCowan (1894). Galvin (1972) offers a complete review. McCowan derived a limiting value of $\eta/d_b = 0.78$ (see Fig. 5 for definition sketch) from solitary wave theory. The numerical value of 0.78 remains in common use although it is generally associated with the ratio, $\alpha = H_b/d_b$. Laboratory studies have demonstrated a dependency of α upon beach slope, m :

$$\frac{1}{\alpha} = 0.92 \quad \text{for } m \geq 0.07$$

$$= 1.40 - 6.85 m \quad \text{for } m \leq 0.07$$
Galvin (1969) (1)

$$\alpha = 0.724 + 5.6 m, \quad \text{Weggel (1972) (2)}$$

$$\alpha = 0.75 + 25 m - 112 m^2 + 3870 m^3, \quad \text{Camfield and Street (1969) (3)}$$

RESULTS. Three ratios, η/d_b , H_b/d_b , and H_b/d_t (Fig. 5) were examined with the data set of 116 waves, which were segregated into plunging and non-plunging. The results are shown in Table 1.

TABLE 1

SUMMARY OF WAVE HEIGHT TO WATER DEPTH RATIOS

Ratio	Total Sample (116)		Plunging Waves (70)		Non-plunging Waves (46)	
	Mean	Std. Dev.	Mean	Std. Dev.	Mean	Std. Dev.
η/d_b	0.69	0.31	0.73	0.27	0.67	0.32
H_b/d_b	0.79	0.36	0.87	0.33	0.68	0.37
H_b/d_t	0.89	0.46	1.03	0.53	0.69	0.31

Application of the Student "t" test indicates that the difference between the means of the plunging versus non-plunging waves is significant ($P < 0.01$) for the ratios H_b/d_b and H_b/d_t . In all cases the standard deviations are relatively large. It is of interest to note that the average value of H_b/d_b for the entire sample is very close to the value commonly used in engineering practice. The histograms for H_b/d_b are shown in Figure 6.

The observed values of H_b/d_b were also compared with the three relationships denoting slope dependency (Eqs. 1-3) using the local slope in the region of breaking. All the plots exhibited wide scatter as a result of the wide variation in H_b/d_b for a very small slope range. This data set is inappropriate to independently test for the effect of slope on relative breaking depth.

CLASSIFICATION OF BREAKER TYPE

Visual inspection of waves breaking in the nearshore or on the foreshore leaves even the casual observer with the impression that there are characteristic differences between the modes of breaking which range between a condition where the waves cascade foam down the foreface of the crest as they approach the foreshore to conditions where, on steeper slopes, the waves simply surge up the foreshore without "breaking". The qualitative dependence of wave breaker type on beach slope and wave steepness has been recognized for several decades. Perhaps the most important difference between breaker characteristics is the varying rates of wave energy dissipation as the wave interacts with the nearshore and beach morphology. Galvin (1968) formulated a quantitative classification of breaker type based upon laboratory studies which demonstrated a dependence upon beach slope, wave period, and deep water or breaking wave height. Battjes (1974), in the development of a general similarity parameter for breaking wave behavior, also presented a basis for breaker classification. Both authors formulated offshore and inshore parameters.

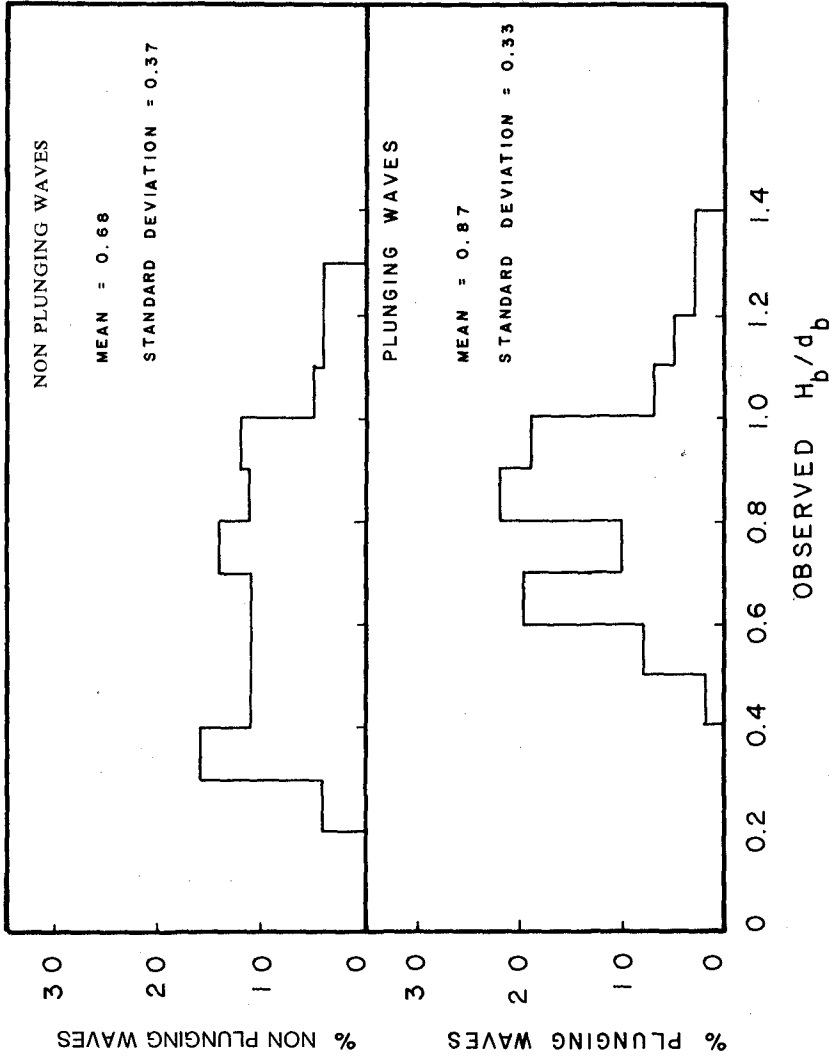


FIGURE 6. HISTOGRAMS OF H_b/d_b .

Offshore

$$\frac{H_0}{L_0 m^2} \quad , \quad \text{Galvin (1968)} \quad (4)$$

$$\xi_0 = \frac{m}{(H_0/L_0)^{1/2}} \quad , \quad \text{Battjes (1974)} \quad (5)$$

As noted by Battjes

$$\frac{H_0}{L_0 m^2} = \frac{1}{\xi_0^2}$$

Inshore

$$\frac{H_b}{gmT^2} \quad , \quad \text{Galvin (1968)} \quad (6)$$

$$\xi_b = \frac{m}{(H_b/L_0)^{1/2}} \quad , \quad \text{Battjes (1974)} \quad (7)$$

Galvin's results are shown in Figure 7. Battjes reexamined Galvin's data in terms of his classification parameters and suggested the following limits:

Offshore

surging	$\xi_0 > 3.3$
plunging	$0.5 < \xi < 3.3$
spilling	$\xi_0 < 0.5$

Inshore

surging	$\xi_b > 2.0$
plunging	$4.0 < \xi_b < 2.0$
spilling	$\xi_b < 0.4$

The purpose of this section is to test the criteria of Galvin and Battjes with the Virginia Beach data set.

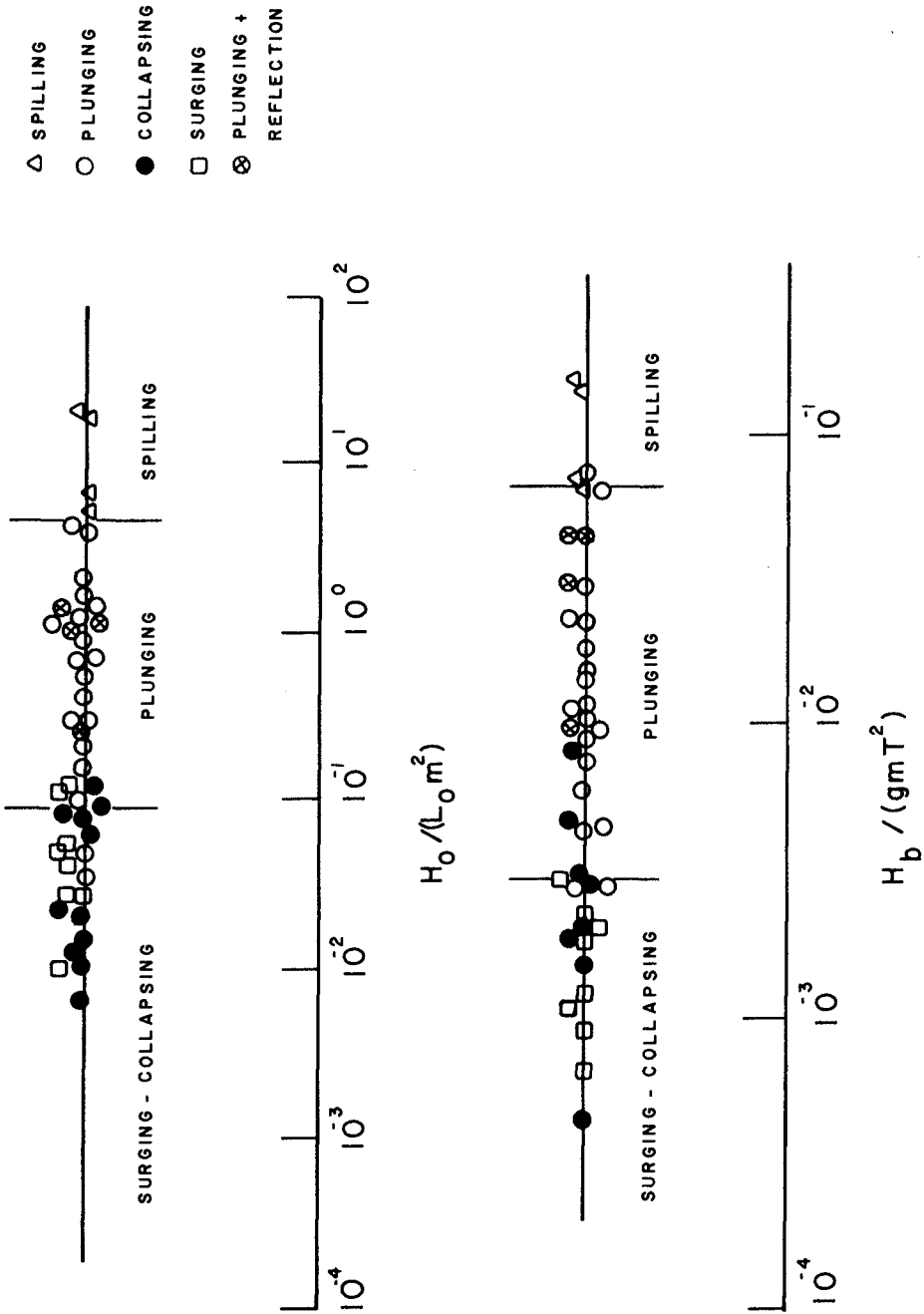


FIGURE 7. BREAKER TYPE AS A FUNCTION OF OFFSHORE AND INSHORE PARAMETER AFTER GALVIN, 1968.

RESULTS. It is important to note that the criteria being tested were formulated under laboratory conditions with uniform slopes whereas the Virginia Beach data set represents conditions of small, but continuously variable slope. In the principal breaking region the average bottom slope was about 0.02 . The slope of the upper foreshore was 0.10 . The slope values entered in the parameter calculations were those of the local bottom slope at the breaker position. This procedure does not take into account the fact that the wave shape is conditioned by the slope conditions prior to the zone of breaking.

The results for the breaker type classification are shown in Figure 8. The most striking result is that the criteria do not separate plunging waves from spilling waves. Although the sample size for spilling waves is much smaller than that for plunging waves, the distribution of spilling waves does not favor the ranges of the parameters suggested by Galvin (1968) or Battjes (1974). On the other hand, most of the plunging waves do fall, or cluster, within the ranges found under laboratory conditions. Furthermore, it is to be noted that the data for plunging waves exhibit closer clustering on the basis of Battjes' criteria relative to those of Galvin. Finally, it may be noted that the "interference" plungers cluster with the "well-defined" plungers.

EVALUATION OF PLUNGE DISTANCE

As an aid in the design of coastal structures, Galvin (1969) presented results of laboratory experiments on the distance a plunging wave travels from the point of breaking to and including the splash region excited by the falling lip of the crest. Part of this distance is the plunge distance which is defined as the distance covered from the inception of breaking to the point where the falling, forward lip touches down in the preceding wave trough (Fig. 9). The results presented in this section offer a comparison of field observations with Galvin's laboratory study.

Galvin's analysis is based on the assumptions that the internal particle velocities are given by the solitary wave phase speed, and that the falling forward face of the plunging wave can be approximated by a free fall trajectory (ballistics) model.

Thus, P , the plunge distance is given by the product of the phase speed, C_b , at breaking, and, t_p , the plunge time. For the free fall parabolic path condition, the time of fall is given by

$$t_p = 1/4 (H_b)^{1/2} \quad (8)$$

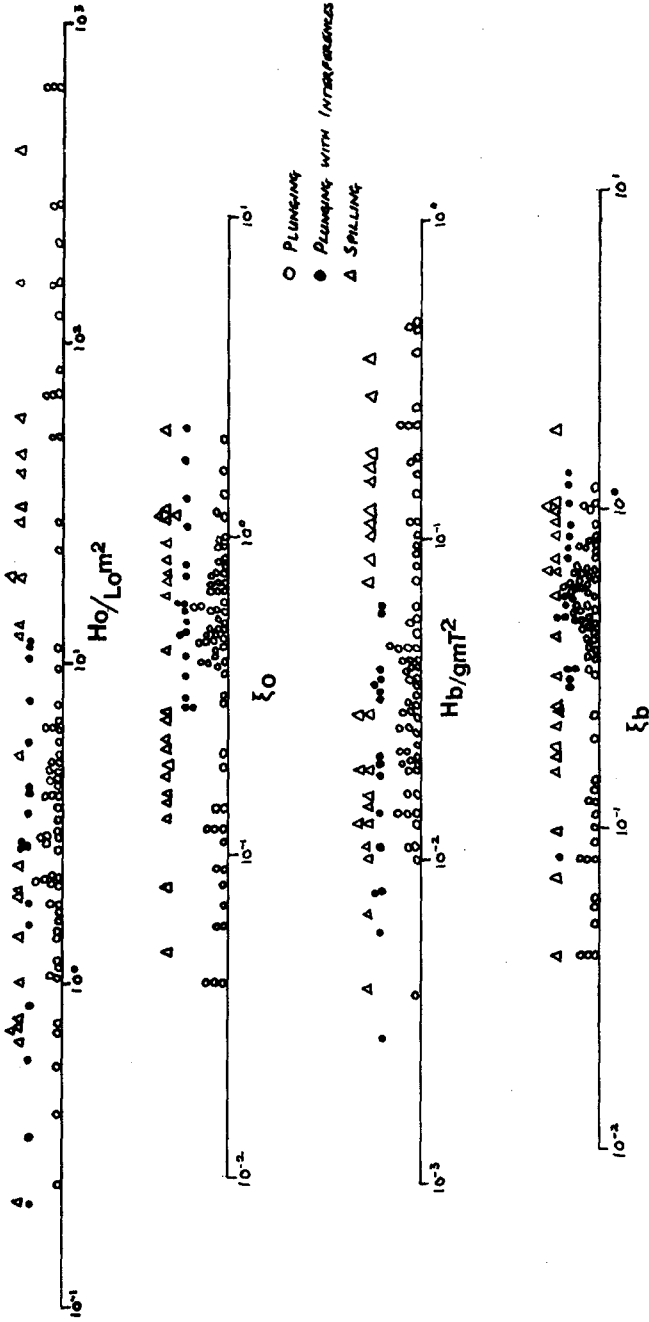


FIGURE 8. VIRGINIA BEACH BREAKER TYPES COMPARED WITH CRITERION OF GALVIN (1968) AND BATTJES (1974).

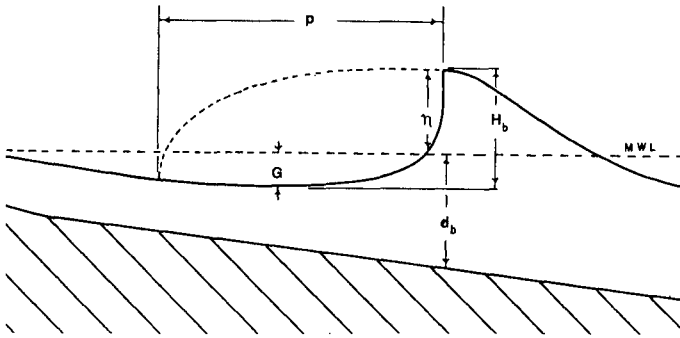


FIGURE 9. DEFINITION SKETCH FOR PLUNGE DISTANCE.

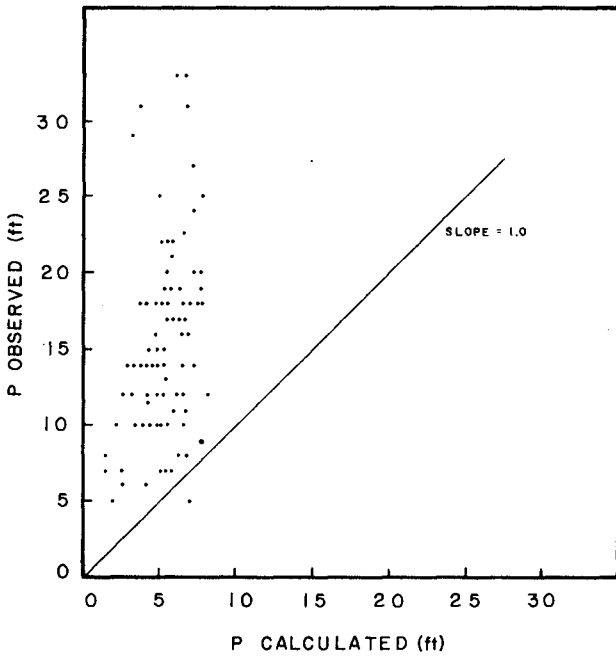


FIGURE 10. COMPARISON BETWEEN CALCULATED AND OBSERVED PLUNGE DISTANCE AT VIRGINIA BEACH.

The wave speed at breaking, C_b , is assumed to be (Fig. 9)

$$C_b = \{g (H_b - G + d_b)\}^{1/2} \quad (9)$$

Taking as approximations, $G \approx 0.25 H_b$ and $d/H_b \approx 1.25$ substitution yields in units of feet per second

$$C_b \approx 8 (H_b)^{1/2} \quad (10)$$

Finally, combining Equations 8 and 10 yields

$$P/H_b \approx 2 \quad (11)$$

Galvin (1969) recognized that the crest foreface has an upward velocity component at breaking and he expected Equation 11 to underestimate the plunge distance. His laboratory measurements showed P to range up to 4.5 with $\bar{P} \approx 3$. Moreover, he found a dependency on bottom slope, P/H_b decreasing as slope increases. This dependency was attributed to the fact that on steeper slopes breaking occurs closer to the shore and the waves may have increasing interaction with the swash-backwash zone. From his averaged values on slopes of 0.05, 0.10 and 0.20, he found

$$P/H_b = 4.0 - 9.25 m \quad (12)$$

Thus, for a horizontal bottom the expected $P/H_b = 4$.

RESULTS. The comparison of expected versus observed values of P is shown in Figure 10. The average value of P/H_b was 5.9 with the range extending from 1 to 10. The poor correspondence between the observed and "expected" values is obvious. In order to investigate the source of error, the observed breaker celerity, C_b , was compared with the calculated celerity using Equation 9. The average error between observed and expected was 12%, with the calculated celerity underestimating the observed at higher values. However, comparison of the calculated t_p (Eq. 8) with the observed t_p indicated an average error of 64% (Fig. 11). The principal source of error is thus in the calculation of plunge time. In order to determine the validity of the equation for plunge distance, $P = C_b t_p$, the observed plunge distance was compared with product of the observed values of breaker celerity and plunge time. These results are shown in Figure 12, wherein a close correspondence is observed. The remaining scatter is attributed to errors in determining the exact breaker position and the observed parameters, breaker celerity and plunge time.

The observations and analysis indicate that the free fall trajectory assumption is an incomplete model as an estimator for the trajectory of the plunging wave. A more complete model would have to include the vertical velocity components at breaking. The results presented for conditions of small beach slope do approximate, on the

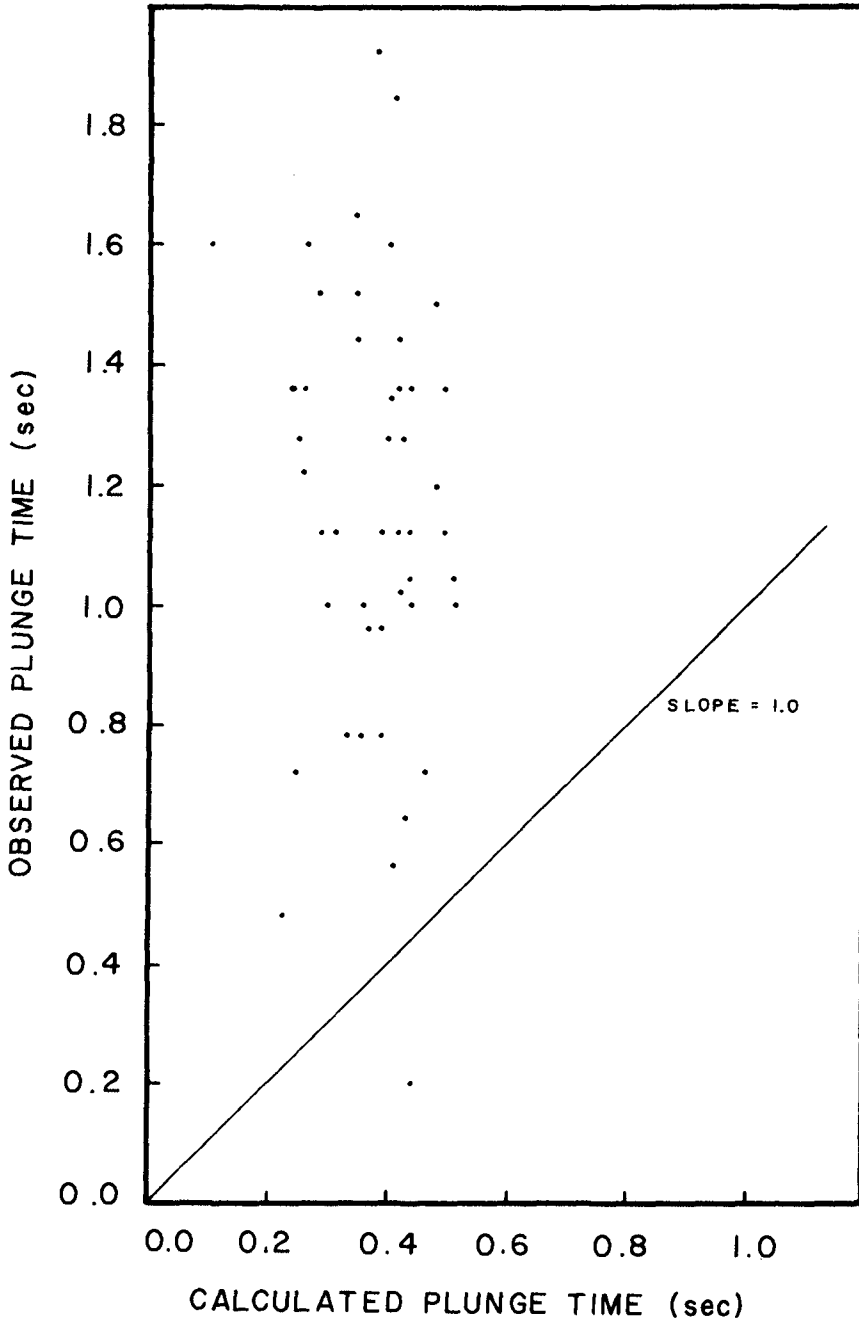


FIGURE 11. COMPARISON OF OBSERVED PLUNGE TIME WITH THAT EXPECTED FROM EQ.8.

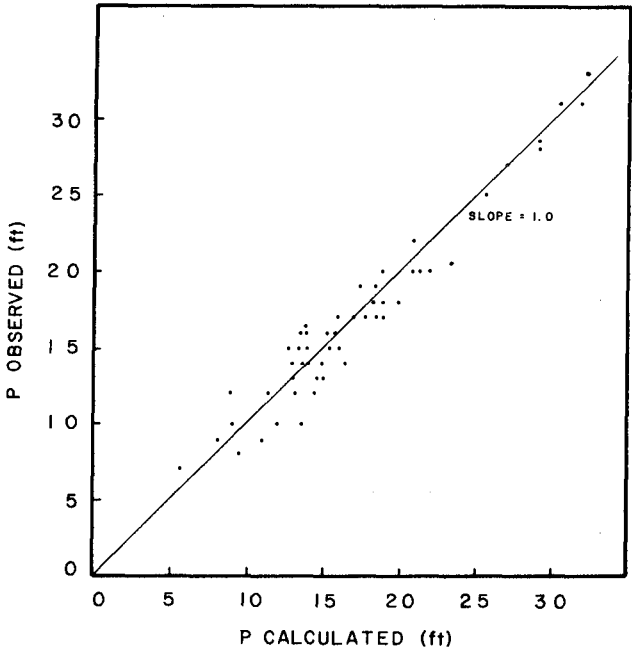


FIGURE 12. COMPARISON OF OBSERVED PLUNGE DISTANCE WITH THAT CALCULATED FROM THE CHARACTERISTIC EQUATION, $P = C_b b^2$.

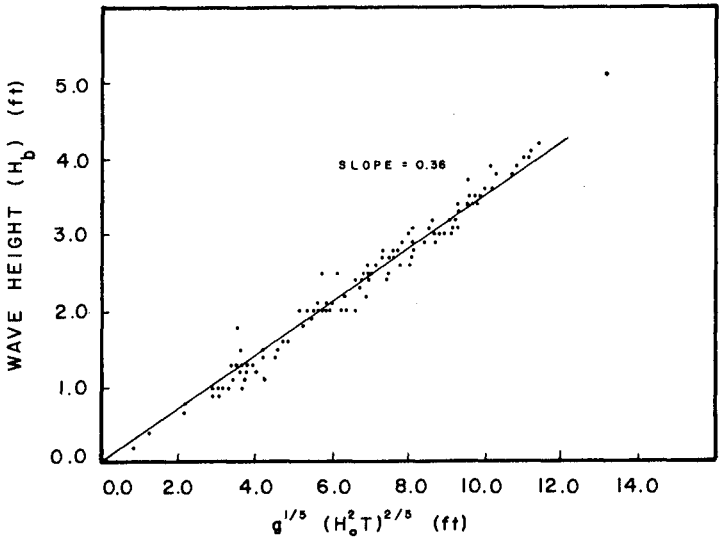


FIGURE 13. OBSERVED BREAKER HEIGHT AS A FUNCTION OF EQ. 17. REGRESSION GIVES $K=0.36$.

average, the experimental results of Galvin (1969) for small slope. Further field research on steeper beaches should clarify whether the level of approximation is consistent with experimental results.

PREDICTION OF BREAKING WAVE HEIGHT

Many engineering applications entail the estimation of wave breaker height given the deep water wave characteristics. Komar and Gaughan (1972) tested three sets of laboratory data and one set of field data from the California coast (Scripps pier) against a formulation for breaker height prediction using linear wave theory combined with a similarity criterion for relative breaking depth, H_b/d_b . The resulting relationship, empirically fitted to the data, was found to be an adequate predictor for breaker height over the range from small laboratory waves to the field data set consisting of breaker heights ranging from 1.2 to 3.5 m. Since the wave heights observed at Virginia Beach fall in the range intermediate to those tested, an independent evaluation was considered worthwhile.

From Komar and Gaughan (1972), the conservation of energy flux is,

$$(E C_\eta)_b = (E C_\eta)_o \quad (13)$$

From linear wave theory,

$$E_b = 1/8 \rho g H_b^2 \quad (14)$$

$$\text{and } C_b = \sqrt{g d_b} \quad (15)$$

Substitution of deep water characteristics and Equations 14 and 15 in Equation 13 yields, with reduction,

$$H_b^2 (g d_b)^{1/2} = \frac{g}{4\pi} (TH_o^2) \quad (16)$$

Using $\alpha = H_b/d_b$ gives the results of Komar and Gaughan

$$H_b = K g^{1/5} (H_o^2 T)^{2/5} \quad (17)$$

where $K = \frac{\alpha}{5} (4\pi)^{2/5}$

A best fit comparison with the experimental data yielded $K = 0.39$. In passing, the predicted value of α for the combined data set of Komar and Gaughan is then 0.71.

Also, if

$$C_b = \{g (\eta + d_b)\}^{1/2}$$

from this study $\eta = 0.92 H_b$; $d_b = 1.26 H_b$

then the expected $K = 0.31$. Regression analysis of the Virginia Beach data yields $K = 0.36$ (Fig. 13).

The combined results of Komar and Gaughan, which compares the laboratory results of Komar and Simmons and Munk (1949), with the Virginia Beach data is shown in Figure 14. It appears that the relationship

$$H_b = 0.39 g^{1/5} (TH_0^2)^{2/5}$$

provides a reasonable estimation of breaker height as a function of wave period and deep water wave height. However, it is to be noted that the effects of wave refraction or frictional dissipation are not incorporated. In the laboratory results the deep water wave height is calculated from linear wave theory. In the case of the data from Scripps pier H_0 is an approximation as the shoaling coefficient varied between 0.99 and 1.44 . A more severe approximation applies for the Virginia Beach data set as the nearshore slope is slight and the effects of wave refraction and dissipation may be expected to be significant. Consequently, the fit to the deduced relationship should be viewed as a relationship between breaker height and the "apparent" deep water wave height with refraction and frictional effects ignored. The degree to which the relationship is an artifact borne of circular reasoning will await further testing which includes refraction and frictional effects. It should be further noted that calculation of the deep water parameters involved the use of the near breaking wave period which for individual waves bears an unknown, and perhaps indeterminate, relationship to deep water period for even "simple" wave trains.

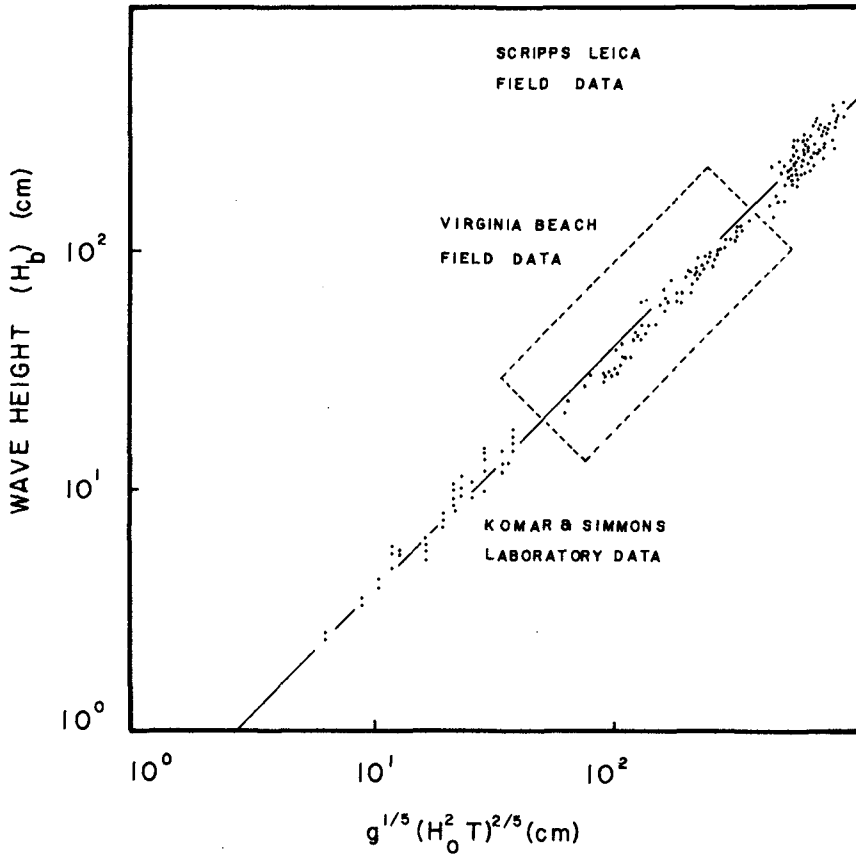


FIGURE 14. COMPOSITE DATA FOR BREAKING WAVE HEIGHT.

REFERENCES

- Battjes, J.A., Surf Similarity, 14th Conf. on Coastal Engr., Chapt. 26, 467, 1974.
- Camfield, F.E. and R.L. Street, Shoaling of Solitary Waves on Small Slopes, Proc. Amer. Soc. Civil Engr., 95(WW1), 1, 1969.
- Galvin, C.J., Jr., Breaker Type Classification on Three Laboratory Beaches, Jour. Geophys. Res., 73(12), 3651, 1968.
- _____, Breaker Travel and Choice of Design Wave Height, Proc. Amer. Soc. Civil Engr., 95(WW2), 175, 1969.
- _____, Wave Breaking in Shallow Water; in Waves on Beaches and Resulting Sediment Transport, Academic Press, 413, 1972.
- Komar, P.D. and M.K. Gaughan, Airy Wave Theory and Breaker Height Prediction, 13th Conf. on Coastal Engr., Chapt. 20, 405, 1972.
- McCowan, J., On the Highest Wave of Permanent Type, Phil. Mag. (5)38, 351, 1894.
- Munk, W.H., The Solitary Wave Theory and Its Applications and Surf Problems, New York Acad. Science Annals, 51, 376, 1949.
- Weggel, J.R., Maximum Breaker Height for Design, 13th Conf. on Coastal Engr., Chapt. 21, 419, 1972.
- Weishar, L.L., An Examination of Shoaling Wave Parameters, Unpublished M.S. Thesis, College of William and Mary, Williamsburg, Va., 1976.

CHAPTER 28

PROBABILITY DENSITY FUNCTIONS OF BREAKING WAVES

By

Edward B. Thornton¹ and George Schaeffer²

ABSTRACT

Waves in the surf zone are a highly nonlinear process which is evident by the appearance of secondary waves. The secondary waves appear as strong peaks in the period PDFs corresponding to the first harmonic of the peak of the wave spectrum. The strong first harmonic period peak is also reflected in the highly correlated height and velocity PDFs. Due to the high probability of the secondary waves, the mean wave period for breakers is a poor descriptor of the average period of the offshore incident waves.

The joint probability density functions for periods and heights of the breaking waves show high correlation (0.60-0.80) which says that greater wave periods are associated with larger breaker heights. The joint PDFs of period and particle velocity, and velocity and height, suggest that the maximum onshore particle velocities are correlated with both the wave periods and wave heights.

I. INTRODUCTION

Studies of the PDFs of period, height, and wave lengths have been conducted over the last 20 years. The majority of these studies have been mainly concerned with theoretical or deep water aspects of the problem.

The theoretical distribution of wave amplitudes for a narrow-banded Gaussian surface elevation in deep water, was shown by Longuet-Higgins (1952) to be a Rayleigh distribution. Tayfun (1977), in studying the transformation of deep water waves to shallow water waves, showed that the Rayleigh distribution for wave amplitude was generally applicable to all bandwidths.

¹Associate Professor, Naval Postgraduate School, Monterey, California, 93940

²Lieutenant, United States Navy

Longuet-Higgins (1975) extended his earlier work on narrow-banded Gaussian surface elevations in deep water and derived an expression for the joint distribution of wave periods and amplitudes

$$p(\xi, \eta) = \frac{\xi^2}{(2\pi)^{\frac{1}{2}}} \exp(-\xi^2(1+\eta^2)/2) \quad (1)$$

where ξ and η are the normalized amplitudes and periods as defined by,

$$\xi = a/\mu_0^{\frac{1}{2}} \quad (2)$$

and

$$\eta = (T - \langle T \rangle) / v \langle T \rangle \quad (3)$$

where $\langle T \rangle$ is the mean period and v is proportional to the spectral width where

$$v = (\mu_2/\mu_0)^{\frac{1}{2}} (\langle T \rangle / 2\pi) \quad (4)$$

and μ_0 and μ_2 are the zero and second moments of the energy spectrum. The wave periods are defined by their zero up-crosses. It is noted that the marginal distribution of wave periods in deep water is bell shaped (but not Gaussian). Longuet-Higgins (1975) compared this theoretical distribution of ocean waves to that of the deep water data obtained by Bretschneider (1959) and found good agreement. He found that for the marginal wave height distribution there is a slight excess of waves with heights near the middle of the range and a deficit at the two extremes. Since much of the high frequency portions of the wave records are filtered out by the pressure transducer, he suggests that the narrow-band approximation may not be as applicable for the unfiltered records. In shallow water with much steeper waves, the distribution can again be expected to be less applicable due to the non-linearities which become increasingly important.

Chakrabarti and Cooley (1977) compared the theoretical joint distribution of Longuet-Higgins (1975) with wave data recorded during a 1961 storm in the North Atlantic. The spectrum of these waves did not fall in the category of narrow-band. Through the comparison, it was found that there was a considerable agreement at the higher wave heights, but a definite trend away from the theoretical curve at the lower wave heights.

Bretschneider (1959) investigated the PDFs of wave heights, H , wave lengths, L , and wave periods, T . He concluded from his empirical study that in deep water wave systems, the PDFs of wave heights and lengths can be approximated by a Rayleigh distribution. Using the relationship, wave length proportional to period squared for deep water linear waves, he concluded that the PDF of periods squared is a Rayleigh distribution.

Assuming that the marginal PDFs are Rayleigh, Bretschneider (1959) examined the extreme cases of 0 and +1 correlation. For the case of zero correlation, the marginal Rayleigh PDFs are given by

$$p(\zeta) = \frac{\pi}{2} \eta \exp(-\pi\zeta^2/4) ; \quad \zeta = H/\bar{H} \quad (5)$$

$$p(\lambda) = \frac{\pi}{2} \lambda \exp(-\pi\lambda^2/4) ; \quad \lambda = L/\bar{L} \quad (6)$$

For zero correlation, i.e. total independence, the joint PDF of heights and lengths is given by

$$p(\zeta, \lambda) = \frac{\pi^2}{4} \zeta \exp(-\pi\zeta^2/4) \cdot \lambda \exp(-\pi\lambda^2/4) \quad (7)$$

In terms of heights and periods,

$$p(\zeta, \tau) = 1.35 \zeta \exp(-\pi\zeta^2/4) \cdot \tau^3 \exp(-0.675 \tau^4)$$

where $\tau = T/\bar{T}$. (8)

For the case of total dependence, the correlation coefficient is equal to one. For a correlation coefficient of one, all data points on a plot of joint Rayleigh PDFs fall on a 45 degree straight line passing through the origin.

Koele and de Bruyn (1964), Goda (1967), and Siefert (1970) have observed that the distribution of wave heights in shallow water does not correlate well with the Rayleigh distribution. Kuo and Kuo (1974) have suggested that this is due to: 1) the non-linear effects of wave interactions yielding more larger waves, 2) the effect of bottom friction yielding a reduction in the low frequency components, and 3) the effects of wave breaking, which would truncate the distribution and transfer some of the kinetic energy to the high frequency components. Therefore the PDFs of wave heights with a certain intensity, may be considered to approximate a conditional Rayleigh distribution truncated by the local breaking height.

A zero-up-cross analysis was conducted on waves measured on a reef by Black (1978), who then compared the observed distribution with the Rayleigh, truncated Rayleigh, and the Weibull distributions. He observed that the truncated Rayleigh distribution fit well for those waves in the breaker zone when the heights were depth limited. The truncated Rayleigh distribution did not fit well for those waves measured either inshore or offshore of the breaker zone. He has found that a Weibull distribution more closely approximated these measured distributions.

It would be expected that the Weibull distribution would yield the better fit. The Rayleigh distribution is a function of the variance of the data, whereas the Weibull distribution is a function

of higher moments about the mean. Neither theoretical distribution adequately describes observed distributions which are multi-modal.

Black's (1978) observations of wave periods show distributions which are skewed to the right. This does not fit well with the symmetrical Longuet-Higgins (1975) distribution. It was found that the period distribution more closely followed the Rayleigh distribution than the period square as proposed by Bretschneider (1959). It was found that the Weibull distribution most closely fit the empirical PDF, but there is considerable variation in the peakedness parameter. His attempts in relating the period statistics to the position on the reef were unsuccessful. He feels that this is due to the non-linearities of the waves in shallow water.

In this paper, the empirical data collected for breaking waves are compared with the Rayleigh distribution.

II. EXPERIMENT AND ANALYSIS

Three different California experimental sites were used to obtain data on the three types of breaking waves--plunging, spilling, and collapsing. Plunging and spilling waves were measured on Del Monte Beach, Monterey, California; collapsing breakers were measured on the Carmel River Beach, which is located approximately five miles south of Monterey, California. Due to the steepness of the beach and the rapidity of breaking of the shoaling waves, reflected waves are found to be present. Spilling breakers on a gently sloping beach were measured at Torrey Pines Beach, a site just north of La Jolla, California.

Capacitance type gauges were used to measure the change in the sea surface elevation. The velocity of the water particles was measured with Marsh-McBirney Model 721 and 722 Electromagnetic Current meters. The meters were calibrated in the laboratory prior to use in the field. The instruments were placed on towers in the surf zone at low tide at the expected point of breaking of the waves for the subsequent high tide. Each tower held a capacitance wave gauge and an electromagnetic flowmeter. The flowmeter was placed below the wave gauge, approximately 0.5 m from the bottom, to insure constant submergence. Data were collected within an hour or two on both the ebb and flow sides of high tide. Details of the experiments are given in Thornton *et al* (1976).

Record lengths of approximately 30 minutes from each data set were analyzed. It was desired to only examine the sea-swell band of frequencies lying between 0.03-1.0 Hz (30 sec-1 sec). Hence, the data were passed through both a high and low pass digital filter. The high pass filter had a cut-off frequency of 0.03 Hz (30 sec). The high pass filter used a Fast Fourier Transform (FFT) algorithm to obtain the Fourier spectrum of the entire 30 minute record. The Fourier coefficients corresponding to 0-0.03 Hz were then used to synthesize a low frequency time series which was subtracted from the wave record. The low pass filter was a 25 weight inverse transform

filter. A cut-off frequency of 1.2 Hz was used with a terminal frequency of 1.8 Hz. The mean and variance of sea surface elevations were calculated for each record as well as the mean and variance of the heights, periods and maximum velocities.

Wave heights were determined from the surface elevation record by means of the zero-up-cross method. The zero-up-cross technique defines a wave period as the interval between adjacent upcrosses. The maximum and minimum of the surface elevation within the interval defines the crest and trough of a wave. Maximum onshore particle velocities were calculated from the flowmeter records. Maximum onshore velocity was defined as the maximum velocity amplitude occurring between successive zero upcrossings as defined by the sea surface elevation record. Joint PDFs of wave height and period, wave height and maximum velocity, and maximum velocity and period were calculated from the analyses.

Heights and maximum velocities were normalized by dividing by their respective standard deviations of the surface elevations and particle velocities respectively. The periods were normalized by dividing by their mean period. Histograms were calculated for the normalized heights, periods, and maximum velocities. The histograms were transformed into PDFs by dividing the number of values over an interval by the total number of values in the array and by dividing by the interval width.

Joint probability density functions of periods versus heights, velocities versus heights and periods versus velocities were calculated in a similar fashion. A 15 by 15 grid was used to determine the frequency of values which simultaneously fill each joint interval.

The energy density spectrum (power spectrum) was obtained by means of a Fast Fourier Transform (FFT) algorithm. The energy density spectrum tells how the variance is distributed with respect to frequency. The spectral width parameter was calculated using the equation:

$$\epsilon = \sqrt{\frac{m_0 m_4 - m_2^2}{m_0 m_4}} \quad (9)$$

where m_0 , m_2 , and m_4 are the spectral moments (Cartwright and Longuet-Higgins, 1956). For $\epsilon = 0$ the waves have only one frequency and the energy spectrum would be represented by a spike. As $\epsilon \rightarrow 1$

the sea surface can be described as a broad-band process for which the distribution would be Gaussian and the spectrum would approach a horizontal line. Swell can therefore be described as a narrow-band process and seas as broad-band. Due to the appearance of secondary waves, a narrow-banded deepwater spectrum of waves broadens in the surf region.

The correlation coefficients of the joint values were calculated to obtain a measure of the amount of linear relationship of random pairs of values of periods and heights, velocities and heights, and periods and velocities.

III. DISCUSSION

Data measured on 16 March 1977 for the case of spilling breakers at Torrey Pines Beach is chosen for subsequent discussion. The off-shore waves on this date appeared as narrow-band swell. But spectral analysis of the surface elevation records in the surf zone yielded spectral width parameters ranging from 0.94-0.97, suggesting a broad-band spectrum in the surf zone. The broad spectral width can be attributed to the non-linear wave-wave interactions yielding harmonics in the breaking zone.

In order to determine the origin of the large spectral width parameter, ϵ was calculated in the ranges of 0-0.25 Hz, 0-0.50 Hz, 0-1.0 Hz and 0-nyquist frequency. The analysis revealed that large values of the spectral width parameter occurred in all cases. In the case of 0-0.25 Hz which contains the first three harmonics, ϵ was greater than 0.7, which was the case with the smallest ϵ . It is concluded that the change from a narrow deep water spectrum to a broad-band shoaling spectrum is primarily due to generation of secondary waves at harmonic frequencies.

Probability Density Functions of Period and Height

Bretschneider (1959) made the assumption that the wave lengths were Rayleigh distributed; using this assumption and the linear wave theory relationship

$$L = \frac{g}{2\pi} T^2 \quad (11)$$

the wave periods squared would be Rayleigh distributed in deep water. Bretschneider's analysis can be extended to the shallow water case using the shallow water approximation for wave length

$$L = \sqrt{gh} T \quad (12)$$

Assuming the wave lengths are Rayleigh distributed, the periods in shallow water would be expected to be Rayleigh distributed since period and wave length are directly proportional.

The period PDF is shown in Figure 1 and it is noted to have a definite skewness. The Rayleigh PDF has been superimposed on the period PDFs for comparison. The period PDFs only loosely follow the Rayleigh PDF. The Rayleigh PDF overpredicts the wave periods greater than the Rayleigh mode value, and underpredicts the observed periods less than the peak Rayleigh value. The observed period PDF has the mode lying close to the maximum of the superimposed Rayleigh PDF.

The mode of the breaking wave distribution is located at a period (7 sec) corresponding to the first harmonic of the offshore peak wave period (14 sec). A peak corresponding to the peak offshore wave period is absent. The waves periods as determined by a zero-up-cross of the surface elevation record for breaking conditions yields a poor indication of the peak of the energy spectrum which corresponds to the mean offshore wave period. The mean periods corresponded to the first harmonic periods or even to a valley between the primary and first harmonic periods. The appearance of strong peaks at one-half the offshore wave period is indicative of the importance of nonlinearities in the form of secondary waves in the surf zone.

The wave height PDF is shown plotted against the theoretical Rayleigh PDF at the top of Figure 1. The height PDF is loosely described by the Rayleigh PDF. The major height peak is centered at 2.2. The Rayleigh PDF overestimates the density of the small wave observations and tends to underestimate the density of the large waves. The heights are truncated at approximately six standard deviations. Since the wave gauge is stationary and therefore the depth of the water is essentially fixed, this truncation occurs due to the breaking of the large waves seaward of the wave gauge. The calculated mean height value on 16 March 1977 lies at 2.7, which actually corresponds to a dip in the PDF relative to the peak intervals on either side. The bimodality was very commonly observed and is attributed to the very narrow band incident wave system and the generation of secondary waves at the first harmonic.

The joint PDF of periods and heights is contoured in Figure 1. It is noted that the longest wave periods are associated with the greatest wave heights suggesting strong correlation between periods and heights. The correlation coefficient was calculated for all cases and varied between 0.60 and 0.80. The area of maximum joint density is found to be associated with the first harmonic of the offshore wave period, and the mode of the observed breaker heights.

Greater density was found at short periods and heights for all records than predicted by the Rayleigh PDF. A high frequency wave riding on a long period wave causes an additional zero crossing as the longer wave passes through zero. Most previous comparisons of heights or periods of waves have been done using pressure sensors which greatly filter the high frequencies due to hydrodynamic attenuation. Capacitance wave staffs and electromagnetic flowmeters have good response times and thus measure high frequencies. Therefore, even though the data were filtered at 1 Hz, all records showed peaks at the shortest periods and heights.

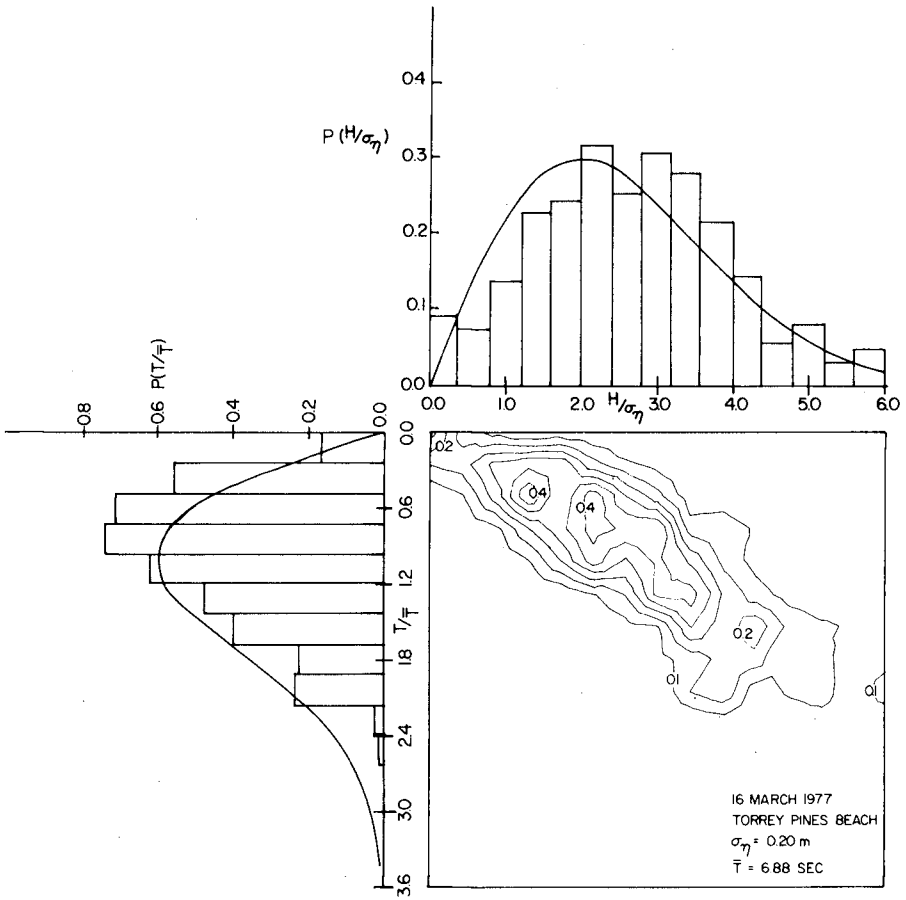


Figure 1. PDFs of Wave Heights and Periods, 16 March 1977

Joint Probability Density Functions of Velocities

The velocity PDFs were calculated as the maximum onshore velocities within the period segments determined by the zero-up-crosses of the surface elevation record shown in Figure 2. Using this technique can result in both positive and negative maximas for onshore particle velocities.

The theoretical Rayleigh PDF is superimposed on the same graphs for comparison and it is apparent that the velocity PDF is not adequately described by the Rayleigh PDF. The velocity PDF for spilling breakers appears to be symmetrical, with the mode value falling at the bin with center velocity of 1.5. There also appears to be a small peak value at 0.3.

The joint probability distributions of velocities and heights shown in Figure 2 show high correlation between velocities and heights. The high positive correlation (0.7) suggests that the larger maximum onshore velocities are correlated with the larger wave heights.

Figure 3 shows the joint PDF of periods and velocities in which the periods were determined from the zero-up-crosses of the wave gauge record and the coincident maximum onshore velocities are determined from the flowmeter record. The results are similar to the joint PDF of period and heights. The maximum spilling probability is found at the intersection of period 0.84 and velocity 1.5.

The negative values of the maximum velocity indicate that, during a wave period defined by the zero-up-crosses of the surface elevation, the maximum velocity can be negative. The joint PDF of wave height and velocity shows that the negative velocities are associated with the low wave heights. The joint PDF of velocity and period shows that small negative velocities are correlated with the short periods. Therefore, it is concluded the negative velocity maxima are associated with short periods and low wave heights. The secondary waves occur after the passage of the primary wave crest and have a peak near the trough of the primary wave; the velocities associated with the primary wave would be negative maximum in this region so that the measured velocity, which is a sum of the primary and secondary waves, can be small or negative.

IV. CONCLUSIONS

Waves in the surf zone are a highly non-linear process which is evidenced by the appearance of secondary waves. The secondary waves appeared in the PDFs at the first harmonic of the primary period.

The joint probability density functions of the breaking wave properties show high correlations. The correlation factor ranged between 0.60-0.80 for periods and heights and suggests that the greater the wave period, the higher the breaker height will be. High correlation between the periods and velocities and the heights

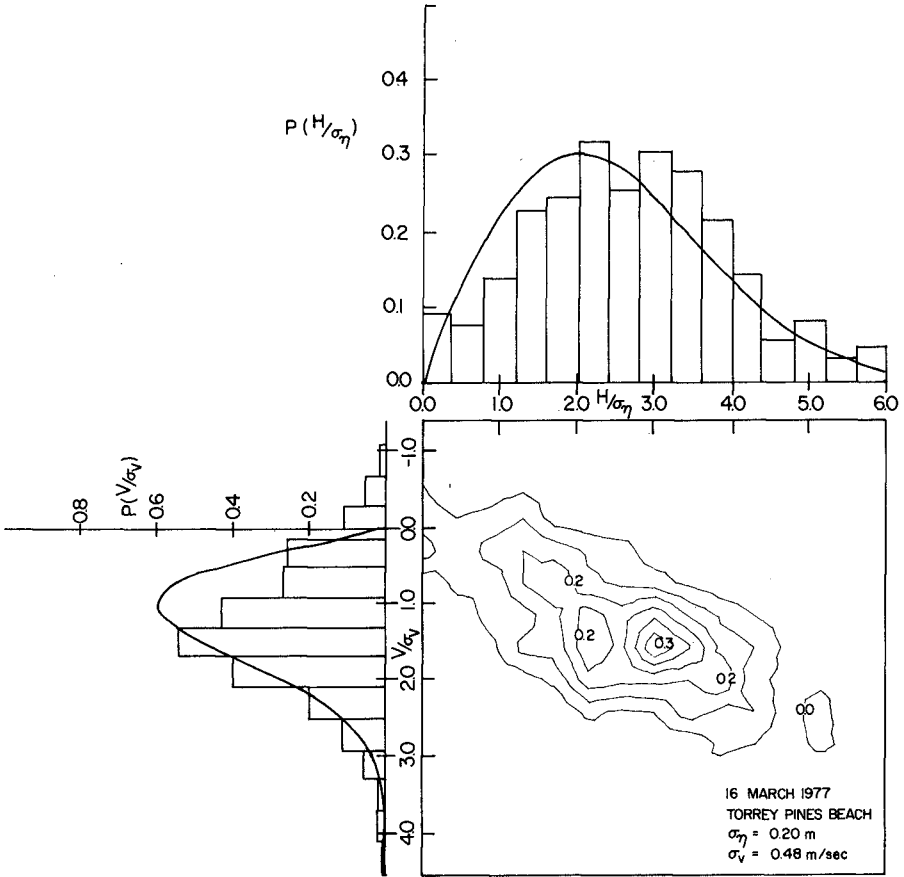


Figure 2. PDFs of Wave Heights and Velocities, 16 March 1977

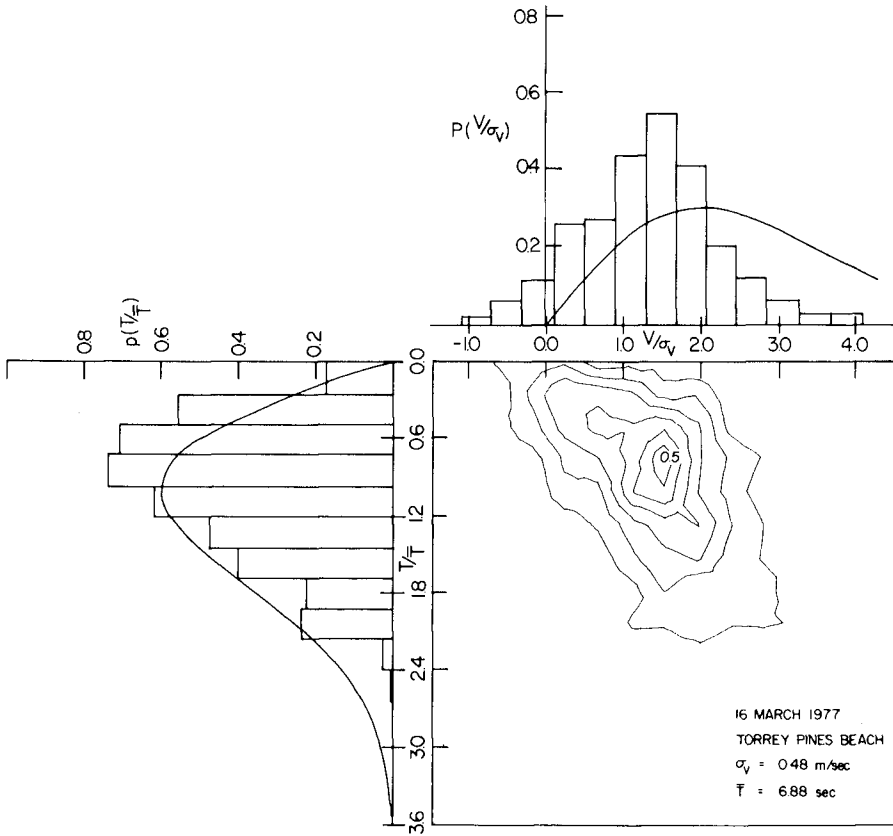


Figure 3. PDFs of Velocities and Periods, 16 March 1977

and velocities suggests that the maximum onshore velocities are a function of wave periods and breaker heights.

A truncated Rayleigh PDF was found to loosely approximate the empirical period and the height PDFs of spilling breakers. This truncation seems to be the result of long period waves with their associated larger breaker heights breaking prior to the arrival at the wave gauge.

The velocities PDFs of breaking waves, where the velocity maxima are associated with the periods defined by the surface elevation, yields a symmetrical distribution with some negative onshore velocities present. Since the Rayleigh distribution is undefined for negative values, the resulting fit of observed data with the theoretical Rayleigh distribution is poor.

The mean wave period as obtained by the zero-up-cross method in the surf zone is a poor indicator of the mean offshore wave period. Spectral analysis of the breaking waves shows an energy peak corresponding to the primary offshore wave period, but the period PDFs of breaking waves have a strong peak at the first harmonic of the wave spectra peak. The joint PDF ($p(T,H)$) of breaker waves showed a maximum density at a wave period equal to one half the peak period of the wave energy density spectrum, i.e. the first harmonic. The corresponding velocities ($p(v,T)$) or heights ($p(H,T)$) likewise were found to have a peak density associated with the first harmonic wave period. The mean period of breaking waves therefore is a poor estimation of the mean period of the incident waves offshore.

ACKNOWLEDGEMENTS

The data collected at Torrey Pines Beach was measured in cooperation with Robert T. Guza and the Shore Processes Laboratory at Scripps Institution of Oceanography. This work was supported by the Office of Naval Research, Geography Branch, under contract NR 388-114.

BIBLIOGRAPHY

- Black, K. P., "Wave Transformation over Shallow Reef, (Field Measurements and Data Analysis)," James K. K. Look Laboratory of Oceanographic Engineering, Department of Ocean Engineering, University of Hawaii, Technical Report No. 42, March 1978.
- Bretschneider, C. L., "Wave Variability and Wave Spectra for Wind Generated Gravity Waves," U. S. Army Corps of Engineers, Tech. Memo 118, 1959.
- Cartwright, D. E., and M. S. Longuet-Higgins, "The Statistical Distribution of the Maxima of a Random Function," Proc. Roy. Soc., Ser A, 237, pp. 212-232, 1956.
- Chakrabarti, S. K. and R. P. Cooley, "Statistical Distributions of Periods and Heights of Ocean Waves," Jour. of Geophysical Research, Vol. 82, p. 9, 20 March 1977.
- Goda, Y., "Some Results of Observations on Wave Statistical Properties," Rept. of Port and Harbor Res. Inst., No. 39, 1967.
- Koele, L. A. and P. A. de Bruyn, "Statistical Distribution of Wave Heights in Correlation with Energy Spectrum and Wave Depth," Proc. of 9th Conf. on Coastal Eng., A.S.C.E., 1964.
- Kuo, C. T. and S. J. Kuo, "Effect of Wave Breaking on Statistical Distribution of Wave Heights," Proc. Conf. on Coastal Engineering (Copenhagen, Denmark, June 1974), pp. 377-389, 1974.
- Longuet-Higgins, M. S., "On the Statistical Distribution of the Heights of Sea Waves," Journal of Marine Resources, Vol. 11:3, pp. 245-266, 1952.
- Longuet-Higgins, M. S., "On the Joint Distribution of the Periods and Amplitudes of Sea Waves," Journal of Geophysical Research, Vol. 80:18, pp. 2688-2694, 20 June 1975.
- Siefert, W., "Wave Investigation in Shallow Water," Proc. of 12th Conf. on Coastal Engineering, A.S.C.E., 1970.
- Tayfun, M. A., "Linear Random Waves on Water of Nonuniform Depth," Ocean Engineering Report No. 16, Part II, Department of Civil Engineering, University of Delaware, Newark, DE, August 1977.
- Thornton, E. B., J. J. Galvin, F. L. Bub and D. P. Richardson, "Kinematics of Breaking Waves Within the Surf Zone," Proc. of the 15th Conf. on Coastal Engineering, pp. 461-476, A.S.C.E., Jul 1976.

CHAPTER 29

WAVE CHARACTERISTICS IN THE SURF ZONE

I.A. Svendsen¹ P.Å. Madsen² J. Buhr Hansen¹

ABSTRACT

The equations describing conservation of mass, momentum and energy in a turbulent free surface flow are derived for a controle volume extending over the whole depth. The effect of the turbulent surface oscillations are discussed but neglected in the following analysis, where the equations are applied to the energy balance in a surf zone wave motion. This leads to results for the wave height variation and the velocity of propagation. The results cannot be reconciled completely with measurements and the concluding discussion is aimed at revealing how the model can be improved.

1. INTRODUCTION

Wave breaking and wave development in the surf zone are topics that have given raise to numerous investigations in the past, and yet much remains to be done before a satisfactory understanding has been obtained and real prediction is possible.

The present paper describes a combined experimental and theoretical work. We concentrate on the development of the gross parameters of wave motion after breaking on a gently sloping beach, and first of all on the phase velocity c and the energy dissipation, i.e. the attenuation of the wave height.

From visual observation aided by photography in laboratory flumes and in the nature it appears that immediately after the wave has started to turn over from the breaking point a violent transition takes place over a horizontal distance of several times the water depth at the breaking point. In this region, which we term the outer breaking region, the motion still shows large scale patterns that are repeated with only small variations from wave to wave (in regular waves) though they of course differ radically with the type of breaking and hence also from wave to wave in an irregular train of waves as on a natural beach. This feature of the breaking process is most significant in a plunging breaker.

From this description it is natural to conjecture that the process is dominated almost entirely by the wave data at the breaking point, i.e. the water depth h_b and wave height H_b . In other words that for a wide range of wave parameters the horizontal scale for the development in this

¹Assoc. Professor, ²Ph.D.-student.

Institute of Hydrodynamics and Hydraulic Engineering (ISVA),
Technical University of Denmark, Building 115, DK-2800 Lyngby.

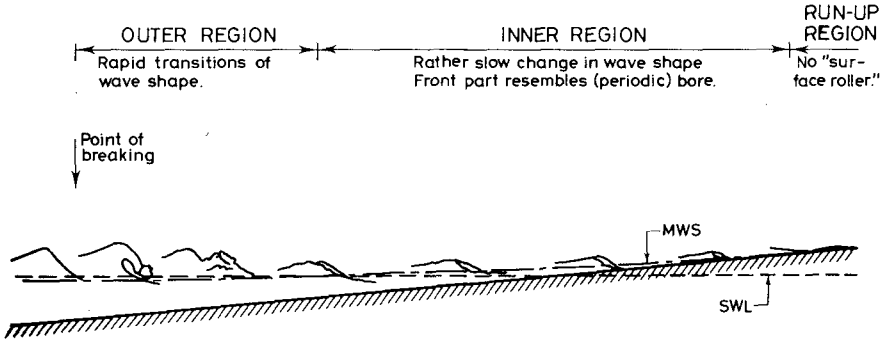


Fig. 1 Wave characteristics in the surf zone.

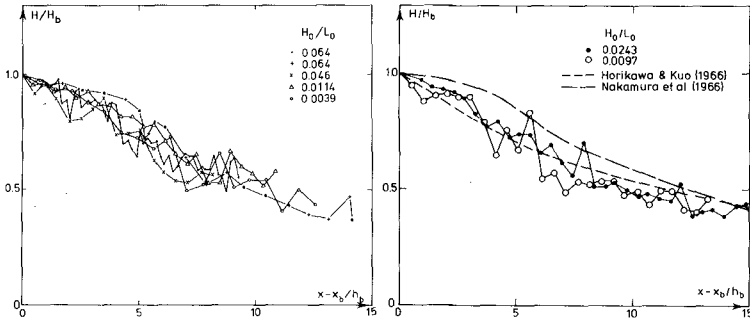


Fig. 2 Relative change in wave height right after breaking.

region is h_b . This is actually confirmed in Fig. 2 which shows the relative change in wave height H/H_b versus the distance from the breaking point measured in units of h_b .

The figure also includes data obtained by Horikawa & Kuo (1966) and by Nakamura et al (1966) on a similar slope (1 in 30 against ours 1 in 34) though the above mentioned conjecture implies that the effect of the slope is insignificant. It is worth noticing that the wide range of wave parameters in Fig. 2 means that the wave height variation is independent of the breaker type (spilling or plunging). Considering the actual differences in the motion one must question the adequacy of the notion "wave height" as a means of description.

As the wave propagates further the large scale deterministic flow breaks up into small scale details which gradually become of a random turbulent nature. During this process the front of the wave becomes

very similar to a moving bore or a hydraulic jump, and we may speak of a system of periodic bores. We term this the inner breaking region and it extends to the shoreline where the run-up starts.

It should perhaps be emphasized that if the wave breaks at or near the shoreline (as e.g. a collapsing or surging breaker) this region is absent and the outer region is immediately followed by the run-up. The description also fails to apply if the depth starts to increase shorewards so the breaking ceases.

One of the remarkable features of the inner region is that the waves or bores from a plunging breaker cannot be distinguished visually from those originating from a spilling breaker.

Thus the water motion at each depth seems to be strongly locally controlled in the sense that local depth and bed slope determines the characteristics of the flow and hence the energy dissipation, the shape of the wave including energy flux, and consequently the decrease in wave height. This hypothesis will find further support in the measurements reported in § 2, where we shall find that for a particular wave train the height to depth ratio H/h is only slowly decreasing and the shape is almost constant in the case of a constant slope.

The internal flow pattern has been studied by Peregrine and Svendsen (1978) who describe the resemblance with in particular hydraulic jumps and single bores occurring in front of a propagating change in water depth. Based on a new flow visualization method they concluded that the turbulence associated with a hydraulic jump or a bore is not limited to a surface roller. In fact there is nothing that separates the surface roller from the rest of a region of highly turbulent flow which originates from the toe of the roller. From there the turbulence develops, in the beginning much like in a turbulent mixing layer. The thickness of the turbulent region increases gradually with distance behind the toe of the roller but remains attached to the free surface. At some distance it reaches the bottom too. These conclusions are supported by the measurements made in a hydraulic jump by Resch et al. (1976).

It is the purpose of this paper to try to explain analytically the basic features phase velocity, energy dissipation rate and wave height attenuation. For this purpose we develop in § 3 the integrated forms of equations describing conservation of mass, momentum and energy and discuss the assumptions made, in particular with respect to the turbulent surface fluctuations.

§ 4 describes how the energy equation can be used to determine the wave height variation and the measurements are used as guidance in the choice of velocity and pressure profiles required in the computations. This also applies to the determination of the velocity of propagation c which turns out to be an important quantity in the description.

The conclusions are not satisfactory yet, and the analysis is succeeded by a discussion of the inaccuracies and possible improvements (§ 8).

2. EXPERIMENTAL RESULTS

The experiments were performed in one of ISVA's 60 cm wide wave flumes (length 32 m) with a water depth at the wave generator of 36 cm's. The waves were of the very regular type deprived of their free second harmonic components (Buhr-Hansen and Svendsen, 1974). The waves broke on a plane slope 1:34 (see Fig. 3) and the surface variations were measured

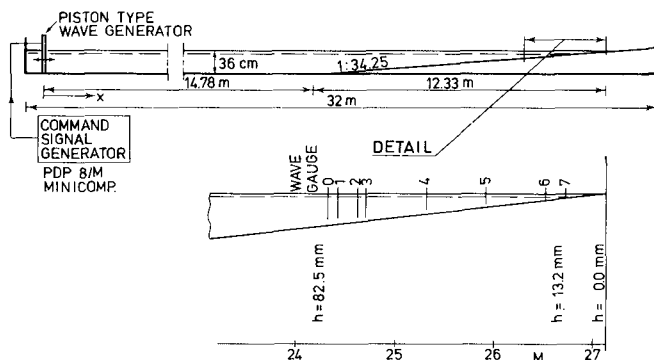


Fig. 3 Experimental set-up.

by resistance gauges (two goldplated silver wires, 0.17 mm diameter, 5 mm apart) and recorded digitally. Eight fixed wave gauges (denoted channel 0, ..., 7) were used, positioned as shown in Fig. 3. Only surface elevations were measured and the depth (excluding set-up) range from about 82 mm at channel 0 to about 13 mm at channel 7.

The following account of measurements is only a preliminary presentation. Results of a more detailed and systematical investigation will follow.

First it is worth mentioning that resistance wave gauges can not without further notice be used in water with air entrained as bubbles as we find it around the front of the broken waves. However, detailed investigations have been made in a vessel with controlled air entrainment. The results show that the gauges used to the accuracy required here measure solid water, i.e. measure the elevation we would have had if the air had been absent. Furthermore visual observations of the bubble-water mixture were compared with photos of the front of the waves indicating that the actual air content in the most densely entrained parts of the laboratory wave is only 2-4 per cent.

Thus the surface elevations reported in the following may be regarded as the elevation of water with normal density.

The digital registration makes it possible to identify data points separated an integral number of wave periods, and thus an ensemble average over many waves can be obtained for the profile at each measur-

ing point. Fig. 4 shows such profiles (η) and the standard deviation $\sigma(\eta)$. The results were obtained over 20 wave periods. As expected the

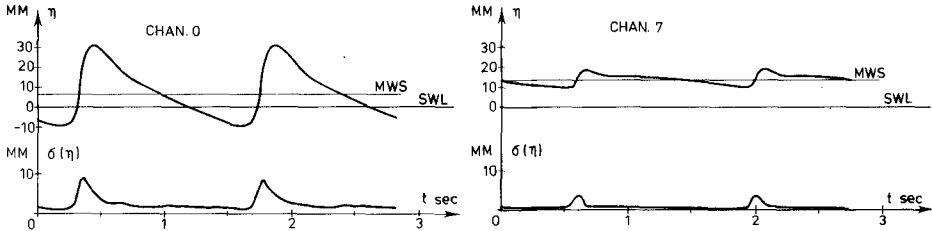


Fig. 4 Mean and standard deviation of measured profiles for experiment with $T = 1/7$ sec, $H_i = 100$ mm.

standard deviation is maximum (about $0.2H$, H being wave height) at the front and very small elsewhere. Notice that the variations at the front may well be fluctuations in the horizontal position interpreted as vertical fluctuations by the ensemble averaging procedure.

Fig. 5 shows wave height to mean water depth H/h_{MWS} versus still water depth h_{SWL} in the region considered. The experiments reported have deep water steepnesses H_0/L_0 between 0.0088 and 0.034. Thus the distance from the breaking point varies from test to test. The figure shows that H/h is decreasing slowly and that the value depends on H_0/L_0 . Yet the scattering for tests with similar data is considerable, so further investigations are obviously needed for a systematical understanding of this point.

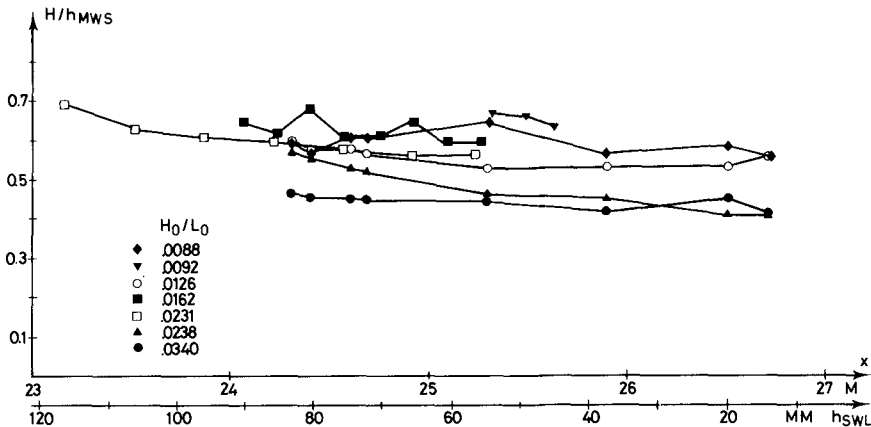


Fig. 5 Variation of wave height to water depth ratio versus still water depth.

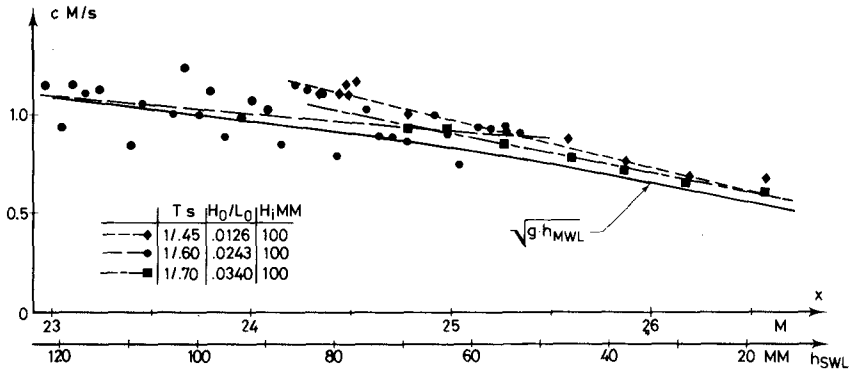


Fig. 6 Measured propagation velocity c .

The measurements of c reported in Fig. 6 were obtained from a trolley moving along the wave flume with two wave gauges 20 cm apart. This set-up measured the propagation time between the two gauges for a point of the wave with a fixed chosen elevation. Results for c versus mean water depth are shown in Fig. 6 with \sqrt{gh}^{MWS} as reference curve. It is tempting though - as we shall see - irrelevant to conclude that the linear shallow water result is a fair approximation (i.e. c/\sqrt{gh}^{MWS} is almost equal to unity).

For each of the 8 recording points (channel 0 through 7) the (ensemble) mean profiles have been determined in each test and Fig. 7 shows such profiles at 4 of the points for 4 different tests, and Fig. 8 shows a comparison of the profiles at the first and the last measuring point. Notice that the abscissa corresponds to increasing time at fixed x so that the wave profiles are "propagating towards the left". The vertical coordinate is scaled with the local wave height to make a direct comparison possible.

The striking feature of these figures is the remarkable similarity of the profiles, not only from point to point in a particular test, but also at the same point for different deep water data (Fig. 8). In fact the only significant development seems to be a decrease in the height of the crest and an increase in depth of the trough as the wave propagates shorewards. Since the surface elevation η is adjusted so that $\int_0^T \eta dt = 0$ (i.e. η is measured from the local MWS) these changes do of course correspond to a systematical change in shape. It may be noticed that this development goes in the direction of a linear variation of η between crest and trough.

In the following sections we try to understand the physical flow conditions behind these results on the basis of the fundamental equations of hydrodynamics.

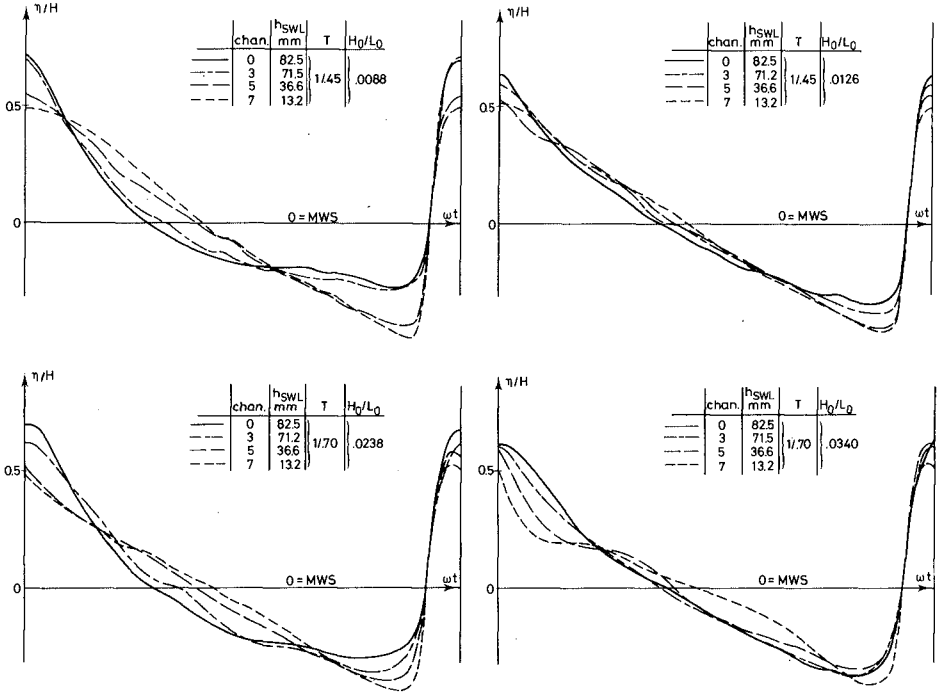


Fig. 7 Mean profiles at four different points.

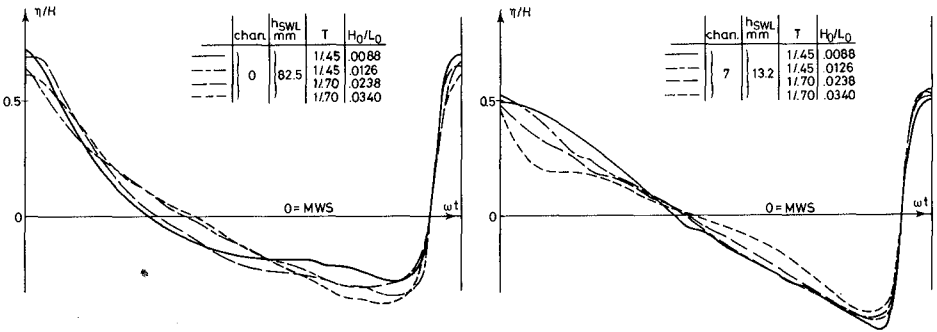


Fig. 8 Mean profiles for different experiments at channel 0 and channel 7.

3. THE INTEGRATED EQUATIONS

As described in the introduction the motion of the waves in the inner region of the surf zone resembles periodic bores or hydraulic jumps. Thus it is natural to start a theoretical analysis by applying the same methods as have been used with great success on particularly hydraulic jumps, i.e. using the integrated equations of mass and momentum to determine the velocity of propagation c and the integrated energy equation to find the dissipation.

Before doing so it is profitable to consider the form of these basic equations. In this context we briefly mention some effects at the free surface which are due to the turbulence, and which do not seem yet to be widely appreciated.

The coordinates and notation used in the following are shown in Fig. 9, which also indicates the type of problem considered.

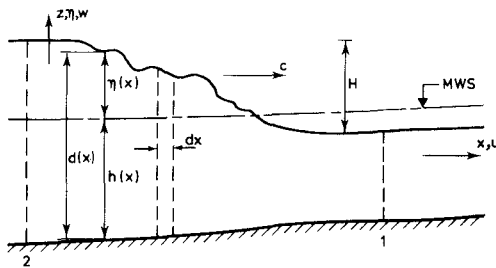


Fig. 9 Definition sketch.

The integrated equations for conservation of mass, momentum and energy may be derived from the general formulation of these principles given by Jeffrey (1965) for volumes with boundaries moving arbitrarily relative to a fixed frame of reference.

For reference these equations are quoted in our notation and for our conditions, i.e. an incompressible fluid without interval energy (nuclear, chemical, etc.).

Equation of continuity

$$\frac{\partial}{\partial t} \int_{V(t)} \rho \, d\omega + \int_{S(t)} (\vec{u} - \vec{v}) \cdot d\vec{S} = 0 \quad (1)$$

Equation of momentum

$$\frac{\partial}{\partial t} \int_{\Omega(t)} \rho \vec{u} \, d\omega = - \int_{S(t)} p \, d\vec{S} - \int_{S(t)} \rho \vec{u} (\vec{u} - \vec{v}) \cdot d\vec{S} + \int_{\Omega(t)} \rho \vec{g} \, d\omega \quad (2)$$

Equation of energy

$$\begin{aligned} \frac{\partial}{\partial t} \int_{\Omega(t)} \rho \vec{u}^2 / 2 \, d\omega = & - \int_{S(t)} p \vec{u} \cdot d\vec{S} - \int_{S(t)} \rho u^2 / 2 (\vec{u} - \vec{v}) \cdot d\vec{S} \\ & + \int_{\Omega(t)} \rho \vec{u} \cdot \vec{g} \, d\omega - \int_{\Omega(t)} D_V \, d\omega \quad (3) \end{aligned}$$

Here $S(t)$ is the surface of the control volume $\Omega(t)$, \vec{u} is the fluid velocity and \vec{v} the velocity of the surface element dS (for a volume changing in time) positive along the outward normal. D_v is the energy dissipation per unit volume due to viscous forces. In the equation of momentum viscous stresses along the surface have been neglected in this formulation.

For waves on a sloping bottom it appears to be simplest to use a control volume (see Fig. 9) following the free surface but otherwise being fixed in space, at first of length dx , later on integrated over a finite horizontal distance. (Thus the first step corresponds to an integration over depth of the differential form of the three equations).

The continuity equation

From (1) the continuity equation becomes

$$\frac{\partial}{\partial t} \int_{-h}^{\eta} \rho dz + \frac{\partial}{\partial x} \int_{-h}^{\eta} \rho u dz = 0 \quad (4)$$

which results in the well known

$$\frac{\partial}{\partial x} \int_{-h}^{\eta} u dz = -\eta_t \quad (5)$$

In this equation we now extract the turbulent fluctuation denoted by $'$. Thus we in general introduce

$$(u, w, p, \eta) = (\bar{u}, \bar{w}, \bar{p}, \bar{\eta}) + (u', w', p', \eta') \quad (6)$$

where $\bar{\quad}$ means time mean value.

In (5) this yields after turbulent time averaging (i.e. disregarding the time variation of the mean values)

$$\frac{\partial}{\partial x} \int_{-h}^{\bar{\eta}} u dz = -\frac{\partial \bar{\eta}}{\partial t} - \frac{\partial}{\partial x} \int_{\bar{\eta}}^{\bar{\eta}+\eta'} u dz \quad (7)$$

The last term here actually corresponds to the extra term found by Hasselmann (1971) in the kinematic free boundary condition in a situation with wavelets superimposed on larger scale wave motions.

Notice that the result (7) is readily obtained by an integration over depth of the continuity equation $\nabla \cdot \vec{u} = 0$ if Hasselmann's kinematic boundary is used at the turbulent mean surface $\bar{\eta}$.

Obviously similar terms must occur in the equations of momentum and energy. Hasselmann also showed that the dynamic free surface condition at $z = \bar{\eta}$ is not $\bar{p}(\bar{\eta}) = 0$, but

$$p(\bar{\eta}) = -\rho \overline{w'^2} \quad (8)$$

a change which is again a result of the fluctuations at the turbulent mean water surface $\bar{\eta}$.

In all published investigations on bores and hydraulic jumps known to the authors (as e.g. Resch, Leutheusser and Coantin, 1976, Rouse, 1958, Tsubaki, 1950) the fluctuations in η seem to have been neglected, corresponding to omission of the last term in (7) and similar terms in the other equations. In an ordinary free surface turbulent flow these

terms are probably small, but this can hardly be expected to apply to the region with the surface roller in a hydraulic jump or a bore.

Thus being aware of the possible errors it may lead to, we shall in the present investigation allow ourselves to make the same approximation (i.e. neglect the effect of the surface fluctuations) in order to be able to pursue other ideas. We therefore assume that the continuity equation reads

$$\frac{\partial}{\partial x} \int_{-h}^{\bar{\eta}} \bar{u} dz = - \bar{\eta}_t \quad (9)$$

in which we may substitute the definition

$$U \equiv \frac{1}{d} \int_{-h}^{\bar{\eta}} \bar{u} dz \quad (10)$$

to get

$$\frac{\partial}{\partial x}(Ud) = - \bar{\eta}_t \quad (11)$$

The equation of momentum

From (2) we get

$$\frac{\partial}{\partial t} \int_{-h}^{\bar{\eta}} \rho dz = - \frac{\partial}{\partial x} \int_{-h}^{\bar{\eta}} (\rho u^2 + p) dz + h_x p(-h) - \tau_b \quad (12)$$

which is exact since $p(\eta)$ is zero. τ_b is the bottom shear stress. Introducing the turbulent description by substituting (6), and neglecting the fluctuations of the free surface yields after turbulent averaging

$$\frac{\partial}{\partial t} \int_{-h}^{\bar{\eta}} \bar{u} dz + \frac{\partial}{\partial x} \int_{-h}^{\bar{\eta}} (\bar{u}^2 + \overline{u'^2} + \bar{p}) dz - \frac{1}{\rho} h_x p(-h) + \tau_b = 0 \quad (13)$$

For further applications it is convenient to express the integrals in terms of coefficients, which we define as

$$\alpha = \frac{1}{d} \int_{-h}^{\bar{\eta}} (\bar{u}/U)^2 dz, \quad \alpha' = \frac{1}{d} \int_{-h}^{\bar{\eta}} \overline{u'^2}/U^2 dz \quad (14)$$

$$\kappa^+ = \frac{1}{\rho g d^2} \int_{-h}^{\bar{\eta}} p^+ dz \quad \text{where} \quad p^+ = \bar{p} + \rho g z \quad (15)$$

Thus (13) may be written

$$\rho \frac{\partial}{\partial t}(Ud) + \frac{\partial}{\partial x} [\rho(\alpha + \alpha')dU^2 + \rho g \kappa^+ d^2 - \frac{1}{2} \rho g \bar{\eta}^2] - h_x p^+(-h) + \tau_b = 0 \quad (16)$$

Here the $\partial/\partial t$ - term can not be integrated with respect to x without information or assumptions about the changing shape of the wave. This is discussed in the following paragraphs.

The energy equation

Here it is useful first to consider the \vec{g} - term in (3). This term

in fact represents the potential energy and may conveniently be re-written as follows

$$\int_{\Omega(t)} \rho \vec{u} \cdot \vec{g} d\omega = - \int_{\Omega(t)} \rho \vec{u} \cdot \nabla g z d\omega$$

which invoking the continuity equation $\nabla \cdot \vec{u} = 0$ becomes

$$= - \int_{\Omega(t)} (\nabla \cdot g z \vec{u}) d\omega = - \int_{S(t)} E_p \vec{u} \cdot d\vec{S} \quad (17)$$

$$\text{with } E_p \equiv g z \quad (18)$$

We further notice that the rate of change of potential energy inside the volume is

$$\frac{\partial}{\partial t} \int_{\Omega(t)} E_p d\omega = - \int_{\Omega(t)} \rho \vec{u} \cdot \vec{g} d\omega + \int_{S(t)} E_{pot} (\vec{v} - \vec{u}) \cdot d\vec{S} \quad (19)$$

where the minus sign of the first right hand term indicates that gravity has to do negative work to increase the potential energy. Combining (17) and (19) yields

$$\int_{\Omega(t)} \rho \vec{u} \cdot \vec{g} d\omega = - \frac{\partial}{\partial t} \int_{\Omega(t)} E_p d\omega + \int_{S(t)} E_p (\vec{v} - \vec{u}) \cdot d\vec{S} \quad (20)$$

When substituted into (3) this can be written

$$\begin{aligned} \frac{\partial}{\partial t} \int_{\Omega(t)} (E'_k + E_p) d\omega = & - \int_{S(t)} p \vec{u} \cdot d\vec{S} - \int_{S(t)} (E'_k + E_p) (\vec{u} - \vec{v}) \cdot d\vec{S} \\ & - \int_{\Omega(t)} D_v d\omega \end{aligned} \quad (21)$$

with

$$E'_k \equiv \frac{1}{2} \rho \vec{u}^2 \quad (22)$$

For the particular control volume considered here we get in the first step (length dx , see Fig. 9)

$$\rho \frac{\partial}{\partial t} \int_{-h}^{\eta} (E'_k + E_p) dz = - \frac{\partial}{\partial x} \int_{-h}^{\eta} (p + E'_k + E_p) u dz - \int_{-h}^{\eta} D dz \quad (23)$$

When we in (23) substitute the turbulent description (6) and average, a large number of turbulent fluctuation terms result. These, however, all belong to the category which we in this context include in the dissipation term D . Thus we concentrate our attention on the ordered mechanical energy only and therefore get

$$\frac{\partial}{\partial t} \int_{-h}^{\bar{\eta}} (E_k + E_p) dz = - \frac{\partial}{\partial x} \int_{-h}^{\bar{\eta}} (p + E_p + E_k) u dz - \int_{-h}^{\bar{\eta}} D_t dz \quad (24)$$

with

$$E_k \equiv \frac{1}{2} \rho (\bar{u}^2 + \bar{w}^2) \quad (25)$$

in which D_t now includes both viscous dissipation and turbulent energy

not yet dissipated, and we recognize the well known expression for the flux of ordered mechanical energy

$$E_f(t) = \int_{-h}^{\bar{\eta}} (\rho g z + \bar{p} + \frac{1}{2}\rho(\bar{u}^2 + \bar{w}^2))\bar{u} dz \quad (26)$$

Thus the energy equation may be written

$$\frac{\partial \mathcal{E}}{\partial t} = - \frac{\partial}{\partial x} E_f(t) - \mathcal{D} \quad (27)$$

with the definitions

$$\mathcal{E} = \int_{-h}^{\bar{\eta}} (E_k + E_p) dz ; \mathcal{D} = \int_{-h}^{\bar{\eta}} D_t dz \quad (28)$$

which simply states that the rate of change of energy inside the control volume is the difference between net flux over the boundary and the loss due to dissipation.

Again it is useful to express the integrals in terms of coefficients which we define as

$$\beta = \frac{1}{d} \int_d (\bar{u}^3 + \bar{w}^2 \bar{u})/U dz \quad (29)$$

$$\delta = \frac{1}{\rho g d^2} \int_d (\bar{u} - U)p^+/U dz \quad (30)$$

Then the energy flux $E_f(t)$ may be written

$$E_f(t) = \int_{-h}^{\bar{\eta}} (p^+ + \frac{1}{2}\rho(\bar{u}^2 + \bar{w}^2))\bar{u} dz = \rho g d^2 U(\delta + \kappa^+) + \rho \beta d U^3 \quad (31)$$

and the energy equation becomes

$$\frac{\partial \mathcal{E}}{\partial t} = - \frac{\partial}{\partial x} [\rho g d^2 U(\delta + \kappa^+) + \rho \beta d U^3] - \mathcal{D} \quad (32)$$

Thus it has been shown how the three fundamental equations integrated over depth can be expressed in terms of velocity and pressure profiles under the assumptions mentioned. In the following these equations are applied to waves.

4. AVERAGED ENERGY EQUATION

One of the important features in the surf zone is the wave height attenuation due to the turbulence generated by the breaking.

For this purpose we average (27) over a mean period (assuming periodicity in time) to get

$$\bar{\mathcal{D}} = - \frac{\partial \bar{E}_f}{\partial x} \quad (33)$$

where $\bar{\mathcal{D}}$ is the mean dissipation per m^2 of bottom and \bar{E}_f is the time mean of $E_f(t)$. We define a non dimensional energy flux B in analogy to ordinary wave theory and using (26) find

$$E_f = \frac{1}{T} \int_0^T \int_{-h}^{\bar{\eta}} (\bar{p}^+ + \frac{1}{2} \rho (\bar{u}^2 + \bar{w}^2)) \bar{u} dz dt \equiv \rho g c H^2 B \quad (34)$$

Similarly we define a nondimensional energy dissipation D and since we want to relate this quantity to the hydraulic jump or bore conditions it is convenient to let D represent the energy dissipation per wave length. Thus we write

$$\bar{D} \equiv \rho g \frac{c}{L} \frac{H^3}{4h} D \quad (35)$$

a form which is closely related to the expression for the hydraulic jump.

Substitution of (34) and (35) into (33) and rearrangement of the terms yield

$$\left(\frac{H}{h}\right)_X = - \left(\frac{h_X}{h} + \frac{c_X}{2c} + \frac{B_X}{2B}\right) \frac{H}{h} - \frac{h_0}{8L} \frac{D}{B} \left(\frac{H}{h}\right)^2 ; \quad X = \frac{x}{h_0} \quad (36)$$

which is a first order nonlinear differential equation in H/h . Notice that (36) itself is fairly general. It is only assumed that the motion is periodic and that D includes the turbulent energy. It also turns out to be a quite convenient basis for studying the effect of simplifying assumptions, also in the related expressions (31) and (34) for B . Solution, however, requires information of the coefficients, and this is the purpose of the following analysis.

The h_X/h term includes the wave set-up so that determination of this term requires integration of the averaged form of the equation of momentum (16). This is perfectly possible but is considered beyond the scope of the present paper. Since the set-up in most of the surf zone is only a small fraction of the still water depth we use an estimate of h_X/h based on the bottom slope and experimental results for the set-up.

The $c_X/2c$ and $B_X/2B$ are more interesting terms, and we first tackle the determination of c .

5. THE VELOCITY OF PROPAGATION

For simplicity the method by which c can be determined for a breaking wave is described for constant depth only. It should be mentioned, however, that it is fairly straightforward to show that the effect of a sloping bottom is negligible on c .

We also assume that the wave motion is of constant form to avoid the complications of defining a speed of propagation for a changing wave form and include the associated effects in the analysis. With a proper choice of c (speed for $\eta = 0$, say) the effect would again be negligible.

None of these assumptions in fact remove from the problem the effects we want to study, namely the influence of the velocity and pressure variation over the depth (i.e. the magnitude of α and κ and for the energy dissipation of β and δ).

Under these conditions it is convenient to change to a frame of reference moving with the wave, and in which the horizontal particle velocity is termed v . Thus

$$\begin{aligned}
 v &= u - c \quad ; \quad V = U - c \\
 \alpha^v &= \frac{1}{d} \int (v/v)^2 dz
 \end{aligned}
 \quad \left. \vphantom{\begin{aligned} v &= u - c \\ \alpha^v &= \frac{1}{d} \int (v/v)^2 dz \end{aligned}} \right\} (37)$$

In a wave of constant form we have

$$\int_d u dz = U d = c \bar{\eta} \quad (38)$$

if i) $\bar{\eta}$ is measured from the mean water level

ii) there is no net mass flux

(see Svendsen, 1974, p. 164 ff).

The continuity equation (11) yields

$$V d = \text{const} = (U - c)d = c \bar{\eta} - c d$$

or

$$V = -c h/d \quad (39)$$

h being the mean water depth.

The equation of momentum (16) becomes (neglecting the bottom friction)

$$\frac{\partial}{\partial t} (V d) + \frac{\partial}{\partial x} [(\alpha^v + \alpha') d V^2 + g \kappa^+ d^2 - \frac{1}{2} g \bar{\eta}^2] = 0 \quad (40)$$

in which the constant form assumption implies that $\partial/\partial t = 0$ so that the equation can be integrated from x_2 to x_1 (see Fig. 9) to yield

$$(\alpha^v + \alpha') d V^2 + g \kappa^+ d^2 - \frac{1}{2} g \bar{\eta}^2 \Big|_2^1 = 0 \quad (41)$$

or with V from (39)

$$c^2 h^2/d (\alpha^v + \alpha') + g \kappa^+ d^2 - \frac{1}{2} g \bar{\eta}^2 \Big|_2^1 = 0 \quad (42)$$

For a wave of constant form c is the same for any choice of x_1 and x_2 . Hence (42) is an equation from which c may be determined, the proper information given. (A check on a solitary wave, say, rapidly confirms this).

In numerical computations, however, the most accurate results are obtained when x_2 and x_1 are placed at the (instantaneous) position of the crest and trough, respectively (Fig. 9).

As a special case we first consider a periodic bore with static pressure and v uniform over the depth. Placing x_2 so far down the stream that there is no turbulence we have

$$\alpha^v = 1 \quad ; \quad \alpha' = 0 \quad ; \quad \kappa^+ = \eta/d \quad (43)$$

Solving for c we then get

$$\frac{c_{\text{bore}}^2}{gh} = \frac{1}{2} \frac{d_1 d_2}{h^3} (d_1 + d_2) \quad (44)$$

$$\text{or with } \zeta = d_2/d_1 \quad ; \quad \zeta_t = d_1/h \quad (45)$$

$$\frac{c_{\text{bore}}^2}{gh} = \frac{1}{2} \zeta_t^3 \zeta (\zeta + 1) \tag{46}$$

which transforms into the well known expression for a single bore if we choose $h = d_1$ (i.e. $\zeta_t = 1$).

In the more general case the direct solution of (42) yields

$$\frac{c^2}{c_{\text{bore}}^2} = A_1 \left[1 + 2 \frac{\kappa_2 \zeta - \kappa_1}{\zeta^2 - 1} \right] \tag{47}$$

where by definition

$$\kappa \equiv \kappa^+ - \bar{\eta}/d \quad ; \quad A_1 \equiv \frac{\zeta - 1}{(\alpha_1^V + \alpha_1') - (\alpha_2^V + \alpha_2')}$$

index $1, 2$ referring to x_1 and x_2 respectively and c_{bore} given by (46).

In (47) may now be introduced various assumptions for the α^V and κ coefficients and the outcome compared with the measurements reported in § 2. Fig. 10 shows the result of such computations. Here three different sets of coefficients have been used, and for reference \sqrt{gh} is shown too.

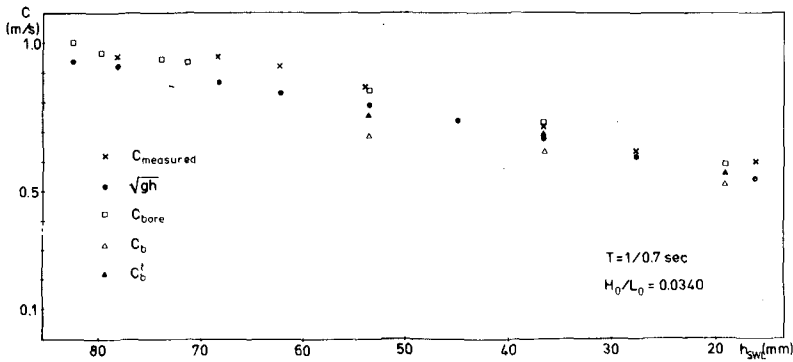


Fig. 10 Measured and computed values of c .

The results denoted c_{bore} correspond to (46). The values of $\bar{\eta}$ used in the computation were taken from the measured profiles and we see that the agreement is good, but of course this can not be taken as a proof of static pressure and uniform velocity.

The points denoted c_B have been obtained by assuming a deviation from static pressure corresponding to a Boussinesq approximation. Thus for \bar{u} we have used

$$\bar{u} = c \bar{\eta}/d + \frac{1}{2} \left(\frac{1}{3} - \left(\frac{z+h}{d} \right)^2 \right) h \bar{\eta}_{xx} \tag{48}$$

and for \bar{p}

$$\bar{p} = \rho g [(\bar{\eta} - z) + \frac{1}{2} (1 - (\frac{z+h}{d})^2) h \bar{\eta}_{xx}] \quad (49)$$

Again the values of $\bar{\eta}$ and $\bar{\eta}_{xx}$ have been determined from the measured mean profiles.

As Fig. 10 shows the resulting c -values are smaller than the bore velocity. In general a non uniform velocity profile under the wave crest (x_2) (as (48)) yields $\alpha^v > 1$, which tends to increase c , whereas a pressure lower than static ($\kappa < 0$) will reduce c . (In the trough (x_1) the value of $h\bar{\eta}_{xx}$ is too small to give significant contributions).

In c_{bore} and c_B the turbulence has been neglected by assuming $\alpha' = 0$.

The last set of points (denoted c_B^t) shows the effect of the turbulent velocity fluctuations. The value of α' has been chosen as 0.10, which is the approximate value one can derive from Rasch et al. (1976) who report results for u'^2 in a hydraulic jump.

The turbulent velocity fluctuations act as an additional momentum and hence increase c . In the figure α' has been applied to the case where α^v and κ were determined by a Boussinesq approximation (so c_B^t should be compared with c_B). In the classical sense this is inconsistent since the Boussinesq theory is usually based on potential theory. However, the formula (49) may also be derived simply by assuming a linear variation of the curvature of the mean stream lines, and (48) may be regarded as simply a parabolic approximation for u .

In general the effect of turbulence (i.e. α') on c can be extracted from (47) as

$$\frac{c^{\text{turb}}}{c^{\text{potential}}} = (1 - \frac{\alpha'}{\zeta - \alpha})^{-1/2} \quad (50)$$

It is emphasized here that $\alpha' = 0.10$ is not much more than an arbitrary guess used to illustrate the nature of the problem.

6. THE ENERGY FLUX

The non dimensional energy flux B can be determined from (34) using the same type of information required to find c . When (31) is substituted B is expressed in terms of the coefficients β, δ and κ^+ and by $U, c^2/g h$ and H , and the result can be tidied for waves of constant form using the continuity equation.

Here it suffices to mention that for sections (x_2, x_1) at crest and trough $\bar{w} \sim 0$, and if we introduce the linear shallow water assumptions

$$u \sim c \bar{\eta}/h \quad ; \quad p^+ \sim \rho g \bar{\eta} \quad (51)$$

we get as first approximation for B

$$B = \frac{1}{T} \int_0^T (\bar{\eta}/H)^2 dt \quad (52)$$

Let us for a moment consider improvements of this result using the

Boussinesq approximation introduced above. Then (52) is the first term in an expansion in η/H . Further analysis shows that the next term with $(\eta/H)^3$ yields contributions only a few percent of (52), for measured values of η .

Therefore in the following considerations it seems reasonable at the present stage to rely upon (52) for B.

7. WAVE HEIGHT VARIATION AND ENERGY DISSIPATION

The application of (36) to determine the wave height variation requires input for the energy dissipation described by D, and considering that c was found to be nearly equal to c_{bore} the first natural choice is also to use the bore result for the energy dissipation. For a periodic bore this corresponds to

$$D = h^2/d_1d_2 \tag{53}$$

Fig. 11 shows the resulting variation in the wave height compared with

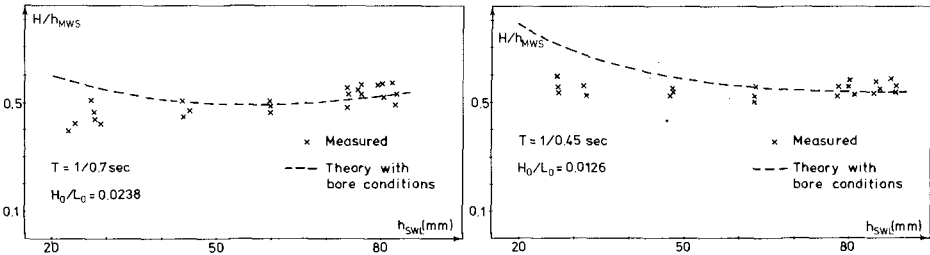


Fig. 11 Measured and computed ratios of wave height to water depth H/h.

measured results. As input to the computations is used the wave height at the first measuring point (largest depth). The agreement is poor and obviously the energy dissipation can not be determined by simple bore relations.

To further illustrate this (36) has been reversed by solving with respect to the D-term which is then determined by using measured values of the other terms including $(H/h)_X$. We define

$$\begin{aligned} \Delta E_{\text{measured}} &\equiv \frac{h_0}{8L} \left(\frac{H}{h}\right)^2 \frac{D}{B} \\ &= -\left(\frac{H}{h}\right)_X - \frac{H}{h} \left(\frac{h}{c} \frac{X}{h} + \frac{c}{2c} + \frac{B}{2B} \frac{X}{h}\right) \end{aligned} \tag{54}$$

Fig. 12 shows a comparison between $\Delta E_{\text{measured}}$ and ΔE_{bore} which clearly confirms the conclusion above.

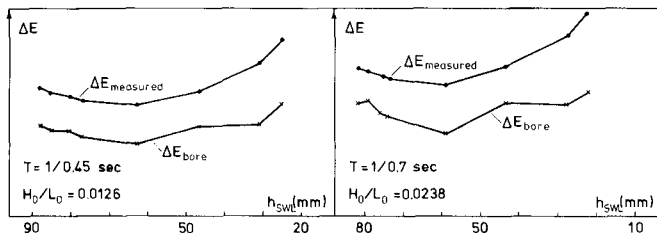


Fig. 12 Measured and computed values of ΔE defined by Eq. 54.

The actual energy dissipation may be determined from (32) for simplifying assumptions similar to those introduced to find (47) for c . And again these represent a good approximation locally. Thus neglecting the changing form of the wave and assuming a horizontal bottom $\partial \mathcal{E} / \partial t$ becomes equal to $-c \partial \mathcal{E} / \partial x$ and (32) integrates directly from x_2 to x_1 . The result represents an equation with the term $\int_{x_2}^{x_1} \mathcal{E} dx$ as unknown. This term represents the total energy dissipation between x_2 and x_1 . The solution can be written in terms of D introduced above as

$$\frac{D}{D_{\text{bore}}} = 1 + \frac{2}{(\zeta-1)^2} (\zeta^2 \kappa_2 + \kappa_1) + A_3 \left(\frac{\zeta+1}{\zeta-1} \right)^2 \left[1 + \frac{2}{\zeta^2-1} (\zeta^2 \kappa_2 - \kappa_1) \right] - 4 \frac{\zeta}{(\zeta-1)^3} (\zeta \delta_2^V - \delta_1^V) \quad (55)$$

where

$$A_3 = A_1 \frac{\zeta^2 \beta_1^V - \beta_2^V}{\zeta^2 - 1} - 1$$

with β^V and δ^V defined from (29) and (30) in analogy with (37), and κ and A_1 by (15) and (47) respectively.

In (55) a uniform velocity distribution corresponds to $\delta = 0$, $A_3 = 0$ and $A_1 = 1$, and static pressure implies $\kappa = 0$, $\delta = 0$.

8. DISCUSSION

Eqs. 47 and 55 have been evaluated for a variety of velocity and pressure conditions in order to obtain agreement with the measurements. This would require a D/D_{bore} value of 1.4 to 1.6 corresponding to the ratio between the two curves in Fig. 12, and at the same time c must be close to c_{bore} as indicated by Fig. 10.

In this context the physical picture of the process suggested by Peregrine and Svendsen (1978) (see description in § 1) has been invoked.

This model implies that at the bottom between x_2 and x_1 the flow is not influenced by the (surface) turbulence, so that the Bernoulli equation yields a simple relation between the bed velocities at x_2 and x_1 , (pressure specified). In all cases considered the conditions at the wave trough were fixed at static pressure and uniform horizontal velocity.

The following general properties may be extracted from these investigations:

- a) D/D_{bore} increases for increasing values of α_2^v . On the other hand any physically relevant velocity profile yields α^v not much larger than unity. The opposite applies to the pressure variation where pressures smaller than the static at x_2 reduce D/D_{bore} .
- b) In this respect D/D_{bore} follows c/c_{bore} . It also appears that the largest value of D/D_{bore} for a fixed value c/c_{bore} is obtained if $|\beta^v|$ is minimized for fixed α^v .
- c) None of the relevant velocity profiles and the associated pressure variations, however, lead to D/D_{bore} larger than about 1.2 as long as $\alpha' = 0$ (i.e. as long as the momentum of the turbulent velocity fluctuations are omitted).
- d) Notice that the energy dissipation (55) includes the turbulent energy generated between x_1 and x_2 and subsequently convected out of the volume through section 2 (see Fig. 9). But (55) does not include the energy lost by generation of turbulent energy behind section 2. This amount is difficult to estimate but may account for some of the deficit in energy dissipation.
- e) Finally it turns out that D/D_{bore} given by (55) increases rapidly with increasing α' , i.e. if the momentum of the turbulent fluctuations are included, even though we have seen that the velocity of propagation c is relatively insensitive to this factor.

Though a more detailed investigation of this is required it seems obvious that the significant deviations between measured and calculated energy dissipations shown in Fig. 12 are primarily associated with the momentum of the turbulent velocity fluctuations represented by α' . Further analysis, however, will also require that the effect of the free surface fluctuations are included.

9. REFERENCES

- Buhr Hansen, J and Svendsen, I.A. (1974). Laboratory generation of waves of constant form. Proc. 14'th Coast. Engng. Conf., Copenhagen, vol. I, p. 321-339.
- Hasselmann, K (1971). On the mass and momentum transfer between short gravity waves and larger-scale motions. Jour. Fluid Mech., 50, p. 189-205.
- Horikawa, K. and Kuo, C. (1966). Wave transformation after a breaking point. Proc. 10th Coast. Engng. Conf., Tokyo, chap. 15, p. 217-233.

- Jeffrey, A. (1965). A note on the integral form of the fluid dynamic conservation equations relative to an arbitrarily moving volume. *ZAMP*, vol. 16, p. 835-37.
- Nakamura, M. et al. (1966). Wave decaying due to breaking. *Proc. 10th Coast. Engng. Conf., Tokyo*, chap. 16, p. 234-253.
- Peregrine, D.H. and Svendsen, I.A. (1978). Spilling breakers, bores and hydraulic jumps. *Proc. 16th Coast. Engng. Conf., Hamburg*.
- Resch, F.J., Leutheusser, H.J. and Coantic, M. (1976). Etude de la structure cinematique et dynamique du ressaut hydraulique. *Journal of Hydraulic Research*, 14, 4, p. 293-319.
- Rouse, H., Siao, T.T. and Nagaratnam, S. (1958). Turbulence characteristics of the hydraulic jump. *Transaction for the Asce*, vol. 124, p. 926-950.
- Svendsen, I.A. (1974). Cnoidal waves over a gently sloping bottom. Series paper no. 6, *Inst. Hydrodyn. and Hydraulic Engrg., Tech. Univ. Denmark*.
- Tsubaki, T. (1950). Theory of hydraulic jump. *Reports, Research Institute for Fluid Engineering, Kyushu University, Fukuoka, Japan*, vol. VI, no. 2.

CHAPTER 30

Spilling breakers, bores and hydraulic jumps

D H Peregrine

Reader in Mathematics, University of Bristol, England

and

I A Svendsen

Associate Professor, Institute of Hydrodynamics and
Hydraulic Engineering (ISVA), Technical University of Denmark

Quasi-steady breaking waves

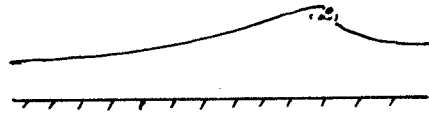
On gently sloping beaches, almost all water waves break. After the initial breaking the water motion usually appears quite chaotic. However, for a moderate time, for example two or three times the descent time of the "plunge" in a plunging breaker, the flow can be relatively well organised despite the superficial view which is largely of spray and bubbles. If waves continue to break the breaking motion, or "white water" soon becomes fully turbulent and the mean motions become quasi-steady.

A reasonable definition of a quasi-steady wave is one which changes little during the time a water particle takes to pass through it. We exclude water particles which may become trapped in a surface roller and surf along with the wave.

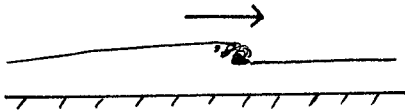
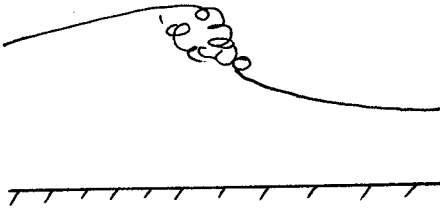
At this stage in its development a wave on a beach may be described as a spilling breaker or as a bore. In fact, there is a range of these waves from those with a little white water at the crest to examples where the whole front of the wave is fully turbulent. In investigating the properties of such waves it is desirable to start by looking at the whole range of related motions. The most obvious extension is to the hydraulic jump; since, in the simplest view, it is equivalent to a bore but in a frame of reference moving with the wave. It is also an example where the mean flow is steady rather than quasi-steady. It takes little further imagination to see that a range of steady and quasi-steady breaking flows is more or less as follows:

- spilling breakers in deep water
- spilling breakers in shallow water
- bores
- hydraulic jumps
- flow below sloping weirs
- waterfalls.

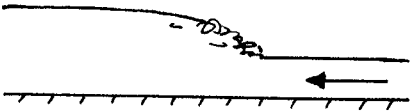
These are illustrated by sketches in figure 1. Within and between each example given there is a considerable variety of flows, not least, because of the differing physical sizes on which they may be realized, from a scale of a centimetre to a scale of ten metres. Other examples



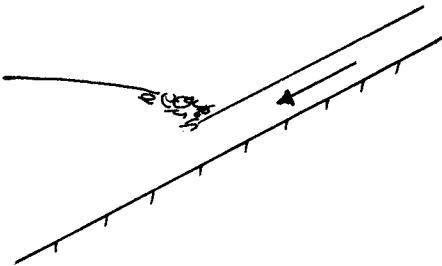
(a) spilling breaker (deep water) (b) spilling breaker (finite depth of water)



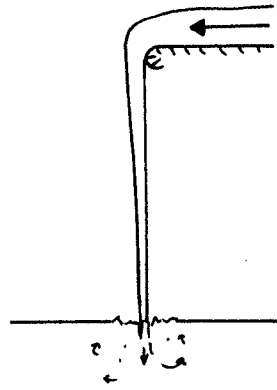
(c) spilling breaker/bore (d) bore



(e) hydraulic jump



(f) weir flow



(g) waterfall

Figure 1. A spectrum of quasi-steady breaking waves.

may be found; for example the white water at the bows of a ship.

Our aim is to increase understanding of the fluid motions in these waves. The only theoretical work on spilling breakers we are aware of is that of Longuet-Higgins and Turner (1974). They focus attention on the aerated surface roller falling down the front face of the wave. We started with ideas based on this model but after observing experimental waves modified our views, as described below. There is rather more work on hydraulic jumps (including a review paper by Rajaratnam (1967), some of which is discussed below.

Experiments and flow visualization

We have studied the motion and surface configuration of breakers, bores and hydraulic jumps in flumes with transparent sides. Photography and direct visual observation have been used. As well as observing entrained air bubbles we observed the motion of buoyant particles on small scale hydraulic jumps. This latter example induced some doubts about the importance of the downward flow in the surface roller of a hydraulic jump since the mean motion down the surface roller appeared to be very slight compared with the random motions. The scale of the flow observed was such that the roller had a height of a few centimetres, surface tension was important and there was only a small amount of aeration.

A few drops of dye in the roller of the hydraulic jump were very rapidly diffused and showed the extent of the turbulent motion. An attempt to minimise the effect of surface tension led us to a technique of flow visualization which enabled us to see the extent of the turbulent motion in propagating breaking waves as well.

The flow visualization method involves forming a layer of tiny bubbles on the free surface of the water. Best results are obtained by a layer which is rather less than a monolayer of bubbles. The bubbles are formed by adding detergent, we found a few parts per million to be satisfactory, to the water in a closed circuit flume. The flume is then run with air entrainment into the pump. This forms many bubbles of a diameter much less than a millimetre. When the pump is stopped the bubbles very slowly rise to surface and form a layer with clear water beneath.

When a breaking wave propagates over such a layer the bubbles indicate the motion of the surface layer of water after it is engulfed by the toe of the surface roller. The bubbles are sufficiently small that their rate of rise under gravity is almost negligible compared with the turbulent velocities. They give an indication of the extent of the turbulence, though it should be remembered that in liquids momentum diffuses much more readily than matter so that the turbulence may spread a little further than the bubbles. However, the spread of turbulence is not a diffusive but a convective process.

Visual and photographic observation, see figures 2 and 3, shows that the strong turbulence rapidly mixes the surface layer into an increasing

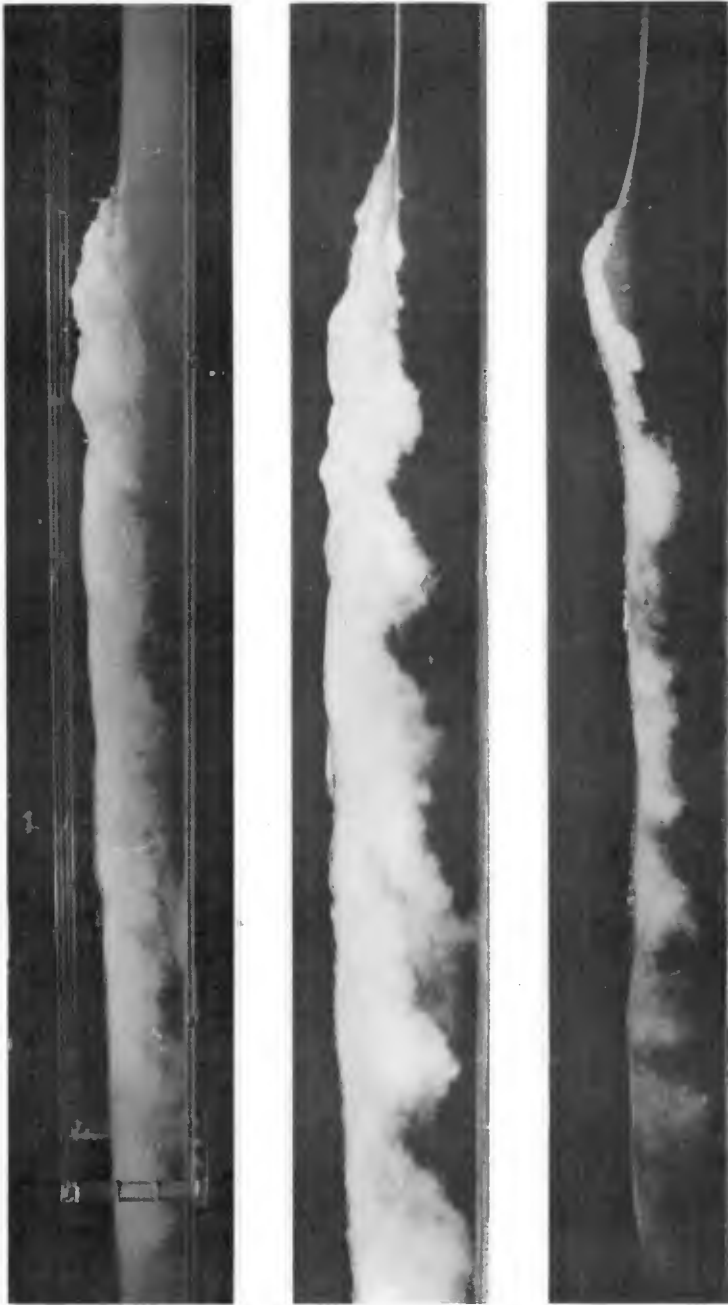


Figure 2. Visualization of the turbulence in propagating breaking waves - distant view.



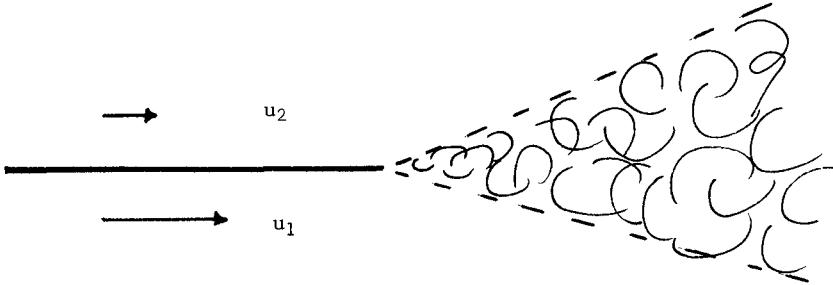
Figure 3. Visualization of the turbulence in propagating breaking waves - near view.

volume. This volume appears to commence from a point at the toe of the roller and forms a wedge which in an instantaneous view has "billows" on its under surface. For waves in moderate and shallow depths of water the turbulent region soon fills the whole depth. On the other hand, for deeper water, or for waves which are only just breaking, the breaking region is followed by a "wake" just below the free surface which only slowly thickens.

A model for the flow field

Our observations indicate that the surface roller does not play a dominant role in the dynamics of the wave. It is only a small part of the region of highly turbulent flow and is in no way separate from it. We consider that it acts as a trigger to initiate the turbulence. In many ways the initial volume of turbulent flow resembles a turbulent mixing layer.

A turbulent mixing layer occurs when two uniform parallel streams of velocities u_1 and u_2 are allowed to meet, for example by passing the end of a partition between them.



There have been numerous studies of turbulent mixing layers, some of which will be referred to shortly.

Consider the water motion in a frame of reference moving with the wave. The smooth water approaching the breaking wave has a velocity u_1 say. It means the toe of the surface roller which has a velocity u_2 which is not very different from zero. Mixing of the incoming water and the water already in the breaker ensues. The similarity to a mixing layer is enhanced by considering u_2 to be zero. There is then no need to have an upper fluid present except for that which is entrained into the mixing-layer. This small amount can be supplied by the reverse flow in the surface roller.

Alternatively, we note that for the toe of the surface roller u_2 is small and negative. In a true mixing layer u_2 is never quite as small as zero because there is always entrainment leading to a small adjustment of the velocity field. Thus if u_2 nominally equals zero

there is still some positive flow towards the mixing layer. In our imagination we can suppose u_2 to be nominally small and negative so that there is then no net flow towards the mixing-layer. This is the situation in a breaking wave.

A well documented property of turbulent mixing layers is that they spread linearly with distance in a wedge. The angle of spread depends largely on the velocity difference between the layers, however, for the case where u_2 is nominally zero there is a large scatter of recorded angles. See for example, Brown and Roshko (1974) which confirms the linear growth of mixing layers, and in figure 10 illustrates a scatter from 0.145 to 0.22 for one measure of the tangent of angle of spread with u_2 zero. The argument of the above paragraph indicates that for u_2 nominally equal zero, some small positive or negative values for u_2 might be more appropriate.

Another aspect of the flow in breakers which attracts attention is the air entrainment. This certainly leads to a lower mean density of fluid, but we consider this to be of secondary importance in the mechanics of the breaking wave. The eye, and camera, can only see one drop or bubble in any direction - vision beyond is obscured, thus it is very difficult to estimate the proportion of air and water. However, on the scale of 10 cm there is only a little air entrainment and yet breakers otherwise appear similar in structure to those on a much larger scale. Even with appreciable air entrainment the above mixing layer resemblance still holds. As Brown and Roshko (1974) show, by measuring mixing layers between helium and nitrogen, there are only quantitative differences when fluids of differing densities mix.

After the initiation of the turbulence it spreads until, at its upper boundary the effect of gravity becomes dominant towards the crest of the wave, and at its lower boundary interaction with the bottom becomes important. Exactly where these interaction regions are depends strongly on the type of breaking wave. Figure 4 is a sketch of these regions.

In the only case where there are measurements, the hydraulic jump, there is a considerable difference in the mean flow when a thick bottom boundary layer exists and when the flow is nearly uniform with depth, as is well shown by the work of Resch and Leutheusser, summarized in Resch et al (1976). This clearly indicates that these "interaction" regions can be important.

Behind the breaking region there is a long 'wake' in which the turbulence spreads, if the water is deep enough, and decays. The first part of this region is that which is most likely to be affected in a qualitative manner by entrained air.

Discussion

The model of flow in a quasi-steady breaker which is given above is not entirely new. We have found that Rajaratnam (1965) shows the

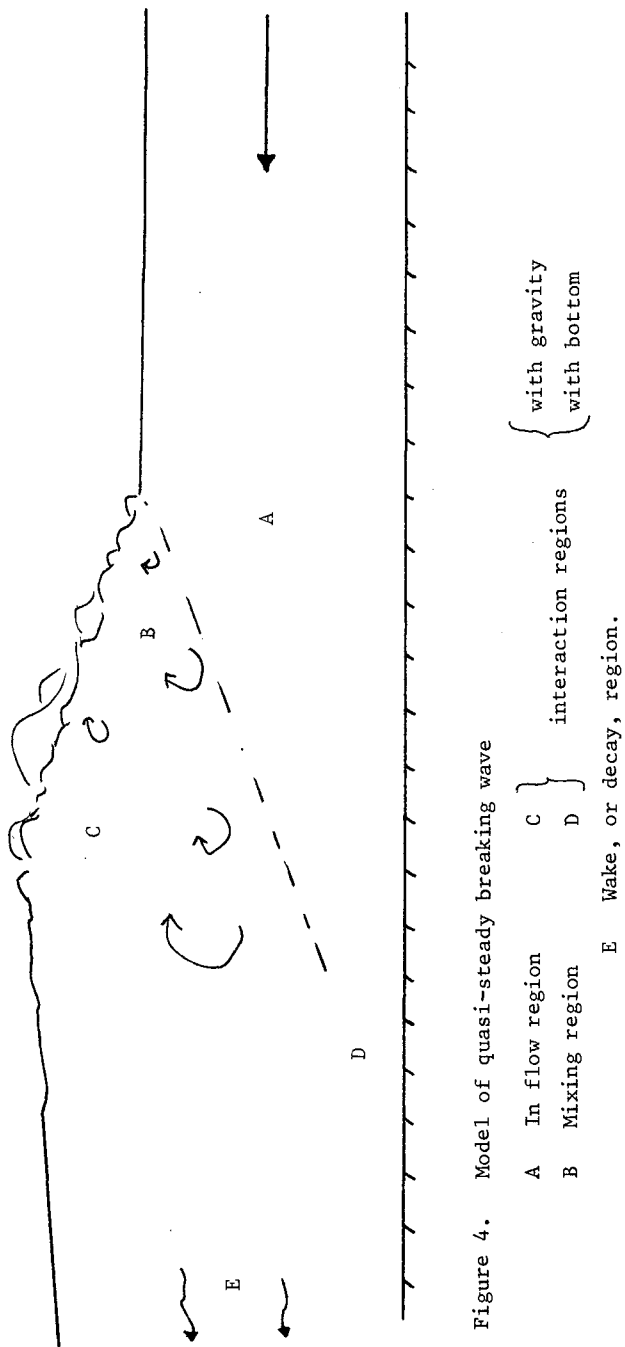


Figure 4. Model of quasi-steady breaking wave

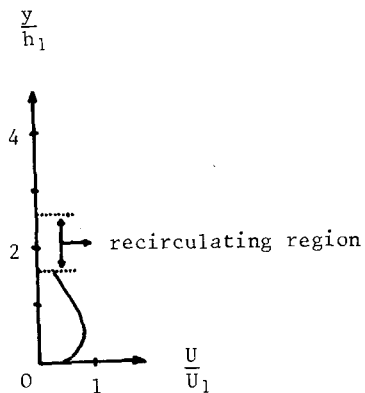
similarity between a strong hydraulic jump and a wall jet, and that Ogris (1975) has likened the hydraulic jump to a succession of vortices and also used the term 'mixing zone' to describe our 'mixing region' and our 'interaction regions'.

In studying any turbulent flow it is very helpful if it can be shown to be similar to other well known flows. Here we have made a hypothesis that flow in a breaking wave is in part like a mixing layer and part may be like a wake. Clearly it is important to assess the accuracy of this hypothesis with actual flow measurements since if the hypothesis proves reasonable then it will be of value in many studies relating to wave breaking such as air/sea interaction, sediment motion and wave forces on structures.

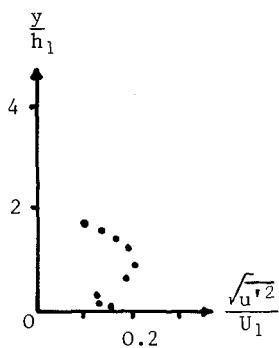
It is possible that some pressure and velocity measurements taken below breakers are of a quality to show the turbulent 'wake' of a spilling breaker, but we are unaware of them. This model of the wake from a spilling breaker is however supported by a laboratory investigation of sediment transport under waves (Nielsen et al 1978, final section).

Measurements of mean flow and turbulent fluctuations in hydraulic jumps are reported by Resch and others in a sequence of papers. Unfortunately they only consider very strong jumps. However, one can examine their weakest example which is for a Froude number of 2.85, that is a depth ratio of 3.6. The only measurements which appear to be relevant to our mixing layer hypothesis are those for a potential inflow at a distance of approximately 7 times the entry depth from the toe of the roller. These are shown in figure 5. From the measures of $\sqrt{u'^2}$ it appears that interaction with the bottom boundary-layer has already commenced. However, the upper part of the mean velocity profile does have an almost constant gradient as one finds through the centre of a mixing layer profile (eg Brown & Roshko, 1974, Fig 9) and the maximum intensity of $\sqrt{u'^2}$ is $0.19U_0$, which is not very different from the values for a mixing layer of around $0.17U_0$, found by several experimenters (see Champagne et al, 1976, figure 5). Examination of Resch and Leutheusser's figures for $\sqrt{v'^2}$ shows one very extreme point, in this profile only, so that we do not consider it reliable for comparison.

We hope this paper will help to stimulate further measurements and would particularly like to point out that it is possible to have quasi-steady breaking waves without air entrainment. The scale simply needs to be small enough. If the breaking front is of a height 1 to 2cm then, depending on the water quality and the particular type of wave, there may be no air entrainment and yet there is a very turbulent flow with all the other qualitative characteristics of a breaking. Without air entrainment laser-doppler anemometer measurements should be straight forward and able to show how far the ideas of this paper can be exploited.



(a) mean velocity profile from Resch et al (1976), figure 8.



(b) intensity of turbulent velocities in the mean flow direction from Resch and Leutheusser (1972), figure 5.

Figure 5. Velocity measurements in a hydraulic jump of depth ratio 5.6. h_1 and U_1 are the depth and mean velocity of the approximately uniform undisturbed flow. The measurements are at a point $7.2h_1$ from the toe of the surface roller.

We suspect that order of magnitude estimates from this model may be quite useful in some circumstances. For example to estimate the strength and scale of turbulence reaching the bottom from a bore on a beach, one could use results corresponding to a mixing layer with u_1 =bore velocity, $u_2=0$ and thickness approximately equal to the total height of the bore (note, bores on a beach only rarely have a depth ratio as great as 2, eg see Svendsen et al, 1978). Alternatively if a spilling breaker is causing the turbulence, one might assume that at the wave crest the mixing layer had a width approximately equal to the height of the roller, then estimate the relative momentum deficit and patch this on to the corresponding wake flow, assuming the free surface represented a symmetric plane at the centre of the wake. When the wake half width equals the depth of water the turbulence affects the bottom.

The authors wish to acknowledge, with thanks, financial support from the U K Science Research Council, The British Council, and Institute of Hydrodynamics and Hydraulic Engineering, Denmark, which has enabled them to meet in order to discuss and experiment together.

References

- G L Brown and A Roshko (1978) On density effects and large structure in turbulent mixing layers. *J Fluid Mech* 64, 775-816.
- F H Champagne, Y H Pao and I J Wygnanski (1976) On the two-dimensional mixing region. *J Fluid Mech* 74, 209-250.
- M S Longuet-Higgins and J S Turner (1974) An 'entraining plume' model of a spilling breaker. *J Fluid Mech* 63, 1-20.
- P Nielsen, I A Svendsen and C Staub (1978) Onshore-offshore sediment movement on a beach. *Proc 16th Internat Conf Coastal Eng.*
- von H Ogris (1975) Die Deckwalze - eine Wirbelstrasse. *Österreichische Ingen Zeitsch* 18 (2), 37-43.
- N Rajaratnam (1967) Hydraulic jumps. *Adv in Hydrosience* 4, 197-280
- N Rajaratnam (1965) The hydraulic jump as a wall jet. *Proc Amer Soc Civ Eng. J Hydr Div* 91, 107-132.
- F J Resch and H J Leutheusser (1972) Reynolds stress measurements in hydraulic jumps. *J Hydraulic Res* 10, 409-430.
- F J Resch, H J Leutheusser and M Coantic (1976) Etude de la structure cinématique et dynamique du ressant hydraulique. *J Hyd Res* 14, 293-319.
- I A Svendsen, P A Madsen and J B Hansen (1978) Wave characteristics in the surf zone. *Proc 16th Internat Conf Coastal Eng.*

CHAPTER 31

ESTIMATION OF WATER PARTICLE VELOCITY OF BREAKING WAVE

by

Tetsuo Sakai
Associate Professor

and
Yuichi Iwagaki
Professor

Department of Civil Engineering
Kyoto University, Kyoto, 606 Japan

ABSTRACT

A possibility to estimate the water particle velocity of breaking wave on beaches by giving only the values of the beach slope i and the deep-water wave steepness H_0/L_0 is investigated. The data of the water particle velocity and profile of breaking wave on the beaches measured by Iwagaki, Sakai, Tsukioka and Sawai(1974) are used for this purpose. A method of using empirical curves relating the coefficients of Dean's stream function to i and H_0/L_0 does not give good results. The relations between the asymmetric breaking wave profile, i and H_0/L_0 are examined. As well as the front face of the profile, the slope behind the crest above some level is found to become steep when H_0/L_0 becomes small. The breaking wave profiles are reproduced by using the empirical curves relating the parameters characterizing the breaking wave profile to i and H_0/L_0 . The velocity of Dean's stream function calculated from the reproduced profile explains the measured velocity better than that of Stokes waves. It is therefore possible to estimate the water particle velocity of breaking wave on beaches by giving only the values of i and H_0/L_0 .

INTRODUCTION

The water particle velocity of breaking wave on beaches is very important in discussing the wave forces on coastal structures and the sediment movement in surf zone. However, one can find few investigations on this subject(for example, Adeyemo(1970) and Thornton, Galvin, Bub and Richardson(1976)). This is because the measurement of the water particle velocity of breaking wave is very difficult.

Recently the horizontal water particle velocities of

breaking waves on the beaches with the slopes of 1/10, 1/20 and 1/30 were measured in a wave tank with a high speed camera (Iwagaki, Sakai, Tsukioka and Sawai (1974)). It was found that the existing small and finite amplitude wave theories can not explain the measured water particle velocities. The velocities of small amplitude waves agree roughly with the measured ones in average, but the vertical distributions of small amplitude waves were more uniform than those of the measured ones. The vertical distributions of the horizontal velocity under the crest phase of the breaking wave were found to be classified by the breaker types.

The water particle velocities of Dean's stream function (Dean (1965)) were calculated by giving the simultaneously measured asymmetric breaking wave profiles (the wave record at the breaking point) (Iwagaki and Sakai (1976)). Although Dean's stream function is based on the assumption of permanent type waves on the horizontal bottom, the calculated velocities of Dean's stream function explained the measured velocities better than the existing theories of symmetric wave profile. It was concluded that the asymmetric breaking wave profile dominates the water particle velocity field of the breaking wave on beaches.

From the view point of practical use, it is desirable that the water particle velocities of breaking waves on beaches can be estimated by giving only the values of parameters such as the beach slope and the deep-water wave steepness or Iribarren number (Battjes (1974)). This investigation is one approach to this problem.

RELATIONS BETWEEN COEFFICIENTS OF DEAN'S STREAM FUNCTION, BEACH SLOPE AND DEEP-WATER WAVE STEEPNESS

Dean's stream function represents the permanent waves on the horizontal bottom:

$$\psi = \frac{L}{T}z + \sum_{n=4,6,8,\dots}^{N-1} \frac{\sinh \frac{(n-2)\pi(h+z)}{L}}{L} x \times \left(X_n \cos \frac{(n-2)\pi x}{L} + X_{n+1} \sin \frac{(n-2)\pi x}{L} \right) \quad (1)$$

in the reference x-z moving with the waves, where L is the wave length, T the wave period, x-axis in the direction of wave propagation, z-axis vertically upward from the still water level, h the water depth, X_n the unknown coefficients. The sine terms in Eq. (1) are introduced so as to represent the asymmetric wave profile. At the water surface $z = \eta$, the value of the stream function $\psi(x, \eta)$ becomes constant (= X_3).

The wave profile η is therefore expressed as follows:

$$\eta = \frac{T}{L} X_3 - \frac{T}{L} \sum_{n=4,6,8,\dots}^{N-1} \frac{\sinh \frac{(n-2)\pi(h+\eta)}{L} x}{L} \times (X_n \cos \frac{(n-2)\pi x}{L} + X_{n+1} \sin \frac{(n-2)\pi x}{L}). \quad (2)$$

As seen from Eq.(2), the wave profile is determined by giving the unknown coefficients X_n . The relations between the coefficients and Iribarren number ξ_0 are examined at first.

The horizontal water particle velocity u is obtained by differentiating ψ with respect to z . The obtained horizontal water particle velocity in the fixed reference is expressed in non-dimensional form as follows:

$$\frac{u}{\sqrt{gh}} = -\frac{Y_2}{Y_1} \sum_{n=4,6,8,\dots}^{N-1} (n-2)\pi \cosh \left\{ (n-2)\pi Y_1 \frac{h+z}{h} \right\} \times (Y_n \cos \{ (n-2)\pi \theta \} + Y_{n+1} \sin \{ (n-2)\pi \theta \}), \quad (3)$$

where $Y_1 = h/L$, $Y_2 = H/L$, $Y_4 = X_4/LH\sqrt{g/h}$,, $Y_n = X_n/LH\sqrt{g/h}$,, $\theta = x/L - t/T$. Table 1 shows the experimental conditions of 39 cases in which the breaking wave profiles were measured by Iwagaki, Sakai, Tsukioka and Sawai(1974). In this table hb is the breaking depth and H_b is the breaking wave height. In 20 cases among them the measured horizontal water particle velocities were compared with the theoretical velocities. Dean's stream functions were already calculated for all 39 cases. Fig.1 shows two examples of the relations between the non-dimensional coefficients Y_n and Iribarren number ξ_0 for 39 cases. The quantity ξ_0 is defined as $i/\sqrt{H_0/L_0}$, where i is the beach slope and H_0/L_0 is the deep-water wave steepness.

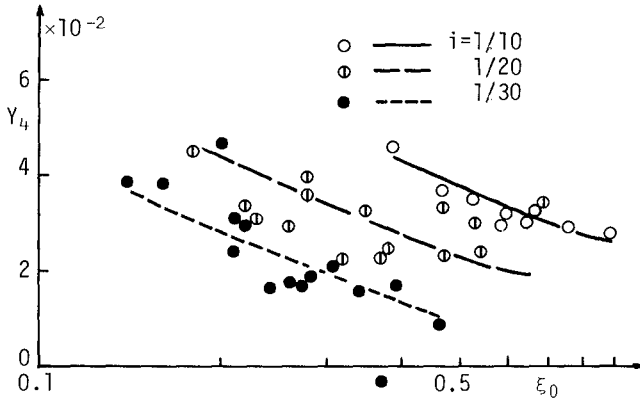
As seen from Fig.1, the data scatter considerably as well as in the relations between the breaking depth, the breaking wave height and the deep-water wave steepness. On the other hand, it is clear that the non-dimensional coefficients of Dean's stream function are not determined by Iribarren number only. The data for the different beach slope have a different trend. Empirical curves were drawn through the plotted points for each beach slope. Using these curves for all non-dimensional coefficients and Eq.(3), the horizontal water particle velocities at crest phase were calculated for the same 20 cases by giving the values of the beach slope and the deep-water wave steepness in each case. Fig.2, (1), (7) and (12) show three examples of the compari-

Table 1 Experimental conditions of analyzed data
(Iwagaki, Sakai, Tsukioka and Sawai(1974))

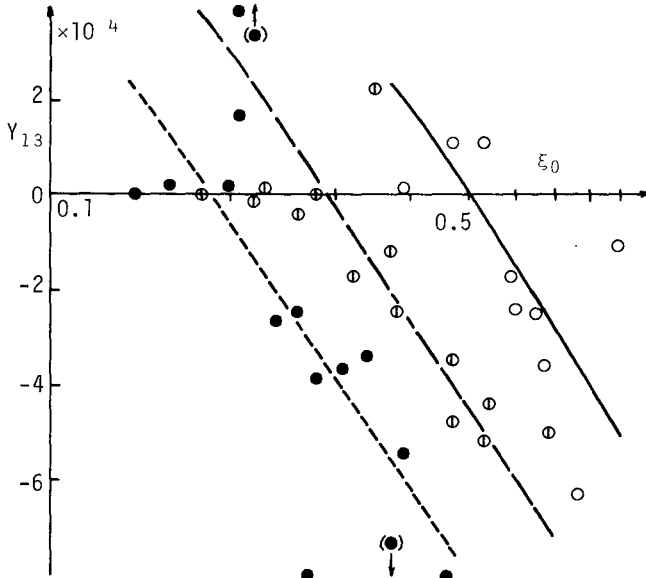
No.	i	T(sec)	H_0/L_0	h_b (cm)	$T\sqrt{g/h_b}$	H_b (cm)	H_b/h_b	**
* 1-1-1	1/10	1.00	0.066	11.2	9.4	9.7	0.87	1
* 2		0.96	0.046	7.4	11.0	6.7	0.91	2
* 3		1.01	0.029	6.2	12.7	5.3	0.85	3
2-1		1.26	0.035	10.5	12.2	10.3	0.98	
2		1.23	0.024	8.3	13.4	6.6	0.80	
3		1.27	0.017	6.5	15.6	6.4	0.98	
* 3-1		1.37	0.028	11.9	12.4	10.0	0.84	4
* 2		1.38	0.022	9.6	13.9	9.0	0.94	5
* 3		1.50	0.013	6.8	18.0	6.8	1.00	6
* 2-1-1	1/20	1.00	0.074	16.0	7.8	8.7	0.54	7
* 2		1.00	0.051	10.6	9.6	8.2	0.77	8
* 3		1.00	0.031	6.9	11.9	6.1	0.88	9
2-1		1.26	0.048	14.3	10.4	12.7	0.89	
2		1.24	0.038	11.0	11.7	9.4	0.85	
3		1.24	0.019	11.5	11.5	4.6	0.40	
* 3-1		1.49	0.032	14.7	12.2	12.5	0.85	10
* 2		1.48	0.020	10.4	14.4	8.3	0.80	11
* 3		1.46	0.012	6.2	18.4	5.7	0.92	12
4-1		1.64	0.025	14.5	13.5	11.5	0.79	
2		1.65	0.018	11.0	15.6	9.6	0.87	
3		1.65	0.009	6.8	19.8	5.8	0.85	
5-1		1.94	0.011	11.5	17.9	8.8	0.77	13
2		1.94	0.009	9.7	19.5	8.1	0.84	14
3		1.96	0.005	6.9	23.4	6.0	0.87	15
* 3-1-1	1/30	1.01	0.057	11.8	9.2	8.2	0.69	16
* 2		0.98	0.043	9.7	9.9	6.6	0.68	17
* 3		0.98	0.029	6.8	11.8	4.4	0.65	18
2-1		1.24	0.026	11.5	11.5	8.6	0.75	
2		1.23	0.024	8.5	13.2	7.0	0.82	
3		1.25	0.015	6.2	15.7	5.5	0.89	
* 3-1		1.49	0.025	12.8	13.6	10.9	0.85	19
* 2		1.50	0.016	10.1	14.8	7.6	0.75	20
3		1.46	0.009	6.3	18.2	4.5	0.71	
4-1		1.64	0.020	12.6	14.5	9.9	0.79	
2		1.60	0.014	9.7	16.1	7.6	0.78	
3		1.60	0.007	6.0	20.5	5.0	0.83	
* 5-1		1.92	0.012	12.2	17.2	9.6	0.79	21
* 2		1.98	0.008	9.9	19.7	8.1	0.82	22
* 3		1.92	0.005	6.6	23.4	5.9	0.89	23

* case in which the water particle velocity is discussed

** No. used in Iwagaki, Sakai, Tsukioka and Sawai(1974) and Iwagaki and Sakai(1976)



(1)



(2)

Fig.1 Examples of relations between coefficients of Dean's stream function and Iribarren number ξ_0

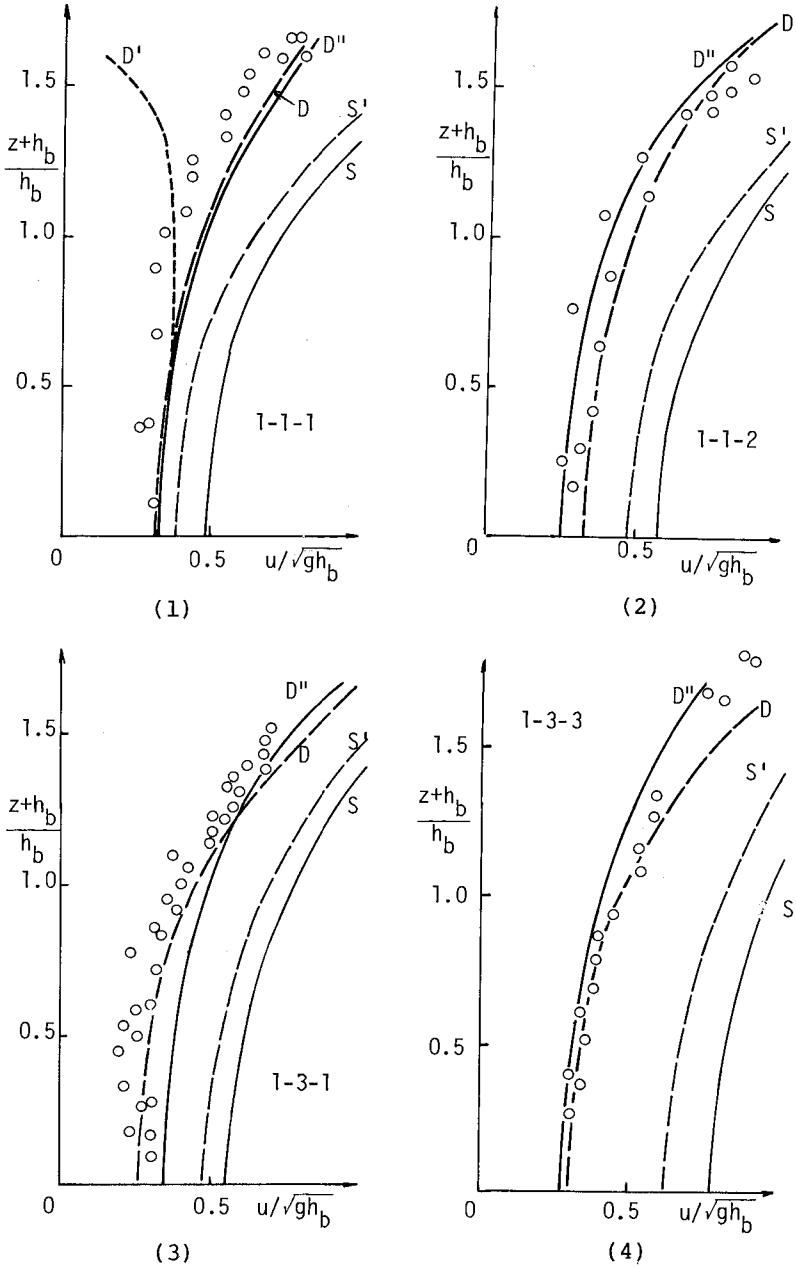
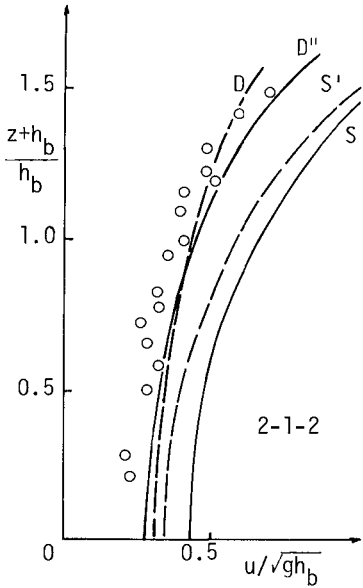
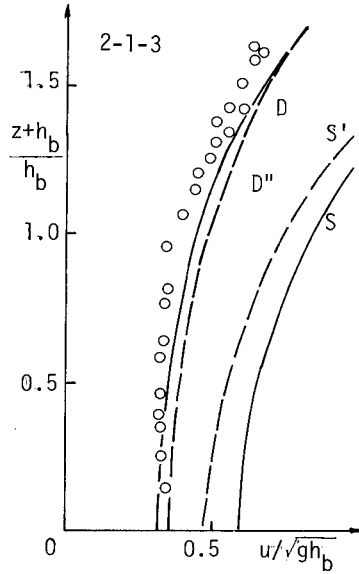


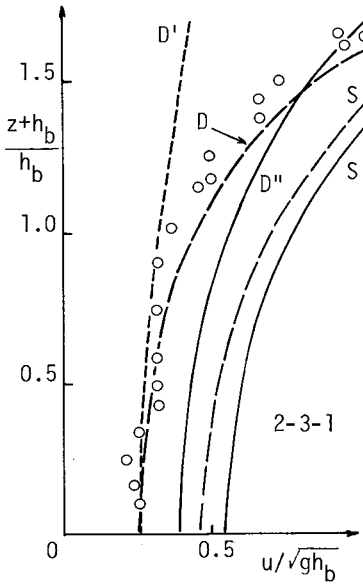
Fig.2, (1)~(4) Examples of comparisons between calculated and measured water particle velocities



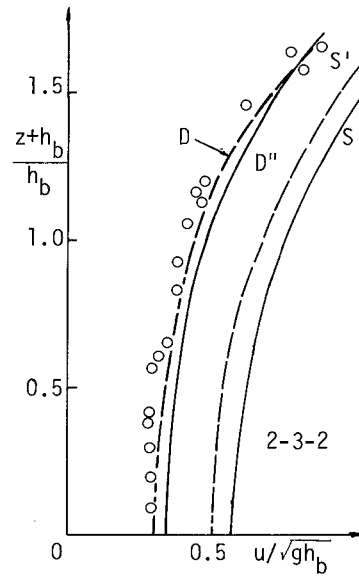
(5)



(6)

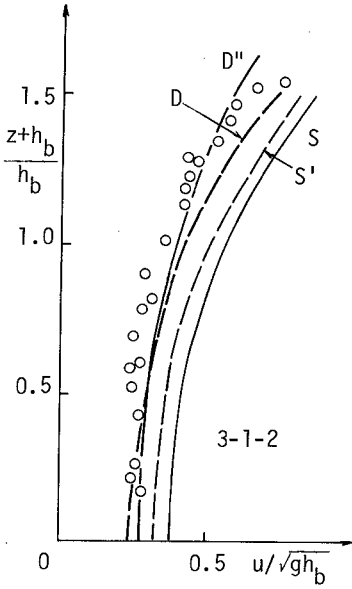


(7)

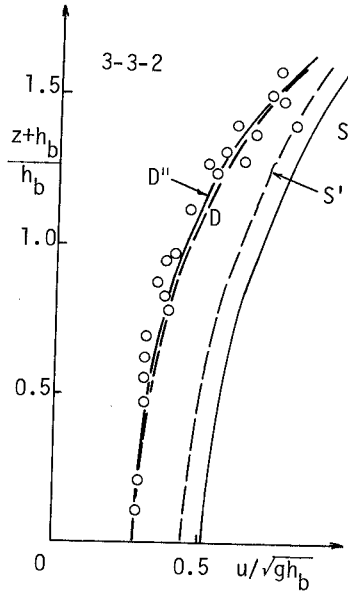


(8)

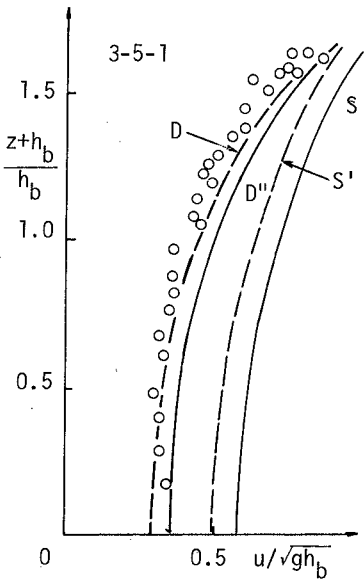
Fig.2, (5) ~ (8) Examples of comparisons between calculated and measured water particle velocities



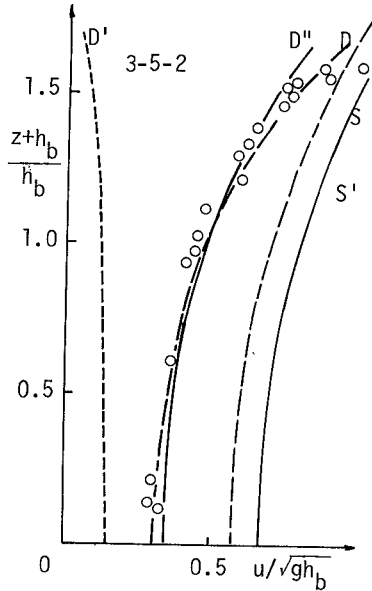
(9)



(10)



(11)



(12)

Fig. 2, (9) ~ (12) Examples of comparisons between calculated and measured water particle velocities

sons between the measured horizontal water particle velocities at crest phase and the calculated velocities denoted by D' . In these figures are also shown several theoretical velocities as follows (Iwagaki and Sakai (1976)):

- S : Stokes waves with first definition of wave celerity
- S' : Stokes waves with second definition of wave celerity (Tsuchiya and Yamaguchi (1972))
- D : Dean's stream function with measured wave profile
- D' : Dean's stream function with determined coefficients
- D'' : Dean's stream function with reproduced wave profile (explained later)

Unfortunately the calculated velocities by using the empirical curves for the non-dimensional coefficients (D') are in general smaller than the measured ones. In Figs. 2, (1) and (12), the velocity near the water surface is rather smaller than that near the bottom. One reason is of course the scatter of the values of the non-dimensional coefficients. Furthermore, the term in the summation of Eq. (3) contains $(n-2)\pi \cosh\{(n-2)\pi Y_1(h+z)/h\}$. Therefore, even if the value and the scatter of Y_n of large n are small, the error of estimating the term of large n (the higher order term) becomes large as n becomes large. The contribution of the higher order term to the water particle velocity is confined near the water surface. This is why the slope of the vertical distribution is reversed near the water surface.

RELATIONS BETWEEN BREAKING WAVE PROFILE, BEACH SLOPE AND DEEP-WATER WAVE STEEPNESS

Considering that the water particle velocity field of the breaking wave is dominated by the asymmetric breaking wave profile, it is tried to relate the measured breaking wave profiles (the wave record at the breaking point) to the beach slope and the deep-water wave steepness. Adeyemo (1970) proposed four parameters on the wave profile asymmetry. They were the relative positions of the crest during one wave period, the crest height and the slope of wave profile. In order to represent the asymmetric wave profile exactly, such a rough parameterization is not sufficient. 39 measured breaking wave profiles were characterized with 25 parameters shown in Fig. 3. Two parameters t_a and η_a are respectively the phase and the level of the point on the profile behind the crest where the slope changes abruptly. Fig. 4 shows the relations between the representative 9 parameters, the beach slope and the deep-water wave steepness. Although the scatter

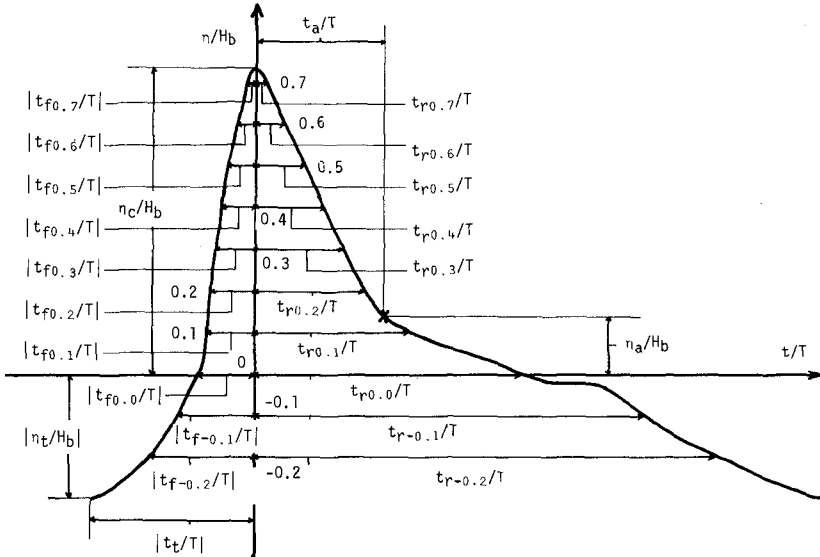
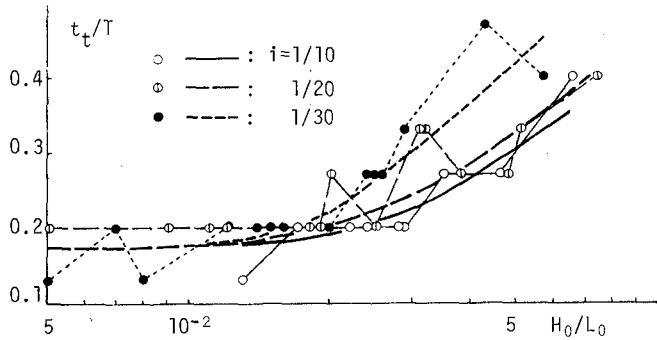
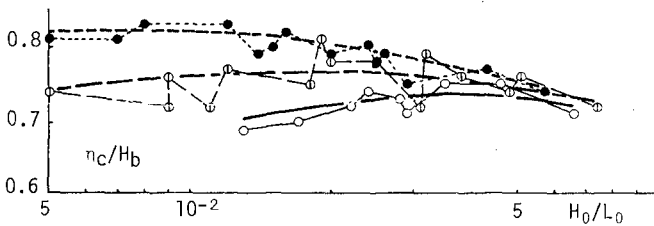


Fig. 3 25 parameters characterizing breaking wave profile



(1)



(2)

Fig. 4, (1), (2) Examples of relations between parameters of breaking wave profile, beach slope and deep-water wave steepness

of the data in each figure is considerable, empirical curves were drawn through the plotted points for each beach slope.

It is well known, from the classification of the breaker types, that the front face of the breaking wave profile becomes steep and the slope behind the crest becomes gentle as the beach slope becomes large and the deep-water wave steepness becomes small. This trend is seen in Figs.4,(1) (the phase of the front trough $|t_t/T|$), (3) (the phase of the front face at $z/H_b = -0.1$ $|t_f-0.1/T|$) and (7) (the phase of the profile behind the crest at $z/H_b = 0.0$ $t_r0.0/T$). The same trend is seen in all phases of the front face and the slope behind the crest below the level of $z/H_b = 0.0$.

In Fig.4,(4), however, the experimental results of the phase of the slope behind the crest at $z/H_b = 0.3$ $t_r0.3/T$ show a different trend. The phase at $z/H_b = 0.3$ slightly decreases as the deep-water wave steepness decreases. Also as for other phases of the profile behind the crest above $z/H_b = 0.3$, the same trend is seen. This fact means that the slope behind the crest above $z/H_b = 0.3$ becomes steep as well as the front face when the deep-water wave steepness becomes small. On the other hand, the relations between the beach slope and the phases of the slope behind the crest above $z/H_b = 0.3$ are not clear.

At $z/H_b = 0.2$, as shown in Fig.4,(5), only in the case of $1/10$ beach slope, the phase behind the crest becomes large as the deep-water wave steepness becomes small. At $z/H_b = 0.1$ (Fig.4,(6)), in two cases of $i = 1/10$ and $1/20$, the phase becomes large as the deep-water wave steepness becomes small. Thus, the beach slope has the effect on the level where the relation between the phase of the slope behind the crest and the deep-water wave steepness reverses. Fig.4,(9) on η_a/H_b explains the effects of the beach slope and the deep-water wave steepness on this level. The level (the value of η_a/H_b) becomes high as the beach slope becomes large and the deep-water wave steepness becomes small.

As seen from Fig.4,(8), the phase of the point of abrupt slope change t_a/T becomes small as the deep-water wave steepness becomes small. That is, the width of the base of the crest of the breaking wave profile becomes narrow as the deep-water wave steepness becomes small. The effect of the beach slope is not clear. The crest height η_c/H_b , as seen from Fig.4,(2), shows complicated trends.

REPRODUCTION OF BREAKING WAVE PROFILE

The empirical curves relating 25 parameters to the beach slope and the deep-water wave steepness in Fig.4 are used to

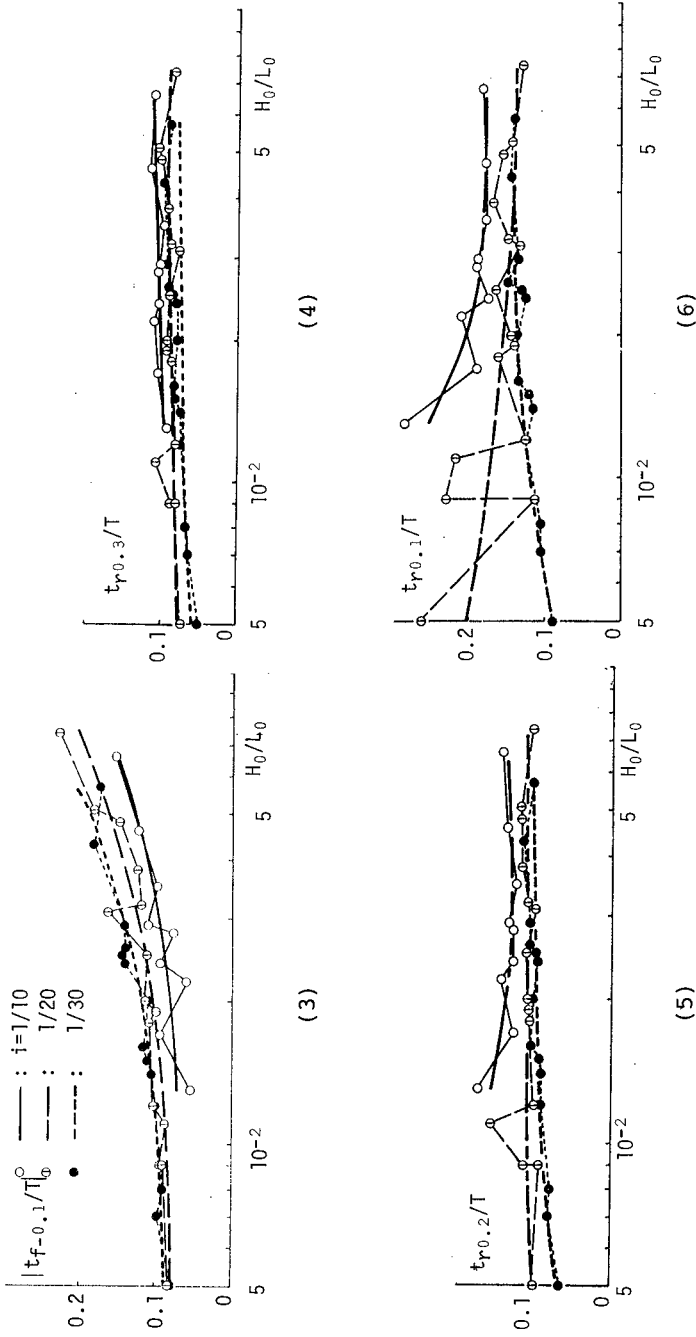
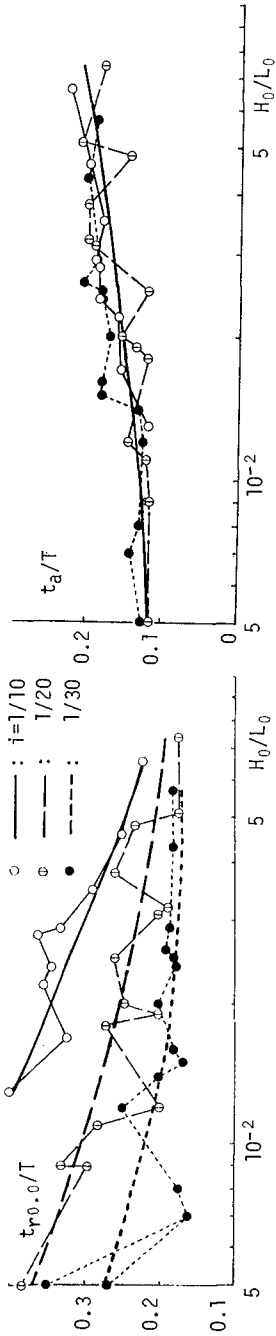
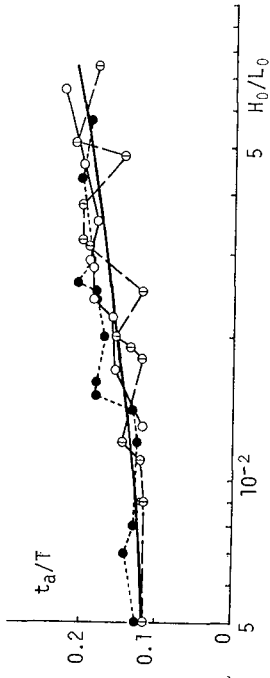


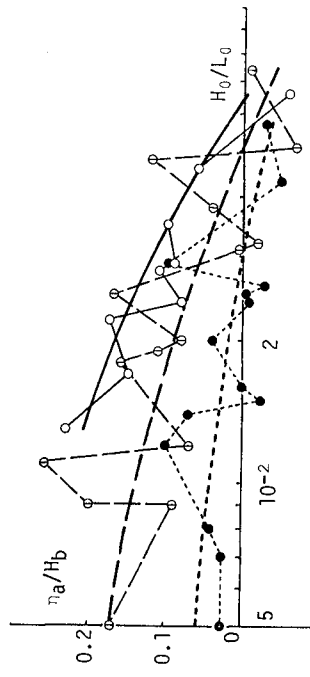
Fig. 4, (3)~(6) Examples of relations between parameters of breaking wave profile, beach slope and deep-water wave steepness



(7)



(8)



(9)

Fig. 4, (7) ~ (9) Examples of relations between parameters of breaking wave profile, beach slope and deep-water wave steepness

reproduce the breaking wave profiles by giving the values of the beach slope and the deep-water wave steepness. In some cases, the phases of the front and back faces at $z/H_b = 0.7$ $|t_f - 0.7/T|$ and $t_r - 0.7/T$ are given, while the crest height η_c/H_b is smaller than 0.7 because of using the empirical curves. In these cases the crest height is adopted. Also in some cases, the position of abrupt profile change (t_a/T and η_a/H_b) is far from the neighboring points determined by the values of t_r/T . In these cases, only the value of t_a/T is adopted.

Figs. 5, (1)~(3) show three examples of the comparisons between the reproduced and measured breaking wave profiles. In general, the reproduced breaking wave profiles coincide with the measured profiles except for the small deviations.

ESTIMATION OF WATER PARTICLE VELOCITY OF BREAKING WAVE ON BEACHES

The reproduced breaking wave profiles were used to calculate Dean's stream functions. The wave profile as the input to calculate the stream function is dimensional. The measured wave period and breaking wave height were used to convert the non-dimensional reproduced profiles into the dimensional ones. The water levels of the reproduced profiles were read at 15 points of equal distance on the time axis. The value of N was set equal to 13 which corresponds to Stokes waves of the fifth order. The calculations determining the unknown coefficients were 5 times repeated.

The curves denoted by D'' in Figs. 2, (1)~(12) are the velocities obtained from the calculated Dean's stream functions with the reproduced breaking wave profiles. In these figures, are also shown the velocities obtained from the calculated Dean's stream functions with the measured profiles (D) and the velocities of Stokes waves of two different definitions of wave celerity (S and S'). The velocities of cnoidal waves are not shown because the vertical distributions are too steep compared with the measured ones. Also the velocities of small amplitude waves are not shown because the vertical distributions are more uniform than the measured ones.

As well as the velocities based on Dean's stream functions with the measured profiles, the velocities based on Dean's stream function with the reproduced profiles explain the measured velocities better than those of Stokes waves. Table 2 shows the relative errors of the calculated velocities at the still water level of 20 cases in which the water particle velocities were measured. u_F is the measured velocity at the still water level. After all, it is possible to calculate the

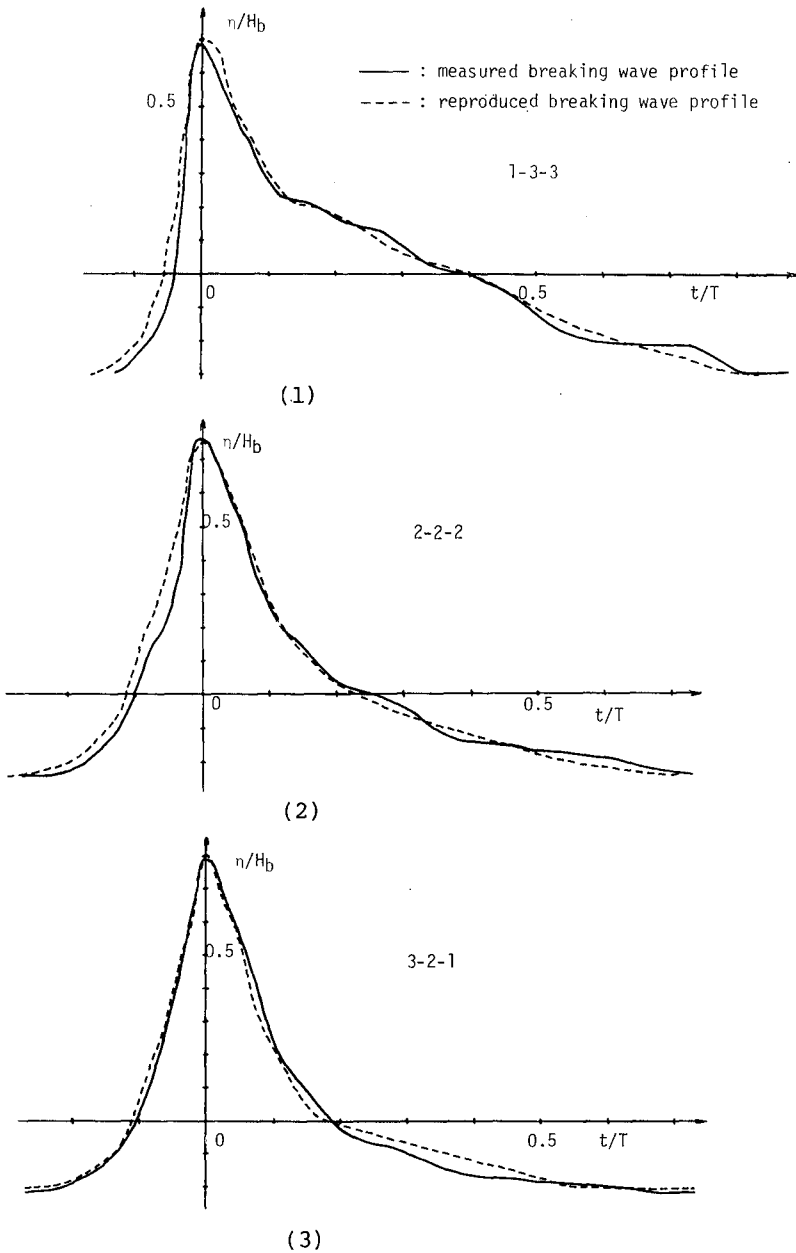


Fig.5 Examples of comparisons between reproduced and measured breaking wave profiles

Table 2 Relative errors of calculated velocities at still water level

No.	i	H_0/L_0	$(u_D - u_E)/u_E$	$(u_{D''} - u_E)/u_E$	$(u_{S1} - u_E)/u_E$
1-1-1	1/10	0.066	0.27	0.37	0.78
2		0.046	0.14	0.05	0.76
3		0.029	-0.06	-0.14	0.45
3-1		0.028	0.15	0.20	0.79
2		0.022	0.16	0.42	0.93
3		0.013	0.04	-0.15	0.74
2-1-1	1/20	0.074	0.27	0.71	0.53
2		0.051	0.08	0.13	0.51
3		0.031	0.26	0.20	0.90
3-1		0.032	0.15	0.51	0.79
2		0.020	0.02	0.23	0.60
3		0.012	-0.07	-0.26	0.42
3-1-1	1/30	0.057	-0.10	0.08	0.28
2		0.043	0.14	0.10	0.38
3		0.029		-0.22	
3-1		0.025	0.14	0.26	0.61
2		0.016	0.10	0.07	0.50
5-1		0.012	0.12	0.28	0.56
2		0.008	0.00	0.09	0.58
3		0.005	-0.02	-0.18	0.47
average of absolute values			0.12	0.23	0.61

horizontal water particle velocity at crest phase of the breaking wave on the beach more exactly by giving only the values of the beach slope and the deep-water wave steepness than with Stokes wave theory.

CONCLUSIONS

The possibility to estimate the horizontal water particle velocity at crest phase of breaking wave on beaches by giving only the values of the beach slope and the deep-water wave steepness was examined. The data of the velocities of breaking waves on the sloping beaches in the wave tank measured by Iwagaki, Sakai, Tsukioka and Sawai(1974) were used. The following conclusions are obtained:

- 1) The coefficients of Dean's stream function are not determined by Iribarren number only.
- 2) The velocity calculated by using the empirical curves relating the coefficients of Dean's stream function to the beach slope and the deep-water wave steepness can not explain the measured velocity.
- 3) As well as the front face, the slope behind the crest of the breaking wave profile above the level($z/H_b = 0.1 \sim 0.3$) which is determined by the beach slope and the deep-water wave steepness becomes steep when the deep-water wave steepness becomes small.
- 4) The breaking wave profile can be reproduced from the empirical curves for the parameters of the profile by giving only the values of the beach slope and the deep-water wave steepness.
- 5) The velocity based on Dean's stream function calculated from the reproduced breaking wave profile explains the measured velocity, as well as the velocity based on Dean's stream function calculated from the measured wave profile.
- 6) It is therefore possible to estimate the water particle velocity of breaking wave on sloping beaches by giving only the values of the beach slope and the deep-water wave steepness.

ACKNOWLEDGEMENTS

The authors wish to express their gratitudes to Mr. T. Asano, Mr. E. Otsuka and Mr. M. Tanaka for their assistances through the data analysis. This work was partly supported by Scientific Research Funds from the Ministry of Education.

REFERENCES

- Adeyemo, M. D. : Velocity fields in breaker zone, Proc. 13th Conf. Coastal Eng., pp.435-460, 1970.
- Battjes, J. A. : Surf similarity, Proc. 14th Conf. Coastal Eng., pp.466-480, 1974.
- Dean, R. G. : Stream function representation of nonlinear ocean waves, Jour. Geophy. Res., Vol.70, No.18, pp.4561-4572, 1965.
- Iwagaki, Y., T. Sakai, K. Tsukioka and N. Sawai : Relationship between vertical distribution of water particle velocity and type of breakers on beaches, Coastal Eng. in Japan, Vol.17, pp.51-58, 1974.
- Iwagaki, Y. and T. Sakai : Representation of water particle velocity of breaking waves on beaches by Dean's stream function, Memo. Fac. Eng. Kyoto Univ., Vol.38, Part 1, pp.11-20, 1976.
- Thornton, E. B., J. J. Galvin, F. L. Bub and D. P. Richardson : Kinematics of breaking waves, Proc. 15th Conf. Coastal Eng., pp.461-476, 1976.
- Tsuchiya, Y. and M. Yamaguchi : Some considerations on water particle velocities of finite amplitude waves theories, Coastal Eng. in Japan, Vol.15, pp.43-58, 1972.

CHAPTER 32

ENERGY LOSS AND SET-UP DUE TO BREAKING OF RANDOM WAVES

J.A. Battjes¹⁾ and J.P.F.M. Janssen²⁾

ABSTRACT

A description is given of a model developed for the prediction of the dissipation of energy in random waves breaking on a beach. The dissipation rate per breaking wave is estimated from that in a bore of corresponding height, while the probability of occurrence of breaking waves is estimated on the basis of a wave height distribution with an upper cut-off which in shallow water is determined mainly by the local depth. A comparison with measurements of wave height decay and set-up, on a plane beach and on a beach with a bar-trough profile, indicates that the model is capable of predicting qualitatively and quantitatively all the main features of the data.

INTRODUCTION

Quantitative predictions of wave-induced mean sea level variations and currents in the nearshore region require a specification of the variation of the mean wave energy density (E) in that region. Battjes (1972) and Goda (1975) have presented methods to that effect applicable to random, breaking waves. In these models, E is forced to follow in some sense, to be described below, the variation of the local depth. The energy dissipation rate due to breaking is not estimated independently in these models. This is a shortcoming, since it immediately precludes the use of an approach based on the energy balance. Such an approach is physically more sound, and would e.g. be needed in applications to profiles where the depth is not monotonically decreasing shoreward, such as in the commonly occurring bar-trough profiles. For these reasons an attempt was made to develop a model for the dissipation of wave energy in random waves, breaking on a beach.

The outline of the paper is as follows. Existing models for the prediction of the energy variation across the surfzone are discussed first. Following that, the various elements of a new dissipation model for random waves are described. The results are combined with a conventional model for the prediction of wave-induced variations in mean water level. Subsequently, experiments are described which were carried out to test the model, and to determine the magnitude of a coefficient which in the theory can be estimated in order of magnitude only. Finally, a comparison is given of the results of the theoretical model to the experimental data.

1),2) Associate Professor (1) and Graduate Student (2), Dept. of Civil Engineering, Delft University of Technology, The Netherlands.

EXISTING MODELS

We consider a two-dimensional situation of waves normally incident on a beach with straight and parallel depth contours.

For given incident wave parameters and beach profile, the variation of mean wave energy density (E) with distance to the shoreline can in principle be calculated from the wave energy balance, written as

$$\frac{\partial P_x}{\partial x} + D = 0, \quad (1)$$

in which P_x is the x -component of the time-mean energy flux per unit length, x is a horizontal coordinate, normal to the still-water line, and D is the time-mean dissipated power per unit area. Knowing the dependence of P_x and D on E and on known parameters such as local mean depth (h), wave frequency (f), mass density (ρ) and gravity acceleration (g), it is possible to integrate (1), subject to the initial condition of the given incident wave, to find E as a function of x .

Outside the surfzone, the wave decay is rather weak, and D can often be neglected entirely. If not, the only contributions to it are from such mechanisms as the formation of a boundary layer near the bed, percolation in a porous bottom, etc., for which the dependence of D on E can be estimated reasonably well. In either case, (1) can in fact be used outside the surf zone.

Inside the surf zone, the dissipation of wave energy in the breaking process is dominant. Because the details of these processes are so little understood, the energy balance is usually abandoned in the surf zone. An exception must be made for LeMéhauté (1962), Divoky et al (1970), and Hwang and Divoky (1970), who do apply an energy balance to breaking solitary or periodic waves, by using a bore model for the dissipation rate. Usually, however, instead of solving the energy balance equation, a self-similarity in the surf zone is assumed (for solitary or periodic waves), such that the wave height (H) decays in constant proportion to the mean depth, or

$$H(x) = \gamma h(x), \quad (2)$$

in which γ is a coefficient of $O(1)$, whose actual magnitude can vary with beach slope and incident wave steepness.

For *random* waves breaking on a beach, a model based on (1) does not seem to have been published. An approach based on (2), using it as an upper bound to the local wave height distribution, has been presented by Battjes (1972) and Goda (1975). Goda's model is similar to Battjes' model in essence, though different in the details.

The use of (1), rather than (2), is in principle much to be preferred for a number of reasons, the most fundamental one being that (1) has a sound physical basis, whereas (2) is assumed ad hoc. Associated with this are the following items:

- Assumption (2) relates the local wave height to the local mean depth. This introduces an unrealistically large dependence of dissipation rate on local bottom slope (Battjes, 1978b). In (1), the local wave height is found from an integration, so that it not only depends on the local depth but also on those further seaward, which is more realistic.
- If necessary, other dissipation mechanisms than that due to breaking can be incorporated in (1) in a straightforward manner, whereas this is not the case for (2).
- Eq. (2) is restricted to profiles in which the depth decreases monotonically in the shoreward direction. This is not the case for (1), which in principle can be applied in bar-trough profiles as well.

A DISSIPATION MODEL FOR RANDOM WAVES

Introduction

As noted above, no model based on the energy balance seemed to be available for the prediction of the energy variation in random waves, breaking on a beach. The preceding comments should make it clear that such a model is in fact desirable. One such model which has been developed will be described in the following.

Before turning to the specifics, some general remarks will be made about the philosophy of approach which has been adopted.

Firstly, since at present there is virtually no systematic quantitative knowledge of the internal structure of breaking waves, the approach used herein is based on knowledge of external, macroscopic properties of breakers only.

Secondly, it was deemed prudent to build a rather crude model at first, containing the simplest possible elements which would still represent those aspects of the problem which were considered essential. A confrontation of such model with real data should serve to indicate whether the model is sufficiently realistic to warrant further refinements. Examples of choices made on this basis are an abrupt upper cut-off of the wave height distribution, the use of a simple, linear approximation for the energy flux P , and the omission of all dissipation mechanisms other than that due to breaking. The results presented in the following represent only the first steps in the sense just described. However, at several places it will be indicated how refinements could possibly be made.

A third point to be mentioned has to do with terminology. When reference is made to a "breaking wave", this could be interpreted as a wave at the moment of incipient breaking, defined in one way or another, or it could perhaps be taken to refer to the turbulent, aerated bore-like structure some time after the onset of breaking. To avoid this possible semantic confusion, we shall here refer to the latter as a broken wave; the breaking itself is then taken to correspond to the transition of the unbroken mode to the broken mode, according to the definition adopted for such transition.

Wave height distribution

Consider a fixed point on a beach, with mean depth h , in the presence of a random incident wave field. It is impossible for waves with heights considerably in excess of h to pass the point being considered, since those which otherwise would do so are reduced in height as a result of breaking. The limited depth effectively limits the larger wave heights in the distribution. A simplified model of this is obtained by defining for each depth h a maximum possible wave height H_m (to be specified subsequently), and to assume that the heights of all^m the waves which are breaking or broken at the point considered, and only those, are equal to H_m .

The assumption just stated is of course a simplification. Not all the heights of broken waves passing a fixed point are equal, nor are they all necessarily larger than those of the non-broken waves. The first of these two aspects can be remedied by providing for a smoother cut-off, as in Goda's model (1975). For the time being the simpler model described here was used. After all, our purpose is not to estimate the details of the wave height distribution in the range near H_m ; it is to derive mean square values from a distribution of wave heights which is somehow suppressed in its upper region by the local depth.

The assumption stated above will now be written in terms of the probability distribution of the wave heights, $F(H)$. The shape of $F(H)$ for the lower, non-broken wave heights is assumed to be the same as it is in absence of wave breaking, i.e. of the Rayleigh-type, with modal value \hat{H} , say. This leads to

$$\begin{aligned}
 F(H) \equiv \Pr\{\underline{H} \leq H\} &= 1 - \exp(-\frac{1}{2}H^2/\hat{H}^2) && \text{for } 0 \leq H < H_m \\
 &= 1 && \text{for } H_m \leq H,
 \end{aligned}
 \tag{3}$$

in which the underscore indicates a random variable. The local value of the parameter \hat{H} is left unspecified for the moment.

Eq. (3) represents a probability distribution with two parameters, \hat{H} and H_m . All the statistics of the wave heights can therefore be expressed in terms of (\hat{H}, H_m) . Among those are the rms value (H_{rms}), defined by

$$H_{rms} = \left\{ \int_0^{\infty} H^2 dF(H) \right\}^{\frac{1}{2}}, \quad (4)$$

and the probability that at a given point a height is associated with a breaking or broken wave (Q_b), which on the assumption stated above equals

$$Q_b = \Pr\{\underline{H} = H_m\}. \quad (5)$$

Substitution of (3) into (4) and (5) gives

$$H_{rms}^2 = 2(1 - Q_b)\hat{H}^2 \quad (6)$$

and

$$Q_b = \exp(-\frac{1}{2}H_m^2/\hat{H}^2). \quad (7)$$

Instead of using (\hat{H}, H_m) as the two parameters of $F(H)$, it is equally possible to use (H_{rms}, H_m) , which have a clearer physical meaning. This can be achieved by eliminating \hat{H} between (6) and (7), which yields for Q_b

$$\frac{1 - Q_b}{\ln Q_b} = - \left(\frac{H_{rms}}{H_m} \right)^2. \quad (8)$$

From this transcendental equation, Q_b can be solved as a function of H_{rms}/H_m :

$$Q_b = f(H_{rms}/H_m). \quad (9)$$

This is a key element in the whole model. It expresses the fraction of waves which at any one point are breaking or broken, in terms of the ratio of the rms wave height (equivalent to mean energy density, E) actually present, to the maximum wave height which the given depth can sustain. The local value of H_{rms} is not known a priori; it is found by integrating the differential equation (1). The importance of Q_b for this equation is due to the fact that the average local energy dissipation rate D is proportional to it, at least in the dissipation model to be described below. It is mainly through Q_b that this model reacts to changes in depth.

In very deep water, where $H_{rms}/H_m \rightarrow 0$, (8) gives $Q_b \rightarrow 0$, as expected. If the waves are shoaling then the ratio H_{rms}/H_m tends to increase, and so does Q_b . In the limit $H_{rms}/H_m \rightarrow 1$, $Q_b \rightarrow 1$, which is a degenerate case since it corresponds to all the waves being broken, and all the wave heights being equal to H_m .

Breaker height

So far the quantitative estimation of H_m was left unspecified. This will be considered next.

The form chosen is based on Miche's criterion for the maximum height of periodic waves of constant form:

$$H_m \approx 0.14 L \tanh(2\pi h/L) \approx 0.88 k^{-1} \tanh kh, \quad (10)$$

in which $k = 2\pi/L$ is the positive real root of the dispersion equation

$$(2\pi f)^2 = gk \tanh kh. \quad (11)$$

Eq. (10) as it stands would predict $H_m \approx 0.88 h$ in shallow water. In application to waves on beaches we want to use a similar functional relationship as in (10) but we also want some freedom of adjustment, to allow for effects of beach slope and of the transformation to random waves, such that in shallow water our expression for H_m reduces to $H_m = \gamma h$, in which γ is a (slightly) adjustable coefficient. In order that the deep-water limit shall not be influenced by the bottom slope the following form was finally adopted:

$$H_m = 0.88 k^{-1} \tanh(\gamma kh/0.88). \quad (12)$$

In application to random waves, (12) will be used, with f in (11) being given a single, representative value, such as \bar{f} , a mean frequency defined as the ratio of the first moment of the surface elevation spectrum about $f = 0$ to the zeroth moment.

It should be pointed out that neither the frequency-dependent transition from deep water to shallow water, as expressed by the tanh-function in (10) or (12), nor the representative frequency to be used, needs to be estimated with great accuracy, inasmuch as most of the wave breaking takes place in shallow water anyway, where $H_m \approx \gamma h$, regardless of the frequency used (within reasonable limits). For the same reason, the use of only one representative value of f is deemed sufficient. In principle it is possible to use a distribution of f -values, leading to a distribution of H_m -values for given h . (A distribution of H_m has in fact been used by Goda (1975), though it was chosen ad hoc.)

Energy dissipation in a broken wave

Following LeMéhauté (1962), the energy dissipation rate in a broken wave will here be estimated from that in a bore of corresponding height.

Consider a bore connecting two regions of uniform flow, with depths Y_1 and Y_2 , respectively (fig. 1a). The macroscopic bore properties are determined by the conservation of mass and momentum across the bore. The power dissipated in the bore per unit span, written as D' , can then be calculated, with the result (Lamb, 1932)

$$D' = \frac{1}{4} \rho g (Y_2 - Y_1)^3 \left\{ \frac{g(Y_1 + Y_2)}{2 Y_1 Y_2} \right\}^{\frac{1}{2}}. \quad (13)$$

This expression will be used to estimate the power dissipated in the crest region of a broken wave. If, as is the case here, the broken wave is one of a sequence on a sloping beach, then the flow conditions on either side of it are non-uniform. Thus, (13) cannot be expected to apply in any exact sense, but at most in order of magnitude. For this reason it is felt to be justified to use further order-of-magnitude estimates in (13) (written as \sim), if applied to broken waves on a beach. In this respect the treatment here deviates from that of LeMéhauté (1962). These order-of-magnitude estimates are (see fig. 1b)

$$Y_2 - Y_1 \sim H \quad (14)$$

and

$$\left\{ \frac{g(Y_2 + Y_1)}{2 Y_1 Y_2} \right\}^{\frac{1}{2}} \sim \left\{ \frac{g}{h} \right\}^{\frac{1}{2}}. \quad (15)$$

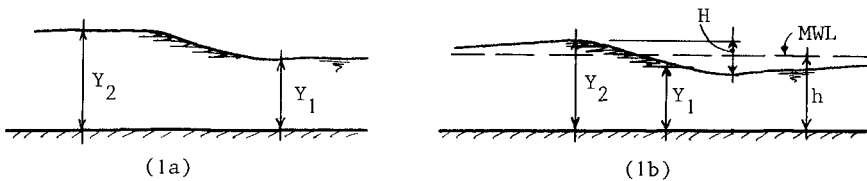


Fig. 1 - Sketch of a single, steady bore (1a) and of one out of a sequence of broken waves on a beach.

Substitution of these in (13) yields the following estimate for the power dissipated per broken wave, per unit span:

$$D' \sim \frac{1}{4} \rho g H^3 \left(\frac{g}{h}\right)^{\frac{1}{2}}. \quad (16)$$

If the waves were periodic with frequency f , then the average power dissipated in the breaking process, per unit area, would be

$$D = \frac{D'}{L} = \frac{fD'}{c} \sim \frac{fD'}{(gh)^{\frac{1}{2}}} \sim \frac{1}{4} f \rho g \frac{H^3}{h}, \quad (17)$$

where L and c denote wavelength and phase speed, respectively.

A more refined estimate for the relation between bore strength ($Y_2 - Y_1$) and wave height H than that in (14) has been given elsewhere, and applied to solitary and periodic broken waves (Battjes, 1978a). However, that refinement has not yet been implemented in the present model for random waves.

Mean energy dissipation in a random breaking wave field

In application to random waves, we are interested in the expected value of the dissipated power per unit area. This can be estimated by applying (17) to the broken waves, and to those only. In the model adopted above these have a height equal to H_m , and a probability of occurrence (at a fixed point) equal to Q_b . Furthermore, the mean frequency (\bar{f}) of the energy spectrum is used again as a representative value of f . If lastly the ratio H_m/h is dropped from the order-of-magnitude relationship, as being of order one in the region where most of the dissipation occurs, we obtain for the overall mean dissipation rate per area

$$D \sim \frac{1}{4} Q_b \bar{f} \rho g H_m^2, \quad (18)$$

or, written as an equality

$$D = \frac{\alpha}{4} Q_b \bar{f} \rho g H_m^2, \quad (19)$$

in which - if the model is good - α is a constant of order one.

In interpretations of (19), it is important to note that Q_b , representing the fraction of broken waves passing any one point, was seen to be a function of H_{rms}/H . Thus, the combination of (8) and (19) determines the power dissipated in the breaking process, D , as a function of the unknown local H_{rms} (or the local energy density E), the known local depth (through H_{rms}), and some constants. This is a key result of the present model, enabling the application of the energy balance (1) to the surf zone.

At first sight, it might seem from (19) as if D were decreasing with decreasing H_m (decreasing h), but this is not normally the case. As long as a random wave train of low or moderate steepness is in relatively deep water, Q_b will be virtually zero, and therefore also D . When, upon approaching the beach, the depth becomes less than 2 to 3 times the rms wave height, Q_b increases strongly, such that its increase in fact more than compensates for the reduction in H_m^2 , so that D also increases. Near the limit of very shallow water, Q_b ultimately approaches unity (except for extremely mild slopes), in which case D decreases, ultimately in proportion to H_m^2 .

Likewise, if the wave train passes a bar, then the increase in depth (and consequently in H_m) shoreward of the bar crest, causes a reduction in Q_b which more than offsets the increase in H_m^2 , so that the dissipation rate in the model can become virtually zero again in the trough shoreward of the bar. Examples of this situation will be given below.

Energy balance

Having established a dependence of the dissipation rate D on the rms wave height, it remains to do the same for the energy flux P in order to be able to integrate the energy balance, eq. (1). A simple linear approximation will be used, viz.

$$P_x = P = E c_g, \quad (20)$$

in which

$$E = \frac{1}{8} \rho g H_{rms}^2 \quad (21)$$

and

$$c_g = \left[\frac{2\pi f}{k} \left(\frac{1}{2} + \frac{kh}{\sinh 2kh} \right) \right]_{f = \bar{f}}. \quad (22)$$

This closes the system of equations for H_m . For given depth profile $h(x)$, given incident wave parameters, and a (suitable) choice of the model parameters α and γ , eq. (1) can be integrated to find $H_m(x)$.

From trial calculations it was found that the damping contained in the model appeared to be insufficient to prevent the ratio H_m/H_m from tending to blow up as the waterline (zero depth) was approached. This phenomenon is reminiscent of the classical shoreline singularity for dissipationless progressive waves. As such it need not be of great concern in the sense that it would invalidate the model away from the waterline. However, the wave height distribution assumed here limits H_m to values not exceeding H_m , so that an internal incompatibility arises.

The situation could have been remedied by simply terminating the calculation where the condition $H_{rms} \leq H_m$ is first violated, or, rather more fundamentally, by incorporating additional physical mechanisms of energy dissipation in eq. (1), which would be predominant near the waterline, and of such strength that $H_{rms}/H_m \leq 1$ as $h \rightarrow 0$. In the preliminary results to be given below, neither of these was done. Instead, the integration of (1) was ceased at the point where the condition $H_{rms} \leq H_m$ is first violated. Shoreward of this point, $H_{rms} = H_m$ was assumed.

MOMENTUM BALANCE

We have so far assumed that the mean-depth profile $h(x)$ was given. Normally, only the depth of the bottom below some reference plane, $d(x)$, is given. In the experiments to be described subsequently, the still-water level was chosen as the reference plane for d , which therefore represents the still-water depth.

The height of the mean water level above the reference plane, written as $\bar{\eta}(x)$, can be determined from the mean momentum balance. Following Longuet-Higgins and Stewart (1962) the mean balance of x -momentum is written as

$$\frac{dS_{xx}}{dx} + \rho gh \frac{d\bar{\eta}}{dx} = 0, \quad (23)$$

in which

$$h = d + \bar{\eta} \quad (24)$$

and

$$S_{xx} = \left(\frac{1}{2} + \frac{2kh}{\sinh 2kh} \right) E, \quad (25)$$

the component of the radiation stress tensor normal to planes $x = \text{constant}$. As an initial condition for the integration of (23), it is common to choose $\bar{\eta} = 0$ in a reference point in deep water.

In the applications given below, the energy balance and the momentum balance have been integrated simultaneously, by a process of iteration.

The most important reason for the inclusion of the wave-induced variations in $\bar{\eta}$ in the model is not to correct d (the energy dissipation model could be checked by working from the outset with h), but to provide an independent check on the validity of the model. As noted in the

introduction, the variation of the wave energy density E in the surf zone is important because the radiation stresses are proportional to E , and the gradients of these stresses provide driving forces for the mean flow. It is therefore very useful to have a check of the capability of the present model to predict such driving forces. A limited but nevertheless useful way to do this is to calculate the wave-induced set-up $\bar{\eta}$, and to compare the results with measurements. This then is one purpose of the experiments to be described in the following chapter, the other one being a more direct check on the model through measurements of H_{rms} .

EXPERIMENTS

Arrangements and procedures

The experiments referred to above were carried out in a flume in the Laboratory of Fluid Mechanics, Department of Civil Engineering, Delft University of Technology. The flume has an overall length 45 m, width 0.8 m, and height 1 m.

The flume is equipped with a hydraulically driven random-wave generator. The control signal was obtained by filtering a random noise signal.

At the end of the flume opposite the wave generator, two beaches with different profiles have been built, viz. a plane beach with a 1:20 slope, and a beach with an idealized bar-trough profile, consisting of two 1:20 plane sections sloping seawards, connected by a 1:40 plane section, sloping shoreward, 4.4 m in length, (Fig. 2).

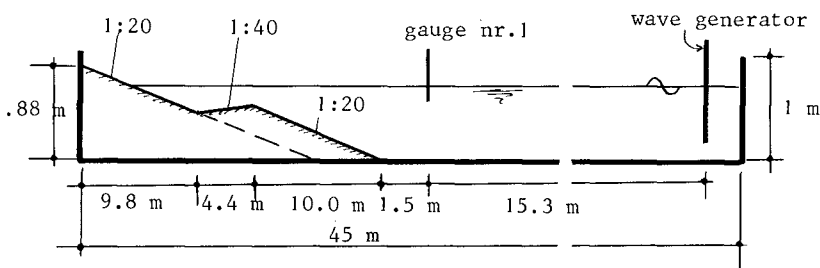


Fig. 2 - Sketch of wave flume with bar-trough beach profile (plane slope indicated by dashed line)

The height of the bar crest was about 0.50 m above the flume bottom, and the depth of the trough below the bar crest was about 0.11 m. The beaches occupied the entire flume width, one at a time. They consisted of compacted sand, finished with a smooth cement-sand mortar layer.

Measurements of the free surface fluctuations were made with 7 parallel-wire resistance gauges. One of these was placed in the constant-depth section, 1.5 m seaward of the toe of the beach; this gauge served as the reference gauge for the incident waves. The other gauges, shoreward of the beach toe, were placed at intervals of 2 m. After a recording time of about 90 min., they were moved by 1 m, so as to obtain an effective interval between adjacent measurement points of 1 m.

The gauges were calibrated immediately before and after each run. Deviations from linearity were less than 0.5%, provided the minimum submergence exceeded 4 cm. This was guaranteed by placing the gauges in the beach, in those points where the minimum required submergence was not available above the beach face (i.e., in the points relatively high on the slope).

The gauge signals were analyzed with respect to the variance (σ^2) and its spectral distribution. To this end they were fed to an eight-channel Pulse Code Modulation recorder, and afterwards from there, at 16 times the recording speed, to a digital correlator and a hybrid spectral analyzer. A total of 2^{15} points per signal were sampled, at intervals of 0.01 s (0.16 s true time). The corresponding Nyquist frequency (f_N) is 50 Hz (50/16 Hz true frequency). Per spectrum, 100 spectral estimates were made, at a separation of $0.01 f_N$, each with about $2^{15}/100 \approx 328$ degrees of freedom.

Values of σ^2 , obtained from the digital correlator, were used to estimate H_{rms} according to

$$H_{rms} = 8^{\frac{1}{2}} \sigma, \quad (26)$$

which is consistent with (21) and with

$$E = \rho g \sigma^2. \quad (27)$$

Paper chart recordings were made incidentally for visual inspection; they were not used in the quantitative analyses.

Wave set-down and set-up were measured indirectly, through the mean piezometric level at the beach face, which in turn was detected by means of 1.5 mm ID tappings placed at intervals of 1 m.

The tappings were flush with the beach face. However, in addition a deviating arrangement was made for some of the higher points, which were above the instantaneous waterline during parts of the time (during draw-down). During such time intervals, conventionally placed tappings at these points would experience a piezometric level equal to the local level of the beach face, even though the point would be momentarily "high and dry" above the water. This would lead to a systematic over-estimation of the wave set-up in that region.

To remedy this situation, a narrow slot, 1 cm wide and 10 cm deep, was gouged into the beach face, parallel to the side walls of the flume. The slot covered an interval of the beach face from a point above the highest run-up expected, to a point which was always submerged. Because the water in the slot can draw down to below the beach face, tappings which were provided in the bottom of the slot can experience piezometric levels lower than the beach face at the local cross section. A comparison of the set-up so obtained with that obtained from a conventional tapping in the same cross section, in a cross section where the latter reading was not suspect, showed them to agree to within the random experimental error (0.1 to 0.2 mm).

The system of measuring the mean water level with tappings in the slot is somewhat similar to another conceivable way of achieving the same objective, viz. through measurements of the mean piezometric level in the pores of a porous beach. If the permeability of such beach is low enough, though not zero, then the beach is virtually impermeable to water motions in the frequency band of the waves. The wave motion would then be the same as on a strictly impermeable beach, while the beach would be permeable to the mean component, making a MWL-measurement possible.

All the piezometer tappings were connected via 9 mm ID plastic tubes to 86 mm ID stilling wells. The waterlevel in the wells was read with a point gauge to 0.1 mm accuracy.

The energy in the frequency band of the incident waves was filtered out to imperceptible values by the system tube-stilling well. However, some lower-frequency oscillations were noticeable in the wells, particularly for the higher points on the beach. For this reason about 10 readings per well were made for each run, with intervals of about 15 min. The arithmetic average of these readings was taken to represent the local mean water level, and the height of this above the still-water level, which was read in the stilling wells before and after each run, was taken as the local set-up. The difference between individual readings was largest for points high on the slope, but even there the maximum deviation from the average was less than 10% of the local set-up.

Tests and results

As mentioned above, tests have been carried out on a plane beach and on a bar-trough beach. A summary of the independent parameters used is given in the following table.

Run	Profile	d_j (m)	d_c (m)	\bar{f}_j (Hz)	σ_j (m)	H_{rmsj} (m)	H_{rms_o} (m)	s_o	d_c
2	plane	.705	-	.544	.051	.144	.157	.030	-
3	plane	.697	-	.407	.043	.121	.126	.013	-
4	plane	.701	-	.463	.050	.142	.152	.021	-
11	bar	.702	.209	.479	.051	.143	.148	.022	1.41
12	bar	.645	.150	.471	.043	.121	.128	.018	1.17
13	bar	.762	.267	.497	.037	.104	.113	.018	2.35
14	bar	.732	.236	.512	.042	.118	.129	.022	1.83
15	bar	.616	.120	.530	.051	.143	.154	.028	0.78

The subscript 1 refers to the reference gauge, 1.5 m seaward of the toe of the beach; d_c is the still-water depth above the bar crest; H_{rms_0} is a deep-water rms wave height, defined as

$$H_{rms_0} = H_{rms1} / K_{s1} = 8^{1/2} \sigma_1 / K_{s1}, \quad (28)$$

in which K_{s1} is the linear shoaling coefficient for depth d_1 and frequency f_1 ; s_0 is a deep-water steepness defined by

$$s_0 \equiv 2\pi f_1^2 H_{rms_0} / g, \quad (29)$$

and

$$\tilde{d}_c \equiv d_c / H_{rms_0}. \quad (30)$$

The incident wave spectrum was rather narrow (half-power bandwidth about 25% of peak frequency), and virtually unimodal, except for a bulge in the range of frequencies about twice the peak frequency.

For the tests on the plane beach, of given slope which was not varied, the deep-water steepness is the most important independent variable. Three such runs were made, with s_0 -values of 1%, 2% and 3% approximately. The results for the run with 2% steepness were intermediate between those of the runs with 1% and 3% steepness. Only the results of the latter two are presented here, the wave heights in figs. 3a and 4a and the set-up in figs. 3b and 4b. These have been plotted against the still-water depth. The variables have been normalized as follows:

$$\begin{aligned} \tilde{H} &\equiv H_{rms} / H_{rms_0} \\ \tilde{\eta} &\equiv \bar{\eta} / H_{rms_0} \\ \tilde{d} &\equiv d / H_{rms_0} \end{aligned} \quad (31)$$

Five runs were made with a bar-trough profile. The most important independent variable in this case is \tilde{d}_c , the relative depth at the bar crest. It was varied from 2.35 to 0.78. In the first case relatively few waves break on the bar, and in the latter case the majority does. Virtually no waves were breaking in the trough region, regardless of the relative depth over the bar crest.

Only the results of the two runs with the largest and the smallest value of \tilde{d}_c are presented here, the wave heights in the figs. 5a and 6a, the set-up in the figs. 5b and 6b. These have been plotted against the relative distance seaward of the still-water line, denoted by

$$\tilde{x} \equiv x / H_{rms_0} \quad (32)$$

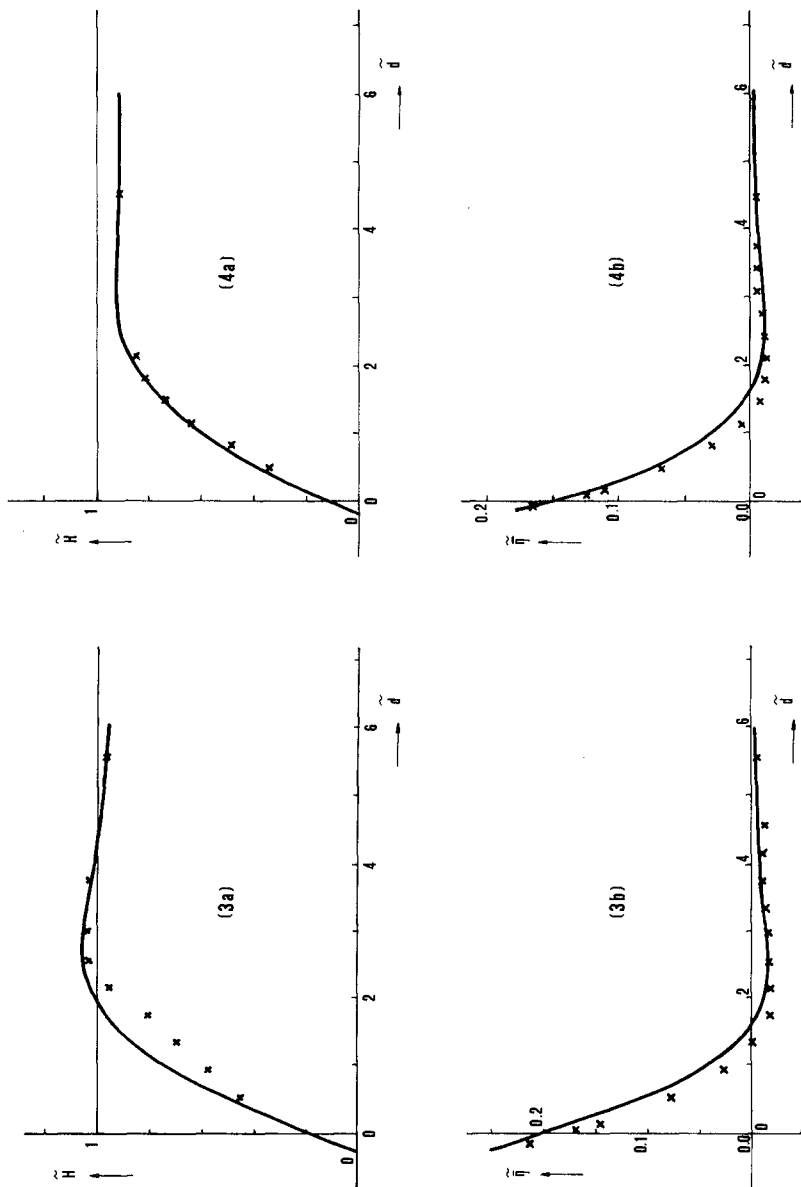


Fig. 3 - Run 3; experimental values (x); theoretical values for $\alpha = 1, \gamma = 0.8$ (—)

Fig. 4 - Run 2; experimental values (x); theoretical values for $\alpha = 1, \gamma = 0.8$ (—)

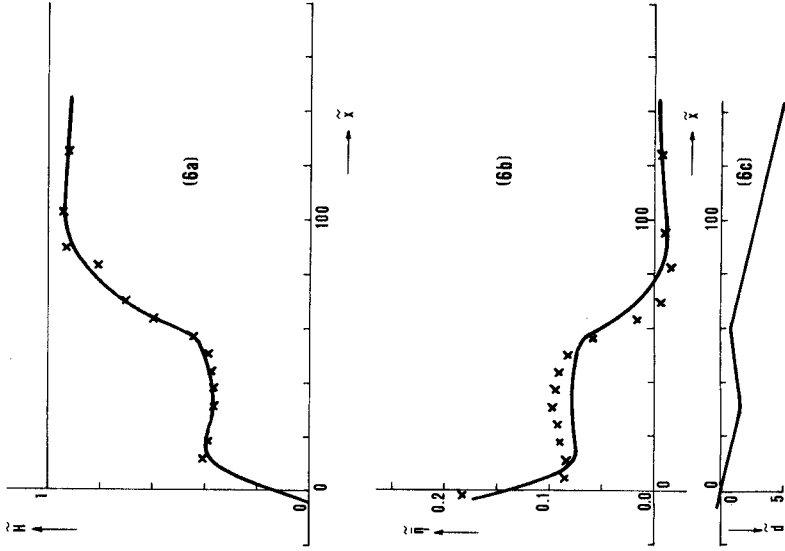


Fig. 5 - Run 13; experimental values (x); theoretical values for $\alpha = 1, \gamma = 0.8$ (—)

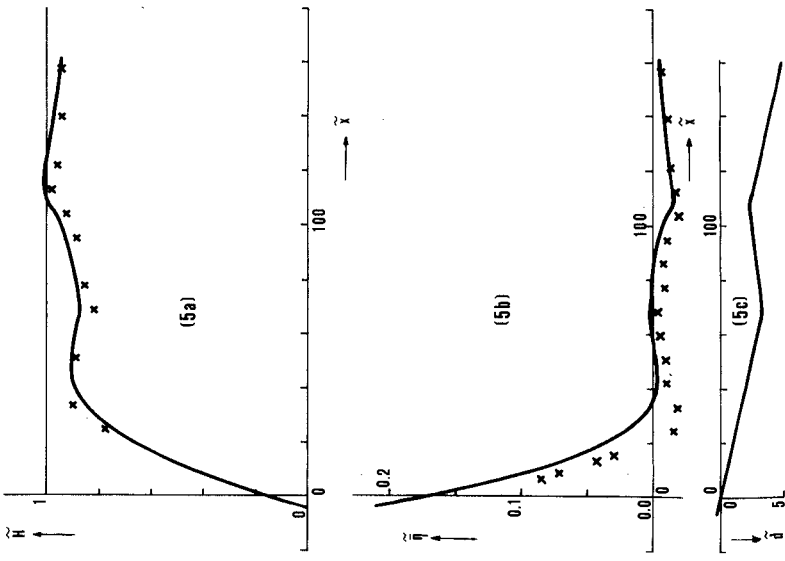


Fig. 6 - Run 15; experimental values (x); theoretical values for $\alpha = 1, \gamma = 0.8$ (—)

As an aid in the interpretation, the beach profile has also been plotted, in the figs. 5c and 6c.

In all the plots, except figure 5, the most seaward data point is that of the reference gauge in the constant-depth section of the flume.

Discussion of experimental results

The wave height decay on the plane slope (figs. 3a and 4a) shows a slight steepness effect, in the sense which might be expected. For the lower steepness ($s_0 \approx 0.01$), there is a noticeable enhancement, in fact to values exceeding the deep-water wave height, before the decay due to breaking sets in. No enhancement has been measured for the steeper waves.

For both steepnesses, the maximum set-down occurs near $\tilde{d} = 2$. The maximum relative set-up, occurring at the waterline, and estimated by extrapolation of measured values, decreases with increasing incident wave steepness.

The wave height data for the bar-trough profile (figs. 5a and 6a) show a slight enhancement, followed by a more or less severe decay on the bar, depending on the relative depth over the bar crest. In both cases there is a wave height minimum in the trough of the beach, as would be the case for dissipationless waves in shallow water. This pattern is consistent with the visual observation that there was virtually no breaking going on in the trough region. The fact that the mean water level has a maximum near the trough is also consistent with this.

The mean water level gradient just shoreward of the bar crest is far greater than further toward the trough, but still on the same slope. (This is particularly clear in fig. 6b.) This is due to the fact that in that region there is still dissipation, though the depth is already increasing. The dissipation contributes to the mean water level gradient in the same sense as the increasing depth (both tending to decrease S_{xx}).

COMPARISON OF THEORETICAL MODEL TO EXPERIMENTAL DATA

Results of theoretical model

The equations of the theoretical model described in previous chapters were programmed for numerical evaluation on a digital computer.

The nearshore beach profiles used in the calculations were the same as those used in the experiments. The seaward portion of the profiles was a constant-depth section in the experiments, but in the calculations this section was replaced by a 1:20 slope extending to deep water. The calculations were started in a point of effectively deep water, using experimental values of \bar{f}_1 and H_{rms0} as input parameters.

Due to the finite size of the flume, the wave-induced set-up on the beach causes a lowering of the mean water level in the constant-depth section. Thus, instead of having an initial value for the integration of the set-up equation (23), the constancy of mass in the flume must provide the integration constant. However, there were indications that water was not only stored on the beach, but also behind the wave generator. The latter amount was not predicted. For this reason, the measured set-down in the constant-depth section was used as the reference value for the calculations of the mean water level.

The calculations cannot be initiated until the parameters (α, γ) have been assigned certain values. It is planned to determine a single pair of (α, γ) -values such that the fit of the calculated results for H_{rms} and $\bar{\eta}$ to the complete data set is optimised in some sense. This has not yet been done. In the calculations performed so far, the coefficients α and γ were given some plausible values a priori.

For γ , which indicates a breaker height-to-depth ratio, the value 0.8 was chosen.

The coefficient of proportionality in the expression for the dissipation rate is expected to be of order unity. A logical a priori choice for it would therefore be 1. This has in fact been done in a previous formulation, in which however a coefficient has been used which was a factor 2 smaller than the coefficient α used here, defined in eq. 19. Thus, the initial calculations were in fact performed for $\gamma = 0.8$, $\alpha = 0.5$. The calculated decay rate proved to be too low. The calculations were then repeated with $\gamma = 0.8$, $\alpha = 1$. The results of these calculations have been superimposed on the plots of the experimental data in the figs. 3 through 6.

Discussion of results

A comparison of the theoretical results to the experimental data leads to the following conclusions.

In general, the wave height variation across the surf zone is predicted reasonably well. In some cases, the agreement between model predictions and experimental data is quite good, such as in the figs. 4a and 6a. In other cases the agreement is less good, though still fair.

The set-down and set-up appear to be less well predicted than the wave heights. Although the overall agreement is fair, the model consistently predicts the transition from set-down to set-up in regions somewhat too far seaward. The fact that this discrepancy exists even where the wave height variation is predicted well, suggests that in the breaking process S_{xx} decreases not as fast as the potential energy of the waves, perhaps due to a local relative surplus of kinetic energy of organized wave motions and turbulent motions together. Data obtained previously have given similar indications (Battjes, 1974).

The probability that an arbitrary wave passing a given point shall be a breaking or broken wave, is an important quantity in the description of random waves on a beach. It has not been measured quantitatively.

However, a comparison of theoretical results with qualitative observations is possible, particularly for the runs with a bar-trough profile. In all cases, the calculated value of Q_b in the trough was virtually zero, even though it could be considerable on the bar crest ($Q_b = 0.06$ in run 13, with $\tilde{d}_c = 2.35$, and $Q_b = 0.46$ in run 15, with $\tilde{d}_c = 0.78$). These variations agree at least qualitatively with the visual observations.

Summarising: the model, when given a single pair of plausible values for the coefficients α and γ , appears capable of predicting qualitatively and quantitatively the main features of the complete set of data, both with respect to the wave heights and to the mean water level variations, both on a plane beach and on a beach with a bar-trough profile. This lends strong support to the usefulness of the model proposed herein.

REFERENCES

- Battjes, J.A., Set-up due to irregular waves, Proc. 13th Intern. Coast. Eng. Conf., Vancouver, B.C., 1972, III, p. 1993-2004.
- Battjes, J.A., Computation of set-up, longshore currents, run-up and overtopping due to wind-generated waves, Comm.on Hydraulics, Dept.of Civil Eng., Delft Univ. of Technology, nr. 74-2, 1974.
- Battjes, J.A., Energy dissipation in breaking solitary and periodic waves, manuscript, 14 p., April 1978 (a).
- Battjes, J.A., A critical review of conventional models for some surf zone phenomena, with special reference to the calculation of longshore currents, Paper presented at Euromech 102, Surf and run-up, Bristol, 1978 (b).
- Divoky, D., B. LeMéhauté, and A. Lin, Breaking waves on gentle slopes, J. of Geophys. Res., 75, 9, March 1970, p. 1681-1692.
- Goda, Y., Irregular wave deformation in the surf zone, Coastal Engineering in Japan, XVIII, 1975, p. 13-26.
- Hwang, Li-San and D. Divoky, Breaking wave set-up and decay on gentle slopes, Proc. 12th Intern. Coast. Eng. Conf., Washington, D.C., 1970, I, p. 377-389.
- Lamb, H., Hydrodynamics, Dover Publications, 1932.
- LeMéhauté, B., On non-saturated breakers and the wave run-up, Proc. 8th Intern. Coast. Eng. Conf., Mexico, 1962, p. 77-92.
- Longuet-Higgins, M.S. and R.W. Stewart, Radiation stress and mass transport in gravity waves, with applications to "surf-beats", J. Fluid Mech., 13, 1962, p. 481-504.

CHAPTER 33

THE ENERGY SPECTRA OF SURF WAVES ON A CORAL REEF

by
Theodore T. Lee^{1/} and Kerry P. Black^{2/}

ABSTRACT

The transformation of waves crossing a coral reef in Hawaii including the probability density function of the wave heights and periods and the shape of the spectrum is discussed. The energy attenuation and the change of height and period statistics is examined using spectral analysis and the zero up-crossing procedure. Measurements of waves at seven points along a 1650 ft transect in depths from 1 to 3.5 ft on the reef and 35 ft offshore were made.

The heights were tested for Rayleigh, truncated Rayleigh and Weibull distributions. A symmetrical distribution presented by Longuet-Higgins (1975) and the Weibull distribution were compared to the wave period density function. In both cases the Weibull probability density function fitted with a high degree of correlation. Simple procedures to obtain Weibull coefficients are given.

Fourier spectra were generated and contours of cumulative energy against each position on the reef show the shifting of energy from the peak as the waves move into shallow water. A design spectrum, with the shape of the Weibull distribution, is presented with procedures given to obtain the coefficients which govern the distribution peakedness. Normalized non-dimensional frequency and period spectra were recommended for engineering applications for both reef and offshore locations.

A zero up-crossing spectrum (ZUS) constructed from the zero up-crossing heights and periods is defined and compared with the Fourier spectrum. Also discussed are the benefits and disadvantages of the ZUS, particularly for non-linear wave environments in shallow water. Both the ZUS and Fourier spectra are used to test the adequacy of formulae which estimate individual wave parameters.

Cross spectra analysis was made to obtain gain function and squared coherency for time series between two adjacent positions. It was found that the squared coherency is close to unity near the peak frequency. This means that the output time series can be predicted from the input by applying the gain function. However, the squared coherency was extremely small for other frequencies above 0.25 Hz.

INTRODUCTION

Most coastal areas of Hawaii, Australia and other tropical regions are protected naturally by a coral reef. Due to complex bathymetry, large energy losses by breaking, friction, scattering and the highly non-linear behavior of impinging waves, the fringing reef presents an extremely complex environment. As a result, the wave transformation on the coral reef is distinctly different from that on sandy coasts. The wave heights, wave

^{1/} Researcher, J.K.K. Look Laboratory of Oceanographic Engineering, Department of Ocean Engineering, University of Hawaii, Honolulu, Hawaii

^{2/} Formerly Research Associate, Department of Ocean Engineering, and Graduate Student, Dept. of Oceanography, Univ. of Hawaii, Honolulu, Hawaii

periods, and energy spectra are thus modified significantly but information on such a modification is very limited (Bushing, 1976), particularly for correlated field measurements. Knowledge of wave characteristics leeward of a reef is necessary in numerous engineering endeavors, such as the assessment of beach stability, design of coastal structures, prediction of dynamic response of small boats in marinas in waters partly protected by a reef, artificial shoal, and submerged breakwaters. Lack of such knowledge has led to grave uncertainties for designing an economical and sound structure. Also, wave transformation is associated with the living coral environment studied by the marine biologists and wave-induced currents are central to the mechanism of food transformation. This paper will provide some new light concerning the transformation and modification of ocean waves as they progress from deep water through breaking on a reef and on into the shallow water beyond.

FIELD EXPERIMENT

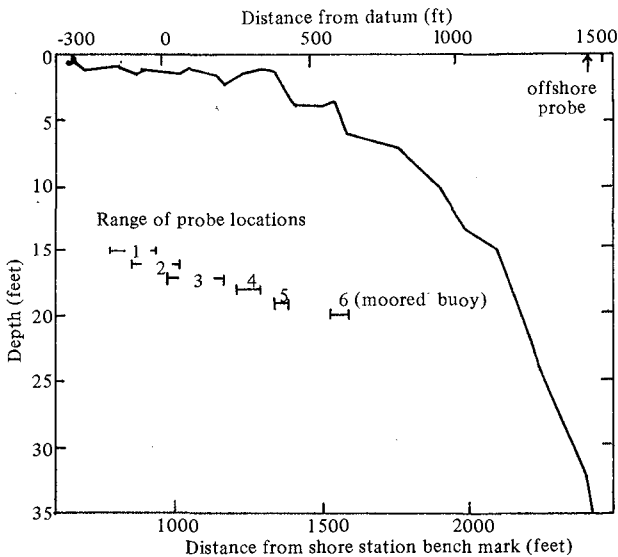


Fig. 1(a) Instrumentation location and bathymetry of Ala Moana reef

was mounted on a tower in 35 ft of water (Fig. 1(b)). A floating buoy (number 6) was moored on the outer edge of the reef (6-8 ft depth) and data was recorded by filming the motion of the buoy. The bathymetry with range of location of instruments is shown on Fig. 1(a). All instruments and recording equipment were transported and deployed from a mobile platform equipped with four jack-up legs. At the project site the legs were lowered to the reef to form a fixed platform which allowed the waves to pass underneath. Wave information was cabled back and recorded on a Sangamo Model 3400, 16-channel tape recorder. A portable electric

Field measurements of water level versus time were made in the ocean at seven points (Fig. 1(a)) along a 1650 ft long transect at the Ala Moana Beach on the southern shore of the island of Oahu ($21^{\circ}17'N$, $157^{\circ}52'W$) in Hawaii from July through September 1976. Five capacitance-type probes (numbered 1 to 5, with number 1 most shoreward) were supported on tripods in shallow water on the reef in depths from 1.0 to 3.5 ft. Another capacitance probe (number 9)

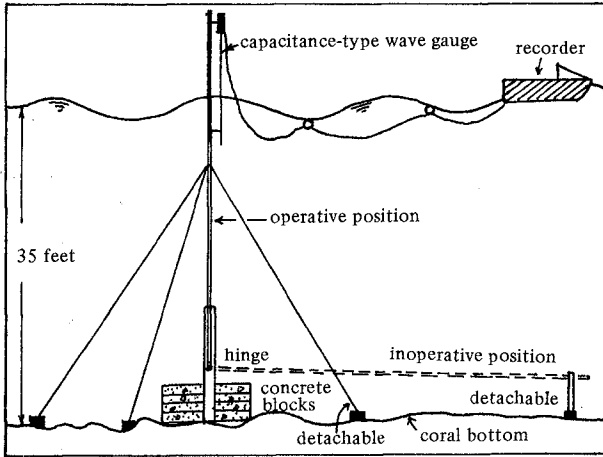


Fig. 1(b) Schematic of offshore wave measurement system

generator was used as a power source. Offshore data was cabled to a Sanborn strip chart recorder using a catamaran as a recording station.

TIME SERIES

A typical time series is shown on Fig. 2. A qualitative schematic of the wave transformation is shown on Fig. 3. The waves impinging on the reef had primary period of 12 to 18 seconds and significant height up to 3 ft. Offshore, the waves tend to arrive in groups, modulated at a beat frequency. As they shoal on the reef, secondary waves are formed indicative of a highly non-linear process. The shoaling waves typically plunge and produce a saw-tooth profile (Probe 4, Fig. 2). The reformed waves inside the breaker zone have a shortened period, due to the formation of multiple crests.

The random nature of ocean waves is usually described as a stationary Gaussian process. Figures 4 and 5 show the probability density of sea-level elevation against the theoretical Gaussian distribution for offshore and near-shore probes respectively. Note that the shallow water data deviates significantly from the theoretical distribution due to the modified wave profile which has long shallow troughs and peaked crests.

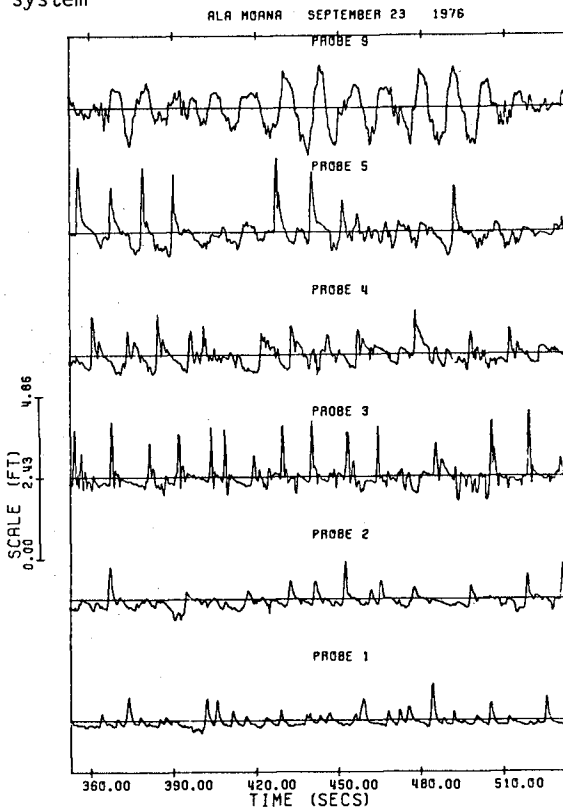


Fig. 2 Wave records, Ala Moana, September 23, 1976.

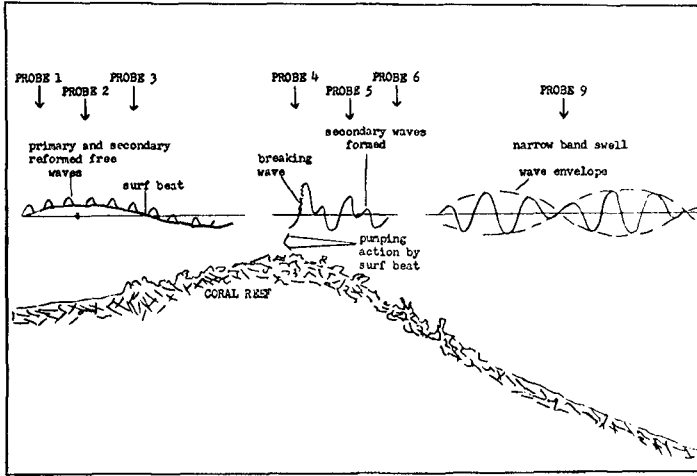


Fig. 3 Qualitative schematic of wave transformation across a reef, with typical probe locations, Ala Moana, 1976.

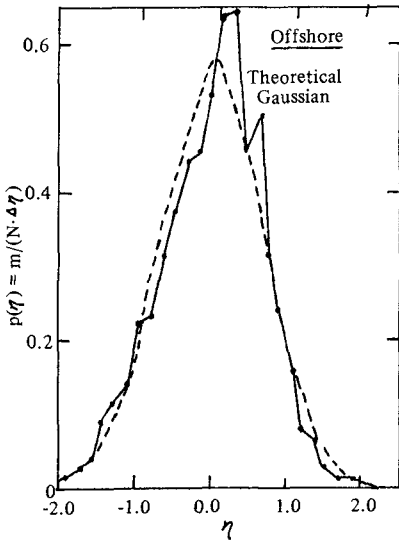


Fig. 4 Probability density of sea level elevation, September 14, offshore probe with Gaussian distribution, Ala Moana, 1976.

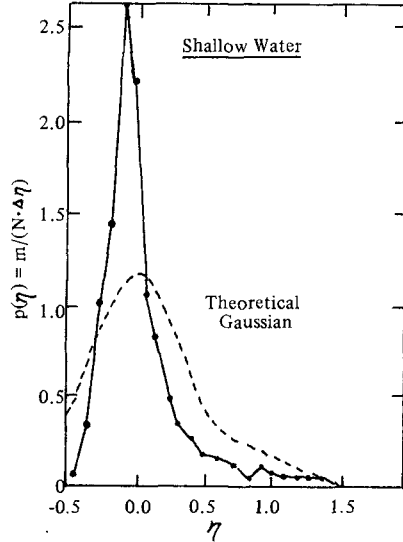


Fig. 5 Probability density of sea level elevation, September 7, probe 4 with Gaussian distribution, Ala Moana, 1976

WAVE HEIGHT

The significant wave height normalized by the offshore significant wave height plotted against the position on the reef is shown on Fig. 6. Due mainly to bottom friction and also to breaking, the ratio decreases

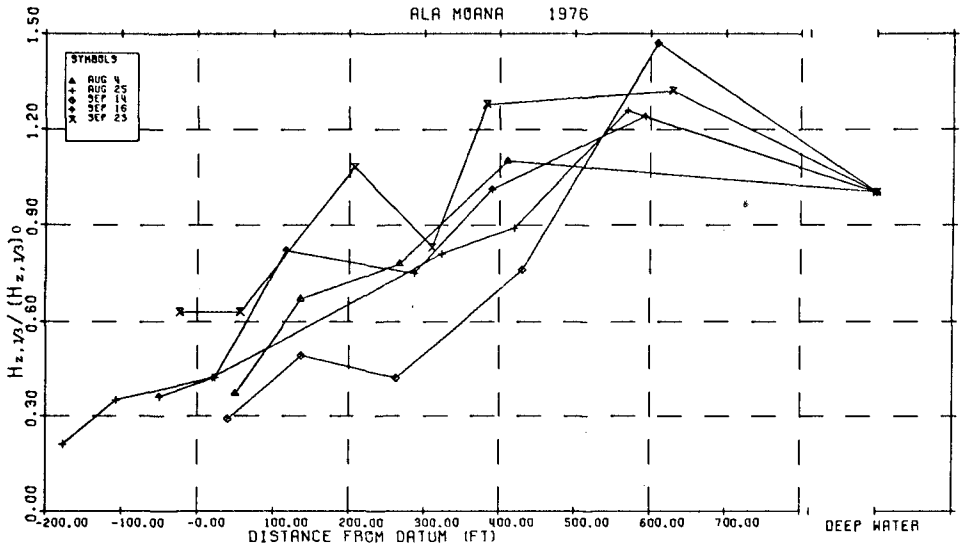


Fig. 6 The significant height normalized by the offshore value against position on the reef, Ala Moana, 1976.

such that the wave height is reduced by approximately 50% every 500 ft travelled on the reef. (The waves generally break at 380 ft from the datum.)

A zero up-crossing analysis was performed on a total on 35 time series and wave height statistics were determined as follows:

$$\begin{aligned}
 H_{z,1/3} / \bar{H}_z &= 1.70 \pm 0.13 && \text{shallow reef} \\
 &1.72 \pm 0.11 && \text{offshore} \\
 &1.64 \pm 0.04 && \text{probes exhibiting Rayleigh distribution} \\
 \text{(NOTE: } 1.60 &&& \text{theoretical Rayleigh)}
 \end{aligned}
 \tag{1}$$

$$\begin{aligned}
 H_{z,max} / H_{z,1/3} &= 1.80 \pm 0.13 && \text{offshore} \\
 &2.60 && \text{shoreward of the breaker zone} \\
 &1.60 && \text{breaker zone} \\
 \text{(NOTE: } 1.74 &&& \text{theoretical ratio given by Longuet-Higgins)}
 \end{aligned}$$

$$\begin{aligned}
 H_{z,1/3} / \sigma &= 3.88 \pm 0.52 && \text{shallow water} \\
 &3.56 \pm 0.13 && \text{offshore} \\
 \text{(NOTE: } 4.00 &&& \text{theoretical Rayleigh)}
 \end{aligned}$$

Rayleigh Distribution. In each case, there is significant deviation from the theoretical Rayleigh value. This coincides with a poor fit of the data to the Rayleigh distribution. Typical distributions are shown in Fig. 7. Using a Chi-squared goodness of fit test, the 35 height distributions were compared to the Rayleigh probability density function and 23 did not fit at the 0.025 level of significance. Two out of the five offshore time series did not exhibit Rayleigh distribution due to an excessive number of short period waves (<2 seconds). After filtering of these waves all offshore height distributions were Rayleigh distributed.

Truncated Rayleigh Distribution. The heights were compared to the truncated Rayleigh distribution (Kuo and Kuo, 1975, Battjes, 1974). The

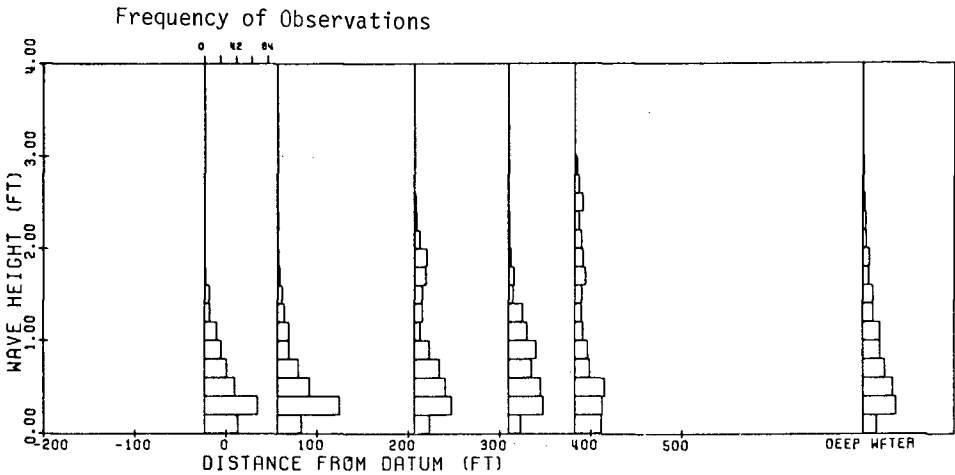


Fig. 7 Distribution of wave heights plotted as height versus frequency of occurrence against position on the reef, Ala Moana, September 23, 1976.

fit was excellent in the breaker zone, but poor both offshore and shorewards of this region. This means that the truncated distribution can only be applicable on certain parts of the reef.

Weibull Distribution. A more general distribution which fits at all positions on the reef for various meteorological conditions was needed. The Weibull distribution given by

$$f(H) = \alpha \beta H^{\beta-1} \exp(-\alpha H^\beta) \tag{2}$$

was selected, and the correlation coefficient, ρ_{12} , which is unity for a perfect fit exceeded 0.98 at most positions on the reef. Arhan and Ezraty (1975) also used Weibull distribution successfully to fit their wave data in shallow water.

It should be noted that Rayleigh is a special case of the Weibull distribution with $\beta=2$ and $\alpha=1/H_{rms}^2$. Procedures to determine β (peakedness coefficient), and α follow:

(1) Curve fitting.

The probability of exceeding $x=x_n$ is

$$G(x_n) = \int_{x_n}^{\infty} f(x) dx = \exp(-\alpha x_n^\beta) = n/N \tag{3}$$

where n waves exceed x_n of a total of N waves. Taking logarithms twice gives

$$\ln[\ln(N/n)] = \ln(\alpha) + \beta \ln(x_n) \tag{4}$$

which is a linear equation with intercept at $\ln(\alpha)$ and gradient β . The coefficients β and α can be determined using standard linear regression techniques or by plotting the double logarithm term against $\ln(x)$ and fitting a straight line.

(2) Distribution width function.

The distribution width function is defined (Black, 1978) as

$$Q_H = 4 \int_0^{\infty} H f(H)^2 dH \tag{5}$$

For a Weibull distribution.

$$Q_H = \beta \tag{6}$$

The approximate value of β for data divided into bins of width ΔH

$$Q_H = \beta = \frac{4}{N^2 \Delta H} \sum_{i=1}^{NBINS} H_i m_i^2 \tag{7}$$

where N is the total number of waves, $NBINS$ is the number of bins, and H_i and m_i are the heights and number of occurrences respectively in the i^{th} bin. The squared probability density term in the distribution width function tends to magnify small deviations from the theoretical distribution and Q_H is sensitive to the choice of the number of bins which should be selected such that

$$NBINS < N/10$$

(3) Determination of β without curve fitting.

The ratio of two height (or period) statistics is uniquely defined by the peakedness so β may be easily determined using any two statistics such as $H_z, 1/3/H_z$ or $\sigma(H)/H_z$ (which are most stable). To facilitate this approach, the theoretical values of several ratios were plotted against β (Fig. 8). One enters the figure with any of the ratios and reads β . The theory is derived by Black (1978).

Procedures to determine the other coefficient, α , follow:

(i) The Weibull coefficient α may be determined as

$$\alpha = [\Gamma(1 + 1/\beta)/H_z]^\beta \tag{8}$$

where Γ is the gamma function, and H_z is the mean height of the distribution. Figure 9 presents a family of curves for various α using Eq. (8). α may be determined if one enters the figure with β and H_z .

(ii) Another useful equation to determine α which does not

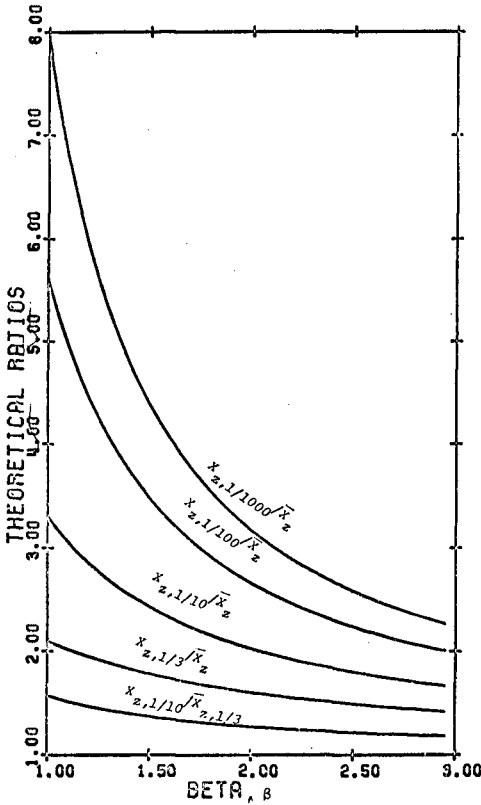


Fig. 8 Theoretical ratios of wave height (period) statistics for waves exhibiting the Weibull distribution against beta, β . (X may be height or period.)

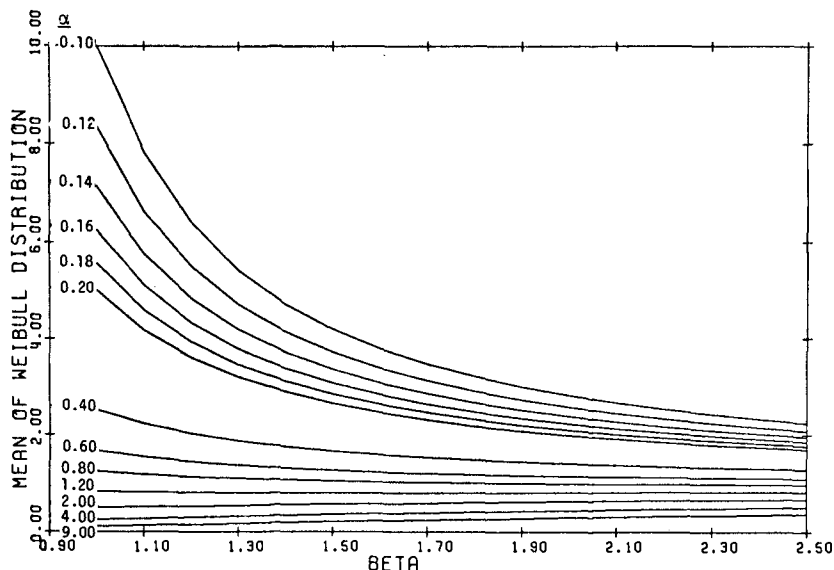


Fig. 9 Theoretical mean of Weibull distribution against β , beta for various α . (Alpha can be determined if given beta and the mean wave height.)

include the gamma function is

$$\alpha = \frac{\beta-1}{\beta} H_p^{-\beta}, \text{ or } [\alpha = \frac{\beta+1}{\beta} f_p^\beta \text{ where } f_p = \left(\frac{\beta-1}{\beta+1}\right)^{1/\beta} T_p^{-1}] \tag{9}$$

The exact solution for the average of the largest n^{th} of waves was determined to be

$$H_{z,n}/N = \frac{N}{n} \bar{H}_z \left(1 - \int_0^{\ln(N/n)} f_G(y) dy\right) \tag{10}$$

where $y = \alpha H^\beta$, \bar{H}_z is given by Eq. (8) and $f_G(y)$ is the incomplete gamma function ratio,

$$f_G(y) = \frac{1}{\Gamma(1+1/\beta)} e^{-y} y^{1/\beta} \tag{11}$$

An approximate solution was also obtained as

$$H_{z,n}/N = \frac{C_1}{2} [(\ln(N)/\alpha)^{1/\beta} + (\ln(N/n)/\alpha)^{1/\beta}] + C_2 \tag{12}$$

where C_1 and C_2 are arbitrary constants, and for $C_2=0$.

Then

$$H_z = \frac{0.65}{2} [\ln(N)/\alpha]^{1/\beta}$$

$$H_{z,1/3} = \frac{0.79}{2} [\ln(N)/\alpha]^{1/\beta} + (\ln(3)/\alpha)^{1/\beta} \tag{13}$$

$$H_{z,1/10} = \frac{0.87}{2} [\ln(N)/\alpha]^{1/\beta} + (\ln(10)/\alpha)^{1/\beta}$$

$$H_{z,\max} = 1.01[\ln(N)/\alpha]^{1/\beta} \quad (13)$$

(cont)

WAVE PERIODS

The significant period normalized by the offshore deep-water period decreases generally as waves cross the reef toward the shoreline due to the formation of multiple crests and a diminishing height to period correlation; the mean values of the ratio are:

$$\frac{T_{H_z,1/3}}{[T_{H_z,1/3}]_0} = \begin{cases} 0.704 \pm 0.176 & \text{shallow reef for offshore wind} \\ 0.642 \pm 0.168 & \text{shallow reef for onshore wind} \\ 0.853 \pm 0.110 & \text{breaker zone} \\ 0.763 \pm 0.103 & \text{outer edge of the reef (4'-8' depth)} \\ 1.000 & \text{offshore in deep water (35 ft depth)} \end{cases} \quad (14)$$

It was found that the rate of change of significant period is small and the correlation is poor ($\rho_{12}=0.31$).

The ratio of the average of the top third of the periods over the significant period is:

$$\frac{T_{z,1/3}}{T_{H_z,1/3}} = \begin{cases} 1.35 \pm 0.14 & \text{shallow reef} \\ 1.11 \pm 0.04 & \text{offshore} \end{cases} \quad (15)$$

The ratio of significant period to mean period is

$$\frac{T_{H_z,1/3}}{\bar{T}_z} = \begin{cases} 1.30 \pm 0.13 & \text{shallow reef} \\ 1.56 \pm 0.12 & \text{offshore} \end{cases} \quad (16)$$

The period distribution was compared to the Weibull probability density function,

$$f(T) = \alpha\beta T^{\beta-1} \exp(-\alpha T^\beta) \quad (17)$$

which offers the best fit with correlation coefficient exceeding 0.98 in most cases. The Weibull coefficients β, α can also be found from Figs. 8 and 9 or from Eq. (5) as the periods and heights were fitted to the same distribution.

The approximate solution for the average of the largest one third of the periods is

$$T_{z,1/3} = \frac{0.77}{2} [(\ln(N/\alpha))^{1/\beta} + (\ln(3)/\alpha)^{1/\beta}] \quad (18)$$

Further, the wave periods were fitted to a symmetrical distribution presented by Longuet-Higgins (1975). The fit is poor due mainly to a positive skewness in the actual period distribution. This symmetrical distribution is generally useful for the narrow spectrum case.

WAVE SPECTRUM

The energy spectra of surf waves on the coral reef were examined in detail by: (1) Fourier spectrum analysis, and (2) zero up-crossing analysis procedures. The transformation of the Fourier spectrum as the waves cross the reef can be seen typically on Fig. 10. Offshore (probe 9), the spectrum has low energy in the high and low frequency ranges which

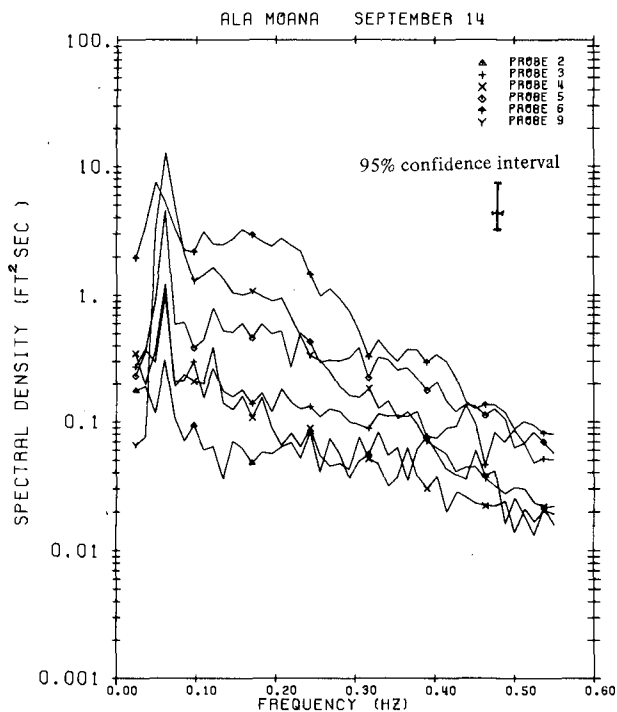


Fig. 10 Fourier spectrum for time series of 4096 data points digitized at 2.5 points per second. Each spectral estimate has 40 degrees of freedom, Ala Moana, September 14, 1976.

increases as the waves enter shallow water when energy shifts from the peak. The shift results in the production of multiple crests and periodic sea level changes at beat frequencies. Harmonics of the peak frequency are evident.

Cumulative energy (Fig. 11) and response function (Fig. 12) against position on the reef were compared. The contours of cumulative energy showing seven frequency ranges between 0 and 1.25 (Nyquist frequency) were presented so that the energy attenuation or amplification in the low, middle, and high frequency ranges can be examined in greater detail (Black, 1978). It showed that low frequency energy (below 0.05 Hz) increases from the offshore probe but it is not attenuated on the reef. Most of the energy is at frequencies less than 0.4 Hz and virtually no energy lies above 0.81 Hz. There is a decrease in variance from the offshore probe to the most seaward shallow water probe even though an increase is expected due to shoaling friction attenuates the waves over this section. The peak of the spectrum is at approximately 0.075 Hz. The peak always attenuates but high frequency energy ($0.21 < f < 1.25$ Hz) gains occur when waves first enter shallow water and break. The breaker zone is at approximately 380 ft from the datum (Fig. 11) where the gradient of the curves is greatest, which means there is maximum energy loss per unit distance traveled across the reef in this region. Shorewards of the breaker zone, there is attenuation at all frequencies. However, interesting behavior was noted for some days that the total variance is greater just shorewards of the breaker zone than in the breakers due to a significant increase in high frequency energy. This is caused in part by local wind-waves but it is most likely caused by wave refraction which introduces energy from the sides of the transect in this region. This suspicion is based on the fact that this phenomena was not observed in the simulated laboratory experiments (Lee, 1978).

It is interesting to note that energy gains at low frequency are larger if the offshore spectrum has a split peak due to wave-induced set-up at beat frequencies in shallow water.

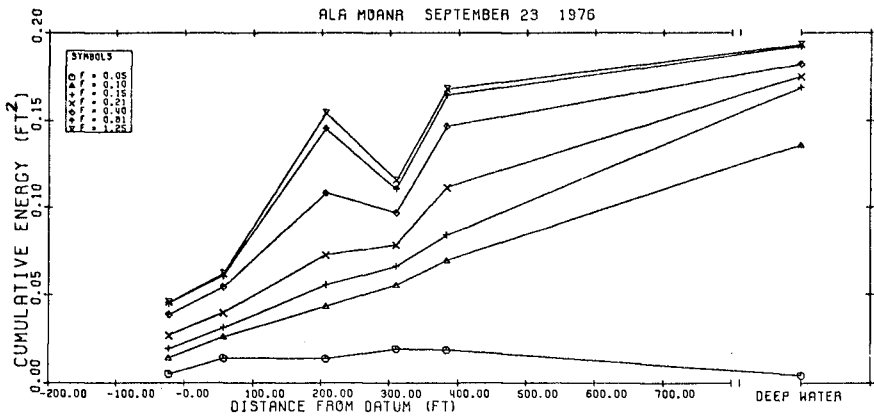


Fig. 11 Contours of cumulative energy from frequency 0.0 to F, where F is given on the symbol table, against position on the reef, Ala Moana, September 23, 1976.

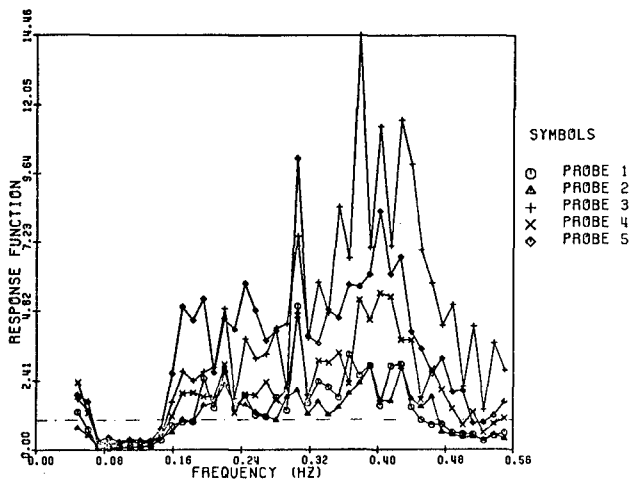


Fig. 12 Response function, $R(f)$, against frequency, where $R(f) = S(f)_x / S(f)_g$. $S(f)_x$ is the spectral density at probe x and $S(f)_g$ is the spectral density at the offshore probe, Ala Moana, September 23, 1976.

(A) Fourier Spectrum

The period spectrum at either offshore or shallow-reef areas has the shape of Weibull distribution given by

$$S(T) = E\alpha\beta T^{\beta-1} \exp(-\alpha T^\beta) \tag{19}$$

where E is the total energy in the spectrum, T is the wave period, and S(T) is the spectral density (ft²/Hz), and β, α determine the shape of the distribution and govern the spectrum peakedness.

The frequency spectrum with the shape of Weibull distribution can be obtained by a change of variable,

$$S(f) = S(T) \left| \frac{dT}{df} \right| \tag{20}$$

and $T = f^{-1}, \frac{dT}{df} = -f^{-2}$ (21)

then $S(f) = E\alpha\beta f^{-\beta-1} \exp(-\alpha f^{-\beta})$ (22)

At $f=f_p$, peak frequency

$$\frac{dS(f)}{df} = 0$$

$$f_p^\beta = \frac{\alpha\beta}{\beta+1} \text{ or } \alpha = \frac{\beta+1}{\beta} f_p^\beta \tag{23}$$

then $S(f) = E \left(\frac{\beta+1}{f_p}\right) \left(\frac{f}{f_p}\right)^{-\beta-1} \exp\left[-\left(\frac{\beta+1}{\beta}\right) \left(\frac{f}{f_p}\right)^{-\beta}\right]$ (24)

$$S(f_p) = E \left(\frac{\beta+1}{f_p}\right) \exp\left[-\left(\frac{\beta+1}{\beta}\right)\right] \tag{25}$$

To show the effect of β on the shape of the spectrum, the above equation (24) was plotted with fixed mode ($f_p=0.1$), unit variance and for β=1, 5 on Fig. 13. Note that the spectrum widens as β decreases.

Methods to obtain β will follow.

(1) Curve fitting.

The cumulative energy is

$$E_c = \int_0^f S(f)df = E \exp(-\alpha f^{-\beta}) \tag{26}$$

and taking logarithms twice gives

$$\ln[\ln(E/E_c)] = \ln(\alpha) - \beta \ln(f) \tag{27}$$

which is a linear equation with intercept at $\ln(\alpha)$ and gradient -β.

(2) Iteration.

A simple method was developed to determine β, without curve-fitting, from Eq. (25) using a simple iterative technique.

$$\exp\left[\left(\frac{\beta+1}{\beta}\right)\right]/(\beta+1) = E/[S(f_p) \cdot f_p] \tag{28}$$

With the peak frequency (f_p), energy density at peak frequency [$S(f_p)$], and the total energy in the spectrum E, β can be obtained. This relationship was plotted on Fig. 14, and β may be obtained by

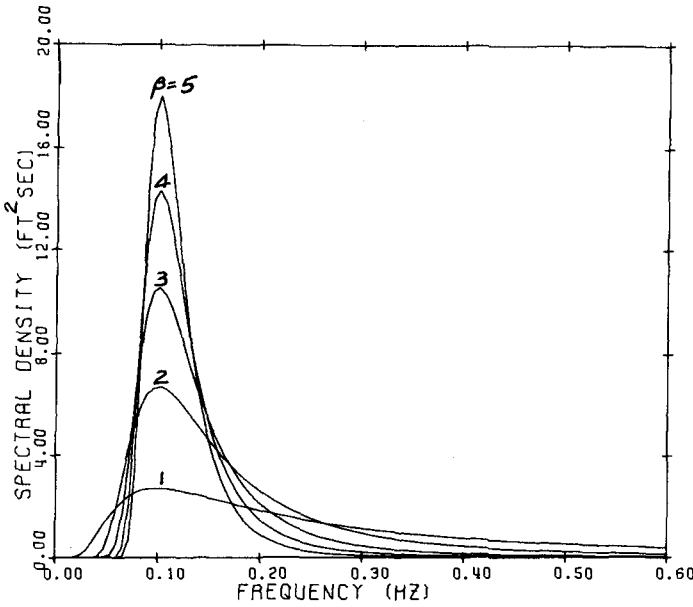


Fig. 13 Theoretical spectra with the shape of Weibull distribution with unit variance, peak frequency $f_p=0.1$ Hz and for $\beta=1,5$.

entering the function $E/[S(f_p) \cdot f_p]$. The other coefficient, α , may be obtained by

$$\alpha = \frac{\beta+1}{\beta} f_p^\beta \quad (29)$$

Analysis showed that the spectrum found in this manner fits the peak exactly but does not necessarily describe the rest of the spectrum well. This method should only be used when an "easy-to-obtain" estimate of β is required or if the spectrum has been highly smoothed. In general, the value of β by iteration is greater than that by curve-fitting.

(3) Goda's spectral peakedness parameter.

Another alternative method to obtain β without curve-fitting employs Goda's spectral peakedness parameters Q_p (Goda, 1974).

$$Q_p = \frac{2}{m_0} \int_0^\infty f S(f)^2 df \quad (30)$$

where m_0 is zeroth spectral moment.

It can be shown for a spectrum with the shape of the Weibull distribution that (Black, 1978)

$$Q_p = \beta/2 \quad (31)$$

In which case, the peakedness β can be found using Q_p .

It was found that Q_p represents the shape of the spectrum much better than the spectral width parameter

$$\epsilon_s = \sqrt{1 - \frac{m_2^2}{m_0 m_4}} \quad \text{or} \quad \epsilon_T = \sqrt{1 - \left(\frac{N_z}{N_c}\right)^2}$$

The spectral width parameters vary considerably with the high frequency cut-off choice, therefore, they are not a good parameter to characterize the spectral distribution.

The design frequency spectrum for engineering applications on coral reef environment is recommended as follows:

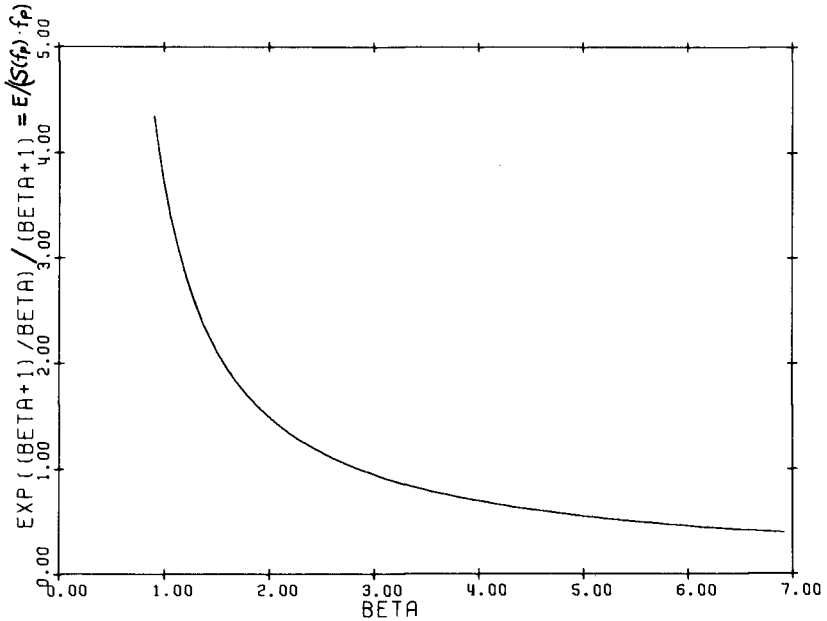


Fig. 14 Theoretical curve to obtain Beta for the spectrum with the shape of the Weibull distribution using the peak energy density, where $\exp(\beta + 1/\beta)/(\beta + 1) = E/(S(f_p) \cdot f_p)$ and E is total energy in spectrum, f_p is peak frequency and $S(f_p)$ is energy density at peak.

(a) Swell spectrum (offshore 35 ft depth)

$$S(f) = 4E_1 f_p^{-1} (f/f_p)^{-4} \exp[-\frac{4}{3}(f/f_p)^{-3}] \tag{32}$$

(b) Shallow water on the offshore side of the reef (5 ft depth)

$$S(f) = 3E_2 f_p^{-1} (f/f_p)^{-3} \exp[-\frac{3}{2}(f/f_p)^{-2}] \tag{33}$$

(c) Shallow water on the shoreward side of the reef (3 ft depth)

$$S(f) = 2E_3 f_p^{-1} (f/f_p)^{-2} \exp[-2(f/f_p)^{-1}] \tag{34}$$

In all three cases f_p is the offshore peak frequency and the total energy $E = (1/4 H_z, 1/3)^2$ where $H_z, 1/3$ is significant wave height.

The normalized non-dimensional frequency spectrum has the general form of

$$\frac{S(f)}{S(f_p)} = [\exp(\frac{\beta+1}{\beta})] (f/f_p)^{-\beta-1} \exp[-(\frac{\beta+1}{\beta})(f/f_p)^{-\beta}] \tag{35}$$

Then, the normalized design frequency spectra are:

(a) Normalized swell frequency spectrum (offshore 35 ft depth)

$$\frac{S(f)}{S(f_p)} = [\exp(\frac{4}{3})](f/f_p)^{-4} \exp[-\frac{4}{3}(f/f_p)^{-3}]; \beta=3 \tag{36}$$

(b) Normalized design frequency spectrum for shallow water on the offshore side of the reef (5 ft depth)

$$\frac{S(f)}{S(f_p)} = [\exp(\frac{3}{2})](f/f_p)^{-3} \exp[-\frac{3}{2}(f/f_p)^{-2}]; \beta=2 \tag{37}$$

(c) Normalized design frequency spectrum for shallow water on the shoreward side of the reef (3 ft depth)

$$\frac{S(f)}{S(f_p)} = [\exp(2)](f/f_p)^{-2} \exp[-2(f/f_p)^{-1}]; \beta=1 \tag{38}$$

These non-dimensional design frequency spectra are plotted on Fig. 15 and they are compared with the following well-known Bretschneider frequency spectrum with $\beta=4$ for deep water,

$$\frac{S(f)}{S(f_p)} = [\exp(\frac{5}{4})](f/f_p)^{-5} \exp[-\frac{5}{4}(f/f_p)^{-4}] \tag{39}$$

The normalized non-dimensional period spectrum can be obtained from Eq. (19),

$$S(T) = E\alpha\beta T^{\beta-1} \exp(-\alpha T^\beta)$$

At $T = T_p$

$$\frac{dS(T)}{dT} = 0 \quad T_p^{-\beta} = \frac{\alpha\beta}{\beta-1} \quad \text{then} \quad \alpha = \frac{\beta-1}{\beta} T_p^{-\beta}$$

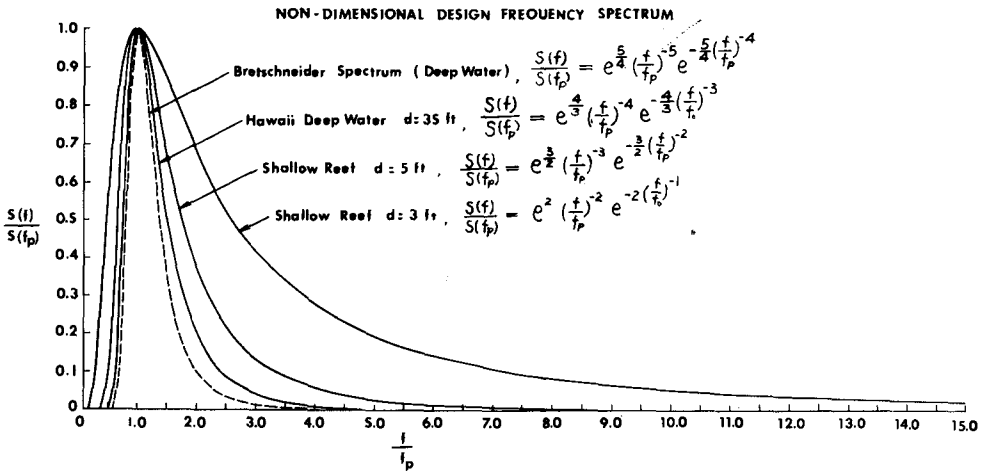


Fig. 15 Non-dimensional design frequency spectra

Then

$$S(T) = E(\beta-1)T_p^{-1}(T/T_p)^{\beta-1} \exp[-(\frac{\beta-1}{\beta})(T/T_p)^\beta] \tag{40}$$

$$S(T_p) = E(\beta-1)T_p^{-1} \exp[-(\frac{\beta-1}{\beta})] \tag{41}$$

The non-dimensional period spectrum has the general form of

$$\frac{S(T)}{S(T_p)} = [\exp(\frac{\beta-1}{\beta})](T/T_p)^{\beta-1} \exp[-(\frac{\beta-1}{\beta})(T/T_p)^\beta] \tag{42}$$

Then, the normalized design period spectra are:

(a) Normalized swell period spectrum (offshore 35 ft depth)

$$\frac{S(T)}{S(T_p)} = [\exp(\frac{2}{3})](T/T_p)^2 \exp[-\frac{2}{3}(T/T_p)^3] \tag{43}$$

(b) Normalized design period spectrum for shallow water on the off-shore side of the reef (5 ft depth)

$$\frac{S(T)}{S(T_p)} = [\exp(\frac{1}{2})](T/T_p) \exp[-\frac{1}{2}(T/T_p)^2] \tag{44}$$

The Bretschneider normalized period spectrum is

$$\frac{S(T)}{S(T_p)} = [\exp(\frac{3}{4})](T/T_p)^3 \exp[-\frac{3}{4}(T/T_p)^4] \tag{45}$$

The shape of the period spectrum was compared in Fig. 16.

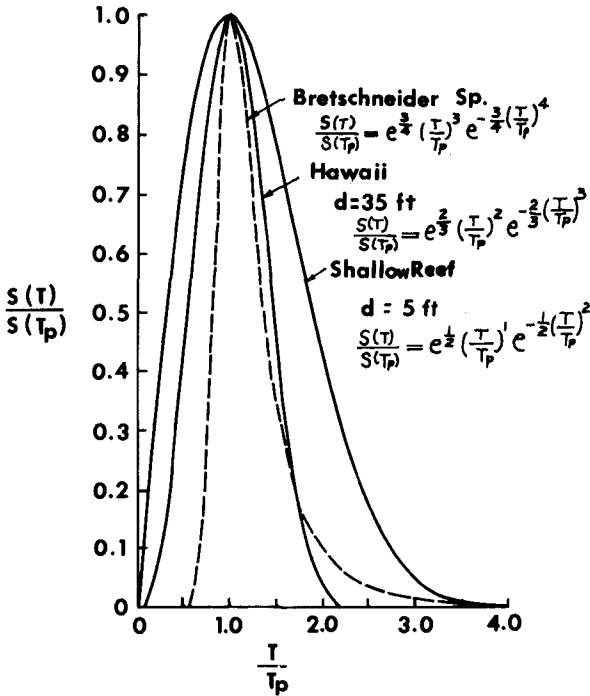
Note that the peak frequency is related to the peak period as follows:

$$f_p^{-1} = (\frac{\beta+1}{\beta-1})^{1/\beta} T_p \tag{46}$$

The relationship between the spectrum and zero up-crossing period statistics was established and compared with others as listed in Table 1.

Ratio	Subject Study			Goda [1974]	Haring et al. [1976]	Manohar et al. [1976]
	range	shallow	offshore			
\bar{T}_z/T_p	0.22-0.58	0.38±0.09	0.46±0.08	0.75	0.52	
$T_{H_z, 1/3}/T_p$	0.28-0.80	0.49±0.13	0.71±0.12	0.94	0.75	0.78
$T_{H_z, 1/10}/T_p$	0.29-0.91	0.54±0.15	0.80±0.10		0.76	
$T_{H_z, max}/T_p$	0.23-1.03	0.66±0.31	0.89±0.11		0.77	
$T_{H_z, 1/3}/T_{m01}$	1.02-2.24	1.47±0.30	1.29±0.06	1.30	1.33	
\bar{T}_z/T_{m02}	1.13-2.46	1.62±0.30	1.16±0.03	1.20	1.15	

Table 1 Range, shallow water and offshore mean values with standard deviations, and comparison with other workers, of Ala Moana results, 1976.



Note that the ratios are significantly reduced by shallow water. This occurs because the peak period of the spectrum is usually constant but the zero up-crossing periods are reduced due to the shifting of energy into the high frequency range. The standard deviation or scattering in the data is much greater in shallow water than offshore.

The spectrum contains a height to period relationship which is linearly dependent on the first spectrum moment (m_1). The best-fit equation with excellent correlation coefficient $P_{12}=0.975$, is

$$\frac{H_z^2}{T_z} = 4.828 m_1 \quad (47)$$

Fig. 16 Non-dimensional design period spectra

Furthermore, comparison of the spectrum peakedness and the

peakedness of the period distribution produced linear correlation. A peaked spectrum (large β) should correspond to a peaked period distribution.

(B) Zero up-crossing spectrum (ZUS)

The zero up-crossing spectrum (ZUS) is defined as

$$S(f) = g(f) \cdot \frac{1}{8} H_{rms}^2(f) \quad (48)$$

which states that the energy density at frequency f is equal to one eighth the square of the zero up-crossing root mean square wave height at that frequency multiplied by the probability that frequency f will occur in the record. For the discrete case

$$S(f) = \frac{\sum_{i=1}^m H_i^2(f)}{8N \cdot \Delta f} \quad (49)$$

where Δf is the frequency interval and includes waves with frequencies from $f - \Delta f/2$ to $f + \Delta f/2$; N is the total number of waves in the record; m is the number of waves of zero up-crossing height H_i with frequencies that lie in the interval defined above. The definition states that the energy is large in a band if many waves fall in the band and if the amplitude of those waves is large.

Under the above definition, the energy of each wave is assumed to be $H^2/8$ which is only true for sinusoidal waves. It is not essential to do

this as $H_i^2(f)/8$ can be replaced by $E_i(f)$ where E_i is the variance of the time series between the two zero up-crossings which defined the height $H_i(f)$. For simplicity, the definition of $H^2/8=E$ is retained here.

The confidence interval for each estimate is

$$\begin{aligned} & \log S(f) + \log m/\chi_m(\alpha/2) , \\ & \log S(f) + \log m/\chi_m(1 - \alpha/2) \end{aligned} \tag{50}$$

at the $1 - \alpha/2$ confidence level, where χ_m is Chi-squared with m degrees of freedom.

The Fourier spectrum (FS) and ZUS are compared on Fig. 17. It showed that the FS and ZUS have distinct similarities but cannot be considered identical. The ZUS is more peaked than the FS. The ZUS allocates most energy over a narrower range than the FS, due to the fact that the zero up-crossing technique selects waves in this range. The ZUS is less stable away from the peak where the number of occurrences in each band decreases and the confidence widens.

The major advantage of the ZUS is that linearity is not required. Because each zero up-crossing wave is isolated from its neighbors, when the spectrum is considered in this manner the problem of interpretation of sinusoidal components at harmonic frequencies in a non-linear environment does not arise. This is useful for shallow water applications. Another advantage is that the spectrum contains a height to frequency relationship which is easily retrieved from the spectrum as

$$H_{rms}^2(f) = \frac{8N \cdot \Delta f \cdot S(f)}{m} \tag{51}$$

The major disadvantage is that if one only had the ZUS it would not be possible to recreate the time series, as the spectrum contains no information about the order in which waves occur. This is unfortunate for

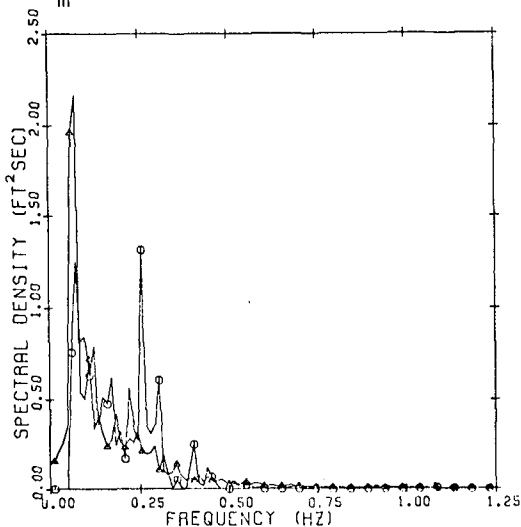


Fig. 17(a) Fourier spectrum (Δ) and ZUS (\circ) for September 7, probe 5, Ala Moana, 1976.

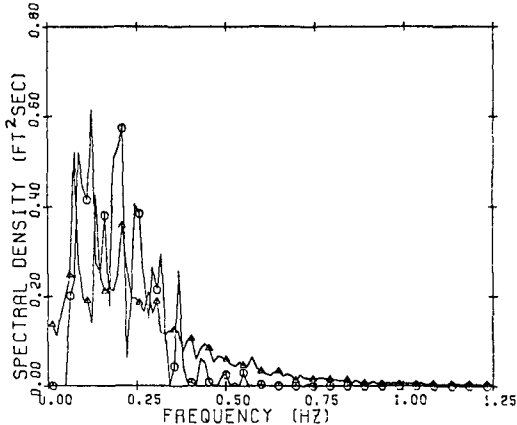


Fig. 17(b) Fourier spectrum (Δ) and ZUS (\circ) for September 7, probe 3, Ala Moana, 1976.

applications where a spectrum is used to generate a sea surface for theoretical studies. Other disadvantages are criticisms aimed at the zero up-crossing procedure in general.

The ZUS is a useful tool for describing ocean waves. For engineering applications, the zero up-crossing analysis in general has some specific advantages and the ZUS is an extension of this approach. It shows the energy partition in a fashion similar to the Fourier spectrum and one can obtain all the statistics such as the significant wave height and period, etc. during the analysis. These cannot be easily obtained in shallow water from the Fourier spectrum.

The ZUS was fitted to the shape of the Weibull distribution given by

$$S(f) = E\alpha\beta f^{-\beta-1} \exp(-\alpha f^{-\beta}) \quad (52)$$

The peakedness, β , varies from 2.17 to 4.18 and is largest just seaward of the breaker zone.

The best-fit ZUS spectrum with Weibull distribution can be used to obtain period parameters from the following relationships

$$T_{m01} = m_0/m_1 = \frac{\alpha^{-1/\beta}}{\Gamma(1-1/\beta)} \quad (53)$$

$$T_{m02} = (m_0/m_1)^{1/2} = \frac{\alpha^{-1/\beta}}{\Gamma(1-2/\beta)} \quad (54)$$

The relationship of mean period (\bar{T}_z) from the zero up-crossing analysis to mean period (T_{m01}) of the ZUS, and to mean apparent period (T_{m02}) of the ZUS are given as follows:

$$\bar{T}_z/T_{m01}(\text{ZUS}) = \begin{array}{ll} 1.106 \pm 0.122 & \text{shallow reef} \\ 0.826 \pm 0.061 & \text{offshore} \end{array} \quad (55)$$

$$\bar{T}_z/T_{m02}(\text{ZUS}) = \begin{array}{ll} 1.303 \pm 0.189 & \text{shallow reef} \\ 0.977 \pm 0.085 & \text{offshore} \end{array}$$

It was shown that the peak of the ZUS occurs at or near the peak of the wave frequency distribution so that the confidence is best near the ZUS peak.

In summary, both the ZUS and Fourier spectra are used to test the adequacy of formulae which estimate individual wave parameters. The results for shallow water deviate significantly from the Rice's (1944 and 1945) theory, which is often used to estimate period statistics.

(C) Cross Spectrum

Cross spectra analysis was made to obtain gain function and required coherency for all time series between the adjacent shallow water probes on the reef. It was found that the squared coherency is close to unity near the peak frequency. This means that the output spectrum near the peak can be predicted from the input by applying the gain function because the system is linear in this frequency range. However, the squared coherency was extremely small for other frequencies above 0.25 Hz. There are energy gains from the probe in the breakers to the next probe shorewards in the mid-frequency range. The relative phase of the two adjacent time series showed that the waves were non-dispersive below approximately 0.25 Hz in shallow water. Typical squared coherency and gain function as a function of probe position on the reef is shown in Fig. 18.



Fig. 18(a) Squared coherency, Ala Moana, September 23, 1976.

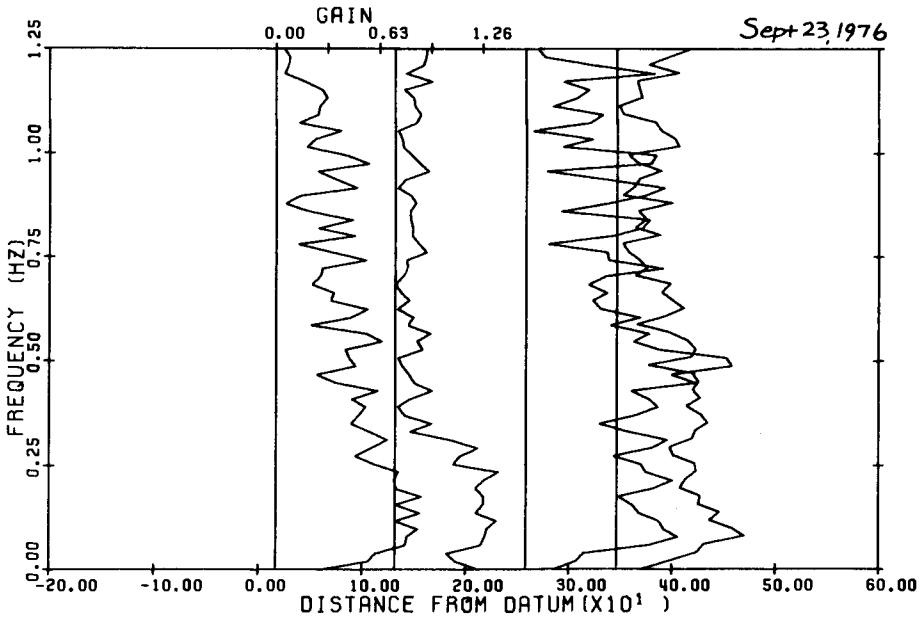


Fig. 18(b) Gain function, G(f), Ala Moana, September 23, 1976.

REFERENCES

- Arham, M., and R. Ezraty (1975), "Saisie et Analyse de Données des Courants Particulaires au Voisinage du Fond Dans La Houle Littorale Proche du Deferlement," La Houille Blanche No. 7/8, 1975, p. 484-496.
- Black, K.P. (1978), "Wave Transmission Over Shallow Reef (Field Measurements and Data Analysis)," Tech. Rep. 78-42, J.K.K. Look Laboratory of Oceanographic Eng., Univ. of Hawaii, March 1978 (Also published as M.S. thesis, "Wave Transformation on a Coral Reef," Univ. of Melbourne, Aust., April 1978).
- Battjes, J.A. (1972), "Set-up Due to Irregular Waves," Proc. of 13th International Conference on Coastal Eng. (July 10-14, 1972, Vancouver, Canada), ASCE, N.Y., 1972, p. 1993-2004.
- Bushing, F. (1976), "Energy Spectra of Irregular Surf Waves," Proc. of 15th International Conference on Coastal Eng. (July 1976, Honolulu), ASCE, p. 539-559.
- Goda, Y. (1974), "Estimation of Wave Statistics from Spectral Info.," Proc. of Int. Symp. on Ocean Wave Measurement and Analysis," (Sept. 1974, New Orleans), ASCE.
- Haring, R.E., A.R. Osborne and L.P. Spenser (1976), "Extreme Wave Parameters Based on Continental Shelf Storm Wave Record," Proc. of 15th Int. Conf. on Coastal Eng. (July 1976, Honolulu), ASCE, p. 151-170.
- Kuo, C.T. and S.T. Kuo (1975), "Effect of Wave Breaking on Statistical Distribution of Wave Heights," Proc. of Civil Eng. in the Oceans III, Vol. 2, p. 1211-1231.
- Lee, T.T. (1978), "Wave Transmission over Shallow Reef (Laboratory Simulation)," Tech. Report 78-44, J.K.K. Look Laboratory of Ocean. Eng., December 1978 (in preparation).
- Longuet-Higgins, M.S. (1975), "On the Joint Distribution of the Periods and Amplitudes of Sea Waves," Jour. Geophys. Res., Vol. 80, No. 18, p. 2688-2694.
- Manohar, M., I.E. Mobarek and N.A. El. Sharaky (1976), "Characteristic Wave Period," Proc. of 15th Int. Conf. on Coastal Eng. (July 1976, Honolulu), ASCE, Vol. 1, p. 273-288.
- Rice, S.O. (1944 and 1945), "Mathematical Analysis of a Random Noise," Bell Systems Tech. Jour., Vol. 23, p. 184-294, 1944; and Vol. 24, p. 133-183, 1945.

ACKNOWLEDGMENTS

This study was jointly supported by Sea Grant, NOAA, the Governor's Office of Marine Affairs, University of Melbourne, and the University of Hawaii. Dr. Edward Thornton of the U.S. Naval Postgraduate School and Dr. J.A. Battjes of the University of Technology, Delft, provided technical assistance while they were at the University of Hawaii as Visiting Colleagues during the academic year 1975-1976 and summer 1976, respectively. Professor F. Gerritsen and George Weber assisted greatly during the course of study.

CHAPTER 34

WIND-GENERATED WAVE DIFFRACTION BY BREAKWATER GAP

by

Hooshang Raissi* and R. L. Wiegel**

SUMMARY

A number of hydraulic laboratory experiments were made of the diffraction of wind-generated waves by a breakwater gap. The directional spectra of the incident wave was used together with the water wave diffraction theory of Penny and Price for a breakwater gap to predict the energy spectra of the diffracted waves.

The difference between the predicted values of the energy spectral density and the measured values demonstrated the limits of using the above techniques. It is likely that this is due to the inadequacy of the diffraction theory of Penny and Price for a breakwater gap for certain ranges of B/L .

INTRODUCTION

For the engineering design and operation of a harbor, the designer often needs to know the wave period and the direction of the wave advance as well as the wave height in certain regions within the harbor.

Until recently, in the design of a harbor one or more predominant wave directions were considered, using the significant wave heights and periods. The effect of diffraction would then be calculated by using the Penny and Price method (1944), which gives a periodic solution for irrotational waves of infinitely long crest, constant amplitude and constant frequency.

Putnam and Arthur (1948) made an experimental study of diffraction by a one-arm ("semi-infinite") breakwater in deep water, using uniform periodic long-crested waves. Their experimental results showed a general agreement with the Penny and Price theory. Blue and Johnson (1949) made a similar experiment using a breakwater gap. Their experimental results also verified the general form of the wave diffraction theory.

* Formerly Graduate Student, University of California, Berkeley.

** Professor of Civil Engineering, University of California, Berkeley.

Due to the development of sophisticated computerized design techniques combined with the availability of new techniques for obtaining estimates of wave directional spectra, it is now desirable for the engineer to predict the power wave spectra at different locations within a proposed harbor during the analysis stages of the design of a harbor.

Mobarek and Wiegel (1967) proposed the use of directional spectra, combined with diffraction theory to determine the wave conditions at any desired location in a harbor. This method was applied to a semi-infinite breakwater and compared with experimental results (Mobarek and Wiegel, 1966; see also Fan, 1968; Fan and Borgman, 1970; Wiegel, Al-Kazily, and Raissi, 1971; Harms, 1975).

After some of these studies had been completed, additional hydraulic laboratory studies were made for the case of a breakwater gap and a new computer program was developed to solve the wave diffraction by a breakwater gap. The results of these studies are presented herein.

THEORETICAL CONSIDERATION

When water waves are intercepted by an obstacle such as a breakwater, diffraction occurs. W. G. Penny and A. T. Price showed in 1948 (see also their 1952 paper) that the solution presented by Sommerfeld in 1896 for the diffraction of light polarized in a plane parallel to the edge of a semi-infinite screen is also a solution of the water wave diffraction phenomenon.

The main assumptions in the Penny and Price solution (see Wiegel, 1964, for a summary of the theory and its verification) are:

1. The motion is irrotational.
2. The water is non-viscous, incompressible and of constant depth.
3. The wave amplitude is infinitely small.
4. The disturbance is propagated without changing form.
5. At the free surface, the pressure is constant.
6. At a fixed boundary, the normal component of the orbital velocity is zero.
7. There is no reflection from the harbor walls.
8. There is no refraction by the harbor bottom.

The water surface elevation, η , can be expressed as (Lamb, 1945):

$$\eta = \frac{A_1 \bar{k} C}{g} e^{i\bar{k} C t} \text{Cosh } \bar{k} d \cdot F(x, y) \quad (1)$$

Assume that the breakwater extends along the x-axis from the origin to infinity and the incident waves are travelling in the direction of the y-axis (Fig. 1). Assume the breakwater to be rigid and impervious. The normal component of the fluid velocity must be zero, there, so that

$$\frac{\partial \phi}{\partial y} = 0, \text{ at } y = 0 \text{ and } x \geq 0 \tag{2}$$

In terms of $f(x,y)$ the condition (2) becomes

$$\frac{\partial f}{\partial y} = 0, \text{ at } y = 0, \text{ and } x \geq 0 \tag{2a}$$

Summerfield's solution of the above problem is

$$f(x,y) = \frac{1+i}{2} \left[e^{-i\bar{y}k} \int_{-\infty}^{\sigma} e^{-\pi i u^2/2} du + e^{i\bar{y}k} \int_{-\infty}^{-\sigma} e^{-\pi i u^2/2} du \right] \tag{3}$$

where

$$\sigma^2 = \frac{4}{L} (\bar{r} - y) \quad \sigma'^2 = \frac{4}{L} (\bar{r} + y) \quad r^{-2} = x^2 + y^2$$

and u is a dummy variable. The signs for σ and σ' depend on the position of (x,y) in the four quadrants (Fig. 1).

The diffraction coefficient, K' , is defined as the ratio of the wave height in the area affected by diffraction to the wave height in the area unaffected by diffraction, which is the height of the incident wave (Penny and Price, 1952); therefore:

$$K' = | F(x,y) |$$

The phase value is given by the argument of $f(x,y)$.

Eq. (3) can be transformed into a form that allows the use of tabulated functions. For detailed mathematical treatment, refer to Putnam and Arthur (1948), Blue and Johnson (1949), and Wiegel (1962).

Penny and Price developed a superposition method by which the problem of diffraction by a gap may be solved by using two solutions for semi-infinite breakwaters, one to the right and one to the left of the opening. Blue and Johnson put the method in a form more convenient to apply, and in an experimental check found that the theory was substantially verified. While Penny and Price and Blue and Johnson studied the

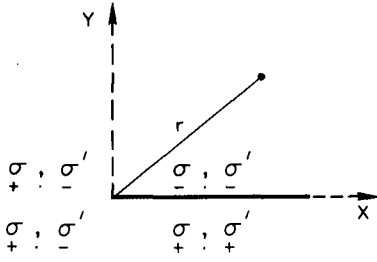


FIG. 1: DEFINITION SKETCH OF SEMI-INFINITE BREAKWATER

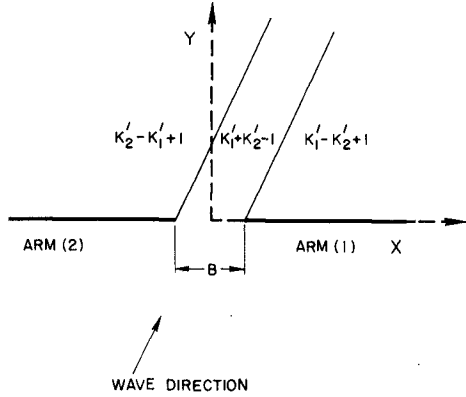


FIG. 2: DEFINITION SKETCH OF A BREAKWATER GAP

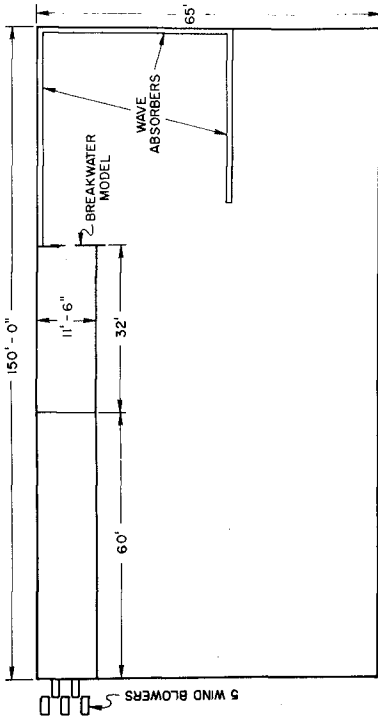
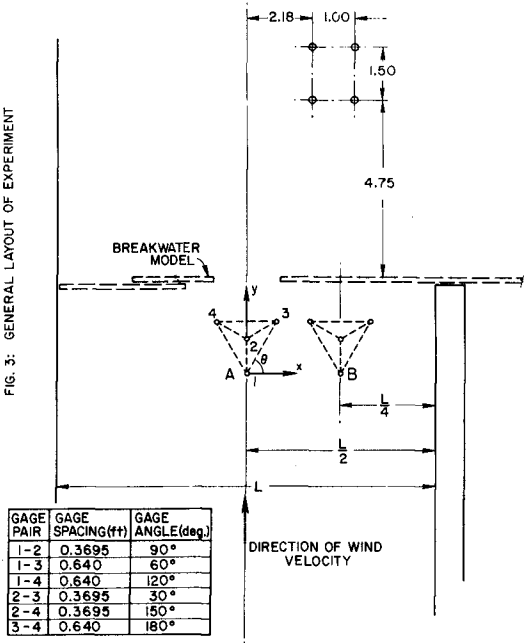


FIG. 3: GENERAL LAYOUT OF EXPERIMENT



GAGE PAIR	GAGE SPACING(ft)	GAGE ANGLE(deg.)
1-2	0.3695	90°
1-3	0.640	60°
1-4	0.640	120°
2-3	0.3695	30°
2-4	0.3695	150°
3-4	0.640	180°

FIG. 4: ARRANGEMENT OF WAVE GAGE ARRAYS

method only for normal incident waves, another study (California Institute of Technology, 1952) shows that the method may be extended to more general angles of incidence.

The two separate values of K' at a given point are combined by very definite rules, depending upon the location of the point.

The rules for combining two values of K' may be explicitly stated, ignoring the diffraction of the reflected wave by breakwater arms (Blue and Johnson, 1948; California Institute of Technology, 1952), as

(a) in the shadow of the right breakwater $K' = K'_1 + K'_2 + 1$

where the subscript 1 and 2 refer to right and left arms, respectively, Fig. 2.

(b) in the geometrically exposed area beyond the gap in the direction of wave travel, $K' = K'_1 + K'_2 - 1$.

(c) in the shadow of the left breakwater $K' = K'_2 - K'_1 + 1$.

The above equations are simple algebraic additions.

A computer program, GAPDFRAK, was developed to calculate the one-dimensional energy spectrum at any specified location inside the breakwater gap, for a measured or assumed two-dimensional ("directional") incident wave spectrum input (Raissi and Wiegel, 1971).

EXPERIMENTAL ARRANGEMENTS

The experiment was conducted in the Hydraulic Engineering Laboratory of the University of California at its Richmond Field Station. Wind waves were generated by means of five blowers located at the one end of a wind-wave tunnel. The blowers were arranged in parallel, each with a 5,000 ft³/min design capacity. The wind-wave tunnel is 11½ feet wide, 2½ feet deep and 60 feet long with its downstream end being connected to an open channel of the same width, but 32 feet long. The tunnel and the channel were both constructed in a corner of the 65 feet by 150 feet by 2½ feet deep wave basin. Wave absorbers were placed all around the basin so that wave reflection was eliminated for all practical purposes (Fig. 3).

Four wave gages in a star-shaped array (Mobarek and Wiegel, 1967) are shown in Fig. 4, and were used to measure the incident waves in front of the breakwater, before the installation of breakwater, in two positions - A and B. Each gage is a parallel wire resistance type made up of two half-round stainless steel wires glued together by an epoxy which has a high electrical resistance.

Also, four wave gages were used to measure the diffracted wave, each gage made of two parallel wires spaced one inch apart. The location of the wave gages are shown in Fig. 4.

Two commercially available four-channel rectilinear writing oscillographs and "Hydra", an electronic digitizer with an 8-channel magnetic tape recorder, were used to record simultaneously the outputs from the wave gages.

A moveable 2 feet by $11\frac{1}{2}$ feet vertical and impervious double-arm breakwater was built. The breakwater was designed in such a way that the size of the gap could be changed (Fig. 5).

EXPERIMENTAL PROCEDURE

Experimental data were taken for two different water depths and for three different wind speeds. Diffracted wave records were obtained for different gap values. The procedure for each run was as follows:

1. The water in the basin was set to the required depth.
2. The breakwater was lifted out of the water.
3. The Sanborn recorder connected to the incident wave gages was balanced.
4. The Sanborn recorder and Hydra were calibrated.
5. A demagnetized tape of 200 density was placed on the Hydra.
6. The required number of blowers were started and allowed to run until equilibrium was achieved.
7. The Sanborn recorders and Hydra were then switched on for a period of 24 seconds.
8. The recorders were switched off and the incident gages were lifted out and disconnected from Hydra.
9. The diffraction wave gages were connected to the recorders and Hydra, and the recorders and Hydra were balanced.
10. The recorders and Hydra were calibrated again.
11. The breakwater gap was set to the required value.
12. The required number of blowers were started and allowed to reach equilibrium.
13. The breakwater was lowered into the proper position very fast (Figs. 6, 7, 8).



FIG. 6: PHOTO SHOWING INCIDENT WIND GENERATED WAVES, BREAKWATER IN PLACE.



FIG. 8: PHOTO SHOWING INCIDENT AND DIFFRACTED WIND GENERATED WAVES.

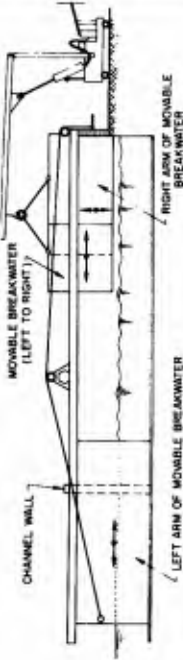


FIG. 5: MODEL BREAKWATER WITH A GAP



FIG. 7: PHOTO SHOWING DIFFRACTED WIND GENERATED WAVES.

14. The recorders and Hydra were started again for 12 seconds (10 seconds after lowering the breakwater gap).
15. Hydra, recorder and blowers were turned off.

RECORD LENGTH, NYQUIST FREQUENCY,
AND CONFIDENCE INTERVAL

Hydra has eight channels; wave gage #1 was connected to channels 1 and 5, wave gage #2 connected to channels 2 and 6, etc. The complete cycle from channel 1 back to 1 took 0.012 seconds. The data used in the analysis were averages of each pair of two measurements, that is, the output from gage #1 on channel 1 and channel 5 were averaged, etc., which resulted in a "smoothing" of the data. The averaging was done as the work of Fan (1968) indicated that it was appropriate to do so.

For the experiment considered herein (incident waves)

$n = 1998$ (total number of data points)

$T_n = 24$ sec (total effective record length)

$\Delta t = 0.012$ (the sampling interval [sec])

and the Nyquist frequency, $F_N = 1/2 \Delta t = 1/2 \times 0.012 = 41.2$ cps. From previous experiments it was found that there was little energy in the wave spectra for large frequency waves; the highest frequency considered in the analysis was taken as 30.

Blackman and Tukey (1958) give the relationships among the number of equivalent degrees of freedom (K), the number of lags (m), the lag interval ($\Delta\tau$), the length of record ($n\Delta t$) and the resolution (R) as

$$R = 1/m\Delta\tau = 1/T_m \text{ cycles per second}$$

$$K = 2 \left[\frac{T_n}{T_m} - \frac{P_d}{3} \right]$$

$$= 2 \left[\frac{T_n}{T_m} - \frac{1}{3} \right] \text{ for one piece of record}$$

where:

$\Delta\tau = h\Delta t =$ lag interval, seconds ($h = 1$ for this case)

$T_m = m\Delta\tau =$ maximum lag, seconds

$P_d =$ number of separate pieces of record = 1 for our case.

For this experiment, $T_m = 0.6$ sec., $R = 1.66$, and $K = 79.4$.

For calculating the confidence limit, a graph in the report of Borgman (1967) was used. For $K = 79.4$, $\hat{S}(f)$ will exceed $1.42 S(f)$ in only 5% of the samples measured, and will be greater than $0.76 S(f)$ in 95% of the samples measured, where $\hat{S}(f)$ is an estimate of $S(f)$.

DATA REDUCTION

After the water surface elevations at constant intervals were recorded on magnetic tape by Hydra, the calibration records were printed out using the computer program developed for this purpose (Raissi and Wiegel, 1971). This program tabulates the time histories of the water surface elevation from a datum.

The tabulated values of the calibration records were then used as a scale to convert the time history records of the wave to a time history of water surface elevation measured in feet from still water level.

Data were obtained for the following conditions:

TABLE 1. INCIDENT WAVE CONDITIONS

Run No.	No. of Blowers Turned On	Depths of the Water (feet)	No. of Data Points per Gage	Position (Fig. 2)
1	2	1.2	1998	A
2	3	1.2	1998	A
3	5	1.2	1998	A
4	2	1.2	1998	B
5	3	1.2	1998	B
6	5	1.2	1998	B
7	2	0.72	1998	B
8	3	0.72	1998	B
9	5	0.72	1998	B
10	2	0.72	1998	A
11	3	0.72	1998	A
12	5	0.72	1998	A

TABLE 2. DIFFRACTED WAVE CONDITIONS

Run No.	No. of Blowers Turned On	No. of Data Points per Gage	x (feet)	y (feet)	D Gap Size (feet)	Water Depth (feet)
1	2	856	2.45	5.5	1.56	1.2
2	3	856	2.45	5.5	1.56	1.2
3	2	856	2.45	5.5	1.87	1.2
4	3	856	2.45	5.5	1.87	1.2
5	2	856	2.45	5.5	2.18	1.2
6	3	856	2.45	5.5	2.18	1.2
7	2	856	2.45	5.5	2.50	1.2
8	3	856	2.45	5.5	2.50	1.2
9	2	856	2.45	5.5	3.00	1.2
10	3	856	2.45	5.5	3.00	1.2

The data for these conditions were recorded on magnetic tapes No. 4941 and 5957, respectively, which are presently stored at the Computer Center and at the Hydraulic Engineering Laboratory, University of California, Berkeley, California, 94720.

RESULTS AND DISCUSSION

The incident energy spectra were computed for each of the records, and also the directional spectra using the computer programs WAVEIN and TRANSFORM (Raissi and Wiegel, 1971). Then, from the directional spectra the diffracted energy spectra were computed using the computer program GAPDIFF (Raissi and Wiegel, 1971).

Also, from the measured diffracted waves records, the diffracted energy spectra were computed using the computer program DFSPEC (Raissi and Wiegel, 1971). Finally, the predicted energy spectra were plotted against frequency.

A few samples of predicted and measured wave spectra behind the breakwater gap are shown in Figs. 9a through 9t.

The results of the predicted wave spectra appear to be smaller than the measured values. Considering the results of Wiegel, Al-Kazily, and Raissi (1971), which shows good agreement between the highest calculated points of the predicted spectra with its equivalent value on the measured spectra, for a single-arm breakwater, together with the experimental results of diffraction coefficient for a gap by Blue and Johnson (1948), the following conclusions can be made:

- (a) For the case: $B = 1.56$ ft. (gap size); $L = 1.56$ ft.
(wave length with highest energy spectral density; $B/L = 1.0$.)

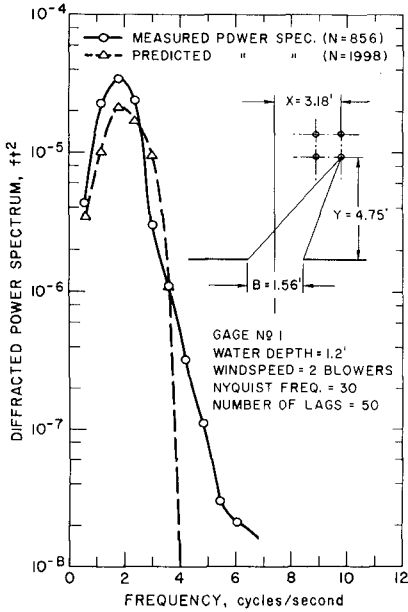


FIG. 9a: COMPARISON OF MEASURED AND PREDICTED POWER SPECTRA FOR B=1.56 FT.

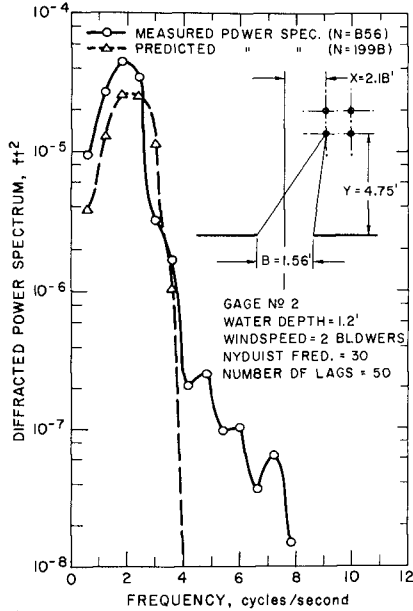


FIG. 9b: COMPARISON OF MEASURED AND PREDICTED POWER SPECTRA FOR B=1.56 FT.

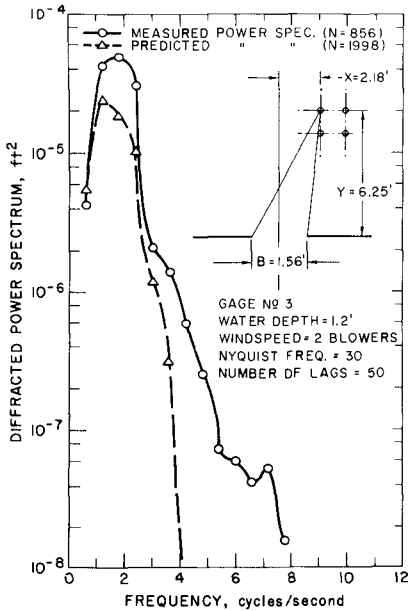


FIG. 9c: COMPARISON OF MEASURED AND PREDICTED POWER SPECTRA FOR B=1.56 FT.

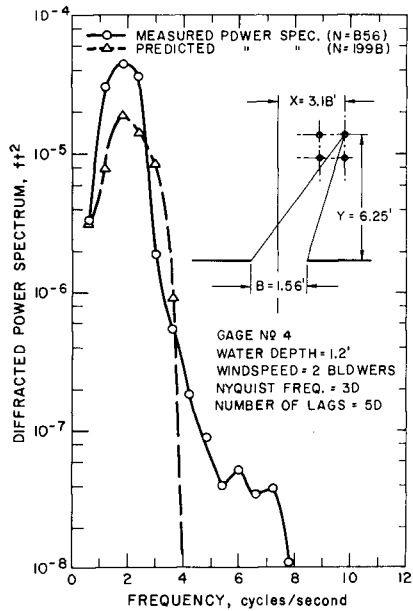


FIG. 9d: COMPARISON OF MEASURED AND PREDICTED POWER SPECTRA FOR B=1.56 FT.

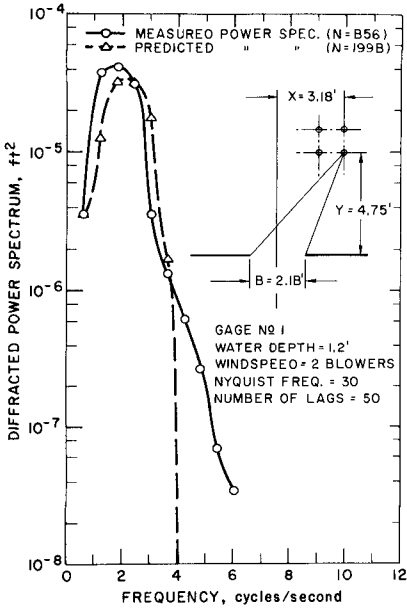


FIG. 9e: COMPARISON OF MEASURED AND PREDICTED POWER SPECTRA FOR $B=2.18$ FT.

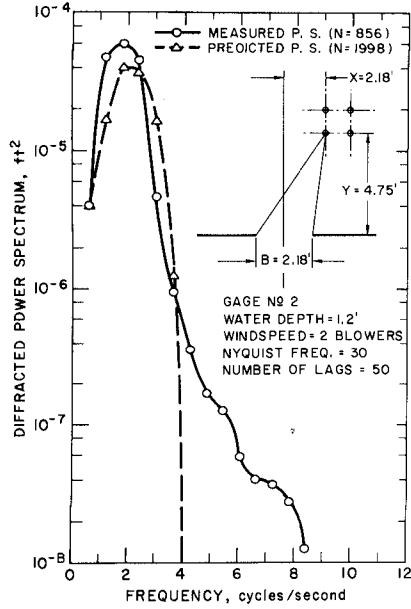


FIG. 9f: COMPARISON OF MEASURED AND PREDICTED POWER SPECTRA FOR $B=2.18$ FT.

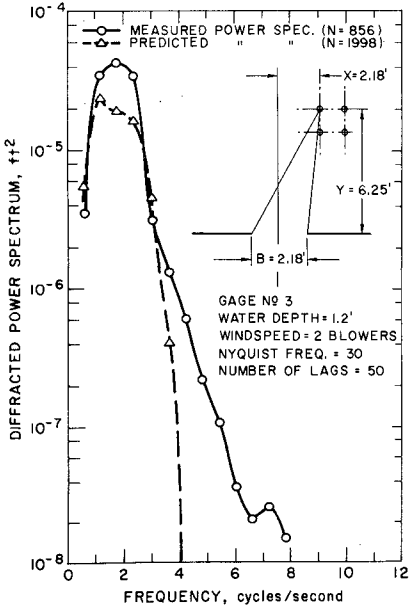


FIG. 9g: COMPARISON OF MEASURED AND PREDICTED POWER SPECTRA FOR $B=2.18$ FT.

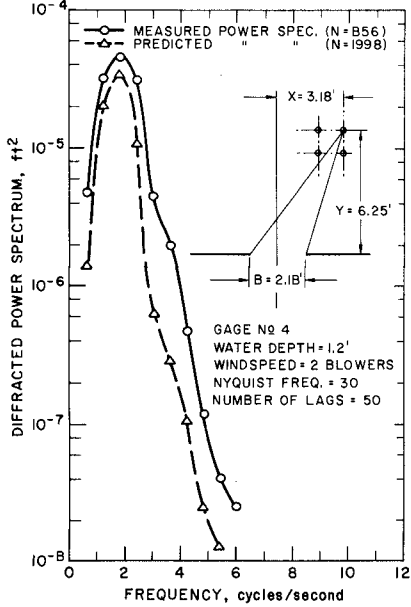


FIG. 9h: COMPARISON OF MEASURED AND PREDICTED POWER SPECTRA FOR $B=2.18$ FT.

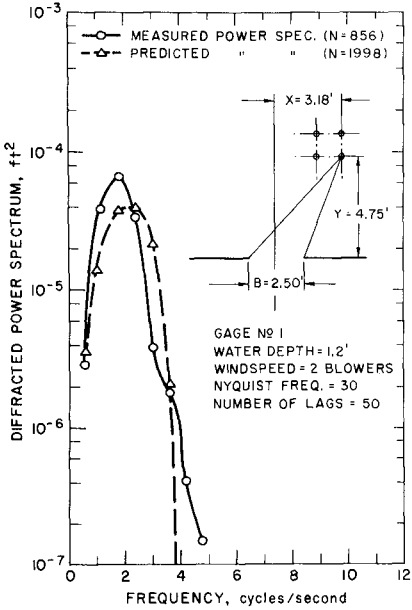


FIG. 9f: COMPARISON OF MEASURED AND PREDICTED POWER SPECTRA FOR B = 2.50 FT.

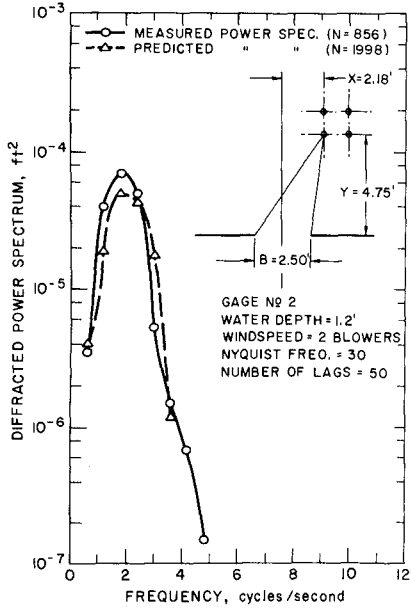


FIG. 9g: COMPARISON OF MEASURED AND PREDICTED POWER SPECTRA FOR B = 2.50 FT.

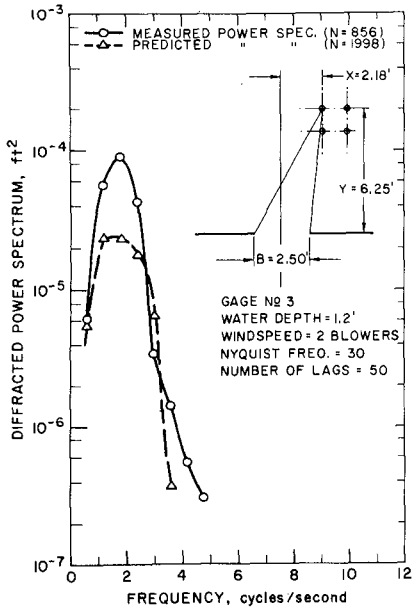


FIG. 9h: COMPARISON OF MEASURED AND PREDICTED POWER SPECTRA FOR B = 2.50 FT.

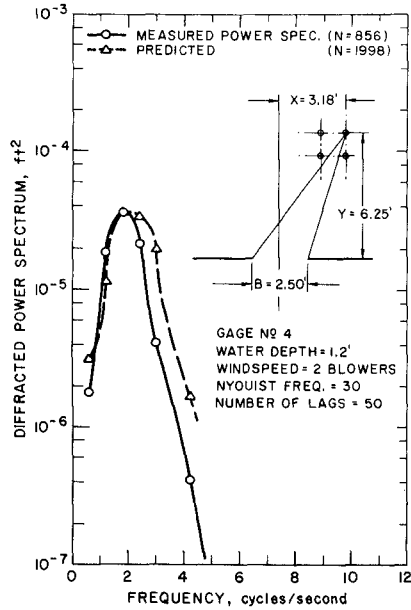


FIG. 9i: COMPARISON OF MEASURED AND PREDICTED POWER SPECTRA FOR B = 2.50 FT.

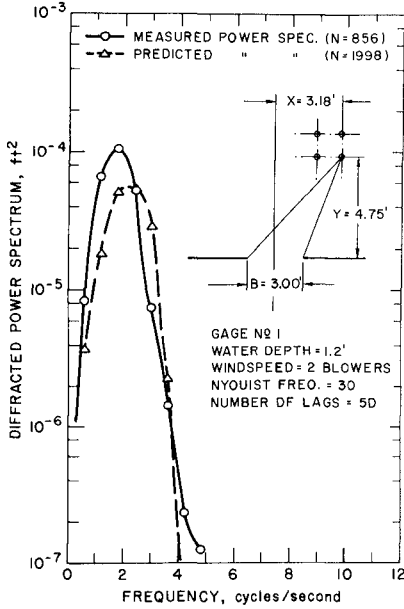


FIG. 9m: COMPARISON OF MEASURED AND PREDICTED POWER SPECTRA FOR $B=3.00$ FT.

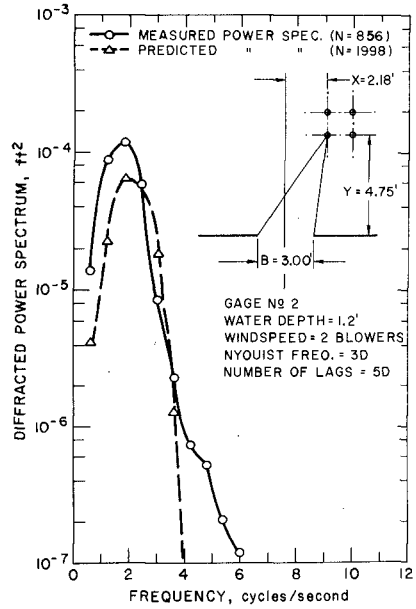


FIG. 9n: COMPARISON OF MEASURED AND PREDICTED POWER SPECTRA FOR $B=3.00$ FT.

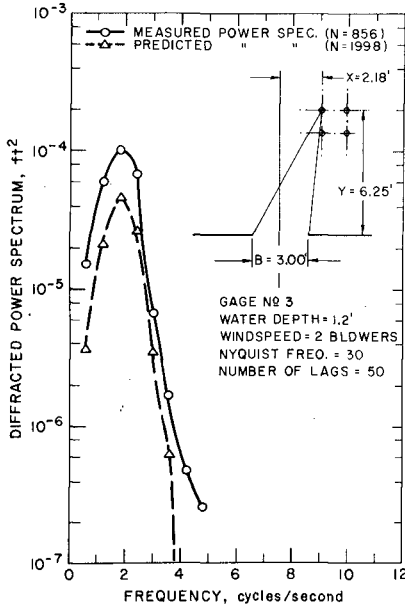


FIG. 9o: COMPARISON OF MEASURED AND PREDICTED POWER SPECTRA FOR $B=3.00$ FT.

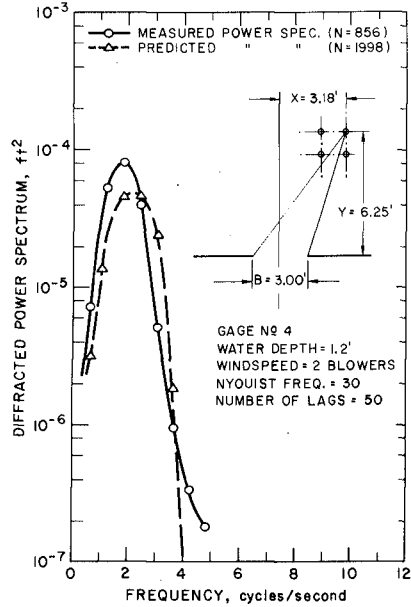


FIG. 9p: COMPARISON OF MEASURED AND PREDICTED POWER SPECTRA FOR $B=3.00$ FT.

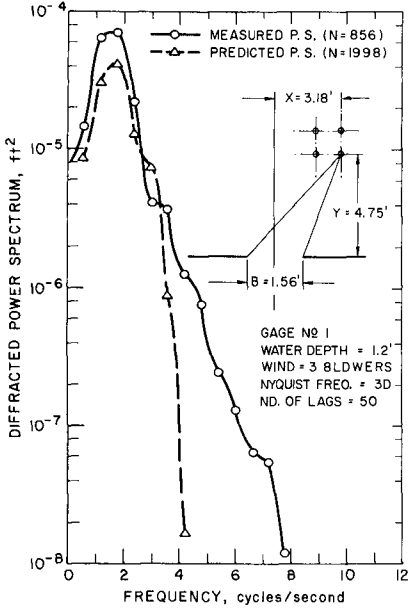


FIG. 9q: COMPARISON OF MEASURED AND PREDICTED POWER SPECTRA FOR $B=1.56$ FT.

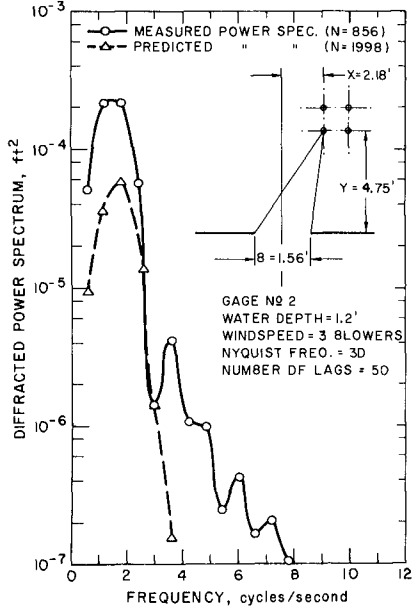


FIG. 9r: COMPARISON OF MEASURED AND PREDICTED POWER SPECTRA FOR $B=1.56$ FT.

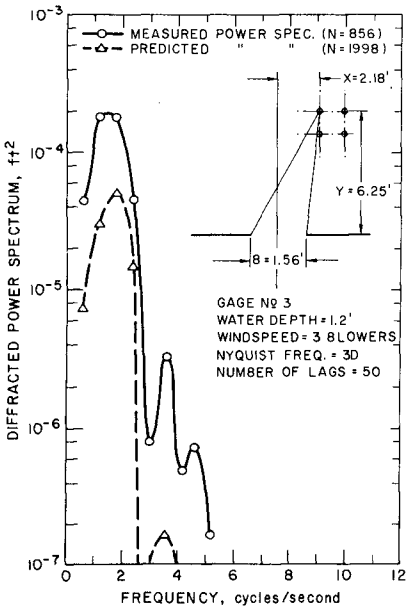


FIG. 9s: COMPARISON OF MEASURED AND PREDICTED POWER SPECTRA FOR $B=1.56$ FT.

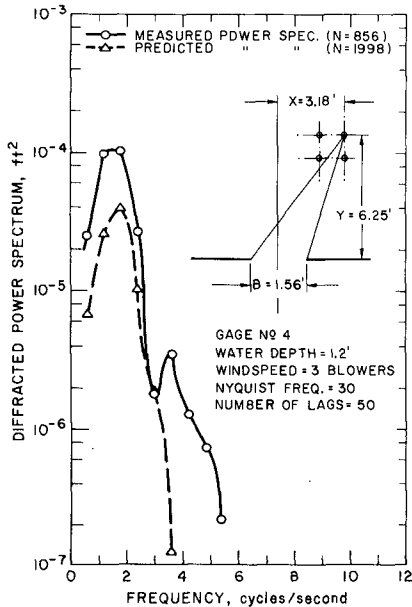


FIG. 9t: COMPARISON OF MEASURED AND PREDICTED POWER SPECTRA FOR $B=1.56$ FT.

The Penny and Price theoretical solution does not meet the exact boundary conditions along the breakwater, and the main difference between the measured power spectra and the predicted one (the ratio M.P.S/P.P.S. is as high as 2 for some cases) is mainly due to the poor results of Penny and Price theory for this particular condition ($B/L = 1$). The Morse-Rubenstein diffraction theory would be more accurate for small gaps (California Institute of Technology, 1952).

- (b) For the case: $B = 2.18$ ft. (gap size); $L = 1.56$ ft.
(wave with highest energy spectral density); $B/L = 1.4$.

The experimental results verify the predicted values of diffracted wave power spectra. Blue and Johnson obtained good results for the above conditions for regular waves.

- (c) For the cases, $B = 2.50$ ft.; $L = 1.56$; $B/L = 1.6$; and $B = 3.00$;
 $L = 1.56$; $B/L = 1.92$.

The experimental results of power spectra for diffracted wave seem to be higher than the predicted one. This difference was also obtained by Blue and Johnson. They found in areas not very close to the center line (where the wave recording gages of this experiment were located), there is a distinct tendency for experimental values of K' (the diffraction coefficient) to exceed the theoretical ones. This might be due to the increased curvature of the wave crests in the regions of steepest waves which cause greater outward flow of the wave energy from the center line than indicated by the theory. This results in decreased K' values near the gap center line and increase in K' quantities towards the flanks.

In the case of steeper incident waves (wave generated with higher wind velocity) and larger breakwater gap, the tendency of the wave energy to flow outward from the centerline is more, causing greater difference between theoretical K' and the experimental one (experimental results verify it).

For discussion regarding the techniques of measuring directional spectra of incident wave which has been used in this paper, the reader is referred to Wiegel, Al-Kazily, and Raissi (1971).

ACKNOWLEDGMENT

The work presented herein was performed under contract DACW 72-68-C-0016 between the Coastal Engineering Research Center Corps of Engineers, U. S. Army, and the University of California.

REFERENCES

Blackman, R.B., and J.W. Tukey, *The Measurement of Power Spectra*, Dover Publications, New York, 1958.

- Blue, R.L. and J.W. Johnson, "Diffraction of Water Waves Passing Through a Breakwater," *Trans. Amer. Geophys. Union*, Vol. 29, 1948, pp. 481-590.
- Borgman, Leon E., *Statistical Time Series Analysis, Short Course in Statistical Time Series Analysis for Engineers*, March 20-25, 1967, Univ. Extension, Univ. of California, Berkeley, Calif.
- Borgman, Leon E., *Directional Spectra Models for Design Use for Surface Waves*, Tech. Rept. HEL 1-12, Hyd. Eng. Lab., Univ. of California, Berkeley, June 1969.
- California Institute of Technology, *Wave Protection Aspects of Harbor Design*, Report No. E-11, August 1952.
- Fan, Shou-shan, and Leon E. Borgman, "Computer Modelling of Diffraction of Wind Waves," *Proc. Twelfth Conf. on Coastal Engineering*, Washington, D.C., Sept. 13-18, 1970, ASCE, Vol. 1, Chap. 29, pp. 473-476.
- Harms, Volker, *Diffraction of Water Waves by Cylindrical Structures of Arbitrary Shape*, Tech. Rept. HEL 1-23, Hyd. Eng. Lab., Univ. of California, Berkeley, Dec. 1975.
- Lamb, H., *Hydrodynamics*, Dover Publications, 1945.
- Mobarek, Ismail, and Robert L. Wiegel, "Diffraction of Wind Generated Waves," *Proc. Tenth Conf. Coastal Engineering*, ASCE, Vol. 1, 1967, pp. 185-206.
- Panicker, N.N., *Determination of Directional Spectra of Ocean Waves from Gage Arrays*, Tech. Rept. HEL 1-18, Hyd. Eng. Lab., Univ. of California, Berkeley, 1971.
- Penny, W.G., and A.T. Price, "The Diffraction Theory of Sea Waves by Breakwater and the Shelter Afforded by Breakwater," *Phil. Trans. Royal Soc. (London)*, Ser. A, Vol. 244, March 1952, pp. 253-263.
- Putnam, J.A., and R.S. Arthur, "Diffraction of Water Waves by Breakwaters," *Trans. Amer. Geophys. Union*, Vol. 29, 1948, pp. 481-490.
- Raissi, Hooshang, and R. L. Wiegel, *Diffraction of Wind Generated Waves by a Breakwater Gap*, Tech. Rept. HEL 1-20, Hyd. Eng. Lab., Univ. of California, Berkeley, Dec. 1971.
- Sommerfield, A., "Mathematische Theorie der Diffraction," *Math. Ann.*, Vol. 47, 1896, pp. 317-374.
- Van Wijngarden, A., and W. L. Scheen, *Table of Fresnel Integrals*, Rept. R49, Computation Dept., Mathematical Center, Amsterdam, 1949.
- Wiegel, R.L., "Diffraction of Wave by Semi-infinite Breakwater," *Jour. Hyd. Div., Proc. ASCE*, Vol. 88, No. HY1, Jan. 1962, pp. 27-44.

Wiegel, R.L., M.F. Al-Kazily, and H. Raissi, *Wind Generated Wave Diffraction by a Breakwater*, Tech. Rept. HEL 1-19, Hyd. Eng. Lab., Univ. of California, Berkeley, 1971.

Wiegel, R.L., *Oceanographical Engineering*, Prentice-Hall, 1964.

Wiegel, R.L., "Parallel Wire Resistance Wave Meter," *Proc. First Conf. on Coastal Engineering Instruments*, Berkeley, California, Oct. 31-Nov. 2, 1955, Council on Wave Research, The Engineering Foundation, 1956, pp. 39-43.

NOTATION

A	= a constant in linear wave theory, ft ² /sec
B	= breakwater gap size, ft
d	= water depth, ft
f	= wave frequency, 1/wave period, 1/sec
F_N	= Nyquist frequency, 1/2 Δt , 1/sec
g	= gravitational acceleration, ft/sec ²
i	= $\sqrt{-1}$, dimensionless
\bar{k}	= wave number, 2π /wave length, 1/ft
K'	= diffraction coefficient, ratio of diffracted wave height to incident wave height, dimensionless
L	= wave length, ft
m	= maximum number of lags, dimensionless
n	= number of data points in each record, dimensionless
P_d	= number of separate pieces of record, dimensionless
\bar{r}	= $[x^2 + y^2]^{\frac{1}{2}}$, ft
R	= resolution, 1/m $\Delta\tau$, 1/sec
S(f)	= one-dimensional wave energy spectral density, ft ² -sec
$\hat{S}(f)$	= estimate of S(f), ft ² -sec
t	= time, sec
T	= length of record, sec

- T_m = $m\Delta\tau$, length of maximum lag, sec
 T_n = $n\Delta t$, total effective record length, sec
 u = a dummy variable, dimensionless
 x = horizontal coordinate along breakwater, ft
 y = horizontal coordinate, normal to breakwater, ft
 Δ = time lag between consecutive recording on Hydra for wave gages 1-2, 2-3, 3-4, 1-4, etc., as specified, sec
 Δt = increment to time, time spacing between successive data samples in digitized record, $\Delta t = T/n$, sec
 $\Delta\tau$ = increment of lag, sec
 η = elevation of varying wave surface measured from mean water surface, ft
 θ = angle between x axis and direction of wave advance, deg
 ρ = mass density of water, slugs/ft³
 σ = $[4(\bar{r} - y)/L]^{1/2}$, dimensionless
 σ' = $[4(\bar{r} + y)/L]^{1/2}$, dimensionless
 ϕ = wave phase angle, deg

CHAPTER 35

DIFFRACTION DIAGRAMS FOR DIRECTIONAL RANDOM WAVES

Yoshimi Goda, Tomotsuka Takayama, and Yasumasa Suzuki

Marine Hydrodynamics Division, Port and Harbour Research Institute
Ministry of Transport, Nagase, Yokosuka, Japan

ABSTRACT

Conventional wave diffraction diagrams often yield erroneous estimation of wave heights behind breakwaters in the sea, because they are prepared for monochromatic waves while actual waves in the sea are random with directional spectral characteristics. A proposal is made for the standard form of directional wave spectrum on the basis of Mitsuyasu's formula for directional spreading function. A new set of diffraction diagrams have been constructed for random waves with the proposed directional spectrum. Problems of multi-diffraction and multi-reflection within a harbour can also be solved with serial applications of random wave diffraction.

INTRODUCTION

Since the proof by Penny and Price [1] that the diffraction of water waves by breakwaters can be analyzed with Sommerfeld's solution, wave heights behind breakwaters have been estimated with the aid of several diffraction diagrams [2~6]. The phenomenon of wave diffraction is a typical problem for which the solution of velocity potential can be applied with accuracy. Published as well as unpublished laboratory investigations have provided the proof of the validity of wave diffraction theory. Disagreement between the theory and experiment if any is usually attributed to inaccuracy in laboratory measurements. The only exception is the appearance of secondary waves around the tip of a breakwater owing to an excessive gradient of wave energy density there [7].

Such a success of theory, however, should be accepted with a caution when the theory is applied for sea waves characterized with irregularity. Most of diffraction diagrams currently available are those prepared for monochromatic waves with a single period from a single direction. The irregularity of sea waves especially of directional spreading produces the pattern of wave diffraction quite different from conventional diffraction diagrams. An experimental study by Mobarek and Wiegel [8] seems to be the first in demonstrating the application of directional wave spectrum to diffraction problems, though they did not present general diffraction diagrams for engineers' usage.

Being aware of these facts, Nagai [9,10] constructed diffraction diagrams for sea waves in 1972, which have been utilized by harbour engineers in Japan. Figure 1 is one of his diagrams, which shows the diffraction diagram for sinusoidal (monochromatic) waves in the left half and that for spectral waves in the right half for the opening width

of five times the wavelength; the difference between them is very clear. The directional wave spectrum employed for computation was of SWOP type [11], which is primarily for wind waves. In the present paper, recalculation is made of diffraction diagrams of random waves with a new proposal of directional wave spectrum, which is a modification of the spectrum originally formulated by Mitsuyasu et al. [12]. Though these diagrams were previously published in Japanese [13], slight corrections have been found necessary and they are duly corrected hereon. The present paper also discusses the behaviour of waves reflected by breakwaters, which can be deduced from Sommerfeld's solution as proved by one of the authors [14]. With the above knowledge, the problem of multi-diffraction and multi-reflection within a harbour can be solved numerically.

SPECTRAL CALCULATION OF WAVE DIFFRACTION

Random waves in the sea are described with a directional wave spectrum under the presumption that random wave profiles are the result of linear superposition of infinite number of infinitesimal wavelets with various frequencies and directions. According to this presumption, the spectrum of diffracted waves at a point (x,y) is calculated as

$$S_d(f|x,y) = \int_{\theta_{\min}}^{\theta_{\max}} S_i(f,\theta) K_d^2(f,\theta|x,y) d\theta, \quad (1)$$

where $S_i(f,\theta)$ denotes the directional spectrum of incident waves and $K_d(f,\theta|x,y)$ is the diffraction coefficient at a point (x,y) for waves with the frequency f and the direction θ . The spectrum of diffracted waves is given here in the form of frequency spectrum only, because the directional spreading of diffracted waves is limited by the aperture of the breakwater gap looked from the point (x,y) .

The representative heights of incident and diffracted waves are derived from the zeroth moment of spectrum by the theory of Longuet-Higgins [15]. For example, the significant heights are given by

$$(H_{1/3})_i = 4.0\sqrt{(m_0)_i}, \quad (2)$$

$$(H_{1/3})_d = 4.0\sqrt{(m_0)_d}, \quad (3)$$

where,

$$(m_0)_i = \int_0^{\infty} \int_{\theta_{\min}}^{\theta_{\max}} S_i(f,\theta) d\theta df, \quad (4)$$

$$(m_0)_d = \int_0^{\infty} S_d(f) df. \quad (5)$$

Though the constant of 4.0 in Eqs. 2 and 3 is better replaced by that of 3.8 for waves observed in the sea on the average, it does not affect the coefficient of diffraction for random waves, which is defined as

$$(K_d)_{\text{eff}} = (H_{1/3})_d / (H_{1/3})_i = \sqrt{(m_0)_d / (m_0)_i}. \quad (6)$$

The representative periods of diffracted waves are not necessarily the same with those of incident waves. The change of wave period by diffraction can be estimated by the theory of Rice [16] as

$$K_{dT} = \sqrt{\frac{(m_0)_d / (m_2)_d}{(m_0)_i / (m_2)_i}} \quad (7)$$

where,

$$(m_2)_d = \int_0^{\infty} f^2 S_d(f) df \quad (8)$$

$$(m_2)_i = \int_0^{\infty} \int_{\theta_{\min}}^{\theta_{\max}} f^2 S_i(f, \theta) d\theta df \quad (9)$$

The effect of the wave spectrum upon diffraction coefficient is demonstrated in Fig. 2, which shows the diffraction diagrams of a breakwater gap with the relative opening of $B = 3L$ for oblique incident waves with the angle of approach of 60° . The diffraction coefficient is calculated with the approximate method by superposition of Sommerfeld's solutions for two semi-infinite breakwaters. The upper diagram is for monochromatic waves and uni-directional irregular waves (with frequency spectrum only). The difference between them is small, thus indicating unimportance of frequency-wise irregularity. The lower diagram is for uni-frequency random waves with directional spreading and very random waves with a directional spectrum, which corresponds to the case of $S_{\max} = 10$ to be discussed in the next chapter. The difference between them is small, but the both are quite different from those in the upper diagram. Thus, Fig. 2 indicates that the directional spreading rather than the frequency-wise irregularity is important in the diffraction of random waves.

PROPOSAL OF DIRECTIONAL WAVE SPECTRUM

Functional Form

The directional wave spectrum is generally expressed as the product of a frequency spectrum $S(f)$ and a directional spreading function $G(f, \theta)$, that is,

$$S(f, \theta) = S(f) G(f, \theta) \quad (10)$$

The frequency spectrum $S(f)$ is given the unit of $m^2 \cdot \text{sec}$ or its equivalent one, while $G(f, \theta)$ is normalized so as to yield the unit value without a dimension when integrated over the full range of wave direction.

The functional form of $S(f)$ can be taken as Bretschneider's spectrum [17] modified by Mitsuyasu [18] to satisfy the condition of Eq. 2. Thus,

$$S(f) = 0.257 H_{1/3}^2 T_{1/3}^{-4} f^{-5} \exp[-1.03 (T_{1/3} f)^{-4}] \quad (11)$$

This is a type of two-parameter spectrum designated by an arbitrary combination of significant wave height and period, $H_{1/3}$ and $T_{1/3}$. The modal frequency or the frequency at spectral peak is set to satisfy the following relation:

$$f_p = \frac{1}{1.05 T_{1/3}} \quad (12)$$

This relation was proposed by Mitsuyasu [18] and has been confirmed to be representative of sea waves [19]. Spectral forms other than Eq. 11 are also eligible as the standard spectrum, but the change of frequency-wise spectral form will affect little the diffraction of random waves as suggested by Fig. 2.

As to the directional spreading function, the formula proposed by Mitsuyasu et al. [12] on the basis of their detailed observations seems most reliable at present. In a slightly modified form, it is written as

$$G(f, \theta) = G_0 \cos^{2S}(\frac{\theta}{2}), \quad (13)$$

where,

$$G_0 = \left[\int_{\theta_{\min}}^{\theta_{\max}} \cos^{2S}(\frac{\theta}{2}) d\theta \right]^{-1}, \quad (14)$$

$$S = \begin{cases} S_{\max} \cdot (f/f_p)^5 & : f \leq f_p, \\ S_{\max} \cdot (f/f_p)^{-2.5} & : f \geq f_p. \end{cases} \quad (15)$$

The term of G_0 is so introduced to normalize $G(f, \theta)$. The directional concentration parameter S has the maximum value at $f = f_p$ and decreases at the both sides of spectral peak.

Selection of S_{\max}

Figure 3 is a demonstration of wave patterns, which shows the contours of surface elevations above the mean water level; the portion of wave troughs is left as blank. This figure is a result of numerical simulation by the principle of linear superposition with the spectrum of Eqs. 10 to 15. The maximum directional concentration parameter S_{\max} is subjectively chosen as 10 and 75, respectively. It will be seen that $S_{\max} = 10$ yields the wave pattern quite random and somewhat resembling that of wind waves, while $S_{\max} = 75$ may corresponds to the wave pattern of swell.

The original proposal of Mitsuyasu et al. [12] for S_{\max} is to relate it with the nondimensional frequency parameter as

$$S_{\max} = 11.5 (2\pi f_p U/g)^{-2.5}, \quad (16)$$

where U denotes the wind speed and g is the acceleration of gravity. Equation 16 is not readily applicable for engineering problems because the design wave height and period are often designated without reference to the wind speed. The knowledge of wave growth depicted in the SMB method suggests that the increase of the parameter $2\pi f_p U/g (= U/C_p)$ is associated with the decrease in the wave steepness H_0/L_0 . Thus, S_{\max} can be assumed to increase as the wave steepness decreases. The assumption is supported by the example of Fig. 3 discussed in the above.

From the above discussions, the authors propose the following values of S_{\max} for engineering applications:

$$S_{\max} = \begin{cases} 10 & : \text{for wind waves,} \\ 25 & : \text{for swell with short to medium decay distance,} \\ 75 & : \text{for swell with medium to long decay distance.} \end{cases} \quad (17)$$

Though the above proposal is somewhat subjective, $S_{\max} = 10$ for wind waves is not without ground because it yields the overall directional distribution almost the same with the law of $(2/\pi)\cos^2\theta$ and the formula of SWOP. Figure 4 shows the nondimensional cumulative curves of wave energy calculated for the directional wave spectrum of Eqs. 10 to 15. The term of $P_E(\theta)$ is calculated by

$$P_E(\theta) = \frac{1}{m_0} \int_{-\pi/2}^{\theta} \int_0^{\infty} S(f, \theta) df d\theta. \quad (18)$$

The diagram can be utilized to allocate the relative wave energy to several wave directions such as expressed in sixteen points bearings. Calculation of $P_E(\theta)$ also yields the approximate relation of

$$\ell = 0.11 S_{\max} : \ell \geq 2, \quad (19)$$

for the type of $G(f, \theta)$ of the following:

$$G(f, \theta) \equiv G(\theta) = \frac{2\ell!!}{\pi(2\ell-1)!!} \cos^2\ell\theta, \quad (20)$$

where $2n!! = 2n \cdot (2n-2) \cdots 4 \cdot 2$ and $(2n-1)!! = (2n-1) \cdot (2n-3) \cdots 3 \cdot 1$.

When applying the above spectrum in shallow water, some correction to S_{\max} is necessary because the phenomenon of wave refraction makes the directional spreading to lessen. Calculation of wave refraction in the water of parallel straight bathymetry has yielded the diagram for the change of S_{\max} in shallow water as shown in Fig. 5. The angle $(\alpha_p)_0$ denotes the incident wave angle to the boundary of deep to shallow waters. As the effect of $(\alpha_p)_0$ is small, the diagram may be utilized for waters of general bathymetry.

RANDOM WAVE DIFFRACTION BY A SEMI-INFINITE BREAKWATER

With the directional wave spectrum specified in the above, the computation of random wave diffraction is straightforward so long as the value of diffraction coefficient for monochromatic waves corresponding to spectral components are computable. The integrals in Eqs. 1, 4, and others are to be evaluated in the form of finite series. The number of frequency components does not need to be great, but the number of directional components should be carefully selected in consideration of the trade-off between the accuracy and computation time. When the diffraction coefficient in the area far distant from the breakwater is to be calculated, a large number of directional components are required.

Examples of the diffraction diagrams of semi-infinite breakwater are shown in Fig. 6 for the case of normal incidence for waves with $S_{\max} = 10$ and 75. The diffraction coefficient of wave heights, or $(K_d)_{\text{eff}}$, is shown with contours of solid lines, while the ratio of wave period is shown with contours of dashed lines. A characteristic feature of Fig. 6 is that the diffraction coefficient takes the value of about 0.7 along the boundary of geometric shadow. This value is about 1.4 times the coefficient of monochromatic wave diffraction. In the sheltered area, the random wave diffraction yields the coefficient far larger than that of monochromatic waves.

An verification of the superiority of random diffraction analysis has been provided by Irie [20] with the wave data at Akita Port. Two wave recorders of inverted echo sounder type were set outside and inside a long breakwater as shown in Fig. 7, and the simultaneous observation was carried out in November and December, 1973. The principal direction of waves incident to the breakwater were read from the images of a radar with the wavelength of 8.6 mm, which is commonly employed in Japan for detection of wave direction since around 1962. During the period of observation, the principal wave direction varied in a narrow range of N85°W to N110°W and the direction of N106°W was employed in the calculation of diffraction coefficient. The result of analysis is summarized in Fig. 8. The observed data were classified by Irie into three categories of dispersive, median, and concentrated wave patterns as judged on the radar image. In the computation of random wave diffraction, the maximum directional concentration parameter of Eq. 17 was subjectively applied for these wave categories with the correction of shallow water effect by Fig. 5. Though the scatter of data makes difficult the assessment of the accuracy of random diffraction analysis, it yields quite reasonable estimates of wave heights behind the breakwater. The monochromatic wave analysis, on the other hand, yields the diffraction coefficient being one half to one quarter of the observed value, thus revealing its inapplicability to the problem of sea wave diffraction.

RANDOM WAVE DIFFRACTION THROUGH A GAP OF BREAKWATERS

Another example of the effectiveness of random diffraction analysis has been given by one of the authors [21]. Wave observation were carried out at three stations in Nagoya Port from 1967 to 1970, which is located at the recess of Ise Bay, Japan. As indicated on the inset of Fig. 9, the stations A and B were positioned outside and inside of a long mole of caisson type. The diffraction coefficient for monochromatic waves at the station B is plotted in this figure for predominant wave period of $T = 3$ sec. The waves diffracted from the east entrance penetrate to the station only when the incident wave direction is from SSSW to SSE, and the waves from the west entrance is appreciable for the incident direction of NW to WNW only. Thus the diffraction coefficient for monochromatic waves is very sensitive to the incident wave direction.

Observed wave records did not exhibit such a directionality, as shown in the example of Fig. 10, where the wave spectra at the stations A and B are compared. The wave direction is estimated as SW from the wind record. As the diffraction coefficient for monochromatic waves is about 0.07, the spectral density of the station B would have been about 1/200 of the density of the station A if the diffraction were to be calculated for monochromatic waves. The observed spectrum at B had the density of about 1/10 to 1/20 of the spectrum at A, and it was nearly in agreement with the spectrum calculated as the random wave diffraction phenomenon although the directional spreading function of $(2/\pi)\cos^2\theta$ was employed in the calculation for the sake of simplicity. The agreement of observed and calculated spectra is an evidence of the necessity of introducing random wave analysis in diffraction problems.

Figures 11 to 14 are the result of the computation of random wave diffraction with the directional spectrum described by Eqs. 10 to 15.

The left half of each diagram is for the change of wave period, while the right half is for the wave height ratio. The abscissa and ordinate are normalized with the opening width B instead of the wave length L . In applying these diagrams, appropriate selection of S_{\max} is to be made and interpolation of the diffraction coefficient from the diagrams for $S_{\max} = 10$ and 75 will be required.

COMBINATION OF WAVE REFLECTION AND DIFFRACTION

In the analysis of wave tranquility in a harbour, wave reflections from quaywalls and other solid structures often become the source of troubles. Breakwaters with vertical faces may also cause additional agitation in the area outside the breakwaters. The height of waves reflected by a semi-infinite rigid breakwater can be estimated by means of the well known Sommerfeld's solution. To illustrate the applicability of the solution, it is rewritten in the following form:

$$F_d(r, \alpha, f, \theta) = F_{id}(r, \alpha, f, \theta) + F_{rd}(r, \alpha, f, \theta) \quad (21)$$

where $F(r, \alpha, f, \theta)$ denotes the dimensionless complex wave amplitude at the point P with the distance r and the angle α from the tip of a semi-infinite breakwater for the incident wave with the frequency f and the direction θ (see Fig. 15). The complex amplitudes F_{id} and F_{rd} are expressed respectively as

$$\begin{aligned} F_{id} &= \frac{1}{\sqrt{2}} \exp[i\{kr \cos(\alpha - \theta) + \frac{\pi}{4}\}] \times [\{C(\gamma_1) + \frac{1}{2}\} - i\{S(\gamma_1) + \frac{1}{2}\}] \\ &= \exp[i\{kr \cos(\alpha - \theta)\}] \\ &\quad + \frac{1}{\sqrt{2}} \exp[i\{kr \cos(\alpha - \theta) + \frac{\pi}{4}\}] \times [\{C(\gamma_1) - \frac{1}{2}\} - i\{S(\gamma_1) - \frac{1}{2}\}], \end{aligned} \quad (22)$$

$$\begin{aligned} F_{rd} &= \frac{1}{\sqrt{2}} \exp[i\{kr \cos(\alpha + \theta) + \frac{\pi}{4}\}] \times [\{C(\gamma_2) + \frac{1}{2}\} - i\{S(\gamma_2) + \frac{1}{2}\}] \\ &= \exp[i\{kr \cos(\alpha + \theta)\}] \\ &\quad + \frac{1}{\sqrt{2}} \exp[i\{kr \cos(\alpha + \theta) + \frac{\pi}{4}\}] \times [\{C(\gamma_2) - \frac{1}{2}\} - i\{S(\gamma_2) - \frac{1}{2}\}], \end{aligned} \quad (23)$$

where,

$$\left. \begin{aligned} \gamma_1 &= \sqrt{\frac{4kr}{\pi}} \cos \frac{\alpha - \theta}{2}, \\ \gamma_2 &= \sqrt{\frac{4kr}{\pi}} \cos \frac{\alpha + \theta}{2}, \end{aligned} \right\} (24) \quad \left. \begin{aligned} C(\gamma) &= \int_0^\gamma \cos \frac{\pi}{2} x^2 dx, \\ S(\gamma) &= \int_0^\gamma \sin \frac{\pi}{2} x^2 dx. \end{aligned} \right\} (25)$$

In the derivation of the second expressions from the first ones of Eqs. 22 and 23, the following equality is employed:

$$\begin{aligned} \{C + \frac{1}{2}\} - i\{S + \frac{1}{2}\} &= [\{C - \frac{1}{2}\} - i\{S - \frac{1}{2}\}] + [1 - i] \\ &= [\{C - \frac{1}{2}\} - i\{S - \frac{1}{2}\}] + \sqrt{2} \exp[-i \frac{\pi}{4}]. \end{aligned} \quad (26)$$

As the distance r increases infinitely, the Fresnel integrals defined by Eq. 25 converge to the values listed in Table 1 depending on

the regions in question. Referring to Table 1, it will be readily understood that F_{id} represents the sum of the incident waves and the associated scattered waves, while F_{rd} represents the sum of the reflected waves and the associated scattered waves. Moreover, the primary reflected waves exist only in the region I, whereas the region III is primarily occupied by scattered waves.

Table 1. Behaviour of Fresnel Integrals at $r = \infty$

Region	$C(\gamma_1)$	$S(\gamma_1)$	$C(\gamma_2)$	$S(\gamma_2)$	Primary Waves
I	1/2	1/2	1/2	1/2	incident, reflected, and scattered waves
II	1/2	1/2	-1/2	-1/2	incident and scattered waves
III	-1/2	-1/2	-1/2	-1/2	scattered waves

The above decomposition of Sommerfeld's solution leads to the calculation of reflected waves by means of F_{rd} . If the reflective boundary is finite in its extension, the amplitudes of reflected waves can be approximately calculated by superimposing the two solutions of F_{rd} for the both tips of the reflective boundary as in the technique of calculating wave diffraction through a gap of two semi-infinite breakwaters. For a partially reflective boundary, the coefficient of wave reflection is introduced to linearly reduce the amplitudes of reflected waves. For example, wave pattern around a semi-infinite breakwater with partial wave reflectivity can be calculated by

$$F_d(r, \alpha, f, \theta) = F_{id}(r, \alpha, f, \theta) + K_r F_{rd}(r, \alpha, f, \theta), \quad (27)$$

where K_r denotes the reflection coefficient. Equation 27 remains as an approximation because K_r usually does not carry the information of phase relation except for the cases of $K_r = 1$ and 0.

An experimental verification of the above analysis [14] has been done for the layout of model breakwaters shown in Fig. 16. The breakwaters are made of vertical walls. Incident waves are diffracted by the right breakwater, but some of them are reflected by the rear face of the left breakwater. Experiments were carried out with uni-directional irregular waves, which had the significant height and period of $H_{1/3} = 1.8$ cm and $T_{1/3} = 1.08$ sec; their spectrum could be approximately expressed by Eq. 11. The result of measurements are shown in Fig. 17 for comparison with the theoretical calculation. Good agreement between them is observed except along the line of $x = 8$ m. The difference is due to an assumption employed in the calculation that the source area of wave reflection can be specified by the principle of geometric optics in order to simplify the procedure of calculation. The error due to such simplification is expected to decrease when the directional spreading characteristic of sea waves is introduced.

The analysis of the reflection of diffracted waves can be proceeded for much complicated harbour layout, even though the algorithm needs to be carefully established. Wave diffraction by overlapping breakwaters can also be solved with the knowledge of decomposed Sommerfeld's solution of Eqs. 21 to 23. An example of wave tranquility analysis for a complicated harbour layout is shown in Fig. 18, which represents

the Port of Yokohama in a slightly simplified form. Wind waves with the significant period of $T_{1/3} = 6.0$ sec are considered to come from the direction of SSE. The maximum directional concentration parameter of $S_{\max} = 10$ is employed in the computation. The specification of wave reflectivity of the boundaries is made somewhat subjectively in order to simplify the process of analysis of multi-reflection and multi-diffraction. Though the field data to verify the calculation is not available yet, Fig. 18 demonstrates the capacity of analyzing wave tranquility in a real harbour. It should be noted that the present analysis has no upper bound of application with regards to the size of harbour relative to wavelengths because of the nature of the theory of wave diffraction.

SUMMARY

The present paper has discussed the diffraction of sea waves with directional spectral characteristics. Major conclusions are as follows:

1. The inapplicability of diffraction analysis by monochromatic wave approach has been demonstrated by two examples of field observation data, which at the same time have proved the effectiveness of random diffraction analysis.
2. A standard form of directional wave spectrum is derived on the basis of the directional spreading function proposed by Mitsuyasu et al. Though the selection of directional concentration parameter is left to somewhat subjective judgement of engineers, it can deal with various stages of wind waves to swell.
3. Several diffraction diagrams are presented for a semi-infinite breakwaters and a breakwater gap for the case of normal incidence of directional random waves. The technique can be extended to the case of oblique incidence as well.
4. Sommerfeld's solution of diffracted wave amplitudes is decomposed into the terms of incident, reflected, and scattered waves. The decomposed solutions can be employed for analyzing the behaviour of waves reflected by rigid breakwaters and other reflective structures.
5. Wave tranquility in a harbour of large dimension can be analyzed by serial calculations of random wave diffraction and reflection.

It is mentioned here that the above technique of random wave diffraction analysis is daily utilized by harbour engineers in Japan with the aid of computer program operatable at the Computation Center of the Port and Harbour Research Institute, Ministry of Transport.

REFERENCES

- [1] Penny, W. G. and Price, A. T.: Diffraction of sea waves by breakwater, Artificial Harbour, Dire. Misc. Weapon Tech. His. No. 66, 1944.

- [2] Blue, F. L. and Johnson, J. W.: Diffraction of water waves passing through a breakwater gap, *Trans. A.G.U.*, Vol. 30, No. 5, 1948, pp.705-718.
- [3] Johnson, J. W.: Generalized wave diffraction diagrams, *Proc. 2nd Conf. Coastal Engg.*, Houston, 1952.
- [4] Wiegel, R. L.: Diffraction of waves by semi-infinite breakwater, *Proc. ASCE*, Vol. 88, No. HY1, 1962, pp.27-44.
- [5] Morihira, M. and Okuyama, I.: Computing method of sea waves and diffraction diagrams, *Tech. Note of Port and Harbour Res. Inst.*, No. 21, 1965, 60p. (in Japanese).
- [6] Takai, T.: The diffraction diagrams of sea waves by a breakwater gap, *Tech. Note of Port and Harbour Res. Inst.*, No. 66, 1969, 42p. (in Japanese).
- [7] Biesel, F.: Radiating second-order phenomena in gravity waves, *Proc. IAHR 10th Congress*, London, 1963, pp.197-203.
- [8] Mobarek, I. E. and Wiegel, R. L.: Diffraction of wind generated water waves, *Proc. 10th Conf. Coastal Engg.*, Tokyo, 1966, pp.185-206.
- [9] Nagai, K.: Computation of refraction and diffraction of irregular sea, *Rept. Port and Harbour Res. Inst.*, Vol. 11, No. 2, 1972, pp.48-119 (in Japanese)
- [10] Nagai, K.: Diffraction of the irregular sea due to breakwaters, *Coastal Engineering in Japan*, JSCE, Vol. 15, 1972, pp.59-67.
- [11] Cote, L. J. et al.: The directional spectrum of a wind generated sea as determined from data obtained by the Stereo Wave Observation Project, *Meteorological Papers*, Vol. 2, No. 6, New York Univ., 1960, 88p.
- [12] Mitsuyasu, H. et al.: Observation of the directional spectrum of ocean waves using a cloverleaf buoy, *J. Geophys. Res.*, Vol. 5, No. 4, 1975, pp.750-760.
- [13] Goda, Y. and Suzuki, Y.: Computation of refraction and diffraction of sea waves with Mitsuyasu's directional spectrum, *Tech. Note of Port and Harbour Res. Inst.*, No. 230, 1975, 45p. (in Japanese).
- [14] Takayama, T. and Kamiyama, Y.: Diffraction of sea waves by rigid or cushion type breakwaters, *Rept. Port and Harbour Res. Inst.*, Vol. 16, No. 3, 1977, pp.3-37.
- [15] Longuet-Higgins, M. S.: On the statistical distribution of the heights of sea waves, *J. Marine Res.*, Vol. XI, No. 3, 1952, pp. 245-265.

- [16] Rice, S. O.: Mathematical analysis of random noise, 1944 and 1945, reprinted in Selected Papers on Noise and Stochastic Processes, Dover Pub., Inc., 1954, pp.132-249.
- [17] Bretschneider, C. L.: Significant waves and wave spectrum, Ocean Industry, Feb. 1968, pp.40-46.
- [18] Mitsuyasu, H.: On the growth of the spectrum of wind-generated waves (I), Rept. Res. Inst. for Applied Mech., Kyushu Univ., Vol. XVI, No. 55, 1968, pp.459-482.
- [19] Goda, Y.: Statistical interpretation of wave data, Draft Contribution to the Committee Rept. I.1 to the 7th Int. Ship Structures Congress to be held in Paris, 1979.
- [20] Irie, I.: Examination of wave deformation with field observation data, Coastal Engineering in Japan, JSCE, Vol. 18, 1975, pp.27-34.
- [21] Goda, Y., Nagai, K., and Ito, M.: Wave observation at the Port of Nagoya (3rd Rept.), Tech. Note of Port and Harbour Res. Inst., No. 120, 1971, 24p. (in Japanese).
- [22] Bretschneider, C. L.: Wave variability and wave spectra for wind-generated gravity waves, U.S. Army Corps of Engrs., Beach Erosion Board, Tech. Memo., No. 113, 1959, 192p.

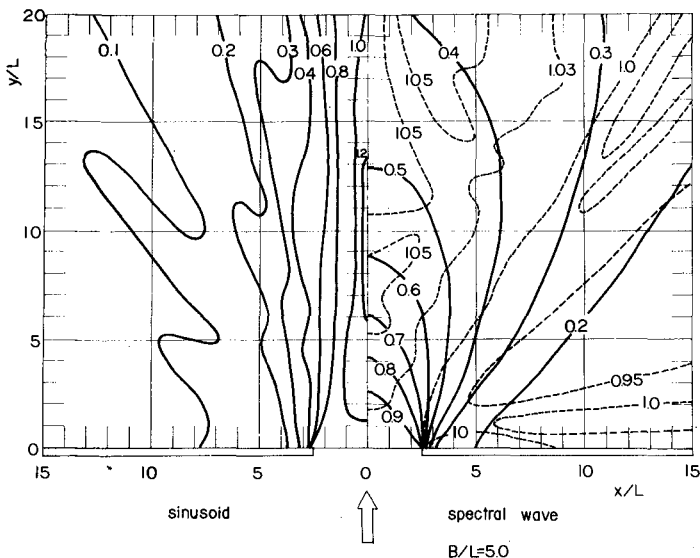
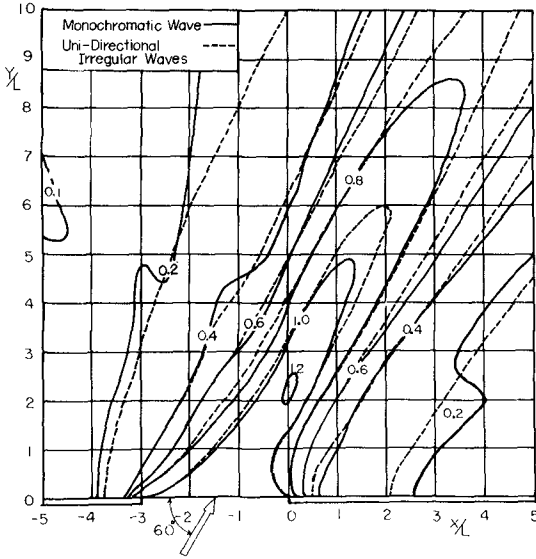
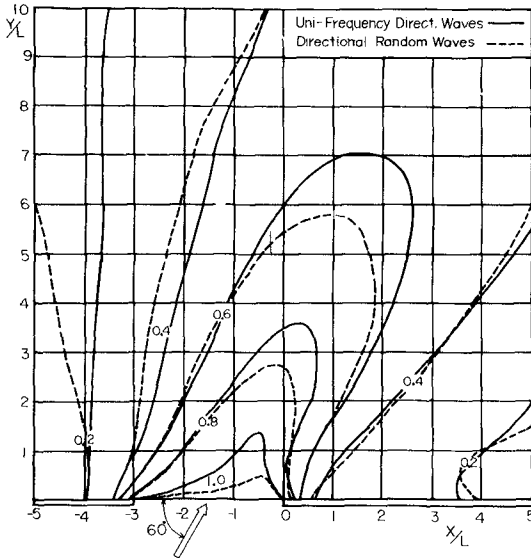


Fig. 1 Comparison of Monochromatic and Random Diffraction Diagrams for the Case of $B/L=5.0$ (after Nagai [9])



(a) monochromatic waves and uni-directional irregular waves



(b) uni-frequency directional waves and directional random waves

Fig. 2 Effect of Directional Spreading Characteristic upon Wave Diffraction through a Breakwater Gap

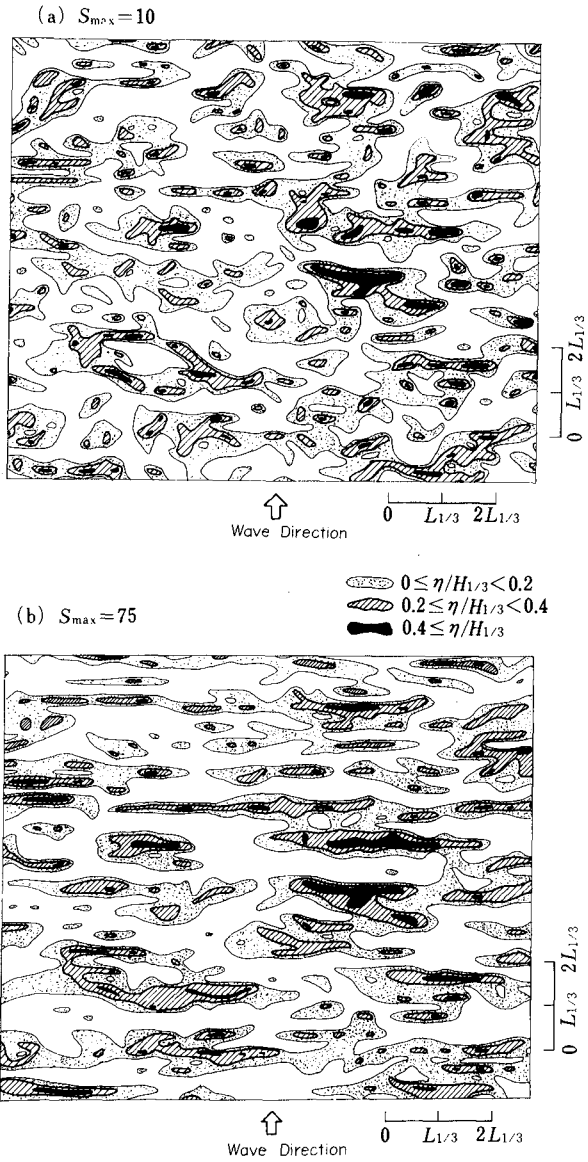


Fig. 3 Surface Elevation Contours of Random Waves by Numerical Simulation

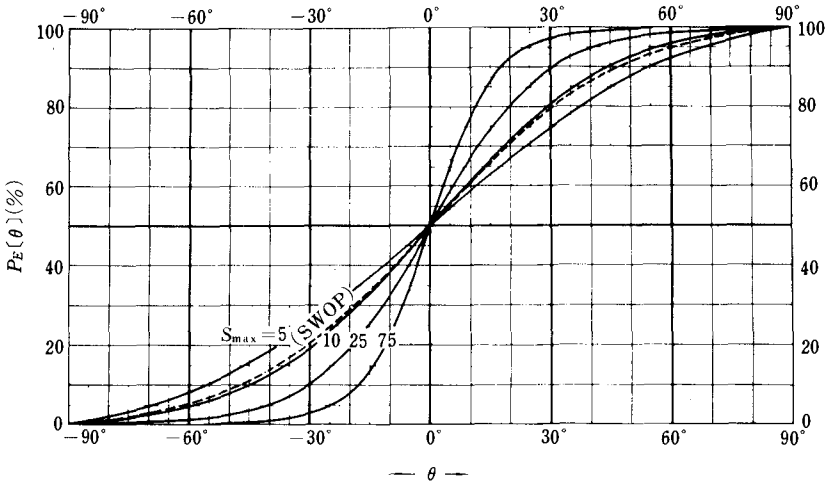


Fig. 4 Cumulative Curves of Relative Wave Energy with Respect to Azimuth from the Principal Wave Direction

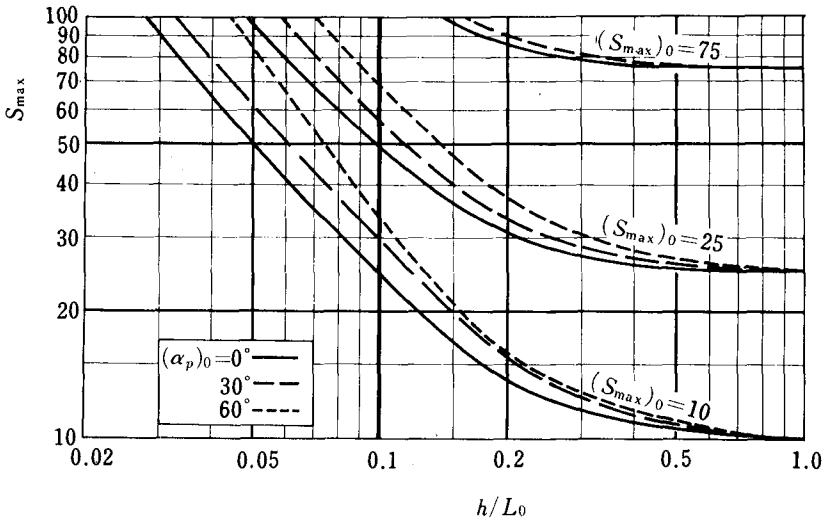


Fig. 5 Change of Maximum Directional Concentration Parameter, S_{max} , Due to Wave Refraction in Shallow Water

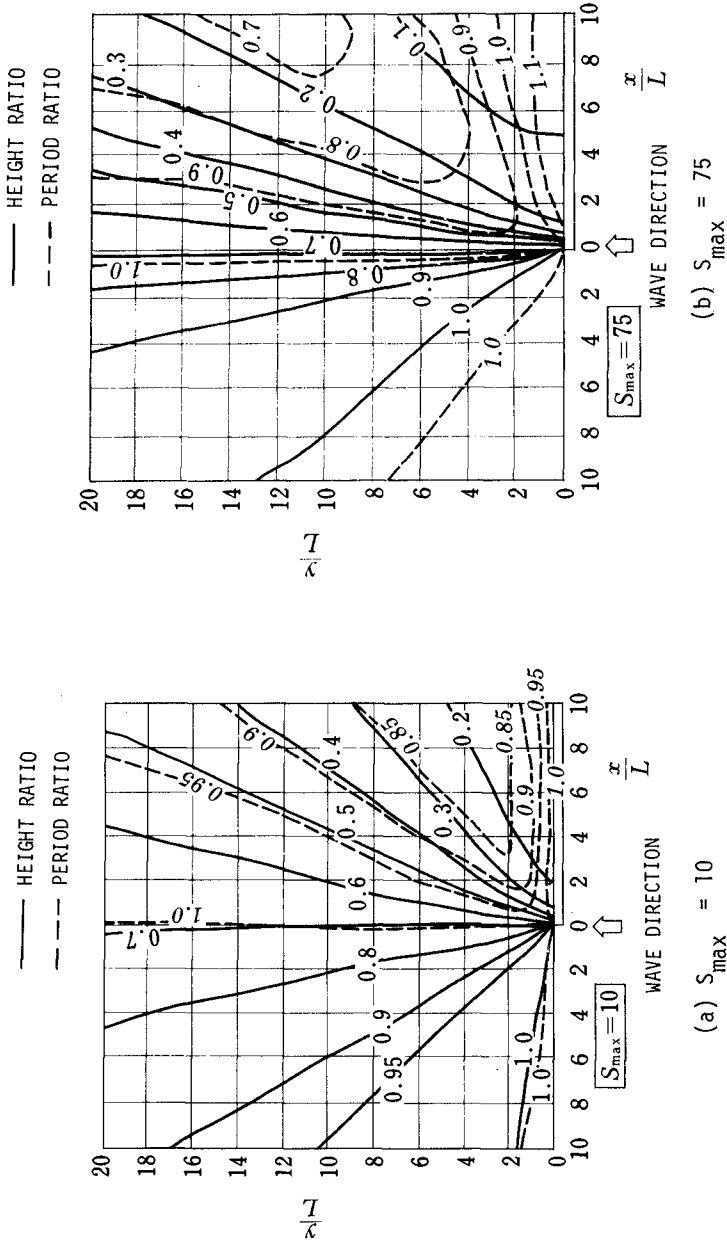


Fig. 6 Diffraction Diagrams of a Semi-Infinite Breakwater for Directional Random Waves of Normal Incidence

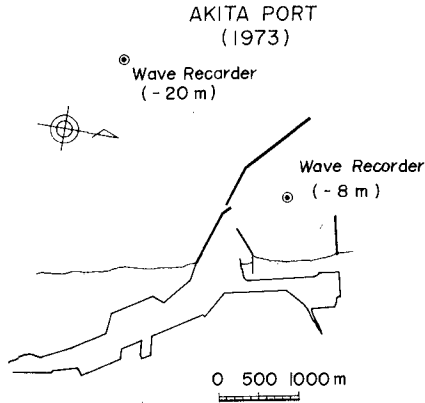


Fig. 7 Sketch of Akita Port in 1973

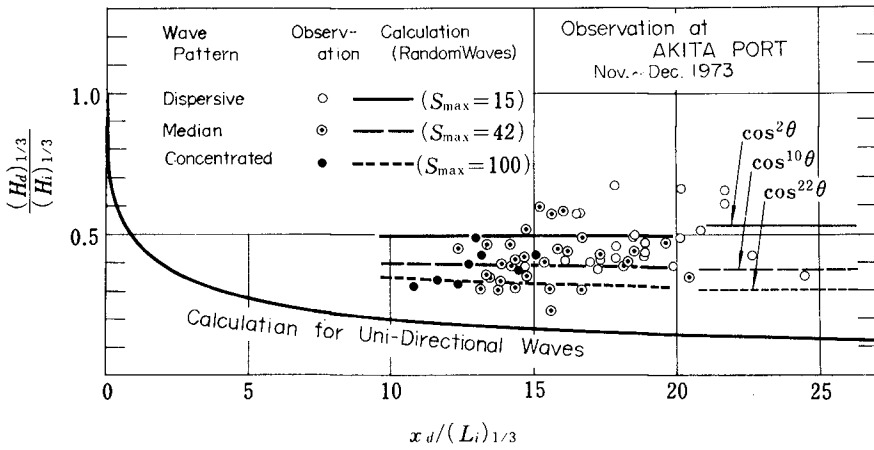


Fig. 8 Diffraction Coefficient Observed at Akita Port in Comparison with Calculation

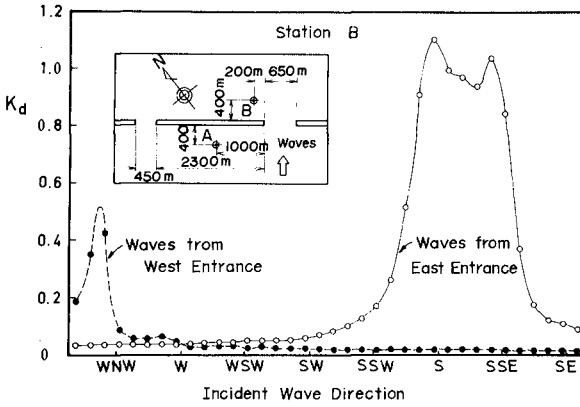


Fig. 9 Diffraction Coefficient by Monochromatic Wave Analysis for the Station B in Nagoya Port

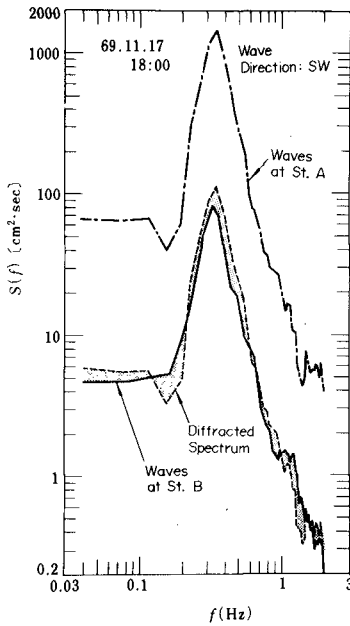
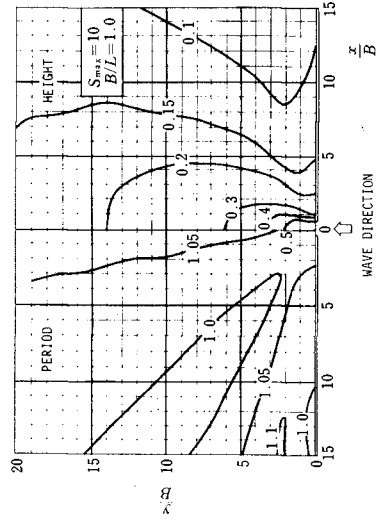
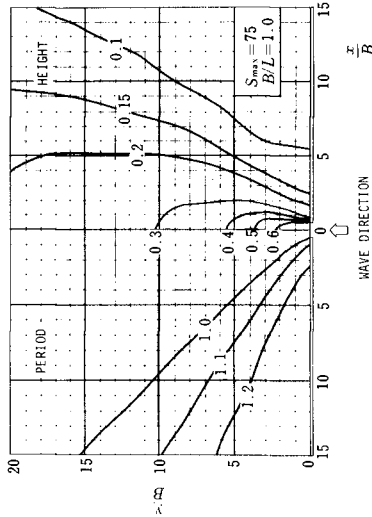


Fig. 10 Wave Spectra Observed at the Stations A and B in Nagoya Port (Wave Direction of SW)



(1) $S_{max} = 10$



(2) $S_{max} = 75$

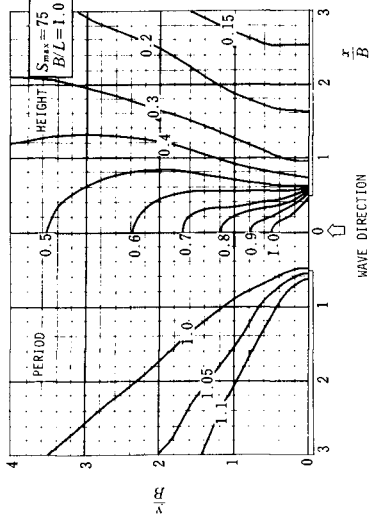
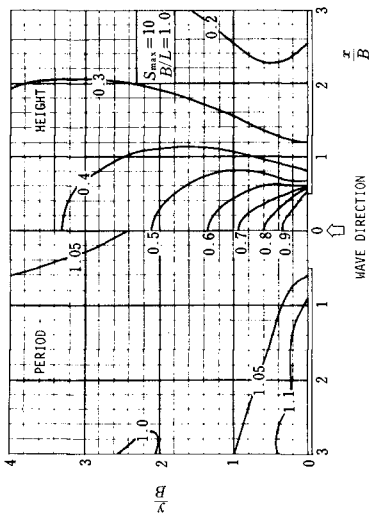
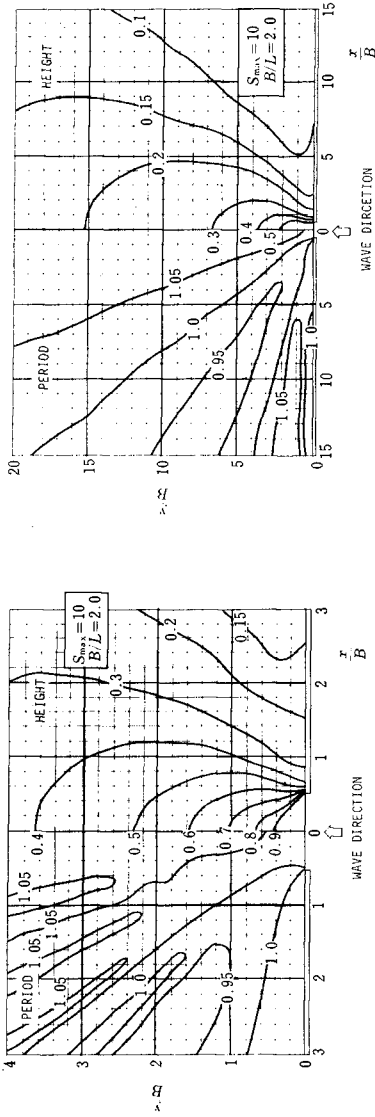
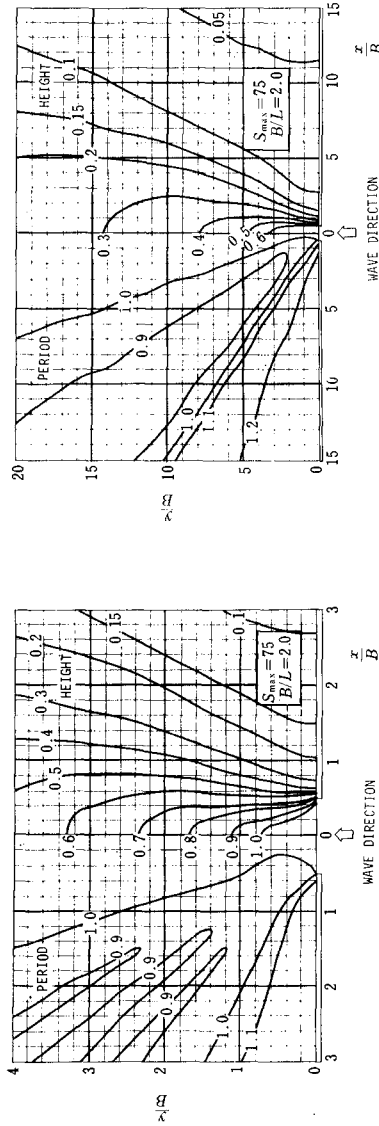


Fig. 11 Diffraction Diagrams of a Breakwater Gap with $B/L = 1.0$ for Directional Random Waves of Normal Incidence

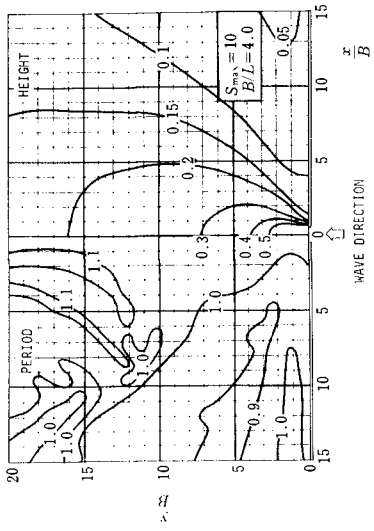


(1) $S_{max} = 10$

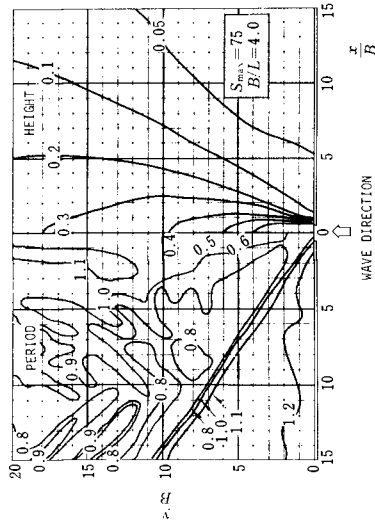


(2) $S_{max} = 75$

Fig. 12 Diffraction Diagrams of a Breakwater Gap with $B/L = 2.0$ for Directional Random Waves of Normal Incidence



(1) $S_{max} = 10$



(2) $S_{max} = 75$

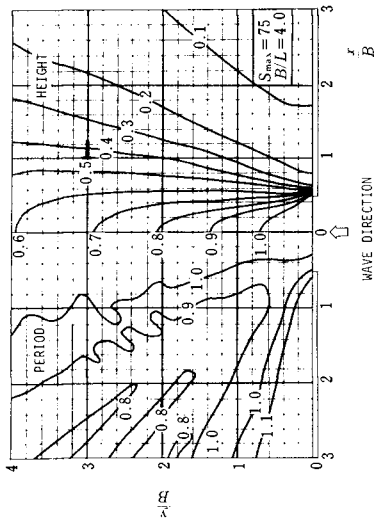
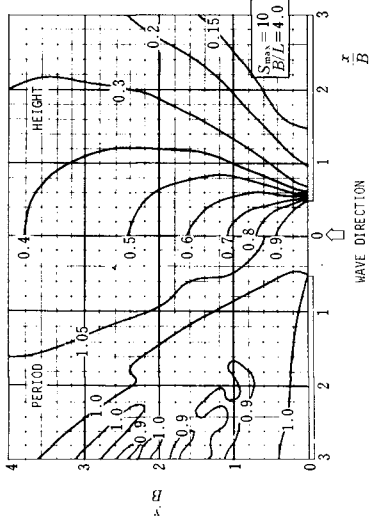
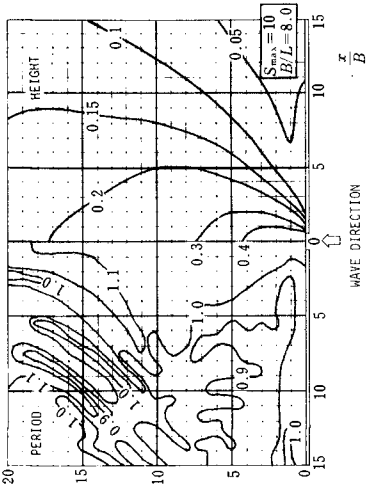
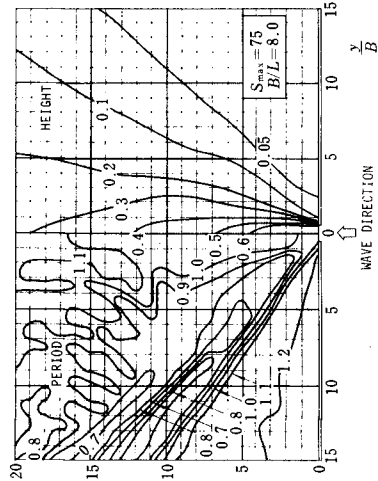


Fig. 13 Diffraction Diagrams of a Breakwater Gap with $B/L = 4.0$ for Directional Random Waves of Normal Incidence

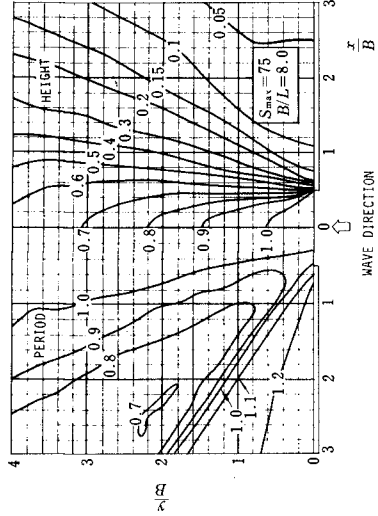
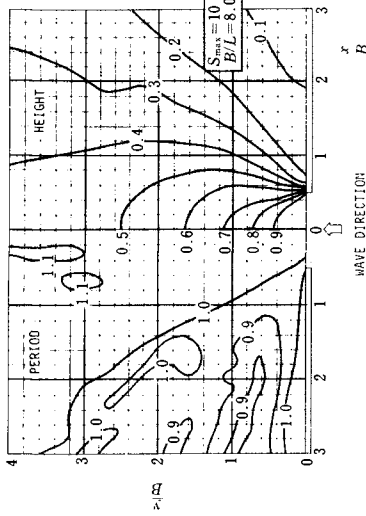


(1) $S_{max} = 10$



(2) $S_{max} = 75$

Fig. 14 Diffraction Diagrams of a Breakwater Gap with $B/L = 8.0$ for Directional Random Waves of Normal Incidence



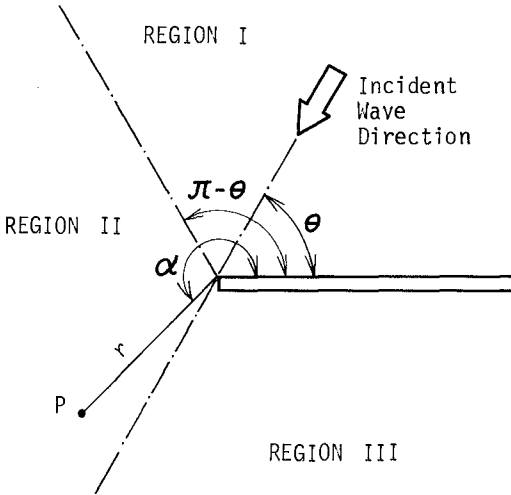


Fig. 15 Definition Sketch

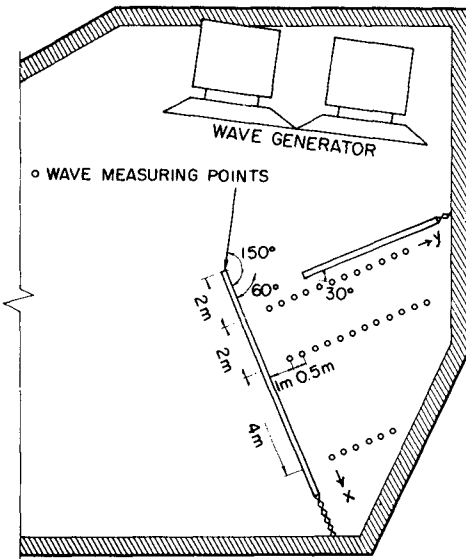


Fig. 16 Experimental Setup for Measurements of Wave Diffraction and Reflection

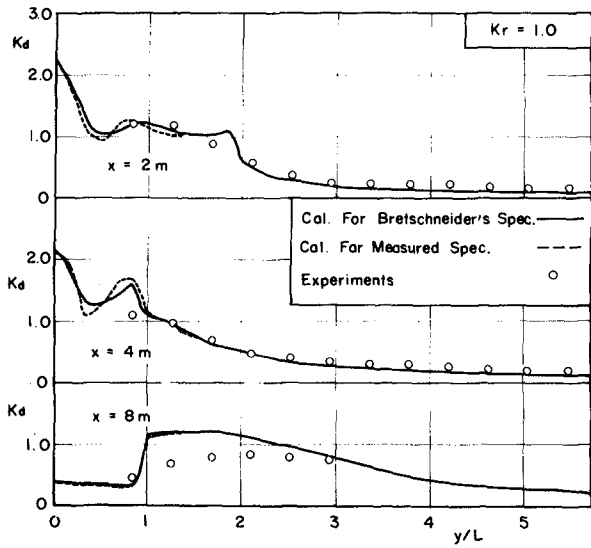


Fig. 17 Measured and Calculated Coefficients of Diffraction by Model Breakwaters

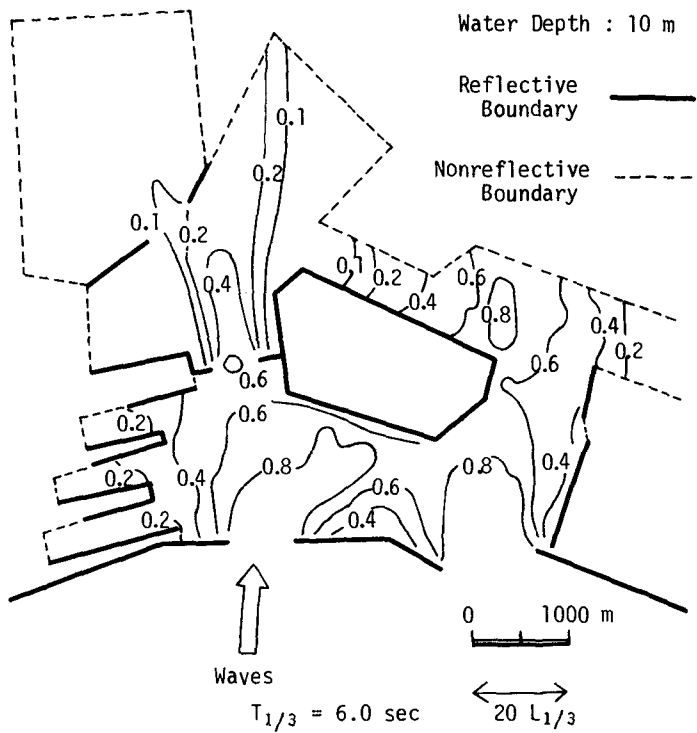


Fig. 18 Estimated Equi-Contours of Wave Height Ratio in Yokohama Port for Wind Waves with $T_{1/3} = 6.0$ sec from SSE

CHAPTER 36

INFLUENCE OF BREAKWATER-REFLECTION ON DIFFRACTION

by

Karl-Friedrich Daemrich and Sören Kohlhase

Franzius-Institut, Technical University of Hannover, Germany

ABSTRACT

Diffraction calculations for breakwaters are often based on SOMMERFELDS solution, which is mathematically exact for thin full-reflecting walls. For breakwaters with low reflecting front-sides, and if guidewalls are used, commonly a modified solution is applied, reducing the second term of the solution-formula proportional to the degree of reflection.

It could be shown that this approach is not sufficient in the region just behind the breakwater, especially for small angles of wave attack.

Regarding the exact solution for wedges it was possible to determine a special weighing factor for the second term of the SOMMERFELD solution, dependent on the degree of reflection and the wave direction, which leads to a better agreement between model tests and theoretical results.

INTRODUCTION

Within the scope of basic research on wave diffraction at harbour entrances with overlapping or displaced breakwaters [1] model tests with simple breakwater gaps and normal wave direction were performed, to get an impression on the comparability between theoretical results and wave heights measured in the hydraulic model.

The investigations were carried out in the wave basin of the SFB 79 (18.45 m) at the Franzius-Institut. The model-breakwaters were constructed of thin plates. Either a low reflecting rip-rap protection at the breakwater front-side, or a guidewall from the breakwater-tip to the wave generator was used, to diminish distortions by rereflected waves.

The theoretical results were calculated by the method of PENNEY and PRICE [3], who superimposed the mathematically exact solution of SOMMERFELD [4] to a solution for simple

breakwater gaps.

The SOMMERFELD solution is as follows (symbols see Fig. 1):

$$F(r, \theta) = f(\sigma) \cdot e^{-ikr \cdot \cos(\theta - \theta_0)} + f(\sigma') \cdot e^{-ikr \cdot \cos(\theta + \theta_0)}$$

with

$$\sigma = 2 \cdot \sqrt{\frac{k \cdot r}{\pi}} \cdot \sin\left(\frac{\theta - \theta_0}{2}\right)$$

$$\sigma' = -2 \cdot \sqrt{\frac{k \cdot r}{\pi}} \cdot \sin\left(\frac{\theta + \theta_0}{2}\right)$$

$$f(\sigma) = \frac{1+i}{2} \int_{-\infty}^{\sigma} e^{-i\pi t^2/2} dt$$

$$f(\sigma') = \frac{1+i}{2} \int_{-\infty}^{\sigma'} e^{-i\pi t^2/2} dt$$

(The modulus of $F(r, \theta)$ is equal to the diffraction coefficient K').

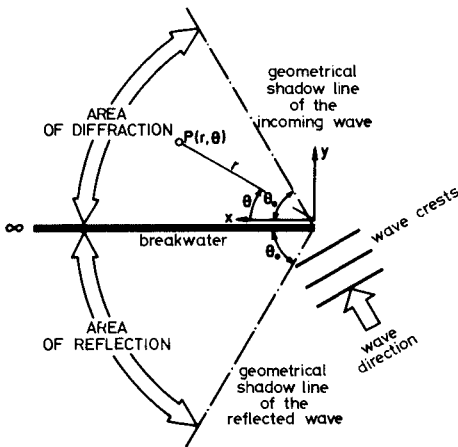


Fig. 1

Definition sketch for the SOMMERFELD solution

The solution is derived and valid for full reflecting breakwaters and cannot be used without restrictions in the case of low reflecting structures.

However, the formula consists of two terms, and because the second term includes the wave field reflected at the breakwater frontside, this term is usually related to the influence of reflection even in the region of diffraction.

As several authors (e.g. [5] , [6]) have suggested, the theoretical results were calculated with a modified formula with the second term reduced proportional to the degree of reflection. For the case, that guidewalls were used, consequently, the second term was neglected and the solution reduces to the so-called "simplified solution".

It shall be pointed out already here, that only the total solution fulfills the boundary condition exactly. If the second term is reduced or neglected the solution is not longer mathematically exact.

Fig. 2 shows exemplarily typical results for an opening width of two wavelenghts for the case, that guidewalls were used. Plotted are relative wave heights in lines parallel to the breakwater.

In the region just behind the breakwater typical differences between theoretical results and wave heights measured in the hydraulic model can be seen. The wave heights should be about zero theoretically, but they reach considerable values in the model. (Similar deviations were observed in the tests with a rip-rap-protected breakwater frontside).

These differences between theory and experiment have been the reason to deal more intensively with the diffraction theories under the special consideration of the influence of reflection.

SOLUTION FOR A BREAKWATER WITH GUIDEWALL

For the case, that guidewalls or wave splitters are used, an appropriate solution is available from the exact solution for semi-infinite vertical wedges.

MITSUI and MURAKAMI [2] have derived solutions for different wedge angles and all wave directions. For an example, the solution for a rectangular wedge is given (symbols acc. to Fig. 3):

$$F(\rho, \theta)_{\nu=\frac{3}{2}\pi} = \frac{4}{3} J_0(\rho) + \frac{8}{3} \sum_{n=1}^{\infty} e^{in\pi/3} \cdot J_{2n/3}(\rho) \cdot \cos^{\frac{2}{3}n\alpha} \cdot \cos^{\frac{2}{3}n\theta}$$

with

$J_0(\rho)$, $J_{2n/3}$ = BESSEL functions, first kind

$$\rho = k \cdot r = \frac{2\pi}{L} \cdot r$$

(The solution has to be halved for wave directions parallel to one wall)

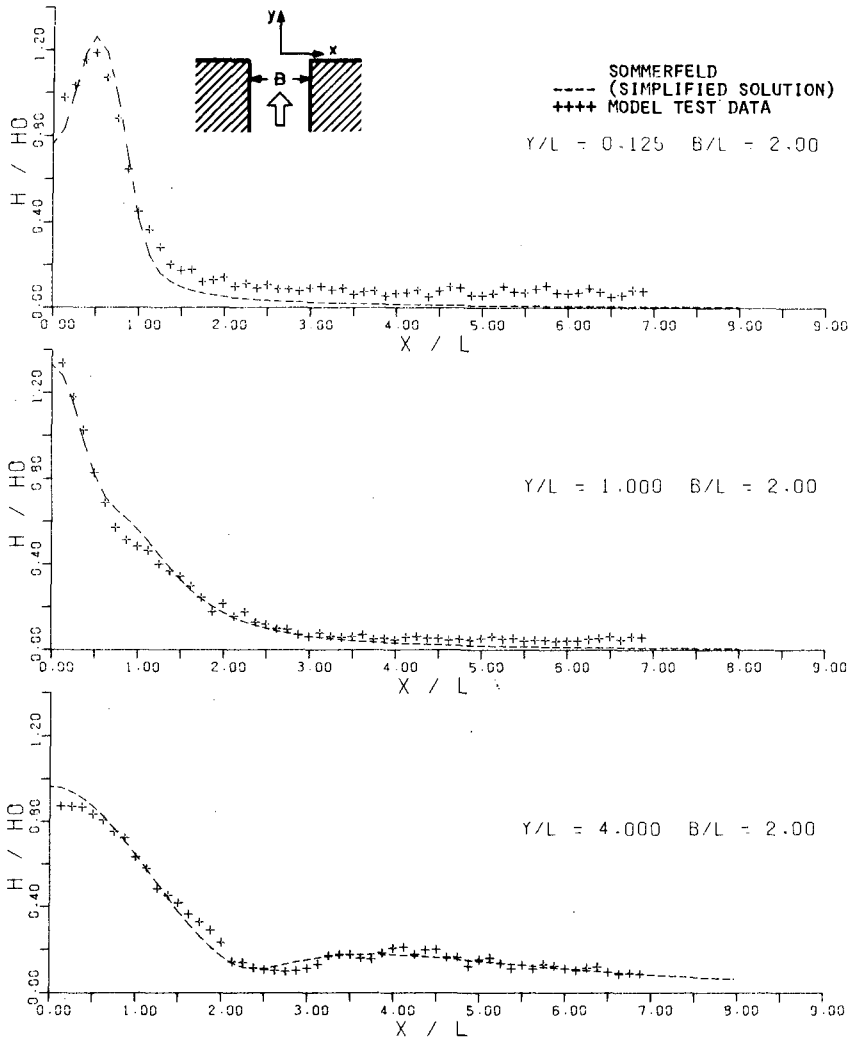


Fig. 2 Comparison of theoretical results with hydraulic model tests

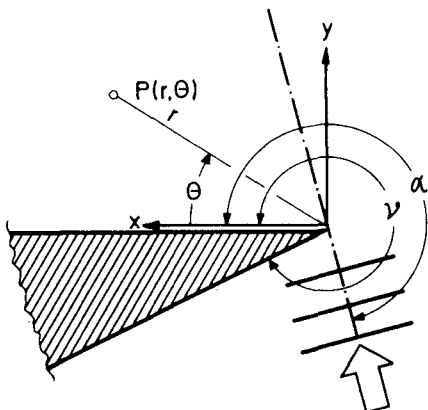


Fig. 3
Definition sketch for
the MITSUI solution

Fig. 4 shows exemplarily the wave heights in the region of diffraction for perpendicular wave approach for different theories.

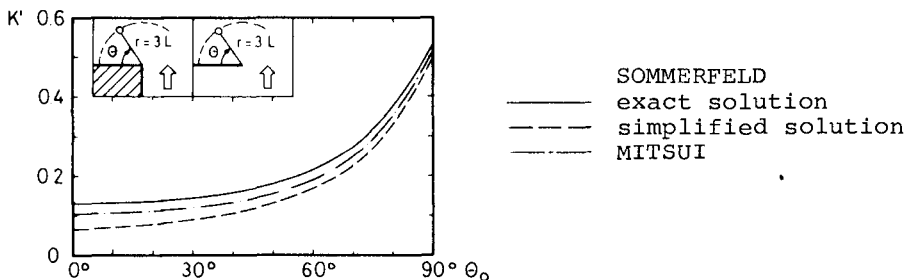


Fig. 4 Comparison of the diffraction coefficient K' for different theories

It can be seen, that the results according to the MITSUI solution are typically heigher than the results according to the simplified SOMMERFELD solution.

Furthermore, it can be seen that the MITSUI solution may be approximated by a modified SOMMERFELD solution. The difference between total solution and simplified solution corresponds to the influence of the second term of the SOMMERFELD solution and therefore a weighing of this second term may be a good approximation.

Fig. 5 gives a comparison of experimental results with results according to the MITSUI solution. The characteristic better agreement confirms the validity of this solution.

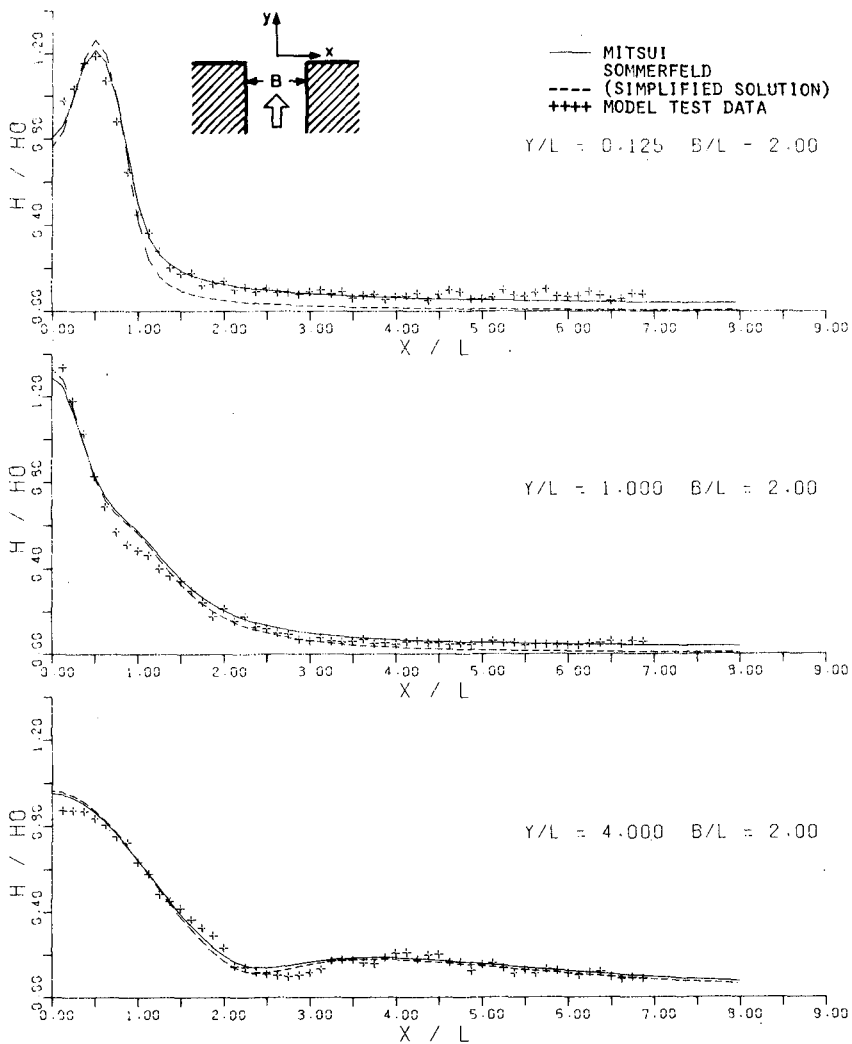


Fig. 5 Model tests in comparison with theoretical results

SOLUTION FOR A BREAKWATER WITH NON-REFLECTING FRONTSIDE

As a basis, the SOMMERFELD solution and the MITSUI solution were used for the theoretical considerations. For illustration, the SOMMERFELD solution shall be briefly discussed.

As mentioned before it consists of two terms. Each term represents a part of the wave field around the breakwater and can be divided mathematically into a straight-crested wavefield, according to the laws of geometrical optics, and a nearly circular scattered wave field. This wave fields, represented by their wave crests, are shown schematically in Fig. 6.

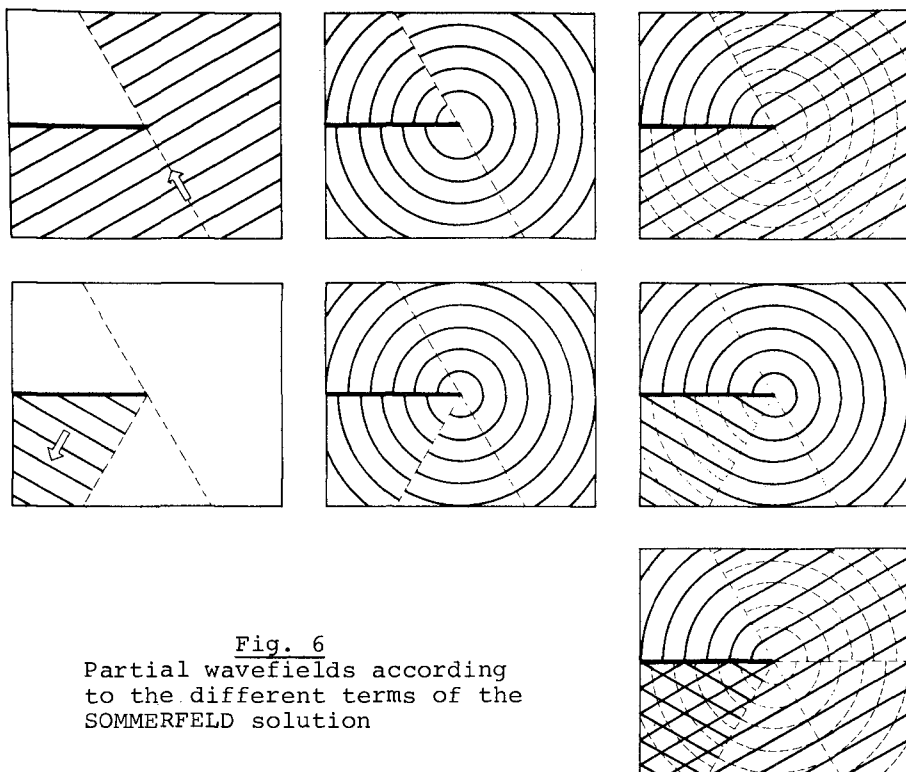


Fig. 6
Partial wavefields according
to the different terms of the
SOMMERFELD solution

The incoming wave field and the pertinent scattered wave field together are represented by the first term of the solution, the reflected wave field and the pertinent scattered wave field by the second term. The characteristics of the scattered wave fields are influenced as well by the boundary condition "breakwater" as by the distribution of the wave heights of the generating straight crested wave field in its geometric shadow line.

Going back to the problem and regarding the wave systems in the upper part of Fig. 6, which correspond to the first term of the SOMMERFELD solution, apparently this case is physically in accordance with the case of a non-reflecting breakwater. There are only incoming waves, together with a pertinent scattered wave system.

However, it must be noticed, that the two scattered wave systems of the two terms of the SOMMERFELD solution fulfill the boundary condition at the breakwater only combined. Each scattered wave field alone does not fulfill the boundary condition, except for a wave direction $\theta_0 = 180^\circ$.

In the following, a similar solution shall be derived for the condition, that the incoming waves are not reflected at the (non-reflecting) breakwater frontside, whilst the pertinent scattered wave system is in accordance to the boundary condition at an impermeable full-reflecting breakwater.

Exemplarily for a given wave direction three similar constellations shall be compared (Fig. 7)

- a non-reflecting thin breakwater according to the above definition, where a solution is searched for (Fig. 7a)
- a breakwater with wave direction parallel to the breakwater, where an exact solution exists, and no reflection can occur (Fig. 7b). (The SOMMERFELD solution has to be halved in this case)
- and a rectangular wedge with wave direction parallel to one wall, where also an exact solution, the MITSUI solution, is known (Fig. 7c)

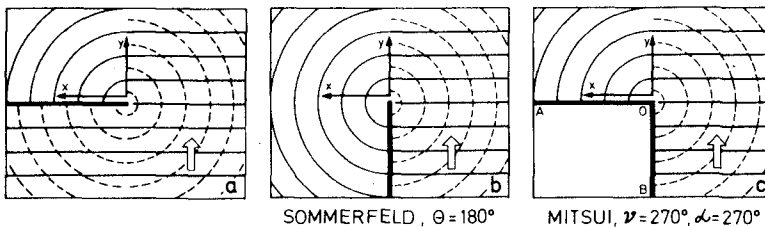


Fig. 7 Wave crests for different breakwater constellations

By comparing the wave fields according to Fig. 7b and c it is possible to determine the alteration of the scattered wave field for the case that the wall \bar{AO} is moved towards the wall \bar{BO} , i.e. if we subtract the wave system at the right from the wave system in the middle we get a "difference scattered wave system", which represents the effect of the spreading or diffraction of the scattered wave field at the wedge into the region of the wedge.

In the same manner, as the solution for the case "wave direction parallel to the breakwater"(Fig. 7b) can be derived from the case "wedge" (Fig. 7c) by adding the difference scattered wave field to the scattered wave field at the wedge, it is possible to derive the searched solution for the non-reflecting breakwater (Fig. 7a) by adding a difference scattered wave field, representing the spreading of the scattered wave field into the region of the wedge at the line \overline{OB} .

From the fact that the wave heights of the scattered wave field in the line \overline{OB} are relatively exact one third of the corresponding wave heights in the line \overline{OA} , we can conclude, that the characteristic form of the difference scattered wave field is the same as mentioned before. The wave heights, however, are one third only for this special wedge angle.

In Fig. 8 the development and the wave height distribution of the difference scattered wave field is shown.

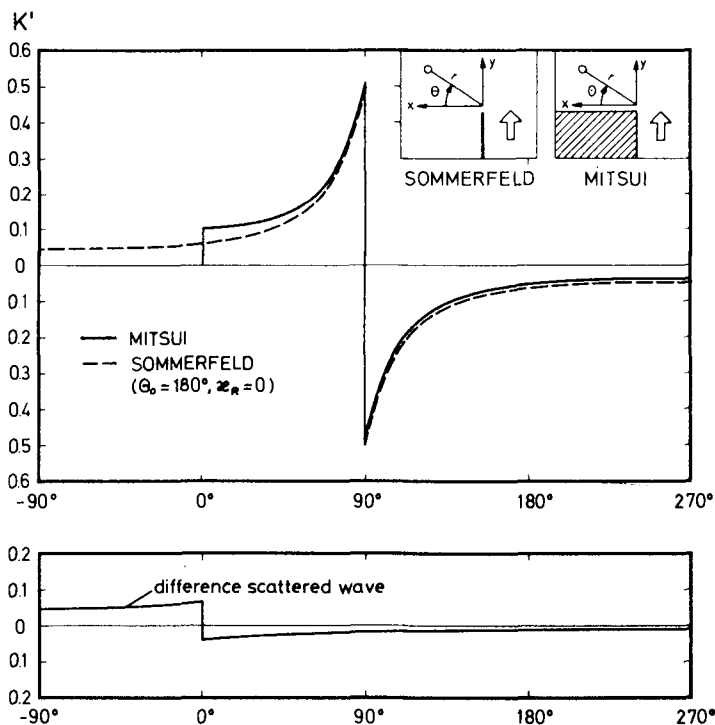


Fig. 8 Wave heights of the scattered waves according to the constellations b and c in Fig. 7, and pertinent "difference scattered wave" (exemplarily for $r = 3 \cdot L$)

In the upper part the wave heights of the both exact solutions are shown, in the lower part the difference scattered wave heights.

Fig. 9 shows finally the wave height distribution of the scattered wave field for the non-reflecting breakwater, and a remarkable difference can be seen in the region of diffraction in comparison to the up to now recommended simplified SOMMERFELD solution with neglected second term.

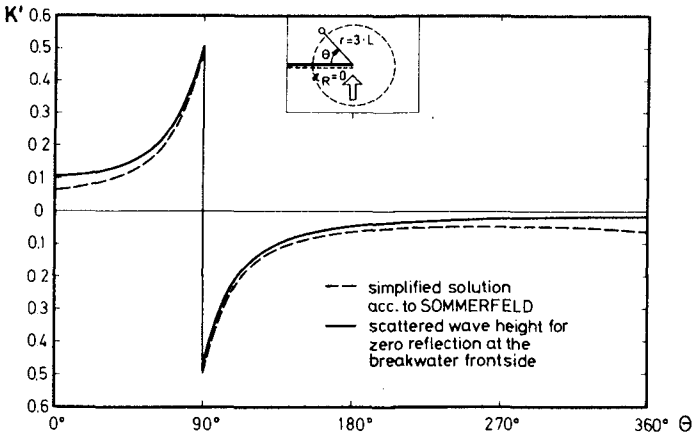


Fig. 9 Diffraction coefficient K' of the scattered wave for zero-reflection in comparison to results from the "simplified solution"

APPROXIMATE METHODS BASED ON THE SOLUTIONS OF MITSUI AND SOMMERFELD

The new solution for non-reflecting breakwaters is very similar to the corresponding solution of MITSUI in the region of diffraction. Therefore, the MITSUI solution for wedges with wave direction parallel to one wall can be used as a good approximation.

(The condition - "breakwater with guidewalls or wave splitters" - is equivalent to the condition - "breakwater with non-reflecting frontside" - in the region of diffraction, as it was assumed by different authors before).

Furthermore comparative calculations have shown, that the difficult solutions according to MITSUI can be approximated well in the region of diffraction, by an adequate modified SOMMERFELD solution, which needs only a half percent of the computer time. This modification consists in a weighing of

the second term of the SOMMERFELD solution depending on the wave direction θ_0 (Fig. 10).

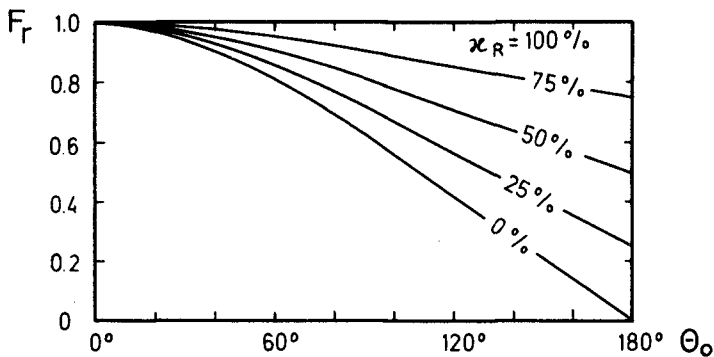


Fig. 10 Weighing factor F_r for the second term of the SOMMERFELD solution for various degrees of reflection

The lowest line in Fig. 10 shows this weighing factor for zero-reflection as a function of the wave direction which has been determined by comparative calculations. It can be readily seen the difference to the up to now recommended method, taking this factor for zero for a non-reflecting breakwater without regarding the wave direction.

This modification, weighing the second term of the SOMMERFELD solution, has furthermore the advantage, that partial reflections can be considered easily by linear interpolation between the weighing factors for zero reflection and total reflection.

Finally, Fig. 11 shows a comparison of experimental results with rip-rap protected breakwater front-sides and theoretical results according to MITSUI and to this modified solution.

The weighing factor for the modified solution was chosen to 0.65 for a wave direction of 90° and a degree of reflection of approx. 10%. (The results of the MITSUI solution are given in addition for comparison only)

CONCLUSION

To consider the effect of a low-reflecting breakwater front-side on the wave heights in the diffraction area, it is usually recommended to reduce the second term of the SOMMERFELD solution proportional to the degree of reflection.

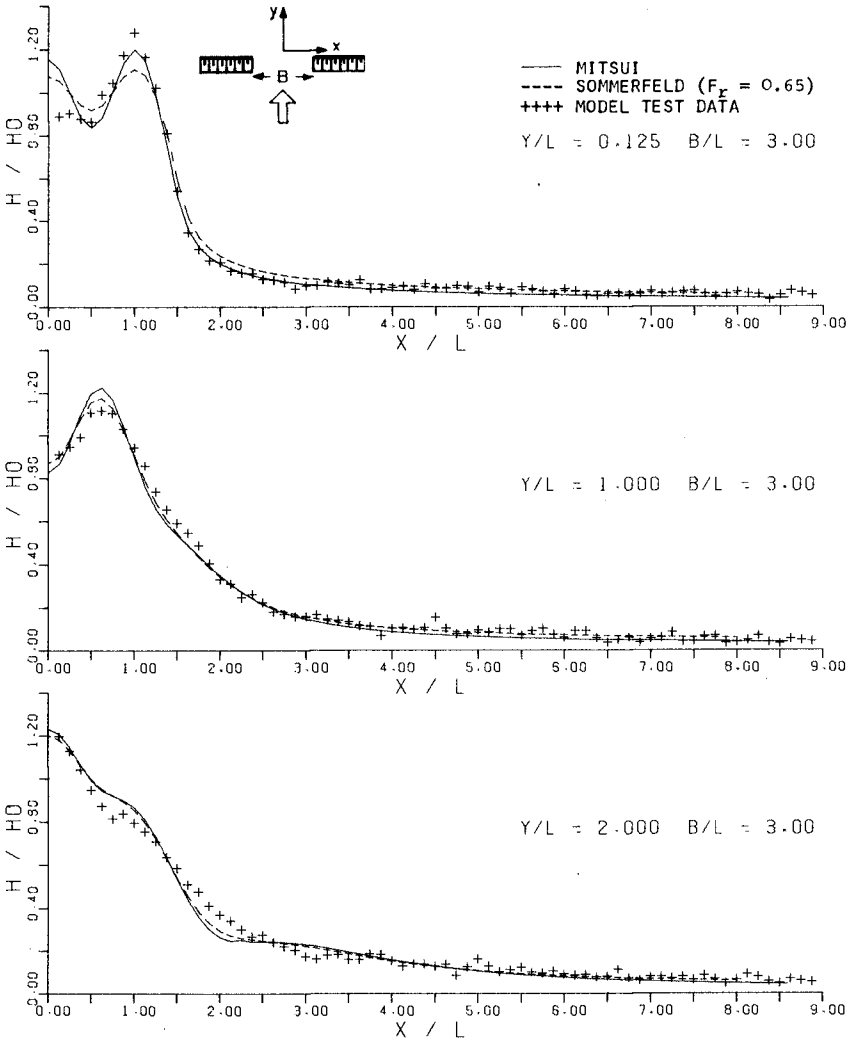


Fig. 11 Model tests in comparison with theoretical results

Within model tests with low-reflecting breakwaters and breakwaters with guidewalls, typical differences between this theoretical approach and the experimental results were observed, specially in the region just behind the breakwater.

It was shown, that the theoretical results according to the MITSUI solution and the developed solution for non-reflecting thin breakwaters are in a better agreement with the experimental results.

Although the commonly used theoretical approach is not acceptable in the region of diffraction just behind the breakwater, it can be used as an appropriate solution introducing a special weighing factor for the second term.

This weighing factor has to be determined with regard to the wave direction and the degree of reflection.

A diagramm with recommended weighing factors is presented (Fig. 10).

REFERENCES

- [1] DAEMRICH, K.-F.: Diffraction gebeugter Wellen
- Ein Beitrag zur Untersuchung der Wellenunruhe in Häfen -
Mitteilungen des Franzius-Instituts für Wasserbau und Küsteningenieurwesen der Technischen Universität Hannover, Heft 47, 1978
- [2] MITSUI, H. and MURAKAMI, H. : Wellenhöhenverteilung an diskontinuierlichen Teilen von Küstenbauwerken
(2. Bericht) Kaigan Kôgagu Kôenkai Kôenshû 14, 1967 (in Japanese)
- [3] PENNEY, W.G. and PRICE, A.T. : The Diffraction Theory of Sea Waves and the Shelter Afforded by Breakwaters
Philos. Transactions of the Royal Society of London, Series A, No. 882, Vol. 224, March 1952
- [4] SOMMERFELD, A. : Mathematische Theorie der Diffraction
Mathematische Annalen, Bd. 47, 1896
- [5] SILVESTER, R. and TECK-KONG LIM : Application of Wave Diffraction Data
Proc. 11th Conf. Coastal Eng., 1968
- [6] WORTHINGTON, H.W. and HERBICH, J.B.: Comp. Progr. to Estimate the Combined Effect of Refraction and Diffraction of Water Waves, Texas A&M University, COE Report No. 127, 1970

A NUMERICAL APPROACH FOR THE DETERMINATION
OF THE WAVE HEIGHT DISTRIBUTION IN A HARBOUR

by

S. Kohlhase, K.-F. Daemrich, U. Berger

E. Tautenhain, O. Burkhardt

Franzius-Institut, University of Hannover

ABSTRACT

The paper deals with a mathematical method to calculate wave heights in harbours caused by diffraction and reflection. Using the complete SOMMERFELD-solution for a semi-infinite breakwater, a linear superposition method is applied. The reflections of the harbour boundary are taken into account using a geometric mirroring principle.

The computer-programme allows the phase-correct superposition of any number of wave systems and, therefore, also the consideration of re-reflections which can be important in the presence of vertical walls. For the presentation of results (K'-lines) an interpolation-plot-programme is used.

The computer-programme has been applied to the harbour Greenville extension (Liberia) (BURKHARDT, 1977). Hydraulic model tests were performed to check the programmes, especially with respect to the influence of harbour reflections and the layout of the breakwater head.

INTRODUCTION

Hydraulic model tests are a reliable aid to investigate the wave height distribution in a harbour, but, with respect to scale effects, normally the model must get considerably large dimensions. The expenditure of construction and operation-time is often high because normally different wave directions have to be checked and the wave heights have to be measured in a narrow grid to allow an objective comparison of results for different wave and harbour-layout conditions.

Because of the simple geometric conditions of the Harbour of Greenville and to save costs a numerical model was used to investigate the wave height distribution in the harbour. The programmes adopted were developed within a special research project (SFB 79) of the GERMAN RESEARCH COUNCIL (DFG).

Fig. 1 shows a plan-view of the Harbour of Greenville which has been built in the 50th and which is now going to be extended. It is planned to elongate the existing breakwater

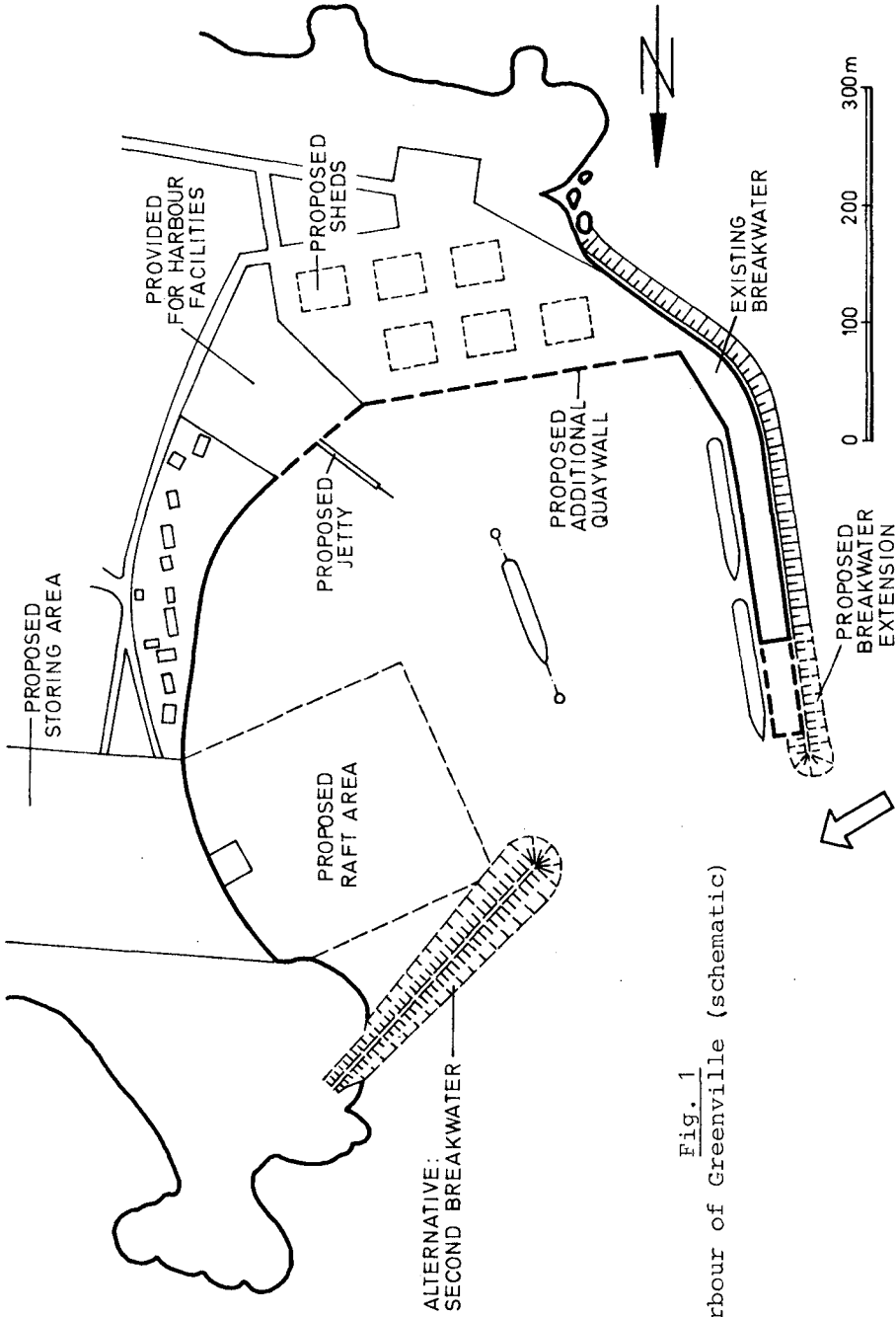


Fig. 1
Harbour of Greenville (schematic)

of the harbour to provide an additional cargo berth. The construction of a second breakwater is considered (RRI, 1976). The breakwater is built as a vertical wall with a rip-rap protected frontside. For the harbour boundaries different alternatives have been discussed.

The directions of the incoming waves are - of course - variable as well as wave heights and periods. The arrow corresponds approximately to the main wave direction.

PRINCIPLE OF CALCULATION

The numerical procedure is based on a simple geometrical mirroring which has been published already by CARR (1952) generally.

The principle of the method used is as follows (Fig. 2): The incoming waves are diffracted at the breakwater head. Diminished by diffraction the waves are propagating into the harbour area and will be reflected at the harbour boundaries.

The diffracted waves are superimposed by the reflected waves, which will be re-reflected at the harbour quays again.

To calculate the influence of reflection and re-reflection the harbour boundaries are idealized as a polygonal course of n elements.

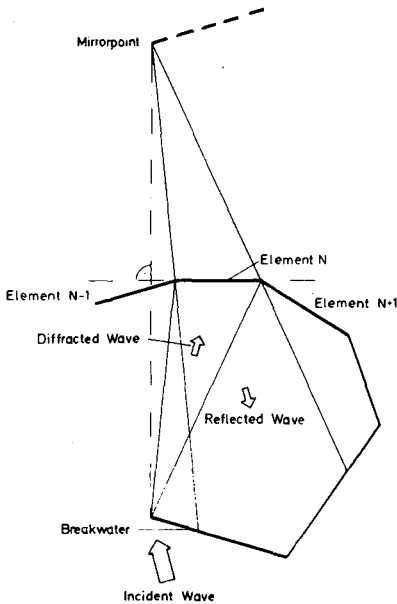


Fig. 2
Explanation of
mirroring principle

According to the rules of the geometric optics the wave reflected at the boundary element $n = N$ can be seen as a diffraction wave starting from the geometric mirror point of the breakwater tip.

The consideration of a reflected wave as a diffraction wave is equivalent to the consideration of the reflecting boundary element as an opening, which implies, that additionally scattered wave systems will be formed at the joints to the neighbouring elements $N-1$ and $N+1$, which have to be superimposed to the other wave systems. These scattered waves provide for a balancing of wave height differences in the lines of geometric shadows.

The calculation of wave systems to be superimposed is based on the SOMMERFELD-solution of the diffraction at a semi-infinite breakwater. The solution-function is as follows (Fig. 3):

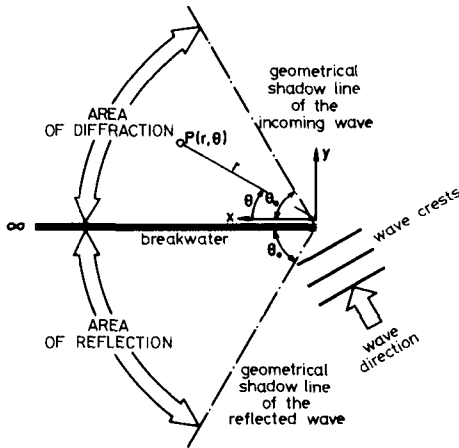


Fig. 3

Co-ordinate system and notations

$$F(r, \theta) = f(\sigma) \cdot e^{-ikr \cdot \cos(\theta - \theta_0)} + f(\sigma') \cdot e^{-ikr \cdot \cos(\theta + \theta_0)}$$

with

$$\sigma = 2 \sqrt{\frac{k \cdot r}{\pi}} \cdot \sin\left(\frac{\theta - \theta_0}{2}\right)$$

$$\sigma' = -2 \sqrt{\frac{k \cdot r}{\pi}} \cdot \sin\left(\frac{\theta + \theta_0}{2}\right)$$

$$f(\sigma) = \frac{1+i}{2} \int_{-\infty}^{\sigma} e^{-i\pi t^2/2} dt$$

$$f(\sigma') = \frac{1+i}{2} \int_{-\infty}^{\sigma'} e^{-i\pi t^2/2} dt$$

Details of calculation are outlined in DAEMRICH (1978) and BERGER (1976) respectively.

The programme allows the phase correct, linear superposition of any number of partial wave systems, but to save computer-time for the calculations of the Greenville harbour only 5 elements and not more than about 15 partial wave systems were used. The degrees of reflection, which must be determined before, are variable.

K'-values are calculated in a cartesian grid. For the graphic representation of the wave pattern a plot programme was used, which plots lines of constant K'-values by means of interpolation.

SOME RESULTS OF CALCULATION

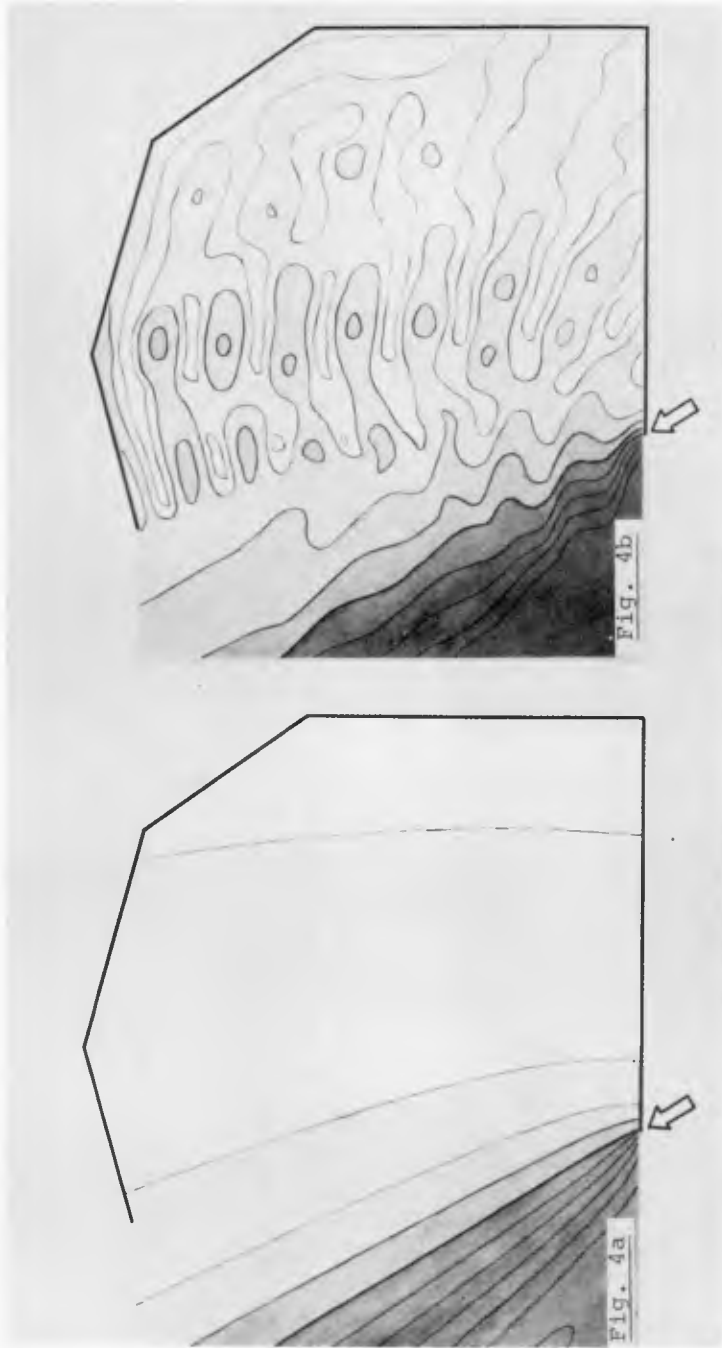
Calculations have been carried out for different harbour configurations and wave conditions. But special results for the harbour of Greenville shall not be reported here, rather it shall be demonstrated in which way the resulting wave system is influenced by reflection and diffraction effects.

Fig. 4a shows the pure diffraction at the breakwater and - in this initial stage - reflections and higher order reflections were not considered. In the line of the geometric shadow the wave height is about 50 % of the incident wave height; the wave heights are decreasing rapidly in the area of the geometric shadow and are in the order of 10 to 20 % of the incident wave height.

The influence of reflection at the harbour boundaries is shown exemplarily in Fig. 4b. The degree of reflection was chosen constant with $K_R = 0.3$. Not considered are the additional scattered wave systems at the corners of the harbour boundaries caused by diffraction as outlined before. Also re-reflections at the harbour side of the breakwater have been neglected.

The comparison of the calculations given by the examples of Fig. 4 shows that the wave pattern - as was to be expected - will become very irregular even with small degrees of reflections. The wave heights become throughout higher within the harbour area. The influence of reflection reaches even into the area outside the geometric shadow line.

The influence of re-reflection at the breakwater can be seen exemplarily in Fig. 5.



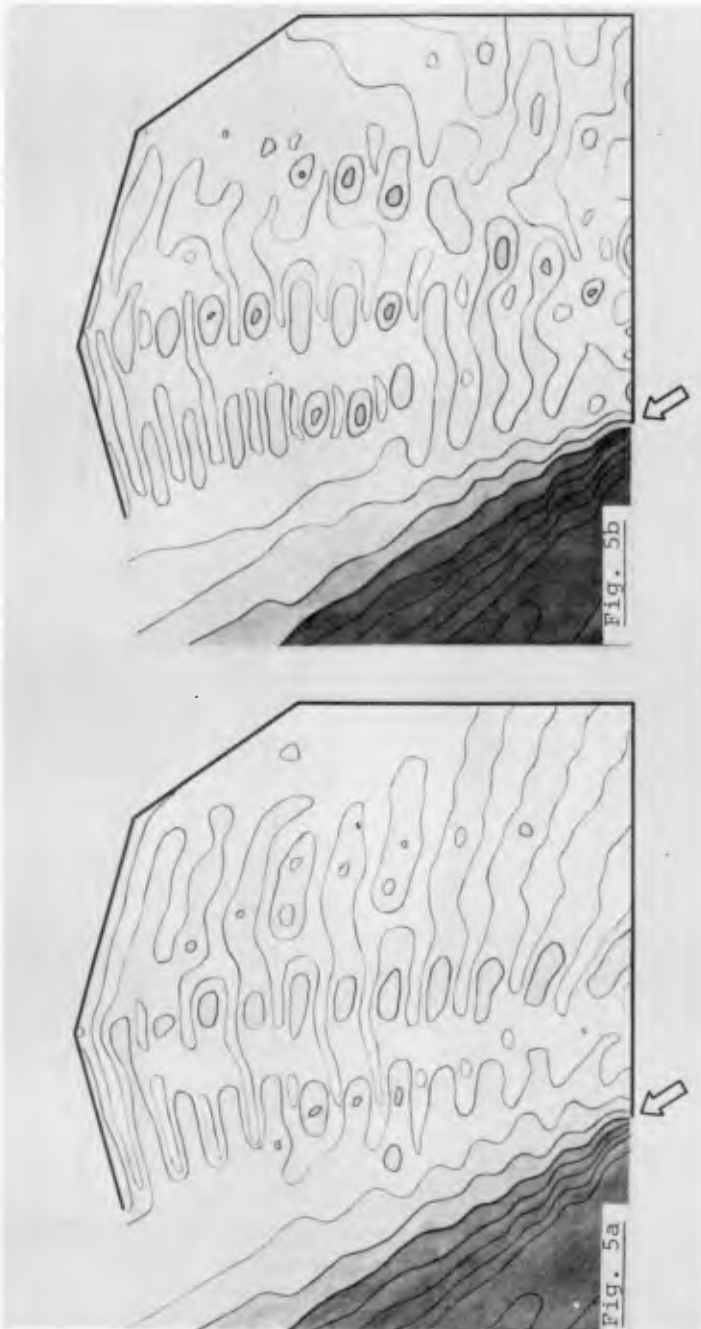
REINE DIFFRAKTION

L=112m 230°

MSPIEG = 0 CASAB = 0,3 APPAB 6/13 = 0.0

L=112m 230°

Fig. 4



MSPIEG = 0 CASAB = 0.3 APPAB 6/13 = 0.0
L = 75m 230°

MSPIEG = 1 CASAB = 0.3 APPAB 6/13 = 0.0
L = 75m 230°

Fig. 5

On the left (Fig. 5a) the condition without re-reflection, on the right (Fig. 5b) with re-reflection is shown. The degree of reflection has been taken as $\kappa_R = 1.0$ at the breakwater. In other respects, the boundary conditions are the same on both Fig. 5a and Fig. 5b, i.e. same wave lengths and periods and uniform degrees of reflection at the harbour boundaries ($\kappa_R = 0.3$). Additionally occurring scattered waves are not considered.

The effect of re-reflected waves running back into the inner part of the harbour can be clearly seen. Lines of equal K' -values which are relatively smoothed in the left part of Fig. 5 are broken up more and more. This break up is specially marked in the breakwater area due to the geometrics of the harbour.

Only in exceptional cases comparable forms on the left and the right side of Fig. 5 can be found.

The influence of additional occurring scattered waves can be seen exemplarily from Fig. 6.

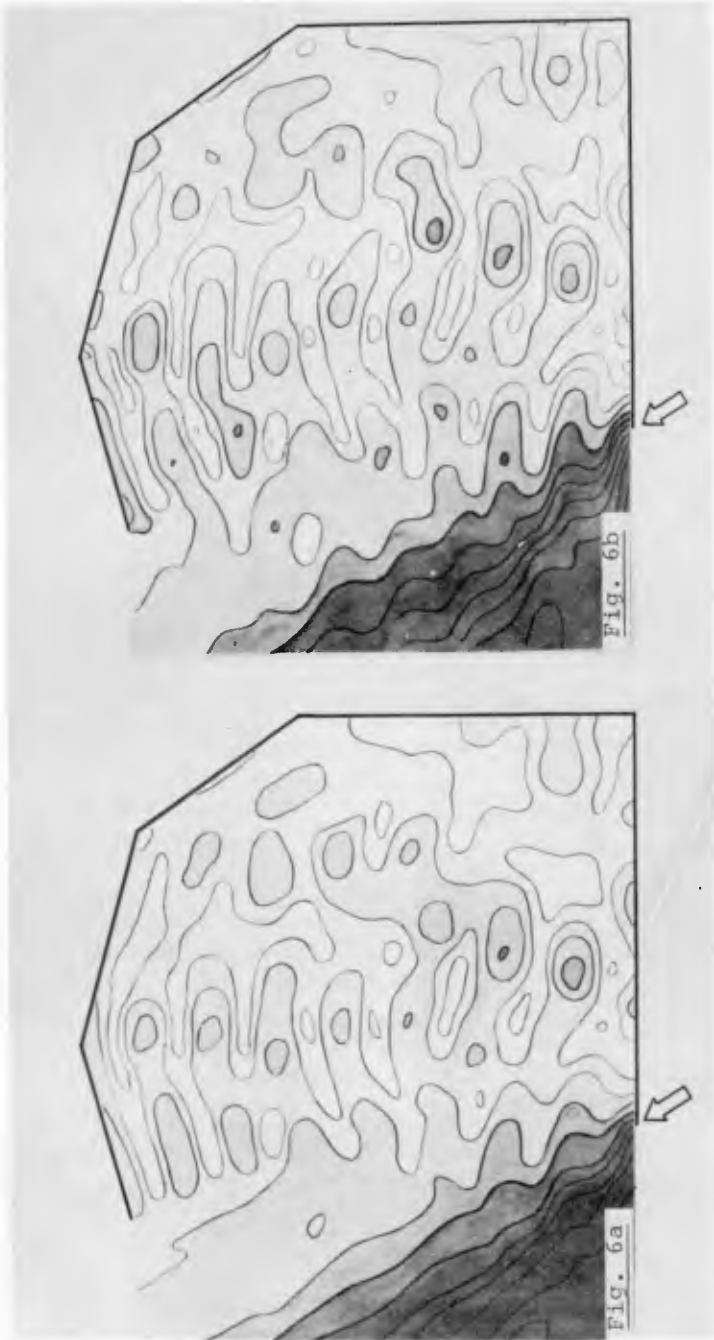
On the left we have an example without scattered waves caused at the boundary corners, on the right with scattered waves.

Differences of the wave height distribution can be seen quite well, although single forms of K' -lines can be found. As shown in the preceding Figures the consideration of any additional influence causes local increases of the wave heights in the harbour area.

Two more examples of the calculations may show qualitatively the significant influence of the wave parameters period and direction.

In Fig. 7 the wave-direction has been changed by 30° . In other respects the conditions are the same left (Fig. 7a) and right (Fig. 7b) and as well re-reflections at the breakwater as additional scattered waves were considered for calculations.

In this example it is nearly impossible to find again single forms of K' -lines just as in the example of Fig. 8 which shows the influence of the wave-length or period. It can be seen once more, how complicated the wave height distribution can be even in the case of a very simple harbour.



MSPiEG = 1 CASAB = 0,3
L = 112 m 230°

MSPiEG = 1 CASAB = 0,3 APPAB 6/13 = 0,0
L = 112 m 230°

Fig. 6

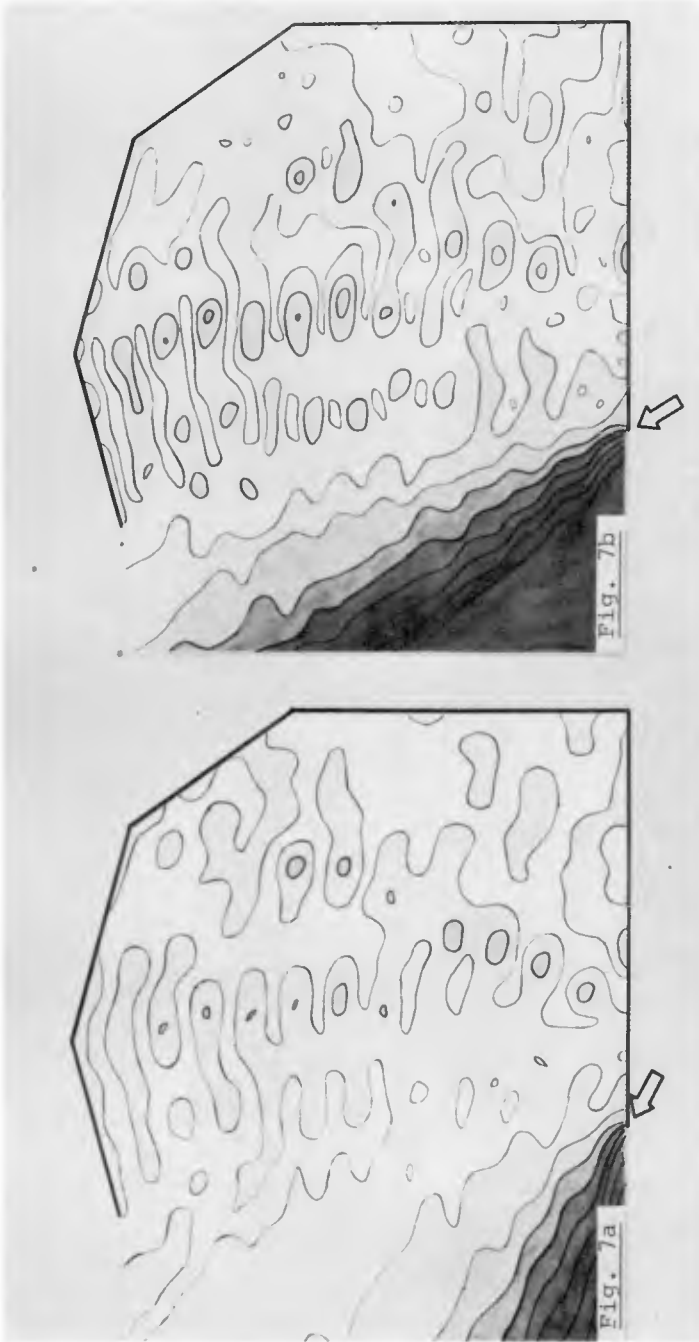


Fig. 7

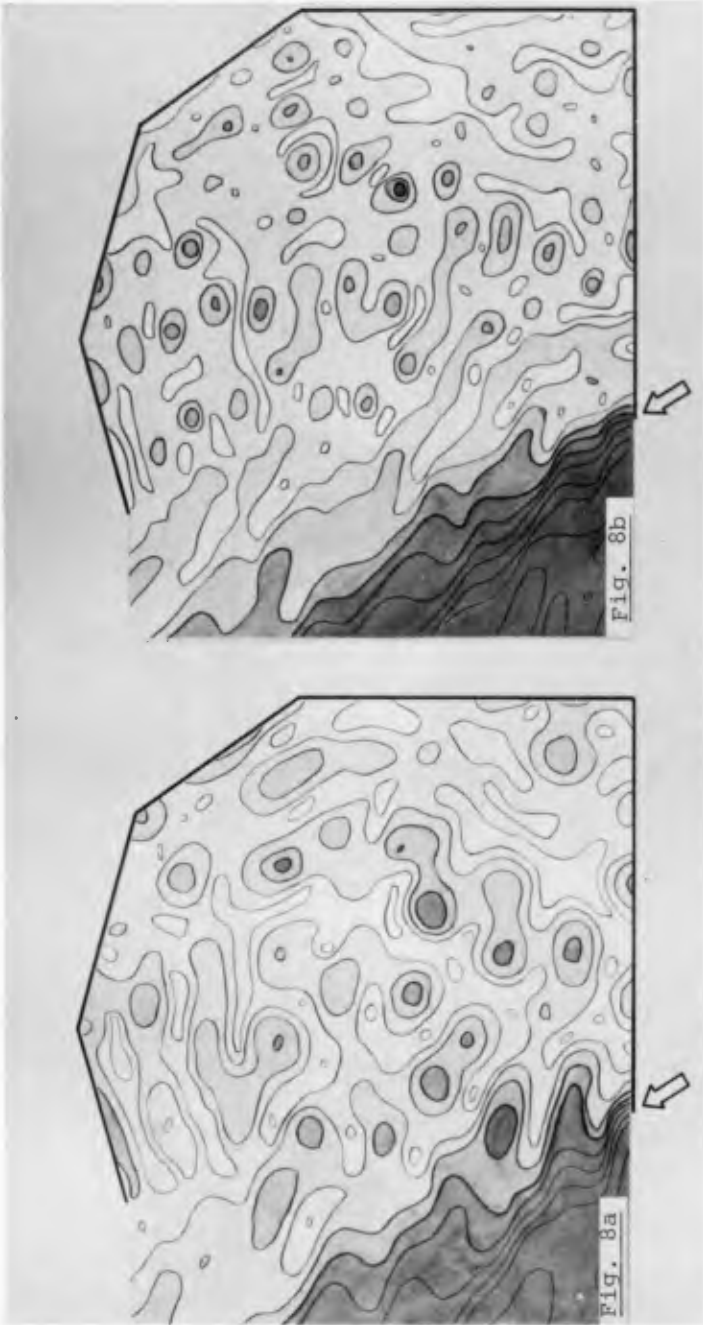


Fig. 8

CONCLUDING REMARKS

A numerical procedure to calculate the wave height distribution in a harbour is presented. The method has been applied to the harbour of Greenville. It has been tested using a schematic hydraulic model showing a fair agreement with the theoretical results. But some general restrictions of the method should be mentioned:

- The method requires a constant water depth and does not include refraction effects within the harbour. This simplification is often but not always permissible.
- The influence of the degree of reflection of the breakwater is considered but not the influence of the breakwater head. The design of the breakwater head can have an influence on the wave heights in the harbour, which - in certain cases - will not be negligible as shown by some comparative model investigations.
- The method allows the superposition of any number of wave systems but the computer time is increasing over-proportional with the number of harbour boundary elements, because of the necessary consideration of re-reflections and scattered waves.

Therefore, the number of elements should be restricted which includes some subjectivity and requires some experiences.

The main advantage of the method is its flexibility, i.e. wave directions, periods, degrees of reflection in connection with or structural changes of quays berth etc. can be varied in the model easily.

In this respect the numerical method can also be a good help to select the test conditions of a hydraulic model.

Finally some remarks on the performance of hydraulic model investigations should be given.

The calculations have shown, that the wave height distribution reacts sensitively on small modifications of the boundary conditions of the numerical model. A hydraulic model will do this too but this sensitivity is not always realized.

To compare the results of a hydraulic model fortuities of measurements must be excluded.

Measurements at a few fixed points in a threedimensional model are therefore useless for comparing purposes, because the position of nodal points of the wave oscillation is changing.

For the performance of hydraulic model test this signifies that the wave data have to be measured in a appropriate narrow grid, which is often ignored.

REFERENCES

1. BURKHARDT, O.: Wellenverhältnisse im Hafen Greenville, Liberia (1977), gutachtliche Stellungnahme (unveröffentlicht)
2. RHEIN-RUHR ING.-GES. (RRI): Extension of the Harbour of Greenville Additional Investigations (1976), (unveröffentlicht)
3. CARR, H.J.: Wave Protection Aspects of Harbour Design Hydrodynamics Laboratory, Hydraulic Structures Division California Institute of Technology, Pasadena, California, Report-Nr. E-11, 1952
4. SOMMERFELD, A.: Mathematische Theorie der Diffraktion Mathematische Annalen, Bd. 47, 1896
in: Vorlesungen über theoretische Physik, Bd. 4, Optik, 1950
5. DAEMRICH, K.-F.: Diffraktion gebeugter Wellen Ein Beitrag zur Berechnung der Wellenunruhe im Hafen Mitteilungen des Franzius-Instituts für Wasserbau und Küsteningenieurwesen der Technischen Universität Hannover, Heft 47, 1978
6. BERGER, U.: Mach-Reflexion als Diffraktionsproblem Mitteilungen des Franzius-Instituts für Wasserbau und Küsteningenieurwesen der Technischen Universität Hannover, Heft 43, 1976

A COMPARISON BETWEEN MODEL AND PROTOTYPE WAVES IN HARBOURS

by Sverre Bjørdal¹ and Alf Tørum²

INTRODUCTION

A common method of estimating the sheltering effects of different breakwater locations and layouts is to carry out physical model wave disturbance tests. Such tests have been carried out in different laboratories throughout the world for many years. But to our knowledge no reports are available in the literature showing comparison between model measurements and field measurements.

The trend is that we know more and more on the wave climate along our coasts. Hence we have a better basis to make our economical calculations on breakwaters. We therefore also want to operate our models on a more absolute basis rather than on a comparative basis. The trend in recent years has also been to study breakwater locations and layouts in order to minimize mooring forces and ship movements.

On this background VHL found a comparison between model test results and field measurements necessary. Full scale measurements of waves were carried out in two harbours by VHL during the winter 1976/77. This paper will present the results of the comparison of the model and the full scale measurements in Berlevåg and Vardø fishing harbours on the open coast of Finnmark in the northern part of Norway (Fig. 1). The model tests, as well as the full scale measurements, have been sponsored by the Norwegian State Harbour Authorities.

BERLEVÅG FISHING HARBOUR

Model tests

In 1960-61 VHL carried out model tests on the breakwater layouts for Berlevåg fishing harbour, and in 1976 the construction of the chosen breakwater layout was completed (Fig. 2). The model tests were carried out in scale 1:110 and regular waves were used, as was usual in every laboratory at that time. Due to the use of regular waves, wave spectra could not be compared from model and field measurements. The input waves during the model tests were based on hindcast and refraction analysis, and the sheltering effects of the breakwaters against waves from N and ENE (deep water) were tested with periods corresponding to $T = 9$ sec and 13 sec. The height of the incoming waves were mostly 5 m but in some tests they were 3 m at the wave generator. The water level during the model tests were +2.5 m.

1) Senior Research Engineer,

2) Head, Department of Harbour and Marine Technology,

both at VHL, the River and Harbour Laboratory at the Norwegian Institute of Technology, Trondheim, Norway.

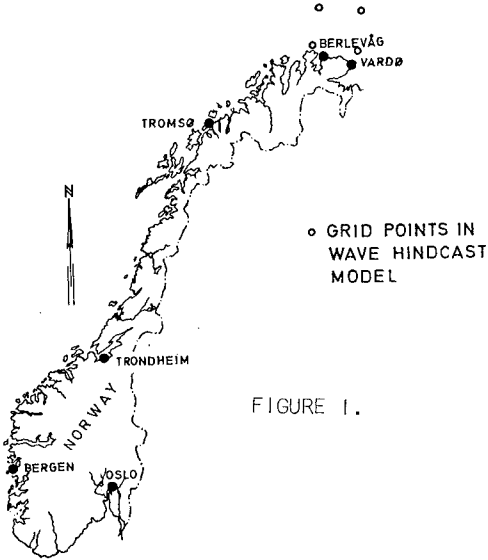


FIGURE 1.

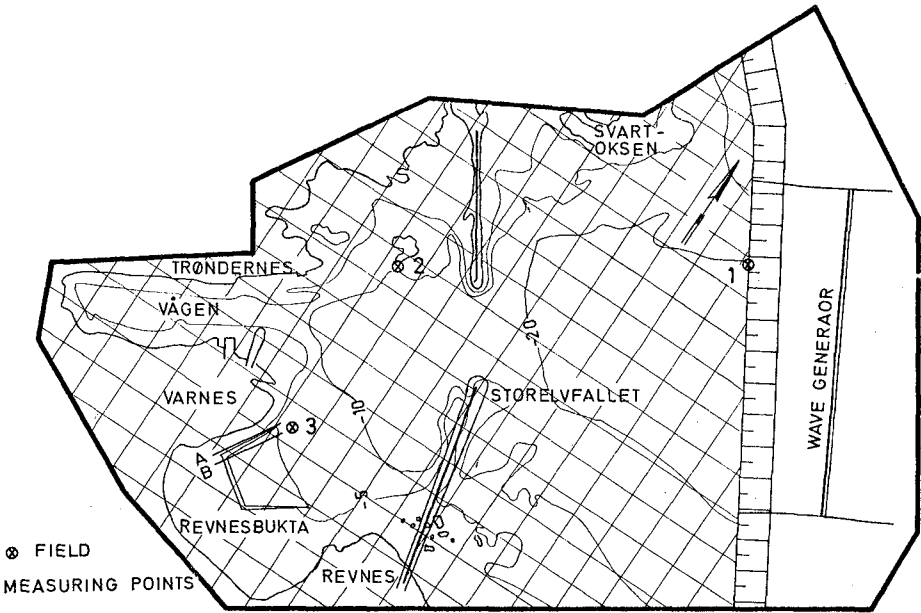


FIGURE 2.

Fig. 3 shows some of the refraction analysis carried out for waves from directions E and ENE. It is seen that although differences in direction in deep water are large, the differences in direction in front of the breakwaters are only some few degrees.

Fig. 2 shows the model plan for Berlevåg harbour. The waves were mainly measured in the grid points, the distance between each point was approximately 100 m. Detailed measurements were carried out at lines A and B, which are in front of a proposed quay site. These measurements showed that the wave heights varied significantly within short distance and also with time in the model.

During the full scale measurements (see later) the position of the wave meters would vary depending on wave and wind conditions. Hence for the basis of comparisons of model tests and field measurements an average wave height of the grid points closest to the wave meter was used. The three field measurement points are shown in Fig. 2. Since the measurements were carried out in more detail in position 3 than in position 2, we consider the model values more accurate for position 3 than for position 2.

In Table 1 is shown the average wave heights for the different measuring points.

TABLE 1. Average wave heights in meters outside and inside Berlevåg harbour based on model tests.

Wave direction deep water	Wave period sec.	Water level m	Wave height position 1 m	Wave height position 2 m	Wave height position 3 m
ENE	9	+ 2.5	5	1.86	1.21
	9	+ 2.5	3		0.88
	13	+ 2.5	5		1.48
	13	+ 2.5	3		0.83
N	9	+ 2.5	5	1.03	1.96
	9	+ 2.5	3		1.04
	13	+ 2.5	5		2.44
	13	+ 2.5	3		0.99

Field measurements

The wave measurements in Berlevåg harbour was carried out during the time period 20 October - 26 November 1976. Three wave gauges of the Datawell Waverider Buoy type were placed in the positions shown in Fig. 2. The wave meters have some freedom to move, and this is to

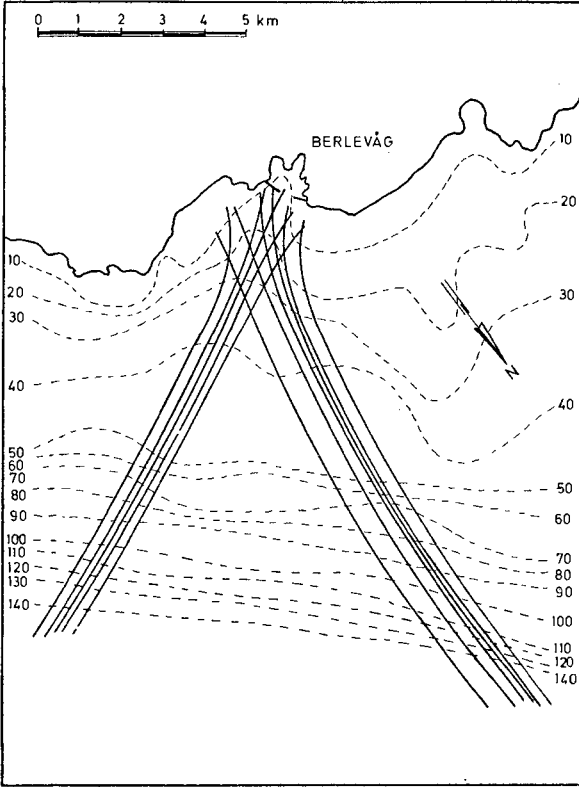


FIGURE 3. Refraction analysis. Wave period $T = 13$ s. Depth contours in meters.

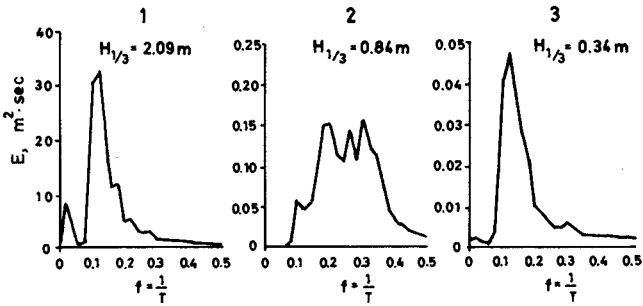


FIGURE 4. Wave spectra at Berlevåg 21 October 1976 at 1000.

some extent considered when comparing the field and model data. The wave gauge outside the harbour was placed as close as possible to the reference point for wave measurements in the model and with due considerations to the navigation in the area.

The weather conditions during the measuring period was, however, good with very little waves for that time of the year.

The waves recorded on 21 October, 25-26 October and 24-25 November 1976 had maximum heights of approximately 4 m, and the waves from these days have been used in our comparison.

The waves were recorded on magnetic tape and the wave recordings were analysed by a computer program.

The wave analysis was based on 300 consecutive waves. A Fast Fourier Transform was used to calculate the wave spectra. 4096 data points were used. The time interval between each data point $\Delta t = 0.5$ s. 2048 components were calculated in the frequency range 0-1 Hz. The averaging was made over 41 components giving data points at frequency intervals $\Delta f = 0.02$ Hz. The 90% confidence interval for each spectral value is within 0.78-0.55 of the calculated value.

Figs. 4 and 5 show simultaneous wave spectra at the three stations.

The main wave directions were visually judged during the measurements. However, wave directions were also calculated by the Norwegian Meteorological Institute using a numerical hindcast model. The wave directions by this numerical model were calculated at grid points 150 km apart. The closest grid points to Berlevåg are shown in Fig. 1. The wave hindcast models give the wave direction in deep water. When considering the wave refraction from deep water to the harbour area, the visually observed wave directions corresponded fairly well to the hindcasted wave direction.

Table 2 shows results of the wave measurements in Berlevåg.

It is also interesting to notice the transfer of energy to higher frequencies of the wave spectrum as shown for position 2 in Fig. 4. The spectra of Fig. 4 are for easterly waves, while the ones in Fig. 5 are for more northerly waves. No significant transfer of energy to higher frequencies is observed for the spectra of Fig. 5.

The reason for the high frequency wave energy at position 2 in Fig. 4 is inferred to be due to waves breaking at the head of the western breakwater. In the breaking process, new short waves are generated. This is a case often observed in model.

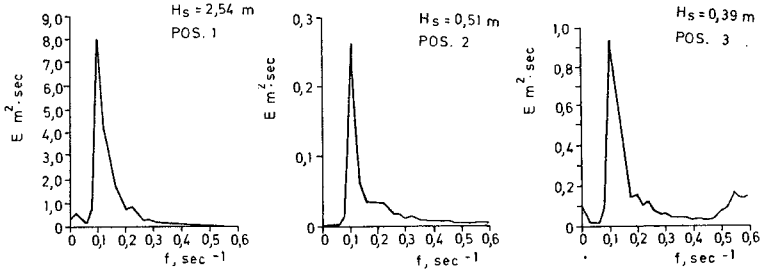


FIGURE 5. Wave spectra at Berlevåg 26 October 1976 at 1030. Deep water wave direction N.

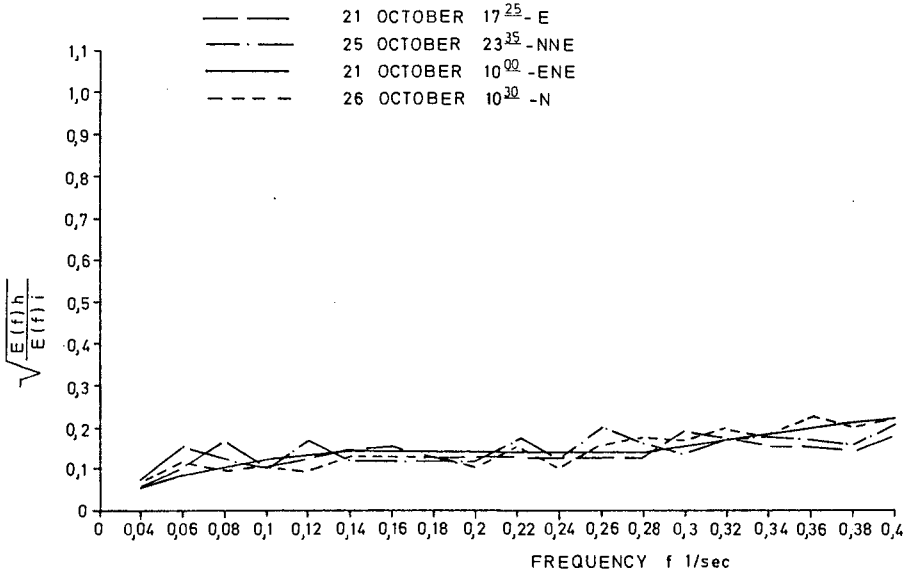


FIGURE 6. Berlevåg - Transfer functions. Position 3.

TABLE 2. Measured waves at Berlevåg harbour. 1976.

Position	Date	Time	H_s m	H_{max} m	T_p sec.	Deep water wave direction	Water level m
1	21 Oct.	1000	2.09	3.93	10.0	ENE	+1.0
	21 Oct.	1725	2.09	3.36	8.5	E	+1.7
	25 Oct.	2325	2.17	3.68	10.0	NNE	+0.3
	26 Oct.	1030	2.54	3.88	10.0	N	+0.7
	24 Nov.	2130	1.56	2.70	7.0	WNW	+1.6
2	21 Oct.	1000	0.73	1.13	4.5		
	21 Oct.	1725	0.84	1.18	4.0		
	25 Oct.	2325	0.45	0.66	10.0		
	26 Oct.	1030	0.51	0.75	10.0		
	24 Nov.	2130	0.26	0.38	7.0		
3	21 Oct.	1000	0.33	0.51	8.5		
	21 Oct.	1725	0.34	0.52	8.5		
	25 Oct.	2325	0.34	0.66	10.0		
	26 Oct.	1030	0.39	0.70	10.0		
	24 Nov.	2130	0.27	0.45	7.0		

$T_p = 1/f_p$; f_p = frequency of maximum energy density;

H_s = significant wave height.

Comparison of waves in the field and the model

Since the waves in the model were regular while the waves in the field are irregular and of different heights than in the model, it is not possible to compare directly the waves in the field and in the model. However, to compare we have defined a sheltering coefficient $K_d = H_h/H_i$, where H_h = wave height in the harbour and H_i = wave height outside the harbour. For irregular waves the significant wave height has been used. It should, however, be noted that the sheltering coefficient varies for different frequencies of the wave spectrum (see later).

In Table 3 is shown the sheltering coefficients from the field measurements and the model tests.

Generally speaking the calculated sheltering coefficients are smaller from the field measurements than from the model tests. This is especially the case for position 2. There may be different reasons for this that will be dealt with in the general discussion.

To obtain some feeling for how the sheltering coefficient varies with the frequency, we have calculated a transfer function for the waves defined as:

TABLE 3. Berlevåg - sheltering coefficients from field and model wave measurements.

	Position 1		Position 2		Position 3		Water level m	Calculated deep water wave direction
	H m	T _p sec	K _d	T _p sec	K _d	T _p sec		
Field H = H _s , T = T _p	2.09	10.0	0.35	4.5	0.16	8.5	+1	ENE
	2.09	8.5	0.40	4.5	0.16	8.5	+1.7	E
	2.17	10.0	0.21	10.0	0.16	10.0	+0.3	NNE
	2.54	10.0	0.20	10.0	0.15	10.0	+0.7	N
	1.56	7.0	0.167	7.0	0.17	7.0	+1.6	WNW
Model, regular H, T	5	9.0	0.41	-	0.24	-	+2.5	ENE
	3	9.0	-	-	0.29	-	+2.5	
	5	13.0	-	-	0.30	-	+2.5	
	3	13.0	-	-	0.28	-	+2.5	
	5	9.0	0.26	-	0.39	-	+2.5	
	3	9.0	-	-	0.35	-	+2.5	N
	5	13.0	-	-	0.49	-	+2.5	
	3	13.0	-	-	0.33	-	+2.5	

$$|T(f)| = \sqrt{\frac{E(f)_h}{E(f)_i}}$$

where $E(f)_h$ = power density spectrum within the harbour

$E(f)_i$ = power density spectrum outside the harbour.

This transfer function is very much used for linear systems.

The calculated transfer functions are shown in Figs. 6 and 7 for measuring stations positions 2 and 3. Apparently the sheltering effect is less for higher frequencies than for lower frequencies contradictory to linear theory. However, as pointed out during the description of the field measurements, there was apparently a transfer of wave energy to higher wave frequencies due probably to wave breaking around the breakwater head.

Thus the transfer functions rather reflect non-linearity effects than physical contradictions. It should also be noted that there is a larger uncertainty of the values of the transfer functions for the higher frequencies because of the rather small values the power density spectra have for the higher frequencies.

It is interesting to note that the transfer function for position 2 for 21 October shows a somewhat lower sheltering coefficient in the frequency range of the peak frequency (0.1-0.15 Hz) than obtained from the ratio of the significant wave heights shown in Table 3.

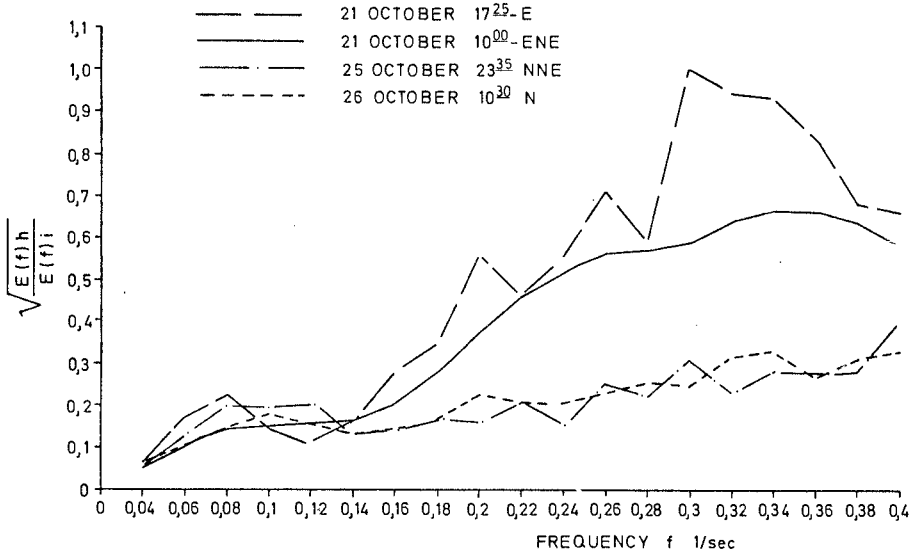
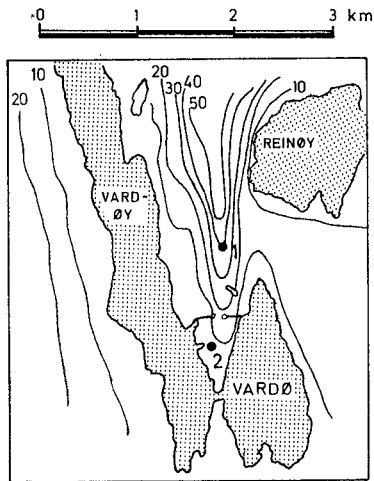


FIGURE 7. Berlevåg - Transfer functions. Postion 2.



● FIELD MEASURING POINTS,
DEPTH CONTOURS IN m.

FIGURE 8. Vardø harbour

The wave sheltering in Berlevåg is apparently better than indicated by the tests with regular waves. How much better is, however, difficult to assess.

VARDØ HARBOUR

Field measurements

The wave measurements at Vardø harbour were carried out prior to the model tests. Fig. 8 shows the area at Vardø harbour and Fig. 9 shows the model plan with depth contours and with the field measuring points.

Waves were measured in Vardø during the time period 1 March - 24 May 1977.

Outside the harbour waves were measured with a Datawell wave rider buoy. At the dock, within the harbour the waves were measured by a pressure type wave gauge. Individual waves are not so easily obtained by pressure wave gauges. However, the wave spectrum is fairly well measured by a pressure gauge, taking into account the wave pressure attenuation with depth.

The waves from the two gauges were recorded on magnetic tape. The wave analysis was based on 300 consecutive waves. The procedure for the spectral analysis was the same as for the waves measured in Berlevåg.

The significant wave heights from the Datawell wave rider buoy was calculated from the wave record, while the significant wave height from the pressure wave gauge was taken as $H_s = 4\sqrt{m_0}$, where m_0 = spectral area. Fig. 10 shows wave power spectra for some of the recorded waves.

Table 4 shows some of the results of the measured waves in Vardø. The wave directions in paranthesis are those calculated by the Norwegian Meteorological Institute, in deep water, while the others are those visually observed.

Model tests

The model tests for Vardø harbour were carried out to improve the wave conditions within the harbour. The model scale was 1:100. Fig. 9 shows the model plan for Vardø harbour with the breakwaters as they were built many decades ago and as they were during the field wave measurements.

Most wave energy will enter the harbour from the north. Hence this wave direction was chosen for the model tests.

Irregular waves were used during the tests. The wave generator had one straight flap. Hence the wave crests were straight when they left the wave generator.

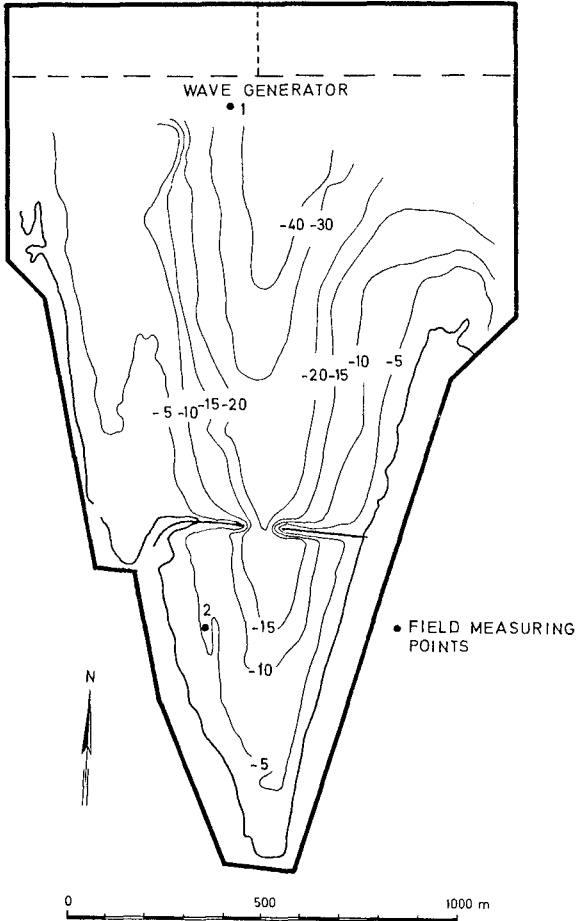


FIGURE 9. Vardø harbour model.

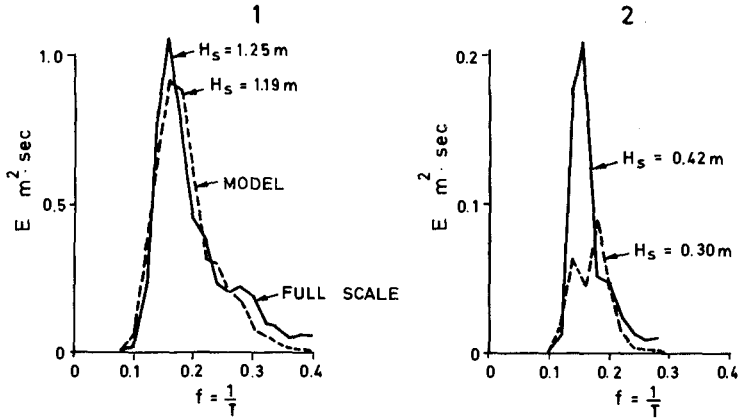


FIGURE 10. Vardø harbour. Field and model wave spectra.

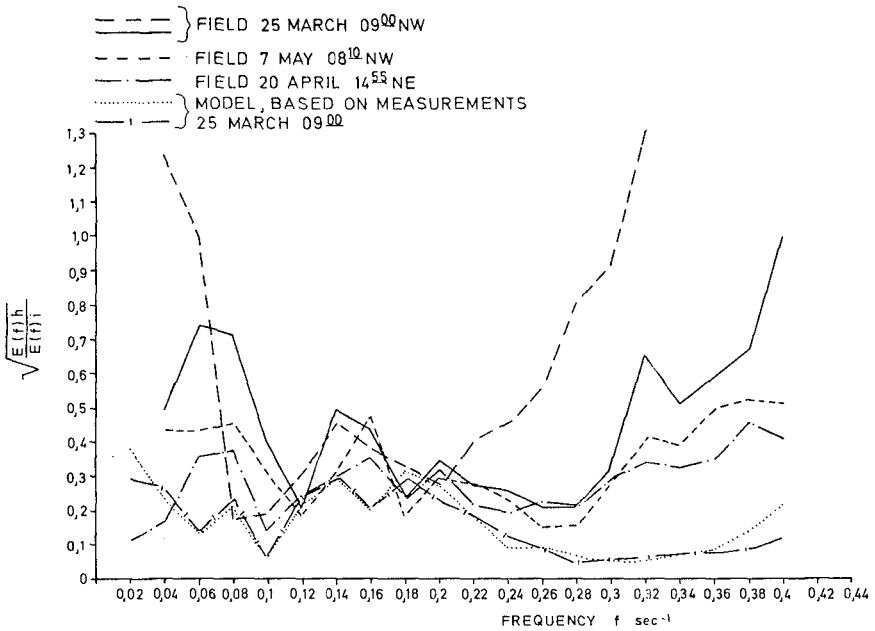


FIGURE 11. Vardø harbour - Transfer functions. Position 2.

TABLE 4. Waves measured at Vardø. 1977.

Position	Date	Time	H_s m	H_{max} m	T_p sec.	Direction	Water level m
1	3 March	1700	1.35	2.8	6.85	NW (W)	+2.5
	5 "	2115	1.01	1.65	7.1	NW	+0.8
	6 "	0915	0.83	1.51	8.3	NW	+1.0
	6 "	1415	1.31	2.12	8.3	N	+1.8
	18 "	0600	1.65	3.37	8.3	SE	+2.4
	24 "	2136	1.03	1.86	5.6	NW	+2.3
	24 "	2315	0.98	1.62	7.1	NW	+1.1
	25 "	0905	1.20	1.84	6.25	NW	+2.8
	25** "	0905	1.08	1.90	6.75	NW	+2.8
	20 April	1445	1.51	2.33	7.1	NE (ENE)	+1.7
	20** "	1445	1.59	2.68	7.1	NE (ENE)	+1.7
	7 May	0810	1.41	2.53	8.3	NW (NNW)	+2.8
	2	3 March	1700	0.28	0.51	6.25	
5 "		2115	0.15	0.27	8.3		
6 "		0915	0.12	0.22	8.3		
6 "		1415	0.40	0.72	7.1		
18 "		0600	0.25	0.47	10		
24 "		2136	0.33	0.60	5.0		
24 "		2315	0.33	0.60	7.1		
25 "		0905	0.37	0.68	7.1		
25** "		0905	0.39	0.71	6.25		
20 April		1445	0.41	0.74	7.1		
20** "		1445	0.42	0.75	7.1		
7 May		0810	0.50	0.90	8.3		

**) Based on 1000 consecutive waves.

Different wave spectra were used for the model tests. Basically the peak frequencies of the model spectra corresponded to the wave periods $T_p = 5.7$ sec, 7.5 sec, 9.0 sec, 10.5 sec and 12 sec. All spectra were relatively narrow, except the spectrum with $T_p = 5.7$ sec. which was based on measured waves in Vardø. The significant wave heights close to the wave generator were in most tests 4.0 m, but for the wave spectrum with $T_p = 5.7$ sec the significant waves at the wave generator were close to the waves measured at Vardø.

In Table 5 is shown some of the wave parameters measured in the Vardø harbour model.

TABLE 5. Significant and maximum measured waves in the Vardø model

Wave direction	Water level m	Position 1			Position 2		
		H_s m	H_{max} m	T_p sec	H_s m	H_{max} m	T_p sec
N	+2.5	1.20	2.33	6.25	0.29	0.46	5.55
N	+2.5	1.19	2.23	6.25	0.30	0.53	5.55
N	+2.5	1.49	3.01	6.25	0.34	0.56	5.55
N	+2.5	1.37	2.30	6.25	0.38	0.61	5.55

Comparison of waves in the field and in the model

Some of the model tests were carried out with waves corresponding to the waves measured in Vardø on 25 March 1977. These waves had rather short periods, and on model scale they were in the order of magnitude 0.5 sec and hence almost on the lower limit of the wave generator.

In Table 6 is shown the sheltering coefficient, $K_d = H_{ns}/H_{is}$, both for the field measurements and from the model tests.

TABLE 6. Vardø - Sheltering coefficient in the field and in the model.

	Position 1		Position 2		Water level m	Calculated deep water wave direction
	H_{is} m	T_p sec	K_d	T_p sec		
Model	1.20	6.25	0.23	5.55	+2.5	N
	1.19	6.25	0.25	5.55	+2.5	N
	1.49	6.25	0.23	5.55	+2.5	N
	1.37	6.25	0.28	5.55	+2.5	N
	2.12	6.25	0.33	5.55	+2.5	N
Field	1.20	6.25	0.31	7.1	+2.8	NW
	1.08	6.25	0.36	6.25	+2.8	NW
	1.51	7.1	0.27	7.1	+1.7	NE
	1.31	8.3	0.31	7.1	+1.8	NW
	1.41	8.3	0.35	8.3	+2.8	NW

Fig. 10 shows the wave spectra from the model and the field for the waves with peak period 6.25 sec.

The sheltering coefficients of Table 6 show that the sheltering is larger in the model than in the field.

Fig. 11 shows the transfer function for different wave conditions. The sheltering varies with the frequency, most for the field measurements. In the model the minimum sheltering is obtained for frequencies around the peak frequencies ($T = 5-8$ s). For higher and lower frequencies the sheltering effect is less. The full scale measurements show the same tendency, except for the highest and lowest frequencies, $T < 3$ s and $T > 10$ s. The field measurements within the harbour were carried out with a pressure type wave gauge. There are uncertainties in calculating high frequency waves from such measurements. This could be one reason for the apparent low sheltering at high frequencies. But it has also to be born in mind that transfer of energy from low to high frequencies has been observed due to breaking of waves at the breakwater heads.

The transfer functions show that the sheltering in the model is better than in the field for almost every frequency. Comparison of the sheltering coefficient based on the significant waves and the transfer function show that the sheltering coefficient is lowest for significant waves both in the model and in the field.

DISCUSSION

The results of the field and model measurements show that there are apparently discrepancies between the field and model measurements. The Berlevåg harbour measurements show that the sheltering is apparently less in the model than in the field, while the opposite is apparently the case in the Vardø harbour measurements. However, there could be different reasons for these apparent discrepancies.

Regular and irregular waves

In the Berlevåg harbour measurements the tests were carried out with regular waves, while in the field measurements the waves were irregular. This makes direct comparisons difficult. Special emphasis is made on the fact that there are some transformation of wave energy from lower to higher frequencies.

In the Vardø harbour tests the waves in both the field and the model were irregular.

Wave direction

The waves were unidirectional in the model at the wave generator flap. In the field the waves were multidirectional at the position of the wave flap. The directional spread at this position was probably, due to refraction effects, not as wide as in the open ocean. The directional spread in the ocean is not fully established yet, but $\cos^n \alpha$ is often used. α is the angular direction from the main direction, n is an exponent, a value of n of 2-4 is often used.

From the refraction analysis shown in Fig. 3 is inferred that although the waves may have almost 90° difference in direction in deep water, the difference in direction at the wave generator flaps is much less. There are, however, still a multidirectionality at the breakwater flap.

There is an uncertainty in the visually observed and hindcasted wave direction from the field measurements at the Berlevåg harbour. This uncertainty can certainly contribute to the discrepancy between the model and the field measurements.

At the Vardø harbour we assume that the main direction of the waves from deep water northerly direction will be from north at the wave generator flap also. The orientation of the flap is such that maximum wave energy will enter into the harbour from that direction. Although we have no wave directional spectrum at the wave generator, there will be some directionality at this place, in the field. However, we believe that the wave direction in the model and the lack of wave directionality in the model is such that we would have relatively higher waves in the model than in the harbour, while the measurements show the opposite.

Another effect that was observed during the model tests was that there was a tendency of cross waves in front of the flap, generated by the flap. These cross waves had a rather short wave period. To what extent the model results are affected by these crossoscillations are not known. However, it is believed that the effect is small.

Another effect that is present at Vardø is a strong refraction effect due to the rather deep "trench" towards the harbour entrance. This effect was particularly observed in the model tests. Also, the depth contours were not true in the vicinity of the wave generator, where the depth corresponded to approximately 40 m along the whole length of the generator. In front of the ends of the generator, the rate of decrease of water depth was larger in the model than in the field to obtain the true depth. This has an effect on the waves, although it is not possible to quantify this effect.

Reflections

There could certainly be different shore and structural wave reflection effects in the field and in the model causing differences in model and field measurements. Different field boundary and gravel shores were tested in the Vardø model, but no significant effects from the different shores were observed. Hence it is inferred that reflection was probably no major cause for differences in the field and model results.

Viscous scale effects

Viscous effects on the wave propagation and wave variation is present both in the field and the model. We have calculated the viscous damping effect in the model using the "Stokes shear wave theory". Over a length with constant water depth the wave damping due to viscous effects is [1]:

$$\frac{H}{H_0} = e^{-\alpha x}$$

where

$$\alpha = \frac{a \cdot 4\pi}{\beta L^2 (\sinh kd + kd)}$$

a = empirical coefficient

d = water depth

$$\beta = \left(\frac{\omega}{2\nu}\right)^{\frac{1}{2}}; \quad \omega = 2\pi/T$$

ν = the water kinematic viscosity

x = wave travel distance

Assuming a water depth of 0.25 m, the average depth in the model from the wave generator to the breakwater, a distance of 9 m, the damping along this distance due to viscous effects is only approximately 2% for a wave with period 0.6 s. If we assume a water depth of 0.05 m, the wave height reduction due to viscous effects is approximately 12% for the same wave period, 0.6 s.

Although there are some effects from viscosity in the model, this effect is almost negligible in our comparisons of field and model wave measurements.

CONCLUSIONS

Although there is a fair agreement between field and model measured waves, it is doubtful if we can use the results from harbour sheltering tests on breakwater layouts on an absolute basis. It is though believed that we will obtain very useful information from such tests on a relative basis.

To improve our model testing technique to obtain information on a more absolute basis, we have to improve our knowledge of field waves, particularly directional wave spectra, especially in shallow water, and general wave climates. We have also to improve our testing equipment. The first basins with directional wave spectra generators have appeared and we need to have a development to use such spectra also for harbour sheltering models.

ACKNOWLEDGEMENTS

We appreciate highly the interest and financial support of the Norwegian State Harbour Authorities who made this study and paper possible.

REFERENCES

- [1] Ippen, A.T.: Estuary and Coastline Hydrodynamics, McGraw-Hill, New York, 1966.

CHAPTER 39

WAVE HEIGHT DISTRIBUTION AROUND PERMEABLE BREAKWATERS

by

Shintaro Hotta*

ABSTRACT

By superimposing solutions due to Sommerfeld, a calculation was made to obtain the wave height distribution around permeable breakwaters in a constant water depth. The cases dealt with were a semi-infinite breakwater, a single relatively large gap in a long breakwater and a single detached breakwater all with incident waves normal to the breakwater. Some cases were verified through experiments in a shallow water basin.

INTRODUCTION

There are many kinds of permeable breakwater systems. In particular, as a countermeasure against beach erosion, the construction of permeable detached breakwater systems has become widely popular. However, the functioning of such breakwater systems has not yet been fully understood.

Even the wave height distribution around a permeable breakwater, which should be first considered in its construction, has received little effort not in comparison with that made for impermeable breakwater systems, because of the complicated phenomena associated with the former.

Up to data, interest in connection with permeable breakwaters has mainly concentrated on wave reflection and transmission phenomena. Only for some special cases in three dimensions has the study of the wave height distribution and related problems already been carried out. For instance, Ijima, Chou and Yumula(1974) studied the scattering of waves around arbitrary shape permeable bodies and gave figures for the wave height distributions around circular, ellipsoid and rectangular cells. Their methods are applicable to arbitrary shape breakwaters, but it seems that the method requires complicated numerical calculations. The studies above may not give satisfaction to engineers who are faced with problems in practice.

* Research Associate, Dept. of Civil Engineering Tokyo Metropolitan University, Setagaya-ku, Tokyo, JAPAN

The purpose of this study is to attempt to clarify the wave height distribution around permeable breakwater systems. However the phenomena are so complicated that applying Sommerfeld's solution for widely deployed breakwater systems was considered as a first stage in the study.

An advantage of the method used in this study, superposition of Sommerfeld's solution, is that wave heights can be calculated very easily by addition and subtraction, if we have the Fresnel Integrals. At present, even on small computers, Fresnel Integrals are prepared as a subroutine or as a function. A few second calculation gives the wave height distribution. Another advantage is that the time lag of waves transmitted through the breakwater can be easily considered in equations, although this was not done here.

Disadvantages of this method are that the boundary conditions are not satisfied and the wave height becomes discontinuous on the x and y axis and on the lines which divide the regions considered. Calculated results, however, show that the discontinuity in wave height on the x and y axis and the otehr lines was small. So, we may close our eyes to this discontinuity. Experimental or field verification of the calculated results are not yet sufficient, but this method may be acceptable for engineering use to predict the wave height roughly, although further laboratory and field verification under various conditions must still be made.

Brief Summary of Sommerfeld's Solution:

For the case of an infinitely thin, vertical, rigid, impermeable, semi-infinite breakwater as drawn in Fig. 1, Penny and Price have shown that Sommerfeld's solution of the optical diffraction problem is also a solution of water wave diffraction.

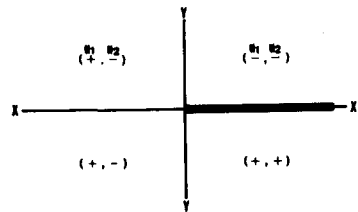
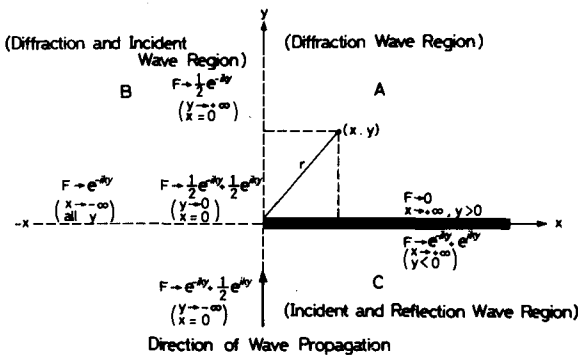


Fig. 2. Signs of u_1 and u_2

Fig. 1. Nomenclature for wave diffraction analysis at semi-infinite breakwater end.

The following is a brief summary of the solution by Penny and Price(1952).

$$\phi = A e^{ikz} \cosh kh \cdot F(x, y) \dots\dots\dots (1)$$

$$\eta = \frac{A k z}{g} e^{ikz} \cosh kh \cdot F(x, y) \dots\dots\dots (2)$$

$$\frac{\partial^2 F}{\partial x^2} + \frac{\partial^2 F}{\partial y^2} + k^2 F = 0 \dots\dots\dots (3)$$

$$f(u) = \frac{1}{\sqrt{2}} e^{i\pi/4} \int_{-\infty}^{u_1} e^{i\pi w^2/2} dw \dots\dots\dots (6)$$

$$g(u_2) = \frac{1}{\sqrt{2}} e^{i\pi/4} \int_{-\infty}^{u_2} e^{i\pi w^2/2} dw \dots\dots\dots (7)$$

where

$$i = \sqrt{-1} \quad k = 2\pi/L$$

L = wave length c = phase velocity

h = water depth g = gravity acceleration

$$f(u) = g(u) = \frac{1}{\sqrt{2}} e^{i\pi/4} \int_{-\infty}^u e^{i\pi w^2/2} dw$$

$$= \frac{1}{2} \{ (1 + C(u) + S(u)) + i(C(u) - S(u)) \} \dots\dots (8)$$

$$f(-u) = g(-u) = \frac{1}{\sqrt{2}} e^{i\pi/4} \int_{-\infty}^{-u} e^{i\pi w^2/2} dw$$

$$= \frac{1}{2} \{ (1 - C(u) - S(u)) + i(S(u) - C(u)) \}$$

$$= S + iW \dots\dots\dots (9)$$

$$F(x, y) = \frac{1}{\sqrt{2}} e^{i\pi/4} \int_{-\infty}^{u_1} e^{i\pi w^2/2} dw$$

$$+ \frac{1}{\sqrt{2}} e^{i\pi/4} \int_{-\infty}^{u_2} e^{i\pi w^2/2} dw$$

$$= e^{i\pi/4} f(u_1) + e^{i\pi/4} g(u_2) \dots\dots\dots (4)$$

$$C(u) = \int_0^u \cos \frac{\pi}{2} w^2 dw, \quad S(u) = \int_0^u \sin \frac{\pi}{2} w^2 dw \dots\dots (10)$$

$$u_1 = \pm \sqrt{\frac{4(r-y)}{L}}, \quad u_2 = \pm \sqrt{\frac{4(r+y)}{L}} \dots\dots\dots (5)$$

$$r = \sqrt{x^2 + y^2}$$

$$S = \frac{1}{2} \{ 1 - C(u) - S(u) \}$$

$$W = \frac{1}{2} \{ S(u) - C(u) \} \dots\dots\dots (11)$$

The diffraction coefficient, K, is defined as the ratio of wave height in the area affected by diffraction to the wave height in the area unaffected by diffraction, and given by the modulus of F(x, y) for the diffracted wave: taht is

$$K = |F(x, y)| = \sqrt{R^2 + I^2} \dots\dots\dots (12)$$

R: Real component of F(x, y)

I: Imaginary component of F(x, y)

The final forms of $F(x, y)$ for numerical calculation for a breakwater located on the + x axis as shown in Fig. 1 are:

Region A, $x > 0, y > 0$

$$\begin{aligned}
 F_0^A(x, y) &= e^{-iky} f(-u_1) + e^{iky} g(-u_2) \\
 &= (S_1 + S_2) \cos ky + (W_1 - W_2) \sin ky \\
 &\quad + i[(W_1 + W_2) \cos ky + (-S_1 + S_2) \sin ky] \text{-----} (13)
 \end{aligned}$$

Region B, $x < 0,$

$$\begin{aligned}
 F_0^B(x, y) &= e^{-iky} f(u_1) + e^{iky} g(-u_2) \\
 &= (1 - S_1 + S_2) \cos ky + (-W_1 - W_2) \sin ky \\
 &\quad + i[(-W_1 + W_2) \cos ky + (-1 + S_1 + S_2) \sin ky] \text{-----} (14)
 \end{aligned}$$

Region C, $x > 0, y < 0$

$$\begin{aligned}
 F_0^C(x, y) &= e^{-iky} f(u_1) + e^{iky} g(u_2) \\
 &= (2 - S_1 - S_2) \cos ky + (-W_1 + W_2) \sin ky \\
 &\quad + i[(-W_1 - W_2) \cos ky + (S_1 - S_2) \sin ky] \text{-----} (15)
 \end{aligned}$$

As a matter of convenience later, we shall give the final forms of $F(x, y)$ for numerical calculation for a breakwater located on the - x axis as shown in Fig. 3.

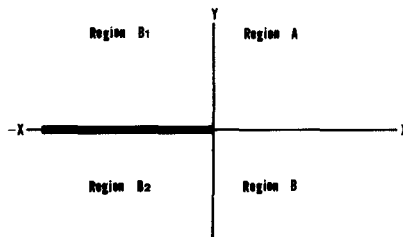


Fig. 3. Nomenclature for wave diffraction analysis at breakwater when located on -x axis.

Region A and C

$$\begin{aligned}
 F_i^A(x,y) &= e^{-iky} f(u_1) + e^{iky} g(-u_2) \\
 &= (1 - S_1 + S_2) \cos ky + (-W_1 - W_2) \sin ky \\
 &\quad + i [(-W_1 + W_2) \cos ky + (-1 + S_1 + S_2) \sin ky] \text{-----} (16)
 \end{aligned}$$

Region B1

$$\begin{aligned}
 F_i^{B1}(x,y) &= e^{-iky} f(-u_1) + e^{iky} g(-u_2) \\
 &= (S_1 + S_2) \cos ky + (W_1 - W_2) \sin ky \\
 &\quad + i [(W_1 + W_2) \cos ky + (-S_1 + S_2) \sin ky] \text{-----} (17)
 \end{aligned}$$

Region B2

$$\begin{aligned}
 F_i^{B2}(x,y) &= e^{-iky} f(u_1) + e^{iky} g(u_2) \\
 &= (2 - S_1 - S_2) \cos ky + (-W_1 + W_2) \sin ky \\
 &\quad + i [(-W_1 - W_2) \cos ky + (S_1 - S_2) \sin ky] \text{-----} (18)
 \end{aligned}$$

NUMERICAL CALCULATIONS OF WAVE HEIGHT DISTRIBUTION
FOR PERMEABLE BREAKWATER

- (1). A single small gap in a long permeable breakwater as shown in Fig. 4.

The heights of waves which have passed through a single gap small compared with the wave length of a long impermeable breakwater have been already given by Lamb (1945).

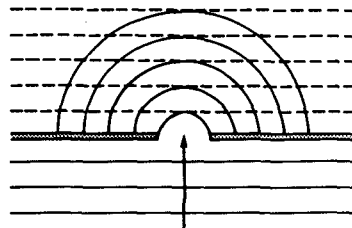


Fig. 4. Diffraction at small gap

The solution is:

$$F_a(x, y) = \frac{\sqrt{\frac{L}{4r}}}{\left(\log \frac{kb}{4} + \gamma + \frac{\pi}{2}i\right)} e^{-i\left(\frac{\pi}{4} + kr\right)} \dots\dots\dots (19)$$

γ : Constant of Euler

$$F_b = \alpha e^{-ky} \dots\dots\dots (20)$$

This equation shows a wave which concentrically spreads from a gap. When the breakwater is permeable we assume that the wave heights inside the breakwater can be express of by superimposing Equations (19) and (20). That is:

$$F = F_a + F_b$$

$$= \alpha e^{-ky} + \frac{\sqrt{\frac{L}{4r}}}{\left(\log \frac{kb}{4} + \gamma + \frac{\pi}{2}i\right)} e^{-i\left(\frac{\pi}{4} + kr\right)}$$

The superimposed result is:

$$F = \alpha \cos ky + \frac{\sqrt{\frac{L}{4r}} \sqrt{C_r^2 + C_i^2}}{2kr} \cos\left(\frac{\pi}{4} + kr - \theta\right) - i \left\{ \alpha \sin ky + \frac{\sqrt{\frac{L}{4r}} \sqrt{C_r^2 + C_i^2}}{2kr} \sin\left(\frac{\pi}{4} + kr - \theta\right) \right\} \dots\dots\dots (21)$$

where

$$C_r = \frac{\log \frac{kb}{4} + \gamma}{\left(\log \frac{kb}{4} + \gamma\right)^2 + \frac{\pi^2}{4}}$$

$$C_i = \frac{-\frac{\pi}{2}}{\left(\log \frac{kb}{4} + \gamma\right)^2 + \frac{\pi^2}{4}}$$

$$\theta = \tan^{-1} \frac{C_i}{C_r}$$

The wave heights are given by:

$$R = \alpha \cos ky + \frac{\sqrt{\frac{L}{4r}} \sqrt{C_r^2 + C_i^2}}{2kr} \cos\left(\frac{\pi}{4} + kr - \theta\right)$$

$$I = - \left\{ \alpha \sin ky + \frac{\sqrt{\frac{L}{4r}} \sqrt{C_r^2 + C_i^2}}{2kr} \sin\left(\frac{\pi}{4} + kr - \theta\right) \right\}$$

$$K = \sqrt{R^2 + I^2}$$

Diagrams for a gap width b, b/L ratios of 0.1 and 0.2 and transmission coefficients, α , from 0.1 to 0.5 are given in Appendix 1.

(2) A semi-infinite permeable breakwater

For the waves on the shore side of the breakwater, regions A and B1 ($y > 0$) as shown Fig 5-(3), superposition of waves as shown in Fig 5-(1) and the waves as shown in Fig 5-(2) is assumed.

On the other hand, for the waves on the offshore side of the permeable breakwater, regions B2 and C ($y < 0$), it is assumed that the waves can be expressed by where the reflection coefficient, β , multiplies a free wave propagating in the $-y$ direction, e^{iky} .

$$e^{-iky}f(u_1) + \beta e^{iky}g(u_2) \text{-----(22)}$$

Equations based on those assumptions in their final forms are:

Region A $x > 0, y > 0$

$$F_0(x, y) = e^{iky}f(-u_1) + e^{iy}g(-u_2)$$

$$F_1(x, y) = e^{iky}f(u_1) + e^{iy}g(-u_2)$$

$$F = F_0 + \alpha F_1$$

$$F_2^A = \{\alpha + (1-\alpha)S_1 + (1+\alpha)S_2\} \cos ky + \{(1-\alpha)W_1 - (1+\alpha)W_2\} \sin ky + i\{(1-\alpha)W_1 + (1+\alpha)W_2\} \cos ky - \{\alpha + (1-\alpha)S_1 - (1+\alpha)S_2\} \sin ky \text{-----(23)}$$

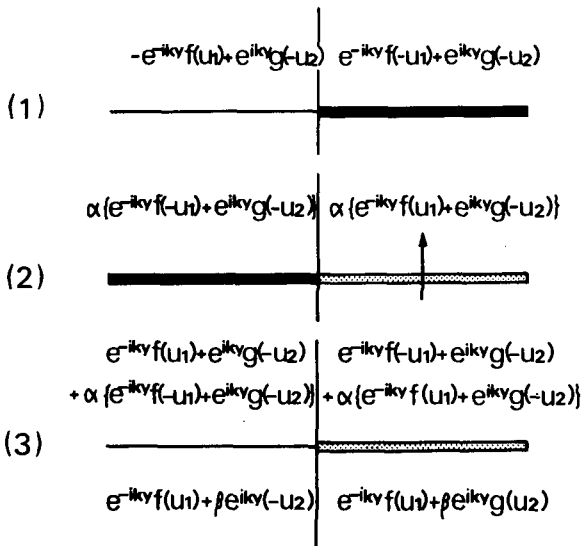


Fig. 5. Superposition of waves for semiinfinite permeable breakwater.

Region B₁ $x < 0, y > 0$

$$F_0(x, y) = e^{-ky}f(u_1) + e^{ky}g(-u_2)$$

$$F_1(x, y) = e^{-ky}f(-u_1) + e^{ky}g(-u_2)$$

$$F = F_0 + \alpha F_1$$

$$F_2^{B_1} = (1 - (1 - \alpha)S_1 + (1 + \alpha)S_2) \cos ky + \{- (1 - \alpha)W_1 - (1 + \alpha)W_2\} \sin ky + i \{ \{- (1 - \alpha)W_1 + (1 + \alpha)W_2\} \cos ky - [1 - (1 - \alpha)S_1 - (1 + \alpha)S_2] \sin ky \} \quad \text{----- (24)}$$

Region B₂ $x < 0, y < 0$

$$F = e^{-ky}f(u) + \rho e^{ky}g(-u_2)$$

$$F_2^{B_2} = (1 - S_1 + \rho S_2) \cos ky + (-W_1 - \rho W_2) \sin ky + i \{ \{- W_1 + \rho W_2\} \cos ky + [-1 + S_1 + \rho S_2] \sin ky \} \quad \text{----- (25)}$$

Region C $x > 0, y < 0$

$$F = e^{-ky}f(u_1) + \rho e^{ky}g(u_2)$$

$$F_2^C = (1 + \rho - S_1 - \rho S_2) \cos ky - (W_1 - \rho W_2) \sin ky - i \{ (1 - \rho - S_1 + \rho S_2) \sin ky + (W_1 + \rho W_2) \cos ky \} \quad \text{----- (26)}$$

$$\alpha + \rho = 1$$

$$S_1 = 1 - C(u_1) - S(u_1) \quad , \quad W_1 = C(u_1) - S(u_1)$$

$$S_2 = 1 - C(u_2) - S(u_2) \quad , \quad W_2 = C(u_2) - S(u_2)$$

where

$$C(u) = \int_0^u \cos \frac{\pi}{2} w^2 dw \quad , \quad S(u) = \int_0^u \sin \frac{\pi}{2} w^2 dw$$

If we ignore the energy loss when waves pass the breakwater, α the transmission coefficient plus β , the reflection coefficient equal unity. Taking α equal to zero, the final equations agree with the solution of a impermeable breakwater. However, if α is not zero, the waves becomes discontinuous on the x-axis. Calculated results with $\alpha = 0.0$ through $\alpha = 0.5$ are given in Appendix 2.

(3) A single relatively large gap in a long permeable breakwater.

For the case of an impermeable breakwater, Penny and Price(1952) have already given the solution by superimposing Eqs. (13), (14) and (15) and Eqs. (16), (17) and (18). Johnson(1952; 1953), Morihira and Okuyama(1966) and others have given detailed diagrams for engineering practice.

We shall write again here the final forms of the solution for numerical calculation because they will be needed the in succeeding sections. Suffixs r and l, indicating the cases when the breakwater is located at the + x and - x regions(Fig. 1 and Fig. 2), will be added.

The final forms are:

Region A1, $0 < x < b/2, y > 0$

$$\begin{aligned}
 F_3^{A1}(x,y) &= e^{-iky} f_r(u_1) + e^{iky} g_r(-u_2) + e^{-iky} f_l(u_1) + e^{iky} g_l(-u_2) - e^{-iky} \\
 &= (1 - S_{r1} - S_{l1} + S_{r2} + S_{l2}) \cos ky + (-W_{r1} - W_{l1} - W_{r2} - W_{l2}) \sin ky \\
 &\quad + i [(-W_{r1} - W_{l1} + W_{r2} + W_{l2}) \cos ky \\
 &\quad + (-1 + S_{r1} + S_{l1} + S_{r2} + S_{l2}) \sin ky] \text{ ----- (27)}
 \end{aligned}$$

Region A2, $b/2 < x, y > 0$

$$\begin{aligned}
 F_3^{A2}(x,y) &= e^{-iky} f_r(-u_1) + e^{iky} g_r(-u_2) + e^{-iky} f_l(u_1) + e^{iky} g_l(-u_2) - e^{-iky} \\
 &= (S_{r1} - S_{l1} + S_{r2} + S_{l2}) \cos ky + (W_{r1} - W_{l1} - W_{r2} - W_{l2}) \sin ky \\
 &\quad + i [(W_{r1} - W_{l1} + W_{r2} + W_{l2}) \cos ky \\
 &\quad + (-S_{r1} + S_{l1} + S_{r2} + S_{l2}) \sin ky] \text{ ----- (28)}
 \end{aligned}$$

Region C2, $x > b/2, y < 0$

$$\begin{aligned}
 F_3^{C2}(x,y) &= e^{-iky} f_r(u_1) + e^{iky} g_r(u_2) + e^{-iky} f_l(u_1) + e^{iky} g_l(-u_2) - e^{-iky} \\
 &= (2 - S_{r1} - S_{l1} - S_{r2} + S_{l2}) \cos ky + (-W_{r1} - W_{l1} + W_{r2} - W_{l2}) \sin ky \\
 &\quad + i [(-W_{r1} - W_{l1} - W_{r2} + W_{l2}) \cos ky \\
 &\quad + (S_{r1} + S_{l1} - S_{r2} + S_{l2}) \sin ky] \text{----- (29)}
 \end{aligned}$$

In the case of a permeable breakwater, the same idea described in the preceding section (2) is assumed. To express the waves on the shore side as show in Fig. 6-(4), the waves in Figs. 6-(2) and 6-(3) are superimposed on the waves as shown Fig. 6-(1). On the offshore side of the breakwater, a reflection coefficient, β , multiplies all terms, e^{iky} .

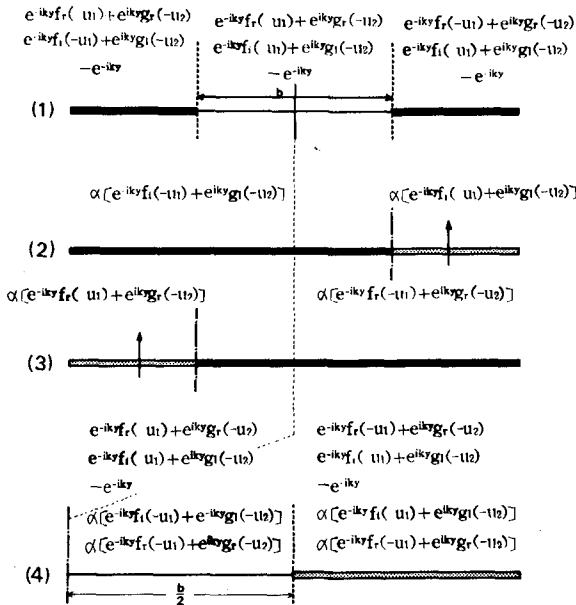


Fig. 6. Superposition of waves for a relatively large gap in permeable breakwater.

According to this assumption. The $F(x,y)$ which should be added to $F_3(x, y)$ because the breakwater is permeable are:

Region A1, $0 < x < b/2, y > 0$

$$F(x,y) = \alpha [e^{-iky} f_l(-u_1) + e^{iky} g_l(-u_2)] + \alpha [e^{-iky} f_r(-u_1) + e^{iky} g_r(-u_2)]$$

$$= \alpha [F_1^{Bl}(x,y) + F_0^A(x,y)] \text{ ----- (30)}$$

Region A2, $b/2 < x, y > 0$

$$F(x,y) = \alpha [e^{-iky} f_l(u_1) + e^{iky} g_l(-u_2)] + \alpha [e^{-iky} f_r(-u_1) + e^{iky} g_r(-u_2)]$$

$$= \alpha [F_1^A(x,y) + F_0^A(x,y)] \text{ ----- (31)}$$

We shall rewrite the function $F_0^A, F_1^A,$ and F_1^{Bl} , adding the suffixes, $r, l.$

$$F_0^A(x,y) = (S_{r1} + S_{r2}) \cos ky + (W_{r1} - W_{r2}) \sin ky$$

$$+ i [(W_{r1} + W_{r2}) \cos ky + (-S_{r1} + S_{r2}) \sin ky] \text{ ----- (14)'}$$

$$F_1^A(x,y) = (1 - S_{l1} + S_{l2}) \cos ky + (-W_{l1} - W_{l2}) \sin ky$$

$$+ i [(-W_{l1} + W_{l2}) \cos ky + (-1 + S_{l1} + S_{l2}) \sin ky] \text{ ----- (16)'}$$

$$F_1^{B1}(x, y) = (S_{\ell 1} + S_{\ell 2}) \cos ky + (W_{\ell 1} - W_{\ell 2}) \sin ky + i [(W_{\ell 1} + W_{\ell 2}) \cos ky + (-S_{\ell 1} + S_{\ell 2}) \sin ky] \text{-----}(17)'$$

Now, we shall consider the coordinate system. For Eq. (28), (29) and (27)

$$r_r = \sqrt{(x - b/2)^2 + y^2}$$

$$r_\ell = \sqrt{(x + b/2)^2 + y^2}$$

On the other hand, for Eq. (14)', (16)' and (17)'

$$r_\ell = \sqrt{(x - b/2)^2 + y^2}$$

$$r_r = \sqrt{(x + b/2)^2 + y^2}$$

If we exchange the suffixes r and ℓ in Eqs. (14)', (16)' and (17)' we can use the same coordinate system in Eqs. (28), (29), (27), (14)', (16)' and (17)'.

Finally, we have:

Region A1, $0 < x < b/2, y > 0$

$$F_{3p}^{A1}(x, y) = F_3^{A1}(x, y) + \alpha [F_1^{B1}(x, y) + F_0^A(x, y)]$$

$$= \{1 - (1 - \alpha)S_{r1} - (1 - \alpha)S_{\ell 1} + (1 + \alpha)S_{r2} + (1 + \alpha)S_{\ell 2}\} \cos ky$$

$$+ \{- (1 - \alpha)W_{r1} - (1 - \alpha)W_{\ell 1} - (1 + \alpha)W_{r2} - (1 + \alpha)W_{\ell 2}\} \sin ky$$

$$+ i \{[- (1 - \alpha)W_{r1} - (1 - \alpha)W_{\ell 1} + (1 + \alpha)W_{r2} + (1 + \alpha)W_{\ell 2}\} \cos ky$$

$$+ \{-1 + (1 - \alpha)S_{r1} + (1 - \alpha)S_{\ell 1} + (1 + \alpha)S_{r1} + (1 + \alpha)S_{\ell 2}\} \sin ky]$$

----- (32)

Region A2, $x > b/2, y > 0$

$$\begin{aligned}
 F_{3P}^{A2} &= F_3^{A2} + \alpha [F_1^A + F_0^A] \\
 &= \{ \alpha + (1-\alpha)S_{r1} - (1-\alpha)S_{l1} + (1+\alpha)S_{r2} + (1+\alpha)S_{l2} \} \cos ky \\
 &\quad + \{ (1-\alpha)W_{r1} - (1-\alpha)W_{l1} - (1+\alpha)W_{r2} - (1+\alpha)W_{l2} \} \sin ky \\
 &\quad + i [\{ (1-\alpha)W_{r1} - (1-\alpha)W_{l1} + (1+\alpha)W_{r2} + (1+\alpha)W_{l2} \} \cos ky \\
 &\quad + \{ -\alpha - (1-\alpha)S_{r1} + (1-\alpha)S_{l1} + (1+\alpha)S_{r2} + (1+\alpha)S_{l2} \} \sin ky] \\
 &\quad \text{----- (33)}
 \end{aligned}$$

Region C2, $x > b/2, y < 0$

$$\begin{aligned}
 F_{3P}^{C2} &= e^{-iky} f_r(u_1) + \beta e^{iky} g_r(u_2) + e^{-iky} f_l(u_1) + \beta e^{iky} g_l(-u_2) - e^{-iky} \\
 &= \{ 1 + \beta - S_{r1} - S_{l1} + \beta(-S_{r2} + S_{l2}) \} \cos ky \\
 &\quad + \{ -W_{r1} - W_{l1} + \beta(W_{r2} - W_{l2}) \} \sin ky \\
 &\quad + i [\{ -W_{r1} - W_{l1} + \beta(-W_{r2} + W_{l2}) \} \cos ky \\
 &\quad + \{ -1 + \beta + S_{r1} + S_{l1} + \beta(-S_{r2} + S_{l2}) \} \sin ky] \text{----- (34)}
 \end{aligned}$$

(4) A single impermeable detached breakwater.

For a single detached breakwater or an insular breakwater that allows waves to diffract around both ends as shown in Fig. 7, Morse and Rubenstein (1938) and Goda, Yoshimura, Ito (1971) developed an exact theory. Numerical calculations for the theory can be done in terms of Mathieu functions. Detailed figures for this have been prepared by Goda et al. (1971). However, if the length of the breakwater is relatively large compared with the wave length, it could be considered that the each end of the breakwater is the end of a semi-infinite breakwater.

The following are the final forms arrived at from this assumption. Detailed diagrams are not given here because of limited space. However, such diagrams may easily be reproduced from the equations.

Region A1, $0 < x < b/2, y > 0$

$$F_4^{A1} = (S_{r1} + S_{l1} + S_{r2} + S_{l2}) \cos ky + (W_{r1} + W_{l1} - W_{r2} - W_{l2}) \sin ky \\ + i[(W_{r1} + W_{l1} + W_{r2} + W_{l2}) \cos ky + (-S_{r1} - S_{l1} + S_{r2} + S_{l2}) \sin ky] \\ \text{----- (35)}$$

Region A2, $x > b/2, y > 0$

$$F_4^{A2} = (1 + S_{r1} - S_{l1} + S_{r2} + S_{l2}) \cos ky + (W_{r1} - W_{l1} - W_{r2} - W_{l2}) \sin ky \\ + i[(W_{r1} - W_{l1} + W_{r2} + W_{l2}) \cos ky + (-1 - S_{r1} + S_{l1} + S_{r2} + S_{l2}) \sin ky] \\ \text{----- (36)}$$

Region C1, $0 < x < b/2, y < 0$

$$F_4^{C1} = (2 - S_{r1} - S_{l1} - S_{r2} - S_{l2}) \cos ky + (-W_{r1} - W_{l1} + W_{r2} + W_{l2}) \sin ky \\ + i[(-W_{r1} - W_{l1} - W_{r2} - W_{l2}) \cos ky + (S_{r1} + S_{l1} - S_{r2} - S_{l2}) \sin ky] \\ \text{----- (37)}$$

Region C2, $x > b/2, y < 0$

$$F_4^{C2} = (1 - S_{r1} - S_{l1} - S_{r2} + S_{l2}) \cos ky + (-W_{r1} - W_{l1} + W_{r2} - W_{l2}) \sin ky \\ + i[(-W_{r1} - W_{l1} - W_{r2} + W_{l2}) \cos ky + (-1 + S_{r1} + S_{l1} - S_{r2} + S_{l2}) \sin ky] \\ \text{----- (38)}$$

When the breakwater is permeable. We assume that the wave in regions A and B ($y > 0$) are the superimposed waves arising from an impermeable breakwater as described above, and the waves multiplied by α passing through a gap as described in (3) [Fig. 8].

In region $y < 0$, the idea is the same in the proceeding sections.

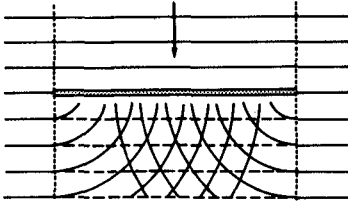


Fig. 7. Diffraction around detached breakwater.

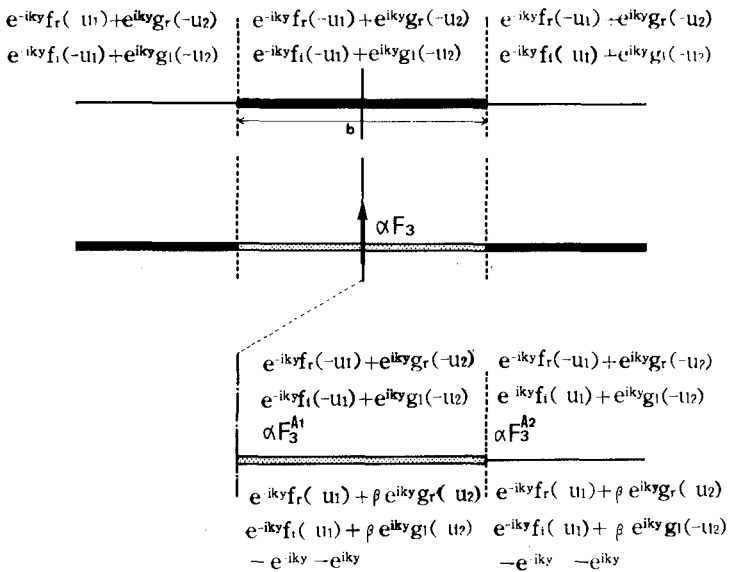


Fig. 8. Superposition of waves for permeable detached breakwater.

We again review the coordinate system.

In Eqs. (36), (37), (38) and (35)

$$r_{\ell} = \sqrt{(x - b/2)^2 + y^2} \qquad r_r = \sqrt{(x + b/2)^2 + y^2}$$

In Eqs. (27), (28) and (29)

$$r_{\ell} = \sqrt{(x + b/2)^2 + y^2} \qquad r_r = \sqrt{(x - b/2)^2 + y^2}$$

To use the same coordinate system, we must exchange the suffixes r and ℓ in Eqs. (27), (28) and (29). Exchanging suffixes r and ℓ in Eqs. (27) and (28) and adding Eq. (36) and Eq. (28) to Eq. (37).

We have finally:

$$\begin{aligned} F_5^{A1} &= F_4^{A1} + \alpha F_3^{A1} \\ &= \cos ky \{ \alpha + (1-\alpha)S_{r1} + (1-\alpha)S_{\ell1} + (1+\alpha)S_{r1} + (1+\alpha)S_{\ell2} \} \\ &\quad + \sin ky \{ (1-\alpha)W_{r1} + (1-\alpha)W_{\ell1} - (1+\alpha)W_{r2} - (1+\alpha)W_{\ell2} \} \\ &\quad + i [\cos ky \{ (1-\alpha)W_{r1} + (1-\alpha)W_{\ell1} + (1+\alpha)W_{r2} + (1+\alpha)W_{\ell2} \} \\ &\quad + \sin ky \{ -\alpha - (1-\alpha)S_{r1} - (1-\alpha)S_{\ell1} + (1+\alpha)S_{r2} + (1+\alpha)S_{\ell2} \}] \end{aligned} \tag{39}$$

$$\begin{aligned} F_5^{A2} &= F_4^{A2} + \alpha F_3^{A2} \\ &= \cos ky \{ 1 + (1-\alpha)S_{r1} - (1-\alpha)S_{\ell1} + (1+\alpha)S_{r2} + (1+\alpha)S_{\ell2} \} \\ &\quad + \sin ky \{ (1-\alpha)W_{r1} - (1-\alpha)W_{\ell1} - (1+\alpha)W_{r2} - (1+\alpha)W_{\ell2} \} \\ &\quad + i [\cos ky \{ (1-\alpha)W_{r1} - (1-\alpha)W_{\ell1} + (1+\alpha)W_{r2} + (1+\alpha)W_{\ell2} \} \\ &\quad + \sin ky \{ -1 - (1-\alpha)S_{r1} + (1-\alpha)S_{\ell1} + (1+\alpha)S_{r2} + (1+\alpha)S_{\ell2} \}] \end{aligned} \tag{40}$$

$$\begin{aligned}
 F_5^{c1} &= e^{-iky} f_r(u_1) + \beta e^{iky} g_r(u_2) + e^{-iky} f_l(u_1) + \beta e^{iky} g_l(u_2) - e^{-iky} - \beta e^{iky} \\
 &= \cos ky \{1 + \beta - S_{r1} - S_{l1} - \beta(S_{r2} + S_{l2})\} + \sin ky \{-W_{r1} - W_{l1} + \beta(W_{r2} + W_{l2})\} \\
 &\quad + i[\cos ky \{-W_{r1} - W_{l1} - \beta(W_{r2} + W_{l2})\} + \sin ky \{-1 + S_{r1} + S_{l1} + \beta(1 - S_{r2} - S_{l2})\}] \\
 &\quad \text{----- (41)}
 \end{aligned}$$

Preliminary experiments

Preliminary experiments were carried out in a small water basin 0.5 m deep, 1.0 m wide and 11 m long. Vertical homogeneous crib-style walls of 8 cm thickness filled with glass ball in diameter were used as the model breakwater.

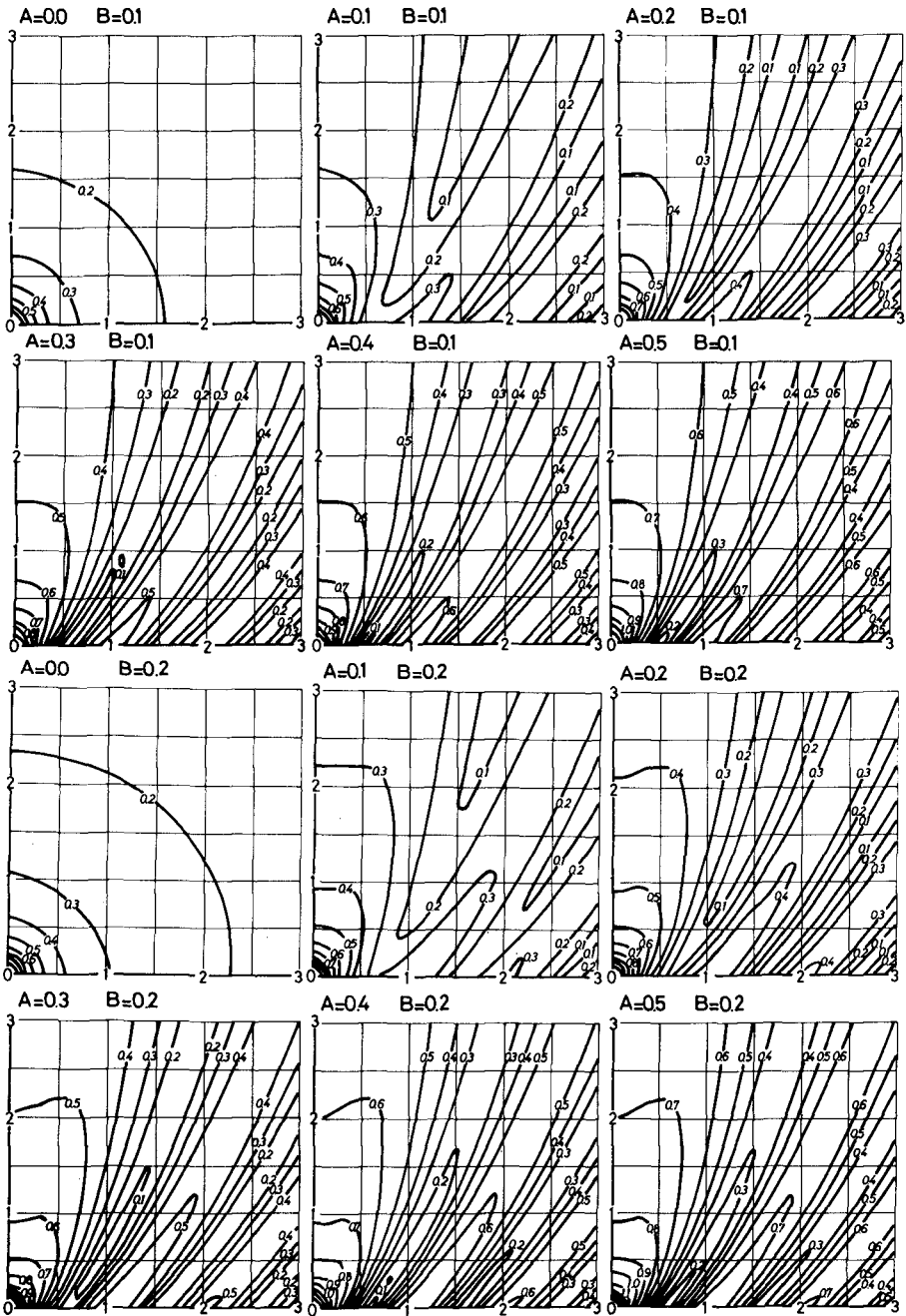
Because of the limited basin width, standing waves appeared on the shore side of the breakwater and the results were not considered adequate for examining the theoretical development. The following are some general experimental results.

- (1) Eq. (21) is acceptable for situations where the ratio between the gap width and wave length is less than 0.2.
- (2) After the distance of one wave length, calculated diffraction patterns by Eqs. (23) and (24) were similar to the experimental patterns.
- (3) Wave heights at the gaps were not constant when the widths of gaps were less than one wave length.
- (4) Energy transmitted to the shore side region of the breakwater was proportional to the ratio of the gap width, to the wave length, within the range less than a ratio of 0.5.

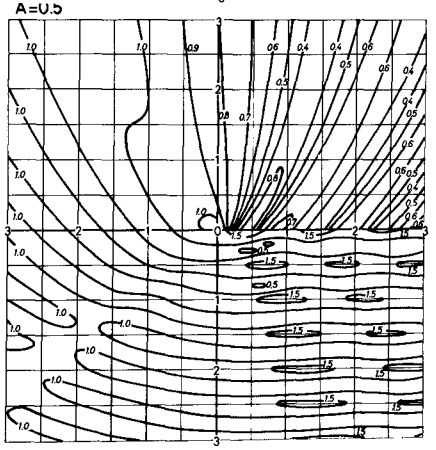
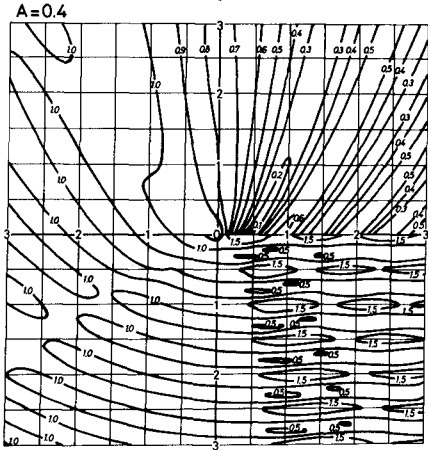
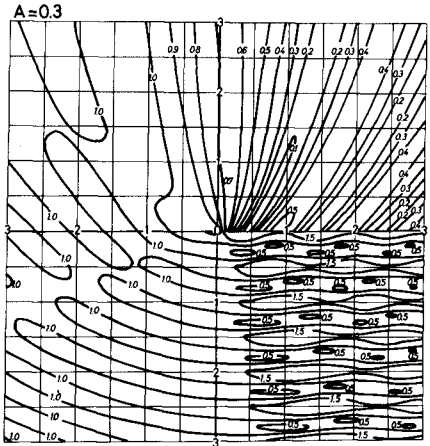
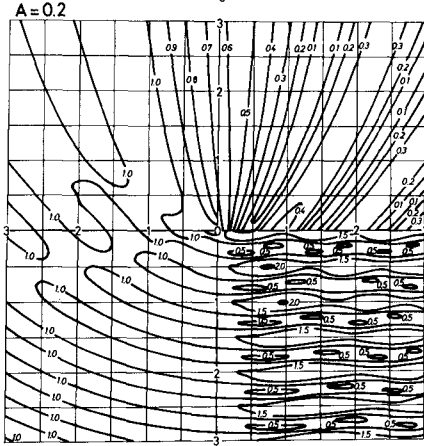
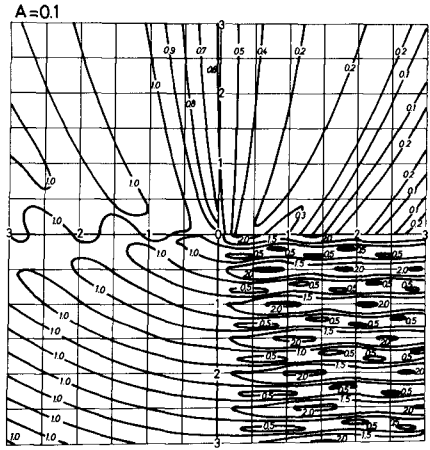
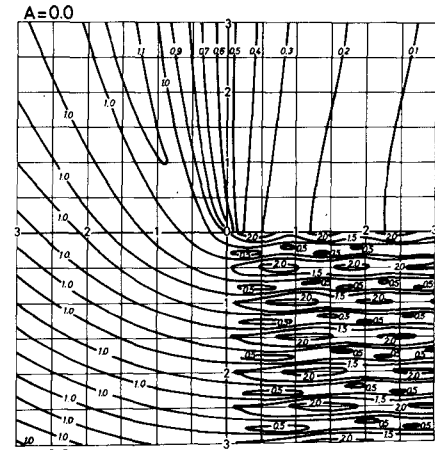
REFERENCES

- Ijima, T., C.R. Chou, Y. Ymura(1974): Scattering of waves by permeable and impermeable breakwater of arbitrary shape, Proc. of the Japan Society of Civil Engineers, No. 225, 31-42. (in Japanese)
- Lamb, Sir Horace(1945): Hydrodynamics, 6th ed., New York, Dover Publication, 533.
- Penny, W.G. and A.T. Price(1952): The diffraction theory of sea waves by breakwaters and the shelter afforded by breakwaters, Phil. Trans., Roy. Soc. London, Ser. A, 244, 236-53.
- Johnson, J.W.(1952): Generalized wave diffraction diagrams, Proc. 2nd Conf. Coastal Eng., 6-23.
- Johnson, J.W.(1953): Engineering aspects of diffraction and refraction, Trans. A.S.C.E. 118, 617-648.
- Goda, Y., Y. Yoshimura, and M. Ito(1971): Reflection and diffraction of water waves by an Insular Breakwater, Report of Port and Harbour Research Institute, Minister of Transport Vol. 10, No. 1, 3-52.

APPENDIX 1



APPENDIX 2



CHAPTER 40

A COMBINED FE-BIE METHOD FOR WATER WAVES

by
A. HAUGUEL*

ABSTRACT

The finite element method and boundary integral equation method are general approximation processes applicable to a wide variety of engineering problems. After a brief description of the combined method, several examples are given for water waves problems : tides, harbour oscillations and waves diffraction and refraction.

INTRODUCTION

Most of the studies in coastal engineering are in relation with water waves coming from deep sea (tides, long and short waves). The difficulty is to take into account the influence of deep sea (infinite or supposed to be so) as exciting and receiving domain.

COMBINED FE-BIE METHOD

The assumption of simple harmonic linear waves yields elliptic partial differential equations. These equations may be solved by :

(i) the boundary integral equation method (BIE) based on Green's identity which leads, under certain conditions, to an integral equation relating the solution and its normal derivative on the boundary.

(ii) the finite element method (FE) in which the region is divided into a number of elements.

The first one is usefull for simple geometric domains because integral equations can be simpliflicated before integration. The second method is fitted for complex geometric domains owing to elements.

Many anthors (Zienkiewicz, Berkhoff, C.C.Mei...) have already described the combined method. So the purpose of this paper will be to present new results showing its advantages.

In few words, the infinite or semi-infinite domain is divided into two regions where each method is applied.

In the external region, where the water depth is assumed to be a constant, the solution will be a superposition of the incident wave and an outgoing wave which is due to the presence of an harbour or any obstacle. This outgoing wave will be represented by a superposition of waves coming from

* Division Hydraulique Maritime. Laboratoire National d'Hydraulique. Electricité de France. Chatou. France.

point sources at the boundary Γ between the sea and the area of interest and must satisfy the conditions at the other boundaries : full reflection on rigid walls and radiation condition of Sommerfeld at sea. So the solution in the external region can be written in the general form :

$$\alpha (f(P) - \psi(P)) = \int_{\Gamma} \frac{\partial G}{\partial n} (P, M) (f(M) - \psi(M)) dM - \int_{\Gamma} G (P, M) \frac{\partial}{\partial n} (f(M) - \psi(M)) dM \quad (1)$$

where

f is the total potential

ψ is the incident potential

G is the Green function of the problem.

The expression is also correct on the boundary Γ ($M \in \Gamma$) by taking the limit (only α changes).

The solution f must be continuous through the boundary with respect to wave height and phase.

So equation (1) can be interpreted as a boundary condition for the internal region.

In this one, the finite element procedure is possible by direct coupling of the solution f and its normal derivative on the common boundary Γ .

The system is solved only in the internal region but the influence of the external one is taken into account thanks to the boundary integral condition.

APPLICATIONS

Some examples of results from the combined FE-BIE method are briefly described here.

The tides in a semi-enclosed sea opened to a semi-infinite ocean are simulated using a linearized, vertically integrated, dissipative form of the Laplace Tidal Equation. A linear bottom friction is used. The tide is modelled by setting the tide-generating force terms to zero and specifying the free surface elevation to infinity as a Kelvin wave. So the equations can be written as follows :

$$-i\omega\eta + \frac{\partial}{\partial x} (h\mu) + \frac{\partial}{\partial y} (h\nu) = 0$$

$$-i\omega\mu + g \frac{\partial \eta}{\partial x} - \Omega\nu + \rho\mu = 0$$

$$-i\omega\nu + g \frac{\partial \eta}{\partial y} + \Omega\mu + \rho\nu = 0$$

where η , μ , ν are the complex amplitude of surface elevation and current components.

h is the mean water depth
 g is the gravity acceleration
 Ω is the Coriolis number
 ρ is the bottom friction coefficient
 ω is the tide pulsation.

These three equations can be transformed in one :

$$\frac{\partial}{\partial x} \left[h \left(A \frac{\partial \eta}{\partial x} + B \frac{\partial \eta}{\partial y} \right) \right] + \frac{\partial}{\partial y} \left[h \left(A \frac{\partial \eta}{\partial y} - B \frac{\partial \eta}{\partial x} \right) \right] + \eta = 0 \quad (2)$$

where A and B are complex functions of ω , Ω , g and ρ .

In the external region, the water depth is assumed to be a constant, so equation (2) is simplified (the B factors disappear) and it can be shown that the Green function of the problem is an Hankel function.

In the internal region, the finite element procedure is easily applied to equation (2).

The M_2 constituent of the tide in the North sea has been calculated by this way. The numerical results (fig. 1) are in good qualitative agreement with the observations, particularly in the reproduction of the amphydromic points. An important thing to point out, is that there is only two parameters to calibrate to solve this problem :

- the wave direction in the ocean, but its influence is very weak
- the bottom friction coefficient which fixes the position of the amphidromic points.

The repartition of amplitude and phase on the common boundary is obtained from the model.

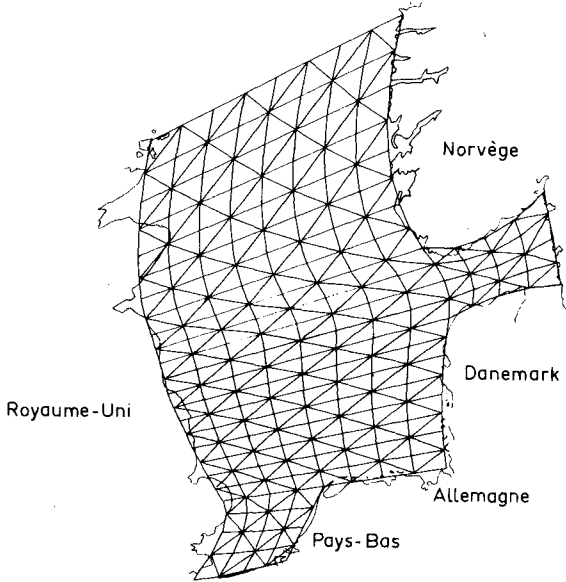
The response of harbours to long waves of different frequencies coming from deep sea can be obtained by the same way. The oscillations are simulated using the same Laplace equation but Coriolis effects and bottom friction can be neglected. In this case, the B factor disappears in equation (2).

The method yields eigen frequencies and correspondent amplification factors of the harbour opened to the sea (see fig. 2 in the case of Marseille Harbour). This is particularly usefull to study seiches in harbours.

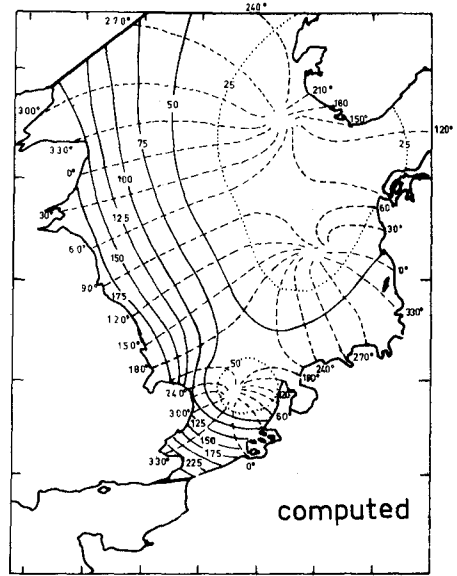
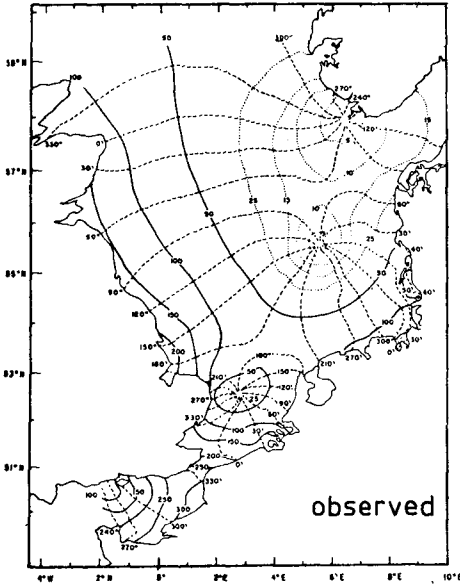
In decreasing the wave length, the last example is the computation of wave diffraction and refraction. In this case the governing equation is

$$\frac{\partial}{\partial x} \left(n \frac{\partial f}{\partial x} \right) + \frac{\partial}{\partial y} \left(n \frac{\partial f}{\partial y} \right) + nk_0^2 f = 0 \quad (3)$$

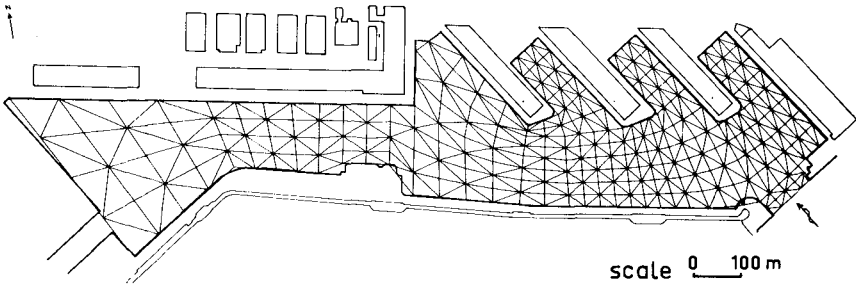
where k_0 is the wave number



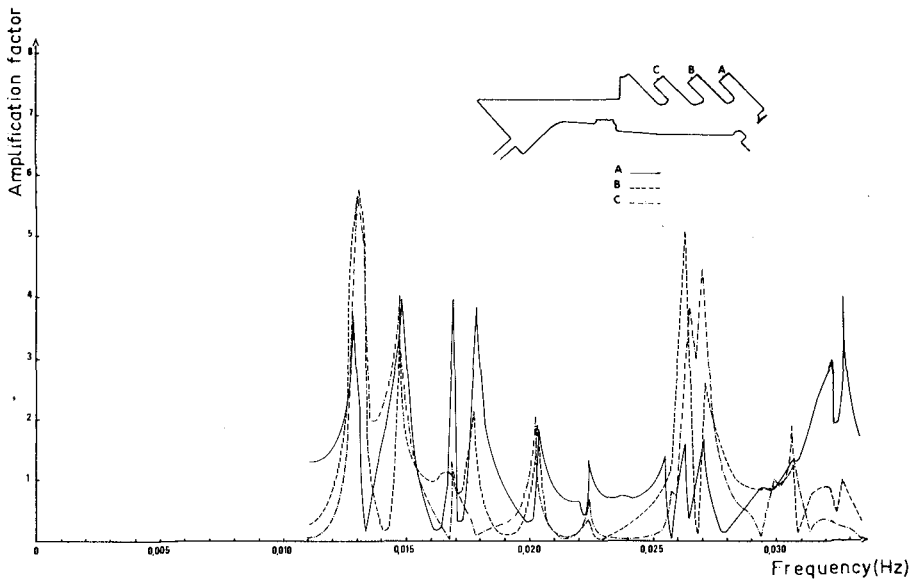
TIDES IN NORTH SEA
CONFIGURATION OF ELEMENTS



M₂ TIDAL CHART
Fig.1



SEICHES IN MARSEILLE HARBOUR
CONFIGURATION OF ELEMENTS



HARBOUR OSCILLATION CURVES

Fig.2

n is the shoaling number

f is the potential.

Equation (3) is similar to equation (2). When the depth and consequently the shoaling number are constant the Green function is also an Hankel function. The same procedure can be applied.

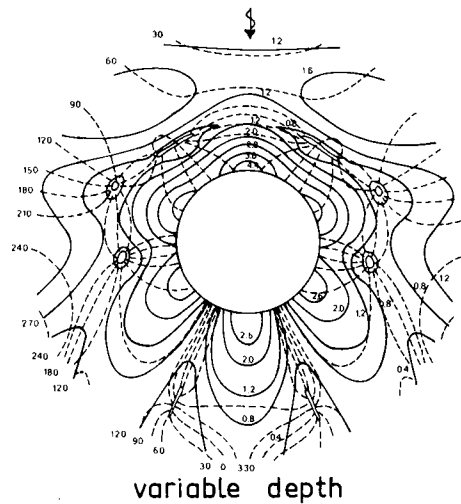
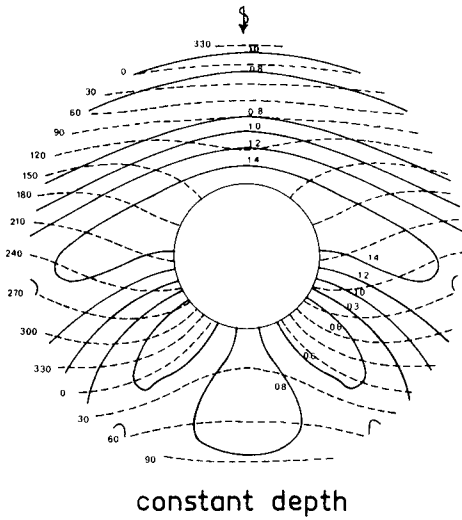
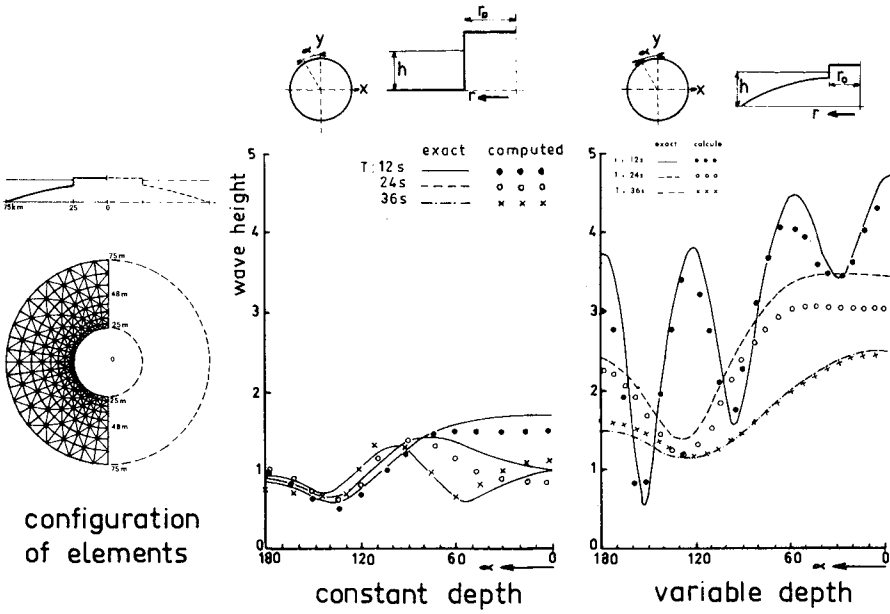
The main restriction of the model is the numerical requirement of about five computing points over one wave length to compute the surface elevation with a sufficient accuracy. Figure 3 shows the solution of wave diffraction and refraction for the case of an island on a flat or parabolic shoal. The numerical results are in good qualitative agreement with the analytical solution. Amplitudes are generally underestimated mainly for short wave lengths (probably in relation with the number of computing points).

CONCLUSIONS

The mathematical model for linear simple harmonic waves described in this paper can be of great help to give some quantitative or qualitative information about waves coming from deep sea (tides and waves). The main restriction of the model is the numerical requirement with respect of large area compared with the mean wave length (especially for short waves) but the rapidity of the resolution, the development of the finite element method and the reduced number of parameters to calibrate the model (one or two for tides) give quite good informations very quickly.

REFERENCES

- Zienkiewics, O.C., Kelly, D.W. and Bettess, P., The coupling of the finite element method and boundary solution procedures. Int. J. Num. Meth. Engng. Vol. 11, n° 2, 1977, pp 355-375.
- Berkhoff, J.C.W. Linear wave propagation problems and the finite element method. Ch. 13, Finite element methods in fluid mechanics (Ed. R.H. Gallagher, J.T. Oden, C. Taylor and O.C. Zienkiewicz). Wiley, 1975.



WAVE REFRACTION DIFFRACTION
AROUND A CIRCULAR ISLAND

Fig.3

CHAPTER 41

WAVE REFRACTION ACROSS A SHEARING CURRENT

Ivar G. Jonsson¹ and Ove Skovgaard²

ABSTRACT

Conservation of wave crests and wave action is introduced to yield the new wave length L_2 and new wave height H_2 as a wave train of plane incidence crosses a shearing current; refraction angle α_2 is determined by Snell's law. Input parameters are water depth h (assumed constant), absolute wave period T_a , angle of incidence α_1 , current velocities U_1 and U_2 (see Fig 1), and initial wave height H_1 . Solution domains are also given, analytically and graphically. The numerical results for L_1 , L_2 , α_2 , and H_2 are presented non-dimensionally in a number of figures, with dimensionless input parameters. As a direct illustration of the effect of the shearing current, a sequence of graphs are presented, showing in dimensional form the variation of L_2 , α_2 , H_2 , and steepness $S_2 = H_2/L_2$ with U_2 for fixed values of h , α_1 , U_1 , T_a , and H_1 . Large positive and negative currents can increase the steepness significantly. The variation of S_2/S_1 with T_a and h is finally depicted, demonstrating the "filtering" effect of a shearing current on waves.

A numerical example shows how simple it is to calculate accurately quantities L_1 , L_2 , α_2 , and H_2 .

1. INTRODUCTION

The purpose of this study is to examine the transformation of waves advancing across a shear layer, from a region of current velocity U_1 to one of current velocity U_2 , see Fig 1. Changes will occur in wave length and height, and in direction and speed of propagation. The results are presented in a number of graphs.

Studies of this kind were initiated by Longuet-Higgins and Stewart (1961), who considered the special case of deep water waves progressing from still water into a region with a steady, uniform current. Here we shall consider the general case of waves on an arbitrary (constant) depth, with arbitrary (steady and uniform) current velocities on both sides of the shear layer. Large-scale currents are considered, i e the current gradient is assumed small everywhere.

In region 1 we prescribe regular and plane incoming waves, and thus also the transmitted waves in region 2 will be plane. The two regions of flow are denoted by subscripts 1 and 2. In these regions current velocities are therefore specified as U_1 and U_2 . Assuming linear theory, solutions are sought for wave lengths L_1 and L_2 , refraction angle α_2 (see

¹ Associate Professor, Institute of Hydrodynamics and Hydraulic Engineering (ISVA), Bldg. 115, Technical University of Denmark, DK-2800 Lyngby.

² Associate Professor, Laboratory of Applied Mathematical Physics (LAMF), Bldg. 303, same address.

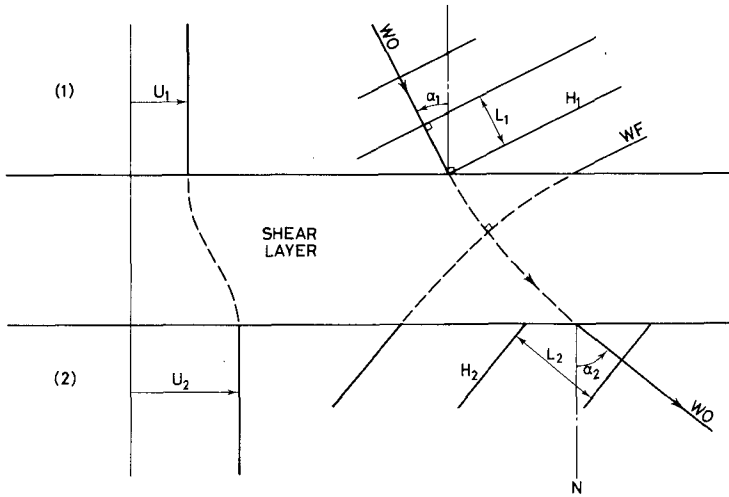


Fig 1. Waves advancing across a shearing current, from region 1 to region 2. WF and WO mean wave front and wave orthogonal. Horizontal sketch.

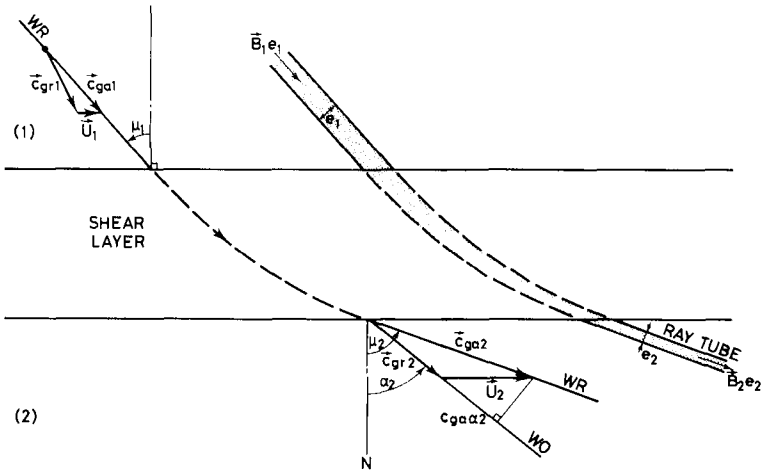


Fig 2. Wave ray WR and ray tube passing a shear layer, from region 1 to region 2. Horizontal sketch.

Fig 1), and wave height H_2 . Given values are water depth h , current velocities U_1 and U_2 , absolute wave period T_a , angle of incidence α_1 (see Fig 1), and incoming wave height H_1 .

Velocities U are taken positive in the direction of wave travel. If we then consider only positive α -values, a positive (i.e. following) current is one running towards the right in Fig 1.

Since large-scale currents are assumed, reflection is excluded a priori, and the waves are purely progressive in both regions. This means in principle that the width of the shear layer must be several wave lengths. In practice this needs not be so, however. This can be seen from Evans (1975), who found transmission and reflection characteristics for a current discontinuity in deep water. He showed "that the amplitude of the transmitted wave as a function of the angle of incidence and current strength is very close to that obtained by Longuet-Higgins and Stewart [1961] on the assumption of small smooth changes in current velocity". This is not immediately expected, since in the former case the flow is not matched in detail at the discontinuity. Only for larger angles of incidence wave transmission was significantly affected by the no-reflection assumption. Reference is made to Evans' Fig 1 and Peregrine's (1976) Fig 12. So although the correct solution to the general problem has not been found yet (Peregrine, 1976, p 73), there is hope that the wave heights presented herein are good approximations also for narrow shear layers. (The only thing for certain is that the height found for the transmitted wave is too large).

We have also excluded the effect of turbulence generated by the shear layer. Here Evans (1975) concluded on the basis of Savitsky's (1970) investigations that turbulence thus generated will have a smaller influence than the mean velocity gradients in the flow. Another more important aspect (for narrow shear layers) is that they are unstable, so that steady solutions here cannot be expected to give more than somewhat crude approximations (Peregrine, 1976, p 71).

The current is assumed constant over depth. The effect of a possible vorticity was examined by Jonsson et al (1978). Dissipation is neglected, but can be included as described in Chapter 3.

The general case of current depth refraction has been studied elsewhere, see for instance Skovgaard and Jonsson (1977), Jonsson and Wang (1978), and the two review articles by the senior author (Jonsson, 1977, 1978b):

For completeness it is mentioned that fundamentally it is not a requirement that regions exist in which U_1 and U_2 are constant; the results obtained are in fact valid going from any point with current velocity U_1 to any other point with velocity U_2 , the flow being parallel over a horizontal bed, and disregarding dissipation.

2. SOME BASIC CONCEPTS

Since wave motion in a moving medium is so different from that in still water, it is worth while starting with the introduction of some concepts, which are important for this type of flow.

In each region we have two frames of reference. One is a coordinate system fixed on a plane earth, in which the wave period (T_a) is constant. This is the common absolute frame of reference, in which we use subscripts 'a'. The other is a Galilean transformation of the first where

the transformation velocity is the current velocity. Observations in the moving system(s) are referred to as relative, and subscripts 'r' are used here.

It is obvious that an important quantity as for instance the relative wave period is not the same in the two systems. The relation is found in the following way. Looking at Fig 1, it is seen that in the absolute frame, the wave front during time T_a has travelled distance

$$L = c_a T_a \quad (2.1)$$

where L is the wave length, and c is the phase speed (here absolute) of the wave. Seen from the moving observer the front has travelled distance $c_r T_a$ during the same time interval. At the same time, the observer him/herself has travelled distance UT_a in the current direction. By projecting this on the wave orthogonal, we hereafter find for the absolute phase speed, after having divided by T_a

$$c_a = c_r + U \sin \alpha \quad (2.2)$$

where α is the angle between the normal N to the streamlines and the wave orthogonal. Since we also by definition have

$$L = c_r T_r \quad (2.3)$$

we get from (2.1) and (2.2) for the relative period T_r

$$\frac{1}{T_r} = \frac{1}{T_a} - \frac{U \sin \alpha}{L} \quad (2.4)$$

It appears that for a following current ($U \sin \alpha > 0$) we have $T_r > T_a$, as expected. In the literature (2.4) is often written $\omega_r = \omega_a - \vec{k} \cdot \vec{U}$ ('conservation of wave crests'), where $\omega = 2\pi/T$, the angular frequency, and \vec{k} is the wave number vector, which is a vector of magnitude $2\pi/L$ going in the wave orthogonal direction.

In Fig 1 α_1 is the angle of incidence and α_2 the refraction angle.

In current wave systems it is important to distinguish between three sets of curves: Streamlines, wave orthogonals, and wave rays. A streamline gives the (local) mean flow direction. A wave orthogonal is normal to the wave front, and gives the direction of wave travel. Finally a wave ray gives the direction of the absolute group velocity, i e of

$$\vec{c}_{ga} = \vec{c}_{gr} + \vec{U} \quad (2.5)$$

where the relative group velocity \vec{c}_{gr} goes in the orthogonal direction, see Fig 1. Wave rays determine wave heights since the so-called wave action, defined as

$$\text{Wave action} \equiv \frac{E}{\omega_r} \quad (2.6)$$

is conserved along wave rays, see Chapter 3.

In (2.6) E is the specific wave energy

$$E = \frac{1}{8} \rho g H^2 \quad (2.7)$$

and ω_r is the relative angular frequency. In (2.7) ρ is density, g gravity acceleration, and H is the wave height.

The component of (2.5) in the direction of the orthogonal is also an important quantity. It is given by

$$c_{ga\alpha} = c_{gr} + U \sin \alpha \quad (2.8)$$

The complete differential equations for wave orthogonals and wave rays for a general system are presented in the Appendix.

3. THE GOVERNING EQUATIONS

Since linear theory is assumed, the relative phase speed is given by

$$c_r = \sqrt{\frac{g}{k} \tanh kh} \quad (3.1)$$

where $k = 2\pi/L$, the wave number, and h is the water depth. Similarly we have for the relative group speed

$$c_{gr} = \frac{1}{2} c_r (1+G) \quad (3.2) \quad \text{with } G \equiv \frac{2kh}{\sinh 2kh} \quad (3.3)$$

REGION 1 - Wave length L_1 can be found by eliminating c_{a1} and c_{r1} from (2.1), (2.2), and (3.1). The (implicit) result is

$$\sqrt{\frac{h}{L_1} \tanh k_1 h} = \sqrt{\frac{h}{L_0}} \left[1 - \frac{U_1 \sin \alpha_1 T_a}{L_1} \right] \quad (3.4)$$

in which $k_1 = 2\pi/L_1$, and L_0 is the deep water wave length in the absence of currents, i e

$$L_0 = \frac{g}{2\pi} T_a^2 \quad (3.5)$$

Equation (3.4) is identical with (3.5) in Jonsson et al (1971). In a dimensionless representation it gives L_1/L_0 as a function of h/L_0 and $U_1 \sin \alpha_1 / c_0$, where c_0 is the deep water phase speed in the absence of currents, i e

$$c_0 = \frac{g}{2\pi} T_a \quad (3.6)$$

Solutions to (3.4) are depicted in Fig 6. Values of L_1/L_0 can also be read in Tables 6-a and 6-b in Jonsson et al (1971), remembering that entry parameter q^* there equals $(h/L_0)(U_1 \sin \alpha_1 / c_0)$. Also Tables 3.2-I and 3.2-II in Jonsson (1978b) can be used.

REGION 2 - Equation (3.4) is valid for this region also, if subscript 1 is replaced by subscript 2. Inserting Snell's law

$$\frac{L_1}{\sin \alpha_1} = \frac{L_2}{\sin \alpha_2} \quad (3.7)$$

into the "new" (3.4) then yields for the determination of L_2

$$\sqrt{\frac{h}{L_2} \tanh k_2 h} = \sqrt{\frac{h}{L_0} \left[1 - \frac{U_2 \sin \alpha_1 T_a}{L_1} \right]} \quad (3.8)$$

in which $k_2 = 2\pi/L_2$, the wave number in region 2. This determines L_2/L_0 as a function of h/L_0 , $U_1 \sin \alpha_1/c_0$, and $U_2 \sin \alpha_1/c_0$. Solutions to (3.8) are depicted in Figs 7-10.

Note that (3.8) can be solved in quite another way than (3.4). Since we assume that L_1 has now been calculated, the right-hand side of (3.8) is known. Ratio h/L_2 can therefore be found from a conventional table for surface gravity waves (e.g. Wiegel, 1964, Appendix 1) using the square of the right-hand side of (3.8) as entry in the column " h/L_0 ". L_2 is hereafter found as $h/(h/L_2)$; it cannot be found from $L = L_0 \tanh kh$!

Refraction angle α_2 is determined from Snell's law as

$$\alpha_2 = \text{Arcsin} \frac{L_2 \sin \alpha_1}{L_1} \quad (3.9)$$

This equation gives α_2 as a function of h/L_0 , α_1 , U_1/c_0 , and U_2/c_0 , as shown in Figs 11-26.

Wave height H_2 is found from wave action conservation. In the general case this principle reads, see Christoffersen and Jonsson (1979) and Jonsson (1978b)

$$\nabla \cdot \left(\frac{\mathbf{E}}{\omega_r} \frac{\vec{c}}{g a} \right) + \frac{E_d - \vec{\tau}_b \cdot \vec{U}}{\omega_r} = 0 \quad (3.10)$$

where ∇ is the horizontal gradient operator ($\partial/\partial x$, $\partial/\partial y$), \mathbf{E} , and \vec{c}_{ga} are given by (2.7) and (2.5), ω_r is the relative angular frequency, E_d is the dissipation per unit horizontal area, and $\vec{\tau}_b$ the (mean) bed shear stress (wind shear is neglected). It is repeated that \mathbf{E}/ω_r is wave action. The wave action flux is often termed \vec{B} , i.e.

$$\vec{B} \equiv \frac{\mathbf{E}}{\omega_r} \frac{\vec{c}}{g a} \quad (3.11)$$

A simple proof of the wave action conservation principle for irrotational flow has been given by the senior author, Jonsson (1978a). In Christoffersen and Jonsson (1979) the general expression (3.10) was deduced.

In this study dissipation is neglected, and (3.10) reduces to $\nabla \cdot \vec{B} = 0$. Looking at the ray tube in Fig 2 we then find using Gauss' theorem

$$B_1 e_1 = B_2 e_2 \quad (3.12)$$

where $B = |\vec{B}|$ and e is the tube width. Thus we find for H_2 , using (3.11) and (3.12)

$$\frac{H_2}{H_1} = \sqrt{\frac{\omega_r}{\omega_r} \frac{r_2}{r_1} \frac{c}{c} \frac{g a_1}{g a_2} \frac{1}{\sqrt{\beta_r}}} \quad (3.13)$$

where β_r is the ray separation factor $e_2/e_1 = \cos\mu_2/\cos\mu_1$; μ is the angle between the ray and the normal N in Fig 2. From this figure we also have $c_{ga} \cos\mu = c_{gr} \cos\alpha$. Introducing c_{gr} through (3.2) and further using that $c_r/\omega_r = 1/k$ and that $k_2/k_1 = \sin\alpha_1/\sin\alpha_2$ (Snell), we find from (3.13)

$$\frac{H_2}{H_1} = \sqrt{\frac{1+G_1}{1+G_2}} \sqrt{\frac{\sin 2\alpha_1}{\sin 2\alpha_2}} \quad (3.14)$$

Equation (3.14) gives H_2/H_1 as a function of h/L_0 , α_1 , U_1/c_0 , and U_2/c_0 . It shows that in this approach H_2 is a linear function of H_1 . The variation of H_2/H_1 is depicted in Figs 11-26. In deep water ($G = 0$) (3.14) reduces to Longuet-Higgins and Stewart's (1961) expression $H_2/H_1 = (\sin 2\alpha_1/\sin 2\alpha_2)^{1/2}$.

In the special case considered here, the wave height can also be found by a simple momentum consideration. The "shear stress" in a section parallel with the streamlines is according to Jonsson (1978a) or (1978b, Section 3.2.3.2) $F_m \sin\alpha$, where $F_m = 1/16 \rho g H^2 (1+G)$, the momentum part of the radiation stress. Since this "shear stress" must be the same on the two sides of the shear layer, (3.14) follows directly.

As α_2 approaches 90° , H_2 goes towards infinity according to (3.14), and the theory breaks down. The physical situation is U_2 being so much larger than U_1 that the waves are "swept" along the "first" U_2 streamline, and wave orthogonals and rays run parallel with it. The ray separation factor then goes towards zero. In practice this will give a strong reflection, which is disregarded in the theory.

The wave steepness S_2 ($\equiv H_2/L_2$) is given both directly (Fig 30) and relative to S_1 (Fig 31), for one set of parameters.

MEAN WATER LEVELS - There will be a slight difference in mean water level between regions 1 and 2. Using the formulae in Jonsson (1978a) or (1978b, Section 3.2.3.2), equilibrium at right angles to the streamlines gives

$$\frac{1}{2} \rho g h_1^2 + F_{p1} + F_{m1} \cos^2\alpha_1 = \frac{1}{2} \rho g h_2^2 + F_{p2} + F_{m2} \cos^2\alpha_2 \quad (3.15)$$

in which $F_p = 1/16 \rho g H^2 G$, the pressure part of the radiation stress, and F_m is the previously given momentum part. After some manipulations, hereunder using (3.14), we find for the difference in mean water level, defined as $b = h_2 - h_1$

$$b = \frac{H_1^2}{16h} G_1 \left[1 - \frac{G_2(1+G_1)}{G_1(1+G_2)} \frac{\sin 2\alpha_1}{\sin 2\alpha_2} + \frac{1+G_1}{G_1} \frac{\cos\alpha_1 \sin(\alpha_2 - \alpha_1)}{\sin\alpha_2} \right] \quad (3.16)$$

correct to second order. Since the factor to the square bracket is recognized as the conventional wave set-down (over a varying bottom) it appears that b is indeed a small quantity, by order of magnitude 1 cm. For normal incidence ($\alpha_1 = 0^\circ$), and in deep water, b vanishes.

4. SOLUTION DOMAINS

REGION 1 - As shown by Jonsson et al (1971, p 493), there are no solutions to the wave length expression (3.4), if the wave orthogonal component c_{ga}

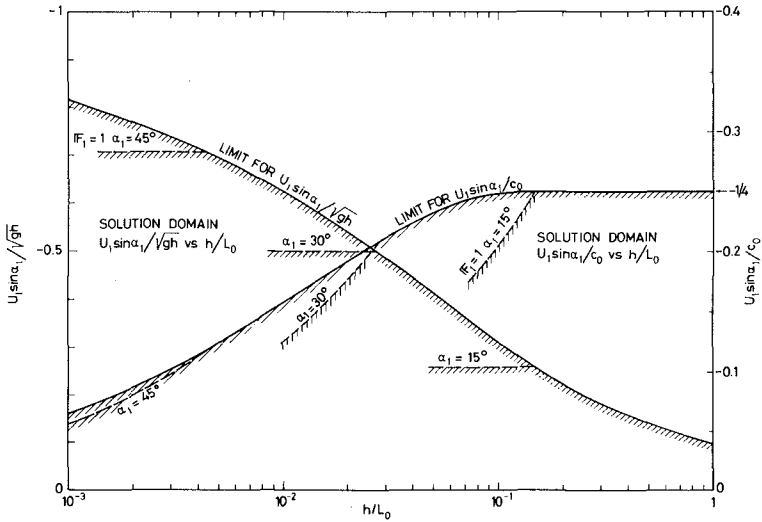


Fig 3. Solution domains for region 1, corresponding to the component $c_{ga\alpha_1}$ in the orthogonal direction of the absolute group velocity being positive (below full curves), or the Froude number F_1 being smaller than one (below dotted curves).

(2.8) of the absolute group velocity c_{ga} is negative. So in the limit $c_{ga\alpha} = 0$ the ray goes in the wave front direction, and we have from (2.8)

$$c_{ga\alpha_1} = c_{gr1} + U_1 \sin \alpha_1 = 0 \tag{4.1}$$

We further have from (3.10) in the above reference

$$\left(\frac{h}{L}\right)_{lim} = \frac{(1 - G_1)^2}{8\pi} k_1 h \tanh k_1 h \tag{4.2}$$

Combining this with (4.1) gives

$$\left(\frac{U_1 \sin \alpha_1}{c_0}\right)_{lim} = -\frac{1 - G_1^2}{4} \tanh k_1 h \tag{4.3}$$

(Equation (4.1) is in fact a consequence of (4.2) and (3.4).) Equations (4.2) and (4.3) are the bases of the limiting curves in Fig 3. In the limit we attain minimum values of L , see Jonsson et al (1971). (Note: In that reference $c_{ga\alpha}$ was for brevity denoted c_{ga} . This is unfortunate, since c_{ga} should be reserved for the magnitude $|\tilde{c}_{ga}|$ of the absolute group velocity. So in this study we have from Fig 1 $c_{ga\alpha} = c_{ga} \cos(\mu - \alpha)$.) In deep water we find the well-known limit $U_1 \sin \alpha_1 / c_0 = -1/4$.

In Fig 3 we have also shown $(U_1 \sin \alpha_1 / \sqrt{gh})_{lim}$ versus h/L_0 . For the latter going towards zero, the former goes towards $-1+$. It is seen, ge-

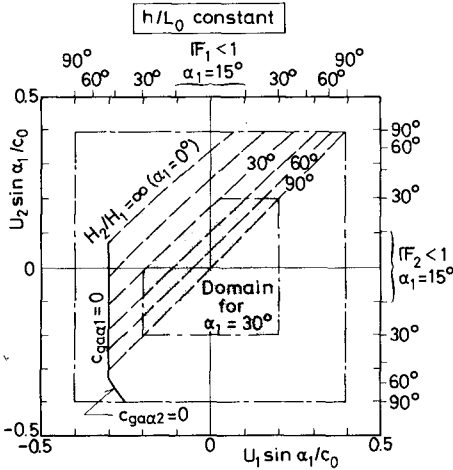


Fig 4. Solution domains for region 2, corresponding to L_2/L_0 -figures. Schematic.

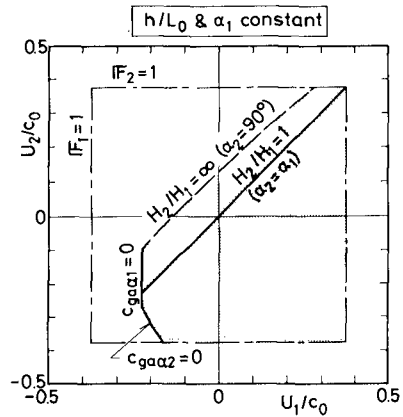


Fig 5. Solution domains for region 2, corresponding to α_2 - and H_2/H_1 -figures. Schematic.

nerally, that if we restrict ourselves to consider Froude numbers F_1 (defined as $|U_1|/\sqrt{gh}$) smaller than one, then this requirement can be 'stricter' than the limiting curve in Fig 3, especially so for the smaller α_1 -values. Also for the $U_1 \sin \alpha_1 / c_0$ solution domain, some $F_1 = 1$ limits are sketched.

To sum up, the full curves in Fig 3 both correspond to (a) wave rays being orthogonal to wave orthogonals and (b) wave lengths attaining their minimum value. The dotted curves correspond to $F_1 \equiv |U_1|/\sqrt{gh} = 1$, for different angles of incidence.

The position of the limit $c_{ga\alpha_1} = 0$ is sketched in Fig 4 (L_2/L_0 solutions) and Fig 5 (H_2/H_1 and α_2 solutions). It naturally corresponds to negative U_1 -values. In these figures also the $F_1 = 1$ (and $F_2 = 1$) limits are shown. In Fig 4 the position of the (chosen) $F = 1$ limits depend on α_1 . Note also in this figure that with the requirement $F < 1$, there are never solutions outside the " $F = 1; \alpha_1 = 90^\circ$ frame". The limits can be recognized in the figures in Chapter 5. It appears from these that the mutual positions of the limiting curves in Figs 4 and 5 are not absolute. Thus the $F = 1$ curves in Fig 5 can lie outside the chosen $U_1/c_0 - U_2/c_0$ frame. And the $c_{ga\alpha_1} = 0$ limit can lie to the left of the $F = 1$ limit.

REGION 2 - In this region there is one further restriction on the input parameters: The wave height H_2 must remain finite, corresponding to $\alpha_2 < 90^\circ$. Thus there are restrictions on the current strength, whether negative or positive. In the former case, one obvious condition is the same as that in region 1, that $c_{ga\alpha}$ be positive. In this limit we thus have from (2.8)

$$c_{ga2} = c_{gr2} + U_2 \sin \alpha_2 = 0 \quad (4.4)$$

stating that the ray goes in the direction of the wave front. So (4.2) and (4.3), and Fig 3, are also valid with subscripts 2. Fig 3 is not directly applicable, however, since α_2 is not known beforehand. The position of the limit $c_{ga2} = 0$ is sketched in Figs 4 and 5, and can be found again in the figures in Chapter 5.

It should be observed that - in contrast to plane shoaling, see Jonsson et al (1971) - minimum wave length here does not correspond to infinite wave height. This is because in our case $c_{ga2} = 0$ ($\Rightarrow L_{2,\min}$) does not yield $c_{ga2} = 0$. (Moreover, c_{ga2} can never vanish here.) If, however, U_2 is much larger than U_1 , the waves cannot "penetrate" through the shear layer, and H_2/H_1 tends to infinity. This case was already discussed in Chapter 3, and it corresponds to $\mu_2 = 90^\circ$, giving ray separation factor $\beta_x = 0$. Fig 2 shows that here we must also have $\alpha_2 = 90^\circ$, which is in accordance with (3.14).

The corresponding limiting curves are depicted in Figs 4 and 5, and can be found again in the figures in Chapter 5. Note that in Fig 4 the position is a function of α_1 . The $\alpha_1 = 0^\circ$ limit is peculiar, since it also corresponds to $L_2/L_0 \rightarrow \infty$.

In shallow water the $\alpha_2 = 90^\circ$ limit corresponds to

$$\frac{U_2 - U_1}{c_0} = \frac{1 - \sin \alpha_1}{\sin \alpha_1} \sqrt{\frac{2\pi h}{L_0}} \quad \text{or} \quad \frac{U_2 - U_1}{\sqrt{gh}} = \frac{1 - \sin \alpha_1}{\sin \alpha_1} \quad (4.5)$$

So here, where there is no dispersion, the critical condition - for a fixed value of α_1 - only depends on the current velocity difference.

In the figures, also the limits corresponding to $F_2 \equiv |U_2|/\sqrt{gh} = 1$ are shown.

5. NUMERICAL RESULTS

WAVE LENGTHS L_1/L_0 - Solutions to (3.4) are presented in Fig 6, which clearly demonstrates the "stretching" effect of a positive current, and the "compressive" effect of a negative ditto. Other things being equal, wave length increases with increasing current velocity and depth. The deep water limit ($U_1 \sin \alpha_1 / c_0$, L_1/L_0) = (-1/4, 1/4) is clearly seen. The thin full curve connecting this point with origo corresponds to - for every fixed value of h/L_0 - the minimum value of L_1/L_0 (i.e. $c_{ga1} = 0$). To every angle of incidence the $F = 1$ limit yields two curves - the solution domain lies between these. The solution domains were also illustrated in Fig 3.

WAVE LENGTHS L_2/L_0 - Solutions to (3.8) are presented in Figs 7-10, corresponding to four dimensionless water depths h/L_0 . Note that $\sin \alpha_1$ - not $\sin \alpha_2$ - appears together with U_2 on the ordinate axis. It is seen that other things being equal, wave length in region 2 increases with increasing current velocity, as expected. The variation of L_2 with U_2 gets slower as U_1 grows. As to the solution limit, we can inspect Fig 7; starting at the bottom and going anti-clockwise the limits correspond to:

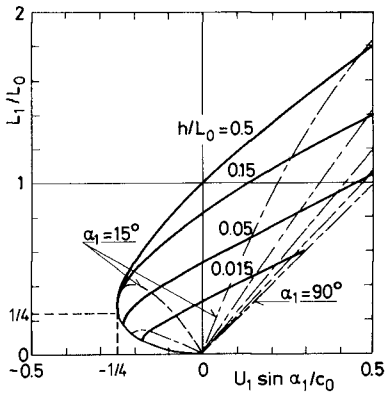
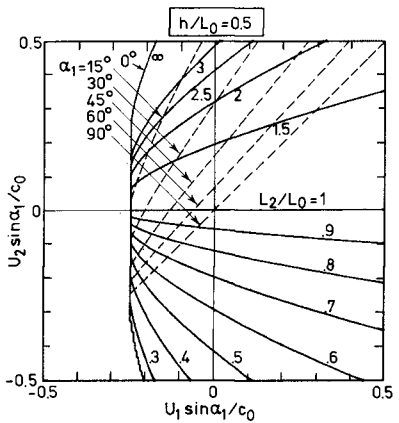
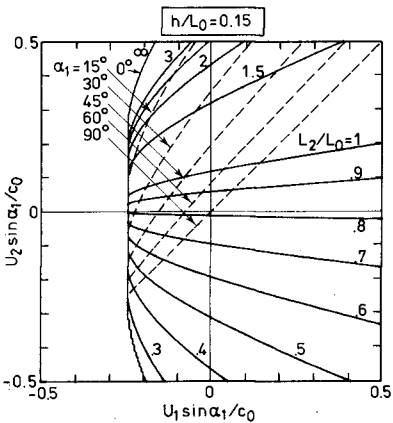
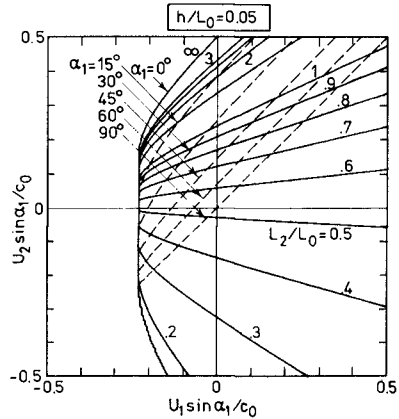
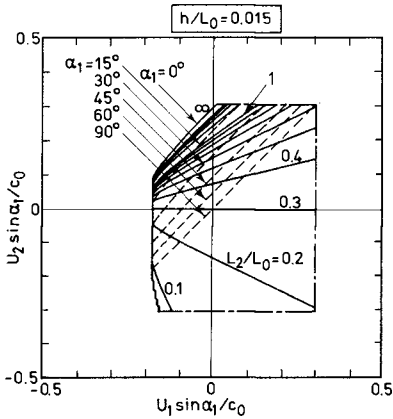


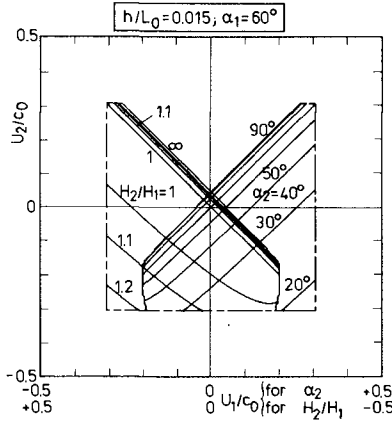
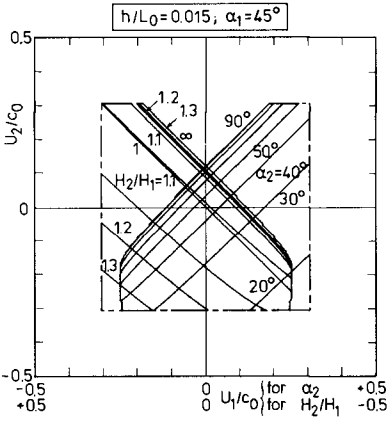
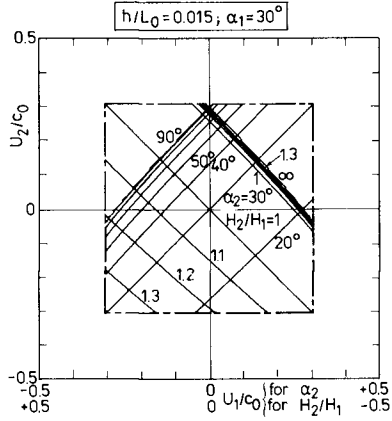
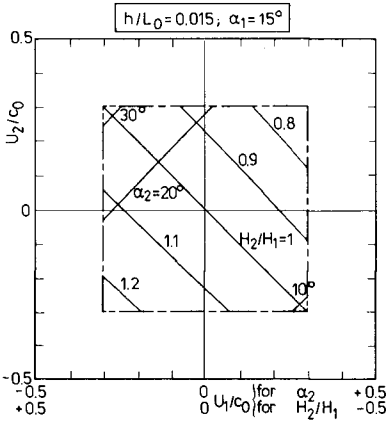
Fig 6

Dimensionless wave length L_1/L_0 in region 1 vs $U_1 \sin \alpha_1 / c_0$ for $h/L_0 = 0.015, 0.05, 0.15, \text{ and } 0.5$. For $U_1 \sin \alpha_1 / c_0 < 0$ the two dot-and-dash lines correspond to $F_1 = 1$ for $\alpha_1 = 15^\circ$ and 30° . For $U_1 \sin \alpha_1 / c_0 > 0$ the five dot-and-dash lines correspond to $F_1 = 1$ for $\alpha_1 = 15^\circ, 30^\circ, 45^\circ, 60^\circ, \text{ and } 90^\circ$.

Figs 7-8
9-10

Contours for dimensionless wave length L_2/L_0 in region 2 vs $U_1 \sin \alpha_1 / c_0$ and $U_2 \sin \alpha_1 / c_0$. For $L_2/L_0 \leq 1$ the contours are plotted with intervals of 0.1. For $1 \leq L_2/L_0 \leq 3$ the contours are plotted with intervals of 0.5. Dot-and-dash lines correspond to $F_1 = 1$. Dotted curves correspond to $H_2/H_1 = \infty$.

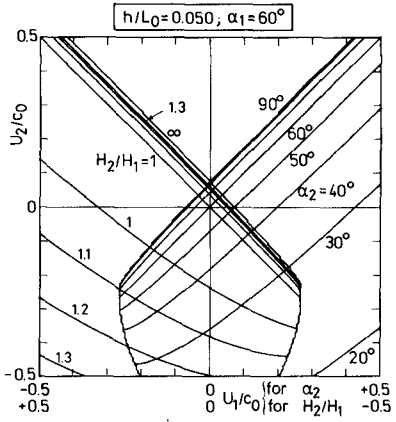
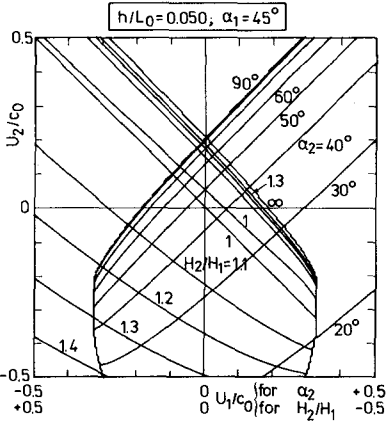
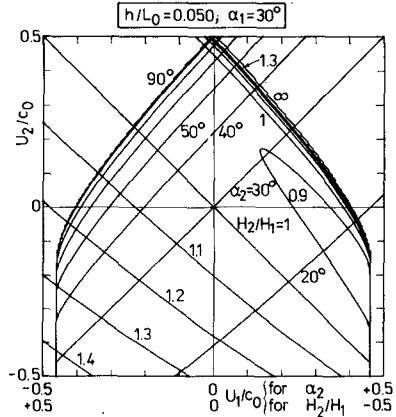
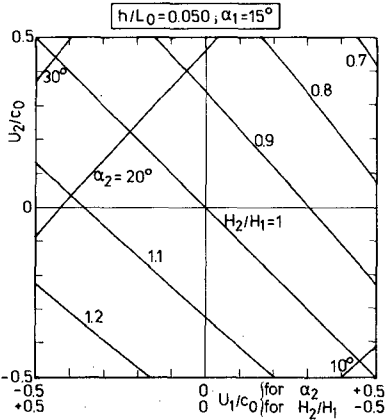




Figs 11-12
13-14 Contours for refraction angle α_2 and relative wave height H_2/H_1 in region 2 vs U_1/c_0 and U_2/c_0 . For α_2 the contours are plotted with intervals of 10° . For $H_2/H_1 \leq 1.3$ the contours are plotted with intervals of 0.1. Dot-and-dash lines correspond to $F=1$. Note that the abscissa axis is reversed for H_2/H_1 .

$F_2 = 1, F_1 = 1, F_2 = 1, H_2/H_1 = \infty, c_{ga\alpha 1} = 0,$ and $c_{ga\alpha 2} = 0$. For details see Chapter 4 and Fig 4. In Figs 8 - 10 the $F=1$ limits lie outside the chosen frame. Some of the limiting curves appear jagged because of the discretization used in the computer software, which was used to plot these curves.

REFRACTION ANGLES α_2 - Solutions to (3.9) are presented in Figs 11 - 26, corresponding to four water depths (same as for L_2/L_0), and four angles of incidence. (H_2/H_1 is shown laterally reversed in the same figures). It appears that the variation of α_2 is slowest for the smallest angle of in-

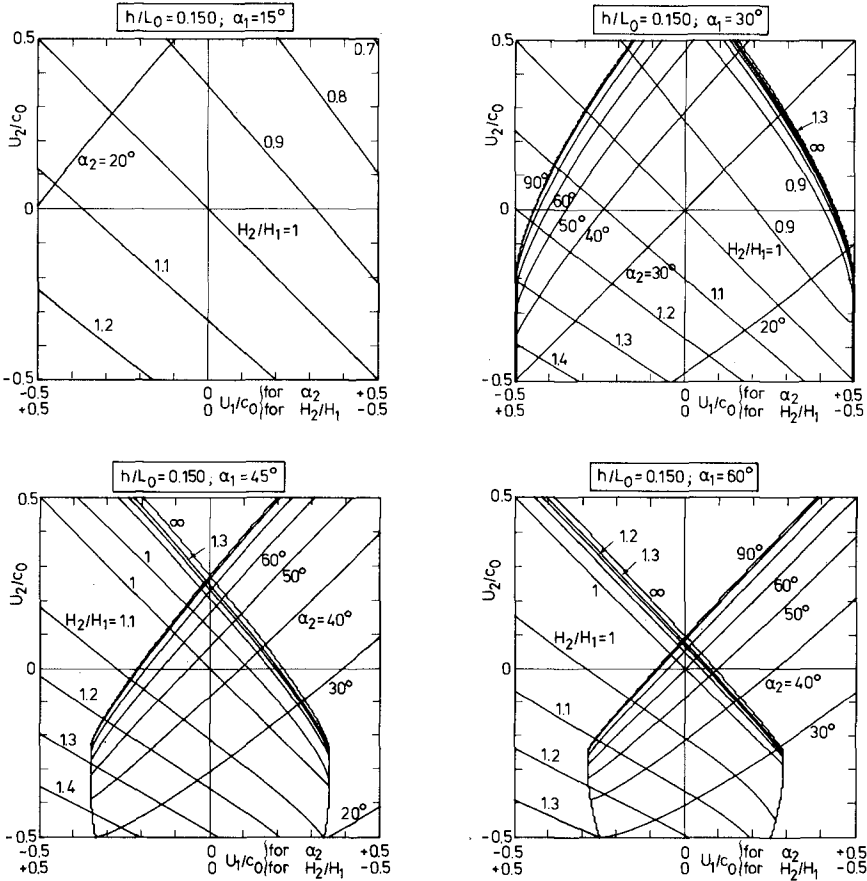


Figs 15-16
17-18

Contours for refraction angle α_2 and relative wave height H_2/H_1 in region 2 vs U_1/c_0 and U_2/c_0 . For α_2 the contours are plotted with intervals of 10° . For H_2/H_1 the contours are plotted with intervals of 0.1 up to 1.3 above the diagonal, and 1.4 below it.

cidence α_1 chosen. Everywhere α_2 increases with increasing U_2 . It can also be seen that (naturally) for $U_2 = U_1$ we have $\alpha_2 = \alpha_1$. Only for the smallest water depth, the $F = 1$ limits lie within the chosen frame. The other limits are discussed in Chapter 4 and illustrated in Fig 5.

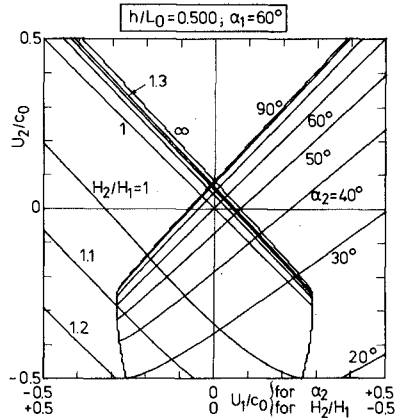
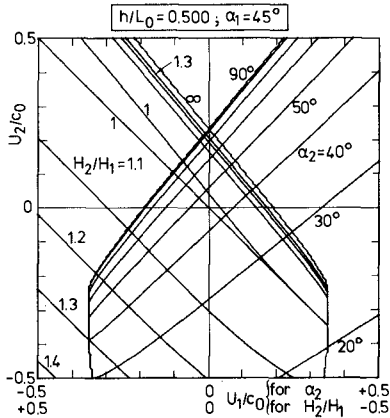
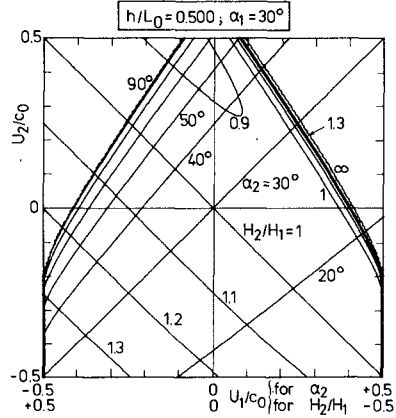
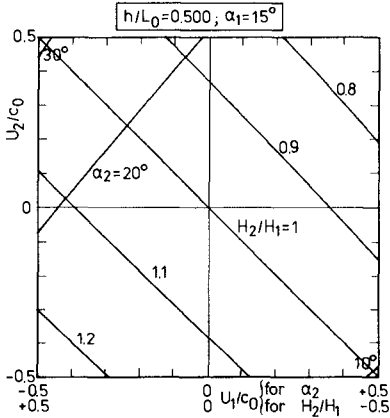
WAVE HEIGHTS H_2/H_1 - Solutions to (3.14) are presented (laterally reversed) in Figs 11 - 26, for four water depths and four angles of incidence. It appears that the variation of H_2/H_1 is slowest for the smallest angle of incidence α_1 chosen. It is also seen that - except for this value of α_1 - the variation with U_2 exhibits a minimum for H_2/H_1 within the chosen



Figs 19-20
21-22 Contours for refraction angle α_2 and relative wave height H_2/H_1 in region 2 vs U_1/c_0 and U_2/c_0 . For α_2 the contours are plotted with intervals of 10°. For H_2/H_1 the contours are plotted with intervals of 0.1 up to 1.3 above the diagonal, and 1.4 below it.

frame. This will be discussed later. For $U_2 = U_1$ we have $H_2 = H_1$. The limits are discussed in Chapter 4 and illustrated in Fig 5.

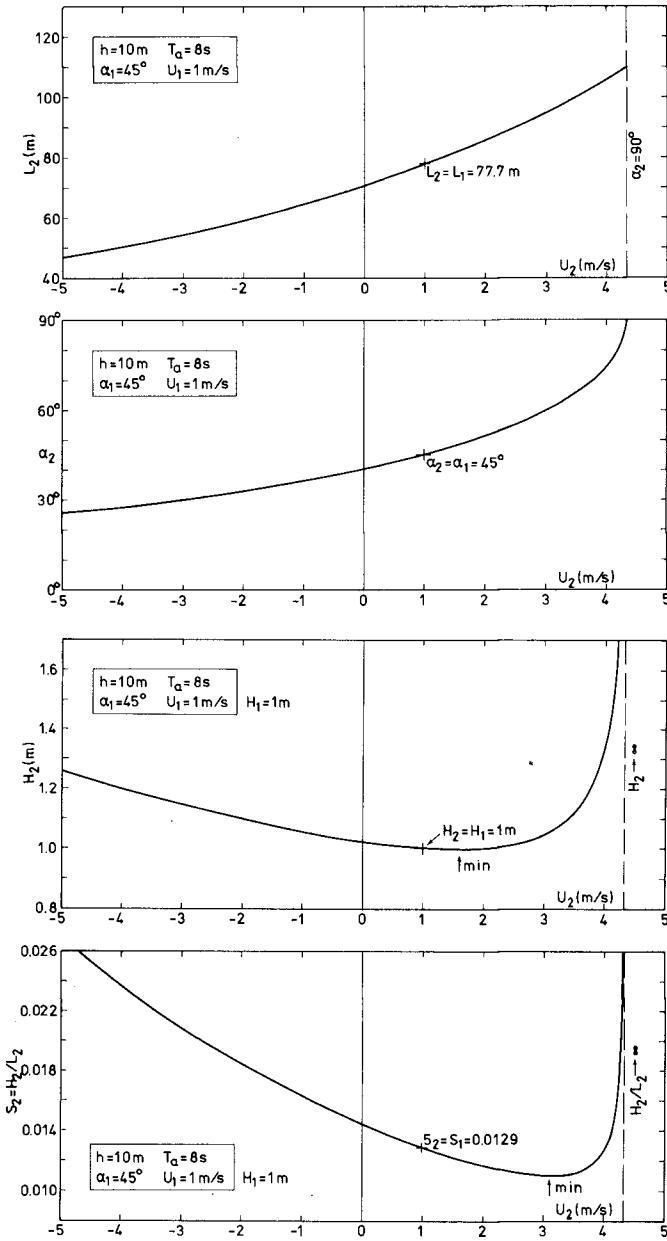
VARIATIONS OF L_2 , α_2 , H_2 , S_2 , and S_2/S_1 - A physical discussion of the transforming effect of the shear layer is facilitated by looking at a few concrete examples. Consider first the sequence in Figs 27 - 30, giving the variation of region 2 quantities with U_2 . Fig 27 shows how L_2 increases monotonously with increasing U_2 ; the maximum value is attained for $\alpha_2 = 90^\circ$. Also α_2 (Fig 28) varies in this way; for $U_2 > 4.3$ m/s (approx) $\alpha_2 = 90^\circ$, and waves cannot penetrate into region 2. In the limit H_2 theoretic-



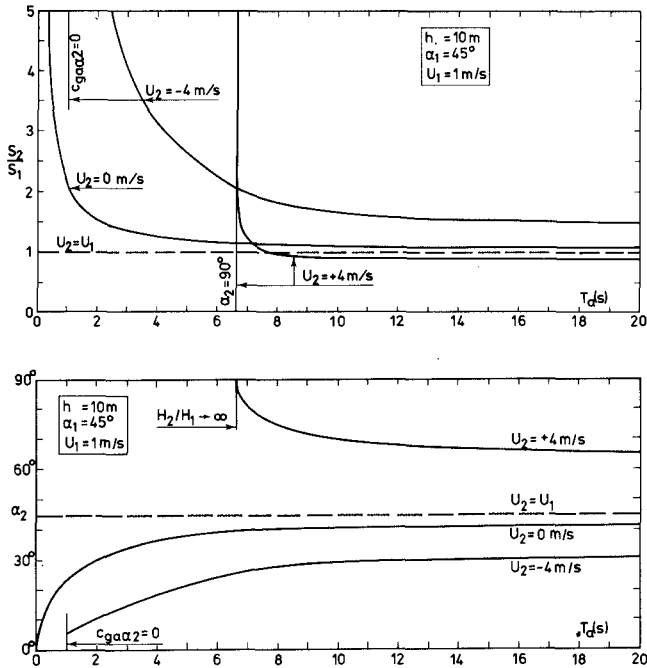
Figs 23-24
25-26 Contours for refraction angle α_2 and relative wave height H_2/H_1 in region 2 vs U_1/c_0 and U_2/c_0 . For α_2 the contours are plotted with intervals of 10° . For H_2/H_1 the contours are plotted with intervals of 0.1 up to 1.3 above the diagonal, and 1.4 below it.

cally tends to infinity (Fig 29). It is also seen from this figure that H_2 has a minimum. This can be anticipated by looking at (3.12); H_2 can become large, if c_{ga} becomes small (Fig 29, left), or if ray width e (see Fig 2) becomes small (Fig 29, right), so a minimum in between is expected. Fig 30 shows that the wave steepness S_2 has a sharper minimum. This is because L_2 is decreasing as U_2 decreases. The figure shows that both a large negative and a large positive current can have a strong steepening effect on the wave; eventually it may break.

The influence of the (absolute) period is illustrated in Fig 31, which gives the ratio between steepnesses in regions 2 and 1. It appears that



Figs 27-30 Wave length L_2 (Fig 27), refraction angle α_2 (Fig 28), wave height H_2 (Fig 29), and wave steepness $S_2 \equiv H_2/L_2$ (Fig 30) vs current velocity U_2 for fixed values of water depth h , absolute wave period T_a , angle of incidence α_1 , current velocity U_1 , and wave height H_1 (Figs 29-30).



Figs 31-32 Relative wave steepness $S_2/S_1 \equiv (H_2/L_2)/(H_1/L_1)$ (Fig 31) and refraction angle α_2 (Fig 32) vs absolute wave period T_a for fixed values of water depth h , angle of incidence α_1 , and current velocity U_1 .

both a large negative and a large positive current have a dramatic steepening effect on waves of smaller period, either because the group speed and wave length become small (opposing current), or because the ray separation factor becomes small (following current), opposing current here meaning $U_2 - U_1 < 0$. In both cases the effect is due to the fact that "short waves are slow waves". This steepening and thus filtering effect was illustrated by Isaacs (1948); in the photo in his Fig 1 the current discontinuity shows up as a foam line because of short wave breaking. Fig 31 also shows that the steepness ratio is remarkably constant for the higher periods.

The period influence on the refraction angle is shown in Fig 32. For $U_2 = +4\text{ m/s}$ the variation towards $\alpha_2 = 90^\circ$ as T_a tends to 6.6 s (approx), reflects that here the ray separation factor goes towards zero.

Finally the influence of the (constant) water depth on S_2/S_1 is shown in Fig 33. It appears that (naturally) the effect is largest on smaller depths, because other things being equal here the phase speed is smallest. For $h > 10\text{ m}$ the variation is quite small in the case considered.

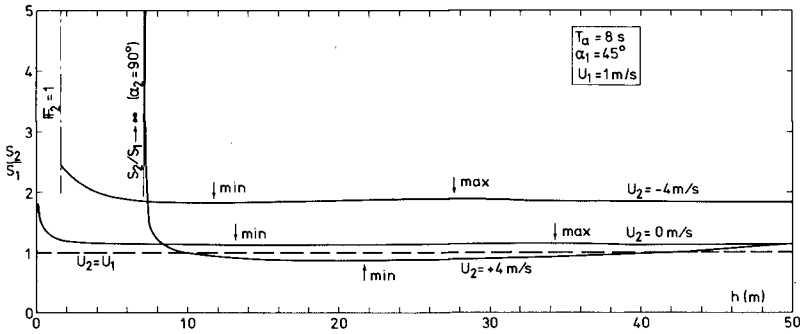


Fig 33 Relative wave steepness $S_2/S_1 \equiv (H_2/L_2)/(H_1/L_1)$ vs water depth h for fixed values of absolute wave period T_a , angle of incidence α_1 , and current velocity U_1 .

EXAMPLE - It can be difficult to read the quantities in the dimensionless delineations in Figs 6 - 26 with any great accuracy (also a number of interpolations are necessary). These figures illustrate the trends, but can give only approximate values. It is not altogether difficult, however, to find the exact figures by calculation. This will be demonstrated in the following. Consider the case with $h = 10$ m, $T_a = 8$ s, $\alpha_1 = 45^\circ$, $U_1 = 1$ m/s, $U_2 = -2$ m/s, and $H_1 = 1$ m (Figs 27 - 30). ($g = 9.80665$ m/s $^2 \Rightarrow g/2\pi \approx 1.561$ m/s 2). Calculation of L_1 - $c_0 = 1.561 \cdot 8 = 12.49$ m/s, $L_0 = 1.561 \cdot 8^2 = 99.90$ m $\Rightarrow h/L_0 = 0.1001$; $q^* = 10 \cdot 1 \cdot \sin 45^\circ / (12.49 \cdot 99.90) = 0.00567$. Table 6-a in Jonsson et al (1971) (or Table 3.2-I in Jonsson, 1978b) then gives $L/L_0 = 0.778 \Rightarrow L_1 = 0.778 \cdot 99.90 = 77.7$ m. (Without a current we find $L = 70.9$ m - the wave is "stretched" by the positive current.) Calculation of L_2 - The right hand side of (3.8) squared is $0.1001(1 - (-2) \cdot \sin 45^\circ / 8 / 77.7)^2 = 0.1314$. Using this as entry in the column " h/L_0 " in a conventional wave table, we find $h/L = 0.1677 \Rightarrow L_2 = 10 / 0.1677 = 59.6$ m, which agrees with Fig 27. (The wave is "compressed" in region 2 by the opposing current). Calculation of α_2 - From (3.9) we find $\alpha_2 = \text{Arcsin}(59.6 \sin 45^\circ / 77.7) = 32.08^\circ$, which agrees with Fig 28. Calculation of H_2 - $h/L_1 = 10 / 77.7 = 0.1287$; $h/L_2 = 0.1677$. From a conventional wave table we then find $G_1 = 0.6682$ and $G_2 = 0.5200$. Then from (3.14) $H_2 = 1 \cdot \sqrt{1.6682 / 1.5200} \cdot \sqrt{\sin 90^\circ / \sin 65.06} = 1.098$ m, which agrees with Fig 29. ($S_2 \equiv H_2/L_2 = 1.098 / 59.6 = 0.0184$, which agrees with Fig 30).

6. CONCLUSIONS

Analytical expressions are presented for the determination of wave length L_2 (3.8), refraction angle α_2 (3.9), and wave height H_2 (3.14), as a wave passes a large-scale shearing current over a horizontal bed. The current velocity is assumed constant in time and over depth. Dimensionless results are presented in Figs 7 - 10 (L_2) and 11 - 26 (α_2 and H_2). The direct effect of the current velocity U_2 in region 2 (see Fig 1) is illustrated in a concrete example in Figs 27 - 30. The most interesting feature here is the display of a wave height (and steepness) minimum. The "filtering" effect of a shear layer on a wave motion is illustrated in Figs 31 and 32, and the influence of the water depth on wave steepness change appears from Fig 33.

The wave length L_1 at the initial state (region 1, see Fig 1) is determined by (3.4); solutions in dimensionless form are illustrated in Fig 6. Solution domains for region 1 appear from Fig 3. Solution domains for region 2 are sketched in Figs 4 (applicable to L_2 -figures) and 5 (applicable to α_2 - and H_2 -figures).

A detailed example of how to obtain numerical results using tables and handcalculations, is given in Chapter 5.

APPENDIX: ORTHOGONALS AND RAYS

In the general case the wave orthogonals are determined by

$$Dx/Ds = \cos A \quad (A.1) \quad Dy/Ds = \sin A \quad (A.2)$$

$$DA/Ds = (\sin A \partial c_a / \partial x - \cos A \partial c_a / \partial y) / c_a \quad (A.3)$$

in which x and y are horizontal Cartesian coordinates, s is distance along the orthogonal, A is the angle from the x -axis to the positive direction of the orthogonal (DA/Ds is the orthogonal curvature), and c_a is the absolute phase speed

$$c_a = c_r + u \cos A + v \sin A \quad (A.4)$$

In (A.4) c_r is the relative phase speed (3.1) and $\vec{U} = (u, v)$ is the current vector. In (A.1) to (A.3) time t can be introduced through $Ds = c_a dt$. Thus formally the wave orthogonal equations are the same as for pure depth refraction, see Skovgaard et al (1975).

In the general case the wave rays are determined by

$$Dx/Dr = \cos \mu \quad (A.5) \quad Dy/Dr = \sin \mu \quad (A.6)$$

$$D\mu/Dr = \cos^2 \mu D(\tan \mu) / Dr \quad (A.7)$$

in which r is distance along the ray and μ is the angle from the x -axis to the positive direction of the ray determined by

$$\tan \mu = (c_{gr} \sin A + v) / (c_{gr} \cos A + u) \quad (A.8)$$

In (A.8) c_{gr} is the relative group speed (3.2). Note that according to (A.8) $\mu = A$ for $(u, v) = (0, 0)$; however, (A.7) does not transform to (A.3) in this limit. This is because (A.7) presupposes (A.3) to be known and solved, giving angle A . (The ray separation factor is determined by (31) in Skovgaard and Jonsson, 1977).

REFERENCES

- Christoffersen, J.B., and I.G. Jonsson, 'A note on wave action conservation in a dissipative medium', manuscript submitted for publication, 1979.
- Evans, D.E., 'The transmission of deep-water waves across a vortex sheet', *J. Fluid Mech.*, 68, 389-401, 1975.
- Isaacs, J.D., Discussion of 'Refraction of surface waves by currents' by J.W. Johnson. *Trans.Am.Geophys.Un.*, 29, 739-742, 1948.
- Jonsson, I.G., 'The dynamics of waves on currents over a weakly varying bed', in 'Waves on Water of Variable Depth', eds. D.G. Provis and R. Radok. *Lecture Notes in Physics*, 64, 133-144, Springer-Verlag, Berlin, 1977.

- Jonsson, I.G., 'Energy flux and wave action in gravity waves propagating on a current', *J. Hydr.Res.*, 16, 223-234, 1978 a.
- Jonsson, I.G., 'Combinations of waves and currents', in 'Stability of Tidal Inlets' by Per Bruun, 162-203. Elsevier, Amsterdam, 1978 b.
- Jonsson, I.G., and J.D. Wang, 'Current depth refraction of water waves', *Inst.Hydrodyn. and Hydraulic Engng. (ISVA)*, Series Paper No.18, 48 pp., 1978.
- Jonsson, I.G., O. Brink-Kjær, and G.P. Thomas, 'Wave action and set-down for waves on a shear current', *J. Fluid Mech.*, 87, 401-416, 1978.
- Jonsson, I.G., C. Skougaard, and J.D. Wang, 'Interaction between waves and currents', *Proc. 12th Coastal Engng. Conf.*, Wash., D.C., Sep. 1970. *Am. Soc.Civ.Engrs.*, New York, 1, 489-507, 1971.
- Longuet-Higgins, M.S., and R.W. Stewart, 'The changes in amplitude of short gravity waves on steady non-uniform currents', *J. Fluid Mech.*, 10, 529-549, 1961.
- Peregrine, D.H., 'Interaction of water waves and currents', in 'Advances in Applied Mechanics', ed. C.-S. Yih, Academic Press, New York, 16, 9-117, 1976.
- Savitsky, D., 'Interaction between gravity waves and finite turbulent flow fields', *Proc. 8th Symp. on Naval Hydrodyn.*, 389-446, Arlington, Virginia: Office of Naval Research, 1970.
- Skovgaard, O., and I.G.Jonsson, 'Current depth refraction using finite elements', *Proc. 15th Coastal Engng. Conf.*, Honolulu, Hawaii, July 1976. *Am.Soc.Civ.Engrs.*, New York, 1, 721-737, 1977.
- Skovgaard, O., I.G. Jonsson, and J.A. Bertelsen, 'Computation of wave heights due to refraction and friction', *J. Waterways, Harbors and Coastal Engrg. Div.*, *Am.Soc.Civ.Engrs.*, New York, 101, WW1, 15-32, 1975 + closure: 102, WW1, 100-105, 1976.
- Wiegel, R.L., 'Oceanographical Engineering', Prentice-Hall, Inc., Englewood Cliffs, N.J., 1964.

CHAPTER 42

EXPERIMENTAL STUDY OF WIND WAVES GENERATED ON CURRENTS

by

Hajime Kato and Hiroichi Tsuruya*

Port and Harbour Research Institute
Ministry of Transport
Yokosuka, Japan

ABSTRACT

This paper presents some experimental results of wind waves generated on currents in a wind-wave channel with a water circulation pump system. The waves were measured at fetches less than 27.8 m by using resistance-type wave gauges. Surface velocities as well as velocity profiles in water were also measured elaborately and true frequency wave spectra were obtained from observed apparent spectra which were modified by the doppler effect of current.

Significant wave heights $H_{1/3}$ computed from $\overline{\eta^2}$ and peak frequencies of true spectra f_{0m} were examined with emphasis. It was inferred from the variation of true spectra that the most prominent effect of water current is to change the effective fetch length. Then an idea of equivalent fetch length was proposed to express the current effect on the development of total wave energy.

By using the equivalent fetch F' in place of the natural fetch it is shown that $H_{1/3}$ and f_{0m} measured under various current conditions can be represented by the non-dimensional fetch relations, respectively, which were originally obtained in the case of no current.

* Present address: Shimonoseki Investigation and Design Office,
Fourth District Bureau for Port Construction,
Higashiyamato-Cho, Shimonoseki, Japan.

1. Introduction

It seems to have been known since old times that in the sea where a tidal current exists the wind-generated waves are greatly changed with the direction of current. There was a remark by Lord Rayleigh (1911) in this connection. Francis and Dudgeon (1967) conducted experiments of pilot nature and demonstrated that the water currents actually have an intense effect on the generation of wind waves. Such an effect of current is considered not negligible in the prediction of wind waves in the sea area where a tidal or ocean current exists. However, the effect of current upon the development of wind waves has not been made clear so much quantitatively, and to our knowledge no method is known to evaluate the current effect in the prediction of wind waves.

In order to shed some light on the effect of current and to find some clues to the prediction of waves in the current field we have investigated wind-generated waves on currents in a wind-wave channel which is equipped with a water circulation pump system. A difficult problem in this kind of experiment is the measurement of the waves. In the experiments of Francis and Dudgeon (1967) the waves were measured photographically and crudely averaged. They state that a more sophisticated method of determining the wave characteristics might be justified in the further work.

In our experiments the waves were measured by means of wave gauges. Therefore what are directly computed from the wave records are the apparent spectra with respect to the apparent frequency modified by the doppler effect of current. For exploring intrinsic wave properties, especially the growth rates of component waves, we calculate (as substitutes for the wavenumber spectra) the true spectra defined with respect to the true frequency by making use of the dispersion relation corresponding to the actual current conditions.

In this paper we mainly discuss the non-dimensional representation of significant wave heights $H_{1/3}$ computed from the total wave powers and peak frequencies of true spectra f_{0m} measured under various current conditions. For this purpose we introduce an idea of the equivalent fetch length and show that it is effective for expressing the current effect on the development of wind waves.

2. Experimental procedures

2.1 General description

Rough sketches of the wind-wave channel used for the experiments are shown in Figs. 1 and 2. The uniform test section is 1.5 m wide, 1.3 m high and 28.5 m long. The side walls and most of the ceiling consist of glass plates. On the windward (right hand) side of the test section over the waterway is a wind blower, where wind is generated by an axial fan driven by 50 KW variable-speed motor. Passing through guide vanes, a fine mesh screen and honeycombs the wind is

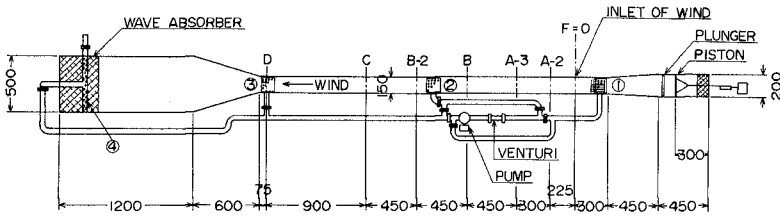


Fig. 1. A plan of the wind-wave channel

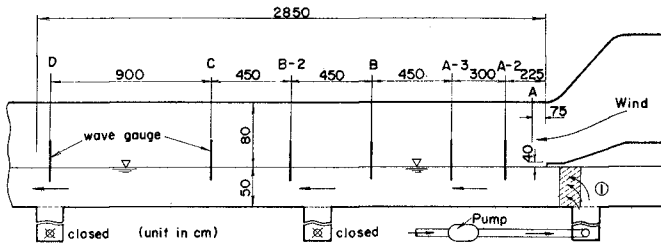


Fig. 2. A side view of the test section

Table 1. Current conditions in the experiments

	Δh (cm)	Q (l/sec)	\bar{U} (cm/sec)
Favorable current	130	224	+29.9
	60.0	152	+20.3
	15.0	76	+10.1
No current	0	0	0
Adverse current	15.0	76	-10.1
	30.0	108	-14.4
	60.0	152	-20.3

allowed to flow onto water of 50 cm depth by means of an adjustable-height guide plate at the inlet section (see Fig. 2), where the wind velocity profile is quite uniform. The wind speed was set up by regulating the speed of fan (rpm). In the experiments the winds at rpm 200, 300 and 400 were used, and the corresponding cross-sectional average wind speeds \bar{U}_a at the inlet section were nearly 5.6, 8.2 and 11.0 m/sec, respectively.

The water currents were generated by a pump between (1) and (4) shown in Figs. 1 and 2. The current condition in each run was controlled by adjusting the flow rate Q accurately by means of a venturimeter. The experimental current conditions are listed in Table 1, where Δh is the differential pressure head of venturi and \bar{U} is the average cross-sectional velocity. The measurements of waves and currents were made at six stations A-2, A-3, B, B-2, C and D shown in Figs. 1 and 2, and the fetches were 2.25 to 27.75 m. Wind velocities were measured at A-2, B, C and D stations.

2.2 Methods of measurement

The waves were measured by means of resistance-type wave gauges. The sensors were made of two parallel platinum wires 0.1 mm in diameter with 2 mm spacing. Wind velocity profiles over the water surface were measured by using a pitot static tube and a differential pressure transducer. A digital data recorder (DATAC-2000B) was used for recording the output voltages of wind and waves on line, and the later data processing was performed by using a computer. A sampling interval for the wave data was taken as $\Delta t = 1/51.2$ second considering the convenience in the computations of wave spectra by FFT.

Current velocities were measured by means of a small propeller-type current meter both with and without wind. The surface current velocities u_0 were measured by using paraffin flakes in the shape of disk about 6 mm in diameter. In order to check the drift current profile near the water surface a hot-film anemometer was also used in several cases with small amounts of detergent mixed in water to suppress wind waves, for otherwise the hot-film could not detect the horizontal velocity component correctly.

2.3 Method of analysis

As mentioned earlier, what are directly obtained from the wave data are the apparent spectra with respect to the apparent frequency f_A which is expressed as

$$f_A = c / L \quad (1)$$

where c is the wave speed for the wavelength L in the actual current field. From the apparent spectra we calculate the true spectra with respect to the true frequency f_0 given by

$$f_0 = \frac{c_0}{L} = \frac{k}{2\pi} \left[\left(\frac{g}{k} + \frac{T_1 k}{\rho} \right) \tanh kd \right]^{1/2} \quad (2)$$

where c_0 is the wave speed under no current for wavelength L , k the wavenumber ($=2\pi/L$), T_1 the surface tension, ρ the density of water, g the acceleration due to gravity, and d the depth of water. If the wave speed c is expressed as a function of wavelength L for a particular current condition, then f_A and f_0 are related by (1) and (2).

In the calculation of c the effect of drift current must be taken into account in addition to various general currents. For this purpose we used the wave speed solution for a logarithmic drift current obtained by Kato (1974). That is, the drift current profile was assumed to be represented by the logarithmic distribution

$$U(y) = u_0 - U_r \ln [(z_{0w} - y)/z_{0w}] - by \quad (3)$$

where y is the vertical position measured upward from the water surface, u_0 is the surface drift current, and U_r , z_{0w} and b are arbitrary constants which are to be determined corresponding to the actual drift current profile. In practice z_{0w} was taken to be 0.01 cm for all cases (cf. Kato (1974) and Duncan et al (1974) for the measured values in the wind-wave channel), and U_r and b were determined by using the observed current velocity profiles.

Since the wind waves have the angular spreading the actual relation between f_A and f_0 is considerably complicated as discussed by Cartwright (1963) and Barnett and Wilkerson (1967) for somewhat different cases where the wave sensor was transferred with a uniform speed. However, the angular spreading is relatively small for the waves in the wind-wave channel, especially for the dominant wave components which are mainly concerned in this paper. If we neglect the angular spreading, then the relation between the true spectrum ϕ_0 and the apparent spectrum ϕ_A is expressed as

$$\sum \phi_0(f_0) \left| \frac{\partial f_0}{\partial f_A} \right| = \phi_A(f_A) \quad (4)$$

where the summation is taken for all possible combinations of f_0 and f_A . In our experiments f_0 and f_A were uniquely related in all cases and the relation (4) can be simplified to

$$\phi_0(f_0) \cdot \Delta f_0 = \phi_A(f_A) \cdot \Delta f_A \quad (5)$$

By using the relation (5) we calculated the true spectra from the apparent spectra.

3. Experimental results

3.1 Data of winds and currents

The values of wind friction velocity u_{*a} which were determined from the wind velocity profiles are shown in Table 2. In general u_{*a} are larger in the cases of adverse current than in the cases of favorable current reflecting the water surface conditions.

Table 2. Values of u_{*a} (cm/sec).

Wind	Station	Currents			
		+29.9	+20.3	$\bar{U} = 0$	-20.3
5.6 (m/sec)	A-2	19.8	20.7	23.3	30.6
	B	23.5	24.2	26.1	30.8
	C	21.4	21.7	25.7	27.8
	D	19.0	21.2	26.6	22.3
8.2	A-2	34.8	34.3	40.0	49.2
	B	31.5	35.3	46.1	47.9
	C	29.9	31.3	41.2	48.7
	D	27.5	30.4	44.6	43.1
11.0	A-2	59.1	68.2	71.1	
	B	55.7	64.3	72.3	
	C	54.4	67.3	78.1	
	D	61.7	76.2	89.9	

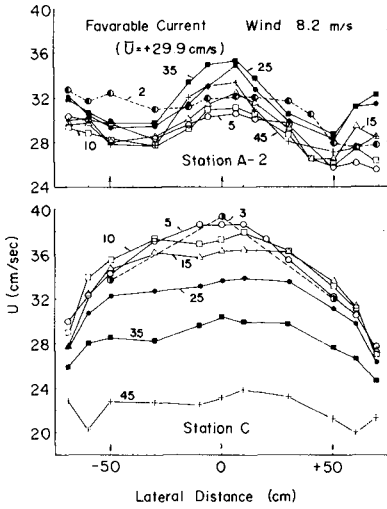


Fig. 3 Lateral current distribution in a case of favorable current.

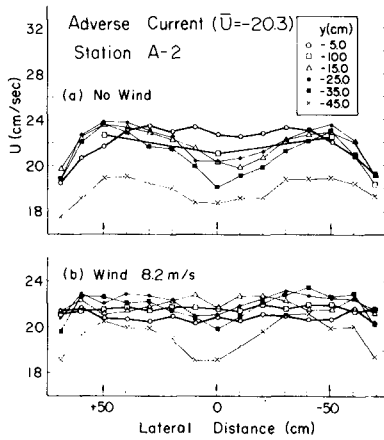


Fig. 4 Lateral current distribution in a case of adverse current.

The lateral distributions of current velocity at A-2 and C stations in the case of favorable current $\bar{U}=+29.9$ cm/sec at wind 8.2 m/sec are shown in Fig. 3. As seen from this figure, in the cases of relatively large favorable currents ($\bar{U}=+20.3$ and $+29.9$ cm/sec) the velocities near the water surface at C and D stations became somewhat larger at the central part than those at the both sides. On the other hand, in the cases of adverse current the lateral velocity distributions were almost uniform at every station. The distributions with and without wind at A-2 station in the case of $\bar{U}=-20.3$ cm/sec are shown in Fig. 4. Obviously the distributions near the surface were made more uniform by the action of wind.

The values of surface current velocity u_0 under various current conditions at wind 8.2 m/sec are shown in Fig. 5. The measurement of u_0 was so difficult in the case of adverse current $\bar{U}=-20.3$ cm/sec that it was performed in that case by suppressing the waves with detergent mixed in water.

3.2 Variation of wave heights

The measurements of waves at each station were conducted at three lateral positions; at the center of channel width and 50 cm apart from it to both sides. As a parameter to represent the total wave energy we use the significant wave height $H_{1/3}$ evaluated from $\bar{\eta}^2$, the average of the three lateral values, where η is the water surface displacement. Fig. 6 shows the variation of $H_{1/3}$ with fetch under various current conditions at wind 8.2 m/sec.

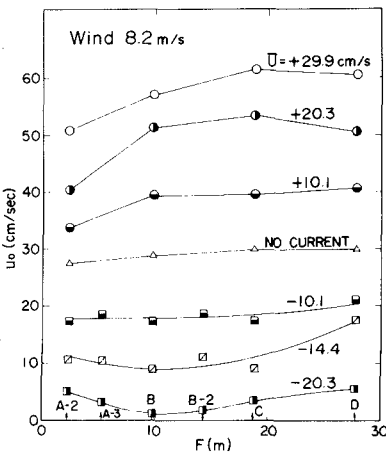


Fig.5 Values of surface current velocity u_0 .

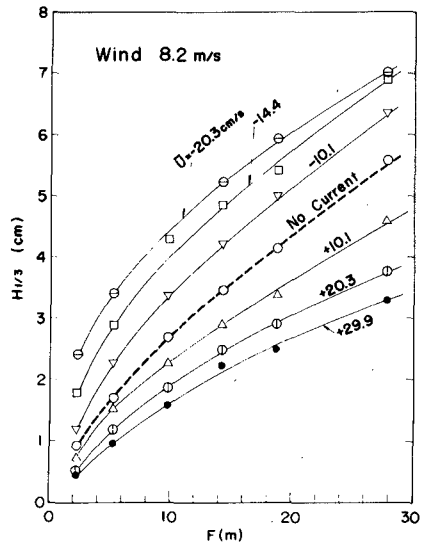


Fig.6 Variation of $H_{1/3}$.

In the cases of large adverse current the peculiar waves propagating obliquely grew with time at short fetches and the total power there became unusually large. The frequencies of such waves were smaller than those of usual wind waves, and the powers (spectral densities) of such oblique waves were excluded approximately in the computation of $H_{1/3}$. As seen from Fig. 6 the wave heights $H_{1/3}$ change systematically with currents, being small for favorable currents and large for adverse currents.

3.3 True spectra and the peak frequencies f_{0m}

As some examples of the obtained true spectra the results in the cases of $\bar{U}=+29.9$ and -14.4 cm/sec at wind 8.2 m/sec are shown in Figs. 7 and 8. From Fig. 7 it is seen that the low frequency wave components develop remarkably from A-2 to B stations. In Fig. 8 the spectra at short fetches such as A-2 and A-3 have two peaks, respectively. The right peaks of them correspond to the usual wind waves. Concerning the left peaks the obtained spectral densities may not be correct so much, but they correspond to the obliquely propagating waves mentioned above.

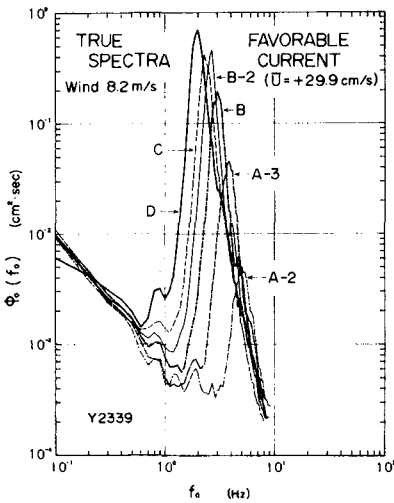


Fig. 7 True spectra ; $\bar{U}=+29.9$ cm/sec, Wind = 8.2 m/sec.

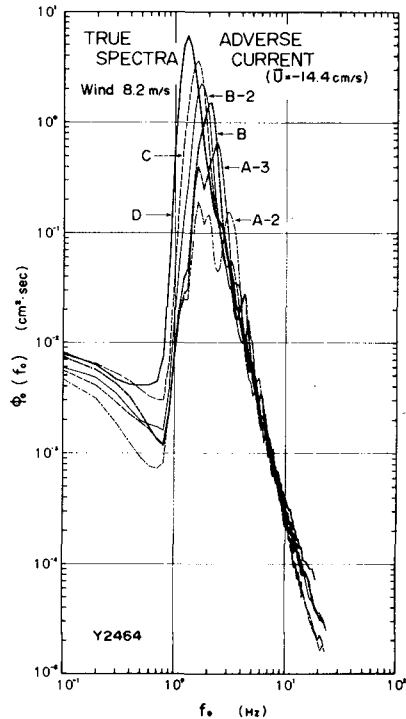


Fig. 8 True spectra ; $\bar{U}=-14.4$ cm/sec, Wind = 8.2 m/sec.

We define a dominant wave at each fetch corresponding to the peak frequency of true spectrum f_{0m} . Then the dominant wave length L_m can be calculated from f_{0m} by using the relation (2). Fig. 9 shows the obtained values of L_m under various current conditions at wind 8.2 m/sec. As seen from this figure the dominant wave lengths L_m are just like $H_{1/3}$ small for favorable currents and large for adverse currents. This variation of wavelength with current is quite contrary to the behavior of the waves moving from still water to a region of current. Huang et al (1972) calculated the wave spectra on currents by considering the kinematic and dynamic interaction between a component wave and current and also using the Pierson-Moskowitz spectrum. However, we must be aware of the distinct difference between the waves generated on a current and the waves propagated into the current from still water.

The values of L_m in each case could be represented as a function of fetch F in the form

$$L_m = \alpha F^n + L_0 \tag{6}$$

where α , n and L_0 are constants. The curves in Fig. 9 show the relation (6) applied to the data in each case, where at short fetches in the cases of adverse current the values of L_m measured photographically (but not shown in Fig. 9) were taken into consideration in order to exclude the influence of the oblique waves mentioned earlier.

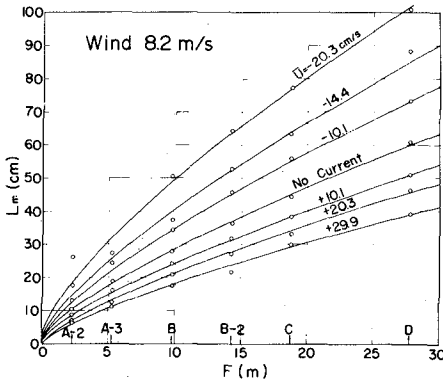


Fig. 9 Variation of dominant wave-lengths L_m with fetch.

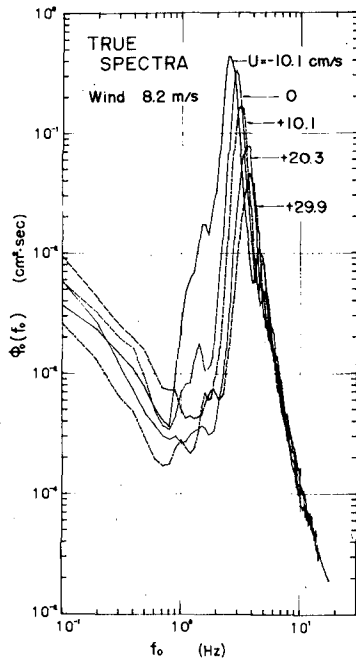


Fig. 10 True spectra under different current conditions.

3.4 Equivalent fetch length

Fig. 10 shows the true spectra obtained under different current conditions at the station A-3 (fetch = 5.25 m) at wind 8.2 m/sec. The high frequency parts of these spectra almost coincide in a curve and the variation of these spectra with currents resemble closely the variation of the spectra with fetch under no current. This fact suggests that the most prominent effect of water current on the development of wind waves is to change the effective fetch length. This effect must be caused by the change of the wave energy transfer velocity due to the current.

Concerning the development of a particular wave component, a fetch length F_1 and a wind duration time t_1 related by

$$t_1 = F_1 / c_g \quad (7)$$

are regarded as equivalent dynamically (Phillips and Katz, 1961), where c_g is the group velocity of the component wave. t_1 of eq. (7) represents the time required for the energy of the component wave to propagate over the distance F_1 . In the sense similar to (7) we assume that the wind duration time which substantially controls the total wave energy at fetch F under a particular current condition is directly proportional to the time \hat{t} given by

$$\hat{t} = \int_0^F \frac{1}{c_{gm}(x)} dx \quad (8)$$

where c_{gm} is the group velocity of the dominant wave at each fetch; \hat{t} of (8) is the time required for the energy of dominant wave to arrive at the measuring spot concerned. Then we can define the effective fetch length F' which is equivalent to fetch F under no current in respect of the development of total wave energy as follows:

$$F' = F \cdot [\hat{t} / \hat{t}_0] \quad (9)$$

where \hat{t}_0 is the value of \hat{t} under no current. In our experiments the values of \hat{t} were calculated numerically by using the empirical relation (6) as well as the current data measured at six stations.

3.5 Non-dimensional representation of $H_{1/3}$ and f_{0m}

Concerning the growth of wave spectra under no current it has been found by Mitsuyasu (1968) that the total wave energy E ($=\overline{\eta^2}$) and the spectral peak frequency f_m are represented in the non-dimensional forms such as

$$g\sqrt{E} / u_{*a}^2 = 1.31 \times 10^{-2} (gF / u_{*a}^2)^{0.504} \quad (10)$$

$$u_{*a} f_m / g = 1.00 (gF / u_{*a}^2)^{-0.330} \quad (11)$$

These fetch relations were obtained using the wind and wave data in a bay as well as in a wave tank and the similar relations were also obtained from the wave data of JONSWAP (Hasselmann et al, 1973). Recently it was found by Mitsuyasu and Rikiishi (1975) that the wave data in a wind-wave channel only are more fitted to the following relations:

$$g\sqrt{E} / u_{*a}^2 = 6.70 \times 10^{-3} (gF/u_{*a}^2)^{0.641} \quad (12)$$

$$u_{*a} f_m / g = 1.19 (gF/u_{*a}^2)^{-0.357} \quad (13)$$

By replacing \sqrt{E} with $H_{1/3}$ the relation (12) can be rewritten as

$$\frac{g H_{1/3}}{u_{*a}^2} = 0.0268 \left(\frac{g F}{u_{*a}^2} \right)^{0.641} \quad (14)$$

Using the equivalent fetch F' of eq. (9) in place of the natural fetch F together with the wind friction velocity u_{*a} , experimental data of $H_{1/3}$ and f_{0m} were plotted in the non-dimensional forms stated above, respectively. Fig. 11 shows the results for $H_{1/3}$. In this figure, at the higher wind speeds (8.2 and 11.0 m/sec) the data from different current conditions are consistent very well in a line and this indicates that the non-dimensional representation by the equivalent fetch F' is adequate. On the other hand, the data at the lowest wind speed (5.6 m/sec) deviate from the points at the higher wind speeds. Such inconsistency, however, has already been reported in the case of no current by Mitsuyasu and Honda (1975), and it is supposed to be due to the undeveloped wave condition. A straight line in Fig. 11, which was determined for the data at the higher winds, is represented by

$$\frac{g H_{1/3}}{u_{*a}^2} = 0.0222 \left(\frac{g F'}{u_{*a}^2} \right)^{0.669} \quad (15)$$

The dotted line in Fig. 11 shows the relation obtained by Mitsuyasu and Rikiishi (1975), eq. (14), and the two relations coincide very well.

Fig. 12 shows the results for the peak frequency f_{0m} . Also in this figure the data at the higher two wind speeds are represented pretty well by a straight line in the figure which is given by

$$\frac{u_{*a} f_{0m}}{g} = 0.939 \left(\frac{g F'}{u_{*a}^2} \right)^{-0.354} \quad (16)$$

The relation (13) by Mitsuyasu and Rikiishi (1975) is also shown in Fig. 12 by the dotted line. Although there is some difference between our result and (13), it is mostly attributed to the effect of drift

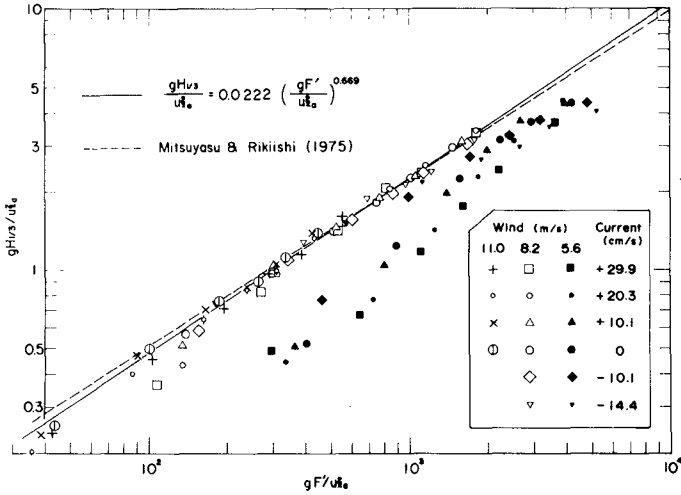


Fig. 11 Experimental results of $H_{1/3}$ represented in the non-dimensional form.

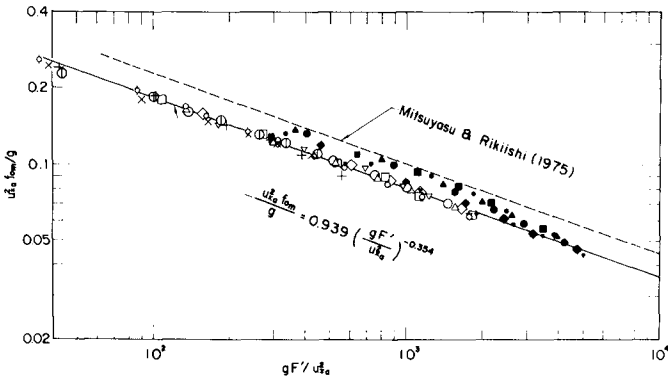


Fig. 12 Experimental results of the peak frequency f_{0m} represented in the non-dimensional form.

current; in our experiments the effect of drift current was completely corrected, while no correction was made for the data of Mitsuyasu and Rikiishi (1975). Since, however, it is rather customary under no current to use the frequency data including the effect of drift current, we must notice it in case of extrapolating the present relation (16) up to a field scale.

4. Conclusions

We have described the experiments conducted in a wind-wave channel to investigate the effect of water current upon the development of wind waves.

From the experimental results it was inferred at first that a water current has an effect to change the substantial (effective) fetch length; an adverse current increases the effective fetch and a favorable current decreases it. Considering the change of energy transfer velocity due to the current, we proposed an idea of equivalent fetch length to express the current effect on the development of wind waves.

It was shown that the non-dimensional fetch relations, which were originally obtained for the wind waves under no current, can equally be applied to the wave data, $H_{1/3}$ and f_{0m} , under various current conditions if the equivalent fetch length is used in place of the natural fetch.

The idea of equivalent fetch length is expected to be of use in the prediction of wind waves in the sea when there is a current, although some assumptions will be necessary in the case of adverse current.

Finally the authors are grateful to Mr. Y. Miyazaki and Mr. T. Doi for their assistance in the experiments.

REFERENCES

- Barnett, T. P. and Wilkerson, J. C. (1967). On the generation of wind waves as inferred from airborne radar measurement of fetch limited spectra. *J. Mar. Res.*, 25, 292 - 328.
- Cartwright, D. E. (1963). The use of directional spectra in studying the output of a wave recorder on a moving ship. *Ocean Wave Spectra*, Prentice-Hall, 203 - 218.
- Duncan, J. R., Keller, W. C. and Wright, J. W. (1974). Fetch and wind speed dependence of Doppler spectra. *Radio Sci.*, 9, 809 - 819.
- Francis, J. R. D. and Dudgeon, C. R. (1967). An experimental study of wind-generated waves on a water current. *Quart. J. Roy. Met. Soc.*, 93, 247 - 253.
- Hasselmann, K. et al. (1973). Measurements of wind-wave growth and swell decay during the Joint North Sea Wave Project (JONSWAP). *Deut. Hydrogr. Z.*, 12, 1 - 95.
- Huang, N. E., Chen, D. T. and Tung, C. C. (1972). Interactions between steady non-uniform currents and gravity waves with applications for current measurements. *J. Phys. Oceanog.*, 2, 420 - 431.
- Kato, H. (1974). Calculation of the wave speed for a logarithmic drift current. *Rep. Port and Harbour Res. Inst.*, Vol. 13, No. 4, 3 - 32.
- Lord Rayleigh, O. M. (1911). *Hydrodynamical Notes*. *Phil. Mag.*, 21, 177 - 195.
- Mitsuyasu, H. (1968). On the growth of the spectrum of wind-generated waves (I). *Rep. Res. Inst. Appl. Mech.*, Kyushu Univ., Vol. 16, No. 55, 459 - 482.
- Mitsuyasu, H. and Honda, T. (1975). The high frequency spectrum of wind-generated waves. *Rep. Res. Inst. Appl. Mech.*, Kyushu Univ., Vol. 22, No. 71, 327 - 355.
- Mitsuyasu, H. and Rikiishi, K. (1975). On the growth of duration-limited wave spectra. *Rep. Res. Inst. Appl. Mech.*, Kyushu Univ., Vol. 23, No. 72, 31 - 60.
- Phillips, O. M. and Katz, E. J. (1961). The low frequency components of the spectrum of wind-generated waves. *J. Mar. Res.*, 19, 57 - 69.

CHAPTER 43

VARIABILITY OF LONGSHORE CURRENTS

BY

R. T. Guza¹ and E. B. Thornton²

ABSTRACT

Simultaneous measurements were made of the offshore directional spectra of gravity waves, and longshore currents within the surf zone. The goal was to test theories which suggest a direct relationship between mean longshore currents (\bar{V}) in the surf zone and offshore values of the off-axis component of radiation stress (S_{xy}). Seventeen minute averages of both S_{xy} and \bar{V} showed considerable temporal variation, and little S_{xy} or no tendency to vary together. There was also considerable longshore spatial variability of the longshore current. Attempts to measure gradients of S_{xy} in the surf zone failed because of small errors in instrument orientation. The measurements suggest that considerable temporal and spatial averaging will generally be required to obtain a representative picture of longshore currents, even if no rip currents are present, due to the presence of "eddy" motions or long edge waves.

INTRODUCTION

Following the introduction of the concept of radiation stress (Longuet-Higgins and Stewart, 1964) many detailed theories for mean longshore currents in the surf zone region have been advanced (for example: Bowen, 1969a; Thornton, 1970; Longuet-Higgins, 1970). Earlier work (Putnam et al (1949), Inman and Quinn (1951) contained much of the essential physics but lacked a quantitative formulation. The newer formulations are fundamentally similar to each other in that they propose a longshore momentum balance between forcing terms related to the mean lateral thrust exerted on the surf zone by non-normally incident incoming gravity waves, and retarding forces associated with bottom drag. Lateral mixing complicates the picture by diffusing longshore momentum across horizontal shear currents. Different authors use

¹Asst. Professor, Shore Processes Lab, Scripps Inst. Oceanography, La Jolla, California

²Assoc. Professor, Naval Postgraduate School, Monterey, CA

different assumptions about the behavior of waves inside the surf zone and about the detailed forms for drag and mixing terms. As a result, the predictions of the magnitude of mean longshore currents and the distribution across the surf zone are somewhat different for identical incident wave conditions. The different theories do agree that for plane parallel contours the total lateral thrust on the surf zone is given by the off-axis term of the offshore radiation stress tensor, S_{xy} , or equivalently by, S_{xy}^B , the "break point" radiation stress value. Evaluation of S_{xy}^B involves estimation of a significant breaker angle, period and height, subjective quantities prone to gross errors (different observers on the same day report values of S_{xy}^B commonly differing by more than 100%). Therefore, in order to test the theories for longshore current with observation we have simultaneously measured S_{xy} offshore (10 m. depth) and longshore currents within the surf zone.

Instrumentation

A large scale field experiment was conducted at Torrey Pines Beach near San Diego, California during the month of March 1977. Properties of the incident gravity wave directional spectrum were measured with a 400 m. long, 5 element linear array of Statham pressure sensors; their mean depth was about 9.5 m. Six biaxial Marsh-McBirney electro-magnetic current meters were installed in the surf zone during low tide. A plan view of instrument positions is shown in Fig. 1A. The pressure sensor signals were telemetered to shore using the SAS system described in Lowe et. al (1972). The current meters were powered and sampled from shore using armored cables. The sampling frequency was 64Hz; the data was immediately block averaged and decimated to 2 Hz.

Figure 1B shows typical shallow water depth profiles for range lines A, C, D on East-West transects. The profiles overlay other when put in a coordinate frame rotated $4^\circ N$ of E (the orientation of the pressure sensor array) suggesting approximately plane parallel contours in this coordinate frame. Contours between the offshore array (not shown) and the current meters show no marked deviation from plane parallel ($4^\circ N$ of E) suggesting that refraction does not lead to significant alongshore gradients of breaker height.

Incident Wave Field

The offshore directional spectrum was analyzed using Fast Fourier transforms in the time domain to obtain phase lags for each frequency band. These phase lags were analyzed using maximum likelihood estimation techniques to obtain the direction distribution of wave energy in each frequency band. Steve Pawka did the offshore wave analysis and subtleties of the analytic methods are discussed extensively in his soon to be completed Ph.D. thesis. We thank him for kindly providing directional spectra for use in this

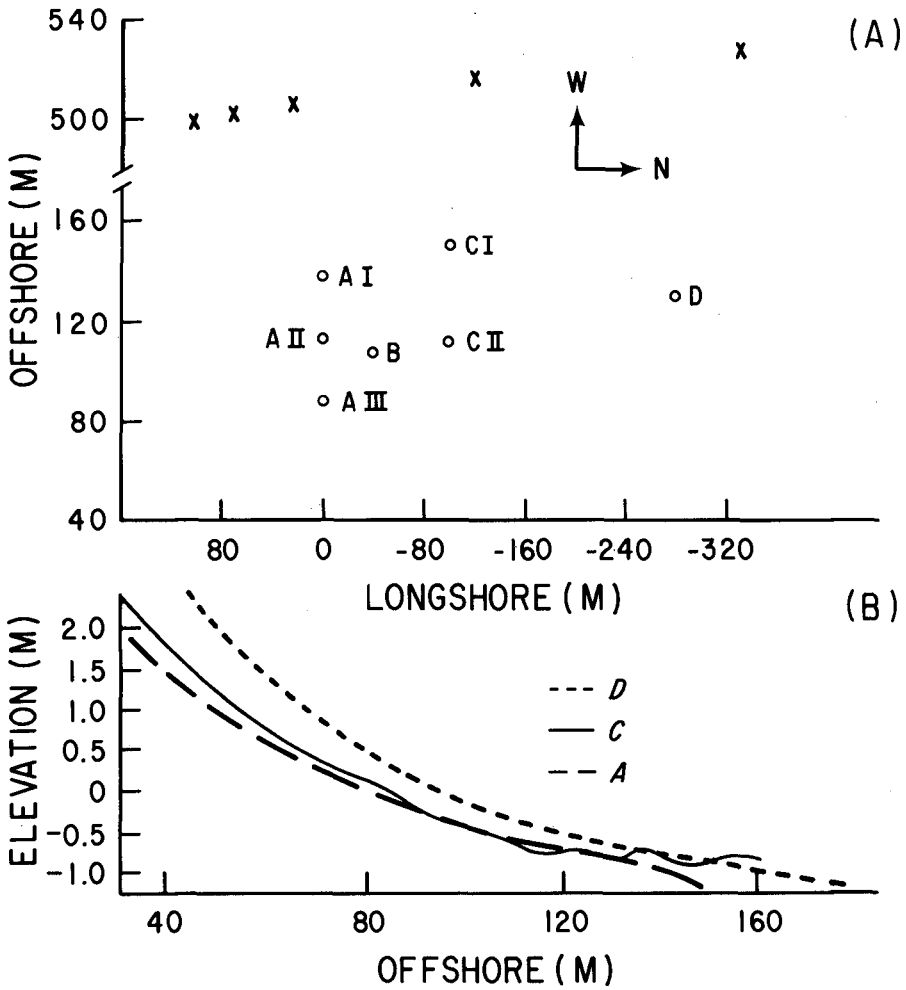


Figure 1. (A) Plan view of instrument locations. x = pressure sensors, 0 = current meters
 (B) Depth profiles for various range lines on E-W transect.

discussion of offshore radiation stress terms. Fig. 2A shows a typical distribution of variance per frequency band. Each band is .0078 hz wide and has 16 degrees of freedom. The record length is 1024 sec. The energy is centered around periods of about 14 sec., with a background of higher frequency waves. Given the directional distribution of energy in each frequency band, $E(f, \alpha)$, the relevant off-axis component ($S_{xy}(f)$) of the radiation tensor is given by

$$S_{xy}(f) = \int_{-\pi}^{\pi} E(f, \alpha) n(f) \sin \alpha \cos \alpha \, d\alpha \quad (1)$$

where $n(f)$ is the ratio of group and phase velocities (assumed given by linear theory) at the array depth and α is the deviation from normal incidence. On plane parallel contours S_{xy} is a conserved quantity if no dissipation occurs (Bowen, 1969b; Thornton, 1970) so S_{xy} at the array gives S_{xy}^{∞} , the deep water value. The entire topography seaward of the array is not plane parallel, but for simplicity we have assumed that it is. Fig. 2B shows that $S_{xy}^{\infty}(f)$ is maximum at the peak energy frequencies. However, the relatively broader frequency band of high frequency "chop" makes a significant contribution to the total $S_{xy}^{\infty T}$. In this example, the principal peak contributes -5.7×10^3 g/sec² while the "chop" contributes $+3.5 \times 10^3$ g/sec². Thus, the total lateral stress exerted on the surf zone by all frequencies,

$$S_{xy}^{\infty T} = \int_0^{\infty} S_{xy}^{\infty}(f) \, df \quad (2)$$

contains significant contributions from a very broad range of frequencies. Visual observations of a significant breaker height and period generally pick out the swell peak and ignore the chop. In certain cases, strong locally wind generated high frequency waves with large angles of incidence may produce a true S_{xy}^T , which is opposite in sign to S_{xy}^T estimated by visual observations biased towards long swell. This may explain some (but probably not all) of Nummedal and Finaley's (1978) observations showing a stronger correlation between local wind and longshore current than between visual observations of S_{xy} and longshore current. More concisely, the eye simply is not a very good directional spectrum estimator when the incident wave field is broadbanded in both frequency and direction. Figure 2C shows the "principal stress angle of approach" $\hat{\alpha}_{\infty}(f)$ defined (rather arbitrarily) using (1),

$$\sin \hat{\alpha}_{\infty}(f) \cos \hat{\alpha}_{\infty}(f) = \frac{S_{xy}^{\infty}(f)}{n_{\infty}(f) E_{\infty}(f)} \quad (3)$$

where $S_{xy}^{\infty}(f)$ and $E_{\infty}(f)$ are the radiation stress and energy per frequency band in deep water. As is obvious from $S_{xy}(f)$,

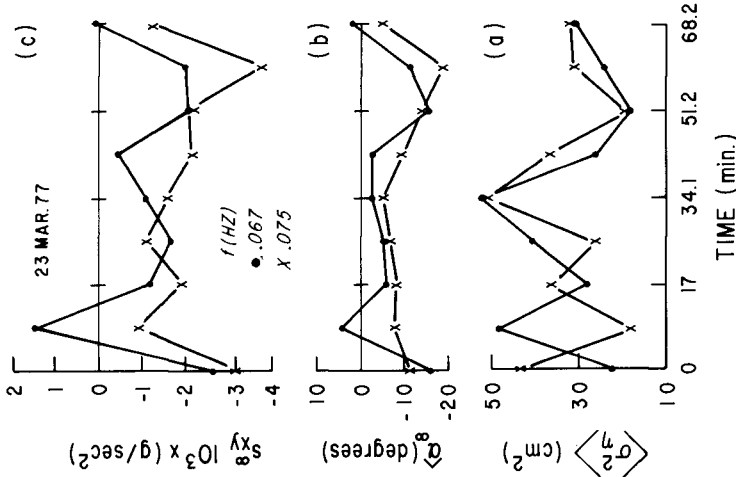


Figure 3. Time series of successive values from records, 1024 secs long, for two adjacent frequency bands in swell peak (Fig. 2) of (a) variance in each band, (b) principal stress angle, (c) radiation stress

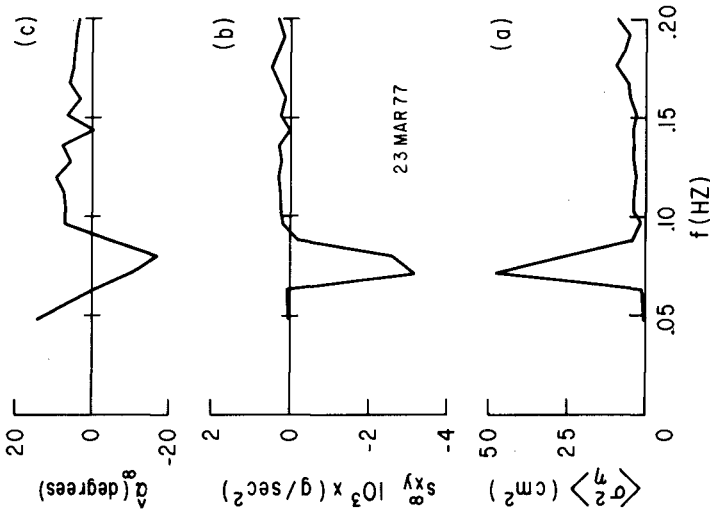


Figure 2. (a) Variance Spectrum, $\langle \sigma^2 \rangle$ per frequency band. (b) Offshore radiation stress, s_{xy}^∞ per frequency band. (c) Equivalent deep water principal stress angle of incidence for each frequency band.

$\hat{\alpha}_{\infty}(f)$ shows the swell and chop approach from different quadrants.

Measurements of $S_{xy}^{\infty, T}$ on several different days show it to be a statistically noisy quantity. This is not surprising because each $S_{xy}^{\infty}(f)$ depends on both the variance and directional distribution of energy in that band. Figure 3 shows the time history of variance (Fig. 3a), $\hat{\alpha}_{\infty}$ (Fig. 3b), and $S_{xy}^{\infty}(f)$ (Fig. 3c) for the two adjacent bands in the swell peak S_{xy}^{∞} shown in figure 2a. The energy dances about, as does $\hat{\alpha}_{\infty}$. The combination of the two fluctuating quantities going into $S_{xy}^{\infty}(f)$ leads to statistical variation of $S_{xy}(f)$. We note that the behavior of $\hat{\alpha}_{\infty}$ and $\langle \sigma^2 \rangle$ are somewhat correlated for these adjacent frequency bands, but that $S_{xy}(f)$ is apparently less correlated. Considering that S_{xy}^T is made up of many $S_{xy}(f)$ which all fluctuate, it is not surprising that S_{xy} is statistically unstable. We have done no further statistical analysis of S_{xy} and only make the general comment that, at Torrey Pines Beach, 1024 secs (17.1 min) does not appear to be a long enough sampling time to adequately measure the forcing function $S_{xy}^{\infty, T}$.

Surf Zone Longshore Currents

Fig. 4 shows 1024 sec means of longshore currents inside the surf zone and of offshore measurements of $S_{xy}^{\infty, T}$. Fig. 4a demonstrates the significant temporal fluctuations of S_{xy} discussed previously. Visual observations (whatever they may or may not signify) did not indicate any obvious non-stationarity of the incident wave field. Large breakers (1.5 m. height) were present with pronounced angles of approach. All current meters were in the inner half of the surf zone. No obvious permanent rips were observed between A and D ranges. Figs. 4b, c, d show mean values of longshore current for sensors at various longshore and on-offshore locations (Fig. 1). At this particular tidal stage (during high tide with little mean depth change) the shallowest and deepest current meters were in depths of about 60 cm. and 120 cm. respectively. The instruments on the same on-offshore range line show some tendency to vary together, but range lines 100 m. apart in the longshore direction (A and C for example) show little tendency to vary together (Fig. 4). Furthermore, no instrument showed an obvious covariation with $S_{xy}^{\infty, T}$.

Referring back to theory (Longuet-Higgins, 1970, eqs. 54-55) for guidance, we should actually expect the surf zone width to vary with $E^{\infty, T}$, and the current strength at a fixed location (always inside the breakpoint) to vary with $\hat{\alpha}_{\infty}^T$, some measure of an approach angle characteristic of the entire directional spectrum across all frequency bands (recall $\hat{\alpha}_{\infty}(f)$ represents the principal stress angle for a given frequency band). We made an extremely crude estimate of $\hat{\alpha}_{\infty}^T$ using

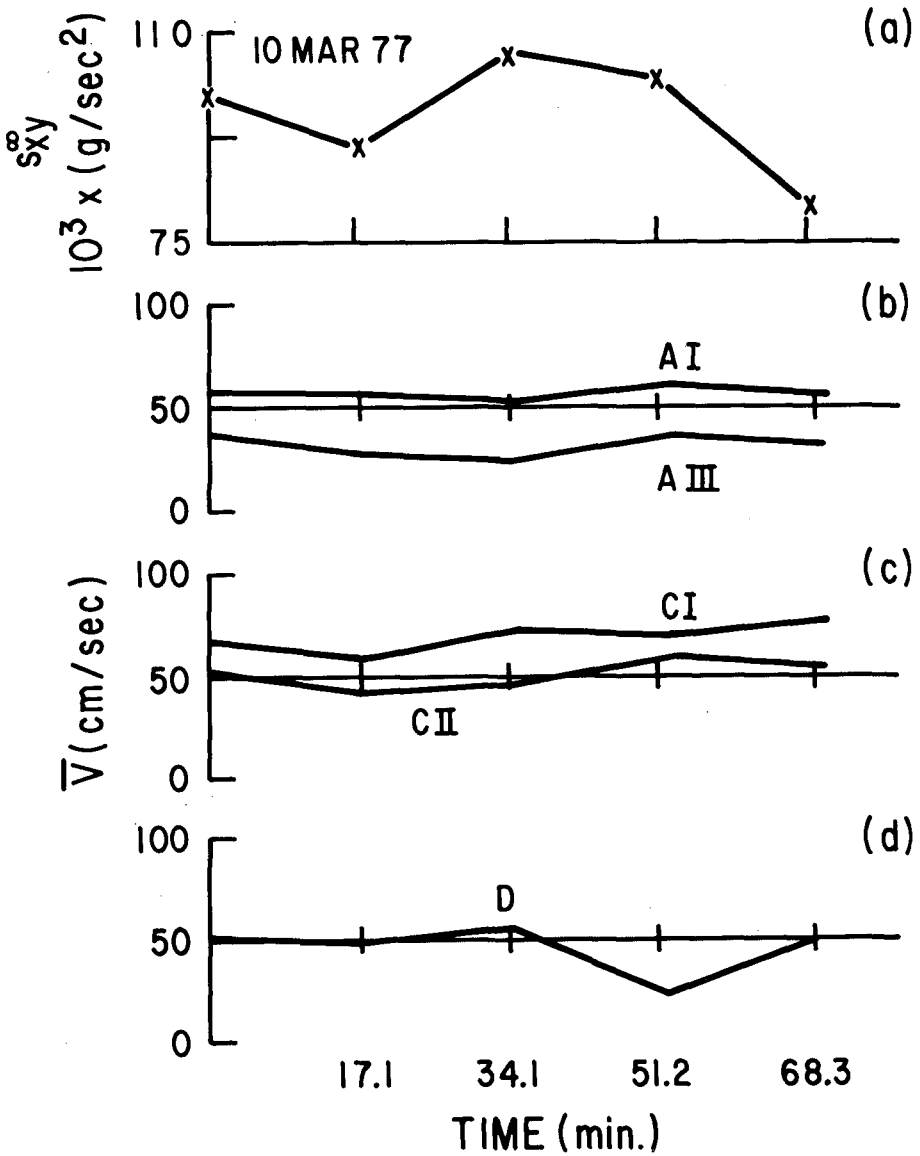


Figure 4. Temporal (1024 secs) averages on 10 March 1977 of
 (a) Total offshore radiation stress
 (b,c,d) Longshore current at different surf zone locations

$$\sin \hat{\alpha}_{\infty}^T \cos \hat{\alpha}_{\infty}^T = \frac{S_{xy}^{\infty, T}}{E_{\infty}^T n_p} \tag{4}$$

where n_p is given by the frequency of the spectral peak. No longshore currents showed an obvious covariation with $\hat{\alpha}_{\infty}^T$. Our conclusion is not a welcome one: considerable longshore variation of mean (temporal) longshore currents can occur even on a relatively straight beach with no obvious rip structures. A large (unknown) amount of longshore spatial averaging, as well as temporal averaging, may be necessary to determine the "mean longshore current" on a given depth contour.

The dominant term in the longshore momentum balance is on-offshore gradients of S_{xy} inside the surf zone, regardless of the contribution of S_{xy} nonlinear terms (for example $\bar{v} \partial v / \partial y$) or alongshore variations in breaker height. If nonlinear terms, longshore variations in mean sea level, and lateral mixing are neglected, the longshore momentum is simply

$$\frac{\partial S_{xy}^T(x)}{\partial x} = \frac{1}{2} \rho C_f \overline{|\vec{U}(x,t)| v(x,t)} \tag{5}$$

where C_f is a Chezy' drag coefficient, $\vec{U}(t)$ and $v(t)$ are the instantaneous total and longshore velocities respectively, $||$ is absolute value, and the overbar indicates time averaging.

Assuming no vertical variations in fluctuating horizontal velocities ($u'(x,t)$ and $v'(x,t)$),

$$S_{xy}^T(x) = \rho h(x) \overline{u'(x,t)v'(x,t)} \tag{6}$$

The usual simplifications of the drag term (Eq. 5) necessary for analytic progress (for example, that $u' > v'$) are not necessary when measured time series are available. We simply computed $S_{xy}^T(x)$ at different offshore locations on the same range line, and solved for C_f

$$C_f = \frac{2(S_{xy}^T(x_2) - S_{xy}^T(x_1))}{\rho \overline{|\vec{U}(x_i,t)| v(x_i,t)}}$$

different values of C_f result from calculating the friction term at location 1 or 2. Fig. 5 shows measured offshore variance, $S_{xy}^{\infty, T}$ and low passed means of surf zone radiation stress gradients. There seems to be a similarity between $S_{xy}^{\infty, T}$ and $\frac{\partial S_{xy}^T}{\partial x}$ in the surf zone. Calculated values of C_f

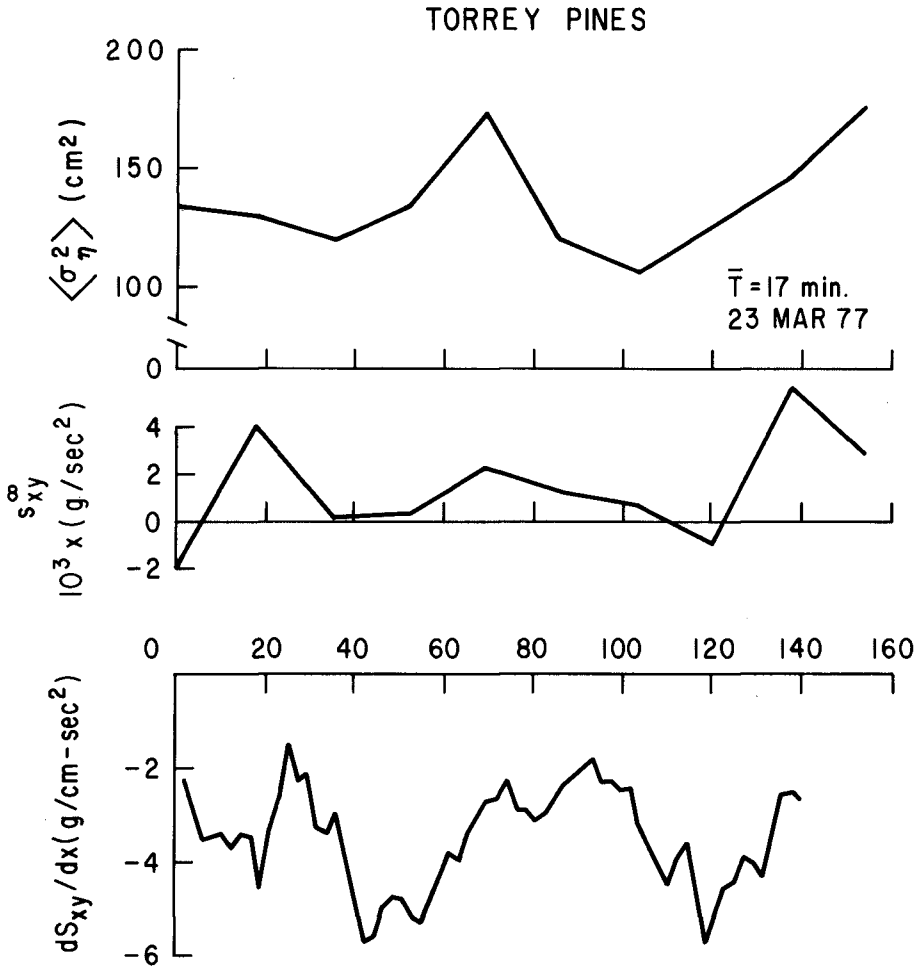


Figure 5. Temporal (1024 sec) averages on 23 March 1977 of total offshore variance, total offshore radiation stress, and running means of dS_{xy}^T/dx inside the surf zone from instruments AII, AIII.

are shown in Fig. 6a. Different C_f values occur depending on whether time series from A II (mid surf zone) or A III (inner) are used in calculating drag terms. Averaging C_f (mid) and C_f (inner) for the whole data set gives $C_f \approx .003$, which is not considerably different than the commonly used value of .01. This was the first data set analyzed and we thought some of the low value of C_f could be due to neglected nonlinear terms, or longshore and vertical variations in S_{xy} . It was more worrisome, however, that the actual magnitudes of S_{xy} at surf zone locations (also shown in Fig. 6) indicated a larger S_{xy} at mid-surf zone than at the offshore array. This does not seem possible since S_{xy} is conserved quantity during non-dissipative shoaling, and theoretically decays monotonically across the surf zone.

We attempted to test the assumption of no vertical variation in $u|v|$ in another experiment (July, 1978) using 6 flow meters horizontally closely spaced. Three meters were installed on the same depth contour, separated by 1 m. in the longshore direction, at different elevations off the bottom. To insure that no interference between closely spaces electromagnetic current meters occurred, the magnet drivers operated in a synchronous master-slave configuration. The flow meters were dynamically calibrated over the entire frequency range of interest using an oscillating arm. Considerable effort was made to carefully align the current meters. The current meters were mounted on a bracket that allowed three degrees of rotation. A special jig was used to orient the mounting bracket vertically with a bubble level and horizontally with a compass. Tests were conducted to insure that deflections of the compass needle by the ferrous mounting bracket were minimized.

The measurements were initially encouraging in that all instruments showed virtually the same on-offshore velocity spectra. For example, the spectra of instruments the same depth above the bottom, and separated by 7 m. in the on-offshore direction (a total depth difference of 8 cm.) are given in Fig. 7; the spectra show similar variance, a very high coherence, and a phase speed slightly faster than \sqrt{gh} with h the measured mean depth. Fig. 8 shows the similarity between longshore velocity spectra.

Particular note in Fig. 8 should be paid to the large low frequency components in the longshore velocity spectra; this is similar to the low frequency longshore current oscillations described in Inman and Quinn (1951), Woods and Meadows (1975), Woods (1976), and more recently by Holman et al. (1978). Without exception every longshore velocity spectra of the hundred or so we examined (corresponding to about 60 hours of observations over a month long period) showed this tendency towards spectral redness, regardless of record length. The longshore current temporal fluctuations are not site or wave regime specific since the present

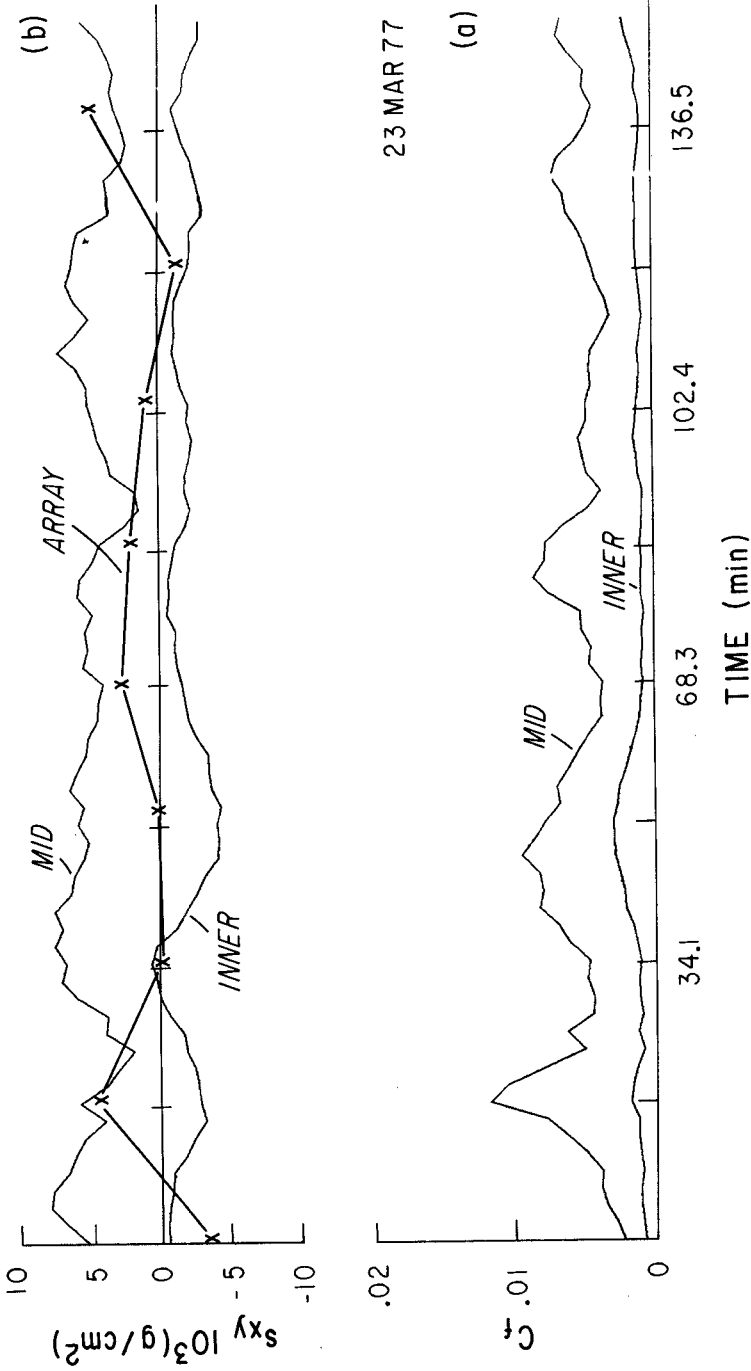


Figure 6. (a) Calculated values of drag coefficient, C_f , at mid and inner current meters
(b) Measured values of S_{xy}^T at the offshore array and mid and inner surf zone locations.

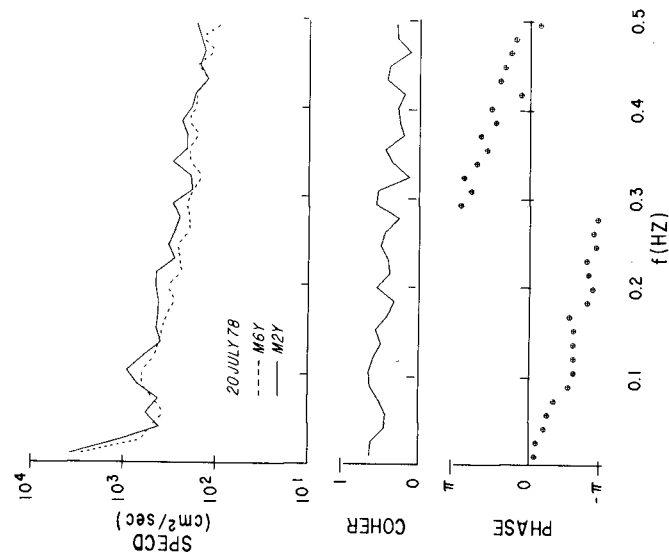


Figure 8. Longshore velocity spectra coherence and phase for the same instruments as in Fig. 7.

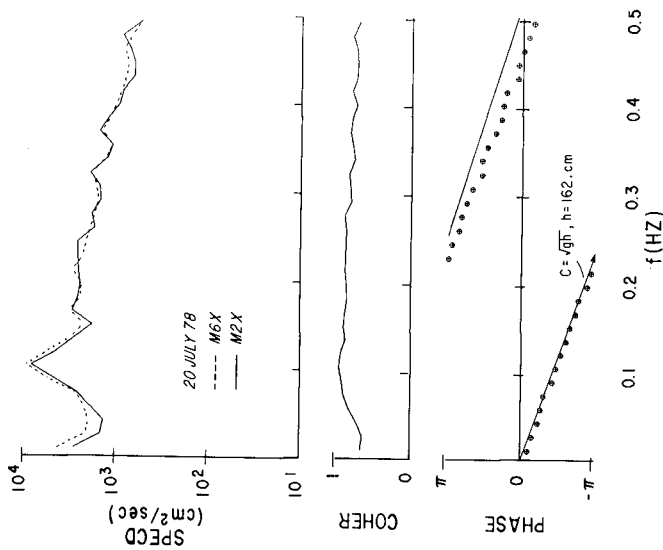


Figure 7. On-offshore velocity spectra, coherence and phase for instruments in depths differing by 8 cm. with an on-offshore separation of 7 m. Record length is 1024 sec. There are 32 degrees of freedom. Solid lines shown on phase curve is for a phase speed given by \sqrt{gh} , $h' = 160$ cm. The actual mean depth was 120 cm.

observations are from Southern California, Woods and Meadows observations are from the Great Lakes, and these of Holman et al. are from the wilds of Atlantic Nova Scotia. This mass of data suggests a grave danger in any assumptions of temporal stationarity such as are implicitly made when profiling "mean" currents with a movable sled or other such device. An appropriate temporal averaging time for mean longshore currents is not known. Woods and Meadows (1975) show 4 successive 15 minute means, and these averages, about 60 cm/sec, differ from each other by less than 5 cm/sec. Clearly, in this case, 15 mins. is a long enough time to obtain a stable average. On the other hand, Fig. 9 shows sequential 256 sec. (4.3 min) averages from 5 closely spaced instruments at Scripps Beach. The instruments vary together suggesting that the observed fluctuations are not due to sensor malfunction. Sequential means at the same location typically vary by as much as 20 cm/sec., so a single 4.3 min. average is not a representative value of the mean over longer time scales.

Upon calculating S_{xy}^T from these current meter records Figs. 7,8, instead of finding very similar values as anticipated, we found order of magnitude difference, sign reversals, and a general scatter suggestive of useless data! The reason for this is as follows. It can easily be shown that, at a particular current meter

$$\begin{aligned} S_{xy}^T &= \rho h(x) \int_0^\infty C_{xy}(f) df \\ &= \rho h(x) \int_0^\infty (E_u(f)E_v(f))^{1/2} \gamma_{uv}(f) \cos\theta(f) df \quad (7) \end{aligned}$$

$E_{u,v}(f)$ are the energy densities of (u and v) respectively, $\theta(f)$ is the phase angle between u and v, and $\gamma_{uv}(f)$ is the coherence between u and v. Figs. 10 and 11 show these spectral quantities for two closely spaced instruments. Although the spectral values are similar (Figs. 7,8), the values of coherence and phase are not. For example, around the spectral peak at .1 hz, Fig. 10 shows a narrower band of higher coherence than Fig. 11, and a phase of about $\pi/2$ compared with π in Fig. 11. This is typical of the difference between sensors and clearly shows (eq. 7) why S_{xy}^T is so different for the two instruments. Why is this occurring?

Large errors in radiation stress can occur due to even small errors in resolving the direction of fluid motion associated with the angle of incident waves. In terms of the measured spectra, the total energy density and the quadrature-spectrum are invariant with coordinate rotation, but the cospectrum used to calculate radiation stress is very sensitive to coordinate rotation.

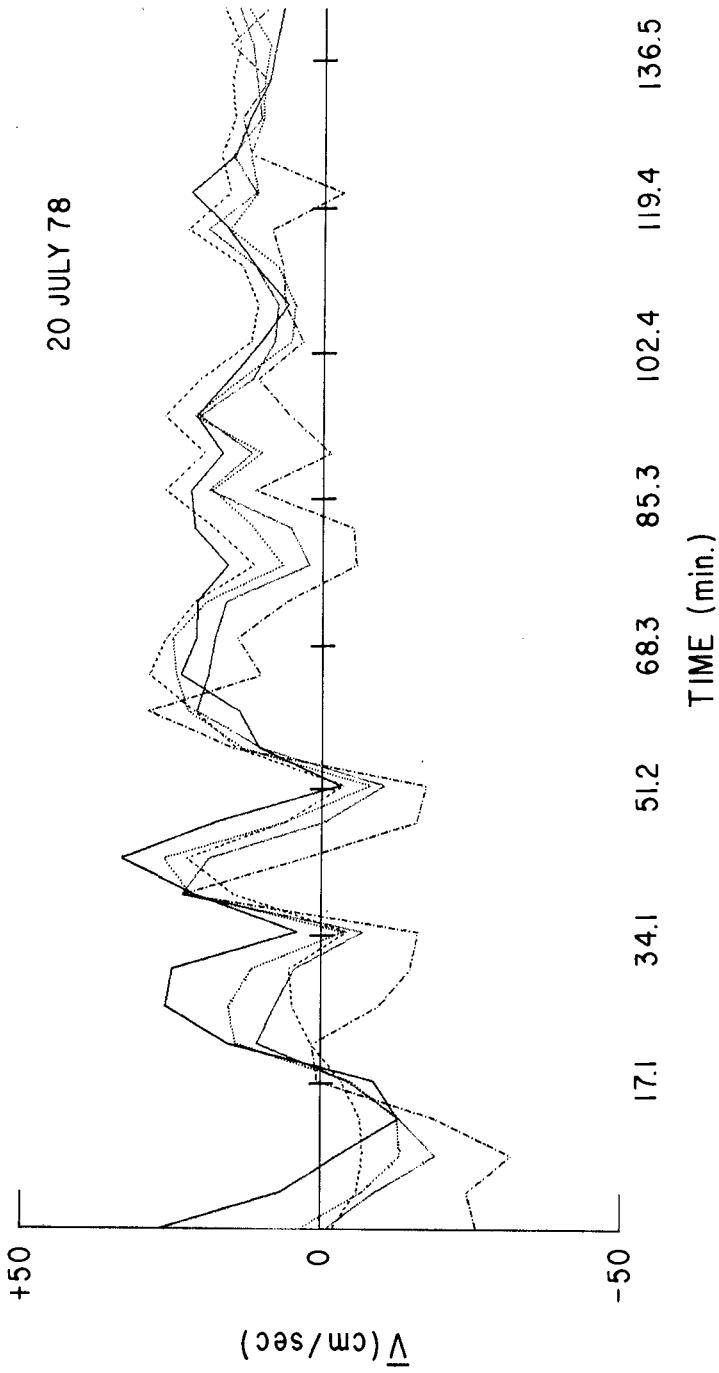


Figure 9. Time history of 256 sec. averages of longshore current from 5 closely spaced current meters, maximum separation is 14 m.

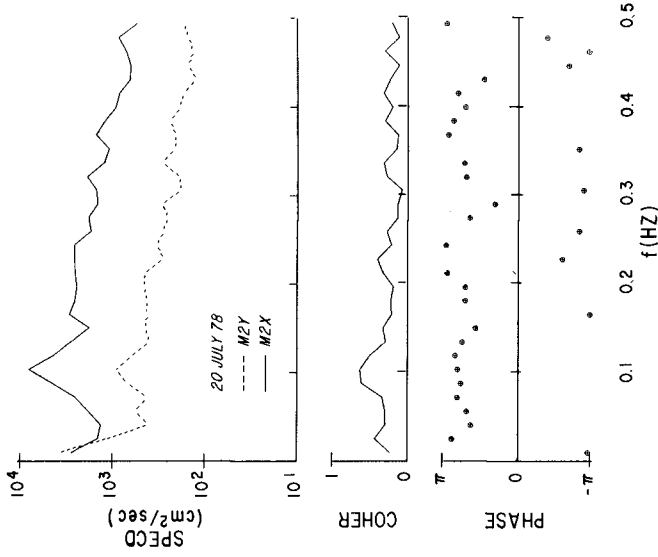


Figure 11. Same as Fig. 10, but the instrument is 7 m shorewards.

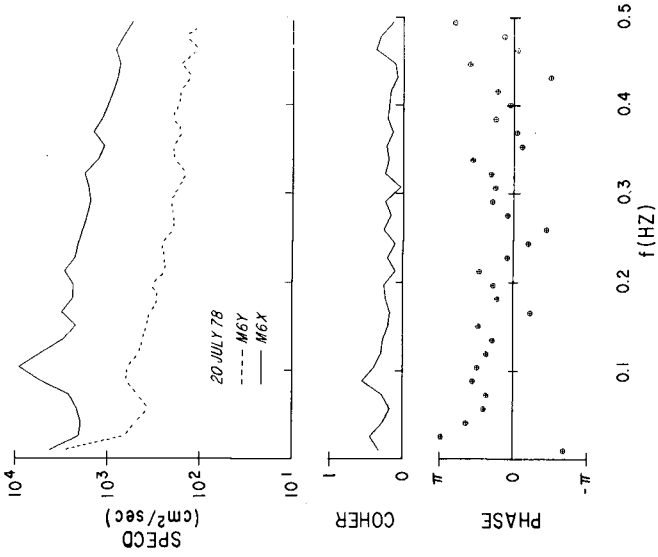


Figure 10. Spectral values, coherence, and phase for on-offshore and longshore currents at one location.

A simple application of Snell's law to a monochromatic plane wave with period 12.6 sec. shows that refraction reduces a deep water angle of incidence (α_∞) to a local angle (α) in a depth of 1 m. given by

$$\frac{\alpha}{\alpha_\infty} = .17$$

Thus, even a relatively large deep water approach angle of 20° is reduced to a small angle of 3.4° . Now consider correctly measured velocity components (u, v) and incorrectly measured velocity components (u_r, v_r) due to a coordinate rotation of angle Δ as shown in Figure 12. Assuming either all waves approach from the same direction or using a monochromatic wave argument, the radiation stress using equation 6 can be stated proportional to

$$S_{xy}^T(x) \propto \overline{u'(x,t)v'(x,t)} = \overline{u'(x,t)}^2 \tan \bar{\alpha}$$

Assuming small angles of approach and small rotation errors, the incorrectly measured radiation stress is proportional to

$$\begin{aligned} S_{xy}^T(x)_r &\propto \overline{u'_r(x,t)v'_r(x,t)} \\ &= \overline{u'(x,t)v'(x,t)} - \overline{u'(x,t)}^2 \sin \Delta \end{aligned}$$

The relative percent error is given by

$$1 - \frac{S_{xy}^T(x)_r}{S_{xy}^T(x)} = \frac{\sin \Delta}{\tan \bar{\alpha}} \approx \frac{\Delta}{\bar{\alpha}}$$

Therefore, since refraction reduces the local angle of incidence to the size of the orientation errors, the error in radiation stress can be very large.

Given perfect instrument directional response and perfect orientation, there is also the more fundamental problem of defining the longshore direction. What spatial scales should be averaged over to determine a contour orientation? Errors associated with choosing a longshore direction even on the relatively straight and parallel contours of Torrey Pines appear to be on the order of several degrees minimum. Therefore, our calculations of C_r (Fig. 6) are probably nonsensical.

Fortunately the small orientation errors discussed above do not introduce serious errors in measurement of mean longshore current because \bar{V} is generally larger than \bar{U} , so the projection of small fractions of \bar{U} onto the \bar{V} signal is not a large error. Our conclusion is that without further sophistication in instrument orientation and design and a better understanding of length scales, it is not possible to measure radiation stress in the surf zone.

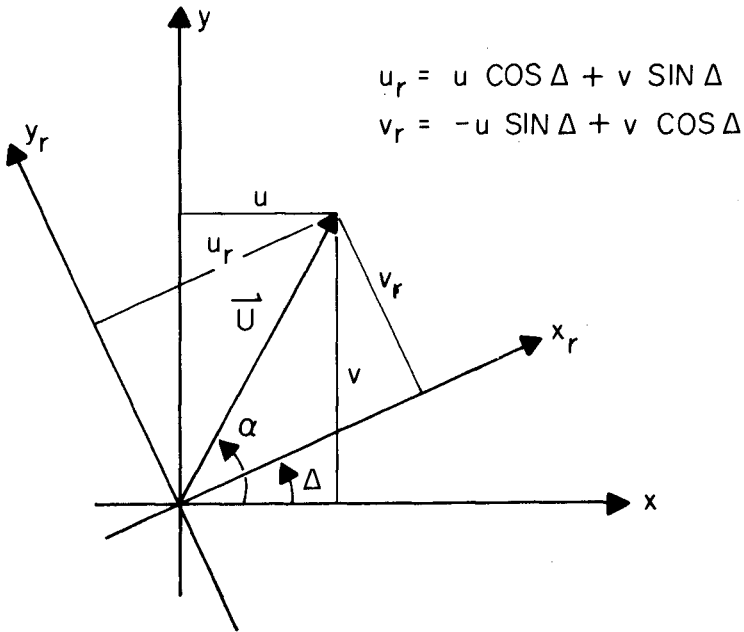


Figure 12. Rotation of coordinate axis for investigation of its influence on radiation stress.

CONCLUSIONS

1. Offshore measurement of radiation stress (the theoretical total lateral thrust exerted on the surf zone) show it to be statistically noisy. This is a preliminary result and it may be site and wave climate specific. Nevertheless, until demonstrated otherwise, short time interval measurements of S_{xy} cannot be considered as necessarily giving an accurate \bar{S}_{xy} estimate of the true mean S_{xy} .
2. Mean longshore currents at a fixed surf zone location are temporally noisy. This has been previously observed by several authors. Mean longshore currents are also spatially noisy, even with no obvious rips, suggesting that nonlinear terms and local short term variations in alongshore breaker height are important in the equations of motion. Free "eddy" motions may also be present in the surf zone.
3. Measurements of S_{xy}^T in the shallow portions of the surf zone are seriously contaminated by even small ($\pm 2^\circ$) sensor orientation errors. This is also true for vertical velocities.
4. A closing philosophical-historical point: the pioneering studies during the early 1950's of Sverdrup, Munk, and Stommel presented a rather simple picture of large scale ocean circulation. The forcing by wind, was represented by a simple long term average. The predicted currents were generally weak and horizontally smooth. The equations used by these authors are basically identical to the standard surf zone equations. They even discussed the relative importance of drag and eddy diffusivity terms, just as is currently done in surf zone dynamics. Nonlinear terms were necessary to explain the jet-like Gulf Stream, just as we currently need these terms to get appropriately strong and narrow rip currents (Arthur, 1962; Bowen, 1969b). Observations with Swallow floats showed, however, that while these theories might correctly predict yearly means, instantaneous (compared to a year) measurements showed large temporal and spatial fluctuations. Even though an enormous amount of energy and money has since been spend on experiments like MODE and POLYMODE to try to determine the importance of shorter scale fluctuations on the longer scale flows, these questions remain unresolved. Considering the strong analogy between developments so far, and the gross nonlinearity of the surf zone, it is probably overly optimistic to hope that out task of accurately difining and understanding mean nearshore flows will be simple.

BIBLIOGRAPHY

- Arthur, R. S., 1962, "A note on the dynamics of rip currents", Jour. Geophys. Research, 67 (7), p 2777-2779.
- Bowen, A. J., 1969a, "The generation of longshore currents on a plane beach", Jour. of Marine Research, 27, 2: p 206-125.
- Bowen, A. J., 1969b, "Rip Currents (1), Theoretical Investigations", Jour. Geophys. Research, 74 (23) p 4567-5478.
- Holman, R. A., D. A. Huntley, and A. J. Bowen, 1978, "Infragravity waves in storm conditions", Proc. 16th Conf. on Coastal Eng.
- Inman, D. L. and W. H. Quinn, 1951, "Currents in the surf zone", Proc. 2nd Coast. Eng. Conf., p 24-36.
- Longuet-Higgins, M.S. and R. W. Stewart, 1964, "Radiation stresses in water waves: a physical discussion with applications", Deep Sea Research, p 529-562.
- Longuet-Higgins, M. S., 1970, "Longshore currents generated by obliquely incident sea waves", Jour. Geophys. Research, 75: 33; p 6778-6789.
- Lowe, R. L., D. L. Inman and B. M. Brush, 1972, "Simultaneous data system for instrumenting the shelf", Proc. 13th Conf. Coast. Eng., p 95-112.
- Meadows, G. A., "Time Dependent Fluctuations in Longshore Currents", Proc. 15th Coast. Eng. Conf., 660-680, 1976.
- Nummedal, D. and R. J. Finley, 1978, "Wind-generated longshore currents", Proc. 16th Conf. Coastal Eng.
- Putnam, J. S., W. H. Munk and M. A. Traylor, 1949, "The prediction of longshore currents", Trans. Amer. Geophys. Union, 30: p 337-345.
- Thornton, E. B., 1970, "Variation of longshore current across the surf zone", Proc. 12th Coast Eng. Conf. p 291-308.
- Wood, W. L. and G. A. Meadows, 1975, "Unsteadiness in longshore currents", Geophys. Res. Letters, 2(11), p 503-505.

Acknowledgements

Surf zone measurements were supported by the Office of Naval Research, Geography Branch, under contract number NR 388-114 (E. B. Thornton) and N000014-75-C-0300 (R. T. Guza). The collection of offshore array wave measurements were supported by the Jet Propulsion Laboratory as part of the West Coast Experiment. Analysis of the offshore wave records were performed by Steve Pawka under ONR sponsorship. The July, 1978 mini-experiment was supported by Sea Grant, Natl. Sed. Transport Study, project R/CZ-N3. Basic overall logistics support for the experiments were provided by the Shore Processes Laboratory.

CHAPTER 44

LONGSHORE CURRENTS DUE TO SURF ZONE BARRIER

by

Bettess, P.^{*}, Fleming, C.A.^{**}, Heinrich, J.C.^{*}, Zienkiewicz, O.C.^{*}

and Austin, D.I.^{*}

* Department of Civil Engineering, University College of Wales, Swansea.

** Sir William Halcrow and Partners.

INTRODUCTION

We consider a straight coastline exposed to large regular waves, of typical wave length, 100 m amplitude 1.6 m, and period 12 sec. The radiation stress gradients in the extensive (up to 2 km wide) surf zone cause set up and long-shore currents. Despite these currents, the beach is known to be fairly stable. If now a cooling water intake basin is introduced on the coast, it is required to determine first whether the wave induced currents in the vicinity of the basin will affect the circulation of cooling water and second, whether sediment transport will occur, leading to a dredging requirement for the basin.

An extensive programme of physical model testing and numerical studies is being undertaken, in order to answer the above questions, and this paper will survey the progress made to date. At the 15th Coastal Engineering Conference a paper on the application of a mathematical model to the prediction of dredging properties inside a cooling water intake basin was presented by Fleming and Hunt, which described the first stage of this work. In that paper a sediment transport model was combined interactively with numerical models of wave refraction, wave diffraction, long shore currents and circulation currents. The last of these numerical models was used to evaluate the current patterns due to the interruption of the continuity of the longshore currents, together with the cooling water flows in the vicinity of the basin. In this paper we describe the development of more sophisticated numerical models for the first three stages of the process.

An understanding of the process of longshore current and set up creation, depends on the concept of radiation stress, introduced by Longuet-Higgins and Stewart,^{12,13,14,15} in a series of papers. A number of workers have since used the radiation stress to determine coastline phenomena, and we now describe a few of the relevant papers, without any attempt at a comprehensive survey. Bowen^{5,6} considered a straight coastline with parallel contours, and determined near shore circulation patterns, using a stream function formulation of the shallow water equations, for normally incident waves, with a sinusoidal coastwise variation in wave amplitude. He used a finite difference method to solve for the stream function. Longuet-Higgins^{10,11} criticized Bowen's use of a constant mixing length (horizontal) viscosity, and introduced a viscosity which varied directly with the distance from the shore, in his one dimensional analytical model for obliquely incident waves. He was able to obtain analytically longshore velocity profiles, which he plotted for a range of viscosities. Sonu¹⁸ showed a wide range of field observations of currents and wave patterns. Recently Dalrymple et al⁸ have

given a comparison of experimental and numerical results for near shore circulation effects.

Probably the most comprehensive numerical attack on the problem is that of Noda^{16,17}. As in the present approach, the calculations fall into two main stages, the determination of the wave pattern, and the determination of the resultant circulation and set up. Noda calculates the wave patterns by using wave ray computations. Subject to the normal restrictions of wave ray theory, which are well known, this method is an efficient method of determining the wave pattern, where there are no wave diffraction, reflection or caustic effects. Noda used the Miche steepness wave breaking criterion to determine the extent of the surfzone. The next stage was the solution of the shallow water equations with radiation stress derivatives as forcing terms. This was done in a domain, whose longshore dimension was unknown a priori, and Noda used an iterative method to determine the extent of the model and to apply the correct boundary condition. A regular finite difference grid was used, and the equations were solved for stream function values using the Gauss-Seidel method.

Most previous attempts to predict near shore circulation have been applied to straight or periodically undulating coastlines. In the present case however, the introduction of the harbour (see Figure 1) complicates the geometry. In order to be able to model such geometries it was decided to use the finite element method for both the wave calculations and the current calculations. It was thought that current refraction effects would not be important, and no attempt has been made to iterate, to see how the currents would modify the wave pattern. The wave calculation is linear and does not require iteration. The use of a finite element model has the advantages over the ray method that wave diffraction, wave reflection and wave absorption are all modelled accurately. Caustics of course are still a problem for any linearised theory.

The calculation of the currents using finite elements usually requires several iterations, because the equations are non-linear. The finite elements can accommodate any problem geometry.

METHOD

DETERMINATION OF WAVE PATTERNS

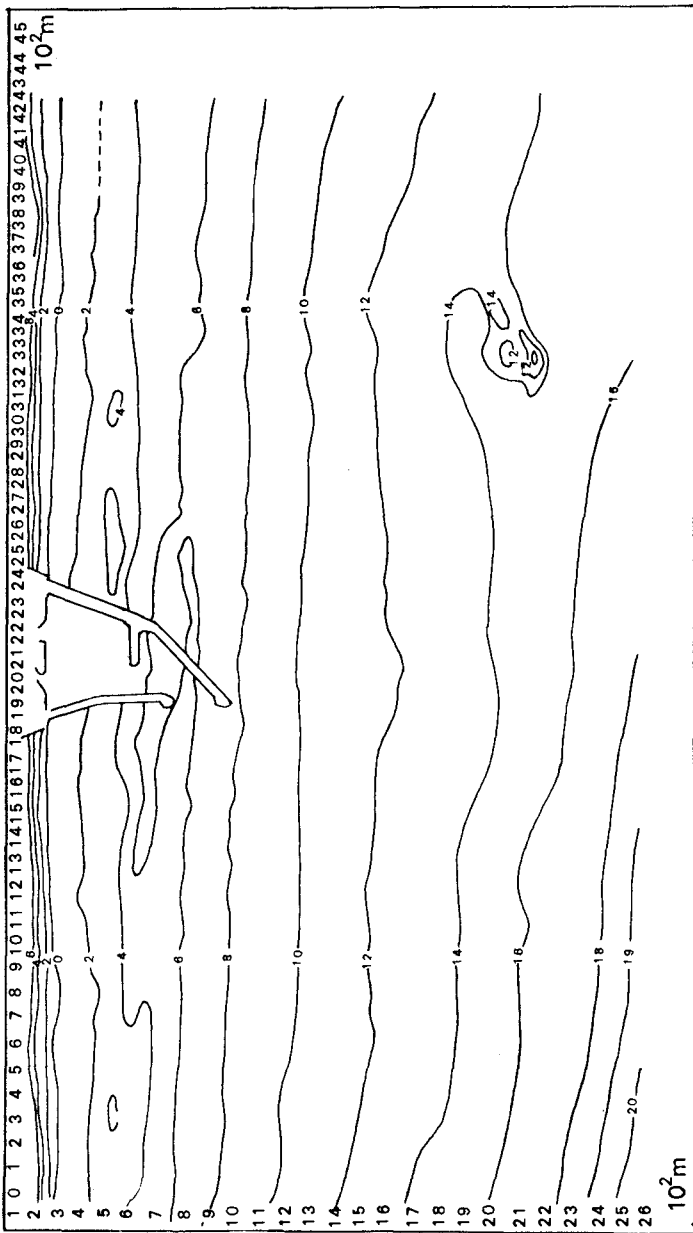
The shallow water wave equations, or Berkhoff's^{2,3} modification of them for intermediate depths are used in the wave model. The governing equation, in terms of the complex velocity potential ϕ (which is factored by $\exp(i\omega t)$), is⁴

$$\nabla_{\sim} \cdot C C_g \nabla_{\sim} \phi + \frac{\omega^2 C_g}{C} \phi = 0 \quad (1)$$

where C is wave celerity, given by ω/k , where ω is angular frequency, and k is wavenumber $= 2\pi/L$, where L is wavelength. C_g is group velocity, given by

$$C_g = \frac{C}{2} (1 + 2kH/\sinh 2kH) \quad (2)$$

and the dispersion relation



Problem Geometry with depth contours

Fig. 1

$$\omega^2 = gk \tanh kH, \quad (3)$$

holds, where g is acceleration due to gravity, and H is the depth of water. Equation 1 can be recast in a variational form as explained in reference 4, and then discretized by the usual finite element method. This evidently enables the discretization of any finite domain of shallow water. Nodal variables are complex values of the velocity potential, or wave elevations. It is clear therefore that the basis functions used in the elements must actually model the variations in the elevation of the water surface. The elements used are quadratic. It is possible to model quite accurately the sine wave using three or four such elements. Fewer than 3 elements in 1 wavelength leads to increasing inaccuracy in the modelling. The resulting equations are complex and symmetrical.

Two problems in the modelling of the unbounded real problem are the extent of the numerical domain, both normal to the shore, and along it. The radiation condition

$$\frac{\partial \phi}{\partial n} - ik \phi = 0 \quad (4)$$

which is derived in detail in reference 4, must be imposed on the non physical boundaries of the model, in order to eliminate extraneous incoming waves. In reference 21 the various methods of applying this boundary condition, using boundary dampers, series solutions, boundary integrals and infinite elements are all discussed. The efficacy of curved boundary dampers is shown in reference 20. For boundaries normal to the shore a method using dampers to eliminate the longshore components of the incident waves was devised, after considerable numerical experimentation. This device enabled us to analyse any portion of an infinite coastline, without reflection or excessive absorption of waves at the non physical ends of the numerical model. The finite element model had the boundary conditions

$$\frac{\partial \phi}{\partial n} \pm ik_s \phi = 0 \quad (5)$$

enforced at the two ends (+ for one end, - for the other), by the addition of line dampers, where k_s was the longshore component of the incident wave number k . (That is for a wave originally incident at an angle θ to the normal to the coast, prior to any refraction, with wave number, k , then

$$k_s = k \sin \theta \quad (6)$$

The energy dissipation in the surf zone is not at present dealt with exactly. Instead the numerical model ends at a small but non zero depth, at the shore line. Here it is assumed that all waves are effectively normal, and they are completely absorbed by line dampers, with a damping constant depending upon the local wave number¹.

The program can easily accommodate breakwaters that partially or totally absorb waves incident upon them. This is done by using line dampers.

DETERMINATION OF RADIATION STRESS DERIVATIVES

Because most of the waves in the model are progressive all standing wave effects are ignored in calculating radiation stresses¹. This simplifies the computations. The output from the wave program are the complex wave

elevations throughout the mesh of elements⁷. At each point the derivatives of the radiation stress components in the two global co-ordinate directions are determined and they are then supplied to the currents program as forcing terms. The calculation is as follows. At each point the direction of zero phase change is found. This is orthogonal to the direction of wave propagation. The radiation stresses and their derivatives can be found in the curvilinear co-ordinate system so defined. Then using tensor transformations the radiation stress derivatives in the global x-y co-ordinate system can be obtained. Longuet Higgins¹⁵ expression for the stress tensor is

$$S_{\alpha\beta} = E \begin{bmatrix} \frac{2kH}{\sinh 2kH} + \frac{1}{2}, & 0 \\ 0, & \frac{kH}{\sin 2kH} \end{bmatrix} \quad (7)$$

where E is total energy density, $= \frac{1}{2} \rho g a^2$, a being wave amplitude, and ρ density of water. If the curvilinear co-ordinates are θ_1 and θ_2 , and the global co-ordinates are x_1 and x_2 , then the required forces f_i are

$$f_i = S_{ij,j} = S_{\alpha\beta\eta} \frac{\partial\theta\alpha}{\partial x_i} \frac{\partial\theta\beta}{\partial x_j} \quad (8)$$

and the forces can be obtained in the two global co-ordinate directions. (Because of the curvilinear nature of the local co-ordinates defined by the waves, the transformations of the derivatives are fairly complicated).¹

In the surf zone a breaking criterion of wave height proportional to depth is used, as is done by Longuet-Higgins¹⁰. The constant of proportionality, obtained from model tests was 0.4.

DETERMINATION OF CURRENTS

The program for the current calculations uses a version of the shallow water equations²².

$$H \left(u \frac{\partial u}{\partial x} + v \frac{\partial u}{\partial y} - \Omega v + g \frac{\partial \eta}{\partial x} \right) + C \sqrt{(u^2 + v^2)} \cdot u = \frac{2}{\rho} \frac{\partial}{\partial x} \mu \frac{\partial}{\partial x} H u + \frac{1}{\rho} \frac{\partial}{\partial y} \mu \left(\frac{\partial}{\partial y} H u + \frac{\partial}{\partial x} H v \right) + \frac{1}{\rho} f_x \quad (9)$$

$$H \left(u \frac{\partial v}{\partial x} + v \frac{\partial v}{\partial y} + \Omega u + g \frac{\partial \eta}{\partial y} \right) + C \sqrt{(u^2 + v^2)} v = \frac{1}{\rho} \frac{\partial}{\partial x} \mu \left(\frac{\partial}{\partial y} H u + \frac{\partial}{\partial x} H v \right) + \frac{2}{\rho} \frac{\partial}{\partial y} \mu \frac{\partial}{\partial y} H v + \frac{1}{\rho} f_y$$

and

$$\frac{\partial}{\partial x} H u + \frac{\partial}{\partial y} H v = 0 \quad (10)$$

where u , v are horizontal velocities, η is the mean wave elevation, H is the water depth, Ω is the Coriolis parameter, C is the Chezy bed friction coefficient, μ is horizontal mixing length viscosity, ρ is density and f_x and f_y are the forcing terms.

The Galerkin weighted residual method is used to obtain a finite element formulation of these equations. The resulting non-linear equations are solved using the Newton-Raphson method. The penalty function approach was used to include the continuity equation, 10. Details are given elsewhere²², suffice it to note that an appropriate penalty factor must be chosen, and reduced integration must be used for the penalty.

In this case 8 noded isoparametric quadrilateral elements were used. A much coarser mesh of elements can be used than is needed for the wave solution, because the element shape functions have only to model the expected velocity profiles, not the actual wave shapes.

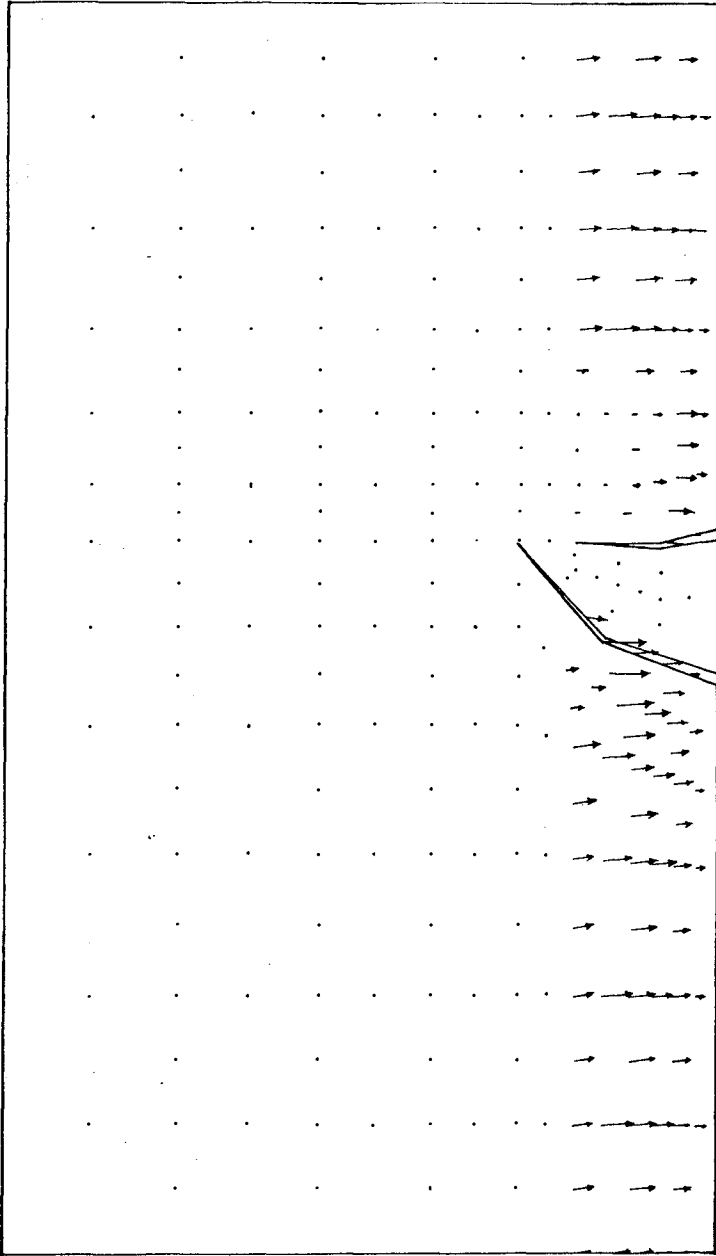
RESULTS

As was explained earlier the requirement of about 3 elements per wavelength in the finite element wave model leads to a very fine mesh of elements. For the geometry of the problem of interest such a mesh has not yet been generated or run, although similar large problems have been solved^{4,21}. The simpler problem of waves incident upon a parallel straight beach has been solved using the program¹, and no particular difficulties are envisaged, in the extension to large problems.

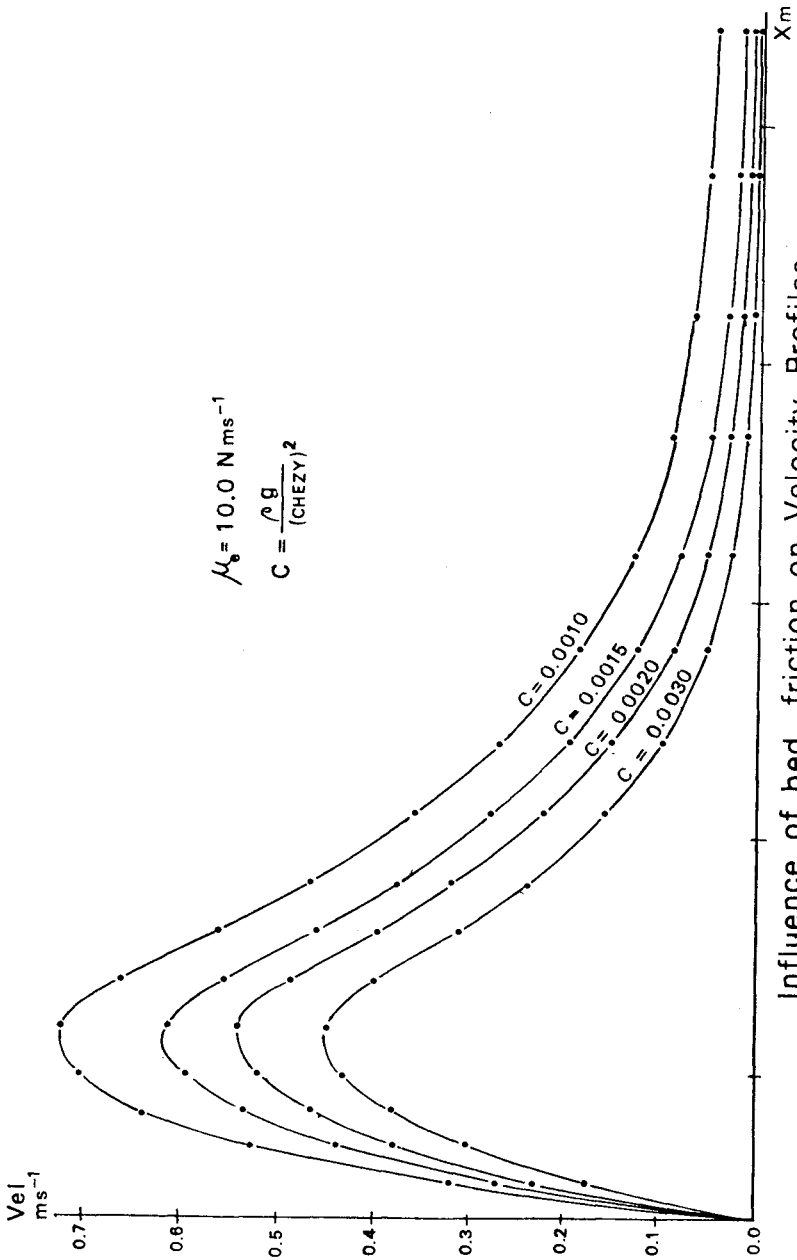
At present the radiation stresses are computed from wave elevations and directions obtained from model tests. The derivatives of the radiation stresses give the force vectors to be input to the currents program. Figure 2 shows a typical pattern of such forces. The main component of the radiation stresses is the onshore component, which would normally only lead to a set up. In the 'lee' of the breakwater, because the waves are smaller the surf line is much closer inshore, and the forces are much smaller. There is thus a rapid change in the onshore component of force in the lee of the breakwater.

The most problematical feature of the current calculations is the determination of appropriate value of the horizontal viscosity and the bed friction constant. A suitable value for the bed friction constant, $C = .002$ in equation 9, was suggested by model tests carried out by the laboratory. This was used in the numerical model. In addition a one dimensional model, using only one row of elements was run, with values of the bed friction constant, C , ranging from 0.001 to 0.003. The resulting velocity profiles are shown in Figure 3. It can be seen that changing the constant has very little qualitative effect on the velocity profile, and it was concluded that the behaviour of the numerical model was not too sensitive to this parameter.

The information available on values of the horizontal viscosity is rather sketchy. Bowen⁵ takes eddy viscosity to be constant throughout the numerical model and presents circulation patterns for a range of Reynolds Numbers. Longuet-Higgins¹⁰ argues that an eddy viscosity which is proportional to the distance from the shore is more realistic, and he uses this assumption in deriving his one dimensional velocity profile. In our case both constant and linearly varying eddy viscosities have been used. Typical flow patterns for the two cases are shown in Figures 4 and 5. For constant viscosity we took $\mu = 10 \text{ Ns/m}^2$, and for linearly varying viscosity, $\mu = 10^{-6} \rho |x| \sqrt{gh}$.

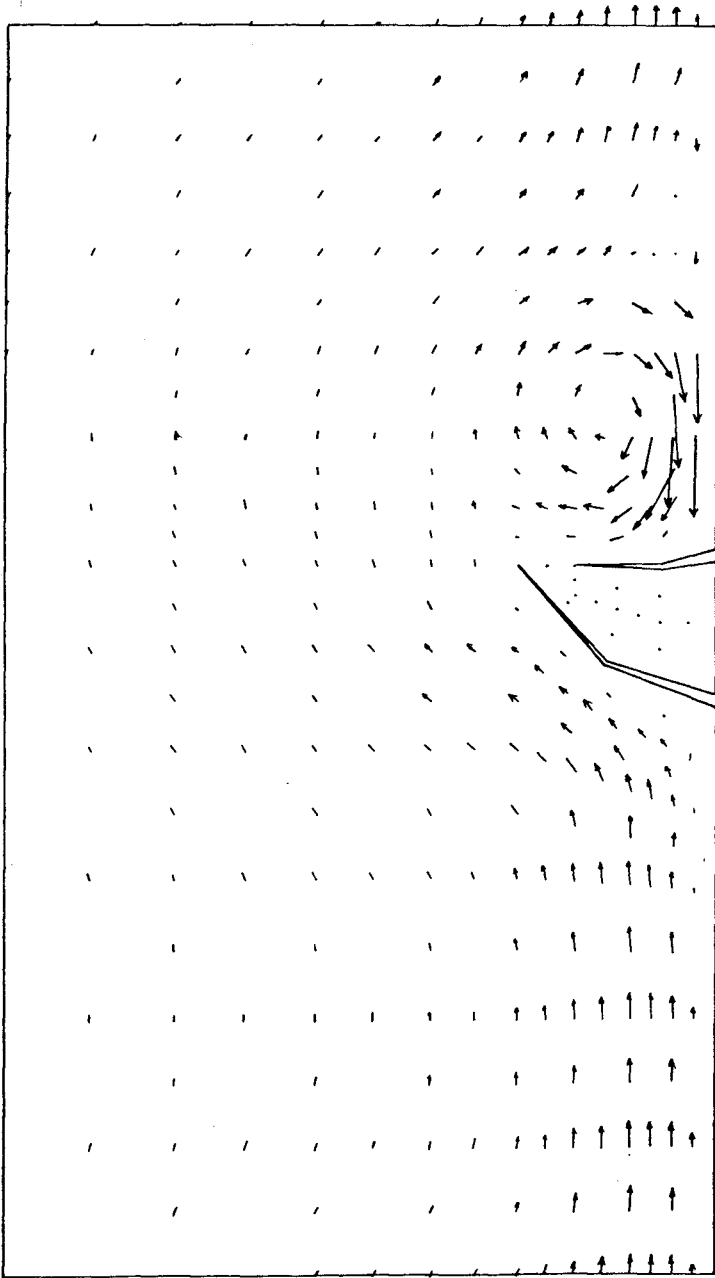


Radiation Stress Resultants
Fig. 2



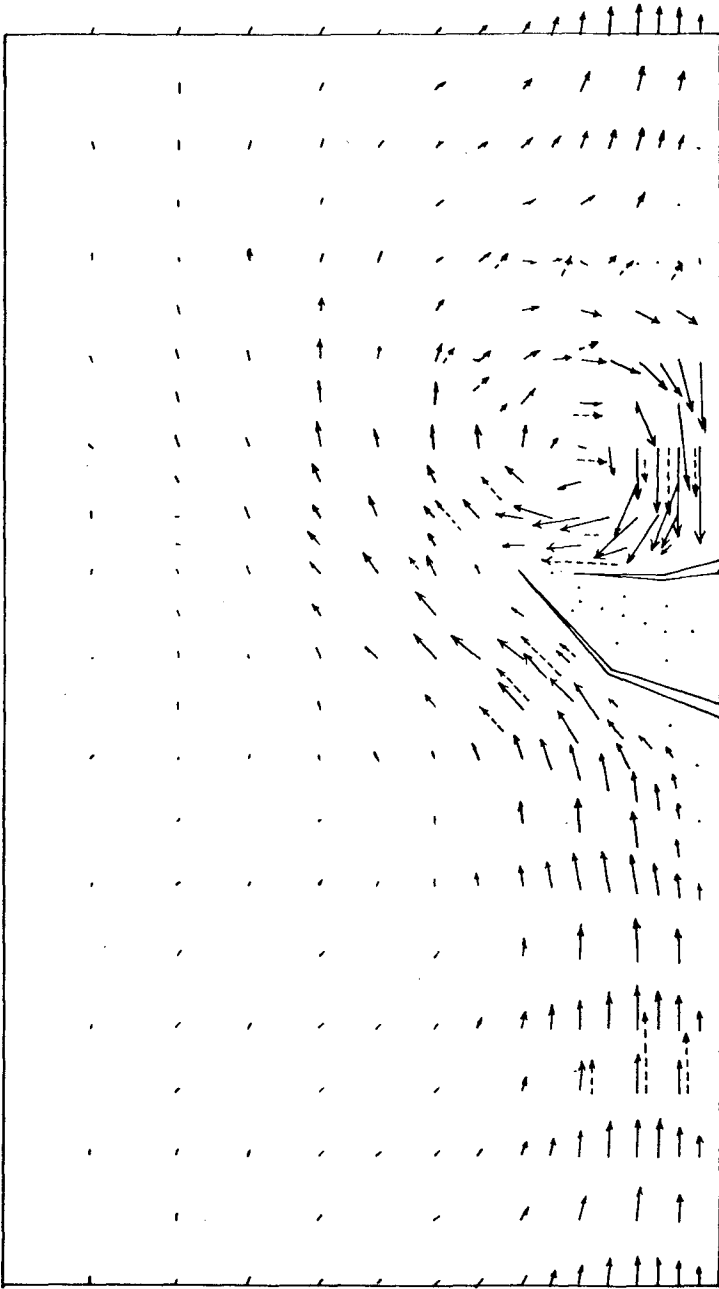
Influence of bed friction on Velocity Profiles

Fig.3



Nearshore Circulation Pattern, linearly varying viscosity

Fig. 4.



Nearshore Circulation Pattern, constant viscosity
Physical Model Pattern shown dotted

Fig. 5

For both types of viscosity variation we encountered difficulties at low values of viscosity, because the dominance of the inertia terms in the shallow water equations led to unrealistic spatial oscillations upstream of the breakwater. Experience with the convection-diffusion equations leads us to believe that these oscillations could be removed by upwinded finite elements, if such low viscosities are physically correct¹⁹.

On Figure 5 we have superposed the currents obtained in model tests. The main feature of both flows is the large strong eddy in the lee of the breakwater, and the agreement obtained is quite reasonable. This eddy seems to be driven by the changes in the onshore component of radiation stress resultant in the lee of the breakwater. While agreeing with Longuet-Higgins' criticism of Bowen's constant viscosity assumption, it seems to us that a viscosity which increases without limit away from the shore is inappropriate for the present geometry. The numerical model would probably be improved if, in determining the eddy viscosity, a mixing length proportional to the distance to the nearest boundary were used, instead of the distance to the shoreline. We conjecture that this would increase the offshore currents adjacent to the downstream breakwater. However, some upper limit should also be put on the eddy viscosity at large distances from the shore. These however, are short term modifications, but what is wanted in the long term is a better mathematical model of turbulence in shallow water problems. Some work along these lines is currently in progress.

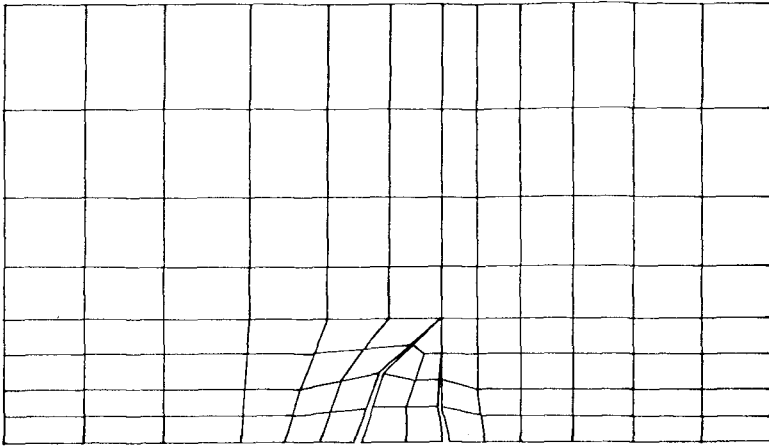
The same problem was also run using a longer numerical model by stretching both end layers of elements. The two meshes of elements used are shown in Figure 6. The velocity profile obtained at the end of the model was then closer to that for the one dimensional problem (of an infinite straight coastline without breakwater), as shown in Figure 7. Presumably the presence of the breakwater and the repeatability condition act as a "roughness" on the coast, retarding the entire flow. As the length of the numerical model is increased presumably the velocity profile tends to that of the coast without breakwater.

CONCLUSIONS

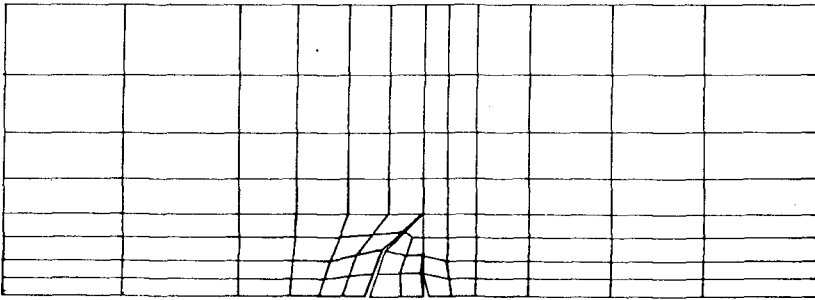
The results obtained so far indicate that the patterns of wave induced near shore circulation can be predicted by numerical means. The main difficulties are the uncertainties in the values of bed friction and viscosity. Problems remaining are i, the wave attenuation in the surf zone of the waves model ii, more accurate calculation of radiation stresses, including standing wave effects iii, an improved model for turbulence.

ACKNOWLEDGEMENTS

The authors express their appreciation to the Electricity Supply Commission of South Africa for permission to publish this paper. They are grateful to Watermeyer Halcrow and Partners for providing details of the problem shown in Figure 1, and to NRIO, Stellenbosch, for data from experimental model results.

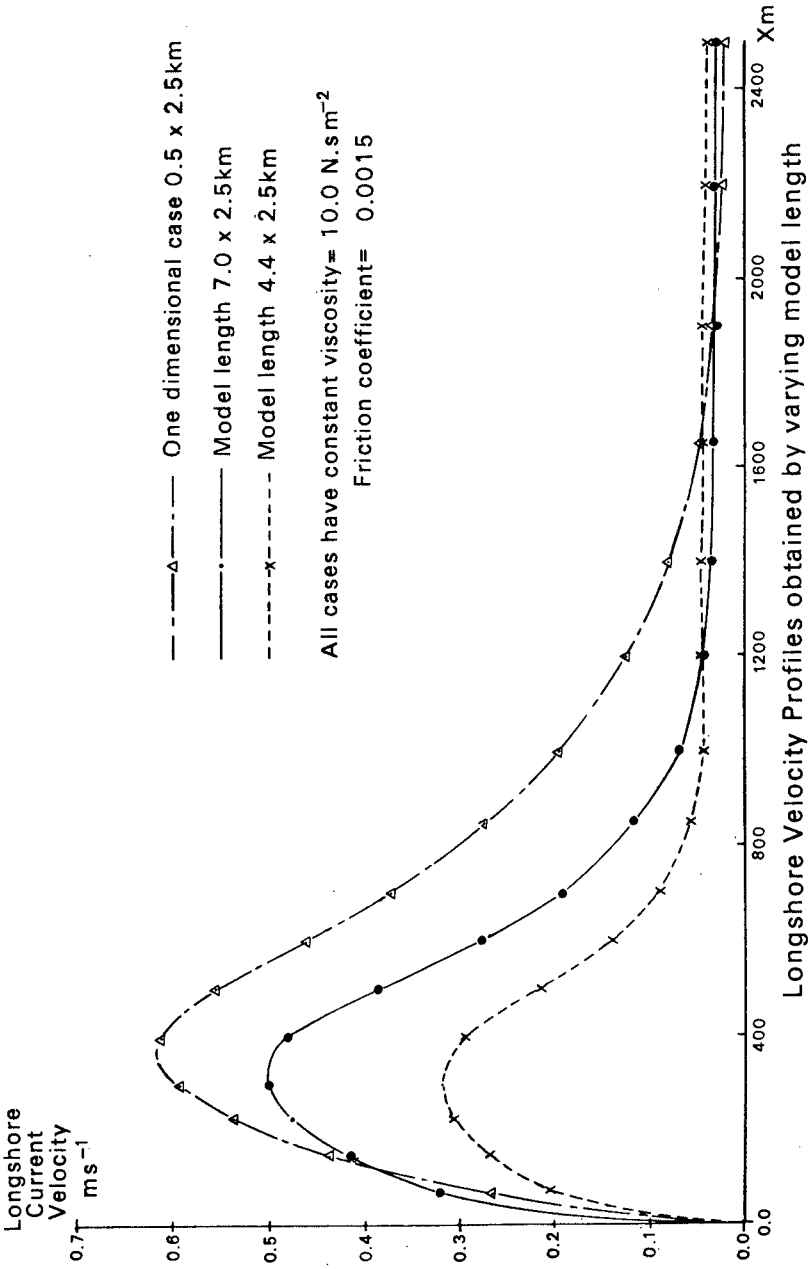


Element mesh used for current calculations, 8 noded quadrilateral elements 4.4 x 2.6km model



Element mesh for 7.0 x 2.6km model

Fig. 6.



Longshore Velocity Profiles obtained by varying model length
Fig. 7

REFERENCES

1. Austin, D.I. 'A finite element program for calculating longshore forces generated by breaking sea waves', M.Sc. thesis, University College of Wales, Swansea, 1977. C/M/128/77
2. Berkhoff, J.C.W. 'Computation of combined diffraction-refraction' 13th Int. Conf. Coastal Engng., Vancouver. (1972).
3. Berkhoff, J.C.W. 'Linear wave propagation problems and the finite element method', Finite Elements in Fluids, Vol.1. (Eds. R.H. Gallagher et al), Wiley, London, 1975. P.251.
4. Bettess, P. and Zienkiewicz, O.C. 'Diffraction and Refraction of Surface Waves using Finite and Infinite Elements', Int. J. for Numerical Methods in Engineering, Vol. 11, pp.1271-1290, (1977).
5. Bowen, Anthony J. 'Rip Currents, 1. Theoretical Investigations', Journal of Geophysical Research, Vol. 74, No. 23, October 1969, pp. 5467-5478.
6. Bowen, Anthony J. and Inman, Douglas L., 'Rip Currents, 2. Laboratory and Field Observations', Journal of Geophysical Research, Vol. 74, No. 3, October 1969, pp. 5479-5490.
7. Computer Report No. 81, Department of Civil Engineering, University College of Wales, Swansea, 'WAVE, A finite element program solving the wave equation', (1976).
8. Dalrymple, Robert A., Eubanks, Robert A. and Birkemeir, William A., 'Wave Induced circulation in shallow basins', Proceedings of the American Society of Civil Engineers, WW1, February 1971, pp.117-135.
9. Fleming, C.A. and Hunt, J.N. 'An application of a sediment transport model', Proc. 15th Coastal Engineering Conference, Hawaii, 1976.
10. Longuet-Higgins, M.S., 'Longshore currents generated by obliquely incident sea waves - Part 1', Journal of Geophysical Research, Vol.75, pp. 6778-6789, 1970.
11. Longuet-Higgins, M.S. 'Longshore currents generated by obliquely incident sea waves - Part 2', Journal of Geophysical Research, Vol. 75, pp.6790-6801, 1970.
12. Longuet-Higgins, M.S. and Stewart, R.W., 'Changes in the form of short gravity waves on long waves and tidal currents', JFM, Vol. 8, pp. 565-583, (1960).
13. Longuet-Higgins, M.S. and Stewart, R.W., 'The changes in amplitude of short gravity waves on steady non-uniform currents', J.F.M., Vol. 10, pp. 529-549, (1961).

14. Longuet-Higgins, M.S. and Stewart, R.W. 'Radiation stress and mass transport in gravity waves, with application to 'surf beats'', J.F.M. Vol. 13, pp. 481-504, (1962).
15. Longuet-Higgins, M.S. and Stewart, R.W. 'Radiation stresses in water waves; a physical discussion with applications' Deep-Sea research, 1964, Vol. 11, pp. 529-562.
16. Noda, Edward K., 'Wave-Induced Nearshore Circulation', Journal of Geophysical Research, Vol. 79, No. 27, September 20, 1974, pp. 4097-4106.
17. Noda, E.K., 'Wave induced circulation and longshore current patterns in the coastal zone', Report TETRAT-P-72-149-3, Tetra Tech, Pasadena, California, 1972.
18. Sonu, Choule, J., 'Field Observation of Nearshore Circulation and Meandering Currents', Journal of Geophysical Research, Vol. 77, No. 18, June 20, 1972.
19. Zienkiewicz, O.C. and Heinrich, J.C. 'The Finite Element Method and Convection Problems in Fluid Mechanics', Chap. 1 of finite elements in fluid mechanics, Vol. 3, Wiley, London, 1978, edited by Gallagher, R.H. et al.
20. Zienkiewicz, O.C., Kelly, D.W. and Bettess, P., 'The Sommerfeld (Radiation) Condition on Infinite Domains and its modelling in numerical procedures', Institute for Numerical Methods, Swansea, Report C/R/302/77, presented at IRIA Third International Symposium on Computing Methods in Applied Sciences and Engineering, Versailles, December, 1977.
21. Zienkiewicz, O.C., Bettess, P. and Kelly, D.W., 'The Finite Element for Determining fluid loadings on rigid structures, Two and Three dimensional formulation', Chap. 4 of Numerical Methods in Offshore Engineering, Wiley, London, 1978, (eds. O.C. Zienkiewicz et al).
22. Zienkiewicz, O.C. and Heinrich, J.C., 'A unified treatment of steady state shallow water and two dimensional Navier Stokes equations. Finite element penalty function approach', Department of Civil Engineering, University College of Wales, Swansea, Report C/R/321/78. Presented at FENOMECH, 1978.

CHAPTER 45

OBSERVATION OF NEARSHORE CURRENT AND EDGE WAVES

by

Tamio O. Sasaki* and Kiyoshi Horikawa**

ABSTRACT

Nodal lines normal to the shoreline of infragravity low mode edge waves in the nearshore zone were observed with eleven wave staffs simultaneously with the nearshore current spatial velocity field on a gently sloping beach. About five peaks were found in the energy spectrum and their frequencies agreed well with cut-off mode edge waves [Huntley(1976)]. Based on the above observation, conceptual models of nearshore current patterns for the infragravity domain are proposed and general current patterns for the three domains are discussed by combining the horizontal patterns of Harris(1969) and the vertical patterns of Sasaki et al.(1976).

INTRODUCTION

Since the publication of the rip current theories of Bowen(1967) and Harris(1967) which attribute the generation mechanism of rip currents to the interaction between incoming waves and gravity edge waves, numerous theories on rip current generation have been proposed regarding causes of longshore perturbations: these are wave perturbations due to synchronous edge waves [Harris(1967), Bowen(1967)], bottom perturbations [Bowen(1969), Sonu(1972), Noda(1972), Sasaki(1975), Birkemeier and Dalrymple(1975)], cross waves [Dalrymple(1975), Maruyama(1976)], infragravity low mode edge waves [Sasaki(1974), Sasaki and Horikawa(1975), Sasaki et al.(1976), Horikawa(1978a)], surf beats [Bowen and Inman(1969)], wave diffraction [Liu and Mei(1974), Hashimoto and Uda(1974)], an instability mechanism [Hino(1973)], Mizuguchi(1976), Dalrymple(1978)], and wave-current interaction [Dalrymple(1978)]. The numerousness of such generation theories implies the complexity of the phenomena, and multiple causes would be possible simultaneously.

Through use of the Battjes'(1974) surf similarity parameter, Sasaki (1974) pointed out that Bowen and Inman's(1969) gravity edge wave mechanism is applicable to steep beaches where synchronous and subharmonic edge waves are excited [Guza and Inman(1975)] and proposed the Infragravity Domain Hypothesis for gentle beaches where infragravity low mode edge waves should control rip current spacing.

* Chief Engineer, Nearshore Environment Research Center, 1203 Famille Hongo Bldg., 1-20-6 Mukohgaoka, Bunkyo-ku, Tokyo, 113 Japan.

** Professor, Department of Civil Engineering, University of Tokyo, Bunkyo-ku, Tokyo, 113 Japan.

Recently, more dynamical and comprehensive models have been proposed by Chappel and Wright(1978), Wright, Thom, and Chappel(1978), and Short(1975, 1978) regarding the interaction between incident wave spectrum, currents, and beach morphology, and they uncovered the role of infragravity waves on the morphodynamics of dissipative beaches [Guza and Inman(1975)], or in the authors' terminology, beaches in the infragravity domain. Also, several researchers have shown that the previously termed surf beats are in fact infragravity low mode edge waves [Sasaki, Horikawa, and Hotta(1976), Meadows(1976), Huntley(1976), Sasaki, Horikawa, and Kubota(1977), Fujinawa, Okada, and Watabe(1977), Huntley, Guza, and Bowen(1977), Bowen and Guza(1978), Holman, Huntley, and Bowen(1978), Nakamura et al.(1978)].

In the present paper the authors deal with the simultaneous observation of the spatial nearshore current field and infragravity low mode edge waves, carried out in the end of August, 1976, on Ajigaura Beach, Japan. Also, the unsteady current pattern change was observed with a newly adopted Hasselbrad 100 ft magazine in place of the previously used smaller 15 ft magazine. Based on these observations a conceptual model of nearshore current patterns is proposed in considering infragravity low mode edge waves.



Figure 1. Overview of Ajigaura Beach(1:30 p.m., 21st October, 1976).

STUDY SITE

The field observation was carried out on Ajigaura Beach which faces the Pacific Ocean (Fig. 1), and which is located 100 km north-east from Tokyo. On this beach is sited a sediment research pier 200 m long (Fig. 1), built by the Public Works Research Institute, Ministry of Construction [Hashimoto and Uda (1976)]. A headland is located about 1 km from the pier, as shown in the Figure. The beach slope is $1/40 \sim 1/70$. Under ordinary wave conditions, the pier head extends outside of the surf zone.

Figures 2 and 3 show the results of a previous current spacing survey taken on February, 1973 [Sasaki and Horikawa (1975)]. The current speed and direction were measured at midsurf by divers with a tethered float, at a wading depth of about 1 m. In this example, rip currents were equally spaced at 400 m intervals. Figure 3 shows the longshore distribution of longshore components of measured current speeds. The location of rip currents can be defined where the curve crosses the horizontal axis. With close examination of the velocities between rip currents, several seemingly periodic fluctuations can be observed. The authors felt this fluctuation could be due to the coexistence of multiple edge waves existing at that time. Concerning spatial longshore current velocity fluctuations as in this case, Meadows (1976) also presented time dependent fluctuations recorded with flowmeters, attributed to low mode edge waves.

Figure 4 shows a photograph taken with a balloon-borne camera system, BACS [Sasaki et al. (1976)], launched from the pier seen at the center of the photograph, on the 29th August, 1976. This day is the last Sunday of the Japanese school summer vacation. A surfing contest was being held on the right-hand side of the pier, and many cars were parked on the beach. Unfortunately STEREO-BACS to obtain wave height fields [Sasaki et al. (1976)] was failed.

The breaker height and period were 1.2 m and 13 sec respectively, and the wind speed was 3m/s from the south-east. The width of the surf zone was about 100 m, and two waves were observed in the surf zone. Because the pier is 200 m long, the size of the coverage is about 400 m alongshore by 250 m offshore. Eleven letters, from A to K, give the locations of wave staffs, and all of them except "I" on the pier are in the surf zone. The staff array is distributed in an area that covers 200 m alongshore and 140 m offshore. There are 4 staffs attached to the pier piles (K, G, H, and I) in the offshore direction. The water surface fluctuations were filmed with 16 mm memo-motion movie cameras, Bolex H16-SBM, at one second intervals.

The surf zone beach topography up to 3 m depth (Fig. 5) was measured just after the current and wave measurements. No clear rip channels could be defined but the 1 m depth contour-line showed a depression around the pier. The average beach slope up to 2 m was about 1/60. The depth of the furthest offshore wave staff "I" was about 2.5 m.

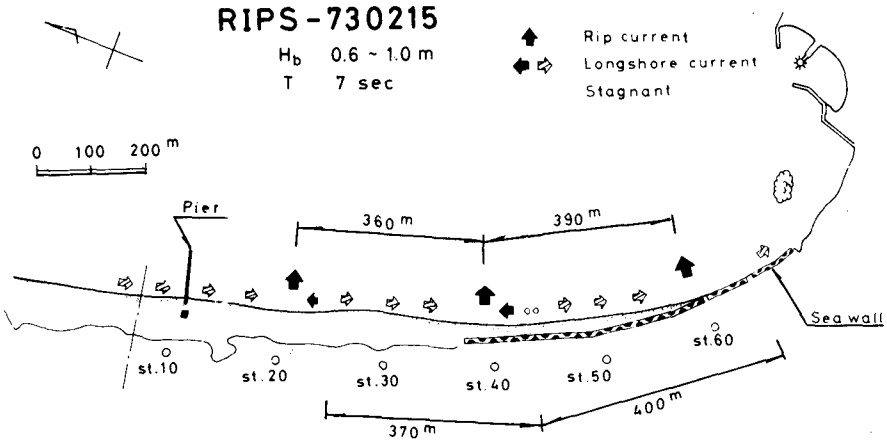


Figure 2. Evenly spaced rip currents on Ajigaura Beach(RIPS-730215), (Sasaki and Horikawa(1975)).

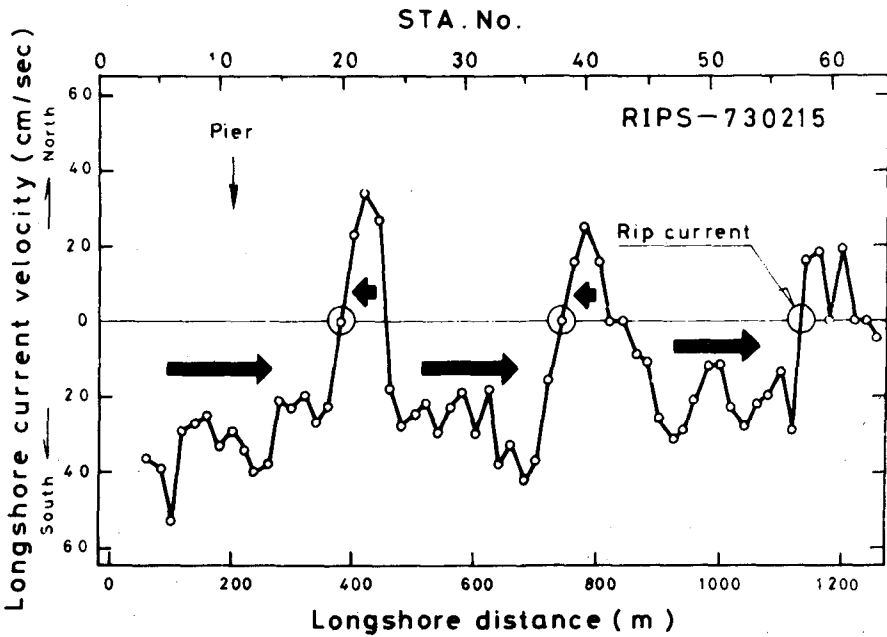


Figure 3. Alongshore distribution of longshore current velocities (RIPS-730215), Sasaki and Horikawa(1975).

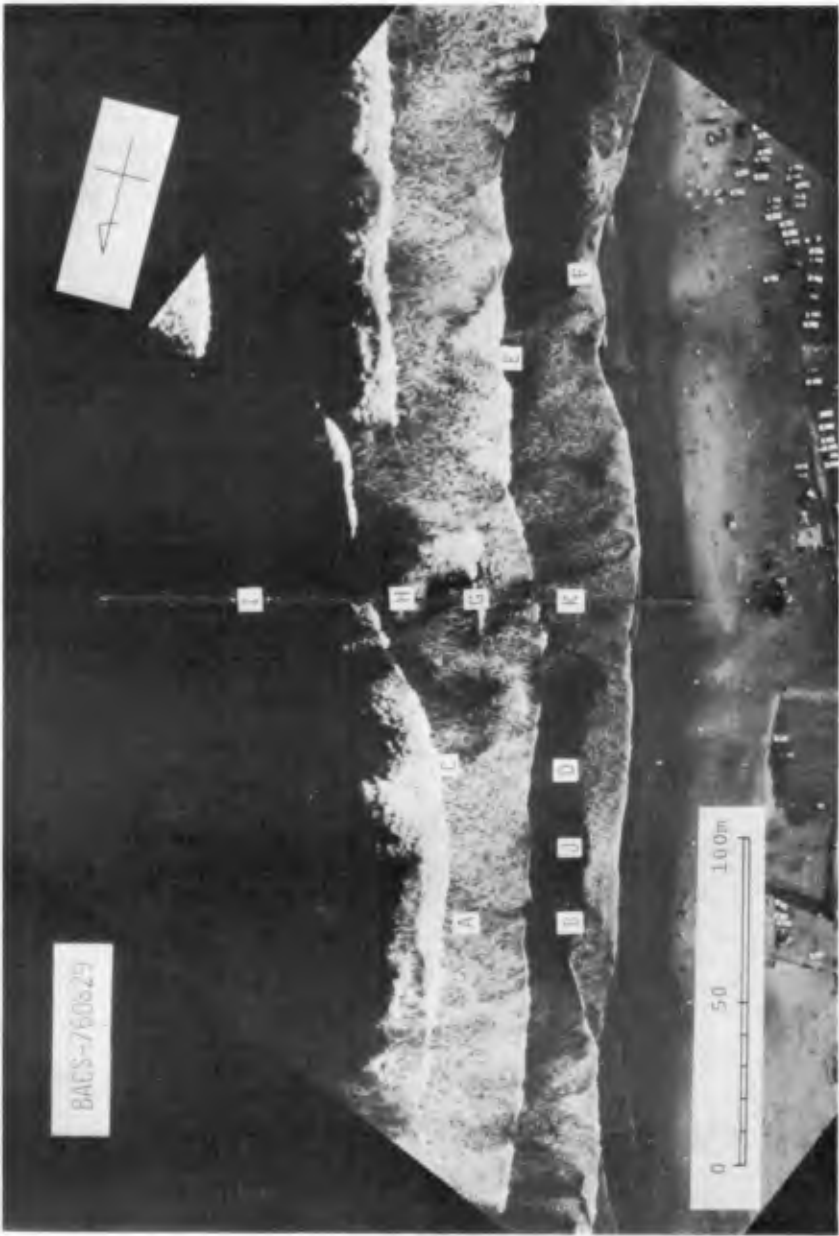


Figure 4. Observation area and instrument locations, August 29, 1976, Ajigaura Beach.

NEARSHORE CURRENT PATTERN FLUCTUATION

Up to 1975, the authors had used a Hasselblad 15 ft magazine which permitted only 70 frames. Because the shutter interval adopted is close to the wave period, i.e., 10 s to 15 s, the observation time was therefore limited to a synoptic measurement of only 10 min to 15 min. However, a longer observation period became possible by utilizing a newly developed 100 ft magazine which allows 480 frames. This enabled a 37 minute continuous measurement at 15 s intervals at an altitude of 240 m. The resultant 150 frames were split into 3 stages, each consisting of 50 frames, and the nearshore current pattern change during these 3 stages over 37 minutes was analyzed.

Figure 6 shows float velocity vectors for the 3 stages. The water enters the surf zone from the left-hand side of the pier, and branches off to the left and to the right forming longshore currents. A part of the latter longshore current enters a small rip current around the pier, and the remaining longshore current moves away further to the right. The maximum longshore current velocity is about 70 cm/s and the average velocity range is 40 to 50 cm/s. The sparse distribution of floats at Stage III is due to diver fatigue from the strenuous work maintained over half an hour.

There is no major rip current or well defined rip channel in this coverage. The rip current seen around the pier is weak and not a major

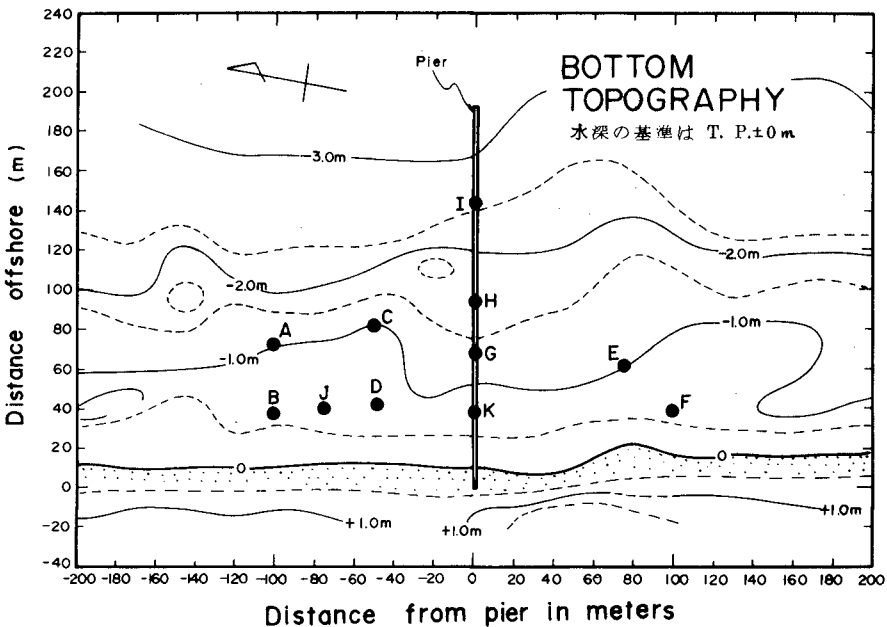


Figure 5. Surf zone topography surveyed on 29th August, 1976.

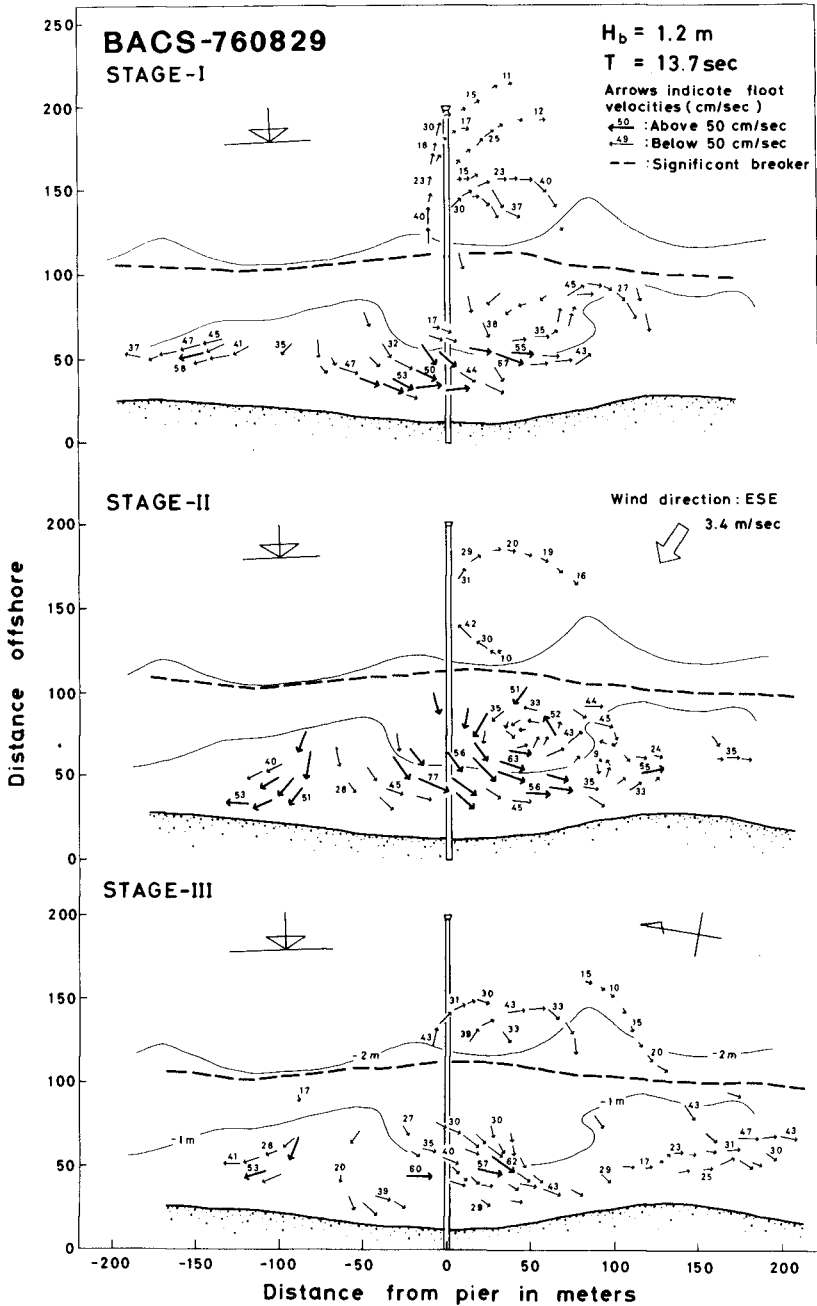


Figure 6. Float velocity vectors for the three 12 min. observation.

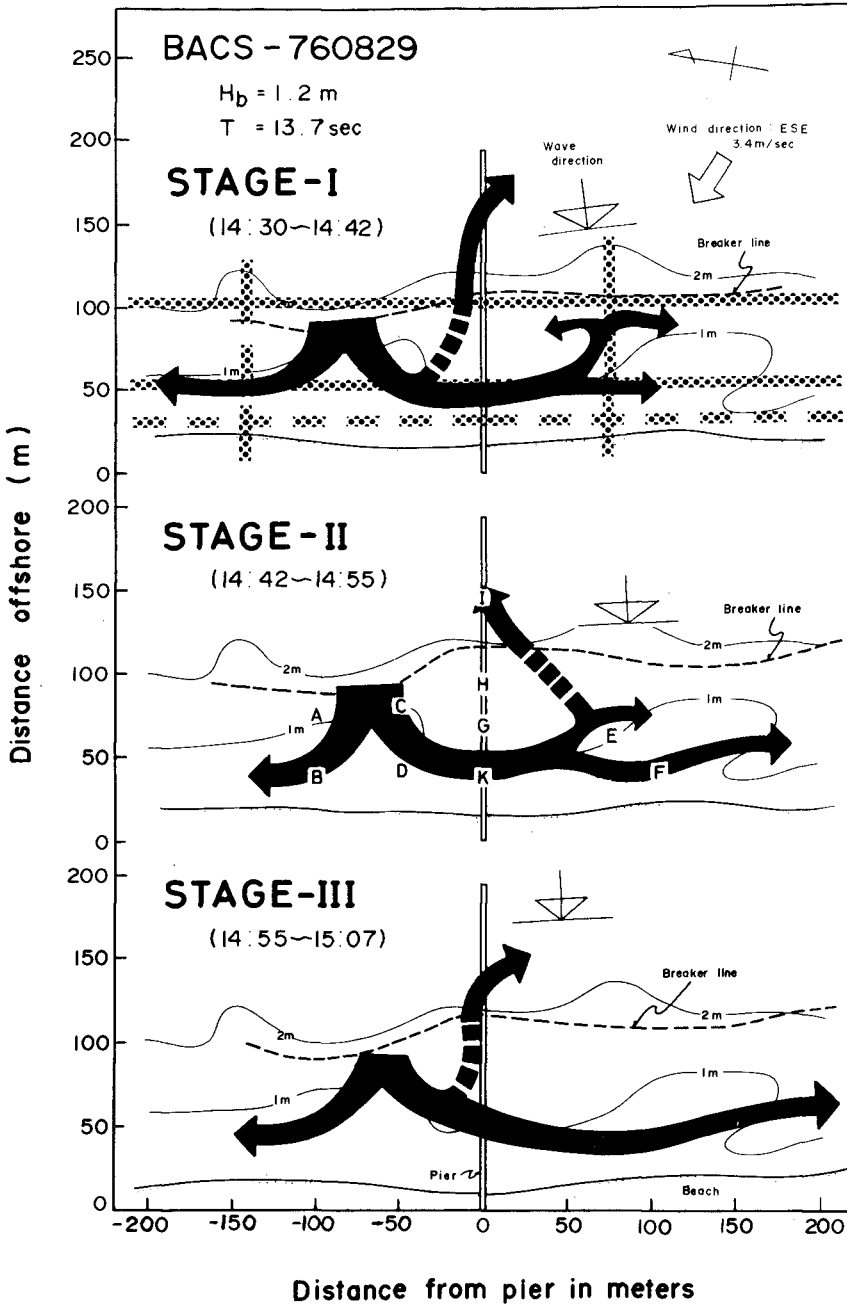


Figure 7. Nearshore current pattern change and associated nodal lines.

one; the current path also seems to be very unstable and unsteady. The maximum velocity is about 40 cm/s.

Figure 7 shows the current pattern change. The longshore current is strong and steady throughout the 3 stages. The reason that the weak rip current is very unsteady may be due to absence of a clear rip channel. A rather wider embayment is formed as seen on the 1 m depth contour line at both sides of the pier. The width of the bottom depression in the surf zone makes the small rip current fluctuate.

The thatched lines in the top diagram indicate the observed nodal lines of edge waves to be mentioned later. The shore parallel nodal line nearest to the shoreline should lie in the swash zone ("swash node"), the second one appears to correspond to the main stream of the longshore current ("longshore current node"), and the third one appears to coincide with the breaker line ("breaker node").

OBSERVATION OF INFRAGRAVITY LOW MODE EDGE WAVES

Observation of the water surface fluctuations was carried out simultaneously with that of the nearshore current. The data obtained from the eleven wave staffs were digitized and analyzed by BMD-02T, i.e., cross-spectrum analysis with $\Delta t = 1$ s.

Figure 8 shows the spectra of input waves around the breaker line "H" and swash zone "K". In the breaker wave spectrum of "H", a broad peak from 6 to 14 s is seen, which, when closely examined, reveals three peaks at 7, 9, and 13 s. In contrast to the input waves, a maximum peak appears in the infragravity wave region, that is, around 40-50 s. Then, to increase the resolution for infragravity waves, data were resampled with $\Delta t = 3$ s after smoothing, and a cross-spectrum analysis was applied.

The power spectra, coherence squared, and phase angle, respectively, for the 11 wave staffs are shown in Figure 9. The left-hand diagram shows the onshore-offshore array attached to the pier, and the middle and the right-hand diagrams are the results from the longshore array. The middle one is the result from the array arranged about 50 m from the shoreline (A, C, G, and E), and the right side is from the array 15-20 m from the shore (B, J, D, and F). In the left-hand diagram,

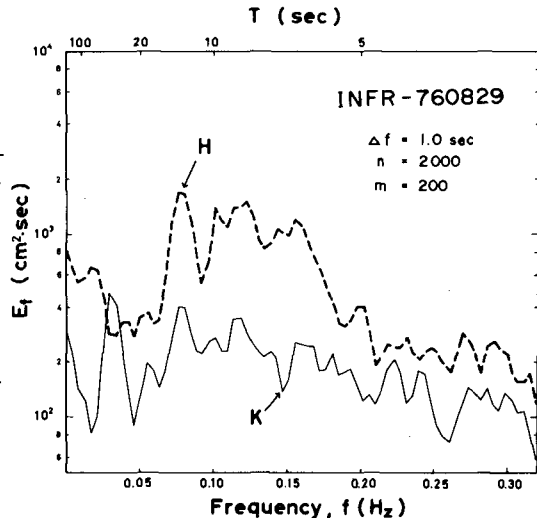


Figure 8. Input wave (H) and swash wave (K) spectra.

Table 1. Nodal lines parallel to the shoreline(INFR-760829).

Peak frequency (Hz)	Wave period T(sec)	Distance of nodal line from shoreline, x(m)			
		n = 1	n = 2	n = 3	n = 4
0.010 (n = 1)	100	90			
0.020 (n = 2)	50	20	100		
0.030 (n = 3)	33	(10)	50	130	
0.039 (n = 4)	26	(6)	30	80	(150)

$\tan\beta = 1/40$, n: offshore modal number, (): inferred.

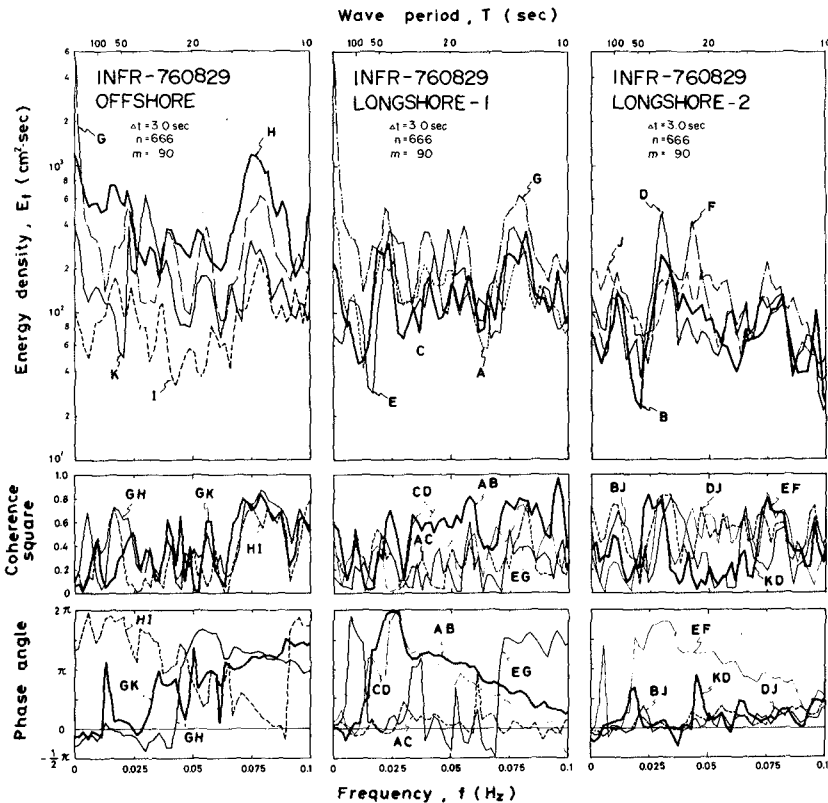


Figure 9. Wave energy density, coherence squared and phase angles for 11 wave staffs.

i.e., the spectrum along the pier, "I" is located the furthest offshore and distant from the surf zone, while "K" is located nearest to the shoreline.

From phase angles, the characteristics of standing waves appear in those waves longer than about 20 s (0.05 Hz). The lowest oscillation occurs in the "G" spectra, which is located along the pier at the mid-surf position. In the power spectrum, about five peaks around 0.01, 0.02, 0.03, 0.04, and 0.05 Hz can be found.

From the phase angles, it is interpreted that each peak is associated with one or two nodal lines parallel to the shore as shown in Table 1. The distance from the shoreline is evaluated from Eckert's (1951) edge wave theory by using a beach slope of $\tan\beta = 1/40$. The distances in parenthesis in the Table indicate inferred nodal lines which could not be confirmed due to the wave staff arrangement. The quantity "n" is an offshore modal number, and each peak frequency corresponds to $n = 1, 2, 3$ and so forth, respectively.

Regarding the nodal lines normal to the shore, proof of edge wave existence can be found in the 0.04 Hz and 0.05 Hz peaks. For lower frequency waves, nodal lines normal to the shore could not be detected due to the narrow distribution of the wave staffs. Huntley (1976) presented the excitation of cut-off low mode edge waves by applying Ball's (1967) edge wave theory for concave beach profile to his field observation. Ball gave a solution for the exponential bottom profile defined as

$$h/h_{\infty} = 1 - e^{-\alpha x} \tag{1}$$

where h is the water depth, x is the distance offshore, and h_{∞} and α are constants determined from the bottom profile. When x tends to infinity, αh_{∞} tends to $\tan\beta$, the beach slope. Defining ν as a peak frequency, ν is simply given as a function of n and bottom profile, that is α and h_{∞} , as shown by Huntley (1976)

$$\nu = \frac{\alpha \sqrt{gh_{\infty}}}{2\pi} \sqrt{n(n+1)} \tag{2}$$

Here, n and g are the offshore modal number and acceleration due to gravity, respectively. Equation (2) was derived from a critical condition of Ball's edge wave excitation, that is, the cut-off mode edge waves. This expression means that if the bottom profile or topogra-

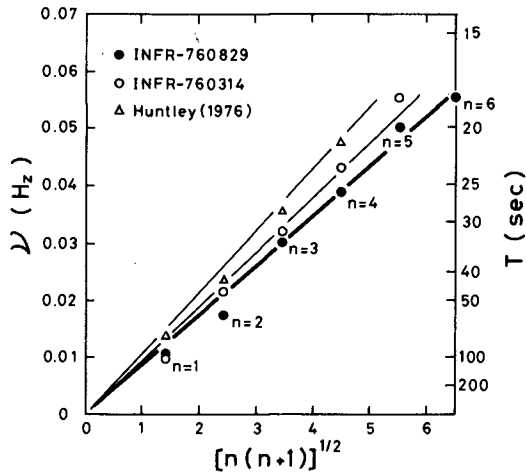


Figure 10. Peak frequency ν verses edge wave modal number n .

graphy were given, the peak frequency of edge waves could be obtained, and also suggests a coexistence of multiple modes of edge waves as suggested in Figure 3.

Figure 10 is a plot of v and n . Also shown in this figure are the infragravity low mode edge waves observed on March, 1976 [Sasaki et al. (1976)] on Ajigaura Beach, as well as Huntley's (1976) results. These results agree well with the empirical fact that in many of our field observations, we have found several minor rip currents between two neighboring major rip currents or, in other words, rip currents are strengthened selectively by the super-position of multiple mode infragravity low mode edge waves. Figure 11 is an example from a 1972 observation on Kujuukuri Coast, east of Tokyo. Very large rip currents developed evenly with a 600 m spacing in the middle part of the stretch, and between them, several minor rip currents are seen.

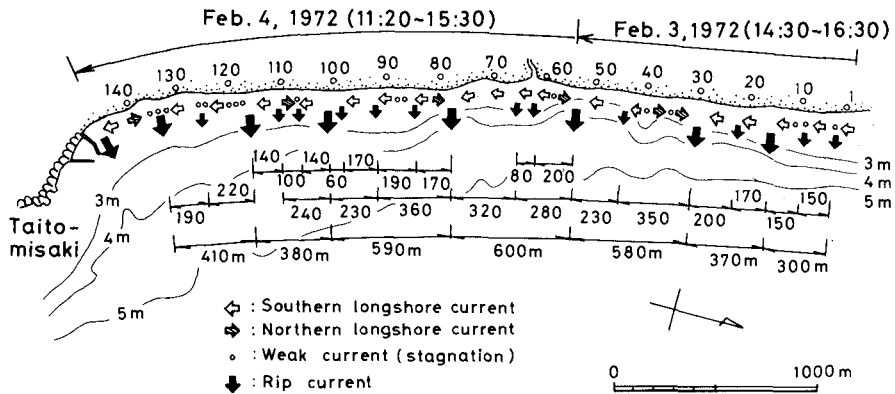


Figure 11. Rip current spacing distribution observed on February, 1972, on southern end of Kujuukuri Coast, Horikawa, Sasaki and Igarashi (1972), Horikawa (1978b).

TRANSFORMATION OF POWER SPECTRUM ACROSS THE SURF ZONE

In the morning of the same day as the above described current and edge wave observation, observation of the onshore-offshore transformation of the power spectrum across the surf zone was performed using 4 wave staffs along the pier, to study the behavior of such infragravity low mode edge waves near the surf zone. Power spectra from 4 wave staffs arranged along the pier, that is, "E", "G", "H", and "I" and plotted in Figure 12. Only "I" is located outside the surf zone, and "E" is located in the swash zone. A very wide spectrum exists outside the surf zone, but in the surf zone higher frequency waves above 0.2 Hz (5 s) are attenuated due to breaking; further, only waves lower than 0.05 Hz (20 s) exist in the swash zone. In contrast with these, waves below 0.05 Hz are not seen outside the surf zone. These infragravity waves are believed to be

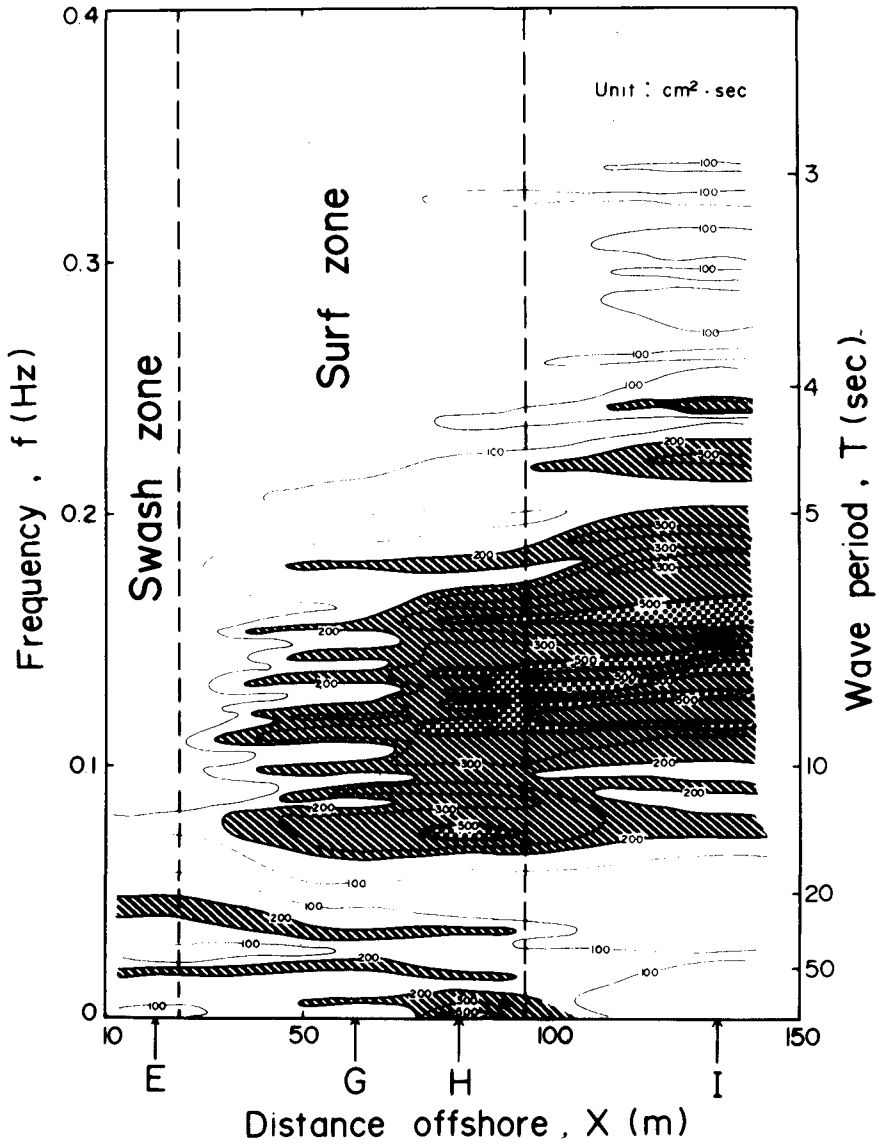


Figure 12. Onshore-offshore wave energy density transformation along the pier.

excited in the surf zone by receiving energy from the gravity waves outside of the surf zone.

CONCEPTUAL MODEL OF THE NEARSHORE CURRENT PATTERN

In conclusion, a conceptual sketch of the nearshore current pattern in the infragravity domain is presented (Fig. 13). Firstly, assuming the existence of multiple mode infragravity edge waves, it is possible to explain in the super-position of major and minor rip currents. Here, a "major" and a "minor" rip current are defined respectively as one which penetrates the breaker line from the surf zone and one which is totally confined to the surf zone. The shapes of the corresponding rip heads differ as illustrated. The number of minor rip currents contained between neighboring major rip currents depends on the frequency of the modes. The major three nodal lines parallel to the shore could be termed as

- 1) "breaker node"
- 2) "longshore current node", and
- 3) "swash node"

since the breaker node appears around the breaker line, the longshore current node appears to correspond to the location of the main stream of the longshore current and the swash node appears to be located in the swash zone.

In our experience, waves break close to the shoreline in the lee of a rip current, because the rip channel is deep and does not satisfy breaking criteria under ordinary wave conditions. Thus the plan shape of a shoreline behind a rip channel is somewhat embayed and has a steep foreshore slope. Two longshore currents from opposite directions meet almost midway in the surf zone resulting in a rip current, and behind this a stagnant zone is produced as shown in the Figure.

Figure 14 gives a more general conceptual model of nearshore current patterns for the three domains [Sasaki(1974), and Sasaki and Horikawa (1975)] combined with the plan view of Harris(1969) and the cross sectional view of the surf zone of Sasaki, Horikawa and Hotta(1976). These three conceptual models can be connected in a probabilistic sense. However, the model proposed here appears to be rather static. From the recent morphodynamic results of Wright, Thom, and Chappel(1978), and Short(1978), various dynamical transition patterns are suggested for the instability domain or asymmetrical cellular circulation system between two typical current patterns, i.e., the infragravity domain and the edge wave domain.

Both domains can be connected with their beach types or stages as in Table 2. To link with the beach type evolution models of Wright et al. (1978) and Short(1978) and to clarify current field associated with them would produce fruitful understanding of the precise coupling mechanism between edge waves, currents and beach topography.

Table 2. Comparison of terminology on wave, current and beach types

Sasaki(1974)	Guza and Inman (1975)	Wright et al. (1978)	Short(1978)
Infragravity domain	Dissipative system	Type 1	Stage 6
Edge wave domain	reflective system	Type 6	Stage 1

CONCEPTUAL MODEL OF NEARSHORE CURRENT IN INFRAGRAVITY DOMAIN

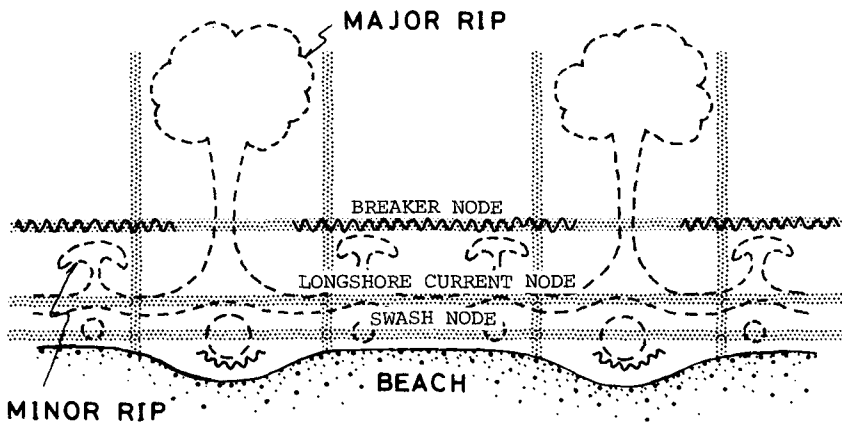
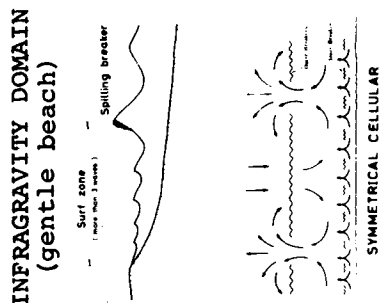
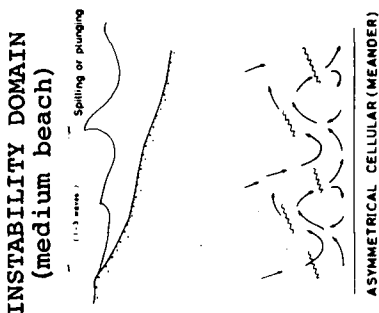
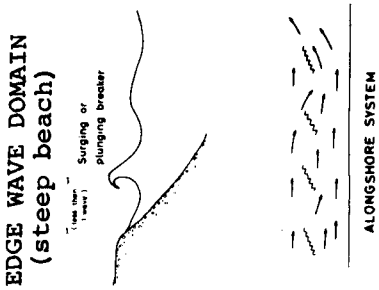


Figure 13. Conceptual model of nearshore current in infragravity domain.



BREAKER PATTERN,
Sasaki et al. (1976)

NEARSHORE CURRENT PATTERN, Harris (1969)

RIP CURRENT SPACING,
Sasaki (1974)

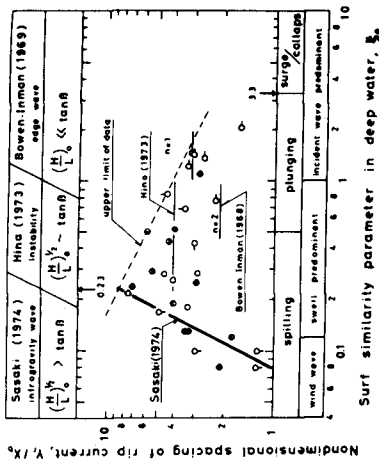


Figure 14. Conceptual model of three typical nearshore current patterns

ACKNOWLEDGEMENTS

The field observations of the nearshore current pattern fluctuation and infragravity low mode edge waves were supported by the Science Research Fund of the Ministry of Education under the name of the second author, and the field observation of the power spectrum transformation was partly supported by the Public Works Research Institute(PWRI), Ministry of Construction under contract with INA Civil Engineering Consulting Co., Ltd., Tokyo.

The authors acknowledge the permission given by the PWRI for reproduction of the data. Also thanks are due for proofreading by Dr. Nicholas C. Kraus, field operations and drawings by Mr. Susumu Kubota, computations by Mr. Sohichi Harikai, and typing by Miss Michiyo Itoh.

REFERENCES

- Ball, F. K.(1967): Edge waves in an ocean of finite depth, Deep Sea Res. Oceanogr. Abstr., 14, 79-88.
- Battjes, J. A.(1974): Surf similarity, Proc. 14th Coastal Eng. Conf., 466-480, Copenhagen.
- Birkemeier, W. A. and R. A. Dalrymple(1975): Nearshore currents induced by wind and waves, Proc. Modeling'75, ASCE, San Francisco, 1062-1081.
- Bowen, A. J.(1967): Rip currents, Ph.D. Thesis, Univ. of Calif., San Diego.
- Bowen, A. J. and D. L. Inman(1969): Rip currents, 2. Laboratory and field observations, J. Geophys. Res., 74(23), 5479-5490.
- Bowen, A. J. and D. L. Inman(1971): Edge waves and crescentic bars, J. Geophys. Res., 76, 8662-8671.
- Bowen, A. J. and R. T. Guza(1978): Edge waves and surf beat, J. Geophys. Res., 83(C4), 1913-1920.
- Chappel, J. and L. D. Wright(1978): Surf beach bar-trough resonance and coupled periodic morphology, Summaries 16th Conf. Coastal Eng., Hamburg., Paper No. 24.
- Dalrymple, R. A.(1975): A mechanism for rip current generation on an open coast, J. Geophys. Res., 80(24), 3485-3487.
- Dalrymple, R. A.(1978): Rip currents and their genesis, Summaries 16th Conf. Coastal Eng., Hamburg, Paper No. 140.
- Eckart, C.(1951): Surface waves in water of variable depth, S10 Wave

- Rep., 100 Ref. 51-12, 99, Scripps Inst. Oceanogr., La Jolla, Calif..
- Fujinawa, Y., K. Okada, and I. Watabe(1977): Some properties of surf beat, Part 2, the Report of the National Research Center for Disaster Prevention, No. 17, National Research Center for Disaster Prevention, Hiratsuka, Kanagawa Pref., 111-166 (in Japanese).
- Guza, R. T. and D. L. Inman(1975): Edge waves and beach cusps, J. Geophys. Res., 80, 2997-3012.
- Guza, R. T. and E. B. Thornton(1978): Longshore current variability, Summaries 16th Conf. Coastal Eng., Hamburg, Paper No. 82.
- Hansen, U. A.(1978): Wave set-up in the surf zone, Summaries 16th Conf. Coastal Eng., Hamburg, Paper No. 27.
- Harris, T. F. W.(1967): Field and model studies of nearshore circulations, Ph.D. Thesis, Univ. of Natal, South Africa, 188.
- Harris, T. F. W.(1969): Nearshore circulation, Field observations and experimental investigations of an underlying cause in wave tanks, Symposium on Coastal Engineering, South Africa.
- Hashimoto, H. and O. Yamaguchi(1978): On long period waves near the surf zone, Proc. 33rd. Annual Conf. JSCE, II-402, 776-777 (in Japanese).
- Holman, R. A., D. A. Huntley, and A. J. Bowen(1978): Infragravity waves in storm condition, Summaries 16th Conf. Coastal Eng., Hamburg, Paper No. 11.
- Horikawa, K., T. Sasaki, and H. Igarashi(1972): Marine recreation and its environment, Proc. 19th Conf. on Coastal Eng. in Japan, 83-91, (in Japanese).
- Horikawa, K.(1978a): Nearshore current treatments and their applications to engineering problems, Proc. 4th Conf. on Port and Ocean Eng. in Arctic Conditions, Memorial Univ. of Newfoundland, 84-114.
- Horikawa, K.(1978b): Coastal Engineering, Univ. of Tokyo Press, Tokyo, 402.
- Huntley, D. A.(1976): Long-period waves on a natural beach, J. Geophys. Res., 81, 6441-6449.
- Huntley, D. A., R. T. Guza, and A. J. Bowen(1977): A universal form for shoreline run-up spectra?, J. Geophys. Res., 82(18), 2577-2581.
- Huntley, D. A. and A. J. Bowen(1978): The 3 dimensional flow field on a natural beach, Summaries 16th Conf. Coastal Eng., Hamburg, Paper No. 28.

- Liu, P. L-F. and C. C. Mei(1974): Effects of a breakwater on nearshore currents due to breaking waves, Ralph M. Parsons Lab. Rep., No. 192, MIT.
- Meadows, G. A.(1978): Time dependent fluctuations in longshore currents, Proc. 15th Conf. Coastal Eng., Honolulu, 660-680.
- Mizuguchi M. and K. Horikawa(1976): Physical aspects of wave-induced nearshore current system, Abstracts of 15th Coastal Eng. Conf., Honolulu, Hawaii, 798-800.
- Nakamura, T., K. Horikawa, T. O. Sasaki, and Y. Jujinawa(1978): Currents in and near the surf zone on Ohkuma Beach, Fukushima, Japan, Proc. 25th Conf. on Coastal Eng. in Japan, 465-469, (in Japanese).
- Noda, E. K.(1972): Rip-currents, Proc. 13th Coastal Eng. Conf., 653-668.
- Sasaki, T.(1974): Field investigations of nearshore currents on a gently sloping bottom, Doctorial thesis in Civil Eng., Univ. of Tokyo, 240, (in Japanese); English edition is available from Nearshore Environment Research Center, Tech. Rep. No. 3, TR-77-2, May, 1977.
- Sasaki, T. and K. Horikawa(1975): Nearshore current system on a gently sloping bottom, Coastal Eng. in Japan, 18, 123-142.
- Sasaki, T., K. Horikawa, and S. Hotta(1976): Nearshore current on a gently sloping beach, Proc. 15th Conf. Coastal Eng., Honolulu, 626-644.
- Short, A. D.(1975): Multiple offshore bars and standing waves, J. Geophys. Res., 80(27), 3838-3840.
- Short, A. D.(1978): Sequential model of beach changes, Summaries 16th Conf. Coastal Eng., Hamburg, Paper No. 60.
- Sonu, C. J. (1972): Field observation of nearshore circulation and meandering currents, J. Geophys. Res., 77(18), 3232-3247.
- Wright, L. D., B. G. Thom, and J. Chappel(1978): Morphodynamic variability of high energy beaches, Summaried 16th Conf. Coastal Eng., Hamburg, Paper No. 35.

CHAPTER 46

COMPARISON OF MODEL AND OBSERVED NEARSHORE CIRCULATION

by

James H. Allender, John D. Ditmars, Wyman Harrison
and Robert A. Paddock*

ABSTRACT

Results from a two-dimensional numerical model for nearshore circulation induced by waves and wind are compared with observations made during two storms at a beach on Lake Michigan. Model-input data include bathymetry, offshore wave characteristics, wind histories, and local water-level changes. The predicted locations of the breaker zone are in rough accord with those observed during the storms. Data for comparison with model results consist of wave and current observations across the surf zone, especially those acquired by using a towed, instrumented sled. The comparisons show that the model often predicts peak currents near the breaker zone quite well, but underestimates the decay of wave height and the strength of longshore currents across the surf zone. Wave breaking on the bar-trough beach structure prevalent in this study apparently is not well represented by the model. An improved breaking criterion, treatment of breaking waves as traveling bores, and inclusion of horizontal mixing of momentum might add to better simulation of surf-zone currents.

1. INTRODUCTION

Numerous efforts to observe nearshore circulation have been undertaken and reported, and recently, numerical models to simulate nearshore circulation have been developed and described. Seldom, however, have attempts been made to evaluate model simulations against observational data. Two major field studies at a beach on Lake Michigan were planned to provide data for the assessment of the simulative capabilities of a two-dimensional numerical model for nearshore circulation induced by wind and waves. The first field study was scheduled to take place during a fall storm, while the second study was scheduled for a spring storm. The second study was planned to provide an independent data set and to allow for changes in observational techniques suggested by analysis of the data from the first study and application of a model to those conditions.

The numerical model considered in this study was developed by Birkemeier and Dalrymple (1975). It is based on a finite-difference solution of the vertically-averaged equations of motion which are averaged in time over a wave period producing radiation stress terms. Given bottom topography, deep-water wave characteristics, and wind, the model simulates in two dimensions (on a relatively fine horizontal grid), the

*Energy and Environmental Systems Division, Argonne National
Laboratory, Argonne, IL, 60439, U.S.A.

nearshore circulation field, the wave field, and mean water surface elevations. Wave heights and directions in the computational grid are determined by the refraction procedure of Noda *et al.* (1974), that includes wave-current interaction. The merits and failings of the model are discussed in terms of extensive comparisons with the wave and current data acquired in this study.

2. MODEL DESCRIPTION

The numerical model used in this study was described in detail by Birkemeier and Dalrymple (1975). The salient features of the model and the modifications made to it for the present application are noted here.

An explicit finite-difference scheme was used to solve the vertically-integrated equations of motion including radiation stresses. The wave refraction part of the model includes wave-current interaction and was described by Noda *et al.* (1974). No-flow conditions were imposed at the beach and at the last offshore row of the computational domain. Periodic boundary conditions for all variables were imposed at two remaining boundaries, thus defining a periodic length of beach.

Quadratic bottom friction was represented as the product of water density, a friction coefficient, the magnitude of the velocity vector, and the velocity vector itself. This friction formulation was modified to include numerical integration over a wave period of the total velocity vector (orbital wave motion and mean current). This modification resulted in more realistic values of bottom friction for large incident wave angles and for mean currents that were the same order of magnitude as the orbital velocities (Liu and Dalrymple, 1978). The friction coefficient is the only free parameter in the model. Its value was 0.01 for most cases. A dissipation term was added in the equation for wave height as the time average of the product of bottom shear stress and orbital wave velocity. This dissipation term was made zero wherever breaking was predicted by the model. The breaking criterion was a modified Miche formula in which breaking wave height was proportional to the hyperbolic tangent of water depth divided by wavelength at breaking (Noda *et al.* 1974). The model also allowed for flooding of dry beach to occur as a result of set-up and changes in lake level.

In summary, the model formulation included wave refraction, wave-current interaction, anisotropic bottom friction, wave set-up, wind effects, and coastal flooding. An improved representation for bottom friction was used and wave height dissipation outside of breaking areas was added. Finally, the model was applied to a much more complex nearshore environment than in the developmental study of Birkemeier and Dalrymple (1975).

Model application requires site-specific input data. These include deep-water wave characteristics, viz., wave height, period, and direction, detailed bathymetry for the given study area, local still-water-level changes during the study period, and wind data. The

simulated variables (nearshore circulation, wave field, and mean-water-level changes) require other data for model evaluation. These include primarily wave and current measurements in the surf zone. The methods for acquiring all of these data and specific examples of processed information are discussed in the next section.

3. FIELD PROGRAM

The study site covers 0.5 km of sand beach near Zion, Illinois, along the western shore of Lake Michigan. Inland of the beach are low marshlands and dunes that rise about 3 m above lake level. The lake bottom immediately offshore is composed mainly of sands and silty sands. Portions of the sandy beach contain coarse pebbles that are often exposed near the waterline. The shoreline is almost straight in the study area. Longshore sand bars lead to surf zone widths of 40-60 m, typically, and outer bars often result in another breaker zone about 150 m offshore.

The first major field study was conducted during a storm in November, 1977. This study was designed specifically to obtain the required model-input data and to gather data on waves and on currents in the surf zone for comparison with model results. Figure 1 shows a plan view of the nearshore study area, which extends about 0.3 km lakeward. Offshore wave information for the model was obtained from a Wave-Rider buoy moored in 20 m of water about 4 km offshore. Wave data at a transitional depth were obtained from a bottom-mounted pressure cell fixed in 4.4 m of water at the outer extent of the nearshore study area. The cell also was equipped with an integrated output to allow measurement of local still-water-level changes throughout the storm.

Detailed bathymetric surveys were conducted before and after the storm to provide depth data for the model and to assess net changes in bottom topography. Bottom soundings were made on a 20 x 20 m grid using digital, position/depth recording equipment aboard an Argonne survey boat. Standard surveying techniques were used to collect beach topographic data on a 5 m (offshore) x 20 m (alongshore) grid in the region from the storm berm to about 60 m lakeward of the still water line.

Waves across the surf zone were measured with four helically-wound, resistance-wire wavestaffs. The staffs were placed on a line perpendicular to shore in 0.5, 0.75, 1.5, and 2.5 m of water with 1.2 m of their 2-m active element above the still water level. The outermost staff was about 70 m offshore. Longshore-current profiles were measured by using a towed sea sled similar to the one developed by Teleki *et al.* (1975). As shown in Fig. 1, the sled traversed the surf zone on a cable-winch system. The sled was equipped with two Bendix B-10, ducted-impeller current meters, placed at 0.5 and 1.0 m above the bottom of the sled and oriented approximately shore-parallel. The signals from the current meters were electronically averaged over several wave periods. A 4-m wavestaff also was mounted on the sled to provide additional data on waves across the surf zone. In addition, a 10-m meteorological tower was erected on the beach to measure wind speed and direction, and air temperature; steel reinforcing bars (rebars) were jettied

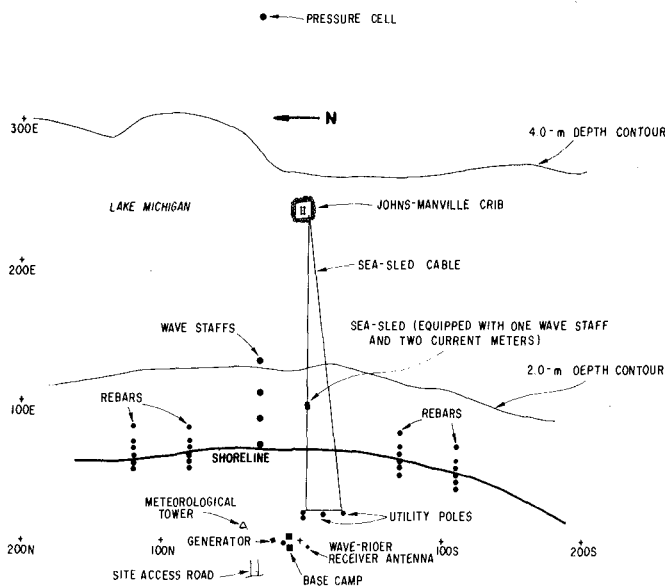


Fig. 1. Plan View of Experiment Site and Horizontal Coordinate System.

into the beach face along four separate transects to allow depth profiling during the storm; dye tracking in the surf zone was used to provide additional information on currents; and aerial photography was conducted during the daylight hours of the storm to provide estimates of wave direction.

Sets of observational data were gathered every three hours over the 27-hr storm period. Each set of data contained: 5-min records taken at each of six locations across the surf zone with the sled-mounted current meters and wavestaff, 5-min records taken with the fixed wavestaffs and the pressure cell when the sled was at the beginning and end of its traverse; and ancillary data taken using the other equipment described above. All wave and current data were recorded on strip charts and subsequently digitized to allow computer analysis. Hourly-averaged wind speeds ranged from 9-15 m/s during the storm. Off-shore significant wave heights and periods varied from about 0.5-2.5 m and 3.8-6.5 s, respectively. Significant breaker heights varied from 0.5-1.5 m, incident breaker angles were 20-30° off normal (ESE), and both spilling and plunging breakers were present. Longshore currents near the breaker line varied from about 0.6-1.5 m/s. The spatial

distributions of longshore current across the surf zone was highly variable. Significant bar movement occurred as a result of the storm, and depth changes as great as 0.8 m were found in the extreme nearshore area.

The second major field study was conducted in April, 1978. It provided an independent data set and allowed for improved observational techniques. The experimental set-up and procedures were similar to those in the first study with the following notable exceptions. The fixed wave staffs were placed outside the breaker zone in a directional array, although only minimal information was acquired due to damage incurred early in the storm. Additional rebar transects were installed. A multi-channel digital data logger was used to record all of the instrument data on magnetic tape at 0.1-s intervals, thus eliminating the need for strip chart recorders. Most data records were still of 5 min duration, but some 17-min wave records were acquired at 3-hour intervals during the storm. For most of the experiment the sled-mounted current meters were oriented perpendicular to each other, thus allowing measurement of the current vector during the sled's transits of the surf zone. Finally, the sled was equipped with a dye-dispensing system to allow the introduction of patches of dye into the surf zone.

Figure 2 shows the pre-storm bathymetry inferred from shipboard soundings and from standard surveying techniques. The beach is characterized by a steep face, a persistent longshore trough, and a somewhat disorganized bar structure that repeats itself on the order of several hundreds of meters. Depth contours beyond 2.0 m are highly convoluted, although a pattern of outer bars exists about 150 m offshore. Depth contours greater than 4.0 m tend to be much more regular.

Observational data during the storm again were gathered at approximately 3-hr intervals over a 24-hr period. Hourly-averaged wind speeds ranged from 7-16 m/s. A summary of offshore (Wave-Rider buoy) and transitional-depth (pressure cell) wave data is given in Fig. 3. Significant wave heights and periods measured by the Wave-Rider buoy (4 km offshore) varied from about 1.25-2.25 m and 4.5-6.3 s, respectively. Significant wave heights as measured by the pressure cell at the outer extent of the nearshore study area (0.35 km offshore) varied from about 0.60-1.25 m before that instrument failed due to storm damage. Wave approach was very oblique (70° off normal incidence, NNE) with breaking angles as large as 45° off normal. Figure 4 summarizes current-meter data acquired by the towed sled during nine different transits of the surf zone. The following specific points should be noted: 1) peak currents near the breaker line ranged from 1.0-1.8 m/s; 2) on/offshore flow was small; 3) the differences between currents measured at 0.5 and 1.0 m above the bottom were small (cycles 1-3); and 4) a relatively strong flow was observed across the entire surf zone in most cases, probably as a result of the bar-trough structure of the beach (note inset showing depth profiles along sled path). Most of the data to be discussed below are taken from this second study, although they are generally representative of the first study, too.

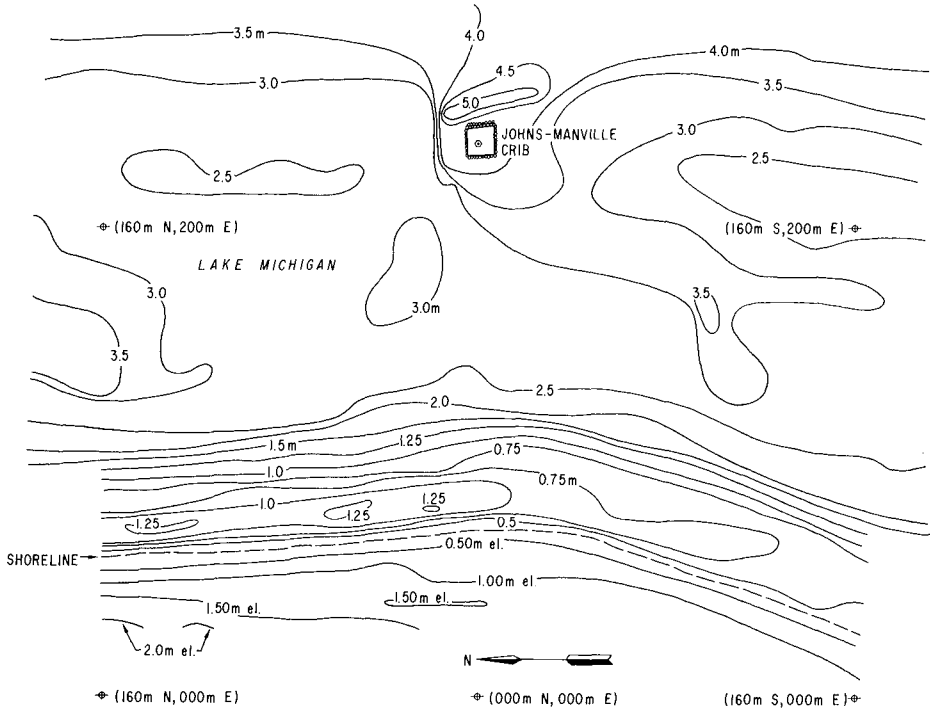


Fig. 2. Pre-storm Bathymetry of Nearshore Study Area, April, 1978.

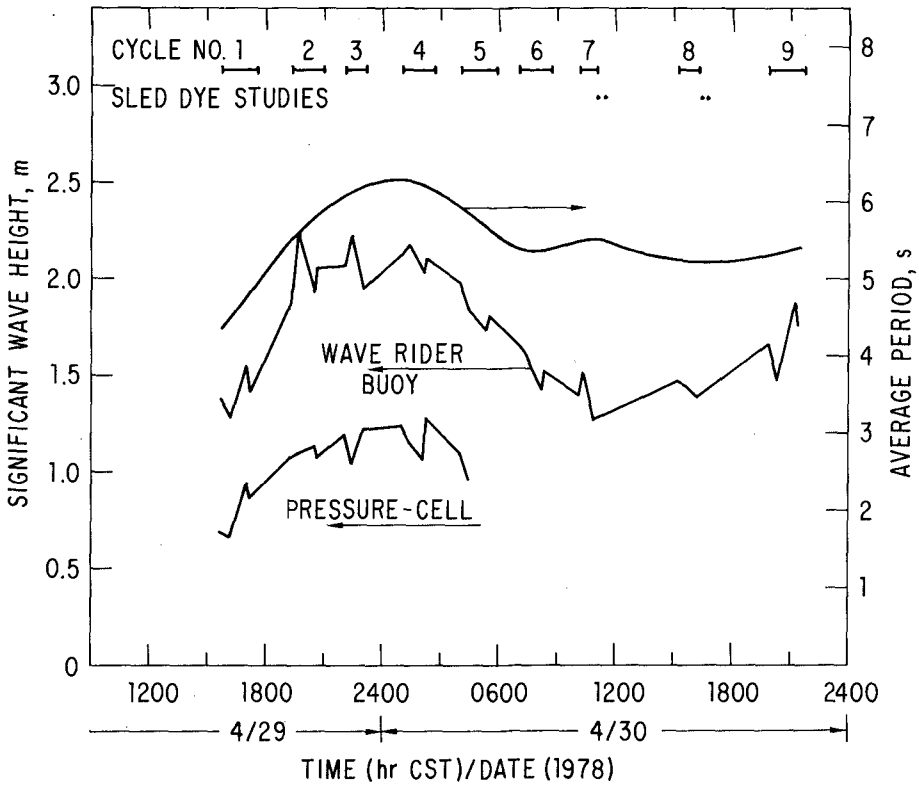


Fig. 3. Offshore (Wave-Rider buoy) and Transitional-Depth (pressure cell) Wave Data, Second Field Study. Data Acquisition Periods (Cycles No. 1-9) are Indicated.

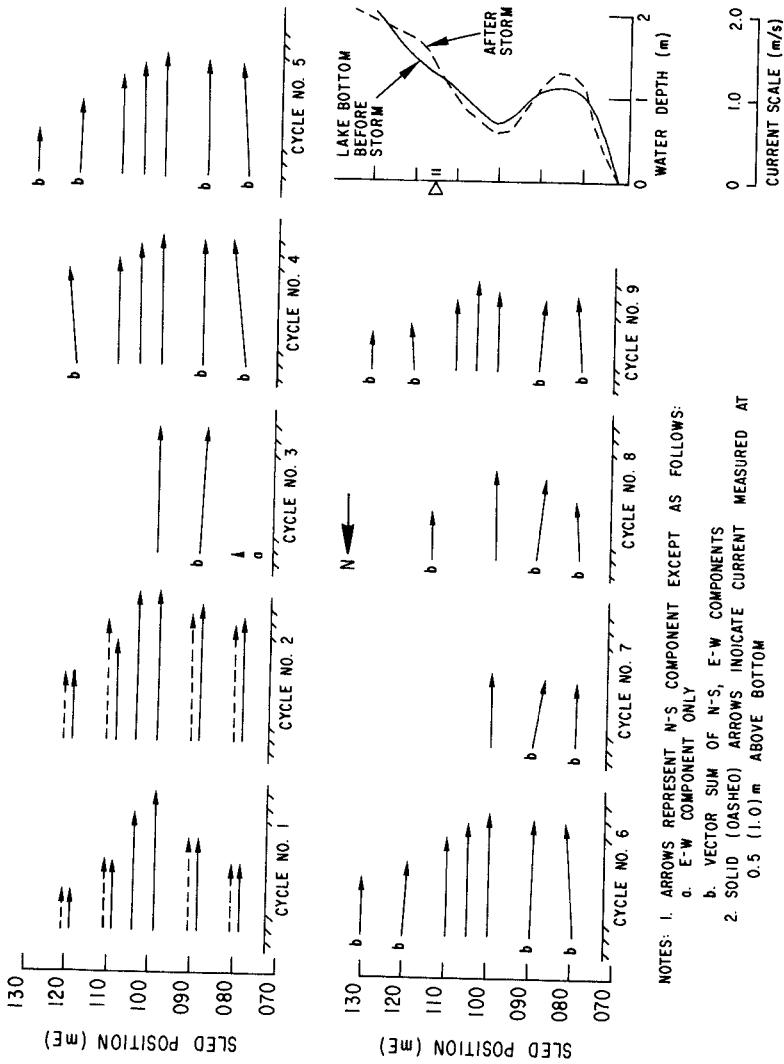


Fig. 4. Current-Meter Data Across Surf Zone Acquired with Towed Sled, and Water Depth Along the Sled Path, April 1978 Study.

4. MODEL APPLICATION

a. Adaptation to Study Site

Model-input data gathered during the fall and spring field efforts were used to make a site-specific application of the numerical circulation model. The alongshore grid spacing was chosen to be 10 m, while a 5-m spacing was used in the offshore direction to provide the necessary resolution of typical depth profiles. Still-water depths from the bathymetric survey were specified for this grid and were adjusted for calculations made during the storm with local lake-level data from the pressure cell. A conservative time step of 0.5 s was selected based on the linear stability criterion, and a quasi-steady model solution was found for given wind and wave conditions by integrating for 1000 time steps. Root-mean-square (rms) wave heights inferred from the Wave-Rider data were used to drive the model. The incident wave field was increased linearly from zero to full strength over the first 100 iterations to minimize water-level oscillations at the natural frequency of the basin defined by the model topography. The total energy and water-level fluctuations were monitored for as many as 2000 iterations in some numerical experiments before 1000 steps was chosen as a good compromise between a quasi-steady solution and computational expediency. The offshore extent of the model was about 200 m, which was far enough to include the outer bars. The effect of model alongshore extent (and the imposed periodicity) on the model currents near the center of the grid is shown in Fig. 5. The sensitivity of the model currents to alongshore extents greater than about 200 m was found to be small compared to changes produced by uncertainties in other model parameters. An extent of 260 m was chosen for most numerical experiments.

Deep-water wave angle was found to be an important parameter that was difficult to estimate accurately based on the observed data. The model, as formulated, used Snell's law and the given deep-water wave characteristics to estimate incident wave height and direction at the offshore extent of the model grid. The following procedure was adopted to find consistent estimates of offshore wave angle: depth contours were assumed parallel from deep water to transitional depth (5 m); standard refraction and shoaling calculations were used to find the deep-water wave angle that would transform the measured deep-water wave height into the wave height measured at transitional depth. The deep-water wave angles calculated by this procedure were found to bear no simple relation to the contemporary wind directions. However, the resulting wave angles at transitional depth did agree with those inferred from the limited aerial photography conducted during the studies, within the errors inherent in these measurements.

Various numerical experiments were performed to test the sensitivity of the model results to small changes in wave height, wave angle, still water level, and friction coefficient. Discussion of these tests and selected comparisons with observed waves and currents are given in the next subsection.

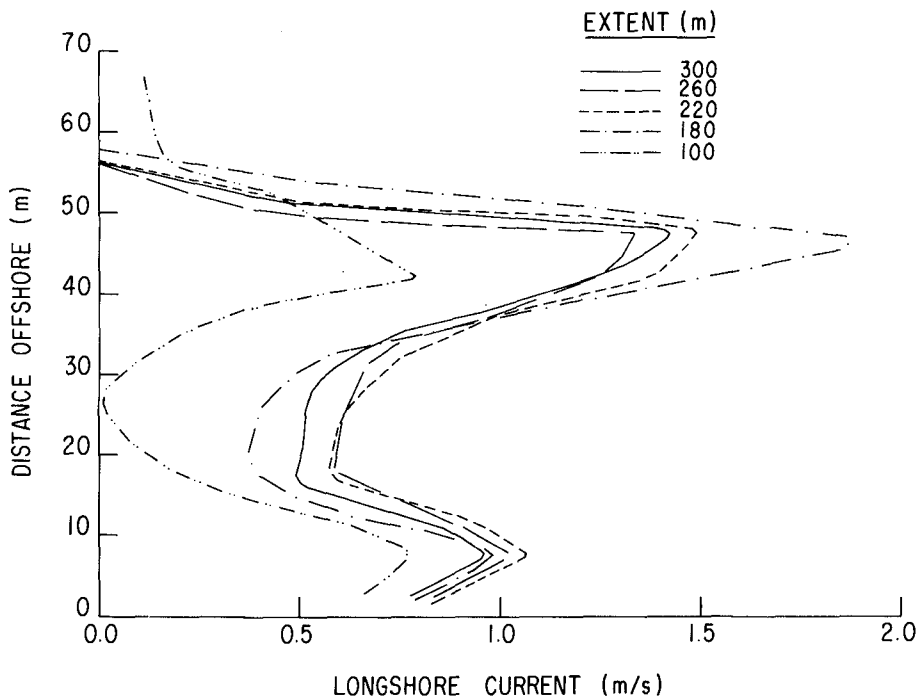


Fig. 5. Effect of Variation of the Model Alongshore Extent on Model Current Profiles (along computation row corresponding to 000 N).

b. Comparisons with Observed Data

Two-dimensional simulations of waves and currents were generated for many of the different wind and deep-water wave conditions observed during the field program. As stated previously, rms wave heights were used to drive the model. Figure 6 is a representative plot of the velocity field predicted by the model, subject to a 1.44-m wave field (5.3 s period) approaching from 73° off normal incidence. A wind of 15 m/s at 80° off normal also was acting, and local still-water level had risen about 0.2 m above the level assumed for the depths given in Fig. 2. The offshore distance in Fig. 6 represents about one-third of the total model extent. The strongest currents are predicted just inside the breaker zone (40 m offshore) and in the trough region (10 m offshore). The overall pattern is highly two-dimensional and the effects of the inner bars are quite apparent (Fig. 2).

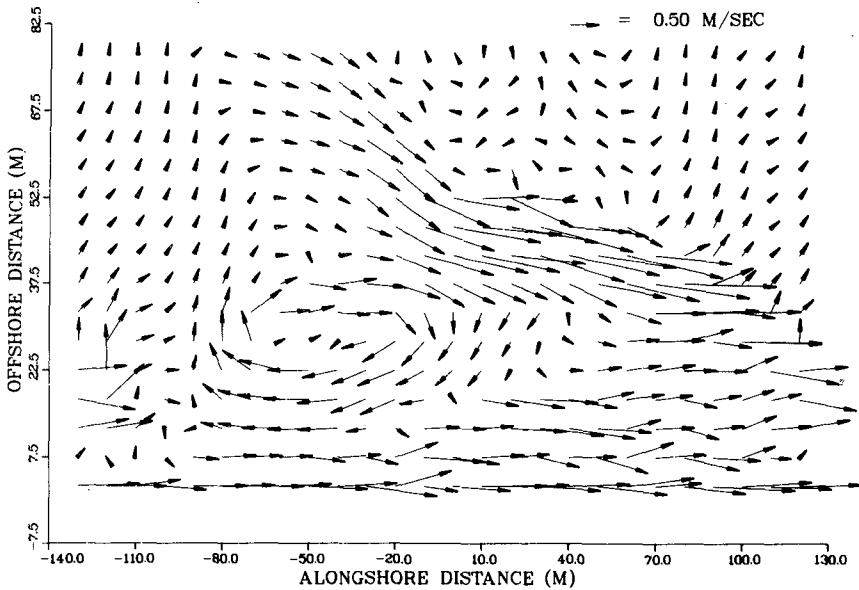


Fig. 6. Model Velocity Field for Second Storm Bathymetry, 1.44 m and 5.3 s Deep-Water Waves from 73° Off Normal and 15 m/s Winds from 80° Off Normal (NNE). (Offshore coordinate stretched for clarity.)

Comparisons of model and observed variables are presented in Figs. 7-11, for observational data acquired during six different transits of the surf zone with the towed sled. Profiles of the alongshore component of model currents at two adjacent rows in the grid are shown in Fig. 7a along with current-meter data acquired from the sled (along 000 N). The model results do not show high variability between adjacent rows. Observed current speeds outside the breaker zone (60-70 m) are much stronger than those in the model. However, other contemporary current studies in the lake, outside the surf zone, showed average lake currents of 0.2-0.3 m/s. It is unlikely that the model boundaries represent a periodic segment of the lake itself, and thus, it is expected that inclusion of lake currents in the model would improve comparisons outside the breakers without significantly changing computed results inside the breakers. Figure 7b shows model and observed wave heights, indicating that the height near breaking is in close agreement for this case, although the heights inside of the breaker zone are somewhat over estimated.

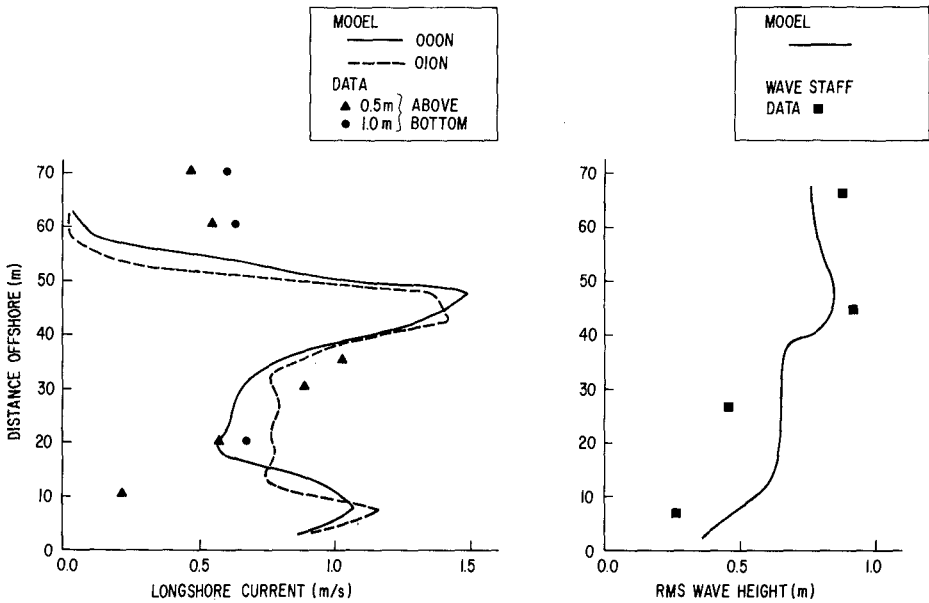


Fig. 7. Comparison of Model and Observed Current Profiles (a) and Wave Heights (b). Model Results for Adjacent Computational Rows are Shown in (a).

Changes in wave climate during the time required for the sled to traverse the surf zone (30-45 min) lead to significant changes in the location of the breaker zone predicted by the model. Figure 8a shows the measured currents for a particular sled transit and the model longshore current profile resulting from the observed wave conditions at the beginning (Case A) and end (Case B) of that transit. The location of the breaker zone in the model shifts about 10 m between these two cases, although model currents inside of the breaker zone are essentially unchanged.

Smaller uncertainties in model-input data result in better agreement with observations for some occasions during the study. Figure 8b gives comparative results for an occasion when wave angle is known with more certainty due to the availability of aerial photos, model topography (based on post-storm surveys) is more likely representative because these current data were acquired near the end of the storm, and the wave climate is less severe with little or no breaking over the trough region. The combination of these conditions appears to result in better agreement between model and observations inshore of the breaker zone than in other comparative cases.

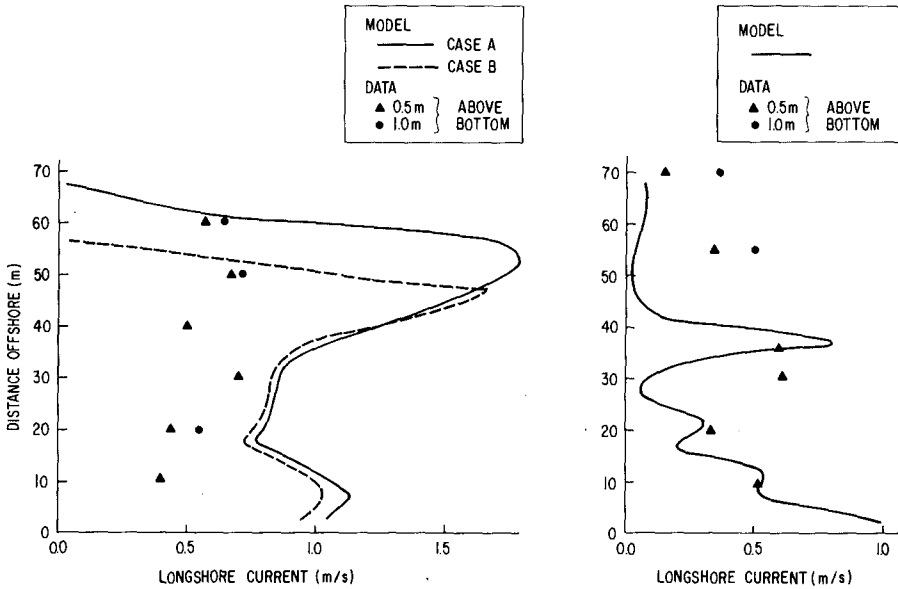


Fig. 8. Comparison of Model and Observed Current Profiles for Different Wave Climates at the Beginning (Case A) and End (Case B) of a Sled Transit (a) and for a Less Severe Wave Climate (b).

The model seems to underestimate the *difference* between wave heights near breaking and heights inshore of the breaker zone as evidenced in Fig. 9b. These wave height discrepancies contribute in part to a model current profile that is more sharply peaked than the observed data profile (Fig. 9a). Several numerical experiments were tried in this case and in others to alleviate these discrepancies. Small changes in incident wave angle ($10-15^\circ$) led to 30% or greater changes in calculated wave heights near shore (for large incident angles), but current profile shapes were essentially unchanged. Model lake current profiles also were largely unaffected by moderate changes in lake level (0.3 m) and changes in the model friction coefficient. Model friction might be adjusted to effect agreement between observed and model peak currents. However, discrepancies between observed and model peak currents could also be accounted for by the discrepancies between observed and model wave heights near breaking. Therefore, fine adjustments in the value of the friction coefficient appear unjustified.

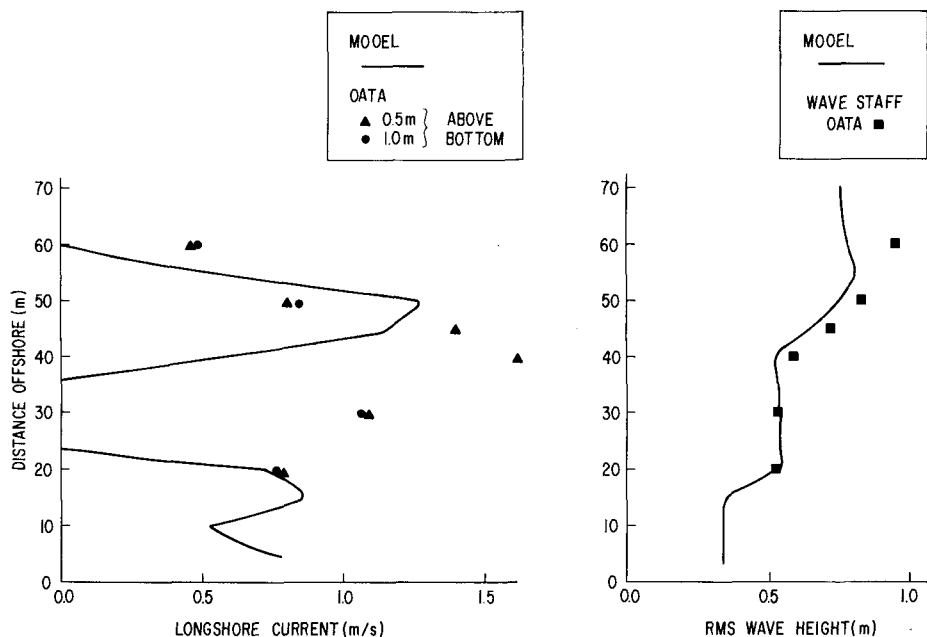


Fig. 9. Comparison of Model and Observed Current Profiles (a) and Wave Heights (b). Model Underestimates Differences between Wave Heights Near Breaking and Heights Inshore of Breaker Zone (b) Resulting in Sharply Peaked Model Current Profiles (a).

A further example of the underestimate of wave height decay in the surf zone model is shown in Fig. 10b. For this case, the observations indicate about a 50% reduction in wave height across the surf zone, whereas model heights decay only about 25%. Again model current profiles (Fig. 10a) deviate significantly from observations, although peak currents agree quite well. The proportionality constant in the model breaking criterion was varied over wide limits in an attempt to better imitate the main features of the observations. In effect, the ratio of breaking wave height to mean-water depth at breaking was varied from 0.65 to 0.95. Results were quite different, of course, but were no more or less in agreement with observations than the results shown here.

In Fig. 11 a final comparison of waves and currents reaffirms the previous statements. Observed currents are relatively strong across the surf zone in contrast to the model results (Fig. 11a). This is due in part to the fact that the model does not predict the observed breaking over the trough region (20-30 m offshore) along the sled path. Observed wave heights suggest that considerably more energy is extracted from the wave field in this region than predicted by the model.

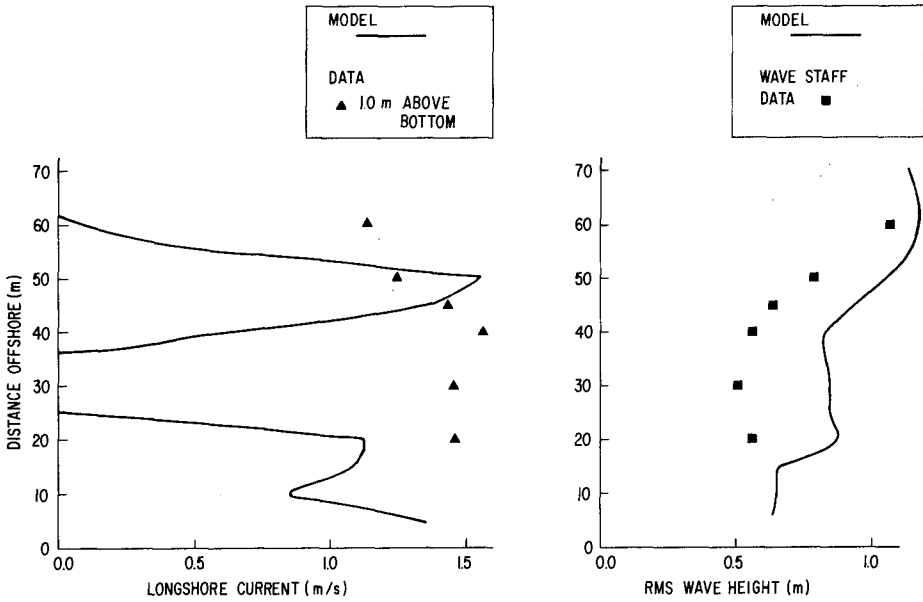


Fig. 10. Sharply Peaked Model Current Profiles (a) Result From Underestimation of Wave Height Decay (b) Across the Surf Zone.

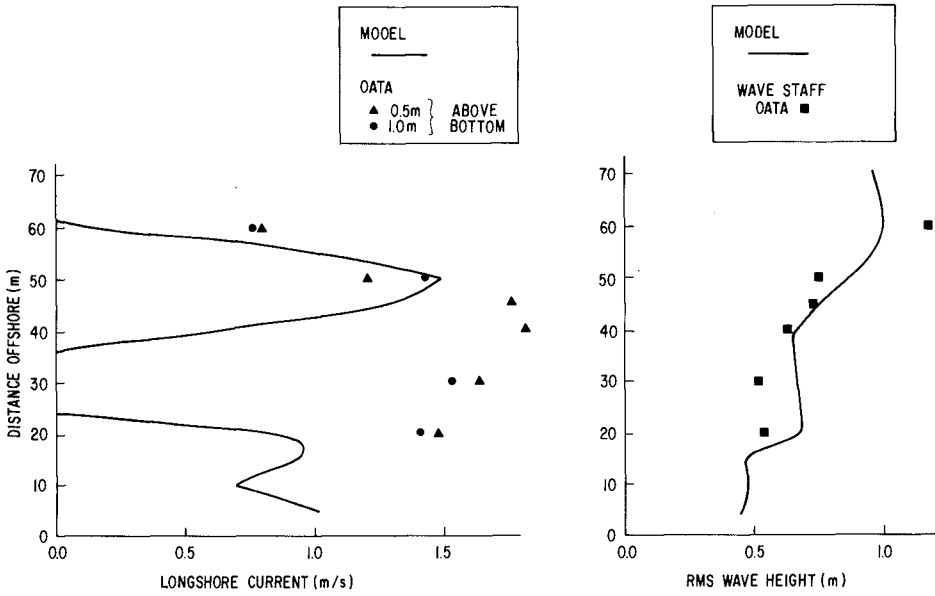


Fig. 11. Additional Comparisons of Model and Observed Current Profiles (a) and Wave Heights (b) Suggest That More Energy is Extracted from the Wave Field Inshore of the Breaker Zone Than the Model Predicts.

5. SUMMARY

New data on waves and currents in the surf zone during two storms were collected. Extensive comparisons were made between these data and results from a state-of-the-art, two-dimensional, numerical model for near-shore circulation. Model current fields showed a highly two-dimensional pattern for all cases that were studied. The tracking of dye packets and relatively large dye clouds in the surf zone also revealed a two-dimensional structure with some regions of stagnant flow and others with strong on/offshore flow. Significant variations in model results were caused by uncertainties in model-input data, such as wave angle, topography, and still-water level. These inherent variations preclude the quantification of the extent to which the model results match the observations. Comparisons do show, however, that the model often predicts peak currents quite well, but underestimates the decay of wave height and also the strength of longshore currents inside of the breaker zone. That is, predicted wave heights lakeward of the breaker zone are often in fair agreement with observed heights. The predicted location of the breaker zone is in rough accord with the location inferred from aerial photos and other visual observations. Thus peak current predictions are quite good. Within the surf zone, however, more energy is extracted from the actual wave field than is predicted in the model. As a result, the distribution of longshore momentum across the model surf zone does not agree well with observations. Apparently, model simulation of waves does not adequately represent the behavior of waves in a region of barred topography. An improved breaking criterion that includes reflection off the bar, or the treatment of a breaking wave as a traveling bore, as suggested by Battjes and Janssen (1978), might improve model results. The present model formulation does not include a specific representation for horizontal mixing of momentum, and provision for such mixing might lead to better simulation of the observed currents within the surf zone.

ACKNOWLEDGMENTS

Studies such as the present one require unusual dedication in the field data-acquisition phases. We wish to acknowledge the assistance of the following colleagues, without whom this study would have been impossible: A.A. Frigo, D.L. McCown, K.D. Saunders, C. Tome, and L.S. Van Loon. We thank the U.S. Army's Coastal Engineering Research Center for loan of their towed sled for our first field experiment. Dr. R.A. Dalrymple is thanked for his continued interest in this work and for his many helpful suggestions.

Funding for this study was provided by the U.S. Nuclear Regulatory Commission.

REFERENCES

- Battjes, J.A. and Janssen, J.P.F.M., *Energy and Loss and Set-Up Due to Breaking of Random Waves*, Proceedings 16th International Conference on Coastal Engineering, 1978.

- Birkemeier, W.A. and Dalrymple, R.A., *Nearshore Water Circulation Induced by Wind and Waves*, Proceedings, Modeling '75,' Symposium on Modeling Techniques, American Society of Civil Engineers, New York, pp. 1062-1081, 1975
- Liu, P.L-F., and Dalrymple, R.A., *Bottom Frictional Stresses and Longshore Currents Due to Waves with Large Angles of Incidence*, Jour. Marine Research, 36, pp. 357-375, 1978
- Noda, E., Sonu, C.J., Rupert, V.C., and Collins, J.I., *Nearshore Circulations Under Sea Breeze Conditions and Wave-Current Interactions in the Surf Zone*, Tetra Tech Report TC-149-4, Feb. 1974.
- Teleki, P.G., Musialowski, F.R., and Prins, D.A., *Data Acquisition Methods for Coastal Currents*, Proceedings, Civil Engineering in the Oceans/III, American Society of Civil Engineers, New York, pp. 1190-1210, 1975.

CHAPTER 47

RIP CURRENT SPACING AS AN EIGENVALUE

by
Noriyuki Iwata*

Abstract

Mass, momentum and wave action conservation laws, including the radiation stress, are used to obtain a rip current spacing as an eigenvalue. A coastal region is divided into two parts: offshore region and surf zone separated by a breaker line. Only the case of normal incidence of the waves is considered. From the matching conditions of the two horizontal velocity components at the breaker line, we can obtain rip current spacing as a function of a nondimensional parameter characterizing the surf zone, for an arbitrary value of a parameter indicating the strength of horizontal mixing.

Introduction

A coastal region with a linear bottom slope is divided into two parts: offshore region and surfzone separated by a breaker line. Wave set-up, wave energy and mean current are assumed to be composed of basic state, which is a function of only the distance from the shore and of superposed two dimensional perturbations.

In the case of normal incidence of the waves, basic steady current system vanishes and perturbations are found to be cellular. When we take into account the horizontal mixing in the surf zone, as LONGUET-HIGGINS(1970) did in the case of the steady longshore current, stream functions of the perturbed motions, which satisfy the boundary conditions at the coastline, can be represented by series expansion, wherein only one of the four roots of the indicial equation is selected. This selected one reduces to the value of the confluent hypergeometric function when the horizontal mixing is ignored(IWATA 1976):i. e. we have in the surf zone chosen a solution corresponding to the confluent hypergeometric equation modified by horizontal mixing, and the other solutions of the differential equation of fourth order are disregarded, partly because of the boundary conditions at

* Director, Institute of Coastal Oceanology, National Research Center for Disaster Prevention, Hiratsuka, Kanagawa, 254 Japan

the coast, partly to take account of the effect of the horizontal eddy viscosity due to wave breaking upon the solution of the inviscid model.

In the offshore region, where wave breaking does not occur, we disregard from the outset horizontal mixing so that the stream function can be represented by the modified Bessel function (IWATA 1976).

The matching conditions at the breaker line must be continuity of the two horizontal velocity components as well as surface elevation and energy. The continuity of energy follows immediately from the energy equation, but the elevation becomes discontinuous, because our model includes the effect of horizontal mixing only in the surf zone mainly due to the wave breaking, so that the elevations do not coincide with each other at the breaker line.

From the matching conditions of the two velocity components at the breaker line, we can obtain rip current spacing numerically as a function of a nondimensional parameter composed from bottom friction coefficient, bottom slope and the ratio of the breaker height to the depth for an arbitrary value of a parameter indicating a ratio of the horizontal mixing to the bottom stress as used by LONGUET-HIGGINS (1970).

§1. Basic equations

Mass, momentum and wave action conservation equations are given as follows,

$$\rho \frac{\partial \zeta}{\partial t} + \nabla \cdot \mathbf{M} = 0, \quad (1.1)$$

$$\frac{\partial \mathbf{M}}{\partial t} + \nabla \cdot (\mathbf{M}\mathbf{U} + \mathbf{s}) + \rho g h \nabla \zeta + \tau - \nabla \cdot (\mu h \nabla \mathbf{U}) = 0, \quad (1.2)$$

$$\frac{\partial}{\partial t} \left(\frac{E}{\sigma} \right) + \nabla \cdot [(\mathbf{U} + \mathbf{C}_g) \frac{E}{\sigma}] + \frac{D}{\sigma} = 0. \quad (1.3)$$

Here ρ is the density of water assumed constant, $h = d + \zeta$ where d is local still water depth and ζ is the mean water level perturbation due to the presence of current and waves, \mathbf{M} and \mathbf{U} denotes the total mean momentum and the mean current respectively

$$\mathbf{M} = \tilde{\mathbf{M}} + \rho h \tilde{\mathbf{U}}, \quad \mathbf{U} = \frac{\tilde{\mathbf{M}}}{\rho h},$$

where $\tilde{\mathbf{U}}$ shows the basic current, supposed independent of the depth and $\tilde{\mathbf{M}}$ denotes the mean wave momentum

$$\tilde{\mathbf{M}} = \left\langle \int_d^{\zeta} \rho \mathbf{u} dz \right\rangle$$

where u is the velocity vector associated with the wave motion. $\nabla (=i\partial/\partial x + j\partial/\partial y)$ is the two dimensional gradient operator. μ denotes the eddy viscosity coefficient, D is the rate of energy dissipation mainly due to wave breaking. E shows the wave energy

$$E = \frac{1}{2}\rho g a^2 ,$$

where a is the local wave amplitude.

$$\sigma = \tilde{\sigma} - k \cdot U$$

σ is the frequency relative to a coordinate system moving with the current velocity U and $\tilde{\sigma}$ is the frequency relative to a fixed coordinate system. k shows wave number. C_g denotes group velocity and its magnitude is

$$C_g = \frac{\partial \sigma}{\partial k} = \frac{1}{2}c \left[1 + \frac{2kh_0}{\sinh 2kh_0} \right]$$

$$c^2 = \frac{g}{k} \tanh kh_0$$

where $h_0 = d + \zeta_0$ and ζ_0 is, as later shown, steady wave set-up.

The radiation stress tensor s and its components referred to the coordinate system shown in Fig.1 are

$$s = \begin{pmatrix} E \left[\frac{C_g}{c} (1 + \cos^2 \theta) - \frac{1}{2} \right] & E \frac{C_g}{c} \frac{\sin 2\theta}{2} \\ E \frac{C_g}{c} \frac{\sin 2\theta}{2} & E \left[\frac{C_g}{c} (1 + \sin^2 \theta) - \frac{1}{2} \right] \end{pmatrix}$$

The bottom stress averaged over one cycle τ is given by (IWATA 1976)

$$\tau = f \begin{pmatrix} U(1 + \cos^2 \theta) + v \frac{\sin 2\theta}{2} \\ V(1 + \sin^2 \theta) + u \frac{\sin 2\theta}{2} \end{pmatrix}$$

where $f = \frac{2}{\pi} \rho K v$, $v = \frac{a}{h_0} c$.

The bottom friction coefficient K is given by (KAJIURA 1968)

$$K = \alpha \left(\frac{v}{\sigma z_0} \right)^{-2/3} , \quad \alpha = \text{const} ,$$

where z_0 is the roughness length of the bottom material.

For the coastal water considered now, we make the

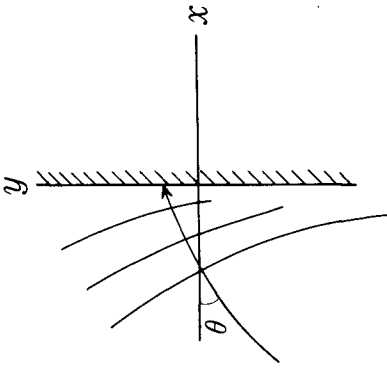


Fig.1 Coordinate axis and incident angle.

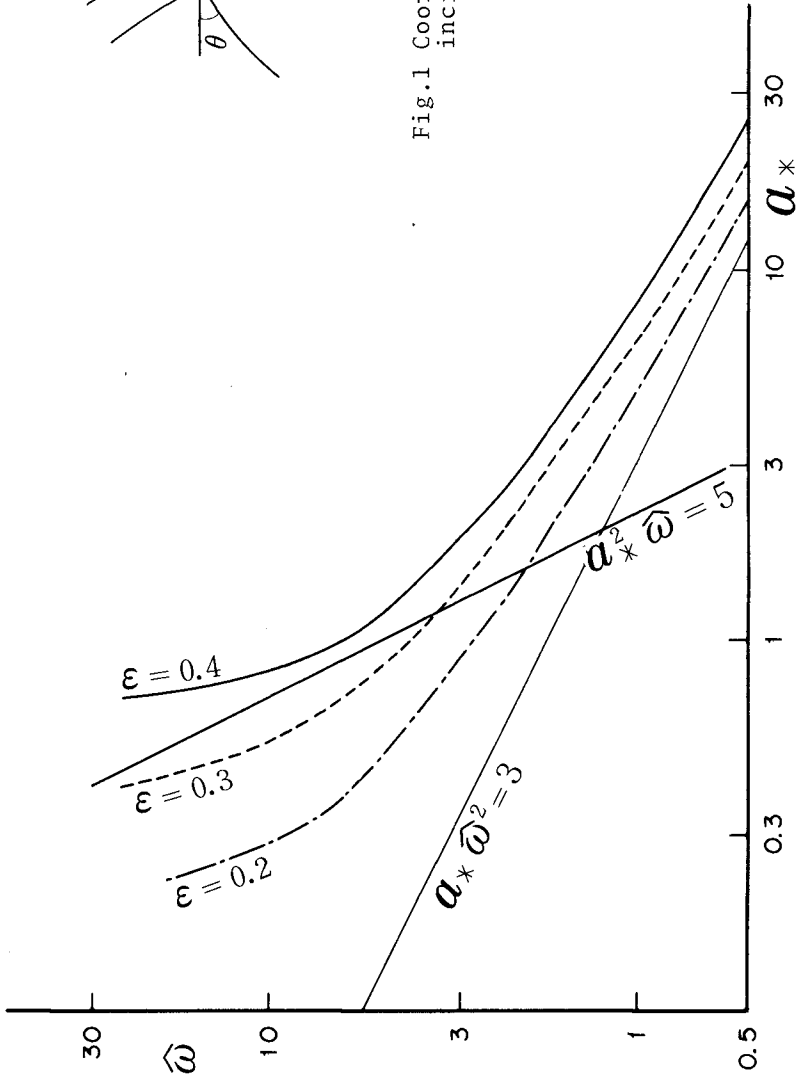


Fig.2 Nondimensional rip current wave number $\hat{\omega}$ as functions of a characteristic parameter a^* .

longwave approximation so that $c^2 = gh_0$, moreover in the surf zone we assume $\alpha = \gamma h_0$, $\gamma = 0.4$. From the above approximations we get (IWATA 1976)

$$f = \begin{cases} f_0 \sqrt{z} & ; z < 1 \\ f_0 & ; z > 1 \end{cases}$$

$$\text{where } z = \frac{h_0}{h_*}, \quad f_0 = \frac{2}{\pi} \rho \gamma K_* \sqrt{gh_*}, \quad K_* = \alpha \left(\frac{\gamma}{kz_0} \right)^{-2/3},$$

where h_* is the water depth at the breaker line. K_* is the bottom friction coefficient in the surf zone and becomes constant. μ denotes the horizontal mixing coefficient and we assume (LONGUET-HIGGINS 1970)

$$\mu = \begin{cases} \rho N |x| \sqrt{gh_0} & ; h_0 \leq h_* \\ \rho N |x| \sqrt{gh_*} & ; h_0 > h_* \end{cases}$$

where N is constant.

From now on we consider a straight coastline where the local still water depth is linear: $d = -sx$, and assume that the field variables are composed of basic steady state as well as superposed perturbations,

$$U = U_0(x) + \delta U_1(x, y, t),$$

$$\zeta = \zeta_0(x) + \delta \zeta_1(x, y, t),$$

$$E = E_0(x) + \delta E_1(x, y, t), \text{ etc.}$$

For the steady state we have

$$\nabla \cdot M_0 = 0, \quad (1.4)$$

$$\nabla \cdot S_0 + \rho g h_0 \nabla \zeta_0 + \tau_0 - \nabla \cdot (\mu h_0 \nabla U_0) = 0, \quad (1.5)$$

$$\nabla \cdot \left[(U_0 + C_g) \frac{E_0}{\sigma_0} \right] + \frac{D_0}{\sigma_0} = 0. \quad (1.6)$$

To study the perturbations we consider conveniently a case of normal incidence of the waves ($U_0 = 0$), as well as steady state ($\partial/\partial t = 0$),

$$\nabla \cdot M_1 = 0, \quad (1.7)$$

$$\nabla \cdot S_1 + \rho g h_0 \nabla \zeta_1 + \tau_1 - \nabla \cdot (\mu h_0 \nabla U_1) = 0, \quad (1.8)$$

$$\nabla \cdot \left[C_g (E_1 + E_0) \frac{k \cdot U_1}{\sigma_0} \right] + U_1 E_0 + \frac{k \cdot U_1}{\sigma_0} D_0 = 0. \quad (1.9)$$

To derive the above equations we have assumed,

$$\frac{k \cdot U_1}{\sigma_0} D_0 \gg D_1, \quad h_0 \nabla \zeta_1 \gg \zeta_1 \nabla \zeta_0$$

where $D = D_0 + \delta D_1$.

Before we proceed to the rip current system, let us consider the basic state. For the case of normal incidence there is no basic current, $U_0 = 0$, so that eqs(1.5) and(1.6) can be transformed as follows,

$$\rho g h_0 \frac{\partial \zeta_0}{\partial z} + \frac{3 \partial E_0}{2 \partial z} = 0, \quad (1.10)$$

$$\frac{\partial}{\partial z}(E_0 C g) + x_* D_0 = 0, \quad (1.11)$$

where $h_* = -s x_*$.

(i) In the surf zone ($h_0 \leq h_*$) we assume as usual

$$E_0 = E_* z^2, \quad E_* = \frac{1}{2} \rho g \gamma^2 h_*^2,$$

then eq.(1.10) gives the basic wave set-up,

$$\zeta_0 = \zeta_* + \frac{3}{2} \gamma^2 h_* (1-z), \quad (1.12)$$

where ζ_* shows the value at the breaker line. In this case eq.(1.11) shows simply the rate of energy dissipation mainly due to the wave breaking, because the energy dissipation by the bottom stress is given by

$$\hat{D}_0 = \frac{8}{3\pi} K \frac{\nu}{h_0} E_0,$$

whereas(1.11) gives

$$D_0 = \frac{5s}{2h_0} E_0 \sqrt{gh_0},$$

that is, energy dissipation by the bottom stress is much smaller than that due to wave breaking.

(ii) Outside the breaker zone ($h_0 \geq h_*$) we can neglect energy dissipation, $D_0 = 0$, so that the energy flux becomes constant, $E_0 C g = \text{const}$. It follows then

$$E_0 = E_* z^{-0.5}, \quad (1.13)$$

introducing (1.13) into (1.10) we have at once,

$$\zeta_0 = -\frac{\gamma^2 h_*}{4} z^{-1.5}, \quad (z \geq 1) \quad (1.14)$$

From now on we take a new coordinate system with origin at the basic wave set-up shore line.

§2. Rip current system

From eq.(1.7) we get stream function as follows,

$$hU_1 = \frac{\partial \psi}{\partial y}, \quad hV_1 = -\frac{\partial \psi}{\partial x}.$$

From eqs.(1.8) and (1.9) we can derive an equation for the stream function. We can put in general $\psi = \psi \cos my$, $E_1 = E_1 \sin my$ and $\zeta_1 = \zeta_1 \sin my$, where m denotes the wave number of the rip current circulation cells.

(i) In the surf zone we have,

$$\tau_1 = f_0 \sqrt{z} \left(\frac{2}{h_0} \frac{\partial \psi}{\partial y}, \quad -\frac{1}{h_0} \frac{\partial \psi}{\partial x} \right), \quad \mu h_0 = f_0 \varepsilon |x_*|^2 z^{2.5},$$

where
$$\varepsilon = \frac{\pi s N}{2 \gamma K_*}.$$

This particular mixing parameter ε denotes essentially the ratio of horizontal mixing to the bottom friction and plays an important role in the rip current system.

$$\eta \psi'' - \left(\frac{1}{4} + \eta \right) \psi' - \left(\frac{1}{2a_*} - \frac{1}{4} \right) \psi = \varepsilon P, \quad (2.1)$$

$$P = 4\eta^3 \psi'''' + 9\eta^2 \psi'' - \left(1 + \frac{2\eta}{a_*} \right) \eta \psi'' - \frac{1\eta}{4a_*} \psi' + \frac{1}{8a_*} \left(1 + \frac{2}{a_*} \eta \right) \psi,$$

where
$$a_* = \frac{\pi s \gamma}{8 K_*}, \quad \eta = \frac{1}{2} a_* (\hat{\omega} z)^2, \quad \hat{\omega} = \sqrt{2} m |x_*|.$$

When we ignore horizontal mixing ($\varepsilon=0$) eq.(2.1) turns out to be confluent hypergeometric equation (IWATA 1976).

The solution of eq.(2.1) can be put in the series,

$$\psi = A \eta^\rho \sum g_n \eta^n, \quad (2.2)$$

where
$$g_0 = 1,$$

$$g_n h_0(\rho+n) + g_{n-1} h_1(\rho+n-1) + \dots + g_0 h_n(\rho) = 0,$$

$$h_0(\rho) = \rho [(\rho-1) \left\{ (\rho-2) \left(\rho - \frac{3}{4} \right) - \frac{1}{4} \right\} + \frac{1}{4} \varepsilon \left(\frac{5}{4} - \rho \right)],$$

$$h_1(\rho) = \frac{1}{2a_*} \left(\frac{1}{16} + \frac{7}{8} \rho - \rho^2 \right) + \frac{1}{\varepsilon} \left\{ \frac{1}{8} \left(\frac{1}{a_*} - \frac{1}{2} \right) + \frac{1}{4} \rho \right\},$$

$$h_2(\rho) = \frac{1}{16a_*^2}.$$

In general the indicial equation $h_0(\rho)=0$ gives four roots. For the case of no horizontal mixing $\rho=0$ and $\rho=5/4$ are obtained, however from the boundary conditions at the coast only $\rho=5/4$ was selected.

In order to see the effect of horizontal mixing upon the inviscid solution, we choose in this study one particular root of the indicial equation, which reduces to $\rho = 5/4$ for the case of no horizontal mixing, and the other roots are all omitted.

Energy in the surf zone can be obtained from eq.(1.9),

$$E_1 = \frac{1}{\sqrt{z}} \int_0^z Q dz \tag{2.3}$$

where $Q = \beta \hat{\omega} E_* z (\frac{\partial \psi}{\partial z} - \frac{1}{2z} \psi)$; $\beta = \frac{s}{h_*^2 \sqrt{2gh_*}}$.

Perturbed wave set-up can also be expressed by the stream-function as follows,

$$\zeta_1 = \frac{-f_0}{\rho g h_* z} [\frac{1}{2f_0} E_1 + \frac{1}{\hat{\omega}} (\frac{z}{z})^{0.5} \frac{\partial \psi}{\partial z} - \epsilon L(\frac{1}{z} \frac{\partial \psi}{\partial z})] \tag{2.4}$$

where $L(\phi) = (z^{1.5} \frac{\partial^2 \phi}{\partial z^2} + \frac{1}{2} z^{0.5} \frac{\partial \phi}{\partial z} - \frac{1}{2} \frac{1}{\sqrt{z}} - \frac{\hat{\omega}^2}{2} z^{1.5}) \phi$

(ii) Offshore region.
Outside the breaker zone we can put $E_0 = E_* z^{-0.5}$ and $f = f_0$. Moreover in this region we can neglect horizontal mixing compared to the surf zone, where the mixing is vigorous owing to breaking of the waves.

$$\xi^2 \frac{\partial^2 \psi}{\partial \xi^2} - (2 + a_* \hat{\omega}^2) \xi \frac{\partial \psi}{\partial \xi} - (\xi^2 - 3a_* \hat{\omega}^2) \psi = 0 \tag{2.5}$$

where $\xi = \hat{\omega} z$.

The solution of the above equation is expressed by the modified Bessel function,

$$\psi = B \xi^\alpha K_\nu(\xi), \tag{2.6}$$

where $\alpha = \frac{1}{2}(3 + a_* \hat{\omega}^2)$, $\nu = \frac{1}{2}(3 - a_* \hat{\omega}^2)$.

The energy in the offshore region is given by

$$E_1 = \frac{1}{\sqrt{z}} [\int_1^z R dz + E_1^*] \tag{2.7}$$

where $R = \beta \hat{\omega} E_* z^{-1.5} (\frac{\partial \psi}{\partial z} - \frac{3}{z} \psi)$; $E_1^* = \int_0^1 Q dz$.

Perturbed wave set-up can be expressed,

$$\zeta_1 = -\frac{f_0}{\rho g h_*^2} \left[\frac{1}{2} \frac{h_* E}{f_0} + \frac{1}{\hat{\omega}} \left(\frac{z}{z_*} \right)^{0.5} \frac{\partial \Psi}{\partial z} \right] \quad (2.8)$$

The matching conditions at the breaker line are the continuity of two horizontal velocity components as well as perturbed wave set-up. As we can see from eq.(2.7), energy is always continuous. Perturbed wave set-up outside the breaker zone is obtained under the assumption of no horizontal mixing, so that it becomes discontinuous on the breaker line even if two horizontal velocities are continuous on it.

At the breaker line $z = 1$, $\eta = \eta_0 = 1/2\alpha_* \hat{\omega}^2$ and $\xi = \hat{\omega}$, accordingly the continuity condition of velocity components are

$$\begin{vmatrix} \Sigma g_n \eta_0^n & 1 \\ 2 \Sigma g_n (\rho+n) \eta_0^n & \frac{\alpha + \nu - \hat{\omega} K_{\nu+1}(\hat{\omega})}{K_{\nu}(\hat{\omega})} \end{vmatrix} = 0. \quad (2.9)$$

The eigenvalues $\hat{\omega}$ are numerically obtained and represented in Fig.2 as functions of α_* from eq.(2.9) for $\epsilon=0.2 \sim 0.4$. In Fig.2 is also shown an empirical formula $\hat{\omega} = 5\alpha_*^{-2}$. Another curve $\hat{\omega} = \sqrt{3}\alpha_*^{-0.5}$ is reproduced from the previous paper (IWATA 1976), which is obtained for the limiting case of no horizontal mixing $\epsilon=0$. Fig.3 shows experimental results (HORIKAWA and MIZUGUCHI 1975) from which the above experimental formula is derived.

From Fig.2 we can see remarkably good agreement with the empirical formula is obtained for the case $\epsilon = 0.3$. It must be noticed this value $\epsilon=0.3$ is also obtained for the basic longshore current, when we consider obliquely incident waves (LONGUET-HIGGINS 1970). For a practical application we can put for the range $\epsilon = 0.3 \sim 0.4$,

$$\hat{\omega} = \begin{cases} 5.0\alpha_*^{-2} & ; \alpha_* < 1.5, \\ 2.7\alpha_*^{-0.5} & ; \alpha_* > 1.5. \end{cases}$$

In Fig.4 and Fig.5 we show an example of calculated stream function for $\epsilon = 0.3$, $\alpha_* = 0.6$ and $\hat{\omega} = 8.4$.

Conclusion

Some of the numerous studies of the near shore circulations insist that irregular bottom topography always exerts complete control over the water circulation, that is,

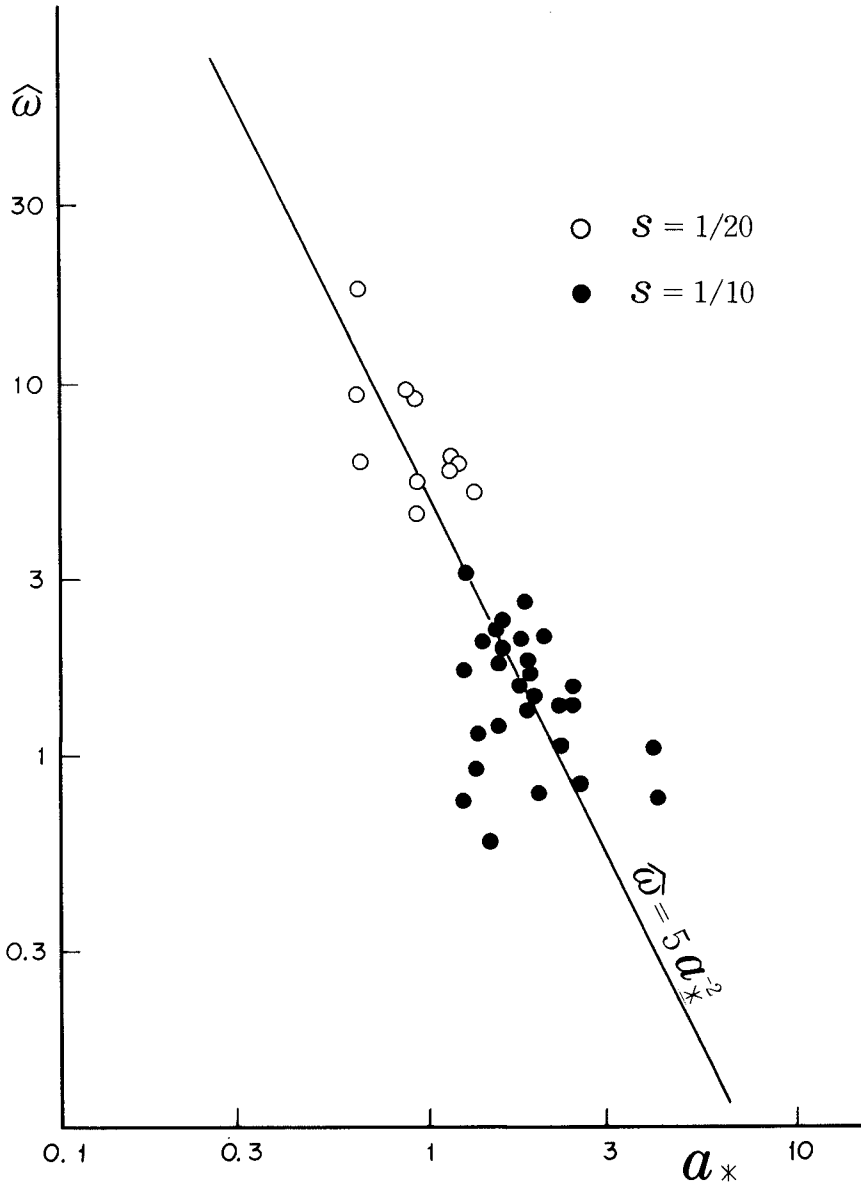


Fig.3 Experimental data and empirical relationship between rip current wave number $\hat{\omega}$ and a_* , where $z_0=1/30z_1, z_1=0.005$ cm are assumed to compute K_* .

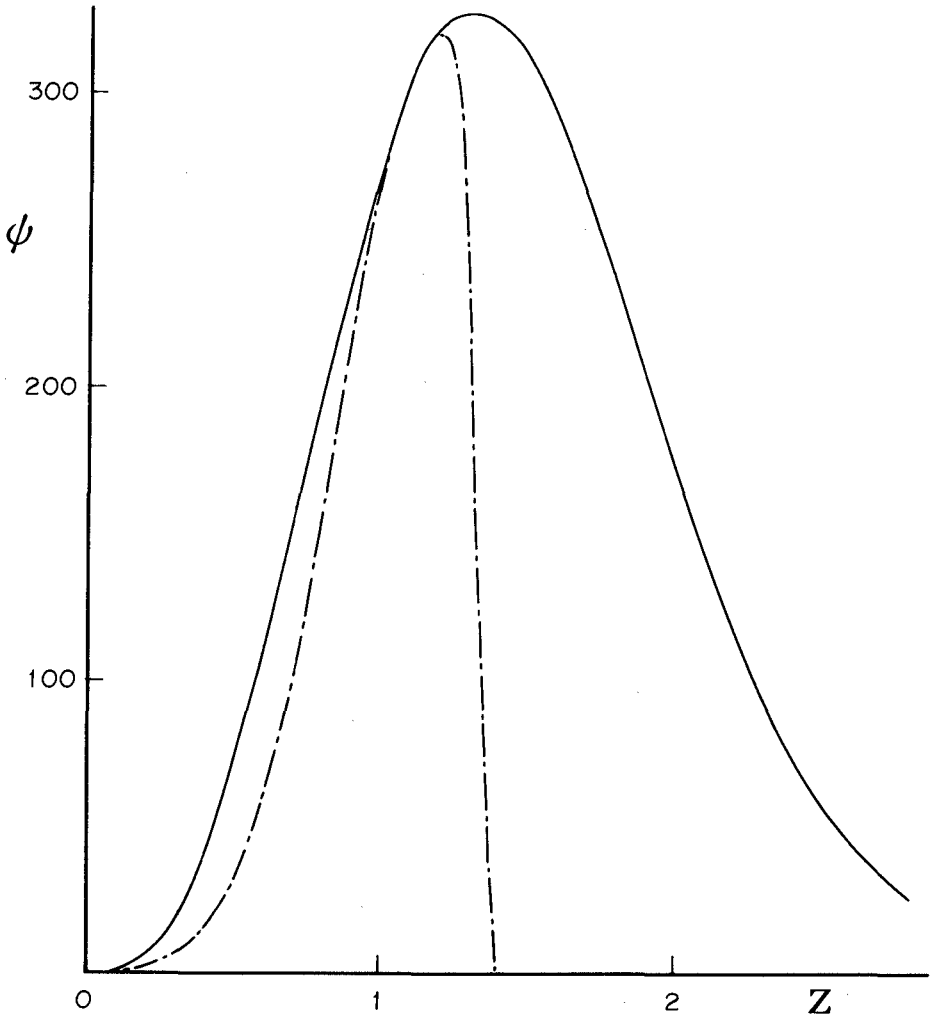


Fig.4 An example of stream functions on either side of breaker line $z=1$.

— Obtained from offshore equation.

- - - Obtained from surfzone equation.

$\alpha_* = 0.6$, $\epsilon = 0.3$ and $\hat{\omega} = 8.4$.

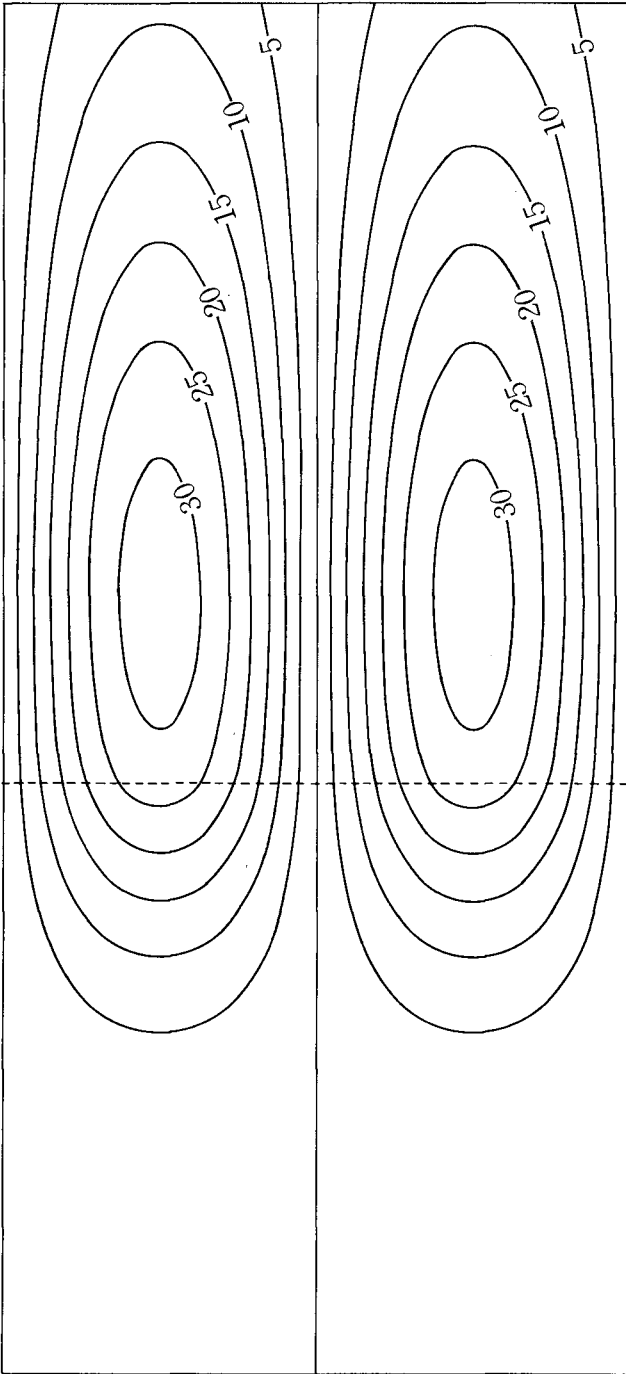


Fig. 5 An example of rip current pattern for $\alpha_*=0.6$, $\epsilon=0.3$ and $\hat{\omega}=8.4$.

the topography is a primary cause to generate nearshore circulation. But there remains the basic question of how the original bottom deformation was formed if not by a cell circulation. Rip current can develop on smooth beaches without any bottom irregularities, presumably cause sediment transport and produce bottom topography. At some later stage the deformed bottom topography may be eventually effective to control the nearshore circulation pattern. Based on these reasonings attempt has been made to clarify the rip current spacing as an eigenvalue of a vorticity equation.

Our model is not self-consistent as far as we do not consider the horizontal mixing in the offshore region. When we take into account the effect of this horizontal mixing, right-hand side of eq.(2.5) is not zero but must be

$$\varepsilon[\xi^4 \psi'''' - 2\xi^3 \psi'' + (2-\xi^2)\xi^2 \psi'' - (2-\xi^2)\xi \psi' + \frac{1}{4}\xi^4 \psi]$$

To find the solution which tends to zero at infinity and reduces to eq.(2.6) in the limiting case of $\varepsilon=0$ is a future problem.

Acknowledgment: Many thanks are due I.Watabe for his helpful programmings of the numerical computations.

REFERENCES

- HORIKAWA,K and M.MIZUGUCHI(1975):Laboratory experiments on nearshore current system, Proc. 22nd Conf.Coastal Eng. in Japan, 141-147(in japanese).
- IWATA,N.(1976): Rip current spacing, Journ. Oceanogr. Soc. Japan, 32(1),1-10.
- KAJIURA,K.(1968):A model of the bottom boundary layer in water waves, Bull. Earthquake Res. Inst.,46,75-123.
- LONGUET-HIGGINS,M.S.(1970):Longshore current generated by obliquely incident waves,2, J.Geophy.Res.,75, 6790-6801.

WIND-INDUCED WATER SURFACE SET-UP AND DRIFT CURRENTS

by

Frederick L.W. Tang¹, Jin Wu², Charles C.C. Chang³,
and Shan-Hwei Ou⁴

ABSTRACT

A systematic experiment to study the wind-induced flow phenomena was conducted in a laboratory tank. The results are related to the wind friction velocity and subsequently scaled for applications at various fetches under different wind velocities. The wind-stress coefficients are found to be well scaled by the Froude number. The bottom friction is measured with an effective shear gauge. The ratios between the bottom stress and the wind stress are obtained. The complete profiles of wind drift current are measured under various wind velocities. A tentative distribution of drift currents in the whole water depth is proposed. The results from the experiment are used to examine the wind-induced flow phenomena in a closed basin.

INTRODUCTION

The water motions induced by wind are involved in many dynamical processes of the mutually-interacting air-sea system. Previous studies on the air-sea interaction, however, seem to concentrate on the atmospheric surface layer and the surface waves. In the past, the wind-induced water-surface set-up and drift currents were measured and analyzed separately. For the surface set-up, it was assumed that the wind stress was balanced by the difference of the hydrostatic pressure due to the surface inclination [Refs. 4 & 7]. Other factors involved were ignored and their influences have not been carefully evaluated. For the drift currents, no systematic experiment has been conducted except for those within the upper layer below the water surface [Refs. 6 & 14]. In the present study, a systematic experiment has been conducted in the wind-wave tank under various wind velocities and wind fetches.

¹ Professor, Dept. of Hydraulic Engineering, National Cheng Kung University, Tainan, Taiwan 700, Republic of China

² Professor, College of Marine Studies and Dept. of Civil Engineering, University of Delaware, Newark, Delaware 19711, U.S.A.

³ Chief Engineer, Taichung Harbour Bureau, Taichung, Taiwan 435, Republic of China

⁴ Visitor, Dept. of Ocean Engineering, University of Hawaii, Honolulu, Hawaii; formerly, Associate Professor, Dept. of Hydraulic Engineering, National Cheng Kung University, Tainan, Taiwan 700, Republic of China

The measurements include the wind profiles, surface waves, surface set-up, current profiles, and bottom friction. All the parameters shown in the free-body diagram of Fig. 1 were measured simultaneously in laboratory wind-wave tank of uniform depth. Various techniques of measurements were illustrated. The results were related to the wind-friction velocity and the wind fetch. The results obtained from all the measurements are substituted into the balancing expression from the free-body diagram; and, the relative importance of each term was also discussed.

EXPERIMENTAL EQUIPMENT AND PROCEDURES

Wind-Wave Tank

Experiments were conducted in the wind-wave tank at the Taichung Harbour Bureau, Taiwan. The tank is 1.5m wide, 2.0m deep and 100m long. Wind is generated by a 75 hp variable-speed fan mounted at the upstream end of the channel. The maximum available wind velocity with a cross section of 0.8m x 1.5m of air passage is above 20 m/s. Wave absorbers were installed at the both ends of the channel to reduce the effect of wave reflection.

Measurements of wind profiles and surface waves were performed at six different fetches: 22^m, 31^m, 37^m, 46^m, 52^m, 58^m and at four different water depths: 1.2^m, 0.9^m, 0.6^m and 0.4^m. Drift current profiles were measured at the fetches of 22^m, 31^m and 37^m, while the bottom frictions were measured only at the middle bottom between fetch 22^m and 31^m.

Fig. 2 is the general outline of the wind-wave tank and the air-water motions. The water motion is assumed to be two-dimensional flow. Select the origin of the axis at the mean water level with x along the channel axis and y vertical and drawn upwards as in Figure 2.

Wind and Wave Measurement Devices

The wind velocities in the channel were measured by pitot-static tube in conjunction with a micromanometer. The tube was supported at the central top of the tank and traversed vertically across the boundary layer of the airflow. The wind velocities were directly read out from the micromanometer.

The surface waves were measured with conductivity probes. The wave signals were recorded on tapes, which were subsequently played back on the analog computer, HP 1000, to determine the wave heights, wave periods, mean water surface elevations and wave spectra. The time interval for the surface data is 0.1 second and the total number of data in each station is 1200.

Current Measurements

Surface drift current was measured by the punched computer cards, 1 cm square saturated with paraffin. The cards were dropped from the channel roof. The surface drift velocities were obtained by timing the

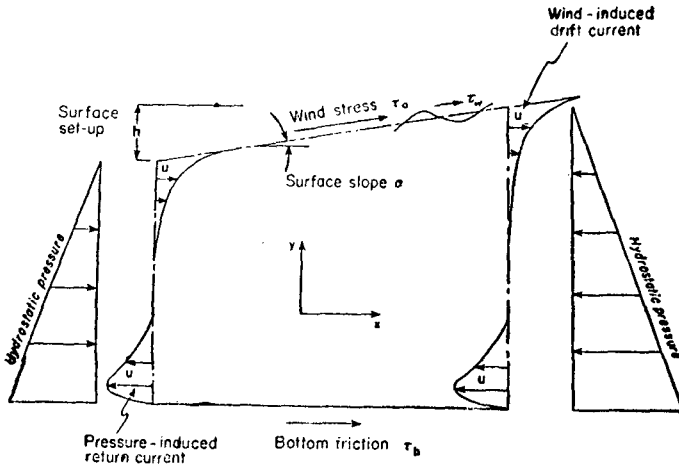


Figure 1. Free-body forces diagram

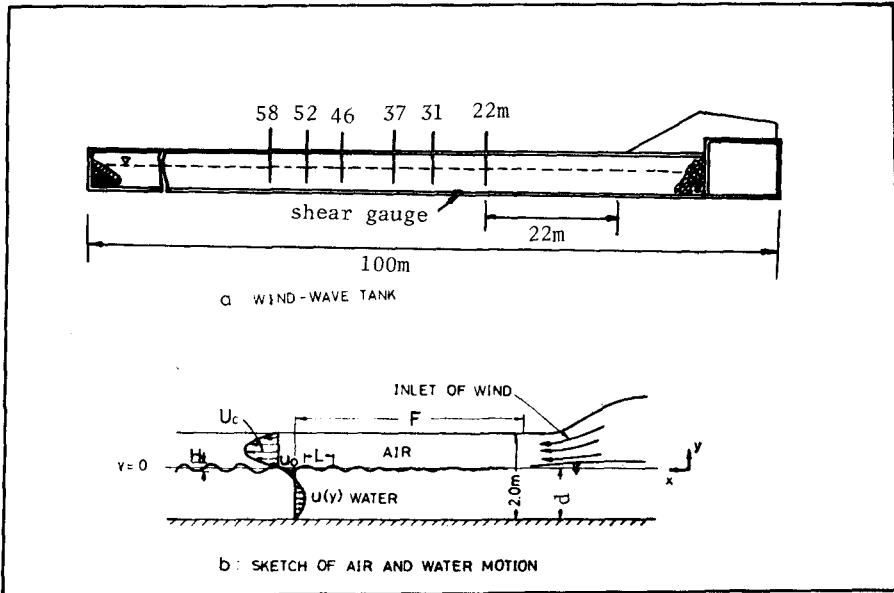


Figure 2. Sketch of wind-wave tank and air-water motions

movements of the cards along a 3m distance. At least five readings were taken for each condition.

The subsurface drift current profiles were measured by dye method. On injecting the dye from the holes on a pvc tube at various elevations, the dye motions were photographed with an 8mm movie camera from the side of the tank. A clear grid was placed outside the channel on the plate-glass sidewall and an electronic clock is placed just below the grid within the camera's view. The dye motion was not laminar, and the velocity flow patterns were confused about ten seconds after the injection of the dye.

The horizontal distances of dye motion at the various depths within time duration were read out from the grid while the time duration was obtained from the electronic clock. The experiments were repeated five to eight times each wind velocity and the average values were taken at the various depths.

Shear Gauge

The shear stress on the tank bottom induced by the return current was measured by a shear gauge, as shown in Figure 3. It consists of three main parts: shear plates, strain gauge, and supported block. The shear plates contain the upper and the lower plate, both 55 cm wide, 65 cm long, and 0.12 cm thick. The lower plate is hung on the supported block by four steel wires (0.5mm diameter) of equal length. The shear plate is sensitive only to the horizontal forces.

The strain gauge is pasted on a steel sheet which is mounted at both ends on the lower plate and the supported block. The steel sheet is carefully adjusted through the screw such that no bending moment is exerted on it when at rest. The shear force acting on the upper plate is transferred to the bending moment on the steel sheet and is recorded on tapes which are then played back on the analog computer. The steel sheet is 0.5mm thick and 7 cm long, which are experimentally examined. The clearance gaps is 1mm along four sides. The shear gauge was statically calibrated.

WIND STRESS AND SCALING CRITERION

The surface set-up and drift currents are governed by the wind stress acting at the air-sea interface. A model scaling criterion for the wind stress coefficient is necessary for the laboratory studies of the field phenomena.

An equation for scaling the wind stress coefficient was given as [Ref. 11]

$$\frac{1}{\sqrt{C_y}} = \frac{1}{k} \ln \left(\frac{1}{0.0112 C_y F_r^2} \right) \quad (1)$$

in which C_y is the wind stress coefficient defined as $C_y = \tau_o / \rho_a U_y^2$;
 F_r is the Froude number defined as $F_r = U_y / \sqrt{g y}$; k is the Karman's constant;

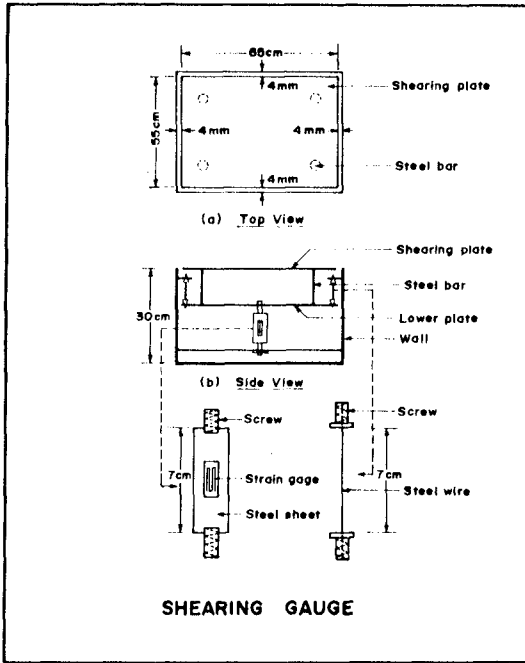


Figure 3. Shear gauge

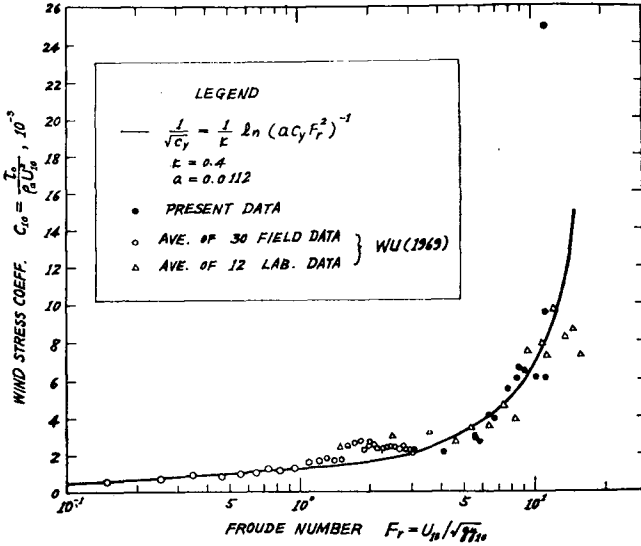


Figure 4. Froude number scaling of wind stress coefficients

and τ_0 is the wind stress, U_y the wind velocity at elevation y , ρ_a the density of air, and g the gravitational acceleration.

This Froude scaling criterion for wind-stress coefficient has been verified by Wu [Ref. 11] with the results of 12 laboratory and 30 oceanic independent data. The present result is given in Figure 4. Good agreement with Froude scaling law was shown.

Since the Froude number scaling law is derived from the logarithmic wind profile [Figure 5], the reference height, y , should be within the inner region of the atmospheric boundary layer. Wu [Ref. 12] proposed the anemometer height in Froude scaling as

$$y = \begin{cases} 10 \text{ cm; for } R < 5 \times 10^7 \\ 7.35 \times 10^{-5} R^{2/3} \text{ cm; for } 5 \times 10^7 < R < 5 \times 10^{10} \\ 10 \text{ m; for } R > 5 \times 10^{10} \end{cases} \quad (2)$$

where R is the fetch Reynold number given as $R = \frac{U_y F}{\nu_a}$, and F denotes the wind fetch, ν_a the kinematic viscosity of air.

Therefore, with a single wind velocity either in the field or in the laboratory at a suggested anemometer height, one can calculate the Froude number, which in turn is given to obtain the wind-stress coefficient. The wind stress and the wind friction velocity can also be obtained.

The dependence of the wind stress coefficient, C_{10} , on fetch was plotted in Figure 6, in which C_{10} indicates the C_y at $y = 10$ cm. In general, C_{10} decreases as F increases for the small wind velocities, while for the high wind velocities, C_{10} decreases first, then increases as F increases. The dependence of the wind friction velocity, U_* , on fetch shows the same tendency as C_{10} does.

BOTTOM FRICTION

The total forces on the test plate before and after the experiment were recorded digitally and analyzed through the analog computer to obtain the mean readings and the time-mean forces. By dividing the area of shear plate, the shear stress was obtained.

Since the bottom friction is oscillatory, the inertial force of the shear plate is involved. An attempt was made to lower reasonably the natural frequency of the steel sheet during the development of the shear gauge.

Figure 7 is the definition sketch of the data in which p indicates the mean reading of oscillatory shear stress after the experiment, q the same reading before the experiment, and A the time-mean range of the force waves. Since the resultant bottom stress is in the same direction as the wind stress [Fig. 1], the average bottom stress, τ_b , is interpreted as $(A/2 + p - q)$, which would correct the inertial force.

The measured values of the average bottom stress were shown in Figure 8 as the function of wind friction velocity. The average bottom stress increases slightly as the wind friction velocity increases. It is also seen that the bottom friction increases remarkably as the water depth decreases. Figure 9 shows the ratio between average bottom stress

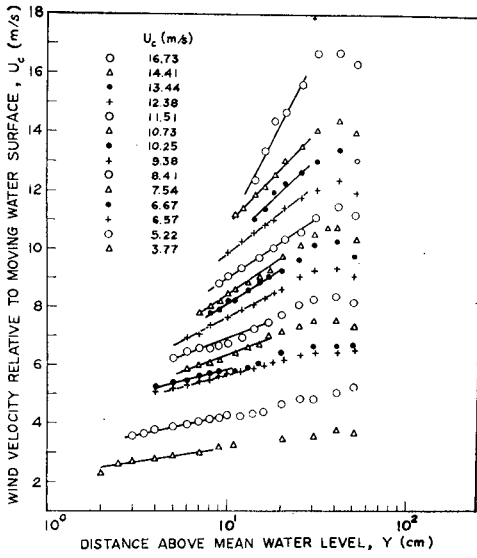


Figure 5. Vertical wind profiles

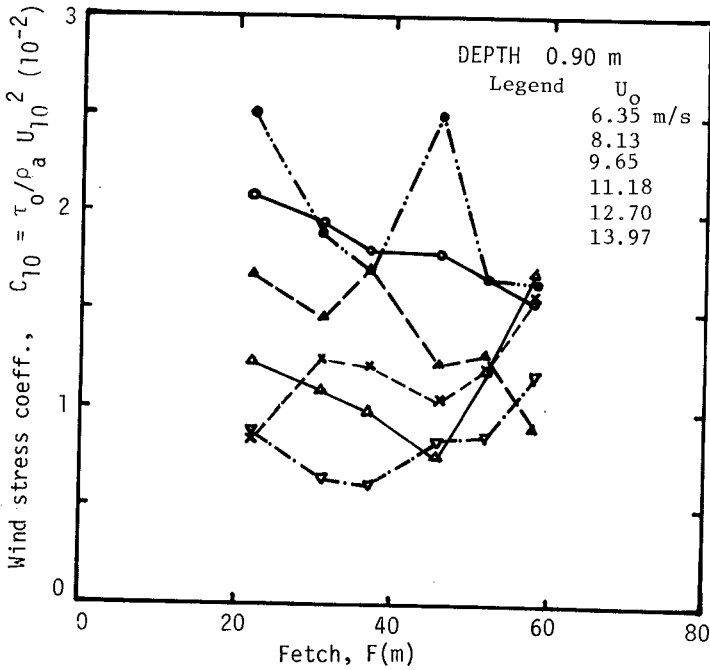


Figure 6. Variation of wind stress coefficient with fetch

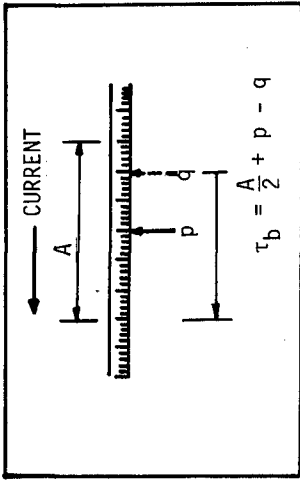


Figure 7. Sketch of data reading of bottom shear

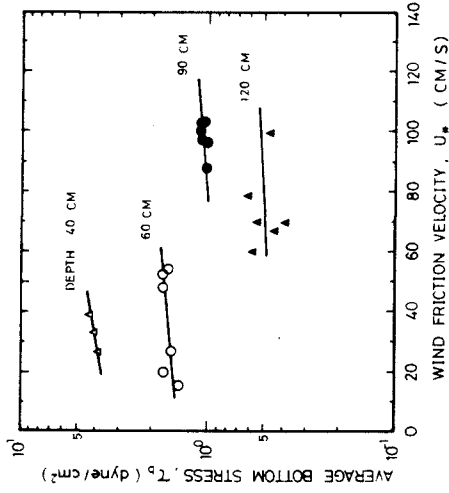


Figure 8. Variation of average bottom stress with wind friction velocity

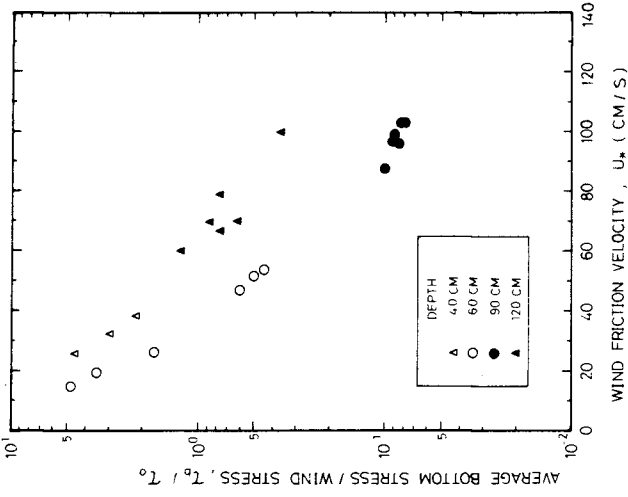


Figure 9. Variation of τ_b/τ_0 with U_*

and wind stress in relation to the wind friction velocity. This ratio has strong dependence on the wind friction velocity, as might be expected because the wind stress is calculated from the square of the wind friction velocity. The measured values of the ratio range from 5 to 0.08 according to the wind velocity and water depth. The value 0.5 assumed by Keulegan [Ref. 4] and 0.1 deduced by Baines & Knapp [Ref. 1] should follow their catalog. This deviation indicates the necessity of measuring rather than calculating the bottom friction when working with a force balance of the free body force diagram.

DRIFT CURRENTS

Surface Drift Currents

The surface drift currents were measured in the plate-glass section of the tank at fetch $F = 31\text{m}$. The measured ratio of the surface drift velocity to the wind velocity was calculated as 0.0311. Table 1 gives the ratio of several sets of experiments in which parts of the wind velocity were referred to the free stream wind velocity.

TABLE 1: Ratio of u_0/U_0

Author	Method	u_0/U_0 (%)
Keulegan	Paraffin particle	3.3
Tickner	Dye	3.0
Plate et. al.*	Paper disc	2.60
Shemdin *	Paper disc	2.89
Kato et. al. *	Hydrogen bubble	2.80
Wu	Floats	3.95
Present data	Paper	3.11

*Wind velocity is referred to as free stream wind velocity

The measured surface drift velocity is plotted in Figure 10 in which Figure (a) shows the variation of u_0 with U_* , Figure (b) shows the variation of u_0/U_* with U_* . The variation of the surface drift with the wind velocity is not fully understood. In this study, the ratio u_0/U_* is around the value of 0.45 at the high wind velocity. It is somewhat lower than the previous results of one of the authors [Ref. 12].

The Stokes transport at the water surface was expressed as [Ref. 2]

$$V_0 = C_0 \left(\frac{\pi H}{L} \right)^2 \quad (3)$$

where H is the wave height, L the wave length, C_0 the phase velocity calculated from Airy wave. The surface Stokes transport is also shown in Figure 10(a).

The wind-induced surface drift is the difference between the total surface drift u_0 and the surface Stokes drift V_0 . This leads to $(u_0 - V_0)/U_* = 0.38$, which is lower than the previous results. This is

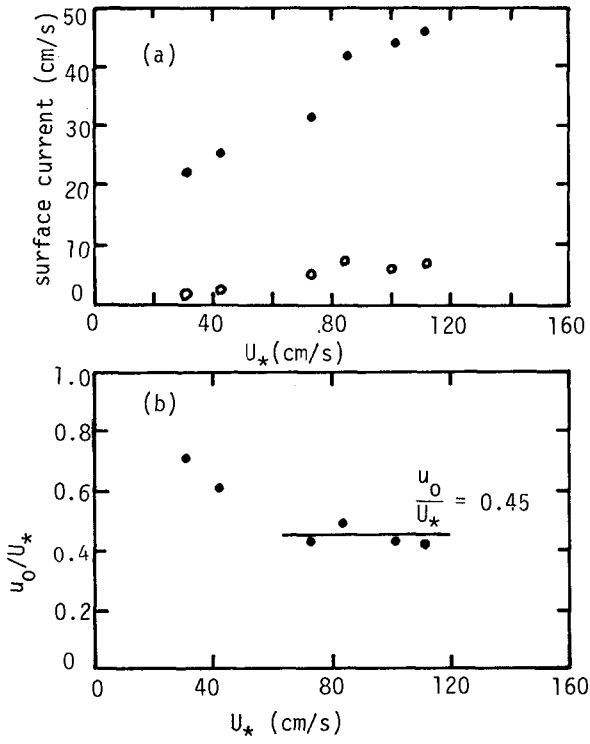


Figure 10. Surface drift velocity for various wind friction velocity
 (Solid: total drift;
 Open : wave-induced)

where more study is needed.

Measurement of Current Profiles

The measurement of the drift current profile is difficult. No complete data have been reported except for Tickner [Ref. 10] and Baines & Knapp [Ref. 1], both of whom made the measurements in shallow water channel at low wind velocities.

Five wind velocities of current profile measurements were conducted in the present study [Ref. 8]. For every wind velocity the profile was worked out from the average of five to eight runs. The current profiles vary with the wind velocity. Five profiles of different velocities were averaged to give the result as the curve E in Figure 11, where previous results are also shown in the figure for comparison.

Curve A in Figure 11 is summarized from the twelve drift current measurements of Wu [Ref. 14] while Curve B is compiled from three profiles of Shemdin [Ref. 6]. The measurements by Wu and Shemdin were aimed at the near surface region. Two curves are very close when y/d is larger than -0.2 , where d denotes the uniform water depth in the tank. Curve C was proposed by Kato [Ref. 3] with the assumption that current velocity at the bottom was equal to that at the half-depth. Curve D was obtained by Tickner [Ref. 10] at the small wind velocities of 3 m/s, in which detergent was added to the water to inhibit the formation of waves.

It is obvious that all of the results show a considerably different shape. In this result, the area under the return current is larger than that under downwind region. The continuity equation of net transport in vertical section is not satisfied. The lateral flow in the channel could cause the inaccuracies.

Analytical Result of Current Profile

Wind stress acting on the water surface causes a forward current in the upper layer and a backward current in the bottom, as shown in Fig. 12. Assuming that the wind stress is steadily and uniformly acting on the water surface, the drift current velocity will change gradually. As a result, the current profile can be separated into two regions: the upper region and the lower region being separated at $y = -\delta$ where $u = u_{\max}$.

The detailed configuration in the upper region is more complicated than the lower region. The wave drag will cause momentum transfer from air to water fluid. However, it is not expected that these effects will penetrate deeply into the fluid. The wind stress exerted on the fluid is like the roughness effect of a boundary. It is convenient to take this flow motion as a semi-pipe flow with the water surface as the pipe-wall. Similarly, the flow in the lower region is taking the flow motion as the semi-pipe flow with the bottom as its pipewall.

Taking the above into consideration, the current profile can be solved as the pipe flow problem. Tang [Ref. 9] solved this turbulent flow by Nikuradse's mixing length formula. The current profiles are given as:

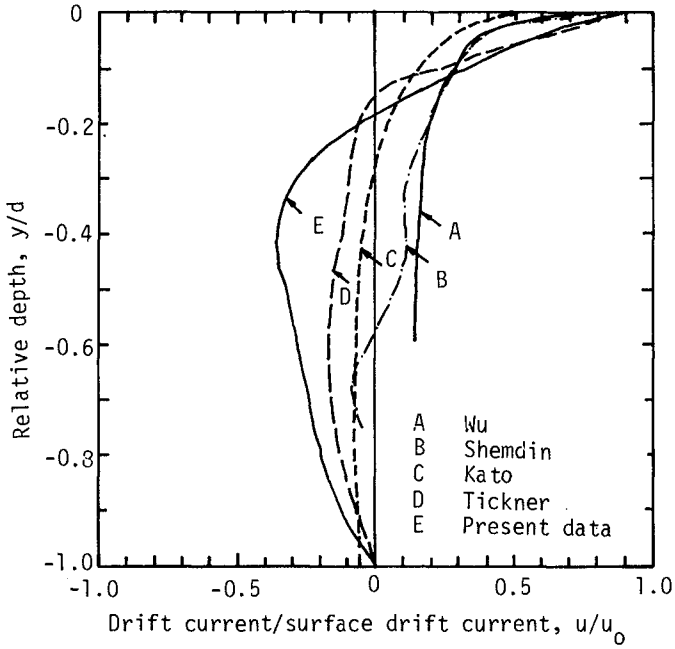


Figure 11. Comparison of drift current profiles

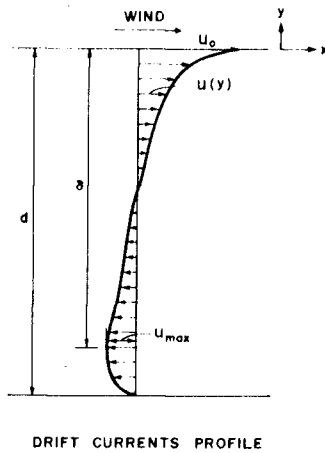


Figure 12. Drift current profile

$$\frac{u_{\max} - u}{u_*} = 2.5 \ln \left(\frac{y}{\delta} \right) + 1.5 \left(\frac{\delta + y}{\delta} \right) - 0.08125 \left(\frac{\delta^2 - y^2}{\delta^2} \right) + 0.06541 \left(\frac{\delta^3 + y^3}{\delta^3} \right) ; \text{ for } -\delta < y < 0 \quad (4)$$

and

$$\frac{u}{nu_*} = 2.5 \frac{d+y+Y}{Y} + 1.5 \left(\frac{d+y}{d-\delta} \right) - 0.08125 \left(\frac{d+y}{d-\delta} \right)^2 + 0.06541 \left(\frac{d+y}{d-\delta} \right)^3 ; \text{ for } -d < y < -\delta \quad (5)$$

where

$$Y = \frac{dn^2}{1+n^2} \exp \left[- \frac{1.760(1+n^3) + 1.484(1-n)}{2.5n(1+n^2)} \right]$$

$$n = \sqrt{\frac{|\tau_b|}{\tau_s}}$$

$$\tau_s = \tau_o - \tau_w$$

u_* = current friction velocity in the upper region

$$\tau_w = \text{wave drag}$$

The computations of Equations (4) and (5) were carried out for cases corresponding to the available experimental results. Good agreement was found, as shown in Figures 13 and 14, with some measured current profiles.

SURFACE SET-UP

The water surface set-up was computed from the data of the surface elevations. The mean water elevation at a station during the test is computed through the computer by sampling the data of surface elevations. The difference between this mean water elevation and the still water level is interpreted as the surface set-up. Surface set-up at the fixed point is sometimes expressed by the surface slope.

Figure 15 shows the relation between the surface slope and the wind friction velocity in the interval of fetches 22^m and 31^m. In general, the surface set-up at the fixed station increases with the increase of wind friction velocity. But the scattered data limit further examination.

The dependence of the surface set-up on the fetch is not clear in this study due to the water oscillation in the tank. Figure 16 gives the relative surface set-up, h/F , as a function of Froude number, including the data from different water depths and different fetches.

The forces exerting on the water body between two sections include the wind stress, bottom friction, momentum flux of drift currents, and hydrostatic pressures at the two sections. For steady condition, the force balance equation can be expressed as

$$\frac{\partial}{\partial x} \int_{-d}^0 \rho_w u^2 dy = -\rho_w g d \tan \alpha + \tau_o + \tau_b \quad (6)$$

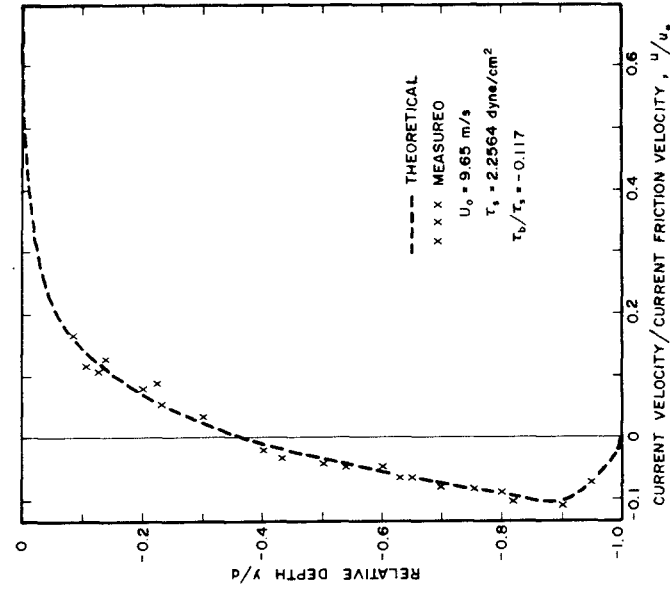


Figure 13. Comparison between proposed current distribution and measured

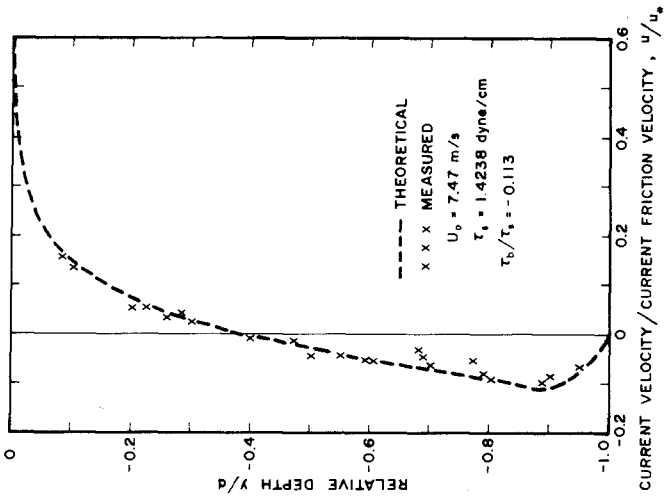


Figure 14. Comparison between proposed current distribution and measured

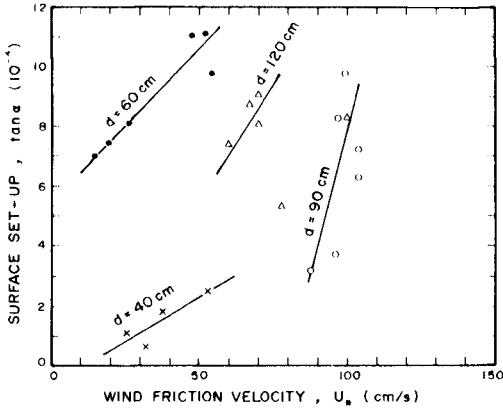


Figure 15. Relation between surface set-up and wind friction velocity at fetch 22^m

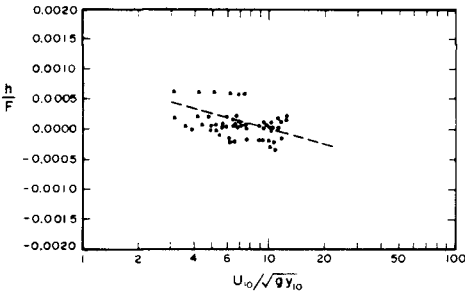


Figure 16. Surface set-up as a function of Froude number

where the left term represents the change of momentum flux due to drift currents and α is the inclination of the water surface between two sections.

Table 2 summarizes the various forces measured at fetch 22^m. If the left term in Equation (6) is neglected, the surface set-up can be estimated as

$$\tan\alpha = \frac{\tau_o + \tau_b}{\rho_w g d} \quad (7)$$

Figure 17 shows the comparison of surface set-up between the measured values and that estimated from Equation (7).

As shown in the figure, the actual water surface set-up is larger than those estimated from the wind stress and bottom friction. In other words, the determination of the wind stress from the water surface slope, which has often been used by the oceanographers, seems to be over-estimated.

TABLE 2: Various Stresses Measured at Fetch 22M

Depth (cm)	Wind friction velocity U_* (cm/s)	Wind stress τ_o (dyne/cm ²)	Bottom stress τ_b (dyne/cm ²)	Surface set-up $\rho_w g d \tan\alpha$
40	25.9	0.87	3.91	4.36
	32.5	1.37	4.01	2.61
	38.8	1.95	4.29	7.40
60	15.0	0.29	1.43	38.55
	19.4	0.49	1.69	43.77
	26.5	0.91	1.56	47.69
	53.9	3.76	1.65	57.49
	52.1	3.51	1.76	65.99
	47.7	2.94	1.72	65.33
90	87.5	9.90	1.02	28.42
	95.9	11.89	1.01	43.12
	102.7	13.64	1.07	55.86
	102.5	13.58	1.08	63.70
	96.7	12.09	1.10	73.50
	99.4	12.78	1.11	86.24

CONCLUSIONS

An attempt has been made for a systematic experiment covering all the dynamical forces on the water free body. Main findings are as follow:

1. Froude scaling criterion for the wind stress coefficient is confirmed, enabling the present results to be scaled for general application.
2. The bottom friction increases slightly with the increase of wind friction velocity, while the ratio between the bottom stress and the wind

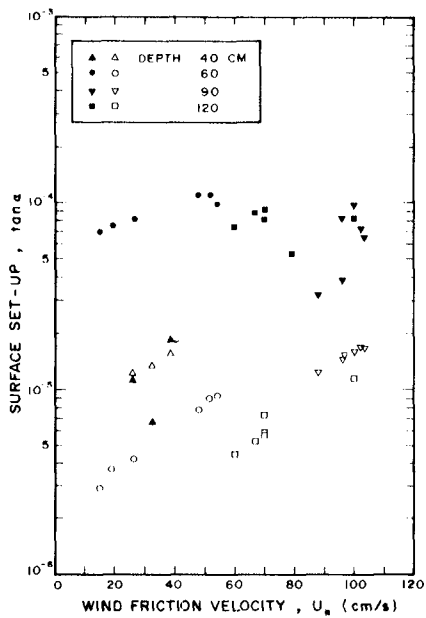


Figure 17. Surface set-up from measured and estimated
 (Solid: measured
 Open : estimated)

stress decreases rapidly with the increase of wind velocity.

3. A complete distribution of the mean current velocity is proposed for prediction of drift currents.

4. The wind stress determined from the inclination of the mean water surface is found to be larger than that obtained from the wind profiles.

ACKNOWLEDGEMENTS

This work was supported by both the National Science Council, Republic of China (Contract No. NSC 66-0501-0202(-17)), and the National Science Foundation, United States of America (Grant No. NSF OIP 75-15806).

REFERENCES

1. Baines, W.D. and D.J. Knapp (1965): Wind driven water currents, J. Hydraulics Division, ASCE 91, p. 205-221.
2. Chang, M.S. (1969): Mass transport in deep-water, longcrested random gravity waves, J. Geophysics Res. 74, p. 1515-1536.
3. Kato, H. (1974): Calculation of the wave speed for a logarithmic drift current, Rept. Port and Harbour Research Inst. 13, No. 4, p. 4-32.
4. Keulegan, G.H. (1951): Wind tides in small closed channels, Journal Res. National Bureau Standards 46, p. 358-381.
5. Plate, E.J., P.C. Chang and G.M. Hidy (1969): Experiments on the generation of small water waves by wind, J. Fluid Mechanics 35, p. 625-656.
6. Shemdin, O.H. (1972): Wind-generated current and phase speed of wind waves, J. Physical Oceanogr. 2, p. 411-419.
7. Sibul, O.J. and J.W. Johnson (1959): Laboratory study of wind tides in shallow water, J. Waterways and Harbour Division, ASCE 97, WW1, p. 1210-1 to 1210-32.
8. Tang, F.L.W., S.H. Ou, C.C.C. Kao, J. Wu, C.C.C. Chang (1977): Wind-induced water surface set-up and drift currents (I), Proc. First Conf. on Ocean Engineering, Taipei, Taiwan, p. 165-189.
9. Tang, S.Y. (1977): Research on velocity profile of wind drift current, MS Thesis under supervision of F.L.W. Tang, National Taiwan University, Republic of China.
10. Tickner, E.G. (1961): Transient wind tides in shallow water, TM-123, U.S. Army Corps of Engineers, Beach Erosion Board, Washington, D.C.
11. Wu, J. (1969): Froude number scaling of wind stress coefficients, J. Atmospheric Science 26, p. 408-413.
12. Wu, J. (1971): Anemometer height in Froude scaling of wind stress, J. Waterways, Harbors and Coastal Engineering Div., ASCE 97, WW1, p. 131-137.
13. Wu, J. (1973): Prediction of near-surface drift currents from wind velocity, J. Hydraulics Division, ASCE 99, p. 1291-1302.
14. Wu, J. (1975): Wind-induced drift currents, Journal of Fluid Mechanics 68, p. 49-70.

CHAPTER 49

DRIFT SPEED OF BUOYS IN WAVES

by

John H. Nath, F. ASCE⁽¹⁾

with an Appendix by M.S. Longuet-Higgins

Abstract

The drift speed of small floating objects subjected to periodic waves was investigated experimentally. Although data scatter is evident, the results show reasonably good agreement between Stokes third order mass transport drift speed and the drift speed of small surface floats, for the lower wave amplitudes. For the steepest waves there is good agreement between the data and recent developments of Longuet-Higgins. Surprisingly, the objects of deeper draft, such as a small spar-type buoy, drifted *faster* than the Stokes drift speed in the lower amplitude wave region of the tests. In the steepest waves the deeper buoys drifted a bit slower than the small objects.

1.0 INTRODUCTION

Mass transport currents on the surface of the ocean are sometimes estimated by tracking small floating discs or oceanographic research buoys. The NOAA Data Buoy Office has developed drifting buoys similar to that shown in Fig. 1 for tracking certain oceanographic parameters, such as water temperature, salinity, etc., as a function of the buoy position, commonly called the Lagrangian movement of the buoy. The buoy is often attached to a deeply submerged drogue by means of a tether and it is hoped that the drogue follows the currents at the depths desired. The buoy provides the reserve buoyancy for the system, as well as a habitat for sensors, recorders, transmitters, etc. Such a floating system is acted upon by wind, waves and currents. An ultimate objective is to be able to predict the motion of the system due to the forces of the environment. As part of this goal, it is desired to be able to predict the influence on the motion of the system from the waves alone.

Instead of the complete system, sometimes the buoy is drifted alone in order to more accurately track the surface currents. Floating discs and other objects are also used by engineers and oceanographers to track littoral drift currents near the breaker zone along the shoreline. Frequently, the motion of such drifters is taken as being equal to the speed of the surface currents acting upon them. However, this study shows that the speed of such drifters is significantly influenced by the water waves alone.

- (1) Professor of Civil and Ocean Engineering and Director of the Environmental Fluid Dynamics Laboratory, Oregon State University, Corvallis, Oregon.

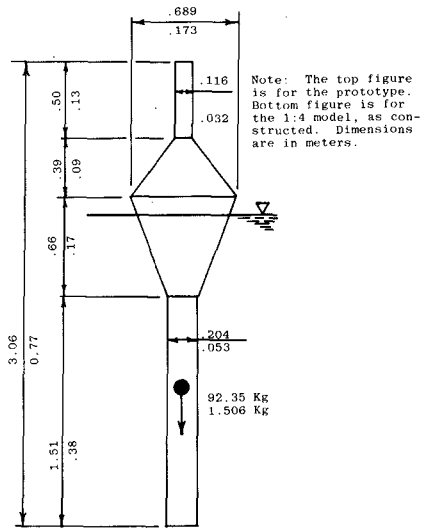


Fig. 1 Drifting Buoy Dimensions

One early part of this work was to develop a time domain numerical model (9) for predicting the motion response of the drifting system to periodic waves, wind and current. A lumped parameter approach for the buoy, tether and drogue was utilized. For the buoy alone, at a particular time step, the forces and moments acting on the buoy are determined, thence the accelerations from Newton's second law of motion. The displacements and velocities at the end of the next time step are then determined with Runge-Kutta and predictor-corrector integration methods. The forces are estimated by dividing the buoy into useful discrete elements and applying a Morison-type equation. Therefore, the predicted buoy motion is dependent on certain coefficients. They were determined experimentally as explained in (10) and the total calculation was checked by comparing numerical model results to laboratory testing for buoy drift speed. The emphasis in this paper is on the laboratory results.

1.1 Purpose and Scope

The purpose of this study was to determine the drift speed in periodic waves for the oceanographic research buoy used by the NOAA Data Buoy Office and for smaller objects. A validation of the numerical program which predicts buoy drift speed was desired as well as a comparison with theoretical predictions of mass transport velocities from waves. Ultimately, it is hoped to be able to predict the average drift speed of buoys in a wave spectrum.

The amount of work at this stage is limited to the experimental determination of the drift of such objects in periodic waves. Of prime importance was to gather experimental evidence of such drift speeds for the first time. It was found that Stokes third order mass transport drift speed fairly well predicts the speed for very small objects. However, for the spar-type drifting buoy, the drift speed was faster than for the small surface float for waves not approaching the limiting steepness. Such a surprising outcome was fairly well predicted by the numerical model which predicts the motion of the buoy to periodic waves. Evidently the accelerations in the waves act upon the buoy in such a manner as to more than overcome the additional restraining drag from the lower extremities of the buoy. The lower extremities of the buoy were in depths of smaller particle trajectory.

1.2 Literature Review

A complete systematic study of the drift speed of objects in waves, either in the laboratory or in the field, has not been done to the writer's knowledge. However, several studies have been made of mass transport in waves using dye and neutrally buoyant particles, in the laboratory. In addition, some theoretical developments have been made.

Stokes (12) showed that wave particle orbits are not closed and that the drift term for deep water ($kh \gg 1$) second order computations is

$$\bar{U} = A^2 \sigma k e^{-2Kz} \quad (1)$$

where A is a wave amplitude, σ is the radian frequency, $2\pi/T$, T is the wave period, and k is the wave number, $2\pi/L$, where L is the wave length. The usual axes are considered here with x positive to the right and z positive upward and $z = 0$ at the still water level. In addition, z may be taken as the mean depth of the particle trajectory below the mean surface level.

Wiegel (3) presents a summary of third order equations for wave motion, and the Lagrangian particle displacements yield a steady state term for deep water, at $z = 0$, of

$$\frac{\bar{U}}{gT} = \frac{1}{4\pi} [1 + (ka)^2] [2(ka)^2 - \frac{20}{8}(ka)^3 + \frac{50}{64}(ka)^4] \quad (2)$$

where a is defined from

$$\frac{H}{L} = 2 \frac{a}{L} + 3\pi^2 \left(\frac{a}{L}\right)^3 \quad (3)$$

and at the breaking wave condition (deep water) H/L , 0.1412 and $a/L = .0666$.

These expressions are valid on the assumption that viscous effects are negligible, or have had not time to act, and that the motion is strictly irrotational and thus free of vorticity.

The viscous effects in laminar motion were considered by Longuet-Higgins (5) who presented a derivation based on boundary layer and vorticity concepts for the "conduction" solution ($A \ll \zeta$, where ζ is the

boundary layer thickness) which is sometimes used successfully in practice (2) regardless of the original small amplitude assumption. For a progressive wave in a uniform depth the solution is

$$\bar{U}(z/h) = A^2 \sigma k F(z/h) \quad (4)$$

$$\begin{aligned} \text{where } F(\mu) = & \frac{1}{4\sinh^2 kh} \{2\cosh[2kh(\mu-1)] + 3 + kh(\sinh 2kh)(3\mu^2 - 4\mu + 1) + \\ & + 3\left(\frac{\sinh 2kh}{2kh} + \frac{3}{2}\right)(\mu^2 - 1)\} \end{aligned} \quad (5)$$

Equation 5 is used successfully for predicting wave mass transport speeds near the bottom (2), but near the surface in deeper water it is not applicable. This is because the flow requires a long time, of order (h^2/ν) , to become established, where ν is the kinematic viscosity.

For large kh

$$F(\mu) = \frac{1}{2} kh (3\mu^2 - 4\mu + 1) + e^{-2kh\mu} \quad (6)$$

and

$$F(0) = \frac{kh}{2} + 1 \quad (7)$$

so that, for unbounded water depth, Eqs. 4 and 7 are unbounded.

It is also interesting to compare drift speeds with the maximum calculated particle velocity at the crest of a wave. The kinematic criterion for breaking is that the wave height increases to the point where the crest particle velocity is equal to the phase speed of the wave.

The phase speed relation for small amplitude waves in deep water is

$$c_0 = \frac{gT}{2\pi} = \frac{g}{\omega} \quad (8)$$

Phase speed for Stokes third order theory (12) is very close to that for fifth order theory and Dean's stream function theory, and is given by Eq. 9 for the maximum wave height condition. This is also the particle velocity at the crest of the wave.

$$c_0^2 = gk_0 [1 + (ka)^2] \quad (9)$$

However, the actual mean speed of advance of the water particles at the surface in a limiting finite amplitude wave is calculated by Longuet-Higgins in the Appendix as

$$\frac{\bar{U}}{c} = 1 - \frac{L}{c\tau} = 0.274 \quad (10)$$

where τ is the period for a pendulum with arm length equal to the wave

length. It is also shown in the Appendix that there is a small negative drift velocity compensating for the total mass-transport in the wave. The magnitude of this drift velocity is

$$U = -\frac{1}{h} = \frac{0.070 (g/k)^{1/2}}{kh} \tag{11}$$

where 1 is the total momentum in a highest deep water wave. For the shallowest condition in the wave tank testing, $\tanh kh \approx 0.83$, so that $kh \approx 1.2$ for that condition. Thus, the total drift for this shoaling case, also taking into account the reduction in phase speed, is $\bar{U}/C_0 = 0.16$. So, for this testing one might expect \bar{U}/C to be from about 0.16 to 0.27.

2.0 METHOD

It was desired to obtain experimental values of buoy drift speed in the laboratory under carefully controlled conditions and to compare these with the various predictors.

2.1 Laboratory Facilities and Procedure

The Wave Research Facility at Oregon State University is described in (4) and (11). For this study, a constant water depth of 3.51 m was used in the constant depth test section. It was found in (11) that the measured wave kinematics for periodic waves are fairly well predicted by Stokes third order wave theory. For the conditions investigated, the Stokes third order wave theory, fifth order wave theory and Dean's stream function theory all give nearly the same results. The maximum periodic wave characteristics in the flume test section are shown in Fig. 2.

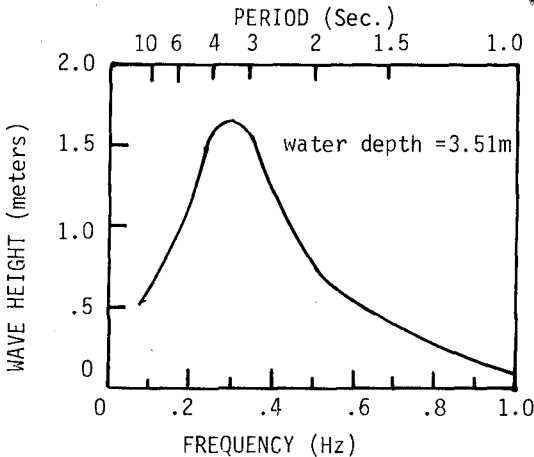


Fig. 2 OSU WRF Periodic Wave Limiting Curve

The drift tests were performed in the laboratory on two experimental buoys, one small discus and one very small sphere. Thus, four objects were tested. The buoys were a prototype 92.4 kg buoy and a 1:4 scale model weighing 1.5 kg, as shown in Fig. 1. The small buoy is labeled Buoy No. 2 and the prototype buoy is labeled Buoy No. 3. [Buoy No. 1 is reported on in (9).] The discus and sphere are shown in Fig. 3. The discus measured 15 cm in diameter, 2.5 cm thick and weighed 150 g so that it floated horizontally at mid-thickness. The small ball was 3.7 cm in diameter and weighed 29 g so that it just barely floated.

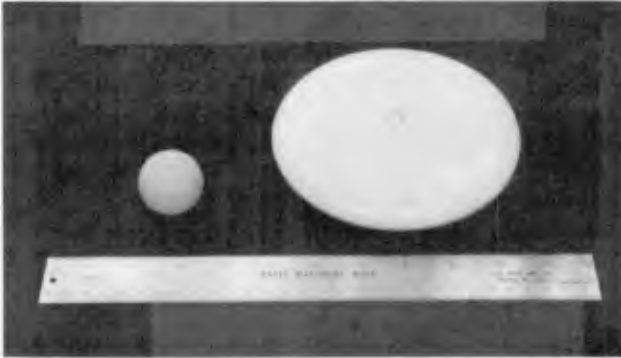


Fig. 3 Small Sphere (3.7 cm) and Small Discus (15 cm dia.) Drift Test Specimens

For each run the specimen was individually subjected to a long series of periodic waves. In the later stages of the testing with the discus and the sphere, a concerted effort was made to provide a long series of waves just prior to performing a drift test so that steady state dynamic conditions would be achieved. However, in the early stages of the testing with the two buoy specimens, such long periods may not have been achieved in each case.

After the wave system was established, the specimen location in the flume was noted just as it appeared at the crest of a wave by placing a marker on the wall in line with that particular wave crest. A stop watch was then started and several waves were allowed before the location was again marked in a similar manner at the crest of another wave. A photo of a typical test is shown in Fig. 4. The elapsed time was noted and the drift distance measured. The average drift speed was calculated therefrom.

2.2 Error Sources

In an experimental study of this sort several sources of error can enter into the measurements. The obvious errors were minimized by making the measurements carefully. Wind currents can create significant surface drift speeds in the shear layer between the wind and water which can

seriously influence the drift speed of small floating objects. In addition, the wind can act on large floating objects and influence their drift merely by the wind drag acting on the object. Therefore, when the wind was blowing at a level which influenced the results, the testing was suspended. In addition, the method of measuring the distance of buoy drift was subject to various sources of parallax which was minimized by using relatively long drift distances which occurred over relatively long periods of time. Thus, the division of these two quantities to obtain the drift speed resulted in a good average value.



Fig. 4 Typical Test Run with Buoy No. 3

In some runs a stray force would initiate a roll motion to the buoy, in a strict nautical sense. It was possible for this motion to become accentuated even though the wave period was not equal to the roll (same as pitch) period of the buoy, or two times that period. This precession was severe in only a few cases. Of course, any precession created a three-dimensional problem from a two-dimensional one. This stray motion was probably a major contributing factor to scatter in the data for the buoys. It will be noted that much more scatter exists for Buoy 3 than for Buoy 2.

It is not known from either theory or experiments how much time is required to establish steady state dynamic conditions in a wave flume. The transient time must be a function of wave board motion characteristics, flume length, water depth, beach absorption and many other variables. In the latter parts of this study, several waves were allowed to pass (20 or 50) prior to starting a test. Thus, it is possible the mass transport circulations had not reached a steady state motion condition prior to a test, and this could conceivably contribute to some of the scatter.

Therefore, a more subtle source of error is in the value and vertical distribution of the reverse flow that must exist in the closed

system wave flume. This reverse flow is a function of the characteristics of wave dissipation at the beach and any reflections that occur. Literature has already been cited that deals with the vertical distribution of mass transport, but an intensive study of the reverse flow, or circulation, mechanism of mass transport in a *closed system wave flume* of the kind used has not been made to the writer's knowledge. According to the results obtained, such reverse flow may not have affected the measurements unduly.

2.3 Data Analysis

The data analysis was quite simple. It was merely necessary to divide the distance traveled by the floating object by the associated period of time. The drift speed results are presented in a non-dimensional form on the graph by dividing the drift speed by gT . It is noted that by multiplying the result by 2π , the resulting values are V/C_0 , where C_0 is the value of wave celerity in deep water from Airy theory.⁶ The buoy drift speed is designated as V . In addition, it may be that the major factor in the motion generation of the buoy is the vertical acceleration of the water particles. They are non-dimensionalized as follows:

$$\frac{\text{particle acceleration}}{g} \approx \frac{H\sigma^2}{g} \quad (12)$$

The linear wave dispersion relation, $\sigma^2 = gk \tanh kh$, is then used, for simplicity, to change the form of Eq. 12 to

$$\frac{\text{particle acceleration}}{g} \approx Hk \tanh kh, \quad (13)$$

which gives some account to shoaling. In the OSU Wave Research Facility tests, most of the waves were deep water waves for which $\tanh kh = 1.0$. The lowest value of $\tanh kh$ was greater than 0.80. It is realized that Eq. 13 is rather crude but refinements from this seem to be lost in the noise of the experiments. By trial, the data collapsed fairly well into coherent plots with this technique. However, it should be noted that the limiting value of $Hk \tanh kh$ in deep water is 0.89, but that the maximum theoretical value of particle acceleration of the wave crest is 0.5 g for a progressing wave.

The nonlinearity of the waves and the influence of shoaling is sometimes approximated by considering the Ursell parameter in the manner similar to that suggested by Hudspeth (3). In this work the Ursell parameter, Ur , is defined as

$$Ur = \frac{H L^2}{h^3} \quad (14)$$

It should be noted that this parameter has little meaning in deep water.

3.0 RESULTS

The general range of wave parameters used for this test are shown in Fig. 5. The basic laboratory results are summarized in Table 1.

Table 1. Basic Laboratory Measurements

Run No.	Wave Period (sec.)			Wave Height (ft.)			Drift Speed (ft./sec.)					
	Object			Object			Object					
	Sphere	Discus	Buoy 2	Buoy 3	Sphere	Discus	Buoy 2	Buoy 3	Sphere	Discus	Buoy 2	Buoy 3
1	1.00	1.00	1.00	1.00	0.32	0.32	.46	.20	0.140	0.200	0.360	.10
2	1.00	1.00	1.00	0.56	0.56	0.56	.27	.31	0.480	0.560	.160	.28
3	1.25	1.25	1.00	0.25	0.25	0.25	.20	.40	0.085	0.110	.087	.38
4	1.25	1.25	1.45	0.43	0.43	0.43	.48	.15	0.150	0.160	.375	.11
5	1.25	1.25	1.45	0.61	0.61	0.61	.27	.38	0.380	0.340	.100	.37
6	1.49	1.49	1.22	0.35	0.35	0.35	.52	.51	0.067	0.620	.360	.47
7	1.49	1.49	1.22	0.64	0.64	0.64	.26	.72	0.240	0.280	.052	.51
8	1.49	1.49	1.75	0.93	0.93	0.93	1.74	.33	0.380	0.460	.650	.33
9	1.67	1.67	1.75	0.43	0.43	0.43	1.42	.71	0.070	0.048	.490	.42
10	1.67	1.67	1.49	0.80	0.80	0.80	1.97	.93	0.260	0.240	.240	.46
11	1.67	1.67	1.75	1.10	1.10	1.10	.64	1.20	0.460	0.420	.120	.59
12	2.00	2.00	1.75	0.97	0.97	0.97	.35	.98	0.230	0.140	.045	.26
13	2.00	2.00	1.85	1.87	0.97	0.97	2.01	1.44	0.370	0.250	.760	.40
14	2.50	2.00	1.85	0.93	1.47	1.47	1.45	1.93	0.100	0.480	.480	.64
15	2.50	2.50	1.85	1.80	0.93	1.80	1.00	1.06	0.310	0.140	.170	.26
16	2.50	2.50	1.85	2.60	1.80	1.80	.51	2.18	0.500	0.330	.093	.44
17	3.00	2.50	1.85	0.93	2.60	2.60	.37	2.94	0.006	0.680	.070	.50
18	3.00	3.00	2.00	1.87	0.93	1.87	1.98	1.04	0.140	0.058	.690	.12
19	3.00	3.00	2.00	2.67	1.87	1.87	.96	2.09	0.350	0.200	.280	.14
20	3.33	3.00	2.00	0.96	2.67	2.67	.57	2.61	0.026	0.390	.200	.22
21	3.33	3.33	2.78	1.93	0.96	0.96	2.93	1.90	0.140	0.011	.660	.17
22	3.33	3.33	2.78	2.80	1.93	1.93	1.09	.95	0.250	0.210	.190	.13
23	4.00	3.33	2.78	1.01	2.80	2.80	2.09	2.57	0.008	0.390	.440	.12
24	4.00	4.00	3.45	2.13	2.13	2.13	3.86	2.86	0.077	0.220	.650	.32
25	4.00	4.00	3.45	3.00	3.00	3.00	1.08	4.10	0.230	0.350	.150	.35
26	--	--	3.45	--	--	--	3.60	.95	--	--	.087	.18
27	--	--	3.45	--	--	--	2.84	2.42	--	--	.410	.32
28	--	--	3.45	--	--	--	2.09	4.00	--	--	.250	.55
29	--	--	4.00	--	--	--	4.29	--	--	--	.680	--
30	--	--	4.00	--	--	--	2.57	--	--	--	.250	--
31	--	--	4.00	--	--	--	1.03	--	--	--	.170	--

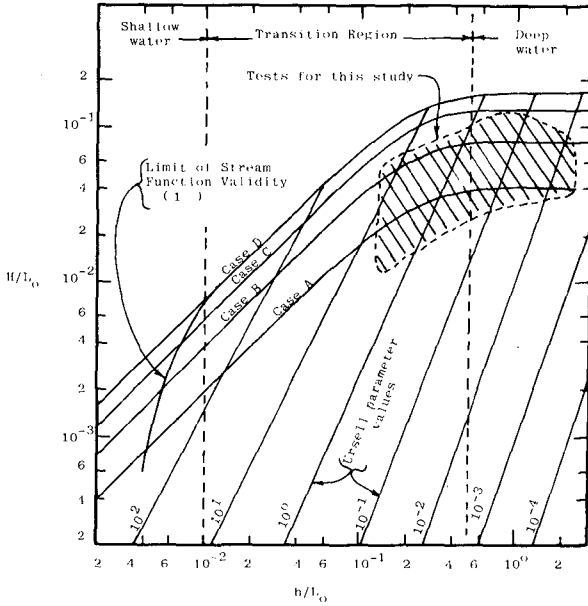


Fig. 5 Range of Periodic Waves with Drifting Objects

The results for the drift speeds for each of the buoys or floating objects are shown in Figs. 6 through 9. The dashed lines drawn through the data are the regression curves of

$$\frac{V}{gT} = B (Hk \tanh kh)^C \quad (15)$$

Table 2. Values of B and C, for Eq. 15, from data.

Model	$B \times 10^2$	C
Sphere	3.05	1.97
Discus	2.92	1.72
Buoy 2 - physical	1.79	1.23
Buoy 2 - numerical	2.85	1.60
Buoy 3 - physical	1.66	1.07
Buoy 3 - numerical	3.78	1.71

Figure 10 shows a comparison of the regression curves for each of the four physical models. If the regression lines for the small sphere and disc are extended to the deep water breaking wave condition, (a

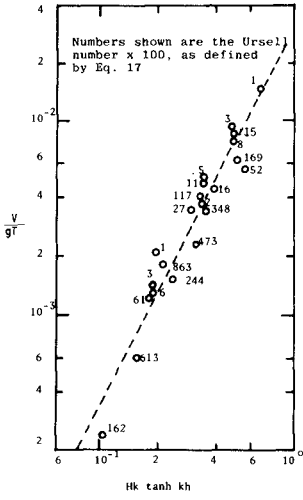


Fig. 6 Drift Speed of Small Sphere

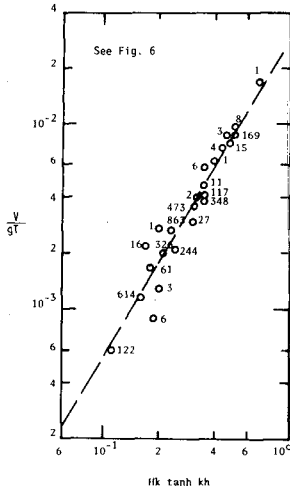


Fig. 7 Drift Speed of Small Discus

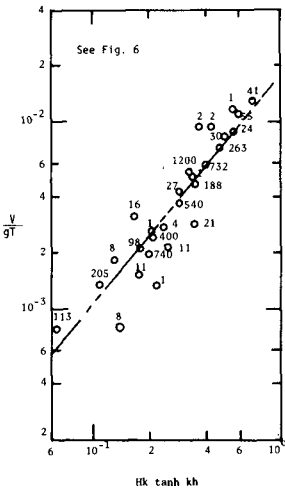


Fig. 8 Drift Speed of Buoy 2 Physical Model

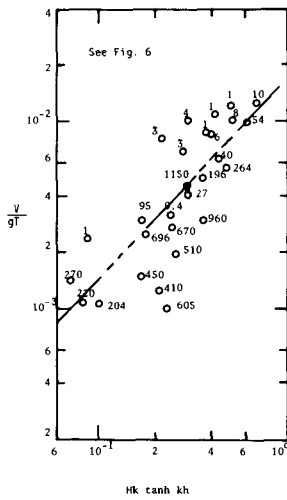


Fig. 9 Drift Speed of Buoy 3

questionable practice, but nonetheless tempting since data were not obtained in the region of very steep, breaking and nearly breaking waves) values of V/gT of 0.2435 and .02403 are obtained, respectively, so that $V/C_0 = 0.153$ and 0.151, respectively. These values compare very closely with those predicted by Longuet-Higgins if one assumes that $\tanh kh \approx 0.8$. However, the high values of V/gT generally can be attributed to runs with relatively short wave lengths so that $\tanh kh \approx 1.0$.

The numerical model of buoy motion was also used in a manner similar to the wave flume tests. A typical example of plotted computational results is shown in Fig. 11, for quick reference to Fig. 10. The total set of runs contains some scatter because the numerical model was probably not run for a long enough time, in some cases, to reach steady state response. This came from a desire to minimize computer costs. A same regression curve as Eq. 15 is shown and the regression curve for laboratory results is superimposed. The force coefficients for the numerical model could perhaps be slightly modified to achieve better agreement. However, the results appear to be quite good and modification of the coefficients have not been made to date.

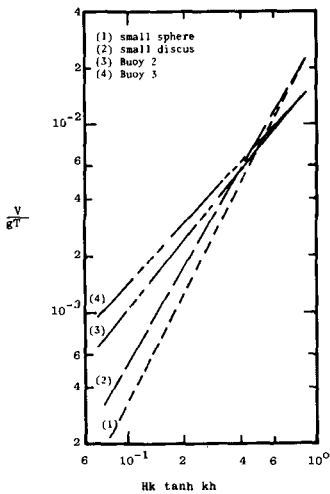


Fig. 10 Regression Curves of Four Laboratory Experiments

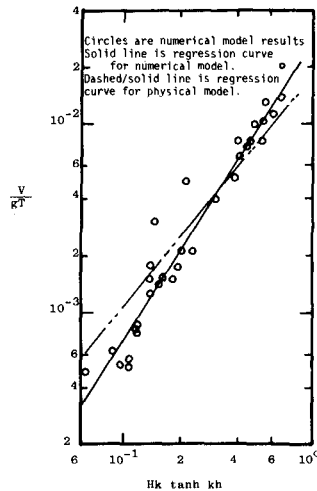


Fig. 11 Drift Speed of Buoy 2 Numerical Model

The regression lines from Fig. 10 are redrawn on Fig. 12, along with other theoretical information for comparative purposes. It could be considered that a limiting case of specimen drift speed would be when the wave breaks and the specimen surfs with the waves, and thus travels with the phase speed of the wave. This could not be tested for periodic waves in the wave flume because the waves could not be made to break continuously at the incipiently breaking condition. However, the particle crest speed is shown for Dean's stream function theory and Stokes third and fifth order theories, for $\tanh kh = 1.0$ and $\tanh kh = 0.80$, for the breaking conditions, on Fig. 12.

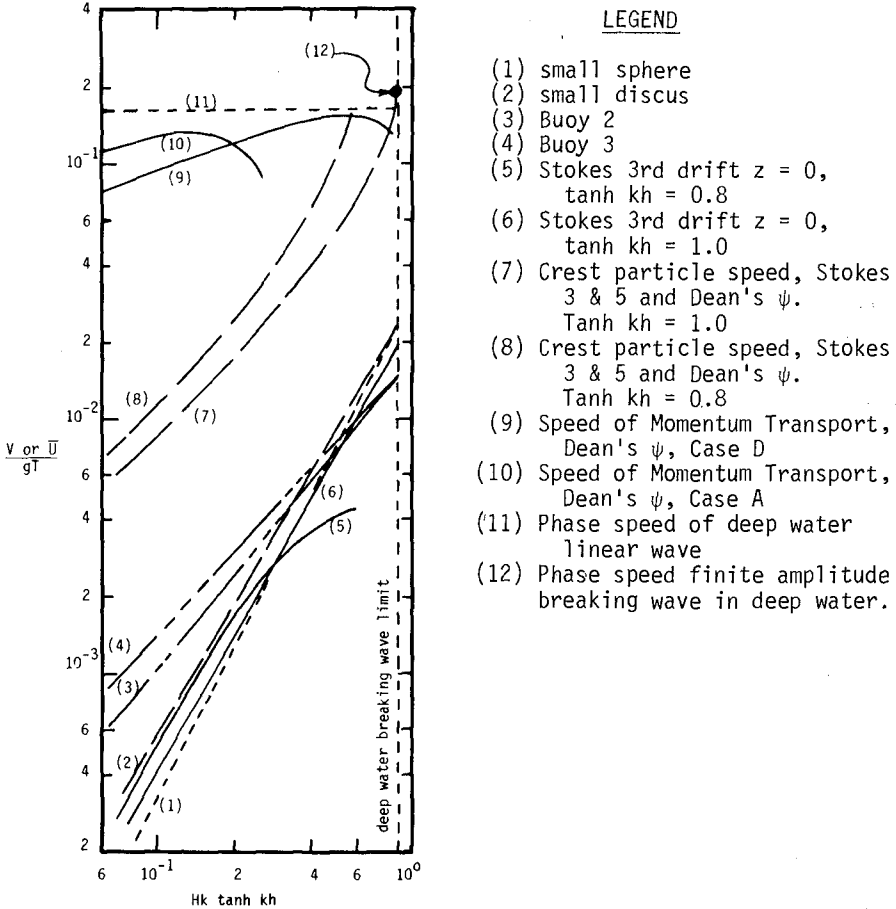


Fig. 12 Composite of Theories vs. Laboratory Results

DISCUSSION

The small discus and sphere drift speeds appear to be fairly closely approximated by the Stokes drift speed as predicted by third order theory. In addition, the drift speed predicted by Longuet-Higgins, with appropriate assumptions for kh , appear to predict the mass transport quite well for very steep waves.

In general, the drifting buoys and other objects tend to be in the region of the predictions by Stokes and Longuet-Higgins. The crest particle horizontal speed is considerably higher than the mass transport drift speed, evaluated at $z = 0$, and approaches the breaking wave phase speed for large kh . The slope of the drift speed curves in Fig. 12 for

the larger buoys is more parallel to the slope of the curves for the crest particle velocity than the slope of Stokes drift.

The regression curve describing the data trends for the large buoy and the small buoys are remarkably close together. In fact, for large wave heights the buoys and the small objects have approximately the same drift speed, in a non-dimensional sense.

The time domain numerical model predicts the drift speed of the buoys quite well. A small modification of the drag and added mass coefficients could be obtained for a closer correlation.

The non-dimensional drift speeds of each object, whether small or large, seem to be independent of Ursell parameter or wave period. Experimentally, at least within the noise of the measurements, widely different Ursell parameters plotted close to one another, indicating that the non-dimensional drift speed is independent of wave length, given other variables are held constant.

Although the information in this research is illuminating, it does not predict the drift of objects in random waves. In order to be able to predict the drift of such buoys in the ocean, one must be able to relate the calculations to the random wave conditions. Since the drift speed is nonlinearly related to the wave amplitudes, it may not be a straight forward matter to develop a nonlinear transfer function to be able to predict buoy drift speed from a random wave spectrum. Until a more careful determination can be made, one might get an estimate of the drift of a buoy in a random sea by working with the modal period, hence the modal wave length, for a narrow wave spectrum. In addition, testing with random waves may be required within the test facility.

ACKNOWLEDGEMENTS

This study was supported by the NOAA Data Buoy Office at the Space Technology Laboratories, Bay St. Louis, Mississippi, through contract 03-78-G03-0500. Part of the effort on this research was supported by the National Science Foundation through contract ENG-76-1623 regarding the slow drift characteristics of moored breakwaters in random waves. I am grateful for the energetic and careful work on the computations from Mr. Cheng-Wen Lin. The laboratory work and model construction was carried out by Mr. Lawrence Crawford and Mr. Terence Dibble, who performed much of the testing independently while I was on leave of absence in Japan. Their careful work and concerned attitude are very much appreciated. In particular, I want to thank Professor Longuet-Higgins for his helpful advice and fascinating Appendix to this paper.

REFERENCES

1. Dean, R.G., "Evaluation and Development of Water Wave Theories for Engineering Application," Vols. 1 & 2, U.S. Army Corps of Engineers, Coastal Engineering Research Center, Special Report #1, November 1974.
2. Horikawa, K., "Coastal Engineering," University of Tokyo Press, 1978.
3. Hudspeth, R.T., "Effects of Nonlinearities on Wave Power Estimates," Journal of the Power Division, ASCE, July 1977.

4. Hudspeth, R.T., Jones, D.F. and Nath, J.H., "Analysis of Hinged Wavemakers for Random Waves," Proceedings of 16th International Conference on Coastal Engineering, Hamburg, September 1978.
5. Longuet-Higgins, M.S., "Mass Transport in Water Waves," Proceedings of the Cambridge Philosophical Society, 245, No.903,535-581,1953.
6. Longuet-Higgins, M.S., "Mass Transport in the Boundary Layer at a Free Oscillating Surface," Journal of Fluid Mechanics, Vol.8,1960.
7. Longuet-Higgins, M.S., See Appendix.
8. Longuet-Higgins, M.S., "Integral Properties of Periodic Gravity Waves of Finite Amplitude," Proceedings of Royal Society of London, A342, 1975.
9. Nath, J.H., "Laboratory Validation of Numerical Model Drifting Buoy-Tether-Drogue System," Engineering Report for NOAA Data Buoy Office, July 29, 1977.
10. Nath, J.H., "Laboratory Model Tests of Drifting Buoy and Drogue," Research Report for NOAA Data Buoy Office, Ocean Engineering Wave Research Facility TR2, Oregon State University, Corvallis, Oregon, September 1977.
11. Nath, J.H. and Kobune, K., "Periodic Theory Velocity Prediction in Random Waves," Proceedings of 16th International Conference on Coastal Engineering, Hamburg, September 1978.
12. Stokes, G.G., "On the Theory of Oscillatory Waves," Mathematical and Physical Papers, Cambridge University Press, London, Vol.1, 1847.
13. Wiegel, R.L., "Oceanographical Engineering," Prentice Hall, Inc.1964.

APPENDIX: THE ORBITAL MOTION IN STEEP WATER WAVES⁽¹⁾by Michael S. Longuet-Higgins⁽²⁾

For a steady, irrotational wave of maximum height in deep water, a rough but possibly useful formula for the orbital motion may be found as follows.

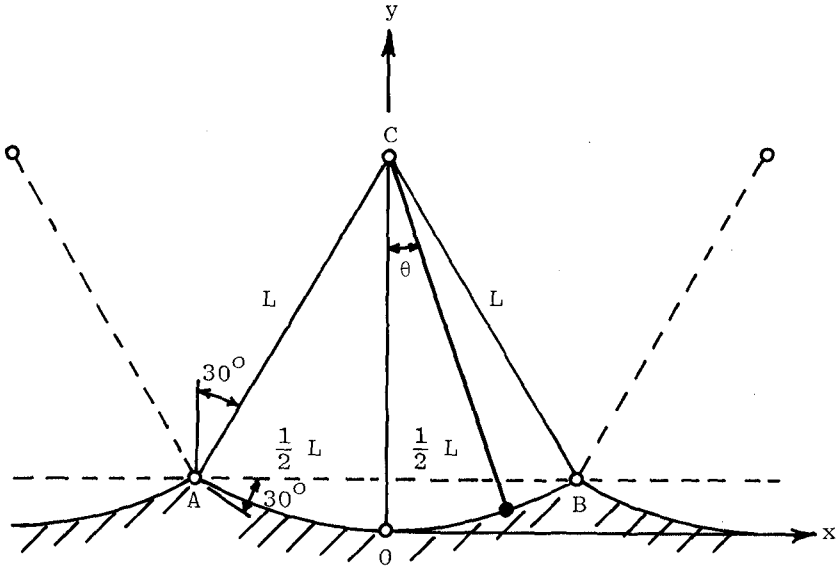


Figure A1

In Figure 1A a wave of length L travels to the right with speed c . We can approximate the free surface between the two adjacent crests A and B by the arc of a circle centre C . To agree with the slope angle of 30° at the crests ($A2$) the arc must correspond to a 60° sector. Hence the triangle ABC is equilateral, and the radius of the arc equals the wave length L . This gives a crest-to-trough wave height $L(1 - \cos 30^\circ)$ or $0.1340 L$, which differs from the accurate ($A3$ and $A4$) value $0.1412 L$ by only $0.0072L$.

At the free surface the pressure is constant, so that the pressure gradient is always normal to the surface. A particle travels from B to A in one half-period

(1) Presented at the 16th International Conference on Coastal Engineering, Hamburg, 1978, as a discussion of the paper by John H. Nath, "Drift Speed of Buoys in Waves."

(2) Royal Society Research Professor, Dept. of Applied Mathematics and Theoretical Physics, Silver Street, Cambridge, England and Institute of Oceanographic Sciences, Wormley, Surrey.

$$\tau \doteq \pi (L/g)^{\frac{1}{2}}$$

At A it comes to rest relative to the profile, and assuming it does not surf-ride, it then transfers, like a trapeze artist, onto a similar pendulum at the left of A. In a reference frame which is at rest relative to deep water the particle has advanced a distance $(c\tau - L)$ in time τ . Its mean speed of advance is therefore

$$U = \frac{c\tau - L}{\tau} = c(1 - \frac{L}{c\tau}).$$

Using the expression $c \doteq (gL/2\pi)^{\frac{1}{2}}$ for deep-water waves of low amplitude gives

$$U/c = 1 - \frac{L}{c\tau} \doteq 1 - (\frac{2}{\pi})^{\frac{1}{2}}$$

The more accurate values $c = 1.0923 (gL/2\pi)^{\frac{1}{2}}$ and $\tau = 1.0174\pi(L/g)^{\frac{1}{2}}$ for waves of maximum height (A3 and A4) and for a pendulum of swing $\pm 30^\circ$ (A5) gives $U/c = 0.282$. Thus the average speed of advance is about 0.28 times the phase-speed.

The particle orbits are given approximately by

$$x = ct - L \sin\theta$$

$$y = L(1 - \cos\theta)$$

where t = time, and (A6)

$$\sin \frac{1}{2} \theta = k \sin(k\sqrt{g/L} t), \quad k = \sin 15^\circ$$

(see Figure A2). After describing each orbit the particle has

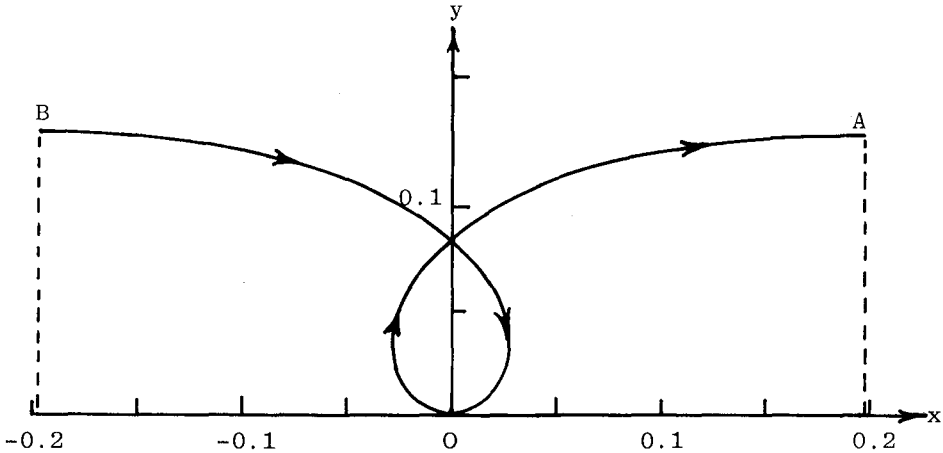


FIGURE A2

advanced a distance X where

$$\frac{X}{L} = \frac{cT - L}{L} = \left(\frac{cT}{L} - 1\right) = 0.393.$$

Precise numerical calculations (A6) based on the profile of the highest deep-water waves as given numerically by Yamada (A3) yield, respectively,

$$U/c = 0.274 \text{ and } X/L = 0.377$$

quite close to the values we have found.

To summarize, the orbital motion of a particle at the surface of a deep-water gravity wave consists very nearly of a uniform horizontal translation superposed on the backwards swing of a pendulum.

However, it can be shown (A6) that the drift velocity U in waves of slightly less than the maximum steepness is significantly less than the steepest wave. Also that in the steepest wave the gradient of the drift velocity near the surface becomes large. Thus, bodies submerged to a depth of only $0.02 L$ may be expected to drift at about half the speed of particles in the free surface.

Lastly, in wave channels of finite length, the effect of a return flow to compensate for the forward mass flux must be considered. For instance, in steep gravity waves in deep water, the total volume flux I is given by

$$I = 0.070 (g/k^3)^{\frac{1}{2}}$$

approximately [see Figure 2 of reference (A7)] where k is the wave number. Hence, in water of moderate depth h such that e^{-kh} is negligible but not $(kh)^{-1}$, there must be a backwards flow of order

$$U' = -\frac{I}{h} = \frac{0.07 (g/k)^{\frac{1}{2}}}{kh}$$

If kh is about 1.2, then there will be a net reduction in the effective phase-speed of about 6 percent, in addition to other changes arising from the finite depth of water, which may be about 9 percent. Such changes together would be enough to reduce U/c from 0.27 to about 0.16, close to the limiting values found by Nath.

In other words, the net drift-speed is very sensitive to finite-depth effects, particularly the compensating backwards flow, which diminishes only like $(kh)^{-1}$, not e^{-kh} , when kh is large.

The application of these results to irregular sea waves, both swell and waves under the action of wind, will be discussed elsewhere.

REFERENCES

- A1. Lamb, H. Hydrodynamics, pp.419 (Cambridge Univ. Press, 1932.)
- A2. Stokes, G.G. Mathematical and Physical Papers 1, 326 (1880).
- A3. Yamada, H. Rep. Res. Inst. Appl. Mech, Kyushu Univ. 5, 37-57,(1957).
- A4. Schwartz, L.W. J. Fluid Mech. 62, 553-578 (1974).
- A5. Bowman, F. Elliptic Fluctions, New York, Wiley p. 28 (1953).
- A6. Longuet-Higgins, M.S. The trajectories of particles in steep, symmetric gravity waves. Submitted to J. Fluid Mech. Oct. 1978.
- A7. Longuet-Higgins, M.S. Integral properties of periodic gravity waves of finite amplitude. Proc. R.Soc. Lond. A342, 157-174 (1975).

CHAPTER 50

NEAR-BOTTOM CURRENT MEASURED BY ACOUSTIC SENSORS

K.A. Selanger[†] and T. Carstens[†],
River and Harbour Laboratory, Trondheim, Norway.

ABSTRACT

A vertical current profile has been measured with three acoustic meters 60 cm, 100 cm and 200 cm from the sea bottom. The depth at the measuring site was 84 metres. The profile is found to depend on the time scale of the water particle motion. An Ekman-like turning of the current is also observed, and the thickness of friction layers is estimated. Comparison of the current data with wave measurements indicates that the vertical transfer of surface wave energy is 30-50 per cent less than first order wave theory prescribes.

INTRODUCTION

To extrapolate a current profile through the bottom friction layer is often requested, but very difficult to do with satisfying accuracy and reliability of the result. One important reason is that there is still a great shortage of field data to support theoretical works on this subject (1,2) or to cover the wide variety of practical situations. The present work is mainly intended to contribute with results and experiences from profiling the near-bottom current by acoustic sensors under natural conditions.

[†] Address: Klaebuvegen 153, N-7034 NTH-Trondheim, Norway.

ARRANGEMENT

The location of the station is illustrated in Fig. 1. The bottom mooring was located at 84 m depth slightly off-shore the south-west part of the Norwegian coastal zone. The geographical position was $N59^{\circ}16'$ $E05^{\circ}04'$. In this area the bottom falls smoothly off at a ratio of about 1:100. One kilometre to the west the slope increases towards the Norwegian trough.

The mooring and the instrument setup is sketched in Fig. 2. Three selfrecording acoustic current meters were mounted on a tetrahedral framework. The measuring levels were $z=60$ cm, 100 cm and 200 cm. Each instrument measured the current simultaneously in two orthogonal directions parallel to the bottom. The power and logging unit also synchronized the measurements of the three instruments.

In the top of the rig, 3 m above the sea bed, an Aanderaa current meter of the integrating type measured absolute-values of the current velocity and the direction of the mooring. None of the instruments were able to rotate.

Wave data were logged from a Datawell Waverider buoy 12 km west of the bottom mooring. This was a permanent wave measuring station, but the bottom topography in that area was too irregular to be suitable for the near-bottom current measurements. Later measurements indicate that the wave power spectrum may be reduced as much as 50 per cent from the location of the waverider to the bottom mooring. The periods of the waves, however, seem to be very similar in the two positions.

Wind observations were made at the island Utsira, see Fig. 1. These data were kindly supplied to us by the Norwegian Meteorological Service.

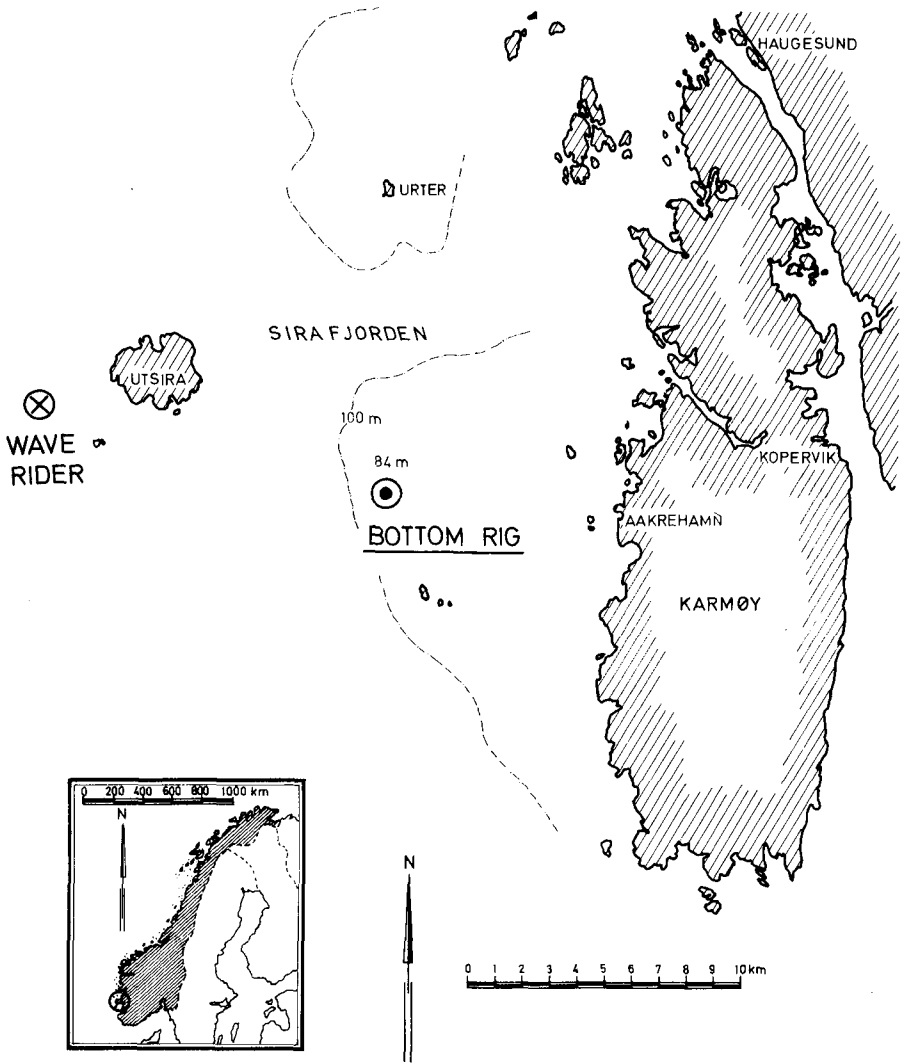


Fig. 1. Location of the bottom mooring and the waverider buoy.

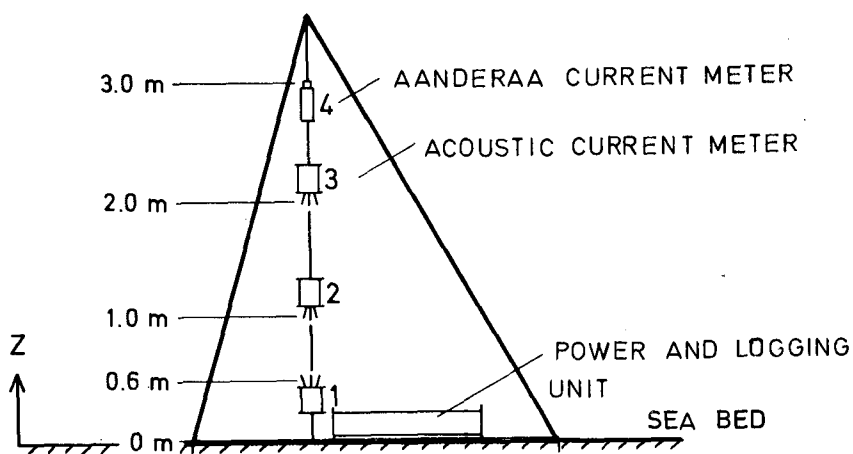


Fig. 2. The bottom mooring with instruments for profiling the current near the sea bed.

DATA SAMPLING AND OBSERVATIONS

The common logging unit of the acoustic sensors is programmable, and to measure the water particle movements on various time scales a broken-series sampling was chosen. One time sequence consisted of 60 equal-spaced registrations each third second. This gives 3 minutes long sampling periods, which were repeated four times an hour. The field experiment lasted 8 days, starting the 17th of March 1975 at 10 a.m. and ending the 25th of March at 12 a.m.

Nearly half a million data were stored on a magnetic tape, which was about sixty per cent of the total storage capacity. Of course, a selection of data for presentation here has to be done. Fig. 3 shows the sequential average velocities (u_{jk}, v_{jk}) , while the details from the single sequence $j=696$ are shown in Fig. 4.

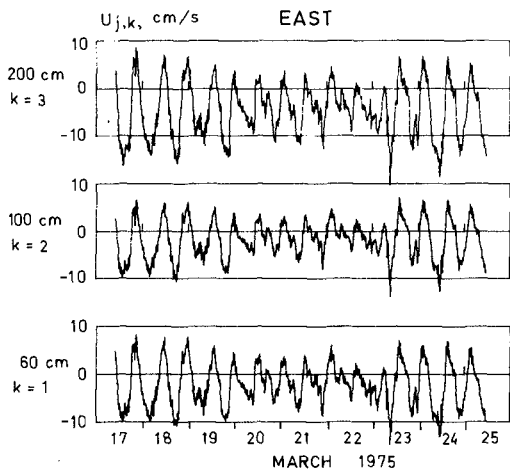
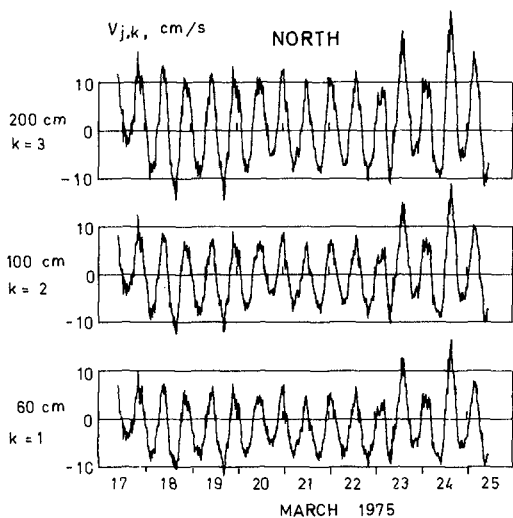
At this point an account for the notation may be appropriate. The current vector number i measured in sequence j by instrument k is denoted

$$\vec{w}_{ijk} = (u_{ijk}, v_{ijk}) \quad (1)$$

In our case $i=1,2,\dots,60$, $j=1,2,\dots,775$ and $k=1,2$ and 3 , where k increases with the distance from the bottom. The axis of each instrument were directed 97 degrees and 7 degrees from north, but in this presentation all data are transformed into a uv reference system with positive values of u and v directed to the east (90°) and north (0°), respectively. When polar coordinates (w_{ijk}, ϕ_{ijk}) are used the angle ϕ is identical with the compass direction. By time averaging the indexing is left out. Further, the large symbol W is reserved for absolute-value averaging, while the small letter w is used in conjunction with vector averaging, e.g. $w_{jk} = |\vec{w}_{jk}|$.

The wave height measurements are shown in Fig. 5. The upper curve shows the maximum wave height, H_{\max} , and the lower one is the $H_{1/3}$ parameter. At the time when these measurements were done the wave registration system had a low regularity, which resulted in loss of valuable data both at the start and the end of the registration period.

The presentation of data is closed by the wind observations from Utsira, see Fig. 6. The diagram shows the average wind velocity for the last 6 hours.



3. Sequential mean values of the current velocity components, u_{jk} and v_{jk} , at the three levels z_k from the bottom. $z_1=60$ cm, $z_2=100$ cm and $z_3=200$ cm. A unit increment of the time index j corresponds to 15 minutes.

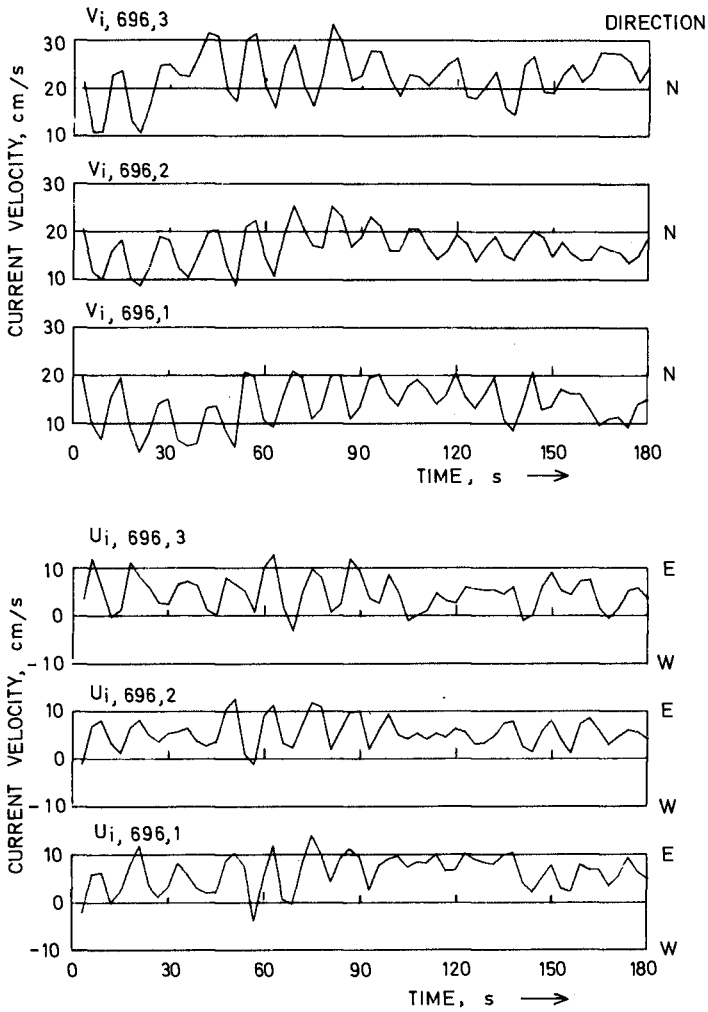


Fig. 4. The acoustic current measurements of the sequence $j=696$, $u_{i,696,k}$ and $v_{i,696,k}$. $k=1,2$ and 3 indicate the distances 60 cm, 100 cm and 200 cm from sea bed, respectively. Sampling interval is 3 s. The measurements were performed the 24th of March, 1975 at 4 p.m. at a station depth of 84 m.

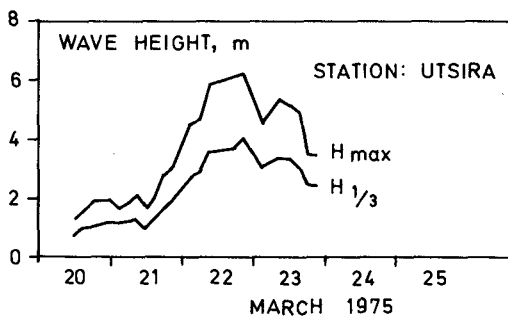


Fig. 5. The measured wave heights H_{max} and $H_{1/3}$.

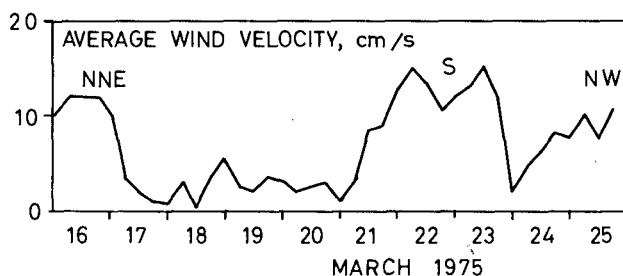


Fig. 6. Wind observations. The diagram shows the mean wind speed for the last six hours.

THE MEAN CURRENT AND THE EKMAN-LIKE TURNING

The analysis is started with the slowest varying motions of the water. These are illustrated by the progressive vector diagrams in Fig. 7. In fact these curves show the same data u_{jk} and v_{jk} as Fig. 3, but this time the z -dependence of the mean current vector is exposed more clearly. The

characteristic tidal loops are also easily seen.

The average current speeds for the entire registration period are $w_1=2.5$ cm/s, $w_2=1.8$ cm/s and $w_3=4.8$ cm/s. Hence, w_2 is less than w_1 , while w_3 is about twice of w_1 .

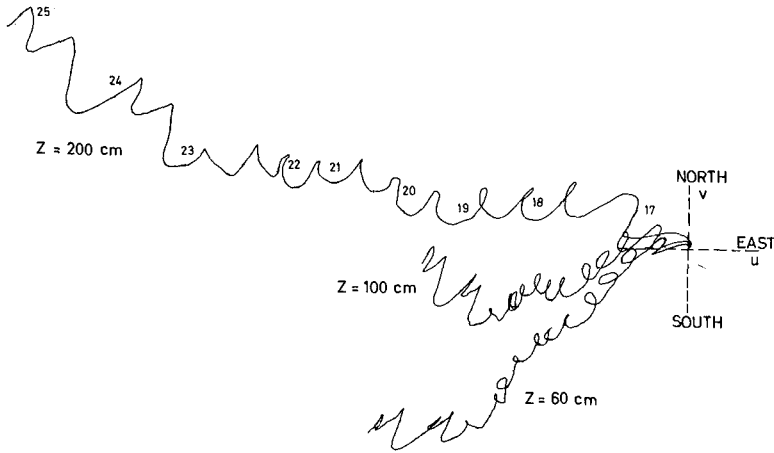


Fig. 7. Progressive vector diagrams of the bottom current.

During the five days long period from the 18th to the 22nd of March the flow was reasonably steady towards the east and the south. We therefore use this period for a closer inspection of the turning effect which is so clearly demonstrated in this figure. The mean velocity for these days is listed in Table 1 both on vector component form and as polar coordinates. The vectors are drawn with solid lines in Fig. 8.

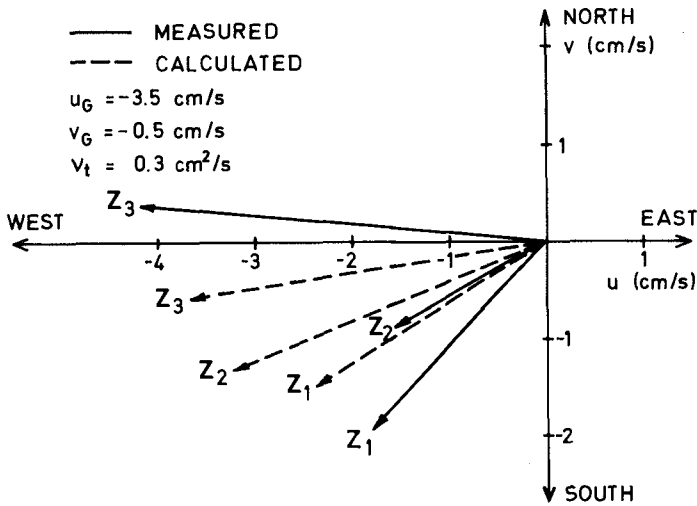


Fig. 8. Comparison of the mean velocity measured between the 18th and the 22nd of March with current values calculated from Ekman's theory.

According to Ekman's theory the Coriolis force causes a turning of the current to the left as the distance from the bottom is reduced. The differential equations are well known and shall not be repeated here. Suggesting a geostrophic current $w_G = (u_G^2 + v_G^2)^{1/2}$ for large values of z and a no-slip condition at the bottom the turning of the current is described by the integrated equations

$$u = u_G - w_G e^{-\frac{\pi}{D} z} \cos\left(\frac{\pi}{D} z + \beta\right) \tag{2a}$$

$$v = v_G + w_G e^{-\frac{\pi}{D} z} \sin\left(\frac{\pi}{D} z + \beta\right) \tag{2b}$$

where $D = \pi \left(\frac{2 v_t}{f} \right)^{\frac{1}{2}}$ and $\beta = \arctg \left(-\frac{u_G}{v_G} \right)$. D is the

thickness of the frictional layer, v_t is the eddy viscosity and f is the Coriolis parameter. For $z > D$ the current practically attains the constant velocity (u_G, v_G) . It is also underlined that eq. (2) is based upon the assumption that v_t is independent of z .

By systematic variation of the parameters u_G, v_G and v_t a best fit of eq. (2) to the measured current values in Table 1 has been found. The parameter values, the friction layer thickness D and the theoretical values of the current speed $\vec{w}(z)$ are listed in Table 2. In addition the calculated current vectors are drawn by dashed lines in Fig. 8 to visualize the comparison of experiment and theory. A linear z -dependence of the eddy viscosity v_t did not improve the agreement between the theory and the field data.

THE LONG-PERIODIC COMPONENTS OF THE CURRENT

The power density spectra in Fig. 9 show the long-periodic harmonic components of the current. Note that the peak on the frequency f_{15} is broken to blow up the other components. No blocking or filtering has been applied. The power density e_n is equal to

$$e_n = \frac{a_n^2 + b_n^2}{2 \Delta f}, \quad n = 1, 2, \dots, 30 \quad (3)$$

where a_n and b_n are the amplitudes of the cosine- and sine fourier coefficients, respectively, and Δf is the spectral

z (cm)	u (cm/s)	v (cm/s)	w (cm/s)	ψ
200	- 4.2	0.4	4.2	275°
100	- 1.6	- 0.9	1.8	241°
60	- 1.8	- 0.9	2.7	223°

Table 1. The mean current vectors for the periode from the 18th to the 22nd of March.

z (cm)	u (cm/s)	v (cm/s)	w (cm/s)	ψ
200	- 3.7	- 0.6	3.7	261°
100	- 3.3	- 1.3	3.5	248°
60	- 2.4	- 1.5	2.8	238°

$$u_G = - 3.5 \text{ cm/s}, \quad v_G = - 0.5 \text{ cm/s}, \quad v_t = 0.3 \text{ cm}^2/\text{s}, \\ D = 2.2 \text{ m}.$$

Table 2. Theoretical values of the near-bottom current as calculated from eq. (2). The parameters u_G , v_G and v_t are adjusted to obtain as good agreement between measurements and theory as possible, see Table 1 and Fig. 8.

resolution. In our case $\Delta f = 1/186 \text{ hour}^{-1} = 0.0053763 \text{ hour}^{-1}$. The total energy σ^2 of the spectra is shown in each diagram.

The main peak on frequency f_{15} is readily identified as the semidiurnal tide. Nearly 100 % (per cent) of the energy of the tidal component M_2 (period 12.42 hours) is on f_{15} . In addition N_2 (12.66 hours) and S_2 (12.00 hours) contributes

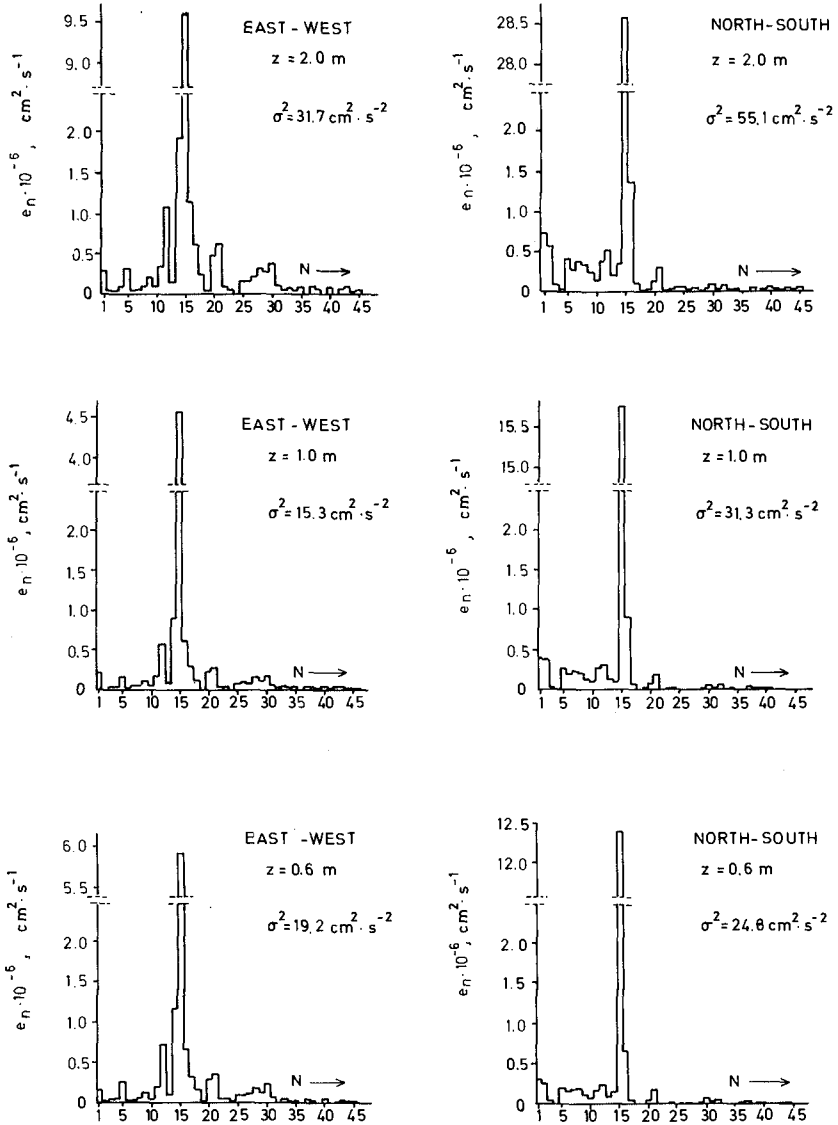


Fig. 9. The longperiodic spectra computed from the data series (u_{jk}, v_{jk}) shown in Fig. 3. σ^2 is the standard deviation of the time series.

by 70 % and 40 %, respectively, of their energy to this frequency. Due to the phase relationship the contribution from S_2 is negative. The energy of f_{14} and f_{16} is mainly due to S_2 and N_2 . The first harmonic component of the main peak, f_{30} , is very weak, but it seems to be significant.

The other spectral peaks are somewhat more difficult to identify. The tidal component M_3 is expected at f_{22} and f_{23} while the nearest top in the spectra is f_{20} and f_{21} . The period of f_5 is 37.2 hours, which is characteristic of the passage of a low pressure. Finally, we compare the period of f_{12} , 15.50 hours, to the inertial period, 13.97 hours.

The attenuation of the longperiodic fluctuations due to the bottom friction is somewhat different from what was observed for the mean current. From 60 cm to 100 cm the energy σ^2 increases very slightly, while the increase of σ^2 is nearly 100 % between 100 cm and 200 cm from the bottom. This corresponds to a difference in velocity of 30-40 %.

The main half axis of the rotational ellipses of the tidal frequencies at f_{15} are about 7 cm/s in the two lowest levels z_1 and z_2 , and 10 cm/s at z_3 . There is no evidence for a turning of the slow periodicities similar to that observed for the mean current.

THE SHORT-PERIODIC FLUCTUATIONS

The variations of the current within each 3-minutes sequence proved to be strongly connected to the windgenerated wave condition on the sea surface, Figs. 5 and 6. Particularly the wind from north the 24th and 25th of March induced horizontal movements of the water particles like those shown in Fig. 4. Spectral estimates of these time series, see

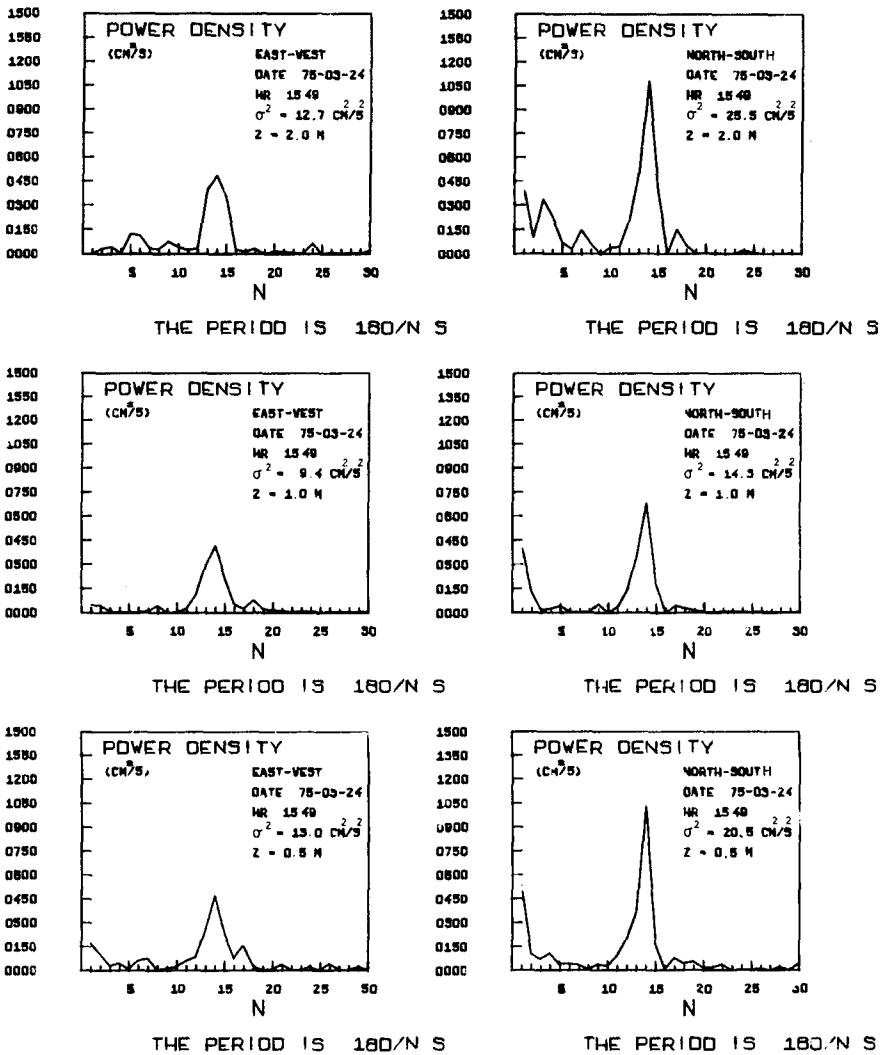


Fig. 10. Power spectra computed from the current measurements ($u_{i,696,k}$, $v_{i,696,k}$). The time series are shown in Fig. 4.

Fig. 10, show a significant peak on typical wave periods between 11 s and 16 s. Only a small part of the spectral energy falls outside this top.

Except for a linear trend reduction the raw data series have been applied for estimating these spectra.

These fast fluctuations seem to be less affected by the bottom friction than the tidal current and the mean velocity. There is a minimum of the peak power as well as the spectral energy 100 cm from the bottom, but from 60 cm to 200 cm the increase of spectral energy is less than 20 %. Similar studies of other time sequences confirm the result that the friction layer thickness for movements on typical wave frequencies is less than 60 cm.

THE VERTICAL TRANSFER OF WAVE ENERGY

According to first order theory the spectral wave power s_η is transferred vertically in the sea as

$$e(\delta) = T_\eta^2(\delta) \cdot s_\eta \quad (4)$$

where δ is the depth and η indicates the wave profile. The transfer function T_η is given by

$$T_\eta = \frac{2\pi f}{\text{sh } kd} \quad (5)$$

where f is the frequency, $k = k(\delta, f)$ is the wave number and d is the total depth. Having measured s_η and a velocity spectrum $e(\delta)$ the transfer function T_η can be tested directly.

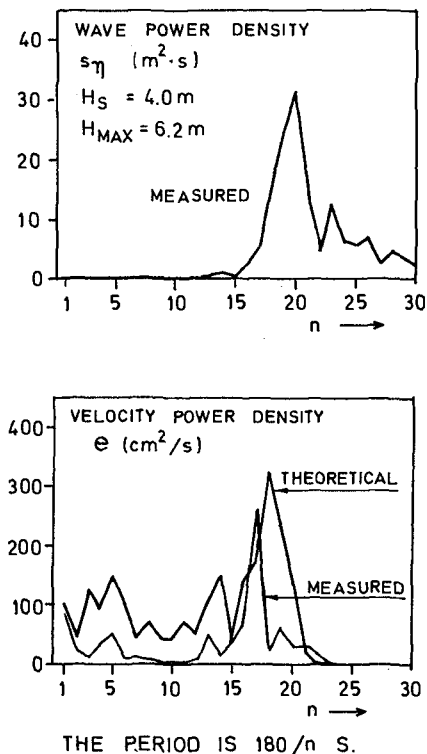


Fig. 11. a) The surface wave spectrum s_η ($\delta=0$ m). H_S and H_{max} are the significant and the maximum wave height, respectively.

b) The theoretical velocity spectrum e ($\delta=82$ m) as computed by eqs. (4) and (5), and the measured spectrum e ($z=2$ m). The measurements were made the 22nd of March at 21 p.m., 1975.

Since the wave measurements stopped by accident too early, the sequence of data shown in Fig. 4 cannot be used for this purpose. Instead, the wave spectrum measured the 22nd of March at 21 p.m. is used, see Fig. 11 a. The theoretical

spectrum computed by eqs. (4) and (5) is shown in the diagram below, Fig. 11 b, together with the power density measured simultaneously 200 cm from the bottom. Hence, the parameters $d = 84$ m and $\delta = 82$ m. The power density of both the u and v direction are included in the current velocity spectrum.

The two spectra in Fig. 11 b indeed show a similar shape in several details. However, there seems to be a greater attenuation of the high frequency flange of the central peak than the theory prescribes. The opposite flange fits quite well at periods between 10 s and 12 s.

The energy of the wave-like motion close to the bottom is found to be about 50 % less than expected from linear wave theory applied to a measured wave spectrum. Some proposals for explaining this discrepancy are discussed in the next chapter.

DISCUSSION AND CONCLUSIONS

The acoustic current measurements have revealed how the profile in the bottom friction layer depends on the characteristic time of the water movement. After having smoothed out the semidiurnal tide from the time series, a mean current remains which increases by 100 % from $z_1 = 60$ cm to $z_3 = 200$ cm above sea bed.

The amplitude of the dominating tidal current increases by 40 % or so, while the oscillations on typical wave frequencies remains nearly constant over the same vertical range. Therefore, one may conclude that the thickness of the bottom friction layer is less than 60 cm for wind-generated wave motions.

A current profile including the result from the Aanderaa current meter has been drawn in Fig. 12. Since the Aanderaa instrument did not rotate it only recorded mean values of the absolute current speed, an operation which has been done mathematically for the acoustic data. The registrations made by the two different types of instruments seem to agree quite well. As shown by a dashed line in Fig. 12 the logarithmic function

$$W = \frac{W_{*}}{\kappa} \ln \frac{z + z_0}{z_0} \quad (6)$$

has been fitted to the data points. In eq. (6) W_{*} is the frictional velocity, $\kappa = 0.4$ is von Karman's constant and z_0 is the roughness parameter. Eq. (6) describes the observations reasonably well with the parameters $W_{*} = 1.8$ cm/s and $z_0 = 23$ cm. This value of z_0 is high and characterizes a hydrodynamically rough bottom. However, when interpreting such a current profile, one should have in mind how the friction layer thickness has been shown to depend on the period of the motion.

An Ekman-like turning of the mean current has been demonstrated, see Fig. 7. In Fig. 8 the experimental result is compared with the idealized Ekman theory where the parameter values $v_t = 0.3$ cm/s, $u_G = -3.5$ cm/s and $v_G = -0.5$ cm/s are used. The Ekman friction layer is estimated to be 2-3 m thick. The observed turning is greater than the theory prescribes, and the measured average current for $z = 100$ cm has only half the expected value. This disagreement may be due to a) topographical effects, b) calibration errors, or c) that v_t depends on z and t and also is influenced by the tide. It should also be pointed out that since the mean current is weak small inaccuracies may result in large relative errors.

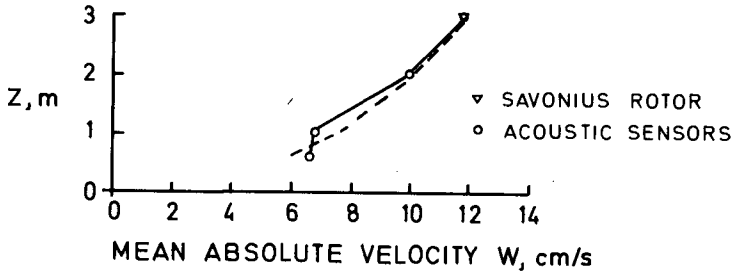


Fig. 12. The current profile including the registrations by the Aanderaa meter. The broken line shows a logarithmic profile, eq. (6), with $W_{*} = 1.8$ cm/s and $z_0 = 23$ cm.

Later experiments indicate that stratification effects are negligible. The boundary condition (u_G, v_G) was not measured.

A velocity component closely related to the wind-generated surface waves is also observed. The intensity of these fast fluctuations is about 50 % less than expected from linear wave theory. This trend, suggesting a weaker wave action near the bottom than classical theory predicts, is in accord with earlier results obtained with pressure sensors, summarized by Silvester, (3). However, the attenuation we have observed seems to be somewhat stronger, and this discrepancy may be caused by the different location of the Waverider buoy and the bottom mooring. The influence of the bottom friction on these fast fluctuations is found to be insignificant beyond $z = 60$ cm.

REFERENCES

- [1] : Weatherly, G.L.: A Study of the Bottom Boundary Layer of the Florida Current. J. Phys. Osc. Vol. 2. pp 54-72. Jan. 1972
- [2] : Knight, D.W.: Review of Oscillatory Boundary Layer Flow. J. Hydr. Div. ASCE. Vol. 104 No HY6. pp 839-855. June 1978.
- [3] : Silvester, R.: Coastal Engineering I. Elsevier Publ. Comp. 1974, pp 275-290.

CHAPTER 51

OSCILLATORY LAMINAR FLOW ABOVE A ROUGH BED

by

C.B. George¹ and J.F.A. Sleath²

Summary

Measurements are reported of the velocity distribution in the laminar boundary layer above a rough bed oscillating in its own plane in still air. The measurements were made with a hot-wire anemometer and the beds consisted of spheres packed closely together on flat plates. Particular attention was paid to the jets of fluid associated with individual roughness elements reported by Keiller & Sleath (1976). The probe used by Keiller & Sleath could be traversed vertically but not parallel to the bed. Consequently it is not known whether or not the velocities which they measured represent the maximum jet velocity at a given height since the probe was not necessarily in the vicinity of the jet at the moment at which it was maximum. In these new tests the probe could be traversed horizontally as well as vertically. It is found that one jet is formed by each roughness element during each half cycle. This jet is directed upwards from the bed. Its intensity shows relatively little variation with Reynolds number for the range of conditions investigated but increases significantly with the relative roughness parameter βD . The moment in the half cycle at which the jet is formed and the location of its axis appear to vary with both βD and Reynolds number. Visual observations suggest that the jet is associated with incipient vortex formation. The variation in velocity with height in the jets of fluid is significantly different from that given by Stokes' theoretical solution for a flat bed. Except in the immediate vicinity of the bed, the jet velocity predominates over that during the rest of the cycle.

Introduction

A knowledge of the velocity distribution close to the sea bed is of importance in several areas of coastal engineering. The attenuation of waves approaching the shore, the steady drift currents produced by the waves (and hence the dispersion of pollutants) and the transport of sediment are all affected by conditions in the boundary layer at the bed.

Measurements of the velocity distribution close to the bed in oscillatory flow have been made by Jonsson (1963), Kalkanis (1964), Horikawa & Watanabe (1968), Sleath (1970), Jonsson & Carlsen (1976) and

¹ Sir M. Macdonald and Partners, Cambridge, England

² Department of Engineering, University of Cambridge, England

Keiller & Sleath (1976). These measurements show that, except for flat beds of very fine sediment, the velocity distribution is quite different from Stokes' (1851) theoretical solution for flow over a flat bed, even when the flow is laminar.

Only the measurements of Keiller & Sleath were made with a probe small enough to examine the detailed flow structure around individual roughness elements. These showed the existence in laminar flow of a jet of fluid thrown up from the bed by each roughness element. The measurements were made with a stationary probe and an oscillating bed. Unfortunately the probe could not be traversed horizontally and consequently it is not known whether or not the velocity which they measured was the maximum for the jet at a given height since the probe was not necessarily in the vicinity of the jet at the instant at which it reached its maximum. It is also possible that there were other jets which were unrecorded by the probe. The object of the tests described in this paper was to carry out a more complete investigation of this phenomenon.

Experimental apparatus

The apparatus was similar to that described by Keiller & Sleath (1976). A flat plate 2.70 m long and 0.30 m wide was caused to oscillate with simple harmonic motion in its own plane by a Scotch Yoke mechanism driven by a variable speed motor. It is well known that relative to axes fixed in the bed the velocity distribution above an oscillating plate is the same as that produced by waves over a stationary bed provided that both the plate and the length of the waves are effectively infinite. Such an apparatus does not, of course, reproduce second-order effects such as mass-transport which occur when the wave length is not infinite.

The plate was enclosed in a wooden chamber 3.15 m long x 0.77 m high x 0.32 m wide. The clearance between the plate and the bottom of the chamber was 0.18 m except at the ends where the floor of the chamber was raised so that the plate was in continuous sliding contact with its surface. This arrangement prevented vortex shedding from the ends of the plate. Although oscillation of the fluid outside the boundary layer at the bed was not entirely eliminated, in no case did it exceed 5% of the amplitude of oscillation of the bed.

The central 1.65 m in length of the oscillating plate was covered with uniform spheres tightly packed together in a hexagonal array. The distance between sphere crests in the direction parallel to the short edge of the plate was equal to the sphere diameter D . In the direction of oscillation the crest-to-crest distance was $D(3)^{1/2}$. Five different beds were used with sphere diameters of 3.10, 6.32, 12.34, 18.60 and 37.80 mm.

All of the measurements were made in air using a DISA 55D01 constant temperature hot-wire anemometer and 55F31 miniature probe. The output was passed through a DISA 55D10 linearizer to a Thermionic Instruments T3000 tape recorder. The recorded signal was subsequently analysed on an IBM 1130 computer using a WDV analog-to-digital converter. Great care was taken to eliminate all extraneous sources of vibration during the experiments and consequently it was not found necessary to filter the

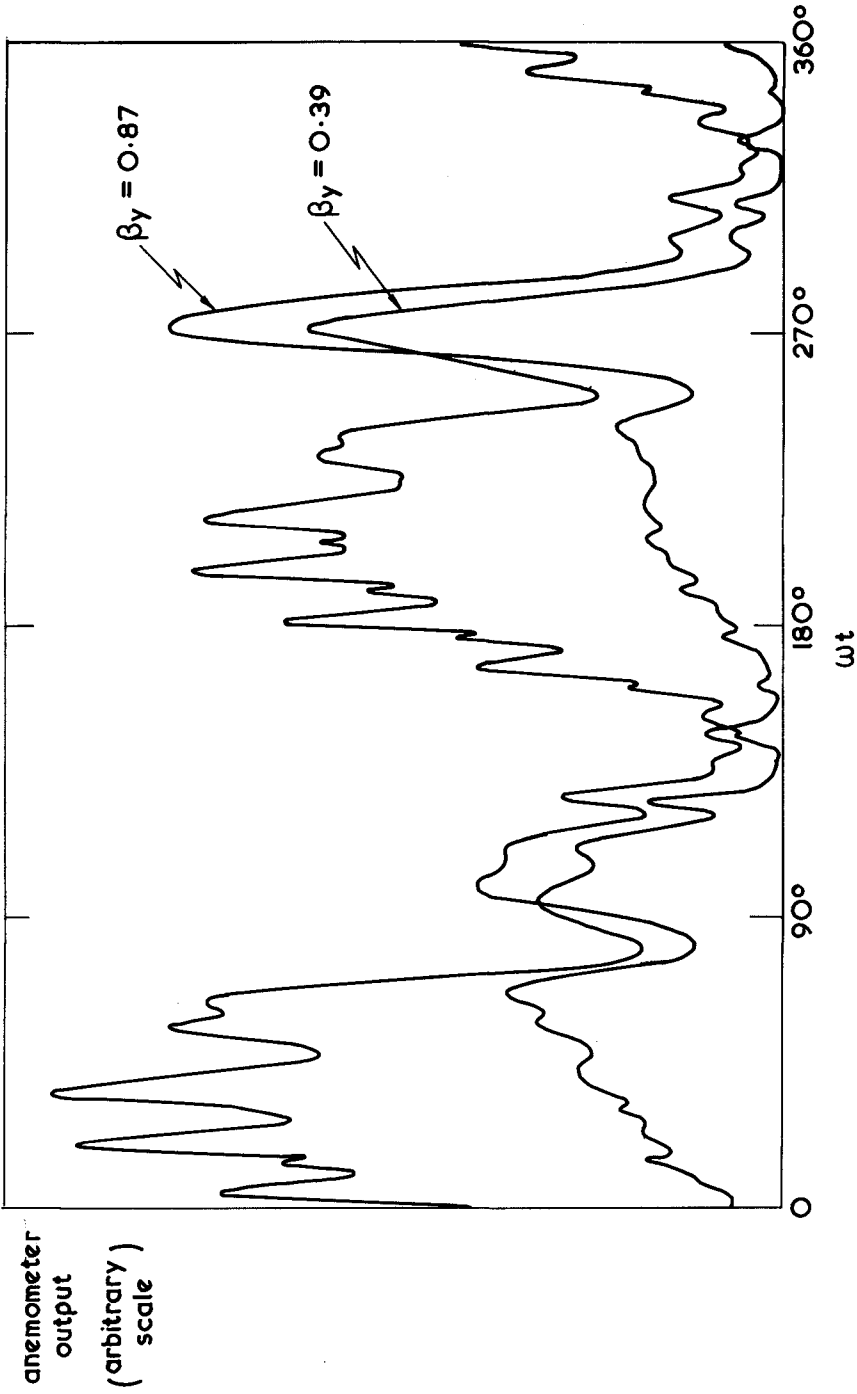


Fig. 1. Anemometer output during one cycle at $\beta D = 6$, $U_o/\omega D = 6.84$

signal. The probe projected vertically down towards the bed and the wire was aligned at right angles to the direction of oscillation of the bed. With this arrangement the recorded signal represents the resultant velocity in the vertical plane containing the direction of oscillation. The length of the wire was 1.2 mm and its diameter 5 μm . Calibration was carried out after each set of tests by oscillating the probe in still air at various known frequencies and amplitudes.

The normal test procedure was for the apparatus to be started up and left for at least two hours to achieve equilibrium. Velocity measurements were then made at various heights above the bed and at various horizontal positions. In this way a complete record of the flow in time and space could be built up. Velocity measurements were only made in laminar flows, i.e. in which the velocity record was effectively identical from one cycle to the next.

In addition to the velocity measurements with the hot-wire anemometer, visual observations were carried out with a similar bed of spheres in an oscillating water tunnel. A hydrogen bubble device was used to visualize the flow.

Test results and discussion

Fig. 1 shows a typical example of the recorded output from the hot-wire anemometer at two different heights above the bed. Since the calibration curve is highly non-linear the actual velocity record would be somewhat different but the main features are the same. In this figure t is time measured from the instant at which the velocity of the bed is maximum, ω is the angular frequency of oscillation, y is height measured vertically from the crest of a sphere, U_0 is the amplitude of the bed velocity and $\beta = (\omega/2\nu)^{1/2}$, where ν is kinematic viscosity, is inversely proportional to the thickness of the viscous boundary layer. The record is different in the two half cycles because the probe was not symmetrically placed relative to the bed in the two half cycles. If we concentrate our attention on the second half cycle ($180^\circ \leq \omega t < 360^\circ$) we observe the following features:

- (1) There is a pronounced peak in the record in the vicinity of $\omega t = 270^\circ$. This is caused by the jet referred to by Keiller & Sleath.
- (2) The record also shows a fairly high frequency oscillation. This is due to the fact that, by continuity, the velocity over the crest of a wavy bed must be greater than over a trough. Since $U_0/\omega D$ is the ratio of amplitude of oscillation of the bed to sphere diameter it follows that eight spheres pass under the probe as the bed moves from one extremity of its stroke to the other for the conditions of Fig. 1. Close examination of the record shows that the velocity rises to a maximum as a crest passes directly under the probe, falls to a minimum, and then rises to a second maximum when the probe is mid-way between crests, and so on. The reason for this second maximum is that, because the spheres are packed in a hexagonal array, the distance between crests in the direction of oscillation is $D(3)^{1/2}$ but the distance between rows of spheres is only $D(3)^{1/2}/2$. In other words the flow is speeded up when the probe is mid-way between

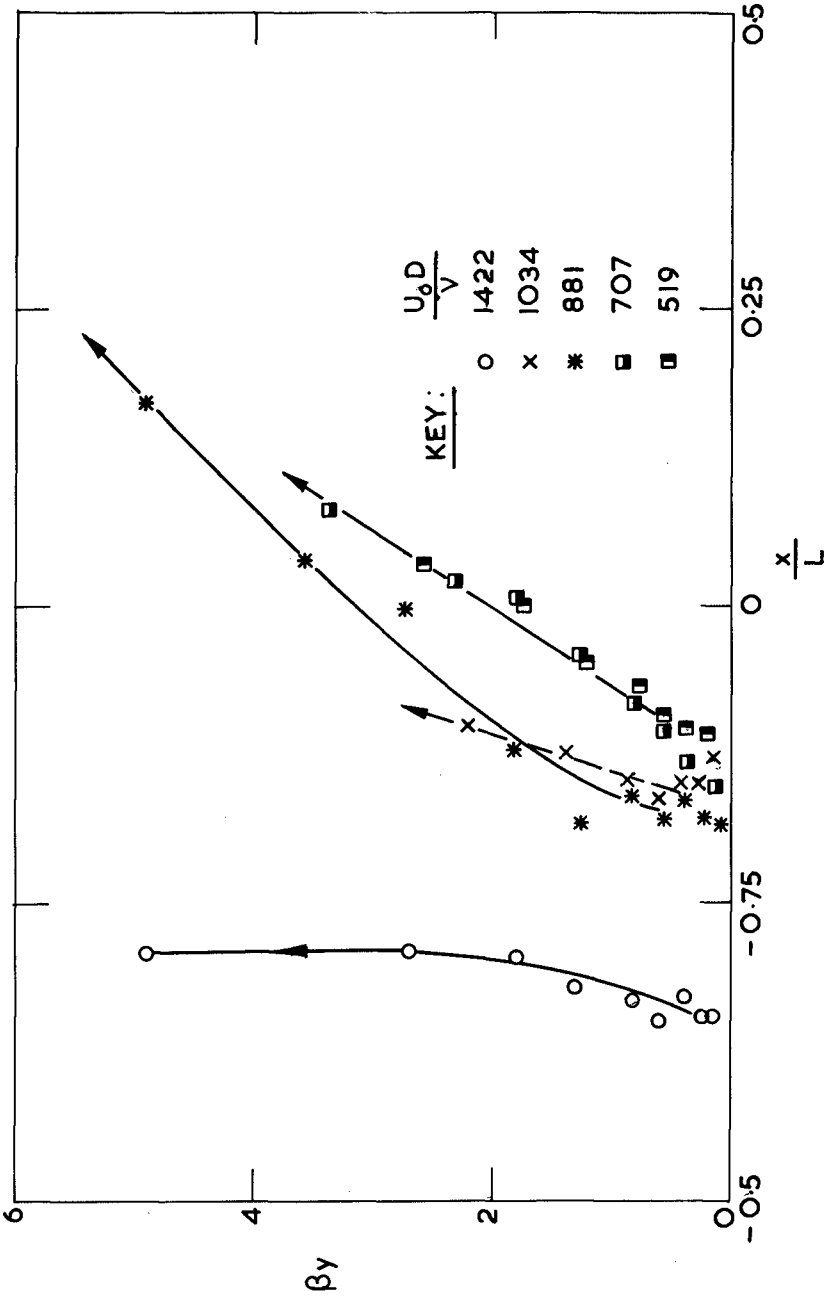


Fig. 2. Horizontal position relative to the bed at which the maximum velocity in the jet is found at various heights above the bed. $\beta D = 20$

crests in the direction of oscillation because the probe is then directly in line with a second row of spheres. The increase in velocity over the crest in the first row is, of course, greater than the increase in the gap between spheres in the second row but this difference becomes less marked as height above the bed increases.

When the thickness of the viscous boundary layer is small compared with the roughness diameter (i.e. $\beta D \gg 1$) this component of velocity is accurately given by the potential flow solution for the bed, except within the thin viscous layer itself.

(3) When the peak in the vicinity of $\omega t = 270^\circ$ and the high frequency fluctuation are excluded, there remains a component of velocity which varies nearly sinusoidally with time. Keiller & Sleath showed that the variation with height of this component is close to that given by Stokes' theoretical solution for flow over a flat plate.

As stated in the Introduction, the object of the present paper is to examine the peak in the vicinity of $\omega t = 90^\circ, 270^\circ$ etc. The visual observations in the oscillating water tunnel showed that this peak appeared to be associated with incipient vortex formation. As the flow near the bed reverses, the remains of the incipient vortex formed during the preceding half cycle is carried back towards the crest and hurled out into the fluid above. If it is assumed that the locus of the maximum velocities in the peak recorded by the probe represents the axis of the jet hurled up from the bed we can determine the path of this jet. Fig. 2 shows examples of the locii of the maxima recorded at $\beta D = 20$. In this figure x is the horizontal distance measured from the crest of a sphere in the direction of oscillation and L is the distance between adjacent crests, which is equal to $D(3)^{1/2}$ in the present case. The axes have been plotted so as to have the same scale for horizontal and vertical distances. We see that at low values of the Reynolds number $U D/\nu$ the jet is angled at about 60° to the horizontal but that at higher Reynolds numbers the angle becomes steeper. Also, as the Reynolds number increases the axis of the jet moves further out into the trough between crests. The arrow heads marked on the curves drawn through the experimental points indicate the direction of increasing phase. The fact that the maxima are found progressively later in the half cycle as distance from the bed increases is consistent with the visual observation of a jet of fluid hurled up from the bed. The measurements shown in Fig. 2 were obtained during one half cycle. During the next half-cycle the jets would, of course, originate on the other side of the crest and be tilted in the opposite direction.

It should be mentioned in passing that George (1977) drew a distinction between a "crest" jet and a "trough" jet. The reason for this is that at large values of the relative roughness parameter βD the flow in the jet decays only slowly with time. Consequently, the actual maximum velocity in the jet may be followed by a decline and then by a second maximum as the jet is carried over a crest or over the second row of spheres mid-way between crests where the velocity is reinforced by the high frequency fluctuation mentioned during the discussion of Fig. 1.

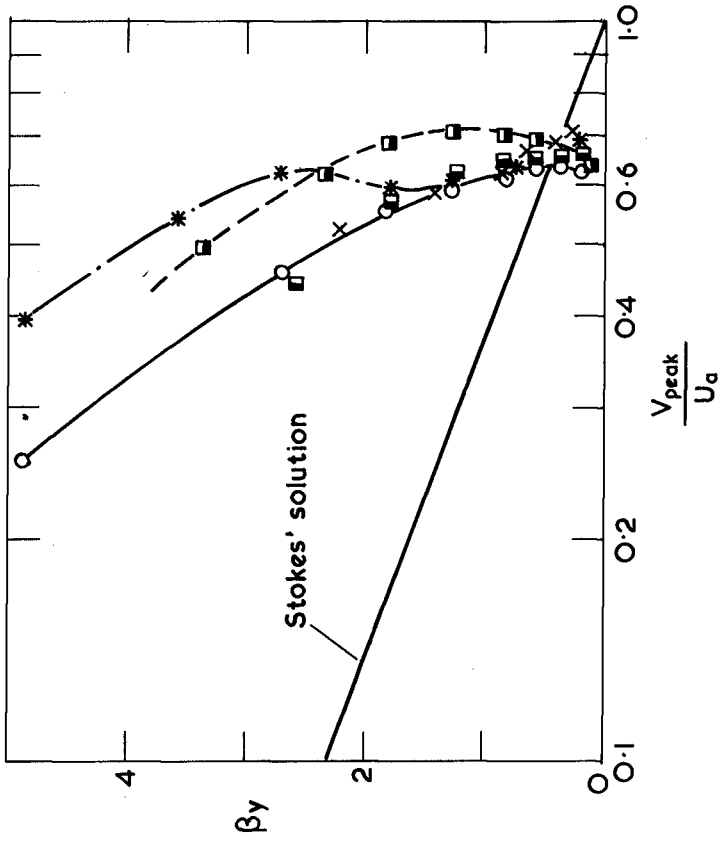


Fig. 3. Variation with height of the maximum velocity in the jet. $\beta D = 20$. (Symbols as for Fig. 2)

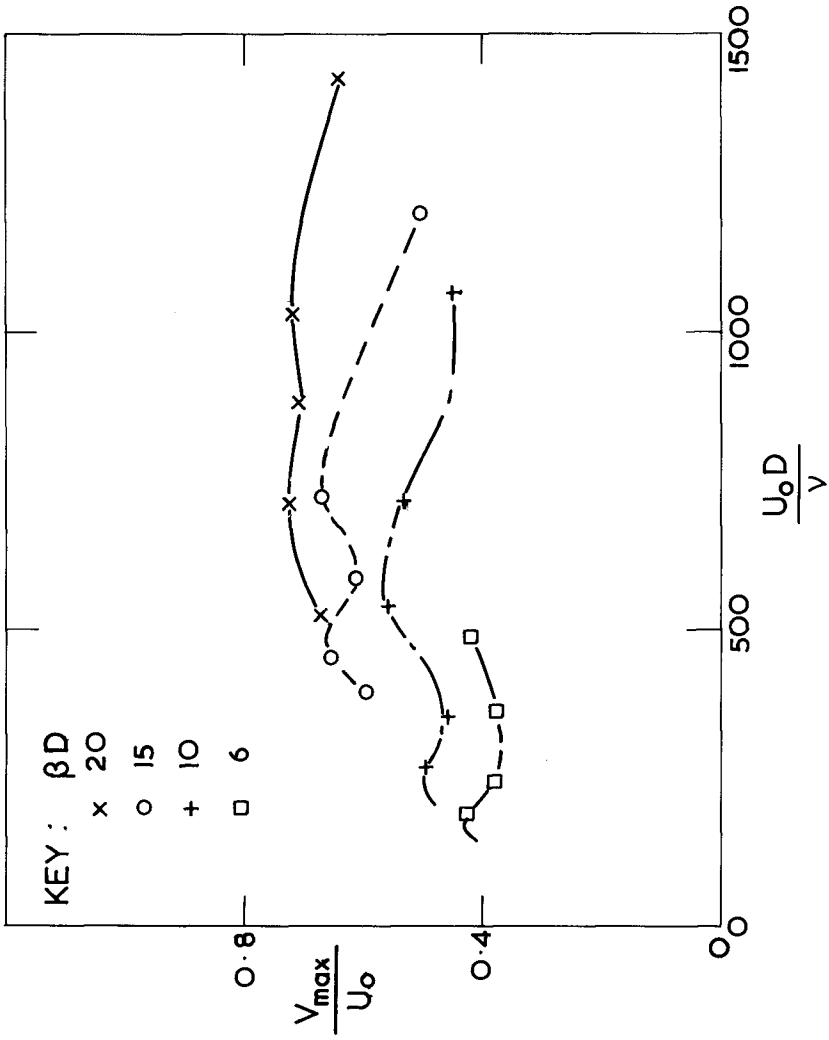


Fig. 4. Variation of the maximum jet velocity with βD and Reynolds number

In reality, there is only one jet whose maximum may, as shown by Fig. 2, be found either over a crest or over a trough depending on the value of $U_0 D/\nu$. At smaller values of βD the jet decays much more rapidly with time after passing its maximum and consequently only one maximum is observed.

An example of the way in which the maximum velocity V_{peak} in the jet varies with height is given in Fig. 3. For purposes of comparison, Stokes' theoretical curve for a flat plate is also shown. It is clear that, except very close to the bed, the velocity in the jet is much greater than that given by Stokes' solution. The peak velocity does not tend to zero at $y = 0$ because, as shown by Fig. 2, the jet does not originate at the crest but some way down in the trough (i.e. below the $y = 0$ level).

The way in which the maximum value, V_{max} , of V_{peak} varies with βD and $U_0 D/\nu$ is shown in Fig. 4. There is clearly significant variation in jet intensity with βD but surprisingly little variation with $U_0 D/\nu$ for the range of values covered. However, the curves must tend to zero as $U_0 D/\nu \rightarrow 0$ if, as suggested above, these jets are associated with incipient vortex formation.

At large distances from the bed the variation of V_{peak} with y tends towards a curve of the form

$$\frac{V_{\text{peak}}}{U_0} = \text{const} \times \exp(-\beta y/X) \quad (1)$$

where X is a constant for given $U_0 D/\nu$ and βD . The way in which the value of X obtained from the present measurements varies with βD and $U_0 D/\nu$ is shown in Fig. 5. The numerical calculations made by Sleath (1974) for two-dimensional bed roughness showed that when βD is sufficiently large a reasonable approximation for X at large distances from the bed is

$$X = \beta D/2\pi \quad (2)$$

The curves obtained for the various values of βD from Eq. (2) are shown in Fig. 5 for purposes of comparison. Although there does appear to be some measure of agreement it should be emphasised that since the bed profiles are very different in the two cases it would be wrong to attach too much significance to it. However, it does seem that the value of X depends mainly on βD and varies only slowly with $U_0 D/\nu$.

Finally, it should be mentioned that although the initiation of the jets is linked with the reversal of flow close to the bed, the phase at which the jet velocities reach a maximum at a given height may vary significantly with βD and $U_0 D/\nu$. For example, Fig. 6 shows the variation in phase of V_{peak} at $\beta y = 0.5$. The numbers over the experimental points at $\beta D = 20$ are the values of $U_0 D/\nu$. The phase is clearly dependent on Reynolds number. At smaller values of βD the spread of values obtained in the various tests is indicated by the error bands. At these smaller values of βD there appears to be a tendency for the phase at which the maximum jet velocity is found to increase with βD .

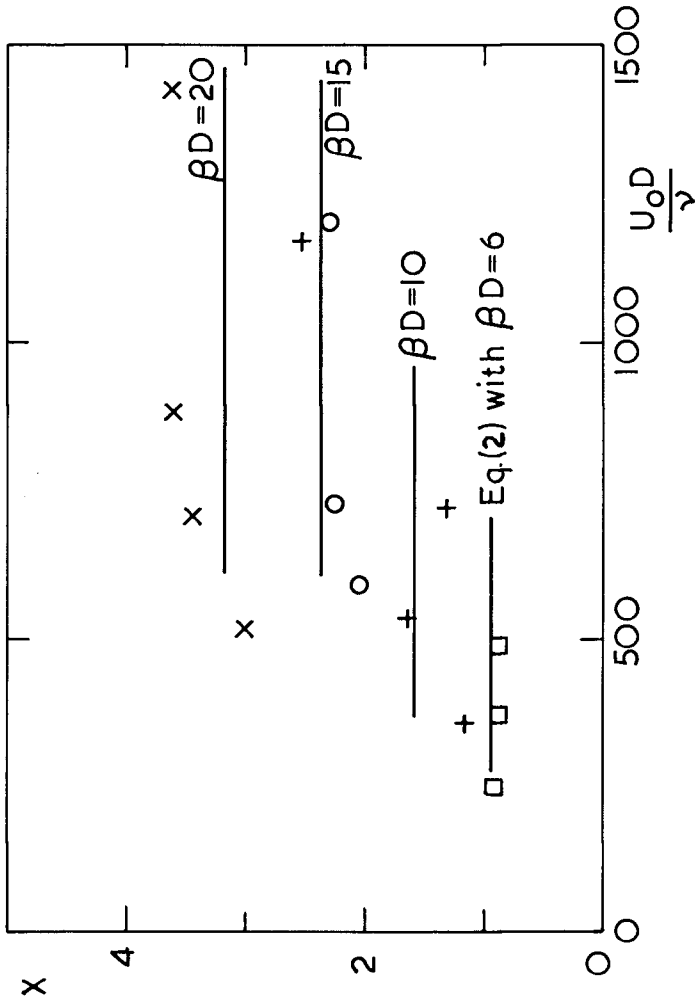


Fig. 5. Variation of X for the jet velocity with βD and Reynolds number. (Symbols as for Fig. 4)

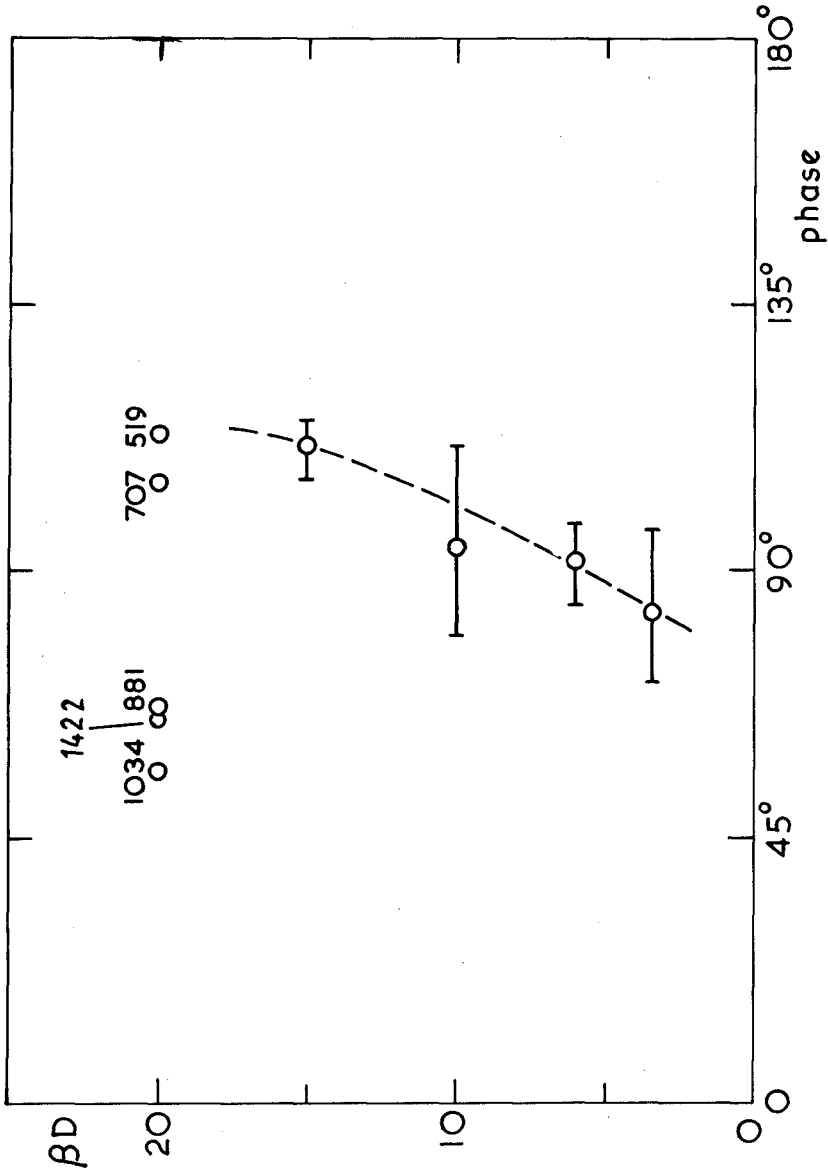


Fig. 6. Phase of maximum jet velocity at $\beta y = 0.5$

Further details of these tests are given by George (1977).

Conclusions

One of the most important conclusions from the present work is that for oscillatory flow over a rough bed there is a range of Reynolds numbers for which the flow remains laminar, in the strict sense of that term, but in which the velocity profile is significantly different from that over a smooth bed. It has usually been assumed in the past that the flow regime at the sea bed is either fully developed turbulence or that the velocity distribution for laminar flow over a smooth bed applies. It is clear from the present work that a third regime which may be called "rough laminar" may also be important.

It was suggested above that the jets of fluid are associated with incipient vortex formation around each roughness element on the bed. It is well known that vortex formation around bluff bodies is found in turbulent as well as laminar flow. This being the case, effects similar to those investigated here may also occur in rough turbulent flow.

Finally it may be noted that, relative to axes fixed in the free stream, both Kalkanis (1957, 1964) and Sleath (1970) found that the velocity distribution in oscillatory flow above beds of sand followed a similar distribution to that of Eq. (1). Since the roughness of beds of sand is very different from that considered here only qualitative agreement between the two sets of results is to be expected. Nevertheless it is possible that what Kalkanis and Sleath were actually measuring was the velocity distribution of the jets of fluid produced by the grains of sand on the surface of the bed.

Acknowledgement

One of the authors (CBG) wishes to acknowledge the financial support of the Science Research Council.

References

- George, C.B. (1977) Flow close to a rough plate oscillating in its own plane. Ph.D. thesis, University of Cambridge.
- Horikawa, I. & Watanabe, A. (1968) Laboratory study on oscillatory boundary layer flow. Proc. 11th Conference on Coastal Engineering, London, pp 467-486.
- Jonsson, I.G. (1963) Measurements in the turbulent wave boundary layer. Proc. 10th Congress IAHR, London, Vol. 1, pp 85-92.
- Jonsson, I.G. & Carlsen, N.A. (1976) Experimental and theoretical investigations in an oscillatory rough turbulent boundary layer. J. Hyd. Res. Vol. 14, no. 1, pp 45-60.

- Kalkanis, G. (1957) Turbulent flow near an oscillating wall.
Beach Erosion Board, Tech. Memo. No. 97.
- Kalkanis, G. (1964) Transport of bed material due to wave action.
US Army Coastal Engineering Res. Center, Tech. Memo. No. 2.
- Keiller, D.C. & Sleath, J.F.A. (1976) Velocity measurements close to a rough plate oscillating in its own plane. *J. Fluid Mech.* Vol. 73, pp 673-691.
- Sleath, J.F.A. (1970) Velocity measurements close to the bed in a wave tank. *J. Fluid Mech.* Vol. 42, pp 111-123.
- Sleath, J.F.A. (1974) Velocities above a rough bed in oscillatory flow. *Proc. ASCE, J. Waterways, Harbors & Coastal Eng. Div.* Vol. 100, No. WW4, pp 287-304.
- Stokes, G.G. (1851) On the effect of the internal friction of fluids on the motion of pendulums. *Trans. Camb. Phil. Soc.* Vol. 9, pp 20-21.

CHAPTER 52

EXTREME SEA LEVELS FROM TIDE AND SURGE PROBABILITY

D. T. PUGH* and J. M. VASSIE*

ABSTRACT

This paper considers a method of deriving the probability of occurrence of extreme sea levels by combining the probability functions of surge and tide. As a result the quantity of data required is less than with traditional methods. The philosophy of the method is discussed and the conditions under which the theory can be applied are examined. Finally the technique is applied to a number of ports in the United Kingdom and the results are compared with known estimates of extreme levels.

1. INTRODUCTION

Realistic estimates of the probability, or inversely the 'return period', of extremely high sea levels are necessary, for example, for the design of harbours and coastal defences. Estimates of the probability of extreme low levels, although not so widely used, are needed by the nuclear power industry for example to site cooling water intakes. Other applications came from the harbour authorities and the shipping industry for dredging approaches to ports or for towing deep draught oil rigs from their moorings across shallow banks to the open sea.

There are many ports particularly in northern Britain from which a few years of sea level data are available but not the several decades of data that one associates with traditional studies of extreme levels. It was our intention to make use of some of this data. Traditional estimates of extremes are made by considering the distribution of annual maximum and minimum sea levels (for example Lennon 1963 or Suthons 1963). In general curves are fitted to the distributions to produce a linear function and the sea level corresponding to a particular return period is estimated by linear extrapolation.

The technique developed in this paper enables estimates to be made from a few years of data by considering separately the probability distributions of the tidal and the surge (non-tidal residual) components of sea level. By extracting the surge component a continuous record of all surges that occur during the period is made available and these can be used to reinforce the statistics that otherwise would be generated from a single annual extreme value. For example large positive surges

* Institute of Oceanographic Sciences,
Bidston Observatory,
Birkenhead,
Merseyside,
U.K.

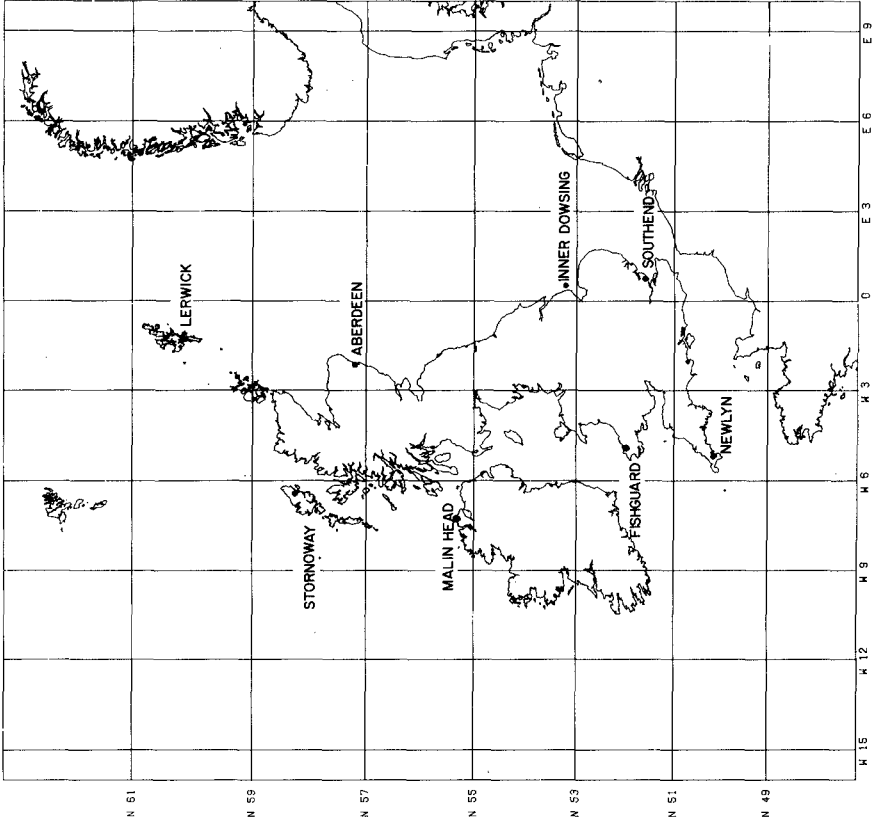


FIG. 1.

that occur at low tide, which do not produce extreme total levels, are included in our analyses. Ackers and Ruxton (1974) used a similar technique for the Essex coastline, but only for surges that occurred at high water, in which they added the surge distribution at high water to the predicted tide at high water.

Our study had two main aims:

- a) To produce estimates of extreme sea levels from data whose duration was much shorter than the return periods by examining tide and surge probability functions separately and combining them in the appropriate way.
- b) To apply the method to a group of ports that would give a reasonable coverage of conditions round the United Kingdom.

The ports for which the technique was applied and the amount of data that was available were Newlyn (19 years), Fishguard (9), Malin Head (12), Stornoway (15), Lerwick (14), Aberdeen (10) and Southend (19). The location of each port is shown in figure 1. Southend was included to study the effect of the strong interaction between tides and surges which exists in the southern North Sea. At the other ports our investigation showed that there was little or no interaction and so tide and surge were treated as independent variables.

One advantage of the technique developed here was that mean sea level was eliminated from the computations. Of course it was defined relative to a local benchmark which in most cases had been levelled to Ordnance Datum Newlyn. Trends in the mean level had little effect because of the short lengths of data used. Rossiter (1966) and more recently Thompson (in preparation) have studied mean sea level trends and these may be easily incorporated into the extremal statistics on the assumption that they are statistically independent of the extremes.

2. Philosophy of the Method

At any time (t) the observed sea level (ξ) can be considered as the sum of a tidal component (x), a surge component (y) and a mean level (Z_0)

$$\xi(t) = x(t) + y(t) + Z_0 \quad 2.1$$

This is illustrated diagrammatically in figure 2.

The tidal component is the coherent part of the sea level that responds directly or indirectly to astronomical forcing. It was removed from the observed sea level records as the finite sum of harmonic constants which had the form:

$$x(t) = \sum_{n=1}^N H_n \cos(\sigma_n t + V_n - g_n) \quad 2.2$$

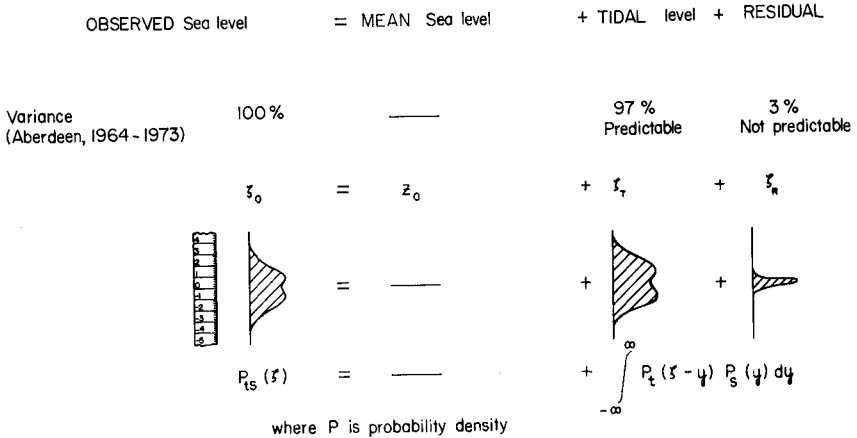
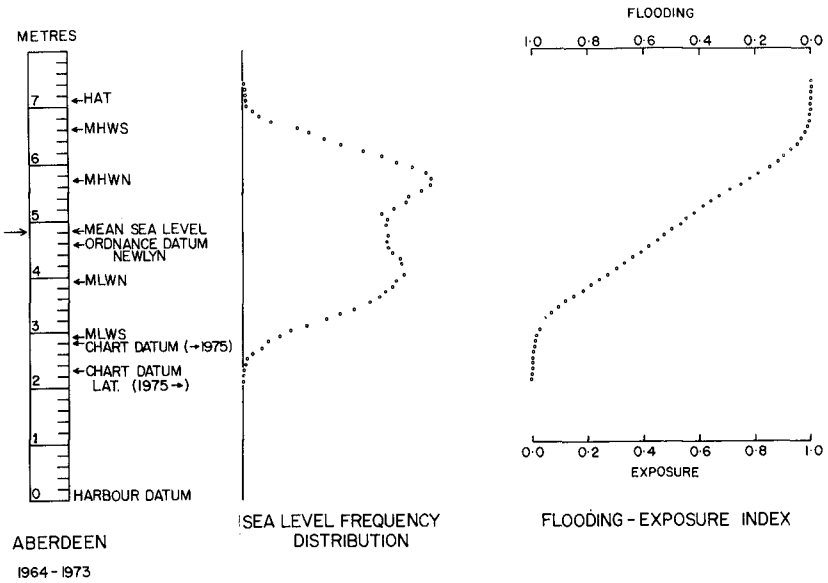


FIG. 2.

where H_n = amplitude of each constituent
 σ_n = speed " "
 V_n = equilibrium phase
 g_n = phase lag of constituent on the
 equilibrium tide

Removal of the tide did not require an excessive amount of data as a satisfactory tidal analysis was obtained from 1 year of observations.

The surge or non-tidal component is that part of the sea level which remains once the tide and mean level have been removed.

Over a long enough period the surge is a random variable. Obviously over a short period of say one month very few surges are likely to occur and any that do will not produce a random phase. Under these circumstances some of the surge energy is likely to appear in the harmonic constants and be depleted from the surge component. With longer data sets of say one year or more the effect is minimal and the surge is well separated from the tide. Only a few percent of the variance of sea level movements is attributable to the surge for typical shelf measurements. The remainder is tidal. Of course considerable damage is caused if the surge coincides with a high tidal level.

Unlike traditional methods the method of tide surge separation is not one of extrapolation. In this method it is intrinsically assumed that the available surge record is a representative sample of the population of all possible surges and that the surges could occur in a different configuration such that, for example, the largest surge could coincide with equinoctial spring tide. Of course the probability of these two coinciding is very small and should show as a correspondingly low probability in the final statistics.

Whether the above assumption is true is considered later but if it is, which is akin to saying that tide and surge are independent, the tidal and surge probability density functions (p.d.f.) can be combined as the sum of two independent variables (see for example Cramer 1971) to give the p.d.f. for total sea level.

If $p_t(x)$ = p.d.f. for tidal component

$p_s(y)$ = p.d.f. for surge component

and $p(\xi)$ = p.d.f. for total sea level

then $p(\xi) = \int_{-\infty}^{\infty} p_t(\xi - y) \cdot p_s(y) \cdot dy$ 2.3

In simple terms equation 2.3 states that the probability of sea level reaching say 10 metres is the sum of all surge and tidal probabilities that combine to produce a level of 10 m. For example a surge of 2 m and a tide of 8 m, or a surge of 1 m and a tide of 9 m.

The integral is taken over an interval which includes all possible tidal and surge levels.

From $p(\xi)$ the probability of exceedance of a particular level can be evaluated by generating the cumulative distribution function $F(\eta)$, where

$$F(\eta) = \int_{\eta}^{\infty} p(\xi) \cdot d\xi \quad 2.4$$

The 'return period' for the level η is given by the reciprocal of the function $F(\eta)$ provided that the time series representing the surge is not auto-correlated.

In a similar fashion the probability of exposure of a low level is given by

$$F(\eta) = \int_{-\infty}^{\eta} p(\xi) \cdot d\xi \quad 2.5$$

Essentially the method consisted of a tidal analysis of the data for the harmonic constants and a prediction of the tide from these harmonic constants. From this the function p_t was generated and from the difference between sea level and the tidal time series the function p_s was generated. These were combined according to equation 2.3 and finally equations 2.4 and 2.5 were used to generate the cumulative distributions from which the return period and corresponding sea level were extracted.

3. THE DATA

The data consisted of hourly values of sea level digitised from tide gauge charts in the normal way. Each year comprised therefore on average 8766 values of hourly heights of sea level measured relative to the local tide gauge benchmark. The length of the records varied from a minimum of 9 years for Fishguard to 19 years for Newlyn and Southend. For these latter ports an extended record covering 50 years was available but only part of it was chosen for the present study. A summary of the data used is given in Table 1.

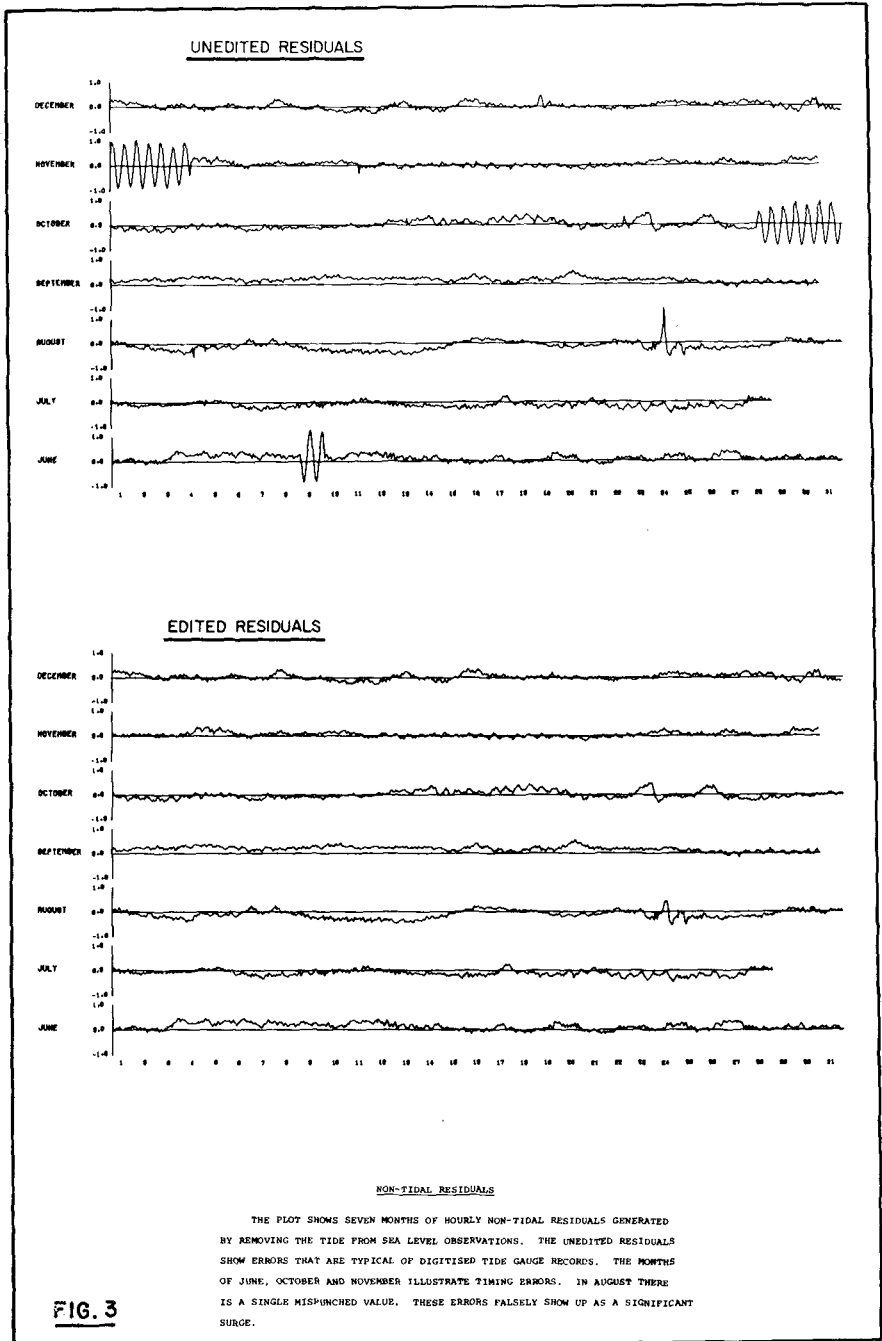


FIG. 3

TABLE 1

Newlyn	19 years	1951-69	continuous
Fishguard	9	1963-71	a few gaps
Malin Head	12	1960-71	sections of the record dubious
Stornoway	15	1957-72	a few gaps
Lerwick	14	1959-72	a few gaps
Aberdeen	10	1964-73	many gaps
Southend	19	1951-69	continuous

Most of the records were fairly complete except for short periods when the tide gauges malfunctioned. Malin Head gauge had two breakdowns and three sections lasting several months where the record was dubious for tidal analysis but adequate for surge statistics. The record from Aberdeen had many gaps but the data from the periods when the gauge was working was satisfactory.

The fact that gaps did exist in the data was of no consequence to the analysis procedure which was designed to deal with this. It might have had some effect on the surge statistics if the gaps had been systematic and had occurred only at particular times of the year. For example, if records had been available only from summer months the statistics would have been biased downwards because the surges were more frequent in the winter.

A typical surge record is shown in figure 3. This was produced by subtracting the tidal signal from the sea level record and there was therefore a need for careful editing of the data. This is not so critical in the annual extremes method which deals only with absolute levels.

When the charts were removed from the tide gauge drum they usually contained seven or fourteen days data and were such that every day occupied the same portion of the chart. Occasionally it happened that the chart was digitised erroneously by following the wrong part of the trace. Another fairly common type of error was due to timing, the chart was placed on the drum offset from the timing zero.

In the annual extremes method neither of the above errors would have had any effect as the absolute levels would not have been changed. However when the tide was removed both types of error produced a large tidally varying residual giving the false impression of a surge of significant height. Errors in reading the absolute height of the sea level curve would have affected the annual extreme and surge methods equally.

When the original tide gauge records were digitised they were at that time subjected to error checking routines. A Lagrangian interpolation curve was fitted to adjacent observations and a check was made for discontinuities between the smooth curve and the digitised level. This was found inadequate for detecting all the possible errors to the accuracy required.

The method chosen to examine the sea level record consisted fundamentally of plotting the surge as a function of time and of examining the plotted values by eye for irregularities. Errors were then corrected by referring to the original tide gauge chart.

The method of data editing is summarised below.

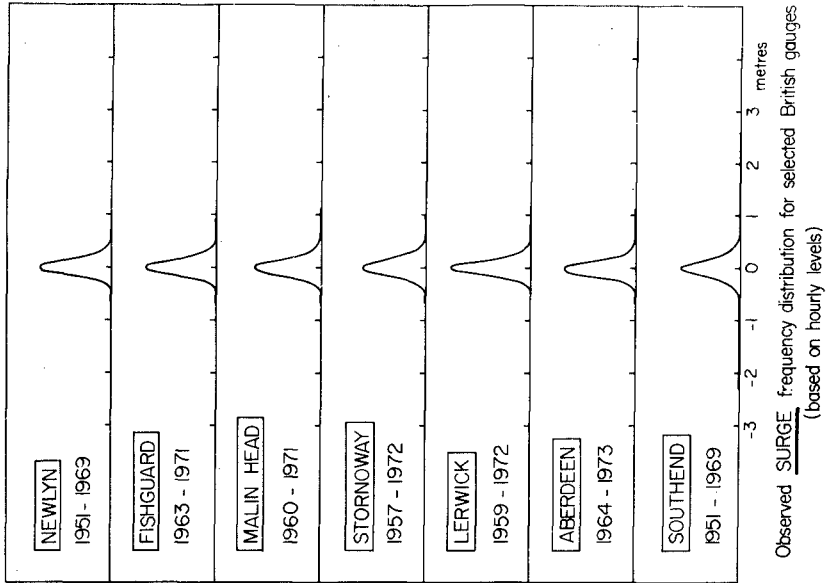
1. Pilot tidal analysis from 1 year of data.
2. Generate non-tidal residuals and plot as in figure 3.
3. Identify major extremes and areas of dubious record.
4. Refer to original tide gauge charts to correct errors.
5. Check weather records during periods of extremes.
6. Edit original sea level record.
7. Tidal analysis of the full period of data.
8. Reproduce non-tidal residuals.

This method was found to be very powerful for detecting errors and less time consuming than orthodox methods in cases where the record was consistently bad. Timing errors of a few minutes were easily detectable.

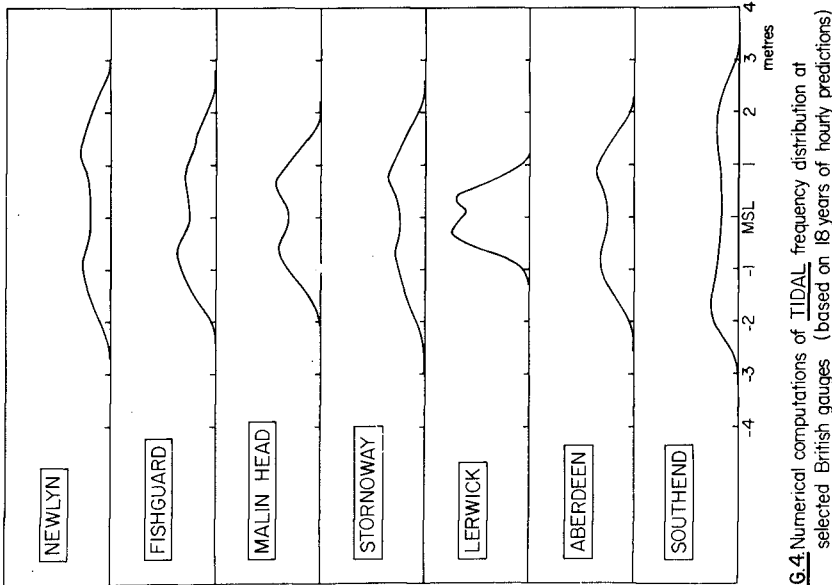
If there was some area of doubt such as a large surge when weather conditions were calm the data concerned was omitted from the analysis, but this rarely happened.

4. THE ASTRONOMICAL TIDES

The tidal part of the record was represented by the harmonic constants given in equation 2.2. From these constants a tidal time series was generated using the same equation and incrementing t from zero in units of one hour. The time series extended over a period of 19 years which is the time of regression of the moon's nodes, a fundamental period in the orbital motion of the Earth-Moon system. 19 years was necessary to generate the correct probability density function (p.d.f.) for the tides as the modulation in tidal elevation due to nodal motion could have been as much as 4%. The resulting p.d.f. for each port is shown in figure 4. These were generated numerically from the tidal time series in class intervals of 0.1 metre.



Observed SURGE frequency distribution for selected British gauges (based on hourly levels)



Numerical computations of TIDAL frequency distribution at selected British gauges (based on 18 years of hourly predictions)

It was possible to get some way towards an analytical expression for the tidal probability distribution from the harmonic constants using the sum of independent sinusoids but all such attempts produced a symmetric distribution whereas almost all the measured tidal distributions were asymmetric.

The measured distribution was always bimodal, the two peaks, or modes, occurring near mean high water neaps and mean low water neaps, but with a considerable tail above and below these levels. The tails did not of course extend to infinity, they terminated at Highest and Lowest Astronomical Tide (HAT and LAT) which in the general case were not evenly distributed about mean sea level. The values of HAT and LAT were extracted from the tidal time series and their values are presented in Table 2 relative to the mean level at each port.

	<u>HAT(m)</u>	<u>LAT(m)</u>
Newlyn	2.914	-2.928
Fishguard	2.791	-2.429
Malin Head	2.177	-2.128
Stornoway	2.626	-2.904
Lerwick	1.188	-1.272
Aberdeen	2.281	-2.576
Southend	3.311	-3.131

One interesting feature of the tidal distribution was the asymmetry of the modes, i.e. they were of different heights. This has been positively related to the shallow water tides M_4 and S_4 which are at exactly twice the frequency of the main lunar and solar tides M_2 and S_2 . It can be shown that the asymmetry is a maximum when the fourth-diurnal tides are in quadrature phase to the semi-diurnal tides. The asymmetry was noticeable even at Lerwick where the non-linear tides were fairly small in relation to the main tide.

5. THE SURGE OR NON-TIDAL RESIDUAL

The mean surge level for all ports was necessarily zero because of the manner in which the tides were removed from the observations of sea level. The time series (figure 3) had the appearance of a background noise continuum with occasional large surges protruding above the noise level. As with the tides the p.d.f. for the surges was generated

numerically from the time series. Figure 4 contains examples of the surge p.d.f's.

The p.d.f's had a Gaussian appearance, but with some asymmetry, which varied in width depending on location. In some cases, particularly Southend, the tail of the distributions were very wide indicating large surges but of infrequent occurrence.

TABLE 3

	<u>maximum</u>	<u>minimum</u>	<u>standard deviation</u>	<u>Skewness</u>	<u>Kurtosis</u>
Newlyn	0.877m	-0.639m	0.149m	0.0016	0.0019
Fishguard	0.962	-0.734	0.156	0.0019	0.0024
Malin Head	1.123	-0.682	0.169	0.0023	0.0034
Stornoway	0.957	-0.739	0.169	0.0016	0.0030
Lerwick	0.756	-0.524	0.136	0.0010	0.0012
Aberdeen	1.054	-0.743	0.155	0.0024	0.0026
Southend	2.638	-2.307	0.230	0.0057	0.0247

Statistics of surge distributions based on hourly values

Table 3 contains the principal moments of the surge distribution for each port in the form of the standard deviation, the coefficients of Skewness and Kurtosis and the maximum and minimum levels reached during the period. The coefficients were defined as follows:

$$\text{rth moment} = \mu_r = \frac{1}{N} \sum_{i=1}^N (y_i)^r \quad \text{where } y_i = \text{ith surge level}$$

$$\text{standard deviation} = \sigma = (\mu_2)^{\frac{1}{2}} \quad N = \text{total number of observations of surge level.}$$

$$\text{coefficient of skewness} = \mu_3 / \sigma^3$$

$$\text{coefficient of kurtosis} = \mu_4 / \sigma^4 - 3$$

The standard deviation increased down the east coast from 13.6m at Lerwick to 23.0 cm at Southend. On the west coast the variation was found to be smaller lying between 14.9 cm and 16.9 cm. The distributions in all cases showed a positive skewness indicative that extreme high levels (positive surges) were more probable than low levels. This was reflected in the maximum and minimum levels which in all cases showed

extremes on the positive rather than negative side. The kurtosis which is a measure of the flattening of a distribution relative to a normal distribution was always positive, more so where the standard deviation was large, but in general was small.

No allowance was necessary in the moments for Sheppard's corrections due to grouping. These were insignificant in comparison to the moments themselves because of the small class interval used in computing each p.d.f.

Tests were carried out on the variation of the p.d.f. over subsets of a year. These showed a remarkable stability in the main parameters of the p.d.f. except for the very extremes of the distribution with which of course this work was primarily concerned. This was expected because the extremes occurred infrequently during the period of even the longest data set and did not occur during every year.

6. ADDITION OF SURGE TO HAT AND LAT

This section is included in the paper not because it is part of the main theme but because it gave upper bounds to the extreme statistics. Also it was found to be a useful technique in cases where safe design criteria were essential. The method consisted of adding the surge extremes to Highest Astronomical Tide instead of combining surge and tide in the manner discussed in section 8. The procedure is illustrated in figure 5 where Fishguard is used as an example.

To estimate the extremes of surge p.d.f. the upper part of the cumulative distribution, shown in the lower part of the diagram, was linearised by fitting a logarithmic curve. This curve proved adequate even although the uppermost surges, which were only three in number, deviated slightly from it. An extrapolation of the curve gave the surge levels associated with return periods of between 1 year and 1000 years.

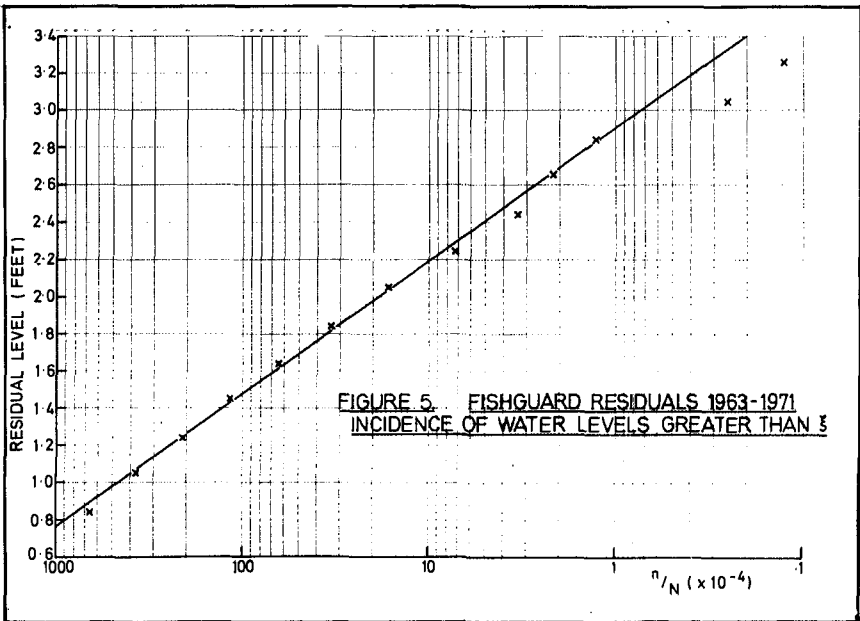
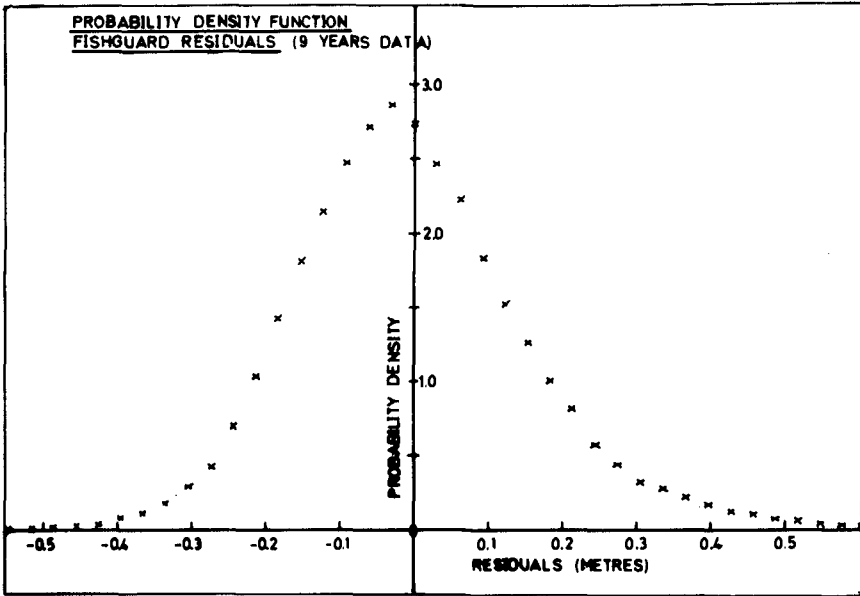
The total sea level appropriate to each return period was then derived by adding the surge statistics to HAT.

This technique of estimating extremes tended to overestimate the probability values and therefore gave, as expected, pessimistic results for the levels associated with each return period. The results are discussed in section 9.

7. INDEPENDENCE OF TIDE AND SURGE

The equation for the combination of tidal and surge distributions (2.3) assumes independence between the two and it is important to consider whether or not they can be treated as statistically independent variables.

One form of possible dependence stems from the fact that surges are more prevalent in the winter than at other times of the year and maximum



tides occur at the equinoxes. However this is liable to be of secondary importance because the levels of the tides at the equinoxes are reached by spring tides at other times of the year to within a few tens of centimetres. Also the extreme surges with which we are primarily concerned do occur at times of the year other than winter. For example, one of the highest surges at Avonmouth occurred close to the spring equinox in March 1947. Fortunately it occurred very near low water or it would have caused extensive damage.

The main cause of dependence that has to be considered is surge/tide interaction such as occurs in the southern region of the North Sea. It is well known that at Southend the peak of the surge occurs on the rising tide and is somehow prevented from coinciding with high water.

To find if interaction was a problem at the six other ports a study was made of the moments of the surge distributions as a function of tidal level. Any interaction would have caused a variation of the moments with the height of the tide. Table 4 reproduces the results for two stations, Aberdeen and Southend.

TABLE 4a

<u>INTERACTION STATISTICS FOR ABERDEEN</u>				
The moments of the surge distribution are shown as a function of tidal height.				
<u>TIDAL LEVEL</u>	<u>SURGE MOMENTS</u>			
(metres)	<u>MEAN</u>	<u>VARIANCE</u>	<u>SKEWNESS</u>	<u>KURTOSIS</u>
to m.s.l.	m	m ²		
-2.4	0.011	0.024	0.001	0.002
-2.0	0.007	0.023	0.003	0.003
-1.6	0.0	0.022	0.002	0.002
-1.2	-0.002	0.024	0.003	0.003
-0.8	-0.003	0.025	0.003	0.003
-0.4	-0.002	0.026	0.003	0.003
0.0	0.0	0.025	0.002	0.003
0.4	0.002	0.024	0.002	0.003
0.8	0.005	0.024	0.002	0.002
1.2	0.001	0.023	0.002	0.002
1.6	-0.001	0.022	0.002	0.002
2.0	-0.001	0.025	0.001	0.002
2.4	-0.025	0.020	-0.001	0.001

For Aberdeen there was little variation in any of the first four moments. The mean level was of course small but should have been zero. The second moment which is the most important as a test of interaction because it represents the square of the amplitude of the surge, was remarkably constant at 0.024 m² with an increase of only 2 mm² near the mid-tide level.

Southend on the other hand showed a marked increase in the second, third and fourth moments towards the mid-tide level and a decrease in

the mean surge level. The second moment for example increased by a factor of two between the top and middle of the tidal range.

The other ports, although not reproduced here, were very similar to Aberdeen. It was concluded that, except for Southend, any interaction effects were of second order and that tide and surge could be treated as statistically independent variables.

TABLE 4b

INTERACTION STATISTICS FOR SOUTHEND				
TIDAL LEVEL (metres) to m.s.l.	SURGE MOMENTS			
	MEAN m	VARIANCE m ²	SKEWNESS	KURTOSIS
-3.2	0.121	0.043	-0.007	0.008
-2.8	0.052	0.040	0.002	0.011
-2.4	0.014	0.039	0.004	0.011
-2.0	-0.005	0.047	0.009	0.022
-1.6	-0.006	0.054	0.010	0.025
-1.2	-0.013	0.061	0.012	0.036
-0.8	-0.011	0.064	0.009	0.034
-0.4	-0.013	0.072	0.009	0.043
0.0	-0.005	0.069	0.008	0.040
0.4	-0.008	0.066	0.004	0.030
0.8	-0.001	0.066	0.004	0.033
1.2	0.019	0.057	0.002	0.020
1.6	0.021	0.052	-0.002	0.018
2.0	0.012	0.047	0.001	0.017
2.4	0.006	0.041	0.0	0.010
2.8	-0.020	0.039	-0.001	0.010
3.2	-0.086	0.035	-0.007	0.012

8. COMBINED TIDAL P.D.F. AND SURGE P.D.F.

The sea level probability distribution was derived from the combined tide and surge distributions according to equation 2.3. In practice a discrete form of the integral was used because of the need to generate the individual distributions in discrete bands or class intervals.

$$p(\xi) = \sum_{i=-N}^N p_t(\xi - ih) \cdot p_s(ih) \quad 8.1$$

where $h = \text{class interval} = 0.1\text{m}$.

Summation was over a number of bands $2N+1$ which was wide enough to include all possible tidal and surge levels.

The cumulative distributions $F(\eta)$ were also discrete and were calculated as a discrete form of equations (2.4) and (2.5). For the high levels, these distributions gave the probability that a particular level would be exceeded which of course decreased as the level was increased. Table 5 shows the cumulative distribution function for each port but here the probability value is expressed as the return period.

Return period in years = $1/(\text{exceedance probability} \times m)$
 where m is the number of hourly values in a year = 8766

TABLE 5

<u>Return periods in years for exceedance of specified sea levels by combination of tidal and surge distributions</u>						
<u>Level (m)</u> <u>above msl</u>	<u>NEWLYN</u>	<u>FISHGUARD</u>	<u>MALIN HEAD</u>	<u>STORNOWAY</u>	<u>LERWICK*</u>	<u>ABERDEEN</u>
3.6	1670					
3.5	311	926				
3.4	74	261				
3.3	20	81		762		
3.2	5.9	26		182		
3.1	1.9	8.7		50		863
3.0	0.7	3.1	1520	15		248
2.9		1.1	392	4.9		80
2.8			109	1.7	1520	27
2.7			35	0.6	199	9.8
2.6			12		27	3.6
2.5			4.4		4.8	1.4
2.4			1.7		1.0	.

* Lerwick levels are related to Mean sea level + 1 metre

TABLE 6

<u>Return periods in years for exposure of specified sea levels by combination of tidal and surge distributions</u>						
<u>Level (m)</u> <u>below msl</u>	<u>NEWLYN</u>	<u>FISHGUARD</u>	<u>MALIN HEAD</u>	<u>STORNOWAY</u>	<u>LERWICK*</u>	<u>ABERDEEN</u>
-2.3			1.3		.	
-2.4			5.6		1.1	
-2.5		0.8	28		7.2	
-2.6		3.4	178		56	0.7
-2.7		18	1655		641	2.6
-2.8		101				12.4
-2.9		584		0.6		64
-3.0	1.3			2.0		316
-3.1	6.6			7.0		1590
-3.2	42			28		
-3.3	335			120		
-3.4				560		
-3.5						
-3.6						

* Lerwick levels are related to Mean sea level - 1 metre

Table 6 gives the equivalent values for the exposure of low levels again expressed as a return period. In both tables Lerwick has been offset relative to the mean level by 1 metre to fit in the table. The

extremes at Lerwick were very much smaller than those at other ports because the tides had a relatively small range.

The return periods in some cases exceeded 1000 years. This might seem surprising because only a few years of data was used but in fact occurred because the combined probability was the product of two probabilities which near the limits of the distributions were themselves small. The limit of the tidal p.d.f. corresponded to the occurrence of equinoxial tide which lasted only a few hours each year (say $p_t = 0.001$). The surge probability was even smaller than that of the tide as it corresponded to the extreme surge in say 10 years ($p_s = 0.00001$). This gave a product of $(10)^{-8}$ and an equivalent return period of 10000 years. Therefore return periods of 1000 years contained at least 10 samples of surge in the upper levels of the distribution.

It is common practice in extreme levels work to quote return periods of 50 years and 100 years. The combined distribution did not produce these levels automatically. It was necessary to interpolate between height intervals to determine a particular return period. This was best done from the probability function because this was a smoother function of level than the return period. The total levels with a return period of 50 years and 100 years are shown in Table 7.

TABLE 7

<u>Sea levels corresponding to 50 year and 100 year return periods.</u>				
<u>Levels are in metres relative to mean sea level.</u>				
	<u>50 years</u>		<u>100 years</u>	
	<u>Exceedance Level</u>	<u>Exposure Level</u>	<u>Exceedance Level</u>	<u>Exposure Level</u>
Newlyn	3.38	-3.32	3.43	-3.37
Fishguard	3.27	-2.78	3.33	-2.80
Malin Head	2.75	-2.55	2.80	-2.59
Stornoway	3.10	-3.34	3.18	-3.31
Lerwick	1.65	-1.60	1.68	-1.65
Aberdeen	2.87	-2.89	2.93	-2.94

9. DISCUSSION

One reason for the inclusion of Newlyn in this work was that estimates were already available for high levels using the annual extremes method (Blackman and Graff, 1978). These were useful for comparison of the results from the two methods. The calculated levels which had a return period of 50 years and 100 years are reproduced in Table 8 from the annual extremes method, from the combined surge-tide method and from the addition of the surge distribution to Highest Astronomical Tide.

The values derived from each method can only be estimates of the probable extremes and should not be considered as absolute. Indeed, it is debatable whether absolute or correct values exist. The maximum

observed level during the 62 years from 1915 to 1976 was 3.18m which was close to the 50 year level derived from annual extremes. The 100 year level by the same method was a slight underestimate when compared to the overall maximum.

The combined surge-tide probability produced values for the 50 year and 100 year return periods which were higher than those from annual extremes by 24 cm and 27 cm respectively. The agreement is good when the very different ways in which the data have been treated is considered. The 3.18 m level during the 62 years suggests that the method of annual extremes may give slightly low estimates. For engineering applications slight overestimates are preferable.

Our method will tend to produce overestimates because the surges are auto-correlated in that successive hourly samples of the time series are not independent of one another. Surges persist for more than one hour. If this grouping of hourly values had been taken into account then the estimated extreme levels would have been reduced. This problem is being investigated.

Another problem is the interaction between surge and tide. For this reason the results for Southend are not presented in this paper. Estimates produced for Southend were greater than the values calculated from annual extremes by as much as 60 cm which requires further consideration. The surge probability distribution for Southend is a function of tidal height because of surge tide interaction (Prandle and Wolf, 1978) and it is intended to model this function so that surge and tide may be combined correctly.

TABLE 8

<u>Comparison of return levels computed for NEWLYN</u> <u>(above 1951-1969 mean sea level)</u>		
	50 years	100 years
62 years of annual maxima (1915-1976)	3.14m	3.16m
Combined <u>tide-surge</u> probability (1951-1969 observations)	3.38m	3.43m
<u>Highest astronomical tide + surge</u> (1951-1969 observations)	3.90m	3.93m
Maximum observed value 1915-1976	3.18m	

10. CONCLUSIONS

We have developed a method for estimating extreme sea levels by studying the probability distributions of surge and of tide separately and then recombining them in a manner which assumes that they are statistically independent.

The method produces realistic estimates for extreme sea levels by comparison with traditional methods, but from much shorter lengths of data. This is important because few coastal sites have long sea level records. The assumption of independence of surge and tidal levels is proved to be valid for all the ports considered, with the exception of Southend.

The estimates are slightly biased on the high side for the upper extremes by comparison with traditional estimates. Some overestimation is inevitable because of the grouping of hourly surge values. The effects of this auto-correlation are being examined in an attempt to reduce the bias.

Our method also enables estimates of extreme low level probabilities. However, figures are not available from the annual extremes method for comparison.

The problem of surge-tide interaction is also being examined so that the method may be applied to ports such as Southend which are in shallow water and where, in consequence, surge and tide cannot be considered as statistically independent.

ACKNOWLEDGEMENT

The work described in this paper was funded by the Consortium consisting of the Natural Environment Research Council, the Ministry of Agriculture Fisheries and Food and the Departments of Energy, Environment and Industry.

REFERENCES

- Ackers P. and Ruxton T.D. Extreme Levels Arising from Meteorological Surges. Coastal Engineering 1974. Vol. 1 pp 69-86.
- Cramer, H. Mathematical Methods of Statistics. Princeton Univ. Press 1971. pp 190-191.
- Blackman D.L. and Graff J. The Analysis of Annual Extreme Sea Levels at Certain Ports in Southern England. Proc. Instn. Civ. Engrs. Part 2 1978, 65, June. 339-357.
- Lennon G.W. A Frequency Investigation of Abnormally High Tidal Levels at Certain West Coast Ports. Proc. Instn. Civ. Engrs. 1963, Vol. 25, Aug., pp 451-484.
- Prandle D. and Wolf J. The Interaction of Surge and Tide in the North Sea and River Thames. Geophys. Jour. R.A.S. 1978, Vol. 55, No. 1, Oct. pp 203-216.
- Rossiter J.R. An Analysis of Annual Sea Level Variations in European Waters. Geophys. J.R. Astr. Soc. Vol. 12, 1967. pp 259-299.
- Suthons C.T. Frequency of Occurrence of Abnormally High Sea Levels on the East and South Coasts of England. Proc. Instn. Civ. Engrs. 1963 25, Aug., pp 443-449.
- Thompson K.R. Analysis of British Mean Sea Level.(personal communication) Institute of Oceanographic Sciences.

CHAPTER 53

Analysis of maximum sea levels in southern England

J. Graff* & D. L. Blackman*.

Abstract

Along the south coast of England, series of observed annual maximum sea levels, ranging from 16 years to 125 years have been analysed for each of 10 ports. The Jenkinson¹ method of analysis was used to compute the frequency of recurrence of extreme levels. For a number of these ports the series of annual maxima are shown to have significant trends of the same order as those for mean sea level. The Jenkinson method can be simply adjusted to cope with maxima having a component linear trend, making it possible to allow for such trends in computing the frequency of recurrence of extreme levels. If a trend in the annual maxima varies throughout the sample of observations it is shown that difficulties arise in using the Jenkinson method to compute acceptable statistics. It is also shown that for certain ports having long series of observed annual maxima it may be necessary to restrict the sample size of observations in order to compute estimates of the recurrence of extreme levels within reasonable return periods.

Introduction

Around the coastline of England, particularly along the north west, east and south east the occurrence in recent years of abnormal flood levels has created a demand for the reassessment of flood defence levels and a need to revise measures of the frequency of recurrence of extreme levels. Subsequent to the disastrous east coast flooding of 1953, coastal defence levels were established to protect against a further recurrence of these levels. In the past decade, the levels of 1953, which were generally associated with return periods exceeding 100 years, have been overtopped on a number of occasions at certain north west and east coast ports suggesting that factors may have contributed to increase the frequency of occurrence of extreme levels. Lennon² and Suthons³ published studies in 1963 on the analysis of occurrence of observed annual maxima for ports respectively on the west and south east coasts of England. For south east ports Suthons, using Jenkinson's method of analysis, included the effects of a linear trend of 1ft/century, representing an assumed secular trend in mean sea level. The series of observations studied by Lennon and Suthons extended to the average period 1957/60. In recent years the need to update the work of Suthons³ for south east coast ports has led to a number of studies, notably Akers & Ruxton⁴ (1974, Southend), Webber & Davies^{5,6} (1976 Portsmouth, Southampton, Calshot) and Blackman & Graff⁷ (1978). The study⁷ by the authors, covering 10 ports along the south

*Bidston Observatory, Institute of Oceanographic Sciences,
Birkenhead, Merseyside. L43 7RA. U.K.

coast of England forms in part the basic framework of this paper. All the studies mentioned so far (viz. 2, 3, 4, 5, 6, 7) accept that the longest available and reliable series of observed annual maxima should be analysed by extreme level techniques. Although no strict information is available (more so perhaps possible) to indicate how far one may extrapolate the analysis curves showing the frequency of occurrence of extreme levels it is accepted¹⁰ that some reliability can be based on considering a period up to perhaps 4 times the original sample size. It is however not uncommon practice, in considering design criteria for coastal defences that the extrapolated extreme sea level likely to occur once in a period exceeding 15 times the original sample size, is in fact used.

For the coastline of east, south east and south England, secular trends of various order exist in the series of annual maxima. Suthons³ and the authors⁷ included the effects of mean linear trends occurring throughout the sample of observations to provide "more likely" estimates of the recurrence of extreme levels. More recently, in reviewing their work on south coast ports, and extending their studies to other U.K. ports the authors have shown that the use of an analysis method such as the Jenkinson technique can be highly dependent not only on the sample size of observations but also on the nature and linear measure of secular trends in the data. Whereas in the past it was thought acceptable to make an analysis of the full available sample of observed annual maxima, and perhaps adjust these for a mean linear trend, it would now seem that such results can cloud the presence of many anomalies and it may be necessary to make the analysis more detailed in order to provide information of practical use. In this paper the authors present a summary of their already published study⁷ and an account of the more recent work⁸ in the analysis of observed annual sea level maxima.

The form of sea level maxima

An observed sea level can be simply expressed as

$$h_o = h_p + h_w + h_r \quad 1.$$

where h_p is the astronomically generated (predictable) tide.
 h_w is the wave height induced by wind or otherwise.
 h_r is a residual due to non tidal or weather effects.

Tide gauges are generally so designed to filter out the wave height and record only the level h_o^*

$$h_o^* = h_p + h_r \quad 2.$$

In reality however a more explicit form of the recorded level h_o^* should be expressed as

$$h_o^* = h_p + h_R \quad 3.$$

where $h_R = h_r + \epsilon$, ϵ being a small (or sometimes large) error due to effects in the recording mechanism which should be accounted for in the reduction of records.

In considering recorded levels h^* of annual extremes it is not uncommon to find that stresses imposed on the tide gauge often contribute severe perturbations (ϵ) to the recorded tidal trace which can not always be resolved unambiguously from the true level being recorded ($h_p + h_r$).

Equally in instances where the tide gauge breaks down around the time of the extreme level occurring it is necessary to try and extrapolate the recorded trace to the time of the peak level.

In the case of extreme levels being recorded from a tide pole there is inherently a far greater uncertainty in accepting the level to be an accurate height as defined in (2). More likely than not, under associated severe weather conditions (often in the dark) a sea level read from a tide pole, even by an experienced observer, may reflect a significant measure of the superimposed wave effects (h_w).

It seems important to mention the above points here to highlight the form of data being considered in this type of analysis. These data are essentially a measure (often estimate) of the single annual maximum sea level as defined in (2), divorced of wave effects which on such occasions are often of a considerably pronounced form. These single annual maxima can be seen in the context of other peak tidal levels in Figure 1, which shows the distribution of observed monthly maxima over some 20 years for Newhaven, one of the ports studied. This bimodal form of distribution is typical of sea level maxima at many ports around the British Isles.

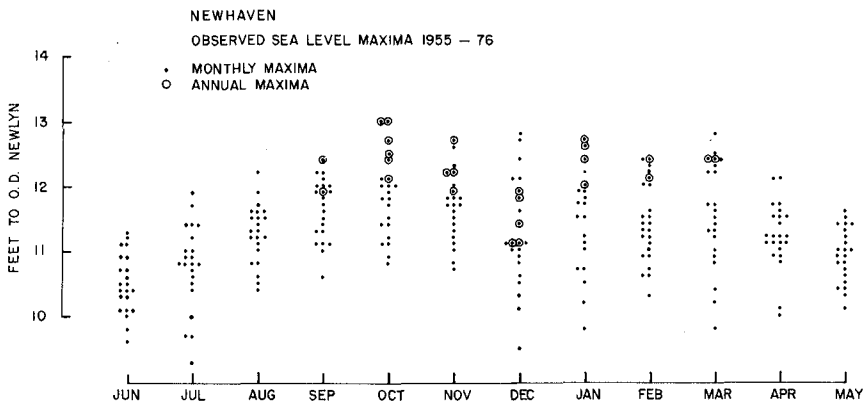


FIG. 1. Observed monthly sea level maxima at Newhaven.

To date only Akers & Ruxton⁴ have endeavoured to analyse the interaction of the components h_p , h_w and h_r in relation to extreme levels, and the complexity of the problem and lack of suitable wave data have shown to present serious limitations. More recently Pugh & Vassie⁹ have approached the problem of investigating the occurrence of maxima by studying the interactive effects of h_p and h_r at hourly intervals, a technique that is hopeful of finding suitable joint probability distributions (of h_p and h_r), based on reasonably short series of a few years, that can be combined to provide information concerning the recurrent frequencies of abnormal levels.

Referring back to the work presented in this paper it is useful again to be reminded that the observed annual maxima studied are principally as defined in (2) although where tide pole data have been used one must accept that some proportional influence of wave effects are included.

Observational data

For each of the 10 ports indicated in Figure 2 the best series of up-to-date annual maxima were obtained, in some cases extending the data studied by Suthons³ by some 30%. Most of these data were based directly on tide gauge records, which for some ports covered a considerable period. All the sea level records were reduced to the national reference datum of Ordnance Datum Newlyn. Table 1 lists the coverage of data for each port.

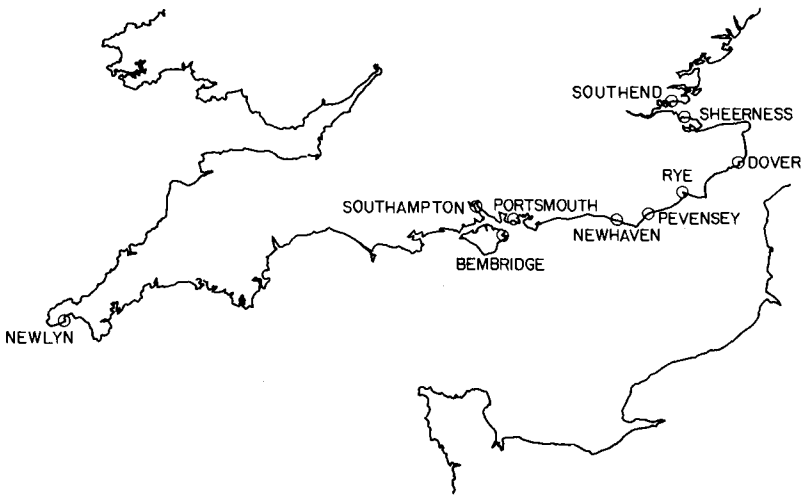


FIG. 2. Location of the 10 ports studied.

TABLE 1

Port	Years	Observed maxima
Newlyn	1916-76	61
Southampton	1924-75	47
Portsmouth	1813-75	105
Bembridge	1947-76	29
Newhaven	1913-76	60
Pevensey	1953-76	24
Rye	1949-74	16
Dover	1912-75	56
Sheerness	1819-70	125
Southend	1929-75	46

The Jenkinson method of analysis

If we assume that any observed annual maximum sea level h is a statistically random extreme event then these data can be analysed by a method such as that suggested by Jenkinson¹ in 1955. If T , the return period of height h is the average interval between occurrences of heights equal to or greater than h , it is easily shown that

$$T = -1/\ln.P \text{ or } \ln T = -\ln(-\ln P) = x$$

where P is the probability that the annual maxima is less than h . Jenkinson suggests that the most general form of curve between h and x is given by

$$x = \frac{1}{k} \ln \left(1 - \frac{h-h_c}{a} \right)$$

where k , h_c and a are constants determined from observations.

k is also a measure of the curve type of the data distribution such that if

$k < 0$, curve bends upwards; Fisher-Typpett Type I

$k = 0$, curve is a straight line; Fisher-Typpett Type II

$k > 0$, curve bends downwards; Fisher-Typpett Type III

Along the south coast of England the nature of the curve changes gradually eastwards, from Fisher-Typpett Type III through Type II to Type I, as seen in Figure 3.

Port diagram curves (Type A)

For the ports shown in Figure 2, the series of observed annual maxima indicated in Table 1 were analysed by the Jenkinson technique, and the results, showing the frequency of recurrence of maxima can be presented in a form as shown in Figure 3. These Port diagram curves are termed type A when related to analysis which do not account for the effect of linear trends.

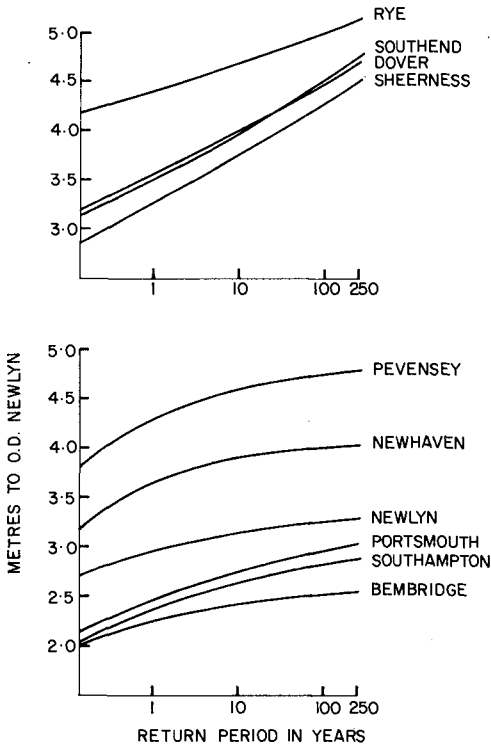


FIG. 3. Frequency of recurrence of observed annual maxima (excluding effects of trends).

Mean trends in observed annual maxima

The series of observed annual maxima for each port were examined for trends. No evidence was found to suggest that any secular fluctuation of data was correlated with long period tidal effects of astronomical origin. Mean linear trends were resolved by simple linear regression analysis, and for several ports where suitable hourly sea level data were available, it was possible to also obtain the linear trend of mean sea level. These trends are shown in Table 2 and it can be seen that in general, the trends in annual maxima are similar to those for mean sea level. For the ports Newhaven, Dover and Sheerness the linear trends in annual maxima are significant.

TABLE 2

Port	Trend in annual observed maxima, mm/year	Trend in mean sea levels, mm/year
Newlyn	1.31 \pm 0.75 (61 years)	1.95 \pm 0.12 (60 years)
Southampton	1.18 \pm 1.62 (47 years)	1.06 \pm 1.11 (15 years)
Portsmouth	0.68 \pm 0.29 (105 years)	8.35 \pm 0.80 (13 years)
Bembridge	-3.38 \pm 2.06	
Newhaven	5.44 \pm 0.94 (60 years)	4.11 \pm 1.65 (18 years)
Pevensey	4.60 \pm 5.39	
Rye	1.53 \pm 5.54	
Dover	4.99 \pm 1.68 (56 years)	4.52 \pm 0.53 (39 years)
Sheerness	2.41 \pm 0.53	2.37 \pm 0.17*
Southend	0.39 \pm 2.92 (46 years)	1.71 \pm 0.29 (49 years)

* Values established by Rossiter,¹¹ based on 85 years.

One could perhaps suggest, in broad terms, that mean trends observed in series of extreme levels reflect the secular trends in mean sea levels, although one should bear in mind that the mean sea levels are based on continuous hourly observations throughout the years whereas the annual maxima represents a single level occurring generally within the "storm months" August-March (See Figure 1).

Port diagram curves (Type B, C)

The Jenkinson method of analysis can be also applied to data which have a component of linear trend, providing that the data are first reduced to some selected epoch. For instance if the epoch is 1900 and a linear trend of .001 m/yr exists in the annual maxima then an observed level of 10.0m in 1850 reduces to a level of 10.05m in 1900, and similarly an

observed level of 10.0m in 1950 reduced to a level of 9.95m in 1900. The resulting port diagram curves, termed type B, accounting for a linear trend component, are similar to those noted as type A. The interpretation of type B curves is strict in the sense that a linear trend has been accounted for up to the base year of the selected epoch and no trend exists in the data beyond this year.

Suthons³ suggested it is possible to make some allowance for including a trend beyond the epoch by adjusting type B curves (into curves termed type C) in the following manner.

If T is a return period of height h_B (type B curve) or h_C (type C curve) where a mean rate of annual rise S is being considered in the data, then

$$h_C = h_B + T.S/2$$

This gives some guidance to interpreting the additive effects of a continuing trend assumed to exist in the data.

Figure 4 illustrates all three Port diagram curve types (A, B, C) for Sheerness.

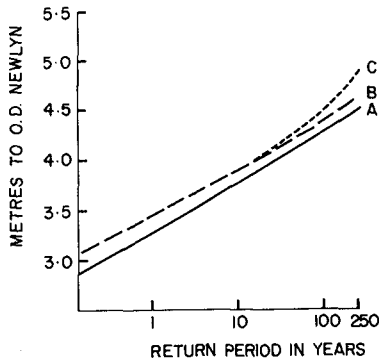


FIG. 4. Frequency of recurrence of observed annual maxima for Sheerness.

Curve A. unadjusted for any trend effects.

Curve B. adjusted to the epoch 1976 for a linear trend of 2mm/yr present only in the data analysed.

Curve C. adjusted to the epoch 1976 for a linear trend of 2mm/yr assumed to persist indefinitely.

As the return period T increases beyond a value equal to about twice the sample size of observations, the expected height h_c increases rapidly to unreal proportions. The format of computing the type C curve is subjective and gives guidance only as a broad illustration of including extrapolated trends. Appendix 1 lists for all 10 ports, data from port diagram curves type A, B, C, related to recurrence periods of 10, 20, 50, 100 and 250 years.

Some further considerations in the analysis of annual sea level maxima

Since in general, only a limited series of observed annual maxima, of the order of 10-20 years, are available for most ports, it is of interest to have some feeling for the response of the analysis method (Jenkinson) to different sample sizes. It is also of considerable interest to understand the nature of secular trends which may exist in the data series since they can have a pronounced effect on the analysis of such data. These considerations are particularly important for ports where a substantial investment is to be made in raising flood defences for protection against abnormal levels, subjectively assessed as being of the order of 1-in-100 years or more. At present the terms "return periods" and the associated "expected levels" are perhaps too freely used in the assessment of design criteria for coastal defences and it seems important to illustrate the drawbacks and limitations of interpreting what may seem to be "standard" port diagram curves.

Before any type of port diagram curve is to be interpreted seriously for practical purposes a number of questions would seem to be of prime importance.

1. How real is the sample of observed data in terms of their measured values.
2. Does a trend exist in the sample data set, and if so what is its form.
3. Will a trend persist in the future and can this trend, and that in a sample data set, be approximated by a constant linear term.
4. What is the confidence in extrapolating port diagram curves and how is this related to the size of the sample set.

Although we would not presume to suggest that any of these questions can be strictly answered we do suggest it is possible to illustrate their significance, hereby gaining a far greater awareness of the problem, thus enabling one to make a more objective interpretation of results.

Reliability of observed data

The uncertainty of measured data has already been discussed earlier and it is a simple fact that for good or bad, most early records of annual maxima proceeding the early fifties must be accepted as the "best measures" available. To review such data in terms of the performance and

stability of the measuring instrument presents considerable problems and frustration in what is often a mass of conflicting historically documented heresay. The national reference level, Ordnance Datum Newlyn, was only introduced as a datum measure to most Ports in Great Britain, in various degrees of accuracy, during the period between the late thirties and early fifties. Diligent checking of the annual tidal records, tide gauge histories and datum levelling exercises is the only sure way of attempting to collate a continuous datum level for series of records dating back through the early part of this century. In a few instances, for portions of data, much of the relevant information has been lost to antiquity.

Trends in annual maxima

With a substantial series of annual maxima one can identify fluctuations that can be resolved as a linear estimate of a mean trend. Table 2 already presents such measures for the 10 south coast ports which leads one to assume it is a simple matter to proceed in computing port diagram curves of type B. If we examine the form of these fluctuations or trends, a little closer it becomes obvious that they are far from linear, and like mean sea level data they vary in an ill defined and unpredictable fashion. Figure 5 shows the annual maxima plotted as 5 year running means for Sheerness and Portsmouth which represent the longest data series available in the study.

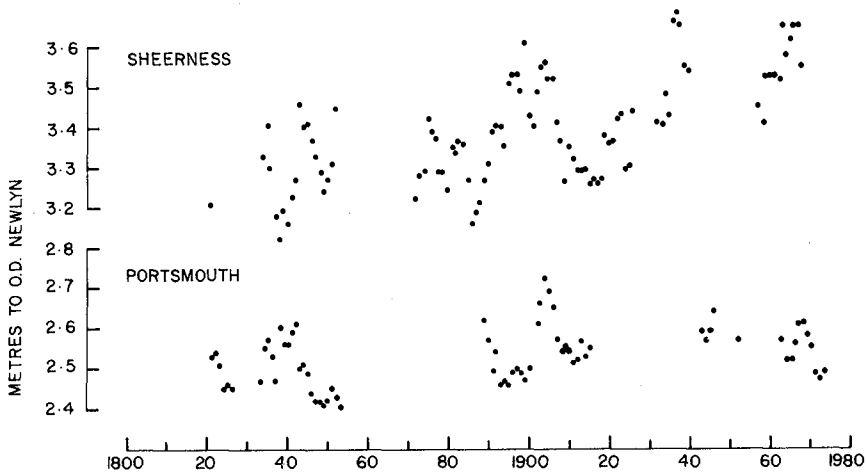


FIG. 5. Observed annual maxima plotted as 5 year running means for Sheerness and Portsmouth.

For some of the 10 ports a significant mean trend can be identified throughout the full data series but moreso in these cases (Sheerness) more pronounced secondary trends also can be identified within both long and short portions of the data set. Simple regression analysis of the annual maxima in cumulative sets to a 10 year base, both forward and backward (in a time wise fashion) readily show the extreme variability of the linear trend estimate and its generally poor fit to the observed data. These results are illustrated for all 10 ports in Appendix 2.

Since one can in fact adjust for linear trends in computing port diagram curves it is easy to see that the question of "what trend do we adjust for" is not a simple one to answer and indeed is a matter for some, if not considerable conjecture.

The confidence in port diagram curves

Bearing in mind that available series of annual maxima may be short or long, some thought should be given to interpreting resulting port diagram curves against the criteria of sample size. Again we split the series of observed data for each port into cumulative 10 year sets as noted earlier and made a systematic analysis to compute port diagram curves of both type A and type B for each block of data, in the same forward and backward fashion as for the regression analysis. To compute the type B curves the appropriate cumulative data sets were adjusted for the associated mean linear trend, to a common epoch. It would be impractical to try and present here even a summary of such results for all 10 ports, a form of analysis ⁸ which is now being systematically applied to data from many other ports around the British Isles. However, it is of some considerable interest to present typical results, for Sheerness, a port of major importance in the Thames estuary. The series of annual maxima for Sheerness show fluctuations in trend as seen in Figure 5 and Appendix 2, these having a significant positive mean linear trend throughout the full series of 125 annual observed maxima.

In Figure 6, the height with a period of recurrence of 100 years, based on type A curve analysis, has been plotted directly against the cumulative size of sample (number of annual maxima) used for the analysis. The cumulative sample sets relate, as shown, to the base year 1819 and 1970, respectively the start and end of the full observed series. It has also been possible to show these estimates based on analysis of 6 independent sets of 20 maxima taken throughout the period of data available. Similarly on the same diagram the results related to a type B curve analysis are shown, each cumulative data set being adjusted for the associated mean linear trend (Appendix 2) to the epoch 1980.

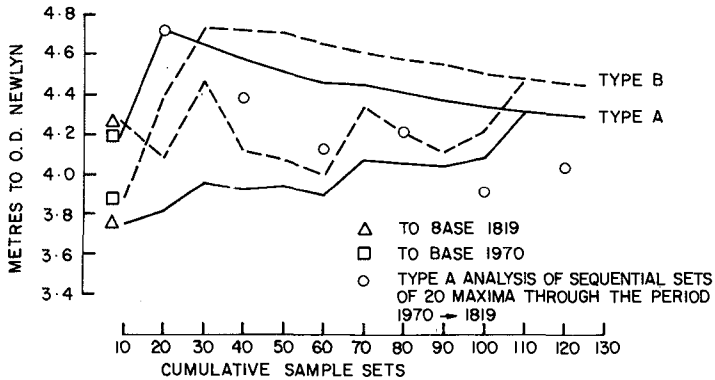


FIG. 6. Frequency of recurrence of observed annual maxima for Sheerness showing the 1-in-100 year event, based on analysis of different subsets of the data.

We would point out that the results shown in Figure 6 are not untypical⁸ of other ports in Great Britain where a far shorter series of annual maxima (up to 60 years) are available. Figure 6 (for Sheerness) highlights two points of particular interest

1. Depending on the sample set of maxima analysed (some multiple of 10) the 1-in-100 yr level can vary within a range of up to 1 metre. This range diminishes only as the sample size approaches its maximum length.
2. There is a pronounced increase in the estimated height of the 1-in-100 yr level throughout the period 1819 to 1970, e.g. there seems to be a general increase in the recurrence of abnormal levels.

This readily illustrates the considerable uncertainty in trying to interpret such results for practical purposes. In the past, and currently, it is often accepted that results based on analysis of a maximum available data series would provide a confident "best estimate" or a recurrence level for basic design level estimates. However this is clearly not the case, and the above results suggest that the assessment of a frequency of recurrence of an abnormal level (design level perhaps) is much more subjective than hitherto suspected, especially if sea level

maxima are subject to some form of secular trends. If the data were truly devoid of significant trend components (as is the case for other ports) then we would expect considerably less divergence in the plots as shown in Figure 6 above, and consequently would have a greater confidence in making an interpretation of such results. Portsmouth is seen to be a case-in-point where the absence of any significant trends produces a relatively stable set of recurrence levels, as illustrated in Figure 7 in the same fashion as for Sheerness. The high anomalous value associated analysis of the 10 earliest maxima reflects in fact the presence of dubious recorded levels.

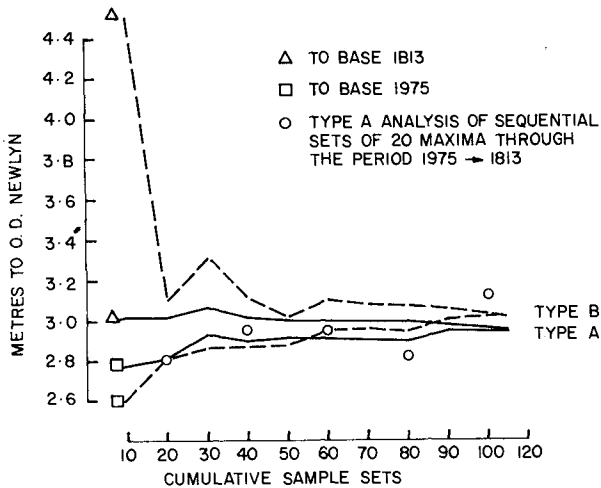


FIG. 7. Frequency of recurrence of observed annual maxima for Portsmouth, showing the 1-in-100 year event, based on analysis of different subsets of the data.

Appendix 3 lists heights associated with recurrence periods of 100 years based on type A curve analysis of 10 year cumulative data sets of the observed annual maxima for all the 10 south coast ports.

Conclusion

This paper has summarised results on the analysis of abnormal sea levels at south coast ports in England, and illustrated the revised level of information that is now necessary in order to provide a meaningful interpretation of the frequency statistics. Hitherto, estimates of recurrence levels have been based purely on analysis of the single full

length sample of annual observed maxima. For certain ports this may be acceptable, but it is suggested that there is a need for a more detailed analysis of the data, as illustrated in this paper. Indeed it may be the case that for some ports, irrespective of the length of available annual observed maxima, one may be restricted to assessing levels with recurrence periods less than 50 years, and these based only on analysis of subsets of the full data series. The analysis procedures are highly sensitive to data which contains secular trends that are not of a strictly linear form. A component of such trends may indeed be due to some corrupting effect of errors in the raw observed data.

Although annual observed sea level maxima provide an attractive basis for analysis procedures, such as Jenkinsons, aimed at forecasting recurrence levels, it is proving more unlikely that such treatment of single annual tidal observations will provide a satisfactory standard level of reliable information for practical design purposes. The interactive effects of tide, wave and weather are complicated to such a degree, that coupled with the uncertainty of sea level measurements of maxima it may be necessary to approach such studies of frequency analysis in a more fundamental way.

Acknowledgements

The work presented here derived from a study undertaken on behalf of Southern Water Authority, England, U.K., and in subsequent support from a Consortium consisting of the Natural Environment Research Council, the Ministry of Agriculture Fisheries and Food, and the Departments of Energy, Environment and Industry.

APPENDIX 1

RECURRENT SEA LEVELS

PORT associated with curve types A, B*, C*
based on analysis of whole data sets of maxima

		10 Yr	20 Yr	50 Yr	100 Yr	250 Yr
NEWLYN	A	3.15	3.19	3.24	3.27	3.30
	B	3.19	3.23	3.27	3.30	3.33
	C	3.20	3.24	3.31	3.37	3.49
SOUTHAMPTON	A	2.65	2.71	2.79	2.84	2.89
	B	2.68	2.74	2.82	2.87	2.93
	C	2.63	2.75	2.85	2.93	3.08
PORTSMOUTH	A	2.75	2.82	2.90	2.96	3.02
	B	2.79	2.87	2.96	3.03	3.12
	C	2.80	2.88	2.98	3.07	3.20
BEMBRIDGE	A	2.43	2.47	2.51	2.53	2.56
	B	2.36	2.38	2.40	2.41	2.42
	C	2.34	2.34	2.31	2.24	2.00
NEWHAVEN	A	3.89	3.94	3.98	4.01	4.04
	B	4.04	4.09	4.13	4.16	4.20
	C	4.07	4.14	4.27	4.44	4.88
PEVENSEY	A	4.60	4.66	4.72	4.76	4.80
	B	4.67	4.73	4.80	4.84	4.88
	C	4.69	4.78	4.91	5.07	5.45
RYE	A	4.72	4.81	4.94	5.03	5.17
	B	4.74	4.83	4.95	5.05	5.18
	C	4.75	4.85	4.99	5.13	5.38
DOVER	A	4.01	4.16	4.35	4.50	4.70
	B	4.16	4.30	4.49	4.65	4.87
	C	4.18	4.35	4.62	4.90	5.50
SHEERNESS	A	3.77	3.93	4.13	4.29	4.51
	B	3.94	4.09	4.29	4.45	4.66
	C	3.95	4.11	4.35	4.57	4.97
SOUTHEND	A	3.98	4.14	4.35	4.53	4.77
	B	3.99	4.15	4.36	4.54	4.77
	C	3.99	4.15	4.38	4.56	4.83

* curve types B, C adjusted to mean linear trend throughout whole data set (Table 2).

Curve type B related to epoch 1980.

APPENDIX 2

LINEAR TREND ESTIMATES (mm/yr) IN CUMULATIVE SETS OF OBSERVED MAXIMA

	10	20	30	40	50	60	70	80	90	100	110	120	130
NEWLYN	△	-3.7	-3.6	2.5	1.4	2.0	1.3						
	□	-4.1	-4.1	0.2	0.3	1.2	1.2	1.3					
SOUTHAMPTON	△	-10.6	-7.1	-2.0	0.5	1.2							
	□	-14.4	9.0	3.6	1.9								
PORTSMOUTH	△	9.5	0.6	1.7	0.7	0.2	0.9	0.8	0.9	0.8	0.7		
	□	14.0	0.0	-1.5	-0.9	-0.9	0.7	1.0	0.6	0.6			
BEMBRIDGE	△	-10.1	-5.1	-3.4									
	□	-9.4*	3.3										
NEWHAVEN	△	18.2*	2.6	5.1	6.4*	7.4*	5.4*						
	□	-1.3	-5.2	1.6	3.9	5.9*							
PEVENSEY	△	50.6*	7.0	4.6									
	□	-22.6	-7.8										
RYE	△	5.3	1.5										
	□	-1.4											
DOVER	△	25.9	-3.3	1.5	4.3	5.8	5.0						
	□	-13.6	6.0	5.3	7.7	4.7							
SHERNESS	△	4.9	2.0	3.6	1.5	1.1	0.8	2.6	1.2	1.6	2.6	2.5	2.4
	□	-18.6	-13.4	2.6	4.3	5.5	4.4	3.0	3.4	2.8	2.5	2.4	
SOUTHEND	△	26.5	5.3	2.6	2.3	0.4							
	□	-23.0	3.8	-0.7	-1.3								

* observed maxima show high correlation with trend estimate
 △ cumulative data sets are to origin of observed maxima (Table 1)
 □ " " " " end " " " "

circled value indicate trend estimate for full sample set of observed maxima (Table 2)

APPENDIX 3

1-in-100 YEAR RECURRENT SEA LEVELS BASED ON TYPE A ANALYSIS OF CUMULATIVE SETS OF OBSERVED MAXIMA

	10	20	30	40	50	60	70	80	90	100	110	120	130
NEWLYN	△ 3.10	3.17	3.21	3.26	3.28	3.27	3.27						
	□ 3.21	3.27	3.31	3.28	3.27	3.26	3.27						
SOUTHAMPTON	△ 2.99	2.88	2.86	2.84	2.84								
	□ 2.74	2.79	2.78	2.78	2.84								
PORTSMOUTH	△ 3.03	3.03	3.07	3.02	3.01	3.01	3.00	3.00	2.98	2.96	2.96		
	□ 2.78	2.82	2.93	2.91	2.92	2.92	2.91	2.91	2.96	2.96	2.96		
BEMBRIDGE	△ 2.57	2.54	2.53										
	□ 2.43	2.39	2.53										
NEWHAVEN	△ 3.84	3.79	3.87	4.01	4.02	4.01							
	□ 4.03	4.01	4.04	4.03	4.02	4.01							
PEVENSEY	△ 4.67	4.77	4.76										
	□ 4.88	4.80	4.76										
RYE	△ 5.13	5.03											
	□ 5.09	5.03											
DOVER	△ 4.01	4.04	4.26	4.53	4.53	4.50							
	□ 4.29	4.34	4.62	4.61	4.53	4.50							
SHERNESS	△ 3.57	3.82	3.96	3.93	3.95	3.90	4.09	4.06	4.05	4.09	4.32	4.31	
	□ 4.22	4.73	4.66	4.58	4.52	4.47	4.46	4.42	4.38	4.35	4.33	4.30	4.29
SOUTHEND	△ 4.35	4.38	4.62	4.56	4.53								
	□ 4.05	4.26	4.64	4.57	4.53								

circled value indicate result from analysis of full sample set of observed maxima (Table 2)

△ cumulative data sets are to origin of observed maxima (Table 1)
 □ " " " " " " " " end " " " " " "

References

1. Jenkinson, A.F. Frequency distribution of the annual maximum (or minimum) values of meteorological events.
Q. J. R. Met. Soc., 1955, 81, 258-177.
2. Lennon, G.W. A frequency investigation of abnormally high tidal levels at certain west coast ports.
Proc. Instn. Civ. Engrs., 1963, 25, Aug., 451-483.
3. Suthons, C.T. Frequency of occurrence of abnormally high sea levels on the east and south coasts of England.
Proc. Instn. Civ. Engrs., 1963, 25, Aug., 443-449.
4. Ackers, P. and Ruxton, T.D. Extreme levels arising from meteorological surges.
Proc. ICCE. 1974. Vol. 1, 70-86.
5. Webber, N.B. and Davies, J.R. Research on exceptional levels in the Solent.
Dock Harb. Auth., 1976, 57, 158-171.
6. Davies, J.R. and Webber, N.B. An investigation of the frequency of occurrence of extreme high water levels at Portsmouth.
Department of Civil Engineering, University of Southampton, 1976, internal report.
7. Blackman, D.L. and Graff, J. The analysis of annual extreme sea levels at certain ports in southern England.
Proc. Instn. Civ. Engrs., Part 2, 1978, 65, June, 339-357.
8. Graff, J. Concerning the recurrence of abnormal sea levels.
(to be published).
9. Pugh, D.T. and Vassie, J.M. Extreme levels from joint Tide/Surge probabilities.
Proc. ICCE 1978.
10. Natural Environmental Research Council. Flood studies report,
Vol. 1, Natural Environment Research Council, London, 1975.
11. Rossiter, J.R. An analysis of sea level variations in European waters.
Geophys. J. R. Astr. Soc., 1967, 12, 259-299.

CHAPTER 53

Analysis of maximum sea levels in southern England

J. Graff* & D. L. Blackman*.

Abstract

Along the south coast of England, series of observed annual maximum sea levels, ranging from 16 years to 125 years have been analysed for each of 10 ports. The Jenkinson¹ method of analysis was used to compute the frequency of recurrence of extreme levels. For a number of these ports the series of annual maxima are shown to have significant trends of the same order as those for mean sea level. The Jenkinson method can be simply adjusted to cope with maxima having a component linear trend, making it possible to allow for such trends in computing the frequency of recurrence of extreme levels. If a trend in the annual maxima varies throughout the sample of observations it is shown that difficulties arise in using the Jenkinson method to compute acceptable statistics. It is also shown that for certain ports having long series of observed annual maxima it may be necessary to restrict the sample size of observations in order to compute estimates of the recurrence of extreme levels within reasonable return periods.

Introduction

Around the coastline of England, particularly along the north west, east and south east the occurrence in recent years of abnormal flood levels has created a demand for the reassessment of flood defence levels and a need to revise measures of the frequency of recurrence of extreme levels. Subsequent to the disastrous east coast flooding of 1953, coastal defence levels were established to protect against a further recurrence of these levels. In the past decade, the levels of 1953, which were generally associated with return periods exceeding 100 years, have been overtopped on a number of occasions at certain north west and east coast ports suggesting that factors may have contributed to increase the frequency of occurrence of extreme levels. Lennon² and Suthons³ published studies in 1963 on the analysis of occurrence of observed annual maxima for ports respectively on the west and south east coasts of England. For south east ports Suthons, using Jenkinson's method of analysis, included the effects of a linear trend of 1ft/century, representing an assumed secular trend in mean sea level. The series of observations studied by Lennon and Suthons extended to the average period 1957/60. In recent years the need to update the work of Suthons³ for south east coast ports has led to a number of studies, notably Akers & Ruxton⁴ (1974, Southend), Webber & Davies^{5,6} (1976 Portsmouth, Southampton, Calshot) and Blackman & Graff⁷ (1978). The study⁷ by the authors, covering 10 ports along the south

*Bidston Observatory, Institute of Oceanographic Sciences,
Birkenhead, Merseyside. L43 7RA. U.K.

coast of England forms in part the basic framework of this paper. All the studies mentioned so far (viz. 2, 3, 4, 5, 6, 7) accept that the longest available and reliable series of observed annual maxima should be analysed by extreme level techniques. Although no strict information is available (more so perhaps possible) to indicate how far one may extrapolate the analysis curves showing the frequency of occurrence of extreme levels it is accepted¹⁰ that some reliability can be based on considering a period up to perhaps 4 times the original sample size. It is however not uncommon practice, in considering design criteria for coastal defences that the extrapolated extreme sea level likely to occur once in a period exceeding 15 times the original sample size, is in fact used.

For the coastline of east, south east and south England, secular trends of various order exist in the series of annual maxima. Suthons³ and the authors⁷ included the effects of mean linear trends occurring throughout the sample of observations to provide "more likely" estimates of the recurrence of extreme levels. More recently, in reviewing their work on south coast ports, and extending their studies to other U.K. ports the authors have shown that the use of an analysis method such as the Jenkinson technique can be highly dependent not only on the sample size of observations but also on the nature and linear measure of secular trends in the data. Whereas in the past it was thought acceptable to make an analysis of the full available sample of observed annual maxima, and perhaps adjust these for a mean linear trend, it would now seem that such results can cloud the presence of many anomalies and it may be necessary to make the analysis more detailed in order to provide information of practical use. In this paper the authors present a summary of their already published study⁷ and an account of the more recent work⁸ in the analysis of observed annual sea level maxima.

The form of sea level maxima

An observed sea level can be simply expressed as

$$h_o = h_p + h_w + h_r \quad 1.$$

where h_p is the astronomically generated (predictable) tide.
 h_w is the wave height induced by wind or otherwise.
 h_r is a residual due to non tidal or weather effects.

Tide gauges are generally so designed to filter out the wave height and record only the level h_o^*

$$h_o^* = h_p + h_r \quad 2.$$

In reality however a more explicit form of the recorded level h_o^* should be expressed as

$$h_o^* = h_p + h_R \quad 3.$$

where $h_R = h_r + \epsilon$, ϵ being a small (or sometimes large) error due to effects in the recording mechanism which should be accounted for in the reduction of records.

In considering recorded levels h^* of annual extremes it is not uncommon to find that stresses imposed on the tide gauge often contribute severe perturbations (ϵ) to the recorded tidal trace which can not always be resolved unambiguously from the true level being recorded ($h_p + h_r$).

Equally in instances where the tide gauge breaks down around the time of the extreme level occurring it is necessary to try and extrapolate the recorded trace to the time of the peak level.

In the case of extreme levels being recorded from a tide pole there is inherently a far greater uncertainty in accepting the level to be an accurate height as defined in (2). More likely than not, under associated severe weather conditions (often in the dark) a sea level read from a tide pole, even by an experienced observer, may reflect a significant measure of the superimposed wave effects (h_w).

It seems important to mention the above points here to highlight the form of data being considered in this type of analysis. These data are essentially a measure (often estimate) of the single annual maximum sea level as defined in (2), divorced of wave effects which on such occasions are often of a considerably pronounced form. These single annual maxima can be seen in the context of other peak tidal levels in Figure 1, which shows the distribution of observed monthly maxima over some 20 years for Newhaven, one of the ports studied. This bimodal form of distribution is typical of sea level maxima at many ports around the British Isles.

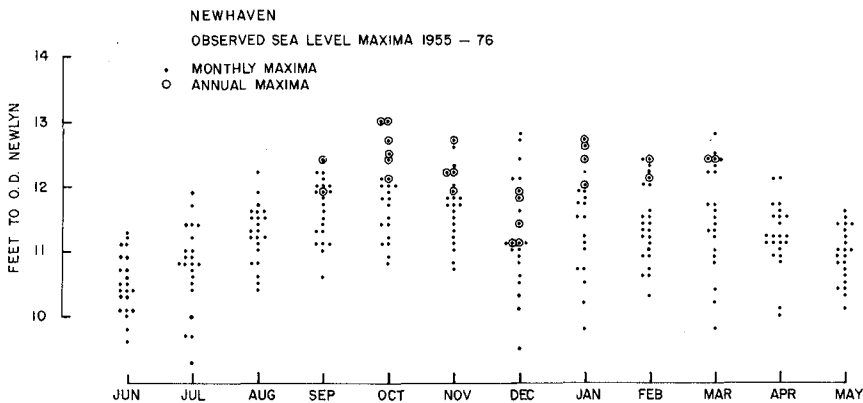


FIG. 1. Observed monthly sea level maxima at Newhaven.

To date only Akers & Ruxton⁴ have endeavoured to analyse the interaction of the components h_p , h_w and h_r in relation to extreme levels, and the complexity of the problem and lack of suitable wave data have shown to present serious limitations. More recently Pugh & Vassie⁹ have approached the problem of investigating the occurrence of maxima by studying the interactive effects of h_p and h_r at hourly intervals, a technique that is hopeful of finding suitable joint probability distributions (of h_p and h_r), based on reasonably short series of a few years, that can be combined to provide information concerning the recurrent frequencies of abnormal levels.

Referring back to the work presented in this paper it is useful again to be reminded that the observed annual maxima studied are principally as defined in (2) although where tide pole data have been used one must accept that some proportional influence of wave effects are included.

Observational data

For each of the 10 ports indicated in Figure 2 the best series of up-to-date annual maxima were obtained, in some cases extending the data studied by Suthons³ by some 30%. Most of these data were based directly on tide gauge records, which for some ports covered a considerable period. All the sea level records were reduced to the national reference datum of Ordnance Datum Newlyn. Table 1 lists the coverage of data for each port.

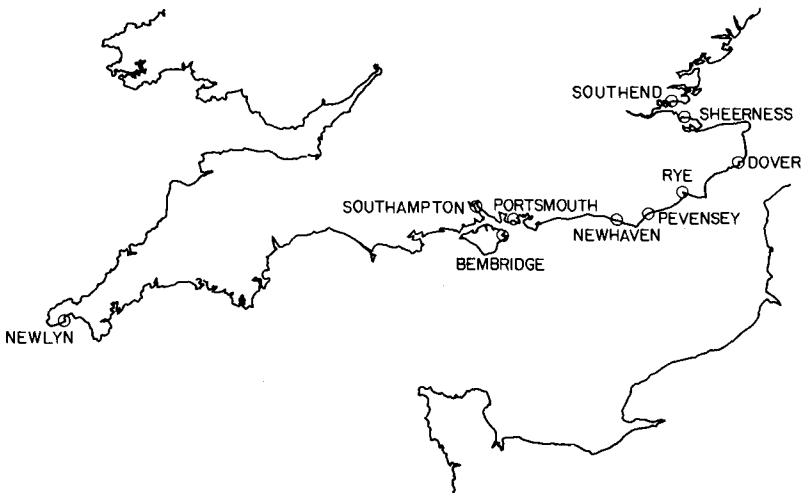


FIG. 2. Location of the 10 ports studied.

TABLE 1

Port	Years	Observed maxima
Newlyn	1916-76	61
Southampton	1924-75	47
Portsmouth	1813-75	105
Bembridge	1947-76	29
Newhaven	1913-76	60
Pevensey	1953-76	24
Rye	1949-74	16
Dover	1912-75	56
Sheerness	1819-70	125
Southend	1929-75	46

The Jenkinson method of analysis

If we assume that any observed annual maximum sea level h is a statistically random extreme event then these data can be analysed by a method such as that suggested by Jenkinson¹ in 1955. If T , the return period of height h is the average interval between occurrences of heights equal to or greater than h , it is easily shown that

$$T = -1/\ln.P \text{ or } \ln T = -\ln(-\ln P) = x$$

where P is the probability that the annual maxima is less than h . Jenkinson suggests that the most general form of curve between h and x is given by

$$x = \frac{1}{k} \ln \left(1 - \frac{h-h_c}{a} \right)$$

where k , h_c and a are constants determined from observations.

k is also a measure of the curve type of the data distribution such that if

$k < 0$, curve bends upwards; Fisher-Typpett Type I

$k = 0$, curve is a straight line; Fisher-Typpett Type II

$k > 0$, curve bends downwards; Fisher-Typpett Type III

Along the south coast of England the nature of the curve changes gradually eastwards, from Fisher-Typpett Type III through Type II to Type I, as seen in Figure 3.

Port diagram curves (Type A)

For the ports shown in Figure 2, the series of observed annual maxima indicated in Table 1 were analysed by the Jenkinson technique, and the results, showing the frequency of recurrence of maxima can be presented in a form as shown in Figure 3. These Port diagram curves are termed type A when related to analysis which do not account for the effect of linear trends.

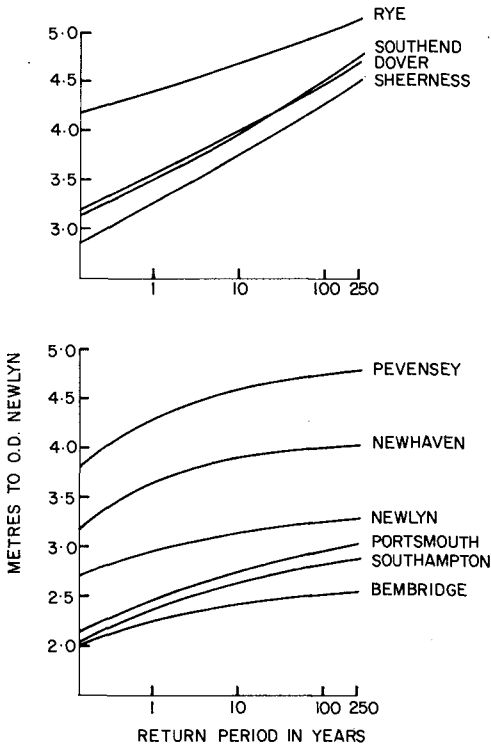


FIG. 3. Frequency of recurrence of observed annual maxima (excluding effects of trends).

Mean trends in observed annual maxima

The series of observed annual maxima for each port were examined for trends. No evidence was found to suggest that any secular fluctuation of data was correlated with long period tidal effects of astronomical origin. Mean linear trends were resolved by simple linear regression analysis, and for several ports where suitable hourly sea level data were available, it was possible to also obtain the linear trend of mean sea level. These trends are shown in Table 2 and it can be seen that in general, the trends in annual maxima are similar to those for mean sea level. For the ports Newhaven, Dover and Sheerness the linear trends in annual maxima are significant.

TABLE 2

Port	Trend in annual observed maxima, mm/year	Trend in mean sea levels, mm/year
Newlyn	1.31 \pm 0.75 (61 years)	1.95 \pm 0.12 (60 years)
Southampton	1.18 \pm 1.62 (47 years)	1.06 \pm 1.11 (15 years)
Portsmouth	0.68 \pm 0.29 (105 years)	8.35 \pm 0.80 (13 years)
Bembridge	-3.38 \pm 2.06	
Newhaven	5.44 \pm 0.94 (60 years)	4.11 \pm 1.65 (18 years)
Pevensey	4.60 \pm 5.39	
Rye	1.53 \pm 5.54	
Dover	4.99 \pm 1.68 (56 years)	4.52 \pm 0.53 (39 years)
Sheerness	2.41 \pm 0.53	2.37 \pm 0.17*
Southend	0.39 \pm 2.92 (46 years)	1.71 \pm 0.29 (49 years)

* Values established by Rossiter,¹¹ based on 85 years.

One could perhaps suggest, in broad terms, that mean trends observed in series of extreme levels reflect the secular trends in mean sea levels, although one should bear in mind that the mean sea levels are based on continuous hourly observations throughout the years whereas the annual maxima represents a single level occurring generally within the "storm months" August-March (See Figure 1).

Port diagram curves (Type B, C)

The Jenkinson method of analysis can be also applied to data which have a component of linear trend, providing that the data are first reduced to some selected epoch. For instance if the epoch is 1900 and a linear trend of .001 m/yr exists in the annual maxima then an observed level of 10.0m in 1850 reduces to a level of 10.05m in 1900, and similarly an

observed level of 10.0m in 1950 reduced to a level of 9.95m in 1900. The resulting port diagram curves, termed type B, accounting for a linear trend component, are similar to those noted as type A. The interpretation of type B curves is strict in the sense that a linear trend has been accounted for up to the base year of the selected epoch and no trend exists in the data beyond this year.

Suthons³ suggested it is possible to make some allowance for including a trend beyond the epoch by adjusting type B curves (into curves termed type C) in the following manner.

If T is a return period of height h_B (type B curve) or h_C (type C curve) where a mean rate of annual rise S is being considered in the data, then

$$h_C = h_B + T.S/2$$

This gives some guidance to interpreting the additive effects of a continuing trend assumed to exist in the data.

Figure 4 illustrates all three Port diagram curve types (A, B, C) for Sheerness.

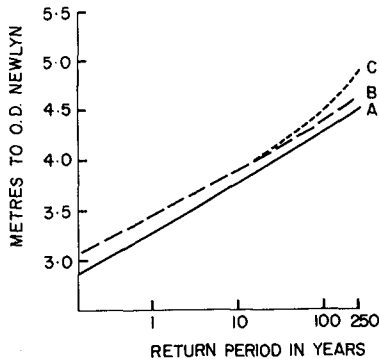


FIG. 4. Frequency of recurrence of observed annual maxima for Sheerness.

Curve A. unadjusted for any trend effects.

Curve B. adjusted to the epoch 1976 for a linear trend of 2mm/yr present only in the data analysed.

Curve C. adjusted to the epoch 1976 for a linear trend of 2mm/yr assumed to persist indefinitely.

As the return period T increases beyond a value equal to about twice the sample size of observations, the expected height h_c increases rapidly to unreal proportions. The format of computing the type C curve is subjective and gives guidance only as a broad illustration of including extrapolated trends. Appendix 1 lists for all 10 ports, data from port diagram curves type A, B, C, related to recurrence periods of 10, 20, 50, 100 and 250 years.

Some further considerations in the analysis of annual sea level maxima

Since in general, only a limited series of observed annual maxima, of the order of 10-20 years, are available for most ports, it is of interest to have some feeling for the response of the analysis method (Jenkinson) to different sample sizes. It is also of considerable interest to understand the nature of secular trends which may exist in the data series since they can have a pronounced effect on the analysis of such data. These considerations are particularly important for ports where a substantial investment is to be made in raising flood defences for protection against abnormal levels, subjectively assessed as being of the order of 1-in-100 years or more. At present the terms "return periods" and the associated "expected levels" are perhaps too freely used in the assessment of design criteria for coastal defences and it seems important to illustrate the drawbacks and limitations of interpreting what may seem to be "standard" port diagram curves.

Before any type of port diagram curve is to be interpreted seriously for practical purposes a number of questions would seem to be of prime importance.

1. How real is the sample of observed data in terms of their measured values.
2. Does a trend exist in the sample data set, and if so what is its form.
3. Will a trend persist in the future and can this trend, and that in a sample data set, be approximated by a constant linear term.
4. What is the confidence in extrapolating port diagram curves and how is this related to the size of the sample set.

Although we would not presume to suggest that any of these questions can be strictly answered we do suggest it is possible to illustrate their significance, hereby gaining a far greater awareness of the problem, thus enabling one to make a more objective interpretation of results.

Reliability of observed data

The uncertainty of measured data has already been discussed earlier and it is a simple fact that for good or bad, most early records of annual maxima proceeding the early fifties must be accepted as the "best measures" available. To review such data in terms of the performance and

stability of the measuring instrument presents considerable problems and frustration in what is often a mass of conflicting historically documented heresay. The national reference level, Ordnance Datum Newlyn, was only introduced as a datum measure to most Ports in Great Britain, in various degrees of accuracy, during the period between the late thirties and early fifties. Diligent checking of the annual tidal records, tide gauge histories and datum levelling exercises is the only sure way of attempting to collate a continuous datum level for series of records dating back through the early part of this century. In a few instances, for portions of data, much of the relevant information has been lost to antiquity.

Trends in annual maxima

With a substantial series of annual maxima one can identify fluctuations that can be resolved as a linear estimate of a mean trend. Table 2 already presents such measures for the 10 south coast ports which leads one to assume it is a simple matter to proceed in computing port diagram curves of type B. If we examine the form of these fluctuations or trends, a little closer it becomes obvious that they are far from linear, and like mean sea level data they vary in an ill defined and unpredictable fashion. Figure 5 shows the annual maxima plotted as 5 year running means for Sheerness and Portsmouth which represent the longest data series available in the study.

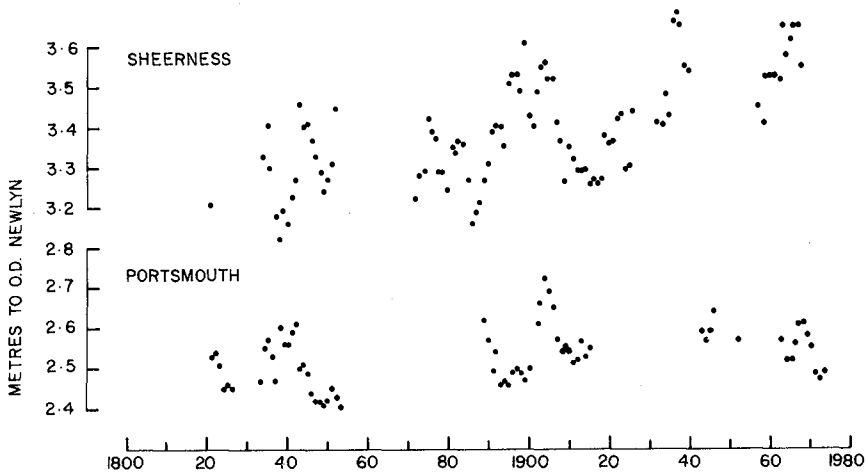


FIG. 5. Observed annual maxima plotted as 5 year running means for Sheerness and Portsmouth.

For some of the 10 ports a significant mean trend can be identified throughout the full data series but moreso in these cases (Sheerness) more pronounced secondary trends also can be identified within both long and short portions of the data set. Simple regression analysis of the annual maxima in cumulative sets to a 10 year base, both forward and backward (in a time wise fashion) readily show the extreme variability of the linear trend estimate and its generally poor fit to the observed data. These results are illustrated for all 10 ports in Appendix 2.

Since one can in fact adjust for linear trends in computing port diagram curves it is easy to see that the question of "what trend do we adjust for" is not a simple one to answer and indeed is a matter for some, if not considerable conjecture.

The confidence in port diagram curves

Bearing in mind that available series of annual maxima may be short or long, some thought should be given to interpreting resulting port diagram curves against the criteria of sample size. Again we split the series of observed data for each port into cumulative 10 year sets as noted earlier and made a systematic analysis to compute port diagram curves of both type A and type B for each block of data, in the same forward and backward fashion as for the regression analysis. To compute the type B curves the appropriate cumulative data sets were adjusted for the associated mean linear trend, to a common epoch. It would be impractical to try and present here even a summary of such results for all 10 ports, a form of analysis ⁸ which is now being systematically applied to data from many other ports around the British Isles. However, it is of some considerable interest to present typical results, for Sheerness, a port of major importance in the Thames estuary. The series of annual maxima for Sheerness show fluctuations in trend as seen in Figure 5 and Appendix 2, these having a significant positive mean linear trend throughout the full series of 125 annual observed maxima.

In Figure 6, the height with a period of recurrence of 100 years, based on type A curve analysis, has been plotted directly against the cumulative size of sample (number of annual maxima) used for the analysis. The cumulative sample sets relate, as shown, to the base year 1819 and 1970, respectively the start and end of the full observed series. It has also been possible to show these estimates based on analysis of 6 independent sets of 20 maxima taken throughout the period of data available. Similarly on the same diagram the results related to a type B curve analysis are shown, each cumulative data set being adjusted for the associated mean linear trend (Appendix 2) to the epoch 1980.

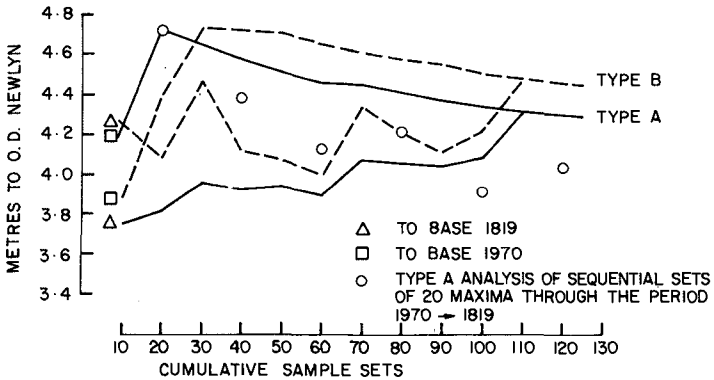


FIG. 6. Frequency of recurrence of observed annual maxima for Sheerness showing the 1-in-100 year event, based on analysis of different subsets of the data.

We would point out that the results shown in Figure 6 are not untypical⁸ of other ports in Great Britain where a far shorter series of annual maxima (up to 60 years) are available. Figure 6 (for Sheerness) highlights two points of particular interest

1. Depending on the sample set of maxima analysed (some multiple of 10) the 1-in-100 yr level can vary within a range of up to 1 metre. This range diminishes only as the sample size approaches its maximum length.
2. There is a pronounced increase in the estimated height of the 1-in-100 yr level throughout the period 1819 to 1970, e.g. there seems to be a general increase in the recurrence of abnormal levels.

This readily illustrates the considerable uncertainty in trying to interpret such results for practical purposes. In the past, and currently, it is often accepted that results based on analysis of a maximum available data series would provide a confident "best estimate" or a recurrence level for basic design level estimates. However this is clearly not the case, and the above results suggest that the assessment of a frequency of recurrence of an abnormal level (design level perhaps) is much more subjective than hitherto suspected, especially if sea level

maxima are subject to some form of secular trends. If the data were truly devoid of significant trend components (as is the case for other ports) then we would expect considerably less divergence in the plots as shown in Figure 6 above, and consequently would have a greater confidence in making an interpretation of such results. Portsmouth is seen to be a case-in-point where the absence of any significant trends produces a relatively stable set of recurrence levels, as illustrated in Figure 7 in the same fashion as for Sheerness. The high anomalous value associated analysis of the 10 earliest maxima reflects in fact the presence of dubious recorded levels.

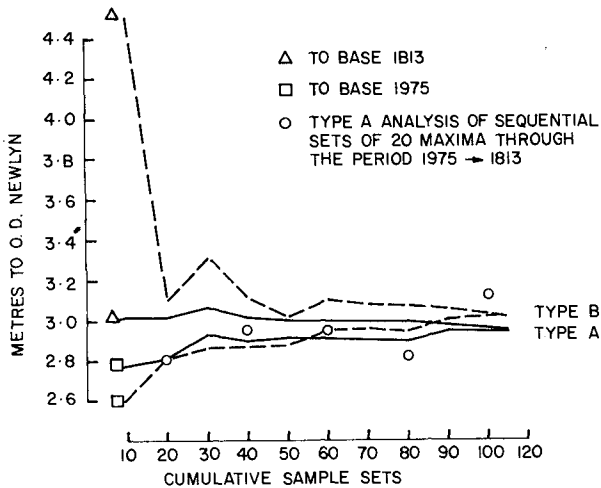


FIG. 7. Frequency of recurrence of observed annual maxima for Portsmouth, showing the 1-in-100 year event, based on analysis of different subsets of the data.

Appendix 3 lists heights associated with recurrence periods of 100 years based on type A curve analysis of 10 year cumulative data sets of the observed annual maxima for all the 10 south coast ports.

Conclusion

This paper has summarised results on the analysis of abnormal sea levels at south coast ports in England, and illustrated the revised level of information that is now necessary in order to provide a meaningful interpretation of the frequency statistics. Hitherto, estimates of recurrence levels have been based purely on analysis of the single full

length sample of annual observed maxima. For certain ports this may be acceptable, but it is suggested that there is a need for a more detailed analysis of the data, as illustrated in this paper. Indeed it may be the case that for some ports, irrespective of the length of available annual observed maxima, one may be restricted to assessing levels with recurrence periods less than 50 years, and these based only on analysis of subsets of the full data series. The analysis procedures are highly sensitive to data which contains secular trends that are not of a strictly linear form. A component of such trends may indeed be due to some corrupting effect of errors in the raw observed data.

Although annual observed sea level maxima provide an attractive basis for analysis procedures, such as Jenkinsons, aimed at forecasting recurrence levels, it is proving more unlikely that such treatment of single annual tidal observations will provide a satisfactory standard level of reliable information for practical design purposes. The interactive effects of tide, wave and weather are complicated to such a degree, that coupled with the uncertainty of sea level measurements of maxima it may be necessary to approach such studies of frequency analysis in a more fundamental way.

Acknowledgements

The work presented here derived from a study undertaken on behalf of Southern Water Authority, England, U.K., and in subsequent support from a Consortium consisting of the Natural Environment Research Council, the Ministry of Agriculture Fisheries and Food, and the Departments of Energy, Environment and Industry.

APPENDIX 1

RECURRENT SEA LEVELS

PORT associated with curve types A, B*, C*
based on analysis of whole data sets of maxima

		10 Yr	20 Yr	50 Yr	100 Yr	250 Yr
NEWLYN	A	3.15	3.19	3.24	3.27	3.30
	B	3.19	3.23	3.27	3.30	3.33
	C	3.20	3.24	3.31	3.37	3.49
SOUTHAMPTON	A	2.65	2.71	2.79	2.84	2.89
	B	2.68	2.74	2.82	2.87	2.93
	C	2.63	2.75	2.85	2.93	3.08
PORTSMOUTH	A	2.75	2.82	2.90	2.96	3.02
	B	2.79	2.87	2.96	3.03	3.12
	C	2.80	2.88	2.98	3.07	3.20
BEMBRIDGE	A	2.43	2.47	2.51	2.53	2.56
	B	2.36	2.38	2.40	2.41	2.42
	C	2.34	2.34	2.31	2.24	2.00
NEWHAVEN	A	3.89	3.94	3.98	4.01	4.04
	B	4.04	4.09	4.13	4.16	4.20
	C	4.07	4.14	4.27	4.44	4.88
PEVENSEY	A	4.60	4.66	4.72	4.76	4.80
	B	4.67	4.73	4.80	4.84	4.88
	C	4.69	4.78	4.91	5.07	5.45
RYE	A	4.72	4.81	4.94	5.03	5.17
	B	4.74	4.83	4.95	5.05	5.18
	C	4.75	4.85	4.99	5.13	5.38
DOVER	A	4.01	4.16	4.35	4.50	4.70
	B	4.16	4.30	4.49	4.65	4.87
	C	4.18	4.35	4.62	4.90	5.50
SHEERNESS	A	3.77	3.93	4.13	4.29	4.51
	B	3.94	4.09	4.29	4.45	4.66
	C	3.95	4.11	4.35	4.57	4.97
SOUTHEND	A	3.98	4.14	4.35	4.53	4.77
	B	3.99	4.15	4.36	4.54	4.77
	C	3.99	4.15	4.38	4.56	4.83

* curve types B, C adjusted to mean linear trend throughout whole data set (Table 2).

Curve type B related to epoch 1980.

APPENDIX 2

LINEAR TREND ESTIMATES (mm/yr) IN CUMULATIVE SETS OF OBSERVED MAXIMA

	10	20	30	40	50	60	70	80	90	100	110	120	130
NEWLYN	△	-3.7	-3.6	2.5	1.4	2.0	1.3						
	□	-4.1	-4.1	0.2	0.3	1.2	1.2	1.3					
SOUTHAMPTON	△	-10.6	-7.1	-2.0	0.5	1.2							
	□	-14.4	9.0	3.6	1.9								
PORTSMOUTH	△	9.5	0.6	1.7	0.7	0.2	0.9	0.8	0.9	0.8	0.7		
	□	14.0	0.0	-1.5	-0.9	-0.9	0.7	1.0	0.6	0.6			
BEMBRIDGE	△	-10.1	-5.1	-3.4									
	□	-9.4*	3.3										
NEWHAVEN	△	18.2*	2.6	5.1	6.4*	7.4*	5.4*						
	□	-1.3	-5.2	1.6	3.9	5.9*							
PEVENSEY	△	50.6*	7.0	4.6									
	□	-22.6	-7.8										
RYE	△	5.3	1.5										
	□	-1.4											
DOVER	△	25.9	-3.3	1.5	4.3	5.8	5.0						
	□	-13.6	6.0	5.3	7.7	4.7							
SHERNESS	△	4.9	2.0	3.6	1.5	1.1	0.8	2.6	1.2	1.6	2.6	2.5	2.4
	□	-18.6	-13.4	2.6	4.3	5.5	4.4	3.0	3.4	2.8	2.5	2.4	
SOUTHEND	△	26.5	5.3	2.6	2.3	0.4							
	□	-23.0	3.8	-0.7	-1.3								

* observed maxima show high correlation with trend estimate
 △ cumulative data sets are to origin of observed maxima (Table 1)
 □ " " " " end " " " "

circled value indicate trend estimate for full sample set of observed maxima (Table 2)

APPENDIX 3

1-in-100 YEAR RECURRENT SEA LEVELS BASED ON TYPE A ANALYSIS OF CUMULATIVE SETS OF OBSERVED MAXIMA

	10	20	30	40	50	60	70	80	90	100	110	120	130
NEWLYN Δ	3.10	3.17	3.21	3.26	3.28	3.27	3.27						
	\square 3.21	3.27	3.31	3.28	3.27	3.26	3.27						
SOUTHAMPTON Δ	2.99	2.88	2.86	2.84	2.84								
	\square 2.74	2.79	2.78	2.78	2.84								
PORTSMOUTH Δ	3.03	3.03	3.07	3.02	3.01	3.01	3.00	3.00	2.98	2.96	2.96		
	\square 2.78	2.82	2.93	2.91	2.92	2.92	2.91	2.91	2.96	2.96	2.96		
BENBRIDGE Δ	2.57	2.54	2.53										
	\square 2.43	2.39	2.53										
NEWHAVEN Δ	3.84	3.79	3.87	4.01	4.02	4.01							
	\square 4.03	4.01	4.04	4.03	4.02	4.01							
PEVENSEY Δ	4.67	4.77	4.76										
	\square 4.88	4.80	4.76										
RYE Δ	5.13	5.03											
	\square 5.09	5.03											
DOVER Δ	4.01	4.04	4.26	4.53	4.53	4.50							
	\square 4.29	4.34	4.62	4.61	4.53	4.50							
SHERNESS Δ	3.57	3.82	3.96	3.93	3.95	3.90	4.09	4.06	4.05	4.09	4.32	4.31	
	\square 4.22	4.73	4.66	4.58	4.52	4.47	4.46	4.42	4.38	4.35	4.33	4.30	4.29
SOUTHEND Δ	4.35	4.38	4.62	4.56	4.53								
	\square 4.05	4.26	4.64	4.57	4.53								

circled value indicate result from analysis of full sample set of observed maxima (Table 2)

Δ cumulative data sets are to origin of observed maxima (Table 1)
 \square " " " " " " end " " " "

.

References

1. Jenkinson, A.F. Frequency distribution of the annual maximum (or minimum) values of meteorological events.
Q. J. R. Met. Soc., 1955, 81, 258-177.
2. Lennon, G.W. A frequency investigation of abnormally high tidal levels at certain west coast ports.
Proc. Instn. Civ. Engrs., 1963, 25, Aug., 451-483.
3. Suthons, C.T. Frequency of occurrence of abnormally high sea levels on the east and south coasts of England.
Proc. Instn. Civ. Engrs., 1963, 25, Aug., 443-449.
4. Ackers, P. and Ruxton, T.D. Extreme levels arising from meteorological surges.
Proc. ICCE. 1974. Vol. 1, 70-86.
5. Webber, N.B. and Davies, J.R. Research on exceptional levels in the Solent.
Dock Harb. Auth., 1976, 57, 158-171.
6. Davies, J.R. and Webber, N.B. An investigation of the frequency of occurrence of extreme high water levels at Portsmouth.
Department of Civil Engineering, University of Southampton, 1976, internal report.
7. Blackman, D.L. and Graff, J. The analysis of annual extreme sea levels at certain ports in southern England.
Proc. Instn. Civ. Engrs., Part 2, 1978, 65, June, 339-357.
8. Graff, J. Concerning the recurrence of abnormal sea levels.
(to be published).
9. Pugh, D.T. and Vassie, J.M. Extreme levels from joint Tide/Surge probabilities.
Proc. ICCE 1978.
10. Natural Environmental Research Council. Flood studies report,
Vol. 1, Natural Environment Research Council, London, 1975.
11. Rossiter, J.R. An analysis of sea level variations in European waters.
Geophys. J. R. Astr. Soc., 1967, 12, 259-299.

FREQUENCIES AND PROBABILITIES OF EXTREME STORM SURGES

(On the Time-Dependent Changes of the Probability of
Extreme Storm Floods at the German North Sea Coast)

by

Alfred FÜHRBÖTER ¹⁾

Abstract

The North Sea as a very shallow sea with high wind set-up effects is acting highly as extremely sensitive measuring equipment for climatic changes, especially for surge producing weather conditions. The flood disaster in the Netherlands 1953, in Germany 1962, the Adolph-Bermphol-Orkan (1967), with mean wind speed of 37 m/sec. over 5 hours, the strong continental storm with high damages in the forests from France till Poland in November 1972, a series of 6 heavy floods in November/December 1973 and two extreme floods in January 1976 with the highest water levels ever registrated in the German bight are indications for some changes in meteorological conditions.

In this paper some hypothetical models shall be introduced which are able to show how extreme storm surge frequencies and probabilities are changing with time.

It is well known, that, on behalf of the high variability and possibilities of superpositions from meteorological parameters (wind velocity, direction, duration a.s.o.) with tidal regimes nobody can give an exact prediction about the highest possible storm surge. As early as in 1939, WEMELSFELDER therefore introduced a method to predict the probability of a storm surge level using the observed frequencies of storm flood levels from long-time series of observations from tidal gauges. In semilogarithmic coordinates, he found for high water levels (= low frequencies) a nearly linear relation between water levels and frequencies; by extrapolation, water levels can be computed which are to be expected - in the average, according to the laws of probability theory! - once, in 100 years, 500 years a.s.o. The basis for this method, however, is, that the stochastic process producing storm surges is a stationary one, i. e. not a time-dependent process.

For these calculations long time series are necessary. They are available on the German North Sea coast at the tidal stations of Cuxhaven (1813 - 1976, n = 164 values), at Wilhelmshaven (1854 - 1976, n = 123 values) and at Husum (1867 - 1971, n = 110 values) as collections of the highest annual storm surge levels.

For Cuxhaven, Fig. 1 shows the logarithmic plotting of this collection for the original values and for the same values adjusted to the year 1975 due to the centennial rise of the water level which was found for

¹⁾ Professor Dr.-Ing., Technical University Braunschweig, Germany,
Director of LEICHTWEISS-Institut für Wasserbau

Cuxhaven to nearly 23 cm/100 years. For all stations, these corrections are necessary in order to eliminate longterm trends which are not connected directly with the actual meteorological conditions. For Cuxhaven, for example, it can be seen that by this correction the storm flood of 1825 was ranked from the third to the second place (fig. 1) in the collection.

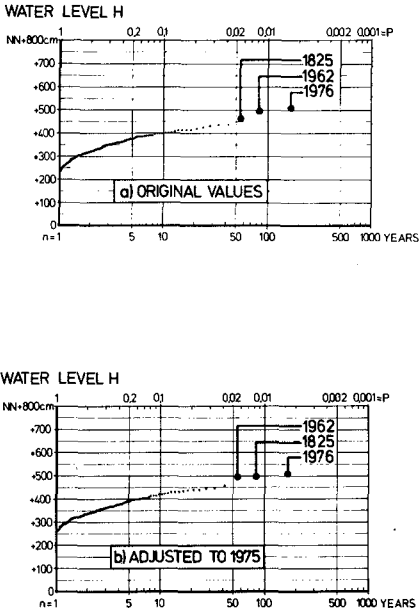


Fig. 1: Frequency curves of annual HW (Harbour diagram) for the station CUXHAVEN from 1813 till 1976 (n = 164 values)
 a) original values
 b) adjusted to 1975 due to centennial rise of water level

Fig. 1 shows observed frequencies; the question is to compute the abstract probability (after POISSON) from these frequencies. It can be seen, that for low frequencies (i. e. extreme surges) the linear approximation by WEMELSFELDER is quite satisfactory.

From the exact theory of probability, always an "event" is defined for instance by a game with dices; also for such a game here the "abstract probability" is exactly known as 1 to 6 when the dice is not "prepared". But for instance in 1973, 6 heavy storm surges occurred inside the German bight during 2 months; it is evident that this, seen from theory of probability, only was one event according to the meteorological conditions. Moreover, it can be assumed that even the meteorological behaviour of sequences of years may not be independent in the light of probability theory.

Contrary to the classical applications of the probability computations (v. MISES 1972) namely in the game of chance e. g. in the game of dice, where every throw represents an

"Event" and the sum of the throw represents the "Collection of Events", in the case of extreme storm floods, the expression "Events" and the connected expression "Collection of Events" have to be defined first, as they do not correspond to discrete events. The chain of storm floods as in 1962, 1973 and 1976 cannot possibly be viewed as independent events in the realm of probability computations.

As the equipments to register storm weather (meteorologically conditioned accidental events) are coupled with other similar equipments in large space and over long years of at least the North Atlantic region, if not globally, it can only be taken as an assumption, and not as a confirmation, to observe for example that an yearly HW is an independent event.

The approach of "Extreme Storm Flood Levels" of WEMELSFELDER results in a simple logarithmic representation of an approximately linear relationship between the water levels and their corresponding frequencies. From the observed frequencies the abstract probabilities for the period of investigation (time series) are interpolated and for the future extrapolated. The abstract probability according to POISSON (1841) is then known already deductively, as for e. g. in a game of dice with $W = 1/6$, for each number it is known; but in the case of storm flood events it must first be calculated from the observed frequencies. An estimate of abstract probabilities from the observed frequencies demands an exact and reproducible definition of "Events" and "Collection of Events" (v. MISES 1972). Irrespective of arbitrary definitions of the expression "Storm Flood", it can be shown through a proof of convergence (FÜHRBÖTER 1976) that the values H_{100} , which represent the abstract probabilities according to POISSON and assign by stationary probability the water levels - in the mean! - occurring once in 100 years, in the form of a function $H_{100}(N)$ for $N > 5$ years, converge to nearly constant values, when the water level HW is assigned as the "Event" in a series of $N = 1, 2, 3, \dots$ up to 20 years in the case of a long series of gauges as in CUXHAVEN, as also till $N = 30$ years. This holds good for the linear approach of WEMELSFELDER. For non-linear fitting functions (GUMBEL, FRECHET, JENKINSON etc.) the convergence can be expected to be already by $N < 5$ years. This proof of convergence which leads from the observed frequencies to abstract probabilities (POISSON) delivers for the three North Sea gauges uniformly asymptotically reaching constant values for H_{100} with $N > 5$ years. As "Event" in the sense of independence an extreme water level HW is to be assigned which occurs in the series of $N = 5$ years.

Fig. 2 shows the convergence test (FÜHRBÖTER 1976) with the behaviour of the functions $H(N)$ with their constant pattern for $N > 5$ years for all 3 stations; on fig. 3 (Cuxhaven), fig. 4 (Wilhelmshaven) and fig. 5 (Husum) it is to be seen that the linear fitting for $N = 5, 10, 15$ and 20 years is nearly the same independently from N (FÜHRBÖTER 1976).

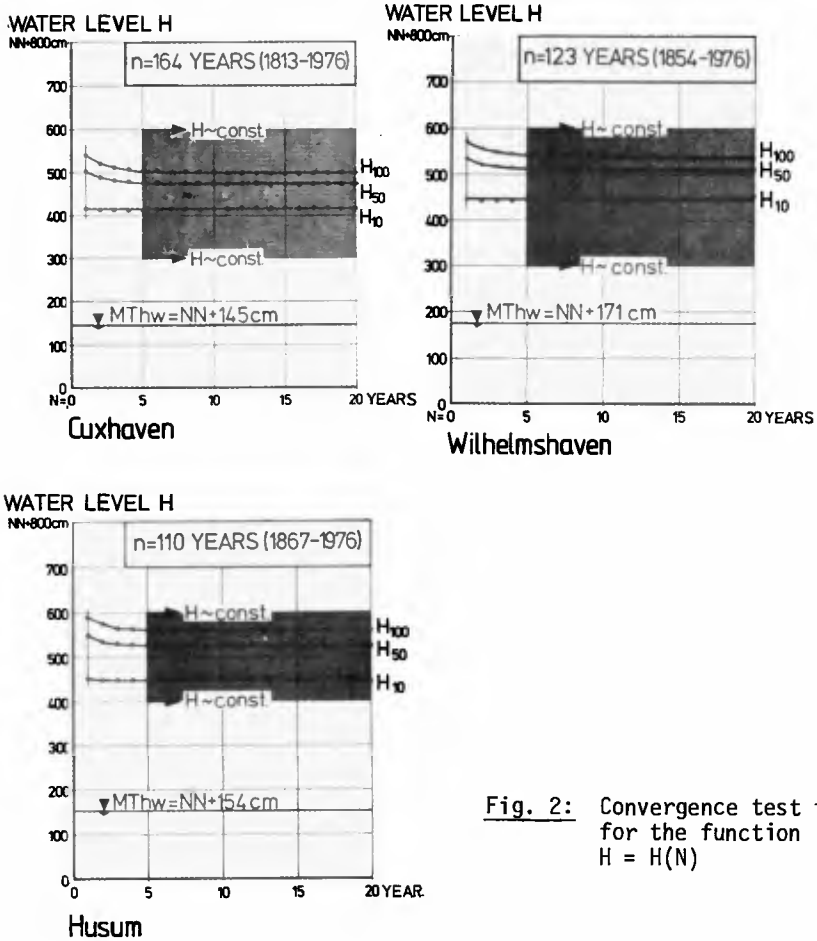


Fig. 2: Convergence test for the function $H = H(N)$

With this the possibility is open for the investigation of the time-dependent changes of the abstract probabilities with a reproducible method which are calculated from the observed frequencies as per WEMELSFELDER method. For the non-stationary applications of WEMELSFELDER method the value H_{100} , the storm flood level - in the mean! - which is reached or exceeded once in 100 years, will be used as the representative value of the corresponding best fit straight line (fig. 2 - 5).

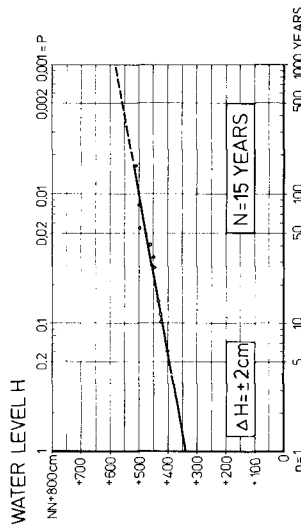
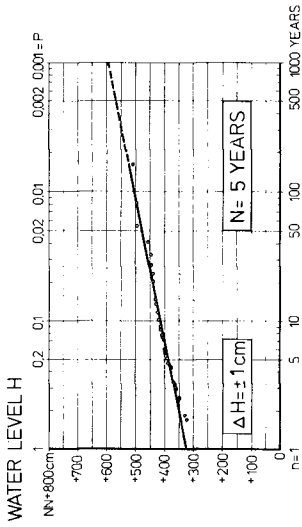
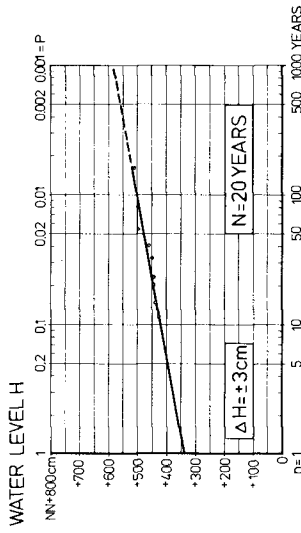
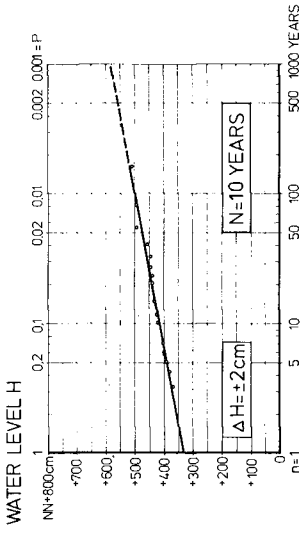


Fig. 3: Convergence test Station CUXHAVEN 1813 - 1976 (n = 164 years)

*

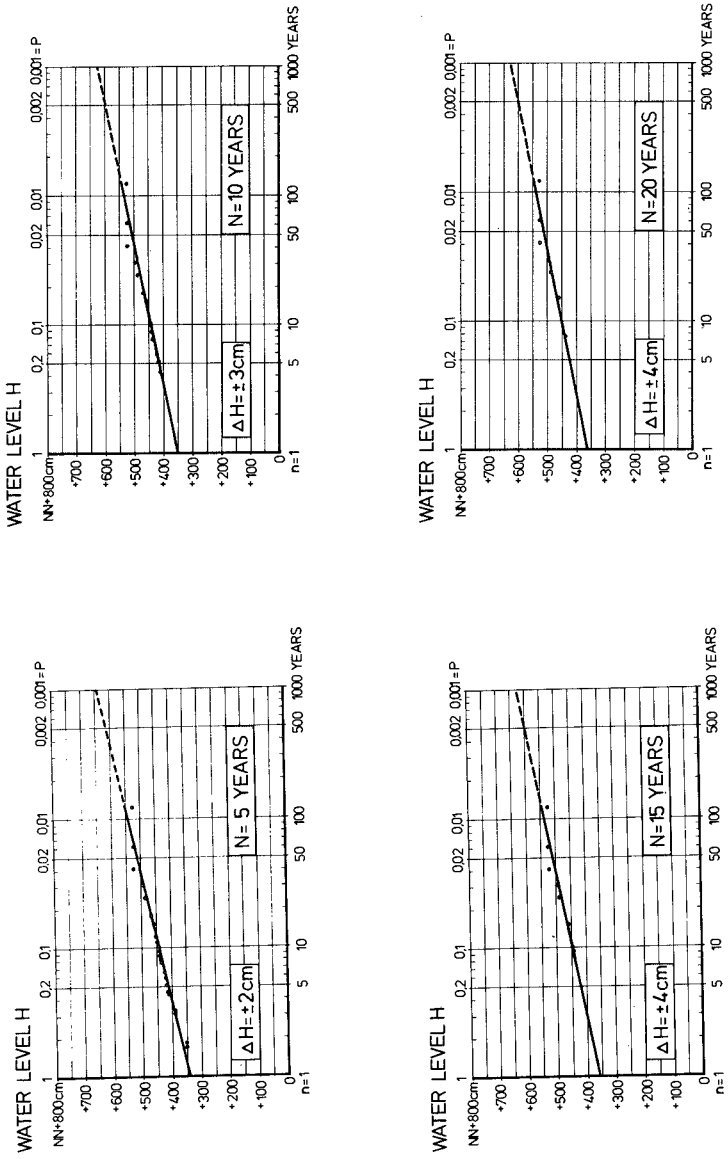


Fig. 4: Convergence test Station WILHELMSHAVEN 1854 - 1976 (n = 123 years)

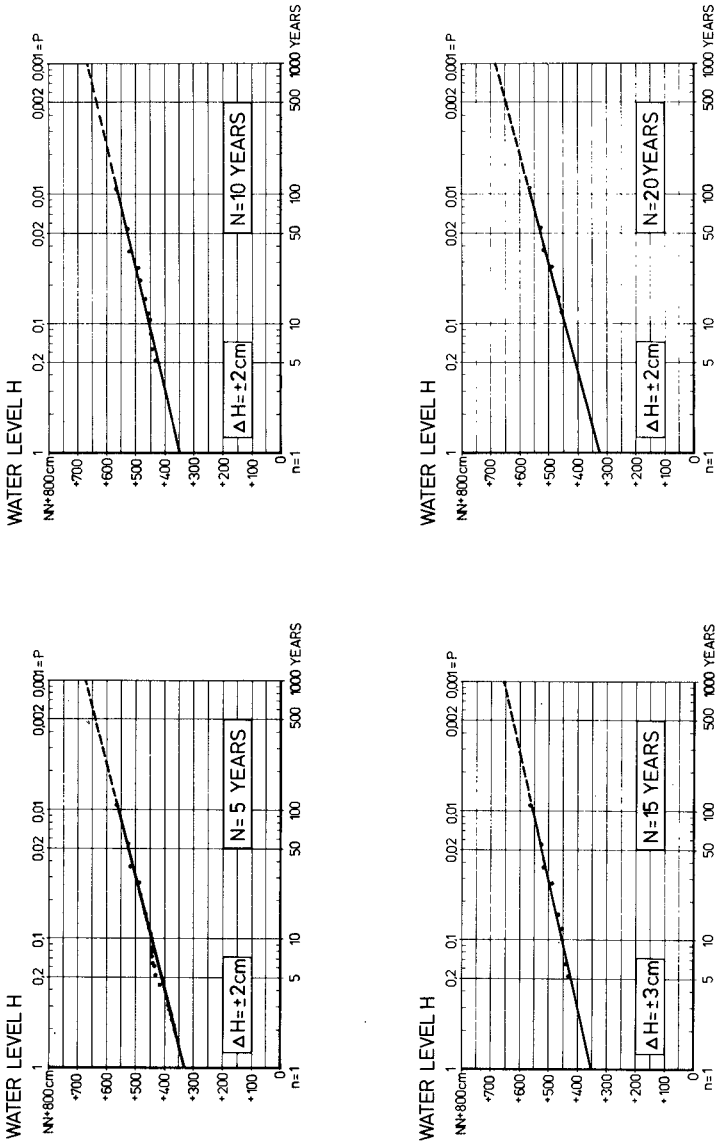


Fig. 5: Convergence test Station HUSUM 1867 - 1976 (n = 110 years)

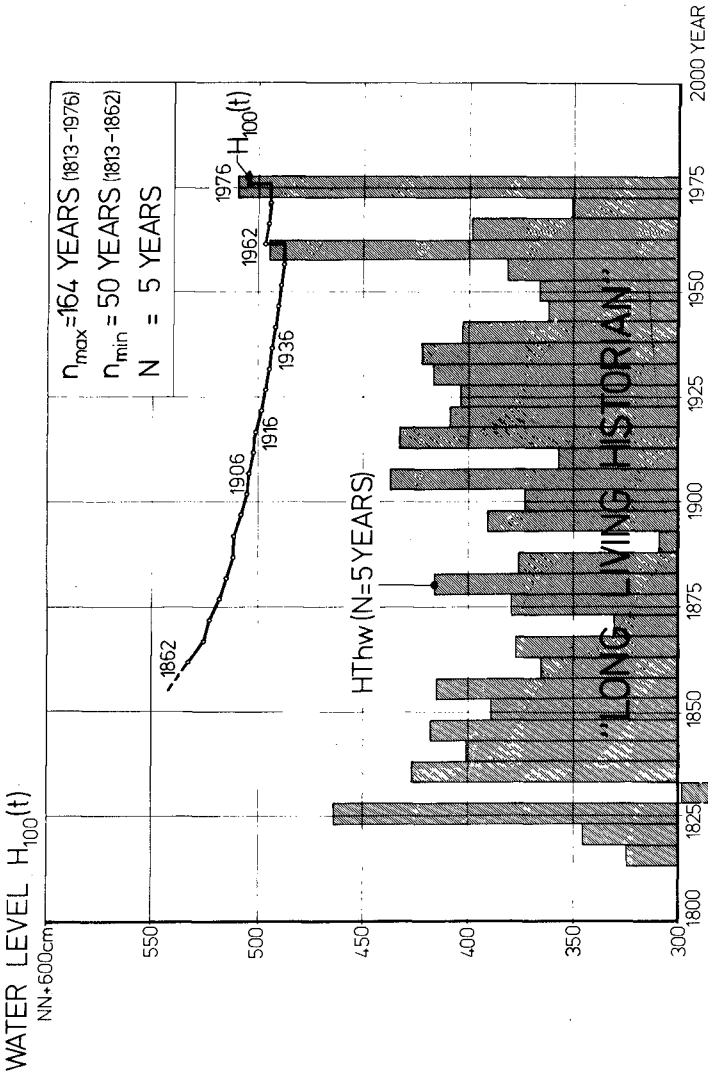


Fig. 6: Hypothetical model: "Long Living Historian" (Station Cuxhaven)

One of the methods of investigation in non-stationary cases is the hypothetical model named "Long living Historian". He begins his work after supplying a 50 years series at the given gauge and examines after every following 5 year period its predictions for the value H_{100} vis-a-vis the new HW of these 5 years. This gives rise to a function $H_{100}(t)$ which can give information about the time-dependent changes of the probability of extreme water levels (FÖHRBÖTER 1976).

Fig. 6 shows the results from the model "Long living Historian" for Cuxhaven; the curve $H_{100}(t)$ ("abstract probability") is combined with the presentation of the HW for each $N = 5$ years ("observed frequency").

It is to be seen here that the function $H_{100}(t)$ has an always falling trend till 1962. Here and 1976 firstly discontinuities occur in form of jumps towards higher levels.

The comparison of the function $H_{100}(t)$ on fig. 6 with this on fig. 7 shows that there is no stationary pattern in the function $H_{100}(t)$ from the "Long living Historian".

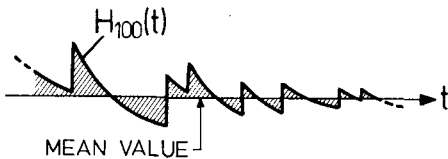


Fig. 7: Example for a function $H_{100}(t)$ from a stationary process

A model opposite to the "Long living Historian" is the "Remembering Historian" who begins his work in 1976 with a 50 year series from 1927 - 1976 and goes than back into the past with his memory.

For Cuxhaven, fig. 8 shows the function $H_{100}(t)$ for this model; here a general rising tendency with some small discontinuities is to be seen.

Another method of investigation is represented by the hypothetical model "Forgetting Historian" (FÖHRBÖTER 1976). He begins with the first 50 year series of the given gauge, similar to the "Long living Historian", but forgets as the time function $H_{100}(t)$ develops all the values that lie behind 50 years, but applies uniformly a 50 year series as moving investigation period. Corresponding to the greater weightage of the events in that period of 50 years in this hypothetical model, the discontinuities since 1962 occur somewhat stronger than in the previous model; at the CUXHAVEN gauge the jumps in 1962 and 1976 result in an increase in the value of H_{100} by about one meter (fig. 9).

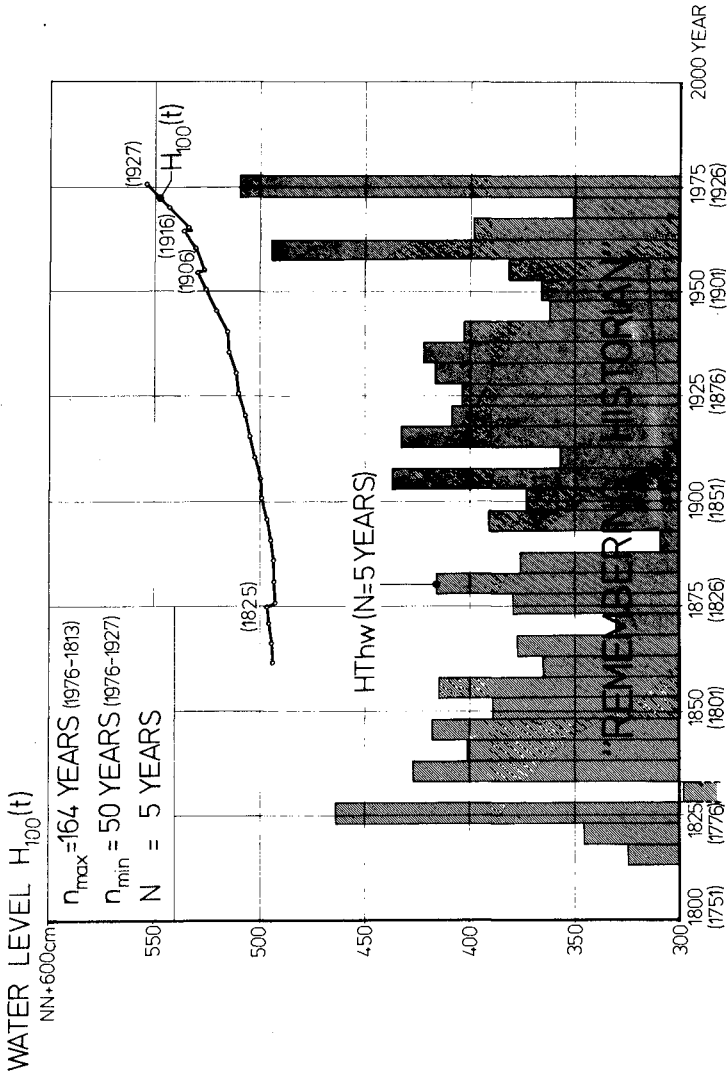


Fig. 8: Hypothetical model: "Remembering Historian" (Station Cuxhaven)

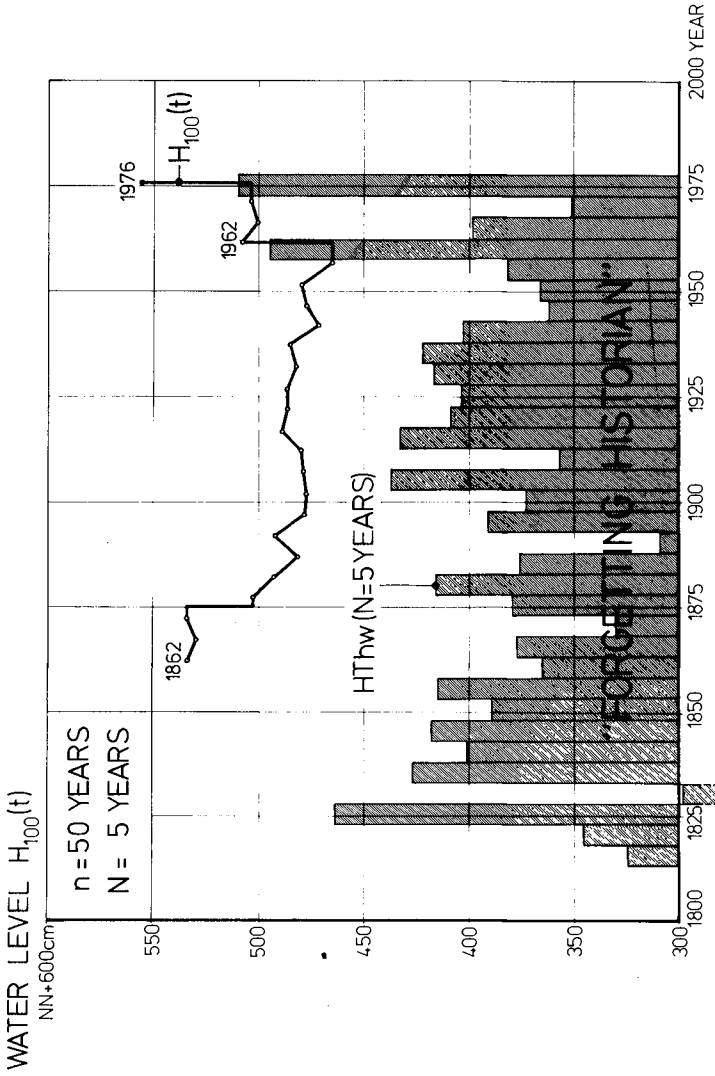


Fig. 9: Hypothetical model: "Forgetting Historian" ($n = 50$ years) (Station Cuxhaven)

Whereas in the "Long living Historian" it is assumed that the meteorological parameters, whose eventual superimposition determines the occurrence of the storm flood, are remaining the same in the mean value, in the model "Forgetting Historian" the meteorological events of the previous 50 years alone are considered as determining the storm flood, also for the period of 100 years, to which the value H_{100} will be extrapolated.

The stations of Wilhelmshaven and Husum show similar trends. It may be of high interest that also on the east coast of England for the harbour of Immingham GRAFF (to be published 1979) found comparable results with time series from 1920 - 1978 (fig. 10).

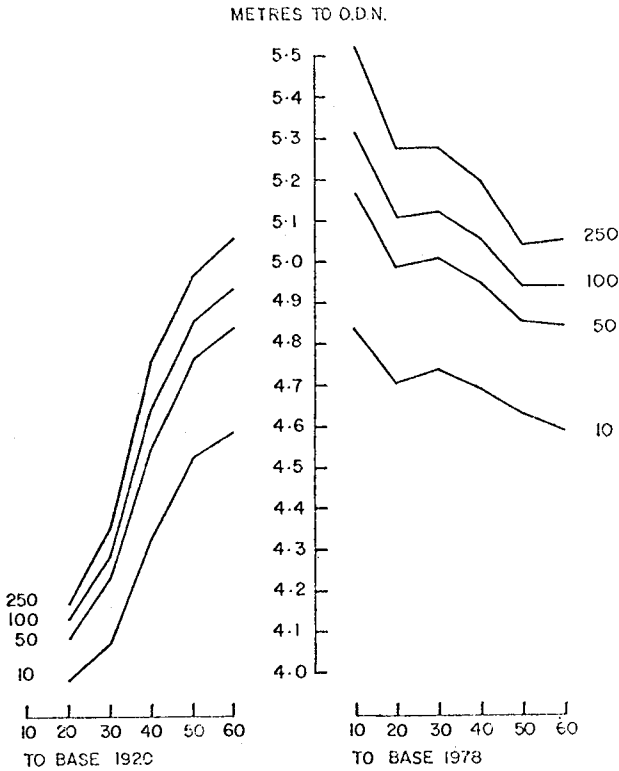


Fig. 10: Sea levels from $H_{250}(t)$ till $H_{10}(t)$ for the harbour of Immingham (from GRAFF, to be published 1979)

The curves "to base 1920" can be compared with the hypothetical model "Long living Historian" (fig. 6), those "to base 1978" with the "Remembering Historian" (fig. 8).

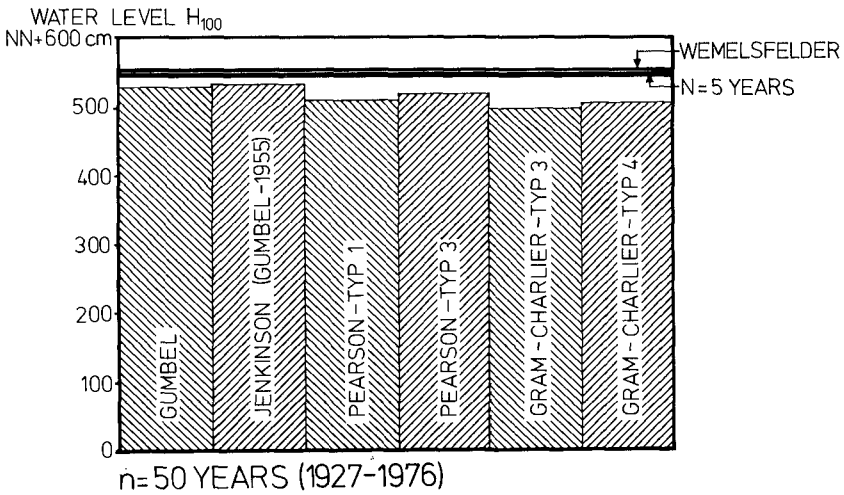
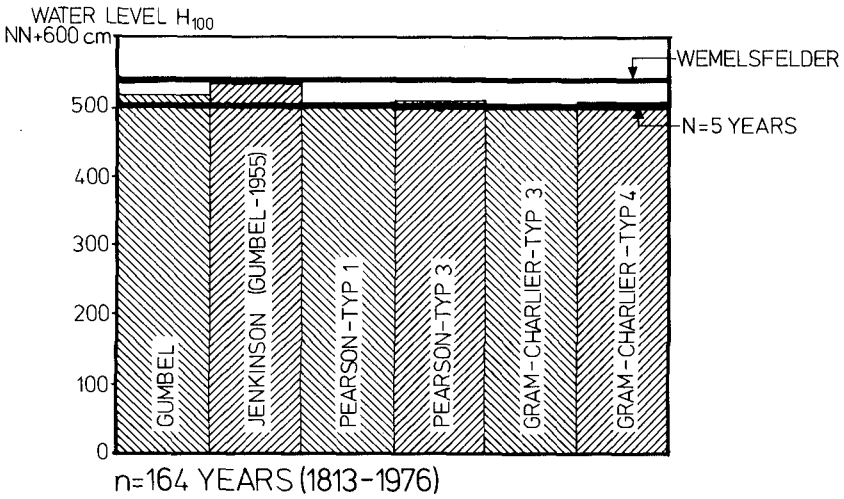


Fig. 11: Comparison of different approximation functions with the value H_{100} for the station of CUXHAVEN (values adjusted to 1975) (from WOLPERS, to be published 1979)

GRAFF used for his computations the distribution function of JENKINSON (1955). On fig. 11, for different probability distributions the values computed after WEMELSFELDER (1939) and with $N = 5$ years (FÜHRBÖTER 1976) are compared for Cuxhaven. It is to be seen that the question which time series are taken for the computation is much more predominant than the question which distribution was used (fig. 11).

The same effect is illustrated for Cuxhaven on fig. 12. The water level H_{100} computed with $n = 50$ years is for the series 1927 - 1976 nearly one meter higher than for the series 1912 - 1961 (FÜHRBÖTER 1976).

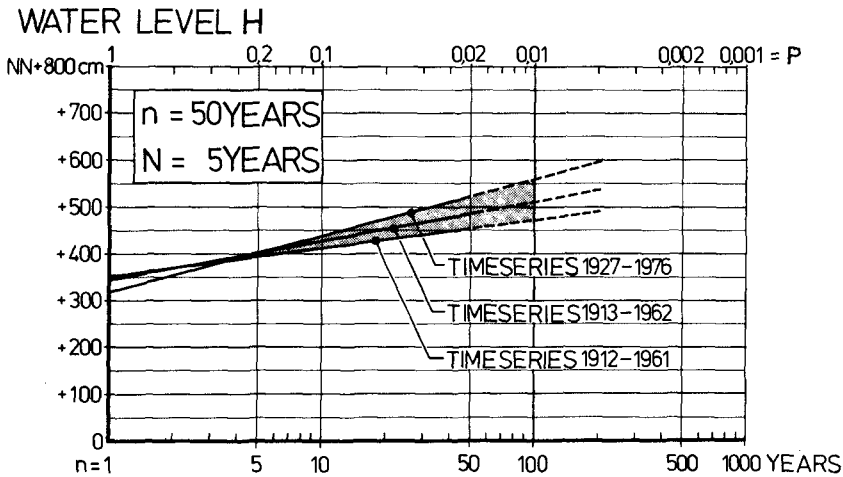
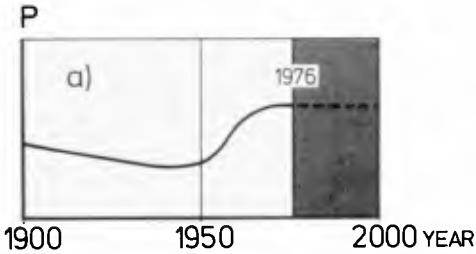


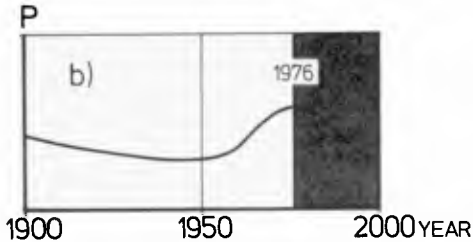
Fig. 12: Changes of $H_{100}(t)$ with different time series for Cuxhaven

The North Sea as a very shallow sea with high wind set-up effects is acting highly as extremely sensitive measuring equipment for climatic changes, especially for surge producing weather conditions. The flood disaster in the Netherlands 1953, in Germany 1962, the Adolph-Bermphol-Orkan (1967), with mean wind speed of 37 m/sec. over 5 hours, the strong continental storm with high damages in the forests from France till Poland in November 1972, a series of 6 heavy floods in November/December 1973 and two extreme floods in January 1976 with the highest water levels ever registered in the German bight are indications for some changes in meteorological conditions.

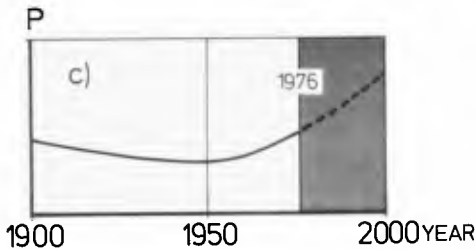
Three possibilities must be taken into consideration for the future (fig. 13);



a) There is a sort of flip-flop mechanism in climate with higher but constant probabilities P for extreme surges for the next future (fig. 13a)



b) Like some periods during the Middle Ages, there is a temporary maximum with a trend of reduction in future (fig. 13b) or



c) the worst development: the probability P shows a furtherly increasing trend (fig. 13c).

Fig. 13: Possibilities of futural development of storm surge probability P

From meteorology, no exact prediction can be given for the next future (see FLOHN 1967, LAMB 1976). Also how far human impacts on the climate may be responsible for the events, cannot be answered at time, but meteorologists and engineers should observe very carefully this development for the future (FÜHRBÖTER 1976).

References:

- FLOHN, H. 1967 Klimaschwankungen in historischer Zeit
Die Wissenschaft, Bd. 122, 1967
- FÜHRBÖTER, A. 1976 Über zeitliche Änderungen der Wahrscheinlichkeit von Extremsturmfluten an der deutschen Nordseeküste (On the Time-Dependent Changes of the Probability of Extreme Storm Floods at the German North Sea Coast)
Mitt. des LEICHTWEISS-Instituts der Techn. Univ. Braunschweig, Nr. 51, 1976
(engl. Edition in press at JJT Madras/India)
- GRAFF, J. 1979 Concerning the Recurrence of Abnormal Sea Levels
(to be published 1979 in "Coastal Engineering")
- JENKINSON, A. F. 1955 The Frequency Distribution of the Annual Maximum (or Minimum) Values of Meteorological Elements
Quarterly Journal Royal Meteorological Society, April 1955
- LAMB, H. H. 1976 Remarks on the Current Climatic Trend and its Perspective
Proceedings WMO/IAMAP
Symposium on Long-Term Climatic Fluctuation, Norwich, August 1975
- v. MISES 1972 Wahrscheinlichkeit, Statistik und Wahrheit
4. Auflage, Springer-Verlag Wien, New York 1972
- POISSON, S. D. 1841 Lehrbuch der Wahrscheinlichkeitsrechnung
Deutsche Übersetzung von Dr. Schnuse
G.E.E. Meier Verlag, Braunschweig, 1841
- WEMELSFELDER, P.J. 1939 Wetmatigheden in het optreden van storm-vloeden
De Ingenieur, Maart 1939
- WOLPERS, F. 1979 Über Wahrscheinlichkeitsverteilungen für extreme Sturmflutereignisse
(to be published 1979 in Mitt. des LEICHTWEISS-Inst. der Techn. Univ. Braunschweig)

CHAPTER 55

STORM SURGE PREDICTION BY COMBINED WIND AND TIDE DATA

by
Hermann Christiansen^{*)} and Winfried Siefert^{*)}

ABSTRACT

The authors suggest a storm tide forecasting method that allows high water predictions for a coastline 3 to 4 hours in advance with an accuracy of ± 30 min in time and ± 20 to 30 cm in height. It is based on actual (not on predicted) data, i.e. exact wind velocity and direction data from a reference station and tide data from two gauges. The method was developed by analysing storm surge curves and wind data of those 50 storm tides that occurred since 1965 in the German Bight. Another 50 storm tides back to the year of 1930 were taken into account, though without exact wind data.

The method was proved at all storm tides since 1965 and applied with good success to the events during fall and winter 1977/78 for the coastline off Cuxhaven.

^{*)} Dr.-Ing. Hamburg River and Port Authority
Coastal Engineering Research Group "Neuwerk"
2190 Cuxhaven, F.R. Germany

INTRODUCTION

Storm tide forecastings and quick propagation of warnings are of high importance for people living at coastlines and tidal rivers behind the dykes. This yields to the demand, that a storm tide forecasting method must satisfy the highest level of scientific solidity that can be reached. Methods that are developed by hindcasting 5 to 10 special storm tides are not serious enough. Our investigations show that we have to live with at least 20 different surge types.

Lots of forecasting methods often remain insufficient as they are based on weather forecasts and these weather forecasts - mainly wind speed and wind direction developments - are not accurate enough.

The other reason for unsatisfactory predictions are the methods in itself, as usually only the peaks of storm tides are taken into consideration, and that is only one point on a curve. Characteristics of tide and surge curves are not developed, and tide/surge interactions are not evaluated.

To exclude such difficulties the presented storm tide forecasting method was developed

1. by analysing storm surge curves of those 100 storm tides that occurred since 1930 at several tide gauges on our coastline. A storm surge curve is defined as the differential curve between storm and mean tide curves;
2. by taking into consideration wind data of 50 storm tides back to 1965 (data from earlier events were not available);
3. by using only exact (not predicted) tide and wind data

STORM TIDE CONDITIONS IN THE GERMAN BIGHT

Fig. 1 shows the situation with the German North Sea coast. In the German Bight the astronomical tide is progressing anti-clockwise. Wind at storm tides comes from western directions like the storm surge wave. By this, a forecast for a point B on this coastline needs informations from a location westward of it. We found this point with the tide gauge A at the Island of Borkum. This gauge A is the so-called input gauge for the forecast gauge B.

Fig. 2 shows in the upper part the storm tide curves for one event at A and B. High water level at A occurs 2 to 3 hours earlier than at point B. A comparison of high water levels at A and B (Fig. 3) shows that there is already a remarkable trend. On the other hand single deviations up to 1 m show that a use only of this trend is not exact enough to forecast high water levels at B. That means that water level informations merely from an input gauge are not sufficient.

FORECASTING METHOD I

Further investigations showed that an explanation for the runaways of Fig. 3 can be given if wind speed and wind direction development in the last 3 hours before high tide at A (Borkum) are taken into account. The wind development in this 3 hours intervall (about 3 hours before the expected high water level at B) is the best indicator for what will happen with the water level changes in the following 3 hours after high tide at A. The conclusion is, that about 3 hours before high tide at B no further wind informations are needed to forecast the highest level at B. These conditions are in agreement with results at the Dutch and British coast.

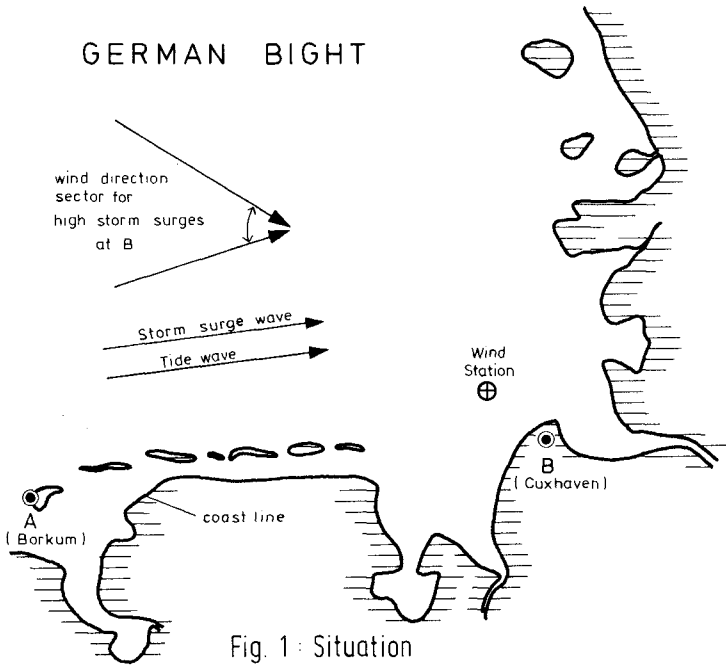


Fig. 1: Situation

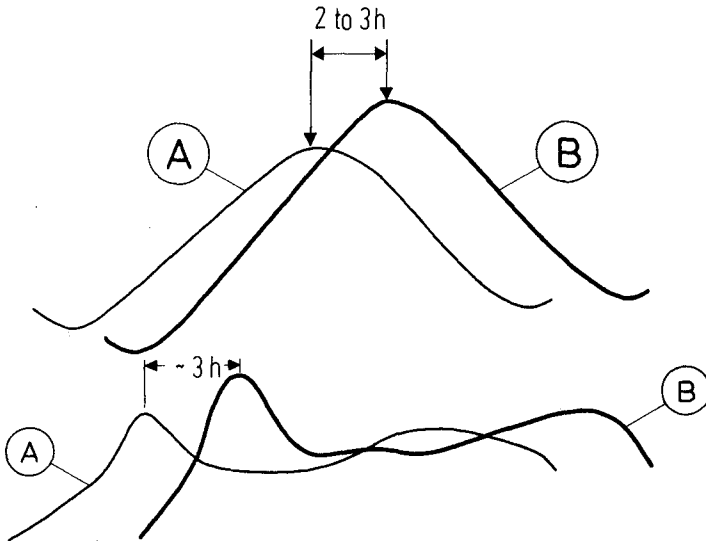


Fig. 2: Tide- and Storm Surge Curves at A and B

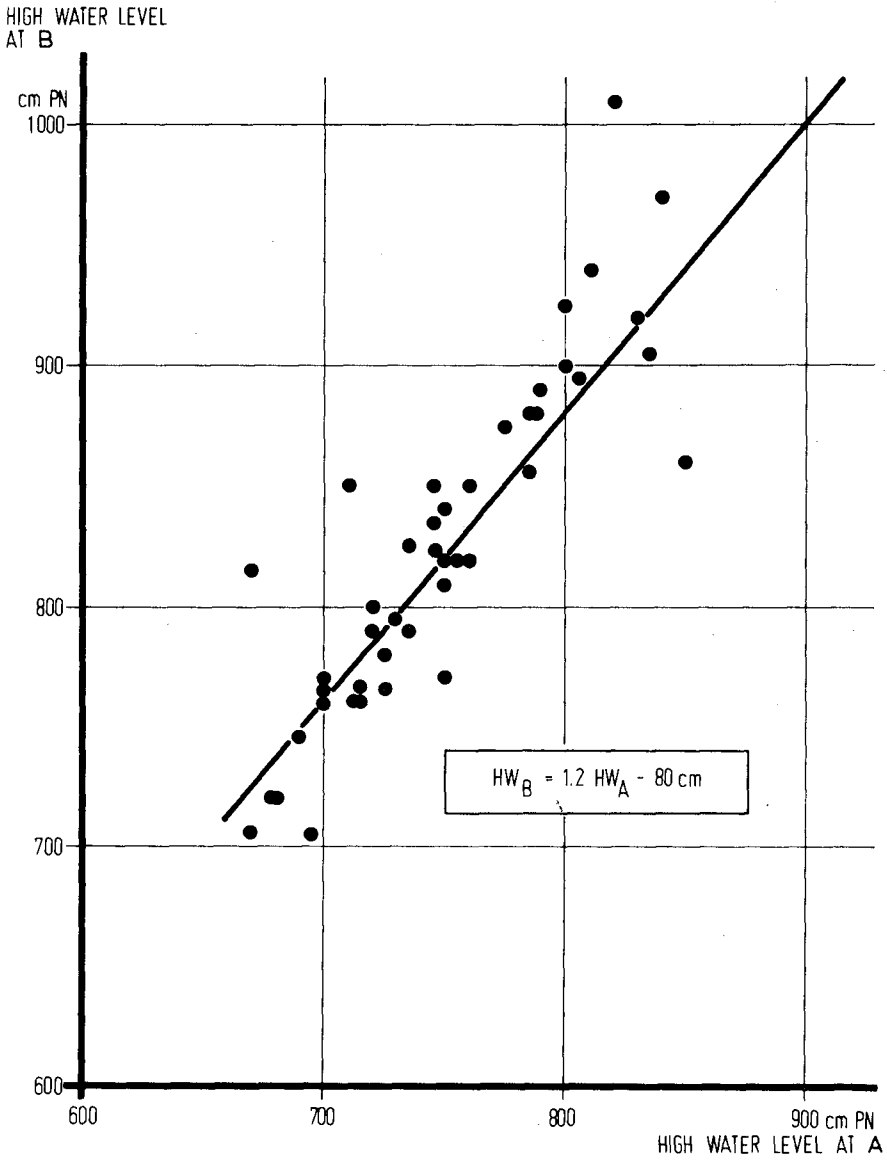


Fig. 3: Comparison of High Water Levels at A and B

The high water level at B (HW_B) can be calculated by the simple formula:

$$HW_B = 1.2 \cdot HW_A + \Delta v + \Delta R - 80 \text{ cm}$$

where

- $1.2 \cdot HW_A - 80 \text{ cm}$ gives the trend of high water level comparison at A and B (Fig. 3) and
- Δv (Fig. 4) and ΔR (Fig. 5) are the partial amounts for wind speed and wind direction developments within 3 hours before forecasting time

The wind data is needed with an accuracy of 1 m/s in speed and 10° in direction. The example in Fig. 4 demonstrates the necessity of exact wind speed data. A change in wind speed from 20 to 24 m/s over the 3 hours intervall gives a positiv amount of $\Delta v = + 40 \text{ cm}$. A change of only 2 m/s more (to 26 m/s) doubles this amount to $\Delta v = + 80 \text{ cm}$.

Fig. 5 shows that highest amounts for wind direction developments are given by changes from other directions to 280° , what is the most effective wind direction for high storm surges at Cuxhaven. Direction changes further northward give high negative amounts, up to $\Delta R = - 80 \text{ cm}$.

FORECASTING METHOD II

There is at least a second chance to forecast high water levels at B to control the first method mentioned above. This possibility is given by analysing the surge curves at A and B. The surge curve (see Fig. 6) is defined as the difference curve between the storm tide curve and the mean tide curve. This curve includes all deviations from the mean tide, such as wind influence, astronomical disproportion, external surges, temperature, atmospheric pressure etc.

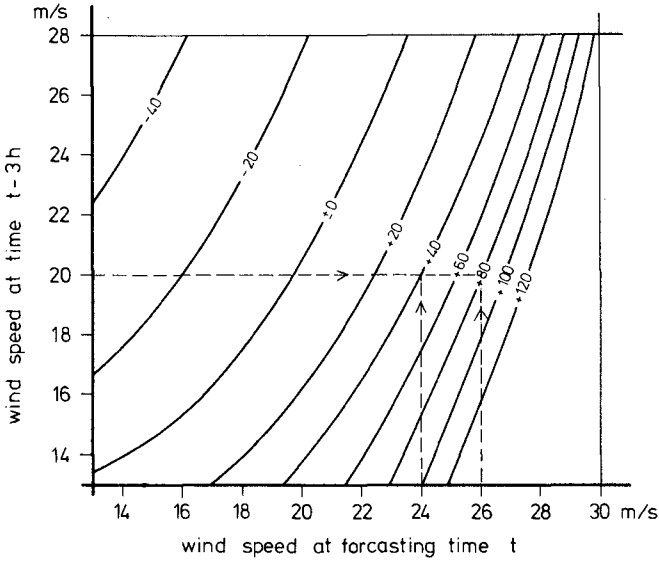


Fig. 4 : Wind Speed Development Value Δv in cm

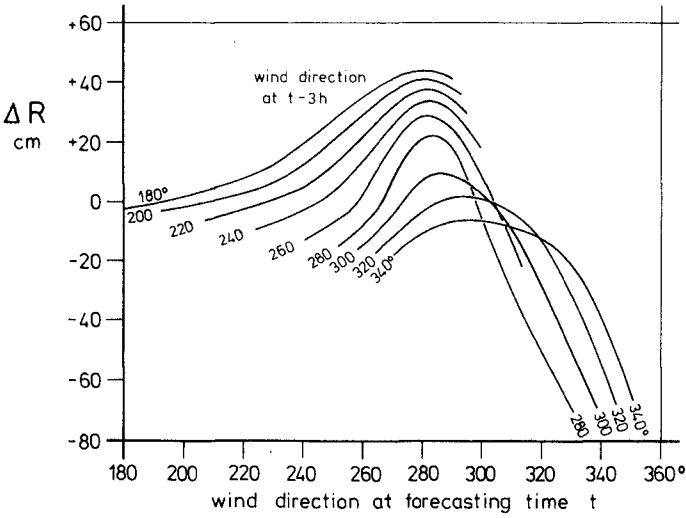


Fig. 5 : Wind Direction Development Value ΔR

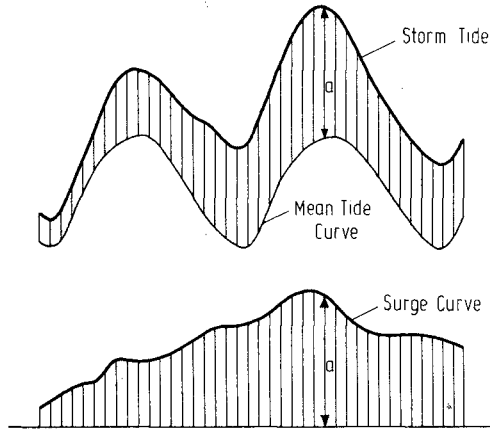


Fig. 6 : Definition Sketch Surge Curve

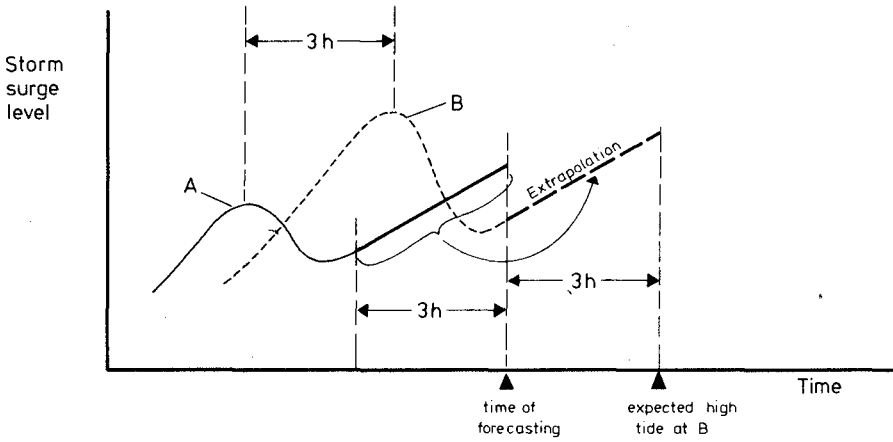


Fig. 7 : Extrapolation of Storm Surge Curve B by the Shape of Curve A

Fig. 2 shows in the lower part, that surge curves of the same event at neighbouring gauges are not only very similar, but there is also a phase lag of about 3 hours between these curves. That means, that what happened in the last 3 hours with the surge curve at A, will happen qualitatively in the same way within the next 3 hours at B. So it is possible to extrapolate the surge curve at B by the trend of A 3 hours in advance (Fig. 7). Addition of the extrapolated surge curve and the attached part of the known mean tide curve gives the expected storm tide curve at B, including the highest peak.

In practice we found, that the mean value of methods I and II gives the best result for the high water level forecast. The comparison of computed and observed HW data for Cuxhaven is given on Fig. 8.

WHAT CAN WE DO IN FUTURE?

To improve and to reform the presented forecasting method, first of all we have to include all informations that can be reached by further storm tides.

While the high accuracy in forecasting is satisfactory we should try to find a way to give the forecasts earlier than 3 or 4 hours in advance. We believe that this is only practicable if we get exact wind forecasts for the next 2 or 3 hours. For better, i.e. earlier storm tide forecastings it would be greatly helpful if programs could be started to research not only in the development of wind conditions for the next 2 or 3 days but also for this short interval we are interested in.

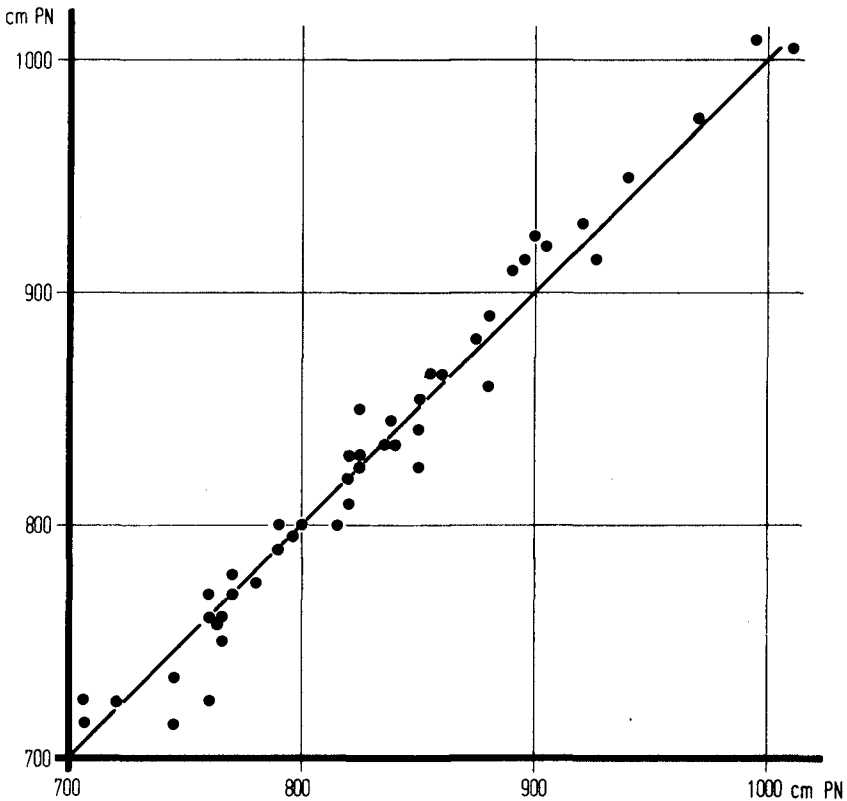


Fig. 8 : Comparison of computed and observed HW-Data Cuxhaven

ACKNOWLEDGEMENT

Acknowledgement is gratefully made to the Town of Cuxhaven and the Federal State of Lower Saxony for their financial support in this research programme and the permission to present this paper.

REFERENCE

- SIEFERT, W.
CHRISTIANSEN, H.: Development of a New Storm Tide Forecasting Method for Cuxhaven. Cuxhaven 1977 (unpublished)

CHAPTER 56

NUMERICAL STORM SURGE FORECASTING

Manfred Engel⁺

Abstract

The present state of the development of an operative storm surge prediction system in Germany is described. It is based on numerical models of the atmosphere and the North Sea. First simulations of the storm surge on Jan. 3, 1976 yield the result, that the observed water levels along the North Sea coasts can be recalculated quite well using a meteorological input derived from observations, whereas the forecasted water levels, using the predicted geostrophic winds of the atmospheric model, are too low since the pressure gradients are too weak. A series of storm surge recalculations with observed and predicted meteorological data shall answer the question, whether parameter fits, applied to the predicted wind stress, lead to satisfying results, suitable for practical applications.

Introduction

After the severe storm surge of January 3, 1976, the German Hydrographic Institute, being responsible for warnings, arranged a meeting with the aim to bring together all people working on numerical modelling of storm surges in Germany.

Meanwhile the Sonderforschungsbereich "Meeresforschung" - special research organisation "Marine Research" - of the University of Hamburg had started a program for the development of a storm surge prediction system. On this

⁺ Institut für Meereskunde, University of Hamburg
Sonderforschungsbereich 94, Meeresforschung

meeting it was concluded that the different activities of numerical modelling of storm surges should be coordinated by a Model Group North Sea. Some of its intentions, its work and some preliminary results shall be discussed in the following. Although e.g. in our institute many storm surge calculations, yielding encouraging results for different events with different models, have been carried out during the past 20 years, it was felt that for the development of a prediction system as a first step it is necessary to get a consistent set of storm surge hindcasts on the basis of observed meteorological data with only one model. Therefore a first goal of the Model Group was the recalculation of a certain number of storm surges.

For this purpose our Sea Weather Office reanalyses very carefully threehourly weather maps, the surface pressure and additionally the air-sea temperature differences. Parallel to this work the meteorological fields for every of these analysed events are hindcasted with a hemispherical prediction model, developed by the Meteorological Institute of the University of Hamburg.

Both data sets are used for storm surge calculations and following analyses of the results.

When these tests are done and when possible improvements of the presently used models are finished, and if it can be shown that the predicted storm surge heights are closer to the observed ones than the conventionally estimated predictions, then we hope that a data link between the German Weather Service in Offenbach, running the meteorological model, and the German Hydrographic Institute, computing the water elevations, will enable us to give better storm surge warnings earlier than it is possible nowadays.

The Models

The North Sea model is a two-dimensional vertically inte-

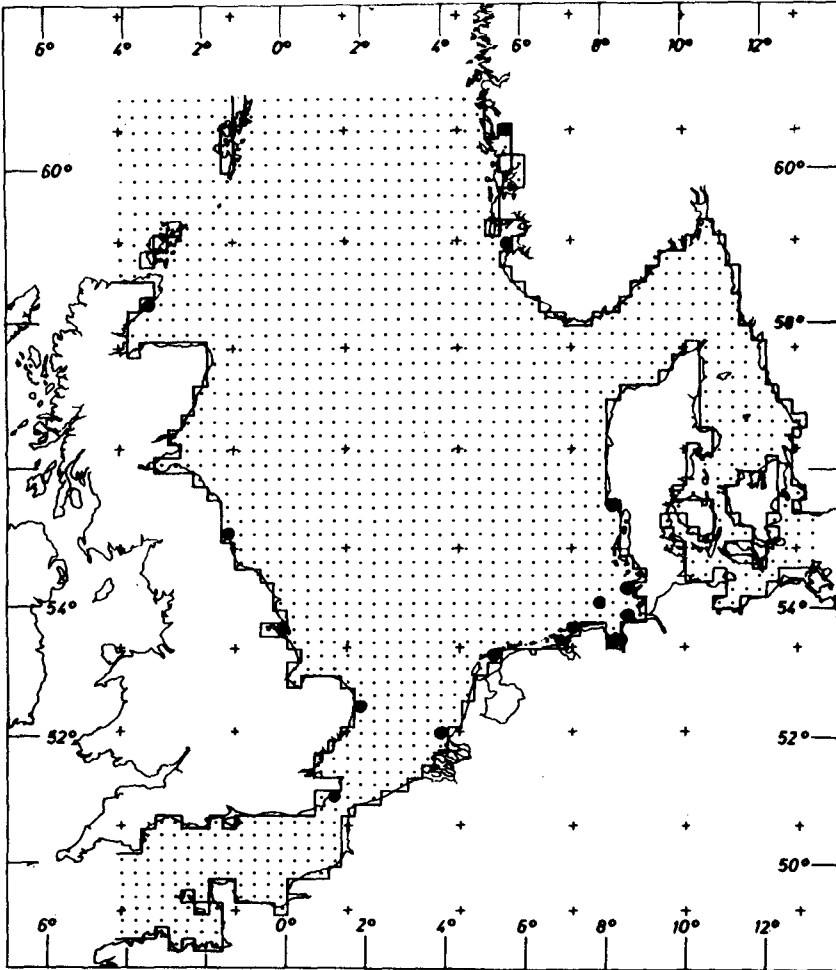


Figure 1 The HN-North Sea model
The crosses (+) denote grid points of the meteorological prediction model.
The dots (•) represent points for comparisons with tide gauge data.

grated HN - model (hydrodynamical-numerical model) with a grid point distance of about 22 km (Fig. 1). It is formulated in spherical coordinates. In addition to an earlier version it now includes parts of the English Channel. On the open boundaries the M_2 - tide is prescribed. It is intended to use later on 10 tidal constituents, but until now the results of such tidal computations are not satisfying since the boundary values are not known exactly enough.

In order to correct for meteorologically induced variations of water levels on the open boundaries a coarser model of parts of the North Atlantic is run parallel to our prediction model.

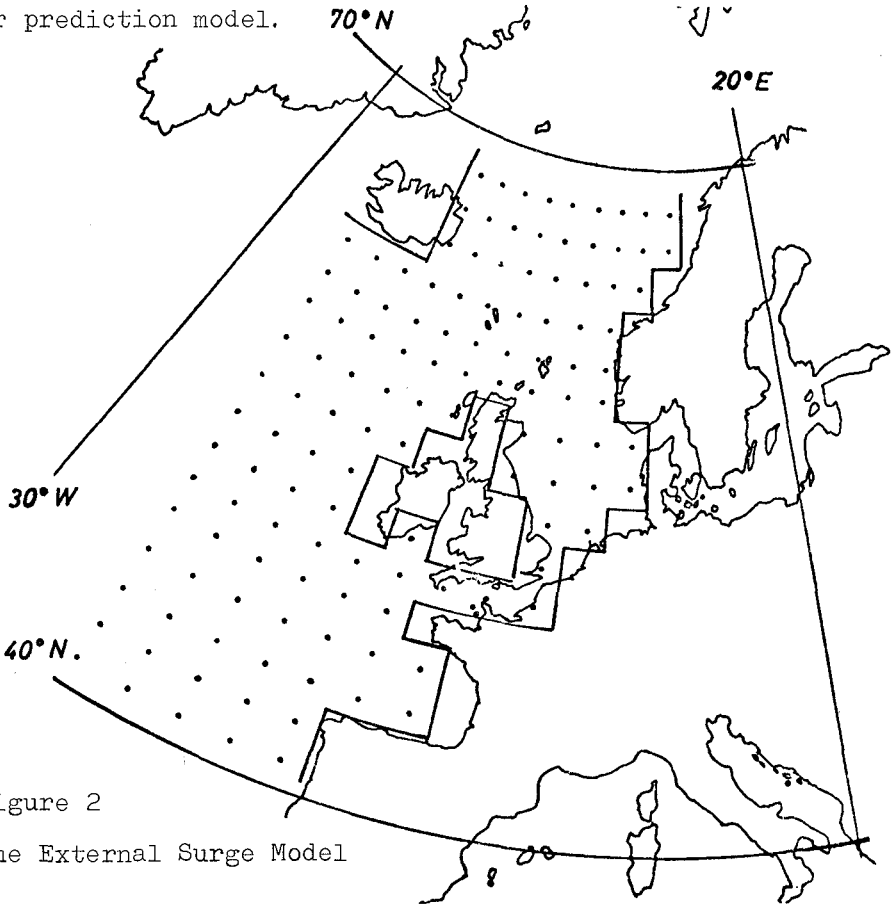


Figure 2

The External Surge Model

The water levels of this model, driven by wind and atmospheric pressure alone, are taken along the open boundaries of the finer model and are added there to the M_2 -tide water levels. It is known that sometimes storm surges are significantly influenced by external surges, yielding contributions to the water levels in the German Bight up to the order of magnitude of one meter.

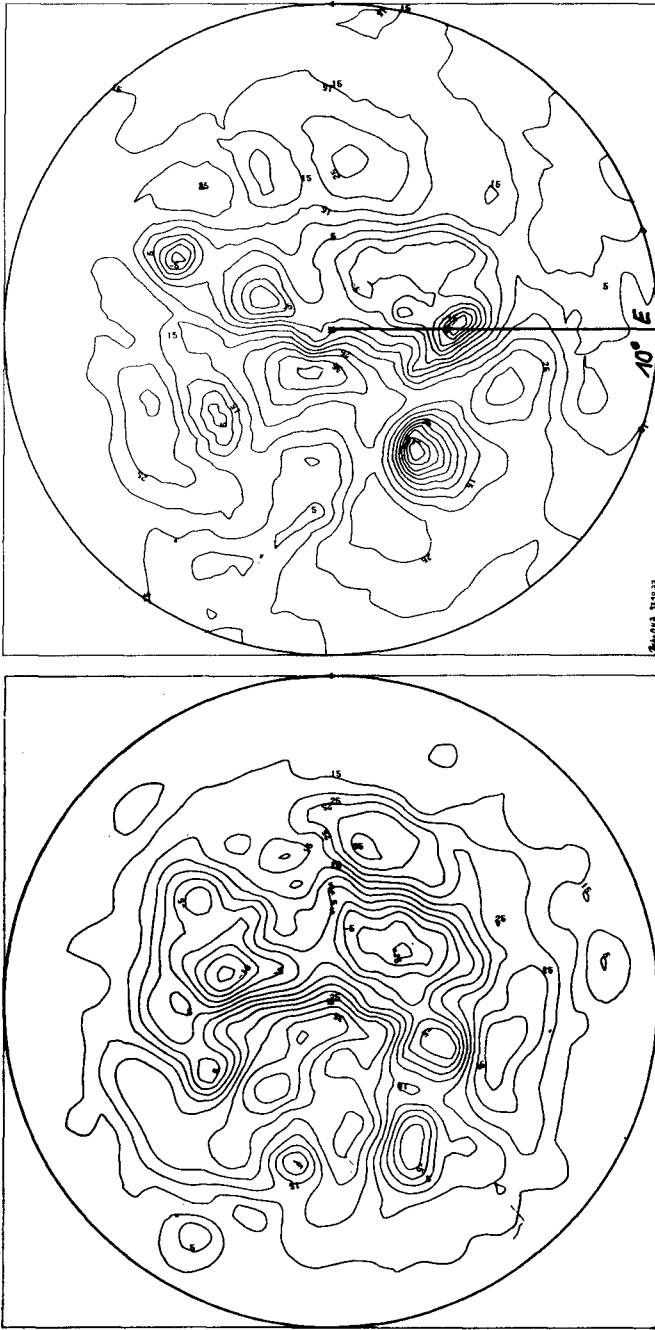
The meteorological model is an 8-layer baroclinic model of the northern hemisphere with an horizontal resolution of 1.4° meridionally and 2.8° zonally, i.e. about 150 km in the North Sea area. The lowest computation layer for wind velocities lies at about 500m height. It predicts wind, pressure, temperature and humidity. Bottom friction is assumed to be different over land and sea areas.

Figure 3a shows the bottom pressure over the northern hemisphere on the 2nd of January at 12⁰⁰ GMT (this information belongs to the set of initial values for the computation) and Fig. 3b gives the predicted field 24 hours later. The cyclone on the 10° meridian lies over the North Sea.

On Figure 4 observations and forecasts of bottom pressure over western Europe are blown up. For a further comparison the predicted bottom pressure of the German Weather Service is added. Both models underestimate the pressure gradients. We will come back to this feature when discussing the predicted storm surge results.

From the meteorological model the pressure is interpolated on the grid points of the North Sea model and then the wind stress is calculated. When using observed meteorological data for surge computations, the pressure information is taken from isobars of weather charts. The pressure gradients are determined as the slope of triangular planes between the isobars and thus can be used directly for stress computations in the North Sea model.

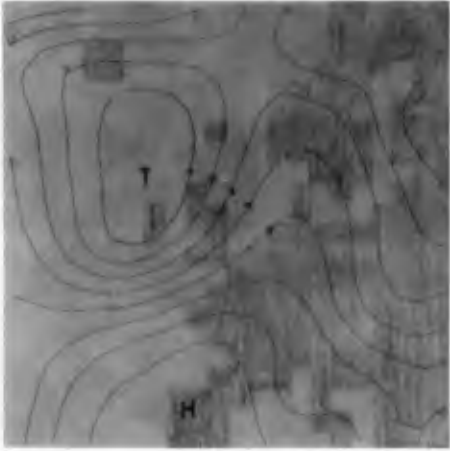
So far we have studied only the already mentioned storm



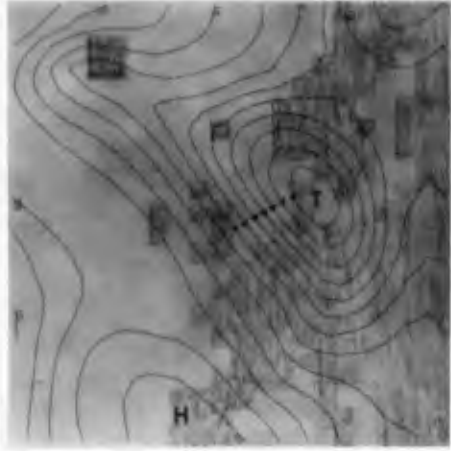
a

b

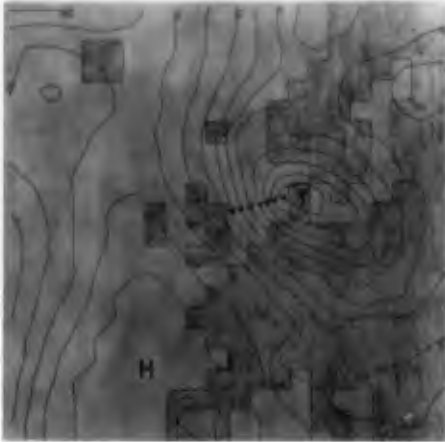
Figure 3 Bottom pressure over the northern hemisphere
(a) Initial values on the 2nd of January 1976, 12⁰⁰ GMT
(b) Predicted bottom pressure field 24 hours later



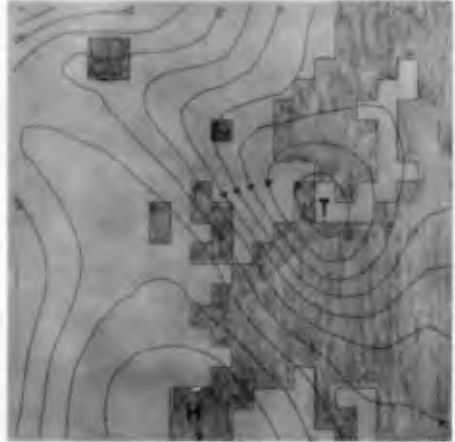
Initial bottom pressure field, 2.Jan. 76, 12⁰⁰GMT



24 hours forecast of the prediction system model



Observation on 3. Jan. 12⁰⁰GMT (24 hours later)



24 hours forecast of the German Weather Service

Figure 4 Observed and predicted bottom pressure fields over western Europe

surge of the 3rd of January in 1976 with this system. This storm surge caused the highest water level, at least at Hamburg, which was ever observed.

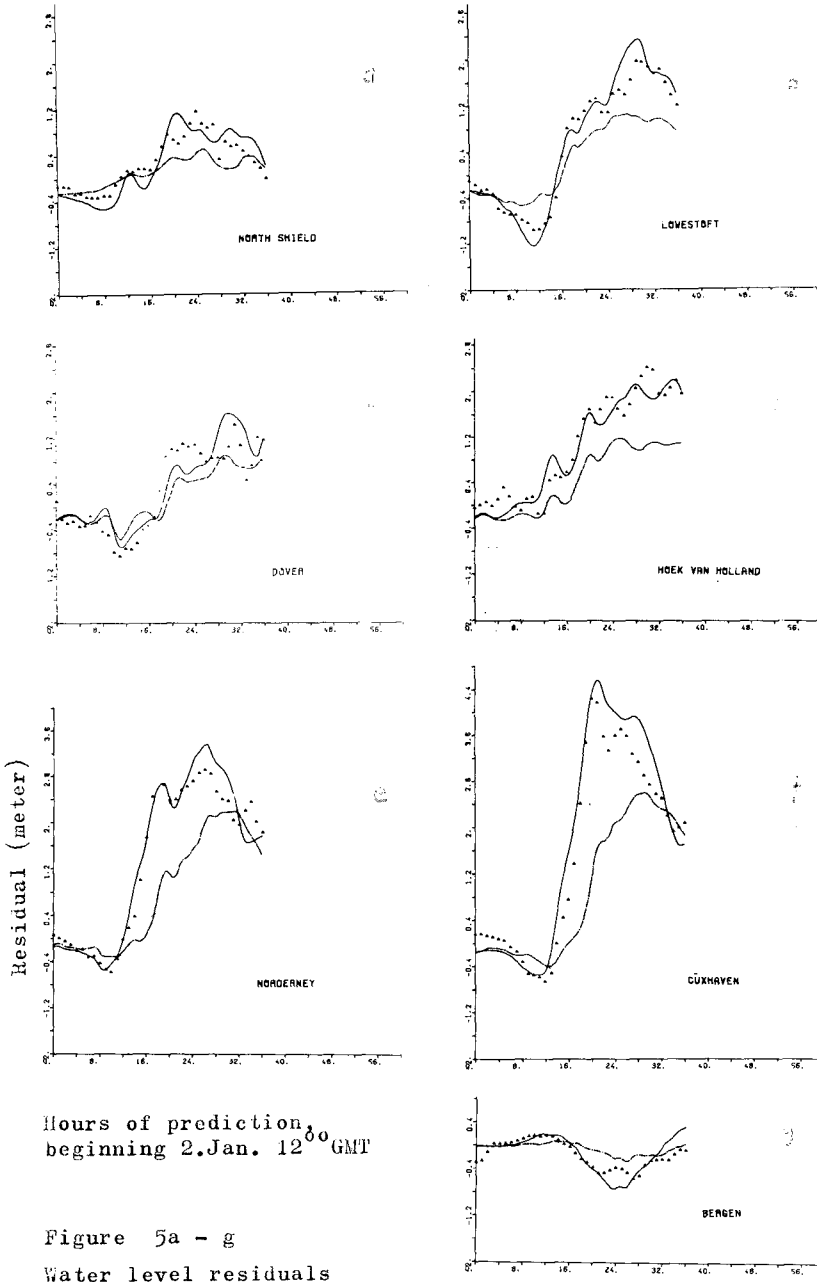
Calculations of a series of storm surges from the 19th through 21st of January, 1976 are under preparation.

Results

On figures 5a-g computed and observed residuals of water levels for different locations around the North Sea are compared. The residual is defined as the difference between water levels as observed or computed with wind, pressure and tides and those which were predicted for the tide or computed in the model for the M_2 -tide alone. All plots show a much better correspondence between observed and hindcasted residuals than between observed and predicted ones. From the results at Dover one can deduce that it is necessary to extend the model into the English Channel.

These first results, yielding the largest prediction errors in the German Bight, are of course not yet suitable to demonstrate the reliability of our prediction system. The discrepancies in the residual forecasts are the direct consequence of the discrepancies of the predicted geostrophic winds, being too weak during the period of interest (Fig. 6).

Both surge computations have been carried out with the same formulation of wind stresses. Since it is a common feature of many atmospheric circulation models to underestimate geostrophic winds, a further surge simulation using the forecasted geostrophic wind and a drag coefficient, tuned at the maximum water levels, has been carried out. The results are looking better, at least up to the maximum water level, but since the predicted low did not decay quickly enough, the following water levels were overestimated.



Hours of prediction,
beginning 2.Jan. 12⁰⁰ GMT

Figure 5a - g
Water level residuals

▲ observed ——— hindcasted - - - - forecasted

Whether such a parameter fit is suitable for our prediction system or not, this can only be decided if we have computed enough events to make a statistical analysis. Beside this attempt, other improvements must be considered to get better meteorological input. For this purpose three projects are under investigation within the Model Group:

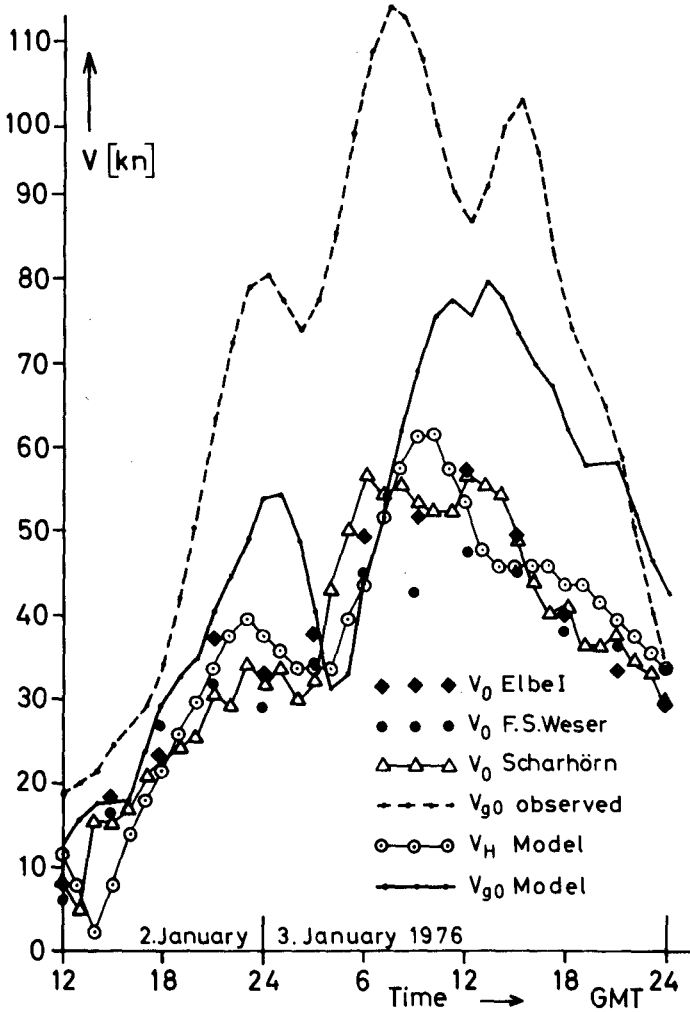


Figure 6 Comparison of observed and predicted geostrophic wind V_{g0}

- (a) to improve the meteorological forecast by means of a nested meteorological model of the North Sea area,
- (b) to test wind stress calculations based on resistance law formulations for the boundary layer,
- (c) to separate the contributions of wind and wave set-up to the storm surge water levels.

In any case it can be concluded that the meteorological data for the North Sea model must be known with high accuracy in order to get satisfying storm surge predictions within the shallow German Bight, which is very sensitive to the meteorological input in nature and in model simulations.

Acknowledgements

The results presented herein were obtained in the course of research supported by the Deutsche Forschungsgemeinschaft. The permission of Prof. Dr. G. Fischer to present the figures of the meteorological model is gratefully acknowledged. Thanks are due to L.F. Dolata, who performed the North Sea simulations and placed the corresponding figures to the authors disposal.

References

Fischer, G.

Results of a 36-hour Storm Surge Prediction of the North Sea for January 3, 1976 on the Basis of Numerical Models
Deutsche Hydrographische Zeitschrift 1, 1979
to be published

CHAPTER 57

STORM SURGE PREDICTION IN TIDAL RIVERS: A NEW CONCEPTION

by Winfried Siefert^{*)}

INTRODUCTION

The heights of extreme storm surges in the North Sea rise up to 4 or 5 m above mean high tide. Warning services are established along the coast, mainly based on empirical connections between weather and tide data. A lot of wrong announcements are given especially for places up the tidal rivers. This can become disastrous for a lot of modern, highly sensitive harbour facilities.

Thus storm surges are the famous plagues of the southern North Sea coast. Moreover, the "ten plagues of Germany" occurred during the last 16 years.

So recently a new conception for storm surge prediction in tidal rivers was developed - with the result of a lot of new understandings of tidal dynamics in rivers (SIEFERT, 1968). We investigated about 130 storm surges, hindcasting all of them and forecasting about 20 of them, and analysed their behaviour in tidal rivers. Now we are able to forecast the upstream heights and even the shape of the surge curve in the Elbe with an accuracy of ± 2 dm, 6 hours in advance. In order to do this, informa-

^{*)}Dr.-Ing., Hamburg Port and River Authority, Coastal Engineering Research Group "Neuwerk", 2190 Cuxhaven, F.R. Germany

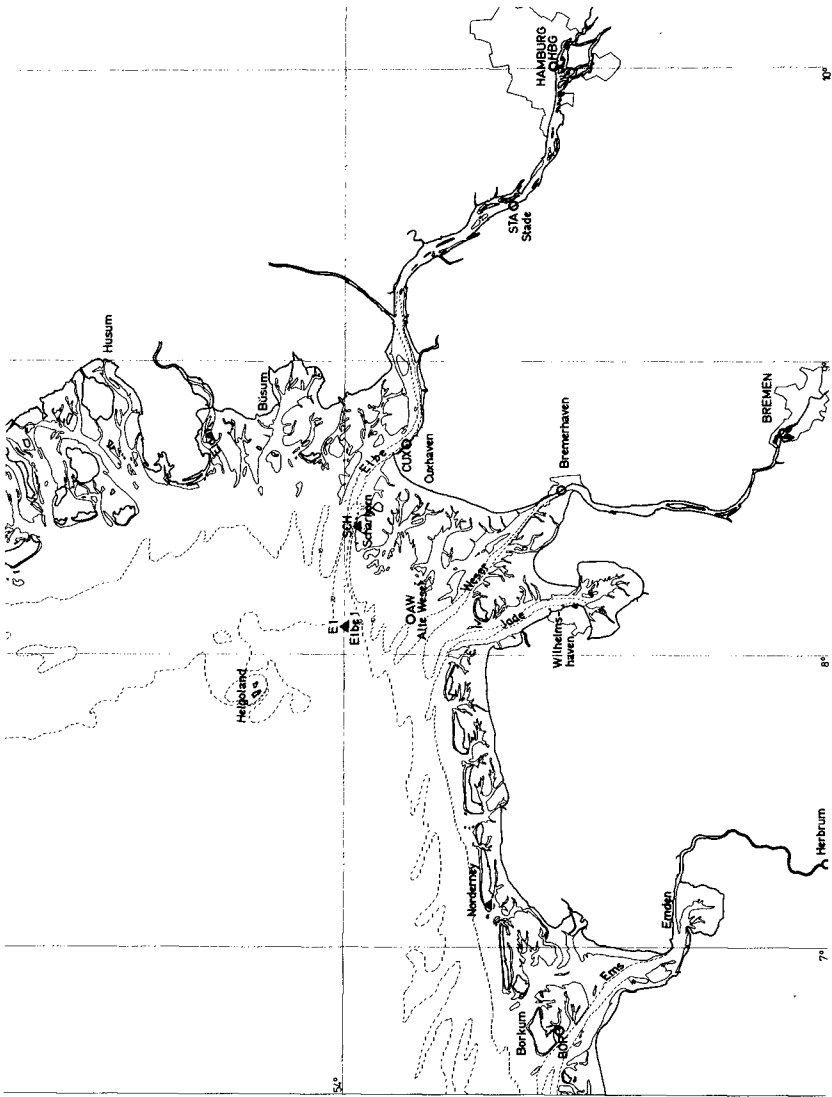


Fig. 1

tions about the boundary values are necessary. We tried to obtain informations from the stations on fig. 1 (circles = tide gauges, triangles = weather stations). It turned out that for a sufficiently exact prediction for the Elbe region data from Borkum (tide), Cuxhaven (tide) and Scharhörn (wind) are necessary.

CONCEPTION

The new conception for understanding the dynamics of storm surges in rivers and for developing a reliable warning system is very simple: Storm surge behaviour in a river is treated as a problem of combination of boundary values and eigenvalues. To solve these problems mathematically, a lot of differential equations have to be treated. This is not yet sufficiently possible. It can easier be solved in a hydraulic model (including all eigenvalues) with variation of the boundary values. This was done for the Elbe (for 200 river-km), with special respect to Hamburg, and thereafter transferred to other rivers (fig. 2).

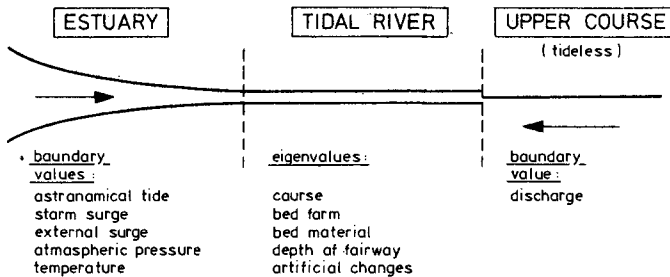


Fig. 2

It turned out that all other than astronomic influences result in a special, individual surge curve in the estuary. So we have to consider as seaward boundary values only two curves: the (more or less regular) tide curve and the (irregular) surge curve. These have to be combined with the eigenvalues by tide-river-dynamics. The latter can be considered constant during individual storm events. They are mainly changed by man (deepening and widening of fairway, course corrections, new dyke lines, weirs, dams, sluices etc.) and so are varying through the decades. The upper boundary value (discharge) can also be treated as constant during a surge.

The identification of the seaward boundary values is done by separation of the astronomical or (in first-order approximation for this area) of the mean tide wave and the surge wave (fig. 3):

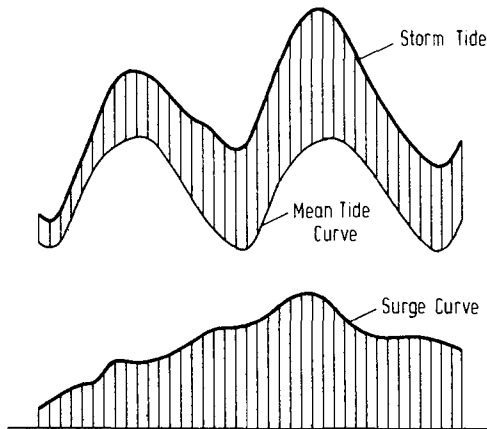


Fig. 3

The surge curve is characterized by 5 parameters as shown in fig. 4. After these treatments we investigated how these curves behave, when they proceed in a river, and especially, how they interact.

CHARACTERISTIC SYSTEM NUMBER

Correlations between storm tide heights of different gauges along a tidal river show no significant coherences. For interpretation of tidal dynamics it is necessary to take into account the complete curves.

HARLEMAN and LEE (1969) give some methods for the solution of tidal propagation in estuaries. The harmonic solution of the linear function equation for the tidal elevation at any x and t

$$\eta = \frac{\eta_{0H}}{2} \cdot e^{-\frac{\delta x}{2}} \cdot (e^{\mu x} \cos(\sigma t + kx) + e^{-\mu x} \cos(\sigma t - kx))$$

contains the amplitude attenuation coefficient μ . The authors computed the damping parameter μx for the Delaware estuary. So did PARTENSKY and BARG (1977) for the rivers Elbe, Weser, Ems and St. Lawrence.

Using μ and the variation of the damping parameter $\frac{d\mu x}{dx}$, the simple equation for wave propagation in shallow water could be modified to

$$c = S \cdot \sqrt{g \cdot d^*}$$

with g = acceleration of gravity

d^* = representative water depth in a river

It turned out that the characteristic system number S of a river can be computed as

$$S = \sqrt{\frac{1}{\mu} \cdot \frac{d\mu x}{dx}}$$

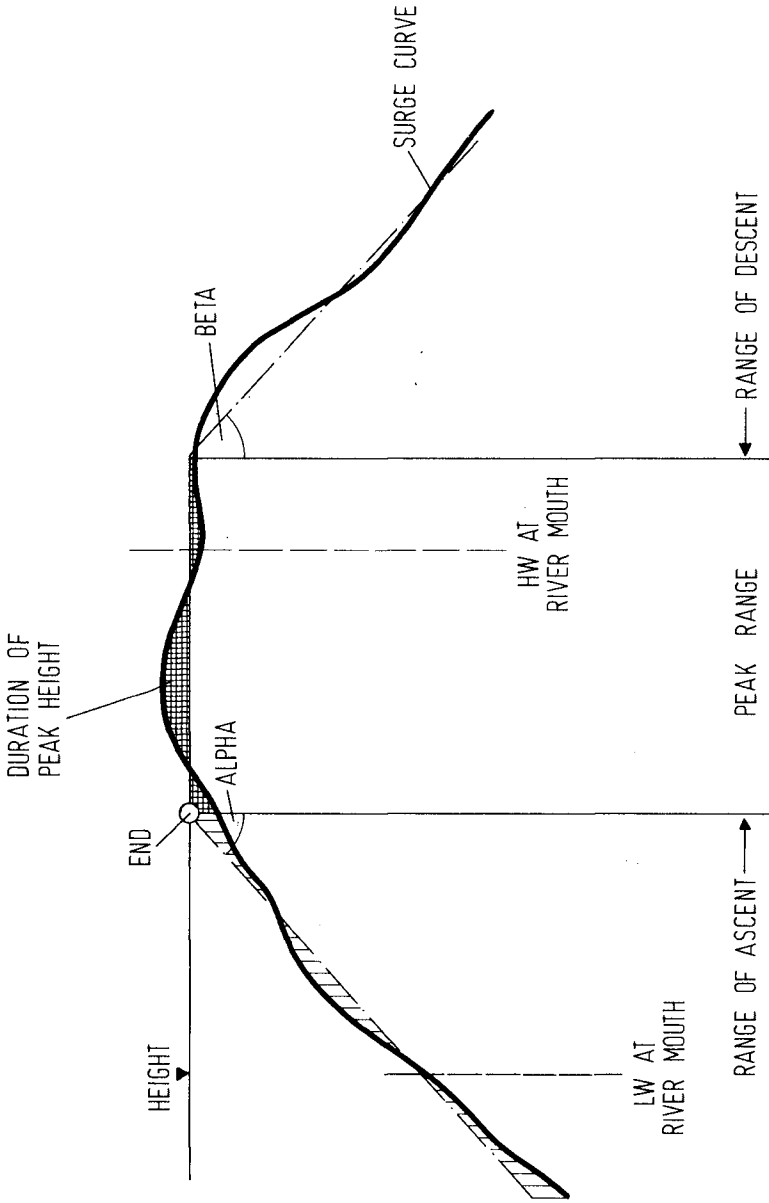


Fig. 4
Storm Surge Parameters

The values vary from 0.56 for the Elbe to 1.11 for the Delaware (SIEFERT, 1978). It changes with time, i.e. with secular changes in the river as were mentioned before.

Computations of a lot of tides and storm surges showed that the "representative water depth" d^* in a river is characterized by the depth of the fairway d_F . This fact is best proved in rivers with a distinct fairway of a certain length, as the tide and storm surge dynamics are the more concentrated at the fairway the deeper it is, relative to the rest of the cross-section.

So the equation

$$c = \sqrt{\frac{1}{\mu} \cdot \frac{d\mu x}{dx} \cdot \sqrt{g \cdot d_F}}$$

shows that c is a function of d_F alone only as long as μ and $\frac{d\mu x}{dx}$ are constant. It can be started from the principle that they are during the time of a storm tide.

LONG WAVE INTERACTIONS

If that is so, the so-called pick-a-back-effect during propagation of tide and surge waves in a river results in special interactions as shown in fig. 5. Thereby it

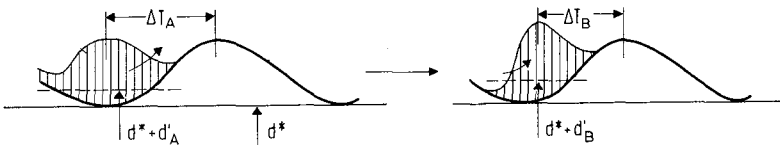


Fig. 5

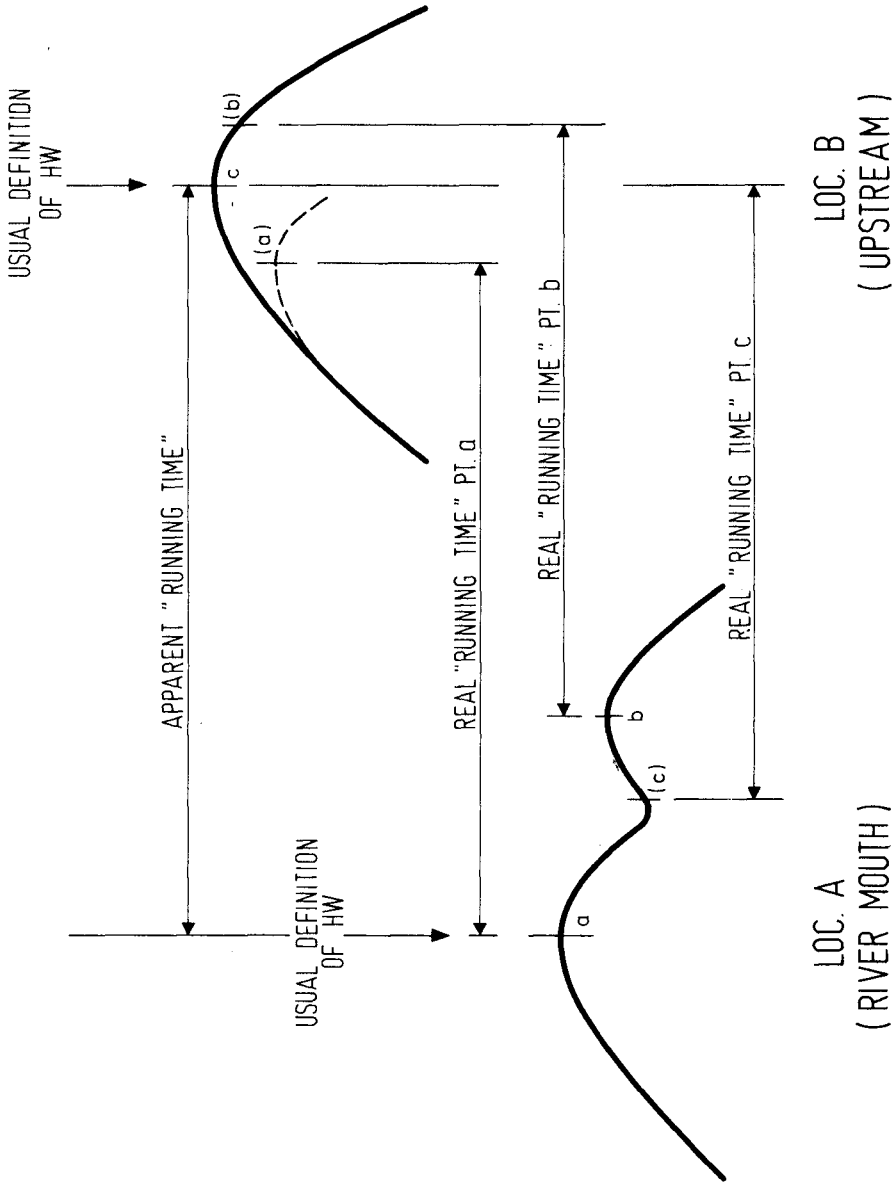


Fig. 6
Example Shape Variation of Tide Curves Between two Locations

becomes very difficult to identify real and comparable peak heights and peak velocity differences between two locations (fig. 6).

The interactions result in differing propagation velocities not only of the surge, but also of the tide waves. This may be illustrated by the shape of the surge curves on fig. 7. They occurred on Jan. 3, 1976 during the highest storm tide ever registered in the Elbe. The comparison of the shapes

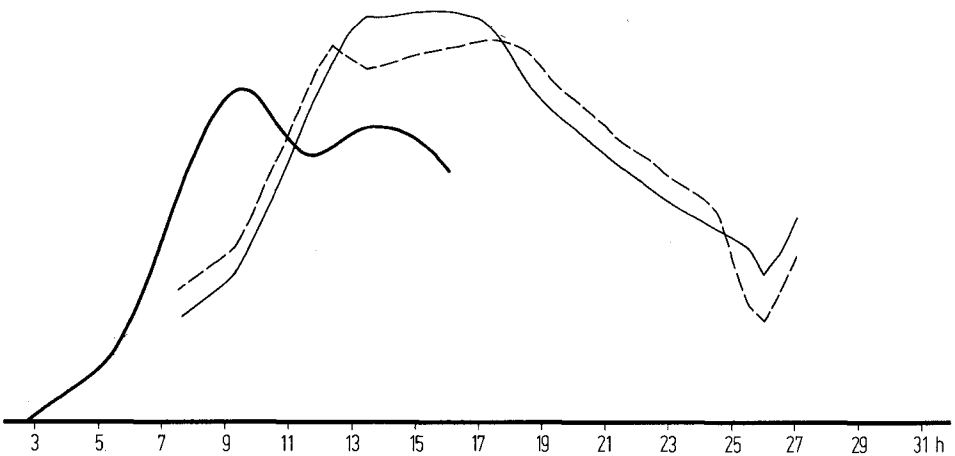


Fig. 7

- Thick solid line: surge wave in Cuxhaven
 Thin solid line : surge wave in Hamburg (101 km upstream),
 evaluated under the hypothesis of un-
 disturbed tide wave propagation
 Dashed line : surge wave in Hamburg, evaluated under
 the hypothesis that tide wave propaga-
 tion from C. to H. lasted 3 h instead
 of (normal) 4 h

give the hint that tide waves must run a lot faster than usual. As only small alterations of the surge curves are to be expected, best fit shifts have to be found. (This is one of the first results of an extensive computer investigation that is still in progress.)

ACCURACY OF PREDICTIONS

At the moment the "Hamburger Sturmflut-Warndienst" (WADI) is working on the basis of data from Borkum and Cuxhaven (tides) and Scharhörn (wind), fig. 1. The evaluation is based on the parametrisation of the surge curve as indicated on fig. 4. This allows predictions of the storm tide maximum in Hamburg 6 to 8 h in advance with an accuracy of

$$\begin{aligned} &\pm 25 \text{ cm in height} \\ &\pm 30 \text{ min. in time.} \end{aligned}$$

All values scatter within these borders.

Note: The results were not only obtained by hindcoasts, but also by about 20 forecasts since 1976.

As soon as the quantitative effects of interaction dynamics will be physically understood, they will be taken as a new basis for predictions of complete storm tide developments in tidal rivers.

DEVELOPMENT OF STORM TIDE HEIGHTS SINCE 1900

The analysis of more than 130 storm tides proved to give a suitable data collection to answer the question, why the heights of storm tides in tidal rivers of the southern North Sea increased so remarkably during the last decades. It is often presumed that this development is an effect of river improvements in Ems, Weser, and Elbe respectively.

For the purpose of finding the real reason, mean heights of high storm surges - each mean height representing about 4 to 12 events in a decade - were calculated. Their heights above mean high water level (MHW) varied considerably, with a resultant increase of about 80 cm from 1900 to 1975 (fig. 8). But variations as well as total increase in Hamburg can be explained by changes of surge curve parameters in Cuxhaven (101 km downstream). On fig. 8 only the influences of ALPHA and HEIGHT (see fig. 4) are taken into account. That yields to the conclusion that the increase in surge heights in Hamburg is almost completely an effect of higher surge curves in the Elbe estuary, i.e. an effect of stronger wind in a critical direction.

REFERENCES

- HARLEMAN, D.R.F. The Computation of Tides and Currents in Estuaries and Canals. Mass. Inst. of Techn., Hydrodyn. Lab., Techn. Bull. No. 16; Cambridge, Mass. 1969
- LEE, C.H.:
- PARTENSCKY, H.-E. Energy Dissipation in Tidal Estuaries. Proc. 15th ICCE, ASCE, New York, N.Y. 1977
- BARG, G.:
- SIEFERT, W.: Sturmflutvorhersage für den Tidebereich der Elbe aus dem Verlauf der Windstaukurve in Cuxhaven. Mitt. Franzius-Inst., Techn. Univ. Hannover, Vol. 30, 1968
- SIEFERT, W.: Über das Sturmflutgeschehen in Tideflüssen. Mitt. Leichtweiß-Inst., Techn. Univ. Braunschweig, Vol. 63 1978

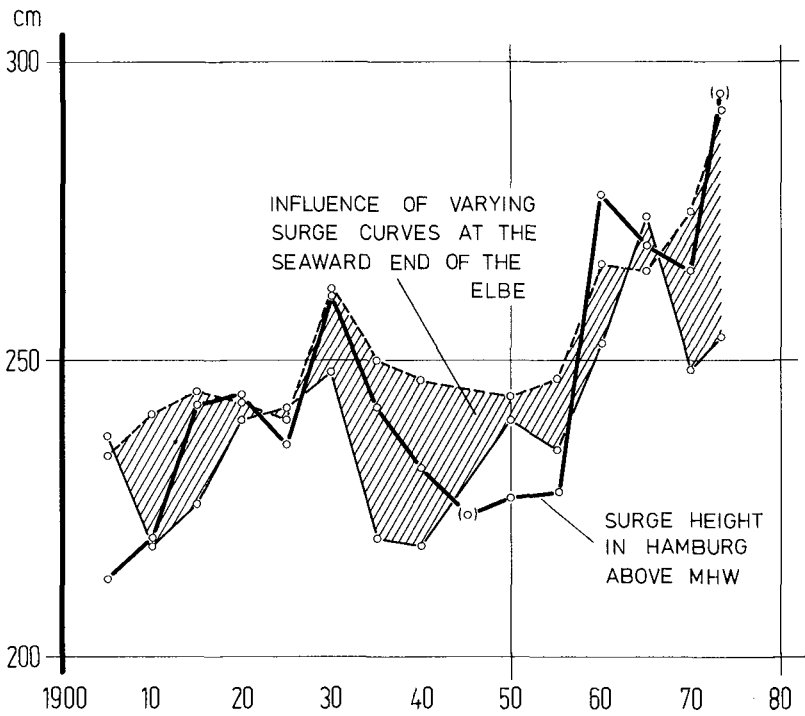


Fig. 8.

Development of Mean Heights of High Storm Surges in Hamburg, Compared with Development of Surge Curve Parameters in Cuxhaven

CHAPTER 58

STORM SURGE FORECASTING METHODS IN ENCLOSED SEAS

P.F. Hamblin

Applied Research Division, National Water Research Institute,
Canada Centre for Inland Waters, Burlington, Ontario, Canada

Storm surges in enclosed seas although generally not as large in amplitude as their oceanic counterparts are nonetheless of considerable importance when low lying shoreline profiles, shallow water depth, and favourable geographical orientation to storm winds occur together. High water may result in shoreline inundation and in enhanced shoreline erosion. Conversely low water levels are hazardous to navigation.

The purpose of this paper is to discuss the problem of storm surge forecasting in enclosed basins with emphasis on automated operational procedures. In general, operational forecasting methods must be based on standard forecast parameters, require a minimum of computational effort in the preparation of the forecast, must be applicable to lakes of different geometry and to any point on the shore, and to be able to resolve water level changes on an hourly basis to 10 cm in the case of high water level excursions associated with large lakes and less than that for smaller lakes. Particular physical effects arising in lakes which make these constraints difficult to fulfill are the reflections of resurgences of water levels arising from lateral boundaries, the stability of the atmospheric boundary layer and the presence of such subsynoptic disturbances as squall lines and travelling pressure jumps.

METHODS AND STUDY AREA

Interest in the study was centred on Lakes Ontario, Erie, and St. Clair as representative examples of large and intermediate sized lakes. Observations of past storm surges were collected from water level recordings over the period 1961 to 1972 at sites at the ends of these lakes (see Figure 1). Meteorological data, namely surface winds at Belle River on Lake St. Clair, and surface barometric pressures at a number of points around the lakes, as well as archived operational forecast elements from the U.S. National Meteorological Center primitive equation model, were gathered for the periods preceeding and during the observed occurrences of storm surges.

In the case of Lakes Ontario and Erie, surface barometric pressures were interpolated to the synoptic grid points of the numerical weather model by means of the nearest three surrounding stations. Longitudinal and transverse winds at the centers of these lakes were calculated from regression relations established between shipboard wind measurement and the various forecast elements computed by the numerical weather model by Feit and Barrientos (1974).

Unfortunately for Lake St. Clair neither the regression relations existed

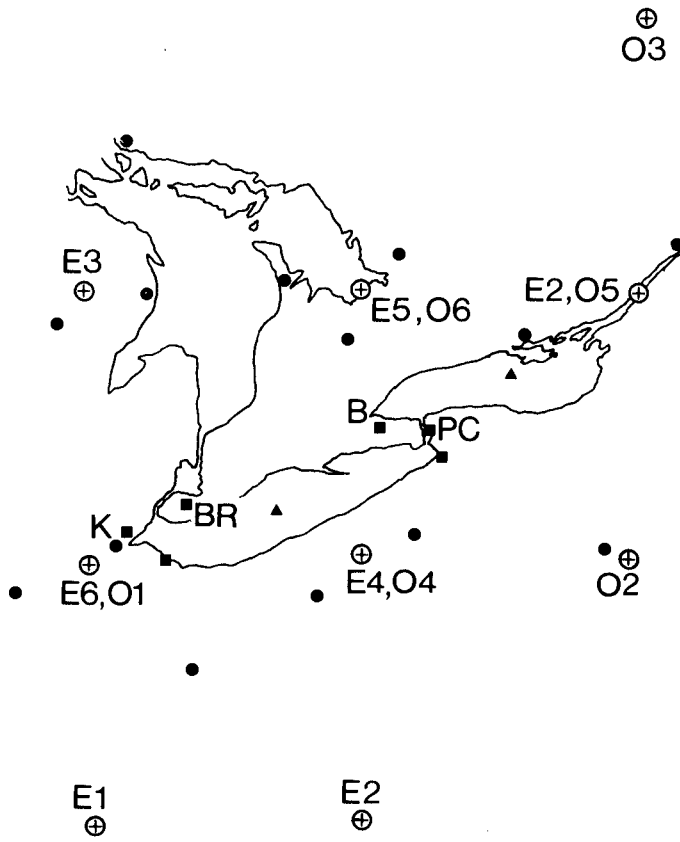


Figure 1. Study area and location of measurement points.

nor did the synoptic grid point pressures account for more than 3% of the water level variance. Relaxing somewhat our requirement for a standard automated forecast parameter, we chose the local hourly winds measured at Windsor Airport as an input parameter.

In Lake St. Clair, and in some cases in Lakes Ontario and Erie, the air-water temperature difference during the storm was computed from measured data.

STATISTICAL METHODS

The most widely employed statistical method for forecasting storm surges is the multiple regression method. It has the advantage of being simple to develop and straightforward to employ, and generally results in a minimum of computational effort in the preparation of the forecast. It has the disadvantage that a relatively long series of data, both water levels and meteorological data, must be available at the point of interest. For details of the development of the multiple regression relations given here the reader is referred to Venkatesh (1974). At the time this study was undertaken, routine forecast variables were available at six hourly intervals and at the synoptic grid points of the Canadian Meteorological Centre weather forecast model which is identical to the U.S. weather model in the Great Lakes region. Therefore, barometric pressure at the time of the surge and six hours previously at the synoptic grid points surrounding the lake were chosen as predictors.

In Lakes Erie and Ontario (also Huron) expressions of the type were developed,

$$\eta_i = A_i + \sum_{ijk} B_{ijk} P_{ijk} + \sum_j C_j \Delta T_j$$

where η_i = surge height at i hours after the time of the pressure forecast ($i = 0, , 5$);

P_{ijk} = surface pressure at grid point j,k and at lag, i , hr;

ΔT_i = air-water temperature differences over the lake at a lag of i hours; and $A, B,$ and C are regression coefficients.

An expression of the type

$$\eta = A + BV^2 + CV^2(\Delta T_0 + D\Delta T_1)$$

was developed for Lake St. Clair, where V^2 is the average of the past three hours of the components of wind squared in the maximum fetch direction. In general two to three dozen storms were used to establish the regression coefficients, A, B, C and D .

A more advanced statistical analysis was undertaken on the Lake St. Clair data only involving a Box-Jenkins transfer function model, (Box and Jenkins, 1970).

As basic input data for this technique, the two normal components of surface wind stress, τ_x and τ_y , corrected for surface stability and wind speed dependence of the drag coefficient (to be outlined later), were prepared for each of the 24 storms. First, the nonstationarity of both the input and output series was removed by first order differencing. Then a transfer function model of the type

$$\Sigma C_j \eta_{t-j} = \Sigma_j A_j \tau_{xt-t-j} + \Sigma_j B_j \tau_y \ t-t-j$$

was fitted to the data.

If at some future time, histories of the past water levels could be made available at the time of forecast, then they could be usefully employed in a statistical procedure known as one-step-ahead forecasting. An autoregressive and moving average model of the type

$$\Sigma C_j \eta_{t-j} = \Sigma_j A_j \tau_{xt-t-j} + \Sigma_j B_j \tau_y \ t-t-j + \Sigma D_j a_{t-j}$$

was determined, where a_t is the observed water level history. For a detailed discussion of these more advanced statistical techniques the reader is referred to Budgell and El-Shaarawi, 1978.

DYNAMICAL METHODS

In enclosed seas on account of the relatively weak flows associated with storm surges, the linearized shallow water equations on a plane of constant rotation ($2f$) serve as the basic mathematical model along with the usual boundary conditions.

$$\frac{\partial u}{\partial t} - fv = -g \frac{\partial \eta}{\partial x} + \frac{\tau_x - \tau_{bx}}{\rho h}$$

$$\frac{\partial v}{\partial t} + fu = -g \frac{\partial \eta}{\partial y} + \frac{\tau_y - \tau_{by}}{\rho h}$$

$$\frac{\partial \eta}{\partial t} + \frac{\partial hu}{\partial x} + \frac{\partial hv}{\partial y} = 0$$

where g is the acceleration of gravity, h is the equilibrium depth, and τ_b is the bottom stress.

The conventional method of integrating this equation set is to discretize the differentials and solve for the free surface, η , and the velocity components, u and v at each point in a horizontal grid and at each time step. The classical computation of this type was performed by Platzman (1963) on Lake Erie in a simulation of nine storm surges. Unfortunately, this form of the dynamical method is too demanding computationally for routine forecasts. In general a large difference exists between the time step required for numerical stability (several minutes) and the forecast time step (here, 6 hrs.)

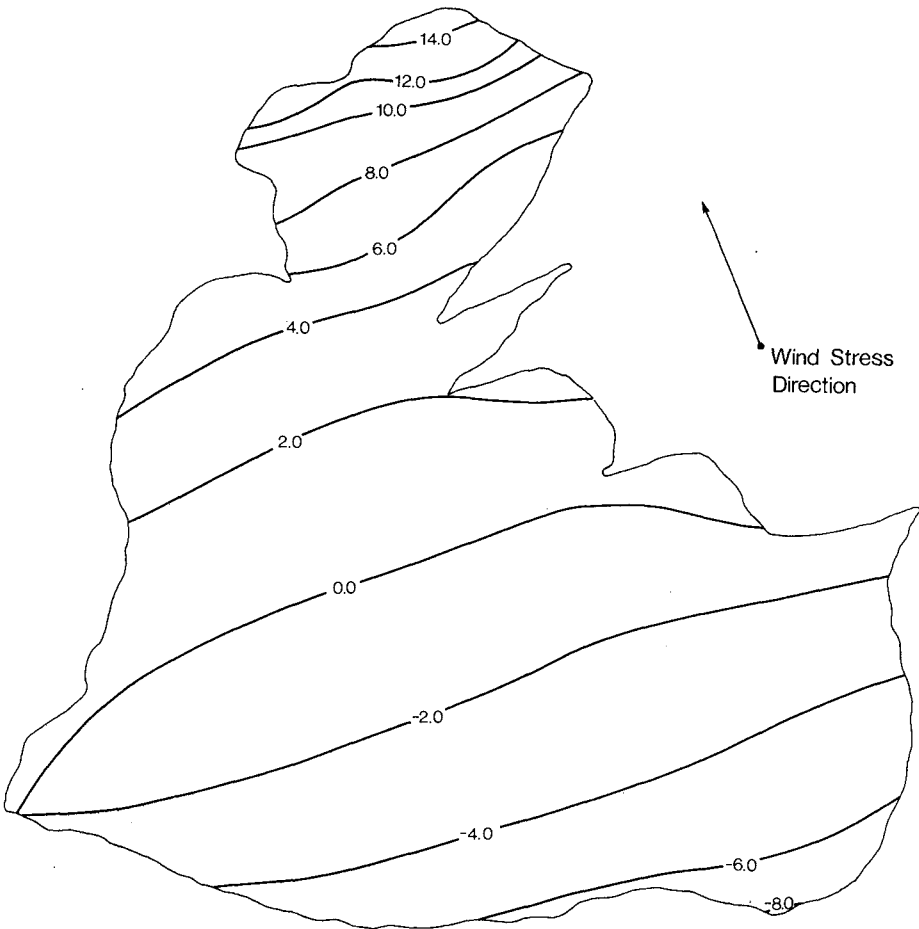


Figure 2. Free surface displacement (cm) for a steady wind stress of 1.0 dyne/cm for Lake St. Clair computed by the finite element method.

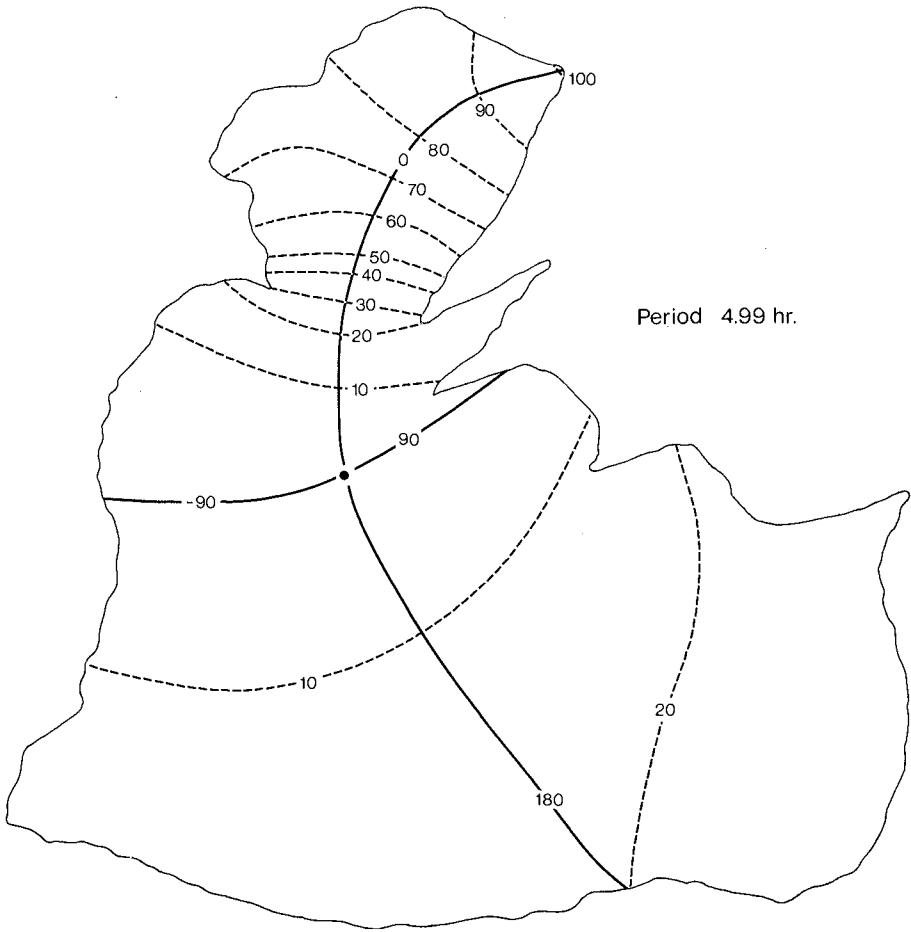


Figure 3. Free surface displacement (amplitude, ---, ———) for the fundamental gravitational seiche of Lake St. Clair computed by the finite element method.

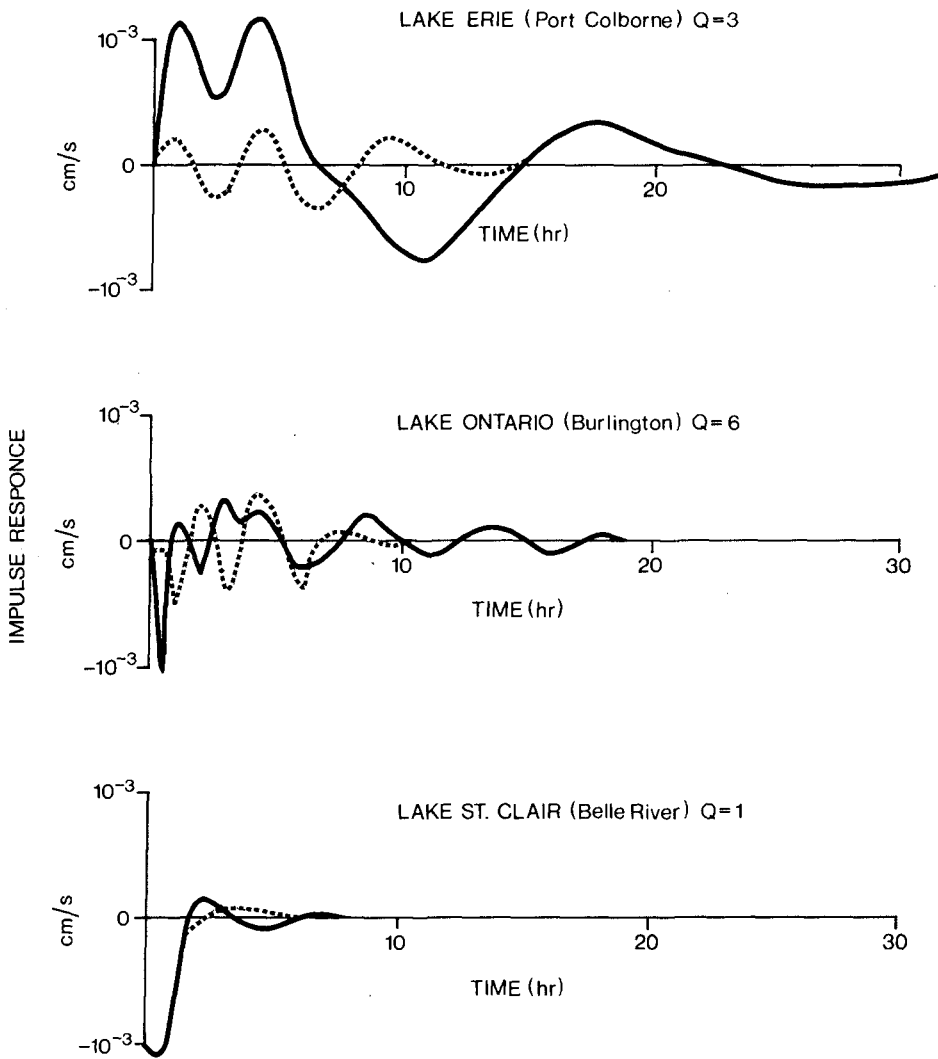


Figure 4. Impulse response functions computed by the spectral method. Lakes Ontario, Erie, and St. Clair, Q refers to the friction assumed.

An alternative approach which avoids the unnecessary routine computation of free surface and velocity components at points at which they are not needed is based upon the computation of the impulse response function or Green's function for the point of interest from a dynamical model such as equation (1). Once this function is determined, then the storm surge at a given point is simply the convolution of the impulse response function for that point with the forecast forcing function. If the weights of the impulse function are considered as regression coefficients, the two methods may be seen to be equivalent in computational effort. Thus the storm surge forecasting problem is reduced to the evaluation of one or more convolution integrals which are essentially digital filters in their discrete form.

Here we adopt the spectral method of determining the impulse response functions in which the impulse response function is expanded in terms of the steady solution and in terms of the lowest six to twelve free modes of oscillation. This number is based on power spectral analysis of water level fluctuations during storm surges which reveals that, in general, only the lowest modes of oscillation are excited at the points of largest storm surge excursion. The complex expansion coefficients are determined from least squares methods but essentially the amplitudes of the oscillation are determined from the steady solution of the free surface and the relative phases from the initial conditions. Both the steady state free surface displacement and the characteristic functions for the basin are computed by finite element methods. The spectral response method is developed in detail by Hamblin (1976) where it is applied to wind generated surges and by Hamblin and Hollan (1978) who applied this technique to excitation of surges by both barometric pressure gradients and winds.

A typical example of a finite element solution for the steady state free surface is given in Figure 2 and of a seiche solution in Figure 3. These solutions may be considered as components of the impulse response. Examples of the computed impulse response functions are given for three lakes of interest in Figure 4. The Q factor refers to the amount of frictional damping assumed in the bottom stress. Alternatively impulse response functions have been obtained for Lake Erie by Schwab (1978) by applying a unit wind stress to a time-stepping model for the first time step only. Results employing the two impulse response functions, determined by the spectral and the time stepping methods are in close agreement in Lake Erie.

SURFACE STRESS

In both the cases of the forecast winds in Lakes Ontario and Erie, and of the observed winds in Lake St. Clair, surface stress is taken as proportional to the product of the wind speed, and the wind vector, v .

$$\tau = \rho_a C_d |\vec{v}| \vec{v}$$

where the air density, ρ_a , is assumed constant and the drag coefficient, C_d , is assumed to be a function of wind speed after the empirical studies

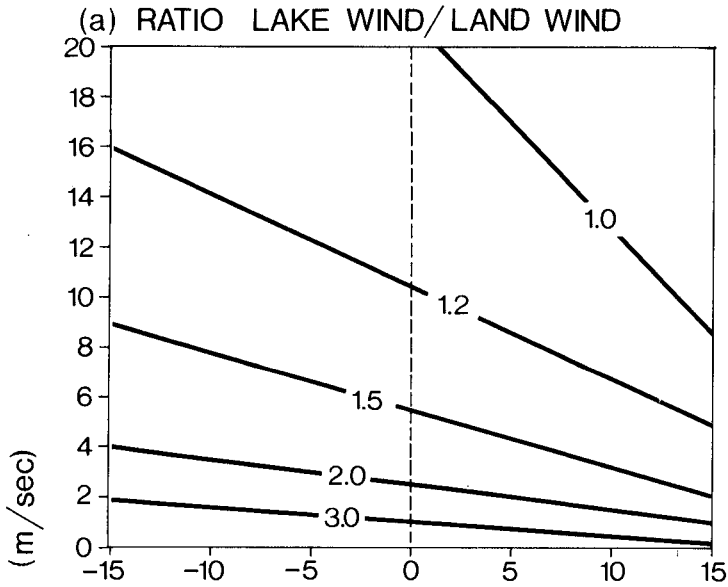


Figure 5a. Ratio of lake wind to land wind after Phillips and Irbe, 1978, as a function of wind speed and air-water temperature.

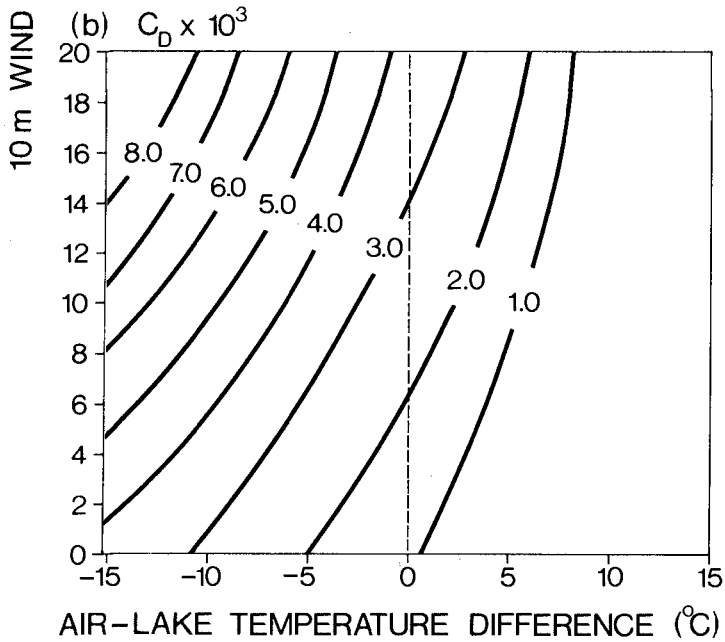


Figure 5b. Dependence of drag coefficient on wind speed and atmospheric stability employed in the study.

of Smith and Banke (1975) and a function of atmospheric stability of the form, $(1-AT_0)$ which has been employed by McClure (1970). The constant A, was arrived at by trial and error. The behaviour of C_d with wind speed and air-lake temperature difference is shown in Figure 5b. For neutral conditions C_d is 3.0×10^{-3} at a wind speed of 14 m/s which is a typical value employed for storm surge studies in enclosed basins. The effect of stability is to increase the effective drag coefficient under unstable conditions and to decrease it under stable conditions. In the case of Lake St. Clair, since the wind data were measured at the shoreline, experiments were performed employing an empirical relation for the overlake wind speed from the land wind which is based on fetch, wind speed, and atmospheric stability, (Phillips and Irbe, 1978). The behaviour of the wind ratio is shown in Figure 5a for the constant fetch case.

RESULTS

Statistical Methods

Multiple regression analysis of barometric pressures and air-water temperature difference accounted for approximately 60% of the variance of water level fluctuation as defined as the deviation from the undisturbed level before the storm and based upon dependent storms. The largest standard errors of the estimates of 20 cm occurred in the case of Lake Erie as a result of the higher excursions in that lake.

In the case of the smallest of the Great Lakes, Lake St. Clair, use of the six hourly temperatures and pressures at grid spacing separated by 380 km explained only several percent of the variation. Based on hourly wind observations one hour before the forecast time and air-water temperature differences the regression approach accounted for 54% of the variation of 24 dependent storms.

For Lake St. Clair a direct comparison was made between the three statistical techniques. The transfer function approach is evidently superior to the standard multiple regression approach, (Table 1), while the one-step-ahead forecast although not suitable for routine forecasting is the best of the three methods. It may be seen from the example shown in Figure 7 the regression method fails to predict the peak immediately following the main surge. It is thought that one reason for the improvement of the transfer function approach over the standard regression techniques is that it can readily account for resurgences or seiches which in certain cases such as Lake Erie form a significant portion of the storm surge response.

The Dynamical Method

An example of a dynamical forecast employing the spectrally determined impulse response function is compared to the standard regression method in Figure 6 for Lake Erie. In general both methods account for disturbances lasting for periods of half a day or more and that when seiches are present the dynamical model alone accounts for these

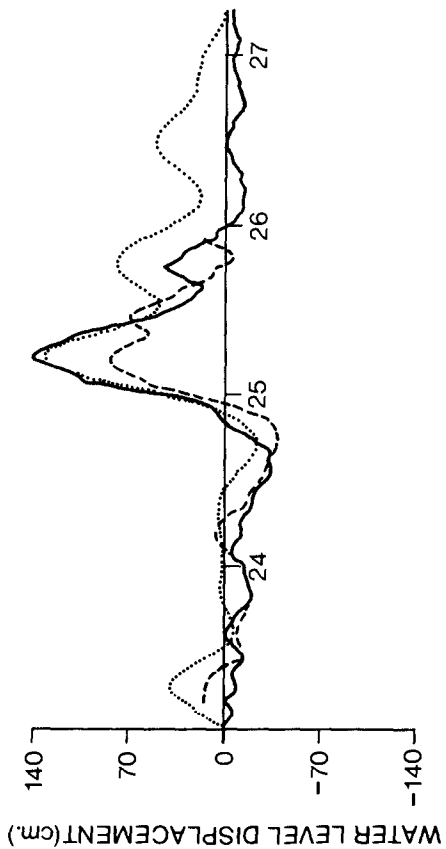


Figure 6. Simulation of a storm surge forecast. Port Colborne, Lake Erie, January 1972.

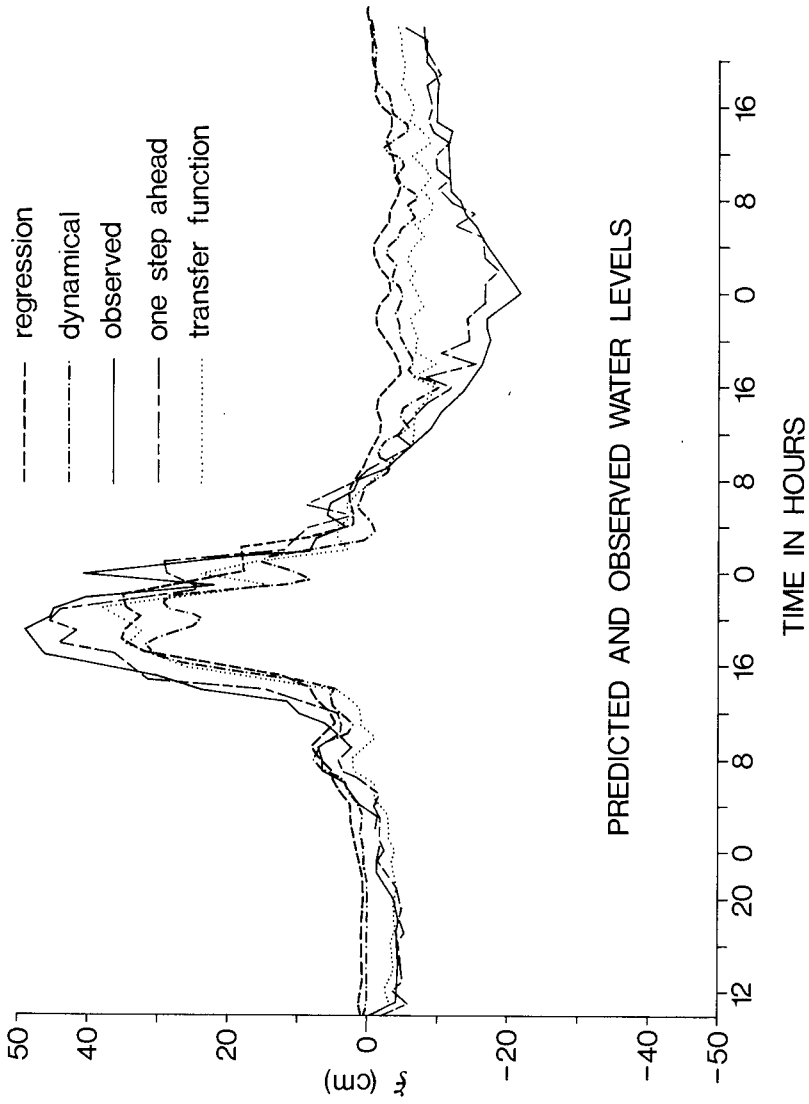


Figure 7. Comparison of various storm surge prediction methods, Lake St. Clair.

TABLE I

% Explained Variance of 24 Storms Lake St. Clair

(1) Dynamical	Unfiltered	49
	Filtered	54
(2) Regression		54
(3) Transfer Function		68
(4) Transfer Function plus one step ahead		90

seiches when the period of the seiche is longer than the six hour forecast period. Of course, neither method can account for seiches when the seiche period is less than the forecast period.

The comparison between the various methods has been examined in most detail for the case of Lake St. Clair. For the purpose of comparison, the storm exhibiting the largest excursion is shown in Figure 7. In this example the dynamical method underestimates the peak slightly more than the other methods. All methods except the one-step-ahead forecast fail to account for the negative surge occurring after the end of the storm. The dynamical method accounts for 49% of the variance of 24 storms. This compares favourably with the regression method when it is considered that the storms are dependent storms as far as the regression technique is concerned and in consideration that no attempt has been made to optimize the coefficients in the stability and wind speed dependence of the drag coefficient.

A characteristic feature of the Lake St. Clair storm surge is the gradual and continuous build up of water level during the storm. The source of these long term trends is not known but it is suspected that they may be due to enhanced river discharge during the storm. In order to remove this influence, both the water levels and winds were filtered by means of a high pass filter. The proportion of explained variance was augmented to 54% in the filtered dynamical forecasts. It may be noted that removal of trends is another reason for the superiority of the transfer function approach.

Finally, it is worth mentioning that correcting the land wind for the overlake effect after the empirical relations of Phillips and Irbe (1978) unexpectedly does not improve the dynamical forecasts. At high wind speeds the lake-land wind ratio approaches unity whereas at low winds, land winds are amplified considerably. Probably at low wind speeds the land winds are more representative of the local conditions on land than over the lake and thus fail to account for the surge.

DISCUSSION

In the regression study treatment of the air-water temperature difference as an independent predictor indicated that taking account of the stability of the atmospheric boundary layer over the water could improve the forecast. The effect of stability is greatest for the smallest lake studied, Lake St. Clair, where 5% of the variance is accounted for by the air-water temperature difference. Taking account of the stability in Lake St. Clair also improved the dynamical forecast results. Unfortunately it was impossible to account for this effect on the dynamical forecasts in the other lakes studied since the air-water temperature difference is not at present a standard forecast element.

Among the storms considered there were frequently cases of sudden changes in water level or shifted peaks in water level that could not be accounted for by either the dynamical or the regression methods.

It is likely that these effects are caused by spatially varying wind fields. In order to examine this method of generation of rapid fluctuations in water level occurring over several hours a simple analytical model was formulated for the generation of storm surges by a travelling stress field.

In a one-dimensional channel of constant depth, h , and length, L , the model equations,

$$\frac{\partial u}{\partial t} = -g \frac{\partial \eta}{\partial x} + \tau / \rho h$$

$$\frac{\partial \eta}{\partial t} + h \frac{\partial u}{\partial x} = 0$$

have the solution for a suddenly turned on uniform wind stress, τ ,

$$\eta(x,t) = -\sum_{m=1,3,5,\dots}^{\infty} \left[\frac{1}{\sigma_m^2} \frac{4\tau}{L\rho} [1 - \cos \sigma_m t] + \eta(0) \cos \sigma_m t + \frac{\partial \eta(0)}{\partial t} \frac{\sin \sigma_m t}{\sigma_m} \right] \cdot \cos \chi_m x$$

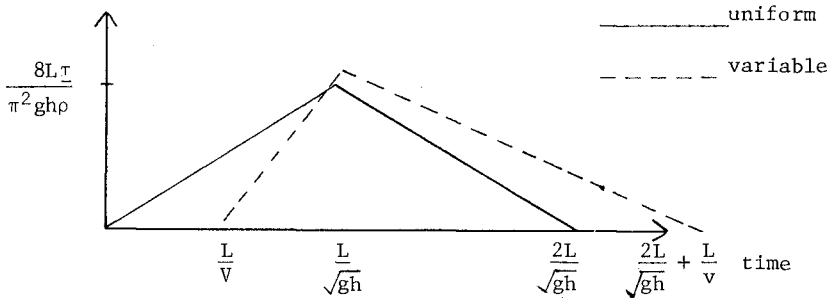
where $\sigma_m = \frac{\sqrt{gh_m \pi}}{L}$ and $\chi_m = \frac{\sigma_m}{\sqrt{gh}}$

In the case of a semi-infinite stress band travelling at a speed $v \neq \sqrt{gh}$, starting from a state of rest,

$$\eta(x,t) = \sum_{m=1,2,\dots}^{\infty} \frac{2\tau}{\sigma_m L \rho} \left[\frac{\cos \sigma_m t - 1}{\sigma_m} + \frac{\cos \chi_m vt \cos \sigma_m t}{2\sigma_m + 2\chi_m v} + \frac{\cos \sigma_m t - \cos \chi_m vt}{2\chi_m v - 2\sigma_m} \right] \cos \chi_m x$$

As seen in the accompanying figure in the case of a semi-infinite wind stress, taking account of spatial variation results in a more sharply rising surge than in the uniform case although the peaks occur concurrently when the wind is measured at the shoreline on the side of the lake opposite to the water level gauge.

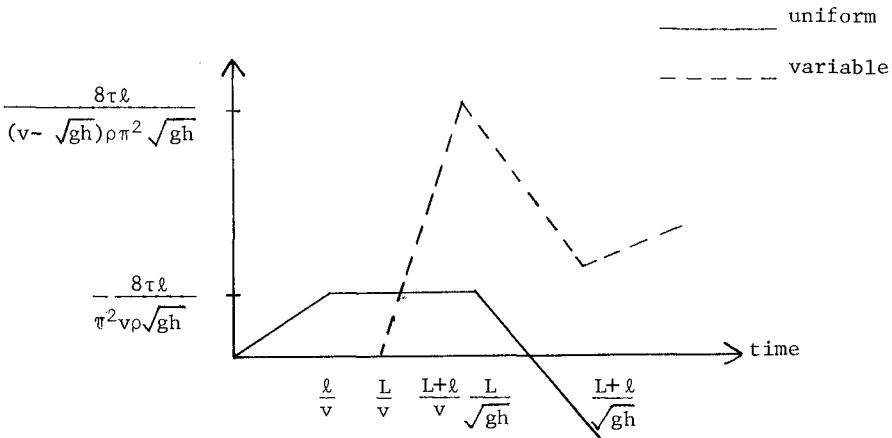
I Semi-infinite Stress Band Travelling at Speed, v



Downwind water level with respect to wind measured on upwind shoreline versus time.

Solutions for a finite stress field may be constructed from a superposition of the fundamental solutions presented above.

II Stress Band of Finite Width $l < L$



In the above example it may be seen that resonant excitation of the surge results in amplitudes much larger, of different shape and time of arrival than in the spatially uniform case.

CONCLUSIONS

Strictly speaking the results are not exactly comparable; for instance, only in the cases of dynamical forecasts in Lakes Erie and Ontario were true storm surge forecasts simulated. Nonetheless it is possible to draw a number of conclusions from the study.

Based on the applications of several statistical methods and a new dynamical approach to the simulation and forecasting of over three dozen storm surges in the Great Lakes reveals that in most cases all methods account for disturbances lasting for periods of half a day or more, that when seiches are present the dynamical and transfer function methods account for the seiche when the period of the seiche is longer than the forecast period and that these methods fail to account for seiches when the seiche period is shorter than the forecast period.

Horizontal variations in the wind field are particularly important in accounting for fairly rapid fluctuations in the water. Operational forecasts may be improved by a more detailed temporal and spatial resolution of the forecast data including the specification of such subsynoptic disturbances as squall lines and atmospheric pressure jumps. In particular, synoptic forecast surface pressures do not offer sufficient resolution in subsynoptic scale lakes such as Lake St. Clair.

Atmospheric stability is a significant factor in storm surge prediction in enclosed seas as it affects the surface momentum transfer, especially in smaller water bodies. At present the air-water temperature difference is not a standard automated forecast element. Wind speed dependence of the drag coefficient is also a significant influence. The question of correction of land winds for overlake modification is not yet resolved for storm surge forecasting in the Great Lakes but does not appear to improve the forecasts in the case of Lake St. Clair.

It is recommended that attention be given to the removal of long term trends in water levels and meteorological input data when developing and testing forecast relations and that trend removal may result in an improved forecast.

It is concluded from a comparison of various approaches to storm surge forecasting that dynamical and statistical methods give comparable errors. The fact that the discrepancy between the methods is less than between observation and forecasts suggests that the main source of error is due to uncertainties in the meteorological forecasts rather than to the failings of the methodology.

ACKNOWLEDGEMENTS

The author would like to thank W.P. Budgell and A. El-Shaarawi for many useful discussions and for allowing him to use some of their results in the preparation of this manuscript.

REFERENCES

- Box, G.E.P., and G.M. Jenkins. 1970. Time Series Analysis Forecasting and Control. Holden Day.
- Budgell, W.P., and A. El-Shaarawi. 1978. Time Series Modelling of Storm Surges on a Medium Sized Lake. Weather and Sea State Prediction. Proc. 10th Internat. Conf. on Ocn. Hydrodyn. Edited J.C. Nihoul. Elsevier, Amsterdam.
- Felt, D.M., and C.S. Barrientos. 1974. Great Lakes Wind Forecasts Based on MDS. Proc. 17th Conf. Great Lakes Research, pp 725-32
- Hamblin, P.F. 1976. Seiches, Circulation and Storm Surges of an Ice-free Lake Winnipeg. J. Fish Res. Bd. Can. Vol. 33, No. 10, pp 2277-2391.
- Hamblin, P.F., and E. Hollan. 1978. On the Gravitational Seiches of Lake Constance and Their Generation. Schweizerische Zeitschrift für Hydrologie.
- McClure, D.J. 1970. Dynamic Forecasting of Lake Erie Water Levels Report No. 70-250-H. Hydro-Electric Power Commission of Ontario. Research Div. Report.
- Phillips, D.W., and J.G. Irbe. 1978. Lake to Land Comparison of Wind Temperature and Humidity on Lake Ontario During the International Field Year for the Great Lakes. Report No. CL1-2-77. Atmospheric Environment, Fisheries and Environment Canada.
- Platzman, S.W. 1963. The Dynamical Prediction of Wind Tides on Lake Erie. Meteor Monogr. Vol 4, No. 26, 44p.
- Schwab, D.J. 1978. Simulation and Forecasting of Lake Erie Storm Surges. Unpublished Report Great Lakes Environmental Research Laboratories. N.O.A.A., Ann Arbor, Michigan.
- Smith, S.D., and E.G. Banke. 1975. Variation of the Sea Surface Drag Coefficient With Wind Speed. Quart. J. Roy. Meteor. Soc. 101.
- Venkatesh, S. 1974. The Development of Manual Techniques for the Real Time Prediction of Storm Surges on the Great Lakes. Unpublished Report Canada Centre for Inland Waters.

CHAPTER 59

Analysis of Storm Tide Waves

by

Volker Barthel*

ABSTRACT

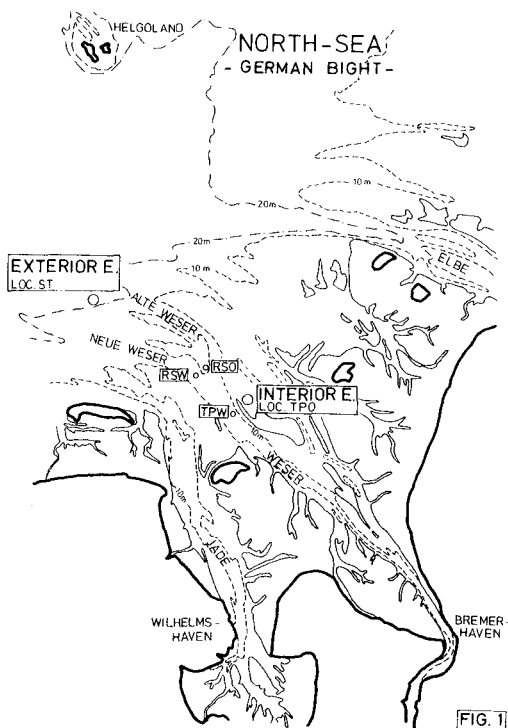
First results of a wave investigation program in the Outer Weser (German Bight of the North Sea) point out, that under storm conditions higher waves than computed by the normal prediction methods are possible in the exterior estuary. In the interior estuary higher waves occur mainly as a sort of swell. The influence of bad weather conditions on the probability of runs of waves with $H^* > H \frac{1}{3}$ is shown in two examples in comparison with a theoretical investigation.

INTRODUCTION

The importance and necessity of field investigations as far as waves are concerned has been underlined by experts again and again. Though there were several investigations in the deep water of the North Sea, in the wadden area and on sandy shores of islands one can't find hardly any in estuaries. There are given computation and prediction methods for straight shores with parallel contours or islands and shores with concentric circular contours, but there is hardly any example for shores, bars and sand-banks with deep channels between them and another bar following a few kilometers behind (1). The knowledge of the often very complicated wave systems in an estuary, i.e. the correlation of water level, tidal currents, waves,

orbital currents and morphological changes leads to an estimation of the effect of waves on structures and morphology (1) in the distinct regions of an estuary and vice versa. For this reason a field investigation program was started in 1975, which is carried out by the Wasser- und Schifffahrtsamt Bremerhaven, an office of the Federal Waterways Administration, and is supported by the Federal Ministry of Research and Technology. FIG. 1 shows a part of the Weser estuary with the locations ST, RSO, RSW, TPO and TPW. The following investigations are planned on this locations in detail:

* Dipl.-Ing., Wasser- u. Schifffahrtsamt Bremerhaven,
2850 Bremerhaven, Federal Republic of Germany



- a. alteration of significant data of waves entering the estuary
- b. distribution of wave energy behind reefs and bars
- c. influence of waves on the morphological shape of the bottom and - vice versa - the influence of morphology on the waves
- d. determination of design data for all structures
- e. influence of waves on the assignment of ships and particularly of long-period-waves on the lurch of deep-drawing ships with a small keel-clearance.

STORM TIDE WAVES

On the 3rd of January, 1976, the wind in the German Bight grew from 16 m/s to nearly 30 m/s (Beaufort 11). The direction changed from 175° (S) to 295° (WNW). The water level at gauge ALTE WESER rose to NPH + 9.10 m, while the mean Low Water (MLW) is NPH + 6.32 m.

STORMTIDE ON JANUARY 2nd/3rd 1967

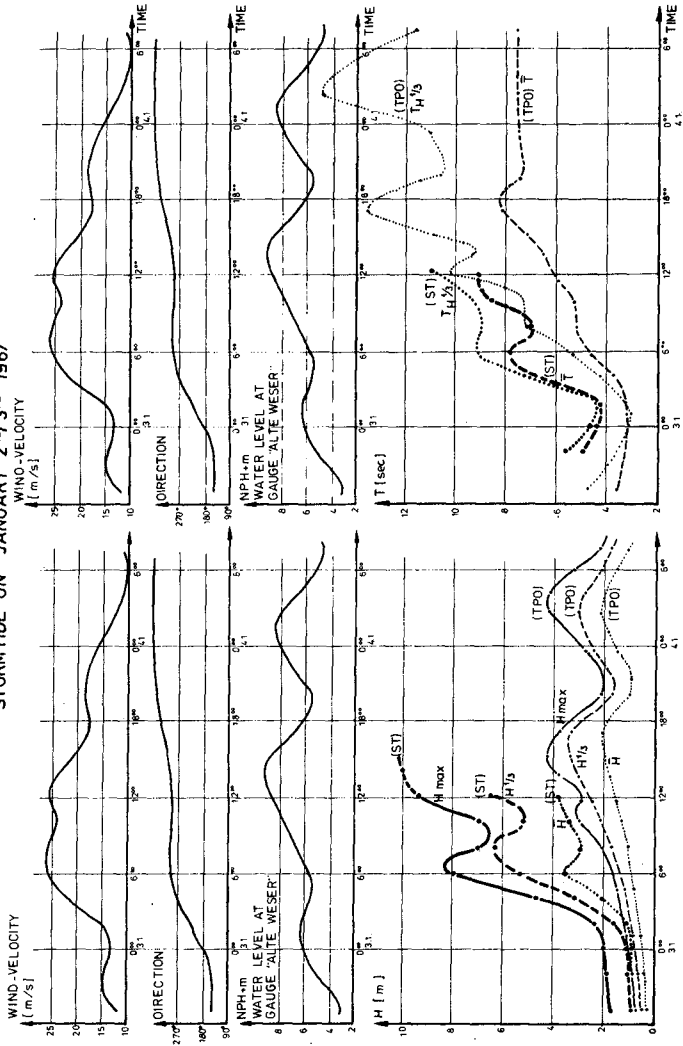
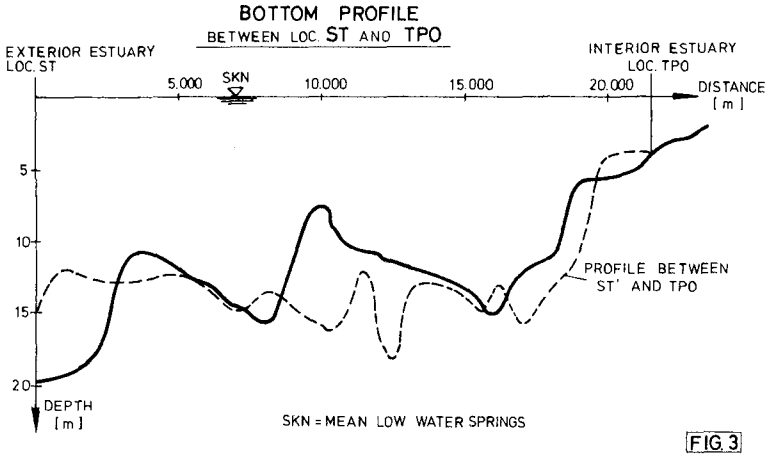


FIG. 2

Though the wave buoys and gauges were not yet installed completely we succeeded in gaining some data at the locations ST and TPO. A third wave gauge failed by collision with a drifting ship.

Loc. ST lies at a water depth of about 22m. It is to record the waves coming from the open sea and produces prototype data for the exterior estuary. Loc. TPO lies in front of a sand-bank at about 4m water depth and represents the interior estuary.



In FIG. 2 the measured values are plotted as a function of time. You can see the mean and significant wave height H and $H 1/3$ in the exterior, growing with increasing wind-velocity very quickly and becoming smaller with decreasing wind-velocity. Unfortunately the recorder broke down at 3.00 p.m. because the measuring range wasn't expected to be so wide. The mean and significant periods T and $T 1/3$ show nearly the same attitude dependent on wind-velocity.

With a time-lag of about two hours the mean and significant wave heights H and $H 1/3$ come to their maximum values in the interior estuary. A second peak was registered on the 4th of January at about 3.00 a.m. It is obvious that in this case the height follows the water depth during a decreasing wind-velocity. Striking is the strong increase of the periods $T_H 1/3$ in the interior estuary up to values of 16 sec. But I'll come back to this phenomenon later on.

ALTERATION OF HEIGHTS AS A FUNCTION OF WIND - VELOCITY AND WATER DEPTH

As there had been a lot of measurements in the meantime, the slope of wave height, wind-velocity and water depth for this region could be investigated more thoroughly. For this purpose records

at an almost coincident water level or wind velocity were combined. FIG. 4 shows, that in the interior estuary the correlation between \bar{H} respectively $H^{1/3}$ and the water depth ($r= 0.85 - 0.87$) is much better than in the exterior ($r= 0.46 - 0.52$).

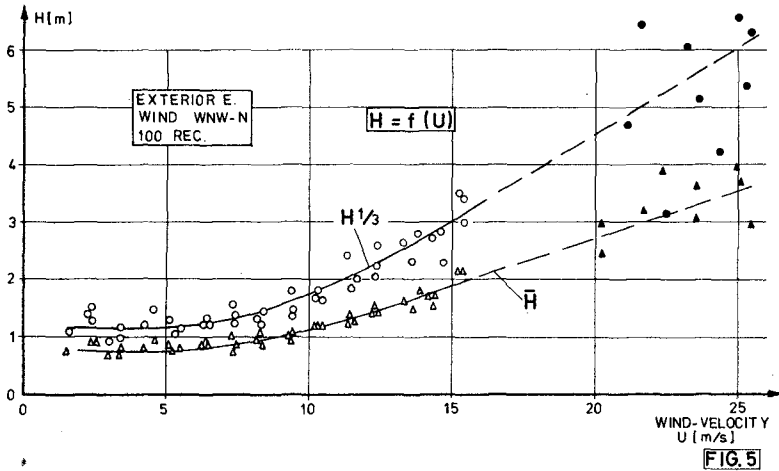
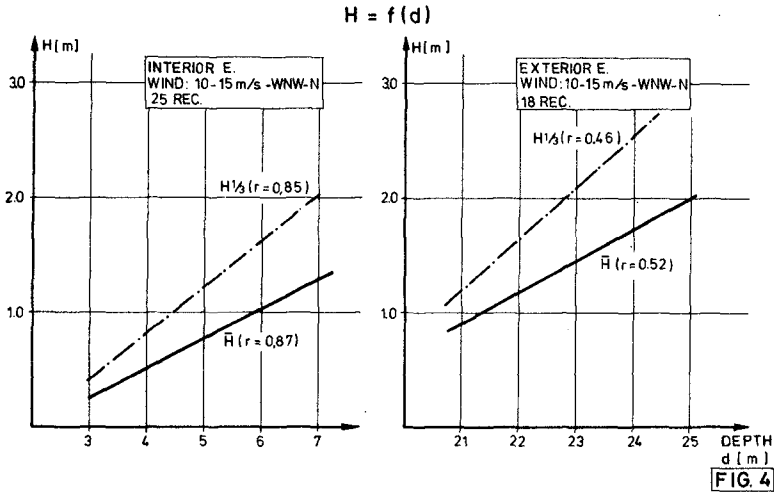
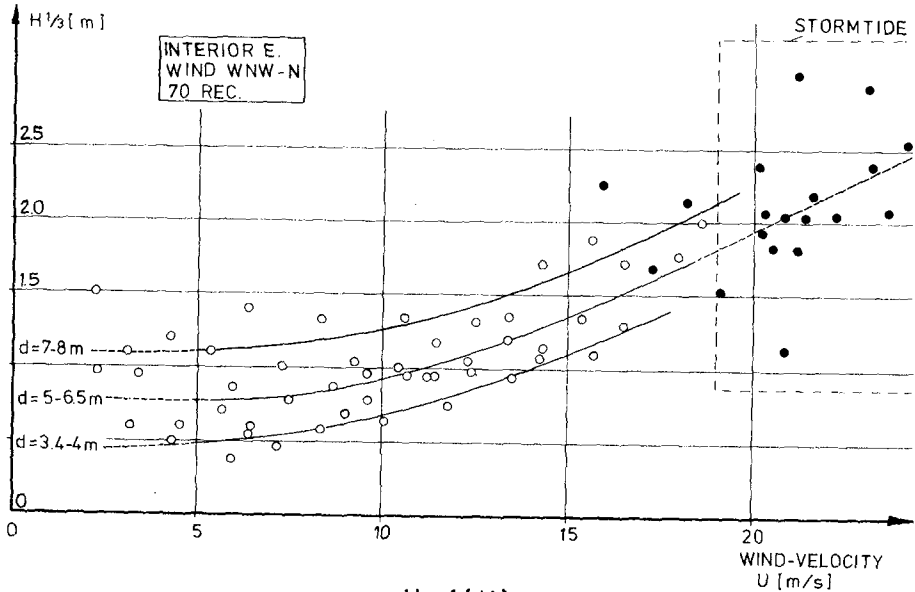
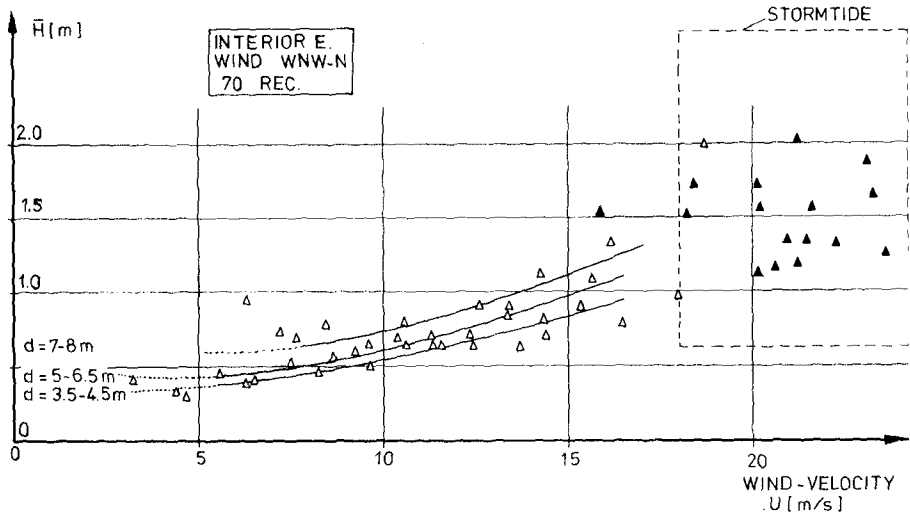


FIG. 5 shows a good correlation between heights and wind-velocity for the exterior e. as it is to be found in literature --- mostly as a linear slope. The values obtained in the storm tide ($U=20 - 25$ m/s) fit this drawing.



$H = f(U)$

FIG 6

In FIG. 6 the same values for the interior e. are plotted, split into single graphs for \bar{H} and $H_{1/3}$. In this case the values can be clearly arranged in groups with different water depths, showing that the depth-dependency is more important than in the exterior estuary.

ALTERATION OF WAVE PERIOD AND STEEPNESS

An astonishing fact gave the strong increase of the wave periods in the interior during the storm tide. The significant period $T_{1/3}$ came up to more than 15 s. The evaluation of more data in this field gave the latest findings, that waves in extraordinary weather conditions occur mainly as swell in this region. With the simplified assumption, that

$$L = \bar{T}^2$$

a mean wave length of 80 m is to be found, which may have a dangerous influence on deep-drawing ships in a narrow channel.

One should believe that - similar to a tidal wave - waves coming from the open sea into an estuary become steeper and shorter by shoaling, refraction and diffraction. Just the opposite seems to be true in this case. After evaluating a lot of additional records it could be pointed out, that as a general principle periods become longer during the penetration of waves into this estuary, though there are deep channels between the shoals. The local wind influence seems to be of subordinate importance.

FIG. 7 shows the alteration of the significant wave period $T_{1/3}$ and the so called steepness factor

$$s = \frac{\bar{H}}{g \cdot \bar{T}^2}$$

for two groups of waves with different height.

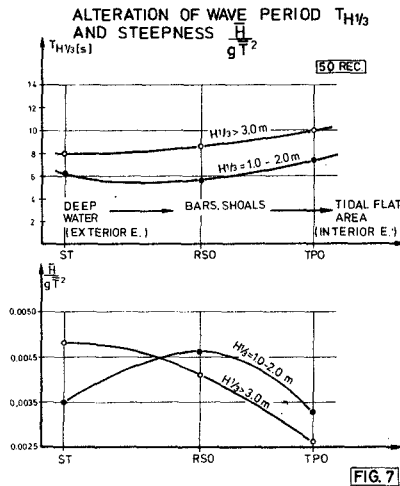
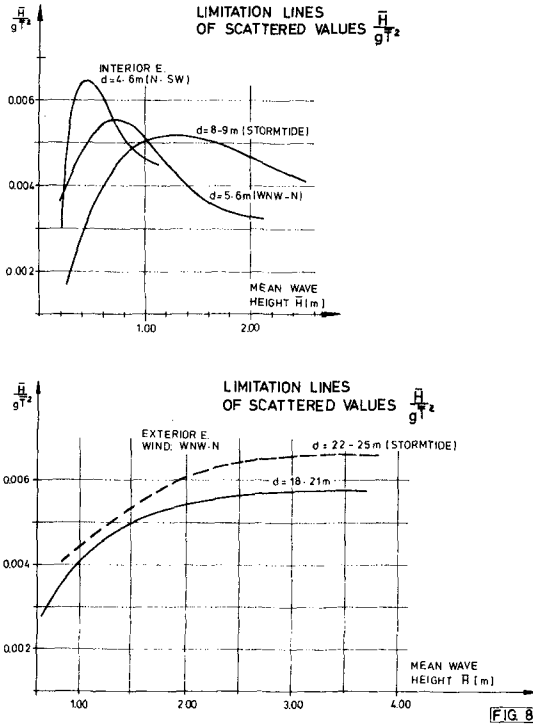


FIG. 7

You can see that the periods increase and the steepness factor becomes small with decreasing water depth, i.e. while the waves approach the interior estuary. The same phenomenon was detected by SIEFERT (10) with measurements in the wadden sea of the Outer Elbe. (Loc. RSO in this case lies on a bar where breaking of waves occurs at a smaller water depth (Fig. 7).



The increasing period of waves penetrating the interior estuary necessarily reduces the steepness factor s with a constant or decreasing height. While in the exterior estuary during a high wind velocity and water depth (that is for example during a storm tide) the steepness increases and comes to a constant value (limitation line of the scattered values of $s = \frac{\bar{H}}{gT^2}$);

the scattering of values with a larger water depth in the interior e. is wider, the maximum values however are smaller. The values for a different wind-direction are plotted in comparison to show the irritability of wave climate against the different factors of influence. Obviously the steepness in the interior e. decreases with increasing mean wave height, dependent on wind-direction

and therefore the fetch-length too. This fact seems to be important for the design criteria of structures.

Alteration of wave parameters

FIG. 9 shows the mean period \bar{T} as a function of the mean wave height \bar{H} . Apart from the differences between the interior and exterior e. on normal conditions one can see, that a storm tide causes a considerable alteration of wave characteristics. By this chance it becomes obvious that abnormal wind conditions evoke shorter periods and steeper waves in the exterior, while in the interior just the opposite is true.

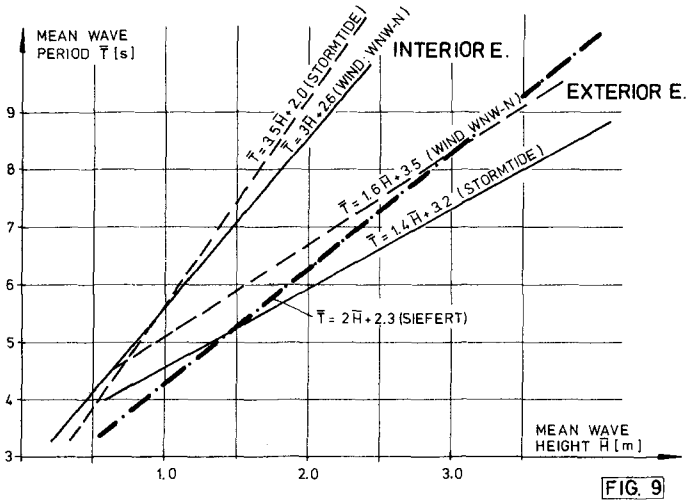


FIG. 10 shows the mean ratio of periods and height in the interior and exterior e. during normal and storm conditions.

TABLE 1 (FIG. 10)

		WAVE HEIGHT				
		AVERAGED VALUES	\bar{H}	$H_{1/3}$	$H_{1/10}$	H_{max}
INTERIOR ESTUARY	FROM 100 RECORDS:		1	1.47	1.75	1.98
	STORM TIDE VALUES: (44 REC)		1	1.55	1.85	1.89
EXTERIOR ESTUARY	FROM 100 RECORDS:		1	1.50	1.86	2.14
	STORM TIDE VALUES: (16 REC)		1	1.55	1.95	2.30

WAVE PERIOD

INTERIOR ESTUARY	}	AVERAGED VALUES	\bar{T}	$T_{H1/3}$	$T_{H1/10}$	T_{Hmax}
		FROM 100 RECORDS:	1	1.27	1.30	1.29
EXTERIOR ESTUARY	}	STORM TIDE VALUES:	1	1.46	2.21	1.34
		(44 REC)				
EXTERIOR ESTUARY	}	AVERAGED VALUES				
		FROM 100 RECORDS:	1	1.12	1.12	1.57
EXTERIOR ESTUARY	}	STORM TIDE VALUES:	1	1.11	1.09	1.08
		(16 REC)				

In a few words:

Interior: The ratio of the mean to the sign. periods increases at a storm tide very much. That is a hint to the transformation into swell. The ratio of the height doesn't change so much; maximum height decreases.

Exterior: Wave periods become smaller, the waves therefore become steeper. The ratio of mean to significant respectively maximum height increases. These results fit the frame of the words said before.

MAXIMUM WAVE HEIGHT

Because in the Outer Weser no investigations in the wave field had been carried out for a long period, the results of the storm-tide records were astonishing and startling at the same time, especially because the high wind-velocities had had only a short-time-occurrence and the direction had changed permanently. After Mc Cowan a theoretical maximum wave height (for deep water) $H_{max} = 0.78 d = \sim 19 \text{ m}$ ($d = 24 \text{ m}$) is possible. But waves with higher wind-velocities in the German Bight with its limited water depth are to be considered as shallow water waves and therefore wall turbulence friction takes effect in addition to the free turbulence friction. Wave energy and height are reduced by this. DRAPER (3) has predicted (for this region of the North Sea) a maximum wave height of 17 m under conditions of a 50-year-design storm with a duration of 12 hours.

If you consider a design storm with

wind-velocity: $U = 40 \text{ m/s}$

duration: $t = 5 \text{ hours}$

fetch-length: $F = 250 \text{ km}$

effective fetch: $w = 150 \text{ km}$

different prediction methods for the German Bight result in a significant wave height

of

$$H_{1/3} = 7.0 - 10.5 \text{ m (8)}.$$

With the revised prediction method of BRETSCHNEIDER (2) for shallow water under the above mentioned conditions a significant wave height of

$$H_{1/3} = 6.70 \text{ m was evaluated for the exterior e.}$$

and with the ratio of

$$\frac{H_{\max}}{H^{1/3}} = \left(145 \frac{g \cdot d}{U^2} \right)^{0.1} \pm 10\% \quad (2)$$

a maximum wave height of 10.0 m is possible.

ROLL (6) deducts a maximum wave height up to 8.0 m from observations on lightships. During the storm tide of January 3rd a significant wave height of

$$H_{1/3} = 6.72 \text{ m was registered in}$$

the exterior estuary until the instrument failed. The max. wave height, which could be read in the incomplete record, was

$$\underline{10.0 \text{ m}} \text{ (end of registration width).}$$

According to the steepness of the wave and its incomplete period one could estimate its height of about

$$\underline{12 - 13 \text{ m.}}$$

The maximum height in the interior estuary can hardly be predicted by well-known methods, because the ratio of

$$\frac{H_{\max}}{d} = f(d, \text{topography}),$$

which is a function of water depth and surrounding topography (10), is very complicated in this area.

The highest possible propagating wave is after KISHI (5)

$$H_{\max} = 0.9 d \quad \text{for } d < 0.1 L$$

$$H_{\max} = 0.146 d \quad \text{for } d > 0.4 L$$

(with a parabolic change between the two borders)

For normal waves with $L = \bar{T}^2$:

$$H_{\max} = 0.9 d \quad \text{for } d < 0.1 T_{H_{\max}}^2$$

$$H_{\max} = 0.146 T_{H_{\max}}^2 \quad \text{for } d > 0.4 T_{H_{\max}}^2$$

and with the given ratio of mean to significant period $\bar{T}/T_H^{1/3}$ respectively max. period $\bar{T}/T_H^{1/3}$ the max. height becomes

$$H_{\max} = 0.9 d \quad \text{for } d < 0.18 \bar{T}^2$$

$$H_{\max} = 0.26 \bar{T}^2 \quad \text{for } d > 0.72 \bar{T}^2$$

The theoretical max. height $H_{\max} = 8.4 \text{ m}$ for gentle slopes.

The comparison between normal and storm conditions in FIG. 12 turns out, that with the investigated wind-directions a higher probability of consecutive waves $H^* > H_{1/3}$ is not to be found. Its obvious that in the interior e. shorter runs of waves occur under bad weather conditions. This seems to be important for the design of all structures in this area.

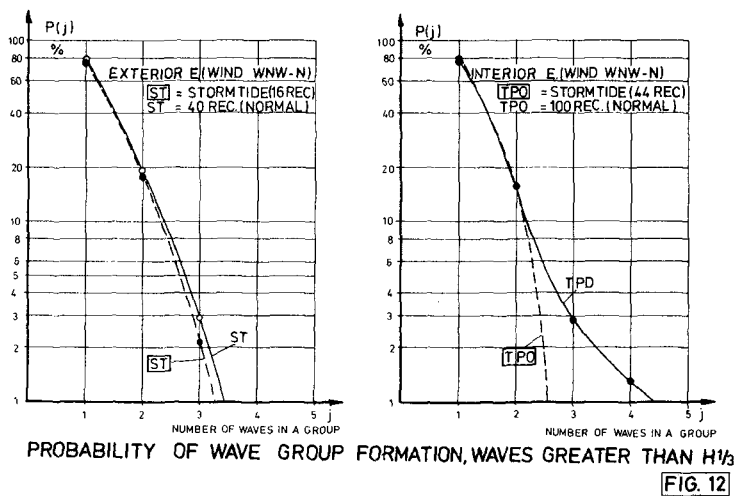


FIG. 12

CONCLUSIONS:

The results of the relatively short measurements during the storm tide in comparison with records under more normal conditions can be comprised as follows:

- The wave heights in the exterior e. are mostly wind-dependent, while the local wind-influence in the interior e. is subordinate to the water depth.
- After wind-velocities more than 15-20m/s the higher waves in the interior e. occur with long periods changing to a sort of swell. Therefore there is a certain danger for deep-drawing ships, which has to be investigated more thoroughly. Max. wave heights are influenced by the reefs and bars in front of the interior e. and are reduced at a rate of about 50 - 60 %.
- The max. heights in the exterior e. came up to a value of more than 10.0 m already in a short storm. Heights of more than 15.0 m are not impossible.
- The wave parameters change with a different range in unusual weather conditions according to the above mentioned facts.
- Runs of waves with $H^* > H_{1/3}$ don't occur more often under bad weather conditions than normally. In the exterior e. the distribution fits a theoretical one; in shallower water it is nearly the same as in the adjacent area of the Outer Elbe.

In the present investigations the influence of tidal currents upon

According to the measurements in question this height cannot be found in the interior estuary, because a considerable transformation of energy occurs on the reefs and bars. During the storm tide the measured max. wave height read

$$H_{\max} = 4.05 \text{ m with a period of } 18.2 \text{ s.}$$

Later on we gained records after two hours with wind from WNW with 20 m/s, in which the max. height was 3.5 m with a period of 12s.

CONSECUTIVE HIGH WAVES

In addition to the highest water level and max. or significant wave height a certain dynamic strain by vibration or perhaps resonance caused by a run of waves of certain height can be important for the design of structures in coastal areas. Because of the unexpected high waves it was of great interest, to analyse the records of the storm tide and those under normal conditions in this regard. The problem has already been treated numerically by GODA (1970) (4) for wide spectra. Evaluations of field data under storm conditions were done by RYE (1975) (7). SIEFERT (1976) (9) determined the probability of consecutive high waves for an adjacent area of the Outer Elbe with its wadden sea. A comparison of the results is plotted in FIG. 11.

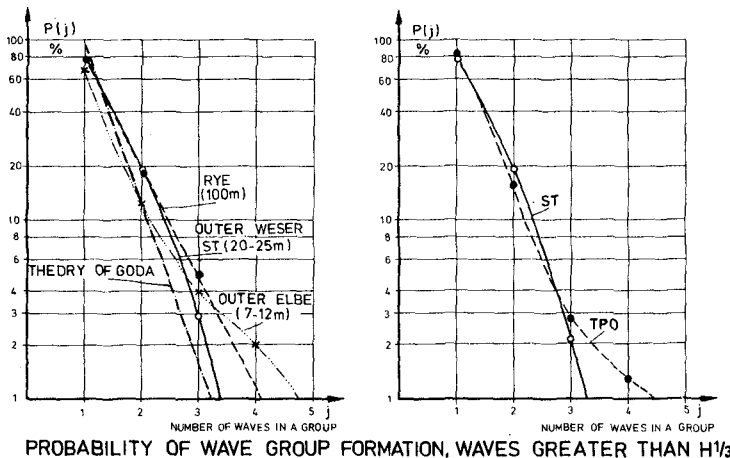


FIG. 11

The drawing in semi-logarithmic scale shows, that the probability of groups of waves greater than the significant wave height $H_{1/3}$ in the exterior estuary best fits the theory of GODA (4). In the computation of 40 records there was no run of more than 3 consecutive waves. The probability in the interior e. shows a good correspondence with the results in the Outer Elbe.

the wave parameters has been neglected. It will be the task for the next time to find out this influence by measurements for distinct regions of the Weser estuary.

REFERENCES:

- 1) Barthel, V.: Stability of Tidal Channels Dependent on River Improvement, CEC 1976, Honolulu, Hawaii, ASCE, New York, 1977
- 2) Bretschneider, Ch.L.: Wave Forecasting Relationships for the Gulf of Mexico, Beach Erosion Board, Technical Memorandum No. 84, 1956
- 3) Draper, L.: Extreme Wave Conditions in British and Adjacent Waters, Proceedings CEC 1972, Vancouver, ASCE, New York, 1973
- 4) Goda, Y.: Numerical Experiments on Wave Statistics with Spectral Simulation. Report of the Port and Harbour Research Institute. Vol. 9, Nr. 3 Japan 1970
- 5) Kishi, T.: The Possible Highest Gravity Waves in Shallow Water. Coastal Eng. in Japan, Jap. Society of Civ. Eng., Tokyo 1959
- 6) Roll, H.-U.: Die Meereswellen in der südlichen Nordsee (aufgrund von Wellenbeobachtungen Deutscher Feuerschiffe), Deutscher Wetterdienst, Seewetteramt, Einzelveröffentlichung Nr. 8, Hamburg, 1956
- 7) Rye, H.: Wave Group Formation Among Storm Waves. Proceedings CEC 1974, Copenhagen, ASCE, New York 1975
- 8) Schüttrumpf, R.: Über die Bestimmung von Bemessungswellen für den Seebau am Beispiel der südlichen Nordsee, Mitt. des Franzius-Instituts für Wasserbau und Küsteningenieurwesen der T.U. Hannover, Heft 39, 1973
- 9) Siefert, W.: Consecutive High Waves in Coastal Waters, Proceedings CEC 1976, ASCE, New York 1977
- 10) Siefert, W.: Über den Seegang in Flachwassergebieten, Mitteilungen des Leichtweiß-Instituts für Wasserbau der TU Braunschweig, Heft 40, 1973
- 11) Wiegel, L.: Oceanographical Engineering, Prentice Hall Inc., Englewood Cliffs, N.Y. 1964

CHAPTER 60

COASTAL FLOOD SIMULATION IN STRETCHED COORDINATES

by

H. Lee Butler
Wave Dynamics Division, Hydraulics Laboratory
USAE Waterways Experiment Station
Vicksburg, Mississippi

ABSTRACT

Coastal flooding in developed areas can be catastrophic. As an essential element in coastal water level prediction, a two-dimensional numerical model of long period wave behavior is presented. The time dependency is treated implicitly for cost-effective simulation of coastal flooding from hurricane surges or other hydrodynamic phenomena such as extratropical storm surges, tides, tsunamis, etc.

An important feature of the model is use of a coordinate transformation in the form of a piecewise exponential stretch. Such a technique permits simulation of a complex landscape by locally increasing grid resolution and/or aligning coordinates along physical boundaries.

The model is applied to Galveston Bay, Texas, for storm surge and coastal flooding from Hurricane Carla 1961. Verification for the Galveston area was accomplished by using physical model data from simulations of free gravity waves (tide and design surge). Subsequent hindcasting of Carla produced good agreement between observed and computed surges with a mean absolute error of 0.18 m for peak elevations.

INTRODUCTION

Reliable prediction of coastal inundation from tidal or hurricane surge is extremely complex and is usually complicated by the presence of channels, barriers, bays, and highly variable bathymetry and topography which redistribute water flooding inland from the open sea. The Corps of Engineers, and in particular, the Waterways Experiment Station (WES), have had to address the problem of providing reliable estimates of coastal flooding in order to make sound engineering decisions regarding the design, operation, and maintenance of various coastal projects. Physical models have been used in the past to simulate free gravity surge, however they have the disadvantage of not being able to effectively simulate wind effects. The need of a more generalized numerical model for treating the flooding from storm surges (Wanstrath et al., 1977) in coastal areas has therefore been apparent for some time. Many two-dimensional storm surge models have been presented in the literature during this decade. Each model has exhibited certain advantages but most models have been developed for application to specific locations. The model presented here has been under development at WES (Butler and Raney, 1976; Butler, 1978) for use in storm surge applications as well as other applications where shallow water wave equations can be employed.

The most popular approach to solving the system of differential equations describing storm driven surges has been the application of finite difference techniques (Reid and Bodine, 1968; Leendertse, 1967, 1970, 1971; Pearce, 1972; Reid et al., 1975; Wanstrath, 1976). The model described herein, known as the WES Implicit Flooding Model (WIFM), employs the implicit solution scheme developed by Leendertse (1967). Dependent variables of the centered, alternating-direction procedure used in the model are the vertically integrated fluid transports and surface elevations as a function of position and time. Included in the model are actual bathymetry and topography, time and spatially variable bottom roughness, inertial forces due to advective and coriolis accelerations, rainfall, and spatial and time-dependent wind fields. Horizontal diffusion terms in the momentum equations are optionally present and can be used, if desired, for aiding stability of the numerical solution. Inundation, drying, and/or draining of low-lying terrain during a hurricane surge is simulated by making the location of a land-water boundary a function of local water depth. The model also is capable of treating subgrid barrier effects. Exposed, submerged, and overtopping barriers can be represented within the grid system permitting proper simulation of surge waters breaching narrow barriers such as elevated highways, railroads, control structures, etc. WIFM uses a coordinate transformation in the form of a piecewise exponential stretch to map real space, discretized with a smoothly varying grid, into computational space employing a regular spaced grid. Such a scheme permits a local increase of resolution in strategic areas while minimizing computational cost.

Calculation of coastal water levels from surges requires an estimation of storm windfields. The hurricane windfield model currently used in WIFM follows that used by Jelesnianski (1965) and Wanstrath (1976). An improved windfield model has been suggested by Cardone (1969) and research is ongoing to extend the work of Resio and Vincent (1977) and Cardone to develop a planetary boundary layer windfield model which also accounts for windfield transformation as the storm propagates from the open ocean across coastal flood-prone lands.

Application to Galveston Bay included verification to physical model data and subsequent simulation of storm surge and coastal flooding from hurricane Carla. An open-coast curvilinear coordinate surge model of the continental shelf (Wanstrath, 1977) was used to specify seaward boundary conditions for WIFM. Hindcast results for Carla indicate WIFM's predictive capabilities.

SHALLOW WATER WAVE EQUATIONS

The hydrodynamic equations used in WIFM are derived from the classical Navier-Stokes equations in a Cartesian coordinate system (Fig. 1). By assuming vertical accelerations are small and the fluid is homogeneous, and integrating the flow from sea bottom to water surface, the usual two-dimensional form of the equations of momentum and continuity are obtained:

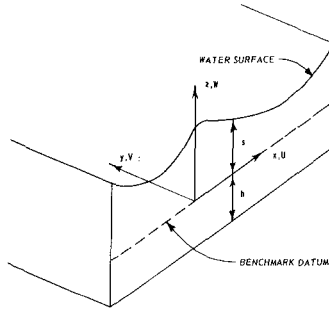


FIGURE 1. CARTESIAN COORDINATE SYSTEM.

MOMENTUM

$$\frac{\partial U}{\partial t} + \frac{\partial}{\partial x} \left(\frac{U^2}{d} \right) + \frac{\partial}{\partial y} \left(\frac{UV}{d} \right) - fV + gd \frac{\partial}{\partial x} (s - s_a) + F_x + \frac{gU}{C^2 d^2} (U^2 + V^2)^{1/2} - de \left(\frac{\partial^2 U}{\partial x^2} + \frac{\partial^2 U}{\partial y^2} \right) = 0 \quad (1)$$

$$\frac{\partial V}{\partial t} + \frac{\partial}{\partial x} \left(\frac{UV}{d} \right) + \frac{\partial}{\partial y} \left(\frac{V^2}{d} \right) + fU + gd \frac{\partial}{\partial y} (s - s_a) + F_y + \frac{gV}{C^2 d^2} (U^2 + V^2)^{1/2} - de \left(\frac{\partial^2 V}{\partial x^2} + \frac{\partial^2 V}{\partial y^2} \right) = 0 \quad (2)$$

CONTINUITY

$$\frac{\partial s}{\partial t} + \frac{\partial U}{\partial x} + \frac{\partial V}{\partial y} = R \quad (3)$$

where s is the water surface elevation; s_a is the hydrostatic elevation corresponding to the atmospheric pressure^a anomaly; U , V are the vertically integrated transports per unit width at time t in the x and y directions, respectively; $d = s - h$ is the total water depth; h is the still water elevation; f is the Coriolis parameter; C is the Chezy frictional coefficient; g is the acceleration of gravity; e is a generalized eddy viscosity coefficient; R represents the rate at which additional water is introduced into or taken from the system (for example, through

rainfall and evaporation); and F_x , F_y are terms representing external forcing functions such as wind stress in the x and y directions.

Many numerical modelers have found it difficult to obtain meaningful solutions to the above equations when advective terms (second and third terms of equations 1 and 2) are included. Current research at WES is underway to assess the role of advective terms in the numerical simulation of long period, large amplitude water wave behavior in coastal regions. These terms are not included in the application presented herein, but have been modeled successfully in other simulations (Butler, 1976, 1978). The last terms in the momentum equations are representative of equivalent internal stress resultants due to turbulent and dispersive momentum flux (Vreugdenhil, 1973). They provide a mechanism for dissipating wave energy of wavelength on the order of twice the spatial step by smoothing curvatures developing in the solution. Since energy is transferred to this scale by the non-linear advective terms and these terms have been neglected in the Galveston Bay application, the flux terms have also been omitted. Both terms are presented here for completeness.

STRETCHED COORDINATES

A major advantage of WIFM is the capability of applying a smoothly varying grid to the given study region. For each direction a piecewise reversible transformation (analogous to that used by Wanstrath, 1976) is independently used to map prototype or real space into computational space. The transformation takes the form

$$x = a + b\alpha^c \quad (4)$$

where a, b, and c are arbitrary constants. The transformation is such that all derivatives are centered in α -space. By applying a smoothly varying grid whose functional as well as first derivatives are continuous, many stability problems commonly associated with variable grid schemes are eliminated. A time-share code has been designed to calculate the mapping defined by equation (4) allowing complete control of grid resolution at any point along each grid axis.

By using equations similar to (4) the equations of motion in α -space can be written as

MOMENTUM

$$\frac{\partial U}{\partial t} + \frac{1}{\mu_1} \frac{\partial}{\partial \alpha_1} \left(\frac{U^2}{d} \right) + \frac{1}{\mu_2} \frac{\partial}{\partial \alpha_2} \left(\frac{UV}{d} \right) - fV + \frac{gd}{\mu_1} \frac{\partial}{\partial \alpha_1} (s - s_a) + F_{\alpha_1} + \frac{gU}{C^2 d^2} (U^2 + V^2)^{1/2} - T_1 = 0 \quad (5)$$

$$\frac{\partial V}{\partial t} + \frac{1}{\mu_1} \frac{\partial}{\partial \alpha_1} \left(\frac{UV}{d} \right) + \frac{1}{\mu_2} \left(\frac{V^2}{d} \right) + fU + \frac{gd}{\mu_2} \frac{\partial}{\partial \alpha_2} (s - s_a) + F_{\alpha_2} + \frac{gV}{C^2 d^2} (U^2 + V^2)^{1/2} - T_2 = 0 \quad (6)$$

CONTINUITY

$$\frac{\partial s}{\partial t} + \frac{1}{\mu_1} \frac{\partial U}{\partial \alpha_1} + \frac{1}{\mu_2} \frac{\partial V}{\partial \alpha_2} = R \quad (7)$$

where

$$\mu_1 = \frac{\partial x}{\partial \alpha_1} = b_1 c_1 \alpha_1^{c_1 - 1} \quad (8)$$

$$\mu_2 = \frac{\partial y}{\partial \alpha_2} = b_2 c_2 \alpha_2^{c_2 - 1} \quad (9)$$

Quantities μ_1 and μ_2 define the stretching of the regular spaced computational grid in α -space to approximate a study region in real space. The terms T_1 and T_2 represent the transformed flux terms.

FINITE DIFFERENCE MODEL

Since obtaining a solution to the governing non-linear equations on a region with highly complex geometry and topography is intractable using a pure analytical approach, a numerical technique is employed. A variable rectilinear grid is first developed for the model area. The appropriate variables are defined on the grid in a space-staggered fashion as depicted in Fig. 2 for a typical cell.

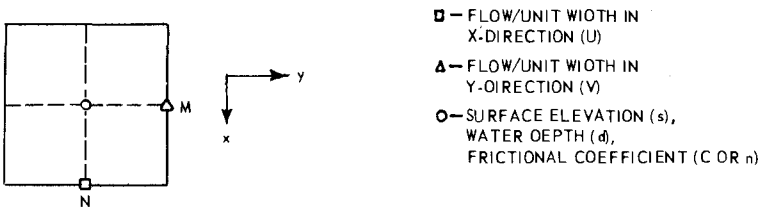


FIGURE 2. COMPUTATIONAL CELL DEFINITION.

An alternating-direction technique (Leendertse, 1967) is used to develop a finite difference scheme for solving the transformed equations (5-7). Computations are separated into two cycles corresponding to a sweep of the grid in both directions. The first cycle consists in solving for s and U implicitly; the second cycle computes s and V implicitly. The omitted transport is assumed constant for that cycle. Applying a centered difference operator to the momentum equation (5), and the continuity equation (7), along a grid line parallel to the x -axis, results in a system of linear algebraic equations whose coefficient matrix is tri-diagonal. The form of the difference equations for the first cycle is given by

$$\begin{aligned}
 U_{n,m+1/2}^{k+1/2} = & U_{n,m+1/2}^{k-1/2} + \Delta t \left\{ f\bar{v}_{n,m+1/2}^k + F_{\alpha_1}^k - \frac{g}{2\Delta\alpha_1} \left(\frac{d^*}{\mu_1} \right)_{n,m+1/2} \right\} s_{n,m+1}^{k+1/2} \\
 & - s_{n,m}^{k+1/2} + s_{n,m+1}^{k-1/2} - s_{n,m}^{k-1/2} - 2 \left[(s_a)_{n,m+1}^k - (s_a)_{n,m}^k \right] \left\{ \right. \\
 & \left. - \frac{g \left(U_{n,m+1/2}^{k+1/2} + U_{n,m+1/2}^{k-1/2} \right)}{2(d^*C^k)^2} \left[\left(U_{n,m+1/2}^{k-1/2} \right)^2 + \bar{v}_{n,m+1/2}^2 \right]^{1/2} \right\} \quad (10)
 \end{aligned}$$

$$\begin{aligned}
 s_{n,m}^{k+1/2} = & s_{n,m}^k - \frac{\Delta t}{2} \left[\frac{1}{\Delta\alpha_1(\mu_1)_m} \left(U_{n,m+1/2}^{k+1/2} - U_{n,m-1/2}^{k+1/2} \right) \right. \\
 & \left. + \frac{1}{\Delta\alpha_2(\mu_2)_n} \left(V_{n+1/2,m}^k - V_{n-1/2,m}^k \right) \right] + \frac{\Delta t}{2} R_{n,m}^k \quad (11)
 \end{aligned}$$

where $d^* = \bar{s}^k - \bar{h}$. In these expressions a single bar represents a two point average and a double bar a four point average. The subscripts m and n correspond to spatial locations and superscript k to time levels. Equations for the second cycle are similar to (10) and (11) and are not presented.

The implicit difference scheme when applied to the linear system of governing equations exhibits unconditional stability as shown by Leendertse (1967). Longer time steps are usually permissible with the implicit scheme in contrast to explicit formulations. In many instances this fact permits a more cost-effective simulation. Inclusion of non-linear terms into the implicit scheme, however, may result in an inherent

instability. As mentioned previously, flux terms have been used to overcome this problem but current research is being directed at finding a more satisfactory solution without giving up advantages of the implicit procedure. Weare (1976) has attempted to analyze conditions under which the system is unstable and has obtained a condition which relates velocity, advection, and friction. A fully time-centered scheme is suggested to avoid the problem.

A variety of boundary conditions are employed throughout the computational grid. These include prescribing water levels or flow rates, fixed or movable land-water boundaries, and subgrid barrier conditions.

Open boundaries. Included in this category are seaward boundaries terminating the computational grid or channels exiting the two-dimensional grid at any point in the system. Water levels or flow rates are prescribed as functions of location and time, and are given as tabular input to the code. For economical storm surge application, an open coast surge model may be used to develop the open sea boundary values to drive the inland flooding model.

Water-land boundaries. These conditions relate the normal component of flow at the boundary to the state of the water level at the boundary. Hence, water-land boundaries are prescribed along cell faces. Fixed land boundaries are treated by specifying $U = 0$ or $V = 0$ at the appropriate cell face. Low-lying terrain may alternately dry and flood within a tidal cycle or surge history. Inundation is simulated by making the location of the land-water boundary a function of local water depth. By checking water levels in adjacent cells a determination is made as to the possibility of inundation. Initial movement of water on "dry" cells is controlled by using a broad crested weir formula (Reid and Bodine, 1968). Once the water level on the "dry" cell exceeds some small prescribed value, the boundary face is treated as open and computations for s , U , and V are made for that cell. The drying of cells is the inverse process. Mass conservation is maintained within these procedures.

Subgrid barriers. Such barriers are defined along cell faces and are of three types: exposed, submerged, and overtopping. Exposed barriers are handled by simply specifying no-flow conditions across the appropriate flagged cell faces. Submerged barriers are simulated by controlling flow across cell faces with the use of a time dependent frictional coefficient. Overtopping barrier is a terminology used to distinguish barriers which can be submerged during one segment of the simulation and totally exposed in another. Actual overtopping is treated by using a broad-crested weir formula to specify the proper flow rate across the barrier. Water is transferred from the high to low side according to this rate. Once the barrier is submerged (or conversely exposed), procedures as described for submerged barriers (or exposed) are followed.

Graphics play an important role in presenting model results. Typical model output and data displays for W1FM include water level hydrographs,

contours of water levels over the computational region, time history plots of velocity and volumetric discharge, and vector plots of either velocities or transports over the computational region. Normally, output from this model is used to produce color slides and color movies facilitating portrayal of the coastal flooding.

APPLICATION TO GALVESTON BAY

Galveston Bay, located in southeast Texas, is a large shallow bay covering more than 1000 square kilometers. There are three Gulf of Mexico entrance channels to the bay system, Galveston Entrance Channel, San Luis Pass Channel, and Rollover Pass Channel. Since Rollover Pass is so narrow and carries no more than one percent of the total discharge, it was not included in the simulation. The major channels in the bay are the Houston Ship Channel, Trinity River Channel, Galveston Channel, Texas City Channel, and the Intracoastal Waterway. The average depth of the bay is 2.75 meters while major channels average over 9 meters depth.

The objective of this application was to evaluate and/or illustrate WIFM's use as a predictive tool in simulating coastal flooding. By hindcasting the storm surge and flooding from hurricane Carla (1961) in the Galveston Bay area, such an assessment could be made. The first step was to verify the model for the study area. A variable grid consisting of 3572 grid cells was developed for the Galveston Bay region. The minimum cell width used was 604 meters and the maximum was 2583 meters. Various subgrid barriers were used throughout the grid system to represent features such as jetties, spoil banks, reefs, and major elevated highways. A one-dimensional channel computation extended 30 kilometers beyond the two-dimensional grid for simulating the Houston Ship Channel. A time step of 180 sec per cycle (permissible in the implicit scheme) was selected for both the verification and hindcast phases of application. Fig. 3 depicts the Galveston Bay grid and gage locations used in establishing high water marks and hydrographs for comparison with observed data.

VERIFICATION

The objective of the verification phase of any model study is to demonstrate the model's ability to produce results that agree with data for known conditions. Such a test gives a reasonable degree of confidence for applying the model as a predictive tool. The difficulty in attempting to verify a model for storm surge is usually a lack of prototype data. In the case of Galveston Bay a physical model study was conducted at WES and reported by Brogdon (1969). A wealth of both prototype and physical model data was available for the verification process. Unfortunately the prototype tide data included wind effects, the magnitude of which were unknown. Consequently, it was decided to use physical model results (both for a normal tide and a design surge) in this phase of the study.

Gage locations for verification purposes are shown in Fig. 3. Seven tide gages and four velocity stations were used, and gages T-A, -B,

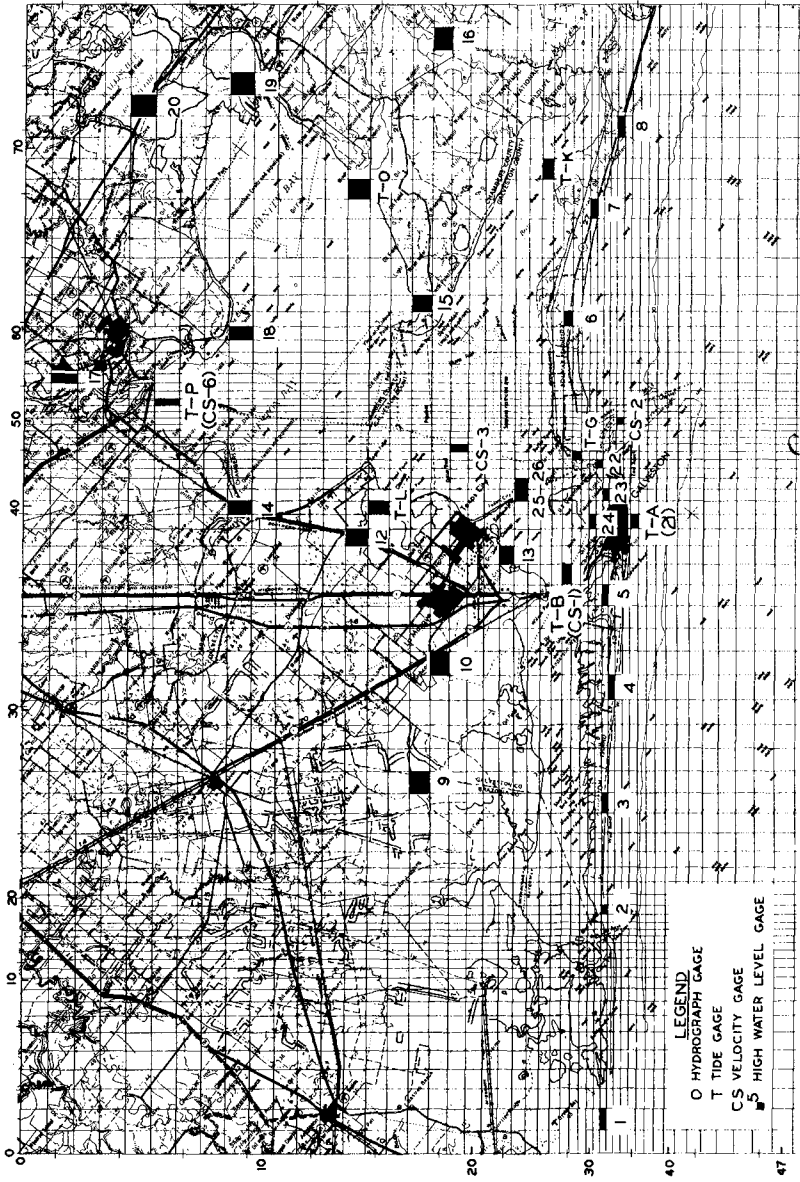


FIGURE 3. COMPUTATIONAL GRID AND GAGE LOCATIONS FOR GALVESTON BAY.

-L, -P and station CS-2 are presented in Figs. 4-8 for displaying sample results. Computation was begun at $t = -2$ hr, setting the entire water surface down to -0.2 meters msl and assuming a quiescent body of water.

As an additional check and test of the model's predictive capability, an application for a large radius high translation design surge (Brogdon, 1969) was performed. The design surge had a peak elevation of 4.4 meters and a duration of 20 hr. The WIFM simulation was terminated at hour 18. Comparison for gages T-A, -B, -L, and -P between physical and numerical model are displayed in Figs. 9-12. The results were in good agreement at most gages indicating that the model was ready for use in a predictive mode.

Experience in using the model has indicated that once proper resolution of the study area is adopted, application can be carried out with minimal adjusting or tuning of the model. The major adjustment made in the verification phase of the Galveston Bay application was a change in frictional characteristics of the Galveston entrance channel.

CARLA HINDCAST

In order to hindcast surge elevations and coastal flooding from hurricane Carla, two major forcing functions were required: time dependent open sea boundary values and a time and spatially dependent wind field describing winds from Carla. Open sea boundary values were developed by first applying an orthogonal curvilinear open-coast surge model (SSURGE 111, Wanstrath, 1977) to the continental shelf region. The curvilinear model avoids necessity of stairstepping the coastline eliminating problems associated with such an approximation. The open-coast model also has a finite-height barrier coast boundary condition and allows for ponding areas. Therefore the boundary conditions computed by SSURGE 111 for WIFM are not contaminated with excess water caused by an infinite wall boundary condition commonly used in open-coast models. Both WIFM and SSURGE 111 employ the same wind model using appropriate modifications to account for wind deformation due to land influence (Shore Protection Manual, 1977). This model and the atmospheric pressure model are given by Jelesnianski (1965) but modified by Wanstrath (1976). An additional parameter, maximum wind speed, is required by the wind model. Values for this parameter cannot always be obtained, an important disadvantage for simulating hurricane winds in a predictive mode. The problem can be resolved by incorporating a wind model, based on the physics of the marine boundary layer, that will provide a windfield as a result of dynamic meteorological computations. The composite model would be appropriate for both forecasting and hindcasting. However, the wind model used in this study did produce results in good agreement with observed meteorological data. Comparison of computed and observed wind speed at the Weather Bureau Office, Galveston, Texas, is depicted in Fig. 13. Wind direction comparison for this station is shown in Fig. 14. The astronomical tide was included in the open coast simulation (and consequently in the driving function for the seaward boundary conditions for the inland flooding model) to eliminate uncertainties due to the linear superposition of tide and surge elevations.

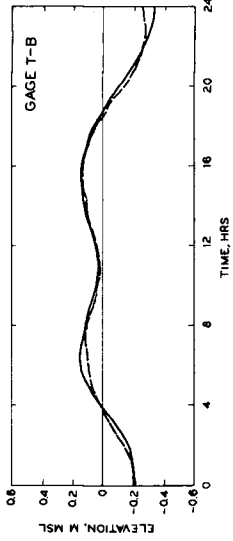


FIGURE 4

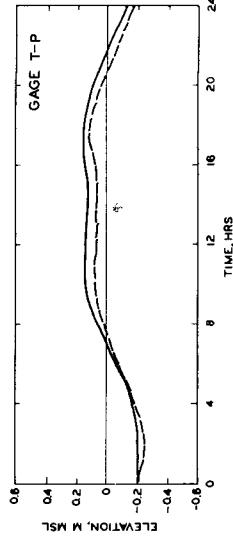


FIGURE 5

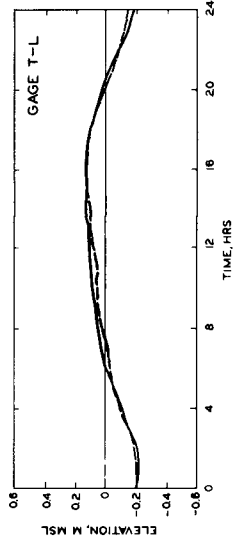


FIGURE 6

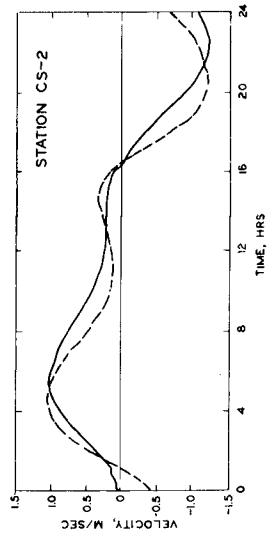


FIGURE 7

LEGEND
- - - PHYSICAL MODEL
— NUMERICAL MODEL (WIFM)

SAMPLE RESULTS FOR TIDAL VERIFICATION.

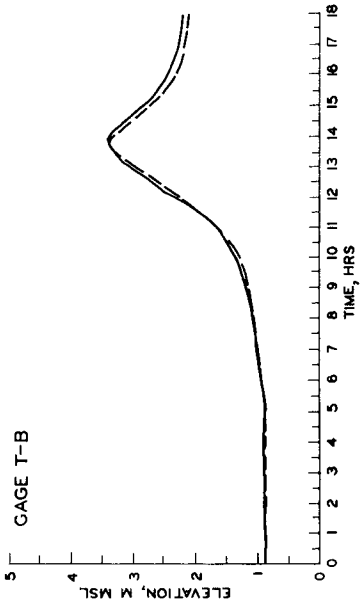


FIGURE 10

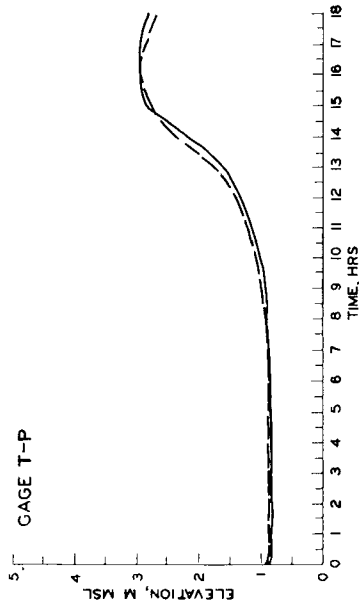


FIGURE 12

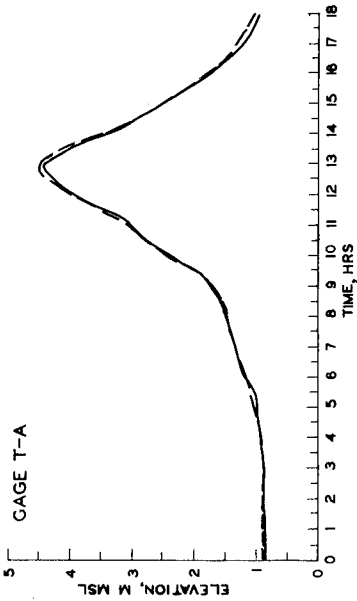


FIGURE 9

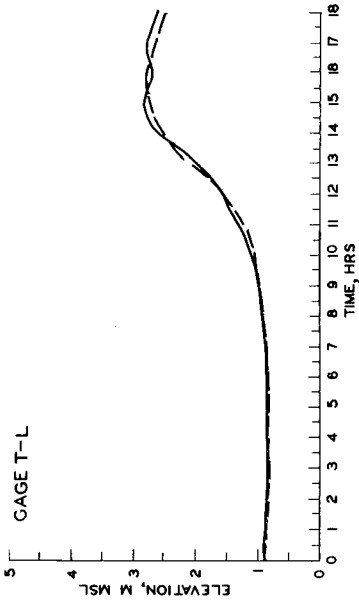


FIGURE 11

LEGEND
- - - - - PHYSICAL MODEL
_ _ _ _ _ NUMERICAL MODEL (WIPM)

SAMPLE RESULTS FOR LARGE RADIUS HIGH TRANSLATION DESIGN SURGE.

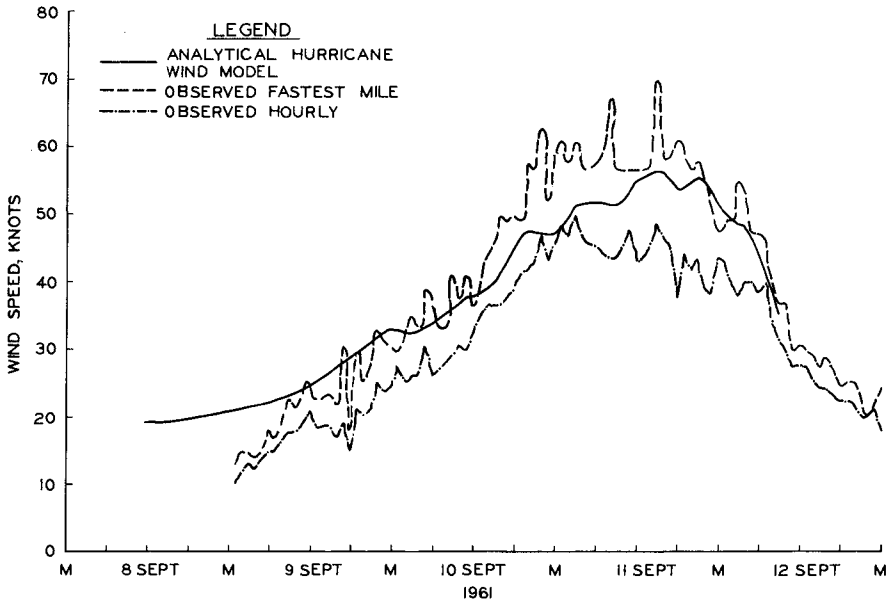


FIGURE 13. COMPARISON OF COMPUTED AND OBSERVED WIND SPEED AT GALVESTON, TEXAS.

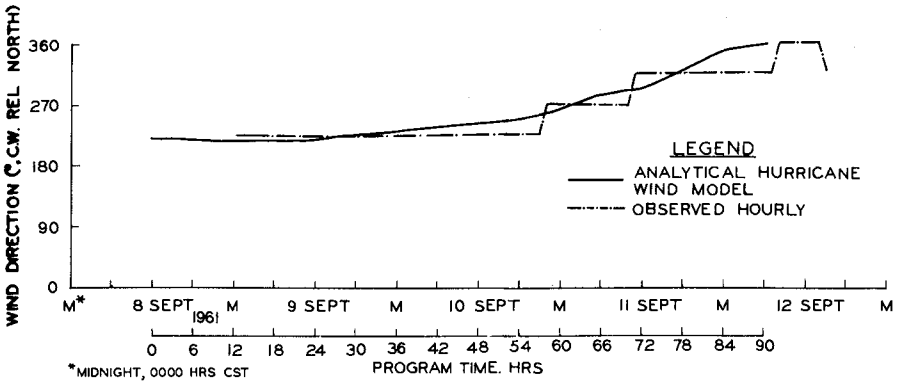


FIGURE 14. COMPARISON OF COMPUTED AND OBSERVED WIND DIRECTION AT GALVESTON, TEXAS.

The variable grid employed by WIFM is of finer resolution and lies askew to the open-coast grid, and thus interpolation of discrete values of water level from the open-coast grid is required. The interpolation scheme is based on a four-point, distance-weighted averaging procedure. The open-coast simulation, began at 12 noon on 8 September 1961, continued for 93 hours to 0900 on 12 September, and was calibrated to give good agreement between observed and model data at Pleasure Pier (gage 21, same as T-A). For economy of application the inland simulation was begun at hour 18 of the open-coast run and continued for 72 hours to hour 90. The water level throughout the model area at hour 18 was approximately 1.1 meters and thus the bay was spun up from a quiescent state with initial elevation of the entire bay at +1.1 meters. No change in model parameters was made after the verification phase was completed. Fig. 15 displays observed and model results at the Pleasure Pier open coast gage 21. Additional hydrograph comparisons are given in Figs. 16 and 17 for gages at Pelican Bridge (24) and Texas City Dyke-North (26). The major difficulty in the application was the calibration of the wind model to simulate Carla's winds. The overshoot in the computed results around program hours 60-66 is possibly due to the inability of the wind model to account for sheltering effects from the city of Galveston (winds were directly on-shore during this period).

Table 1 illustrates a comparison of observed high-water levels at various locations throughout the system with those computed by WIFM. Mean absolute error for 26 gages was 0.18 meters. The largest deviation from observed high water levels at any one gage was 0.64 meters at Sea Isle Beach (gage 3). The observed peak water level at Sea Isle was nearly 0.5 meters higher than that at any neighboring gage, indicating (assuming the data were correct) that some local anomaly existed which was not modeled by WIFM. All observed data were taken from a USAE Galveston District Report (1962). Peak elevation data were obtained from a tide gage reading crest of tide or still high water elevation marks. The reported gages were taken as representative of conditions experienced around the bay.

CONCLUSIONS

The following conclusions can be drawn from the material presented:

1. A two-dimensional implicit finite difference coastal flooding model in stretched coordinates has been developed. It is applicable to predict coastal flooding from storm surges, tides, tsunamis, or any long-period wave phenomena where boundary conditions can be specified.
2. The variable grid characteristic of WIFM (its principle advantage relative to other two-dimensional models) permits the capability to obtain finer resolution in important local areas without sacrificing economical application of the model.
3. A verification of the efficacy of the model was clearly demonstrated through application of the model to hindcast hurricane surge

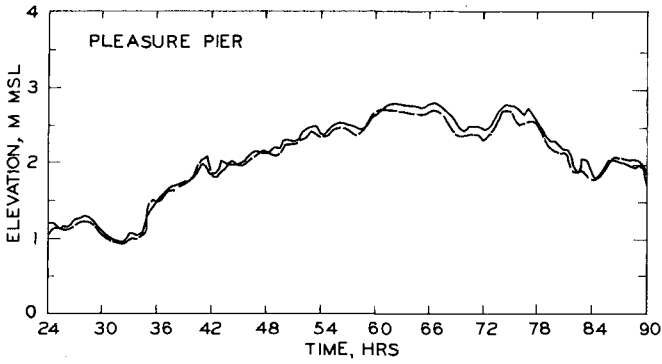


FIGURE 15

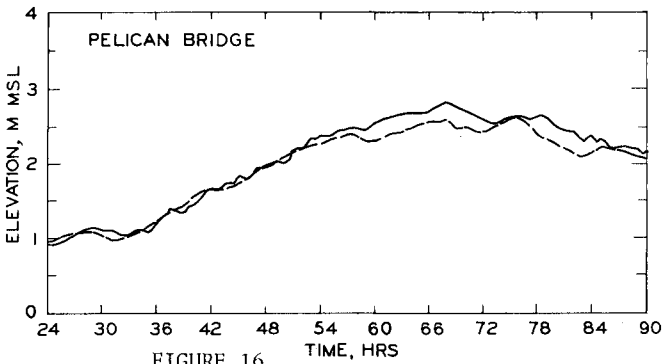


FIGURE 16

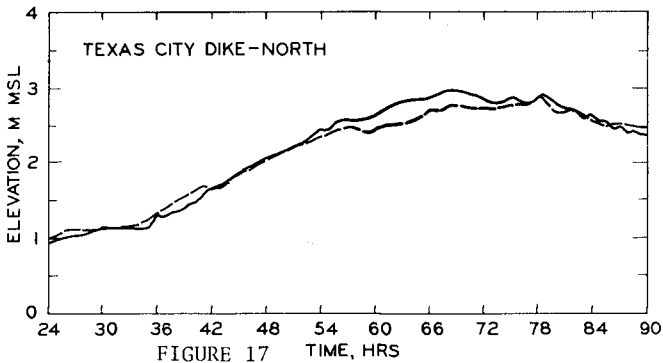


FIGURE 17

LEGEND
 - - - OBSERVED DATA
 — NUMERICAL MODEL (WIFM)

COMPARISON OF COMPUTED AND OBSERVED SURGE ELEVATIONS IN THE GALVESTON BAY AREA.

TABLE 1
COMPARISON OF HIGH WATER LEVELS AT SELECTED GAGE LOCATIONS

GAGE NO.	GAGE LOCATION	OBSERVED m	COMPUTED m	DIFFERENCE m	GAGE NO.	GAGE LOCATION	OBSERVED m	COMPUTED m	DIFFERENCE m
1	OYSTER CREEK	3.11	3.29	+0.18	15	SMITH POINT	2.99	3.17	+0.18
2	SAN LUIS PASS	3.29	3.05	-0.24	16	OYSTER BAYOU	3.20	3.35	+0.15
3	SEA ISLE BEACH	3.69	3.05	-0.64	17	SCOTT BAY	4.33	4.30	-0.03
4	BERMUDA BEACH	3.20	2.99	-0.21	18	HUMBLE DOCKS	4.18	3.84	-0.34
5	SCHOLES FIELD	2.59	2.93	+0.33	19	ANANUAC	3.78	3.87	+0.09
6	BOLIVAR BEACH	2.83	2.83	+0.00	20	WALLISVILLE	4.27	4.26	+0.00
7	CRYSTAL BEACH	2.68	2.87	+0.18	21	PLEASURE PIER	2.83	2.87	+0.03
8	ROLLOVER BEACH	2.93	2.83	-0.09	22	FORT POINT	2.74	2.90	+0.15
9	HALLS BAYOU	4.36	4.30	-0.06	23	PIER 21	2.68	2.90	+0.21
10	HIGHWAY SIX	3.84	3.87	+0.03	24	PELICAN BRIDGE	2.74	2.87	+0.12
11	SIEVERS COVE	3.23	2.83	-0.39	25	TEXAS CITY DYKE (SOUTH)	2.90	3.05	+0.15
12	DICKINSON BAYOU	3.47	3.60	+0.12	26	TEXAS CITY DYKE (NORTH)	2.96	3.05	+0.09
13	CARBIDE DOCKS	3.35	3.17	-0.18					
14	KEMAH	4.33	3.90	-0.43					

MEAN ABSOLUTE ERROR = 0.18 m.

elevations and coastal flooding for Hurricane Carla. The mean absolute difference between observed and computed water levels was 0.18 m and the observed and computed hydrographs (time dependency of surge elevations) were in good agreement.

4. The relative ease of application, variable grid capability, implicit computing scheme, and flexible output characteristics (when considered together) make W1FM a very useful model for performing practical engineering computations to aid in the solution of real-world problems.

RECOMMENDATIONS

A number of recommendations for future efforts are apparent as a result of the work contained herein and are delineated below:

1. Although W1FM has been successfully applied with the nonlinear advective terms incorporated into the solution on several occasions, there are more stability problems associated with their use than desirable. Additional research is needed to develop better methods of treatment of these instabilities. Some work is proceeding along these lines at WES and it is hoped that others also will actively pursue this important problem in order to minimize the time when use of the nonlinear advective terms in practical engineering applications becomes routine.

2. Additional research also is needed to better define the role of the advective terms in problems involving catastrophic flooding (such as storm surges and tsunami inundation). It may turn out that the advective terms have little effect on the extent of catastrophic flooding, in which case, they may be neglected from a practical engineering point of view.

3. Simulation of narrow rivers or channels would be improved in W1FM with even more potential cost savings by incorporation of a scheme similar to that of Reid et al. (1975) which uses the concept of dynamically coupled one-dimensional subgrid channels. It is planned to add this capability to W1FM during the next application of the model.

4. For storm surge predictions, a planetary boundary layer wind-field model which also accounts for windfield transformation from ocean to land would represent a substantial improvement to W1FM and other two-dimensional flooding models.

ACKNOWLEDGEMENTS

The author wishes to acknowledge the Office, Chief of Engineers, for granting permission to publish this paper and Dr. J. J. Wanstrath, Research Oceanographer, Wave Dynamics Division, WES, for his many helpful discussions during the various phases of this study.

REFERENCES

- Brogdon, N. J., "Galveston Bay Hurricane Surge Study, Report 1, Effects of Proposed Barriers on Hurricane Surge Heights," Technical Report H-69-12, U. S. Army Engineer Waterways Experiment Station, CE, Vicksburg, MS, 1969.
- Butler, H. L., "Numerical Simulation of Tidal Hydrodynamics: Great Egg Harbor and Corson Inlets, New Jersey," Technical Report H-78-11, U. S. Army Waterways Experiment Station, CE, Vicksburg, MS, 1978.
- Butler, H. L. and Raney, D. C., "Finite Difference Schemes for Simulating Flow in an Inlet-Wetlands System," Proceedings of the Army Numerical Analysis and Computers Conference, The Army Mathematics Steering Committee, Durham, NC, Mar 1976.
- Cardone, V. J., "Specification of Wind Distribution in the Marine Boundary Layer for Wave Forecasting," Technical Report 69-1, Geophysical Sciences Laboratory, New York University, New York, NY, 1969.
- Jelesnianski, C. P., "A Numerical Calculation of Storm Tides Induced by a Tropical Storm Impinging on a Continental Shelf," MWR, 93, 1965, pp. 343-358.
- Leendertse, J. J., "Aspects of Computational Model for Long-Period Water-Wave Propagation," RM-5294-PR, Rand Corp., Santa Monica, CA., 1967.
- Leendertse, J. J., "A Water-Quality Simulation Model for Well-Mixed Estuaries and Coastal Seas., Vol 1, Principles of Computation," RM-6230-rc, Rand Corp., Santa Monica, CA., Feb 1970.
- Leendertse, J. J., and Gritton, E. C., "A Water-Quality Simulation Model for Well-Mixed Estuaries and Coastal Seas., Vol 2, Computational Procedures," RM-708-NYC, Rand Institute, New York, NY, Apr 1971.
- Pearce, B. R., "Numerical Calculation of the Response of Coastal Waters to Storm Systems," Technical Report No. 12, Coastal and Oceanographic Engineer Laboratory, University of Florida, Gainesville, FL, Aug 1972.
- Reid, R. O., and Bodine, B. R., "Numerical Model for Storm Surges in Galveston Bay," Journal of Waterways and Harbors Division, ASCE, Vol. 94, No. WW1, Feb 1968, Proc. Paper 5805, pp. 33-57.
- Reid, R. O., Vastano, A. C., and Reid, T. J., "Development of Surge II Program with Application to the Sabine-Calcasieu Area for Carla and Design Hurricanes," Contract DACW64-74-C-0015, U. S. Army District, Galveston, CE, Galveston, TX, Dec 1975.

Resio, D. T., and Vincent, C. I., "Estimation of Winds Over the Great Lakes," Journal of the Waterway, Port, Coastal and Ocean Division, ASCE, Vol. 103, No. WW2, Proc. Paper 12951, May 1977, pp. 265-283.

U. S. Army Coastal Engineering Research Center, "Shore Protection Manual," Vol I, 1977, Fort Belvoir, VA.

U. S. Army Engineer District, Galveston, "Report on Hurricane Carla, 9-12 September 1961," January 1962, Galveston, TX.

Vreugdenhil, C. B., "Secondary-Flow Computations," Delft Hydraulics Laboratory, Publication No. 114, Nov 1973.

Wanstrath, John J., "Nearshore Numerical Storm Surge and Tidal Simulation," Technical Report H-77-17, U. S. Army Engineer Waterways Experiment Station, CE, Vicksburg, MS, 1977.

Wanstrath, J. J., Butler, H. Lee, Vincent, C. L., Resio, D. T., and Whalin, R. W., "Use of Numerical Models for Computation of Coastal Water Levels," Proceedings of the 1977 Annual Convention, ASCE, San Francisco, CA, Oct 1977.

Wanstrath, J. J., Whitaker, R. E., Reid, R. O., and Vastano, A. C., "Storm Surge Simulation in Transformed Coordinates, Vol. I-Theory and Application," Technical Report 76-3, U. S. Army Coastal Engineering Research Center, CE, Fort Belvoir, VA, Nov 1976.

Weare, T. John, "Instability in Tidal Flow Computational Schemes," Journal of the Hydraulics Division, ASCE, Vol. 102, No. HY5, May 1976, pp. 569-580.

CHAPTER 61

ADJUSTMENT AND VERIFICATION OF THE RANDELTA II MODEL

A. Langerak,¹ M. A. M. de Ras,² and J. J. Leendertse³

I. INTRODUCTION

In the mid-1950s the Netherlands government embarked on a massive construction program, called the Delta Plan. Its purpose was to enhance protection from floods caused by the North Sea in the estuaries of the Rhine, Meuse and Scheldt. According to the plan, all connections to the sea were to be closed by dams, except the New Waterway to Rotterdam and the Western Scheldt. In 1974 all dams and dikes were complete except the dam closing off the Eastern Scheldt from the sea. In view of growing opposition to a complete closure, plans were revised in 1976, and instead of the dam, a storm surge barrier will be constructed. This barrier will reduce the tidal range in the Eastern Scheldt and will be closed during storm surges.

In support of engineering and environmental studies related to the construction and operation of this barrier, a large numerical model has been developed, which covers the Eastern and Western Scheldt and the adjacent offshore area. The section of the North Sea which is included in the model is about 120 km long and 30 km wide, running from Blankenberghe in Belgium to Scheveningen in the Netherlands (Fig. 1).

The bathymetry of the model area varies widely. In general it slopes from the shore to about 25 m at 30 km from the coast. In certain sections of the offshore area, the bottom is relatively flat; in other areas it has offshore bars and the bottom contains underwater sand dunes with a height of several meters. In the estuaries the tidal flow has scoured deep channels. The tidal flats near the North Sea are generally sandy, but the ecologically important tidal marshes located more inland contain much finer material.

The flow and the water levels in the region which is modeled are generally tide-induced. However, the influence of meteorological effects is always present and sometimes dominates water movements and water levels (storm surges). The influence of the fresh water discharges is of much less importance; generally their effects can only be noticed in the immediate vicinity of the discharge.

The tides in the offshore area of the model are part of the complicated tide system in the North Sea. The semidiurnal tidal wave propagates along the coast in a northeasterly direction. During this propagation the amplitude reduces from about 1.90 m near Blankenberghe to about .85 m near Scheveningen.

¹ Delft Hydraulics Laboratory, The Netherlands

² Rijkswaterstaat, Delta Service, The Netherlands

³ The Rand Corporation, Santa Monica, California, U.S.A.

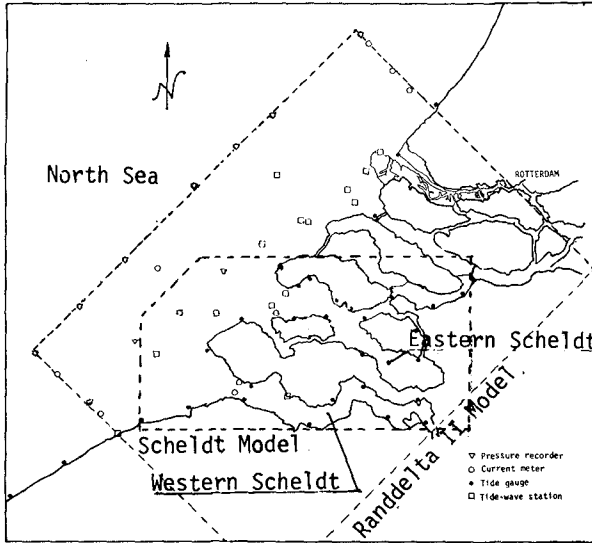
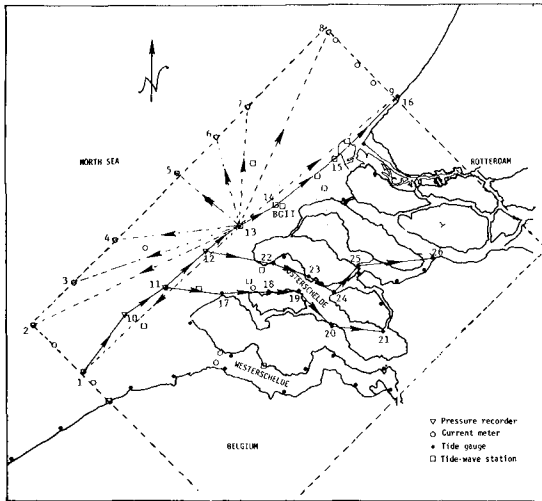


Fig. 1--Layout of models and location of recording stations

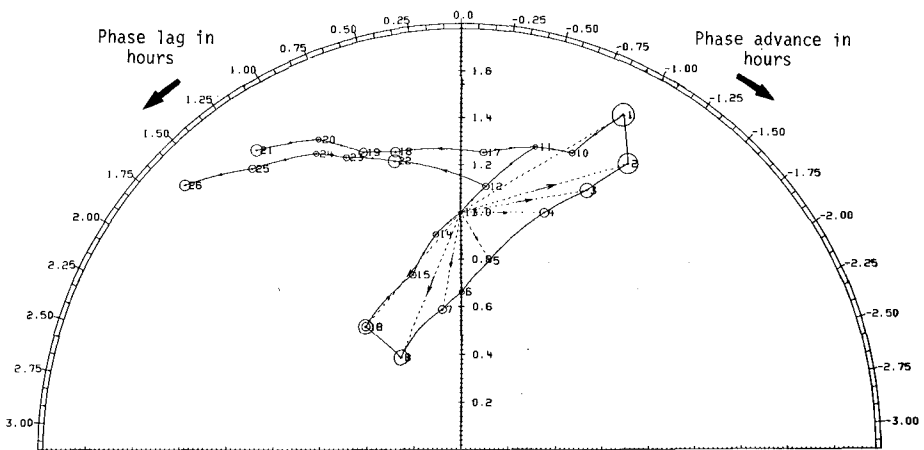
In the Eastern and Western Scheldt, the semidiurnal tidal wave penetrates into the estuary and is partially reflected. In the Eastern Scheldt the amplitude increases from 1.35 m near the mouth to 1.95 m at the eastern extremity; in the Western Scheldt the amplification is from about 1.75 m near Vlissingen to 2.30 m at the Dutch-Belgian border.

As the tides are waves, the best visual representation can be obtained by looking at amplitude and phase relations between stations. In Fig. 2 the results of such an analysis are presented in the form of a polar plot of frequency response estimates for the semidiurnal tide. The top part of the figure shows how the respective amplitude and phase relations were established by cross-spectral analysis and the locations of the recording instruments. All stations are numbered and the respective amplitude and phase are shown in relation to a station in the center of the model. For example, station 26 (Rak Zuid Volkerak) lags 1.6 hours behind the reference station 13 (BG II) and is about 1.6 times as large.

The diurnal tide is much smaller and is not much amplified in the model area. In some parts of the model area, the nonlinearities in the hydrodynamics generates strong overtides. This is particularly the case in the northern part of the model. Figure 3 shows the observed water levels obtained by a bottom pressure recorder during the survey described in Ref. 1, corrected for density variations, settling and atmospheric pressure. In the same graph, the quarter-diurnal tide component is shown. This component was obtained by filtering the tide data with Coulomy's quarter-diurnal bandpass filter, described by Godin [2]. The existence of these strong nonlinearities in the system complicated the modeling work considerably.



- REF B.G. II
- 1 SCHEUR I
- 2 KNIKPUNT I
- 3 NOORD THORTONBANK
- 4 KNIKPUNT II
- 5 KNIKPUNT III
- 6 EURO IA
- 7 KNIKPUNT IV
- 8 KNIKPUNT V
- 9 SCHEVENINGEN
- SCHEUR I
- 10 DEURLOO
- 11 KALDD NOORD
- 12 MIDDENBANJAARO
- 13 B.G. II
- 14 B.G. V
- 15 M.A. III
- 16 SCHEVENINGEN
- KALDD NOORD
- 17 OOSTKAPELLE
- 18 VLIETEPOLDER
- 19 COLIJNSPLAAT
- 20 MEMELDINGE
- 21 RAZERNIJPOLOER
- MIDDENBANJAARO
- 22 BURGHSLUIS
- 23 ZIERDZEE
- 24 STAVENISSE
- 25 KRAMMER
- 26 RAK ZUID VOLKERAK



FREQUENCY = 0.08 PER HOUR

RAND CORPORATION
09/10/7612, 41.15

Fig. 2--Polar plot of the frequency response estimates of the semidiurnal tide from a central station (BG II) to other stations in the model area

The velocities in the model area vary considerably in space and time. The large variations which are present near tidal channels put high demands on the stability of the computation method and the accuracy of the representation of these spatial variations.

In the estuaries the tidal current can be as high as 1.50 m/s in the offshore area; the currents range from 0 to 1 m/sec.

The seaward boundaries of the Randdelta II model are situated at the same location as the boundaries of an earlier model with a much coarser grid. Only the model area at the northern end was reduced. The location of the boundaries of that model were determined on the basis of a numerical model study of the southern North Sea with a model described in Ref. 3. Studies with that model indicated that the influence of the closure dams in the Delta region on the water levels at the boundary of the Randdelta models would be very small--much smaller than the accuracy at which water level data can be obtained at that water depth. In part the exact location of the long open boundary was determined from the feasibility of data collection. As described in Ref. 1, many limitations existed in placing instruments in these heavily traveled waters.

At the boundary, water level and current data was measured, by which the boundary conditions for the model were well determined.

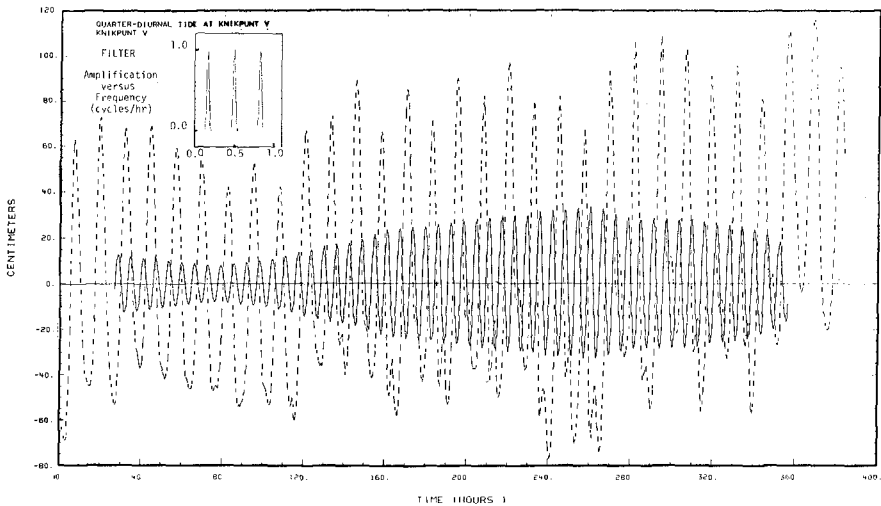


Fig. 3--Observed tides at a station in the corner of the model (Knikpunt V), together with the quarter-diurnal tide obtained from the record by a bandpass filter

II. MODEL FORMULATION

The model is based upon the so-called vertically integrated semi-momentum equations which have been derived in Ref. 4. In this case the atmospheric pressure differences are added as driving forces. The momentum equations now contain a viscosity term and pressure differences due to salinity gradients. The equations are written as

$$\frac{\partial U}{\partial t} + U \frac{\partial U}{\partial x} + V \frac{\partial U}{\partial y} - fV + g \frac{\partial \zeta}{\partial x} + \frac{1}{2}g \frac{H}{\rho} \frac{\partial \rho}{\partial x} + g \frac{U(U^2 + V^2)^{\frac{1}{2}}}{C^2 H} - \frac{\theta \rho_a W^2 \sin \psi}{\rho H} - \frac{\partial P}{\partial x} - k \left(\frac{\partial^2 U}{\partial x^2} + \frac{\partial^2 U}{\partial y^2} \right) = 0 \quad (1)$$

$$\frac{\partial V}{\partial t} + U \frac{\partial V}{\partial x} + V \frac{\partial V}{\partial y} + fU + g \frac{\partial \zeta}{\partial y} + \frac{1}{2}g \frac{H}{\rho} \frac{\partial \rho}{\partial y} + g \frac{V(U^2 + V^2)^{\frac{1}{2}}}{C^2 H} - \frac{\theta \rho_a W^2 \cos \psi}{\rho H} - \frac{\partial P}{\partial y} - k \left(\frac{\partial^2 V}{\partial x^2} + \frac{\partial^2 V}{\partial y^2} \right) = 0 \quad (2)$$

$$\frac{\partial \zeta}{\partial t} + \frac{\partial (HU)}{\partial x} + \frac{\partial (HV)}{\partial y} = 0 \quad (3)$$

$$\frac{\partial (HP)}{\partial t} + \frac{\partial (HuP)}{\partial x} + \frac{\partial (HVP)}{\partial y} - \frac{\partial \left(HD_x \frac{\partial P}{\partial x} \right)}{\partial x} - \frac{\partial \left(HD_y \frac{\partial P}{\partial y} \right)}{\partial y} - R = 0 \quad (4)$$

where D_x, D_y = dispersion coefficients

f = Coriolis parameter

g = acceleration of gravity

h = distance from the bottom to the reference plane

H = temporal depth (= $h + \zeta$)

k = horizontal velocity diffusion coefficient

P = vector of dissolved constituent concentrations

ρ = atmospheric pressure

U = vertically averaged velocity component in x direction

V = vertically averaged velocity component in y direction

W = wind speed

ζ = water level elevation relative to a horizontal reference plane

θ = wind stress coefficient

ρ = density of water

ρ_a = density of air

ψ = angle between wind direction and the positive y direction

Several coefficients can be computed. The Chezy value can be computed from the Manning's coefficients and the temporal depth, and the dispersion coefficient from the temporal depth, the local velocity and the Chezy coefficient.

In the model a horizontal velocity diffusion can be used. From a theoretical point of view, the horizontal momentum diffusion is small, but because of computational effects, it may be desirable to use a value which is larger than we would expect from theory. More sophisticated users of the model would like to see a larger coefficient used only when considerable variations occur in the velocity field, for example, in such areas where we would expect vortex streets which we naturally cannot represent on a grid system. To accommodate such users we have introduced

$$k = k_0 + k' \left| \frac{\partial \omega}{\partial y} \right| (\Delta s)^2 \quad (5)$$

$$\text{where } \omega = \frac{\partial U}{\partial y} - \frac{\partial V}{\partial x}$$

The horizontal density gradient is computed from the salinity distributions and an equation of state. For the equation of state we use

$$\rho = (5890 + 38T - .375T^2 + 3S) / [(1779.5 + 11.25T - .0745T^2) - (3.8 + 0.01T)S + 0.698(5890 + 38T - 0.375T^2 + 3S)] \quad (6)$$

where T = temperature
S = salinity

The temperature differences in the model area appear to be small; also, the influence of temperature on density is small. Consequently, it can be assumed for the computation of density that the temperature is constant in the whole model area.

III. COMPUTATION APPROXIMATIONS

The model is based upon finite difference approximations of the partial difference equations (1)-(4). The grid system and the method of computation are an extension of an earlier computation method described in Ref. 4. To write these finite difference equations, the following notations for averages, derivatives and time shifts are used:

$$\bar{F}^x = \frac{1}{2} \left\{ F[(j+\frac{1}{2})\Delta x, k\Delta y, n\Delta t] + F[(j-\frac{1}{2})\Delta x, k\Delta y, n\Delta t] \right\} \quad (7)$$

$$\delta_x F = \frac{1}{\Delta x} \left\{ F[(j+\frac{1}{2})\Delta x, k\Delta y, n\Delta t] - F[(j-\frac{1}{2})\Delta x, k\Delta y, n\Delta t] \right\} \quad (8)$$

$$\nabla_x^2 F = \frac{1}{(\Delta x)^2} \left\{ F[(j+1)\Delta x, k\Delta y, n\Delta t] - 2F[j\Delta x, k\Delta y, n\Delta t] + F[(j-1)\Delta x, k\Delta y, n\Delta t] + F[j\Delta x, (k+1)\Delta y, n\Delta t] - 2F[j\Delta x, k\Delta y, n\Delta t] + F[j\Delta x, (k-1)\Delta y, n\Delta t] \right\} \quad (9)$$

$$F_+ = F[j\Delta x, k\Delta y, (n+\frac{1}{2})\Delta t] \quad (10)$$

$$F_- = F[j\Delta x, k\Delta y, (n-\frac{1}{2})\Delta t] \tag{11}$$

$$\delta_{+\frac{1}{2}t} F = \frac{2}{\Delta t} \{ F_+ - F \} = \frac{2}{\Delta t} \{ F[j\Delta x, k\Delta y, (n+\frac{1}{2})\Delta t] - F(j\Delta x, k\Delta y, n\Delta t) \} \tag{12}$$

In the finite difference equations variables which are computed by iterations are indicated by special symbols, for example, F_* , F_+ .

By the introduction of iterations in determining the value of certain variables, the user of the model has some choice in the approximations of the partial differential equations. This choice refers mainly to the time level at which the approximation of a certain term is made, thus we can say that the user has certain integration options.

The integrations are performed with two different operations. In one of the operations we are computing the new velocity components and the new water levels at timestep $n+\frac{1}{2}$ from information which is available at timestep n and timestep $n-\frac{1}{2}$ by use of

$$\begin{aligned} \delta_t u - f\bar{v} + 1/3 \left\{ \left(\frac{\bar{u}^x \bar{u}^x}{\bar{u}_*^x \bar{u}_*^x} \right)_x + \frac{1}{2} \left[\bar{u}_* (u_* + \Delta^2 \nabla^2 u_*) \right]_x^{-x} + 2\bar{v} \left(\frac{\bar{u}_*^y}{\bar{v}_*^y} \right)^y + \bar{v}^x \left(\frac{\bar{u}_*^y}{\bar{v}_*^y} \right)^y \right\} \\ + g \frac{\bar{\zeta}^t}{\bar{\rho}_x} + \frac{1}{2} \frac{g}{\rho} (\bar{h}^y + \bar{\zeta}^x) \delta_x \rho + g \frac{\bar{u}^t [(u_*)^2 + (\bar{v})^2]^{\frac{1}{2}}}{(\bar{h}^y + \bar{\zeta}^x) (\bar{C}^x)^2} \\ - \frac{\theta \rho_a W^2 \sin \psi}{\rho (\bar{h}^y + \bar{\zeta}^x)} - \delta_x \rho - k \nabla^2 u_- = 0 \end{aligned} \tag{13}$$

at $j+\frac{1}{2}, k, n$

$$\delta_{+\frac{1}{2}t} \zeta + \delta_x \left[(\bar{h}^y + \bar{\zeta}_+^x) u_+ \right] + \delta_y \left[(\bar{h}^x + \bar{\zeta}_+^y) v \right] = 0 \tag{14}$$

at $j+\frac{1}{2}, k, n$

where $\Delta = \Delta x = \Delta y$

The integration can be made without iteration at which u_* and h_+ are taken at the time level of the last available data, which would be $n-\frac{1}{2}$ for u and n for ζ . The results of this step can also be introduced again into u_* and ζ_+ , for example, by using the average of the newly-found velocity and u . Many options are available to the investigator, as described in Ref. 5.

Generally initially an option is used which results in a second order approximation in time and space of all terms in the equations except the momentum diffusion term. For constituent 1, the mass-balance equation is approximated in finite-difference form at time level n by

$$\begin{aligned}
 & \delta_{+\frac{1}{2}t} \left[\bar{P}_i (\bar{h} + \zeta) \right] + \delta_x \left[(\bar{h}^y + \bar{\zeta}_+^x) u_+ \bar{P}_{i+}^x \right] + \delta_y \left[(\bar{h}^x + \bar{\zeta}_+^y) v_+ \bar{P}_i^y \right] \\
 & - \delta_x \left[(\bar{h}^y + \bar{\zeta}_+^x) D_{x+} \delta_x P_{i+} \right] - \delta_y \left[(\bar{h}^x + \bar{\zeta}_+^y) D_y \delta_y P_i \right] \\
 & + \sum_{\ell=1}^{i-1} (\bar{h} + \zeta_+) K_{i\ell} P_{\ell+} \alpha_i + \frac{\text{---}t/2}{(\bar{h} + \zeta) K_{ii} P_i} + \sum_{\ell=i+1}^{\ell_{\max}} (\bar{h} + \zeta) K_{i\ell} P_{\ell} \beta_i \\
 & + (\bar{h} + \zeta) S_i = 0 \quad \text{at } j, k, n \tag{15}
 \end{aligned}$$

where $\alpha_i = \begin{cases} 0 & i = 1 \\ 1 & 1 < i \leq \ell_{\max} \end{cases}$

$\beta_i = \begin{cases} 0 & i = \ell_{\max} \\ 1 & 1 \leq i < \ell_{\max} \end{cases}$

ℓ_{\max} = maximum number of constituents

K = reaction matrix term

No iteration is required for the computation of the concentrations.

In the second operation, the new velocity component v and the new water levels at timestep n+1 are computed from information which is available at timestep n+1/2 and timestep n by use of

$$\begin{aligned}
 & \delta_t v + f\bar{u} + 1/3 \left\{ 2\bar{u}(\bar{v}_*)^x_x + \bar{u}^y(\bar{v}_*)^x_x + (\bar{v}_*^y \bar{v}_*^y)_y + \frac{1}{2} \left[\bar{v}_* (\bar{v}_* + \Delta^2 \bar{v}_*)^y \right] \right\} \\
 & + g \frac{\delta_y \zeta^t}{\rho} + \frac{1}{2} \frac{g}{\rho} (\bar{h}^x + \bar{\zeta}_+^y) \delta_y \rho + g \frac{\bar{v}^t [(\bar{u})^2 + (\bar{v}_*)^2]^{\frac{1}{2}}}{(\bar{h}^x + \bar{\zeta}_+^y) (\bar{C}^y)^2} \\
 & - \frac{\theta \rho_a W^2 \cos \psi}{\rho (\bar{h}^x + \bar{\zeta}_+^y)} - \delta_x P - kV^2 v_- = 0 \\
 & \text{at } j, k, t+\frac{1}{2}, n+\frac{1}{2} \tag{16}
 \end{aligned}$$

$$\begin{aligned}
 & \delta_{+\frac{1}{2}t} \zeta + \delta_x \left[(\bar{h}^y + \bar{\zeta}_+^x) u \right] + \delta_y \left[(\bar{h}^x + \bar{\zeta}_+^y) v_+ \right] = 0 \\
 & \text{at } j, k, t+\frac{1}{2}, n+\frac{1}{2} \tag{17}
 \end{aligned}$$

It will be noted that u is computed only in the half-integer timesteps,

while v is computed in the integer value of the timestep, and the water levels are computed every half timestep.

The concentrations are also computed every half timestep, and in the second operation of the computation method the following equation is used:

$$\begin{aligned} & \delta_{+\frac{1}{2}t} \left[P_i (\bar{h} + \zeta) \right] + \delta_x \left[(\bar{h}^y + \bar{\zeta}^x) u P_i^x \right] + \delta_y \left[(\bar{h}^x + \bar{\zeta}^y) v P_i^y \right] \\ & - \delta_x \left[(\bar{h}^y + \bar{\zeta}^x) D_x \delta_x P_i \right] - \delta_y \left[(\bar{h}^x + \bar{\zeta}^y) D_y \delta_y P_i \right] \\ & + \sum_{\ell=1}^{i-1} (\bar{h} + \zeta) K_{i\ell} P_{\ell} \alpha_i + \frac{t}{2} (\bar{h} + \zeta) K_{ii} P_i + \sum_{\ell=i+1}^{\ell_{\max}} (\bar{h} + \zeta_+) K_{i\ell} P_{\ell} \beta_i \\ & + (\bar{h} + \zeta) S_i = 0 \qquad \text{at } j, k, n+\frac{1}{2} \end{aligned} \tag{18}$$

The rather extensive fourth order expressions for the advection terms of the momentum equations are required for stability. In the large computational fields with much variation in velocities, simple second order approximation of the advection terms appeared to be unstable, generating interactions between the two momentum equations, and thus generating high vorticities with the dimension of the grid spacing. The Arakawa [6] expression used here prevents this occurrence.

The model requires a large number of time-varying boundaries. At the seaward boundaries, water levels (or currents) are prescribed by linear interpolation of amplitudes and phases between points of prototype measurement, as described in Ref. 1.

If water levels are used as boundary conditions, the advection terms near the seaward boundaries of the model are omitted. This omission simplifies the boundary description. It can be shown that, in addition to the water levels, velocity data is required to describe the boundary when the flow is into the model when the advection terms are included. The contributions of these terms are very small, as the velocities in the Randdelta II model are either nearly perpendicular or nearly parallel to the boundary and the rate of change is also small. More important than the advection terms are the contributions of the pressures induced by salinity differences. The salinities are prescribed during inflow and computed from inside the field during outflow. The transition in the salinity between outflow and inflow is according to half the cycle of a cosine function over a period which can be set.

All discharges into the system, wind intensity and direction and atmospheric pressures are time-varying.

The computations of the tidal marshes and flats are described in Ref. 5.

IV. MODELING SYSTEM

For successful model investigations with numerical models a system of interlocking programs is required for data handling, simulation and graphical representation. The system used in this investigation has three major parts, namely, the Input Data Processor (IDP), the Simulation program (SIMSYS2D) and the Simulation Data Display system (SDD).

One of the functions of IDP is to order the input data from a logical input form into a form that permits it to be readily used by the simulation. For example, discharges and wind speed and direction can be inserted as individual time series. The processor will order all this data in a sequence fit for simulation. Another very important function of this processor is to document the data in an easily readable report and in easily accessible data files for graphical representation.

The system which is used for data display is designed to make charts and graphs of simulation results and inputs for study and reporting purposes. For example, Fig. 4 shows a chart made with the system to indicate which area is under water when the static water level is .50 m above the reference level. Also, comparisons of simulation results with other simulation data or with observed data can be made.

The system is designed to be used by civil engineers. Its operation requires no special knowledge of the computer science aspects of data handling and manipulation other than a thorough understanding of the computation procedures outlined briefly in the previous section of this paper.

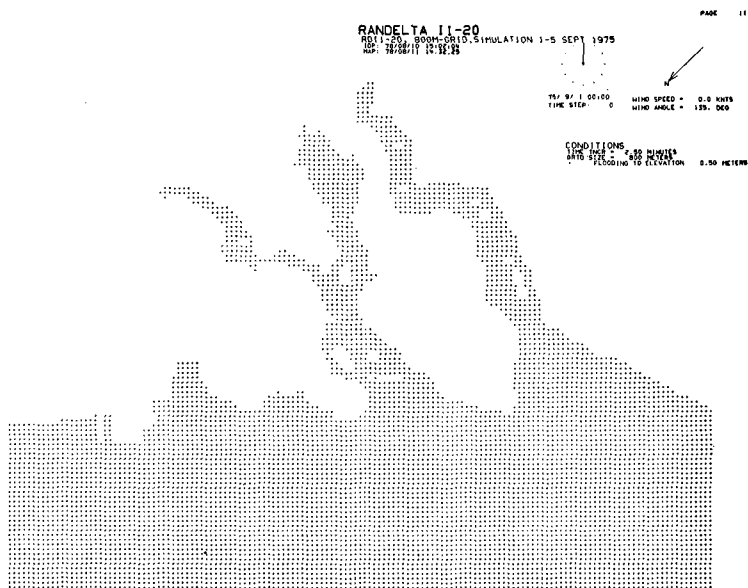


Fig. 4--SDD chart of submerged area at a still water level of 0.5 m above the reference level

V. ASPECTS OF TIDAL WAVE PROPAGATION IN THE MODEL AREA

The tidal flow in the sea area of the Randdelta II model is part of the flow in a much larger system, thus to properly represent this flow in the model area, boundary conditions along the open sides of the model have to be obtained. These boundary conditions can be derived from a model covering a larger area or from a field survey. For some of the studies with the model involving storm surges, results from a larger model are being used, but for the adjustment of the model, results of a large field survey are available in which water levels and currents on each of the open sides of the model were determined. In the computational procedures of the simulation system water levels or currents could be used as boundaries. Consequently, in the beginning of the investigation the question arose as to what would be the best combination of water level and current boundary conditions, taking into account that the boundary data contain errors and that these errors may be amplified. For example, if only flow is used on all boundaries, their errors would lead to a gradual increase or decrease of the water levels in the system. Naturally, it would be better if at least one of the boundaries was prescribed by water levels.

The type of boundary conditions along the seaward sides of the model should be chosen in such a manner that

- o errors in the boundaries have a direct and easily detectable response in water levels and currents of the model results.
- o errors in the boundary are not amplified in the interior of the model.
- o errors in amplitudes should only influence the amplitudes in the system and errors in phase should only influence the phases of the tide.
- o the vertical tide in the sea area just outside the estuary is not much influenced by the choice of the Manning's coefficient and the accuracy of the bathymetry.

If the last condition can be fulfilled, the estuaries can be adjusted more or less independent from the adjustment of the offshore area of the model.

The three open boundaries of the model indicated in Fig. 5 are each in a different position as to the semidiurnal tidal wave, which is the dominating wave in the system. The tidal wave enters the model through boundary (1) and exits through (3). Boundary (2) is nearly parallel to the direction of tidal wave propagation. For each of these three boundaries we have two choices, namely, a water level boundary, designated by H in the following discussion, and a flow boundary, designated by Q.

Table 1 shows the possible combinations of boundary conditions. Note that the combinations a through d are the same as the combinations e through h, except in the condition for boundary (2).

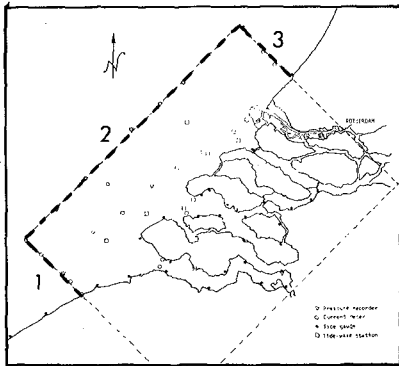


Fig. 5--Boundary designation

Table 1

Combination	Boundary		
	1	2	3
a	H	H	H
b	Q	H	Q
c	Q	H	H
d	H	H	Q
e	H	Q	H
f	Q	Q	Q
g	Q	Q	H
h	H	Q	Q

The following suppositions can be made:

- o The errors are relatively small compared to the measured values.
- o The errors are more or less equally distributed along the boundary.
- o Those errors are gradually diminishing along the perpendicular boundary 2.

These suppositions are partially supported by the fact that in preparing the results of the survey efforts were made to make the results coherent. In section I it is noted that the tide progresses parallel to the coast. This and the aforementioned suppositions make it plausible to first investigate the interaction of boundaries 1 and 3 in a one-dimensional analytic model with the axes along boundary 2, thus leaving the possibility of considerably reducing the number of combinations to be investigated later in connection with boundary 2.

For the one-dimensional analytic model the area in view was schematized to a channel with a constant width and depth. To find an analytic solution to the partial differential equations describing the long-wave motion in a tide, the equations are linearized with respect to the roughness term. Furthermore, the advection term and the Reynolds stresses in the momentum equation and the wave height with respect to the depth are neglected.

The following partial differential equations remain:

$$\frac{\partial Q}{\partial t} + \lambda Q + gDB \frac{\partial \zeta}{\partial x} = 0 \quad (19)$$

$$B \frac{\partial \zeta}{\partial t} + \frac{\partial Q}{\partial x} = 0 \quad (20)$$

where B = width (m)
 D = depth (m)
 g = gravity acceleration (m/s²)
 Q = flow (m³/s)
 ζ = wave height (m)
 λ = roughness parameter (1/s), equal to $\frac{gu}{C^2 D}$, with
 C = Chezy parameter (m^{1/2}/s)
 u = representative velocity (m/s)

These equations have a general solution of the type:

$$Q(x,t) = A_Q(X) \cos [\omega t + P_Q(X)] \quad (21)$$

$$\zeta(x,t) = A_\zeta(X) \cos [\omega t + P_\zeta(X)] \quad (22)$$

By substituting Eqs. (21) and (22) into Eqs. (19) and (20) and by use of boundary conditions, solutions for the amplitudes and phases of the tidal waves can be obtained. As the system is linear, several constituents can be considered, but in the analysis only the semidiurnal tide was considered.

From the field survey, good estimates of water levels and currents of the semidiurnal tide could be made. These were used for the combinations a through d of Table 1. For the depth the average of the region was taken and the friction factor was estimated. In these tests comparisons were made of the horizontal and vertical tide for each combination with increased and decreased amplitudes at one of the boundaries and with phase shifts at that boundary. Also, tests were made with increased and decreased depth and bottom friction. Some of the combinations of boundary conditions were very sensitive to changes in the friction factor. For example, if an H boundary is taken at (1) and a Q boundary at (3), a decrease in the resistance factor of 20% increases the amplitude at boundary (3) by about 50%. The distribution of the error along the model is shown in Fig. 6 for an increase and decrease of the friction factor of 20%. Figure 7 shows the distribution of the error in a similar manner for Q.

The result of this analysis was that water levels at each of the sides of the model was by far the best combination. In that combination the model is insensitive in the water levels to changes in bottom friction and has a relatively small response in the amplitude and phase of the horizontal tide to changes in bottom friction.

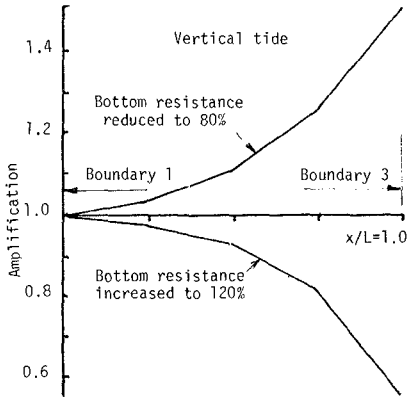


Fig. 6--Influence of change in bottom resistance factor λ on the vertical tide by use of H at boundary 1 and Q at boundary 3

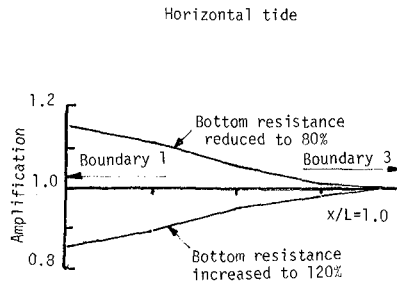


Fig. 7--Influence of change in bottom resistance factor λ on the horizontal tide by use of H at boundary 1 and Q at boundary 3

After having established the best combination of boundary conditions for boundaries 1 and 3, an analysis was made of the long open boundary 2. This analysis was made with a submodel of the Randdelta II model. This submodel, described in section VI, models the offshore area of the Randdelta II model with a grid size of 1600 m. Simulations with flow data obtained from the field survey at boundary 2 indicated that errors in Q had a large effect upon the water levels in the model region. Errors in water levels along boundary 2 appear to have a minimal effect upon water levels in the model area and would affect only the flow field locally. Consequently, a water level boundary condition was also chosen here. The errors in that water level boundary were reduced by procedures outlined in Ref. 1.

The results of the analysis of the boundary conditions for this offshore area are not generally applicable. The optimum choice depends on the size of the offshore area to be modeled, the depth and the bottom friction.

For example, an extensive research effort with one- and two-dimensional models made by the Delft Hydraulic Laboratory, for determining the optimal combination of boundaries for a hydraulic model of an offshore area near the entrance of the New Waterway, indicated that a combination of H and Q boundaries was to be preferred. This model covers a small section of the Randdelta II model.

To assist in the adjustment of the estuary sections of the Randdelta II model, a one-dimensional analysis of the tidal wave propagation into the Eastern and Western Scheldt was also made. As shown in Figs. 8 and 9, incremental increases in depth and the linear bottom resistance term do not give a linear change in amplification and phase shift.

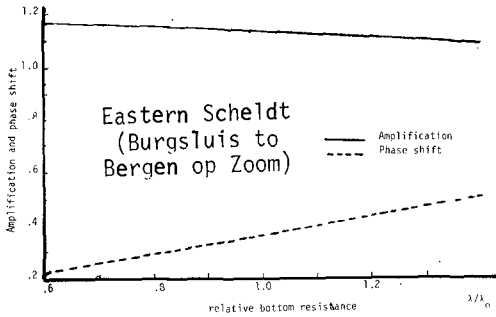


Fig. 8--Influence of change in bottom resistance on amplification and phase lag for the Eastern Scheldt

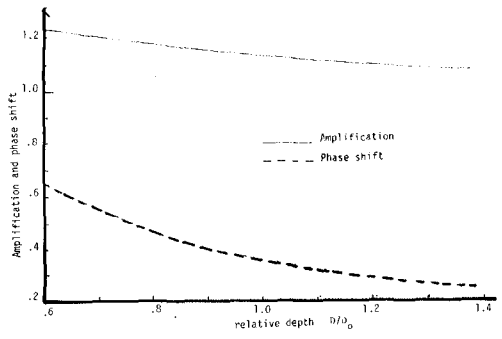


Fig. 9--Influence of change in depth on amplification and phase lag for the Eastern Scheldt

VI. SUBMODELS

The adjustment of tides and currents in the estuaries appeared to be difficult. The estuaries are relatively poorly represented on the 800m grid, certainly in comparison with the offshore area. To progress more rapidly with the adjustments of these sections of the model, several submodels were built based upon data abstracted from the Randdelta II model.

The depth array for the Randdelta II model was obtained by drawing all cross-sections at lines through the depth grid points which are more or less perpendicular to the main current direction. Subsequently depth approximations at the grid points were made in such a manner that the area of the cross-section in the model is about the same as in nature. Care was taken that channels were well represented. With the submodels the opportunity existed to verify the adequacy of this representation.

The first step in the adjustment process is to check the submergence of tidal flats. The criteria used in the flow simulation are quite complicated, mainly due to the demands of conservation of the mass of water and the mass of the constituents.

The submergence is checked by procedures in the SDD system which operate in the same way as in the simulation (Fig. 4). With the SDD system charts can then be made indicating the area which is submerged at certain specified water levels. On these charts it can be checked if small channels become closed by the procedures.

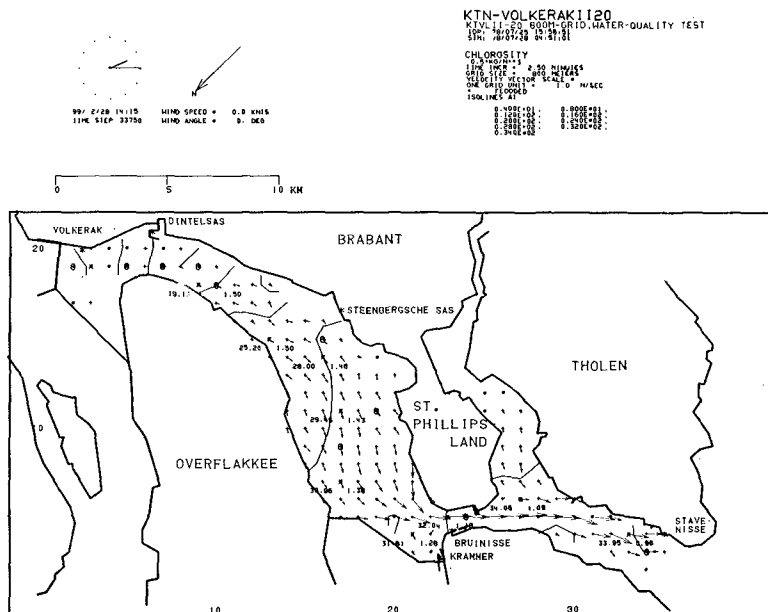


Fig. 10--Chlorosity distributions computed with the KTN-Volkerak II submodel of the Randdelta II model

Figure 10 shows a typical graphical result obtained from a simulation with a submodel. For the adjustment of this submodel observed water levels were used as boundary conditions. The first simulation with this submodel was made with an initial estimate of the Manning's coefficient. Subsequently a simulation was made in which in a certain well-defined region between two water level stations the Manning's coefficient was increased. Also a simulation was made in which the depth in that defined region was increased proportionally 10%, but using Chezy values in that region obtained from the original run of that region. By analyzing the computation results for water levels, functional relationships between changes in Manning's coefficient and depth increases for the amplification and phase lag of the semidiurnal tide in the considered section of the model could be determined. From these relations it was possible to make a good estimate of the required changes to match the propagation in the model with that in the prototype. If depth changes were required, those were made by reviewing the used depth approximation in relation to the actual cross-sections. Other sections of the submodel were adjusted in a similar fashion.

The depth appeared to be rather sensitive in the shallow water areas and the shape of the tidal curve in the eastern part of this submodel is determined to a very large extent by the time of submergence of the tidal marshes. Even though it was realized that only a rough approximation of the flow in this submodel could be obtained, considerable

effort was expended, as the phase of the currents at the boundary of the submodel would be of importance in simulating the Eastern Scheldt proper. In this submodel, fresh water discharges through sluices at the eastern extremity of the model were present. These discharges are of considerable magnitude, and in a part of the submodel area salinity differences in the vertical existed in the simulation period. Consequently, the basic model assumption that the area is well mixed was violated. The salinity differences in the vertical induce vertical circulations which can be represented locally by a larger diffusion coefficient.

To adjust this coefficient long duration simulations were made of a condition in which the discharge into the system was kept approximately constant. The model was started with the salinity of the open boundary everywhere in the whole model. By simulating two months and adjusting the diffusion coefficient in the region with vertical density differences, equilibrium conditions could be obtained which matched quite well the observed conditions.

Dronkers [7] presents an analytical study of the longitudinal dispersion in shallow well mixed estuaries based upon a study of exchange processes in the model area. He concluded that for well mixed systems, in addition to the dispersion process in the main channel, the exchange of water between the channel and the tidal flat or marsh area is of importance, as well as the mixing process on the tidal flat itself. As the water movements and the resultant exchanges are apparently quite well represented even with the relatively coarse grid, no further adjustment of diffusion coefficients in the well mixed region of the model other than the original estimate was required.

This submodel was also used in many experiments for checking and evaluating computation procedures. It was found that the computation is insensitive to the time levels in the advection terms, and that the phase of the tide is influenced when the time step is increased beyond 2.5 minutes.

In addition to the submodels which have the same grid size and depth as the Randdelta II model, a model of the offshore area with a grid size of 1600m was used in the adjustment process. This model had the same seaward boundaries as the Randdelta II model, and it had water level boundaries at the mouths of the Eastern Scheldt and Western Scheldt.

This model was relatively small and inexpensive to run. Many effects in this offshore zone could be studied effectively with this model. For example, the boundary conditions developed by cross-spectral analysis, as described in Ref. 1, were tested and evaluated with this model. Presently it is being used to evaluate the seaward boundaries for storm surge conditions, which were abstracted from a model of a section of the North Sea.

The Randdelta II model will furnish the boundary conditions of a model of the Eastern and Western Scheldt and a small adjacent offshore area with a 400m grid (Fig. 1). This model will be used for more detailed computations. Since this model is very large, submodels are again being used for adjustment and for experiments.

VII. MODEL ADJUSTMENT AND VERIFICATION

Modeling with a numerical model requires large data sets, and setting up the Randdelta II model has been a major effort. Much of the time-varying data for the tidal inputs originated from a field survey (Ref. 1), but also much data from other sources were used.

For example, all the major discharges in the system had to be obtained from the different logs which were kept by government officials at many places. Weather data had to be obtained and digitized. As already mentioned, determining the depth array from various survey charts was a major undertaking, and all data for making charts used for graphical representation of water level, velocity and concentration fields had to be digitized. Furthermore, all coordinates of the measuring stations on the national grid system had to be translated to those on the computational grid so that the closest available grid point can be used for abstracting similar data out of the model.

After the adjustment of the submodels, the depth and Manning's data were transferred back into the Randdelta II model and a series of experiments were made. The studies about the propagation of the semidiurnal tidal wave in the offshore area and in the estuaries gave guidance as to making increasingly better fits between observed and computed data. Even though the model is not considered completely adjusted in all respects, the agreement between observed and computed is good (Fig. 11). In one of the four graphs, the observed as well as the input tide is shown. All other graphs show the observed and computed vertical tides.

The recording station Steenbergse Sas is about 90 km from the closest open boundary and the recording station Baarland about 80 km. The small disturbances shown in the computed record for the station Steenbergse Sas originate from the incremental changes in the land-water boundary by the computation procedures.

The agreement between the observed magnitudes of currents and directions is also good, particularly if one takes into account that the observed currents are obtained at a certain point in a vertical. Figure 12 shows a comparison of currents. The Knikpunt III station is near the boundary and reflects all errors made in the data inserted.

With the simulation system, charts can be made of the velocity distributions at a particular time. Figure 13 shows such a velocity distribution on a much reduced scale. Note that extensive areas in the estuaries are exposed.

Presently, the model has been verified only to a limited extent by use of boundary data not previously used for adjustment. The results are very similar to those shown. Since it is the intention to use the model also for time periods at which no boundary input data are available, the verification process has to include the prediction of the boundaries from the fixed stations.

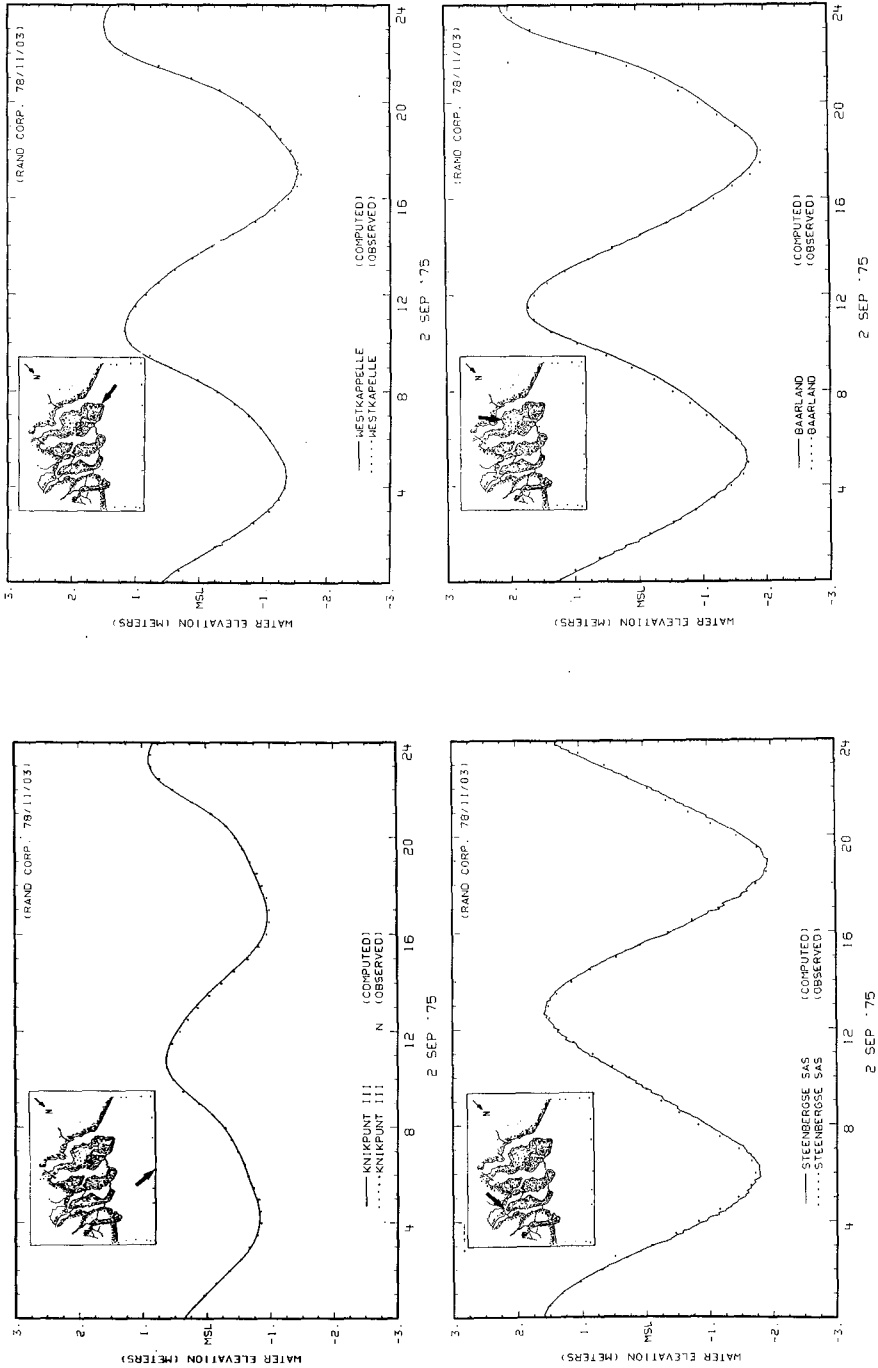


Fig. 11--Computed and observed water levels at four locations for September 2, 1975

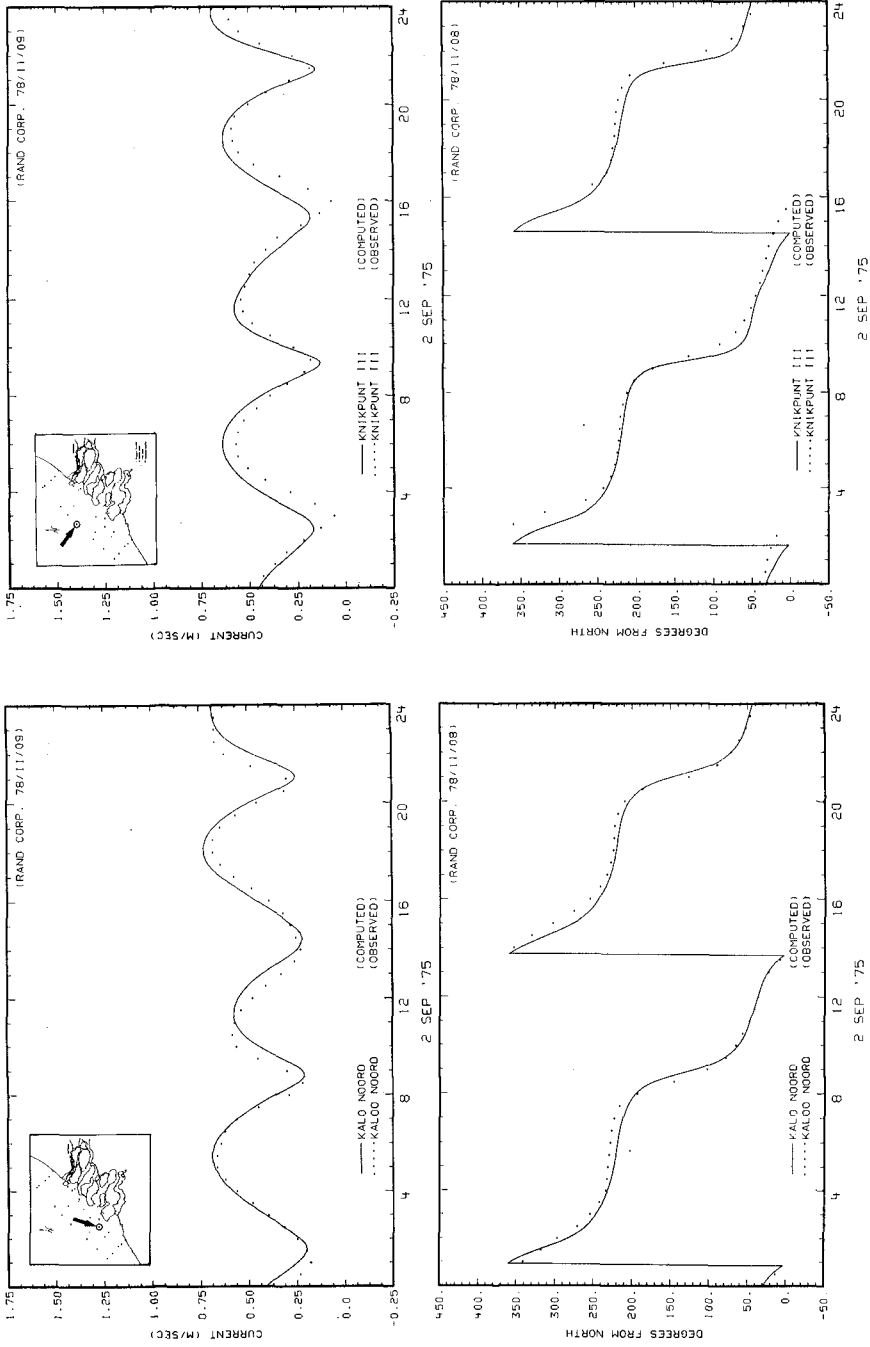


Fig. 12--Computed and observed current magnitudes and directions at two stations for September 2, 1975

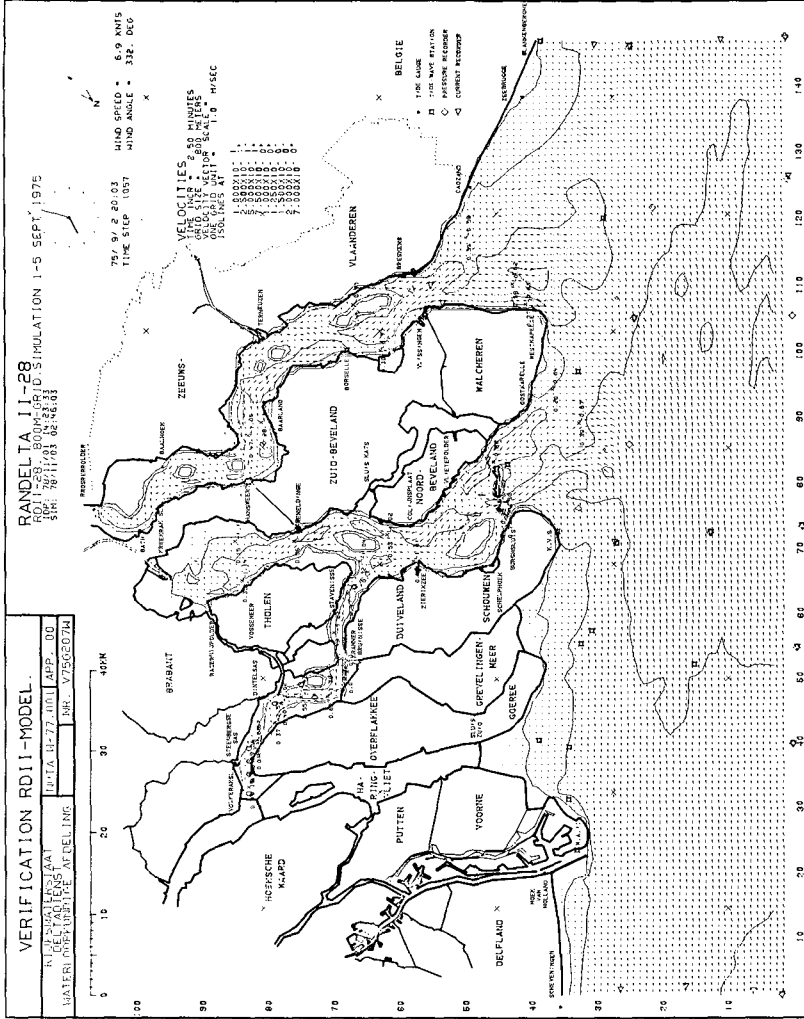


Fig. 13--Computed velocity distribution on September 2, 1975 at 20:03 hrs

REFERENCES

1. Van de Ree, W. J., J. Voogt and J. J. Leendertse, "A Tidal Survey for a Model of an Offshore Area," *Proc. 16th Int. Conference on Coastal Engineering*, 1978.
2. Godin, G., *The Analysis of Tides*, University of Toronto Press, Toronto, 1972.
3. Leendertse, J. J., *Aspects of a Computational Model for Long-Period Water-Wave Propagation*, The Rand Corporation, RM-5294-PR, May 1967.
4. Leendertse, J. J., and E. C. Gritton, *A Water Quality Simulation Model for Well-Mixed Estuaries and Coastal Seas: Vol. II, Computation Procedures*, The Rand Corporation, R-708-NYC, July 1971.
5. Leendertse, J. J., C. N. Johnson, and A. B. Nelson, *The SIMSYS/WAQUA System for Two-Dimensional Modeling of Estuaries and Coastal Seas*, The Rand Corporation, (to be published).
6. Grammelvedt, A., "A Survey of Finite-Difference Schemes for the Primitive Equations for a Barotropic Fluid," *Monthly Weather Review*, Vol. 97, No. 5, May 1969.
7. Dronkers, J., "Longitudinal Dispersion in Shallow Well Mixed Estuaries," *Proc. 16th Int. Conference on Coastal Engineering*, 1978.

CHAPTER 62

WAVE SET-UP IN THE SURF ZONE

by Uwe A. Hansen¹⁾

In designing coastal protective structures the knowledge of the static load due to the water level elevation is as important as that of the dynamic load due to the waves.

The structure, designed at sandy coasts with well formed surf zones on the beach - these areas are the basis of this examination - has to stand against both, the superposition of the static and dynamic load, which are dependent on each other. Undoubtedly a rise in the design water level (a summation of different influences - see figure 1) will cause an increase in the wave heights and the reverse will happen, when the design water level decreases.

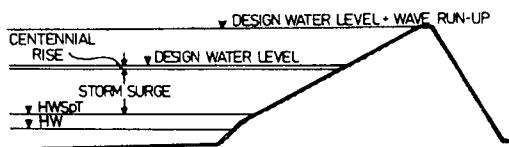


Fig. 1. - Design water level for the determination of the height of a sea dyke

The location of the wave breaking point in the surf zone will also shift with changing water levels and also the magnitude of the wave run-up and the unknown wave set-up. That shows that only the exact knowledge of all possible factors - including wave-

1) Dr.-Ing. Hydraulic Engineer, Heide, Federal Republic of Germany, formerly Leichtweiß-Institut für Wasserbau, Techn. Univ. of Braunschweig

set-up, influencing the height of the design water level, makes a construction safe and economical.

Up to now, the magnitude of the phenomenon wave set-up and its influence on the design water level remains practically unknown. Though formulas exist to compute the magnitude of wave induced set-up in the surf zone, which mainly were developed out of small scaled model tests, e.g. Munk(13), Savage(14), Fairchild(4), Dorrestein(3), and Longuet-Higgins and Stewart(12) and many others (see Hansen(8)), comparisons with measurements show, that the existing wave theories are not adequate to describe the difficult processes in the surf zone as a non-stationary three-phase-flow of water, air and solid particles. Comparisons of measured run-up heights at sea dykes after heavy storms with calculated values showed, that there must be an unknown factor up to now, which could be the wave set-up.

Therefore field measurements were made by the LEICHTWEISS-INSTITUT of the Technical University of Braunschweig, sponsored by the GERMAN RESEARCH FOUNDATION (Bonn), at the west coast of the island of SYLT in the North Sea (see figure 2) in winter 1975/76 to determine the wave set-up in the surf zone under prototype conditions.

The measuring profile is shown in figure 3 with the locations of the measuring points. At stations W_4, W_3 and W_1 wave measurements were made with ultrasonic wave gauges. At the stations in the surf zone wave sensors with pressure cells were installed. The incident significant wave height $H_{0,s}$ was measured at station W_4 , 1280 m seaward of the toe of the dune.

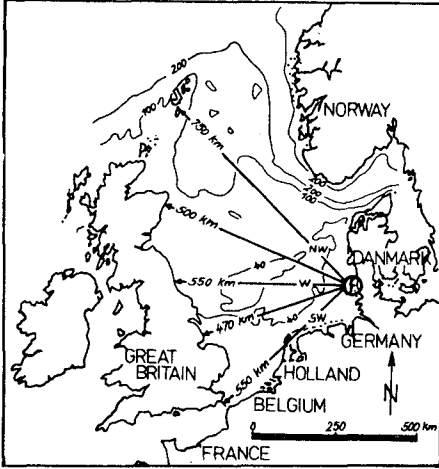


Fig. 2. - Location of the island of SYLT in the North Sea

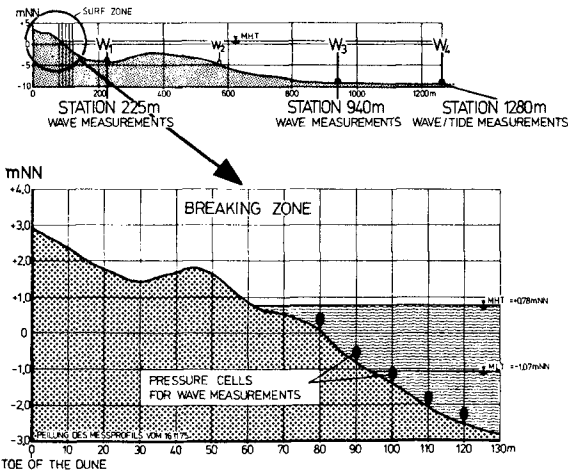


Fig. 3. - Measuring profile at the west coast of SYLT in North Sea

Though the definition of wave set-up is a simple one:

the height difference between MEAN WATER LEVEL
and STILL WATER LEVEL,

the determination of those two different water levels in field measurements under prototype storm conditions is a rather difficult task.

The water level, even under calm conditions and without any movements by waves, changes with the tide.

In the area off SYLT the difference between high and low water is about two meters. To compute or measure wave set-up in the surf zone, the height of the water level, defined as SWL, must first be determined there. As this water level can not be measured directly in the surf zone because of the influence of the unknown wave set-up, the place for registration this SWL must be positioned at a far seaward location where this unknown influence of wave set-up does not exist. As former measurements had shown, that the wave climate at the most seaward measuring point W_4 (1280 m seaward of the top of the dune) is not influenced by the shore and that shelf response effects are negligible there, this tide gauge was used to give the time variations of the SWL, the tide, by filtering out the wave components and translate it into the surf zone.

The second necessary value, the time variation of the MWL, was not defined by one of the well-known methods like "crest-to-crest" method or "zero-crossing" method. The analog wave records, obtained at the five measuring stations in the surf zone were first converted into digital values with a time span of 0.4 seconds.

The water level variations between two extremes, the maximum and the following minimum, was then defined as a wave (see figure 4).

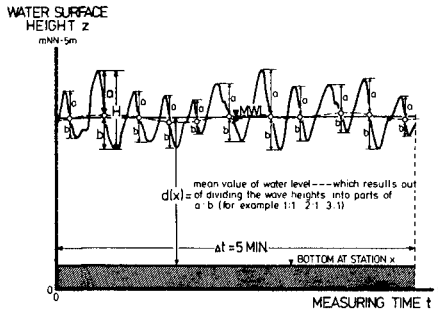


Fig. 4. - Determination of MWL out of prototype wave records by dividing height between wave crest and following trough into parts of $a:b$ after Hansen (8)

Within a time span of 5 minutes measuring time the result was a number of 750 digital values z_i , representing the water level fluctuations, out of which the MWL was computed as the mean value of all these water level variations. This method, done by a computer, is not very difficult and gives good results as comparisons showed.

These comparisons were the following:
 due to the well known behavior of the vertical asymmetry of waves in the surf zone, the part of the wave over the MWL is about 66% to 85% of the total wave height just before breaking (see Gaillard (6), Galvin and Eagleson (7) and Inman and Quinn (10),

so that only 33% to 15% of the wave height remains below the MWL. With these criterions the MWL was determined by dividing the heights in water level fluctuations between wave crests and wave troughs into these parts of percentage. Then the MWL was defined as the mean value of all these resulting points within a designated time span of 5 minutes (see figure 5).

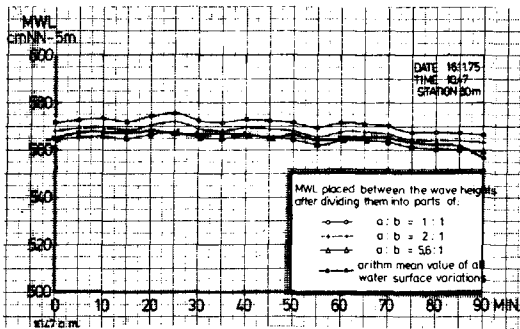


Fig. 5 - Time variation of MWL at station 80 m after dividing all wave heights by differnt parts

The comparison showed, that the results of these more time-consuming methods of dividing all wave heights into parts between 66% to 85% over and 33% to 15% below the MWL differ only a few centimeters from those calculated by taking only the mean values of all water surface variations measured over a certain time span of 5 minutes.

The reason, that this method - the arithmetic mean value of all water surface variations over a certain time span - is equally suitable to yield the MWL for

these irregular waves in the surf zone is due to the great horizontal asymmetry of these waves. Just before breaking the waves have a form with very short leeward and long windward slopes (see figure 6). As a result, balance of the areas in a wave form above and below the MWL - which is equal to the arithmetic mean value of all water surface variations - can only be reached, when the waves steepen in the surf zone.

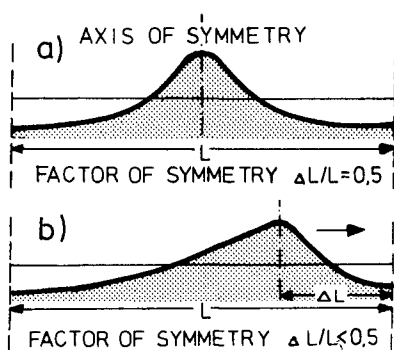


Fig. 6. - Asymmetries: (a) vertical and (b) horizontal of waves in the surf zone after Führböter (5)

Now some results of the field measurements at the west coast of the island of SYLT in the North Sea: The measurement program included 27 separate measurements of about occasionally 60 minutes registration time at different sea and wind conditions. Those who are interested in detail should refer to the report by the writer (8).

Figure 7 shows the spatial variations of wave set-up at a certain time span for run nr. 15 with an incident significant wave height of 1.58m and a

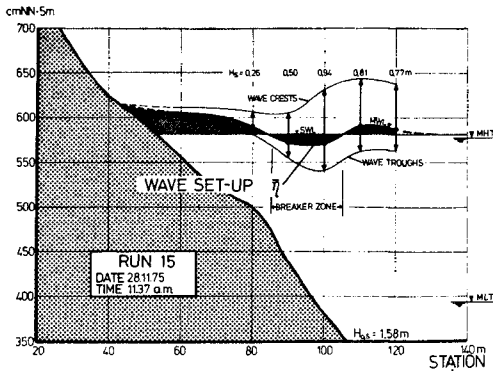


Fig. 7 - Spatial variation of wave set-up in measuring profile at the west coast of SYLT during falling tide

measuring time of about 60 minutes. The envelopes of the wave crests and troughs, measured at the stations in the surf zone are also given in this figure to clearly reveal their relationships with respect to the MWL.

Based on the 27 sets of measurements the maximum wave set-up $\bar{\eta}_{\max}$ on the beach at the so called set-up line is estimated to be

$$\bar{\eta}_{\max} \approx 0.3 H_{0,s}$$

as seen in figure 8, where $H_{0,s}$ is the significant wave height measured at station W_4 , 1280 m seaward of the toe of the dune (see fig. 3). The relationship shows good agreement with theoretical results of Collins (2), but less so with those of Dorrestein (3) and Saville (15).

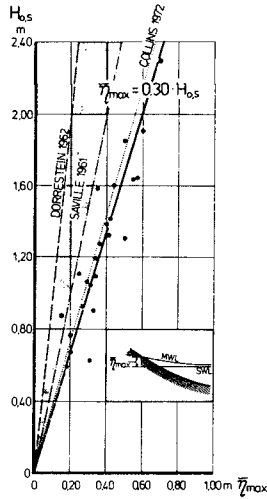


Fig. 8. - Maximum wave set-up in dependence on significant incident wave height after Hansen (8)

In relation to the significant wave height at the breaking point in the surf zone $H_{B,S}$, the maximum wave set-up can be expressed as

$$\bar{\eta}_{max} \cong 0.5 H_{B,S}$$

as seen in figure 9, in which also the theoretical results of Hwang and Divoky(9), Battjes(1) and Jonsson and Jacobsen(11) are given.

Beside these maximum values of the wave set-up, measured at the set-up line on the beach, the values at the breaking point in the breaking zone are of great interest too. The measurements and computations showed in the area of the sandy beach off SYLT, that the wave set-up there not only depends on the height of the incident offshore wave, but also on the width and location of the breaking zone, which varies with the tidal cycle.

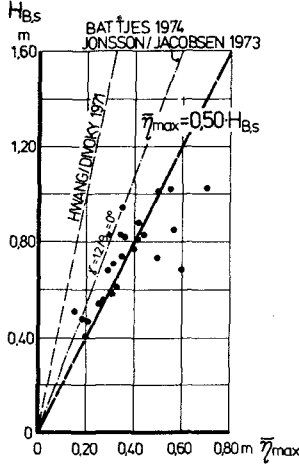


Fig. 9. - Maximum wave set-up in dependence on wave height at breaking point after Hansen(8)

As shown in figure 10, in wide breaker zones mainly intermediate forms of spilling and plunging breakers predominate, whereas in narrow breaker zones plunging breakers occur.

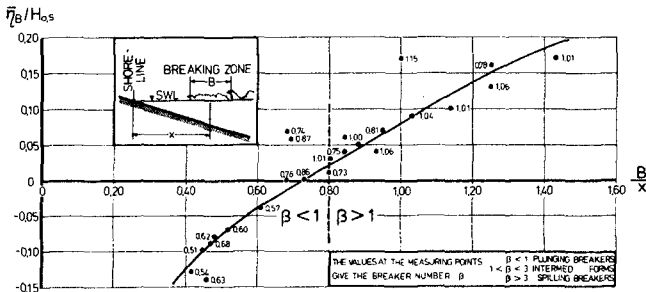


Fig. 10 - Wave set-up at breaking point versus significant wave height in dependence on width of breaking zone versus location of breaking zone after Hansen(8)

With the variation of the width of the breaking zone and the breaker forms (classification after Führböter(5)), the values of wave set-up at the breaking point vary too: values greater than 1 - a rise in water level (MWL above SWL)- were measured in wide breaker zones, values less than 1 in narrow ones (MWL under SWL).

From these interesting results the following conclusions were drawn (see figure 11 - a schematical drawing):

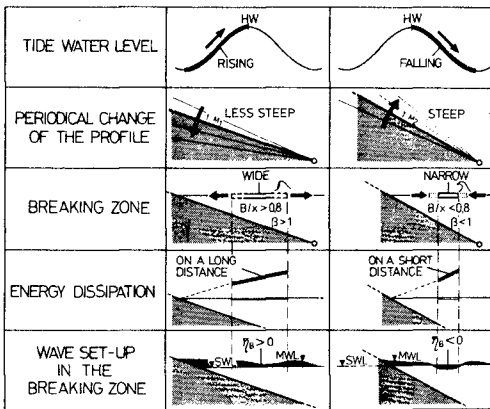


Fig. 11 - Wave set-up in breaking zone in relation to tide, measuring profile, and energy dissipation

As the underwater slope of the sandy beach varies with the tidal cycle, the wave set-up at the breaking point varies too. The reason for this variation of $\bar{\eta}_B$ is that the slope of the underwater profile in the surf zone changes more or less periodically with the tide, as profile measurements at this

sandy coast of SYLT had shown. With falling water levels the slope becomes steeper. With rising water levels it becomes more gentle, so that the position and width of the breaker zone changes.

In wide breaker zones, where plunging and spilling breakers predominate, the rate of energy dissipation is less, so that a greater part of wave energy is preserved to create wave set-up and the MWL in the breaking zone remains above the SWL. On the other hand, the increased energy dissipation in narrow breaker zones, where plunging breakers predominate causes a wave set-down at the breaking point, that means the MWL lies below the SWL (see figure 11).

As a conclusion it can be said, that the field investigations at the sandy coast of the island of SYLT have shown, that the maximum wave set-up on the beach (at the set-up line) can reach values up to 30% of the incident significant wave height and up to 50% of the significant breaker height. For engineering purposes the maximum values are more important, as they directly influence the height of the design water level for coastal protective structures. The results of this study can be used for other areas, when boundary conditions like sandy beach, similar slopes and well formed surf zone are given.

References:

1. Battjes, J.A., "Computation of Set-Up, Long-shore Currents, Run-Up and Overtopping due to Wind-Generated Waves," Communications on Hydraulics, Report No. 74-2, Delft University of Technology, The Netherlands, 1974

2. Collins, J.I., "Longshore Currents and Wave Statistics in the Surf Zone," U.S. Government Report, Feb., 1972.
3. Dorrestein, R., "Wave Set-Up on a Beach," presented at the second Technical Conference on Hurricanes, Miami Beach, Flo., Report No. 50, U.S. Department of Commerce, National Hurricane Research Project, 1962.
4. Fairchild, J.S., "Model Study of Wave Set-Up induced by Hurricane Waves at Narragansett Pier, Rhode Island," Beach Erosion Board, Coastal Engineering Research Center, Bulletin 12, 1958.
5. Führböter, A., "Einige Ergebnisse aus Naturuntersuchungen in Brandungszonen," Mitteilungen des Leichtweiss-Instituts für Wasserbau der Technischen Universität Braunschweig, Federal Republic of Germany, Heft 40, 1974.
6. Gaillard, D.D., "Wave Action in Relation to Engineering Structures," U.S. Army Corps of Engineers Professional Papers No. 31, U.S. Printing Office, Washington, D.C., 1904.
7. Galvin, C.J., and Eagleson, P.S., "Experimental Study of Longshore Currents on a plane Beach," Technical Memorandum No. 10, U.S. Army Coastal Engineering Research Center, Jan., 1965.
8. Hansen, U.A., "Brandungstau und Bemessungswasserstand," Mitteilungen des Leichtweiss-Instituts für Wasserbau der Technischen Universität Braunschweig, Federal Republik of Germany, Heft 52, 1976.

9. Hwang, L.S., and Divoky, D., "Breaking Wave Set-Up and Decay on gentle Slopes," Proceedings, 12th Coastal Engineering Conference, ASCE, Washington, D.C., 1970.
10. Inman, D.L., and Quinn, W.H., "Currents in the Surf Zone," Proceedings, 2nd Int. Conference on Coastal Engineering, Council on Wave Research, Richmond, Calif., 1951.
11. Jonsson, I.G., and Jacobsen, T.S., "Set-Down and Set-Up in a Refraction Zone," Report No.29, 13-22, Instituts of Hydrodynamics and Hydraulic Engineering, Technical University of Denmark, 1973.
12. Longuet-Higgins, M.S., and Stewart, R.W., "Radiation Stress and Mass Transport in Gravity Waves," Journal of Fluid Mechanics, Vol.13, 1962.
13. Munk, W.H., "The Solitary Wave Theory and its Application to Surf Problems," Annals of the New York Academy of Sciences, Vol. 51, Art.3, May, 1949.
14. Savage, R.P., "Model Tests on Wave Run-Up for Hurricane Protection Project," Bulletin, Beach Erosion Board, 1957.
15. Saville, T., jr., "Experimental Determination of Wave Set-Up," Proceedings, 2nd Technical Conference on Hurricanes, Miami Beach, Flo., Report No. 50, U.S. Department of Commerce, National Hurricane Research Project, 1962.

CHAPTER 63

ROLE OF 2D AND 3D MODELS IN JONSDAP '76

by

A. M. Davies

Institute of Oceanographic Sciences, Bidston Observatory,
Birkenhead, Merseyside, L43 7RA, England.

Abstract

This paper describes how a two-dimensional numerical model of the North Sea was used to determine optimum positions for the deployment of off-shore tide gauges during the JONSDAP '76 oceanographic exercise.

A three-dimensional model of the North West European Shelf is also described. Using this model the three-dimensional distribution of the M_2 tidal current over the shelf has been computed. This model has also been used to compute the wind induced circulation of the North Sea for the INOUT period of JONSDAP '76.

1. Introduction

In order to gain a more comprehensive understanding of the physical and biological oceanography of the North Sea, a large scale observational program took place in the northern North Sea during 1976, namely JONSDAP '76 (Joint North Sea Data Acquisition Program 1976), involving a number of European maritime countries.

This paper describes two hydrodynamic North Sea models. The application of one of these in determining optimum positions for off-shore tide gauges, prior to the JONSDAP '76 exercise is described. The use of these models in the interpretation of the physical data collected during the exercise is also considered. Employing a model to determine positions for off-shore tide gauges it is possible to take tidal measurements around its open boundaries at locations which have the greatest influence upon the tidal regime subsequently computed by it. Observational data collected at these points during the exercise constitutes an optimum open boundary data set for use with the model to simulate the motion of the sea for the period of the exercise.

The numerical model used to determine tide gauge sites, is two-dimensional, comprehensively non-linear, with a fine grid resolution of $1/9^\circ$ latitude by $1/6^\circ$ longitude; it covers the North Sea, the Skagerrak, the Kattegat and the eastern half of the English Channel (see Figure 1). The open boundaries correspond to those monitored during JONSDAP '76. Thus, the open boundary in the north runs along the line between the port of Wick and position $59^\circ 20'N$, $0^\circ 0'W$ and then along latitude $59^\circ 20'N$ between this point and the Norwegian coast. The southern open boundary is the line of longitude crossing the English Channel at $2^\circ W$. The southern end of the Kattegat is a very shallow region and has been considered closed.

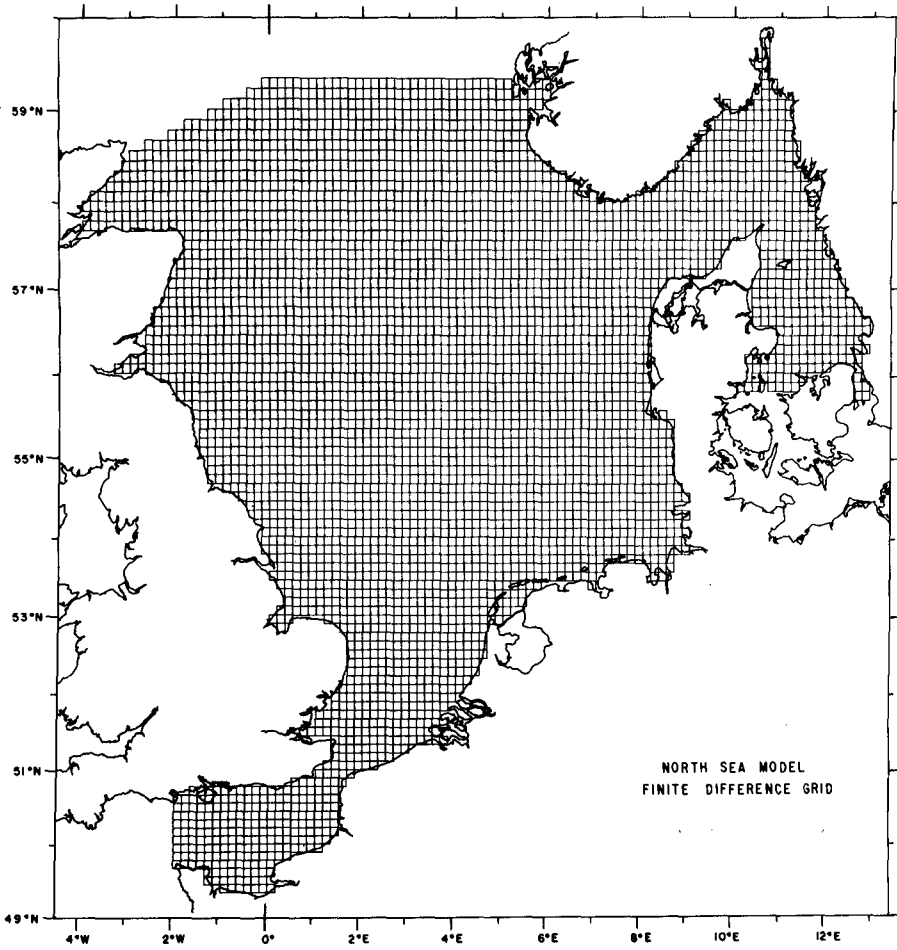


Figure 1. Two-dimensional North Sea model : finite difference grid.

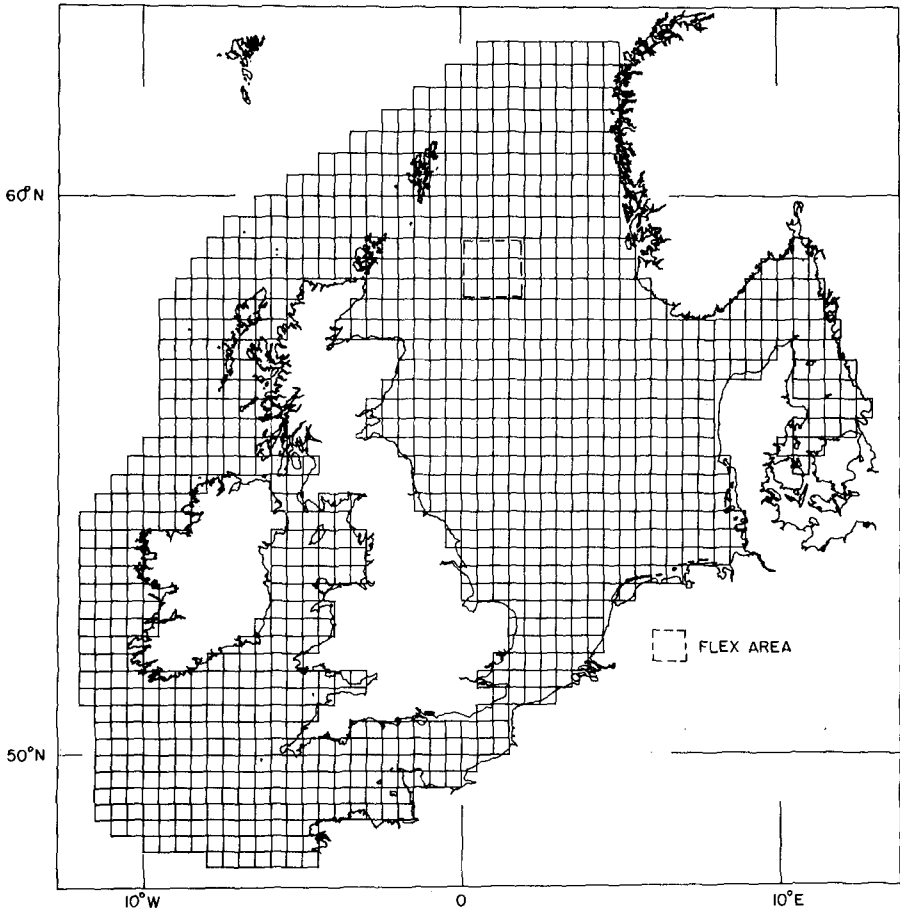


Figure 2. Three-dimensional shelf model : finite difference grid.

The second model employed is three-dimensional with a coarser grid resolution of $1/3^\circ$ latitude by $1/2^\circ$ longitude, covering the continental shelf as shown in Figure 2. The region in the northern North Sea, marked FLEX area on this diagram, denotes the sea area in which an intense biological measurement program took place concurrently with the physical measurements made during JONSDAP '76. The hydrodynamical equations include a quadratic bottom friction but are otherwise linear. Along the open boundaries, a radiation condition is employed to allow disturbances from the interior of the model to pass outwards.

This model is used initially to compute the distribution of the M_2 tide over the continental shelf. In this case boundary forcing is provided by M_2 tidal elevation alone. In a subsequent calculation the wind-induced circulation on the shelf for the period 15 March 1976 to 15 April 1976 (the INOUT period of JONSDAP '76) is computed. Boundary forcing for this case involved the M_2 tidal elevation and a meteorologically-induced elevation computed using the hydrostatic approximation. Meteorological forcing at the sea surface consisted of a time-average wind stress field and a time-averaged field of atmospheric pressure gradients. The time averaging was over the period cited above. The meteorologically induced circulation for the period was computed by subtracting the pure tidal motion from that computed with tide and meteorological forces.

2. Two-dimensional North Sea model (Figure 1)

The depth averaged equations of continuity and motion, including the non-linear advective terms and non-linear bottom friction may be written in polar coordinates as follows :

$$\frac{\partial \xi}{\partial t} + \frac{1}{R \cos \phi} \left\{ \frac{\partial (dU)}{\partial x} + \frac{\partial (dV \cos \phi)}{\partial \phi} \right\} = 0 \quad (1)$$

$$\begin{aligned} \frac{\partial U}{\partial t} + \frac{U}{R \cos \phi} \frac{\partial U}{\partial x} + \frac{V}{R \cos \phi} \frac{\partial (U \cos \phi)}{\partial \phi} - 2\omega \sin \phi V \\ + \frac{R U (U^2 + V^2)^{1/2}}{d} + \frac{g}{R \cos \phi} \frac{\partial \xi}{\partial x} = 0 \end{aligned} \quad (2)$$

$$\begin{aligned} \frac{\partial V}{\partial t} + \frac{U}{R \cos \phi} \frac{\partial V}{\partial x} + \frac{V}{R} \frac{\partial V}{\partial \phi} + \frac{U^2 \tan \phi}{R} + 2\omega \sin \phi U \\ + \frac{R V (U^2 + V^2)^{1/2}}{d} + \frac{g}{R} \frac{\partial \xi}{\partial \phi} = 0 \end{aligned} \quad (3)$$

where the notation is :

λ, ϕ east-longitude and latitude, respectively,

t time,

ξ elevation of the sea surface above undisturbed level,

h undisturbed depth of water

$d = h + \xi$ total depth of water,

R radius of the Earth,

ω angular speed of the Earth's rotation,

R coefficient of bottom friction,

g acceleration due to gravity,

u, v components of current in the directions of increasing λ, ϕ respectively, at a depth z below the undisturbed sea surface,

U, V components of depth mean current given by

$$U = \frac{1}{h + \xi} \int_{-h}^{\xi} u(z) dz, \quad V = \frac{1}{h + \xi} \int_{-h}^{\xi} v(z) dz \quad (4)$$

Equations (1) to (3) are approximated using finite difference methods : details are given by Davies and Flather [1978] and will not be presented here. An explicit finite difference technique is used to generate solutions through time and space over a staggered grid in which ξ, U and V are calculated at different mesh points. Solutions are generated from a state of zero displacement and motion, expressed by,

$$\xi = U = V = 0 \quad (5)$$

Along open and closed boundaries, appropriate dynamical conditions have to be satisfied. Thus, along a closed boundary the normal component of current is set to zero, i.e.

$$U \cos \psi + V \sin \psi = 0 \quad (6)$$

where ψ denotes the inclination of the normal to the direction of increasing λ . Along the open boundaries tidal elevation is specified according to the harmonic theory. Here we consider only the M_2 component of the tide, thus the tidal elevation on the open boundary is given by :

$$\xi = H \cos(\sigma t - g), \quad (7)$$

where for this component, H denotes the amplitude, σ the speed and g the phase.

3. Calculation of the M_2 tide and determination of an optimum deployment pattern for tide gauges.

In principle in order to calculate the M_2 component of the tide throughout the region covered by the two-dimensional model (Figure 1) it is necessary to have a detailed knowledge of the tide along the open boundaries of the model. Obviously prior to the JONSDAP '76 exercise this data was not available, and thus it was necessary to take M_2 tidal input from a numerical model of the continental shelf (Flather [1976]). Input data around the open boundaries of the latter model was derived from the observational data taken by Cartwright [1976]. A distribution of the M_2 tide over the North Sea in good agreement with observation (Davies [1976]) was obtained from the two-dimensional model shown in Figure 1.

Having thus proved the model it was possible to determine the sensitivity of the distribution of the M_2 tide computed with the model to changes in amplitude and phase of the M_2 tidal input along various sections of the open boundary. To this end, the northern open boundary of the model was divided into seven sections. Section 1 spans the seven grid boxes between the Scottish coast and the point ($58^{\circ}40'N$, $2^{\circ}0'W$), Section 2 the seven grid boxes between ($58^{\circ}40'N$, $2^{\circ}0'W$) and ($59^{\circ}0'N$, $0^{\circ}50'W$) and so on up to the seventh section which spans eight grid boxes between point ($59^{\circ}20'N$, $3^{\circ}50'E$) and the Norwegian coast. An eighth section comprised the whole of the southern boundary. In order to test the response of the model, the amplitudes of the M_2 tide in the first section were increased by 10 cm; at the same time the phase in this section and the amplitudes and phases in the other sections were kept constant. The numerical model was then run until the tidal regime was established and differences in amplitude and phase, ΔH and ΔG , between the tides of the new distribution and those of the original one were compared at a number of ports throughout the region. In a similar experiment, the phase of the M_2 tidal input in Section 1 was changed by 10° , and the changes ΔH and ΔG at a number of ports were determined. Similar numerical experiments were performed for all seven northern boundary sections, and for the eighth boundary section across the English Channel.

This sensitivity analysis showed that the tides along the north-east coast of Britain from Aberdeen to Inner Dowsing were particularly sensitive to changes along the north-western part of the boundary. They were also sensitive to changes near the Norwegian coast. Changes in tidal amplitude along this section of boundary also affected the tide along the south-east coast of England and in the Channel.

Obviously it is not practical to measure the tide at each northern boundary point of the model. However based on the results of the sensitivity analysis, it was evident that the most important regions

for tidal specification lay on the western and eastern sections of the Northern boundary and thus a distribution of five off-shore tide gauges that reflected this fact was used (Davies [1976]). Since the gauges were situated along the open boundaries of the model the tidal data measured during JONSDAP '76 can be readily incorporated in the model, and calculations using this data are presently in progress, aimed at determining the distribution of various tidal constituents over the North Sea.

4. Three-dimensional shelf model (Figure 2)

The equations of continuity and motion for homogeneous water, neglecting non-linear terms and shear in the horizontal, may be written in polar coordinates as :

$$\frac{\partial \xi}{\partial t} + \frac{1}{R \cos \phi} \left\{ \frac{\partial}{\partial \lambda} \int_0^h u dz + \frac{\partial}{\partial \phi} \int_0^h v \cos \phi dz \right\} = 0 \quad (8)$$

$$\frac{\partial u}{\partial t} - \gamma v = -\frac{g}{R \cos \phi} \frac{\partial \xi}{\partial \lambda} - \frac{1}{\rho R \cos \phi} \frac{\partial p}{\partial \lambda} + \frac{\partial}{\partial z} \left(N \frac{\partial u}{\partial z} \right) \quad (9)$$

$$\frac{\partial v}{\partial t} + \gamma u = -\frac{g}{R} \frac{\partial \xi}{\partial \phi} - \frac{1}{\rho R} \frac{\partial p}{\partial \phi} + \frac{\partial}{\partial z} \left(N \frac{\partial v}{\partial z} \right) \quad (10)$$

where we denote by :

- P atmospheric pressure at the sea surface,
- N the coefficient of vertical eddy viscosity, assumed to be a function of λ, ϕ, z and t . All other symbols are as defined previously.

In order to solve (8), (9) and (10) for ξ, u, v , boundary conditions have to be specified at the sea surface and at the sea bed. The surface conditions are

$$-P \left(N \frac{\partial u}{\partial z} \right)_0 = F_s, \quad -P \left(N \frac{\partial v}{\partial z} \right)_0 = G_s \quad (11a,b)$$

where F_s, G_s denote the components of wind stress acting on the water surface in the λ and ϕ directions, suffix 0 denoting evaluation at $z=0$.

Similarly at the sea bed, $z=h$, assuming a slip condition and

using a quadratic law of bottom friction, gives

$$\begin{aligned} -\left(N \frac{\partial U}{\partial z}\right)_h &= \bar{k} U_h (U_h^2 + V_h^2)^{1/2} \\ -\left(N \frac{\partial V}{\partial z}\right)_h &= \bar{k} V_h (U_h^2 + V_h^2)^{1/2} \end{aligned} \quad (12a,b)$$

where \bar{k} is the coefficient of bottom friction assumed constant.

We now seek a solution of equations (8), (9) and (10) for ξ, U, V subject to boundary conditions (11) and (12). Expanding the two components of velocity U, V in terms of m depth dependent functions $f_r(z)$ and horizontal-space and time-dependent coefficients $A_r(x, \phi, t)$ and $B_r(x, \phi, t)$ gives

$$U(x, \phi, z, t) = \sum_{r=1}^m A_r(x, \phi, t) f_r(z) \quad (13)$$

$$V(x, \phi, z, t) = \sum_{r=1}^m B_r(x, \phi, t) f_r(z) \quad (14)$$

Using the Galerkin method in the vertical space domain, equations (9) and (10) are multiplied by each of the basis functions f_k , and integrated with respect to z over the interval 0 to h . By integrating the term involving the vertical eddy viscosity, boundary conditions (11a,b) and (12a,b) can be included (Davies [in preparation]) giving

$$\begin{aligned} \int_0^h \frac{\partial U}{\partial t} f_k dz &= \gamma \int_0^h v f_k dz - \frac{g}{R \cos \phi} \frac{\partial \xi}{\partial x} \int_0^h f_k dz - \frac{1}{PR \cos \phi} \frac{\partial P}{\partial x} \int_0^h f_k dz \\ &+ f_k(0) \frac{G_s}{\rho} - f_k(h) \bar{k} U_h (U_h^2 + V_h^2)^{1/2} - \int_0^h N \frac{\partial U}{\partial z} \frac{\partial f_k}{\partial z} dz \end{aligned} \quad (15)$$

and

$$\begin{aligned} \int_0^h \frac{\partial V}{\partial t} f_k dz &= -\gamma \int_0^h u f_k dz - \frac{g}{R} \frac{\partial \xi}{\partial \phi} \int_0^h f_k dz - \frac{1}{PR} \frac{\partial P}{\partial \phi} \int_0^h f_k dz \\ &+ f_k(0) \frac{G_s}{\rho} - f_k(h) \bar{k} V_h (U_h^2 + V_h^2)^{1/2} - \int_0^h N \frac{\partial V}{\partial z} \frac{\partial f_k}{\partial z} dz \end{aligned} \quad (16)$$

for $k = 1, 2, \dots, m$

Consider now the choice of basis functions $f_r(z)$. Davies [in preparation] has demonstrated that an expansion of 10 cosine functions is sufficient to accurately reproduce the depth variation of current, and has successfully applied such an expansion to the computation of the wind induced circulation of the North West European Continental Shelf (Davies [1979]). In this paper we again use an expansion of 10 cosine functions, with $f_r(z)$ given by,

$$f_r(z) = \cos \alpha_r z/h \tag{17}$$

The choice of α_r is quite arbitrary, provided $f_r(h)$ is non zero, and a suitable choice for α_r is,

$$\alpha_r = (r-1)\pi \quad \text{for } r=1, 2, \dots, m \tag{18}$$

Substituting expansions (13) and (14) into equations (15), (16) and (8), gives a set of $2m + 1$ equations, which when integrated forward through time subject to initial and boundary conditions, yields ξ and the set of coefficients A_r, B_r at progressive time steps. Using expansions (13) and (14), the u and v components of current at any depth can be computed from the set of A_r and B_r . Details of the method for the solution of the equations are given by Davies (1979) and will not be repeated here.

In order to solve equations (15) and (16) it is necessary to specify how N will vary with x, ϕ and t . The horizontal variation of N over the North Sea for semi-diurnal tidal motion has been computed by Kraav (1969). He shows that N increases rapidly in the shallow coastal areas, particularly along the east coast of England, where the tidal currents are high, and to a first approximation it is evident that N increases with the square of the tidal current. On the basis of Kraav's results, an appropriate parameterization of vertical eddy viscosity is, using M.K.S. units,

$$N = 0.2 (\bar{u}^2 + \bar{v}^2)$$

where \bar{u} and \bar{v} are depth mean currents given in terms of the present theory by

$$\bar{u} = \sum_{r=1}^m A_r a_r, \quad \bar{v} = \sum_{r=1}^m B_r a_r \tag{19}$$

$$a_r = \frac{1}{h} \int_0^h f_r(z) dz \tag{20}$$

This parameterization of vertical eddy viscosity was used in the tidal computations to be described in Section 5.

Alternatively Heaps (1972), from computations of the wind induced circulation of a simple rectangular basin, suggested that the term $\frac{\bar{K} h}{N}$ should be constant and accordingly this term was fixed in the calculation of the wind induced circulation of the North Sea (see Section 6) in such a way that, in water of depth 65m, N had a value of 650 cm²/s - a value suggested by Heaps (1972). In this calculation a coefficient of bottom friction $\bar{K} = 0.0025$ was assumed over the whole shelf.

Solutions were generated from a state of zero displacement and motion, expressed by,

$$\xi = A_r = B_r = 0 \text{ at } t = 0 \quad (r = 1, 2, \dots, m) \quad (21)$$

Along a closed boundary the normal component of current was set to zero, for all $t \geq 0$, thus,

$$A_r \cos \psi + B_r \sin \psi = 0 \quad (r = 1, 2, \dots, m) \quad (22)$$

where ψ denotes the inclination of the normal to the direction of increasing x .

Consider now the open boundary conditions. For the computation of tidal motion alone over the continental shelf, M_2 tidal input determined from the two-dimensional model of Flather (1976) was used, together with a radiation condition. Details of this radiation condition can be found in Davies (1979). For the computation of the tidal motion, the pressure gradient and wind stress terms in equations (15) and (16) were set to zero.

In computing the wind induced motion over the continental shelf the radiation condition was again used along the open boundaries of the model, with M_2 tidal input as described previously, together with meteorological input along the open boundaries, computed using the hydrostatic approximation.

The meteorological forcing functions, namely the two components of wind stress F_s and G_s , and the pressure gradients $\frac{\partial P}{\partial x}$ and $\frac{\partial P}{\partial \phi}$ were calculated from data supplied by the British Meteorological Office. Hourly values of wind stress and pressure gradients were computed at the grid points of the model for the period 0000h 15 March to 0000h 15 April 1976 from the hourly geopotential height data. From this time series mean values of pressure gradients and wind stresses over the sea area for this period were computed.

The meteorologically induced circulation for the period was computed by subtracting the pure tidal motion (computed using identical values of \bar{K} and N to those used with the meteorological input) from that computed with tide and meteorological forces.

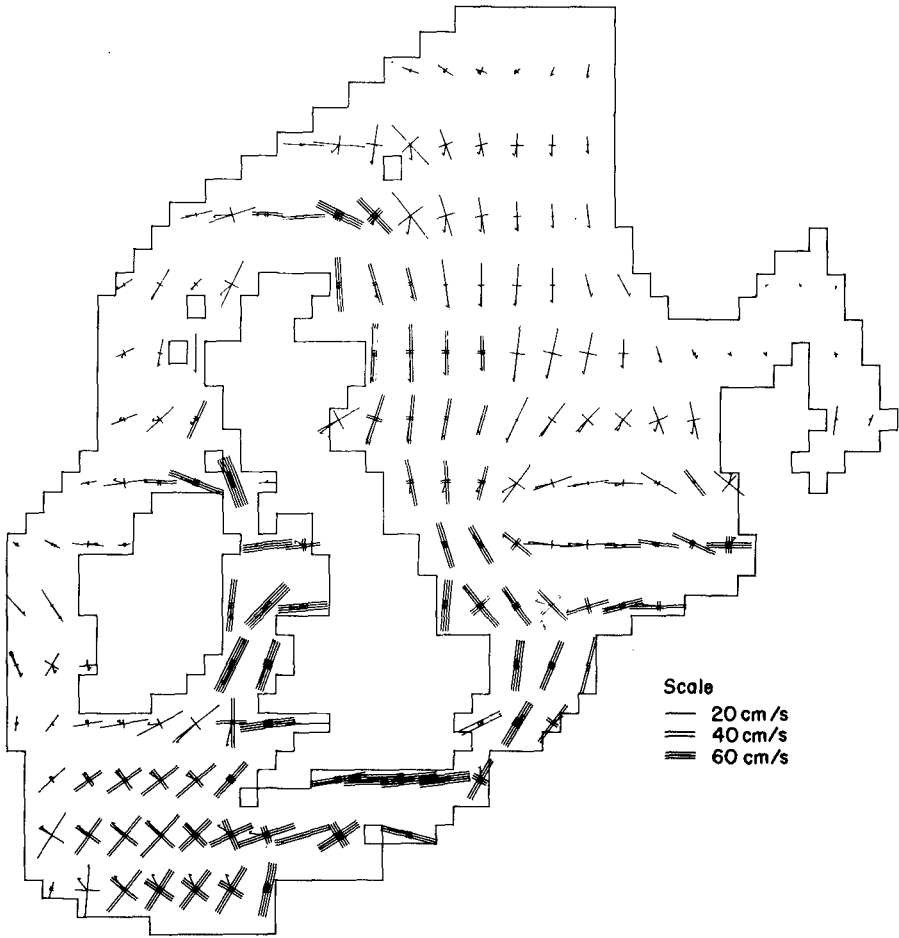


Figure 3a. Distribution over the continental shelf of M_2 current ellipses at sea surface.

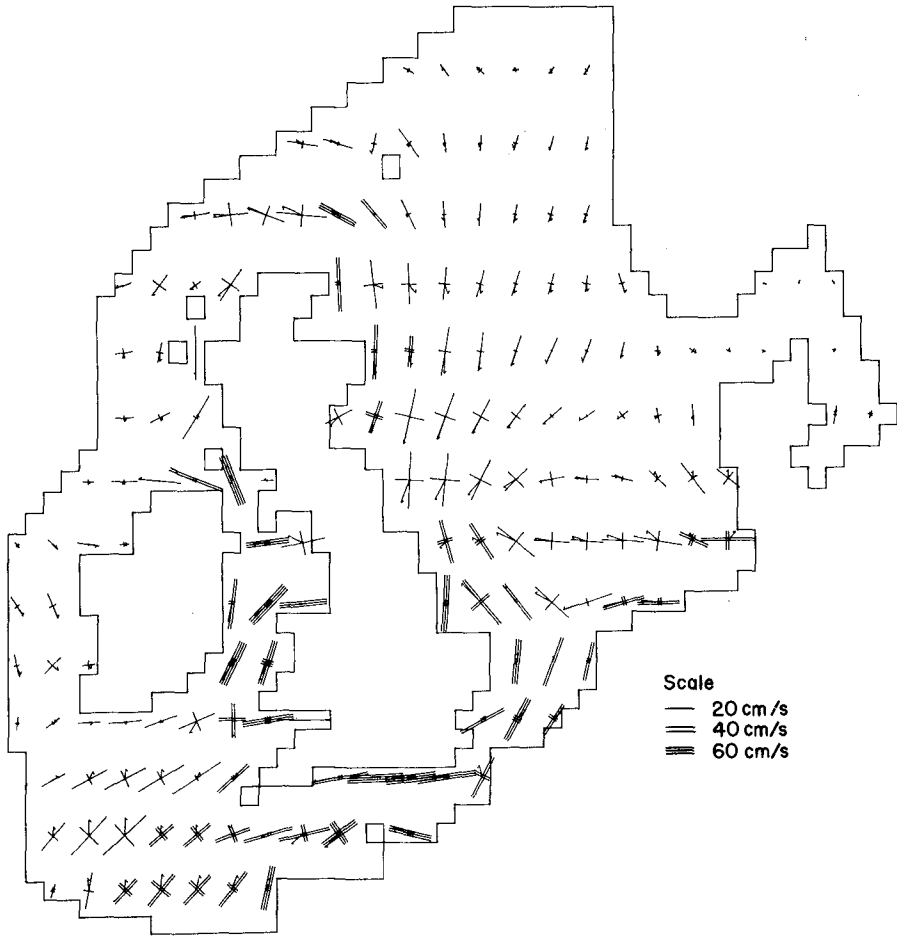


Figure 3b. Distribution over the continental shelf of M_2 current ellipses at sea bed.

5. Computed M_2 tidal currents

The distribution of the M_2 tidal currents over the continental shelf, and through depth were computed using the three-dimensional shelf model described previously. The variation of vertical eddy viscosity with tidal current described in Section 4 was used in the model.

In an initial series of calculations the computed amplitude of the M_2 tidal elevations and currents in shallow areas was found to be sensitive to the value of the coefficient of bottom friction k_b . Using a value of $k_b = 0.0025$ (an appropriate value for a two-dimensional model [Davies 1976]) the amplitude of the tidal velocity in shallow areas was higher than the observed value. However, increasing k_b to 0.0050 reduced the magnitude of these elevations and currents, although currents in the deeper areas were only slightly reduced.

Plots of the magnitude and direction of the major and minor axes of the M_2 tidal current and the sense of rotation of the ellipse computed using $k_b = 0.0050$, together with the time of lunar transit at Greenwich, at every third grid point of the model are given in Figures 3a,b. Figure 3a shows such a plot for the surface current, and the bottom current is presented in Figure 3b.

From Figures 3a,b it is evident that the maximum currents occur in the English Channel, between Cherbourg and the Isle of Wight, where the flow is nearly rectilinear. Tidal surface currents in excess of 100 cm/s occur in this area. Surface velocities of the order of 70-90 cm/s occur along the east coast of England, essentially flowing parallel to the coast. In the northern North Sea, surface tidal velocities are much lower, of order 5-15 cm/s with the orientation of the major axis of the ellipse in a north-south direction. However in the central North Sea, the orientation of the major axis is in a west-east direction, see Figures 3a,b, and the magnitude of the current is of order 25 cm/s.

Comparing Figures 3a and 3b it is evident that over most of the North Sea, both major and minor axes of the tidal current ellipse diminish with depth. However close to the Norwegian coast the computed ellipses do not exhibit this behaviour; the minor axis increases with depth close to the sea bed, and this increase is present in the M_2 current obtained from the harmonic analysis of the observations taken in this area during JONSDAP '76.

It is evident from Figures 3a and 3b that the current ellipses to the east of Aberdeen, rotate in the opposite directions at sea surface and sea bed. Computed current ellipses close to the Norwegian coast also have a different sense of rotation between surface and bottom, and these differences agree well with observational data taken in the area.

As more tidal data becomes available from the JONSDAP '76 program, a more rigorous comparison between computed and observed current ellipses will be possible.

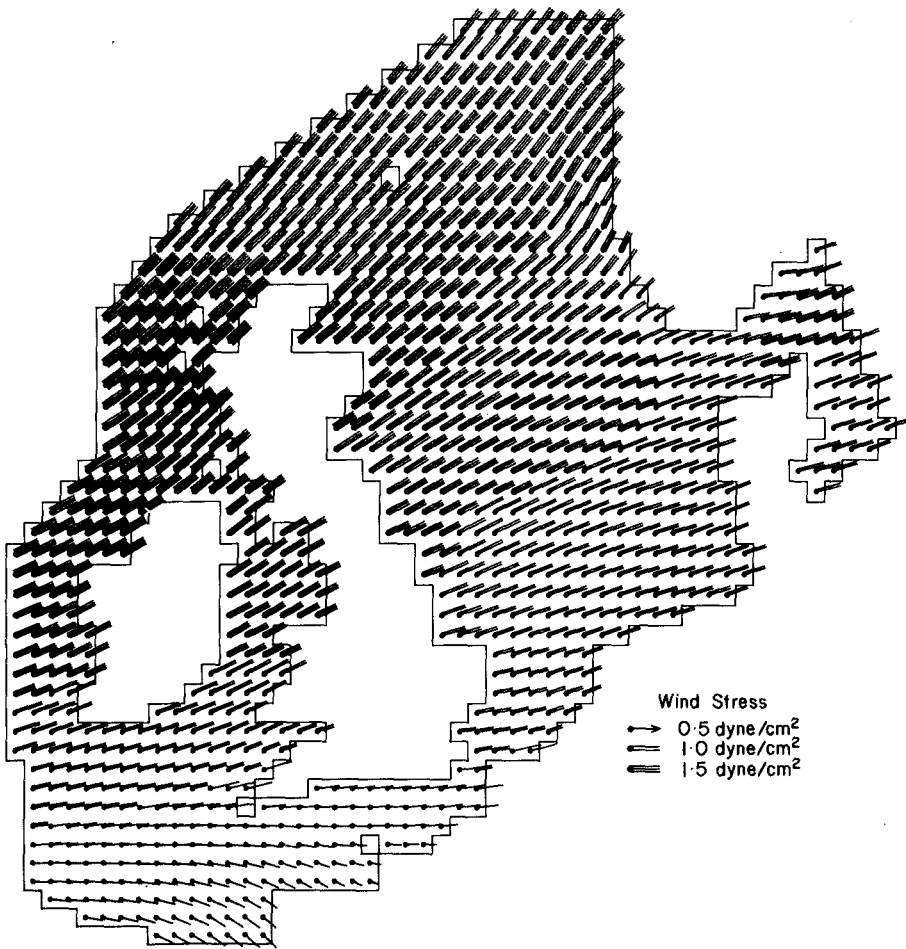


Figure 4. Distribution of mean-wind stress for the period 15 March to 15 April 1976 over the continental shelf.

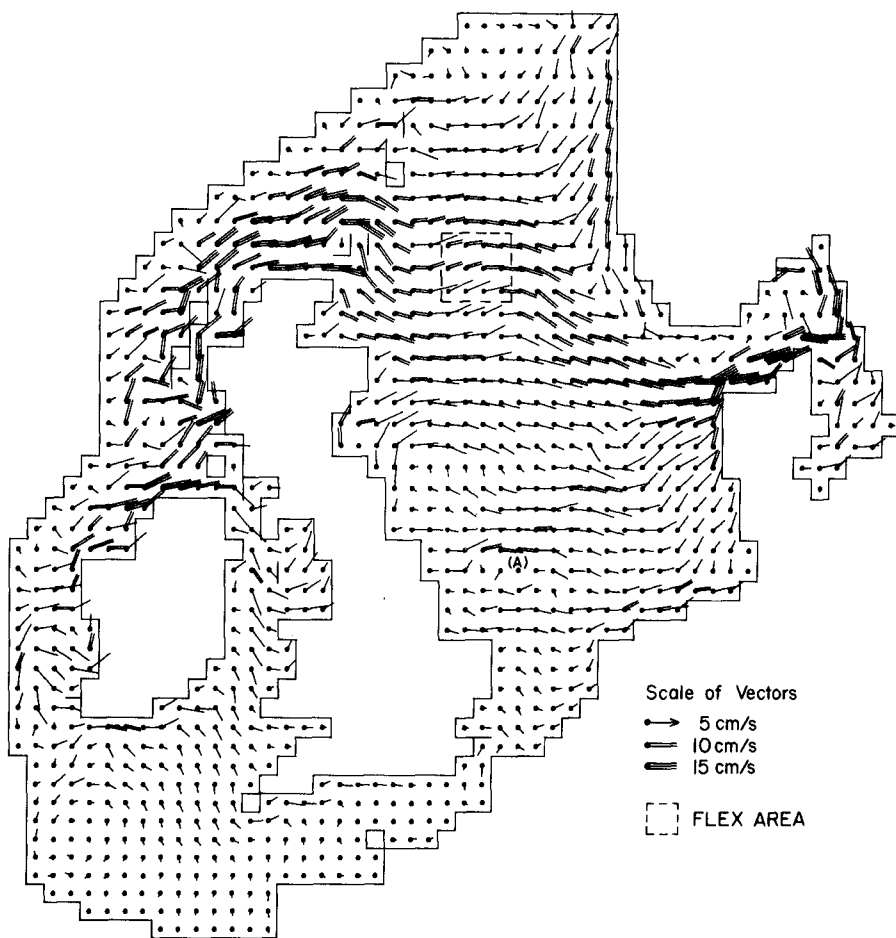


Figure 5a. Meteorologically-induced surface currents, means for the period 15 March to 15 April 1976, computed with the three-dimensional shelf model.

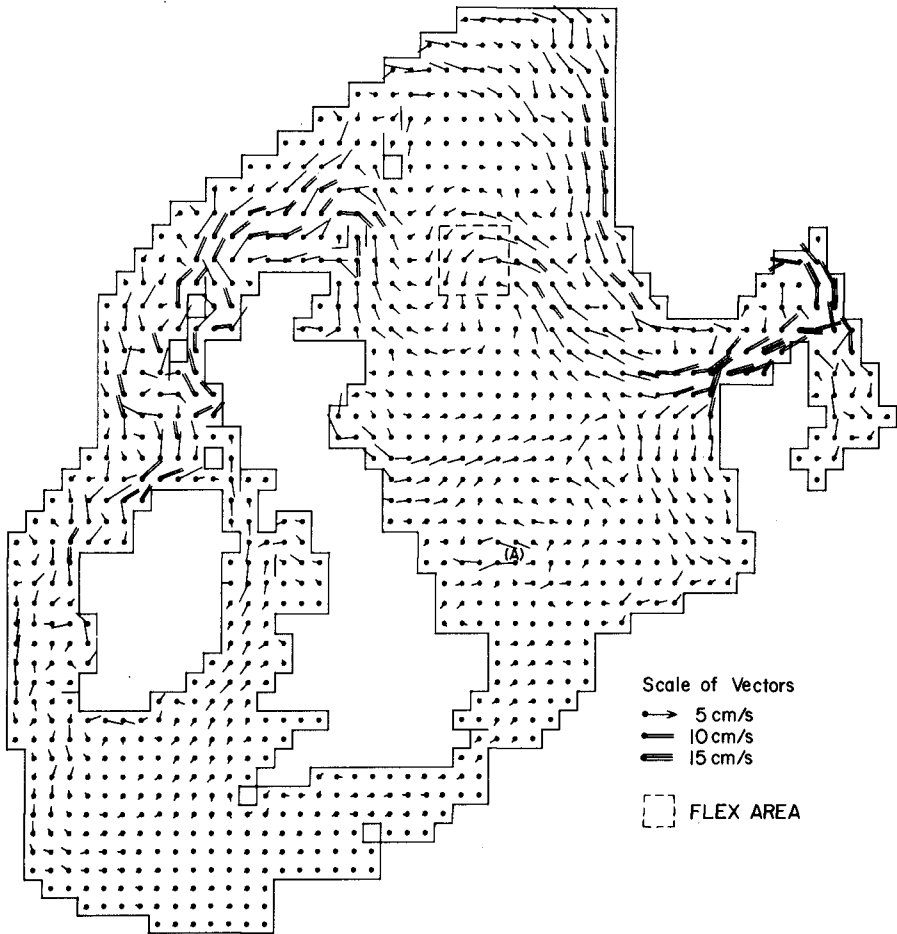


Figure 5b. Meteorologically-induced bottom currents, means for the period 15 March to 15 April 1976, computed with the three-dimensional shelf model.

6. Wind induced circulation for the period 15 March to 15 April, 1976.

Initial conditions corresponding to a state of rest were assumed, and the three-dimensional motion three days after the imposition of the meteorological forcing terms was calculated by integrating equations (8), (15) and (16) forward through time.

The distribution of the mean wind stress over the shelf is given in Figure 4.

The computed spatial distribution of meteorologically induced surface current over the shelf is shown in Figure 5a and comparing this with the computed distribution of bottom current in Figure 5b, it is evident that over most of the shelf the magnitude of the current decreases with depth, and that in certain areas significant differences in current direction, up to 180° , occur between surface and bottom currents.

The horizontal variation of surface current in the region of the FLEX box, to a first approximation is fairly uniform, reflecting the uniform wind stress field, being essentially an eastward flow, at about 45° to the right of the wind field, as would be expected from Ekman theory. However, the bottom flow (Figure 5b) shows a large horizontal variation, being directed southward down the Scottish coast in the sea area to the east of Wick, then flowing eastward at the latitude of Aberdeen, and subsequently turning northward at a point about 100 km to the south of the FLEX box. The flow through the FLEX box shows the current turning from a northward to an eastward flow, which then continues to the south east into the Skagerrak. This high horizontal spatial variation of bottom current in the northern North Sea presumably being due to the influence of bottom topography.

Differences in direction between surface and bottom currents in the German Bight are also evident from Figures 5a and 5b. The surface current is mainly to the north east, moving water towards the coast, whereas the bottom current is to the north west, taking water away from the coast.

A particularly interesting circulation pattern exists off the east coast of England in the region of the grid point marked (A) in Figures 5a and 5b. At grid point (A) the surface current is near zero, while the bottom current is the order of 3 or 4 cm/s towards the coast. The surface currents in the area surrounding point (A) are predominantly off shore, whereas at point (A), and due west of it, the bottom current is towards the coast. This type of circulation has been observed a number of times (Hill [1973]).

Further calculations are presently in progress to compute the daily residual circulation of the North Sea for the period considered here.

7. Concluding Remarks

The results described in Section 3 show that a numerical model can play an important role in the design of an oceanographic exercise. By making measurements at critical points along the open boundaries of the model, an optimum set of open boundary data can be derived and

subsequently used with the model to simulate the motion of the sea during the period of the exercise.

Preliminary comparisons of the three-dimensional tidal currents, computed using the shelf model, with the observational data collected during JONSDAP '76 suggest that the model is reproducing the observed distribution of the tide over the North Sea. As more data becomes available a more rigorous comparison will be possible.

The three-dimensional meteorologically induced circulation of the North Sea, computed with the model, clearly shows the importance of bottom topography and coastal features upon the meteorologically induced circulation of the North Sea.

Further calculations to determine the daily residual flow of the North Sea are in progress and a comparison between these and observed residual flows measured during JONSDAP '76 will provide a rigorous test of the model.

Acknowledgements

The author is indebted to Dr. N. S. Heaps for useful comments during the course of this work. The depth distribution used in the three-dimensional shelf model and the open boundary input data to this model were provided by Dr. R. A. Flather from his two-dimensional shelf model.

The care and effort taken by the Meteorological Office in extracting the meteorological data from their atmospheric model is much appreciated, as is the work performed by Mr. R. A. Smith in preparing the diagrams.

The work described in this paper was funded by a Consortium consisting of the Natural Environment Research Council, the Ministry of Agriculture and Fisheries, and the Departments of Energy and Industry.

References

- Cartwright, D.E. 1976. Shelf boundary tidal measurements between Ireland and Norway. *Mém. Soc. R. Sci. Liège, Ser.6, 10*, 133-139.
- Davies, A.M. 1976. A numerical model of the North Sea and its use in choosing locations for the deployment of offshore tide gauges in the JONSDAP '76 oceanographic experiment. *Dt. hydrogr. Z.* 29, 11-24.
- Davies, A.M. and R.A. Flather. 1978. Application of numerical models of the north west European continental shelf and the North Sea to the computation of the Storm Surges of November-December 1973, in press, *Erganzungshefte Deutsche Hydrographische Zeitschrift*.
- Davies, A.M. 1979. Application of numerical models to the computation of the wind-induced circulation of the North Sea during JONSDAP '76, in press, *Meteor. Forschungsergebnisse*.
- Davies, A.M. (in preparation). On formulating a three-dimensional hydrodynamic model with an arbitrary variation of vertical eddy viscosity.

- Flather, R.A. 1976. A tidal model of the north west European continental shelf. *Mém. Soc. R. Sci. Liège, Ser.6*, 10, 141-164.
- Heaps, N.S. 1972. On the numerical solution of the three-dimensional hydrodynamical equations for tides and storm surges. *Mém. Soc. R. Sci. Liège, Ser.6*, 2, 143-180.
- Hill, H.W. 1973. Currents and Water Masses, pages 17-43 in *North Sea Science* ed. E. D. Goldberg, published M.I.T. Press, Cambridge, Massachusetts 02142.
- Kraav, V.K. 1969. Computation of the Semidiurnal tide and Turbulence Parameters in the North Sea. *Oceanology* 9, 332-341.

CHAPTER 64

A NEW APPROACH FOR TIDAL COMPUTATIONS

C. LE PROVOST

Chargé de Recherche C.N.R.S.

Institute of Mechanics - GRENOBLE (FRANCE)

During the twenty last years, tidal modelling has been intensively developed. Following the growth of engineering needs in coastal areas, more and more accurate models have been established, and this constant research of better accuracy in the representation of real phenomena brings us to very expansive models. One way of reducing these costs is to use variable grids in space, in order to concentrate refined meshes in areas of interest. But the finite difference schemes are not well adapted to this kind of procedure : this is why several attempts have been made recently to use finite element technics : C. TAYLOR and J.M. DAVIS in 1975 [1], C.A. BREBBIA and P.W. PARTRIDGE in 1976 [2], ... But these applications are not easy.

During the same period, since 1975, more complex tentative have been made using Fourier transform of the equations, previously to any kind of numerical integration : tides are effectively quasi periodic phenomena, and their spectra are well known. Two important points arise in doing this :

- time variable is eliminated from the hyperbolic problem of propagation, transformed into a set of elliptic problems.
- for each elliptic problem, a variational formulation is available.

It becomes thus possible to look at the various components of the real tides, and to use finite element technic to integrate numerically these problems in real basins. In this way, B.M. JAMART and D.F. WINTER have used recently a purely numerical procedure based upon the Fast Fourier Transform to carry their tidal computations in fjords, cf. [5], while A. ASKAR and A.S. CAKMAK introduced a perturbation technic to handle the non linearities, very important in such problems, cf. [1]. We have followed a similar approach to study the complete spectrum of the tides in shallow water areas for the european seas : North Sea and English Channel, cf. [9]. The aim of this paper is to illustrate the main ideas of our method applied on an academic one-dimensional problem.

I. THE EQUATIONS.

In the study of the dynamics of tidal waves in shallow waters, the long wave equations are classically used. They are obtained from the Navier Stokes equations by integration over the vertical coordinate, under the assumption that the characteristic vertical scale H is much smaller than the horizontal scale L ($H/L \ll 1$). With this assumption, it can be shown that the pressure is hydrostatic. Without any meteorological effect at the sea surface, and neglecting the horizontal eddy viscosity, the NS equations reduce to :

$$(1.1) \quad \begin{aligned} \frac{\partial \tilde{u}}{\partial \tilde{t}} + \tilde{u} \frac{\partial \tilde{u}}{\partial \tilde{x}} + \tilde{v} \frac{\partial \tilde{u}}{\partial \tilde{y}} - \tilde{f} \tilde{v} + g \frac{\partial \tilde{\zeta}}{\partial \tilde{x}} + \frac{\tilde{c}}{\tilde{h} + \tilde{\zeta}} \sqrt{\tilde{u}^2 + \tilde{v}^2} \tilde{u} &= 0 \\ \frac{\partial \tilde{v}}{\partial \tilde{t}} + \tilde{u} \frac{\partial \tilde{v}}{\partial \tilde{x}} + \tilde{v} \frac{\partial \tilde{v}}{\partial \tilde{y}} + \tilde{f} \tilde{u} + g \frac{\partial \tilde{\zeta}}{\partial \tilde{y}} + \frac{\tilde{c}}{\tilde{h} + \tilde{\zeta}} \sqrt{\tilde{u}^2 + \tilde{v}^2} \tilde{v} &= 0 \end{aligned}$$

Similarly, the continuity equation can be written :

$$(1.2) \quad \frac{\partial \tilde{\zeta}}{\partial \tilde{t}} + \frac{\partial(\tilde{h} + \tilde{\zeta})\tilde{u}}{\partial \tilde{x}} + \frac{\partial(\tilde{h} + \tilde{\zeta})\tilde{v}}{\partial \tilde{y}} = 0$$

with : \tilde{x}, \tilde{y} : horizontal cartesian coordinates in the plane of undisturbed sea surface

\tilde{z} : vertical coordinate

\tilde{t} : time

\tilde{h} : undisturbed depth of water

$\tilde{\zeta}$: elevation of the sea surface

\tilde{u}, \tilde{v} : components of the depth averaged currents in the \tilde{x}, \tilde{y} directions

$$(1.3) \quad \tilde{u} = \tilde{u}(\tilde{x}, \tilde{y}, t) = \frac{1}{\tilde{h} + \tilde{\zeta}} \int_{-\tilde{h}}^{\tilde{\zeta}} \tilde{u}(\tilde{x}, \tilde{y}, \tilde{z}, \tilde{t}) d\tilde{z}, \quad \tilde{v} = \tilde{v}(\tilde{x}, \tilde{y}, t) = \frac{1}{\tilde{h} + \tilde{\zeta}} \int_{-\tilde{h}}^{\tilde{\zeta}} \tilde{v}(\tilde{x}, \tilde{y}, \tilde{z}, \tilde{t}) d\tilde{z}$$

\tilde{f} : Coriolis parameter ($\tilde{f} = 2\tilde{n} \sin \lambda$, with $\tilde{n} = \frac{2\pi}{24h}$ and λ : latitude of point (\tilde{x}, \tilde{y}))

\tilde{c} : coefficient of quadratic bottom friction

g : acceleration due to gravity.

Tidal problems are generally solved in areas \mathcal{D} limited by coastal boundaries Γ_1 and open boundaries Γ_2 . Along Γ_1 the classical boundary condition is $\tilde{v}_n = 0$ (impermeability of coastal lines). Along Γ_2 , several conditions are used :

$$(1.4) \quad \tilde{\zeta} = \tilde{\zeta}^*(\tilde{x}, \tilde{y}, \tilde{t}) \quad \text{or} \quad \tilde{v}_N = v_N^*(\tilde{x}, \tilde{y}, \tilde{t}), \quad \text{normal velocity to } \Gamma_2$$

f^* being a given function on $(\tilde{x}, \tilde{y}) \in \Gamma_2$, for all t .

It should be noted that, with formulation (1.1), tides are assumed to be induced in \mathcal{D} by the open boundaries Γ_2 . But the method here presented can be applied to the more general case of an oceanic basin influenced by the tide generating potential (cf. C. LE PROVOST and A. PONCET, 1977 [8]).

II. GENERAL PRESENTATION OF THE SPECTRAL METHOD.

II.1. Dimensionless equations.

In order to simplify, it is convenient to use non dimensional variables :

$$x = \frac{\tilde{x}}{\tilde{L}}, \quad y = \frac{\tilde{y}}{\tilde{L}}, \quad \zeta = \frac{\tilde{\zeta}}{\tilde{H}}, \quad h = \frac{\tilde{h}}{\tilde{H}}, \quad t = \frac{\tilde{t}}{\tilde{L}/\tilde{c}}, \quad u = \frac{\tilde{u}}{\tilde{c}}, \quad v = \frac{\tilde{v}}{\tilde{c}} \quad \text{with } \tilde{c} = \sqrt{gH}$$

$$\Omega = \frac{\tilde{\Omega}}{\tilde{c}/\tilde{L}}, \quad \omega = \frac{\tilde{\omega}}{\tilde{c}/\tilde{L}}, \quad A = \frac{\tilde{A}}{\tilde{c}}, \quad A' = \frac{\tilde{A}'}{\tilde{H}}, \quad k = \tilde{c} \frac{\tilde{L}}{\tilde{H}}$$

Thus equations (1) are :

$$\begin{aligned} (2.2) \quad & \frac{\partial u}{\partial t} + u \frac{\partial u}{\partial x} + v \frac{\partial u}{\partial y} - 2\Omega \sin \lambda v + \frac{\partial \zeta}{\partial x} + \frac{k}{h + \zeta} \sqrt{u^2 + v^2} u = 0 \\ & \frac{\partial v}{\partial t} + u \frac{\partial v}{\partial x} + v \frac{\partial v}{\partial y} + 2\Omega \sin \lambda u + \frac{\partial \zeta}{\partial y} + \frac{k}{h + \zeta} \sqrt{u^2 + v^2} v = 0 \\ & \frac{\partial \zeta}{\partial t} + \frac{\partial hu}{\partial x} + \frac{\partial hv}{\partial y} + \frac{\partial \zeta u}{\partial x} + \frac{\partial \zeta v}{\partial y} = 0 \end{aligned}$$

which can be written :

$$(2.3) \quad MS = B + E$$

with

$$M = \begin{vmatrix} \frac{\partial}{\partial t} & & -2\Omega \sin \lambda & & h \frac{\partial}{\partial x} \\ & 2\Omega \sin \lambda & & & h \frac{\partial}{\partial y} \\ \frac{\partial}{\partial x} & & & & \frac{\partial}{\partial t} \\ & & \frac{\partial}{\partial y} & & \\ & & & & \frac{\partial}{\partial t} \end{vmatrix} \quad S = \begin{vmatrix} hu \\ hv \\ \zeta \end{vmatrix}$$

$$B = \begin{vmatrix} -h(u \frac{\partial u}{\partial x} + v \frac{\partial u}{\partial y}) \\ -h(u \frac{\partial v}{\partial x} + v \frac{\partial v}{\partial y}) \\ -\frac{\partial}{\partial x} (\zeta u) - \frac{\partial}{\partial y} (\zeta v) \end{vmatrix} \quad E = \begin{vmatrix} -\frac{kh}{h + \zeta} \sqrt{u^2 + v^2} u \\ -\frac{kh}{h + \zeta} \sqrt{u^2 + v^2} v \\ 0 \end{vmatrix} = \begin{vmatrix} f_x \\ f_y \\ 0 \end{vmatrix}$$

II.2. Introduction of small parameters procedure.

We know from the theory of oceanic tides, and from observations, the structure of the tidal spectrum at the open boundary Γ_2 . We can thus suppose that (1.4) are of the form :

$$\begin{aligned}
 \tilde{U}_N &= \sum_{i=1}^{N_p} \tilde{A}_i \tilde{U}_{N_i}^* \cos(\tilde{\omega}_i t + \tilde{\psi}_{N_i}^*) & U_N &= \sum_{i=1}^{N_p} A_i U_{N_i}^* \cos(\omega_i t + \psi_{N_i}^*) \\
 (2.4) \quad \text{or } \tilde{U} &= \sum_{i=1}^{N_p} \tilde{A}_i \tilde{U}_i^* \cos(\tilde{\omega}_i t + \tilde{\psi}_i^*) & \text{i.e.} & \quad \text{or } U = \sum_{i=1}^{N_p} A_i U_i^* \cos(\omega_i t + \psi_i^*)
 \end{aligned}$$

where $U_{N_i}^*$, $\psi_{N_i}^*$, and U_i^* , ψ_i^* are given functions on Γ_2 corresponding to the N_i^p tidal components of pulsation ω_i inducing the movement in \mathcal{D}^p through the open boundary ; the orders of magnitude of each of these components are characterized by parameters A_i or A_i' .

When vectors B and E are neglected, resolution of (2.3) with boundary conditions (2.4) is not difficult (cf. HANSEN, 1962 [4]). But in coastal areas, non linearities are important. In order to handle the different orders of magnitude of these non linearities, we have introduced a perturbation method (cf. J. KRAVTCHENKO and C. LE PROVOST, 1977 [6]). Solutions of (2.3) are considered under the form :

$$(2.5) \quad S = A_i S_{i1} + A_i^p S_{ip} + A_i^q A_j^r S_{ijqr} + \dots$$

where $i, j = 1, 2, \dots, N_p$ and $p, q, r = 1, 2, \dots, \infty$
 Taking (2.5) in (2.3), and gathering the terms of same power in A_i , we obtain for each order of magnitude in A_i a set of equations defining S_{i1} , S_{ip} , S_{ijqr} , ... :

$$\begin{aligned}
 (2.6) \quad M S_{i1} &= 0 \\
 M S_{ip} &= B_{ip} + E_{ip} && \text{with corresponding limit conditions} \\
 M S_{ijqr} &= B_{ijqr} + E_{ijqr} && \text{coming from (2.4)} \\
 &\dots\dots\dots
 \end{aligned}$$

Following a classical procedure in forced vibration theory, solutions of (2.6) are expected under the form :

$$\begin{aligned}
 S_{i1} &= \begin{vmatrix} h u_{i1}(x,y) \cos[\omega_i t + \psi_{i1}(x,y)] \\ h v_{i1}(x,y) \cos[\omega_i t + \chi_{i1}(x,y)] \\ \gamma_{i1}(x,y) \cos[\omega_i t + \varphi_{i1}(x,y)] \end{vmatrix} \\
 (2.7) \quad S_{ip} = S_{ip}^{(a,b,c,\dots)} &= \begin{vmatrix} h u_{ip}^{(a,b,c,\dots)} \cos[(a\omega_1 + b\omega_2 + c\omega_3 + \dots)t + \psi_{ip}^{(a,b,\dots)}] \\ h v_{ip}^{(a,b,c,\dots)} \cos[(a\omega_1 + b\omega_2 + c\omega_3 + \dots)t + \chi_{ip}^{(a,b,\dots)}] \\ \gamma_{ip}^{(a,b,c,\dots)} \cos[(a\omega_1 + b\omega_2 + c\omega_3 + \dots)t + \varphi_{ip}^{(a,b,\dots)}] \end{vmatrix} \\
 S_{ijqr} &= \dots\dots\dots
 \end{aligned}$$

with $a, b, c, \dots = 0, \pm 1, \pm 2, \dots \infty$

The resolution of each system (2.6) is consequently splitted into a set of systems of the following form, of which time is eliminated :

$$\bar{M}_{i1} \cdot \bar{S}_{i1} = 0 \quad (2.8)$$

$$\bar{M}_{ip}(a,b,c\dots) \cdot \bar{S}_{ip}(a,b,c\dots) = \bar{B}_{ip}(a,b,c\dots) + \bar{E}_{ip}(a,b,c\dots)$$

where S_{i1} are vectors of 6 unknowns of two variables x and y :

$$hu_{i1} \cos \psi_{i1}, hu_{i1} \sin \psi_{i1}, hv_{i1} \cos \chi_{i1}, hv_{i1} \sin \chi_{i1}, \zeta_{i1} \cos \varphi_{i1}, \zeta_{i1} \sin \varphi_{i1}$$

(and the same for $S_{ip}(a,b,c\dots), \dots$).

The matrices $\bar{M}_{i1}, \bar{M}_{ip}(a,b,c\dots)$ are easy to deduce from (2.3), (2.6) and (2.7) ; it is the same for vectors $B_{ip}(a,b,c\dots), B_{ip}(a,b,c\dots), \dots$. But an important difficulty arises for vector E , the terms of which are not analytical in the vicinity of small values of the parameters A_i , and impossible "a priori" to develop under a form $E_{ip}(a,b,c\dots)$.

II.3. Development of the quadratic terms of friction.

We have established an approximate development of vector E , in the form of generalized Fourier series (cf. C. LE PROVOST, 1973 [7]), under the assumption of the existence of a "dominant" wave in the complete tidal spectrum over the studied area. This "dominant constituent" must have everywhere in \mathcal{D} a maximum of velocity much bigger than the other constituents in the spectrum. As an example, the M_2 constituent of the tide is the "dominant" wave for the european seas. Taking index l for this "dominant" constituent, f_x and f_y are expanded as follows :

$$f_x = A_i A_j k \sum_{i=1}^N FX_i \cos(\omega_i t + \phi X_i) \quad (2.9)$$

$$f_y = A_i A_j k \sum_{i=1}^N FY_i \cos(\omega_i t + \phi Y_i)$$

where $FX_i, FY_i, \phi X_i, \phi Y_i$ are functions of the amplitude and the phase of the dominant constituent, and of the other constituents of the spectrum. N is theoretically infinite, but in fact it can be limited to a finite value $N_F (> N_0)$.

The aim of this paper is not to present the details of this development. Let us notice only that two classes of terms can be distinguished in (2.9).

a. A first group corresponds to the damping effect played by friction for all the constituents in the tidal spectrum. Considering these terms, it appears that :

- For the dominant wave, this damping can be considered independently of the other constituents of the spectrum, as a first approximation.
- For the other constituents, this damping is strongly influenced by the local characteristics of the dominant wave.

b. A second group of terms corresponds to linear combinations of the pulsations of the different constituents of the complete tidal spectrum : they represent the generating effect of new constituents played by friction in shallow water areas.

II.4. The perturbation method.

In coastal areas, friction is so much important that a simple small parameter method applied as presented in II.2 to solve (2.2) is not rapidly converging towards the real solution within practical limits : this has been noticed in 1971 by B. GALLAGHER and W. MUNK. It is necessary to use a perturbation method in which the first approximation of the solution is already representative of the damped solution. The developments (2.9) show us the way : the first order solution must be the dominant wave studied in the presence of the damping effect of friction, and the other constituents of the tide will appear as perturbations, studied separately as prescribed by a classical process of successive orders of approximation, cf. [6].

III. ILLUSTRATION OF THE PERTURBATION METHOD APPLIED TO A MONO DIMENSIONAL PROBLEM.

Let us consider a channel \mathcal{E} of constant depth h , closed at one end by a vertical wall, and connected with the ocean at the other end. The problem is reduced to a monodimensional one, with the following equations :

$$(3.1) \quad \frac{\partial u}{\partial t} + u \frac{\partial u}{\partial x} + \frac{\partial \zeta}{\partial x} + \frac{kh}{h + \zeta} |u| u = 0$$

$$\frac{\partial \zeta}{\partial t} + \frac{\partial hu}{\partial x} + \frac{\partial \zeta u}{\partial x} = 0$$

The limit conditions are expressed in such a way that they correspond to a monophasic wave coming inside the channel, of pulsation ω , and that every non linear wave induced in \mathcal{E} by non linear processes is coming out of this channel through the limit $x = 0$ without any reflexion. This kind of radiation condition has been established from the theory of characteristics and is formulated as follows :

$$(3.2) \quad \tilde{u} + 2 \sqrt{g(\tilde{h} + \tilde{\zeta})} = 2\tilde{A} \cos \tilde{\omega} \tilde{t} + 2 \sqrt{g\tilde{h}}$$

i.e. $u + 2 \sqrt{1 + \zeta} = 2A \cos \omega t + 2$

III.1. Development of the friction term.

Let us assume that, limited to the second order of approximation, the solution can be written :

$$u = \sum A^p u_p = A u_{11} \cos(\omega t + \psi_{11}) + A^2 [u_{02} + u_{12} \cos(\omega t + \psi_{12}) + u_{22} \cos(2\omega t + \psi_{22}) + u_{32} \cos(3\omega t + \psi_{32}) + \dots] + O(A^3)$$

$$(3.3) \quad \zeta = \sum A^p \zeta_p = A \zeta_{11} \cos(\omega t + \varphi_{11}) + A^2 [\zeta_{02} + \zeta_{12} \cos(\omega t + \varphi_{12}) + \zeta_{22} \cos(2\omega t + \varphi_{22}) + \zeta_{32} \cos(3\omega t + \varphi_{32}) + \dots] + O(A^3)$$

As it was said in § III.3, the friction term :

$$F = \frac{k}{1 + \zeta} |u| u$$

can be expanded into a Fourier serie. We do not present here the details of the analytical development (see. C. LE PROVOST and A. KABBAJ, 1978, [10]) ; let us write only the result of these computations :

$$f = |u| u =$$

second order	≠ damping	$A^2 \cdot \frac{8u_{11}}{3\pi} u_{11} \cos(\omega t + \psi_{11})$
	≠ generation of non linear constituents	$A^2 \left[\frac{8}{15\pi} u_{11}^2 \cos(3\omega t + 3\psi_{11}) - \frac{8}{105\pi} u_{11}^2 \cos(5\omega t + 5\psi_{11}) + \dots \right]$
third order	≠ damping	$A^3 \frac{4u_{11}}{\pi} [u_{02} + u_{12} \cos(\omega t + \psi_{12}) + u_{22} \cos(2\omega t + \psi_{22}) + u_{32} \cos(3\omega t + \psi_{32}) + \dots]$
	≠ generation of non linear constituents	$A^3 \left\{ \frac{4}{\pi} u_{11} u_{22} + \frac{4}{3\pi} u_{11} [u_{12} \cos(\omega t + 2\psi_{11} - \psi_{12}) + u_{32} \cos(\omega t + 2\psi_{11} - \psi_{32})] - \frac{4}{15\pi} u_{11} [u_{32} \cos(\omega t + 4\psi_{11} - \psi_{32}) + u_{52} \cos(\omega t + 6\psi_{11} - \psi_{52})] + \frac{4}{35\pi} u_{11} [u_{52} \cos(\omega t + 6\psi_{11} - \psi_{52}) + \dots] \right\}$

The different terms considered as "damping" terms appear to be a kind of linearization of friction. Using the notations :

$$(3.4) \quad \lambda = \frac{8k}{3\pi} Au_{11} \quad , \quad \lambda' = \frac{4k}{3\pi} Au_{11} \quad , \quad \lambda_{32} = \frac{8k}{15\pi} \quad , \quad \lambda_{52} = -\frac{8k}{105\pi}$$

F can be written :

$$F = \frac{1}{1+\gamma} \left[\lambda Au_1 + \lambda' A^2 u_2 + \lambda_{32} A^2 u_{11}^2 \cos 3(\omega t + \psi_{11}) + \lambda_{52} u_{11}^2 \cos 5(\omega t + \psi_{11}) + \dots + O(A^3) \right]$$

i.e., using development : $(1 + \gamma)^{-1} = 1 - A\gamma_1 + O(A^2)$

$$(3.5) \quad F = \lambda Au_1 - \lambda A^2 u_1 \gamma_1 + \lambda' A^2 u_2 + \lambda_{32} A^2 u_{11}^2 \cos 3(\omega t + \psi_{11}) + \lambda_{52} u_{11}^2 \cos 5(\omega t + \psi_{11}) + \dots + O(A^3).$$

We must notice that coefficients λ and λ' , which can be called "linearized friction coefficients" are not constants and depend on the solution Au_{11} itself.

III.2. Application of the perturbation method.

First order : Following the formulation (2.6), the system giving the first order solution is :

$$(3.6) \quad \begin{aligned} \frac{\partial \zeta_1}{\partial t} + \frac{\partial u_1}{\partial x} &= 0 \\ \frac{\partial u_1}{\partial t} + \frac{\partial \zeta_1}{\partial x} + \lambda u_1 &= 0 \end{aligned}$$

with the limit conditions deduced from (3.2), (using development $(1 + \gamma)^{1/2} = 1 + \frac{\gamma}{2} + \dots$) :

$$(3.7) \quad \begin{aligned} u_1(1) &= 0 \\ u_1(0) + \zeta_1(0) &= 2 \cos \omega t \end{aligned}$$

Notice that, doing this, we introduce in the definition of the first order solution, the damping effect of friction λu_1 which is, strictly speaking, a term of second order.

Let us use the complex notations :

$$(3.8) \quad \begin{aligned} \alpha_{ki} &= \frac{1}{2} \zeta_{ki} e^{j\varphi_{ki}} \\ \mu_{ki} &= \frac{1}{2} u_{ki} e^{j\varphi_{ki}} \end{aligned}$$

$$\begin{aligned} \text{i.e. } \zeta_{ki} \cos(k\omega t + \varphi_{ki}) &= \alpha_{ki} e^{jk\omega t} + \alpha_{ki}^* e^{-jk\omega t} \\ u_{ki} \cos(k\omega t + \psi_{ki}) &= \mu_{ki} e^{jk\omega t} + \mu_{ki}^* e^{-jk\omega t} \end{aligned}$$

with f^* being the conjugate of the complex function f . Equations (3.6) and (3.7) reduce so to :

$$(3.9) \quad \begin{aligned} j\omega \alpha_{11} + \frac{d\mu_{11}}{dx} &= 0 & \mu_{11}(1) &= 0 \\ j\omega \mu_{11} + \frac{d\alpha_{11}}{dx} + \lambda \mu_{11} &= 0 & \alpha_{11}(0) + \mu_{11}(0) &= 1 \end{aligned}$$

which can be written :

$$(3.10) \quad \begin{aligned} \alpha_{11} &= \frac{j}{\omega} \frac{d\mu_{11}}{dx} & \mu_{11}(1) &= 0 \\ \frac{d^2 \mu_{11}}{dx^2} + \omega^2 (1 - j \frac{\lambda}{\omega}) \mu_{11} &= 0 & \mu_{11}(0) + \frac{j}{\omega} \frac{d\mu_{11}(0)}{dx} &= 1 \end{aligned}$$

Finally, we have to solve a second order differential equation of the complex function μ_{11} of one variable only : x . This equation is non linear, because of the presence of $\lambda = \lambda(u_{11})$. We have solved this equation by a numerical finite difference scheme, using a method of successive approximations for the non linearity : as a first approximation, λ is taken equal to zero, which corresponds to the linear solution of (3.1) without friction.

A numerical application has been done with the following numerical values :

$h = 50$ m, $L = 495$ km, $T = 12$ h. 25 mn, $A = 1$ m/s, $c = 3.10^{-3}$ MKSA (which schematically corresponds to the semi-diurnal tidal wave in the English Channel). On figure 1, we have plotted the amplitude of the sea surface elevation and of the current at $x = 0$, $x = L/2$ and $x = L$, obtained at the different steps of the iterative process used for the integration of (3.10). As it can be seen, the solution is stable after five iterations.

In order to check our solution, we have integrated problem (3.1) under the same limit conditions, with the same numerical values by a classical Lax Wendroff finite difference scheme. The solutions $u(x,t)$ and $\zeta(x,t)$ thus obtained have been expanded by Fourier analysis under the form :

$$(3.11) \quad \begin{aligned} u^{LW}(x,t) &= u_0^{LW}(x) + \sum_k u_k^{LW}(x) \cos [k\omega t + \varphi_k^{LW}(x)] \\ \zeta^{LW}(x,t) &= \zeta_0^{LW}(x) + \sum_k \zeta_k^{LW}(x) \cos [k\omega t + \varphi_k^{LW}(x)] \end{aligned}$$

We have plotted on figure 2 and 3 the results for u_1^{LW} and ζ_1^{LW} in order to compare these values with u_{11} and ζ_{11} deduced from the integration of (3.10). The results fit very well.

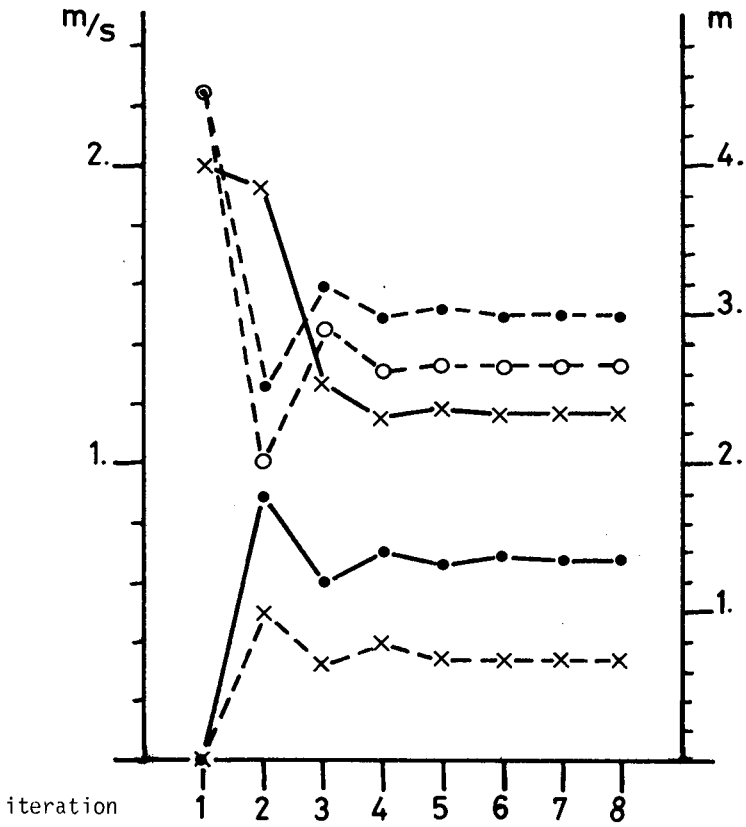
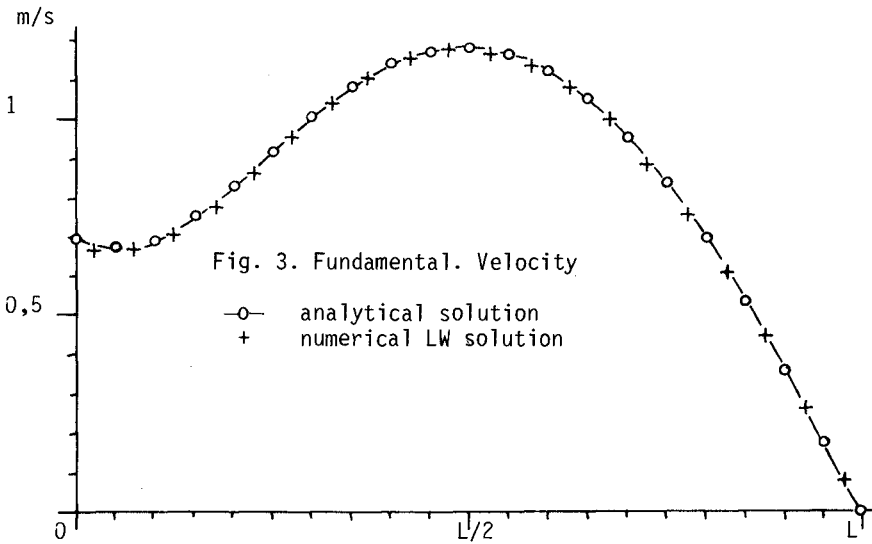
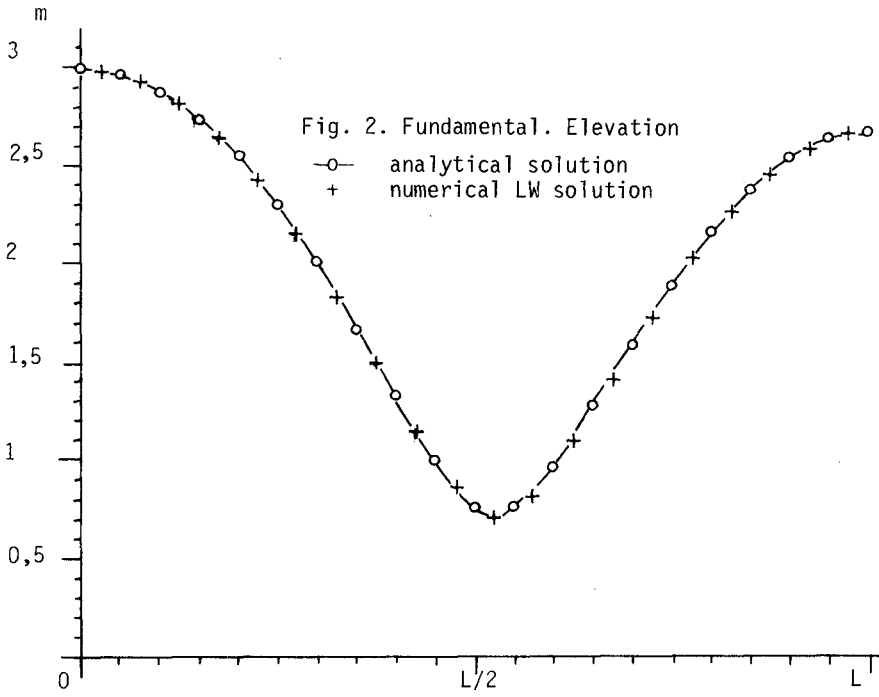


Fig. 1. Convergence of the iterative method

— Velocity - - - - Sea surface elevation
 • mouth of the channel
 x middle of the channel
 o end of the channel



This numerical example illustrates the details of our method : the basic solution used for our perturbation procedure is the damped dominant wave ; it can be seen on figure 1 the important role played by the friction term : iteration 1 corresponds to no damping, and the corresponding solution is 1,8 the exact solution, for the maximum of amplitude of the velocity field. The agreement shown on figure 2 between our approximate solution and the Lax Wendroff solution, which can be considered the exact one, is sufficient to convince of the interest of the proposed method.

Knowing this dominant solution with a good accuracy, we calculate now the second order solution, following formulation (2.6).

Second order : The system giving the second order solutions is :

$$\begin{aligned} \frac{\partial \zeta_2}{\partial t} + \frac{\partial u_2}{\partial x} &= - \frac{\partial (\zeta_1 u_1)}{\partial x} \\ (3.12) \quad \frac{\partial u_2}{\partial t} + \frac{\partial \zeta_2}{\partial x} &= - \frac{1}{2} \frac{\partial u_1^2}{\partial x} - F_2 \end{aligned}$$

$$u_2(1) = 0$$

$$u_2(0) + \zeta_2(0) = \frac{\zeta_1(0)^2}{4}$$

with
$$F_2 = \lambda'_{u_2} - \lambda_{u_1} \zeta_1 + \lambda_{32} u_{11}^2 \cos 3(\omega t + \psi_{11}) + \lambda_{52} u_{11}^2 \cos 5(\omega t + \psi_{11})$$

Using the complex notation defined in (3.8), the second members of (3.12) can be written :

$$\begin{aligned} \frac{\partial \zeta_1 u_1}{\partial x} &= \frac{\partial}{\partial x} (\alpha_{11} \mu_{11}^* + \alpha_{11}^* \mu_{11}) + \left[\frac{\partial}{\partial x} (\alpha_{11} \mu_{11}) e^{2j\omega t} + \text{c.c.} \right] \\ \frac{\partial u_1^2}{\partial x} &= 2 \frac{\partial \mu_{11} \mu_{11}^*}{\partial x} + \left[\frac{\partial \mu_{11}^2}{\partial x} e^{2j\omega t} + \text{c.c.} \right] \quad (\text{c.c. : complex conjugate}) \\ \zeta_1^2 &= 2\alpha_{11} \alpha_{11}^* + \left[\alpha_{11}^2 e^{2j\omega t} + \text{c.c.} \right] \\ (3.13) \quad F_2 &= \lambda'_{u_2} - \lambda [\alpha_{11} \mu_{11}^* + \alpha_{11}^* \mu_{11}] + [\lambda' \mu_{12} e^{j\omega t} + \text{c.c.}] \\ &\quad + [(\lambda' \mu_{22} - \lambda \mu_{11} \alpha_{11}) e^{2j\omega t} + \text{c.c.}] \\ &\quad + [\lambda' \mu_{32} + 2\lambda \mu_{32} \mu_{11}^2 e^{j\psi_{11}}] e^{3j\omega t} + \text{c.c.}] \\ &\quad + [(\lambda' \mu_{52} + 2\lambda \mu_{52} \mu_{11}^2 e^{3j\psi_{11}}) e^{5j\omega t} + \text{c.c.}] \end{aligned}$$

(3.12) is a linear system of equations which therefore can be splitted up into differential systems of the variable x only :

Term of zero frequency H_0 :

$$\begin{aligned} \frac{du_{o2}}{dx} &= - \frac{d}{dx} (\alpha_{11} \mu_{11}^{\bar{x}} + \alpha_{11}^{\bar{x}} \mu_{11}) \\ (3.14) \quad \frac{d\gamma_{o2}}{dx} &= - (\mu_{11} \mu_{11}^{\bar{x}})_x - \lambda' u_{o2} + \lambda (\alpha_{11} \mu_{11}^{\bar{x}} + \alpha_{11}^{\bar{x}} \mu_{11}) \\ u_{o2}(1) &= 0 \\ \gamma_{o2}(0) + u_{o2}(0) &= \frac{1}{2} \alpha_{11}(0) \alpha_{11}^{\bar{x}}(0) \end{aligned}$$

Term of frequency 1 :

No forcing term occur in the corresponding equations deduced from (3.12) and (3.13). The corresponding solution is evidently 0. No correction of solutions u_1 , γ_1 occurs at the second order of approximation.

Term of frequency 2, H_2 :

$$\begin{aligned} \frac{d\mu_{22}}{dx} + 2j\omega\alpha_{22} &= - \frac{d}{dx} (\alpha_{11} \mu_{11}) \\ (3.15) \quad \frac{d\alpha_{22}}{dx} + 2j\omega\mu_{22} &= - \frac{1}{2} \frac{d}{dx} (\mu_{11}^2) - \lambda' \mu_{22} + \lambda \alpha_{11} \mu_{11} \\ \mu_{22}(1) &= 0 \\ \mu_{22}(0) + \alpha_{22}(0) &= \frac{\alpha_{11}^2(0)}{4} \end{aligned}$$

Term of frequency 3, H_3 :

$$\begin{aligned} \frac{d\mu_{32}}{dx} + 3j\omega\alpha_{32} &= 0 \\ (3.16) \quad \frac{d\alpha_{32}}{dx} + 3j\omega\mu_{32} &= -\lambda' \mu_{32} - 2\lambda \mu_{32} \mu_{11}^2 e^{j\psi_{11}} \\ \mu_{32}(1) &= 0 \\ \mu_{32}(0) + \alpha_{32}(0) &= 0 \end{aligned}$$

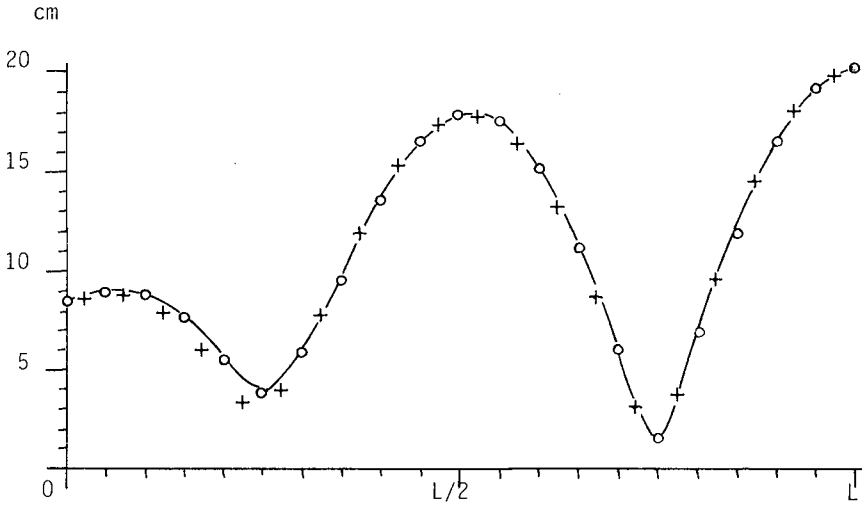


Fig. 4. Harmonic 2. Elevation

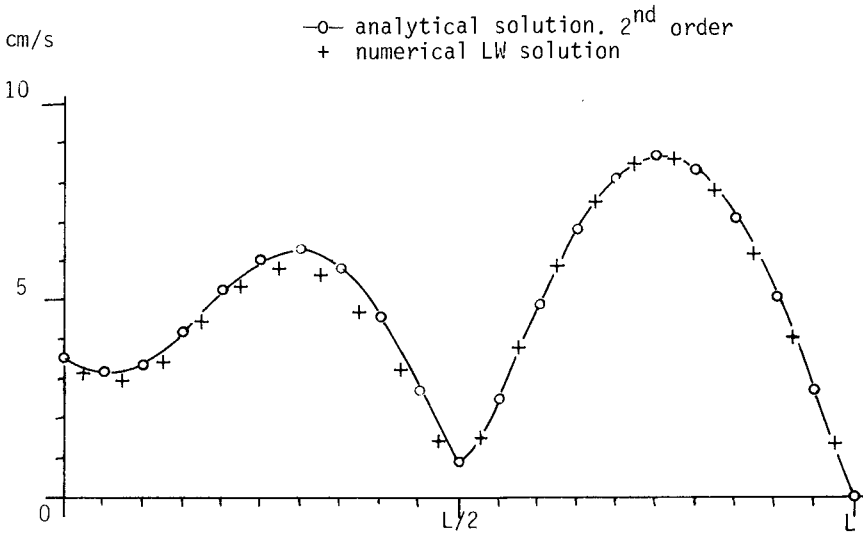


Fig. 5. Harmonic 2. Velocity

—○— analytical solution. 2nd order
 + numerical LW solution

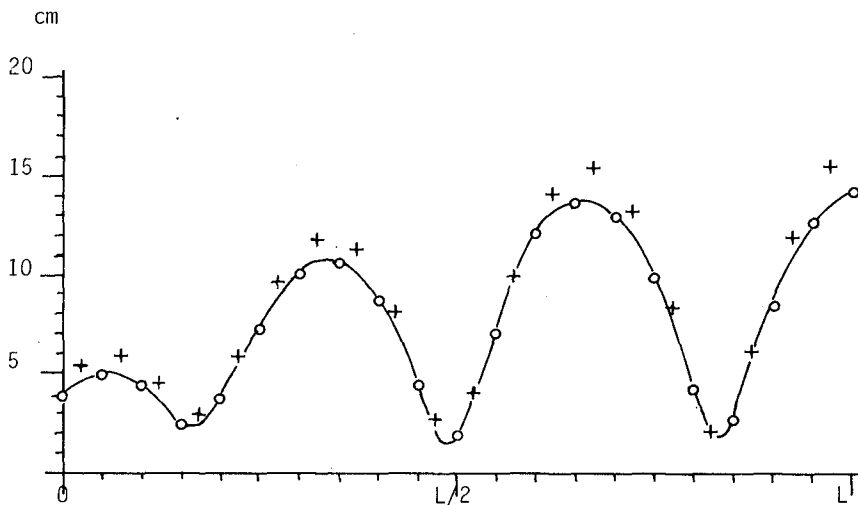


Fig. 6. Harmonic 3. Elevation

—o— analytical solution. 2nd order
 + numerical LW solution

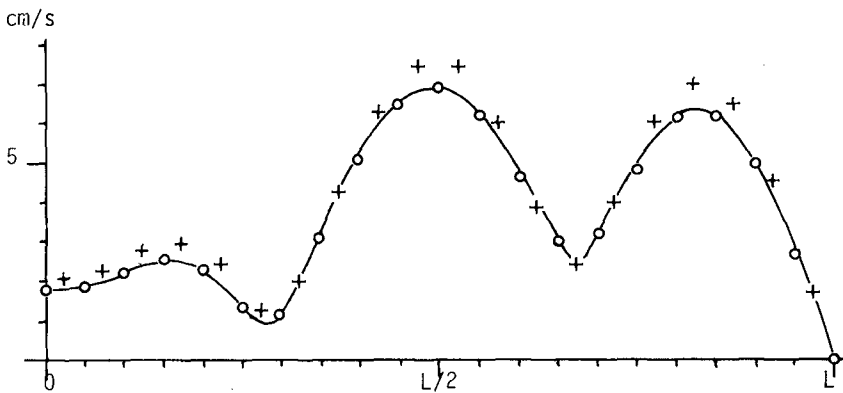


Fig. 7. Harmonic 3. Velocity

—o— analytical solution. 2nd order
 + numerical LW solution

System (3.14) can be numerically integrated without any difficulty. Systems (3.15) and (3.16) are of the same kind as system (3.9), but with second members, and purely linear coefficients (λ' is function of the dominant solution u_{11} only). These systems can be numerically integrated without any difficulty.

With the numerical values already used to illustrate the computation of the dominant wave, we obtain solutions presented on figures 4 and 5 for the harmonic H_2 , and on figures 6 and 7 for the harmonic H_3 (higher harmonics are too small to be considered). As comparison, on the same figures, the numerical solutions obtained from integration of the time dependent problem with the Lax Wendroff scheme are plotted. We can see that the correspondence is quite good. This agreement illustrates the ability of the method to reproduce the non linear harmonic constituents produced by sinusoidal tidal waves propagating in coastal areas. Let us notice in (3.14), (3.15) and (3.16) the presence of damping terms $\lambda' u_{i,j}$, with λ' function of the dominant velocity field u_{11} : as for the definition of the first order dominant wave, it is essential to take into account these damping terms for the computation of the non linear wave of second order.

In the numerical case here considered, the second order is sufficient to correctly represent the complete solution, but for smaller relative depth areas, the non linear contributions can be amplified, and higher order approximations may be necessary.

With this very simple mono-dimensional problem, the principal steps of the perturbation spectral method have been clearly illustrated:

- computation of the "dominant" solution: resolution of a non linear problem (damping coefficient being function of the solution itself) solved by an iterative process
- computation of the other components of the spectrum: resolution of linear problems (with damping coefficients fixed by the dominant solution).

IV. CONCLUSION. EXTENSION TO THE TWO DIMENSIONAL PROBLEM.

No important difficulty arises when the two dimensional problem is considered. Similarly to (3.10), the dominant wave is defined by a second order differential equation of the complex variable α_{11} , corresponding to the sea surface elevation; because of the damping effect of friction, this equation is non linear. It can be shown that a variational formulation is available for this problem (C. LE PROVOST and A. PONCET, 1978 [9]), so that the natural way to realize numerical integrations in real basins is to use finite element methods. A first application has been done for the M_2 tide in the English Channel: the primarily results published in [9] are satisfactory (cf. figures 8, 9). We are actually computing the M_4 constituent in the same area.

With such a procedure, computations are very cheap, because we have to solve a stationary problem for each important component of the tide in the studied area: except the dominant wave, for which an iterative process is necessary to take into account the non linear damping effect of bottom friction, the second order differential equation defining the amplitude of each constituent is solved only one time. It becomes thus

possible to realize a detailed study of all the components of the tidal spectrum in coastal areas, which has still not be realized in any case, because of excessive computing time necessities.

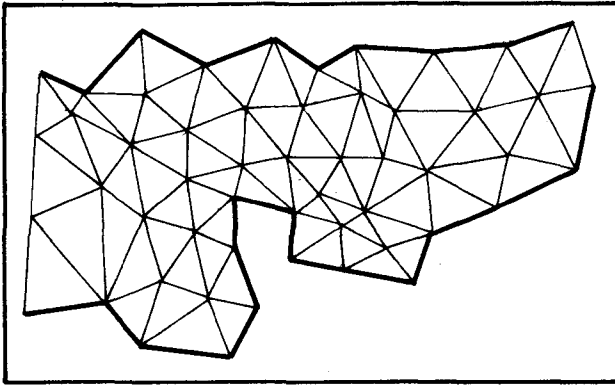


Fig. 8. Finite element grid for the English Channel

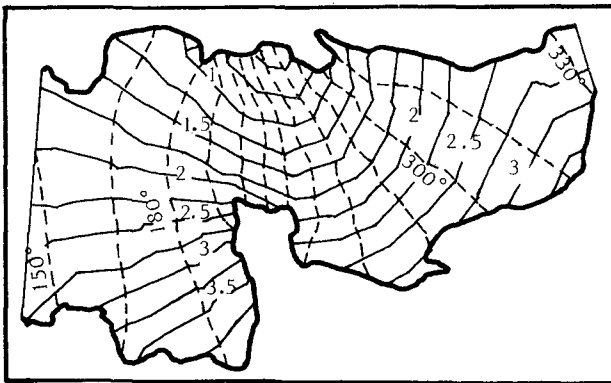


Fig. 9. Cotidal chart for M_2
from C. LE PROVOST and A. PONCET 9

REFERENCES

- [1] A. ASKAR et A.S. CAKMAK (1977). "Studies on finite amplitude waves in bounded water bodies".
Research report 77 SM 5. Princeton University.
- [2] C.A. BREBBIA and P.W. PARTRIDGE (1976). "Finite element simulation of water circulation in the North Sea".
J. Appl. Math. Modelling 1, pp. 101-107.
- [3] B. GHALLAGHER and W. MUNK (1971). "Tides in shallow water : spectroscopy".
Tellus XXIII, 4-5, pp. 346-363.
- [4] W. HANSEN (1962). "Tides".
The Sea, vol. 1, Physical Oceanography. Interscience Publisher.
- [5] B.M. JAMART and D.F. WINTER (1978). "A new approach to the computation of tidal motion in estuaries".
Hydrodynamics of estuaries and fjords. Elsevier. Publishing Company Scientific, Amsterdam.
- [6] J. KRAVTCHENKO et C. LE PROVOST (1977). "Sur la théorie spectrale des marées littorales".
Annales Hydrographiques, 5e série, vol. 5, Fasc. 1, pp. 23-46.
- [7] C. LE PROVOST (1973). "Décomposition spectrale du terme quadratique de frottement dans les équations des marées littorales".
C.R.A.S. t. 276, pp. 571-574 et 653-656.
- [8] C. LE PROVOST et A. PONCET (1977). "Sur une nouvelle méthode numérique pour calculer les marées océaniques et littorales".
C.R.A.S. t. 285, pp. 349-352.
- [9] C. LE PROVOST et A. PONCET (1978). "Finite element method for spectral modelling of tides".
International Journal for numerical methods in engineering, vol. 12, pp. 853-871.
- [10] C. LE PROVOST and A. KABBAJ (1978). "Non linear propagation of tidal waves in rough channels".
Internal Report, I.M.G.
- [11] C. TAYLOR and J.M. DAVIS (1975). "Tidal propagation and dispersion in estuaries".
Finite element in fluids, vol. 1, John Wiley & Sons.

CHAPTER 65

HYDRODYNAMIC MODELLING OF THE SOUTHERN NORTH SEA

by

David Prandle*

ABSTRACT

Numerical modelling of rivers, estuaries and shallow seas has attracted increasing interest over the last two decades. The models have developed from one dimensional (1D) applications to tidal propagation and flood routing through two and, finally, three dimensional applications to motions ranging from "pseudo-turbulence" to annual-mean residual flows. The present account describes the development, over the last five years, of the modelling studies carried out by the author concerning the hydrodynamics of the southern North Sea and River Thames. The objective is to identify those major points which have emerged that may have a wider significance.

1. INTRODUCTION

The modelling work considered is restricted to one and two (horizontal) dimensional applications; explicit finite-difference solutions are used throughout. The motions involved are assumed to be represented by the following shallow water wave equations :

$$\text{motion (-x)} \quad \frac{\partial u}{\partial t} + u \frac{\partial u}{\partial x} + V \frac{\partial u}{\partial y} + g \frac{\partial Z}{\partial x} + \frac{K u (u^2 + V^2)^{1/2}}{(D+Z)} - \Omega V = 0 \quad (1)$$

$$\text{motion (-y)} \quad \frac{\partial V}{\partial t} + u \frac{\partial V}{\partial x} + V \frac{\partial V}{\partial y} + g \frac{\partial Z}{\partial y} + \frac{K V (u^2 + V^2)^{1/2}}{(D+Z)} + \Omega u = 0 \quad (2)$$

$$\text{continuity} \quad \frac{\partial Z}{\partial t} + \frac{\partial [u(D+Z)]}{\partial x} + \frac{\partial [V(D+Z)]}{\partial y} = 0 \quad (3)$$

where u and V are depth-averaged velocities along the respective directions of the orthogonal axes x and y ;

Z the elevation of the water surface above a fixed horizontal datum;

*Principal Scientific Officer, Institute of Oceanographic Sciences, Bidston Observatory, Merseyside, England.

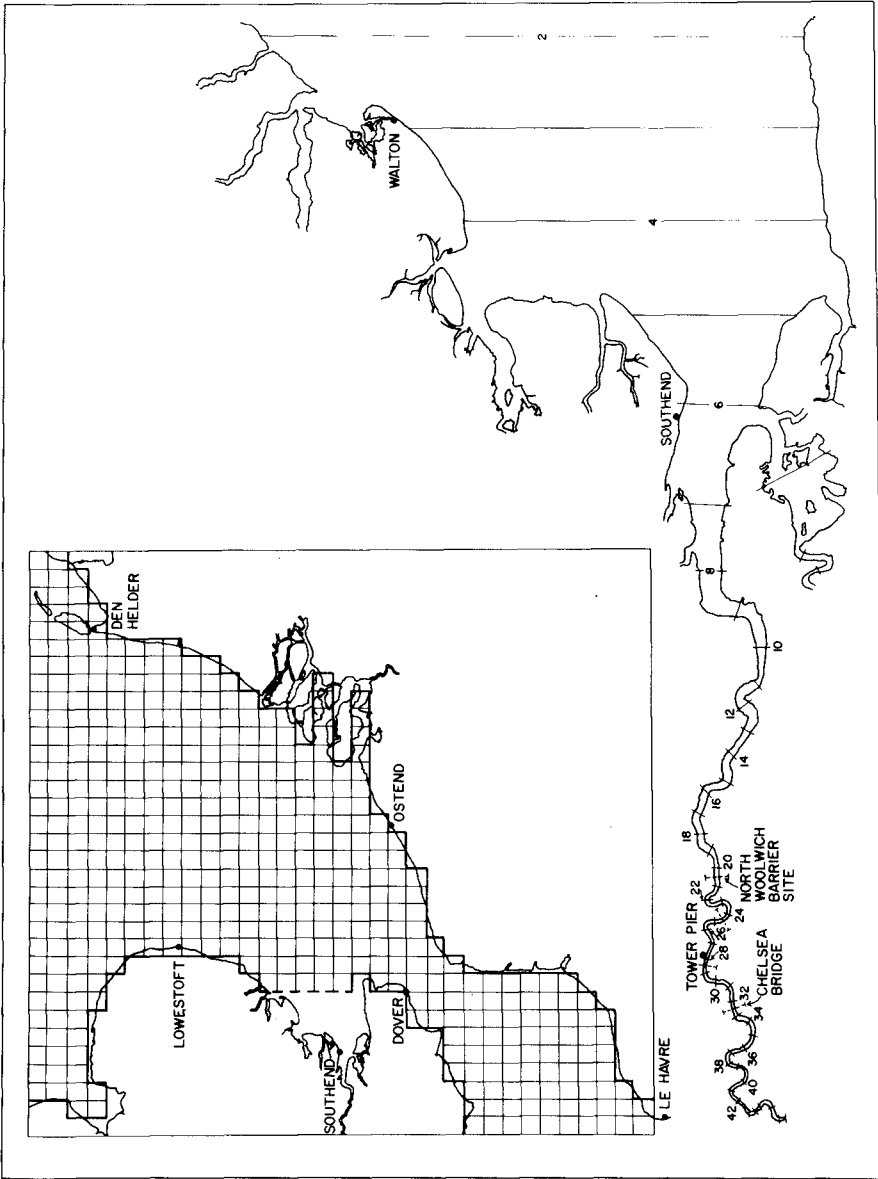


Figure 1. Schematic representation of the southern North Sea and River Thames.

D the depth of the bed below that same datum;
 t time;
 g gravitational constant;
 K friction coefficient;
 and Ω the Coriolis parameter.

The schematic representation of the southern North Sea and River Thames is shown in figure 1.

In using these equations as the basis of the modelling work, the following assumptions have been made : (a) vertical accelerations are negligible (b) variations in the vertical velocity profiles may be neglected (c) density effects may be ignored and (d) energy dissipation may be described by the bed friction formula adopted. Amidst the growing sophistication of numerical models and the competing claims of various numerical methods it is sobering to recognise that the flows produced in a model are limited to those motions which may be described by the original equations. At best, the numerical technique approaches the true analytical solution to the equations subject to the imposed boundary conditions; it cannot in any way improve upon this solution. The discussion of the merits of the various techniques revolve around the question as to which methods minimise the inaccuracies and approximations of numerical solutions. In many three dimensional models it is necessary to specify some additional physical expression concerning the velocity profile or nature of the eddy viscosity. In such cases the dependence of the computed flow values upon this additional restriction should be clearly recognised.

2. DATA

(i) General

In a region as intensively studied as the southern North Sea much of the data is essentially historical providing an important generalised description of the area against which specific modelling applications may be formulated. Flow in this region is dominated by the effects of the M_2 tidal constituent, the amplitude of this constituent exceeding the sum of the amplitudes of all other tidal constituents. The amplitude of this constituent exceeds 3m, since the depth of water in this region is of the order of 10-50m, the region is

characterised by strong tidal mixing with significant non-linearities producing tide-tide interactions. In the winter period surges of up to 3m in height occur fairly frequently with resulting surge-tide interactions. Frictional forces are important in this region, particularly in respect to current magnitudes for which the following general relationship applies :

$$U_{M_2} > U_{SURGE} > U_{RESIDUAL} \quad (4)$$

(ii) Specific

Specific data implies quantitative field measurements used in either calibrating or evaluating the model. The coastline of this region includes over 25 permanent tide gauge stations providing data of excellent quality extending over periods in excess of 50 years. In the off-shore region there have been numerous current measurements and a limited number of tide-gauge deployments, over the last decade the quality and duration of this off-shore data has improved markedly.

In the Dover Strait measurements of the voltage induced across the channel by the flow of sea water across the vertical component of the earth's magnetic field provide an estimate of the net flow through the channel. These measurements have been made using cross-channel telephone cables⁶ and recordings are available over a period of 25 years.

Indications of residual flow patterns over a range of time scales are available from the following sources : (a) movement of drogues and bottom drifters (b) synoptic distributions of salinity and temperature (c) spread of radioactive tracers from the nuclear plant at Cherbourg and (d) observed sand wave movements.

In the following description of modelling studies many comparisons are made between computed and observed measurements, in assessing the validity of these comparisons due regard should be given to the prior filtering involved. In the modelling only a limited part of the spectrum of water movements is considered, the frequency band considered being limited by the validity of equations (1) to (3) and by the specification of the appropriate boundary conditions, some parametric representation of other scales of motion is implicitly

included in the friction coefficients. In the case of observed data, filtering may be deliberately incorporated into the instrument design, for example the use of a tide gauge stilling well, or may be carried out at the data processing stage. Although such filtering techniques may be highly efficient it should be recognised that some mutual contamination of the energy spectra occurs in nature that may be impossible to include in the model. Obvious examples include the interaction between the highly energetic tidal and wind wave bands where tidal currents affect wave heights and, conversely, wind wave propagation is accompanied by changes in mean sea level. Interactions of this type mean that certain errors must be accepted between model results and field measurements, thus manipulation of model parameters to force a more and more exact fit may, in reality, reduce the accuracy to which the model simulates the specific phenomenon.

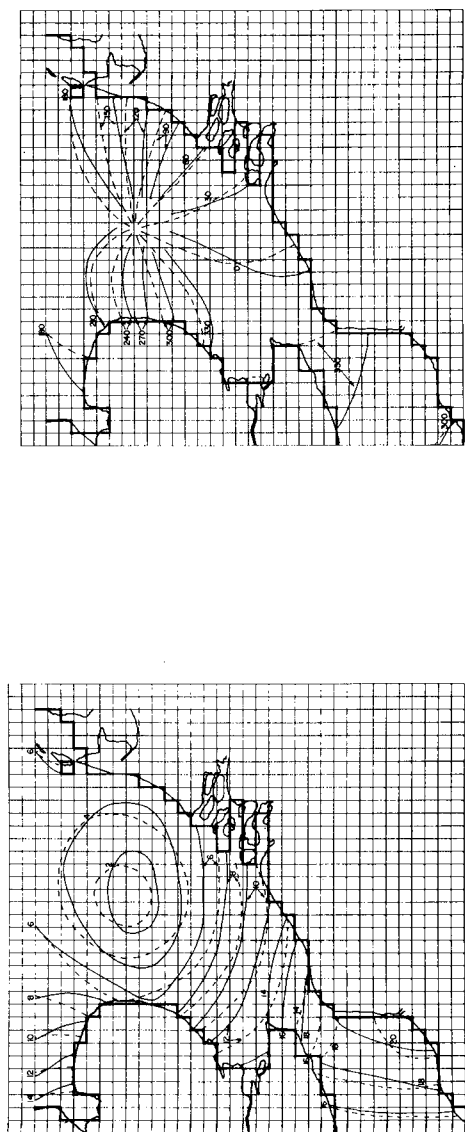
3. TIDES

Because of the predominance of the M_2 tidal constituent it can be shown that it is valid to simulate this constituent in isolation. Likewise in simulating any other tidal constituent it is sufficient to consider only the interaction with M_2 .

(i) Boundary Conditions

Tidal elevations along the two open boundaries of the model were specified using data from the Admiralty Charts and from the German Navy tidal atlas. These charts were originally constructed using the method outlined by Proudman and Doodson¹² whereby interpolation between coastal data points is achieved by using off-shore current measurements. Thus the accuracy of the tidal distributions along the open boundaries is questionable and it seems valid to make any minor adjustments that might improve the agreement between model and recorded results in the interior of the region. In the present application, adjustments to the chart data were found to be ineffective.

At the other extreme, in certain applications the paucity of available data may make it necessary to concoct the tidal distribution along the open boundary by a trial and error procedure



(a)

(b)

Figure 2. Comparison of (a) co-range (ft) and (b) co-tidal charts; ----- Admiralty, ——— computed.

based on improving the observed fit within the model. Some recent investigations have shown that, mathematically, this procedure presents an ill-posed problem and that numerical solutions may well not converge to the true solution.

(ii) Major tidal constituents

The reproduction of the observed M_2 co-tidal and co-range distributions are shown in figures 2(a) and 2(b) respectively.⁴ The agreement shown was achieved using a constant value for the friction factor. Having thus determined a suitable value for this friction factor it is possible to extend the simulation to other major tidal constituents. Tide-tide interactions must then be accounted for by incorporating the influence of the M_2 tide, thus an accurate simulation of, say, S_2 requires the model to be operated for a full 15 days to simulate the complete cycle of M_2 - S_2 interactions. As an alternative, since the interaction via the quadratic friction is predominant it is possible to simulate S_2 alone by using a linearised friction term in which the friction coefficient at each position is determined by reference to the M_2 tidal velocities.

(iii) Higher harmonics

The main concern with higher harmonics is the reproduction of M_4 and M_6 , in the present model it can be shown that these constituents are generated largely by the non-linear shallow water and friction terms, in other regions the convective terms may be of greater significance.³ Although the overall spatial distribution of these constituents in the model is in reasonable agreement with observations, this agreement tends to deteriorate in the very shallow regions where the constituents are largest e.g. in the River Thames as shown in figure 3. In such regions it may be shown that the usual assumption that the shallow water term produces M_4 and the friction term M_6 is invalid, figure 4 shows that M_4 and M_6 may be produced by both terms.

The inaccuracy in the reproduction of these constituents is attributed to the inadequacy of the bed friction formula. In some applications it may be justifiable to include additional terms in the friction formula to force an agreement between model and observed

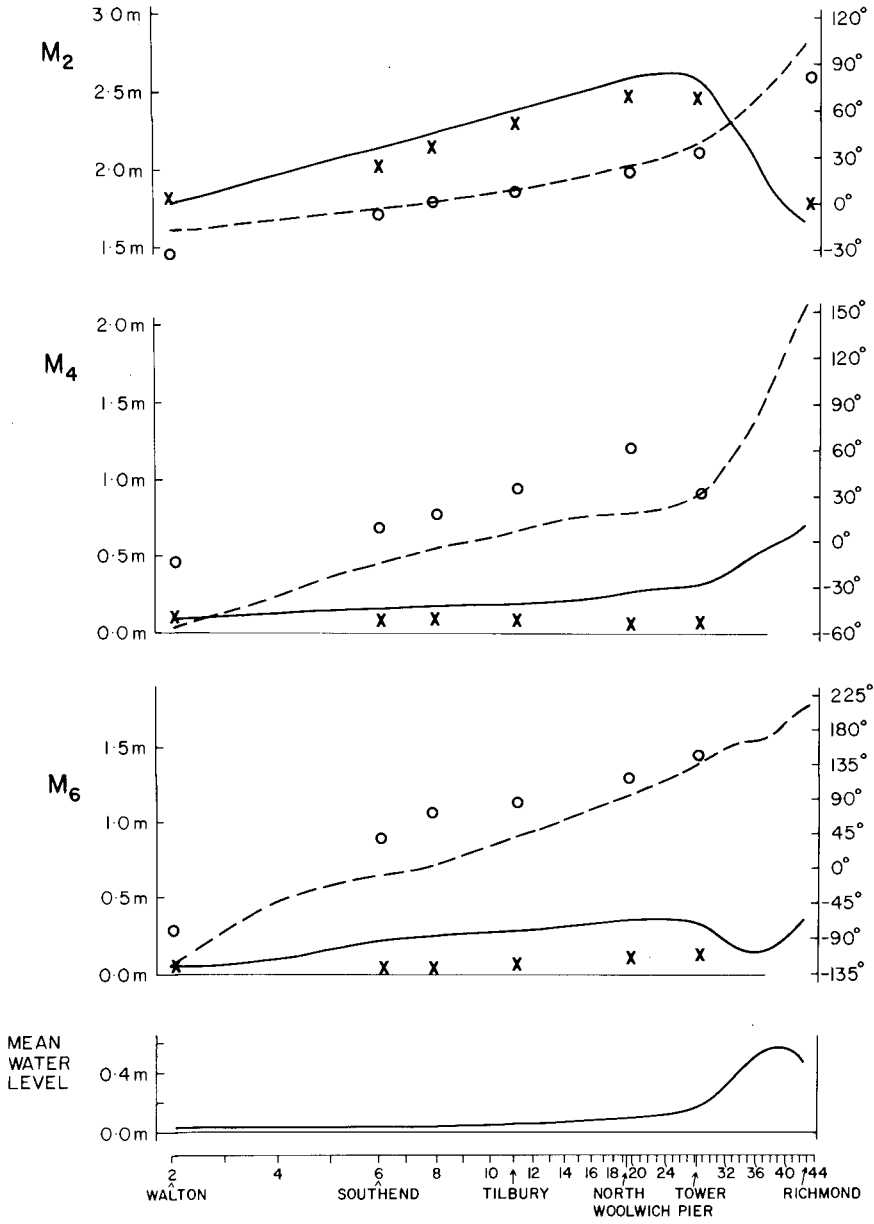


Figure 3. Computed and recorded values of M_2 , M_4 and M_6 along the Thames. Tidal amplitude : ———— computed, X observed; tidal phase : - - - - - computed, O observed.

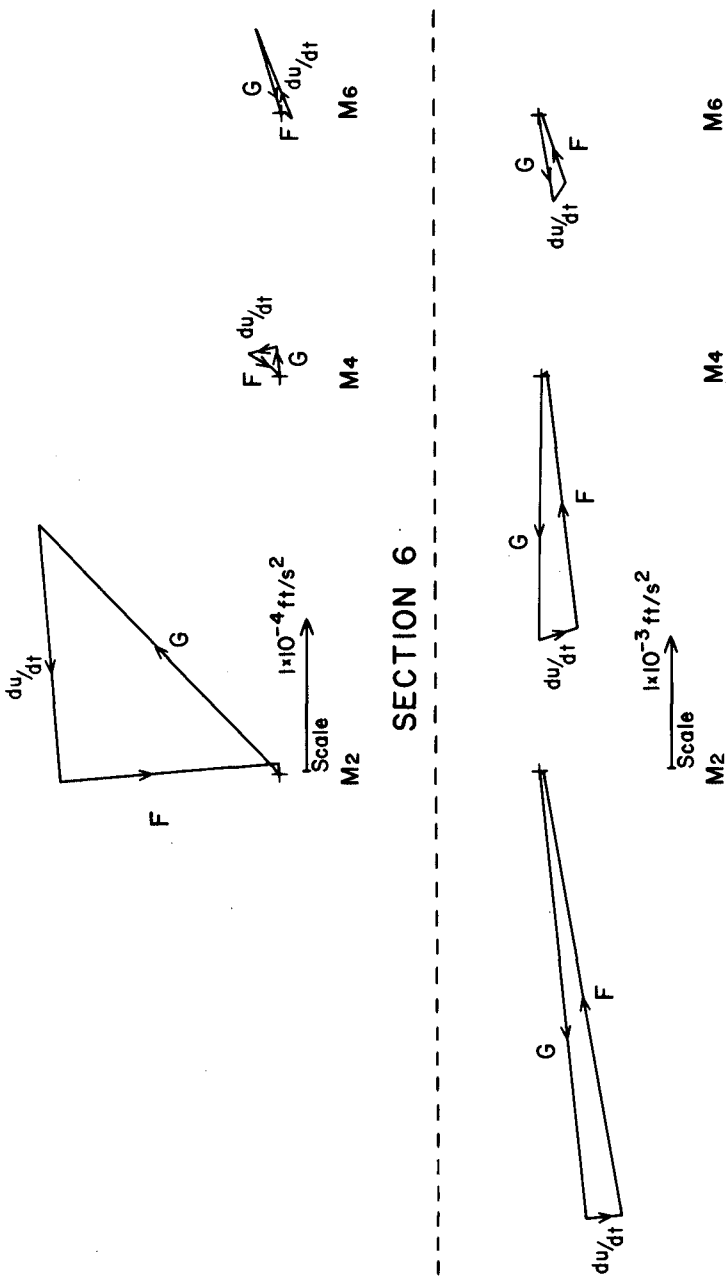


Figure 4. Harmonic constituents for each term in the equation of motion at two positions in the Thames. F - friction term, G - surface gradient, convective term is not labelled.

results. However where there is no clear physical basis for such additional terms the model must be suspect when used for alternative applications i.e. in an extrapolative rather than interpolative mode. An obvious example of this danger is in the simulation of the impact of tidal barriers where, for the River Thames, it has been shown that changes to high and low waters due to barrier construction are more influenced by changes in the M_4 and M_6 constituents than by changes in the predominant M_2 tide.

4. SURGES

(i) 1953 Surge

A detailed examination has been made of the disastrous storm surge of January/February 1953.⁵ The simulation of the surge event involved the addition of four components to the tidal model previously described : (a) the observed surge heights along the northern boundary (b) the observed surge heights along the western boundary (c) the wind stress over the surface of the region and (d) the observed horizontal variation in atmospheric pressure. A comparison of observed and computed surge heights showed that the model could accurately simulate surge propagation. Simulating successively (a) the surge alone, (b) tide plus surge and (c) tide alone, then comparing the results from (a) with the values given by (b) - (c) it was possible to identify the importance of surge-tide interaction.

(ii) Sensitivity analyses

An analysis of the influence of each of the four components, (a) to (d) above, was carried out by operating the model of tide plus surge a further four times and on each occasion omitting a single component. In this way it was shown that the surge from the North is of most significance in the Thames followed by the effect of the local wind field. The rapidity of the water level response, in the Thames, to this local wind field demonstrated the difficulty in using statistical methods for storm surge forecasting.

The influence of the surge component from the West is more significant along the Dutch coast than along the English coasts, this explains why the surge forecasting for the Dutch coast takes account

of this component while the English system does not.

Sensitivity analyses of this type are subject to misuse, strictly it is only appropriate for linearly independent systems. However it is useful in weakly non-linear processes where each of the separate terms omitted is, by itself, a relatively small part of the total system. A frequent application of this approach is to operate models with and without the Coriolis term, the difference in the results is then assumed to represent the influence of the earth's rotation. However the Coriolis term also influences the boundary conditions and hence the physical interpretation of such sensitivity analyses must be questionable.

(iii) Energy budget

The mechanics of energy transfers during the course of the storm were examined, one facet of this examination is shown in figure 5 where the spatial distribution of energy dissipation by bed friction is plotted. This distribution is a representation of $\int u^3 dt$, in a similar fashion functions such as the stratification parameter u^3/D may be readily displayed.

5. RESIDUALS

Interest in residual flows has grown in recent years for such applications as siting of power plants, sewage outfalls, fisheries studies and so on. Field measurements of residual currents suggested considerable spatial and temporal variability in these flows combined with an obvious dependence on wind forcing. However, prior to the modelling study,⁷ the mechanics of the residual circulation and its sensitivity to effects such as wind forcing were poorly understood.

(i) Tidal residuals

The non-linear terms present in the equations of motion which describe the propagation of the M_2 tide produce a time invariant (or residual) flow component that accompanies the oscillating component. An examination of these non-linear terms shows that their magnitude is proportional to the square of the tidal range. Once again, because of the predominance of M_2 it may be shown that

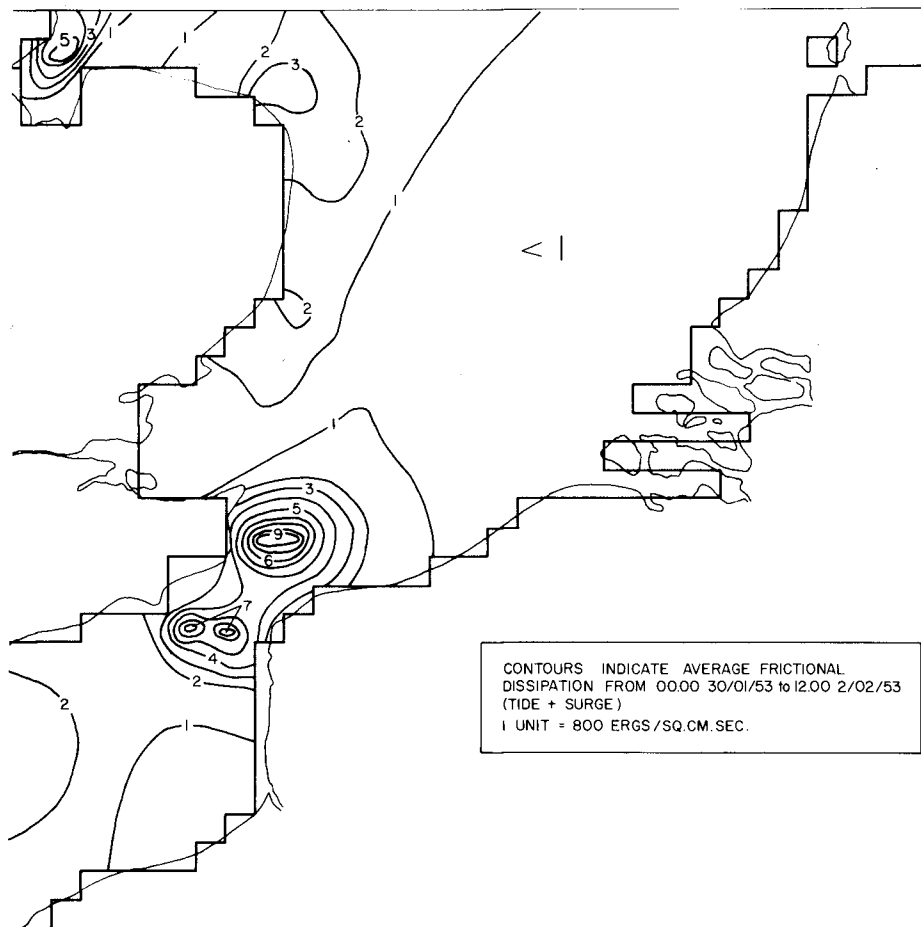


Figure 5. Spatial distribution of frictional dissipation. Mean values over the period 30 Jan to 2 Feb 1953, one unit represents $80 \mu\text{J cm}^{-2}\text{s}^{-1}$.

the average value of the square of the tidal range is equal to the square of the M_2 tidal range and hence an estimation of the M_2 tidal residuals should approximate the net tidal residual.

In extracting residual flow from a time-stepping simulation of the M_2 tide an erroneous residual circulation develops in the vicinity of the open-boundaries. This circulation is due to the assumption of a constant mean sea level along these boundaries, i.e. the neglect of the tidal stress component.² A technique of incorporating a radiation boundary condition was developed to overcome this problem. The tidal residual flow was computed as $8 \times 10^4 \text{ m}^3 \text{ s}^{-1}$ into the North Sea.

(ii) Wind driven residuals

Since the residual flows are much smaller than the tidal flows it is possible to describe these flows using linearised equations in which the friction coefficient is determined by reference to the tidal velocities. It is then possible to use linear superpositioning to combine the separate components of residual flow.

In computing the annual-mean wind driven flow three points of general significance emerged.

(a) Wind data from off-shore (in this case Light Vessels) were found to be much more coherent and therefore representative of spatially averaged surface wind stress than corresponding data from adjacent shore-based stations.

(b) The value of monthly mean wind stress calculated from $\sum_{i=1}^N W_i^2 / N$ for successive 3 hourly wind speed observations W_i was found to be a factor of around 4 times the corresponding value calculated from

$$\left\{ \sum_{i=1}^N W_i \right\}^2 / N$$

(c) The model responds in an irregular fashion to winds from different directions. Thus in order to compute the annual-mean wind driven flow it was necessary to compute separately the response for those periods when the wind was blowing from a particular sector. The net effect was then obtained by adding vectorially the results from each sector. A figure of $4 \times 10^4 \text{ m}^3 \text{ s}^{-1}$ was estimated as the annual-mean wind driven flow. The variability of this component over a twenty five year period has been examined.¹⁰

(iii) Sea surface gradient

Residual flows due to horizontal density gradients were shown to be negligible and, hence, the only remaining residual component was from sea surface gradients. This remaining component was determined by comparing the observed variation in mean sea level along the Continental coast with the corresponding values obtained for the sum of the level variations computed for the tidal and wind driven residual flows. An additional component was then included to obtain the best fit between observed and computed mean sea levels, this component consisted of an imposed sea surface gradient between the two open-boundaries of the model. The flow produced by this additional component was approximately $4 \times 10^4 \text{ m}^3 \text{ s}^{-1}$.

(iv) Total residual flow

Combining the three components gives the total residual flow ($16 \times 10^4 \text{ m}^3 \text{ s}^{-1}$ into the North Sea) and the spatial variation in mean sea level (figure 6). It was then possible to make four quantitative checks on these results.

- (a) A comparison of observed and computed variation in mean sea level along the English Coast.
- (b) An estimate of the level difference between the British levelling datum (O.D.N.) and the French levelling datum (I.G.N.) was calculated and compared with an earlier independent estimate.
- (c) The total residual flow was compared with a corresponding value obtained from 8 years of continuous cable recordings.
- (d) The residual flow in the absence of wind forcing was compared with current meter measurements made in the Dover Strait under tranquil conditions.

6. INTERACTION

An intriguing feature of surge propagation in the Thames is that large surge peaks almost always occur 3 to 4 hours before high tide. This is precisely the time when flood contingency plans have to be decided upon. The existing prediction techniques implicitly assume that the observed surge peak will decrease as high tide approaches.

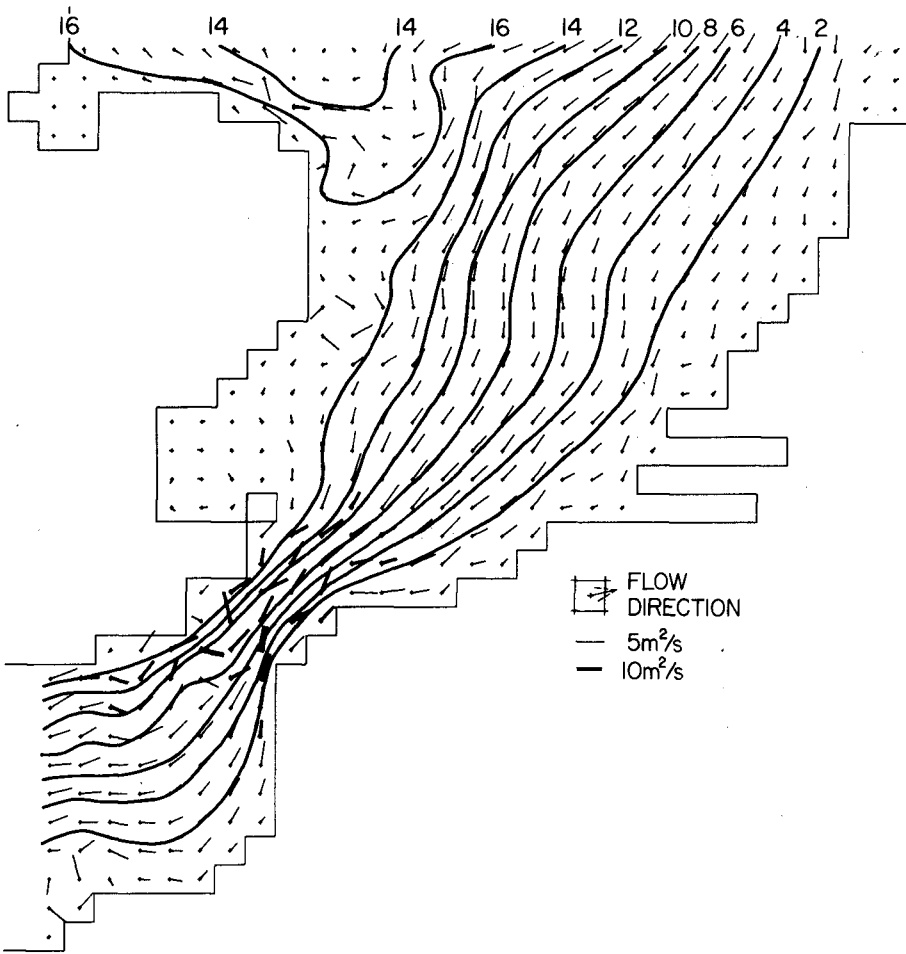


Figure 6. Total residual flow. Streamlines represent $\Psi / (10^4 \text{ m}^3 \text{ s}^{-1}) = \text{constant}$.

However no clear explanation for this phenomenon had been presented and no guidance was available regarding those circumstances under which the surge peak might be sustained.

(i) Surge statistics

A careful examination^{8,9} was made of surge statistics for a number of ports along the east coast of the British Isles and also along the Thames estuary. This showed that surges tend to develop a peak on the rising tide in the Thames irrespective of the phase relationship between the tide and the initial surge development in the northern North Sea. It also showed that although interaction tended to develop progressively as the surges propagated southwards there was an important exception at Lowestoft where interaction appeared to be reduced.

(ii) Parallel models

A new conceptual approach was used to examine the physics of surge-tide interaction, this involved two separate models, one of surge propagation and the other of tidal propagation. The two models are operated simultaneously and interaction, via the non-linear terms, is introduced by cross-linking between the models. To illustrate this consider the quadratic friction term :

$$K (u_s + u_T) |u_s + u_T| = K u_s |u_s + \underline{u_T}| + K u_T |\underline{u_s} + u_T| \quad (5)$$

(combined model) (surge model) (tidal model)

subscripts S and T refer to surge and tide respectively.

Thus in the model of surge propagation the friction term, is modified by the additional term underlined in (5). Similarly the parameter D in the surge model is modified to $D' = D + Z_T$ to represent the shallow water influence of tidal heights on surge propagation. The validity of this approach rests upon the results from these separate models combining to approximate the results from a combined simulation (subscript c), this requires that

$$Z_c = Z_s + Z_T \quad (6)$$

$$u_c = u_s + u_T \quad (7)$$

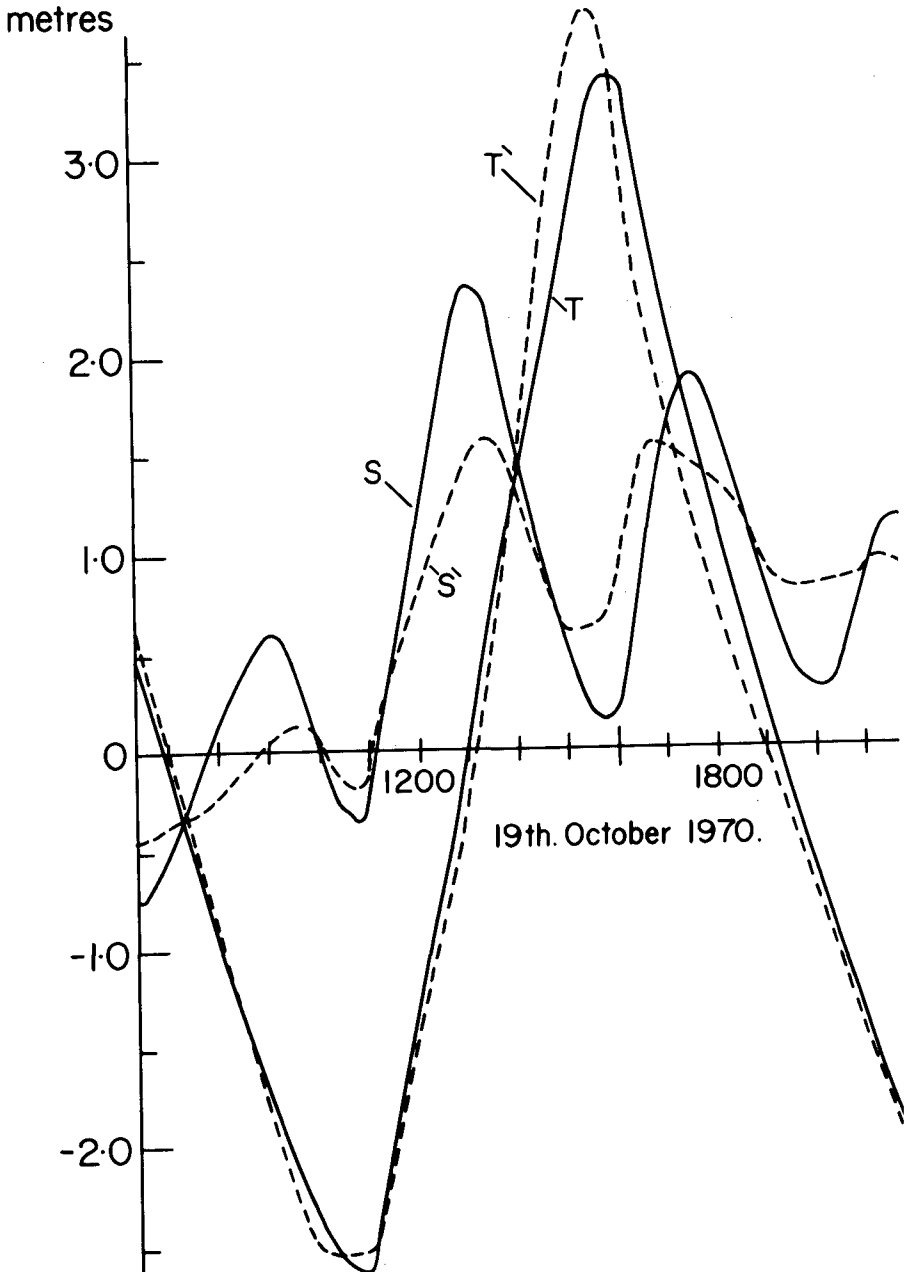


Figure 7. Elevations at Tower Pier.

T - tide alone; S - surge alone; T' tide with interaction from surge; S' surge with interaction from tide.

Figure 7 shows some results for surge and tide elevations at Tower Pier obtained from this approach. The figure contains results from four versions of the model :

- (a) a simulation of tide alone T
- (b) a simulation of surge alone S
- (c) simulation of tide with interaction from the surge T
- (d) simulation of surge with interaction from the tide S } Parallel models

One important result which emerged from this approach was that the magnitude of these cross-linkage terms, and hence the magnitude of the interaction, was shown to be proportional to a product of the tidal amplitude and surge height.

(iii) Conclusions

An analysis of results such as those shown in figure 7 revealed the following features of surge-tide interaction.

- (a) The non-linear friction term is predominant in producing surge-tide interaction, it is particularly effective in reducing higher-frequency surge peaks.
- (b) Shallow water terms produce a phase advance in the tidal component for positive surges and vice versa.
- (c) Interaction can develop rapidly in both space and time. The occurrence of surge peaks on the rising tide in the Thames was attributed to interaction, mainly via the friction term, resulting from the large values of both tidal and surge velocities found in the near-shore region between Lowestoft and Walton.
- (d) At any instant, the separate interactions of tide on surge propagation and of surge on tidal propagation tend to be in opposition. Thus the observed interaction is the small difference between two larger components. This explains why observed interaction appears to include an unexpected high frequency component and, also, why it is so difficult to relate the time series of interaction directly to either surge or tide.

7. FURTHER PROBLEMS

To conclude this summary of recent studies a brief description is

included of current work and some comments included about possible future applications.

(i) Open boundary problem

In a model of limited spatial extent used to examine the impact of some change in channel geometry such as the introduction of a tidal barrier, the problem arises as to the validity of assuming fixed conditions along the open-boundary. An extreme example of this type of problem is the proposed Bay of Fundy tidal power project where it is sensibly suggested that the model might have to extend to the whole of the North Atlantic Ocean in order to overcome this problem. In this particular application, an alternative approach¹ has been developed whereby conditions at the mouth of the model are modified to reflect the combined influences of the model region and the external ocean. A similar approach,¹¹ employing the analogy between tidal flow and A-C electrical circuit theory, has been used to examine the influence of tidal barriers in the Thames and Bristol Channel.

(ii) Inclusion of higher-order physical mechanisms

Previous reference has been made to the inadequacy of the friction formula as used in the shallow water wave equations. Strong arguments can be expressed suggesting that some account should be taken of changing bed formations; turbulent energy levels; temperature, density and stratification of the water mass and so on. Similar arguments might be used to suggest a wind-stress coefficient varying in time and space. However good results have been obtained by the existing, perhaps crude, parameterisation of these other effects. In practical terms an extension into these higher-order effects must be justified on a number of counts. First it must be shown that present methods are inadequate and second some realistic chance of improving the modelling must be shown.

Such extensions may be necessary for applications such as the simulation of sediment transport. However an extension of the spectral range of the model will also imply an equivalent extension of the data base against which the model must be evaluated. Where the objective of this extension in spectral range is to improve the

simulation in the original frequency band it is necessary to have a dynamic feed-back from the higher spectral range into the original. However, in many applications the physics in the higher frequency range are simulated less accurately than is the case for tidal propagation. Hence as the links between different scales of motion become stronger the possibility of reducing the accuracy of tidal propagation is increased.

ACKNOWLEDGEMENTS

The work described in this paper was funded by a Consortium consisting of the natural Environment Research Council, the Ministry of Agriculture, Fisheries and Food, and the Departments of Industry and Energy.

REFERENCES

1. Garrett, C.R.J. & Greenberg, D. 1977. "Predicting changes in tidal regime : the open boundary problem". J. Phys. Oceanography, Vol.7 pp 171-181.
2. Nihoul, J.C.J. and Rood, F.C. 1975. "The influence of the "tidal stress" on the residual circulation". Tellus, Vol.27, pp 484-489.
3. Pingree, R.D. and Maddock, L. 1978. "The M_4 tide in the English Channel derived from a non-linear numerical model of the M_2 tide". Deep-Sea Research, Vol.25, pp 53-63.
4. Prandle, D. 1974. "A numerical model of the southern North Sea and River Thames". Institute of Oceanographic Sciences. Report No.4.
5. Prandle, D. 1975. "Storm surges in the southern North Sea and River Thames". Proc. R. Soc. Lond. A. Vol.344, pp 509-539.
6. Prandle, D. and Harrison, A.J. 1975. "Relating the potential difference measured on a submarine cable to the flow of water through the Strait of Dover". Dt. Hydrogr. Z., Vol.28, 207-226.
7. Prandle, D. 1978. "Residual flows and elevations in the southern North Sea". Proc. Roy. Soc. Lond. A. Vol.359, pp 189-228.
8. Prandle, D. and Wolf, J. 1978. "Surge-tide Interaction in the Southern North Sea". "Hydrodynamics of Estuaries and Fjords" Elsevier Scientific Publishing Company. pp 161-186.
9. Prandle, D. and Wolf, J. 1978. "The interaction of Surge and Tide in the North Sea and River Thames". Geophys. J. R. astr. Soc. v.55.
10. Prandle, D. 1978. "Monthly-mean Residual Flows through the Dover Strait; 1949-1972". J. Mar. Biol. Ass. v.58.
11. Prandle, D. "The open-boundary problem - an application of A-C electrical circuit theory for tidal barriers in the River Thames and Bristol Channel". (in preparation).
12. Proudman, J. & Doodson, A.T. 1924. "The principal constituent of the North Sea". Phil. Trans. R. Soc., A. Vol.224, pp 185-219.

PROCEEDINGS
OF THE

Sixteenth Coastal Engineering Conference

August 27 to September 3, 1978
Hamburg, Germany

Volume II

Sponsored by
ASCE Coastal Engineering Research Council
ASCE Waterway, Port, Coastal and Ocean Division
Ministry for Research and Technology
of the Federal Republic of Germany
Free and Hanseatic City of Hamburg,
Association for Port and Coastal Engineering
and
International Association of the
Physical Sciences of the Oceans



Published by the American Society of Civil Engineers
345 East 47th Street, New York, N.Y. 10017
Net Price: \$50.00

ACKNOWLEDGMENTS

The following engineers served as the Organizing Committee for the Sixteenth International Conference on Coastal Engineering:

KARL-EDUARD NAUMANN, Chairman
Association for Port and Coastal Engineering (Hamburg)

HANS-WERNER PARTENSCKY, Co-Chairman
Technical University of Hannover

WINFRIED SIEFERT, Secretary
Port and River Authority, Cuxhaven

ALFRED FÜHRBÖTER
Technical University of Braunschweig

HARALD GÖHREN
Port and River Authority, Hamburg

JOHANN KRAMER
Board of Maritime Works, Aurich

HANS ROHDE
Federal Institute for Waterways Engineering, Hamburg

JOSEF SINDERN
Waterways and Navigation Board North, Kiel

HANS VOLLMERS
University of Federal German Armed Forces, München

The use of photographs by U. Muuss, N. Rüpke, and H. Engler for use on the Parts title pages is gratefully acknowledged.

PART II
COASTAL SEDIMENT PROBLEMS

Chapter 66 WAVE POWER AND BEACH-STAGES: A GLOBAL MODEL Andrew D. Short	1145
Chapter 67 MATHEMATICAL MODELING OF SHORELINE EVOLUTION Bernard Le Méhauté and Mills Soldate	1163
Chapter 68 MORPHODYNAMIC VARIABILITY OF HIGH-ENERGY BEACHES L. D. Wright, B. G. Thom and J. Chappell	1180
Chapter 69 VARIATIONS OF WAVE-ENERGY LEVELS AND COASTAL SEDIMENTATION, EASTERN NICARAGUA E. H. Owens and H. H. Roberts	1195
Chapter 70 PROCESS-RESPONSE MODELS FOR DEPOSITIONAL SHORELINES: THE GERMAN AND GEORGIA BIGHTS Dag Nummedal and Ian A. Fisher	1215
Chapter 71 MORPHOLOGY OF COASTAL BARRIERS, DELAWARE, U.S.A. John C. Kraft, Chacko J. John and Evelyn M. Maurmeyer	1232
Chapter 72 A NEW METHOD FOR THE REPRESENTATION OF SEDIMENTARY SEQUENCES IN COASTAL REGIONS Hansjörg Streif	1245
Chapter 73 COASTAL PROCESSES AT OREGON INLET, NORTH CAROLINA James T. Jarrett	1257
Chapter 74 MAINTENANCE OF SANTA CRUZ HARBOR, CALIFORNIA, U.S.A. Orville T. Magoon and Don C. Baer	1276
Chapter 75 CASE STUDIES OF DELAWARE'S TIDAL INLETS: ROOSEVELT AND INDIAN RIVER INLETS W. A. Dennis, G. A. Lanan and R. A. Dalrymple	1282

Chapter 76	
NUMERICAL MODEL INVESTIGATION OF SELECTED TIDAL INLET-BAY SYSTEM CHARACTERISTICS	
William N. Seelig and Robert M. Sorensen	1302
Chapter 77	
VELOCITY AND STRESS MEASUREMENTS IN A TIDAL INLET	
David A. Huntley and Dag Nummedal	1320
Chapter 78	
PERIODIC FLOWS FROM TIDAL INLETS	
D. L. Wilkinson	1336
Chapter 79	
THE EFFECT OF OFFSHORE DREDGING ON COASTLINES	
W. A. Price, J. M. Motyka and L. J. Jaffrey	1347
Chapter 80	
SURF ZONE RESONANCE AND COUPLED MORPHOLOGY	
John Chappell and Lynn Donelson Wright	1359
Chapter 81	
BEACH CUSPS AND EDGE WAVES	
D. A. Huntley and A. J. Bowen	1378
Chapter 82	
NEAR-BOTTOM VELOCITIES IN WAVES WITH A CURRENT	
W. T. Bakker and Th. Van Doorn	1394
Chapter 83	
RIP CURRENTS AND THEIR CAUSES	
Robert A. Dalrymple	1414
Chapter 84	
WIND-GENERATED LONGSHORE CURRENTS	
Dag Nummedal and Robert J. Finley	1428
Chapter 85	
VISIBLE-REGION PHOTOGRAPHIC REMOTE SENSING OF NEARSHORE WATERS	
Tsuguo Sunamura and Kiyoshi Horikawa	1439
Chapter 86	
UNDULATED BOTTOM PROFILES AND ONSHORE-OFFSHORE TRANSPORT	
Madhav Manohar	1454
Chapter 87	
ONSHORE-OFFSHORE SEDIMENT MOVEMENT ON A BEACH	
P. Nielsen, I. A. Svendsen and C. Staub	1475

Chapter 88	
USES FOR A CALCULATED LIMIT DEPTH TO BEACH EROSION	
Robert J. Hallermeier	1493
Chapter 89	
DEPTH OF DISTURBANCE OF SAND IN SURF ZONES	
Michael K. Gaughan	1513
Chapter 90	
SCALE RELATIONS FOR EQUILIBRIUM BEACH PROFILES	
Hideaki Noda	1531
Chapter 91	
TRACKED VEHICLE FOR CONTINUOUS NEARSHORE PROFILES	
Richard J. Seymour, Alan L. Higgins and David P. Bothman	1542
Chapter 92	
THE NEARSHORE SEDIMENT TRANSPORT STUDY	
Richard J. Seymour and David B. Duane	1555
Chapter 93	
LONGSHORE SEDIMENT TRANSPORT DATA: A REVIEW	
Matthew N. Greer and Ole Secher Madsen	1563
Chapter 94	
SEDIMENT MOTION CAUSED BY SURFACE WATER WAVES	
A. G. Davies and R. H. Wilkinson	1577
Chapter 95	
DISTRIBUTION OF SAND TRANSPORT RATE ACROSS A SURF ZONE	
Toru Sawaragi and Ichiro Deguchi	1596
Chapter 96	
LITTORAL DRIFT ALONG BAYSHORE OF A BARRIER ISLAND	
Yu-Hwa Wang and T. H. Chang	1574
Chapter 97	
SEDIMENT LOAD UNDER WAVES AND CURRENTS	
D. H. Willis	1626
Chapter 98	
SEDIMENT TRANSPORT AND RIPPLES DUE TO WAVES AND CURRENTS	
Zbigniew Pruszek and Ryszard B. Zeidler	1638
Chapter 99	
A MODEL STUDY OF ALONGSHORE SEDIMENT TRANSPORT RATE	
J. W. Kamphuis and J. S. Readshaw	1656

Chapter 100	
EFFECT OF WAVES ON SAND TRANSPORT BY CURRENTS	
Michael W. Owen and Michael F. C. Thorn	1675
Chapter 101	
FIELD EXPERIMENT ON BEACH GRAVEL TRANSPORT	
Masataro Hattori and Takasuke Suzuki	1688
Chapter 102	
SHINGLE TRACING BY A NEW TECHNIQUE	
Peter Wright, J. S. Cross and N. B. Webber	1705
Chapter 103	
A NUMERICAL MODEL FOR SEDIMENT TRANSPORT	
J. P. Lepetit and A. Hauguel	1715
Chapter 104	
SURF ZONE MEASUREMENTS OF SUSPENDED SEDIMENT	
Timothy W. Kana	1725
Chapter 105	
STORM INDUCED PERIODICITIES OF SUSPENDED SAND MOVEMENT	
Jay E. Leonard and Benno M. Brenninkmeyer	1744
Chapter 106	
SLED SYSTEM FOR PROFILING SUSPENDED LITTORAL DRIFT	
J. P. Coakley, H. A. Savile, M. Pedrosa and M. Larocque	1764
Chapter 107	
ON THE GEOMETRY OF RIPPLES DUE TO WAVES	
M. S. Yalin and E. Karahan	1776
Chapter 108	
THE INFLUENCE OF DUNE AND FLOW PARAMETERS ON THE FRICTION FACTOR	
J. Sündermann, H. Vollmers and W. Puls	1787
Chapter 109	
TIME-LAG OF DUNES FOR UNSTEADY FLOW CONDITIONS	
Horst Nasner	1801
Chapter 110	
PREDICTION OF BEACH PLANFORMS WITH LITTORAL CONTROLS	
Marc Perlín and R. G. Dean	1818
Chapter 111	
ESTIMATION USING A MOVABLE BED MODEL OF SHORELINE CHANGE CAUSED BY A RECLAMATION PROJECTED INTO THE SEA	
Shoji Sato and Hiroaki Ozasa	1839

Chapter 112	
MORPHOLOGIC EFFECTS OF WESTERLAND BEACH NOURISHMENT 1972	
Dieter Wenzel	1859
Chapter 113	
IMPORTANCE OF HANDLING LOSSES TO BEACH FILL DESIGN	
R. D. Hobson and W. R. James	1873
Chapter 114	
SOME FACTS AND FANCIES ABOUT BEACH EROSION	
Richard Silvester	1888
Chapter 115	
DIFFRACTION CALCULATION OF SHORELINE PLANFORMS	
Robert G. Dean	1903
Chapter 116	
CONCENTRATION OF SUSPENDED CLAY IN PERIODIC FLOW	
A. Watanabe, P. Thimakorn and A. Das Gupta	1918
Chapter 117	
SUSPENSION AND TRANSPORTATION OF FLUID MUD BY SOLITARY-LIKE WAVES	
John T. Wells, James M. Coleman and William J. Wiseman, Jr.	1932
Chapter 118	
HYDRODYNAMICS AND SEDIMENT TRANSPORT IN A SALT MARSH TIDAL CHANNEL	
Larry G. Ward	1953
Chapter 119	
TWO-DIMENSIONAL STABILITY ANALYSIS OF TIDAL BASINS AND TIDAL FLATS OF LARGER EXTENT	
Eberhard Renger	1971
Chapter 120	
TIDAL SEDIMENTATION IN GROS-CACOUNA HARBOR	
Georges Drapeau and Guy Fortin	1986
Chapter 121	
FACTORS GOVERNING THE DISTRIBUTION OF DREDGE-RESUSPENDED SEDIMENTS	
W. Frank Bohlen	2001
Chapter 122	
MOVABLE BED MODEL TESTS ON DUNE EROSION	
P. Vellinga	2020

Chapter 123
USING FENCES TO CREATE AND STABILISE SAND DUNES
Brian B. Willetts and Christopher J. Phillips2040

Chapter 124
BEACH GROUND-WATER OSCILLATIONS
Andrzej Lewandowski and Ryszard Zeidler2051



North Friesian Coast

PART II
COASTAL SEDIMENT PROBLEMS

Westerland, Island Sylt



CHAPTER 66

WAVE POWER AND BEACH-STAGES: A GLOBAL MODEL

Andrew D. Short

Coastal Studies Unit, Dept. of Geography

University of Sydney, Sydney, N.S.W. 2006

Australia

ABSTRACT

A three-dimensional morphodynamic model of sequential beach changes is presented. The model is based on variations in breaker wave power generating a predictable sequence of beach conditions. The spectrum of beach conditions from fully eroded-dissipative to fully accreted-reflective is characterised by ten beach-stages. Using the breaker wave power to beach-stage relationship the model is applied to explain temporal, spatial and global variations in beach morphodynamics.

INTRODUCTION

Beach and surfzone morphodynamics have received increasing attention in recent years (for review see Wright and Thom, 1977). While much progress has been made there exists a general lack of understanding and awareness of the total spectrum of beach conditions. Individual beach studies in diverse locations, wave conditions and coastal environments are often difficult to relate or compare, and in general there is no overall conceptual model within which beach studies and their results can be framed. Most studies are of too short a duration and too limited range of wave and beach conditions to generate data for a larger model. This paper presents a model within which all previous beach studies can be framed (Short, in preparation) and which can be applied globally to all microtidal, open coast, sand beaches. The model is the result of more than 2½ years of daily observations of beach morphodynamics (Figure 1) and associated deepwater and breaker wave characteristics. The main field site was located at Narrabeen Beach, New South Wales, a 4km long, medium to fine sand beach ($M\phi = 1.3\phi$) receiving moderate to high power east coast swell on a microtidal coast. These observations are supplemented by ground and aerial surveys and aerial photographs of the 3,300 km southeast Australian coast, a microtidal coast which receives east and west coast swell wave conditions, on beaches composed of fine to coarse sand (Short, 1978).

Using the 30 month time series of wave and beach conditions a three-dimensional model of sequential beach changes was formulated. The model depicts continuous changes in beach morphodynamics, with decreasing breaker wave power leading to onshore bar migration, beach accretion and reflective surfzone conditions, and increasing wave power generating

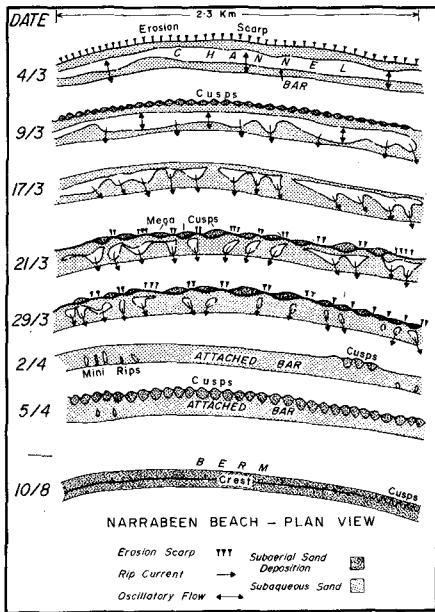


Figure 1 :

An example of the field observations during a four week accretionary period under low wave conditions (4.3 to 5.4.1977 and 10.8.1977) illustrating the migration of a parallel bar (4.3.77) onshore; resulting in crescentic bars (9 and 17.3.77); accretionary rip cells (21 and 29.3.77); welded bar, mini-rips and cusps (2 and 5.4.77); and at a later stage a continuous subaerial berm (10.8.77).

beach erosion, bar-channel formation and dissipative surfzone conditions. The model applies to the subaerial beach and subaqueous surfzone to the seaward slope of the inner bar (~ 3 m at Narrabeen Beach). Second and outer bars are not included.

The model is now briefly presented. It is then applied to explain temporal, spatial and global variations in beach morphodynamics.

THE MODEL

The time series of wave and beach conditions was separated into ten *beach-stages*, four erosional, four accretional with two terminal stages of fully eroded and fully accreted (Figure 2). The ten stages represent ten characteristic beach morphodynamic conditions in a continuum of beach changes. Movement through the model is generated by variations in breaker wave power. At any stage the direction of movement to adjoining erosional or accretionary stages depends on the direction of change in wave power. Increasing wave power causes movement through the erosional stages, decreasing power produces movement through the accretionary stages. The model is now outlined for an idealised situation of continuously decreasing wave power, the accretionary sequence, and increasing wave power, the erosional sequence. It assumes waves arrive normal to shore on an open, microtidal sand coast. For a more complete description of the model see Short (in preparation).

The accretionary sequence (Figure 2a and 3) begins at *beach-stage* 6, a parallel bar-channel system, where the position of the bar is

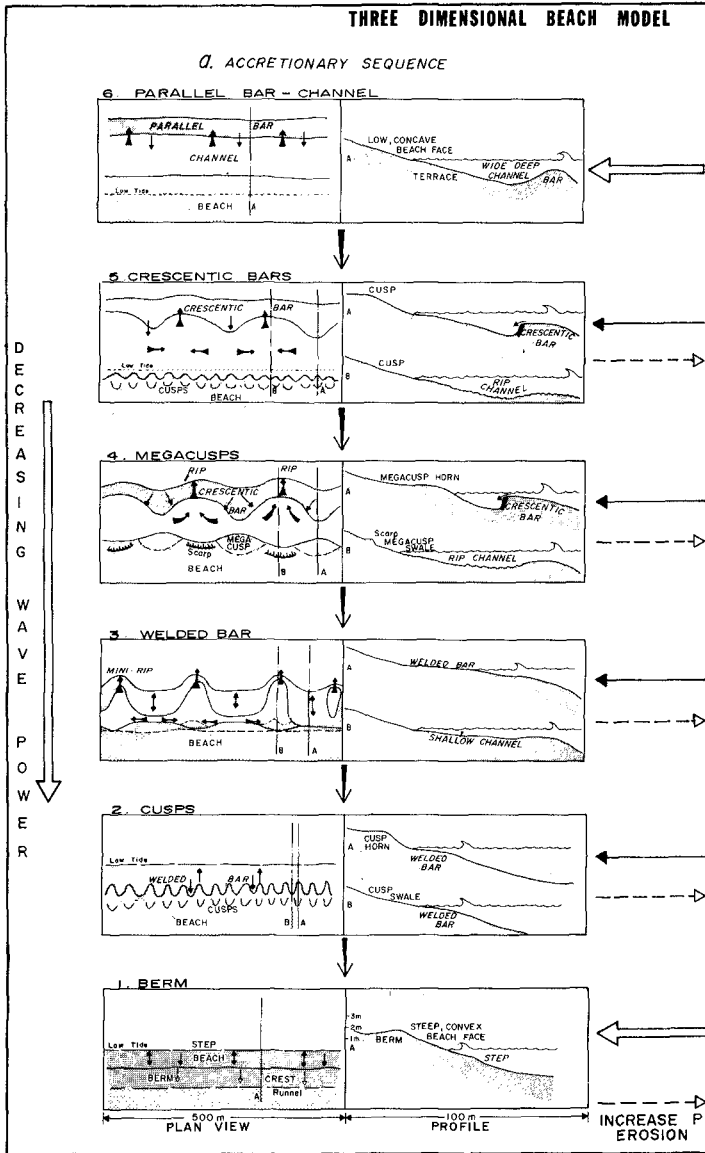


Figure 2 : The three dimensional beach model. Connecting arrows indicate direction of movement within model, solid-decreasing wave power (P) and movement to accretionary stages, broken - increasing power and movement to erosional stages. Within each beach-stage, heavy arrows indicate surfzone current flow at low frequencies, small arrows indicate flow at incident wave frequency. a. The accretionary sequence, beach-stages 6 to 1 generated by decreasing wave power.

(Fig. 2 continued)

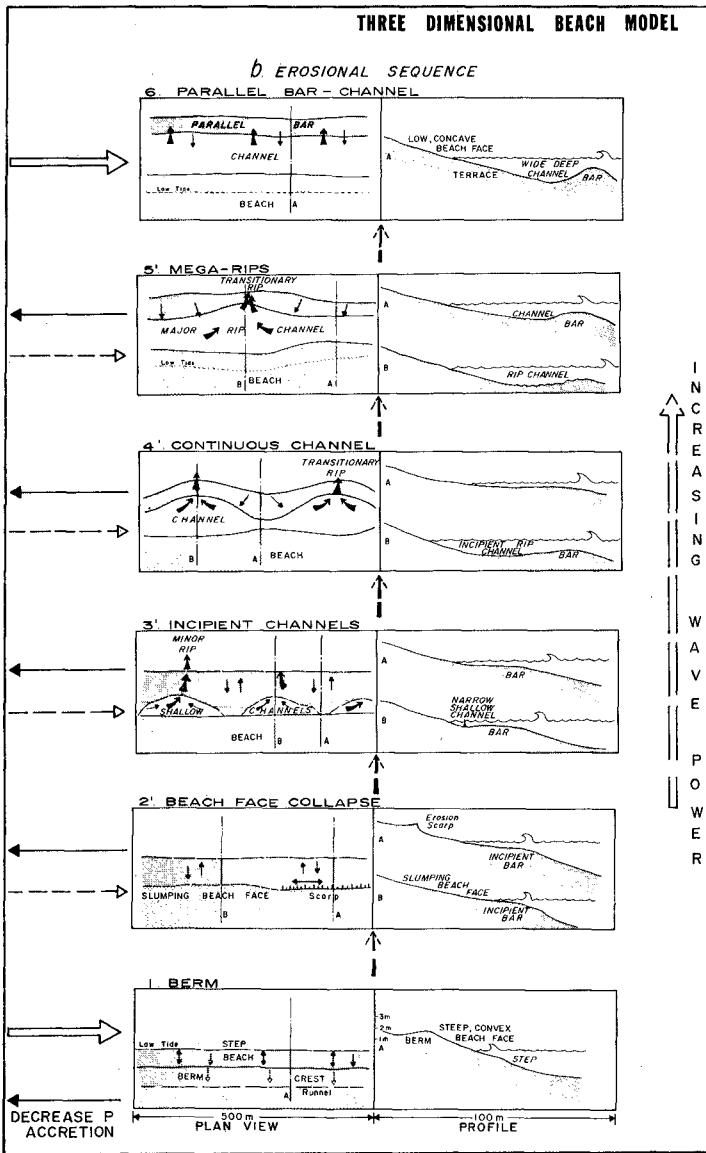


Figure 2 : The three dimensional beach model, continued.

- b. The erosional sequence, *beach-stages 1 to 6*, generated by increasing wave power.



Figure 3 : Examples of accretionary beach-stages from south east Australia. a. Beach-stage 6, The Coorong, South Australia. 3-4m high waves are breaking on the outer bar and flowing into shore parallel channel.



Figure 3 b : Beach-stages 5, Fens Embayment, New South Wales (N.S.W.). Note crescentic bars (spacing approximately 200 m) and beach cusps, with megacusps (indicated by arrows) beginning to form inshore of more shoreward advanced crescentic bars.

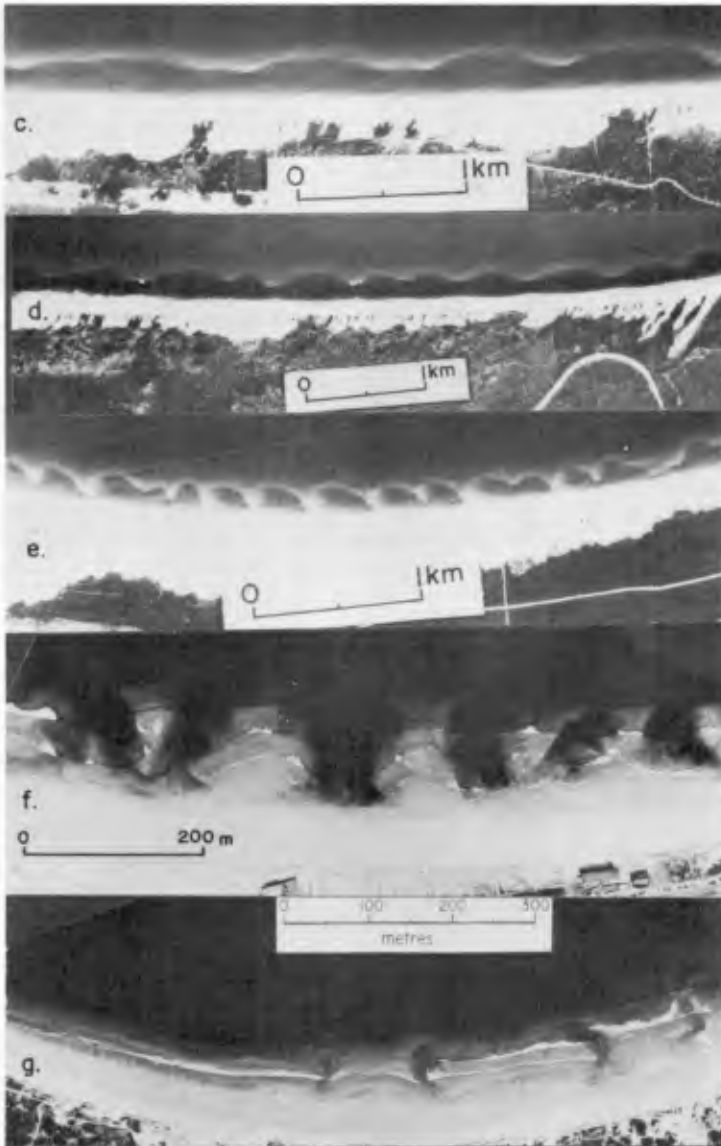


Figure 3 c : Beach-stage 5, Fens Embayment, N.S.W.
 d : Beach-stage 5, Fens Embayment, N.S.W.
 e : Beach-stage 4, Fens Embayment, N.S.W.
 f : Beach-stage 3, Cronulla Beach, N.S.W.
 g : Beach-stage 3 → 2, Cronulla Beach, N.S.W.



Figure 3 h : Beach-stage 3, Narrabeen Beach, N.S.W. Note welded bar and remnants of megacusps.
 i : Beach-stage 2, Narrabeen Beach, N.S.W. Cusps horns indicated by arrows.
 j : Beach-stage 2 \rightarrow 1, Warriwood Beach, N.S.W. Cusps embayments fill as a continuous berm develops.
 k : Beach-stage 1, Narrabeen Beach, N.S.W. Note straight berm crest and backing runnel.

determined by low frequency standing waves generated by waterlevel setup in the channel during high wave power conditions, (Figure 3a). If the offshore slope is gentle multiple bars result. All flow is shore normal and no rips are present, the beach is in 'equilibrium', with no longshore variation in profile or dynamics. With a decrease in wave power, resonance generated by reflection of the incident waves off the beach face, and possibly lower mode reflection against the inside of the bar, results in edge waves that respectively generate systematic longshore variations in waterlevel on the beach face and bar. The longshore variations in waterlevel result in preferential shoreward flow of water across the beachface and bar at the antinodes of the edge waves. This flow in turn produces greater shoreward movement of sediment at those points initiating cusps and crescentic bars (Narrabeen mean bar spacing 150m), (*beach-stage 5*, Figure 2a and 3b, c and d). Decreasing wave power causes the crescentic bars to migrate shoreward during *stage 4*, filling the now overfit channel, (Figure 3 d and e). The increasingly crescentic bar-channel morphology produces marked longshore variations in wave power and direction at the beach face generating a second phase reworking of the beach face as megacusps horns are deposited and embayments eroded. During *stage 3* the accretionary rip channels completely infill as the bar welds to the base of the beach, (Figure 3 e - h). Continuing low wave power conditions moves the 'bar' up the beach face (*stage 2*) where increasing beach steepness and beach reflectivity usually result in edge waves and cusp deposition (Wright, et. al., 1977) (Figure 3 i and j). Finally the cusp swales fill (Figure 3 j and k) and a continuous berm is formed (*stage 1*). The berm face is now too reflective for edge wave generation resulting in a straight berm crest, (Figure 3k). The beach is again in an 'equilibrium' condition with no longshore variation in beach morphology or dynamics. The erosion sequence (Figure 2b) begins with increasing wave power generating saturation and collapse of the steep berm face. The slumping sand is moved immediately seaward of the beach face as a narrow attached bar (*Stage 2'*). As wave power continues to increase in *Stage 3'*, narrow channels are initiated at the apex of the beach face and bar. The channels permit storage and longshore transport of water before it pluses seaward at lower frequencies. In *Stage 4'*, increasing wave power results in greater onshore flow of water which requires larger storage and transport channels. The resulting channel excavation moves the bar and breakpoint further seaward. At this stage relative closely spaced (spacing 200-500m), poorly developed erosional rips are initiated to facilitate seaward return of the water. The spacing of the rips is probably controlled by edge waves generating longshore variation in water level. As wave power continues to increase the size of the edge waves also increases resulting and more widely spaced megarip currents by *Stage 5'* (spacing 500-1,000m). Finally by *Stage 6* the longshore channel is large enough to temporarily store water moving shoreward so as to allow it to return to normal to the shore, instead of being transported laterally into high velocity rip currents. The shore normal return is achieved by a water level set-up in the channel that returns seaward in the form of a low frequency standing wave. It is this standing wave and its seaward effect that in turn determines offshore bar or bars spacing.

In nature wave power rarely moves smoothly between such extremes,

rather depending on the wave environment it oscillates with varying amplitude and frequency around a modal wave power. The effect of these oscillations is to generate smaller cycles within the sequence shown in Figure 2. Cycles of this nature are shown in Figure 4, which plots part of the time-series of deepwater wave power and height, beach-stage and subaerial sand volume over a period of 13 months for Narrabeen Beach. Note the close correlation between all parameters as wave power varies. Increasing wave height and power produces higher beach-stages and erosion of the subaerial beach (January to June, 1978), while decreasing height and power result in low beach-stages and subaerial beach accretion (August-December, 1977). Also note that the transit time between erosional beach-stages is faster than between accretionary stages. This reflects the relative power associated with the erosive and accretive conditions. However, the absolute amount of wave power required to erode a beach is balanced over a longer period by the same magnitude of lower wave power through the accretionary sequence.

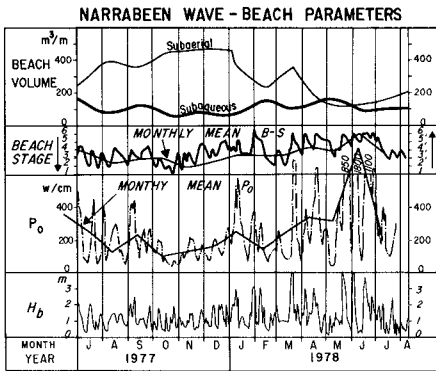


Figure 4 :
A time series of wave and beach parameters at Narrabeen Beach. Note the close correlation between breaker wave height (H_b), deepwater wave power (P_0), beach-stage, and subaerial beach volume. Subaqueous beach volume (0 to - 3 m) reflects the movement of eroded subaerial sediment to beyond the - 3 m depth contour.

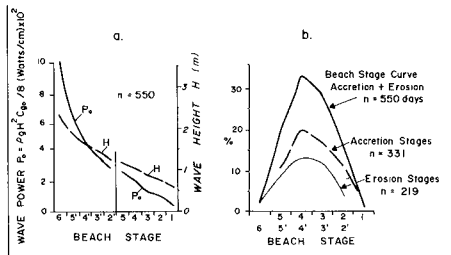


Figure 5 :
a. Correlation between erosional (6 to 2¹) and accretionary (5 to 1) beach-stages and deepwater wave power (P_0) and height (H) for Narrabeen Beach.
b. Narrabeen Beach beach-stage curves, plotting the percent frequency of occurrence of erosion, accretion and combined beach-stages between April 1976 and January 1978.

WAVE POWER AND BEACH STAGES

Absolute Wave Power

The model is based on the response of beach morphodynamics to variations in the level of absolute deepwater and breaker wave power,

Po and Pb respectively, where

$$P_o = \rho g H^2 C_o / 8 \text{ W cm}^{-1} \text{ wave crest}$$

where ρ is seawater density, g gravity, H significant wave height and C_o wave group velocity. Figure 5 a indicates the level of H and P_o associated with the 10 *beach-stages* on Narrabeen Beach. High stages are associated with high wave power, and erosive stages with the highest power. A threshold appears to exist at around $H = 1.2\text{m}$ and $P = 3 \times 10^2 \text{ Wcm}^{-1}$ above which erosive stages dominate and below which accretion dominates. Therefore for a given level of absolute deepwater and breaker wave power a corresponding beach-stage is generated with its associated morphology, dynamics and relative level of subaerial sediment volume.

Temporal Variations in Wave Power

Temporal variations in deepwater wave power produce variations in breaker wave power and thereby temporal variations in beach-stage. Over time the deepwater wave climate, will through its spectrum of wave power affect a corresponding spectrum of beach-stages. The amplitude and frequency of wave power oscillations determine beach-stages cycles. The frequency of occurrence of a particular beach-stage reflects the occurrence of the associated deepwater and breaker wave power. In order to apply this association to the model the beach-stage curve is now presented.

The *beach-stage curve* plots the percent frequency of occurrence of all beach-stages over a given time period for a particular site. Because of the direct linkages between accretion and erosion beach-stages of the same level (Figure 2) they can be combined as one in a total curve. The annual or total beach-stage curve is therefore the summation of the accretion and erosion beach-stage curves, which plot the occurrence of their respective beach-stages. Figure 5b illustrates the beach-stage curve for Narrabeen Beach. The modal breaker wave ($T = 10 \text{ sec}$, $H = 2 \text{ m}$) which arrives 10% of the time explains the modal 4/4' *beach-stage*. Rarer occurrences of very high ($> 3 \text{ m}$, 5%) and low ($< .5 \text{ m}$, 4%) waves explain the infrequent excursions to *stages 6* and *1* respectively. The *mode* and *range* of the beach-stage curve reflect the modal breaker wave power and range of wave conditions respectively. The beach-stage curve depicts quantitatively the morphodynamic character of a beach. It not only provides a mechanism for rigorously classifying and describing a beach but also for comparing it to beaches in other locations and wave environments.

APPLICATION

Temporal variations in wave power account for the morphodynamic character of a beach over time. In order to apply the model more widely the effect of spatial variations in deepwater and breaker wave power are now incorporated.

Spatial Variations in Breaker Wave Power

For a given deepwater wave climate the breaker wave power varies longshore in response to wave attenuation across the shelf (Wright, 1976) and wave refraction and diffraction. Along a coast the deepwater wave power will be attenuated and redistributed at the breakpoint depending on the shelf, nearshore and coastal morphology.

Longshore variations in breaker wave power affect a longshore variation in the relative level of beach-stage generated. In an idealised embayment (Figure 6), the longshore variation in breaker wave power generates a longshore variation in beach-stage, with low wave power producing lower stages, and high power higher stages. This effect is apparent on Narrabeen Beach which is protected in its southern portion (Collaroy Beach) from the dominant southeast swell. As a result when southeast swell dominates Narrabeen has a modal *stage 4*, while Collaroy with significantly lower breaker wave power has a modal *stage 2* (Figure 7a). However during the period of dominant northeast waves, Figure 7b, when the entire beach is equally exposed, the modal beach-stages are more similar. The annual beach-stage curves (Figure 7c) reflect the long term bias toward higher stages at Narrabeen and lower stages at Collaroy.

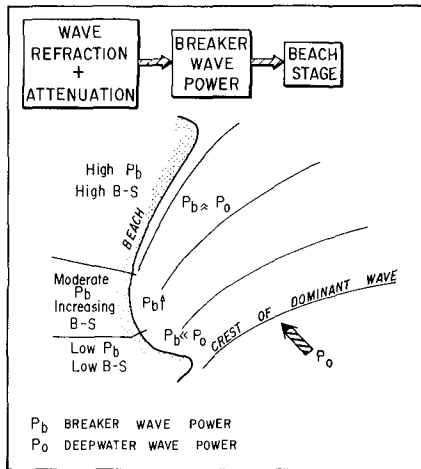


Figure 6 : Idealised coastal embayment showing the relationship between longshore variation in breaker wave power, due to wave refraction and attenuation, and corresponding level of beach-stage.

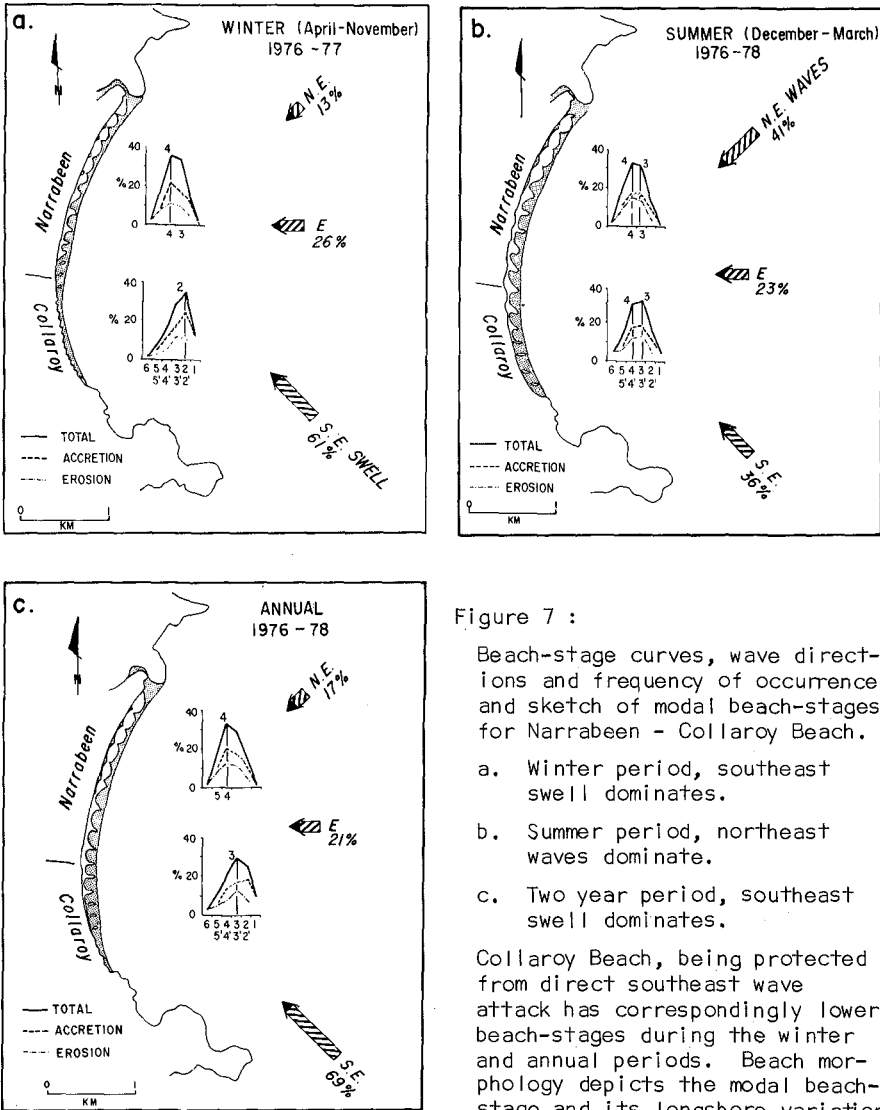


Figure 7 :

Beach-stage curves, wave directions and frequency of occurrence, and sketch of modal beach-stages for Narrabeen - Collaroy Beach.

- a. Winter period, southeast swell dominates.
- b. Summer period, northeast waves dominate.
- c. Two year period, southeast swell dominates.

Collaroy Beach, being protected from direct southeast wave attack has correspondingly lower beach-stages during the winter and annual periods. Beach morphology depicts the modal beach-stage and its longshore variation.

The same effect can occur in longer embayments. The Coorong coast of South Australia is exposed to year round, high power, west coast swell, resulting in very high deepwater wave power. Along The Coorong however breaker wave power varies from very high in the northwest to zero in the southeast (Figure 8) due to nearshore wave attenuation over dunerock reefs in the southeast. The modal beach morphodynamics adjusts accordingly having modal beach-stage 5 to 6 for the first 100 km, then

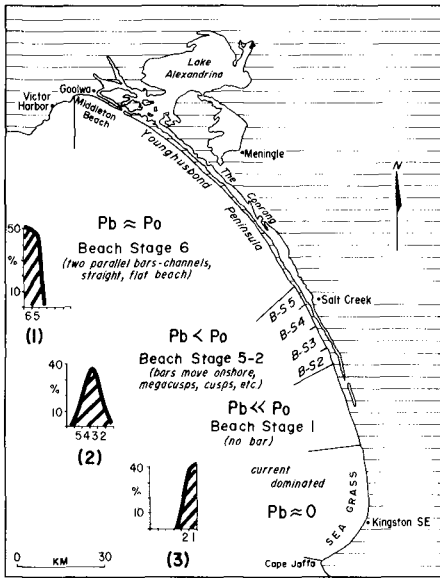


Figure 8 :

The Coorong, South Australia, illustrating the relative levels of deepwater (P_o) and breaker (P_b) wave power, and corresponding effect on modal beach-stage (1), (2) and (3).

as breaker wave power decreases between 100 to 130 km a transition zone occurs with modal *beach-stage* decreasing from 5 to 2, and finally with very low breaker wave power from 130 to 160 km, *beach-stage 1* dominates. Beyond 160 km to Cape Jaffa, breaker wave power is zero and the shoreline is dominated by current-generated sand waves with seagrass growing to the shoreline.

Therefore while deepwater wave power will determine the potential mode and range of beach-stages, breaker wave power governs the actual mode and range for a given location.

Global - Absolute, Temporal and Spatial Wave Power

Global deepwater wave climates are associated with the oceans' wave environments. Davies (1964 and 1973) classified the ocean wave environments into storm wave, west coast swell, east coast swell, trade wind and monsoon influence, and tropical cyclone influence, (Figure 9). Using Davies' basic wave environments, the characteristic deepwater wave spectrum associated with each environment can be used to generate a characteristic beach-stage curve. Figure 10 presents idealised annual and seasonal beach-stage curves for the major wave environments as would be expected on open, microtidal, sand coasts receiving maximum breaker wave power.

Storm wave environments with persistent high wave power have a modal *stage 5 - 6* with rare excursions to lower stages (Figure 10a). West coast swell have high winter wave power and corresponding *stage 6*. In the northern summer low power dominates and *stage 2* and *1* persist

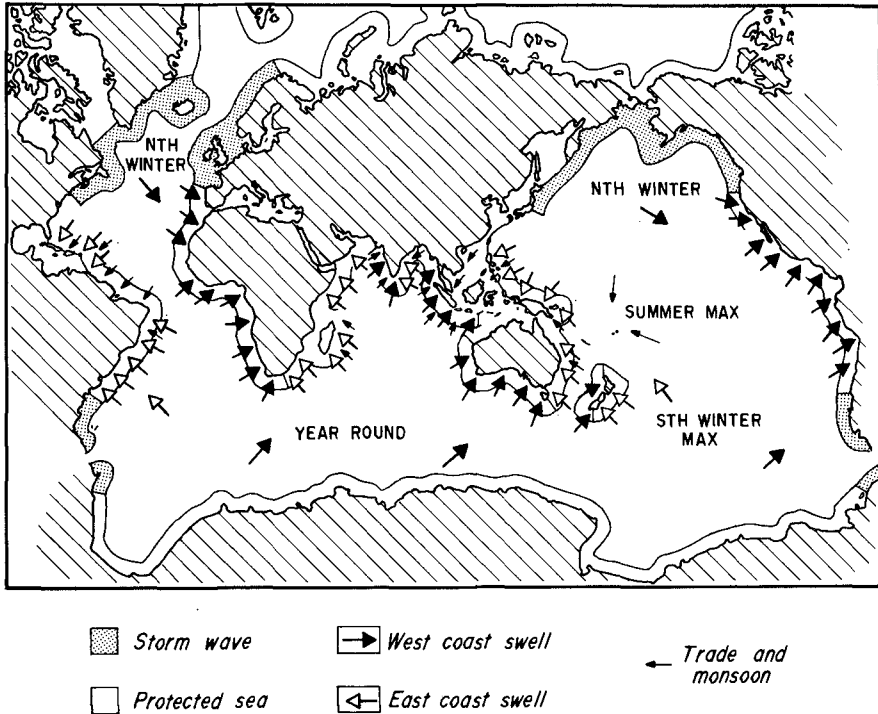


Figure 9 : Global wave environments. (Modified from Davies, 1973). Midocean arrows and lettering indicate direction and season of highest wave power.

(Winant and Aubrey, 1976), however in the southern hemisphere summer power remains high generating *stage 5* and *6* (Figure 10b). East coast swell environments, such as the study area and elsewhere (Wright et.al., in press), have a modal *stage 4* and experience the entire range from *6* to *1*, (Figure 10c). Trade wind coasts have a late summer maximum in wave power generating a modal *stage 4* to *6*, and a lower late winter wave power resulting in a modal *stage 3 - 4* (Figure 10d). Monsoon coasts have a moderate power summer maximum during the onshore monsoon generating a modal *stage 3 - 4*, and low winter wave power producing a modal *stage 2 - 1* (Figure 10e). Protected coasts away from background ocean swell rely on the passage of storms. They are therefore characterised by low beach-stages with infrequent storm generated higher beach-stages, (Figure 10f). Storm generated morphologies often remain as 'relic' forms in the absence of subsequent low waves to return the sand onshore. This is the likely explanation of the common occurrence of multiple parallel bars off relatively low power, through storm prone coasts, including the Mediterranean (King, 1972), Great Lakes (Davis and Fox, 1971) and Alaskan Arctic (Short, 1975).

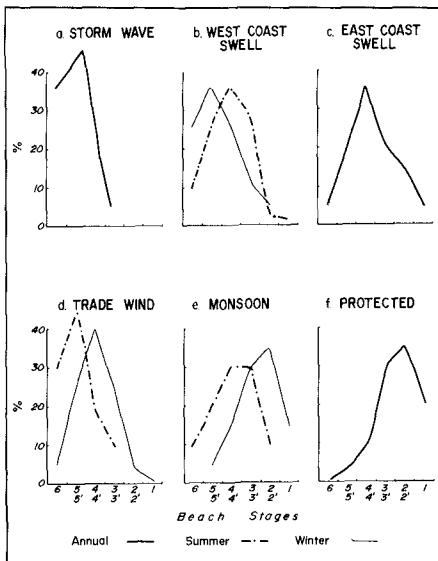


Figure 10 :

Idealised beach-stage curves for the major global wave environments. Curves describe expected occurrence of beach-stages on open coast, sand beaches receiving maximum deepwater wave power.

Other global implications of wave power and the beach-stage model are as follows.

The potential range of beach-stages is determined by the spectrum of absolute P_o , whereas the actual range depends on P_b .

Daily variations in P_o and P_b generate daily adjustments in the associated beach-stages. These adjustments may however have a lag of a few days particularly during low wave power (see Figure 4).

The seasonality of P_o will determine the bias toward erosional or accretionary stages during the seasons. Note that the commonly used terms of 'winter' cut and 'summer' fill are based on studies in California, a northern hemisphere, west coast swell environment. Application of these terms to other wave environments including southern hemisphere west coast swell coast is often inappropriate and has led to much confusion and misunderstanding. Contrary to the west coast U.S.A. beach cycles, one would expect erosion stages to dominate or be significant during the summer season in east coast swell, (see Figure 7a and b), trade wind, monsoonal, and low and high latitude protected sea coasts, with little seasonal variation in southern hemisphere west coast swell environments (Figure 10b). Only in northern hemisphere west coast swell and mid-latitude protected sea coasts, are the terms 'winter' cut and 'summer' fill applicable. Therefore the terms are quite meaningless on a global scale and if must be used, should be with caution. More important than the present grossly simplified, emphasis on seasonal beach cycles, the present model illustrates how in east coast swell environments 'cut' and 'fill' cycles can occur at relatively high frequency throughout the year, though seasonal trends may be apparent (Figure 4 and 7).

To understand the cycles of beach morphodynamics in a particular location we must know the deepwater wave climate, shelf and nearshore wave transformation and associated breaker wave climate. Given a time series of the wave and beach conditions and resultant beach-stages and beach-stage curves, beaches can be understood and compared temporally and/or spatially between and among any suite of open coast environments.

DISCUSSION AND CONCLUSIONS

A beach model is presented which relates three-dimensional changes in beach and surfzone morphodynamics to variations in breaker wave power. The model covers all beach conditions from fully eroded to fully accreted, linked by both erosional and accretionary sequences. The entire cycle of sequences are presented as ten characteristic beach-stages. Using the relationship between wave power and the beach-stages, the beach-stage curve is introduced. The curve plots the percent frequency of occurrence of the ten beach-stages, over a given time period for a given beach site. The beach-stage curve, enables for the first time, the morphodynamic character of the beach to be quantified. The mode, range and shape of the curve all rigorously define the morphodynamic character of the beach over time. Beach-stage curves for different beaches and time periods permit comparison of all sandy beach beaches both temporally and spatially.

Variations in wave power generate the following predictable response in the model and beach morphodynamics in general.

1. Absolute wave power through breaker wave power controls the level of beach-stage present at any point in time.
2. Temporal variations in P_o and P_b affect sequential changes in beach-stages (Figure 1), the greater the variation in P_b the greater the range of stages.
3. Spatial variation in P_b produces longshore variation in beach-stage. Along a section of coast as P_b varies so does the associated beach-stage.
4. Global wave environments (storm wave, west and east coast swell, trade wind, monsoon and protected) through their characteristic P_o spectrum will generate a characteristic beach-stage curve.
5. Locally, the spectrum of P_b at the shoreline will determine for any wave environment the actual beach-stage curve.

The model allows beach morphodynamics to be explained at any point, period or place in the time, and can be used to compare beaches in all open coast wave environments over any time scale. In doing so it provides a framework within which all past, present and future beach studies can be located, so that their results can be seen in the overall context of a single unified model. The model also indicates that the major proportion of beach morphodynamic situations (particularly beach-stages 6, 5', 5, 4', 3', 2') have not been previously identified

or rigorously investigated.

Finally the model illustrates the four-dimensional complexity of the beach and surfzone. This complexity must be taken into account when dealing with the coastal zone whether it be in field, laboratory or mathematical experiments, or in designing management or engineering criterion for safeguard of the zone.

ACKNOWLEDGEMENTS

This project was supported by the Queen's Fellowship Committee and the Australian Research Grants Committee, Department of Science, Canberra, Australia. Thanks to Peter Cozier, Val Barnes, Peter Cowell and Peter Rogers for assistance in the field. The figures were prepared by John Roberts and Maureen Rigney.

REFERENCES CITED

- Davies, J.L., 1964, A morphogenic approach to world shorelines: *Zeit. f. Geomorph.*, v. 8, p. 127-142.
- _____, 1973, *Geographical Variation in Coastal Development*, Hafner, New York, 204 p.
- Davis, R.A., Jr., and W.T. Fox, 1971b, Beach and nearshore dynamics in eastern Lake Michigan, ONR Tech. Rept. No. 4, Contract 388-392, 145 p.
- King, C.A.M., 1972, *Beaches and Coasts*, 2nd ed., St. Martin's, New York, 570 p.
- Short, A.D., 1975, Multiple offshore bars and standing waves: *Jour. Geophys. Res.*, v. 80, p. 3838-3840.
- _____, 1978, Characteristic beach morphodynamics on the southeast Australian coast: Fourth Australian Conf. on Coastal and Ocean Engineering, Adelaide, The Inst. of Engineers, Australia, National Conference Publication No. 78/11, p. 148-152.
- _____, (in preparation) Three dimensional beach model: (submitted to *Jour. Geol.*).
- Winant, C.D., and D.G. Aubrey, 1976, Stability and impulse response of empirical eigenfunctions: *Proc. 15th Coastal Engineering Conf.*, p. 1312-1325.
- Wright, L.D., 1976, Nearshore wave-power dissipation and the coastal energy regime of the Sydney-Jervis Bay region, New South Wales: A comparison: *Australian Jour. Freshwater Res.*, v. 27, p. 633-640.
- _____, Chappell, J., Thom, B.G., Bradshaw, M.P., and Cowell, P.,

(in press), Morphodynamics of reflective and dissipative beach and inshore systems: Southeastern Australia: Marine Geology.

_____, and Thom, B.G., 1977, Coastal morphodynamics: Progress in Physical Geography, v. 1, p. 412-459.

_____, _____, Cowell, P. Bradshaw, M., and Chappell, J., 1977, Field observations of resonant surf and current spectra on a reflective beach and relationship to cusps: Search, v. 8, p. 321-322.

CHAPTER 67

MATHEMATICAL MODELING OF SHORELINE EVOLUTION

Bernard Le Mehaute¹
Mills Soldate²

ABSTRACT

A mathematical model for long term shoreline evolution is developed. The combined effects of variations of sea level, wave refraction, wave diffraction, loss of sand by density currents during storms, by rip currents and by wind, bluff erosion and berm accretion as well as effects of man-made structures such as long groin or navigational structures and beach nourishment are all taken into account. A computer program is developed with various subroutines which permit modification as the state-of-the-art progresses. The program is applied to a test case at Holland Harbor, Michigan.

I. INTRODUCTION

The purpose of this paper is to establish a mathematical model for shoreline evolution and to calibrate it with a test case, located at Holland Harbor, Michigan. The present mathematical model includes many of the characteristics already covered in the literature. In addition, it presents an integrated approach covering a large number of phenomena previously neglected. It is extracted from a more general investigation on three dimensional modeling of shoreline evolution.

It is recalled that three time scales of shoreline evolution can be distinguished:

- (a) Geological evolution taking place over centuries;
- (b) long-term evolution from year-to-year or decade; and
- (c) short-term or seasonal evolution and evolution taking place during a major storm.

Associated with these time scales are distances or ranges of influence over which changes occur. The geological time scale deals, for instance, with the entire area of the Great Lakes. The long-term evolution deals with a more limited stretch of shoreline and range of influence; e.g., between two headlands or between two harbor entrances. The short-term evolution deals with the intricacies of the surf zone circulation; e.g., summer profile-winter profile, bar, rhythmic beach patterns, etc.

For the problem under consideration, long-term evolution is of primary importance, the short-term evolution appearing as a superimposed perturbation on the general beach profile. Evolution of the coastline is characterized by low monotone variations or trends on which are superimposed short bursts of rapid development associated with storms.

¹ Professor and Chairman of Ocean Engineering, Rosenstiel School of Marine and Atmospheric Science, University of Miami. Formerly Senior Vice President of Tetra Tech, Inc.

² Senior Engineer, Engineering Division, Tetra Tech, Inc.

The primary cause of long-term evolution is water waves or wave-generated currents. Three phenomena intervene in the action which waves have on shoreline evolution:

- (a) Erosion of beach material by short period seas versus accretion by longer period swells;
- (b) effect of (lake) level changes on erosion; and
- (c) effect of breakwaters, groins, and other structures.

II. MATHEMATICAL FORMULATION

Let us consider a coastal zone limited by boundaries at a small distance from the surf zone (Figure 1). The bottom topography is defined in a three coordinate system, $oxyz$, by a function $z_b = f(x, y, t)$ where the axis, ox , is parallel to the average shoreline direction, the axis, oy , is perpendicular seaward and, oz , is positive upward from a fixed horizontal datum. The angle of the shoreline with the axis, ox , is small. The shoreline is defined by $y = y_s$, $z = z_s = z_b(x, y_s, t)$ which also defines the sea level as function of time.

The deepwater limit of the beach is, $y = y_c$. (This limit defines the contour line where the sand is no longer moved by wave action). The water depth at $y = y_c$ is D_c . It will be assumed that D_c remains constant as sea level and beach profiles change. Therefore $\partial z_s / \partial t = \partial z_c / \partial t$.

B is the height of the bluff in case of erosion (i.e., when $\frac{\partial y_s}{\partial t} < 0$), and the height of the berm in case of accretion, (i.e., when $\frac{\partial y_s}{\partial t} > 0$),

The quantity of sand over a stretch of shoreline, Δx , unity and bounded by the datum, $z = 0$, $y = 0$, and the beach profile z_b

at time, t , is:
$$V(t) = \int_0^{y_1} z_b(x, y, t) dy$$

Let us assume that, for some reasons, the beach profile changes during an infinitesimal amount of time, dt . Let us further assume that the initial beach profile which is considered at time, $t = t_1$, could be the normal "equilibrium profile".* The departure and modification from this initial beach profile can be characterized by:

(a) A translation in the yz plane defined by an elementary vector of components.

*The "equilibrium profile" may never exist under varying prototype conditions (similarly two-dimensional wave never exists), but it is a convenient idealized concept which could be approached in two-dimensional wave tank experiments. In the present case, it could be defined as the statistical long term average beach profile which exists under a given wave climate. The model presented herewith is actually independent from this definition.

$\frac{\partial y_s}{\partial t}$, $\frac{dD}{dt}$ is the rate of change of sea level.

Note that this translation is independent from the beach profile and in particular, if the beach profile normally exhibits a number of significant bar formations, under normal conditions, this translation will reproduce this characteristic at the same water depth.

(b) A perturbation characterizing the departure or variation from the initial profile. Since the rate of the vertical component of translation is $\frac{dD}{dt}$, the perturbation can be defined by only a horizontal displacement. This effect is neglected in the present layer and will be presented in a sequel at a later date.

Note that this translation is independent from the beach profile and in particular, if the beach profile normally exhibits a number of significant bar formations, under normal conditions this translation will reproduce this characteristic at the same water depth.

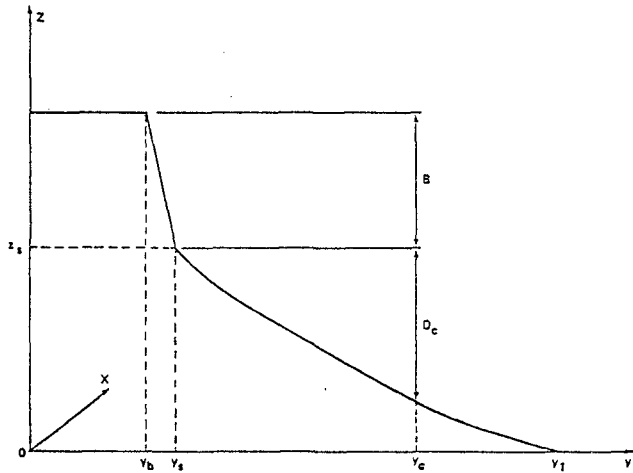


Figure 1 Notation

The variation of sand quantity in the considered domain is:

$$\frac{dV}{dt} = \int_0^{y_l} \left(\frac{\partial z_b}{\partial t} + \frac{\partial z_b}{\partial y} \frac{dy}{dt} + \frac{\partial z_b}{\partial x} \frac{dx}{dt} \right) dy$$

On which if one neglects the variation of z_b with respect to x yields:

$$\frac{dV}{dt} = (B + D_c) \frac{\partial y_s}{\partial t} - (y_c - y_b) \frac{dD}{dt}$$

This variation of volume is due to the variation

of littoral drift along the ox axis and the onshore-offshore motion. The following terms are included:

(a) The discharge of sand leaving the beach per unit of width which includes:

1. Q_{yw} due to loss of sand by wind.

2. $Q_{ys}(x)$ due to the quantity of silt contained in the bluff and which tends to move offshore by suspension. This loss occurs

only in case of erosion $\frac{\partial y_s}{\partial t} < 0$ and is equal to $Q_{ys} = K_s B \frac{\partial y_s}{\partial t}$ where K_s is the percentage of silt in the bluff.

3. Q_{yf} due to the loss of sand from the beach by density current during storm. Q_{yf} is a function of the size distribution and density of material. A beach of fine material ($< 0.1^{mm}$) will tend to erode more rapidly than beach made of coarse material ($> 1^{mm}$). The coarse material tends to move along shore while the fine sand moves offshore.

The determination of these three quantities are given from sand budget investigations.

(b) A general term $M(x,t)$ expressing the local variation in the sand budget due to

1. loss of sand by rip currents along groins.
2. sudden dumping of sand in case of beach nourishment or flood.

(c) The variation of littoral drift along the axis ox which is

$$Q_s(s) - Q_x(x + dx) = - \frac{\partial Q_s}{\partial x} dx$$

$Q_s = 7.5 \times 10^3 P_l$ where Q_s is in yd^3 year. P_l is in $ft - lbs/sec/ft$ of shoreline and is expressed by the relationship:

$P_l = \frac{\rho g^2}{64\pi} H_o^2 T K_R^2 \sin 2\alpha_b$ where K_R is the refraction coefficient from deep water to the line of breaking inception: T is the wave period, H_o is the deepwater wave height, α_o is the angle of the deep water wave with the shoreline, α_b is the angle of breaking with the shoreline.

This formula will be assumed to hold in case of gentle beach curvature. The refraction coefficient K_R and angle α_b can be determined as functions of the deep water wave characteristics H_o , T , α_o (or α) and the angle of the shoreline at breaking, $\approx \frac{\partial y_s}{\partial x}$. At $x \rightarrow -\infty$, the deep-water wave angle α with bottom contours is equal to α since the shoreline has the same direction as the axis ox . In the general case, i.e., for any value of x

$$\alpha_o = \alpha - \tan^{-1} \frac{\partial y_s}{\partial x}$$

The breaking waves characteristic: wave height, H_b , water depth d_b , and the angle breaking α_b , can be obtained from the deepwater wave characteristics, H_o , T , and α_o . α_o is given by the previous equation

in terms of α and $\frac{\partial y_s}{\partial x}$ which takes into account the curvature of the

shoreline. The following equation is valid provided the bottom contours are parallel along a wave ray, (Le Mehaute and Koh, 1967) (Figure 2):

$$\alpha_b \approx \alpha_o \left[0.25 + 5.5 \frac{H_o}{L_o} \right] \text{ where } L_o = \frac{gT^2}{2\pi}$$

Therefore, the refraction coefficient,

$$K_R = \left[\frac{\cos \left(\alpha - \tan^{-1} \frac{\partial y_s}{\partial x} \right)}{\cos \left[\left(\alpha - \tan^{-1} \frac{\partial y_s}{\partial x} \right) \left(0.25 + 5.5 \frac{2\pi H_o^2}{gT^2} \right) \right]} \right]^{1/2}$$

Now it is possible to formulate the variation of littoral drift:

$$\frac{\partial Q_s}{\partial x} = A H_o^2 K_R^2 2 \cos 2\alpha_b \frac{\partial \alpha_b}{\partial x} + A H_o^2 2K_R \frac{\partial K_R}{\partial x} \sin 2\alpha_b$$

where $A = 7.5 \cdot 10^3 \frac{\rho g^2}{64\pi} T$. On the other hand one also has

$$\frac{\partial \alpha_b}{\partial x} = \frac{0.25 + 5.5 \frac{H_o}{L_o}}{1 + \left(\frac{\partial y_s}{\partial x} \right)^2} \frac{\partial^2 y_s}{\partial x^2}$$

In case of wave diffraction, the wave height varies significantly along a wave crest. Then the

previous refraction coefficient K_R has to be replaced by a combined coefficient, say $K_D K_R$. Also, in a diffraction zone, α_b is due to the sum of variation of shoreline direction

$\tan^{-1} \frac{\partial y_s}{\partial x}$ and because of diffraction, the rotation of the wave crest around the end of the groin: θ (Figure 3). θ is the angle which has the end of the groin as apex and extends from the limit of the "shaded" area to the considered location defined, therefore,

$$\alpha_b \approx \tan^{-1} \frac{\partial y_s}{\partial x} + \alpha_o - \tan^{-1} \frac{x}{\ell},$$

$$-\frac{\partial \theta}{\partial x} = \frac{\partial \theta'}{\partial x} = \frac{1}{\ell} \frac{1}{1 + \left(\frac{x}{\ell} \right)^2}$$

An empirical formulation for determining the combined effect of diffraction and refraction is more suitable to quantitative analysis of a real sea spectrum than more exact theories of wave diffraction which are valid for periodic waves over a horizontal bottom and are represented by Fresnel integral.

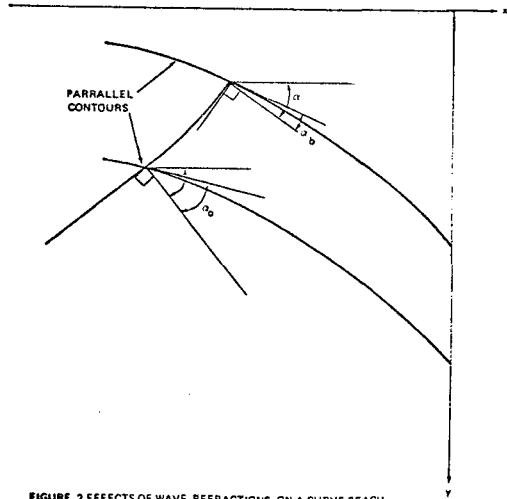


FIGURE 2 EFFECTS OF WAVE REFRACTIONS ON A CURVE BEACH

For this, it will be assumed that the energy travels laterally along a wave crest as well as along a wave ray. This lateral transmission of energy results into a decrease of wave energy from the exposed area to the shaded area,

$$\int_A^C H^2 dx = \int_0^D H_0^2 ds$$

In the case where the long groin is in the previously defined wave diffraction zone as in Figure 3, it is assumed that the wave energy which reaches the groin is absorbed by friction. It is assumed that the combined effects of diffraction refraction of a wave spectrum can simply be represented by a sinusoidal variation of wave height along the breaking line. (Mobarek and Weigel, 1966). One has finally

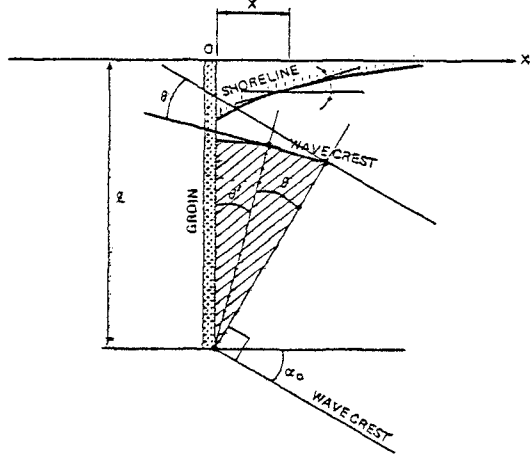


Figure 3 Diffraction Zone Notation

$$K_D(x) = \left(\frac{\sqrt{2}}{2} \frac{\cos(2\alpha_0)}{\sin \alpha_0} \right)^{1/2} \sin \left[\frac{\pi \cos(2\alpha_0)}{4l} (x + l \tan(45^\circ - \alpha_0)) \right]$$

Inserting this value in the littoral drift formula previously described permits us to complete the mathematical model.

III. TRANSFORMATION OF THE PHENOMENOLOGICAL EQUATION AND NUMERICAL SCHEME

Now that all the phenomenological equations have been established we will find it more convenient to express them in dimensionless form. The general equation expressing the sand budget balance can still be written. (The loss terms have been dropped for sake of simplicity and can easily be included whenever necessary).

$$(B(x,t) + D_c) \frac{\partial y_s}{\partial t} + (y_c - y_b) \frac{dD}{dt} = \frac{\partial Q}{\partial x}$$

For purposes of analysis we consider this equation in dimensionless form.

$$\text{let } (\text{length})^{\hat{}} = \frac{\text{Length}}{B_o + D_c} \quad B_o \text{ to be chosen later}$$

$$\hat{t} = \frac{At}{(B_o + D_c)^3}$$

$$Q = \frac{A}{2} K_R^2 K_D^2 \sin 2\alpha_b$$

The general equation is thus transformed to:

$$\frac{B + D_c}{B_o + D_c} \frac{\partial \hat{y}_s}{\partial \hat{t}} + (\hat{y}_c - \hat{y}_b) \frac{d\hat{D}}{d\hat{t}} = \frac{\partial}{\partial \hat{x}} \frac{K_D^2 K_R^2 \sin 2\alpha_b}{2}$$

α_b = function of α_o , say $f(\alpha_o)$, (the function f depends only on H_o/L_o as previously shown). The hats and subscripts will be dropped from all variables from this point on.

$$\text{Therefore } \frac{1}{2} K_D^2 K_R^2 \sin 2\alpha_b = K_D^2 \cos \alpha_o \sin \alpha_b$$

$$\text{Note } \frac{\partial}{\partial x} \cos \alpha_o \sin \alpha_b = \left[\cos \alpha_o \cos \alpha_b \frac{\partial f}{\partial \alpha_o} - \sin \alpha_o \sin \alpha_b \right] \frac{\partial \alpha_o}{\partial x} = F(\alpha_o) \frac{\partial \alpha_o}{\partial x}$$

The general equation then becomes (after some rearrangements)

$$\frac{\partial y}{\partial t} = \frac{B_o + D_c}{B + D_c} F(\alpha_o) \frac{1}{1 + \left(\frac{\partial y}{\partial x}\right)^2} \frac{\partial^2 y}{\partial x^2} + R(x,y,t)$$

$$\text{where } R(x,y,t) = \frac{B_o + D_c}{B + D_c} F(\alpha_o) \frac{\partial \alpha_o}{\partial x} - (y_c - y_b) \frac{dD}{dt} + 2K_D \frac{\partial K_D}{\partial x} \cos \alpha_o \sin \alpha_b$$

$\alpha = \alpha(x)$ in the diffraction zone

The above equation is the general dimensionless form which gives us the time dependent sand budget. This general equation is nonlinear and appears to be impossible to solve analytically. Some numerical results are presented

The uniform depth theory of Penny and Price is used as an approximation (not substantiated) for diffraction about the end of the breakwater. The shoreline is calculated for various multiples of a fixed At (Figure 4a). Of interest is to note that the undulatory patterns of the shoreline seen in Figure 4a disappear in Figure 4b. Hence, diffraction induced undulations in natural shoreline probably rarely appear since offshore wave climates are usually multi-directional.

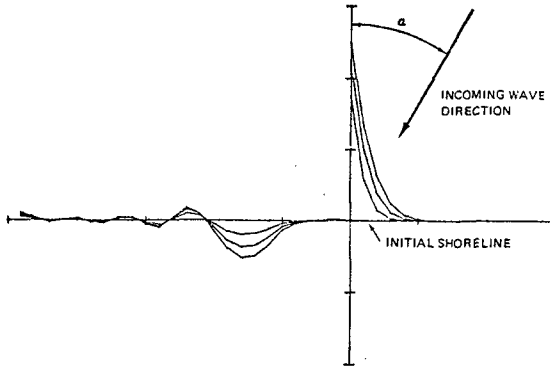


FIGURE 4a SHORELINES AT SUCCESSIVE TIMES 5Δt, 10Δt, 15Δt

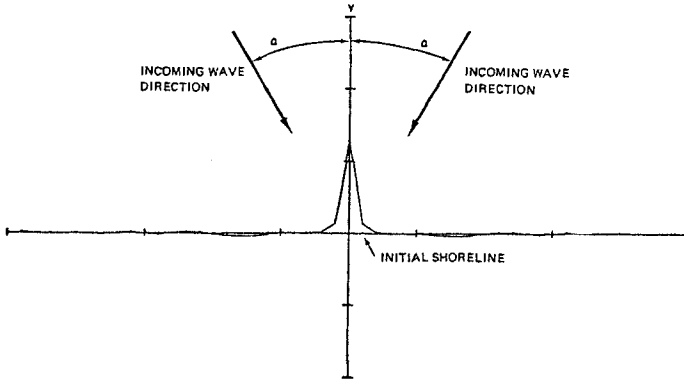


FIGURE 4b SHORELINES FOR TIME 2Δt

The numerical scheme generally used to solve this problem is based on the use of implicit finite differences. Such schemes, whether implicit or explicit, or both, are commonly used to efficiently solve parabolic problems. However, even in the case where only refraction is considered, the boundary condition

$\frac{\partial y}{\partial t} = - \tan \alpha$ at $x = 0$ numerically gives a solution which initially may not conserve mass, i.e., the integrated transport equation

$\frac{\partial}{\partial t} \int_0^L y dx = Q(L)$ may not be satisfied. Unfortunately this feature is unavoidable for most such schemes (the exceptions will be discussed below) as the following will demonstrate. Shown on Figure 5 is an initially straight shoreline. In any finite difference scheme, after 1 time increment the shoreline is bounded below by the solid shoreline of Figure 5.

This shoreline has the least possible area A, where $A = \frac{\Delta x^2}{2} \tan \alpha$

The conservation of mass equation requires $\Delta t Q(L) = \cos \alpha \sin \alpha_b \geq A$

Thus, Δt must satisfy the inequality

$$\Delta t > \frac{1}{2} \frac{\sin \alpha}{\sin \alpha_b} \frac{\Delta x^2}{\cos^2 \alpha} \quad \text{Since the accuracy (and in explicit schemes, stability as well) depends}$$

on the ratio $\lambda = \frac{\Delta t}{\Delta x^2}$ the above inequality places a lower bound on the

accuracy of the solution which may be unacceptable in practice. The finite difference form of the equation for the conservation of mass may be incorporated directly into the numerical scheme. In this case a solution exists which is similar to the previous case but shows a small erosion throughout the reach. For engineering applications the primary quantity of interest is the amount of sand on a given shoreline. It is then more important to conserve mass than to satisfy the shoreline boundary condition as written in the present form. The general equation will now be used to derive an equivalent equation for the transport Q which, even though subject to similar numerical problems, will satisfy the transport boundary conditions exactly.

Consider, for the moment, the situation in which only refraction is important. The general equation then becomes $\frac{\partial y}{\partial t} = \frac{\partial Q}{\partial x}$

where $Q = \cos \alpha_o \sin \alpha_b$

$$\alpha_b = f(\alpha_o)$$

$$\alpha_o = \alpha + \tan^{-1} \frac{\partial y}{\partial x} \quad \text{Differentiating by } x \text{ gives } \frac{\partial}{\partial t} \frac{\partial y}{\partial x} = \frac{\partial^2 Q}{\partial x^2}$$

The transport function Q can be considered as a function of α_o which may be solved for α_o , say $\alpha_o = g(Q)$.

Thus the above transport equation becomes

$$\frac{\partial}{\partial t} \tan(\alpha_o - \alpha) = \frac{\partial}{\partial t} \tan(g(Q) - \alpha) = \frac{\partial^2 Q}{\partial x^2}$$

$$\therefore \frac{\partial g(Q)}{\partial t} = \cos^2(g(Q) - \alpha) \frac{\partial^2 Q}{\partial x^2}$$

$$\text{but } \frac{\partial g(Q)}{\partial t} = \frac{dg(Q)}{dQ} \frac{\partial Q}{\partial t}$$

$$\therefore \frac{\partial Q}{\partial t} = \frac{\cos^2(g(Q) - \alpha)}{dg(Q)/dQ} \frac{\partial^2 Q}{\partial x^2}$$

Assuming a solution for this equation is known, the shoreline y can be calculated from the equation

$$y(t,x) = y(0,x) + \int_0^t \frac{\partial Q}{\partial x}(t,x) dt$$

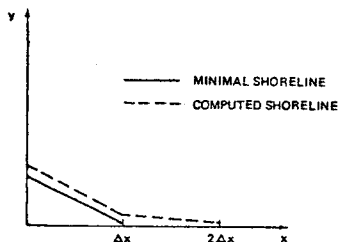


FIGURE 5 COMPUTED AND MINIMAL SHORELINES FOR FINITE DIFFERENCE SCHEME OF TIME = 1Δt

In practice the equation for Q is not solved in the above form. Implicit in the above formulation is the assumption that the function g exists. However, as is illustrated in Figure 6, g is not single valued if the maximum range of the angle α_0 is greater than approximately 41 degrees. This difficulty may be removed by considering the equation for Q and y as a system subject to the boundary conditions for Q .

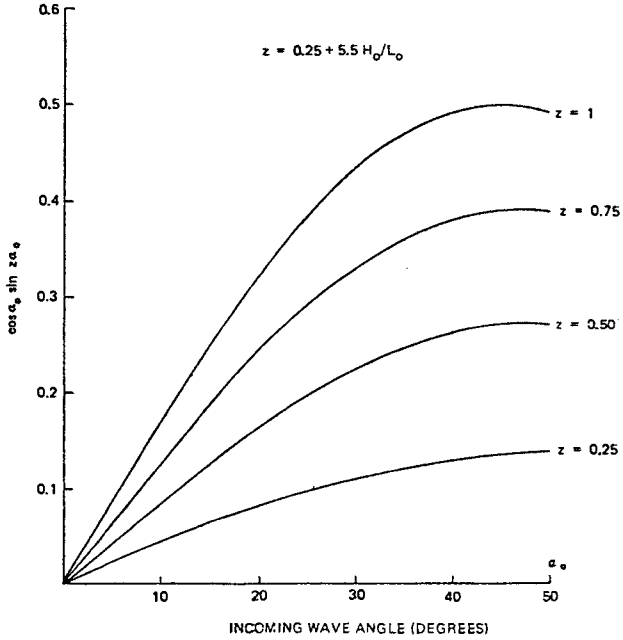


Figure 6: Transport function $Q(\alpha_0) = \cos \alpha_0 \sin z\alpha_0$ for selected values of z .

Note that
$$\frac{\cos^2(g(Q)-\alpha)}{dg(Q)/dQ} = \frac{dQ}{d\alpha_0} \left/ \left[1 + \left(\frac{\partial y}{\partial x} \right)^2 \right] \right.$$

Hence, the equation for Q becomes
$$\frac{\partial Q}{\partial t} = \frac{dQ}{d\alpha_0} \frac{1}{1 + \left(\frac{\partial y}{\partial x} \right)^2} \frac{\partial^2 Q}{\partial x^2}$$

This together with the equation $\frac{\partial y}{\partial t} = \frac{\partial Q}{\partial x}$ is solved in a cyclic scheme.

One possible method is the centered Crank-Nicolson type implicit-explicit scheme discussed in the following. Suppose y is given for all x at a given time t , and that from time t the wave climate is specified by the (constant) triple (α, H_0, T)

$$\text{Let } L(t,x) = \frac{dQ}{d\alpha_0} \frac{1}{1 + \left(\frac{\partial y}{\partial x} \right)^2}$$

$$\lambda = \frac{\Delta t}{\Delta x^2}$$

$L(t,x)$ = an approximation to $L(t,x)$

Integrating the Q equation gives

$$Q(t+\Delta t, x) = Q(t, x) + \frac{\Delta t}{2} \left[L(t, x) \frac{\partial^2 Q}{\partial x^2} \Big|_t + \tilde{L}(t+\Delta t, x) \frac{\partial^2 Q}{\partial x^2} \Big|_{t + \Delta t} \right]$$

where $\frac{\partial^2 Q}{\partial x^2} = \frac{Q(x+\Delta x) - 2Q(x) + Q(x-\Delta x)}{\Delta x^2}$

Integrating the y gives

$$y(t+\Delta t, x) = y(t, x) + \frac{\Delta t}{2} \left[\frac{\partial Q}{\partial x} \Big|_t + \frac{\partial Q}{\partial x} \Big|_{t+\Delta t} \right]$$

where $\frac{\partial Q}{\partial x} = \frac{Q(x+\Delta x) - Q(x-\Delta x)}{2\Delta x}$

The equations are solved numerically, subject to the appropriate boundary conditions, by the cyclic algorithm:

- 1) Let $L(t+\Delta t, x) = L(t, x) \forall x$
- 2) Calculate $Q(t+\Delta t, x) \forall x$ subject to the appropriate boundary conditions
- 3) Calculate $y(t+\Delta t, x) \forall x$
Calculate $L(t+\Delta t, x)$, set this equal to $L(t+\Delta t, x)$
Calculate new Q
- 4) If new Q compares with old Q stop, if not go to step 3

Tests with this scheme have shown that it converges to its limit after one application of step 3.

This method can easily be modified to solve the equation where both diffraction and variations in lake level are allowed, i.e., (s is the beach slope)

$$\frac{\partial y}{\partial t} = \frac{\partial}{\partial x} K_D^2 \cos \alpha_o \sin \alpha_b - \frac{1}{s} \frac{dD}{dt}$$

For convenience let $Q = \cos \alpha_o \sin \alpha_b$

$$\tilde{Q} = K_D^2 Q$$

As before

$$\begin{aligned} \frac{\partial}{\partial t} \frac{\partial y}{\partial x} &= \frac{\partial}{\partial t} \tan (g(Q)-\alpha) \\ &= \frac{1}{\cos^2 (g(Q)-\alpha)} \frac{dg(Q)}{dQ} \frac{\partial Q}{\partial t} - \frac{1}{\cos^2 (g(Q)-\alpha)} \frac{\partial \alpha}{\partial t} \end{aligned}$$

Also $\frac{\partial Q}{\partial t} = K_D^2 \frac{\partial Q}{\partial t} + 2K_D \frac{\partial K_D}{\partial t} Q$

The second term in each of the above two equations are negligible in physical situations of usual interest, where the distance between the shoreline and the tip of the breakwater is large compared to the distance the shoreline changes during a time Δt .

Therefore, the transport equation becomes

$$\frac{\partial \tilde{Q}}{\partial t} = \frac{K_D^2}{dg/dQ} \cos^2(g(Q)-\alpha) \frac{\partial^2 \tilde{Q}}{\partial x^2} \quad \text{and} \quad \frac{\partial y}{\partial t} = \frac{\partial Q}{\partial x} - \frac{1}{s} \frac{dD}{dt}$$

This system is solved using the same type of algorithm as previously employed.

In the present situation where only refraction is important several approximations are possible which produce problems having analytic solutions. The most direct approximation, and essentially the assumption of Pelnard-Considere, is to approximate

$$\frac{\partial y}{\partial t} = \left[z \cos \alpha_o \cos \alpha_b - \sin \alpha_o \sin \alpha_b \right] \frac{1}{\left(\frac{\partial y}{\partial x} \right)^2} \frac{\partial^2 y}{\partial x^2}$$

(subject to the boundary conditions

$$\left. \frac{\partial y}{\partial x} \right|_{x=0} = -\tan \alpha$$

$$y(x,t) = 0 \quad \text{for } x = \infty$$

by $\frac{\partial y}{\partial t} = a \frac{\partial^2 y}{\partial x^2}$ where a is a constant. For the standard breakwater problem, the most logical choice for this constant is given by

$$a = \frac{z}{1 + \tan^2 \alpha} = \left[\quad \right]_{x=0} \quad \text{since the shoreline in this case is principally governed by its behavior at the breakwater. This problem has solution}$$

$$y(x,t) = 2 \tan \alpha \frac{\sqrt{at}}{\sqrt{\pi}} e^{-x^2/4at} - \tan \alpha x \operatorname{erfc}\left(\frac{x}{\sqrt{4at}}\right)$$

which is exactly the same as that of Pelnard-Considere except that the constant a has been changed. This problem however doesn't conserve mass since

$$\frac{\partial}{\partial t} \int_0^\infty y(x,t) dx = z \sin \alpha \cos \alpha \neq \sin \alpha \cos \alpha$$

When this approximation is used in the transport equation for Q , the problem becomes

$$\frac{\partial Q}{\partial t} = a \frac{\partial^2 Q}{\partial x^2} \quad \text{subject to the boundary conditions}$$

$$Q(x=0) = 0$$

$$Q(x=\infty) = \cos \alpha \sin \alpha_b$$

which has solution

$$Q(x,t) = \cos \alpha \sin \alpha_b \operatorname{erf}\left(\frac{x}{\sqrt{4at}}\right)$$

Integrating the equation

$$\frac{\partial y}{\partial t} = \frac{\partial Q}{\partial x}$$

$$\text{gives } y(x,t) = \cos \alpha \sin \alpha_b \left(\frac{\sqrt{2}}{\sqrt{\pi a}} t^{1/2} e^{-x^2/4at} - \frac{x}{a} \operatorname{erfc}\left(\frac{x}{\sqrt{4at}}\right) \right)$$

which is of the same form as the previous solution.

IV. APPLICATION

The evolution of the shoreline at Holland was studied using the present model. The relevant physical data as well as the estimates of offshore sediment losses were used in the analysis (Figure 7). The historical shorelines were interpolated to give the shoreline every 100 feet along the baseline. The results of these computations are not given. The height of the berm is assumed to be 10 feet. The depth to no sediment motion was estimated at 30 feet, based on visual consideration of the offshore bathymetry as well as the use of the method of Weggel (private communication). An offshore line loss of 3.2 yd³/yr/ft of beach is also included.

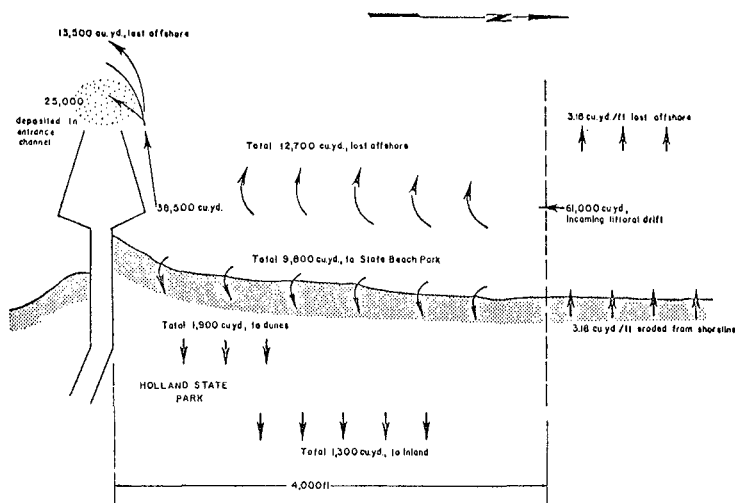


Figure 7: Summary of sand budget north of Holland, Michigan.

Choice of wave climate is the remaining input parameter to be determined, and is the most controversial. The wave climate most desirable for the study of shoreline evolution is a time series giving wave height H, period T, and direction D. Unfortunately, this is almost never available and hence statistical summaries must be used. The monthly statistical summaries given by the SSMO for Lake Michigan South previously described are chosen for use. One possible employment of these summaries is to construct monthly times t for each possible (H,T,D) triple, i.e., t (H,T,D), and then calculate the evolution of the shoreline as the (H,T,D) triples are chosen in some deterministic order or at random. This method would be computationally very expensive and is not used. The most simple approach is to assume that these are but 2 (H,D,T) triples representing the gross transport north and south, each occurring for some length of time per month. The entire shoreline is alternately calculated for an incremental time assuming the direction of the incoming wave is positive, then negative. The period T used is taken to be the average T, i.e.

$$\bar{T} = \frac{\sum p(H,T)T}{\sum p(H,T)}$$
 where the p(H,T) are the (H,T) probabilities given in the SSMO (). The choice of (H,D) for north and south, denoted (H_N,D_N) and (H_S,D_S) respectively, must now be made. This choice is subject to the condition that the actual northerly transport, as calculated using the statistics and given a straight shoreline for the reach of interest, be preserved, i.e., that

$$t_N H_N^2 \bar{T} \cos \bar{\alpha}_0 \sin \bar{\alpha}_b = t_h \sum_{H,T} p(T|H) p(H,D) T H^2 \cos \alpha_0 \sin \alpha_b$$

H,T
D giving north
transport

holds where

- t_h = number of hours in a given month
- $p(T|H)$ = conditional probability T occurs given H
- $p(H,D)$ = probability of (H,D) pair, using SSMO Table 18 as a data base
- α_0 = D_N - shoreline orientation
- α_b = f (α₀)
- t_N = number of hours the "average" wave condition exists
- H_N = "average" wave height
- $\bar{\alpha}_0$ = D_N - shoreline orientation
- D_N = "average" direction

And similarly for the directions giving southerly transport.

The average directions of the shoreline at the breakwater are calculated using the historical records. The directions are chosen for the incoming wave angles since the complex geometry of the harbor breakwater shields the nearby shoreline from waves arriving from most directions. At present, the time duration of waves arriving from the

north is assumed to be the same as from the south. Hence, $t_N = t_S = 0.5 t_h$. The conservation of transport equation is then used to calculate the average wave heights H_N and H_S .

A computer program was used to calculate the evolution of the shoreline from September 1967 to May 1968. The historical 1967 and 1968 shorelines, as well as the computed 1968 shoreline, are shown on Figure 8. The calculation assumed that $\Delta x = 100$ feet with $\lambda \approx y$ which gives a value for Δt which varies from 8 to 20 hours depending upon the month and wave characteristics. The principal discrepancy between the predicted and actual 1968 shoreline occurs in the vicinity of the breakwater. While the shapes agree there is an erosion in the calculated shoreline which is probably due to the approximations used in calculation of the diffraction coefficients, and incoming wave angles which are functions of x in the shadow region of the diffraction zone. The unaltered theory of Penny and Price was incorporated into the numerical scheme since most breakwaters can be represented as line barriers, and hence is almost always useful. However, for the case of Holland Harbor a universally valid prediction of the shoreline would require the detailed calculation of the diffraction effects due to the geometry of the breakwaters. Also, the convenient choice of incoming wave direction obscures the fundamental problem of how to properly use the statistical wave summaries.

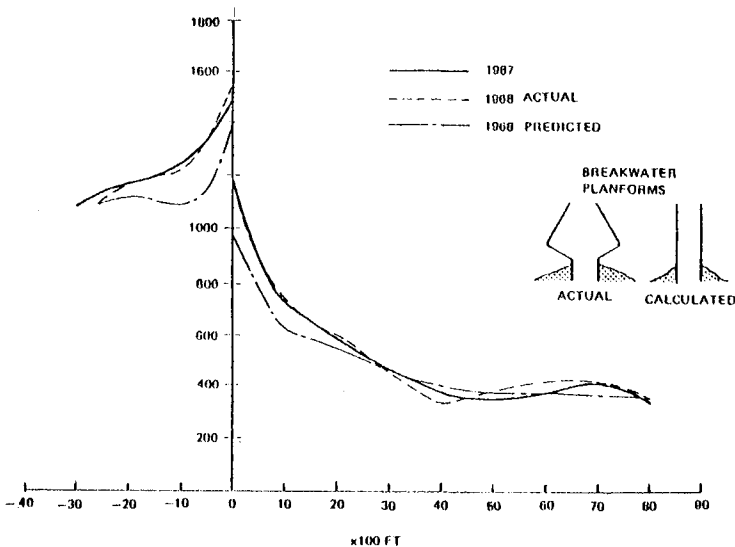


FIGURE 8 COMPUTED vs. ACTUAL DATA

V. CONCLUSION

The basic idea of Pelnard-Consideré, i.e., to investigate shoreline evolution by concentrating on conservation of mass as a spacial one dimensional problem, has been generalized to essentially its limits of applicability. These physical processes of refraction and diffraction (where applicable) have been incorporated, as have deterministic variations in lake level, bluff height and beach slope. The inclusion of refraction makes possible the proper use of the known physical relationships between wave energy and littoral drift on a priori basis without necessarily determining these as results from the past recorded shorelines at a given location. Accurate determination of the behavior of the shore in the lee of a breakwater requires inclusion of diffraction in some form. This could be done in a heuristic manner, as presented here either in the global approximation described in a previous section or in the use of the constant depth theory of Penny and Price. It could also be done in a more rigorous manner which would include the effects of a sloping beach. Thus quantitative predictions of the shoreline can, in theory, be attempted in situations where on-offshore transport of sand in either negligible or as known from other sources of information.

The resulting theory is presented in several equivalent forms, one in terms of the behavior of the shoreline $y(x,t)$ alone, the other expressed explicitly in the longshore transport $Q(x,t)$ and implicitly in $y(x,t)$. The former has the advantage that numerical schemes, such as that of Crank-Nicolson described earlier, can qualitatively indicate the behavior of the shoreline in regions of rapid change. However, the conservation of mass is difficult, if not initially impossible to achieve since any approximation of a transport derived term (i.e. a term arising from $\partial Q/\partial x$) will alter the transport balance. On the other hand, the later form allows employment of analytical or numerical approximations in the transport equation which will not disturb the total sand content of the system, but only its local distribution.

The most severe and unavoidable limitations to the engineering application of these methods is the use of the statistical wave summaries. While one possible use of these was attempted, many others are possible. Efficient and accurate employment of the offshore wave statistics is endemic to the problem of large scale shoreline prediction, and must be achieved before any theory, whether one line, multiple lines, or grid can successfully produce accurate results.

Also, the problem of shoreline evolution sensitivity to time step in the input wave climatology would require further research.

Despite this limitation, it is felt that by taking into account effects of wave refraction, wave diffraction and change of lake level, as done in this paper, a mathematical model with multiple bottom contour lines could be formulated which will, if the problem of wave statistics input is solved, permit us to calculate the evolution of the complete bottom topography.

It is important to point out that wave refraction effect on shoreline evolution have been found particularly important. It is particularly necessary in order to determine a planform stability criteria, which can be established from the present formulation.

ACKNOWLEDGMENT

The writers acknowledge Dr. Rich Weggel of the Coastal Engineering Research Center, and Mr. Charles Johnson of the U. S. Army, Corps of Engineers, Chicago Division for their pertinent remarks during the course of this investigation. Informal discussions with Dr. Robert Dean, University of Delaware, have been very constructive.

REFERENCES

- Le Mehaute, B. and R. Koh (1967). "On the Breaking of Waves Arriving at an Angle with the Shoreline". Journal of Hydraulic Research, Vol. 5, No. 1, pp 67-88.
- Mobarek, I. E. and R. L. Wiegel (1966). "Diffraction of Wind Generated Waterwaves". Proc. 10th Conference on Coastal Engineering, Tokyo, Japan. Sept. Vol. I, pp 185-206.

CHAPTER 68

MORPHODYNAMIC VARIABILITY OF HIGH-ENERGY BEACHES

L.D. Wright (1), *B.G. Thom* (2) and *J. Chappell* (3)

- (1) *Coastal Studies Unit, Dept. of Geography, University of Sydney, Sydney, N.S.W. 2006 Australia*
- (2) *Dept. of Geography, University of New South Wales, R.M.C. Duntroon, Canberra, A.C.T. 2600 Australia*
- (3) *Dept. of Geography, S.G.S., Australian National University, Canberra, A.C.T. 2600 Australia*

Abstract

Field observations of beach and inshore morphology and of surf and inshore current spectra using an array of pressure transducers and low-inertia bidirectional flow meters interfaced with an in-field mini-computer/logging system have been replicated on several beaches in southeastern Australia under a range of energy conditions. Two broad extremes of beach conditions are distinguished spatially and temporally: (1) reflective systems in which much of the incident wave energy is reflected from the beach face; and (2) dissipative systems with wide surf zones and high turbulent viscosity. Reflectivity increases as the ratio of wave steepness to beach (or bed) steepness decreases. Compared to steep, unbarred reflective beaches which are common in deeply indented or partially protected compartments, the topography of exposed dissipative systems is more complex and varied: six time-and-environment-dependent morphologic types with different bar patterns and bar-beach relationships are recognized. The greatest total dissipation prevails in regions of most abundant inshore sediments or during and immediately after severe storms. Between the reflective and dissipative extremes there is a hierarchy of observed resonant frequencies with the highest frequency resonance occurring in the most reflective cases. Results indicate that near the beach face, motions associated with resonance at periods greater than incident wave periods exhibit strong net seaward resultants and are probably important sources of beach erosion. Reflective beaches are sensitive to resonant excitations over a wider range of frequencies and under lower energy conditions than are dissipative beaches. Hence, although reflective beaches represent the accretive end point of a "beach cycle" they are also more delicately poised with a higher potential for erosion.

Introduction

Beach and inshore systems on the New South Wales coast of south-eastern Australia (*Fig. 1*) exhibit pronounced morphologic and dynamic variability with respect to both time and local environment (Wright *et al.*, in press). The coast is characterised regionally by a steep marine-dominated inner shelf. Rocky headlands separate embayed beaches which occupy pronounced coastal compartments, of widely varying dimensions. Inshore processes are dominated by a relatively high energy wave regime with a highly variable wind-wave climate superimposed on persistent long southerly and southeasterly swell. Significant wave heights of 1.5m, 2.5m and 4m are respectively exceeded for 50%, 10% and 1% of the time; storm waves exceed heights of 10m (Lawson and Abernethy, 1975). Semi-diurnal spring tide range is 1.6m.

Field observations of beach and inshore morphology, surf and inshore current spectra, and inshore circulation patterns have been replicated in several contrasting beach environments for a range of energy conditions. An array of pressure transducers and low-inertia bidirectional flow meters interfaced with an in-field mini-computer/data acquisition system was used to obtain wave and current data. The system permits simultaneous logging and analysis of time series from 16 channels. (See Bradshaw *et al.*, 1978 for detailed description of field instrumentation)

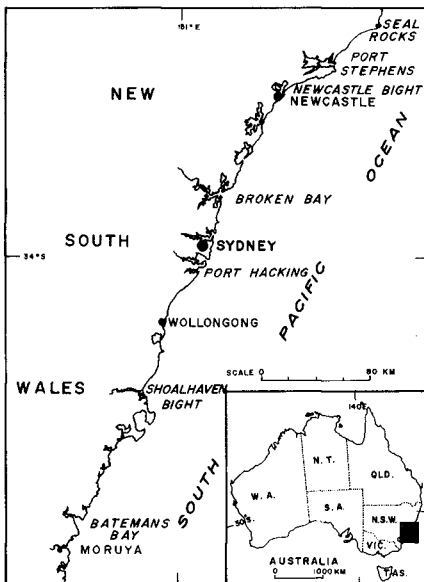


Figure 1: Location Map of study area and major beach sites

Variability of Beach Conditions

Two broad extremes of beach conditions are distinguished spatially and temporally: (1) reflective systems in which much of the incident wave energy is reflected from the beach face; and (2) dissipative systems with wide surf zones and high turbulent viscosity. The degree of reflectivity depends in a gross sense on the surf scaling parameter as defined by Guza and Bowen (1975) by

$$\epsilon = a\omega^2 / g \tan^2 \beta \quad (1)$$

where a is breaker amplitude, ω is radial frequency ($2\pi/T$ where T is period) of the waves, g is the acceleration of gravity and β is beach or inshore slope. Highly reflective conditions are associated with ϵ values less than ~ 2.0 whereas in the case of fully dissipative systems ϵ normally exceeds 30.0 in the vicinity of the breakers. Reflective conditions persist for most of the year in deeply indented compartments, on partially protected estuarine beaches, and on beaches composed of coarse material. Dissipative systems prevail in most of the exposed, open coast situations except after prolonged periods of accretion and low wave energy (Wright et al., in press).

Reflective Beaches

Reflective beaches are characterised by the profile configuration shown in *Figure 2*. Distinguishing features include: (1) a linear, low gradient nearshore (i.e., seaward of break) profile composed of fine sand; (2) a pronounced step composed of the coarsest available material; (3) a steep, linear beach face surmounted by a high berm; (4) well-developed beach cusps; and (5) surging breakers with high runup and minimum setup. The step below the beach face is situated beneath the shore break which is also the position of collision between backwash and incident waves. The depth of the step base increases with increasing wave energy. The reflective condition is normally maintained throughout the tide cycle. Features such as ridge and runnel topography, swash bars, and inshore troughs are consistently absent from such reflective systems. Large-scale inshore (subaqueous) rhythmic topographies are completely absent. Similarly, inshore circulation cells and rip currents are rarely present except during storms. The most conspicuous three-dimensional features are well-developed beach cusps on the beach face and berm. An oblique view of Bracken (McKenzie's) Beach, a typical reflective beach on which many of our experiments were conducted, is shown in *Figure 3*.

Wave height and current spectra (*Figure 4*) from reflective beaches consistently have their dominant peaks at incident wave (T) and subharmonic ($2T$) periods and cross spectra indicate the existence of low-mode edge waves at those periods. Edge wave lengths are consistently well correlated with cusp spacing (Wright et al., 1977, in press). Infragravity peaks are not important. Under low energy conditions subharmonic peaks are low relative to incident wave peaks; however,

Increasing breaker height tends to be accompanied by increasing subharmonic energy. Growth of subharmonic resonance is accompanied by an increase in the strength of seaward flows which pulse at the subharmonic period. Subharmonic seaward pulsing thus appears to be a major mode of erosion of reflective beaches, at least, in the early erosional stages.

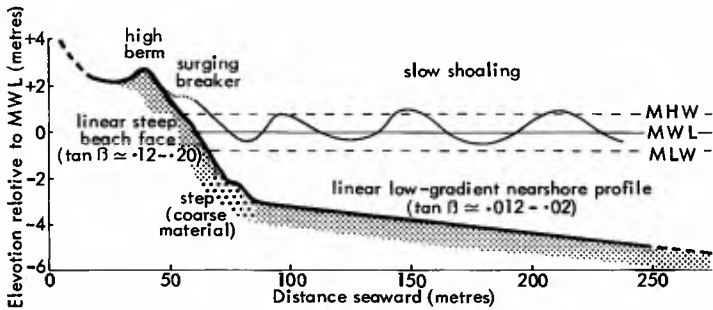


Figure 2 : Typical cross section of a reflective beach



Figure 3 : Oblique Photograph of Bracken (McKenzies) Beach: a predominantly Reflective Beach

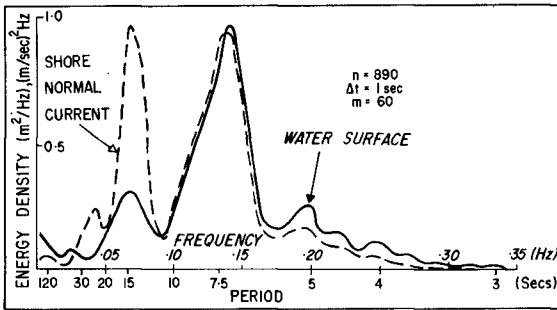


Figure 4:
Typical Power Spectra of wave height and shore normal current time series from a reflective beach (Bracken Beach Dec. 1977; sensors located 3 metres seaward of step)

Dissipative Beach Systems

Dissipative systems are fronted by concave upward nearshore (seaward of break) profiles and wide flat inshore profiles (Figure 5). Waves break 75 to 300+ metres seaward of the beach and dissipate much of their energy before reaching the beach, creating significant radiation stress gradients and setup. Topography is much more complex and varied than in the case of reflective beaches; one or more bars, three-dimensional inshore topography, and different scales of rip cells are frequently present. It is common for dissipative systems to become segregated into subregions of contrasting turbulent viscosity such that a highly dissipative inshore zone may front a moderately reflective beach face. It is therefore necessary to separate the surf scaling parameter into an inshore value, ϵ_s and a beach face value ϵ_b . Wright et al. (In press) have classified dissipative beaches into the six basic types shown in Figure 6. Each type is dominated by a distinctive combination of surf-zone processes and by different scales and frequencies of resonant phenomena.

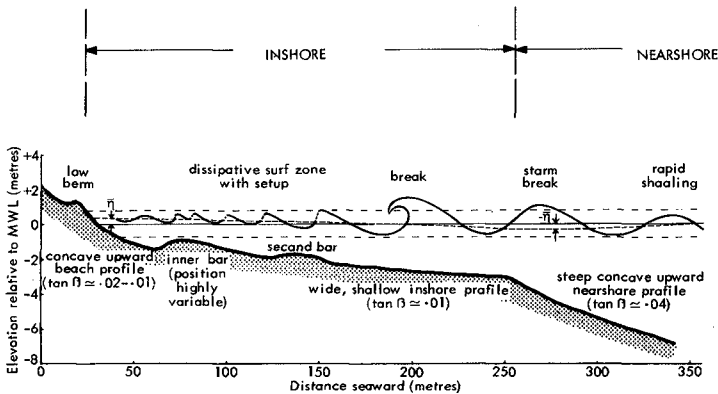


Figure 5 : Typical cross section of a dissipative beach

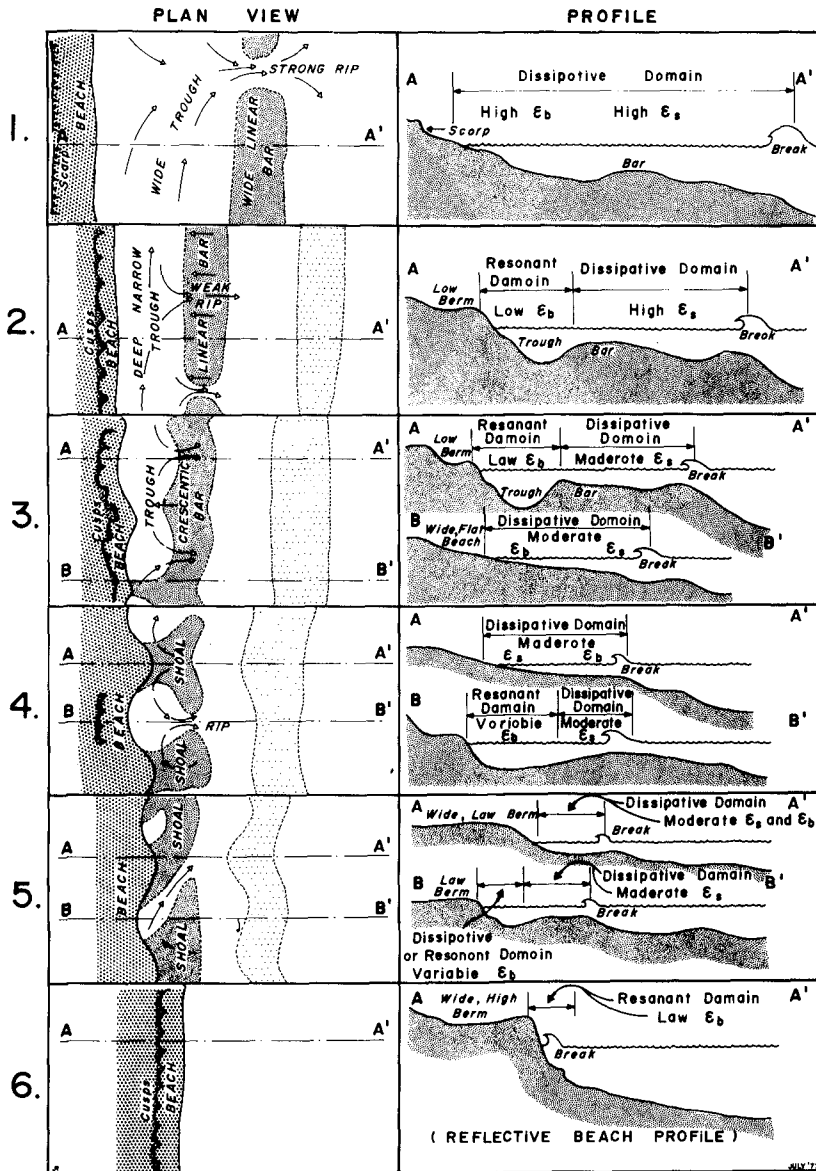


Figure 6 : Six major types of high-energy dissipative beach/inshore systems

The greatest total dissipation is associated with *Type 1* (*Figure 6*) which prevails in the regions of most abundant inshore sediments or during and immediately after severe storms. *Type 1* is dynamically similar to beaches in deltaic regions where abundant inshore sediments sustain very flat profiles. Where it develops on high-energy beaches away from major depositional regions, *Type 1* is a manifestation of sub-aerial beach erosion under extreme energy conditions. At least one well developed bar lies 100-200 metres seaward of a flattened beach face. Additional bars may occur farther seaward. Both the inshore zone and the beach face are highly dissipative. Setup is highest and runup is lowest with *Type 1* and the dominant energy near the beach is at surf beat periods (80-150 sec.). Along longer and straighter beaches multiple longshore bars may remain unbroken by rips. Multiple bars are particularly prominent at the northern ends of large depositional bights (e.g., *Figure 7*) where accumulation of abundant sediments creates wide, flat nearshore/inshore profiles. As in deltaic settings, this situation can result in the maintenance of highly dissipative conditions even under moderately low energy conditions. Under these conditions the parallel bar patterns conform well with patterns predicted from the theory of long-crested leaky-mode infragravity standing waves (Suhayda, 1974; Short, 1975). However, on the more highly compartmented beaches the development of *Type 1* topography is often accompanied by one or two rips which extend up to 1 to 2 km seaward (*Figure 8*). These large, powerful rips commonly exhibit a very low frequency pulsing at periods of 5 to 10 minutes and are very destructive in their effects. Observations of storm-rip pulsing on Palm Beach (*Figure 8*; Cowell, 1975) and on Cronulla Beach (Lees, 1977) show remarkable correspondence with the natural frequency of the compartments.



Figure 7: Multiple Parallel bars related to *Type 1* topography (Shoalhaven Bight, N.S.W.)

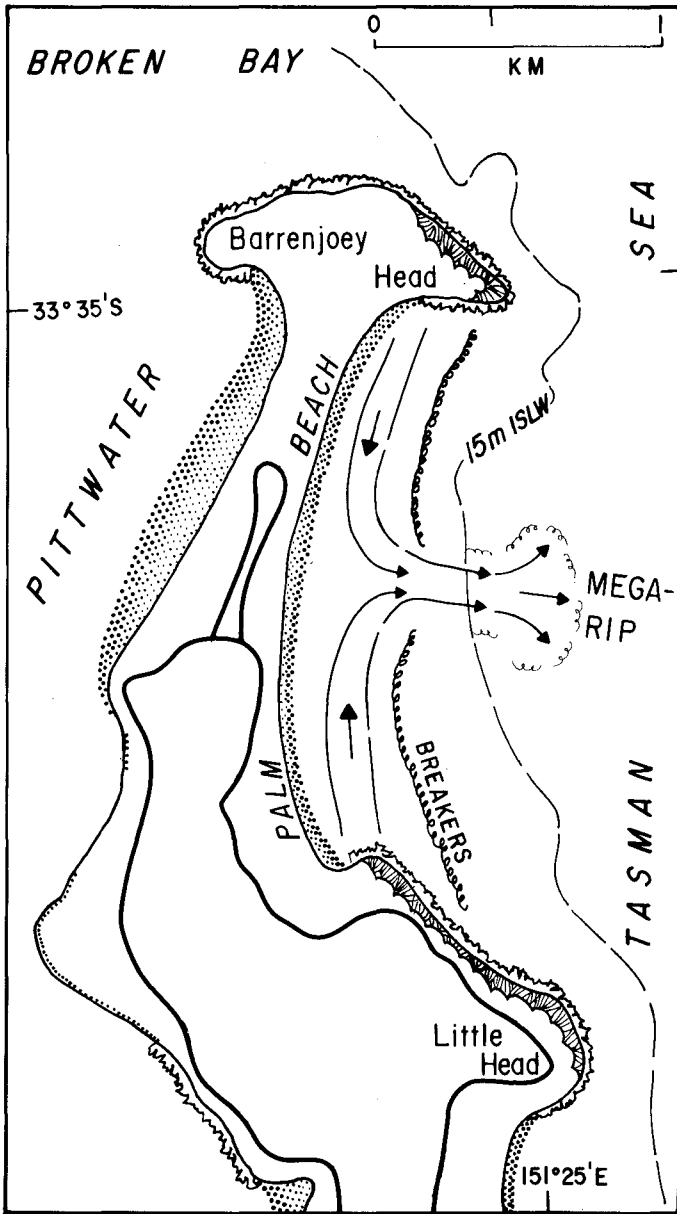


Figure 8 : Large scale "megarip" circulation system related to Type 1 conditions on a highly compartmented beach (Palm Beach, N.S.W.)

Type 2 develops as the bar migrates shoreward under the influence of the progressive shorter period (incident wave period, T and its harmonic $T/2$) components of surf motion when the wave height diminishes to more moderate energy levels. As the bar migrates shoreward the beach face steepens and a deep trough develops within which the partially dissipated waves reform (*Figure 9*). Although the outer surf zone remains dissipative, low turbulent viscosity prevails within the trough and low ϵ_b values characterize the beach face. Synchronous and subharmonic resonance occurs near the beach face, and, as with reflective beaches, low-mode edge waves form beach cusps. A conspicuous feature of *Type 2* and *3* is the occurrence of pronounced resonant spectral peaks at $4T$ (40-50 sec.) within the trough and on the bar. Lower frequency surf beat peaks also remain present but are secondary. An example of power spectra of surf zone surface oscillations over the bar and within the trough of *Type 2* is shown in *Figure 10*. The development of the narrow-band peak at $4T$ within the trough is readily apparent. Rips which pulse at surf-beat periods (100-150 secs.) commonly cross or cut the bar at widely spaced intervals. *Type 2* can persist for several weeks under swell-dominated conditions.

Type 3 is distinguished by a highly regular and rhythmic crescentic bar (*Figure 11*). Shoreline undulations and well-developed circulation cells with evenly spaced rips are also common. Rips and crescentic features have spacings of 100-200 metres. Edge waves with periods corresponding to the observed resonant spectral peaks at $4T$ (40-50 secs) are probably responsible for the crescentic forms and periodic circulation cells. Rip-current spectra exhibit dominant peaks at $4T$ indicating pulsing at that period. As with *Type 2*, the beach face remains relatively reflective, but with the lowest ϵ_b values and highest runup prevailing behind crescentic embayments, where low mode synchronous and subharmonic edge waves commonly exist near the beach face.

Well-developed rhythmic topography with alternating transverse bars and pronounced embayments characterize *Type 4* (*Figure 12*). Transverse bars are frequently anvil-shaped but cusped bars similar to those described by Sonu (1973) may also occur. The topography may also be skewed alongshore under conditions of oblique breaker angles. Narrow, well-defined rips occupy embayments while net shoreward transport occurs over shoals as observed by Sonu (1972, 1973). Where shoals weld to the beach, both ϵ_s and ϵ_b remain high and runup is low; however, the beach face behind embayments remains steep, ϵ_b is normally less than 2, and runup is high. A step is usually present at the base of the beach face. In an accretionary sequence, the spacings of rips and transverse bars appear to be largely inherited from *Type 3*. However, the primary rip circulation cells associated with *Type 4* are probably topographically induced.

Spectra of shore-normal and shore-parallel current motion and water surface oscillations as observed in the presence of *Type 4* topography show dominant, broad surf beat (80-150 secs) peaks near the beach face where the transverse bar attaches to the shore. Rips pulse at corresponding periods. In contrast to transverse bar spectra, current and surface oscillation spectra from the step region behind rip bays also show strong peaks at T and $2T$.



Figure 9 : Shore-parallel bar and deep pronounced trough of Type 2 topography (Moruya Beach, N.S.W.). Note wave breaking and partial dissipation over the bar and reduced turbulence in the trough.

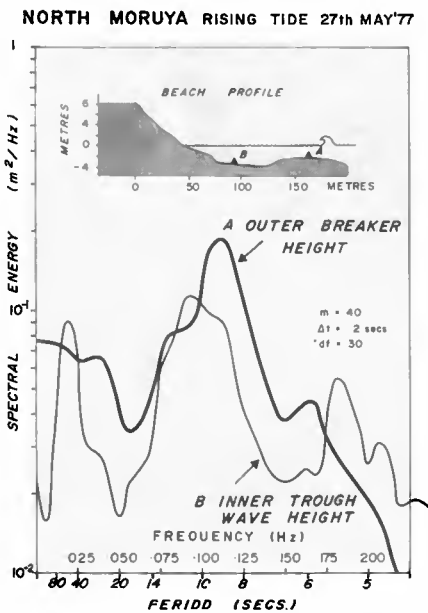


Figure 10 :

Power spectra of water-surface oscillation over the bar and within the trough of Type 2 topography (Moruya Beach, N.S.W.)



Figure 11 :

Rhythmic crescentic bar patterns associated with *Type 3* topography (Erunderee embayment near Seal Rocks, N.S.W.)



Figure 12 : Rhythmic transverse bars and rip embayments of *Type 4* topography (Cronulla Beach, N.S.W.)

Extensive inshore shoals at the base of a moderately steep beach face distinguish *Type 5* (*Figure 13*). The shoals develop following long periods of low energy or in relatively protected regions with abundant inshore sediment. The shoals are crossed at irregularly-spaced intervals by narrow rip channels which atrophy with continued accretion. With *Type 5*, ϵ_b varies appreciably with tide. At low tide dissipation is virtually complete before the waves reach the beach; runup is very low and motion near the beach is dominated by low-energy infragravity oscillations. At high tide, however, runup is high and synchronous and subharmonic resonance occurs. *Type 5* can persist for prolonged periods of 2 to 3 months under sea-breeze dominated summer conditions provided no high energy events occur.

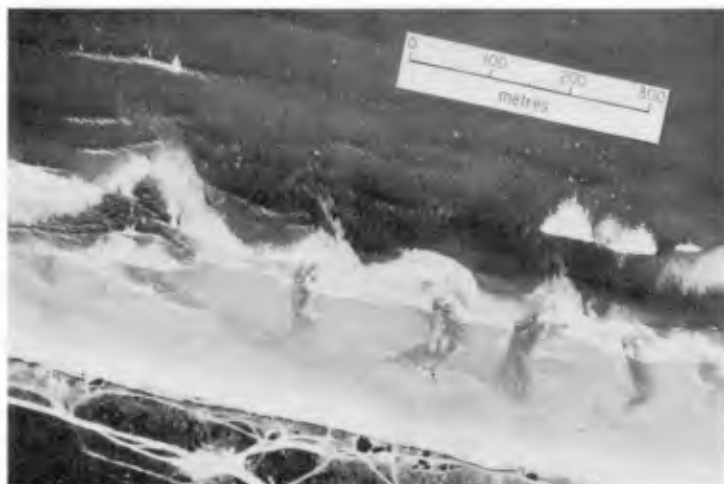


Figure 13 : Intertidal shoals and atrophied rip channels associated with *Type 5* topography

Type 6 morphology (*Figure 14*) represents the fully accreted beach state and occurs after prolonged periods of low swell. It is generally rather rare on exposed, otherwise dissipative surf beaches. *Type 6* is a reflective beach with a steep linear beach face and a very high berm which remains continuous for long distances alongshore; rips are always absent. Wave and current spectra are also similar to those described for reflective beaches.



Figure 14 : Steep Reflective beach and high berm associated with *Type 6* topography (near Port Stephens, N.S.W.)

Discussion

The spectrum of motions in any given surf zone is made up of numerous progressive (dissipative) and standing (reflective) components (Huntley *et al.*, 1977). On a steep reflective beach oscillations at incident wave period are normally standing near the beach; however, with increasing ϵ and increasing surf zone viscosity, high frequency reflection is suppressed and the periods which can be standing increase through a progression of subharmonics (jT ; where $j = 2$ or 4) to surf-beat ($T_b = 80$ -150 secs) to a very low frequency seiching at periods ($T = 5$ -10 min) near the natural compartment period. The standing oscillations can exist either as "leaky" modes in which the reflected energy is re-radiated back to sea (e.g., Suhayda, 1974), or as resonant trapped edge waves; the latter appear to be common except under the most dissipative extremes (*Type 1*) on long straight beaches. Increasing resonant period is accompanied by increasing scale (i.e., spacing between rips and associated rhythmic morphology) and intensity (i.e., rip velocity) of circulations. The progression of resonant modes through a series of discrete frequencies implies firstly that beaches do not vary between reflective and dissipative extremes on a continuum but probably shift abruptly to different states. Secondly, a hierarchy of "nested" circulation and morphologic elements can occur.

Segregation of shore-normal current spectra into shoreward and seaward components (e.g., Wright *et al.*, in press) indicates that on any given beach or inshore slope, significant shoreward movement near the bed is dominated by progressive dissipative bores with periods equal

to those of the incident waves (T) and their harmonics ($T/2$). Near-bed current motions associated with resonant oscillations at periods greater than incident wave period (i.e., $2T$, $4T$, and surf beat) exhibit strong net seaward-directed resultants, suggesting that low frequency resonance plays a major role in causing seaward sand transport. Where synchronous resonance at the dominant incident wave period, T , prevails (e.g., on reflective beaches), the shoreward and seaward velocities are approximately balanced for oscillations at that period. This balance tends to prevail on steep reflective beaches and in the immediate vicinity of the beach face of some dissipative beach types (*Types 2, 3* and *6*, and in the rip embayments of *Type 4*) where incident waves are commonly standing. However, cross spectra reveal that away from the beach face over flat, dissipative inshore profiles the higher frequencies (T and $T/2$) are progressive and dissipative. The shoreward decay of these progressive components is accompanied by a shoreward increase in resonant energy at lower frequencies. The shore-normal direction (i.e. onshore or offshore) of net sediment transport at any given inshore position depends on the energy of the high frequency progressive components relative to the energy of lower frequency resonant components.

On very flat, highly dissipative, profiles resonance at intermediate frequencies ($2T$, $4T$) is suppressed or weak whereas possible resonance at very low frequencies (surf beat or compartment seiching periods) requires high energy dissipation in order to become dominant over the accretive progressive bores. Hence, although the fully dissipative system represents the end point of an erosional sequence, its large inshore sediment storage and flat gradient give it the greatest potential for experiencing future accretion. In contrast, highly reflective beaches (and *Type 6* profiles: the accretive and point) are, owing to their steep gradients and subaqueous sediment deficit, sensitive to resonant excitations over a wide range of frequencies and may experience erosion under moderate swell conditions as soon as resonant energy at $2T$ (first subharmonic) exceeds incident wave energy near the beach. The reflective beach is thus delicately poised with a high erosion potential.

At any specific beach locality the morphodynamic state can vary from *Type 1* to *Type 6* with time and depending on antecedent energy conditions. The most exposed localities show the greatest variability between states. The persistence of a given type also varies spatially with local environment. *Types 1* and *2*, often with multiple bars, are common at the northern ends of large depositional bights, particularly in cases where there is an abundance of sediment. *Types 2, 3* and *4* are frequently encountered in fully exposed middle sections of coastal compartments. *Type 5* is most likely to be persistent on stretches of beach less exposed to high energy swell, but exposed to shorter wind-generated waves. *Type 6* is often present in the partially protected southern ends of compartments in the lee of headlands; it is particularly prominent in the southern arcs of log-spiral or "zeta-curved" compartments. Significantly, although these last environments experience low energy for most of the time, they are chronically susceptible to appreciable erosion under heavy swell conditions.

Acknowledgements

This study is supported by the Australian Research Grants Committee (ARGC). Mr. M.P. Bradshaw, Mr. P. Cowell, and Dr. A.D. Short have provided essential and able assistance in all facets of the study. Long-term surveys of Moruya Beach, which formed the basis of the 6-state model, were initiated by Dr. R. McLean in collaboration with one of us (B.G.T.).

References

- Bradshaw, M.P., J. Chappell, R.S. Hales and L.D. Wright, 1978 "Field Monitoring and real-time analysis for surf and inshore current behavior" Proc. 4th Aust. Coastal and Ocean Engineering Conference (Adelaide) 171-175.
- Cowell, P.J. 1975 Morphodynamic Aspects of the Interactions Between Incoming waves and Bed Topography at Palm Beach, N.S.W. Unpublished B.A. Hons. Thesis, Dept. of Geography, University of Sydney, 179 pp.
- Guza, R.T. and A.J. Bowen, 1975 "The resonant instabilities of long waves obliquely incident on a beach" J. Geophys. Res. 80: 4529-4534.
- Huntley, D.A., R.T. Guza, and A.J. Bowen 1977 "A universal form for shoreline runup spectra?" J. Geophys. Res. 82: 2577-2581.
- Lawson, N.V. and C.L. Abernethy, 1975 "Long term wave statistics off Botany Bay" Proc. 2nd Aust. Conf. on Coastal and Ocean Engineering (Gold Coast, Qld) 167-176.
- Lees, B.G. 1977 The Effects of Compartmentalization on Beach Processes and Forms: Cronulla, N.S.W. Unpublished B.A. Hons. thesis, Dept. of Geography, University of Sydney.
- Short, A.D. 1975 "Multiple Offshore bars and standing waves" Jour. Geophys. Res. 80: 3838-3840.
- Sonu, C.J. 1972 "Field observations of nearshore circulation and meandering currents" J. Geophys. Res. 72: 3232-3247.
- Sonu, C.J. 1973 "Three dimensional beach changes" J. Geol. 81: 42-64.
- Suhayda, J.N. 1974 "Standing waves on beaches" J. Geophys. Res. 79: 3065-3071.
- Wright, L.D., B.G. Thom, P. Cowell, M. Bradshaw and J. Chappell 1977 "Field observations of resonant surf and current spectra on a reflective beach and relationships to cusps" SEARCH 8: 321-322.
- Wright, L.D., J. Chappell, B.G. Thom, M.P. Bradshaw and P. Cowell In press "Morphodynamics of reflective and dissipative beach and inshore systems, Southeastern Australia" Marine Geol.

CHAPTER 69

VARIATIONS OF WAVE-ENERGY LEVELS AND COASTAL SEDIMENTATION, EASTERN NICARAGUA

by

E. H. Owens and H. H. Roberts

Coastal Studies Institute, Louisiana State University,

Baton Rouge, Louisiana 70803

Abstract

High rates of weathering, abundant rainfall, and high discharge rates combine to supply large volumes of sediment to the coastal zone of eastern Nicaragua. This terrigenous sediment is confined to a narrow section of the inner shelf (<30 km wide) due to the circulation pattern within a coastal boundary layer. Sediment transport within the inner shelf and shore zone is to the south. This simple transport pattern is considerably modified by variations in wave-energy levels that are a function of shelf width, bottom friction, and wave sheltering. In northern sections, the shelf is up to 200 km wide but narrows to less than 20 km in the south. A direct result is that wave-energy levels at the shoreline are of the order of three times greater in the south. In the north the Rio Coco delta is prograding seaward in a fluvially dominated environment, whereas the Rio San Juan delta in the south has a wave-dominated morphology characterized by deflected distributaries. Other major accumulation features have developed where wave-shadowing is produced by offshore reefs and cays. Alongshore a spatial variation was recorded, with straight beaches and simple linear bars in the north that change to rhythmic beach topography and crescentic nearshore bars as wave-energy levels increase toward the south.

Introduction

A 2-year multidisciplinary study (1976-77) on the eastern Nicaragua shelf (Figure 1) was directed toward the investigation of macro- and meso-scale shelf and nearshore processes (Murray et al., in preparation). One aspect of the investigations was to determine the regional pattern of sediment supply, transport, and deposition for the shelf and nearshore environments. This subject is considered in more detail elsewhere (Roberts et al., in preparation) but forms the basis for the present discussion, which focuses on an explanation of the variations in the morphology of the beach and nearshore sediments as a function of spatial variations in wave-energy levels at the shoreline.

The primary characteristics of the Caribbean shelf of Nicaragua are (1) persistent northeast trade winds with high average speeds (15 to 20 km/hour) throughout the year; (2) rainfall values in the coastal zone that increase from 2500 mm/year in the north to 5500 mm/year in the south; (3) a large drainage basin of volcanic rocks, with high weathering and erosion rates; (4) high river discharge; (5) a unidirectional wave approach out of the northeast; (6) a dominant system of north to south nearshore and inner shelf currents; (7) a narrowing of shelf width from 200 km in the north to less than 20 km in the south; (8) shallow depths on the shelf, generally less than 30 m; and (9) a microtidal environment (20 to 60 cm range).

Supply of Sediment to the Coast

The continental divide in this section of Central America is adjacent to the Pacific coast (Figure 1), so that the drainage basins that discharge into the Caribbean Sea are relatively large. The eastern Nicaragua drainage basin is approximately 133,000 km², and erosion rates are very high. Intense weathering of the

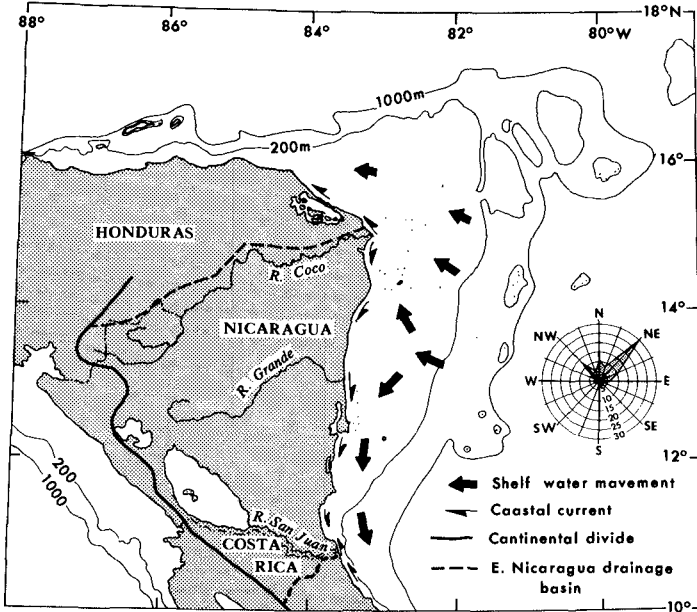


Figure 1. Shelf and coastal currents, Eastern Nicaragua. The wind rose indicates annual frequency (percent) by direction.

volcanic rocks, which are the major geologic outcrop in the mountains of the upper basins, results from high temperatures and large rainfall amounts, coupled with the seasonality of the rainfall distribution. The abundant rainfall also leads to high erosion and high river discharge rates.

Although the data base is limited for this region, extrapolation from available discharge and sediment load measurements indicates a total sediment supply to the shelf by rivers that is in the order of 25 to $30 \times 10^6 \text{ m}^3/\text{year}$ (Table 1). This sediment yield is equivalent to an estimated basin erosion rate of $4.0 \times 10^5 \text{ kg/km}^2/\text{year}$, a rate that is comparable with the high-rainfall, high-temperature, and high-relief areas of southwestern Asia that have erosion rates at the same order of magnitude (Strakhov, 1967).

Table 1
Major Terrestrial Sediment Sources

Drainage Basin	Area (km ²)	Estimated Annual Discharge (m ³ x10 ⁶)	Estimated Annual Sediment Supply (m ³ x10 ⁶)
Coco	24,761	36,460	5.5 - 7.4
Prinzapolka	10,548	20,766	3.1 - 4.2
Grande	17,556	29,104	4.5 - 6.0
Escondido	12,308	26,464	4.0 - 5.4

Estimated total sediment supply to shelf from rivers:
25 - 30 x 10⁶m³/year

For further comparison, in terms of unit lengths of coast, the Nicaragua shelf receives about three times more fresh water and about thirty-three times more sediment from river discharge than does the Atlantic shelf of the United States (Murray et al., in preparation).

Coastal erosion as a source of sediments is limited to a 5- to 10-km section of shoreline in the north, near Puerto Cabezas, where 10-15-m cliffs of sands and gravels are undergoing wave attack. Elsewhere, sections of barrier beaches are subject to erosion, but this process involves redistribution of sediments rather than the supply of new sediments to the coastal zone.

An estimated 16 to 22 x 10⁶ m³/year, the majority of the sediment that is supplied to the shelf, enters the coastal zone in that section to the north of and including the Rio Grande (Figure 1). This northern section accounts for two-thirds of the eastern Nicaragua drainage basin due to the geometry of the Central American isthmus, which narrows from north to south in this region.

Shelf Processes and Sediment Transport

The distribution of terrigenous sediments supplied to the coastal zone and shelf is characterized by two major features. The first is the dominant north to south transport of sediment along the Nicaraguan coast, and the second is the confinement of

the terrigenous sediments to a narrow (less than 30 km) band of the inner shelf adjacent to the coast.

The percentage of calcium carbonate in sediments collected on a transect from the mainland coast (between Punta Perlas and El Bluff) to the shelf edge reflects the rapid facies change to carbonates away from the coast (Figure 2). In less than 20 km terrigenous sediments of the strong longshore drift system are replaced by in situ derived carbonates. Sediments confined to this narrow band along the coast vary from coarse volcanic sands near the river mouths and in the beach and bar systems to fine-grained kaolinitic-montmorillonitic clays in coastal recesses and away from the shoreline. Variations in river discharge and therefore sediment input, as well as perturbations in the strength and direction of the northeast trade winds, cause the sediment-rich coastal plume to expand and contract.

The transition areas between dominantly terrigenous bottom sediments and carbonates are generally found to be rather flat and featureless depositional plains. In these areas, terrigenous clays are deposited in association with in situ generated aragonitic muds derived from the growth and disintegration of numerous varieties of calcareous green algae. Geomorphically, the belt of terrigenous sediments and the terrigenous-carbonate transition areas are associated with a depositional ramp that interfaces with the coast (see zone 1 of Figure 3).

Beyond the limits of the belt of terrigenous sediments (approximately 20 km from the coast), the shelf sediments are generally composed of more than 95% calcium carbonate. The shelf interior consists of vast flat areas blanketed by bimodal sediments consisting of Halimeda-rich carbonate muds. These intermediate shelf areas of carbonate deposition generally have very

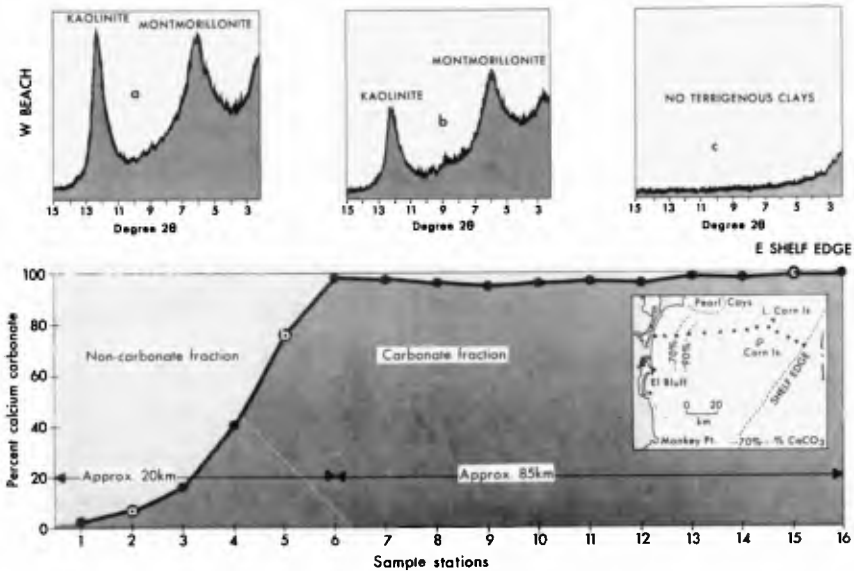


Figure 2. Percent calcium carbonate in bottom sediment samples across the south-central part of the Eastern Nicaragua shelf. Sample locations are given on the inset diagram. X-ray diffraction of representative bottom sediments is shown for sample stations 2, 5, and 15.

little relief and are found in water depths between 20 m and 30 m (see zone 2 of Figure 3).

Extremely rough-bottomed topography, resulting from the growth of coral-algal reefs, is associated with well-defined areas of the shelf (see zone 3, Figure 3). Island platforms such as the Pearl Cays, the Mosquito Cays, and the Corn Islands, as well as submerged topographic highs and a belt along the seaward margin of the shelf, exhibit active reef growth (Figure 3). These reef zones are important source areas for carbonate sediments derived from both biological and mechanical degradation of reef components. In addition to being generation sites for carbonate debris, the extremely irregular bottom topography of these zones is a major factor in the attenuation of open-ocean waves as they intersect the shelf and translate across it. Reefs commonly have

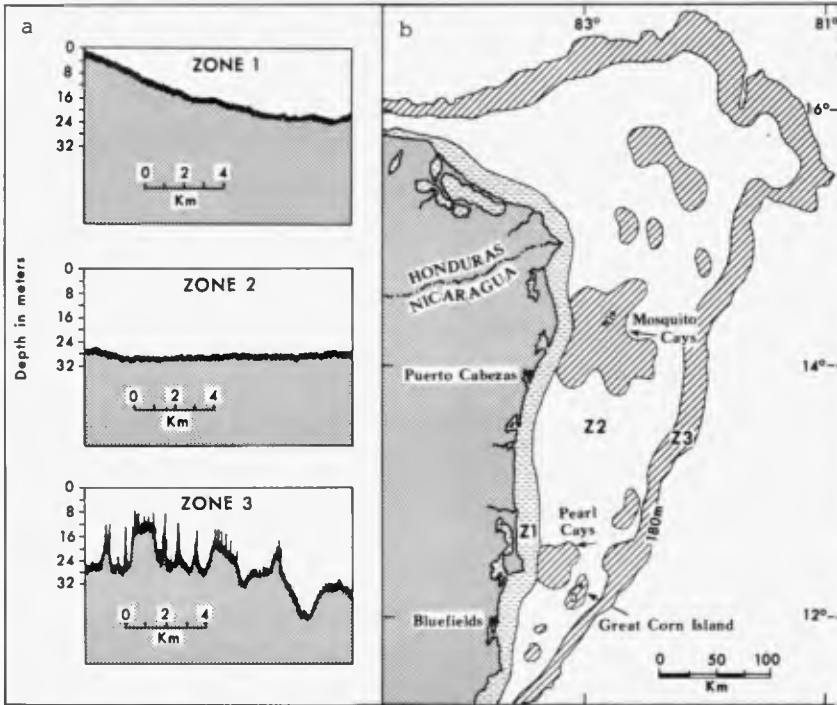


Figure 3. Bottom roughness zonation of the Eastern Nicaragua shelf can be defined by three categories:

Zone 1--Smooth depositional ramp near the coast.

Zone 2--Featureless mid-shelf areas of carbonate deposition.

Zone 3--Rough-bottomed conditions reflecting reef growth on island flanks, mid-shelf platforms, and the shelf margin.

(a) Examples of echo-sounder records for the three zones; (b) geographic distribution of bottom roughness types.

relief of 10 m, and at the shelf margin relief in excess of 20 m is not unusual. The shelf margin reefs are continually bathed in open ocean water and are developing in an environment free of terrigenous sediment, whereas shelf and island platform reefs, for example the Pearl Cays, may be subject to various levels of interaction with terrigenous sedimentation.

The north to south transport of terrigenous sediment is a function of both oceanic and wave-induced currents. In the near-

shore zone the dominant wave approach is out of the northeast, as a result of the effects of the northeast trades, and this situation produces a strong littoral current and longshore drift at the shoreline. Adjacent to the coast wave heights are less than 1.5 m for 75% of the year, with significant periods of 5 to 7 s in the north and 7 to 9 s in the southern areas (Livesey and Henderson, 1968).

Offshore, oceanic currents are characterized by an onshore movement across the shelf of the central Caribbean drift and by a bifurcation of the drift toward the northwest and southwest (Figure 1). Although the mean drift is to the northwest in northern sections of the shelf, the shallow-water countercurrent adjacent to the coast moves toward the south under the influence of the northeast trades and of quasi-geostrophic adjustment to the large freshwater influx along the coast. On the inner shelf the currents are confined to a 10-30-km-wide coastal boundary zone characterized by strong baroclinic structures and by the frictional effects of the northeast trades (Crout and Murray, 1979). In addition, these currents are enhanced by the surface slope of the nearshore waters, so that velocities of 40 to 70 cm/s are common in the upper layers of the coastal currents (Murray et al., in preparation). The primary effect of the oceanic currents is to confine the terrigenous sediments to a relatively narrow (less than 30 km) band adjacent to the coast (Roberts et al., in preparation).

The primary north to south sediment transport system along this 450-km section of coast reverses direction at the Nicaragua borders. In the north the change in coastline orientation from north-south to northwest-southeast at the mouth of the Rio Coco (Cabo Gracias a Dios) leads to a divergence in the littoral drift system and a coastal current that transports sediment to the

northwest along the northern shore of the Coco delta (Figure 1). In the south the coast of Costa Rica also trends northwest-southeast, and this section is affected by easterly and southeasterly winds that become progressively more important toward the south. These winds generate a strong south to north current along the coast of Costa Rica that meets the north to south current in the vicinity of the Rio San Juan delta at the Nicaragua border (Figure 1). The result of these reversals in sediment transport directions is that the Rio Coco delta is a zone of sediment divergence and that the Rio San Juan delta is a zone of convergence.

Coastal Processes and Sedimentary Responses

The macro-scale coastal geomorphology of eastern Nicaragua is characterized by four major sediment accumulation features. Two extensive deltaic systems have developed at the mouths of the Coco and San Juan rivers, and two large cusplate forelands at Punta Gorda and Punta Perlas represent sedimentation in the lee of offshore reef systems. Also, at the regional scale there is a longshore spatial variation in beach and nearshore morphology that is a response to a major change in shoreline processes along this coast.

(a) Comparison of the Coco and San Juan deltas. The variability of shoreline processes on this coast is best exemplified by comparison of these two major deltaic systems. Although only 450 km apart, they represent morphological responses to totally different sets of shoreline processes.

The delta of the Rio Coco (Figure 4a) has assumed a large prograding cusplate shape that reflects the dominance of fluvial over marine processes. The cusplate form has developed as a single river channel has extended the delta by flank deposition. This seaward growth results from the high discharge and high sediment



Figure 4. Generalized morphology of the (a) Coco and (b) San Juan-Colorado deltas.

load of the river (Table 1) and from the inability of marine processes to redistribute the sediments alongshore.

Despite the dominance of fluvial processes, evidence of wave action is given by the relatively smooth outline of the delta. Therefore, applying the terminology of Wright and Coleman (1973), the Coco delta is defined as characterized by a river-dominated morphology with a low level of wave modification. In terms of morphology, this delta is comparable to the Ebro of northeastern Spain (Wright and Coleman, 1973, Fig. 4). The low wave-energy levels at the mouth of the Rio Coco are a function of the wide (up to 200 km), shallow shelf offshore that is characterized by numerous reefs and cays. Incoming waves therefore are subject to considerable frictional attenuation, and at the shoreline waves are generally of short period and low amplitude.

The morphology of the Rio San Juan delta, 450 km to the south, is totally different (Figure 4b). Although the estimated discharge rates and sediment loads of the two rivers are similar (Table 2), and although this is a zone of convergence of the longshore currents, the delta protrudes only slightly onto the adjacent shelf. The river has two major distributaries, both of which

have been deflected toward the north. In particular, at the mouth of the Rio Colorado a series of blocked distributary channels that parallel the shoreline (Figure 4b) are evidence of a seaward progradation that is controlled by marine reworking of the deltaic sediments. The shelf adjacent to the San Juan delta is less than 20 km wide (Figure 1), with a mean slope of 1:80 (cf. the shelf adjacent to the Coco delta, which has a slope less than 1:200, Table 2). The morphology of this delta clearly reflects the dominance of marine over fluvial processes on this section of coast.

The variation that exists between these two delta systems is due to the significant change in the balance between fluvial and marine processes. This change results from a variation in wave-energy levels at the shoreline that is controlled by shelf width. As the shallow shelf narrows toward the south, and as frictional attenuation therefore also decreases, wave energy at the shoreline increases significantly. (Computed values for wave energy show a

Table 2
Comparison between the Deltas of the Rios Coco and San Juan

	Coco	San Juan
Shelf width (km)	150-200	<20
Shelf slope	<1:200	1:80
Wave-energy levels (ergs/m/s)	Low: ~1.2 x 10 ¹⁰	High: ~4.3 x 10 ¹⁰
Discharge (m ³ /year)	~40 x 10 ⁹	~25 x 10 ⁹
Estimated sediment load (m ³ /year)	5.5-7.4 x 10 ⁶	4.0-5.4 x 10 ⁶
Littoral drift	Zone of divergence	Convergence, dominantly to north
Primary processes	Fluvial	Marine (wave dominated)
Delta morphology	Single protruding channel	Straight coast, deflected distributaries

threefold increase, from 1.2×10^{10} ergs/m/s in the north to 4.3×10^{10} ergs/m/s in the south.)

(b) Punta Gorda and Punta Perlas. In addition to the systematic alongshore changes in wave energy at the shoreline, the presence of offshore reef and cay complexes causes local variations in the coastal geomorphology. The Mosquito Cays and Pearl Cays (Figure 3) act as barriers to incoming waves, and accretion of sediments within the longshore transport system has occurred in the lee of these two reef systems. Both Punta Gorda and Punta Perlas have developed on the low-lying swampy coastal plain by the seaward progradation of a series of well-defined beach ridges.

Punta Gorda is in the lee of the Mosquito Cays (Figure 5a) and has developed downdrift of the Coco delta. As much of the sediment supplied by the Coco is diverted to the northwest at the mouth of the delta (Figure 4a), the estimated annual supply of fluvial sediment from the Coco and Ulang rivers is in the order of 3 to 5×10^6 m³/year.

Farther to the south, Punta Perlas (Figure 5b) lies downdrift of several major rivers, including the Prinzapolka and the Grande, so that sediment input in this section is much greater, in the order of 9 to 12×10^6 m³/year. Therefore, although the Pearl Cays are a less effective filter to incoming waves, when compared to the Mosquito Cays, there is more sediment in the longshore transport system. This situation has favored the development of a large cusped feature that now extends 10 km seaward from the general trend of the coast. The Punta Perlas system acts as a large groin-like feature with a resulting downdrift offset of the coast to the south.

(c) Comparison of river-mouth characteristics. As a measure of wave competence and its effect on local coastal geomorphology,

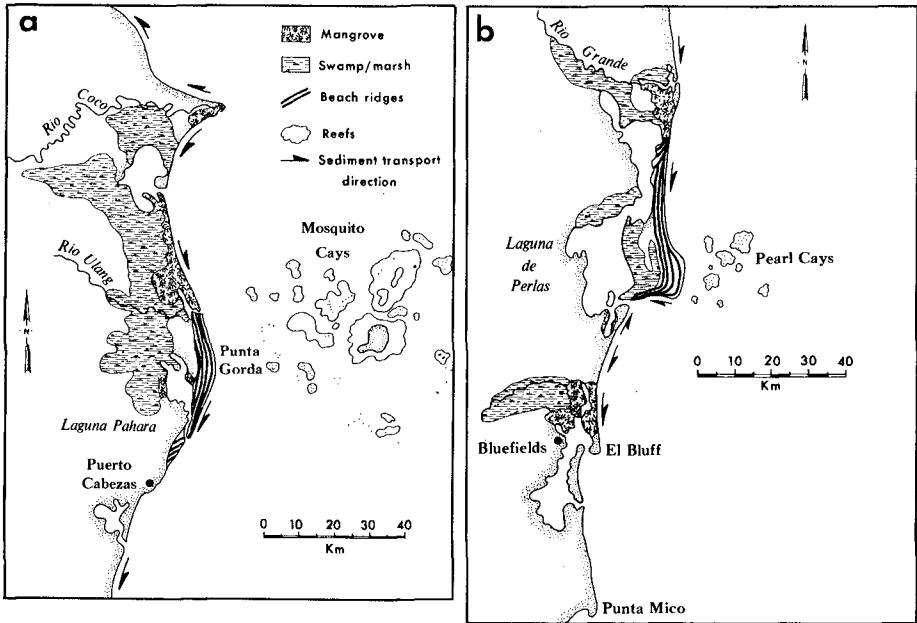


Figure 5. Generalized morphology of (a) Punta Gorda and (b) Punta Perlas (from topographic maps and aerial photographs).

a comparison has been made between the river exits of the Rio Ulang (Figure 5a) and the Rio Indio (Figure 4b). Both rivers have relatively small drainage basins and enter the shore zone at sections of unimpeded sediment transport. Although the Ulang drains an area twice the size of the Indio (Table 3), the increase in annual rainfall amounts between the two areas (from 2500 to 5000 mm) results in similar discharge rates and sediment loads. The Ulang river mouth is characterized by a large ebb-tidal delta system in which the main ebb channel has been deflected to the south by wave-induced littoral currents (Photograph 1). Although this deflected channel system is characteristic of rivers with small drainage basins, such as the Wawa and Kukalaya, the tidal deltas associated with large rivers in the northern half of the shelf (the Prinzipolka and Grande) show no evidence of channel deflection. In

these cases the very high discharge rates are sufficient to counterbalance the processes associated with the longshore transport system.

In contrast to the Ulang, the channel of the Rio Indio has been deflected 15 km to the south due to the effects of strong wave-induced longshore currents. The channel parallels the shoreline and is separated from the sea by a narrow (300-400 m), low (<3 m) barrier (Photograph 2). The mouth of the Rio Indio has become part of the outlet system associated with the northern distributaries of the San Juan delta (Figure 4b).

(d) Beach-nearshore morphology variations. At a smaller scale, field measurements and reconnaissance observations have shown that there is a marked change in beach and nearshore planform morphology from north to south on this coast. This systematic alongshore variation is a direct function of the changes in wave-energy levels at the shoreline.

In northern sections of this coast, to the north of Punta Perlas, the beaches are narrow (~10 m) and straight. A single continuous linear bar is present in the nearshore zone, usually at

Table 3
Comparison Between the Ulang and Indio Rivers

	Ulang	Indio
Drainage basin (km ²)	3830	1820
Discharge (m ³ /year)	5840 x 10 ⁶	5140
Sediment load	0.9-1.2 x 10 ⁶	0.8-1.1
River-mouth morphology	Large ebb-tidal delta - partially deflected channel	River channel deflected 15 km to south
Wave energy at shoreline (ergs/m/year)	-1.2 x 10 ¹⁰	-4.3 x 10 ¹⁰



Photograph 1. Low-altitude aerial photograph of the mouth of the Ulang River. Note the deflection of the main (ebb) channel, which closely follows the south (left in this photo) shore of the estuary.



Photograph 2. Aerial photograph of the lower course of the Rio Indio. The river exit is indicated by the arrow.

about 60 m from the shoreline (Photograph 3). Generally trough and bar depths are in the order of 1.5 and 1.0 m, respectively. Due to the wide shelf (up to 200 km) and shallow gradients, frictional attenuation values are high, particularly as much of the outer shelf is composed of active coral reefs. Computed energy levels at the shoreline are in the range 0.7 to 1.2×10^{10} ergs/m/s.

The central section, between Punta Perlas and Punta Mico (Figure 5b), is a transition zone. Beaches are generally wider and steeper, and the morphology is a series of irregular protuberances and embayments (Photograph 4). The nearshore zone is characterized by rip cells and by a nonlinear bar system with some longshore periodicity that has wavelengths in the order of 50 to 70 m. Trough depths vary between 1.0 and 2.0 m on the landward side of the inner bar, and the inner bar shoals to 1.5 to 2.5 m. Computed shoreline energy levels are between 0.9 and 1.5×10^{10}



Photograph 3. Straight shoreline with a single linear nearshore bar near Laguna de Wounta, to the north of Prinzapolka (12 April 1977).



Photograph 4. Wide breaker zone and irregular beach-nearshore topography north of El Bluff (12 April 1977).



Photograph 5. Well-defined rhythmic topography at Cano El Pescado, approximately 25 km north of the San Juan-Colorado delta (12 April 1977).

ergs/m/s as shelf width decreases to between 100 and 150 km.

The beaches to the south of Punta Mico exhibit a rhythmic morphology (Photograph 5). This configuration is mirrored in the nearshore zone by a well-developed crescentic bar system with wavelengths in the order of 100 to 125 m. No field data were collected in this section, but computed wave-energy values are in the range 2.5 to 4.3×10^{10} ergs/m/s.

The increase in energy levels alongshore results in a distinct transition from simple morphological features to a complex system of rhythmic topography (Table 4).

Table 4
Eastern Nicaragua Beach/Nearshore Morphology

	North	Central	South
Shelf width (km)	200	100-150	20
Wave-energy levels	Low	Moderate	High
Nearshore wave power (ergs/m/sec)	$0.7-1.2 \times 10^{10}$	$0.9-1.5 \times 10^{10}$	$2.5-4.3 \times 10^{10}$
Beach morphology	Straight narrow beaches	Irregular protuberances and embayments	Wide beach, rhythmic morphology
Nearshore morphology	Single linear bar 60 m from shore	Nonlinear bar(s), some longshore periodicity (50-70 m wavelength)	Well-developed rhythmic bar system (100-125 m wavelength)

Conclusions

1. Although the Nicaragua shelf receives an estimated three times more fresh water and thirty-three times more terrigenous sediment per unit length of coast than the Atlantic shelf of the United States, the shelf has developed as a vast carbonate

province with terrigenous sediments confined to a narrow, well-defined belt (<20 km) along the coast.

2. The shelf margin (50-70 m depth), mid-shelf platforms, and island flanks are sites of active coralgall reef growth. These areas of extreme bottom roughness affect energy levels along the shoreline by the combined effects of frictional attenuation and sheltering.

3. Decreasing shelf width and decreasing frictional attenuation from north to south cause a threefold increase in wave-energy levels at the shoreline.

4. The spatial variation in nearshore and shoreline wave-energy levels results in (a) a fluvial dominated deltaic environment at the mouth of the Rio Coco, in the north; (b) a marine (wave) dominated deltaic environment at the mouth of the Rio San Juan, in the south; and (c) a systematic change from straight linear bars and beaches in the north to rhythmic topography in the south.

5. The distribution, transport, and morphology of sediments supplied to the shelf and shore zones on this coast are controlled by shelf and coastal currents and by the spatial variation in shoreline wave-energy levels.

Acknowledgments

The research was performed under a contract between the Geography Programs, Office of Naval Research, Arlington, Virginia, 22217, and the Coastal Studies Institute, Louisiana State University, Baton Rouge. J. N. Suhayda computed the wave-energy values, and Gerry Dunn prepared the illustrations.

References

- Crout, R. L., and Murray, S. P. 1979. Current dynamics in the coastal boundary layer, Caribbean coast of Nicaragua. Proc., 16th Internat. Coastal Eng. Conf., Hamburg, Amer. Soc. of Civil Engr., N.Y. (this volume).
- Livesey, R., and Henderson, A. B. 1968. Atlantic port and harbour study, Republic of Nicaragua. Vol. 7, Hydrographic appendix. Livesey Consulting Co., London.
- Murray, S. P., Hsu, S. A., Roberts, H. H., Owens, E. H., and Crout, R. L. In preparation. Dynamics and sedimentation over a broad shallow bank.
- Roberts, H. H., Owens, E. H., and S. A. Hsu. In preparation. Variability of geomorphology and sediments: Mosquito Bank, Nicaragua (Central America).
- Strakhov, N. M. 1967. Principles of lithogenesis. Vol. 1. Edited by Tomkeieff, S. I., and Hemingway, J. E., Oliver and Boyd, Edinburgh, 245 pp.
- Wright, L. D., and J. M. Coleman. 1973. Variations in morphology of major river deltas as functions of ocean waves and discharge regimes. Amer. Assoc. Petroleum Geologists Bull. 47:370-398.

CHAPTER 70

PROCESS-RESPONSE MODELS FOR DEPOSITIONAL SHORELINES: THE GERMAN AND THE GEORGIA BIGHTS

by

Dag Nummedal
Department of Geology
Louisiana State University
Baton Rouge, Louisiana
70803, USA

and

Ian A. Fischer
Mobil Oil Corporation
1001 Howard Avenue
New Orleans, Louisiana
70113, USA

ABSTRACT

Sediment dispersal patterns in tidal inlets within the German and the Georgia Bights are found to be controlled by three major environmental factors: (1) the tide range, (2) the nearshore wave energy, and (3) the geometry of the back-barrier bay. Both embayments chosen for study are characterized by high wave energies and low tide ranges on their flanks, and low wave energies and high tide ranges in their centers. The spatial variability in inlet morphology, therefore, contains information on the relative role of tides and waves in inlet sediment dispersal. The paper concludes by proposing a simple model for inlet morphologies for successively greater relative role of tidal currents in the sediment dispersal.

INTRODUCTION

Investigations of process-response characteristics of tidal inlets along the southeast coast of the United States (Bruun, 1966; Finley, 1976; FitzGerald *et al.*, 1976; Hubbard *et al.*, 1977; Nummedal *et al.*, 1977) have demonstrated that the geometry of the inlet entrance and the associated sand shoals depends upon three major environmental factors: (1) the tide range, (2) the nearshore wave energy, and (3) the bathymetry of the back-barrier bay.

The relative magnitudes of factors 1 and 2 control to a large extent the inlet stability. Inlets along the Georgia coast, which has high tide range and low wave energy, are much more stable than those along North Carolina's Outer Banks where the wave energy is high and the tide range relatively low. These observations support, in a qualitative sense, Bruun's (1966) stability criterion which is based on the ratio between the tidal prism and the longshore sediment transport rate.

The third factor listed above, the bathymetry of the bay, controls the degree of velocity asymmetry through the inlet gorge (Nummedal and Humphries, 1978). The bays in the southeastern United States are typically filled with intertidal salt marsh (*Spartina alterniflora* being the dominant grass species), leaving only about 20 per cent of the total bay area as open water (tidal creeks). The consequent large variation in water surface area during the tidal cycle tends to develop strongly ebb-dominant flow in such a bay-inlet system. The peak ebb current and the consequent seaward-directed sediment transport, far exceed that moving landward during flood. In cases where the back-barrier bay is essentially all open water (as in the lagoons behind the Outer Banks of North Carolina) there is no such tendency for ebb dominance.

In order to determine the response of the tidal inlets to the three controlling factors one must examine coastal segments within which all factors undergo significant changes in magnitude according to a well-known geographic pattern. The coastal segments chosen for this investigation were the southeast coast of the United States from Cape Hatteras to Cape Canaveral (Fig. 1) and the northwest coast of Europe from the Netherlands to the west coast of the Jutland peninsula in Denmark (Fig. 2). For short, the first region will be referred to as the Georgia Bight, the second one as the German Bight.

TIDE RANGE

Along the east coast of the United States the open coast tide range is primarily a function of shoaling of the tidal wave across the continental shelf. Therefore, the wider the shelf, in the direction of advance of the tidal wave, the larger the tide range (Redfield, 1958; Silvester, 1972). Figure 3 (from Nummedal et al., 1977), shows the regional tide range variation along the U.S. east coast as well as the accompanying variation in shelf width. The tide range dependency on shelf width can clearly be seen.

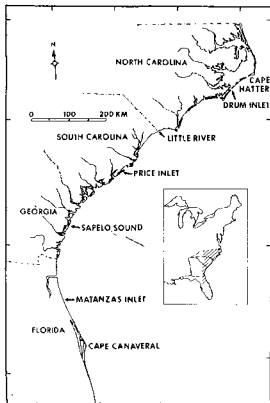


Fig. 1. Location map of the Georgia Bight.

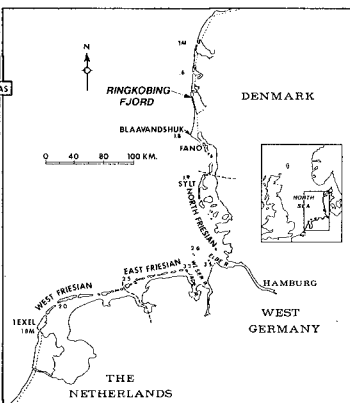


Fig. 2. Location map of the German Bight.

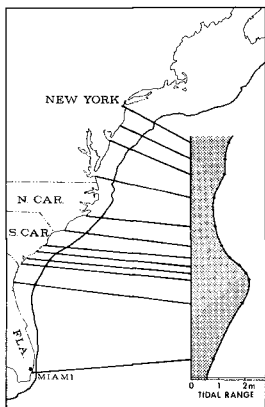


Fig. 3. Mean tide range along the east coast of the United States. Data from: National Oceanic and Atmospheric Administration, 1978.

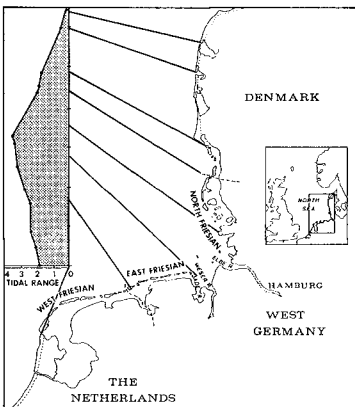


Fig. 4. Mean tide range along the shores of the German Bight. Data from Deutschen Hydrographischen Institut, 1978.

In the North Sea, the entire region is essentially a continental shelf. The variation in open-coast tide range within the German Bight, therefore, is largely controlled by the amphidromic system. Classical models of the M_2 tide within the North Sea (Defant, 1958), demonstrate the existence of a counter-clockwise rotation of the tidal wave in the North Sea around an amphidromic point between Jutland and the east coast of England. Iso-range lines are nearly concentric around this point. Therefore, the central part of the German Bight which is further away from the amphidromic point than is the northwest Netherlands or the coast of Jutland, has the larger tide range. The tide range variability within the coastal segment of interest in this study is plotted in figure 4.

By comparing figures 3 and 4 it is evident that both the Georgia and the German Bights are characterized by low tide range at their flanks and high tide range in the center. Mean tide range in the center of the Georgia Bight exceeds 2 meters; in the center of the German Bight it exceeds 3.5 meters.

WAVE ENERGY

Evaluations of the regional variability in nearshore wave climate is presently impossible because reliable wave records are very scattered and typically of too short duration to be of much use in long-range sedimentation studies. In order to derive a consistent picture of wave energy variability, therefore, it was decided to utilize the Summary of Synoptic Meteorological Observations (SSMO - data) published by the U.S. Naval Weather Service Command (1974, 1975). Wave energy flux distributions within pre-established data squares were calculated by a procedure outlined in Nummedal and Stephen (1978). In this same article the authors have also discussed in some detail the assumptions and problems associated with the utilization of SSMO-data in studies of coastal sedimentation dynamics. Results of the wave energy flux calculations for data squares off the southeast coast of the United States and in the North Sea are summarized in figures 5 and 6, and tables 1 and 2.

The deep water energy flux shows a distinct southward decrease along the U.S. east coast from a total onshore flux at Cape Hatteras of $7.7 \cdot 10^3$ Watts/m to $4.6 \cdot 10^3$ Watts/m at Jacksonville. In spite of this deep water trend, however, the mean annual breaker height in northeast Florida exceeds that of the central part of the Georgia Bight (58 cm at

Daytona Beach versus 12 cm at St. Simon Island; Coastal Engineering Research Center, 1975) probably because of the steeper inner shelf profile off the Florida coast (Nummedal et al, 1977).

Table 1. Deep water wave energy flux values for the southeast U.S. SSMO data squares. Energy flux in units of 10^3 Watts/meter.

Data Square Direction	Cape Hatteras	Charleston	Jacksonville	Miami
N	4.8	3.2	4.2	1.9
NE	3.3	3.5	2.2	2.2
E	1.3	1.9	1.3	2.4
SE	1.2	1.3	1.1	1.2
S	1.9	2.2	1.8	.8
SW	2.8	2.5	1.6	.8
W	3.0	3.2	1.9	.7
NW	2.7	2.6	3.2	1.3

Table 2. Wave energy flux values for SSMO data squares along the margins of the North Sea. Energy flux in units of 10^3 Watts/meter.

Data Square Direction	Edinburg	Grimsby	Rhine Delta	Bremerhaven	Esbjerg	Stavanger
N	2.1	1.5	.8	.7	2.1	5.1
NE	.5	1.5	.7	.3	1.0	1.4
E	3.3	1.5	.5	.8	1.8	4.5
SE	3.4	.8	.3	.3	1.0	7.8
S	1.8	2.1	.7	.5	2.3	3.8
SW	1.7	2.8	2.1	1.5	5.0	5.4
W	3.0	2.3	1.9	2.9	5.5	9.8
NW	3.3	2.7	1.4	2.4	6.3	11.8

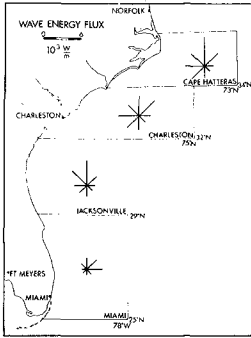


Fig. 5. Wave energy flux distribution off the southeast coast of the U.S.

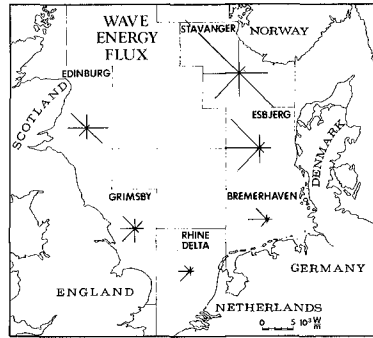


Fig. 6. Wave energy flux distribution along the margins of the North Sea.

Along the southeast coast of the North Sea one also finds a distinct southward decrease in total wave energy flux. This is thought to reflect a combination of a decrease in storm frequency as well as westerly fetch in the same direction. Total onshore wave energy flux in the Esbjerg data square (Fig. 6) is about $17 \cdot 10^3$ Watts/m, compared to $7 \cdot 10^3$ Watts/m along the North Friesian Islands and only $3.5 \cdot 10^3$ Watts/m along the East Friesian Islands.

By combining the information presented on the wave energy and tide range variations one can derive a generalized pattern of wave and tide dominance along the shores of these two bights (Fig. 7). The flanks have high wave energy and low tide range. They are wave dominated. Further towards the center the two factors will both be of major importance; therefore, this will be a zone of mixed energy. In the center of both bights the tidal currents clearly control the sedimentation patterns. These areas are tide dominated.

INLET MORPHOLOGY

Both the Georgia and the German Bights show distinct and similar trends in inlet morphologic changes as one progresses from the flanks toward the centers. These changes provide unambiguous evidence regarding the relative role of tidal and wave induced sediment dispersal in the total inlet circulation pattern. This paragraph will review the characteristics of inlet morphology, moving from the wave dominated embayment flanks to increasing tidal dominance at the embayment centers.

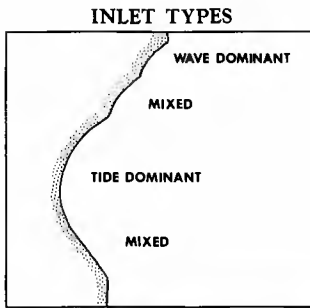


Fig. 7. Generalized distribution of wave and tide dominance along an embayment coast



Fig. 8. Oblique air photo of Drum Inlet, North Carolina. Photo, May 1977, courtesy of Albert C. Hine.

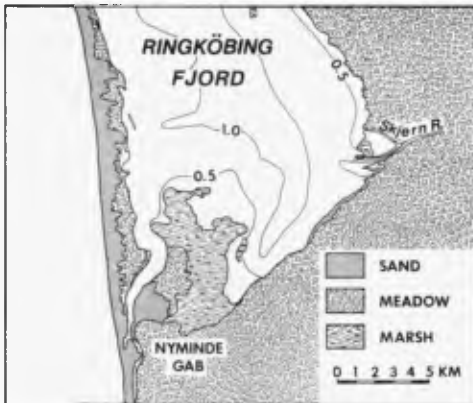


Fig. 9. Map of the southern part of Ringkøbing Fjord, including the old flood-tidal delta at Nyminde Gab. Depth contours in meters.

Inlets along the wave dominated coastal segments of both bights are typified by Drum Inlet, North Carolina, at the northern flank of the Georgia Bight (Figs. 1 and 8). Although the Drum Inlet flood-tidal delta was developed over a very short time immediately after the inlet was artificially opened in 1972 its morphology is typical of the much larger deltas behind Ocracoke, Hatteras and Oregon inlets as well. Today, the Drum Inlet flood-tidal delta is rather inactive (Hubbard, 1977).

Within the German Bight the wave dominated barrier-lagoon coast is restricted to the west coast of Jutland. Furthermore, all these lagoons now have artificially cut and maintained entrances. However, it is clear from old maps and the present lagoon morphology that the natural entrance to Ringkøbing Fjord was associated with a large flood-tidal delta, the remains of which are clearly recognizable at Nyminde Gab (Figure 9).

The morphology of an inlet at a wave dominated coast is summarized in frame 1, figure 10.



Fig. 10. Tidal inlet morphological models. Frames 1 through 6 reflect an increasing role of tidal currents in inlet sediment dispersal.

As illustrated, such an inlet is characterized by sand bodies exclusively on the landward side of the inlet gorge. The gorge itself is relatively stable, the ebb tidal delta (outer shoal) is present only as a minor subtidal shoal.

With an increase in tidal range, and consequent tidal current capacity for sediment transport, one observes an intriguing change in inlet shoal configuration. Both Little River inlet on the North Carolina-South Carolina border

(Fig. 11) and Matanzas Inlet in northeast Florida (Fig. 12) are good examples of this inlet type which will be called mixed energy, low tide range, inlets.

Based on the distribution of sand bodies within these inlets the generalized model shown in frame no. 2, figure 10, was developed. This type of inlet has a smaller, and less continuous, flood-tidal delta than inlet type no. 1, it has a wide and rather unstable inlet gorge, and a significant ebb-tidal delta reflecting main channel ebb-current dominance (Hayes *et al.*, 1973).

The inlets between the East Friesian Islands on the coast of Lower Saxony, Germany, must also be termed mixed energy inlets. However, both tide range (Fig. 4) and wave energy (Fig. 6) exceed those within the Georgia Bight. As the gross differences in morphology appear to reflect primarily the larger tide range, these inlets are classified as mixed energy, high tide range, inlets. Excellent examples would be the inlet between Norderney and Baltrum (Fig. 13), and the Harle Inlet between Spiekeroog and Wangerooge (Fig. 14).

As demonstrated by Luck (1976) these Friesian inlets have a large ebb-tidal delta with a nearly continuous arc of swash bars along its margin, the "reef-bow." The high wave energy appears to cause rapid swash bar migration contributing to the instability of the seaward end of the main ebb channel. The inlets are very wide and the ones that are not yet stabilized by sea walls and groins on the adjacent island shores typically have multiple channels. According to historical studies by Luck (1975) prior to stabilization the Harle Inlet also had multiple sand bars in the gorge section and two or three major channels. Reduction in tidal prism as a function of the reclaiming of large areas of back-barrier tidal flat appears to be the main factor contributing to the changes morphology of the Harle Inlet.

A generalized morphological model of the Friesian inlets is presented in frame no. 3, figure 10. The only essential difference from model no. 2 is the larger ebb-tidal delta, projecting further out to sea in response to much stronger tidal currents. Strong wave action also produces a more continuous series of swash bars along the swash platform margin.



Fig. 11. Oblique air photo of Little River Inlet, North Carolina-South Carolina border. Photo, May, 1977, courtesy of Dennis K. Hubbard.



Fig. 12. Oblique air photo of Matanzas Inlet, Florida. Photo, April, 1977, courtesy of Dennis K. Hubbard.



Fig. 13. Oblique air photo of Wichter Ee, the inlet between Norderney and Baltrum, Lower Saxony. July, 1978.



Fig. 14. Bathymetric map of Harle Inlet, Lower Saxony. The contour interval is 2 meters.

True tide dominance characterizes the inlets of the central part of the Georgia Bight. Although the tide range there is less than that along the Friesian coast, tidal dominance is brought about by the extremely low nearshore wave energies. Though small, Price Inlet (Fig. 15) illustrates well the morphology of the larger tidal inlets along this segment of the coast. Descriptions, photos and maps of numerous other inlets in the central Georgia Bight can be found in Hubbard (1977), Nummedal *et al.* (1977), Oertel (1975), and FitzGerald *et al.*, (1978).



Fig. 15. Oblique air photo of Price Inlet, South Carolina. Photo, March, 1977.

The morphology of tide dominated inlets is generalized in frame no. 4, figure 10. These inlets consist of a single, straight, and deep main ebb channel, a large swash platform projecting far out to sea, and numerous, often large swash bars migrating towards the inlet gorge across the swash platform. There are no sand bodies in the inlet gorge section nor on its landward side, reflecting strong ebb dominance in the main inlet channel.

With a further increase in the ratio between tide range and wave energy, beyond the conditions found in the central part of the Georgia Bight, barrier islands with distinct individual tidal inlets cease to exist. As an example one can consider the central part of the German Bight where the mean tide range in places exceeds 3.5 meters (Fig. 4).

As shown in the bathymetric maps of the entrance to the Weser estuary (Fig. 16 and 17), small, unstable, supratidal sand bodies like Alte Mellum, have replaced the barrier islands of lower tidal range. A series of linear, lunate and sigmoidal shoals dominate the estuary entrance. Their long

axes are typically parallel to the main estuary axis. The total sand body associated with this estuary is large and extends much further out to sea than any of the tidal deltas of the mixed energy inlets between the Friesian Islands further west.

Inlets (or estuary entrances) of this type are summarized in frame 5, figure 10. They are high tide range, tide dominated inlets.



Fig. 16. Bathymetry of the entrances to the Weser and Jade estuaries.



Fig. 17. Bathymetry of the area enclosed by frame in figure 16. Arrows refer to hydrographic data obtained by Barthel (1976). Open arrows indicate flood dominance, solid arrows show ebb dominance.

The high tide range end member of this spectrum of inlet types had to be found outside the German or the Georgia Bights. Hayes (1975) and Hayes and Kana (1976) present maps of Nushagak Bay, Alaska, as an example of a macrotidal embayment. Extremely high tide ranges, as in Nushagak Bay, can only develop in narrow embayments where there is a significant funneling of the tidal wave. The strong tidal currents, in turn, prevent the development of barrier islands across the embayment entrance. As indicated in the simplified morphological model of frame 6, figure 10, the shoal distribution within an embayment like Nushagak Bay is fairly similar to that of the high tide range, tide dominated embayment of frame no. 5. The main difference appears to be the degree of development of the sigmoidal shoals. An increase in tide range, and the associated tidal current strength, appears to develop larger sigmoidal shoals and more distinct flood and ebb segregated channels.

DISCUSSION

The paper demonstrates that there clearly exists a continuum of tidal inlet morphologic types. Examples of most types within this continuum can be found within the Georgia and the German Bights because of large regional variations in tide range and wave energy.

The wave dominated inlets (frame 1, figure 10) typically have the majority of the shoals on the landward side of the inlet gorge because the net direction of wave induced sand transport will be towards the lagoon. Furthermore, the existence of a largely open-water lagoon rather than a marsh or tidal flat in the back-barrier environment will reduce the ebb dominance of the main inlet channel and cause flood dominance of some inlets (Nummedal and Humphries, 1978). Complex wave-current interactions on the swash platform have been found to produce a higher concentration of suspended sediment on flooding than on ebbing tide at one inlet (Hubbard, 1977). This factor might also contribute to the landward-directed net sediment transport at some wave dominated inlets.

The mixed energy inlets within the Georgia and German Bights are all hydraulically ebb dominated, because of the extensive back-barrier marshes and tidal flats (Nummedal and Humphries, 1978). The seaward extent of the swash platform must reflect an equilibrium between the capacity for seaward transport by the ebb flow and landward transport by wave breaking on the platform. Consequently, the primary change in the ebb-tidal delta with an increase in the ratio of tidal range to breaker energy will be its seaward growth. Secondly, the inlet gorge will become better defined and less subject to changes due to bar migration as wave-induced bar development will take place on platform margins further away from the inlet. These patterns of response to increasing tidal influence on the sediment dispersal mechanism are well illustrated in models two, three and four in figure 10.

Barrier islands cease to exist along depositional coast of high tide range because the longshore sediment movement due to wave action becomes completely subordinate compared to the on-offshore movement of sediment by the tides. For the wave energy of the German coast the critical tide range appears to be about 3 meters (Fig. 4). The development of sigmoidal shoals in these high tide range embayments is an expected consequence of the deflection of a current around

the leading face of any sedimentary deposit formed by another current flowing in the opposite direction. This causes strongly segregated channels for ebb and flood flow, hence the sigmoidal shape of the bar crest. This segregation of ebb and flood flow in the Weser estuary has been well documented by Barthel (1976).

CONCLUSIONS

1. The pattern of variability in tidal inlet sand body geometries within the Georgia and the German Bights suggests the existence of continuum of inlet morphologic types. In this continuum the shoals assume a configuration which directly reflects the relative capacity for sediment transport by waves and tidal currents. Six discrete stages of inlet morphology are presented in figure 10.

2. The diagram applied by Hayes (1979) to classify barrier island shorelines is used here to show the relationship between the inlet morphologic types and the two dominant environmental parameters: wave height and tide range (Fig. 18). To establish the boundaries, 19 inlets were classified, based on shoal geometry, as wave dominated, mixed or tide dominated. The mean tide range was well known for each, mean annual breaker heights, however, are much less precisely known. Nevertheless, a distinctive pattern did emerge, permitting the establishment of fairly precise boundaries for each inlet type on this bivariate graph. The boundaries slope such that with an increase in mean annual wave height an increase in tidal range is required to produce the same type of inlet shoal geometry.

3. The regional variability of the inlets within the Georgia and German Bights can be represented by the arrow in figure 18. Towards the center of both bights one finds an increase in tidal range and a decrease in the mean annual wave height. Therefore, the inlet change from wave dominated ones at the flank to tide dominated ones at the centers.

ACKNOWLEDGMENT

Work on the coast of West Germany was sponsored by the Office of Naval Research, Geography Programs, through contract no. N00014-78-C-0612 to L.S.U. Work on the southeast coast of the United States was sponsored largely by the Army Research Office, Division of Terrestrial Sciences, through contract no. DAAG 29-76-6-0111 to the University of South Carolina.

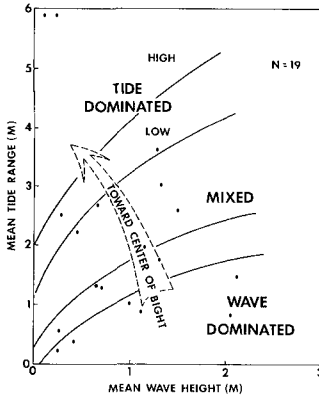


Fig. 18. Inlet morphologic types as functions of mean annual wave height and tide range. 19 barrier island coasts in North America and Europe were used to establish the boundaries.

REFERENCES

- Barthel, V., 1976, Stability of tidal channels dependent on river improvement: Proc., 15th Coastal Engineering Conference, ASCE, Honolulu, Hawaii, p. 1775-1789.
- Bruun, P., 1966, Tidal inlets and littoral drift: Universitetsforlaget, Trondheim, Norway, 193 p.
- Coastal Engineering Research Center, 1973, Shore Protection Manual, 3 vols.: U.S. Government Printing Office, Washington, D.C.
- Defant, A., 1958, Ebb and flow: University of Michigan Press, Ann Arbor, Mich. 121 p.
- Deutschen Hydrographischen Institut, 1978, Gezeitentafeln.
- Finley, R.J., 1976, Hydraulics and dynamics of North Inlet, South Carolina, 1974-75: General Investigation of Tidal Inlets, U.S. Army, Coastal Engineering Research Center, Ft. Belvoir, Va., report no. 10, 188 p.
- FitzGerald, D.M., Hubbard, D.K., and Nummedal, D., 1978, Shoreline changes associated with tidal inlets along the South Carolina coast: Proc., Coastal Zone '78, ASCE San Francisco, p. 1973-1994.

- FitzGerald, D.M., Nummedal, D., and Kana, J.W., 1976, Sand circulation pattern at Price Inlet, South Carolina: Proc. 15th Coastal Engineering Conference, ASCE, Honolulu, Hawaii, p. 1868-1880.
- Hayes, M.O., 1975, Morphology of sand accumulation in estuaries: an introduction to the symposium: in Cronin, L.E., (ed.), Proceedings of the 2nd International Estuarine Research Federation Conf., Myrtle Beach, S.C., p. 3-22.
- Hayes, M.O., 1979, Barrier island morphology as a function of tidal and wave regime: Proc. Annual Mtg. North East GSA, 1978 (in press).
- Hayes, M.O., Owens, E.H., Hubbard, D.K., and Abele, R.W., 1973, The investigation of form and processes in the coastal zone: in Coastal Geomorphology, Coats, D.R. (ed.), State Univ. of N.Y., Binghamton.
- Hayes, M.O., and Kana, T.W., (eds.) 1976, Terrigenous clastic depositional environments: Tech. Rept. CRD-11, Coastal Res. Div., Dept. of Geology, University of South Carolina.
- Hubbard, D.K., 1977, Variations in tidal inlet processes and morphology in the Georgia embayment: Tech. Rept. CRD-14, Coastal Res. Div., Dept. of Geology, University of South Carolina.
- Hubbard, D.K., Barwis, J.H., Nummedal, D., 1977, Sediment transport in four South Carolina inlets: Proc. Coastal Sediments '77, ASCE, Charleston, S.C., p. 582-601.
- Luck, G., 1975, Der Einfluss der Schutzwerke der ostfriesischen Inseln auf die morphologischen Vorgänge im Bereich der Seegaten und ihrer Einzugsgebiete: Dissertation, Mitteilungen des Leichtweiss-Institutes für Wasserbau der Technischen Universität Braunschweig, Heft 47.
- Luck, G., 1976, Inlet changes of the east Friesian islands: Proc. 15th Coastal Engineering Conference, ASCE, Honolulu, Hawaii, p. 1938-1957.
- National Oceanic and Atmospheric Administration, 1978, Tide tables, east coast of North and South America.

- Nummedal, D., and Humphries, S.M., 1978, Hydraulics and dynamics of North Inlet, South Carolina, 1975-76: General Investigation of Tidal Inlets, report no. 16, U.S. Army, Coastal Engineering Research Center.
- Nummedal, D., Oertel, F.G., Hubbard, D.K., and Hine, A.C., 1977, Tidal inlet variability - Cape Hatteras to Cape Canaveral: Proc. Coastal Sediments '77, ASCE, Charleston, S.C., p. 543-562.
- Nummedal, D. and Stephen, M.F., 1978, Wave climate and littoral sediment transport, northeast Gulf of Alaska: J. Sed. Pet., v. 48, p. 359-371.
- Oertel, G.F., 1975, Ebb-tidal deltas of Georgia estuaries: in Cronin, L.E., (ed.), Proceedings of the 2nd International Estuarine Research Federation Conf., Myrtle Beach, S.C., 267-276.
- Redfield, A.C., 1958, The Influence of the Continental Shelf on the Tides of the Atlantic Coast of the United States: Journal of Marine Research, v. 17, 1958, p. 432-448.
- Silvester, R., 1974, Coastal Engineering, v. 2: Elsevier Publ., Amsterdam.
- U.S. Naval Weather Service Command, 1974, Summary of synoptic meteorological observation, Western European coastal marine areas: National Climatic Center, Ashville, N.C.
- U.S. Naval Weather Service Command: 1975, Summary of synoptic meteorological observations, North American coastal marine areas: National Climatic Center, Asheville, N.C.

CHAPTER 71

MORPHOLOGY OF COASTAL BARRIERS, DELAWARE, U.S.A.

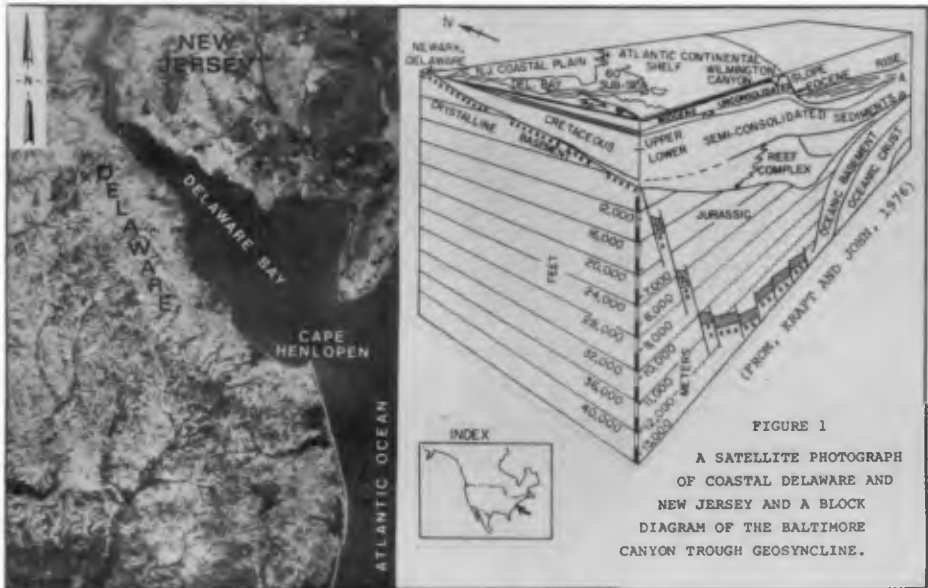
John C. Kraft, Chacko J. John, and Evelyn M. Maurmeyer
Dept. of Geology, University of Delaware
Newark, Delaware 19711

ABSTRACT

The Atlantic Coast of Delaware consists of four separate but continuous segments including (from north to south): (1) a northward-projecting spit complex (Cape Henlopen); (2) eroding Pleistocene headlands; (3) a linear coastal washover barrier; and (4) an area of migrating inlets with associated modern and relict ebb and flood tidal deltas. Coastal process studies show that continuing coastal erosion is accompanied by longshore transport of sand eroded from headlands, offshore transport to the nearshore marine area, and overwash processes transporting sand landward across the barrier. Studies of the adjacent nearshore marine area show that the barrier and its various geomorphic elements lay at the outer edge of the continental shelf approximately 12,000 years ago, and migrated landward and upward to the present position as the Holocene marine transgression continued. The sequence of coastal sediments of the barrier system consist of (landward to seaward) tidal marsh fringe, lagoonal muds and sands, barrier sands (including washover, dune, and beach deposits), and shallow nearshore sand and gravel. Drill-hole studies provide information on the subsurface configuration of the barrier from which the three-dimensional structure and stratigraphy of coastal sedimentary environmental lithosomes may be defined.

INTRODUCTION

The Atlantic coast of Delaware lies on the northwestern flank of the Baltimore Canyon Trough geosyncline of the Atlantic continental shelf of eastern North America (Figure 1). This geosyncline has been subsiding at various rates since Jurassic time (180-135 million years B.P.) and includes marine and non-marine sediments deposited along the eastern edge of the North American continent. There appears to be a geologic "hinge line" near the present Delaware shoreline indicated by different rates of subsidence northwest and southeast of this hinge line (Kraft & others, 1976; Kraft & John, 1976; Belknap & Kraft, 1977). The Atlantic coast of Delaware is presently undergoing a marine transgression causing landward and upward movement of the coastal barrier in time and space. This transgression is the result of a combination of eustatic sea level rise as a consequence of the melting of continental glaciers over the past 12,000-14,000 years, and of tectonic subsidence and compaction.



GЕOMORPHIC DIVISIONS AND COASTAL PROCESSES

The Atlantic coastal barrier of Delaware can be divided into four separate but continuous segments from north to south (Figure 2) as follows:

- (1) A spit-beach-dune complex;
- (2) Barrier against marsh;
- (3) Barrier against pre-Holocene highlands, and
- (4) Linear barrier-ebb and flood tidal delta-lagoon system. (Kraft, 1971; John, 1977).

Studies of the barrier and the nearshore marine area adjacent to the Atlantic continental shelf show that the barrier and its various geomorphic elements at one time lay farther to the east of the present position, towards the outer edge of the continental shelf. Since about 12,000 years before present, this barrier system has been migrating landward and upward as the marine transgression continues. Continuing coastal erosion is accompanied by northward longshore transport of sands eroding from pre-Holocene highlands which crop out along the barrier coastline. Sand and gravel are deposited at the spit, Cape Henlopen, and into deeper water (20 m) at the mouth of the large estuary, Delaware Bay, at the northern end of the barrier system. In addition, sand is trapped in the ebb and flood tidal deltas associated with this barrier system at the Indian River inlet (Figure 2). It is estimated that the net longshore transport to the

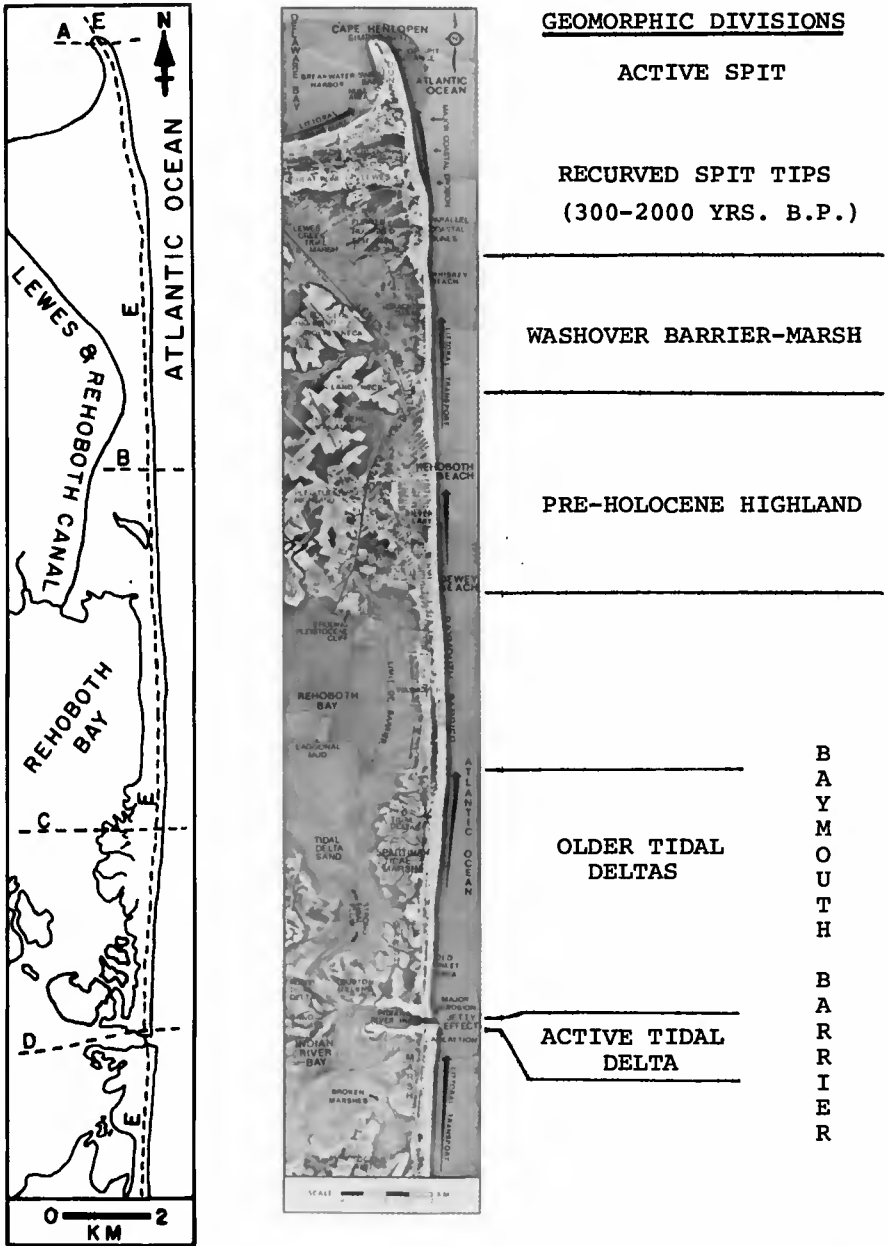


Figure 2. An index map and an aerial photo mosaic of Delaware's coastal zone indicating prominent geomorphic features. Lines of cross-section of figures in this paper are shown.

north along the Atlantic Coast ranges from 100,000-340,000 cubic meters per year (Turner, 1968).

In this area the average wave approach direction is from the east or southeast throughout the year. High intensity storms known as "northeasters" with a northeasterly wave component occur approximately once every two years in this region (Mather, 1965). Depending upon the position of the storm center as it passes the Atlantic Coast of Delaware, the longshore transport during storms may be to the north or south. In addition, large amounts of sand along the edge of the barrier may be transported offshore into the inner shelf region, or washed landward across the barrier into adjacent tidal marshes and coastal lagoons, forming washover fans. The major coastal processes in action are littoral transport of sand along the shoreface of the barrier accompanied by overwash of the barrier during times of high intensity

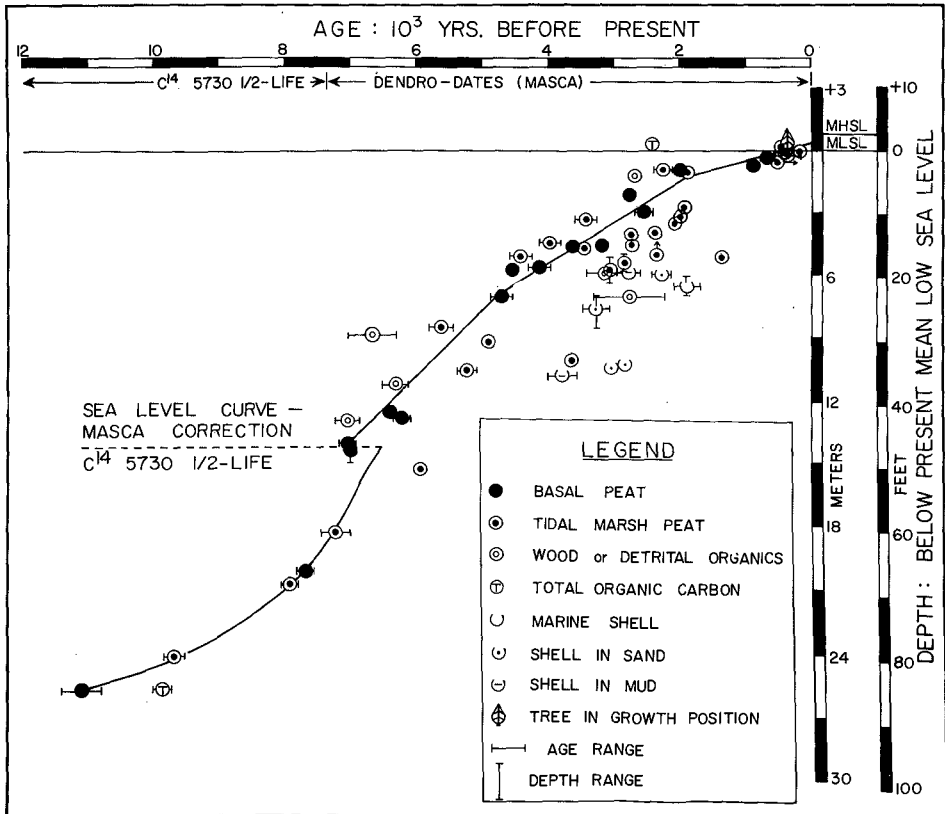


Figure 3. A local relative sea-level rise curve for coastal Delaware (Kraft, 1976).

storms. Transport of sand in the beach-berm and foreshore area can be by littoral transport in northerly or southerly direction, overwash across the barrier, transport by winds into dunes along the barrier, erosion and seaward transport and deposition on offshore bars, and transport through tidal inlets into flood and ebb tidal deltas.

Radiocarbon dates from basal salt marsh peats have enabled the construction of a local relative sea level curve for this area (Figure 3). This curve shows a continuing relative sea level rise in the Delaware Atlantic coastal region. During the Holocene Epoch (past 10,000 years) the local relative sea level shows different rates of change varying initially from 30 cm/century to the present 20 cm/century from approximately 5000 years before present (Kraft, 1976; Belknap and Kraft, 1977).

Tide gage records from the Delaware coastal area supported by tidal information from adjacent areas in New Jersey and Virginia, indicate a relative sea-level rise of approx. 33 cm/century based on an observation over the past 50 years (Figure 4).

Historical map records from various sources including the U. S. Coast and Geodetic Survey, U. S. Army Corps of Engineers, and National Ocean Survey may be used to determine average annual rates of shoreline change (Figure 5). These maps show persistent landward migration of the barrier system as a whole. Erosion rates varied from 0.4 to 3.1 meters per year over the time interval from 1765 to 1972. The only exceptions to these pervasive rates of landward erosion of the coast are those caused by construction of groins and jetties for stabilizing the coastline. However, even in the areas of groin fields net landward migration of the shoreline is occurring.

GEOLOGY

Figure 6 is a schematic representation of coastal processes in action modifying the coastline and the coastal environments undergoing transgression. Surface coastal environments, proceeding from land to sea, include pre-Holocene highlands, a tidal-marsh fringe, lagoonal muds and sands, back-barrier marshes, the Atlantic washover barrier including dunes, and the nearshore marine sands and gravels. Barrier sands tend to fill in the seaward side of the lagoon while tidal marsh sediments form at the leading edge of the Holocene transgression on the landward side of the lagoon. The beach-berm area is one of continual erosion and deposition with infrequent large washovers caused by hurricanes or "northeasters". Drill core studies of the subsurface stratigraphic units that have resulted from the landward Holocene

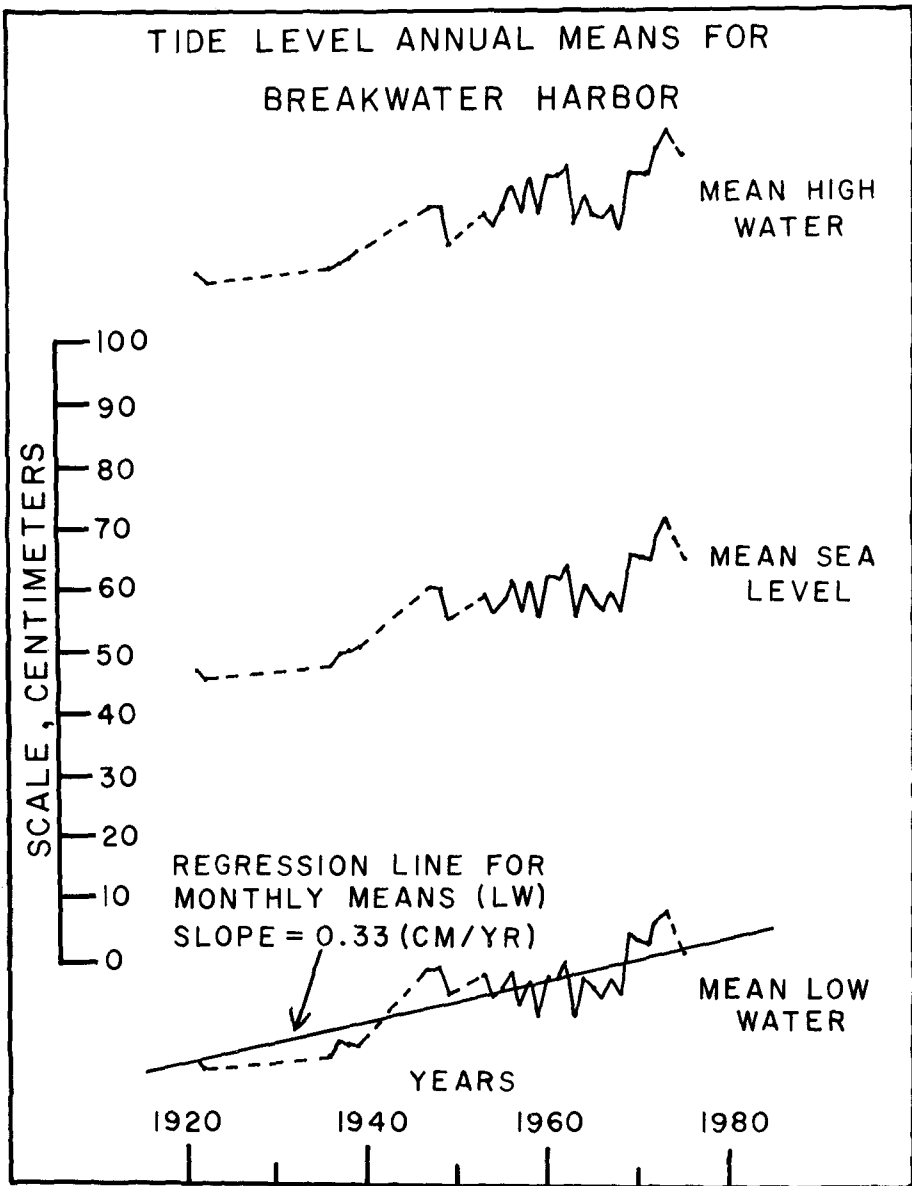


Figure 4. Tidal gage records from Breakwater Harbor at Lewes, Delaware showing relative sea-level rise during the 20th century (modified from Hicks and Crosby, 1974, and Demarest, 1978).

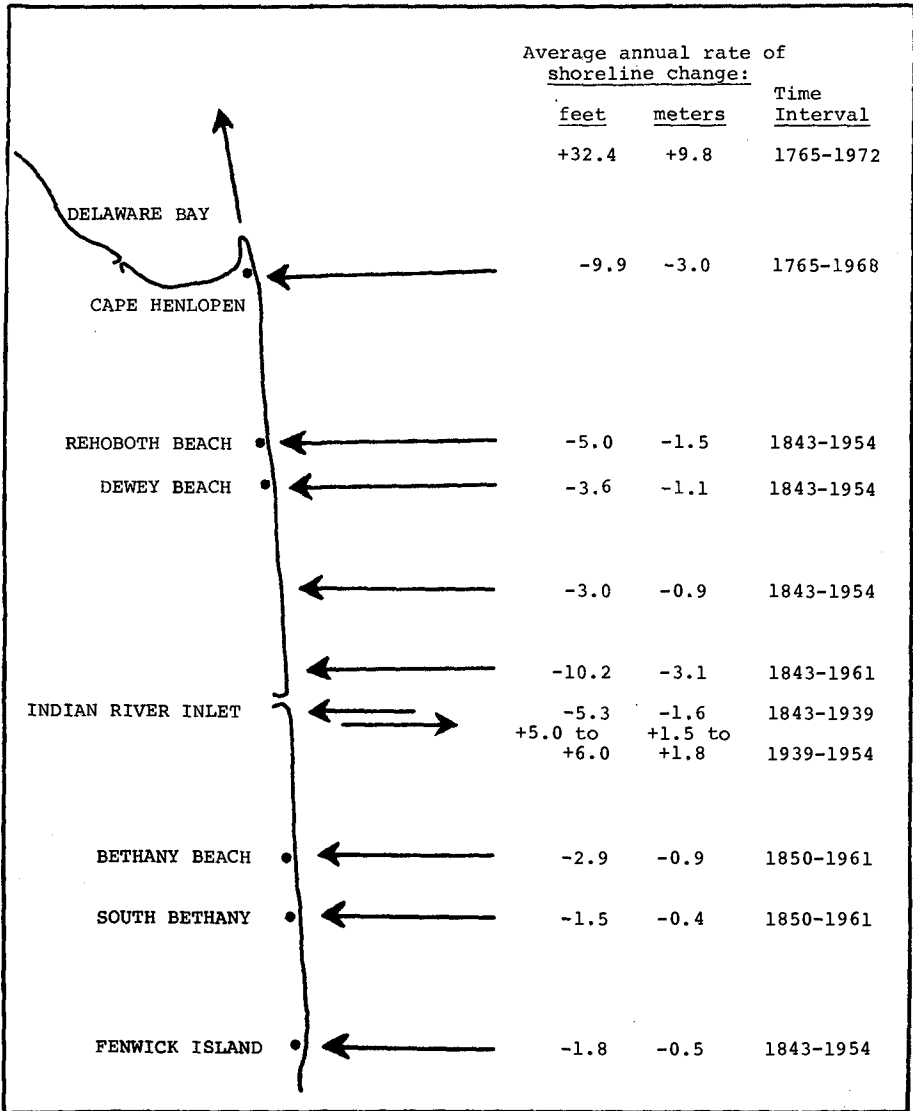


Figure 5. Average annual rate of shoreline changes for the Atlantic coast of Delaware (compiled from Moody, 1964 and U. S. Army Corps of Engineers, 1968).

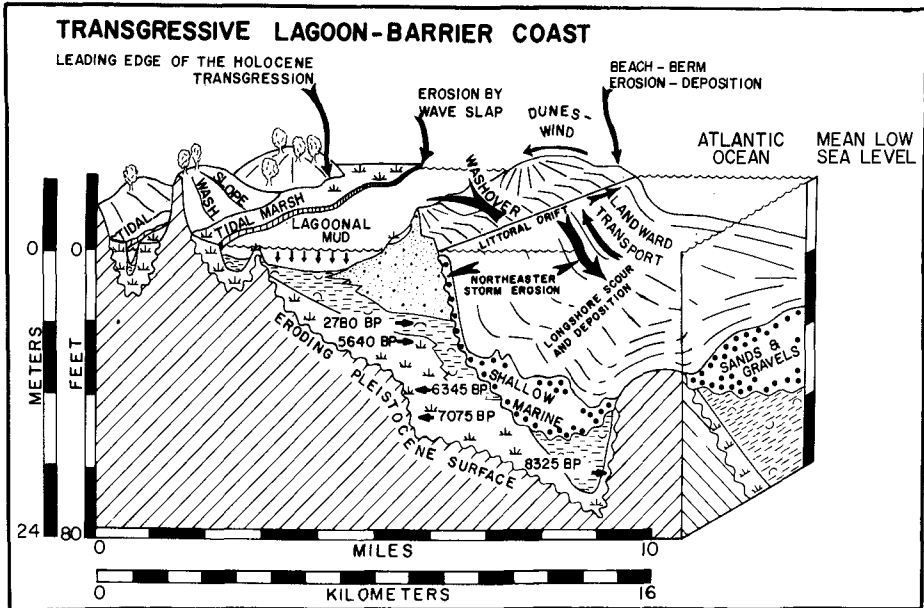


Figure 6. A schematic block diagram illustrating coastal sedimentary facies of the Delaware coastal zone (Kraft and John, 1976).

transgression of the coastal zone indicate that the vertical stratigraphic sequences of sediments seen in cores are equivalent to the lateral surficial sedimentary lithosomes undergoing land transgression (Figure 6). Essentially, this is an excellent illustration of Johannes Walther's Law of Correlation of Sedimentary Facies. In the vertical sequence, barrier sands overlie lagoonal muds and sands overlying a sequence of marsh fringe muds which unconformably overly the pre-Holocene sediments undergoing transgression.

The subsurface structure of this coastal barrier has been clearly delineated with the aid of a large number of drill cores taken along the length of the barrier, in the lagoon, and in the nearshore marine area (Figures 7 and 8). Cross sections of the four geomorphic variations of Delaware's Atlantic coastal barrier, described earlier in this paper, are shown in Figure 7. The Cape Henlopen spit (Fig. 7-A) is advancing rapidly (about 10 m/year averaged over the past 150 years) in a northwest direction into deep waters (20 m) at the junction of Delaware Bay and the Atlantic Ocean, as a result of deposition of sediment moving by littoral transport from the south. Erosion of the coastal barrier and pre-Holocene highlands such as at Rehoboth Beach

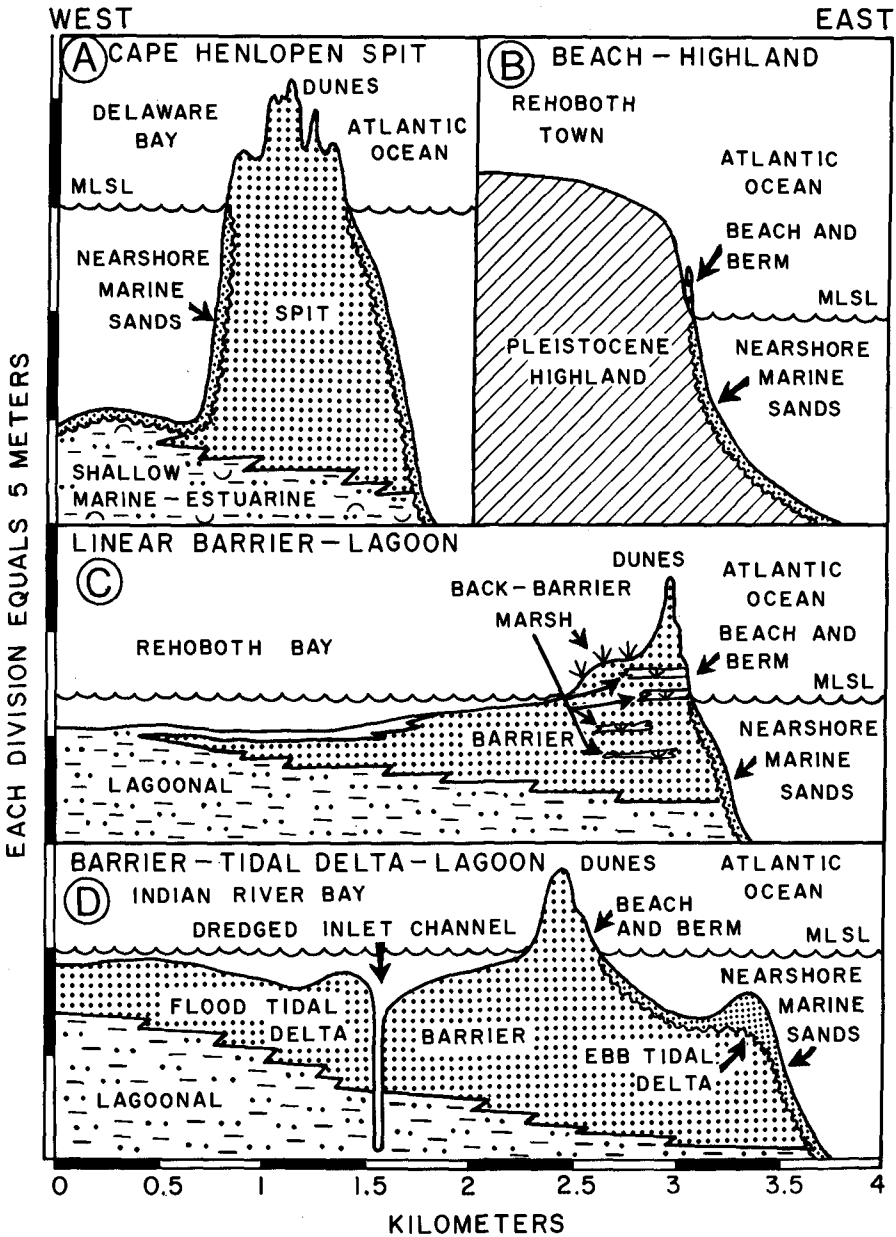


Figure 7. Schematic cross-sections of geomorphic variants of Delaware's Atlantic coastal zone. See Figure 2 for lines of cross-section (modified from John, 1977).

provide sediment to the littoral transport system. Erosion of the Atlantic coast of Cape Henlopen has been relatively constant, averaging approximately 3 m/yr. over the past two centuries (Moody, 1964; U. S. Army Corps of Engineers, 1968). Rates of advance of the spit tip, however, increased steadily from 5 m/yr (in the 18th century) to 30 m/yr (at present) (Maurmeyer, 1974). At present, the Cape Henlopen spit is in the form of a simple linear spit with narrow recurves at its tip and is tending to arc from the north and west around a breakwater built early in the 19th century. Formerly, this spit had the form of a cusped foreland and recurved spit over the past 300 to 2,000 years (Kraft and others, 1978). Ebb tide currents winnow out sand from the spit tip and deposit it on an offshore shoal (Hen and Chickens Shoal) lying to the east and extending southeast of the spit tip into the Atlantic Ocean. The thickness of the spit sands and gravels is 18 m and they overlie shallow marine-estuarine sediments.

Pre-Holocene highlands such as at Rehoboth Beach (Figure 7-B) are encountered at various positions in the landward marine transgression across a pre-Holocene drainage system which includes the large drowned river estuary, Delaware Bay, of the ancient Delaware River of more than 14,000 years before present. The barrier here is in the form of a narrow beach with the beach sediments directly overlying pre-Holocene sediments. The beach in this case is so narrow that it could be completely destroyed by large waves resulting from high intensity storms. However, after such storms abate the thin beach is built back again but this time a little farther landward than its position before the storm.

The internal structure of the linear barrier (Figure 7-C) shows a number of back-barrier marshes in the internal composition of the barrier. These sediments represent the back-barrier marsh positions during the past 3000 years, when the barrier was farther east (seaward) of its present position. As shown in Figure 7-C the barrier sediments extend laterally to about 2.5 km into the Rehoboth Bay lagoon and interfinger with the lagoonal muds and sands and overlie them. In this section of the Atlantic coastal barrier the thickness of the barrier including the dunes and the back-barrier marsh sequences within the barrier is about 10 m.

In some areas along the Atlantic coastal barrier, tidal inlets cut across the barrier and form ebb and flood tidal deltas. Tidal inlets are known to have migrated along the barrier in historic times. Figure 7-D shows the barrier associated with the Indian River inlet which is now stabilized by a rock jetty. The barrier sands in inlet areas, including dunes, are 12 m thick and thin out laterally where they interfinger with the tidal delta and lagoonal sediments. In this case the sub-lagoonal barrier and flood tidal delta extend to about 4 km into the Indian River Bay lagoon (Figure 7-D). In all the four cases illustrated (Figure 7) the

barrier sands unconformably lie against nearshore marine sands on the ocean side.

The present transgression is overriding a pre-Holocene trellis-patterned drainage system incised up to 70 m below sea-level in the Delaware coastal area. As the Holocene transgression continued landward across the Atlantic continental shelf, accompanied by sea level rise, the trellis drainage system was inundated by tidal waters. This led to the highly irregular surface of inundation being filled with sediments of various coastal environments. Lagoonal and marsh sediments were deposited along the axes of the stream valleys. Subsurface studies in the Delaware estuary and in the area of Delaware's Atlantic coast suggest that tidal intrusion commenced approximately 12,000 years before present (Kraft and others, 1976).

A cross section parallel to the Atlantic coastal barrier of Delaware is shown in Figure 8. The nature of the tributary valleys incised in the pre-Holocene surface and the in-fill of lagoonal, salt marsh, and shallow marine-estuarine sediments can be seen in this cross section (Figure 8). It is apparent from this cross section (Figure 8) that the thickest sections of Holocene sediments are found infilling the ancestral stream valleys. Hence, in such areas, the chances of preservation of barrier sediments in the geologic record are much better than at other areas along the barrier.

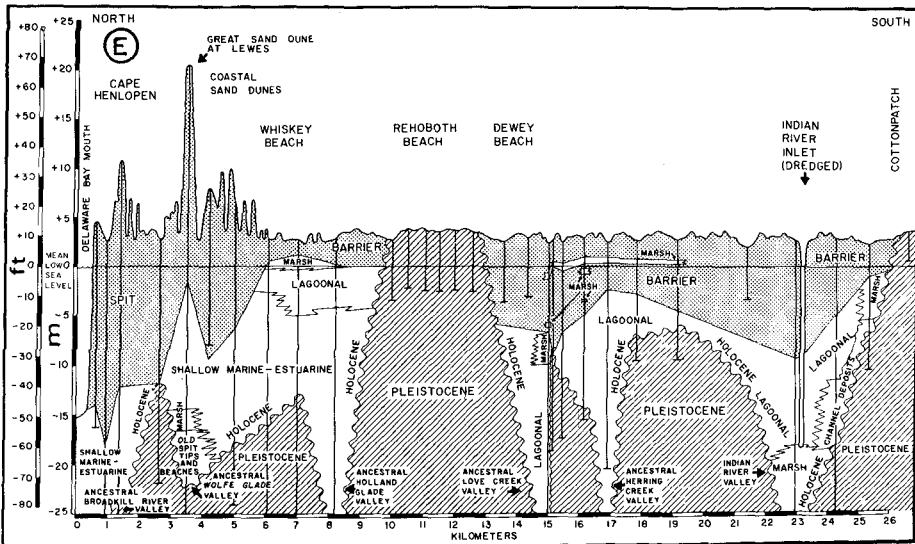


Figure 8. A longitudinal section of Delaware's coastal zone parallel to the shoreline (John, 1977). Holocene coastal sedimentary facies are shown relative to the incised pre-Holocene stream valley topography.

CONCLUSIONS

Based on analysis of the long-term stratigraphic record (past 10,000 years), historic rates of erosion and accretion, and present coastal processes, the nature of coastal change along the Delaware Atlantic Coast may be precisely defined. Thus it should be possible to make logical projections of change in the coastal environments in the short-term future. An understanding of the short- and long-term geological processes in the coastal zone should allow prediction of the impact of engineering structures on the nearshore marine and coastal areas, so that rational plans for the development of the coastal zone can be made.

REFERENCES

- Belknap, D. F. and J. C. Kraft, 1977, "Holocene relative sea-level changes and coastal stratigraphic units on the northwest flank of the Baltimore Canyon trough geosyncline", Jour. Sed. Petrology, v. 47, p. 610-629.
- Demarest, J. M., 1978, "The shoaling of Breakwater Harbor-Cape Henlopen area, Delaware Bay, 1842 to 1971", DEL-SG-1-78, College of Marine Studies, Univ. of Delaware, Newark, 169 p.
- Hicks, S. D., and J. E. Crosby, 1974, "Trends and variability of yearly mean sea level:" NOAA Tech. Memo. NOS-13, Rockville, Maryland, 14 p.
- John, C. J., 1977, "Internal sedimentary structures, vertical stratigraphic sequences, and grain-size parameter variations in a transgressive coastal barrier complex-The Atlantic Coast of Delaware", DEL-SG-10-77, College of Marine Studies, Univ. of Delaware, Newark, 287 p.
- Kraft, J. C., 1971, "Sedimentary facies patterns and geologic history of a Holocene marine transgression", Geol. Soc. Amer. Bull., v. 82, p. 2131-2158.
- Kraft, J. C., 1976, "Radiocarbon dates in the Delaware coastal zone (eastern Atlantic coast of North America)", DEL-SG-19-76, College of Marine Studies, Univ. of Delaware, Newark, 20 p.
- Kraft, J. C. and C. J. John, 1976, "The geological structure of the shorelines of Delaware", DEL-SG-14-76, College of Marine Studies, Univ. of Delaware, Newark, 106 p.

- Kraft, J. C., E. A. Allen, D. F. Belknap, C. J. John and E. M. Maurmeyer, 1976, "Delaware's Changing Shoreline", Tech. Rept. No. 1, Delaware's Coastal Management Program, Delaware State Planning Office, Executive Dept., 319 p.
- Kraft, J. C., E. A. Allen and E. M. Maurmeyer, 1978, "The geological and paleogeomorphological evolution of a spit system and its associated coastal environments: Cape Henlopen spit, Delaware;" Jour. Sed. Petrology, v. 48, p. 211-226.
- Mather, J. R., 1965, "Climatology of damaging storms" in Burton, I., R. W. Kates, J. R. Mather, and R. E. Sneed, eds., The Shores of Megalopolis: Coastal occupance and human adjustment to flood hazard: Pub. in Climatology, v. 18, no. 3, p. 525-549.
- Maurmeyer, E. M., 1974, "Analysis of short- and long-term elements of coastal change in a simple spit system: Cape Henlopen, Delaware", M.S. Thesis, Dept. of Geology, Univ. of Delaware, Newark, 150 p.
- Moody, D. W., 1964, "Coastal morphology and processes in relation to the development of submarine sand ridges off Bethany Beach, Delaware:" Ph.D. dissertation, The Johns Hopkins University, Baltimore, Maryland, 167 p.
- Turner, P. A., 1968, "Shoreline history, Atlantic Coast Delmarva Peninsula", (abs.) 1968 Ann. Mtg., Northeastern Section, Soc. Econ. Paleon. and Mineralogists, Washington, D.C.
- U. S. Army Corps of Engineers, 1968, "Delaware Coast, beach erosion control and hurricanes protection:" Senate Doc. 90, 90th Cong., 2nd Sess., Philadelphia, 110 p.

CHAPTER 72

A New Method for the Representation of Sedimentary Sequences in Coastal Regions

Hansjörg Streif*

1. Introduction

Coastal lowlands usually consist of a body of unconsolidated sediments of up to 30 m thickness which have been deposited under the influence of a rising sea level during the past 10,000 years. These lowlands increasingly are acquiring importance for industrial plants, harbour construction, pipelines, and for the exploration of mineral resources. Consequently a basis for planning is required which will permit an economic exploitation of the coastal zone.

Geological mapping at scale of 1 : 25 000, which has been going on in Germany for more than 100 years, is of fundamental importance for this. Especially the newest type of geologic maps - the sequence map - offers the possibility of classifying and representing (BARCKHAUSEN, PREUSS & STREIF 1977) the coastal deposits in a way that is well suited for technical and scientific purposes.

Its range of application covers tidal flat areas, marshes and coastal bogs, as they occur for example in the coastal zone of the southern North Sea. Combined with a documentation system of the field data and the techniques of automatic data processing this type of map offers new aspects which by far exceed the possibilities of conventional geological mapping.

*Hansjörg Streif, Niedersächsisches Landesamt für Bodenforschung, Stilleweg 2, D 3000 Hannover 51, Federal Republic of Germany.

2. The system of classification and representation

Conventional geological maps - so called surface maps - represent the geographical distribution of individual layers within 2 m of the surface. The sequence map in contrast offers the possibility of representing the spatial extension of complete sedimentary sequences - so called profile types (DE JONG & HAGEMANN 1960, HAGEMAN 1963) - in the body of coastal deposits. This gives the sequence map a three-dimensional character.

A hierarchic system of lithological classification has been developed, based on the vertical succession and the lateral interfingering of clastic sediments on the one hand and peat on the other hand. Three different hierarchic levels can be distinguished in the new system of classification (BARCKHAUSEN, PREUSS & STREIF 1977). Complexes (with 3 profile types), sequences (with 12 subordinate profile types), and facies units (with a variable number of special profile types).

This lithological system has to be linked with a chronostratigraphic system based on radiocarbon ages (BARCKHAUSEN, PREUSS & STREIF, 1978: Fig 4.). As the time interval represented by a specific sedimentary layer or peat horizon varies from place to place, the lithological classification system on the one hand and the chronostratigraphical system on the other hand, must be regarded as two independent methods of subdividing the Holocene. A clarification of the coastal development in terms of time and space, i.e. in a paleogeographic sense, can be done only with a combination of both systems.

2.3. Complexes

In the first level of the hierarchic system the following 3 lithological complexes and 3 profile types have been established (Fig. 1):

- a clastic complex (seaward region)
a body of clastic sediments without intercalated peat layers.

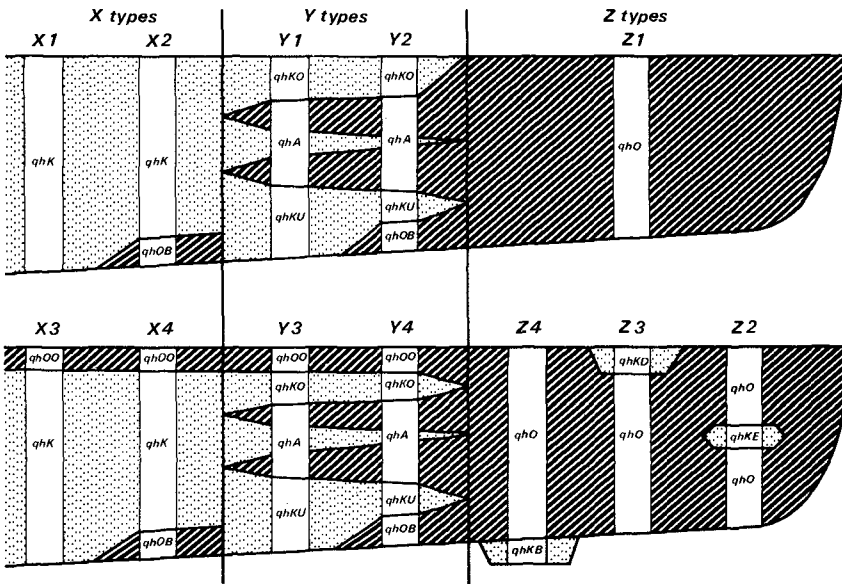


Fig. 1: Schematic cross section through the coastal deposits with the labels for the principal profile types (X_1 , X_2 , X_3 , X_4 , Y_1 , ... etc. Z_4). The sequences are labeled with stratigraphic symbols according to BARCKHAUSEN, LOOK, VINKEN & VOSS (1975). qhK = clastic sequence, qhOB = organic basal sequence, qhOD = organic cover sequence, qhKU = lower clastic sequence, qhA = splitting up sequence, qhKO = upper clastic sequence, qhO = organic sequence, qhKB = clastic basal sequence, qhKE = clastic interbedded sequence, and qhKO = clastic cover sequence.

- Peat may occur, however at the base or on top of the complex. Sediments are dominant in this complex,
- an interfingering complex (transition zone)
a body of coastal deposits in which clastic sediments are intercalated by peat layers. Sedimentary and sedentary deposits are occurring in this complex mutually,
 - a peat complex (back swamp region)
a body of peat and limnic ooze. Thin layers of clastic sediments can either be intercalated in the peat complex or can occur as a single layer at the base or on top of the peat complex. Sedentary organic deposits are dominant in this complex.

These complexes can be represented in sequence maps in the form of principal profile types. Thereby, the clastic complex is labeled as X-profile type, the interfingering complex as Y-type, and the peat complex as Z-type (Fig. 1). Usually the use of the principal profile type without subdivisions is limited to maps at a small scale. A more detailed subdivision of the coastal Holocene deposits can be achieved on the second level of the hierarchic system.

2.2 Sequences

Sequences are units of lithological classification which rank in the middle of the hierarchy. They are subdivisions of the above mentioned complexes and consist of one or more facies units. Some interrelations-hips between organic and clastic deposits can be deduced from the vertical succession and the lateral interfingering of the sequences. The variety of possible interrelations is represented in Fig. 1 in form of a schematic section. The vertical lines indicate the boundaries between the above mentioned complexes. The sequences, which are defined in the following, are looked upon as stratigraphical elements and therefore are labeled with stratigraphic symbols (Fig. 2) according to "Symbolschlüssel Geologie" (Symbol Key Geology, BARCKHAUSEN, LOOK, VINKEN & VOSS 1975).

Nr. des TK 2608		Name	Aufschrift	Nummer	LK-Zahl	Erläuterer		Koordinaten												Höhe über NN (m)		Spalten 1-39 allgemeiner Teil		
1 2 3 4 5 6 7 8 9 10 11 12 13 14 15 16 17 18 19 20 21 22 23 24 25 26 27 28 29 30 31 32 33 34 35 36 37 38 39				2116	0	GEIK	25676605917200	-	0.175												0.175			
Beauftragter		Jahr	W	AA	M	V	Datum/Weite z.B. Fachbereiche												Spalten 40-80 Fachteil					
Baric.khlausen		97	3	1	S	R																		
Tiefe bis [m] bzw. Mächtigkeit		Stratigraphie		Petrog./Gehalte/Farben/Formelemente und Zusatzzeichen/ Proben [Entnahmbereich, Probenmaterial, Untersuchungsmethode, Ergebnis]												Persönliche Notizen [nicht zur ADV] Typ, Monat								
0.50		qhK0		U-fS;k/bo,u																				
1.00				U-fS;t,efle2,k/br,wa/gr																				
1.50				fS;u,t1,wg,efle,k4/wa/gr,rif																				
1.90				U;fs5,wg,t,k/wa/blgr																				
3.80				U;t,fs,lag(wg),lag(T,u),k/wa /blgr-dgr																				
8.75		qhK0		U;t,fs,lag(fS,u),ss,k/br,wa/ gr/XE																				
8.95		qhA		F;pr3,pf																				
9.05				Hc;F,pr3																				
9.15		qhA		Hp;f																				
9.25		qhKU		T;ssmm,pfh,kf/la/dgr																				
9.80				T;pr2,pf																				
10.80				T;pr1,hw,pf,kf/la/bngr																				
11.30				T;pr1,pf4,hwa/la/gr																				
12.30				T;u,hlw1,k2/br/gr																				
12.46		qhKU		T-F/la,l/grbn																				
12.70		qhOB		F;sub(Hl)																				
12.91		qhOB		Hl;Hle////,(Y2)																				
12.95		qp,qh		fS;h2//dgr																				

Fig. 2 Example of a data form for field data capture.

The necessary characteristics of the bore hole are given in a fixed format. The strata description is recorded in a free format, and its various elements (depth, stratigraphy, petrography etc.) are separated from each other by a slash. The symbols of the sequences (qhK0, qhA, qhKU, and qhOB) are given in the column stratigraphy, the profile type (Y2) is given in the lowermost layer of coastal Holocene.

- clastic sequence (qhK): clastic sedimentary succession without intercalation of peat layers. Soil horizons and layers in which rootlets of phragmites are abundant are regarded as a part of the clastic sequence;
- organic basal sequence (qhOB): succession of peat and limnic ooze or organic soil horizons at the base of clastic Holocene deposits;
- organic cover sequence (qhOD): succession of peat or limnic ooze which occurs at the present surface and which is underlain by clastic Holocene sediments.

The organic basal sequence and the organic cover sequence can occur in the clastic complex as well as in the interfingering complex, but which may also be absent. The following elements are found only in the interfingering complex and are characteristic of it:

- lower clastic sequence (qhKU): clastic sedimentary unit at least 5 cm thick, which underlies the lowermost intercalated peat layer and may be underlain by an organic basal sequence;
- splitting up sequence (qhA) sedimentary succession between the bottom of the lowermost intercalated peat layer and the top of the uppermost one. Thus, the splitting up sequence consists of peat layers (in a special case only layer) as well as clastic sediments which lie between the intercalated peat layers;
- upper clastic sequence (qhK0) clastic sedimentary unit at least 5 cm thick which overlies the uppermost intercalated peat and may be overlain by an organic cover sequence.

The following sequences are found in the peat complex and are characteristic of it:

- organic sequence (qh0) succession of peat and limnic ooze with at most one interbedded layer of clastic sediments more 5 cm thick;

- clastic basal sequence (qhKB) clastic sedimentary unit which occurs in the basal part of the coastal Holocene deposits and which is covered by an organic sequence. The thickness of the basal clastic sequence is less than of the covering organic sequence;
- clastic interbedded sequence (qhKE) unit of clastic sediments which is interbedded in the organic sequence unrelated to an upper or lower clastic sequence as defined above or to clastic units of a splitting up sequence. This clastic interbedded sequence may not exceed 50 % of the total thickness of the organic sequence. The qhKE may consist of one individual layer and/or of several thin layers, less than 5 cm thick;
- clastic cover sequence (qhKD) clastic sedimentary unit which occurs at the present surface and which is underlain by the organic sequence. The thickness of the clastic cover sequence must be less than that of the underlying organic sequence.

There are 12 possible arrangements of these sequences as defined above. These possibilities define the 12 subordinate profile types and are labeled (Fig. 2) as X1, X2, X3, X4, Y1, ..., etc. (BARCKHAUSEN, PREUSS & STREIF 1977).

Any bore hole in the coastal zone can be immediately ascribed to one of the 3 main profile types and one of the 12 subordinate profile types in the course of the field data capture or during an evaluation of archive material (Fig. 2). If a bore hole does not penetrate the Holocene deposits, hence incomplete profile types are following. This is indicated by adding an "u" to the label. The following incomplete subordinate types are possible: X1u, X3u, Y1u, Y3u, Z1u, Z2u, and Z3u.

2.3. Facies units

A more detailed subdivision of the sedimentary units can be achieved within the lowest hierarchic level of the system. The above-defined sequences often consist of several facies units; special profile types must then be defined for these cases. In contrast to the first and second levels, with their well-defined elements and their established number of profile types, the lowest level of the system is a variable one.

The facies units are variable in number and in range, so that petrographic, genetic, structural, and other criteria can be taken into account and represented in an unlimited number of special profile types. Thus, the facies units and the special profile types have to be selected or defined individually with respect to the specific objectives and the prevailing local conditions. Besides geological findings, special technical or economic factors can be evaluated and represented in these maps. For instance, the spatial extension of:

- sediments susceptible to compaction and therefore unsuitable for building foundation;
- deposits of special consistency, for which specific excavating and dredging methods are necessary;
- sedimentary units that contain raw material of economic interest such as sand, gravel or mineral deposits.

These examples of possible utilisation of this classification the system might be greatly enlarged. Consequently the lithological subdivision of the coastal deposits combined with the representation of profile types offers totally new aspects which by far exceed the possibility of conventional mapping.

3. Practical application

During the course of field data capture it is nearly impossible to foresee all the aspects which might be of technical or scientific interest. However, most of the information necessary for any application can easily be recovered from the pool of geological

basic data by a systematic evaluation. A selection can be made from an immense amount of basic data within a very short time by computer methods.

A close link between the above-mentioned classification system for coastal deposits on the one hand and data bank management systems on the other hand has been achieved in the following way: All basic data are collected on special data forms (Fig.2) during the field data capture. All information, such as depth, stratigraphy, petrography, genesis, colour and additional remarks, is recorded according to a symbol key (BARCKHAUSEN, LOOK, VINKEN & VOSS1975) on this data form. These strata descriptions are then stored on punch cards magnetic tape or disc. All necessary characteristics of the bore hole (such as bore hole number, longitude and latitude, elevation, etc.) are recorded in "fixed format"; description (depth, stratigraphy, petrography, genesis, colour, additional remarks, and samples) are recorded in a "free format". For instance: for the mapping of sheet Emden West, which is situated by the Ems River estuary, about 650 bore holes have been sunk. Altogether about 10,000 m of sedimentary cores have been described and about 25,000 to 30,000 individual layers have been distinguished and sedimentologically characterized.

The documentaion and retrieval system DASCH has been developed to handle such an immense pool of different data (MUNDRY 1975). The strata descriptions which were recorded and stored in a free format can be converted into a fixed format in so-called documentation lists. The various parts of the description such as depth, stratigraphy, petrography etc. are arranged in these lists in defined fields. The most important part of the DASCH system, however, is retrieval. A selection of specific data can be retrieved from the mass of basic data. This is done by a sequential search of all of the basic data. Those basic data that correspond to a retrieval query can then be printed out or stored on magnetic tape or disc for further processing. For practical use it is very important that the structure of the

query is the same as the structure of the strata description. Thus, the DASCH system can be easily used by field geologists or technicians who are directly involved with the specific problems. Other data processing programs have been developed, especially for the production of geologic maps, profile and cross sections (MUNDRY 1975, BARCKHAUSEN 1973). At present we are able to produce starting the following constructions from the basic data:

- individual profiles, cross sections and profile maps;
- isoline maps (contourlines, isopach plans and geological boundaries constructions);
- signature maps, bore hole symbol maps;
- sequence maps or profile type maps.

These all have two objectives. One is the graphic representation for a general overview. Second, they serve as a base for specialized evaluations, whereby much troublesome and lengthy manual work is avoided.

The first sheet of this new type of geological map, the sequence map sheet Emden West 1 : 25,000, has been published (BARCKHAUSEN & STREIF 1978). Two further sheets, Wilhelmshaven and Emden are in preparation. The advantages of the new map are quite obvious. The system is more flexible and its utilization is easily manageable. Furthermore it offers the possibility of representing the whole sequence of sedimentary deposits in the coastal zone. Consequently, this new type of maps covers scientific and practical requirements much better than conventional geological maps and is of better use for planning purposes. Combined with data bank management systems, the sequence map offers totally new aspects for geological mapping in coastal areas. This concerns the production of the maps as well as their practical evaluation. As the system of the sequence map can be applied to nearly all coastal lowlands, it may be regarded as an important part of the technical and scientific know how of coastal engineering.

4. References

BARCKHAUSEN, J. (1973):

Automatisch gewonnene Informationen aus geologischen Schichtenverzeichnissen und ihre Weiterverarbeitung. - Geol. Jb., A7 : 35 - 50, 4 Abb., 3 Tab., 1 Taf.; Hannover.

BARCKHAUSEN, J., LOOK, E.R., VINKEN, R. & VOSS, H.H. (1975):

Symbolschlüssel Geologie, Symbole für die Dokumentaion und Automatische Datenverarbeitung - ADV - Geologischer Feld- und Aufschlußdaten. Niedersächs. Landesamt f. Bodenforschung und Bundesanstalt f. Geowiss. und Rohstoffe, 135 S.; Hannover.

BARCKHAUSEN, J. & PREUSS, H. & STREIF, H. (1977):

Ein lithologisches Ordnungsprinzip für das Küstenholozän und seine Darstellung in Form von Profiltypen. - Geol. Jb., A 44 : 45-77, 7 Abb., 3 Tab.; Hannover.

BARCKHAUSEN, J. & STREIF, H. (1978):

Erl. geol. Kt. Niedersachsen 1 : 25.000, Bl. 2608 Emden West : 80 S., 5 Abb., 1 Tab., 3 Kt.; Hannover.

DE JONG, J.D. & HAGEMAN, B.P. (1960):

De legenda voor de holocene Afzettingen op de nieuwe geologische Kaart van Nederland, schaal 1 : 50.000. - Geologie en Mijnbouw , 39 : 644-653; Den Haag / 's - Gravenhage.

HAGEMAN, B.P. (1963):

De profiltype - legenda van de nieuwe geologische kaart voor het zeelei - en rivier - kleigebied. - Tydschrift van het Nederlands Aardrykskundig Genootschap, 80 : 217-229; Leiden.

MUNDRY, E. (1970):

Zur automatischen Herstellung von Isolinenplänen. - Geol. Jb. 98 : 77-93, 7 Abb; Hannover.

MUNDRY, E. (1973):

Ein Dokumentations- und Abfrageprogramm für Schichtenverzeichnisse (DASCH). - Geol. JB., A7 : 25 - 33, 1 Tab.; Hannover.

CHAPTER 73

COASTAL PROCESSES AT OREGON INLET, NORTH CAROLINA

James T. Jarrett*, M.ASCE

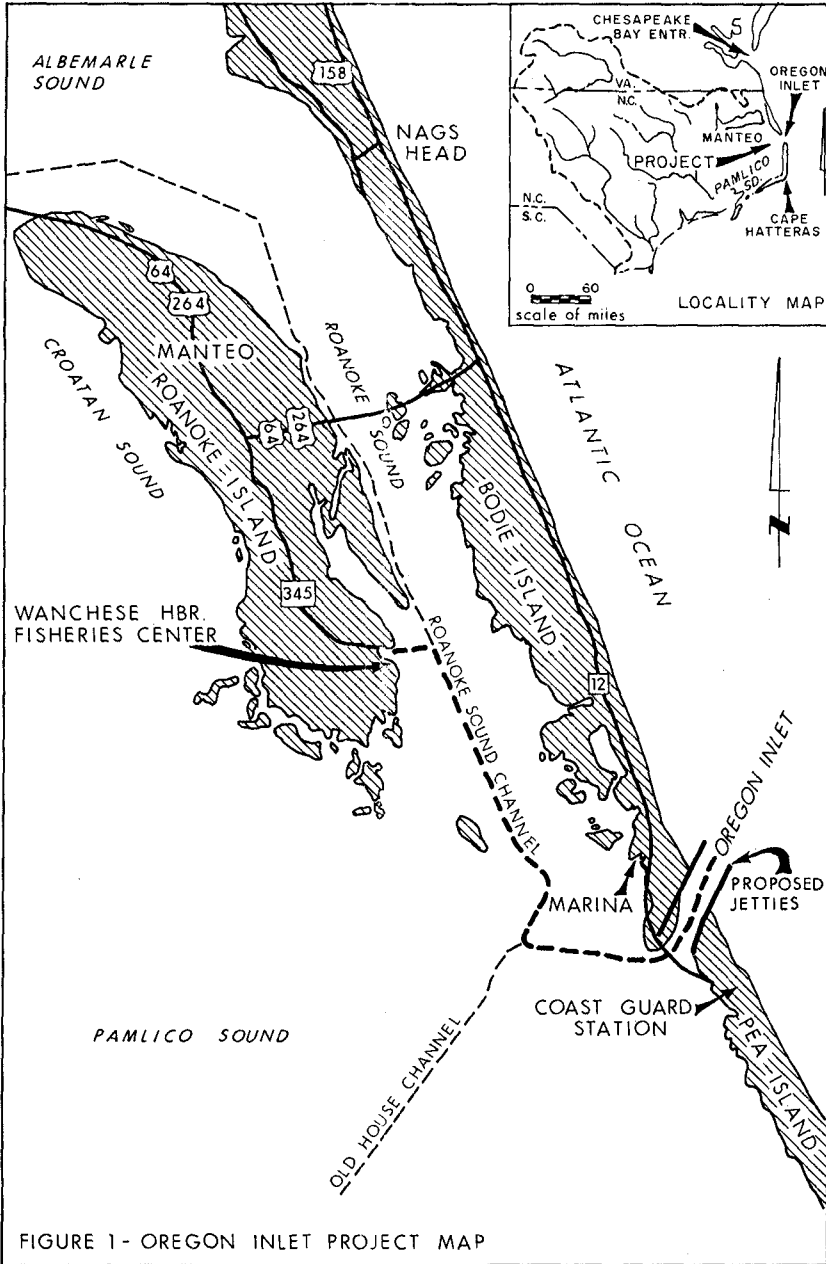
INTRODUCTION

Coastal processes in the vicinity of Oregon Inlet, North Carolina were studied in connection with the design of a dual jetty system for that inlet. Oregon Inlet is the northernmost breach through the "Outer Banks" of North Carolina and is situated approximately 40 miles (64 km) north of Cape Hatteras and 90 miles (145 km) south of the ocean entrance to Chesapeake Bay, see Fig. 1. The improvements planned for this inlet are part of an overall plan of development directed at enhancing the fisheries industry of North Carolina through the provision of a modern fisheries center at the village of Wanchese, located on Roanoke Island, see Fig. 1. The general layout of the proposed jetty system is shown on Fig. 2. Certain aspects of this design will be referred to later in this paper.

In addition to their structural and functional aspects, a major part of the design of the jetties concerns the structure-shore interaction and means whereby adverse shore processes will be prevented in operating the project. Obviously, the construction of jetties or any other type of littoral barrier at an inlet would disrupt the normal movement of and processes associated with longshore sediment transport. Therefore, artificial means of moving littoral materials around a stabilized inlet must be employed to assure that the adjacent beaches are maintained in at least the same state existing prior to any navigation related improvements. The need for a reliable sand bypassing method at Oregon Inlet is accentuated by the fact that the inlet is bounded on the north by the Cape Hatteras National Seashore and on the south by the Pea Island Wildlife Refuge, both of which are Federally owned beach areas managed for the purpose of preserving the natural quality of the Outer Banks environment.

The design of a sand bypassing system must be based on a knowledge of the existing shore and inlet processes, particularly as they relate to the rate and directional distribution of longshore sediment transport. When the existing conditions are known, it is possible to estimate the sediment transport rates with the structures in place and, thus, predict the amount and direction in which material will have to be bypassed. This paper describes the approach taken to evaluate the existing and future longshore sediment transport in the vicinity of Oregon Inlet and briefly discusses the proposed bypassing system for the stabilized inlet.

*Project Engineer, Coastal Engineering Studies Section, U.S. Army Engineer District, Wilmington, N.C.



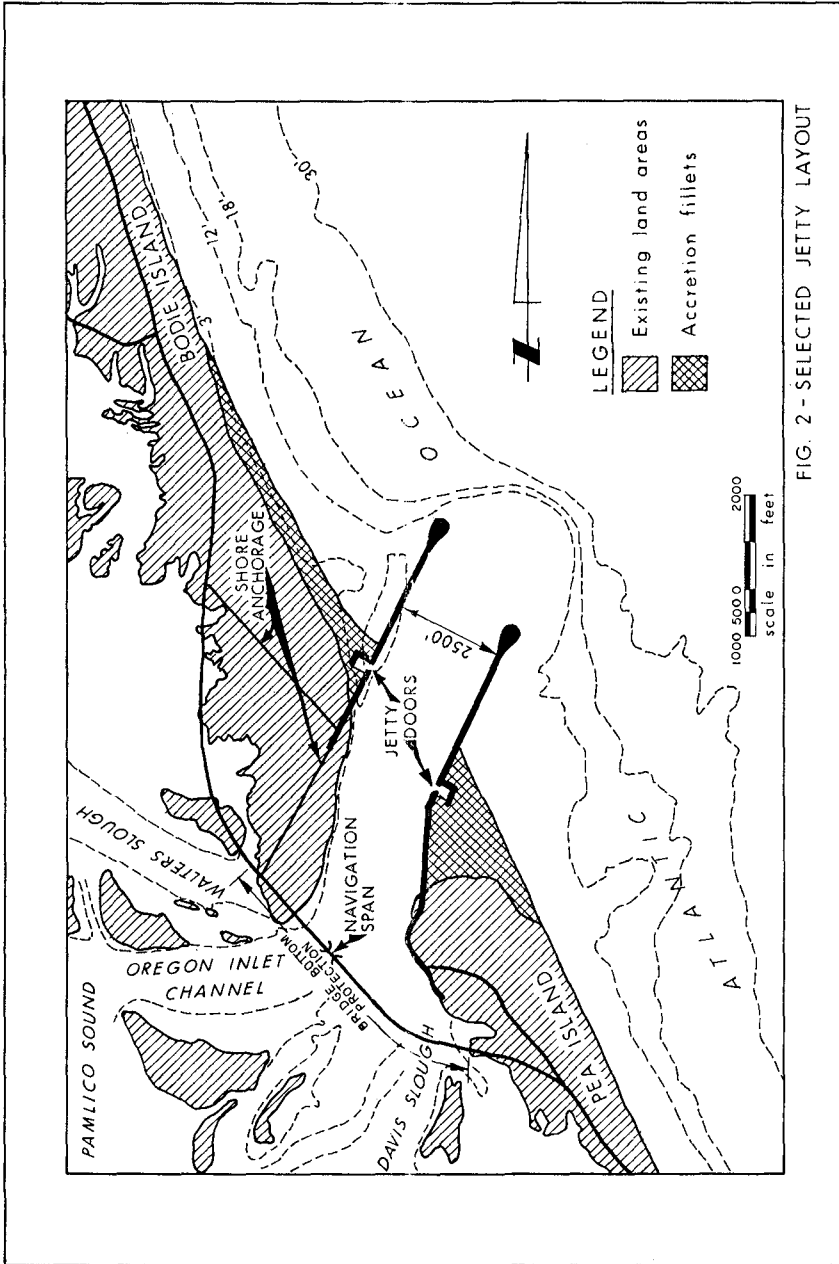


FIG. 2 - SELECTED JETTY LAYOUT

EXISTING LONGSHORE SEDIMENT TRANSPORT RATES

The estimate of the existing rate and directional distribution of longshore sediment transport in the vicinity of Oregon Inlet was accomplished through a sediment budget analysis which involved (1) an estimate of volumetric changes from the beaches and in the inlet for a selected time period, (2) wave refraction analysis to determine the variation of longshore energy flux along the shorelines north and south of the inlet, and (3) an estimate of the transport quantities by correlating the beach and inlet volume changes with the computed longshore energy flux distribution. The time period chosen for this analysis extended from 1965 to 1975, primarily because relatively accurate wave data was available for this period.

Beach Changes.

Changes in the shoreline position for the beaches adjacent to Oregon Inlet were determined from nearshore beach profiles surveyed in 1937 and 1964 and from a comparison of 13 sets of aerial photographs made between 1940 and 1975. As a result of these shoreline comparisons, the study area was divided into six segments or littoral cells, as shown on Fig. 3, based, in part, on the behavior of the beaches during the analysis period and on the relative orientation of the shoreline cells. Also indicated on Fig. 3 are the shoreline changes for the 1965-1975 period selected for the sediment budget analysis.

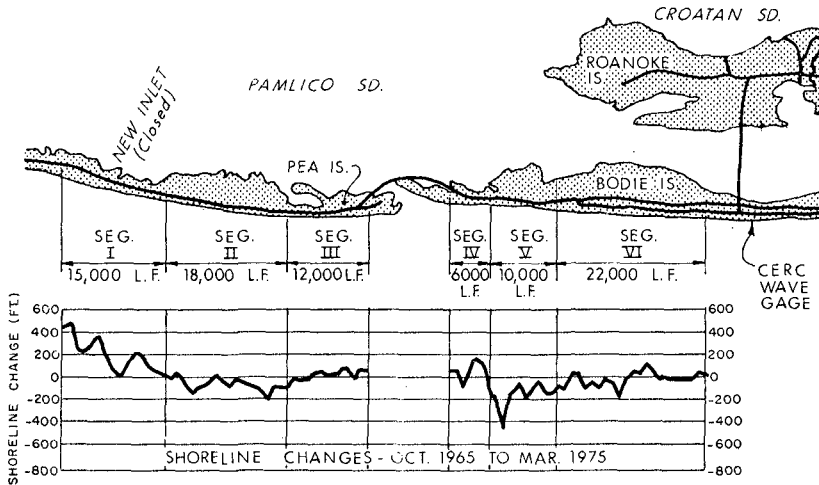


Fig. 3 - Shoreline Segments (or Littoral cells) and 1965-1975 Shoreline Changes

In order to perform the sediment budget analysis, the linear shoreline movements were converted to volumetric changes. This was accomplished by assuming that the entire active profile, i.e., that portion of the nearshore area influenced by wave action, moves at the same rate as the shoreline. In making this assumption, the beach volume changes were directly related to the total vertical distance of the active profile measured from the crest of the berm to some limiting depth. The identification of the limiting depth is difficult without comparative surveys; however, a reasonable estimate of this depth appears to be the deepest depth contour that maintains parallelism with the shoreline. In the case of the immediate study area, outside the influence of tidal currents flowing through Oregon Inlet, the -30 foot (-9.1 m) mean low water (MLW) depth contour satisfied this criterion. The crest elevation of the berm is about +8 feet (+2.4 m) MLW, thus the total vertical distance of the active profile was taken as 38 feet (11.5 m). This resulted in a volumetric equivalent factor (C) of 1.41 cu.yds/lin. ft. of shoreline/foot of erosion or accretion of the shoreline (11.5 m³/m shoreline/m of shoreline change). The equivalent volumetric changes obtained by applying this factor to the 1965-1975 shoreline movements within each segment are given in table 1. Note that no volume changes are given for Segment IV since changes in this segment are included in the estimated volume changes for Oregon Inlet.

TABLE 1
Beach Volumetric Changes, 1965-1975

Segment	Length of Segment		Estimated Total Volume Change ^{1/}		Offshore Losses Due to Rising Sea Level	
	(ft)	(m)	(cy/yr)	(m ³ /yr)	(cy/yr)	(m ³ /yr)
I	15,000	(4,572)	+155,000	(+118,513)	21,000	(16,057)
II	18,000	(5,486)	-188,000	(-143,745)	25,000	(19,115)
III	12,000	(3,658)	+ 10,000	(+ 7,646)	17,000	(12,998)
IV	Volume change included in Oregon Inlet					
V	10,000	(3,048)	-264,000	(-201,854)	14,000	(10,704)
VI	22,000	(6,706)	-127,000	(- 97,104)	31,000	(23,703)

^{1/} + = accretion, - = erosion

The total volume changes given in table 1 include the affects of longshore movements of material and additions or losses associated with material moving normal to the beach such as the amount of sediment transported bayward when the beach is overtopped or onshore-offshore movements by wave activity. During the 1965-1975 analysis period, no overtopping of any consequence occurred along the study area. However, there was undoubtedly some losses offshore. Offshore losses from the littoral cells were estimated by a procedure developed by Bruun (1) in which shoreline erosion is related to sea level rise. These losses are also given in table 1.

Inlet Changes.

The recent history of Oregon Inlet dates from 1846 when the present-day inlet was opened by a hurricane. Prior to 1846 New Inlet, which was located 8 miles (12.9 km) south of Oregon Inlet (see Fig. 3),

was the only inlet through the North Carolina Outer Banks north of Cape Hatteras. Since its opening, Oregon Inlet has migrated an average distance of 10,000 feet (3,050 m) to the south as indicated by the superposition plots of the inlet shoreline positions shown on Fig. 4. This southward migration of the inlet has been accompanied by alternate widening and narrowing of the inlet in response to varying weather patterns. For example, between 1953 and 1962, the Oregon Inlet area experienced one of the most active storm periods of record. Included during this period was the Ash Wednesday Storm of March 1962 which caused considerable damage along the northeastern coast of the United States. As a result of these storms, Oregon Inlet, which has a normal width of about 2,100 feet (640 m), had attained a width of 7,150 feet (2,180 m) following the March 1962 storm. Since 1962, no severe storms have affected the Oregon Inlet area; consequently, the north shoulder of the inlet migrated rather rapidly to the south in the form of an elongated spit as shown by the 1975 shoreline in Fig. 4.

Changes in the volume of material in Oregon Inlet associated with its migratory history were determined from hydrographic surveys made in 1937, 1962, and 1975, and from dredging records associated with the construction and maintenance of the interior bay channels and the ocean bar channel.

Between 1937 and 1962, the ocean bar at Oregon Inlet lost a total of 3,343,000 cubic yards (2,556,000 m³) of material. Since the March 1962 storm occurred just prior to the 1962 survey, it appears that the comparison of the 1937 and 1962 ocean bars reflect more on the losses resulting from the 1962 storm than on the general trend prior to this storm. For example, during the latest time period, 1962-1975, which has been relatively storm-free, the ocean bar has accumulated a gross amount of 2,835,000 cubic yards (2,168,000 m³). This represents an annual accumulation rate of about 218,000 cubic yards/yr (167,000 m³/yr). In addition to the buildup of material on the ocean bar between 1962 and 1975, the volume rate of accumulation associated with the development of the north spit following the Ash Wednesday storm amounted to 452,000 cu.yds./year (345,000 m³/yr). Thus, the total volume rate of change on the ocean bar and north spit between 1962 and 1975 was 670,000 cu.yds/yr (512,000 m³/yr).

With respect to volumetric changes in the bay area, the 1937 survey showed that the main channel connecting Oregon Inlet and Roanoke Sound passed through Walters Slough, see Fig. 1. As Oregon Inlet migrated southward, Walters Slough shoaled to such an extent that it had to be abandoned and a new channel excavated to connect Oregon Inlet with Old House Channel. This new channel, designated as the Oregon Inlet Channel, was dredged in 1960 and followed essentially the same alignment as exists today. As was evident from the comparison of the hydrographic surveys and aerial photographs of the inlet, most of the volume changes in the bay associated with the migration of Oregon Inlet actually occurred prior to 1965. Since 1965, very little net change has taken place in the bay with the average accumulation estimated to be only 20,000 cu.yds/yr (15,000 m³/yr).

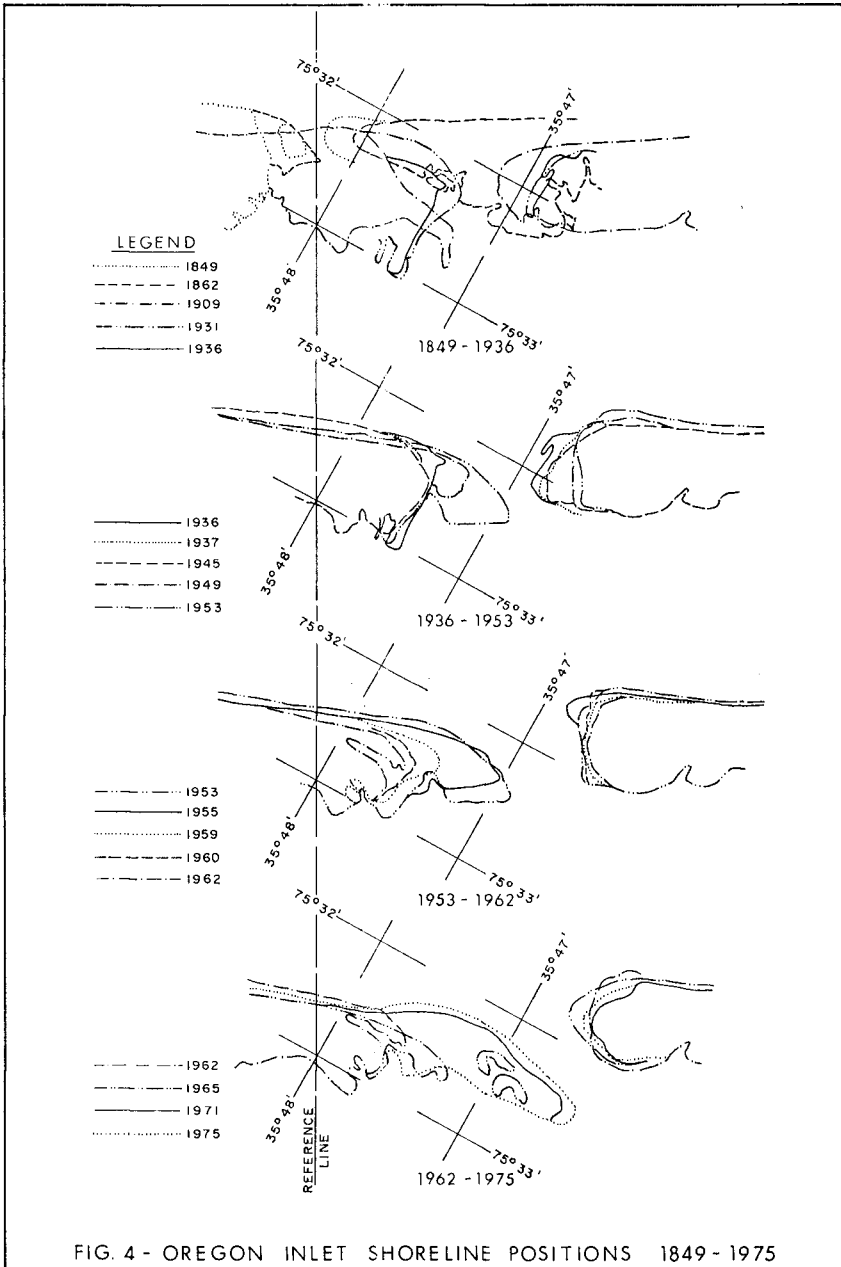


FIG. 4 - OREGON INLET SHORELINE POSITIONS 1849 - 1975

Based on these observed volume changes in Oregon Inlet, a volume rate of accumulation of 690,000 cu.yds/yr. (527,000 m³/yr) was assumed to be representative of the volume changes in Oregon Inlet during the 1965 to 1975 period selected for the sediment budget analysis.

Wave Refraction-Longshore Energy Flux Analysis. The amount of material that moves parallel to the shoreline is directly related to the longshore component of wave energy flux in the surf zone. The computation of longshore energy flux at a particular site requires information on (a) the wave climate at the site, and (b) the effects of wave refraction on the distribution of the longshore energy flux along the shoreline as waves propagate toward shore from deep water.

Wave Climate. The wave characteristics used for this analysis were obtained from a Coastal Engineering Research Center (CERC) wave gage, located on an ocean fishing pier 9 miles (14.5 km) north of Oregon Inlet, see Fig. 3. A summary of the observed waves for the period July 1964 to April 1976 is given in table 2. The wave characteristics measured by this gage represent essentially 100 percent of all the waves (and, consequently, the wave energy flux) reaching the study area at the gage site. However, since the gaged data is non-directional, it was impossible to determine differences in the wave height-period distribution for the various directions of wave approach. Therefore, the same relative height-period distribution was used for all wave directions.

With the gaged wave data representing 100 percent of the wave energy flux from all possible directions at the gage location, this total energy flux was proportioned to the various directions of wave approach based on visual wave observations made by U.S. Coast Guard personnel at the Diamond Shoals (Cape Hatteras) and Chesapeake Bay light towers. The relative directional distribution of the wave energy applicable to the study is tabulated in table 3.

Longshore Energy Flux (P_{1s}). The method used to compute the distribution of longshore energy flux along a given reach of shoreline has been given previously in reference (2) and will not be repeated here. In essence, the computational procedure requires the refraction of a large number of wave rays toward the study area. In this analysis, 101 wave rays were refracted toward shore for each combination of wave period and direction applicable to the study area, resulting in the generation of 7,272 wave rays. For each wave ray pair, the value of the longshore energy flux was computed at the breaking point of eleven wave heights ranging from 0.5 ft. (.15 m) to 11 ft. (3.35 m). The results of each individual longshore energy flux computation for all combinations of wave height, period, and direction was interpolated at specific intervals along the coast and summed to yield the total downcoast and upcoast distributions of longshore energy flux. The resulting longshore energy flux distribution is shown on Fig. 5.

Computation of Littoral Transport Rates. The relationship between longshore sediment transport and longshore energy flux has the form:

$$\begin{aligned}
 Q_s &= \beta P_{1s} \text{ where:} & (1) \\
 Q_s &= \text{the volume of sediment transported per year} \\
 \beta &= \text{constant} \\
 P_{1s} &= \text{annual longshore component of wave energy flux.}
 \end{aligned}$$

TABLE 2
Nags Head Wave Data
Summary of Percent Observations From CERC Wave Gage
Period of Record (Jul 1964 to Apr 1976)

Wave Period (secs)	Significant Wave Height (ft)												Total	
	0-1	1-2	2-3	3-4	4-5	5-6	6-7	7-8	8-9	9-10	10-11	11-12		
0-1.9	0.04													0.04
2-2.9	0	0.11	0.01											0.12
3-3.9	0.09	1.42	1.10	0.25										2.86
4-4.9	0.01	0.84	1.63	0.94	0.27	0.01								3.70
5-5.9	0.09	1.63	2.73	2.72	1.54	0.62	0.27	0.01						9.61
6-6.9	0.15	1.94	2.76	2.50	1.95	1.26	0.59	0.20	0.05					11.40
7-7.9	0.26	3.09	2.27	1.43	1.19	1.04	0.47	0.33	0.16	0.05				10.29
8-8.9	0.87	9.11	5.40	2.38	1.58	0.95	0.51	0.41	0.25	0.09			0.04	21.59
9-9.9	0.41	5.67	3.49	1.83	1.00	0.52	0.29	0.37	0.16	0.05				13.79
10-11.9	0.41	3.80	3.12	2.02	0.91	0.83	0.63	0.27	0.24	0.08				12.31
12-13.9	0.31	2.69	2.01	1.31	1.03	0.74	0.62	0.40	0.16	0.08	0.04			9.39
14-15.9	0.22	1.25	0.78	0.36	0.33	0.21	0.32	0.27	0.16	0.04				3.94
>16	0.04	0.38	0.15	0.11	0.07	0.07	0.05	0.05	0.04	0				0.96
Total	2.90	31.93	25.45	15.85	9.87	6.25	3.75	2.31	1.22	0.39	0.04	0.04	0.04	100.00

TABLE 3
Relative Distribution of Offshore Wave Energy
for the Oregon Inlet Area

	Wave Direction							
	North	NNE	NE	ENE	E	ESE	SE	SSE
% Wave Energy	22.65	20.56	15.24	9.83	5.85	7.78	8.46	9.64

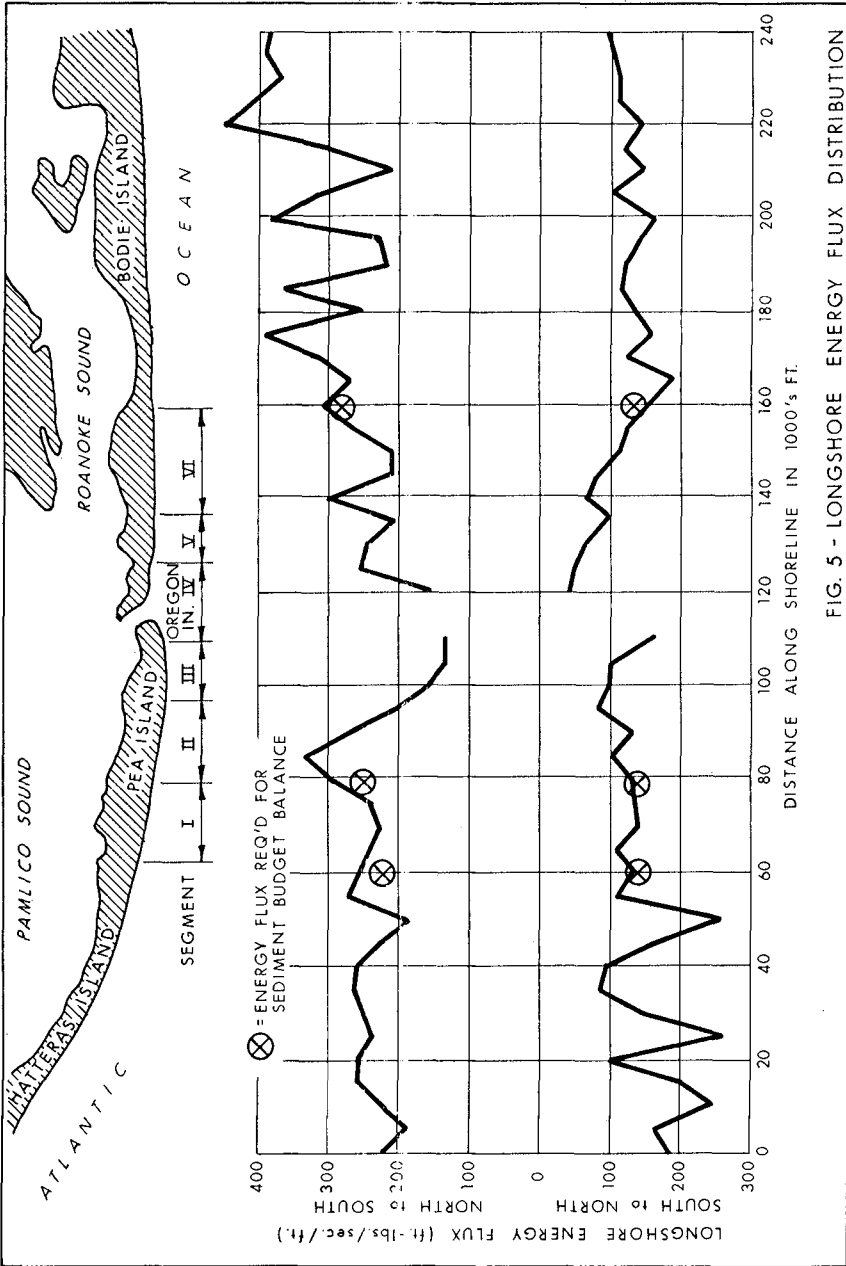


FIG. 5 - LONGSHORE ENERGY FLUX DISTRIBUTION

Although values of β have been proposed based on field and laboratory measurements, in this analysis, β is assumed to be unknown. Also, since the longshore energy flux analysis is not applicable to the immediate area of the inlet, due to the complex bottom and tidal current-wave interactions, two unknowns in addition to β are introduced into the sediment budget analysis to represent the amount of natural bypassing of sediment across the inlet in the downcoast (SB) and upcoast (NB) directions. Thus, with three unknowns, three conditions must be established to solve for these values. This was accomplished by balancing the sediment budget between the inlet cell and the two littoral cells immediately adjacent to the inlet as shown schematically on Fig. 6. It is remarked that the relative longshore transport values expressed as $(P_{1S})\beta$ in Fig. 6 were determined from the results of the longshore energy flux computations at the boundaries of the littoral cells. The solution of the sediment budget for the condition shown in Fig. 6 resulted in a value of β of 6,018 for sediment transport expressed in cu.yds/yr. This gave computed natural bypassing quantities of 1,232,000 cu.yds/yr (942,000 m³/yr) to the south (SB) and 133,000 cu.yds/yr (102,000 m³/yr) to the north (NB).

With the value of β determined, the sediment budgets of the other shoreline segments (or littoral cells) was computed. However, in order to balance the amount of sediment moving into and out of each cell, the assumption was made that the estimated volume rates of change within each cell are absolute and that any adjustments required to obtain a complete sediment balance would be made in the computed values of the longshore energy flux at the cell boundaries. For the most part, the amount of adjustment required to obtain a sediment balance was less than 12 percent. The adjusted values of P_{1S} required to balance the sediment budget for all littoral cells are indicated on Fig. 5, whereas the final results of the longshore transport analysis for the 1965 to 1975 time period is summarized schematically on Fig. 7.

SHORELINE ADJUSTMENTS AND LONGSHORE TRANSPORT RATES FOLLOWING JETTY CONSTRUCTION

Changes in the shoreline configuration and sediment transport rates adjacent to the proposed jetties at Oregon Inlet were estimated based on the assumption that sediment transport would vary in direction proportion to changes in the breaker angle ($\Delta\alpha_b$) relative to the pre-jetty shoreline. If α_b is the average breaker angle relative to the pre-jetty shoreline associated with a longshore transport rate Q_s , then the transport rate along a shoreline reach having an average breaker angle of $(\alpha_b + \Delta\alpha_b)$ would be:

$$Q_{Sn} = \psi_n Q_s \quad (2)$$

where:

Q_{Sn} = transport rate along reach n

$$\psi_n = \frac{\sin 2(\alpha_b + \Delta\alpha_{bn})}{\sin 2\alpha_n}$$

$\Delta\alpha_{bn}$ = change in average breaker angle within reach n.

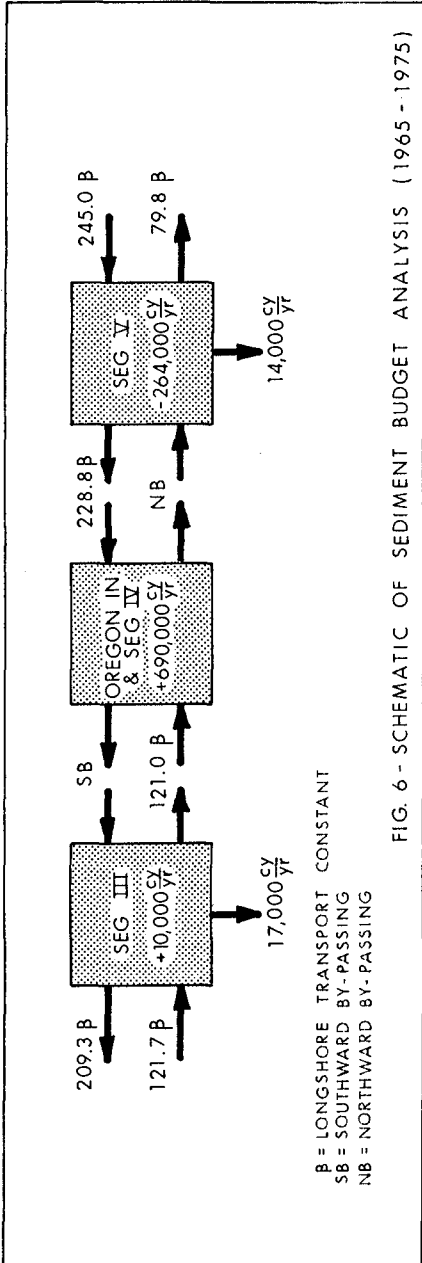


FIG. 6 - SCHEMATIC OF SEDIMENT BUDGET ANALYSIS (1965 - 1975)

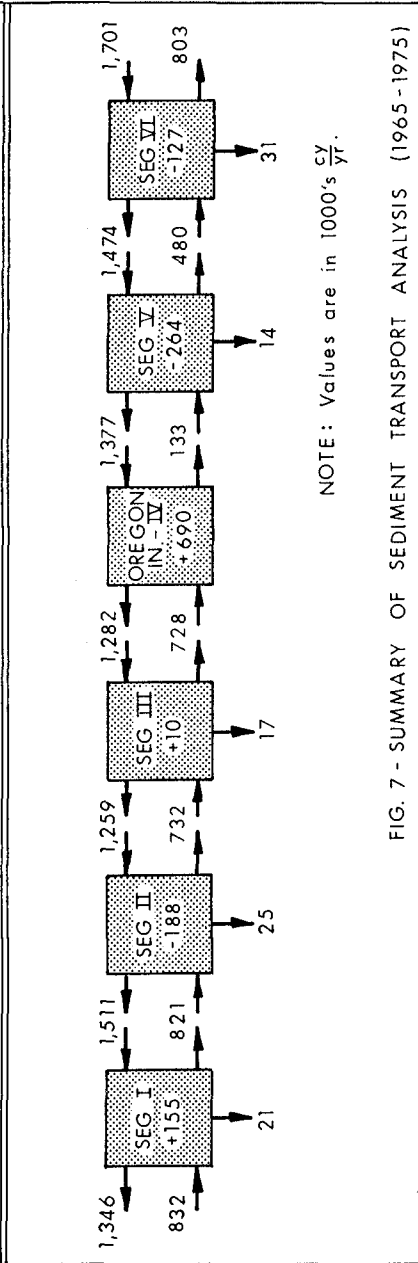


FIG. 7 - SUMMARY OF SEDIMENT TRANSPORT ANALYSIS (1965 - 1975)

In setting up the procedure to compute the shoreline adjustments adjacent to the jetties, the shoreline was divided into reaches of various lengths (L_n) as shown on the definition sketch in Fig. 8, where L_n does not have to be the same for each reach. The midpoint of reach n, measured from the intersection of the pre-jetty shoreline with the jetty, is designated as X_n .

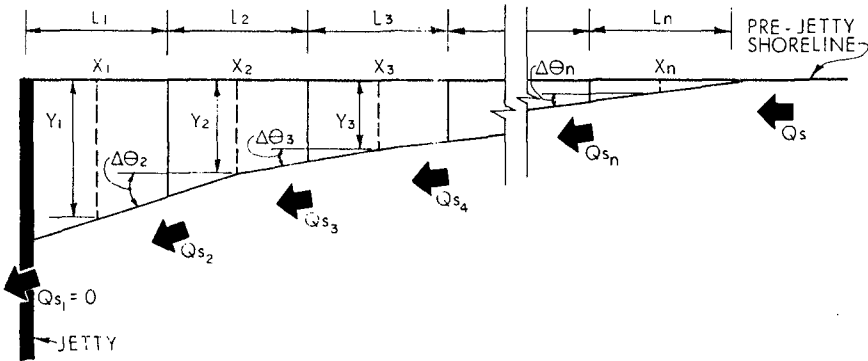


Fig. 8 - Definition Sketch for Shoreline Adjustment Computations

If the volume of material in a reach changes by an amount ΔVOL , during some time interval Δt , then the average seaward or landward movement of the reach, measured at its midpoint, would be:

$$\Delta Y_n = \frac{\Delta VOL}{L_n C} \quad (3)$$

where:

ΔY_n = average movement of reach n occurring during a time interval Δt

L_n = length of reach n

C = volumetric equivalent factor relating volume changes to linear movements (see previous discussion)

$$\Delta VOL = (Q_{sn} - Q_{sn-1})t \Delta t$$

$(Q_{sn} - Q_{sn-1})t$ = difference in the volume rate of longshore transport at the downdrift and updrift boundaries of the reach at time step t.

Δt = time interval between shoreline position computations

At the end of some time period t, the midpoint of reach n would have moved through a total distance Y_n measured from the pre-jetty shoreline. If the rate of longshore transport varies from reach to reach, then the amount of movement of the various reaches would not be the same. This would result in a change of shoreline orientation between the reaches relative to the original shoreline by an angle given by:

$$\Delta\theta_n = \tan^{-1} \left(\frac{Y_{n-1} - Y_n}{X_{n-1} - X_n} \right) \quad (4)$$

Therefore, for the simplified case in which the effects of changes in wave refraction are ignored, the breaker angle in reach n at time t would be:

$$(\alpha_{bn})_t = \alpha_b + \Delta\theta_n \quad (5)$$

and the associated longshore transport within this reach during time step t would be computed as:

$$(Q_{sn})_t = Q_s \left(\frac{\sin 2(\alpha_b + \Delta\theta_n)}{\sin 2\alpha_b} \right) \quad (6)$$

Equation (6) is valid as long as wave angles, relative to the bottom contours are small and the waves are not diffracted by the structure. However, if diffraction does occur, the angle at which the diffracted wave would break relative to the original shoreline (designated as α_b') would differ from the average breaker angle associated with Q_s . Furthermore, the height of the waves in the diffraction zone would be reduced by the diffraction coefficient K' , which in turn would reduce longshore transport by an amount proportional to $(K')^2$. If the shoreline within the diffraction zone has also undergone an angular change ($\Delta\theta$), then the transport rate in the shadow zone of the structure would be:

$$Q_{sn}' = \psi_n' Q_s \quad (7)$$

where:

$$\begin{aligned} Q_{sn}' &= \text{transport rate in the diffraction zone} \quad (8) \\ \psi_n' &= (K')^2 \left(\frac{\sin 2(\alpha_b' + \Delta\theta)}{\sin 2\alpha_b} \right) \end{aligned}$$

In applying the above procedure to Oregon Inlet, an average breaker angle (α_b) of 12° , determined from the wave refraction analysis, was used for the longshore transport rates along the pre-jetty shoreline in both the north and south directions. North of the inlet, the pre-jetty shoreline transport rates (Q_s) used were 1,377,000 cu.yds/yr (1,053,000 m^3 /yr) to the south and 480,000 cu.yds/yr (367,000 m^3 /yr) to the north, whereas south of the inlet, the pre-jetty shoreline transport rates were 1,259,000 cu.yds/yr (963,000 m^3 /yr) south and 728,000 cu.yds/yr (557,000 m^3 /yr) north. These annual longshore drift rates correspond to the rates computed for Segment V and III, respectively, as shown on Fig. 7.

Since the shoreline adjustments and sediment transport rates adjacent to the jetties are time dependent, realistic results can only be obtained if the time increment (Δt) between shoreline position computations is relatively small. For this analysis, the time increment varied from about 1 to 2 weeks, with the amount and direction of longshore transport occurring during a particular time increment being based on a simulated yearly time distribution of the longshore drift as developed from the wave gage and light tower wave records.

For the shoreline updrift of the north jetty, wave diffraction effects associated with waves approaching from the southern quadrants were estimated by using an average angle of wave incidence relative to the north jetty of 60° . This angle of wave incidence was based on the seaward refraction of a wave having an 8.5-second period (approximately the average period for the study area) and a breaker angle of 12° , out to the head of the proposed north jetty. On the south side of the inlet, wave diffraction would be of minor importance as the average angle of wave approach from the northern quadrants is less than the angle the proposed south jetty makes with the shoreline.

The predicted shoreline changes north and south of Oregon Inlet, following jetty construction, are given on Fig. 9(a) and 9(b), respectively. As noted on these figures, the total shoreline changes include some initial adjustments associated with the redistribution of the ocean bar deposits toward shore once tidal flow over these shoal areas is eliminated. On the north side, a total of 3,600,000 cu.yds. ($2,753,000 \text{ m}^3$) of material was distributed along the shoreline in a shape predicted by the shoreline evolution theory developed by Pelnard-Considere (3). This 3,600,000 cu.yds. ($2,753,000 \text{ m}^3$) of fillet material represents approximately 75 percent of the estimated total volume of material north of the inlet that would be subject to redistribution once the jetties are built. This percentage of the total volume was assumed to move on-shore next to the jetty since approximately 75 percent of the gross drift in this area is to the south. On the south side of the inlet, the initial shoreline adjustment simply involved the projection of the shoreline alignment of Segment III from the existing south shoulder of the inlet to the point of intersection with the south jetty. The volume of material required to straighten this portion of the shoreline would be about 1,200,000 cu.yds. ($918,000 \text{ m}^3$), whereas the total volume of material south of the inlet that may eventually be redistributed is estimated to be in excess of 9,400,000 cu.yds. ($7,187,000 \text{ m}^3$). The time required for these initial adjustments to occur is not known; however, since the construction of the jetties will take 3 to 4 years, most of these initial adjustments will probably take place during this period.

With respect to the deposition of the net southward drift of 897,000 cu.yds/yr ($686,000 \text{ m}^3/\text{yr}$) along the shoreline north of the inlet, the shoreline adjustment computations indicated that approximately 50 percent would be deposited within about 5,500 feet (1,676 m) of the north jetty. The balance of the net drift would be spread over about 14,500 feet (4,422 m) of shore further north. On the south side, most of the 531,000 cu.yds/yr ($406,000 \text{ m}^3/\text{yr}$) deficit would be felt within a 6,500-foot (1,981 m) segment immediately south of the jetty. Obviously, in order to maintain a stable shoreline south of Oregon Inlet, an average of 531,000 cu.yds/yr ($406,000 \text{ m}^3/\text{yr}$) would have to be placed along this beach.

SAND BYPASSING AT OREGON INLET

The bypassing plan being developed for Oregon Inlet will require a cutter-suction pipeline dredge to operate on the accretion fillets immediately adjacent to the jetties. In order to limit the dredge to a minimum amount of wave exposure, special openings or "doors," as shown

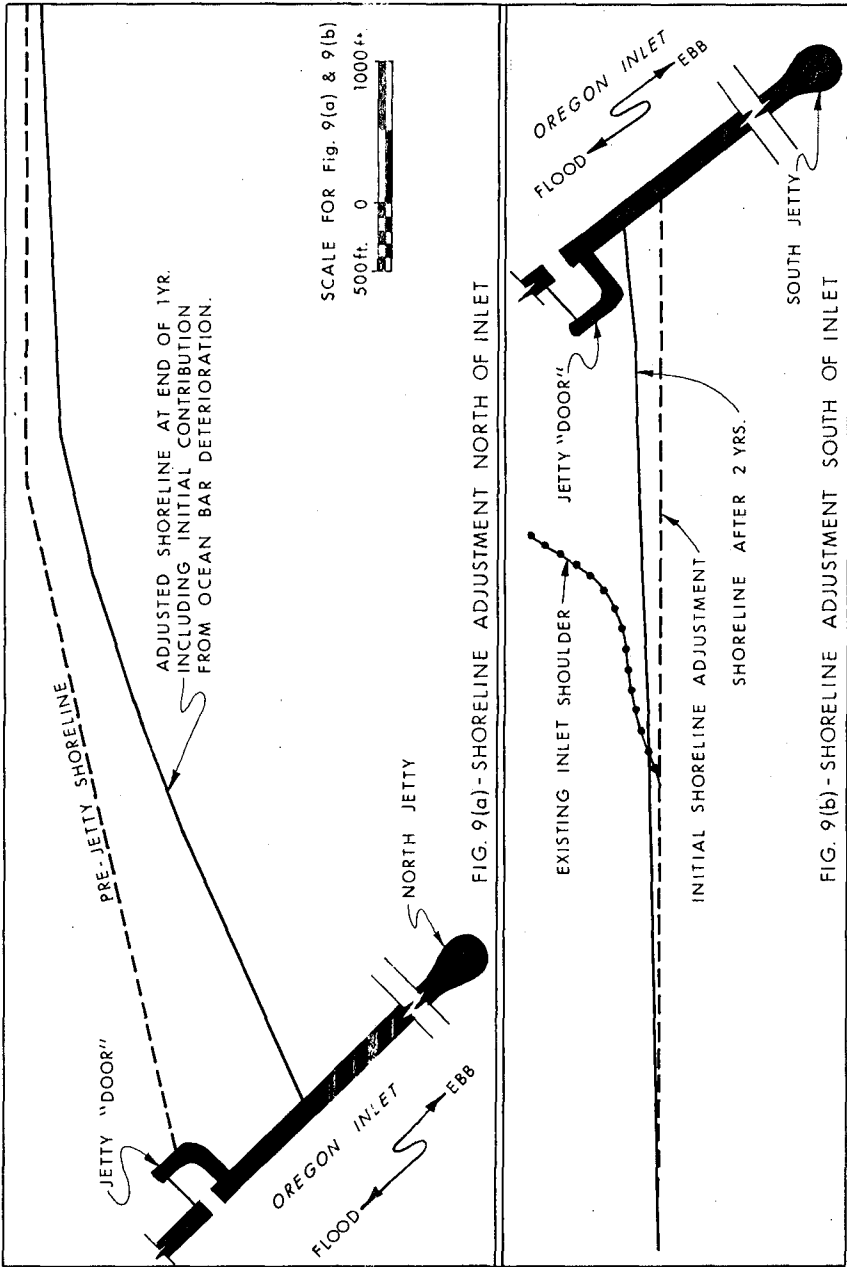


FIG. 9(a) - SHORELINE ADJUSTMENT NORTH OF INLET

FIG. 9(b) - SHORELINE ADJUSTMENT SOUTH OF INLET

on Fig. 2, have been designed near the landward ends of both jetties to permit a dredge to cut its way onto the bayside of the fillets. Note that these openings have been included in both jetties to allow for bypassing from either side of the inlet if conditions so dictate. Although most of the material to be bypassed can be removed from the subaerial fillet accumulations, a certain amount will have to be taken from the normally turbulent nearshore zone in order to prevent the movement of material around the seaward end of the jetty. During this nearshore phase of the bypassing operation, a floating breakwater will be positioned seaward of the borrow area in order to increase the production time of the dredge. A schematic representation of the bypassing operation is shown on Fig. 10. As a result of the bypassing operation, a deposition basin will be created in the fillet area adjacent to the jetty, which would serve to entrap littoral materials for subsequent bypassing operations.

In an attempt to determine the feasibility of this bypassing arrangement, at least from the sediment transport aspects, a simulated sediment trap was imposed on the shoreline immediately adjacent to the north jetty as shown on Fig. 11. The size of this trap equaled a two-year bypassing requirement for the south side of the inlet. By applying the shoreline adjustment procedure outlined above, an estimate was made of the shoreline configuration in the vicinity of the sediment trap at the end of three months, one year, and two years following the bypassing operation. These shorelines are also shown on Fig. 11.

On the basis of this analysis, bypassing directly from the fillet appears feasible in that the sediment trap was essentially filled at the end of the two-year period. Just as important, however, was the indication that material would not be transported around the seaward end of the jetty and that a stable beach would be created for a considerable distance updrift. Some verification of the functional aspects of the fillet deposition basin should be available following movable-bed hydraulic model tests which will be conducted in the near future.

References

- (1) Bruun, P., "Sea Level Rise as a Cause of Shore Erosion," *Journal Waterways and Harbors Division, ASCE*, February 1962.
- (2) Jarrett, J.T., "Sediment Budget Analysis - Wrightsville Beach to Kure Beach, N.C.," *Coastal Sediments 77, Fifth Symposium of the Waterway, Port, Coastal and Ocean Division of ASCE*, November 1977.
- (3) Pelnard-Considere, R., "Essai de Theorie de l'Evolution des Formes de Rivage en Plages de Sable et de Galets," *4th Journees de l'Hydraulique, Les Energies de la Mer, Question III, Rapport No. 1*, 1956.

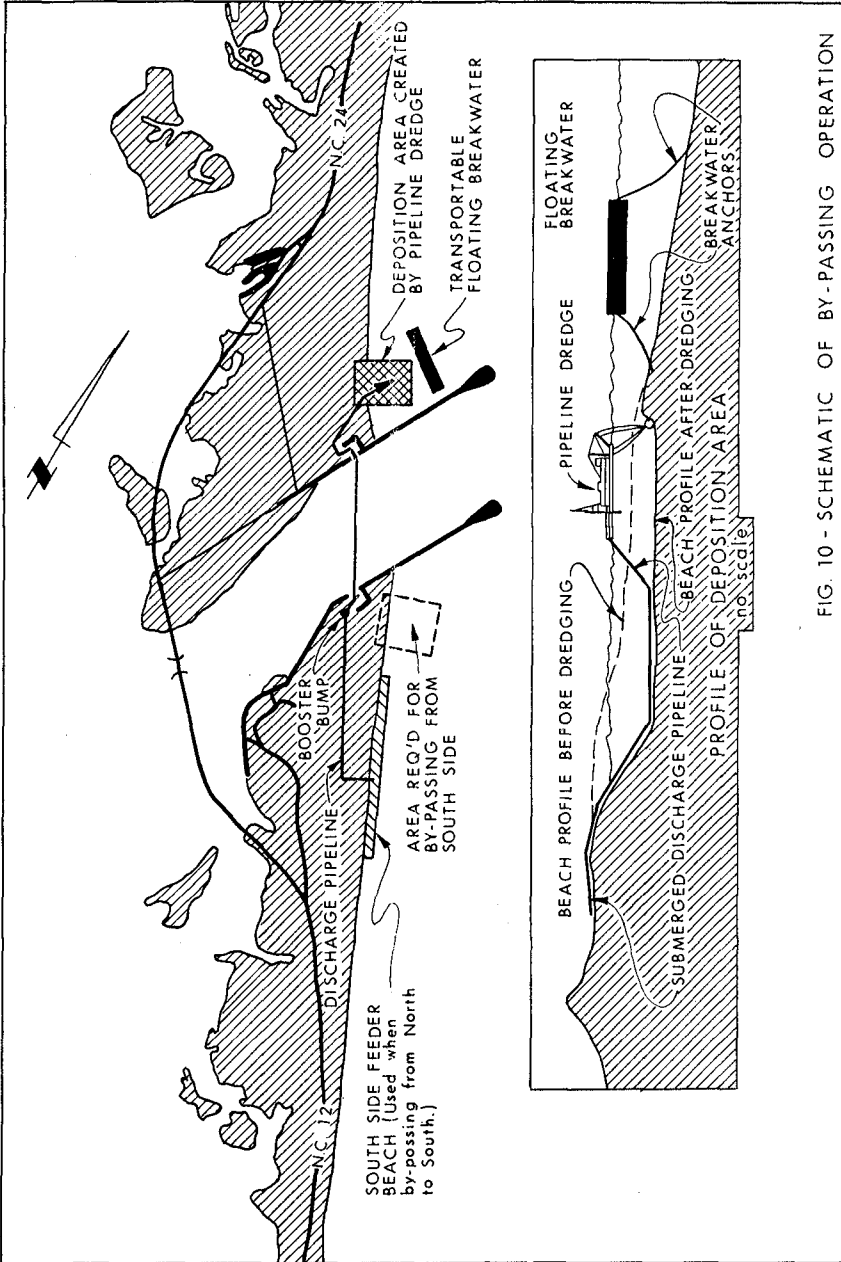


FIG. 10 - SCHEMATIC OF BY-PASSING OPERATION

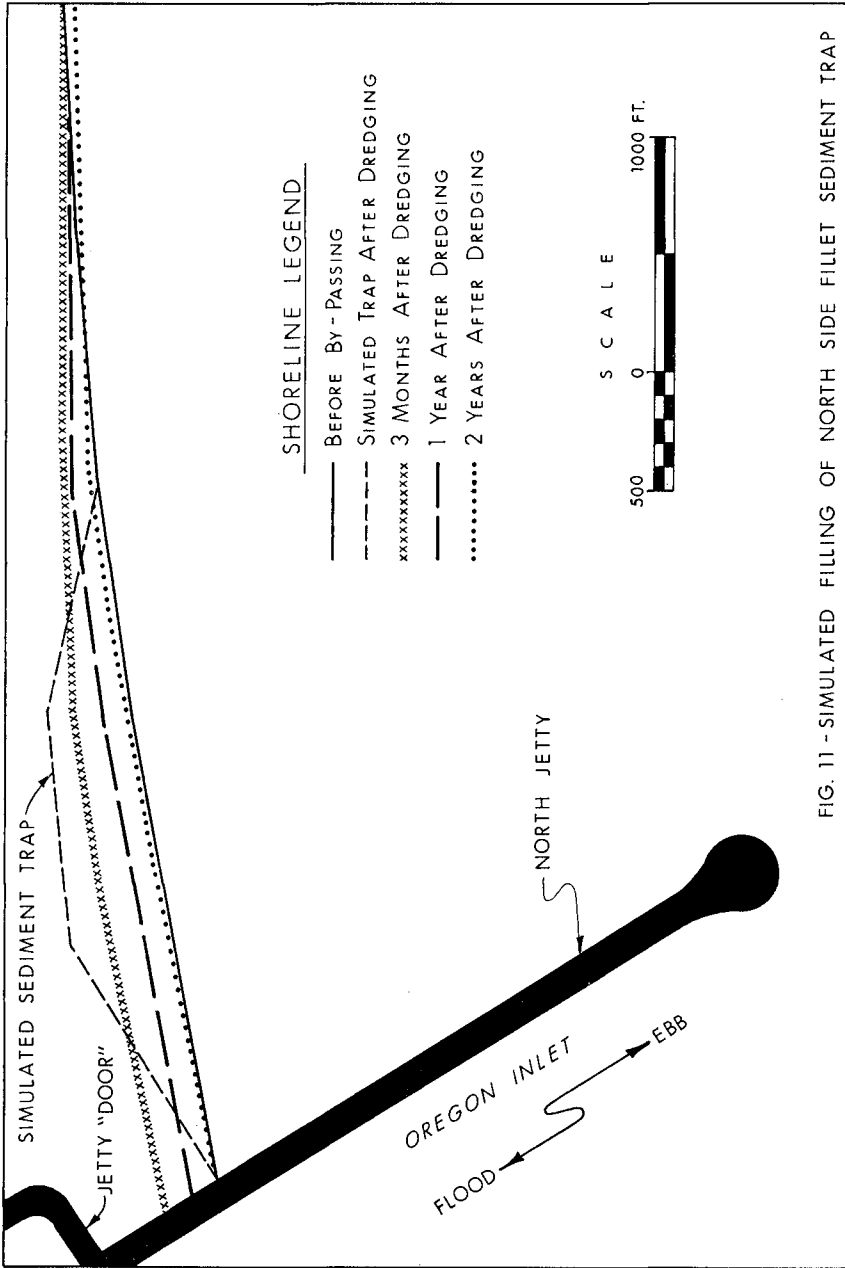


FIG. 11 - SIMULATED FILLING OF NORTH SIDE FILLET SEDIMENT TRAP

CHAPTER 74

MAINTENANCE OF SANTA CRUZ HARBOR, CALIFORNIA, USA

by

Orville T. Magoon¹

Don C. Baer²

ABSTRACT

In planning and operating coastal harbors subjected to shoaling, it is imperative that the characteristics and regime of the sediments which deposit in the harbor entrance be quantified to the maximum extent possible in order that the economic impacts of the channel shoaling and along adjacent shores may be evaluated.

This paper presents a brief progress report on the study of a coastal harbor in an area subjected to shoaling. This study represents the input of many engineers and researchers in the United States.

INTRODUCTION

Santa Cruz Harbor is located at the northern end of Monterey Bay on the California Pacific Coast (Figures 1 and 2). Harbor elements include an entrance channel 100 feet wide and 20 feet deep protected by jetties as well as interior channels and turning basins. The harbor serves as the home port for recreation and commercial fishing vessels. The main (west) jetty is 1,200 feet in length and protected with 28-ton concrete quadripods. The major navigation features of the harbor were completed in 1964. (1)

Inasmuch as the harbor is located in an area of considerable littoral movement, the Federal project authorization included provisions for sand by-passing at the harbor entrance. The harbor entrance has generally been maintained with contract hydraulic cutter pipeline-type dredges. Recently an experimental eductor type sand by-passing system was installed by the US Army Waterways Experiment Station, Vicksburg, Mississippi, and evaluated.

¹Civil Engineer, US Army Engineer Division, South Pacific, San Francisco, California, Chief, Coastal Engineering Branch, Planning Division

²Civil Engineer, US Army Engineer Division, South Pacific, San Francisco, California, Chief, Construction and Operations Division

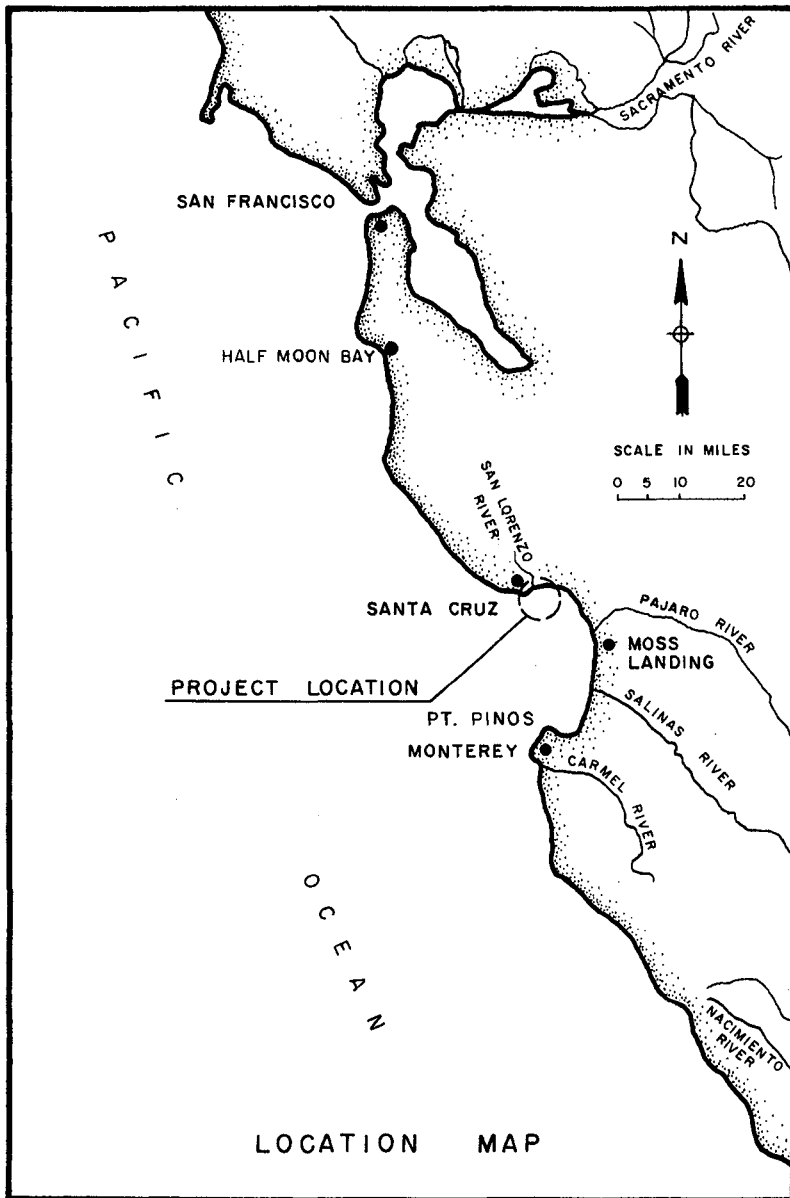


Figure 1. Location Map

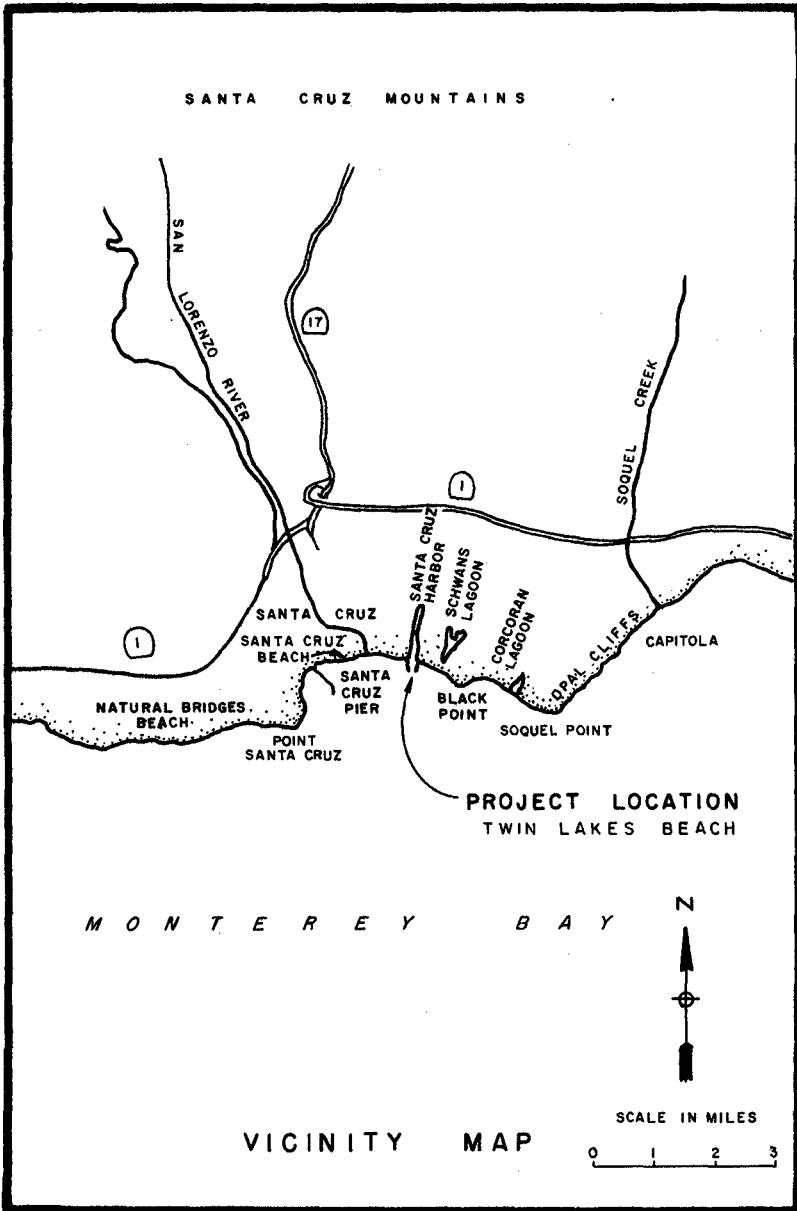


Figure 2. Vicinity Map

In order to quantify the coastal processes at Santa Cruz, an extensive prototype data collection program was initiated. This information includes beach and hydrographic surveys, LEO measurements,⁽²⁾ aerial photography, alongshore energy flux measurements, wave heights^{(3), (4)} at other locations along Monterey Bay, and offshore wave measurements.

CHARACTERISTIC ENTRANCE SHOALING

Shoaling of Santa Cruz Harbor entrance has been documented in a report entitled, "Santa Cruz Harbor Shoaling Study, Santa Cruz Harbor, California," by Walker, et al, of Moffatt & Nichol, Engineers.⁽⁵⁾ Walker found that the harbor entrance shoaling followed a relatively predictable pattern as shown on Figure 3. It should be noted that the harbor entrance experiences only relatively light shoaling until approximately October and relatively rapid shoaling until March or April when the pattern is repeated. Areas of deposition are similarly characteristic.

WAVE REGIME

In order to understand and quantify the movements of sediments at coastal locations, it is necessary to understand and quantify the offshore and nearshore wave regime, with particular emphasis on the determining of the direction and quantity of coastal littoral sediments. Traditionally this has been done through the use of deepwater wave hindcasts followed by appropriate transformation of these deepwater waves to the nearshore area. These nearshore wave characteristics were then translated to littoral drift calculations through the use of relations between the wave energy and the expected alongshore transport. Although these methods are useful in understanding coastal phenomena, they necessitate a complex chain of calculations which are difficult to make and which must often be made with insufficient information.

In order to better understand the littoral regime and to provide a usable technique of quantifying littoral processes at a specific location through in situ measurement, Seymour et al, of the California Department of Navigation and Ocean Development, and the representatives of the Scripps Institute of Oceanography, developed a device for directly measuring the alongshore energy flux (sxy). This device was installed at Santa Cruz Harbor and values of sxy are being calculated routinely. Very preliminary results by Douglas Pirie et al of the San Francisco District of the US Army Corps of Engineers indicate that quantities dredged at Santa Cruz Harbor are related to the sxy values at Santa Cruz as calculated by Seymour.

CONCLUSIONS

Improved technology appears to have provided a path for a major breakthrough in quantifying the alongshore sediment movement which results in shoaling at harbor entrances. If the results of these improved methodologies are substantiated through longterm coastal measurements, a powerful new tool will have been provided coastal engineers.

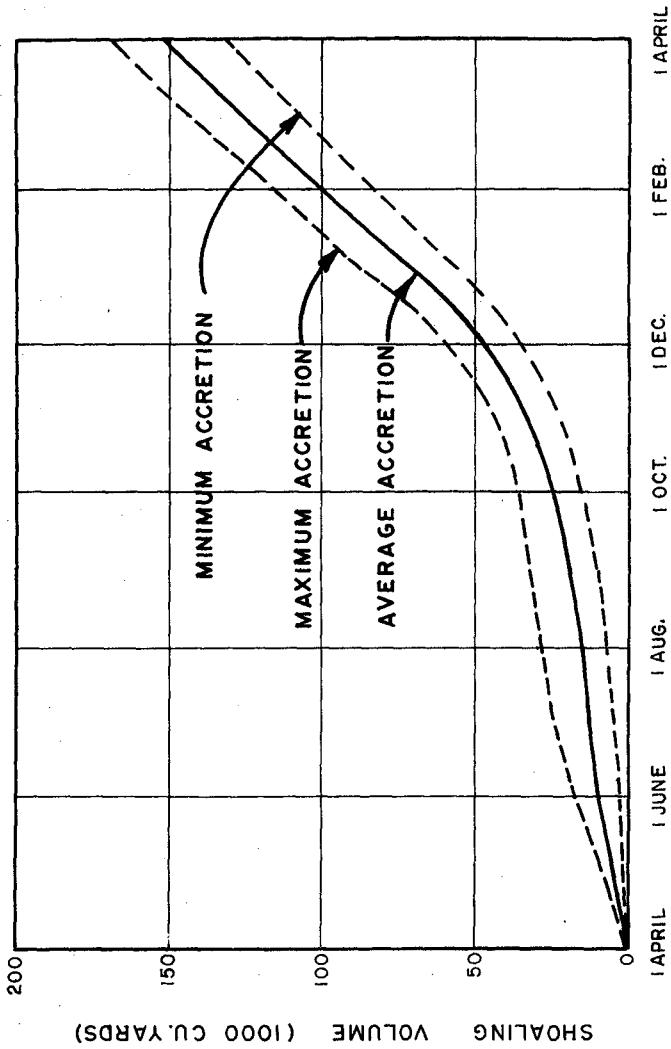


Figure 3. Average, Maximum, and Minimum Monthly Cumulative Rates of Accretion Between Dredging Episodes, 1972 to 1977

ACKNOWLEDGEMENTS

The work summarized in this paper is financially supported through the programs of the California Department of Navigation and Ocean Development, and the US Army Corps of Engineers. The work effort on the project was accomplished through the efforts of Mr. Douglas Pirie et al of the US Army Engineer District, San Francisco; Mr. D. Lee Harris of the US Army Coastal Engineering Research Center, Washington, DC; Mr. Dick Sager and colleagues at the US Army Waterway Experiment Station in Vicksburg, Mississippi; Dr. Richard Seymour of the California Department of Navigation and Ocean Development and A. Higgins, M. Sessions et al at the Scripps Institute of Oceanography; Mr. Milton Millard of the US Army Corps of Engineers Office of the Chief of Engineers, Washington, DC; Mr. Donald C. Baer of the South Pacific Division of the US Army Corps of Engineers; and Mr. Jim Wolfe and Mr. Hank Pape of the US Army Engineer District, San Francisco. The leader for the Santa Cruz Harbor shoaling study was Dr. James (Kimo) Walker of Moffatt and Nichol, Engineers. Continuing cooperation was received by the Santa Cruz Harbor Port District and the California Department of Parks and Recreation.

Acknowledgement is gratefully made to the Corps of Engineers, US Army, for access and permission to use this study material. The views of the authors do not purport to reflect the position of the Corps of Engineers, Department of the Army, or Department of Defense.

LIST OF REFERENCES

1. Weymouth, Olin E. and Magoon, Orville T., Stability of Quadripod Cover Layers, Proceedings, 1968, Coastal Engineering Conference, 1968, p. 787-796
2. Berg, Dennis W., Systematic Collection of Beach Data, Proceedings, Coastal Engineering Conference, 1968, p. 273-297
3. Seymour, R. J. and Sessions, M. H., Regional Network for Coastal Engineering Data, Proceedings, Coastal Engineering Conference, 1976, p. 60-71
4. Seymour, R. J., Defining the Wave Climate for a Harbor, Proceedings, ASCE Ports 77 Conference, Vol. II, p. 218-235
5. Walker et al, Santa Cruz Harbor Shoaling Study, Santa Cruz Harbor, California, USA, Moffatt and Nichol for the District Engineer, US Army Engineer District, San Francisco

CHAPTER 75

CASE STUDIES OF DELAWARE'S TIDAL INLETS: ROOSEVELT AND INDIAN RIVER INLETS

W. A. Dennis¹, G. A. Lanan² and R. A. Dalrymple³

ABSTRACT

Studies were undertaken to document the past and present characteristics and trends of Delaware's two major tidal inlets, Roosevelt and Indian River Inlets.

It was found that both inlet complexes are effective sediment traps causing considerable downdrift erosion. The major mechanism by which sand enters Indian River Inlet is by overtopping the impounded south jetty. At Roosevelt Inlet sediments are readily transported past the severed steel sheet pile jetties.

The results of a one-dimensional hydraulic model, as well as field measurements, predict the presence of a mean southerly flow through the canal and bay system which connects these two inlets. This flow is shown to have a substantial effect on the behavior and stability of these entranceways, causing major asymmetries on the depositional patterns at each location. Roosevelt Inlet was found to have a strong tendency to trap sediment within its throat; whereas, Indian River Inlet, on the opposite end of the system, was found to retain large quantities of sand on its developing ebb tidal shoal.

INTRODUCTION

The state of Delaware's coastline, along the shore of Delaware Bay and the Atlantic Ocean, features two major inlets which are coupled via the Intracoastal Waterway (Figure 1). These inlets, which were recently studied independently by Lanan and Dalrymple (1977) and Dennis and Dalrymple (1978), were shown to have various similar characteristics as shared with most tidal inlets as well as various contrasting features. Roosevelt Inlet, which serves as the northern entrance to the waterway, lies on the extreme southern edge of Delaware Bay, approximately 3 nautical miles west of Cape Henlopen. The inlet is bordered on the

¹Wilmington District, U. S. Army Corps of Engineers, Wilmington, NC.

²Texas Eastern Transmission Company, Houston, TX.

³Department of Civil Engineering, and College of Marine Studies,
University of Delaware, Newark, DE.

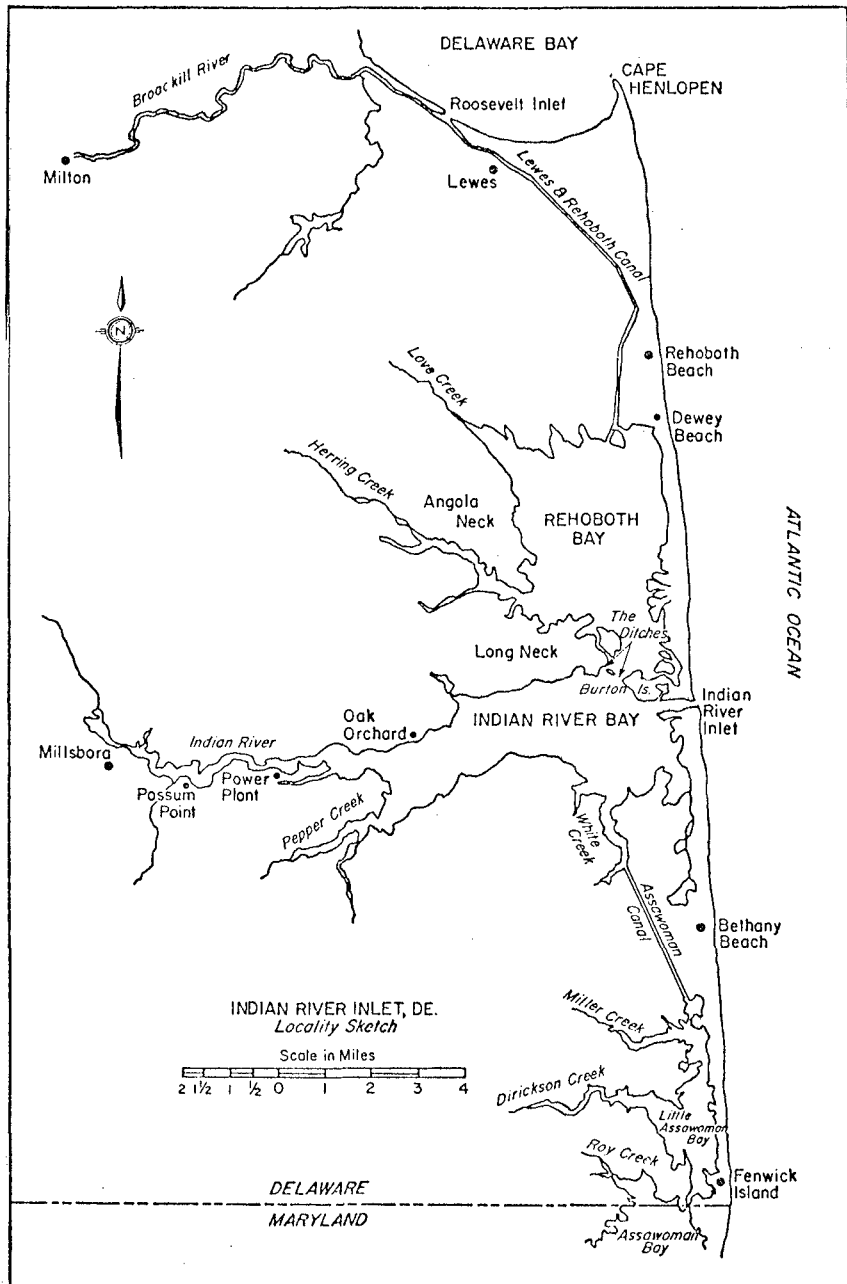


Figure 1 Locality Sketch of Indian River Inlet, Delaware

west by an undeveloped barrier beach known as Beach Plum Island and on the east by the small coastal community of Lewes Beach. Indian River Inlet lies about the midpoint of Delaware's Atlantic coast 11 nautical miles south of Cape Henlopen. The adjacent northern and southern barrier beaches are both contained in the Delaware Seashore State Park. These two inlets are connected by the Lewes and Rehoboth (L&R) Canal and the Rehoboth and Indian River Bays.

The wave climate in the vicinity of each of these inlets varies considerably due to the relative exposure of each location. Indian River Inlet, lying along the fully exposed Atlantic coast, is subjected to waves which average approximately a meter over the year; however, the possibility of two or three moderate-to-intense "northeasters" over that period, or the presence of a hurricane, are always a likelihood. The most effective wave energy arrives out of the southeasterly quadrant, driving the net littoral drift northward toward Cape Henlopen.

Roosevelt Inlet, on the other hand, is situated along a more sheltered shoreline. The wave climate is much less than that of the open ocean coast, with waves rarely exceeding a meter due to the limited fetch of Delaware Bay, particularly in the northeastern quadrant. Waves emanating from this direction are attenuated by the sheltering effect of the Cape as well as by the presence of two detached breakwaters at the southern entrance of Delaware Bay. Generally, the largest waves are generated along the major axis of Delaware Bay as a result of the sustained north to northwesterly winds. The biased wave climate results in an easterly net littoral drift along this reach, again toward Cape Henlopen.

BACKGROUND

Both of the inlets were stabilized about the same time. Roosevelt Inlet was established through the excavation of nearly 522,000 yd³ (399,300 m³) of mud, clay, and sand across the barrier beach commencing in the latter part of 1936. The construction of twin steel sheet-pile jetties followed the excavation and were completed by October 1937. The two structures were each 1,700 ft. (518.5m) in length extending bayward to the 6-foot (1.83m) depth contour, with a parallel spacing of 500 ft. (152.5m). This new inlet was to serve as a dependable and essential navigable northern entranceway of the recently completed L&R Canal after previous attempts at an alternate entrance (Broadkill Inlet), about 2 1/2 miles (4 km) to the west, had failed.

Unlike Roosevelt Inlet, Indian River Inlet occurred naturally, although its history has been one of migration, shoaling and closure. Repeated closure of the inlet in its natural state led to several pertinent problems, the most damaging of which was its effect on the local seafood industry. Not only did the inlet closure render vessel passage impossible, but normal fish migration into the feeding and spawning areas of the Rehoboth and Indian River Bays was disrupted. Furthermore, the large numbers of fish and shellfish trapped in the bays gradually died off as freshwater runoff reduced the salinity of the bay waters beyond tolerable limits. Many unsuccessful efforts were made to alleviate

these problems by both State and local interests through excavation and dredging until, finally, in 1937 a Federal project was approved to stabilize the inlet. Construction of two parallel stone jetties spaced 500 ft. (152.5m) apart was begun in 1938 and completed in 1940. Each structure extended seaward 1,556 ft. (474.6m) to the 14-ft. (4.3m) depth contour. The shoreward 904 ft. (275.7m) on the north side and 890 ft. (271.5m) on the south side were constructed of steel sheet piling for bank protection. For further historical details on Indian River Inlets, the reader is referred to Thompson and Dalrymple (1976).

INLET STABILIZATION AND RESULTING PROBLEMS

For both inlets office, as well as field studies, were undertaken to identify and document the various past and present coastal processes and associated problems. These studies included hydrographic surveys, beach profiles, current measurement, sand tracer experiments, collection and comparison of past and present charts and aerial photographs, as well as the documentation of all dredging and beach nourishment activities for each inlet. The following will present a discussion of the major problems and pertinent processes uncovered by these studies:

a. Downdrift Erosion. As with most tidal inlets along sandy coastlines, the presence of these inlets has resulted in significant erosion experienced by the adjacent beaches. Following the stabilization of Indian River Inlet, the south jetty began to trap sediment until the impoundment capacity was reached. Recent surveys of this area have revealed that approximately $319,000 \text{ yd}^3$ ($244,000\text{m}^3$) have been impounded since 1938 or an annual rate of $8,600 \text{ yd}^3$ ($6,580\text{m}^3$) per year. Presently, the sand passes rather freely around and over the south jetty entering into the confines of the inlet. At this point, the sand is entrained by the strong tidal currents reaching velocities as high as 6 feet/sec (1.8m/sec) and is ultimately deposited in either the flood or more extensive ebb tidal shoals. Thus the inlet complex acts as an effective sediment trap causing major erosion along the downdrift beaches. The shoreline response to the inlet stabilization is shown in Figure 2, which is based on comparison of aerial photographs, 1938 to 1975. In an effort to alleviate the sediment deficit, both the State and Federal governments have been nourishing the beach north of the inlet since 1957. To date, a total of $2,019,549 \text{ yd}^3$ ($1,544,955\text{m}^3$) have been placed along this reach.

The major mechanism by which the sand enters into Indian River Inlet and, to a lesser degree, Roosevelt Inlet, is by overtopping of the jetty. The beach berm crest along the reach adjacent to the south jetty at Indian River Inlet is generally one foot (0.3m) higher than the jetty crest. During periods of high tides, waves sweep up the beach, across and through the jetty, and into the channel, carrying large volumes of sand in the swash (Figure 3). At Roosevelt Inlet sediment occasionally overtops the shoreward portion of the east (downdrift) jetty during periods of northeasterly winds and high tides via a similar swash transport. The jetty at this location is essentially a low crested rubble revetment, primarily functioning as bank protection,

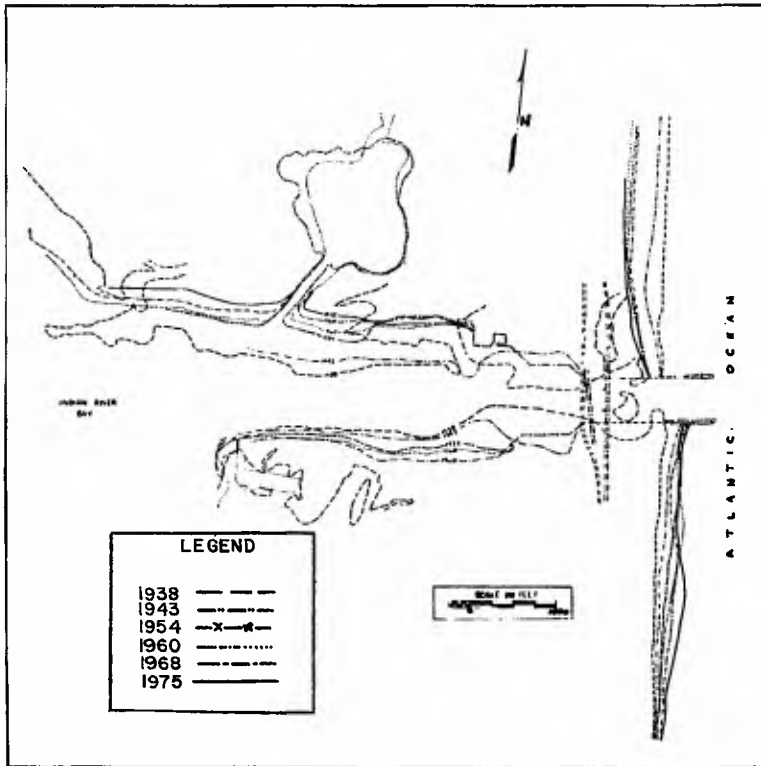


Figure 2 Shoreline Changes at Indian River Inlet



Figure 3 Sand Being Carried Over Indian River Inlet South Jetty by Ocean Waves

the crest of which varies 1-2 feet (0.3-0.6m) below the adjacent beach profile. A similar problem has also been noted to occur at Ocean City Inlet, Md., where the low and permeable inshore portion of the south jetty allows sand to flow downslope past the jetty and onto the northern tip of Assateague Island (Dean and Perlin, 1977).

b. Jetty Corrosion. A problem of greater impact which became apparent within two years after the jetty construction at Roosevelt Inlet was the corrosion and deterioration of the steel sheet-piling. At present no repairs have been made to the ailing structures which have deteriorated well beyond their effectiveness (most of the piling is only visible during low tide). As a consequence of the condition of the jetties, wave action easily moves sand through, around and over the severed sheet pile. Upon entering the inlet channel, the sand is reworked by wave and current action and is usually deposited in lobe-shaped shoals which build along both the east and west banks. The west lobe is usually larger, being on the updrift side of the inlet (Figure 4). Once the sand is worked within Roosevelt Inlet, there appears to be no effective mechanism to return the sand to the littoral regime other than by dredging. Therefore, in its present condition the inlet acts as an effective sink, trapping the gross littoral drift. The mechanism for this trapping will be explored more fully in the Section, Inlet Hydraulics. This trapping action has resulted in major erosion along Lewes Beach, which has again prompted both the State and Federal governments to provide remedial measures in the form of beach nourishment and the construction of nine groins.



FIGURE 4 Sand easily passing the deteriorated jetties at Roosevelt Inlet and depositing along the western bank.

c. Channel Bank Erosion and Channel Enlargement. Another major problem encountered following the stabilization of Indian River Inlet was the flanking of the jetties at the shoreward ends, causing erosion of the channel banks. The flanking probably was caused by the refraction of waves entering the inlet and striking the channel banks obliquely. Also, the expansion of the flood currents, upon exiting from the guides of the jetties, cause eddies to form which may result in scour of the unprotected banks. Following stabilization and the accompanying dredging, the unprotected channel banks began to widen dramatically. At a point about 650 ft. (198m) west of the present highway bridge, the channel widened 580 ft. (176.9m) during the following year and a half. In an effort to curtail the erosion, steel sheet-piling and riprap were extended along the channel banks in 1943 and again in 1963. However, each addition merely displaced the erosion pattern more westward. Today the erosion west of the protected channel banks is still continuing. The progressive widening can be seen by referring back to Figure 2.

Concomitant with the general widening of the unstabilized portion of Indian River Inlet was also a general deepening and thus a trend of increasing cross sectional area. This trend has caused the hydraulic characteristics of the inlet to change over time, including an increase in the tidal prism, enhancing the water quality of the adjoining bays. Comparison of past survey charts has revealed that the average cross sectional area has increased 15 fold since 1936. This increase has been manifested by a three-fold increase in the average width, 380 to 1,160 ft (116 to 354m) and a five-fold increase in the average depth of 3.5 to 18 ft (1.1 to 5.5m).

INLET HYDRAULICS

a. Development of Numerical Model. In order to gain a better understanding of the overall hydraulics, a one-dimensional numerical model was developed which encompassed all the bays and waterways from Indian River Inlet to Roosevelt Inlet. It provided a basis for simulating the tides and the cross sectionally averaged currents at any location within the system. The tides and currents (discharges) predicted by the model were compared with measured field data at specific locations and gave surprisingly accurate results. No effort was made to "fine tune" or calibrate the model to exactly predict the field data since the simplicity of the model would preclude such accuracy and also it was uncertain whether or not these measured data were representative of the average conditions.

The governing equations used in the model are the depth-integrated equations of motion and continuity. The effect of wind and the addition of freshwater inflow were neglected in the application and development of this model, although they are easily added. The vertically integrated differential equation of motion can be written in a semi-linearized form for flow in the x-direction as follows:

$$\frac{\partial q}{\partial t} = -g D \frac{\partial \eta}{\partial x} - \frac{\tau}{\rho} \quad (1)$$

where q = discharge per unit width in the x -direction

t = time

g = gravitational constant

D = total depth = $h + \eta$

h = depth at mean sea level

η = tide displacement above mean sea level

x = horizontal distance coordinate in flow direction

ρ = mass density of salt water

τ = frictional stress on the bottom of water column

$$= \frac{\rho f |q|}{8D^2}$$

f = Darcy-Weisbach friction factor

The continuity equation for one dimension is expressed as:

$$\frac{\partial \eta}{\partial t} + \frac{\partial q}{\partial x} = 0 \quad (2)$$

For computation these equations were cast into finite difference form, and the bays and waterways of the system were divided into finite segments. In the operation of the model a time and space staggered procedure is used in which the equation of motion is applied between mid-points of the adjacent segments (i.e., across segment boundaries) at full time steps, t , and the continuity equation is applied at each segment at half time step increments.

The finite difference form of Equation (1), expressed in terms of total discharge onto the n^{th} segment Q_n , follows, as:

$$Q_n' = \frac{Q_n - \overline{WD} g [\eta_n - \eta_{n-1}] \frac{\Delta t}{\Delta x}}{1 + \frac{\overline{W} \Delta t f |Q_n|}{8(\overline{DW})^2}} \quad (3)$$

where Δt = time step

Δx = space step

W = segment width

The primed quantities indicate unknown quantities whose values are determined at time $t + \Delta t$, from the unknown quantities on the right-hand side of the equation. The over-barred quantities represent averages based on the n^{th} and $(n-1)^{\text{th}}$ segments.

The continuity equation is expressed in finite difference form as:

$$\eta_n' = \eta_n + \frac{\Delta t}{\Delta x} \frac{1}{W} (Q_n - Q_{n+1}) \quad (4)$$

The segment characteristics used in the model are given in Table 1 and their locations, in Figure 5. Where small inlet segments connect two very large bodies of water, such as Indian River Inlet and "The Ditches", a Keulegan (1967) type inlet equation is used. The equation may be expressed as an example for Indian River Inlet as:

$$Q_2 = \frac{A_c \sqrt{2g} |\eta_1 - \eta_2| \text{sign}(\eta_1 - \eta_2)}{\sqrt{K_{en} + K_{ex} + f\ell/4R}} \quad (5)$$

where A_c = cross sectional flow area of Indian River Inlet

Q_2 = flow onto Indian River Bay from the Atlantic Ocean

η_2 = Indian River Bay tide

η_1 = Atlantic Ocean tide (specified)

K_{en} = entrance loss coefficient = 0.3

K_{ex} = exit loss coefficient = 1.0

R = hydraulic radius of the inlet

ℓ = length of the inlet

f = Darcy-Weisbach friction factor

The boundary conditions to be specified are the ocean and Delaware Bay tides at the mouths of Indian River Inlet (3.8 ft (1.2m) mean, 4.6 ft (1.4m) spring) and Roosevelt Inlet (4.4 ft (1.3m) mean, 5.2 ft (1.6m) spring), respectively (NOAA, 1977). The average time lag between each location was calculated to be 0.77 hours based on a month's tidal prediction, with the tides of Roosevelt Inlet lagging behind those of Indian River Inlet.

The development of the model was based on a similar study at Navarre Pass, Florida, (Coastal and Oceanographic Engineering Laboratory, University of Florida, 1973).

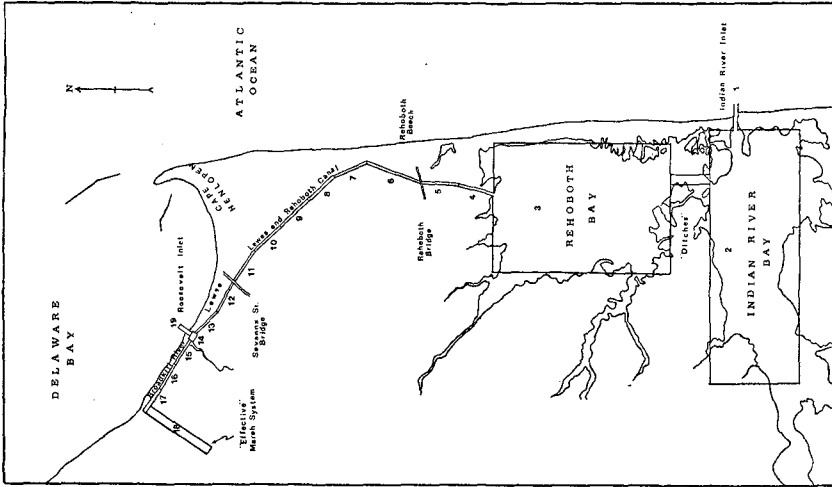


Figure 5 Schematization of the Bay and Waterway Segments, Roosevelt to Indian River Inlet

Bay and Waterway Segments

#	Length(ft)	Width(ft)	Depth(ft)	f	Description
1					Atlantic Ocean Tide
2	31,000	11,000	6	0.03	Indian River Bay
3	21,000	16,000	6	0.03	Rehoboth Bay
4	4,800	100	3	0.03	
5	4,800	100	3	0.03	
6	6,600	75	6	0.03	Lewes and Rehoboth Canal
7	4,500	100	6	0.03	
8	4,500	100	6	0.03	
9	4,500	100	7	0.03	
10	4,500	100	7	0.03	
11	4,500	100	7	0.03	
12	4,000	150	10	0.03	
13	4,000	150	10	0.03	
14	800	500	12	0.03	Canal-Inlet Junction
15	3,700	150	9	0.03	Lower Broadkill River Section
16	3,700	150	5	0.03	
17	3,700	150	5	0.03	
18	9,000	1,000	3	0.03	Effective Marsh System
19					Delaware Bay Tide

Inlet Characteristics

Length(ft)	Width(ft)	Depth(ft)	f	$K_{en} + K_{ex}$	Description
6,000	800	16	0.03	1.3	Indian River Inlet
4,000	1,000	5	0.03	1.3	"Ditches"
2,000	470	12	0.03	---	Roosevelt Inlet

Table 1 Characteristics of Hydraulic Model Segments

b. Results and Data Comparison. The results of the model were compared to tide and current measurements recorded at Roosevelt Inlet and the L&R Canal (Savannah Street Bridge - see Figure 5 for location) during June 1977, as well as with any other readily available source, such as the NOAA tide tables. Generally, the model showed good correlation with the field data but underpredicted the peak discharges and over predicted the peak tidal amplitudes. At Roosevelt Inlet the discharge peaks measured in the field were underpredicted by the model by as much as 40%.

Table 2 lists the predicted flow volumes for various locations in the system. The total volume passing the mouth of the Broadkill River $8.36 \times 10^7 \text{ ft}^3$ ($2.34 \times 10^6 \text{ m}^3$) was adjusted in the model by varying the dimensions of the "effective marsh" Segment No. 18 to match field measurements by DeWitt (1968).

The most apparent result indicated by Table 2 is the net southerly flow present throughout the system. The net volume pumped during each tidal cycle is approximately $6.3 \times 10^6 \text{ ft}^3$ ($1.76 \times 10^5 \text{ m}^3$) for mean tide conditions and $7.8 \times 10^6 \text{ ft}^3$ ($2.18 \times 10^5 \text{ m}^3$) for spring tide conditions. This net volume pumped is represented by a mean flow of 141 and 176 cubic feet (3.9 and 4.9 m^3) per second per tidal cycle for mean and spring tidal conditions, respectively (roughly 0.2-0.3 ft/sec (0.09m/sec) in the L&R Canal). The net volumes listed for all locations seem to indicate that mass is not conserved within the system (i.e., $6.3 \times 10^6 \text{ ft}^3$ enter through Roosevelt Inlet and $7.15 \times 10^6 \text{ ft}^3$ exit through Indian River Inlet for mean tide conditions). This error (18%) is a result of the computer accuracy in performing the integration routine for net volume over the complete tidal cycle and is not reflective of the time marching solution.

The current measurements recorded for this study also indicate the presence of a net southerly flow. For instance, a net southerly flow volume of $1.0 \times 10^7 \text{ ft}^3$ ($2.8 \times 10^5 \text{ m}^3$) was recorded at Savannah Street Bridge, which reduces to a mean flow of $230 \text{ ft}^3/\text{sec}$ ($6.4 \text{ m}^3/\text{s}$). This phenomenon has also been indicated in another set of recent field data (Jensen, 1977). More interestingly, a study dated back to the year 1930, undertaken to determine the effect of the Lewes and Rehoboth and Assawoman Canals on the behavior of Indian River Inlet, also revealed a net southerly flow out of the L&R Canal, which at this time was calculated to be $5.5 \times 10^6 \text{ ft}^3$ ($1.54 \times 10^5 \text{ m}^3$) (Indian River Inlet Commission, 1931).

The mean pumping to the south within the system is due to the combined effect of the mass transport of the two tidal waves entering each inlet, as well as the frictional characteristics of the system. A reasonable approximation of the net discharge quantity through the canal results, if one considers two separate tidal waves entering at each inlet and subtracts the respective mass transports for the net result. From long-wave theory the mass transport per unit width, M , is expressed as:

$$M = \rho q = E/C$$

(6)

TABLE 2. Predicted Flow Volumes* for Various Locations

Location	Mean Tide Conditions				Spring Tide Conditions			
	Volume Over One Tide Cycle $\text{ft}^3 \times 10^{-6}$		Net Volume $\text{ft}^3 \times 10^{-6}$	Mean Flow $\text{ft}^3/\text{s} \times 10^{-2}$	Volume Over One Tide Cycle $\text{ft}^3 \times 10^{-6}$		Net Volume $\text{ft}^3 \times 10^{-6}$	Mean Flow $\text{ft}^3/\text{s} \times 10^{-2}$
	North	South			North	South		
Roosevelt Inlet	59.1	65.4	6.3 S ⁺	1.41	66.6	74.4	7.83 S	1.75
Broadkill River Mouth	41.8	41.8	0	0	47.1	47.1	0	0
Savanna Bridge	13.3	19.6	6.3 S	1.41	14.7	22.6	7.85 S	1.76
Rehoboth Bridge	9.08	15.4	6.3 S	1.41	9.61	17.5	7.86 S	1.76
"Ditches"	253	259	6.6 S	1.49	271	279	8.48 S	1.89
Indian River Inlet	940 (Flood)	947 (ebb)	7.15 (ebb)	1.60	1063 (Flood)	1072 (ebb)	9.10 (ebb)	2.04

* Numbers Rounded Off After Computation
 + S or N indicates direction

where

$$E = \text{wave energy} = \frac{\rho g H^2}{8} \quad (6)$$

$$C = \text{wave celerity} = \sqrt{g h}$$

with all other terms previously defined. Solving for q and expanding:

$$q = \frac{gH^2}{8 \sqrt{g h}} \quad (7)$$

Defining the net discharge per unit width as $q_{\text{net}} = q_c - q_o$ where the subscripts "c" and "o" refer to the canal and Atlantic ocean entrances, respectively, equation (7) may be cast in the following form:

$$q_{\text{net}} = \frac{g}{8} \left[\frac{H_c^2}{\sqrt{g h_c}} - \frac{H_o^2}{\sqrt{g h_o}} \right] \quad (8)$$

Substituting the appropriate quantities of $H_c = 4.4$ ft (1.34m) and $h_c = 10$ ft (3.05m) for the canal and $H_o = 3.8$ ft (1.16m) and $h_o = 16$ ft (4.88m) for Indian River Inlet into equation (8), we find $q_{\text{net}} = 1.77$ ft²/s (0.17m²/s). For the canal, which is approximately 100 feet (30.5m) in width, the net discharge would be 177 ft³/s (5.0m³/s). This estimate is reasonably close to that quantity predicted by the model of 141 ft³/s (4m³/s) for mean tidal conditions.

The effect of friction within the system can be evaluated from the following results. The model predicts that high tide occurs roughly about the same time in Indian River Bay and in the southern end of the L&R canal, with high tide occurring in Rehoboth Bay approximately 1.9 hours later, hence the tidal division line lies within Rehoboth Bay. In addition, low tide in Indian River Bay is predicted to occur nearly 1.4 hours before it occurs at the southern end of the canal. This indicates that Rehoboth Bay starts to drain through "The Ditches" into Indian River Bay long before it drains into the L&R Canal.

Therefore, in summary, it is felt that the mean pumping throughout the system is caused by the dominate southerly discharge, propagating completely through the canal into Rehoboth Bay on flood tide, whereupon during ebb tide Rehoboth Bay drains more favorably toward the south through a less frictionally resistant passage.

c. Effects of Net Flow. The amount of sediment carried into or out of an inlet is dependent on the power available in the ebb and flood flows to move the sediment plus the amount of sediment supplied to the inlet by littoral transport. When a mean flow is present over the tidal cycle, a bias in the tidal power exists, and this can materially affect the depositional characteristics of the inlet. A study by Costa and Isaacs (1975), using both a physical and numerical hydraulic model, showed that the superposition of a small current upon an unbiased tidal flow significantly altered the deposition pattern around the inlet. In fact, the results of their physical movable bed

model indicate that a secondary flow of one percent of the main flow directed in the ebb direction results in at least a twelve percent increase in sediment load being carried seaward.

Following the ideas and developments set forth by Costa and Isaacs, the effect of the anisotropic flow through the bay and canal system on the tidal power available for sediment transport was investigated. Within this development it is assumed that the work done in transporting sediment in the flood and ebb directions can be expressed as:

$$I_{f,e} \sim \int_{f,e} P(t)dt \sim \int_{f,e} \epsilon V^3(t)dt \tag{9}$$

where $I_{f,e}$ = work accomplished in transporting sediment in the flood and ebb directions

$P(t)$ = power utilized in sediment transport

$V(t)$ = velocity in the inlet as predicted by the model

ϵ = transport efficiency

The transport efficiency developed empirically by Costa and Isaacs after data presented by Inman is shown to be a function of the stream power as given by:

$$\epsilon = 0.01 \left[\left(\frac{V}{V_C} \right)^3 \right]^{1.86}, \quad V_C^3 < V^3 < 5V_C^3 \tag{10}$$

where V_C = velocity at which incipient motion begins

It was assumed that for the range of particle sizes present in the inlet, approximately 0.4mm to 1.0mm, that 20 cm/sec or 0.66 ft/sec would be representative of the critical velocity, V_C , based on a curve developed by Hjulström (1935) contained in Graf (1971).

The work done on sediment transport for both flood and ebb tide at Roosevelt Inlet was computed from the numerical integration of Equation 9 with the results given in Table 3.

TABLE 3 Sediment Transport Work Per Tidal Cycle at Roosevelt Inlet

Tide Condition	Available Work Per Tidal Cycle (ft-lbs)			Work Ratio Flood/Ebb
	Flood	Ebb	Net	
Mean	148	26	122 F	5.7
Spring	470	72	394 F	6.2

It is readily apparent that the mean pumping into the inlet results in a significant bias of the available tidal work to transport sediment into the inlet. In fact, the results show that the sediment transport work is approximately six times greater for flood than ebb. Although no investigation of the tidal power at Indian River Inlet was undertaken, it is clear that a similar, but opposite, (ebb to flood) bias exists.

The effects of the sediment transport bias should be reflected in the depositional characteristics of each inlet. At Roosevelt Inlet, the majority of the sediment that enters the channel deposits in lobe-like shoals along both banks (as mentioned previously), eventually clogging the rear of the entrance channel. In addition, strong evidence of the presence of an ebb-tidal shoal was not found (at least within the survey limits of this project). Both of these factors suggest a net flood transport as predicted in the model.

At the other end of the system, indications of a net seaward sediment transport should be evident. One indication of this has been the development of a rather extensive ebb tidal shoal currently estimated to contain 4,884,000 yd³ (3,763,260m³). Secondly, the sediment introduced to the system through erosion and scour of the inlet channel seems to have been dominated by ebb tidal flows since an overall loss within flood tidal shoals has been evident. Estimates of the material within the general vicinity of the flood shoals show slightly over one million cubic yards (7.65x10⁵m³) has been removed.

STABILITY ANALYSIS

In the preceding section it was surmised that the bias of tidal power can significantly influence the depositional patterns and hence the sedimentary stability of the inlets. At Roosevelt Inlet there was a tendency toward closure as sediment was continually trapped within its throat. On the other hand, Indian River Inlet is thought to be quite stable against closure with scour and enlargement present. In this section, the sedimentary stability of these two inlets will be further investigated by adopting the concepts developed by Escoffier (1940), O'Brien (1969) and Jarrett (1976).

A stability curve of maximum inlet velocity, V_{max} , versus the inlet cross sectional area, A_c , based on the concepts first developed by Escoffier, was generated for Roosevelt Inlet through the use of the numerical model discussed previously. Historic cross sections were fed into the computer, and a corresponding V_{max} was calculated using spring tidal conditions. Further cross sectional area data were generated, assuming the area could continually decrease with a minimum width of 200 ft (61m). The resulting curve is shown in Figure 6. It is seen that the inlet has always been in the stable portion of the curve. The change in cross section along this portion of the curve has been principally dominated by dredging activity. A closer look at the data indicates a general trend of increasing cross sectional area following dredging activity prior to June 1963. After this date, reductions in cross sections are evident following dredging activity.

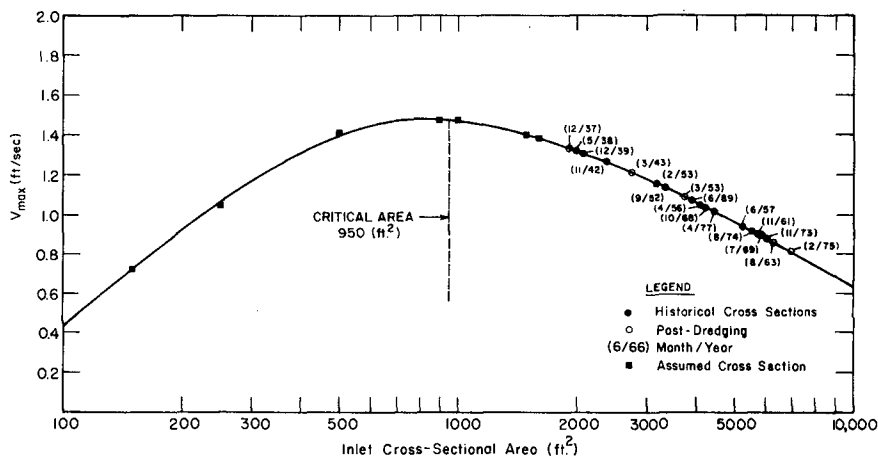


Figure 6 Stability Curve for Roosevelt Inlet

This trend reversal has presumably been caused by the rapid deterioration of the jetties accompanying the devastating 6-8 March 1962 storm which, in turn, altered the nature and rate of deposition.

Other approaches to inlet stability by O'Brien and Jarrett have been based on empirical relationships between the inlet throat cross sectional area and the tidal prism. These relationships are mostly based on data of inlets that connect the ocean with a bay or bays; thus Roosevelt Inlet is a unique case. With this in mind the effect of the mean flow on the sedimentary stability of the inlet may somewhat supersede the prism area relationships at hand.

If it is assumed that the tidal prism can be closely represented by the following:

$$P = A_c \int_0^{T/2} V_{max} \sin \frac{2\pi t}{T} dt = \frac{A_c V_{max} T}{\pi} = \frac{Q_{max} T}{\pi} \quad (11)$$

where T is the semidiurnal period of 44,700 seconds. The tidal prism-area relationships of these investigators may be plotted with the stability curve. Where intersection occurs between the stability curve and the prism-area curve, the inlet is expected to reach an equilibrium satisfying both hydraulic and sedimentary properties. These curves are shown plotted in Figure 7. The figure shows that the stability curve lies below the prism-area curves for all cross sections, indicating a strong tendency for closure to occur. However, the exact position of the stability curve is open to question since: (1) The model used in generating the curve generally underpredicted the peak flows measured

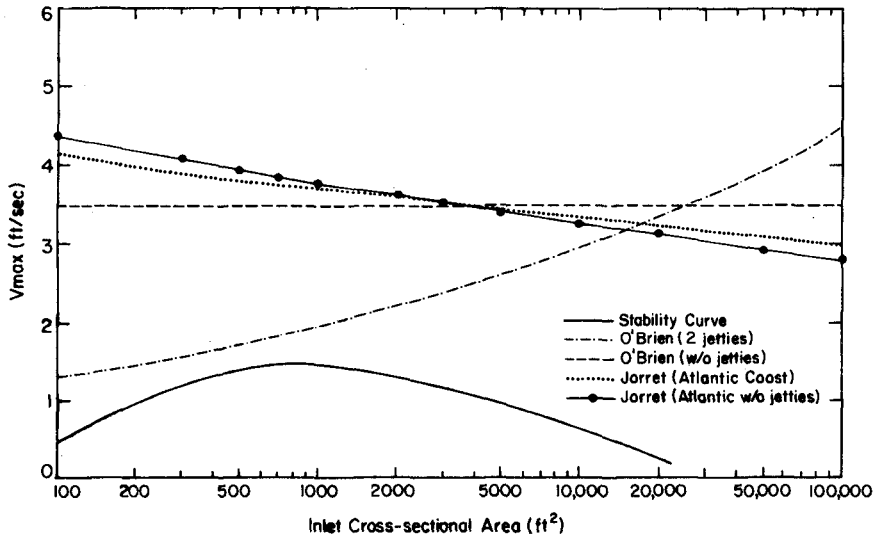


Figure 7 Stability and Prism-Area Curves for Roosevelt Inlet

in the field and (2) the prism-area relationships were developed from inlets on fully exposed coasts unlike Roosevelt Inlet, and (3) the prism-area relationships are not directly applicable since they were derived mostly from inlets without net flows.

Similar curves were also generated for Indian River Inlet through analytical means. Historic average inlet cross sections were plotted, based on theoretical relationships presented by O'Brien and Dean (1972). These points are shown in Figure 8, marked with the appropriate date.

Additional points corresponding to cross sectional areas larger than the present were computed for the inlet deepening but not widening. The solid line was computed, based on a constant rectangular cross sectional shape, the width 20 times the channel depth. It is seen from the figure that the inlet has progressed from the unstable (frictionally dominated) portion of the curve, through the critical area and into the stable portion with a present cross sectional area of about 20,000 ft² (1,860m²).

The solid stability curve was also plotted with the various tidal prism area relationships as shown in Figure 9. All these prism-area curves intersect the stability curve near $A_c = 31,000$ ft² (2,883m³) and $V_{max} = 3.6$ ft/sec (1.1m/sec). As mentioned beforehand, the inlet could be expected to reach an equilibrium state when it suffices both relationships simultaneously. The present enlargement trend of the inlet channel may be an attempt to reach this equilibrium area.

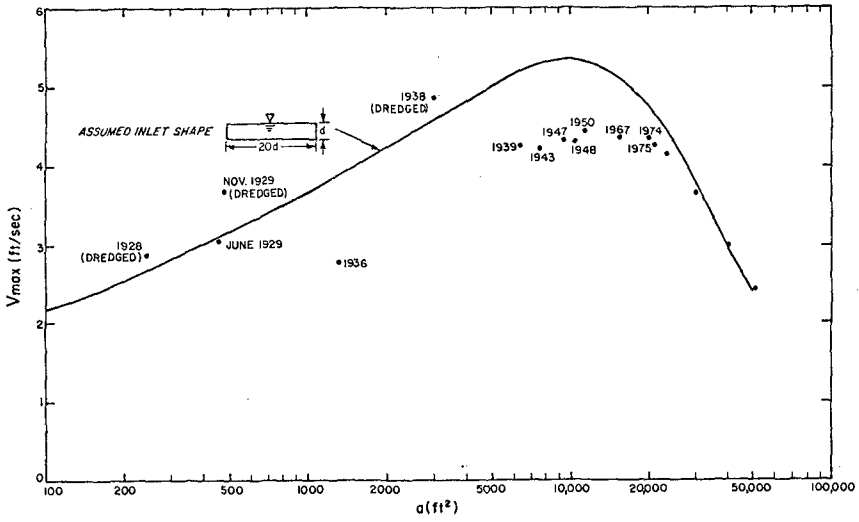


Figure 8 Stability Curve for Indian River Inlet for Historical and Assumed Cross Sections

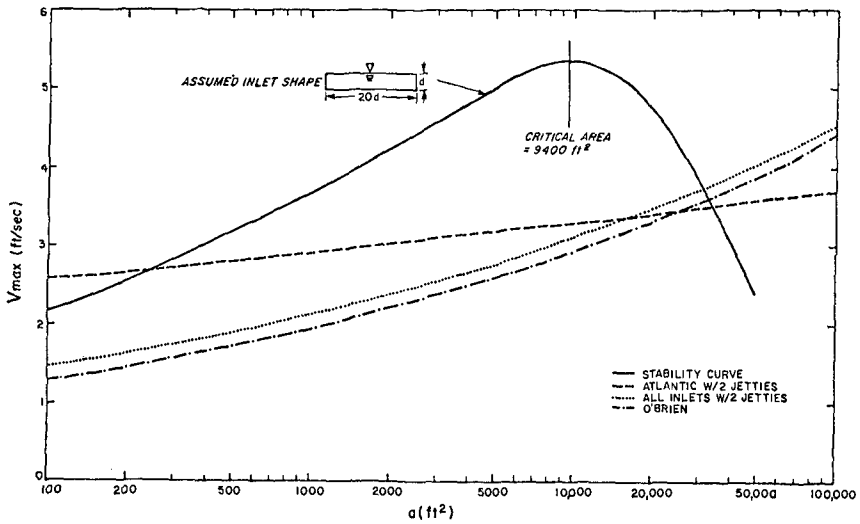


Figure 9 Stability and Prism-Area Curves for Indian River Inlet

Overall, the results of the stability and prism-area concepts reveal that neither of the inlets is presently in equilibrium. For Roosevelt Inlet a tendency for reduction in area is evident, mostly through a decrease in width from the developing sand lobes along the banks. At Indian River Inlet a tendency for cross sectional enlargement is expected to continue, mostly through a general deepening.

A true equilibrium will only exist if there is a zero mass transport through the system. The cross sectional enlargement at Indian River Inlet and decrease at Roosevelt Inlet are possibly natural adjustments to gradually alter the respective flow regimes at each inlet to reach a zero net flow condition.

CONCLUSIONS

1. Downdrift erosion is the major problem that developed after the stabilization of each inlet. In both cases sediments easily enter the inlet channel where they are transported to developing shoals with no apparent natural return to the littoral system. Sand primarily enters Indian River Inlet through the overtopping of the impounded south jetty. At Roosevelt Inlet sediments are readily transported past the badly deteriorated steel sheet pile structures.
2. The results of a one-dimensional hydraulic model, as well as field measurements, predict the presence of a mean southerly flow through the canal and bay system which connect Roosevelt and Indian River Inlets. This flow is believed to cause a major bias in the tidal power available for sediment transport at each inlet (6 to 1 at Roosevelt Inlet), thus significantly influencing the depositional characteristics at both locations.
3. The tidal power bias, as well as stability and equilibrium analyses, indicates that at Roosevelt Inlet a tendency toward closure is evident; whereas, Indian River Inlet seems quite stable against such an occurrence.

REFERENCES

- Coastal and Oceanographic Engineering Laboratory, Florida Engineering and Industrial Experimental Station, "Coastal Engineering Study of Proposed Navarre Pass," University of Florida, Gainesville, 1973.
- Costa, S. L. and Isaacs, J. D., "Anisotropic Sand Transport in Tidal Inlets," Symposium on Modeling Techniques, Vol I, 2nd Annual Symposium of the Waterways, Harbors and Coastal Engineering Division of ASCE, September 1975.
- Dean, R. G. and Perlin, M., "Coastal Engineering Study of Ocean City Inlet, Maryland," Coastal Sediments '77 Specialty Conference, ASCE, Waterway, Port, Coastal and Ocean Division, 1977.

- Dennis, W. A. and Dalrymple, R.A., "The Study of Beach Erosion at Roosevelt Inlet, Lewes, Delaware," Ocean Engineering Technical Report, Department of Civil Engineering, University of Delaware, Newark, 1978.
- DeWitt, W., "The Hydrography of the Broadkill River Estuary," unpublished Masters Thesis, Department of Biology, University of Delaware, Newark, 1968.
- Escoffier, F. F., "The Stability of Tidal Inlets," Shore and Beach, Vol 8, No. 4, pp 114-115, 1940.
- Graf, W. H., Hydraulics of Sediment Transport, McGraw-Hill Book Co., New York, 1971.
- Indian River Inlet Commission, Report of the Indian River Inlet Commission to the 103 Assembly of the State of Delaware, U.S. Engineer Office, Wilmington, DE. 1931.
- Jarrett, J. T. "Tidal Prism -- Inlet Area Relationships," Department of the Army, Corps of Engineers, GITI Report No. 3, 1976.
- Jensen, P.A., Lecturer, College of Marine Studies, University of Delaware, Newark, Field data and personal communication, 1977.
- Keulegan, G. H., "Tidal Flow in Entrances, Water-Level Fluctuations of Basins in Communications With Seas," Committee on Tidal Hydraulics, Department of the Army, Corps of Engineers, Technical Bulletin No. 14, 1967.
- Lanan, G. A., and Dalrymple, R. A., "A Coastal Engineering Study of Indian River Inlet, Delaware," Ocean Engineering Technical Report No. 14, Department of Civil Engineering, University of Delaware, Newark, 227p, 1977.
- O'Brien, M. P., "Equilibrium Flow Areas of Inlets on Sandy Coasts," J. of Waterways, Harbors and Coastal Engineering Division, ASCE, Vol. 95 No. WW1, pp 43-52, 1969.
- O'Brien, M. P., and Dean, R. G., "Hydraulics and Sedimentary Stability of Coastal Inlets," Coastal Engineering, Chapter 41, pp 761-780, 1972.
- Thompson, W. W. and Dalrymple, R. A., "A History of Indian River Inlet, Delaware," Shore and Beach, July, Vol. 44, No. 22, pp 24-31, 1976.

ACKNOWLEDGMENTS

These studies were supported by the Office of Sea Grant Programs under grants to the University of Delaware.

CHAPTER 76

NUMERICAL MODEL INVESTIGATION OF SELECTED TIDAL INLET-BAY SYSTEM CHARACTERISTICS

William N. Seelig (1)
Robert M. Sorensen (2)

Abstract

A spatially integrated one-dimensional numerical model of inlet-bay hydraulics has been combined with a simple sediment transport model to investigate selected tidal inlet-bay system characteristics. A parametric study has been performed using the models to determine the effect of various factors on the net direction and order of magnitude of inlet channel flow and sediment transport. Factors considered include astronomical tide type, storm surge height and duration, variation in bay surface area, time-dependent channel friction factor, and the addition of a second inlet connecting the bay and sea.

Introduction

The purpose of this study is to investigate selected basic flow and sediment transport characteristics of tidal inlets. A simple numerical hydraulic-sediment transport model applied to an idealized inlet-bay system is used to evaluate the time-dependent channel ebb and flood flow velocity and sediment transport rate as well as the net and gross sediment transport rate for a tidal cycle. The independent variables investigated are:

1. Common tidal types found on the Atlantic, Gulf and Pacific coasts of the United States.
2. A normalized storm surge of varying peak height and duration.
3. A water-level dependent variable bay surface area.
4. Time-dependent channel resistance specified by a variable Manning coefficient.
5. A second inlet of varying cross-sectional area.

Inlet-Bay System

The idealized inlet shape used in this study (Figure 1) was designed to have characteristics typical of tidal inlets, but excludes

¹Hydraulic Engineer, Coastal Structures Branch, US Army Coastal Engineering Research Center, Ft. Belvoir, Virginia 22060.

²Chief, Coastal Structures Branch, US Army Coastal Engineering Research Center, Ft. Belvoir, Virginia 22060

any ebb or flood tidal deltas. This idealized shape was developed during a classification study of many inlets throughout the United States.

The bay area is initially taken as independent of bay water level and the tidal wave length in the bay is assumed to be much longer than the longest axis of the bay.

Inlet Hydraulics

The numerical model of inlet hydraulics used in this study was reported earlier in Sorensen and Seelig (1976) and discussed in detail in Seelig et al. (1977). Important characteristics of the model are: (1) the continuity equation is used to relate rate of bay water level change, dh_b/dt to inlet velocity, V , by assuming that the surface water level is uniform throughout the bay at any time. That is

$$VA_c = A_b \frac{dh_b}{dt} \quad (1)$$

where A_b is the bay surface area and A_c is the inlet cross-sectional area. Storage of water in the inlet is neglected. (2) motion of water in the inlet is described by the one-dimensional equation of motion along the inlet channel axis:

$$-g \frac{d\eta}{dx} = \frac{fV|V|}{8R} + V \frac{dV}{dx} + \frac{dV}{dt} \quad (2)$$

where η is the water surface elevation, R is the channel hydraulic radius, x the distance along the channel axis from some reference point, f the channel friction factor, and g the acceleration of gravity. Eq. 2 relates the horizontal driving force due to the water surface slope to the channel frictional resistance, the convective acceleration caused by velocity variation along the channel axis, and the temporal acceleration (or inertia) caused by velocity variation with time.

In this numerical model the inlet is divided into a series of channels and cross-sections to produce a flow net grid. Each grid element is assigned a Manning's n , depth, width, and length. Eq. 2 is written in a finite element form. Equations (1) and (2) are then solved in a time marching procedure for solving differential equations with boundary conditions applied at each time step. Flow is assumed to follow the path of least resistance and the amount of flow in each grid element at each time step is determined accordingly.

This numerical model has been tested for a variety of inlets throughout the United States and found to be a reliable low-cost method for predicting the hydraulics of inlets.

The idealized inlet in Figure 1 was modeled using a semi-diurnal sinusoidal tide with an amplitude, a_o , of 61 cm and period, T , of 12.4 hours for various values of bay surface area. Figure 2 shows results of the hydraulic predictions where the phase lag and the dimensionless maximum velocity, V'_{max} , have been averaged for the flood and ebb portions

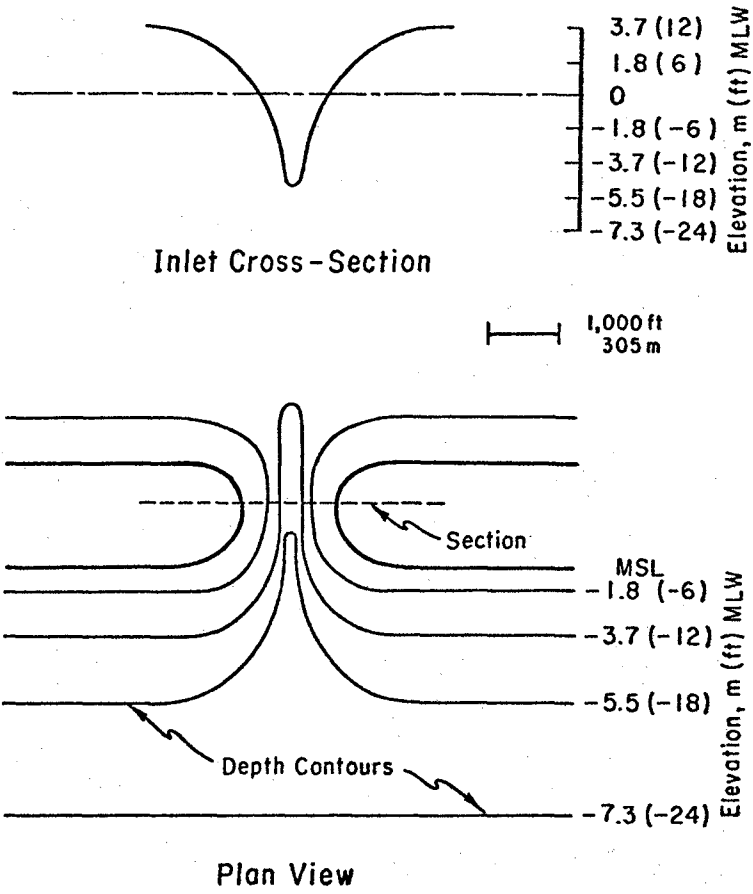


Figure 1. Idealized inlet

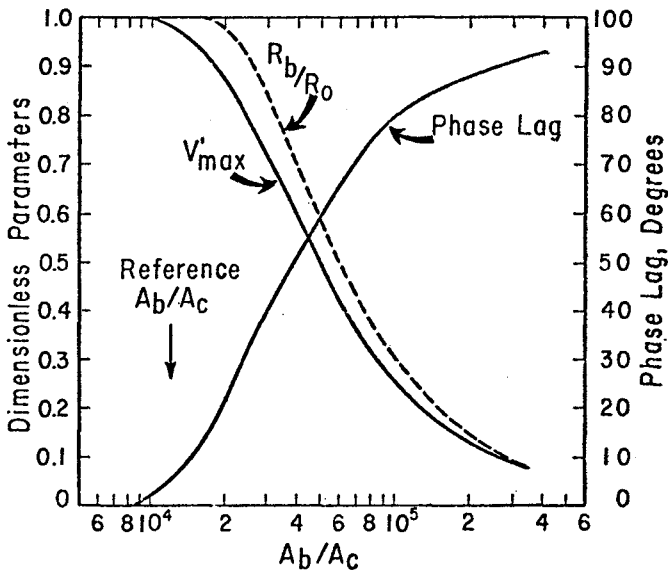
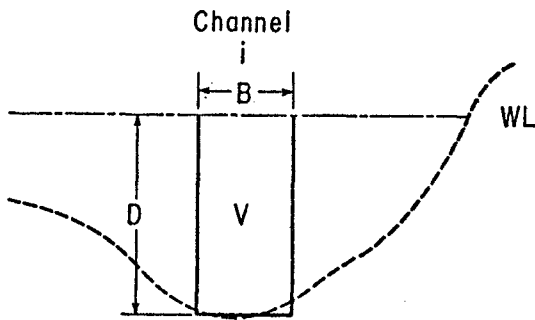


Figure 2. Inlet-bay hydraulic characteristics



Sediment Transport

$$Q_s = k \sum_{\text{cross section}} B (|V| - V_c)^3 \text{sg}(V)$$

Figure 3. Sediment transport calculations

of the tidal cycle. We define

$$V'_{\max} = V_{\max} T A_c / (2\pi a_o A_b) \quad (3)$$

where V_{\max} is the maximum channel velocity averaged across the throat cross section during a tidal cycle. Manning's n used in these calculations is taken as a weak function of channel water depth:

$$n = 0.038 - 0.0022 D \quad (4)$$

where D is the still water depth in meters for each grid.

Jarrett (1976) made a study of tidal inlets throughout the U.S. and presented a relationship between the cross-sectional area of the inlet at still water level and the tidal prism. This condition is satisfied for the idealized inlet where $A_b/A_c = 1.2 \times 10^4$. Conditions at this point are referred to as "the reference condition". For the reference condition the bay tide range is approximately equal to the tide range in the ocean.

Sediment Transport Model

The rate of sediment transport, Q_s , across the minimum cross-sectional area portion of the inlet is taken as:

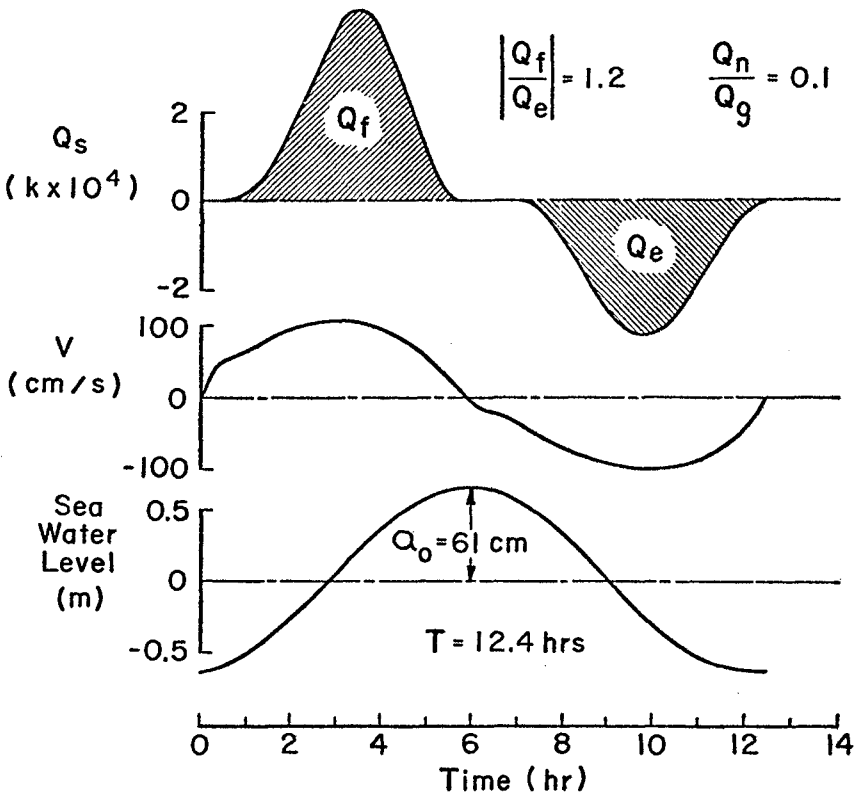
$$Q_s = k \sum_{i=1}^N B (|V| - V_c)^3 \text{sg}(V) \quad (5)$$

where $\text{sg}(\)$ is the sign function, V is the velocity for a grid for a time step, $|V|$ is the magnitude of V , V_c is a critical velocity below which the sediment transport rate can be neglected (V_c is taken as 30 cm/sec in this study), N is the number of grid channels, and k is some unknown function influencing the transport rate (Figure 3) and B is the grid channel width. In this study k is taken as an unknown constant.

Figure 4 shows the predicted rate of sediment transport and average inlet throat velocity for the reference condition. Note that the maximum inlet velocity is slightly higher than 100 cm/sec, which is typical for natural tidal inlets. Changes in depth, cross-sectional flow area and frictional resistance throughout the tidal cycle produce asymmetries in water velocities that are magnified in the predicted rate of sediment transport. For example, the predicted rate of flood sediment transport for this case is higher but generally shorter in duration than for ebb.

The rate of sediment transport is integrated over the flood and ebb portions of the cycle to give volumes of transport, Q_f and Q_e . For the conditions in Figure 4 the flood transport is 20% higher than the ebb transport and the net transport volume is about one-tenth of the gross or total volume of sediment transport.

In the following sections, deviations from the reference conditions are systematically made and the predicted sediment transport volumes are compared to the reference condition.



REFERENCE CONDITION

$A_b/A_c = 1.2 \times 10^4$

$n = 0.038 - 0.0022D$

Figure 4. Hydraulic and sediment predictions for the reference condition

Influence of Tide Type

Astronomical tides are not strictly sinusoidal, as assumed in the reference condition, but are influenced by numerous astronomical and local affects. To obtain some idea of the effect of the astronomical tide type, tides were predicted for three locations (Wilmington, N.C., Galveston, Texas, and Los Angeles, California) using a computer program developed by D.L. Harris of CERC. Tides were predicted for the entire month of January 1981 and normalized by dividing by the root-mean-square of the water levels to give the tides the same energy. The relative amounts of calculated net and gross sediment transport and samples of the tide are given in Figure 5. These results suggest that for a fixed amount of tidal energy a semi-diurnal tide (top curve) produces the largest predicted gross transport with a relatively large net flood sediment transport, while a semi-diurnal tide with a strong inequality has lower gross transport and net transport in the ebb direction.

Storm surges investigated in this study are taken as having a normal shape with range in the ocean, R_0 . The period of the surge is characterized by four times the standard deviation of the normal shape. Figure 6 illustrates a surge of this type and shows the predicted hydraulic response. The inlet velocities are highly asymmetrical due to inertia and non-linear effects.

Predicted sediment transport volumes for storm surges are given in Figure 7 for surges with durations of one to eight hours and various surge amplitudes. The left portion of the figure shows the ratio of predicted flood to ebb sediment transport. For most conditions investigated, the value of this ratio is greater than unity, indicating that more transport occurs on the flood than ebb portion of the tidal cycle. In the right section of the figure the gross amount of sediment transport is normalized by the gross transport predicted for the reference semi-diurnal tide condition. (The superscript (')) indicates sediment transport has been normalized by conditions at the reference condition). The right portion of Figure 4 shows that the amount of transport during a surge can be an order of magnitude more than during astronomical tidal cycle.

The astronomical tide plus a storm surge produces a complicated pattern of sediment motion. The magnitude and direction of the sediment motion depends on the amplitude of the tide and are strongly influenced by the phase relation between the tide and surge. In conditions modeled, the gross transport for a surge plus tide reached as much as three times the value predicted for the surge and tide acting independently. Net transport was as high as one and one-half times larger.

Influence of Bay Surface Area

The bay surface area usually will not be constant with changing water level as was assumed in the reference condition. Flooding of tidal flats and sloping bay shores may dramatically change the bay surface area throughout the tidal cycle. A number of bay area variation models were tested and three are presented in this paper. First, bay area is assumed to be a linear function of bay level (Figure 8) and

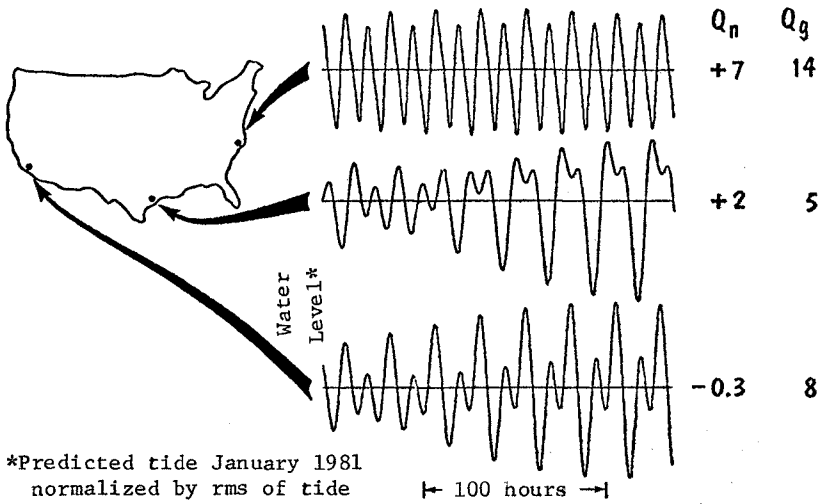


Figure 5. Influence of tide type on sediment transport

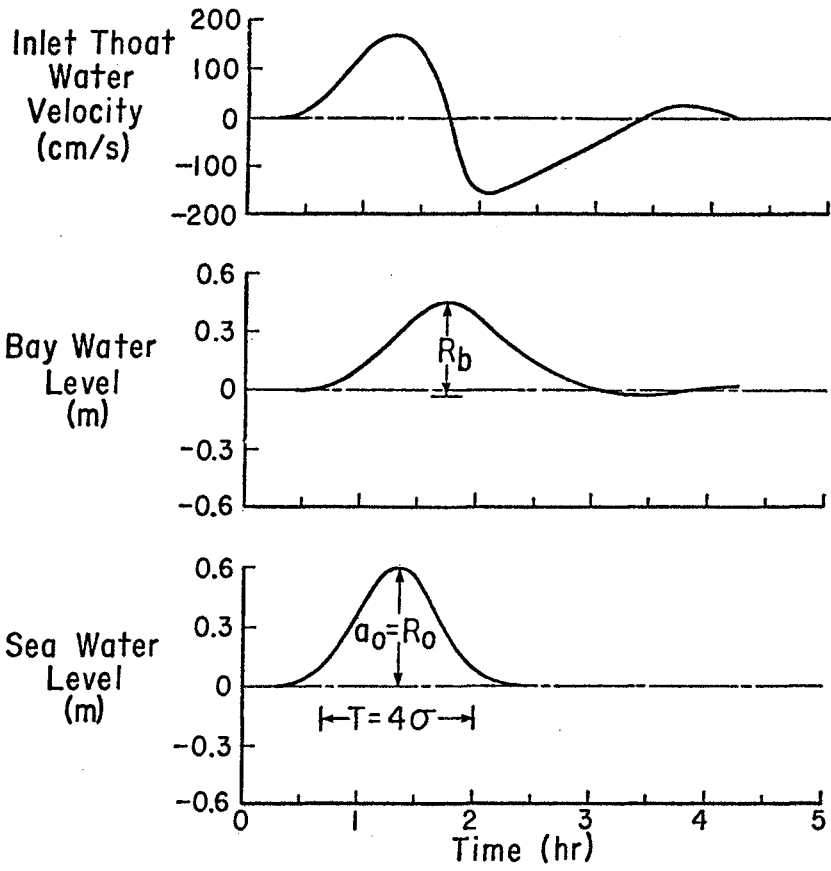


Figure 6. Inlet hydraulic response to a storm surge

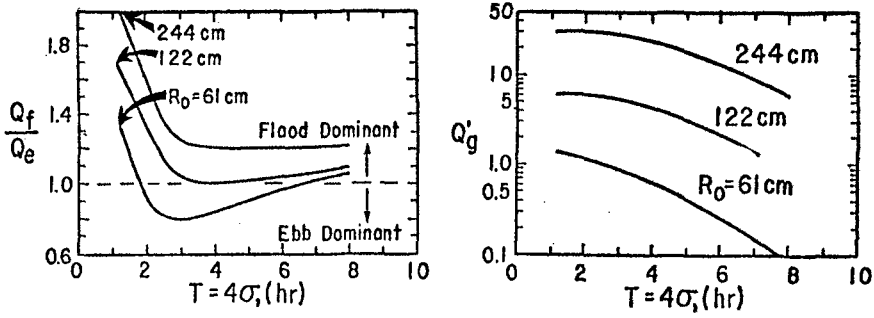


Figure 7. Sediment transport caused by a storm surge

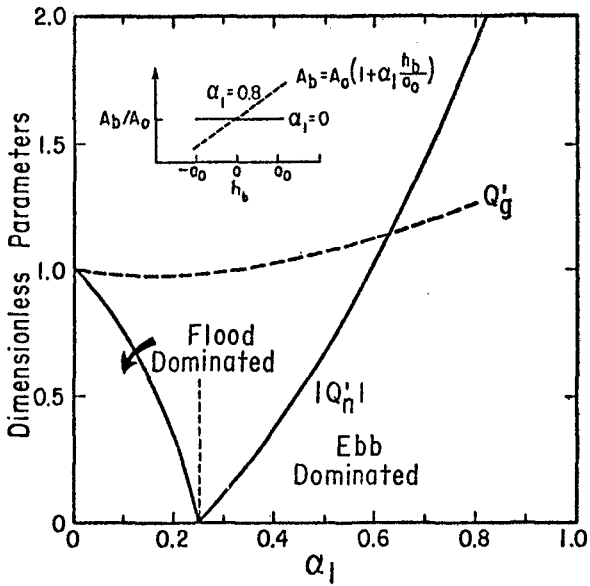


Figure 8. Effect of bay area variation on sediment transport

the amount of variation is characterized by the parameter, α_1 . If $\alpha_1 = 0$, there is no bay surface area variation and the reference condition is reached. As α_1 increases larger variations occur in surface area as the water level changes (upper portion of the figure).

As the rate of surface area change is increased (α_1 gets larger) the amount of gross sediment transport increases while the tidal prism remains approximately constant. Less flood dominance is present, as shown by the net transport, so that for $\alpha_1 = 0.25$ there is no net sediment transport predicted. For $\alpha_1 > 0.25$ net transport is in the ebb direction.

As a second form of bay area variation the bay surface area below the still water level is taken as constant and there is a linear variation above the still water level (Figure 9). This case could correspond to a bay with extensive incised channels and well-developed tidal flats at or above the mean water level. The pattern of trends in sediment motion is similar for this bay area change model to that for the linear case. No net motion occurs when $\alpha_2 = 0.58$.

Results for an exponential bay area variation model are given in Figure 10. The transition between net flood and net ebb sediment transport for this bay area variation model occurs at $\alpha_3 = 0.28$.

Influence of Channel Resistance

In the reference condition the Manning's friction factor, n , was made to weakly decrease with channel depth (Equation 3). This encourages higher flow rates in deeper portions of the inlet channel, so that predicted gross sediment transport is higher than for a constant value of n (Figure 11). Higher values of n decrease gross transport, but actually increase the amount of net transport because asymmetries throughout the flow cycle are enhanced (Figure 11).

Behrens et al. (1977) carried out a field study on Corpus Christi Pass, a tidal inlet dominated by frictional effects. Manning's friction factor was computed for the inlet as a function of time and found to vary strongly throughout the tidal cycle. For most cases studied, n steadily increased until it reached a maximum towards the end of a ebb or flood portion of the tidal cycle. In some cycles the opposite pattern was observed. Both cases were investigated in the idealized inlet (Fig. 12).

The case of the increasing n is characterized by a velocity that rapidly changes at flow reversal and reaches a high value that is retained throughout much of the cycle. The situation where n decreases during the cycle has larger variation in velocity with time (Figure 12). In spite of the differences in the shape of the velocity curves for these two cases, the gross and net amounts of predicted sediment transport are approximately the same. The volumes of sediment transport are approximately the same as if the mean value of n were used throughout the tidal cycle.

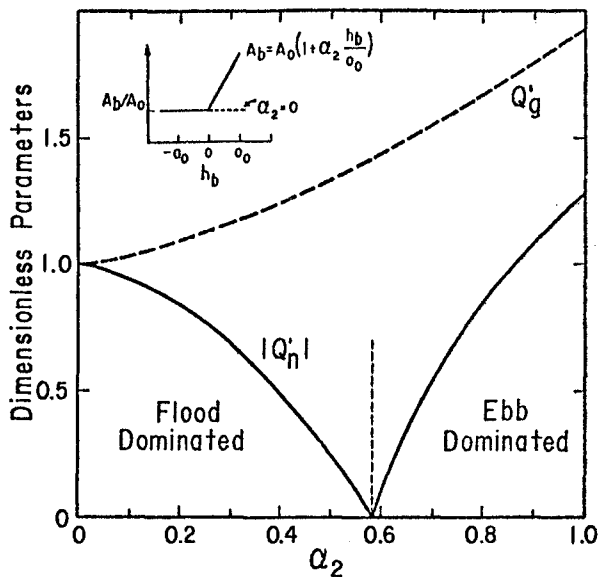


Figure 9. Effect of bay area variation on sediment transport

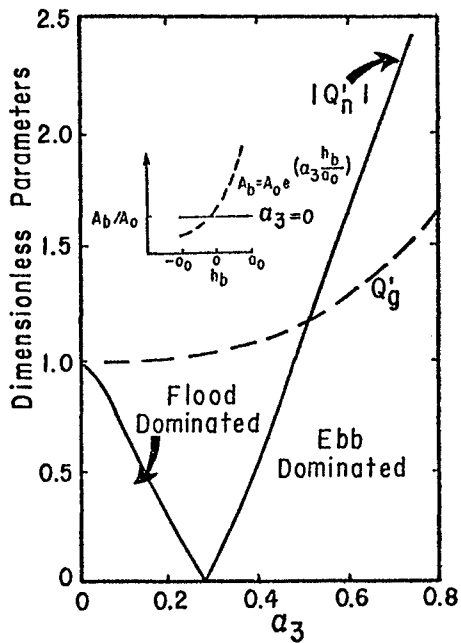


Figure 10. Effect of bay area variation on sediment transport

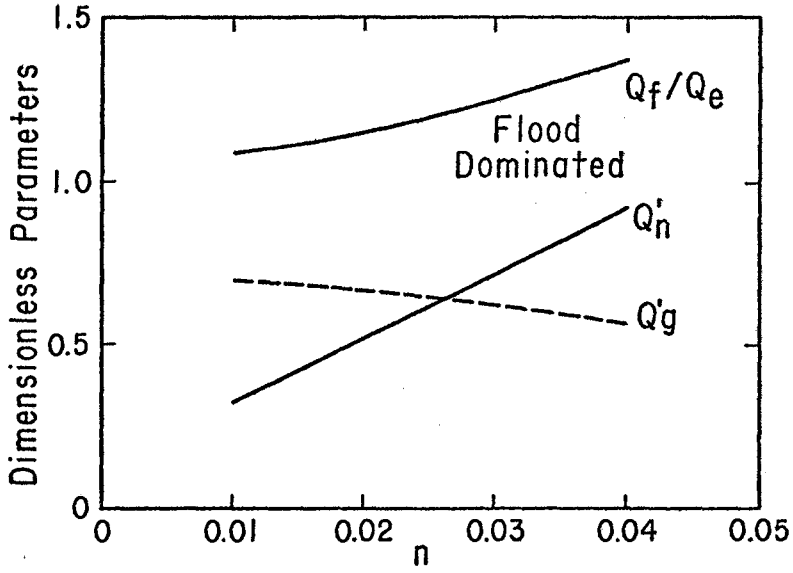


Figure 11. Effect of Manning's n on sediment transport

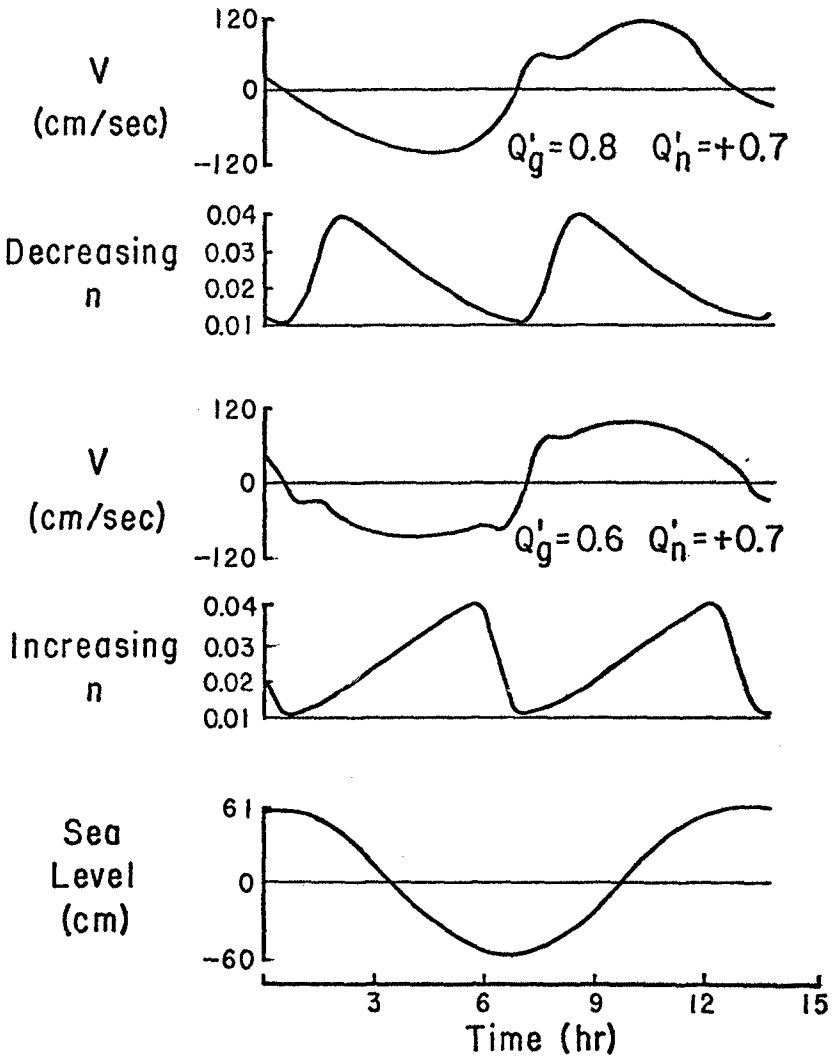


Figure 12. Effect of variable n on inlet hydraulics and sediment transport

Influence of a Second Inlet

A bay may be connected to an ocean by more than one inlet. The effect of a second inlet is examined by adding another inlet to the system with a length equal to the width of the barrier island. The second inlet is taken as prismatic with a width to depth ratio of 50, which was found as most typical for US inlets in an inlet classification study performed by Vincent (1978). Predicted transport volumes for the reference condition tide are shown in Figure 13.

As the size of the second inlet increases, the sediment transport in the idealized inlet rapidly decreases, so that when the cross-sectional areas are equal, $(A_{C1} + A_{C2})/A_{C1}=2$, the transport in the idealized inlet is less than ten percent of that at the reference condition. Total transport in the second inlet increases as its area increases until transport reaches a maximum when the cross-sectional area is approximately half of the idealized inlet. The sediment transport in the idealized inlet is generally larger than in the second inlet because the idealized inlet's deep gorge makes it more hydraulically efficient.

Summary and Conclusions

A numerical model investigation of the sediment transport in a realistic inlet shape shows that:

- (1) A semi-diurnal tide produces the largest amount of sediment motion and gives a net flood sediment transport, when several tides types of equal energy are compared.
- (2) Storm surges can move significantly more sediment than is moved during an astronomical tidal cycle. The phasing of a surge and tide is especially important in determining the amount and net direction of transport.
- (3) If the surface of the bay changes as the bay water level fluctuates there will tend to be less flood sediment motion and more ebb sediment motion than for the case of no bay area change.
- (4) High inlet friction enhances flow asymmetries so net sediment transport increases while gross sediment transport decreases. An inlet with a Manning's n friction factor that varies throughout the cycle produces approximately the same amount of sediment transport as the inlet with the mean value of n.
- (5) A second inlet may greatly reduce the amount of sediment transport in the primary inlet and the total transport of the two inlets can be smaller than if only the first inlet connects the bay and ocean.

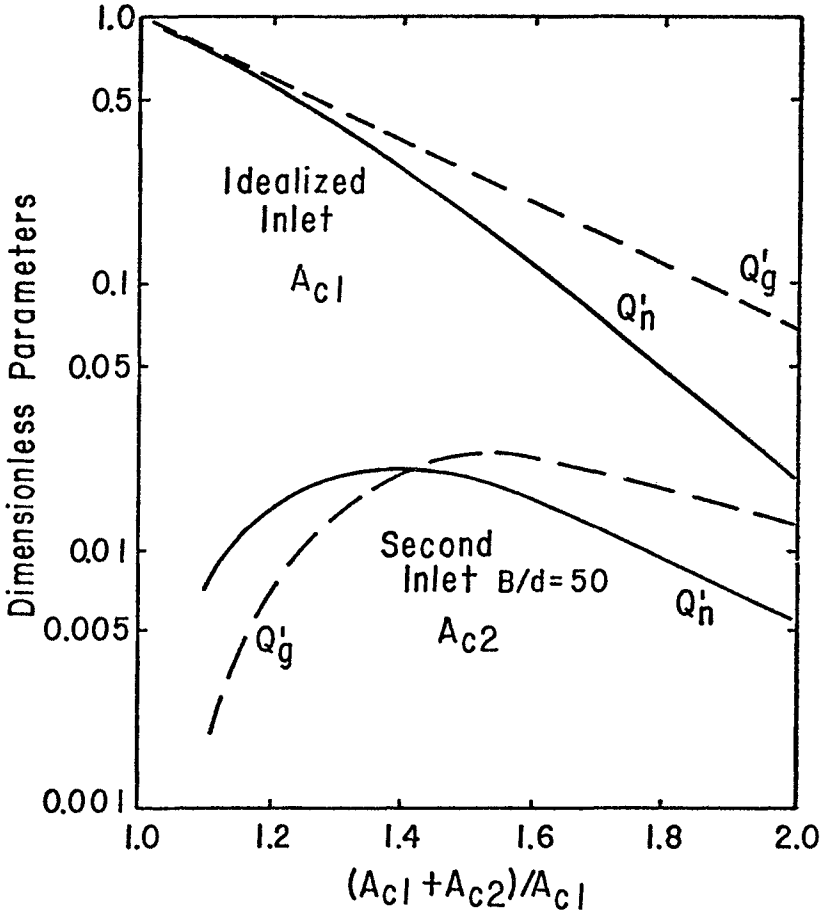


Figure 13. Effect of a second inlet on sediment transport

Acknowledgment

The analysis and results presented in this paper, unless otherwise noted, were based on research conducted at the Coastal Engineering Research Center under the Coastal Engineering Research Program of the U.S. Army Corps of Engineers. The findings of this paper are not to be construed as official Department of the Army position unless so designated by other authorized documents. Permission to publish this information is appreciated.

REFERENCES CITED

- Behrens, E. W., Watson, R. L. and Mason, C., "Hydraulics and Dynamics of New Corpus Christi Pass, Texas: A Case History, 1972-73", GITI Report No. 8, CERC-WES, January 1977.
- Jarrett, J. T., "Tidal Prism - Inlet Area Relationships", CERC-WES General Investigation of Tidal Inlets Report 3, February 1976.
- King, D. B., and Shemdin, O. H., "Modeling of Inlet-Bay Systems in Relation to Sand Trapping", Symposium of the Waterways, Harbors and Coastal Engineering Division, ASCE, 1975, pp 1623-1637.
- Seelig, W., "Computer Program Documentation - INLET2", unpublished report, U.S. Army Coastal Engineering Research Center, Ft. Belvoir, VA. 13 December 1976.
- Seelig, W., Harris, D. L. and Herchenroder, B. E., "A Spatially Integrated Numerical Model of Inlet Hydraulics", CERC-WES General Investigation of Tidal Inlets Report 14, November 1977.
- Sorensen, R. M. and Seelig, W., "Hydraulics of Great Lakes Inlet - Harbors Systems", Proceedings Fifteenth Coastal Engineering Conference, ASCE, July 1976, pp. 1646-1665.
- Vincent, L., "The Geometry of Selected Tidal Inlets", CERC-WES General Investigation of Tidal Inlets Report (in publication), U.S. Army Coastal Engineering Research Center, Ft. Belvoir, VA 22060, 1978.

SYMBOLS

A_b	bay surface area
A_b'	dimensionless bay surface area = A_b/A_c
A_b^*	reference bay surface area
A_c	inlet cross-sectional area at the throat
A_o	bay surface area at the still water level
a_o	sea tidal or surge amplitude
B	inlet grid width
d	water depth
f	channel friction factor
g	acceleration of gravity
h_b	bay water level
k	sediment transport factor (value unknown)
n	Manning's bottom friction coefficient
P	tidal prism
Q_e	ebb sediment transport
Q_f	flood sediment transport
Q_g'	dimensionless gross sediment transport normalized by the reference condition
Q_g^*	reference gross sediment transport
Q_n'	dimensionless net sediment transport normalized by the reference condition
Q_n^*	reference net sediment transport
Q_s	rate of sediment transport
R	hydraulic radius
R_b	bay tidal range
R_o	sea tidal range
t	time
V	instaneous flow velocity
V_c	threshold velocity for sediment motion
V_{max}	maximum inlet velocity at the inlet throat (mean of ebb and flood for periodic flow)
V_{max}'	dimensionless maximum inlet velocity
X	distance
$\alpha_1, \alpha_2, \alpha_3$	bay surface area variation parameters
η	water level

CHAPTER 77

VELOCITY AND STRESS MEASUREMENTS IN A TIDAL INLET

David A. Huntley
Department of Oceanography
Dalhousie University
Halifax, Nova Scotia
B3H 4J1, Canada

Dag Nummedal
Department of Geology
Louisiana State University
Baton Rouge, Louisiana
70803, USA

ABSTRACT

Fast-response electromagnetic flowmeters were used in a marginal flood channel of an ebb tidal delta to assess the importance of wave contributions to the flood dominance of these channels. Measurements were made at a single point in the channel in both ebb and flood currents. The oscillatory motion of waves was a very significant feature of the velocity records, and its magnitude was comparable with the mean flow at all stages of the tide. This observation shows that flowmeters capable of responding accurately to wave velocities are needed to obtain accurate values of mean flow. Some earlier measurements made with slow response flowmeters are probably unreliable. Wave contributions to the mean flow were assessed by looking at the correlation between the low frequency ($>17.5s$) oscillations of the along-channel current and the low frequency envelope of the wave velocities. Surprisingly little correlation was found for any time lag, suggesting that wave effects were not important in the mean tidal currents in the channel studied. However, close to low tide on the ebb, conditions existed which appear to have been favourable for the "wave pump" mechanism suggested by Bruun and Viggisson (1973). Significant correlation between the wave envelope and low frequency fluctuations was observed at this time. It is therefore suggested that wave effects can be important to the mean flow in marginal channels with rapidly converging and shoaling mouths which are oriented towards the dominant incident wave direction.

INTRODUCTION

A tidal inlet is a complex region whose continually changing morphology is the result of the interaction of wave and tidal forces acting on the nearshore sediments. The most prominent feature of an

ebb-tidal delta is a broad relatively deep central channel, usually essentially at right-angles to the coastline, terminating on the seaward side with a deltaic fan of sediment often many kilometres offshore. This channel is flanked on either side by linear bars, and broad sheets of sand known as swash platforms on which shoreward migrating swash bars are commonly observed. On either side of the inlet, between the swash platforms and the beaches adjacent to the inlet, one usually finds marginal channels which are dominated by flood tidal currents (Hayes 1975).

Considerable understanding of the processes responsible for forming and maintaining the topography of these inlets has been gained from study of their morphology, and from measurements of the average tidal and wave parameters, but it is clear that more direct and detailed measurements of wave and tidal forces are needed to clarify some of the dynamic models inferred from these studies. The present investigation was designed as a preliminary look at the relative role of waves and tides in the hydraulics of the marginal flood channels of an inlet.

The dominance of flood currents in marginal channels is generally accepted, on the evidence of bedforms and a few direct measurements of tidal current (Brun and Gerritsen, 1959, Oertel, 1972, 1975, Fitzgerald et al 1977). Clearly the inertia of a jet-like ebb flow through the inlet mouth is likely to result in an asymmetry of the tidal currents on the seaward side, with mean current gyres on either side of the ebb channel tending to enhance flood currents in the marginal channels. Dean and Walton (1975) suggest that flood dominance may also be partly due to entrainment into the ebb jet from the marginal channels.

Fitzgerald et al. (1977) suggest that waves could also be important in contributing to the flood dominance of marginal channels. A longshore variation of the height of waves breaking on the seaward side of the bar which flanks the flood channel creates a longshore gradient of set-up along the bar. Fitzgerald et al. hypothesise that this set-up gradient may be felt over the bar into the flood channel where it could drive a flood-directed current. Waves clearly might also contribute to flood dominance in several other ways. For example, wave refraction over the delta system tends to cause waves to approach the shoreline obliquely towards the inlet throat, so that at breaking they should drive flood-directed longshore currents in a narrow surf zone at the shoreline. In the highly turbulent conditions of a marginal flood channel these surf-zone driven currents might spread beyond the surf zone and influence the overall mean flow in the channel. Similarly longshore currents generated in the surf zone on the seaward side of the outer bar may also spread over the bar into the marginal channel. Also possibly relevant in this context is the

description of a "wave pump" by Bruun & Viggisson (1973) and Brunn & Kjelstrup (1978). In their wave pump, some combination of mass transport and wave set-up in waves breaking in a converging shoaling channel drives a current (more than 1 m/s in large laboratory tests with 1.6m waves) into an open discharge channel ahead of the waves. In a tidal inlet these effects could be important, particularly for waves refracted to travel directly along the marginal flood channel.

As a preliminary test of some of these ideas, fast response flowmeters have been used in a marginal flood channel to measure accurately the wave and tidal currents during both ebb and flood flows.

THE FIELD MEASUREMENTS

The site chosen for this study was Price Inlet, South Carolina, about 15 km north of Charleston Harbour on the Georgian Bight coast of the Southeastern United States (figure 1). An aerial photograph of the inlet a few months before our study shows the general complexity of the region (figure 2). The southern flood channel region is particularly complex. An older flood channel has just been closed to form an isolated pond, and a new flood channel is forming offshore. The



Figure 1: Map showing location of Price Inlet



Figure 2: Price Inlet at Low Tide, March 1977

photograph in figure 2 was taken in March 1977, and by the time of our study in November 1977 the new flood channel had become considerably better defined by continued growth of the offshore bar. The measurements described in this paper were taken in this southern flood channel on November 20th and 21st, 1977.

The flowmeters used in this field study were two-component electromagnetic sensors with a nominal time constant (low pass) of 0.2 seconds (Marsh-McBirney Model 511 OEM). Three of these instruments were mounted on arms attached to an aluminum tripod 0.3m high. Two were mounted so as to measure simultaneously vertical (w) and along-channel (u) flow at 0.75m and 0.35m respectively above the channel floor. The third flowmeter was aligned to measure along-channel (u) and cross-channel (v) flow 0.52m above the channel floor. Figure 3 shows in plan view the location of the instruments and a cross-section showing the position of the flowmeters in relation to the offshore bar and marginal channel. The sensors appear to be well to one side of the channel, though this may be somewhat deceptive since at the tidal height necessary to cover the sensors this displacement would not be so apparent. In any case there was no evidence of spatial asymmetry in the flow at this point, so that flow past the sensors should be representative of the cross-sectional average. (This was not true for the northern marginal channel at this inlet where the strongest ebb current was displaced well towards the seaward side of the channel while the flood current dominated the landward side of the channel.)

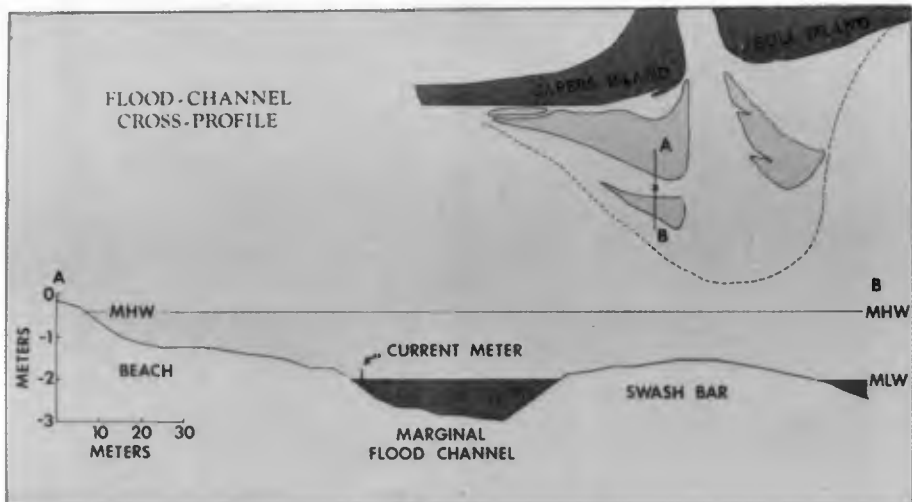


Figure 3: Plan and cross-section of marginal channel

The tripod mount holding the sensors was placed in this location near the time of low water and held onto the channel floor by lead weights placed in a cradle at the base of the tripod. Alignment of the sensor directions was achieved by sighting by eye along a range on the shore defined, from a theodolite survey, to be the across-channel direction; alignment accuracy was estimated to be approximately $\pm 5^\circ$.

Cables ran up the beach from the sensors to a telemetry system at the crest of the beach. This system consisted of a sealed aluminum canister about 2m high and 25cm diameter (designed also to be used as a surface buoy) containing batteries, an analogue multiplexing system for the six data channels and a low power transmitter. The buoy transmitted the data along line-of-sight to a receiving station and analogue data logger at some more convenient location. The receiving stations used in this experiment were either a hut with mains electricity about one km into the inlet or, more commonly for clarity of reception, a boat anchored in the channel throat on which car batteries were used as a power source. The analogue data were subsequently digitized at a sampling interval of 0.3 seconds for computer analysis.

An example of the velocity time series obtained with this system is shown in Figure 4. This record was taken during a flood tide, and a mean current of 62 cm/s in the flood direction has been removed from the along-channel velocity record. Positive velocities represent flood-directed, shoreward, and upward velocities respectively. The great irregularity in the flow is obvious from these records. The incoming waves broke at about 1m height on the margin of the swash platform but were reduced by multiple breaking over the platform to about 0.3m in height as they broke over the bar flanking the seaward side of the marginal channel. The larger of these waves, overtopping the bar, travelled obliquely shorewards in the channel with a large flood-directed component. These can be seen in the velocity records, for example between 38 and 50 seconds in Figure 4, as oscillations of both along-channel and cross-channel flow with a period of about 7 seconds. The time series of the product uv shows that these waves contribute large positive values to the flood-directed stress, for example at 38, 46, and 90 seconds. Superimposed on these waves are smaller higher frequency oscillations of velocity, probably caused by multiple wave crests refracted round the ends of the offshore bar and travelling in both ebb and flood directions along the channel. As is commonly observed in velocities from shoaling waves, the vertical velocity record appears much more spikey than the horizontal velocities, with a proportionally larger high frequency content (c.f. Huntley (in press)). This may in part be simply due to the smaller scale of the trace (peak of 0.25 m/s compared to 1.0 m/s and 0.75 m/s) but is also due to the sharp upward velocity peaks as the steep front of a shoaling wave passes. Notice also the presence of slow variations in the horizontal velocity records at periods much longer than observed wave periods.

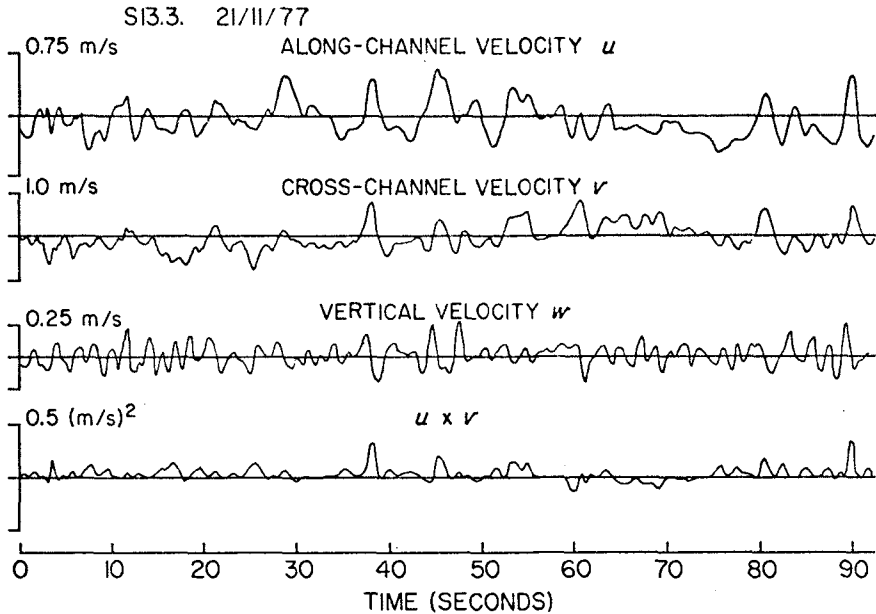


Figure 4: An example of the velocity records

Table 1 summarizes the flow parameters measured in the southern marginal flood channel. The four runs numbered 12. were made between 17:40 hrs and 20:40 hrs local time on November 20th, 1977 during an ebb flow; the three runs numbered 13. were made between 12:50 hrs and 14:45 hrs on November 21st, 1977 during the flood flow. The elevation is relative to chart datum and was measured about 1 km inshore along the ebb channel by a U.S. Department of Commerce NOAA tide gauge. This gauge also was used to give the times of runs relative to high water shown in the second column of Table 1. A second tide gauge was also running on the seaward side of Bull's Island about 1km north of the sensor location. This gave a similar tidal record, with a time lead of only five minutes, so the horizontal distance between tide gauge and sensors was considered unimportant. For reference, the top of the flood channel bar was at about 0.95m above chart datum, so that overtopping was strong only for the records closest to high water. This is reflected in the values of standard deviation of the along channel flow shown in Table 1. The values are large only for runs 12.1 and 13.3. At lower mean water levels the standard deviation has become much smaller and surprisingly constant; these values are probably due predominantly to waves propagating along the channel.

Table of Flow Parameters, Southern Flood Channel, Price Inlet, S. C.

November 20/21, 1977

Run I.D.	Time from H.W. (Hrs Mins)	Elevation (m)	Mean Ebb Flow cm/s	Standard Dev. cm/s	Shoreward Horizontal Stress ₂ (cm.s) ²
12.1	+1h 30m	1.56	+ 60.5	72.4	-----
12.2	+2h 49m	1.07	+ 24.1	17.9	72.1
12.3	+3h 32m	0.84	+ 40.3	14.4	18.0
12.4	+4h 13m	0.60	+ 32.6	15.1	- 12.3
13.1	-4h 01m	0.69	-105.0	17.5	36.3
13.2	-3h 09m	0.98	- 70.5	18.8	109.4
13.3	-2h 25m	1.22	- 61.7	38.3	214.8

The mean flows shown in Table 1 are means over 15 minutes of record. Two things can be concluded from these means.

First, it is clear that they are all of the same order of magnitude as the standard deviations. Thus any current meter used to measure tidal flows at this point in the inlet, and presumably at other positions, must be capable of responding correctly to wave currents so that they can be averaged out of the velocity record properly. It is known that most slow response flowmeters cannot respond quickly enough to fluctuations, particularly of direction, under waves and will tend to rectify wave velocities, thus recording higher than true mean currents. This observation may therefore call into question previous measurements of flow in tidal inlets at locations where wave velocities are significant. In particular the large increase in wave velocities near the time of high water would cause slow-response flowmeters to overemphasise the skewing of maximum flood and ebb currents towards the time of high water (Fitzgerald et al 1977).

The second conclusion from these observed means is that, as expected from previous investigations, flood currents are very much larger than ebb currents at the same water level and time from high water. The tidal range for the ebb was 1.47m while that on the flood was 1.31m, suggesting that the difference in currents would be even greater for the same tidal ranges.

The last column of Table 1 shows the flood directed horizontal stresses uv due to the fluctuations, averaged over 15 minutes. Figure 5 shows these values plotted against tide height and it is clear that they are positive on both flood and ebb for most tide levels, which for these data ranged from about 0.3m to about 1.7m above datum. The radiation stress theory of longshore currents (Bowen 1969, Longuet-Higgins 1970) shows that these positive (flood directed) stresses, if interpreted as radiation stresses, would drive longshore currents in the flood direction in the narrow surf zone on the shoreward side of the flood channel. Estimates of the magnitude of these currents suggest that they reached about 1 m/s near high tide (c.f. Huntley 1977). We will see in the next section how we might estimate the importance of this predominantly surf-zone current to the mean flow in the main channel, seaward of the break point. The observation of larger values of stress on the flood than on the ebb is perhaps to be expected since refraction of incoming flood-propagating waves by the flood and ebb currents will cause this effect. It will not necessarily be reflected in larger longshore currents in the narrow shoreline surf zone where tidal currents are much smaller.

The observation of a negative value on the ebb tide is of some interest. Towards low tide the predominant wave activity in the channel was due to waves which were refracted around the ebb-channel end of the bar and which propagated up the channel in the ebb direction; flood-propagating waves were reduced by the longer shallow path around the opposite end of the bar. The presence of these ebb-propagating waves at this stage of the tide is of particular interest, as we shall see later.

WAVE EFFECTS ON THE MEAN FLOW

Clearly, with current data from a single point we are unable to study directly the importance of longshore variability of wave height in driving flood currents, although such variability clearly existed. Neither are we able directly to measure local mass transport effects since surface elevation measurements were not made along with the flow measurements.

In fact, separation of mean wave and tidal effects is in general going to be extremely difficult without extensive measurements covering a wide range of incident wave climates.

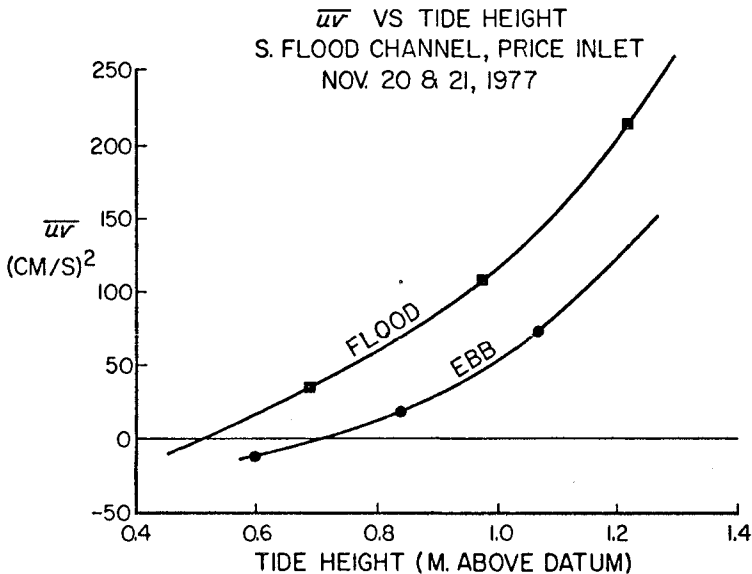


Figure 5:

Nevertheless, we might expect that any wave-driven component of the flow will show variations related to the "groupiness" of the wave record, i.e. to the envelope of wave velocities. This should be true in some sense for currents driven by a set-up gradient over the bar, for longshore current effects and for currents driven by non-local mass transport and set-up in waves propagating along the channel. We have therefore looked at the relationship between the low-passed portion of the along-channel flow and the time series of the envelope of the velocity fluctuations.

In spectral terms this involves dividing an initial spectrum of the alongshore flow (the upper trace of Figure 6) into two portions, using a Cartwright filter of 342 weights, with a half power point at a period of 15 seconds (Cartwright, personal communication). The lower trace in Figure 6 shows the same spectrum as the upper trace, but displaced downwards by an order of magnitude and divided into a low-passed and a high-passed portion. The high-passed portion contains, at each frequency, more than 99% of the spectral energy for periods shorter

than 12 seconds, and therefore includes the incident wave energy as well as the energy of higher frequency turbulent fluctuations. The low-passed portion, with the 99% level at 17.5 seconds, contains the longer period variability which may include wave-induced fluctuations as well as longer period turbulence. To obtain the wave envelope the high-passed time series was then squared and low-passed again with the same Cartwright filter.

Cross-correlation functions, the means of the product of two time series normalized by their standard deviations, were then calculated between the low frequency part of the original current record and the low frequency part of the wave envelope. These functions were calculated for different time lags between the two records to allow, in some average sense, for non-local forcing of the mean flow by the waves.

The result of these computations is, surprisingly, that all but one of the calculated cross-correlation functions have no significance at the 95% level for any time lag. Figure 7 shows an example of the cross-correlation function for run 13.1 and is typical of all runs except run 12.4. This result appears to suggest that wave forcing in the neighborhood of the sensors is of no importance in driving the mean flow under the wave conditions prevailing at the time of measurement. This does not, of course, preclude the possibility of purely local mass transport effects, but in view of the changing wave amplitudes along the channel this seems unlikely. Neither does it preclude the possibility that driving of the currents occurs at a location well removed from the sensor position and that wave breaking, dispersion and interaction destroys the relevant wave groups by the time they reach the sensors, but this too seems unlikely, particularly near high tide when the marginal channel is deep and relatively unobstructed.

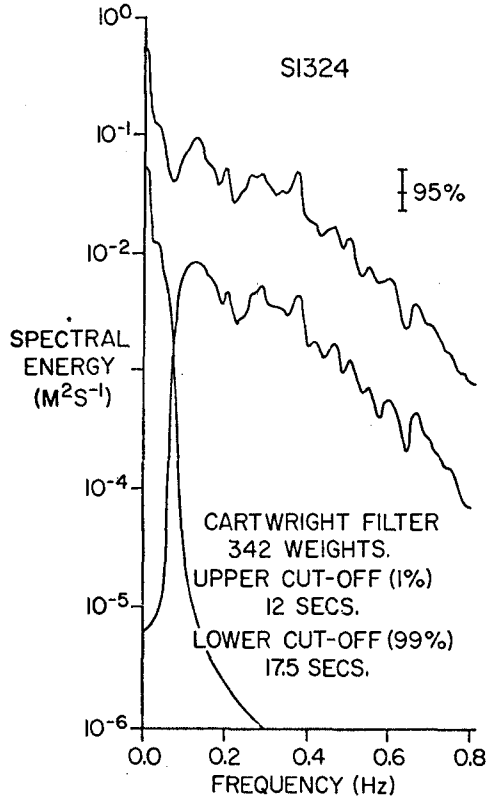


Figure 6: Dividing a spectrum into low and high frequency parts.

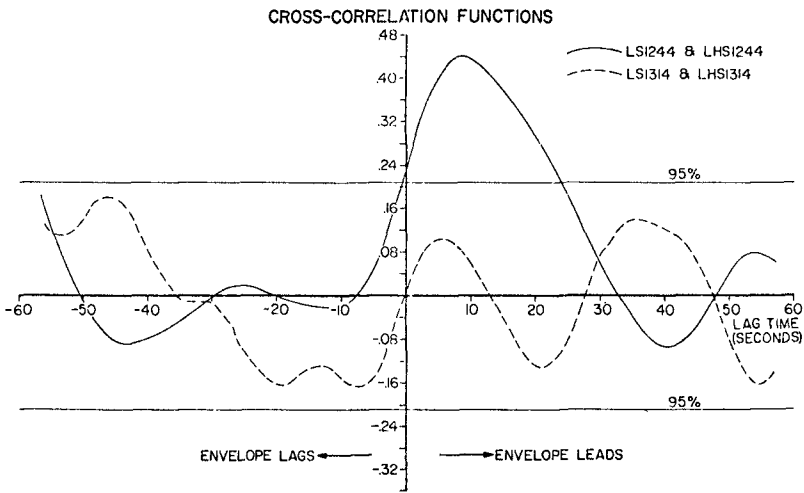


Figure 7: --- Run 13.1
 ——— Run 12.4.

The one exception, showing significant correlation, is run 12.4. Figure 7 shows that the cross-correlation function has a correlation which rises to about 0.44 when the envelope of the waves leads the current by about 9 seconds. Pre-whitening of the time series before forming this function, in the manner prescribed by Jenkins and Watts (1968), reduces the correlation somewhat (to about 0.26), but does not effect the conclusion of significance at this time lag. Cross-spectra between the original time series and the envelope of the high frequency fluctuations were also calculated to see whether significant correlation existed over a broad low frequency band or was confined to a narrow band. Again significant correlation was only found for run 12.4 and at periods longer than about 40 seconds. Figure 8 shows a section of the time series for 12.4; although the calculated correlation coefficient is small, it is nevertheless possible to see correlation between the two lower records, as indicated by the fine diagonal lines.

Run 12.4 is the run at the low-tide end of the ebb current sequence which gave the ebb directed radiation stress shown in Figure 5. In fact, the positive sign of the correlation between wave envelope and current suggests that a large wave group, propagating in this case in the ebb direction, drives an enhanced current in the ebb direction, though the significance of the time lag is not known.

SI244 MEAN FLOW = 0.33 m/s EBB

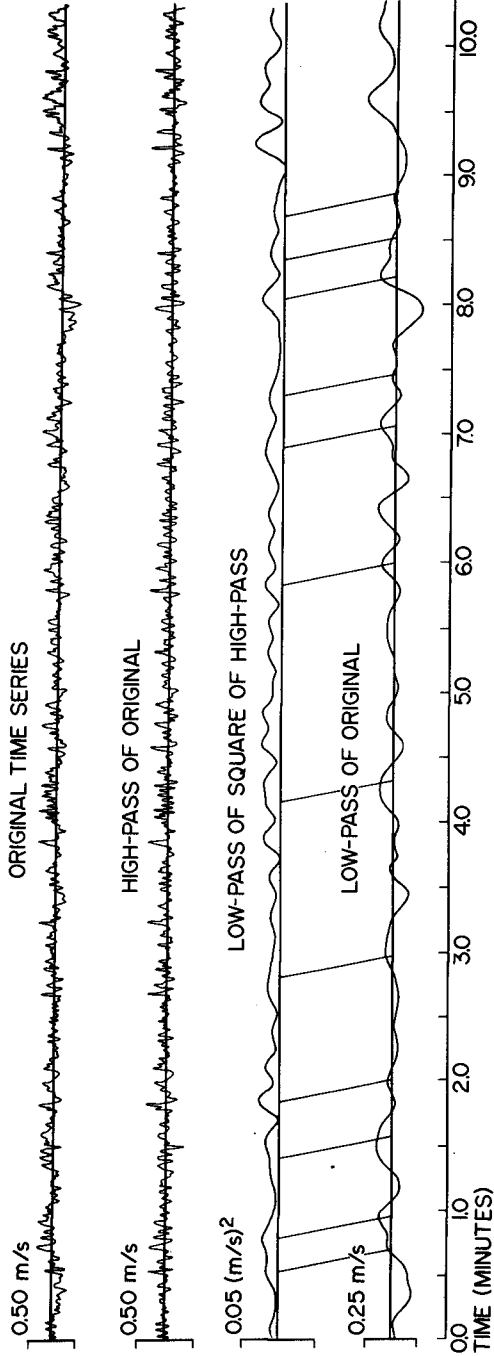


Figure 8: Time series showing correlation between low frequency velocities and the high frequency envelope.

DISCUSSION

It is interesting that wave effects seem to be generally of negligible importance to the mean flow at the measuring point. The significant longshore currents suggested by the calculated stress values must presumably be confined to a narrow region in the vicinity of the surf-zone at the shoreline, and be of no importance at the sensors, except perhaps close to low tide. Surprisingly, the effect of a longshore gradient of wave set up along the outer bar is also probably small; no wave effect in the low-passed flow is observed even when the water level is sufficiently high for significant breaker energy to propagate over the bar into the marginal channel.

Laboratory tests of the "wave pump" effects of set-up and mass transport (Bruun and Viggisson 1973, Bruun and Kjelstrup 1978) show that they are critically dependent on the geometry of the channel along which the waves propagate and on the breaking or non-breaking of the waves. Largest currents are generated when waves propagate directly along a rapidly converging shoaling channel into a basin or channel of constant or increasing depth ahead, and when waves are near to breaking or are spilling. For most of our runs in the southern flood channel none of these conditions seem to have applied. For waves from the flood direction the marginal channel converges very slowly and, except at the entrance, has a relatively flat bed. In addition, since dominant waves approach from the north-east, waves entering the southern flood channel have been refracted a great deal and are therefore relatively small.

However, for the one run that does show some significant correlation, waves from the ebb-channel propagated into the rapidly converging and shoaling mouth of the marginal channel before passing over the sensors a short distance into the channel, and these conditions seem to fit those for wave pump effects quite well. Thus, despite the predominantly null results from these data, it does seem that waves might be important in the marginal flood channels of an inlet if the topographic and wave conditions were right. In fact, the northern marginal channel of Price Inlet has a rapidly converging and shoaling topography at its seaward end (Figure 2) and wave refraction diagrams (e.g. Fitzgerald et al 1977) suggest that waves would propagate much more readily into this channel. Wave effects on the flood dominance of this channel may therefore be much more significant than in the southern marginal channel. Further work is underway to test this idea.

ACKNOWLEDGEMENTS

The help of Rob Holman and Mendel Spencer from Dalhousie, and Tim Kana and others from the Geology Department of the University of South Carolina was vital to the success of this project. Logistic support was provided by the Coastal Research Division, Department of Geology, University of South Carolina, directed by Miles O. Hayes. Mrs. E Magwood and her family generously allowed us to use her home during the field work.

Financial support for the project came from grants from the Army Research Office, administered by the University of South Carolina (DN), and from the Canadian National Research Council (DAH).

REFERENCES

- Bowen, A. J. 1969. The generation of longshore currents on a plane beach, J. Mar. Res. 27, 206-215.
- Bruun, P. and F. Gerritsen. 1959. Natural bypassing of sand at coastal inlets., Jour Waterways and Harbors Division, ASCE, Paper 2301, 75-107.
- Bruun, P. and S. Kjelstrup. 1978. The wave pump., Proc. 4th Conf. on Port and Ocean Engr. under Arctic Conditions. Memorial University of Newfoundland.
- Bruun, P. and G. Viggisson. 1973. The wave pump., Proc. 2nd Conf. on Port and Ocean Engr. under Arctic Conditions, Reykjavik, Iceland.
- Dean, R. G. and T. L. Walton. 1975. Sediment transport processes in the vicinity of inlets, with special reference to sand trapping: in Cronin, L. E. (ed.), Proc. 2nd Int. Estuarine Res. Federation Conf., Myrtle Beach, S. C. pp. 129-150.
- Fitzgerald, D. M., D. Nummedal and T. Kana. 1977. The sand circulation pattern at Price Inlet, S. C., Proc. 15th Coastal Eng. Conf., Hawaii, ASCE, New York.
- Hayes, M. O. 1975. Morphology of sand accumulation in estuaries: an introduction to the symposium: in Cronin, L. E. (ed.), Proc. 2nd Int. Estuarine Res. Federation Conf., Myrtle Beach, S. C., pp. 3-22.
- Huntley, D. A. 1977. Lateral and bottom forces on longshore currents. Proc. 15th Coastal Eng. Conf., Hawaii, ASCE, New York.
- Huntley, D. A. (in press). Edge waves on a crescentic bar system. Geological Society of Canada publication.
- Jenkins, G. M. and D. G. Watts. 1968. Spectral analysis and its applications. Holden-Day Inc., San Francisco. 525 pp.
- Longuet-Higgins, M. S. 1970. Longshore currents generated by obliquely incident sea waves. 1 & 2. J. Geophys. Res., 75, 6778-6801.

- Oertel, G. F. 1972. Sediment transport on estuary entrance shoals and the formation of swash platforms. Jour. Sed. Petrology, 42, 858-863.
- Oertel, G. F. 1975. Ebb-tidal deltas of Georgia estuaries: in Cronin, L. E., (ed.), Proc. 2nd Int. Estuarine Res. Federation Conf., Myrtle Beach, S. C. pp. 267-276.

CHAPTER 78

Periodic Flows from Tidal Inlets

by D.L. Wilkinson *

Introduction

A study was undertaken of the flow produced in the offshore region by tidal currents at the entrance of a coastal inlet. The gross features of the offshore flow structure were examined in an idealised two dimensional model in which a sinusoidally reversing flow was discharged from an open channel into a large stagnant basin. During each period of ebb flow, the discharge from the simulated inlet developed a structure very similar to that of a starting jet, and a vortex pair was observed to form and ultimately became the dominant feature of the flow. Although variable bottom topography and long shore currents will distort the flow pattern, the rotational motions observed in these experiments would be expected to persist.

The study was restricted to coastal inlets in which the sectional area of the entrance channel is several orders of magnitude smaller than the area of water surface inside the inlet.

Length and Time Scales of the Flow

The flow under study is shown schematically in Figure 1.

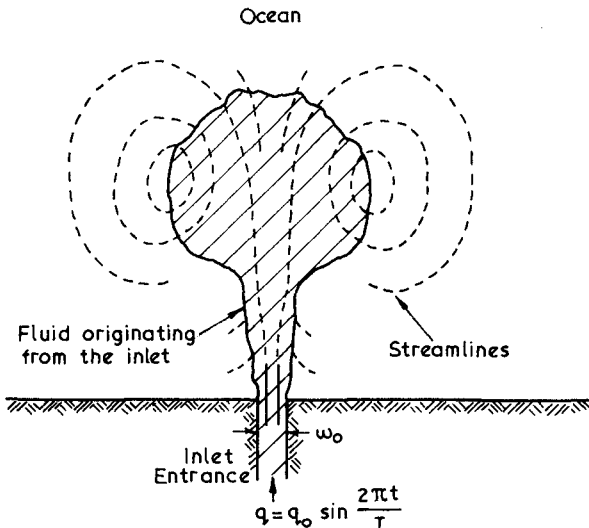


Figure 1: Schematic diagram of outflow from inlet

* Senior Lecturer, The University of New South Wales, Australia.

A periodically reversing flow passed through the entrance channel which joins to a large basin. The depths in the basin and the channel are uniform and the same. The flow per unit depth Q varies with time t according to the relationship

$$Q = Q_0 \sin \frac{2 \pi t}{T} \tag{1}$$

where Q_0 is the maximum flow rate and T is the tidal period.

It is well known that steady jets conserve axial momentum and that no characteristic length scale can be ascribed to them. However, if the strength of the jet is periodic with period T , it can be readily shown that a characteristic length scale exists for the motion. A periodic two dimensional jet at high Reynolds Numbers is fully defined by m_0 the maximum value of the momentum eflux, the period T , the width of the entrance channel w_0 , and the fluid density ρ . The momentum flux m_0 is given by

$$m_0 = \frac{\rho Q_0^2}{w_0} \tag{2}$$

The variables m_0 , T and ρ can be combined to give a characteristic length l which is now defined as

$$l = \left(\frac{1}{\rho} m_0 T^2 \right)^{1/3} \tag{3}$$

This is the appropriate length scale by which the structure of the flow may be described. Experiments have shown that l is of the order of the jet size, one period after the commencement of the ebb flow.

Any other flow parameter, for example the breadth b of the jet, at time t and distance x from the entrance, can be expressed non-dimensionally as

$$\frac{b}{l} = \text{fn} \left(\frac{x}{l}, \tau, \frac{w_0}{l} \right) \tag{4}$$

where τ is the normalised time t/T .

It is well established that the structure of steady jets is independent of the initial velocity structure at distances of 20 or more source widths downstream of the discharge point. Turbulence resulting from Kelvin-Helmholtz type instability in the shear zone, spreads in a direction normal to flow and destroys any initial structure. A similar situation can be expected to exist in the periodic jet provided the dimensions of the inlet are small compared with the size of the flow structures which develop. That is the ratio w_0/l must be small. This being so, it can be expected that periodic jets will have a general structural similarity at similar non-dimensional times.

Experiments

Experiments were conducted with three aims in mind:

- (i) To examine the basic structure of the flow and to check that the characteristic length as defined in Equation (3) was the appropriate scaling parameter.
- (ii) To examine the significance of the entrance width ratio on the normalised flow structure.
- (iii) To determine the proportion of the flow which returns to the inlet having been discharged on the previous ebb tide.

The experiments were performed in a tank 5m square and filled to a depth of approximately 100mm. The width of the entrance channel ranged from 25mm to 97mm and the maximum tidal velocities ranged from 30mm s^{-1} to 110mm s^{-1} in the different experiments. Reynold's numbers in the entrance were never less than 4000 at peak outflow. The periodic flow was achieved using the system shown in Figure 2.

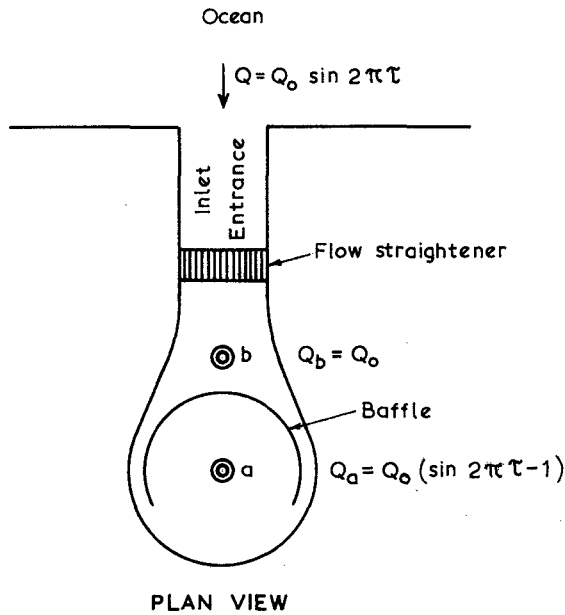


Figure 2: Periodic flow generator

A constant flow Q_0 was discharged through a vertical manifold at b. A flow Q_a was drained from a location a and this flow was regulated by means of a motor driven valve to produce the flow $Q_a = Q_0(\sin 2\pi\tau - 1)$, that is, the withdrawn flow varied sinusoidally between 0 and $2Q_0$. The difference between the flows at a and b discharged into the model ocean and this flow varied sinusoidally between $-Q_0$ and $+Q_0$. The

tidal period used in the experiments was constant at 60s.

It will be noted with this system geometry, the ebb flow can only originate from Q_b and this flow was tabled with a very weak electrolyte solution so that concentrations of water originating from the inlet could be monitored in the ocean by means of conductivity probes. The addition of the electrolyte produced no detectable density stratification in any part of the model.

Structure of the Flow

The photographs in Figure 3 show the structure of the flow at dimensionless times $\tau = 0.25, 0.50, 0.75$ and 1.06 corresponding to

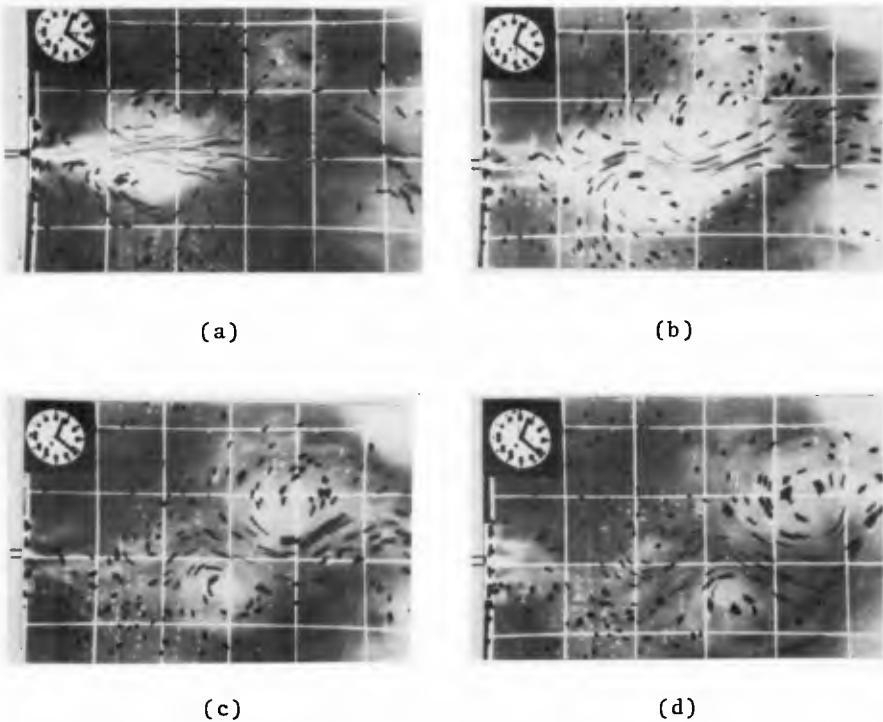


Figure 3: Structure of the flow at various phases

maximum ebb flow, low slack water, maximum flood flow and shortly after high slack water. The structure is revealed by means of streaklines observed by a stationary camera exposed for a time $\tau = 0.03$ (2 seconds). Water originating from the inlet was dyed in these experiments and shows as lighter coloured areas in the photo-

graphs. The grid scale consists of 200mm squares.

The entrance width ratio in this experiment was $w_0/l = 0.02$ which may be considered as small. The first photograph (a) shows the flow when the ebb current in the entrance is a maximum. It will be seen that a vortex pair has formed and is symmetrically placed about the entrance channel. Note that most of the circulation at this stage involves ocean fluid and is uncontaminated with water discharged from the inlet. This implies that the vortical motion is largely irrotational since vorticity can only be introduced from the shear layers at the boundary of the jet.

As time progresses, each vortex is spun up at a rate equal to the moment of momentum of the half jet and in photograph (b) taken at low slack water it will be observed that the areal extent of the vortices has increased and because of their mutual interaction they have moved further away from the entrance. Note also that because of the interaction, velocities are a maximum midway between the two vortices and that the symmetry observed in the previous photograph is no longer apparent. This results from the interaction of the present vortex pair with pairs formed during previous tidal cycles. In photograph (c), taken at maximum flood flow, the vortices are so distant from the entrance that the flow reversal has minimal effect on their motion. It can also be seen that the major portion of the fluid discharged from the inlet on the ebb cycle is now contained within the vortices which continue to move seawards. Photograph d was taken just after high slack water. The new ebb flow has just commenced to flow from the entrance and the vortices from the previous cycle are still clearly visible.

Profiles of the dyed inlet fluid normalised with respect to the characteristic length are shown at several stages of the tide in Figure 4. The physical value of the length scale was different in each of these experiments and the collapse of the data confirms that the scale formulation of Equation (3) is valid. Furthermore, the value of the inlet width ratio in each of these experiments was different but always less than 0.05. This suggests that like steady jets, the structure of periodic jets is independent of the entrance conditions provided the characteristic length of the flow is large compared with the dimensions of the entrance.

Figure 5 shows the normalised velocity structure of the flow at various tidal phases. The velocity maxima was found to always occur between the two vortices, and the distribution of the axial velocity component along a line joining the centres of the vortices at time $\tau = 0.5$ suggests that the flow could be modelled by a pair of interacting Rankine vortices.

It is not evident in the photographs; however, on the flood tide, the flow into the entrance was found to be very similar to that predicted

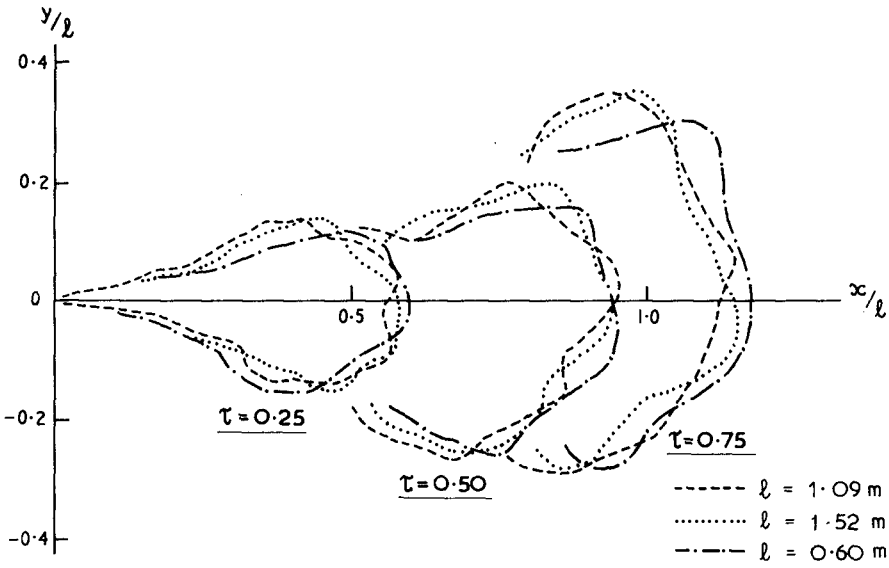


Figure 4: Normalised flow profiles for small values of $w_0/1$

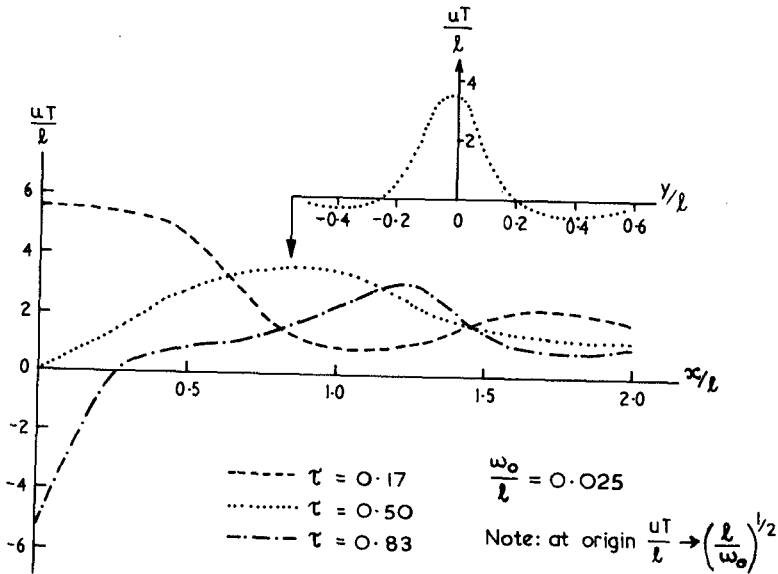


Figure 5: Normalised velocity profiles of ebb flow

by potential flow theory. The flow was radially uniformly distributed about the entrance, and consequently the ocean area affected by the flood tide was very much less than that affected by the ebb tide.

Significance of the Inlet Width Ratio

It has been shown that provided the inlet width ratio is small (less than approximately 0.05), the structure of periodic jets is similar at any given value of the tidal phase. It remains to determine how valid this condition will be in real inlets. It is well established in many tidal inlets that the sectional area of the entrance channel, A , is in almost linear proportion to the mean tidal prism, P (O'Brien 1931). The constant of proportionality in the relationship is found to have a value of approximately $6 \times 10^{-5} \text{ m}^{-1}$ so that

$$A = 6 \times 10^{-5} P \quad (5)$$

In terms of the two dimensional model

$$\begin{aligned} A &\doteq w_0 \\ \text{and } P &\doteq \int_0^{T/2} Q \, dt = \frac{Q_0 T}{\pi} \end{aligned} \quad (6)$$

However, Equations (2) and (3) give

$$Q_0 T = (w_0 l^3)^{1/2} \quad (7)$$

which on substituting into Equation (5) gives

$$\begin{aligned} w_0 &= \frac{6 \times 10^{-5}}{\pi} (w_0 l^3)^{1/2} \\ \text{or } \frac{w_0}{l} &= 4 \times 10^{-10} l^2 \end{aligned} \quad (8)$$

Hence the entrance ratio can only be considered small for inlets with characteristic lengths of approximately 10km or less. This corresponds to tidal prisms of up to a maximum of $2 \times 10^7 \text{ km}^3$ where d is the mean depth of the entrance channel.

The effect of increased entrance width ratio can be seen in Figure 6 where normalised ebb profiles, as defined by dyed fluid emerging from the inlet, are shown for w_0/l ratios of 0.02 and 0.15 at dimensionless times $\tau = 0.25, 0.50$ and 0.75 . The breadth of the ebb discharge is appreciably greater for flows having higher entrance width ratios and this is particularly true in the immediate vicinity of the entrance channel. Therefore it is to be expected that the fraction of water returning to the inlet on the flood tide will increase as the entrance width ratio increases in value.

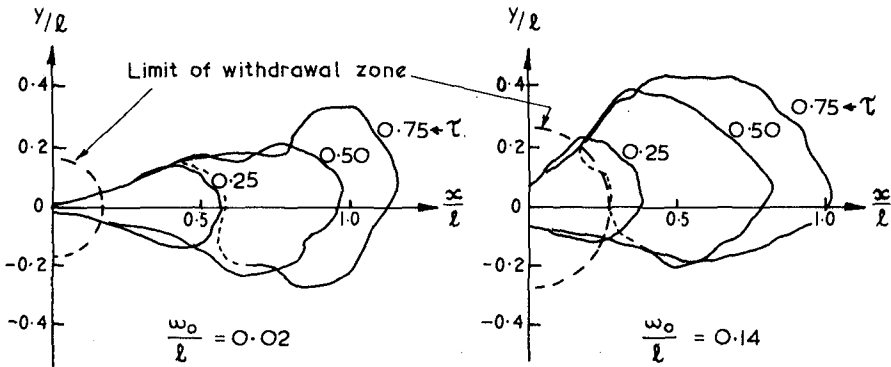


Figure 6: Effect of entrance width on the flow profiles

A further effect reinforces the above trend. The tidal prism P can be used to define a radius of withdrawal R at the channel entrance so that

$$\frac{\pi R^2}{2} = P \tag{9}$$

However, the tidal prism can be expressed in terms of l via Equations (6) and (7) to give

$$\frac{R}{l} = \frac{\sqrt{2}}{\pi} \left(\frac{w_0}{l} \right)^{\frac{1}{4}} \tag{10}$$

Thus the extent of the withdrawal zone increases as the entrance width ratio increases. The limits of the withdrawal regions for the two experiments shown in Figure 6 are indicated by the semi-circles encompassing the entrances.

It is apparent in Figure 6 that the fraction of water which returns to the inlet on the flood tide, having been discharged on the preceding ebb, will increase as the entrance width ratio of the inlet increases. This trend is clearly shown in Figure 7 where the fraction of returning water in the flood flow is plotted against tidal phase. These data were obtained by means of conductivity probes located in the entrance channel which detected the concentration of electrolyte labeled fluid in the incoming flow.

The flushing capacity of an inlet reduced as the entrance width ratio of the inlet increased. This is clearly demonstrated in Figure 8 which shows the fraction of water which returns to an inlet as a function of the entrance width ratio of the inlet. Equation (8) indicates that the flushing ability will reduce as the tidal prism increases for inlets con-

forming to the O'Brien relationship.

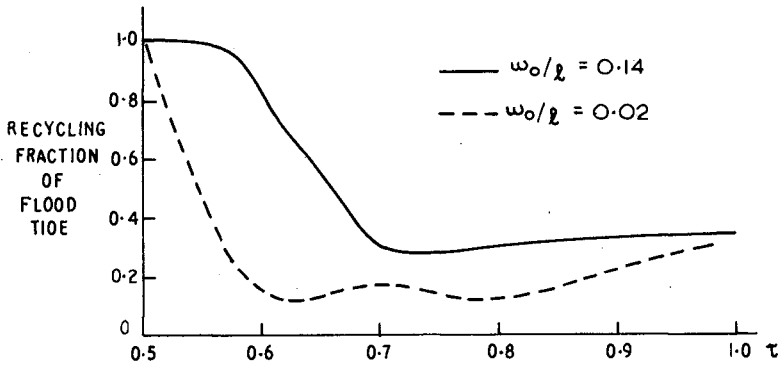


Figure 7: Fraction of water recycling on flood tide as a function of tidal phase

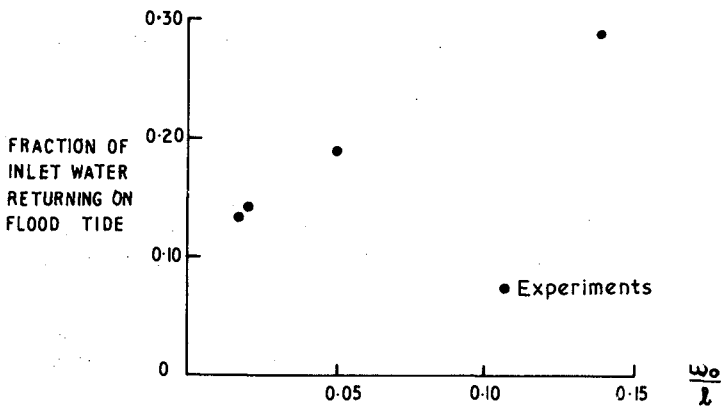


Figure 8: Fraction of inlet water returning on subsequent tide as a function of the entrance width ratio

Bottom Friction

It is to be expected that, in real estuaries, where the water depth would be relatively much less than in the experiments described here, the effect of bottom friction would be proportionately greater.

A measure of the importance of friction in real estuaries may be had by comparing the impulse (I), applied to the flow by bottom friction in one tidal period, with the total momentum M discharged from the inlet on the ebb tide. Thus

$$I = \int_0^T \int^A \frac{\rho g u^2}{C^2} dA dt$$

and
$$M = \int_0^{T/2} m d dt$$

in which C is the Chezy friction coefficient, A is the plan area of the flow associated with the discharge between times t = 0 and T = T, u is the axial velocity component within that area and d is the mean depth of the entrance channel.

Values of the impulse and total momentum can be expressed in terms of the characteristic variables, and the orders of magnitude of these two terms are

$$I = O \left[\frac{g}{10C^2} \left(\frac{1}{w_0} \right) \rho \frac{l^4}{T} \right]$$

and
$$M = O \left[\frac{d}{l} \frac{1}{w_0} \rho \frac{l^4}{T} \right]$$

Thus
$$\frac{I}{M} = O \left[\frac{g}{10C^2} \frac{1}{d} \right]$$

For a typical inlet in which

$$\frac{1}{d} = O [10^3]$$

and Chezy 'C' = 50 m^{1/2} s⁻¹

$$\frac{I}{M} = O [10^{-1} \text{ to } 1.0]$$

Thus substantial frictional effects could be expected in the prototype situation. These would be apparent in the far field (say for X/l > 0.5) where bottom friction will have done more work on the flow.

Conclusions

The off-shore flow structure at a tidal inlet resembles a starting jet during the period of ebb flow, and a potential flow during the flood half of the tidal cycle. The flow pattern is periodic and can be described non-dimensionally in terms of length and time scales based on the maximum value of the momentum flux emerging from the inlet and the tidal period.

The flushing capability of the inlet decreases as the normalised width of the entrance reduces in value.

Real inlets rarely conform to the idealised two dimensional conditions considered in this paper. Bottom friction will exert an appreciable influence on the flow particularly at distances of the order length scale. The offshore slope will also affect the motion tending to increase the angular speed of the vortices while diminishing their size. In spite of these influences, the basic structures observed in the experiments described here could be expected to persist in prototype situations.

Acknowledgements

The author would like to thank Mr. C.A. Miller for suggesting the means of obtaining the periodic flow and to Mr. R.B. Tomlinson for his assistance with the experiments.

Reference

O'Brien, M.P.: Estuary Tidal Prisms Related to Entrance Areas, J. Civ. Eng., 1 (8) pp 738-793 (1931).

THE EFFECT OF OFFSHORE DREDGING ON COASTLINES

W A PRICE J M MOTYKA
AND L J JAFFREY

1. Introduction

The South of England is well endowed with land deposits of river gravel and sand. Nevertheless, the demand for aggregate and the need to conserve agricultural land have increased to the point where in 1976 sea dredged aggregate was accounting for 11% of the total sand and gravel production. In addition to this annual home consumption of about 12 million tonnes of dredged aggregate a further 3.5 million tonnes was exported to Europe in 1976.

Understandably, authorities responsible for coast protection and sea defence view the increase in the removal of marine deposits with concern and a system of licensing by the Crown Estate Commissioners who are responsible for the sea bed from high water to the UK Continental shelf limit has been developed over the years. Dredging by port authorities within their area of jurisdiction, for navigational purposes, is outside this licensing system. Within the three mile limit local authorities have powers under the Coast Protection Act to regulate dredging.

In 1976 a report by an advisory committee to the Department of the Environment⁽¹⁾ recommended, among other things, that further studies should be carried out by HRS aimed at reviewing the existing constraints on marine dredging for gravel. In general, the material which is sought for construction purposes is a 60% shingle, 40% sand mixture, but sand is also needed for reclamation fill and for industrial purposes. The areas dredged at present are shown in Figure 1.

This paper deals briefly with the licensing procedure and at some length with the involvement of the Hydraulics Research Station in assessing how dredging might affect the coastline. The effect on fisheries, navigation, coastal ecology, and other interests is considered by other organisations.

Very little is known of the criteria applied to offshore dredging by other countries, apart from Germany, but with the increased exploitation of the sea bed it is important that information gained by other countries should be used to improve our existing criteria.

2. Consultation Procedure

The licensing system for offshore dredging in the United Kingdom started in 1963. It has now evolved to a stage where a licence is granted only after comprehensive consultations have taken place with many authorities.

After prospecting an area and proving the presence of suitable material the dredging company which is equipped with ships purpose built for gravel extraction submits an application for a licence to the Crown Estate Commissioners to dredge a defined area at a given rate. The Hydraulics Research Station is then asked to give an opinion on whether dredging at the stated rate is likely to effect the adjacent coastline. The questions to be considered and the studies which have assisted in providing some answers are dealt with later in the paper but if our opinion is unfavourable i.e. if damage may result, then the licence application is unlikely to proceed further.

Senior Principal Scientific Officer, Higher Scientific Officer and Principal Scientific Officer respectively at Hydraulics Research Station Wallingford UK

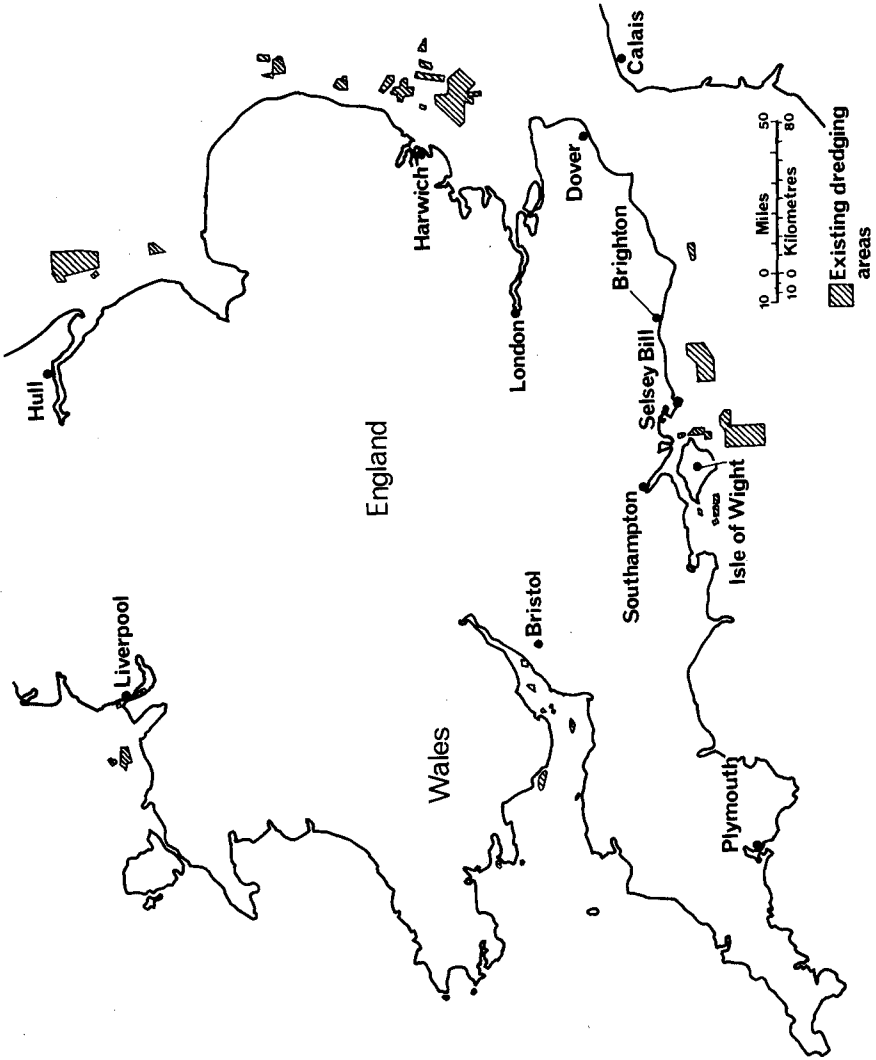


Fig.1 Map showing location of areas dredged

If, on the other hand, we consider that coastal changes will not take place then the following bodies are consulted:—

Department of the Environment (Coast Protection and Petroleum Division)
Ministry of Agriculture, Fisheries and Food (Fisheries Laboratory)
Department of Trade (Navigation)
Post Office (Marine Division)
Local coast protection authorities
Regional Water Authorities

These opinions are received by the Construction Industry Directorate of the Department of the Environment and a view on the issue of a licence is prepared after considering the interests of all parties. There is no right of appeal against a decision. In practice, now that the HRS guidelines are well known and with some measure of early discussion the submission of unreasonable applications is unlikely. Finally a licence is issued by the Crown Estate Commissioners who have the right to levy a charge on each ton of material landed.

3. Evaluation of Proposal by Hydraulics Research Station

In forming an opinion on a licence application HRS aims to answer the following questions:—

- (1) Is the area of dredging far enough offshore so that beach drawdown into the deepened area will not take place?
- (2) Is the dredging to be carried out in deep enough water so that it will not affect possible onshore movement of shingle?
- (3) Does the dredging area include bars and banks which might provide protection to the coast from wave attack?
- (4) Is the area to be dredged sufficiently far offshore and in deep enough water that refraction of waves over it will not cause significant changes in the pattern of alongshore transport of bed material?

Collection of data. A limited amount of information on sea bed levels and tidal currents is available from published Admiralty charts although various other sources are also used for additional information. However, unless an area has been the subject of particular study, the movement of bed material in the zone from low water to say, a depth of 20m, is difficult to quantify, although the general direction of movement can usually be inferred. Such measurements, particularly over a wide area and extending several kilometres offshore, would be extremely difficult to carry out and would almost certainly require time-consuming and high cost radio-active tracking techniques. It is possible that, if the demand for gravel continues to grow, areas where the effects of dredging are difficult to establish may have to be critically re-examined. In such cases a detailed investigation of material movement would be necessary for each particular licence application.

For most of the present applications that we receive, however, existing guidelines are adequate for assessing the effects of dredging on the coastline. These guidelines are

described below. The research carried out at the Station for the development of some of these guidelines is described in the next section, 4.

Beach Drawdown. This usually occurs during storms due to the action of high steep waves. Beach material is eroded from the upper foreshore and moved seawards. However, during periods of calmer weather the material is returned to the beach by long low swell. If the dredged area is too near the coastline then this dynamic equilibrium can be upset; in that material may be transported from the upper portion of the beach into the dredged hole and erosion of the foreshore may result. Some of the most comprehensive information concerning the seasonal offshore—onshore interchange of sand has been recorded by Inman and Rusnak off La Jolla, California⁽²⁾. Observations of sea bed levels were made by divers equipped with scuba who installed a series of rods at water depths of 1.8, 5.5, 9.1, 15.8 and 21.3 metres. The change in sand level at the reference rods was measured over a period of three years. The most inshore site provided very little useful information since the rod was usually completely buried. The rod at a depth of 5.5 metres showed large fluctuations in sea bed level but was lost after a short time, after a period of erosion. In water depths of 9.1 metres or more the vertical variation in level was only ± 0.03 metres or so. At the deeper stations, any seasonal trends were so small as to be masked by fluctuations of a shorter period. From this work it would appear that the active zone of offshore—onshore movement extends to 9.15m, say 10 metres, and beyond this depth seasonal movement takes place intermittently.

Most of the licences are issued for areas on the South and East coasts of the United Kingdom (Figure 1). The wave climate in these areas is certainly less severe than that at La Jolla, California and therefore we believe that dredging in water depths of 10 metres or more will not result in beach drawdown into the dredged hole due to seasonal changes in onshore—offshore movement.

In exceptional circumstances, even this criterion can sometimes be relaxed. For example in the case of beach nourishment from within the 10 metre contour, a redistribution of littoral material takes place but there is no actual loss incurred. Monitoring of beach nourishment projects by Watts, of the US Army Corps of Engineers⁽³⁾ has shown that dredging has been carried out as close inshore as 300 metres with no apparent detriment to the shoreline. Surveys of the borrow pits have shown a general infilling with silt sized material which normally would settle out further offshore. An increase in the proportion of fines can be undesirable from an amenity or fishery point of view and the Station recommends that dredging should not take place within twice that distance from the shoreline, namely 600 metres.

Thus, with respect to beach drawdown there are two criteria — a minimum depth of 10 metres and a minimum offshore distance of 600 metres. These considerations are applied usually to small scale or short term operations for winning sand for beach nourishment or for land reclamation purposes. For the majority of licences which involve longer term working of shingle deposits, a more severe criterion is applied. This is discussed under the next heading.

Interception of sediment. If the beach is being fed from offshore by current and wave action then dredging may trap a proportion of this material and interrupt the supply to the shore. It is very important therefore that dredging should be excluded from any deposits which are moving actively. Research into the threshold of movement of material by waves

and tidal currents forms an important and continuing part of the Station's programme. The first investigations were made using radio-active labelled shingle. The movement of this material was tracked at a number of water depths off Worthing, see next chapter. We concluded that shingle movement seaward of the 18 metre depth contour was negligible at all times. The present criterion therefore applied on the south and east coasts of the United Kingdom for the dredging of shingle is a minimum depth of water of 18 metres. Other ways of predicting the mobility of bed material are currently being pursued. Recently we have completed a study into the threshold of movement of shingle south-east of the Isle of Wight. Wave action and tidal currents here would appear to be strong enough to induce shingle movements in depths as great as 22 metres, see next chapter.

Protection by offshore banks. Offshore banks help to protect the coastline from wave attack either by dissipating wave energy as a result of bed friction, by partial breaking of the waves, by reflection or by any combination of these three. A permanent lowering of the crest of a bank due to dredging or indeed by natural means can result in changes of the wave refraction pattern and hence changes in the net angle of wave attack at the shoreline. Thus, under certain circumstances, dredging from offshore banks can alter the rate of littoral drift and hence affect the stability of the shoreline. Changes in wave refraction whether it be due to an overall lowering of the seabed or dredging from offshore banks are discussed under the next heading.

Where accretion on offshore banks has been well documented and where the coastline is sheltered from wave attack a limited amount of dredging is sometimes allowed. Dredging under such conditions is of course strictly controlled and is only considered on a short term basis. A desk study is first carried out to determine the wave height transformation by bed friction, refraction and shoaling using the method developed by Bretschneider and Reid⁽⁴⁾. The calculation of wave height is very dependent on the value of the friction factor f used in the calculation. Until the present time we have used the value of $f = 0.01$ adopted by Bretschneider for a sand seabed. The latest research from field work and model studies⁽⁵⁾ indicates that the value of the friction factor can be substantially greater than 0.01, and clearly further work is necessary before large values of f can be used with confidence.

Because of the uncertainty in the appropriate value of the friction factor to be used in wave height calculations, dredging of banks adjacent to the coastline is generally not allowed. The only exception to this rule is when the rate of accretion at the coastline is so high that any increase in wave activity and possible reduction in the rate of accretion would have no harmful effect on shoreline stability.

The effect of changes in wave refraction. As waves approach the shore they travel with a group velocity that is dependent upon their period and upon the depth of water. If the water depth increases locally, eg over a dredged hole, the velocity and wavelength change. The local increase in wave celerity due to the increased water depth causes changes in the angle of wave approach to the beach. Such changes result in a variation in the rate of littoral drift along the shoreline and can cause either accretion or erosion. An example of the result of such changes in wave approach took place in Botany Bay, Australia, where severe erosion followed a period of dredging within the Bay. Wave refraction diagrams were plotted showing the angle of wave approach to the beach. Changes in wave angle agreed closely with positions of beach erosion. A beach mathematical model has been developed by Hydraulics Research Station⁽⁶⁾ and is used to predict changes that could occur from offshore

dredging. Results have shown that, in general, the effects of wave refraction are insignificant when dredging takes place in water depths greater than 14 metres. The study is described in the next chapter.

4. Research by HRS

Tracer study off Worthing. In 1968 the Hydraulics Research Station began an investigation, for the Crown Estate Commissioners, into the movement of shingle by using radio-active tracers. This experiment was carried out on the south coast of England off Worthing, some 15 kilometres to the east of Brighton, see Figure 1. The object of the study was to obtain quantitative data on the mobility of shingle under wave action in water depths of 9 to 18 metres. The area was particularly suitable for such a study – firstly, because a number of firms wanted to dredge there and had already applied for licences, and secondly because the bottom topography was uncomplicated and wave conditions were fairly typical of those in British coastal waters.

Previous investigations carried out by Kidson and Carr⁽⁷⁾ off Orfordness on the East Anglian coastline failed to show any significant movement of shingle even under severe weather conditions. The duration of these experiments however was short, 8 weeks or less. The dispersal of radio-active pebbles over this period was small, a maximum of about 50 metres and a minimum dispersal of about 30 metres. It should be noted that the seabed in this area consists of sand, silt or mud and it is possible that the movement of the pebbles was hampered by burial within the soft surface layer.

In the HRS investigation the sea floor was first examined by divers and then radioactive tracer pebbles were placed at mean water depths of 9, 12, 15 and 18 metres.⁽⁸⁾ This operation was carried out in mid-September 1969 and the pebble movement was tracked over a period of 20 months. Wave observations from the Owers Light Vessel, situated off Selsey Bill, were used to relate the rate of movement of shingle to the prevailing wave conditions.

The results clearly demonstrated an increase in shingle mobility with decreasing water depth and also showed the existence of a small net landward movement of shingle inshore of the 12 metre contour. However, even at the inshore sites, in depths of water of 9 metres and 12 metres the quantities of shingle moved towards the shore were very small. The centroid shifts at these two sites indicated that the average pebble would take about 200 years to advance 3 kilometres shorewards from the 12 metre to the 9 metre contour.

It was concluded from the results of this study that the movement of shingle beyond the 18 metre depth contour on the South Coast will be negligible at all times. On this basis, therefore, the Station recommends that dredging of shingle should not take place in depths of water less than 18 metres below low water level.

Numerical model of shoreline changes due to wave refraction over dredged areas. A study financed partly by the Crown Estate Commissioners has been made on the effects that offshore dredging may have on shoreline changes. The Station's wave refraction computer program⁽⁹⁾ was linked to a beach mathematical model⁽⁶⁾. Predictions were made of changes in the plan shape of an initially straight shoreline due to changes in the height and the direction of the waves at breaking. The beach mathematical model is based on the reasoning that the alongshore sediment transport rate is a function of the wave height and

the angle between the breaking wave crest and the beach. For a given set of deep water wave conditions these variables can be easily calculated by the use of the wave refraction program. In the beach mathematical model the following operations are carried out:—

- (1) From the data obtained from the refraction program calculate the wave height and angle at breaking.
- (2) Calculate the rate of alongshore sediment transport rate using the Scripps equation as modified by Komar.⁽¹⁰⁾
- (3) Having determined a stable time step calculate the amount of accretion and erosion from changes in the rate of littoral drift. Distribute these changes over the inshore seabed.
- (4) Return to the wave refraction program to recalculate the input wave conditions i.e. go to (1).

Preliminary results from this study were presented at the 14th Coastal Engineering Conference in Copenhagen, Denmark⁽¹¹⁾. The model showed that the shoreline erosion decreased very rapidly as the area of dredging was moved offshore into deeper water. At this stage it was prudent to “err” on the safe side and we stated that the effects of wave refraction were insignificant in water depths greater than 18 metres in British Coastal Waters. However more work was needed to define the amount of shoreline erosion for different depths of dredging.

After further tests we now consider that the effects of wave refraction are insignificant in water depths of 14 metres or more. Our report to the Crown Estate Commissioners was published in April 1976⁽¹²⁾. This report shows that the mean shoreline erosion plotted against water depth is approximately an exponential curve with the asymptote occurring at 18 metres or so. However for all depths of dredged hole the difference in erosion due to dredging at 14 metres and at 18 metres is negligible. Inshore of the 14 metre depth, erosion was significant even for the shallowest depth of dredging tested (1 metre).

The effect of hole length was investigated for a 4 metre depth of dredging (dredging to greater depths is not generally considered). An increase in hole length, parallel to the shore resulted in a small but measurable increase in erosion. The shoreline recession was found to increase at the rate of about 1.4 metres for every kilometre increase in the length of the dredged hole. For depths of dredging shallower than 4 metres the effects of wave refraction were reduced and hence recession increased more slowly with increased length of hole. These tests were carried out inshore of the 14 metre depth contour. Beyond this depth, these effects can be considered insignificant.

All the results show that the water depth over the dredged area is the controlling factor for any particular wave climate tested. In British coastal waters dredging is not allowed shoreward of the 18 metre contour on sediment supply considerations. This mathematical study shows that a 14 metre depth limit is quite acceptable so far as wave refraction effects are concerned. At present we do not generally allow dredging between the 14 metre and 18 metre water depth. However, if all other criteria are satisfied then we might under some circumstances allow dredging closer inshore than at present.

Movement of shingle under waves and tidal currents. The studies with radioactive tracers off Worthing established a depth limit for no movement under wave action but with weak currents. There are areas where contractors would like to dredge, where currents as well as wave action contribute to the initiation of sediment movement. Such an area is off the Isle of Wight on the South coast of England. If the beaches at the adjacent coastline are being fed from offshore by current and wave action then material might be trapped in the dredged areas and the onshore supply of shingle interrupted. It is necessary to develop new criteria to help decide whether a dredging licence can be granted.

There were two parts to the studies designed to establish a criterion now to be described. A theoretical approach was developed to calculate the shear stress at the seabed due to the combined action of waves and tidal currents. The shear stress was then used to predict the threshold of movement of shingle using a modified form of the Shields curve. Also a field study was carried out to measure the strength of tidal currents south-east of the Isle of Wight — an area of high dredging potential. It was therefore possible to apply the criteria established theoretically to a practical case.

The shear stress due to tidal currents alone was calculated using the Karman–Prandtl velocity profile equations. Using Prandtl's mixing length hypothesis the velocity distribution can be written as:—

$$U = \left[\frac{\gamma_c}{\rho} \right]^{1/2} \cdot \frac{1}{K} \cdot \log_e \left[\frac{33y}{Ks} \right] \quad \dots (1)$$

where U = velocity measured at 0.4 of the water depth (m/s)

γ_c = shear stress exerted at the bed by the current flow (N/m^2)

ρ = density of sea water (kg/m^3)

K = Von Karman's constant, the value taken was 0.4

y = water depth at the height of the current velocity meter (m)

Ks = Nikuradse roughness parameter

The maximum bed shear stress due to wave action was calculated using Jonsson's wave friction factor $f_w^{(1,3)}$. The maximum shear stress being related to the wave conditions by the equation:—

$$\gamma_w = \frac{f_w}{2} \cdot \rho \cdot U_m^2 \quad \dots (2)$$

where γ_w = maximum bed shear stress (N/m^2)

f_w = wave friction factor, a function of the sea bed roughness and the wave conditions

ρ = salt water density (kg/m^3)

U_m = maximum horizontal wave orbital velocity (m/s)

The maximum orbital velocity was found from small amplitude sinusoidal wave theory, and was then used to calculate the water particle displacement at the seabed i.e.

$$A_m = \frac{U_m \cdot T}{2\pi} \quad \dots (3)$$

where A_m = maximum particle displacement (m)

T = wave period (s)

The value of f_w in equation 2 was found from the Jonsson friction diagram where it is plotted against the relative roughness of the seabed A_m/K_s .

So far we have considered the shear stress exerted near the seabed by tidal currents and wave action acting independently of each other. The combined shear stress was determined by considering the general formula for fully turbulent flow

$$\gamma = \rho L \left[\frac{\delta v}{\delta y} \right]^2 \quad \dots (4)$$

where γ = shear stress (N/m^2)

L = Prandtl's mixing length (m)

v = velocity at a small height y above the bed (m/s)

Rearrangement of the equation gave :-

$$\frac{\delta v}{\delta y} = \left[\frac{\gamma}{\rho} \right]^{1/2} \cdot \frac{1}{L} \quad \dots (5)$$

Hence the combined maximum velocity δv at the outer edge of the viscous sublayer with thickness δy is:-

$$\delta v = \left[\frac{\gamma_c}{\rho} \right]^{1/2} \cdot \frac{1}{L} + \left[\frac{\gamma_w}{\rho} \right]^{1/2} \cdot \frac{1}{L} \quad \dots (6)$$

And substituting back into equation (4) we have:-

$$\gamma = \gamma_c + 2 \sqrt{\gamma_c \cdot \gamma_w} + \gamma_w \quad \dots (7)$$

The combined instantaneous maximum shear stress is greater than the straight addition of the shear stress due to waves and tidal currents. Madsen and Grant⁽¹⁴⁾ found that the Shields curve predicted the threshold of movement by waves if the boundary shear stress was replaced by the maximum value of the oscillatory shear stress. It would therefore seem reasonable to use this curve to predict the threshold under the combination of the two and this is the approach used here.

The method has not been checked under prototype or model conditions and further experimental work will be carried out to refine the method.

The field study consisted of tidal current measurements in mean water depths ranging from 16 to 29 metres. The observations were made with a Plessey M021 current meter held at 0.4 of the mean water depth by means of a moored submerged float. This instrument translated the readings of current strength and direction at 10 minute intervals onto a self contained magnetic tape recorder. The data was fed into an HRS computer program which calculated a number of tidal current parameters e.g. magnitude, duration, direction, directional scatter of the velocity readings.

A desk study was then carried out using the tidal current velocity information together with wave data from the nearby Owers Light vessel. This data was used to calculate the threshold of movement of shingle under the combined action of waves and currents using the theoretical approach described above.

Preliminary results from this study show that off the Isle of Wight the mobility of shingle is significantly increased by the action of tidal currents. It is not possible at this stage to give definite recommendations about the minimum depth of dredging. It would appear however that 25mm shingle for example is likely to be mobile in depths of water up to 22 metres. Further research by the Station will indicate whether the existing criterion of 18 metres applicable in areas of weak tidal action needs to be strengthened, and by how much.

5. Conclusions

1. An increasing amount of shingle is being won from the sea. This source accounts for some 11% of the total sand and gravel production in the United Kingdom. In the procedure leading up to the granting of a licence by the Crown Estate Commissioners, the first to be consulted is the Hydraulics Research Station. We are asked to say whether there is a possibility that dredging could affect adjacent coastlines. If the answer is "yes" the application is usually turned down; if "no" then other authorities are consulted. We attempt to answer a number of questions:

- (i) Is the dredging far enough offshore that beach drawdown into the hole cannot take place? The approximate limit for onshore/offshore movement off the South Coast of England is considered to be about 10 metres below low water and this is usually taken as the minimum depth to ensure that beach drawdown will not take place into the hole. We also have a limit in terms of distance offshore of 600 metres. This criteria is hardly ever invoked because it is usually over-ridden by other considerations.
- (ii) Is dredging to be carried out in deep enough water so that the hole will not intercept the onshore movement of shingle? Field tracer studies have shown that for the south coast wave climate and in regions of weak tidal currents shingle will not move in depths greater than 18 metres. A method of including the effect of tidal currents has been developed. We believe it errs on the safe side. As an example, the 18 metre criterion changes to 22 metres for a tidal current of 1.1 m/s. However it is stressed that the method is at an early stage of its development.

- (iii) Does the dredging area include banks which if removed would increase wave activity at the shoreline? In this case it is usual for the application to be turned down. There are exceptions under special conditions. If for example it can be shown that the beach is well protected from wave attack, eg by a very wide fore-shore, then dredging of a limited quantity of material under controlled conditions may be allowed. For such special cases a desk study is carried out by HRS.
- (iv) Is the area sufficiently distant from the shore and in deep enough water so that changes in wave refraction over the dredged area do not lead to changes of littoral transport at the shoreline and hence changes in beach plan shape? A beach mathematical model developed at HRS has shown that in general the effects of wave refraction are insignificant when dredging takes place in water depths greater than 14 metres.

6. Acknowledgements

This paper represents years of effort on the part of many people working both on demanding field studies and physical processes. Although their names were not included as authors we would like to thank Dr A H Brampton, Mr M J Crickmore and Mr M W Owen for their considerable contributions to the studies. We appreciate the assistance of the Crown Estate Commissioners in sponsoring some of the studies and especially we wish to mention Mr John Edwards for his support and encouragement.

This paper is published with the permission of the Director of Hydraulics Research Station, Wallingford, England.

7. References

1. Report of the Advisory Committee on Aggregates. "Aggregates: the way ahead". Department of the Environment Great Britain 1976.
2. Inman D L and Rusnak G S. "Changes in sand level on the beach and shelf at La Jolla, California". US Army, Corps of Engineers. Beach Erosion Board. Technical Memorandum No 82 July 1956.
3. Watts G M. "Behaviour of offshore borrow zones in beach fill operations". Proceedings of the 10th Congress of the International Association for Hydraulic Research. London 1963. Vol 1 pp 17-24.
4. Bretschneider C L and Reid R O. "Modification of wave height due to bottom friction, percolation, and refraction". US Army, Corps of Engineers. Beach Erosion Board. Technical Memorandum No 45 October 1954.
5. Treloar P D and Abernethy C L. "Determination of a bed friction factor for Botany Bay, Australia". Coastal Engineering, 2 (1978) pp 1-20. Elsevier.

6. Price W A, Tomlinson K W and Willis D H. "Predicting changes in the plan shape of beaches". Proceedings of the 13th Conference on Coastal Engineering, 1972. Vol 2, pp 1321–1330.
7. Kidson C and Carr A P. "The movement of shingle over the sea bed close inshore". The Geographical Journal. Vol 125 (1959) pp 380–389.
8. Crickmore M J, Waters C B and Price W A. "The measurement of offshore shingle movement". Proceedings of the 13th Conference on Coastal Engineering, 1972. Vol 2, pp 1005–1025.
9. Abernethy C L and Gilbert G. "Refraction of wave spectra". Hydraulics Research Station, Report INT 117. May 1975.
10. Komar P D. "The longshore transport of sand on beaches". PhD Thesis. University of California, San Diego. 1969.
11. Motyka J M and Willis D H. "The effect of wave refraction over dredged holes". Proceedings of the 14th Conference on Coastal Engineering, 1974. Vol 1 pp 615–625.
12. Hydraulics Research Station. "The effect on coastline changes of wave refraction over dredged areas". Report No EX 728, April 1976.
13. Jonsson I G. "Wave boundary layers and friction factors". Proceedings of the 10th Conference on Coastal Engineering, 1966. Vol 1 pp 127–148.
14. Madsen O S and Grant W D. "Sediment transport in the coastal environment". Ralph M Parsons Laboratory for Water Resources and Hydrodynamics, Massachusetts Institute of Technology. Report 209, January 1976.

CHAPTER 80

SURF ZONE RESONANCE AND COUPLED MORPHOLOGY

JOHN CHAPPELL Department of Geography, School of General
 Studies, Australian National University,
 Canberra, A.C.T., Australia.

LYNN DONELSON WRIGHT Coastal Studies Unit, Department of
 Geography, University of Sydney, Sydney,
 Australia.

ABSTRACT The edge wave hypothesis for periodic inshore morphology and circulation is tested for five beaches and is supported by resulting wave-current spectral and cross-spectral data. Beach types range from a reflective, narrow surf zone, case through various dissipative medium to high energy beaches including some with inshore bar-trough morphology and one broad surf zone troughless one. In all cases beachface reflectivity is moderately high ($E < 2.5$) and inshore resonance occurs, indicated by strong spectral peaks at lower than incident frequency with wave-current co-peaks being 90° out of phase. Several different edgewave frequency and mode combinations are indicated. The reflective beach shows an $n = 0$ subharmonic edgewave (*i.e.* at half incident wave frequency) which Guza and Davis (1974) predict as the most likely case, *viz.* the (0,0) triad. The troughless dissipative case shows a (1,0) edgewave triad; the same occurs in some bar-trough dissipative cases but in other cases is supplanted by the (0,0) sub-harmonic wave and/or by a lower subharmonic wave at $\frac{1}{2}$ incident frequency. The likelihood of a given edgewaveset appears to be regulated by surf friction, and a change of edge wave set appears likely to explain observed changes of inshore circulation.

INTRODUCTION Several models exist for periodic morphology and associated cellular circulation on surf beaches. We present detailed wave and current data which support the edge wave model in the context of rip cells on high energy sandy beaches, and which indicate that inshore morphodynamic patterns change in response to discontinuous change of edge wave mode and frequency. In what follows, we discriminate between two categories of periodic phenomena, rip cells and beach cusp cells on the grounds that rip cells occupy broad dissipative surf zones and can exist in several different morphodynamic states, whereas cusps essentially are intertidal phenomena on reflective beaches and vary in scale rather than in form. We note that cusps frequently coexist with rips, especially where a steep beach face lies behind the inshore trough of a broad dissipative surf zone.

When inshore morphology is rectilinear, initiation of periodic patterns requires periodic variation longshore of wave

height, so that inshore radiation stress gradients can force cellular circulation. Periodic wave height variation has been suggested to be due:

(1) to intersection of two wave trains originating by refraction offshore (*e.g.* Dalrymple, 1975); or (2) to inshore wave edges interacting with the incident waves (*e.g.* Bowen and Inman, 1969); or (3) to a periodic deformation of water surface due to instability in the radiation stress field (Hino, 1975). The refraction hypothesis may have local application, but the widespread occurrence of beach cusps under shore-parallel swell conditions argues against this as a universal mechanism. On the other hand, the existence of edge waves on natural beaches has been supported by analysis of inshore current spectra by Huntley and Bowen (1975), and Guza and Inman (1975) show that beach cusps are coupled with edge wave development. Theoretical argument for edge wave initiation of rip cells was developed by Bowen and Inman (1969), but has been criticised by Hino (1975) - the proponent of the radiation stress instability theory - on the grounds that excitation of sufficiently large edge waves is improbable in a dissipative broad surf zone.

However, Guza and Davis (1974) show that edge wave excitation through resonance with incident waves is possible under reflective conditions when incident wave amplitude (a_i) is such that

$$a_i^2 > \gamma k(N_1, N_2)/\omega_i \quad \dots (1)$$

where γ is kinetic viscosity, ω_i is incident frequency, N_1 and N_2 are mode numbers of a possible edge wave pair, and $k(N_1, N_2)$ is a constant for given N_1, N_2 (note $K(N_1, N_2)$ values tabulated by Guza and Davis were subsequently found by Guza and Inman, 1975, to be too great by a factor of 4. It is debated whether excitation occurs in dissipative situations when the reflectivity parameter

$$\epsilon = a_i w^2/g \tan^2 \beta \quad \dots (2)$$

(where β is beach slope) is greater than about 2.0. This is important for the edge wave initiation of rips. Our results indicate resonance and edge wave existence in several morphodynamically different dissipative and reflective contexts, and indicate conditions where edge wave modes and periods change abruptly, depending on inshore bar morphology, incident wave conditions, and tide. In another paper in this volume (Wright *et al.* 1978) we discuss the morphodynamic associations between six commonly occurring morphologic types, different resonant frequencies, and different scales of inshore circulation. In the present paper we examine evidence for inshore resonance from five selected experiments.

EXPERIMENTAL METHODS

Several sandy surf beaches in N.S.W. Australia (Fig. 1) were chosen to represent a range of hydrodynamic and morphodynamic conditions, ranging from highly reflective steep beaches without a bar, through dissipative cases with either a rectilinear bar-trough system or a crescentic system, to dissipative cases where broad bars have accreted to the beach, forming long and broad inshore shoals (*e.g.* Wright *et al.* 1978; in press). The beaches experience medium to high wave energies, and experiments were done with mean breaker heights typically between .08 and 2 m.

Wave and current measurements were taken on a continuous basis, using pressure transducers for waves and fast-response directional flow meters for currents. Our standard instrument mount includes a pressure transducer plus orthogonal horizontal flow meters (shore-normal and shore-parallel), on a stable portable base, connected by cables to chart recorders, data logger, and a mini-computer in a mobile onshore van. Several instrument mounts can be deployed together. The system is described in detail by Bradshaw *et al.* (1978).

Measurements were made when waves essentially were normally incident (*i.e.* crests shore parallel). Spectral and cross-spectral analysis provide the key for edge wave identification. Standard spectral methods were used employing auto and cross covariance analysis, detrending and use of hanning or cubic filters, and Fourier transformation. Sampling intervals (Δt) of 1 or 2 seconds were used. Spectral and cross spectral analysis (*e.g.* Bendat and Piersol, 1971) are guided by the following points:

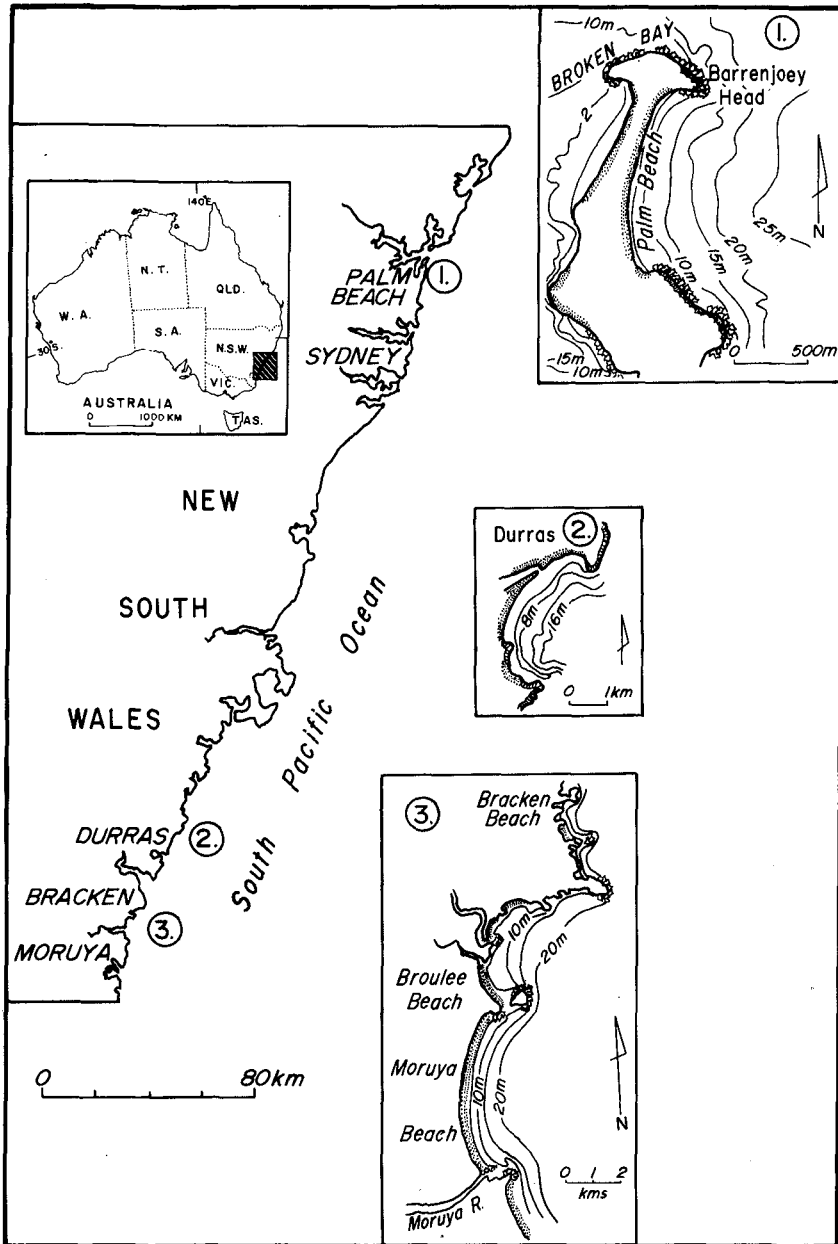
- (i) Auto or cross-correlogram reduction of primary data is repeated with different maximum lag numbers when preparing each spectrum, to establish stability of spectral peaks.
- (ii) We are concerned to identify oscillatory motions at incident wave frequency, subharmonics of this, or at surf beat frequencies, and consider only spectral peaks very significantly above the white noise spectrum.
- (iii) Cross-spectral coherence is a guide to usefulness of phase estimates of cross-spectral peaks, *i.e.* when coherence is low the phase estimate is judged unreliable.

We consider that an edge wave is indicated:

- (i) when phase difference between water surface and horizontal current is close to $\frac{\pi}{2}$, and (ii) when an inferred edge wave spectral peak diminishes in magnitude away from the shore (*i.e.* the same test as used by Huntley and Bowen, 1975).

Magnitude relationships of shorenormal and shore-parallel current components in a rip feeder channel usually differ from those predicted from the edge wave velocity potential (ϕ) field,

Figure 1 Locations of beaches used as experiment sites (Palm, Durras, Bracken, Moruya).



$(u, v) = \Delta\phi$, due to the presence of the current. At some of these sites we separate the bidirectional current time series into component left- and right-flow spectra to show that dominant drift is at edge wave rather than incident frequencies.

In the experiments which follow, not all results are final as some are based on measurements taken when field conditions precluded sampling at several sites, and for others the full analysis of data logs is still in progress.

FIELD EXPERIMENTS

We report from several dissipative beaches plus one reflective beach. The latter is included to furnish a connection between our work and that of Guza and Inman (1975) and others, and to provide a methodologic bridge to the dissipative cases. Locations and maps are shown in Figure 1. The dissipative beaches - Moruya, Durras, Palm Beach - have well sorted medium sand, dominantly quartz with variable but significant quantities of shell fragments. The reflective example - Bracken Beach - had bimodal sediment of coarse sand and gravel. The New South Wales coast experiences a variable wind-wave climate, with strong sea-breeze in summer, superimposed on persistent high energy swell from the southeast. Significant wave height exceeds 1.5 m for 50% of the time and 4 m for 1% of the time. Wave periods around 10 seconds are most common. Tides are semi-diurnal and have an average springtide range of 1.6 m.

Sites were chosen to sample a range of inshore morphologies. Measurements were made generally under swell conditions. Figure 2 shows site details for representative experiments discussed herein. The sites are briefly described in terms of the morphodynamic classification scheme of Wright *et al.* (1978). Primary morphodynamic data are listed in Table 1.

(i) A typical reflective experiment on Bracken Beach is shown in Figure 2a. Typical of reflective beaches (*e.g.* Wright *et al.* in press), Bracken Beach has a linear, low gradient nearshore profile (fine sand) which passes through a pronounced gravel step into the steep beach face of coarse sand. Beach cusps are well developed, the active cusps often being nested within much larger cusps high on the beach face, which are relict from storm waves. Waves break at the gravel step and surge up the beach face with high runup. Features such as transverse or crescentic bars, swash bars and inshore gutters invariably are absent.

(ii) Moruya experiment 1 (Figure 2b) took place in the presence of a long-shore bar-trough system with incipient periodic morphology and a moderately steep beach face. Topography was transitional between the parallel bar-trough system referred to by Wright *et al.* (1978) as Type 2 dissipative beach state, and the crescentic bar-

- TABLE 1 -

MORPHODYNAMIC PROPERTIES OF 5 EXPERIMENTAL SITES

Expt Number	Site	Topo Type*	H _b (m)	T _p (sec)	β (°)	ε _b **	X _s (m)
(i)	Bracken	R	0.6	7.5	6.9	2.3	15
(ii)	Moruya 1	2-3	0.7	9	3.5	2.5	70
(iii)	Moruya 2	3	0.8	11	3.5	1.6	90
(iv)	PaIm	5	1.2	10	3.5	2.3	50
(v)	Durras	2	1.4	10	4.5	1.6	75

* R - reflective; other types a/c classification of Wright, *et al.* (in press).

** calculated for observed inshore wave height near the beach face (*i.e.* after prior dissipation).

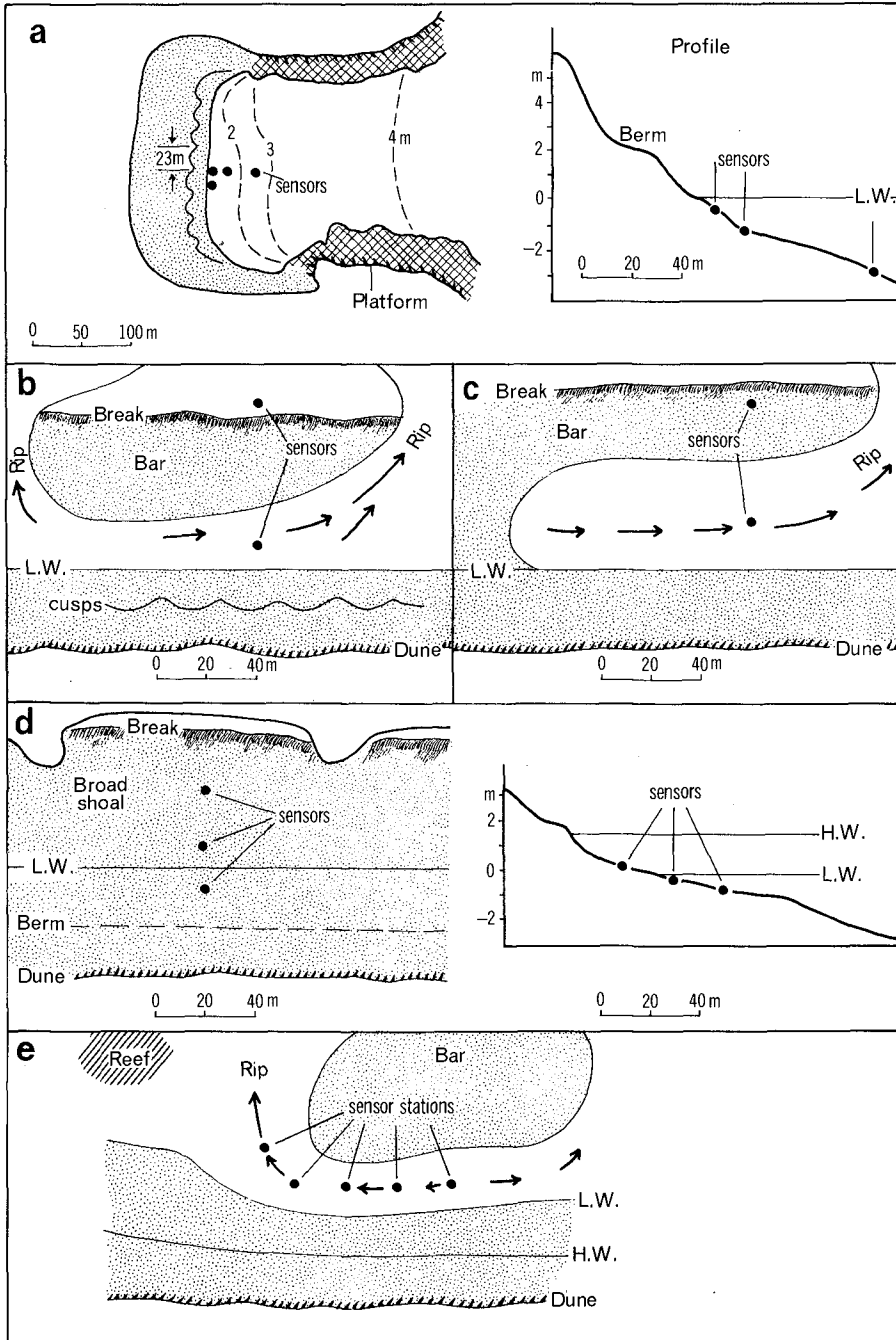
- TABLE 2 -

SURF ZONE PARAMETERS AND POSSIBLE EDGE WAVE DATA, DISSIPATIVE BEACHES

Expt.	1/Te(H ₃)	X _s	n	L _e	β _s (°)	D
Bracken	0.067	2	0	46	-	-
Moruya 1	0.05	11	0	40	1	0.75
		11	1	120	"	0.25
		2.4	0	190	"	0.16
Moruya 2	0.023	3.5	0	190	0.6	0.27
PaIm	0.063	13	1	75	1.4	0.9
	0.03	2.9	0	110	"	0.6
Durras	0.063	14	1	100	1.4	0.9
	0.03	3.2	0	150	"	0.6

(NOTE: X_s must exceed 7.0 for n = 1 to occur)

Figure 2 Inshore morphodynamic states for 5 experiments. (a) Bracken Beach, reflective. (b) Moruya Beach 25 May '77 shore-parallel bar-trough system. (c) Moruya Beach 27 May '77 shore-parallel plus transverse bar system. (d) Palm Beach 9 April '78 broad dissipative shore-tied goal. (e) Durras Beach shore-parallel bar-trough system.



rhythmic shoreline situation of Type 3. The primary break typically was plunging with waves tending to reform as they traversed the trough.

(iii) Moruya experiment 2 (Figure 2c) was representative of a typical Type 3 state, where crescentic bars intermittently tie to the beach through transverse bars. Beach face and inshore wave conditions resembled Moruya experiment 1 (*cf* Table 1).

(iv) Palm Beach experiment (Figure 2d) represents an advanced stage in an accretionary phase where a broad shoal extending the full width of the surf zone had developed through shoreward bar migration (Type 5 of Wright *et al.*). The upper beach face was moderately steep; the lower portion flatter. Reflectivity varied accordingly with tidal stage. The entire surf zone was crossed by spilling bores.

(v) Durras experiment (Figure 2e) was conducted within a parallel bar-trough system. Topography approached Type 2 but was influenced by a nearshore reef at the northern end of the site. The trough is relatively shallow, and larger sets of waves developed spilling bores across the surf zone while small sets reformed inshore of the break. This experiment differed from the others in that measurements were taken at 5 sites alongshore, within the trough.

SURF ZONE RESONANCE

The results of each of the selected experiments described above reveal several distinctive resonant frequencies and modes which appear strongly dependent on the morphology prevailing at the time of the experiments. The resonant phenomena associated with each set of conditions are elucidated by spectral and cross-spectral analyses of the measured time series of water surface and inshore current oscillations.

(1) Reflective case - Bracken experiment (10 December, 1977)

The steep beach face showed pronounced cusps at 23 m spacing. Waves and currents were measured seawards of the shore break at three locations off a cusp horn, and near the step off a cusp bay (Figure 2a). Spectra (from the middle station off the cusp horn) reveal several important features some of which are shown in Figure 3).

(a) Wave spectra show sharp peaks at incident wave frequency (0.13 Hz) at all stations off the cusp horn although this peak weakens at the inner station and off the cusp. Water surface motion at this frequency is dominated by the incident waves, indicated by zero phase difference between horn and bay 0.13 Hz peaks. In this experiment, water surface elevation and currents were in phase at incident wave frequency at all stations.

(b) The shore-normal current spectra show strong peaks at the frequency of the first subharmonic (.067 Hz) at both the middle and inner stations. This peak is also expressed in water surface elevation spectra; it is present as a secondary peak in the middle station but becomes the dominant peak at the inner station. Flow is $\frac{\pi}{2}$ rds out of phase with water surface elevation at this subharmonic frequency.

(c) Segregation of current spectra into offshore and onshore components by separating the primary record into half series indicates that seaward flows had highest spectral energy at subharmonic frequency, while at incident frequency onshore and offshore energies are equal.

A subharmonic edge wave is inferred from the strong peaks at subharmonic frequency and from the $\frac{\pi}{2}$ current-wave phase relationship. Guza and Davis (1974) have shown that subharmonic edge waves are preferentially excited. Guza and Inman (1975) argue that cusp spacing should be one-half edge wave length, L_e :

$$L_e = (g/2\pi) T_e^2 (1 + 2_n) \tan \beta \quad \dots (3)$$

where n = mode number = 0,1,2,3 ... (Bowen and Inman, 1969). Bowen and Inman (1969) also suggest that dominant mode decreases with decreasing dimensionless surf zone width

$$\chi_s = \omega^2 X_s / g \tan \beta \quad \dots (4)$$

where $\omega = 2 / T_e$ and X_s is horizontal distance from the beach face to the break point. For edge waves to be trapped, χ_s must exceed a minimum value, χ_{min} , which Huntley (1976) estimates as

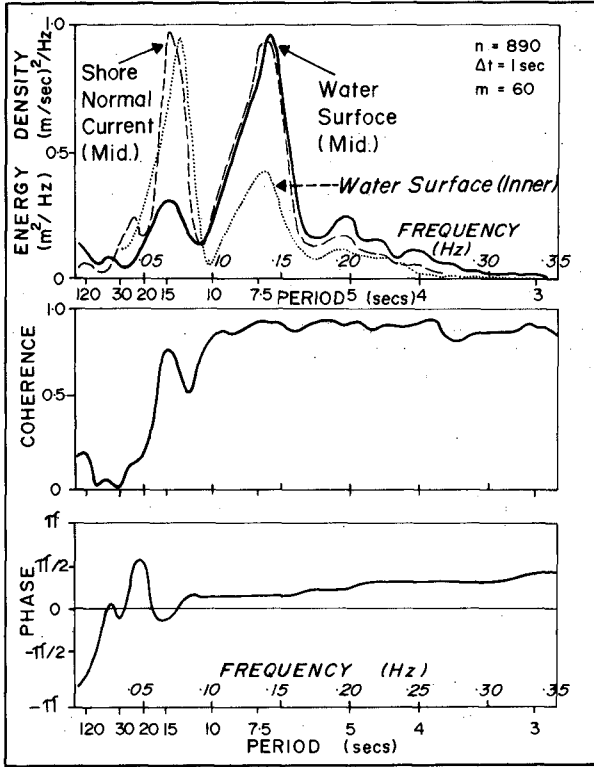
$$\chi_{min} = 3.5 n (n + 1) \quad \dots (5)$$

From χ_s values in Table 1, the cut-off mode at 0.067 Hz is $n = 0$ (from Eq. 5), corresponding to $L_e = 46$ for β values in Table 1 (Eq. 3). This is twice the measured cusp spacing.

(2) Dissipative bar-trough systems - Moruya experiments (ii) and (iii)

Spectra from two dissipative beach experiments on Moruya Beach are shown in Figure 3 from instruments located as shown in Figures 2b, 2c. Salient elements are as follows:

Figure 3 Representative spectra for reflective beach experiment (ref. Fig 2a for instrument locations).



MORUYA RISING TIDE 25th MAY '77

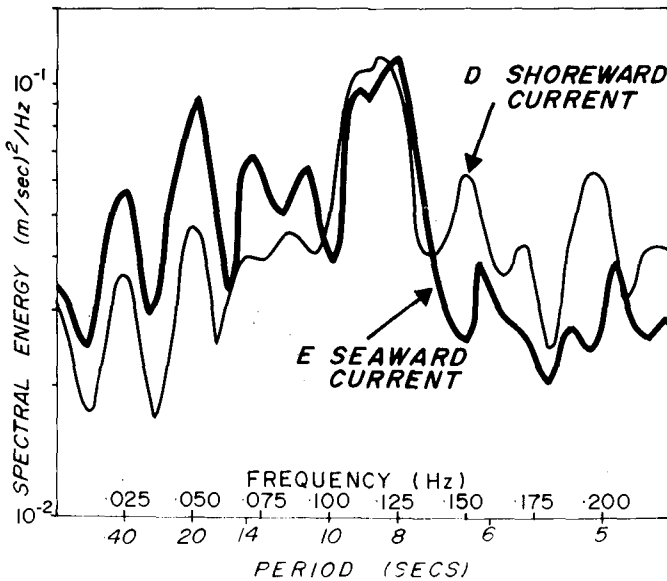
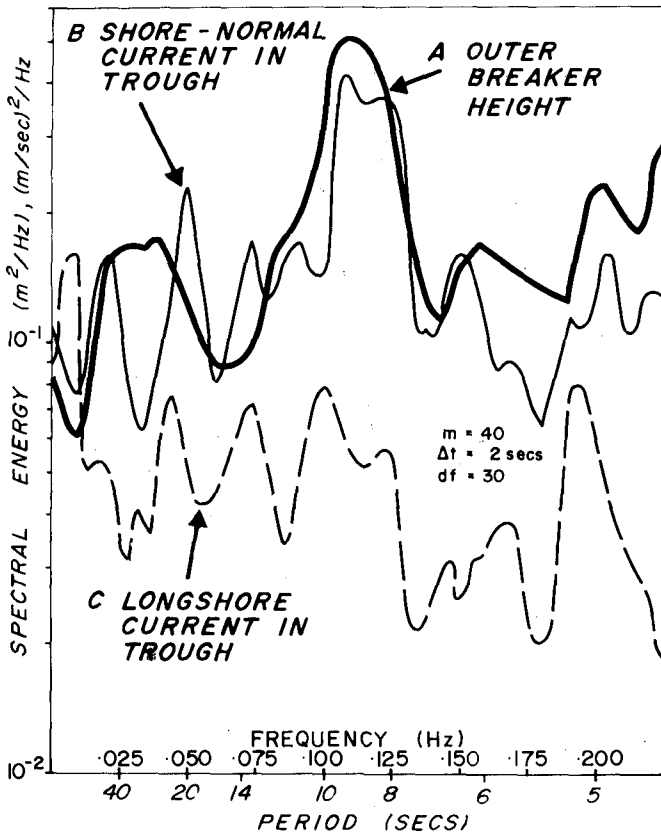
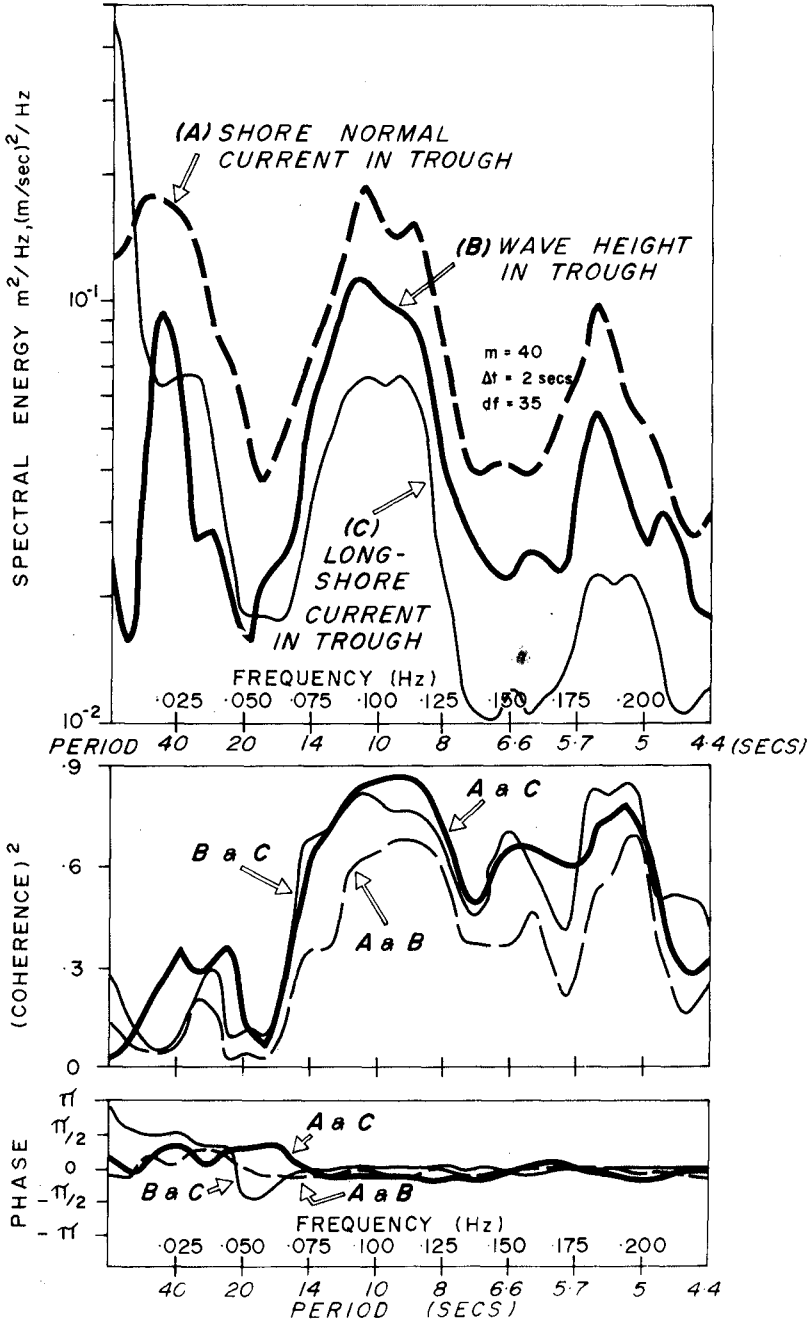


Figure 4 Representative spectra for two dissipative bar-trough systems - Moruya experiments (ii) (25 May) and (iii) (27 May) (ref. figs 2b, 2c for instrument locations).

NORTH MORUYA RISING TIDE 27th MAY '77

FIGURE 4 (iii)



(a) Strong subharmonic components appear in current spectra on both occasions in addition to incident-frequency peaks, but at different multiples of incident wave period. For experiment (ii) the incident frequency is close to 0.1 Hz, and secondary current peaks appear at 0.05 Hz and 0.023 Hz, the 0.05 Hz being the stronger. Experiment (iii), with incident frequency again close to 0.1 Hz but a somewhat broader trough, shows only the lower frequency subharmonic current peak at 0.023 Hz, which is very near to $\frac{1}{4}$ the incident wave frequency. Phase determinations for experiment (iii) show that flow oscillations at .023 Hz are 90° out of phase with water surface oscillations at this frequency, whereas the strong incident-frequency flow is in phase. Progressive motion thus is indicated at incident frequency; standing motion at the $\omega/4$ frequency. The wave record for experiment (iii) at the same point in the trough, shows the same 0.023 Hz ($\omega/4$) peak; this peak is absent in the outer breaker record.

(b) Segregation of the current record from experiment (ii) into on-shore and offshore components shows a similar effect to the reflective beach case, *i.e.* offshore current substantially exceeds the onshore component at $\omega/2$ and $\omega/4$ frequencies.

(c) For the second experiment χ_g for the 0.023 Hz peak is 3.6, indicating that only the zero-mode edge wave is likely at this frequency. The corresponding L_e value is 190 m, which is very close to twice the observed spacing of transverse bars (90 m; data in Table 1). However, this does not constitute "proof" of edge wave determination of coupled circulation and topography: firstly, because several modes below cutoff are possible for resonance at $\omega/2$, and secondly, because estimates of L_e are very sensitive to values of β , which often varies down the beach face and over the surf zone. This allows too much freedom when finding a "fit" between L_e and rip or transverse bar spacing, especially when $\omega/1$ and $\omega/4$ peaks both are present as in the first Moruya experiment.

An interesting result is that the low frequency peak at $\frac{1}{4}$ of incident frequency, which is subordinate to the first subharmonic in Moruya 1, rises to dominance in the second experiment when energy conditions are 20% higher, the trough wider, and the surf zone broader (Table 1). This implies firstly that increasing dissipativeness inhibits excitation of higher frequency edge waves, which is consistent with Guza and Davis (1974) measure (D) of boundary layer dissipation per unit of longshore length, restated as

$$D = E\pi (2\gamma\omega_i)^{1/2}/L_e \tan \beta \quad \dots (6)$$

where E is total wave energy per unit longshore length. When dominant resonance shifts to $\omega/4$, L_g increases fourfold (relative to $\omega/2$) for a given mode (Eq. 3), and sensible dissipation for the edge wave decreases.

Guza and Davis argue that excitation of an edge wave of lower frequency and higher mode than the (0,0) subharmonic is possible only when $ai^2\omega$, $\gamma > 4 K(0,0)$. The corrected value of $K(0,0)$ is ≈ 50 (Guza and Inman, 1975), and from Eq. 1 the minimum incident amplitude at the beach face necessary for growth of higher mode, lower frequency edge waves for our case is $a_i \approx 6$ cm, which is about 1/7 of observed inshore wave amplitude.

Strong resonance at $\omega/4$ is not predicted by conventional edge wave theory and is generally inconsistent with the concept of resonant triad as set out by Guza and Davis (1974). For this reason and because thus far we have only found resonance at $\omega/4$ in situations of pronounced bar-trough topography, we infer that resonance at this frequency is a consequence of topography. In the cases studied the trough has been deep, the bar has been shallow with a steep (and potentially reflective) landward face and the beach face has been locally reflective. Estimated natural trough frequencies are close to the frequency of the first subharmonic ($\omega/2$) at times when $\omega/4$ peaks occur.

(3) Dissipative surf zone without trough - Palm Beach

An important question is whether edge waves occupying the inshore zone of dissipative systems will always be excited when beach reflectivity is high and the condition of Equation 1 is surpassed substantially. This is relevant to rip current initiation under Type 5 conditions when an inshore trough is absent; our observations indicate an absence of regular rip organization in these conditions (c. Figure 2d; see also Wright *et al.* 1978 and in press; Chappell and Eliot, in press). The broad troughless intertidal shoal fronting a moderately reflective high-tide beach ($\Sigma = 2.3$) was monitored for shore-normal currents at 3 sites - mid swag, and at points about 8 m and 20 m seaward of the shore break (Figure 2d). Wave record was obtained only from the inner surf zone site owing to failure of the outer transducer. Neglecting the swash zone record, spectra shown in Figure 5 indicate several interesting points.

The inner surf zone wave spectrum shows a strong incident peak and a minor subharmonic peak ($\omega/2$). This does not appear in the current record, however, which is dominated by a peak at 0.063 Hz with a second peak at 0.03 Hz. Both are close to 90° phase from the water surface oscillations although phase-significance is low. Both peaks exceed the incident-frequency peak at 0.1 Hz which is in phase with the incident wave peak. The mid-surf zone flowmeter shows the 0.063 Hz peak, at lesser amplitude than the

incident frequency peak. We interpret these results as indicating the edge wavepair (1,0) of resonant triad, which, according to Guza and Davis (1974) will have edge wave frequencies of (0.63, 0.3) ω_i *i.e.* very close to our observed frequencies. The (1,0) pair is consistent with χ_s values which indicate that mode 1 is possible at 0.63 Hz and only zero mode can exist at 0.03 Hz for the Palm Beach surf zone. Non-appearance of wave peak at 0.063 Hz suggests that the inner surf zone instruments were close to the mode 1 node. Profiles of edge wave surface, $\eta(x)$, and flow $u(x)$, calculated from $u = d\phi/dx$ and $\eta = (1/g)\delta\phi/\omega$ where $\phi = (ga/\omega)L_n(2Kx) \exp(-Kx)$, L_n is the Laguerre polynomial of mode n , in Figure 5, show that this interpretation is consistent, although the 0.03 Hz wave peak would have been expected.

This result, when compared with the Moruya cases, raises the question of why a particular set occurs. We suggest that answer lies with the dissipation parameter D (Eq. 6), and that the highest frequency, lowest mode set will occur which is consistent with the excitation condition (Eq. 1), and for which D is less than a threshold level D_c . Table 2 lists ω_e permitted modes and L_e values, and estimates of D for the Moruya and Palm Beach experiments. These D values are calculated using the surf zone gradient β_s rather than the beach-face β value. Empirically, it appears the D_c is about 1.0 for dissipative beaches. We note, however, that excitation of the first subharmonic ($\omega/2$), (0,0) set is significantly easier than the (1,0) set and suggest that a similar (0,0) set can be excited at $\omega/4$ in preference to the (1,0) : ($\omega/1.6$, $\omega/3.0$) set when a trough of sufficient width is present.

During the Palm Beach experiment, rips were virtually absent, allowing no test of possible edge wave - circulation relationships. To explore this last problem we turn to the final experiment.

(4) Multiple sites along a bar-trough system - Durras experiment

This experiment is potentially most interesting in that 5 sites at 20 m intervals in a parallel bar-trough system were measured, but unfortunately this was done prior to establishment of the full experimental system. A single instrument set of 2 flow meters and one transducer, logged by chart recorder, was moved to successive sites. This was a preliminary experiment and field work was done largely by a student, Mr E. Wallensky. Figure 6 shows spectral results and net (u , v) velocity components at each site. A longshore current feeding a rip is indicated clearly. There is no transverse or rhythmic topography to influence location of the rip catchment divide. In summary, results indicate a (1,0) edgewave set (0.06 Hz, 0.03 Hz) dominating, with a common node at the rip current and the 0.06 Hz component antinode about 30 m up-trough from the rip, while the 0.03 Hz component has its antinode about 40 m up-trough. These

Figure 5 Spectra for dissipative troughless surf zone, reflective beach face - Palm Beach (ref. fig. 2d). Theoretical edge wave surface and current profiles shown (normalised).

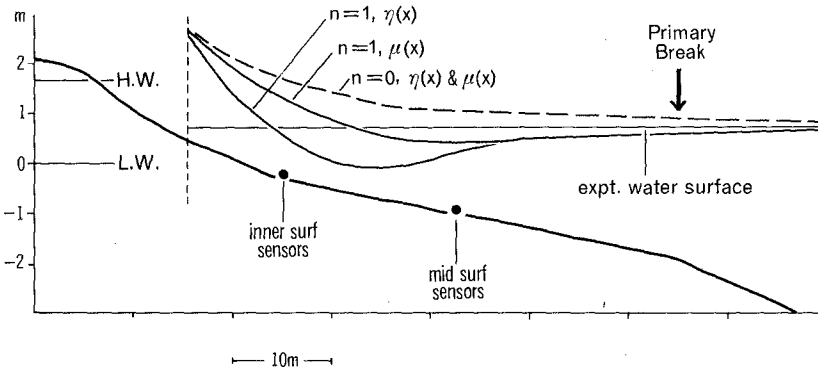
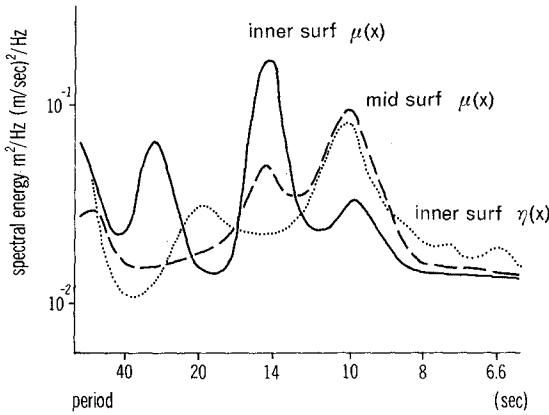
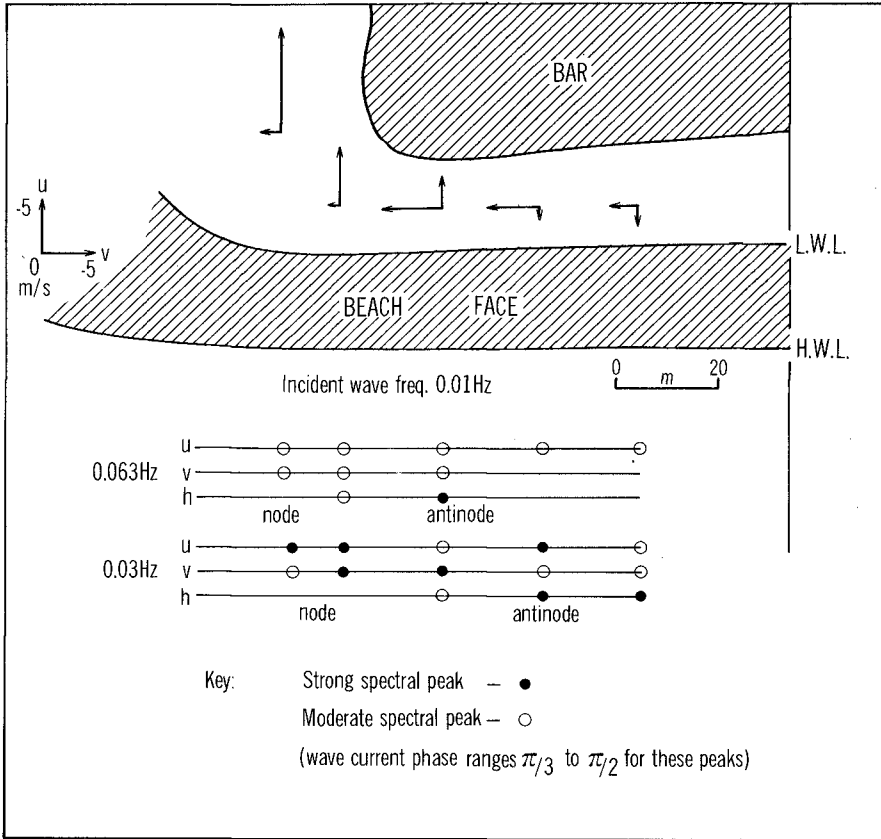


Figure 6 Multiple sites in parallel bar-trough system, showing longshore variation of inferred (1,0) triad spectral peaks and net currents (Durras Beach, ref. fig. 2e).



correspond quite well with predicted quarter-wavelengths (node to antinode) of the (1,0) components, *i.e.* 25 and 38 m.

CONCLUSIONS

The existence of edge waves appears confirmed for dissipative surf beaches, as well as for the simpler reflective case as previously has been argued. Our reflective example supports the hypothesis that beach cusps form from the influence of a stationary zero-mode edge wave at half the incident wave frequency, *i.e.* the first subharmonic. With varying degrees of dissipation it appears that a series of edgewave frequencies can exist with frequencies ω_j/j , where $j = 1, 1.6, 2, 3, 4 \dots$. We include $j = 1$ here to include possible edge waves at incident frequency (although these are less likely, especially as stationary waves: Guza and Inman).

Dissipative surf zones with steep beach faces show a greater range of inshore edge waves, in particular as resonant (0,0) or (1,0) pairs at frequencies of $\omega/2$, or $(\omega/1.6, \omega/3)$ respectively. Further, the single zero-mode form appears to occur at $\omega/4$. Although the zero mode wave at $\omega/2$ is more easily excited, by a factor of 4, the particular edge wave which occurs is limited by inshore dissipation, and that which exists is the lowest mode, shortest period wave for which inshore friction D (Eq. 6) is less than 1.0.

As far as our measurements go, edge waves appear to influence location of inshore circulation systems, with rips tending to locate at nodes. The fact that edge wave length increases discontinuously as inshore dissipation increases offers an explanation of the phenomenon - often observed - that new or secondary rips appear when wave energy conditions change.

ACKNOWLEDGMENTS

This study is supported by the Australian Research Grants Commission (ARGC). We are grateful to Mr M. Bradshaw, Mr. P. Cowell, and Professor B.G. Thom for co-operation and assistance in all facets of the study, and to Mr E. Wallensky for his major part in experiment 5.

REFERENCES

- Bendat, J.S. and A.G. Piersol, 1971, *Random Data : Analysis and Measurement Procedures*, New York, Wiley, 407 pp.
- Bowen, A.J., and D.L. Inman, 1969 "Rip currents 2: laboratory and field observations". *J. Geophys. Res.* 74 (23): 5479-5490.
- Bradshaw, M.P., J. Chappell, R.S. Hales and L.D. Wright, 1978 "Field monitoring and real time analysis for surf and inshore current behaviour". *Proc. 4th Aust. Coastal and Ocean Engineering Conference (Adelaide)*, 171-175.
- Dalrymple, 1975, "A mechanism for rip current generation on an open coast". *Jour. Geophys. Res.*, 80, 3485-3487.
- Guza, R.T., and R.E. Davis, 1974, "Excitation of edge waves by waves incident on a beach". *J. Geophys. Res.* 79 (9) : 1285-1291.
- Guza, R.T., and D.L. Inman, 1975, "Edge waves and beach cusps". *J. Geophys. Res.* 80 (21): 2997-3012.
- Hino, M., 1975, "Theory on formation of rip current and cuspidal coast". *Proc. 14th Conf. Coast Engineering*, 909-919.
- Huntley, D.A., 1976, "Long period waves on a natural beach", *J. Geophys. Res.* 81 : 6441-6449.
- Huntley, D.A., and A.J. Bowen, 1975a, "Comparison of the hydrodynamics of steep and shallow beaches", in Hails, J.R. and A. Carr (eds), *Nearshore Sediment Dynamics and Sedimentation*, London, Wiley and Sons, 316 pp.
- Wright, L.D., B.G. Thom, and J. Chappell, 1978, "Morphodynamic Variability of High Energy Beaches". *Proc. 16th International Conference on Coastal Engineering* (this volume).
- Wright, L.D., J. Chappell, B.G. Thom, M.P. Bradshaw and P. Cowell (in press), "Morphodynamics of reflective and dissipative beach and inshore systems, southeastern Australia." *Marine Geology*.

CHAPTER 81

BEACH CUSPS AND EDGE WAVES

D. A. Huntley & A. J. Bowen

Department of Oceanography
Dalhousie University
Halifax, Nova Scotia
B3H 4J1, Canada

ABSTRACT

Beach cusps are very common, concave-seaward cusped patterns at the shoreline of a beach, which tend to occur with a regular longshore spacing, but which can have a wide range of longshore wavelengths from a few centimeters to several kilometers or more. Edge waves, resonant waves trapped at the shoreline by refraction, have been suggested as the cause of beach cusps but it has proved difficult to establish a definitive link on natural beaches. This paper describes field measurements of nearshore velocities, in all three orthogonal directions, that show the presence of edge wave motion just before the formation of beach cusps of the corresponding wavelength, and thus provides convincing evidence that edge waves are responsible for beach cusps. The magnitude of the observed edge wave oscillatory and drift velocities are found to be large and apparently well able to form cusps of the observed size. The observed edge waves are at the subharmonic of the incident wave frequency and thus are the field equivalent of the laboratory observations of Guza and Inman (1975) and Guza and Bowen (1977). It is not clear, however, whether the developing cusp topography enhanced or suppressed the edge wave motion.

INTRODUCTION

Beach cusps are cusped patterns in beach sediment formed at the shoreline, with longshore wavelengths which are generally relatively constant at a given location and time but which can vary with location and time from around 10 cms on lake shores (Komar 1973) to several hundred meters on long oceanic beaches. Dolan and Ferm (1968) have even suggested that the large-scale features of a shoreline, with capes and bays, may also be described as beach cusps with wavelengths of 100 km or more. The characteristic morphology of beach cusps is of seaward-facing concave embayments separated by relatively narrow seaward-pointing horns. Their relief varies typically from a few centimeters to several meters.

Considerable scientific and coastal engineering interest has centered on beach cusps, not only because of their very common occurrence and the wide scale of features they encompass, but also because they are

clearly the result of on/off-shore movement of sediment. As readily observable features of the shoreline, which are known to form remarkably rapidly where they occur, they may provide an important link in understanding the processes controlling the onshore and offshore movement of sediment on beaches.

Many mechanisms have been proposed to explain the existence of beach cusps, but the most plausible is that they are the response of the beach sediment to the presence of edge waves (Bowen 1969, 1973; Bowen and Inman 1967, 1971; Guza and Inman 1975). Edge waves are resonant waves trapped along the edge of water bodies by refraction. They vary sinusoidally along shore and have an amplitude which decays rapidly offshore. The existence of a regular longshore wave length for an edge wave, and the possibility of edge waves with a wide range of longshore wavelengths makes them very attractive as potential generators of beach cusps.

The laboratory experiments of Guza and Inman (1975) give clear evidence that, at least on reflective beaches where little or no breaking occurs and incoming waves are reflected seaward again, subharmonic edge waves (with period twice that of the incident waves) are generated and form cusped features at the shoreline on an erodable laboratory beach. Extensive laboratory experiments by Guza and Bowen (1977) show that subharmonic edge wave resonance occurs for low incident wave steepness but is suppressed, probably by the increased friction, for wave steepness large enough to produce pronounced plunging or spilling of waves in the surf zone.

In the field a definitive link between edge waves and beach cusps has proved elusive. Komar (1973) describes field observations which show that cusp formation is a result of motion in the water column which has its own intrinsic longshore wavelength, and is not a result of water/sediment feedback at some arbitrary perturbation wavelength. He made visual observations of small cusps of wavelength ranging, from day to day, between 11 and 58 cms on Mono Lake, California. Because of their small size he was able to destroy them by flattening the beach with a ruler. When this was done, cusps of the same wave length reformed on the beach within ten minutes under surging waves of height less than 2 cms. On the basis of their rapid formation, the co-existence of cusps and waves surging on the beach, and the consistency and magnitude of their longshore wavelengths, Komar concluded that the beach cusps were generated by edge wave motion. However, he did not make any direct measurement of the nearshore water motion to prove the existence of edge waves.

Direct observations in the field of edge wave motion, both at subharmonic and much longer periods, have been made on smooth beaches without obvious cusps or longshore rhythmic features, (Huntley and Bowen 1973, 1975a, Huntley 1976, Sasaki et al 1977) and on beaches with

pre-existing rhythmic topography (Huntley (in press), Chappell and Wright (in press)). However, the definitive experiment linking beach cusps to edge waves would be the observation of edge wave motion before and during the formation of beach cusps of the corresponding wavelength. This paper describes a field experiment in which, by good fortune, these conditions occurred.

THE FIELD OBSERVATIONS

Three electromagnetic velocity sensors (two Marsh-McBirney Inc. Model 711 and one Cushing Engineering Inc. Model 612) were used to measure the nearshore velocity fields. These two-component fast response (time constant 0.1 or 0.2 secs) instruments were mounted on an aluminum tripod 0.3m high which was dug into the seabed about 7 cms and held in position using lead weights (Huntley and Bowen 1975b). Two of the sensors, mounted 0.35m and 0.72m above sea bed, were aligned to measure the offshore and vertical components of flow and the third sensor, at 0.61m above the bed, was aligned to measure the offshore and longshore components of flow. In this way the three orthogonal components of flow were simultaneously measured essentially at a single location. Orientation in the horizontal plane was achieved by using a theodolite at the top of the beach to define a line perpendicular to the trend of the beach, and then aligning the offshore direction of the sensors by sighting along range poles placed on this line; accuracy of alignment was estimated to be about 2°. Cables ran up the beach from the sensors to a vehicle parked at the top of the beach which contained battery-powered electronics and a magnetic tape analogue data logger. The data were subsequently digitized at a sampling interval of 0.33s for computer analysis.

In addition, two 135 second time series of water elevation above the sensors were obtained by filming water level against a graduated range pole placed close to the sensor mount.

The field site was Queensland Beach, Nova Scotia, Canada (Figure 1). The beach is located at the head of St. Margaret's Bay, a large sheltered bay opening to the Atlantic. The beach itself forms a tombola about 300 m long facing directly towards the mouth of the Bay and the dominant incident wave direction. Figure 2 shows beach profiles measured at low tide in the vicinity of the instruments. A set of beach cusps remaining from the previous high tide were subaerial when these profiles were measured and gave the trough and cusp profiles shown, with an alongshore separation of about 3.5m. The sensors were placed on the cusp range. The mean sea level marked on Figure 2 gives the approximate level during the measurements of velocities, but a change of approximately 0.4m about this level occurred with the rising tide as measurements were taken.

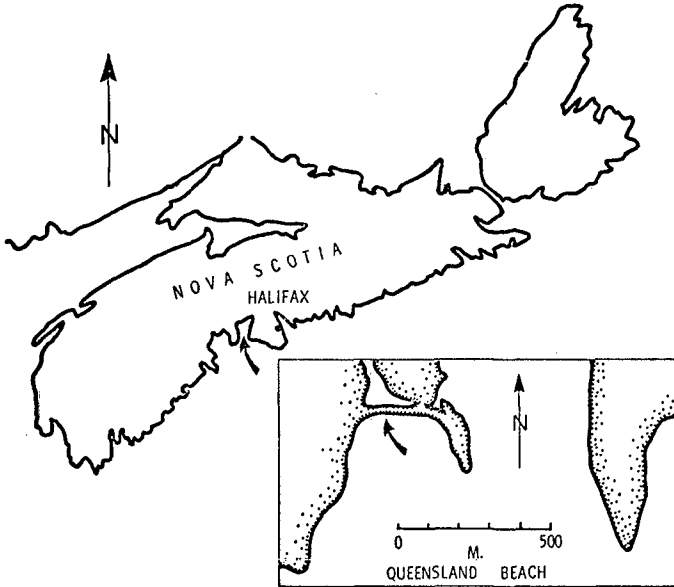


Figure 1: Location map.

An example of the records obtained is shown in Figure 3. The upper time series shows the water elevation as measured by the movie film, and the elevation axis is given relative to the sea bed. The three horizontal lines mark the elevations of the three electromagnetic sensors. This time series shows the incoming waves to have a dominant period of about 7 seconds, but the period is clearly irregular. The sensors at this time were at the break-point for the largest plunging breakers (e.g. at 25 and 40 s) but outside the breakpoint for the smaller waves. The steepest breakers have a height of about 0.7m in a mean depth of 0.9m, in good agreement with the expected value.

The three lower records show the onshore and vertical velocities measured by the flowmeters at 0.72m and 0.35m height. Positive velocities are onshore and downwards respectively. The elevation record shows that the upper sensor came out of the water in wave troughs on several occasions, and the dotted lines in the velocity

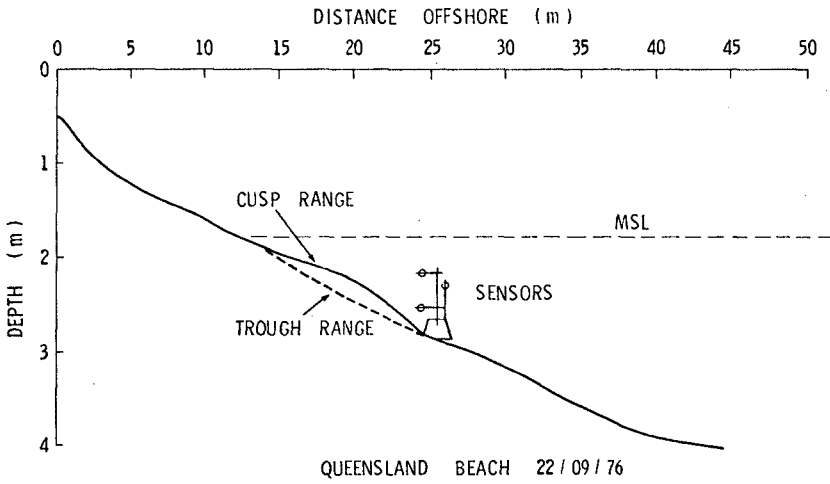


Figure 2: Beach profiles.

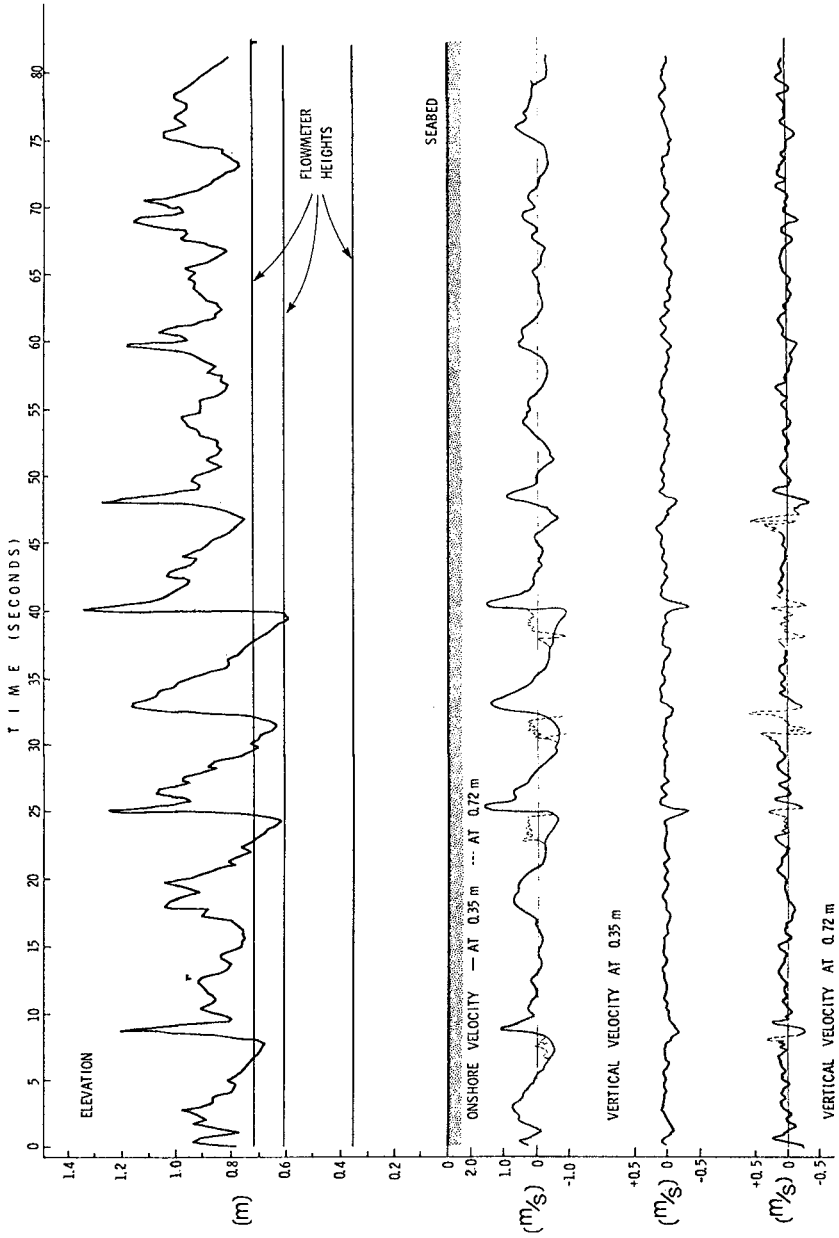


Figure 3: An example of the time series records.

records show the measurements when this occurs. Except when this occurs, onshore velocities at the two flowmeters overlap, and the wave induced vertical velocities decrease with depth in a way consistent with the predicted linear decrease for shallow water waves.

The behaviour of the flowmeter as it comes out of the water and is re-immersed is interesting. The characteristics in the onshore record are most clearly shown in the second event at about 22s (Figure 3). As the flowmeter comes out of the water the sensor output settles rapidly, but with some ringing, to the zero-level (a zero-flow mean voltage equivalent to about 0.23 m/s was present for this sensor). On re-immersion a large spike occurs, either positively or negatively depending on the details of the immersion, followed by rapid recovery to a measurement of the true water velocity. Laboratory tests confirm this typical behaviour and show that, for an instrument with a nominal time constant of 0.2 secs, about 0.8 seconds of immersion are necessary before accurate measurements of water flow can be made. This time interval is clearly sufficiently small to allow the peak onshore velocities in breaking waves at this level to be measured, and further tests to measure the profile of onshore flow closer to the wave crest should be possible and will prove very interesting. For vertical velocities, however, the maximum upward flow occurs on the rising face of the breaker very close to the time of reimmersion and it is clear that the recovery time of the flowmeters is too long to measure this.

EDGE WAVES

The theory of edge waves has recently been reviewed in several papers (Bowen and Inman 1969, 1971, Huntley 1976, Guza and Inman 1975) and it is therefore only necessary here to point out features relevant to these measurements.

For a beach of linear slope angle β , Ursell (1952) finds a dispersion relation of the form

$$L = g \frac{T^2 \sin}{2\pi} (2n+1)\beta \quad (1)$$

where L is the longshore wavelength of the edge wave, T is the period and n is an integer, known as the mode number, which gives the number of zero crossings in the rapid decay of amplitude and velocity with distance offshore. This dispersion relation predicts a whole family of edge wave modes for any specified period, each mode having a distinct longshore wavelength. The work of Guza and Davis (1974), Guza and Inman (1975) and Guza and Bowen (1975, 1977) suggests that, for beaches with surging, collapsing or low plunging breakers, edge waves of subharmonic period (twice the incident wave period) dominate.

Bowen and Inman (1971) and Bowen (1973) show that edge waves which are not synchronous with the incident waves should generate beach cusps with a wavelength $L/2$. This was observed on an erodable laboratory beach by Guza and Inman (1975).

In distinguishing between edge waves and incident waves in near-shore velocity records, the relative phases between the orthogonal velocity components are important. Table 1 shows the phases for four cases based on gravity wave theory and Ursell's edge wave theory. Here "in phase" can mean a relative phase of 0° or 180° and "quadrature" a relative phase of 90° or 270° .

Table 1. Phase relationships between velocity components

Wave type	u	v	u	w	u	w
	offshore	vs longshore	longshore	vs vertical	offshore	vs vertical
Progressive Gravity	in phase		quadrature*		quadrature*	
Standing Gravity	quadrature		quadrature*		in phase	
Progressive Edge	quadrature		quadrature		in phase	
Standing Edge	in phase		in phase		in phase	

*Except near the sea bed where the velocity is linear and follows the bottom slope

In order to identify possible edge wave motion in the present velocity measurements spectra and cross-spectra were calculated, Figure 4 shows spectra for onshore and longshore velocities 0.61m from the bed and Figure 5 for onshore and vertical velocities 0.35m from the bed. For each of the spectra the most prominent peak occurs at about 0.145 Hz (period 6.9 secs) in good agreement with the estimated incident wave period. The fine vertical lines at higher frequencies mark the frequencies of the first, second, and third harmonics of this incident wave period and it is clear that structure is present in the spectra centered around these periods. In fact, for the onshore spectrum of figure 4 the bandwidths of the harmonic peaks increase approximately in proportion to the harmonic number, as might be expected. Of more interest in the present context however is the presence of a peak in each of the spectra at the first subharmonic of the incident wave frequency. Although this peak does not appear to be

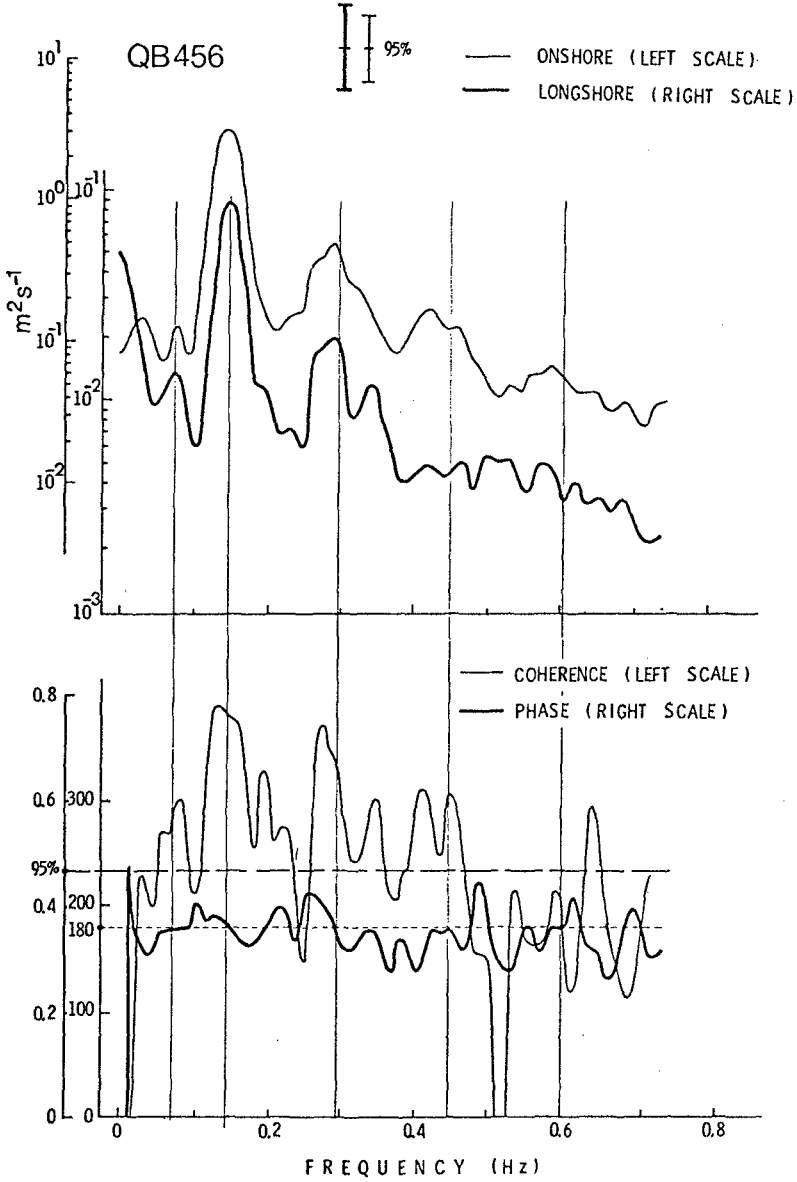


Figure 4: Spectra and cross-spectra of onshore and longshore flows.

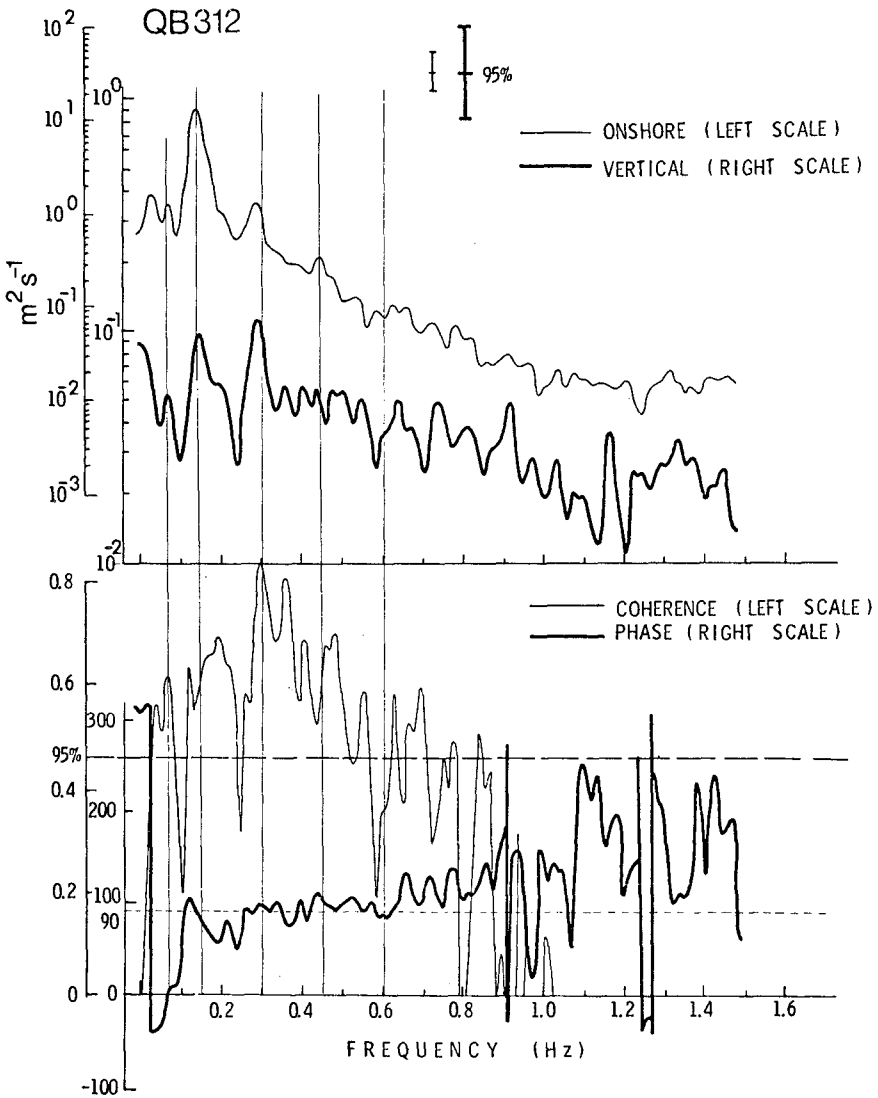


Figure 5: Spectra and cross-spectra of onshore and vertical flows.

significant at the 95% level in any individual spectrum, its persistence in all these and in the other spectra obtained from the present measurements suggests that it is a significant feature of the velocity field. A second low frequency peak also appears in both the onshore records at about 0.03 Hz but cannot be studied in detail with the short record lengths obtained during these measurements.

The significance of the low frequency peaks is confirmed by the calculated coherences between the velocity components. In figure 4 the coherence between the onshore and longshore velocities is well above the 95% confidence level for zero coherence at the incident wave frequency and at the first two harmonic and the subharmonic frequencies; in figure 5 the coherence is, rather surprisingly, higher for the first harmonic than for the incident wave peak, but is also well above the 95% level for the subharmonic (and 0.03 Hz) peak.

The phase plots show that the phase between the onshore and longshore components of flow is close to 180° throughout the frequency range shown; the expected 95% confidence limits for the phases of the incident peak and subharmonic peak are $\pm 12^\circ$ and $\pm 17^\circ$ respectively (Jenkins and Watts 1968) and the phases for each are well within this range about 180° . For the onshore and vertical velocities (Figure 5) the phase is close to 90° for the wind wave band of frequencies (0.1 - 0.9 Hz), though displaying an unexplained slight rise with increasing frequency. Below 0.1 Hz the phase changes dramatically, however, and at the subharmonic frequency has a value of about $+8^\circ$, insignificantly different, at the 95% confidence interval of $\pm 17^\circ$, from a phase of 0° .

When compared with the predicted phases shown in Table 1, the observed phases for frequencies above 0.1 Hz suggest that the spectral energy is predominantly due to the presence of progressive gravity waves approaching the beach, with little reflection occurring. Below 0.1 Hz, and specifically at the subharmonic frequency, the phases of 180° between onshore and longshore and 0° between onshore and vertical show that the subharmonic peak in the spectra is due to the presence of a standing subharmonic edge wave, with a period of around 14 seconds.

The confidence with which these identifications, based on phase, can be made depends to a large extent on accurate alignment of the sensors. For incident waves, which are refracted towards the shore normal as they propagate inshore, the longshore component of flow will be much smaller than the on/offshore, so that misalignment of the sensors in the horizontal plane may cause serious contamination to the assumed longshore record by on/offshore flows. For low mode edge waves, however, misalignment in the horizontal plane is not as serious since, in the offshore variation of amplitudes, away from zero-crossings onshore and longshore flows have comparable magnitudes so the distinction in phase between progressive and standing edge waves should be clear. Misalignment in the offshore/vertical plane may also seriously

contaminate the much smaller vertical velocities with horizontal flows. Thus there will be a tendency for offshore and assumed vertical records to be in phase for both incident waves and edge waves.

For the present data subharmonic edge waves are not predicted to have zero-crossings in either offshore or longshore flow near the sensors, except at high mode numbers, so the 180° phase between these components at the subharmonic frequency rules out the existence of low mode progressive edge waves; we will see later that the offshore variation of amplitude of this subharmonic peak also makes it unlikely to be due to a standing gravity wave. On the other hand, the observation of near 90° phase between onshore and vertical flow for frequencies above 0.1 Hz can only be due to progressive incident waves. This suggests that the sensors were aligned vertically to considerably better than 1° , which is surprising and probably fortuitous. The fact that the phase tends to drop below 90° for frequencies between 0.1 Hz and 0.3 Hz appears to be inconsistent with the possibility of some standing gravity wave energy being present at the incident wave frequency, since the phase between onshore and vertical velocities for standing waves of this frequency and at the offshore distance of the sensor is predicted to be 180° rather than 0° . The phase drop may therefore be the result of a slight shoreward dipping of the assumed on/offshore direction due to misalignment, or a tilt of the current ellipse so that its major axis is inclined slightly out of the horizontal towards the bottom slope.

In order to find the longshore wavelength of the observed subharmonic edge wave we need to know its mode number (equation 1). With the present data this can only be estimated from the offshore decay of the amplitude of the velocity components (e.g. Huntley 1976). The tidal excursion of the shoreline position changed the effective offshore distance of the sensor mount and this was used to map the velocity field for a narrow range of offshore distances, under the assumption that the edge wave velocity field remained essentially constant over the one hour of measurements. Figure 6 shows the result for the on/offshore velocities. Measured values have been scaled to give the best fit to the predicted variation for the mode zero edgewave of subharmonic period on a beach of the linear slope most closely matching the profiles (figure 2). The mode zero curve provides the best fit to the data, but the uncertainty in the levels of the observed velocities is sufficiently large that higher mode numbers would still provide a reasonable fit, despite a zero-crossing at around 14m. Unfortunately the longshore velocity records do not provide additional information. For the two inshore data records the longshore sensor, at 0.61m above the bed, came out of the water in wave troughs and satisfactory spectra could not be calculated. Nevertheless if we assume a mode zero wave and can accept an extrapolation to the shoreline based on a linear beach slope, the shoreline amplitudes shown in Figure 6 are obtained. In calculating these values a half-power band width of 0.035 Hz and a triangular peak shape were assumed for the subharmonic peak. Adjustment of the

velocity has also been made to allow for the fact that measurements were not made at an alongshore antinode of onshore velocity; the relative size of the longshore component suggests that measurements were made about 1.2m from an alongshore antinode. Higher mode numbers would give values within a factor of two of these shoreline values. The predicted total excursion (peak to peak) along the beach face is entirely consistent with observations of the longshore variability of run-up, though no precise observations were made.

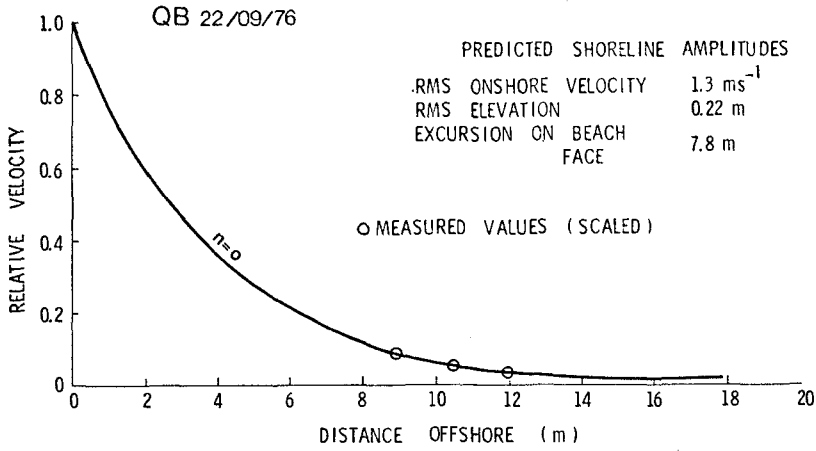


Figure 6: Relative amplitudes of onshore velocity vs. offshore distance.

BEACH CUSPS

TABLE 2: Predicted Cusp Spacing

	wave period. s.	predicted cusp spacing m.		
		n=0	n=1	n=2
Synchronous	6.9	6.0	18.0	30.1
Subharmonic	13.8	12.0	36.1	60.2

Table 2 shows the predicted beach cusp spacings ($L/2$) for subharmonic standing edge waves of the first three mode numbers; for comparison the predicted spacings of cusps formed by synchronous edge waves (L) are also shown.

Two sets of cusps were observed at the beach site.

The first set of cusps, formed on the previous high tide, was found at the start of the field experiment (Figure 2). As the tide rose over the instrument mount, however, these cusps were destroyed and could not be seen by the time velocity measurements were begun. These pre-existing cusps had a longshore spacing, from measurement of 23 cusps, of 6.8m with a standard deviation of 0.7m. They may, therefore, have been formed originally by synchronous edge waves, but were not being actively formed during our measurements.

However, a second set of cusps began to form at the shoreline towards the end of the measurement period. Near the end of our final run, active formation of these cusps was first observed and within one hour the cusps appeared to have reached an equilibrium size. Measurement of the longshore spacings of eight of the cusps gave a mean spacing of 12.7m with a standard deviation of 1.4m, in good agreement with the predicted wavelength from a zero mode subharmonic edge wave.

The fact that subharmonic edge waves were measured in the water column before the formation of cusps of corresponding wavelength provides convincing evidence that beach cusps are the result of edge wave motion.

Unfortunately, the relief of the new cusps was not measured, but since they were of a similar size to the pre-existing cusps, the relief measured by the cusp and trough profiles in Figure 2 was used to provide a rough estimate of the amount of sediment moved in forming cusps of this scale. Based on a simple sinusoidal model of cusp topography, an estimate of about 1m^3 of sand per metre length of beach is obtained. Observations suggest that this amount of sand was moved in a period of about an hour.

The size of the observed edge waves, combined with the incident waves, would appear to be well able to move this sediment. The shoreline oscillatory velocity of the edge wave was about 1.8 m/s in mean amplitude (Figure 6). The maximum bottom drift velocity under the edge wave, calculated using Bowen and Inman (1971) equation 17, is found to be about 35 cm/s offshore.

The actual formation of the cusps seems to depend on having a reasonably steady shoreline position, since cusps did not form during the time of our velocity measurements, when there was a rapid rise of tide level. The shoreline was moving up the beach at a rate of about 6m per hour when our measurements began, but had slowed to 2m per hour by the time cusps began to appear.

A possible generation mechanism for subharmonic zero order edge waves on a plane beach has been shown by Guza and Davis (1974) and

Guza and Bowen (1975) to be the longshore instability of a reflected gravity wave. Guza and Bowen (1977) made a laboratory and theoretical study of the range of incident wave conditions for which subharmonic edge wave resonance was important, and found that a controlling parameter is

$$\epsilon_i = \frac{a_\infty}{gT^2} \left(\frac{2\pi}{\tan \beta} \right)^{5/2}$$

where a_∞ is the incident wave amplitude before shoaling. Subharmonic resonance was observed on their laboratory beach when ϵ_i was less than 9 or 10 but was suppressed for larger ϵ_i because of increased damping due to wave breaking. For our field data, we use the formula of Komar and Gaughan (1972) to estimate a_∞ from our measurements of breaking wave height, and hence find a value of $\epsilon_i \approx 7$ for the incident wave conditions. This value falls well within the range of ϵ_i for which maximum edge wave resonance was observed in the laboratory. Our field observations are therefore directly comparable with the laboratory observations of Guza and Bowen (1977) and Guza and Inman (1975) and confirm that subharmonic edge waves can form beach cusps in the field as well as in the laboratory.

ACKNOWLEDGEMENTS

Financial support for this work was provided by the National Research Council of Canada.

REFERENCES

- Bowen, A. J. 1969. Rip currents, 1, Theoretical investigations, J. Geophys. Res. 74, 5467-78.
- Bowen, A. J. 1973. Edge waves and the littoral environment, in Proceedings of the 13th Coastal Engineering Conference, pp. 1313-1320, Council on Wave Research, London.
- Bowen, A. J. and D. L. Inman. 1969. Rip currents. 2 laboratory and field observations. J. Geophys. Res. 74, 5479-5490.
- Bowen, A. J. and D. L. Inman. 1971. Edge waves and crescentic bars. J. Geophys. Res. 76, 8662-8671.
- Chappell, J. and L. D. Wright. (in press). Surf beach bar-trough resonance and coupled periodic morphology. Proceedings of the 16th Coastal Engineering Conference, Hamburg. ASCE, New York.
- Dolan, R. and J. C. Ferm. 1968. Crescentic landforms along the Atlantic coast of the United States. Science, 159, 627-629.
- Guza, R. T. and A. J. Bowen. 1975. The resonant instabilities of long waves obliquely incident on a beach. J. Geophys. Res. 80, 4529-4534.
- Guza, R. T. and A. J. Bowen. 1977. Resonant interactions for waves breaking on a beach, in Proceeding of the 15th Coastal Engineering Conference, pp. 560-579, American Society of Civil Engineers, New York, N. Y.

- Guza, R. T. and R. E. Davis. 1974. Excitation of edge waves by waves incident on a beach, J. Geophys. Res. 79 (9), 1285-1291.
- Guza, R. T. and D. L. Inman. 1975. Edge waves and beach cusps, J. Geophys. Res. 80 (21), 2997-3012.
- Huntley, D. A. 1976. Long period waves on a natural beach. J. Geophys. Res. 81, 6441-6449.
- Huntley, D. A. (in press). Edge waves on a crescentic bar system. J. Geological Society of Canada.
- Huntley, D. A. and A. J. Bowen. 1973. Field observations of edge waves. Nature 243 (5403), 160-162.
- Huntley, D. A. and A. J. Bowen. 1975a. Field observations of edge waves and discussions of their effect on beach material. Q. J. Geol. Soc. Lond., 131, 69-81.
- Huntley, D. A. and A. J. Bowen. 1975b. Field measurements of nearshore velocities, in Proceedings of the 14th Coastal Engineering Conference, pp. 538-557, American Society of Civil Engineers, New York, N. Y.
- Jenkins, G. M. and D. G. Watts. 1968. Spectral analysis and its applications. Holden-Day, Inc., San Francisco. 525 pp.
- Komar, P. D. 1971. Nearshore cell circulation and the formation of giant cusps. Geol. Soc. Amer. Bull. 82, 2643-2650.
- Komar, P. D. 1973. Observations of beach cusps at Mono Lake, California, Geol. Soc. Amer. Bull., 84, 3593-3600.
- Komar, P. D. and M. K. Gaughan, 1972. Airy wave theory and breaker height prediction, Proceedings of the 13th Coastal Engineering Conference, pp. 405-418. American Society of Civil Engineers, New York, N. Y.
- Sasaki, T., Horikawa, D. and Kubota, S. 1977. A study on nearshore currents (report no. 5); long period fluctuations in nearshore currents, in Proceedings of the 24th Conference on Coastal Engineering in Japan, cited in: Horikawa, K., 1977, Nearshore current treatments and their applications to engineering problems, in Proceedings of the 4th P.O.A.C. Conference, Memorial Univ. of Newfoundland, St. John's, Nfld.
- Ursell, F. 1952. Edge waves on a sloping beach. Proc. Roy. Soc. A., 214, 79-98.

CHAPTER 82

NEAR-BOTTOM VELOCITIES IN WAVES WITH A CURRENT

by W.T. Bakker¹⁾ and Th. van Doorn²⁾

0 Abstract

Bakker (1974) developed a mathematical model concerning the sand concentration and velocity distribution in an oscillatory turbulent flow, with or without resultant current.

The flow is assumed to be uniform in horizontal direction. The present paper reports on an experimental verification of this theory. Furthermore, the numerical accuracy of the model has been investigated and diagrams are presented which enable the computation by hand of global velocity profiles.

1 Introduction

This paper deals with a numerical theory on the near-bottom velocity pattern in parallel-directed waves and current and with the comparison of theory and measurements. The paper is a sequence to an earlier paper (Bakker, 1974); the numerical theory concerning the velocity field developed herein is further refined and, in some respects, revised. For the sake of physical understanding an additional paper, dealing with an approximate analytical theory is in preparation (Bakker, 1979).

Furthermore, a Report is in preparation (Bakker and Van Doorn, 1979) which comprises as well the analytical and the numerical theory, and which goes further into details. This study has to be placed in a general scope of investigations, mentioned in the preceding paper (Bakker, 1974).

The necessary assumptions are mentioned in Ch. 2; in Ch. 3 the mathematical formulation is given. Because several aspects differ from those in the earlier paper, most of the derivations from this paper are repeated for convenience. Ch. 4 deals with the investigations on numerical accuracy. In Ch. 5 experiments are described, carried out in the Delft Hydraulics Laboratory (DHL). Comparison between theory and experimental data is made in Ch. 6. The present theory and the theory of Lundgren (1972) are compared in Ch. 7. After the conclusions (Ch. 8) the acknowledgements (Ch. 9), the literature and the symbols are mentioned.

The theory was developed by the first author; the experimental verification was carried out by the second author, who also reported on this subject.

2 Assumptions

The following assumptions are made:

- a. Apart from turbulent fluctuations a horizontally directed and horizontally uniform current pattern is assumed. The current u is assumed to be only a function of the vertical coordinate z and the time t , but no function of the horizontal coordinate x .

1) Senior Scientific Officer, Technical University of Delft

2) Head of Study Dept. Vlissingen, Rijkswaterstaat, Netherlands

Project Engineer, Delft Hydraulics Laboratory, Netherlands

b. In the fluid a turbulent shear stress is assumed, according to the assumptions of Prandtl (1931) equal to:

$$\tau = \rho \ell^2 \frac{\partial u}{\partial z} \left| \frac{\partial u}{\partial z} \right| \quad (1)$$

in which τ is the shear stress, positive when acting in positive direction from the upper layer on the lower layer, ρ is the specific density of the fluid and ℓ is the mixing length.

c. A reasonable assumption on this mixing length and the distribution of the shear stress as a function of the height is obtained as follows. The equation of motion reads:

$$\rho \frac{\partial u}{\partial t} = \frac{\partial \tau}{\partial z} - \frac{\partial p_r}{\partial x} \quad (2)$$

in which p_r denotes the fluid pressure. A periodical water motion with period T is assumed. By Fourier analysis, one finds that the left-hand side of Eq. (2) will be zero when averaged over period T .

Then one finds from (2):

$$\frac{d\bar{\tau}_{\text{real}}}{dz} = \frac{\partial \bar{p}_r}{\partial x} \quad (3)$$

The bar above the symbol indicates the averaging over the wave period T ; the subscript "real" of τ serves as a distinction from the schematized τ , mentioned later on.

Assuming, that the mean pressure gradient is constant over the height h , one may write for $\bar{\tau}$:

$$\bar{\tau}_{\text{real}} = (h-z) \frac{\partial \bar{p}_r}{\partial x} \quad (4)$$

If only a stationary and no periodic motion would occur, according to well-known methods one finds a logarithmic velocity distribution, starting from a mixing length ℓ_{real} according to:

$$\ell_{\text{real}} = \kappa z \sqrt{1 - \frac{z}{h}} \quad (5)$$

where κ is the Von Karman constant.

For a stationary current, this logarithmic velocity distribution is found also, if the shear stress τ is schematized as a constant (i.e. uniform over the height):

$$\bar{\tau} = h \frac{\partial \bar{p}_r}{\partial x} \quad (6)$$

and the mixing length according to:

$$\ell = \kappa z \quad (7)$$

As the investigated features occur quite near to the bottom, where (4) and (6) on one hand and (5) and (7) on the other hand look very much the same, in the following the relationships (6) and (7) will be assumed.

d. Starting from a mixing length according to (7), generally it will be assumed, that the pressure gradient $\text{grad}(p_r)$ is horizontally directed, i.e. that the pressure is only a function of x and t .

e. The mean velocity, when averaged over the water depth and the wave period is called U_{mean} . It is further assumed that the water mass far from the bottom is in oscillatory motion according to:

$$U_{\text{osc}} = \hat{U}_1 \sin(\omega t - \psi_1) + \hat{U}_2 \sin(2\omega t - \psi_2) + \hat{U}_3 \sin(3\omega t - \psi_3) + \dots \quad (8)$$

\hat{U}_{mean} , \hat{U}_1 , \hat{U}_2 , \hat{U}_3 , ψ_1 , ψ_2 and ψ_3 can be arbitrary chosen. Connected with the solution, a small parasitary fourth harmonic is found, being 5 to 10% of the first one.

A solution with U_{mean} equal to zero can only be found, when also \hat{U}_2 is zero (as all higher even harmonics). In this case, a parasitary fifth harmonic of the order of 5 to 10% of the first one is found.

f. A hydraulically rough bottom is assumed. The velocity at a height z above the theoretical bottom level is assumed to be zero; it is assumed that z_0 equals 1/33 times the Nikuradse roughness r .

3 Computation of water velocities and shear stress

Define a rather arbitrary height z_{max} above the bottom, in this way, that the periodical changes of the shear stress are attenuated at that height. For $z \geq z_{\text{max}}$ the shear stress τ equals $\bar{\tau}$, being assumed constant over the height (assumption c). Thus one finds from (2):

$$\rho \frac{\partial u}{\partial t} = - \frac{\partial p}{\partial x} \quad \text{for } z \geq z_{\text{max}} \quad (9)$$

Let the velocity at $z = z_{\text{max}}$ be U . Thus Eq. (9) remains valid, when u is replaced by U ; let Eq. (9a) be Eq. (9) for $u = U$.

Define a "defect velocity" u_d as:

$$u_d = u - U \quad (10)$$

According to assumption d, subtracting Eq. (9a) from Eq. (9) yields:

$$\frac{\partial u_d}{\partial t} = 0 \quad \text{for } z \geq z_{\text{max}} \quad (11)$$

In (1), one may replace u by u_d , because U is no function of z . Thus, from (1) and (7) can be derived:

$$\bar{u}_d = \frac{\sqrt{\bar{\tau}/\rho}}{\kappa} \ln \frac{z}{z_{\text{max}}} \quad \text{for } z \geq z_{\text{max}} \quad (12)$$

Consider now the area where $z < z_{\text{max}}$. Subtracting Eq. (9a) from Eq. (2) and substituting u_d from (10) yields:

$$\frac{\partial u_d}{\partial t} = \frac{\partial(\tau/\rho)}{\partial z} \quad (13)$$

This equation can be transferred in an equation with the shear stress velocity p as independent variable.

Define p as:

$$p = \text{sign}(\tau) \cdot \sqrt{|\tau/\rho|} \quad (14)$$

Inversely, this implies:

$$\tau = \rho p |p| \quad (15)$$

From (1) and (7) it shows:

$$p = \kappa z \frac{\partial u}{\partial z} \tag{16}$$

In (16) one may replace u by u_d . Differentiation of (13) to z and multiplying with κz yields:

$$\frac{\partial p}{\partial t} = \kappa z \frac{\partial^2(p|p|)}{\partial z^2} \tag{17}$$

For method of computation of u from p is referred to Bakker (1974). The following mainly deals with deviations from this paper. From p , one can find u_d with the aid of (10), which can be written as:

$$u_d = - \frac{1}{\kappa} \int_z^{z_{\max}} \frac{p}{z} dz \tag{18}$$

Eq. (17) can be made dimensionless by introducing the following dimensionless variables:

$$\left. \begin{aligned} p^* &= p/\hat{p}_{b1} \\ t^* &= t/T \\ z^* &= z/Z, \text{ with } Z = \kappa \hat{p}_{b1} T \\ u^* &= u/\hat{p}_{b1} \quad (\text{see note } 1^1) \end{aligned} \right\} \tag{19}$$

in which \hat{p}_{b1} is the amplitude of the first harmonic of the shear stress velocity at the bottom (the index "b" refers to "bottom").

Thus one obtains from (17):

$$\frac{\partial p^*}{\partial t^*} = z^* \frac{\partial^2(p^*|p^*|)}{\partial z^{*2}} \tag{20}$$

As lower boundary condition is assumed:

$$p_b^* = \bar{p}_b^* + \sin 2\pi t^* + \hat{p}_{b2}^* \sin(4\pi t^* - \phi_2) + \hat{p}_{b3}^* \sin(6\pi t^* - \phi_3) \tag{21}$$

for $z^* = 0$

If U_{mean} equals zero, \bar{p}_b^* and \hat{p}_{b2}^* are assumed zero; to the choice of the variables \bar{p}_b^* , \hat{p}_{b2}^* , \hat{p}_{b3}^* , ϕ_2 and ϕ_3 will be referred.

The upper boundary condition is determined by the fact that $\bar{\tau}$ should remain constant over the height according to (6)²; Averaging Eqs. (13) and (17) over the wave period (in which case the left-hand side becomes zero, as can be seen by decomposing u_d and p in harmonics) one finds that

1) Generally, the velocities denoted by a symbol with an added star have been divided by \hat{p}_{b1} .

2) J. van Overeem drew the attention of the author to the fact, that this condition was not fulfilled by the solution for waves and currents, given by Bakker (1974). Therefore the solution in the present paper contains a revision of last-mentioned paper with respect to the case of waves with a current.

the solution of these equations fulfills this condition automatically, if the upper boundary condition is properly chosen. At the upper boundary the shear stress velocity p should be equal to $\sqrt{\tau}/\rho$:

$$p^* = \sqrt{p_b^* |p_b^*|} \quad \text{for } z^* = z_{\max}^* \quad (22)$$

In the case of an oscillatory flow without current (22) degenerates to $p^* = 0$ for $z^* = z_{\max}^*$. In the computer program, initially an approximation is chosen according to:

$$p^* = \sqrt{\pi p_b^* / 4} \quad \text{for } z^* = z_{\max}^* \quad (\text{initially}) \quad (23)$$

This approximation follows from analytical considerations (Bakker, 1979). In the course of the computations, the real value of the right-hand side of (22) is calculated; after each period the upper boundary condition is adapted. This condition changes, because after some periods \hat{p}_b^* , \hat{p}_{b2}^* , \hat{p}_{b3}^* , ϕ_2 and ϕ_3 are adapted by means of an iterative procedure¹⁾, in this way that the upper boundary condition (8) (in dimensionless shape) is fulfilled as good as possible.

In order to check the accuracy of this upper boundary condition, from the shear stress velocity p^* the value of U^* is calculated after some periods by means of numerical integration¹⁾ with the aid of (18), which clearly keeps its validity in the dimensionless shape.

In the following, some attention will be paid to the results with respect to the first harmonic and the mean velocity profile. This gives just a general scope: solutions, which fit rather closely to the wanted boundary conditions can be found by application of the computer program.

With respect to the first harmonic, the dimensionless relationship between \hat{u}_{d1}^* (the amplitude of the first harmonic of the dimensionless defect velocity) and z^* can be transferred into a dimensionless relationship between a kind of friction coefficient \hat{p}_{b1}/\hat{U}_1 and a_1/r , in which a_1 equals $\hat{U}_1 T/2\pi$ and r the Nikuradse roughness. This can be performed as follows.

Consider a certain defect velocity field u_d^* , which has been calculated, starting from certain bottom boundary conditions, defined by harmonics of p_b^* .

In principle every level z^* (at which u_d^* has been calculated) can be taken as a bottom boundary level z_o^* , where u^* is assumed zero. Therefore according to (10) the choice of z_o^* determines U^* , the dimensionless velocity far from the bottom (at $z^* = z_{\max}^*$). Thus one computation of u_d^* determines a great number of velocity fields u^* with various upper boundary conditions and various values of z_o^* . Neglecting (just for the general scope) non-linear interactions between the harmonics of p^* , in first approximation the relationship between dimensionless first harmonic U_1^* and z_o^* can be investigated by taking \hat{p}_b^* , \hat{p}_{b2}^* and \hat{p}_{b3}^* in

¹⁾ cf. Bakker (1974) and Bakker and Van Doorn (1979)

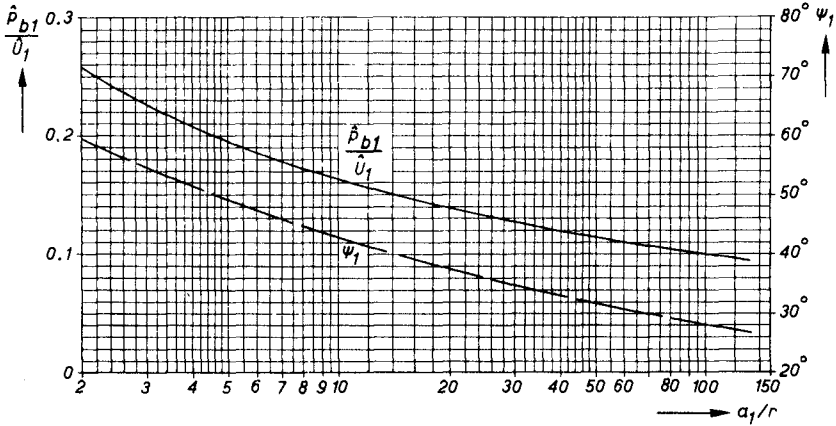


Fig. 1. Ratio \hat{p}_{b1}/\hat{U}_1 between the amplitudes of the first harmonics of the shear stress velocity and the velocity far from the bottom, respectively phase lag ψ_1 between \hat{p}_{b1} and \hat{U}_1 as function of the ratio a_1/r between the stroke length and the ripple height.

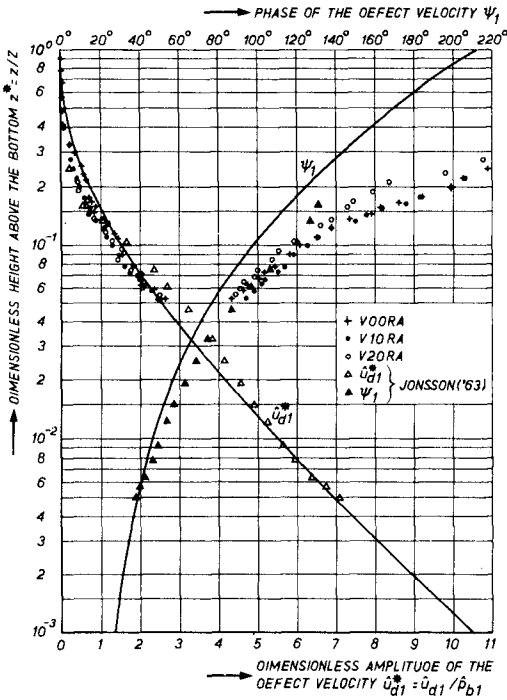


Fig. 2. Dimensionless amplitude \hat{u}_{d1}^* and phase ψ_1 of the defect velocity as function of the dimensionless height above the bottom: according to theory and measurements.

(21) equal to zero and calculating u_{d1}^* under these conditions.¹⁾ On the effect of non-linear interaction will be returned in Ch. 4.

From assumption \underline{f} and (19) the following relationship can be determined:

$$\frac{a_1}{r} = \frac{1}{66\pi\kappa} \cdot \hat{u}_1^* / z_o^* \quad (24)$$

which in turn can be written, using (10):

$$\frac{a_1}{r} = \frac{1}{66\pi\kappa} \hat{u}_{d1}^*(z_o^*) / z_o^* \quad (25)$$

where $\hat{u}_{d1}^*(z_o^*)$ denotes \hat{u}_{d1}^* at the height z_o^* .

Now the ratio \hat{p}_{b1} / \hat{u}_1 , relating the amplitude of the first harmonic of the bottom shear stress velocity to the amplitude of the first harmonic of the oscillatory motion U_{osc} far from the bottom, equals $1/\hat{u}_1^*$, according to (19) which in turn can be written as $1/\hat{u}_{d1}^*(z_o^*)$. According to a similar reason, the phase lag ψ_1 between p_{b1} and u_{d1} equals minus the phase lag between p_{b1}^* and $u_{d1}^*(z_o^*)$. Thus, from the computer results with the mentioned bottom boundary conditions, the choice of a value of z_o^* gives a relationship between a value a_1/r and the belonging values of \hat{p}_{b1}/\hat{u}_1 and ψ_1 . By using z_o^* as a parameter, the general relationship between a_1/r and the last mentioned parameters can be obtained; this is shown in Fig. 1. The same results are plotted in another way in Fig. 2, giving $\hat{u}_1^* (= \hat{u}_{d1}^* \text{ at } z_o^*)$ and ψ_1 as a function of z_o^* .

Now the attention will be turned to the mean velocity profile \bar{u} as function of z . From (10) and (18) for the upper part of the mean velocity profile is found:

$$\bar{u} = \bar{U} + \frac{\sqrt{\tau/\rho}}{\kappa} \ln \frac{z}{z_{max}} \quad \text{for } z \geq z_{max} \quad (26)$$

where \bar{U} is the mean velocity at $z = z_{max}$. Averaging (16) over the wave period and integrating, one finds in the vicinity of the bottom, where $\bar{p} \approx \bar{p}_b$:

$$\bar{u} \approx \frac{\bar{p}_b}{\kappa} \ln \frac{z}{z_o} \quad (\text{near the bottom}) \quad (27)$$

Therefore, plotting \bar{u} on the horizontal scale versus $\ln z$ on the vertical scale, the upper part will be a straight line with a gradient $\arctan(\kappa/\sqrt{\tau/\rho})$, where the curve tends to a straight line with gradient $\arctan(\kappa/\bar{p}_b)$ near the bottom. The last-mentioned gradient is larger than the first-mentioned one: the ratio $\bar{p}_b/\sqrt{\tau/\rho}$ will be called β_{op} and equals approximately $\sqrt{\pi\bar{p}_b^*/4}$ (for $\bar{p}_b^* \ll 1$); this follows from substitution of $\bar{p}_b = \bar{p}_b + \hat{p}_{b1}$ sin ωt into (15) and approximating in an analytical way²⁾³⁾.

1) This has been done earlier by Bakker (1974). In the present paper the conception is left of a coefficient " f_w ", occurring in the former paper, which relates the top-bottom shear stress to the top-orbital velocity. Because of the effect of higher harmonics, this coefficient obscures rather than enlightens the mechanism.

2) This result has already been used for the transition from (22) to (23).

3) Bakker (1979); Bakker and Van Doorn (1979).

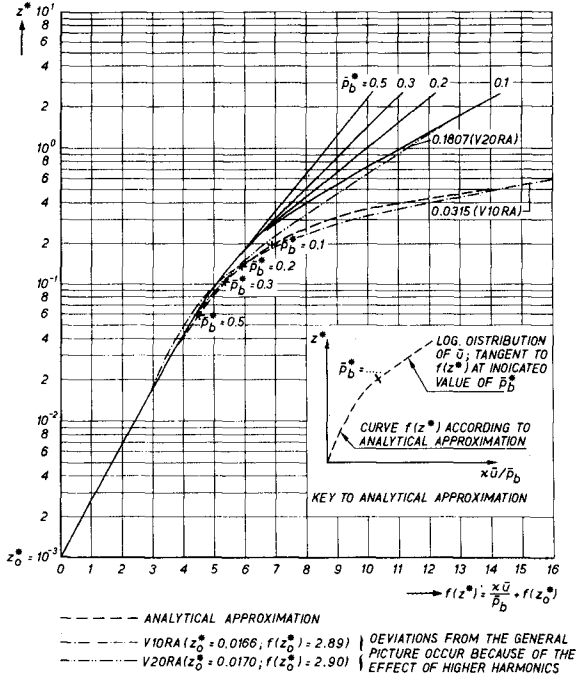


Fig. 3a. Theoretical distribution of mean velocities.

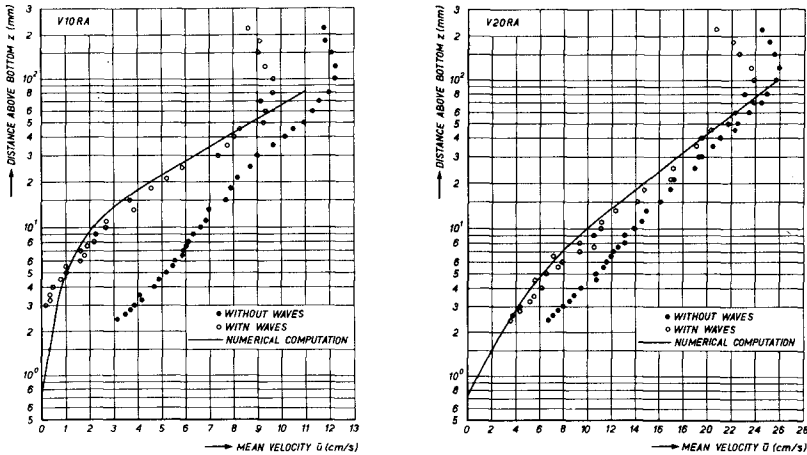


Fig. 3b. Comparison with measurements.

Fig. 3. The mean velocity distribution according to theory and measurements.

Thus it shows, that the velocity profile consists of two logarithmic parts with a transition zone between.

With respect to this transition between the bottom and $z = z_{\max}$, an analytical approximation¹⁾ suggests the occurrence of a universal function $f(z^*)$ in this way, that for small values of z^* the following relationship holds:

$$\frac{\bar{\kappa} \bar{u}}{\bar{p}_b} = f(z^*) - f(z_o^*) \quad (28)$$

When z^* is plotted on a vertical, logarithmic scale and $\bar{\kappa} \bar{u} / \bar{p}_b$ on a linear horizontal scale so that 1 on the horizontal scale corresponds with $\ln e$ on the vertical scale, the lower part of the curve $f(z^*)$ degenerates to a line under an angle of 45° . Thus this part corresponds with the lower logarithmic part of the velocity profile mentioned before. The curve $f(z^*)$ also gives the transition zone; the upper logarithmic part of the velocity profile can be found by drawing the tangent to $f(z^*)$ with a gradient $\sqrt{\pi \bar{p}_b^* / 4}$ with the horizontal (inset Fig. 3).

From the computer results the curve $f(z^*)$ can be found. Starting from certain values of \bar{p}_b^* and assuming \bar{p}_{b2}^* and \bar{p}_{b3}^* equal to zero, the velocity field u_d^* , and thus \bar{u}_d^* , can be calculated; starting from a certain, rather arbitrary²⁾ value of z_o^* , one can find \bar{u}_o^* , and thus $\bar{\kappa} \bar{u} / \bar{p}_b^*$, equal to $\bar{\kappa} \bar{u} / \bar{p}_b$. Indeed it shows, that the lower part of the resultant curves for various values of \bar{p}_b^* coincide, and that the lower part gives a straight line under 45° , whereas the upper parts show a gradient $\sqrt{\pi \bar{p}_b^* / 4}$ (Fig. 3a).

The question remains how \bar{p}_b can be determined from U_{mean} , the velocity averaged over the period as well over the depth h .

Without an oscillatory motion, the relationship would exist:

$$\bar{p}_b = \frac{\bar{\kappa} U_{\text{mean}}}{\ln(h/ez_o)} \quad (\text{without oscillatory motion}) \quad (29)$$

which can be derived in the same manner as the Chezy relationship³⁾.

With oscillatory motion, an approximate calculation of U_{mean} from \bar{p}_b (or inversely: of \bar{p}_b from U_{mean}) could be made by neglecting the effect of the transition zone and the lower logarithmic curve on the mean velocity and extrapolating the upper logarithmic curve in downward direction (Fig. 4). However, this extrapolated line will intersect the (vertical) line of zero-velocity, in a point higher than $z = z_o$, say $z = \alpha z_o$ (Fig. 4). Thus it shows, that the effect of the oscillatory motion is an enlargement of the apparent roughness with a factor α . Furthermore, \bar{p}_b in (29) should be replaced by $\sqrt{\bar{\tau}} / \rho$, which makes a difference of a factor β_{ob} , as stated before in this Chapter. Thus, in case of oscillatory flow, (29) changes into:

$$\bar{p}_b = \frac{\beta_{ob} \bar{\kappa} U_{\text{mean}}}{\ln(h/e \alpha z_o)} \quad (30)$$

1) Bakker (1979); Bakker and Van Doorn (1979)

2) Only should be conditioned, that z_o^* is so small, that it gives a point on the lower straight section (under 45°) of the $f(z^*)$ -curve.

3) This can be easily seen by multiplying both sides of Eq. (29) with $(1/\bar{\kappa}) \ln(h/ez_o)$.

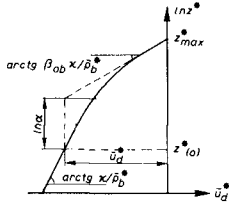


Fig. 4. Relationship between $\ln \alpha$ and \bar{u}_d^*

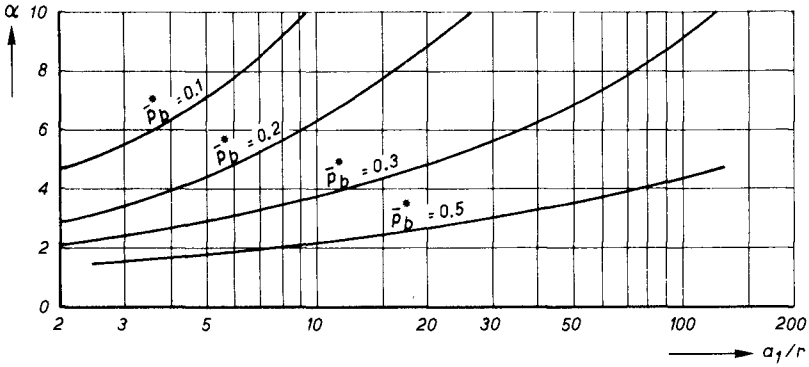


Fig. 5. The coefficient α as function of a_1/r and \bar{p}_b^* .

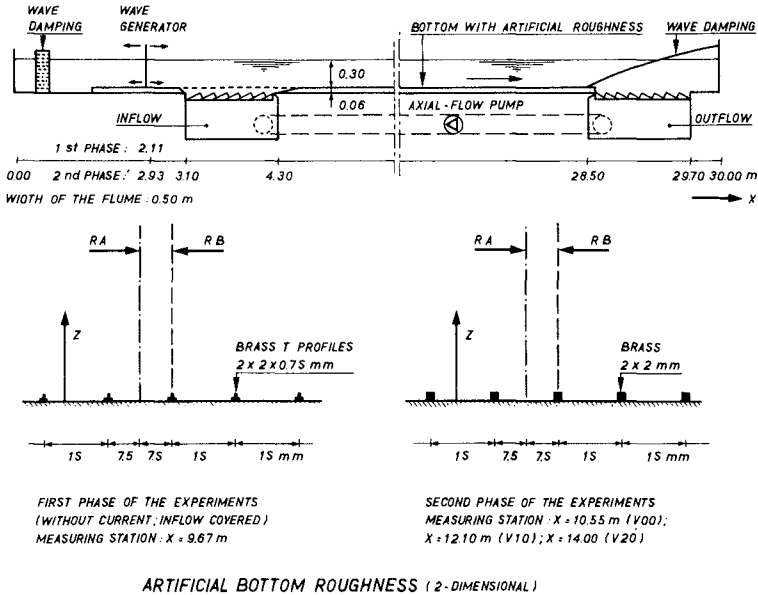


Fig. 6. Wave flume and artificial roughness.

in which $\beta_{ob} \approx \sqrt{\pi \bar{p}_b^* / 4}$ and in which α is derived with the aid of the computer program in the following way.

Analogous to the case with the first harmonic, each level z^* can be considered as a lower boundary condition z_o^* , which determines a_1/r . Fig. 4 shows that α can be found from the following relationship:

$$\ln \alpha = \ln \frac{z_{\max}^*}{z^*} - \frac{\beta_{ob} \kappa}{\bar{p}_b^*} \cdot \bar{u}_d^*(z^*) \quad (31)$$

where $\bar{u}_d^*(z^*)$ denotes \bar{u}_d^* at the level z^* . In this way, with one computer calculation—starting from a bottom boundary condition with a certain value of \bar{p}_b^* and assuming \hat{p}_{b2}^* and \hat{p}_{b3}^* equal to zero—one may find the value of a_1/r for a great number of values a_1/r . Fig. 5 shows α as a function of a_1/r and \bar{p}_b^* .

Now the following rough way of calculation of the mean velocity profile is advised:

- a. Determine a_1/r , using $a_1 = \hat{U}_1 T / 2\pi$
- b. Determine \hat{p}_{b1}^* from the ratio \hat{p}_{b1}^* / U_1 , found in Fig. 1
- c. Calculate \bar{p}_b^* from (30), which may be written as:

$$\bar{p}_b \approx \frac{\pi}{4} \cdot \left[\frac{U_{\text{mean}}}{(\hat{p}_{b1} / \kappa) \ln(h/\epsilon \alpha z_o)} \right]^2 \quad (\text{see note } 2) \quad (32)$$

Here α has to be determined iteratively: assuming for instance first $\alpha = 1$, finding \bar{p}_b^* from (32), finding a better estimation of α from Fig. 5 until the wanted accuracy of \bar{p}_b^* is reached.

- d. The lower part of the profile is a straight line on single-logarithmic paper under an angle $\arctan(\kappa / \bar{p}_b)$ through the point $(u, z) = (0, z_o)$
 - the upper part is a straight line on single-logarithmic paper under an angle $\arctan(\beta_{ob} \kappa / \bar{p}_b)$ or, approximately $\arctan(\kappa \sqrt{\pi} / (4 \bar{p}_b \hat{p}_{b1}))$
 - the transition can be found from Fig. 3a.

As mentioned, more accurate results can be obtained by using the computer program directly; in this case a first estimation of \bar{p}_b^* follows from (32).

4 Numerical accuracy

A number of computations has been carried out in order to check the numerical accuracy. For the details is referred to Bakker and Van Doorn (1979); here the following results may be mentioned.

- a. In the computer program an initial condition can be introduced, which may be different from the one, following from the periodical bottom boundary condition. After 4 periods running, the effect of this initial condition vanished up to 1°/oo of \hat{p}_{b1} ³⁾.
- b. The effect of the upper boundary condition on the ratio \hat{p}_{b1} / \hat{U}_1 is small, as long as z_{\max}^* is 1.5 at least.

1) For $\bar{p}_b^* > .5$ this approximation becomes inaccurate, in which case is referred to Bakker (1979) or Bakker and Van Doorn (1979).

2) In (32) the denominator between the brackets shows a hypothetical mean velocity over the profile, which would occur when the bottom shear stress velocity would have been \hat{p}_{b1} , instead of (a mean value of) $\sqrt{\pi} / \rho$. and when the roughness would have been α instead of r .

3) The ratio between \hat{p}_{b1} and \hat{U}_1 can be found from Fig. 1.

- c. The greatest traceable source of numerical error in the program is found to be caused by the fact, that the present iteration procedure does not extend up to the fourth and fifth harmonic; when the real fourth and fifth harmonic of U are zero, the error is of the order of 20% of \hat{p}_{b1} . Because of this error, the accuracy is not effectively enlarged by taking more than 6 grids (using $z_{\max}^* = 1.5$). The differences in U_1 between the use of respectively 3, 4, 5 grids compared with using 6 grids is respectively 4, 2, 1, 0.3% of \hat{U}_1 when $a_1/r = 129$ ¹⁾. The raising of the grid number by 1 increases the computer time about a factor 2.
- d. Considering the case without resultant current, the effect of a third harmonic of p_b (being so large, that \hat{U}_3 becomes zero) on the first harmonic U_1 is small (about 1% of \hat{U}_1).
- e. The effect of \bar{p}_b (i.e. resultant current) on the first harmonic u_{d1} is relatively small for large values of a_1/r (2.5% of \hat{U}_1 when $a_1/r = 129$ and $\bar{p}_b^* = .23$). For smaller values of a_1/r the effect is larger (6% of \hat{U}_1 when $a_1/r = 3.5$ and $\bar{p}_b^* = .23$).

5 Experiments

The bottom boundary layer under periodic progressive water waves, without and with a superimposed current has been investigated at the Delft Hydraulics Laboratory (DHL). The results of these experiments on the velocity distribution are compared with the present theory. In the theory, assumptions are made for the case of a horizontally oscillating flow such as can be realized in a horizontally pulsating water tunnel. The results of the present investigations, with free surface waves, will in future be compared with results from similar tests in the Oscillating Water Tunnel of the DHL.

Water surface elevation (η) and horizontal water velocity component in the direction of wave propagation (u) have been measured simultaneously in the same cross-section in a 30 m long, 0.5 m wide and 0.5 m high glass-walled flume of the DHL (Fig. 6).

Periodic waves were generated by a flat wave board oscillating horizontally with adjustable amplitudes at the lower and upper side. The wave trains applied in the experiments, obtained by starting the wave generator always from the same position were very well reproducible. In all experiments, the still-water depth (h) was 0.30 m, the wave period (T) with respect to a fixed point 2.0 s and the wave height (H) at the measuring station 0.12 m. Steady currents can be generated by circulating the water (Fig. 6). In view of the presence of secondary waves, the measuring stations were chosen so that the ratio of the amplitudes of the first and second harmonic components of the surface waves approximately showed a maximum. In order to obtain a turbulent boundary layer at the bottom, two-dimensional roughness elements (2 mm high at 15 mm centers) were applied (Fig. 6).

¹⁾ In the present program z_o^* may differ from Δz^* . This is a facility, plugged in the computer program after Appendix A of Bakker (1974) was written. In this way the value of \hat{U}_1^* belonging to an arbitrary value of a_1/r can be calculated, independent of the number of grids. For details, cf. Bakker and Van Doorn (1979).

The experimental study has been performed in two phases. In the first phase 1), waves without a current were considered. The inflow provision in the flume was covered. The artificial bottom roughness was applied only over a distance of 1.5 m at the measuring section. In the second phase of the experiments 2), roughness elements were applied over a distance of 15 m next to the water inlet and currents were generated in the same direction as the wave propagation. The mean current velocities (averaged over the height) were approximately 0.10 m/s (test code V10) and 0.20 m/s (test code V20). In this second phase, tests without a current (test code V00), but with open inlet were repeated for comparison.

For each condition, velocities in two verticals have been measured viz. in between two roughness elements (code RA) and just above one (code RB). In this way, tests series were performed with codes RA, RB (first phase) and VOORA, VOORB, VIORA, VIORB, V2ORA, V2ORB (second phase).

Figure 3b shows the distribution along the vertical of measured current velocities (time average values). It is noted that in the experiments the speed of the pump was the same for the current only and for current with waves, whereas the theory on oscillatory flow with resultant current starts from a given gradient of the mean water level which is supposed to be the same for "current only" and for "current with waves".

For the analysis, only the waves from a wave train were used after the start-up transients and before the first reflected wave reached the measuring station. Three wave trains were applied for every level at which velocities have been measured, from which as an average a more accurate orbital velocity could be determined. In the case of waves with a current, η and u are measured also without waves.

The water surface elevation was measured with a resistance-type wave gauge. The velocities were measured at a series of successive levels above the bottom with a laser-doppler velocity meter (LDV). The application of this technique with its general advantage of measuring accurately and contactless in very small measuring volumes, was highly satisfactory. The error in positioning the level of the LDV was less than ± 0.1 mm. The reference distance to the bottom, determined by means of a measuring rule is less accurate; the error is estimated less than ± 0.3 mm.

The signals from the wave gauge and the LDV were recorded simultaneously on paper and on an analog magnetic tape. From the tape recorder the signals have been processed in two steps:

- a. Digitization by synchronized sampling, exactly 72 times per wave period, i.e. a sampling frequency of 36 Hz. From every wave train, the measured signals have been sampled over the same time interval after the start of the wave generator, so phase relations between velocities measured at different levels could be maintained. In the first phase of the experiments, the accuracy of digitizing was ± 0.025 cm and ± 0.15 cm/s for the signals of the surface waves and the velocities respectively. In the second phase, these values were 10 times smaller.
- b. Harmonic analysis of the digital signals. The results obtained from harmonic analysis of the average wave (i.e. also velocities) of the three wave trains were used for comparison with theory.

Table 1 shows the most important parameters deduced from the tests.

1) Van Doorn and Godefroy (1978)

2) Van Doorn (1979)

TEST	\hat{U}_1 (1) (cm/s)	\bar{U} (2) (cm/s)	s_1 (3) (mm)	a_1/r (4)	Z (5) (mm)	\hat{p}_{b1} (6) (cm/s)	\bar{p}_b (7)	β_{ob} (8)	\hat{p}_{b2} (9) (cm/s)	\hat{p}_{b3} (10) (cm/s)	ψ_1 (11) (degr.)	ψ_2 (12) (degr.)	ψ_3 (13) (degr.)
RA	29.83	-2.6	95.0	4.11	49.8	6.22	-0.054		1.33	1.03	49.5	191.1	0.2
RB													
VOORA	26.5	-3.0	84.5	3.65	45.8	5.72							
VOORB													
V1ORA	25.7	9.6	81.8	3.54	44.7	5.58	0.0315	0.095	1.46	1.18	53.1	196.7	343.7
V1ORB													
V2ORA	24.3	22.7	77.3	3.35	41.5	5.19	0.1807	0.329	1.35	1.23	52.7	193.1	331.3
V2ORB													
JONSSON ('63) (cf. Ch. 6)	211	0.5	2850	112.8	697.8	20.79	0.0121		0.96	1.49	25.4	305.6	76.3

- (1) \hat{U}_1 = amplitude of the 1st harmonic of the velocity just outside the boundary layer
- (2) \bar{U} = mean velocity at $z = z_{max} = 1.5 Z$
- (3) $a_1 = \hat{U}_1 T / 2\pi$; (4) $r = 33 z_0$; (5) $Z = \kappa \hat{p}_{b1} T$
- (6)-(13) These values have been adopted from the numerical solution
- (8) $\beta_{ob} = \hat{p}_b / \sqrt{\bar{U} \rho}$

Table 1 Test parameters

6 Comparison between theory and measurements.

Comparison is made between the theory and the measured mean velocity profiles V1ORA and V2ORA. The results are plotted in Fig. 3b.

The theoretical curves (found from the computer program) differ from the ones which can be interpolated, using Fig. 3a, because of the effect of the strong second harmonic U_2 (about 1/3 of the first harmonic U_1) on \bar{U} , which is not taken into account in the derivation of Fig. 3a.

With respect to the comparison of the first harmonic, apart from the experiments, mentioned in Ch. 5, also the measurements of Jonsson (1963) (see also Jonsson and Carlsen, 1976) will be taken into consideration for the comparison between theory and measurements. The experimental data, as derived from the literature are added to Table 1.

For the various experiments, the dimensionless amplitude and the phase of the defect velocity have been calculated and plotted against the dimensionless height above the bottom. The results are shown in Fig. 2. With respect to the amplitude of the defect velocity there is a rather good agreement between measurements and theory, whereas the phases still show discrepancies.

The comparison between the instantaneous velocity profiles according to the theory and the measurements (starting from a given upper boundary condition) is given in Figure 7.

The general trend is rather well predicted, although the "overshoot" velocity tends to be higher according to the measurements than according to theory. Fig. 8 shows $\sigma(u) / \hat{p}_{b1}$ as function of the dimensionless distance z^* above the bottom for the various tests, $\sigma(u)$ being the standard deviation between the theoretical and measured values of the instantaneous velocities at a certain height. The mean value $\bar{\sigma}$ of $\sigma(u)$, averaged

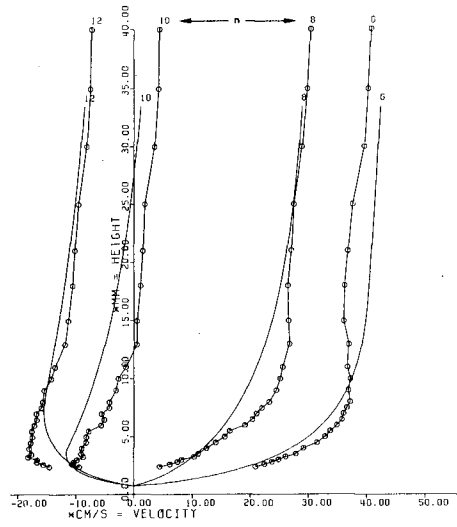
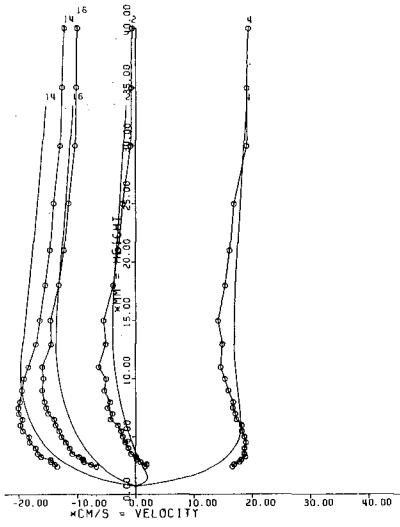


Fig.7a. V10RA $\bar{\sigma} = 2.39$ cm/s

EXPLANATION:
 ○ MEASURED PROFILE, AT $t = \frac{n}{10} T$
 — THEORETICAL PROFILE

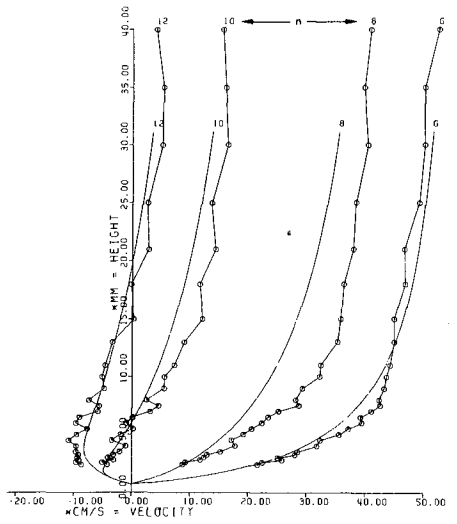
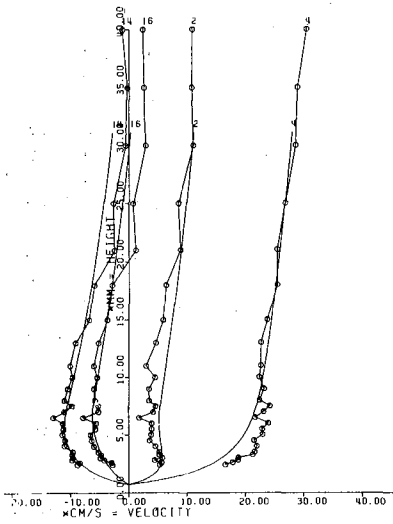


Fig.7b. V20RA $\bar{\sigma} = 2.27$ cm/s

Fig.7. Instantaneous velocity profiles according to theory and measurements.

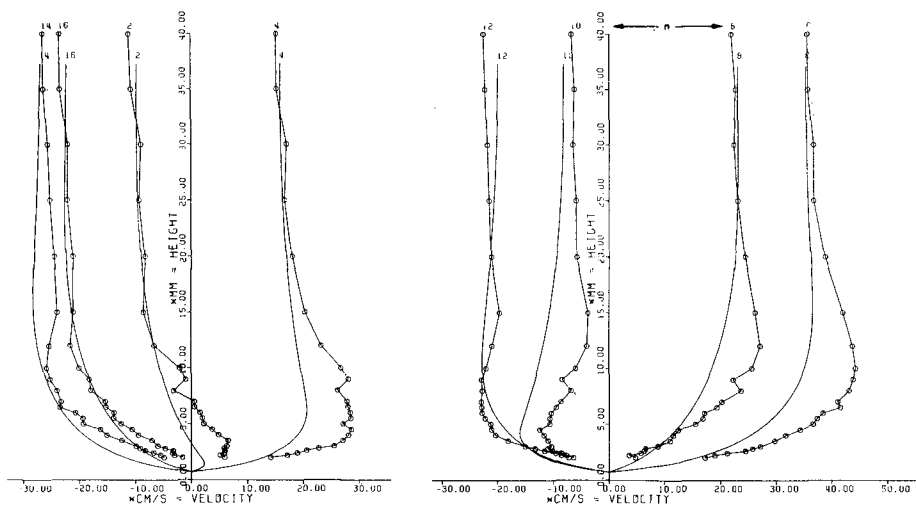


Fig.7c. RA $\bar{\sigma} = 4.71$ cm/s

EXPLANATION
 ○ MEASURED PROFILE, AT $1 - \frac{0.1}{16} T$
 — THEORETICAL PROFILE

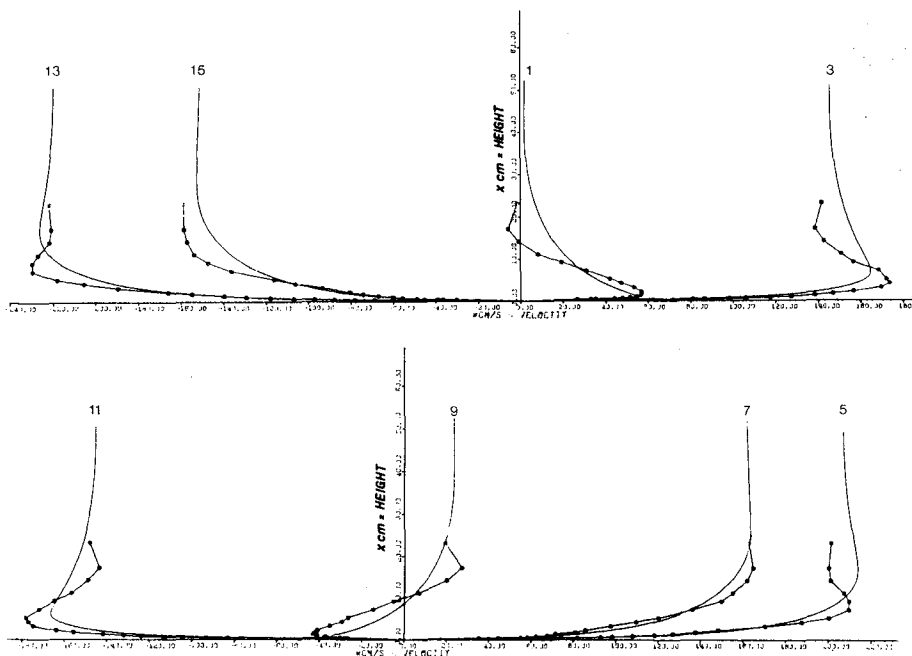


Fig.7d. JONSSON (1963) $\bar{\sigma} = 10.79$ cm/s

Fig.7. Instantaneous velocity profiles according to theory and measurements.

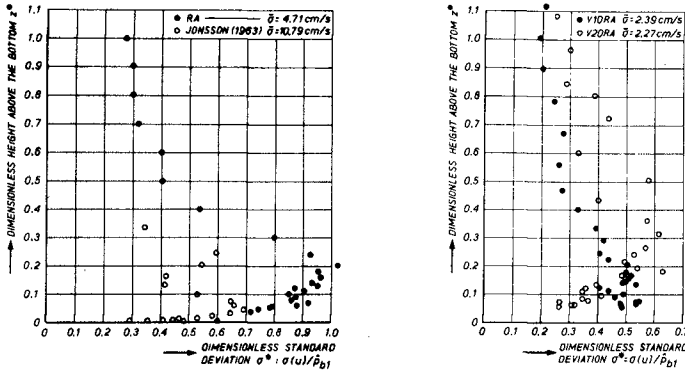


Fig.8. Dimensionless standard deviation as function of the dimensionless distance above the bottom.

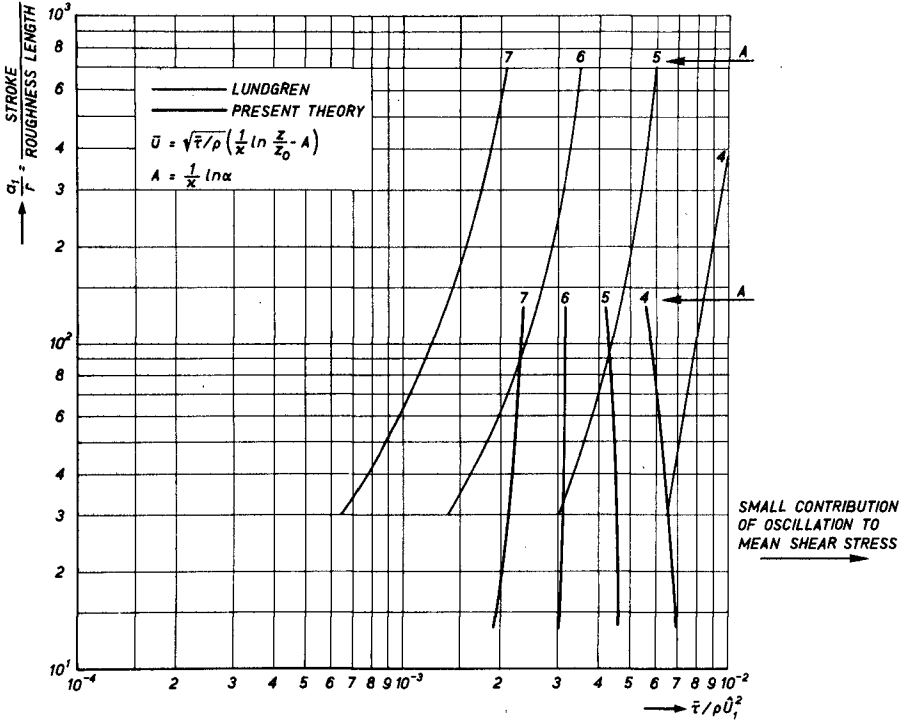


Fig.9. Comparison of the velocity defect according to Lundgren and the present theory.

over the considered levels within the boundary layer, has also been given in Figs. 7 and 8.

7 The mean velocity profile according to the present theory and according to Lundgren

Lundgren (1972) defines a shear stress velocity "U_f" (Eq. (19) of his paper), equal to τ_{cw}/ρ, in which "τ_{cw}" is the period-average of the bottom shear caused by waves and current. Thus "U_f" equals \bar{p}_b/β_{ob} in the present notation.

Lundgren's equation ((23) of his paper) for the mean velocity profile reads, in the notation of the present paper:

$$\bar{u} = \frac{\bar{p}_b}{\beta_{ob}} \left(\frac{1}{\kappa} \ln \frac{z}{z_o} - A \right) \tag{33}$$

in which he calls A the "velocity defect".

In the present theory, the upper part of the velocity profile is given by:

$$\bar{u} = \frac{\bar{p}_b}{\beta_{ob}} \frac{1}{\kappa} \ln \frac{z}{\alpha z_o} \quad (z \gg z_o) \tag{34}$$

Therefore "A" equals (lnα)/κ. In his Fig. 2 Lundgren presents as result of his calculations the value of A as function of "τ_{cw}/ρU_b²", being in the present notation $\bar{\tau}/\rho\hat{U}_1^2$, or in dimensionless notation $(\bar{p}_b^*/\beta_{ob}\hat{U}_1^*)^2$.

In the computer program, \bar{p}_b^*/β_{ob} is known from the upper boundary condition (22). In the computer program for given values of \bar{p}_b^* as well A as $\bar{\tau}/(\rho\hat{U}_1^2)$ can be calculated as function of a₁/r; therefore Fig. 2 according to the lay-out of Lundgren may be reproduced according to the present theory. In Fig. 9 the lines of constant "A" as function of a₁/r and $\bar{\tau}/\rho\hat{U}_1^2$ according to Lundgren and the present theory are drawn together.

8 Summary and conclusions

- a. Bakker (1974) presented a numerical mathematical model of the turbulent bottom boundary layer in periodic waves with (or without) resultant current in the direction of wave propagation. This model starts from the Prandtl assumptions with respect to the relationship between shear stress and the instantaneous velocity gradient. Non-linear interactions are taken into account.
- b. In the present paper the mathematical model has been improved and has been compared with experimental investigations at the Delft Hydraulics Laboratory (DHL). Velocities at a series of successive levels above the bottom under free surface waves without, respectively with resultant current in a wave flume were measured with a laser-doppler velocity meter.
- c. The mathematical model predicts reality rather well although the phases of the first harmonic of the "defect velocity" in model and reality show discrepancies. With respect to the resultant velocity is referred to Fig. 3, with respect to the amplitude and phase of the first harmonic of the defect velocity to Fig. 2 and with respect to the instantaneous velocity profiles to Fig. 7. In Fig. 8 the standard deviation between measurements and theory is given as a function of the height above the bottom in a dimensionless graph. For this, \hat{p}_{b1} has been used as reference velocity (the ratio between \hat{p}_{b1} and the amplitude \hat{U}_1 of the first har-

monic of the velocity outside the boundary layer is given in Fig. 1) and $\kappa p_{bl} T$ as a reference height.

- d. The shear stress, exerted at the bottom according to this model and according to the investigation of Lundgren (1972) appears to be of the same order of magnitude (Fig. 9), although the problem is approached from a different angle.
- e. In the future, the mathematical model will be improved by including higher harmonics than the third in the upper boundary conditions; the measurements will be continued with similar tests in the Oscillating Water Tunnel of the DHL; a (less accurate) analytical theory will be presented, giving more insight in the physics of the matter.

9 Acknowledgement

The authors gratefully acknowledge the important remark of Mr. J. van Overeem, mentioned before. Furthermore, the contribution of Mr. C.J. van Kakum in programming and the valuable assistance of Mr. J. van Overeem and Mr. W. Tilmans should be mentioned. The authors thank Mr. C. Fischer for his linguistic remarks.

References

- BAKKER, W.T. (1974).
Sand concentration in an oscillatory flow.
Proc. 14th Conf. on Coastal Engineering, Copenhagen.
- BAKKER, W.T. (1979).
Analytical computations on the near-bottom velocity field in waves with a current (in preparation).
- BAKKER, W.T. and DOORN, Th. van (1979).
Bottom friction and velocity distribution in an oscillatory flow with resultant current (in preparation).
- DOORN, Th. van and GODEFROY, H.W.H.E. (1978).
Experimental investigation of the bottom boundary layer under periodic progressive water waves.
Report M 1362 (2 parts) of the Delft Hydraulics Laboratory.
- DOORN, Th. van (1979).
Experimental investigation of near-bottom velocities in water waves without and with a current.
Report M 1423 of the Delft Hydraulics Laboratory (in preparation).
- JONSSON, I.G. (1963).
Measurements in the turbulent wave boundary layer.
Proc. of the 10th IAHR Congress, London.
- JONSSON, I.G. and CARLSEN, N.A. (1976).
Experimental and theoretical investigations in an oscillatory turbulent boundary layer.
Journal of Hydraulic Research, Vol. 14, No. 1, pp. 45-60.
- LUNDGREN, H. (1972).
Turbulent currents in the presence of waves.
Proc. 13th Conf. on Coastal Engineering, Vancouver.
- PRANDTL, L. (1931).
Abrisz der Strömungslehre, Braunschweig, 3er Abschnitt.

LIST OF SYMBOLS

a_1	stroke length $\hat{U}_1 T / 2\pi$
e	basic number of neperian logarithms
$f(z^*)$	universal function, from which $\kappa \bar{u} / \bar{p}_b$ can be found (vide (28))
h	water depth
l	mixing length (schematized according to (7))
l_{real}	more realistic value of mixing length
p	internal shear stress velocity ($\sqrt{\tau/\rho}$) in the fluid
P_r	(instantaneous value of the) water pressure
r	Nikuradse roughness
t	time
T	wave period
u	horizontally directed water velocity (uniform in horizontal direction), after averaging turbulent fluctuations
U	velocity u at $z = z_{\text{max}}$
u_d	"defect velocity" $u - \bar{U}$
U_{mean}	mean velocity, averaged over both wave period T and water depth h
U_{osc}	oscillatory water motion above the boundary layer (assumed uniform over the height), i.e. $u - \bar{u}$ for $z \geq z_{\text{max}}$
x	horizontal coordinate
z	vertical coordinate
z_0	$r/33$, the theoretical level where the velocity is assumed to be zero
z_{max}	height, at which the variations of the internal shear stress are attenuated
α	multiplication factor of the apparent roughness, caused by the addition of the oscillation to the current
β_0	ratio between \bar{p} and $\sqrt{\tau/\rho}$ (about equal to $\sqrt{\pi \bar{p}_b^*}/4$ if $\bar{p}_b^* \ll 1$ and if $\hat{U}_2, \dots \ll \hat{U}_1$)
κ	Von Karman constant
ρ	specific density
τ	internal shear stress in the fluid
$\bar{\tau}_{\text{real}}$	more realistic approximation of the shear stress averaged over the wave period than $\bar{\tau}$ (vide (4))
$\phi_2, (3)$	phase angle of harmonics of the shear stress velocity p
$\Psi_1, (2), (3)$	phase angle of harmonics of the velocity U at height $z = z_{\text{max}}$ above the boundary layer
ω	angular frequency of first harmonic of oscillation ($2\pi/T$)

Other symbols added to a variable x :

\bar{x}	average value of x during period T
x^*	"dimensionless variable", i.e. velocity divided by \hat{p}_{b1} , or height divided by $\kappa \hat{p}_{b1} T$, or time, divided by T
x_b	value of x at the bottom ($z = 0$)
$x_1, (2), (3)$	subscript applies to first, (second), (third) harmonic of x
\hat{x}	amplitude of harmonic x (always in combination with subscript 1, 2 or 3)
$ x $	absolute value of x
$\text{sign}(x)$	"+1" if x is positive, "-1" if x is negative
$X(x)$	value of variable X at height x

CHAPTER 83

Rip Currents and Their Causes

by

Robert A. Dalrymple¹

Introduction

"The outworn dogmas of science seem to be particularly concentrated in the discussions of the ocean in geology books". Beginning with this controversial statement, F. P. Shepard in 1936 tried to lay to rest the concept of the undertow, which had been debated in the pages of Science for over a decade. At the same time, he introduced the term, rip current, to describe the rapidly seaward-flowing currents, which were well-known to lifeguards at that time, as these currents were responsible for carrying swimmers offshore at frightening speeds.

Subsequent studies by Shepard and his colleagues (Shepard, Emery and LaFond, 1941; Shepard and Inman, 1950a, 1950b) showed that rip currents (1) are caused by longshore variations in incident wave height, (2) are often periodic in both time and in the longshore direction and (3) increase in velocity with increasing wave height. The major reason put forth to explain the variation in wave height was the convergence or divergence of wave rays over offshore bottom topography (such as submarine canyons) or the forced wave height variability caused by coastal structures, such as jetties.

McKenzie (1958) and Cooke (1970) in their studies corroborated the findings of the Scripps Institution of Oceanography researchers and also pointed out the persistence of rip currents (once high energy waves in a storm had caused rip channels to be cut into the bottom) after the storm had abated. In fact it appears that on coastlines which are affected by major storms which build offshore bars, that the nearshore circulation may be dominated by the storm-induced bottom topography for long afterwards.

The researchers up to the late 1960's who attempted to theoretically model rip currents knew the importance of longshore wave height variability and the wave-induced set-up in the formation of rip currents, but it was not until Longuet-Higgins and Stewart (e.g., 1964) codified the wave momentum flux tensor that great strides were made in providing models for rip currents.

This paper is intended to categorize and review the more recent theories for rip current generation and to discuss a simple model for rip currents on barred coastlines.

¹Associate Professor, Department of Civil Engineering, University of Delaware, Newark, Delaware, U.S.A. 19711

Theoretical Approaches

The various mechanisms proposed to date to explain rip currents can be conveniently placed into two categories: (1) wave interaction and (2) structural interaction. The distinction between the two is that the first category mechanisms can occur on uniformly planar beaches (having no longshore variability), while the second group cannot. Table I lists the categories and the candidate theories within each.

Table I. Rip Current Mechanisms

<u>Wave Interaction Models</u>	<u>Primary Investigators</u>
Incident-edge wave	
Synchronous	Bowen (1969), Bowen and Inman (1969)
Infra-gravity	Sasaki (1975)
Intersecting wave trains	Dalrymple (1975)
Wave-Current Interaction	LeBlond and Tang (1974), Dalrymple and Lozano (1978)
<u>Structural Interaction</u>	
Bottom Topography	Bowen (1969), Noda (1974)
Coastal Boundaries	
Breakwaters	Liu and Mei (1976)
Islands	Mei and Angelides (1977)
Barred Coastlines	Dalrymple, Dean and Stern (1976)

Wave Interaction Models - The first theory in this category is the incident/edge wave interaction model proposed by Bowen (1970), Bowen and Inman (1970) and independently by Harris (1967). This model requires the intersection of synchronous edge waves (traveling along the shore) and the incident wave field to provide the longshore variability of wave heights. The synchronous edge wave forces a nearshore circulation with a longshore periodicity, L_r , equal to the edge wavelength, L_e ,

$$L_r = L_e = L_o \sin\{(2n + 1)\beta\} \quad (1)$$

where $L_o = gT^2/(2\pi)$, the deep water wavelength, g the acceleration of gravity, β is the beach slope and n is the offshore mode number of the edge wave. Clearly the rip current spacing depends strongly on the incident wave period. (Surprisingly, some of Harris' laboratory experiments (Mark II) show no period effects). The length of the rip spacing has a maximum of L_o , for the case of very steep

beaches and/or high mode edge waves. Often, however, for many beaches, such as Silver Strand (see Bowen and Inman (1970)) and the East coast of the U.S., L_r exceeds L_o , or else very high mode numbers are required for Eq. (1), Tait (1970). The origin of synchronous edge waves could be reflection of the incident waves by a structure or headlands or through a nonlinear resonance, but Guza and Davis (1974), theoretically, and Guza and Inman (1975) and Harris (1967), experimentally, showed that the most likely resonant edge wave is the subharmonic edge wave, which does not produce rip currents. A further restriction on the model is that the shoreline must be reflective, requiring the waves to be non-breaking. Guza and Inman (1975) have proposed the requirement for the existence of edge waves as

$$\epsilon = \frac{a_1 \sigma^2}{g \tan^2 \beta} = \left(\frac{2\pi H_o}{L_o \tan^2 \beta} \right) \leq 2 \quad (2)$$

Note that this parameter, ϵ , is directly relatable to the parameter proposed by Irribarren and Nogalles (see Battjes, 1974).

For surf zones, characterized as dissipative ($\epsilon > 2$), which would have a significant width, Bowen and Inman hypothesized that longer period edge waves and surf beat could perhaps interact to cause the longer rip spacings, $L_r > L_o$. Sasaki (1975), noting that there is significant energy in the surf zone at low frequencies (Suhayda, 1975; Huntley, 1976) recommended an empirical equation for the case of infra-gravity waves

$$L_r = 1.27 \times 10^{-2} \epsilon \quad (3)$$

For cases other than those used by Sasaki, Bruno and Dalrymple (1978) found an apparent linear trend with ϵ , but for small ϵ . Additionally the slope of the line was different than that in Eq. 3.

Dalrymple (1975) and Dalrymple and Lanan (1976) generalized the edge/incident wave model to show that rip currents and beach cusps are produced by intersecting synchronous wave trains. The periodic spacing of the rip current is

$$L_r = \frac{L_o}{(\sin \theta_o - \sin \zeta_o)}$$

where θ_o , ζ_o are the deep water angles of incidence made between the wave rays and the beach normal. This model has no theoretical maximum for L_r but has a minimum spacing of $L_r = L_o/2$, thus there is a small region of overlap between the edge wave and the intersecting wave model. While it is clear that this model will generate rip currents when the incident wave field is reflected back on itself or when refraction or diffraction is strong, it is not known what percentage of the time this mechanism is valid on a plane beach when two different synchronous wave systems would have to be present.

A third class in the wave-interaction category is the wave-current interaction models, which have been stimulated by the observations of Arthur (1950, 1962), Harris (1967) and others that rip currents can cause strong refractive effects on the incident wave field.

The concept is that for normally incident waves, the basic state is one of uniform setup along the beach with no nearshore circulation; however, as the investigators of this class of models have discovered, there are other modes that are also possible, which do yield rip currents. LeBlond and Tang (1974) investigated the possibility that the interaction of the nearshore currents and the wave energy would cause a feedback mechanism and a preferential spacing for rip currents. Iwata (1976) used a similar approach; but, as pointed out recently by Dalrymple and Lozano (1978), these models did not predict rip current spacings. Mizaguchi (1976), unable to get rip currents with a fixed bottom friction, introduced an arbitrary variation in the friction coefficient and was able to predict rips; however, the assumed variability in f was somewhat arbitrary. Dalrymple and Lozano (1978) showed that only when the effects of incident wave refraction by the outgoing rip currents are included can a model similar to LeBlond and Tang's predict a rip current spacing. The non-dimensional rip current spacing, $\lambda X_b \cong 2\pi X_b / L_r$, (where λ is the longshore wave number for the circulation and X_b is the surf zone width) is expressed as a function of the parameter $A_D = (\tan \beta \kappa \pi / 8f)$ where κ is the breaking index, $0(1)$, which relates the breaker height to the water depth and f is a Darcy-Weisbach (constant) friction coefficient. This result can be approximated as

$$\lambda X_b \cong \frac{1}{A_D} + 2.8 \quad (4)$$

Note that this result yields an increase in L_r with wave height as X_b directly proportional to H_b , the breaking wave height. The solution obtained by Dalrymple and Lozano was for a beach characterized by a flat sloping surf zone bottom and a flat offshore; the discontinuity in slope at the breaker line caused the development of two circulation cells, one wholly contained within the surf zone and one which extends across the breaker line. Despite this, the results appear to follow the trend of LEO observations, taken by the Coastal Engineering Research Center, with a great deal of scatter (Bruno and Dalrymple, 1978).

A key assumption included in these theories is the manner in which energy dissipation is modelled in the surf zone at each order of the perturbation. For the above studies it was assumed that the form of energy dissipation corresponds to that necessary to give $H = kd$ at the basic state (LeBlond and Tang, 1974), that the relationship between H and d is true for all order of perturbations (Dalrymple and Lozano, 1978) or there is no dissipation beyond the basic state (Iwata, 1976). Recently Miller and Barcilon (1978) have used a hydraulic jump analogy to develop a form for energy dissipation. Their results yield an approximate formula (for their $B = 32$ case)

$$\lambda X_b = 0.03/A_D + 0.6 \quad (5)$$

This result is far smaller than most field observations. Until more studies are made for energy dissipation in the surf zone, no real progress can be made using these techniques.

Another problem that hampers this area of research is the inability to study the instability mechanisms; for example, a small perturbation in the basic state. Since the governing equations have been time averaged (over a wave period), only slowly evolving instabilities can possibly be studied. As yet, even this problem has not been solved.

Finally, Hino (1974) has proposed a model for coastal instability based on a feedback between the deforming bottom and the flow field. His model yields approximately a constant spacing

$$\lambda_{x_b} \cong \pi/2 \quad (6)$$

Significant work still needs to be done in this area.

Boundary Interaction Models - This category of models probably accounts for the majority of rip currents observed on coastlines. As mentioned, the early researchers discerned that longshore variability in the bottom topography would cause rip currents to form. If the bottom variability is periodic in the longshore direction, then periodic nearshore circulation cells may form. The first theoretical model for this case was put forward by Bowen (1969). Numerical and analytical extensions of his work to various bottom bathymetries have verified the basic forcing of the nearshore circulation due to the bottom topography's effect on the wave field, e.g., Sonu (1972), Noda (1974), Noda *et al.* (1974), Birkemeier and Dalrymple (1974) and Mei and Liu (1975). All of these models have utilized linearized models in the sense that the wave field has been characterized by linear water wave theory and the mean equations for the nearshore currents do not include the convective acceleration terms.

In addition to bottom topography, the presence of man-made or natural lateral barriers influence the nearshore circulation also. Dalrymple, Eubanks and Birkemeier (1977) studied the circulation interior to rectangular basins, such as a harbor or, in particular, laboratory wave basins. Liu and Mei (1976) in a series of two papers examined the wave field and the nearshore circulation in the vicinity of breakwaters both shore-connected and detached. Mei and Angelides (1977) examined the wave-induced flow around a circular island, considering refractive effects alone. This problem of circulation around structures is still one that requires a significant amount of study, particularly in determining the wave field in the regions surrounding structures, that not only partially reflect and diffract the waves, but also serve as significant energy sinks. Laboratory studies of structures and the effect on the nearshore circulation have been conducted by Gourlay (1976).

The case of incident waves encountering longshore bars and the associated nearshore current field has been largely neglected in the literature. While the presence of rip channels in bars has been

recognized in longshore current formulae, e.g. Inman and Bagnold (1963) and Bruun (1963), efforts to develop nearshore circulation models in this case are hampered by an inability to correctly predict the wave field over the longshore bar. Recently, Dalrymple, Dean and Stern (1977) indicated that, in addition to the usual continuity assumptions (that is, the mass transport of water over the bar must equal the flow in the rip current), wave reflection from the submerged sand bar provides an important forcing for the circulation system. Since that work has not been clearly expounded upon, a similar approach is presented here for normally incident waves on a bar.

Currents on a Barred Shoreline

The model primarily is presented to examine mean currents behind a longshore bar, including the effect of wave reflection from the bar. There are three equations necessary for the model. The first is the continuity equation, which relates the onshore flow over the bar to the increase in flow in the longshore trough, between the bar and the beach.

$$U h_b = h_t w_t \frac{\partial V}{\partial y} \quad (7)$$

where U is the vertically and time-averaged in-flow, including the mass transport, h_b is the mean depth over the bar, h_t and w_t are the mean depth and the width of the trough, and $V(y)$ is the cross-sectionally and time-averaged longshore current. Figure 1 illustrates the geometry. The second equation is the equation of motion within the trough.

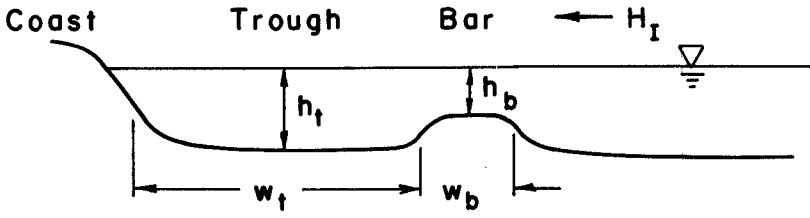
$$v \frac{\partial V}{\partial y} = -g \frac{\partial \bar{\eta}}{\partial y} - \frac{f_t U_m V}{4\pi h_t} \quad (8)$$

where $\bar{\eta}(y)$ is the mean water level within the trough measured from the still water level. The bottom friction term is of the form developed by Longuet-Higgins (1970) for weak currents (see Liu and Dalrymple, 1978, for a generalization for strong currents), U_m is the wave-induced water particle velocity over the trough.

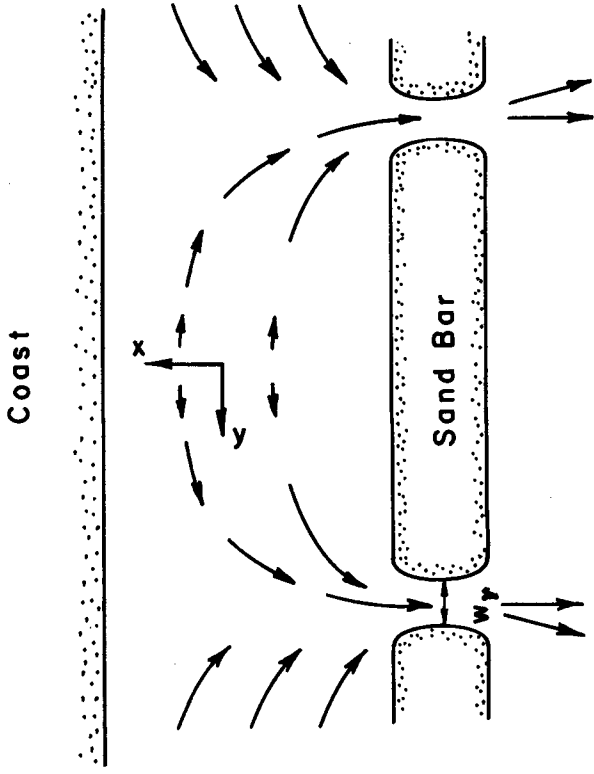
$$U_m \approx \frac{H_t \sqrt{gh_t}}{2 \cdot h_t} \quad (9)$$

and f_t is the Darcy-Weisbach friction factor in the trough.

The final equation is the onshore/offshore momentum equation, which includes the mean excess momentum flux due to the presence of the waves (the radiation stresses), denoted S_{xx} , as well as the force exerted on the submerged bar by the waves. The basic premise here is that the portion of the incident wave reflected by the bar induces a force as its momentum flux has been reversed. This force is provided by the reaction force of the bar but also by a set-up of water inside the bar (Longuet-Higgins, 1967) or bottom friction across the bar. The set-up of water, which only exists where the bar is reflecting waves and which is much smaller where the rip channel exists, provides the longshore variation in water level to drive the longshore flow. Therefore, the force balance on each side of the bar is



ELEVATION



PLAN

Fig. 1

$$S_{xx,I} + S_{xx,R} + \frac{1}{2} \rho g h_t^2 - F = S_{xx,T} + \frac{1}{2} \rho g (h_t + \bar{\eta})^2 + \tau_b \omega_b \quad (10)$$

where the subscripts on the radiation stresses denote incident, reflected and transmitted, F is the mean wave force on the bar and $\tau_b \omega_b$ is the shear force exerted on the bar.

If the longshore bar is uninterrupted by rip channels, then the set-up, $\bar{\eta}$, would be uniform in the longshore direction and will be denoted as $\bar{\eta}_p$, where the subscript p indicates the potential set-up. For this case the friction term would be absent (no flows over the bar) and F can be determined (Longuet-Higgins, 1976). If, on the other hand, rip channels exist and $\bar{\eta}$ is drawn down below the $\bar{\eta}_p$ level necessary to provide the force balance, then a shear stress is developed by an in-flow across the bar. Therefore, if we define

$$\bar{\eta}_D = \bar{\eta}_p - \bar{\eta} \quad (11)$$

where $\bar{\eta}_D$ is the deficit in the set-up between the maximum potential set-up and the actual set-up, η , and substituting into the previous equation, we have remaining,

$$\rho g h_t \bar{\eta}_D = \tau_b \omega_b \quad (12a)$$

or

$$\rho g h_t \bar{\eta}_D = \frac{f_b U_m}{2\pi} (U - \bar{u}) \omega_b \quad (12b)$$

where the mean flow is reduced by mass transport velocity, \bar{u} , which does not contribute to the bottom friction (Iwata, 1970).

Using the last equation and the continuity equation, $\bar{\eta}_D$ may be eliminated from the longshore equation of motion, with the assumption that the geometry is fixed and all second order terms may be neglected (including the convective acceleration terms), leaving

$$\frac{d^2 v}{dy^2} - \gamma^2 v = 0 \quad (13)$$

and

$$\gamma^2 = \left(\frac{f_t U_m h_b}{2f_b U_m h_t \omega_b \omega_t} \right) \quad (14)$$

A solution to this equation, which is zero at $y = 0$, the midpoint between two rip channels, is

$$v = v_m \frac{\sinh \gamma x}{\sinh\left(\frac{\gamma b}{2}\right)} \quad (15)$$

where V_m is the maximum of V which is assumed to occur at $l/2$, the location of the rip channel. The distance l is the longshore length of the bar.

The deficit, $\bar{\eta}_D$, can be found from the linearized Eq. (8), subject to the condition that $\bar{\eta}_D = 0$ at $x = 0$.

$$\bar{\eta}_D = \frac{f_t U_m V_m (\cosh \gamma x - 1)}{4\pi g h_t \gamma \sinh\left(\frac{\gamma l}{2}\right)} \quad (16)$$

and also, from the continuity equation,

$$U = \frac{\gamma h_t \omega_t V_m \cosh \gamma x}{h_b \sinh\left(\frac{\gamma l}{2}\right)} \quad (17)$$

The V_m can be found from the bottom stress, Eq. (12b), to yield

$$V_m = \left(\frac{h_b}{h_t \omega_t}\right) \frac{\bar{u}}{\gamma} \sinh\left(\frac{\gamma l}{2}\right) \quad (18)$$

Thus

$$V = \frac{\bar{u} h_b}{\gamma h_t \omega_t} \sinh \gamma y \quad (19)$$

For small y , the longshore current V can be approximated as

$$V = \frac{\bar{u} h_b}{\omega_t h_t} y \quad (20)$$

which indicates initially the longshore current increases due to the inflow over the bar by mass transport. However, as the mean water level drops from its potential value at $y = 0$, the inflow U increases above the \bar{u} value.

$$U = \bar{u} \cosh \gamma y \quad (21)$$

Further

$$\bar{\eta}_D = \frac{f_b \omega_b U_m \bar{u} (\cosh \gamma y - 1)}{2\pi g h_t} \quad (22)$$

The flow out of the rip channel is

$$U_r = \frac{2V \omega_t h_t}{\omega_r h_r}$$

by continuity considerations, where the r subscripts refer to rip variables.

It is expected that the maximum upper limit for $\bar{\eta}_D$ is $\bar{\eta}_p$; that is, $\bar{\eta} = 0$, which would occur at $y = \ell/2$. With this upper limit, an estimate may be made for ℓ . For the case of no wave breaking over the bar, Longuet-Higgins (1965) showed

$$\eta_p = \frac{\alpha E}{\rho g h_t}$$

where $\alpha = (1 + K_r^2 - K_T^2)$, where K_r and K_T are the reflection and transmission coefficients. For other cases, where breaking occurs on the bar, $\bar{\eta}_p$ would be larger.

Since $\bar{u} = E_b / (\rho C_b h_b)$ and $U_{m_b} = \kappa \sqrt{g h_b} / 2$, we can write Eq. (22) as

$$\frac{2\pi g h_t \bar{\eta}_p}{f_b \omega_b U_{m_b} \bar{u}} = \cosh\left(\frac{\gamma \ell}{2} - 1\right) = 2 \sinh^2\left(\frac{\gamma \ell}{4}\right) \quad (23a)$$

or

$$\frac{\pi \alpha h_b}{f_b \omega_b \kappa \beta} = \sinh^2 \frac{\gamma \ell}{4} \quad (23b)$$

where β relates E_b to E_{incident} .

$$\text{Finally} \quad \ell = \frac{4}{\gamma} \sinh^{-1} \left(\sqrt{F \frac{h_b}{\omega_b}} \right) \quad (24)$$

where F is a constant, of order (125).

$$F = \frac{\pi \alpha}{f_b \kappa \beta}$$

Now, h_b can be related to H_b by the breaking index κ and ω_b is presumed to be a fixed fraction of the wavelength $\omega_b \sim \mu L$, therefore

$$\ell = \frac{4}{\gamma} \sinh^{-1} \sqrt{\frac{F}{\mu \kappa} \left(\frac{H_b}{L} \right)}$$

Recall from Eq. (14)

$$\gamma = \sqrt{\frac{f_t}{2f_b} \frac{U_{m_t}}{U_{m_b}} \frac{h_b}{h_t} \frac{1}{\omega_b \omega_t}} \approx \varepsilon \frac{1}{L}$$

where

$$\epsilon = \left(\frac{f_t}{2f_b} \frac{\omega_b}{L} \frac{\omega_t}{L} \left(\frac{h_b}{h_t} \right)^{1/2} \right)^{1/2}$$

assumed to be a constant.

From the preceding results and assumptions, it is logical to expect the dimensionless rip spacing (ℓ/L) to be related to the wave steepness, H/L , with some effects due to sediment characteristics (f). It remains to be proven whether this is in fact true; however, laboratory experiments to date have shown (1) gaps in bars to produce longshore and rip currents and (2) there is a longshore gradient in water surface slope as predicted by the theory.

A significant assumption is the neglect of the convective acceleration terms which certainly play a role, particularly in the deceleration in the base of the rip current. Another critical assumption is the neglect of wave-current interaction which plays an important role in varying the wave direction offshore of the rip channel and in the longshore trough.

Conclusions and Recommendations

In the fifty years that rip currents have been the study of coastal engineers and scientists, numerous theories have been proposed to explain their occurrence. Most of these theories have appeared in the last ten years and yet, owe their origin to different mechanisms. These theories can be grouped into two broad generic categories, the wave-interaction models and the boundary interaction models. Of the various theories within each group, it is not yet entirely clear during which percentage of time they may occur for a particular coastal type or wave climate, if they occur at all. This question, which, of course, bears on the validity of the various theories, must be addressed by field observations of nearshore circulation for many coastal types. Some work has been undertaken in this area (Sonu, 1972, Fox and Davis, 1974 and Allender, et al. in this volume), yet more detailed and thorough studies remain to be conducted, to include all relevant variables and many coastal geometries.

Significant research needs to be conducted to provide a general model for the shoaling, refraction and diffraction of water waves, so as to provide a unifying basis on which a general model can be built.

Finally the hydrodynamics must be melded to the sediment transport, in order that the feedback mechanism of bottom topographic changes can be incorporated into the models. This development would provide the bridge between the two classifications of rip currents, thus allowing a model of the wave-interaction category to develop perturbations in a previously planar bottom, which would then force a reinforcing circulation of the boundary interaction type.

Acknowledgments

This research was supported in part by funds from the Office of Naval Research, Geography Programs, and the National Sea Grant Program. This paper was written while the author was a sabbatical visitor at the Scripps Institution of Oceanography's Shore Processes Laboratory and their hospitality is appreciated.

References

- Arthur, R. S., Refraction of Shallow Water Waves: The Combined Effect of Currents and Underwater Topography, Trans., A. G. U., 31, 549-557, 1950.
- Arthur, R. S., A Note on the Dynamics of Rip Currents, J. Geophys. Res., 67, 2777-2779, 1963.
- Battjes, J. A., Surf Similarity, Proc. Fourteenth Coastal Eng. Conf., ASCE, Copenhagen, p. 466-480, 1974.
- Birkemeier, W. A. and R. A. Dalrymple, Nearshore Currents Induced by Wind and Waves, Proc. Symposium on Modelling Techniques, ASCE, San Francisco, 1062-1080, 1975.
- Bowen, A. J., Rip Currents, I. Theoretical Investigations, J. Geophys. Res., 74, 5467-5478, 1969.
- Bowen, A. J. and D. L. Inman, Rip Currents, II. Laboratory and Field Observations, 74, 5479-5490, 1969.
- Bruno, R. O. and R. A. Dalrymple, Field Observations of Rip Currents, in preparation, 1978.
- Bruun, P., Longshore Currents and Longshore Troughs, J. Geophys. Res., 68, p. 1065-1078, 1963.
- Cooke, D. O., The Occurrence and Geological Work of Rip Currents Off Southern California, Mar. Geol., 9, 1973-186, 1970.
- Dalrymple, R. A., A Mechanism for Rip Current Generation on an Open Coast, J. Geophys. Res., 80, 3485-3487, 1975.
- Dalrymple, R. A., R. G. Dean and R. I. Stern, Wave-Induced Currents on Barred Coastlines (abs.), EOS, 57, Dec. 1976.
- Dalrymple, R. A., R. A. Eubanks and W. A. Birkemeier, Wave-Induced Circulation in Shallow Basins, J. Waterway, Port, Coastal and Ocean Division, ASCE, Vol. 103, p. 117-135, 1977.
- Dalrymple, R. A. and G. A. Lanau, Beach Cusps Formed by Intersecting Waves, Bull. Geol. Soc. Amer., 87, 57-60, 1976.
- Dalrymple, R. A. and C. J. Lozano, Wave-Current Interaction Models for Rip Currents, J. Geophys. Res., Paper 8C0556, in press.

- Fox, W. T. and R. A. Davis, Beach Processes on the Oregon Coast, July, 1973, ONR Tech. Rept. No. 12, Williams College, 85 pp., 1974.
- Guza, R. T. and R. E. Davis, Excitation of Edge Waves by Waves Incident on a Beach, J. Geophys. Res., 79, 1285-1291, 1974.
- Guza, R. T. and D. L. Inman, Edge Waves and Beach Cusps, J. Geophys. Res., 80, 2997-3011, 1975.
- Gourlay, M. R., Non-Uniform Alongshore Currents, Proc. Fifteenth Conf. on Coastal Eng., ASCE, 701-720, Honolulu, 1976.
- Harris, T. F. W., Field and Model Studies of the Nearshore Circulation, Ph.D. Dissertation, University of Natal, 183 pp., 1967.
- Hino, M., Theory on the Formation of Rip Current and Cuspidal Coast, Proc. 14th Conf. on Coastal Eng., ASCE, Copenhagen, 901-919, 1974.
- Huntley, D. A., Long Period Waves on a Natural Beach, J. Geophys. Res., 81, 6441-6449, 1976.
- Inman, D. L. and R. A. Bagnold, Littoral Processes, The Sea, Vol. 3, M. N. Hill, eds., Interscience Pub., N. Y., 529-553, 1963.
- Iwata, N., A Note on the Wave Set-Up, Longshore Current and the Undertow, J. Oceanographical Society of Japan, Vol. 26, 233-236, 1970.
- Iwata, N., Rip Current Spacing, J. Ocean. Soc. Japan, 32, 1-10, 1976.
- LeBlond, P. H. and C. L. Tang, On Energy Coupling Between Waves and Rip Currents, J. Geophys. Res., 79, 811-816, 1974.
- Liu, P. L.-F. and R. A. Dalrymple, Bottom Frictional Stresses and Longshore Currents Due to Waves With Large Angles of Incidence, J. Mar. Res., Vol. 36, p. 357-375, 1978.
- Liu, P. L.-F. and C. C. Mei, Water Motion on a Beach in the Presence of a Breakwater, I and II, J. Geophys. Res., Vol. 81, 3079-3094, 1976.
- Longuet-Higgins, M. S., On the Wave-Induced Difference in Mean Sea Level Between Two Sides of a Submerged Breakwater, J. Mar. Res., 25, 148-153, 1967.
- Longuet-Higgins, M. S., Longshore Currents Generated by Obliquely Incident Sea Waves, 1, J. Geophys. Res., 75, 6778-6789, 1970.
- Longuet-Higgins, M. S., The Mean Forces Exerted by Waves on Floating or Submerged Bodies, with Applications to Sand Bars and Wave Power Machines, Proc. Roy. Soc. London, Series A, V06, June 1976.

- Longuet-Higgins, M. S. and R. W. Stewart, Radiation Stress in Water Waves, A Physical Discussion with Applications, Deep Sea Res., 11, 529-562, 1964.
- McKenzie, P., Rip-Current Systems, J. Geology, Vol. 66, p. 103-113, 1958.
- Mei, C. C. and D. Angelides, Longshore Circulation Around a Conical Island, Coastal Engineering, 1, 31-42, 1977.
- Mei, C. C. and P. L.-F. Liu, Effects of Topography on the Circulation in and Near the Surf Zone; Linearized Theory, J. Est. and Coastal Mar. Sci., 5, 25-37, 1977.
- Miller, C. and A. Barcelon, Hydrodynamic Instability in the Surf Zone as a Mechanism for the Formation of Horizontal Gyres, J. Geophys. Res., Vol. 83, 4107-4116, 1978.
- Mizuguchi, M., Eigenvalue Problems for Rip Current Spacing, Trans., Japan Soc. Civil Engg., 248, 83-88, 1976 (in Japanese).
- Noda, E. K., Wave-Induced Nearshore Circulation, J. Geophys. Res., 79, 4097-4106, 1974.
- Noda, E. K., C. J. Sonu, V. C. Rupert, and J. I. Collins, Nearshore Circulation Under Sea Breeze Conditions and Wave-Current Interaction in the Surf Zone, TETRA-72-149-4, Tetra Tech, Inc., 216 pp., 1974.
- Sasaki, T., Simulation on Shoreline and Nearshore Current, Proc. Civil Engineering in the Oceans, III, ASCE, Newark, DE, 179-196, 1975.
- Shepard, F. P., Undertow, Rip Tide or "Rip Current", Science, Vol. 84, 181-182, Aug. 21, 1936.
- Shepard, F. P., K. O. Emery and E. C. LaFond, Rip Currents. A Process of Geological Importance, J. Geology, Vol. 49, p. 337-369, 1941.
- Shepard, F. P. and D. L. Inman, Nearshore Circulation, Proc. First Conf. on Coastal Engineering, Council on Wave Research, Berkeley, Oct. 1950a.
- Shepard, F. P. and D. L. Inman, Nearshore Water Circulation Related to Bottom Topography and Wave Refraction: Trans., A. G. U., Vol. 31, 196-213, 1950b.
- Sonu, C. J., Field Observations of Nearshore Circulation and Meandering Currents, J. Geophys. Res., 77, 3232-3247, 1972.
- Suhayda, J. N., Determining Nearshore Infra-gravity Wave Spectra, Int. Symp. on Ocean Wave Measurement, ASCE, New Orleans, Louisiana, 1975.
- Tait, R. J., Edge Wave Modes and Rip Current Spacing, Ph. D. Dissertation, Scripps Institution of Oceanography, 123 pp., 1970.

CHAPTER 84

WIND-GENERATED LONGSHORE CURRENTS

by

Dag Nummedal
Department of Geology
Louisiana State University
Baton Rouge, Louisiana
70803, USA

and

Robert J. Finley
Bureau of Economic Geology
University of Texas
Austin, Texas
78712, USA

ABSTRACT

This paper evaluates, through the use of a stepwise multiple regression procedure, whether parameters descriptive of the surf-zone wave field adequately explain the variability in longshore current velocities, or if the inclusion of additional physical environmental parameters could significantly improve the ability to predict such currents. The data set consists of 250 LEO - observations, collected on a seasonal basis over one year, at Debidue Island beach, South Carolina.

A regression analysis was performed both on linear combinations of all measured wave parameters, and on non-linear parameter combinations proposed in various semi-empirical predictive equations. Invariably, in all the regression analyses, the longshore component of the wind velocity proved to be the independent variable explaining most of the observed variance in the current velocity. Therefore, the statistical data analysis presented in this paper strongly suggests that wind stress can be a most significant factor in surf-zone current generation.

INTRODUCTION

Longshore current velocities measured in the surf-zone at Debidue Island, South Carolina, are the vector resultant of velocity components due to the oblique approach of the

breaking wave, the nearshore cell circulation system, currents generated directly in the nearshore zone by wind stress and, perhaps, components of a regional circulation system. It is generally assumed that the dominant factor in the generation of longshore currents is the oblique approach of the breaking wave. Accordingly, the two most important parameters determining the longshore current velocity are the wave height and the angle between the wave crest and the shoreline (U.S. Army, Corps of Engineers, Coastal Engineering Research Center, 1973). A number of theories explain the generation of such currents and predict their magnitude. These theories are grouped according to their considerations of (a) conservation of mass, (b) conservation of energy flux, or (c) conservation of momentum flux (Galvin, 1967). Empirical equations, based on statistical analysis of parameters describing the breaking wave, have also been constructed (Harrison, 1968; Fox and Davis, 1972), though such equations are generally of limited value outside the specific area of formulation.

The objective of this study was to evaluate, through the use of a stepwise multiple-linear regression procedure, whether parameters descriptive of the surf-zone wave field adequately explain the observed variability in longshore currents, or if the inclusion of additional environmental parameters could significantly improve the ability to predict such current velocity. Linear combinations of breaker parameters and four proposed equations for prediction of longshore current velocity were used in the evaluation.

Galvin (1963), basing his model on the continuity of water mass, arrived at the following equation

$$V = k \cdot g \cdot m \cdot T_b \cdot \sin 2\alpha_b \quad (1)$$

where V is longshore current velocity, g is the acceleration of gravity, m is beach slope, α_b is breaker angle, T_b is breaker period, and k is a parameter of the breaker form, here taken as 1.0 (Galvin and Eagleson, 1965).

Longuet-Higgins (1970) derived an equation by considerations of the conservation of momentum flux for breaking waves. The U.S. Army, Corps of Engineers, Coastal Engineering Research Center (1973) empirically determined the proportionality constant in Longuet-Higgins' equation by fitting it to laboratory data by Galvin and Eagleson (1965)

and field data from Putnam et. al (1949). Thus, the "modified" Longuet-Higgins equation reads:

$$v = 20.7 \text{ m } (g H_b)^{\frac{1}{2}} \sin 2\alpha_b \quad (2)$$

Fox and Davis' (1972) empirical equation for their Lake Michigan data set is:

$$v = 2.98 \frac{H_b}{T_b} \sin 4\alpha_b \quad (3)$$

Another empirical equation, derived by Harrison (1968) from analysis of surf-zone data at Virginia Beach, reads:

$$v = 0.17 + 0.037 \alpha_b + 0.032 T_b + 0.24 H_b \quad (4)$$

Equations 1 through 4 formed the basis for the statistical evaluation of the role of breaker parameters in explaining the observed variability in the longshore current.

MEASUREMENTS

Descriptive summary statistics for all longshore current velocity readings obtained between July 1974 and March 1976 are presented in Table 1. The mean longshore current is stronger to the south (35.8 centimeters per second versus 23.8 centimeters to the north). Extreme variability in current velocities is demonstrated by the fact that the standard deviation almost equals the mean. Inman and Quinn (1952) also found in their study of longshore current variability on the Pacific coast that the standard deviation often equalled or exceeded the mean. There is an indication in the data that fall current velocities are slightly higher than those at other seasons.

The data set includes only those velocity readings which were obtained at least 3 hours after sudden reversals in wind direction. It was determined that there was a lag of about 2 to 3 hours between reversals in the longshore wind component and corresponding reversals in the current.

Table 1. Longshore current velocities at Debidue Island
(in centimeters per second)

	Direction ¹	N ²	Mean	Std. Dev.	Median
Jul. 1974 - Mar. 1976	N	176	23.8	17.0	19.6
	S	271	35.8	27.9	28.4
Analysis by season					
Jul. 1974	N	0	----	---	3
	S	0	----	----	
Jun. 1975	N	120	22.6	15.0	
	S	98	37.3	28.7	
Sept. 1974	N	21	13.8	0.0	
	S	152	46.4	33.0	
1975	N	58	26.3	16.1	
	S	137	45.5	30.7	
Jan. 1975	N	61	22.7	14.0	
	S	107	33.8	21.4	
1976	N	57	17.2	13.2	
	S	136	34.9	25.6	
Mar. 1975	N	72	24.4	18.3	
	S	64	27.1	17.4	
1976	N	117	31.3	19.7	
	S	103	25.7	16.3	

¹Current direction along shoreline. N is to the north, S to the south.

²Number of observations.

³No reading.

All measurements were made by observers on the beach in accordance with specifications set forth in the Littoral Environments Observation program by the Coastal Engineering Research Center. As demonstrated in figure 1, the southern end of Debidue Beach, where the measurements took place, is characterized by a straight, gently sloping beach. Bathymetric profiles (Humphries, 1977) demonstrate that

the nearshore region has straight shore-parallel depth contours. Although the North Inlet tidal delta is only about 2 km south of the study site, no measureable influence of tidal currents was detected.



Fig. 1. Oblique aerial view to the south along the shore of Debidue Island

ANALYSIS

Three regression procedures were utilized in this data analysis:

(1) Simple correlation was used to test for linear relationships between any pair of variables. The Pearson correlation coefficient is a measure of the degree of proportionality between two variables.

(2) Stepwise regression enters one independent variable at a time until all are entered simultaneously. Their order of inclusion is determined by the computer - the independent variable which explains the largest amount of variance in the dependent variable is entered first. The others are then entered in order of decreasing variance explained. The proportion of the total variance in the dependent variable explained by an independent variable, or a combination of variables, is expressed by the multiple correlation coefficient, r^2 .

(3) Multiple regression enters one independent variable at a time in any order specified by the investigator. Thus, the amount of variance explained by any independent variable of particular interest can be assessed.

The variable names used in the computations and the following analysis are defined in Table 2.

Table 2. Variable names used in multiple regression analysis of littoral processes.

Name	Definition
VEL	Observed longshore current velocity (in centimeters per second). (+) indicated current to the right (south); (-) indicates current to the left (north).
HGT	Breaker height (in centimeters).
PER	Breaker period (in seconds).
WINDL	Longshore component of wind velocity (m.p.h.)
WAVL	Sine of the breaker angle.
VGAL	Velocity calculated by Galvin's (1963) formula (eq. 1), (centimeters per second).
VELH	Velocity calculated by Longuet-Higgins (1970) formula (eq. 2)
VEFD	Velocity calculated by Fox and Davis' (1972) formula (eq. 3)
VHAR	Velocity calculated by Harrison's (1968) formula (eq. 4).

Table 3 is a matrix of the Pearson product-moment correlation coefficients for these 9 variables for the 1975-76 data set of 250 observations.

Table 3. Pearson correlation coefficients between littoral variables defined in Table 2.

	VEL	HGT	PER	WINDL	WAVL	VGAL	VELH	VEFD
VEL	--							
HGT	0.37	--						
PER	-0.11	-0.06	--					
WINDL	0.83	0.36	-0.07	--				
WAVL	0.68	0.27	-0.09	0.68	--			
VGAL	0.64	0.27	-0.01	0.66	0.97	--		
VELH	0.69	0.38	-0.07	0.70	0.97	0.95	--	
VEFD	0.70	0.46	-0.12	0.69	0.88	0.81	0.93	--
VHAR	0.68	0.39	0.05	0.69	0.98	0.97	0.97	0.88

Bivariate data plots produced by computer give further information on the nature of these correlations. The plots of wave height and period versus current velocity show hardly any discernible trend. Clearly, these parameters do not exert any dominant control on the current velocity. The sine of the breaker angle shows a moderate correlation with the current velocity. The scatter is particularly large for small angles of breaker approach. Wind velocity shows a moderate correlation with the current velocity, again scatter is at a maximum for relatively moderate winds. By far the best correlation is that between the longshore component of the wind velocity and the observed current velocity. The correlation coefficient equals 0.83 and the scatter is small, and uniform, over the entire range of the independent variable. If the surf-zone wave parameters are combined as suggested in equations (1), (2), (3) and (4), the predicted and observed longshore velocities show correlations ranging from r equals 0.64 for Galvin's (1963) formula to r equals 0.70 for Fox and Davis' (1972) formula.

If the longshore component of the wind is considered to be the only independent variable, one can write a simple regression equation for the longshore current velocity as:

$$VEL = 3.42 \cdot WINDL + 6.3 \quad (5)$$

This is a wholly empirical equation, and all parameters affecting the longshore current velocity are lumped into WINDL. Equation (5) does not indicate how much is due to the oblique breaking of the wind-generated waves. However, the equation is of predictive value for longshore currents off Debidue Island (and probably elsewhere under similar environmental conditions).

The correlation coefficients between observed current velocity and that predicted by the tested equations are all reasonably high. This indicates proportionality. However, the magnitude of the predicted velocity generally differs substantially from that observed, as evidenced by the proportionality factors in the following regression equations (all velocities are in centimeters per second).

$$VEL = 0.33 VGAL + 5.18, r = 0.64 \quad (6)$$

$$VEL = 0.45 VELH + 4.6, r = 0.64 \quad (7)$$

$$VEL = 2.0 VEFD + 4.1, r = 0.70 \quad (8)$$

$$VEL = 0.71 \overline{VHAR} - 14.4, \quad r = 0.68 \quad (9)$$

Galvin's (1963) and Longuet-Higgins' (1970) equations are both semiempirical, both predict current velocities higher than those observed at Debidue Island. The empirical equation of Fox and Davis (1972) predicts current velocities which are generally too low by a factor of $\frac{1}{2}$. Harrison's (1968) equation predict currents of essentially the correct magnitude.

To test for the relative importance of the independent variables in explaining the variance in the dependent one, a stepwise regression analysis was used. The test was performed both for the pooled annual data and for each seasonal data set. Results are summarized in Table 4.

Table 4. Percent of the variance in VEL explained by each of four independent variables entered successively in a stepwise regression analysis.

Variable	Annual	1975		1976	
		June	Sept.	Jan.	Mar.
WINDL	70	81	63	57	69
VGAL	1	0	0	2	2
VELH	2	0	1	2	4
VEFD	4	0	7	1	6

For all data sets, the longshore component of the wind velocity, WINDL, proved to be the independent variable explaining most of the observed variance in current velocity, VEL. The multiple correlation coefficient (r^2), for VEL versus WINDL ranged from 0.81 for the June 1975 data set to 0.57 for the January 1976 data. Expectedly, data noise was at a maximum in January and minimum in June because of the different weather conditions under which the field observers had to operate. It is quite significant to note that for the data set which was expected to be the most reliable, (June 1975), WINDL alone explained 81 percent of the variance. For this data set, the inclusion of breaker parameters combined into the predictive equations of Galvin (1963), Longuet-Higgins (1970), and Fox and Davis (1972), does not improve the multiple correlation coefficient. For the other data sets, these variables add a few percents of explained variance.

A series of regression equations can be developed depending on which variables or combinations of variables are included. Table 5 summarizes the two types of equations derived in this study; the first (equation 10) is the regression equation derived by treating each measured environmental parameter as an independent variable; the three subsequent equations (equations 11, 12, 13) are derived by combining the pertinent breaker parameters as suggested in Galvin's (1963), Longuet-Higgins' (1970), and Fox and Davis' (1972) predictive formulas. Breaker parameters not accounted for in the predictive formulas are included as independent variables. The amount of variance in VEL explained by each parameter combination is constant, about 72 percent. Typically, the longshore component of the wind speed, WINDL, alone explains 70 percent of the variance. All other parameters combined can improve the predictability by a mere two percent.

Based on a similar analysis, Harrison (1968) derived a regression equation for longshore current velocity at Virginia Beach, Virginia. However, simultaneous wind measurements were not obtained in his study, and the question of wind stress or breaking wave dominance in longshore current generation could not be assessed.

Table 5. Multiple regression equations for measured longshore current velocities. The equations are all based on the same data set, but utilize different combinations of independent parameters.

$$VEL = 2.78 WINDL + 44.2 WAVL + 0.12 HGT - 0.85 PER + 5.94 \quad (10)$$

$$VEL = 2.73 WINDL + 0.69 VEFD + 4.72 \quad (11)$$

$$VEL = 2.83 WINDL + 0.13 VELH - 0.94 PER + 13.28 \quad (12)$$

$$VEL = 2.91 WINDL + 0.06 VGAL + 0.12 HGT - 1.15 \quad (13)$$

CONCLUSION

Based on measurements of longshore currents at Debidue Island beach, South Carolina, it appears that the parameters descriptive of the surf-zone wave field do not explain a significant amount of observed current variance. In fact, the longshore component of the wind velocity explains more of the observed current variance than any

single parameter, or combination of parameters, descriptive of the breakers.

ACKNOWLEDGMENTS

Financial support for this study was obtained from the Coastal Engineering Research Center through contract no. DACW 72-74-C-0018 to the University of South Carolina (M.O. Hayes, principal investigator). Stan Humphries contributed valuable assistance in both data collection and analysis.

REFERENCES

- Fox, W. T., and Davis, R. A., Jr., 1972, Coastal processes and beach dynamics at Sheboygan, Wisconsin, July 1972; Technical Rept. no. 10, ONR contract 388-092, Williams College, Williamstown, Mass. 1971.
- Galvin, C. J., Jr., 1963, Experimental and theoretical study of longshore currents on a plane beach: Ph.D. thesis, Department of Geology and Geophysics, Massachusetts Institute of Technology, Cambridge, Mass.
- Galvin, C. J., Jr., 1967, Longshore current velocity: a review of theory and data: Rev. Geophysics, v. 5, p. 287-304.
- Galvin, C. J., Jr., and Eagleson, P. S., 1965, Experimental study of longshore currents on a plane beach: U. S. Army Corps of Engineers, Coastal Engineering Research Center, TM-10.
- Harrison, W., 1968, Empirical equation for longshore current velocity: Jour. Geophysical Research, v. 78, p. 6929-6936.
- Humphries, S. M., 1977, Morphologic equilibrium of a natural tidal inlet: Coastal Sediments '77, ASCE, p. 734-753.
- Imman, D. L., and Quinn, W. H., Currents in the surf zone: Proc. 2nd Coastal Engineering Conference, ASCE, p. 24-36.

- Longuet-Higgins, M. S., 1970, Longshore currents generated by obliquely incident sea waves: Jour. Geophysical Research, v. 75, p. 6788-6801.
- Putnam, J. A., Munk, W. H., and Traylor, M. A., 1949, The prediction of longshore currents: Transactions, Am. Geophysical Union, v. 30, p. 337-345.
- U. S. Army, Coastal Engineering Research Center: 1973, Shore Protection Manual: Superintendent of Documents, Washington, D. C.

CHAPTER 85

VISIBLE-REGION PHOTOGRAPHIC REMOTE SENSING OF NEARSHORE WATERS

Tsuguo Sunamura *Institute of Geoscience, University of Tsukuba,
Ibaraki 300-31, Japan*
Kiyoshi Horikawa *Department of Civil Engineering, University of
Tokyo, Tokyo 113, Japan*

ABSTRACT

By use of a synchronized camera system, multiband black-and-white photographs and conventional color photographs were taken respectively with the purposes of testing filters available for shallow-water photographic bathymetry, and of checking the availability of low-cost process imagery for the study of coastal processes. Kodak Wratten filters 29, 58, and 90 were employed for the multiband photography. A Wratten 90 filter provided the best correlation between water depth and the photographic density. The low-cost imagery, obtained in a laboratory from the color photographs by applying ordinary filters without using any expensive image processing devices, proved to be useful.

INTRODUCTION

Since minimum attenuation of light in water occurs in the visible region of electromagnetic spectrum, i.e., 400-700 nm in wavelength, the remote sensors available in this region are effective for the aerial investigation of nearshore waters, especially of underwater environments. The photographic sensors covering the visible region are (1) black-and-white photographs, (2) color photographs, and (3) multiband or multispectral photographs; these sensors have been widely used in the field of coastal engineering (Stafford, 1972).

The feasibility of nearshore bathymetry using multiband photographs has recently investigated (Stafford, 1972), and several studies have been conducted to explore optimum film/filter combinations for the bathymetric use (e.g., Lockwood et al., 1974; Magoon and Pirie, 1972; Pestrong, 1969). However, sufficient data on this point are unavailable. One of two purposes of the present study is to furnish a basic data on filters used for the multiband

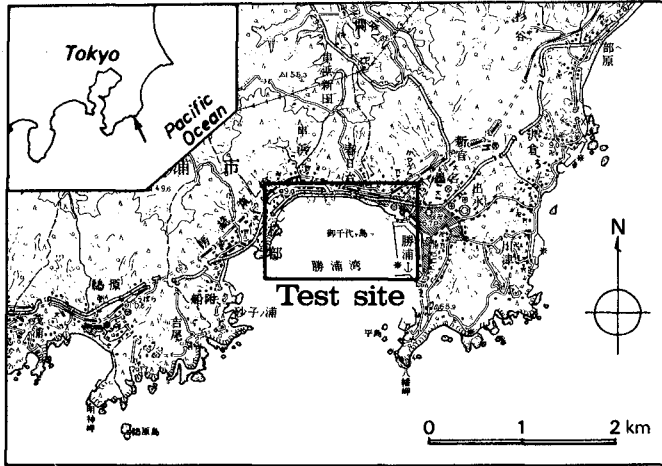


Figure 1 Test site.

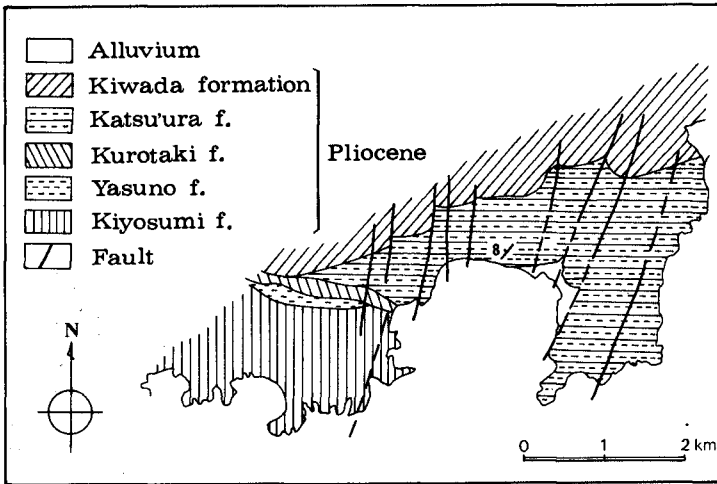


Figure 2 Geology around the test site.

photography with the aim of sounding a shallow-water area.

The process imagery through the image enhancement or processing devices has been widely used to extract various information from photographs (American Society of Photogrammetry, 1975, pp. 611-813). However, these devices are expensive. The imagery processed from conventional color photographs by applying only filters without using any expensive equipment is also considered to be useful. But, the availability of this low-cost process imagery has not yet been tested with the exact sea or ground truths. The second purpose of the present study is to examine this availability from the view point of the data acquisition for coastal processes studies.

TEST SITE

The test site is a shallow-water area at the head of the Katsu'ura Bay located on the Pacific coast of Japan (Fig. 1). The bay is a semicircular shape bordered by coastal cliffs made of Pliocene sedimentary rocks (Fig. 2). The alternation of sandstone and siltstone strata of Katsu'ura formation (strike: N40-50E, dip: 5-10N) forms the cliff at the test site. A narrow bay-head beach develops with an alongshore distance of 1.3 km. The direction of wave approach is nearly normal to the beach. Approximate tidal range at spring tide is 1.5 m, while at neap tide is 0.7 m.

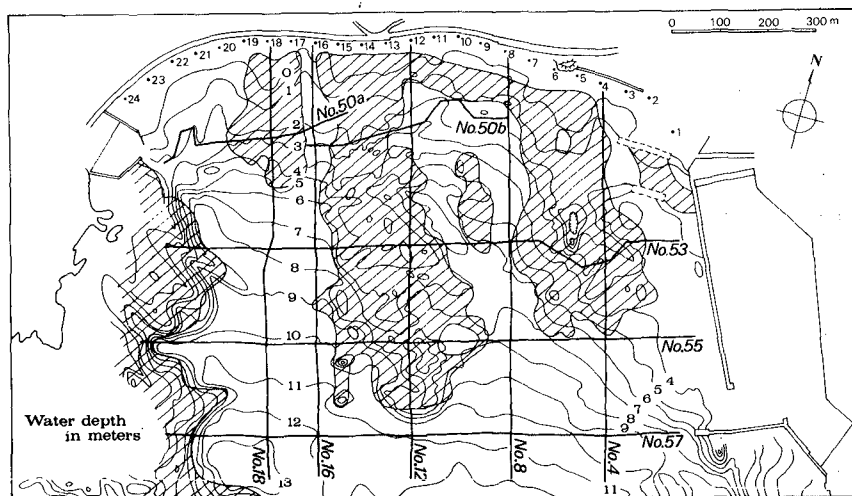


Figure 3 Submarine topography and the area of exposed bedrock (hatched area).

Underwater topographical and geological characteristics of the test site are that (1) the seabed consists of portions made of medium sand and of exposed bedrock (Katsu'ura formation) (Fig. 3), and (2) the bedrock region is located higher than the adjacent sand bottom, forming an abrasion platform (Fig. 4). The higher bedrock-region induces the convergence of wave energy (Sunamura and Horikawa, 1976); the energy convergence produces breaking waves even in a calm sea.

The main reasons for the selection of this area as the test site are that (1) water is clear, and (2) both the bedrock and the sandy areas have no regional color variations, respectively.

AERIAL PHOTOGRAPHY

The flight plan was made paying much attention to the exclusion of the sun's glitter on aerial photographs. Along the flight lines (Fig. 5), the test site was photographed by using a Cessna aircraft at an altitude of about 1,000 m during three days from November 27 to 29, 1974, under different wave conditions. Approximately 60 per cent overlap along the flight lines and 30 per cent side lap were obtained.

A synchronized camera system consisting of four Hasselblad cameras was employed. One of them was used for color photographs, and the remaining three cameras were used for multiband photographs, i.e., 3-band black-and-white photographs applying Kodak Wratten filters 29, 58, and 90, respectively (Fig. 6). Films for the color and the multiband photographs were Kodak Aerocolor Negative 2445 and Kodak Tri-X Aerographic 2403, respectively. Table 1 shows the film/filter/camera combinations and additional photographic data.

GROUND AND SEA TRUTH MEASUREMENTS

Prior to photographing, two kinds of work were made for the water depth determination test: (1) a bathymetric survey and (2) submarine installation of white targets. The former was done along 32 ranges 25 m apart, set up perpendicularly to the shoreline; the inshore region including the backshore and foreshore was measured by using a transit, staff, and tape, while the offshore region up to a water depth of several meters was surveyed with the aid of an echo sounder. The latter was done by using five squares with a length of 1.8 m each (Fig. 7), which were placed at a water depth of 1 to 5 m with a vertical interval of 1 m (Fig. 8). The location of the target installation is shown in Fig. 9.

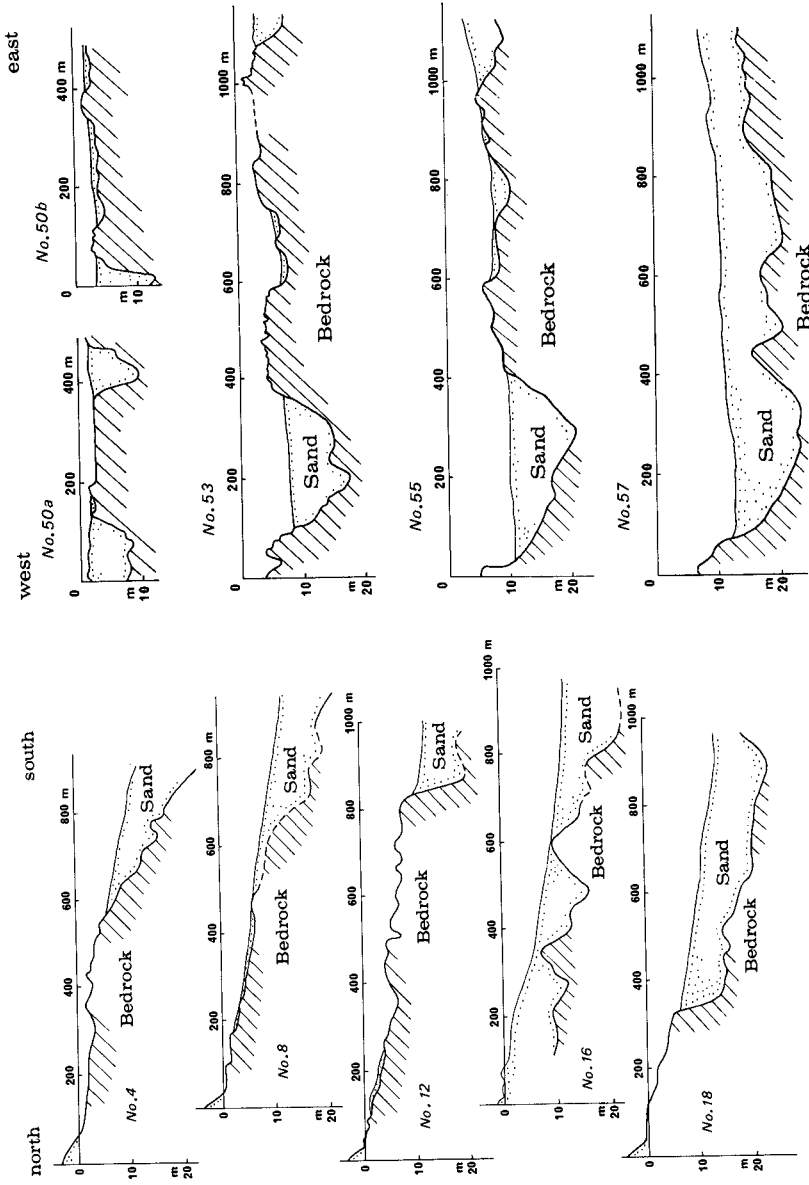


Figure 4 Geological cross-sections along survey lines shown in Fig. 3.

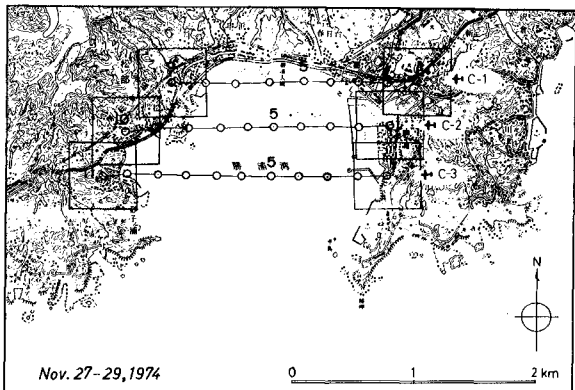


Figure 5
Flight lines.

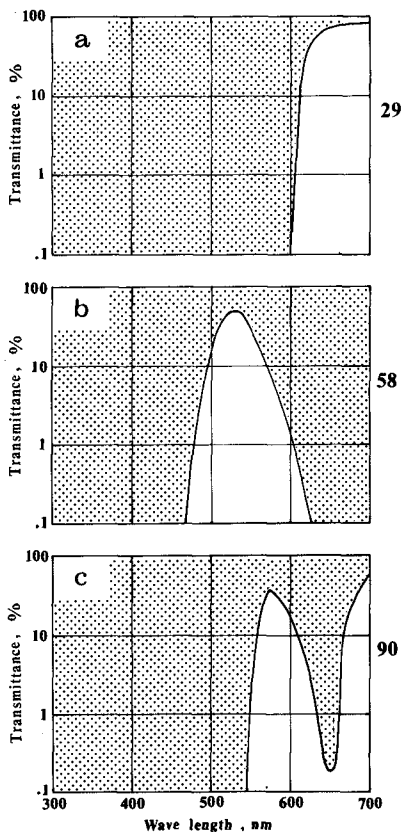


Figure 6
Filters used for the multiband
photography.

Table 1 Film/filter/camera combinations.

Film*	Filter**	Camera***	Lens† & focal length	f	Shutter speed	Remarks
2403	58	MK 70	100.94 mm	5.6	1/250	Multiband photo
2403	90	500EL	100	4	1/250	
2403	29	500EL	100	5.6	1/500	
2445	2B	500EL	100	8	1/500	Color photo

* Kodak

** Kodak Wratten

*** Hasselblad

† Zeiss

Figure 7
Sketch showing a submerged target.

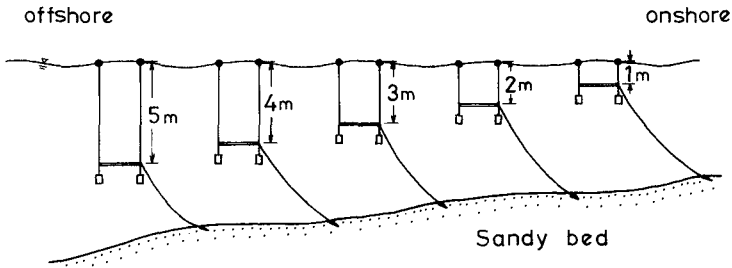
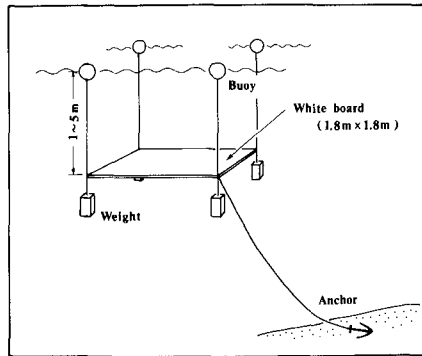


Figure 8 Schematic diagram showing underwater installation of targets.

Table 2 Wave and tidal conditions at the time of photography.

Time and date	Waves		Tide level
	Breaker height	Period	
	H_b	T	
12:00-13:00 Nov. 27, 1974	ab. 1 m	9 - 10 sec	0.4 - 0.5 m above MSL
12:00-13:00 Nov. 28, 1974	ab. 2	10 - 11	0.4 - 0.5 above MSL
12:00-13:00 Nov. 29, 1974	ab. 1.5	ab. 10	0.35-0.45 above MSL

The wave condition during the aerial photography is summarized in Table 2. The test site is characterized by the existence of an alongshore variation in the height of breaking waves: higher breakers are observed in the bedrock region compared to the adjacent sand area. The "breaker height" in Table 2 denotes a time-averaged value in the bedrock region.

DATA ANALYSES AND RESULTS

(1) Filter Test for Water Depth Determination

Two methods have been developed concerning the quantitative photographic bathymetry (American Society of Photogrammetry, 1975, pp. 1574-1584): (1) photogrammetric method using stereoscopic (three-dimensional) measuring techniques, and (2) transparency method using photographic-density measuring techniques. The present study applied the latter method for the availability check of the filters used in the multiband photography. Photographs with no influence of suspended material are needed for the quantification of the photographic density-water depth relation. The photographs of November 27 were used here, because the degree of sediment suspension was the lowest due to the calmest sea during the three-day investigation (see Table 2). The photographic density was measured by applying a micro-densitometer (Rhesca Model PPA-250) on the positive transparencies. The density output was expressed in terms of volts.

Figure 10 shows a linear relationship between water depth and the photo-density on the submerged targets; this relation was obtained from the photographs with a Wratten 90 filter. Results from the Wratten 29- and 58-filtered photographs presented the similar relation to Fig. 10, although a considerable scatter of the data

points was seen.

Two measuring lines, C-16 and C-30 (see Fig. 9), were sorted out from the 32 survey ranges for the photo-density measurement over the natural submarine bottom: C-16 traverses the bedrock area, while C-30 the sandy area. Both lines have little influence of sediment suspension. The correlation between the density and water depth becomes worse in order of the Wratten 90-, 58-, and 28-filtered photographs. Figure 11 is the best result, obtained from the Wratten 90-filtered photographs, showing some scatter of the data points. The lack of data points in the bedrock region shallower than a water depth of 1.5 m is due to the presence of surf zone. The result of the natural seabed shows the exponential relation (Fig. 11), while the target test presents the linear one (Fig. 10). The reason for this difference is unknown.

The light transmission characteristics of coastal water show that maximum transmittance occurs with the 500-600 nm (green) range of electromagnetic spectrum (Duntley, 1963; Lockwood et al., 1974). Therefore, one can expect that a Wratten 58 filter having a bandwidth of 460-620 nm (see Fig. 6(b)) could be optimum for the bathymetric use. However, the present study indicates that a Wratten 90 filter was the best. The possible reason for this is as follows:

In the visible-region electromagnetic spectrum, the shorter wavelength radiation is more sensitive to the scattering by fine particles suspended in the atmosphere and the ocean than the longer wavelength radiation. A Wratten 58 filter transmits wavelengths of 460-500 nm (a part of blue region), allowing the record of the atmospheric and oceanic scattering; this masks the underwater information recorded by the green-region electromagnetic waves. Therefore a perfectly blue-cut filter like a Wratten 90 filter would produce the best result.

(2) Availability Check of Low-Cost Process Imagery

Three kinds of images were processed in a laboratory from the color photographs by utilizing blue (Kodak Wratten filter 94), green (93) and red (92) filters, respectively (see Fig. 12). In this processing, was used a separation film whose sensitivity covered a wavelength range of 400-700 nm. The imagery, printed on the separation film at first, was finally printed out on the ordinary printing paper. This was black-and-white negative imagery. Figure 13 shows one example of the process imagery.

Figure 13(a) shows a low-contrast image, produced by the atmos-

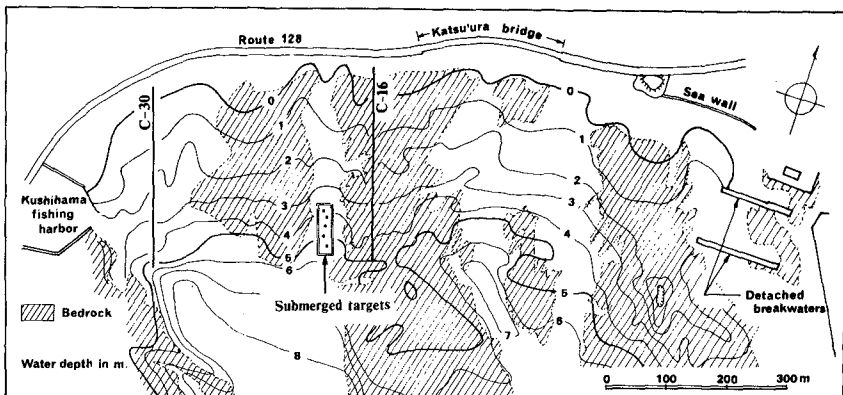


Figure 9 Locations of the submerged targets and the survey lines (C-16 and 30), used for water depth determination test.

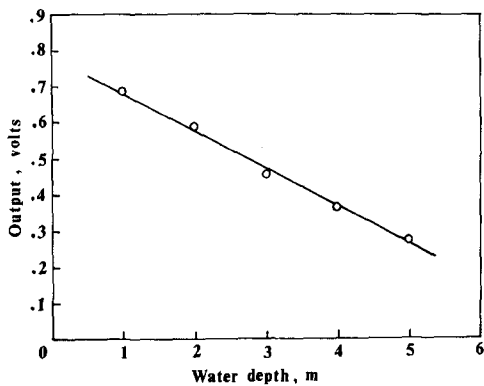


Figure 10 Water depth vs. photographic density on the submerged targets.

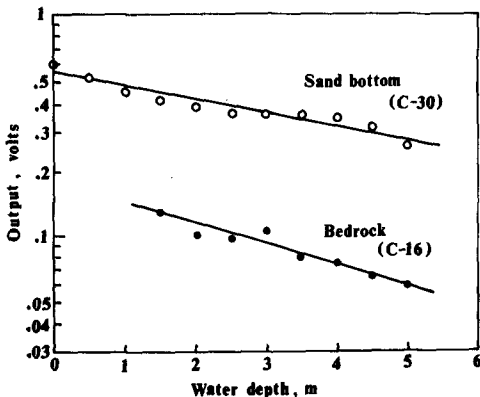


Figure 11 Water depth vs. photographic density on the natural seabed.

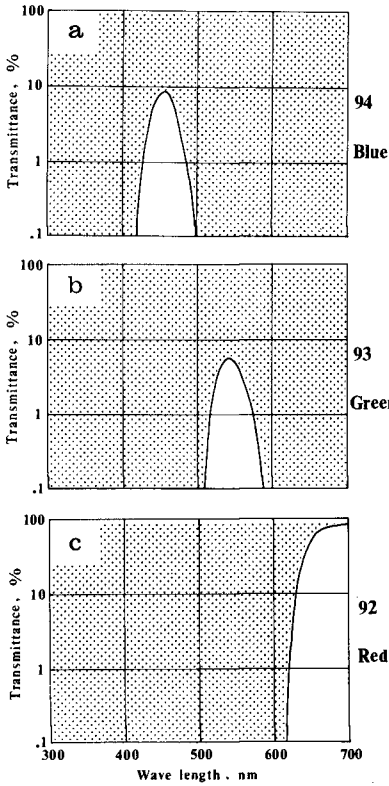


Figure 12
 Filters used for image processing
 from the color photographs.

pheric and oceanic scattering of the 400 to 500 nm-length waves. This indicates that blue-filtered photographs are not available for use in the interpretation of a shallow-water environment.

Figure 13(b) allows the visualization of submarine bedrock features, because the green filter transmits wavelengths of 510 to 580 nm, which have the capability of recording underwater details to maximum depth. Since wave breaking and sediment suspension deteriorate the underwater information, the photographs taken under the calmest sea condition should be used for the submarine investigation. The green-filtered images of November 27 were applied for the delineation of the linear features on the exposed bedrock; the result is shown in Fig. 14.

Figure 13(c) exhibits a clear image of rip current pattern, i.e., flow pattern of water discolored by suspended material. In



(a) Blue-filtered



(b) Green-filtered



(c) Red-filtered

Figure 13 Process imagery from the color photograph taken on November 28, 1974, by using blue, green, and red filters.

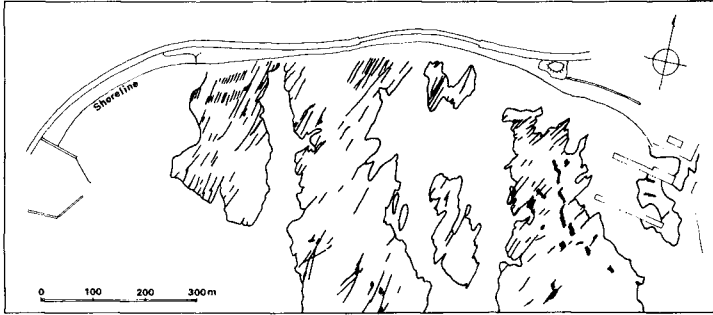


Figure 14 Linear features on exposed submarine bedrock, depicted from the green-filtered imagery of November 27, 1974.

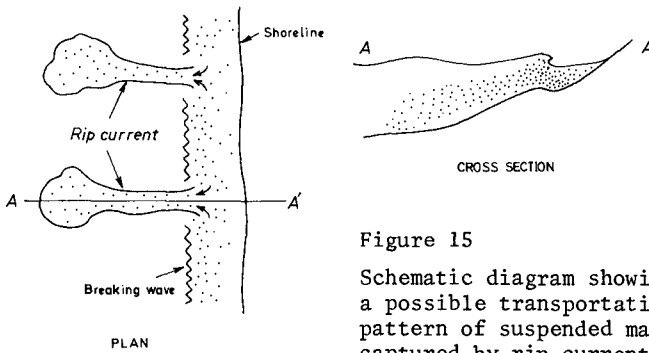


Figure 15 Schematic diagram showing a possible transportation pattern of suspended matter captured by rip currents.

the red region of electromagnetic spectrum, the degree of water penetration is inferior as compared to the green-region wavelengths. This means that the red-filtered imagery supplies shallower-water information than the green-filtered imagery does. The material transported offshore by rip currents would probably be suspended to a certain height over the seabed (Fig. 15). Therefore the red-filtered imagery is preferable for tracing the pattern of sediment-laden rip currents. Figure 16 shows the rip current patterns depicted from the red-filtered images of the three-day data; the solid lines indicate certainty and the dashed lines show uncertainty as to the delineation of the flow pattern. The degree of rip current development increases with increasing breaker height.

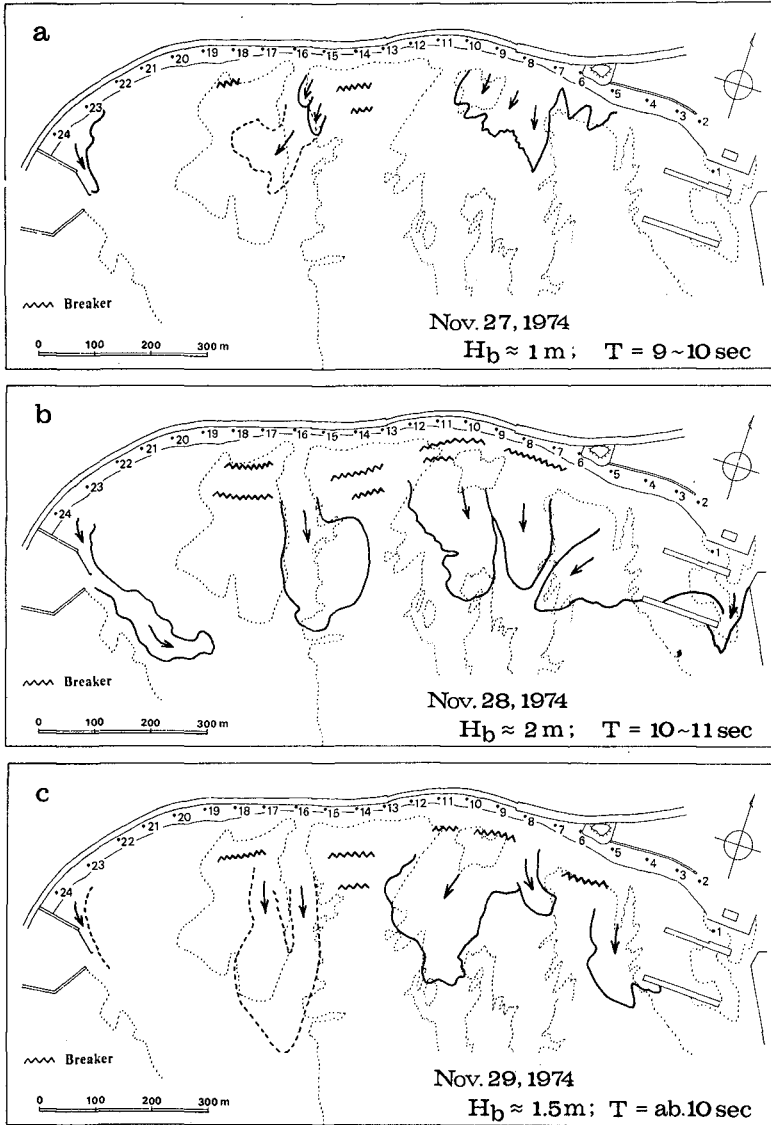


Figure 16 Rip current patterns depicted from the red-filtered imagery.

CONCLUSIONS

A perfectly blue-cut filter is useful for the multiband photography having the purpose of shallow-water bathymetry by the transparency method. However, there is a limitation that the photographs should be taken under calm sea conditions, because suspended material and surf zone make it difficult to read accurately the photographic density.

The low-cost process imagery from conventional color photographs by using pertinent filters is available for use in the study of coastal processes.

ACKNOWLEDGMENTS

This study was financially supported by National Institute of Resources, Science and Technology Agency, Japan. Helpful information of photographic engineering given by Dr. Y. Shima of Chiba University is greatly appreciated.

REFERENCES

- American Society of Photogrammetry, 1975, Manual of Remote Sensing. R. G. Reeves, Editor-in-chief, American Society of Photogrammetry, Falls Church, Virginia, 2144 pp.
- Duntley, S. Q., 1963, Light in the sea. Jour. Optical Soc. Am., vol. 53, pp. 214-233.
- Lockwood, H. E., Perry, L., Sauer, G. E., and Lamar, N. T., 1974, Water depth penetration film test. Photogrammetric Eng., vol. 40, pp. 1303-1314.
- Magoon, O. T. and Pirie, D. M., 1972, Remote sensing in the study of coastal processes. Proc. 13th Coastal Eng. Conf., Vancouver, pp. 2027-2043.
- Pestrong, R., 1969, Multiband photos for a tidal marsh. Photogrammetric Eng., vol. 35, pp. 453-470.
- Stafford, D. B., 1972, Coastal engineering applications of aerial remote sensing. Proc. 13th Coastal Eng. Conf., Vancouver, pp. 2045-2064.
- Sunamura, T. and Horikawa, K., 1976, Field investigation of sediment transport pattern in a closed system. Proc. 15th Coastal Eng. Conf., Honolulu, pp. 1240-1257.

CHAPTER 86

UNDULATED BOTTOM PROFILES AND ONSHORE-OFFSHORE TRANSPORT

Madhav Manohar*

ABSTRACT: Underwater bars, the characteristic features of oceans and lakes occur singly or in a series along the coast. Nearest bar to the shore, namely the break-point bar moves shoreward in summer, joins the coast and is replaced by another bar in its original place. The other seaward bars are storm bars, more or less permanent though they may shift slightly in orientation, position and shape depending upon the wave climate and state of the coastal processes. With the sediment and bottom profiles changing constantly with differing wave characteristics and beach exposure, a rigorous mathematical analysis for long range variability of profiles and therefore coastal processes is not possible. Therefore, the concept of medium depth and steepness characteristics is introduced to distinguish the profiles and their major dimensions.

Onshore-offshore sediment motion is sometimes far in excess of longshore transport mostly confined in the breaker zone. When submarine bars are present, such motion is considerable mainly as a result of the hydrodynamic reaction between the rotating eddies generated over the bars and the bar surface. By means of dimensional analysis, it is possible to relate the quantity of onshore-offshore motion to the bar dimensions, wave period, water depth and transport direction by profile steepness characteristics.

The above two concepts are then applied to the Nile Delta coastal processes with satisfactory results.

INTRODUCTION: Longshore bars, are a series of submerged sand bars which often form parallel or nearly parallel to the coast. They occur either singly or in a series in the nearshore and offshore zones extending many kilometers into the sea or lake. They develop in both tidal and tideless seas, moving back and forth in the former depending upon the water level fluctuations and are more or less stationary in the latter. A common feature of both is a breakpoint bar - a well developed high and narrow bar at the point of breaking. Offshore of this bar, one, two or three storm bars also develop depending upon the wave climate and they are more or less low in height and wide at base. Lake Michigan (Hands, 1976) and Chesapeake Bay (Ludwick, 1972) areas manifest bars belonging to the tidal seas, whereas Nile Delta coast of the Mediterranean Sea (UNESCO et al 1973) is a typical example having more or less stationary bars of a sea of small tides.

*Visiting Professor, Civil Engineering Department, Pahlavi University, Shiraz, Iran.

Waves are known to be the main agents for bar development. Longshore currents may modify them but are not essential for their formation (Keulegan (1948)). The shape of bars depends greatly on wave, beach and sediment characteristics. Overnourished profiles (accretion areas) have flat slopes and fine sediment, whereas undernourished profiles (erosion areas) are steeper with coarser sediment. The bars on the former have wide base unlike the latter. Bars on equilibrium profiles (a stable profile with maximum steepness - Bruun and Manohar, 1963) have features similar to the undernourished profiles. The number of bars is greater on flatter profiles. Generally, the break-point bars and storm bars can be considered as independent features supposedly related to separate events. Further bars over accretion profiles are highly variable in shape, position, orientation and stability whereas those on erosion profiles are known for their regularity.

Whereas within the breaker zone, longshore transport is the predominate transport mode, seaward of the breaker zone, longshore currents unless external, are negligible and therefore in such cases longshore sediment motion may be insignificant. However, in areas where fine sediment and considerable swell and storm activity exist, intense onshore-offshore motion with consequent formation of submarine bars, and they (bars) acting as focus, and area between them acting as transport zone, can be expected. In many coastal area devoid of source nourishment for longshore motion, onshore-offshore transport seaward of the break-point bar is several times larger than the longshore movement landward of it.

One of the first laboratory experiments (Manohar, 1955) on onshore-offshore sediment motion emphasized on the nature of the boundary layer at the bottom, the type of bars generated by oscillatory motion at the bottom, and the sediment transport mechanism and the resulting rates. Subsequent laboratory research (Rector, 1954; Eagleson, 1961; Nayak, 1970) showed beach profile characteristics to be functions of wave steepness, height and sediment characteristics. Sitarz (1963) analyzed swell built profiles without bars theoretically and found the shape to be parabolic. Swarts (1974) in his laboratory studies on offshore barless profiles, obtained from regular waves and uniform sand, found them (called D-profile) to be functions of deep-water wave characteristics and sediment size. He found all such transport from his studies, to be offshore. Unfortunately in nature, every variable involved in the generation of profiles, bars and in onshore-offshore motion changes continuously and even for short term variability, no two analyses seem to agree as to the exact relationships between the variables (Saville, 1957). Therefore, these and other similar laboratory studies, though useful for an understanding of the mechanisms involved in the coastal processes, are not of much value in the study of natural beach profiles.

Assuming that onshore-offshore motion is considerable, it is necessary to know its direction. According to Carter et al (1973), some degree of beach reflection is always present and it is related to the foreshore slope and offshore topography which in turn depends upon the profile type existing in the area. For flat slopes with bed sediment being smaller than the boundary layer thickness, net sand transport

is mainly onshore because of weak reflection. If reflection coefficient is large (Moraes, 1970) as on steep slopes or with low amplitude waves, sand movement may occur offshore eventually stopping in sufficiently deep water when mass transport becomes negligible at the bottom.

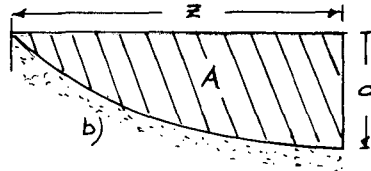
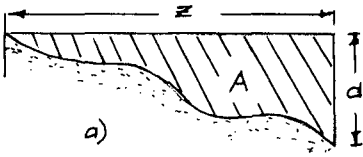
Keulegan (1948), in his experimental study of submarine sand bars, found the following: Water depth remaining constant, depth of bar base and consequently bar position formed by a singly system of waves, is a function of wave height and wave steepness. If the water depth and wave steepness are constant, an increase in wave height will move the bar seaward. If the water and wave height are constant, an increase in wave steepness will move the bar shoreward. If the wave height and wave length are constant, any increase in water depth will move the bar seaward.

VARIABILITY OF PROFILES: Beach profiles being variable in character can be studied by repeated observations over time spans of varying duration. But to interpret the variations one must know the variables causing the changes namely the characteristics of waves, currents, sediments and other interrelated quantities which themselves vary from time to time. Further the controlling processes are different in the nearshore and offshore zones. No doubt statistical analysis of waves may indicate a pattern in its behavior but, such analysis will need many years of data rarely available. Thus analysis on short-term variability basis (Zeigler and Tuttle, 1961; Harrison, 1969), though useful to a limited extent may not be of much help in the analysis of coastal changes on long term basis.

PROFILE VARIABILITY ON LONG TERM BASIS: As already stated, a dynamic equilibrium gradient of a natural beach continuously adjusts itself to the changing variables on which it depends. But, it is safe to assume that its dynamic state will fluctuate within some inner, outer and mean limits for a long term time span. The same may be said to occur on over-nourished and under-nourished beaches also. The concept of medium depth and steepness characteristics of profiles used to define beach steepnesses of the North Sea coast (Bruun, 1954) may be used with advantage to determine the nature of the profiles.

Consider two profiles, namely one of erosion (under-nourished) and another of accretion (over-nourished) (Fig. 1) with the distance of the outer depth limit from the shoreline being the same in both cases. In the former, medium profile depth ($d_m = A/Z$) will be larger than in the latter and the profile steepness s_t ($s_t = A/Z^2$) defined as the medium depth divided by the distance from the shoreline will be larger also. For an equilibrium profile, it will have a constant value.

The importance of these two parameters is that when the analysis of profiles in the field which fluctuate continuously with even a small change in wave and sediment characteristics is difficult, they (the two parameters) give a valuable insight in the dynamic nature of the profiles on a long term basis. Their advantage lies in the fact that changes within area "A" need not be taken into consideration except



a) Overnourished profile

b) Undernourished profile

$$\text{Medium Profile Depth} = d_m = \frac{A}{z}$$

$$\text{Profile Steepness} = S_t = \frac{A}{z^2}$$

FIG.1: PROFILE DEPTH AND STEEPNESS DEFINITION

the knowledge as to whether they are eroding or accreting which in turn can be determined from a few hydrographic surveys. This approach, therefore, avoids the analysis of profile changes as functions of wave and sediment characteristics. The latter analysis will result in so many numbers of profile shapes (mostly smooth shapes without bars) that it will be difficult to interpret the results for long term analysis. No doubt, each coast will have its own limiting medium depth and profile steepness characteristic but, these can be obtained from a few surveys.

NEARSHORE SEDIMENT MOVEMENT: In the analysis of nearshore processes, as stated earlier, it is preferable to study the changes within and beyond the breaker zone separately. It is also necessary to determine the influence of the various bars on sediment transport and its direction.

Out of the two or three bars developed on beach profiles, the nearest one (break-point bar), frequently joins the shore in summer since swells with longer periods and smaller wave steepnesses cause a net shoreward sediment transport. When this bar joins the coast, a new bar is formed at its previous location and the process is repeated. This onshore sediment in motion trapped between the break point bar and the shore is the primary sediment source for alongshore transport unless external sources such as river sediments are available. Further, the nearshore circulation systems being more regular in summer than in winter, localize the coastal processes. Also the alongshore transport is much less in summer than winter, the major summer process being the shoreward transport.

With relatively large waves of the winter (large wave steepness), angle between the breaker line and shoreline in the breaker zone becomes the controlling factor for longshore current direction. Similarly, there is greater turbulence in the surface zone which keeps the sediment in suspension particularly in the shallow water zone. With mass transport from high waves being greater, substantial translation waves are also generated on wave breaking resulting in shoreward flow of water at the surface and seaward current at the bottom. Thus in winter, these flow systems cause formation of undulations, large and small, at the bottom.

Seaward of the break point bar, the onshore-offshore sediment exchange is likely to be as follows: When deep water waves travelling towards the shore start feeling the bottom (approx. when $d/L < 0.5$), ripples are formed which eventually become large size bars in the nearshore zone orienting themselves parallel to the wave crests. With the passage of waves, sediments will move from one side by the bar crest to the other (Fig. 2). When depth decreases, bottom velocity distribution with time changes from approximately sinusoidal to one that has a high shoreward component associated with the brief passage of wave crest and smaller seaward velocities associated with the longer time interval of the trough passage (CERC, 1973). When the shoreward velocity decreases with the crest passage and begins to reverse direction, sediment is placed in suspension from the landward side of the bar and this is transported with the seaward flow under the trough. Generally landward flow drops material shoreward as bed load and suspended load

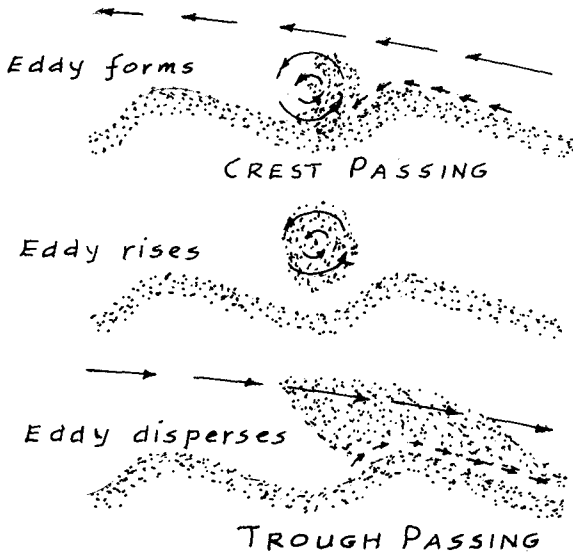


FIG. 2: ONSHORE-OFFSHORE EXCHANGE
AROUND BARS

goes seaward. Thus in areas having coarser sand and lesser fines, net shoreward movement may be higher. Vice versa is likely to occur for more fines and less coarse material. Further, most storms move large amounts of sediment from the beach offshore but after each storm, the smaller waves which follow, tend to restore this loss shoreward to some extent unless another storm intervenes in the process. Successive storms in the same area may generate sufficient transport in the opposite directions causing insignificant net coastal changes whereas if the transportation direction before, during and after the storms is the same, changes can be considerable.

FACTORS AFFECTING ONSHORE-OFFSHORE TRANSPORT OVER BARS

In his classical analysis of onshore-offshore sediment transport over the bars, Keulegan (1948) showed that correlation exists between the sediment transport rate and total displacement of water surface during the passage of a wave. Using dimensional analysis, it can be shown that:

$$\frac{QT}{\rho_s g d^2} = f \left(\frac{\Delta H}{d}, \frac{\rho_w}{\rho_s}, \frac{\sqrt{gd} D}{\nu}, \frac{d}{gT^2}, \frac{D}{d}, m, \sigma_\phi \right)$$

defining the laws of sediment motion. In this,

Q = sediment transport rate

ρ_w & ρ_s = densities of water and sediment resp

ΔH = total displacement of water during the passage of a wave

d = depth of water at the seaward toe of the bar

T = wave period

D = characteristic grain size

ν = kinematic viscosity of water

m = bed slope

σ_ϕ = sand dispersion coefficient

Assuming other quantities to be constant for a given wave condition,

$$\frac{QT}{\rho_s g d^2} = f \left(\frac{\Delta H}{d} \right).$$

Since the total displacement ΔH is composed of the maximum elevation of the surface above the undisturbed water level and the corresponding maximum depression during the passage of a wave, it may be further approximated, to be the breaking wave height over the bar. Further assuming the breaking wave height = depth of water at the point of

breaking, ΔH is equal to the depth H on top of the bar. In other words

$$\frac{QT}{\rho_s g d^2} = f \left(\frac{H}{d} \right)$$

The significance of this equation (as confirmed by model experiments) can be understood if one looks at each of the quantities in the equation. The wave period T , specifies the type of waves, density ρ_s , the weight characteristics of the sediment; d , the depth seaward of the bar; and H , the depth of water over the bar. These basic variables govern the sediment transport rate. The term $(d-H)$ namely the height of the bar governs the hydrodynamic reaction between the rotating eddies between the bars and the sediment surface of the bars.

DIRECTION OF ONSHORE-OFFSHORE TRANSPORT: The influence of water depth, wave height, and wave steepness in moving the sediment seaward or shoreward has already been mentioned. Unfortunately, because of their continuous variability, their use for long range interpretation of direction of transport is impractical. One likely solution to this problem is again the use of medium depth and profile steepness concept. If the value of the steepness characteristic decreases as compared to its previous value, the predominant transport will be onshore and vice versa will occur for offshore transport. Similar use of medium depth is possible.

APPLICATION TO FIELD DATA

The above concepts were applied by the author on the Nile Delta coastal studies spanning from 1971 to 1977. During that period, annual and semi-annual hydrographic surveys were conducted, waves and currents were measured, and erosion and accretion trends of the 240km long coastal stretch (Fig. 3) were monitored and continuously analysed.

BAR ANALYSIS: The characteristic feature of the Nile Delta coast of the Mediterranean Sea is that it has a series of longshore bars, typical of a tideless sea. In general, there are three bars, one nearest to the shore being the break-point bar in one to two meter depth, with the middle one (in three to four meter depths) and the outer one (in five to six meter depths) being the storm bars. The breaker zone bar is mobile and shifts landward during summer accretional processes, joins the coast and is replaced by another similar bar. The other two bars are permanent features adjusting back and forth consistent with wave climate. Field observations confirm that the first bar is formed by the short steep waves and swells with the middle and outermost bars being formed by storm waves. As regards to their heights, there is no regular pattern. They may be as high as one meter and sometimes wide at base and low. Generally, greater heights cause greater onshore-offshore motion. Typical barred profiles are shown in Fig. 4.

UNDERWATER PROFILES: All three types of profiles, namely undernourished, equilibrium and overnourished profiles exist on the Nile Delta coast (Fig. 5), though equilibrium profiles are found only on very short stretches.

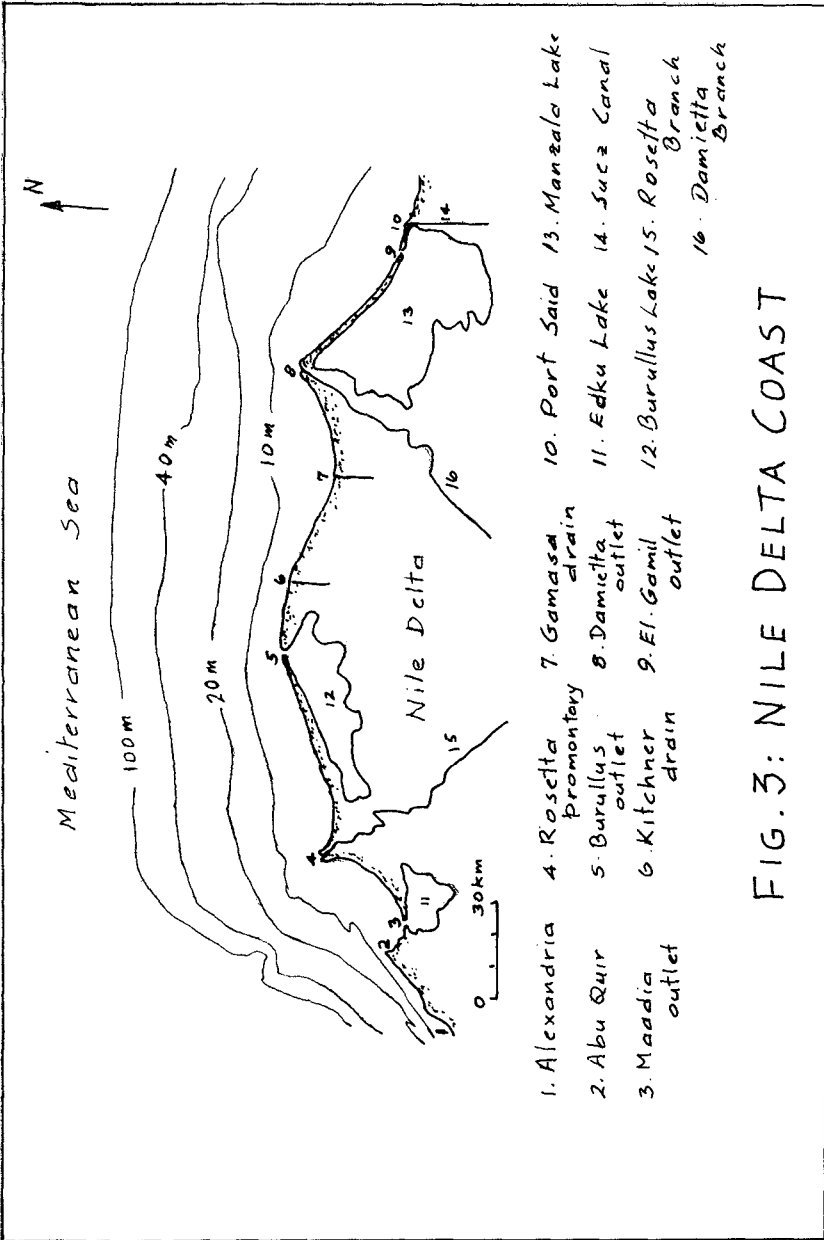


FIG. 3: NILE DELTA COAST

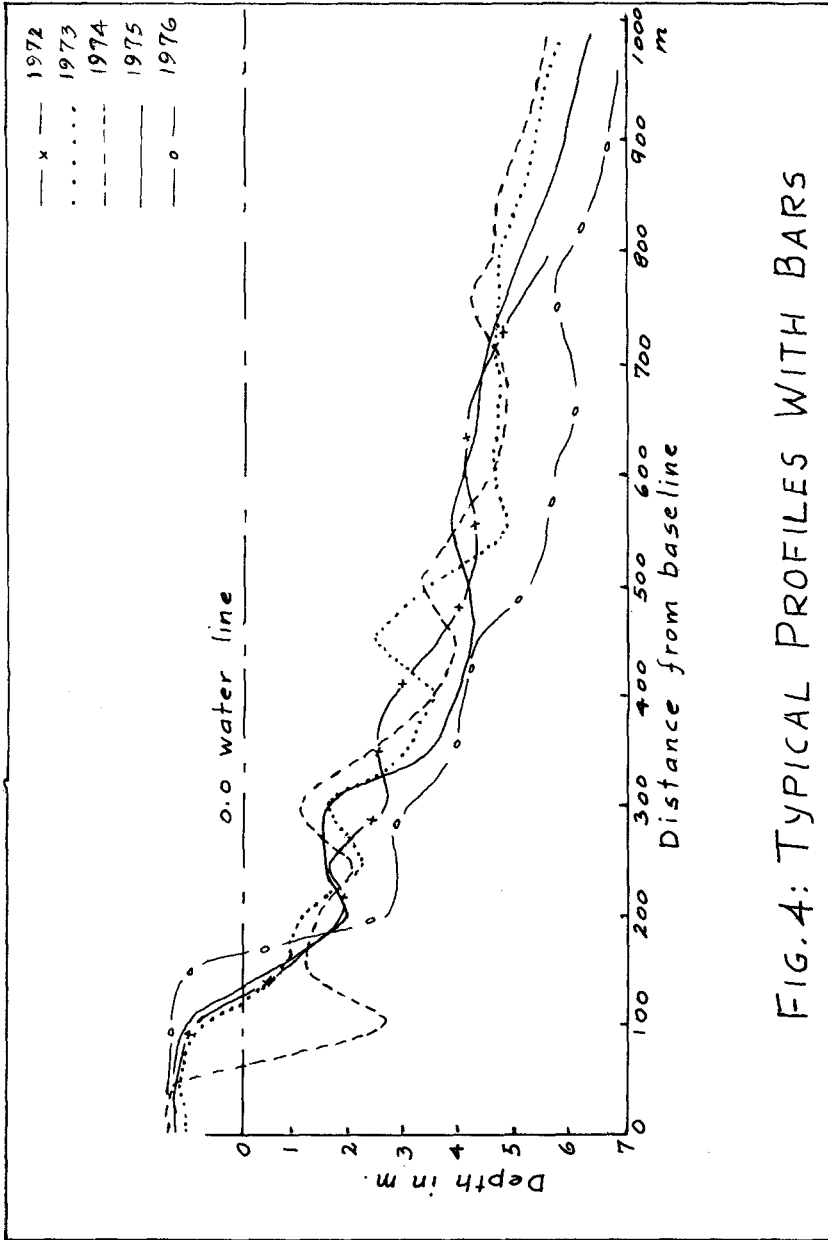


FIG. 4: TYPICAL PROFILES WITH BARS

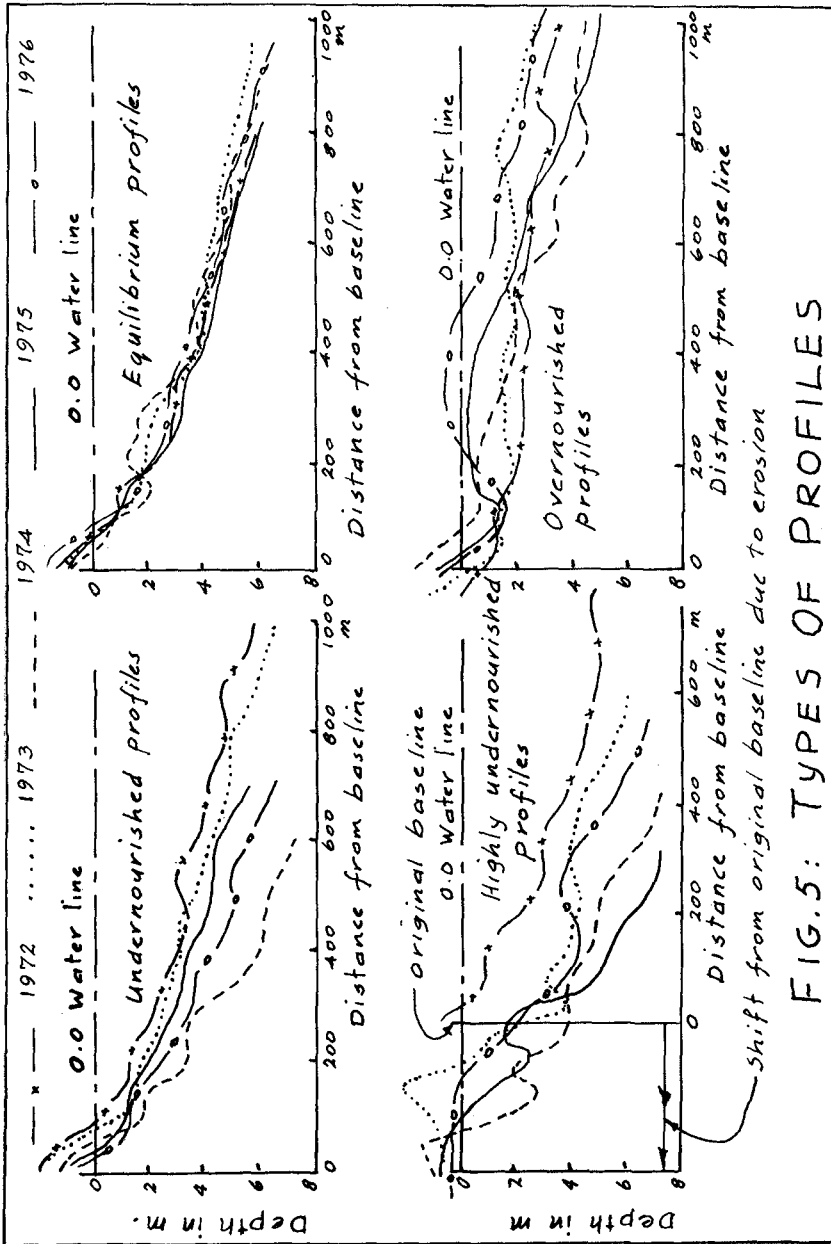


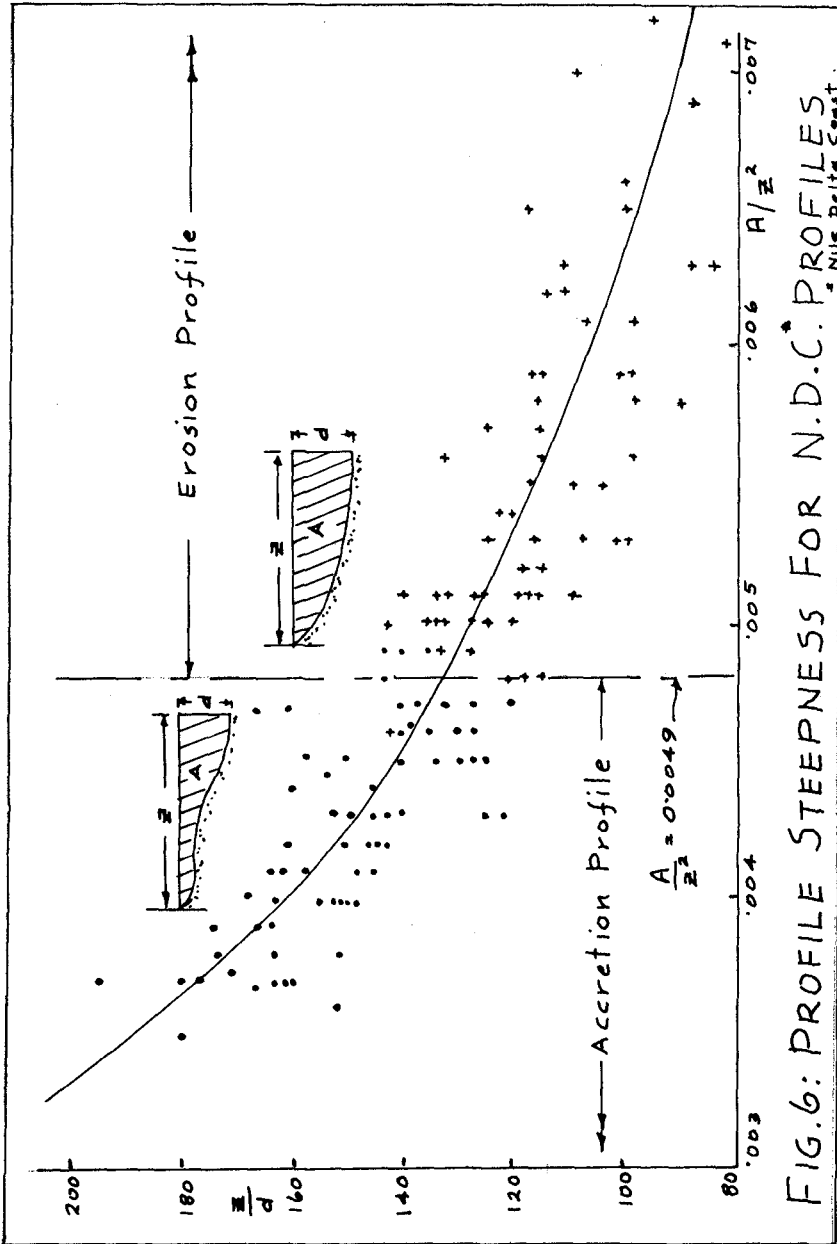
FIG.5: TYPES OF PROFILES

Analysis based on medium depth and steepness criteria shows that the limiting value of profile steepness represents equilibrium profiles with a value of $A/Z^2 = 0.0049$ with accretion profiles having lower values and erosion profiles having higher values (Fig. 6). Medium depth criterion for different types of profiles is shown in Fig. 7. Fig. 6 is also useful for preliminary determination of area A and type of profile from a measurement of depth d beyond the bars and the corresponding distance from the shoreline. Fig. 8 shows the status of the Nile Delta coast profiles based on profile steepness.

SEDIMENT TRANSPORT: Continuous monitoring of the coast for six years, analysis of yearly and semi-annual hydrographic surveys, calculation of gross volume and net volume changes, determination of alongshore transport by actual measurements and refraction analysis in the breaker zone, and analysis of sediment movement patterns by T-X diagram (a 3-dimensional representation with time on the vertical axis and baseline distance along the shore on the horizontal axis) indicate the following:

- i) alongshore transport in the breaker zone is small compared to the total sediment in motion;
- ii) bottom changes do not follow any set pattern or alongshore direction;
- iii) there is no predominant direction in which the sediment moves;
- iv) net volume changes appear independent of time, that is, volume changes in an interval of four to five years is not anywhere equal to the volume change per year multiplied by time even if overall change in wave climate is insignificant;
- v) movement is compartmentalized in various stretches (physiographic units) and;
- vi) changes beyond the breaker zone in the onshore-offshore direction within the physiographic units are several times more than the alongshore changes.

Using the already described dimensional analysis as the tool and assuming the sediment trapped between the bars is mainly the result of onshore-offshore transport, quantity Q , in movement between the bars was calculated as a function of height of the bars ($d-H$), wave period T and depth d seaward of the bars. Figs. 9, 10, and 11 show that relationships do exist between them. Fig. 9 also shows that beyond a certain increase in bar height, the rate of increase in quantity trapped, drops considerably because under those conditions, waves are liable to break on the bars and the transport mechanism becomes different. The quantities so calculated, agree well with the erosion and accretion rates calculated from hydrographic surveys using the bar steepness criterion for finding the transport directions.



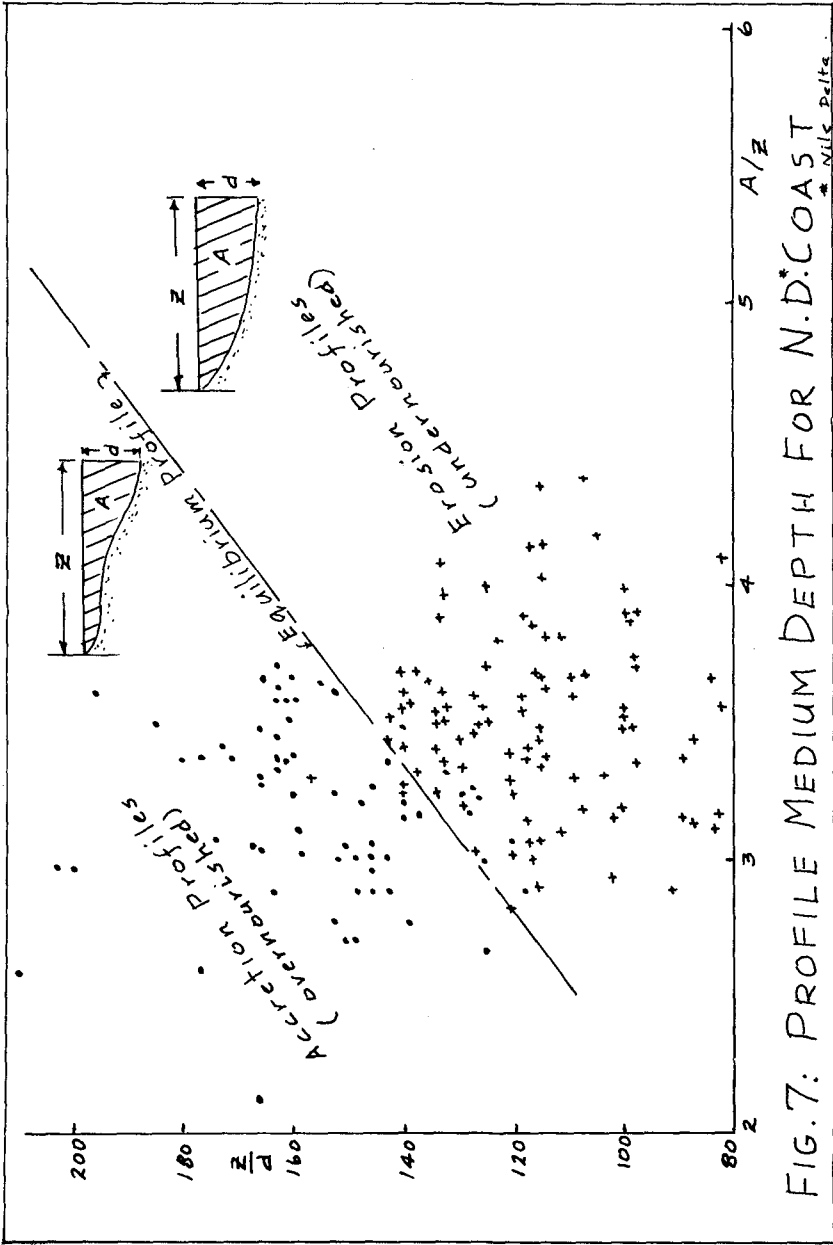
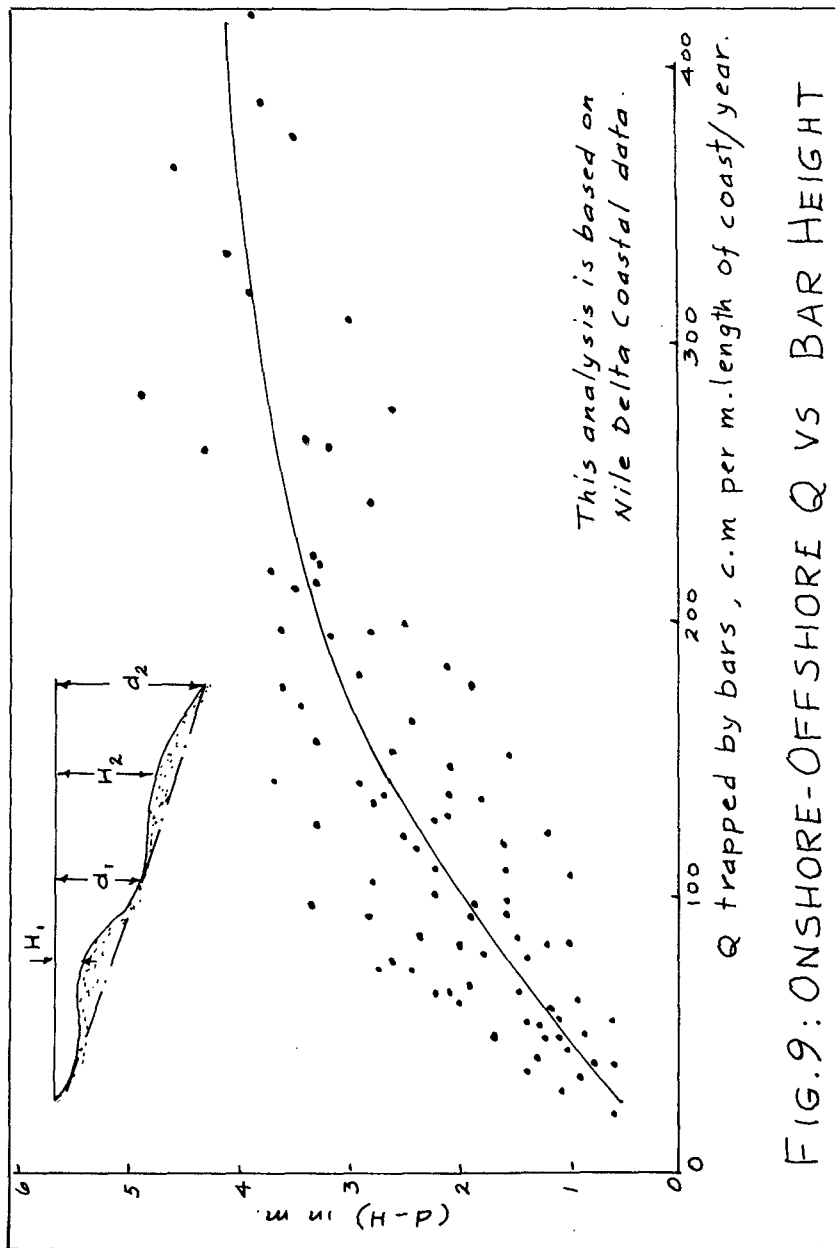


FIG. 7: PROFILE MEDIUM DEPTH FOR N.D. COAST

WILKINSON



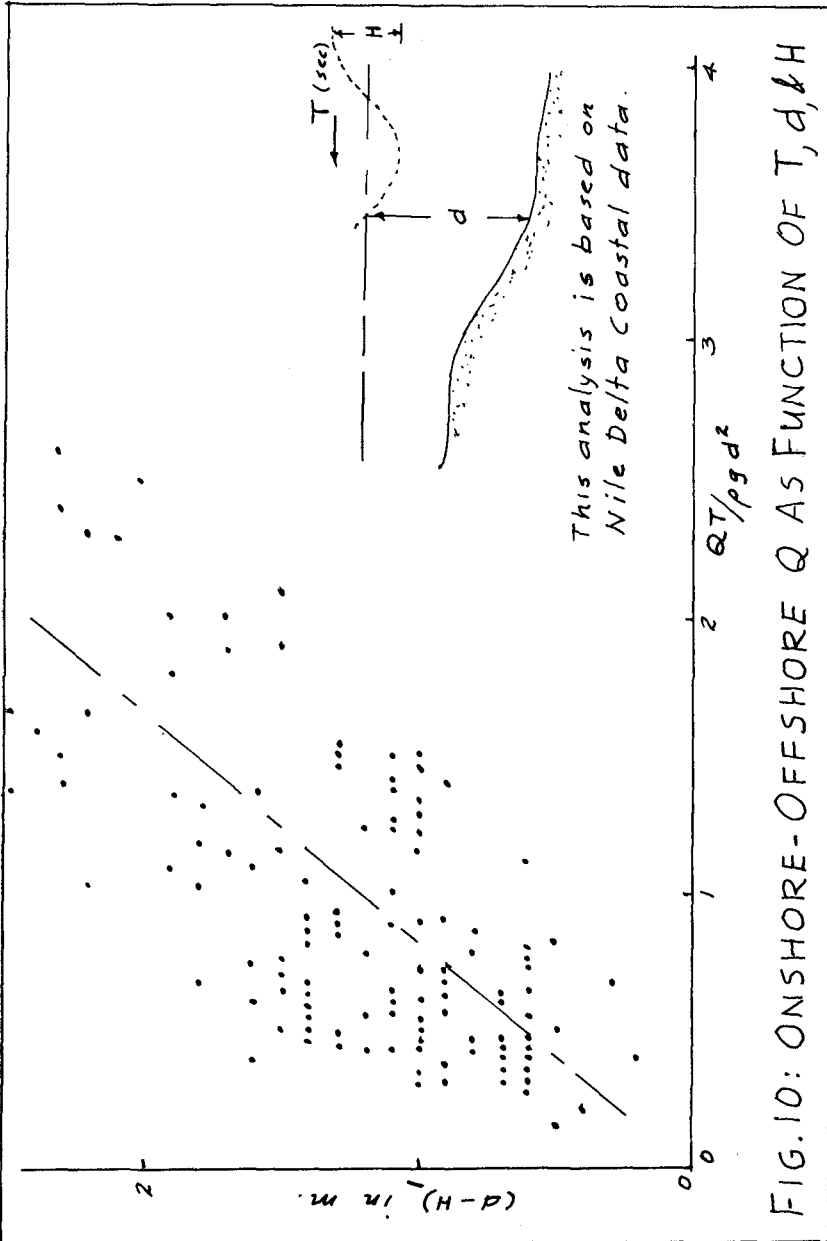
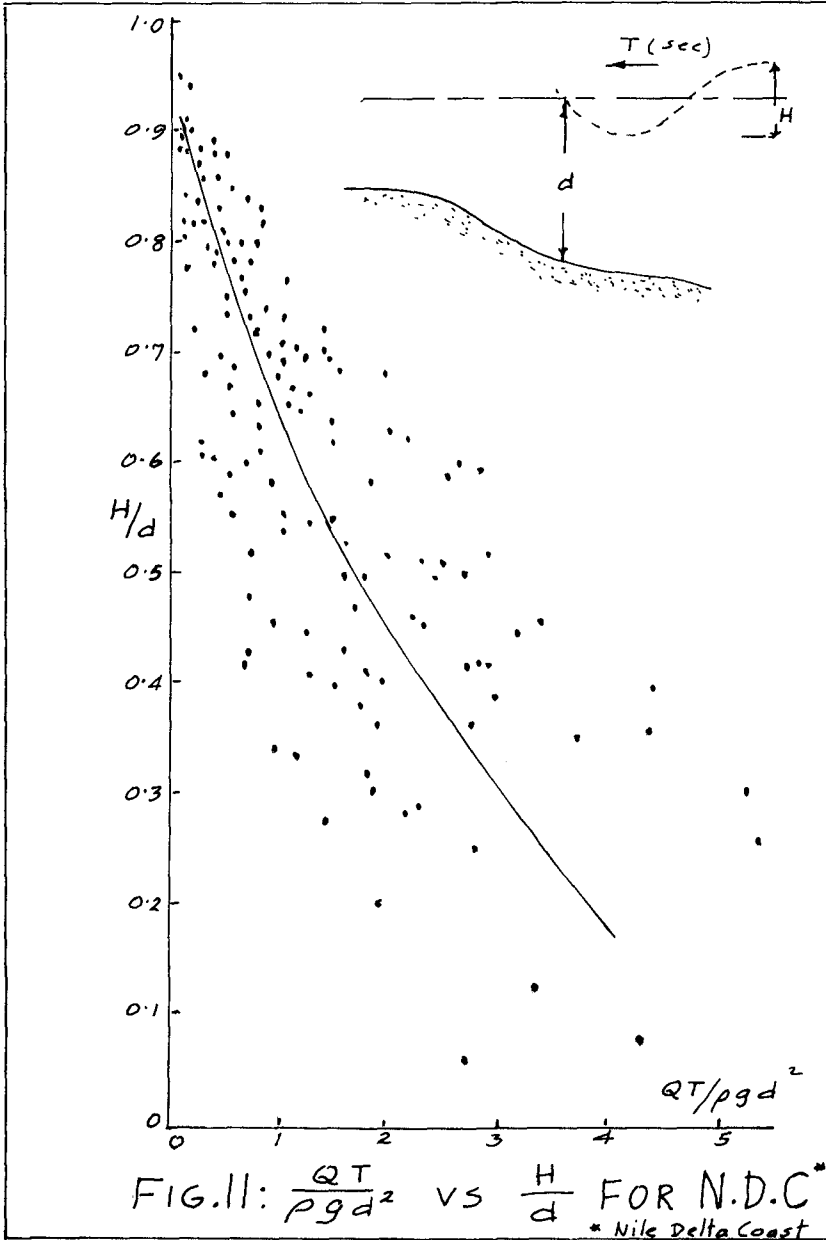


FIG.10: ONSHORE-OFFSHORE Q AS FUNCTION OF T, d, & H



CONCLUSIONS

1. Characteristic features of majority of coasts facing seas with moderate or no tidal action are the existence of one or more submarine bars beyond the breaker zone and a break point bar in the breaker zone.

2. Underwater profiles with or without bars can be divided into three categories, namely, undernourished profiles in erosion areas, equilibrium profiles in dynamically stable areas and overnourished profiles in accretion areas.

On long term basis, they can be distinguished by medium depth and profile steepness criteria which will have certain limiting values for different types of profiles for a particular coast.

3. Though alongshore transport may predominate in the breaker zone, onshore-offshore transport beyond may be many times more influencing the coastal processes on a far bigger scale than has been anticipated at present. Submarine bars influence such motion to a considerable extent. Using dimensional analysis as the tool, onshore-offshore motion or vice versa can be calculated as functions of bar height, sediment density, wave period and depth behind the bars.

4. The methods described in 2. and 3. are applied to the Nile Delta coast where a comprehensive study of coastal processes has been in existence since 1971.

5. The fact that the coastal processes beyond the breaker zone especially in the onshore-offshore direction influence the erosion and accretion patterns much more than the alongshore transport, emphasizes the view held by many coastal engineers that the engineering project study of a coast should be extended far into the offshore zone.

ACKNOWLEDGEMENTS

This study is based on the field data taken by the author and his colleagues during his assignment as UNESCO expert on Nile Delta coast studies. The author wishes to thank the UNESCO, UNDP and Academy of Scientific Research and Technology, Egypt for the opportunity given to him.

REFERENCES

1. Bruun, P. "Coastal Stability," Danish Technical Press, Copenhagen, 1954.
2. Bruun, P. and Manohar, M. "Coastal Protection for Florida," Bul. Ser. 113, Fla. Engg. and Indus. Expt. Station, University of Florida, Gainesville, Fla., August 1963.
3. Carter, T.G., et al. "Mass Transport By Waves and Offshore Sand Bedforms," WW2, Am. Soc. of Civil Engineers, New York, May 1973.
4. CERC. "Shore Protection Manual - Vol. I," Coastal Engineering Research Council, U.S. Army Corps of Engineers, Fort Belvoir, Va., 1973.
5. Eagleson, P.S. et al. "Equilibrium Characteristics of Sand Beaches in the Offshore Zone," Tech. Memo 126, Beach Erosion Board, U.S. Army Corps of Engineers, Washington, D.C., 1961.
6. Hands, E.B. "Observations of Barred Coastal Profiles Under the Influence of Rising Water Levels, Eastern Lake Michigan, 1967-71," Tech. Rpt. 76-1, Coastal Engineering Research Center, U.S. Army Corps of Engineers, Fort Belvoir, Va., Jan. 1976.
7. Harrison, W. "Empirical Equations for Foreshore Changes over a Tidal Cycle," Marine Geology, Vol. 7(6), 1969.
8. Keulegan, G.H. "An Experimental Study of Submarine Sand Bars," Tech. Rpt. No. 3, Beach Erosion Board, U.S. Army Corps of Engineers, Washington, D.C., 1948.
9. Ludwig, J.C. "Migration of Tidal Sand Waves in Chesapeake Bay Entrance," Shelf Sediment Transport, Dowden, Hutchinson and Ross, Stroudsburg, Pa., 1972.
10. Manohar, M. "Mechanics of Bottom Sediment Motion Due to Wave Action," Tech. Memo. 75, Beach Erosion Board, U. S. Army Corps of Engineers, Washington, D.C., 1955.
11. Moraes, C. "Experiments of Wave Reflection on Impermeable Scopes," Proc. of XII Conf. on Coastal Engg., Am. Soc. Civil Engineers, New York, 1970.
12. Nayak, I.V. "Equilibrium Profiles of Model Beaches," Report HEL 2-25, Univ. of California, Berkeley, Cal., 1970.
13. Rector, R.L. "Laboratory Study of Equilibrium Profiles of Beaches," Tech. Man. 41, Beach Erosion Board, U.S. Army Corps of Engineers, Washington, D.C., 1954.
14. Saville, T., Jr. "Scale Effects in Two Dimensional Beach Studies," Proc. Seventh General Meeting, Inter. Assoc. of Hydr. Research, Delft, Holland, 1957.

REFERENCES (Continued)

15. Sitarz, J.A. "Contribution a l'etude de R'evolution des plages a partir de la consistance des profile d' equilibre," Trav. Centre Etud. Rech. Oceanogr., 1963.
16. Swartz, D.H. "Schematization of Onshore-Offshore Transport," 14th Conf. Coastal Engineering, Copenhagen, Am. Soc. Civil Engineers, New York, 1974.
17. UNESCO/ASRT/UNDP. "Detailed Technical Report, Oct. 1973," Project EGY/70/581, UNDP/ASRT/UNESCO, Alexandria, Egypt, 1973.
18. Zeigler, J.M. and Tuttle, S.D. "Beach Changes Based on Daily Measurements of Four Cape Cod Beaches," Journ. of Geology, Vol. 69, 1961.

CHAPTER 87

ONSHORE-OFFSHORE SEDIMENT MOVEMENT ON A BEACH

P. Nielsen¹ I. A. Svendsen² C. Staub³

ABSTRACT

A theoretical model is developed for the movement of loose sediments in oscillatory flow with or without a net current. In the present formulation the model is two-dimensional, but may readily be extended to three dimensions.

It is assumed that all movement of sediments occurs in suspension, and exact analytical solutions are given for the time variation of the concentration profile, the instantaneous sediment flux and the net flux of sediment over a wave period. The model requires as empirical input a diffusion coefficient ϵ and pick-up function $p(t)$, for which experimental data are presented. Two examples are discussed in detail, illustrating important aspects of the onshore-offshore sediment motion.

1. INTRODUCTION

The motion of loose sediments perpendicular to the coastline is one of many unsolved problems in sediment transport due to waves and currents. Yet it is generally agreed that this particular phenomenon plays a vital part in the sorting of sediments on a coast and hence has important bearing on the question of which grain sizes are present in the surf zone, where the bulk of the longshore transport takes place.

In nature the lateral sediment transport depends strongly on three-dimensional effects which are responsible for the often significant net water motions that occur in particular in the surf zone. Here the net water flux is shorewards in areas where the bottom configuration creates heavy breaking, and seawards (sometimes as rip-currents) in the often deeper areas where the breaking is weak or absent, moving as a longshore current between these regions. Also appreciable time variations occur over some minutes and may even dominate the spatial variations.

Though obviously crucial for the net movement of sediments it is beyond the scope of the present paper to analyse this water motion further. In the following we shall assume that the water motion is known. This is further justified by the observation that the processes involved in the local movement of sediments, which we are going to analyse, are almost exclusively governed by the local flow conditions. The purpose of the present paper is to formulate a theory that as closely as possible models the important part of the processes which can be observed to occur in sediment motion under waves.

¹Ph.D.-student, ²Assoc. Professor, ³Graduate student
Institute of Hydrodynamics and Hydraulic Engineering (ISVA),
Technical University of Denmark, Building 115, DK-2800 Lyngby.

2. PHYSICAL DESCRIPTION

To do so it is important first to describe the nature of the phenomenon.

Bottom configuration

One of the basic aspects is the bottom configuration generated by the water motion. It is well known that for a wide range of wave and sand parameters ripples are formed on the bed. The size, steepness and shapes of these have been measured by numerous authors (see e.g. Inman (1957) and Dingle (1974)), and lately Nielsen (1977) showed that the steepness of the ripples (measured ratio between height η from trough to crest over distance λ between two successive crests) is almost constant (0.15 to 0.20) for a value of the Shields' parameter θ' less than about 0.4, where θ' is defined as

$$\theta' \equiv \frac{1}{2} a^2 \omega^2 f_w / (s-1) g d \quad (1)$$

with a the amplitude of water particle motion at the bottom, $\omega = 2\pi/T$, T being the wave period. f_w is a friction factor, s and d are specific gravity and mean diameter, respectively, of the sand grains. g is the acceleration of gravity.

For θ' increasingly larger than 0.4 the steepness of the ripples decreases rapidly, and for $\theta' > 1$ the bed is virtually plane with relatively gentle undulations.

These are general trends subject to considerable scattering in the individual cases, in particular when field conditions in irregular waves are considered. Nevertheless it shows that except for very high storm waves, the sand on natural beaches (most often having $d \approx 0.2 - 0.3$ mm) will yield θ' -values not larger than 1. (A wave height $H = 10$ m, say, on a water depth $h = 15$ m yields $\theta' \sim 5$), which again implies that most often the bed will be covered by ripples.

Since it turns out that the ideas presented later in this paper can readily be adopted to a plane bottom, we first focus on the flow over a ripple bed.

Oscillatory flow over a ripple bed

The ripples formed by the oscillatory particle motion under waves are entirely different from the bed forms known from steady flow (see e.g. Allen (1968)). Also the oscillatory flow itself and the mechanisms by which the sediment is moved show little resemblance with unidirectional flow patterns.

This is due to the strong pressure gradients associated with the oscillatory flow which create strong lee eddies during the phase where the main flow is retarded, i.e. twice every wave period. Successively at the turn of the flow these eddies are 'washed' out into the main flow, thus yielding dominant contribution to the general turbulence level, and carrying appreciable amounts of sediment out in suspension (Fig. 1). Excellent photos showing details of the development of the eddy and a description of the process were presented by Bijker et al. (1976). Also Nakoto et al. (1977) describe the sequence.

One of the important features is the large velocities in the lee eddy. In fact the adverse velocity is of the same magnitude as the

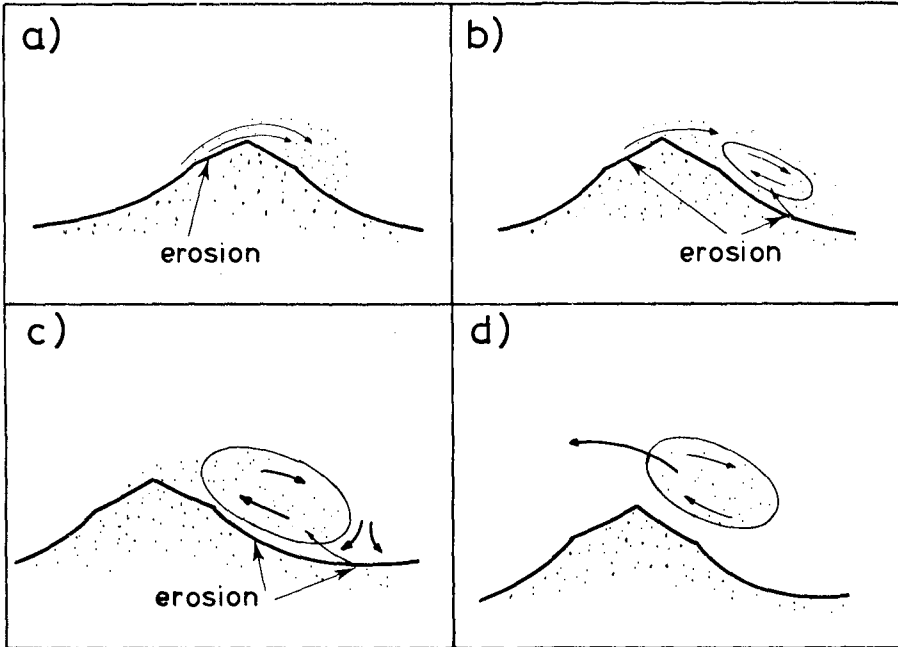


Fig. 1 Pick-up mechanism over a rippled bed. a) Velocity increasing, no separation, no effective pick-up. b) Velocity decreasing, separation started, sand accumulation in vortex. c) Water velocity vanishing, the vortex is fully developed. d) Water velocity reverses, the vortex is lifted out. This is when the effective pick-up takes place.

velocity in the main flow outside (Tunsdall and Inman (1975)), in contrast to the back flow in lee eddies in a steady unidirectional flow, which is usually only a fraction of the velocity in the main flow.

Another point is worth mentioning. The total excursion of the main water flow is often less than twice the ripple length.

Thus the flow pattern above the level of the ripple crests does not, as one might expect, attain the character of an oscillatory boundary layer in the known sense with the ripple height as a measure of the bed roughness. In fact the flow structure is entirely dominated by the regular eddies, their interaction and decay into turbulence.

Finally direct visual observations and high speed movies of the motion of the sand particles indicate that actual bed load transport as known from unidirectional flow hardly occurs. In fact one gets the impression that once a sand grain has started to move it goes into suspension (often via the eddy) before it settles again. This is also in disagreement with Longuet-Higgins (1972, p. 213) who (quoting Inman) claims that 'most of the weight of sediment is indeed in bed load, and not in suspended load.'

3. OUTLINE OF A THEORETICAL MODEL

We assume on the basis of these observations that *all* sediment is moved in suspension. The sediment is brought into suspension by a pick-up mechanism (as described above), which is further discussed in § 6. In the model it is described by the amount of solid sediment $p(t)$ being picked up per unit area of bottom per second, and the mean value of $p(t)$ over one period will be determined experimentally.

We further assume that the balance between the agitating processes tending to keep the sediment in suspension, and the settling of sediment (described by settling velocity w) has the nature of a diffusion process (irrespective the above mentioned regular nature of the eddy motion) with a diffusion coefficient ϵ , which is independent of time and horizontal coordinate x . (In fact the latter corresponds to averaging over a ripple length.) Thus the concentration $c(z,t)$ of suspended sediment satisfies the diffusion equation

$$\frac{\partial c}{\partial t} - w \frac{\partial c}{\partial z} - \frac{\partial}{\partial z} \left(\epsilon \frac{\partial c}{\partial z} \right) = 0 \quad (2)$$

z being the vertical coordinate.

The assumption of a pick-up mechanism $p(t)$ implies that the process of bringing the sand into suspension is independent of the settling of the sediments. In the mathematical formulation this function acts as the source for the diffusion equation (2), thus representing the boundary condition at the bottom level z_b

$$- \epsilon \frac{\partial c}{\partial z} = p(t) \quad \text{at} \quad z = z_b \quad (3)$$

One advantage of this formulation is that it is considered easier to suggest physically realistic descriptions for the pick-up function $p(t)$ (which could e.g. be proportional to the bottom shear stress) than for e.g. the bottom concentration c_b , often used as a boundary condition in suspension models.

As the second boundary condition in z is used $c(z) \rightarrow 0$ for $z \rightarrow \infty$ (though the water depth is h), and the system is closed in time by a periodicity assumption

$$c(z, t+T) = c(z, t) \quad (4)$$

When $c(z,t)$ has been determined the instantaneous flux $Q(t)$ of sediment through a vertical section is readily determined from the horizontal water velocity $u(z,t)$ by

$$Q(t) = \int_0^h u(z,t) c(z,t) dz \quad (5)$$

and the net sediment flux then follows from

$$\bar{Q} = \frac{1}{T} \int_0^T Q dt \quad (6)$$

At this point the model is more detailed than e.g. the approach used by Madsen and Grant (1976) who only consider the net motion of sediments. A closer inspection of the system shows that the clear separation of the pick-up and settling processes yields a memory effect in the model which implies that the maximum of sediment in motion occurs later than the

maximum of p , and also that the sediment motion does not vanish with p , which may itself show a phase difference relative to the fluid motion. This is a generalization of the idea of a phase lag between shear stress and sediment motion introduced by Kennedy (1963), and used in waves by Kennedy and Falcon (1965). It will be shown that this effect is crucial for the understanding of the onshore-offshore transport.

4. GENERAL SOLUTION

In the general solution the pick-up function $p(t)$ is considered in terms of its fourier series, which is assumed to have the form

$$\left. \begin{aligned} p(t) &= \sum_0^N P_n \cos n(\omega t - \psi_n) \\ p(t) &= \text{Re} \left\{ \sum_0^N P_n e^{in(\omega t - \psi_n)} \right\} \end{aligned} \right\} (7)$$

The z coordinate is zero at the level of the ripple crests which is also chosen as the level for the boundary condition (3), i.e. $z_b = 0$.

The phase angle ψ_n in (7) accounts for the phase difference between p and the water motion which will be assumed to vary as $e^{in\omega t}$.

The equation is solved by separation of variables, and to facilitate the calculations the physical concentration is considered to be the real part of the complex function

$$c(z,t) = \sum_0^N C_n e^{in\omega t} \zeta_n(z) \tag{8}$$

where for simplicity we assume

$$\zeta_n(0) = 1 \tag{9}$$

Inserting (8) in the diffusion equation (2) leads to

$$\zeta_n'' + \left(\frac{w + \epsilon'}{\epsilon} \right) \zeta_n' - i \frac{n \omega}{\epsilon} \zeta_n = 0 \tag{10}$$

where $\epsilon' = d\epsilon/dz$. The experiments presented later show that ϵ does not vary with z in non-breaking waves. If this is introduced into (10), an equation with constant coefficients results

$$\zeta_n'' + \frac{w}{\epsilon} \zeta_n' - i \frac{n \omega}{\epsilon} \zeta_n = 0 \tag{11}$$

which can be solved by standard methods.

Invoking (11) and the boundary condition $\zeta_n \rightarrow 0$ as $z \rightarrow \infty$ we get

$$\zeta_n(z) = e^{-\frac{w}{\epsilon} \alpha_n z} \tag{12}$$

where

$$\alpha_n = \frac{1}{2} + \sqrt{\frac{1}{4} + i \frac{n \omega \epsilon}{w^2}} \tag{13}$$

The complex coefficients C_n in (8) are determined by the boundary condition (3), which using (8) becomes

$$-\epsilon \frac{\partial}{\partial z} \left(C_n e^{in\omega t} \zeta_n \right) = P_n e^{in(\omega t - \psi_n)} \tag{14}$$

from which we get

$$C_n = \frac{P_n}{w \alpha_n} e^{-in\psi_n} \tag{15}$$

For $n = 0$ this yields a relation between the steady part of $c(o,t)$ and the steady part of $p(t)$

$$C_o = \frac{P_o}{w} \tag{16}$$

which enables us to determine P_o from measurements of $C_o = \overline{c(o,t)}$, where the bar denotes mean value over a wave period.

Thus the complete solution for the concentration profile as a function of time becomes

$$\left. \begin{aligned} c(z,t) &= \sum_0^\infty \frac{P_n}{w \alpha_n} e^{in(\omega t - \psi_n)} e^{-\frac{w}{\epsilon} \alpha_n z} \\ \alpha_n &= \frac{1}{2} + \sqrt{\frac{1}{4} + i \frac{n \omega \epsilon}{w^2}} \end{aligned} \right\} \tag{17}$$

We note that $\epsilon\omega/w^2$ is an important parameter, which represents the ratio of the response time for the concentration profile ϵ/w^2 over the wave time scale $T/2\pi$. This information could, of course, also be extracted directly from (2) by non-dimensionalization.

The physical concentration is obtained as the real part of (17), which is

$$c(z,t) = \sum_0^\infty \frac{P_n}{w |\alpha_n|} \cos n \left[\omega t - \psi_n - \frac{1}{n} \left(\arg \alpha_n + \frac{wz}{\epsilon} \text{Im}\{\alpha_n\} \right) \right] e^{-\frac{wz}{\epsilon} \text{Re}\{\alpha_n\}} \tag{18}$$

Fig. 2 shows the variation of α_n , and Fig. 3 that of $|\alpha_n|$, $\arg \alpha_n$, $\text{Re}\{\alpha_n\}$, and $\text{Im}\{\alpha_n\}$.

Finally the sediment flux Q is determined from (5). Here we assume that the ripple length λ is small, i.e. $\lambda \ll L$, where L is the wave

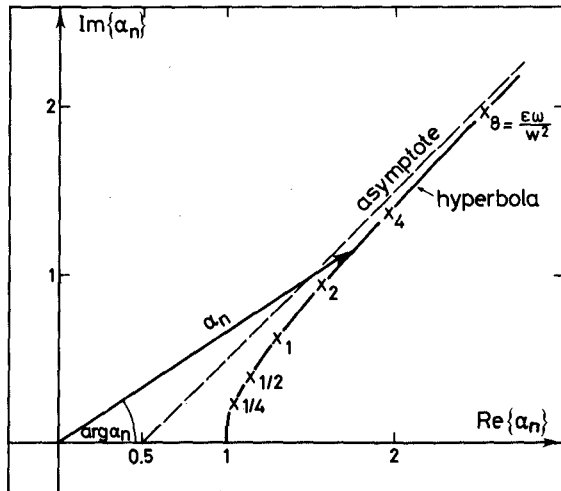


Fig 2
The position of α_n
in the complex plane.

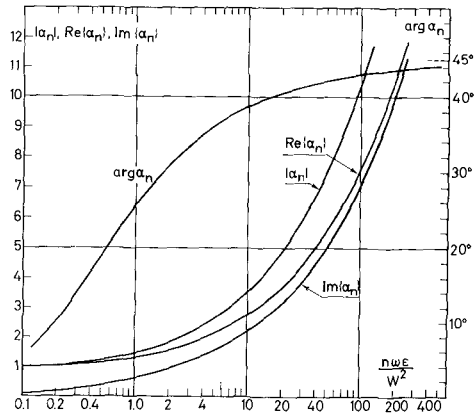


Fig. 3
The magnitude of $|\alpha_n|$, $\text{Re}\{\alpha_n\}$, $\text{Im}\{\alpha_n\}$ and $\text{arg } \alpha_n$ versus $n\omega\epsilon/w^2$.

length, so that the horizontal water velocity is approximately constant over λ , and the averaging over a ripple length introduced earlier can be executed with a constant $u(z,t)$. Thus for convenience we assume that u has the form

$$u(z,t) = \sum_0^N u_n(z) \cos n \omega t \tag{19}$$

which include a term $u_0(z)$ constant in time. Substituting this and (8) into (6) yields

$$\bar{Q} = \frac{1}{T} \int_0^T \int_0^T \sum_0^N c_n(z,t) u_n(z,t) dz dt \tag{20}$$

which is a general expression for Q . To get practical results from this expression we must specify the value of the diffusion coefficient ϵ , a problem which is discussed in § 5. We must also know the form of the pick-up function p (i.e. the fourier-coefficients P_n in (7) and the phase angle ψ_n). This is discussed in § 6. And finally $u_n(z)$ is required. However, the formulation above is actually too general for detailed discussion, and a number of useful conclusions can be obtained from studying special examples. This will be discussed in § 7.

5. PREDICTION OF THE DIFFUSIVITY

One of the basic assumptions behind this model is that the upward flux of sediment at any level is due to diffusion as expressed by the term $-\epsilon \partial c/\partial z$.

To test this assumption and to obtain results for ϵ , the sediment concentrations were measured over a sand bed subjected to waves in a 60 cm wide wave flume with a water depth of about 40 cm. The water/sand mixture was sucked out through thin pipes (1,5 mm diameter) at different levels, and the concentration determined from the sample. Thus all measurements represented mean values over several wave periods. In addition to these results, measurements published by Nakato et al. (1977), and some unpublished results performed in the pulsating water tunnel described by Lundgren and Sørensen (1958), have been used in the following analysis.

The value of ϵ for each experiment was determined graphically from a semilogarithmic plot of the measured concentrations versus the vertical coordinate z . Fig. 5 shows examples of such plots which clearly illustrate that ϵ is nearly constant under non-breaking waves, and also may be taken as a support of the assumption that the phenomenon may be approximated by a diffusion process with $\epsilon = \text{constant}$.

The results thus obtained for ϵ have been analysed in several ways. First it is worth to notice that Svendsen et al. (1977) analysed the motion of suspended particles in accelerated flow and found that sand grains would follow the oscillatory water motion practically identically (apart from the settling due to gravity). From their results for sinusoidal oscillations may be deduced that even in the relatively low frequency turbulence in the flow in question, the grains must very nearly follow the water flow, from which we can conclude that the diffusivity ϵ is equal to the turbulent eddy viscosity ν_T .

ϵ or ν_T are often considered as the product of a typical length scale l_ϵ and a typical velocity u_ϵ .

A natural length scale (of vertical motion) in the flow over a ripple bed is the ripple height η .

When no ripples are present, the scale is $\kappa \delta$, where κ is Von Karman's constant and δ the boundary layer thickness. δ may then be calculated from the equation

$$\delta/a = 0.072 (2.5 d/a)^{0.25} \quad (21)$$

as given by Jonsson and Carlsen (1976).

For the characteristic velocity u_ϵ , is normally used the friction velocity $u_f = \sqrt{\tau_{\max}/\rho}$. One might then conjecture a simple relation like

$$\epsilon = F(u_f[\eta + \kappa \delta]) \quad (22)$$

where $\kappa \delta \ll \eta$ in situations with noticeable ripples.

In fact it turns out that the best empirical correlation in the results for ϵ is obtained if we use

$$\frac{\epsilon}{(\eta + \kappa \delta) g T} = f\left(\frac{U_m}{w}\right) \quad (23)$$

as shown in Fig. 4. The physical background, however, of this correlation is not clear, and the subject obviously needs further consideration.

The diffusivities mentioned above are all determined in non-breaking waves and from measurements of concentrations within about 5 ripple heights from ripple crest level. Above this level there is hardly any bed material in suspension.

If, however, the waves are just gently breaking as spilling breakers, the turbulence generated by the breaking will reach the bottom after 4 - 6 wave periods, and significantly change the shape of the concentration profile, down to a few ripple heights (centimeters) above the bed. As a result the suspended material is spread from surface to bottom. The effect is surprisingly strong, particularly for fine materials with large u/w , and indisputable as shown in Fig. 5, where the concentration profile from under a spilling breaker is shown together with that of an unbroken wave with the same height. It also forms a remark-

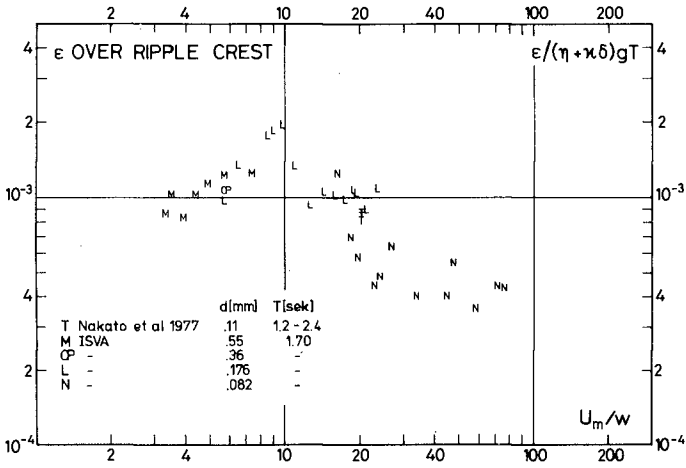


Fig. 4 A plot for semi-empirical determination of ϵ from U_1/w and the vertical length scale $(\eta + \kappa \delta)$.

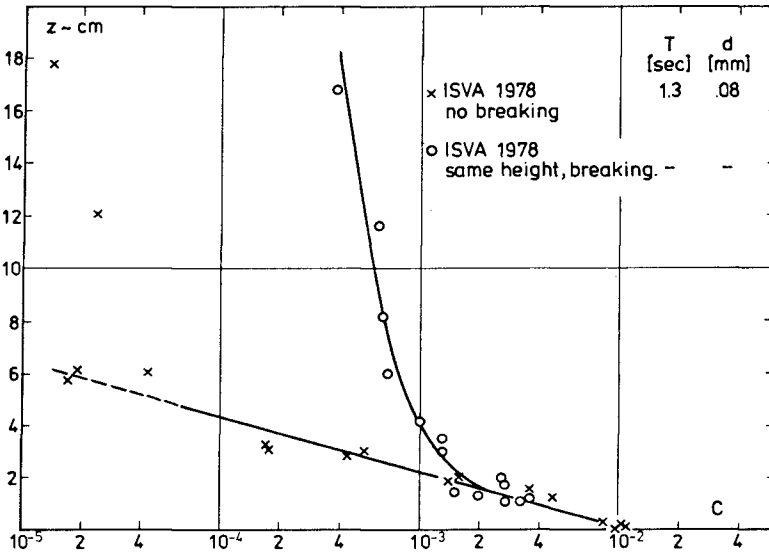


Fig. 5 The distributions of suspended sediment under breaking and non-breaking waves of equal heights. Breaking gives much larger diffusivities but slightly smaller concentrations at the bed level.

able illustration to the ideas about the turbulence conditions in spilling breakers presented by Peregrine and Svendsen (1978).

It should be noticed that the concentrations at the bed level are nearly unchanged by the breaking, and the measurements show that the total amount of sediment in suspension is practically unchanged too. This indicates that the pick-up process is only moderately affected by the surface turbulence, which has been decaying over 4 - 6 wave periods before it reaches the bottom. On the other hand, the relative change in turbulent intensity is large from the surface down to about 5 times the ripple height above the bed, and the already suspended sand is easily spread over a whole depth of water.

6. ANALYSIS OF PICK-UP FUNCTION

The pick-up function $p(t)$ is always non-negative and therefore has a positive time mean value P_0 . In the following we divide the discussion between P_0 , which is determined experimentally, and the time variation of $p(t)$ (i.e. the rest of fourier-coefficients in (7)).

The time mean value of $p(t)$

In the solution for $c(z,t)$ we found in § 4 that the true mean value P_0 of $p(t)$ was equal to wC_0 where C_0 is the time mean value of the concentration at $z = 0$. This means that P_0 can be determined directly from the measurements described in the previous paragraph.

A closer analysis of these shows that C_0 depends on the horizontal position of the measuring point relative to the ripple. C_0 is larger over the crest than over the trough. We find that $C_{0,crest} \approx 1.8 \cdot C_{0,trough}$.

However, the net transport \bar{Q} must be the same through any vertical section. And since we have chosen our reference level $z = 0$ at the level of the ripple crest to be consistent, we must also in the calculations use the C_0 values obtained over the ripple crest.

Fig. 6 shows the measured values of $C_{0,crest}$ as a function of the Shields' parameter θ' (i.e. the non-dimensional shear stress) given by (1), in which we have used Swart's (1974) empirical fit to the experimental results for f_w in an oscillatory boundary layer, i.e.

$$f_w = \exp\{5.213 (2.5 d/a)^{0.195} - 5.977\} \quad (24)$$

It is important here that f_w is based on grain-roughness, not on the ripple-height, say.

As we see from the figure, the results for C_0 varies fairly consistently with θ' .

The time variation of $p(t)$

As mentioned in § 2 most of the sediment grains that move over a rippled bed are ripped off the upstream side of the ripples, pass over the crest into the lee eddy, and are then washed out into real suspension with that eddy. Thus we must expect the pick-up function $p(t)$ to show significant peaks twice every wave period. No measurements are available to quantify this, but observations in a wave flume or on a beach clearly show strong puffs with high concentration of sediments

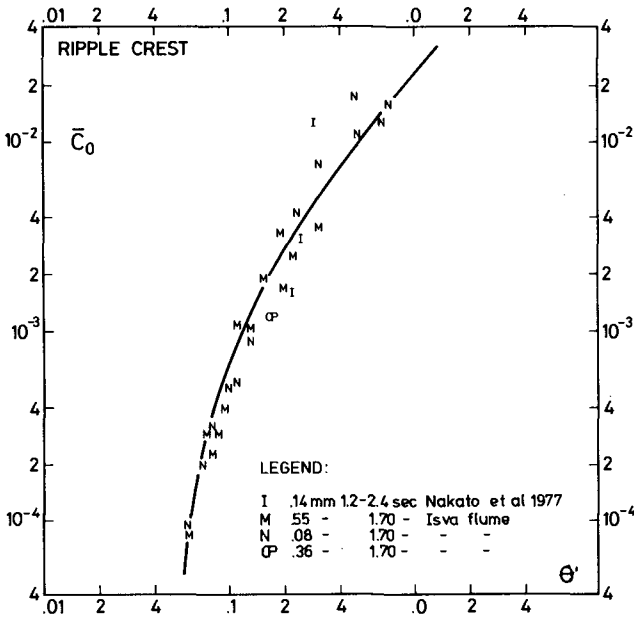


Fig. 6 The steady part of the concentration at ripple crest level is a function of θ' .

emerging in the general 'pea soup' over each ripple, and at the right time. Often the puffs occurring right after the wave crest has passed (i.e. after the highest velocities) are more significant than those produced after the weaker return flow in the wave trough.

Tentatively this can be modelled by a pick-up function of the form

$$p(t) = \frac{P_0}{1+\beta} \frac{(2m)!!}{(2m-1)!!} \left[\cos^{2m} \frac{1}{2}(\omega t - \psi^+) + \beta \cos^{2m} \frac{1}{2}(\omega t - \psi^-) \right] \quad (25)$$

where m is a positive integer,* and β is accounting for the difference between crest and trough velocities. β may be determined as

$$\beta = \left(\frac{u_{\text{trough}}}{u_{\text{crest}}} \right)^2 \quad (26)$$

with the u 's as maximum values of the bottom velocities in the water motion (notice that weak currents may be included here).

According to the description above the phase angles ψ^+ and ψ^- are determined as the phases where the velocity in the main flow is changing direction. Notice that this choice, however surprising, may also be expected to apply as an approximation to the case of a plane bed. Then the thin boundary layer adhering to the bottom separates shortly before the time of velocity shift, yielding a situation similar (though less pronounced) to the release of eddies over the ripple bed.

* $(2m)!! = 2 \cdot 4 \cdot \dots \cdot 2m$; $(2m-1)!! = 1 \cdot 3 \cdot 5 \cdot \dots \cdot (2m-1)$.

Thus ψ^+ and ψ^- depend on the wave motion considered. In the examples in the following paragraph $\psi^+ = \psi^- - \pi = \pi/2$ for sinusoidal waves (example (1)), whereas $\psi^+ < \pi/2$ and $\psi^- > 3\pi/2$ for second order Stokes waves with zero mass flux (example (2)).

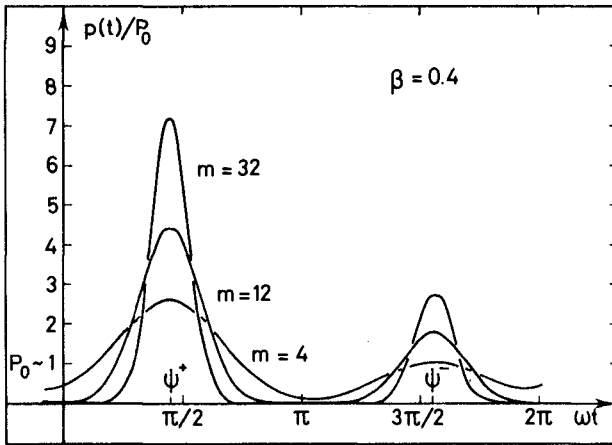


Fig. 7 The time-variation of the pick-up function for different values of the power $2m$.

The exponent $2m$ gives the shape of the pick-up function. For $m \rightarrow \infty$ (25) corresponds to two δ -functions at $\omega t = \psi^+$ and ψ^- , respectively. Fig. 7 shows some examples for different choices of m . The important point, however, how much the choice for m is influencing the results for \bar{Q} is analysed in more details in example (2).

7. EXAMPLES

(1) Sinusoidal wave motion

The simplest example one can think of is that of a sinusoidal wave, where

$$u(t) = U_1 \cos \omega t \tag{27}$$

Here $p(t)$ must have two peaks, equal in height and with a phase difference of π , i.e. $\beta = 1$ in (25), so that $p(t)$ is

$$p(t) = P \cos^{2m}(\omega t - \psi) \tag{28}$$

Without loss of generality we can take $m = 1$ to obtain

$$p(t) = P_0 (1 + \cos 2(\omega t - \psi)) \tag{29}$$

Fig. 8 shows the variation of the pick-up function and the concentration at the bed level in this case.

We see from (15) that the phase shift is $\frac{1}{2} \arg \alpha_2$, and that $c(o,t)$ does not go to zero as $p(t)$ does. Hence this important property of

the suspension mechanism is modelled correctly because of the separation between the pick-up and settling process.

Equation (20) shows that $\bar{Q} \approx 0$ because of the symmetry of the problem. Note that this result is independent of ψ and of the power $2m$ in (28).

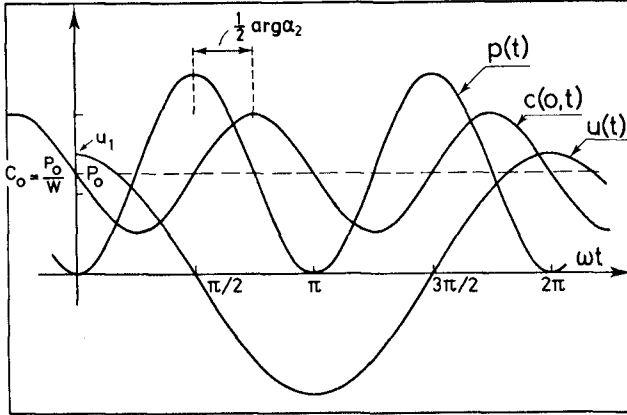


Fig. 8 The variation mode of $p(t)$ and $c(o,t)$ when $u(t)$ is simple harmonic. Note that $c(o,t)$ is not in phase with $p(t)$, and that $c(o,t)$ does not go to zero as $p(t)$ does.

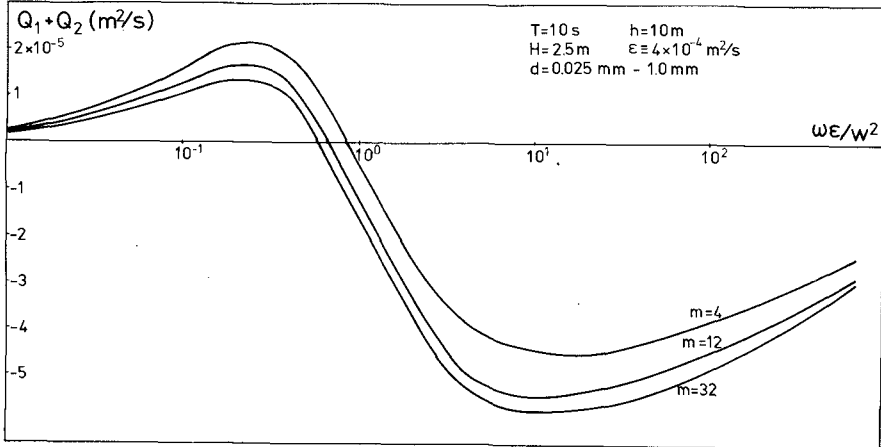


Fig. 9 The choice of m is not critical for $Q_1 + Q_2$. (Q_o is independent of m).

(2) Second order Stokes' wave

In the second example we assume a second order Stokes' wave motion, i.e. a velocity u at the bottom given by

$$u = U_0 + U_1 \cos \omega t + U_2 \cos 2\omega t$$

with

$$U_1 = \frac{\pi H}{T \sinh kh} \quad U_2 = \frac{3}{16} c \frac{(kH)^2}{\sinh^4 kh} \quad \left. \vphantom{U_1} \right\} (30)$$

i.e. we neglect the z -variation of u . Notice that U_0 can represent a 'return flow' corresponding to a zero net mass transport (i.e. (30) will represent a pure wave motion), if

$$U_0 = -\frac{1}{8} \frac{gH^2}{ch} \quad (31)$$

If (30) is substituted into (20) together with (25), we get the following expression for the net sediment flux

$$\begin{aligned} \bar{Q} &= \frac{U_0 P_0 \epsilon}{2w^2(1+\beta)} \left[2(1+\beta) - \sum_{n=1.2} \frac{a_n U_n}{U_0 |\alpha_n|^2} \left(\cos(n\psi^+ + 2 \arg \alpha_n) + \beta \cos(n\psi^- + 2 \arg \alpha_n) \right) \right] \\ &\equiv Q_0 + Q_1 + Q_2 \end{aligned} \quad (32)$$

The parameters of this expression are the wave data H/L and $T\sqrt{g/h}$, the grain diameter d , and m . Fig. 9 shows for a particular wave the influence on the oscillatory part of \bar{Q} (i.e. $Q_1 + Q_2$) of three choices for m in the range, which is considered realistic. $m \rightarrow \infty$ yields less than 10% change in \bar{Q} relatively to $m = 32$. The dependence on m is moderate, and we choose $m = 12$ in the following.

The results for the ripple height η required for evaluation of ϵ from Fig. 7 have been obtained from the mean curve shown in Fig. 10, which gives η/a (a being the water particle amplitude at the bottom determined from linear theory) versus $U_1^2/(s-1)gd$, s being the relative density of the sand.

Figs. 11 through 14 show the variation of $Q_1 + Q_2$, Q_0 and the net discharge \bar{Q} for waves with $T\sqrt{gh} \approx 10$ and height up to 4 metres (0.4 times depth of water), and four typical grain diameters $d = 0.1, 0.2, 0.4$ and 1 mm. In these calculations U_0 has been determined from (31), i.e. the \bar{Q} represents zero net transport in the water motion. Some characteristic values of ϵ and θ' obtained in the computations are shown in the figures too.

The figures show that under these conditions the sediment will move seawards under almost all wave conditions ($\bar{Q} < 0$).

A number of other observations and conclusions may be extracted from the results.

(i) The rather sharp decrease in the numerical value of all Q -curves corresponds to the region between $\theta = 0.4$ and $\theta = 1.0$, where the ripples suddenly disappear and ϵ , as given by Fig. 4 and Fig. 10, consequently decreases by a factor of 10.

(ii) For the larger grains sizes the oscillatory contributions are positive (shoreward movement) for high waves, and of the same order of magnitude as Q_0 . Thus if Q_0 had been less negative (or even positive) -

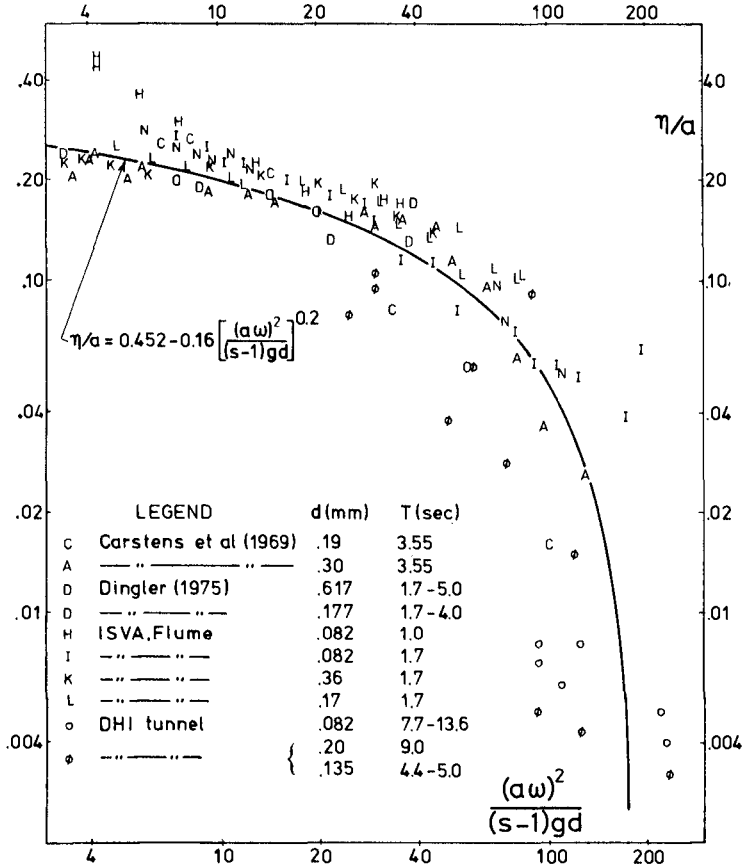


Fig. 10 Semi-empirical plot for determination of the ripple height η for instance due to three-dimensional effects, vide the introduction — \bar{Q} might well have been positive.

(iii) The finer the material, the less important the oscillatory part, and for $d = 0.1$ mm net sediment discharge is entirely dominated by Q_0 , i.e. U_0 . Then the net sediment flux may be determined by

$$\bar{Q} \approx Q_0 = U_0 P_0 \epsilon / w^2 \tag{33}$$

and this corresponds to situations where the variation of c over a wave period is small.

(iv) The values obtained for ϵ by the procedure described above appear in a wide region without ripples to be close to $1/4 \kappa U_f \delta$ (κ von Karman's constant, U_f friction velocity, δ boundary layer thickness). This esti-

mate can in fact be inferred from Kajiura (1968) (Jonsson, private communication). Since part of this region is outside the region where measurements for ϵ are available, this is taken as an indication that our extrapolations in the computations are reasonable.

Finally it is emphasized that all these results apply to non-breaking waves only.

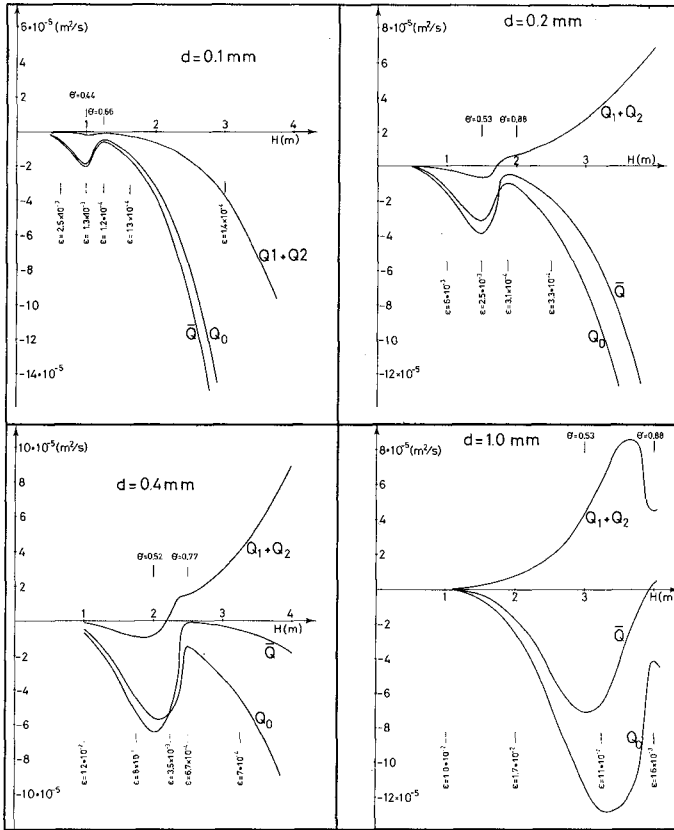


Fig. 11 - 14 Transport versus wave height for different grain diameters. ($U_0 = -gH^2/8ch$).

Comparison with experiments

The model has also been compared with measurements in a wave flume. Fig. 15 shows measurements of \bar{Q} obtained on a horizontal bottom from the changes in bed elevation over a recorded number of waves. Fig. 16 shows the corresponding measurements of the mean water velocity U_0 . When this is used in the calculation of \bar{Q} , we get the value shown by the dotted line in Fig. 15. (The straight line approximation in Fig. 16 was used for U_0).

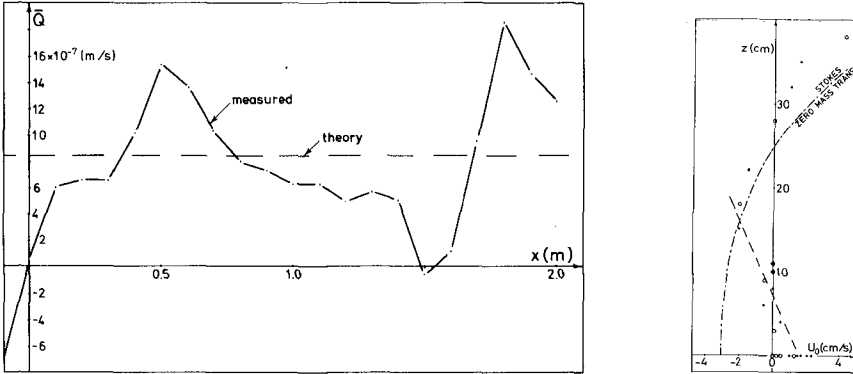


Fig. 15 - 16 Calculated and measured transport for a flume experiment. (ISVA, 1978).

8. CONCLUSIONS

A theoretical model has been developed which yields analytical results for the instantaneous distribution of sediment concentrations $c(z,t)$, when the oscillatory water motion (the wave) and the net mass flux (the current) is prescribed. The result for c is given by (17). Also the sediment flux (instantaneous and time mean) is determined (Eqs. 5 and 6).

Experiments are used to determine the diffusion coefficient ϵ (§ 5) required as input to the model (Fig. 4), and the results indicate that it is reasonable as done to assume the suspension of sediment can be approximated by a diffusion process. The actual physics of the sediment motion is described and discussed in detail in § 2.

In the solution a pick-up function $p(t)$ occurs. Mathematically it acts as the boundary condition at the sea bed for the diffusion equation (§ 3-4). Physically it accounts for the process (also described in § 2) of picking up the sand and bringing it into suspension. The mean value of $p(t)$ is determined experimentally in § 6 where also the time variation of this process is discussed, and equation (25) is a heuristic suggestion for $p(t)$ and further discussed in example (2) in § 7.

In § 7 two examples are analysed, showing the consequences of the model for the onshore-offshore sediment flux in two different wave motions. The first (a simple sinusoidal wave) always yields zero net sediment movement.

In the second example a second order Stokes' wave with specified mass flux is considered. Here the results are far more complicated. For a wave motion with zero net mass flux, the net sediment motion \bar{Q} is always against the wave direction. The balance, however, is delicate, and in a pure oscillatory flow (no return flow) the motion may go in either direction (Figs. 11 through 14).

Finally the model is compared with a measurement of \bar{Q} in a wave flume with zero net water flux, using a second order Stokes' wave model and a measured mean water velocity profile (Fig. 16). In Fig. 15 the computed and measured values of \bar{Q} are shown to compare within the accuracy of the measurements.

References

- Allen, J.R.L. (1968) *Current Ripples*. North-Holland Publ. Co., Amsterdam.
- Bijker, E.W., E. van Hijum and P. Vellinga (1976) Sand transport by waves. Proc. 15th Coastal Engrg. Conf., Hawaii, pp. 1149-1167.
- Dingler, J.R. (1974) *Wave Formed Ripples in Nearshore Sands*. Ph.D. thesis, Univ. Calif., San Diego, 136 pp.
- Fredsøe, J. (1978) Natural backfilling of pipeline trenches. Proc. 10th Offshore Tech. Conf., Houston, Texas, OTC 3073, pp. 225-232.
- Inman, D.L. (1957) Wave generated ripples in nearshore sands. Tech. Memo 100, Beach Erosion Board, 55 pp.
- Jonsson, I.G. and N.A. Carlsen (1976) Experimental and theoretical investigations in an oscillatory turbulent boundary layer. J. Hydr. Res., Vol. 14, No. 1, pp. 45-60
- Kajiura, K. (1968) A model of the bottom boundary layer in water waves. Bull. Earthquake Res. Inst., Univ. Tokyo, Vol. 46, Ch. 5, pp. 75-123.
- Kennedy, J.F. (1963) The mechanics of dunes and antidunes in erodible-bed channels. J. Fluid Mech., Vol. 16, No. 4, pp. 521-544.
- Kennedy, J.F. and M. Falcon (1965) Wave generated sediment ripples. MIT, Hydrodyn. Lab., Rep. No. 86, 55 pp.
- Longuet-Higgins, M.S. (1972) Recent progress in the study of longshore currents. In: *Waves on Beaches and Resulting Sediment Transport*, Proc. Adv. Sem., Madison, Wisconsin. Ed. R.E. Meyer. Academic Press, pp. 203-248
- Lundgren, H. and T. Sørensen (1958) A pulsating water tunnel. Proc. 6th Coastal Engrg. Conf., Florida, pp. 356-358.
- Madsen, O.S. and W.D. Grant (1976) Sediment transport in the coastal environment. MIT, Ralph M. Parsons Lab. Water Res. Hydrodyn., Rep. No. 209, 120 pp.
- Nakato, T., F.A. Locher, J.R. Glover and J.F. Kennedy (1977) Wave entrainment of sediment from rippled beds. ASCE, Vol. 103, WW1, pp. 83-100.
- Nielsen, P. (1977) A note on wave ripple geometry. ISVA, Tech. Univ. Denmark, Prog. Rep. 43, pp. 17-22.
- Peregrine, D.H. and I.A. Svendsen (1978) Spilling breakers, bores and hydraulic jumps. Proc. 16th Coastal Engrg. Conf., Hamburg.
- Svendsen, I.A., P. Nielsen and C. Staub (1977) The motion of suspended particles in oscillatory flow. ISVA, Tech. Univ. Denmark, Prog. Rep. 44, pp. 13-18
- Swart, D.H. (1974) Offshore sediment transport and equilibrium beach profiles. Delft Hydr. Lab., Publ. No. 131.
- Tunsdall, E.B. and D.L. Inman (1975) Vortex generation by oscillatory flow over rippled surfaces. J. Geophys. Res., Vol. 80, No. 24, pp. 3475-3485.

CHAPTER 88

USES FOR A CALCULATED LIMIT DEPTH TO BEACH EROSION

by

Robert J. Hallermeier

Oceanographer, U.S. Army Coastal Engineering Research Center,
Fort Belvoir, Virginia 22060

Abstract. A sediment entrainment parameter is used to calculate maximum water depth for intense bed agitation by shoaling linear waves of given height and period. Calculated limit depths agree with available laboratory measurements of water depth at an erosive wave cut into slopes of quartz and other fine sediments. Ignored variables have small effects on the agreement between calculations and laboratory measurements. On natural seasonal beaches, available measurements of seaward limit to appreciable sand level changes agree with limit depths calculated for extremely high waves expected 12 hours per year. The apparent accuracy and lack of scale effect in the calculated limit depth justify several applications in field and laboratory projects.

THE CALCULATED LIMIT DEPTH

In considering sediment transport by water waves on a beach, it is useful to divide the onshore-offshore profile into zones related to physical processes. The simplest division distinguishes two zones: a nearshore or littoral zone; and an offshore zone. In the offshore zone, wave shoaling is the dominant process and bed agitation remains relatively moderate. The littoral zone is characterized by increased bed stresses and sediment transport, caused by waves near breaking and induced fluid circulations.

The hypothetical boundary between these two zones is the seaward limit of intense bed agitation by shoaling wave action. Hallermeier (1977) proposed that the onset of intense bed agitation might be described as a critical value of a sediment entrainment parameter. This parameter has the form of a Froude number:

$$\phi = U_b^2 / \gamma' g \epsilon d \quad (1)$$

where U_b is maximum horizontal water velocity near the bed, g is the acceleration of gravity, d is water depth, ϵ is a number less than unity, and γ' is the ratio of the density difference between sediment and fluid to fluid density. This Froude number is peak near-bottom wave energy per unit sediment grain volume, divided by the energy needed to raise an immersed grain a distance $(\epsilon d/2)$. Two order-of-magnitude choices, $\epsilon = 0.03$ and $\phi = 1$, are taken to describe the onset of intense wave agitation for fine sands (diameter, D , between 0.06 and 0.5 mm).

With these assumptions and linear theory for shoaling waves, equation 1 can be written as

$$\xi \sinh^2 \xi \tanh^2 \xi \left(1 + \frac{2\xi}{\sinh 2\xi} \right) = (329 H_o^2 / \gamma' L_o^2) \quad (2)$$

where H_o and L_o are wave height and wavelength in deep water, and $\xi = (2\pi d_s / L_s)$ gives the limiting water depth, d_s , in a form normalized by local wavelength, L_s . For a certain γ' , H_o and $L_o = (gT^2/2\pi)$, where T is wave period, the ξ solving equation 2 can be conveniently computed using either a graph or an iterative root-finding procedure on a programmable calculator. The maximum water depth for intense bed agitation is $d_s = (\xi \tanh \xi)(L_o/2\pi)$.

The primary evidence for the usefulness of the calculated d_s is provided by laboratory tests with constant waves on an initially plane slope of sediment. The many published profiles developed in such tests provide a data base on sediment transport towards an equilibrium profile in controlled wave conditions. A common profile feature with fine sediment is a submarine cut by erosive waves into the initial slope, with sediment deposition offshore. The well-defined water depth at this wave cut, d_c , is the limit depth to the erosive action of the surface waves. The wave cut sometimes lies on the landward side of a bar, but more commonly is on a gently sloping terrace.

Figure 1 shows the good agreement of measured d_c with calculated d_s for 46 laboratory tests of profile development with an initially plane sediment slope. The filled points in Figure 1 denote tests with sediments having γ' appreciably different from quartz in water. The Appendix gives references and test conditions for the 46 profiles,

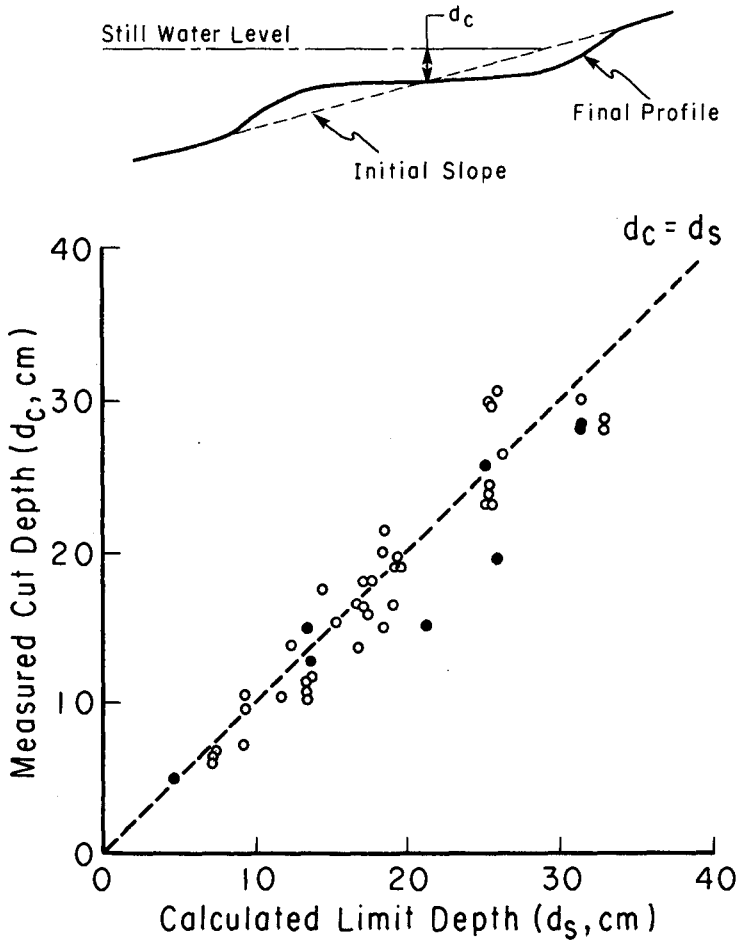


Figure 1. Measured profile cut depth, d_c , versus calculated limit depth, d_s . Conditions for 46 laboratory tests from 13 studies are presented in the Appendix.

selected as ideal cases of a wave cut. In each case, there is only sand deposition on the initial slope offshore of the cut depth.

Table 1 presents results of linear regressions on the Figure 1 points. For each regression line (including those of the data set halves discussed in the following section), the correlation coefficient, r , is large enough to reject the possibility of no linear relationship between d_c and d_s with at least 99.99% confidence, presuming the data points are random samples from a bivariate normal population (Freund, 1962). In each case, the intercept of the fit line is fairly near zero and the slope is near unity. The agreement between measurement and calculation is most ideal for the 38 tests with quartz sands. With the sediments of other densities (glass, coal, bakelite, maselite, and oolitic aragonite), agreement is still good, providing additional confidence that the calculated d_s is the limit depth to the erosive action of various waves causing offshore deposition of various fine sediments.

The footnote to Table 1 emphasizes the fact that d_s is approximately a linear multiple of incident wave height, for any given γ' . The measured d_c is well described by a linear dependence on H_o , but the fit is considerably better with the exact calculated d_s , which includes a slight effect of wave period.

It may be noted that a similar physical viewpoint is involved in the d_s calculated using the equation 1 consideration of sand entrainment energetics and in a limit depth arising in the empirical eroding-profile schematization of Swart (1974). That work considers an "equilibrium D-profile" geometry, with offshore water depth, d_1 , at the lower limit stated to be related to the first occurrence of suspended-load transport. For the 6 tests considered in Figure 1 and in Swart (1974), $0.69d_1 < d_s < 0.78d_1$; this narrow range helps confirm a similar phenomenon is involved in d_s and d_1 .

EFFECTS OF IGNORED VARIABLES

The laboratory data base was divided into approximate halves to isolate effects of larger or smaller: tank water depth; number of waves; initial slope; Stokes number, describing the nonlinearity of the

Table 1. Results of Linear Regressions: $d_c = \alpha + \beta d_s$.

<u>Data Set</u>	<u>Number of Points</u>	<u>Correlation Coefficient, r</u>	<u>Intercept, α, cm</u>	<u>Slope, β</u>
All Data	46	0.946	0.61	0.93
Quartz Sands*	38	0.950	-0.01	0.98
Other γ'	8	0.954	1.56	0.83
$(d_t L_s / d_s L_t) \leq 1.7$	23	0.923	1.53	0.88
$(d_t L_s / d_s L_t) > 1.7$	23	0.958	-0.72	1.04
<u>Quartz Sands*</u>				
10K to 400K Waves	19	0.933	2.01	0.91
>400K Waves	19	0.969	-1.67	1.05
Slope $\geq 1/12$	19	0.949	-0.80	1.07
Gentler Slopes	19	0.972	0.30	0.92
11 < S < 21	20	0.927	1.23	0.91
21 < S < 119	18	0.966	-0.84	1.03
$D \leq 0.21$ mm	18	0.956	-2.77	1.15
$D \geq 0.22$ mm	20	0.923	3.69	0.83
$125 < (H_s / D) < 375$	19	0.906	0.09	0.94
$415 < (H_s / D) < 710$	19	0.855	4.44	0.81
$7 < \phi < 24$	19	0.919	-0.47	1.00
$24 < \phi < 43$	19	0.858	2.90	0.87
$95 < (a_s / D) < 300$	19	0.928	-1.10	1.06
$300 < (a_s / D) < 950$	19	0.945	0.17	0.97

* Also, $d_c = 1.97 \text{ cm} + 1.70 H_o$, with $r = 0.875$, for quartz sands

waves; and sand diameter. The separation criteria are given in Table 1 along with the linear regression results; data subsets of nearly equal size facilitate comparison of results. In Table 1, the relative tank depth is given in dimensionless form as $(d_t / L_t) / (d_s / L_s)$, where d_t is maximum water depth and L_t is linear wavelength in that depth for the

given T ; this form seems more appropriate than (d_t/d_s) for considering wave geometry effects. The Stokes number is $S = (H_s L_s^2 / 2d_s^3)$, where H_s is calculated wave height at d_s , according to linear theory for wave shoaling. Ignoring sand size is thought to be a significant assumption in the calculation procedure, so the influence of sand diameter was examined using four parameters: D directly; (H_s/D) , suggested by Bagnold (1940) as a similarity parameter for beach profile development; and two useful parameters from dimensional analysis of oscillatory-flow interaction with a sediment bed (Lofquist, 1978), $\phi = (U_b^2 / \gamma' g D) = (\epsilon d_s / D)$ and $(a_s / D) = (H_s / 2D \sinh \xi)$, where a_s is near-bottom horizontal fluid orbit amplitude.

There are differences in the fit lines and the correlation coefficients between each data subset of the eight pairs in Table 1. The quantity r^2 measures the amount of variance in d_c attributable to the derived linear dependence on d_s . This ranges between 73% and 95%, and differs somewhat between the two members of each of the eight pairs. In seven of the eight cases, the larger r occurs for the fit line in better agreement with the present model, i.e., α nearer zero and β nearer unity. (Results with gentler and steeper slopes show practically the same agreement with the model.)

For each of these eight cases, a nonparametric statistical test was applied to assess the parallelism of the two regression lines. This test (Hollander and Wolfe, 1973) compares two sets of slope estimators from pairs of points within each data base half, using the Wilcoxon signed rank test, with no assumptions about the distribution of deviations from linearity. Inferences from repeats of this test may differ slightly because a random pairing of slope estimators is involved.

The tank water depth was found to affect the slope at the 0.13 level of significance. This result implies there is a 0.13 probability that the parallelism of the fit lines has been rejected, when in fact they are parallel. With relatively large water depth, $(d_t L_s / d_s L_t) > 1.7$, the $(d_s d_c)$ data shows better agreement with the present model. Because 6 of 8 tests with non-quartz sands were done with relatively small water depth, these 8 points were deleted from the further analyses.

The number of waves was found to affect the slope at the 0.04 level of significance. More waves result in a better agreement between calculated and test results. For 25 of the 38 quartz-sand tests, the profile development in time was available, and d_c is found to oscillate somewhat but generally to increase slightly with running time. On the average, it is clear that d_s provides a useful estimate for the limit depth on an eroding profile approaching equilibrium.

The statistical test gave no conclusive indications of effects of initial slope and of Stokes parameter on the regression line slopes. Initial slope appears to have insignificant consequences for the present consideration, considering the large and nearly equal r for these two data subsets. However, the lack of a discernible effect of the Stokes parameter on the fit between d_c and d_s requires comment. Linear wave theory can be valid only if correction terms arising in second-order theory are negligible compared to the linear solution; an approximate form for this requirement is that the Stokes parameter be much less than about 50 (Madsen, 1976). The stream function results in Dean (1974) show that for $(HL^2/2d^3)$ greater than about 10, the calculated U_b is appreciably greater than that given by linear wave theory, although the difference is not monotonic with the Stokes parameter, clearly depending on (d/L) . These results are for waves over an ideal immobile bed, and the present data base includes only $S > 11$. These facts might account for lack of a definite effect with larger Stokes parameter for the calculation procedure to underestimate U_b and thus d_s (equation 1), as the wave condition becomes increasingly non-linear.

The examinations of sand size effects gave some interesting results. Splitting the data base directly according to reported D was found to affect the regression-line slope at the 0.18 level of significance; finer sands result in slightly better agreement between the model and measurements. When the data base is split using either (H_s/D) , $(U_b^2/\gamma'gD)$ or (a_s/D) , the parallelism of the two regression lines cannot be rejected even at the 0.4 level of significance.

The separation of the data base according to (H_s/D) appears to be the least constructive, because the fit line for each data subset shows

relatively poor agreement with the present model. Bagnold (1940) suggested the change of bed material behavior from shingle to sand takes place for (H_s/D) on the order of 2,000, but the present consideration suggests the transition value is on the order of $(H_s/D) = 200$, if this is the proper descriptive parameter. A limited range of relatively fine sands are represented in the present data base. Bagnold (1940), Rector (1955), Popov (1960), and van Hijum (1974) have reported laboratory tests with waves acting on coarse quartz sediments: $3 \leq D \leq 7$ mm. A near-horizontal shelf or wave cut commonly occurred at water depth ranging from $(0.7 H_o)$ to $(2 H_o)$. These tests with coarse sediments all have (H/D) on the order of 40, but no clear conclusion is possible on the limit depth to the wave's erosive action. However, it seems clear that the calculated d_s should be an upper bound to the actual limit depth with erosive waves acting on coarser, less mobile sediments.

Although results are not too decisive when the data base is separated according to $(U_b^2/\gamma'gD)$ or (a_s/D) , it is somewhat paradoxical that measurements appear in better agreement with the model for relatively small $(U_b^2/\gamma'gD)$ and for relatively large (a_s/D) , because these two parameters are strongly and positively correlated in the present data base. Others of the ignored variables might cause this. $(U_b^2/\gamma'gD)$ roughly measures the intensity of sand motion, and the values of $(U_b^2/\gamma'gD)$ and (a_s/D) in the present data base indicate that $\phi = 1$ may correspond to the onset of intense bed agitation as revealed by the decline of bed forms with increasing bed agitation (cf. Figure 32 in Lofquist, 1978).

In summary, the variables ignored in calculating the limit depth appear to have small or negligible effects. Emphasizing the non-negligible effects, d_s has been seen to agree better with the limit depth of equilibrium profile erosion for fine sands and unconstrained water depth. Each data subset gives less ideal agreement between d_c and d_s than the entire data base for quartz sands. The excellent agreement between d_c and d_s in the larger data base evidently results from an averaging of effects of ignored variables.

YEARLY LIMIT DEPTH TO PROFILE ACTIVITY ON SEASONAL BEACHES

Because d_s is calculated from a critical value of a Froude number, this limit depth should pertain to eroding natural beach profiles of fine sand, with comparable (H_o/L_o) and Φ , as well as to profiles developed in smaller-scale laboratory tests. This is partially confirmed by several profiles obtained by Saville (1957) in large-scale laboratory tests, as discussed in Hallermeier (1977). However, application of this calculated limit depth to natural beaches must consider complicating effects occurring in nature, including changing wave action.

For natural sand beaches, one limit depth useful in coastal engineering is the yearly limit to the very active nearshore profile, beyond which repetitive surveys reveal little sand level change throughout the seasonal wave climate changes. This profile close-out depth can be estimated using the cut depth calculated for a yearly extreme wave condition. Such high waves erode the nearshore and deposit sand offshore; the estimated yearly extreme cut depth should be a minimum limit to water depth for appreciable sand level changes. An appropriate extreme wave condition is proposed to be that exceeded for 12 hours per year (0.137%). This duration should permit moderate adjustment towards profile equilibrium and moderate quantities of sand deposited beyond the limit depth. Also, Maksimchuk (1976) stated the beach profile in varying wave action is dominated by a similar wave condition, that having a cumulative frequency of 0.2% (0.73 days per year).

To calculate limit depth for such extreme waves, an accurate approximation for equation 2 is convenient:

$$d_{se} = 2.28 H_e - 68.5 (H_e^2 / g T_e^2) \quad (3)$$

Here γ' has been taken as 1.6 (quartz sand in salt water), H_e and T_e are nearshore significant height and period of the extreme wave condition, and g is acceleration of gravity in appropriate units.

H_e is the dominant input in calculating d_{se} . Thompson and Harris (1972) reported measured nearshore wave heights for a complete yearly cycle occur according to a modified exponential distribution, and

height of extreme waves is best estimated using the mean height, \bar{H} , and standard deviation of height, σ , defined by a full year of at-least-daily nearshore wave measurements. According to the exponential distribution, the 12-hour-per-year height is

$$H_e = \bar{H} + 5.6 \sigma \quad (4)$$

T_e should be taken to be the typical period of measured high waves.

Any near-bed velocities above those caused by linear waves are ignored in calculating the limit depth in equation 3. Use of linear wave theory is warranted because of its simplicity and agreement with available field measurements of peak near-bed velocity (Grace (1976)). However, any flows superposed on surface waves must increase the peak near-bed fluid kinetic energy, the numerator of equation 1, and thus increase the calculated limit depth in the denominator. To counteract this, it is proposed that the calculated d_{se} be used as a minimum estimate of profile close-out depth with respect to mean low(er) tide level.

Table 2 presents estimated profile close-out depths along with recorded close-out depths from published field studies including repetitive nearshore profile and wave measurements. The estimated water depths are calculated using equations 3 and 4, and measured depths are for profile superposition throughout a yearly cycle to within 1 foot, a typical resolution for nearshore surveys. In each case, the estimated close-out depth is quite close to and usually less than the measured depths. There is about the same agreement with measurement if limit depth is calculated using, rather than equation 3, the exact form of equation 2 ignoring shoaling wave height change (given in Hallermeier, 1977). Each field study in Table 2 was done on a different sea coast, with very different extreme wave conditions, increasing confidence in the usefulness of the calculated yearly limit depth. Agreement between calculated and measured depths is best for the most ideal data set, Torrey Pines Beach, where three profiles were surveyed monthly over a two-year interval.

On the other hand, Table 2 summarizes a very small amount of field investigation, and the present treatment has ignored several possibly important factors in considering only two-dimensional wave action.

Table 2. Comparison of estimated and measured profile close-out depths from field studies reporting repetitive nearshore profiles and wave measurements. Water depths are with respect to local mean low(er) tide level, and sand sizes are near estimated limit depths.

Locality; Reference	Description of Data Set: Profiles	Design Wave:		Eq. 3 Limit Depth, Ft	Measured Close-out Depth*, Ft	Profile Line Name
		H _e , Ft	T _e , Sec			
Gold Coast, Australia, S. Pacific Ocean; Delft Hydr. Lab., 1970 (D = 0.2 mm)	5 lead-line surveys Jun 66-Dec 68	4/day records (1 year) from deep-water waveriders	14.5	8	26.1	28.5 (>25.5) Tugun Palm Broadbeach The Spit
Avondale, Fla., U.S., Gulf of Mexico; Balsillie, 1975; Poche, 1972 (D = 0.3 mm)	8 lead-line surveys, Jan-Aug 70	97% daily breaker observations (1 year)	7.9	5.4	13.5	14.8 Pier
Torrey Pines, Cal., U.S., N. Pacific Ocean; Nordstrom & Inman, 1975; Pawka et al., 1976 (D = 0.12 mm)	24 fathometer surveys, Jun 72-Apr 74	64% daily breaker observations (2 years); 4/day pressure records (16 months)	11	14	23.8	22.8 24.3 24.8 North Indian South

* Profiles superpose to within ± 0.5 ft; depth is average of two yearly cycles, except for Balsillie (1975).

Swart (1974) considered the effects on the onshore-offshore equilibrium beach profile of wave-induced longshore and rip currents; in erosive waves, each effect theoretically deepens the profile due to increased bed shear. Bijker (1967) reported the measured increase of bed shear in a uniform current due to wave action could be expressed as an empirical function of: angle between wave and current; the ratio of their peak near-bed speeds; and the bed roughness. These factors must be considered in predicting alongshore and onshore-offshore sediment transport within the nearshore beach zone.

However, the beach profile near d_{se} ($\approx 2 H_e$) should be beyond the influence of intense wave-induced nearshore circulations. Wave breaking usually occurs at water depth on the order of wave height, i.e., in water appreciably shallower than d_{se} . Beyond wave breaking, the seaward extent of the induced currents seems a useful way to define the extent of the nearshore zone. Available theory and experiment on the wave-generated alongshore current give maximum current speed on planar fixed beds within the breakers, with monotonically decreasing current speed offshore of the maximum (Longuet-Higgins, 1970; James, 1974; Jonsson et al., 1974). The onshore-offshore profile of the longshore current evidently depends on wave condition and on the mechanisms of energy dissipation and lateral fluid mixing. There remains considerable uncertainty about the seaward extent of significant near-bed alongshore currents and rip currents, especially in extreme events, but the water depth d_{se} seems a reasonable estimate for the extreme extent of the nearshore zone, intensely active due to wave action.

At such water depth, tidal or wind-induced currents may significantly add to wave-induced velocities. Interaction of water waves and currents is a complex topic (Peregrine, 1976), and available results on bed agitation and suspended sediment provide no guidance on modifying equation 1 to account for the combined effect of wave action and a current. For this reason, the simple geometric correction has been proposed for the effect of tidal action: d_{se} is to be taken with respect to mean low(er) tide level for estimating minimum limit depth to the very active profile on natural seasonal beaches.

APPLICATIONS TO FIELD PROJECTS

The yearly limit depth from equations 3 and 4 has several applications in coastal engineering:

a. Any nearshore hydrographic survey should extend further seaward than the estimated limit depth, to ensure coverage of the very active zone of a sand beach. Minimum definition of conditions at a seasonal beach requires two such surveys, conducted when the beach shows maximum summer-wave accretion and winter-wave erosion.

b. For subaqueous beach nourishment, suitable material should be placed landward of the estimated limit depth to the active seasonal profile during the summer-wave accretionary beach phase. This guidance is consistent with field offshore nourishment attempts judged successful (Vera-Cruz, 1972; Mikkelsen, 1977; Schwartz and Musialowski, 1977) and unsuccessful (Harris, 1954; Hall and Watts, 1957; Wiegel, 1964). Nearshore wave measurements (Thompson, 1977) indicate average summer-wave height is about $(0.8 \bar{H})$, and the estimated yearly limit depth is about half the maximum water depth for motion initiation with fine sands, summer waves, and the motion threshold criterion of Komar and Miller (1974).

c. For effective offshore disposal, material should be placed far seaward of the limit depth to the very active beach profile, so that it does not enter the nearshore system.

The estimated limit depth to the nearshore zone might also find applications in the design of coastal structures in sandy regions. It seems an offshore mound-type breakwater must be situated in water deeper than this limit for the nearby region, if it is to provide wave shelter while minimizing its effect as a littoral barrier. Also, it seems that dual jetties at a navigation channel extending to the limit depth may be expected to intercept almost all the littoral drift during a typical yearly cycle of waves. However, regions near navigation channels and structures are three-dimensional and have significant currents in addition to waves (Liu and Mei, 1975), factors not considered in the present treatment. Also, coastal structure design must consider the economics of construction and maintenance, as well as functional performance. Further research is needed before the

estimated limit depth can be applied with confidence to structure design.

APPLICATION TO LABORATORY TEST DESIGN

Laboratory investigations of nearshore sediment transport can potentially provide valuable information for coastal engineering, since regulated experiments on sand response to controlled hydraulic forces are permitted in the laboratory. Interpretation of laboratory results requires consideration of scale effects in replicating prototype processes (Bijker, 1967; Kamphuis, 1975), and obtaining meaningful experimental results requires that laboratory effects, e.g., constrained geometry, be minimized (Chesnutt, 1978).

The previously discussed results (Table 1) on parameters influencing the cut depth by erosive waves clarify one requirement for unconstrained geometry in laboratory experiments on nearshore processes: water depth must be adequate to accommodate an equilibrium nearshore profile. The wave cut in laboratory sand slopes is a distinct geometrical feature with erosive waves, and the elevation of this feature on a two-dimensional profile approaching equilibrium is generally better explained by d_s from equation 2 with relatively large tank water depths: $(d_t L_s / d_s L_t) > 1.7$. Some profiles obtained by Monroe (1969) and by Masuda and Ito (1975) indicate untypical forms are associated with dimensionless water depths much less than this. Using typical laboratory values of $d_s = 2H$ (quartz sand) and $(L_t/L_s) = 1.5$, it seems water depth should be at least five times generated wave height for vertically unconstrained tests with fine quartz sand in water. For sediments of lower density, larger water depth is required (equation 1) for meaningful tests.

The laboratory requirements for a horizontally unconstrained beach profile remain somewhat uncertain, but appear harder to accommodate in general. Two-dimensional profiles developed by erosive waves commonly have a gently sloping terrace centered at the cut point in the initial slope. The profile developments in time reported by Sunamura and Horikawa (1974) and by Chesnutt (1978) show an approximately logarithmic increase in the length of this terrace with running time. The

terrace slope is on the order of 1° (comparable to offshore slopes on natural beaches), and an equilibrium eroding profile must be very long, because the terrace should extend to a depth where sediment movement ceases, to include the entire active beach profile.

A practical alternative is to truncate the offshore profile, while including the entire nearshore zone in the laboratory situation. Kemp (1960) has noted that dynamic similarity between laboratory test and prototype is more likely within the turbulent breaker zone than offshore. In designing the profile truncation, provision must be made for the offshore-zone function as a source or sink of nearshore sands, in various wave conditions. Also, the truncation cross-section should be shaped to minimize wave reflection, which has deleterious effects on laboratory beach studies (Chesnutt, 1978). Available laboratory results on perched beach designs (Chatham et al., 1973) provide a data base for further research on offshore profile truncation.

SUMMARY

The sediment entrainment parameter (equation 1) does not figure in any reported research results on wave propagation or interaction with sand beds. However, with linear wave theory, and two coupled order-of-magnitude assumptions, this parameter can be used to calculate a limiting water depth to the erosive action of waves causing offshore deposition of fine sands (equation 2). This calculated depth agrees well, over a wide range of conditions, with the elevation of the wave cut commonly occurring on eroding laboratory sand slopes (Figure 1). Also, for extremely high waves expected 12 hours per year, the estimated limit depth (equations 3 and 4) agrees well with recorded close-out depth to significant profile activity at seasonal beaches on several sea coasts (Table 2). The calculated limit depth has several types of application in field and laboratory projects, although further analysis and tests are clearly required.

ACKNOWLEDGEMENTS

For kindly providing beach profiles, I thank J. Nicholson, National Research Institute for Oceanology, South Africa; T. Sunamura, University of Tokyo, Japan; C.H. Hulsbergen and J.J. Vinje, Delft Hydraulics Laboratory, Netherlands; and S. Masuda and M. Ito, Meijo University, Japan.

Also, I thank C.B. Chesnutt and C. Mason for review of this manuscript, and K.L. Jacobs and M.W. Leffler for assistance in data analysis. Results presented herein, unless otherwise noted, are based on research conducted at the Coastal Engineering Research Center under the Coastal Engineering Research Program of the U.S. Army Corps of Engineers. The findings reported are not to be construed as an official Department of the Army position unless so designated by other authorized documents. Permission to publish this information is appreciated.

REFERENCES

- Bagnold, R.A., "Beach Formation by Waves; Some Model Experiments in a Wave Tank", J. Institution Civil Engineers, Vol. 15, 1940, pp. 27-52.
- Balsillie, J.H., "Analysis and Interpretation of Littoral Environment Observation (LEO) and Profile Data Along the Western Panhandle Coast of Florida", Coastal Engineering Research Center, Ft. Belvoir, VA., Tech. Memo. 49, 1975.
- Bijker, E.W., "Som Considerations about Scales for Coastal Models with Movable Bed", Delft Hydraulics Lab., Netherlands, Pub. 50, 1967.
- Chatham, C.E., Jr., D.D. Davidson, and R.W. Whalin, "Study of Beach Widening by the Perched Beach Concept: Santa Monica Bay, California, Hydraulic Model Investigation", Waterways Experiment Station, Vicksburg, Miss., Tech. Rep. H-73-8, 1973.
- Chesnutt, C.B., "Laboratory Effects in Beach Studies. Volume VIII. Analysis of Results from 10 Movable-Bed Experiments", Coastal Engineering Research Center, Ft. Belvoir, VA., Misc. Rep. 77-7 (VIII), 1978.
- Collins, J.I., and C.B. Chesnutt, "Grain Shape and Size Distribution Effects in Coastal Models", Coastal Engineering Research Center, Ft. Belvoir, VA., Tech. Paper 76-11, 1976.
- Dean, R.G., "Evaluation and Development of Water Wave Theories for Engineering Application, Coastal Engineering Research Center, Ft. Belvoir, VA., Spec. Rep. 1, 1974, 2 Vols.
- Delft Hydraulics Laboratory, "Gold Coast, Queensland, Australia. Coastal Erosion and Related Problems", 3 Vols., Rep. R257, Delft, Netherlands, 1970.
- Eagleson, P.S., B. Glenne, and J.A. Dracup, "Equilibrium Characteristics of Sand Beaches in the Offshore Zone", Beach Erosion Board, Washington, DC., Tech. Memo. 126, 1961.
- Freund, J.E., Mathematical Statistics, Prentice-Hall, Englewood Cliffs, NJ., 1962.
- Grace, R.A., "Near-Bottom Water Motion Under Ocean Waves", Proc., 15th Coastal Eng. Conf., 1976, pp. 2371-2386.
- Hall, J.V., Jr., and G.M. Watts, "Beach Rehabilitation by Fill and Nourishment", Trans., ASCE, Vol. 122, 1957, pp. 155-177.
- Hallermeier, R.J., "Calculating a Yearly Limit Depth to the Active Beach Profile", Coastal Engineering Research Center, Ft. Belvoir, VA., Tech. Paper 77-9, 1977.
- Harris, R.L., "Restudy of Test - Shore Nourishment by Offshore Deposition of Sand. Long Branch, New Jersey", Beach Erosion Board, Washington, DC., Tech. Memo. 62, 1954.
- van Hijum, E., "Equilibrium Profiles of Coarse Material Under Wave Attack", Proc., 14th Coastal Eng. Conf., 1974, pp. 939-957.
- Hollander, M., and D.A. Wolfe, Nonparametric Statistical Methods, Wiley, New York, 1973.

- Horikawa, K., T. Sumamura, and H. Kitoh, "A Study of Beach Deformation by Wave Action", Proc., 20th Japanese Conf. on Coastal Eng., 1973, pp. 357-363 (in Japanese).
- James, I.D., "A Non-linear Theory of Longshore Currents", Estuarine and Coastal Marine Science, Vol. 2, 1974, pp. 235-249.
- Jonsson, I.G., O. Skovgaard, and T.S. Jacobsen, "Computation of Longshore Currents", Proc., 14th Coastal Eng. Conf., 1974, pp. 699-714.
- Kamphuis, J.W., "Coastal Mobile Bed Model - Does It Work?", Proc., Sym. on Modeling Techniques, 1975, pp. 993-1009.
- Kemp, P.H., "The Relationship Between Wave Action and Beach Profile Characteristics", Proc., 7th Coastal Eng. Conf., 1960, pp. 262-277.
- Komar, P.D., and M.C. Miller, "Sediment Threshold Under Oscillatory Waves", Proc., 14th Coastal Eng. Conf., 1974, pp. 756-775.
- Liu, P. L-F., and C.C. Mei, "Effects of a Breakwater on Nearshore Currents Due to Breaking Waves", Coastal Engineering Research Center, Ft. Belvoir, VA., Tech. Memo. 57, 1975.
- Lofquist, K.E.B., "Sand Ripple Growth in an Oscillatory-Flow Water Tunnel", Coastal Engineering Research Center, Ft. Belvoir, VA., Tech. Paper 78-5, 1978.
- Longuet-Higgins, M.S., "Longshore Currents Generated by Obliquely Incident Sea Waves, 2", J. Geophysical Research, Vol. 75, 1970, pp. 6790-6801.
- Madsen, O.S., "Wave Climate of the Continental Margin: Elements of its Mathematical Description", Marine Sediment Transport and Environmental Management, Wiley, New York, 1976, pp. 65-87.
- Maksimchuk, V.L., "Model Studies of the Beach Processes and Similarity Requirements", Proc., Diamond Jubilee Sym., Central Water and Power Research Station, Poona, India, Vol. I, 1976, pp. A12-1 - A12-18.
- Masuda, S., and M. Ito, "Analysis of Beach Processes by Means of the Design of Experiments", Coastal Eng. in Japan, Vol. 18, 1975, pp. 75-93.
- Mikkelsen, S.C., "The Effects of Groins on Beach Erosion and Channel Stability at the Limfjord Barriers, Denmark", Proc., Coastal Sediments '77, 1977, pp. 17-32.
- Monroe, F.F., "Oolitic Aragonite and Quartz Sand: Laboratory Comparison Under Wave Action", Coastal Engineering Research Center, Washington, DC., Misc. Paper 1-69, 1969.
- Nicholson, J., "A Laboratory Study of the Relationship between Waves and Beach Profiles", Proc., 3rd Australasian Conf. on Hydraulics and Fluid Mechanics, 1968, pp. 33-37.
- Nordstrom, C.E., and D.L. Inman, "Sand-Level Changes on Torrey Pines Beach, California", Coastal Engineering Research Center, Ft. Belvoir, VA., Misc. Paper 11-75, 1975.
- Paul, M.J., J.W. Kamphuis, and A. Brebner, "Similarity of Equilibrium Beach Profiles", Proc., 13th Coastal Eng. Conf., 1972, pp. 1217-1236.
- Pawka, S.S., D.L. Inman, R.L. Lowe, and L. Holmes, "Wave Climate at Torrey Pines Beach, California", Coastal Engineering Research Center, Ft. Belvoir, VA., Tech. Paper 76-5, 1976.
- Peregrine, D.H., "Interaction of Water Waves and Currents", Advances in Applied Mechanics, Vol. 16, Academic Press, New York, 1976, pp. 9-117.
- Poche, D., "Selective Sorting of Sediment by Waves: The Influence of Grain Shape", Ph.D. Thesis, University of Virginia, Charlottesville, 1972, 99 pp.

- Popov, I.J., "Experimental Research in Formation by Waves of Stable Profiles of Upstream Faces of Earth Dams and Reservoir Shores", Proc., 7th Coastal Eng. Conf., 1960, pp. 282-293.
- Raman, H., and J.J. Earattupuzha, "Equilibrium Conditions in Beach Wave Interaction", Proc., 13th Coastal Eng. Conf., 1972, pp. 1237-1256.
- Rector, R.L., "Laboratory Study of Equilibrium Profiles of Beaches", Beach Erosion Board, Washington, DC., Tech. Memo. 41, 1954.
- Saville, T., Jr., "Scale Effects in Two Dimensional Beach Studies", Proc., 7th General Meeting, International Association of Hydraulic Research, 1957, pp. A3-1 - A3-10.
- Schwartz, R.K., and F.R. Musialowski, "Nearshore Disposal: Onshore Sediment Transport", Proc., Coastal Sediments '77, 1977, pp. 85-101.
- Shinohara, K., T. Tsubaki, M. Yoshitaka, and C. Agemori, "Sand Transport Along a Model Sandy Beach by Wave Action", Coastal Eng. in Japan, Vol. I, 1958, pp. 111-130.
- Sunamura, T., and K. Horikawa, "Two-Dimensional Beach Transformation Due to Waves", Proc., 14th Coastal Eng. Conf., 1974, pp. 920-938.
- Swart, D.H., "Offshore Sediment Transport and Equilibrium Beach Profiles", Delft Hydraulics Lab., Netherlands, Pub. 131, 1974.
- Thompson, E.F., "Wave Climate at Selected Locations Along U.S. Coasts", Coastal Engineering Research Center, Ft. Belvoir, VA., Tech. Rep. 77-1, 1977.
- Thompson, E.F., and D.L. Harris, "A Wave Climatology for U.S. Coastal Waters", Paper OTC 1693, 4th Offshore Technology Conf., 1972.
- Vera-Cruz, D., "Artificial Nourishment of Copacabana Beach", Proc., 13th Coastal Eng. Conf., 1972, pp. 1451-1463.
- Watts, G.M., and R.F. Dearduff, "Laboratory Study of Effect of Tidal Action on Wave-Formed Beach Profiles", Beach Erosion Board, Washington, DC., Tech. Memo. 52, 1954.
- Wiegel, R.L., Oceanographical Engineering, Prentice-Hall, Englewood Cliffs, NJ., 1964.

Appendix. Test conditions for profiles showing ideal wave cut.

Test I.D.	Initial Slope	D, mm	γ'	Ho, cm	T, sec	Total Waves	d_t/L_t	d_s/L_s	d_s , cm	d_c , cm	$\frac{H_s L_s^2}{2d_s^3}$	a_s/D
(Chesnut, 1978)												
70X-06	1/10	0.23	1.65	11.88	1.9	398K	0.164	0.0886	25.25	23.2	31.3	484
70X-10	1/10	0.23	1.65	11.88	1.9	332K	0.164	0.0886	25.25	23.2	31.3	484
71Y-06	1/10	0.23	1.65	11.88	1.9	711K	0.164	0.0886	25.25	23.8	31.3	484
71Y-10	1/10	0.23	1.65	11.88	1.9	635K	0.164	0.0886	25.25	24.4	31.3	484
72A-06	1/10	0.22	1.65	8.56	3.75	130K	0.074	0.0439	25.90	30.5	18.3	946
72C-10	1/10	0.21	1.65	13.72	1.5	336K	0.227	0.1158	25.28	29.7	19.6	397
72D-06	1/10	0.22	1.65	11.88	1.9	341K	0.164	0.0886	25.25	29.8	31.3	477
(Collins and Chesnut, 1976)												
14A	1/10	0.3	1.42	2.0	0.82	101K	0.320	0.0876	4.60	4.95	29.6	60
238	1/10	0.45	1.42	7.0	1.00	94K	0.224	0.1274	13.20	15.05	15.5	83
(Delft Hydraulics Laboratory; Swart, 1974)												
71-09A	1/20	0.22	1.65	11.4	1.15	423K	0.213	0.1353	19.28	19.5	15.2	254
71-09B	1/20	0.16	1.65	11.4	1.15	423K	0.213	0.1353	19.28	19.0	15.2	349
71-11A	1/20	0.22	1.65	10.7	1.15	423K	0.213	0.1314	18.39	21.5	15.9	247
71-11B	1/20	0.16	1.65	11.2	1.15	423K	0.213	0.1342	19.03	19.0	15.4	349
71-12A	1/10	0.22	1.65	9.6	1.15	451K	0.213	0.1252	16.96	18.0	17.2	237
71-12B	1/10	0.16	1.65	9.3	1.15	451K	0.213	0.1234	16.56	16.5	17.6	322
(Eggleston, Glenne and Dracup, 1961)												
2	1/30	0.37	1.67	9.57	1.15	523K	0.258	0.1247	16.84	16.4	17.4	143
3	1/20	0.37	1.67	9.91	1.15	429K	0.253	0.1266	17.29	16.0	17.0	143
(Horikawa, Sunamuro and Kifoh, 1973)												
1	1/24	0.2	1.65	6.4	1.4	591K	0.168	0.0883	13.60	11.7	31.5	289
2	1/24	0.2	1.65	5.3	1.4	617K	0.168	0.0815	11.74	10.6	36.4	267
3	1/24	0.2	1.65	7.3	1.4	123K	0.168	0.0934	15.07	15.2	28.5	299
4	1/24	0.2	1.65	6.1	1.7	415K	0.132	0.0791	16.41	13.5	32.2	317
(Masuda and Ito, 1975)												
II-1	1/10	0.33	1.3	9.80	2.30	13K	0.099	0.0730	25.86	19.8	39.7	349

(Monroe, 1969)												
1A	1/15	0.26	1.585	16.57	1.19	106K	0.231	0.1569	26.19	26.5	11.8	253
18	1/15	0.27	1.81	16.57	1.19	106K	0.231	0.1522	24.97	25.8	13.2	255
2A	1/15	0.26	1.585	17.11	1.77	96K	0.133	0.1113	32.87	28.0	20.5	424
28	1/15	0.27	1.81	17.11	1.77	96K	0.133	0.1081	31.24	28.3	23.1	426
8A	1/15	0.26	1.585	17.11	1.77	161K	0.133	0.1113	32.87	28.8	20.5	424
88	1/15	0.27	1.81	17.11	1.77	161K	0.133	0.1081	31.24	28.0	23.1	426
(Nicholson, 1968)												
79	1/10	0.42	1.61	8.23	1.00	50K	0.229	0.1332	14.21	17.5	15.4	98
(Paul, Kamphuis and Brebner, 1972)												
5a	1/10	0.357	1.67	4.15	1.29	100K	0.183	0.0785	9.30	9.5	39.3	124
5e	1/10	0.357	1.67	10.33	1.29	100K	0.183	0.1165	18.87	16.7	19.5	175
6e	1/10	0.525	0.60	5.15	0.91	47K	0.182	0.1467	13.76	12.8	8.1	38
(Raman and Earattupuzha, 1972)												
1	1/8	0.3	1.65	6.8	1.0	144K	0.246	0.1216	12.20	13.9	18.0	130
3	1/12	0.3	1.65	11.08	1.0	155K	0.246	0.1516	17.53	18.0	12.7	155
(Shinohara, Tsubaki, Yoshitaka and Agemori, 1958)												
Fig. 2a	1/10	0.2	1.66	3.84	1.40	15K	0.154	0.0710	9.10	10.5	47.2	232
Fig. 2b	1/10	0.2	1.66	4.95	0.89	24K	0.299	0.1170	9.05	7.3	19.3	147
Fig. 2c	1/10	0.3	0.29	4.30	1.65	13K	0.126	0.0939	21.12	15.6	11.8	117
(Sunamura and Horikawa, 1974)												
2	1/10	0.2	1.65	3.4	1.0	576K	> 0.200	0.0898	7.16	6.2	30.6	305
4	1/10	0.2	1.65	7.6	1.0	576K	> 0.274	0.1278	13.27	10.2	16.6	203
6	1/10	0.2	1.65	7.6	2.0	288K	0.116	0.0702	18.16	20.0	48.1	473
8	1/20	0.2	1.65	3.4	1.0	576K	> 0.178	0.0898	7.16	6.4	30.6	305
10	1/20	0.2	1.65	7.6	1.0	576K	> 0.241	0.1278	13.27	10.7	16.6	203
12	1/20	0.2	1.65	7.6	2.0	288K	> 0.114	0.0702	18.16	15.2	48.1	473
14	1/30	0.2	1.65	3.4	1.0	576K	> 0.143	0.0898	7.16	6.7	30.6	305
16	1/30	0.2	1.65	7.6	1.0	576K	> 0.200	0.1278	13.27	11.6	16.6	203
(Watts and Dearduff, 1954)												
Fig. 7	1/20	0.22	1.65	15.24	2.0	108K	0.160	0.0943	31.30	29.9	28.0	567

CHAPTER 89

DEPTH OF DISTURBANCE OF SAND IN SURF ZONES

Michael K. Gaughan¹

ABSTRACT

A coring technique employed during wave action allowed accurate measurement of the depth of vertical mixing b_m of fluorescent sand tracer grains within the surf zone of a gently sloping Pacific Ocean beach (beach slope tangent $s = 0.012$). The depth b_m is the distance from the sediment surface to the lower limit of observed tracer grains within the inner portion of the core. Although this definition is only strictly applicable to a rectangular distribution of tracer concentration with depth, the b_m results were quite similar to those using concentration-weighted depth averages of Crickmore (1967). For one winter regime experiment, vertical cross-sectional contour maps of tracer concentration normalized by the local core maximum were drawn with concentrations computed for each 0.4cm slice. Trends present are (1) in the onshore-offshore direction the maximum concentration is at the bed surface shorewards of the mid-surf position and 0.4 cm to 1.2 cm below the bed seaward of the mid-surf position, and (2) in the longshore direction (at the mid-surf position) the maximum concentration lies 0.4 cm to 1.6 cm below the bed surface. For spilling breaker heights H_b between 75 cm and 150 cm, histograms of b_m were clearly different for spring/summer and fall/winter experiments: the mean and standard deviation (in parenthesis) are 0.5 cm (0.5 cm) and 1.1 cm (0.5 cm), respectively. These results are substantially less than both the 3.0 cm and the 20 cm to 40 cm disturbance depths per 100 cm of H_b reported by King (1951) and by Otvos (1965) and Williams (1970). The discrepancy with Otvos and Williams is due to the much different breaking process; in their experiments small breakers ($H_b = 5$ cm to 30 cm) plunged directly onto steep beach slopes ($s = 0.1$) causing large b_m . The tracer grain's longer exposure to bottom stresses of passing surf bores may explain King's greater disturbance depths. Her sampling interval was one semi-diurnal tidal period T versus the span $0.02 T$ to $0.32 T$ in this study.

INTRODUCTION

It is well accepted that waves breaking on a beach are the prime mechanism for transporting sand. However, quantitative measurements of the waves and moving sand are scarce

¹CICESE, 843 Espinoza Ave., Ensenada, Baja Calif., Mexico

(e.g., Komar, 1969). Several methods of measuring the volume of moving sand are available (e. g., sand tracers, bedload and suspension traps, periodic surveys). Because of the successes of the sand tracer technique in estimating sand transport in rivers (Crickmore, 1967) and in narrow surf zones (10 m) with large tidal ranges (8 m) (Komar, 1969), the present study investigates its usefulness in wide surf zones (100 m) with moderate tidal ranges (2 m) typical of many Pacific Ocean beaches. A few experiments of this nature were also carried out by Komar (1969).

For non-steady, two-way transport the spatial integration method is to be preferred over both the time integration and steady dilution methods when using sand tracer to calculate sediment transport (Crickmore, 1967); these are essentially the conditions normally present within surf zones. Following Komar (1969) the mean velocity of transport is calculated from the tracer concentration distribution by taking moments of the tracer concentration in the direction of interest. For example, the mean longshore velocity of the tracer centroid is given by

$$V = \frac{\sum_{x=0}^{x_b} \sum_{y=-\infty}^{\infty} y C_{(x,y)} / t}{\sum_{x=0}^{x_b} \sum_{y=-\infty}^{\infty} C_{(x,y)}} \quad (1)$$

where $C_{(x,y)}$ is the concentration at a longshore distance y from the injection line and at an offshore distance x , and t is the time between release and sampling. The bulk volume sand transport is then

$$S_1 = b \cdot X_b \cdot V_1 \quad (2)$$

where b is the depth of disturbance and X_b is the surf zone width. Preliminary field studies of the depth of disturbance are described in this report.

FIELD SITE AND METHODS

Because much of the surf zone remains covered with water at low tide on the beach of interest, a method was devised of obtaining samples under these conditions. It consists of a coring pipe with a transparent sampling tube inserted into the bottom end (Figure 1). This beveled transparent tube is then forced into the sand by leaning on and rotating the coring pipe. The coring pipe is withdrawn slowly, and once the transparent tube holding the sand sample surfaces, it is immediately inspected for sand movement. If there is any, the sample must be retaken. Although the method is not extremely rapid, the cores provide accurate measurements of the depth of disturbance and the tracer concentration.

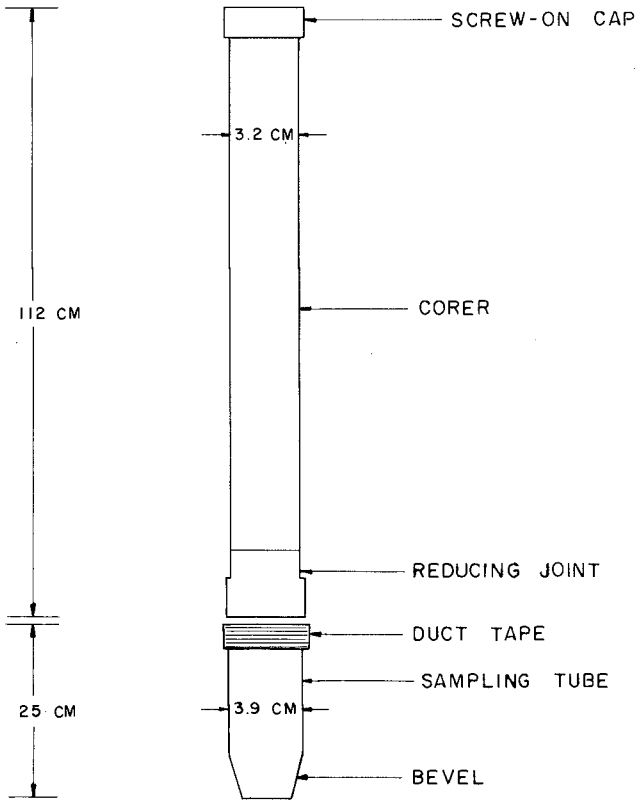


Figure 1.- Sand coring apparatus.

The beach is 15 km long with a lagoon entrance located midway between the rocky headlands at both ends (Figure 2). It is backed by small sand dunes along most of its length. At the site of interest the foreshore sand is relatively fine-grained (Figure 3) with the beach slope tangent $s = 0.012$. Most of the time the waves form spilling breakers, with the larger waves occurring from fall through spring. Waves from the south are blocked by Punta Banda and Todos Santos Island. Several sampling intervals and grid sizes were tested to gain familiarity with the surf zone time and length scales. During all nine of the field studies a single point source of tracer sand (20 kg to 50 kg) was injected at an estimated mid-surf position.

RESULTS AND DISCUSSION

A comparison was made of three definitions of the depth of disturbance. (1) b_{max} is the maximum depth below the sand surface of tracer grains observed in the sample. (2) A second disturbance depth b_2 is given by

$$b_2 = h(c_1 + c_2 + c_3 + \dots) / c_{max} \quad (3)$$

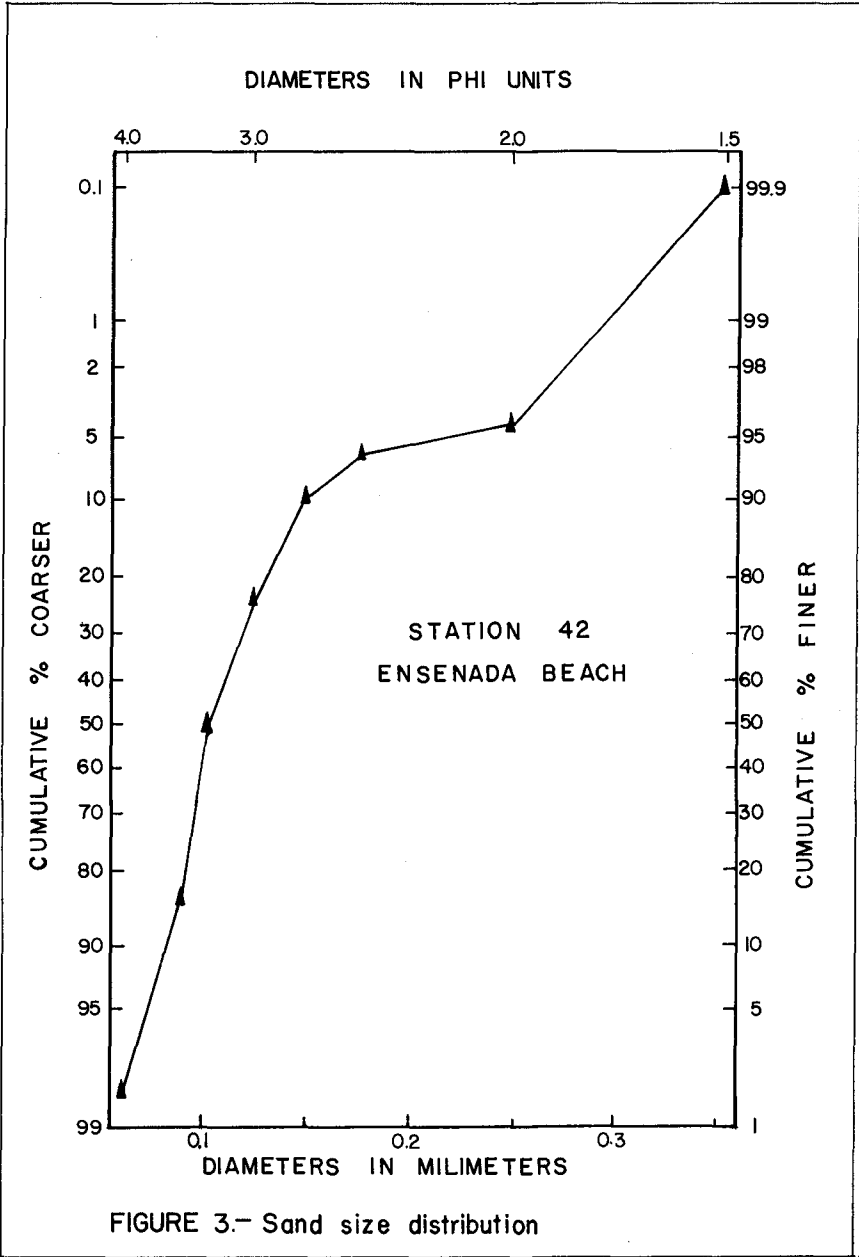
where h is the core slice thickness (0.4 cm), c_1, c_2 are the concentrations of core slices, 1,2 where 1 denotes the top slice, c_{max} is the maximum concentration in the core under study. This equation is only directly applicable when the concentration/depth distribution has a continuous negative gradient, with the concentration decreasing sequentially with depth (Crickmore, 1967). The more irregular tracer distributions were first simplified to eliminate any positive gradients and then treated as above (Crickmore, 1967). Figure 4 illustrates this procedure for various forms of concentration distributions (Crickmore, 1967), and it also defines the types of distributions. (3) A third definition of the depth of disturbance b_3 is computed from equation (3) by using the mean concentration (averaged over the number of cores) for each slice where c_{max} is the maximum of these averages. For 60 core samples from the 9DEC experiment the results are

$$\begin{aligned} \bar{b}_{max} &= 1.1 \text{ cm} \\ \bar{b}_2 &= 1.0 \text{ cm} \\ \bar{b}_3 &= 1.2 \text{ cm} \end{aligned}$$

where $\bar{}$ indicates mean value. Since there is less than ten percent difference between b_{max} and the concentration-weighted disturbance depths, b_{max} is used throughout the remainder of this paper.



Figure 2.- Study area near Ensenada, Baja California, Mexico.



$$b_2 = h (C_1 + C_2 + C_3 \dots) / C_{max}$$

where

h = core thickness (mm)

c = tracer concentration in number of grains per gram of sand

CONCENTRATION

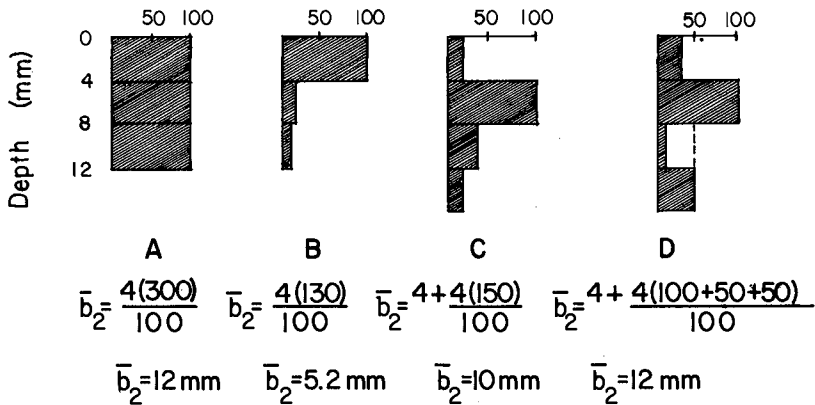


Figure 4.- Calculation of depth of mixing from core distribution. A. Abrupt decrease. B. Continuous negative gradient. C. One positive gradient. D. Two positive gradients (Crickmore, 1967).

The most frequently occurring concentration distribution type is Type C, which has the maximum concentration in the slice one layer below the surface. It is predominant offshore of the mid-surf position, while Types A and B, which have maxima at the surface slice, occur in nearly half of the samples shoreward of the mid-surf position (Figure 5). The near-to-shore occurrence of Types A and B may be due to sand deposition in the upper swash zone which is continually receding seaward during the ebbing tide. In addition, although the distribution type and b_{max} may be a function of bedform, in this case the vertical scale of the bedforms was very similar. The ripple height of both the usual sand ripples and the backwash ripples was approximately 0.5 cm to 1.0 cm. For the sheet flow-flat bed conditions the depth of the mobile layer was likely less than 0.5 cm, but it is possible some grains mixed to greater depths.

The apparent independence of the disturbance depth on time for wave exposures of 15 min to 240 min is seen in Figure 6. These samples were within 5 m of the mid-surf release site. The 18MAR data have two b_{max} greater than 2.0 cm, and these may be due to sampling within the dyed sand patch before it has had time to disperse; indeed after 80 min the release site still contained much of the tracer sand below a thin moving surface layer (0.3 cm) of undyed sand. The 26MAR samples ($b_{max} = 0.8$ cm) were cored under very strong current conditions ($H_b \approx 2$ m) resulting in a very rapid dispersion of tracer sand. On this occasion the bed was always flat. Careful measurements of stake heights within 20 m of the release site showed erosion of less than 0.5 cm. Unfortunately the coring technique had not been sufficiently mastered and only 19 cores were acceptable for analysis. The 31MAY data also display very little trend of increasing burial with time.

Figures 7 to 11 are the results of sampling 3 hours after tracer release. Again the tracer sand was exposed to breakers during an ebbing tide. Due to the approximate nature of the mid-surf position, it was considered inappropriate to combine data from separate field studies. Individually some of the measurements do show b_{max} to vary with distance from the injection site; the 25NOV data show a slight tendency to decrease with distance from the injection site.

The disturbance depth seems to show a marked dependence on the incident wave conditions (Figure 12). These histograms represent two classes of field experiments; (1) the spring/summer regime and (2) the fall/winter regime. As yet unprocessed wave measurements may generate a hypothesis attempting to explain these observations.

Vertical cross-sectional contour maps were drawn to study the horizontal variation of the tracer concentration versus depth. Figure 13 demonstrates the effectiveness of this presentation as shorewards of the release site, the maximum con-

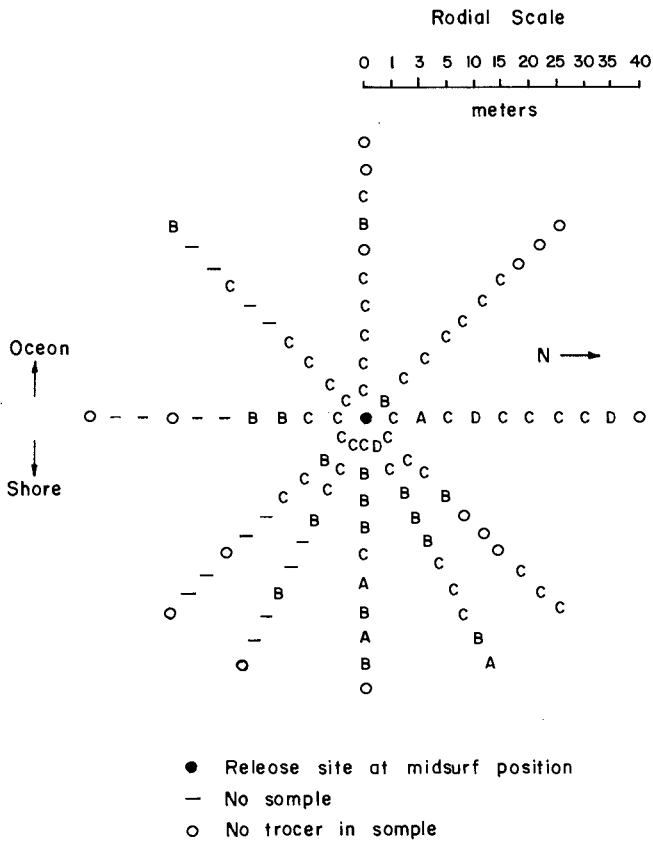


Figure 5.- Map of core concentration distribution types .

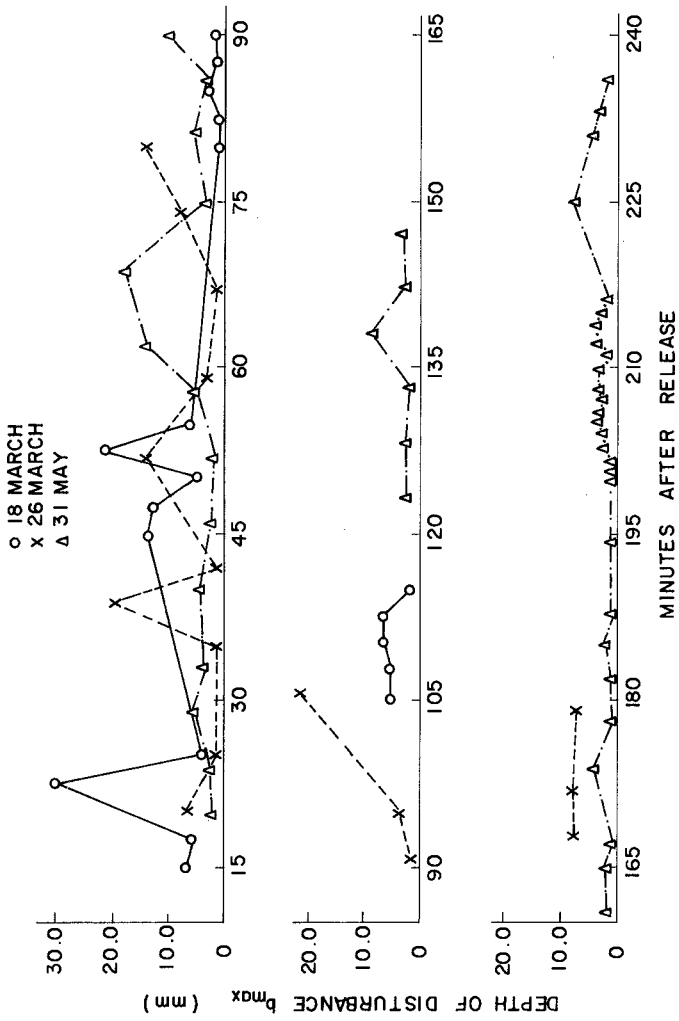


Figure 6.- Depth of disturbance versus time after release within 5 m. of release site at midsurf position.

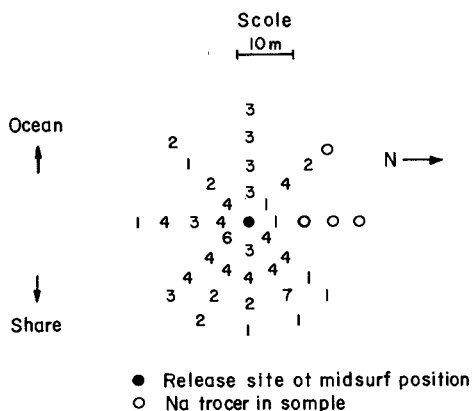


Figure 7.- Map of b_{max} for 13 June (mm)

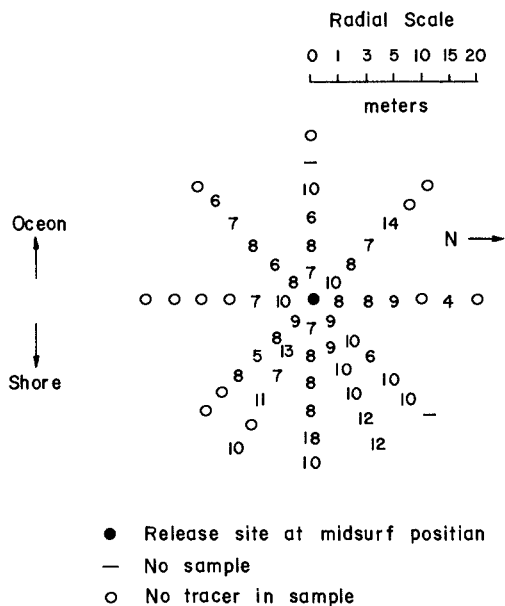


Figure 8.- Map of b_{max} for 13 Oct. (mm)

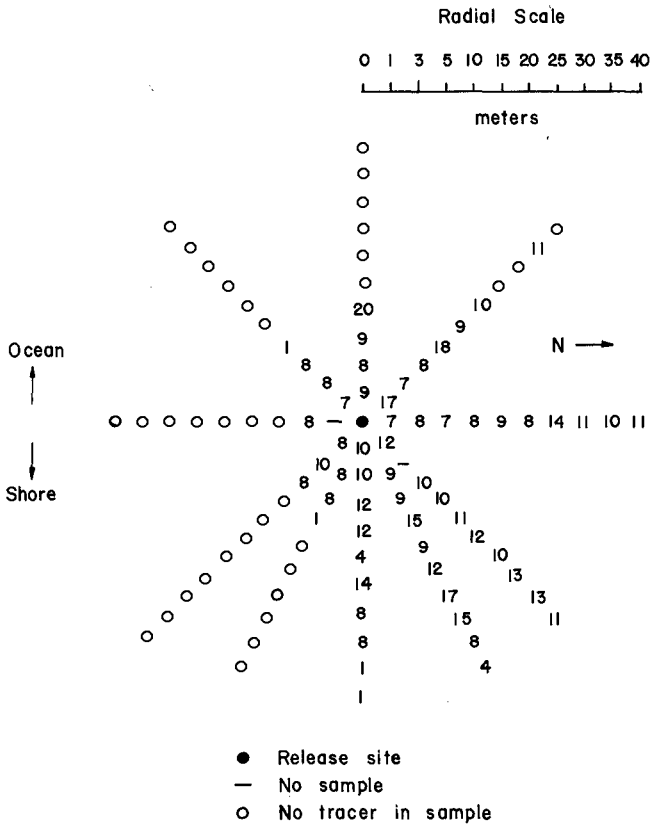


Figure 9.- Map of b_{max} for 10 Nov. (mm) .

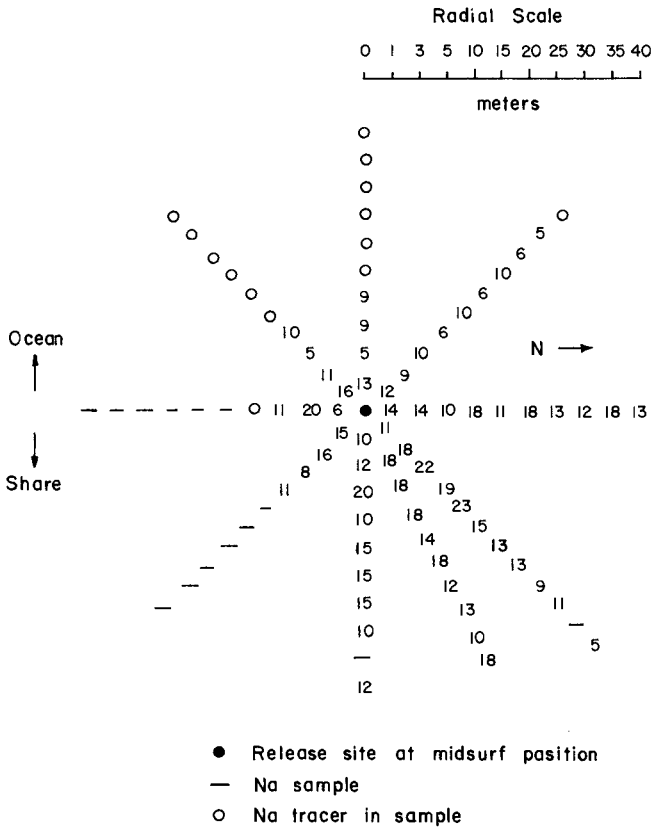


Figure 10.- Map of b_{max} for 25 Nov. (mm) .

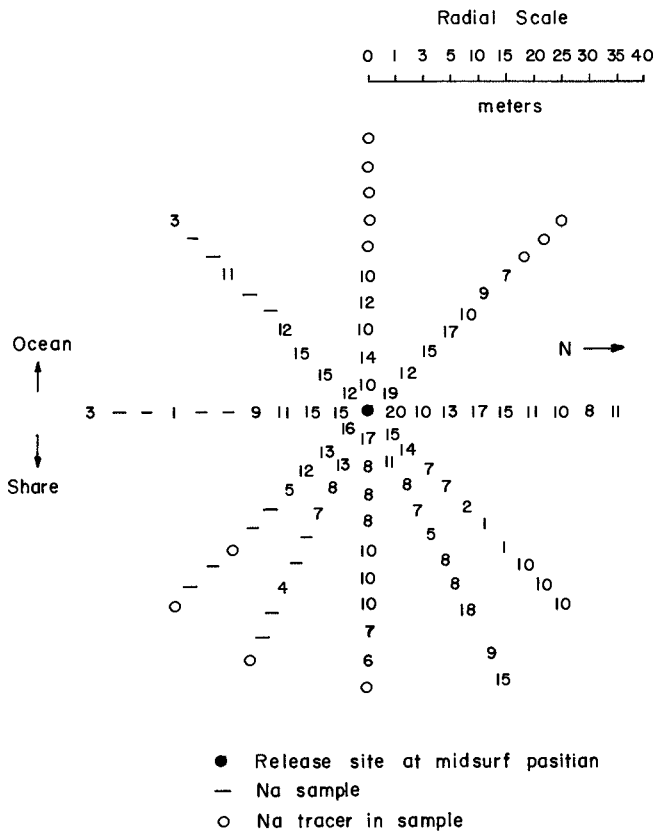


Figure 11.- Map of b_{max} for 9 Dec. (mm) .

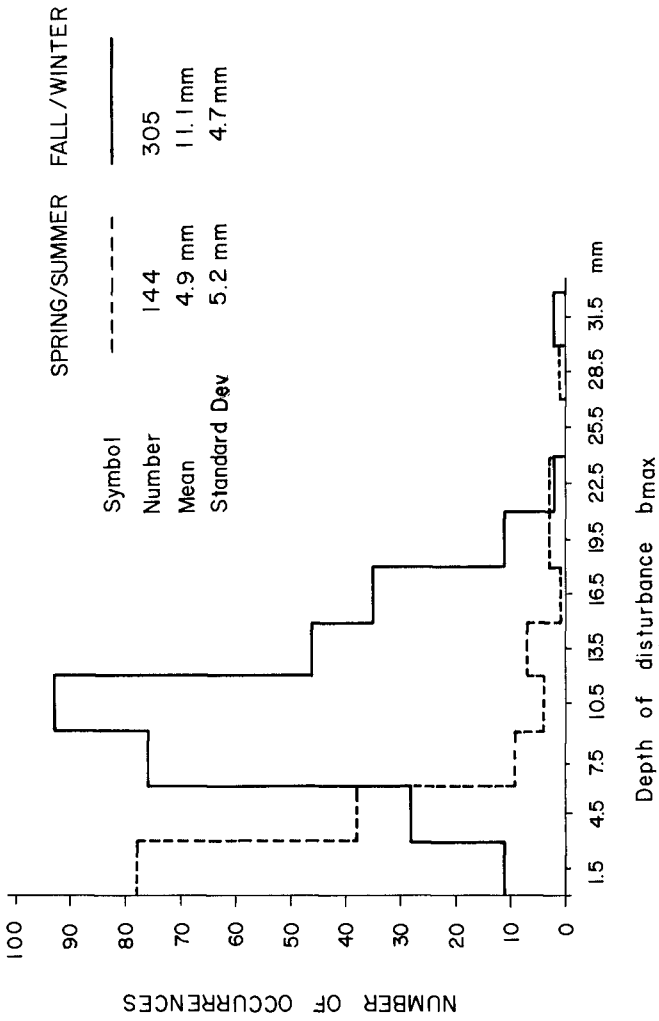


Figure 12 - Histograms of the depth of disturbance bmax for the spring/summer and fall/winter regimes .

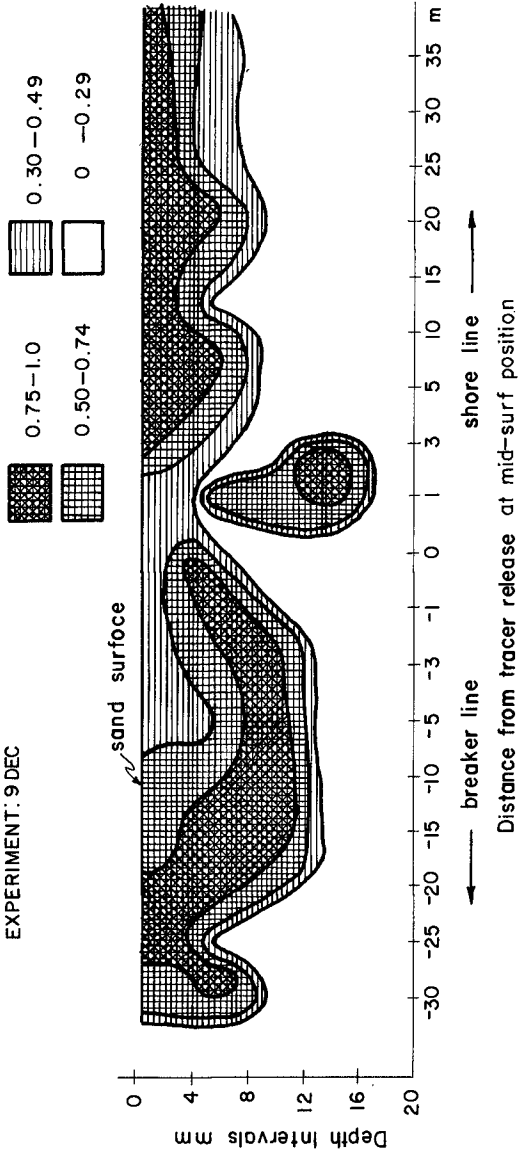


Figure 13.— Cross-sectional contour map of tracer concentration in the onshore-offshore — direction. Each concentration has been divided by the maximum in its core sample.

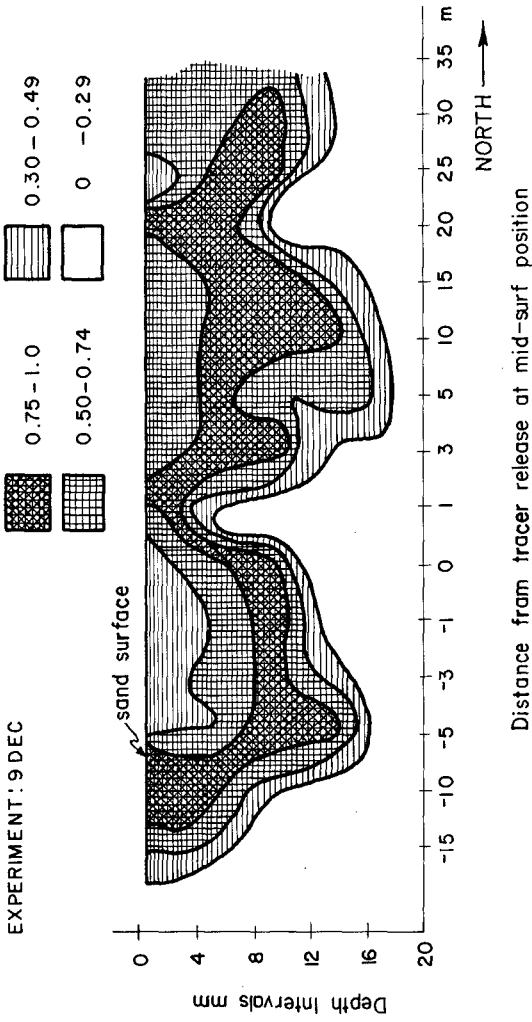


Figure 14.- Cross-sectional contour map of tracer concentration in the alongshore direction. Each concentration has been divided by the maximum in its core sample.

centration is clearly at the bed surface, while seaward of the release site, it is below the surface. The maximum concentration is nearly always below the bed surface along a line parallel to the shoreline located at the mid-surf position (Figure 14).

SUMMARY

All field experiments involved sand tracer exposure to waves in the surf and swash zones during an ebbing tide. For these conditions some important observations are:

1. For breaker heights between 75 cm and 150 cm, the disturbance depth b_{max} averaged much less than in previous experiments of King (1951), Otvos (1965), and Williams (1970).
2. A comparison of b_{max} to concentration-weighted disturbance depths showed less than 10% difference for 60 cores from one field study.
3. Maxima of tracer concentration were located at the bed surface shoreward of the mid-surf release site and just below the bed seawards of the release site. The indication of deposition in the receding upper swash limit leads to hypothesis regarding the calculation of the longshore transport. Obviously, as this tracer sand leaves the longshore transport zone, the longshore transport would be underestimated if these samples were included in the calculation of the moments about the injection line.
4. b_{max} did not show any strong trends either with time near the release site nor with distance from the release site three hours following injection.

REFERENCES

- Crickmore, M. J., 1967, Measurement of sand transport in rivers with special reference to tracer methods, *Sedimentology*, 8, 175 - 228.
- King, C. A. M., 1951, Depth of disturbance of sand on sea beaches by waves, *Jour. Sed. Petrology*, 21, 131 - 140.
- Komar, P. D., 1969, The longshore transport of sand on beaches, Phd. Thesis, Univ. of California at San Diego, 143 pp.
- Otvos, E. G., 1965, Sedimentation-erosion cycles of single tidal period on Long Island Sound beaches, *Jour. Sed. Petrology*, 35, 604 - 609.
- Williams, A. T., 1971, An analysis of some factors involved in the depth of disturbance of beach sand by waves, *Mar. Geology*, 11(3), 145 - 158.

CHAPTER 90

SCALE RELATIONS FOR EQUILIBRIUM BEACH PROFILES

Hideaki NODA*

ABSTRACT

The scale relation for modeling natural beach profiles in the laboratory and selecting size of model sediments is examined. The results are shown for relating scale law to the dimensionless fall velocity and the model law for selecting sand size is proposed.

INTRODUCTION

There are many practical problems related to coastal engineering, which may be solved by using movable bed scale models of the coastal zone. The scale model must obey the laws of sediment transport in order to obtain satisfactory results. However, sediment transport in the coastal zones is so complex that the mechanism is not fully understood.

Some authors have attempted to find a model law relationship for equilibrium beach profiles. Yalin¹⁾ derived a scale law for the offshore zone using a bed velocity based on laminar boundary conditions. Brebner, Kamphuis and Paul²⁾ have performed extensive experimental tests on movable-bed models using light weight sediment, and Le Méhauté³⁾ presented a scaling law for coastal movable-bed models in the breaker zones.

The purpose of this study is finally to determine the scale law relationship for coastal movable-bed model. As first step, this paper concerns itself with the derivation of proper scale laws for modeling of equilibrium beaches.

DIMENSIONAL ANALYSIS AND SCALE RELATIONS

The depth of beach profiles, h may be expressed as a function of

$$H_0, T, D, \rho, \rho_s, g, \nu, x$$

where H_0 the deepwater wave height, T the period of waves, D the representative diameter of sediments, ρ the fluid density, ρ_s the sediment density, i_0 the initial slope of the beach, g the acceleration of gravity, ν the kinematic viscosity of fluid, and x the horizontal distance measured from the initial shoreline as shown in Figure 1.

The beach profile may be expressed as

$$h = f (x, H_0, T, D, \rho, \rho_s, i_0, g, \nu) \dots\dots\dots(1)$$

By using the relation of $L_0 = gT^2/2\pi$ and neglecting the fluid viscosity,

* Professor, Department of Civil Engineering, Faculty of Engineering, Tottori University, Tottori, Japan

Equation (1) may be rewritten in the dimensionless form as

$$\frac{h}{L_0} = f \left(\frac{x}{L_0}, \frac{H_0}{L_0}, \frac{H_0}{D}, \frac{\rho_s}{\rho}, i_0 \right) \dots \dots \dots (2)$$

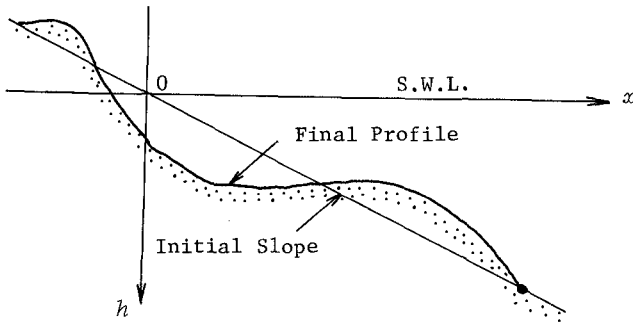


Figure 1 Definition sketch

The author⁴⁾ previously indicated that the deepwater wave steepness H_0/L_0 and the ratio of the deepwater wave height to the median diameter of sediment H_0/D_{50} are important parameters governing generation of longshore bars. It appears that these two parameters also are useful to describe the equilibrium beach profiles formed in the simplified conditions of onshore-offshore sediment motion due to wave action.

From Equation (2), the following scale laws may be derives as

$$\left. \begin{aligned} n_h &= n_{L_0}, n_x = n_{L_0}, n_{i_0} = 1 \\ n_{H_0} &= n_{L_0}, n_{D_{50}} = n_{H_0}, n_{\rho} = n_{\rho_s} \end{aligned} \right\} \dots \dots \dots (3)$$

where n is the scale expressed as model value over prototype one. Equation (3) implies that the horizontal and the vertical scales of beach profiles must be identical with those of wave motion, that is, the models cannot be distorted, and that $n_{\rho} = n_{\rho_s} = 1$, i.e. the density of model sediment must be selected so as to be identical with that of prototype one, since it is necessary to use water in model, while particle sizes must be scaled down geometrically.

By taking the effect of the fluid viscosity into account, the another expression of the beach profiles was presented by Brebner and others²⁾ as

$$\frac{h}{L_0} = f \left(\frac{x}{L_0}, \frac{H_0}{L_0}, \frac{H_0}{D_{50}}, \frac{D_{50}\sqrt{gH_0}}{\nu}, \frac{\rho_s}{\rho}, i_0 \right) \dots \dots \dots (4)$$

As pointed out by them, the effect of $D_{50}\sqrt{gH_0}/\nu$ is negligible when the value of $D_{50}\sqrt{gH_0}/\nu$ is large enough to ensure a turbulent flow around the grain in both prototype and model. However, it will be shown that

the effect of the Reynolds number cannot be negligible in the scale of laboratory. On the other hand, scale laws on H_0/L_0 and $D_{50}\sqrt{gH_0}/\nu$ yield conflicting values for n_{D50} , i.e. the former is $n_{D50} = n_{H_0}$ and the latter $n_{D50} = n_{H_0}^{-0.5}$. Therefore, both conditions of similarity cannot be satisfied concurrently.

Dean⁵⁾ presented a model for the shift from a storm to a swell profile and found that the dimensionless parameter $\pi w_f/gT$, where w_f is the fall velocity of grains, is important in governing the equilibrium beach profiles. Therefore, an equation of the equilibrium beach profiles is expressed as

$$\frac{h}{L_0} = f \left(\frac{x}{L_0}, \frac{H_0}{L_0}, \frac{\pi w_f}{gT}, i_0 \right) \dots\dots\dots (5)$$

From Equation (5), the following scale laws may be derived as

$$\begin{aligned} n_{H_0} = n_{L_0}, \quad n_{w_f} = n_T = n_{L_0}^{1/2} \\ n_h = n_{L_0}, \quad n_x = n_{L_0}, \quad n_{i_0} = 1 \end{aligned} \dots\dots\dots (6)$$

The fall velocity of a grain w_f is expressed as

$$w_f = \left\{ \frac{4}{3} \left(\frac{\rho_s}{\rho} - 1 \right) \frac{gD}{C_D} \right\}^{1/2} \dots\dots\dots (7)$$

where C_D is the drag coefficient of sphere grain and a function of Reynolds number $w_f D/\nu$. If it is assumed that

$$C_D = \alpha \left(\frac{w_f D}{\nu} \right)^{-m} \dots\dots\dots (8)$$

the fall velocity w_f is given by

$$w_f^{2-m} = \frac{4}{3\alpha} \left(\frac{\rho_s}{\rho} - 1 \right) \frac{g}{\nu^m} D^{1+m} \dots\dots\dots (9)$$

where α and m are constants. Substituting Equation (9) into dimensionless parameter $\pi w_f/gT$, this quantity may be rewritten as follows:

$$\frac{\pi w_f}{gT} = \beta \left(\frac{\rho_s}{\rho} - 1 \right)^{1/(2-m)} \left(\frac{D_{50} g H_0}{L_0} \right)^{m/(2-m)} \left(\frac{H_0}{L_0} \right) \left(\frac{H_0}{D} \right)^{1/2} \dots\dots (10)$$

where $\beta = \sqrt{\pi/2} \cdot (4/3\alpha)^{1/2-m}$.
 If $D = D_{50}$, the dimensionless parameter is a function of $(\rho_s/\rho)-1$, H_0/L_0 , H_0/D_{50} and $D_{50}\sqrt{gH_0}/\nu$. Therefore it is evident that the application of Equation (5) for the scale law coordinates the contradiction mentioned above.

EXPERIMENTAL EQUIPMENT

Laboratory experiments of the equilibrium beach profiles were made using a steel wave tank 20m long, 0.5m wide and 0.6m deep at the Hydraulic Laboratory, Tottori University. Waves were generated by a

flatter type generator with a 2 HP electric motor. Incident wave heights were measured by a capacitance type wave gage which was installed at the part of constant water depth, $h = 0.4\text{m}$.

Two kinds of the well-sorted sand were used in the experiments and the median diameters of these sands were 0.3mm and 0.6mm, respectively.

All tests were carried out in the initial slope of 1:10, for sufficient time to form an equilibrium beach. The equilibrium beach profiles were measured with a point gage along the flume centerline.

EXPERIMENTAL RESULTS

(a) Scale relations based on Equation (3)

Figure 2 shows that the different model beach profiles are compared

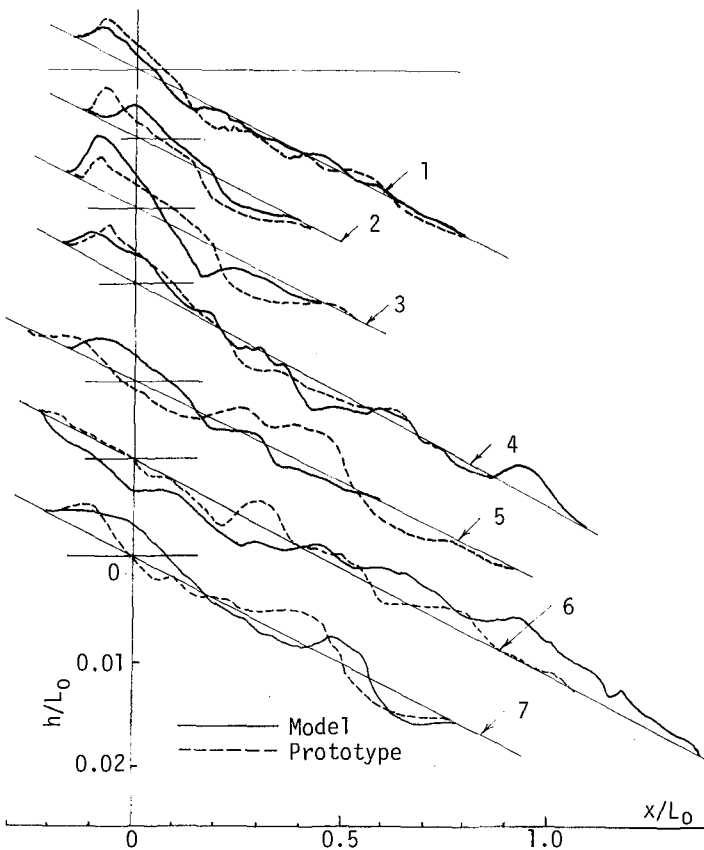


Figure 2 Comparisons of dimensionless profiles between prototype and model, based on Eq.(3)

Table 1 Test conditions and scale relations

NO.	H_0 (cm)	T (sec)	D_{50} (mm)	H_0/L_0	H_0/D_{50}	n_{H_0}	$n_{D_{50}}$
P-1	9.00	2.54	0.34	0.0089	264	1/1.88	1/2
M-1	4.78	1.85	0.17		281		
P-2	2.68	1.04	0.60	0.0155	44	1/2	1/2
M-2	1.32	0.74	0.30				
P-3	5.38	1.46	0.60	0.0163	90	1/2	1/2
M-3	2.70	1.03	0.30				
P-4	10.98	2.06	0.60	0.0165	183	1/2	1/2
M-4	5.50	1.46	0.30				
P-5	6.15	1.13	0.60	0.0309	103	1/2	1/2
M-5	3.08	0.80	0.30				
P-6	13.24	1.60	0.60	0.0332	221	1/2	1/2
M-6	6.62	1.13	0.30				
P-7	5.40	0.90	0.60	0.0427	90	1/2	1/2
M-7	2.70	0.64	0.30				

with their corresponding prototype beach profiles, and Table 1 indicates the test conditions and the scale relations represented by Equation (3). Since the tests were carried out using natural sand in both prototype and model, the scale was selected in values of $n_{H_0} = n_{L_0} = n_{D_{50}} = 1/2$, in order to avoid the use of the cohesive range for the model sand.

The comparisons in the test results indicate a closer similarity between prototype and model of foreshore berm in No. 4, but significant differences still exist beyond wave breaking zone. Furthermore considerable differences are observed for the other test results. Therefore, it is evident that the scale laws based on Equation (3) cannot be adopted.

It seems that the differences between comparable profiles depend upon the influence of fluid viscosity. The values of H_0/L_0 and H_0/D_{50} are same for each comparable profiles, but the model value of $D_{50}\sqrt{gH_0}/\nu$ cannot be equivalent to prototype one for each test. From the test results of No. 4, 5 and 6, it is apparent that the lower limit of model beaches, which is related to beginning sand movement due to wave motion, makes a considerable difference from that of prototype beaches. This fact shows that the difference is related to Reynolds number $D_{50}\sqrt{gH_0}/\nu$.

(b) Scale relations based on Equation (6)

Figure 3 shows model and prototype beach profile data plotted in the dimensionless form x/L_0 versus h/L_0 , and Table 2 indicates the test conditions and the scale ratios of H_0 and D_{50} . These results were obtained by using the scale laws represented by Equation (6). The comparisons between the test results indicate a closer similarity. From these figures, however, a few differences of profiles between prototype and model are observed. The reason is due to a few difference of the value of $\pi\omega_f/gT$ as shown in Table 2. Therefore, it should be noted that the dimensionless parameter $\pi\omega_f/gT$ must be severely preserved in model tests.

Figure 4 shows that the various model beach profiles are compared with a prototype beach profile (DP) in order to clarify the effect of

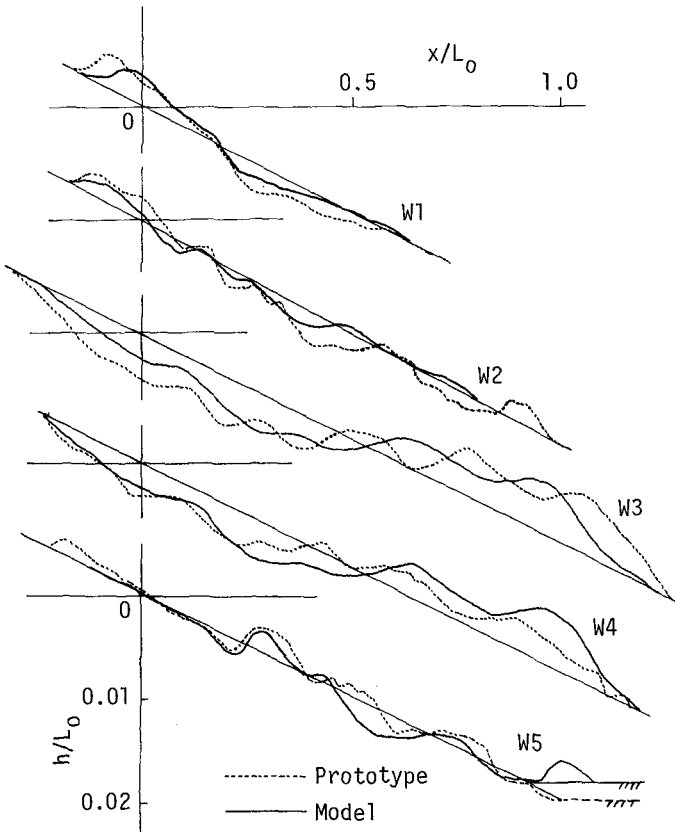


Figure 3 Comparisons of dimensionless profiles between prototype and model, based on Eq. (6)

Table 2 Test conditions and scale ratios

NO.	H_0 (cm)	T (sec)	D_{50} (mm)	H_0/L_0	$\frac{\pi W_f}{gT}$	n_{H_0}	$n_{0.50}$
W1-P	10.98	2.06	0.60	0.0166	0.0132	1/8.32	1/2
W1-M	1.32	0.74	0.30	0.0155	0.0153		
W2-P	5.50	1.64	0.30	0.0165	0.0085	1/2.62	1/1.76
W2-M	2.10	0.90	0.17	0.0166	0.0071		
W3-P	5.83	1.07	0.28	0.0326	0.0099	1/2.41	1/1.65
W3-M	2.42	0.70	0.17	0.0312	0.0092		
W4-P	6.62	1.13	0.30	0.0332	0.0088	1/2.74	1/1.76
W4-M	2.42	0.70	0.17	0.0312	0.0092		
W5-P	13.24	1.60	0.60	0.0332	0.0196	1/2.00	1/1.25
W5-M	6.61	1.12	0.48	0.0337	0.0215		

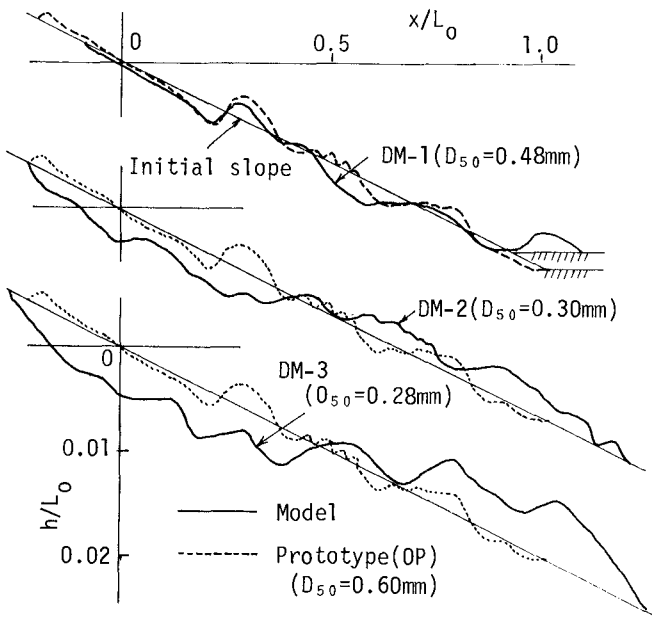


Figure 4 Comparisons of influence of sand size

Table 3 Test conditions for Figure 4

NO.	H_0 (cm)	T (sec)	D_{50} (mm)	H_0/L_0	$\frac{\pi W F}{gT}$	n_{H_0}	$n_{D_{50}}$
DP	13.24	1.60	0.60	0.0332	0.0196		
DM-1	6.61	1.12	0.48	0.0337	0.0215	1/2	1/1.25
DM-2	6.62	1.13	0.30	0.0332	0.0088	1/2	1/2
DM-3	5.83	1.07	0.28	0.0326	0.0099	1/2.27	1/2.14

size of model sediment. From this figure, it is evident that the upper model profile (DM-1) is coincident with the prototype one (DP), but the middle (DM-2) and the lower (DM-3) model profiles do not reproduce the prototype profiles correctly. In the upper case of Figure 4, it is apparent that the value of $n_{D_{50}}$ is less than that of n_{H_0} . From these test results, sand size used in model may be chosen so as to reproduce prototype beach profiles.

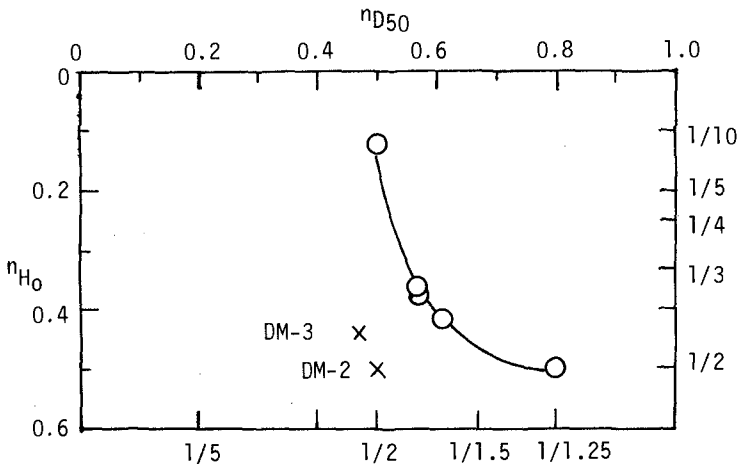
Figure 5 Relationship between n_{H_0} and $n_{D_{50}}$

Figure 5 indicates the relationship between n_{H_0} and $n_{D_{50}}$ to be recommended when using the sand in model. In this figure, it is apparent that the test results of DM-2 and 3 do not reproduce the prototype beach profiles.

(c) Possibility of distorted movable-bed models

Figure 6-a indicates dimensionless comparison between equilibrium beach profiles obtained by Watts⁶⁾ (prototype) and Iwagaki and Sawaragi⁷⁾ (model), and their test conditions are presented in Table 4. From Table 4, it is evident that the horizontal and the vertical scales with respect to wave motion are $n_{H_0} = 1/4$ and $n_{L_0} = 1/8$ respectively, and $n_{D_{50}} = 1/2.14$. Therefore, $N_w = n_{H_0}/n_{L_0} = 2$, where N_w is the model distortion of wave motion. On the other hand, model scale of distortion with respect to beach profile, N is expressed as

$$N = n_x/n_h \dots\dots\dots(11)$$

where n_x and n_h are the horizontal and the vertical scales of the beach profiles, respectively.

Figure 6-b shows that the model beach profile is coincident with the prototype one, if $N = N_w^{0.7}$. The relationship among N , N_w and $n_{D_{50}}$ is not clear and therefore no general conclusion can be drawn as to validity of the distorted models. However, it is recognized that it is possible to use the distorted models in practical purpose.

CONCLUSIONS

The following conclusions may be derived from the laboratory test results developed in this paper:

- 1) Two dimensional equilibrium beach tests, based on the scale laws preserving the parameters H_0/L_0 and H_0/D_{50} , indicate that it is impossible to obtain closer similarity between prototype and model beach profiles.
- 2) Closer similarity between the profiles are obtained when dimensionless fall velocity is preserved and the sediment size may be modeled by Figure 5 when using the sand in model.
- 3) Based on the experimental results, it is found that the coastal movable-bed model may be distorted. However, no general conclusion can be drawn as to the validity of the distorted models.

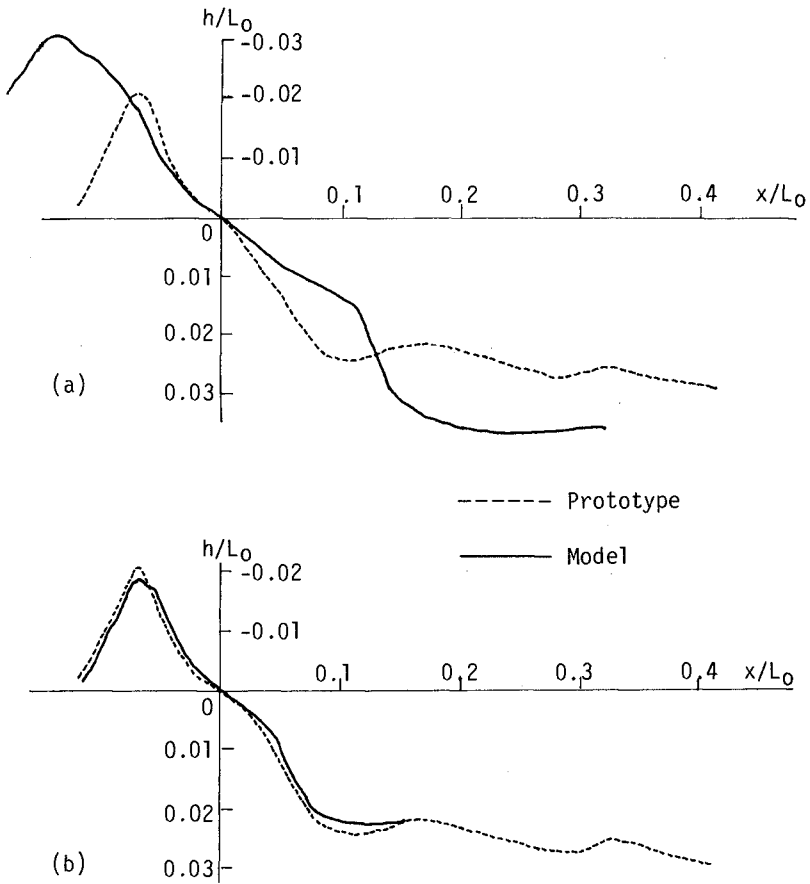


Figure 6 An example of distorted model profile

Table 4 Test conditions for distorted model

	H_0 (cm)	T (sec)	D_{50} (mm)	i_0
prototype	12.66	2.68	3.44	1/20
model	3.17	0.95	1.61	1/10

REFERENCES

1. Yalin, S., Method for Selecting Scales for Models with Movable Bed Involving Wave Motion and Tidal Currents, Proc. of 10th Congress of IAHR, Vol. 1, 1963.
2. Paul, M.J., Kamphuis, J.W. and Brebner, A., Similarity of Equilibrium Beach Profiles, Proc. of 13th Conference on Coastal Engineering, 1972, pp.1217-1236.
3. Le Mehaute, B., A Comparison of Fluvial and Coastal Similitude, Proc. of 12th Conference on Coastal Engineering, 1970, pp.1077-1096.
4. Iwagaki, Y. and Noda, H., Laboratory Study of Scale Effects in Two-dimensional Beach Processes, Proc. of 8th Conference on Coastal Engineering, 1962, pp.194-210.
5. Dean, R.G., Heuristic Models of Sand Transport in the Surf Zone, Proc. of Conference on Engineering Dynamics in the Surf Zone, 1973, pp.208-214.
6. Watts, G. M., Laboratory Study of Varying Wave Periods on Beach Profiles, BEB, Tech. Memo., No. 53, 1954.
7. Iwagaki, Y. and Sawaragi, T., Laboratory Study of Equilibrium Beach Profiles and Sand Transport by Breaking Waves, Proc. of 2nd Conference of Coastal Engineering in Japan, 1955, pp.99-106, (in Japanese).

CHAPTER 91

TRACKED VEHICLE FOR CONTINUOUS NEARSHORE PROFILES

Richard J. Seymour*
Alan L. Higgins**
David P. Bothman***

INTRODUCTION

The measurement of nearshore profiles has been the traditional method for evaluating on- and offshore transport of beach sand by waves. The measurement on that portion of the beach face which is dry at low tide presents no particular problems and can be effectively accomplished with conventional rod and level surveying techniques. Once the measurement location moves into the wet part of the foreshore, however, the problems rapidly increase. In general, it requires an extremely dedicated rod man to remain on position in breakers larger than a meter, although measurements in breakers up to 2 meters in height have been accomplished on a nonroutine basis. When waves exceed this height, or when the water depth exceeds the ability of a man to stand and hold the rod, this method must be abandoned. In deeper water, and well outside the surf zone, a boat and fathometer approach is normally employed with considerable loss in vertical and horizontal accuracy. In particular, the vertical resolution is decreased by the uncertainties in knowledge of the instantaneous sea level because of the combination of tides, waves and storm surge. If the tides are large and the waves small, it is possible to achieve an overlap between the boat survey and the shore survey. When the wave height exceeds the ability of the boat to operate, this method also must be abandoned. Although larger boats can operate in larger waves, they are generally also restricted to deeper water.

The result of all of the restrictions described above is that profiles can be measured with reasonable accuracy only during periods of low waves. Unfortunately, the episodes of greatest interest are the rapid cutting back of the beach face and the accompanying offshore bar building which occur during times of high waves. The technology to measure the storm waves has been available for many years. The ability to correlate wave parameters with offshore transport rates requires the ability to make accurate profiles from the dry beach through and beyond the breaker line under storm wave conditions. This paper describes a vehicle that was developed to meet this need.

*California Department of Navigation and Ocean Development

**Scripps Institution of Oceanography

***Scripps Institution of Oceanography

PROFILER VEHICLE

The approach selected to obtain storm wave profiles was to use a remotely controlled tracked vehicle capable of traversing to a sufficient distance offshore to pass well beyond the breaker line. Design limits were set at 450 meters maximum offshore excursion and 10 meters maximum operating depth.

The basic vehicle is a small tractor originally used for light construction work. The 7.5 horsepower internal combustion engine was replaced by an electric motor of the same power which is powered from an umbilical cable. The motor is run totally immersed in the reservoir of hydraulic fluid to protect it from sea water. This reservoir is maintained at ambient pressure by a large flexible diaphragm. The electric motor drives the hydraulic pump in the tractor which in turn powers the tracks through a hydraulic motor driving through a transmission and mechanical clutches and brakes on each tread. The manual controls for steering the tractor were replaced by hydraulic rams controlled by solenoid valves.

The profiler is shown in Figure 1. The mechanism above the tractor provides for cable tension control when the profiler is returning to shore. The simplest maneuver is for the profiler to be stopped at the end of the profile and then returned on the same line. Eliminating turns avoids any concern with running over the cable in the case where strong longshore currents may exist and also provides for a second realization of the profile. Since the cable drag over the bottom is large, it dominates the tension at the land end so that the winch operator cannot tell if the cable is slack at the profiler from measuring tension on shore. A cable tension measuring system is provided utilizing a hydraulic cylinder and a pressure measuring transducer as the load sensing element. This tension is displayed onshore on a meter and is used to adjust the winch takeup speed. The cable, which contains 16 conductors, is jacketed in plastic and uses Kevlar strength members to reduce weight. Its diameter is 2.5 cm and its length is 450 meters.

SUPPORT EQUIPMENT

The profiler is transported on a military surplus ten-wheel-drive truck capable of traversing sandy beaches. This truck also mounts a 75KVA diesel powered generator which delivers 220 v, 3 phase power to the electric motor and 110V current to the instruments and controls. Two aluminum ramp sections are stored below the truck bed and are used to load and unload the profiler. Also mounted on the truck bed is a winch powered by a 3HP variable speed direct current



PROFILER DESCENDING FROM
TRANSPORT VEHICLE
PRIOR TO BEACH SURVEY.
THE PROFILER WILL BE
TURNED THROUGH 180° BEFORE
BEGINNING A RUN.

FIGURE 1

motor which is used to unwind and wind the umbilical cable. The truck and other support equipment is shown in Figure 2.

INSTRUMENTATION

Consideration was given initially to using a stadia rod on the profiler so that conventional surveying methods could be extended into deeper water. However, it was decided that the poor visibility associated with flying spray from heavy wave breaking, plus the great distance offshore, would make optical tracking very difficult. Therefore, the decision was made to utilize onboard instruments that would not require any penetration of the surface.

Horizontal position as well as vertical profiles are obtained from the on-board instrumentation. A two-axis vertical gyroscope, a flux gate compass, and an odometer for each tread are sampled once per second. These data are multiplexed, converted to serial format, and transmitted by cable to the beach. The on-board instruments are contained in a waterproof enclosure.

The shielded cable used for data transmission is jacketed together with the power cable. All conductors of both cables are connected to slip rings to allow rotation of the winch. Double rings are provided for data conductors. At the stationary slip rings, the power conductors leading to the diesel generator and control box branch away from the data lines.

The serial multiplexed data are transmitted asynchronously over a single line. On the beach, it is immediately recorded on a digital cassette tape recorder. An electronic monitor box decodes the data, either as it is recorded, or from tape recorder playback. Any channel can be selected for binary display on LED panel lights. The control box used for vehicle control and data recording is shown in Figure 3.

Motions of the profiler are calculated relative to its starting position, which is a fixed point on the beach of known position. Distance traveled along the path is obtained from the odometers, assuming a constant, empirically determined slippage rate. At each observation, the odometer and compass azimuth readings form the magnitude and direction of a displacement vector. Horizontal position is updated by adding this vector to the previous position fix.

Vertical excursions are tracked in the same manner. The two-axis vertical gyro measures pitch and roll. The sine pitch angle is integrated with respect to odometer output to obtain profiles. Roll



THE TRANSPORT VEHICLE FOR THE PROFILEK
IS A TEN-WHEEL DRIVE TRUCK.
A DIESEL POWERED GENERATOR AND A
VARIABLE SPEED WINCH MAKE THE SYSTEM
COMPLETELY SELF-CONTAINED.

FIGURE 2



THE PROFILER CONTROL CONSOLE
CONTAINS TRACTOR DIRECTIONAL CONTROLS,
A PLOTTER FOR POSITION VISUALIZATION,
THE DATA RECORDER AND INSTRUMENT
STATUS CHECKOUT EQUIPMENT.

FIGURE 3

angle is not used in position calculations but is valuable for construction of topography between transects.

$$x(t) = \sum_{i=1}^t l_i \cos \theta_i \cos \phi_i$$

$$y(t) = \sum_{i=1}^t l_i \sin \theta_i \cos \phi_i$$

$$z(t) = \sum_{i=1}^t l_i \sin \phi_i$$

l_i = distance traveled in i^{th} observation period

θ = azimuth

ϕ = pitch

Since the profiles will ideally be measured along a straight line, the course is plotted in printer-plot style with a compact thermal printer. A commercial programmable calculator has been modified so that data can be entered remotely. An interface circuit is used to bypass the buttons. Program steps required to calculate and plot the course are stored on a magnetic card. Each time the tractor moves a fixed distance, its new position is approximated from the reported azimuth and plotted. Although the plotted position is not exact, it indicates to the operator when course corrections are necessary. The control console is shown in Figure 3.

After the beach experiment is over, the cassette tape is played back through an interface circuit, into an IBM 1800 computer. This interface, like the decoder box on the beach, converts the data back to parallel form and generates synchronization pulses as external interrupt. Computation of courses and profiles and interpolation of topography is done after the data are transferred.

PERFORMANCE

Initial evaluations have been performed on the handling characteristics and profile measurement capabilities at Scripps Beach, California. Figure 4 shows the profiler entering the ocean on a calibration run. In order to provide verification of the actual profile traversed, a mast was added temporarily to support a standard surveyor's stadia rod. A base line was set up on the beach with a surveyor's level on the profile range line and a transit for measuring angles at the other end of the base line. The tractor was stopped at approximately 5 m intervals to allow recording of the position and elevation. Observations have shown that no track slippage occurs, even on steep and soft beach slopes. Further, no vertical elevation changes occur even when the tractor remains stopped for long periods under breakers greater than one meter in height as illustrated in Figure 5 and Figure 6.

The results of one of the calibration runs at Scripps Beach is shown in Figure 7. The agreement between the measured and computed profiles is excellent, with a maximum error of only a few centimeters. The actual slope measurement record is also depicted to illustrate how the apparently noisy slope signal integrates to a smooth profile.

Figure 8 shows the profiler returning on a calibration run.

ACKNOWLEDGEMENTS

The development of this profiler was undertaken with financial support from the Nearshore Sediment Transport Study (described by Seymour and Duane in these proceedings) and from the Naval Ocean Systems Center, San Diego, California.



THE PROFILER
ENTERING THE SURF ZONE
ON A CALIBRATION TRIAL.
THE STADIA ROD IS MOUNTED FOR CALIBRATION
PURPOSES ONLY AND IS NOT NORMALLY USED
WITH THE PROFILER.

FIGURE 4



THE PROFILER
TRAVERSING THE BREAKER ZONE

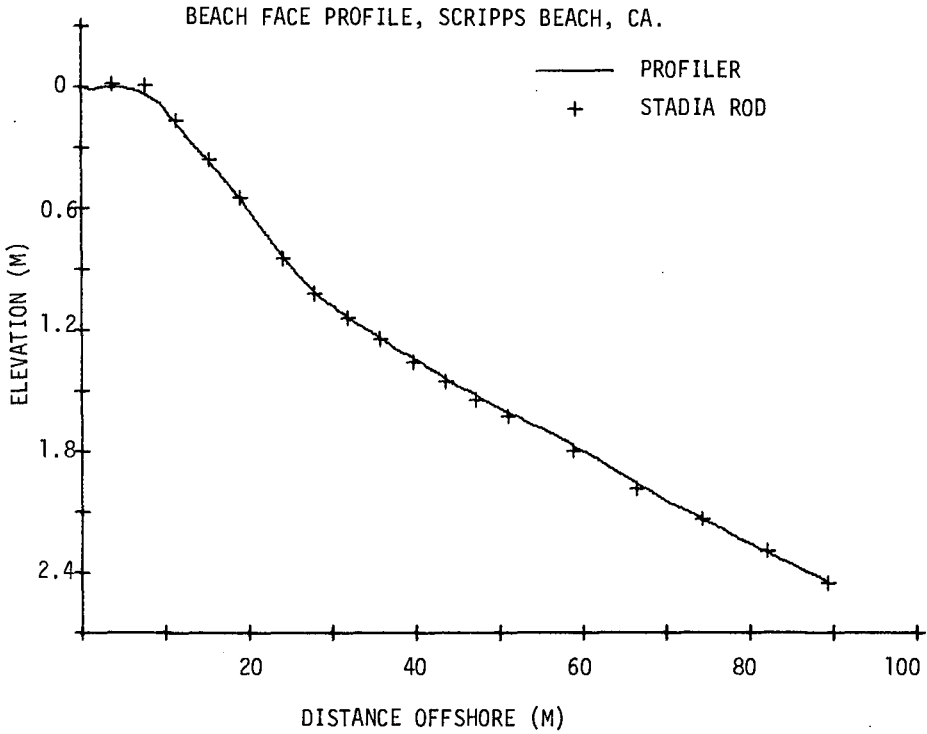
FIGURE 5



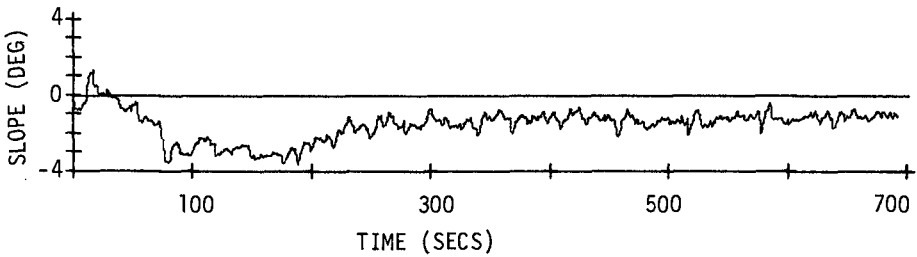
AN UNDERWATER VIEW
AT A DEPTH OF APPROXIMATELY 2 M.

FIGURE 6

FIGURE 7



COMPARISON OF BEACH PROFILE MEASURED WITH STADIA ROD AND LEVEL WITH THAT OBTAINED FROM INTEGRATING THE PROFILER RECORD BELOW.



RECORD OF SLOPE OBTAINED FROM PROFILER INSTRUMENTATION. RECORD DURATION CORRESPONDS WITH DISTANCE TRAVERSED IN TOP FIGURE.



THE PROFILER
COMPLETING A RETURN RUN AT SCRIPPS BEACH

FIGURE 8

CHAPTER 92

THE NEARSHORE SEDIMENT TRANSPORT STUDY

Richard J. Seymour*
David B. Duane**

INTRODUCTION

The models for predicting longshore transport of sediment along straight coastlines that are presently in general use were derived empirically from very sparse measurements of both the forcing function (waves and currents) and the response function (sediment motions). A detailed treatment of these data sets is contained in Greer and Madsen (1978). In addition to the generally unsatisfactory nature of the basic measurements upon which they were based, the models may be deficient because they fail to employ such potentially significant factors as wind stress, sediment size distribution, bottom slope and spatial variations in waves and currents, including the effects of rip currents. Although these models have served certain engineering needs, there is a strong measure of uncertainty in the coastal engineering community about their general applicability. Certainly, because they are empirical rather than physically reasoned models, there is no rational means for extending their usefulness to predicting transport where coastlines are not straight -- such as the case of a tidal inlet.

The economic impact of sediment transport in the nearshore regime is enormous and the need for improved predictive tools appears to be universally accepted. To be most useful, these improved models must be globally applicable. This implies very strongly that they must be based upon a thorough understanding of surf zone dynamics and the details of the response of the sediment. The surf zone flow fields are highly complex and nonlinear, implying an equally complex and difficult system of sediment responses. Characterizing the entire forcing and response functions simultaneously requires large and expensive field measurement programs that greatly exceed the present state of the art of measurement and analysis. The approach of the last two decades of single investigators working at laboratory scale or in the ocean with a few single point measurements would not appear to ever meet these needs. However, the present costs for coastal dredging and shoreline protection, which can be measured in billions of dollars on a world scale, argue for a major undertaking to develop better predictive tools.

In an attempt to satisfy these needs, an ad hoc group was formed at the Fifteenth Coastal Engineering Conference in Honolulu to plan a large scale and coordinated series of investigations leading to improved sediment transport predictive models. Less than a year later, the Nearshore Sediment Transport Study was initiated under the sponsorship of the Office of Sea Grant. The program began as a focused

*California Dept. of Navigation and Ocean Development, Scripps Institution of Oceanography, UCSD, La Jolla, California
**Office of Sea Grant, Washington, D. C.

cooperative effort among four Sea Grant universities and several government agencies. With the advent of new legislation authorizing national Sea Grant projects to meet national needs, the NSTS program has recently been designated as the first such national program.

OVERALL OBJECTIVES

The major objective of the NSTS program is to produce improved engineering models for predicting the motion of sediment along straight coastlines under the action of waves and currents in the nearshore regime. From its inception, the program has been directed towards the development of models that can be simply employed, without recourse to large computers, and which will depend upon measurements or observations that can be obtained at reasonable cost.

PROGRAM ORGANIZATION

Management of a technically complex program and the effective coordination of a large and diverse group of investigators required the creation of a management concept substantially different from existing Sea Grant programs. The program employs a two tier management structure which is shown schematically in Figure 1. The Sea Grant Director has appointed an advisory group referred to as the NSTS Review Committee. This group, all experienced in nearshore processes, reviews proposals and makes funding recommendations to the Director, formulates overall program direction and reviews the progress of the investigators. A second tier group, known as the NSTS Steering Committee, is formed of the senior investigators. The chairman of this group functions as the Project Manager and is an ex officio member of the Review Committee. The Steering Committee formulates the details of the project program, plans and executes cooperative field programs and conducts workshops to promulgate the findings of the study to the coastal engineering community.

The NSTS program will have a duration of five years and is anticipated to cost more than \$4 million. During this period, four major functional elements will be completed. These are:

1. The development of necessary instruments and measurement and analysis techniques.
2. The determination by field investigation of the parameters which are significant to nearshore sediment transport and the collection of sufficient data to allow characterization of these significant parameters.
3. The formulation of models to characterize the forcing and response functions and overall engineering models for predicting transport.
4. The verification of these models using field data obtained in this program.

These functions, although they are logically sequential, will be undertaken with a certain level of concurrence as indicated by their schedule in Figure 2.

NSTS PROGRAM MANAGEMENT

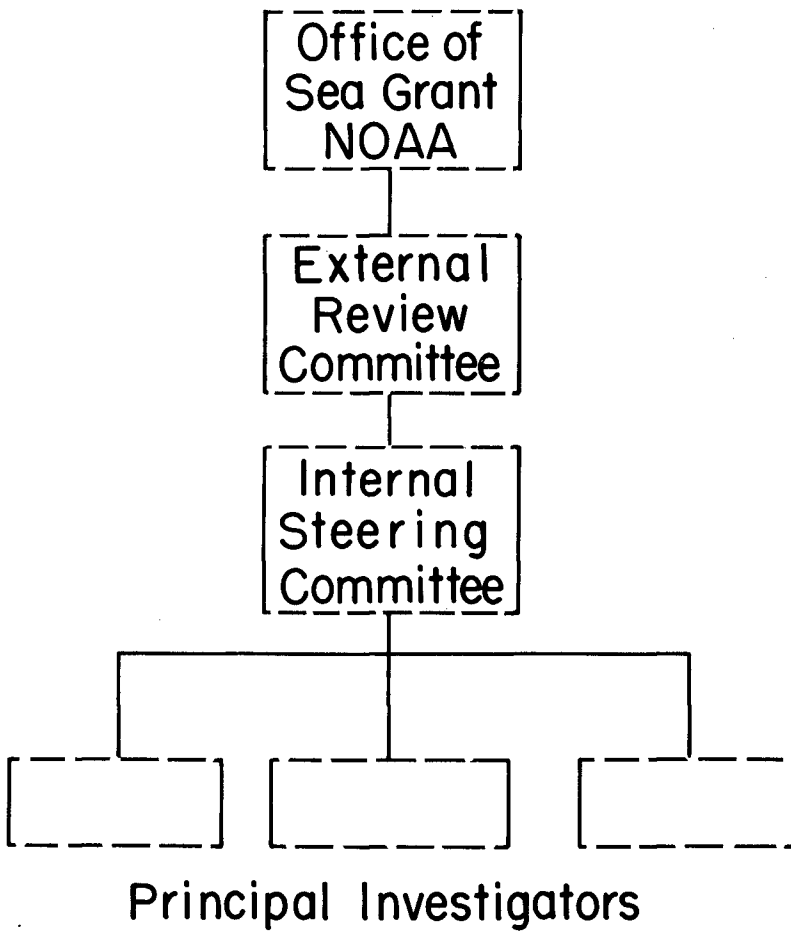


FIGURE 1

FUNCTIONAL SCHEDULE

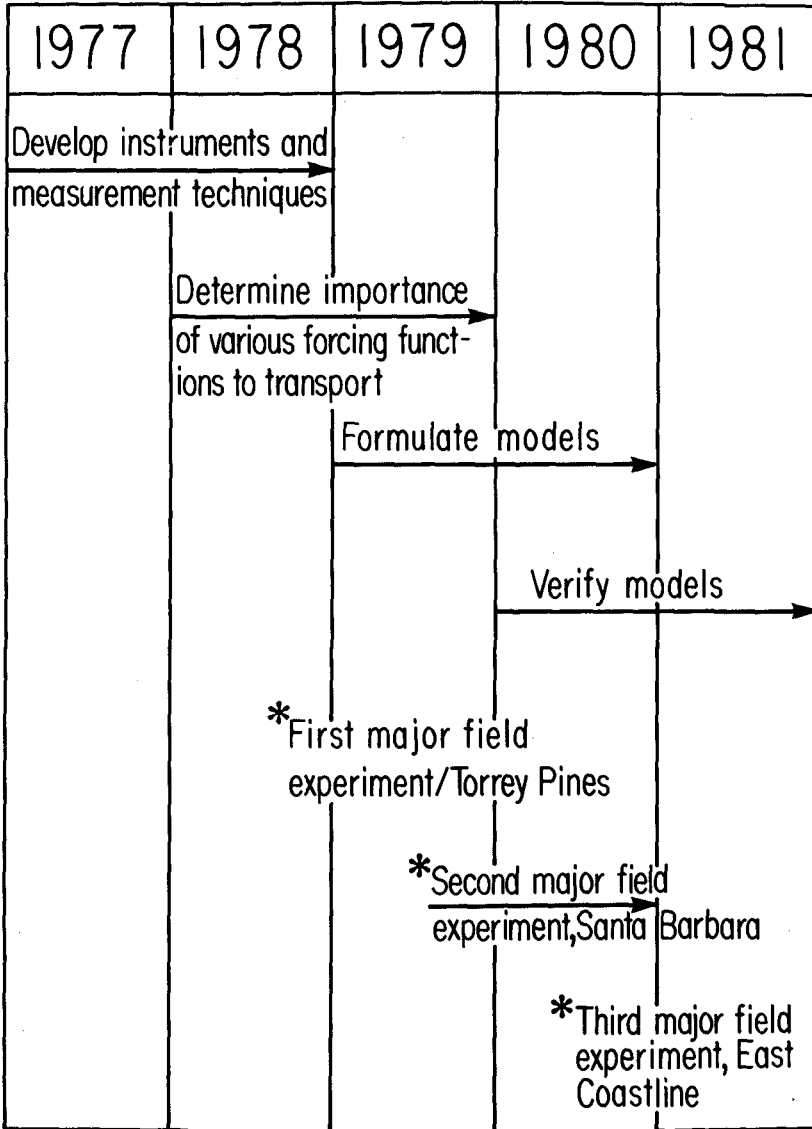


FIGURE 2

PROGRAM ATTRIBUTES

To accomplish the NSTS objectives, it was understood from the earliest planning sessions that the program must contain certain attributes which would set it apart from many prior efforts. Among the most important of these attributes are:

1. NSTS is a broad-based program with many investigators from a large number of institutions. It is an attempt to bring together many experienced practitioners to plan and execute a series of major experiments which would vastly exceed the capabilities of a single investigator.
2. NSTS is a field-oriented program. Laboratory or numerical modeling are not foreseen as significant elements of the project.
3. The NSTS field experiments will attempt to measure, simultaneously, the details of both the velocity field within the surf zone and the sediment response to these velocities. This is in recognition of the fact that there are significant spatial variations in sediment transport within the nearshore regime and that the ability to understand and predict these variations is a prerequisite to developing a universally applicable engineering model.
4. The NSTS measurement program will encompass a large number of parameters that are potentially significant to a predictive model.
5. The NSTS predictive model is intended to be two-dimensional. That is, it will predict on-offshore movement as well as longshore movement of sediment.

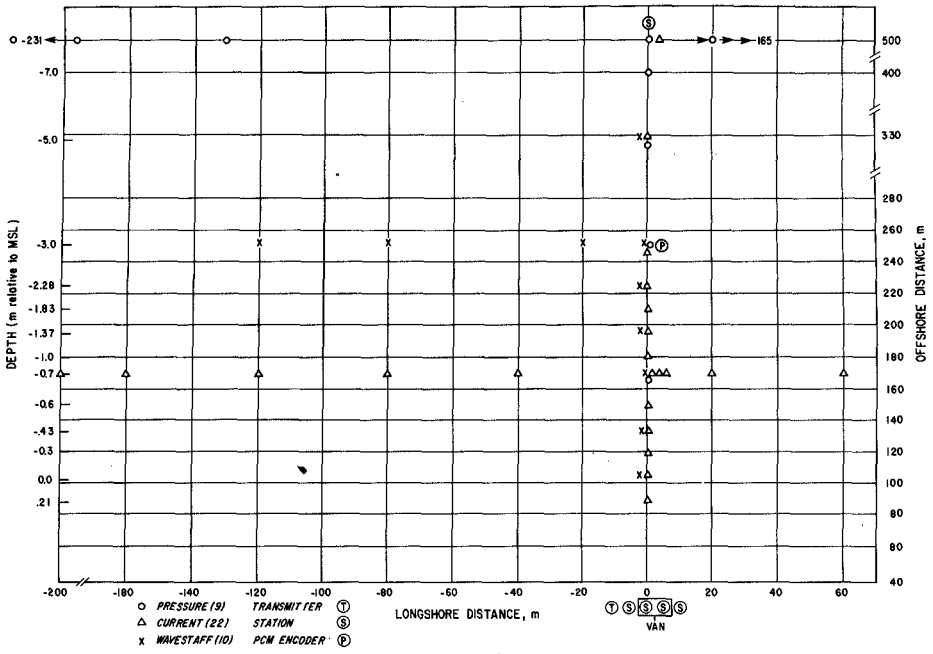
TASK ORGANIZATION

The overall NSTS program is composed of a large number of tasks, each one of which addresses a major element in the project and which is under the direction of one or more principal investigators. In the following sections, the tasks which were funded in 1977 and 1978 will be described followed by those which are anticipated to be funded in 1979 and subsequent years.

TASKS PRESENTLY FUNDED

.....Field Investigation of Currents and Surface Elevation Within the Surf Zone. This task is under the joint direction of R. T. Guza of Scripps Institution of Oceanography and E. B. Thornton of the Naval Postgraduate School. Guza and Thornton (1978) describes the type of measurements and analyses undertaken in this task. A typical instrumentation plan is shown in Figure 3. The major objective of this task is to characterize the three-dimensional velocity field within the surf zone and to relate this to the observed incident wave climate.

.....Field Investigation of Rip Currents, under the direction of R. A. Dalrymple of the University of Delaware. This task is concerned with the measurement and characterization of rip currents, determination of



TYPICAL PLAN FOR INSTRUMENT PLACEMENT IN A LARGE FIELD
EXPERIMENT TO DEFINE SURF ZONE DYNAMICS
FIGURE 3

the mechanism for their formation and their correlations with the incident wave climate. A general treatment of the approach is contained in Dalrymple (1978).

.....Development of a Model Characterizing Surf Zone Dynamics. This task, under the direction of O. S. Madsen of Massachusetts Institute of Technology, will undertake the synthesis of a simplified model for predicting the surf zone velocity field from known incident wave and wind characteristics. This model will then be verified using the data sets from Guza and Thornton, and Dalrymple.

.....Field Investigation of Longshore Sediment Transport, under the direction of D. L. Inman of Scripps Institution of Oceanography. This task has as its major objective the characterization of longshore transport using fluorescent tracers, point samplers of suspended concentrations and continuous measurement of bedload transport with monitoring instruments.

.....Field Investigation of Suspended Sediment, under the direction of R. W. Sternberg at the University of Washington. This is a complementary project to the Inman task and is concerned with the development and deployment of monitoring instruments to obtain continuous measurements of suspended sediment concentrations.

.....Field Investigation of On-Offshore Transport, under the direction of R. J. Seymour of Scripps Institution of Oceanography. This task is concerned with the characterization of on-offshore transport by means of precision profiling. Seymour, Higgins and Bothman (1978) describes a remotely controlled profiling tractor developed in this task.

.....Evaluation of Candidate Experimental Sites, under the direction of R. G. Dean of the University of Delaware. This task is concerned with identifying and ranking potential sites along the United States coastlines for large scale field experiments.

1978 FIELD EXPERIMENT

The first major experiment under the NSTS program is scheduled for October - November 1978 at Torrey Pines Beach in Southern California. All of the field investigations described above will be undertaken jointly in this one-month-long effort. Approximately 90 channels of data will be sampled at 16 Hz for at least four hours each day for the 30-day period.

TASKS TO BE FUNDED IN 1979 AND SUBSEQUENT YEARS

.....Field Investigation of Tidal Currents. In this task, long-term (on the order of months) measurements of longshore current will be made at locations through the surf zone and correlated with surface tides. The objective is to determine if tidal current is a significant factor within the surf zone.

.....Field Investigation of the Effect of Winds. In this task, the wind stress on the surf zone will be characterized and correlated with the surface elevation and velocity fields measured in other tasks. The objective is to determine under what conditions the wind is a significant parameter in nearshore transport.

.....Field Investigation of the Interactions with Periodic Planform Changes. In this task, rhythmical changes in beach contour in the longshore direction will be measured and correlated with changes in the velocity field measured by others. The objective is to determine if these planform shapes must be accounted for in the transport model.

.....Field Investigation of Three-Dimensional Velocity Structure. This task is a continuation of the present effort associated with characterizing the nearshore velocity field.

.....Field Investigation of the Incident Directional Wave Field. In this task, directional arrays will be employed to characterize the incident wave field. These data will form the basis for models that predict velocity or transport rates from known wave data.

.....Field Investigations of Longshore Transport. This task is a continuation of the two present programs on longshore transport with increased emphasis on the use of continuously monitoring instruments.

.....Field Investigation of On-Offshore Transport. This is a continuation of the present program using beach profile data with emphasis on rapid offshore movement under storm waves.

.....Develop an Improved Engineering Model for Nearshore Sediment Transport. This is the task in which all of the other findings of the program are synthesized into a single model.

FUTURE FIELD EXPERIMENTS

The major field experiment for 1979 will occur at Leadbetter Beach, west of the harbor at Santa Barbara, California. The experiment sites for 1980 and beyond are presently under study. However, it is planned that one East Coast site will be selected.

AVAILABILITY OF DATA

Under the NSTS management plan, data are exchanged freely between investigators. The investigator collecting the data has proprietary publishing rights for a period of one year. After that time, all data becomes available to the public. In addition to the normal papers, texts and reports, all of the raw data will be archived through the National Oceanographic Data Center and will be available on magnetic tape.

REFERENCES

- Dalrymple, R. A.: 1978. "Rip Currents and Their Genesis." Proc., 16th Int'l. Conf. on Coastal Engr., Hamburg, September 1978.
- Greer, M. N. and O. S. Madsen: 1978. "Longshore Sediment Transport Data: A Review." Proc., 16th Int'l. Conf. on Coastal Engr., Hamburg, September 1978.
- Guza, R. T. and E. B. Thornton: 1978. "Longshore Current Variability." Proc., 16th Int'l. Conf. on Coastal Engr., Hamburg, September 1978.
- Seymour, R. J., A. L. Higgins and D. P. Bothman: 1978. "Tracked Vehicle for Continuous Nearshore Profiles." Proc., 16th Int'l. Conf. on Coastal Engr., Hamburg, September 1978.

CHAPTER 93

LONGSHORE SEDIMENT TRANSPORT DATA: A REVIEW

by

Matthew N. Greer⁽¹⁾ and Ole Secher Madsen⁽²⁾

INTRODUCTION

Siltation rates anticipated at harbor entrances, in navigation channels and at inlet structures as well as possible adverse effects caused by these and other coastal engineering constructions are often assessed based on considerations of longshore sediment transport rates. The ability to predict the longshore sediment transport rate is consequently of considerable importance in many coastal engineering problems. The engineering need for an ability to predict longshore sediment transport rates is evidenced by the fact that the development of empirical relationships preceeded, by decades, any attempts at rigorous analyses of the mechanics of sediment transport processes in the surf zone.

A predictive relationship for longshore sediment transport rates, which enjoys considerable popularity in the United States, is the empirical relationship suggested by the U.S. Army (1973), Coastal Engineering Research Center (CERC) in their Shore Protection Manual (SPM-73). This relationship suggests the longshore transport rate, Q_{ℓ} , to be proportional to the wave energy flux factor, $P_{\ell S}$, and is given by the formula

$$Q_{\ell} = 7.5 \cdot 10^3 P_{\ell S} \quad (1)$$

in which Q_{ℓ} is in cubic yards per year and $P_{\ell S}$ is evaluated based on the significant wave characteristics in the ft-lb-sec system. The wave energy flux factor is given by

$$P_{\ell S} = \frac{1}{16} \rho g H_b^2 C_{g,b} \sin 2\theta_b \quad (2)$$

in which ρ is the fluid density, g is gravity, H , C_g and θ are the wave height, group velocity and angle of incidence, respectively, all evaluated at breaking as denoted by the subscript b .

(1) Grad. Res. Assist., MIT-WHOI Joint Program in Oceanographic Engineering, R.M. Parsons Lab., Dept. of Civil Engineering, MIT, Cambridge, Massachusetts

(2) Doherty Associate Professor in Ocean Utilization, R.M. Parsons Lab., Dept. of Civil Engineering, MIT, Cambridge, Massachusetts

Earlier versions of the CERC formula suggested Q_{ℓ} to be proportional to some power of $P_{\ell s}$. Arguments based primarily on dimensional considerations (Bagnold, 1963) have, however, been used to justify the linear relationship suggested by Eq. (1). The absence of sediment characteristics (grain size), beach characteristics and the sole dependency of the longshore sediment transport rate on wave characteristics suggest the limited validity of Eq. (1). The data used in establishing Eq. (1) were obtained in three independent studies (Watts, 1953; Caldwell, 1956; Komar, 1969) covering a relatively wide range of conditions (grain sizes from 0.175 mm to 0.6 mm) and using quite different techniques for the determination of Q_{ℓ} as well as $P_{\ell s}$. Although some justification for the type of relationship suggested by Eq. (1) has been given, it should be regarded as a purely empirical relationship established by plotting points of Q_{ℓ} versus $P_{\ell s}$ on log-log paper. Such a plot is presented in SPM-73, and reproduced in Figure 1. Considering the fact that we are dealing with the problem of sediment transport, the data points show a remarkably low degree of scatter around the relationship given by Eq. (1). In fact, it is reported in SPM-73 that "the average difference between the plotted points from field data and the prediction given by Equation (1) is at least 28 percent of the value of the prediction". Even in the context of the much simpler problem of sediment transport in unidirectional open channel flow such an agreement between predictions and observations would be considered extremely good. Thus, one is left with the impression that Eq. (1) is a reasonably accurate relationship. Being empirical it can, however, be no more accurate than the data on which it is based. To assess the degree of confidence one can have in the data points used to establish Eq. (1) it was therefore decided to critically review the methods used by Watts (1953), Caldwell (1956) and Komar (1969) for the determination of Q_{ℓ} and $P_{\ell s}$.

The review emphasizes a critical evaluation of the different methods used for the determination of the longshore sediment transport rate. The assumptions underlying the use of a particular method are discussed and the degree to which these assumptions are violated or not is investigated from the reported data. It is realized that there are several unanswered questions regarding the validity of the significant wave concept as an equivalent representation of a random sea. This problem is not addressed in the review of the manner in which the wave energy flux factor was determined. Comments on the determination of wave characteristics are therefore limited to comments on how the significant wave characteristics were obtained and used to determine the wave energy flux factor.

REVIEW OF THE DATA BASE

WATTS (1953)

In this study a sediment trap north of the jettied South Lake Worth Inlet on the east coast of Florida was assumed to catch the long-

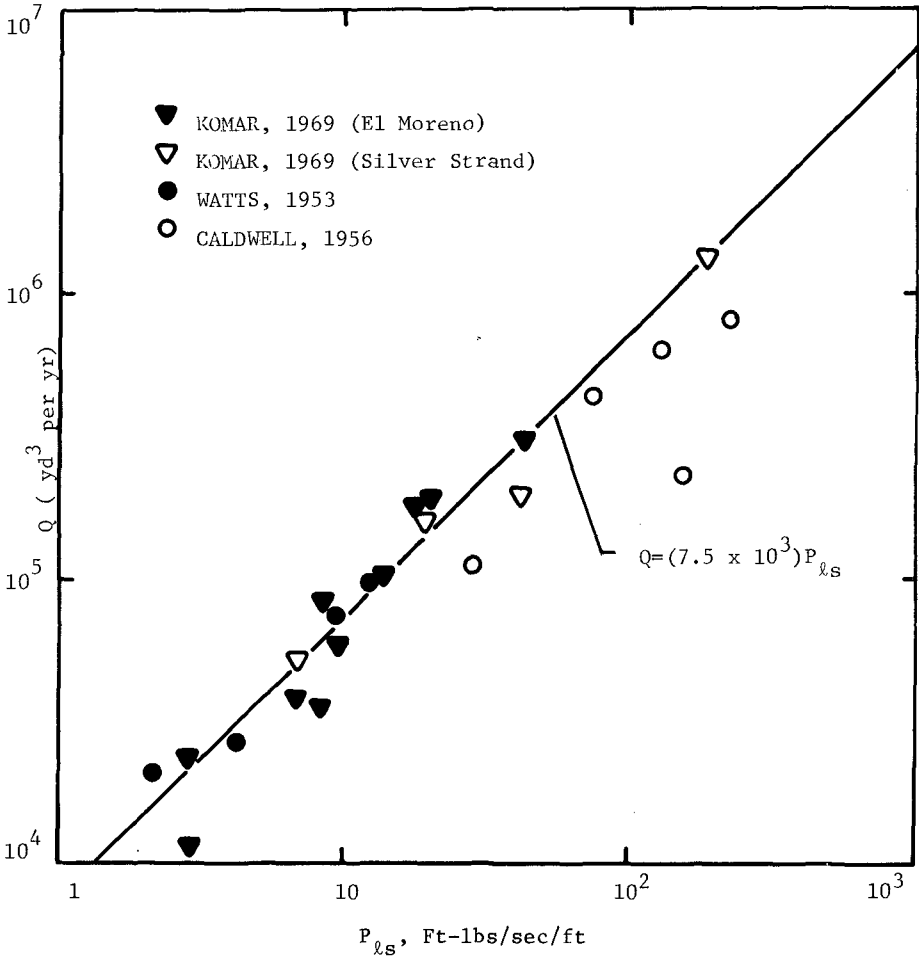


Figure 1: Plot of Data Points and Empirical Relationship for Longshore Sediment Transport Rates. (From U.S.Army, Shore Protection Manual, 1973)

shore sediment transport during periods of waves out of the north. The rate of southerly transport was estimated from pumping rates reported by a sand by-passing plant at the inlet. Wave heights and periods were obtained at 4-hour intervals from a wave gage located in 17 ft. of water some 10 miles north of the study area. Wave directions were determined twice daily by sighting from the top of a hotel 3.5 miles north of the study area using an engineer's transit. The estimated pumping rate over a given time interval, Q_ℓ , was related to the southerly wave energy flux, P_ℓ , during the same interval. Both short term ("daily" averages) and long term ("monthly" averages) were reported. Only the monthly averages (4 points) are used in SPM-73 to establish Eq. (1).

The use of a sand trap to determine longshore sediment transport rates is, in principle, appealing. The method does, however, rely on several assumptions some of which are discussed in the following.

For waves out of the north the

- (A) sand trap must be 100 percent effective and catch only the longshore transport.

In general it appears to be extremely difficult to ascertain whether or not this assumption is violated. During Watts' experiment wave heights were quite moderate (2 ft. or less) which may justify assumption (A) provided the trap caught only the longshore transport.

For waves out of the south the

- (B) sand trap should not catch any significant amount of material.

If significant amounts of sediment are caught by the sand trap during periods of waves out of the south this is indicative of the sand trap catching not only longshore transport. Presumably, this would also be the case during periods of waves out of the north, thus violating assumption (A). In the analysis of the data averaged over long periods Watts correlated the total pumping rate with the wave energy flux factor computed from wave observations including only the energy flux during times of waves out of the north. This clearly makes the monthly average data meaningful only if assumptions (A) and (B) are satisfied.

Erosion north of the jetty during periods of waves out of the south

- (C) does not affect the longshore transport rate when waves are out of the north.

If it is assumed that the jetties act as a littoral barrier for waves out of the south, the beach north of the inlet is deprived of sediment during periods of waves out of the south. To the north of the jetty there would be a stretch of beach along which the longshore sedi-

ment transport would be increasing with distance from the jetty until it attains its equilibrium value. This would cause some erosion to take place north of the jetty during periods of waves out of the south. Once the wind and waves swing around to be out of the north, a southerly transport would be initiated. If this southerly transport is affected by the erosion which took place during waves out of the south, by repairing the damage done, the sand trap would not catch the southerly longshore transport until equilibrium conditions were re-established. It appears to be extremely difficult to ascertain to which extent assumption (C) is violated; however, the use of sand traps for the determination of longshore sediment transport rates relies heavily on this assumption.

To examine the degree to which the assumptions discussed above are violated in the field experiment performed by Watts the complete tabulation of wave data given by Das (1971) as well as the pumping rate reported by Watts (1953) have been plotted in Fig. 2. The sign convention for angles of incidence, θ , is that $\theta > 0$ for waves out of the north. At the start of the experiment, it is seen that the waves were quite high (H^2) as were the pumping rates (Q). During the period of March 7 to 9 waves were out of the north ($H^2 \sin\theta > 0$) but swung around to be out of the south from March 10 to 15. From the ideal behavior of the sand trap discussed in conjunction with assumption (B) it is noted that the change in wave direction, somewhat disturbingly, is practically unnoticeable in the reported pumping rate during this period. Similar evidence of significant transfer of sediment into the sand trap during periods of waves out of the south is observed around March 23, April 10, and April 24. The conclusion reached from the presentation of Watts' data in Fig. 2 is that assumption (B) is violated, thereby invalidating the manner in which the data points corresponding to monthly averages were obtained. Furthermore, the results presented in Fig. 2 suggest that the sand trap may catch sediment not considered to be part of the longshore sediment transport during periods of waves out of the north. Thus, the daily averages, obtained over the periods indicated in Fig. 2, may not represent the short term longshore transport. In addition, the short term average pumping rates are more sensitive to errors arising from pumping rates not corresponding exactly to the amount of material deposited in the sand trap.

The wave data (height and period) were obtained in 17 ft. of water. No specific mention of the depth of water where the wave direction was obtained can be found in the original report. Since the direction was observed visually it would be tempting to assume that the direction was the angle of incidence at breaking. Several directional observations, however, report values of θ in excess of 20° (up to 49°). Since waves of 5 sec. period breaking in 1.5 ft. of water will have an angle at breaking less than 15° , it does not appear reasonable to assume that the reported angle of incidence corresponds to the angle at breaking. Examining the nature of Eq. (2) this may be written in the form

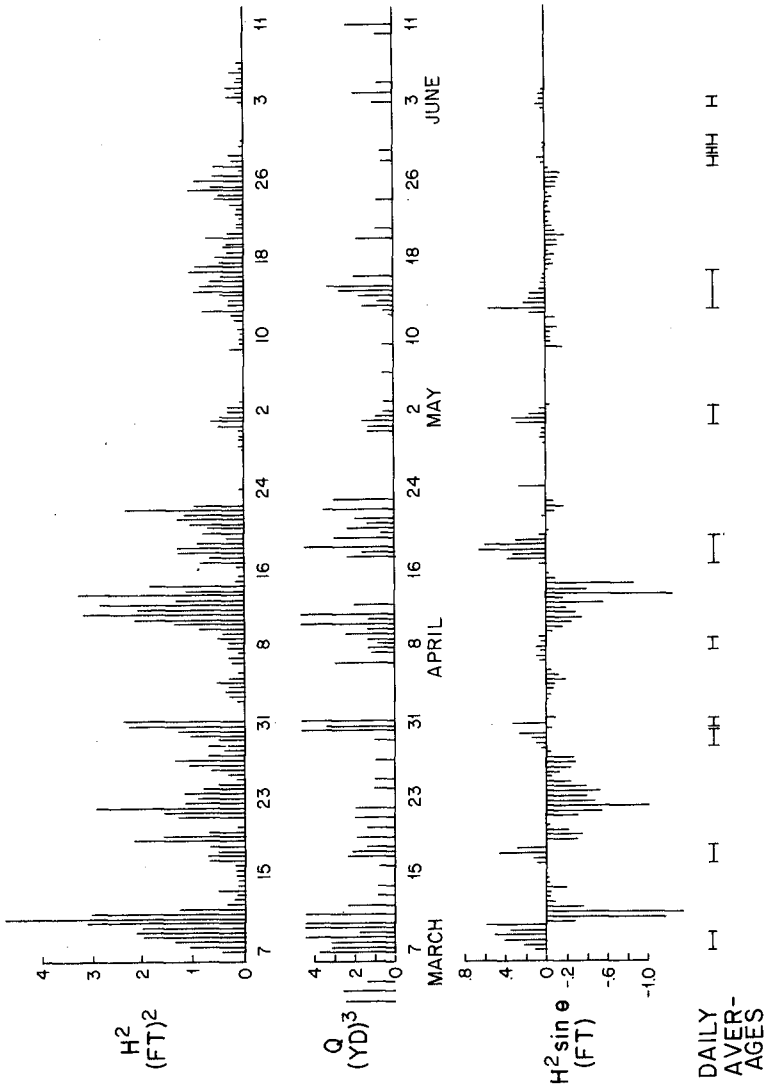


Figure 2: Plot of Wave Intensity (H^2), Pumping Rates (Q), and Directional Wave Intensity ($H^2 \sin \theta$) During Watts' (1953) Experiments.

$$P_{\ell s} = \left\{ \frac{1}{8} \rho g H_b^2 C_{g,b} \cos \theta_b \right\} \sin \theta_b \quad (3)$$

The bracketed terms represent the shore normal energy flux and assuming Snell's Law to be valid this quantity is customarily assumed to remain constant. Thus, the bracketed terms may be evaluated in any water depth, for example, corresponding to $h = 17$ ft. where H and T were obtained. The uncertainty about the location where θ , as reported by Watts, was obtained is of relatively minor importance in the evaluation of the bracketed term in Eq. (3). It is, however, of extreme importance that the angle at breaking be used to evaluate $\sin \theta_b$. It is evident that Watts evaluated Eq. (3) using a water depth of 17 ft. and assuming all wave parameters to correspond to this water depth. If the reported value of θ does indeed correspond to $h = 17$ ft. Watts' evaluation of $P_{\ell s}$, which is used in SPM-73, could potentially be off by a factor of the order 5.

CALDWELL (1956)

In this study the erosion rate "downdrift" of a littoral barrier was determined by surveying 21 transects spaced at 500 ft. intervals. Surveys were repeated every 2 to 3 months. The net amount of sediment volume change within the study area between consecutive surveys was used to determine an average daily net sediment transport rate at the transect furthest away from the littoral barrier. Wave characteristics were determined from a combination of wave gage records, obtained 6 miles away in 20 ft. of water, and from hindcasts. Wave direction was obtained from refraction diagrams based on hindcast deep water wave characteristics. This study produced six points of Q_{ℓ} versus P_{ℓ} ; however, one of these points showed a negative relationship between Q_{ℓ} and P_{ℓ} and it was consequently discarded.

Using the erosion or deposition rate "downdrift" of a littoral barrier to quantify the longshore sediment transport rate is based on the assumptions that

(D) The littoral barrier is 100 percent effective.

No transport out of or into the
(E) study area through its offshore boundary.

The longshore sediment transport
(F) through the downdrift boundary of the study area is unaffected by the presence of the littoral barrier.

As discussed in conjunction with the discussion of assumption (C), the longshore transport rate requires some distance downdrift of a littoral barrier to achieve its equilibrium value. The same applies for sedi-

ment transport towards the littoral barrier. The spatially varying longshore sediment transport rate in the vicinity of the littoral barrier suggests an erosion or deposition pattern which approaches a zero volume change between transects close to the "downdrift" boundary of the study area. This required behavior of the erosion pattern appears self-evident since the net volume change within the study area and hence the inferred longshore transport rate otherwise would depend on the location of the "downdrift" boundary.

The observed volume changes within the study area of Caldwell are plotted in Fig. 3 for the six survey periods. It is evident that the erosion patterns for all survey periods conform rather poorly to the expected ideal pattern discussed above. Only the erosion and deposition patterns during the survey periods Nov. 9 to Jan. 25 and Jan. 25 to April 8 exhibit the features resembling those required. The two data points corresponding to these survey periods, with $P_{\ell S}$ evaluated in the manner to be discussed, happen to indicate a significant decrease in Q_{ℓ} with increasing $P_{\ell S}$, hardly a comforting result.

The wave characteristics (height and period) were determined from a combination of wave gage measurements in 20 ft. water depth and hindcasts, used whenever results from the wave gage were unavailable. A comparison between hindcast and measured wave characteristics is reproduced in Table 1.

Table 1: Comparison between hindcast and observed (wave gage) wave heights (from Caldwell, 1956, Table 4).

H_{gage} (ft.)	3.6	0.5	2.0	1.1
H_{hindcast} (ft.)	1.4	1.5	1.5-1.8	1.5

Recalling that the wave height enters the determination of $P_{\ell S}$, Eq. (2), essentially to the $5/2$ power, it is seen from the comparison of measured and hindcast wave heights that $P_{\ell S}$ obtained from hindcast wave characteristics may deviate considerably from the values obtained from measured wave characteristics.

Refraction diagrams were used to determine the wave directions in 12 ft. water depth for waves out of the west to northwest and for waves out of the south. For waves out of the west to northwest hindcast directions varying between 4° to 15° were obtained, and an "average" value of $\theta = 9^{\circ}$ was used for all waves from this direction. For hindcast waves out of the south an average direction of 21° , representing a directional spreading of $16^{\circ} < \theta < 23^{\circ}$, was used for all waves.

The value of the wave energy flux factor was evaluated from Eq. (2) using the hindcast or observed wave height and period corre-

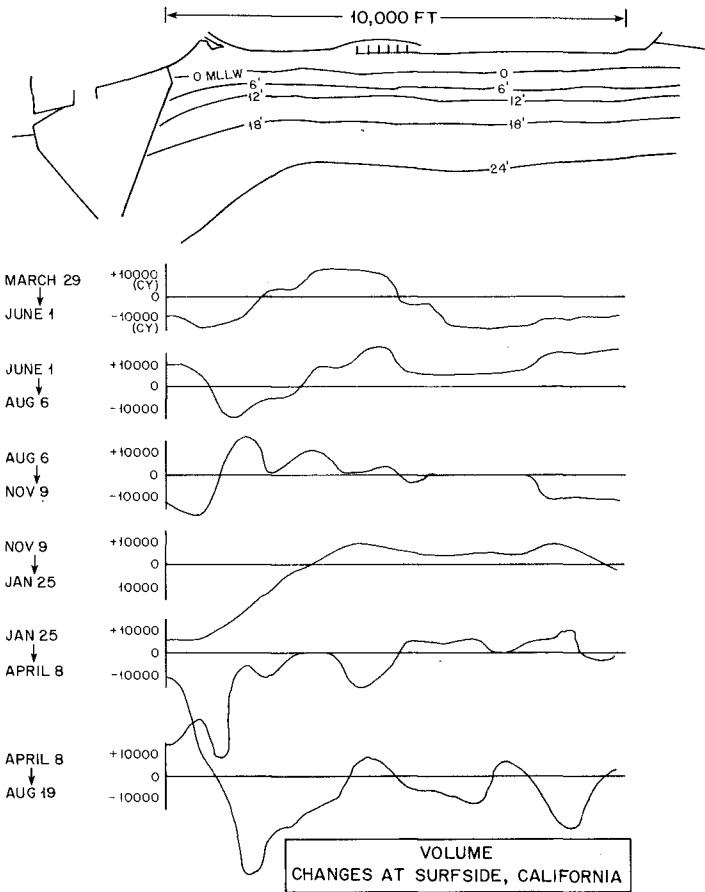


Figure 3: Plot of Volume Changes Observed During Caldwell's (1956) Experiments.

sponding to 20 ft. water depth with the angle θ taken as the constant average value determined from refraction diagrams and corresponding to a water depth of 12 ft. Thus, the values obtained by Caldwell for $P_{\ell S}$ are not based on breaking wave characteristics, and Caldwell's values can readily be imagined to be off by factors of 10 or more. Nevertheless, the values for $P_{\ell S}$ obtained by Caldwell (1956) are the values used in the SPM-73 plot of Q_{ℓ} versus $P_{\ell S}$.

KOMAR (1969)

In this study sand tracers (fluorescent) were injected on the beach face (El Moreno Beach) or across part of the surf zone (Silver Strand Beach). Sampling at some time following injection gave contours of equal tracer concentration from which the centroid movement of the tracers was determined. From the distance traveled, $\Delta\ell$, and the time, Δt , the average centroid velocity, $V = \Delta\ell/\Delta t$, was obtained and used as the average velocity of moving sediment. The longshore transport rate was then obtained from the formula

$$Q_{\ell} = V b X_B \quad (4)$$

in which b is the thickness of the moving layer of sediment and X_B is the width of the surf zone. The thickness of the moving layer was taken to be the burial depth of tracers as obtained from core samples taken close to the injection line. Wave characteristics were determined from a wave gage array located some distance seaward of the surf zone. Breaking wave characteristics were either predicted by shoaling the measured waves until breaking or by direct observation of the breaker characteristics.

When applying tracer techniques for measuring sediment transport a number of assumptions are made.

(G) The tracer should behave as the native material.

This is most readily satisfied by coating material from the study area as done by Komar.

(H) The transporting system is stationary.

This basically requires conditions to be steady during the experiment. Clearly, conditions are far from steady in the surf zone. However, one may view the transport process in the surf zone as consisting of a series of events, each event corresponding to the passage of a breaking wave. The stationarity requirement therefore does not apply to the time scale of the wave motion. Rather it should be interpreted to mean that wave conditions do not change during the experiment. At Silver Strand Beach injection was made in the surf zone around high

tide and sampling was performed 1 to 3 hours after injection. Although the tide introduces some changes during the duration of an experiment of this type, it appears that this lack of stationarity is minimized by conducting the experiments in the manner used by Komar at Silver Strand Beach. At El Moreno Beach, the experimental procedure was, however, somewhat different. Here the tidal range is considerable (about 20 ft.) so the steep beach face was exposed during low tide. Tracer was injected in a trench on the beach face during low tide. As the tide came in the surf zone would move across the injection site. The same would happen as the tide went out. When the beach face was exposed again sampling was performed. It is evident that the conditions during experiments at El Moreno Beach hardly can be considered to have been stationary. We are not aware of any investigations which allow us to assess the possible effects of lack of stationarity on results obtained from tracer experiments. All we can say is that the crucial assumption (H) was violated for Komar's experiments on El Moreno Beach and the quality of his data on sediment transport rates obtained at this location is therefore somewhat uncertain.

An additional assumption is that

- Sufficient time following injection should
(I) be allowed to ensure that the tracer behavior is
independent of the manner in which it was introduced.

If one models tracer dispersion based on the diffusion equation the spatial integration method used by Komar was shown by Lean and Crickmore (1963) to be applicable at any time following injection. The dispersal patterns observed by Komar are, however, not indicative of a transport system which is adequately modeled as a simple advective diffusion process. If this were the case the region of high tracer concentrations would move downdrift and at the same time spread out. Contrary to this behavior many of Komar's dispersal patterns show that the area of high tracer concentrations, at the time of sampling, had remained at the location of the initial injection. Such a behavior of tracer dispersal following an instantaneous line injection is to some extent modeled by a simple model which considers the transporting system to consist of two layers. In this two-layer model the top layer is a transporting layer and exchanges particles with an immobile bed layer. Based on a model of this type tracer particles would appear in the bed layer downdrift of the injection site because they had been "picked up" by the transporting layer and subsequently deposited in the bed layer. This two layer model predicts that the area of high tracer concentration in the bed would remain at the injection site for some time following time of injection. It also predicts that the centroid velocity immediately following injection is zero and with time approaches a constant value. If the centroid velocity obtained by Komar corresponds to this equilibrium value the two layer model suggests that the transport indeed may be obtained from Eq. (4). The only change from a diffusion model is that b , rather than being inter-

puted as the thickness of moving sediment, should be interpreted as the thickness of the non-moving bed layer which exchanges tracer particles with the moving layer. It is not possible to ascertain whether or not the time between injection and sampling used by Komar at Silver Strand Beach was sufficient to satisfy assumption (I). The determination of V obtained from a single measurement of $\Delta R/\Delta t$ can therefore not be accepted without some reservation.

Since the longshore transport rate represents the transport across the entire width of the surf zone it is, of course, necessary that the entire surf zone participates in the dispersal of the tracer particles. A certain distance must therefore be allowed downdrift of the injection site for complete mixing to take place, if the injection covers only part of the width of the surf zone. Komar (1969) comments on this point in conjunction with a discussion of the uncertainties associated with his experiments at Silver Strand Beach.

A final requirement, when tracer techniques are used in sediment transport studies, is that all the tracer particles initially injected must be accounted for. In the context of Komar's longshore sediment transport study this translates into the assumption that there can be

(J) No transport of tracer particles out of the sampling area.

The degree to which this assumption was satisfied in Komar's experiments was assessed by evaluating the amount of tracer accounted for by the sampling program. It is, however, difficult to interpret the significance of a tracer mass balance which accounts for, say, 80 percent of the tracer initially injected. Is the discrepancy experimental error or did tracer particles leave the sampling area? And, if the latter explanation is adopted, to which extent does this loss of tracers affect the results obtained?

The quantity b in the transport equation, Eq. (4), was obtained by Komar from core samples. The values obtained for b in a single experiment were reported to vary greatly with location of the core sample relative to the initial injection line. Thus, Komar reports that fairly large burial depths of tracers could be observed near the injection site whereas tracers were found only near the bed surface further away from the injection. This observed variation in b necessitates a choice of which value to use in the evaluation of Eq. (4). The larger burial depth observed close to the injection site is explained by Komar to be associated with the relative abundance of tracers in this region over a relatively long period of time. Thus, near the injection site tracers are more likely to have sufficient time to "diffuse" vertically into the bed. This explanation does appear very plausible indeed. It does not, however, appear to justify Komar's use of the large values of b obtained close to the injection site when Eq. (4) is evaluated. It is our feeling that the determination of b

represents one of the major difficulties in sediment transport studies using tracer techniques.

Komar's determination of the wave energy flux factor, as defined by Eq. (2), appears to be quite accurate when one accepts the equivalent wave concept without detailed considerations of the influence of directional wave characteristics.

CONCLUSIONS

The data base used by the U.S. Army (1973) in their SPM-73 to establish the empirical longshore transport relationship given by Eq. (1) has been reviewed.

The review revealed that the data points obtained from the studies by Watts (1953) and Caldwell (1956) are of questionable quality. Fundamental assumptions regarding the methods used for the determination of the longshore sediment transport rates appear to have been violated to the extent that one can have no confidence in the values of Q_{ℓ} reported in these studies. The values obtained for the wave energy flux factor should, according to Eq. (1), correspond to breaking wave conditions. The values of the wave energy flux factor reported by Watts (1953) and Caldwell (1956) are used in SPM-73 as if they corresponded to breaking wave conditions whereas they in fact do not. It is not possible to quantify the errors associated with each of the data points obtained by Watts and Caldwell. However, they appear to be sufficiently uncertain in terms of both Q_{ℓ} and $P_{\ell s}$ to justify their exclusion from any analysis aimed at establishing empirical longshore sediment transport relationships.

Removing Watts' and Caldwell's data from Fig. 1 leaves the data points obtained by Komar (1969) and removes the comfort of the argument that Eq. (1) is based on data from three independent studies. The degree of confidence one can have in the accuracy of Eq. (1) is therefore intimately related to the accuracy of the methodology used by Komar in his experiments. The critical review of Komar's use of tracer technology for the determination of longshore sediment transport rates revealed that several of the basic assumptions underlying the use of tracers in sediment transport studies appear to have been violated in this study. The lack of stationarity of the transporting system during the experiments at El Moreno Beach renders the quality of these data points uncertain. The uncertainty about whether or not sufficient time was allowed between injection and sampling to make the determination of the centroid velocity meaningful during the experiments at Silver Strand Beach casts doubts on the accuracy of these data points. In all experiments the ambiguity in the determination of the "thickness of moving sand" introduces a significant uncertainty in the results obtained. It does not appear possible to quantify the magnitude of the errors resulting from the noted violations of the

basic assumptions. The fact that several basic assumptions were violated does, however, suggest that it is unjustified to rely too heavily on the accuracy of the sediment transport rates obtained in Komar's investigation.

The conclusion of our review is therefore that coastal engineers using Eq. (1) for the calculation of longshore sediment transport rates should regard their results as no better than order of magnitude estimates.

ACKNOWLEDGMENT

The present investigation is part of ongoing studies of Longshore Sediment Transport and Surf Zone Hydrodynamics carried out at the R.M. Parsons Laboratory, Department of Civil Engineering, MIT, and the Ocean Engineering Department, WHOI, as part of the MIT Sea Grant Program, supported by NOAA's Office of Sea Grant, U.S. Department of Commerce under grant number 04-7-158-44079. The second author (Madsen) acknowledges the general support of the Doherty Foundation as the Third Doherty Associate Professor in Ocean Utilization. The U.S. Government is authorized to produce and distribute reprints for governmental purposes notwithstanding any copyright notation that may appear hereon.

REFERENCES

- Bagnold, R.A. (1963), "Mechanics of Marine Sedimentation," The Sea, Vol. 3, Wiley, New York, pp. 507-528.
- Caldwell, J.M. (1956), "Wave Action and Sand Movement Near Anaheim Bay, California," TM-68, U.S. Army, Corps of Engineers, Beach Erosion Board, Washington, D.C.
- Das, M.M. (1971), "Longshore Sediment Transport Rates: A Compilation of Data," MP1-71, U.S. Army, Corps of Engineers, Coastal Engineering Research Center, Fort Belvoir, Virginia.
- Komar, P.D. (1969), "The Longshore Transport of Sand on Beaches," Ph.D. Thesis, Scripps Institution of Oceanography, University of California, San Diego.
- Lean, G.H. and M.J. Crickmore (1963), "Methods for Measuring Sand Transport Using Radioactive Tracers," Radioisotopes in Hydrology, International Atomic Energy Agency, Tokyo, pp. 111-131.
- U.S. Army (1973), "Shore Protection Manual," U.S. Army, Corps of Engineers, Coastal Engineering Research Center, Fort Belvoir, Virginia.
- Watts, G.M. (1953), "A Study of Sand Movement at South Lake Worth Inlet, Florida," TM-42, U.S. Army, Corps of Engineers, Beach Erosion Board, Washington, D.C.

CHAPTER 94

SEDIMENT MOTION CAUSED BY SURFACE WATER WAVES

by

A G DAVIES* AND R H WILKINSON*

Abstract

This paper describes an experimental study of sand motion on the seabed caused by surface water waves. The observations were made close to a beach, but outside the breaker zone and in a location where steady currents were small. Measurements of water velocity components were made at various heights above both rippled and flat beds, together with measurements of the pressure gradients at the seabed, in order to examine the threshold of motion of the natural coarse sand ($D_{50} \approx 1.4\text{mm}$). This motion was monitored with an under-water television system. The flow conditions were predominantly laminar and no flow separation occurred above the lee slopes of the ripples.

Sediment motion was of 'bed load' type and was confined to the crests when the bed was rippled. This motion has been found to be caused by waves having an orbital velocity amplitude (measured in the free stream flow) of about one half of that required to cause motion on a flat bed of the same material. Wherever possible the threshold measurements have been compared with results obtained in the laboratory.

The relative importance of forces on the seabed induced by velocity and pressure gradients has been assessed. It appears that the latter effects are of little or no importance in situations of the kind described, as suggested elsewhere in the literature.

1. Introduction

Most previous experimental work on the threshold of sediment motion by waves has been carried out in the laboratory. Typically, this has involved the definition of 'critical waves' of single frequency which are just capable of causing sediment motion on a flat bed, such waves being defined by their velocity amplitudes and periods, and the bed material by its size and density. Sediment motion arises primarily as a result of the near-bed velocity field; however, a secondary influence which must be investigated is the possible role of pressure gradients at the bed surface. The velocity induced bed shear stresses are expected to lead the oscillation in the free stream in phase, on account of bottom boundary layer effects; whereas the additional forces on the grains due to the direct action of the fluid pressure field are expected to be in phase with the pressure

*Institute of Oceanographic Sciences, Crossway, Taunton, Somerset, UK,
TA12DW

gradients in the free stream outside the boundary layer. Unfortunately, in laboratory work little attention has been given to these phase relationships and, in particular, to the phase angles in the wave cycle between which to- and fro- motion of sediment has been observed. This makes the interpretation of field observations difficult.

A study of incipient sediment movement requires ultimately an understanding of the shear stress distribution in the flow, accompanied by a knowledge of the instantaneous velocity profile in the boundary layer through a wave cycle. Both of these quantities will depend upon the seabed topography; the development of ripples complicates the flow pattern close to the bed, alters the amount of sediment in motion and causes the breakdown of the 'critical wave' formulae derived for flat beds in the laboratory. An important part of such a study involves determining whether the flow in the boundary layer is laminar or turbulent. The transition from laminar to turbulent flow occurs near the threshold of motion for sands and, furthermore, differs for flat and rippled beds (see Davies and Wilkinson (1977)).

In this paper we are concerned with the relevance of laboratory formulae for threshold motion, when applied in the sea where the bed is normally rippled; also with the secondary problem of whether forces induced by pressure gradients in the flow are important at the threshold of motion. We make no attempt here to model the bottom stress and the resulting sediment transport directly. Instead we concentrate on studying the causal link between observations of sediment motion on the seabed and measurements of the flow parameters in the free stream outside the boundary layer. In particular, an attempt has been made to identify the critical conditions which exist instantaneously in the free stream flow at the threshold of motion of coarse sand.

2. Field Studies

Two experiments have been carried out at Blackpool Sands, Start Bay, Devon, England: the first on 22 March 1975 (Davies, Frederiksen and Wilkinson (1977)); the second on 25 - 26 March 1976. Measurements were made at positions close to the beach but well outside the breaker zone (Fig 1). Tidal currents and the effects of shoaling were shown to be of secondary importance at the experimental site, and the flow near the seabed was due primarily to an incoming ocean swell on both occasions. The bottom slope at the position of the rig was about 1 : 17 and the mean water depth was about 5m (Fig 2).

In the first experiment measurements of velocity were made above the crest of a ripple of height about 10 cms, and wavelength about 100 cms; and in the second above the crest of a ripple of height 12 cms and length 85 cms, as well as above an artificially flattened bed. When the bed was rippled, the to- and fro- motion of grains was always confined to the region of the ripple crests, and was of bed load type only. The bed features were almost certainly fossil ripples in both experiments, not in equilibrium with the existing flow field but formed by some previous more active wave-induced flow conditions.

BLACKPOOL SANDS, START BAY.

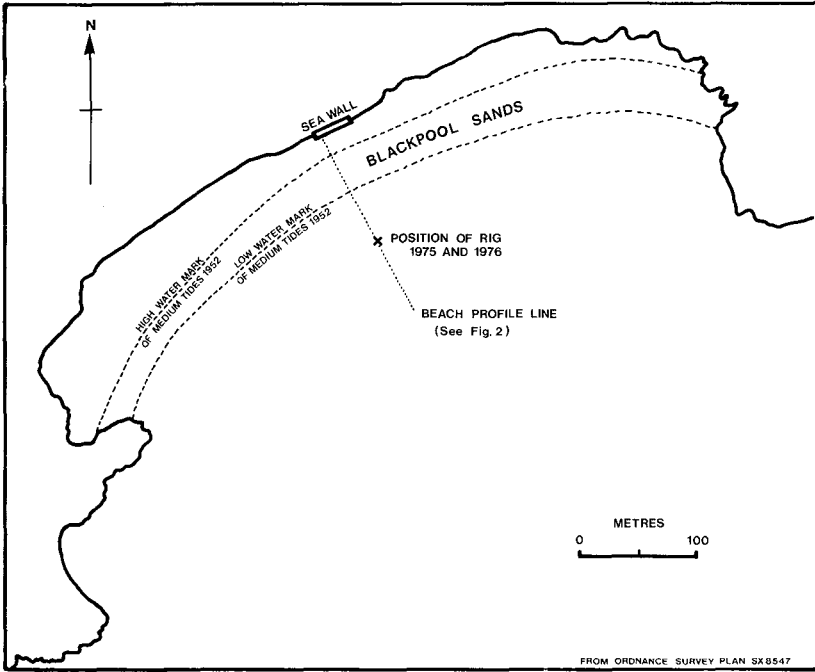


Fig.1

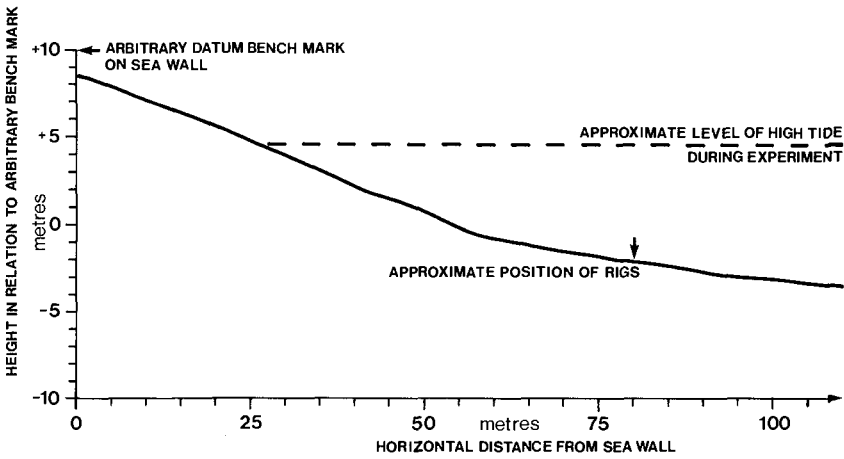


Fig.2 BEACH PROFILE AND NEARSHORE BOTTOM TOPOGRAPHY.

No flow separation was observed above the lee slopes of the ripples, judging from the behaviour of visible particulate matter in the water, nor was there any obvious sign of turbulent exchange in the flow. Indeed conditions, at least well away from the bed, appeared to be predominantly laminar in both experiments. When the bed had been flattened, grain motion occurred more generally over the bed surface, and again the flow appeared to be laminar.

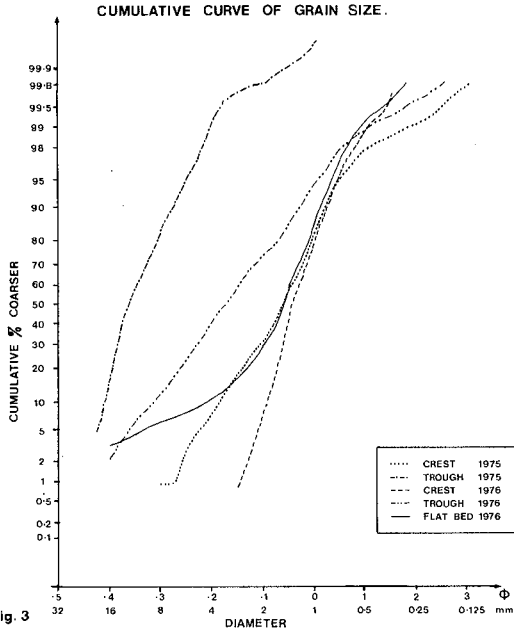
In both experiments, the surface bed material was a coarse sand on the ripple crests and an even coarser material in the troughs, see Fig 3. In the second experiment, the material on the surface of the artificially flattened bed was predominantly of crest type.

The deployment of the apparatus was carried out by divers; its layout on the seabed is shown in Fig 4, together with the definition of axes and the symbols adopted for the flow parameters. Velocity measurements were made using two electromagnetic flowmeters with 10cm diameter Colnbrook measuring heads, mounted on a tetrahedral frame. These were positioned to measure the horizontal and vertical components of velocity in the vertical plane in the direction of wave advance; one flowmeter was at a height of 1m above the seabed, and the other at a height of 30cms in the first experiment and at a variable height between 15 and 60cms in the second. It was possible also to position the 'lower' flowmeter in a horizontal plane above the rig; this was done before and after runs in the second experiment in order to monitor the directional characteristics of the waves. In this paper, we concentrate for the most part on measurements of the horizontal velocity made with the 'upper' flowmeter.

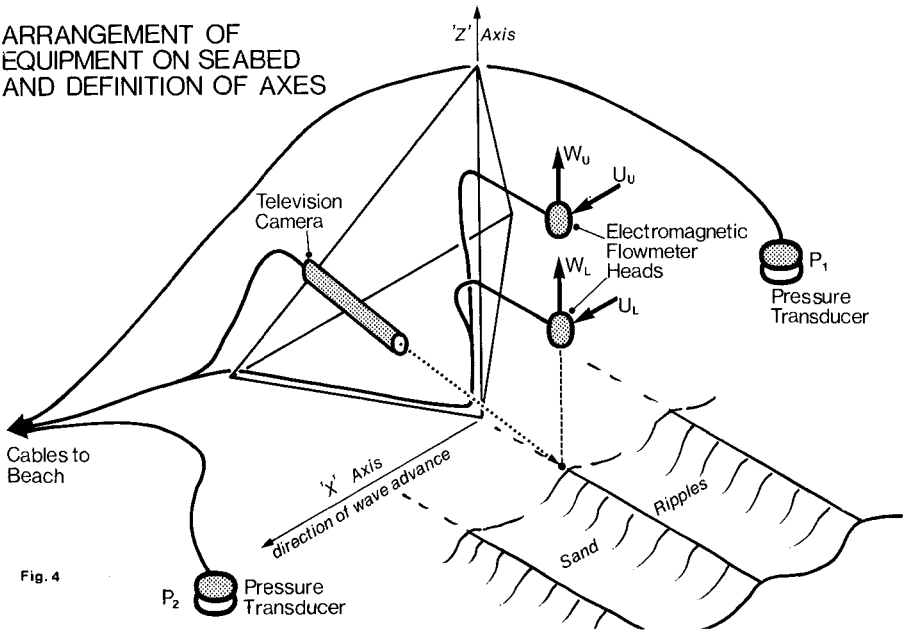
Also attached to the rig was an underwater television camera, with which an area of the seabed about one half a metre square vertically below the flowmeters was viewed. The resolution of the camera was such that individual sand grains could be detected clearly and, when the bed was rippled, a view along a crest was obtained (as shown schematically in Fig 4). At distances of 5m on either side of the rig, in the direction of wave advance, FM-pressure transducers were positioned in order to obtain a direct estimate of the pressure gradient in the flow. The separation of the transducers was less than one quarter of the expected surface wavelength in order to avoid spatial aliasing.

The velocity and pressure signals were logged on a Bell and Howell FM-tape recorder. In addition, a synchronous video record showing the sediment motion was made with the underwater television system. The first experiment provided continuous data over a two hour period, while, in the second, four forty-minute runs were made on each of two consecutive days.

Before and after the experiments, the FM-flowmeters were calibrated in a towing tank. However, in the second experiment, zero points on the velocity scales were also determined in the field by placing shrouds over the measuring heads; this enabled the drift in the system to be corrected for. The noise of the flowmeter system was equivalent to a pk-pk velocity of about 1 cm/sec, and the pressure transducers could each resolve to about 1 cm of water.



ARRANGEMENT OF EQUIPMENT ON SEABED AND DEFINITION OF AXES



3. The Sediment Threshold Analysis

One of the main objectives of the experiments was to determine the values of the measured parameters at the instants when sediment motion started and stopped in both shoreward and seaward directions. This aspect of the investigation required the times of occurrence of grain motion to be obtained from the video records, and these times were then used to obtain critical velocities from the FM-flowmeters, as well as critical pressure values from the two FM-pressure recorders.

The method adopted was to replay the video tapes to three observers, each of whom recorded automatically an opinion as to whether sediment movement was taking place (for details, see Davies, Frederiksen and Wilkinson (1977)). The three sets of opinions were then averaged in such a way that a series of times was obtained at which sediment motion was considered to have either started or stopped, in both shoreward and seaward directions. These times were used to obtain critical instantaneous values of velocity and pressure from the synchronous analogue data. The means and variances of the critical values were calculated and, due to the subjective nature of the sediment threshold analysis, it was not surprising to find that they contained a considerable amount of scatter. It has been shown that the distribution of the critical values around their means was Gaussian for each parameter.

Under the experimental conditions, the sand on the ripple crest and, even more so, the sand on the flattened bed, remained stationary for most of the time. Sediment movement was observed only occasionally and it was usually associated with a group of higher amplitude surface waves. The number of instances of sediment motion in both shoreward and seaward directions, together with the percentage of the total time that sediment was in motion are shown in Table 1. The most striking feature here is the almost complete inhibition of sediment motion which was brought about by flattening the bed, even though the wave conditions were essentially the same.

For the first experiment, the number of instances of motion has been broken down into values for succeeding intervals of duration 10 minutes. In this form they display a considerable variability which can be associated with the changing wave conditions which were experienced during the experiment. To illustrate this, the number of instances of motion in an interval has been plotted against the variance of u_x , the horizontal velocity at a height of 30 cms, in that interval (see Fig 5). There is clearly an increase in the number of instances of motion with variance as expected; the scatter in the results indicates merely that variance is a crude measure of wave intensity for the present purpose and does not bear any direct relationship to sediment transport. Similar results were obtained by taking the variances of u_v , p_x and w_x (see Fig 4).

4. Energy Spectra and Probability Density Functions

The analogue velocity and pressure data recorded on the magnetic tape, having been filtered and then digitized at a rate of 5 Hz, was examined from a general statistical point of view. Firstly, the energy content of the signals was investigated by computing variances over intervals of duration 10 mins, and then the frequency composition of these variances was studied using standard spectral analysis techniques

BED TYPE	EXPERIMENT 1		EXPERIMENT 2			
	RIPPLED BED		RIPPLED BED		FLATTENED BED	
Data Collection Period (mins.)	130		125		145	
Direction of Sediment Motion	Seaward (-)	Shoreward (+)	Seaward (-)	Shoreward (+)	Seaward (-)	Shoreward (+)
Number of Occurrences of Motion	214	232	303	260	12	9
% of Total Time that Sediment was in Motion	S-5	5-9	S-3	4-2	0-15	0-13
% of Total Time in which NO Motion Occurred	BB-6		90-S		99-72	

TABLE 1

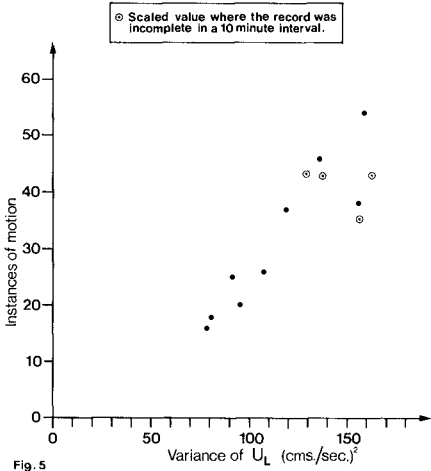


Fig. 5

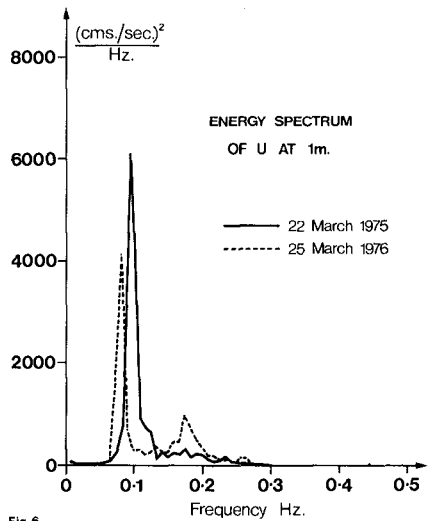


Fig. 6

based on the use of a Fast Fourier Transform. In forming energy spectra, adjacent harmonics were grouped such that spectral estimates were obtained every $1/120$ Hz in the frequency domain.

Typical energy spectra of u_x for the two experiments are shown in Fig 6. For the first experiment, the spectrum is dominated by a single peak centred on 0.088 Hz, corresponding to a wave of 11.4 secs period. For the second, in addition to the main peak at 0.080 Hz, a smaller peak can be seen in the range (0.17, 0.19)Hz; this was typical during the experiments on both the rippled and flattened beds. Relatively little activity was measured at frequencies above 0.3 Hz. Thus conditions in both experiments can be seen to have been dominated by a low frequency swell, with a higher frequency contribution also present in the second experiment.

For the purpose of further classifying the observed phenomena, the digitized data from a 10 minute interval is presented in Fig 7 in the form of normalized probability density functions for both u_x and u_y . The normalized Gaussian curve is included for comparison and, since the distributions for both velocity components shown are approximately Gaussian, the signals can be classified as narrow band random noise. This is consistent with the wave group behaviour noted in the velocities and pressures measured during the experiment.

5. Results of Threshold of Motion Studies

(i) The instantaneous threshold of sediment motion

After critical values of the measured velocities and pressures at the times of sediment threshold motion had been established (as described in Section 3), these were sorted into four groups of starting (α) and stopping (Ω) of motion, in the shoreward (+) and seaward (-) directions. Mean values and standard deviations were calculated for each group. Threshold results from the two experiments for u_x , the horizontal velocity measured at a height of 1m above the ripple crest, are shown in Table 2. At threshold the critical velocities in the '+' and '-' directions were approximately equal, and the large standard deviations show that the differences between the magnitudes of the threshold values in the two directions have no statistical significance. Also the results suggest that the asymmetry introduced by an overall beach slope of 1 : 17 did not significantly enhance sediment motion seawards. However smaller critical speeds occur at termination of motion than at initiation. This suggests the persistence of grain motion after the current speed had fallen below the initiation threshold value, possibly as a result of the inertia of the grains in motion. Differences between results for the two experiments can be accounted for in terms of differences in ripple steepness.

The same procedure was carried out on sets of data reduced in such a way that instances of motion were retained for analysis only if the time interval (ΔT) between the initiation of one motion and the cessation of the previous motion exceeded some specified value. This was aimed at studying possible differences in threshold values caused by a "settling of the bed" during a period of no grain motion. It was thought that the longer the interval, the more time the bed would have to "settle out" and become increasingly resistant to subsequent erosion. Results for an interval $\Delta T = 5$ secs are given in Table 2. These show an increase in the initiation threshold values of u_x in both directions, as anticipated. Different values of the interval, ΔT , have been taken for

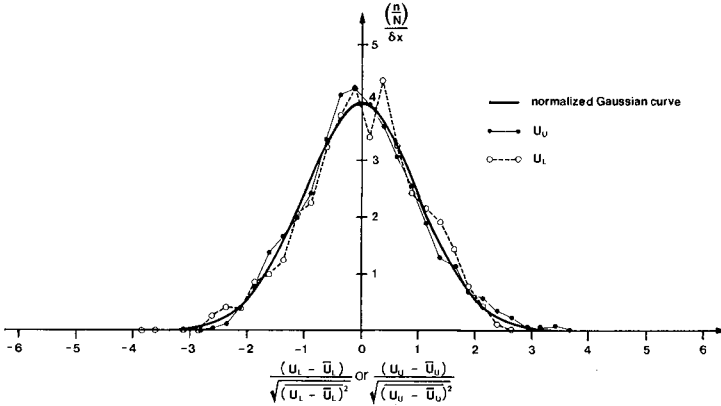


Fig.7 NORMALIZED PROBABILITY DENSITY FUNCTIONS OF U_L AND U_U , PLOTTED TOGETHER WITH THE NORMALIZED GAUSSIAN CURVE. (Notation: n occurrences of the N digitized values overall, lying in a band of width $\delta x = \frac{1}{2} \times \{\text{standard deviation of the signal}\}$).

THRESHOLD VALUES OF HORIZONTAL VELOCITY MEASURED AT A HEIGHT OF 1M. ABOVE THE CREST OF A SAND RIPPLE
 RIPPLE STEEPNESS: $\frac{1}{10}$ IN EXPERIMENT 1, $\frac{1}{7}$ IN EXPERIMENT 2

TYPE OF EVENT	EXPERIMENT 1				EXPERIMENT 2				
	- α	- Ω	+ α	+ Ω	- α	- Ω	+ α	+ Ω	
Mean Velocity	-16.48	-9.37	16.23	11.79	-14.20	-12.97	14.55	12.75	ALL MOTIONS INCLUDED
Standard Deviation	7.93	8.69	7.67	8.24	4.38	4.77	4.97	4.53	
Mean Velocity	-19.41	-8.44	18.17	10.11	-16.65	-12.10	17.22	12.86	REDUCED DATA: No Motion Interval $\Delta T = 5$ secs.
Standard Deviation	6.12	9.19	6.64	8.56	3.36	4.31	4.30	4.26	

TABLE 2.

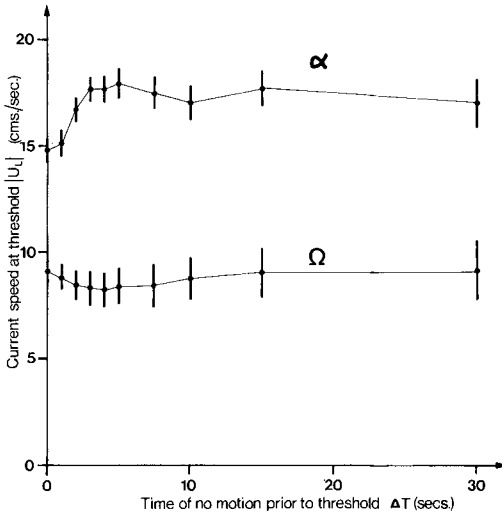


Fig. 8 VARIATION OF THRESHOLD SPEED WITH ΔT AT INITIATION AND TERMINATION OF MOTION FOR THE CASE OF U_L (NEGATIVE). Standard errors are indicated by vertical bars.

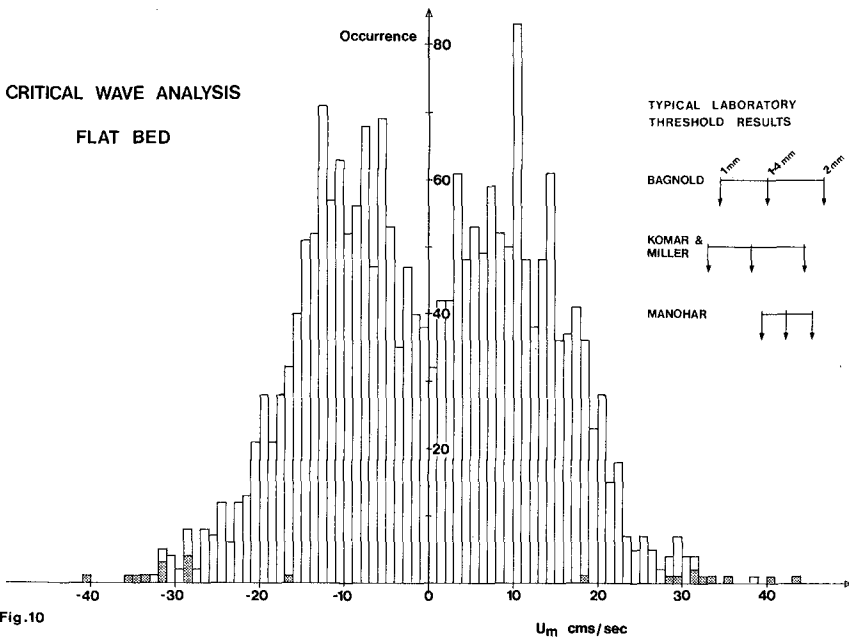
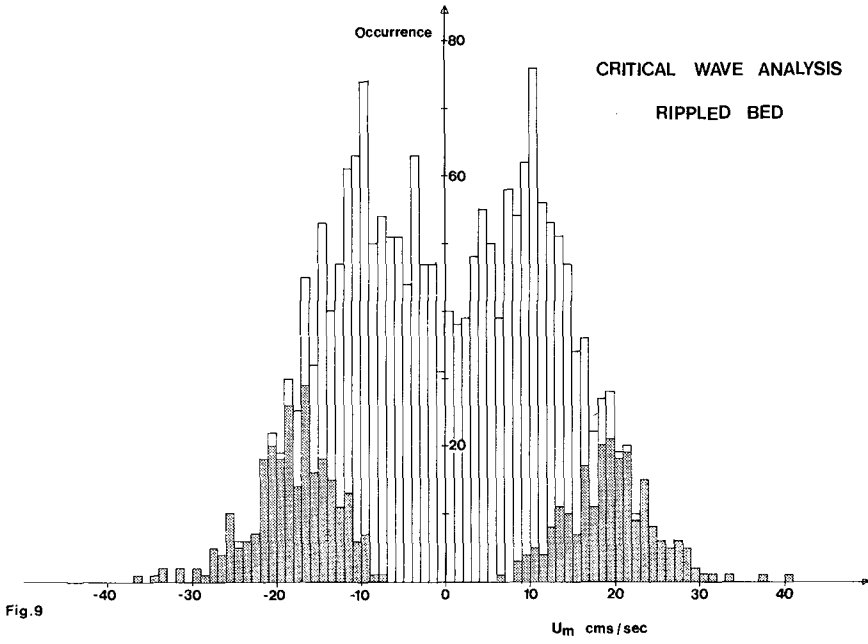
the case of u_w , for motion in the (-) seaward direction during the first experiment (Fig 8). For critical current speeds at the initiation of motion (α), a sharp increase can be seen in the range $0 \leq \Delta T \leq 3$ secs but, thereafter, no further statistically significant increase occurs. Standard errors are indicated by vertical bars, and the t-Test for the Two Sample Case (Dayton and Stunkard (1971)) has been used to show that the mean values obtained for u_w with $2 \leq \Delta T \leq 15$ secs, are different from the overall mean value ($\Delta T = 0$) within 95% confidence limits. On the other hand the mean \bar{u}_w -values, indicating termination of motion, display no such trend as ΔT is varied; for these values, the t-Test indicates that none of the mean values in $1 \leq \Delta T \leq 30$ secs has arisen from a population having a different mean value from the overall mean at $\Delta T = 0$ again within 95% confidence limits. From these typical results (similar results being obtained in the shoreward direction, as well as in u_v) it does seem possible that a sand bed takes a certain length of time to "settle out". However the subjective nature of the sediment threshold analysis might have had a bearing here; in particular, the possibility must be admitted that the longer the grains on the bed surface remained stationary, the slower were the reactions of the observers watching the TV-replay when they eventually moved.

(ii) The critical wave analysis

The critical times indicating the occurrence of sediment motion were used also for a wave by wave analysis. In this case, the aim was to classify individual wave half-cycles in a record according to their velocity amplitudes and periods, noting which waves moved sediment and which did not. This analysis was performed to enable direct comparisons to be made with laboratory findings, and the results described in this section are based on the horizontal velocity data obtained at the 1m height above the bed.

Typical results from the second experiment for the rippled and artificially flattened beds are shown in Figs 9 and 10 respectively, in which the peak velocity (U_m) achieved in a wave half cycle has been plotted against the number of half cycles during the record which had U_m falling within each unit range. The full histogram indicates the distribution of U_m for all waves in the record, and the shaded one is a subset of this indicating only those waves which moved sediment. Positive values indicate the shoreward direction. Fig 9 shows results for a 110 minute data collection period on a rippled bed, and Fig 10 for a 120 minute period on a flat bed.

It can be seen from Figures 9 and 10, firstly, that there is a marked difference between threshold conditions on rippled and flat beds, the measured threshold velocity amplitudes in the latter case being higher by a factor of about two than in the former. Secondly, as expected, the figures show that the waves having high free stream orbital velocity amplitudes moved sediment, and those with low velocity amplitudes did not. Less predictable is the existence of the "transition ranges" between these two situations, in which only a proportion of the waves achieving a particular value of U_m moved sediment. In the case of the rippled bed, the transition range was (-7, -21) cms/sec in the - direction, and (6, 23) cms/sec in the + direction. For the flattened bed, the wave conditions measured in the free stream during the experiment were such that very little motion occurred, despite the



fact that these conditions were essentially the same as those during the experiment with the rippled bed; however the start of a transition range can be seen in Figure 10.

Also shown in Fig 10 for the case of the flattened bed are some typical threshold velocity amplitudes obtained on flat beds in the laboratory. The values shown are from the formulae of Bagnold, Manohar, and Komar and Miller (see Table 3). In the calculations the sand grain size has been varied through the range 1 - 2mm, the D_{50} value in the second experiment being 1.4mm. The wave period has been taken equal to 9 seconds, which was a representative mean value obtained from an analysis of zero crossing periods (see Fig 11); in fact, each of the formulae shown is relatively insensitive to wave period, and Manohar's is independent of it. The observed sediment motion can be seen to have occurred at slightly lower values of velocity amplitude than predicted by the three formulae, even allowing for the uncertainty as to which grain size in the range shown was actually moving. It should be realized however that, although an attempt was made to achieve a consistent sediment threshold criterion in the present experiment, it is not possible to compare this criterion objectively with those adopted by the other workers. Nevertheless it can be seen that the parameter U_m does go a considerable way towards explaining the sediment threshold observations on the flattened bed.

(iii) Discussion of the sediment threshold results

The main questions emerging from the critical wave analysis were, firstly, why did the change from a rippled to a flat bed inhibit sediment motion; and, secondly, what was the explanation for the existence of the transition regions, which were particularly evident in the rippled bed results and in which only a fraction of the waves achieving a particular U_m moved sediment.

A quantitative explanation of the apparent discrepancy between the threshold values on flat and rippled beds has been achieved by performing an analysis of the frictionless flow over both real and idealized finite amplitude ripple shapes, assuming a non-separating deep oscillatory flow over the prescribed bed surface. The results of this work have indicated that the measuring height of 1m was well outside the zone of (frictionless) influence of the ripples, and the velocities at this height can, therefore, be said to have been obtained in the unperturbed free stream flow. Calculations of the velocity at the surface of the ripple crest have shown that, for the real sand ripples over which the measurements were made in the second experiment, almost a doubling of the velocity in relation to the unperturbed flow is to be expected (Davies, in prep). This would explain the apparent discrepancy in the sediment threshold findings.

A number of explanations can be proposed for the appearance of the transition regions in the histograms, involving factors of secondary importance in the problem:

- (a) the subjective nature of the sediment threshold analysis;
- (b) sedimentological considerations of various kinds:- the uncertainty about the grain size in the range (1, 2)mm which was moving at any one time, possible effects of the "settling" of the bed, and changes in the threshold velocity due to the continual changes occurring in the ripple shape during an experiment;

TYPICAL SEDIMENT THRESHOLD FORMULAE FROM THE LABORATORY FOR OSCILLATORY FLOW OVER A FLAT BED

BAGNOLD (1946) $\frac{\omega^{1/4} U_M^{3/4}}{\gamma^{1/2} D^{0.325}} = 21.5$ (c. g. s. units)

MANOHAR (1955) $\frac{U_M}{(\gamma g)^{0.4} (vD)^{0.2}} = 8.2$

KOMAR AND MILLER (1973) $\frac{\omega^{1/4} U_M^{7/4}}{\gamma g D^{3/4}} = 1.45$ (for $D > .05$ cms.)

where

- U_M = velocity amplitude in the free stream
- ω = wave frequency = $(2\pi/T)$
- D = representative grain diameter
- $\gamma = (\rho_s - \rho_f) / \rho_f$
- ρ_f = density of water
- ρ_s = density of sediment
- g = acceleration of gravity
- v = viscosity of water

TABLE 3

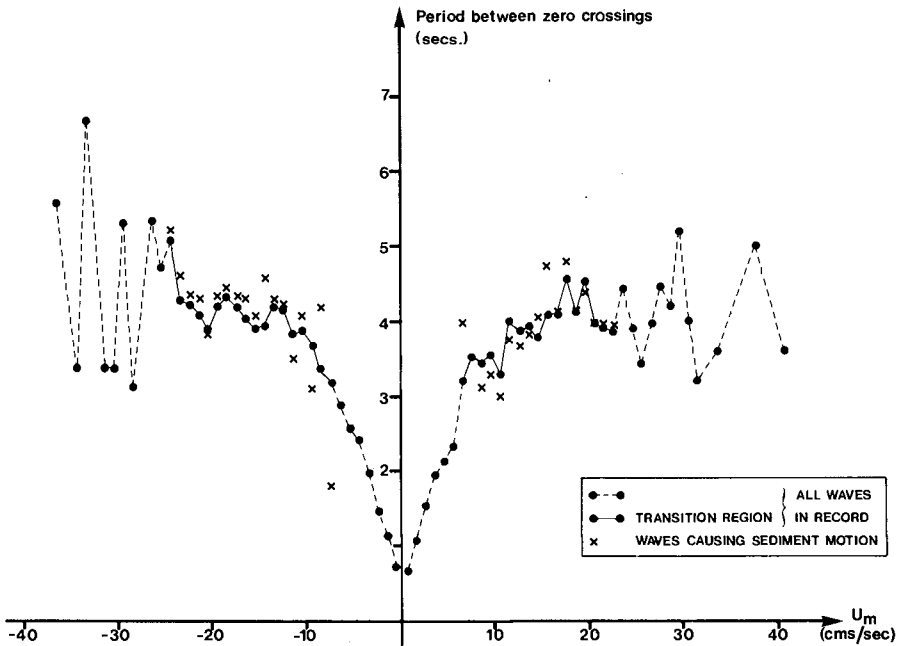


Fig. 11

MEAN PERIOD BETWEEN ZERO-CROSSINGS OF WAVE HALF CYCLES DEFINED BY VALUES OF U_m (IN INTERVALS OF UNIT WIDTH)

- (c) slight changes in wave direction - in particular, the transverse velocity component in the direction normal to the plane of the measuring head has been assumed small compared with u and this may not always have been the case;
- (d) finally, and probably most important of all, the forces at work at threshold are not being considered directly in concentrating attention on U_m . In particular, an analysis involving bed shear stress is more likely to yield a solution to the problem than one based on the velocity amplitude U_m . However, another possible secondary perturbing influence at threshold is the fluid pressure field, which will give rise to forces on the grains on the bed over and above those forces caused by the fluid velocity field. The discussion in the next section is concerned with the importance of the spatial pressure gradient $\partial p / \partial x$ in the direction of wave advance.

6. The Importance of Pressure Gradients in the Fluid at the Threshold of Sediment Motion

The role of spatial pressure gradients in the fluid acting on individual grains at the initiation of sediment motion is likely to be of secondary importance only and depends, essentially, on whether or not fluid molecular viscosity is an active agent in determining the nature of forces on the exposed sand grains on the bed surface. Davies, Frederiksen and Wilkinson (1977) in discussing a related topic have shown that, depending upon whether fluid momentum is transferred to sand grains on the bed by dynamic pressure effects or by skin friction acting on the exposed top surfaces of grains, the role of pressure gradients is likely to be negligible or of small secondary importance respectively. In deciding which case is relevant in the present problem, it is possible to look for guidance at the comparable and well documented situation of uniform fluid flow past a single sphere; however, unfortunately, the Reynolds number of the flow past the sphere equivalent to the sand grains in question, lies in the intermediate region between linear and quadratic drag law behaviour. The nature of the forces on grains of mixed size on a sand bed is also unclear, and for this reason the data analysis described in this section has been pursued.

In examining the importance of forces resulting from the fluid pressure field at threshold, the analysis of the data has again been carried out both on a wave by wave basis and on the basis of an examination of instantaneous values of the relevant parameters at the initiation of sediment motion.

(i) Further results of the critical wave analysis

The aim in performing this analysis was to determine from the measured parameters whether any decisive difference could be found in the transition regions, between the waves which did and did not move sediment at each value of U_m . Before the measured pressure field was examined, consideration was given to the fluid acceleration. This was done on account of the presence in certain of the laboratory threshold formulae (Table 3) of the wave frequency, in addition to the velocity amplitude, indicating the possible importance of accelerative effects at threshold. In carrying out the analysis, it was assumed

that the behaviour of the velocity field in individual wave half cycles in the transition range was approximately sinusoidal, and that a measure of acceleration in a particular wave half cycle could thus be obtained by noting the interval between zero crossing values of velocity. The purpose of proceeding in this way was to see whether the waves in the transition ranges which moved sediment were, on an overall basis, those which displayed shorter periods (and, therefore, greater accelerations) between zero crossings at each value of U_m . It was not possible to seek directly peak values of acceleration itself during half cycles defined by zero-crossing times of measured velocity, due to the quadrature phase relationship between these quantities.

The results of the investigation are shown in Fig 11, in which average values of the interval are plotted against U_m for the rippled bed data in the second experiment. It can be seen that there was no systematic difference of the type sought, the waves moving sediment in the transition regions having a similar interval between zero-crossings to the assembly of all waves in the record. In other words, the examination of the transition regions has revealed that, at a particular U_m , the mean period of the waves causing sediment motion was not significantly different from that of the waves which did not cause motion. In addition, Figure 11 shows that the waves in the transition regions had a half-period of approximately $\frac{1}{2}$ seconds, or period of 9 seconds.

As argued above, a direct examination of the peak acceleration in each wave half cycle was not possible on account of the phase relationship between u and $\partial u / \partial t$. Clearly, the same phase relationship exists between u , the horizontal velocity measured in the free-stream flow, and $\partial p / \partial x$, the spatial pressure gradient in the direction of wave advance, since, in a frictionless zone and on a linearized analysis, the fluid acceleration is proportional to the pressure gradient. This was approximately so in the field, as can be seen in the typical scatter plot shown in Figure 12. The 3000 points plotted are pairs of digitized values of $\partial u / \partial t$ and $\partial p / \partial x$ from a 10 minute period during the second experiment. Although a general linear relationship is clear in these results, there was thought to be sufficient scatter about the mean line to justify an examination similar to the one described above, but now taking the peak pressure in each wave half cycle instead of the period between zero crossings of u . This was possible on account of the approximately in-phase behaviour of u and p , the waves measured being predominantly of progressive wave type; the pressure was taken as the mean value $\bar{p} = \frac{1}{2} (p_1 + p_2)$. Then, again at each U_m in the transition regions, the mean peak pressures of the waves which moved sediment were compared with peak pressures for the assembly of all waves in the record.

Figure 13 shows the results obtained for the rippled bed data in the second experiment. It is apparent that the waves which moved sediment were associated at certain values of U_m with higher than average peak pressures through the transition ranges in both shoreward and seaward directions. However, to argue from this that pressure gradients in wave half cycles associated with sediment motion were also generally greater than average, requires further assumptions; these relate both to the sinusoidal nature of individual wave half

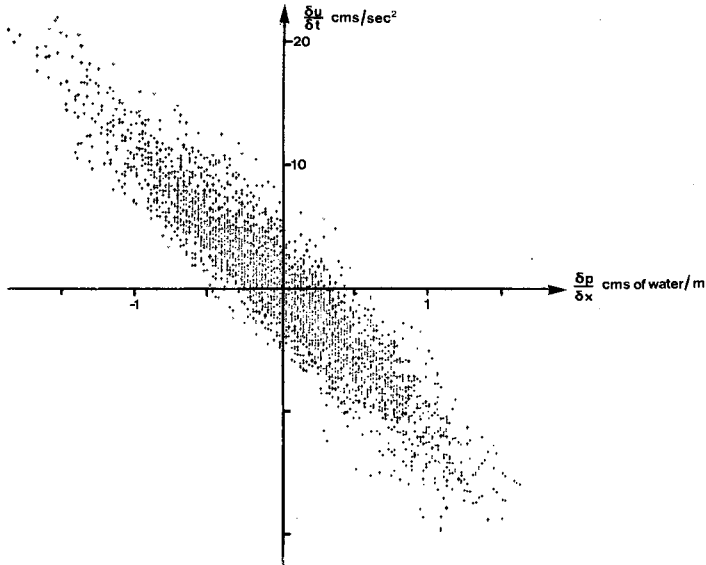


Fig.12 A SCATTER PLOT OF ACCELERATION AGAINST SPATIAL PRESSURE GRADIENT
(3000 values from a 10min run)

MEAN VALUES OF PEAK PRESSURE IN WAVE
HALF CYCLES DEFINED BY VALUES OF U_m
(IN INTERVALS OF UNIT WIDTH)

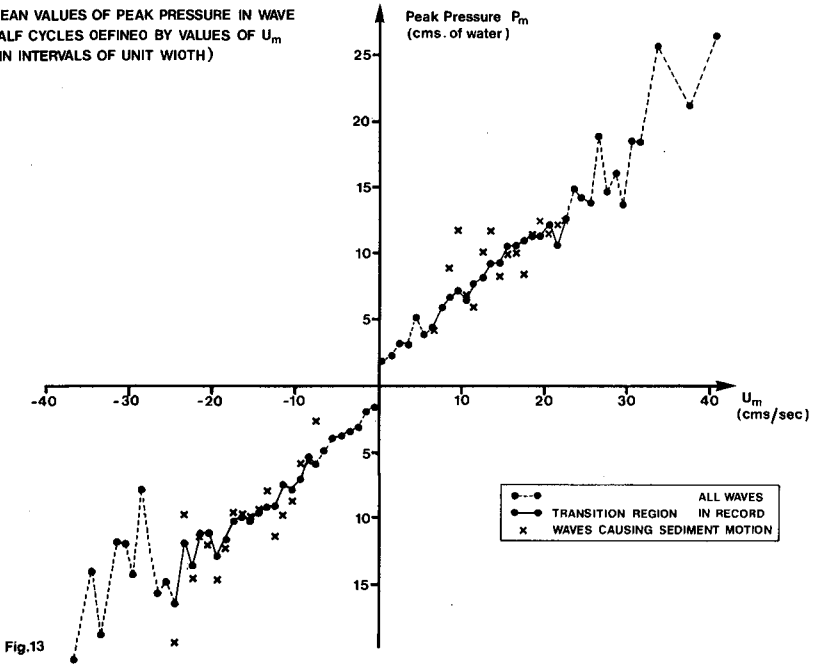


Fig.13

cycles, but more importantly to whether the flow can truly be regarded as two-dimensional. For it is possible that the degree of correlation between β and the total horizontal velocity may have been better than that between β and u ; no suitable experimental evidence was obtained to test this. Thus, on the basis of Figure 13, it cannot be shown that pressure gradients were a significant perturbing influence at threshold, and to resolve this area of ambiguity an analysis of the instantaneous sediment threshold data has been carried out.

(ii) Further results of the instantaneous threshold of motion study

Corresponding to the instantaneous threshold values of u_0 , quoted in Table 2 for the case of the rippled bed in the second experiment, mean values of the pressure gradient $\partial p / \partial x \approx (\bar{p}_1 - \bar{p}_2) / \Delta x$ were found to be -0.75 and $+0.81$ cms of water/metre, at the initiation of motion in the shoreward and seaward directions respectively; the standard deviations were 0.76 and 0.69 cms of water/metre respectively.

In order to assess the importance of pressure gradients at threshold, an attempt has been made to reduce the considerable amount of scatter in the critical values of u_0 and $\partial p / \partial x$ on a systematic basis, by combining pairs of critical values to form empirical expressions for the total force on the bed surface, firstly of the type

$$F_1 \Big|_{\nu} = C_1 u_0 \Big|_{\nu} + C_3 \frac{\partial p}{\partial x} \Big|_{\nu}$$

and secondly,

$$F_2 \Big|_{\nu} = C_2 \{ u_0 | u_0 | \} \Big|_{\nu} + C_3 \frac{\partial p}{\partial x} \Big|_{\nu}$$

where the subscript ν indicates the ν th data value at threshold. The expressions relate to the cases of linear and quadratic velocity drag law behaviour respectively, and C_1 , C_2 and C_3 are appropriate force coefficients. The aim of this exercise was to determine whether the scatter in $F_{1,2}$ could be shown to be significantly smaller than the scatter in the critical values of $F_{1,2}$ with $C_3 = 0$, by adopting some optimum value of the ratio $C_1 : C_3$ or $C_2 : C_3$ respectively. The method used was a perturbation procedure to determine values of these ratios according to the criterion that the variance in $F_{1,2}$ over all ν , should be minimized.

The investigation was carried out for the rippled bed data in the second experiment, over successive data collection periods of 10 minutes. Occurrences of motion in the shoreward and seaward directions were examined separately. The results showed that, although the variance in $F_{1,2}$ could be reduced substantially in almost all the data portions examined by a particular choice of the ratios $C_1 : C_3$ and $C_2 : C_3$, no systematic behaviour was evident in these ratios. In particular, the general trend in the results was for the minimization of variance to be accomplished by a pressure gradient force acting always in one direction regardless of the direction of grain motion. In other words, while the minimization of variance was of numerical significance, it had no physical significance. It is thought that this offers

substantial evidence that the pressure gradients in the present problem were of no importance in mobilizing grains on the seabed, despite a weak suggestion in Section 6(ii) to the contrary.

7. Discussion and Conclusions

From the critical wave by wave analysis, two main conclusions have been drawn. Firstly, that for the real sand ripples in the present experiment there was an apparent doubling in the threshold velocity amplitude (measured in the free stream) for sediment motion on a flat bed compared with motion on the crest of a sand ripple. However, a quantitative explanation for this has been obtained from a model of the potential flow over real sand ripple shapes.

Secondly, there was not found to be just one value of velocity amplitude associated with the initiation of grain motion; rather, a wide (transition) range of velocity amplitude values has been identified in which only a fraction of the measured waves moved sediment. Sedimentological considerations, the somewhat subjective nature of the sediment threshold analysis and possible effects of three-dimensionality in the flow, have been proposed as factors of secondary importance in the problem which may go some way towards explaining the presence of the transition regions. Accelerative effects in the flow do not appear to provide an explanation. However more recent work has suggested that a significant narrowing of the transition regions can be accomplished by working a critical wave by wave analysis in terms of bottom stresses at threshold, rather than velocity amplitudes measured in the free stream flow. Despite the improvement in an understanding of the phenomenon which can be achieved in this way, it is thought encouraging that the measured critical velocity amplitude values in the present experiment (when the bed was flattened, or when allowance was made for the effect of ripples) were in reasonable agreement with various well known laboratory threshold results.

The instantaneous threshold of motion study has been used to isolate the critical instants in time at which sediment motion started or stopped, with a view to understanding in more detail the processes at work at the initiation of sediment motion. The study conducted on the importance as a perturbing influence at threshold, of pressure gradients in the flow, has led to the conclusion that pressure induced forces on the surface grains on the bed are of little or no importance in the transport of coarse sands by swell waves. The same may not be true during and after the breaking of waves, where the pressure gradients are much higher at certain instants in each wave cycle. However, outside the breaker zone, it appears that sediment movement by waves is capable of explanation in terms of the near-bed velocity field alone.

Acknowledgments

The authors would like to thank the electronics engineers and the diving team at IOS Taunton for the essential part they played in performing the experiments. Dr K R Dyer is thanked for his comments during the preparation of this paper.

References

- Bagnold, R A (1946). Motion of waves in shallow water. Interaction with a sand bottom. Proceedings of the Royal Society, London. Series A, 187, 1 - 185.
- Davies, A G and Wilkinson, R H (1977). The movement of non-cohesive sediment by surface water waves, Part I : Literature survey. Institute of Oceanographic Sciences Report Number 45 (Unpublished manuscript).
- Davies, A G, Frederiksen, N A and Wilkinson, R H (1977). The movement of non-cohesive sediment by surface water waves, Part II: Experimental study. Institute of Oceanographic Sciences Report Number 46 (Unpublished manuscript).
- Dayton, C M and Stunkard, C L (1971). Statistics for problem solving. McGraw-Hill Inc. 290 pp.
- Komar, P D and Miller, M C (1973). The threshold of sediment movement under oscillatory water waves. Journal of Sedimentary Petrology, 43 (4) 1101 -1110.
- Manohar, M (1955). Mechanics of bottom sediment movement due to wave action. US Army Corps of Engineers. Beach Erosion Board Technical Memorandum 37.

CHAPTER 95

DISTRIBUTION OF SAND TRANSPORT RATE ACROSS A SURF ZONE

Toru Sawaragi

Professor of Civil Engineering
Osaka University, Osaka, Japan

and

Ichiro Deguchi

Research Associate of Civil Engineering
Osaka University, Osaka, Japan

ABSTRACT

The distributions of longshore and on-offshore sediment transport rates in a surf zone were measured by an apparatus which was able to separately record both components of the sediment transport rate. The characteristics of their distributions were discussed from the bottom shear stresses which were measured by the shear meter under the same wave conditions as the laboratory experiment of the sediment transport.

The maximum bottom shear stress took place at the depth between the breaking depth of waves and the depth where the velocity of the longshore current showed a maximum. On the other hand, the maximum on-offshore and longshore sediment transport rates occurred at the depth slightly shallower than the depth where the maximum bottom shear stress took place. What's more, the longshore sediment transport rates were represented by the longshore current velocity and the bottom shear stress generated by waves and the longshore current. However, the distribution of the on-offshore sediment transport rates showed more complicated profile than that of the longshore sediment transport rates because there were no eminent unidirectional flow in the direction normal to the shore line. Therefore, the on-offshore sediment transport rates could not be formulated by the bottom shear stresses.

1. Introduction

In the problems of the coastal sediment, the sediment transport is usually considered to be divided into the longshore and the on-offshore components for convenience. The longshore sediment transport rate has been investigated from an energy principle approach, and the on-offshore sediment transport has been investigated in the process of equilibrium beach profiles. However, the sediment in the surf zone do not move in the directions normal and parallel to the shore line independently. Although some investigations concerning the distribution of the longshore sediment transport rate in the surf zone based on both energy and force principle approach have been proposed (Thornton(1972)

and Komar(1977)), those theories have not been verified thoroughly by fields or model beach experiments because of the lack of information about wave deformations and wave-induced flow conditions, and the difficulty of the measurement of the longshore sediment transport rate in the surf zone.

The authors devised an apparatus which was able to separately record the longshore and the on-offshore sediment transport rates, the distributions of each component of the sediment transport rate along a line normal to the shore line across the surf zone were measured by using this apparatus in a field as well as in a laboratory model beach. Furthermore, the distribution of bottom shear stresses, which directly cause sediment movements on a sea bottom, along a line normal to the shore line was also measured by a shear meter on a fixed bed in a laboratory under the same wave conditions as the laboratory experiment of sediment transport rates.

The characteristics of a bed load caused by waves and wave-induced longshore current were discussed with respect to the distribution of the bottom shear stress and the formula on the rate of longshore sediment transport was proposed.

2. Equipments and procedures to measure the sediment transport rate.

In the surf zone where the wave-induced longshore current occurs, sediment particles at the bottom are moved by the water-particle-motion combined waves and the longshore current. As a results, the directions of sediment movements change with time according to the phase of the wave motion or the relative velocity of the water particle due to waves to the velocity of currents. The authors devised the method to analyze the longshore and the on-offshore sediment transport rates by measuring the sediment volume which are moved by uprush and downrush separately, by using a sand trap as shown in Fig.1. During the measurement, this sand trap was buried in the sea bottom till the upper part of the trap and its surrounding sea bottom were on the same level. Pebble stones were also put around the trap to prevent local scouring due to waves in the field. In Fig.1, the following symbols are used:

a : the diameter of the sand trap

$|\vec{q}_u|$ and $|\vec{q}_d|$: the sediment transport rates per unit length per unit time when sediment are moved by uprush and downrush,

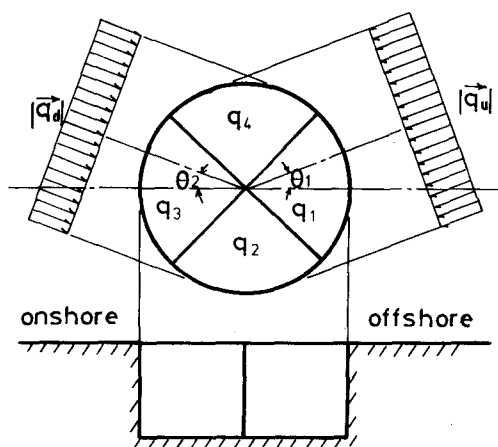


Fig.1 Sand trap

respectively.

θ_1 and θ_2 : the angles between a line normal to the shore line and the directions of the sediment movement (the clockwise position being positive), respectively.

where q_{u1} and q_{d1} are defined by assuming the following model of the sediment transport:

a) When the sediment moves toward the shore line, the volume of the sediment which can be transported by any current per unit area at the bottom is q_{u1}^* and the velocity of the sediment transport is $|\vec{u}_{s1}|$, the direction of which makes an angle θ_1 with the normal to the shore line. Hence the sediment transport rate per unit length per unit time when the sediment is moved by uprush equals $|\vec{q}_{u1}| = q_{u1}^* \cdot |\vec{u}_{s1}|$ and the longshore and the on-offshore components of the velocity of the sediment transport equal $|\vec{u}_{s1}| \sin \theta_1$ and $|\vec{u}_{s1}| \cos \theta_1$, respectively.

b) When the sediment is moved toward offshore by downrush, the volume of the sediment which can be transported is q_{d1}^* and the velocity of the sediment transport is $|\vec{u}_{s1}|$, the direction of which makes an angle θ_2 with the normal to the shore line. Here, the sediment transport rate when the sediment is moved by downrush equals $|\vec{q}_{d1}| = q_{d1}^* \cdot |\vec{u}_{s1}|$ and the longshore and the on-offshore components of the velocity of the sediment transport equal $|\vec{u}_{s1}| \sin \theta_2$ and $|\vec{u}_{s1}| \cos \theta_2$, respectively.

Based on these assumptions, the longshore and the on-offshore sediment transport rates per unit length per unit time, q_x and q_y , are given as follows:

$$\begin{aligned} q_x &= q_{u1}^* |\vec{u}_{s1}| \sin \theta_1 - q_{d1}^* |\vec{u}_{s1}| \sin \theta_2 = |\vec{q}_{u1}| \sin \theta_1 - |\vec{q}_{d1}| \sin \theta_2 \\ q_y &= q_{u1}^* |\vec{u}_{s1}| \cos \theta_1 - q_{d1}^* |\vec{u}_{s1}| \cos \theta_2 = |\vec{q}_{u1}| \cos \theta_1 - |\vec{q}_{d1}| \cos \theta_2 \end{aligned} \quad (1)$$

In these equations, $|\vec{q}_{u1}|$, $|\vec{q}_{d1}|$ and θ_1 , θ_2 can be calculated volumetrically from the sediment which were trapped in the individual compartments of the sand trap by using the following relations:

For $0 < \theta_1, \theta_2 < \pi/4$

$$\begin{aligned} q_1 &= |\vec{q}_{u1}| \sqrt{2} \cos \theta_1, \quad q_2 = |\vec{q}_{u1}| a (1 - \cos(\theta_1 + \pi/4)) + |\vec{q}_{d1}| a (1 - \cos(\pi/4 - \theta_2)) \\ q_3 &= |\vec{q}_{d1}| \sqrt{2} \cos \theta_2, \quad q_4 = |\vec{q}_{d1}| a (1 - \cos(\theta_2 + \pi/4)) + |\vec{q}_{u1}| a (1 - \cos(\pi/4 - \theta_1)) \end{aligned} \quad (2)$$

For other values of θ_1 and θ_2 , similar relations as eq. (2) are used to calculate $|\vec{q}_{u1}|$, $|\vec{q}_{d1}|$ and θ_1 , θ_2 except when $-\pi/2 < \theta_1 < -\pi/4$, $\pi/4 < \theta_2 < \pi/2$ and $\pi/4 < \theta_1 < \pi/2$, $-\pi/2 < \theta_2 < -\pi/4$. In these case, the velocity of the longshore current is greater than the water-particle velocity due to the wave, and the on-offshore sediment transport can be neglected.

3. Field measurements of the sediment transport rate in the surf zone.

The authors conducted the measurements with this sand trap in the two natural beaches shown in Fig. 2. Isonoura Beach looks out on the Pacific Ocean and has a straight beach of about 1 km, the slope of which is about 1/80. The median grain size of the beach materials is about 0.2 mm. The incident wave steepnesses are usually flat and wave heights are relatively high. Matsuho Beach is located at the southern end of Awaji Isl. and has a convex beach of about 50 m, the slope of which is about 1/15. The median grain size of the beach materials is about 2.0 mm. The incident wave steepnesses are usually steep and wave heights are

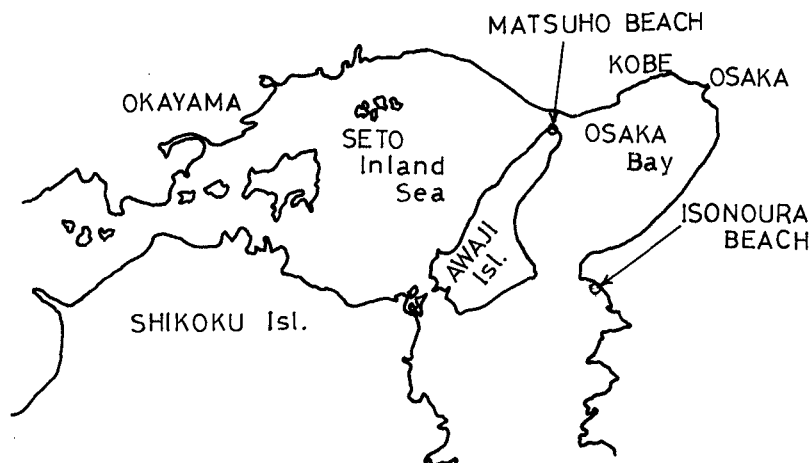


Fig.2 Sites of field measurements of sediment movements.

relatively small. The diameter of the sand trap used in these field experiments was 50cm and the depth was 30cm – 40cm . 10 sand traps were buried equi-distance between the wave run-up height and about 3.0m below the mean water level. The incident wave characteristics were also recorded by the pressure-type wave gauge.

Figs.3 and 4 show examples of the distributions of the longshore and the on-offshore sediment transport rates along beach profiles measured in these two beaches.

Figs.3(a) and (b) indicate the results obtained at different times in Isonoura Beach. This beach has a large surf zone of about 100m width because of the gentle slope and flat and high incident wave height. The distribution of the longshore and the on-offshore sediment transport rates shown in Fig.3(a) indicates one peak slightly seaward from the shore line. While the profile of the distribution of the longshore sediment transport rate shown in Fig.3(b) indicates two peaks near the shore line and a location slightly shallower than the breaking depth of the significant incident wave.

Figs.4(a) and (b) indicate the results obtained in Matsuho Beach. Since Matsuho Beach has a steep beach slope which consists of relatively large beach materials, and furthermore, since the incident wave heights are usually small, the length of the surf zone is small (about 5m). So, as shown in Fig.4, the longshore and the on-offshore sediment transport were concentrated in a narrow range near the shore line. And the profiles of the distribution of the longshore and the on-offshore sediment transport rates indicated one keen peak which was sometimes above the shore line.

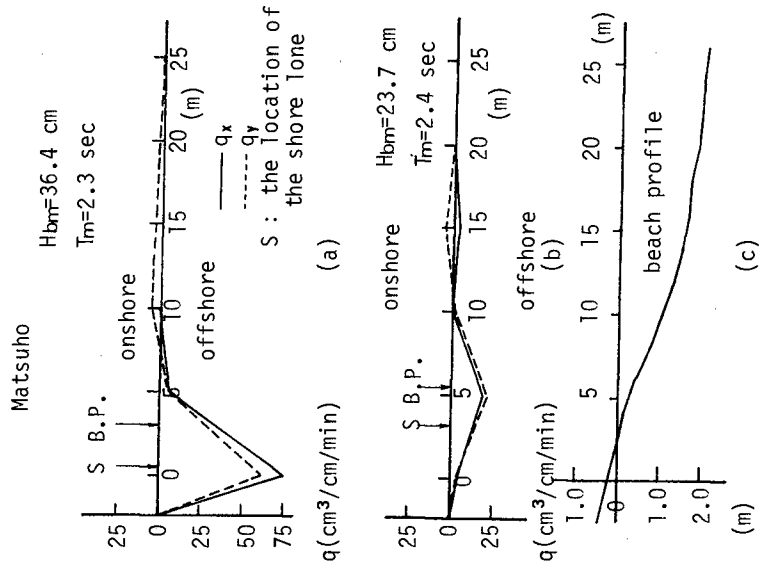


Fig. 4 Distribution of sediment transport rate measured at Matsuho Beach.

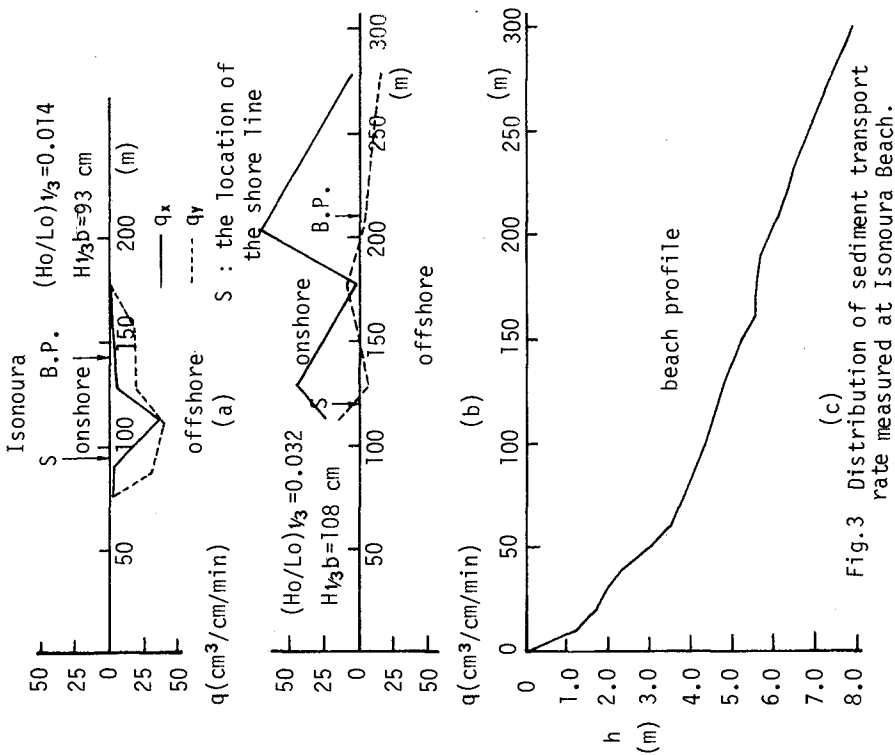


Fig. 3 Distribution of sediment transport rate measured at Isonoura Beach.

4. Measurements of the sediment transport rate and bottom shear stresses on a model beach.

It appears very difficult to find the general characteristics of the sediment transport from the field data as shown in Figs.3 and 4 because of the irregularities of incident waves and the changes of the still water level due to tides. Therefore, the authors conducted measurements of the sediment transport rates in the surf zone on a model beach with a movable bed. In addition, bottom shear stresses which directly cause sediment movements on a fixed bed were measured in order to make more detailed investigation of the mechanism of the sediment transport in the surf zone.

4-1. Measurements of the sediment transport rate on a model beach.

Movable bed experiments were conducted by using a wave basin of 20^m width, 30^m length and 0.6^m depth. At one end of the basin was equipped a straight 12^m long model beach with a slope of 1/20. At the other end of the basin was installed a flap-type wave generator which generated an incident wave making an angle 30° with the shore line of the model beach at the water depth of 38^{cm}. Three kinds of waves of which the steepness in a deep water were about 0.02, 0.04, and 0.06 were propagated. Two kinds of beach materials, median grain size d_{50} being 0.34^{mm} and 0.68^{mm}, were used. However, the wave height in deep water was kept constant at about 6^{cm}.

Sediment transport rates were measured by 10 sand traps buried between the shore line and at the depth of 10^{cm}. The diameter of the sand trap was 10^{cm} with a depth of 7^{cm}. Wave height distributions in the surf zone were measured by capacitance-type wave gauges, and the longshore current velocity and the wave direction were recorded by 16^{mm} high-speed cine camera equipped at a height of 4^m above the wave basin.

4-2. Equipments and procedures to measure bottom shear stresses.

The bottom shear stress was measured by a shear meter which is shown in Fig.5. In Fig.5, a shear force acting on the shear plate ① is measured by converting the force into a moment of the supporting shaft ②. The shear plate is subjected to a resultant force due to wave pressure gradient force and the shear force. Thus, the shear force is calculated by subtracting pressure gradient force, measured by the pressure tube ③ equipped at both ends of the shear plate, from the resultant force measured by the shear plate.

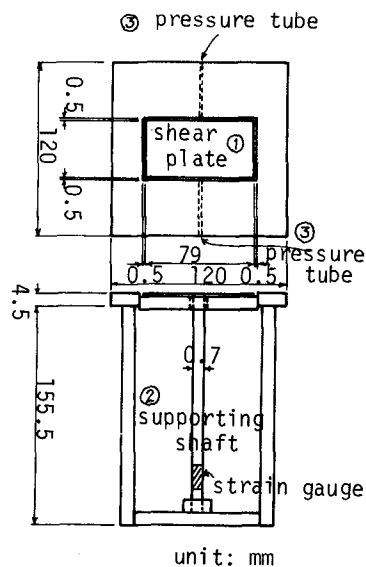


Fig.5 Shear plate

However, in the experiments, the bottom shear stresses were caused by waves and currents and the direction of their respective water-particle-motion made an angle of about 90° . Therefore, it was assumed that the water-particle movements normal to the direction of the shear stress do exist. Then the authors made many concave gratings under the shear plate to prevent these water-particle movements. And the bottom shear stress was measured as the longshore and the on-offshore components separately at about the same point as the measurement of the sediment transport. Hereafter, these components of the bottom shear stress are represented by τ_x and τ_y , respectively.

5. Experimental results.

5.1 Distributions of q_x and q_y .

The distributions of averaged q_x and q_y measured twice within 10^{min} after wave propagation in the experiments of $d_{50} = 0.34^{\text{mm}}$ and $d_{50} = 0.68^{\text{mm}}$ are shown in Figs.6 and 7, while Fig.8 shows the distributions of the velocity of the longshore current U and wave height H . In these Figs., q_{xm} and q_{ym} indicate the maximum value of q_x and q_y . And U_m is the maximum longshore current velocity and H_b is the breaking wave height. Y is the distance from the shore line and Y_b is the distance from the shore line to the breaking point.

When $d_{50} = 0.68^{\text{mm}}$ ($H_0/d_{50} = 88$) as shown in Figs.6 and 8(a), the maximum q_x and q_y occurred at $Y/Y_b = 0.6$ which was slightly seaward than the point where the velocity of the longshore current showed a maximum value regardless of H_0/L_0 . Besides, the direction of the on-offshore sediment transport was almost offshore. According to the continuous equation for the sediment transport, the distribution of q_y as shown in Fig.6(b) causes the following modes of beach deformation as erosion in the range of $Y/Y_b < 0.6$ and accretion in the range of $Y/Y_b > 0.6$ and these modes of beach deformation were confirmed in our experiments.

On the other hand, in the case of $d_{50} = 0.34^{\text{mm}}$ in Fig.7(a), maximum q_x took place at $Y/Y_b = 0.8$, which was more toward the seaward side than the former case and the profiles of the distribution showed saddle shapes in the region of $Y/Y_b < 0.6$, while the distribution of q_y shown in Fig.7 (b) indicates complicated figures, maximum q_y occurring at the same point as q_x . Furthermore, it can be seen from Fig.7 that a fair amount of sediment transport occurred in the region of $Y/Y_b > 1.0$.

5-2. Profiles of the distribution of τ_{xm} and τ_{ym} .

Fig.9 shows an example of the distribution of measured maximum bottom shear stresses in nondimensional form by dividing by $\rho g H_b$ along a beach profile together with the distribution of the velocity of the longshore current and the wave heights measured at the same time, where ρ is the density of the water and g is the acceleration due to the gravity.

In the region of $Y/Y_b > 0.8$ in Fig.9, both $\tau_{xm}/\rho g H_b$ and $\tau_{ym}/\rho g H_b$ increase monotonously as Y/Y_b decreases. And in the region of $Y/Y_b < 0.8$,

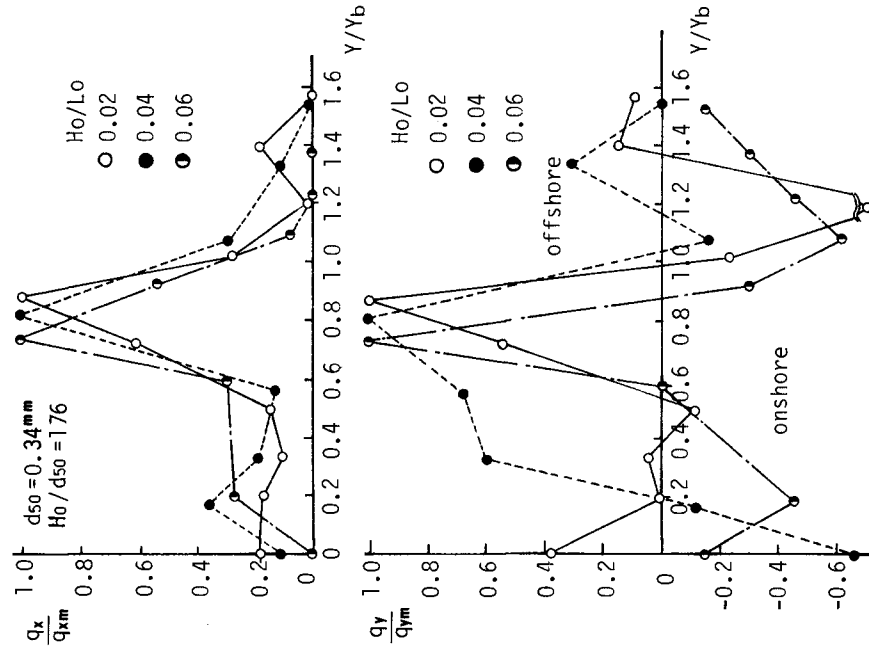


Fig.6 Distribution of sediment transport rate.

Fig.7 Distribution of sediment transport rate.

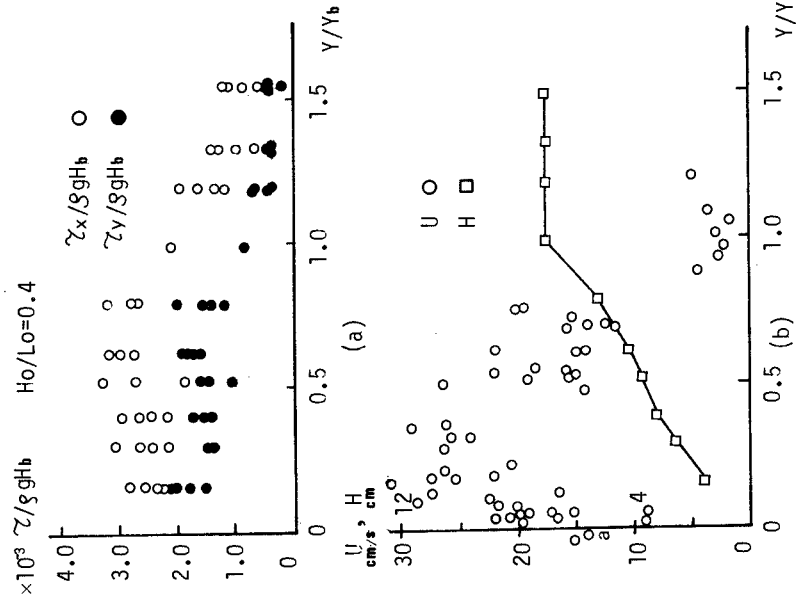


Fig. 9 Distribution of bottom shear stress, longshore current velocity and wave height.

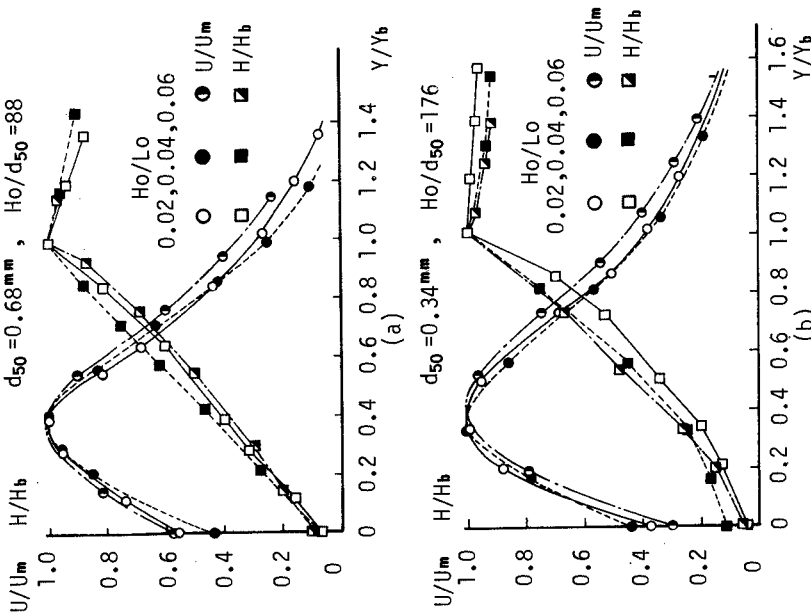


Fig. 8 Distribution of longshore current and wave height.

$\tau_{ym}/\rho g H b$ indicates almost constant values. On the other hand, the distribution of $\tau_{xm}/\rho g H b$ in this region is minimum at $Y/Y_b=0.6$ and maximum at $Y/Y_b=0.3$ where the velocity of the longshore current became significant as shown in Fig.9(b).

Bijker(1966) studied the problem of the bottom shear stress due to a combined wave and current action when they were given independently. In his theory, the bottom boundary layer was mainly determined by a current. So, when his results were applied to our experiments τ_{xm} surpasses τ_{ym} ($\tau_{xm}/\tau_{ym}>5$) in the whole range of the surf zone. However, because the longshore current is caused by waves, it can be thought reasonably that the boundary layer in the surf zone is determined almost by the wave characteristics and Bijker's theory can not be applied in the surf zone.

Therefore, the authors assume the effects of the longshore current on the bottom shear stress as follows:

Consider the water particle velocity which is composed of the wave and the longshore current just outside the bottom boundary layer as shown in Fig.10. In this figure, the following symbols are used:

U : the velocity of the longshore current.

u_{bm} : the maximum water-particle velocity by waves.

θ : the angle between the direction of wave propagation and a line normal to the shore line.

V : the composite water-particle velocity of the wave and the longshore current.

β : the angle between the direction of the composite bottom shear stress and a line normal to the shore line ($=\tan^{-1}(\tau_{xm}/\tau_{ym})$).

and \rightarrow indicates a vector. It is now assumed that the maximum bottom shear stress acts in the direction of the vector sum of the longshore current and the maximum water-particle velocity by the wave, which makes an angle $(\pi/2-\theta_m)$, and is expressed by the following relation,

$$\tau_m = \rho f |\vec{V}_m|^2$$

$$\text{where } |\vec{V}_m|^2 = (u_{bm} \cos \theta_m)^2 + (u_{bm} \sin \theta_m + U)^2 \quad (3)$$

and f is the friction factor. In this case, the longshore and the on-off-shore components of τ_m become

$$\tau_{xm} = \tau_m (u_{bm} \cos \theta_m) / |\vec{V}_m|$$

$$\tau_{ym} = \tau_m (u_{bm} \sin \theta_m + U) / |\vec{V}_m| \quad (4)$$

and the following relation can be obtained,

$$\frac{\tau_{xm}}{\tau_{ym}} = (\tan \theta_m + \frac{U}{u_{bm}}) \sec \theta_m \quad (5)$$

Now, let $(\tau_{xm}/\tau_{ym})_0$ be the ratio when there is no current ($U=0$), $(\tau_{xm}/\tau_{ym})_0 = \tan \theta_m$ from eq.(5), and eq.(5) can be written as

$$\left(\frac{\tau_{xm}}{\tau_{ym}} - \left(\frac{\tau_{xm}}{\tau_{ym}} \right)_0 \right) \cos \theta_m = \frac{U}{u_{bm}} \quad (6)$$

Fig.11 shows the relation of eq.(6) where u_{bm} was calculated from the relation

$$u_{bm} = \sqrt{g(h+H)} (H/2h) \quad (7)$$

and H in eq.(7) was obtained from the experimental results.

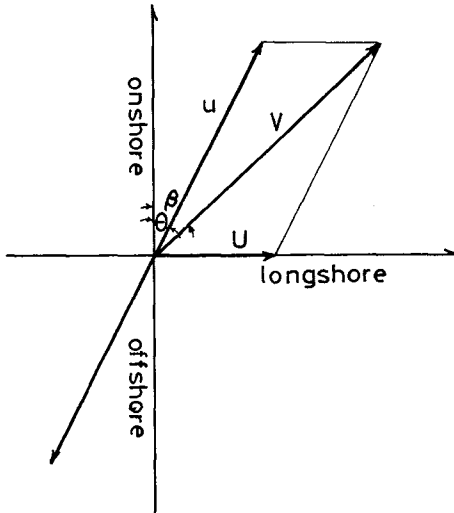


Fig.10 Composite water-particle velocity

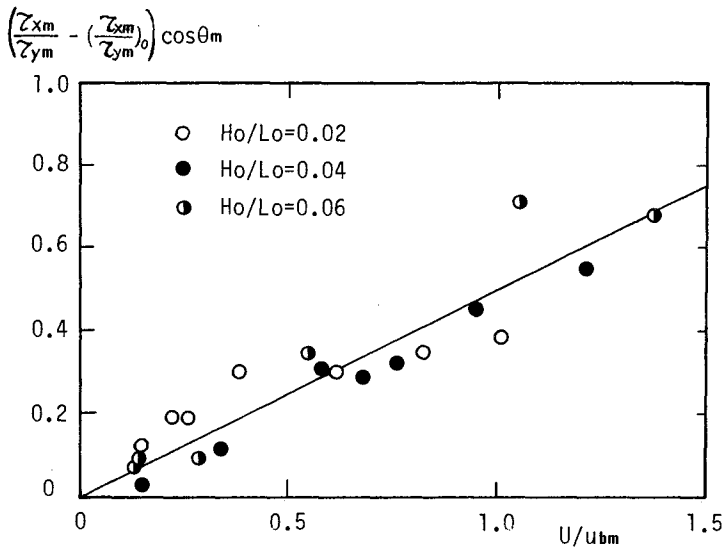


Fig.11 Increase of the longshore component of bottom shear stresses due to longshore current.

It can be seen from Fig.11 that $(\tau_{bm}/\tau_{gm} - (\tau_{bm}/\tau_{gm})_0)\cos\theta_m$ increase linearly as U/u_{bm} increase regardless of H_0/L_0 . However, the gradient of the straight line drawn in Fig.11, which indicates the approximate relation between the two quantities of eq.(6), is about 1/2. From this fact, the velocity of the longshore current just outside the boundary layer assumes a value about half of the velocity at the surface and the following expression for τ_{bm}/τ_{gm} and τ_{bm} can be obtained,

$$\frac{\tau_{bm}}{\tau_{gm}} = \frac{U}{2u_{bm}\cos\theta_m} + \tan\theta_m \quad (8)$$

$$\tau_{bm} = (\tau_{bm}^2 + \tau_{gm}^2)^{1/2} = \left\{ \left(\frac{U}{2u_{bm}\cos\theta_m} + \tan\theta_m \right)^2 + 1 \right\}^{1/2} \tau_{gm} \quad (9)$$

However, there are some complexities involved calculating these components of the bottom shear stress according to eqs.(3) and (4), and the authors tried to express τ_{gm} by using the wave characteristics only as defined by

$$\tau_{gm} = \rho f_y u_{bm}^2 \quad (10)$$

Fig.12 shows the relation between f_y calculated from eq.(10) and the Reynolds' number $Ret = u_{bm}^2 T/\nu$, where T is the wave period, ν is a coefficient of the kinetic viscosity of the water, a_s is an amplitude of the water-particle movement just outside the boundary layer and k_s is the equivalent roughness element. The full line in this figure indicates the relation obtained from the laminor theory and the dotted line indicates the limit of the transitional range from laminor to turbulent flow condition obtained by Reidel et.al.(1972). It can be seen from Fig.12 that f_y calculated from our experiments are a few times larger than those in the laminor boundary layer.

From the results mentioned above, it can be seen that bottom shear stresses can be calculated easily from Fig.12 and eqs.(8),(9) and (10).

5-3. Relations between q_x and the bottom shear stress.

As shown in Figs.6.7 and 8, there exists a certain relation between q_x and the bottom shear stress. Therefore, the authors investigated the distribution of the longshore sediment transport rate along the beach profile, based on the measured results of the bottom shear stress by considering the velocity of the longshore current as a velocity of the sediment transport. However, since the bottom shear stress was measured on a smooth-fixed bottom, there still remains some questional problems as to whether the same bottom shear stress as measured on a fixed bed can be applied to a movable bed or not. According to Kajiura(1968), the flow condition in the bottom boundary layer in the surf zone was laminor or smooth-turbulent when the bottom was flat, and rough-turbulent when sand ripples were formed in a movable bed. However, in the surf zone, large turbulence was brought into the water from the surface by breaking. And it was estimated that the wave energy loss in the surf zone was some hundred times the amount of energy dissipated due to the bottom shear stress(Sawaragi et.al.(1974)). Therefore, the flow condition in the surf zone seems to determined by the intensity of the turbulence by wave breaking regardless of the bottom configurations. Hence, the application of the results in a fixed bed to the movable bed is justified. Figs.8 and 9(b) may verify the above-mentioned consideration to some extent.

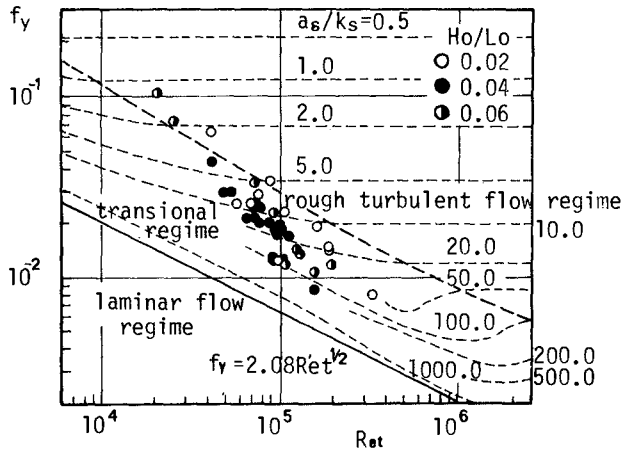


Fig.12 Friction factor calculated from the on-offshore component of the bottom shear stress and water-particle velocity.

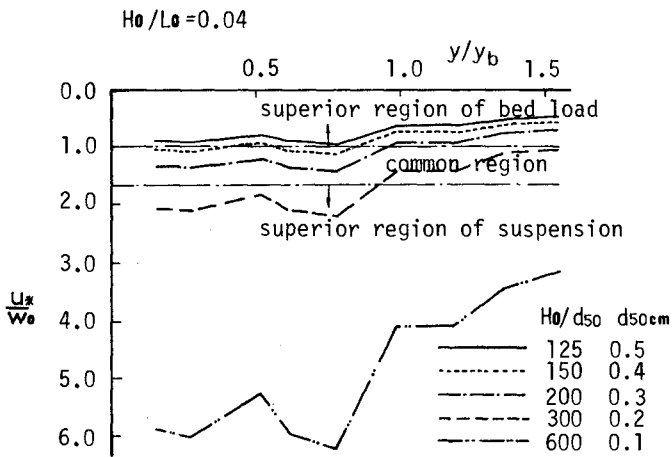


Fig.13 Distribution of u_x/W_o

That is, the conditions of the wave attenuation in the surf zone are similar and there seems to be no significant difference between the distribution profiles of the velocity of the longshore current of various bottom configurations. Therefore, the authors considered that the bottom shear stresses, as measured on the fixed bed, acted with almost the same intensity on the movable bed in the surf zone. Hence the longshore sediment transport rate can be expressed as a function of the bottom shear stress and the velocity of the longshore current.

Based on the above-mentioned way of thinking, the maximum longshore sediment transport takes place at the same location regardless of the size of the beach materials. However, this fact is different from the experimental results in that the location where the maximum longshore sediment transport of $d_{50} = 0.68^{mm}$ took place was shallower than that of $d_{50} = 0.34^{mm}$.

The sand trap shown in Fig.1 was used in our experiment for the purpose of recording the volume of the sediment which were transported as the bed load. In the region where the turbulence at the bottom is strong enough to bring the sediment into suspension from the bed, this kind of sand trap does not function effectively. Therefore, it is worthwhile to clarify the region where both bed materials of $d_{50} = 0.34^{mm}$ and 0.68^{mm} in the model beach experiments could be suspended in the surf zone.

It has been recognized that the criterion for the start of the suspension is determined by the ratio u_* / w_o where u_* is the bottom shear velocity and w_o is a falling velocity of the sediment and the region where the suspended load surpasses the bed load is also determined by u_* / w_o in the field of the open channel flow. For example, these limits concerning the suspension are given by Engelund(1965) and Shinohara (1959) as follow:

$$\begin{aligned} u_* / w_o > 1.0 & \dots \text{the start of suspension} \\ u_* / w_o > 1.7 & \dots \text{suspended load surpasses bed load} \end{aligned} \quad (11)$$

Fig.13 shows u_* / w_o against Y/Y_b calculated from the bottom shear stresses measured on a fixed bed and Rubey's formula for w_o with the parameter d_{50} and H_o/d_{50} . As can be seen from Fig.9, measured bottom shear stresses were scattered, u_* were calculated by using the averaged values of τ_{zm} and τ_{ym} at the same Y/Y_b from the relation

$$u_*^2 = \tau_m / \rho = (\tau_{zm}^2 + \tau_{ym}^2)^{1/2} / \rho$$

The criterions given by eq.(11) are indicated in Fig.13 by the dotted and the chain lines. According to these criterions, it is clear that when $H_o/d_{50} < 125$ ($d_{50} > 0.5^{mm}$), no suspension of the sediment can occur in the whole range of the surf zone, while in the case of $H_o/d_{50} > 200$ ($d < 0.3^{mm}$) the sediment is suspended in the surf zone and in the case of $H_o/d_{50} > 300$ ($d_{50} < 0.2^{mm}$), the volume of the sediment transported in suspension is larger than the volume of the sediment transported as bed load at the phase of the maximum bottom shear stress taking place. From these considerations, it can be assumed that in our experiments of the measurements of the sediment transport rates, sediment were transported almost as the bed load. However, a certain amount of the sediment

particles, which can not be predicted by the informations the authors have, were suspended in the region of $Y/V_b < 0.8$ in the case of $d_{50} = 0.34^{mm}$.

Taking account the above-mentioned considerations about the sediment transport, the authors tried to obtain the relationship between nondimensional longshore sediment transport rates q_x/Ud_{50} and nondimensional force of the sediment transport, $F = (u_*^2 - u_{*c}^2) / (\rho/\rho_s - 1)gd_{50}$, as shown in Fig.14, where u_* is given by eq.(12), ρ_s is the density of the sediment particle and u_{*c} is given by Iwagaki(1956) as follows:

$$\begin{aligned}
 u_{*c}^2 &= 80.9d_{50}^3, & \text{for } d_{50} > 0.303^{cm} \\
 &= 134.6d_{50}^{3/4}, & \text{for } 0.303^{cm} > d_{50} > 0.118^{cm} \\
 &= 55.0d_{50}, & \text{for } 0.118^{cm} > d_{50} > 0.0565^{cm} \\
 &= 8.41d_{50}^{1/2}, & \text{for } 0.0565^{cm} > d_{50} > 0.0065^{cm} \\
 &= 226d_{50}, & \text{for } 0.0065^{cm} > d_{50}
 \end{aligned}
 \tag{13}$$

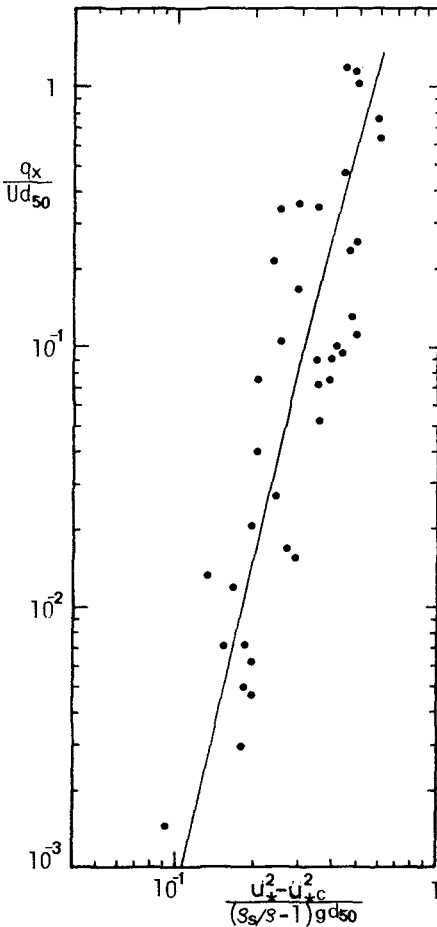


Fig.14 Relation between non-dimensional longshore sediment transport rate and nondimensional force of sediment transport.

Although the data shown in Fig.14 are somewhat scattered, they can be approximately represented by the following two straight lines:

$$\begin{aligned} \frac{q_x}{U_{d50}} &= 86F^{3.7}, & \text{for } F \geq 0.3 \\ &= 23F^{4.5}, & \text{for } F < 0.3 \end{aligned} \quad (14)$$

In eq.(14), u_* in F can be predicted by eqs.(9) and (10). Therefore, the distribution of q_x can be calculated if the velocity of the longshore current is given.

The predicted distribution of q_x calculated from eq.(14) are compared with the measured distribution of q_x in the case of $H_0/L_0=0.04$ in Fig.15. Here, the longshore current velocity was calculated by the theory of Longuet-Higgins(1970). The parameter p defined by Longuet-Higgins in his theory was fixed at 0.4 based on the consideration that the location where the longshore current shows the maximum is at about $Y/Y_b=0.4$ as shown in Fig.9(b). In Fig.15, the predicted q_x is indicated as a non-dimensional quantity by dividing by the predicted maximum value. From Fig.15, it is found that the distribution of the measured q_x in the case of $d_{50}=0.68^{mm}$ where any suspension did not occur in the entire region of the surf zone coincides fairly well with the distribution predicted by eq.(14) and the longshore current velocity presented by Longuet-Higgins. However, the distribution of q_x in the case of $d_{50}=0.38^{mm}$ differs from the predicted distribution in the profile. In such conditions of the sediment transport as in the case of $d_{50}=0.38^{mm}$, a certain amount of sediment was brought into suspension in the surf zone and it seems necessary to clarify the mechanism of suspension of the bed materials in the surf zone and take account of the quantity of the sediment in suspension in eq.(14)

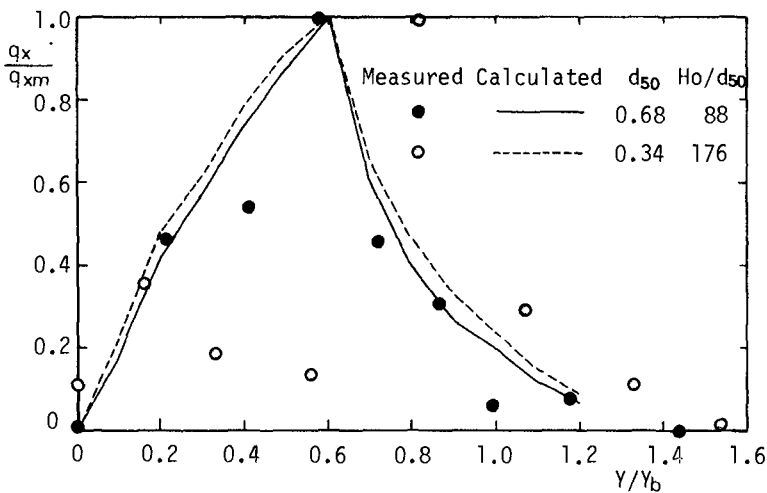


Fig.15 Comparison of the predicted and the measured longshore sediment transport rate.

6. Conclusion

The method to separately record the longshore and the on-offshore sediment transport rates, as the bed load, in the surf zone is developed, and the characteristics of the sediment transport in the surf zone are discussed from the bottom shear stresses measured on a fixed model beach.

The following conclusions are drawn from the foregoing study:

1. The distribution of the longshore sediment transport rate as the bed load shows a steep profile compared with the distribution of the longshore current and the maximum longshore sediment transport occurs at the place between the breaking point of incident waves and the location where the velocity of the longshore current shows the maximum value.

2. The maximum on-offshore sediment transport takes place at about the same place as the longshore sediment transport. However, the distribution of the on-offshore sediment transport rate shows more complicated profiles than that of the longshore sediment transport rate; the direction of the on-offshore sediment transport at any location changes with wave characteristics and beach slope from offshore direction to onshore direction.

3. The locations where the maximum longshore and on-offshore sediment transport take place are mainly controlled by the sediment size relative to the wave height.

4. The longshore current has less influence on the on-offshore component of the bottom shear stress than the longshore component, and within the range of the measurements where the wave directions at the breaking points are less than 20° , the on-offshore component of the bottom shear stress is greater than the longshore component of the bottom shear stress. This result differs from the result obtained by Bijker under the condition where waves and currents are given independently. However, the magnitude of the longshore component of the bottom shear stress is not so small as assumed by many investigators in the theory of the longshore current.

5. The longshore sediment transport rate when there are no suspended sediment can be represented by the function of the maximum bottom shear stress and the velocity of the longshore current. However, the estimation of the on-offshore sediment transport rate can not be represented by the maximum bottom shear stress. Further, there still remain some problems with regards estimating the on-offshore sediment transport rate and suspended load quantitatively.

References

- Thornton, E.B. (1972) : Distribution of sediment transport across the surf zone. Proc. 13th conf. Coastal Eng., pp.1049~1068.
- Komar, P.D. (1977) : Beach sand transport: Distribution and total drift. Proc. ASCE. Vol.103, No.WW2, pp.225~239.
- Bijker, E.W. (1966) : The increase of bed shear in a current due to wave motion. Proc. 10th conf. Coastal Eng., pp.746~765.
- Riedel, H.P., Kamphuis, J.W. and Brebner, A. (1972) : Measurement of bed shear stress under waves. Proc. 13th conf. Coastal Eng., pp.587~604.
- Kajiura, K. (1968) : A model of the bottom boundary layer in water wave. Bull. Earthquake Research Institute, Tokyo Univ., Vol.46, pp.75~123.
- Sawaragi, T. and K. Iwata (1974) : On wave deformation after breaking. Proc. 14th conf Coastal Eng., pp.481~479.
- Engelund, F. (1965) : Turbulent energy and suspended load. Basic Research Progress Report, Technical Univ. of Denmark, No.10.
- Shinohara, K and T. Tsubaki (1959) : On the characteristics of sand waves of the open channels and rivers. Reports of Research Institute for Applied Mechanics, Kyushu Univ., Vol.7, No.25, pp.15~45.
- Iwagaki, Y. (1956) : Basic study on the critical shear velocity for sediment movement in the open channels. Proc. JSCE. Vol.41. (in Japanese)
- Longuet-Higgins, M.S. (1970) : Longshore current generated by obliquely incident sea waves, 1. Journal of Geophysical Research. Vol.75, No.33, pp.6778~6789.

CHAPTER 96

LITTORAL DRIFT ALONG BAYSHORE OF A BARRIER ISLAND

Yu-Hwa Wang* and T.H. Chang**

INTRODUCTION

A barrier island is an easily recognized geographical land feature along the south-east Atlantic and Gulf of Mexico coasts of the United States. It is characterized by a large ratio of length to width. It has a bay on one side and an ocean on the other. The inlets, on the ends, connect the bay to the ocean. The sand movement along the bayshore side is subjected to steeper and shorter waves which respond to local wind conditions. The physical boundary constraint of a bay is also different from open coast shorelines. Virtually no information exists with regard to the littoral drift rate on a bay shoreline. This paper tries to answer the question of whether or not the drift on the bay shoreline is different from that of the open coast since it is under different wave climates and physical constraints.

STUDY AREA

Santa Rosa Island is a barrier island situated on the west end of the Florida panhandle. It has the Gulf of Mexico on its south side and Santa Rosa Sound to its north. This barrier island has 48 miles of sand beaches on its Gulf and bay shores, which stretch eastward from Pensacola Beach to Fort Walton Beach. The average width, however, is approximately 1.5 miles. Santa Rosa Sound is 44 miles long and 2 miles wide. The study area was a highly-developed recreational community. A location map of the study area is given in Figure 1.

FIELD MEASUREMENTS

The breaker height, breaker angle and the longshore current were measured during the sampling operation (Wang et al, 1977). They are shown in the following table.

TABLE I

Date Mon./day	Breaker height (cm)	Breaker angle (degree)	mean longshore current u(cm/sec.)
2/15	15.2	11	7.4
2/15	12.7	10	7.0
2/16	10.2	9	7.4
2/16	11.4	10	6.2
2/17	8.9	12	10.5
2/17	10.2	7	5.7
2/18	15.2	10	5.1
2/18	12.7	12	8.8
2/19	15.2	13	7.2

* Associate Professor, Coastal and Oceanographic Engineering Laboratory, University of Florida, Gainesville, Florida 32611

** Graduate Assistant, Coastal and Oceanographic Engineering Laboratory, University of Florida, Gainesville, Florida 32611

The sand tracing method was used for determining the littoral transport rate. Sand was collected from the study site shortly before the tracing operation. This sand was coated with four colors of fluorescent dye in the Coastal and Oceanographic Engineering Laboratory (COEL), University of Florida. One hundred pounds of each of the four colored tracers were then injected back into the shoreline. A dredge-type sand sampler was used for collecting the samples, and the sampling stations were according to the predetermined coordinate system shown in Figure 2. Each sample was put into a sampling cloth bag with the station number marked on the label, and then sorted into sample sets for shipping to COEL for tracer counts in Gainesville. A series of equal concentration contour maps were produced. Figure 3 shows equal concentration contours for the blue tracer. The centroids of each contour map were calculated, and their longshore co-ordinates $(y_{\ell})_i$ were determined. $i = 1, 2, 3, \dots$

A tide gage and a wind anemometer were installed near the study area. Tidal curves and wind roses can be found in the report by Wang et al, 1977.

ESTIMATION OF LITTORAL TRANSPORT RATE

The water depth at the study site was shallow. The shoreline slope was rather flat with transverse bars at an angle with the shoreline (Wang et al, 1977). Wave conditions and currents at the study area correspond directly to the local winds. In order to account for the wind and tide induced currents it is considered that Bagnold's (1963, p. 518) formulation would be more appropriate for the present study,

$$I_{\ell} = K' w \frac{u}{u_m} \tag{1}$$

where the immersed transport rate is I_{ℓ} , the wave power $w = (EC)_b \cos \alpha_b$, E is the wave energy density, C the wave group velocity, α the breaking angle, subscript b meaning at wave breaking condition; the maximum orbital velocity $u_m = \sqrt{(2E/\rho h)}$; ρ is the water density; h , the water depth, and u is the average longshore current in the surf zone. The quantity $w(u/u_m)$ may be calculated from the field measurements in Table 1. I_{ℓ} is determined through the sand tracing technique. The longshore component of the advective velocity of the beach sand (considered same as the tracer sand) is calculated as

$$v = \frac{(y_{\ell})_2 - (y_{\ell})_1}{t} \tag{2}$$

where t is the time between sampling operations. The active depth d of the moving layer of beach sand was obtained by examining the eroding depth of a buried tracer column. It was determined to be 1/8 of an inch for the study area. The volume transport rate S_{ℓ} is then,

$$S_{\ell} = v d B$$

where B is the surf zone width. This volume transport rate S_{ℓ} is related to I_{ℓ} by $I_{\ell} = (\rho_s - \rho) g \beta S_{\ell}$. ρ_s and β stands for the density and the porosity correction of sand respectively.

The transport coefficient K' in equation (1) was determined by the data which were derived from the four color tracers; each color consisting

of nine sample sets. Only the blue tracer is presented here in Table 2.

TABLE 2

Sample sets	Date Mon/day/year	Time EST (hour)	I_s NT/Sec.	$W(u/u_m)$ Joules/Sec. M	K'
1	2/15/77	14:00	1.64	7.25	0.23
2	2/15/77	21:00	0.44	4.75	0.09
3	2/16/77	10:00	0.69	3.25	0.21
4	2/16/77	15:00	0.24	3.40	0.07
5	2/17/77	10:00	0.29	3.60	0.08
6	2/17/77	16:00	0.28	2.50	0.11
7	2/18/77	10:00	0.77	5.10	0.15
8	2/18/77	16:30	1.46	6.08	0.24
9	2/19/77	12:00	1.39	7.00	0.20

I_s 's for the blue tracer in Table 2 as well as for other three colors were then plotted against the quantity of $w(u/u_m)$. A regression line through the data points was drawn and shown in Figure 4. The regressional transport coefficient was determined to be $K' = 0.18$. The statistical analysis of the data, including the test of fit of the data, may be found in Chang (1978), Chang and Wang (1978).

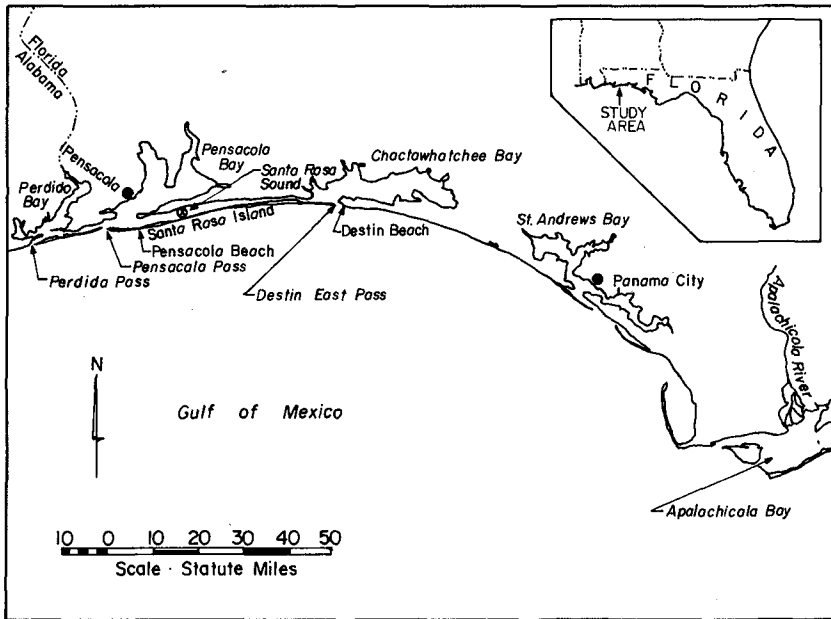


Figure 1. Study Area Map

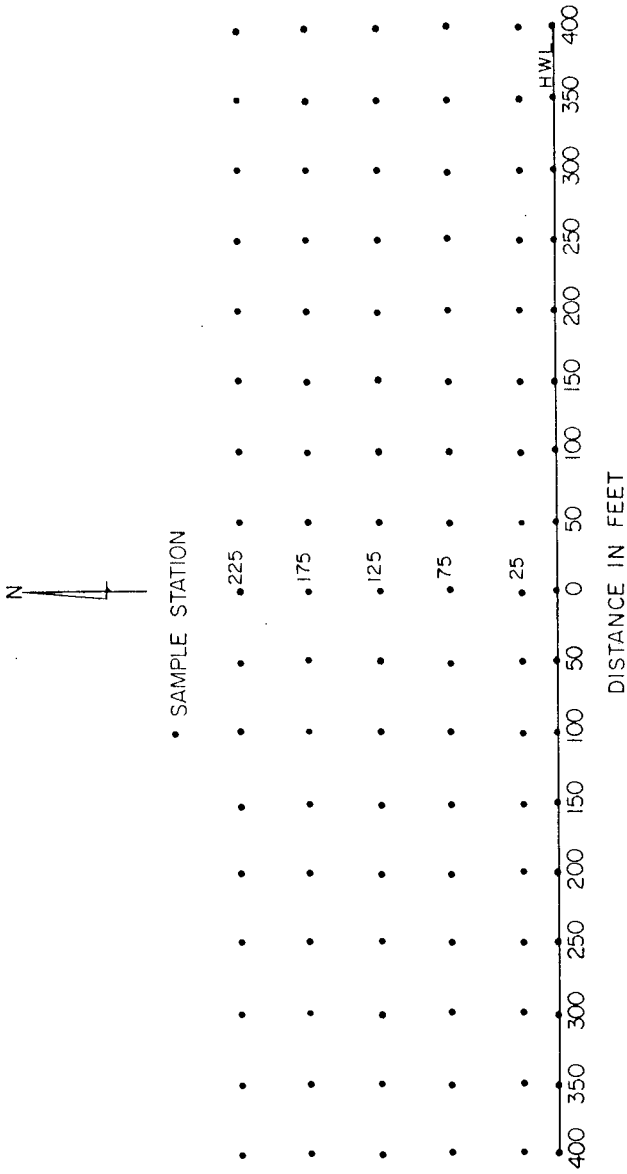


Figure 2. Grid Coordinate System

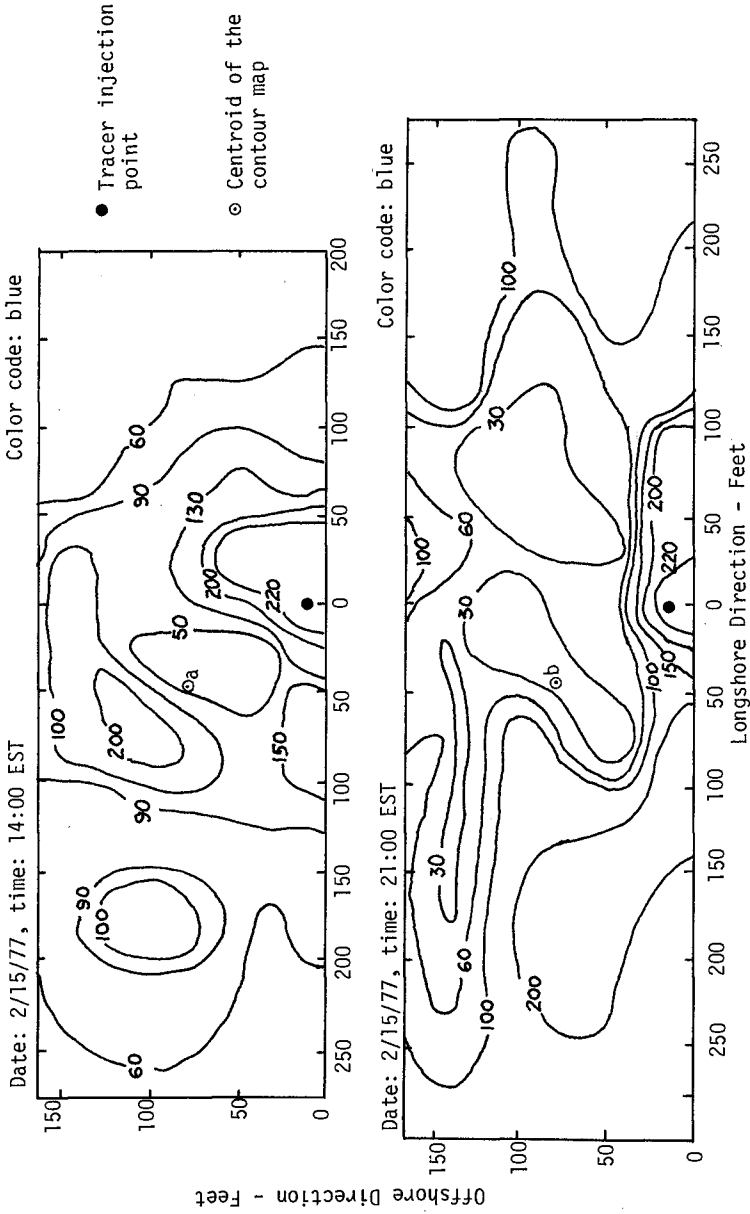


Figure 3. a and b, Equal Concentration Contour Maps

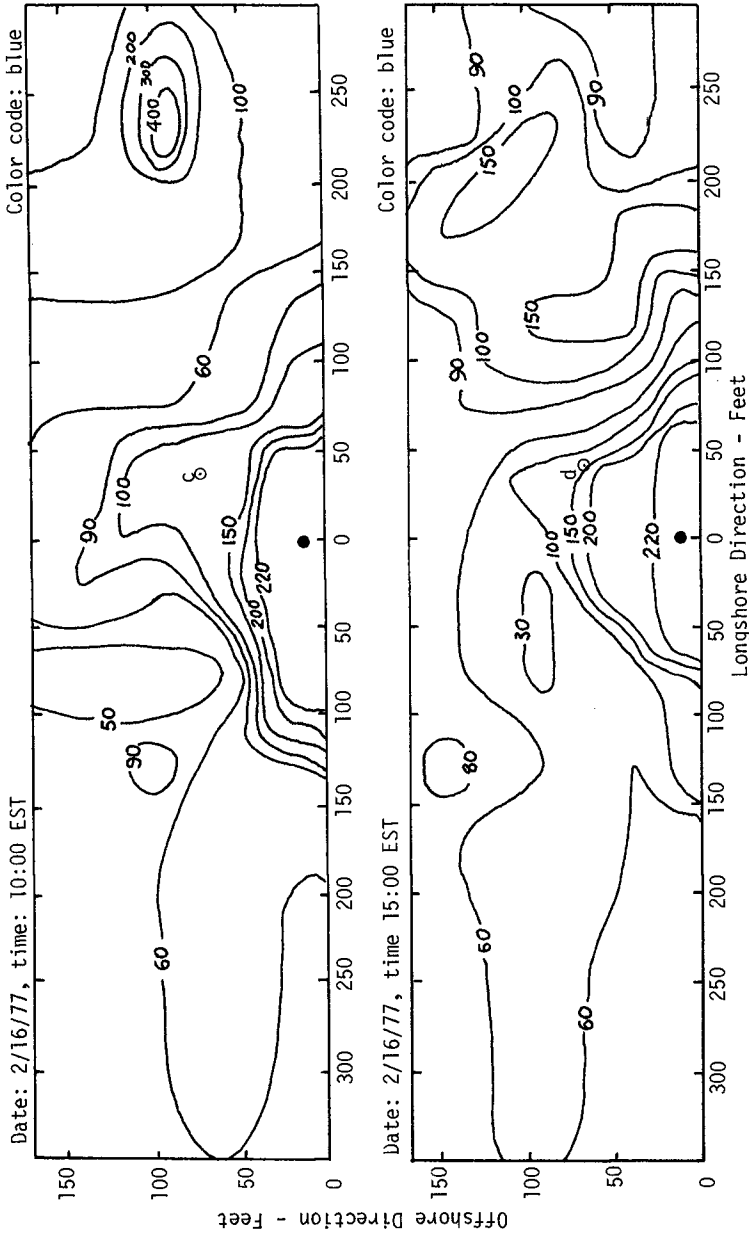


Figure 3. c and d, Equal Concentration Contour Maps

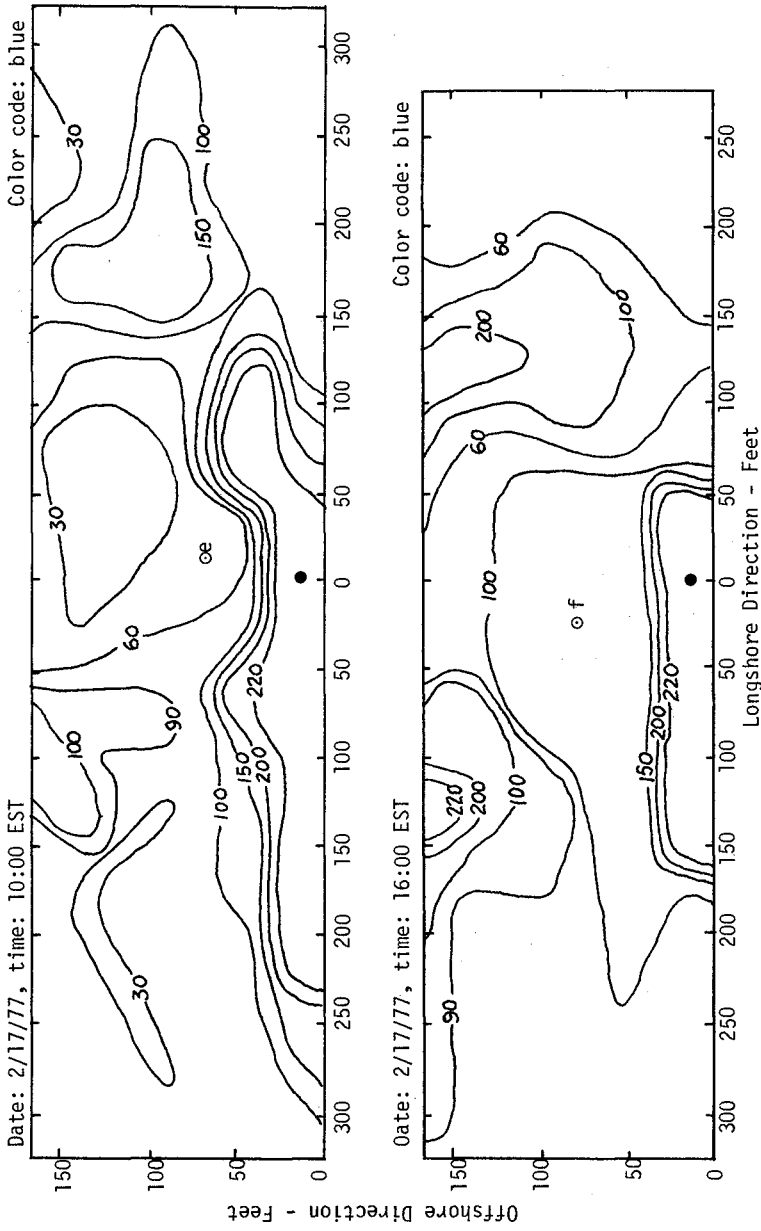


Figure 3. e and f, Equal Concentration Contour Maps

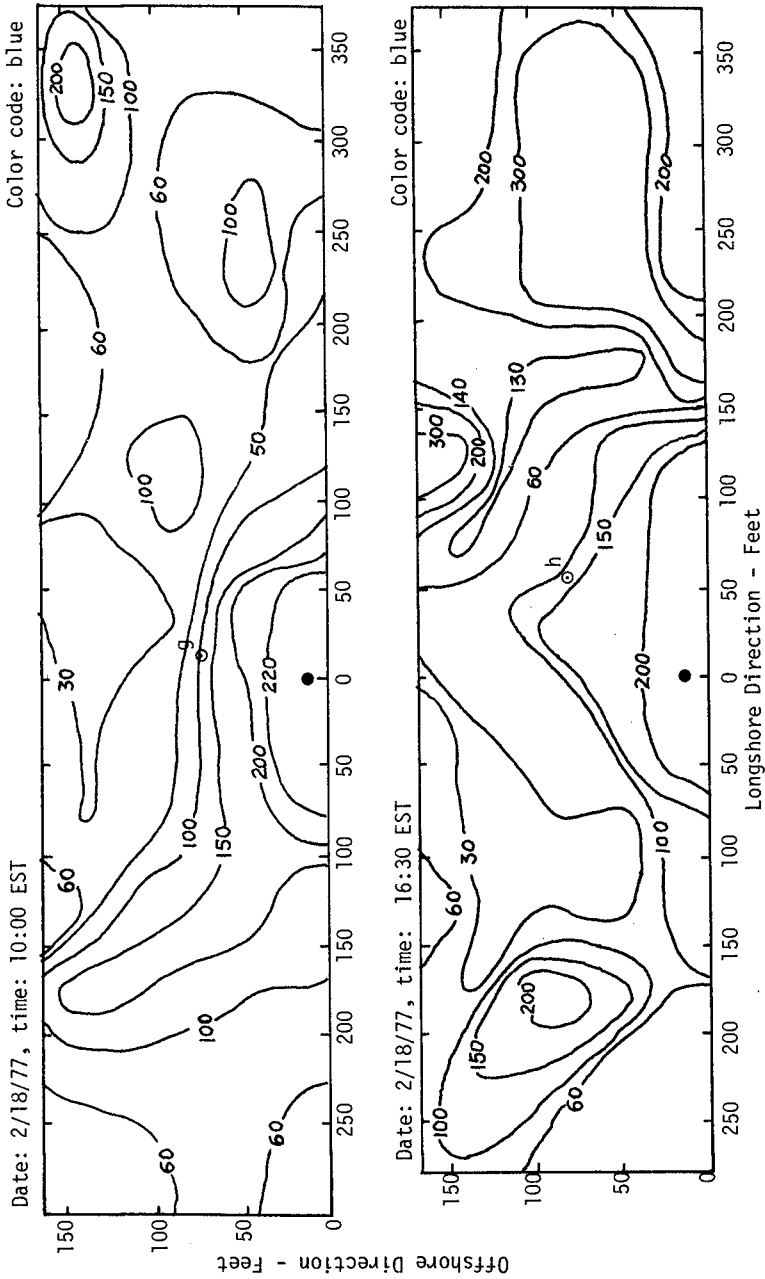


Figure 3. g and h, Equal Concentration Contour Maps

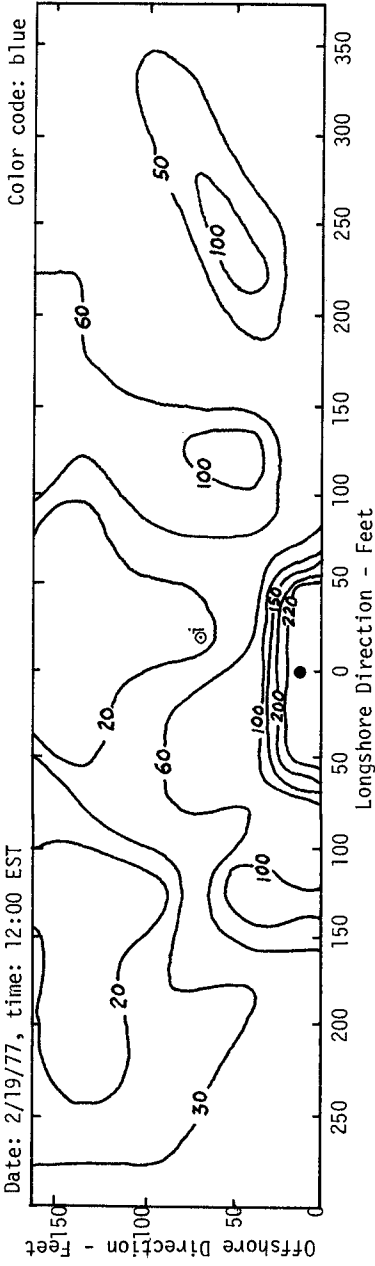


Figure 3. i, Equal Concentration Contour Maps

- For blue tracer
- For other color tracers

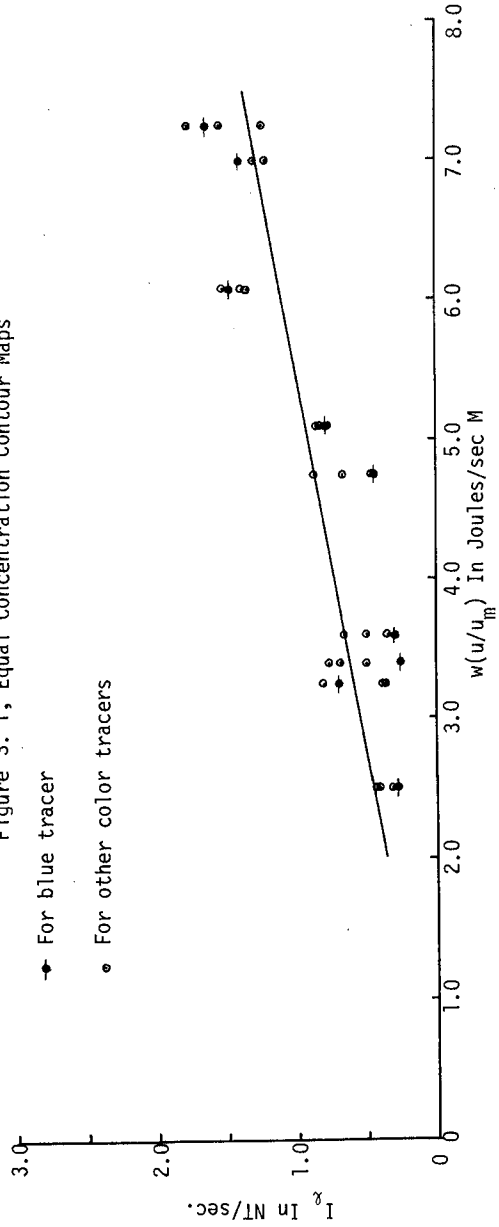


Figure 4. I_x Versus $w(u/u_m)$

DISCUSSION OF RESULTS

1. The calculated regression coefficient $K' = 0.18$ is approximately 36% smaller than the value 0.28 for open coast given by Komar in 1969.
2. There are, in general, two difficulties involved in a sand-tracing operation. First, the conservation of the tracer within the sampling area is often violated due to (a) loss of tracer seaward of the surf zone, (b) tracer moving out of the sampling area and (c) tracer loss due to burials. Secondly, the determination of the active moving layer depth and its vertical variations are uncertain. However, these were not the problems in the present study. Following a single injection of 100 pounds each of the four colors of fluorescent tracer; there were nine consecutive sampling operations covering a time span of five days. The nine equal concentration contour maps of the blue tracer (the other 3 colors as well) have shown that much of the tracers remain in the sampling region after 5 days. The depth of active moving sand layer on the bayshore was small (1/8 inch), and therefore there was very little or no loss of tracer due to burial.
3. The tide and wind induced currents were taken care of by using Bagnold's formula for sediment transport rate calculations.
4. The tracer dispersal pattern was characterized by closed loops and islands in the equal concentration contour maps. These peaks and valleys on the maps correspond to the bathymetry configurations. The low transverse bar tends to collect tracer on its troughs and less tracer on its broad crests (Wang et al, 1977).
5. The concentration of tracers in the injection area were noticeably increased in Figure 3. i, from the previous contour map. This indicated a strong onshore movement which may have been induced by an onshore wind-driven current.
6. All nine centroids of equal concentration contour maps were collected and plotted in Figure 5. The centroids are marked with letters which correspond to the sequence of the contour maps in Figure 3. A study of the movement of these centroids revealed the following interesting observations.
 - (a) The tracers were injected 25 feet from the water's edge (see Figure 3). Four hours after the injection the centroid #a moved out a distance approximately 80 feet from the water's edge.
 - (b) Several reversals of the drift direction during the five day period were clearly observable. The sand transport was longshore dominant. The on/off shore transport was relatively small compared to their longshore component.
 - (c) All nine centroids were in the region approximately 65 to 80 feet from the water's edge. This peculiar character may be explained by the fact that the coating of the local sand with fluorescent dye resulted in an increase of sand particle volume, consequently, a decrease of the specific gravity. When tracers were injected back in to the shoreline they were subjected to a wave-sorting process and moved bayward

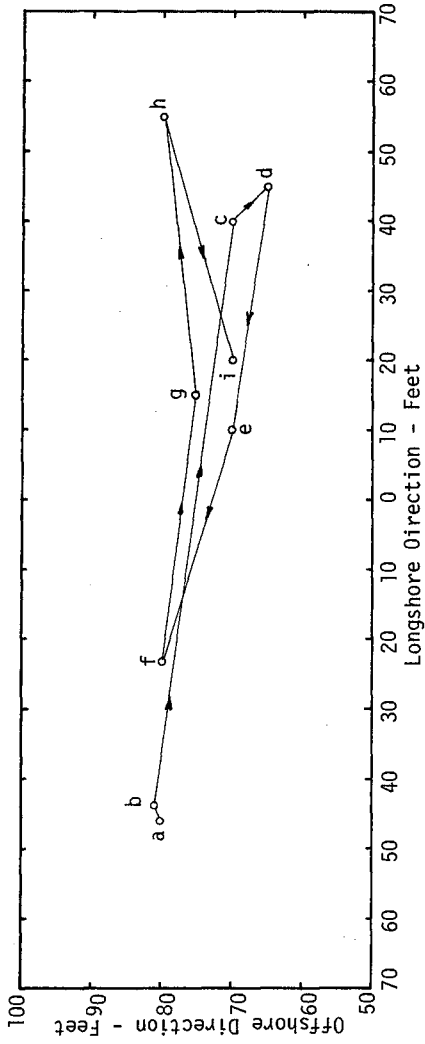


Figure 5. A Collection Of The Centroids From Figure 3

because the tracers were lighter than the local sand at the injection point. This may raise a question concerning the accuracy of the convective velocity V defined in equation (2). Perhaps the distance between the injection point and the centroid of the first contour map should be adjusted to account for the wave sorting effect. It is however not clear how one can perform this adjustment properly.

ACKNOWLEDGEMENT

The field data collection work was sponsored by Corps of Engineers, Mobile District, Alabama. The analysis was supported by Engineering and Industrial Experimental Station, University of Florida. Their financial assistance is gratefully acknowledged.

REFERENCES

1. Bagnold, R.A. (1963), "Mechanics of Marine Sedimentation" in The Sea ed. M.N. Hill, Vol. 3, Interscience, New York.
2. Komar, P.D. (1969), "The Longshore Transport of Sand on Beaches", Ph.D. Dissertation, University of California, San Diego, P. 68.
3. Chang, T.H. (1978), "Littoral Drift Along the Bayshore of a Barrier Island", M.S. Thesis, University of Florida, Gainesville, Florida.
4. Chang, T.H. and Y.H. Wang (1978), "Field Verification of Sediment Transport Model", Proceedings of 26th Speciality Conference of Hydraulic Div., ASCE, University of Maryland, Maryland.
5. Wang, Y.H., T.H. Chang and S.L. Harrell (1977), "Determination of Direction of Littoral Transport Along the Northshore of Santa Rosa Island", Technical Report UFL/COEL - 77/001, Coastal and Oceanographic Engineering Laboratory, University of Florida.

CHAPTER 97
SEDIMENT LOAD UNDER WAVES AND CURRENTS

by

D.H. Willis
Associate Research Officer
National Research Council of Canada

ABSTRACT

A technique is proposed for calculating sediment load, the mass concentration of sediment in motion, under combinations of waves and currents. The technique is based on the unidirectional flow method of Ackers and White, Ref. 1. The calibration of the technique against measurements of sediment load under waves has only just begun.

SEDIMENT LOAD

Sediment load is not sediment transport. It is an essential part of sediment transport, the concentration by mass of sediment in motion, but it requires the presence of a current to transport it from one place to another.

Although I will primarily deal with sediment load under waves, or waves and currents, the concept is best grasped for the case of currents alone. In this case there is, of course, always a current and therefore always a sediment transport. Sediment load is then the mass rate of sediment transport divided by the mass rate of current discharge.

The sediment load concept is however most useful when there are only very small currents, for example the mass transport associated with water waves. Here the sediment load due to the oscillatory wave motion may be quite high, but because of the very small currents involved, sediment transport calculations frequently fail. It is still handy to know how much sediment is available to fill in your navigation channel, even if you remain unsure of the rate at which infilling takes place.

We, at the Hydraulics Laboratory of the National Research Council of Canada, have therefore undertaken a program to develop a technique for calculating sediment loads under combinations of waves and currents, covering the range from currents only to waves only. We are initially aiming for a technique applicable seaward of the breaker line, but will not be at all disappointed if it turns out to be useful in the surf zone as well.

Like Swart in Ref. 13, I chose as a basis the method of Ackers and White, Ref. 1, for calculating sediment load in currents only. Their method has proved to be very

successful in predicting sediment loads in rivers, see for example Fleming and Hunt, Ref. 3. The theoretical modification of the Ackers and White method for the presence of waves is virtually complete. But in making that modification, I added a new empirical coefficient, the calibration of which has only just begun. This then is a report on work in progress.

ACKERS AND WHITE METHOD

The technique of Ackers and White, see Ref. 1, was developed for calculating the sediment load in unidirectional flow over an alluvial bed. Ackers and White take a transporting power approach: the work done in moving sediment is the product of the power available to move the sediment and the efficiency of the system.

Despite its being a total load concept, their derivation does make a distinction between bed load and suspended load. But the distinction is made, not on the basis of position in the water column, but rather on dimensionless grain size,

$$D_{gr} = D \left(\frac{g(s-1)}{v^2} \right)^{\frac{1}{3}} \quad (1)$$

Coarse material, $D_{gr} \geq 60$, is considered to be moved as bed load. Grains are rolled along the surface of the bed by the component of bed shear parallel to the local bed surface,

$$\tau_{cg} = \rho \frac{V^2}{C_{hcg}^2} \quad (2)$$

$$\text{where } C_{hcg} = 5.75 \log \frac{11d}{D} \quad (3)$$

Fine material, $D_{gr} \leq 1$, is moved as suspended load. The turbulence which keeps the grains in suspension is a function of the total shear on the bed,

$$\tau_{fg} = \rho \frac{V^2}{C_{hfg}^2} \quad (4)$$

$$\text{where } C_{hfg} = 5.75 \log \frac{11d}{r} \quad (5)$$

The total shear includes components both parallel and normal to the local bed surface

The power per unit area available to move sediment then becomes

$$\begin{aligned} P_{cg} &= \tau_{cg} V \\ \text{and } P_{fg} &= \tau_{fg} V \end{aligned} \quad (6)$$

It is not my purpose to repeat the derivation by Ackers and White here. You are instead referred to Ref. 1. It will I hope suffice to say that they develop two sets of relationships, one for coarse grains and one for fine grains. Transition sizes, $1 < D_{gr} < 60$, are handled by mixing the relationships using an exponent, n . This is illustrated by the Ackers and White mobility number,

$$F_{gr} = \frac{u_{*fg}^n u_{*cg}^{1-n}}{\sqrt{gD}(s-1)} \quad (7)$$

where the shear velocity is as usual,

$$u_* = \sqrt{\frac{\tau}{\rho}} \quad (8)$$

An important feature of the method, and one which makes it almost unique, is the inclusion of a criterion for the beginning of sediment motion, the threshold of movement. This is expressed as a critical value of the mobility number, F_{gr_c} , below which no sediment motion takes place. They then derive the following expression for sediment load:

$$X = C \left(\frac{F_{gr}}{F_{gr_c}} - 1 \right)^m \frac{sD}{d} \left(\frac{\rho^{\frac{1}{2}} P_{fg}}{\tau_{fg}^{\frac{3}{2}}} \right)^n \left(\frac{P_{cg}}{\tau_{cg} V} \right)^{1-n} \quad (9)$$

In the currents only case of Ackers and White, this reduces to

$$X = C \left(\frac{F_{gr}}{F_{gr_c}} - 1 \right)^m \frac{sD}{d} C_{hfg}^n \quad (9a)$$

At this point, the values of C , F_{gr_c} , m and n are still undefined. Ackers and White considered them to be empirical coefficients and calibrated them against over 1000 field and laboratory measurements of sediment load, obtaining

$$\log C = 2.86 \log D_{gr} - (\log D_{gr})^2 - 3.53, \quad (10)$$

$$2.95 \times 10^{-4} \leq C \leq 0.025$$

$$F_{gr_c} = \frac{0.23}{\sqrt{D_{gr}}} + 0.14, \quad 0.17 \leq F_{gr_c} \leq 0.37 \quad (11)$$

$$m = \frac{9.66}{D_{gr}} + 1.34, \quad 1.5 \leq m \leq 11.0 \quad (12)$$

$$n = 1 - 0.56 \log D_{gr}, \quad 0 \leq n \leq 1 \quad (13)$$

MODIFICATION FOR WAVES

My principal criterion in modifying the Ackers and White method for the presence of both waves and currents, was that the basic method as set out in Ref. 1 should remain intact

when no waves were present. Ackers and White have, after all, calibrated their method against more than 1000 measurements, and such a wealth of data can not be lightly tossed aside.

Vector addition of wave and current velocities produces a shear relationship which meets that criterion. Shear is proportional to the instantaneous velocity squared:

$$V_{TOT}^2 = (V + u_o \sin \frac{2\pi t}{T} \cos \alpha)^2 + (u_o \sin \frac{2\pi t}{T} \sin \alpha)^2 \quad (14)$$

Averaging V_{TOT}^2 over a wave period,

$$\overline{V_{TOT}^2} = V^2 + \frac{u_o^2}{2} \quad (15)$$

which is independent of direction.

If we assume that the unidirectional Chézy friction factor can be applied to the unidirectional term only, the Jonsson wave friction factor, $f_w/2$ see Ref. 6, to the oscillatory term only, and that f_w is independent of wave phase, we obtain for the combined bed shear

$$\tau = \rho \left(\frac{V^2}{C_h^2} + \frac{f_w}{4} u_o^2 \right) \quad (16)$$

Power is a scalar, and therefore we only need obtain an expression for the wave power available to move sediment and add that to the unidirectional term, Equation (6). The wave power per unit area, available to move sediment is

$$P_w = E \frac{dC_g}{dx} + C_g \frac{dE}{dx} \quad (17)$$

Since a locally horizontal bed is assumed in the Ackers and White method, C_g does not vary with distance and

$$P_w = C_g \frac{dE}{dx} \quad (17a)$$

There are a number of factors affecting the wave energy attenuation, dE/dx : bed friction, bottom percolation, surface contamination, to name a few. But we are only interested in that part of dE/dx available to move sediment, the part due to bottom friction or bed shear. Therefore

$$P_w = C_g \rho \frac{f_w}{4} u_o^2 \quad (17b)$$

The total power per unit bed area under waves and currents then becomes

$$P_w = \rho \left(\frac{V^2}{C_h^2} V + C_g \frac{f_w}{4} u_o^2 \right) \quad (18)$$

Subscripts have been dropped from Equations (16) and (18) but there are fine grain and coarse grain versions, analogous to Equations (2), (4) and (6). In both Equations (16) and (18), the first term is that for currents only, as in the Ackers and White method, with the second term adding the wave effect.

One further modification is necessary to compensate for the fact that the threshold of sediment motion is different under waves than under unidirectional flow. If the expression for F_{grc} , Equation (11), is modified, as Swart has done in Ref. 12, then it ceases to be a function of D_{gr} alone; it also becomes a function of the flow conditions. However, the flow conditions are already contained in the mobility number, F_{gr} Equation (7), by way of the modified shear stress of Equation (16). I therefore decided to leave the threshold of movement criterion alone, and further modify the shear stress to compensate for differences in wave and current thresholds. A new empirical coefficient, W_c , was added to the wave terms of Equation (16) and (18), which become respectively:

$$\tau = \rho \left(\frac{V^2}{C_h^2} + W_c^2 \frac{f_w}{4} u_o^2 \right) \quad (19)$$

$$P = \rho \left(\frac{V^2}{C_h^2} V + W_c^2 C_g \frac{f_w}{4} u_o^2 \right) \quad (20)$$

THRESHOLD OF MOVEMENT

Equations (19) and (20) not only reduce to their unidirectional flow forms when no waves are present, but when no currents are present they also reduce to their wave terms. It should therefore be possible to calibrate W_c against measurements of sediment load under waves alone.

Twenty-seven suitable measurements of sediment load under waves were found in the literature, 4 field measurements of which one included a current velocity, and 23 laboratory measurements. "Suitable" simply means that enough data were presented to allow an Ackers and White calculation of sediment load to be made and a value of W_c to be determined. Even for such "suitable" measurements, it was usually necessary to make one or more of the following assumptions:

1. Mass density of sea water, 1020 kg/m^3 , or of fresh water, 1000 kg/m^3 .
2. Mass density of sand, 2650 kg/m^3 .
3. Kinematic viscosity of laboratory water, $1 \times 10^{-6} \text{ m}^2/\text{s}$ (20°C), or of sea water $1.3 \times 10^{-6} \text{ m}^2/\text{s}$ (10°C).
4. Ripple dimensions given by the design curves of Mogridge, Ref. 10.

The 27 measurements are summarized in Table I. In all cases, sediment load was presented as a plot of concentration vs. depth. I integrated these plots, either analytically or numerically, from water surface to bed to obtain the total load, X , shown on Table I. The column headed " F_{grC} Required" is the value of the threshold of movement necessary to make the computed sediment load agree with the measured, and "Equivalent W_c " is the adjustment required to the wave shear.

The computed thresholds are plotted on Fig. 1 as Shields parameter, θ , against dimensionless grain size, D_{gr} . The Shields parameter is simply the square of the Ackers and White mobility numbers, F_{gr} or F_{grC} . The following are also plotted on Fig. 1.

1. The Shields curve, Ref. 11, for threshold of movement under unidirectional flow over a plane bed. Threshold was determined by observation and is somewhat subjective. It may be useful to note that, plotted in this way with D_{gr} as the abscissa rather than shear Reynolds Number, the Shields curve can be used without iteration to determine a critical shear stress for a given sediment.
2. The Ackers and White threshold of movement criterion, Equation (11), for unidirectional flow over a rippled bed. This criterion has been inferred from measured rates of sediment transport, and may therefore be more objective than the Shields curve.
3. Thirty-five points presented by Komar and Miller, Ref. 8, for threshold of movement under oscillatory flow. These points come from a variety of sources, but in general are the result of observation of the initiation of motion on a plane bed.

Most of the oscillatory flow points lie above the two curves for unidirectional flow. However, the data of Bhattacharya, Ref. 2, which forms the majority of my 27 calibration points, seems to require a significantly lower threshold of movement than either the unidirectional criteria or the rest of the oscillatory flow data. Thirteen of the 21 points from Ref. 2 fall below both the Shields and the Ackers and White curves, while only one of the remaining 41 points does so. This may be a bed slope effect, Bhattacharya did his measurements on a laboratory beach, but whatever the reason, it was with some regret that I decided to ignore his data for the rest of the analysis.

The remaining oscillatory flow points on Fig. 1 show no clear trend, other than that there appears to be a higher threshold of movement under oscillatory than under unidirectional flow. Madsen and Grant, Ref. 9, concluded that the Shields curve adequately described the threshold in oscillatory flow. Certainly for large grains, $D_{gr} \geq 100$, the Shields

TABLE I
SUMMARY OF CALIBRATION DATA

Ref.	Water Depth D	Wave Height H	Wave Period T	Current Velocity V	Sediment Load X	D _{gr}	F _{grc} Req'd	Equiv. W _c	Symbol on Fig. 1
--	m	m	s	m/s	--	--	--	--	--
5	11.3	2.05	8.0	0.25	1.07×10^{-4}	1.99	0.574	0.528	+
14	4.6	0.6	7.0	0.0	3.1×10^{-5}	1.54	0.433	0.751	○
14	6.4	0.6	7.0	0.0	3.9×10^{-5}	1.54	0.443	0.734	○
7	0.25	0.146	1.0	0.0	4.4×10^{-4}	3.54	0.302	0.868	△
4	0.3	0.165	1.3	0.0	7.2×10^{-4}	2.53	0.314	0.907	□
4	7.8	1.05	6.2	0.0	2.4×10^{-5}	5.22	0.243	0.992	□
2	0.137	0.119	1.5	0.0	7.8×10^{-4}	5.31	0.284	0.843	*
2	0.155	0.116	1.5	0.0	6.3×10^{-4}	5.31	0.295	0.813	*
2	0.184	0.110	1.5	0.0	5.8×10^{-4}	5.31	0.258	0.928	*
2	0.209	0.107	1.5	0.0	6.6×10^{-4}	5.31	0.220	1.090	*
2	0.223	0.104	1.5	0.0	4.3×10^{-4}	5.31	0.224	1.069	*
2	0.244	0.101	1.5	0.0	4.1×10^{-4}	5.31	0.204	1.177	*
2	0.279	0.101	1.5	0.0	2.5×10^{-4}	5.31	0.203	1.180	*
2	0.300	0.098	1.5	0.0	2.8×10^{-4}	5.31	0.181	1.325	*
2	0.140	0.107	1.04	0.0	9.0×10^{-4}	5.31	0.263	0.911	*
2	0.157	0.122	1.04	0.0	9.8×10^{-4}	5.31	0.262	0.914	*
2	0.189	0.098	1.04	0.0	6.2×10^{-4}	5.31	0.199	1.204	*
2	0.198	0.094	1.04	0.0	8.3×10^{-4}	5.31	0.171	1.401	*
2	0.221	0.091	1.04	0.0	6.3×10^{-4}	5.31	0.158	1.519	*
2	0.238	0.101	1.04	0.0	4.4×10^{-4}	5.31	0.175	1.373	*
2	0.250	0.091	1.04	0.0	3.2×10^{-4}	5.31	0.162	1.482	*
2	0.143	0.101	1.04	0.0	1.8×10^{-3}	5.31	0.208	1.155	*
2	0.171	0.129	1.04	0.0	4.8×10^{-4}	5.31	0.300	0.800	*
2	0.210	0.105	1.04	0.0	8.0×10^{-4}	5.31	0.180	1.332	*
2	0.218	0.110	1.04	0.0	6.8×10^{-4}	5.31	0.188	1.274	*
2	0.261	0.115	1.04	0.0	4.8×10^{-4}	5.31	0.174	1.377	*
2	0.304	0.105	1.04	0.0	2.8×10^{-4}	5.31	0.151	1.587	*

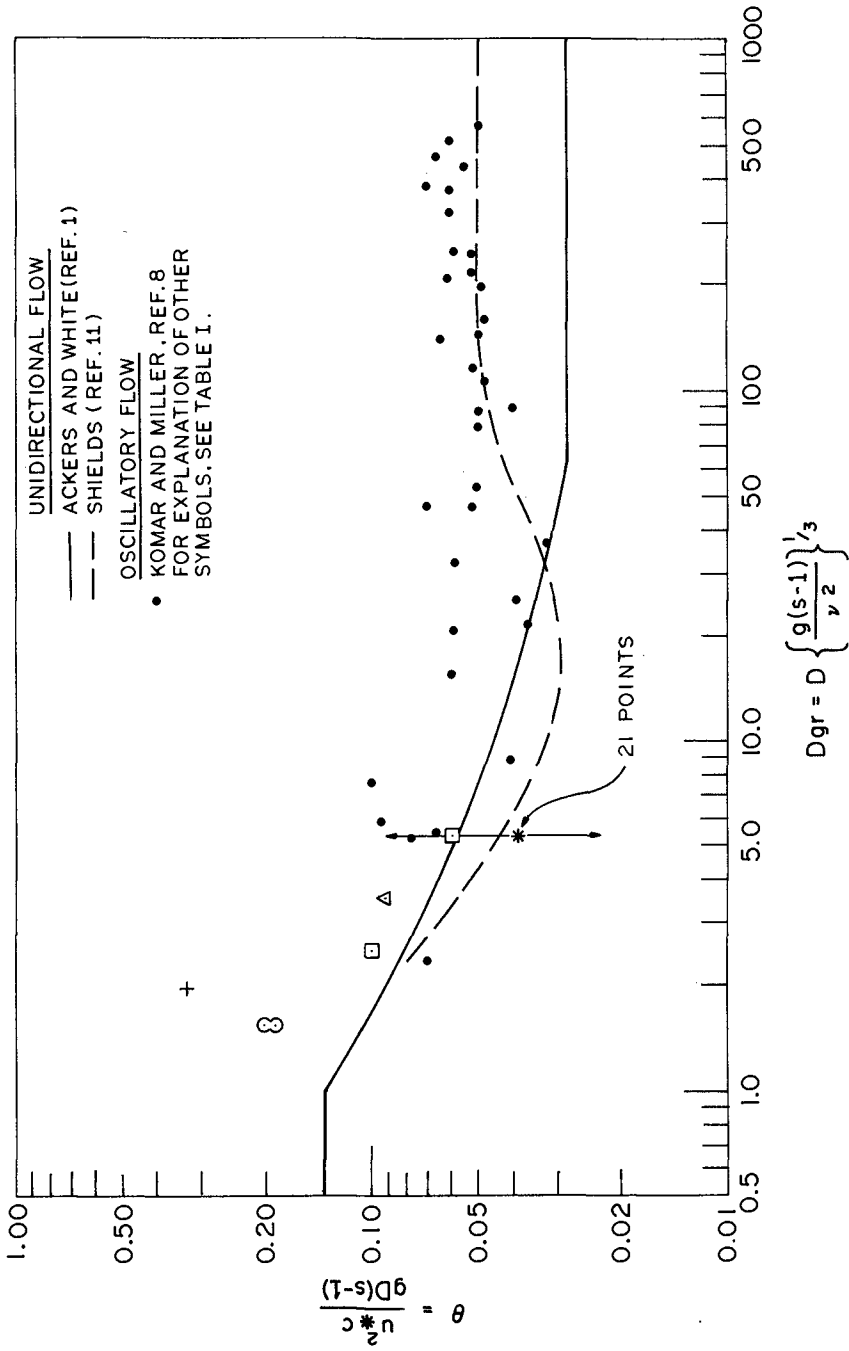


FIG.1 THRESHOLD OF MOVEMENT

curve is a better lower envelope to the oscillatory flow threshold than the Ackers and White curve. The value of W_c needed to make the two curves coincide here is 0.76. However, at the lower end, $D_{gr} \leq 10$, the Ackers and White criterion is a better lower envelope, implying $W_c = 1$. Perhaps overall W_c varies inversely with D_{gr} , but as an interim measure, I have taken it as a constant, $W_c = \sqrt{0.6}$, in Equations (19) and (20), making them

$$\tau = \rho \left\{ \frac{V^2}{C_h^2} + 0.6 \frac{f_w}{4} u_o^2 \right\} \quad (21)$$

$$P = \rho \left\{ \frac{V^2}{C_h^2} V + 0.6 C_g \frac{f_w}{4} u_o^2 \right\} \quad (22)$$

FUTURE WORK

There is clearly a need for more data, in particular for a consistent set of sediment load measurements covering the full range of dimensionless grain sizes. We at the National Research Council of Canada are presently collecting that data in a wave flume, varying grain size and density, water depth, and height and period of the regular waves. Sediment load is determined by counting particles in the narrow column illuminated by a vertical laser beam.

I must emphasize again that the work reported here is still very much in progress. The quoted value of $W_c = \sqrt{0.6}$ must be regarded as a temporary measure until either confirmed or replaced by something better as a result of the on-going flume tests.

ACKNOWLEDGEMENTS

I particularly want to thank Dr. C.A. Fleming for pointing out that what really needed modification for waves in the Ackers and White method was the threshold of movement criterion.

My thanks also go to Ir. J. Moes and Dr. G.R. Mogridge for their day-to-day help and advice, and for their critical reading of this paper.

REFERENCES

1. ACKERS, P. and WHITE, W.R., "Sediment transport: new approach and analysis", Proceedings of the American Society of Civil Engineers, Vol. 99, No. HY11, November 1973, pp. 2041-2060.
2. BHATTACHARYA, P.K., "Sediment suspension in shoaling waves", Ph.D. Thesis, University of Iowa, 1971.

3. FLEMING, C.A. and HUNT, J.N., "A mathematical sediment transport model for unidirectional flow", Proceedings of the Institution of Civil Engineers, Great Britain, Part 2, Vol. 61, 1976, pp. 297-310.
4. HOM-MA, M. and HORIKAWA, K., "Suspended sediment due to wave action", Proceedings of the 8th Conference on Coastal Engineering, 1962, Vol. I, pp. 168-191.
5. JENSEN, J.K. and SORENSEN, T., "Measurement of sediment suspension in combinations of waves and currents", Proceedings of the 13th Conference on Coastal Engineering, 1972, Vol. II, pp. 1097-1104.
6. JONSSON, I.G., "Wave boundary layers and friction factors", Proceedings of the 10th Conference on Coastal Engineering, 1966, Vol. I, pp. 127-148.
7. KENNEDY, J.F. and LOCHER, F.A., "Sediment suspension in water waves", in "Waves on Beaches and Resulting Sediment Transport", R.E. Meyer (ed.), Academic Press, New York, 1972, pp. 249-295.
8. KOMAR, P.D. and MILLER, M.C., "Sediment threshold under oscillatory waves", Proceedings of the 14th Conference on Coastal Engineering, 1974, Vol. II, pp. 756-775.
9. MADSEN, O.S. and GRANT, W.D., "The threshold of sediment movement under oscillatory waves: a discussion", Journal of Sedimentary Petrology, Vol. 45, No. 1, March 1975, pp. 360-361.
10. MOGRIDGE, G.R., "Bedforms generated by wave action", National Research Council of Canada, Quarterly Bulletin of the Division of Mechanical Engineering, April-June 1973, Report No. DME/NAE 1973(2), pp. 21-41.
11. SHIELDS, A., "Anwendung der Aehnlichkeitsmechanik und der Turbulenzforschung auf die Geschiebewegung", Mitteilungen der Preuszischen Versuchsanstalt für Wasserbau und Schiffbau, Heft 26, Berlin 1936.
12. SWART, D.H., "Weighted value of depth of initiation of movement", Stellenbosch, South Africa, August 1977.
13. SWART, D.H., "Coastal sediment transport, computation of longshore transport", Delft Hydraulics Laboratory, Report No. R968, Part 1, 1976.
14. WANG, H. and LIANG, S.S., "Mechanics of suspended sediment in random waves", Journal of Geophysical Research, Vol. 80, 1975, No. 24, pp. 3488-3494.

APPENDIX I

GENERAL NOTATION

- C coefficient in sediment load function (Equation 10)
- C_g wave group velocity $\left(\frac{L}{T}\right)$
- C_h dimensionless Chézy coefficient
- D typical grain diameter [L]
- D_{gr} dimensionless grain size
- d water depth [L]
- d_o maximum water particle excursion at the bed [L]
- E wave energy $\left(\frac{M}{T^2}\right)$
- F_{gr} sediment mobility number
- f_w Jonsson wave friction factor, Ref. 6
- g acceleration due to gravity $\left(\frac{L}{T^2}\right)$
- H wave height, trough to crest [L]
- m exponent in sediment load function (Equation 12)
- n transition exponent (Equation 13)
- P power per unit bed area $\left(\frac{M}{T^3}\right)$
- r ripple roughness, a function of ripple geometry, see for example Ref. 13 [L]
- s ratio of mass density of sediment to that of the fluid
- u_o maximum wave orbital velocity at the bed $\left(\frac{L}{T}\right)$
- u_* shear velocity (Equation 8) $\left(\frac{L}{T}\right)$
- V mean unidirectional flow velocity $\left(\frac{L}{T}\right)$
- W_c empirical wave shear coefficient
- X sediment load
- x horizontal co-ordinate [L]
- α horizontal angle between wave orbital velocity and mean current velocity

- θ Shields parameter, see Fig. 1
 ν kinematic viscosity of the fluid $\left(\frac{L^2}{T}\right)$
 ρ mass density of the fluid $\left(\frac{M}{L^3}\right)$
 τ shear stress at the bed $\left(\frac{M}{LT^2}\right)$

Subscripts

- c critical for initiation of sediment motion
 cg coarse grain
 fg fine grain
 TOT total
 w due to waves

APPENDIX II

SUMMARY OF METHOD

1. Calculate D_{gr} from Equation (1)
2. Calculate empirical coefficients, C , F_{grc} m and n from Equations (10), (11), (12) and (13)
3. Calculate the dimensionless Chézy coefficients Ch_{cg} and Ch_{fg} using Equations (3) and (5).

4. Calculate the Jonsson wave friction factors,

$$f_{w_{cg}} = \exp(-5.98 + 5.21 \left(\frac{d_o}{2D}\right)^{-0.19}) \quad \left. \vphantom{f_{w_{cg}}} \right\} f_w \leq 0.30 \quad (23)$$

$$f_{w_{fg}} = \exp(-5.98 + 5.21 \left(\frac{d_o}{2r}\right)^{-0.19}) \quad (24)$$

These approximate formulae are from Swart, Ref. 13.

5. Calculate bed shears, τ_{cg} and τ_{fg} , using Equation (21) and convert to shear velocities, u_{*cg} and u_{*fg} , with Equation (8).
6. Calculate powers, P_{cg} and P_{fg} , using Equation (22).
7. Calculate the mobility number, F_{gr} , using Equation (7).
8. Calculate sediment load by Equation (9).

CHAPTER 98

SEDIMENT TRANSPORT AND RIPPLES DUE TO WAVES AND CURRENTS

Zbigniew PRUSZAK* and Ryszard B. ZEIDLER**

ABSTRACT

Water velocities and shear stresses have been determined for a laminar boundary layer of a progressive wave travelling over a regular series of ripples. The Lavrentiev variational method was used to transform conformally the water area with ripples into a strip with flat bottom, while the Lin approach permitted solution of the boundary layer equation.

The theoretical prediction of the bed friction was verified experimentally with a new mechanical apparatus.

By coupling the theoretical shear stress at the rippled bed with laboratory data for ripple parameters one can expose the friction conditions that control the growth and decay of ripples. If waves develop higher values of shear stress, the rippled bed becomes gradually washed out. For known shear stresses, basing on the Frijlink-Bijker formula one can compute sediment transport rates. In the respective diagram, a curve of s.t. rate versus bottom friction consists of two branches. The stages of the growth and decay of ripples are reflected in the lower and upper branches of the curve. For identical ripple height there are two values of s.t. rate, for two different wave intensities, likely to differ by as much as 25 per cent.

Three-dimensional ripples have been analyzed with regard to bed friction and compared with two-dimensional conditions.

* Polish Academy of Sciences' Institute of Hydro-Engineering, Gdansk, Sen. Research Scientist

** ibidem, Asst. Prof.

BOUNDARY LAYER ON RIPPLES

The dynamics of sediment and ripples depends on the characteristics of boundary layer. In order to analyze this dynamics it is reasonable to map conformally the area of motion over ripples, solve equation of motion in the basic flow region, use this solution as a background for a boundary layer equation, and determine motion inside the boundary layer. The following assumptions were made in the analysis :

- 1 Regular series of impermeable sinusoidal ripples preserve their form during motion
- 2 Ripples are exposed to regular progressive small-amplitude waves with wave height h and period T
- 3 Oscillatory boundary layer is laminar
- 4 Regular eddies are generated by waves in ripple troughs.

As shown by experiments, laminar flow at rippled bed under oscillatory motion is fairly stable. The assumption on eddies is an outcome of the studies by Sleath [6] .

A method derived by Lavrentiev [3] has been employed in our conformal mapping. The method is particularly suitable for cases with slightly different original and mapped areas of motion. Two subsequent stages of mapping, from original area with ripples, of depth H , to an elementary strip with flat bottom, are presented in Fig.1.

In the dimensionless form, the formula of mapping reads

$$w=f(z) \approx \left[\bar{x} + \frac{\eta}{2} \coth\left(\frac{2\pi H}{\lambda}\right) \sin\frac{2\pi\Delta x}{\lambda} \cosh\frac{2\pi\Delta y}{\lambda} \right] + \dots 1$$

$$+ i \left[\bar{y} + \frac{\eta}{2} \coth\left(\frac{2\pi H}{\lambda}\right) \cos\left(\frac{2\pi\Delta x}{\lambda}\right) \sinh\left(\frac{2\pi\Delta y}{\lambda}\right) \right] = u(x,y) + iv(x,y)$$

in which $z = \bar{z} + \Delta z$ with the following intervals of variation

$$\begin{array}{ll} -\infty < \bar{x} < \infty & - \eta/2 \leq \Delta y \leq \eta/2 \\ 0 < \bar{y} < H & - \lambda \leq \Delta x \leq \lambda \end{array}$$

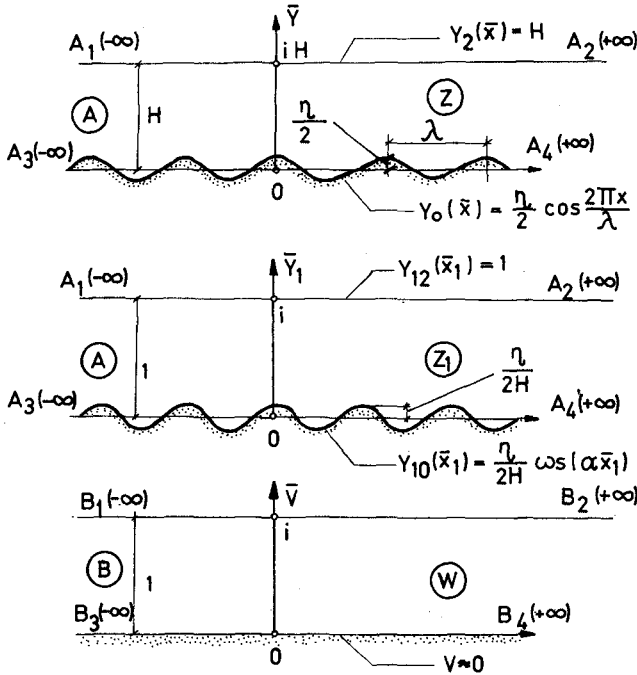


Fig.1 - Conformal Mapping

The complex velocity potential in the strip w can be chosen as

$$W(w) = \phi(u, v, t) + i \psi(u, v, t) = \frac{h \omega \cosh kv}{2k \sinh kH} \sin(ku - \omega t) + \dots 2$$

$$+ i \frac{h \omega \sinh kv}{2k \sinh kH} \cos[ku - \omega t]$$

By substituting (1) in (2) and assuming $v \approx 0$ for the lower boundary in the strip w , or $\sinh^2 kv(x, y) \approx 0$, one obtains the following velocity at the upper limit of the boundary layer

$$\begin{aligned}
 u_1(x,y,t) = & \frac{\cosh kv(x,y)}{\sinh kH} \cos[ku(x,y) - \omega t] \left\{ 1 + 2\pi \frac{\eta}{\lambda} \coth\left(\frac{2\pi H}{\lambda}\right) x \right. \\
 & \times \cos\left(\frac{2\pi \Delta x}{\lambda}\right) \cosh\left(\frac{2\pi \Delta y}{\lambda}\right) + \pi^2 \left(\frac{\eta}{\lambda}\right)^2 \coth^2\left(\frac{2\pi H}{\lambda}\right) \cos^2\left(\frac{2\pi \Delta x}{\lambda}\right) \times \dots 3 \\
 & \left. \times \cosh^2\left(\frac{2\pi \Delta y}{\lambda}\right) + \pi^2 \left(\frac{\eta}{\lambda}\right)^2 \coth^2\left(\frac{2\pi H}{\lambda}\right) \sin^2\left(\frac{2\pi \Delta x}{\lambda}\right) \sinh^2\left(\frac{2\pi \Delta y}{\lambda}\right) \right\}^{1/2}
 \end{aligned}$$

One can now proceed to solution of a boundary layer equation. In 1957 Lin presented the following approximation for an unsteady laminar boundary layer:

$$\frac{\partial u}{\partial t} = \frac{\partial U}{\partial t} + \nu \frac{\partial^2 u}{\partial y^2} \dots 4$$

The well-known boundary conditions are

$$u = 0 \text{ at } y = 0 \text{ and } u = U \text{ at } y \rightarrow \infty \text{ (or } y \rightarrow \delta \text{)}$$

It is possible to determine the error of the linearization inherent in Eq.4. Using Eq.3 and by comparison of the nonlinear term $U \frac{\partial U}{\partial x}$ to $\frac{\partial U}{\partial t}$ one can find the linearization errors for various values of ripple steepness. They are shown in Fig.2, for the most inaccurate situation with U_1 , at the upper limit of the boundary layer.

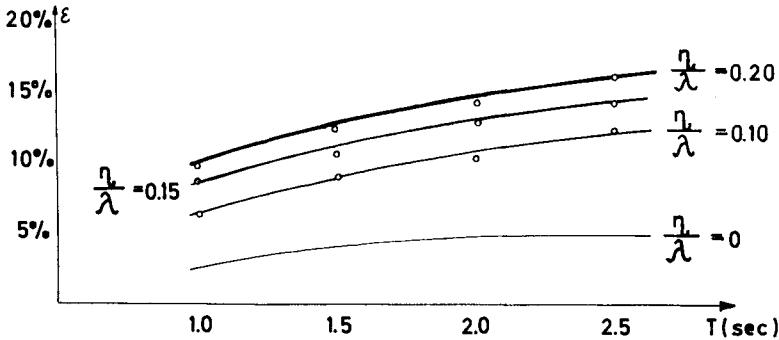


Fig.2 - Linearization Error

In general, the Lin method proves to be acceptable for fairly small bed microforms, under the studied conditions with wave periods from 1 to 2.5 (5) seconds.

The following solution [4] can be obtained from Eq.4

$$u(x, y, t) = U_{max}(x) \left\{ \cos[ku(x, y) - \omega t] - \exp(-\beta y_1/X) \cos[ku(x, y) - \omega t + \beta y_1/X] \right\} \quad \dots 5$$

in which

$$U_{max}(x) = \frac{h\omega}{2} \frac{\cosh kv(x, y)}{\sinh kH} \times \sqrt{1 + 2\pi \frac{R}{\lambda} \coth\left(\frac{2\pi H}{\lambda}\right) \cos\left(\frac{2\pi \Delta x}{\lambda}\right) + \cosh\left(\frac{2\pi \Delta y}{\lambda}\right) + \pi^2 \left(\frac{R}{\lambda}\right) \coth^2\left(\frac{2\pi H}{\lambda}\right) \cos^2\left(\frac{2\pi \Delta x}{\lambda}\right) \cosh^2\left(\frac{2\pi \Delta y}{\lambda}\right) + \pi^2 \left(\frac{R}{\lambda}\right)^2 \coth^2\left(\frac{2\pi H}{\lambda}\right) \sin^2\left(\frac{2\pi \Delta x}{\lambda}\right) \sinh^2\left(\frac{2\pi \Delta y}{\lambda}\right)} \quad \dots 6$$

and X is the vortex-effect parameter introduced by Sleath. By analogy, one can suggest the following formula for the bed friction

$$\tau_o^* = \frac{2\sqrt{2}}{\omega h} \frac{U_{max}}{X_o} \cos\left[ku(x, y) - \omega t + \frac{\pi}{4}\right] \quad \dots 7$$

in which $X_o \neq X$.

In order to determine the parameter X_o we used the data measured by Kalkanis [2]. From the comparison of this data and the results predicted by formula (7) it follows that X_o depends on $R = U_{max} \cdot \eta^2 \cdot \beta \cdot \nu^{-1}$

$$X_o \approx 0.3 R^{0.165} \quad \dots 8$$

An example of the computed velocity profiles is presented in Fig. 3. From analysis of the velocity fields it is clear that both velocities and their gradients above

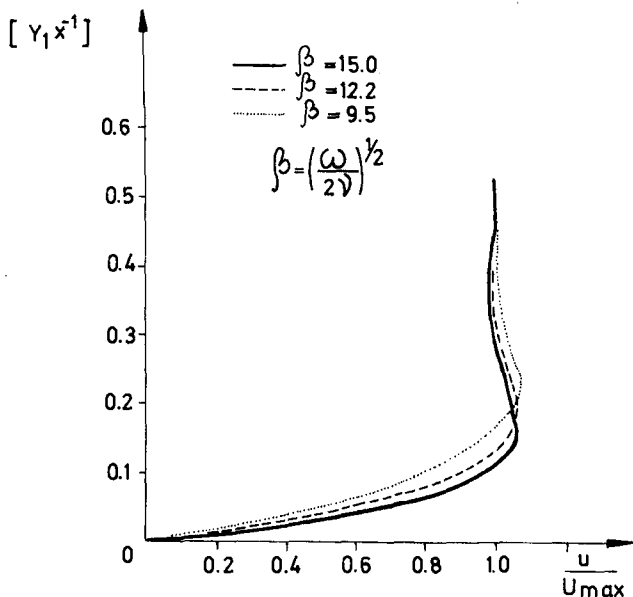


Fig.3 - Velocity Profiles in Boundary Layer

the ripple crests increase with decreasing depth of water and increasing height of water waves. The magnitudes above ripple troughs are much lower than those over the crests. The local excess of u over U , for $1.5 \leq y_1 \cdot \beta \cdot x^{-1} \leq 4.0$, is likely to be caused by the eddies generated about ripples.

The distribution of computed bed friction on ripples, both in time and space, is shown respectively in Figures 4a and 4b. In Fig.4a it can be seen that the maximum bed friction is shifted by $\omega t = \frac{\pi}{4}$ with regard to the wave crest. The values drawn in the diagram correspond to strictly defined instants, different for various points on the ripples, as if independent of the conditions in their neighborhood. On the other hand, presented in Fig.4b is the distribution generated over a certain section with ripples, as if the

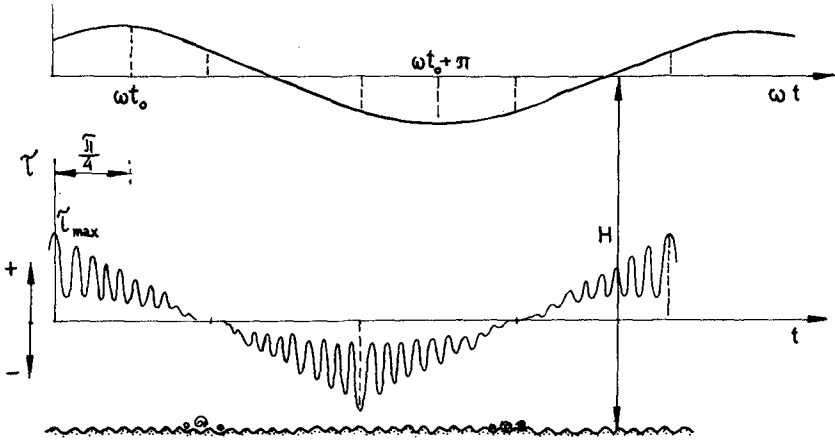


Fig.4a - Temporal Variation of Bed Friction During Consecutive Wave Phases ωt

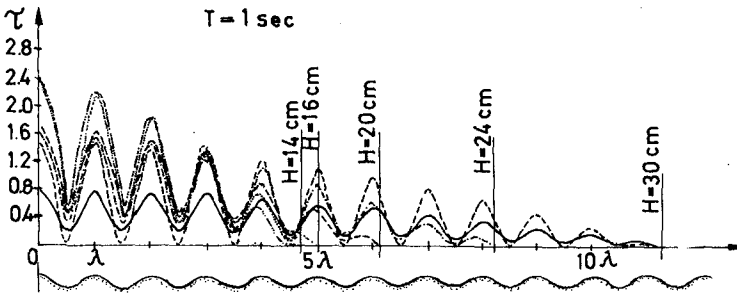


Fig.4b - Distribution of Maximum Bed Friction (for $\omega t = \frac{\pi}{4}$)

wave crest occurred at each ripple. In reality, the distributions vary in time and space, and both figures have to be combined.

EXPERIMENTAL VERIFICATION

The theoretical prediction of the bed friction on ripples was checked experimentally with a new device shown in Fig.5.

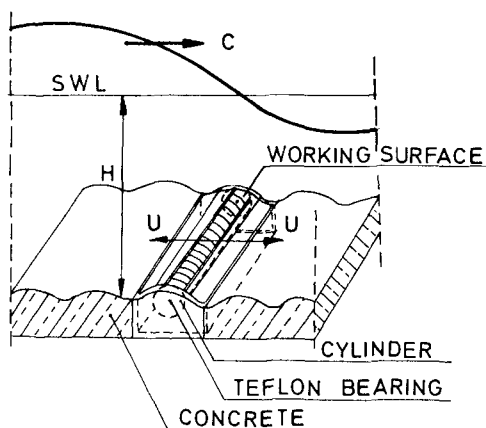


Fig.5 - Apparatus for Measurement of Bed Friction

The apparatus consists of an organic-glass cylinder, mostly sheltered in its body, the latter being flush with the crest of a ripple. The forces induced by waves are exerted in a narrow upper part of the cylinder, in the slit of the concrete ripple segment. The principle of operation consists in an angular displacement of the cylinder under the action of water. The mass of the cylinder is distributed so accurately that it moves even if minute forces are applied to its surface and returns very fast to its original position after the force is removed. Owing to a system of transverse scratches, the roughness of the exposed surface of the

cylinder is identical with that of the concrete ripples. At present, measurements of displacements of the cylinder are conducted by visual means; the calibration curve permits translation of displacements into forces. The bearing friction and the drag forces acting on the working surface of the cylinder are deducted from the total force measured with the apparatus.

The measurements of the bed friction were carried out in a wave flume with the rippled bed, a section of which is depicted in Fig.5. The waves generated in the flume had periods from 1.5 to 2.7 seconds. Because of technical difficulties, it was only a few ripple-and-wave combinations that corresponded to each other: the concrete ripple segments had forms identical with those generated by their water wave counterparts. Other pairs were incoherent, so that the results obtained for them should be treated with caution. In Table 1 they are marked with asterisks. - As can be seen from the comparison in Table 1, the computed bed friction exceeds the measured values by 10 to 40 per cent. These figures are yet smaller, below 30 percent, if one takes into account the resistance at the bearings of the measuring device. Thus, it can be claimed that the theoretical prediction of the bed friction presented in the previous section is close to reality and that the apparatus, even in its prototype version, is a promising tool in laboratory investigations.

BED FRICTION AND SEDIMENT TRANSPORT ON RIPPLES

By coupling the theoretical bed friction at rippled bed with laboratory data for ripple parameters one can expose the friction conditions that control the growth and decay of ripples. The findings for ripple height are shown in Fig.6. Four different zones, separated by three critical lines of bed friction, can be distinguished. For bed friction lower than τ_{1c} it is only the movement of single sand grains, on a flat bed, that is possible. The zone of the generation of eddies and single ripples (whichever come first) stretches

Table 1

Bed Friction : Computed (C) Versus Measured (M)

T s	h cm	H cm	L cm	$U_{\max} \frac{\text{cm}}{\text{s}}$	(C) τ_{\max}	(M) τ_{\max}	$\frac{\tau_{\max}}{\tau_{\max} \text{ c/m}}$
1.5	9.2	25.0	250.0	41.2	8.85	5.8	1.53*
1.5	10.5	25.0	250.0	47.1	10.12	5.8	1.74*
1.5	10.8	35.0	216.0	38.35	8.23	5.8	1.42
1.5	11.4	35.0	216.0	40.48	8.69	6.6	1.31
2.0	8.6	25.0	320.0	44.82	8.33	5.88	1.41
2.0	10.0	35.0	349.0	39.61	7.36	6.59	1.11
2.3	13.35	35.0	408.0	54.61	9.47	11.54	0.82*
2.5	11.5	25.0	388.0	58.92	9.81	8.24	1.19
2.5	11.9	35.0	445.0	49.20	8.19	8.96	0.915*
2.7	16.0	35.0	483.0	66.88	10.72	11.68	0.915*

between τ_{1cr} and τ_{2cr} , while series of ripples are formed between τ_{2cr} and τ_{3cr} . The line of τ_{3cr} marks the conditions under which the growth of ripples is completed. If waves generate higher stresses at the ripples, the latter become gradually washed out. For the sand used in our wave flume (with $D_{50} = 0.025$ cm and density of 2.65 gram per cubic cm) the ripples created by lower waves are unable to withstand (without irreversible deformations) shear stresses over 0.005 to 0.006 $\text{kg cm}^{-1}\text{s}^{-2}$. It can be assumed that ripples become completely destroyed if shear stresses at the bed reach 0.01 $\text{kg cm}^{-1}\text{s}^{-2}$. Under these conditions, with reconstructed flat bed, water carries suspended sediments of high concentrations.

One of the opportunities offered by the theoretical prediction of shear stresses consists in the computation

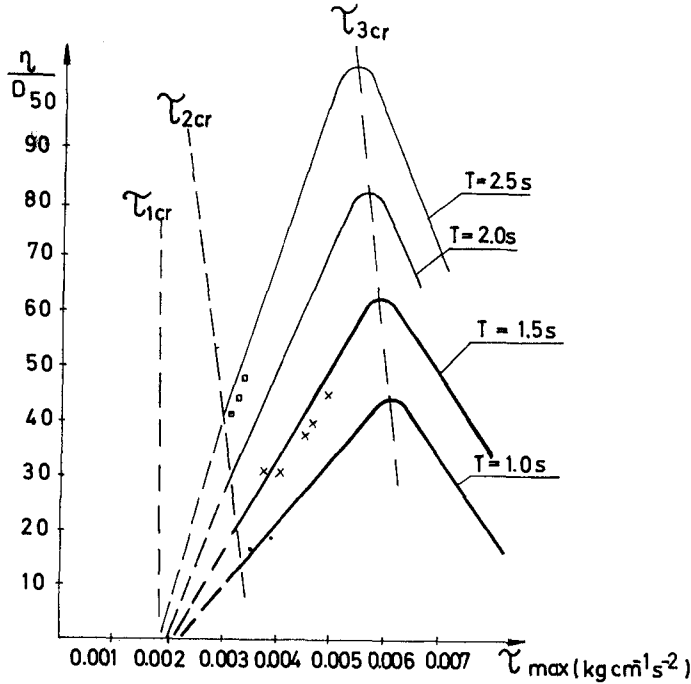


Fig.6 - Ripple Height Versus Bed Friction

of sediment transport rate, one of the most important quantities in the coastal dynamics. The computation can be based on the Frijlink formula (which is also used by Bijker [1]). Some results are presented in Fig.7 for various wave periods and velocities of longshore currents. The latter have been included in order to generalize the findings, but they are not necessary to draw the conclusions presented below. The picture illustrates general trends only, because the values of s.t. rates are local, as they were computed for the crest of the "first" ripple (where the boundary layer begins to develop). The s.t. rates averaged over the ripple length are smaller by three orders of magnitude. For comparison, analogous rates are also given for flat bed (dots for D_{50}). It should be mentioned that higher s.t. rates for rippled bed (than for flat bed) are not paradoxical: higher ripples

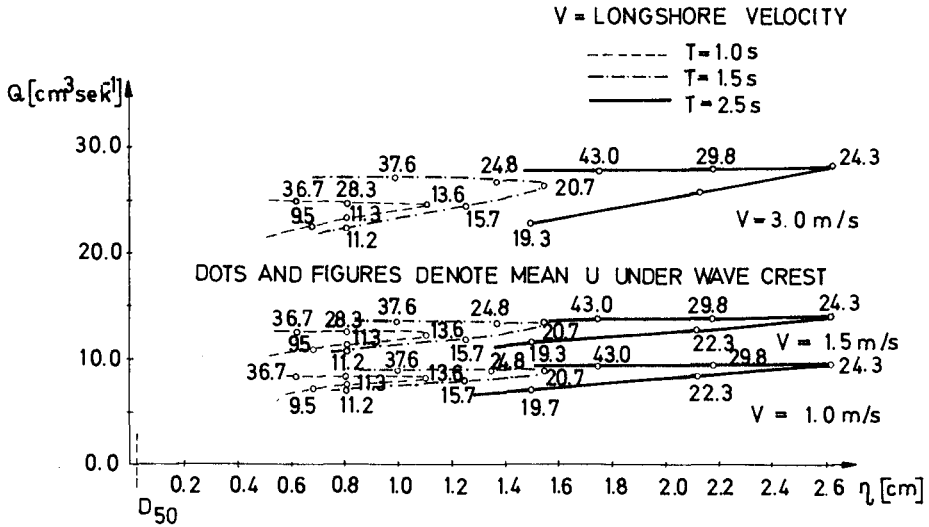


Fig.7 - Sediment Transport Rate Versus Ripple Height

bring about more resistance to motion of water but it must be remembered that, at the same time, they are produced by stronger waves.

The stages of the growth and decay of ripples are reflected respectively in the lower and upper branches of the curves. From a similar trend observed in the wave tank it can be inferred that sediment transport sometimes differs considerably for seemingly close bed roughness conditions. For the same ripple height there occur two different values of the sediment transport rate. Depending on the strength of wave motion, which is coupled with shear stresses at the bed, a given ripple with a certain height can be in the stage of growth or washout, and the corresponding s.t.rates can differ by as much as 25 per cent.

In many existing formulas for sediment transport rates (for example, those derived by White and Ackers, Engelund and Hansen, and Bijker) the rippled bed is represented by the equivalent roughness height r . The results of this study can be used to substantiate the choice of this parameter and to revise the assumptions on r made hitherto.

THREE - DIMENSIONAL EFFECTS

Under complex conditions of coastal zones, with various systems of currents and waves and diversified configuration of beach, bed microforms are usually three-dimensional (Fig.8).

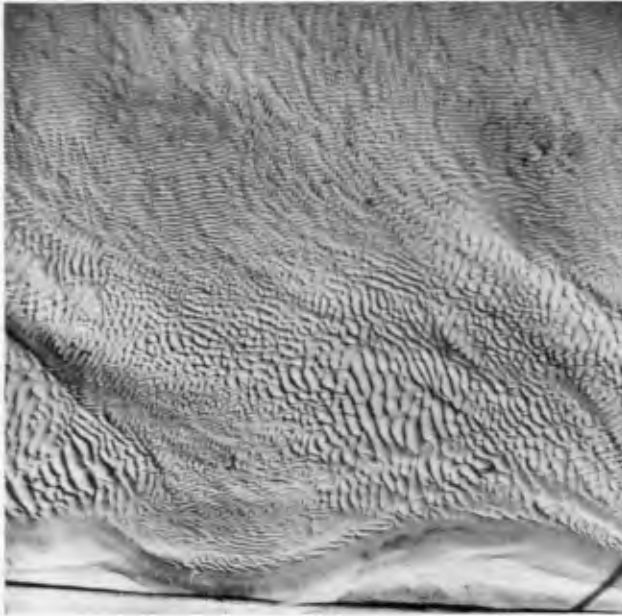


Fig.8 Three-dimensional Bed Forms in PAS-IHE Wave Tank

It is interesting to determine the origin and transformation of these forms and expose general relationships of the type $\eta, \lambda = f(\tau)$, as shown for two-dimensional forms.

Parameters of three-dimensionality can be chosen in a dozen of ways. In our analysis of the results obtained in a wave tank for two angles of wave incidence, 45° and 0 to 5° , we confined ourselves to three parameters: ripple height η , ripple length λ and the angle between ripple and local wave crest (Fig.9), Δ .

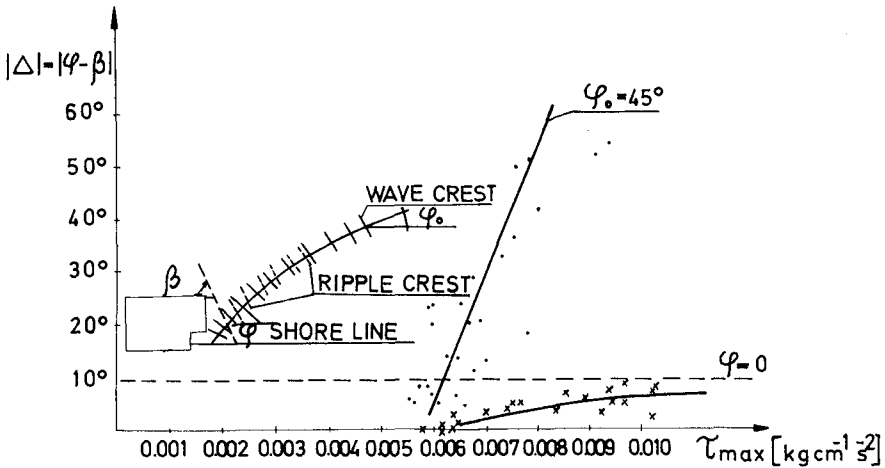


Fig.9 Ripple Misalignment Angle versus Shear Stress

The three parameters have been investigated as functions of shear stresses computed as if the ripples were two-dimensional. Thus, our definition of three-dimensionality is fairly arbitrary : 3-D conditions differ from 2-D configurations mostly by oblique layout of ripples. The angles $0 \leq \psi \leq 5^\circ$ are usually linked with 2-D ripples, provided however that coastal currents are secondary (although the reverse is encountered most often).

As can be concluded from Fig.9, small angles of wave incidence (normal attack) are connected with minor misalignment of ripples, but even small changes in the layout of ripples induce considerable increase in shear stress. These situations embody local gradential currents. For oblique incidence of waves, with more pronounced longshore currents, the misalignment

angle Δ increases much stronger as the waves approach beach, and shear stress at the bed also increases. Both curves in Fig.9 merge at the abscisae axis about the shear stress $\tau = 0.006 \text{ kg}\cdot\text{cm}^{-1}\cdot\text{s}^{-2}$. This marks the limit at which three - dimensional ripples begin to appear in the wave tank.

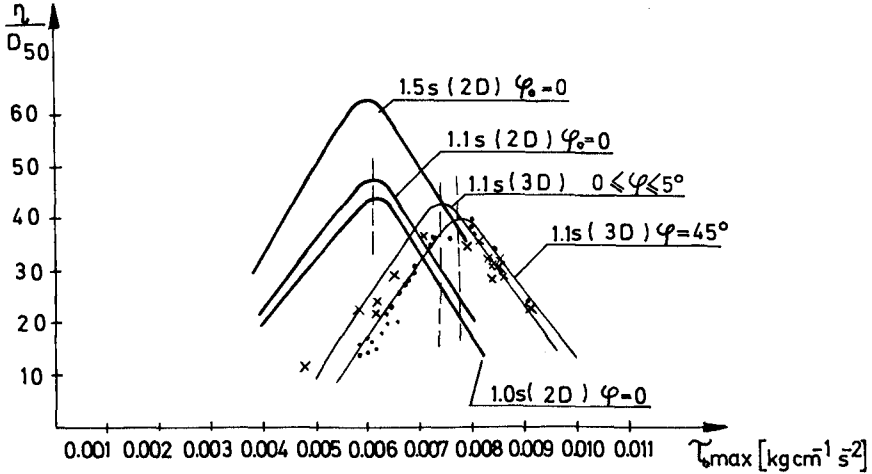


Fig.10 Height of 3-D and 2-D Ripples

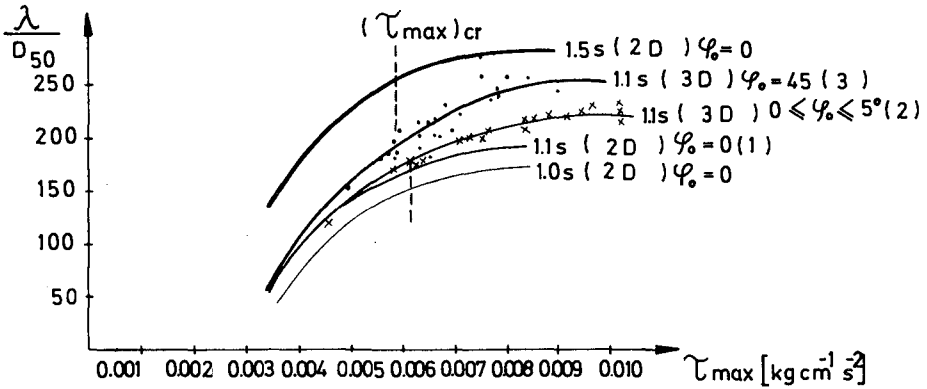


Fig.11 Length of 3-D and 2-D Ripples

Figures 10 and 11 present heights and lengths of three-dimensional ripples; 2-D ripples are also shown for comparison. The curves suggest that the processes of the generation and decay of ripples are similar for 2-D and 3-D forms. The shift of 3-D curves, with regard to 2-D curves, is partially caused by cementing of sediments in the open-air wave tank, attacked by plankton and silt.

Three-dimensionality of bed microforms in the presence of waves and currents becomes more pronounced with higher angles of wave incidence, Ψ . Even though the shift of curve (2) with regard to (1) in Fig.10 can be attributed to cementing, the discrepancies of curves (2) and (3) are due to different Ψ . It should be noted that the scatter of the measured results around curve (3) depends on the ratio of oscillatory and longshore velocities, $U_{max} : V$. For the ratios smaller than 1 the scatter is considerable, while for $U_{max} : V > 2$ the results lie close to the curve, especially at its apex.

The three-dimensional effects in the ripple length (Fig.11) are reflected in relative increase in the length, for a given shear stress. The differences of the lengths of 2-D and 3-D ripples increase with higher shear stress. The 3-D length also increases with higher Ψ .

An important role in the generation of 3-D microforms is played by interrelations of waves and currents in the coastal zone. The effect of these factors is inherent in the angle Ψ , which determines, among others, the longshore current due to wave breaking. The variation of ripple parameters with the velocity of longshore current depends on local vectors of longshore current and wave motion. Thus, the angle Ψ determines the ripple length λ on greater depths, seawards of the breaking zone, where refraction of waves and ripples is similar, so that their directions are parallel. In the surf zone, where the effect of currents is pronounced, the three-dimensional effects become significant. Fig.12 illustrates the influence of Ψ and Δ on the increase in the length of 3-D ripples, compared to 2-D forms.

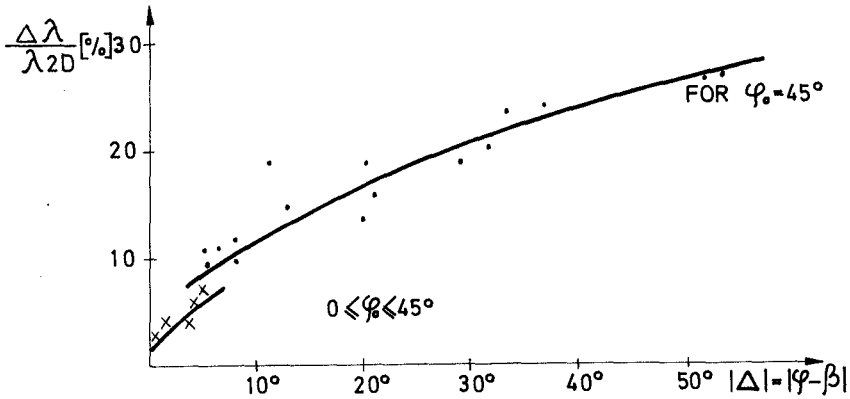


Fig.12 Relative Increase in Length of 3-D Ripples

ACKNOWLEDGEMENTS

This study has been carried out under the Polish Academy of Sciences MR I.15.3.1 programme.

The sponsorship of the Claude W.Nash Foundation, both moral and financial, is highly and sincerely appreciated.

NOTATION

h = wave height

H = depth of water

$k = \frac{2\pi}{L}$

L = wavelength

T = wave period

U_{max} = velocity at the upper limit of boundary layer,
due to water wave in the crest phase

η = ripple height

λ = ripple length

ν = kinematic coefficient of viscosity

$$\omega = \frac{2\pi}{T}$$

REFERENCES

- 1 Bijker E.W., Some considerations about scales for coastal models with movable bed, Publ.No 50
Delft Hydraulics Laboratory, 1967
- 2 Kalkanis G., Transportation of bed material due to wave action, Technical Memorandum No 2, Beach Erosion Board, 1964
- 3 Lavrentiev M.A., Shabat B.W., Methods of the functions of complex variable /in Russian/, Moscow 1965
- 4 Pruszek Z., Processes of the formation, growth and decay of ripples in oscillatory flow /in Polish/, Rozprawy Hydrotechniczne, No 39, 1978
- 5 Pruszek Z., Zeidler R., Bed friction and sediment transport rate in coastal zone with bed microforms /in Polish/, PRACE Inst.Bud,Wodnego PAN No 4, Gdańsk 1978
- 6 Sleath J.F.A., A contribution to the study of vortex ripples, Journal of the Intern. Assoc.Hydr. Research, vol.13 No 3, 1975

CHAPTER 99
A MODEL STUDY OF ALONGSHORE SEDIMENT TRANSPORT RATE

by

J.W. Kamphuis
Queen's University
Kingston, Canada

and

J.S. Readshaw
Western Canada
Hydraulics Laboratories
Vancouver, Canada

ABSTRACT

Alongshore sediment transport rate was studied in a 3-dimensional mobile bed coastal model and was found to depend on the beach profile and rate of wave energy dissipation in addition to the normal wave and sediment parameters. Alongshore sediment transport rate was found to be strongly related to the surf similarity parameter, a single parameter simplistically describing beach profile and breaker type.

INTRODUCTION

Tests have been performed at Queen's University for a number of years using the concept of "dynamic equilibrium profiles" (6,7,8) denoting the profile response to a simply simulated annual wave climate. A detailed description of "dynamic equilibrium" may be found in Ref. 6.

The earlier tests were concerned with beach profile formation, application of artificial beach nourishment and redistribution of grain sizes. This particular paper deals with littoral drift rates.

SIMPLE EXPRESSIONS

Many expressions have been developed to relate littoral transport to wave conditions. The simplest of these are based on either energy or momentum principles.

The energy approach in its simplest form relates littoral transport to alongshore energy flux

$$Q_s = K_p P_{ab} \quad (1)$$

where Q_s is the littoral transport rate, K_p is a constant and P_{ab} is the alongshore component of wave power in the breaking zone in N-m/s/m of beach.

$$P_{ab} = \frac{1}{2} n_b C_b E_b \sin 2 \alpha_b \quad (2)$$

Here C is the velocity of wave propagation, E is the wave energy density, α is the angle of wave approach and

SEDIMENT TRANSPORT RATE

$$n = \frac{1}{2} \left[1 + \frac{4\pi d/L}{\sinh 4\pi d/L} \right] \quad (3)$$

while the subscript b denotes the breaking zone. This approach is described in detail in Shore Protection Manual (11) and is often referred to as the CERC formula. The constant K_p is dimensionless if Q_s is expressed as weight flux (N/s). In this paper Q_s will be expressed as mass rate of transport and thus K_p has the dimensions of (1/g) or, defining a new constant K'_p ,

$$Q_s = K'_p \left(\frac{P_{ab}}{g} \right) \quad (4)$$

The momentum approach uses the concept of "radiation stress", the excess momentum flux resulting from the presence of waves (10). The stress component of interest is the alongshore component

$$S_{xy} = n E \sin \alpha \cos \alpha \quad (5)$$

If an onshore gradient in this component exists, an alongshore force is present:

$$F_a = - \frac{\partial}{\partial x} (S_{xy}) dx \quad (6)$$

Such an onshore gradient only exists in the breaking zone, where the wave energy is dissipated. Assuming the radiation stress at the shore to be zero the total lateral thrust available to move sediment is

$$F_a = (S_{xy})_b = \frac{1}{2} n_b E_b \sin 2 \alpha_b \quad (7)$$

Sediment transport may be related to wave thrust in its simplest form as:

$$Q_s = K_t F_a \quad (8)$$

where K_t is not dimensionless but has units of time. Some experimental evidence in support of an equation such as Eq. 8 is presented by Bruno and Gable (2). It is to be noted that

$$P_{ab} = F_a C_b \quad (9)$$

and thus Eqs. 4 and 8 are very similar. Equation 8 is easier to use since F_a does not include a difficult estimate value of C_b

DIMENSIONAL ANALYSIS

Sediment transport is a function of water, wave and beach parameters

$$Q_s = f(\mu, \rho, g, H, T, \alpha, \rho_s, D, t, n) \quad (10)$$

where μ and ρ are the viscosity and density of the water,

g the gravitational acceleration, H the wave height, T the wave period, α the angle of wave approach, ρ_s and D the density and size of the sand, t is time and η is the beach shape. The quantity η is included simply as a reminder that beach shape is important.* In a later section it will be seen that η is a complicated combination of many geometrical parameters.

Dimensional analysis yields:

$$\frac{Q_s}{\rho H^2 \sqrt{gH}} = \Phi \left(R, \frac{H}{L_o}, \alpha, \frac{\rho_s}{\rho}, \frac{D}{L_o}, \frac{t}{T}, \eta^* \right) \quad (11)$$

where
$$R = \frac{\hat{u}_\delta a_\delta}{v} = \frac{\pi H^2}{4\sqrt{T}}$$

the maximum amplitude Reynolds number (4), while η^* denotes the dimensionless version of η .

During the present tests, α , ρ_s/ρ and D/L_o were not varied.

The effect of using light weight (or heavy weight) material has been discussed earlier in detail (5) and consequently sand was used in the model. This introduces scale effect in the model since the initiation of motion and sediment transport characteristics have now changed (5). This scale effect will be denoted by m_ρ . The scale effect resulting from improper scaling of the material size has also been discussed (5) and it is expected that a scale effect (m_η) is present in this model.** Since tests were only performed with one generated angle of approach of the waves the effect of α has been assumed to be as shown in Eqs. 2 and 7. This assumption is based upon the experimental results of Refs. 2 and 11. Thus Eq. 11 may be rewritten for purposes of this study as:

$$\frac{Q_s}{\rho H^2 \sqrt{gH}} = m_\rho m_D \sin 2\alpha_b \Phi_1 \left(R, \frac{H}{L_o}, \frac{t}{T}, \eta^* \right) \quad (12)$$

The value of C_b in Eq. 2 is difficult to determine and may be expressed as

$$C_b = \sqrt{\kappa g d_b} \quad (13)$$

* In a strict dimensional analysis sense, the quantity η should not be included here since η is not independent of D and ρ_s , hence the term "reminder".

** Note that these are scale effects in addition to the influence of different profiles as a result of using incorrectly scaled ρ_s and D. The effect of profile differences is included in η^* .

$$\text{where} \quad 1.0 < \kappa < 1.78 \quad (14)$$

depending on whether linear, cnoidal or solitary wave theory is used. A careful interpretation of Iversen's (3) and Battjes' (1) results would indicate that both H_b/d_b and κ may be approximated by unity, yielding:

$$\frac{Q_s}{\rho H_b^2 \sqrt{g H_b} \sin 2 \alpha_b} = \frac{Q_s}{P_{ab/g}} = K'_p = m_\rho m_D \Phi_1 \left(R, \frac{H}{L_0}, \frac{t}{T}, \eta^* \right) \quad (15)$$

and what was assumed constant in Eqs. 1 and 4 is seen to be a function of the wave Reynolds number, the wave steepness, the time and the beach shape.

The effect of R is small in a turbulent flow region such as near the breaking zone and thus the investigation concentrated on wave steepness, time and beach shape.

EXPERIMENTS

The experiments were carried out in the wave basin shown in Fig. 1, essentially the same as used by Kamphuis and Myers (7) except that the generator was placed further away from the beach to improve re-reflection patterns. Circulation was allowed to take place in the breaker zone and under the generator to achieve an "infinitely long beach". The sediment feeder was placed on a track to facilitate dropping the feed material in the breaker zone at all times. The sediment trap was suspended with 3 load cells to allow continuous weighing of the trapped material. The material entered the traps through narrow slots. The end of the beach was supported by a template which had approximately the same shape as the profile line in the middle of the beach. Sediment was pumped from the trap to the feeder at the end of each test using a diaphragm slurry pump.

The tests performed are summarized in Table 1. The wave climates for tests 1 through 4 are the same as used by Bridgeman and by Myers (6,7). In tests 5 through 7 the summer waves were 20% larger but with the same steepness and the winter waves were 5% smaller and somewhat steeper. In test 8, the winter wave period was substantially reduced to produce a very steep wave.

A distinction must be noted in Table 1 between series types S and D, denoting steady state and dynamic equilibrium tests. In the steady state tests a number of summer (or winter) storms were repeated immediately following each other.

TEST RESULTS

The rates of sediment feeding and trapping were carefully measured and matched. A sample plot is included in Fig. 2. A number of

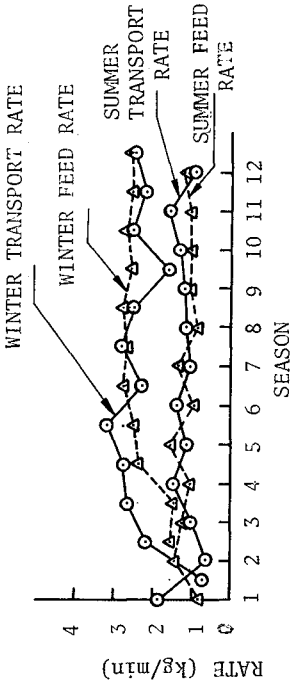


FIGURE 2 MEAN TRANSPORT RATE AND FEED RATE PER SEASON FOR TEST SERIES 8S AND 8W

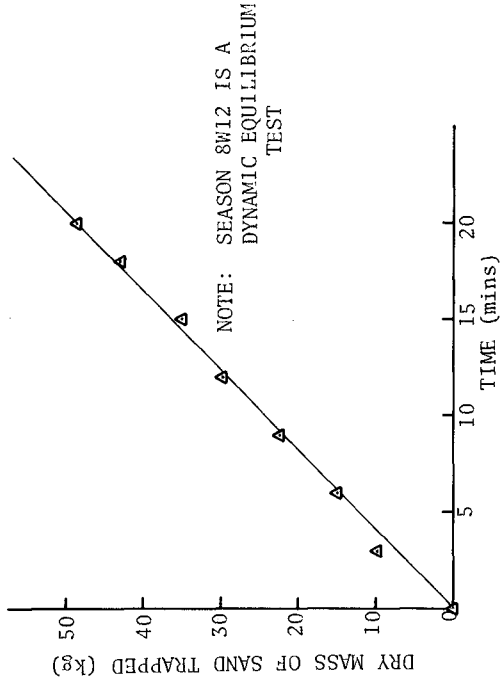


FIGURE 3 MASS OF SAND TRAPPED VS TIME WITHIN SEASON 8W12

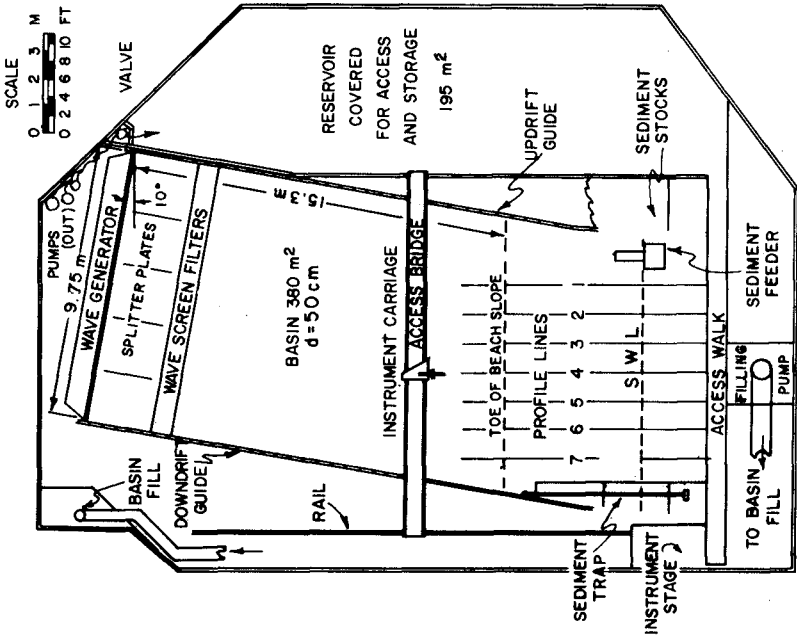


FIGURE 1 BASIN LAYOUT

NOTE: SEASON 8W12 IS A DYNAMIC EQUILIBRIUM TEST

SEDIMENT TRANSPORT RATE

1661

TABLE 1

TEST RESULTS

TEST SERIES	TEST SEASON	H _o (m)	T (s)	H _o /L _o	SEASON LENGTH (min)	TYPE	NUMBER OF SEASONS	Q _i	Q _{tr}	Q _{eq}	ξ _b
1	1S	0.047	1.17	0.022	110	S	10			1.9	2.2
	1W	0.124	1.4	0.035	15	S	8			5.1	1.1
2	2S	0.047	1.17	0.022	110	S	5			2.0	3.1
	2W	0.12	1.5	0.035	15	S	20			9.9	1.1
3	3S	0.047	1.17	0.022	110	D	27	1.4	3.1	0.8	0.7
	3W	0.12	1.5	0.035	15	D	27			9.7	1.1
4	4S	0.047	1.17	0.022	60	S	4			0.4	.4
5	5S	0.056	1.31	0.021	110	S	18			2.2	2.2
	5W	0.114	1.37	0.039	20	S	22			5.9	.7
6	6S	0.056	1.31	0.021	110	D	13	0.5	1.5	1.3	1.0
	6W	0.114	1.37	0.039	20	D	12			8.4	.7
7	7S	0.056	1.31	0.021	60	S	6			0.9	.7
8	8S	0.056	1.31	0.021	150	D	12	0.3	3.0	1.1	.7
	8W	0.093	1.0	0.060	20	D	12			2.4	.5

discrepancies occurred which were corrected as the tests progressed and with respect to modelling of beaches the following was learned:

1. If the model study is meticulously controlled, *it is possible* to investigate alongshore sediment transport in a model which is carefully set up to simulate an infinitely long beach.
2. The *model boundary conditions* affect the measured littoral transport rate.
 - a. The *end (downdrift) template* must closely match the existing beach profile. If the template is too high, the beach will accrete locally at the downdrift end and with time will turn and decrease the breaking angle. If the template is too low, an alongshore beach gradient will be formed as the beach erodes near the template. This will increase the littoral transport rate as the sand is removed and with time will cause the breaking angle to increase.
 - b. Small variations in the *feed rate* had a negligible direct effect on the littoral transport rate. Dissimilarities between the littoral transport rate and the feed rate did, however, cause the beach profile to change. This in turn changed the nature of the interaction between the beach profile and the breaker and changed the littoral transport rate.
 - c. The *feeder position* must be continuously adjustable so that the feed material is always introduced at the breaker point. Only then are the sand grains distributed over the entire width of the surf zone.

With respect to sediment transport rates it was learned that:

3. Sediment transport rates are *not the same* for steady state and dynamic equilibrium tests (Table 1) and are also different for component storm waves when paired with different storm waves (Table 1, tests 6S and 8S).
4. The rate of sediment transport for the *steady state equilibrium profiles* increased slowly until it reached a constant value for the smaller summer storm waves. For the large winter storm waves, a constant sediment transport rate was reached almost immediately after startup.
5. For the *dynamic equilibrium tests* the transport rate was

constant throughout the winter storm portion of the cycle (Fig. 3). For the summer storms, the transported volume exhibited an S curve indicating a small "initial" transport rate, followed by a large "transitional" transport rate, followed by a smaller "equilibrium" transport rate (Fig. 4). Tangents may be drawn to the curve (Fig. 5) and these tangential sediment transport rates have been recorded in Table 1 for the dynamic tests 3, 6 and 8.*

In order to understand the mechanism that results in the S-curve of sediment transport a test series was run in which the beach profiles were measured at short intervals. It was found that:

6. *Beach profiles* and equilibrium transport rates are very closely related and the transport rate responds rapidly to changes in beach profile.
 - a. The transport rate for the steep *winter storm waves* (Fig. 3) was constant because the profile resulting from summer storms was rapidly reshaped into a bar profile by the first few waves and subsequently only small adjustments took place to achieve more complete equilibrium.
 - b. For the *summer storm waves* (Fig. 4), the first stage of the reshaping cycle consisted of removing sand from the offshore bar into the trough and into the swash zone. This resulted in a long, flat shelf, a very gentle breaking wave and a low initial transport rate. The material was subsequently remoulded into a summer step and during this "transitional" stage a violent breaker and large littoral drift rate was evident. Eventually, the summer step increased in length to its ultimate equilibrium length and an equilibrium beach with "equilibrium" transport rate resulted.

BEACH PROFILE AND BREAKER

Further study was made of the beach profile and its important influence on sediment transport rate as outlined in conclusion 6 above. In the dimensional analysis, the term η was used. This

* Note that for waves of small steepness, "equilibrium" littoral transport rate cannot be measured accurately unless the material transported is trapped and weighed continuously. The average transport rate \bar{Q} for the summer storm waves is meaningless since it depends on when the test is completed. In Fig. 5 two such rates corresponding to test durations t_1 and t_2 are shown.

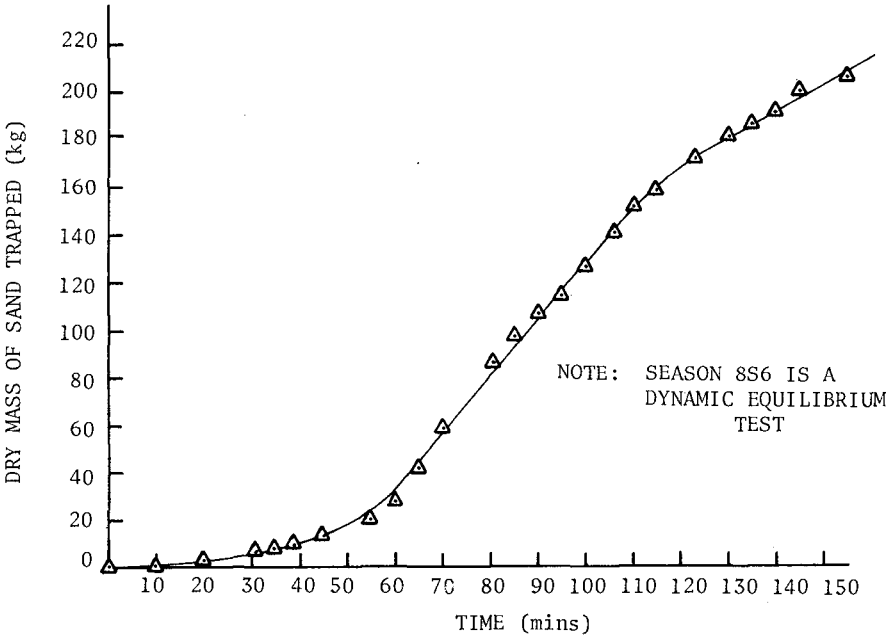


FIGURE 4 MASS OF SAND TRAPPED vs TIME WITHIN SEASON 86

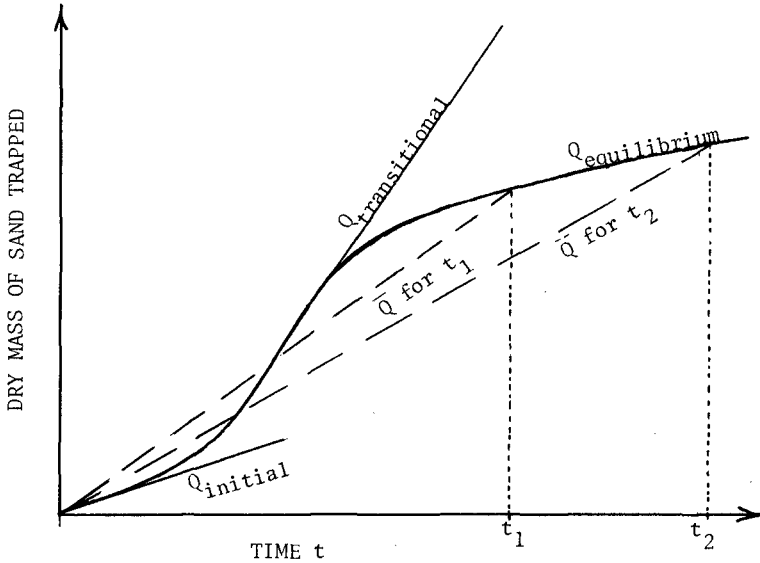


FIGURE 5 TRANSPORT RATE DEFINITIONS

η is a combination of a number of levels and distances on the beach profile and nomenclature for the beach profile is introduced in Figures 6 and 7. The beach is divided into a turbulent zone and a swash zone and several geometrical distances are defined as shown in Fig. 7 where S refers to beach slope, initially (S_0), on the foreshore (S_{FS}) and offshore (S_{OS}), λ is the length of the summer step (λ_s) or the distance to the bar (λ_w) - defined as distances between tangents S_{FS} and S_{OS} , Σ is the depth of water over the summer step and β the depth of water over the bar.

In the following, Q_s refers to the equilibrium sediment transport rate both for the steady state and dynamic equilibrium tests.

Whenever a beach profile and a sediment transport rate were measured simultaneously, comparisons were made between the sediment transport rate and the individual beach parameters of Fig. 7. Figures 8, 9, 10 and 11 indicate little relationship between Q_s and S_{FS} , S_{OS} , Σ and β . This leaves λ , the length of the summer step or distance to the bar. A measurement of the evolution of λ_s for test 3S (Fig. 12) indicates an S curve somewhat similar to Figure 4 and when Q_s is plotted against λ there is a definite relationship as shown in Fig. 13. The scatter is a result of simultaneous variation of the other parameters. Figure 13 indicates that as λ lengthens, the sediment transport rate decreases and this corresponds with observation as well as with conclusion 6b above. This also explains why the dynamic equilibrium tests produced higher sediment transport rates in summer than the identical steady state tests and why there was a discrepancy between tests 6S and 8S.

It was also noticed that as λ increased, the breaker type became less violent, tending to change from plunging to spilling characteristics.

Extensive work on breaker types on a plane slope has been done by Battjes (1) who relates breaker type to the surf similarity parameter

$$\xi_b = \frac{\tan \theta}{\sqrt{H_b/L_0}} \quad \text{or} \quad \xi_0 = \frac{\tan \theta}{\sqrt{H_0/L_0}} \quad (16)$$

where θ is the slope of the plane beach. This parameter combines beach slope, essentially a simplification of beach profile and of η , with wave steepness. Obviously if this parameter were to be used in the present study, it should include λ and thus for this study

$$\xi_s = \frac{\Sigma/\lambda_s}{\sqrt{H/L_0}} \quad \text{and} \quad \xi_w = \frac{\beta/\lambda_w}{\sqrt{H/L_0}} \quad (17)$$

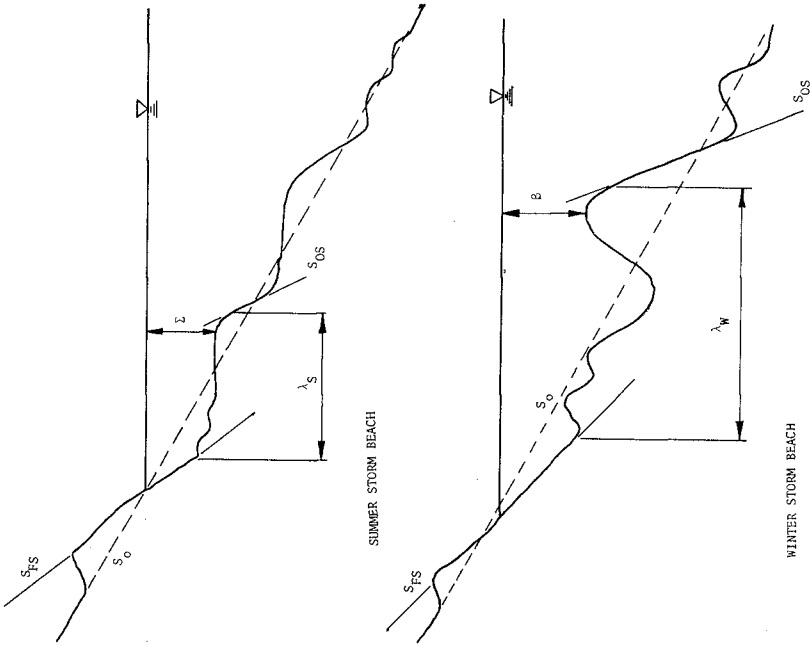


FIGURE 7 PROFILE DEFINITIONS

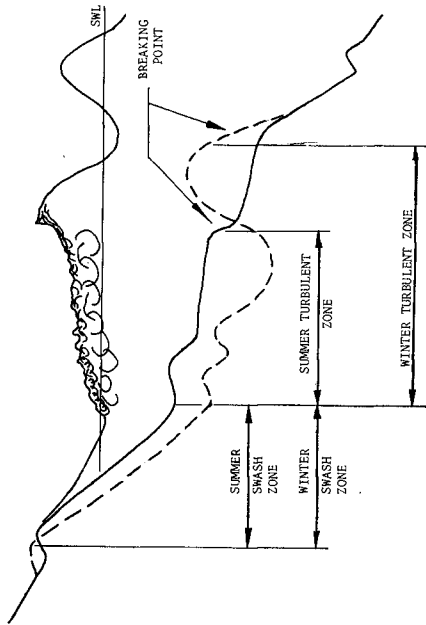


FIGURE 6 TYPICAL TURBULENT AND SWASH ZONES

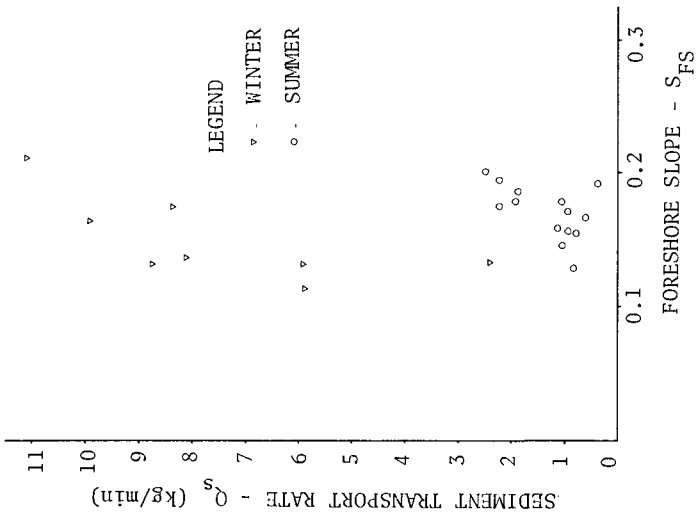


FIGURE 8 SEDIMENT TRANSPORT RATE AS A FUNCTION OF FORESHORE SLOPE

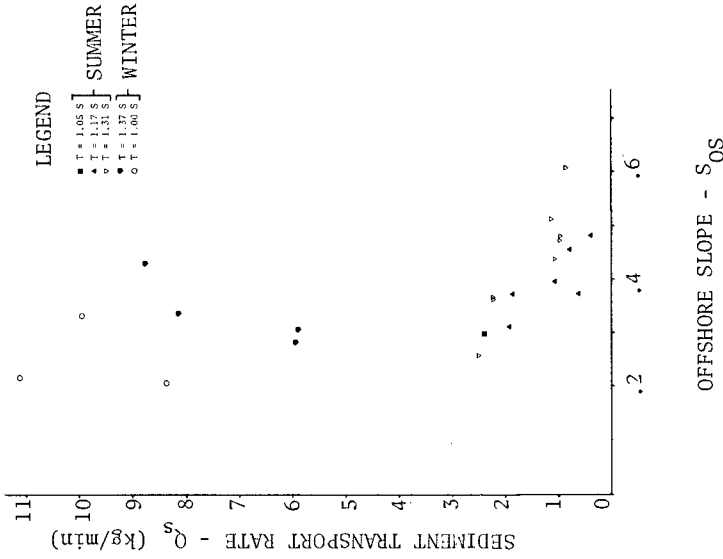


FIGURE 9 SEDIMENT TRANSPORT RATE AS A FUNCTION OF OFFSHORE SLOPE

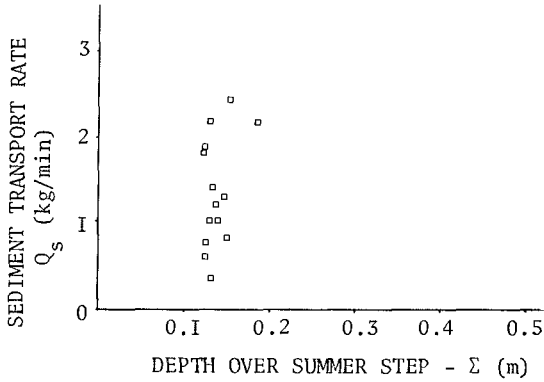


FIGURE 10 SEDIMENT TRANSPORT RATE AS A FUNCTION OF DEPTH OVER THE SUMMER STEP

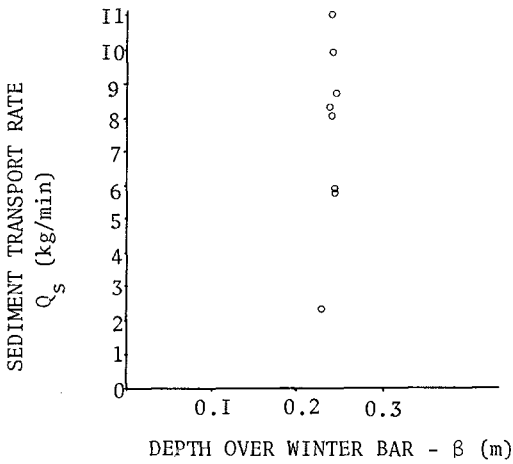


FIGURE 11 SEDIMENT TRANSPORT RATE AS A FUNCTION OF DEPTH OVER THE WINTER BAR

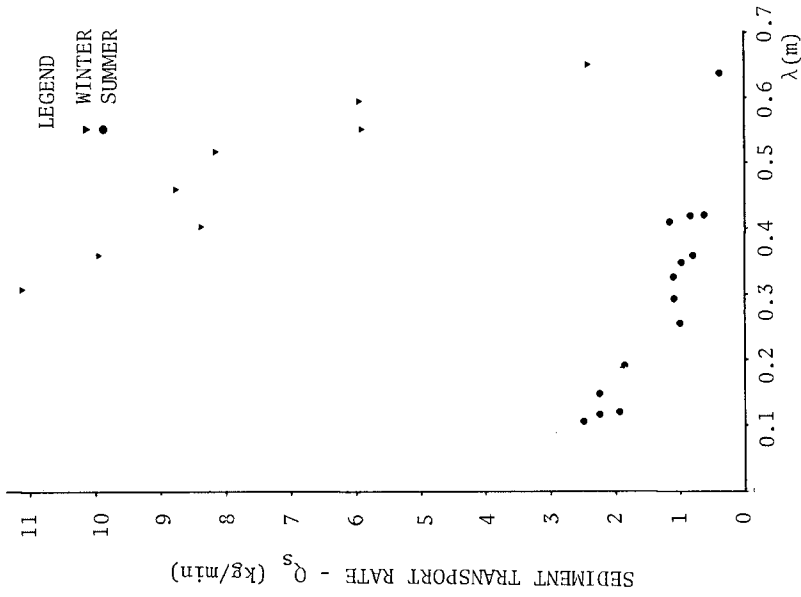


FIGURE 13 SEDIMENT TRANSPORT RATE AS A FUNCTION OF λ (SUMMER STEP LENGTH OR DISTANCE TO THE WINTER BAR)

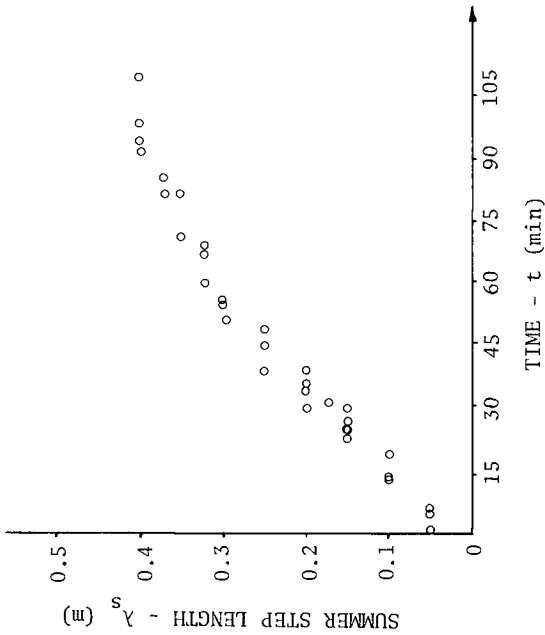


FIGURE 12 EVOLUTION OF SUMMER STEP LENGTH IN TEST 3S

where Σ/λ_s and β/λ_w are simplifications of η^* and are estimates of the beach slope of the active portion of the beach, i.e. in the turbulent zone and the swash zone for summer and winter respectively.

The rate of sediment transport is plotted against ξ_b in Fig. 14 and it may be seen that there is a strong relationship indicating that the replacement of η^* in Eq. 11 by ξ_b is a valid step, especially since Σ and β can be shown to be independent of λ_s and λ_w . Introducing the above simplification, it is now possible to plot the dimensionless sediment transport $Q_s/\rho H_b^2 \sqrt{gH_b}$ against ξ_b as was done in Fig. 15. Breaking wave heights were used in the formulation of dimensionless sediment transport to correspond to ξ_b . Use of deep water wave heights and ξ_0 introduced further scatter in the results. Figure 15 indicates a single, very strong relationship, suggesting that the variation with R , H/L_0 and α for equilibrium values of $Q_s/\rho H_b^2 \sqrt{gH_b}$ is small. In a further step, K'_p of Eq. 15 was plotted against ξ_b using values of α_b obtained by refraction analysis and checked by overhead photography. It may be seen from Fig. 16 that the K'_p is not a constant but is strongly related to ξ_b .

The straight line shown in the diagram indicates that

$$K'_p \approx 0.7 \xi_b \quad \text{for} \quad 0.4 < \xi_b < 1.4 \quad (18)$$

with a correlation coefficient, $r^2 = 0.73$. This correlation is an improvement over Fig. 15 where a similar line would yield $r^2 = 0.56$. Thus Eq. 15 improved upon Eq. 11 and the term $(\sin 2 \alpha_b)$ removes a considerable portion of the variance present in Fig. 15.

The constant K'_p as determined by Komar and Inman (9) has also been shown on Fig. 16. It may be seen that the test results and the constant value of K'_p correspond very well for high values of ξ_b . Indeed, Komar and Inman state that the breakers at their most intensively studied beach (El Moreno) were violently plunging and that the beach was steep. This would indicate a high value of ξ_b for these tests. Their other beach (Silver Strand) was much flatter, but the measurements were made for swell of small height, thus again indicating possibly high values of ξ_b . The fact that for lower values of ξ_b , K'_p is a function of ξ_b may be why Komar and Inman's work and the CERC formula overestimate littoral transport rate for many situations, especially those involving gently sloping beaches and low swell.

Equation 8 surmises that littoral transport rate may be presented as a simple function of wave thrust. Figure 17 indicates this proportionality also to be a function of ξ_b . The straight line in the figure is

$$K_t \approx 0.08 \xi_b \quad \text{for} \quad 0.4 \xi_b < 1.25 \quad (19)$$

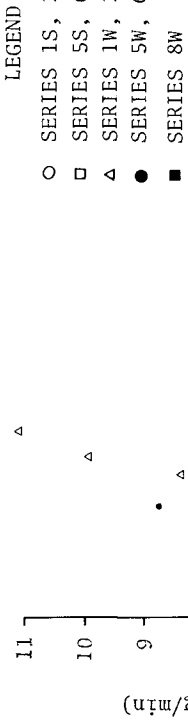


FIGURE 14 SEDIMENT TRANSPORT RATE AS A FUNCTION OF THE SURF SIMILARITY PARAMETER

- LEGEND
- SERIES 1S, 2S, 3S, 4S
 - SERIES 5S, 6S, 7S, 8S
 - △ SERIES 1W, 2W, 3W
 - SERIES 5W, 6W
 - SERIES 8W

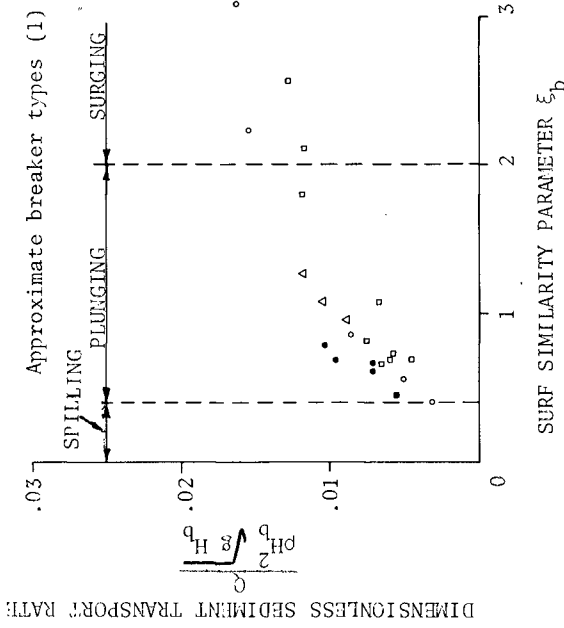


FIGURE 15 DIMENSIONLESS SEDIMENT TRANSPORT RATE AS A FUNCTION OF THE SURF SIMILARITY PARAMETER

LEGEND

- SERIES 1S, 2S, 3S, 4S
- SERIES 5S, 6S, 7S, 8S
- △ SERIES 1W, 2W, 3W
- SERIES 5W, 6W
- SERIES 8W

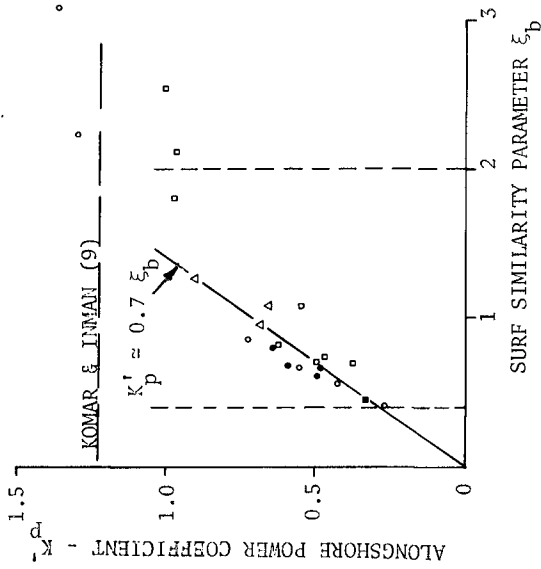


FIGURE 16 ALONGSHORE POWER COEFFICIENT AS A FUNCTION OF SURF SIMILARITY PARAMETER

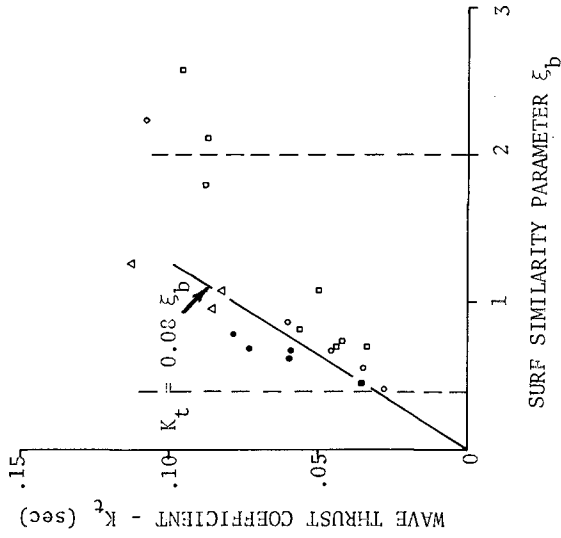


FIGURE 17 WAVE THRUST COEFFICIENT AS A FUNCTION OF SURF SIMILARITY PARAMETER

with a correlation coefficient $r^2 = 0.62$ indicating that this relationship contains more scatter than Eq. 18. Field results obtained by Bruno and Gable (2) have not been shown on Figure 17 since no wave and beach profile data were available from their paper and since their field results for K_t showed much more scatter than the experimental results in Fig. 17.

Figures 14 to 17 yield the following conclusions:

7. The rate of littoral transport was closely related to the beach shape, the type of breaker and the rate of energy dissipation in the breaking zone. These quantities may be simply represented by the surf similarity parameter and the dimensionless littoral transport was found to increase linearly with the surf similarity parameter over the range $0.4 < \xi_b < 1.4$.
8. The CERC formula can be used to estimate littoral transport rate only for beaches where the breakers are violently plunging or surging. For gently sloping beaches or for low swell, resulting in spilling to plunging breakers, the beach profile must be taken into account using the surf similarity parameter and the CERC formula overestimates littoral transport rate.

DISCUSSION

It is worthwhile to note the following points:

Sediment transport rate is closely related to the rate of energy dissipation in the breaker zone, i.e. breaker type, which in turn is related to beach shape. The surf similarity parameter may therefore be estimated either by inspection of the beach shape or by inspection of the breaker type. This yields two estimates of ξ_b and should facilitate determination of this parameter and hence of sediment transport rate on more complex beach profiles with multiple bar systems.

Recently much discussion has centred on the usefulness of the CERC expression and the dependence of its "constant" on grain size and density. This paper has shown that the CERC expression is valid for simple model conditions, but that the "constant" is a variable. The value of K_p' was shown to be strongly related to ξ_b , but ξ_b in turn depends strongly on grain size and density. Thus, although m_D and m_ρ explain some of the dependence of K_p' on ρ_s and D , most of the dependence on ρ_s and D is taken care of via ξ_b .

Finally, although out of experimental necessity equilibrium values of Q_s and ξ_b were used to define Figs. 16 and 17, the relationships are general and can be used for beaches which are not in equilibrium, except for short-term storm durations where a transition sediment transport rate can occur which is several times the equilibrium rate.

REFERENCES

1. Battjes, J.A., (1974) "Computation of Set-up, Longshore Currents, Run-up and Overtopping due to Wind-generated Waves", *Report 74-2, Delft Technological University*, 244 pp.
2. Bruno, R.O. and Gable, C.G., (1976) "Longshore Transport at a Total Littoral Barrier", *Proceedings, 15th Conference on Coastal Engineering*, Honolulu, Hawaii, pp. 1203-1223.
3. Iversen, H.W., (1952) "Laboratory Study of Breakers", *National Bureau of Standards, Circular 521*, p. 9.
4. Kamphuis, J.W., (1975) "Friction Factor Under Oscillatory Waves", *Waterways, Harbours and Coastal Engineering Journal*, A.S.C.E., Vol. 101, WW2, May 1975, pp. 135-144.
5. Kamphuis, J.W., (1975a) "The Coastal Mobile Bed Model", *Queen's University C.E. Report No. 75*, August 1975, 113 pp.
6. Kamphuis, J.W., and Bridgeman, S.G., (1975b) "Placing Artificial Beach Nourishment", *Proceedings, Oceans III Conference*, Delaware, 1975, pp. 197-216.
7. Kamphuis, J.W., and Myers, R.M., (1976) "Three Dimensional Tests on Dynamic Equilibrium and Artificial Nourishment". *Proceedings, 15th Conference on Coastal Engineering*, Honolulu, Hawaii, 1976, pp. 1532-1551.
8. Kamphuis, J.W., and Moir, J.R., (1977) "Mean Diameter Distribution of Sediment Sizes before and after Artificial Beach Nourishment", *Proceedings Coastal Sediments '77*, Charleston, S.C., Nov. 1977, pp. 197-210.
9. Komar, P.D., and Inman, D.L., (1970) "Longshore Sand Transport on Beaches", *Journal of Geophysical Research*, Vol. 75, No. 30, pp. 5514-5527.
10. Longuet-Higgins, M.S., (1972) "Recent Progress in the Study of Longshore Currents", *Contribution to Waves on Beaches*, Academic Press, New York.
11. Shore Protection Manual (1977) *Coastal Engineering Research Centre*, U.S. Corps of Engineers.

ACKNOWLEDGEMENTS

The authors thank the National Research Council and the Ontario Graduate Scholarship Programme for financial support.

CHAPTER 100

EFFECT OF WAVES ON SAND TRANSPORT BY CURRENTS

by

Michael W Owen* and Michael F C Thorn*

The effect of waves on the transport of sand in suspension by currents can be especially important in the outer regions of estuaries and tidal inlets. Two series of field experiments are therefore being carried out to investigate the transport of sand under the combined action of waves and currents.

In the first series of tests, measurements were taken from a specially constructed tower located just off the Maplin Sands in the outer Thames Estuary, England, (Fig.1). The tower stands in about 1.5m of water at lowest tide levels, and the mean spring tidal range is about 4.5m. Average tidal velocities are about 0.6m/s, with peak values up to about 0.9m/s. The tower has a completely open structure (Fig.2) below the water line, with the exception of the four corner piles penetrating the sea bed, and a vertical trackway which stops approximately 1m above bed level. A series of instruments were fixed to a trolley which could be winched up and down the trackway, thus allowing measurements at any height above bed level. The annual wave climate at a waverider buoy position some 900m from the tower is summarised in Fig.3: Fig.3a shows the percentage occurrence of different wave heights, and it can be seen that the tower is at a fairly sheltered site, with less than 2 per cent of the waves exceeding 1m in significant height. Fig.3b shows the percentage occurrence of given wave periods which, as one would expect, are correspondingly short, with less than 2 per cent exceeding 4.5s mean-zero crossing period.

The second series of field tests are presently being carried out at the seaward end of Boscombe Pier, located in Poole Bay, England, (Fig.4). Water depths at this site are about 2.5m at low tide, with a mean spring tidal range of about 1.7m. Maximum tidal velocities are only about 0.3m/s, although during prolonged storms the tidal currents are enhanced by strong wind-induced currents. This site is significantly more exposed than Maplin, which was the reason for the choice of this second location. Annual wave statistics are not available for Boscombe Pier itself, but a waverider buoy some 3000m from the pier (Fig.4) has been operated by the University of Southampton for several years, and Fig.5 shows the percentage occurrence of given wave heights for the year 1977. Some 17 per cent of waves were greater than 1m significant height, and 2 per cent greater than 2m. Fig.6 shows the percentage occurrence of given wave periods: 5 second waves are the most common, but with periods of longer than 10 seconds being recorded. Despite initial appearances, Fig.7, Boscombe Pier is a relatively open structure below the water line, with only vertical columns 0.4 x 0.4m, spaced at 5.5m centres. As at Maplin, a vertical trackway is provided, and an instrument trolley can be winched up and down.

*Principal Scientific Officers, Hydraulics Research Station
Wallingford, England.

The actual instrumentation used at Maplin and Boscombe was very similar, (Fig.8). To measure time-averaged and also instantaneous velocities an electro-magnetic current meter was mounted in the horizontal plane, giving the two horizontal velocity components. A sampling nozzle connected to a pump enabled large-volume samples of the suspended sediment to be taken. On its delivery side the pump was connected to a pressure filter which separated off all sediment coarser than $40\mu\text{m}$ (microns), with the volume flow rate being measured by flow-meter. At Maplin these two instruments were augmented by a Braystoke propeller current meter to give time-averaged velocities during the first few months of the experiment when the electro-magnetic current meter was unavailable. At Boscombe the two basic instruments were augmented by a light-extinction turbidity meter, which it was hoped would give a qualitative indication of instantaneous sediment concentrations. At both Maplin and Boscombe wave heights were measured by bottom-mounted pressure recorders. Output from all the instrumentation was recorded in digital form on magnetic tape, and also in analogue form on paper chart.

The experimental procedure at both sites is first to lower the instrument trolley until a bed sensor locates the seabed. At this position the instruments were 0.05m above the bed. Velocities were then measured at this level over a 100s period, and a 20 litre sample of the suspension taken and filtered. The filtered sand was then removed ready for return to the laboratory where it was to be sub-divided into 5 size fractions by dry sieving. The trolley was then unclamped from the trackway and moved up to place the instruments at 0.1m above seabed level. Measurements were then repeated at this level and also at 0.15 , 0.25 , 0.5 , 1 , 2 , 3 and thence every metre up to the water surface. Measurement of the complete profile of velocity and sediment concentration generally takes about 20 minutes. Profiles are taken at about 30 minute intervals during typical calm conditions, and also an attempt was made to man the experiments during periods when storms were forecast. All the field measurements have been completed at Maplin Tower, and the equipment has been removed and transferred to Boscombe Pier. Here a good number of measurements were obtained during the winter of 1977/78 but at the time of writing analysis of these results has hardly begun. The results presented in this paper are therefore based almost entirely on the Maplin measurements.

Each data set consists essentially of vertical profiles of time-averaged velocities of the root-mean-square of the velocity fluctuations and of the suspended sediment concentrations of each of 6 size gradings. For the earlier readings at Maplin, when the electro-magnetic current meter was not available, the rms velocity was calculated from the recorded wave spectrum. When the e.m. current meter finally became available a comparison between the measured and calculated rms velocities could be made: the agreement was remarkably good as the example in Fig.9 shows, indicating that the velocity fluctuations were primarily due to the orbital motion of the waves. Altogether some 250 complete sets of good data were obtained at Maplin: faced with this quantity of information the decision was first taken to sub-divide the data into groups corresponding to the range of the tide during which the particular measurements were taken. Secondly it was decided to try a simple "bulk -flow" analysis of the data. For this purpose a classical

logarithmic expression was fitted to the velocity profile and the profile integrated from bed to water surface to give the depth-averaged velocity. An exponential expression of the Rouse type was then fitted to the sediment concentration profiles for each sediment size grading. The product of the fitted velocity and sediment concentration expressions was then integrated numerically from bed to surface to give the sediment discharge in each size grading. The total discharge of sand-sized sediments ($> 40 \mu\text{m}$) was then obtained by summation. This sand discharge was then plotted against depth-averaged velocity, with the rms of the velocity fluctuations at 0.05m above the bed as the third variable. One plot was prepared for each of the tidal range groups of data, and on each plot it was found that for small values of the rms velocity the sand discharge T (g/s/m width) was uniquely related to the depth-averaged velocity V (m/s) by the expression

$$T = 1400 V^4$$

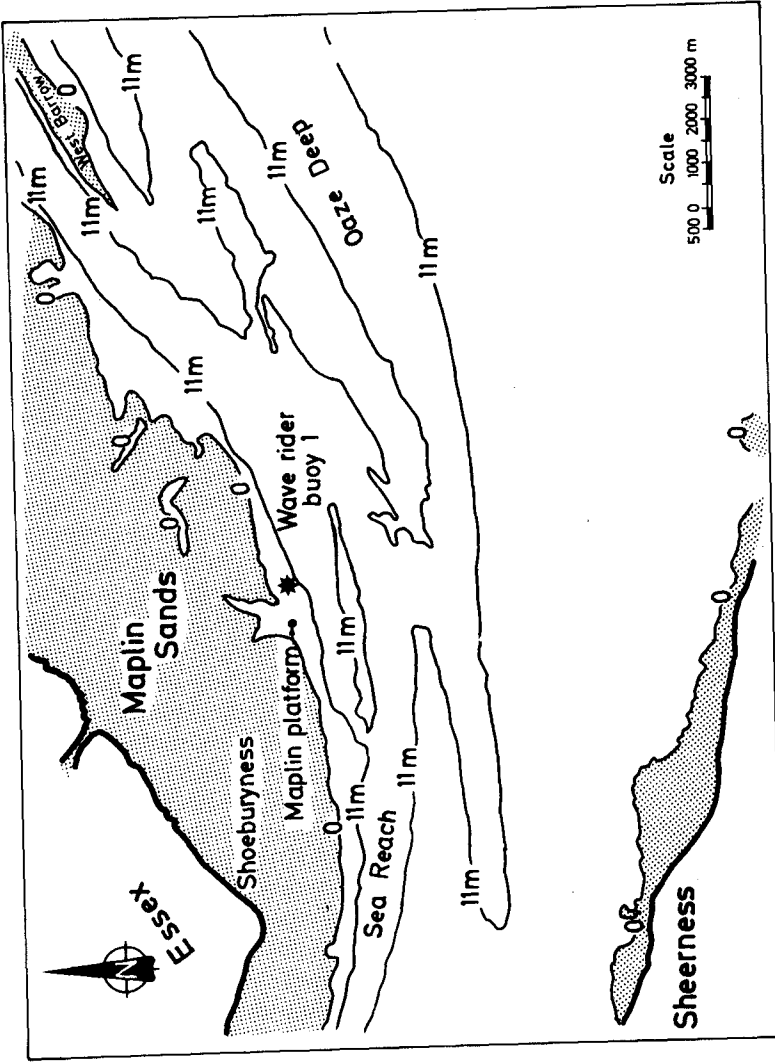
Fig.10 shows the plot for Group A tides - these having a tidal range of about 4.5m and a peak tidal velocity of about 0.8m/s. Neither tidal range, water depth nor rms velocity affected this expression provided that the rms velocity was less than about 50mm/s. Altogether some 210 sets of good data fell within this range of rms velocities. Although there were, inevitably, significantly fewer sets of data with rms velocities greater than 50mm/s it was evident that the sand discharge was substantially increased when there was pronounced wave activity. When lines were drawn on the sand discharge/depth-averaged velocity plot joining points of equal value of rms velocity it was found that they were broadly parallel to the base or 'no-waves' line, Fig.11. In other words, the expression relating sand transport to velocity was still of the basic form $T = \text{const} \times V^4$, but with the constant as a function of the rms orbital velocity. By plotting this constant derived from the various plots against the corresponding rms orbital velocity, Fig.11 it appears that the sand transport can be expressed as

$$T = 1400 \left(\frac{U_{\text{rms}} - 0.05}{0.05} \right)^2 V^4$$

where U_{rms} is the rms value of the velocity fluctuations at 0.05m above the bed, V and U_{rms} are in m/s, and T is in g/s/m width.

It is evident that although such a simple analysis of the data gives a usable expression for sand discharge at the Maplin site, it gives little insight into the actual effect of the waves, for example in possibly enhancing suspended concentrations or in distorting the velocity profile. In addition the analysis does not make use of the data on each size of sediment. Further detailed analysis of the results is therefore presently underway to obtain a better understanding of the processes involved.

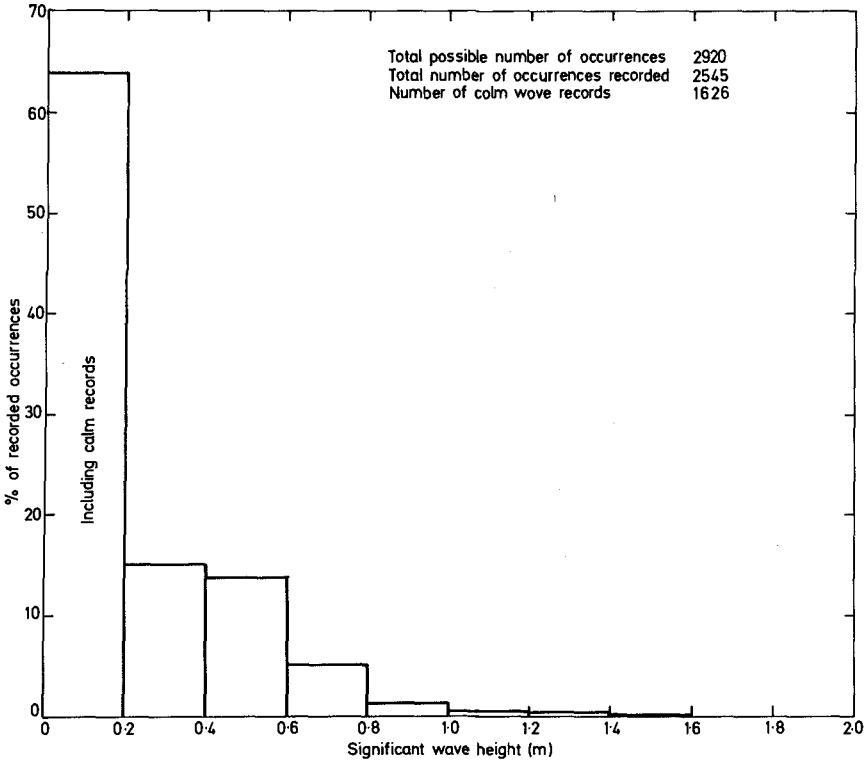
The work described in this paper is being undertaken as part of the research programme of the Hydraulics Research Station, Wallingford, England, and is published with the permission of the Director of Hydraulics Research.



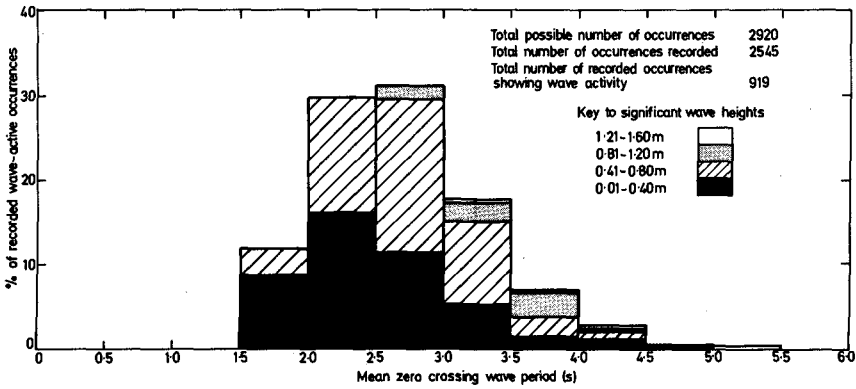
**Fig.1 Maplin Tower
Location map**



Fig 2 Maplin Tower



(a) Distribution of significant wave height, 1st April 1973-31st March 1974



(b) Distribution of mean wave period, 1st April 1973-31st March 1974

Fig 3 Twelve-month wave statistics at wave-rider buoy site 1

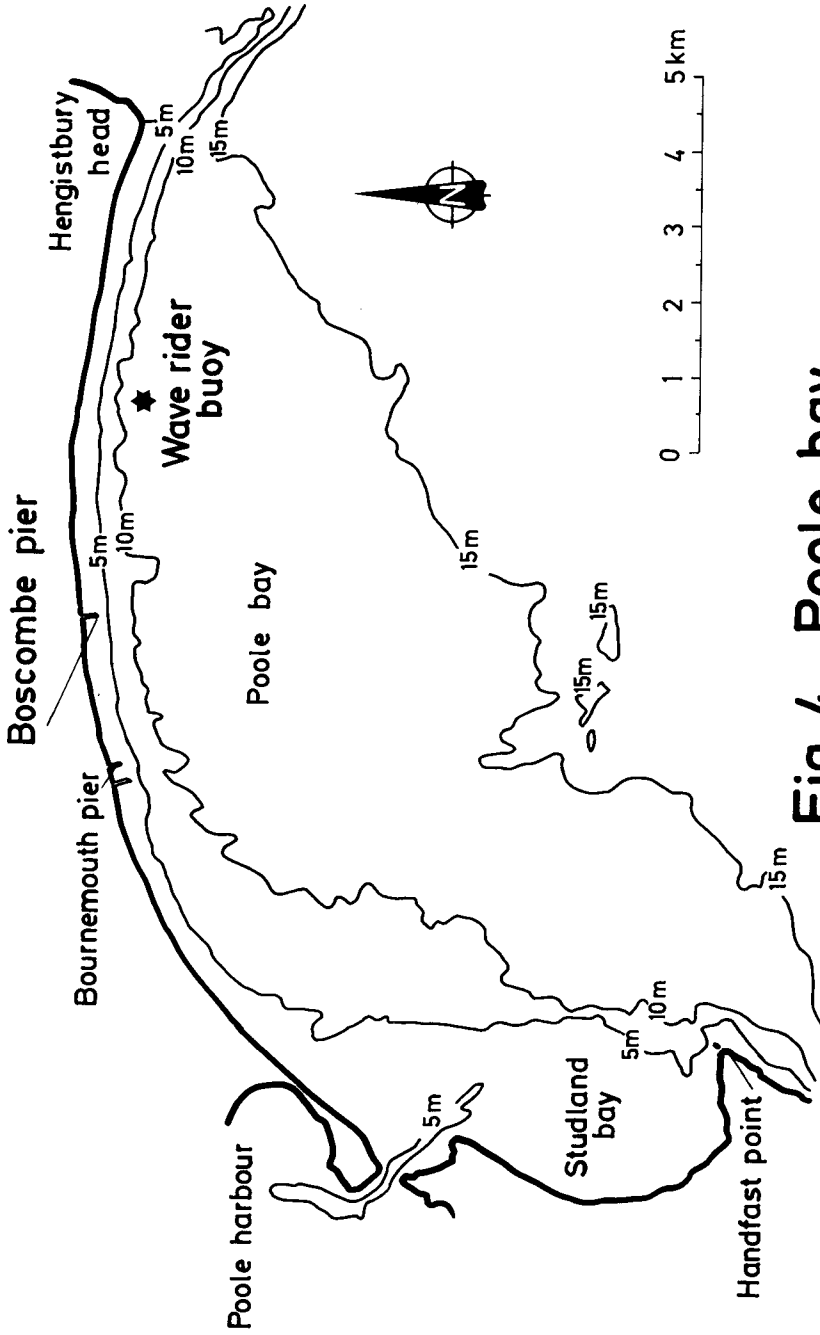


Fig. 4 Poole bay

Location of Boscombe pier and wave rider buoy

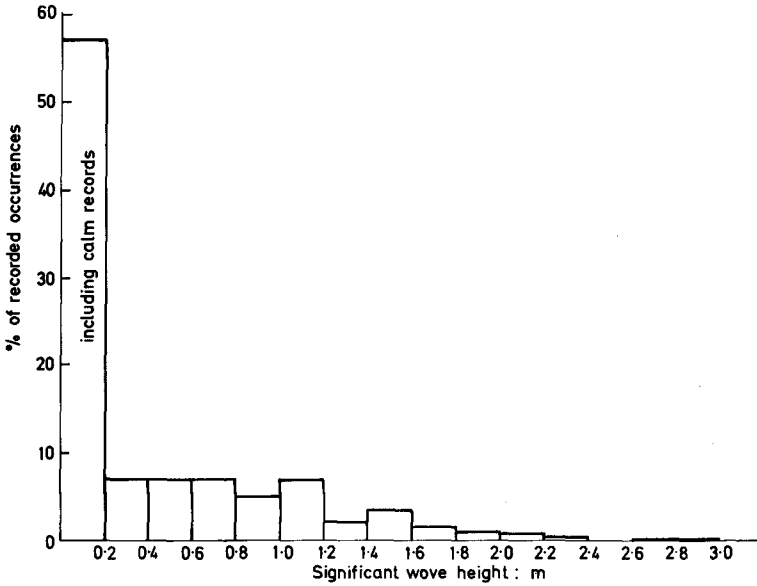


Fig.5 Poole Bay
Distribution of significant wave height ,1977

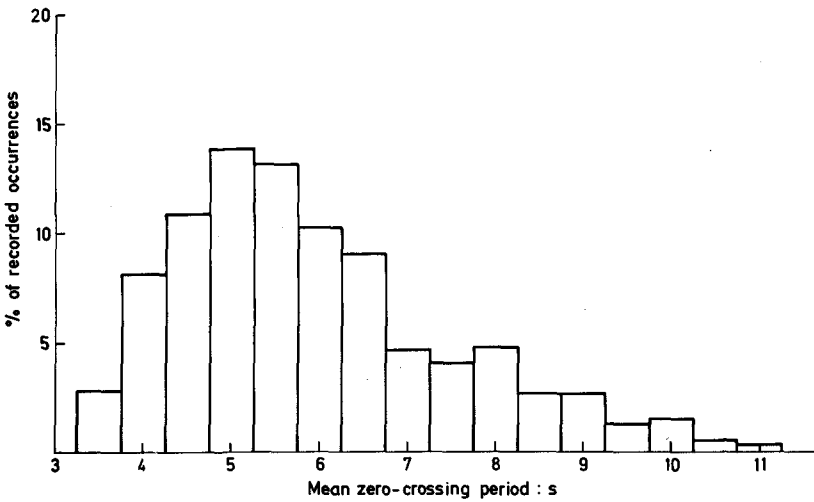


Fig.6 Poole Bay
Distribution of mean zero -crossing period, 1977



Fig.7 Seaward end of Boscombe Pier



Fig.8 Instrumentation trolley

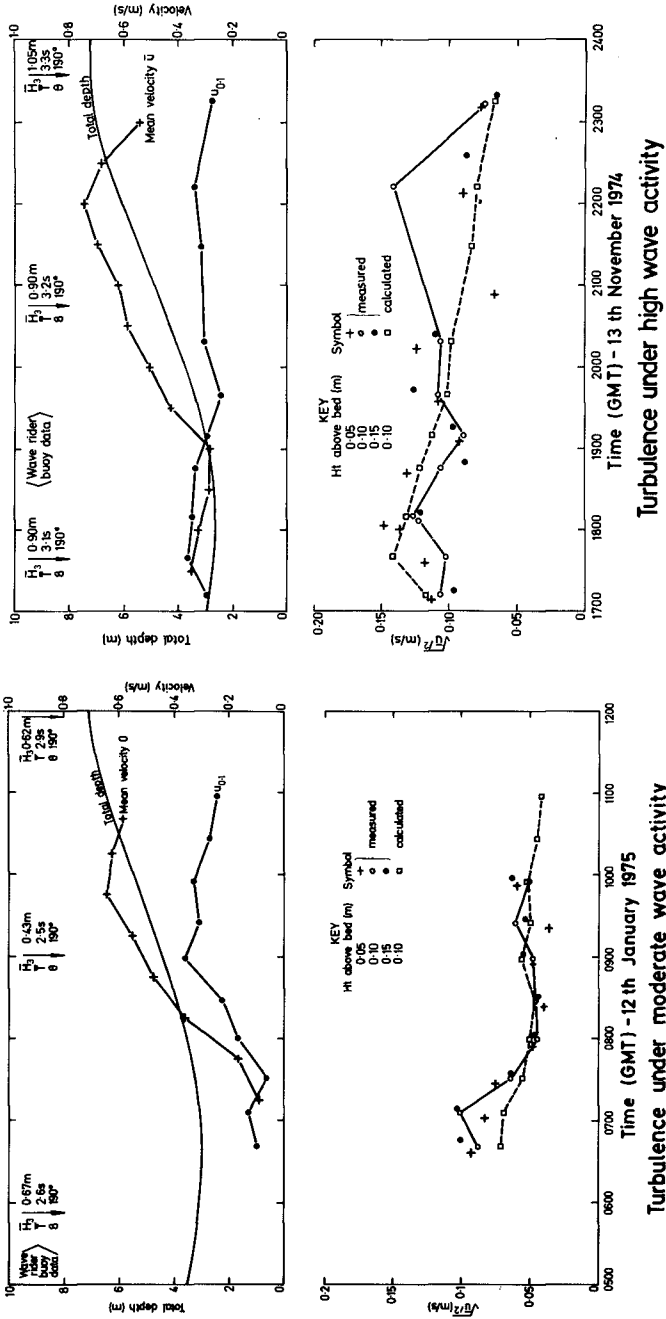


Fig.9 Comparison of measured and calculated turbulence intensities

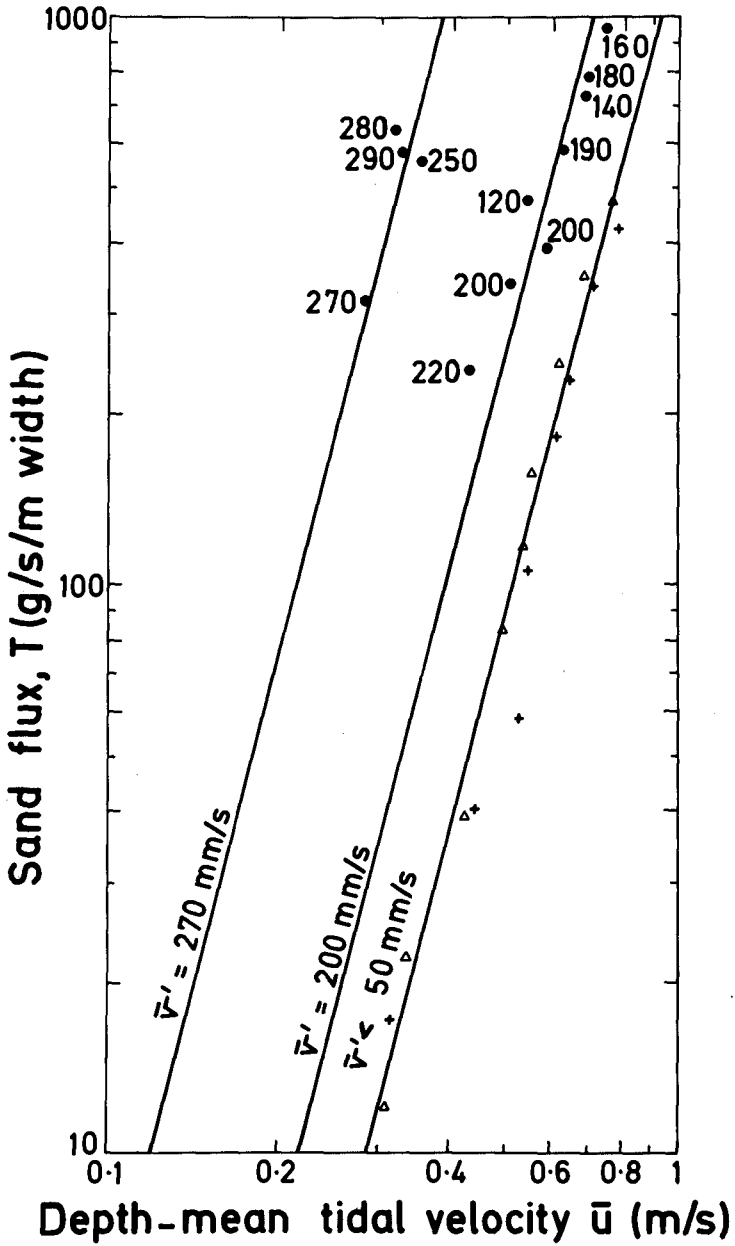


Fig.10 Sand flux for group A tides

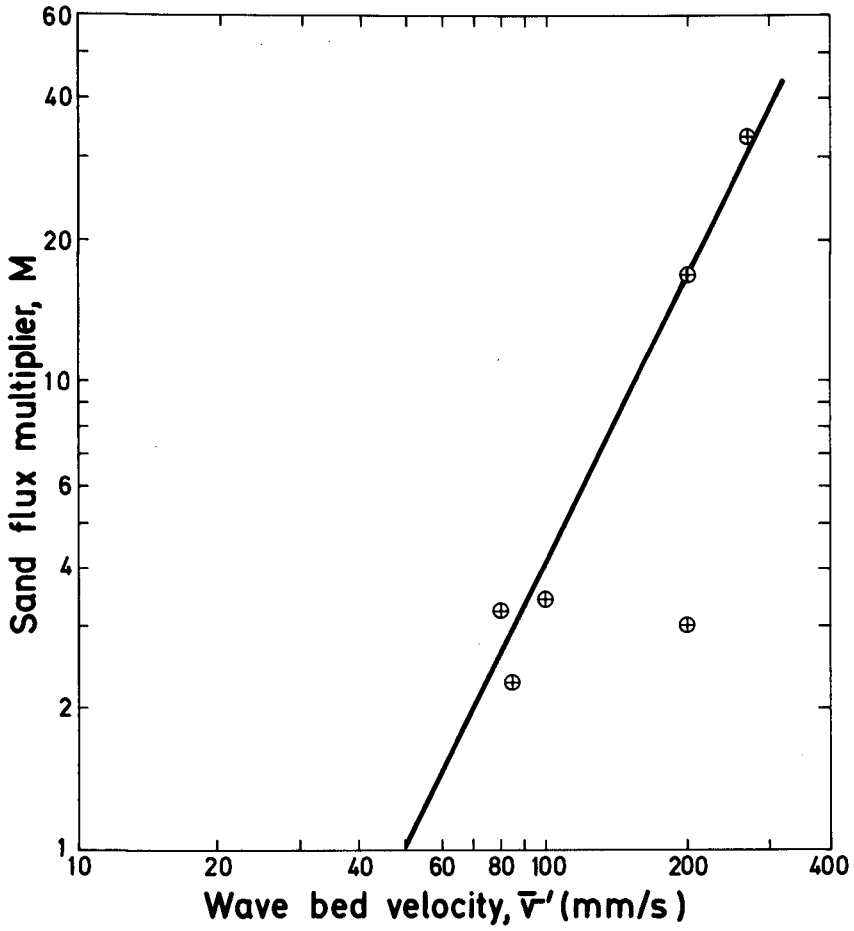


Fig.11 Sand flux multiplier for waves

CHAPTER 101

FIELD EXPERIMENT ON BEACH GRAVEL TRANSPORT

by

Masataro Hattori* and Takasuke Suzuki**

* Department of Civil Engineering

** Institute of Geoscience

Chuo University
Bunkyo-ku, Tokyo, Japan

Abstract

To examine the longshore transport processes of beach gravels under wave action, a field experiment was performed by tracing the dacite blocks injected on Fuji Coast, Shizuoka Prefecture, Central Japan.

The mean dislocating velocity of the tracer was 2 to 3 m/day under normal sea conditions, while under storm conditions it reached about 400 m/day. This velocity was fairly proportional to the longshore component of incident wave energy flux.

The longshore variations of the size and shape of beach gravels were mainly resulted from the progressive attrition and impact breakage of beach gravels rather than from the selective transport.

INTRODUCTION

This paper describes a field experiment carried out to obtain a better understanding of the littoral transport of beach gravels under wave action.

The mechanism of littoral transport of sand by waves and wave-induced currents has been extensively investigated and the beach processes have also been discussed by many researchers (1)*. On the other hand, our knowledge of the processes of beach gravel transport seems to be very limited in comparison with that of the sand transport, because it is very difficult to study the gravel transport by the laboratory experiments.

* : The figure in parentheses represents the reference cited at the end of this paper.

The transport processes of beach gravels have been studied by the tracing experiment using marked beach materials (2,3,4). According to previous studies, the transport processes are controlled by the size of gravels and the location of the zone in which the transport occurs.

Some researchers have inclined to the view that the longshore variation in beach gravel size can be produced by the selective transport processes. On the other hand, a number of field studies (5) demonstrates that beach gravels decrease in size, and change in shape due to the progressive attrition during their travel.

The present writers suggested in the previous paper(6) that the predominant direction and intensity of littoral sediment transport were more easily determined from longshore variations of beach gravel properties than from those of sand properties. More detailed informations on this subject are required to substantiate the writers' concept.

The principal purposes of this experiment were as follows:

1. To examine the longshore dislocating velocity of beach gravels,
2. To obtain the relation between the dislocating velocity and the longshore component of incident wave energy flux.
3. To elucidate the processes of the size and shape changes of beach gravels during their travel.

OUTLINE OF THE STUDY AREA

The experiment was performed on Fuji Coast located at the head of Suruga Bay, Shizuoka Prefecture, Central Japan (Fig.1). The study beach is the eastern reach of Fuji Coast which extends about 15 km from Tagonoura Port on the west to Numazu Port on the east.

The beach is about 150 m in width and is composed of sand and gravels. They are derived mostly from Fuji River on the west and slightly from Kano River on the east.

Suruga Bay is extremely deep and faces the Pacific Ocean in the south-west direction. Since the head of a submarine canyon is located near the coastline, the near-shore slope is so steep, up to about 1 on 10, that breaking waves plunge and form an intense swash with a narrow surf zone. The longshore current is not strong under normal wave conditions.

According to the tide observation of Fuji Coast (7), the tidal range during a spring tide is about 1.5 m, and the greatest resultant velocity of tidal current in the east-west direction is about 9 cm/day.

The littoral drift is in the east direction, which is the dominant one along Fuji Coast, and it has been intercepted by a navigation channel at Tagonoura Port. This has

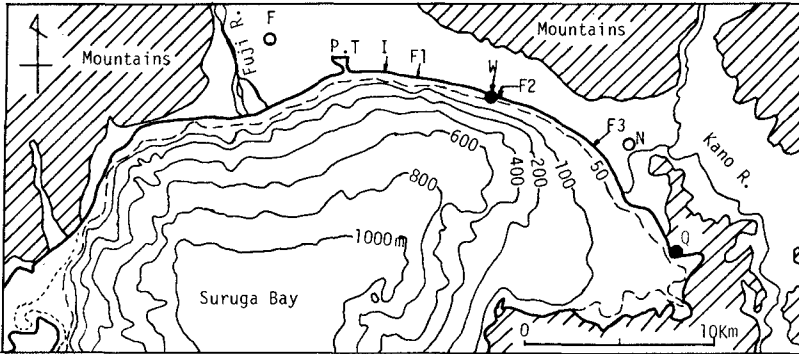


Fig. 1 Location of the study area.

I: Tracer injection site, W: Hara Wave Observatory, Q: Dacite block quarry, P.T.: Tagonoura Port, N: Numazu City, F: Fuji City, F1, F2 and F3: Outlet works.

resulted in severe beach erosion on the up-drift side of the study beach.

To prevent further beach erosion, wave defense works, a kind of offshore breakwater system, have been constructed along the shoreline in the vicinity of the Tagonoura Port. There are no other coastal structures on the beach, except for three diversion outlet works, whose locations are denoted by F1, F2 and F3 in Fig.1. Their effect on the shoreline configuration is not so large.

Figure 2 shows the two-dimensional bottom profile

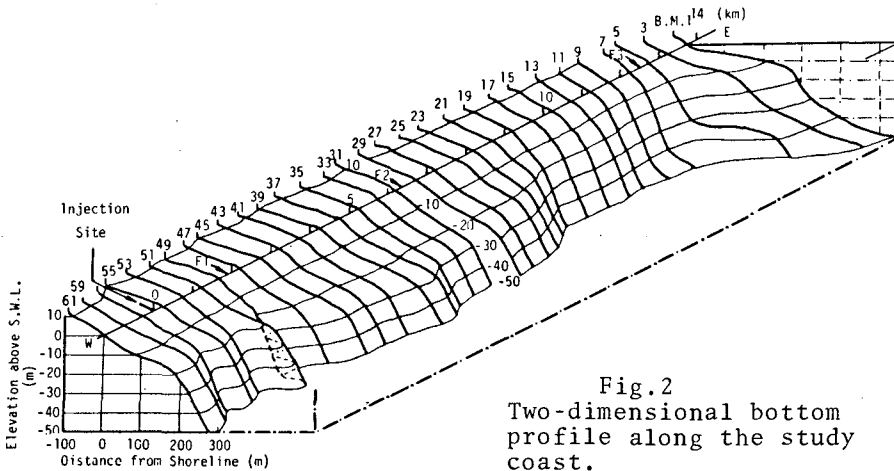


Fig.2 Two-dimensional bottom profile along the study coast.

along the study beach from the west to the east. Figures attached to the profile represent the bench mark number.

Due to the submarine topography of Suruga Bay, swells and huge waves generated by typhoons often attack the beach. The predominant wave direction is almost constant with respect to seasonal changes. The wave energy level along the study beach is considered to be almost constant, except for the vicinity of Numazu Port.

METHODS OF FIELD EXPERIMENT

Various labelling techniques of beach materials for the tracing experiment have recently developed to examine the nature and dislocating velocity of sediment transport (8). In this experiment, dacite blocks from a quarry, Q in Fig. 1, were used as the tracer.

This dacite is whitish yellow in color and homogeneous in texture, and have the physical and mechanical properties as shown in Table 1. This type of dacite gravels are not found on the study beach and also on the bed of Fuji and Kano Rivers. Therefore, the dacite blocks could be easily distinguished from the indigenous beach gravels, most of which are sandstone, granite, slate and basalt. The tracer is slightly softer and lighter than these indigenous gravels.

Table 1 Physical and mechanical properties of dacite blocks.

Initial Tracer Properties	Water Condition	Number of Specimen	Mean	S.O.
apparent specific gravity		5	2.68	0.01
dry bulk weight (gr/cm ³)	dry	10	2.41	0.02
porosity (%)	dry	5	10.1	0.80
maximum water content (%)	wet	10	3.8	0.17
P-wave velocity (km/sec)	dry	5	3.2	0.06
	wet	5	3.3	0.07
S-wave velocity (km/sec)	dry	5	2.5	0.1
	wet	5	2.5	0.2
dynamic modulus of elasticity (x10 ⁵ kg/cm ²)	dry	5	3.5	0.6
	wet	5	3.1	0.7
compressive strength (kg/cm ²)	dry	5	615	41
	wet	5	341	44
tensile strength (kg/cm ²)	dry	5	70	4.5
	wet	5	29	3.8
weight loss percentage by Los Angeles test (%/500gr)	wet	1	18.3	-----

Some 7000 dacite blocks were injected on the beach face from the shoreline at low tide-level to the backshore berm line in the shape of a jetty 42 m long, 3 m wide and 0.3 m high. The injection site, I in Fig. 1, was about 1.5

km east of Tagonoura Port. The initial size and shape indices of the injected blocks are shown in Table 2. The injected blocks were larger in size and more angular in shape than the indigenous beach gravels.

Table 2 Initial size and shape indices of the injected blocks

Initial tracer parameters	maximum	minimum	mean
long diameter : a (cm)	85	10	26.0
intermediate diameter : b (cm)	40	7	19.2
short diameter : c (cm)	29	4	13.2
nominal volume : $V_n(=axbxc)(cm^3)$	6.4×10^4	2.8×10^2	5.8×10^3
flatness : axb/c^2	16.1	1.2	2.7
elongation : a/c	5.0	1.2	2.0
Krumbein's roundness	0.5	0.3	0.32

Surface sampling of the tracer was carried out across the entire beach profile along the beach every field survey. Every sampled block of tracer was measured for its long, intermediate and short diameters, and its sampling location on the beach was recorded in terms of the longshore distance from the injection site and the seaward distance from the bench mark. Its picture was also taken to determine the roundness on the basis of Krumbein chart of roundness. After measurement, the tracer was returned to its sampling point.

The tracer recovery rate was two or three percent for every field survey. In the discussion of the experimental results, it is assumed that the distribution of sampled tracer on the beach surface represents that of the whole transported tracer.

Wave data at Hara Wave Observatory, W in Fig. 1, were obtained from a pressure wave gage placed on the sea bottom at a depth of 20 m and lined to an analogue recorder on land. The measurements were made for twenty minutes every two hours.

Figure 3 shows a temporal change in wave height using the data for the first 70 days after injection. Two typhoons, Nos.5 and 6, attacked the beach 11 days and 17 days after injection. The greatest wave height of 11.6 m was recorded during Typhoon No.6.

Figure 4 shows the distributions of wave height and period. From these histograms, prepared using the data

during the experiment, the significant wave height and period are read as 0.5 m and 8 seconds, respectively.

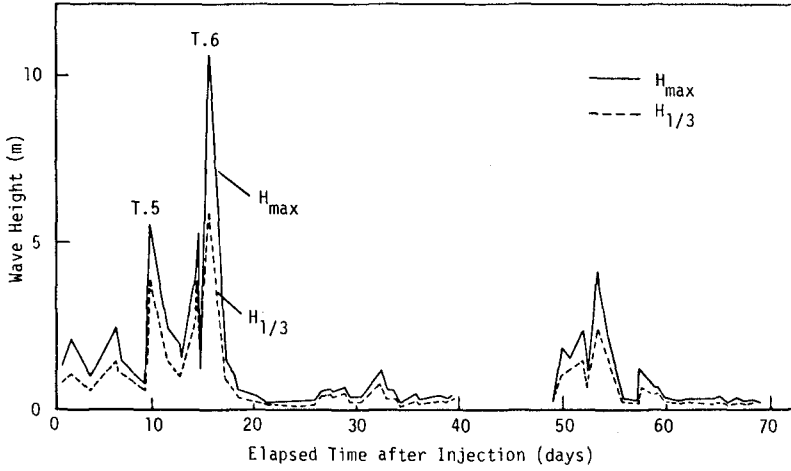


Fig. 3 Temporal change of wave height during the first 70 days after injection.

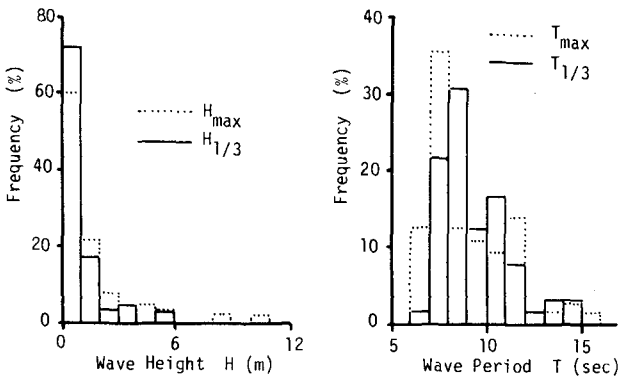


Fig. 4 Distributions of wave height and period.

DISLOCATING VELOCITY OF TRACER

Figure 5 shows the distribution of displaced blocks three days after injection. At that time, three quarters of the injected blocks still remained at the injection site. The drift piling zone, indicated by a thin dotted line, is considered to represent the upper limit of uprush at high tide-level.

Asymmetrical distribution indicates that the beach drift direction is eastward. Most of displaced blocks are distributed in the median zone between the top of foreshore and the upper limit of uprush.

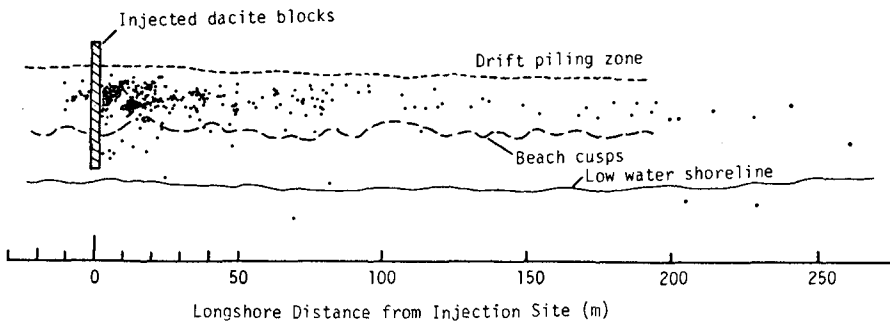


Fig. 5 Distribution of displaced blocks three days after injection.

The mean longshore distance of transport was calculated from the longshore distribution of displaced blocks by taking the first moment of the tracer distribution in the longshore direction about the injection site.

The greatest or maximum distance was estimated from the sampling location of the furthest travelled block.

The mean longshore dislocating velocity was calculated by dividing the mean transport distance by the elapsed time during which the transport occurred. The maximum velocity was also obtained in the same manner.

Experimental results of the longshore transport distance and the dislocating velocity are summarized in Table 3. Figure 6 shows the time changes of the greatest and mean longshore distances of tracer transport.

It is noticed from these results that the predominant direction of littoral transport was westward and the exceptional displacements occurred during the two typhoon attacks on the beach. The furthest blocks reached 14 km east of the injection site in about a half year after

Table 3 Transport distance and dislocating velocity.

Elapsed Time (days)	The Number of Sampled Tracer		Longshore Distance from Injection Site (m)		Dislocating Velocity (m/day)		Median Diameter (ϕ -scale)	
			Xmax	\bar{X}	Vmax	\bar{V}		
0	(7000)		0	0			- 7.5	
1	E	300	E	147		147		
	W	8	W	5	E	8.7	6.7	-----
3	E	320	E	255		54		
	W	15	W	13	E	35	13.2	
10	E	355	E	520		44		
	W	12	W	5	E	54	3.2	- 7.4
11*	E	9	E	865	E	380		
12*	E	20	E	1265	-----		400	-----
36	E	123	E	6250	E	1535		44.4
89	E	148	E	5960	E	1640		2.0
174	-----		E	14000	-----			96
364	E	138	E	14000	E	4800		
730	E	240	E	14000	-----			
Mean Dislocating Vel. During the Experiment							80	13.2

Xmax and \bar{X} : the maximum and mean transport distances, Vmax and \bar{V} : the maximum and mean dislocating velocities, E: the eastward transport, W: the westward transport, *: the storm conditions under Typhoon No.5.

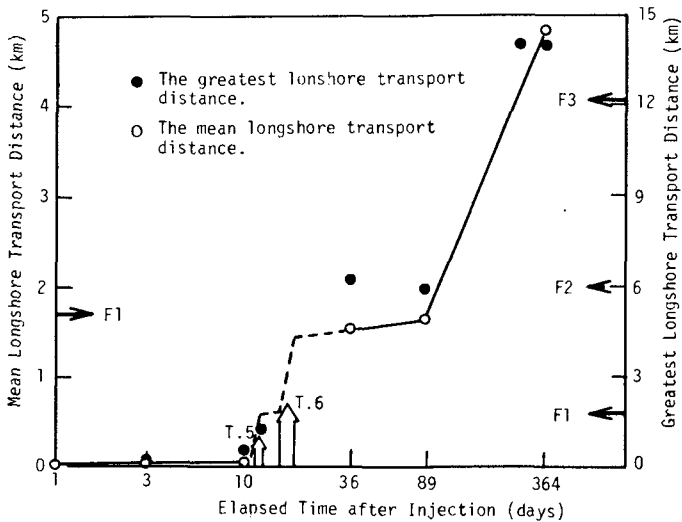


Fig. 6 Temporal changes of the longshore distance of the tracer transport.

injection.

The dislocating velocities under various sea conditions are estimated from these results as follows:

The mean dislocating velocity was between 2 and 3 m/day under normal sea conditions, while under storm conditions it reached about 400 m/day. The maximum velocity under normal sea conditions was estimated to be 50 to 60 m/day, and during Typhoon No.6 it produced about 1 km/day.

Table 4 shows that the mean velocity seems to increase with tracer-size decrease. Phillips (9) also reported a similar tendency, whereas, Evans (10) and Kindson and Carr (11) stated that the larger gravels were transported faster than the small. However, the problem is very complicated, because in the present experiment the tracer decreased in size due to the progressive attrition and impact breakage, as discussed later. Hence, the result shown in Table 4 does not necessary imply the size effect on the dislocating velocity.

Table 4 Relation between the tracer size and mean dislocating velocity.

Mean Diameter (ϕ -scale)	- 8	- 7	- 6	- 5	- 4
Mean Velocity \bar{V} (m/day)	6	14	19	--	23

The relation between the mean dislocating velocity and the longshore component of incident wave energy flux is shown by Fig. 7, which was prepared using the data collected during the first 89 days after injection.

This shows a fairly good linear relationship between the two quantities. A similar relationship between the rate of sand transport and wave energy flux has also been reported (12).

From Fig. 7, an empirical relation is obtained as

$$\bar{V} = 0.0025 \bar{E} - 3.75,$$

where \bar{V} is the mean dislocating velocity in m/day, and \bar{E} is the longshore component of incident wave energy flux in ton·m/day·m.

Using this relation, the threshold wave height for the tracer movement is calculated to be about 0.2 m, for which the wave period is assumed to be 8 seconds.

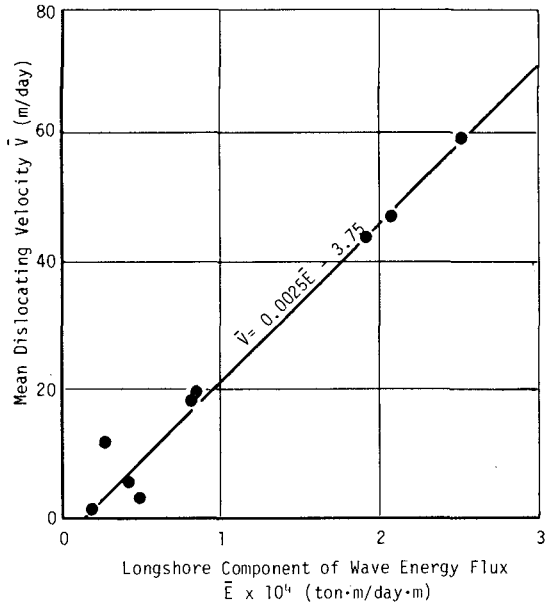


Fig. 7 Relation between the mean dislocating velocity and the longshore component of wave energy flux.

CHANGES IN TRACER SIZE AND SHAPE

Figure 8 shows the temporal changes of the mean long and short diameters and the mean nominal volume of the tracer. Figure 9 is the cumulative curves of the tracer nominal volume for each field survey.

These figures indicate the following facts:

1. During the two typhoon attacks, there occurred considerable volumetric decreases, reaching about 70 percent of the initial mean volume (Fig.8), and all fraction of blocks seemed to lose volume uniformly (Fig.9).
2. Over the 70 days after the typhoons, the tracer size seemed to be almost constant (Fig.8), because the sea conditions during this period were very calm.
3. Over the 275 days between 89 days and 364 days after injection, only the small size fraction of the tracer decreased in volume (Fig.9).
4. The whole fraction of tracer decreased in volume in the next year (Fig.9).
5. The rates of decreases of the long and intermediate diameters were slightly greater than that of the short diameter (Fig.8).

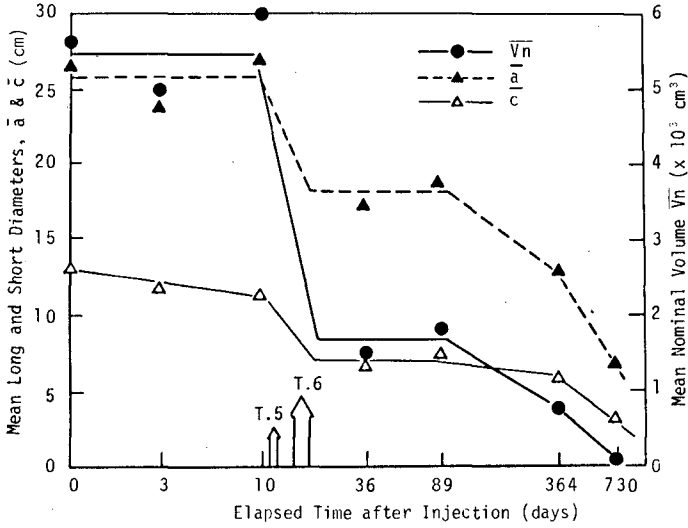


Fig. 8 Temporal changes of the mean long and short diameters and the mean volume.

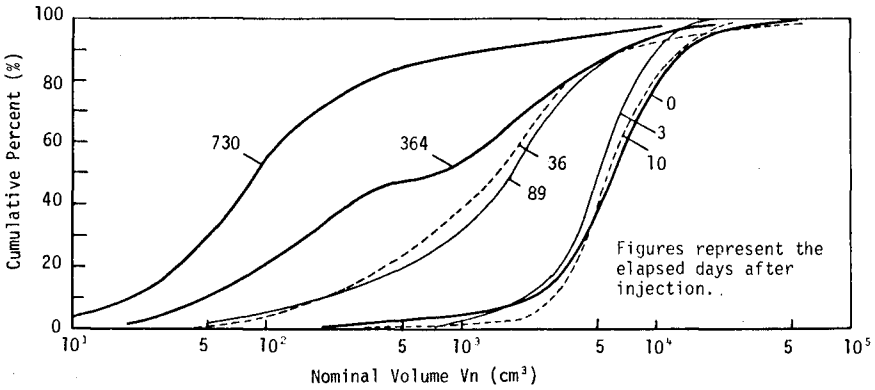


Fig. 9 Cumulative curves of tracer volume.

Figure 10 shows the longshore variations of the long and short diameters 36 days, 89 days and 364 days after injection. Abrupt decreases in diameters are found about 3 km east of the injection site. The location of the abrupt decrease moved progressively eastward with the elapsed time.

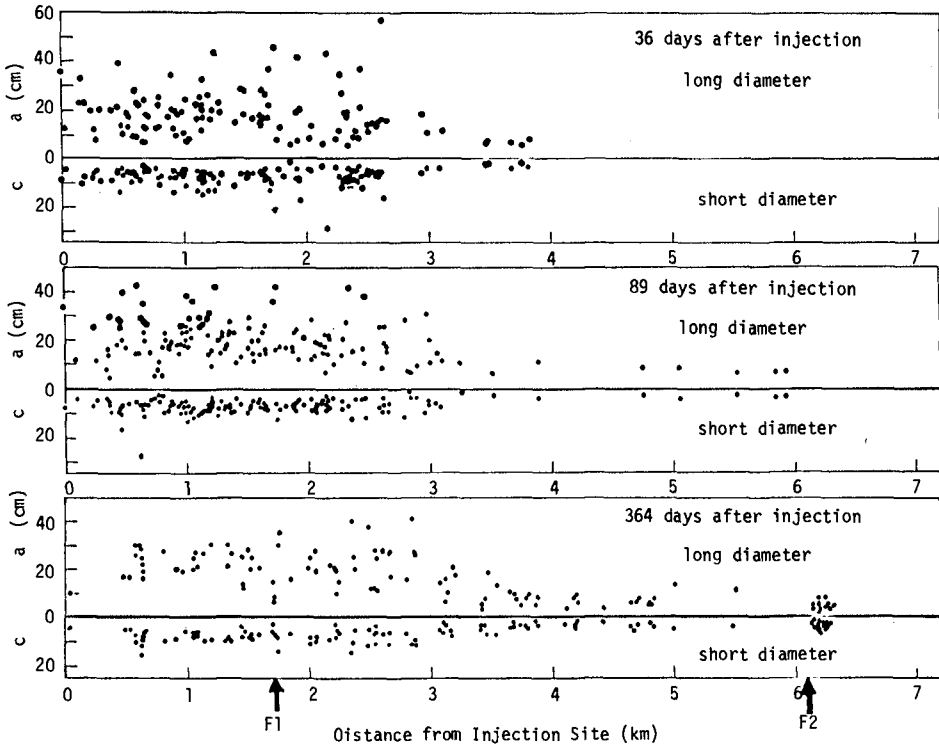


Fig. 10 Longshore variations of the long and short diameters.

Figure 11 shows the longshore variations of the mean nominal volume of the ten largest blocks. In comparison with Fig. 10, it is found from this figure that the abrupt decrease in the tracer volume also occurs at almost the same location as the case of the long and short diameters.

The temporal changes of the elongation and flatness of the tracer are shown in Fig. 12. These shape indices increased progressively with the elapsed time. After attaining their maximum values about 100 days after injection, they tend to decrease. The increases in these indices suggest also that the short diameter decreased faster than the long and intermediate diameters.

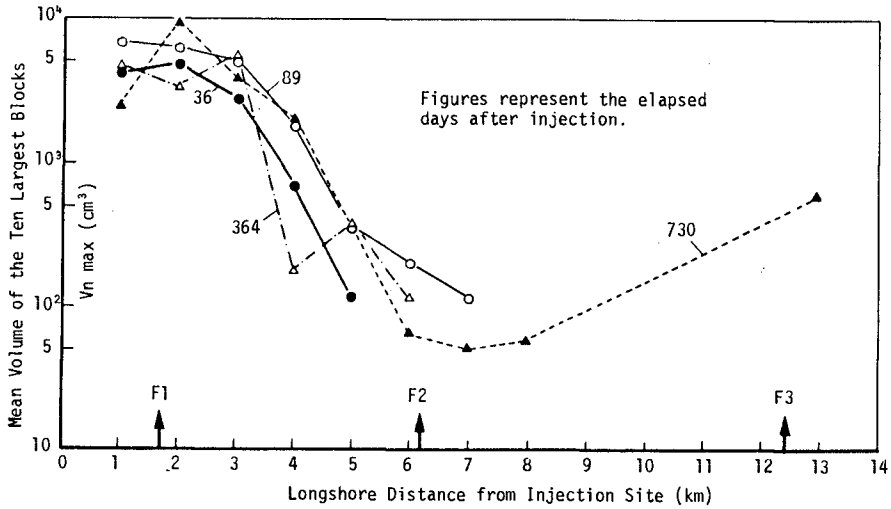


Fig. 11 Longshore variations of the ten largest tracer blocks.

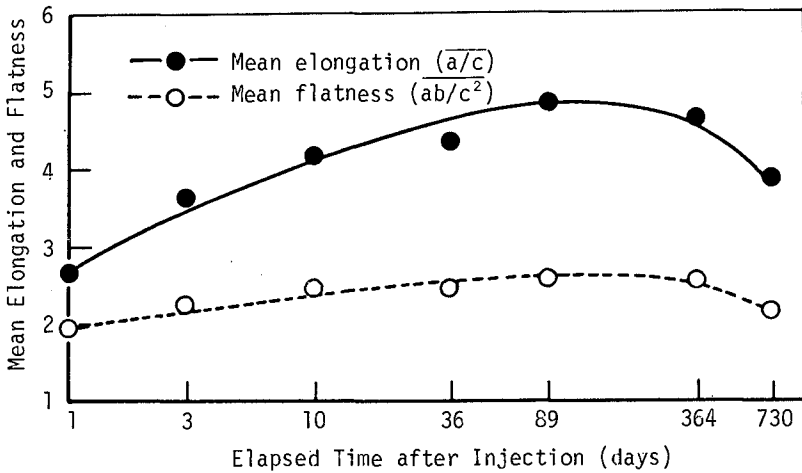


Fig. 12 Temporal changes in the elongation and flatness of the tracer.

The evidences deduced from the experimental results suggest that the large blocks tended to be displaced by sliding motion, and that as the blocks became smaller in size, they tended to be rolled and tossed by waves.

Figure 13 shows the typical longshore distributions of the elongation and flatness of the tracer 36 days after injection. These distributions indicate that the two indices increase with longshore distance until a point about 2 km east of the injection site. Beyond this point they abruptly decrease, and then again increase gradually. Based on these longshore variations, it is concluded that the abrupt decreases in the shape indices of the tracer are caused by tracer breakage due to collisions with beach gravels.

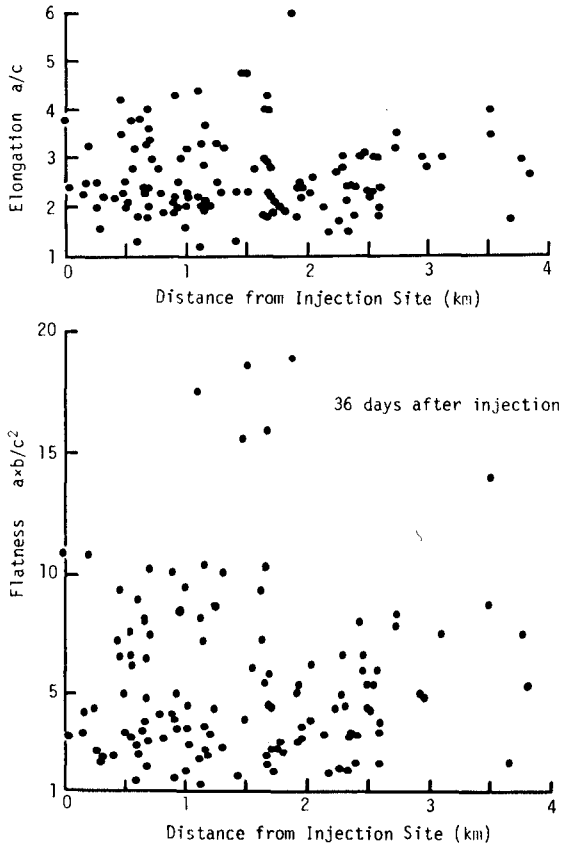


Fig. 13 Longshore distributions of the elongation and flatness 36 days after injection.

Figure 14 shows the longshore variations of the tracer roundness. The upper figure indicates that the injected blocks having sharp edges were soon rounded due to the grinding with the indigenous gravels and sand. As shown in the bottom figure, the roundness of about two thirds of the tracer 364 days after injection is more than 0.7.

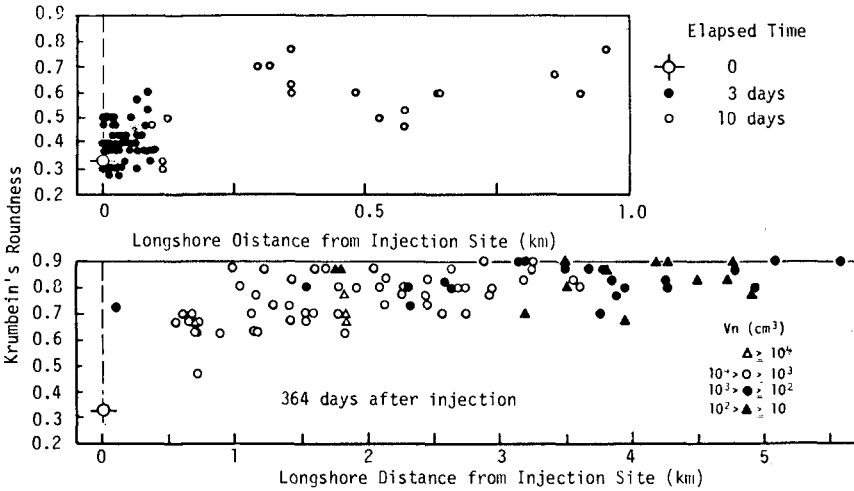


Fig. 14 Longshore variations of the roundness.

In conclusion, a possible process of the size and shape changes of the tracer can be inferred from the results of the present experiment, as follows:

Over initial period after injection, the blocks are displaced through sliding motion due to wave action. Then, the blocks decrease in size and become rounder, flatter, and more slender through sliding abrasion.

When their shape indices attain certain values, for example, 4 to 5 for elongation and 10 to 15 for flatness, the block must be broken into two pieces by collisions with beach gravels. As a result, the elongation and flatness become about a half of these values before the impact breakage occurs.

As the blocks decrease in size due to both attrition and breakage, they are rolled and tossed by waves and thus they experience wearing on all sides.

Figure 15 is a comparison of the longshore variation of the mean nominal volume of the tracer with that of the main indigenous beach gravels. Abrupt changes in the indigenous gravel volume were observed at almost the same location as that giving abrupt decreases in tracer volume.

The tracer became smaller rapidly than the indigenous beach gravels. This fact depends on 1) the weaker resistance of the dacite blocks to the attrition and breakage, 2) the initial angularity of the tracer, and 3) the limited supply of the tracer.

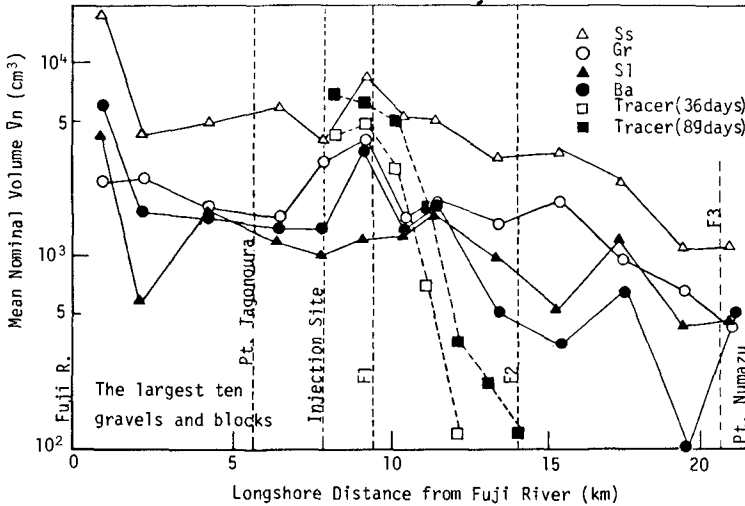


Fig. 15 Longshore variations of the mean volume of tracer and beach gravels.

Ss: sandstone, Gr: granite,
Sl: slate, Ba: basalt.

CONCLUSIONS

The mean dislocating velocity of the tracer was 2 to 3 m/day under normal sea conditions, while under storm conditions it reached about 400 m/day. This velocity was fairly proportional to the longshore component of incident wave energy flux.

The longshore variations of the size and shape of beach gravels were mainly resulted from the progressive attrition and impact breakage of beach gravels rather than from the selective transport.

REFERENCES

- 1) Horikawa, K.: Coastal Engineering - An introduction to Ocean Engineering - , University of Tokyo Press, pp.269-274, 1978.
- 2) Zenkovich, V.P.: Processes of Coastal Development, edited by J.A.Steers, Oliver & Boyd, pp. 317-322, 1967.
- 3) King, C.A.M.: Beaches and Coasts, Edward Arnold, pp.290-292, 1972.
- 4) Komar, P.D.: Beach Processes and Sedimentation, Prentice-Hall, pp. 351-363, 1976.
- 5) Komar, P.D.: loc. cit. 4).
- 6) Hattori, M. and T. Suzuki: Concept for inferring the littoral drift trend, Proc. 15th Conf. on Coastal Engineering, pp. 1223-1239, 1976.
- 7) Shuto, N., J. Taguchi and T. Endo: Field observation of sand drift at Fuji Coast, Proc. 24th Conf. on Coastal Engineering in Japan, pp. 211-215, 1977. (in Japanese)
- 8) Kidson, C. and A.P. Carr: Marking beach materials for tracing experiment, Jour. of the Hydraulic Division, Proc. of ASCE, Vol. 88, No. HY 4, pp. 43-60, 1962.
- 9) Phillips, A.W.: Tracer experiments at Spurn Head, Yorkshire, England, Shore and Beach, 31(2), pp.30-35, 1963.
- 10) Evans, O.F.: Sorting and transportation of material in the swash and backwash, Jour. of Sedim. Petrol., Vol. 9, No.1, pp. 28-31, 1939.
- 11) Kindson, C. and A.P. Carr: Beach drift experiments at Bridgewater Bay, Somerset, Proc. Bristol Nat. Soc., Vol. 30, No. 2, pp. 163-180, 1961.
- 12) Horikawa, K.: loc. cit. 1).

CHAPTER 102

SHINGLE¹ TRACING BY A NEW TECHNIQUE

Peter Wright, J.S. Cross and N. B. Webber
Department of Civil Engineering
University of Southampton, England

Abstract

A major drawback of all existing tracer techniques for monitoring shingle movement, except that of labelling with radioactive isotopes, is that tracer recovery rates are invariably low, (commonly less than 15% of the total injected) because recovery is limited to the beach surface. Investigations were made into the possibilities of developing a new tracer that might overcome this problem.

The paper describes the results of, and the conclusions drawn from two trial field experiments carried out using metal tracer pebbles. These had specific gravities, size and shape similar to the indigenous beach pebbles, and were recovered both on and beneath the beach surface using metal detectors. By assessing the relative merits and drawbacks of the technique it was concluded that the use of metal pebbles as tracers for shingle beaches is more practical than other methods for most tracing purposes. At present the technique is best suited to investigations ranging in length from a few days to a few months and requiring small to medium-scale injections of 5000 tracer pebbles or less. The considerable scope for the further development and application of the technique is discussed.

Introduction

Most techniques for investigating shingle transport on beaches depend either on some method of marking the indigenous beach material, on the introduction of beach pebbles and cobbles of a different petrological type or pebble and cobble substitutes and monitoring their movement after injection. The relative merits and drawbacks of existing tracer techniques are well documented in the literature by Kidson and Carr (1962). A more recent but less comprehensive review of shingle tracing is contained in Hails (1974).

A major drawback of all existing tracer techniques except that of labelling with radioactive isotopes, is that tracer recovery is limited to the beach surface. Consequently tracer recovery rates are seldom

SHINGLE¹ - used here in the context defined by Carr (1971), that is as encompassing all sediment particles whose long diameter, 'a', lies within the range 4-256mm, and as such includes the pebble and cobble categories of the Wentworth Scale.

greater than 30% and commonly less than 15% of the total quantity of tracer injected. This situation in which tracer recovery rates are low and little, if anything, is known of the tracer distribution beneath the beach surface is clearly unsatisfactory for seeking a detailed understanding of the behavioural patterns of shingle beaches.

Investigations were made into the possibilities of developing a new tracer for shingle beach studies that might overcome these difficulties.

Metal Pebbles: A New Type of Tracer for Shingle Beaches

The potential merits of using metal pebbles as a new type of tracer for shingle beaches were considered to be:

1. With the use of metal detectors it would be possible to detect the tracer pebbles beneath the beach surface which would not only increase tracer recovery rates but also provide information on the vertical distribution of the tracer.
2. Metal tracer pebbles could be manufactured to reproduce the specific gravity, size and shape of the indigenous beach pebbles.
3. Of importance when investigating beaches which are popular with the general public, they would be unobtrusive and present no health risk.

The specific gravity of the indigenous pebble-sized material found on the beaches to be investigated directly governed the metal used for the manufacture of the tracer pebbles. The pebble and cobble fractions of these beaches are composed of 90+% of flint and chert, both have specific gravities of 2.7. Aluminium was chosen as the metal most suitable for the purpose, not only because it has a specific gravity of 2.7, but also because it is easy to work with. The tracer pebbles used in the first trial field experiment were manufactured using the "full mould" or "cavityless" method of casting (Waring, 1965). Those used in the second trial field experiment were manufactured using a "sand-casting" technique (Fig.1).

Full details of the manufacturing procedures and the methods of tracer pebble detection and recovery in the field, including a discussion of the relative merits of the various types of metal detectors and search procedures, are contained in Wright, et al (1978).

Field Trials of the New Tracer

Aims of the field trials

1. To establish estimates of "expected" tracer recovery rates when using aluminium tracer pebbles.



Fig.1. Aluminium tracer pebbles manufactured using a "sand-casting" technique (first and third columns). Indigenous beach pebbles used as patterns (second and fourth columns).

2. To gain a clearer insight into the practicalities of undertaking a larger-scale field investigation using this tracer technique.
3. To ascertain the purpose and scale of tracer experiments to which this new tracing technique would be best suited.
4. To assess the corrosive and corrasive qualities of the aluminium tracer pebbles under field conditions.

It was hoped to assess whether or not the behaviour of the aluminium pebbles differs significantly from that of the indigenous beach pebbles by releasing simultaneously with the aluminium tracers, and at the same site, marine-painted or fluorescent-coated beach pebbles. However, due to financial restrictions this was not possible.

Conduct and results of the field trials

Field trials were undertaken at Hengistbury Long Beach, Poole Bay, Dorset (Fig.2), during the periods 9/5/77 - 25/5/77 and 20/2/78 - 11/3/78.

In both experiments the tracer pebbles were injected at one-pebble depth (40-50mm) on the upper foreshore at the seaward foot of the shingle scarp face of the backshore zone. The background indigenous pebble population incorporated the full size range of the artificial aluminium pebbles. The dimensions of the tracer pebbles injected in the two experiments are given in Table I.

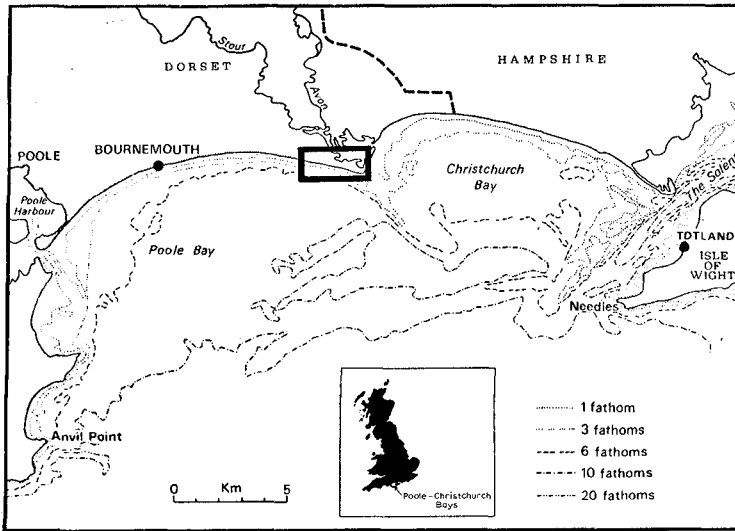


Fig.2. Location of field trial site.

TABLE 1

Size and shape parameters of the tracer pebbles used in the field trials (measurements in millimetres).

Pebble batch	Quantity injected	Length of 'a', 'b', and 'c' axes			Sphericity index value (c/\sqrt{ab})
		a	b	c	
<u>Field Trial 1</u>					
L	25	60	50	45	0.82
M	25	45	40	30	0.71
S	25	40	35	25	0.67
<u>Field Trial 2</u>					
LA	70	70	55	35	0.56
MA	70	67	38	25	0.50
SA	90	58	45	24	0.47
LR	70	57	49	44	0.83
MR	70	61	34	30	0.66
SR	90	44	34	31	0.80

TABLE II

Classification of wind and wave conditions during the field trials (all observations were made at the field site).

No. of tides after injection	Wind states		Wave states		
	direction	force (Beaufort)	breaker height (m)	period (sec)	orientation
<u>Field Trial 1</u>					
0-4	SW-W	4-5↑7-8	0.6↑1.5	4-6	+5° to +12°
5-6	NW	4	2.0↓0.8	8-10	+7° to +14°
7-29	N-NE	4-5	0.3-0.5	5	-17° to -27°
<u>Field Trial 2</u>					
0-8	E-SE	6↓2-3	1.1↓0.9	4-6	-17° to -29°
9-14	SW	4-5	1.5↓1.2	12	-18° to -20°
15-20	SE	3-4	1.0	4-6	-23° to -29°
21-25	NE-N	4↓2-3	0.4	6-8	+1° to -6°
26-27	SSE	2	2.0	18	0° to +4°
28-33	S-WNW	2	0.7	6	+10° to +12°
34-37	WNW↘SE	2	0.8	6	+1° to +8°

Key

- ↑ - increasing
- ↓ - decreasing
- ↘ - wind backing
- ↙ - wind veering

Wave orientation is expressed as the angle which the orthogonals of waves approaching the shore make with an imaginary line drawn at right-angles to the same shoreline. Angles measured to the west of the line are prefixed +, and those measured to the east, prefixed -.

During the first field trial the tracer pebbles were subjected to movement under three distinct sets of wave conditions. During the second experiment however conditions were much more varied. Wind and wave conditions during the two field trials are summarized in Table II. During the first field trial tracer recoveries of 41% (no lower foreshore search), 63%, 59% and 61% were made on the four days of full sweeping of the tracer-spread area. During the second trial tracer recoveries of 38%, 27%, 28%, 30%, 34% and 43% were made. Tracer recovery rates for both field trials are fully tabulated in Table III.

TABLE III

Tracer recovery rates during the field trials (values are expressed as percentages of the total number of tracer pebbles injected).

No. of tides after injection	Total	Tracer recoveries					
		Pebble Batches					
<u>Field Trial 1</u>		L	M	S			
6	41*	45	64	12			
12	63	72	84	32			
14	59	76	72	28			
29	61	80	58	40			
<u>Field Trial 2</u>		LA	MA	SA	LR	MR	SR
2	38*	49	31	34	44	39	31
6	27*	27	39	32	20	22	21
8	28*	27	30	36	22	29	22
17	30*	34	37	26	31	26	23
27	34*	42	44	30	34	34	22
37	43	54	54	32	43	41	33

* - No lower foreshore search possible

The lower rates of tracer recovery made during the second field trial were attributed to three main causes. Firstly, only on the occasion of the final full sweep of the backshore and foreshore zones was the lower foreshore sufficiently exposed for an adequate search to be made. Secondly, the area of beach through which the tracer spread was 18540m², four times greater than that during the first field trial (Table IV). Consequently, with the limited personnel available, searches of the beach were insufficiently thorough. Finally, the depth of beach through which the tracer spread was 1.3m, 2.5 times greater than that during the first field trial (Table IV). Consequently, a high proportion of the tracer pebbles were buried at depths exceeding the maximum penetration depth of 0.4m of the metal detectors. The validity of the latter explanation is illustrated by the data presented in Table V. Although tracer recoveries during any one search of the beach averaged only 30-35% of the total quantity injected, the majority of the remaining tracer pebbles had not been "lost" either longitudinally or transversely beyond the search area. After only two tides the tracer pebbles were thoroughly distributed through the backshore and foreshore zones. Subsequent reworking of the beach material by wave action successively returned tracer pebbles to within 0.4m of the beach surface, where they could be readily detected. Table V shows that in this way an overall average of 72% of the tracer pebbles injected had been recovered at least once since injection (The tracer pebbles were number stamped so that the movement of individual pebbles could be monitored).

TABLE IV

Comparison of tracer recovery rates with the volume of beach through which the tracer had spread.

No. of tides after injection	Total tracer recoveries	Tracer spread area (m ²)	Depth of beach through which tracer spread (m)
<u>Field Trial 1</u>			
6	41	2620	0.50
12	63	2960	0.45
14	59	3080	0.45
29	61	4800	0.45
<u>Field Trial 2</u>			
2	38	4080	0.8
6	27	7040	0.8
8	28	9850	0.8
17	30	14210	0.7
27	34	16680	1.3
37	43	18510	1.2

TABLE V

Cumulative percentage of tracer pebbles within each batch recovered at least once since injection.

No. of tides after injection	Tracer recoveries						
	<u>Total</u>	<u>Pebble Batches</u>					
		LA	MA	SA	LR	MR	SR
<u>Field Trial 2</u>							
2	28.1	39	21	24	34	29	21
6	40.8	46	46	44	43	36	30
8	49.6	61	54	56	46	43	38
17	55.3	67	61	59	51	49	44
27	59.0	73	64	61	59	51	46
37	66.8	74	77	69	67	60	53
57	69.3	77	79	72	67	64	57
97	71.7	80	80	76	69	66	60

During both field trials recovery rates for the larger size tracer pebbles were, for the most part, greater than that for the smaller pebbles because the former have a greater surface area than the latter and are consequently detectable at greater depths. Further discrepancies in the recovery rates of tracer pebbles of differing size and shape were attributable to pebble sorting by wave action. For example, angular tracer pebbles, irrespective of size, tended to be carried up on to, and remain on, the upper foreshore and backshore zones, whereas rounded tracer pebbles under the same wave action were more likely to be returned with the backwash to the lower foreshore.

The use of metal detectors better suited to the conditions of operation should result in higher recovery rates.

Conclusions

From our investigations carried out to-date the application of metal pebbles as a tracer for shingle beaches offers the following merits:

1. The most valuable capability of the new technique is the ease of detection of the tracer beneath the beach surface. This provides:
 - a) a direct, and consequently more reliable means of studying beaches as three-dimensional features.
 - b) a higher rate of tracer recovery upon which to base statistical inferences.
2. The ability to manufacture tracer pebbles with similar specific gravity, size and shape to that of the indigenous beach pebbles is a considerable advantage over many previously devised artificial tracers.
3. Number stamping the tracer pebbles can provide a means of tracking the movement of individual pebbles.
4. Of prime importance when investigating beaches which receive use by the general public are the considerations that:
 - a) aluminium pebbles present no health risk. Whilst the use of radioactive isotopes provide a means of tracer pebble detection and recovery from beneath the beach surface they should not be used on popular public beaches.
 - b) they are also unobtrusive, and as such are unlikely to arouse public interest in the same way that painted pebbles might. Therefore losses and redistribution due to interference should be minimal.
5. The new technique provides a means of pebble detection, although not necessarily recovery, in the unexposed swash zone.
6. Tracer contamination of the beach is no particular problem because pebbles used in successive experiments can be colour-coded with small resin plugs poured into holes, either cast or drilled, in the individual pebbles. Tracer contamination

is a problem when using mass injection of "foreign" beach pebbles, because the range of pebbles of different petrological types which have similar specific gravity, size and shape characteristics to that of the indigenous beach pebbles is normally very limited.

7. Tracer pebbles recovered at the end of an experiment are reusable in subsequent investigations.

Four possible drawbacks of the technique can be identified:

1. Cost. At current British prices 1000 tracer pebbles 50x40x35mm in size can be manufactured, using a "sand-casting" technique, at a cost of £200 sterling (380 U.S. dollars). This cost may be considered high by researchers working on a low budget. However, the cost of using aluminium tracer pebbles compares favourably with that of other tracer techniques when one considers that:
 - a) in order to achieve comparable results, the number of tracer pebbles required using the new technique is less than that by any other method because of the higher recovery rates one can normally expect
 - b) the tracer pebbles are reusable on recovery.
2. Tracer pebbles not recovered at the end of an experiment are liable to be unnecessarily detected in subsequent experiments carried out on the same length of beach. However, in the normal sequence of events the longer the tracer pebbles remain on the beach the more diffused they become, i.e. spread longitudinally beyond the limits of later experiments and buried to depths exceeding the maximum penetration depth of the metal detectors.
3. The background metal content of the beach can be a problem if the beach being investigated is highly contaminated with metal objects.
4. Losses and redistribution of the tracer during field experiments due to public interference arising from the fact that treasure hunting using metal detectors has become a popular minority pastime in Britain in recent years. The majority of these treasure hunters are members of regional clubs, which when approached, are very pleased to co-operate and even give assistance during field experiments.

Summary

By assessing the relative merits and drawbacks of the technique, we have concluded that the use of metal pebbles as tracers for shingle beaches is more practical than other methods for most tracing purposes. At present the technique is best suited to investigations ranging in length from a few days to a few months and requiring small to medium-scale injections of 5000 tracer pebbles or less. It is of particular value when a knowledge of the movements of individual pebbles is required.

Refinements to the efficiency of the technique would greatly increase its value. The efficiency to be gained from improvements to the field application of the technique are small compared to that attainable by improvement to the detection equipment. Two such improvements to the latter are of prime importance and both are within the bounds of present technology. There is a need to increase the depth of sensitivity of the search heads, and to increase the reliability of metal discrimination devices that are currently built into detectors. There is a future need for a detector capable of differentiating between various grades of tracer pebbles on the basis of size and/or shape differences. This might be achieved in one of two ways, either with a programmable detector in which the differentiation could be carried out internally or with a detector with an inbuilt display panel upon which it could display an outline of the detected metal object which could then be classified by the operator.

There is considerable scope for the further development and application of the technique both for use on beaches and in the near-shore and offshore zones.

Acknowledgements

The authors are grateful to N. H. Babbedge for his innovations, to Messrs. J. Blizzard, A. L. Clarke and S. Horrill of Southampton College of Technology and to Haworth Castings Ltd. of Romsey for advice and practical assistance in the manufacture of the aluminium pebbles, and to Messrs. J. and R. Compton for the kind loan of metal detectors.

The research was undertaken as part of a large coastal-engineering research project sponsored by the Department of the Environment and co-ordinated by Sir. W. Halcrow and Partners in which the Hydraulics Research Station, and Bournemouth, Christchurch, and New Forest District Councils are participating. The authors gratefully acknowledge the assistance given by the engineering staff of Bournemouth Corporation in connection with the field trials.

References

- Carr, A.P., 1971. Experiments on longshore transport and sorting of pebbles: Chesil Beach, England. *J. Sedim. Petrol.*, 41: 1084-1104.
- Halls, J.R., 1974. A review of some current trends in nearshore research. *Earth-Sci. Rev.*, 10: 171-202.
- Kidson, C. and Carr, A.P., 1962. Marking beach materials for tracing experiments. *J. Hydraulic Div., Proc. Am. Soc. Civ. Eng.*, 3189: HY4: 43-60.
- Waring, J., 1965. The development of the full mould casting process. *J. Aust. Inst. Met.*, 10(4): 313-322.
- Wright, P., Cross, J.S. and Webber, N.B., 1978. Aluminium pebbles: a new type of tracer for flint and chert pebble beaches. *Mar. Geol.*, 27: M9-M17.

CHAPTER 103

A NUMERICAL MODEL FOR SEDIMENT TRANSPORT

by

J.P. LEPETIT and A. HAUGUEL*

ABSTRACT

We introduce here a numerical two dimensional model for sediment transport which permits to compute the impact of a coastal structure on the bottom evolution.

The introduction of current disturbance and some assumptions using difference of time scale between current and bottom evolutions permits to obtain a propagation equation driving the bottom evolution. The model has been calibrated in the case of the local scour around a jetty. At last, it has been applied to the bottom evolution in the vicinity of the new port of Dunkerque.

INTRODUCTION

One of the impacts of a large coastal structure is its effect on current pattern in the vicinity of the structure. These changes in current conditions will induce changes in the sediment transport pattern and may disturb an existing equilibrium thus causing large changes in bottom topography in the vicinity of the structure. To assess the severity and extend of topographical changes induced by the structure the interaction of the resulting fluid motion with the bottom evolution must be properly reproduced.

The study of sediment drifting and movable bed evolution is a difficult problem from a physical and mechanical point of view. But the sediment transport relationship admitted, the problem is reduced to the study of a conservative phenomena.

An other problem is the difference of time scale between current and bottom evolution. It is impossible (because of cost), to compute simultaneously the bottom evolution and the current by the classical way. Nevertheless, the interaction between the two is fundamental for the bottom evolution.

This paper presents a two dimensional mathematical sediment transport model taking into account the influence of the bottom evolution upon the current pattern and shows how this particular aspect of the interaction drives the ripples propagation.

THEORETICAL ANALYSES

Bed continuity equation and sediment transport relationship

Let \vec{T} be the sediment transport vector and ξ the bottom elevation ; the bed continuity equation may be expressed as

* Division Hydraulique Maritime. Laboratoire National
d'Hydraulique. Electricité de France. Chatou. France.

$$\frac{\partial \xi}{\partial t} + \text{div } \bar{T} = 0$$

How express \bar{T} as a function of the velocity? That is a real problem. Many relations can be found taking into account waves or not. For ourselves we have used the Meyer-Peter relationship for the sediment transport vector \bar{T} which is supposed in the direction of the current bottom shear stress which is evaluated using Chezy's relationship.

So the bed continuity equation can be transformed into :

$$\frac{\partial \xi}{\partial t} + T_{Xu} \frac{\partial u}{\partial x} + T_{Xv} \frac{\partial v}{\partial x} + T_{Yu} \frac{\partial u}{\partial y} + T_{Yv} \frac{\partial v}{\partial y} = 0$$

with

$$T_{Xu} = \frac{u}{W} \frac{\partial T}{\partial u} + T \frac{v^2}{W^3}, \quad T_{Yu} = \frac{v}{W} \frac{\partial T}{\partial u} - T \frac{uv}{W^3}$$

$$T_{Xv} = \frac{u}{W} \frac{\partial T}{\partial v} - T \frac{uv}{W^3}, \quad T_{Yv} = \frac{v}{W} \frac{\partial T}{\partial v} + T \frac{u^2}{W^3}$$

$$T = \left. \begin{array}{l} 8\sqrt{\frac{g}{\varpi}} \frac{1}{\varpi_S - \varpi} (\tau - \tau_C)^{3/2} \text{ if } \tau > \tau \\ 0 \text{ if } \tau < \tau_C \end{array} \right\} \text{ sediment transport}$$

$$\tau_C = A (\varpi_S - \varpi) D_M \quad (0,02 < A < 0,06 \text{ Shields}). \text{ Critical bottom shear stress}$$

$$\tau = \varpi \frac{W^2}{C^2} \text{ bottom shear stress}$$

u, v are the two components of the depth averaged current

$$W^2 = u^2 + v^2$$

ϖ, ϖ_S specific weight of water and sediment

D_M mean diameter of sediment.

Influence of bottom evolution upon the current pattern

With the initial bottom shape ξ_0 and the new geometric conditions the depth averaged flow pattern is (u_0, v_0) .

This current modifies the bottom shape which in turn modifies the current by $(u_1(t), v_1(t))$.

At time t , the current pattern is given by $(u_0 + u_1(t), v_0 + v_1(t))$ and the bottom level by $\xi(t)$ ($\xi_S = \xi - \xi_0$ is the bottom evolution).

The resulting disturbance (u_1, v_1) is assumed to be without effect upon the surface elevation z_0 . This assumption is equivalent to neglect the characteristic response time of the surface wave propagation compared to the characteristic response time of the bottom evolution.

The resolution of the fluid continuity equation shows that the current disturbance (u_1, v_1) can be written in two different terms :

- the first one (\bar{u}_1, \bar{v}_1) comes directly from the bottom elevation ξ and expresses the flow conservation along the stream lines of the undisturbed field of currents (u_0, v_0)

$$\bar{u}_1 = u_0 \frac{\xi - \xi_0}{z_0 - \xi} = u_0 \frac{\xi_s}{h} \quad \bar{v}_1 = v_0 \frac{\xi - \xi_0}{z_0 - \xi} = v_0 \frac{\xi_s}{h}$$

- the second one (\tilde{u}_1, \tilde{v}_1) is a deviation of the flow due to the bottom slope. It is governed by :

$$\frac{\partial}{\partial x} \left[\tilde{u}_1 (z_0 - \xi) \right] + \frac{\partial}{\partial y} \left[\tilde{v}_1 (z_0 - \xi) \right] = 0$$

Bottom equation

These two terms are introduced in the bed continuity equation (1) which can be written :

$$\frac{\partial \xi_s}{\partial t} + C \left(\frac{u}{W} \frac{\partial \xi_s}{\partial x} + \frac{v}{W} \frac{\partial \xi_s}{\partial y} \right) = - T_{Xu} \left[\frac{\partial}{\partial x} (u_0 + \tilde{u}_1) + \xi_s \frac{\partial}{\partial x} \left(\frac{u_0}{h_0} \right) \right]$$

$$\begin{aligned} & - T_{Xv} \left[\frac{\partial}{\partial x} (v_0 + \tilde{v}_1) + \xi_s \frac{\partial}{\partial x} \left(\frac{v_0}{h_0} \right) \right] \\ & - T_{Yu} \left[\frac{\partial}{\partial y} (u_0 + \tilde{u}_1) + \xi_s \frac{\partial}{\partial y} \left(\frac{u_0}{h_0} \right) \right] \\ & - T_{Yv} \left[\frac{\partial}{\partial y} (v_0 + \tilde{v}_1) + \xi_s \frac{\partial}{\partial y} \left(\frac{v_0}{h_0} \right) \right] \end{aligned} \quad (2)$$

with $C = \frac{1}{h} \left(u \frac{\partial T}{\partial u} + v \frac{\partial T}{\partial v} \right)$

Equation (2) governs a ripples propagation in the direction of the initial current pattern with the celerity C. This phenomena comes directly from the adaptation of current disturbance (\bar{u}_1, \bar{v}_1). By neglecting the disturbance it is impossible to reproduce the ripples propagation.

The second member can be divided in two different parts :

- contribution of the initial current pattern which is conserved at time t
- contribution of the deviation of the flow (\tilde{u}_1, \tilde{v}_1) which drives a ripple deformation.

Fluid equation

To determine the current disturbance (u_1, v_1) an other assumption is required; an irrotational current disturbance pattern ($\hat{u}_1 + \hat{u}_1, \hat{v}_1 + \hat{v}_1$) is assumed. So \hat{u}_1 and \hat{v}_1 are obtained from the three-dimensional stream function ψ , which yields a Poisson type equation (3).

So the actual current pattern is defined by :

$$u = u_0 + u_0 \frac{\xi_s}{h} + \frac{\hat{u}_1}{h} \frac{\partial \psi}{\partial y}$$

$$v = v_0 + v_0 \frac{\xi_s}{h} - \frac{\hat{v}_1}{h} \frac{\partial \psi}{\partial x}$$

$h = z_0 - \xi$ actual depth and ψ obtained from

$$\Delta \psi = + h \frac{\partial}{\partial x} \left(v_0 \frac{\xi_s}{h} \right) - \frac{\partial}{\partial h} \left(u_0 \frac{\xi_s}{h} \right) + \hat{u}_1 \frac{\partial h}{\partial y} - \hat{v}_1 \frac{\partial h}{\partial x} \quad (3)$$

NUMERICAL MODEL

A finite difference scheme is used to solve equations (2) and (3). The computational grids ψ and u, v, ξ are shifted. The initial conditions (u_0, v_0, z_0, ξ_0) are obtained with an other numerical model or recorded on a scale model.

Each time step involves two stages :

- computation of the bottom level ξ ; equation (2) is solved by the characteristic method. All functions are explicit but the scheme is stable.
- computation of the new velocities ; only \hat{u}_1, \hat{v}_1 have to be computed. Equation (3) is solved by an iterative process.

NUMERICAL EXAMPLESLocal scour around a jetty

Several numerical examples have been computed. In figures 1 and 2, the local scour around a jetty, and the flow pattern evolution are shown. The conditions are : flat initial bottom, far field mean velocity = 41 cm/s, water depth = 20 cm, width = 46 cm, ratio jetty length over flume width = 1/3 and particle diameter 4,5 mm. The initial current pattern has been computed with an other numerical model. In figure 3, comparison between computed and measured scour is shown.

Study of new port of Dunkerque

The Port Autonome of Dunkerque has built a new port able to receive 22 metters draught ships. Many studies have been

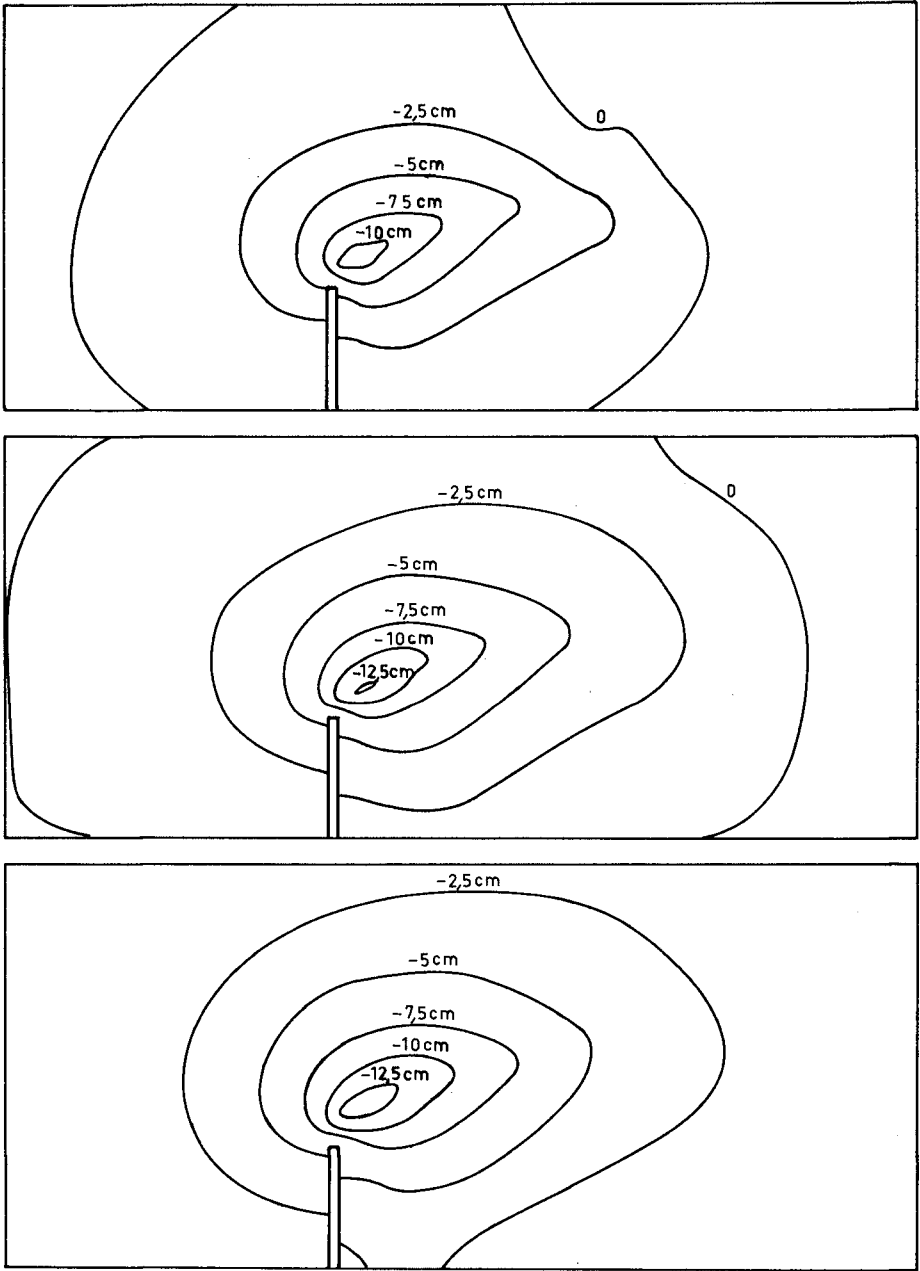


Fig.1_EROSIONS AFTER 1,2 AND 3 HOURS

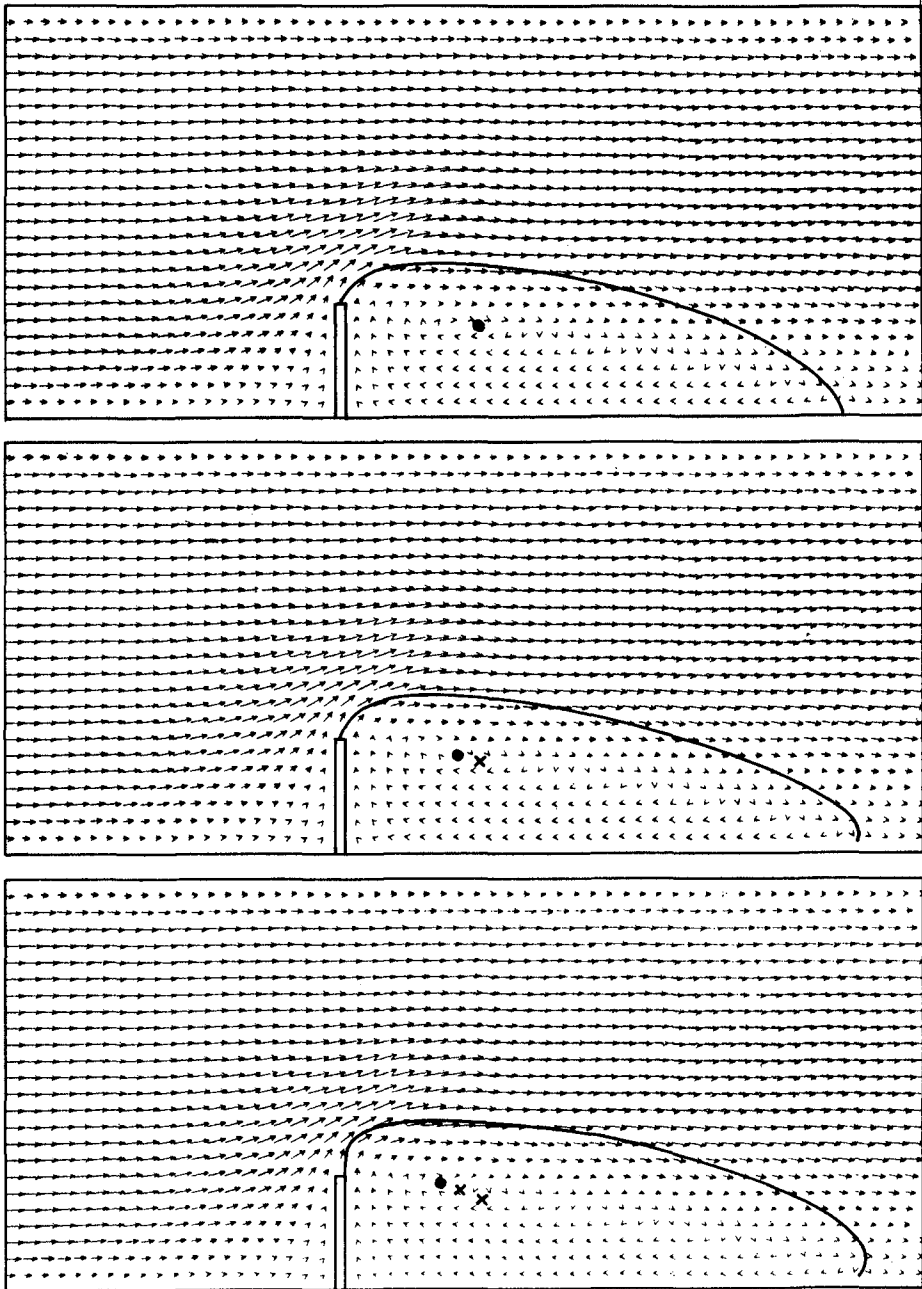
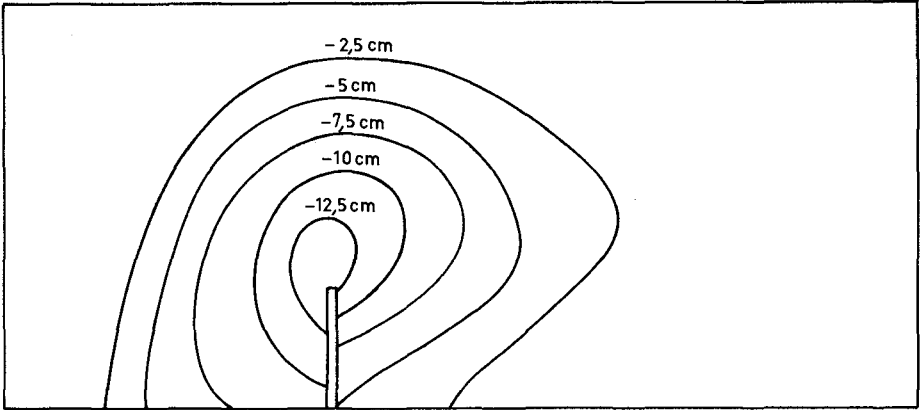
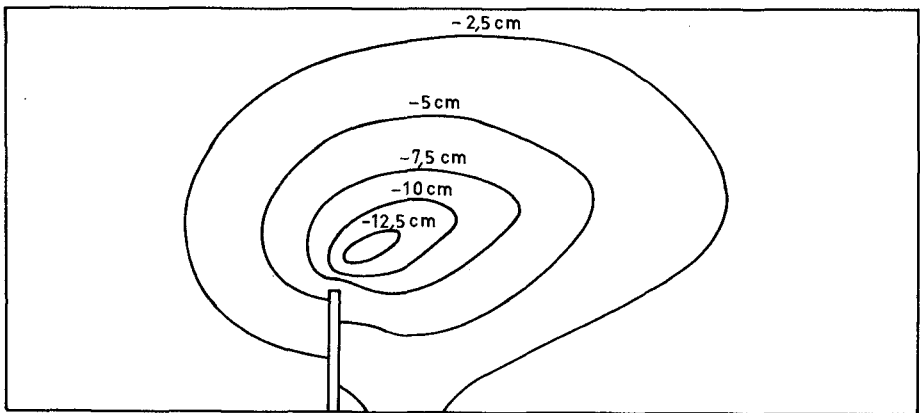


Fig.2_ CURRENT PATTERN AFTER 1,2 AND 3 HOURS



EXPERIMENT



COMPUTATION

Fig.3 _COMPARISON BETWEEN MEASURED
AND COMPUTED EROSIONS

carried on during ten years. Particularly, a movable bed model have been built to study the bottom evolution due to tidal currents near the new port.

The numerical model has been used in this particular case, but to decrease the cost of computation the second kind of disturbance has been neglected. Only equation (2) was solved. The initial current pattern used for the computation was recorded on the scale model.

The comparison between the computed and mesured erosions and accretions is presented on figures 4 and 5. The main difference takes place near the jetties and it probably comes from the initial current pattern which was not conservative because of the precision of measurements on the scale model.

CONCLUSION

A simple kinematical study of the sediment transport equation has shown how can the ripples propagation be obtained. It has also allowed a numerical integration on a computer. The characteristic response time of the surface wave propagation compared to the characteristic response time of the bottom evolution put a stop to any sort of computation of the disturbed current in the classical way. The introduction of current disturbance and several assumptions permit the computation of the bottom evolution during a long time. This kinematical and mathematical aspect almost understood, studies are going on a more physical and dynamical point of view to determine the influence of the different parameters in transport relationship and to find a best dynamical approximation of the current disturbance. In the same time, a mean of averaging the tide in tidal problems is investigated.

REFERENCES

- Daubert, A., Lebreton, J.C., Marvaud, P., Ramette, M., 1966. Quelques aspects du calcul du transport solide par charriage dans les écoulements graduellement variés. Bulletin du CREG n° 18.
- Zaghoul, N.A., Mc Corquodale, J.A., 1975. A stable numerical model for local scour. Journal of Hydraulic Research.
- Bonnefille, R. Essai de synthèse des lois de début d'entraînement des sédiments sous l'action d'un courant en régime continu. Bulletin du CREG n° 5.
- Lepetit, J.P., 1974. Nouvel avant-port de Dunkerque, étude sur modèle réduit sédimentologique d'ensemble de l'évolution des fonds au voisinage de l'avant-port. Rapport Electricité de France, Direction des Etudes et Recherches.
- Gill, M.A., 1972. Erosion of sand beds around spur-dikes. Journal of Hydraulic Division.

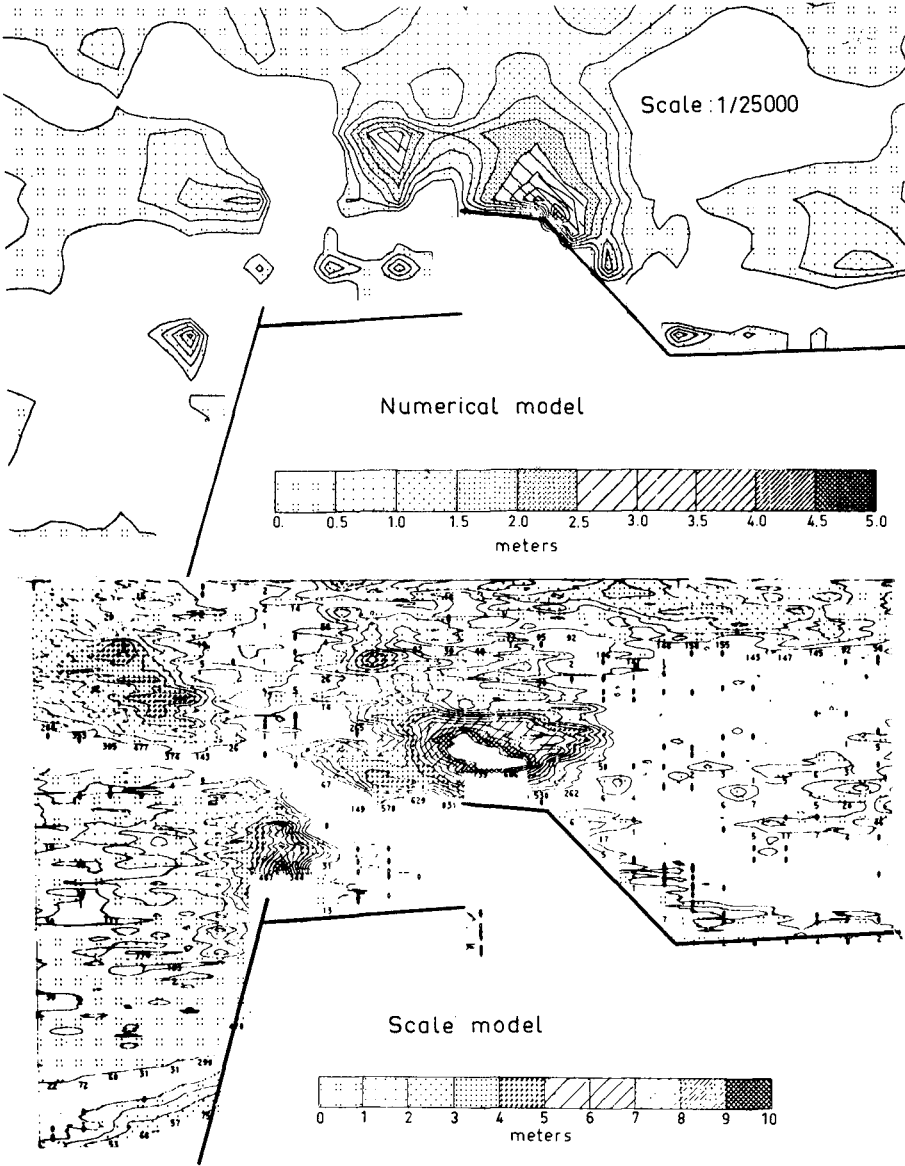


Fig.4. EROSIONS NEAR DUNKERQUE PORT

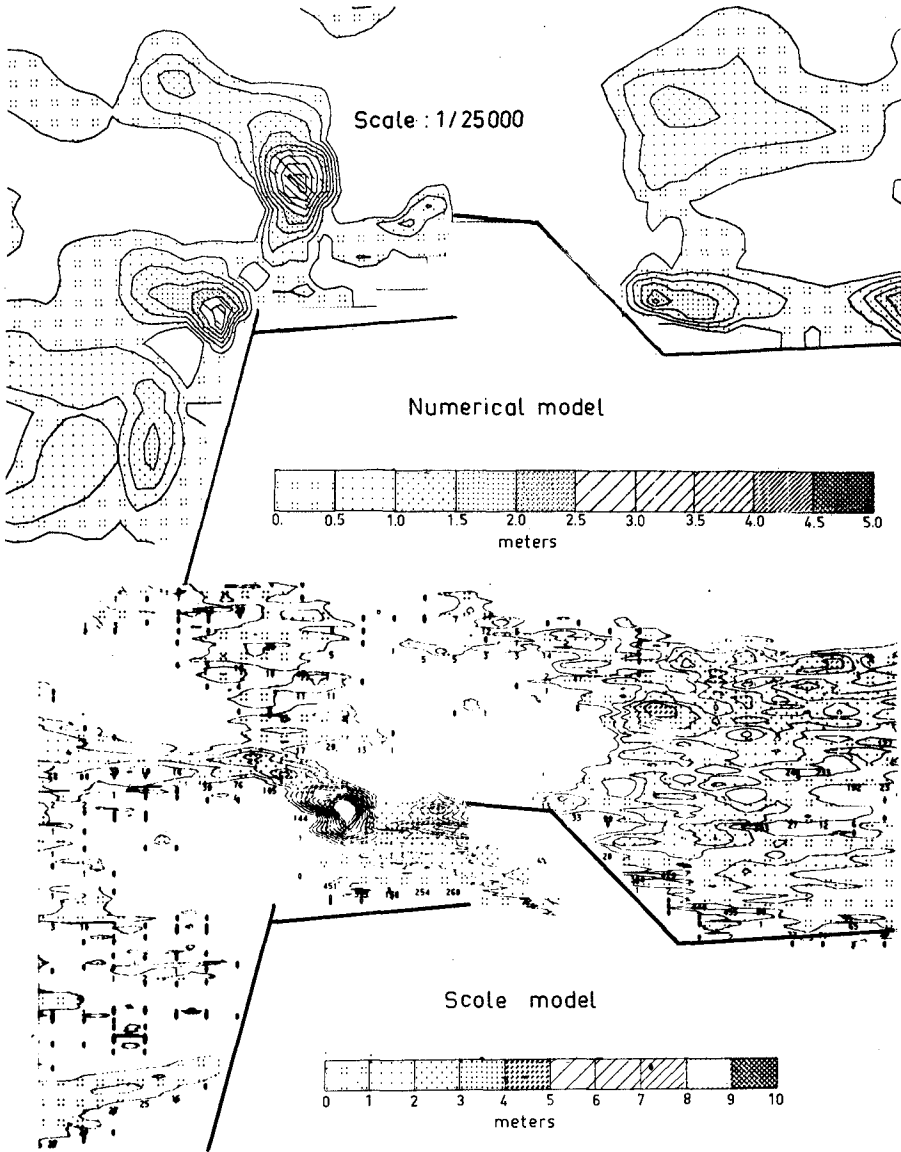


Fig. 5 . ACCRETIONS NEAR DUNKERQUE PORT

CHAPTER 104

SURF ZONE MEASUREMENTS OF SUSPENDED SEDIMENT

Timothy W. Kana¹

ABSTRACT

Suspended sediment concentration was measured in approximately 250 breaking waves on undeveloped beaches near Price Inlet, South Carolina, U.S.A., using portable *in situ* bulk water samplers. As many as 10 instantaneous 2-liter water volumes were obtained in each wave for a total of 1500 samples. Concentrations of suspended sediment were determined at fixed intervals of 10, 30, 60 and 100 cm above the bed for various surf zone positions relative to the breakpoint. The majority of waves sampled during 22 days in June and July, 1977 were relatively long crested, smooth, spilling to plunging in form, with breaker heights ranging from 20 to 150 cm. Surf zone process variables measured included breaker height and depth, breaker type, wave period, surface long-shore current velocity, wind velocity and direction.

Scatter plots of mean concentration against various process parameters indicate the amount of sediment entrained in breaking waves is primarily a function of elevation above the bed, breaker type, breaker height and distance from the breakpoint. Concentration ranged over 3 orders of magnitude up to 10 gm/l, but varied less than 1 order for samples collected under similar conditions with regard to elevation and breaker type. Plunging breakers generally entrain 1 order more sediment than spilling breakers equal in height. Despite considerable scatter, these data indicate concentration decreases with increasing wave height for waves 50 to 150 cm high, suggesting that small waves can be important in the transport of sand on gently-sloping open coasts.

INTRODUCTION

Over 1500 instantaneous suspended sediment concentrations have been determined from water samples collected in the surf zone near Price Inlet, South Carolina, U.S.A. The purpose of this study was to determine the spatial distribution of suspended sediment near the breakpoint under various wave conditions in order to identify the wave parameters which control the amount of sediment entrained from the bed. This work represents one of several experiments conducted by the Coastal Research Division of the University of South Carolina designed to increase our understanding of sediment entrainment and transport processes in waves and eventually to construct a predictive model of suspended sediment concentration in the surf zone.

¹Coastal Research Division, Department of Geology,
University of South Carolina, Columbia, S. C. 29208

METHODS FOR MEASURING SUSPENDED SEDIMENT CONCENTRATION

Only a few workers have attempted to measure concentration of suspended sediment in breaking waves, undoubtedly due to the relative difficulty of sampling in a high energy environment. Three basic methods for measuring concentration in oscillatory flows have been used: pump systems for obtaining a time-integrated sample of water and sediment (Watts, 1953; Fairchild, 1972, 1977; and Coakley, *et al.*, 1978, this volume); *in situ* collecting traps for obtaining relatively instantaneous bulk water samples (Kana, 1976; Inman, 1977); and indirect measures which relate turbidity to light attenuation, back scatter of light, or gamma absorption (Homma, *et al.*, 1975; Hattori, 1969; Horikawa and Watanabe, 1970; Kennedy and Locher, 1972; Basinski and Lewandowski, 1974; Brenninkmeyer, 1976a; and Leonard and Brenninkmeyer, 1978, this volume). There are obviously certain disadvantages to any of these techniques, most important of which is the influence of the sampling apparatus on the flow field. Any device which remains fixed to the bed, or utilizes a supporting structure or pier, is likely to monitor artificially-induced suspensions (Inman, 1977).

Pump samplers were not suitable for the present study because they provide time-averaged water samples making it difficult to determine the effect of a single wave on sediment suspension. Since concentration generally fluctuates at a period approximating that of the incident wave field, relatively instantaneous values were required.

Indirect monitors of concentration, such as the almometer (Brenninkmeyer, 1976a), have the advantage of providing detailed time series information on turbidity changes, but most of these devices are difficult to calibrate for field use. Such external conditions as cloud cover, air entrainment in the surf zone, and the presence of varying amounts of organic matter in the water column, affect turbidity and, therefore, the output of these devices. Also, in some cases, the threshold for detecting sediment bursts from the bed is significantly higher than the typical concentrations found in the surf zone by Watts (1953) in California, or Kana (1977) in South Carolina.

According to Inman (1977), the best way of overcoming the limitations of presently available suspended sediment samplers is by using portable *in situ* samplers activated by swimmers in conjunction with remote recording turbidity sensors. This combination may be ideal, but it is difficult to coordinate and expensive to deploy. However, for the past 3 years, we have used a portable *in situ* water sampler which has proven to be an efficient and inexpensive means of obtaining suspended sediment samples in the surf zone under a variety of wave conditions. Concentrations obtained directly from *in situ* water samples have been combined with littoral observations to estimate suspended sediment transport rates along two undeveloped beaches (Kana, 1977).

The apparatus used in the present study collects several closely spaced simultaneous water samples in a vertical array above the bed (Kana, 1976). It consists of a 2 meter-long mounting pole, support brackets and several 2-liter cast acrylic bottles closed off by hinged

doors (Fig. 1). To ready the sampler for use, the operator opens the bottle doors and attaches them to a trigger assembly on the mounting pole, similar to rigging a Van Dorn-type water sampler. Then as the bottles are held open, the device is carried into the surf zone and positioned vertically above the bed until the sampling instant. At the desired sampling time, the apparatus is thrust into the bed, forcing the trigger open and allowing the bottles to shut simultaneously, trapping each sample. The device has a relatively fast response time of less than one-half second, remaining off the bed until the sampling instant. Tests have shown that the collecting bottles are drawn shut before sediment thrown up by the apparatus reaches each sampling position. The typical array of samples collected in this study were centered at 10, 30, 60 and 100 cm above the bed. Because of the relatively broad, stubby shape of each collecting bottle, the lowermost sample obtains sediment suspended between 4 and 16 cm above the bottom. Inman (1977) has recently developed a portable device for "coring" the water column to obtain a similar vertical array of instantaneous water samples; however, detailed results were not available in time to be included in this report.

PREVIOUS RESULTS

It is generally recognized from laboratory studies that in oscillatory flow, suspended sediment concentration decreases exponentially above the bed (Hattori, 1971; Kennedy and Locher, 1972; and MacDonald, 1977). Field measurements in the surf zone by Inman (1977; Fig. 5) and Kana (1977; Figure 5) tend to confirm this relation. A relatively constant suspension wash load of fine-grained particles exists throughout the water column in the nearshore. However, in the breaker and swash zones, intermittent suspensions of relatively coarse bed material are thrown up by waves to cause the observed vertical distribution of concentration. The frequency and magnitude of these intermittent suspensions are of primary interest because of their importance in the transport of sand on beaches. In general, the timing of bursts of sediment from the bed corresponds to the time of wave breaking, with some delay as the particles lag behind the water motion (Hattori, 1969; Brenninkmeyer, 1976b).

Fairchild (1972), working from ocean piers at Ventnor, N. J. and Nags Head, N. C., has measured a slight increase in concentration with breaker height and a decrease away from the breakpoint for time-integrated pump samples. Additionally, he has shown that concentration increases with the ratio of breaker height to breaker depth and is more variable with low waves than high. His samples were collected in waves ranging from 40 to 120 cm, yielding concentrations up to 4.0 parts per thousand. The sampler intake was varied between 8 cm and 75 cm above the bed. Since most of the samples were pumped over a 3 minute time period, it is difficult to isolate the effect of a single wave and establish any quantitative relationships from these data. However, Fairchild was apparently correct in concluding that suspended sediment concentration is a function of elevation above the bed, wave height and position in the surf zone.

Brenninkmeyer (1976b), using arrays of photoelectric sensors in the surf at Point Mugu, California, found that the zone of maximum suspension occurs near the stillwater level in the swash zone. He reported that suspensions of sand more than 15 cm above the bed are rare in the outer surf zone and appear to be influenced by the stage of the tide and the elevation of the ground water table. Bursts of sediment from the bed or "sand fountains" have durations of the order 2 to 10 seconds, apparently corresponding to the period of incident waves.

Kana (1977) reported a dependency of concentration on elevation above the bed and breaker type, based on instantaneous in situ bulk water samples collected along two South Carolina beaches. Using a visual classification, he reported that plunging-type waves entrain almost one order more sediment than spilling breakers.

None of these studies is complete enough to establish a quantitative relationship between suspended sediment concentration and commonly measured surf parameters. However, they provide a basis to continue research designed to isolate and identify the important factors controlling the entrainment of sediment in the surf zone. The present paper is, at most, an attempt to describe some relations of common surf parameters to suspended sediment concentration under a variety of moderate wave conditions. As such, it applies to a relatively specific wave climate, beach morphology, sediment size and bed packing.

STUDY AREA

The field measurements for this study were obtained at two beach sites, each approximately 2 km from Price Inlet, on Bulls Island and Capers Island, South Carolina (Fig. 2). This portion of the South Carolina coast is under the influence of dominant waves from the northeast, causing net longshore transport to the south (estimated rate is $1.2 - 1.5 \times 10^5 \text{ m}^3/\text{yr}$; Kana, 1977). Wave energy is moderate with breaker heights ranging from 20 to 160 cm under non-storm conditions, with a mean of 60 cm. The beaches at these two sites are composed of well-sorted, fine sand (mean diameter = 0.22 mm) and are gently sloping and relatively featureless (mean beach face slope = 0.018). During average swell conditions, the surf zone is approximately 50 meters wide, but due to the mean tide range of 1.5 meters, a much wider portion of the beach face is periodically exposed to the impact of breaking waves. The bed in the active surf zone is tightly compacted and rarely exhibits small scale bedforms. Slope changes along the beach face are minor and generally controlled by the formation of low amplitude ridges or bars parallel to shore.

EXPERIMENTAL DESIGN

During 22 sampling days in June and July, 1977, multiple arrays of water samples were collected in the littoral zone near Price Inlet, South Carolina, during a variety of swell conditions using the sampler in Figure 1. Up to three arrays providing as many as 10 water samples were used in the same wave to detect suspended sediment concentrations

Figure 1. Apparatus used to collect water samples in the surf zone. A 2 m-long pole supporting several 2 l. bottles is emplaced vertically in the surf zone. When thrust into the bed, a foot pad moves the trigger assembly up, simultaneously tripping each bottle. Top two bottles are rigged for sampling. Bottom bottles are in the tripped position.

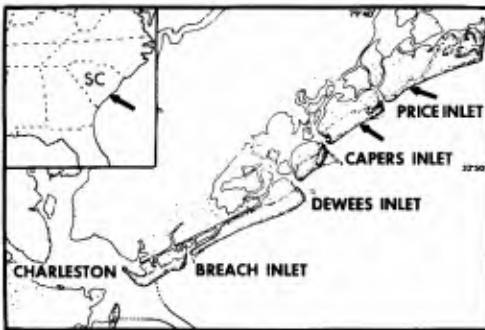


Figure 2. Study area near Charleston, South Carolina, U.S.A. Suspended sediment samples were collected at stations located along two undeveloped beaches near Price Inlet (arrows).

across the surf zone and along individual wave crests. A four-to six-man field team was required in order to simultaneously collect the water samples, make littoral process observations, and photograph each wave sampled.

Two ranges were established at the experiment sites and periodically surveyed to the low tide breaker line to establish the beach slope at each sampling point. Each day, stakes were set throughout the surf zone as reference points for sampling location and wave position. Each suspended sediment sample was positioned in relation to: 1) the bed, by means of the sampling apparatus, 2) a bench mark on land, by means of the reference stakes, 3) the wave breakpoint, by measuring the distance seaward or landward to each array, and 4) the time of passage of each wave sampled. Figure 3 is a sketch of a typical sampling arrangement.

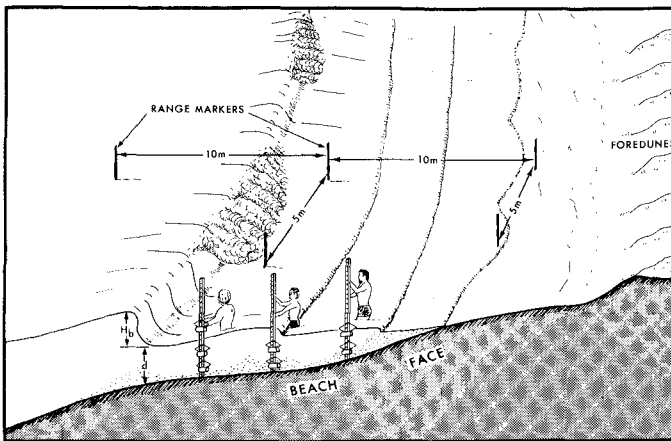


Figure 3. Sketch of the sampling arrangement showing samplers in place. Operators stood downdrift from sample point holding apparatus above bed until sampling instant.

In order to minimize the number of variables affecting the distribution of concentration, sampling was performed during swell conditions with wind velocities less than 5 m/s. Generally at these beach sites, waves are more "classically" formed and long crested in the morning before the diurnal sea breeze is established. As onshore wind velocity increases, wave crests become shorter and more irregular, making it difficult to distinguish the breakpoint. The beaches at these two sites were chosen for the experiment because their profiles are generally featureless, small scale bed forms are essentially nonexistent, and they are away from any artificial structures which may influence turbidity.

All samples reported herein were collected approximately 2 seconds after the passage of the wave bore by each sampler. Previous results indicate that, in general, the maximum concentration at a point occurs just after the passage of a wave (Kana, 1977). Thus, with 3 operators, it was possible to follow one wave toward shore and, to some extent, determine the change in concentration across the surf zone. Multiple arrays were also collected along individual wave crests to determine the range of variability of concentration within a single wave. Each wave sampled was photographed at several positions during breaking to maintain a record of wave types and provide a means of checking visual estimates of height and depth. A typical photographic sequence is shown in Figure 4.

The following surf parameters were measured for each sample array:

1. Breaker height (H_b) and water depth at breaking (d) - visually, by means of a graduate staff held in place at the breakpoint and checked by scaling photographs taken during sampling. Limit of error ± 10 cm.

2. Wave period (T) - by averaging the time of travel between the wave crest prior to, and the crest following, the wave sampled. Limit of error ± 1 second.

3. Surface longshore current velocity at mid-surf position (V) - by timing the travel of small floats between range markers set 10 m apart in the alongshore direction.

4. Breaker angle (α_b) - visually, by means of a protractor, sighting the acute angle between wave crest and shoreline. Limit of error ± 2 degrees.

5. Breaker type - qualitatively, by visual observations in the field, verified by photos taken while sampling and checked against various breaker-type parameters (e.g., Galvin, 1968; Battjes, 1974).

6. Wind velocity and direction - by means of a hand-held anemometer.

Suspended sediment samples were processed by normal filtration techniques to determine concentration as a weight per unit volume (gm/l).

Using up to 3 samplers in each wave, over 250 individual waves were sampled during the study yielding approximately 1500 concentration values. Over 1000 of the samples were collected at 10 and 30 cm above the bed.

Table 1 summarizes the range of surf conditions and number of samples by wave type and wave height collected during the experiment.

Figure 4. Four successive photographs of one of the breaking waves sampled at 3 positions inside the surf zone. Arrays of suspended sediment samples taken 3 m, 7 m, and 10 m landward of A. the breakpoint. Concentrations are listed below.

A. Wave beginning to break 3 m seaward of sampler operator #1.

$H_b = 90$ cm; $d = 95$ cm; $T = 8$ s; $V = 0$ cm/s; $m = 0.011$; breaker type: spilling; Time = 0 s.

B. Wave fully broken, bore at Operator #1.

Bore height = 70 cm; Depth under bore = 90 cm; Time ~ 1 s.

C. Bore approaching operator #2.

Bore height = 60 cm; Depth = 65 cm; Time ~ 2½ s.

Just before sampling instant array #1 (seawardmost).

D. Bore at operator #3.

Bore height = 55 cm; Depth = 60 cm; Time ~ 4 s.

Just before sampling instant Array #2.

Results:

Array #	Elev. above bed (cm)	Conc. (gm/l)
1	60	.135
	30	.256
	10	.329
2	30	.261
	10	.234
3	30	.170
	10	.231



TABLE 1

Breaker height Hb (cm)	Breaker Type - # Waves Sampled			# Vertical arrays of* susp. sediment samples
	Spilling	Spill/Plunge	Plunging	
0-35	5	4	2	29
35-45	7	1	3	32
45-55	15	2	5	56
55-65	12	4	1	46
65-75	15	8	10	92
75-85	29	6	7	118
85-95	13	11	18	115
95-105	8	9	5	63
105-115	10	3	2	45
115-125	6	2	1	27
125-160	11	0	0	33
Totals	131	50	54	656

* 3 vertical arrays of 1 to 4 samples each were collected in each wave to yield a total of approximately 1500 concentration values.

RESULTS

Previously reported field results by Watts (1953), Fairchild (1972) and Kana (1977) have shown that the concentration of suspended sand in the surf zone can vary by several orders of magnitude. Therefore, it is necessary to compare samples collected under similar conditions with regard to wave position and height above the bed in order to determine the effect of individual waves. By grouping samples according to elevation, breaker type or distance from the breakpoint, it is possible to eliminate much of this variation. As a first attempt at establishing the relation between common surf parameters and concentration, it was decided that a comparison of mean values obtained under similar conditions was the best (and perhaps only) way of isolating any trends. There will be no attempt in this paper to rigorously test these relationships. Instead, they are presented as a description of a given set of field conditions.

Plotted on a log scale, suspended sediment concentration is normally distributed by sample elevation for the data set reported herein (Fig. 5). From Figure 5, it can be seen that the mean concentration 10 cm above the bed is approximately 2 times higher than the mean concentration at 30 cm. The range of concentrations at each sample elevation spans roughly 2 orders of magnitude.

Figure 6 shows mean suspended sediment concentration by elevation for three breaker types classified by visual and photographic interpretation. Two dominant wave types, plunging and spilling, occur at the experiment sites. However, we identified and plotted an intermediate type exhibiting characteristics of both spilling and plunging

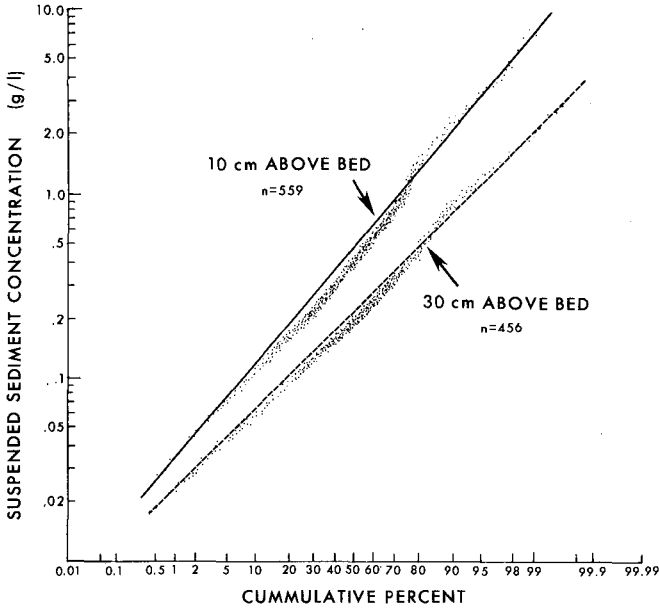


Figure 5. Normal probability plot of concentration for all samples collected 10 cm and 30 cm above the bed irrespective of breaker types.

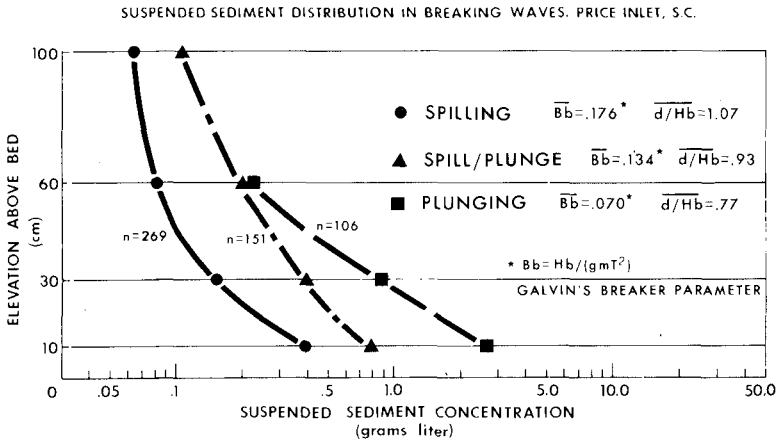


Figure 6. Suspended sediment distribution in the outer surf zone between 1 and 10 m landward of the breakpoint. Mean concentrations are plotted by elevation above the bed for spilling and plunging type breakers. An intermediate wave type exhibiting characteristics of spilling and plunging waves is also plotted (triangles).

waves. The visual classification of wave types tends to agree with Galvin's (1968) breaker classification, which is given by a dimensionless parameter, (B_b), based on wave steepness and beach slope*. Galvin reports a cut off from spilling to plunging waves at $B_b = 0.068$ versus 0.070 for these data. The depth at breaking generally decreases from spilling to plunging waves, and this agrees with mean values of the ratio breaker depth to height, (d/H_b), listed in Fig. 6. Note that plunging waves, on average, entrain almost one order more sediment than spilling breakers. Concentration decreases exponentially up to 60 cm above the bed, then appears to reach a constant value, reflecting the type of suspension: intermittent close to the bed, resulting from periodic bursts of coarse, bed material; continuous near the surface, due to the dominance of suspended wash load.

Since breaker type is an important factor controlling the magnitude of intermittent bursts of sand from the bed, it is desirable to test concentration against parameters which quantify the variation in wave type. No universally accepted breaker classification exists, but several have been proposed. Probably the most widely known are Galvin's (1968), which was already mentioned, and Battjes' (1974), which is also based on wave steepness and beach slope. Based on laboratory waves, Galvin has determined cutoffs between spillings and plunging waves at $B_b = 0.068$ and for plunging and collapsing waves at $B_b = 0.003$. Galvin's inshore parameter is plotted against mean suspended sediment concentration for samples collected 10 cm above the bed (Fig. 7). There is a general trend of increasing concentration from spilling to plunging waves, but due to considerable scatter, and the relatively flat slope of the regression line, this relation is not satisfactory as a predictor of concentration for these data.

The poor fit of the data to Galvin's breaker classification may be due to the dependence of B_b on wave period (T). A plot of concentration versus period shows essentially no dependence of suspended sediment on T (Fig. 8). This suggests that the periodicity of waves has little effect on sediment entrainment for this range of waves. This is not surprising, considering the characteristics of waves as they are transformed at breaking. Munk (1949) recognized that wave length, a function of T , has little to do with the shape of waves near the breakpoint since waves in very shallow water commonly have long, shallow troughs and steep, sharp crests. Consequently, he recommended applying solitary wave theory for describing waves near breaking. This theory differs from the classical Airy or Stokes

* B_b is Galvin's inshore parameter given by $B = H_b / (gmT^2)$, where H_b is breaker height; g is acceleration of gravity; m is beach slope; and T is wave period.

Figure 7. Mean concentration at 10 cm above the bed versus Galvin's (1968) inshore breaker type parameter ($B_b = H_b / (gT^2)$). The defined cut off between spilling and plunging waves is 0.063. Although there is a trend toward high concentrations in plunging waves, this parameter is not an adequate predictor for these data.

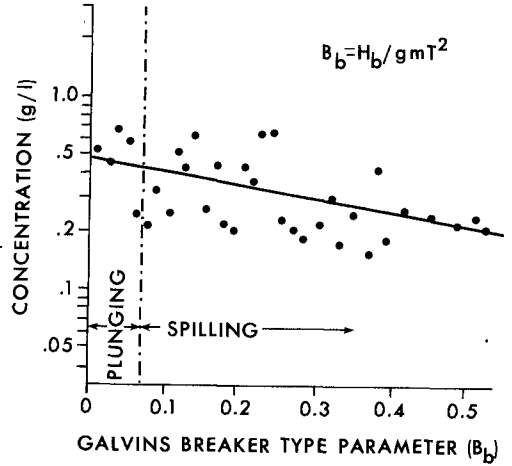


Figure 8. Mean concentration at 10 cm above the bed versus wave period for plunging and spilling breakers. Bars on each point represent the range in concentration values to ± 1 standard deviation. Suspended sediment appears to be independent of wave period for moderate wave conditions.

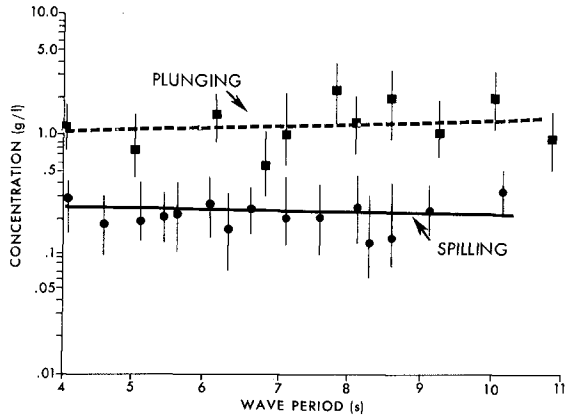
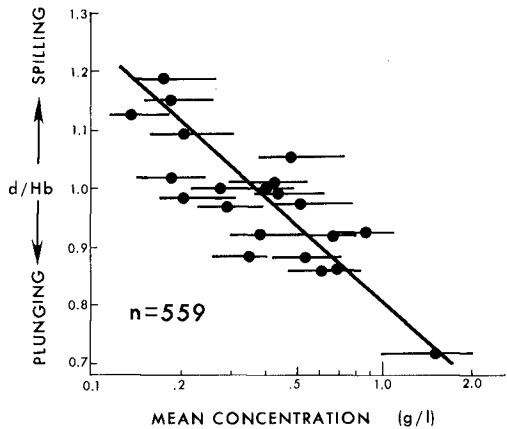


Figure 9. Mean concentration at 10 cm versus the ratio of breaker depth (d/H_b). Bars on each point are ± 1 standard deviation. This parameter, independent of wave period, is useful for distinguishing breaker types and predicting concentration.



wave theories because it contains only one fundamental parameter independent of wave length: relative wave height, or the ratio, H_b/d .

In Figure 9, d/H_b has been plotted against mean concentration for the 10 cm above the bed samples. There is still considerable scatter in the plot, but the data show better separation of breaker types by this parameter alone. Relative wave height, which is independent of wave steepness, appears more useful for classifying the present set of waves. Bars on each data point represent the range of variation in concentration to ± 1 standard deviation.

It would be useful to establish a relation between wave height and suspended sediment concentration for purposes of prediction, since H_b is a commonly measured surf parameter. Fairchild (1972) reported an increase in concentration with wave height, and it is commonly believed that sediment suspension increases directly with wave energy. The data in Figure 10, breaker height versus concentration by wave type, do not support this contention. The means for samples collected 10 cm above the bed show a clear distinction between breaker types, but the shape of each curve is different. Figure 10 shows an increase in concentration for spilling waves up to approximately 90 cm, then a significant decrease for higher waves up to 150 cm. This suggests a concentration maximum in wave heights between 50 and 90 cm for moderate swell conditions. Plunging waves, on the other hand, show a generally continuous decrease in concentration with increasing breaker height. It is not clear why this unexpected result occurs, but it may be related to the increased interaction of the wash uprush and backrush with smaller waves. The width of the surf zone is a function of breaker height such that higher waves tend to break in deeper water considerably seaward of the zone of maximum backrush. This is especially true for relatively flat beaches similar to those in South Carolina. If concentrations corresponding to waves less than 50 cm in height are not considered, there remains a trend of decreasing concentration with H_b for both breaker types.

Concentration is plotted against distance from the breakpoint in Figure 11, showing the variation in mean values across the surf zone. Again, there is a clear distinction between breaker types, with plunging waves entraining higher amounts of sediment. Spilling waves show a sudden increase in concentration within 1-2 m landward of the breakpoint and then appear to maintain a relatively steady suspension across the surf zone. Plunging waves similarly show a rapid increase in concentration just landward of the breakpoint, then a gradual decrease with distance toward shore. The shapes of these distributions seem reasonable if one considers that plunging waves dissipate their energy more rapidly (Führbötter, 1970), and, consequently, should show a peak close to the breakpoint.

Other parameters tested against concentration included wind velocity, longshore current velocity and beach slope; however, none was found to be a useful predictor for these data. This is due in

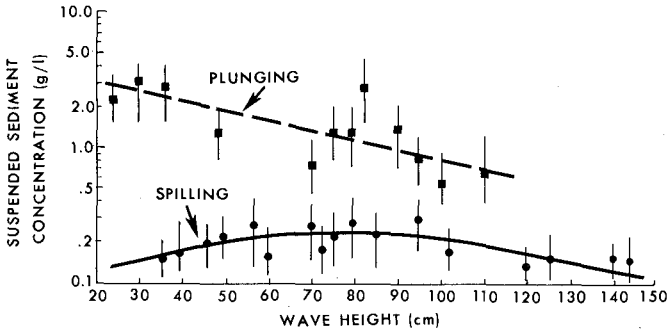


Figure 10. The variation in concentration with wave height for spilling and plunging waves. In general, suspended sediment decreases with increasing wave height during moderate wave conditions on gently sloping ($m = 0.018$), fine-grained beaches. Plunging waves entrain approximately 1 order more sediment than spilling waves equal in height.

Figure 11. Distribution of mean concentration at 10 cm above the bed, relative to wave breakpoint. Suspended sediment increases sharply 1-2 m landward of the breakpoint, then remains relatively constant in spilling waves. Plunging waves tend to peak close to the breakpoint then gradually decrease due to more rapid energy dissipation.

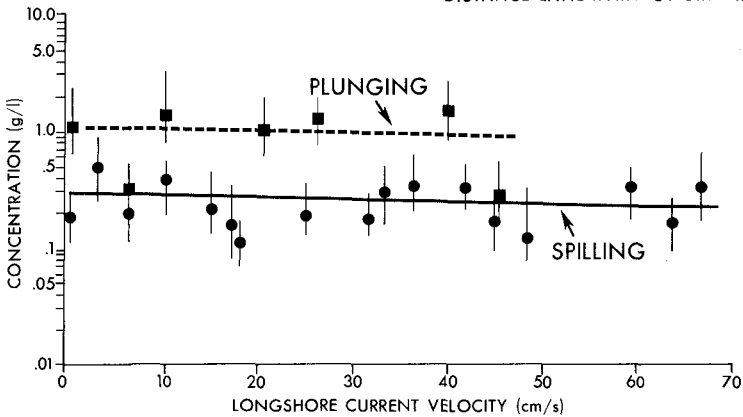
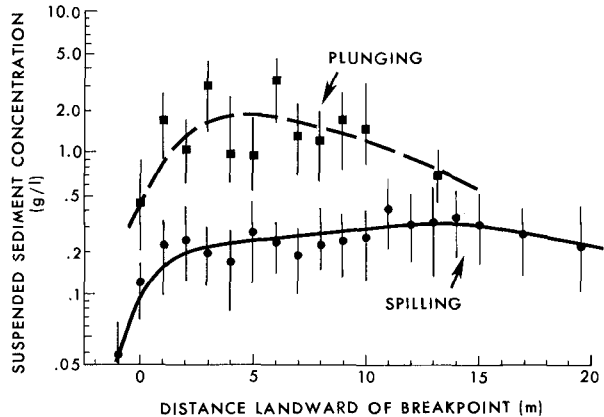


Figure 12. Suspended sediment concentration appears to be independent of longshore current velocity for these data. Samples were collected during a variety of moderate wave conditions over 22 days.

part to the moderate weather conditions prevailing during the study and the attempt to sample only during swell conditions. Beach slope remained relatively constant during the experiment, and surface wind velocity never exceeded 5 m/s. Longshore currents were variable, but as shown in Figure 12, they do not explain concentration variability for these data. This is probably due to the imprecision of our current measurements, as much as the relatively low velocities recorded. It is probable that wind and longshore current velocity become very important during storms.

DISCUSSION

Despite the lack of measurements during storms (a perennial omission with experiments in the surf zone), a major problem in the present study is the range of variability of wave conditions even during relatively ideal swell conditions. To isolate the effect of a single process variable on concentration, repeat sampling under identical conditions is necessary. This may be an impossible task, since not only do successive waves vary in form on a given day, but individual waves exhibit considerable variation along their crests. This is further magnified by small scale changes in bottom topography. It was the intention in this experiment to sample well formed, swell waves with easily definable breakpoints to minimize the influence of such secondary effects as surface wind stress or small scale bedforms. Obviously, these external factors can be important. Even under controlled situations in the laboratory, suspended sediment can be as variable as turbulent flows.

Although concentration varies by several orders of magnitude in the surf zone, these data show that samples taken under similar conditions with respect to elevation, breaker type or wave height vary by much less. As indicated by the ranges in each figure, the standard deviation around the means is significantly less than one order of magnitude for most of these samples. Thus, with increased control over sampling, it should be possible to define a smaller range of concentration values for a given set of wave and beach conditions.

These results tend to confirm several widely held notions concerning sediment suspension in the surf zone, including the dependence of concentration on elevation above the bed and breaker type. But at the same time, they present relations which are not easily explained based on our present understanding, especially the decrease in concentration with breaker height. A possible explanation for the results reported herein may be found in the laboratory studies of Miller (1976), who photographed the entrainment of air in breaking waves. Figure 13, reproduced from Miller's work, shows the distribution of air bubbles entrained in plunging and spilling waves. Note that in spilling breakers, bubbles remain near the surface; whereas, in plunging waves, air is entrained all the way to the bed. Since this distribution of bubbles is an indication of turbulence, it is evident that plunging waves

will effect sediment entrainment from the bed more readily than spilling breakers. The concentration data of the present study verify this.

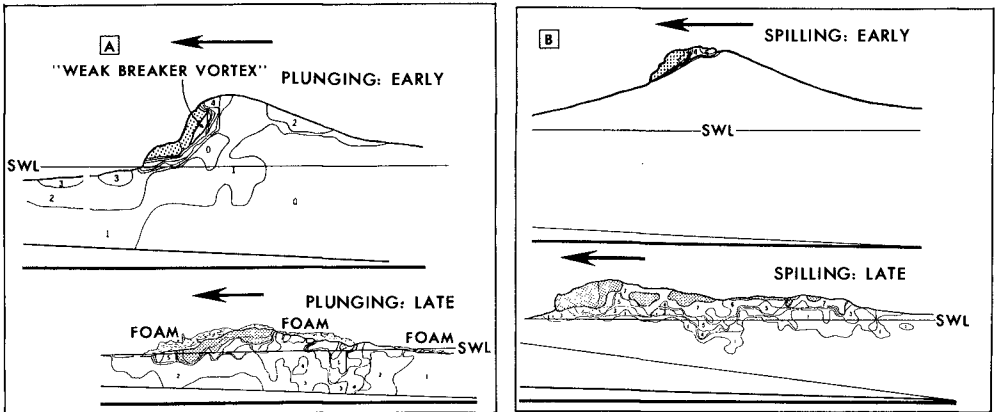


Figure 13. Cross-sectional contour diagrams of bubble concentration in plunging (A) and spilling (B) breakers. Numbers represent percentage estimate of the number of 1 mm scale units containing one or more bubbles (on a scale of 1 to 10). A 5 means 50% of the scale units contain bubbles, a 10 represents 100% bubble concentration. Note that bubbles penetrate to the bed in plunging waves but remain close to the surface in spillers. This suggests more turbulence reaches the bed in plunging waves contributing to the observed higher concentrations of suspended sediment for this breaker type (Miller, 1976).

Miller's diagrams may also explain lower concentrations with increasing breaker heights. If one considers that waves generally break at a depth approximately equal to wave height, turbulence in higher waves must penetrate deeper water to impact the bed. Just as the air bubbles in Miller's spilling waves remain near the surface, the energy to suspend sediment may move away from the bed as water depth increases with higher waves. Although wave energy increases with breaker height, it may be counteracted by the absorbing "cushion" of water which increases with trough depth. Also, on gently sloping coastlines like South Carolina, the largest waves tend to spill, gradually dissipating their energy over a wider surf zone.

An important implication of these results is the apparently significant role of smaller waves on sediment suspension. During moderate swell conditions, there may be less sediment moved by the largest waves breaking in the outer surf zone than is moved by small secondary waves close to the swash zone. And, as Brenninkmeyer (1966) suggests, sediment suspension may be the dominant mode of transport only in the inner surf zone.

Inman (1977) has stated that studies of suspended sediment in the surf zone are generally deficient due to the lack of simultaneous measurements of the velocity and turbulence fields. While this is certainly true, the problem will remain until better measurement techniques are developed. Obtaining simultaneous, accurate measurements of the suspended load and velocity field is a formidable and expensive proposition. The techniques used in the present study offer a less rigorous but efficient and inexpensive method of studying suspended sediment in moderate wave conditions.

CONCLUSIONS

Based on the above results for plunging and spilling waves, under moderate swell conditions, the following conclusions are offered:

1. Suspended sediment concentration in the breaker zone is primarily dependent on elevation above the bed, breaker type, wave height and distance from the breakpoint.
2. Concentration decreases exponentially above the bottom to approximately 60 cm elevation as a function of the intermittent suspension of coarse sediment from the bed.
3. Relative breaker height (d/H_b) is useful for quantifying breaker types and predicting concentration at a given elevation.
4. Concentration decreases with wave height in the range 50 to 150 cm for spilling and plunging waves, but the relationship for waves less than 50 cm is not adequately resolved.
5. In spilling waves, concentration rapidly increases inside the breakpoint, then remains relatively constant under the bore as it propagates toward the beach. In plunging waves, concentration peaks within a few meters of the breakpoint, then decreases gradually toward shore.

ACKNOWLEDGEMENTS

Support for this study was provided by the U.S. Army Research Office Grant No. DAAG-29-76-G-0111 (Miles O. Hayes and Dag Nummedal, principal investigators). Dan Domeracki, Jerry Sexton and Robert Logan provided enthusiastic and efficient assistance in the field. Pris Ridgell and Nanette Muzzy helped prepare the manuscript. I'm indebted to Dag Nummedal, Miles Hayes and members of the Coastal Research Division for their continued help and advice.

REFERENCES CITED

- Basinski, T. and Lewandowski, A., 1974, Field investigations of suspended sediment: Proc. 14th Conf. on Coastal Engr., A.S.C.E., p. 1096-1108.
- Battjes, J. A., 1974, Surf similarity: Proc. 14th Conf. on Coastal Engr., A.S.C.E., p. 466-480.
- Brenninkmeyer, B., 1976a, In situ measurements of rapidly fluctuating, high sediment concentrations: Marine Geology, 20, p. 117-128.
- _____, 1976b, Sand fountains in the surf zone: in Davis, R. A., Jr. and Ethington, R., (eds.), Beach and Nearshore Sedimentation, S.E.P.M. Spec. Pub. 24, p. 69-91.
- Coakley, J. P., Savile, H. A., Pedrosa, M., and Larocque, M., 1978, Sled system for profiling suspended littoral drift: Proc. 16th Conf. on Coastal Engr., A.S.C.E., Hamburg, West Germany.
- Fairchild, J. C., 1972, Longshore transport of suspended sediment: Proc. 13th Conf. on Coastal Engr., A.S.C.E., p. 1062-1088.
- _____, 1977, Suspended sediment in the littoral zone at Ventnor, New Jersey and Nags Head, North Carolina: C.E.R.C. Tech. Paper No. 77-5, U.S. Army Corps of Engrs., 97p.
- Führbötter, A., 1970, Air entrainment and energy dissipation in breakers: Proc. 12th Conf. on Coastal Engr., A.S.C.E., p. 381-398.
- Galvin, C. J., Jr., 1968, Breaker type classification on three laboratory beaches: J. of Geophys. Res., 73(12), p. 3651-3659.
- Hattori, M., 1969, The mechanics of suspended sediment due to standing waves: Coastal Engr. in Japan, 12, p. 69-81.
- _____, 1971, A further investigation of the distribution of suspended sediment concentration due to standing waves: Coastal Engr. in Japan, 14, p. 73-82.
- Hom-ma, M., Horikawa, K., and Kajima, R., 1965, A study on suspended sediment due to wave action: Coastal Engr. in Japan, 8, p. 85-103.
- Horikawa, K. and Watanabe, A., 1970, Turbulence and sediment concentration due to waves: Proc. 12th Conf. on Coastal Engr., A.S.C.E., p. 751-766.
- Inman, D. L., 1977, Status of surf zone sediment transport relations: Proc. Workshop on Coastal Sediment Transport with Emphasis on the National Sediment Transport Study, manuscript, 12p.
- Kana, T. W., 1976, A new apparatus for collecting simultaneous water samples in the surf zone: J. Sed. Petrology, 46, p. 1031-34.

- Kana, T. W., 1977, Suspended sediment transport at Price Inlet, S. C.: Proc. Coastal Sediments '77, A.S.C.E., Charleston, S. C., p. 366-382.
- Kennedy, J. F. and Locher, F. A., 1972, Sediment suspension by water waves: in Meyer, R. E. (ed.), Waves on Beaches and Resulting Sediment Transport, Academic Press, New York, p. 249-295.
- Leonard, J. E. and Brenninkmeyer, B. M., 1978, Periodicity of suspended sand movement during a storm: Proc. 16th Conf. on Coastal Engr., A.S.C.E., Hamburg, West Germany.
- MacDonald, T. C., 1977, Sediment suspension and turbulence in an oscillating flume: C.E.R.C. Tech. Paper No. 77-4, U.S. Army Corps of Engrs., 80p.
- Miller, R. L., 1976, Role of vortices in surf zone prediction: sedimentation and wave forces: in Davis, R. A., Jr. and Ethington, R., (eds.), Beach and Nearshore Sedimentation, S.E.P.M. Spec. Pub. No. 24, p. 92-114.
- Munk, W. H., 1949, The solitary wave theory and its application to surf problems: Annals of the N. Y. Acad. of Sciences,, 51(3), p. 376-424.
- Watts, C. M., 1953, Development and field tests of a sampler for suspended sediment in wave action: Beach Erosion Board Tech. Memo. No. 34, U.S. Army Corps of Engrs., 41p.

CHAPTER 105

STORM INDUCED PERIODICITIES OF SUSPENDED SAND MOVEMENT

JAY E. LEONARD¹

AND

BENNO M. BRENNINKMEYER, S.J.²

SUMMARY

An array of electronic sensors was installed on Nauset Light Beach, Cape Cod, Massachusetts, U.S.A., in order to provide a description of the sediment movement during storm conditions. These sensors included two sediment concentration indicators (almometers) which monitor sediment movement as a function of elevation and time, one bidirectional electromagnetic current meter, and a resistive wave staff.

Prior field studies performed during "normal" conditions have indicated that surf-zone suspended sediment movement is a low-frequency phenomenon, with the relatively high-frequency component (normal wave period) contributing little to the amount of total sediment transported. Development of a computational technique based upon discrete Fourier analysis and digital filtering called *Spectrally Filtered Integration* (SFI) provides the calculation and filtering of true units of sediment change in grams-per-liter. Moreover, the SFI technique eliminates the possibility spurious sediment information created by the presence of air bubbles in the water column.

Generally, higher-frequency sediment movement is more common during storm conditions than during normal non-storm conditions. This movement is controlled not by the prevailing wave and swell periods, but by a longer period which may be due to water interactions below the surface.

INTRODUCTORY REMARKS

The nature and periodicity of sedimentation during storm conditions

¹Department of Geology, Rensselaer Polytechnic Institute, Troy, N.Y.
12181 U.S.A.

²Department of Geology and Geophysics, Boston College, Chestnut Hill,
MA 02167 U.S.A.

in the nearshore zone is virtually unknown. At no other time do the processes of erosion, transportation and deposition operate with such a degree of efficaciousness. Therefore, the relationships among storm waves and currents to the movement of sedimentary material is one of the major problems prevalent in the nearshore zone.

A major limitation, however, in understanding these relationships is the lack of reliable storm-garnered quantitative field data. This dearth of data has led workers to rely upon models based on mechanics, hydrodynamics, flume studies and empirically derived non-storm data. Therefore, the ability to make real-time field measurements during storm conditions is essential. The purpose of this report is to present results and interpretations concerning the periodicities of sediment movement based upon a series of five-experiments performed during the rising tide of a coastal storm.

FIELD TECHNIQUES

Instrumentation

To measure nearshore sediment movement and processes, an array consisting of two almometers, a bidirectional electromagnetic current meter and resistance wave-staff was utilized. The almometer (Brennk-meyer 1973, 1975, 1976) is a series of electro-optical sensors which instantaneously and continuously measure the change in opacity of the lower one meter of water column caused by sediment concentration. A sealed fluorescent bulb at a distance of one meter provides constant illumination. This distance prevents the coalescing of scour pits around each almometer. Each photoresistor was fitted with a 1.5 cm copper tube internally darkened so that its field of "vision" was limited and controlled (see Table 1). The data were recorded on a FM and direct seven-channel analog tape recorder operating at 3.75 ips. The data were gathered between 2400 and 0600 hours so that sunlight could not affect the incident light on the photocells.

Study Area

The instrumentation was emplaced as shown in figure 1 at low tide on Nauset Light Beach in late October of 1975. Nauset Light Beach, located on outer Cape Cod, Massachusetts, U.S.A., trends northerly and faces the open Atlantic Ocean. The major storms are "noreasters" since their principal direction is from the northeast. The tides on the outer Cape are semi-diurnal and have a mean range of 2.3 m and a spring range of 2.7 m. Although the outer Cape has an erosion rate slightly less than 1 m/y (Marindin, 1889; Zeigler, 1964), the beaches are relatively narrow indicating that a large amount of sediment is transported along-shore (Leonard and others, 1976).

Sea State

The original intention of the study was to measure sediment movement during "normal" sea conditions; however, during the latter part of the study a severe storm arose so quickly that the equipment could not

Table 1

Elevation in cm	Vision in liters
0	56.2
5	72.0
10	88.4
15	99.6
20	106.6
25	110.4
30	112.0

Cone of "vision" (in liters of water) for the various almmeter photocell elevations (in cm).

removed from the water. During the storm, the primary breakers were approximately 500 m from shore. Breaker height was estimated to be 4 m, with long-period variations caused by at least two principal swell directions. The array usually stood in the area of secondary and/or tertiary breakers which were considered normal to the beach. These breakers coupled with short-period wind-chop, translational-bores and turbulent-surf defined an extremely confused nearshore hydrodynamic condition. The largest peak in the unusually noisy wave spectra occurred at about 8 seconds.

Zones

Most authors follow the ideas of Shepard and Inman (1951) in dividing the water motion on the foreshore and offshore regions of a beach into three dynamic zones: swash, surf and breaker zones. Schiffman (1965) added another, "the transition zone," between the swash and surf. This zonal concept is valuable in placing a complex environment into a logical reference framework. These dynamic zones, however, are only well-defined during fair-weather conditions. In the conditions extant during a storm, with different period waves arriving at a shore simultaneously from different angles, the boundaries between the zones become indistinct and may even be absent. During this study the breaker zone was relatively far out to sea, and the nearshore was a mass of turbulence caused by the interaction of locally derived wind waves, swell, as well as bore-surf and backwash. In this paper, the operational definition "time zones" will be used. Each zone (Fig. 2) represents a one hour time slice of a rising tide. During this time the array went from partially underwater to completely underwater.

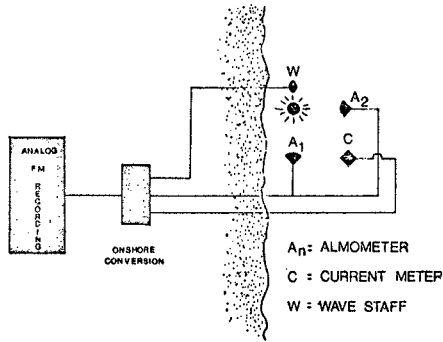


Figure 1. The configuration of the sensor array, onshore conversion station and the recording station (not to scale). W is the wave staff attached to the light source. C is the electromagnetic current meter. A₁ is the onshore/offshore almometer. A₂ is the longshore almometer. The distance of A₁ and A₂ from the light source is one meter.

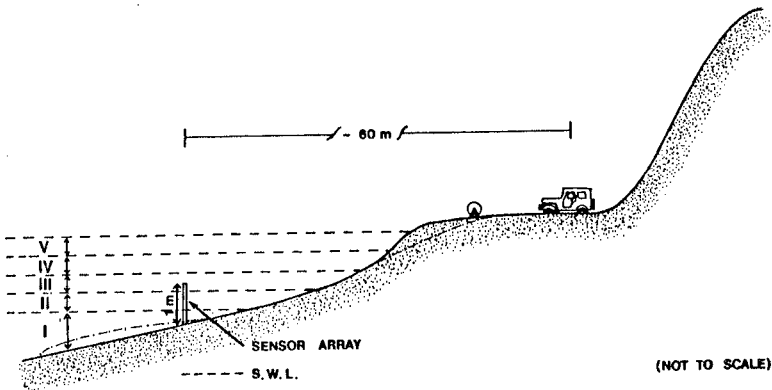


Figure 2. A schematic of the sensor array and its relative position to the time zones described in the text. I-V refer to the approximate still water elevation of each time zone.

ANALYTICAL METHODSAnalog to Digital Conversion

Conversion of the analog data to a digital form was performed subsequent to the field experiments. Each data point of all sensors was twelve-bit resolution at a frequency of 2 kilohertz. Brenninkmeyer (1975) digitized four different key almometer concentrations: 40, 75, 135, and 365 grams-per-liter of sediment at their corresponding elevation in the water column. Each point was sampled at a 5-Hertz interval, thereby showing a time-history of the elevation of a particular sediment concentration. He then Fourier-transformed each concentration's elevation to find its individual spectrum. This method offers information on both the geometry of sand suspension events, and the frequency of particular concentrations of suspension as a function of elevation. A major drawback to this technique is that the mode of digitizing was such that the almometer record was scanned for these key concentrations from the top of the water column to the bottom. If a sediment concentration inversion occurs, the digitizing records only the highest point of this event and indicates a continuous sand fountain.

By contrast, the almometer information for this study was digitized in a different manner. Each discrete elevation above the bottom was recorded with respect to changing sediment concentration, in order that the fluctuations of concentration, not the fluctuations of elevation, could be Fourier-transformed. Although this technique provides little immediate information on the geometry of sand suspension events, it gives an excellent appraisal of the time-history of a discrete elevation. One can, therefore, see the frequency of all sediment concentration as a function of elevation.

A major drawback is inherent in this technique: one must make assumptions as to the location of the dynamic bottom and constantly update these assumptions since the elevations must remain discrete. However, sediment concentration inversion can be found and analyzed.

Time Series Analysis Applied to Experimental Data

The data chosen for Fourier analysis included the wave record and the two current meter records for the five time zones. In addition, 30 elevations above the bottom were selected for the analysis of periodic sediment movement. In all, 2079 points, or 13.86 minutes, of real-time data from each elevation in each time zone were transformed. The Fourier routine used in the analysis was a modification of the FORTRAN program, FILTRAN (Cohn and Robinson, 1975). FILTRAN is based upon the Fast Fourier Transform of the Gentleman and Sande (1966) algorithm as modified from Good (1958) and Cooley and Tukey (1965). This algorithm provides faster and more accurate manipulation of the data arrays and is considered as a significant advancement over the standard Cooley-Tukey techniques.

Digital Filtering and the SFI Technique

Filtering is a process by which a portion of a signal is removed by

suppressing amplitudes of certain frequencies. Filtering in the time-domain is defined as convolution (Blackman and Tukey, 1959). In one-dimension this operation can be expressed as:

$$O(x) = \int_0^{\infty} I(x-\lambda)S(\lambda) d\lambda \quad (1)$$

where $I(x)$ is the input function, $S(\lambda)$ is the lagged filter, and $O(x)$ is the filtered output. The Fourier-Transform of the convolution integral is:

$$O(\omega) = I(\omega) \cdot S(\omega) \quad (2)$$

where $I(\omega)$ is the input function in the frequency-domain, $S(\omega)$ is the filter, and $O(\omega)$ is the filtered output. Filtering in the frequency-domain requires only that the components of the filter be multiplied by those of the input function, whereas filtering in the time-domain is more complicated in that it requires folding, multiplication, shifting and summation (Cohn, 1975).

The actual filtering process, whether convolution in the time-domain or multiplication in the frequency-domain, simply changes the amplitudes of some of the component sinusoids. Digital filtering enhances the interpretation of a particular waveform by suppressing the amplitudes of conflicting sinusoids that fall outside the desired frequency range. This process is analogous to the action of an automobile suspension, where the springs and shock absorbers filter out the short-period undulations while passing long-wavelengths bumps and hills without change (Robinson, 1968).

For digital filtering in the frequency-domain, all that is necessary is to compute the one-dimensional Fourier-Transform, delete undesired frequencies (noise) by multiplying by zero, then return to the time-domain through the inverse-transform (Cohn and Robinson, 1975).

Because filtering in the frequency-domain is achieved with much greater speed and efficiency than its time-domain convolution counterpart, a technique utilizing both numerical integration and digital frequency-domain filtering was developed. This method called the *Spectrally Filtered Integration* technique (SFI) (Leonard, 1977), is used to differentiate the true "unit-valued" amount of sediment moved by various process agents at given frequencies.

Simply, given a function $f(t)$ (in this case, grams-per-liter of sediment movement versus time), the total amount of sedimentation over a particular time span or zone can be expressed as:

$$\int_a^b f(t) dt \quad (3)$$

which is step (A) in Fig. 3.

Taking Fourier-Transform of this function and deleting the mean value (Fig. 3, B) produces the function $f(\omega)$ or the frequency-domain spectrum of the original amount of grams-per-liter of movement (Fig. 3, C).

By deleting the amplitudes at various frequencies (Fig. 3, D) and substituting zeros in both the real and imaginary coefficients, one in effect places a filter on the data. Figure 3, D, shows a simple band pass filter that is applied to the frequency spectrum.

Next (Fig. 3, E) one applies the inverse-transform to this data and reassesses the effect of the deleted D.C. component while reordering the data matrix and considering the effects of the imaginary components. This operation results in $f'(t)$, or the filtered reconstruction of the original data (Fig. 3, F).

Since the units are maintained as an end-product, the integration:

$$\int_a^b f'(t)dt \quad (4)$$

gives the amount of transported material at all frequencies except the ones filtered.

By mere subtraction the residual area of the filtered frequencies is calculated (Fig. 3-G). This is the spectrally filtered integration method. In other words, the contribution of periodic stimuli (i.e., waves, edge waves, and other processes) to the sediment movement can be selectively removed and the resulting sediment concentrations can be calculated.

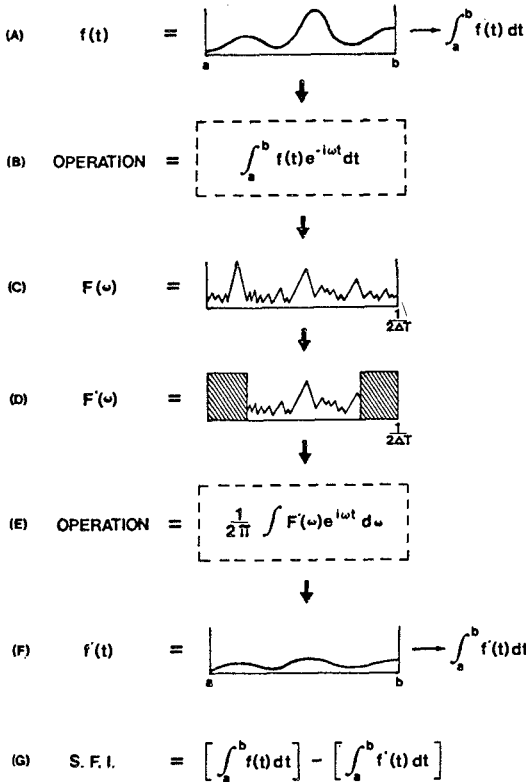
In this study it was chosen to determine and quantify the amount of sediment moved at low-frequencies (<0.01 Hz. or >100 seconds). The stimulus for this came from Brenninkmeyer (1975) who observed low-frequency movement in his data. The SFI analysis of this data included the application of a bandpass filter. The periodicities greater than 100 seconds were nulled along with the higher-frequency "noise." This "noise" included all frequencies greater than 0.5 Hertz (2 seconds). The variance within this high-frequency band can be attributed to the random variations of air bubbles present in the water column. This effect can be shown through visual observations of the almometer oscilloscope record where bubbles and surface foam exhibit a high-frequency variation. Another cause of high-frequency fluctuations is the vibration of the almometer and the anchoring auger in the presence of waves. We believe the construction of the 0.5 Hertz cutoff will eliminate all but a small portion of the error caused by the presence of air bubbles and vibrations. Therefore, the filtered data should contain only information on sediment movement.

Figure 3. The SFI technique in schematic form (below):

- A. The second order integration of the time-domain function $F(t)$.
- B. The Fourier Transformation of the function $F(t)$.
- C. The transformed function $F(\omega)$ to $F(\omega)$.
- D. The frequency-domain filter applied to the function $F(\omega)$.
- E. The inverse-transform of the function $F(\omega)$.
- F. The resultant time-domain function $F'(t)$ after frequency-domain filtering and the second-order integration of this function $F'(t)$.
- G. The determination of the residual amount of time-domain data, represented by the contribution of the filtered frequencies.

Note $1/2 T =$ the Nyquist frequency.

This diagram implies continuous functions; however, the analyses for this study were performed with discrete functions. Implicitly, the complex conjugant of the Fourier transform must be included in the SFI technique.



RESULTS

In order to determine sediment concentration as a function of elevation, the position of the bottom (datum) must be monitored. Bottom is defined, operationally, as that elevation which attained a time-averaged concentration of greater than 500 grams per liter. Bottom changes not only occur dynamically at high-frequencies, but also may exhibit an established trend. Figure 4 shows the changing absolute position of the bottom as a function of time zones during the increasing tide. At first glance, a disproportionate amount of burial appears in the onshore/offshore almmometer at Zone IV. This is interpreted as a sand bar created from the eroding berm.

By performing the Fourier transformation of the autocorrelation function of the time-domain records for the various changing sediment concentrations, information on the frequency or its reciprocal periodicity can be determined at elevations of high concentration variance throughout each time zone. A precise breakdown of contributions appears in Appendix I, A-E, which shows percentage contribution to the total variances (power) of selected bandwidths. The bandwidths chosen include: greater than 120 seconds, 120 to 60 seconds, 60 to 30 seconds, 30 to 15 seconds, 15 to 12 seconds, 12 to 10 seconds, 10 to 8 seconds, 8 to 6 seconds, and 6 to 4 seconds.

The bandwidth of greater than 120 seconds indicates the long periodicities of sediment movement. This change can perhaps be characterized as transient suspension events occurring within the sampling period. Some of these may be due to shelf waves (Munk, 1962). This band may also indicate the long term change of data string (i.e., fluctuations in bottom topography).

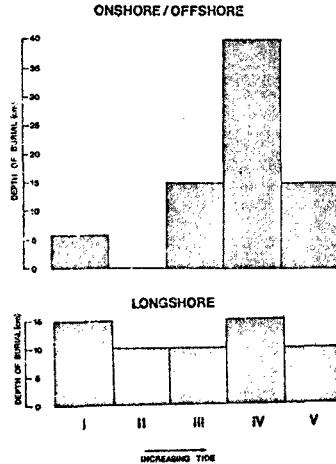


Figure 4. Depth of burial of the bottom of the almmometer in both the longshore and onshore/offshore for each zone.

The bandwidth between 60 and 120 seconds represents movement or changes that may be caused by surf beat (Munk, 1949; Tucker, 1950). Surf beat is the systematic low-frequency fluctuation in wave height created when two sets of small waves arrive simultaneously from two different storm sources. The constructive and destructive interference of these wave trains gives the impression of rhythmically varying wave heights on the beach.

The 60-to-30 second bandwidth input during storm conditions is difficult to explain. The processes that contribute to this moderately low-frequency may include the following: (1) The shore face is reflecting surging water. (2) The variations in the components of both standing and progressive edge waves (Bowen and Inman, 1969; and Huntley and Bowen, 1973, 1975). Huntley and Bowen (1973, 1975) measured edge waves in the field and found them to be subharmonic of the incoming waves. In the case of storm conditions, the various wave trains arriving may cause variations in these subharmonic edge waves. (3) Finally, the input process to this bandwidth may include the phase difference or time lag between the incoming bore (swash) and the returning backwash. Emery and Foster (1948) have observed this phenomenon, and suggest that it may be attributed to the interaction with the ground water table. Waddell (1976) also sees this relationship.

The possible causes of the remaining moderate-frequencies which are also the middle-periods of 30 to 4 seconds, may include combinations of the previously mentioned process with the addition of the major swell, breaker, and wave periods. The 10-to-8 and 8-to-6 second bands indicate the periods of the major wave and water velocity variance as indicated by their respective spectra.

Zonal Periodicity

Zone 1. The sediment power spectra for Time Zone 1 show similar characteristics, and generally appear in one form. Appendix I-A indicates a breakdown of percentage contribution of the total power to the various bandwidths. Generally, in the onshore/offshore direction, a majority of the variance of sediment movement occurs within the large band between 60 and 120 seconds. Just (0-5 cm) above the bottom, a major portion of the movements occur every 60 to 30 seconds with the highest peak at 40 seconds. This peak represents a contribution of slightly over 6 percent. As the elevation increases, the frequency of movement also increases with the preponderance of power residing in the 30-to-15 second bandwidth. At 10 centimeters and above, the 15-to-12 second band shows some activity, but not nearly as much as the 30-to-15 second band. Also, from 5 to 25 centimeters (above the bottom), approximately 30 percent of the remaining variances occur between 10 and 4 seconds. Seemingly, the major factor contributing to sand movement in this zone is the interaction of wave surges, which are exhibited as a subharmonic of the wave period.

In the longshore direction, the same trend can be seen with a majority of the power residing in the 30-to-15-second bandwidth. The bottom

sediment here also moves at a lower-frequency than the material in the water column.

Little information could have been gained from the wave and current records because of the noisy spectra created by instruments' poor response in alternating wet and dry conditions.

Zone II. During Time Zone II, the power spectra (Appendix I-B) reveal a general trend toward low periodic sediment movement. In the onshore/offshore direction, the strongest peaks are all longer than 120 seconds. Above 1 minute, approximately 30 percent of all the variances (power) for all the onshore/offshore elevations can be explained (Appendix I-B). Approximately 40 percent of the remaining variances lie within a band between 15 and 60 seconds, indicating some long-period water interaction creating sediment suspension events. Very little contribution came from the normal wave period (10 to 8 seconds).

The same trend exists for the longshore direction, except that it is more magnified. Approximately 50 percent of the sediment movement is explained at a frequency of greater than 120 seconds. No major contributions occur at a period of less than 15 seconds.

In contrast, the current and wave instruments show their strongest peaks at a band between 8 and 4 seconds. Therefore, the contribution to sediment movement by the normal wave and current activity in this zone is minimal.

Zone III. The spectra of Time Zone III (Appendix I-C) indicate peculiar properties. In the onshore/offshore direction at the 5 centimeter level, more than half the power is located in the greater than 120-second band. This is due to the long-term burial of the lower sensors. The resulting bands at this (5 cm) elevation are virtually undifferentiated. At the 15 centimeter elevation, however, the greatest contribution lies between 30 and 12 seconds, indicating that at this height, movement is still controlled by an interaction of the translational bore with the seaward returning water. At 25 centimeters, the greatest power is in the greater than 120-second band, but a strong peak is present in the 30-to-15 second interval.

In the longshore direction almost 80 percent of the contribution exists in the greater than 120-second band.

Zone IV. In Time Zone IV, the power spectra appear to take on diverse forms. In the onshore/offshore direction less contribution (Appendix I-D) comes from the greater than 120-second band than for the previous time zones. Generally, in upper elevations, more power is concentrated between 8 and 4 seconds, indicating the frequencies of waves and currents. Strong peaks do occur, however, in the water interaction band of 30 to 15 seconds. At 5 and 10 centimeters, the greatest contributions lie in the low-frequencies, with major peaks at greater than 120 seconds. Some sediment movement variance is seen in the 30 to 15 second band, as a response of translational water interaction. A small (10.8 percent) peak is found at the 5 centimeter level, showing that near the bottom normal

wave activity contributes to sediment movement.

In the longshore direction, the near bottom elevations of ≈ 0 and 5 centimeters show movement occurring at low-frequencies. A major break exists at 10 centimeters where the frequency of the major contributors occurs in the 8 to 4 second band. Only 5 centimeters above this level however, at 20 centimeters, sediment movement periodicities increased to between 60 and 5 seconds. At present no explanation can be given for this 10 centimeter anomaly.

Zone V. In the onshore/offshore direction of Time Zone V, the sediment power spectra (Appendix I-E) indicate generally low-frequency movement. At all elevations, approximately 20 percent of the contribution can be placed in the wave and current bandwidth. The water interaction band of 30 to 15 seconds shows greater than 10 percent contribution at elevations of 10 and 15 centimeters.

The longshore direction spectrum at 5 centimeters indicates approximately 75 percent of the contribution occurring above 30 seconds. The current and wave sensors spectra indicate that the strongest peaks occur between 10 and 4 seconds.

Amount of Sediment Moved

The integration of the time-domain records of sediment movement provides a reasonable estimate of the total sediment moved during each time zone. Figure 5 illustrates the total amount of sediment moved in the onshore/offshore direction as a function of near bottom elevation for each time zone.

In Time Zone I, the expected pattern of decreasing sediment movement with increasing elevation is present. Total movement on the bottom is over 350 kilograms per 13 minutes of "almometer-sensed" water volume (Table 1), whereas at an elevation of 25 centimeters, only 75 kilograms of sediment move. The decrease from bottom to top is linear, except at 15 centimeters, where the slope steepens, and movement decreases at a lower rate.

Zone II indicates the same trend in movement, although less movement is present at the bottom and at 5 centimeters than in Time Zone I. Interestingly, greater amounts of sediment were moved at the 10 centimeter level in Time Zone II than in Time Zone I, perhaps due to the presence of minor sediment concentration inversions at this level.

Zone III shows a peculiar divergence from the previous zones. At an elevation of 25 centimeters, approximately 250 kilograms of material moved, whereas below this level at 15 centimeters, only 170 kilograms moved. This phenomenon probably occurs because of sediment concentration inversions. Generally, more material was moved in Zone III than in Zones I and II.

In Time Zone IV, the total amount of movement decreases significantly and follows a pattern of decreasing quantity with increasing elevation.

Zone V also indicates less movement than the previous zones, except for a concentration inversion at 10 centimeters. This inversion may be the response of the oceanward flow of water present in a rip-current observed at this time by the array.

In the previous section, it was stated that the low-frequency, long period bands normally contained the most power contribution. It should be mentioned, however, that phase relationships play an extremely important role in determining what the percentage contributions really mean in terms of total material moved. If, for example, a band contains two large power spikes, the percentage contribution would also be large, but if these two peaks were 180 degrees out of phase, the resulting movement would be zero. This reasoning led to the development of the SFI method.

Utilizing the SFI technique, Table 2 presents a summary of the "time-averaged" quantity of sediment moved in each of the respective time zones. The "O" column represents the integrated total quantity (in grams corrected to one liter of water) seen by a photocell in respect to the volume of its particular field of "vision" (Table 1). In other words, these numbers are the grams of sediment per liter of water, one would statistically expect to find in any given second.

ZONE I	Elevation (cm)	TABLE 2			F O
		O	F	O-F	
Onshore- Offshore	25	.497	.107	0.39	0.22
	15	.621	.128	0.49	0.21
	10	1.29	.216	1.07	0.17
	5	3.70	.280	3.42	0.08
	≥0	6.36	.310	6.05	0.05
Longshore	20	.200	.038	0.16	0.19
	10	.302	.057	0.24	0.19
	5	.744	.146	0.60	0.20
ZONE II					
Onshore- Offshore	10	1.71	.274	1.44	0.16
	5	2.31	.536	1.77	0.23
	≥0	4.20	.636	3.57	0.15
Longshore	5	.938	.338	0.60	0.36
	≥0	7.05	.311	6.74	0.04
ZONE III					
Onshore- Offshore	25	2.23	.652	1.58	0.29
	15	1.79	.431	1.36	0.24
	5	5.29	.981	4.31	0.18
Longshore	5	1.91	.609	1.30	0.32
ZONE IV					
Onshore- Offshore	20	.315	.146	0.17	0.46
	15	.643	.251	0.39	0.39
	10	1.61	.459	1.15	0.28
	5	1.91	.522	1.39	0.27
Longshore	20	.147	.039	0.11	0.26
	10	.054	.022	0.03	0.41
	5	.595	.182	0.41	0.31
	≥0	4.28	.245	4.04	0.06
ZONE V					
Onshore- Offshore	25	.484	.269	0.22	0.56
	20	.757	.360	0.40	0.48
	15	.390	.205	0.18	0.53
	10	.828	.382	0.45	0.46
	5	1.51	.610	0.90	0.40
Longshore	5	2.25	.385	1.86	0.17

Table 2. Various parameters derived from the SFI technique

A. O equals the "time-averaged" total amount of sediment moved expressed in grams-per-liter per second.

B. F equals the "time-averaged" quantity of material moved at a periodicity greater than 100 seconds.

C. O-F equals the "time-averaged" quantity of sediment moved at periodicities between 2 and 100 seconds.

D. The ratio of F to O.

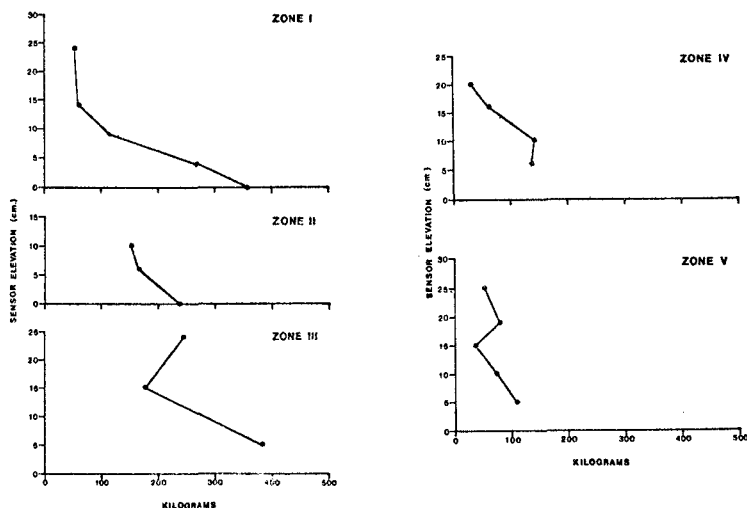


Figure 5. Corrected total amount of sediment movement in the onshore/offshore direction as a function of elevation for each zone.

The data taken from elevations in excess of 10 cm above the bed are in reasonable agreement with values of surf-zone sediment suspension measurements reported by other workers (Komar, 1978, Table 1); utilizing more direct measurement techniques. Those values include .13 g/l at Torrey Pines, California (Thornton, 1977), 0.26 g/l in spilling breakers at Price Inlet, South Carolina (Kana, 1976), 0.39 g/l at Nags Head, North Carolina (Fairchild, 1973), 0.53 g/l at Ventnor, New Jersey (Fairchild, 1973), 0.68 g/l at Pacific Beach, California (Watts, 1953) and 1.09 g/l at Price Inlet in plunging breakers (Kana, 1976).

Below 10 cm, however, the values of sediment concentration increase by several orders of magnitude. This is not surprising, since our data were obtained close to the bed in storm conditions. The "F" value is the amount of sediment moved at a periodicity greater than 100 seconds. Various other derived parameters contained in these tables are explained in the figure captions.

Low Period Contribution to Sediment Movement

Figure 6 illustrates the relationship between the percentage-ratio of the material moved at a periodicity greater than 100 seconds to the total amount of material moved. It can be seen that for the onshore/offshore direction for Zone I, the high-frequency contribution decreases with increasing elevation. This relationship is expected because sediment movement in the higher elevations should be less common than in the lower. In the longshore direction, the low frequency contribution seems to be undifferentiated as a function of depth.

Onshore/offshore sediment movement in Time Zone II indicates high-to mid-frequency motion on the bottom, with increasingly low-frequency

contribution to an elevation of 5 centimeters. This trend then reverses, and the contribution of lower-frequency decreases to an elevation of 10 centimeters. The longshore direction shows that low-frequency increases with increasing elevation.

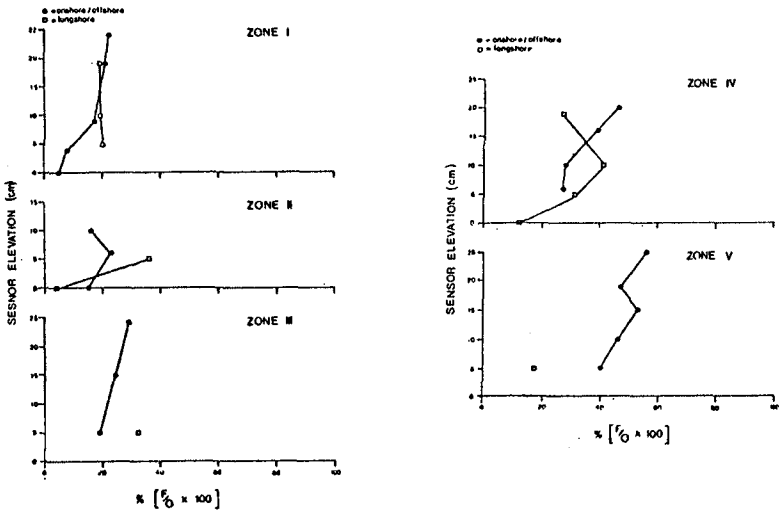


Figure 6. The ratio between the sediment moved at periodicities greater than 100 seconds (F) and the total sediment moved (O) for the five zones, as a function of elevation (in cm), in both the onshore/offshore and longshore directions. Note: Dark circles indicate onshore/offshore.

Zone III (onshore/offshore) also shows the expected relationship with 20 percent of sediment movement accounted for by the greater than 100-second periods at 5 centimeters above the bottom. This figure then increases to 30 percent at 25 centimeters.

As the water deepens, the low-frequency contributions tend to become more important. In Time Zone IV, the onshore/offshore direction reflects this expected relationship, but the total curve shifts to the right, indicating a generally more significant contribution by the low-frequencies. An anomalous trend occurs, however. In the longshore direction of Zone IV, at above the 10 centimeter elevation, the lower-frequencies become approximately a factor of 2 less significant. This reduction may be explained by sediment shedding off a sand bar, which buried the onshore/offshore sensors, but not those of the longshore.

In Zone V, the curve shifts further to the right, indicating a greater lower-frequency contribution in deeper water. A small shift to the left (higher-frequency contribution) can be seen at the 20 centimeter elevation, and is probably due to sediment "jetting" from the higher bar

elevation bounding the throat of a rip current.

In contrasting the five time zones for the onshore/offshore direction with the contribution of low-frequency movement, Figure 7 illustrates the relationship between the total sediment moved (expressed in decibels) and the ratio of sediment moved at low-frequencies (expressed in decibels). The decibel scale [$10 \log (\text{ratio})$] was chosen since it compacts both data sets to the same scales of the same order of magnitude. For the total sediment movement (TdB), the ratio was determined by contrasting the total amount moved in kilograms to a nominal movement of 1 kilogram, hence eliminating division by zero.

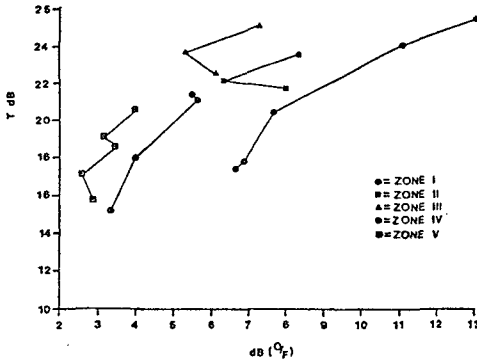


Figure 7. Relationship between the ratio of the total sediment moved (TdB) and the ratio of the total amount moved at low frequencies (dB O/F) for the onshore/offshore direction.

The zonal grouping shown indicates that, during storm conditions, high-frequency sediment movement decreases as the tide rises. This diagram also indicates that as time progresses, this relationship is virtually constant, i.e., it shows little if any differentiation due to the traditional dynamic zones.

CONCLUSIONS

Some general impressions can be extracted from the analysis of data concerning the nature and periodicity of sediment movement in the nearshore zone during storm conditions. A summary of the more salient conclusions follow:

(1) Standard time series analysis is insensitive to the study of quantitative periodic sediment transport in the nearshore zone. A technique has therefore been developed (the SFI method) which will isolate certain sediment movement frequencies caused by explained and inferred stimuli; wave period, edge waves, surf beat, shelf waves and interference of uprush and backwash. This method allows an analysis of the absolute amount of material moved by each of these inputs.

(2) During severe storm conditions sediment suspension and resuspension is more prevalent through the five time zones than during times

of milder wave conditions.

(3) The power spectra of sediment movement throughout various elevations, various zones and different directions exhibit diverse forms. Typically, however, during severe storm conditions, throughout all time zones, the power contained in the lower-frequencies is not as strong as that during normal (non-storm) conditions. If one were to characterize the most common process based upon the spectra, it would be the frequency of the water collision and interaction of two opposing velocity distributions. This is substantiated by current meter measurements. However, this relatively higher-frequency movement decreases as water deepens and lower frequency contributions tend to become more important to sediment transport. Nevertheless, contrasted to non-storm conditions sediment movement during storms is at a much higher-frequency.

Because these experiments represent only conditions which occurred during one storm event, much more data of this type must be acquired in order to characterize the processes interacting with the dynamic beach environment. This study is, therefore, more of a starting point than an end in itself.

ACKNOWLEDGMENTS

Many people and institutions have contributed to the fulfillment of the project. We thank the National Park Service, Cape Cod National Seashore, the computer centers of Boston University, Bryn Mawr College, Haverford College and Rensselaer Polytechnic Institute. Many thanks to B. Cohn, J. Filor, G. Hoffman, C. James, A. Niedoroda, and C. Rouleau. Financial support was provided by the Office of Naval Research Geography Program and the National Oceanographical and Atmospheric Administration (NOAA).

REFERENCES

- Blackman, R.B. and Tukey, J.W., 1958, The measurement of power spectra from the point of view of communications engineering: Dover, New York, 148 p.
- Bowen, A.J. and Inman, D.L., 1969, Rip currents, 2: laboratory and field observations: Jour. Geophys. Res., v. 74, p. 5479-5490.
- Brenninkmeyer, B.M., 1973, Synoptic surf zone sedimentation patterns: Ph. D. dissertation, Univ. Southern California, 274 p.
- Brenninkmeyer, B.M., 1975, Mode and period of sand transport in the surf zone: Proc. 14th Conf. on Coastal Engineering, p. 812-827.
- Brenninkmeyer, B.M., 1976a, In situ measurements of rapidly fluctuating high sediment concentrations: Marine Geol., v. 20, p. 117-128.
- Brenninkmeyer, B.M., 1976b, Sand fountains in the surf zone: in Davis, R. A. and Ethington, R.L. (eds.), Beach and nearshore sedimentation: Soc. Economic Paleontologists and Mineralogists Spec. Paper, 24, p. 69-91.
- Cohn, B.P., 1975, A forecast model for Great Lakes water levels: Ph.D. dissertation, Syracuse Univ., 235 p.

- Cohn, B.P. and Robinson, J.E., 1975, Cyclic fluctuations of water levels in Lake Ontario: Computers and Geosciences, v. 1, p. 105-108.
- Emery, K.O., and Foster, J.F., 1948, Water tables in marine beaches: Jour. Marine Res., v. 3, p. 644-654.
- Fairchild, J.C., 1973, Longshore transport of suspended sediment: Proc. 13th Conf. on Coastal Engineering, p. 1069-1088.
- Gentleman, W.M. and Sande, G., 1966, Fast Fourier transforms -- for fun and profit: A.F.I.P.S., Proc. Fall Joint Computer Conf., v. 29, p. 563-578.
- Good, I.J., 1958, The interaction algorithm and practical Fourier series: Jour. Roy. Statistical Soc., v. 20, p. 361-372.
- Huntley, D.A. and Bowen, A.J., 1973, Field observations of edge waves: Nature, v. 243, p. 160-161.
- Huntley, D.A. and Bowen, A.J., 1975, Comparison of the hydrodynamics of steep and shallow beaches: in Hails, J. and Carr, A. (eds.), Near-shore sediment dynamics and sedimentation: Wiley, New York, p. 69-110.
- Kana, T.W., 1976, Sediment transport rates and littoral processes near Price Inlet, S.C.: in Hayes, M.O. and Kana, T.W. (eds.), Guidebook, terrigenous clastic depositional environments: p. II-158-171.
- Komar, P.D., 1978, Relative quantities of suspension versus bed-load transport on beaches: Jour. Sedimentary Petrology, v. 48, p. 921-932.
- Leonard, J.E., 1977, Space-time sediment relationships in the nearshore zone: the case of storm conditions: Ph.D. dissertation, Boston University, 540 p.
- Leonard, J.E., Fisher, J.J., Godfrey, P.J., Leatherman, S.P., Goldsmith, V., Kaye, C.A., Nilson, H., Oldale, R.N. and Rosen, P.S., 1976, Coastal geology and geomorphology of Cape Cod: an aerial and ground view: in Cameron, B.W. (ed.), Geology of the Boston Area: Science Press, Princeton, N.J., p. 224-264.
- Marindin, H.L., 1889, Encroachment of the sea upon the coast of Cape Cod, Mass., as shown by the comparative studies, cross-sections of the shores of Cape Cod between Chatham and Highland Lighthouse: U.S. Coast and Geod. Survey Rept. for 1889, app. 12, p. 403-407.
- Munk, W.H., 1949, Surf beats: Trans. Am. Geophys. Union, v. 30, p. 849-854.
- Munk, W.H., 1962, Long ocean waves: in Hill, M.N. (ed.), The sea: Inter-science, New York, v. 1, p. 647-663.
- Robinson, J.E., 1968, Analysis by spatial filtering of some intermediate scale structures in southern Alberta: Ph.D. dissertation, Univ. Alberta, 193 p.
- Schiffman, A., 1965, Energy measurements of the swash-surf system: Limnology and Oceanography, v. 10, p. 255-260.
- Shepard, F.P. and Inman, D.L., 1951, Nearshore circulation: Proc. First Conf. on Coastal Engineering, p. 50-59.
- Thornton, E.B. and Morris, W.D., 1977, Suspended sediments measured within the surf zone: Coastal Sediments '77, p. 655-668.
- Tucker, M.J., 1950, Surf beats, sea waves of 1-5 min. period: Proc. Roy. Soc. London, Series A, v. 202, p. 565-573.

Waddell, E., 1976, Swash-groundwater-beach profile interactions: in Davis, R.A. and Ethington, R.L. (eds.), Beach and nearshore sedimentation: Soc. Economic Paleontologists and Mineralogists Spec. Publ. 24, p. 115-125.

Zeigler, J.M., 1964, Erosion on the cliffs of outer Cape Cod: tables and graphs: Woods Hole Oceanographic Inst., ref. no 64-21, 30 p.

APPENDIX I

(SECTION A-E)

Percent Contribution of Total Sediment Variance (Power) from the Spectra for Zones I-V at Selected Bandwidths

APPENDIX I-A
Zone I

ELEVATION	Bandwidth in Seconds								
	>120	120-60	60-30	30-15	15-12	12-10	10-8	8-6	6-4
Onshore/Offshore									
25 cm	4.4	3.8	9.3	21.3	12.7	6.7	10.1	10.7	13.5
15 cm	5.1	5.1	8.5	23.3	12.3	5.7	8.9	11.1	13.7
10 cm	6.9	5.4	7.9	18.6	16.7	7.6	10.9	10.7	9.7
5 cm	7.1	8.5	11.2	18.2	8.7	7.3	12.1	9.9	9.4
>0 cm	4.3	11.8	20.2	16.3	8.8	7.4	8.2	7.3	9.9
Longshore									
20 cm	4.7	5.3	10.0	24.0	12.9	5.3	11.9	10.6	11.0
10 cm	15.1	4.7	12.7	25.5	11.4	6.2	11.1	8.6	11.0
5 cm	11.1	5.3	18.1	23.6	12.2	4.6	8.8	6.8	7.0

APPENDIX I-B
Zone II

ELEVATION	Bandwidth in Seconds								
	>120	120-60	60-30	30-15	15-12	12-10	10-8	8-6	6-4
Onshore/Offshore									
10 cm	15.2	14.0	18.3	18.7	7.6	4.2	4.3	6.7	2.9
5 cm	22.0	13.9	19.2	19.1	6.3	2.6	3.3	5.6	5.1
>0 cm	21.0	16.0	19.1	17.1	5.7	2.1	4.2	6.0	5.1
Longshore									
5 cm	48.6	16.5	11.3	13.5	2.7	1.8	2.6	1.8	2.1
>0 cm	50.9	11.1	8.0	11.9	1.8	3.1	2.9	2.6	3.7

APPENDIX 1-C
Zone III

ELEVATION	Bandwidth in Seconds								
	>120	120-60	60-30	30-15	15-12	12-10	10-8	8-6	6-4
Onshore/Offshore									
25 cm	47.9	8.4	6.7	11.3	6.8	3.5	4.3	4.4	4.1
15 cm	23.2	12.0	7.3	14.2	11.6	6.4	8.1	8.6	5.3
5 cm	59.1	6.2	2.3	7.3	6.6	3.4	3.6	4.2	4.0
Longshore									
5 cm	79.7	4.8	3.7	4.7	1.8	0.7	1.0	1.7	1.0

APPENDIX 1-D
Zone IV

ELEVATION	Bandwidth in Seconds								
	>120	120-60	60-30	30-15	15-12	12-10	10-8	8-6	6-4
Onshore/Offshore									
20 cm	7.7	6.3	5.3	17.2	7.2	8.8	8.0	18.8	14.0
15 cm	10.0	5.7	11.2	15.2	13.3	6.0	5.7	16.4	10.4
10 cm	23.0	18.9	13.6	12.7	5.3	3.2	4.5	8.9	5.3
5 cm	21.9	12.9	15.5	11.3	7.3	4.4	5.5	10.8	5.4
Longshore									
20 cm	12.9	11.6	16.6	10.4	6.1	6.1	9.0	9.1	9.6
10 cm	8.4	11.6	2.9	13.6	9.8	5.0	11.8	17.1	10.6
5 cm	42.8	12.6	11.6	9.6	2.6	3.0	3.6	7.8	4.0
20 cm	53.4	10.1	11.4	7.9	1.7	1.9	1.9	2.9	2.3

APPENDIX 1-E
Zone V

ELEVATION	Bandwidth in Seconds								
	>120	120-60	60-30	30-15	15-12	12-10	10-8	8-6	6-4
Onshore/Offshore									
25 cm	33.7	18.4	11.4	8.3	5.3	1.9	3.9	5.8	7.1
20 cm	41.5	7.7	8.1	8.2	4.2	2.4	4.9	8.4	9.2
15 cm	19.9	11.9	8.4	14.2	9.5	1.7	7.6	10.4	11.5
10 cm	26.1	7.3	10.8	13.7	8.0	2.0	5.4	11.0	9.8
5 cm	39.8	5.6	9.3	8.6	6.1	2.9	5.5	10.8	7.2
Longshore									
5 cm	56.1	8.9	9.5	9.9	3.7	2.1	3.9	2.7	2.0

CHAPTER 106
SLED SYSTEM FOR PROFILING SUSPENDED
LITTORAL DRIFT

by

J. P. Coakley¹, H. A. Savile², M. Pedrosa², and M. Larocque²

INTRODUCTION

There are many factors which suggest that littoral zone processes in the Great Lakes differ substantially from those of the marine coasts described in the existing coastal research literature. Among these factors are the lack of an appreciable tidal cycle; the predominance of relatively short, steep, waves; the virtual absence of swell waves; and the presence of shore fast ice in winter. As a result, many of the empirical relationships derived for marine coasts might be of questionable applicability to Great Lakes coasts. The present study, which represents only one phase of a long-term project designed to develop more specific littoral transport relationships, is aimed at obtaining accurate, direct estimates of the actual littoral transport at an experimental site located at the western end of Lake Ontario.

This paper will describe a mechanical system designed to collect a series of time-averaged samples of suspended sediment for concentration determinations as well as flow velocity and water depth at locations across the surf zone. Some preliminary results of the field program using the system will also be presented and discussed.

BACKGROUND

A number of researchers in the U.S.A. (Watts, 1953; Fairchild, 1972; Brenninkmeyer, 1974), Japan (Hom-ma and Horikawa, 1962; Noda, 1967), and other countries (Aibulatov, 1957; Jensen and Sorensen, 1972; and Kilner, 1976) have published techniques for measuring suspended sediment transport in the nearshore zone. Because of the variety of process factors operating there and the presence of breaking waves, this is usually not an easy task. From an operational point of view, the two most common problems involved in such measurement are the physical spanning of the zone (usually more than 100 m in width), and the designing of a measurement platform rugged enough to withstand the highly turbulent conditions that typify this area. Most of the work cited above has involved the use of pump samplers manipulated along a pier or a specially constructed tramway, or cumulative samplers such as the moored bamboo samplers used in the Japanese research. From an interpretation point of view, the main problem lies in the unsteadiness of the phenomenon both in time and space, due to the periodic or oscillatory nature of the driving processes in sediment suspension. This unsteadiness contributes to making the establishment of theoretical models of the process very difficult.

¹Hydraulics Research Division

²Scientific Support Division
National Water Research Institute
Canada Centre for Inland Waters
Burlington, Ontario

Nevertheless, the concept of relating quantitatively the total suspended sediment transport to the total littoral transport rate is generally recognized to be a valid one (Dean, 1973) and has the potential of improving considerably on previous direct techniques such as sand tracers. Simply stated, the concept entails the determination of the suspended sediment volume along a transect normal to the longshore currents of the littoral zone. By coupling these data with concurrent measurement of the flow velocity of the water column in a manner analogous to river discharge measurements, it should be possible to obtain a good estimate of the rate and direction of littoral transport. The word "estimate" is deliberately chosen since the unknown proportion of total transport in the form of bed load is not taken into account. Our experience with profile changes in the Great Lakes, however, leads us to believe that the dominantly bed load transport which occurs between storms is relatively minor, so by concentrating on storms when most of the material transported is suspended above the bed for some period of time at least, we feel that the estimate we obtain still represents an improvement on other techniques described to date in the literature. Three important factors, however, must be taken into account. One; the unsteady nature of the process means that the suspended sediment concentrations at a given location vary with time at a frequency related mainly to the orbital motions of the water particles under the waves (Brenninkmeyer, 1974), so care must be taken to obtain measurements over a period long enough for these variations to be averaged out. The variation produced by unsteadiness should also be significantly reduced if measurements were taken during fully developed turbulent conditions, i.e. during storms of moderate intensity. Two; the distribution curve for both sediment concentration and flow velocity with respect to the vertical (or depth) axis is well-known to be of a quasi-exponential form with values for both changing rapidly in the lower part of the curve, and becoming more uniform in the upper part. This makes it essential that measurements be biased toward obtaining sufficient readings near the bed. Finally; studies by Komar (1971) and Aibulatov (1957) demonstrate that the littoral transport rate varies across the surf zone as well. Thus, measurements must be spaced at intervals along the surf zone transect so that this horizontal distribution can be taken into account. Furthermore, since a proper measurement of instantaneous depth values is critical in a zone where rapid bottom topographical changes are occurring continually, the system must be designed to also measure depth, or height of the water column.

In summary, if the above constraints are successfully met, then the estimated total longshore sediment flux (Q_{long}) could be expressed as:

$$Q_{long} = \int_{j=0}^x \int_{i=0}^z (C_{ij} V_{ij} dz) dx$$

where: x = width of transect; V_{ij} = longshore component of the flow at level i and horizontal position, j ; z = vertical axis (or depth); C_{ij} = concentration of suspended sediments at level i and position j ; and dz, dx = vertical and horizontal gradient, respectively.

It is evident that, in such an experiment, onshore-offshore sediment transport would at best be only qualitatively indicated, mainly from the flow direction measurements. Also, variations in longshore transport rate parallel to the shore would require additional transects. Such a three-dimensional approach is beyond the scope of this experiment.

DESIGN OF THE PROTOTYPE SYSTEM

After a thorough investigation of all the techniques described in the literature, we finally chose the profiling system described below. The system consists of a low-slung, rugged sled towed and positioned along a fixed cableway by a shore-based winch (Figure 1). The system was designed and constructed at the National Water Research Institute and was used for the first time during a program of field measurements carried out in late 1977. The main components of the system are:

1. The Surf Sled Instrument Platform

The Surf Sled, shown in Figure 2, was adapted from a similar concept described in Reimitz and Ross (1971) and Teleki *et al* (1976). It measures 2.84 m in length, 1.68 m in width, and stands approximately 30 cm high. Because of its open-work frame and welded 0.5 cm gauge aluminium plate construction, its total displacement in water was only 340 kg. The sled was fitted with wide (35 cm) runners or skis to minimize excess loading and penetration into the sand substrate. Hinged towing yokes are attached to both ends for towing the sled out and in. The flat, open-work top surface carries the sampling accessories, power and electronics packages, and recorder cylinders.

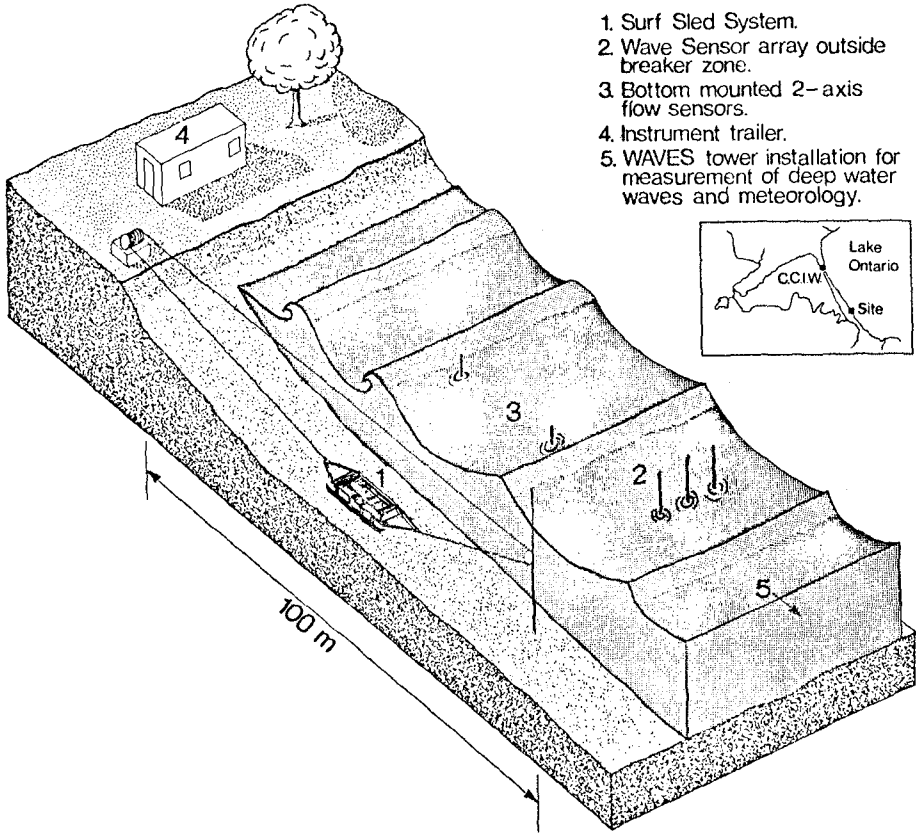
Protruding forward from one of the corners of the sled, and aligned parallel to its length, is a 1.5 m long rigid boom, framed in the shape of an elongated parallelogram, and articulated at the base. At the end of this boom is located the two-axis current sensors and the intake for the sampler pump. During field operations, the sled was intended to be configured with the boom pointing lakeward or in front of the sled body.

At each sampling position the boom is programmed to move to three vertical sampling/sensing positions: 10 cm, 30 cm, and 100 cm above the lake bottom. The lake bottom is defined as being 5 cm above the forward projection of the sled runners, to allow for some settling of the sled into the sand substrate. The power and switching systems for moving the boom are described in a later section.

2. Sampling System

The sampling pump used presently, a Jabsco 12 V D.C. Mini Puppy model, is mounted inside the power distribution box and draws through a sample intake at the end of the boom. The intake is equipped with a 2 mm mesh strainer to remove large objects which might damage or clog the system. From the pump, which provides twice the desired flow, the sample goes to a flow splitter. One half goes to waste and the other goes to the distribution valve. This is a rotary, 60 position, valve driven by a commercially available, air operated rotary table. This table is operated via a solenoid valve operated by a momentary, 0.1 second, 12 V pulse from the sequencer through a monostable circuit. The valve output is divided alternately into 30 waste and 30 sample positions. In operation the valve is held in the waste position for 15 seconds while the pump purges the lines and is then shifted to a sample position to fill a sample bag in the rack at the stern of the sled. The sample bags are slightly modified urinary

LITTORAL TRANSPORT EXPERIMENTAL SITE



1. Surf Sled System.
2. Wave Sensor array outside breaker zone.
3. Bottom mounted 2-axis flow sensors.
4. Instrument trailer.
5. WAVES tower installation for measurement of deep water waves and meteorology.

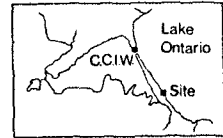


Figure 1 Sketch of the physical layout of the site where the system for profiling littoral drift was installed, showing winch-driven cableway and Surf Sled (not to scale). Other sensors for monitoring littoral processes are shown.

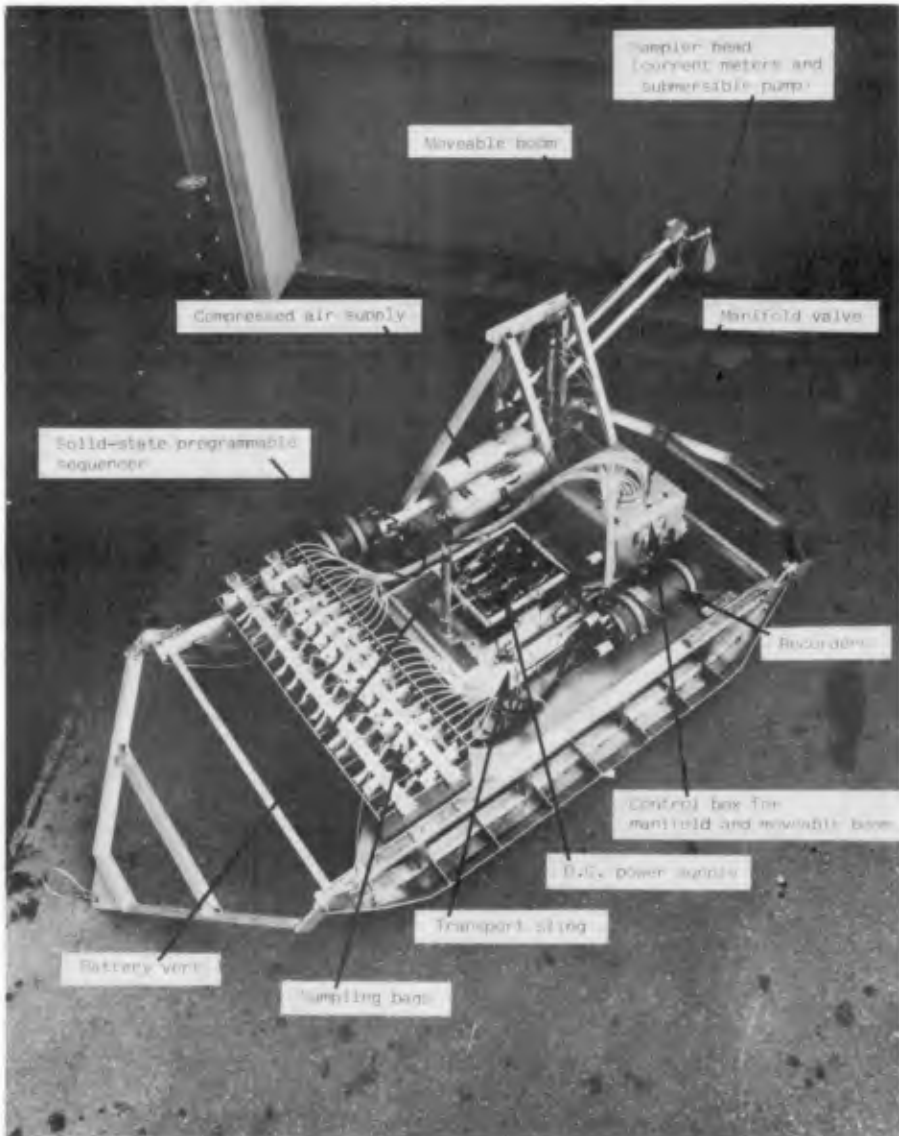


Figure 2 The Surf Sled, showing labelled major components. Overall length: 2.84 m.

catheterization bags, cutter Resiflex #950-19, with the air vent heat-sealed off. Sample size ranges from 1200-1800 ml of sand/water suspension.

3. Sensing and Recording Sub-System

The sensing of water flow is performed by two (Bendix B10 ducted impeller type) flow sensors mounted orthogonally, one above the other, at the end of the sled's 1.5 m moveable boom. The sensors have their central axes parallel to the horizontal plan and sense the water flow bidirectionally at the three preprogrammed boom positions, while suspended sediment samples are taken automatically just beneath them. The impellers of the sensors rotate and produce five pulses for each revolution. These pulses are converted to analog output which is 1 mV per 5.14 cm/s.

The sensing of instantaneous water depth is performed by a sensitive and fast (<.1 s response) pressure transducer (Gould PA 822-15) mounted on the sled platform 32 cm above the bed. The amplifier output is 18.4 mV/m.

The analog recording of water flow (two bidirectional axes "x" and "y") and the depth of the sled track is carried out by two Rustrak Potentiometric recorders (Model 3400 - dual channel for the x and y flow components, and model 400 - single channel for depth).

Two event markers are also used to record each boom position at a station on the x-y recorder and the arrival at each station on the depth recorder.

4. Programmable Sequencer and Control System

This apparatus controls, via timed electronic impulses to the various solenoid or on-off switching units, the sequence of functions performed by the sled during a sampling/sensing traverse of the surf zone. In brief, the system is activated on the beach prior to immersion and after a pre-determined time lapse (sufficient to enable it to reach the first station), goes through the following sequence:

- i) Pump is switched "on" at the exhaust mode; sampler arm is lowered by solenoid-controlled pneumatic action of both air cylinders to the lowest position (position 1-0.10 m above the bed). At this position, a switch on the moveable boom closes and causes an event mark to be made on the recorder chart. Exhaust mode lasts for 15 seconds exactly. This time is sufficient to purge the lines of water/sediment from the previous sample.
- ii) Sampler is then switched (by solenoid impulse) to the sample mode and collects a sample over a period of 44 seconds.
- iii) Solenoid switches sampler to exhaust mode; sampler arm rises to position 2 (0.30 m above the bed). This event is marked again on recorder. Exhaust cycle lasts for 15 seconds.
- iv) Sampler is switched to sample mode, and collects a sample over a period of 44 seconds.

- v) Sampler is switched to exhaust while the arm moves to position 3 (1.0 m above the bed); exhaust time - 15 seconds.
- vi) Event marker indicates arrival at position 3 and sample mode is activated. Sample collected over a period of 44 seconds.
- vii) Sequence ends and pump is shut off; event marked on both pressure and current records; sampler arm stays in "up" position; sampler itself switched to exhaust mode but this is not activated until the arrival at the next station when the pump is switched on again.
- viii) Sled is towed to the next station where the above sequence is repeated. After the last station (up to 10 stations possible), all systems are shut down and the sled is returned to the beach for unloading and reactivation for the next run.

5. Power Supply Systems

- i) The 12 V D.C. supply consists of two 150 A lead acid batteries arranged in parallel. The tops of the batteries are potted with polyester to electrically insulate all connections. Venting and pressure compensation are achieved by manifolding together all the battery vents and running the common vent line to the top of a sealed reservoir which is open at the bottom. The power is supplied through "E.O." connectors to the distribution box.
- ii) The 115 V A.C. supply consists of an inverter, "Abbott KNGT-115-60, which draws 12 V D.C. from the terminal bus in the power distribution box and outputs up to 60 VA of 115 V 60 Hz sine wave power for driving the chart recorders.
- iii) The compressed air supply consists of a pair of 224 m³ capacity "SCUBA" cylinders and associated reducing valves. One cylinder is used to pressure compensate the power distribution box. The other provides air at 0.83 M Pa to move the sampling arm and the distribution valve via the solenoid valves.

6. Winch and Cableway

The sled is moved by means of a cableway extending 100 m out into the surf zone. The shore end terminates above the maximum wave runup point on the beach. Both ends of the cableway are secured to jettied-in piles which penetrate 5 m into the soil. The piles are in two parts joined with a bolted flange connection at ground level. A middle pile is located at the top of the beach 1 m away from the centreline of the cableway and carries an arm with sheaves to lift the cable over the abrupt change in slope at that point. The winch is housed in a sheet metal garden-type shed on shore and is of the friction wheel type having a 2.2 KW S.C.R. controlled motor through reduction gearing. The winch is free to move fore and aft on teflon sliders and tension is applied to the system by means of a counterweight and multiple purchase. The tension in each leg of the 9.5 mm diameter wire rope is approximately 7.8 KN which is sufficient to provide traction on the winch drive wheel and to avoid whipping caused by wave action yet provide an adequate safety factor.

The offshore pile is guyed to eight anchors jettied into a depth of 5 m and the two onshore piles are unguyed. Grease nipples and bronze sleeves are fitted to all sheaves.

An electronic meter wheel indicates the position of the sled to the nearest 1 m. The cable is also marked to give an emergency stop point should the meter wheel fail.

FIELD OPERATIONS

The system described above was tested and used in littoral drift studies during the fall of 1977. The field operations were located at Hamilton Beach at the western end of Lake Ontario (see inset, Figure 1). Length of the surf zone transect was approximately 100 m (cableway length was 135 m) and the transect terminated in roughly 3.5 m of water.

During the period October 21 - December 5, 1977, a total of 16 experiments, covering moderate to storm-wave conditions, were carried out. In spite of breaking waves as high as 3 m, the system suffered no structural damage. Seven of the runs yielded complete data sets, i.e. full sample bags and complete depth/flow records.

PRELIMINARY RESULTS

1. Reproducibility

In order to test the reproducibility of the measured data, the sled was positioned at a station roughly midway across the transect (depth 1.4 m) over a full cycle. Figure 3 shows the plotted results from a series of seven complete vertical profiles taken at that location. In spite of the small sample size, the results show reasonable internal consistency.

2. Effect of Sled on Flow and Suspension

Two tests of this effect were carried out. One involved the visual inspection of the sled operation by divers. This test was, of necessity, carried out in moderate wave conditions. However, the divers noted no resuspension phenomena that were obviously related to the presence of the sled in the oscillating flow field caused by the waves.

The second test was carried out during a storm and involved the reversing of the sensor/sampler boom position with respect to the sled, i.e. the sled's normal confirmation was altered so that these components were on the landward side. This placed them in the lee of the propagation direction of the wave bore. The discharge results obtained in this configuration were more than double those of a run immediately preceding it, in which the normal forward configuration of the sensor/sampler head was used (1050 m³/hr versus 440 m³/hr). This indicates clearly that there is a sled effect on the discharge quantities calculated, and that the reversed configuration clearly overestimates the actual discharge. However, we do not yet know whether there is an appreciable sled effect on discharge values obtained using the normal configuration during storms. Experiments are presently being planned to investigate this further using a scale model and simulated wave conditions inside the HRD wind/wave flume.

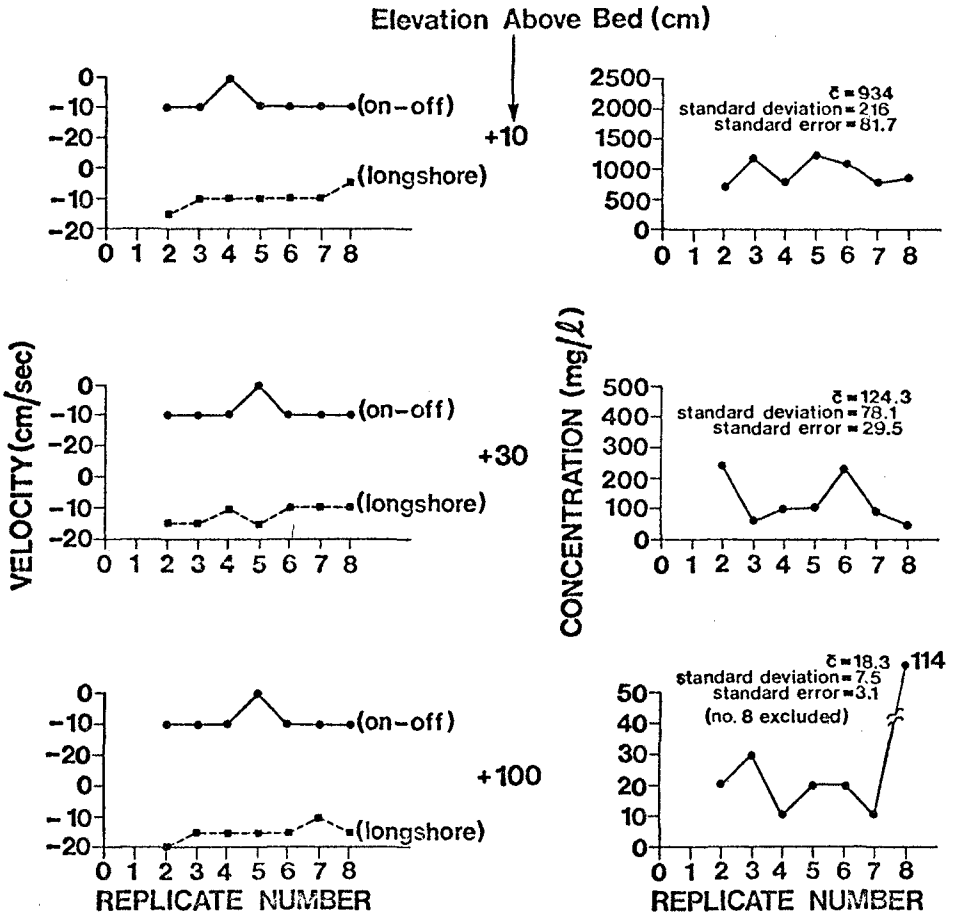


Figure 3 Plot of replicate measurements of two-axis flow velocity and concentration at a single station along the surf zone transect. The station was located 50 m from the shoreline at a depth of 1.4 m. Wave parameters during the run were: significant wave height - 0.8 m, and period - 2.5 s. For the flow values, negative indicates on-shore (on-offshore component) or toward the North (longshore component).

3. Magnitude and Distribution of Suspended Sediment Discharge

As stated previously, the number of complete data sets (flow velocity/suspended sediment concentration couples) is at this time too small to allow any broad statement on transport rates to be made. Furthermore, due to the fact that dry-weight/volume concentrations were used, we might want to revise the analysis procedure at some later date to make it more comparable with other studies. Nevertheless, in order to illustrate the final results of the system, we present a plot of the variables (concentration, longshore component of flow, calculated discharge versus distance along the surf-zone transect for a single experiment conducted during a severe storm on December 5, 1977 (Figure 4). Wave statistics were as follows: H -186 cm, T -6.1 sec, and wave angle -1.8° . These wave data were measured during the experiment at a three-staff wave array just outside the breaker zone in 5 m of water (Figure 1). Waves at the time were mostly of the plunging type. The value shown for discharge is based on a dry weight-to-volume conversion factor of 1600 kg to 1 m³.

The data appear to have an expectedly high variability both in time and space, so any further discussion of the results ought to await the collection of a more statistically valid data base. To this end, we are continuing our data collection into at least the winter of 1978 and spring of 1979.

CONCLUSIONS

The system described above was designed and constructed to collect profile data on suspended sediment concentration and flows velocity across a transect spanning the surf zone of western Lake Ontario. Experiments carried out to date have demonstrated that the system functioned well under conditions which at times exceeded the design criteria.

Because of the small data base compiled thus far, a full data analysis is still in the initial stages. However, preliminary analysis indicates that the figures obtained are reasonable and internally consistent.

REFERENCES

- Aibulatov, N. A. 1957. "Determination of the Magnitude of Suspended Sand Currents along Seashores". DOKL. AKAD. NAUK. SSSR, Vol. 116, No. 5, pp. 1-6. (Engl. Trans.)
- Brenninkmeyer, B. M., 1974. "Mode and Period of Sand Transport in the Surf Zone". Proc. 14th Conf. Coastal Eng., Chap. 46, pp. 812-827.
- Dean, R. G., 1973. "Heuristic Models of Sand Transport in the Surf Zone". Sydney Australia, 1973. (Abstract) Inst. of Eng.
- Fairchild, J. C., 1972. "Longshore Transportation of Suspended Sediment". Proc. 13th Coastal Eng. Conf., Vancouver, pp. 1069-1087.
- Hom-ma, M. and K. Horikawa, 1962. "Suspended Sediment due to Wave Action". Proc. 8th Coastal. Eng. Conf., ASCE, Mexico City, pp. 168-193.

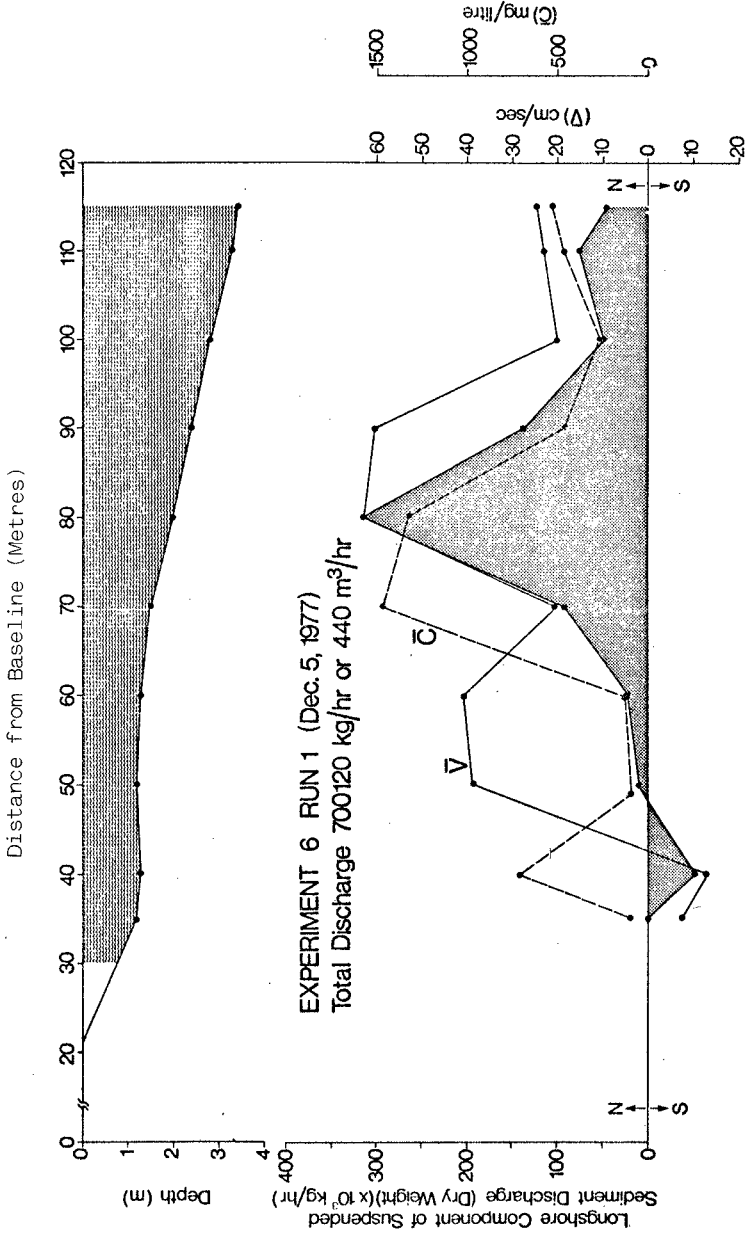


Figure 4 Sample distribution of depth-averaged longshore current velocity, suspended sediment concentration, and calculated suspended sediment discharge (shaded) across the surf zone transect for a single profiling run. At the top is shown the depth profile recorded by the sled.

- Jensen, J. K. and T. Sorensen, 1972. "Measurement of Sediment Suspension in Combinations of Waves and Currents". Proc. 13th Conf. Coastal Eng., Vol. 2, pp. 1097-1104.
- Kilner, F. R., 1976. "Measurement of Suspended Sediment in the Surf Zone". Abstract, 15th Conf. Coastal Eng., pp. 329-332.
- Komar, P. D., 1971. "The Mechanics of Sand Transport on Beaches". J. Geophys. Res., Vol. 76, No. 3.
- Noda, H., 1967. "Suspension of Sediment due to Wave Action". Proc. 14th Conf. on Coastal Eng. in Japan, pp. 306-314.
- Reimitz, E. and D. A. Ross, 1971. "The Sea Sled - A Device for Measuring Bottom Profiles in the Surf Zone". Marine Geology, Vol. 11, pp. M27-M32.
- Teleki, P. G., R. K. Schwartz and F. R. Musialowski, 1976. "Nearshore Waves, Currents and Sediment Response". Proc. 15th Coastal Eng. Conf., pp. 569-572.
- Watts, G. M., 1953. "Development and Field Tests of a Sampler for Suspended Sediment in Wave Action". B.E.Bd.T.M. 34.

CHAPTER 107

ON THE GEOMETRY OF RIPPLES DUE TO WAVES

by

M.S. YALIN¹ and E. KARAHAN²

ABSTRACT

The present paper is an attempt to determine a single curve for the prediction of the length of ripples forming due to wind waves in shallow waters. The curve is revealed by normalising the field and laboratory data supplied by various authors. The concept of the unified plot embodied by the single curve mentioned is developed by using dimensional methods and by considering the fact that the specific weight and the density of the cohesionless bed material do not affect the length of ripples in a detectable manner. It is shown that the present formulation of the length of ripples due to waves satisfies the requirement of transition into the corresponding formulation of the unidirectional flow ripples when the period and the amplitude of the oscillatory motion increase indefinitely, while their ratio (implying "the velocity") remains finite.

INTRODUCTION

The occurrence of ripples alters the roughness of the movable bed and thus exerts a considerable influence on the mechanical structure of the flow and on sediment transport. Hence it is not surprising that the formation of ripples has attracted the attention of many researchers for many years. In spite of this, however, our knowledge of the origin of ripples and our methods of predicting their dimensions is far from complete, and therefore some further contributions on the topic cannot be regarded as superfluous. The present paper concerns the prediction of the length (Λ) of ripples generated by short waves (wind waves) in shallow waters. It is assumed that the initial surface of the horizontal movable bed is flat, that the granular material is cohesionless, and that the oscillatory motion of the two phases (transporting fluid and transported sediment) is two-dimensional. Furthermore, it is assumed that this oscillatory motion is completely symmetrical, i.e. that no "not drift" is present.

DIMENSIONLESS FORMULATION OF RIPPLE LENGTH

If the internal geometry of a granular material (i.e. the shape of its grains and the shape of its sieve curve) is specified, then, under the conditions stated above, the oscillatory two-phase

¹ Professor of Hydraulics, Queen's University, Kingston, Canada.

² Tech. Univ. Istanbul, Post Doctoral Fellow, Queen's University, Kingston, Canada.

motion in the vicinity of the bed is determined by the following dimensionless variables (Refs. [1] and [2])

$$X = \frac{\gamma_s D^3}{\rho \nu^2} \quad Y = \frac{\rho D}{\gamma_s T^2} \quad Z = \frac{a}{D} \quad W = \frac{\rho_s}{\rho} \quad (1)$$

Here	$\rho =$ fluid density $\nu =$ kinematic viscosity $\rho_s =$ density of grains $\gamma_s =$ specific weight of grains in fluid $D =$ typical grain size (usually D_{50}) $T =$ period of the oscillatory fluid motion $a =$ orbit length of fluid motion at the boundary layer level] fluid] granular material] fluid kinematics
------	--	--

The dimensionless variables (1) ensure the possibility of determining any quantitative property of the oscillatory two-phase motion. This, however, does not mean that all four of these variables must necessarily be present in the expression of every property. The number of variables that must be present and the form of their appearance vary depending on the property under consideration.

The graphs produced to date for the prediction of ripple length Λ , or of its dimensionless version Λ/D , are in the form of a family of curves plotted versus the orbit length a or $Z = a/D$. (See e.g. Figs. 1 and 2 reproduced from Ref. [3] and [2] respectively.) Thus, contemporary practice is to treat Λ/D as a function of two variables, i.e. as

$$\frac{\Lambda}{D} = f(Z, \theta) \quad (2)$$

say, and to plot it by using Z as the abscissa and θ as a parameter differentiating individual curves (each curve corresponding to a constant value of θ). There is general agreement that Z is the most important variable in the expression of Λ/D . There is, however, no agreement yet as to what is exactly the "parameter θ ", i.e. how it should be expressed in terms of the remaining variables X , Y and W ; (see e.g. from Figs. 1 and 2 that in Ref. [2] the parameter θ is identified with the variable Y , whereas in Ref. [3] the curves are classified simply by using the grain size D). The next section is an attempt to reveal the expression of θ .

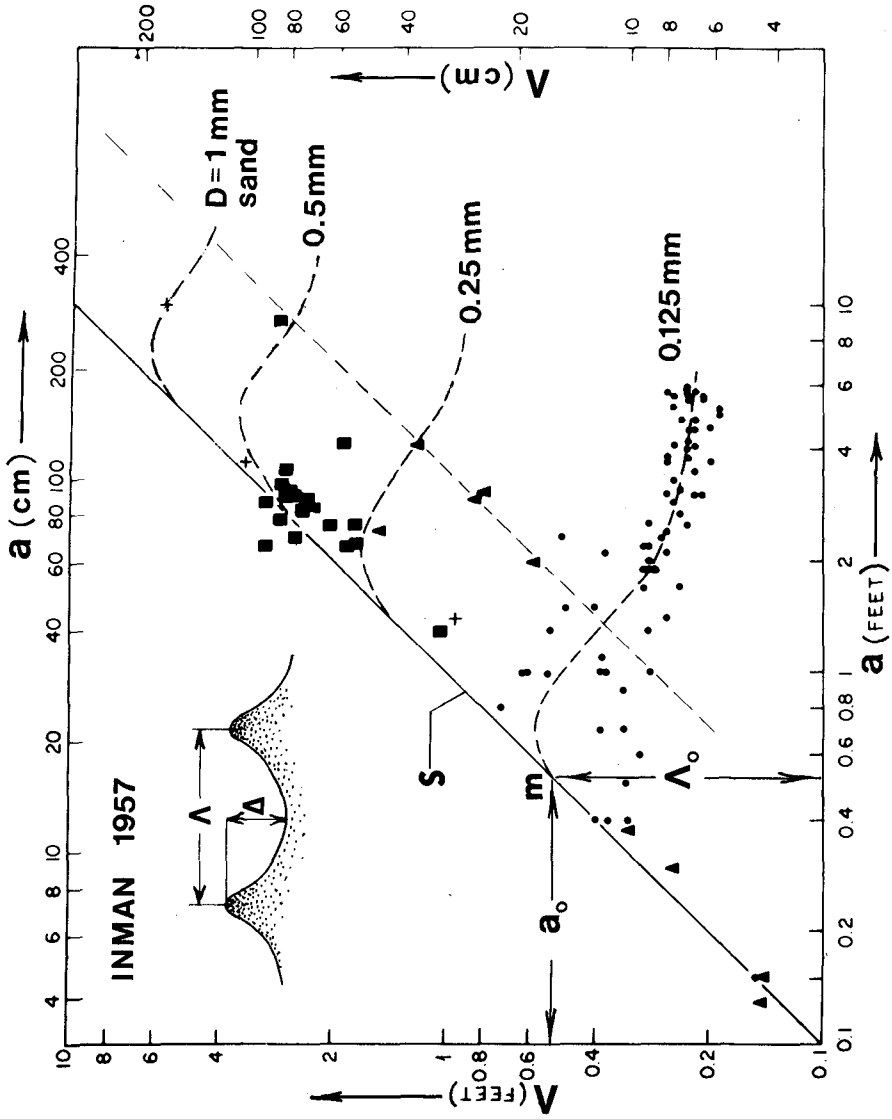


Fig. 1

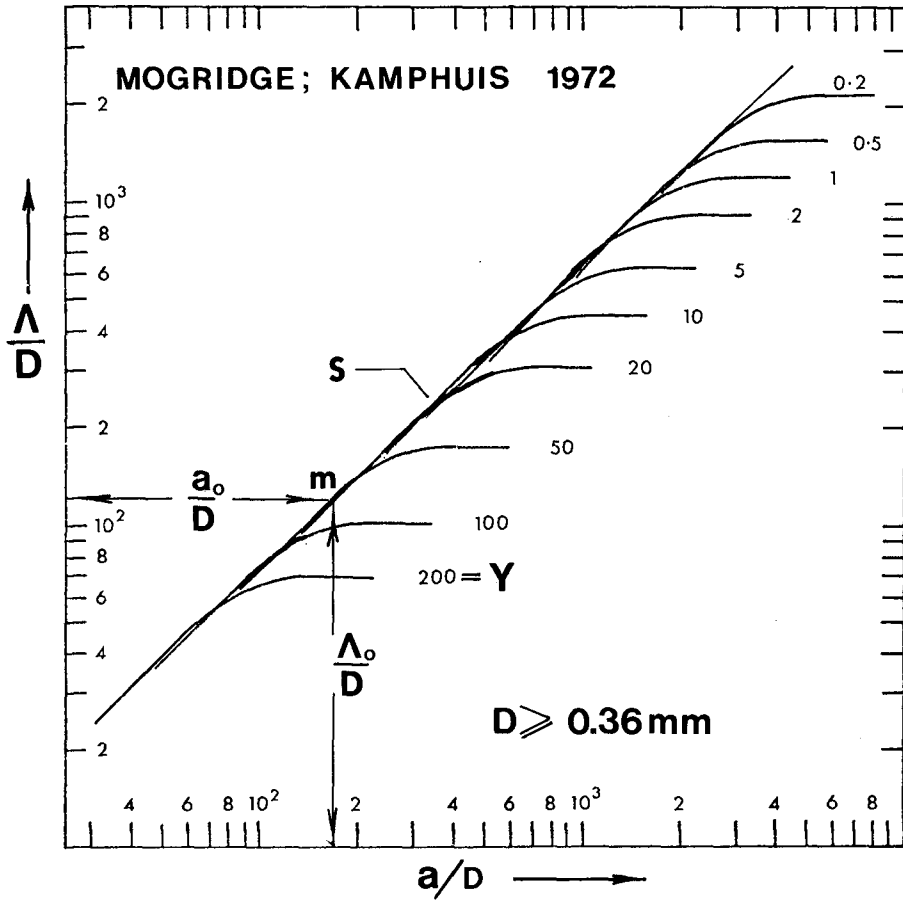


Fig. 2

PARAMETER Θ

Consider the information supplied by experiment.

In Ref. [4] the measurements of the ripple length were carried out for three different granular materials: quartz ($\gamma_s/\gamma = 1.65$); coal ($\gamma_s/\gamma = 0.50$) and steel ($\gamma_s/\gamma = 6.6$). No influence of γ_s or ρ_s was detected in the behaviour of the curves representing the variation of the ripple length Λ with the orbit length a . (See e.g. the three curves corresponding to the same grain size $D = 0.36$ mm in Fig. 1 of Ref. [4]).

Similarly from Fig. 3 of Ref. [1] it can be seen that the variation of Λ/D with Z for sand ($\gamma_s/\gamma = 1.65$) and perspex ($\gamma_s/\gamma = 0.19$) is almost the same if the period is the same ($T = 1.82s$) and if their grain size is comparable. (Compare e.g. the patterns of the points corresponding to $D = 0.52$ mm sand and $D = 0.48$ mm perspex in Fig. 3 of Ref. [1] (last two lines in the table on this graph)). These are only a few of the examples which indicate that the length Λ of ripples does not depend on the nature of the granular material, i.e. on its specific weight γ_s and density ρ_s . But the quantities γ_s and ρ_s can only disappear from the expression of Λ if W is excluded, while X and Y appear in the form of the product

$$X \cdot Y = \left(\frac{\gamma_s D^3}{\rho v^2} \right) \cdot \left(\frac{\rho D}{\gamma_s T} \right) = \frac{D^4}{v^2 T^2} \quad (3)$$

(or any power thereof). Accordingly, the relation determining Λ/D can be expressed in the form

$$\frac{\Lambda}{D} = f\left(Z, \frac{vT}{D}\right) \quad (4)$$

From the comparison of (4) and (2) it follows that

$$\Theta = \frac{vT}{D^2} = (X \cdot Y)^{-1/2} \quad (5)$$

DISCUSSION

(i) The parameter Θ which reflects the influence of T in conjunction with v is, at the same time, an indicator which shows how the viscous effect (at the bed) compares with that of turbulence. Indeed, let δ_v and δ_t be the boundary layer thicknesses of viscous and fully turbulent flows respectively. If the flows are oscillatory and the bed is flat, then

$$\delta_v \sim \sqrt{\nu T} \quad (6)$$

$$\text{and} \quad \delta_t \sim K_s \sim D \quad (7)$$

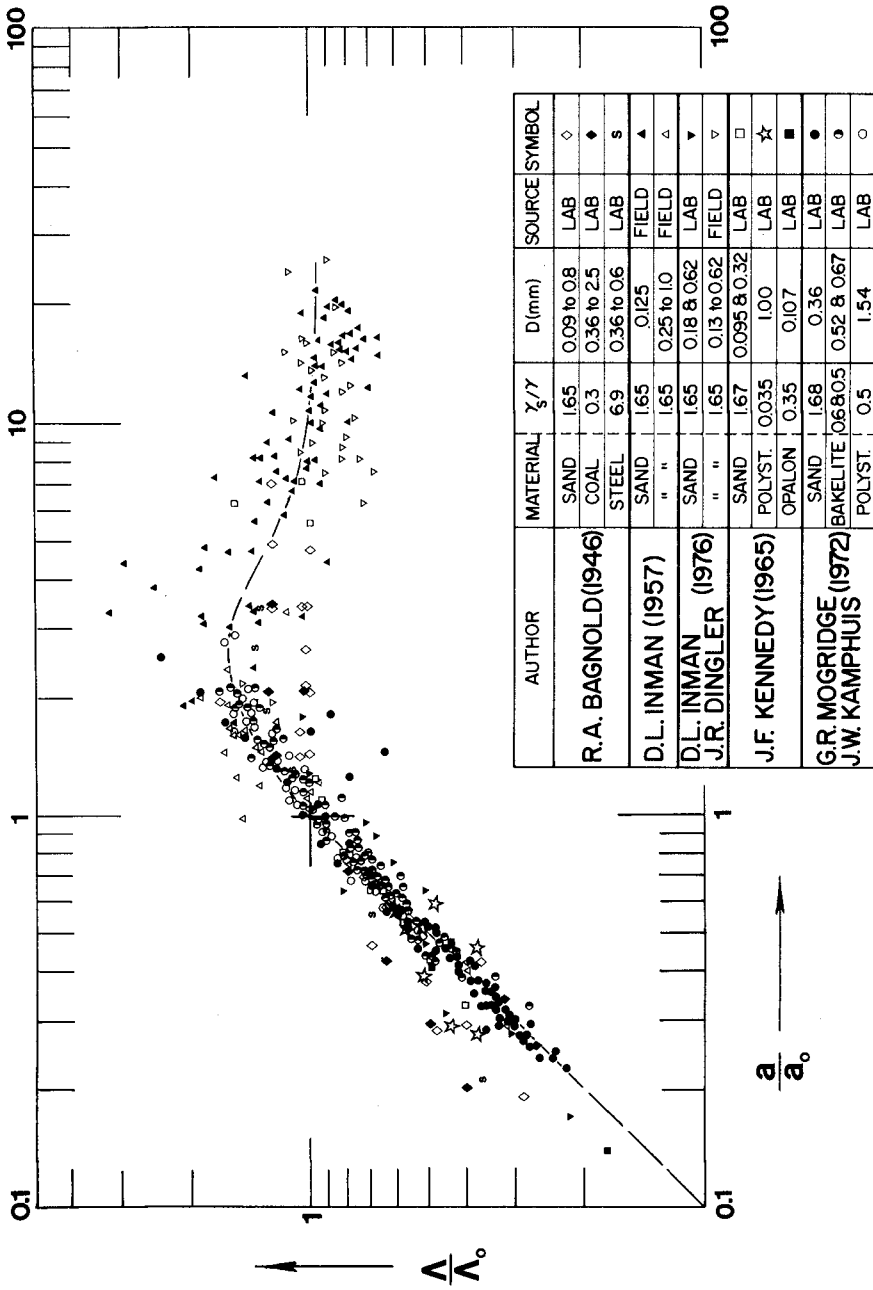


Fig. 3

Thus

$$\theta \sim \left(\frac{\delta v}{\delta t} \right)^2 \quad (8)$$

(If the "geometry" of the oscillatory motion over the flat (initial) bed is given (by $Z = a/D$) then the subsequent wave-like deformation of this bed appears to be dependent only on the comparative degree of turbulence.)

(ii) In the field of unidirectional flows it is well known that the length (Λ) of sand waves does not depend on γ_s or ρ_s . Indeed, none of the expressions produced to date for the length of ripples, dunes or antidunes contain γ_s or ρ_s ; (these quantities affect only the speed of their development). In particular the length of ripples forming in a (two-dimensional) unidirectional flow is determined only by the parameters v_* , D and v (Ref. [5]):

$$\frac{\Lambda}{D} = \phi \left(\frac{v_* D}{v} \right) \quad (9)$$

Consider now an oscillatory flow having

$$(a \rightarrow \infty, T \rightarrow \infty) \quad \text{but} \quad \left(\frac{a}{T} \text{ finite} \right) \quad (10)$$

Suppose that the (finite) mean orbital velocity $U = 2(a/T)$ of this flow is as sufficiently large as to induce the transport of sediment and consequently to generate ripples. Clearly the ripples generated by such an oscillatory flow must be virtually the same as those of a unidirectional flow. But if so, then the function (4) (of two variables) must in the limit (10) reduce into the function (9) (of one variable). In other words, the function (4) must possess the property

$$\lim_{\substack{a \rightarrow \infty \\ T \rightarrow \infty}} \left[f(Z, \theta) \right] = \phi \left(\frac{v_* D}{v} \right) \quad (11)$$

If a and T are very large, then their individual influence vanishes and they affect the phenomenon in the form of the ratio a/T meaning "the velocity" ($u \sim a/T$). But the ratio a/T can only appear in the expression of Λ/D if two variables Z and θ of the function (4) merge into a single variable Z/θ , which means that

$$\lim_{\substack{a \rightarrow \infty \\ T \rightarrow \infty}} \left[f(Z, \theta) \right] = \phi \left(\frac{Z}{\theta} \right) \quad (12)$$

must also be valid. From comparison of (11) and (12) it follows that the necessary expectation in the limit (10) can only be satisfied if Z/θ has the same meaning as the Reynolds number $v_* D/v$. Observe that this is indeed so

$$\frac{Z}{\Theta} = \frac{(a/D)}{(\sqrt{T/D^2})} = \frac{(a/T) \cdot D}{v} \sim \frac{UD}{v} \sim \frac{v_* D}{v} \tag{13}$$

(An analogous transition into the Reynolds number $v_* D/v$ (which does not contain γ_S or ρ_S) cannot be achieved by any other expression of Θ (other than (5)), as any combination of X , Y and W (other than $(X Y)^n$) will inevitably contain γ_S and/or ρ_S).

NORMALISED PLOT

When the values of Λ/D corresponding to a constant value of Θ are plotted versus Z , then the experimental points first follow a common 45°-straight line S , then they diverge from it and form some curves (Figs. 1 and 2). These curves (point patterns) are rather similar to each other and it is very likely that each of them is in fact "the same curve shifted in the 45°-direction". Let m be the point (location) where an individual curve diverges from the common straight line S , and a_0 and Λ_0 be the coordinates of m (Fig. 1). If the individual curves are indeed the shifted versions of each other, then one can normalise the curve family (i.e. one can make all the curves collapse into a single unified curve) by plotting Λ/Λ_0 versus a/a_0 . Estimating the locations m from the data available (Refs. [2], [3], [4], [6], [7]) such a normalised plot was produced and it is shown in Fig. 3. The scatter is considerable (especially that due to the field data) and yet the points (symbols) do not tend to form some patterns of "their own". Thus the idea of a normalised plot appears to be feasible. It would certainly be desirable if some further (laboratory) measurements were carried out in the range

$$\approx 2 < \frac{a}{a_0} < \approx 20$$

(in order to reveal more clearly the position of the curve in this region).

The graph in Fig. 3 can only be used for the prediction of Λ if one knows the values of a_0 and Λ_0 . Since the divergence points m lie on the straight line S (Figs. 1 and 2) a_0 and Λ_0 are interrelated by the simple proportion

$$a_0 = (\text{const}) \cdot \Lambda_0 \tag{14}$$

$$\text{where} \quad \approx 0.75 < (\text{const}) \leq \approx 1 \tag{15}$$

(In fact it is only the curve family of Ref. [2] which yields $(\text{const}) \approx 0.75$. The curve families of the rest of the authors quoted yield $(\text{const}) \approx 1$, and therefore with regard to practical purposes it would be only reasonable to adopt simply $a_0 \approx \Lambda_0$).

Thus it remains to reveal the value of Λ_0 . Since the

divergence point m is displaced together with the curve (Figs. 1 and 2), and since the position of each curve is determined only by the parameter Θ , the value of Λ_0/D must also be determined by Θ only.

$$\frac{\Lambda_0}{D} = \psi(\Theta) \quad (16)$$

Plotting the ordinates Λ_0/D of the points m (estimated from the data available) versus the corresponding values of $\Theta = \sqrt{T/D^2}$ one arrives at the graph in Fig. 4. (Note from this graph that the points corresponding to different γ_s and ρ_s do not tend to form different patterns).

Hence, knowing D , v and T (and consequently Θ) one determines from Fig. 4 the value of Λ_0 , and then from Eqn. (14) the value of a_0 . Knowing a (and thus a/a_0) one can predict Λ/Λ_0 (and thus Λ) from Fig. 3.

REFERENCES

- [1] Yalin, M.S. and Russell, R.C.H.: "Similarity in Sediment Transport Due to Waves", Proc. 8th Conf. on Coastal Eng., Mexico City, pp. 151-167 (1962).
- [2] Mogridge, G.R. and Kamphuis, J.W.: "Experiments on Bed Form Generation by Wave Action", Proc. 13th Conf. on Coastal Eng., Vancouver, pp. 1123-1142 (1972).
- [3] Inman, D.L.: "Wave Generated Ripples in Nearshore Sands", Beach Erosion Board, Tech. Memo. 100 (1957).
- [4] Bagnold, R.A.: "Motion of Waves in Shallow Water, Interaction between Waves and Sand Bottoms", Proc. Roy. Soc. London, Series A, Vol. 187, pp. 1-15 (1946).
- [5] Yalin, M.S.: "On the Determination of Ripple Length", Proc. A.S.C.E., Vol. 103, No. HY4, pp. 439-442, April 1977.
- [6] Dingle, J.R. and Inman, D.L.: "Wave-Formed Ripples in Nearshore Sand", Proc. 15th Conf. on Coastal Eng., Honolulu, pp. 2109-2126 (1976).
- [7] Kennedy, J.F. and Falcon, M.: "Wave Generated Sediment Ripples", M.I.T. Hydrodynamics Lab. Rep. No. 86 (1965).

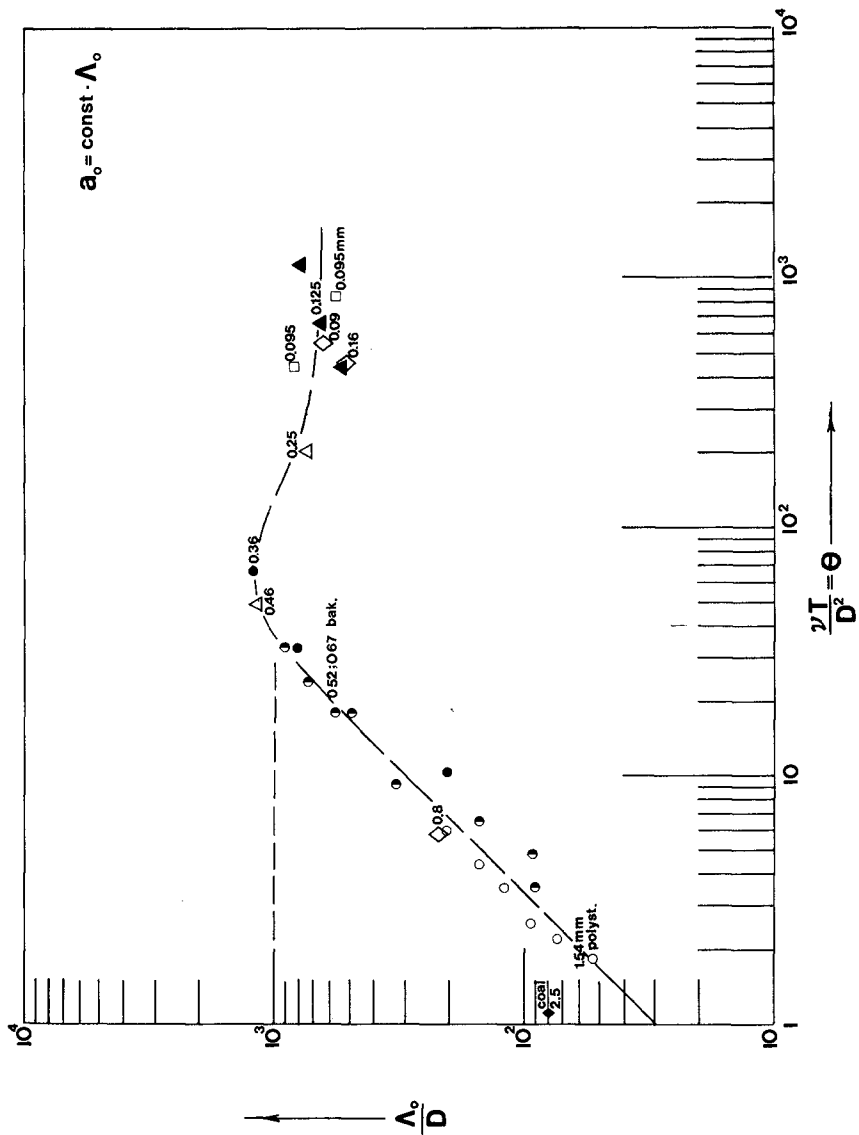


Fig. 4

LIST OF SYMBOLS

ρ	fluid density
ν	kinematic viscosity
ρ_s	density of grains
γ_s	specific weight of grains in fluid
D	typical grain size (usually D_{50})
T	wave period
a	orbit length of the oscillatory fluid motion due to waves at the boundary layer level
$U = 2a/T$	mean orbital velocity at the boundary layer level
K_s	height of the granular roughness of the (initial) flat bed
v_*	shear velocity of the unidirectional open channel flow
Λ	ripple length
δ_v	boundary layer thickness of the viscous oscillatory flow
δ_t	boundary layer thickness of the fully turbulent oscillatory flow
X, Y, Z, W	dimensionless variables of the two dimensional oscillatory two-phase motion at the mobile bed, as defined by Eqns. (1)
$\Theta = \nu T/D^2$	dimensionless combination reflecting the influence of period (in conjunction with viscosity)
a_o and Λ_o	upper limits of the proportionality between a and Λ which correspond to a given $\Theta = \text{const}$

CHAPTER 108

THE INFLUENCE OF DUNE AND FLOW PARAMETERS ON THE FRICTION FACTOR

by

J. Sündermann¹

H. Vollmers²

W. Puls³

Taking for example the flow over a ripple, some results of a hydrodynamic numerical model are presented and compared with experimental results. Special importance is attached to the pressure. On the basis of the used equations the physical reason for the horizontal pressure gradient is investigated. The influence of some dune and flow parameters on the friction is examined.

Introduction

Less is known about tidal bedforms than there is known about bedforms in unidirectional flow. Therefore, a project having in mind the investigation of tidal bedforms must at first be sure to give a good description of the simpler conditions. The investigation, a part of which is presented here, is divided into two branches: a hydraulic and a numerical one. The following only concerns the numerical model.

For sediment transport over dunes a special model has been formulated and some calculations of bed deformations have been performed (/1/, /2/). Before tackling the bed, there must be a good knowledge about the flow over this bed. The major work until now was concentrated on this subject.

Numerical model

The numerical model is two-dimensional (horizontal (x)-vertical(z)). It calculates the pressure p , the horizontal

1. Prof. Dr. rer. nat., University of Hamburg, FRG

2. Prof. Dr.-Ing., Hochschule der Bundeswehr München, FRG

3. Dipl. Phys., SFB 79 Hannover, Fed. Rep. of Germany

velocity u and the vertical velocity w . There is a free surface, and the natural bed is approximated by a rectangular polygon (Fig. 1).

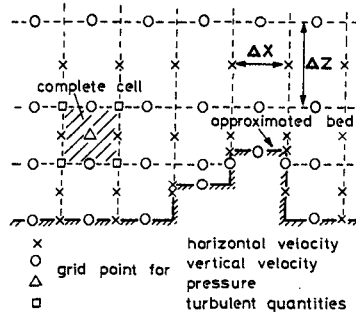


Fig. 1 Grid and approximated bed

There are about twenty grid points in a vertical section. Near the bed, the grid is refined. The grid is rigid, whereas the bed can move within the grid. A variation of the bed, caused by flow-induced sediment transport, in turn leads to a variation of the flow.

The flow is calculated from the primitive equations ($\zeta = 1$)

$$\frac{\partial u}{\partial t} + u \frac{\partial u}{\partial x} + w \frac{\partial u}{\partial z} - \frac{\partial}{\partial z} \left(A_v \frac{\partial u}{\partial z} \right) + \frac{\partial p}{\partial x} = 0 \quad (1)$$

$$\frac{\partial w}{\partial t} + u \frac{\partial w}{\partial x} + w \frac{\partial w}{\partial z} + \frac{\partial p}{\partial z} = 0 \quad (2)$$

$$\frac{\partial u}{\partial x} + \frac{\partial w}{\partial z} = 0 \quad (3)$$

The eddy viscosity A_v is calculated from a turbulence model (/3/). It is variable both in the horizontal and in the vertical direction. The turbulence model is a two-equation model; the calculated quantities are the turbulent kinetic energy k and the dissipation rate ϵ . A_v is a function of k and ϵ . The turbulence model has not only the task to calculate A_v . The knowledge of turbulence is an important tool for the determination of sediment transport.

Verification of calculated results

In order to be sure that one has a productive model for the flow, one has to compare the calculated results with measurements. For this comparison several experiments were carried out in the hydraulic model and data from literature was also used. The basis for the following comparison is an experiment that was performed by Raudkivi (/4/, /5/).

A short description of the experiment: There is a chain of ripples (length $\Lambda \approx 38\text{cm}$, height $\Delta \approx 3\text{cm}$) in a rather narrow flume (mean water depth $H \approx 13\text{cm}$). The flow is stationary (mean velocity $u_m \approx 30\text{cm/sec}$). The topography of the rippled bed as well as the measured quantities have been taken from drawings. This, of course, can be a source of error. Another point producing discrepancies is the fact, that there are periodic conditions in the numerical model (also a question of costs), which is not totally true for the experiment.

The comparison of measured and calculated quantities is shown in Fig. 2, 3, 4, and 5.

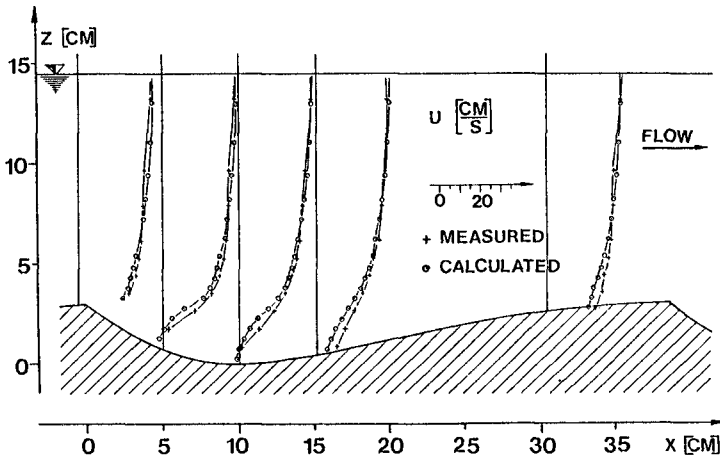


Fig. 2 Comparison of horizontal velocities

In Fig. 2 a measured profile at $x \approx 23\text{cm}$ could not be

taken, because the drawn values were obviously wrong (/5/, Fig. 12.13). The agreement of the other profiles in Fig. 2 is quite good, except perhaps at $x \approx 15\text{cm}$ and $x \approx 30\text{cm}$, where the calculated velocities near the bed are too small.

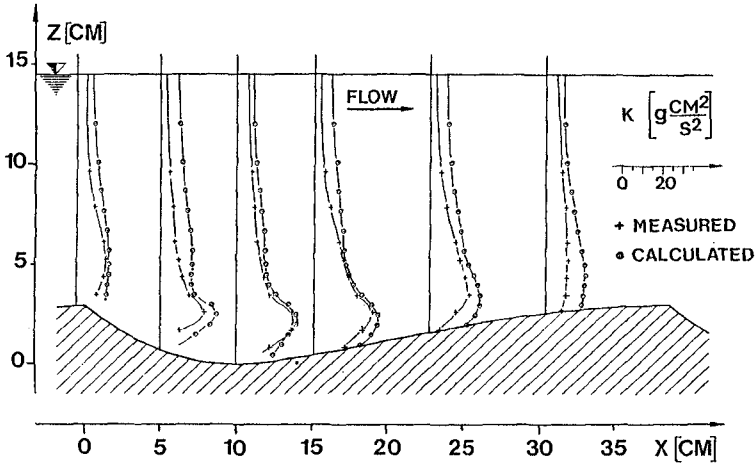


Fig. 3 Comparison of turbulent kinetic energy

Fig. 3: The measured quantities are $\overline{u'^2}$ and $\overline{w'^2}$, whereas the corresponding calculated quantity is $k = (\overline{u'^2} + \overline{v'^2} + \overline{w'^2}) \cdot 0.5$. For the comparison, it was supposed that $\overline{v'^2} = \overline{w'^2}$. For the turbulent quantities, a quantitative agreement can hardly be expected (due to both insufficiencies in measurements and calculations). So a difference of 50% in some places is not surprising. The good qualitative agreement must be emphasized, however.

The same is true for Fig. 4, with the additional difficulty, that the identification of $-\overline{u'w'}$ with $A_v \frac{\partial u}{\partial z}$ is problematic (turbulent viscosity concept of Boussinesq). It is interesting to see that near the bed there is a

decrease of $-\overline{u'w'}$, contrary to the behaviour over a flat bed.

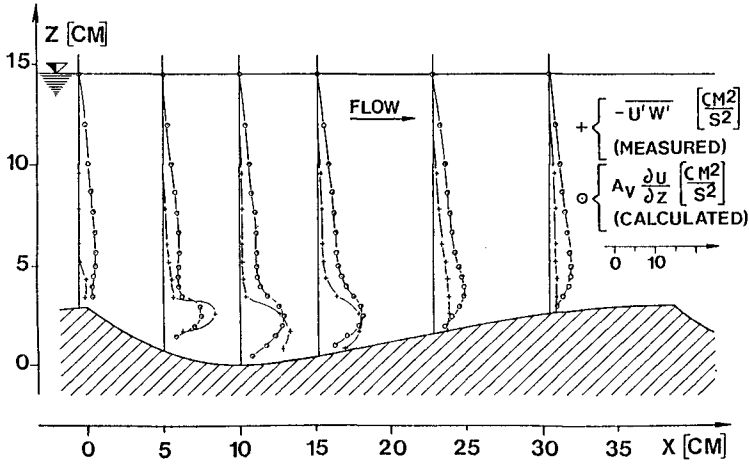


Fig. 4 Comparison of shear stress

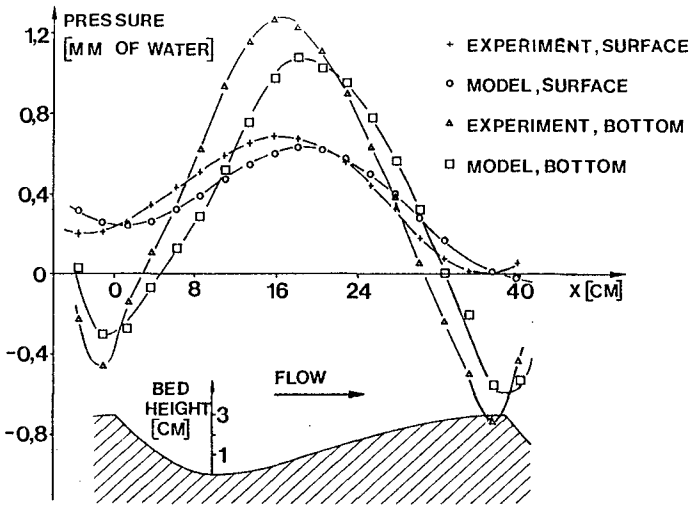


Fig. 5 Comparison of pressure

Fig. 5: The agreement of pressures is satisfying. At $x \approx 33\text{cm}$ the measured and the calculated surface pressures were set to zero. Both for the water surface and for the bottom pressure there are the same tendencies: the amplitude of the calculated pressure is too small and there is a shift to the right. Above all, this can be noticed for the bottom pressure. The influence of the walls of the flume had to be separated for the experimental curves.

On the whole, the comparison of the calculated and the measured quantities show, that the model is able to reproduce sufficiently the flow over dunes. Other flows, like that over a block or the flow behind a negative step have also been calculated. They too were found to be in acceptable agreement with experimental results.

Analysis of the pressure gradient

In principle, there are two methods to determine the pressure gradient S of the flow over a periodic bed:

1.
$$S = \frac{p(x_1 + \Lambda, z_1) - p(x_1, z_1)}{\Lambda} \quad (4)$$

(x_1, z_1 arbitrary within the fluid)
2. Measuring tangential and normal stresses at the bed; subsequent determination of S .

In the case of a stationary flow, the two methods must lead to identical results for S (principle of actio and reactio). This was also a test for the correctness of the model.

Knowing S , one is usually content. In this view-point, however, the flow is like a black box. One knows S , but one doesn't know it's origin. An advantage of computer calculations is the possibility to look at what happens in detail in the flow.

The flow is a result of the equations (1), (2), (3) (apart from boundary and initial conditions). We are interested in $\partial p / \partial x$ which appears in (1). Every term A, B, C, D in (1) represents a positive or negative horizontal acceleration of the fluid. The spatial distribution of the effects of the terms A and B can be taken from Fig. 6 and 7. Acceleration means an acceleration in the positive x -direction. The

dotted lines indicate the regions where the effect is highest.

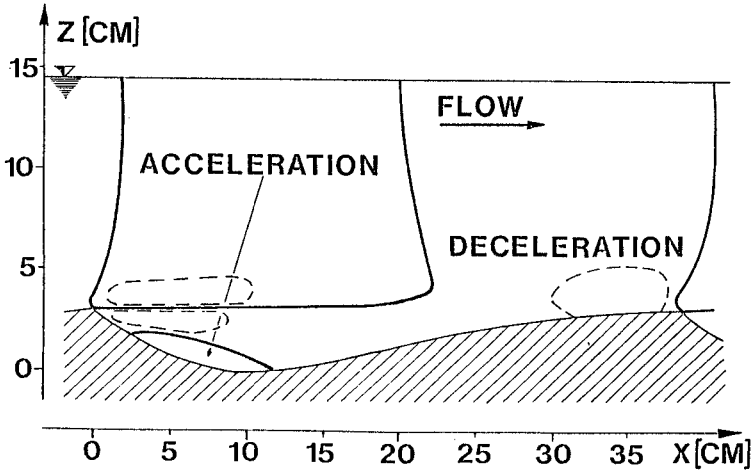


Fig. 6 Effect of term A

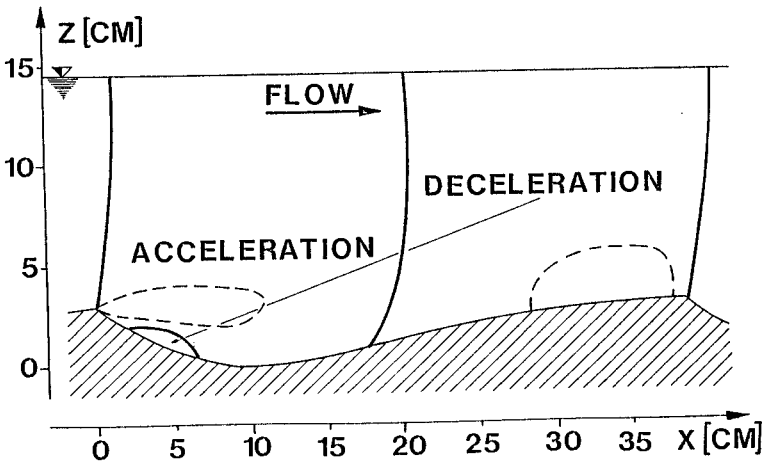


Fig. 7 Effect of term B

Fig. 6: The predominant effect of A is a deceleration of the flow which comes from the trough between the ripples. At the lee slope u is small, whereas at the luff slope u is large. Apart from the eddy, the flow transports small u into a region of large u , which means deceleration. In the main flow we have both acceleration and deceleration; the net effect in this part is relatively small.

Fig. 7: In the lee of the ripple crest w has a great negative and $\partial u / \partial z$ a great positive value. Thus the vertical velocity transports large u into a region of small u , which means acceleration. The opposite effect is found in the luff region. On the whole, acceleration is the predominant effect of B.

The influence of the diffusion term C can be imagined from Fig. 4. Due to C, there is a deceleration of u in the most part of the flow and an acceleration near the bed. These two effects nearly compensate each other.

Because $A_v \partial u / \partial z = 0$ at the water surface, we have the following pressure gradient due to C over one ripple length ($h(x)$ = actual water depth):

$$S_c = \frac{1}{\Lambda} \int_0^{\Lambda} \frac{1}{h(x)} \left(A_v \frac{\partial u}{\partial z} \right)_{Bd} dx$$

As can be seen from Fig. 4, $(A_v \partial u / \partial z)_{Bd}$ is small everywhere. S_c is the value that is expected theoretically. Because of numerical influences the model gives a value S_c^{model} , that is different from S_c . This difference can reach about 50%, which is relatively large. But assuming the absolute smallness of S_c , it is not so bad. In the following, we will use S_c , so we have to put up with a small error.

Now we want to pass over to quantitative examinations. For this we take equation (1) and integrate it vertically. Now the single terms in (1) depend on x only. Expressing the influences of the integrated terms A, B, C, D with pressure gradient terms $\partial \bar{p}_A / \partial x, \dots, \partial \bar{p}_D / \partial x$, the curves $\bar{p}_A(x), \dots, \bar{p}_D(x)$

give an impression of the effect of the single terms (Fig. 8). The pressure gradient due to A for one ripple length Λ is

$$S_A = \frac{\bar{p}_A(\Lambda) - \bar{p}_A(0)}{\Lambda}$$

The corresponding is valid for the other terms. It is $S_D \approx -S_A - S_B - S_C$ ("≈" because $S_C \neq S_C^{\text{model}}$).

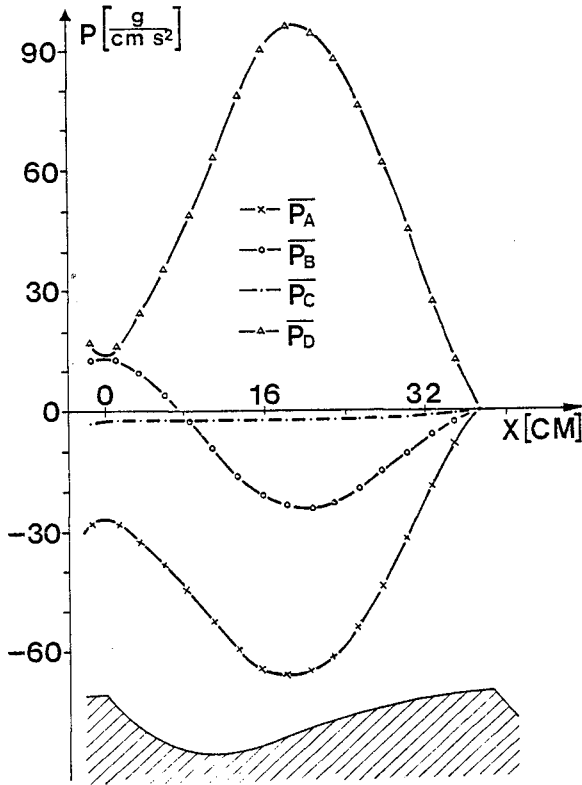


Fig. 8 Representative pressures due to the terms of (1)

The vertical integration of (1) leads to an additional difficulty. This can be seen from Fig. 9 (compare with Fig. 1).

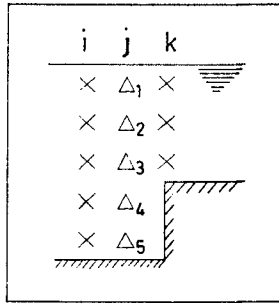


Fig. 9 For the explanation of effect E

The numerical integration of p in column j gives $\tilde{p} := \frac{1}{5} \sum_{n=1}^5 p_n$. \tilde{p} acts on the u -points in column i . The u -points in column k , however, are only affected by $\hat{p} := \frac{1}{3} \sum_{n=1}^3 p_n$.

If $\tilde{p} \neq \hat{p}$, the gradients $\partial \tilde{p} / \partial x$ for the u -points in i and k have not the same "basis" in j . This effect (which we call E) leads to a difference between S from equation (4) and S_D . E is no physical effect, but a consequence of vertical integration. In accordance with S_A etc., S_E is the pressure gradient due to E for one ripple length. Then we have:

$$S = S_D - S_E$$

$$\text{and } S \approx -S_A - S_B - S_C - S_E$$

The total and the partial pressure gradients for Raudkivi's conditions are given in the first column of the table. There is also given the friction factor (Darcy-Weisbach), taken from the law

$$|u_m| = \sqrt{\frac{8}{f}} \sqrt{\frac{1}{5} H |S|}$$

The results of the numerical model can be compared with theoretical considerations of Yalin (/6/). Yalin gives expressions for the pressure gradients due to skin and form effects. Deducing the formula for the form drag, he says, that the pressure gradient over a dune is mainly due to the

expanding part (lee slope), the effect of the contracting part (luff slope) being negligible.

This seems to be too rough. From Fig. 8 we see that both the expanding and the contracting zones are influencing the behaviour of pressure. It is the net effect that represents S . Compared with this net effect, the single contributions of the expanding and the contracting zones are considerably large.

Yalin's formula for the form drag is:

$$\left(\left| \frac{\partial p}{\partial x} \right| \right)_{\text{form}} = \frac{1}{2} \frac{\Delta^3 u_m^2}{H^2 \Lambda} \quad (5)$$

For Raudkivi's conditions this gives $0.62\text{g}/(\text{cm}^2\text{s}^2)$. Our corresponding value is $S_A + S_B + S_E$, which is also $0.62\text{g}/(\text{cm}^2\text{s}^2)$.

Yalin's formula for the skin friction gives a pressure gradient of $0.11\text{g}/(\text{cm}^2\text{s}^2)$, whereas we get $S_c = 0.085\text{g}/(\text{cm}^2\text{s}^2)$. A remark: Yalin assumes constant skin friction over the luff slope. In the numerical model, the skin friction is about zero in the lower part of the luff slope (reattaching and developing zone), whereas it is relatively high near the crest (see the curve for \bar{p}_c in Fig. 8).

Influence of the flow and bed parameters

The effects of the parameters u_m , H and Λ were investigated in the numerical model: Case I includes the original conditions of Raudkivi; there are six variations of case I, that can be taken from the table (all values of S in $10^{-2}\text{g}/(\text{cm}^2\text{s}^2)$).

The table gives the total pressure gradient S , the partial pressure gradients S_A , S_B , S_C , S_E and the friction factor f for the different cases.

In case II, u_m gets a factor of 1.25 compared with case I. As a result, every pressure gradient gets a factor of about $(1.25)^2$; f remains nearly constant. This is well known, of course also (5) gives this dependance. Case II can be thought to be a test for the model.

The cases III-V include three calculations where only H differs from case I. Yalins formula (5) gives a proportionality to H^{-2} . This can be noticed here too, though it is not unequivocal. Approximately we have $S_A \sim H^{-2}$, $S_B \sim H^{-1.5}$, $S_E \sim H^{-1}$.

Case	I	II	III	IV	V	VI	VII
$u_m \left[\frac{\text{cm}}{\text{s}} \right]$	28.7	35.9	28.7	28.7	28.7	28.7	-28.7
$H \text{ [cm]}$	13.2	13.2	9.2	17.2	28.7	13.2	13.2
$\Delta \text{ [cm]}$	2.95	2.95	2.95	2.95	2.95	4.43	2.95
S	-66.8	-102.1	-132.0	-42.6	-17.8	-102.7	130.8
S_A	73.1	111.1	149.6	44.4	16.5	95.0	-25.6
S_B	-33.2	-50.5	-58.4	-22.2	-10.2	-19.1	-42.5
S_C	8.5	12.4	17.3	5.4	2.2	2.3	-18.1
S_E	22.0	34.8	30.7	17.5	10.7	28.5	-53.9
$r \text{ [} 10^3 \text{]}$	8.6	8.4	11.8	7.1	5.0	13.2	16.8

Compared with S_A however, the effect of the sum $S_B + S_E$ is small, and thus the final result is nearly due to the effect of A alone. Of course this is a rough approximation, usable perhaps as a rule of thumb.

A variation of Δ is only examined for one case (VI). Compared with case I, the bed height (see Fig. 5) gets the factor 1.5. As a result, the sum of S_A , S_B , S_E is nearly proportional to Δ . The tendencies for the single terms, however, is quite different: $|S_A|$ and $|S_E|$ become larger, $|S_B|$ becomes smaller. This behaviour is a result of the expansion of the lee eddy. For the same reason (expansion of the recirculating and the developing zone) the skin friction has decreased in case VI. From this comparison of only two cases one cannot say that $S_A + S_B + S_E \sim \Delta$ is valid, but it is a reference point. Yalin's formula (5) gives a different result: a proportionality to Δ^2 .

On the whole, from the numerical experiments we get the rough formula for the friction factor (the influence of skin friction produces an additional uncertainty):

$$f \sim \frac{\Delta}{H} \quad (6)$$

The versions II-VI are more or less small variations of Raudkivi's original experiment. The dominating influence always comes from A. This is not true if we take the same geometry, but a reversed direction of the flow (case VII). Here the effect of B has the same sign as A, C, E, and together with E it is dominating.

This investigation does not take into account variations of the length and the shape of a ripple. A tidal dune, for instance, can lead to totally other results, which is indicated by case VII. Thus the "law" (6) can be thought to be valid for conditions like Raudkivi's only. What about the dependence $S \sim \Delta$, which is contrary to Yalin, this work can perhaps give an impuls for further investigations concerning this point.

REFERENCES

- /1/ PULS, SÜNDERMANN, VOLLMERS, "A numerical approach to solid matter transport computation", Proc., XVIIth Congress of IAHR, Baden-Baden, Vol. 1, 1977.
- /2/ PULS, "Ein mathematisches Modell für die Wechselwirkung Strömung-Feststofftransport-Sohldeformation in einem Gerinne", Dipl.-Arbeit, Univ. Hamburg, 1976.
- /3/ LAUNDER, SPALDING, "Mathematical Models of Turbulence", Academic Press, London, 1972.
- /4/ RAUDKIVI, "Study of sediment ripple formation", ASCE, HY 6, 1963.
- /5/ RAUDKIVI, "Loose boundary hydraulics", Pergamon Press, 1st edition, 1967.
- /6/ YALIN, "On the average velocity of flow over a movable bed", La houille blanche, No. 1, 1964.

CHAPTER 109

TIME-LAG OF DUNES FOR UNSTEADY FLOW CONDITIONS

by

Horst Nasner*

1. Introduction

Many publications based on theoretical considerations or model tests, give utterance to the demand that there should be unequivocal relations between hydraulic conditions and bed form characteristics which should be generally applicable. These relationships determined for steady conditions and limited water depths should be handled with care when being applied to natural rivers. The bed configurations do not immediately fit themselves to the varying flow conditions. The bed forms need a certain reconstruction time in case of a changing discharge. The time-lag of dunes was observed on numerous rivers, in the past. A general review of investigations made in this field is given by ALLEN (1976 b).

In the following contribution, an attempt is made to describe the magnitude of the time lag of bed forms for unsteady flow conditions.

2. Bed forms and flow conditions

The formation and migration of the different bed forms which may occur, were investigated in many basic theoretical studies and laboratory tests for stationary conditions and restricted water depths. The terms for different bed configurations are explained by the graph in Fig. 1 (ENGELUND and HANSEN, 1967). For the relation between bed shear stress and flow velocity it shows the bed forms which occur for an increasing velocity of flow.

* Head of Hydraulic Engineering, Engelbrecht Consult, Hamburg /Germany

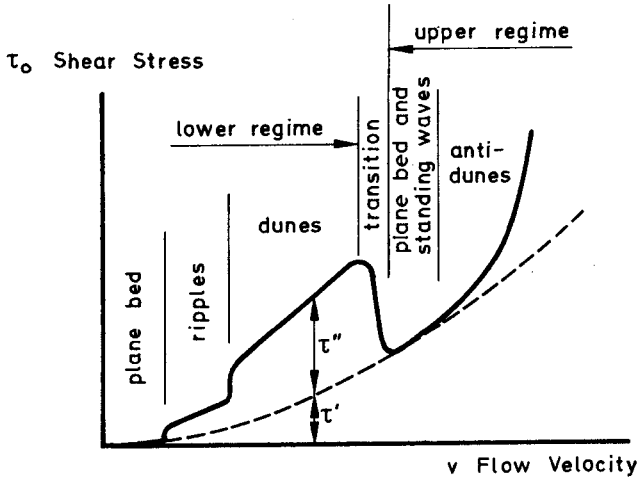


Fig. 1 Bed Shear Stress, Flow Velocity and Bed Forms

(ENGELUND and HANSEN, 1967)

In the lower regime, with streaming flow, ripples or dunes are formed when a certain velocity is exceeded. For a further increase of the flow velocity in the transition zone, the dunes are drawn out.

In the upper regime, standing waves or antidunes may be observed which move against the direction of flow. The upper regime is apparent for Froude numbers $Fr > 1$ (shooting flow).

Deep water rivers and tidal channels are characterized by low Froude numbers. Following the preceding example, large dunes should be formed with increasing flow velocities.

For unsteady conditions, the maximum dune dimensions should appear with a time-lag, after the maximum flow.

3. Change of bed forms with tidal motion
- 3.1. Shifting during the tide

From model tests with tidal currents it is known, that the shape of the current ripples adapts itself to the prevailing flood - or ebb-current direction - within a short time (DILLO, 1960).

TERWINDT analyzed on 923 dune fields in tidal channels of the Netherlands (1970) up to what height the tidal dunes change their general shape with the alternating currents.

These observations led to the following result: "The asymmetry of the ripples ($H = 30 - 100$ cm) may change with the turn of the tidal currents, but this is not always the case. The asymmetry of the ripples ($H = 100 - 200$ cm) most times does not change with the turn of the tides." From this result it may be concluded that the adaption time or time-lag of the smaller forms is less than one flood - or ebb current phase - which are shorter than 6 hours as the tides at the North Sea coast are semidiurnal. The general shape of the larger dunes ($H > 1$ m) is not affected by tidal motion, that means the time-lag exceeds 6 hours. There are only local redistributions in the crest area due to the tidal currents (NASNER, 1974 a).

- 3.2. Fresh-water flow and dune height

In the upper part of a tidal river, the mean current velocities are influenced by the fresh-water discharge. Analyses of many years on four significant dune fields in the navigation channel of the River Weser between Bremen und Bremerhaven (Fig. 2), proved that the height and migration of the ebb predominant sand waves are influenced significantly by the long-term change of the mean ebb-current velocities as a consequence of the change of the fresh-water discharge Q_0 (NASNER, 1974 a, 1974 b). The characteristics of the bed forms are not influenced by the tidal motion. The mean wave length is in the order of 50 m, the mean height reaches values of more than 2,5 m in mean water depths of about 10 m. The semidiurnal tides are quite regular with a tidal range of approximately 3,5 m.

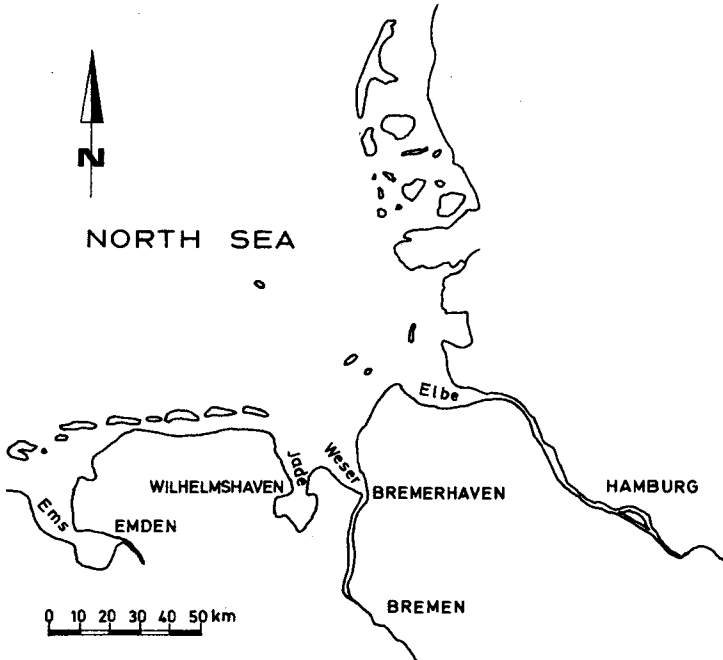


Fig. 2 German North Sea Coast

4. Phase diagrams

4.1. Preliminary remark

A possibility to determine the time-lag between the change of the flow parameters and the adaption of bed form characteristics is given by phase diagrams (ALLEN, 1973; 1976 a; 1976 b; JACKSON II 1976). This can be done by plotting, for example dune height against fresh-water discharge, where both parameters are also functions of the time. Such graphs are loops which ideally are closed, whereas the time may run clockwise or anticlockwise.

4.2. Dune height discharge diagram for the River Weser

By way of example the mean dune height \bar{H} (about 40 dunes are analysed) was plotted as a function of the fresh-water discharge in a phase diagram for the River Weser, from September, 1966 till October, 1967 (Fig. 3). The time-lag between maximum discharge and maximum dune height is extremely large for the River Weser with values up to 7 - 9 months (ALLEN, 1976 b). However, this result is not relevant to the behaviour of dune characteristics and discharge, as the following explanations will show.

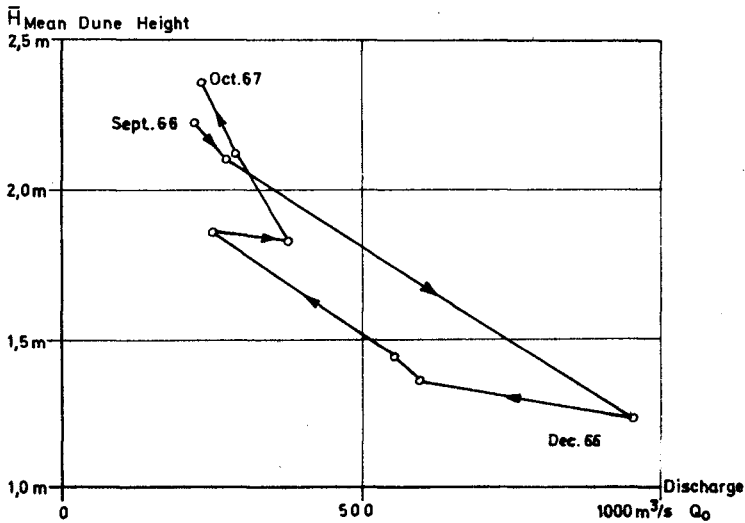


Fig. 3 Mean Dune-Height Discharge Curve for River Weser

According to the preceding description of possible bed forms (Fig. 1), the river bottom of the Weser is far-off the transition zone, as the Froude number compares with $Fr = 0,1$. For the water depth of approximately 10 m the Froude number obviously is no longer the determinative factor. The dune height H is governed by the mean ebb-current velocity over the dune crest. A state of equilibrium is given, when the flow velocity over the crest reaches a limiting value, which is a function of the sediment characteristics. For the dunes in the River Weser, the limiting velocity is about 1,0 m/sec (NASNER, 1974 a; 1974 b).

The conditions for the River Weser are represented ideally in Fig. 4. Due to the unsteady situation, there are no unique relationships between dune height and fresh-water flow. One value of discharge ($Q_{a,b}$) corresponds to two values of dune height (H_a ; H_b) and inversely.

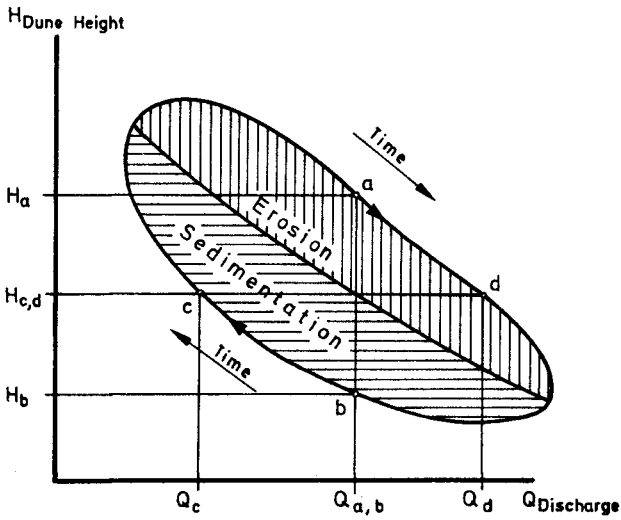


Fig. 4 Schematic Dune-Height Discharge Curve for River Weser

With increasing fresh-water discharge, the limiting ebb-current velocity is exceeded and erosion is caused. The dunes are higher than they should be (lag of erosion). With decreasing discharge, dunes are smaller than they should be (lag of sedimentation). It is mentioned elsewhere that a state of equilibrium is reached in the River Weser, when there is a quasi steady fresh-water discharge for about 30 days.

As a result, the tidal dunes of the River Weser are to be assigned to the transition zone in Fig. 1. This may be seen from the shape and time sequence of the diagram in Fig. 4. The smaller dunes thus are related to the higher discharge. The assumption that higher bed forms are built up with a higher discharge, is refuted by the preceding descriptions.

The adapting of the dunes to the fresh-water discharge in the River Weser is clearly given in the time-series in Fig. 5. For the hydrological years 1966 to 1972, the daily fresh-water discharges Q_0 of the River Weser are compared with the mean dune heights \bar{H} . The example shows the continuous creation-destruction process to which the bed forms are subjected.

The model tests carried out by Simons and Richardsor. (1960) are quite interesting in this connection. Fig. 6 shows the flow velocities, water depths and different bed forms as functions of the Froude number. Even for water depths of only 0,3 m the beginning of transition was measured for a flow velocity of about 1,0 m/sec. Similar results were found by model tests in a circuit flume with water depths of approximately 1 m and sand from the River Weser (ZANKE, 1976). As the prototype investigations have shown, the limiting value for the flow velocity may be extrapolated to greater water depths.

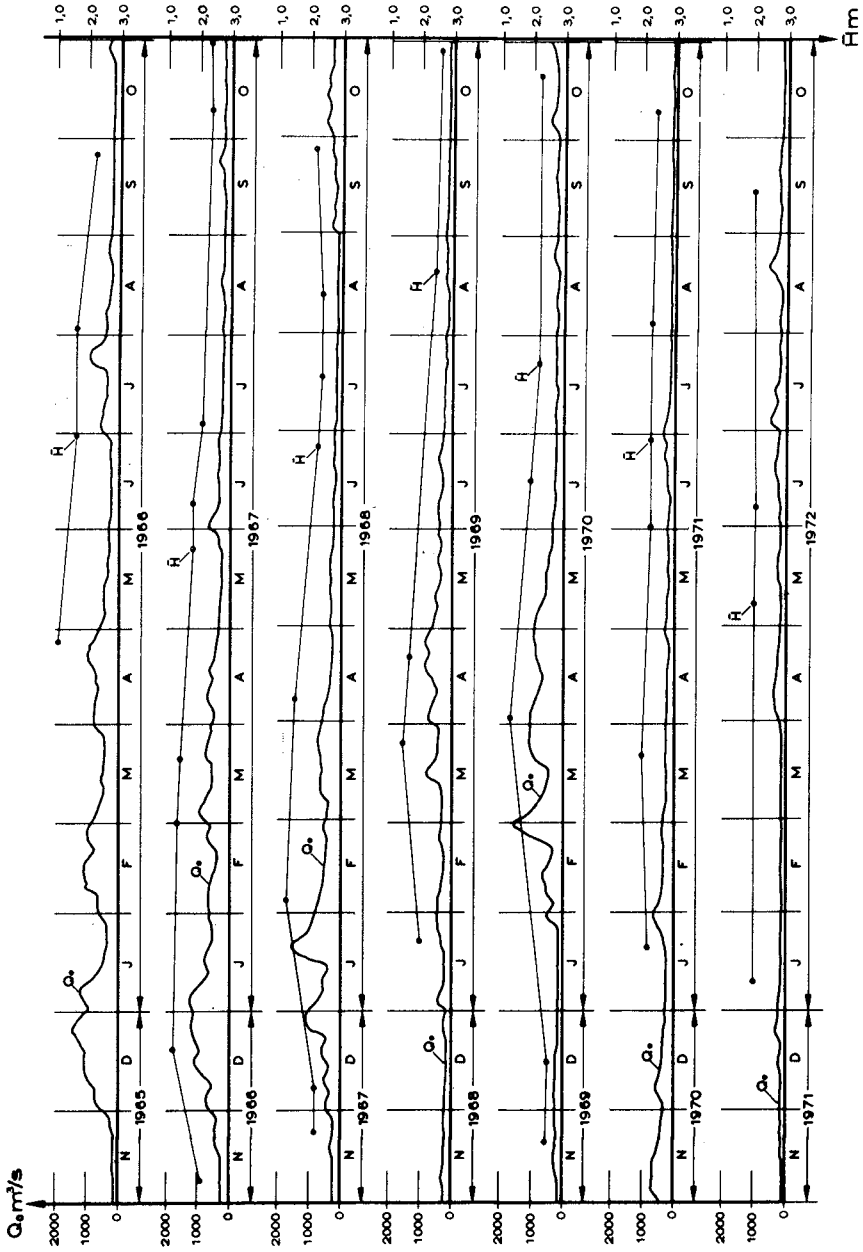


Fig. 5 Progress Line of Discharge Q_0 and Mean Dune Height \bar{H} for River Weser

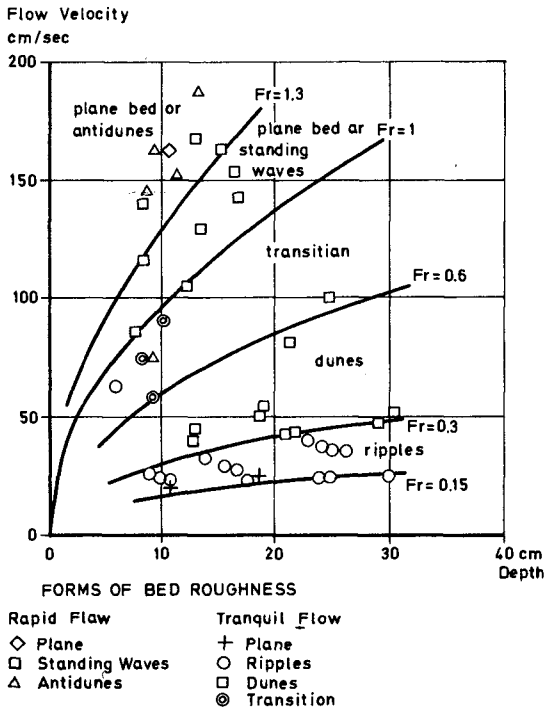


Fig. 6 Flow Velocity, Water Depth and Bed Form (SIMONS and RICHARDSON, 1960)

5. Comparison with other rivers

The results found for the River Weser, can be generalized as they also apply to other rivers, where with raising water levels due to the increasing flow velocities, there occur smaller dunes (phase of erosion) than with falling water levels (phase of sedimentation). Examples are given for rivers without tidal motion by the investigations of NEDECO (1959) on the River Niger and of STÜCKRATH (1969) on the Rio Paraná (Fig. 7 and 8).

In a 40 km river stretch of the River Niger, soundings were performed by NEDECO. In Fig. 7 the frequencies of dune heights at low water and at high water are plotted. The dunes are smaller at the raising stage (A) than at the falling stage (B).

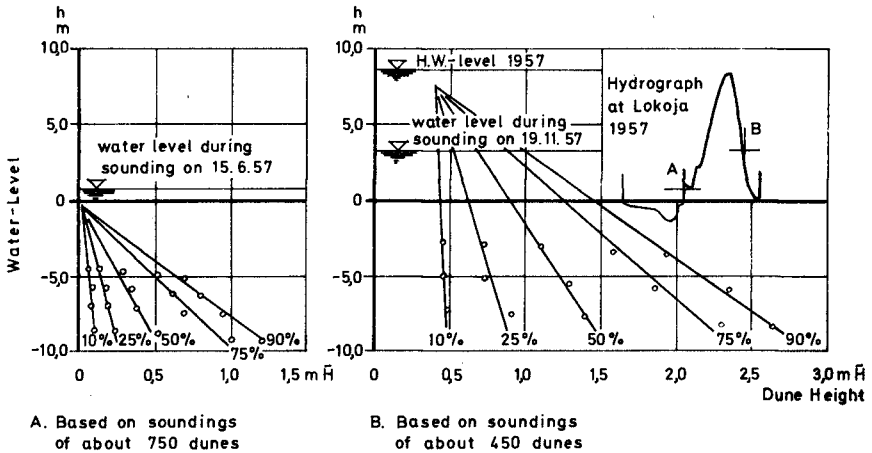


Fig. 7 Dune Heights on the Niger at Low Water and at High Water (NEDECO, 1959)

STÜCKRATH analyzed soundings on the Rio Paraná from May, 1967 up to December, 1968 (Fig. 8). The time progress is indicated by the arrows in Fig. 8. In general, there is a decrease in dune height with an increase of the water level and flow velocities. The Froude number is smaller than $Fr = 0,1$. The range of the mean flow velocities, which is between 0,9 and 1,1 m/sec comparable with those in the River Weser, is of special interest. It can be stated from Fig. 8 that the dunes on the bottom of the Rio Paraná are in transition.

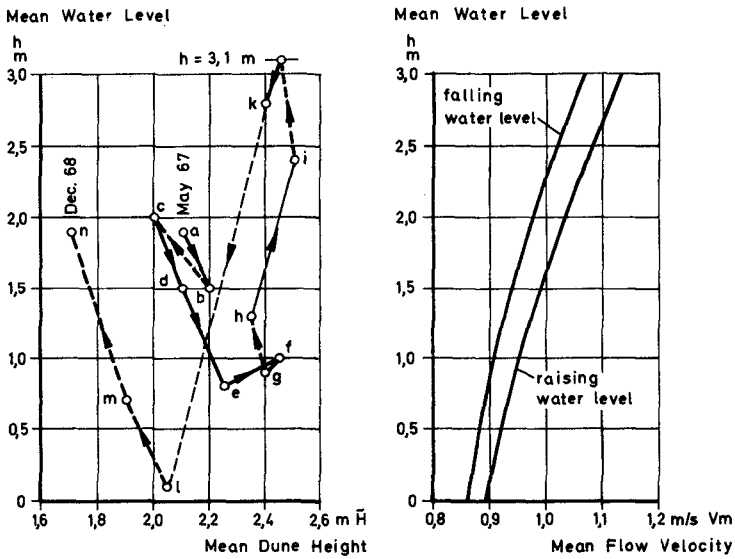


Fig. 8 Mean Dune Height, Flow Velocity and Water Levels in the Rio Paraná (STÜCKRATH, 1969)

Mean water level and dune height

In Fig. 9, besides the progress line of the daily fresh-water discharge and the measured dune heights, the monthly mean tide levels are plotted. Again the continuous adaption of the dunes to the changeable discharges is shown as well as the fact that the time-lag is a short-term event.

A remarkable result is the circumstance that the fixed boundary (dune height) reacts to changed flow conditions in a more sensitive way than the free surface. The fluctuation of the mean tide is significantly smaller than the variation of the dune height. The height variation is caused mainly by erosion and sedimentation in the crest area with a nearly constant through level (NASNER, 1976 a). The significant parameter is the flow velocity to which the river bottom adjusts itself. It is of interest, in this connection, that in many formulas on sediment transport, the bed-form contribution is considered by an additional friction factor.

The stability of a dune-covered bed against discharging is subject to the transport mechanism of the bed forms, by which the bed load is considerably reduced in comparison with a flat bed (FÜHRBÖTER, 1967). Investigations in the prototype have proved that the sand transport in a dune field is effected essentially through a local redistribution of the bed material corresponding to about the migration velocity of the dunes (NASNER, 1976 b).

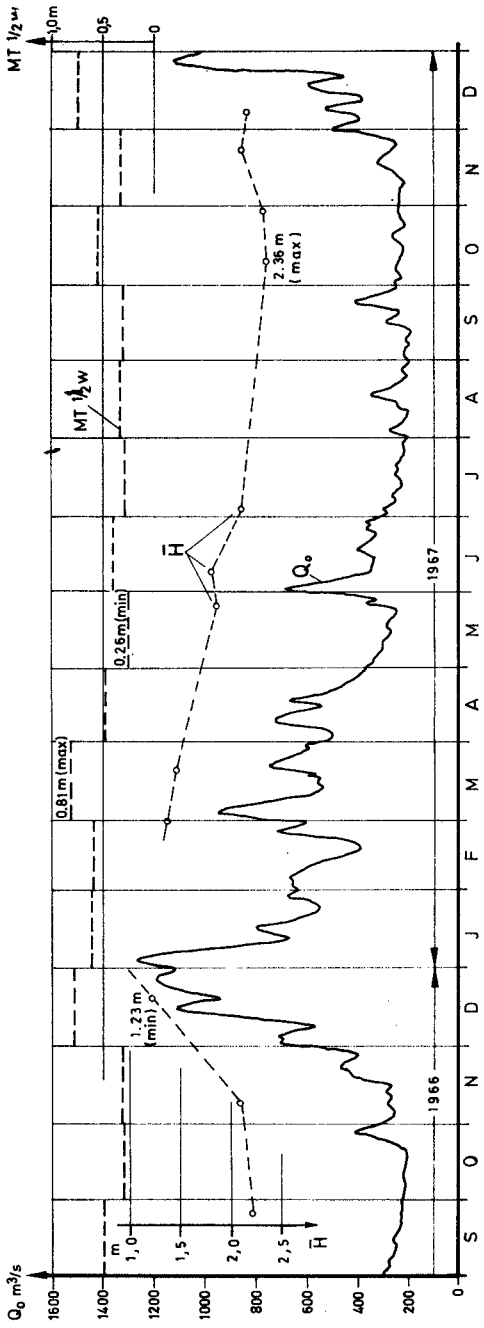


Fig. 9 Progress Line of Discharge Q_0 , Mean Dune Height \bar{H} and Mean Tide Level $MT \frac{1}{2} w$ for River Weser (1966-1967)

7. Concluding remarks

In this paper, the time-dependent behaviour of dunes as a function of the governing hydraulic conditions have been described. The results can be summarized as follows:

- It has been proved that it is difficult to apply the results from experiments on models, to natural rivers. A clear-cut relationship between bed form properties and flow conditions may be given for steady circumstances. In nature where unsteady flows prevail, the bed configuration adjusts itself to the changing hydraulic conditions with a time-lag. However, also for significant dunes in deep-water rivers, this is a short-term process.
- The knowledge gathered from laboratory tests, according to which for low Froude numbers and increasing velocities, higher dunes will be established, obviously applies to limited water depths only. The governing parameter for rivers of greater depths is the flow velocity which determines the limiting dune height - depending on the sediment characteristics. In spite of the low Froude numbers, the river bottom may be situated in the transition zone. The dunes become smaller by erosion, for increasing discharges and flow velocities. In case of falling water levels and lower current velocities, the bed forms may be enlarged again by sedimentation.
- The investigations revealed that the river bottom shows a very sensitive reaction to changed discharge and flow conditions. The variations of the dune height are of a remarkably greater order of magnitude than the fluctuations of the mean water level. On principle, the dunes cause a stabilization of the bottom so that the sediment removal is reduced. Compared with a flat bed, the sand transport is considerably reduced by the merely local redistribution of the bed material. In this respect, the dune height is of minor significance, as the height as well as the migration velocity of the bed forms is governed by the mean velocity of the flow and not inversely.

8. Bibliography

- ALLEN, J.R.L.: Computational models for dune time-lag: general ideas, difficulties and early results
Sediment. Geol., 15: 1-53
- ALLEN, J.R.L.: Time-lag of dunes in unsteady flows: an analysis of Nasner's data from the river Weser, Germany
Sediment. Geol., 15: 309-321
1976 b
- ALLEN, J.R.L.: Phase differences between bed configurations and flow in natural environments, and their geological relevance
Sedimentology, 20: 323-329
1973
- DILLO, H.G.: Sandwanderung in Tideflüssen
Mitteilungen des Franzius-Instituts für Grund- und Wasserbau
Technische Hochschule Hannover
Heft 17
1960
- ENGELUND, F. and
HANSEN, E.: A Monograph on Sediment Transport in Alluvial Streams
Copenhagen
1967
- FÜHRBÖTER, A.: Zur Mechanik der Strömungsriffel
Mitteilungen des Franzius-Instituts
Technische Hochschule Hannover
Heft 29
1967

- JACKSON II, R.G.: Largescale ripples of the Lower
Wabash River
Sedimentology, 23: 593-623
1976
- NASNER, H.: Über das Verhalten von Transport-
Körpern im Tidegebiet
Mitteilungen des Franzius-Instituts
Technische Hochschule Hannover
Heft 40
1974 a
- NASNER, H.: Prediction of the Height of Tidal
Dunes in Estuaries
Proceedings 14th International
Conference on Coastal Engineering
Copenhagen
1974 b
- NASNER, H.: Regeneration of Tidal Dunes after
Dredging
World Dredging Conference
WODCON VII
San Francisco
Proceedings WODCON VII
1976 a
- NASNER, H.: Transport Mechanism in Tidal Dunes
Proceedings 15th International
Conference on Coastal Engineering
Honolulu
1976 b
- NEDECO: River Studies and Recommendations
on Improvement of Niger and Benue
Amsterdam
1959
- SIMONS, D.B. and
RICHARDSON, F.V.: Resistance to Flow in Alluvial
Channels
Proceedings ASCE
Vol. 86, HY 5
1960

- STÜCKRATH, T.: Die Bewegung von Großriffeln an
der Sohle des Rio Paraná
Mitteilungen des Franzius-Instituts
für Grund- und Wasserbau
Technische Hochschule Hannover
Heft 32
1969
- ZANKE, U.: Über den Einfluß von Kornmaterial,
Strömungen und Wasserständen auf
die Kenngrößen von Transportkörpern
in offenen Gerinnen
Mitteilungen des Franzius-Instituts
Technische Universität Hannover
Heft 44
1976

CHAPTER 110

PREDICTION OF BEACH PLANFORMS WITH LITTORAL CONTROLS

by

Marc Perlin⁽¹⁾ and R. G. Dean⁽²⁾

ABSTRACT

Three numerical models representing shoreline response are described and applied to a number of problems of coastal engineering interest. Included are: (1) a one-line explicit model, (2) a one-line implicit model, and (3) a two-line explicit model. Simplified refraction and diffraction schemes are incorporated into the models. The models allow grid elements to be activated and deactivated as sand is initially deposited in or the last sand removed from a grid at a jetty inclined to the shoreline. The one-line explicit model and two-line explicit model are similar to those described by Bakker, Breteler and Roos⁽³⁾. The one-line implicit model offers the advantage of stable computations for much longer time steps.

Example applications of shoreline response are presented to illustrate the utility of the model including: permeable versus impermeable jetties, shoreline perturbations caused by jetties which are aligned with the incoming waves versus jetties perpendicular to shore, shoreline response inside a groin compartment and the effect of a littoral barrier. In addition, the one-line implicit model is applied to predict the shoreline response in the vicinity of an offshore breakwater at Channel Islands Harbor, California where sediment is accumulated and dredged periodically. In this case, excellent shoreline response data are available from the prototype; however, only visual wave observations were available for this comparison and it was found necessary to increase the sediment transport relationship fourfold to achieve even approximate correspondence.

Numerical models offer a powerful means which, when combined with good judgement, should strengthen the coastal engineer's ability to predict the effects of a coastal engineering design. The research needs to improve numerical modeling capabilities are presented.

INTRODUCTION

In considering the installation of a coastal structure it is important to know the impact of the structure on shoreline fluctuations. Theoretical solutions are available for idealized cases of simple littoral barriers, unidirectional waves and linearized transport. Most actual conditions are considerably more complex due to reversals

(1) Hydraulic Engineer, Evaluation Branch, Coastal Engineering Research Center, Fort Belvoir, Virginia 22060.

(2) Professor, Department of Civil Engineering and College of Marine Studies, University of Delaware, Newark, Delaware 19711.

of longshore transport, a time-varying wave height and possibly more than one structure present. Numerical modeling has been developed to a fairly high degree of reliability for some applications such as tidal wave propagation in estuaries. Conversely, the numerical modeling of shoreline evolution must be considered in a relative state of infancy, however, it does appear to offer the potential of providing a substantial improvement to existing design and assessment capabilities. Moreover, it is anticipated that the use of numerical models will identify those critical sediment transport mechanisms requiring improved understanding and will provide the framework which, when applied in conjunction with well-designed and instrumented laboratory and/or field experiments, will allow these mechanisms to be better defined.

In this paper, three numerical models to represent shoreline evolution will be described and examples illustrating their application presented. Two of these models are quite similar to those developed and described by Bakker, Breteler and Roos⁽³⁾ and by Hulsbergen, Bakker and van Bochove⁽⁹⁾. The third utilizes an implicit approach and allows much longer time steps to be utilized. Additionally, the latter model is applied to several interesting coastal engineering problems not previously treated by this approach.

REVIEW OF PREVIOUS WORK

Analytical Approaches

Previous efforts to predict shoreline evolution include both analytical and numerical approaches. The earliest approach was that of Pelnard Considère⁽¹³⁾ in which the linearized longshore sediment transport equation and conservation of mass equation were combined to yield the diffusion equation in terms of a shoreline coordinate, y

$$\frac{\partial y}{\partial t} = A \frac{\partial^2 y}{\partial x^2} \quad (1)$$

and where A incorporates the wave and beach characteristics. Eq. (1) has been solved for a number of conditions including that of a long littoral barrier, the spreading out of a deposit of sand on an otherwise straight shoreline, etc.

Bakker, Breteler and Roos⁽³⁾ have extended the theory of Pelnard Considère by representing the beach profile by two contours, say y_1 and y_2 . In this case, there are two governing equations which incorporate the effect of the onshore or offshore motion between the two contours due to a non-equilibrium beach slope. Bakker has solved these equations for a number of interesting cases including those of single and multiple groins along a shoreline. Accumulation occurs at a groin until the accretion of the shoreline results in a profile that is so steep that the offshore gradient causes the sand to be diverted to the offshore contour where it is transported around the tip of the groin.

There have been a number of laboratory experiments^{(3) (4) (9) (16)} of shoreline evolution; the results of these experiments are generally in good agreement with the analytical solutions.

Numerical Approaches

In order to avoid the assumptions and limitations associated with the analytical approaches, a number of studies (2) (3) (9) (15) (16) (18) have been carried out to investigate the application of numerical models to shoreline evolution problems. The advantages of numerical modeling include the capability to readily incorporate many features, including: changes in wave conditions, the full (nonlinear) equations, complicated structure geometry, wave diffraction, structure permeability, crest elevation, etc. Almost any feature or mechanism for which a relationship is known (or is suggested) can be incorporated into the numerical model.

METHODOLOGY

Three numerical models will be described and illustrated by examples. These include: (1) a one-line explicit model, (2) a one-line implicit model, and (3) a two-line explicit model.

One-Line Explicit Model

This type of numerical model has been applied by a number of investigators to the problem of shoreline response. The governing equations include the sand transport equation and the conservation of mass equation.

Sand Transport Equation. The relationship governing the transport of sand along a straight shoreline as expressed by Inman and Bagnold⁽¹⁰⁾ is

$$I = K P_{\ell s} \quad (2)$$

in which I is the immersed weight transport rate, K is a dimensionless constant (≈ 0.8) and $P_{\ell s}$ is the longshore component of wave energy flux at the breaker line, given by

$$P_{\ell s} = \rho g \frac{H_b^2}{8} C_{G_b} \sin \delta_b \cos \delta_b \quad (3)$$

in which ρ is the mass density of water, g is the gravitational constant, H_b is the breaking wave height, C_{G_b} is the group velocity at the breaker line and δ_b is the breaking wave crest angle relative to the shoreline,

$$\delta_b = \beta_B - \beta' - \alpha_b$$

and α_b is the azimuth from which the waves propagate, β_B is the azimuth of the outward normal of the baseline and β' is the inclination of the shoreline relative to the baseline. One advantage of Eq. (2) over other forms is that I and $P_{\ell s}$ have the same dimensions. The immersed weight sand transport rate, I , and the volumetric sand transport rate, Q , are related by

$$Q = \frac{I}{\rho g (S-1) a} \quad (4)$$

in which S_s is the specific gravity of the sediment relative to the fluid and a is the complement of the porosity ($a \approx 0.6$ to 0.7).

Conservation of Mass Equation. The conservation of mass equation, considering only longshore transport is

$$\frac{\partial \Psi}{\partial t} + \frac{\partial Q}{\partial x} = 0 \tag{5}$$

in which x is the longshore coordinate and Ψ represents the total volume of the beach profile per unit length.

Solution. The one-line explicit model utilizes a time-marching space and time-staggered procedure in which the shoreline orientation is held fixed for one time step (from $n\Delta t$ to $(n+1)\Delta t$) and the sand transport calculated, and the transport held fixed over a time step (from $(n+\frac{1}{2})\Delta t$ to $(n+\frac{3}{2})\Delta t$) and the changes in shoreline position are determined. The finite difference equations are

$$Q_i^{n+1} = K \left(\frac{H_b^2}{8} \right)^n \frac{C_b^n}{(S_s - 1)a} \sin \delta_b^{n+\frac{1}{2}} \cos \delta_b^{n+\frac{1}{2}} \tag{6}$$

$$y_i^{n+\frac{3}{2}} = y_i^{n+\frac{1}{2}} - \frac{\Delta t}{D\Delta x} \left[Q_{i+1}^{n+1} - Q_i^{n+1} \right] \tag{7}$$

where the superscripts denote the time level at which the variable is evaluated and D represents the total depth of the "active" beach profile which is assumed to be displaced landward or seaward without change of form. The shoreline orientation β' relative to the baseline is determined by

$$(\beta'_i)^{n+\frac{1}{2}} = \tan^{-1} \left(\frac{y_{i+1}^{n+\frac{1}{2}} - y_i^{n+\frac{1}{2}}}{\Delta x} \right) \tag{8}$$

Figure 1 presents the grid system for the one-line model.

Wave Refraction. The orientation of the deep water waves is considered known. The waves are then refracted to the breaking depth in accordance with Snell's Law, where the orientation of the contour at breaking is assumed to be the same as that of the shoreline for the same grid.

Wave Diffraction. An approximate diffraction procedure is incorporated in the model, based on the results of Penny and Price⁽¹⁴⁾. The reader is referred to Perlin⁽¹⁵⁾ for greater detail on the manner of representing diffraction in the model.

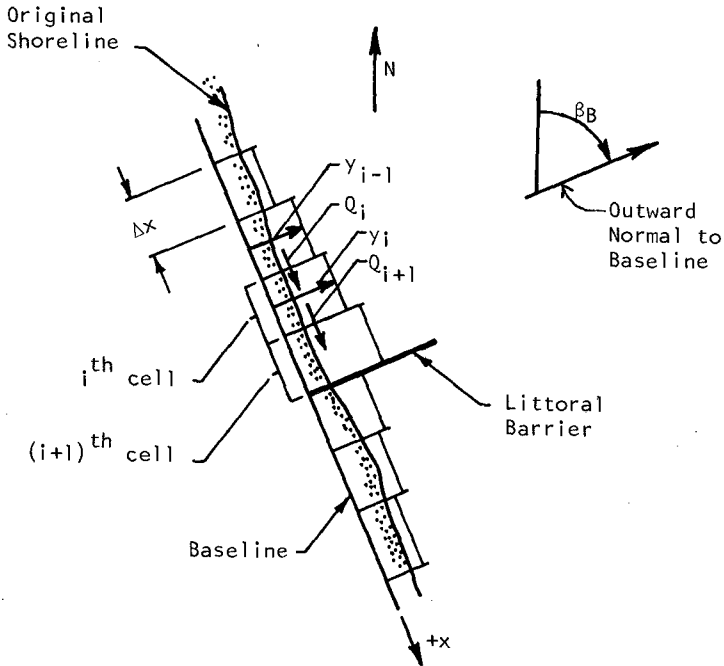


Figure 1. Shoreline Representation for One-Line Numerical Model.

One-Line Implicit Model

The one-line implicit model is based on the same equations (Eqs. (5) and (6)) as the one-line explicit model; however, for the implicit model they are solved simultaneously and thus greater numerical stability results. The main features of the implicit model will be described in detail, since this type of model does not appear to have been applied before for shoreline evolution.

Sand Transport Equation. The sand transport equation is the same as introduced earlier and is written below in abbreviated form as

$$Q = \Gamma H_b^{5/2} \sin 2\delta_b \quad (9)$$

where

$$\Gamma = \frac{K\sqrt{g}}{16(S_s - 1)\sqrt{k} a}$$

in which the shallow water approximation $C_{G_b} = \sqrt{gh_b}$ and the usual spilling breaking assumption $H_b = kh_b$ have been introduced. The quantity h_b

represents the breaking depth. Considering that the appropriate sand transport value for establishing changes between the n^{th} and $(n+1)^{\text{th}}$ time step as that at $(n+\frac{1}{2})\Delta t$, expanding Eq. (9) and accounting for first order effects of changes in y

$$Q_i^{n+\frac{1}{2}} = \Gamma(H^{\frac{5}{2}})^n \left[\sin 2(\beta_B - \alpha_{b_i})^n \cos(2\beta_i')^n - \cos 2(\beta_B - \alpha_{b_i})^n \frac{y_i^{n+1} + y_i^n - y_{i-1}^{n+1} - y_{i-1}^n}{\sqrt{(\Delta x)^2 + (y_i^n - y_{i-1}^n)^2}} \right] \quad (10)$$

Other forms for $Q_i^{n+\frac{1}{2}}$ could be equally valid or more valid.

Conservation of Sand Equation. The equation for the conservation of sand is

$$y_i^{n+1} = y_i^n - \frac{\Delta t}{D\Delta x} \left[Q_{i+1}^{n+\frac{1}{2}} - Q_i^{n+\frac{1}{2}} \right] \quad (11)$$

Solution to Equations. Prior to describing the equations to be solved, they will be rewritten in the following forms

$$A_i y_i^{n+1} + Q_i^{n+\frac{1}{2}} - A_i y_{i-1}^{n+1} = D_i \quad (12)$$

$$B_i Q_{i+1}^{n+\frac{1}{2}} + y_i^{n+1} - B_i Q_i^{n+\frac{1}{2}} = E_i \quad (13)$$

where

$$A_i = \Gamma(H^{\frac{5}{2}})^n \frac{\cos 2(\beta_B - \alpha_{b_i})^n}{\sqrt{\Delta x^2 + (y_i^n - y_{i-1}^n)^2}} \quad (14)$$

$$D_i = \Gamma(H^{\frac{5}{2}})^n \left[\sin 2(\beta_B - \alpha_{b_i})^n \cos 2(\beta_i')^n - \cos 2(\beta_B - \alpha_{b_i})^n \frac{y_i^n - y_{i-1}^n}{\sqrt{\Delta x^2 + (y_i^n - y_{i-1}^n)^2}} \right] \quad (15)$$

$$B_i = \frac{\Delta t}{D\Delta x} \quad (16)$$

$$E_i = y_i^n \quad (17)$$

and Eqs. (12) and (13) represent the sand transport and conservation of sand equations respectively.

Eqs. (12) and (13) are solved by the so-called double-sweep method⁽¹⁾⁽¹⁶⁾ in which it is assumed that the adjacent Q and y values are related linearly, i.e.

$$Q_{i+1}^{n+\frac{1}{2}} = G_i y_i^{n+1} + H_i \quad (18)$$

$$y_i^{n+1} = G_i^* Q_i^{n+\frac{1}{2}} + H_i^* \quad (19)$$

It is clear that if the G , G^* , H and H^* values were known for all i and if either y or Q were also known at one boundary, it would be possible to calculate all Q and y values from Eqs. (18) and (19). The double-sweep method proceeds by substituting Eq. (18) into Eq. (13) and solving for y_i^{n+1} , which results in

$$y_i^{n+1} = \frac{B_i}{B_i G_i + 1} Q_i^{n+\frac{1}{2}} + \frac{E_i - B_i H_i}{B_i G_i + 1} \quad (20)$$

and substituting Eq. (19) into Eq. (12) yields

$$Q_i^{n+\frac{1}{2}} = \frac{A_i}{A_i G_i^* + 1} y_{i-1}^{n+1} + \frac{D_i - A_i H_i^*}{A_i G_i^* + 1} \quad (21)$$

Comparison of Eqs. (20) and (21) with (18) and (19) establish a relationship between the unknowns, G_i , H_i , G_i^* and H_i^* and the knowns A_i , B_i , D_i and E_i as

$$G_i = \frac{A_{i+1}}{A_{i+1} G_{i+1}^* + 1}, \quad H_i = \frac{D_{i+1} - A_{i+1} H_{i+1}^*}{A_{i+1} G_{i+1}^* + 1} \quad (22), (23)$$

$$G_i^* = \frac{B_i}{B_i G_i + 1}, \quad H_i^* = \frac{E_i - B_i H_i}{B_i G_i + 1} \quad (24), (25)$$

As an example, the solution proceeds from the right-hand boundary ($i = I$) where either Q_I or y_I is specified. If Q_I is known, then $H_{I-1} = Q_I$ and $G_{I-1} = 0$. If y_I is specified, then $H_I^* = y_I$ and $G_I^* = 0$. To illustrate the process further, suppose Q_I is specified, then H_{I-1} and G_{I-1} can be determined, and from Eqs. (24) and (25) it is possible to establish G_{I-1}^* and H_{I-1}^* . Continuing in a stepwise fashion, from Eqs. (22) and (23), G_{I-2} and H_{I-2} are calculated, etc. Considering that Q_I is the value stated at the left-hand end of the grid system the determination of G_1^* and H_1^* complete the first "sweep" from right to left. The second "sweep" is from left to right and comprises the establishment of the sand transport values $Q_i^{n+\frac{1}{2}}$ and y_i^{n+1} for all i using Eqs. (18) and (19). This completes the procedure for one time step and the process is repeated for subsequent time steps.

Unless otherwise stated all examples presented subsequently will be based on the implicit model.

A M-Line Model

A M-line model is an extension of the similar two-line explicit model presented by Bakker, Breteler and Roos⁽³⁾. The displacements of M contours are calculated at each time step including onshore-offshore transport due to the beach slope being milder or steeper than the equilibrium, respectively, see Figure 2. A multi-line model provides a much better representation of shoreline response in the vicinity of structures where, for example, the steepening of the profile on the updrift side causes offshore transport and bypassing of the structure before the mean water level contour has advanced to the tip of the structure.

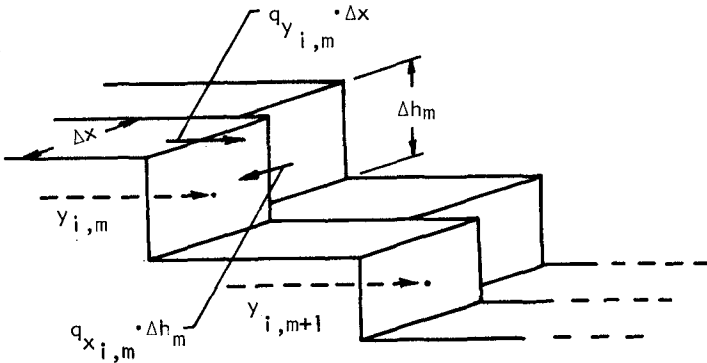


Figure 2. Beach Profile and Transport Representation For Multiple-Line Numerical Model.

Sand Transport Equations. The longshore sand transport equation for the m^{th} line is

$$Q_{x_{i,m}} = \mu_m Q$$

where Q is the value given by Eqs. (2) and (4) and μ_m is the proportion of the transport associated with the m^{th} line and it follows that

$$\sum \mu_m = 1 \tag{26}$$

The equation for offshore transport per unit beach length, q_{y_m} from the $(m-1)^{th}$ to the m^{th} contour is

$$q_{y_m} = K_{y_m} (y_{m-1} - y_m + W_m) \tag{27}$$

in which K_{y_m} is a transport coefficient for the m^{th} contour line and W_m is the equilibrium separation distance for the $(m-1)$ and m contours. It follows that if the profile is steeper or milder than the equilibrium the transport will be offshore or onshore respectively. In the two-line

model utilized here, the equilibrium distance, W , was based on an analysis of equilibrium profiles by Dean⁽⁸⁾ and the sand transport coefficient, K_y , was based on wave tank tests by Saville⁽¹⁷⁾.

Conservation of Sand Equation. The sand conservation equation, for the m^{th} contour, including the effects of onshore-offshore transport, is

$$\Delta h_m \frac{\partial y_m}{\partial t} + \frac{\partial Q_x}{\partial x} - q_{y_m} + q_{y_{m+1}} = 0 \quad (28)$$

Solution to Equations. In the present study, the equations for the two-line model were solved explicitly; however, there should be no difficulty in utilizing a mixed (explicit-implicit) procedure.

APPLICATIONS

As with any model, a complete evaluation requires comparison with as many other analytical and physical model results as possible. First a comparison between explicit and implicit one-line models will be demonstrated to provide confidence in the implicit solution followed by a comparison between the numerical model and the theory of Pelnard Considère, using two different transport equations in the numerical model. This is followed by specific applications which demonstrate the utility of the model.

In addition to intercomparison of numerical and analytical models, the model developed here is compared with the results from two physical model tests. Finally, the model predictions are compared with the results of a field measurement program.

Explicit Versus Implicit Schemes

To evaluate the implicit scheme, comparisons were carried out with results obtained from the explicit model. The wave conditions used in both models were a breaking wave height of 5 ft., an angle of wave approach of 45° from the north, and a duration of 1.39 days. The jetties were 1500 ft. long, and both the north jetty and the south jetty were oriented at angles of 20° to the shoreline. The time step in the explicit and implicit models are 600 and 6000 seconds, respectively. Because the differences between predicted shoreline changes by the two methods are small, rather than presenting plots, the results are tabulated in Table 1. The accretion is represented as a positive change and the erosion as negative. Both the x-distances (distance from shore end of the jetty at the baseline) and the y-coordinates have been rounded to the nearest tenth of a foot. Also, y-coordinates which did not change due to being outside the region of jetty influence are not presented in Table 1.

The distances proceed outwards in both directions from the jetty. Note that grid point 50 has a value of 176.2 ft. which is less than the value at grid 48. The explanation is simply that 176.2 ft. is the distance from the baseline to the jetty at grid 50 (i.e., the jetty is impounded with sand at this point). It is also worth noting that the south beach is affected for a larger distance from the jetty because

the diffraction changes the wave heights along this stretch of beach and, therefore, the transport rate is not uniform even for the straight beach condition until the beach is out of the diffraction shadow zone.

TABLE 1
COMPARISON OF EXPLICIT AND IMPLICIT ONE-LINE MODELS
SHORELINE CHANGES ADJACENT TO JETTIES AT AN INLET

Grid Point	Distance From Base of Respective Jetty (ft.)	Shoreline Changes		Percent Difference (Explicit vs. Implicit)
		Explicit (ft)	Implicit (ft)	
North Jetty				
50	64.1	176.2	176.2	0.0
48	192.4	276.4	265.6	3.9
46	320.6	182.2	171.8	5.7
44	448.9	114.2	106.5	6.7
42	632.0	47.0	42.4	9.8
40	870.1	12.0	10.9	9.2
38	1108.0	2.4	2.3	4.2
36	1346.3	0.4	0.4	0.0
34	1158.4	0.1	0.1	0.0
South Jetty				
62	119.0	-16.8	-16.4	2.4
64	357.1	-13.7	-13.4	2.4
66	595.2	-29.0	-28.6	1.4
68	833.3	-55.6	-55.3	0.5
70	1071.4	-91.2	-90.9	0.3
72	1309.4	-126.9	-124.6	1.8
74	1547.5	-117.7	-114.5	2.7
76	1785.6	-55.9	-53.1	5.0
78	2023.7	21.1	22.9	-8.5
80	2261.8	13.1	12.9	1.5
82	2499.8	5.1	5.1	0.0
84	2737.9	16.0	1.6	0.0
86	2976.0	0.4	0.4	0.0
88	3214.1	0.1	0.1	0.0

The last column on the table, which gives percent differences demonstrates that the two methods are reasonably close. The error in the explicit procedure is due to the fact that the y values are computed using Q values determined at previous time steps whereas in the implicit scheme, they are solved simultaneously. As a summary statement of this comparison, the two approaches yield results which are in generally good agreement.

Theory of Pelnard Considère, Numerical Model With Pelnard Considère Transport Equation, and Comparison to Both With One-Line Implicit Scheme

The solution of Pelnard Considère has been plotted on Figure 3 for the following conditions: $\alpha_0 = 22^\circ$, $A = 1.045 \text{ ft}^2/\text{sec}$, $t = 86,400 \text{ sec.} = 1 \text{ day}$.

As a check of the numerical model, the linearized transport equation of Pelnard Considère was introduced into the numerical model and the solution obtained as indicated by the dash-dot line in Figure 3. Also presented on Figure 3 is the solution resulting from the one-line implicit model. As expected, the shoreline has not accreted as far as with the other two models because the angle of wave attack is modified along the beach such that the sine of twice the difference between the wave angle and the shoreline decreases, thereby reducing the sediment transport. This exercise demonstrates that the finite-difference equations approach the analytic solution.

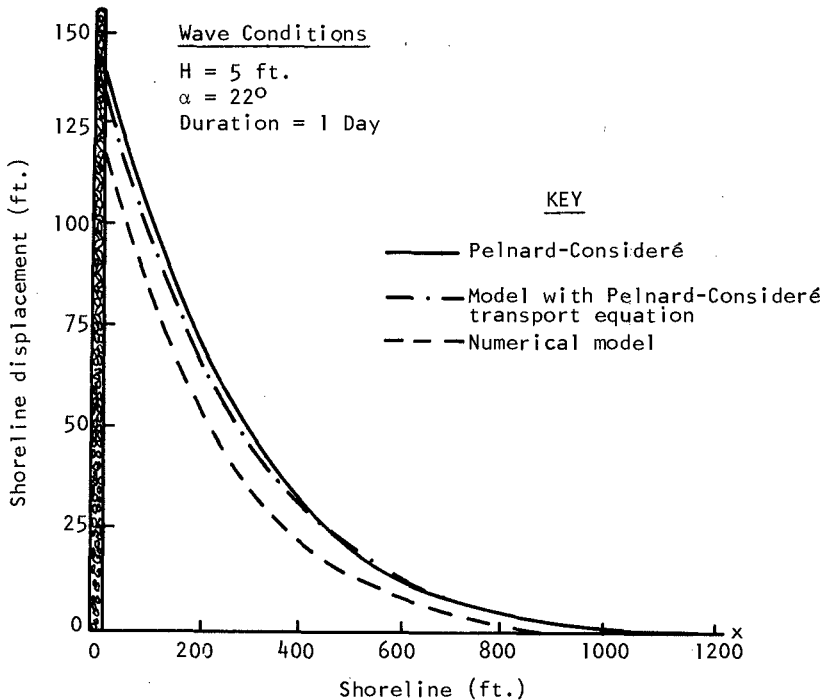


Figure 3. Comparison of the Three Predictions for Sand Accumulation Against a Littoral Barrier

Jetties Oriented Directly Into the Dominant Waves Versus Jetties Perpendicular to the Original Shoreline, With and Without Permeable Jetties

It appears that shoreline fluctuations adjacent to jetties could be minimized by orienting the jetties into the dominant wave approach, rather than perpendicular to the shoreline. In order to examine this problem, particular waves and jetty orientations were selected for modeling. The breaking wave height was 5 ft. incident on the beach at a +20° angle, with a period of 8 seconds and a duration of 1 day. Then, the wave angle was shifted to -20° for another day, +20° for a third day and finally back to -20° for the fourth and final day. First, these conditions were run with the 1500 ft. jetties perpendicular to the original baseline, and then the 1500 ft. jetties were oriented inward, each at an angle of 20°, i.e. into the incoming waves.

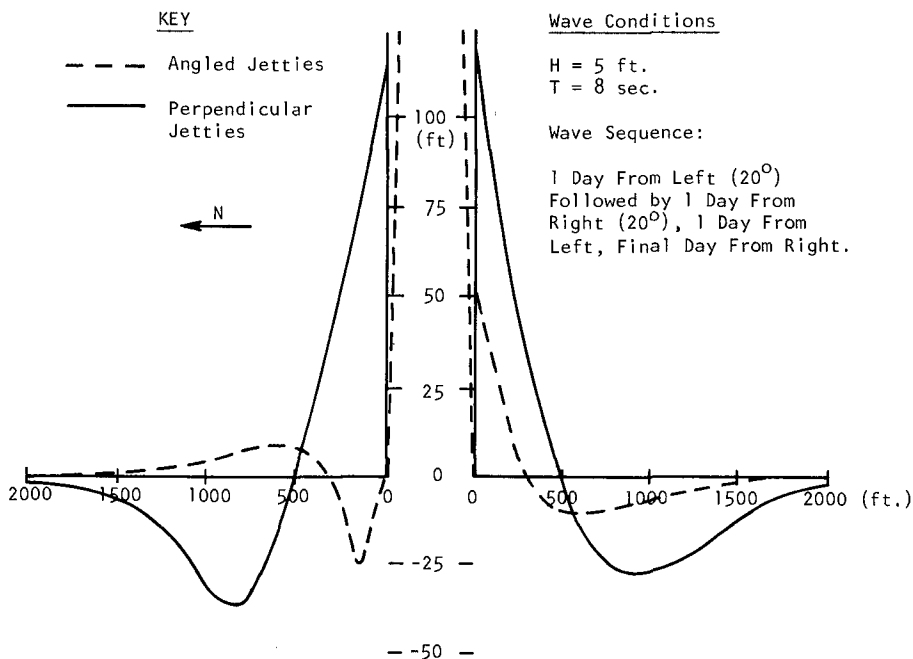


Figure 4. Comparison of Shoreline Response Due to Jetties Perpendicular to the Shoreline Versus Jetties Oriented Into Oncoming Waves.

The results of the simulation are presented graphically in Figure 4. Note the significant differences in magnitude in the shoreline changes for the two cases. With the angled jetties (the dashed lines in the diagram), the disturbance is considerably less, i.e., the shoreline changes for the perpendicular jetty case is modified more by the presence

of the jetty. This is due to the redistribution of wave energy caused by the diffraction, or lack of diffraction in the perpendicular and angled jetty cases, respectively. Because each of the two wave directions causes shadow zones on the instantaneous downdrift beach, the sand is displaced on both sides and once the fillets have developed the waves are not able to transport the sand readily; therefore, the fillets remain.

In nature, waves are not monochromatic, nor do they originate from two directions, however, this simulation suggests that a structure should be designed considering the perturbations that different jetty orientations would cause to adjacent beaches.

Another application of the numerical model is to represent jetties which are not sand tight (i.e., permeable). The permeability characteristics of a particular barrier are, by far, not easy to determine. However, for the purpose of the model, a jetty with a permeability of 20% was selected. The definition of permeability, as used here, is that 20% of the sand which arrives at the grid adjacent to the barrier is carried through and lost to the system. In the case of two jetties, the sand is only carried through the respective jetty during periods when the wave conditions are such as to transport sediment toward that jetty.

Using the same wave conditions as were used for the comparison of perpendicular jetties and angled jetties, and a permeability for both jetties of 20%, the resulting beach in planform is shown in Figure 5.

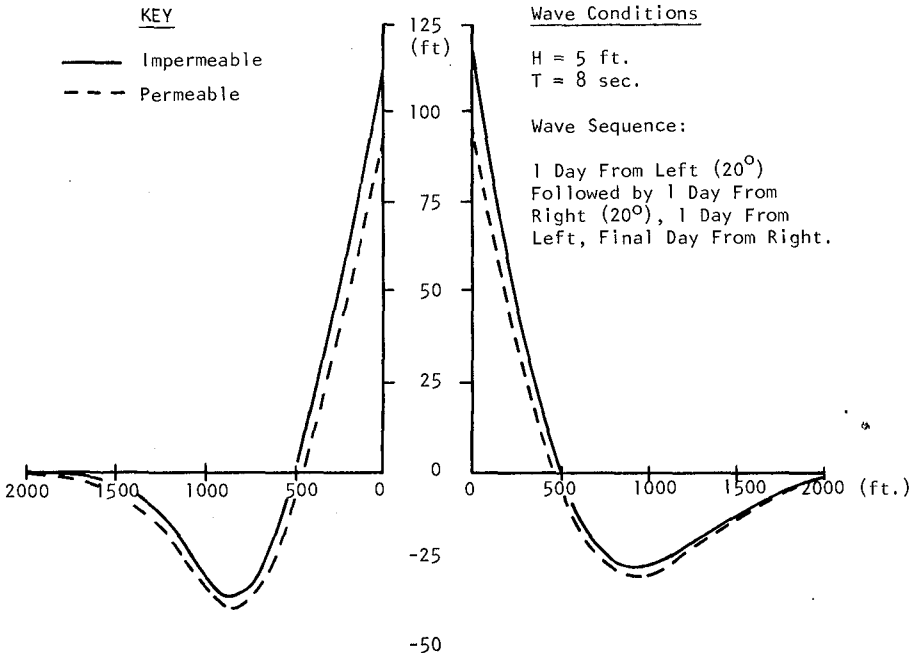


Figure 5. Effect of Permeable Versus Impermeable Jetties Oriented Perpendicular to Shore.

The difference between the total sand accumulation in the impermeable and permeable simulations for 1 day is 16%. The explanation of the difference between the permeability (20%) and the 16% difference is that only the grid adjacent to each jetty allows sand through it. As the beach accretes in the fillets, the transport rates in the adjacent grids to the jetty decrease due to the angle changes which occur. Therefore, a difference of 4% seems reasonable.

The effect of permeability on accretion of the fillets is of interest. Examining the south jetty, it is seen that the impermeable barrier impounded sand extending out from the original shoreline a distance of 112.5 ft., while the permeable barrier's beach extended out to approximately 92.5 ft. This is a change of slightly less than 18% which again seems reasonable.

The Physical Model of Barceló as Compared With the Numerical Model Prediction

One of the few physical models presented in the literature which contains sufficient information to model is that of Barceló⁽⁴⁾. Numerical model predictions for this hydraulic model test have been presented by Hulsbergen, Bakker and van Bochove⁽⁹⁾. In Barceló's model, two groins were present on each side of a beach which measured slightly less than 45 ft. in length. The updrift groin was approximately 18 ft. from his original shoreline with the downdrift groin approximately 7 ft. The beach was composed of pumice stones.

In order to simulate his model conditions, several of the constants had to be calculated and many other parameters had to be scaled from the figures in his article. The beach slope used was 8%, the length of the first jetty which caused the diffraction and was perpendicular to the original beach was 18.27 ft., the total beach length (including groin compartment) was 88.58 ft., and the length of time the model was run was 35 hours.

The depth, D , of the active profile was not given explicitly in the paper, however, examining the offshore profiles suggested an approximate value of 0.33 ft. with very small changes occurring for depths greater than 0.20 ft. For reasons to be discussed later, runs were carried out with $D = 0.33$ ft. and $D = 0.72$ ft.

The constant used in the sediment transport equation was changed because the mass density of pumice stone is different than quartz.

The results of the runs are shown in Figure 6. The most obvious differences are that for $D = 0.33$ ft. the numerical model predicts more rapid changes than measured in the physical model and it is noted that the beach in the immediate vicinity of the jetty adjacent to the eroded portion of the beach has a slightly different shape than the numerical model. The first difference is expected because different D values can be interpreted as different time scales (or transport proportionality factors) and laboratory data fall significantly below the field data on the curves used to establish the transport constant, see the Shore Protection Manual, 1973. Since the value of K used in the model ($K = 0.77$), was determined from field data, it is reasonable that the

numerical model would predict higher degrees of erosion and accretion.

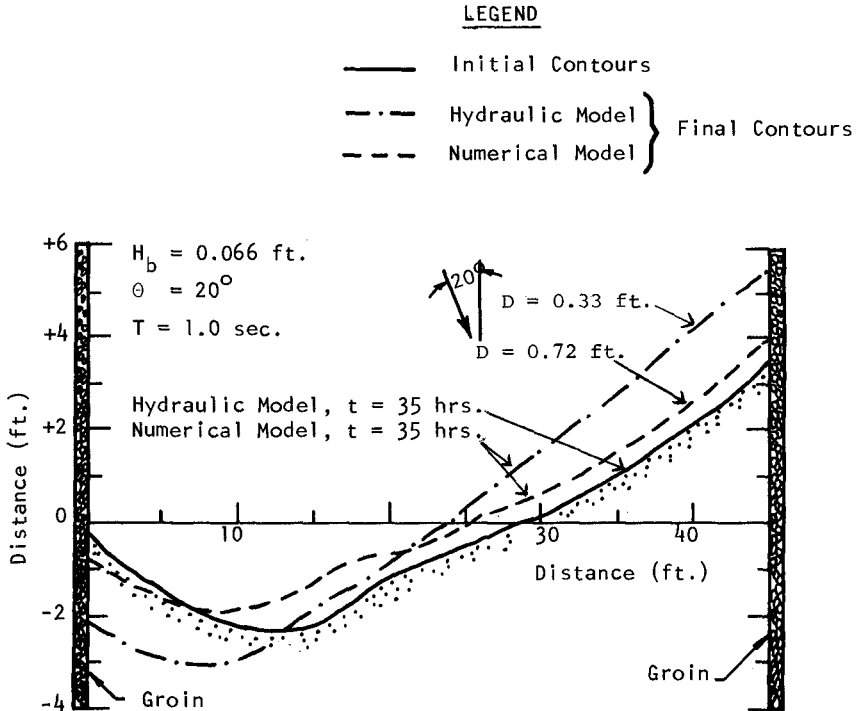


Figure 6. Comparison of One-Line Numerical Model Predictions with Hydraulic Model Tests by Barceló. Groin Compartment.

Comparison of a Two-Line Physical Model and the Two-Line Numerical Model

In order to evaluate the ability of the two-line numerical model to predict shoreline changes, the two-line physical model of Hulsbergen, Bakker and van Bochove⁽⁹⁾ was simulated. Test "T22" was the run chosen to model because it was stated in the article as one of their best runs. The length of the beach was approximately 106.6 ft. and the duration of the test was 50 hrs. The beach material was comprised of dune sand and was fed into the model at the updrift boundary.

A list of the constants used is presented in Table 2. The sediment transport constant, T , was taken as 0.326 and the other required input data were taken or scaled from the article. It should be noted that a plane beach was not used in this model, but rather the idealized beach profile (Dean⁽⁸⁾) discussed earlier. Also, the value of "w" used in the numerical model was obtained by scaling from Figure 14 of the paper by Hulsbergen, Bakker and van Bochove. "w" represents the equilibrium distance between the two lines and the lines in this figure at $t = 0$ are supposed to be at equilibrium (the model was first run without the

groins to reach equilibrium). The value scaled from the diagram was an average value of 5.97 ft., this being the value used in the numerical model.

TABLE 2

<u>Constants</u>	<u>Value Used in Two-Line Model</u>
Length of Groin	13.78 ft.
Length of Beach	106.63 ft.
Angle of the Groin	0°
Shape Factor for Equilibrium Profile Dependent on Bed Material, see Reference 8	0.0778 ft ^{1/3}
Reciprocal Depth of Closure	0.802 ft ⁻¹
Constant of Proportionality, Γ , in Sediment Transport Equation	0.326
Equilibrium Distance Between Two Lines	5.97 ft.
Height of Breaking Wave	0.246 ft.
Wave Period	1.55 sec.
Direction of Wave Attack	5°
Time Step	0.5 min.
Duration	6000 iterations (= 50 hours simulated)

The values input as "y₁" and "y₂" initial conditions were scaled from an enlarged version of Figure 14 of their paper. The only other change made in the numerical model was the boundary condition at the groin. The only way in which sand would be moved in the model with a wave height of only 0.246 ft. was by onshore/offshore sediment motion because breaking waves only occurred inshore of Line 2. This seemed to be realistic except at the boundary (groin) between the two beaches. Here, the amount of transport across the boundary was computed in the following manner. The distance from the tip of the groin to the y₂ grid point was divided by the total distance between the two lines, y₁ and y₂. This portion of the total offshore transport at the groin became the value of sediment transported around the barrier (i.e., at Line 2) and the remaining portion resulted in a seaward advancement of the first line, y₁. The sediment transported around the end of the barrier is used as the transport at the second line. This sand is then moved onshore accordingly.

Results of the comparison between the physical model tests and the numerical model tests are shown for the test duration of 50 hours in Figure 7. The prediction seems quite good with the exception of the smoothing that took place as expected. Certainly, the magnitude of the changes are approximately the same along with the general shapes. As noted in Reference 9, some of the perturbations apparent in the physical model could be due to rip currents which are not included in the numerical model.

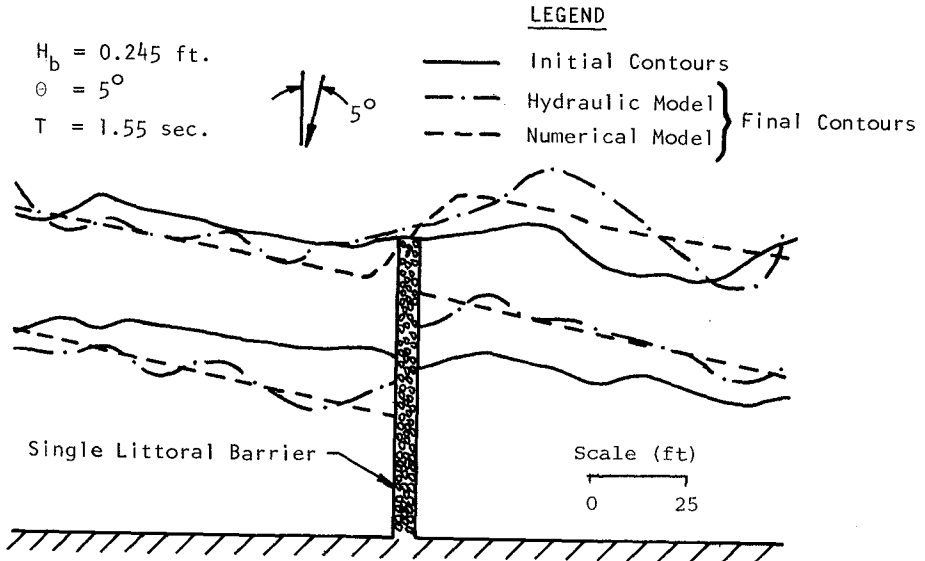


Figure 7. Comparison of Two-Line Numerical Model Predictions With Hydraulic Model Tests of Hulsbergen, Bakker and van Bochove.

Channel Islands Harbor Simulation

As a final application/evaluation of the model, it is desirable to compare model predictions with field data. Channel Islands Harbor was selected because concurrent wave data and planform change data exist. The wave data available at the time of writing this paper are LEO (Littoral Environmental Observational) visual data collected by the Coastal Engineering Research Center (CERC). The Channel Islands Harbor area of interest consists of two entrance jetties and an overlapping offshore breakwater. This structure system was idealized as shown in Figure 8. Two modeling efforts were carried out. The first utilized the recommended K value (c.f. Eq. (2)) of 0.77 and it was found that the amount of sediment accumulation behind the jetty was much too small. The second modeling was with a fourfold increase in K ($= 3.08$) and the results shown in Figure 8 were determined, which still indicates that not enough sediment is being transported and deposited behind the breakwater.

The Channel Islands Harbor study is being conducted by the Coastal Engineering Research Center as a full-scale sediment trap to attempt to determine the value of the constant, K (c.f., Eq. (2) of this paper). To date, it has been the general finding of that study that the constant ($K = 0.77$) is too small and perhaps should be increased by as much as twofold, Bruno and Gable⁽⁵⁾. There are various possibilities for the differences noted. The constant in the sediment transport equation could be too small for the transport at Channel Islands Harbor. Also, it is possible that on ebb tide a cell circulation is set up such that sand is transported toward the jetty by forces other than just those of the waves. The wave data were observed visually and a consistent underestimate in

wave height by 25% would result in a sand transport which was too low by 51%. The effect of the dredged area would be to cause sand transport behind the breakwater, a three-dimensional effect not accounted for in the present sand transport relationship.

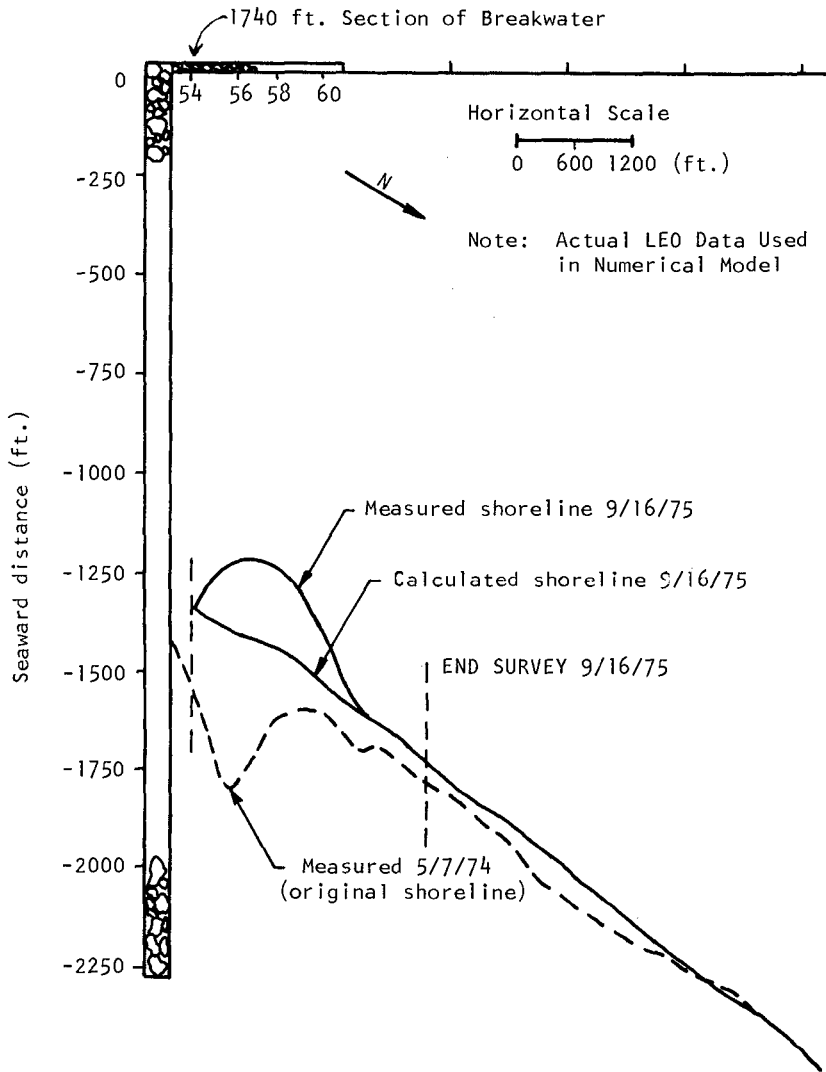


Figure 8. Comparison of Calculations With Field Surveys at Channel Islands Harbor, California. Longshore Transport Constant, $K = 3.08$.

SUMMARY

The governing equations and solution algorithms are presented for three types of numerical models developed to represent shoreline response to coastal structures. The models include: (1) a one-line explicit model, (2) a one-line implicit model, and (3) a two-line explicit model. This appears to be the first application of the implicit model for shoreline representation. In addition, the one-line models allow for activation and deactivation of grids adjacent to a structure oriented at an angle to the shoreline.

A number of problems of relevance to coastal engineering are investigated by the models including: permeable jetties, shoreline effects due to jetties aligned with the incoming waves compared with jetties perpendicular to the beach, shoreline response inside a groin compartment, and the effect of a littoral barrier. In addition, the one-line implicit model was applied to predict the shoreline response at Channel Islands Harbor, California where sediment is accumulated and dredged periodically from behind an offshore breakwater. Although in this case, only visual wave observations were available, it was necessary to increase the proportionality factor in the sediment transport relationship by a factor of four to obtain even approximate agreement between measurements and predictions.

The results of this paper are in accordance with those of other investigators of numerical models (3) (9) (12) (16) (18), namely that the potential is good for predicting shoreline response. Particular research needs to improve numerical modeling are:

- (1) An improved understanding of the distribution of longshore sediment transport across the surf zone,
- (2) An improved understanding of the mechanics of onshore-offshore sediment transport as affected by beach slopes milder and steeper than the equilibrium slopes, respectively,
- (3) The effects of longshore bottom slopes such as would exist in the vicinity of a dredged hole, and
- (4) Quantification of the sand transport processes in close proximity to structures. Of particular interest is the transport over a sill which is lower than the natural equilibrium profile elevation, and the transport through a permeable structure.

There appear to be no major difficulties in developing a "m-line" model and this should allow a more detailed description of shoreline response in the vicinity of structures.

REFERENCES

1. Abbott, M. B., "Numerical Methods", International Course in Coastal Engineering, Delft University, 1971, pp. 69-71.
2. Bakker, W. T., "The Dynamics of a Coast With a Groin System", Proceedings of the Eleventh Conference on Coastal Engineering, ASCE, 1968, pp. 492-517.
3. Bakker, W. T., E. H. J. Klein Breteler and A. Roos, "The Dynamics of a Coast With a Groyne System", Proceedings of the Twelfth Conference on Coastal Engineering, ASCE, 1970, pp. 1001-1020.
4. Barcelo, J., "Experimental Study of the Hydraulic Behavior of Groin Systems", Proceedings of the Eleventh Conference on Coastal Engineering, ASCE, 1968, pp. 526-548.
5. Bruno, R. O. and C. G. Gable, "Longshore Transport at a Total Littoral Barrier", Proceedings of the Fifteenth Conference on Coastal Engineering, ASCE, 1976, pp. 1203-1222.
6. Carnahan, B., H. A. Luther and J. O. Wilkes, "Applied Numerical Methods", John Wiley and Sons, 1969, pp. 429-450.
7. Dean, R. G., "Beach Erosion: Causes, Processes and Remedial Measures", CRC Critical Reviews in Environmental Control, Vol. 6, Issue 3, 1976, pp. 259-296.
8. Dean, R. G., "Equilibrium Beach Profiles: U. S. Atlantic and Gulf Coasts", Ocean Engineering Report No. 12, University of Delaware, 1977, pp. 1-45.
9. Hulsbergen, C. H., W. T. Bakker and G. van Bochove, "Experimental Verification of Groyne Theory", Proceedings of the Fifteenth Conference on Coastal Engineering, ASCE, 1976, pp. 1439-1458.
10. Inman, D. L. and R. A. Bagnold, "Littoral Processes", in The Sea; Ideas and Observations, Vol. 3, The Earth Beneath the Sea (Edited by M. N. Hill) Interscience Publications, pp. 529-553.
11. Komar, P. D. and D. L. Inman, "Longshore Sand Transport on Beaches", Journal of Geophysical Research, Vol. 75, 1970, pp. 5914-5927.
12. Le Mehaute, B. and M. Soldate, "Mathematical Modeling of Shoreline Evolution", A Literature Survey, Tetra Tech Report No. TC-831, January, 1977.
13. Pelnard-Considère, R., "Essai de Theorie de l'Evolution des Formes de Rivages en Plages de Sable et de Galets", U. S. Army Corps of Engineering Map Service Translation, 1954.
14. Penny, W. G. and A. T. Price, "The Diffraction Theory of Sea Waves and the Shelter Afforded by Breakwaters", Philosophical Transactions of the Royal Society of London, Ser. A, Z44, March, 1952, pp. 236-253.

15. Perlin, M., "A Numerical Model to Predict Beach Planforms in the Vicinity of Littoral Barriers", M. S. Thesis, Department of Civil Engineering, University of Delaware, June, 1978.
16. Price, W. A., K. W. Tomlinson and D. H. Willis, "Predicting Changes in the Plan Shapes of Beaches", Proceedings of the Thirteenth Conference on Coastal Engineering, ASCE, 1972, pp. 1321-1329.
17. Saville, T., "Beach Profile Laboratory Tests, Large Wave Tank", Coastal Engineering Research Center, unpublished.
18. Willis, D. H., "An Alongshore Current Evolution Model", National Research Council of Canada, Hydraulics Laboratory, Report No. H4-92, March, 1978.

CHAPTER 111

ESTIMATION USING A MOVABLE BED MODEL OF SHORELINE CHANGE CAUSED BY A RECLAMATION PROJECTED INTO THE SEA

by

Shoji SATO and Hiroaki OZASA
Port and Harbour Research Institute, Ministry of Transport,
1-1, 3-chome, Nagase, Yokosuka, Japan

INTRODUCTION

Recently, many local airports in Japan are considering to extend their runways, so accomodating passenger traffic. But most airports are obliged to extend their runways into the sea on account of the shortage of land and complaints from their neighbors about jet-plane noise. Tokushima Airport is one of such local airports, which is situated on the coast along the Kie-Suido Channel as shown Figure 1. The length of the runway of Tokushima Airport is 1500 m at present, so a plan to extend the runway by 600 m into the sea has been proposed by the local government. However, Matsushige beach, where the airport is located, is now so seriously eroded that offshore breakwaters are being constructed in the south and the northern part is used for sea-bathing. Therefore, it is necessary to estimate the change of beach profiles, especially of the shoreline, caused by the extension of the runway, and to find countermeasures against unfavourable change.

A movable bed model was constructed to estimate such changes, because no numerical simulation using a computer has been developed to estimate changes of a complicated beach topography. Of course, the universal dynamic similarity does not hold for model studies on sand transport problems. Therefore, the characteristics of sand transport at the site are first clarified through analysis of the field observation data, and then the model scale, bed material, and test waves are determined in such a manner that the topographic variation in the model sea bed will become similar to that in the prototype. But, in general, it is difficult to make all of the variations of the sea bed in the model similar to that in the prototype. In this model experiment, the long term changes of the shoreline has been taken as the most important phenomena to be reproduced in the model.

CHARACTERISTICS OF LITTORAL SEDIMENT TRANSPORT

The Matsushige coast, where the airport is located, is a sandy beach of 4000 m long bounded by the breakwaters of Imagiri and Awazu Ports. Waves from SSE-SE are overwhelmingly predominant, as seen in Table 1 which shows the deep water wave energy from each direction based on wave hindcasting using weather maps during the period from January 1971 to December 1975. Their wave heights, however, are usually less than 1.5 m as seen in Table 2, which shows waves of significant height more than one meter recorded on a wave recoder in 15 meters of water, from November 1975 to November 1976. Waves of more than 2 m high occur only when the typhoon passes near by the coast. Northerly waves occur

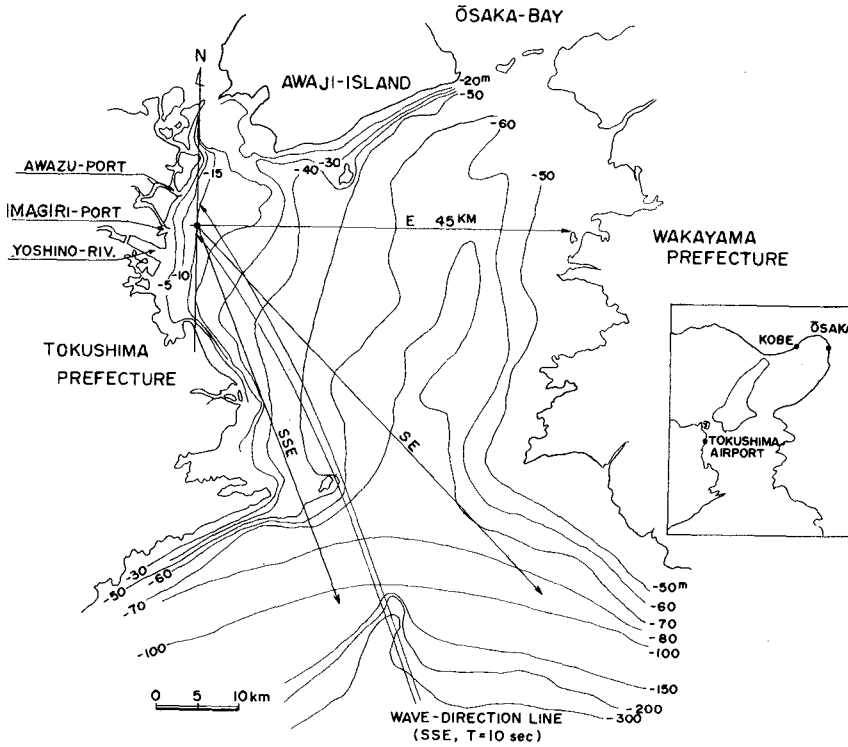


Figure 1. Situation of Tokushima Airport

DEEP WATER WAVE DIR.	WAVE ENERGY ($1 \cdot m/m$)
N E	1 2 0 2 0
E N E	3 4 0 0
E	5 3 0 0
E S E	1 2 5 4 0 0
S E	4 9 2 8 5 0
S S E	2 1 0 8 4 0 0
S	1 1 5 4 3 0

Table 1. Deep water wave energy based on wave hindcasting (Jan. 1971 to Dec. 1975)

DATE	$H_{1/3}$ (m)	$T_{1/3}$ (sec)
23 NOV. 1975	1.14	15.4
22 FEB. 1976	1.06	7.2
25 MAY 1976	1.31	15.1
24 JUL. 1976	1.42	10.8
13 SEP. 1976	1.31	7.0

Table 2. Observed waves of $H_{1/3}$ 1 m at the 15 m contour (nov. 1975 to Nov. 1976)

mostly in winter, but their height is usually less than one meter.

From the above wave characteristics, it is clear that the sand is predominantly transported along the coast from south to north. The Matsushige coast is located on the delta formed by the material discharged from the Yoshino River, the mouth of which is at about 2 km south of Imagiri Port. At present, however, littoral material transported into the coast from the south and transported out northward from the coast is very small in volume, on account of the construction of dams in the upstream areas of the Yoshino River and the completion of the breakwaters of Imagiri and Awazu Ports. So, the coast can be considered to be a nearly isolated beach from the standpoint of littoral sediment transport.

Figure 2 shows a contour map of the coast. At present, there is no sand beach within 1600 m from Imagiri Port, but from there it gradually appears, becoming 100 m wide at Awazu Port. Looking at the contours, 5 m line runs parallel to the coast from Awazu Port until the center of bay, and then turns seaward, and reaches the tip of the breakwater at Imagiri Port. Shallower contours tend to be parallel to the beach for a greater part of the bay, those less than 2 m being parallel all along it. Longshore bars occur only in the half of the bay near Awazu Port and are between 2 and 3 m deep. These contours also prove that the littoral transport is overwhelmingly northward in direction as mentioned above. The median diameter of the bed material is 0.3-0.36 mm on the beach, 0.2-0.24 mm on the bed at 5 m deep, and 0.1-0.13 mm on the bed at 10 m deep, as shown in Figure 2. A sea dike with crest height of 7 m above the datum level exists along all this stretch of the coast.

PRELIMINARY TEST

Method of The Preliminary Test

The waves for the main test which are able to cause littoral transport similar to that in the prototype clearly have SSE-direction in deep water, as seen in Table 1. Waves from SSE in deep water become SE in direction on 15 m contour owing to the refraction shown in Figure 1. Therefore, the bottom topography from the sea dike to the 15 m contour between Imagiri and Awazu Ports was produced in a wave basin with a scale of 1/200 horizontal and 1/50 vertical. The model area is shown in Figure 2. The part between 10 and 15 m contours was a fixed bed of concrete and the shallower part was made as a movable bed of sand with median diameter of 0.29 mm. The grain size distribution of the sand is shown in Figure 3.

This model test aim was to estimate long term changes of the bottom topography, especially of shoreline, caused by the extension of the runway. Past data on the long term changes of the bottom topography near the shoreline, therefore, are necessary in order to determine the wave condition for the main test. Unfortunately, no field surveys of the beach have not conducted in the past, except for a three years in recent, so that the past changes of the shoreline have been investigated using aerial photographs taken in different years. Figure 4 shows the shorelines in May 1964 and May 1969 which were found by that method.

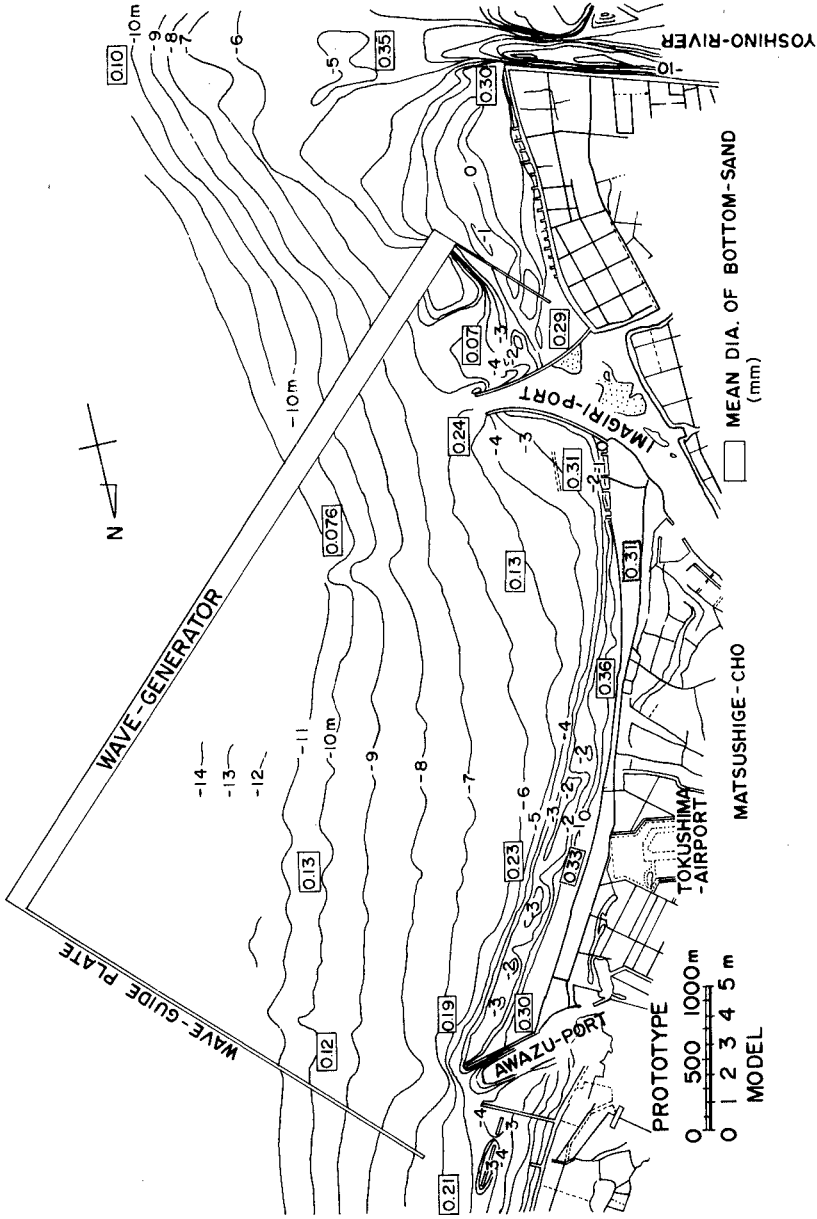


Figure 2. Contour map and the area of hydraulic model

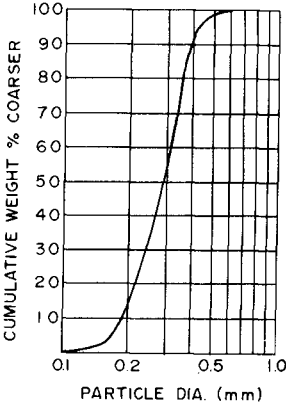
The breakwater of Imagiri Port had already been completed in May 1964, while the the south breakwater of Awazu Port was extend by 400 m, from 150 m long in May 1964 to 550 m long in May 1969. During those 5 years, the beach disappeared in the 1000 m nearest Imagiri Port and widen near Awazu Port.

The preliminary test was conducted by a trial and error method to find the most suitable SE-wave to produce the shoreline changes shown in Figure 4. Each wave, as shown in Table 3, was generated in the model where the bed topography was made to correspond to that of May 1964. The structures such as breakwaters were modeled to correspond to their state in May 1969. The bottom topography of May 1964 was obtained by the method shown in Figure 5, that is, the position of the shoreline investigated by using the aerial photograph of May 1964 was plotted with the beach profile of May 1975. Then the profile near the shoreline was drawn so that the same shape should be similar to that of May 1975. In order to check how the plan shape of the beach in the model approached that of the profile in May 1969 after wave action, the standard deviation of the former against the latter was calculated by the method shown in Figure 6. The position of the model was measured at 50 cm intervals (100 m in the prototype). The test was conducted at the level of M.W. which is one meter above the datum level. The scale of the wave period was taken as the square root of the vertical scale.

Result of The preliminary Test

Figure 7 shows changes of the above mentioned standard deviations during the experiment. The standard deviations, for all cases, decreased with the duration of the wave action, reaching a minimum value after some hours, then increasing. Among these cases, the standard deviation reached its smallest value for the case of waves of 5.3 cm in height and 1.13 sec period and its second smallest value for the case of the wave of 8.5 cm and 1.41 sec. Figure 8 shows the relation between H_o/L_o and H_o/d_{50} for each case, where H_o is the deep water wave height and d_{50} the median diameter of sand. The boundary lines between storm and normal beaches of Johnson (1949)¹⁾ and Iwagaki-Noda (1963)²⁾ are also shown in the figure. Comparing the test data with these boundary lines, it is found that Cases 1 and 5 which have the smaller minimum values of standard deviation are nearly on the boundary lines, but Cases 2 and 6, having larger values are a long way from them. Figure 9 shows the shorelines for each case at the time when it approached nearest the position of the prototype in May 1969. Cases 1 and 5 coincide with the shoreline of May 1969 fairly well, but Cases 2 and 6 deviate respectively seawards and landwards. The waves of Cases 2 and 6 are considered to be respectively accumulative and erosive waves.

In order to determine the wave condition for the main test, it is also necessary to the quantity of sand movement in the offshore zone as well as the comparison of the shorelines as mentioned above. In Case 5, which has waves of 5.3 cm in height and 1.13 sec period, sand ripples were not seen in some areas of the offshore zone deeper than about 16 cm (8 m in the prototype). On the other hand, in Case 1, which has waves of 8.5 cm in height and 1.41 sec period, they were seen in all area of



CASE	MODEL		PROTOTYPE	
	H (cm)	T (Sec)	H (m)	T (Sec)
1	8.5	1.41	4.3	10
2	6.2	1.71	3.1	12
3	5.8	1.41	2.9	10
4	6.8	1.41	3.4	10
5	5.3	1.13	2.7	8
6	7.4	1.13	3.7	8

Table 3. Dimension of the waves in the preliminary test

Figure 3. Grain size distribution of the sand used as movable material

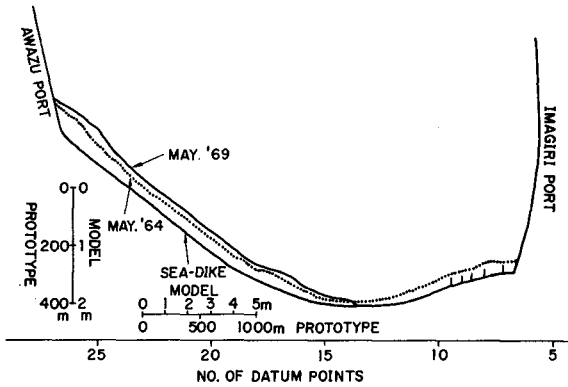


Figure 4. Shorelines of 1964 and 1969 found by using aerial photographs

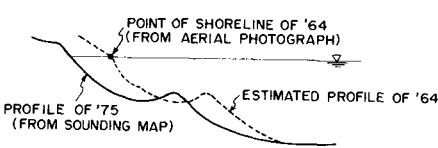
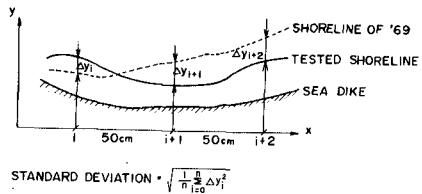


Figure 5. Method of estimating the bed topography of May 1964



$$\text{STANDARD DEVIATION} = \sqrt{\frac{1}{n} \sum_{i=1}^n \Delta y_i^2}$$

Figure 6. Calculation of the standard deviation of the shoreline

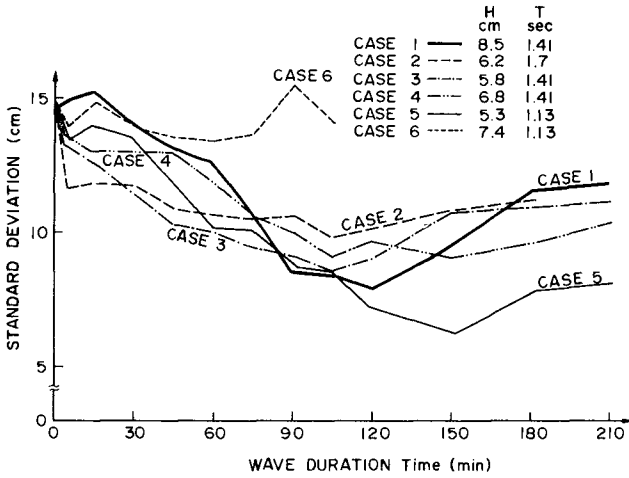


Figure 7. Changes of the standard deviations of the shorelines due to the wave action

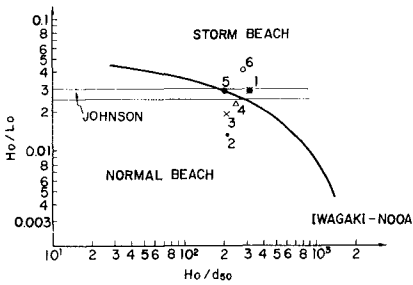


Figure 8. Relation between model waves and the boundary lines between storm and normal beach

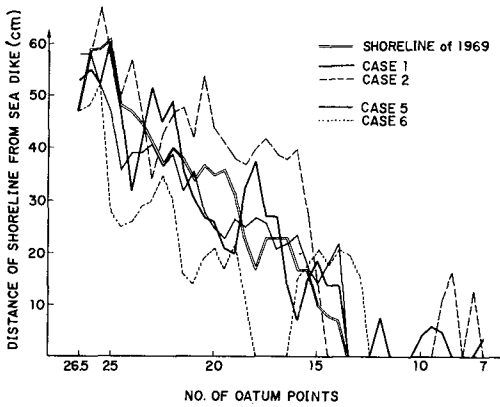


Figure 9. Comparison of the model shorelines when they approached nearest the actual shoreline of May 1969

the movable bed.

The critical water depth h , where all sand particles of the surface layer of the sand bottom are moved collectively in the direction of the wave propagation on the open sea without strong currents, is expressed by Sato-Ijima-Tanaka (1962)³ as follows:

$$\frac{H_o}{L_o} = 1.35 \left(\frac{d}{L_o}\right)^{1/3} \left(\sinh \frac{2\pi h}{L}\right) \left(\frac{H_o}{H}\right) \quad (1)$$

Where H_o and L_o are the height and the length of deep water waves, H and L are the height and the length of the waves at the critical water depth h , and d the diameter of bottom sand. The calculation diagram of Equation (1) is shown in Appendix. The length of the deep water wave of $T = 1.41$ sec is

$$L_o = 1.56 \times (1.41)^2 = 3.10 \text{ m}$$

Using small amplitude wave theory, the dimension of the deep water wave for $H = 8.5$ cm and $T = 1.41$ sec at 30 cm deep is obtained to be $H_o = 9.13$ cm. Using $d = 0.29$ mm in the model,

$$\frac{H_o}{L_o} = \frac{0.0913}{3.10} = 0.0295, \quad \frac{d}{L_o} = \frac{0.29 \times 10^{-3}}{3.10} = 9.35 \times 10^{-5}$$

According to Figure (A-3) in Appendix, $h/L_o = 0.038$. So,

$$h = 0.038 \times 310 = 11.8 \text{ cm}$$

The critical water depth $h = 11.8$ cm corresponds to $h = 5.9$ cm in the prototype. The critical wave height H_o for $T = 10$ sec, $h = 5.9$ m, and $d = 0.23$ mm in the prototype is calculated as follows:

$$\frac{d}{L_o} = \frac{0.23 \times 10^{-3}}{156} = 1.47 \times 10^{-6}, \quad \frac{h}{L_o} = \frac{5.9}{156} = 0.038$$

By the same figure in Appendix, $H_o/L_o = 0.0075$ is given. So,

$$H_o = 0.075 \times 156 = 1.2 \text{ m}$$

That is, the waves of Case 1 nearly correspond to a significant wave of $H_o = 1.2$ m and $T = 10$ sec in the prototype from the standpoint of the sand movement in the offshore zone. Also, it is found that the critical water depth for Case 5 is 6 cm and that the waves of Case 5 nearly correspond to a significant wave height of $H_o = 0.7$ m and period of $T = 10$ sec in the prototype from the same standpoint.

On the other hand, according to the observation data shown in Table 2, the wave height in the normal storm would be expected to be 1.0–1.5 m. Therefore, the wave for the main test was determined to be the wave from SE of 8.5 cm height and 1.41 sec period. This wave reproduced the shoreline change from 1964 to 1969 after 120 minutes of the run, as shown in Figure 7; the time scale for the shoreline changes would be approximately 120 minutes in the model to 5 years in the prototype.

MAIN TEST

Test Cases

The determined wave condition was generated for 6 hours on each of the following four cases:

- Case 1: The present bottom configuration which was surveyed in 1975
- Case 2: Reclamation for the runway extension is added to Case 1
- Case 3: A single line of offshore breakwaters along the coast south of the runway reclamation and a long offshore breakwater along the north coast are added to Case 2

Case 4: Double lines of offshore breakwaters along the southern part of the coast and three short offshore breakwaters along the northern part are added to Case 2

The models of offshore breakwaters are rectangular boxes of wire netting filled by small gravel, so they are permeable. The crest height is 8 cm (4 m in prototype) above the datum level, though that of the prototype actually is 2.5 m. This is because the model wave height is larger than 1/50 of the prototype wave height for a normal storm as mentioned before. Where the beach was eroded so severely that waves struck directly on the sea dike, same gravel was placed in front of it. The sea wall around the runway reclamation was faced by wave absorbers of gravel. The water level was set at the mean water level, the same as that in the preliminary test.

Changes of The Shoreline

The lines of the mean water level are shown in Figure 10 for before the wave action and after 360 minutes of it. Not that longitudinal and lateral scales are different. Using the time scale obtained in the preliminary test, 360 minutes of wave action nearly corresponds to 15 years in the prototype. The following changes of the shoreline can be deduced from the figure.

(1) The coast between the runway reclamation and Imagiri Port
From the result of Case 1, it can be seen that the coast will carry on eroding if it remains in the present state without any countermeasures; the beach above M.W.L. would disappear moreover over a stretch of about one kilometer after 15 years. But, if the runway reclamation is carried, the coastal erosion would be cease in some areas; the loss of the beach above M.W.L. after 15 years only occurs over half the stretch affected in Case 1. Moreover, if the offshore breakwaters are added as in Case 3, the distance over which the beach would disappear reduces to 300 m. In Case 4 with the double lines of offshore breakwaters set in zigzag-pattern, the beach would be formed to the south of the present one.

(2) The coast between the runway reclamation and Awazu Port
From the result of Case 1, the beach is clearly going to continue accreting if it remains in the present state. On the other hand, if the runway reclamation is constructed, the width of the beach would increase near the breakwater of Awazu Port and the reclamation, and decrease a little between them. As a result, the shape of the beach line would become concave. Though such a concave shoreline was not considered to be inconvenient for sea-bathing, measures to keep the shoreline straight were researched in Cases 3 and 4. In Case 3 with a long offshore breakwater, the beach erodes near Awazu Port and accumulates elsewhere. In Case 4 with three short offshore breakwaters, the beach accumulates throughout, keeping an almost straight shoreline. The distance between the offshore breakwaters and the shoreline, however, becomes so small as to be inconvenient for sea-bathing.

Changes of The bottom Topography

Figure 11 shows the contours for Case 1. (a) in the figure, which

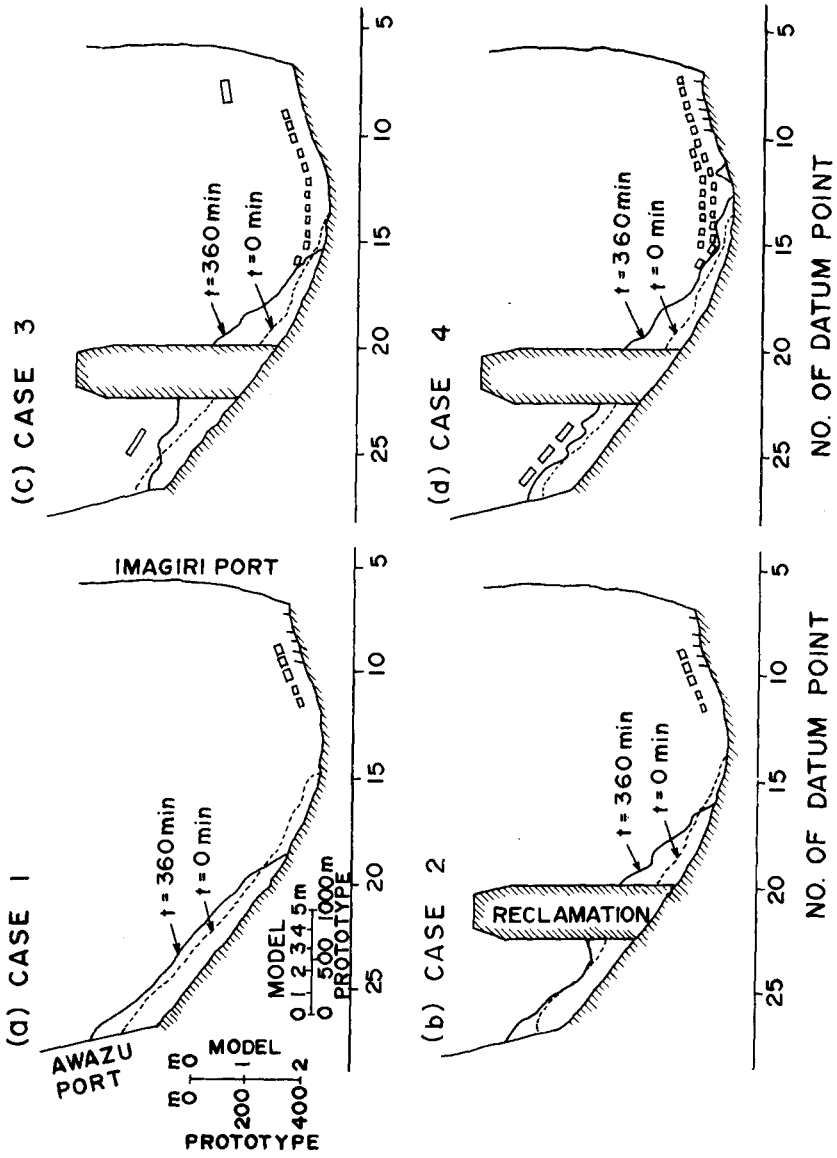


Figure 10. Changes of the lines of m.w.l.

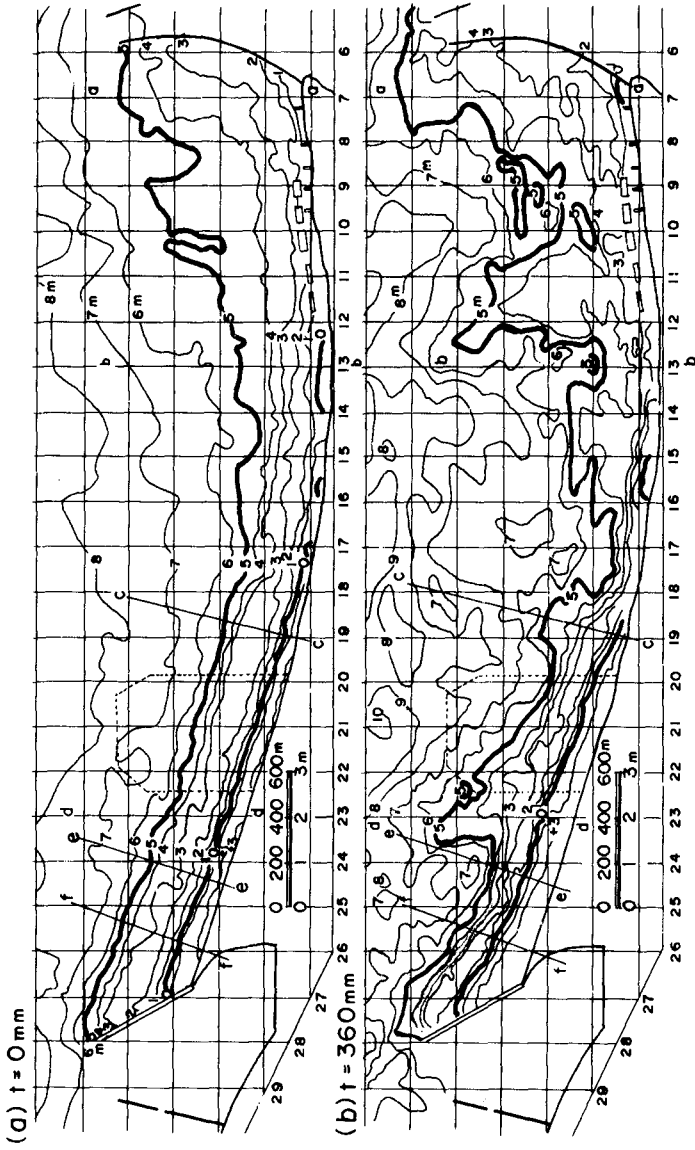


Figure 11. Changes of the bottom topography

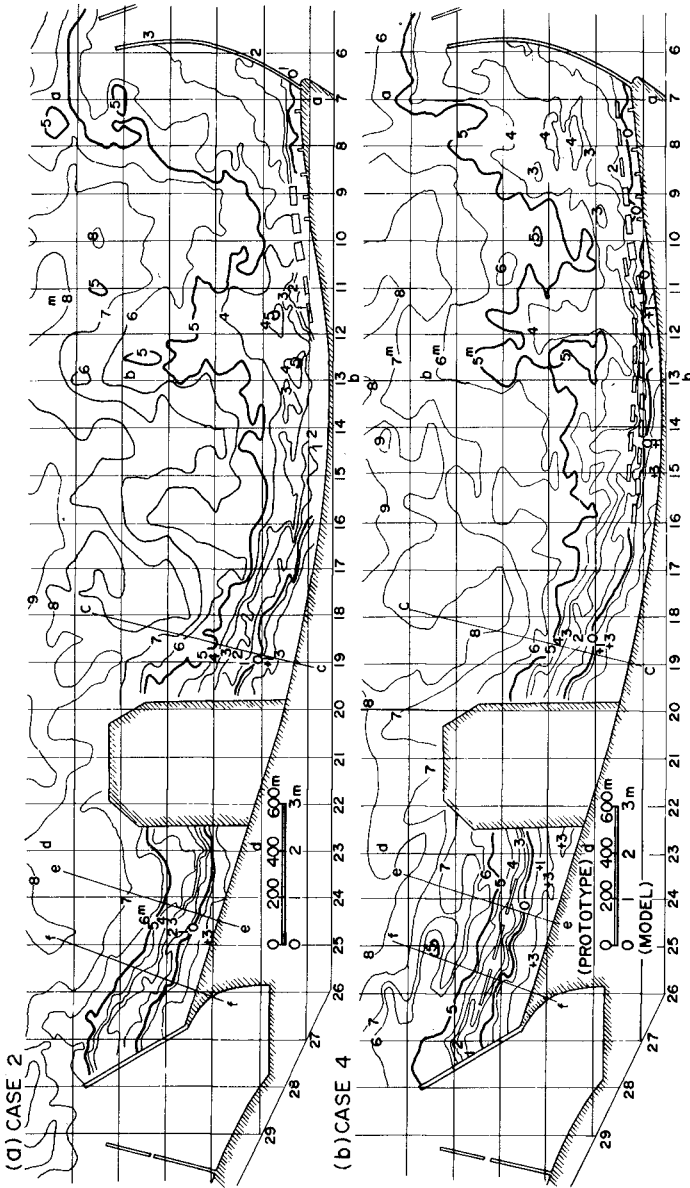


Figure 12. Contours after 360 minutes of wave action for Cases 2 and 4

is before wave action, is the bottom topography of 1975. The beach above 0 m is not exposed over a stretch of 1100 m near the south end of the bay and has a width of 100 m at the north end. In the contour map after 360 minutes of the run shown in (b) of the figure, the 5 m contour recedes landwards considerably in the areas near datum points Nos. 9-10 and 13 at the south end and Nos. 16-18 in the central part. It advances seawards considerably at the area of points Nos. 11-12 and 22-23. The contour of 5 m also advances seawards in the vicinity of the tips of the breakwaters of Imagiri and Awazu Ports. In the area near the shoreline, there is clearly a tendency of erosion in the south and of accumulation in the north; the beach above 0 m is not exposed for a stretch of 2200 m near Imagiri Port but increases to 200 m in width in the vicinity of Awazu Port.

Figure 12 shows the contours after 360 minutes of the run for Cases 2 and 4. Needless to say, the contours before the run for the both cases are the same as (a) in Figure 11. The followings can be deduced from (a) of Figure 12 in comparison with (a) of Figure 11:

(1) The 5 m contour recedes landwards in the area of Nos. 9-10 and advances seawards in the area of Nos. 11-12 as remarkably as in Case 1 but does not recede in the areas of Nos. 13 and 16-18. It, in fact, advances seaward in the vicinity of the runway extension.

(2) In the vicinity of the shoreline, a wide beach appears just at the south side of the runway reclamation, and the width of the beach between the reclamation and the south breakwater of Awazu Port becomes a littil narrower than in Case 1.

(3) The 5 m contour recedes landwards a littil at the tip of the south breakwater of Awazu Port, which is different from Case 1.

Comparing (a) and (b) in Figure 12, the points of difference points between Cases 2 and 4 are as follows:

(1) In the area between the runway reclamation and Imagiri Port, a beach above 0 m appears in front of the sea dike almost along its length in Case 4 and the contours between 1 and 5 m recede a littil further landwards in Case 4 than in Case 2.

(2) In the area between the runway reclamation and Awazu Port, the line of 0 m advances further seawards in Case 4 than in Case 2, though it runs in a rather straighter line.

Figure 13 shows the changes of the beach ploffiles after 360 minutes of wave action for Cases 1, 2, and 4. The profiles shown in the figure are along the lines a-a, b-b, c-c, d-d, e-e, and f-f of Figure 11 and 12. The profile a-a, which is near Imagiri Port, accumulates most in Case 1. The profile b-b, which is about 1300 m from the north breakwater of Imagiri Port, erodes in Cases 1 and 2, but accumulates at the shoreline of Case 4. The profile c-c accumulates in all cases, but more so in Cases 2 and 4 as a result of the runway extension. The profiles d-d, e-e, and f-f accumulate more in Case 1 than in Cases 2 and 4, and, comparing Cases 2 and 4, the area in the vicinity of the shoreline accumulates more in Case 4 than in Case 2.

The Rate of Littoral Sediment Transport

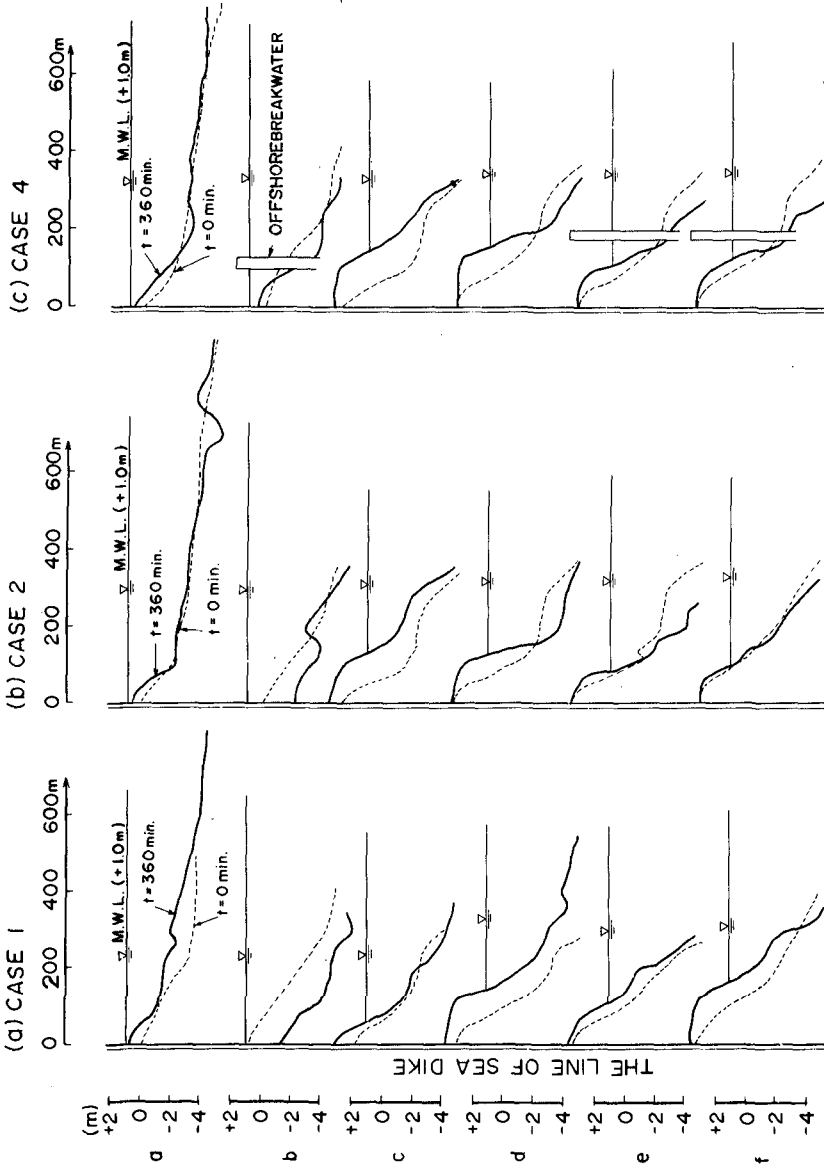


Figure 13. Changes of the beach profiles

The littoral sediment transport was measured in Cases 1 and 2 by using sand traps. A unit of the sand traps is a stainless steel box of 10 cm high and 30 cm wide, and has wings of 15 cm long on both sides, as shown in Figure 14. In Case 1, from minutes 120 to 130 of the run, the sand traps were set from the sea dike to the 7 m contour, in perpendicular to the shoreline on the line passing datum point No. 20 which lies on the proposed runway reclamation. In Case 2, from minutes 200 to 210 of the run, they were set seawards from the 7 meters contour on the same line as Case 1. These results are shown in Figure 15, where the volume of sand trapped in each trap is shown by dry weight. Most littoral transport is found to be concentrated landwards of the longshore bars as in the prototype. The peak values of trapped sand at the seaward end, in Cases 1 and 2, are considered to be caused by sand entering the trap from its offshore edge. On the other hand, the peak value at the landward end in Case 2 is thought to be due to sand travelling along the sea wall of the runway reclamation from the south.

From the results mentioned above, the total littoral transport rate in the case without the runway reclamation can be deduced to be the sum of the following two volumes:

11800 g/10 minutes minus the peak value of the seaward end (in Case 1)

and

2200 g/10 minutes minus the peak value of the landward end (in Case 2)

This gives 1200 g/minute. In the case with the runway reclamation, the transport is 2200 g/10 minutes from Case 2, that is, 220 g/minute.

The apparent specific gravity of sand in the sea bottom is supposed to be 1.6. 24 minutes in the model corresponds to one year in the prototype on the basis of the preliminary test. Considering, moreover, that the volume ratio of the prototype against the model is $200^2 \times 50$, the littoral sediment transport rate in the prototype would be calculated as follows:

(1) For the case without the runway reclamation

$$1200 \times \frac{1}{1.6} \times 24 \times 200^2 \times 50 \times 10^{-6} \doteq 36000 \text{ m}^3/\text{year}$$

(2) The littoral transport rate passing the offshore side of the runway reclamation

$$2200 \times \frac{1}{1.6} \times 24 \times 200^2 \times 50 \times 10^{-6} \doteq 6600 \text{ m}^3/\text{year}$$

On the other hand, the longshore wave energy which was calculated by using weather maps in period from 1971 to 1976 is shown in Table 4. The net longshore wave energy flux per year, according to Table 4, is approximately 1.9×10^5 ton·m/m northward. The relation between the littoral transport rate Q_i and the longshore wave energy flux E_i , on the basis of the diagram of Savage (1964)⁴, is given as follows:

$$Q_i = 0.21 E_i$$

Where Q_i is in unit of cubic meters and E_i ton·m/m. Substituting the value of 1.9×10^5 mentioned above for E_i in this equation, the littoral

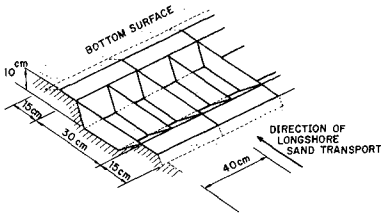


Figure 14. Sketch of the sand traps

Direction of Deep-water wave	Longshore Energy Flux at the Breaking Line ($t \cdot m/m$)
NE	- 3,450
ENE	- 1,440
E	- 2,020
ESE	- 13,020
SE	+ 63,080
SSE	+ 867,300
S	+ 32,550
Total	+ 943,000

Table 4. Longshore wave energy flux calculated on the basis of waves estimated during 5 years from Jan. 1971 to Dec. 1975

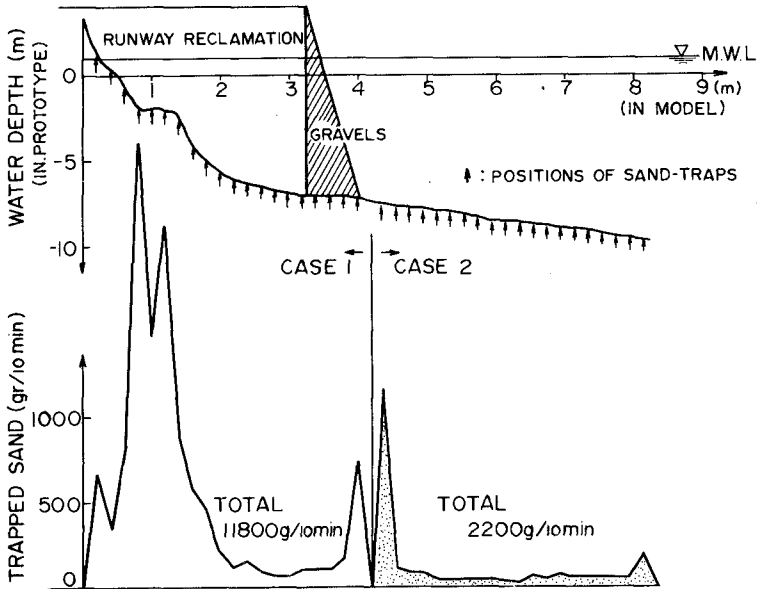


Figure 15. Volume of sand trapped by the sand traps

transport rate is obtained to be $40000 \text{ m}^3/\text{year}$. This value is of the same order as that obtained in the model test. Therefore, the model test would also be considered to be similar to the prototype from the viewpoint of sand transport rate.

CONCLUSIONS

A movable bed model test has been conducted in order to estimate the changes of the bottom topography, mainly in the vicinity of the shoreline, which are caused by a reclamation of 600 m long injected into the sea for the extension of the runway of Tokushima Airport. The Matsushige coast, where the airport is located, is a sandy beach of nearly 4000 m long which is bounded by the breakwater of Imagiri Port to the north and by that of Awazu Port to the south. The model scale is 1/200 horizontal and 1/50 vertical, the sand with median diameter of 0.29 mm was used as movable material. The wave condition for the main test was selected so that the shoreline changes for the past five years from 1964 to 1969 would be reproduced and the quantity of the sand movement in the offshore zone of the model would be similar to that during the normal storm condition in the prototype.

From the main test using the above mentioned wave condition, the following points would be estimated:

(1) The volume of the net longshore sediment transport is about several ten thousands cubic meters per year on the basis of the volume trapped by sand traps, which agrees with the volume calculated from wave energy data

(2) The area where the beach disappears would gradually extend northward, if the coast remains in the present state without any countermeasures.

(3) The reclamation for the runway extension makes the length of the beach which will disappear less than in the case without reclamation.

(4) Double lines of offshore breakwaters are much more effective than a single line of them for restoring the eroded beach in the southern part of the coast.

(5) The area between the runway reclamation and the breakwater of Awazu Port will have a concave shoreline with slight erosion in the center. Offshore breakwaters are useful to prevent this change.

(6) The runway reclamation also decreases the littoral transport entering Awazu Port from the south, after passing the tip of its breakwater.

ACKNOWLEDGEMENTS

The authors express grateful thanks to the members of the Komatsujima Port Construction Office and the Kobe Investigation and Design Office of the 3rd Port and Harbour Construction Bureau, who conducted the field observation for this study, and Mr. Toshihiko Nagai of the same as the authors who engaged in this study.

REFERENCES

- 1) Johnson, J. W. (1949): Scale effects in hydraulic model involving

- wave motion, Trans. Am. Geophys. Union, Vol. 30, No. 4, pp. 517-525
- 2) Iwagaki, Y. and H. Noda (1963): Laboratory study of scale effects in two dimensional beach processes, Proc. 8th Conf. on Coastal Eng., pp. 194-210
 - 3) Sato, S., T. Ijima, and N. Tanaka (1963): A study of critical depth and mode of sand movement using radioactive glass sand, Proc. 8th Conf. on Coastal Eng., pp. 304-323
 - 4) Savage, R. P. (1962): Laboratory determination of littoral transport rate, Proc. Am. Soc. Civil Engrs. No. WW2, pp. 69-92
 - 5) Sato, S. (1963): Study of sand drift phenomena related to new port projects, Tech. Note of The Port and Harbour Research Inst., No. 5 (Japanese)

APPENDIX

Surface Layer Movement and Completely Active Movement of Bottom Sand

Sato-Ijima-Tanaka (1963)³ have classified the distribution patterns by waves of radioactive glass sand injected in the offshore zone into the following four groups shown in Figure A-1:

(1) The first group This is the case that the point of the maximum count moves in the direction of the wave propagation and all equi-count lines also extend in the same direction.

(2) The second group This is the case that the point of the maximum count does not move, but all equi-count lines extend in the same direction of the wave propagation.

(3) The third group This is the case that the point of the maximum count does not move and only a part of equi-count lines extends in the direction of wave propagation. This group also contains the case that the count decreases markedly in total, despite the distribution of equi-count lines scarcely changes.

(4) The fourth group This is the case that the distribution of equi-count lines remains unchanged and the count also does not decrease significantly. The cases that all equi-count lines extend in the same direction as the tidal current or in the direction opposite to the wave propagation are also included in this group.

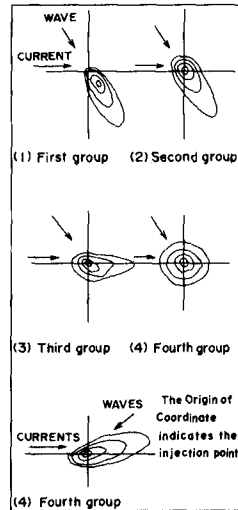


Figure A-1

Then, classifying the field data into these four groups, the results that they have been related with the wave characteristics are shown in Figure A-2⁵. This figure was obtained by Sato (1963)⁵, who plotted additional data in the similar figure by Sato-Ijima-Tanaka (1963)³. In the figure, wave height H and wave period T are those of the maximum significant wave at the injection point of glass sand during the period when the change of count-lines was monitored, and depth h the mean water

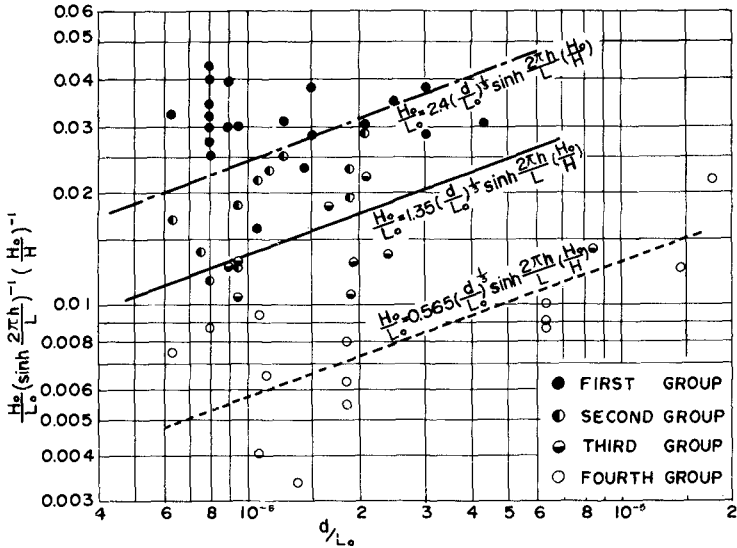


Figure A-2. Relation between the wave characteristics and the median diameter of sand for each distribution of radioactive glass sand (Sato-Ijima-Tanaka 1963 and Sato 1963)

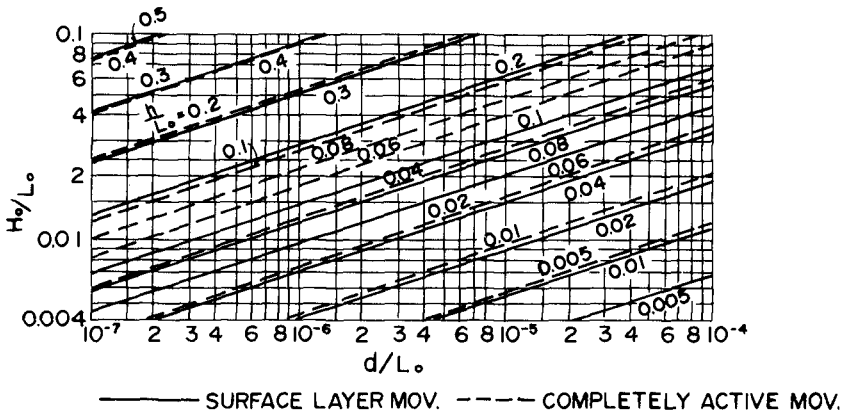


Figure A-3. Calculation diagram of Eqs. (A-1) and (A-2)

depth at the injection point. H_0 and L_0 are the height and length of the deep water wave for H and T , d the median diameter of the glass sand which is the same as the bottom sand in the vicinity. In this figure, the transition from the second group to the third group is shown by the following equation:

$$\frac{H_0}{L_0} = 1.35 \left(\frac{d}{L_0}\right)^{1/3} \sinh \frac{2\pi h}{L} \cdot \left(\frac{H_0}{H}\right) \quad (A-1)$$

and the critical condition on which points enter into the first group is shown by the following equation:

$$\frac{H_0}{L_0} = 2.4 \left(\frac{d}{L_0}\right)^{1/3} \sinh \frac{2\pi h}{L} \cdot \left(\frac{H_0}{H}\right) \quad (A-2)$$

That is, Equation (A-1) corresponds to the state where all sand particles on the surface layer of the sea-bed move collectively in the direction of wave propagation and Equation (A-2) corresponds to such great movement of the bottom sand as to produce the change of water depth. The former is called the surface layer movement and the latter the completely active movement by Sato and Tanaka. Figure A-3 shows the calculation diagrams of those equations.

CHAPTER 112

MORPHOLOGIC EFFECTS OF WESTERLAND BEACH NOURISHMENT 1972

Dieter WENZEL ¹

Abstract

In 1972, a beach nourishment scheme was to delay the steady coast erosion near Westerland (Germany). Morphologic investigations state the development of the fill and its effects to adjacent beaches, and yield recommendations for another nourishment scheme in 1978.

The morphologic analyses are related to two different profile areas. They show that the effects of the nourishment were quite confined in space and time. Particularly the island base and the bar remained unaffected by the fill.

The analysis becomes more instructive and perhaps easier by the use of special means, such as the differential morphometric characteristic and the mean profile depth instead of mass computations or mass balances. The standard mean depth in the morphologic system of the investigation area is found to be NN-4,1 m.

1. Initial Situation

The west coast of the island of Sylt, Germany (fig. 1), is built up of sand and subject to an important erosion. The mean regression rate between 1793 and 1952 was 1,6 to 1,9 m per year. The urban area of the town of Westerland, adjacent immediately to the beach, had been protected by a vertical wall. This wall itself, built between 1907 and 1923, is threatened by the erosion of the shore and foreshore (fig. 2). A beach nourishment in 1972 provided a stock of about 750.000 m³ of sand, pumped on the beach in the form of a large groyne.

The typical beach profile in this central part of the coast consists in: beach - trough - bar - sea-bottom (fig. 3). It is likely to form a constant morphologic system produced by the specific hydrodynamic conditions. These are characterized by a normally

¹ Diplomingenieur, Civil Engineer, Department of Hydrology, Amt für Land- und Wasserwirtschaft Husum, D-2250 Husum, Federal Republic of Germany

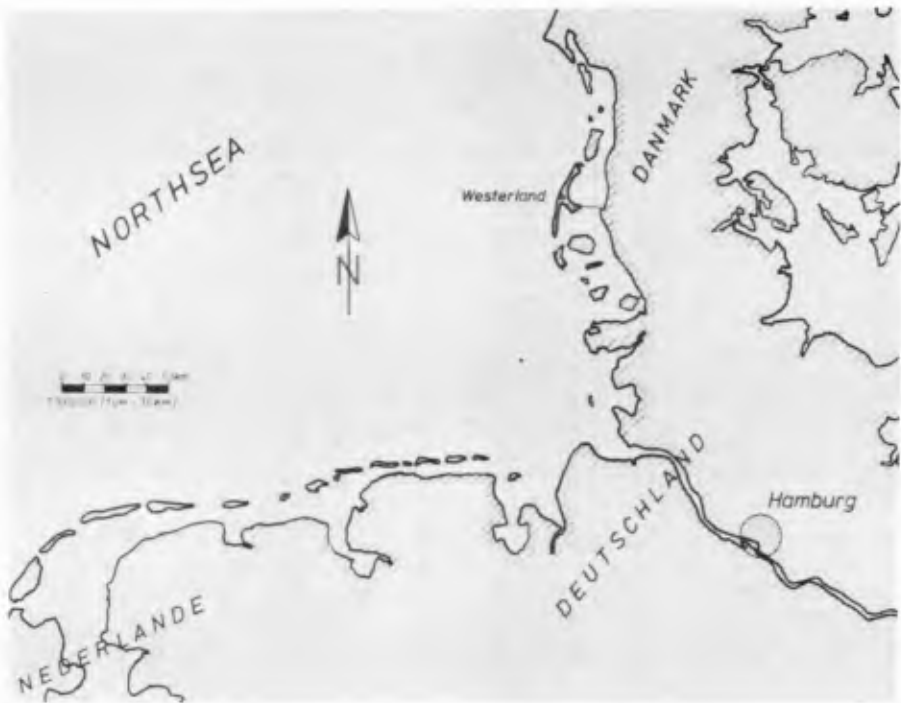


Fig. 1. The situation of the investigation area



Fig. 2. Westerland sea-wall and its protection by tetrapods (14.01.76)

medium to high wave impact with variable incident angles, moderate current velocities of changing sense, and a mean tidal range of 1,85 m. The periods of calm sea surface normally do not exceed a total of 6 weeks per year, caused by seaward winds.

2. Investigations

The basic data for the morphologic investigations were collected by a lot of soundings and beach surveys. The soundings included an area till 1000 m offshore and down to a depth of NN-8 to -9 m.

These data were worked up to bathymetric charts and further on to differential bathymetric charts, profiles, maps of contour line shifting, mass calculations, and morphometric diagrams. For checking the reliability of the data obtained, an error estimate took into account especially the possible or existing systematic errors, so those influencing a whole survey or major parts of it in one sense.

It was found that the elevation error in the maps used has the following values:

	maximum	mean values
proportional error	5 %	2,5 %
constant error	0,35 m	0,01 m
+ temporary constant error	0,15 m	0,04 m

Respective error ranges are shown in the diagrams fig. 6 to 8.

The conclusion from this error estimate was, that overall mass balances are no good means to state shore and foreshore evolution. Moreover they suffer from being the result of records of an instantaneous, possibly singular shape and from neglecting the drifting sediments.

To render the statement of mass calculations persuasive, adequate marginal terms have to be chosen. For the present study, two different areas have been defined (fig. 3 and 4):

- the stock comparison area, limited by fixed boundaries or stationary lines, informing about the volume of the available sand masses and their distribution with regard to the coastal structures,
- the system comparison area, limited by defined contour lines (+1,5 m and -7,0 m), thus informing about the volume of sand contained within the morphologic system.

The length of shoreline computed is 1,5 km. The investigation period covers the years 1970 till 1978. Outstanding events during this period were:

- the beach nourishment in 1972
- a series of six heavy storms in November/December 1973, straining the shore with a wave energy superior to that of the whole winter 1971/72 (63100 versus 40700 kWh per 1 m shoreline)
- two heavy storm surges in January 1976, during which the water levels reached those of the catastrophic surges in 1962.

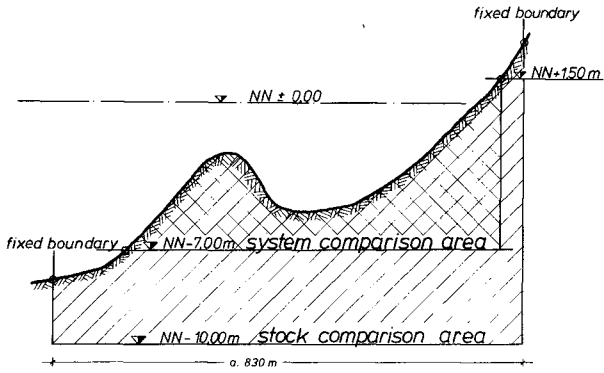


Fig. 3. Morphologic system and mass comparison areas

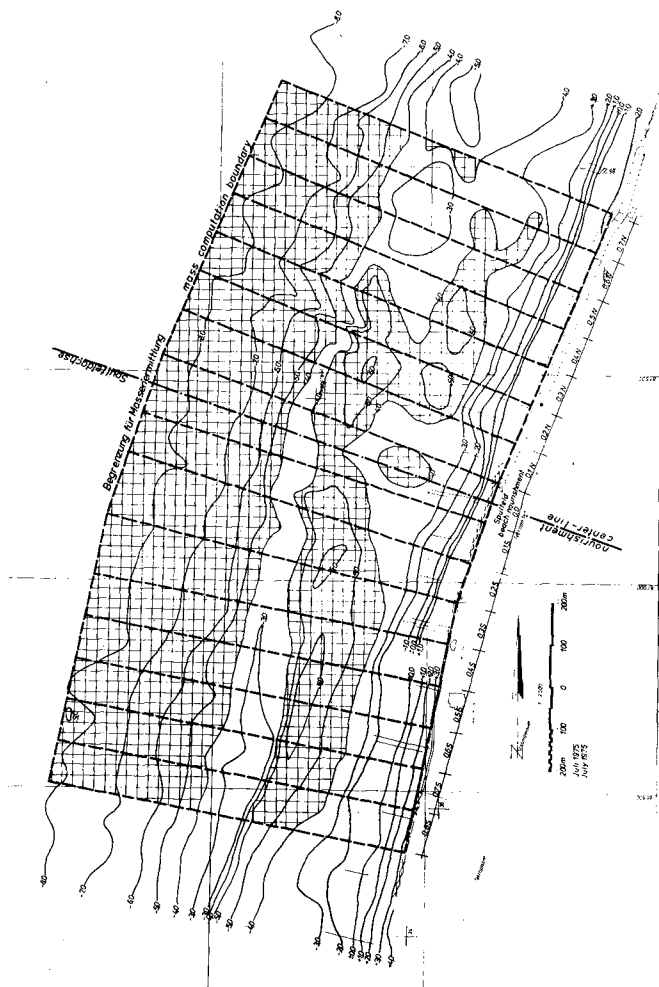


Fig. 4. Bathymetric chart July 1975 and plan of mass computation cells (strips)

3. Sounding and Morphologic Data Analysis

The characteristic phenomena before the filling action 1972 - decreasing beach width, increasing trough dimensions, bar diminution - were partially neutralized: the beach became larger in the immediate vicinity of the fill, and the trough became less wide and deep (fig. 4). But the holes just ahead of the beach continued to exist in their place, though somewhat less deep, and the bar remained unaffected by the fill.

At once after the fill, the situation started to develop towards the former condition, a fact which turns out more evident by the differential bathymetric charts (fig. 5). They show that in 1976 the sand stock in the beach is nearly consumed and the trough is even deeper (by 1 ... 1,5 m) than in 1972. The bar, however, did not change significantly.

The existence of seasonal effects (winter shape - summer shape) is here confirmed, too. They are accentuated by the occurrence of winter storms: The shape in March '76, after the January storm-surges, presents clearly a steeper seaward bar slope, a higher bar crest (by 0,5 m against August '76), a deeper trough (by 0,5 m against August '76), and a stronger erosion of the beach (up to 2 m deeper).

The mass computations within the stock comparison area (fig. 6) show a more pronounced erosion in the central part (0 ... 0,2N) of the investigation area before the fill. Towards the ends, at a distance of about 800 m from the filling center-line, the differences between the lines are rather small, meaning that a measurable deposition disappears. The line for February '74 runs near the former lines, meaning that the storm series of 1973 drifted the main part of the fill away.

The mass computations within the system comparison area (fig. 7) show little variation in time, apart from the stations 0 ... 0,2 N before the fill, where even the system had started to dissolve by losing of its specific volume.

But in principle there seems to be a substantial constancy of masses within the morphologic system. On the other hand it proves a small form variation capability, particularly when comparing it to the conditions at other sand coasts subject to heavy wave attack.

In order to identify the morphologic changes, which occurred nevertheless, in a simple and reliable way, the morphologic magnitude "mean profile depth h_m " is defined:

$$h_m = NN - 7 + d_m \quad [m]$$

$$\text{with } d_m = \frac{\text{mass of the profile strip } [m^3]}{\text{surface area of the profile strip } [m^2]} \quad [m]$$

NN = Normal Null, German Normal Chart Datum

The analysis of the mean depth diagram (fig. 8) gives a standard value of NN-4,1 m for the investigation area. In the central part,

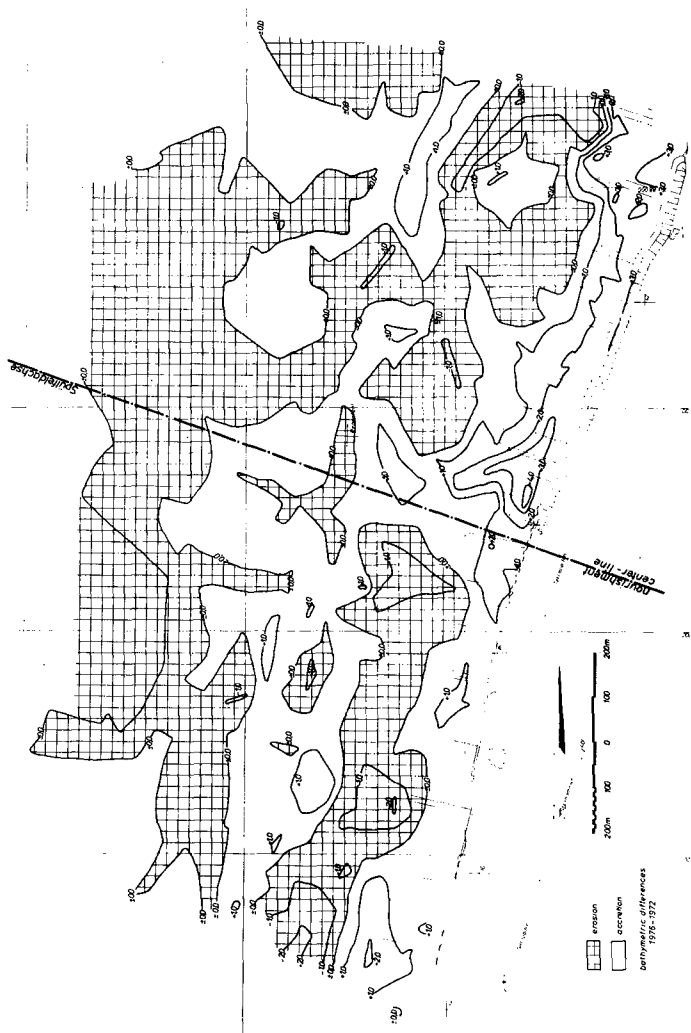


Fig. 5. Differential bathymetric chart 1976-1972 (before the fill). Differences indicated in metre.

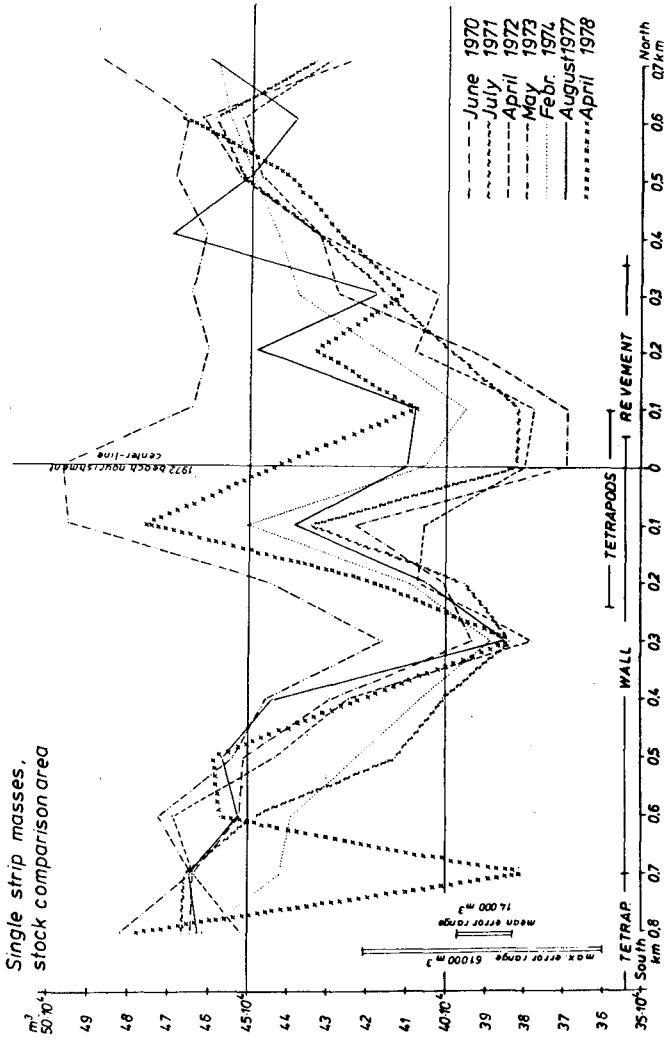


Fig. 6. Distribution of sand masses within the stock comparison area along the coast

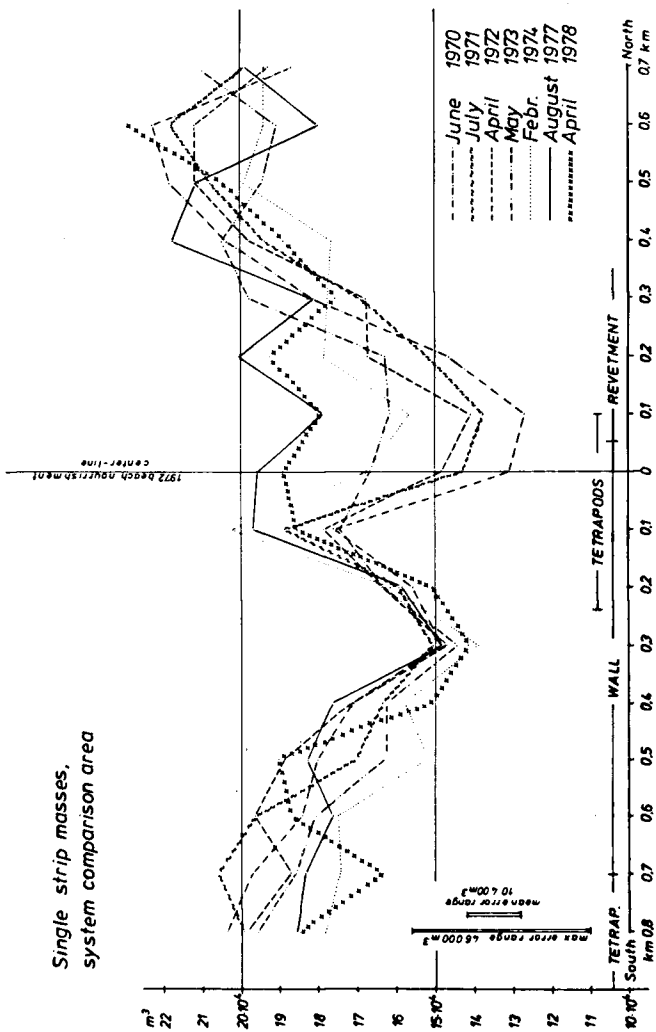


Fig. 7. Distribution of sand masses within the system comparison area along the coast

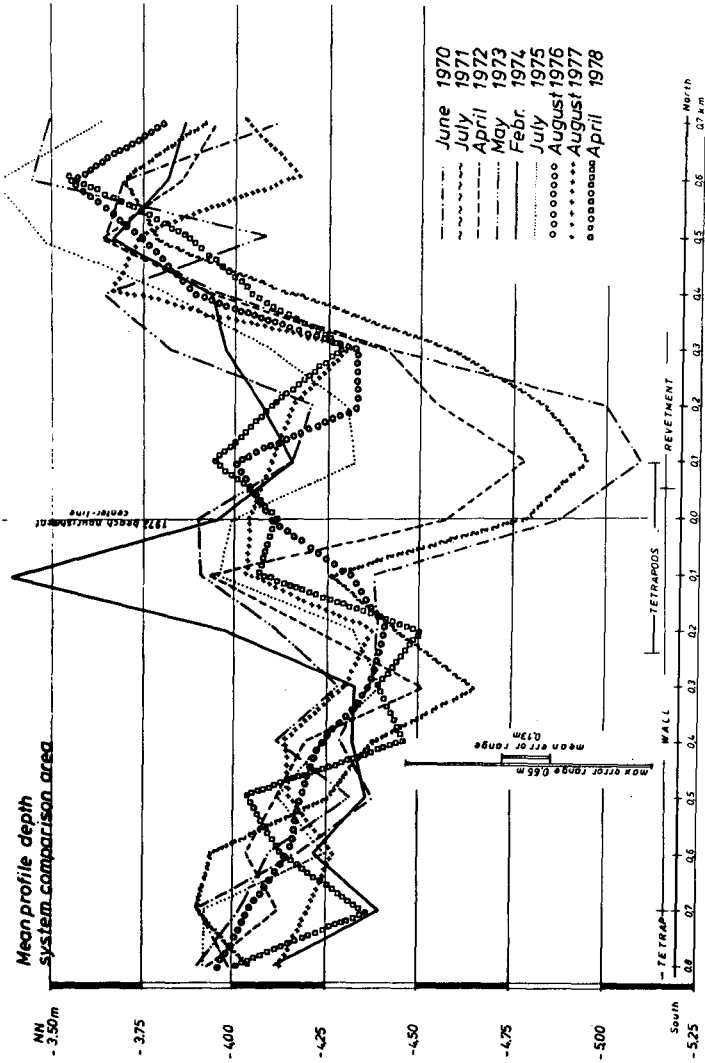


Fig. 8. Mean profile depths of each profile strip within the system comparison area

subject to particular hydrodynamic stress, it increased up to NN-4,85 m before the fill, and afterwards it returned to its normal value again. Two potential danger areas may be indicated in 1975-78 by minima in stations 0,4 ... 0,2S and 0,2 ... 0,3N, and it is here (0,2N ... 0,7S) where the fill 1978 has been executed.

The mean depth informs about the development due to erosion or accretion of this one-bar system and thus indicates the "state of health" of a certain coast section.

The morphometric characteristic (according to RENGGER) represents the typical depth distribution by a generalized vertical section (fig. 9). It can be imagined as being obtained by shifting all the horizontal layers horizontally towards the island.

For easier analysis, the differences versus the mean values of the years 1970/71 have been drawn up (fig. 10). The application of this method to the shore and foreshore reveals that the effect of the beach nourishment, increasing the contour line areas, was confined to the zone above NN-5 m. Below NN-6 m, the 1973-line runs in the negative and even deeper than the 1972-line, meaning that the erosion of the deeper island base continued even during the filling action and afterwards. In these depths, accretion can be observed only in the immediate vicinity of the filling site.

The storm surges of November/December '73 caused a considerable erosion, most significantly between NN-3 m and NN-6 m. In the following years, a certain recovery took place in the deeper parts, but the tendency is obvious, that the slope of the overall profile is going to approach the former slope of 1970-72.

4. Conclusions

The simultaneous analysis of the morphologic data suggests the conclusion, that the morphologic effect of the beach nourishment extended only to the beach zone down to a depth of about NN-5 m. Particularly the bar of the central 1,5 km shoreline remained unaffected by the fill. Moreover the actual erosion tendency seems to point now to the southern part of the investigation area, affecting now a good length of the shoreline, where it already caused considerable losses of material.

The recommendation deducted from these analyses for the nourishment 1978 was to realize a longshore fill on a distance of 900 m, and in fact, this plan was adopted for execution.

Information about the development of a sand coast subject to erosion is necessary for planning and design of shore protection works. Reliable information can be obtained, rather than from overall mass balances, from the morphologic variations as found by the analysis of bathymetric charts and, more easily, from the interpretation of morphologic indicators, such as the mean profile depth.

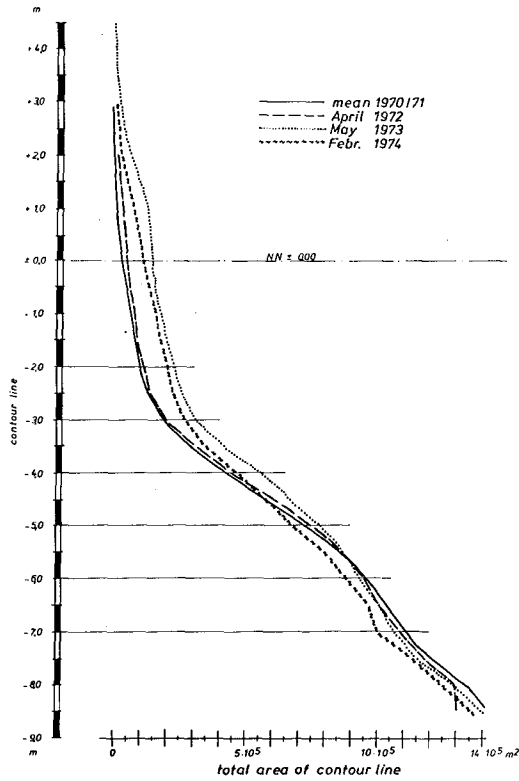


Fig. 9. Adaptation of Renger's morphometric characteristic to Westerland shore and foreshore, total investigation area

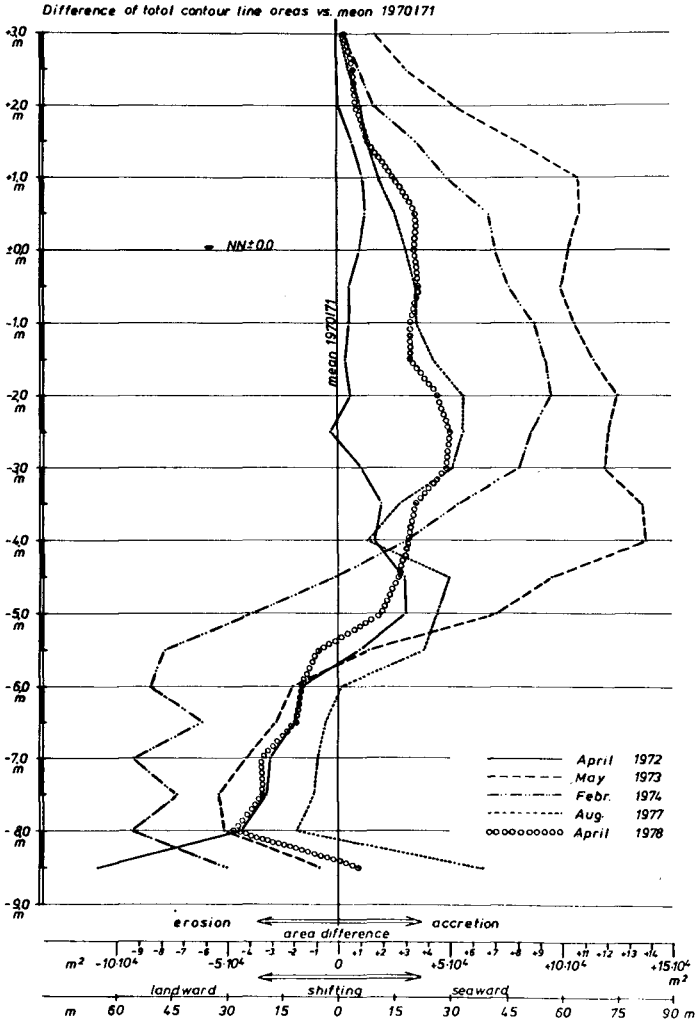


Fig. 10. Differential morphometric characteristic versus mean 1970/71, total investigation area

5. References

1. Amt für Land- und Wasserwirtschaft Husum: Untersuchungen zur Sandbewegung vor der Insel Sylt, Bereich Westerland: Veränderungen im Strand- und Vorstrandbereich (Author: Wenzel). Hydrologic Report no 2/77, Husum, 1977
2. Figge, K.: Das Sandriffsystem vor dem Südtteil der Insel Sylt (Deutsche Bucht, Nordsee). Deutsche Hydrographische Zeitschrift, vol. 29, no 1, 1976
3. Küstenausschuß Nord- und Ostsee, Gutachtergruppe Sylt: Gutachten zur Vorbereitung und Durchführung der vom Land Schleswig-Holstein für das Jahr 1971 geplanten Sandvorspülung am Weststrand der Insel Sylt. Teilgutachten D: Beurteilung der Sandvorspülung 1972 und Empfehlungen für die künftige Stranderhaltung am Weststrand der Insel Sylt. Die Küste, no 29, Heide, 1976
4. Nachtigall, K.H.: Über die Unterwasserhangmorphologie vor Rantum und Kampen auf Sylt. Meyniana 18, Kiel, 1968
5. Renger, E.: Quantitative Analyse der Morphologie von Wattenzugsgebieten und Tidebecken. Mitteilungen des Franzius-Instituts für Wasserbau und Küsteningenieurwesen der TU Hannover, no 43, Hannover, 1976
6. Swart, D.H.: Offshore Sediment Transport and Equilibrium Beach Profiles. Delft Hydraulics Laboratory Publication no 131, 1974
7. Vollbrecht, K.: Der Küstenrückgang an der Insel Sylt. Deutsche Hydrographische Zeitschrift, vol. 26, no 4, Hamburg, 1973
8. Zenkovich, V.P.: Processes of Coastal Development. London, 1967

CHAPTER 113

IMPORTANCE OF HANDLING LOSSES TO BEACH FILL DESIGN

R. D. Hobson^{*} and W. R. James^{**}

ABSTRACT

Beach nourishment models commonly employed by the U.S. Army Corps of Engineers compare textural properties of native beach and dissimilar borrow sediments to determine overflow and renourishment requirements for beach fill projects. It is assumed for these comparisons that the texture of borrow sediments is unchanged by dredging and handling operations but investigations have shown that significant handling losses do, in fact, occur.

This paper presents results from four field studies that document textural changes caused by dredging and sediment handling at Rockaway Beach, NY, and at New River Inlet, NC. Errors associated with calculating volumes of sediment dredged and lost using standard surveying and production methods are discussed and an alternate method is presented as a handling-loss model that compares bottom and dredged sediment texture to determine volumes lost.

The results of the studies presented are that handling operations do create significant changes in bottom sediment texture which, in turn, do affect beach fill model calculations by generally improving the predicted performance of these sediments as fill. The proposed handling-loss model predicts volumetric losses that greatly exceed losses generally anticipated during project construction. Discrepancies between loss estimates are discussed in terms of possible inadequacies of the model and of mechanisms that might consistently minimize losses using the standard methods for determining dredged sediment volumes.

INTRODUCTION

Beach nourishment is a commonly selected method of shore protection in the United States. Nourishment projects often receive substantial federal government support and they not only protect against loss and damage caused by storms and ongoing erosion, but also provide recreational benefits to an area while maintaining its natural aesthetics. Sand for beach fills is typically won offshore and may be pumped directly from the dredge to the beach when the borrow site is nearby. When the site is too far away for direct pumping, the sand is loaded into hoppers or barges, rehandled and pumped onto the beach from a location closer to the project.

* Coastal Engineering Research Center, Fort Belvoir, Virginia.

** U.S. Geological Survey, Reston, Virginia.

Studies of longshore transport, erosion rates, wave climate and storm history provide the kinds of data needed by the engineer to design a fill section that will withstand anticipated waves and water levels during storms as well as contain a sufficient volume of sand to meet expected erosion losses (U.S. Army Coastal Engineering Research Center, 1977). Renourishment needs are also considered in the design since most eroded beaches will continue to erode after nourishment and the fill section must also provide sufficient sand to meet these losses. Since beach fill design elements are determined using data from process-response studies of waves and currents interacting with native beach sediments, it is important to appreciate that the resulting fill volume requirements are for sediments similar to those found on the native beach. Dissimilarities between native beach and potential borrow sediments require adjustments to the designed volume which are commonly accomplished by applying beach fill models to calculate initial overflow and adjusted renourishment estimates (James, 1975). For these models, native beach sand serves as a standard for comparison with potential borrow sediments. The comparisons are between representative samples called composites (Hobson, 1977a) of the native beach and potential borrow sediments. Grain size distributions (gsd's) of these composites are expressed as phi sizes (Krumbein, 1938) and their phi means (M_ϕ) and phi sorting (S_ϕ) values commonly serve as input for the models.

HANDLING LOSS STUDIES

When applying the beach fill models, it is assumed that the volume and texture of sediment dredged from a borrow site is unchanged during project construction. However, sediment losses are commonly observed in the form of turbid water surrounding a dredge or as plumes extending seaward of a beach during nourishment. The term "handling loss" is used here to describe these project-related sediment losses. If significant, handling losses might modify the texture of borrow sediments enough to affect their performance as predicted by the beach fill models.

Handling losses are commonly caused by removal of sediment in suspension (elutriation) from the water-sediment slurry. These slurries commonly contain 10 to 25 percent solids and elutriation losses can occur during dredging on the bottom, during the overflow process used to fill hoppers with sediment, during recharge of sediment with water to allow hoppers to be pumped out, and during hydraulic placement of sediments on the beach. Documentation of this kind of loss has been minimal. Taney (1965) suggests losses in excess of 80 percent caused by prolonged overwashing of a dredge's hoppers and Mauriello (1968) reports that handling losses resulted in a fill sediment that was 0.2 mm coarser than the borrow sediment dredged. Neither of these studies was directly designed to examine handling losses and clearly there is a need for studies that both document these losses and assess their possible effects upon beach fill design.

Four handling loss examples are discussed below where suitable sedimentary data sets are available. Three of these sets were collected during field studies designed to investigate handling losses and these studies were conducted at New River, North Carolina, in the summers of 1976 and 1978, and at Rockaway Beach, New York, in 1977 (Figure 1). The fourth data set was also collected at Rockaway Beach but in 1975 during one phase of that project's construction, and by personnel from the New York Army Corps District office. For simplicity, these four examples are henceforth referred to as Rockaway (1975), Rockaway (1977), New River (1976) and New River (1978). Each example is briefly described below. Detailed descriptions of the Rockaway project are provided by Nersesian (1977) and Hobson (1977b), and the New River experiments by Hobson (1977b) and 1977c).

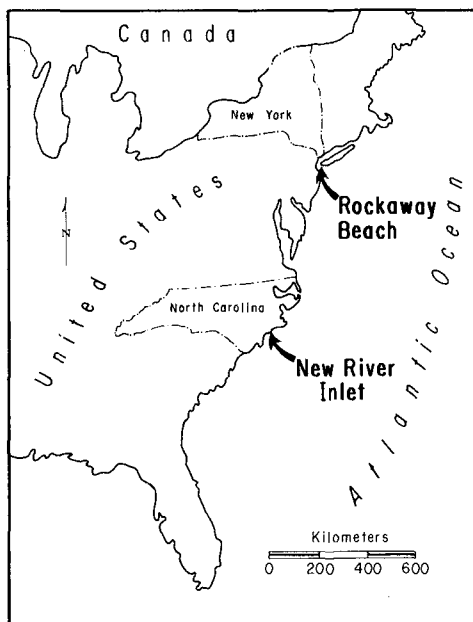


FIGURE 1. Location map - Rockaway Beach and New River Handling-loss studies.

Description and Sampling: Rockaway Beach is a barrier island with a morphology that has evolved over the past century in response to multiple episodes of artificial nourishment. The latest episode was accomplished in three phases during the summer months of 1975, 1976, and 1977. The beach was nourished along its 16 kilometer length with approximately 5,500,000 m³ of sand obtained from local offshore borrow sites. During the first phase (Rockaway 1975), borrow sediments were

dredged and loaded into scow barges offshore, transported 13 km to the leeward side of the barrier where they were recharged, and pumped hydraulically onto the beach. For phases two and three (Rockaway 1976, 1977), a suction dredging barge was used to load the sand, transport it to an offshore discharge point, recharge the load with water, and pump the slurry onto the beach. Sampling for Rockaway (1975) was conducted by the U.S. Army Corps of Engineers and consisted of coring bottom sediments at the borrow site using vibratory-type equipment, and collecting surface or grab samples from 26 of the scow barge loads and, of fill sediments at the 26 beach locations where the barged sediment loads were discharged. A three meter long, suction-assisted coring device was used to collect cores of bottom and barged sediments during the Rockaway (1977) study. Native beach sediments were sampled during pre-construction investigations of the area.

New River Inlet is periodically dredged to maintain a shallow access channel for small boats. A side-casting suction dredge and a split-hull barge have been employed by the Wilmington Corps of Engineers District office to accomplish this work. Studies were conducted by the Coastal Engineering Research Center (CERC) in 1976 and 1978 to evaluate sediment losses incurred during dredging. In 1976, the side-caster was used to fill the split-hull barge which then carried the dredged sediments to a nearshore dump site located downdrift of the inlet. By 1978, the split-hull barge had been equipped with suction drag heads and was able to perform all loading and dumping operations by itself. Sampling during both studies consisted of using divers to collect surface sediment samples from the bottom prior to a pass of the dredge, and using the suction corer to sample the entire thickness of the barged loads where sediments located near the bottom were subjected to less elutriation effects than upper layers. Three cores were taken from the hopper loads sampled and at least 10 surface samples were obtained to characterize each load. In addition, samples of sediments overwashed from the hoppers were collected as were samples of native beach sediments (e.g. 45 beach samples in 1976 and 22 in 1978). In both cases the beach was sampled at the downdrift dump area along profile lines that extended offshore from the storm berm to water depths of approximately 4.5 meters below MSL.

Discussion: Figures 2 and 3 are presented as typical plots of grain size distributions sampled during the Rockaway and New River studies, respectively. Table I is a summary of textural changes and beach fill model predictions for the four cases studied and it is evident from inspection of this table that in all cases, dredging and handling operations have coarsened dredged sediments (decrease in M_{ϕ} , Table I). The degree of coarsening varies but it is the kind of textural change anticipated where considerable overwashing is required to fill a scow or hopper. The smallest change in grain size occurred at Rockaway (1975) during the recharging and placement phase of handling where less overwashing was required to recharge the scow loads and where losses to the offshore were low during placement because the "fill" sampled included all sand placed on the beach within elevation limits of +3 to -5.5 m, sea level datum.

	TEXTURAL PARAMETERS				BEACH FILL MODEL PREDICTIONS	
	Native Sediments		Borrow Sediments		Overfill Factor	Renour. Factor
	M_ϕ	S_ϕ	M_ϕ	S_ϕ	R_A	R_J
ROCKAWAY 1975	1.69 0.72					
Native vs. Bottom			1.85	0.86	1.24	1.00
Native vs. Barged			1.31	0.66	1.00	0.64
Native vs. Placed			1.24	0.64	1.00	0.56
ROCKAWAY 1977	1.63 0.70					
Native vs. Bottom			2.23	1.02	1.20	0.58
Native vs. Barged			1.33	0.73	1.00	0.25
NEW RIVER 1976	2.39 0.80					
Native vs. Bottom			1.51	0.91	1.00	0.29
Native vs. Barged			1.04	1.02	1.00	0.13
NEW RIVER 1978	2.24 0.82					
Native vs. Bottom			1.20	1.25	1.01	0.14
Native vs. Barged			0.26	1.46	1.00	0.10

TABLE I Textural parameters describing native beach and handling-altered sediment gsd's, and beach fill model predictions for Rockaway Beach and New River handling loss studies. The symbols M_ϕ and S_ϕ are the phi mean and phi sorting values, respectively.

The observed coarsening should reflect selective removal, by washing, of finer sized sediments. The gsd's of elutriated sediments sampled during the New River experiments support this interpretation with mean sizes of 0.11 mm finer than bottom sediment means in 1976 and 0.21 mm finer in 1978. Losses of fine sediments should also improve the sorting of barged or placed sediments. Sorting does decrease with each handling episode for the Rockaway studies (Table I). However, at New River, sorting values were observed to increase with handling even though the mean grain sizes of barged sediments were significantly

coarser than for bottom sediments, and sediments overwashed were fairly fine grained. These curious changes in sorting at New River may reflect inadequate sampling of bottom sediments but they cannot be explained here using the data available from the experiments.

In all cases, the textural changes produced by handling do lower the overfill and renourishment estimates provided by the beach fill models (Table I) which suggests that handling improves a sediment's performance as fill. These changes are more striking for the Rockaway examples where borrow sediments were finer grained and more poorly sorted than native beach sediments than for the New River cases where borrow sediments were dredged from a high energy shoal complex and were significantly coarser than native beach sediments. At Rockaway, changes to the overfill ratios (R_A 's, Table I) of 0.20 (1977) and 0.24 (1975) indicate that losses of fines from the borrow material during construction will produce a fill sediment that will match the performance of native beach sand. Thus no overfill is predicted and project volumes are reduced by 17 and 20 percent, respectively. It is also predicted from the renourishment values (R_J 's) that the same winnowing losses will generally double the time span required between renourishment operations.

Rockaway Beach, NY (1977)

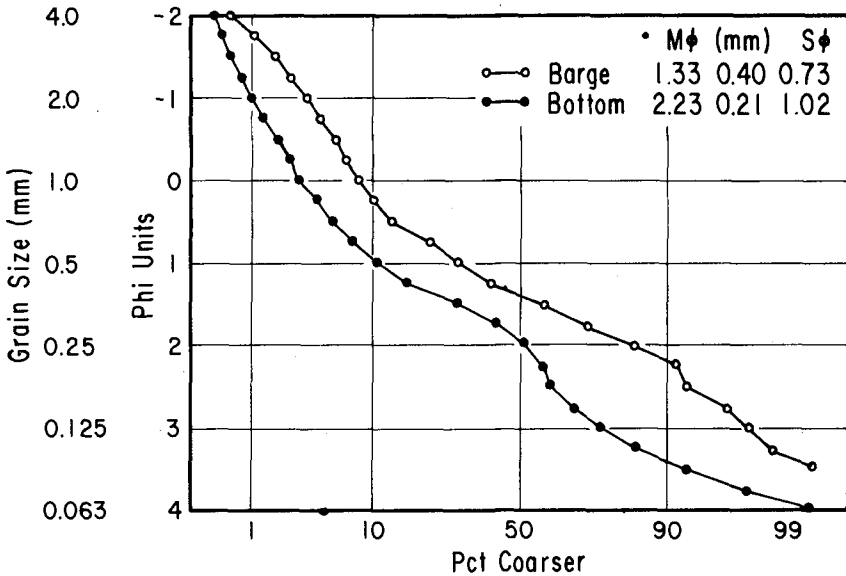


FIGURE 2 Grain size distributions (gsd's) showing textural differences between dredged (barged) and bottom sediments, Rockaway Beach (1977).

New River Inlet, NC (1978)

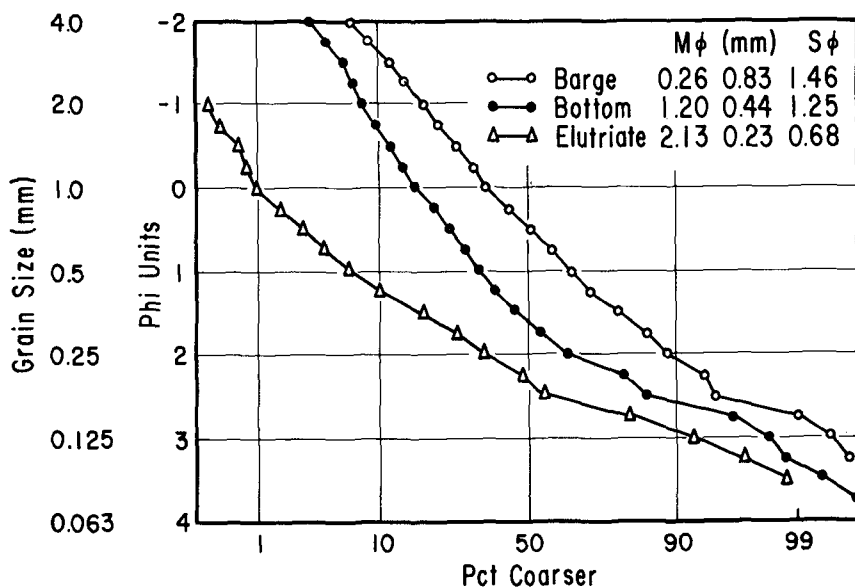


FIGURE 3 Grain size distributions (gsd's) showing textural differences between dredged (barged), bottom, and sediments overwashed during hopper filling (elutriate) at New River, NC (1978).

VOLUMETRIC CALCULATIONS

The experiments described provide some documentation of textural modifications to dredged sediments caused by handling operations. Sediments placed as fill contain a smaller fine-grained fraction than the same sediments contained prior to dredging, and thus initial fill volumes may be reduced and slower erosion rates may be expected. The effects of these potential changes upon project design and performance can be further evaluated by determining actual volumes lost during construction.

Handling loss volumes can be determined using estimates of the volumes of sediments dredged from the borrow site, volumes loaded into hoppers or rehandling sites, and volumes placed as fill on the beach. These volumetric estimates are typically calculated using data obtained by surveying, from plant production specifications, or from hopper load measurements. A general evaluation of these data sources reveals

potential problems with each and demonstrates the need for improved calculation procedures.

Surveying: Volumes of sediment placed on a beach or dredged from a borrow site are commonly calculated by multiplying differences in elevations surveyed along profile lines by some spacing factor between the profiles. Both land and hydrosurvey techniques are often used and errors in the volumes calculated are usually the result of inaccurately measured elevations or locations, and by inadequate profile spacing. Improvements in equipment are gradually reducing the measurement errors and are providing for quicker data collection as well. Nevertheless, considerations of time and costs often result in surveys with fewer profiles than needed for areas of irregular topography. For example, the self-loading suction barge used at Rockaway (1977) changed the fairly smooth bottom topography of the offshore borrow site into a surface irregularly dotted with cone-shaped depressions of varying diameter and depth (up to 6 meters deep). Obtaining an adequate estimate of the volume of sediment dredged in this case would have required that more profiles be surveyed than would have been possible during the time available to the crews assigned to the project.

Plant Production: Although slurry concentration and slurry flow meters are available for dredging plants, this equipment is seldom installed on American dredges. Determining production values therefore requires estimates of these factors which are usually provided as a slurry density constant for particular types of sediment (sand, silt, etc) and rating values for pump performance in clear water. No general factors are applied to account for density changes caused by variations in texture, bottom firmness, topography, and the like, nor for factors that affect the pump such as water depth or the degree of impeller wear. The result is that a competent leverman knows how to maintain a dredge's efficiency by watching his suction and engine performance gages but it is extremely difficult translating this kind of efficiency into actual volumes of sediment dredged, or lost, during a filling operation.

Hopper Loads: These kinds of data are fairly accurate with volumes determined from the number of containers filled (hoppers, scows, etc) or from the mass of sediment loaded into a container as metered by displacement-types of equipment. Although bulking and density changes can often be determined, these volume estimates still give no method for determining the total volume of solids lost overboard during the filling process. Clearly, alternate methods to surveying, plant production and load metering are desirable for calculating more accurate estimates of the volumes of sediment dredged and lost during handling.

HANDLING-LOSS MODEL

Comparing the properties of grain size distributions provides another method for estimating handling loss volumes. Losses are mostly from the finer grain sizes of a sediment and occur because the fines are carried away with the fluid phase of a dredged slurry to leave a coarser sediment in the hopper or on the beach. Only sizes small enough to be transported by fluids at the velocities present are removed. The result

should be that the smallest sizes are most affected and that losses should progressively decrease with increasing grain size until a critical size is reached that is too large to be transported. All grains larger than the critical size should therefore be retained and their relative proportion increased in the resulting gsd as compared to their proportion in the gsd of the pre-dredged sediments. These relationships lead to the following handling-loss model.

During dredging it is assumed that all sediments encountered on the bottom are picked up by the dredge head so that the volume dredged from the bottom (V_B) equals the sum of the volumes placed (V_P) and lost (V_L) during handling. A simple mass-balance equation provides the relation

$$V_B F_B(\phi) = V_P F_P(\phi) + V_L F_L(\phi) \quad (1)$$

where ϕ is a measure of grain size (Krumbein, 1938) and $F(\phi)$ is the proportion of material coarser than ϕ in each gsd. It is assumed that all losses are due to elutriation, that abrasion is negligible, and that losses are restricted to particle sizes finer than some critical size (ϕ^*). The result is that handling losses will effectively increase the proportion of sediments coarser than ϕ^* in the gsd and that for these coarse sizes $F_L(\phi)$ is zero value so that equation (1) leads to the relation

$$\frac{V_B}{V_P} = \frac{F_P(\phi)}{F_B(\phi)} = K, \quad (2)$$

where K is a constant reflecting the proportion of material lost. Therefore, inspection of the ratios of cumulative frequencies for all sizes coarser than ϕ^* should be fairly constant (Figure 4) and the percentage volume lost is given by

$$V_L = \left(1 - \frac{1}{K}\right) \times 100. \quad (3)$$

Evaluation of the Model: The textural data describing sediments collected during the handling-loss experiments were used to evaluate the model. The results of this evaluation are summarized as Table II. Figure 5 is presented as a typical plot of gsd ratios and is for the cumulative size distributions of barged and bottom sediments (Figure 3) collected at New River (1978). In general, the ratios of gsd's for each pair of composites plotted like those in Figure 5 and showed the kind of pattern predicted by the model (Figure 4) of fairly constant frequency ratios for an initial range of coarse sizes followed by a gradual decrease of the ratios to unity as grain size became finer. The only real variation to this pattern is that on some plots, the gsd ratios were quite variable (of both low and high value) for the very coarsest grain size fractions. These "irregularities" are interpreted to mainly reflect sampling errors as they usually occurred when cumulative weight percentages were less than five percent which is in that portion of a gsd where a very few grains constitute each size fraction and where grain number is easily affected by splitting and sieving

operations. Nevertheless, the presence of these fluctuations had little effect upon the calculated K-values (loss constants, Table II).

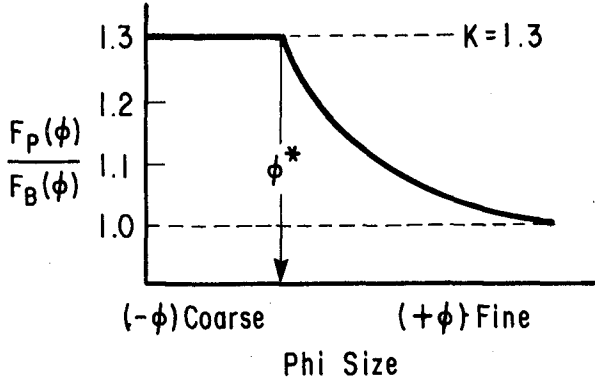


FIGURE 4 Relationship of K and ϕ^* for schematized plot of ratios of gsd's for bottom, $F_B(\phi)$ and pumped, $F_P(\phi)$, sediments as predicted by the proposed handling-loss model (for case of $K=1.3$ representing a 23 percent volume loss).

New River Inlet, NC (1978)

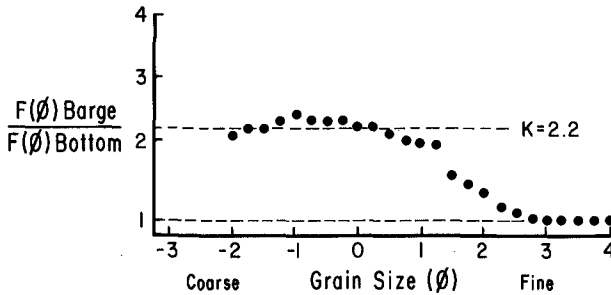


FIGURE 5 Observed ratios between gsd's for barged and bottom sediments, New River, 1978.

	ϕ^* Critical Size (mm)	K Constant of Loss	V_L Estimate of Loss	Increase in Mean (mm)
BOTTOM VS PLACED				
Rockaway 1975	0.39	2.10	52%	0.14
BOTTOM VS BARGED				
Rockaway 1975	0.33	1.71	42%	0.12
Rockaway 1977	0.55	2.96	66%	0.19
New River 1976	0.92	2.70	63%	0.47
New River 1978	0.46	2.33	58%	0.39
BARGED VS PLACED				
Rockaway 1975	0.46	1.23	19%	0.02
AVERAGED VALUES	0.52	2.17	50%	0.22

TABLE II Critical Size (ϕ^*), Loss Constants (K's) and Volume Loss estimates (V_L 's) predicted by the proposed handling-loss model for Rockaway Beach and New River studies (Mean grain size increases also shown).

The data presented in Table II suggest that handling losses for the cases studied: (a) tend to increase the average size of sediments handled by about 0.2 millimeters; (b) are from grain sizes finer than about half of a millimeter; (c) and average about 50 percent. The first suggestion simply reports those changes observed during the field studies. The second suggestion comes from estimates of the critical grain size (ϕ^*) determined from plotted gsd ratios and this suggestion is generally supported by inspection of the grain size distributions for three overwash samples collected during the studies. In these cases, 95 percent of the samples overwashed were finer than 0.64 mm (vs $\phi^* = 0.92$ mm) at New River (1976), finer than 0.70 mm (vs $\phi^* = 0.55$ mm) at Rockaway Beach (1977), and finer than 0.50 mm (vs $\phi^* = 0.46$ mm) at New River (1978). The third suggestion of fifty percent handling losses is

at least twice that expected and claimed during dredging operations at Rockaway (Nersesian, personal communication, 1977).

The discrepancy between handling loss volumes predicted by the proposed model versus losses estimated during construction may reflect inadequacies in the model; problems associated with sampling and analytical procedures, or possibly, greater losses do occur during project construction than have been generally recognized. A few different models have been examined which, using these same textural data, have not significantly narrowed the gap between predicted and estimated losses. New field studies are generally needed to collect adequate data for evaluating most other models.

The textural properties of nearshore zone sediments are typically quite variable over short distances and thus sampling procedures should be considered as possibly contributing to the textural differences found between bottom and dredge-modified sediments. Sampling procedures that might affect textural properties include the number and spacing of sample locations, the type of samples collected (e.g., surface vs. cored samples) to characterize sediment sources (bottom, barged, or placed), and the kind of equipment used to collect the samples. Evaluation of these procedures used in the studies reveals a need to investigate potential losses of fine sizes during core sampling operations and the desirability of increasing the bottom sampling density in future studies where suction, drag head plants are used to dredge over fairly large areas. Still it is tentatively concluded here that elements of sampling have not significantly affected the results of these dredge-loss studies since results from each study are similar in type and magnitude even though the sampling procedures varied from study to study.

Perhaps handling losses are greater than generally recognized. Potential errors in calculating sediment volumes using survey, production and hopper load data have been noted but no reasonable explanation is apparent for why these kinds of errors would consistently minimize losses. Other explanations are needed.

One possible explanation for the discrepancies in loss estimates is that handling operations not only cause sediment losses but that they also change the internal arrangement of dredged sediments in a way that creates a false impression of dredged volumes. For example, Turnbull and Mansur (1974) have shown that dredging tends to decrease the bulk density of sandy sediments in cases where the material is not well drained (as in hoppers below the water line?) whereas Poulos and Hed (1973), and Youd (1973), showed that the volume of solids in clean sands decreased with improvements in sorting and decreases in angularity, respectively. These relationships were applied using the Rockaway (1977) samples and the results are summarized in Table III.

Relative densities of the sediment sources at Rockaway (1977) were not measured in the field and thus estimates of their values are required for the following calculations. A relative density of 50 percent is assigned to the barged sand which is the average for hydraulically-

placed fills as measured by Paulos and Hed (1973), and a 78 percent value is calculated for the bottom sediments in-place that have been assigned a void ratio of 0.40. The percent of solids per unit volume of sediment determined using these relative densities is 64 percent for the barged sediment versus 71.4 percent for the sediment in-place. Volume differences like the 7.4 percent shown in this example would not be apparent during the construction phase of a beach fill but could become quite important at a later time when this uncompacted material was under attack by storm waves.

	Roundness (Powers, 1953)	Uniformity Index	Maximum Void Ratio (Youd, 1973)	Minimum Void Ratio (Youd, 1973)
Bottom Sand	0.37	3.00	0.62	0.34
Barged Sand	0.33	1.91	0.77	0.38

TABLE III Textural and Bulk properties of bottom and dredged (barged) sand collected at Rockaway Beach, NY, 1977.

Increased handling losses of 5 to 10 percent don't equalize volume losses estimated during construction with those predicted by the model. For Rockaway (1977) the predicted losses (model) are at least double those claimed during construction. Nevertheless, it is clear that many factors affect the volume of handling losses such as changes in textural and bulk properties and that interrelationships among these factors are not well understood even though they affect both the design and the economics of a beach fill project.

CONCLUSIONS

The following remarks summarize results, to date, of investigations of handling effects upon sediment properties and beach fill design. These investigations are part of an effort that will continue and that will hopefully explain those problems that remain unsolved.

1. Significant changes in sediment texture are caused by dredging and handling operations. For all cases studied, the winnowing (elutriation) of finer sizes produced a dredged sediment that was coarser (0.22 mm average increase) than bottom sediments. Sorting values decreased in some cases (Rockaway) and increased in others (New River).

2. Textural changes produced through handling can effect the estimates of overfill and renourishment elements of beach fill design. In all cases studied, the changes improved the predicted performance of sediments as beach fill.

3. Traditional methods of measuring beach fill volumes (surveys, plant production records, and hopper load measurements) often provide unreliable results and therefore, a need exists for improved or alternate methods.

4. A handling-loss model that compares textural differences between dredged and bottom sediments provides handling-loss estimates that are approximately double the losses estimated using the methods listed in item 3 above. These discrepancies are being evaluated by testing alternate handling-loss models, by evaluating different sampling procedures, and by considering mechanisms that explain handling losses of the magnitudes shown with the model.

5. Changes in the bulk properties of sediments caused by dredging can affect sediment volume calculations. These changes warrant further investigation as they may well affect the sediment's performance as beach fill.

ACKNOWLEDGEMENTS

The analysis and results presented in this paper were based on research conducted at the Coastal Engineering Research Center of the U.S. Army Corps of Engineers. Permission to publish this information is appreciated.

REFERENCES

1. Hobson, R. D., "Review of design elements for beach fill evaluation", T.P. 77-6, U.S. Army Coastal Engineering Research Center, Ft. Belvoir, VA, (Jun 1977a).
2. Hobson, R. D., "Dredging-induced modifications to sediment texture and their influence on beach fill requirements", proceedings, 2nd International symposium on dredging technology, Texas A&M University, (Nov 1977b).
3. Hobson, R.D., "Sediment handling and beach fill design", Coastal sediments '77, 5th Symposium of the Waterway, Port, Coastal and Ocean Division of ASCE, Charleston, SC, (Nov 1977c).
4. James, W. R., "Techniques in evaluating suitability of borrow material for beach nourishment", TM 60, U.S. Army Coastal Engineering Research Center, Ft. Belvoir, VA (1975).
5. Krumbein, W. C., "Size frequency distributions of sediments and the normal phi curve", Jour. Sed. Pet., V. 4, pp. 84-90, (1938).
6. Mauriello, L. J., "Experimental use of a self-unloading hopper dredge for rehabilitation of an ocean beach", ASCE, ww2, pp. 368-395, (1968).

7. Nersesian, G. J., "Beach fill design and placement at Rockaway Beach, New York, using offshore borrow sources", Coastal Sediments '77, 5th Symposium of the Waterway, Port, Coastal and Ocean Division of ASCE, Charleston, SC, (1977).
8. Poulos, S. J. and Hed, A., "Density measurements in a hydraulic fill", in evaluation of relative density and its role in geotechnical projects involving cohesionless soils, ASTM STP 523, pp. 402-424, (1973).
9. Powers, M. C., "A new roundness scale for sedimentary particles", Jour. Sed. Pet., V. 23, No. 2, pp. 117-119, (1953).
10. Taney, N. E., "A vanishing resource found anew", Shore and Beach, V. 33, No. 1, pp. 22-26, (1965).
11. Turnbull, W. J. and Mansur, C. I., "Compaction of hydraulically placed fills", Jour. of the Soil Mechanics and Foundations Division, ASCE, V. 99, No. SM11, pp. 939-955, (1973).
12. U.S. Army, Corps of Engineers, Coastal Engineering Research Center, "Shore Protection Manual", V. II, U.S. Government Printing Office, Washington, DC (1977).
13. Youd, T. L., "Factors controlling maximum and minimum densities of sands", ASTM STP 523, p. 98-112, (1973).

CHAPTER 114

SOME FACTS AND FANCIES ABOUT BEACH EROSION

by

Richard Silvester

Associate Professor of Civil Engineering,

University of Western Australia,

Nedlands, 6009 W.A.

ABSTRACT

Coastal defense up to the present has employed seawalls, groynes and renourishment, all of which do not tackle the basic problem of lack in sediment supply from upcoast. The need is for sufficient sand to be continually available for the formation of the defensive offshore bar. If means are provided for this material to be returned directly on shore by subsequent swell, a stable situation ensues. Such normal re-deposition occurs within bays formed between headlands which have reached equilibrium shape or nearly so. Comparisons are made between various stabilization procedures. The influence of sand characteristics in renourishment is discussed.

Stabilization of coasts has been carried out over many decades. The remedies have taken three major forms, namely, seawalls, groynes, and in more recent times sand renourishment. Whilst shapes and orientation of these structures have been varied in order to optimise protection, engineers in the main have relied upon bigness for greater reliability. Investment in dredging to supply sediment "temporarily" to beaches is growing prodigiously. It is now time to sit back and re-assess the situation, so as to determine a change of outlook, be it only slight, that may effect greater long term economies.

AXIOMS OF BEACH PROCESSES

There are certain theorems respecting beach processes which, although proved separately, are not normally considered conjointly in the stabilization issue. These are:

- (a) On oceanic margins and even along coasts of enclosed seas there is a predominant or resultant wave direction which is usually oblique to the coastline.
- (b) The longshore component of wave energy both in the surf zone and offshore can transport a specific load of sediment across a given bed profile normal to the beach.
- (c) Flunctuations in river discharge of sediment, in wave incidence along the coast, in man's interception of littoral drift, and in storm

activity, cause continual variations in supply of material from upcoast on any section of shoreline.

(d) The transfer of sand from beach to offshore and back again in an oceanic margin during storm and swell sequences results in different beach and nearshore profiles than on shores of enclosed seas where swell is minimal.

(e) Waves reflected obliquely from walls, cliffs or submerged reefs create a short-crested wave system that generates strong vortices, resulting in increased macro-turbulence which magnifies sediment suspension in a situation of excessive mass transport.

(f) Groynes have no influence on bed erosion beyond their toes and cannot retain material collected between them during storms because of their promotion of rip currents.

(g) If waves arrive nearly normal to the coast the offshore slope must be very flat before the waves can effect longshore transport of sediment at the rate it is being supplied.

(h) An eroded shoreline will absorb a large proportion of sand re-nourishment supplied to it in order to construct the equilibrium profile appropriate to the wave energy normally present.

(i) Persistent swell arriving obliquely to alignments of headlands will form crenulate-shaped bays between the fixed points which have a limiting indentation and specific curved shape.

By combining the effects in these truisms one may be led to a solution of beach erosion which is economic in both investment and maintenance. It is the purpose of this paper to examine the real problems in littoral drift and suggest a comprehensive plan for management of the coast.

PAST MISTAKES

Remedial measures for beach recession have taken various forms, with periodic changes similar to those in womens' fashions. The reason for this copying sequence in engineering might be blamed on the control effected by some eminent or prominent person. The neophytes of the profession tend to emulate their peers, for purposes of promotion if nothing else. It is very difficult in a conservative atmosphere to introduce innovations. Engineering suffers as much from this as the medical profession where the caution is "Be not the first to adopt the new, nor the last to cast the old aside". This leads to the sequence: "When first discovered it is not proved. Twenty years later it is proved but not important. Thirty years more it is proved and important, but it is fifty years old - we have something better now!"

The phases in coastal engineering have been seawalls, groynes and the latest panacea is renourishment. It is well to see where these three concepts went astray, or to compare the disadvantages against the purported benefits.

Seawalls It was believed, even by eminent oceanographers and presumably by many engineers, that if the energy of incident waves could be thrown back to the sea all was well on the coastal front. Little was it realised that re-application of this energy to the seafloor, particularly if it involved oblique reflection, would expedite sediment removal and

suspension. (1) Not only does scour occur in front of a wall but also downcoast of it, where the diffracting reflected waves combined with the incident to continue the short-crested wave system. (See Figure 1) The rapid removal of material results in a shoal further downcoast because the incident waves cannot cope with the increased load removed and hence a shoal and even shoreline protuberance occurs. The sight of erosion between an accretion and the wall extremity has prompted the extension of walls downcoast and the displacement and expansion of the problem.

Even rubble-mound structures can reflect a large proportion of the wave energy, particularly that of the longer period components of the spectrum. Also submerged walls or reefs will reflect the lower sections of the wave motion and hence create water particle motions equivalent to short-crested waves at the surface. (2) This is a problem not fully realised with pipe outfalls experiencing angled waves, which fail due to scour, some little distance back from their extremities. The local phenomenon of vortex generation at sharp ends of walls or objects is another matter, but a very serious one for caisson type breakwaters.

Groynes Since man could observe the excessive turbulence and suspension of sediment in the surf zone, plus the current produced by oblique breaking of the waves, it was assumed that all important transport of material was occurring in this water strip at the beach margin. It was concluded, therefore, that an impediment placed across this pathway should retain sand on that section of coast. Thus groynes have been constructed out to the limit of normal breaking waves on the beach.

In recent years the importance of the offshore zone in transmitting sediment downcoast has been illustrated in the knowledge of mass transport and the influence of multiple wave trains in disturbing the bed. The added effect of swell waves angled to each other has not been examined thoroughly enough to date but the possible increase in transmission can be surmised. It has been propounded that the complete continental shelf can serve as a highway of this transport. (3)

Beyond the tip of a groyne the waves move sediment and hence any imbalance between material removed and that replenished from upcoast is unaffected by this structure. Many cases can be cited of continued deepening and steepening of the bed offshore from a field of groynes, which were constructed due to an erosive tendency, which will continue. (4). This offshore deepening permits subsequent waves, be they storm or swell in character, to approach at a more oblique angle and at a greater celerity, both adding to the longshore transporting capacity of the system.

But even the material blocked in transit by the groynes adjacent to the beach is in jeopardy during a storm. Waves will arrive from all seaward directions as the low pressure centre traverses the coast. Thus whilst they consume the adjacent beach to form a protective offshore bar the associated changeable longshore drift is deflected seawards by groynes to form strong rip currents. Material is thus carried seawards and when brought back to the beach by subsequent swell waves is deposited much further downcoast than if it had been just offshore. (See Figure 2)

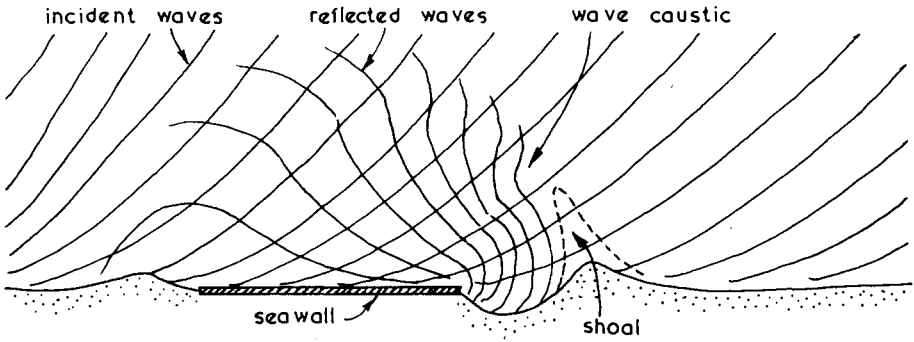


Fig. 1 Interaction of incident and reflected waves at a seawall

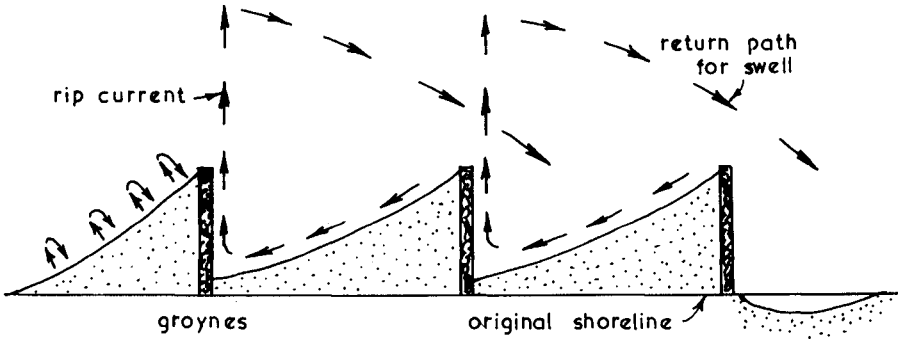


Fig. 2 Groynes with erosion beyond toe and rip formation

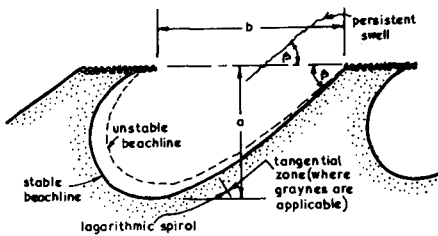


Fig. 3 Crenulate shaped bay in stable and unstable condition

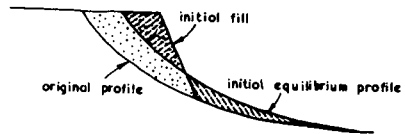


Fig. 4 Profile of stable beach profile plus fill

Groynes could thus be considered to enhance downcoast drift.

Because more than normal volumes of sand are removed between groynes the subsequent filling process during the swell season results in erosion downcoast of the groyne field.

There is one location where a structure running normal to the shoreline can be effective in accreting a beach. This is along the tangent section of a crenulate shaped bay, but this is unlikely to be in an erosive situation because the waterline is controlled by the downcoast headland. (See Figure 3) This tangential zone is little affected even when the bay is becoming more indented due to reduction or cessation of littoral drift upcoast. Instances can be cited where fluctuations in littoral drift have either buried groyne systems or inundated them as though they did not exist.

Renourishment This is the latest panacea of the erosion problem, with the more expensive alternative of dredging from the sea being promoted. Since the whole shelf can be considered the highway for transport any substantial holes dug in it can influence the sediment somewhere along the coast, not necessarily in the affected area. (5) But it is the benefit to the community as a whole from such artificial widening of a beach that should be of concern.

That there is a strong longshore drift resulting from oblique predominant waves must be accepted, otherwise there would be no erosion problem. This downcoast component will still exist after the refill and hence will transmit sooner or later (more likely the former) this expensive material in the same manner as the original coast. In fact, it will move it more rapidly, especially at first, because it is perched against the coast with a steeper than normal profile, almost the angle of repose of the sediment. (See Figure 4) Even just swell waves will spread this material both downcoast and over the eroded offshore region in an attempt to produce the original equilibrium profile appropriate to the wave climate for the area. Initial losses of 30 to 50% have been recorded (6)

Renourishment is a palliative which eases the problem but does not remedy the cause. This can be likened to the pill prescribed by the medical profession to get rid of the pain without attacking the root of the disease. Whilst the pain is gone there is less incentive to work on the real problem. Most engineering "doctors" applying this solution recognise the transitory nature of the benefit and recommend annual additions of the pain killer, possibly of 10 to 20% (6).

BASIC REQUIREMENTS

The essence of the beach erosion problem, or its solution, is to have sufficient sand on the beach to form an adequate offshore bar during any severe storm sequence. This natural defense mechanism cannot be bettered by man. Even if he were to place a fixed mound parallel to the coast to replicate this bar, it would serve as a reflecting wall during periods of swell and hence expedite transport of sand downcoast. Thus it is the swift construction of this feature in times of need that is so helpful to mankind, and its subsequent dismantling by the swell waves a few days later.

Whilst man cannot assist nature in this valued erosion limiting process he can assist by providing milder slopes to the offshore profile of the beach. Such a flatter bed requires less beach material to construct a bar of sufficient size to break incoming storm waves. It is a case of more material being maintained in the region, with a large proportion of it being submerged. This mode of storage inhibits the possibility of wind blowing it inland to form sand dunes.

The question is how to create this seaward accretion without it being subject to longshore wave energy and hence transport downcoast. Again nature has provided the answer because where the coast is so oriented that it is parallel to the crests of the persistent swell waves the offshore bed is mildly sloped, as can be gauged by the number of simultaneous breakers visible in the surf zone. (7) This is also understandable because a near-normal approach of waves makes it difficult for them to transmit material downcoast. Material is deposited until the depths are reduced to such a degree that the waves can disturb the bed sufficiently to balance the energy available with the load to be carried.

CRENULATE SHAPED BAYS

This necessary reshaping of the coast for it to receive the persistent swell (or predominant waves in the case of enclosed seas with little or no swell) normally has been carried out by nature over geologic time. When headlands or control points exist the sedimentary shoreline between has been sculptured into bays with specific curved outlines. Where the waves of greatest duration arrive obliquely to the headland alignment such bays assume a crenulate or zeta shape. (See Figure 3) These are the most abundant physiographic features on all coastlines of the world, whether they be on oceanic margins, in enclosed seas, or inland waterways where wave action is significant. (8)

Although these bays can be of any dimensions, hundreds of metres between headlands or even kilometres, they will be exact models of each other if the obliquity (β) of the persistent waves is the same. For a specific angle of approach to the headland alignment and a condition of no sand supply from upcoast or within the bay certain characteristics of the bay are now known. (9) (10). These are the ratio of maximum indentation (measured normal to the headland alignment) to the clear distance between the headlands, and the curvature of the logarithmic spiral which is applicable to the curved section of the bay. (See Figure 5) With knowledge of the limiting values of these parameters for specific wave obliquities (which angle is the same as that between the downcoast tangent section of the crenulate shape and the headland alignment) a tool is available to check the stability of any bayed coastline. (See Figure 3) If the values plotted do not fall on the equilibrium line further erosion can be expected if and when sand supply decreases or ceases in the future. Complete cessation is prevalent in modern times with the need for dredging deep channels across the shoreline to ports.

When a bay is nearing this final stable shape the incoming persistent swell will diffract and refract in the lee of the upcoast headland in such a way that it will break simultaneously around the whole

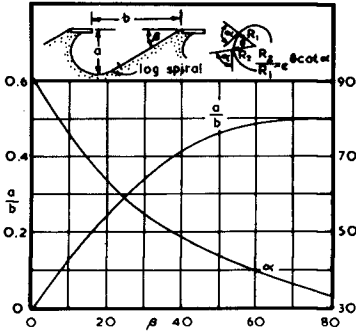


Fig. 5 Stability criteria for equilibrium shaped bay

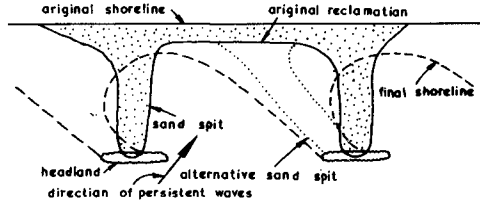


Fig. 7 Utilization of sand spit for headland construction

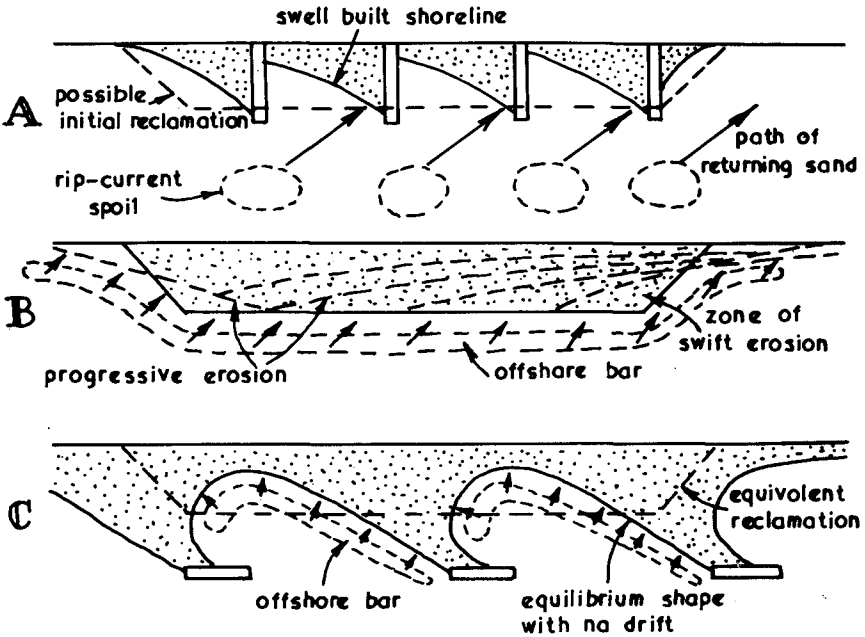


Fig. 6 Comparison of renourishment schemes A: with groynes B: with no assistance and C: with headland control

periphery of the bay. This has been proven in model studies (11), as well as in this field (12). At this stage longshore drift cannot occur. Hence any offshore bar formed during a storm will be carried back to the beach by the swell and placed in its original position. Certainly there will be negligible loss of material between one bay and the next.

COMPARISON OF DEFENCE PROCEDURES

Consider a reasonably short section of straight coast requires stabilizing because of the investments already in jeopardy along the beach. The basic need as stated above is to maintain a reserve of sand in the area, which is readily available from year to year, to service the storm waves in constructing the defensive offshore bar. The alternative of building seawalls or revetments instead of providing this sand reserve is not worthy of discussion, because of the high maintenance cost, the high risks taken and the lack of aesthetic appeal.

Thus the solutions to be compared are plain renourishment, a field of groynes, or several headlands (offshore breakwaters). With sand placed on the beach in the affected area there will be a downcoast extremity to the widened beach. This will involve a more oblique approach of the waves in this region and therefore swifter removal than along the general shoreline. (See Figure 6). This in time will reorient the whole renourished beach to a more oblique line and hence downcoast removal is expedited. This will result in a hump of sand proceeding along the shoreline which could well silt up waterways and other marine facilities. Continual maintenance of this fill will be necessary.

The second alternative of groynes, even if provided concurrently with renourishment, will retain perhaps half the volume during the subsequent swell season. However, when the storm waves arrive they will take portion of the reserve to form a bar and the remainder will be carried further out to sea by rip currents. This latter material will be re-deposited on the beach beyond the field of groynes by the oblique swell. (See Figure 6) This means that the groyne field must now be partly refilled by littoral drift coming from upcoast. During this process the downcoast region will suffer erosion.

The third alternative of headland control implies structures which will be positioned further offshore than the tips of the groynes discussed above. Their spacing also should be great enough for the bays to be significant features on the coast. (See Figure 6) In this way a new equilibrium shape can be developed which involves milder offshore bed slopes. The reserve of sand, which may again be that available from renourishment, is not only stored on the beach but also under water. Less is taken from the beach during a storm and what is can be replaced directly back whence it came. No sand is exchanged between bays except the net littoral drift that existed in the first place. This drift will still pass through the bay system and hence give the same supply downcoast as before, but without the eroded load from the short section of beach being stabilized. The security obtained is that if all littoral drift ceases the bays in front of the important beach site will indent to a predictable limit and no further.

An ultimate aim by coastal engineers should be to reduce littoral drift along the whole coast to zero. If this could be accomplished the cost could in the long term be met by the savings in erosion, silting, by-passing and bar formation at river mouths and harbours. In this procedure new land could be won from the sea, which would be stable enough for maximum employment in recreation, housing or industry.

COMBINED RENOURISHMENT AND CONTROL

It is often recommended that groynes should accompany renourishment (6) (13). The author is not against such reclamation per se, but would recommend structures other than groynes for retaining this newly won but costly material in position. He has written on several occasions to local authorities, where renourishment has just been reported in the technical literature, suggesting that headlands be spaced along the resulting waterline. By such an economical expedient it would immediately be learned that about half the material would be kept as beach, probably one quarter would be stored offshore, and the remainder might possibly go downcoast. This would be a better balance sheet than 100% lost in a matter of three to five years. The cost of dumping rubble-mound rock or its equivalent at around mean tide level would be minimal compared to the overall investment in transitory reclamation.

It is instructive to discuss a method of headland control in combination with a renourishment scheme. Since dredging generally involves pipeline discharge onto the beach it is most inconvenient to concentrate deposition at certain points on the coast rather than spreading uniformly. (See Figure 7) In fact, this economical mode of operation has been utilised for filling beaches within a groyne field (14). If stone were deposited promptly at the tip of the sand spit the man-made tombols could intercept littoral drift from upcoast, whilst the downcoast beach would be sculptured into a logarithmic spiral, to connect with the adjacent downcoast headland. This spit construction could be aided by earthmoving equipment. The head and sides could be quickly protected if necessary by blocks placed there temporarily and later shifted to the main structure.

When it is realised that a reef at low-low-water is sufficient to maintain a shoreline in place, the design of headlands can be quite economical. Natural or fabricated armour units can be dumped on the beach face in the knowledge that they will progressively slump seawards as waves reflect obliquely from them. Sufficient material should be supplied initially to cater for this spreading action, to ensure that waves are broken even at the highest tide and storm surge. Random placement and shape can make the structure appear as a natural feature.

To reduce the use of stone, which continually becomes harder to obtain and more expensive to transport, sand sausages are an alternative worth considering (15). Membrane materials are now becoming available which can be welded or sewn into large diameter tubes which can be filled with sand, cement mortar or concrete. The advantage is that the bulk of the material is available at the site and only requires some technique of pumping into the sausage skin located in position offshore.

The massive infra-structure of roads, trucks and cranes is thus obviated, which is particularly beneficial at remote points of the coast.

Another economical construction method for headlands, or other coastal structure for that matter, is the large bag which again can be filled with sand, mortar or concrete (16). The size of this armour unit is limited only by the size and strength of the bag that can be handled underwater or in the surf. The stability of such structures has only been tested in prototype situations, where they have withstood waves from some of the fiercest hurricanes in the Gulf of Mexico. Comparative tests with fabricated concrete units should be carried out, but it can be rationalised that such bags filled in situ develop very close contact, unlike monoliths which have only point contacts. Particularly difficult is it for a wave to overturn or dislodge a flexible mass such as a bag filled with sand.

Tubes of 1m diameter have been used to form groynes and pseudo-seawalls (17), but if used on a lattice fashion as depicted in Figure 8B each sausage could be safe from displacement by the largest waves. The alternative larger sausage is not cylindrical in shape (15) but assumes a profile as illustrated in Figure 8A. Such structures need only be built to mean-low-water for them to break waves at all times. The construction procedure lends itself to this reef concept because it is not necessary to provide access some meters above high tide to transport armour units. Its width also can be planned to meet the hydraulic needs rather than those of construction equipment.

DUNES VERSUS EMBAYMENTS

The real comparison to be made is between sand dunes, as the currently believed stalwarts against the sea, and crenulate shaped bays, formed between headlands of natural or man-made origin.

Because dunes are built by wind blowing dry sand from the beach berm into vegetation closest to the beach, it is believed they are God's given gift for defense of the coastline. When a particularly prolonged storm arrives the beach berm disappears offshore together with the face of the first dune. Later, when swell waves return this bar material to the shore (swiftly at first and then more slowly) the berm is wider than usual, thus providing a greater width from which the wind can lift sand and deposit it against the damaged dune.

But it is not the most erodable beach that has the highest dunes available. A large proportion of the bar material here does not return because it is compensating for the offshore deepening that is continuing in this erosive situation. On the other hand, in a stable or accretory situation the constant supply of sand to the beach permits an extra high first dune to exist. Seldom is such a feature attached and hence the anomaly that where least needed Nature provides the largest safeguard and where most needed this back-up structure is not well developed.

The idea is often expressed that it costs nothing to let Nature, through its dunes, provide us with our factor of safety, or more appropriately our factor of ignorance. Like the equivalent reserve in the

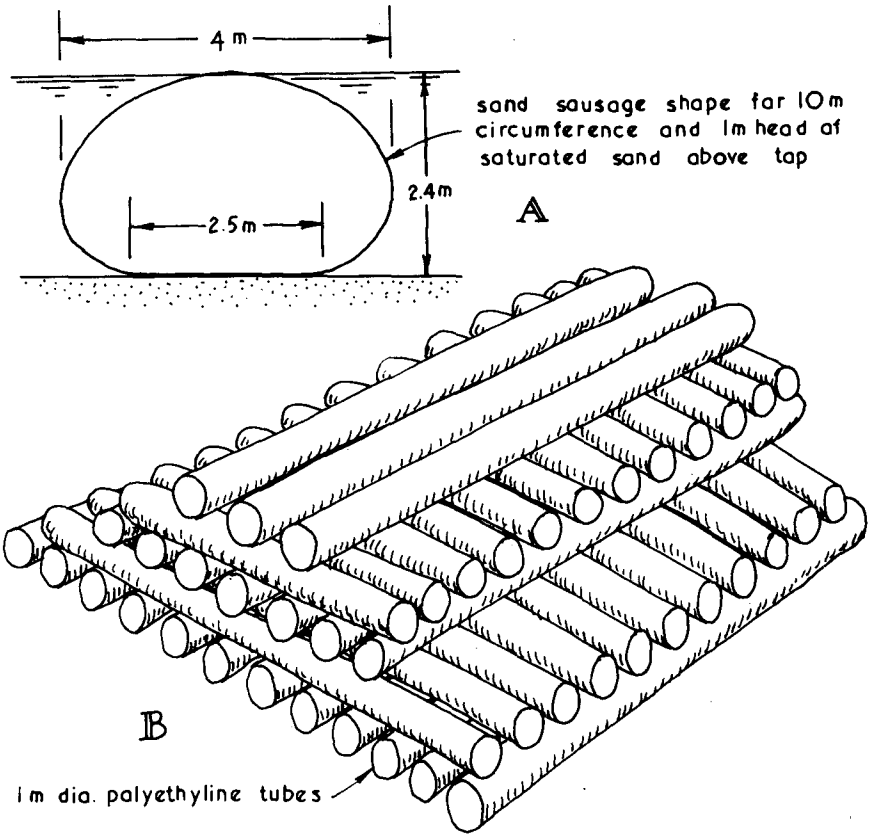


Fig. 8 Sand filled membranes A: large version, B: multiple tube construction

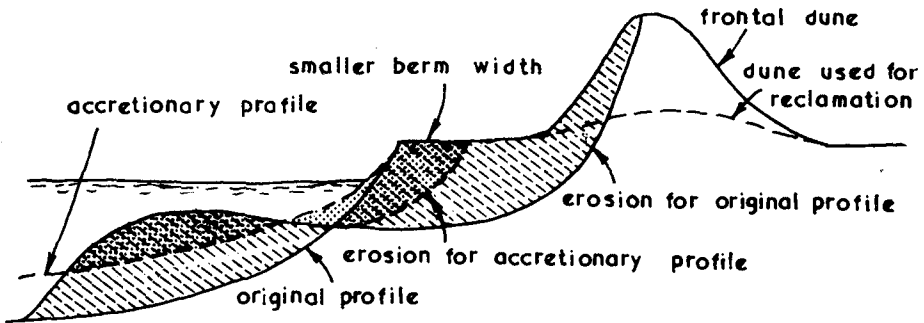


Fig. 9 Relative erosion for steep and mild offshore slopes

bank it costs money, because some of the most valuable coastal real estate is not available for development by the community for residential, recreational or commercial purposes. The sparsely vegetated white sedimentary hills create their own peculiar problems of wind blown sand and inaccessibility to the water.

It should be kept in mind that the real defense of the coast is to have sufficient sand continually available for the offshore bar to be constructed by the storm waves. Dune storage involves loss to the inland by wind erosion. If the required volume of sand can be retained at the shoreline, partly as beach berm and the remainder offshore as a shoal then the acelian denudation is minimised, with all its secondary problems. (See Figure 9) The advantages of providing this storage in an equilibrium bay feature is that material removed from the beach to form the bar is returned by the swell directly to its original position. Hence the same berm is available for the next year or the next decade. Because the bulk of the material is stored offshore, in its flattened slope, less demand is made upon the beach for an adequate structure to be built for stopping further erosion. The berm therefore is narrower and hence reduces the problem of wind blown sand.

Besides the aesthetic value of breaking the coastline into beautifully curved beaches there are many other benefits (18). The wave energy around each bay periphery varies considerably, so providing bathing conditions for the toddler to the surf-board rider. On oceanic margins, where persistent swell is ever present, the calmer zones in the lee of the upcoast headland can serve as launching sites for small craft, including those of the surf-life savers. The predictable limit of bay indentation (See Figure 5) gives an encroachment or usability line that is dependable, hence permitting full utilisation of the coastal strip. This situation should be compared with the dune system where people are prevented from walking for fear of blow outs or despoilation of the massive hills of sand that have insufficient nutrients to support vegetation.

SAND FOR RENOURISHMENT

Some papers have concentrated on the characteristics of sand to be used for renourishment, whether it should be coarser or finer in order to minimise removal downcoast. To the author this consideration is very unimportant, the waves will resolve this matter. The fines will be removed offshore, leaving the coarsest proportions on the beach face and berm. (12) If only coarse material is used the beach face will become steeper so promoting greater wave reflection, and thus increasing the energy available to transport this larger size material.

As stressed before, the most important factor for retaining or losing reclaimed land is the approach angle of the most persistent waves, generally the swell, to the beachline. When this is normal or near normal the longshore energy component is negligible and hence littoral drift in the surf zone, plus longshore movement further seawards, is zero or very low. Whether the sand is coarse or fine makes little difference to the overall profile. If very fine the bulk of the material will migrate offshore to make a wide shoal.

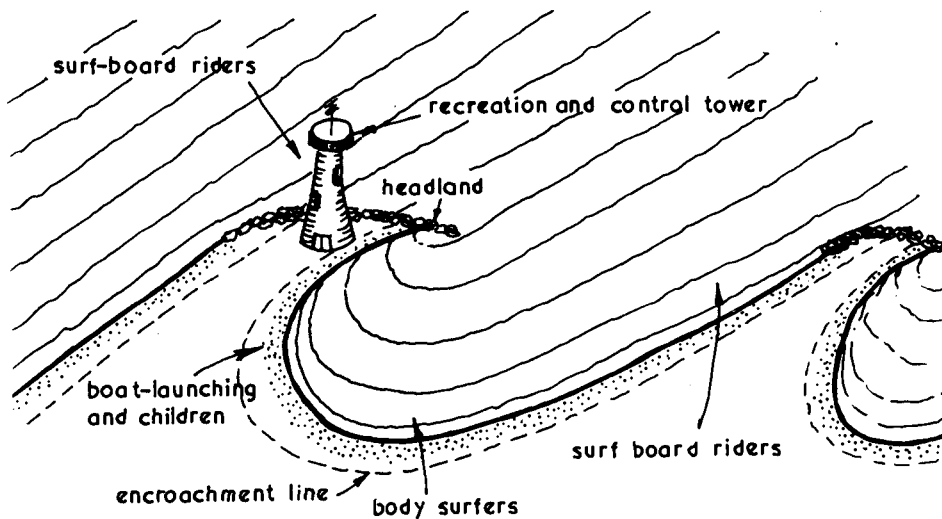


Fig. 10 Advantages from bayed beaches.

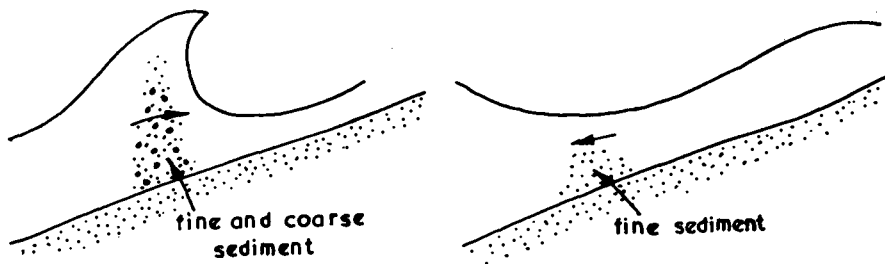


Fig. 11 Mechanism of sand sorting nearshore

If more coarse the bulk will be stored above water as beach berm, but because of the narrow exposed area and the larger diameter these grains are not so subject to wind transport.

Hence it would appear that a mixture of fine and coarse sand can serve the purposes desired, of providing material on hand for the construction of the natural defensive bar. The offshore zone of fine material is a ready foundation whilst the coarser fraction can form the top of this mound. During the transitional period of being returned shoreward both the fine and coarse grains will be mixed, until the waves can sort them once again. This makes the timing of sediment sampling for comparisons extremely important.

CONCLUSIONS

1. There are certain axioms or facts that can be accepted without question which, when considered together, point to new methods of coast stabilization.
2. Many mistakes have been perpetrated in the past because novel approaches to old problems are not readily accepted in conservative quarters of the engineering profession.
3. The basic requirement of coast stabilization is to have available from year to year sufficient sand to form an offshore bar which dissipates incoming storm waves.
4. The return of bar material to its original location (instead of downcoast) can be achieved in crenulate shaped bays where the persistent swell arrives normal to all points of the periphery.
5. Reclamation on its own suffers swift degradation, groynes expedite the transmission of sand downcoast, whilst headlands provide stable bays that can be used to the full.
6. When renourishment is carried out insurance against swift removal can take the form of headland construction which still permits the passage of littoral drift to downcoast areas.
7. The sand storage alternatives of dunes or shoals within embayments, indicate the need to seriously consider the latter for their long-term economic advantages.
8. When a shoreline is reoriented to receive normally the persistent swell, or resultant wave vector, the characteristics of the sand in a renourishment scheme are of little consequence.

REFERENCES

1. Silvester R. "Wave reflection on seawalls and breakwaters" Proc. Instn. Civil Engrs. 51, 1972, 123-131.
2. Silvester R. "The role of wave reflection in coastal processes. Proc. Coastal Sediments 77 (ASCE) 1977, 639-654.

3. Silvester R. Coastal Engineering Vol II Elsevier Publ. Co., Amsterdam, 1974.
4. Mikkelsen S.C. "The effects of groins on beach erosion and channel stability at the Limfjord barriers, Denmark" Proc. Coastal Sediments 17, (ASCE), 1977, 17-32.
5. Willis D.H. and Motyka J.M. "The effect of wave refraction over dredged holes". Proc. 14th Conf. Coastal Eng. II 1974, 615-625.
6. Newman D.E. "Beach replenishment: sea defences and a review of the role of artificial beach replenishment" Proc. Instn. Civil Engrs. Pt. 1, 1976, 60, 445-460.
7. Silvester R. "What makes a good surfing beach" Proc. 2nd Austral. Conf. Coastal Eng. 1975, 30-37.
8. Silvester R. "Sediment movement around the coastlines of the world" Proc. Conf. Instn. Civil Engrs. (London) 1962, 289-315.
9. Silvester R. "Development of crenulate shaped bays to equilibrium" Proc. ASCE J. Waterways & Harbours Divn 96 (WW2) 1970, 275-287.
10. Silvester R. "Headland defense of coasts" Proc. 15th Conf. Coastal Eng., Vol II, 1976, 1394-1406.
11. Ho S.K. "Crenulate Shaped bays" M.Eng. Thesis No. 346, Asian Inst. Tech., Bangkok, 1971.
12. Silvester R. and Ho S.K. "Use of crenulate shaped bays to stabilize coasts" Proc. 13th Conf. Coastal Eng. 2, 1972, 1347-1365.
13. Kramer J. "Beach rehabilitation by use of beach fills and further plans for the protection of the Island of Norderney" Proc. 7th Conf. Coastal Eng. 1960, 847-859.
14. Dette H.H. "Effectiveness of beach deposit nourishment" Proc. Coastal Sediments 77 (ASCE), 1977, 211-227.
15. Silvester R. and Liu G.S. "Sand sausages for beach defense work" Proc. 6th Conf. Austral. Hyd. and Fl. Mech., 1977, 340-343.
16. Porraz M. "Textile forms slash cost of coastal zone structures" Ocean Industry II, 1976, 61-66.
17. Jakobsen P.R. and Nielsen A.H. "Some experiments with sand filled flexible tubes" Proc. 12th Conf. Coastal Eng. 1970, 1513-1521.
18. Silvester R. and Ho S.K. "New approach to coastal defense" Civil Engineering (ASCE), Sept. 1974, 66-69.

CHAPTER 115

DIFFRACTION CALCULATION OF SHORELINE PLANFORMS

by

Robert G. Dean⁽¹⁾

ABSTRACT

A method is presented, and illustrated with examples, for calculating planforms for a class of "pocket" beaches. This type of pocket beach is formed of mobile sediment due to waves diffracting through an opening in erosion resistant material, for example behind a break in a revetment or behind closely spaced offshore breakwaters. The opening is considered as a series of sources with circular wavelets radiating landward from each element. The height and phasing of each wavelet is varied depending on whether the depth at the element limits the wave height and on the wave direction relative to the opening, respectively. Based on reasonable, but not complete, considerations of sediment transport, the equilibrium bathymetry is considered to exist when the wave front is everywhere tangent to the local bottom contours. A differential equation is developed for the local orientation of the contours; this equation is solved numerically starting from a reference transect and extending the contour until it intersects the line defining the opening.

Examples are presented illustrating the method for the following cases: (1) normally incident waves diffracting through a single relatively narrow opening, (2) obliquely incident waves diffracting through a single relatively narrow opening and (3) spiral bays which are contained by two relatively widely spaced headlands. In addition, a procedure is suggested for applying the results to the case of normally and obliquely incident waves diffracting through the openings formed by a series of offshore breakwaters.

INTRODUCTION

Wave diffraction is known to play an important role in the determination of the equilibrium planforms of pocket beaches particularly when the waves propagate through a restricted opening. An ability to predict the planforms for this type of beach would allow improved design for recreation and beach erosion protection and would also assist in the interpretation of the "effective" wave climates which form existing pocket beaches.

REVIEW OF PREVIOUS WORK

A number of studies have been concerned with the prediction of beach planforms under conditions where diffraction effects are significant. Yasso (1965) studied four beaches for which there is an updrift

¹Professor, Dept. of Civil Engineering and College of Marine Studies, University of Delaware, Newark, DE 19711.

headland and very little sand supply. These features were termed "headland bay beaches" by Yasso and it was demonstrated that the planforms could be fit very well by a logarithmic spiral equation of the form

$$r = e^{\theta} \cot \alpha \quad (1)$$

in which r is the radius from the log spiral center, θ is the horizontal angle from the origin, and α is a characteristic of the particular logarithmic spiral and represents the angle between a radius vector and tangent to the curve at that point.

Silvester and his co-workers (1970), (1972) have conducted studies of spiral bays lending further credence to the empirical fit provided by the logarithmic spiral. Based on an examination of planforms in nature and those evolved through laboratory studies, the conclusion has been reached that the planforms consist of three segments: (1) a circular arc segment in the lee of the updrift headland, (2) a log-spiral segment, and (3) a straight segment extending to the downdrift headland or other littoral control. It was also concluded that both refraction and diffraction effects significantly influence the beach planform. Silvester and Ho (1972) have utilized the spiral bay concept in which artificial headlands were constructed of gabions and rubble in an attempt to stabilize a landfill.

LeBlond (1972) has developed a numerical model to simulate the evolution of a straight shoreline to a spiral bay. Numerical stability problems occurred and the model was not successful in predicting the equilibrium beach planform characteristics. O'Rourke and LeBlond (1972) utilized the equations of motion including the radiation stress terms to investigate the water circulation patterns in a semi-circular bay. No attempt was made in the latter study to infer the associated beach planform.

Rea and Komar (1975) have developed a numerical model to simulate the formation of a crenulate bay. Diffraction effects were parameterized with the wave crests in the "shadow zone" described as circular arcs with the relative wave height decreasing from unity outside the shadow zone to progressively reduced values further in the lee of the headland. The unique feature of this model is that shoreline elements of two different orientations were used. In proximity to the updrift headland, the displacements of the elements were parallel to the axis of the headland and approximately perpendicular to the local wave crest. Outside of the shadow zone, the elements were perpendicular to those just described so that again the shoreline displacement was generally perpendicular to the local wave front. Good qualitative agreement was found with the general form of logarithmic spiral beaches.

Font, Sanabria and Silva (1976) have included the effect of the longitudinal gradients of breaking wave heights and the associated currents. The total longshore current consists of that due to the obliquity of the waves and that due to the gradient of the wave setup. The condition adopted for the equilibrium beach planform is zero total current. This is in contrast to the observations of Silvester (1970) that the waves break with crests parallel to the shoreline for

the equilibrium planform.

Walton (1977) has analyzed beach planforms of the spiral bay type and the associated waves and has concluded that the planform is everywhere perpendicular to the local wave energy vector. A family of possible beach planforms is determined and the planform selected which provides a best fit to the beach of interest. The method does not allow for diffraction and has the disadvantage of predicting that in the "gap" between two headlands, a wave system characterized by a single height and direction would result in a straight beach planform perpendicular to the incoming waves.

Dean and Maurmeyer (1977) have presented an approach to calculating the beach planforms resulting from "narrow" and "wide" openings between littoral controls. The method was compared with two measured planforms and demonstrated reasonably good agreement. One limitation of the method was that for the "narrow" gaps, it was necessary that the waves approach perpendicular to a line connecting the two headlands. The present paper presents an extension of that just described, including: (1) waves can approach the opening from any direction, and (2) an improved calculation procedure is utilized.

METHODOLOGY

General

The approximate method to be presented considers waves incident on an opening between two control points or headlands with a connecting sill of arbitrary depth, see Figure 1. The effects of diffraction are accounted for by using a simple representation of a series of wave sources distributed along the sill. The equilibrium beach and contour planforms are defined as coinciding with lines of constant wave phase; the effects of wave refraction are accounted for directly by the method in an approximate manner. The effect of currents due to gradients of breaking wave heights are not included. Although other authors, for example Font, Sanabria and Silva (1974) and LeBlond (1972) have emphasized the importance of these currents, other investigators, for example Silvester (1970), have noted that the equilibrium planform occurs when the wave breaks at normal incidence to the beach. My observations of beach planforms in apparent equilibrium tend to verify the latter assessment. Future studies will attempt to address the relative importance of these currents.

Headlands and Connecting Sill

The two headlands are considered to be separated by a distance, b , and to be connected by a non-erodible sill. For computational purposes, the sill is subdivided into N segments, each of which will be considered as a wavelet source radiating outward with a circular crest.

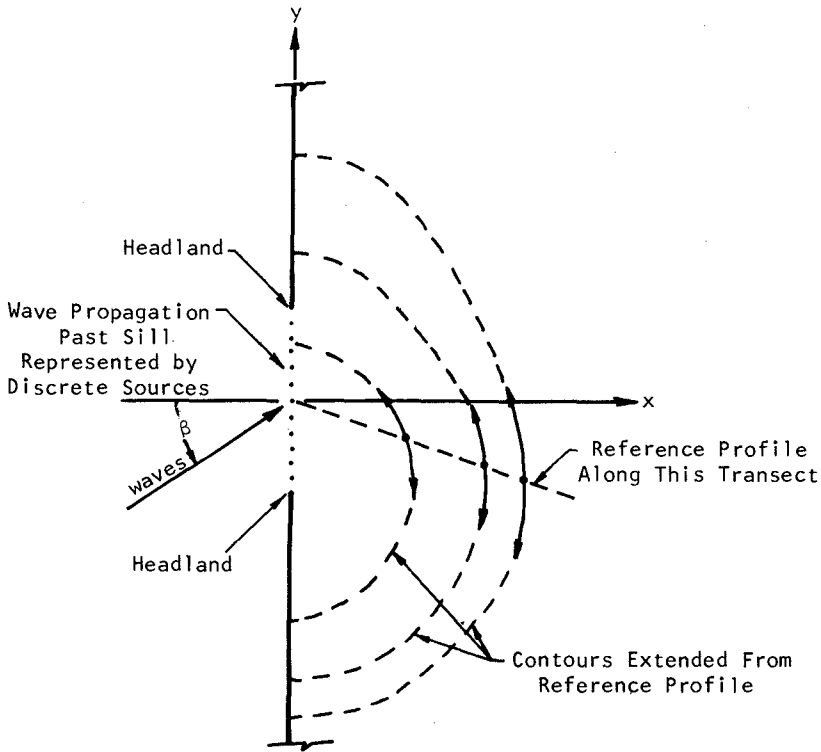


Figure 1. Definition Sketch Showing Method of Extending Contours From Reference Profile.

Incident Wave Representation

The incident wave, $\eta(x,t)$, is represented as the sum of M incident waves of height, H_{I_m} , angular frequency, $\sigma_m (= 2\pi/\text{wave period})$, wave number, $k_m (= 2\pi/\text{wavelength})$, and phase, ϵ_m , propagating in a direction, β_m , with respect to a line joining the two headlands forming the pocket beach, see Figure 1.

Reference Profile

The computations are initiated and extended from specified depths along a reference transect as shown in Figure 1. The depths, $h(x)$, along this reference transect could be based on measurements or could be based on an idealized form

$$h(x) = A(x_{\max} - x)^{2/3} \quad (2)$$

as found by Dean (1977) in an analysis of 502 beach profiles from the Atlantic Coast and the Gulf of Mexico. In Eq. (2), the parameter, A, depends on sediment properties, primarily the fall velocity.

Wave Propagation Into Bay

The wave height, H_s , radiating out from the sill elements is considered to be equal to the incident wave height if no breaking at the sill occurs or to be limited by breaking in accordance with the usual assumptions for spilling breakers.

$$\left. \begin{aligned} H_{S_m} &= \kappa h_s, H_{I_m} > \kappa h_s \\ H_{S_m} &= H_{I_m}, H_{I_m} \leq \kappa h_s \end{aligned} \right\} \quad (3)$$

As noted, the wave height and phase at any location in the bay are determined from the linear sum of all contributions from the sill elements. The resulting water surface displacement in the bay can be expressed as

$$\eta(x,y,t) = [\eta(x,y)]_{\max} \cos[\sigma t - \epsilon(x,y)] \quad (4)$$

in which $\epsilon(x,y)$ is the phase angle associated with the maximum water surface displacements as defined by

$$\tan \epsilon = \frac{S_2}{S_1} \quad (5)$$

where

$$S_1 = \sum_{m=1}^M \sum_{n=1}^N \frac{H_{n,m}}{2} \cos \mu_{n,m} \quad (6)$$

$$S_2 = \sum_{m=1}^M \sum_{n=1}^N \frac{H_{n,m}}{2} \sin \mu_{n,m} \quad (7)$$

and

$$\mu_{n,m} = k_{s_{n,m}} x_{n,m} \cos \beta_m + k_{s_{n,m}} y_{n,m} \sin \beta_m + \sigma_m r_n / \bar{C}_m \quad (8)$$

In these equations, the outer and inner summations are carried out over the number of incident wave components, M, and sill elements, N, respectively. The subscript s refers to conditions at the sill, \bar{C}_m is the average propagational speed of the mth wave component from source element to contour point of interest, a distance r_n , where

$$r_n \equiv \sqrt{(x - x_{s_n})^2 + (y - y_{s_n})^2} \quad (9)$$

The average propagational speed for a shallow water wave directed normally along a profile as given by Eq. (2) can be shown to be

$$\bar{c} = \frac{(\Delta x)_* \sqrt{gA^3}}{1.5[h_* - h']} \quad (10)$$

where h_* and h' are the depths just bayward of the sill and at the water depth of interest, respectively, and Δx_* is the normal distance along that contour separating the two end depths, h_* and h' . It is assumed that the propagational speed from the sill element to the location of interest is the same as if the wave were propagating normally along a profile given by Eq. (2).

Although not necessary for computation of the equilibrium planform contours, it is noted that the resultant wave height, $H(x,y)$, at any location is

$$H(x,y) = 2 \sqrt{S_1^2 + S_2^2} \quad (11)$$

Since the consideration for the locus of an equilibrium contour is that the contour be parallel to the wave crest, this is equivalent to establishing the locus of isolines of constant $\epsilon(x,y)$ (or $\tan \epsilon(x,y)$). Expressed analytically, using Eqs. (5), (6), and (7),

$$d(\tan \epsilon) = \frac{\partial(\tan \epsilon)}{\partial x} dx + \frac{\partial(\tan \epsilon)}{\partial y} dy = 0 \quad (12)$$

which can be simplified to the differential equation for the locus of a line of constant $\epsilon(x,y)$

$$\frac{dy}{dx} = - \frac{S_1 \frac{\partial S_2}{\partial x} - S_2 \frac{\partial S_1}{\partial x}}{S_1 \frac{\partial S_2}{\partial y} - S_2 \frac{\partial S_1}{\partial y}} \quad (13)$$

Contour Determination

The phase $\epsilon(x,y)$ to be held fixed along a given contour is first determined at the contour of interest on the reference profile through direct application of Eq. (5). The contour is next extended from the reference profile by a selected increment Δs in accordance with the direction established by Eq. (13), see Figure 2. The incremental Δx and Δy are

$$\left. \begin{aligned} \Delta x &= \Delta s \cos \delta \\ \Delta y &= \Delta s \sin \delta \end{aligned} \right\} \quad (14)$$

where

$$\delta = \tan^{-1} \left(\frac{dy}{dx} \right) \quad (15)$$

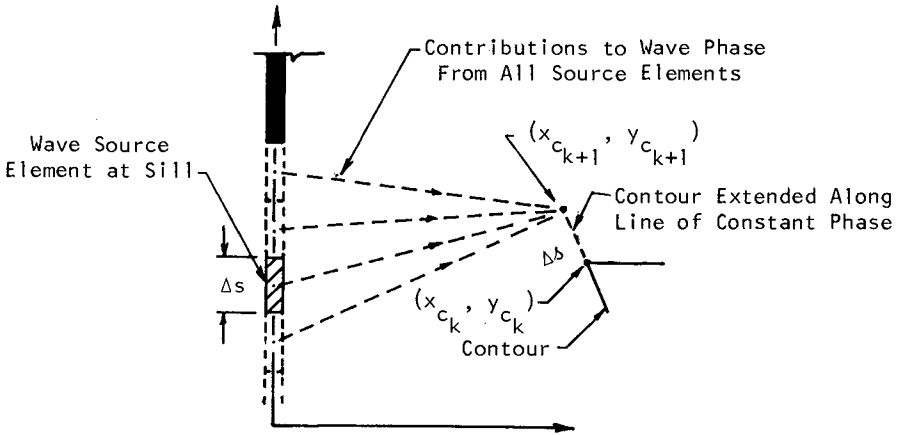


Figure 2. Step-Wise Extension of Contour Along Line of Constant Wave Phase.

The values of the (k+1) coordinates are now

$$\begin{aligned} x_{k+1} &= x_k + \Delta x \\ y_{k+1} &= y_k + \Delta y \end{aligned} \tag{16}$$

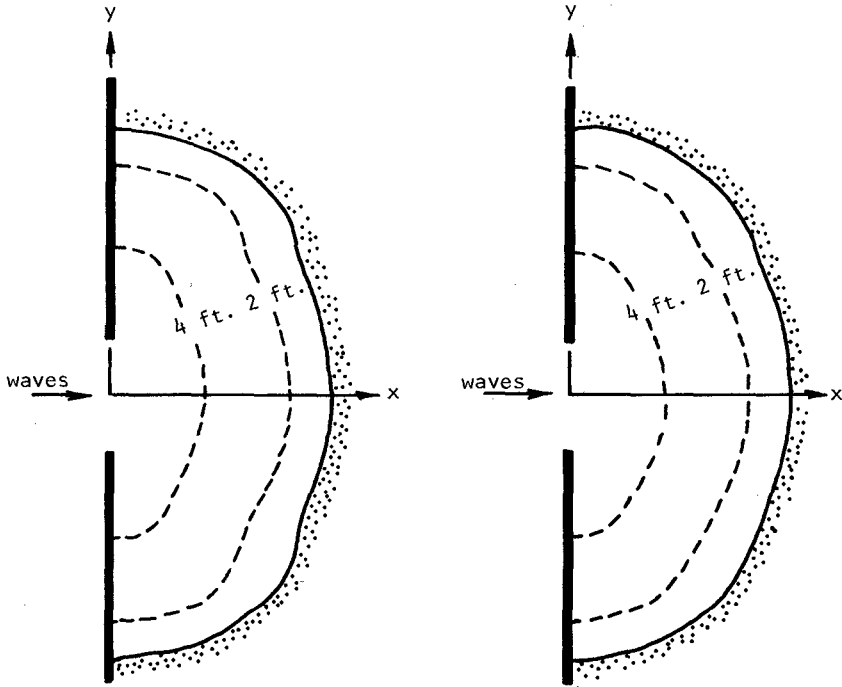
With estimates of the location of the extended contour now available, improved values of (x_{k+1}, y_{k+1}) are determined by applying a Newton-Raphson procedure repeatedly to establish the "target" value of $\epsilon(x,y)$. This involves modifying (x_{k+1}, y_{k+1}) along a direction which is perpendicular to the local value of (dy/dx) as determined from Eq. (13). In the results to be presented, this correction procedure was applied eight times for each point. It was usually possible to achieve the "target" value of $\epsilon(x,y)$ within 0.5° . In this manner the contour is progressively extended until it intersects the line connecting the two headlands. Each successive contour of interest is then calculated in the manner described. This completes the calculation of the embayment planform.

APPLICATIONS

In this section the method will be applied to several idealized cases of interest.

Normal Wave Incidence

A number of cases of varying relative gap width have been computed for normally incident waves. For an incident wave of a single period, it was found that the contours were somewhat irregular; the irregularities were reduced when the incident wave was represented by two components of slightly different periods. Figure 3a presents the planform associated with an incident wave of a single period of 8 seconds.



a) Planform for a Single Incident Wave, $T = 8$ sec. b) Planform for An Incident Wave System Comprising Two Components. Reference Wave Period is 8.0 sec.

Figure 3. Calculated Pocket Beach Planforms. Distance Between Headlands is 120 ft.

The contours contain slight irregularities characteristic of diffracted wave fields. Figure 3b presents the planform for the same case except that the incident wave system comprises two individual waves of equal height but of different periods: 8.0 and 8.8 seconds. For all examples presented hereafter, the incident wave system will consist of two components of the same height and two periods equal to 1.0 and 1.1 times the "reference" period.

The effect of wave period, relative gap opening, and sill discretization were examined. It was found that for the longer

periods, the planforms were smoother and less elliptical (i.e. more circular) in shape. Figure 4 presents the calculated planform for the same case as Figure 3b, except the reference period is 24 seconds, and the differences noted above are evident.

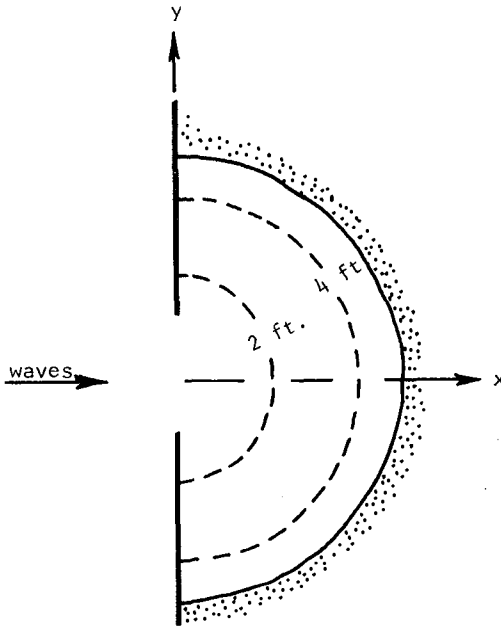


Figure 4. Calculated Planform for a Reference Wave Period of 24 Seconds. Distance Between Headlands is 120 ft.

The ratio of the major-to-minor semi-axis, a_2/a_1 , was evaluated as a function of ratio of half gap width to minor semi-axes, $b/2a_1$, for three reference wave periods. Based on simple geometric considerations, an approximate relationship for these variables is

$$\frac{a_2}{a_1} = 1 + \frac{b}{2a_1} \tag{17}$$

Figure 5 presents the calculated planform results where it is seen that Eq. (17) represents an upper limit. For any given relative gap width, the ratio of major to minor semi-axis (a_2/a_1) is larger for the shorter periods. The irregularities in the results are believed to be associated with the previously described characteristics of diffraction patterns.

The effect of finer discretization of the sill width was found to reduce slightly the irregularities in the calculated planforms.

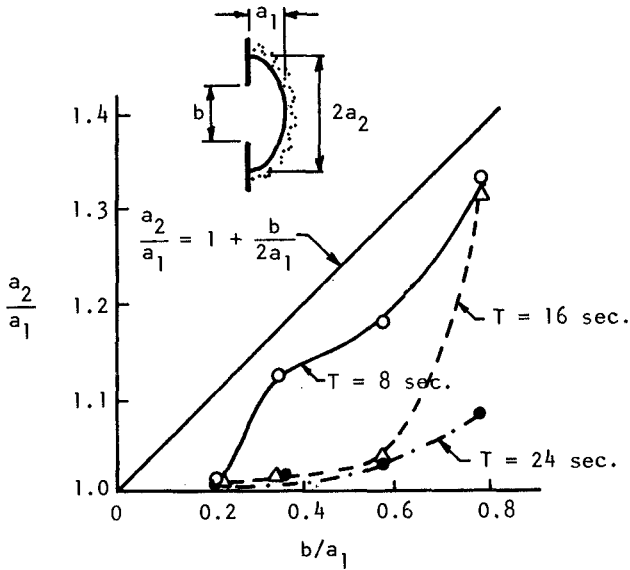


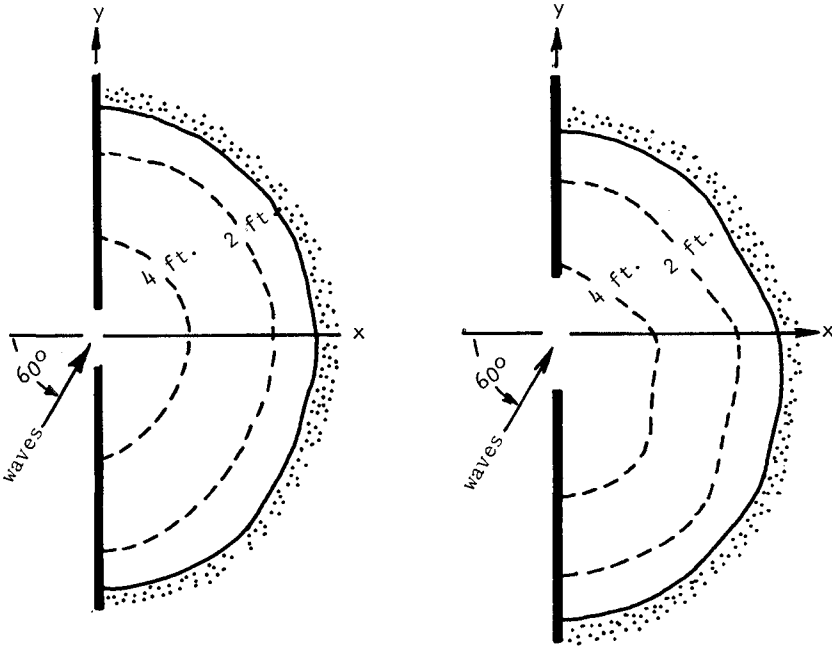
Figure 5. Variation in Calculated Ratios of Major to Minor Semi-Axes for Cases of Normal Wave Incidence and Various Wave Periods.

Oblique Wave Incidence

Figure 6 presents the calculated planforms for waves propagating at a 60° angle with respect to the x-axis and for two gap openings. For the relatively narrow gap opening ($b/2a_1 = 0.11$), it is seen that there is little asymmetry in the two major semi-axes, the ratio of the down-wave to up-wave semi-axes being 0.88. For the wider gap opening ($b/2a_1 = 0.29$), the ratio of the major down-wave to up-wave semi-axes is reduced to 0.71. It is also of interest that in the vicinity of the opening, the 4 ft. contour is oriented approximately normal to the incident wave direction for the wider gap.

Spiral Bays

The method was applied to the calculation of two spiral bay planforms for incident wave angles of 30° and 60° respectively, see Figures 7 and 8. The planforms are in qualitative agreement with the characteristics of spiral bays as produced in laboratory experiments and as found in nature.



- a) Planform for Relatively Narrow Opening, $b/2a_1 = 0.11$. b) Planform for Relatively Wide Opening, $b/2a_1 = 0.29$.

Figure 6. Calculated Beach Planforms for Oblique Wave Incidence. Reference Wave Period is 8.0 sec. The Minor Semi-Axis = 235 ft. in Both Cases.

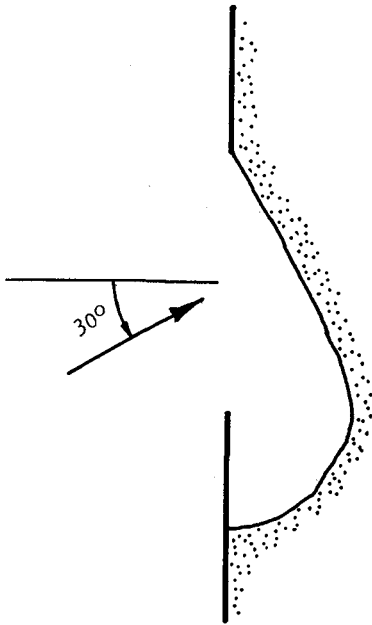


Figure 7. Calculated Spiral Bay Type Planform for 30° Wave Obliquity. Reference Period = 16 sec. Distance Between Headlands = 840 ft.

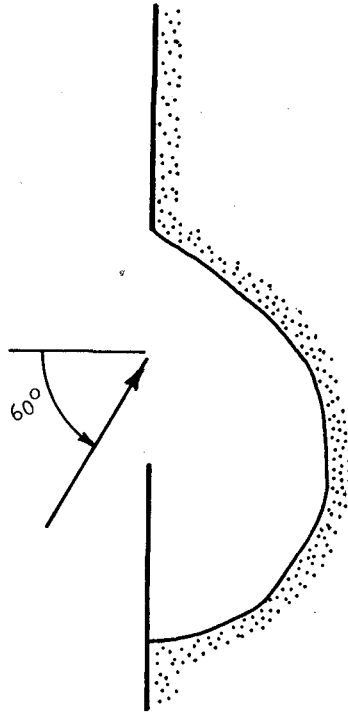
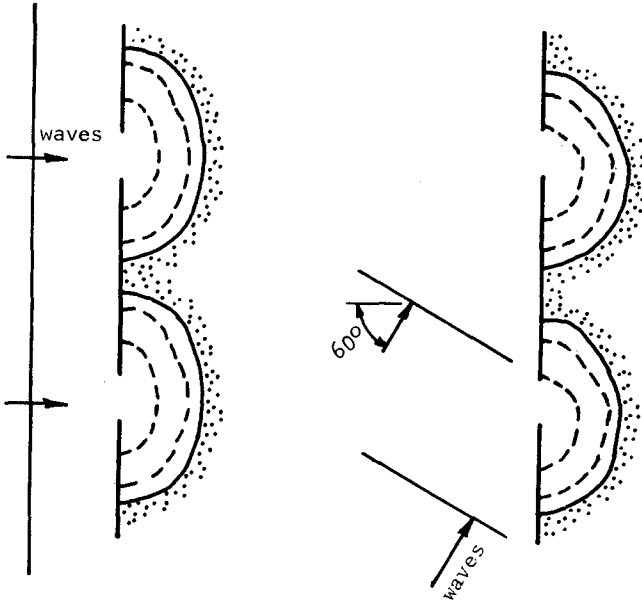


Figure 8. Calculated Spiral Bay Type Planform for 60° Wave Obliquity. Reference Wave Period = 16 sec. Distance Between Headlands = 380 ft.

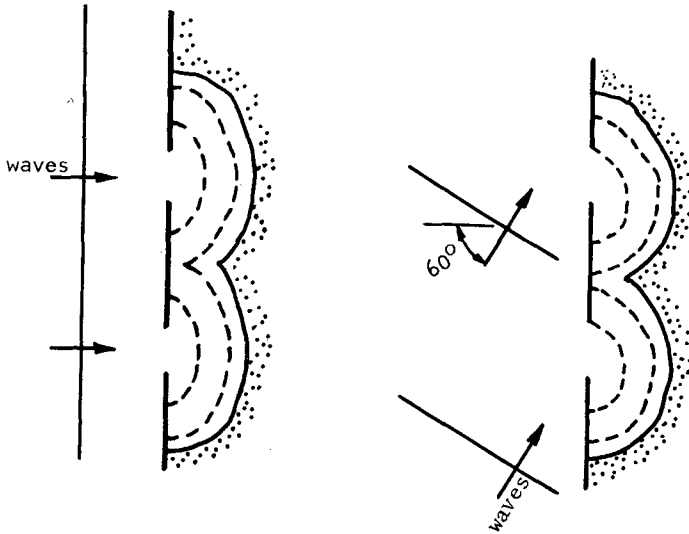
Application to Planforms Associated With Offshore Breakwaters

The planforms computed as described herein can be extended in a very approximate graphical manner to the case of offshore breakwaters. The procedure is first applied to planform computation for a single opening, the wave conditions of interest and with the reference transect representing the proper offshore distance of the breakwater. These planform results are then transferred to an overlay with the offshore breakwaters shown. If the spacing of the breakwater gap centerlines is greater than the major axis of the planform, then a tombolo is indicated, see Figure 9. If the spacing of the breakwater gap centerlines is less than the major axis of the planform, then the breakwater is not connected to the shoreline, see Figure 10. In order for this approach to be approximately valid, the reference transect must be correct and there must be adequate sand in the system to form an equilibrium planform in the proper geometric relationship to the profile along the reference transect.



a) Normal Wave Incidence. b) Oblique Wave Incidence.

Figure 9. Shore-Connected Planforms Associated With Offshore Breakwaters. Gap Opening is 120 ft. Reference Wave Period is 8 sec.



a) Normal Wave Incidence. b) Oblique Wave Incidence.

Figure 10. Planforms Associated With Offshore Breakwaters With a Relatively Large Ratio of Gap Opening to Breakwater Length. Gap Opening is 120 ft. Reference Wave Period is 8 sec.

SUMMARY AND CONCLUSIONSSummary

A method has been presented and illustrated with examples for calculating the equilibrium planform characteristics of pocket beaches contained by erosion resistant features, herein called headlands. In accordance with the observations of some investigators, the method considers the planform contours to coincide with lines of equal wave phase. The opening between the headlands is represented as a series of sources from which circular wavelets radiate landward. The water surface displacement at any location in the bay is considered as the linear sum of the contributions from all sill elements. Starting from the known contours on a reference transect, the contour is extended in accordance with a differential equation defining the locus of that contour. Examples presented include planforms for relatively narrow openings with normally and obliquely incident waves. In addition planforms are calculated for spiral bays which are associated with reasonably wide openings.

Conclusions

There are irregularities associated with the calculated planforms of lines of equal wave phase. These are found to be reduced somewhat for an incident wave system comprising two waves of differing periods. It appears that planforms in nature may be smoothed by a range of effective wave periods and directions. The general characteristics of the calculated planforms are reasonably representative of those found in nature. However, a full evaluation of the method will require additional laboratory and field data.

REFERENCES

- Dean, R. G., "Equilibrium Beach Profiles: U. S. Atlantic and Gulf Coasts", University of Delaware Ocean Engineering Report No. 12, Jan. 1977.
- Dean, R. G. and E. M. Maurmeyer, "Predictability of Characteristics of Two Embayments", Proc., ASCE Specialty Conference on Coastal Sediments '77, p. 848-866, Nov. 1977.
- Font, J. B., P. Sanabria and A. Silva, "Geometria des Playas Protegidas en Equilibrio", Proc., VI Congreso Latino Americano de Hidraulica, p. C3-1 to C3-12, July 1974.
- LeBlond, P. H., "On the Formation of Spiral Beaches", ASCE Proc., Thirteenth International Conference on Coastal Engineering, Chapter 73, p. 1331-1345, 1972.
- O'Rourke, J. G. and P. H. LeBlond, "Longshore Currents in a Semi-Circular Bay", J. Geophy. Res., Vol. 77, p. 444-452, 1972.
- Rea, C. C. and P. D. Komar, "Computer Simulation Models of a Hooked Beach Shoreline Configuration", J. of Sedimentary Petrology, Vol. 45, No. 4, p. 866-872, Dec. 1975.

Silvester, R., "Growth of Crenulate Shaped Bays to Equilibrium", J. Waterways and Harbors Div., Proc. ASCE, Vol. 96, WW2, p. 275-287, May 1970.

Silvester, R. and S. Ho, "Use of Crenulate Bays to Stabilize Coasts", ASCE Proc., Thirteenth International Conference on Coastal Engineering, Chapter 74, p. 1345-1365, 1972.

Walton, T. L., "Equilibrium Shores and Coastal Design", Proc., ASCE Specialty Conference on Coastal Structures, p. 1-16, Nov. 1977.

Yasso, W. E., "Plan Geometry of Headland-Bay Beaches", J. of Geology, Vol. 73, p. 702-713, 1965.

CHAPTER 116

CONCENTRATION OF SUSPENDED CLAY IN PERIODIC FLOW

BY

- A. Watanabe - Associate Professor, University of Tokyo, Japan, formerly Associate Professor, Asian Institute of Technology, Thailand
- P. Thimakorn - Associate Research Professor, Asian Institute of Technology, Thailand
- A. Das Gupta - Assistant Research Professor, Asian Institute of Technology, Thailand

SYNOPSIS

A diffusion model of clay-water flow is formulated to determine the time dependent concentration distribution of suspended clay in a two dimensional periodic flow. Taking into account the entrainment rate of the clay particle from the bed, the integrated diffusion equation to yield a solution of the time-variation of the clay concentration in the vicinity of the channel bed is derived. In addition the original diffusion equation is solved by means of the finite element method. An experiment was conducted in a recirculating two dimensional channel where sinusoidal current variation was generated upon the clay-water mixture. Results obtained from the experiment are compared with those derived from the model.

INTRODUCTION

Transport of fine cohesive clay over a mud bed always appears in the form of full suspension. This phenomena is mostly found in the estuaries of large rivers which flow through flat alluvial flood plain into the sea. Under the influence of tide from the sea the flow in the estuary becomes periodic. Estimation of the sediment transport in the estuarine environment of this nature is practically dependent on four predominant factors, namely, tide, velocity, cross sectional area and concentration of suspended solids in the flow. Though factors influencing the suspended clay transport in an estuary, such as effect of salinity on flocculation, mixing of salt and fresh water (well mixed, partially mixed or stratified flow) and others are important, it is however useful to consider at the beginning the dynamic of the transport process only so that the phenomena can be understood. This dynamic characteristic of the clay-water flow is recognized by the two factors, the velocity and the concentration.

This phenomena was noted by Postma [1] in which the periodicity of the suspended clay in the periodic flow field in the Wadden Zee in Holland was shown. Later on Krone [2] found that in a steady flow the concentration of suspended clay when expressed in the form of percent of deposition attains

an inversely linear relationship with the bed shear stress. Similarly Metha and Partheniades [3] showed that the equilibrium concentration of clay-water mixture under a steady flow has a logarithmic relationship with the relative bottom shear stress. Recently Thimakorn and Gupta [4] correlated the two periodic parameters by means of cross correlations of the velocity and concentration data collected from field measurements in an estuary in Thailand. In this paper a diffusion model of a two dimensional clay-water flow is formulated to find out the response of the clay concentration under a periodic flow condition of simple sinusoidal type. The time variation concentration obtained from the experiment is compared with the diffusion model results.

THE MODEL

The definition sketch of the instantaneous suspended concentration profile, $C(y,t)$ within a two-dimensional time dependent flow, $u(t)$, is shown in Fig. 1. From the figure the governing equation of the vertical diffusion is:

$$\frac{\partial C}{\partial t} = \frac{\partial}{\partial y}(w_o C) + \frac{\partial}{\partial y}(K_v \frac{\partial C}{\partial y}) \quad (1)$$

where C is the concentration at any depth y , w is the terminal fall velocity of clay and K_v is the vertical diffusion coefficient.

Two boundary conditions are valid. One at the free surface where there is no net flux of the sediment across it is:

$$\text{at } y = h; \quad w_o C + K_v \frac{\partial C}{\partial y} = 0 \quad (2)$$

And at a reference level, y_o , near the bed the vertical diffusion is replaced by the variation of the entrainment rate, $q(t)$:

$$\text{at } y = y_o; \quad K_v \frac{\partial C}{\partial y} = -q(t) \quad (3)$$

Integration of Eq. (1) from $y = y_o$ to $y = h$ thus yields:

$$\frac{d}{dt} \int_{y_o}^h C dy = q - w_o C_b \quad (4)$$

which becomes:

$$(h - y_o) \frac{d\bar{C}}{dt} = q - w_o C_b \quad (5)$$

where \bar{C} is the vertical average of concentration and C_b is the concentration near the bottom ($y = y_o$).

Under steady flow, after some time the concentration reaches its equilibrium, and the entrainment rate, q , is balanced by the settling rate of the particles, or Eq. (5) becomes:

$$q = w_o (C_b)_{eq} = \text{constant} \quad (6)$$

where $(C_b)_{eq}$ is the nearbed concentration at equilibrium.

Assume that the entrainment rate thus evaluated can be applied to the time dependent flow at any instant time, t , which is analogous to the gradually varied flow (quasi steady) such as tidal current.

Introducing:

$$\beta = \frac{\bar{C}}{C_b} \quad (7)$$

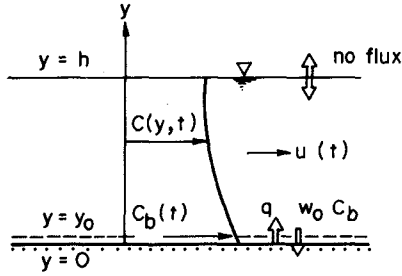


Fig. 1 Definition Sketch of Concentration Field Time Dependent Concentration.

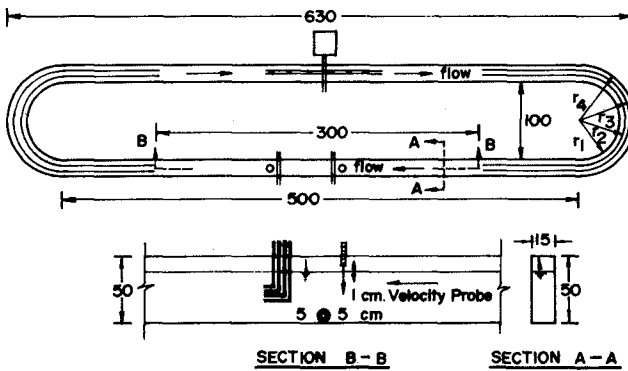


Fig. 2 The Circulating Channel.

and assuming further that it is nearly constant, Eq. (5) is transformed into:

$$\frac{dc_b(t)}{dt} = \gamma [(C_b)_{eq}(t) - C_b(t)] \tag{8}$$

which expresses the time variation of the bottom concentration in the form of the integrated diffusion equation of the original equation, Eq. (1).

The parameter γ is derived from:

$$\gamma = \frac{w_o}{\beta(h-y_o)} \tag{9}$$

In a steady flow condition, the general solution of Eq.(8) becomes:

$$C_b(t) = (C_b)_{eq} + [C_b(0)-(C_b)_{eq}] \exp(-\gamma t) \tag{10}$$

which is then:

$$\ln \frac{C_b(t)-(C_b)_{eq}}{C_b(0)-(C_b)_{eq}} = -\gamma t \tag{11}$$

This equation is used to determine the value of γ from the asymptotic variation of the concentration measured at time intervals before it reaches equilibrium.

To determine the time dependent bottom concentration, Eq. (8) is solved numerically by means of the Runge-Kutta method. In order to obtain the numerical result, values of β , γ , w_o and q are needed, which can be obtained from the steady flow experiments.

The result obtained from the integrated diffusion equation, Eq. (8), gives only the time variation of the bottom concentration in a periodic flow. In order to determine the vertical distribution of concentration at any time, Eq. (1) must be solved.

Here we shall apply the finite element analysis to Eq. (1).

First an approximate expression for $C(y,t)$ is introduced as:

$$C(y,t) = \sum_{i=1}^I N_i(y) C_i(t) \tag{12}$$

in which N_i , is the interpolation function and C_i the nodal concentration. By means of the Galerkin's method, the original diffusion equation, Eq. (1), with the two boundary conditions, Eqs (2) and (3) is expressed as:

$$\int_{L_e} N_i \left[\frac{\partial C}{\partial t} - \frac{\partial}{\partial y} (w_o C) - \frac{\partial}{\partial y} \left(K_y \frac{\partial C}{\partial y} \right) \right] dy = 0 \tag{13}$$

governing the behavior of a line element, L_e .

Integrated by parts Eq. (13) becomes:

$$T_{ij} C_j + (W_{ij} + K_{ij}) C_j + F_i = 0 \tag{14}$$

which is the finite element expression to give the behavior of C_i in one element only, where $C_j = dC_j/dt$,

$$T_{ij} = \int_{L_e} N_i N_j dy, \quad W_{ij} = \int_{L_e} w_o \frac{dN_i}{dy} N_j dy$$

$$K_{ij} = \int_{L_e} K_y \frac{dN_i}{dy} \frac{dN_j}{dy} dy, \quad F_i = \begin{bmatrix} f_i \\ 0 \\ 0 \\ -f_r \end{bmatrix}$$

$$\text{and } f_i = (w_0 C + K \frac{\partial C}{\partial y}), \quad y = y_i$$

After some manipulations and assembly procedure, the final equation for solution takes the form of:

$$P_{ij} \dot{C}_j + Q_{ij} C_j + R_i = 0 \quad (15)$$

where the explicit forms of P_{ij} , Q_{ij} and R_i are omitted since they are readily obtained.

Note that the influence matrix P_{ij} is constant in time and symmetric, while the other two matrices Q_{ij} and R_i are time dependent and in particular Q_{ij} is unsymmetric. Time derivatives in Eq. (15) are expressed in the finite difference form as:

$$\begin{aligned} & [P_{ij} + \frac{\Delta t}{2} Q_{ij}^{(n+1)}] C_j^{(n+1)} \\ & = [P_{ij} - \frac{\Delta t}{2} Q_{ij}^{(n)}] C_j^{(n)} - \frac{\Delta t}{2} [R_i^{(n)} + R_i^{(n+1)}] \end{aligned} \quad (16)$$

In order to solve this equation it is assumed that the diffusion coefficient K_y is given by the modified Rouse's formula

$$\begin{aligned} K_y &= u^* K_y (1 - \frac{y}{h}) & \text{for } y \leq \frac{h}{2} \\ &= \frac{1}{2} u^* K_h & \text{for } y > \frac{h}{2} \end{aligned} \quad (17)$$

and the vertical velocity profile is logarithmic:

$$u = u^* (3.0 + 5.75 \log \frac{u^* h}{v}) \quad (18)$$

THE EXPERIMENT

The objectives in conducting the experiments are three-faced; namely: 1) to demonstrate the physical behavior of the clay-water mixture under periodic flow; 2) to determine numerical values, β , γ , w_0 and q to be used in solving Eq. (8); and 3) to compare the time dependent concentration with that of the model result. A two-dimensional recirculating channel, Fig. 2, having the width of 15 cm and the depth of 40 cm is used in the experiment. Clay-water mixture is moved by a rotating paddle wheel which can generate both steady flow velocity and sinusoidal velocity by means of a sine-current regulator derived from a rotating linear potentiometer. Flow velocity is measured by an impulse generating 1 cm diameter propeller current meter. Samples of water are collected to find the concentration from a series of five 2 mm diameter syphons. A long scale galvanometer reads the current from the photo transistor receiving the light through the measuring sample cell from the light emitting diode (LED). The following is the steps of the test:

1) Steady Flow: By means of generating different velocities, maintaining the steady flow condition of each velocity, and taking samples at different time intervals it was found that;

- The concentration reaches the equilibrium state within one hour, no matter whether the initial concentration is higher or lower than the equilibrium value, (Fig. 3);

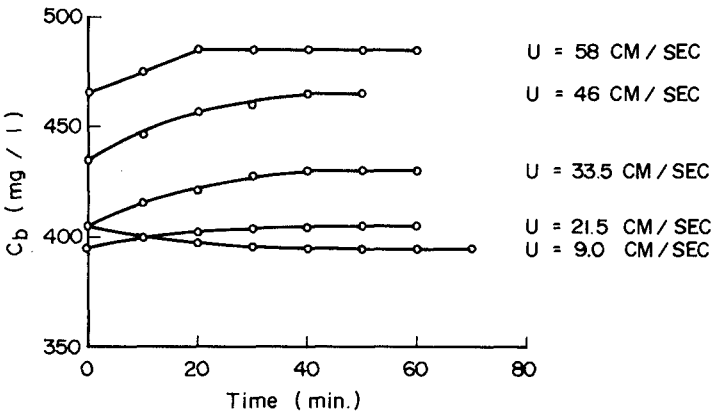


Fig. 3 Bottom Concentration in a Steady Flow.

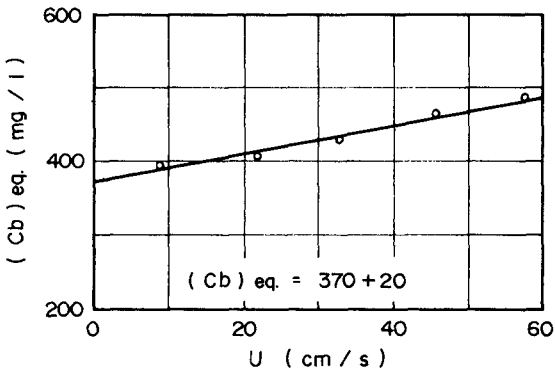


Fig. 4 Equilibrium Concentration in a Steady Flow.

- A linear relationship between the bottom concentration at equilibrium condition and the flow velocity exists as, (Fig. 4):

$$(C_b)_{eq} = 370 + 2u \text{ (mg/liter) (u:cm/sec)} \quad (19)$$

The bias value of 370 mg/liter can be considered as the base concentration corresponding to very fine particles of almost zero fall velocity; and

- The time variations of the bottom concentration in a transient period before the equilibrium is plotted as shown in Fig. 5. It shows a good agreement with Eq. (11). The value of γ obtained from this plot is 0.06 min^{-1} or 0.001 sec^{-1} .
- 2) Periodic Flow: The results obtained from tests with periodic flow conditions are:-
 - The velocity profiles illustrate similar logarithmic profile and that the sinusoidal velocity curve is obtained as $u(t) = |u_{\max} \sin \frac{2\pi t}{T}|$, (Fig. 6);
 - Change of the concentration is relatively small for a short period of a cycle when compared to a larger change found in a longer time period, Fig. 7. This is because the effect of time response in the transport process which is represented by the coefficient γ in Eq. (8);
 - Time lag between the maximum concentration and the maximum velocity is larger in a short period flow than that in a long period flow, Fig. 8. Again this phenomenon is demonstrated by the time response factor γ ;
 - Vertical distribution of the concentration is almost uniform except near the bed and it shows that the difference between the concentrations for different phase angles increases as the period, T , increases. The parameter $\beta = C/C_b$ is about 0.95 for all conditions, Fig. 9; and
 - By means of plotting the time variation of the bottom concentration, for comparison between the flow having 2 hour, 6 hour and 12 hour periods, taking the phase angle equal to zero at zero velocity and 90° at maximum velocity, Fig. 10, it is shown that the larger relative concentration variation is found in the 12 hour period compared to those of the 6 hour and 2 hour periods. On the other hand the time lag is larger in the 2 hour periods than those found for the 6 hour and 12 hour periods.

MODEL ASSESSMENT

In order to determine the validity of the model, an exercise is carried out to find the concentration variation in two ways; namely the solution of the integrated diffusion equation, Eq (8), which gives the time variation of the bottom concentration, $C_b(t)$, and the solution of the original diffusion equation by means of the finite element method, Eq.(16), which determines the depth-time dependent concentration variation, $C(y,t)$. The two consecutive solutions are as follows:

1) Time Variation of Bottom Concentration: From the experimental data, the values of the necessary parameters, namely β and γ are first obtained as

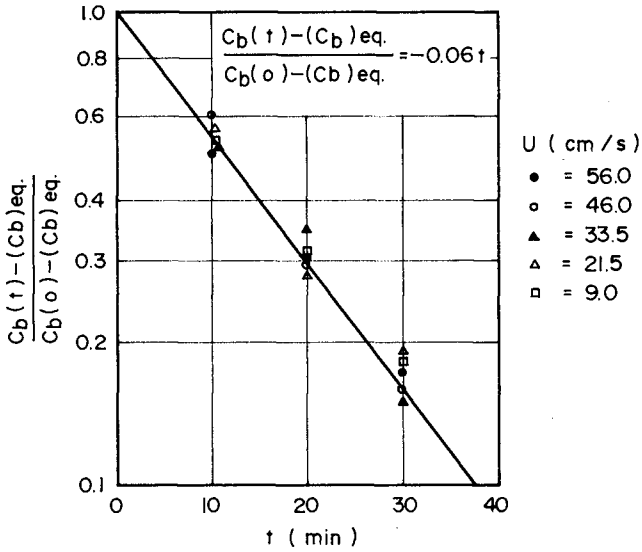


Fig. 5 Concentration Variation in a Transient Period in Steady Flow.

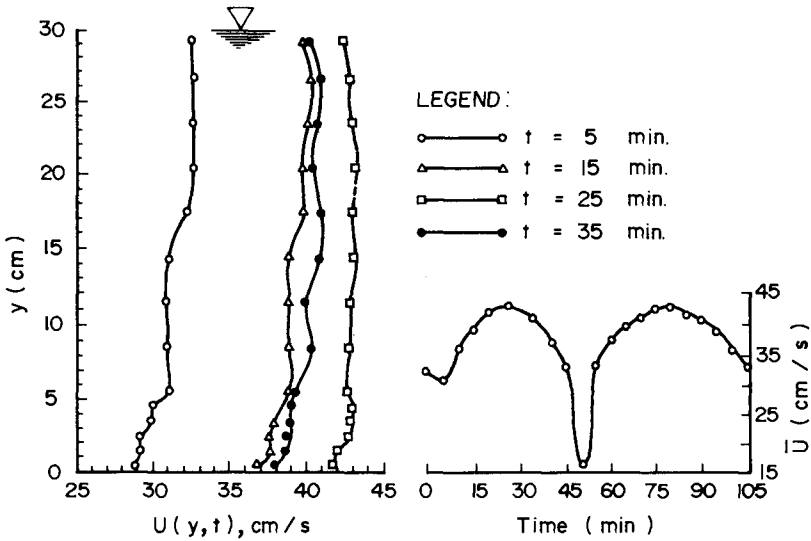


Fig. 6 Velocity Profiles and the Sine-Velocity Variation

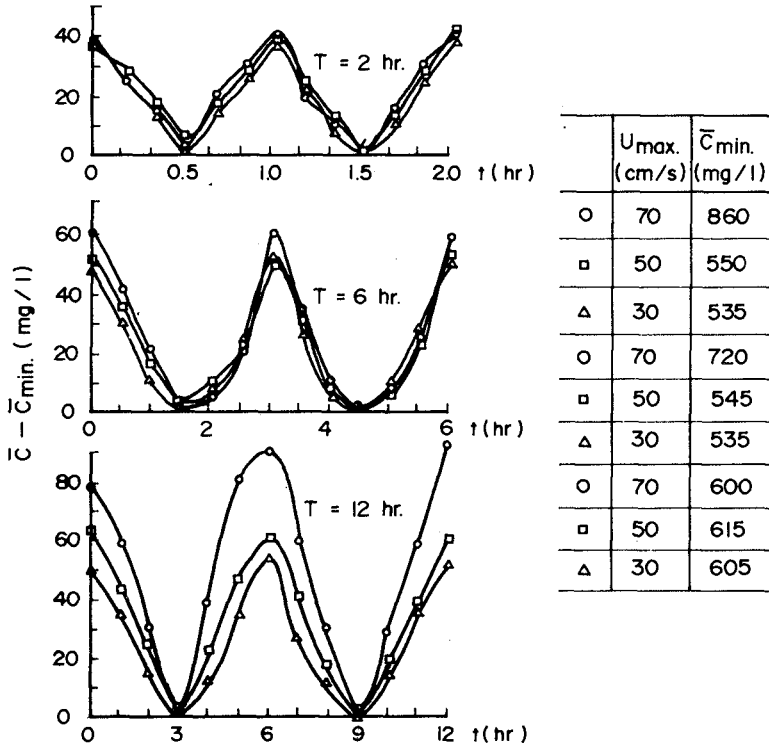


Fig. 7 Concentration Variation at Different Periods.

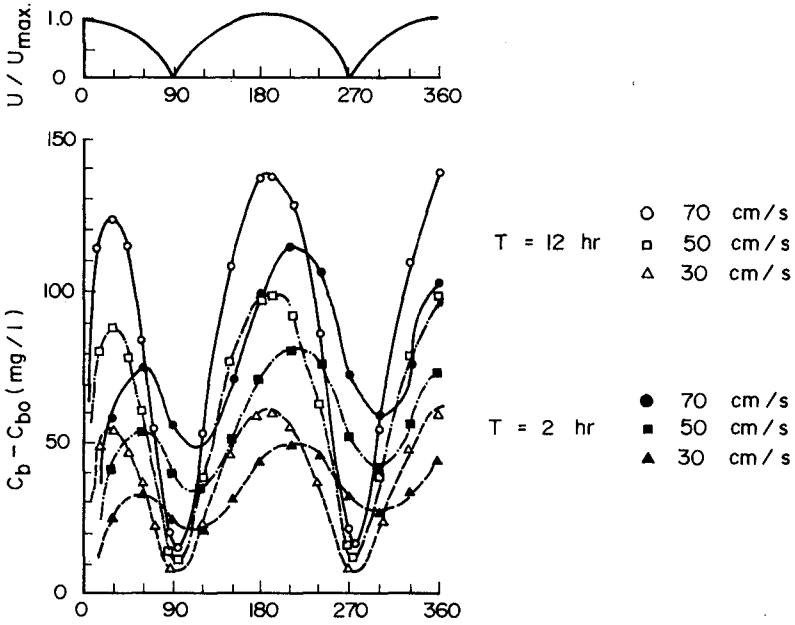


Fig. 8 Effect of Time Period on Lag Time of Peak Values.

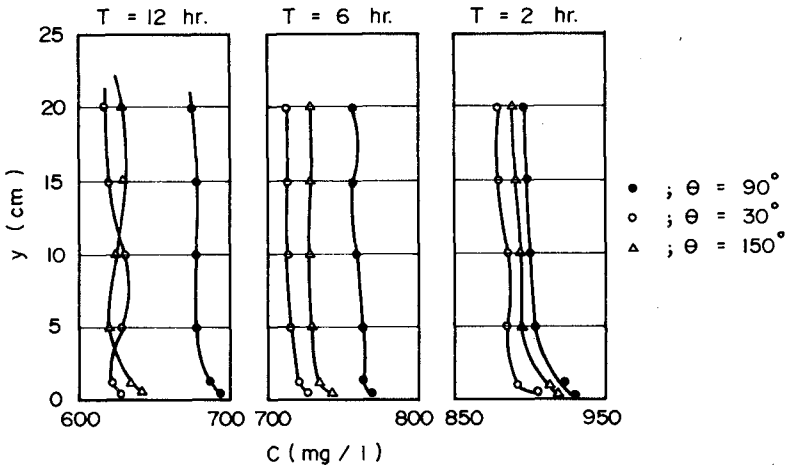


Fig. 9 Vertical Distributions of Concentration for Periodic Currents.

mentioned in the former section. In addition the fall velocity, w_o , is obtained from Eq. (9), which is about 0.024 cm/s. Introducing the empirical formula which shows the relationship between the velocity, u , and the equilibrium concentration, $(C_b)_{eq}$, as shown in Eq. (19) and with the sinusoidal velocity variation, the final form of Eq. (8) becomes:

$$\beta(h - y_o) \frac{dC_b}{dt} = A + \alpha |u_{\max} \sin \sigma t| - w_o C_b \quad (20)$$

where A and α are the constants relating to the linear relation between the entrainment rate, q , and velocity, u , as:

$$q = A + \alpha u \quad (21)$$

Although the solution of this equation is an initial value problem, the effect of the initial concentration disappears rather rapidly so that any arbitrary initial value can be chosen. Solution to Eq. (20) for 2 hour, 6 hour and 12 hour tidal periods with assumed initial concentration is shown in Fig. 11. The plotted results show similar tendencies in both magnitude and phase lag as those obtained from the experiment (Fig. 10).

2) Solution of the Original Diffusion Equation: The final form of the diffusion equation, Eq. (16) is solved for $C(y,t)$. The value of the base concentration is taken as zero for the simplicity in this model. Two solutions are shown in Fig. 12 for the near bed ($y = 0.5$ cm) and mid-depth ($y = 10$ cm) concentrations for the case of 2 hour, 6 hour and 12 hour tidal periods. Again similar tendencies of both magnitude and time variation are observed with the experimental results. In addition the concentration profiles given in Fig. 13 show a slight difference from the experimentally obtained profiles, particularly the concentration gradient near the bed. However, the trend of the calculated profiles is similar to the experimental ones.

CONCLUSIONS

The one-dimensional diffusion model, or its integrated form, proposed in this paper was found to give reasonable estimation of the concentration variation of suspended clay particles in a periodic flow, which is needed for estimating the sediment transport in tidal estuaries. The parameter, γ , the ratio of the fall velocity to the water depth plays a significant role as the time response factor in the transportation process of clay together with the rate of entrainment from the bed. Further investigation is necessary in particular, to establish the universal relationship between the entrainment rate, sediment properties and flow conditions, and to evaluate the diffusion coefficient properly.

REFERENCES

1. Postma, H., "Sediment Transport and Sedimentation in the Estuarine Environment", in Estuaries, Pub. No. 83, ASAS, Washington D.C., 1967.
2. Krone, R.B., "Flume Studies of the Transport of Sediment in Estuarial Shoaling Processes", Final Report, Hydro. Engr. Lab and San. Engr. Res. Lab., University of California, pub. year 1963.

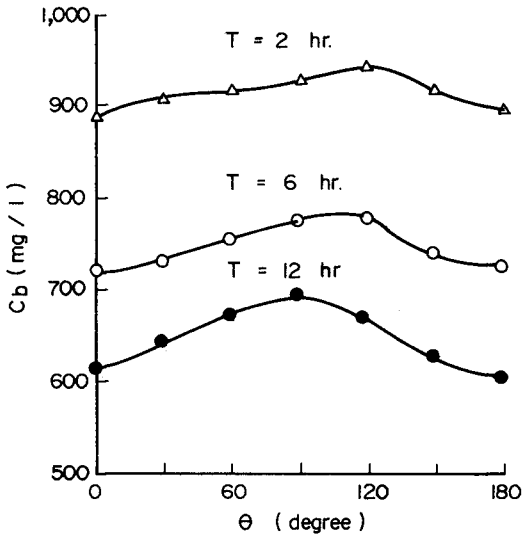


Fig. 10 Concentration Variation in Periodic Currents (Measured data)

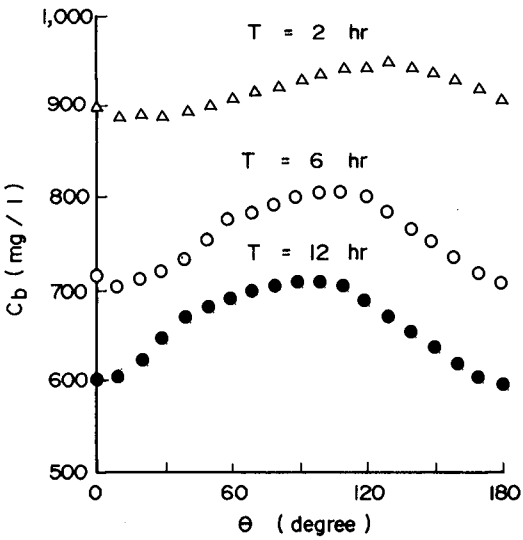


Fig. 11 Concentration Variation in Periodic Currents (Computed values)

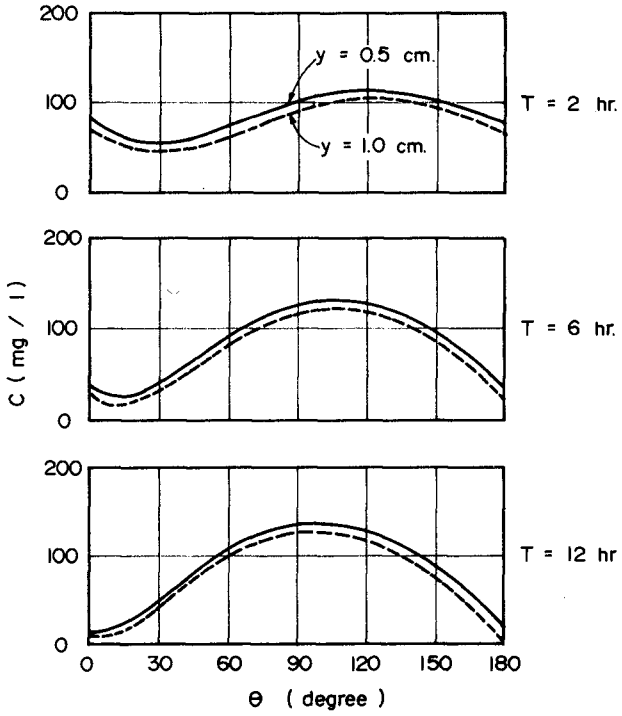


Fig. 12 Solution of the Depth-Time Dependent Concentration.

3. Metha, A.D. and Partheniades, E., "Effect of Physico-Chemical Properties of Fine Suspended Sediment on the Degree of Deposition", Proc. IAHR, January 1974, Thailand.
4. Thimakorn, P. and Gupta, A.D. "Concentration of Suspended Clay in Tidal Estuary", Proc. Int. Conf. Water Resources Eng., IAHR, January 1978, Thailand.

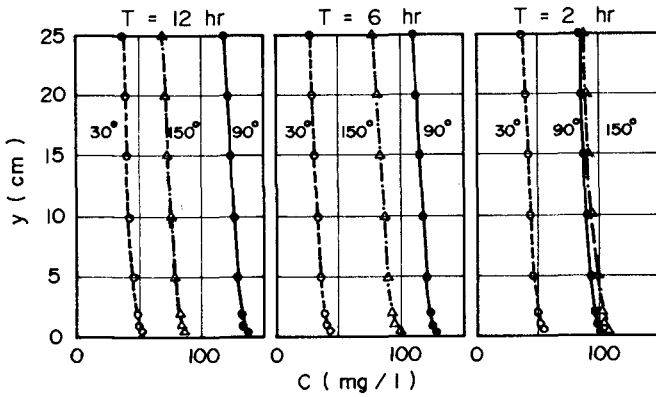


Fig. 13 Estimated Concentration Profiles.

CHAPTER 117

SUSPENSION AND TRANSPORTATION OF FLUID MUD

BY SOLITARY-LIKE WAVES

John T. Wells, James M. Coleman, and Wm. J. Wiseman, Jr.

Coastal Studies Institute, Louisiana State University

Baton Rouge, Louisiana 70803

ABSTRACT

The suspension and transportation of fluid muds in the near-shore zone by shallow-water, solitary-like waves has been investigated along the coast of Surinam, South America. Accumulations of fluid mud which front the coast at a spacing of 30-60 km affect incoming swell by changing the wave profile from sinusoidal to solitary-like and by preventing wave breaking except for occasional spilling. Simultaneous time-series measurements of wave height and period, fluid-mud density, and tide elevation, along with results of suspended-sediment measurements, indicate that in cases when the bulk density is less than 1.20 g/cm^3 and where water depths are less than 5 m fluid mud is suspended from the bottom in two frequency modes: wave-by-wave suspension (~10 sec) and tide-related suspension (~12.4 hr). Surface-water suspensate concentrations exceed $3.4 \times 10^3 \text{ mg/l}$ as up to 0.5 m of fluid mud is periodically removed from the bottom.

High concentrations of suspended fluid mud, together with solitary-like waves from the northeast throughout the year, can lead to extraordinarily high sediment transport volumes. Calculations based on solitary wave theory and on data obtained from this study indicate that $15\text{-}65 \times 10^6 \text{ m}^3$ of mud can move along shore each year without involving breaking waves, the concept of radiation stress and a nearshore circulation cell, or bed-load transport. These values are 10 to 100 times greater than typical transport rates along sandy coasts.

INTRODUCTION

As a generalization, research on fluid muds prior to the 1970s was restricted almost entirely to the laboratory, and even today field data are scarce. In this study we report results of field measurements conducted along the open, unprotected coast of northeastern South America, where incoming waves are affected by mud shoals composed partly of thixotropic, gel-like fluid muds. Our primary objectives were to examine the interaction between incoming waves and fluid mud and to assess the role of waves in the suspension and transportation of fluid mud.

The lack of field data can be explained partly by the difficulties encountered in obtaining direct measurements of near-bottom processes such as suspension and deposition. Several innovative techniques for studying fine-grained sediment dynamics, including acoustic systems (Kirby and Parker, 1974; Orr and Hess, 1978), a sea-floor flume (Young and Southard, 1978), and nuclear densimeters (Parker et al., 1975), have been utilized in recent years with varying degrees of success. As part of the present study an instrument was developed that could be used as a combination wave gage and sediment-density sensing device. By assuming that variations in mud density must be related to suspension, deposition, and near-bottom transport processes, we have been able to examine the details of fluid-mud dynamics in both intertidal and subaqueous hydrologic settings. Based on actual field measurements and reasonable assumptions, an explanation for transport by waves of suspended fluid mud is presented.

FIELD AREA AND METHODS

During field seasons in 1975 and 1977 data were collected at ten sites off the coast of Surinam, South America, on a section located midway along the 1,600 km of muddy coast that extends from the Amazon River in Brazil to the Orinoco River in Venezuela (Fig. 1). Climatic conditions and coastal processes in the study section are generally representative of those in northeastern South America. The warm tropical climate is controlled by the northeast trade wind system and periods of high and low wind speeds, each several months in duration, alternate throughout the year. During the months of data acquisition, August through October, conditions are typically dry and winds are low to moderate (~10-15 km/hr).

Formed during the Holocene by Amazon-derived muds, the coastline of the Guianas is both interesting and somewhat unique. Linear mud shoals, tens of kilometers long, front the coast at a 30-60-km interval and form a buffer to wave attack, thus controlling the distribution of nearshore wave energy. A spectacular alongshore cycle of erosion and accretion results; in interbank areas, plunging breakers may impinge directly upon stands of mangroves at high tide, whereas in shoal, fluid-mud regions waves are virtually absent at the shoreline and coastal progradation proceeds rapidly. As a result of alongshore mudbank migration, this erosion/accretion system moves to the northwest at an average rate of 1.5 km/yr, suggesting that any given segment of coast has undergone many cycles of erosion and accretion during the last 5,000 yr (Augustinus, 1978).

Simultaneous measurements of wave height and period, fluid mud density variations, suspended-sediment concentration, and tide

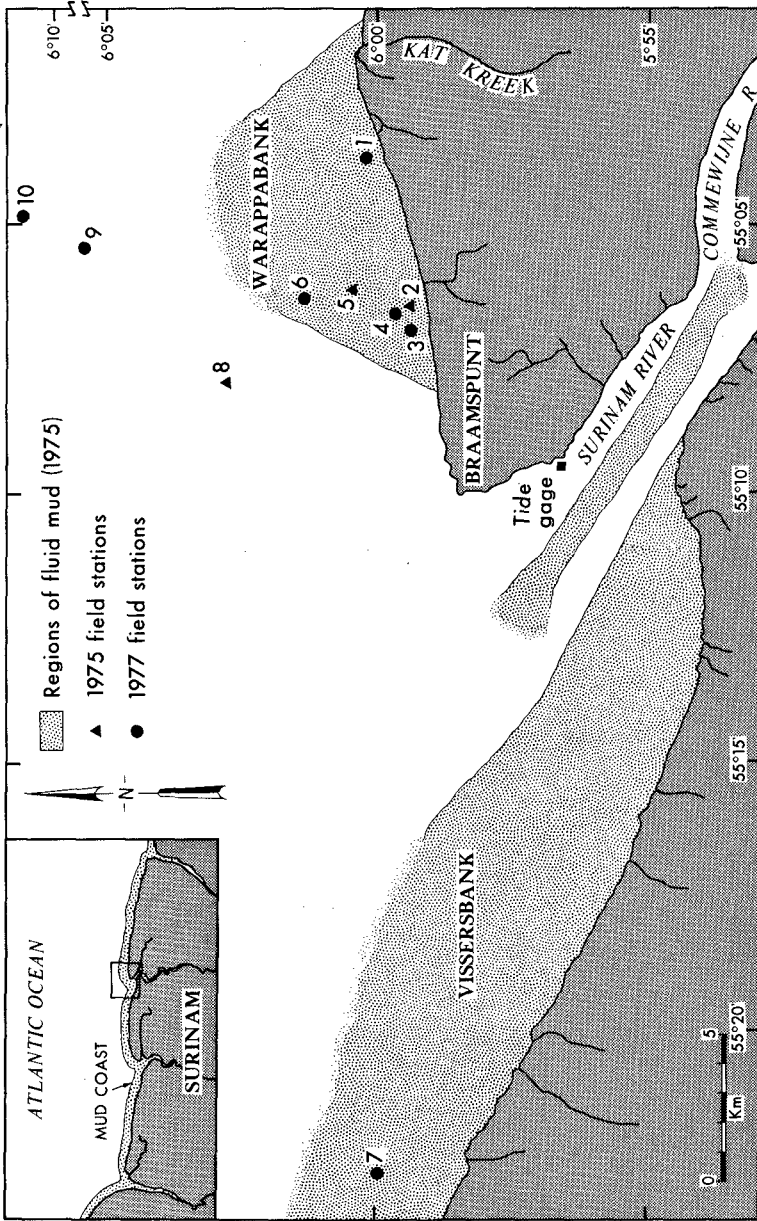


Figure 1. Index map of station locations.

elevation were made at field sites located over Warappabank and Vissersbank, regions where fluid mud up to 1.5 m thick blankets the bottom (stations 1-7, Fig. 1). Wave data were also taken farther offshore where substantial quantities (<0.1 m) of fluid mud are lacking (stations 8-10, Fig. 1). A moderate tide range (~3.2 m at spring tide), combined with a gentle offshore slope, leads to the exposure of a wide expanse of fluid mud at low tide (Fig. 2). Several of our field sites were located in these intertidal regions where water depths never exceeded 2 m (stations 1-3, Fig. 1). At other field sites water depths ranged from 1 to 10 m depending on the location and the stage of the tide.

Fluid mud is defined as a fine-grained sediment-water mixture in which the sediment concentration is greater than 1.0×10^4 mg/l (Krone, 1962). Where fluid mud is present the bottom is taken to be the upper surface of the fluid-mud layer, even though survey instruments may penetrate through this layer to more consolidated sediments (Odd and Owen, 1972). Properties of coastal fluid muds in the study area are given in Table 1.

Two Statham Model PA-506 Amplibrigde pressure transducers, fastened securely to an adjustable sleeve on pipe that was driven into the bottom, formed the sensing unit of the wave/fluid mud pressure (density) sensing device (Fig. 3). Pressure under a wave, less atmospheric pressure, is given by

$$P = \rho g (\eta K_z - z) \quad (1)$$



Figure 2. Prograding mudflat photographed at low tide, eastern Surinam coast.

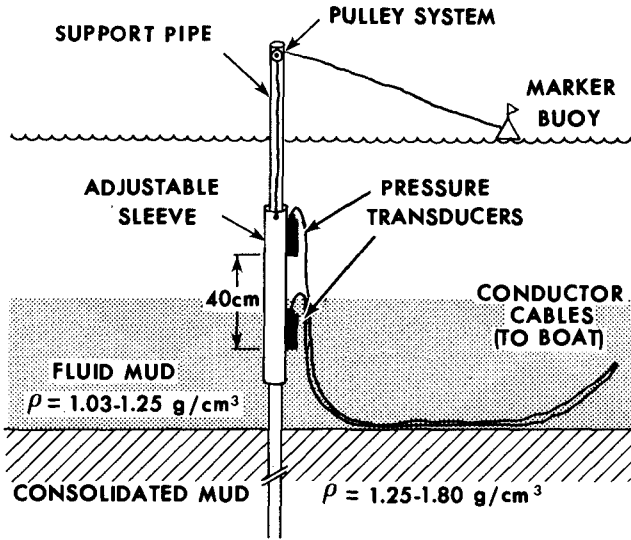


Figure 3. Schematic of field setup for wave/fluid mud pressure-sensing device, showing typical arrangement of pressure transducers relative to fluid-mud layer.

where, in the linearized case,

$$\eta = \frac{H}{2} \cos\left(\frac{2\pi x}{L} - \frac{2\pi t}{T}\right) \quad (2)$$

and the pressure response factor, K_z , is given by

$$K_z = \left(\frac{\cosh [2\pi(z+h)/L]}{\cosh (2\pi h/L)}\right). \quad (3)$$

In equations (1) - (3), ρ = density of seawater, g = acceleration resulting from gravity, z = distance below still-water level, h = water depth, L = wave length, H = wave height, t = time, T = wave period, and x = horizontal distance. For shallow-water waves such as the tide, $h/L \ll 0.05$, $K_z \rightarrow 1$, and equation (1) reduces to

$$P = \rho g(\eta - z) = \rho g z' \quad (4)$$

where z' can be considered a depth below the time-varying surface. If pressure is measured simultaneously at two depths below the surface, z_A' and z_B' , then

$$P_B - P_A = \rho g (z_B' - z_A') \quad (5)$$

Table 1
Properties of Coastal Fluid Muds, Surinam, South America

Bulk density	1.03-1.25 g/cm ³ (1030-1250 kg/m ³)
Water content	64-96%
Voids ratio	4-62
Median particle size	0.5-1.0 micron (disaggregated)
Viscosity	0.02-210 poises

and, provided that $z_B' - z_A'$ is constant with time, any variation in $P_B - P_A$ is directly proportional to a density variation.

For higher frequency gravity waves, say $T = 1-15$ sec, K_z becomes significant and density can be obtained from equation (5) only if K_z is known at depths z_A' and z_B' . From linear theory, K_z between pressure sensors ranges from 0.01 to 0.07 for wave frequencies encountered in this study. However, observational data indicate that values of K_z are not in perfect agreement with linear theory (Hom-ma et al., 1967; Tubman and Suhayda, 1977), and a correction factor m is usually applied to equation (1). In this study m ranges from 1.0 to 1.05. The determination of density variation from pressure variation is further complicated by the fact that attenuation rate is altered when one transducer is placed in a denser medium than the other, as depicted in Figure 3. Although these problems have been largely overcome by running field tests to determine differential attenuation in clear water and in fluid muds over a range of frequencies, an empirically determined differential density scale has been assigned in cases where $K_z < 1$.

Applying the above concepts in the field, $P_B - P_A$ is nulled out of each transducer electronically by a potentiometer located on the instrument panel (Fig. 4). Once this step is completed, any deviation from the zero null position is directly proportional to a density change. By using 10 or 20 sec time constant filters, high frequency noise is removed from the signal and, if desired, resolution of the signal can be increased up to 0.004 g/cm³.

In order to obtain useful time-series data, waves were recorded in real time from transducer A simultaneously with the filtered pressure differential between transducers A and B. All data were recorded as analog signals on strip chart recorder. The final step, conversion of differential pressure into absolute density units, required that sediment samples be taken between instrument sensors for initial calibration.

SHALLOW-WATER WAVES

Examination of approximately one hundred and fifty 20-min wave records, taken over all stages of the tide, indicates that waves undergo a severe shoaling transformation when propagating over a fluid-mud bottom. In addition to the rapid height attenua-



Figure 4. Wave/fluid mud pressure-sensing device (recorder not shown).

tion, described qualitatively in previous reports as a major factor in natural sea defenses (Delft Hydraulics Laboratory, 1962; NEDECO, 1968; Augustinus, 1978), waves are deformed from sinusoidal into solitary-like profiles, similar to that which can be observed in gentle swell just prior to breaking. Long, flat troughs separate sharp, isolated crests and, on days when local winds and associated sea chop are low, waves with periods of 15 sec can be recorded.

Information obtained from spectral analysis shows spectral peaks in the frequency range 0.07-0.25 Hz ($T = 15 - 4$ sec) and H_{rms} of 0.2-1.2 m for waves in water 1-5 m deep. Typical analog wave records and pressure spectra are given in Figure 5 for the consolidated interbank area (station 8), the soft mudbank area (station 5), and for solitary waves given by theory. Note the similarity in profile for waves recorded over a fluid-mud bottom and waves given by solitary wave theory. Wave spectra for solitary-like waves show a wide distribution of variance density with peaks often occurring at harmonic frequencies. Multiple peaks for true solitary waves occur exactly at harmonic frequencies. In interbank areas or farther offshore the spectra display a single well-defined peak in variance density.

In general the boundaries of a mudbank can be delineated simply by the appearance of surface waves (Moni, 1971; Nair, 1976). Height attenuation in the areas between mudbanks is substantially

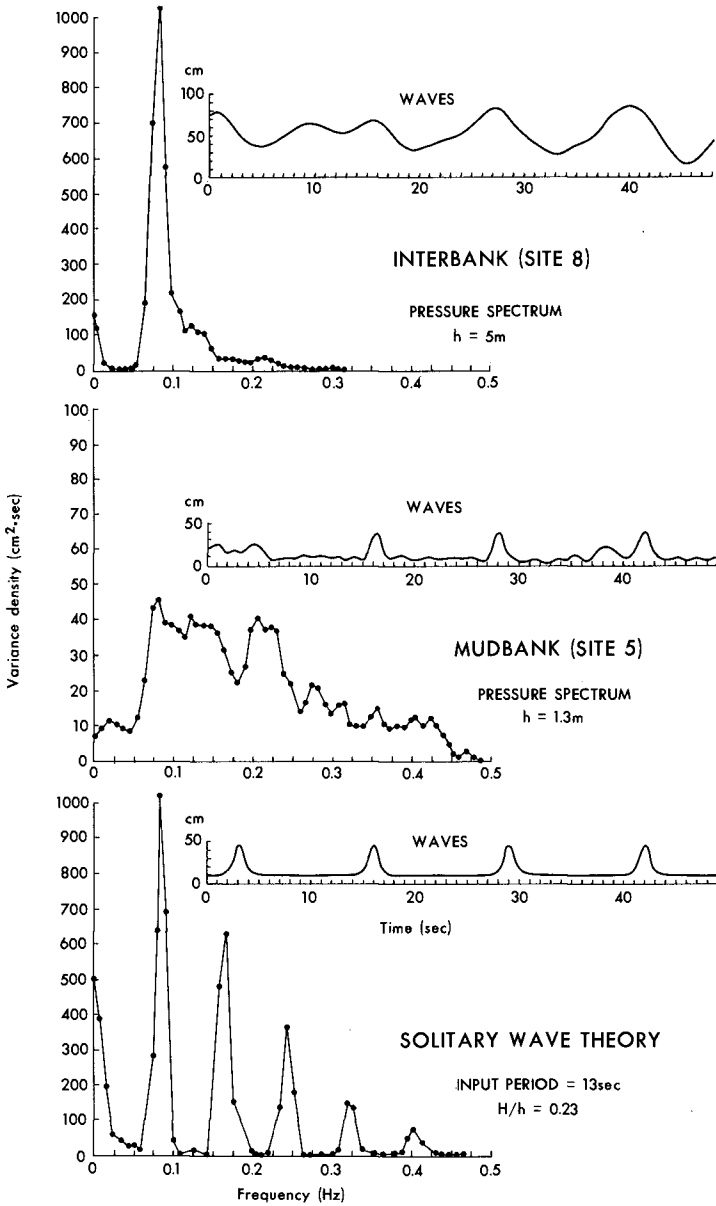


Figure 5. Typical wave records and pressure spectra from inter-bank area (consolidated bottom, site 8), mudbank area (fluid mud, site 5), and from solitary wave theory.

less and, for a given water depth, wave height may vary by as much as 100% from mudbank to interbank areas. The above generalizations become more complicated in the direction of propagation as waves encounter variations in thickness and density of fluid mud. Analysis currently underway suggests that wave height, period, and form are extremely sensitive to spatial and temporal variations in bottom consistency.

Three features of the solitary-like waves are important with respect to sediment transport. First, they maintain a nearly constant wave height to water depth ratio, $H_{rms}/h = 0.23$, a value that is considerably less than the 0.78 given as the limit of solitary wave theory. In a true solitary wave the volume of water transported is a function of H/h and higher ratios lead to greater transport rates. Second, although spilling breakers have been noted near the shoreline, solitary-like waves over a fluid mud bottom seldom break; rather, they decrease in height until they disappear at the shoreline, indicating that breaking waves and the conventional momentum flux approach to sediment transport problems may not be applicable. Third, waves become noticeably more like true solitary waves in appearance as sediment concentration in water increases. The most solitary-like waves have been observed from mid-tide to mid-tide during the lower half of the tidal cycle.

SEDIMENT SUSPENSION

In the broadest sense, shallow-water waves propagating over a soft muddy bottom maintain a large volume of sediment in suspension. Wells and Coleman (1977) have shown that suspensate concentrations in regions of fluid-mud bottom are orders of magnitude higher than in interbank areas and may attain surface-water values of several thousand milligrams per liter. Some spatial (depth) and temporal (stage of tide) variability also has been observed. Data from that study, combined with data obtained since publication of those results, are given in Table 2. Generally, inshore waters are more turbid than offshore and near-bottom are more turbid than surface waters.

Much of our information concerning suspension processes has been obtained by monitoring density variations in the upper 0.5 m of fluid mud. In general, variations in mud density can result from suspension or deposition, gain or loss of pore waters, and from advection of sediment past instrument sensors. By obtaining measurements over a range of fluid-mud densities (1.03 - 1.24 g/cm³) with sensors at several depths relative to the surface of the fluid-mud layer, we have been able to examine details of near-bottom processes in a variety of situations, from which generalizations have been made concerning sediment suspension.

Suspension of sediment by solitary-like waves takes place in two predominant frequency modes: tide-related suspension (~12.4 hr) and wave-by-wave suspension (~10 sec). In mud with a bulk density less than 1.20 g/cm³ and with water depths less than 5 m, an exchange process between the fluid mud and overlying water operates at the tidal frequency. Data from several field sites (stations 2, 3, and 5) indicate that on a falling tide, near mid-tide level, 10-50 cm of fluid mud is dispersed into water. This

Table 2
Maximum and Minimum Surface Suspended-sediment Concentration,
Coast of Surinam

Field Site	Range in Water Depth (m)	Concentration (10^2 mg/l)	
		Maximum	Minimum
1	0.0- 2.0	3.33	0.21
2	0.0- 2.0	2222.85*	26.57
3	0.0- 2.0	52.34	1.09
4	0.5- 2.5	17.75	0.67
5	1.0- 3.0	37.49	0.34
6	1.5- 4.0	11.19	0.82
7	0.5- 2.5	24.51	2.75
8	4.0- 7.0	0.81	0.16
9	4.5- 8.0	0.34	0.14
10	9.0-11.5	No	data taken

*Sampled from surface of fluid mud exposed at low tide.

NOTE: A total of 183 samples was collected. A least squares best fit to all data indicates that concentration varies with height (m) above the bottom, y , as $c = 5.31 e^{-1.80 y}$, where c is in milligrams per cubic meter. Coefficient of determination, r^2 , is 0.38 ($P < 0.001$).

dispersion is concurrent with the time that waves initially change to the pronounced solitary-like wave profile. Suspended-sediment concentrations increase rapidly and coastal waters become noticeably more turbid. Maximum concentrations of suspended sediment occur at or near low water. On a rising tide concentrations decrease and fluid mud is, presumably, redeposited during the period between mid-tide and high water.

In muds where bulk density exceeds 1.20 g/cm^3 , such as inter-bank areas or the more consolidated eastern edges of mudbanks, less than 1 cm of the bottom is suspended by incoming waves (this value assumes that mass of sediment dispersed into the water reflects the volume of known density removed from the bottom).

Figure 6 shows results of a 3-hr experiment beginning at low tide on an intertidal flat composed of fluid mud with initial density of 1.16 g/cm^3 . Five time-series sections, each approximately 20 min, show that bulk density decreased from approximately 1.16 to 1.05 g/cm^3 as water level rose and incoming waves suspended the fluid mud. Figure 7 shows diagrammatically the suspension process. At the termination of this experiment nearly 50 cm of fluid mud had been suspended. The considerable variation in bulk density of fluid mud prior to the first impingement of waves (Fig. 6, sections A and B) was the result of interstitial pressure waves from offshore which, in low density muds, generally precede

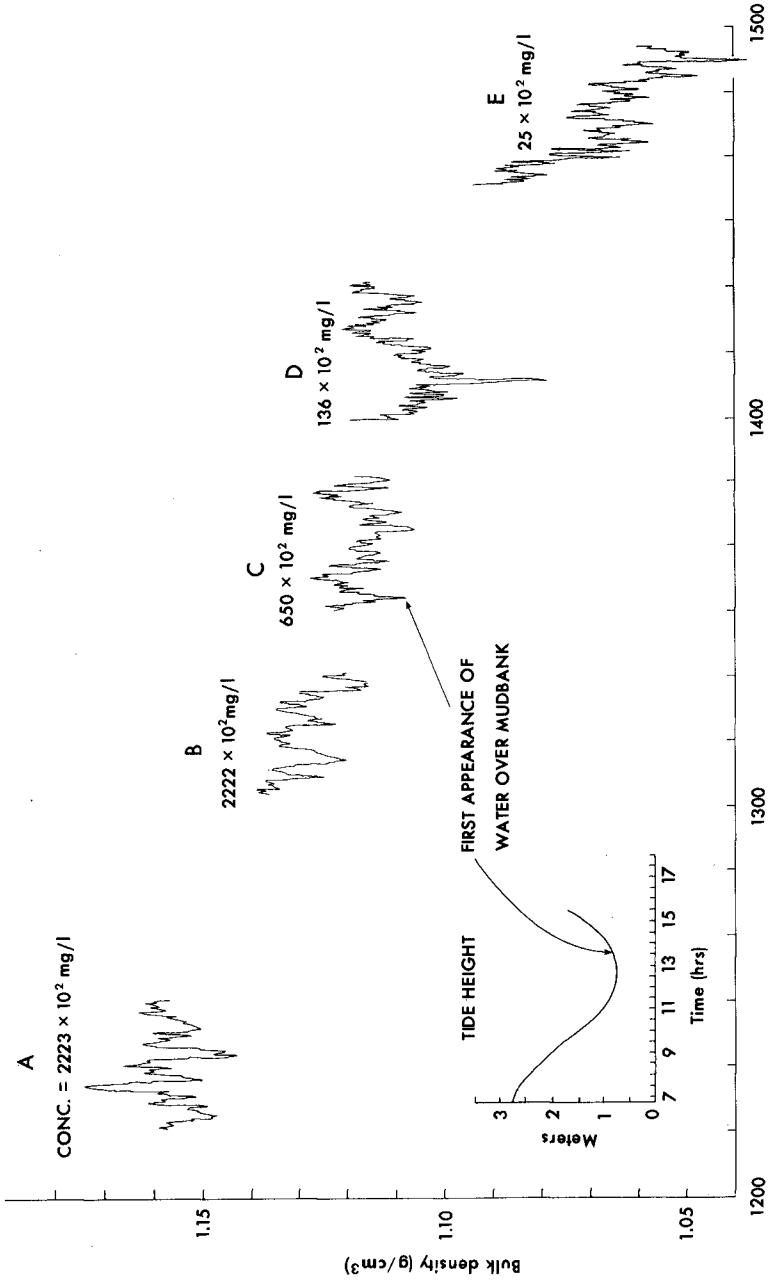


Figure 6. Time series of bulk density variations in upper 0.5 m of fluid mud, beginning at low tide, 8 October 1975. Numbers above each time-series section are surface suspended-sediment concentrations.

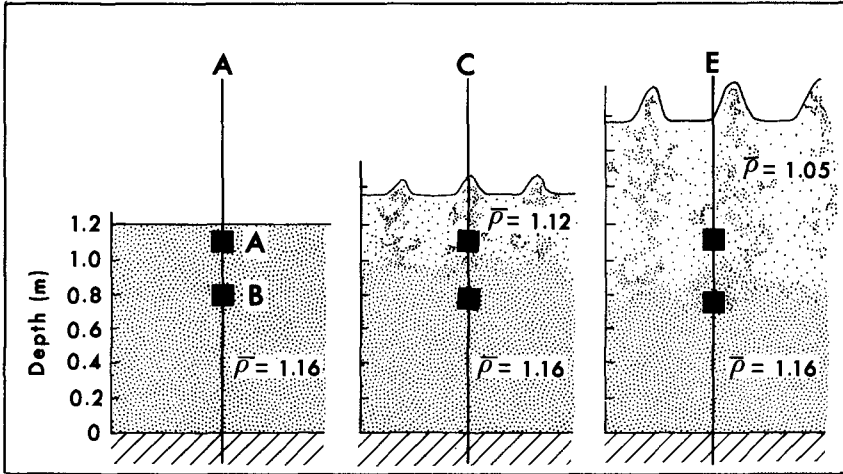


Figure 7. Suspension of Fluid mud by solitary-like waves.

the arrival of surface waves.

The relatively stable wave height to water depth ratio, $H_{rms}/h = 0.23$, may be partly a result of adjustment of the bottom to the amplitude of incoming waves. On days when stronger winds from the northeast produced local waves that were larger than the solitary-like swell waves, suspended-sediment concentrations increased rapidly. Thus, at a given stage of the tide, higher waves suspended more sediment. An example of this process is given in Figure 8. Following a wind shift from southeast to northeast (1200 hr), waves increased in height rapidly and suspended sediment concentration increased by an order of magnitude as fluid mud was suspended at field site #6. The suspension of mud from the bottom was manifested as an overall decrease in bulk density between 1200 and 1400 hr. Field site #9, farther offshore over a relatively consolidated bottom, was unaffected.

Wave-by-wave suspension, often superimposed on the longer term processes described above, is shown in four sections of time series data in Figure 9. As each wave crest passed instrument sensors differential density rose rapidly, then fell gradually; the process repeated when the following wave arrived. The initial explanation of these density variations (Wells, 1977) hypothesized that a cloud of sediment was instantly suspended, followed by rapid settling of this densely flocculated sediment. Based on previous laboratory and field results (Partheniades, 1971; Krone, 1972), it is difficult to explain such rapid settling, which in this case would require that the center of mass settle at 10 cm/sec. In light of the apparent nonlinear properties of waves, a more plausible explanation may be the advection of this sediment cloud past the sensors. Theoretical bottom particle velocities under solitary waves exceed 100 cm/sec for the range of wave heights observed in this study. The persistence of high-frequency

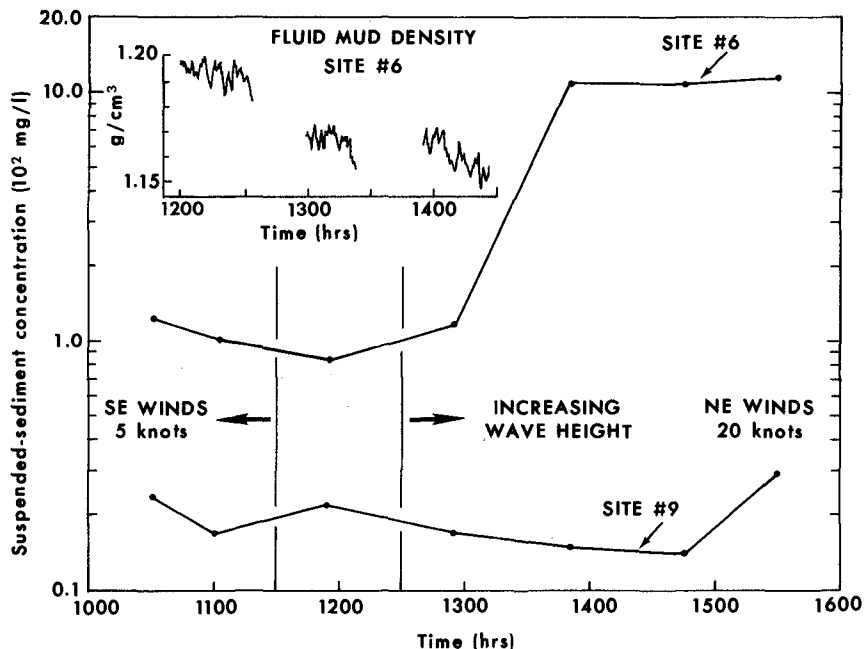


Figure 8. Surface suspended-sediment concentration and fluid-mud density variations, 20 August 1977.

suspension and transport by waves results in temporary or even permanent removal of fluid mud from the bottom. During 3.5 hr of observation (Fig. 9) average density in the upper 0.25 m of fluid mud decreased by 0.04 g/cm^3 , an amount that could be achieved only by the removal of 10 cm of fluid mud from the bottom. The possible fate of this suspended fluid mud will be discussed in the next section.

MUD TRANSPORT

Recent estimates of sediment transport along the mud coast of northeastern South America indicate that approximately 20-40% of the total sediment load from the Amazon River makes its way northward along the coastlines of French Guiana, Surinam, and Guyana (Eisma and van der Marcel, 1971), resulting in one of the highest littoral transport rates in the world. Approximately $150 \times 10^6 \text{ m}^3/\text{yr}$ of "through transport" takes place in the form of suspended sediment, and another $100 \times 10^6 \text{ m}^3/\text{yr}$ moves as a result of the propagation of coastal mudbanks to the northwest (summarized from Delft Hydraulics Laboratory, 1962; Gibbs, 1967; Allersma, 1968; NEDECO, 1968; and Eisma and van der Marcel, 1971). Previous investigators have generally attributed these exceedingly high longshore transport rates to suspension of mud by wave orbital

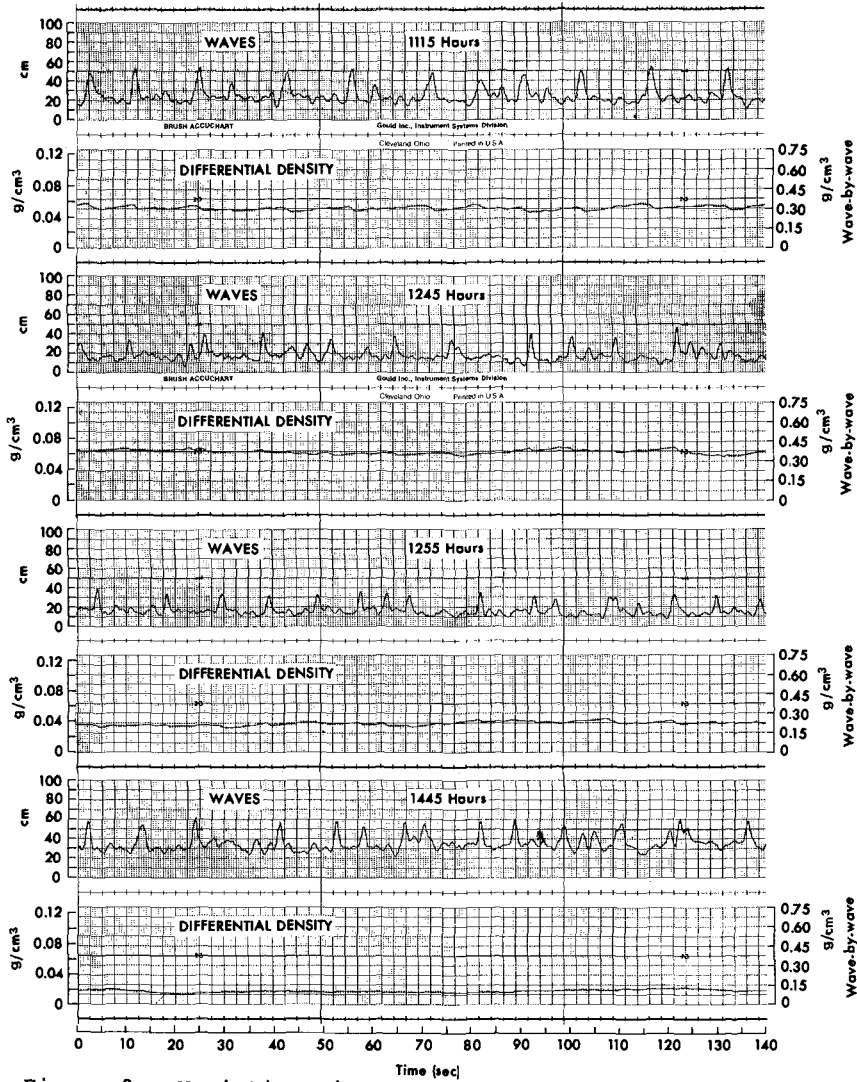


Figure 9. Variations in near-bottom fluid-mud density. Recorded during the passage of waves from HW + 4.5 hr to LW + 2 hr, 26 September 1975. The attenuation of high-frequency signals (less than 100 sec) resulting from a 20-sec time-constant filter requires that a separate scale be used for wave-by-wave variations.

scour, followed by transport to the northwest by the Guiana Current.

The finding in this study that suspensate concentrations are highest in fluid-mud regions where solitary-like waves occur, combined with the fact that 93% of sea and swell arrive at the coastline between N30°E and east (NEDECO, 1968), suggests that a tremendous potential exists for sediment transport by waves acting alone. In theory a solitary wave is a wave of translation whereby water particles move only in the direction of wave travel. Laboratory studies on solitary waves have shown that if wave profile is similar to that given by theory, then particle trajectories are unidirectional and each wave clearly produces a mass transport (Daily and Stephen, 1953). Numerous observations in this and other field studies (for instance, Inman et al., 1963) have provided qualitative verification that particle velocity is greater in the onshore than in the offshore direction for solitary-like waves. In the following paragraphs a simple model for explaining sediment transport, based on results of this study and above-mentioned rationale, is examined.

Consider mass transport of suspended sediment, as applied to surf zone problems, to be given by

$$T_M = \iint_A c V \sin \alpha \, dA \quad (6)$$

where $dA = dx dy$, c = suspended-sediment concentration, V = current velocity, and α = angle of wave approach.

Cross-sectional area through which transport takes place (Fig. 10a, b) varies with water elevation, h , and is given by

$$A_i = \int_0^{x_i} h \, dx \quad (7)$$

where horizontal distance, x_i , is determined by h and offshore slope is given by β . As a simplification, regional variations in water depth that result from fluid-mud suspension and deposition processes (as discussed in the last section) are ignored.

The most justifiable estimate for suspended-sediment concentration is given by the least squares best fit to all suspended-sediment data

$$c = 5.31 e^{-1.80 y} \quad (8)$$

where c is concentration in kilograms per cubic meter and applies to any location offshore, y is height above the bottom in meters, and $0 \leq y \leq h = 5$ m.

Assuming pure solitary waves, total volume of a wave per unit crest length above still water level can be obtained as

$$Q = 2 \int_0^{\infty} \eta \, dx \quad (9)$$

where

$$\eta = H \operatorname{sech}^2 \left[\sqrt{\frac{3}{4}} \frac{H}{h^3} (x - Ct) \right] \quad (10)$$

and H = wave height, C = wave speed, and t = time. Substituting equation (10) into equation (9) and integrating, Munk (1949) gives

$$Q = 4h^2 \sqrt{\frac{1}{3}} \frac{H}{h} \quad (11)$$

which, averaged over one wave period from the surface to the bottom, gives

$$\bar{v} = \frac{Q}{hT} = \frac{4h(1/3 H/h)^{1/2}}{T} \quad (12)$$

as volume transport rate. Investigation of analytical solutions indicates that there is little velocity shear in the vertical, thus a uniform surface to bottom transport rate is reasonable.

Mass transport, averaged over a wave period, now becomes

$$T_M = \sin \alpha \int_X \bar{v} \int_0^{h(x,t)} c \, dy \, dx \quad (13)$$

Average mass transport over a tidal cycle

$$\langle T_M \rangle = \frac{1}{T} \int_0^T \sin \alpha \int_X \bar{v} \int_0^{h(x,t)} c \, dy \, dx \, dt \quad (14)$$

can now be approximated through numerical integration by taking a 2-min time step, an average tide range of 2.5 m, and a water elevation (depth in meters) to be given as

$$h = 3.75 + 1.25 \cos \omega \quad (15)$$

where $\omega = 2\pi t/T$.

Finally, if bulk density of the transported mass, including pore space of static grains, is known or assumed, then volume transport is found by dividing by sediment concentration at that density

$$T_v = \frac{T_M}{\rho_c} \quad (16)$$

This allows mass transport values to be converted into units of volume transport that are useful in assessing coastal accretion or erosion.

Volume transport in cubic meters per year is plotted as a function of wave period for angles of wave approach from 6° to 12° ,

taking $H/h = 0.23$, $\rho_c = 375 \text{ kg/m}^3$ ($\rho = 1.25 \text{ g/cm}^3$), and $\beta = 0.001$ (Fig. 11). Only transport during one-half of the tidal cycle, that half extending from mid-tide through low water to the following mid-tide, has been considered since this is the time that the most solitary-like waves are observed.

The range in transport spans roughly from 15 to $65 \times 10^6 \text{ m}^3/\text{yr}$. Higher angles of wave approach lead to higher transport rates, as do shorter wave periods (more pulses of water per unit of time). Values for H/h , ρ_c , and β have been determined from field data and any realistic variations in these parameters will produce small changes in transport values.

Longshore transport rate is most sensitive to horizontal and vertical variations in suspended sediment. Unfortunately, processes controlling the distribution of suspended sediments are more complex and varied than presented here. Thirty-eight percent of the variability in suspended-sediment concentration ($P < 0.001$) can be explained by water depth, leaving 62% to be explained by such factors as local wind-generated waves and density and thickness of the fluid-mud layer. However, inasmuch as most studies of this nature (Galvin, 1973; Komar, 1976) take an average concentration for the entire surf and breaker zone, equation (8) provides an equally good or better estimate.

Values reported in Figure 11 at first appear considerably lower than littoral transport estimates for the coast of northeastern South America, leading one to believe that, even if waves are indeed solitary, only one-quarter or less of the transport can be explained by this mechanism. However, close examination indicates that the total estimated sediment transport rate, cited by previous investigators as $250 \times 10^6 \text{ m}^3/\text{yr}$, has been determined for a 30-km-wide band extending offshore. If one-sixth of this volume moves alongshore in a band that is only 5 km wide, the width of the hypothetical mudbank in Figure 10a, then the rate becomes $42 \times 10^6 \text{ m}^3/\text{yr}$ and a remarkable similarity can be seen.

Several simplifications that require qualitative evaluation have been introduced into these transport calculations. First, the shoreward component of net drift assumes a return flow to satisfy continuity considerations. If return flow is taken perpendicular to the coastline in the area between mudbanks (Fig. 10a), then longshore transport may be unaffected. This is a logical pattern of onshore/offshore transport since solitary-like waves, which break only by spilling, produce a greater setup over mudbanks than do plunging breakers in areas between mudbanks. In support of this concept, Sonu (1972) has shown that, on the west coast of Florida, wave-induced currents move shoreward over shoals where waves break by spilling and a return flow occurs in troughs where waves break by plunging.

Second, the transport model considers only that transport which occurs in regions of fluid mud, yet assumes that these rates reflect transport in interbank areas as well. This results in an overestimation, even though some transport may take place in interbank areas as a result of an oblique wave approach or by longshore currents produced by breaking waves through the concept

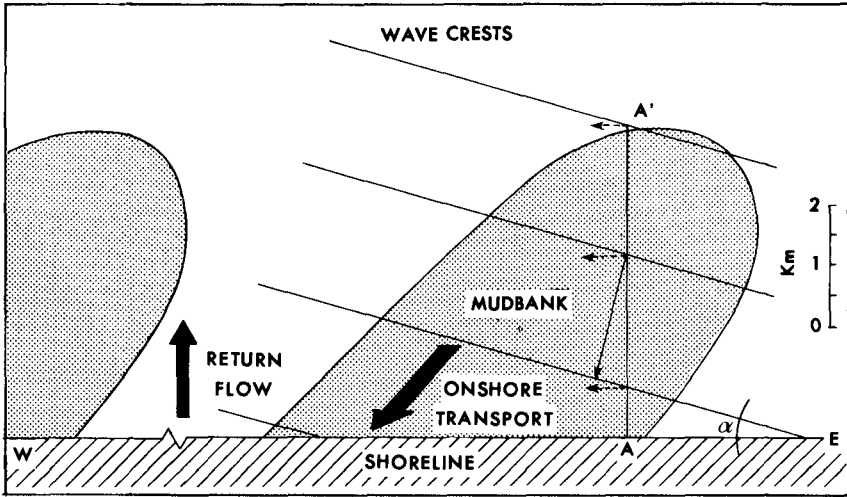


Figure 10a. Plan view of idealized mudbank used in transport calculations. Dashed lines represent longshore component of wave drift.

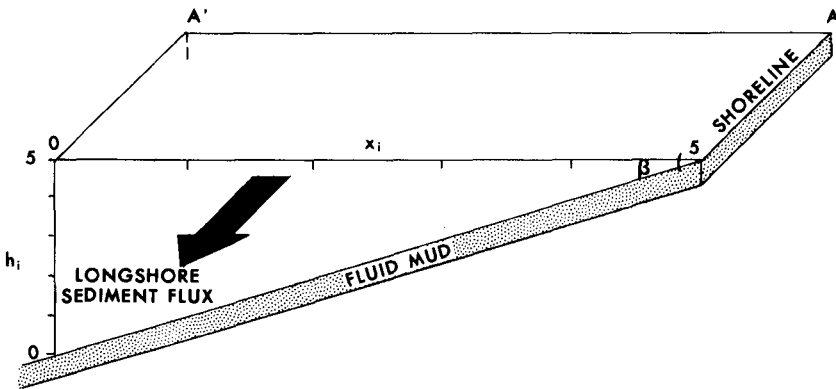


Figure 10b. Cross section along line A-A' (Fig. 10a). Maximum area coincides with high tide when $h = 5$ m and $x = 5$ km.

of radiation stress, as normally applied to sandy coasts (Komar, 1976, p. 190). Moreover, all waves over mudbanks are not solitary and probably do not have particle velocities of true solitary waves. Thus, the longshore volume transport rate given in Figure 11 should be considered as an upper bound for that which can be explained by solitary-like waves.

Third, large-scale circulation patterns along this coast are unknown and have been neglected. Such circulation patterns may

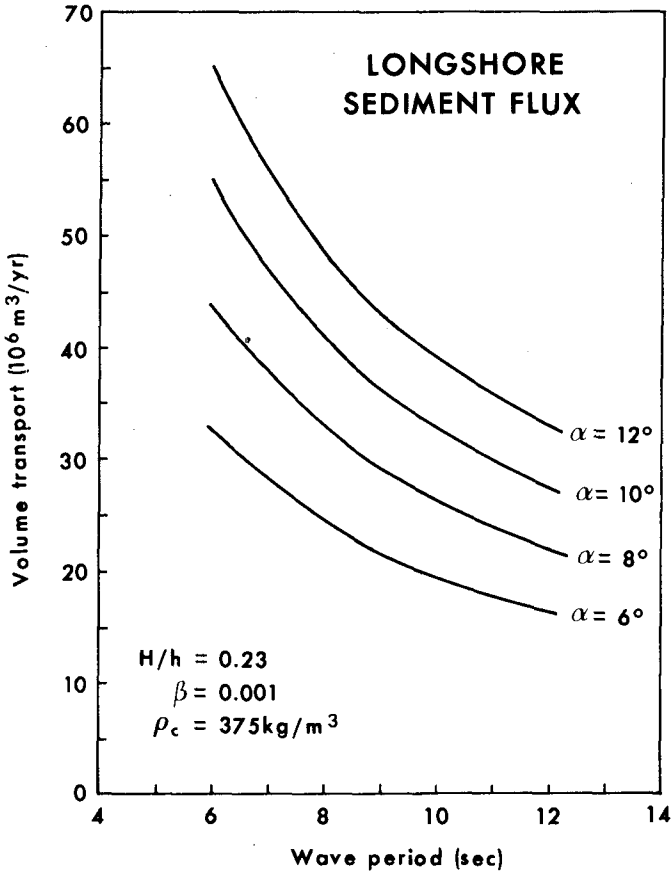


Figure 11. Longshore volume transport as a function of wave period.

provide avenues for moving sediment both onshore and offshore.

Despite the simplifications and unknown processes, the basic conjecture remains that if waves in high suspended-sediment regions have hydromechanical properties of true solitary waves, then sediment transport by waves alone needs to be considered as an explanation for high volume transport rates. The fact that the littoral zone has been taken in this study to extend 5 km offshore, rather than a few meters or a few hundreds of meters, is responsible for longshore sediment transport rates that are orders of magnitude higher than those reported for sandy environments. These estimates, taken across the entire zone in which waves appear to be solitary, may be more realistic than estimates along sandy coasts where only that volume moved by waves in the swash zone is considered.

Finally, we believe the idea presented in this paper, namely

that solitary waves can suspend and transport large volumes of fine-grained sediment without utilizing breaking waves, the concept of radiation stress and a nearshore circulation cell or sediment moving as bed load should be vigorously checked along the world's muddy coastlines. A logical next step would be to take field measurements for determination and verification of orbital speeds under solitary-like waves.

ACKNOWLEDGMENTS

This research was performed under a contract between the Geography Programs, Office of Naval Research, Arlington, Virginia 22217, and the Coastal Studies Institute, Louisiana State University, Baton Rouge. Cooperation and field support were provided by Drs. R. A. Cambridge, E. H. Dahlberg, and Th. E. Wong, Government Service for Mining and Geology, Ministry of Development, and Mr. A. M. Suttmuller and his staff, Hydraulic Research Division, Ministry of Public Works and Traffic, Paramaribo, Surinam. Technical assistance in the field was provided by Mr. R. G. Fredericks, and Mrs. A. F. Dunn prepared the illustrations. Drs. S. P. Murray and E. H. Owens reviewed the manuscript and offered helpful suggestions.

REFERENCES

- Allersma, E. 1968. Mud on the oceanic shelf off Guyana. Paper contributed to Symposium on Investigations and Resources of the Caribbean Sea and Adjacent Regions, CICAR Conference, Curacao (Delft Hydraulics Laboratory, Delft, The Netherlands, unpublished), 20 pp.
- Augustinus, P. G. E. F. 1978. The changing shoreline of Surinam. Unpublished thesis, University of Utrecht, Holland, 232 pp.
- Daily, J. W., and S. C. Stephan, Jr. 1953. The solitary wave-its celerity, profile, internal velocities and amplitude attenuation in a horizontal smooth channel. Proc., 3rd Conf. Coastal Engr., Cambridge, Mass., pp. 13-30.
- Delft Hydraulics Laboratory, 1962, Demerara coastal investigation. Delft, The Netherlands, 240 pp.
- Eisma, D., and H. W. van der Marel. 1971. Marine muds along the Guyana coast and their origin from the Amazon Basin. Contributions in Mineralogy and Petrology 31:321-334.
- Galvin, C. J. 1973. A gross longshore transport formula. Proc., 13th Conf. Coastal Engr., Vancouver, B.C., Canada, pp. 953-970.
- Gibbs, R. J. 1967. Geochemistry of the Amazon River system. Part I. The factors that control the salinity and the composition and concentration of the suspended solids. Bull. Geol. Soc. Am. 78:1203-1232.
- Hom-ma, M., K. Horikawa, and S. Komori. 1967. Response characteristics of underwater wave gage. Proc., 10th Conf. Coastal Engr., Tokyo, Japan, pp. 99-114.
- Inman, D. L., W. R. Gayman, and D. C. Cox. 1963. Littoral sedimentary processes on Kauai, a subtropical high island. Pacific Science XVII:106-129.

- Kirby, R., and W. R. Parker. 1974. Seabed density measurements related to echosounder records. Dock and Harbour Authority 54:423-424.
- Komar, P. D. 1976. Beach processes and sedimentation. Englewood Cliffs, New Jersey (Prentice-Hall), 429 pp.
- Krone, R. B. 1962. Flume studies of the transport of sediment in estuarial shoaling processes. University of California Hydraulic Engr. Lab. and Sanitary Research Lab., Berkeley, 110 pp.
- Krone, R. B. 1972. A field study of flocculation as a factor in estuarial shoaling processes. Committee on Tidal Hydraulics, Corps of Engr., Vicksburg, Miss., Tech. Rept. 16, 62 pp.
- Moni, N. S. 1971. Study of mudbanks along the southwest coast of India. Proc., 12th Conf. Coastal Engr., Washington, D.C., 2:739-750.
- Munk, W. H. 1949. The solitary wave theory and its applications to surf problems. Ann. N. Y. Acad. Sci. 54:376-424.
- Nair, R. R. 1976. Unique mud banks, Kerala, Southwest India. Bull. Am. Assoc. Petrol. Geologists 60:616-621.
- NEDECO. 1968. Surinam transportation study. Netherlands Engr. Consultants, The Hague, 293 pp.
- Odd, N. V. M., and M. W. Owen. 1972. A two-layer model of mud transport in the Thames estuary. Proc. Inst. Civ. Engr., Supplement Paper #7517S, pp. 175-205.
- Orr, M. H., and F. R. Hess. 1978. Remote acoustic monitoring of natural suspensate distributions, active suspensate resuspension, and slope/shelf water intrusions. J. Geophys. Res. 83:4062-4068.
- Parker, W. R., G. C. Sills, and R. E. A. Parke. 1975. In-situ nuclear density measurements in dredging practice and control. 1st Internat. Symp. on Dredging Tech., pp. B3-25 - B3-42.
- Partheniades, E. 1971. Erosion and deposition of cohesive materials. In (H. W. Shen, ed.) River mechanics. Boulder (Colorado State Univ. Press), pp. 25-1 - 25-91.
- Sonu, C. J. 1972. Field observation of nearshore circulation and meandering currents. J. Geophys. Res. 77:3232-3247.
- Tubman, M. W., and J. N. Suhayda. 1977. Wave action and bottom movements in fine sediments. Proc., 15th Conf. Coastal Engr., Honolulu, 2:1168-1183.
- Wells, J. T. 1977. Shallow-water waves and fluid-mud dynamics, coast of Surinam, South America. Ph.D. dissertation, Coastal Studies Inst., Louisiana State Univ., Baton Rouge, 99 pp.
- Wells, J. T., and J. M. Coleman. 1977. Nearshore suspended sediment variations, central Surinam coast. Marine Geology 24:M47-M54.
- Young, R. N., and J. B. Southard. 1978. Erosion of fine-grained marine sediments: sea-floor and laboratory experiments. Bull. Geol. Soc. Am. 89:663-672.

CHAPTER 118

HYDRODYNAMICS AND SEDIMENT TRANSPORT IN A SALT MARSH TIDAL CHANNEL

Larry G. Ward
Coastal Research Division
Department of Geology
University of South Carolina
Columbia, South Carolina 29208

ABSTRACT

Processes and sediment transport were investigated in a salt marsh drainage system at Kiawah Island, South Carolina. A general survey of the tidal current was done in the major tidal channel (Bass Creek) for a 10 tidal cycle period in August, 1977. Detailed determinations of current velocity, discharge, and suspended load were conducted during 15 tidal cycles in March, 1977 and again during 8 tidal cycles in July-August, 1977. For each of these periods, mass budget for the total suspended load were computed.

The tidal currents have a pronounced time velocity asymmetry with the maximum current velocity occurring nearer high slack water and the peak ebb velocity being 20 - 30% stronger than the flood. Suspended load transport is significantly affected by the time velocity asymmetry. Peak current occurring nearer high slack water causes a net displacement of suspended material in an ebb or seaward direction under normal conditions. This process is enhanced by the stronger ebb currents. Mass budgets reflect the ebb dominance of the system showing a net export of combustible (organic) material during the March sampling period and a net export of both noncombustible (inorganic) and combustible material during the July-August period. Also important to suspended load transport in marsh systems are stressed meteorological conditions. High winds or heavy rains increase suspended load concentration and can cause significant import or export of fine-grained material.

INTRODUCTION

The physical and sedimentological processes occurring in a salt marsh tidal channel system were studied at Kiawah Island, South Carolina (Fig. 1). The purpose of the investigation was to monitor hydrodynamic processes and determine their effect on suspended material transport. Therefore, the tides, currents, and suspended load were monitored within the tidal channel system, and mass budgets for the total suspended load computed.

Physical Setting

Study area. - The investigation was conducted in a small marsh system (5 km²) on the northeastern end of Kiawah Island (Fig. 2). The marsh is enclosed on three sides by Holocene beach ridges (Hayes,

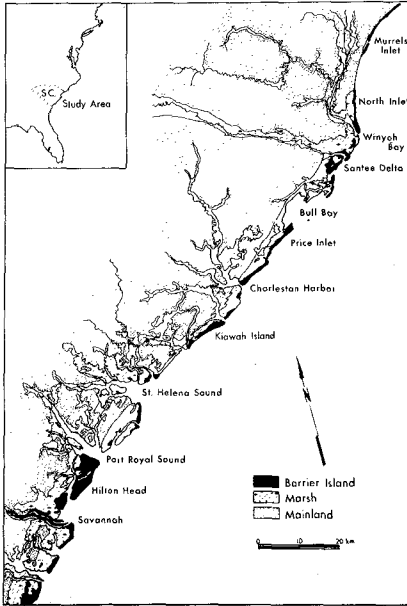


Figure 1. Location map of Kiawah Island, South Carolina.

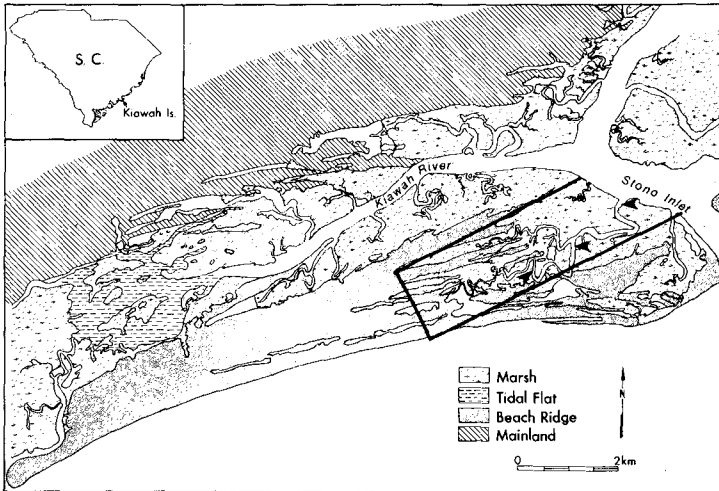


Figure 2. Map of Kiawah Island, South Carolina. The study was conducted in the Bass Creek marsh system outlined by the black line. Arrows point to locations where currents were monitored. Mass budgets for suspended material loads were done at the western-most station.

1975) which isolates it from any other major drainage system. One main tidal channel, Bass Creek, and its small tributaries, form the entire drainage network. The Bass Creek marsh system was chosen because it is unpolluted, essentially undisturbed by man, has no fresh water influx and has a simplified drainage system.

The primary marsh vegetation is Spartina alterniflora with Salicornia ambigua and Borrchia frutescens found at higher elevations. The marsh is composed of silt and clay-sized sediments (kaolinite and illite) except adjacent to abandoned beach ridges which have a high quartz sand content. Underlying the marsh sediments are fine-grained cohesive tidal flat sediments that have abundant oyster shell (Crassostrea virginica) deposits. The tidal channels normally have beds composed of fine sands, and the banks are composed of silts and clays. The channels are relatively unstable, showing numerous abandoned channels (cutoffs, oxbows, etc.). Channel migrations of up to 75 m in 24 years have occurred at locations where the channels have eroded into abandoned beach ridges (Ward and Domeracki, 1978).

Climate. - Kiawah Island has a marine subtropical climate modified by the Atlantic Ocean (Kjerfve, 1975). The monthly average temperatures for the period from 1935-1974 range from 10.2°C in January to 27.5°C in July with a mean of 18.9°C (Fig. 3). The average precipitation ranges from 6 cm in November to 18 cm in July, totaling 124 cm per year (data obtained from the National Weather Service).

Kiawah's climate is greatly influenced by frontal systems moving across the United States in an eastward direction (Kjerfve, 1975). During the winter months, when polar air masses traverse portions of the southeast, cold fronts produce west and northwest winds of considerable velocity. During the summer months, the Bermuda High creates anti-cyclonic circulation off the South Carolina coast causing southerly winds. The dominant winds are associated with the passage of low pressure systems or northeast storms.

The weather conditions that most affect marsh and tidal channel processes (observed in this study) are the occurrence of frequent afternoon and evening thundershowers. During the late spring and summer, severe thundershowers occur on a regular basis. During a single storm, several inches of rainfall and winds of over 50 km/hr may occur.

Tides. - The tides at Bass Creek are semi-diurnal with a strong diurnal component. The mean tidal range for 28 weeks of tidal data measured within Bass Creek is 1.75 meters. Two week averages vary from 1.54 to 1.92 meters. Individual tidal cycles have ranges from a maximum of 2.40 meters during spring tides to 0.84 meters during neap tides.

CHARLESTON HARBOR 1935 - 1974

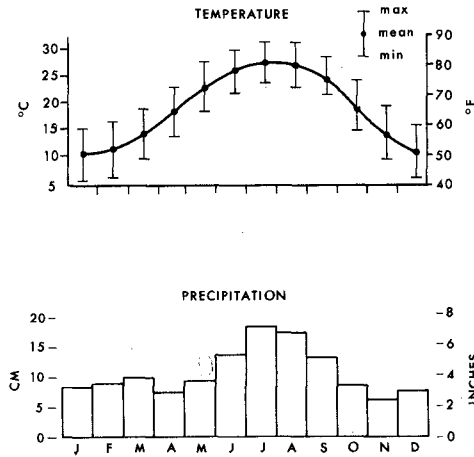
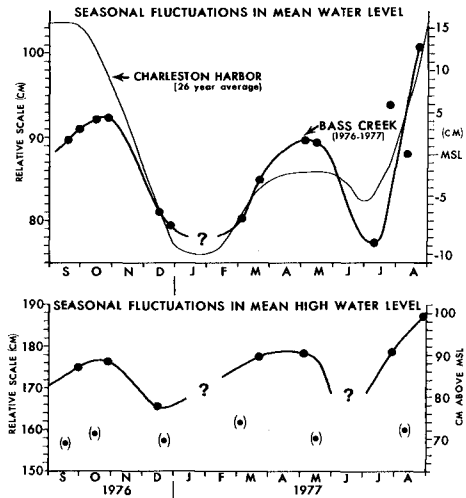


Figure 3. Average monthly temperatures and precipitation for Charleston Harbor, South Carolina, from 1935-1974.

Figure 4. Seasonal fluctuations in water levels for Bass Creek and Charleston Harbor. Mean water levels for Bass Creek were determined by averaging hourly readings during two week periods. MSL is the mean water level at Bass Creek for 1976-1977. The curve for Charleston Harbor is from Hicks and Crosby (1974).



The mean water level, determined for 14 two-week periods by averaging $\frac{1}{2}$ hour water level readings, shows a yearly variation of 22 cm (Fig. 4). The highest mean water level occurs during the late summer and early fall; while the minimum values occur during mid-winter. Similar trends have been reported by Humphries (1977) and Kjerfve, *et al.* (in press) for tidal creeks at North Inlet and by Hicks and Crosby (1974) for Charleston Harbor, South Carolina. The fluctuations in mean water level have been attributed to steric sea level changes (Patullo, *et al.*, 1955).

During periods when the mean water level is at a maximum, the height and consequently the duration to which the marsh surface is flooded increases (as illustrated by the two-week averages for mean high water levels in Figure 4). Kjerfve, *et al.* (in press) found that due to higher autumn water levels at North Inlet, South Carolina, the marsh surface is inundated 42% of the time in October compared to 27% of the time in January. The length of time the marsh surface is covered is important to both depositional processes and nutrient exchanges. The marsh vegetation acts as a baffle, increasing sedimentation rates while it is covered with water. In addition, the marsh surface is the primary source of decaying vegetation. Increased flooding facilitates the removal of this material into the estuarine system where it can be utilized by the aquatic food chain.

Previous Studies

Physical and sedimentological processes in salt marsh tidal channels have been studied by a number of investigators trying to determine the flux of suspended material and dissolved substances. An excellent review of many of these articles is given by Frey and Basan (1978). Probably the most precise study was conducted by Boon (1973) in a marsh tidal creek in Virginia. The results of his work indicate that small low order tidal channels act as conduits, transporting both inorganic and organic particulate matter in a seaward (ebb) direction. His conclusions were based on sediment flux measurements done at a single channel cross section. Settlemyre and Gardner (1975) computed mass budgets for a larger tidal channel in an enclosed marsh in Charleston Harbor, South Carolina. Their results, contrary to Boon's, show an influx of inorganic particulate matter and an export of organic particulate matter. Hackney (1977), working in a marsh tidal channel in Mississippi, found an import of both organic and inorganic material during the summer and an export of both during the winter. Odum and de la Cruz (1967) computed mass budgets for organic detritus and found that it was exported from a Georgia salt marsh during all seasons.

A number of studies pertinent to understanding the processes in salt marsh tidal channels have been conducted on tidal flats. Some of

the earlier investigations were done in the Dutch and German North Sea by Van Straaten and Kuenen (1957), Van Straaten (1961), Postma (1967) and Groen (1967). The results of these investigations indicate a landward increase in the fine-grained suspended material concentrations in tidal channels due to a "settling lag" and "scouring lag" effect. Coupled with this is a tidal current asymmetry, with the peak flood and ebb velocities occurring nearer low slack water. The effect of this asymmetry is that suspended material can be transported for a longer period on flood than ebb tides. Therefore, over a number of tidal cycles, there is a net landward displacement of the suspended load. They argued that, under normal conditions, this would cause a build-up of fine-grained material toward land with the North Sea being the source. Pestrong (1972a, 1972b) studied tidal flats and salt marshes in the San Francisco Bay area. His work suggests that tidal flats are overgrown by salt marshes by eroding sediment from the head of the marsh and flushing it seaward by ebb flow. Thus, the growth of the marsh onto the tidal flat is partially cannibalistic. Anderson (1972) has shown the importance of wave activity on the tidal flats in New Hampshire. At this location, it was illustrated that even small amplitude waves resuspend significant amounts of fine-grained sediment.

PROCESSES AND SEDIMENT TRANSPORT

Tidal Currents

Methods. - The current was monitored for a 10 tidal cycle period in August, 1977 at three locations within Bass Creek ranging from the mouth to a position 4 km in the flood direction (Fig. 2). At each location, a General Oceanics current meter was moored near the bottom (less than 1 meter) at mid-channel. Velocity and direction readings were taken at approximately 4 minute intervals for the 10 tidal cycle period.

Results. - The current velocity at all three locations has a pronounced time asymmetry (Fig. 5). Maximum current velocity normally occurs 1 to 3 hours before and 1 to 2 hours after high slack water. The current velocity at the two stations in Bass Creek away from the mouth also has a velocity asymmetry with the ebb current being much stronger than the flood. The average ratios of the maximum flood velocity (F max) to maximum ebb velocity (E max) at the two stations located 2 km and 4 km away from the mouth are 0.64 and 0.68 respectively for the 10 tidal cycles monitored. The station located in the mouth of Bass Creek shows no velocity asymmetry, having an average F max/E max ratio of 0.98.

In addition to the time velocity asymmetry of the currents, there is an asymmetry or difference in the duration of the flood and ebb flow. Inspection of Figure 5 shows that the flood currents normally occur for over $6\frac{1}{2}$ hours, while the ebb currents flow for less than 6 hours. This

difference in duration is further verified in the 28 weeks of tide data analyzed in Bass Creek. The average duration of the flood component of the tide is 6.54 hours; while the average duration of the ebb is 5.69 hours. It should be pointed out that only half-hour readings were taken from the tidal records and used to compute these averages. Therefore, there may be some error. To determine the reliability of these figures, a number of tidal cycles were measured directly to obtain accurate flood and ebb durations. The results indicate that there is a large amount of variability in the duration of individual cycles, but the averages compare well to the 2-week averages (within 0.1 - 0.2 hours). Similar duration asymmetries in tidal inlets and marsh channels have been reported by Boon (1973), FitzGerald, et al., (1976), and Nummedal and Humphries (1978), and were attributed to distortion of the tidal wave and the formation of overtides. Nummedal further pointed out that if the flood and ebb discharges are similar, then because of the shorter duration, the ebb velocities would have to be higher than the flood to transport the same volume of water in a shorter period. This process contributes to the velocity asymmetry of the current.

Suspended Load Transport and Mass Budgets

Method. - The current, discharge, and suspended load were monitored during 23 tidal cycles in Bass Creek at a location that transmitted the entire tidal prism to an isolated area of the marsh (Fig. 2). The first sampling session was conducted in March, 1977, during which 15 out of 18 consecutive cycles were monitored. The other 8 tidal cycles were monitored during July-August, 1977. These two periods were chosen because March is representative of winter conditions in the southeastern United States, having minimum temperatures and precipitation (Fig. 3); while July-August represents summer conditions having maximum temperatures and precipitation.

Prior to these sampling sessions, preliminary surveys were done to assess the accuracy at which the mean current, discharge, and suspended load could be determined. This information was then used to determine the experimental error involved in computing the instantaneous and total flux of suspended material over a flood or ebb portion of a tidal cycle. It was found that the mean current could be estimated within $\pm 4.2\%$ to $\pm 8.5\%$ and the suspended load within $\pm 6.3\%$, if measurements were made at $1/5$, $1/2$, and $4/5$ the distance across the channel and at 0.2 and 0.8 the relative depth at each location (Figs. 6 and 7). The error involved in computing the instantaneous flux is the combined error for the current and suspended load or approximately ± 7.6 to $\pm 10.6\%$ (Ward, 1978). The error for determining the total flux of suspended material over a flood or ebb portion of a tidal cycle is slightly less (Boon, 1973). Therefore, any net or residual flux of material

INSTRUMENT ARRAY

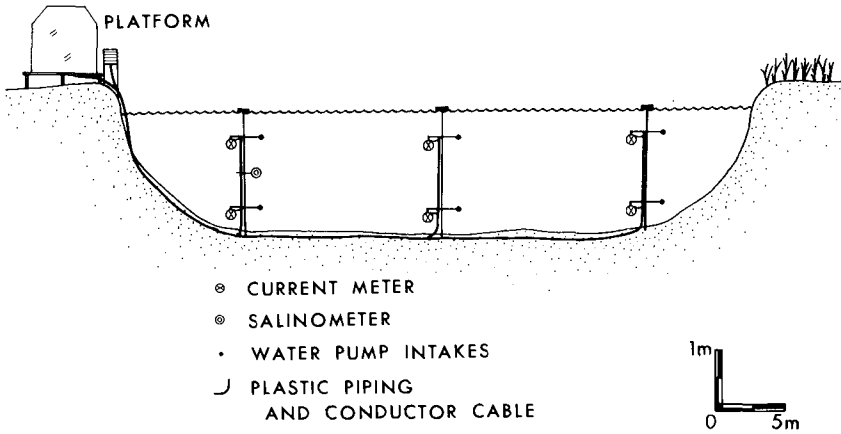


Figure 6. Schematic of the instrument array. The channel was approximately 50 meters wide, and the instrument frames were located $1/5$, $1/2$ and $4/5$ the distance across the channel. The current meters and intakes for the water pumping system were able to rotate freely and were always aligned into the current. The current velocity, temperature, and salinity readings were taken inside a tent located on the platform. The water samples were taken at the out-flow valves of the pumping system also located on the platform.

INSTRUMENT FRAME

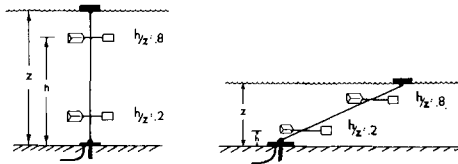


Figure 7. Schematic of the instrument frame. The base was augered into the channel and a float attached to the top. A hinge allowed the frame to raise and lower with changes in tidal height, keeping instruments at 0.2 and 0.8 of the total depth at all stages of the tide.

greater than $\pm 10\%$ for the mass budget is considered to be significant and not the result of sampling errors.

Results. - The suspended load concentrations during the March sampling session are normally between 10 - 20 mg/l except during periods of high wind or heavy rain when concentration exceed 50 mg/l. During the July-August sampling session, the total suspended loads range from 20 - 200 mg/l, but are normally between 50 - 100 mg/l. The organic fractions range from 0 to 70% but have a mode at about 20%.

Time series data of the suspended load and current for the first two tidal cycles monitored during the July-August session illustrates the relationship between highest sediment transport and maximum current velocity (Fig. 8). During the first tidal cycle, highest suspended load concentrations during flood tide occur simultaneously with the strongest current. The suspended load concentration is over 160 mg/l, but drops to about 30 mg/l as high slack water approaches, and the coarser material settles out. After the ebb current reaches a maximum, the suspended load increases to 160 mg/l again.

Mass budgets of the suspended load for the tidal cycles monitored in March are shown in Figure 9. The first 6 cycles (TC1-6) are during spring tides, 7-10 during mean, and 13-18 during neap tides. In general, the spring tides are much more dynamic than neap tides in respect to sediment transport. Fluxes for the total suspended load are normally greater than 5×10^6 grams for any half cycles during the spring tides, while neap tide fluxes are normally closer to 1.0×10^6 grams. These higher transport rates result from greater discharges and stronger currents that occur during spring tides.

The flux of material for tidal cycles 1-6 was summed in order to determine the net movement of material for that period. The net mass budget for the 6 cycle periods shows an export of 2.3×10^6 grams or about 5% of the total suspended load flux. Results of the error analysis indicate that fluxes this low are not reliable, as they may be accounted for by experimental error. Therefore, the budget is considered to be in balance. Inspection of the components of the total suspended load indicates there is also a balance of the non-combustibles (inorganic) fraction, but an export or ebb-directed net flux of 1.5×10^6 grams of combustibles (organics) fraction. The net export of combustibles accounts for a residual transport of approximately 16% which is considered reliable.

The effects of the meteorological conditions on suspended load transport become evident when individual tidal cycles are inspected. During cycles 1-4, when there were only light winds and no rainfall, the mass budgets reflect the movement of material due to the large tidal prisms associated with spring tides. As the tidal range and tidal

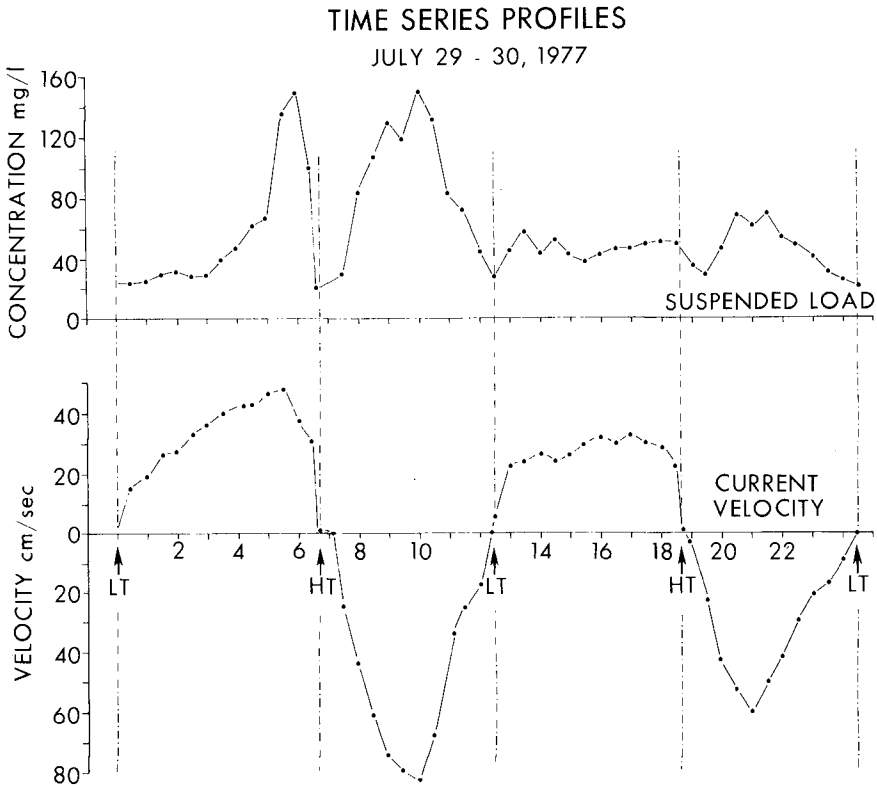


Figure 8. Time series profiles of the mean suspended load and current velocity in Bass Creek during the July, 1977 session. Note that the maximum suspended load concentrations occur with peak current velocity. Also note the time velocity asymmetry of the current.

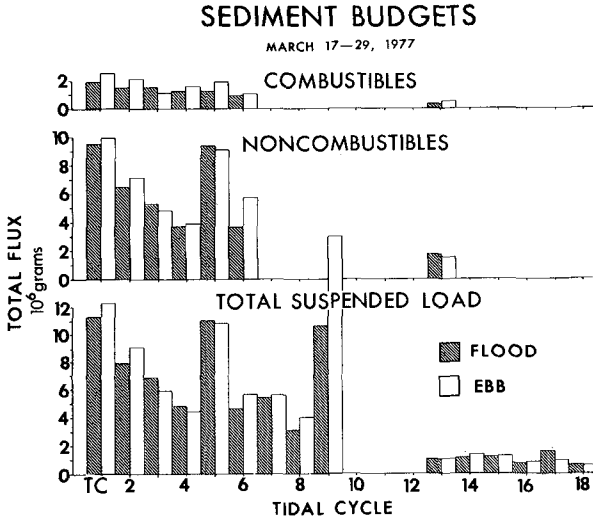


Figure 9. Mass budgets for the suspended load in Bass Creek during March, 1977. Tidal cycles 1-6 were during spring tides while 13-18 were during neap tides. Hatched columns represent the flood fluxes; open columns represent ebb fluxes.

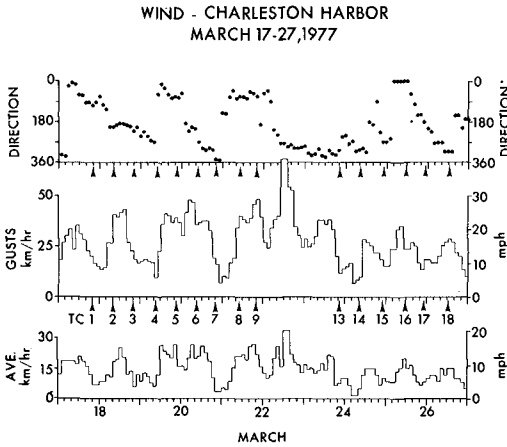


Figure 10. Wind velocity and directions for Charleston Harbor, South Carolina. The times that correspond to the tidal cycles monitored are labelled TC1-18. Note the strong gusting winds from the north-east during TC-9.

prism decrease, sediment transport reduces. During tidal cycle 5, winds gusting to 40 km/hr from the northeast and east (Fig. 10) caused a slight set-up in the tidal height and an increase in wave activity within the tidal channels. The wave activity eroded material from the channel margin, increasing the total suspended load and the mass budgets. During the following tidal cycle, the winds remained strong, but began blowing from the south. The marsh system is orientated such that winds from the northeast are most effective in increasing the wave activity and causing a set-up in the tides. Winds from other directions seem to have only a minor effect on marsh processes; therefore, the sediment flux for tidal cycle 6 is markedly reduced.

The relationship between meteorological conditions and sedimentary processes is again demonstrated during tidal cycle 9. During the ebb portion of tidal cycle 8, the wind began to blow consistently from the northeast at about 25 km/h. During the flood portion of tidal cycle 9, the winds remained from the northeast, but increased in velocity reaching nearly 50 km/h. This caused a water level nearly 40 cm higher than would normally be expected and a flood duration of over 7 hours. These increases resulted in the water elevation being abnormally higher than the ocean level which produced an abnormally steep hydraulic slope. When the tide turned, the increase in the hydraulic slope created currents of over 75 cm/sec which were greater than those measured during maximum spring tides. Due to the set-up, wave activity, and high ebb currents resulting from the northeast winds, much more material was transported than in any of the previous cycles. Over 10.6×10^6 grams and 16.9×10^6 grams were transported on the flood and ebb respectively.

Mass budgets for the summer show similar trends as the March budgets except for the quantity of material being transported (Fig. 11). During the winter sampling period, the maximum amount of material transported over any $\frac{1}{2}$ tidal cycle past the channel cross-section is 20×10^6 grams. During the summer sampling period, the maximum value reaches 87×10^6 grams. This dramatic increase may be attributed to three factors. Steric sea level is at a maximum which would conceivably increase the tidal prisms (Fig. 4). Second, the warmer water temperatures may reduce the cohesiveness of the fine-grained material, making it more erodable. Finally, there is an increase in biologic activity during the summer. Observations in the field show that the activity of the fiddler crab (*Uca pugnax*) and other organisms is greatly increased. This, in addition to the increase in the floral growth, increases the turbidity and suspended load and, consequently, the mass budgets. In all probability, it is a combination of these factors.

The net flux of material for the five tidal cycles monitored during the spring tides (TCL-5; Fig. 11) indicate that there is an export of both the combustible and noncombustible fractions of the suspended load. A residual of approximately 40.7×10^6 grams (35%) of noncombustible and 2.9×10^6 grams (10%) of combustible material was exported.

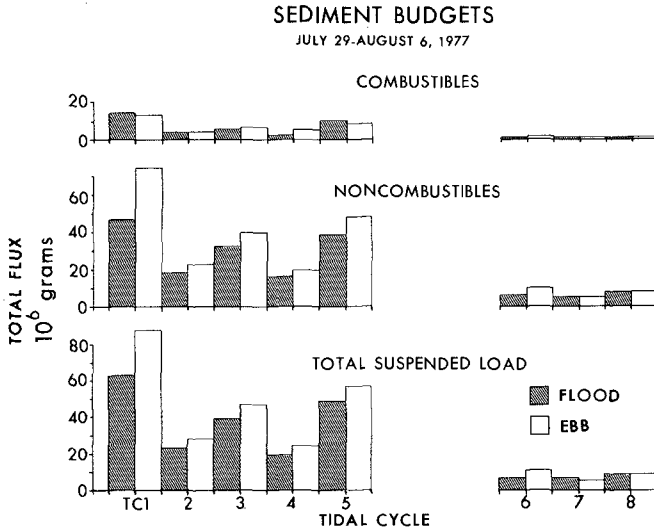


Figure 11. Mass budgets for the suspended load in Bass Creek during July-August, 1977. Tidal cycles 1-5 were during spring tides while 6-8 were during neap tides. Hatched columns represent flood fluxes; open columns represent ebb fluxes.

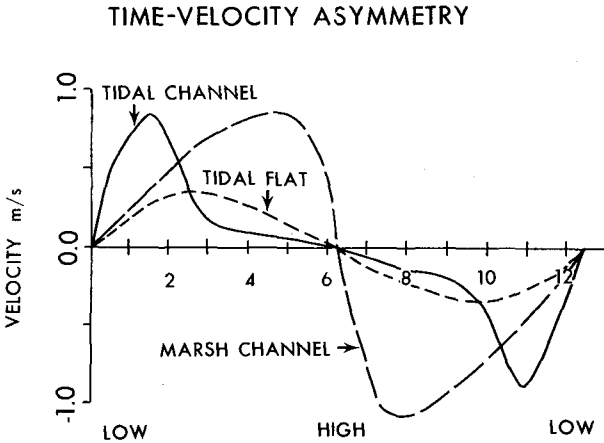


Figure 12. Representative current profiles from tidal channels and tidal flats in the Wadden Sea (Postma, 1967) and the marsh channel at Bass Creek, South Carolina. Note the shifting of peak current velocity from being asymmetric toward low slack water in the Wadden Sea to high slack water in Bass Creek.

Discussion

The time velocity asymmetry strongly affects the movement of sediment within tidal channels and ultimately controls the flux of particulate matter under normal meteorological conditions. As illustrated in Figure 8, the strongest current occurs 1-2 hours before and 2-3 hours after high slack water, and the maximum ebb current velocity can be between 50 to 100% stronger than the flood. The net effect of the time asymmetry is that a parcel of water can be transported at maximum velocity only 1-2 hours during the flood. Conversely, the same parcel of water can be transported up to 3-4 hours on the ebb tide. Consequently, even without the maximum currents being unequal, the water parcel undergoes a net seaward or ebb-directed displacement. This effect is further enhanced by the stronger ebb currents. The suspended load reaches a peak simultaneously with the current and therefore would be displaced in a similar manner as a water parcel. Thus, the time velocity asymmetry causes a net movement of material seaward. This same relationship, but, in reverse, is used along with "settling and scouring lag" to explain a net landward transport of suspended material in the Wadden Sea (Van Straaten and Kuenen, 1957; Postma, 1967; Groen, 1967). Data published by Postma (1967) shown in Figure 12 illustrates the time velocity asymmetry measured in the Wadden Sea. The maximum current velocity occurs near low slack water causing a net displacement of water and suspended material landward. If the period of maximum current is shifted toward high slack water as in the southeastern United States, then there is a seaward flux of material.

CONCLUSIONS

This study of the physical and sedimentological processes in the Bass Creek salt marsh tidal channel system illustrates the complex relationship between the tidal regime and, consequently the tidal currents, the meteorological conditions, the biologic activity, and the transport and deposition of sediment. The major findings of this study based on the two extended sampling periods and the general monitoring of the tides and currents at Bass Creek, S. C. are:

1. Sediment transport varies nearly an order of magnitude from the high transport period of the summer to the low transport period of the winter. This variation is primarily attributed to steric sea level fluctuation and changes in biologic activity.
2. Sediment transport varies a great deal from tidal cycle to tidal cycle under normal conditions due to changes in tidal prisms or discharge.
3. There is a net export of combustible (organic) suspended material during both the summer and winter in the marsh tidal channel.

4. There is an export of noncombustible (inorganic) suspended material during the summer and a balance during the winter.
5. The net export of material under normal conditions can be attributed to the time velocity asymmetry of the currents.
6. Stressed meteorological events (such as heavy rains or strong winds) increase sediment transport in marshes dramatically.

ACKNOWLEDGEMENTS

Financial support for this study was given by the South Carolina Wildlife and Marine Resources Department and by a National Science Foundation Doctoral Dissertation grant. Exceptional field and laboratory assistance was given by John Barwis, Daniel Domeracki, Michael Waddell, Chris Ruby, Stephanie Ward, Mary Ann Capria, and Ian Fischer. The drafting was done by Nannette Muzzy, and the final text typed by Priscilla Ridgell. I would also like to acknowledge Frank Stapor for the use of the General Oceanic current meters and the Kiawah Island Company for access to their property.

REFERENCES

- Anderson, F. E., 1972, Resuspension of estuarine sediments by small amplitude waves: *Jour. Sed. Petrology*, v. 42, p. 602-607.
- Boon, J., 1973, Sediment transport processes in a salt marsh drainage system: Unpubl. Ph.D. Dissertation, College of William and Mary, Williamsburg, Va., 225p.
- FitzGerald, D. M., D. Nummedal, and T. W. Kana, 1976, Sand circulation pattern at Price Inlet, South Carolina: *Proceedings of the Coastal Engineering Conference, Honolulu, Hawaii, July 11-17*, p. 1868-1879.
- Frey, R. W. and P. B. Basan, 1978, Coastal salt marshes: *in Coastal Sedimentary Environments*, R. A. Davis, Jr. (ed.), Springer-Verlag, p. 101-159.
- Groen, P., 1967, On the residual transport of suspended matter by an alternating tidal current: *Netherlands Jour. Sea Res.*, v. 3, p. 564-574.
- Hackney, C. T., 1977, Energy flow in a tidal creek draining an irregularly flooded *Juncus* marsh: Ph.D. Dissertation, Mississippi State Univ., Starkville, Mississippi, 83p.
- Hayes, M. O., 1975, Geology and coastal processes: *in Environmental Inventory of Kiawah Island*, W. M. Campbell and J. M. Dean, Directors, Environmental Research Center, Inc., Columbia, S. C., G1 - G165.

- Hicks, S. D., and J. E. Crosby, 1974, Trends and variability of yearly mean sea level 1893-1972: U. S. Dept. Commerce, N.O.A.A. Tech. Memo., NOS 13, 16p.
- Humphries, S. M., 1977, Seasonal variation in morphology at North Inlet, South Carolina: Unpubl. Master's Thesis, Univ. South Carolina, Columbia, S. C., 97p.
- Kjerfve, B., 1975, Climatology: in Environmental Inventory of Kiawah Island, W. M. Campbell and J. M. Dean, Directors, Environmental Research Center, Inc., Columbia, S. C., C1 - C34.
- _____, J. E. Greer. and R. L. Crout, in press, Low frequency response of estuarine sea level to non-local forcing: in Estuarine Interactions, M. L. Wiley (ed.), Academic Press, p. 497-513.
- Nummedal, D., and S. M. Humphries, 1978, Hydraulics and dynamics of North Inlet, South Carolina, 1975-76: GITI Rept. 16, U. S. Army Coastal Eng. Res. Center, Fort Belvoir, Va.
- Odum, E. P. and A. D. de la Cruz, 1967, Particulate organic detritus in a Georgia salt marsh-estuarine ecosystem: in Estuaries, G. H. Lauf (ed.), Amer. Assoc. Advancement Science, Wash., D. C., p. 383-393.
- Patullo, J., W. Munk, R. Revelle, and E. Strong, 1955, The seasonal oscillation in sea level: Jour. Mar. Res., v. 14, p. 88-155.
- Pestrong, R., 1972a, Tidal flat sedimentation at Cooley Landing, southwest San Francisco Bay: Sediment. Geol., v. 8, p. 251-288.
- _____, 1972b, San Francisco Bay tidelands: Calif. Geol., v. 25, p. 27-46.
- Postma, H., 1967, Sediment transport and sedimentation in the estuarine environment: in Estuaries, G. H. Lauf (ed.), Amer. Assoc. Advancement Science, Pub. 83, Wash., D. C., p. 158-179.
- Settlemyre, J. L., and L. Gardner, 1975, A chemical and sediment budget for a small tidal creek, Charleston Harbor, South Carolina: Water Resources Res. Inst., Rept. No. 57, Clemson University, Clemson, S. C., 50p.
- Van Straaten, L.M.J.U., and P. H. Kuenen, 1957, Accumulation of fine-grained sediments in the Dutch Wadden Sea: Geologie Mijnb., v. 19, p. 329-354.
- _____, 1961, Sedimentation in tidal flat areas: Jour. Alberta Soc. Petroleum Geologist, v. 9, p. 203-213.

Ward, L. G., 1978, Hydrodynamics and sediment transport in a salt marsh tidal channel, Kiawah Island, South Carolina: Unpubl. Ph.D. Dissertation, Univ. South Carolina, Columbia, South Carolina.

_____, and D. D. Domeracki, 1978, The stratigraphic significance of back barrier tidal channel migration: (abs.), Annual Convention of Southeastern Geol. Soc. Amer., Chattanooga, Tenn.

CHAPTER 119

TWO-DIMENSIONAL STABILITY ANALYSIS OF TIDAL BASINS AND TIDAL FLATS OF LARGER EXTENT

by
Eberhard Renger ^{*)}.

Abstract

Stability studies of natural tidal basin system demand a regime-oriented analysis and a characteristic quantification of the morphological values. Hence it was necessary to create relative form parameterization dependent on the location by means of a two-dimensional system of natural coordinates (z = elevation, s = gully length coordinate).

The underlying logic for the determination of the equilibrium of the tidal basins and tidal flats is as follows:

When the continuity equation for non-steady flow at any cross-section (s_i, z_i) of a tidal basin, within the mean tidal range is applied, a dimensionless relationship between horizontal and vertical cross-sections (A and F) and tide-generated mean velocities of current (\bar{u}) and tidal rise and fall ($\pm v$) can be derived with an accuracy of more than 90 %:

$$\frac{u}{v} \approx \frac{A}{F}$$

The analysis of the term on the right-hand side of this equation showed a characteristic vertical distribution of the relationship for all investigated tidal basins of the German Bight and look rather similar. The reference values of the corresponding relationships depend on the area of the tidal basin (E) at MHW and the mean tidal range (H).

The influence of the horizontal extent has been elaborated by varying the line of intersection systematically along the gully-length-coordinate (s). In addition it was possible to point out the differences between the characteristics of stable and (well-known) non-stable conditions by means of a two-dimensional analysis of the dammed-off tidal river EIDER/German Bight.

The relations derived may prove to be useful in the planning of future constructions and even in understanding and influencing the disadvantageous changes in running systems.

^{*)} Dr. Ing. E. Renger, Senior Research Engineer,
Landesamt für Wasserhaushalt und Küsten, Kiel, Germany,
Head of Teilprojekt B3, Sonderforschungsbereich 79, Technical
University, Hannover

Introduction

Stability conditions of tidal basins and tidal flats have been mainly observed from natural systems of minimum morphological change. Some well-known basic relationships between morphological and hydrological components have been empirically derived by making wider comparisons of similar systems. As a fundamental result several investigations have pointed out the most important equilibrium relationships between the cross-sectional area of a tidal basin inlet and the associated tidal prism or the area of the tidal basin (see Ref.).

However, the entrance is only one particular part of a tidal basin or estuary. Cross-sections and tidal prisms show a characteristic variation during tidal rise and fall (z) and along the gully axis (s). As a consequence, and in addition to earlier stability investigations, the local distribution and the relationship between horizontal (s) and vertical (z) components of the system have to be taken into account.

The present paper concerns a two-dimensional analysis which has been elaborated in order to obtain basic informations about the forecasting-modelling of morphological change, i.e. the proof of stability and the calculation of sand balances.

Because of the complicated interactions within these "tidal basins with movable bed" attention is focussed on the following three aspects which in author's view are the most instructive with the knowledge that is available to us at the moment:

1. The method of analysis
2. The comparison of the derived form parameters due to stability conditions
3. The proof of instability and time-dependent change of the representative form parameters by means of the regime of the EIDER, a tidal river in the inner German Bight.

It is hoped that the relations derived may prove to be useful in the planning of future constructions and even in understanding and influencing the disadvantageous changes in running systems.

Basic assumptions and analysis

In contrast to the results of former investigations carried out by various authors, this investigation had to elaborate a two-dimensional approach to quantifying the tidal-hydrodynamic and morphological characteristics of the system as a whole. Therefore natural coordinates were assumed within the area of the tidal basin both vertically (z = elevation) and horizontally (s = gully length coordinate).

The horizontal and vertical cross-sections (A and F) were measured and calculated from the maps at a scale of 1 : 10 000. They were mainly analyzed within the mean tidal range for the 6 different tidal basins at the seaward boundary at the bar with the help of computers (Fig.3). It must emphatically be pointed out that a comparison of tidal basins as a whole can only be successful if they are taken as a physiographic unit within the seaward boundary at the bar! RENGER, (5,7)

The physical behaviour of the tidal wave within the basin may be easily described by the continuity equation for non-steady flow.

$$u = \frac{\tilde{A}}{\tilde{F}} \cdot \frac{dh}{dt} \quad (1)$$

On the right-hand side of Fig. 1 there is a schematical cross-section over a plan view.

In this elementary tidal basin (section)

- the inflow volume ($Q \cdot dt$) equals the increase of the tidal volume ($\tilde{A} \cdot dh$) and
- the flow (Q) equals the term ($\tilde{F} \cdot u$).
- The mean velocity of tidal rise and fall (dh/dt) is substituted by (v) - as seen on the left hand side of Fig. 1.

When these basic equations are combined the mean current velocity (u) in the cross-section (\tilde{F}) is derived within a good accuracy as

$$u = \frac{\tilde{A}}{\tilde{F}} \cdot v \quad (2)$$

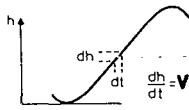
When this equation is transformed into a dimensionless expression, the hydrodynamical components are separated from the morphological ones (Fig. 2)

$$\frac{u}{v} = \frac{\tilde{A}}{\tilde{F}} = \frac{A}{F} \quad (3)$$

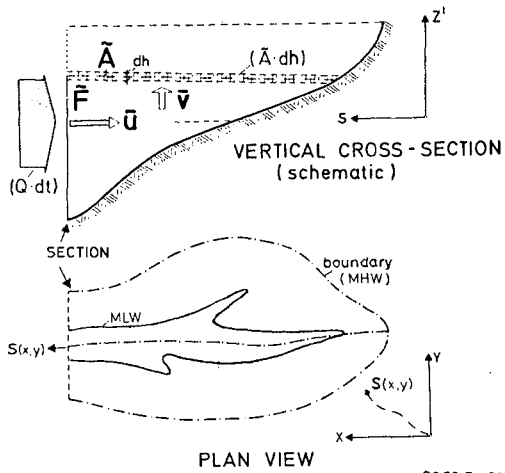
\swarrow morphological
 \downarrow hydrological

As the values depend exactly on three variables of space and time $f(z,s,t)$ a restriction on two variables of space is very useful in this first approach. Thus the term on the right-hand side of this equation was preferred for analysis. In addition the morphological system shows an integrating character from the morphogenetic point of view because of its much greater inertia of change.

TIDAL CURVE



TIDAL BASIN



CONTINUITY

(1) $Q \cdot dt = \tilde{A} \cdot dh$

(2) $Q = \tilde{F} \cdot \tilde{u}$

(3) $\tilde{u} = (\tilde{A}/\tilde{F}) \cdot \tilde{v}$

CURRENT VELOCITY

08 78 Re 01

Fig. 1

from $\tilde{u} = (\tilde{A}/\tilde{F}) \cdot \tilde{v} \rightsquigarrow$

$\frac{U}{V} \approx \frac{A}{F}$	-- HORIZONTAL
	-- VERTICAL

MEAN VELOCITIES CROSS-SECTIONS
HYDROLOGY MORPHOLOGY

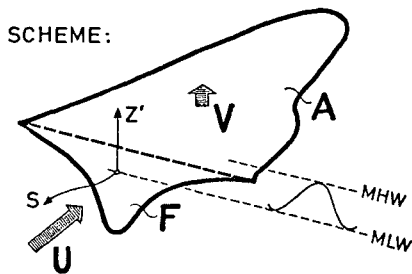


Fig. 2

08 78 Re 02

TIDAL BASINS

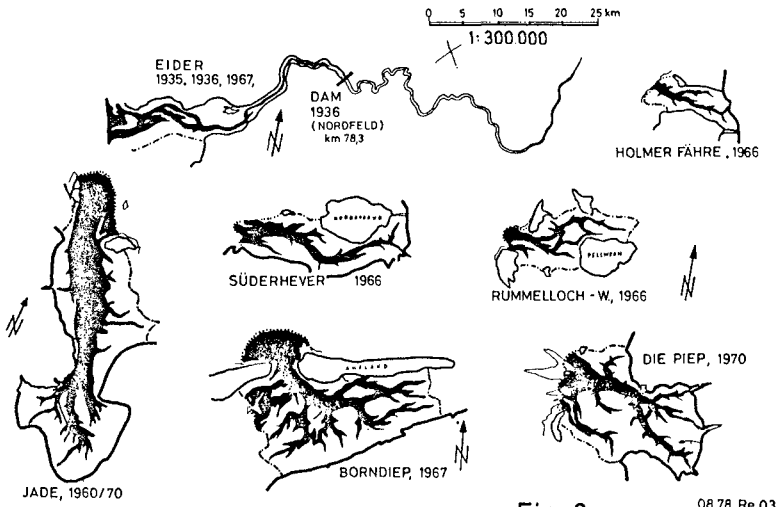


Fig. 3

08 78 Re 03

TIDAL BASINS

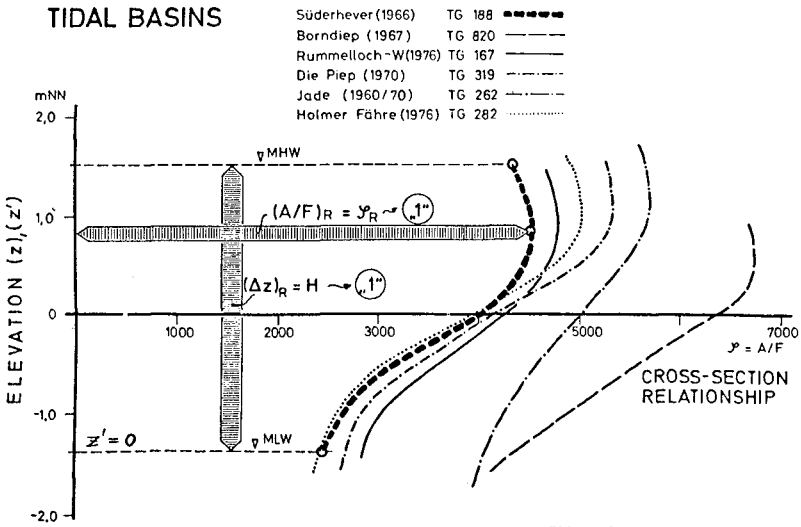


Fig. 4

08 78 Re 04

One-dimensional comparison of tidal basins as a unit (E_{σ})

The vertical distribution of the corresponding relationships (A/F) are shown in Fig. 4.

As a first result it can be pointed out that

- the curves show a characteristic distribution in the vertical and look rather similar,
- the (A/F) varies from about 2,500 at MLW up to 7,000 and more at MHW, and that
- there is an optimum near MHW, which has to be pointed out for future analysis.

In order to make the systems comparable the distribution functions were made uniform in both variables. Therefore the vertical component (z) was shifted to MLW (z') and related to the mean tidal range (H), with ($\zeta = z'/H$). (4)

The abscissa (A/F = \mathcal{J}) was related to the optimum value of (\mathcal{J}), with $\mathcal{J}^* = [(A/F)/(A/F)_R]$. (5)

This dimensionless relationship

$$\mathcal{J}^* = f(\zeta) \quad (6)$$

is used as a basic relationship for every further comparison (see Fig. 5).

The following 4 parameters are of main interest for the stability analysis:

- the vertical distribution curve ($\mathcal{J}^*(\zeta)$)
- the range of the (\mathcal{J}_R)
- the range of the corresponding (A_R) (meaning a "measuring area" for modelling purposes)
- the mean tidal range (H)

As a first result of this investigation about morphological similarity it was possible to work out some significant attributes:

- The vertical distribution-curve ($\mathcal{J}^*(\zeta)$) shows a rather uniform characteristic.
- The (\mathcal{J}_R) (at the optimum) was found to have an average value of about 5,200 for the inner German Bight with a mean tidal range of about 3 m (cf. table on Fig. 5 and upper graph of Fig. 10).
- One investigated tidal basin of an area with a smaller mean tidal range of about 2,2 m (Borndiep, The Netherlands) showed a greater \mathcal{J}_R -value.
- The A_R -value was found nearly to be almost equal with the area of the tidal basin (E) at MHW-level.

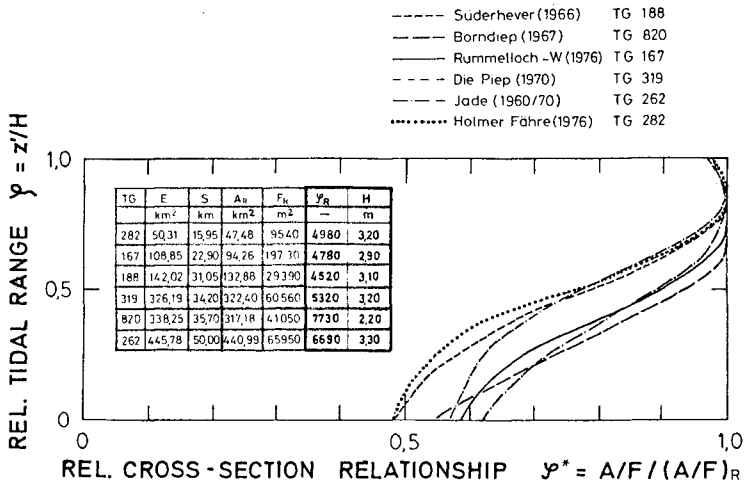


Fig. 5

0878 Re 05

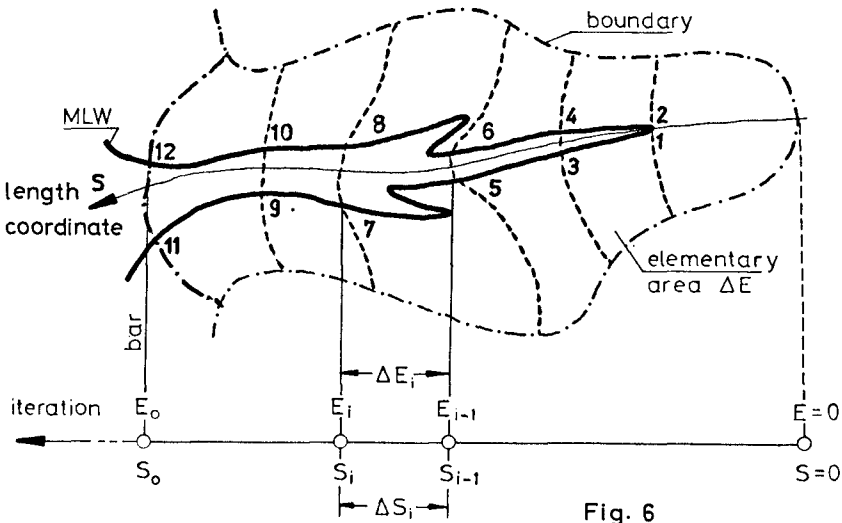


Fig. 6

Two-dimensional comparison of tidal basins within the physiographical unit (E_0)

In order to ascertain the horizontal variation of the relationships within the tidal basins, the sections were iteratively varied along the gully axis (see Fig. 6); in other words:

the $A(z)$ becomes an increasing variable due to the gully-length coordinate (s) (Ref. 7). Precisely the procedure of analysis was carried out at every section as explained before.

The vertical variation ($\mathcal{Y}^*(\mathcal{Y})$) due to the gully length (s) of three investigates tidal basins of very different size and type is shown in the next three graphs (Figs. 7,8,9).

Fig.	Tidal basin	Area at MHW (E_0)	Mean tidal range (H)
7	Süderhever, 1966	142 km ²	3,0 m
8	Born-diep (NL)1967	320 km ²	2,2 m
9	Jade-Estuary 1960/70	446 km ²	3,3 m

One most important result is that in every example the set of curves look rather similar and the curves always coincide very well.

The horizontal variation of the morphological characteristics only shows differences in the \mathcal{Y}_x -value. The dimensionless reference parameter seems to depend mainly on the mean tidal range (Fig. 10). On the one hand it is dependent on the order of the tidal range in general and on the other hand it seems to increase due to the decreasing tidal range along the gully length coordinate from land to sea.

The proof of instability

Referring to the last graphs on Fig. 10 we find some irregularities and deviations which may be of different origins, such as:

- methodical errors or mistakes
- influence of simplification (2 variables of space)
- individual attributes of the system that are not covered by the approach
- or even a certain degree of instability.



SÜDERHEVER 1966

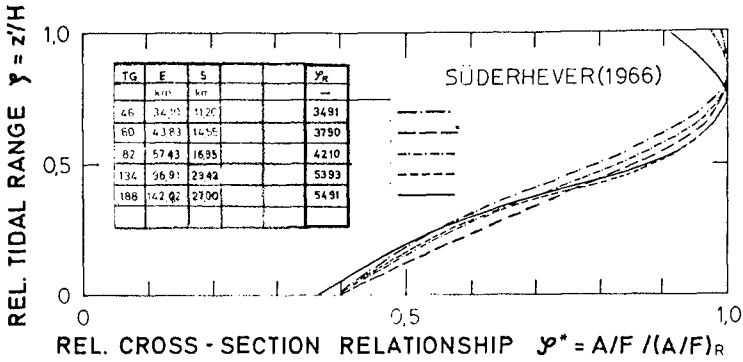
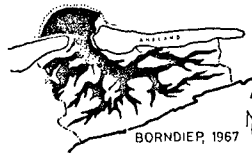


Fig. 7



BORNDIEP, 1967

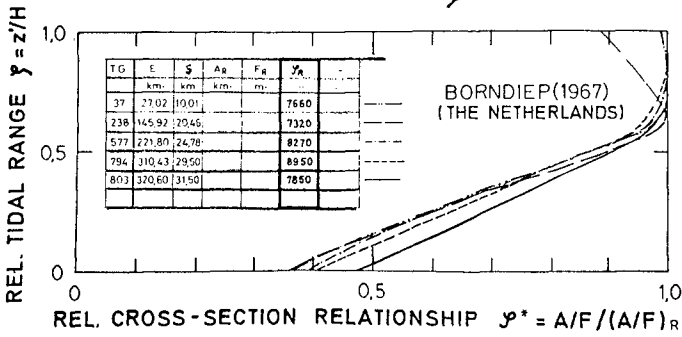


Fig. 8

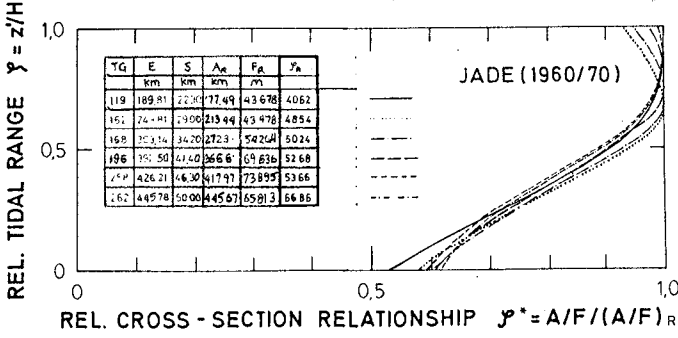
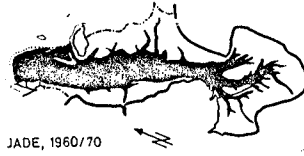


Fig. 9

0878 Re 08

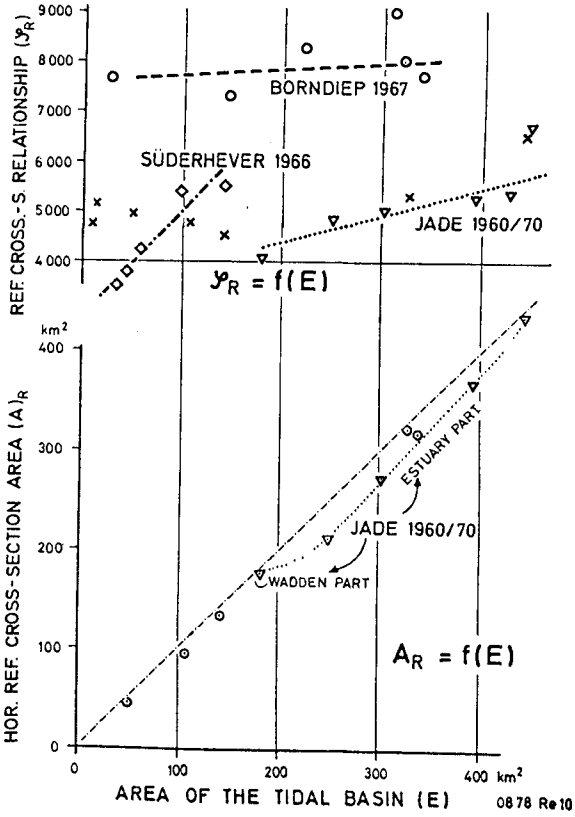


Fig. 10

0878 Re 10

However, this is an open question at the present, and the deviations must be analyzed systematically by future investigations.

For these reasons we have to appreciate all the more the measurements of a tidal regime in the nature of which the non stability is well-known from its time-dependent change in the past towards an equilibrium state. The change of the characteristic form parameters are to be proved by the tidal river EIDER in the inner German Bight, which was dammed off at km 78 in 1936 (note the black part on Fig. 11.)

To get some idea about the change of the regime during the following 30 years the very heavy accumulation of about 50 Mio m³ of silt has been observed outside the barrage over an area of about 25 km² and 30 km length.

In the lower part of the graph 3 time-stages of the investigated change of the regime are shown schematically (1935, 1936 and 1967). As an example the three time-stages are pointed out for the selected profiles nos. 78 and 115 at km 10 and km 20 in front of the barrage which are to be discussed subsequently in the next two graphs (Figs. 12 and 13).

The related (A/F)-distribution $\mathcal{Y}^*(\zeta)$ is nearly the same just before and just after the damming off in 1935 and 1936 as can be shown on both profiles. But in contrast, the $\mathcal{Y}^*(\zeta)$ -curve of the situation 31 years later in 1967 after the heavy accumulation mentioned above is not quite similar.

The corresponding \mathcal{Y}_R -distribution due to the length-coordinate (s) is given in the next graph (Fig. 14). It is surprising to find that the \mathcal{Y}_R -values of the non-influenced tidal river EIDER as a constant almost exactly the same as the average value of about 5,200 that was analyzed from tidal basins, although the $\mathcal{Y}^*(\zeta)$ -curve was very different.

At the second time-stage just after the damming-off the reference values were found to be drastically diminished, as can be seen from the dotted line near the abscissa. Within the next 31 years the values had increased slowly towards the original level of 5,200 due to the accumulation of silt that had taken place.

At the moment we are not quite sure about the degree of non-stability (instability) because the type of the tidal basin has changed too much. But for other reasons a certain accumulation in consequence of the damming-off is still to be expected.

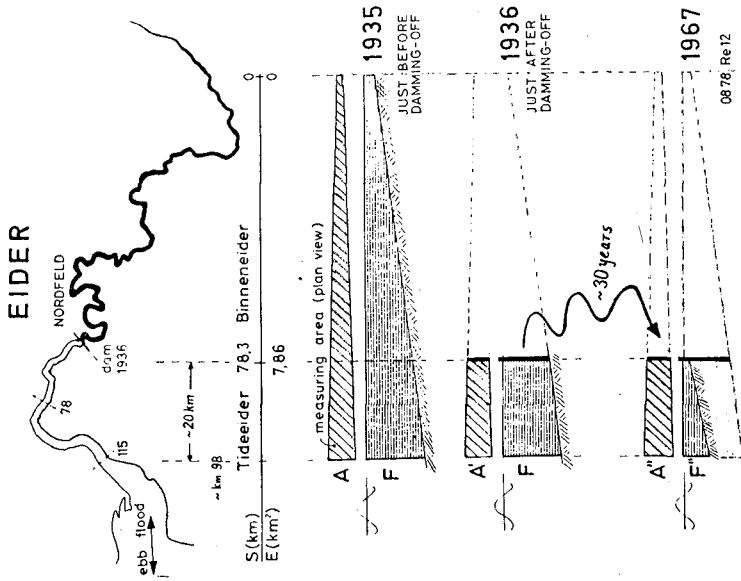


Fig. 11

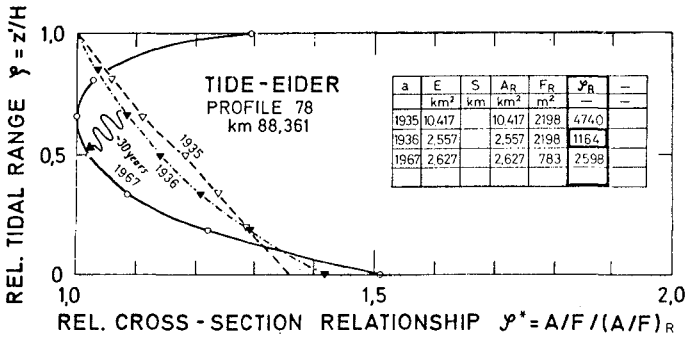


Fig. 12

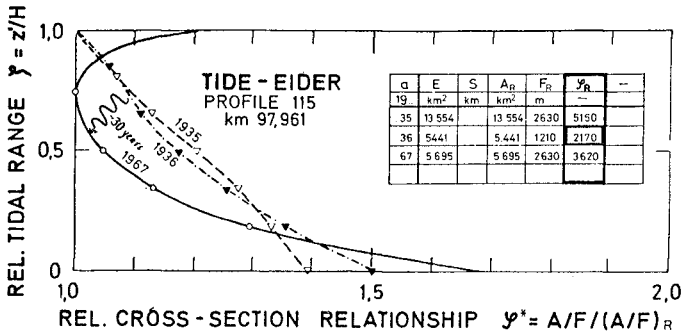


Fig. 13

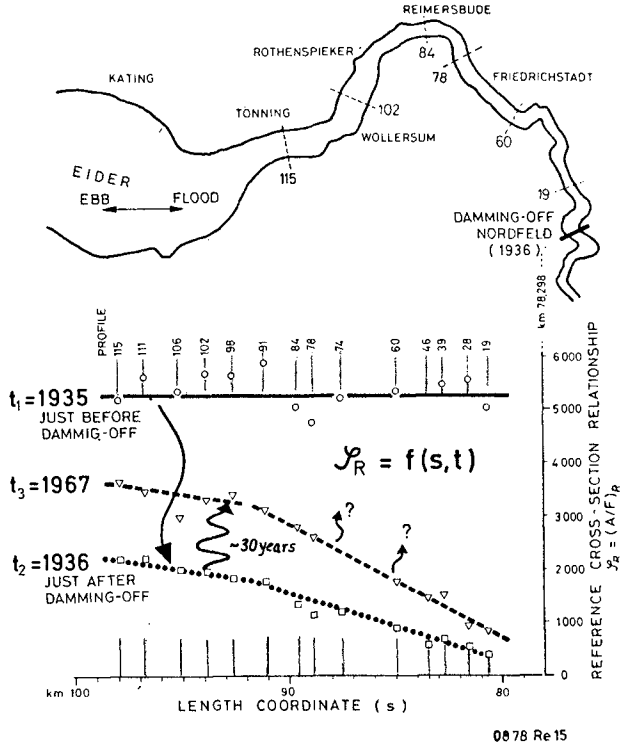


Fig. 14

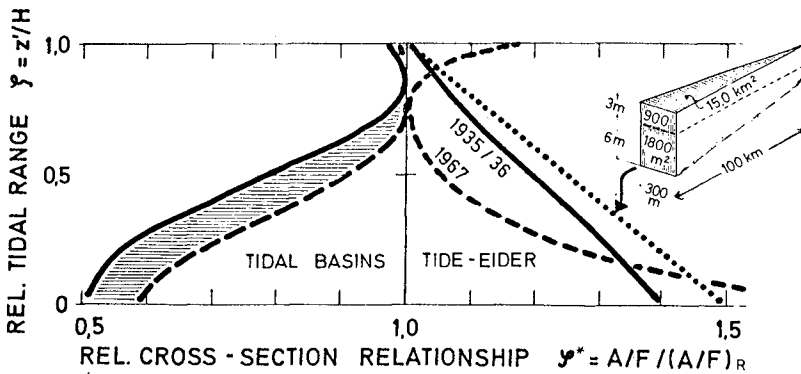


Fig. 15

Conclusions

Morphological change of tidal regimes is, to be precise, dependent on four variables:

- 3 variables of space and
- 1 variable of time

In addition complicated boundary conditions of the regime have to be covered. As a consequence a certain simplification due to the approach and a certain selection of parameters as well as a drastic data reduction is necessary and even possible.

In order to apply the method, morphological data (maps) in particular, as well as mean tidal conditions, must be known. The extensive quantity of data can only be handled with the help of computers, as has been pointed out in earlier publications.

Because of open boundary conditions in tidal flats, stability criteria must be specified by further systematic investigations, and with reference to the boundary conditions. The universal application of these investigations to other tidal basin systems may result in similar equilibrium characteristics.

At the moment there are only a few results, and these have only exemplary significance. But these first results promise to be a good tool in stability analysis and forecasting modelling of tidal flats and tidal basins due to man-made influences on the regime.

Acknowledgements

This study is part of the Research Project "Morphological Analysis of Tidal Basins" which is carried out in the Special Research Center 79 of the Technical University of Hannover. The research upon which this paper is based was supported by the Deutsche Forschungsgemeinschaft which is gratefully acknowledged by the author.

Morphological data was provided by various coastal administrations of Germany, The Netherlands, Denmark and Great Britain. Special thanks are due to my colleagues Dipl.-Ing. H. Messal and R. Dieckmann who were always available for help and discussion.

References

- 1) BRUUN, P., GERRITSEN, M.: Stability of Coastal Inlets. Journal of the waterways and Harbors Division. Proc. of the ASCE WW3, May 1958
- 2) HENSEN, W.: Ausbau der seewärtigen Zufahrten zu den deutschen Nordseehäfen, Hansa Nr. 15, 1971
- 3) O'BRIEN, M.P.: Equilibrium Flow Areas of Inlets on Sandy Coasts. Journal of Waterways and Harbors Div. Proc. of the ASCE. Vol. 15, No. WWI, Feb. 1969
- 4) RENGGER, E., PARTENSKY, H.-W.: Stability Criteria for Tidal Basins. Proc. 14th Int. Conf. on Coastal Engineering, 1974
- 5) RENGGER, E.: Quantitative Analyse der Morphologie von Wateinzugsgebieten und Tidebecken. Mitteilungen des Franzius-Instituts für Wasserbau und Küsteningenieurwesen der TU Hannover, H. 43, 1976
- 6) RENGGER, E.: Grundzüge der Analyse und Berechnung der Morphologie von Wateinzugsgebieten und Tidebecken. Mitteilungen des Franzius-Instituts für Wasserbau und Küsteningenieurwesen der TU Hannover, H. 44, 1976
- 7) RENGGER, E.: Quantitative Geomorphological Analysis of Erosional Topography with Respect to the Morphology of Tidal Basins. XVII Int. Conf. Ass. for Hydr. Res. 1977
- 8) RODLOFF, W.: Über Wattwasserläufe. Mitteilungen des Franzius-Instituts für Grund- und Wasserbau der TU Hannover, H. 34, 1970
- 9) VOLLMERS, H., GIESE, E.: On the Reproduction of morphological Changes in a Coastal Model with movable Bed, Proc. XVI. IAHR Congress, Sao Paulo, Vol. I., 1975
- 10) WALTHER, Fr.: Zusammenhänge zwischen der Größe der ostfriesischen Seegaten mit ihren Wattgebieten sowie den Gezeiten und Strömungen. Forschungsstelle Norderney der Niedersächsischen Wasserwirtschaftsverwaltung, Jahresbericht 1971, Band 23, 1972

CHAPTER 120

TIDAL SEDIMENTATION IN GROS-CACOUNA HARBOR

by

Georges Drapeau¹ and Guy Fortin²

ABSTRACT

The harbor of Gros-Cacouna on the South shore of the St. Lawrence Estuary has been silting at the rate of 31 cm/yr. since it was dredged at the depth of 14 meters in 1968. Measurements of temperature, salinity, turbidity, current speed and direction were carried out as well as bottom sampling and reflection seismic profiling. A model of suspended sediment transport combines the tidal volumes and the current profiles at the harbor entrance.

During a period of high turbidity (Spring) in the St. Lawrence Estuary, 54.2 tons of suspended sediments entered the harbor during the flood phase, while 41.1 tons were carried out during the ebb phase of a semi-diurnal tide, leaving 13.1 tons of sediments in the harbor. The transfer coefficient is 0.24 indicating that one quarter of the suspended sediment load settles in the harbor during one tidal cycle. In September, the turbidity is low in the Estuary and the suspended sediment budget in the harbor is 4 times smaller but the ratio of deposited sediments versus the total quantity of sediments transported in suspension is the same.

INTRODUCTION

The harbor of Gros-Cacouna is located on the south shore of the St. Lawrence Estuary at latitude 47°55'42" North and longitude 69°31'12" West, 230 kilometers downstream Quebec city (Fig. 1).

The St. Lawrence Estuary is 20 km wide and 70 meters deep off Gros-Cacouna. Water temperature varies between 10°C and freezing.

-
1. INRS-Océanologie, Université du Québec, Rimouski, Qué. Canada G5L 3A1
 2. Section d'Océanographie, Université du Québec à Rimouski.

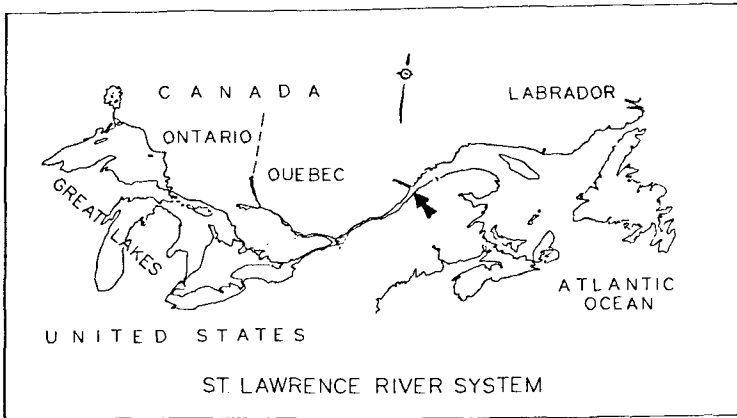


FIGURE 1 The location of Gros-Cacouna harbor on south shore of St. Lawrence River system is shown by an arrow.

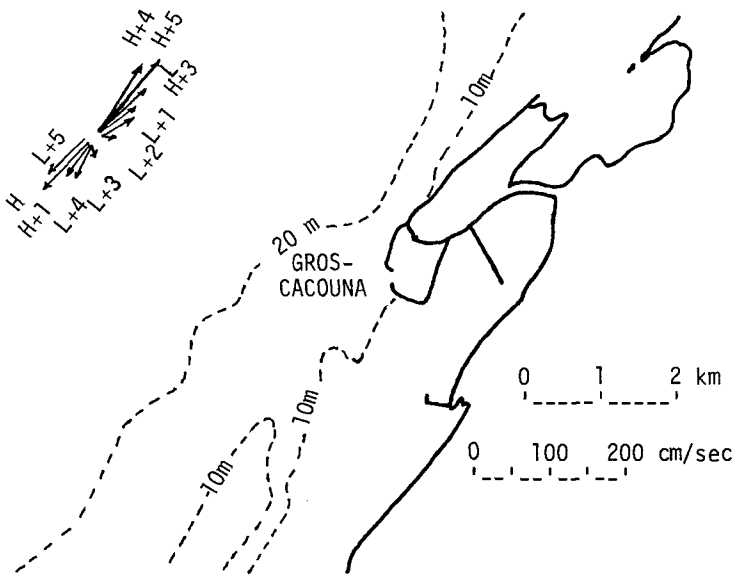


FIGURE 2 Location of Gros-Cacouna harbor at the southern end of Gros-Cacouna Island and rose of offshore tidal currents (H: high tide, L: low tide, H+1: one hour after high tide, etc). (Canadian Hydrographic Service, 1939).

The harbor is often surrounded by drifting ice in winter. Salinity varies seasonally and also with depth and ranges between 20 ‰ and 29 ‰. The limited fetch across the Estuary and the presence of islands along the southern coast prevent the formation of large waves. During the windiest month (January), 4 meter waves are expectable 5% of the time and only if the Estuary is not ice covered.

Tide is mixed, dominantly semi-diurnal, and ranges from 3.7 m (neap) to 5.7 m (spring). The difference between day and night tide reaches one meter at some phases of the lunar month.

Tidal currents in the St. Lawrence Estuary are strong and reverse with the semi-diurnal tide. Off Gros-Cacouna the surface currents reach 130 cm/sec during the ebbing tide and 100 cm/sec during the flood (fig. 2). The circulation is typically estuarine; the water column is stratified and the two layers are flowing in opposite directions most of the time, as observed outside the harbor during this survey as well as some 3 km offshore by d'Anglejan and Ingrassia (1976).

The rubble-mound jetties of Gros-Cacouna harbor were built in 1966. They enclose an area of $5.3 \times 10^5 \text{ m}^2$. A $2 \times 10^5 \text{ m}^2$ basin was dredged at a depth of 14 meters in 1968 (fig. 3). As the harbor was not yet complemented with wharves in 1976, it was an ideal hydraulic model where experiments could be carried out at the 1:1 scale.

Previous studies (E.R.S.L., 1973) indicated that the suspended sediment concentration was relatively high (10 to 19 mg/l) in the harbor and that siltation was progressing rapidly in the basin dredged in 1968. By contrast, essentially no sediment transport is taking place in the intertidal zone in this area. A small wharf at Cacouna Village did not retain sediments on either side since it was built 30 years ago.

FIELD INVESTIGATIONS AND METHODS

The suspended sediment load varies considerably in the St. Lawrence Estuary and is related to the fresh water run off of the St. Lawrence drainage Basin although that run off is regulated to 1.7:1 (Neu, 1976). Two cruises were organized to survey the harbor during periods of high turbidity (31 May - 4 June 1976) and low turbidity (30 August - 3 September 1976).

Precise measurements of temperature, salinity, turbidity, current speed and direction were carried out at the entrance and both inside and outside the harbor. Bottom samples were taken as well as continuous reflection seismic profiles to gain a thorough understanding of the harbor sedimentation dynamics. The precision of measurements was $\pm 0.02^\circ\text{C}$ for temperature, $\pm 0.02 \text{ mmhos/cm}$ for conductivity and $\pm 25 \text{ cm}$ for depth. Shipborne current measurements permitted to obtain continuous profiles of current speed and direction versus depth.

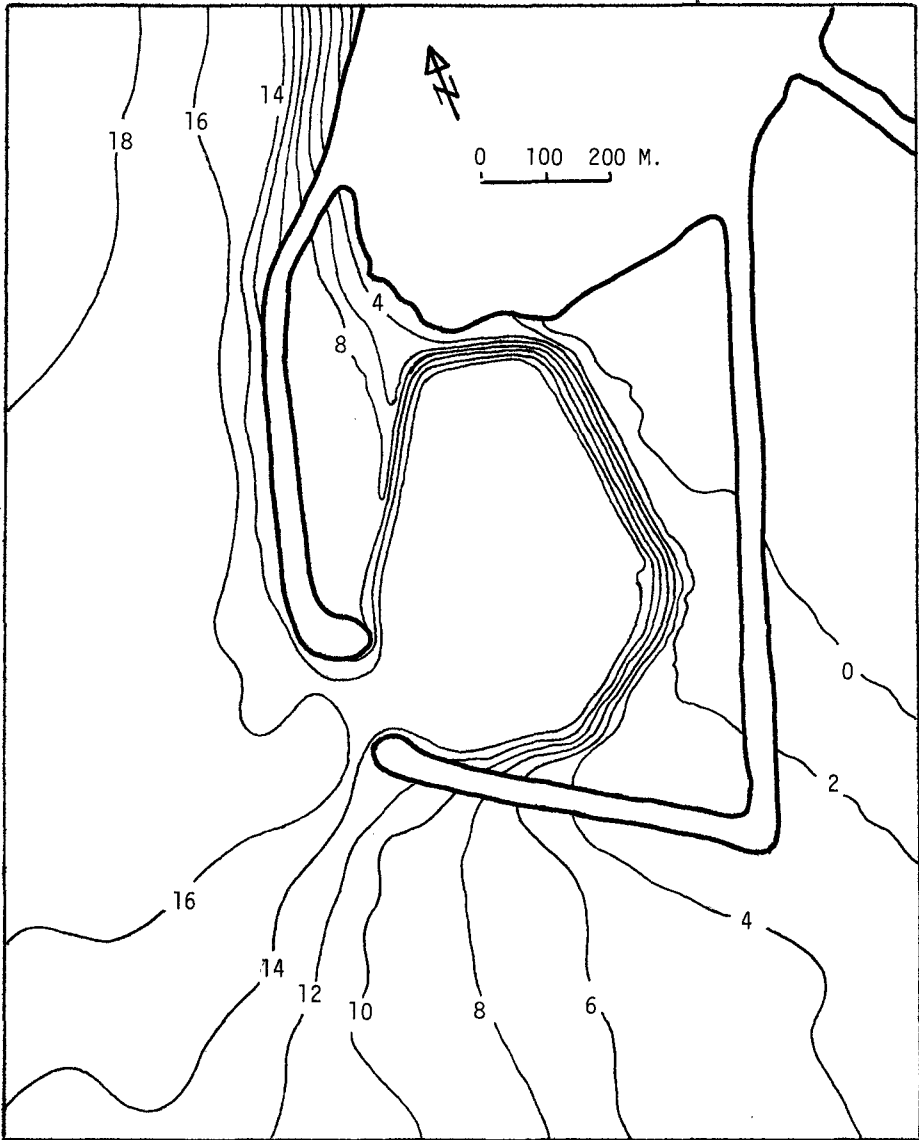


FIGURE 3 Bathymetry of Gros-Cacouna harbor (depth contours in meters).
The depth contours at two-meter intervals outline the basin dredged at a depth of 14 meters.

The concentration of suspended sediment particles was determined with a turbidimeter during the May-June cruise. Calibration of the instrument specifically for that cruise showed that the transmissivity for a 10 cm beam was linear within a range from 10 mg/l to 100 mg/l. During the August-September survey the suspended sediment concentration was too low to use a turbidimeter and the concentration of suspended sediments was determined by filtration of 250 ml water samples on 0.45 micron filters.

TIDAL CIRCULATION IN THE HARBOR ENTRANCE

The variation of current speeds and directions as a function of depth and time is shown in the upper portion of figure 4 for the day-time tide of September 1st, 1976. At high tide (09:00 hrs) water is flowing out of the harbor through the upper half of the entrance and inward at the bottom. The flow pattern evolves through the tidal cycle and at low tide (15:00 hrs) it has reversed and water flows inward through the upper half and flows out at the bottom of the entrance. This two-layer flow across the harbor entrance reflects the main features of the tide-induced circulation in the Estuary. The circulation of water masses across the harbor entrance more than compensates for changes of water levels due to the propagation of the tide in the harbor.

SEDIMENTATION RATE IN GROS-CACOUNA HARBOR

Continuous reflection seismic profiles were surveyed at the completion of the dredging of the harbor basin in 1968 and were repeated along the same base lines in 1971 and 1972 and during this survey, in 1976. Bottom samples were taken to determine the nature of the sediments deposited on the bottom of the basin since 1968. These data were used to determine the rate of sedimentation in the harbor. The results appear on table 1.

TABLE 1

SEDIMENTATION IN GROS-CACOUNA HARBOR ($2 \times 10^5 \text{ m}^2$ basin dredged in 1968)

	Volume ($\times 10^3 \text{ m}^3$)	Weight ($\times 10^3$ tons)	Sedimentation rate (cm/yr)
1968-72:	314.7	535	39
1972-76:	248.8	423	31
1968-76:	563.5	958	35

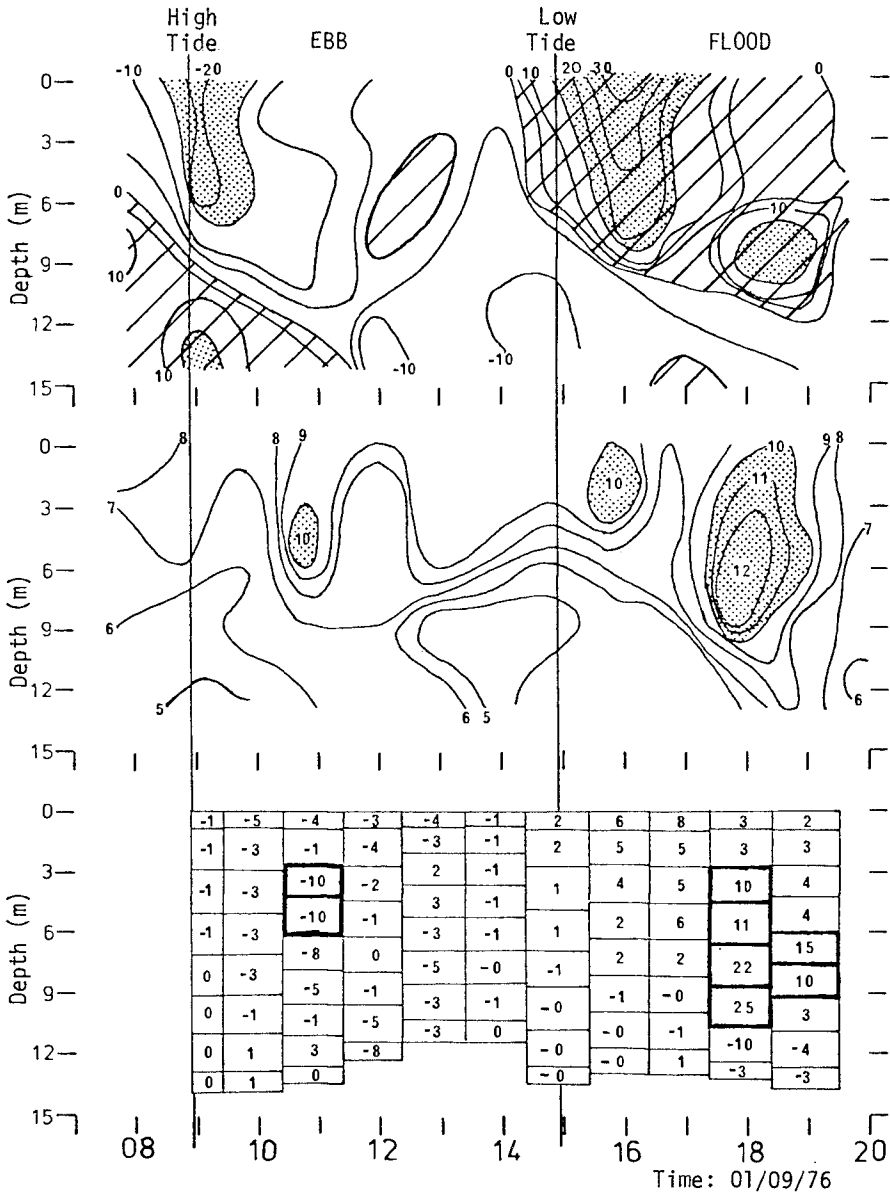


FIGURE 4 Top: Current speed profiles (cm/sec) as a function of time (ebb and flood) at the harbor entrance. Inflowing currents are positive and are outlined by inclined lines. Middle: Suspended sediment concentration (mg/l); inflow is positive. Bottom: Suspended sediment transport in hundreds of kilograms (+:inflow) corresponding to current velocities and suspended sediment concentrations shown above.

The texture of these sediments ranges from sand to clay-size particles. On the basis of textural analyses of the sediments deposited in the basin, the total suspended load is estimated to be in the order of 268×10^3 tons (Fortin et Drapeau, 1979).

TRANSPORT MODEL FOR SUSPENDED SEDIMENTS

The tide being the dominant phenomenon, the objective of the model is to determine the net quantity of sediments that remain inside the harbor at the end of a tidal cycle. The problem is simplified by the fact that no rivers flow in the harbor, the jetties are impermeable and the harbor has only one entrance.

Firstly the flow pattern at the entrance is determined and secondly the measurements of suspended sediment concentration are used to calculate the transport of sediments based on the flow pattern.

Flow at the harbor entrance

The proposed model is empirical and integrates two types of data: 1) tidal volumes of the harbor, that is the net quantity of water flowing through the harbor entrance calculated on the basis of changes of water level during given time intervals, and 2) current velocity profiles measured at the harbor entrance for the same time intervals.

The net volume of water (W_i) either entering or flowing out of the harbor during a specific time interval (ΔT_i) is the product of the change of height (ΔH_i) of the water level during that time interval by the area of the water surface of the harbor (A_i):

$$W_i = \Delta H_i A_i \quad (1)$$

To be significant in terms of sediment transport, it is essential at the end of the tidal cycle analysed that exactly the same volume of water flows in and out the harbor that is:

$$\sum W_i = 0 \quad (2)$$

Current speed and direction profiles were monitored at the harbor entrance with a shipborne current meter and recorded at 8 to 10 depths depending on the height of the tide. These current measurements are transformed into a matrix of current vectors $[V_{i,d}]$ perpendicular to the entrance of the harbor. The vectors are positive (+) for inflow.

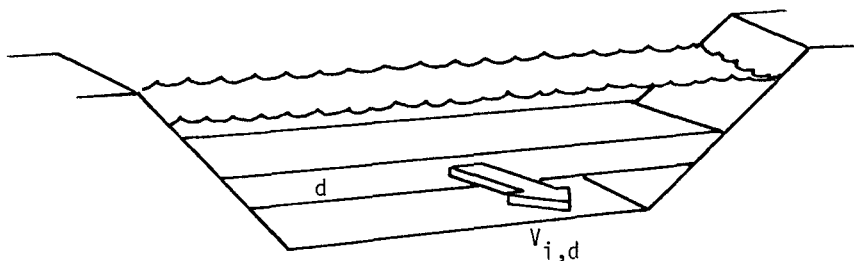


FIGURE 5

The cross-sectional area of the harbor entrance is divided into a given number (d) of horizontal layers corresponding to each current measurement. L_d is the cross-sectional area of each horizontal layer (see fig. 5).

During a given time interval ΔT_i , the volume of water ($Q_{i,d}$) flowing through one layer is:

$$Q_{i,d} = V_{i,d} L_d \Delta T_i \quad (3)$$

and the net flow of water through the entrance during the interval ΔT_i is:

$$Q_i = \left(\sum V_{i,d} L_d \right) \Delta T_i \quad (4)$$

In theory Q_i and W_i are equal. In practice hundreds of current measurements would be necessary to make Q_i consistently equal to W_i . This difficulty is overcome by calibrating the current vectors ($V_{i,d}$). A correction factor (C_i) is determined for each series (i) of measurements:

$$C_i = \frac{W_i}{Q_i} \quad (5)$$

This correction factor is used to generate a calibrated matrix of current vectors $[V_{i,d}^*]$

$$V_{i,d}^* = C_i V_{i,d} \quad (6)$$

These corrected current vectors are introduced in equations (3) and (4)

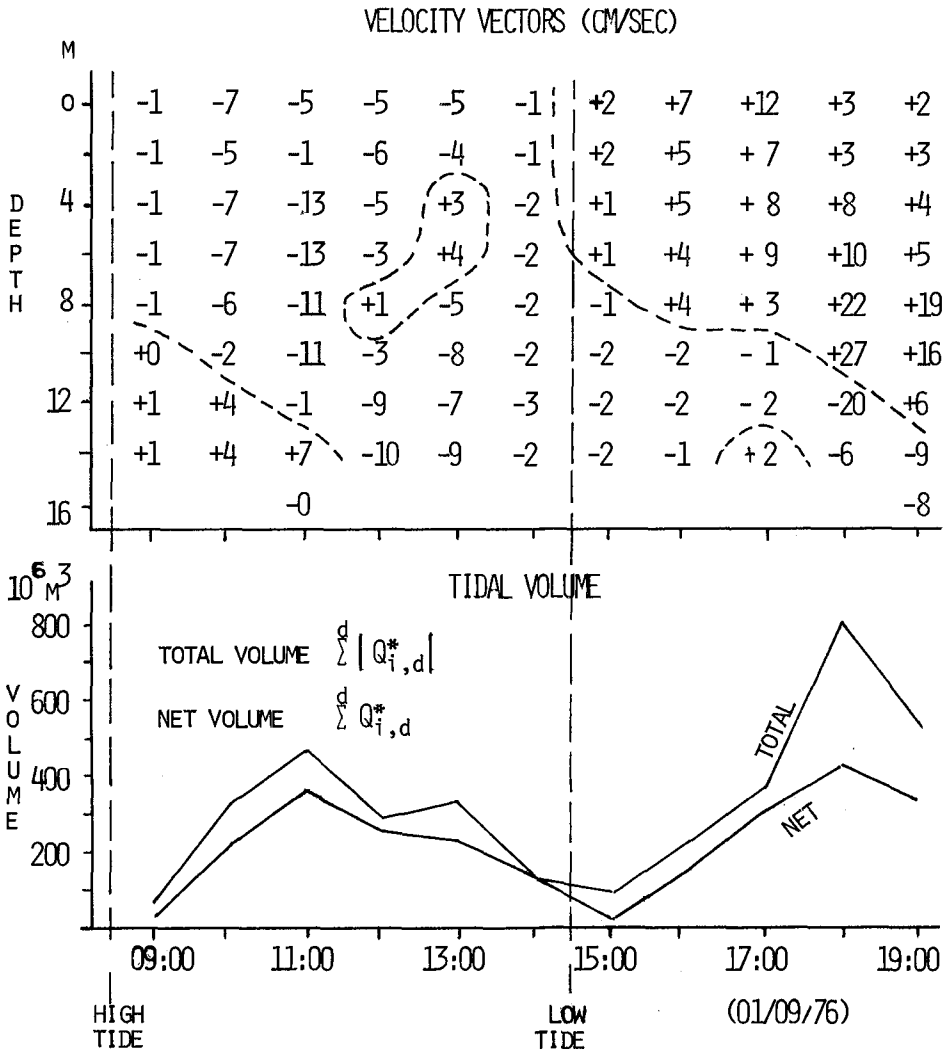


FIGURE 6 Top: Current vectors perpendicular to the cross-sectional area of the harbor entrance and calibrated according to the tidal volume of the harbor. Bottom: Diagram showing the net and the total volume of water flowing through the entrance of the harbor at different phases of the tide.

$$Q_{i,d}^* = V_{i,d}^* L_d \Delta T_i \quad (7)$$

$$Q_i^* = \left(\sum^d V_{i,d}^* L_d \right) \Delta T_i \quad (8)$$

These calibrated data fulfill the requirement that at the end of a tidal cycle, that is when the water level reaches the same height as at the beginning of the tidal cycle:

$$\sum Q_i^* = 0 \quad (9)$$

As already mentioned, the validity of the model is based on equation (9). The model has to be in accordance with the fact that tide in the harbor is a purely harmonic phenomenon.

The matrix of calibrated current vectors $[V_{i,d}^*]$ for September is tabulated on figure 6. It schematizes the circulation at the entrance of the harbor. The flow pattern has the same characteristics as those shown on the upper portion of fig. 4, except that the individual velocities are calibrated to fulfill the requirements of equation (9). The matrix outlines the two-layer circulation and its evolution with the progression of the tide. Only at station 33 is the whole water column flowing in the same direction. During all other time intervals the flow is bi-directional, that is, more water than necessary to compensate for the tide flows through the entrance of the harbor. The difference between the total flow ($\sum |Q_{i,d}^*|$) and the net flow ($\sum Q_i^*$) is outlined on the lower half of figure 6. Summation of these data indicates that 1.57 time the water necessary to compensate for the tidal volume of the harbor did flow through the entrance during that tidal cycle.

Transport of suspended sediments

Calculations for the transport of suspended sediments are based on the calibrated flow matrix $[Q_{i,d}^*]$ and the suspended sediment concentration measurements $(F_{i,d})$. The quantity of sediments $(S_{i,d})$ transported through one layer during a given time interval (ΔT_i) :

$$S_{i,d} = Q_{i,d}^* F_{i,d} \quad (10)$$

The net suspended sediment transport through the entrance during a given time interval is:

$$S_i = \sum^d Q_{i,d}^* F_{i,d} \quad (11)$$

The net suspended sediment transport during one tidal cycle is:

$$S = \sum S_i \quad (12)$$

TABLE 2

SUSPENDED SEDIMENT TRANSPORT, 1 JUNE 1976

Time (EDT)	Flow ($\times 10^3$ m ³)	Transport (kg)	Total Transport (kg)	Net Transport (kg)
High tide				
07:36-08:06	-200.7	-5,193		
08:06-08:35	-238.	-6,259		
08:35-09:00	-193.4	-4,532		
09:00-09:30	-246.5	-6,192		
09:30-10:00	-218.5	-6,195	-41,060	
10:00-10:24	-140.6	-3,894		
10:24-11:00	-147.8	-4,077		
11:00-11:27	- 95.9	-2,415		
11:27-11:58	- 71.1	-2,303		
11:58-12:27	0	458		13,138
Low tide				
12:27-12:58	46.3	2,146		
12:58-13:30	74.0	2,578		
13:30-13:56	102.4	3,782		
13:56-14:27	197.2	7,815		
14:27-14:59	201.8	8,820		
14:59-15:28	192.8	7,048	54,198	
15:28-15:57	208.0	7,344		
15:57-16:26	184.7	6,023		
16:26-16:56	143.3	4,375		
16:56-17:27	132.2	4,155		
17:27-18:00	67.7	- 346		

TABLE 3

SUSPENDED SEDIMENT TRANSPORT, 1 SEPT. 1976

High tide				
08:55-09:25	- 32.2	- 275		
09:25-10:27	-225.5	-1,624		
10:27-11:24	-385.1	-3,628		
11:24-12:23	-278.7	-2,422	-10,346	
12:23-13:23	-219.2	-1,716		
13:23-14:25	-111.6	- 681		3,466
Low tide				
14:25-15:26	13.8	350		
15:26-16:24	169.0	1,680	13,812	
16:24-17:24	317.5	2,487		
17:24-18:26	430.7	5,971		
18:26-19:37	322.1	3,324		

The results of these calculations for each time interval (S_i) and for the net transport during a tidal cycle (S) are shown on Table 2 for the June survey and on Table 3 for the September survey.

TRANSFER COEFFICIENT

Table 2 shows that during the tide studied in June, 54.2 tons of suspended sediments were transported inside the harbor during the flood of the tide while 41.1 tons were carried out during the ebb; leaving 13.1 tons in the harbor. This survey coincided with a period of high turbidity in the Estuary. The second survey (September) was carried out during a period of low turbidity and the suspended sediment transport rates were lower, as shown on Table 3. The net transport for a comparable tidal cycle was only 13.8 tons, that is 4 times less than in June. The proportion of sediments that remained in the harbor at the end of a tidal cycle is the same in both cases however. The term "transfer coefficient" is used to describe that characteristic.

Transfer coefficient:

June:	13138/54198 = 0.24
September :	3466/13812 = 0.25

The transfer coefficient bears some analogy with the "equilibrium concentration" defined by Mehta and Partheniades (1974) to discuss the depositional properties of estuarine sediments. The equilibrium concentration is a parameter defined experimentally while the transfer coefficient is empirical and would need further investigation.

COMPARISON OF SUSPENDED LOAD TRANSPORT WITH MEASURED SILTATION

The total accumulation of sediments in the harbor basin is in the order 95.8×10^4 tons over a period of 8 years, that is an average sedimentation of 164 tons per tidal cycle. A large proportion of these sediments is too coarse to be transported in suspension and the average transport in suspension is estimated to be 45.8 tons per tidal cycle (Fortin and Drapeau, 1979). That quantity of sediments is much higher than what was measured during June (13.1 tons) and September (3.5 tons) surveys.

The suspended sediment concentration most reach higher values in Gros-Cacouna area than those observed in June 1976 (24-48 mg/l). Although the turbidity maximum of the St. Lawrence Estuary is further upstream, the suspended sediment longitudinal gradient is 1.5 mg/l per kilometer in April-May in Gros-Cacouna area (Poulet and Chanut, 1979). High concentrations of suspended sediments are then susceptible to reach Gros-

Cacouna harbor and produce high siltation rates during these periods of high turbidity.

Differences in ranges of successive tides (1 meter at neap tides) can lengthen the residence of water masses in the harbor and favor the deposition of suspended sediments. The importance of this phenomenon is difficult to evaluate however at the present stage of the investigations.

SUSPENDED SEDIMENT TRANSPORT MECHANISMS

Distribution of suspended sediments

Figure 4 shows simultaneously the currents, the suspended sediment concentration and the transport of sediments across the entrance of the harbor during a tidal cycle. The suspended sediments are concentrated in streams in the upper half of the water column. This phenomenon has also been observed outside the harbor (Fortin, 1978). D'Anglejan and Ingram (1976) have sampled mid-depth concentration maxima once each semi-diurnal tidal cycle at seven stations surveyed in the Middle St. Lawrence Estuary. They relate these maxima to both the turning time of tidal currents from ebb to flood and the intensity of cross-channel flow.

Floculation

Floculation of fine sediment particles is playing an important role in Gros-Cacouna harbor. On the basis of a settling velocity of 0.5 mm/sec determined by Migniot (1977) for the muds of many estuaries, the flocculated suspended sediments could fall a distance of 7 meters (centrum of harbor depth) in 4 hours. If macro-flocs are formed, the settling velocity could be higher. Such mechanisms must be particularly efficient in Gros-Cacouna harbor considering the high rate of sedimentation.

Tidal volume

The concept of tidal basins as used by Renger and Partenscky (1974) and Renger (1978) is useful to evaluate the importance of tidal movements in the nearshore zone. The nearshore zone can be divided according to natural tidal basins or into more arbitrary cells. As shown on figure 7 a cell of width A , the size of the harbor, is delineated perpendicularly to the coast. The change of tidal volume of that cell is calculated for different heights of the tide. If the cross-sectional area A is considered, less water is flowing through that cross-section because of the presence of the harbor that prevents the free movement of water.

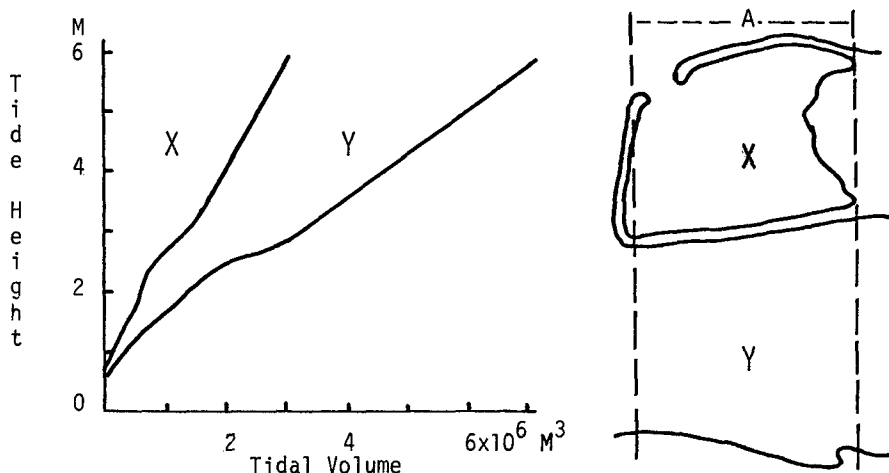


FIGURE 7

The diagram on figure 7 shows the volume of water flowing in the harbor as well as the total volume of water that would otherwise flow through the cross-sectional area A. Less than half the initial volume of water is now flowing over the harbor area. It disrupts the hydraulic equilibrium that used to prevail. Although water is flowing faster at the very entrance of the harbor, the water mass is more tranquil and sedimentation is favored.

ACKNOWLEDGEMENT

This research was supported by the National Research Council of Canada, CNRC Grant A-8862.

REFERENCES

- D'Anglejan, B. and R.G. Ingram, 1976, Time-depth variations in tidal flux suspended matter in the St. Lawrence Estuary: *Estuarine and Coastal Marine Science*, V.4, p. 401-416.
- Canadian Hydrographic Service, 1939, Tidal current Charts, St. Lawrence Estuary, Orleans Island to Father's Point, Tidal Publication No. 21.
- E.R.S.L., 1973, Etude des paramètres hydrauliques du port de Gros-Cacouna, Ministère des Travaux Publics du Canada: Etude des Rives du St-Laurent, 42 p.

- Fortin, G., 1978, Etude de la sédimentation dans le port de Gros-Cacouna, Estuaire du St-Laurent: Master of Sciences Thesis, Université du Québec, 112 p.
- Fortin, G. and G. Drapeau, 1979, Envasement du port de Gros-Cacouna, Estuaire du St-Laurent: *Naturaliste Canadien* (in press).
- Mehta, A.J. and E. Partheniades, 1974, On the depositional properties of estuarine sediments: Proc. 14th Conf. on Coastal Engr., p. 1232-1251.
- Migniot, C., 1977, Action des courants, de la houle et du vent sur les sédiments: *La Houille Blanche*, 1-1977, p. 9-47.
- Neu, H.J.A., 1976, Runoff regulation for hydro-power and its effect on the ocean environment: *Bull. Sci. Hydrol.* V. 31, p. 433-444.
- Poulet, S.A. and J.P. Chanut, 1979, Analyse factorielle des particules en suspension II. Variations dans l'Estuaire et le Golfe du Saint-Laurent (in preparation).
- Renger, E., 1978, Two-dimensional stability analysis of tidal basins and tidal flats of larger extent: 16th International Conf. on Coastal Engineering, paper 62, Hamburg, Aug. 27-Sept. 3, 1978.
- Renger, E. and H.W. Partenscky, 1974, Stability criteria for tidal basins: Proc. 14th Conf. on Coastal Engr. Vol. 2, p. 1605-1618.

CHAPTER 121

Factors Governing The Distribution of Dredge - Resuspended Sediments

W. Frank Bohlen

Marine Sciences Institute
and
The Department of Geology and Geophysics
University of Connecticut
Avery Point
Groton, Connecticut
U. S. A.

ABSTRACT

Field observations are analyzed to determine the primary factors governing the distribution of sediments suspended by clam-shell bucket dredge operations. These data show the plumes produced under typical estuarine conditions to be relatively small scale features having maximum longstream dimensions of approximately 700 m. Plumes can be considered to consist of three contiguous zones: an initial mixing zone, a secondary zone and a final mixing zone. The initial mixing zone immediately adjacent to the dredge has dimensions governed by bucket induced mixing and suspended material concentrations determined by dredge efficiency. Observations indicate that dimensions can be reasonably estimated using wake theory and that efficiencies result in the introduction of 2-4% of the sediment mass contained in each bucket load. Resultant concentrations range between 200 and 400 mg/ℓ. Progressing downstream into the secondary mixing zone concentrations decay rapidly due primarily to gravitational settling. The observed decay rates indicate an average settling velocity of 4.7cm/sec well in excess of values based on the grain size characteristics of the dredged sediment. The behavior suggests significant particle agglomeration within this area. At the downstream limit of this zone distributions become essentially exponential in character and remain so through the final mixing zone. In this area concentrations progressively approach the upstream background levels and variations are governed primarily by diffusion. In each of these zones the observed distributions appear amenable to relatively straightforward modeling.

Introduction

In many coastal areas of the United States routine channel dredging represents the most common marine engineering operation. Much of the sediment removed during these projects is contaminated by a variety of organic and inorganic compounds, and as a result dredge-induced suspensions have the potential to perturb water quality and impact local biota. During the past few years a variety of investigations have been conducted to assess both the short and long term character of these impacts (see the review by Morton, 1976). In addition some investigations have examined dredge efficiency (Yagi, et. al., 1977) and developed schemes intended to reduce and/or predict project related turbidity (Huston and Huston, 1976; Barnard, 1978). The majority of these studies however, provided little quantitative information concerning the distribution and dispersion of materials suspended by the dredge. This paucity of data has tended to limit the development of predictive schemes applicable within coastal and estuarine waters.

During the summer and early fall of 1977 several detailed surveys of dredge-induced suspended material plumes were conducted within the lower Thames River estuary near New London, Connecticut (Bohlen, et. al., 1978). Suspended material distributions were sampled and both concentration levels and composition were analyzed. These data provide a reasonably comprehensive view of the longstream character of the dredge-induced plume and permit evaluations of both dredge efficiency and some of the primary factors governing the distribution and dispersion of the suspended sediments. This paper presents the results of these evaluations.

Study Area and Project Characteristics

Long Island Sound (Fig. 1) represents one of the major embayments along the eastern coast of the United States. Extending a distance of approximately 120 Km to the east of New York City, the Sound has a varied coastline providing several major port areas and numerous smaller, recreational anchorages. Regional hydrography dominated by the interactions between freshwaters supplied by three river systems entering along the northern margin and the local tidal currents favors nearshore deposition of fine grained sediments and requires regular dredging to maintain port and harbor viability. These dredging operations typically employ one of three methods; hydraulic, dragline or clamshell bucket. Hydraulic and dragline techniques have typically been restricted to relatively small volume projects. Major projects involving the removal of more than 100,000 m³ of material generally have employed clamshell buckets and hopper barges to transport spoils for disposal at selected offshore sites.

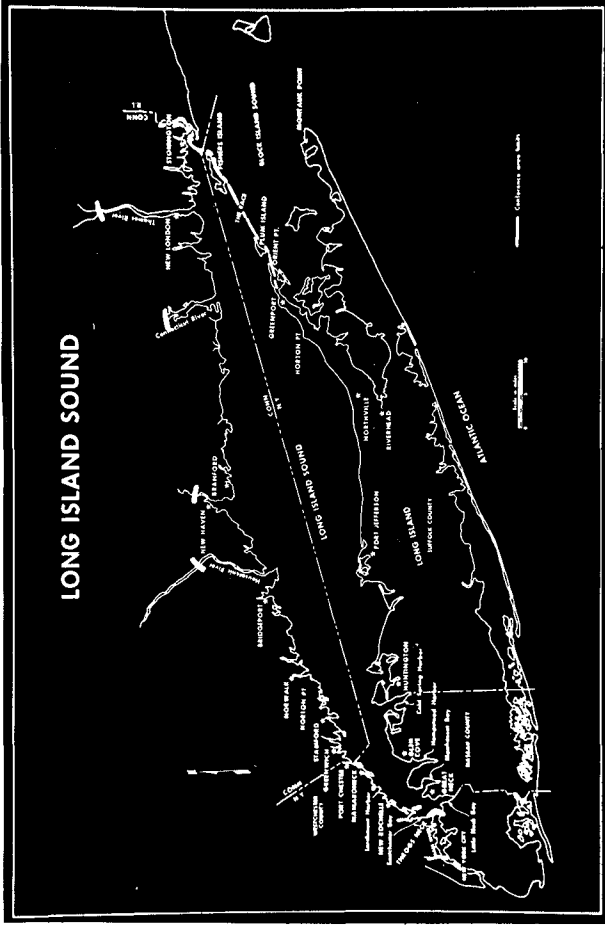


Fig. 1. Long Island Sound. Note the location of the Thames River entering near the eastern limit in the vicinity of New London, Connecticut.

Since 1974 the lower Thames River (Fig. 2) has been the site of a major dredging project intended to increase the depth of the main navigational channel to approximately 10 - 12 m. This stream is a typical small estuary having an annual average streamflow of approximately $75 \text{ m}^3/\text{sec}$ and tidal range of 0.78 m at New London. The combination produces a density field displaying persistent vertical stratification and an evident seasonal variability. Wind stress effects are generally negligible.

In July of 1977 dredging of the northern reach of the project area (outlined in Fig. 2) was initiated. Local sediments consisting primarily of fine-grained sands and silts (Fig. 3a) were removed using a floating barge-mounted crane equipped with a 10 m^3 open clamshell bucket (Fig 3b). Spoils were placed in a 1500 m^3 hopper barge typically moored alongside the operating dredge. This operation served to introduce sediments into the water column due primarily to bottom impact and washover from the open bucket during the subsequent ascent phase (Fig. 4a). The volumes of material supplied by overflow from the barge were negligible.

Survey Methods and Procedures.

In August and September, 1977 the suspended material plume extending downstream of the operating dredge was surveyed in detail (see Fig 2 for dredge locations). Hydrographic conditions during both survey periods were essentially identical although a slight increase in streamflow in September caused a decrease in near surface salinity and increased the degree of vertical stratification characteristic of the local density field (Fig. 4b).

The field methods and analytical procedures used in these surveys have been described in detail in an earlier paper (Bohlen, et. al., 1978). Very briefly, optical techniques were used to define the limits of the plume and to establish a network of stations along the defined centerline. At each station the suspended material field was sampled directly using 5ℓ van Dorn bottles. These samples were returned to the laboratory and vacuum filtered using dried and pre-weighed Nuclepore filters (0.40μ pore-size-57mm dia.). After careful washing, the filters were dried and re-weighed to determine the by-weight concentration of total suspended solids. Both surveys were conducted during the ebb tidal cycle.

Results and Conclusions.

The suspended material distributions along the centerline of the plume downstream of the operating dredge for each survey period are

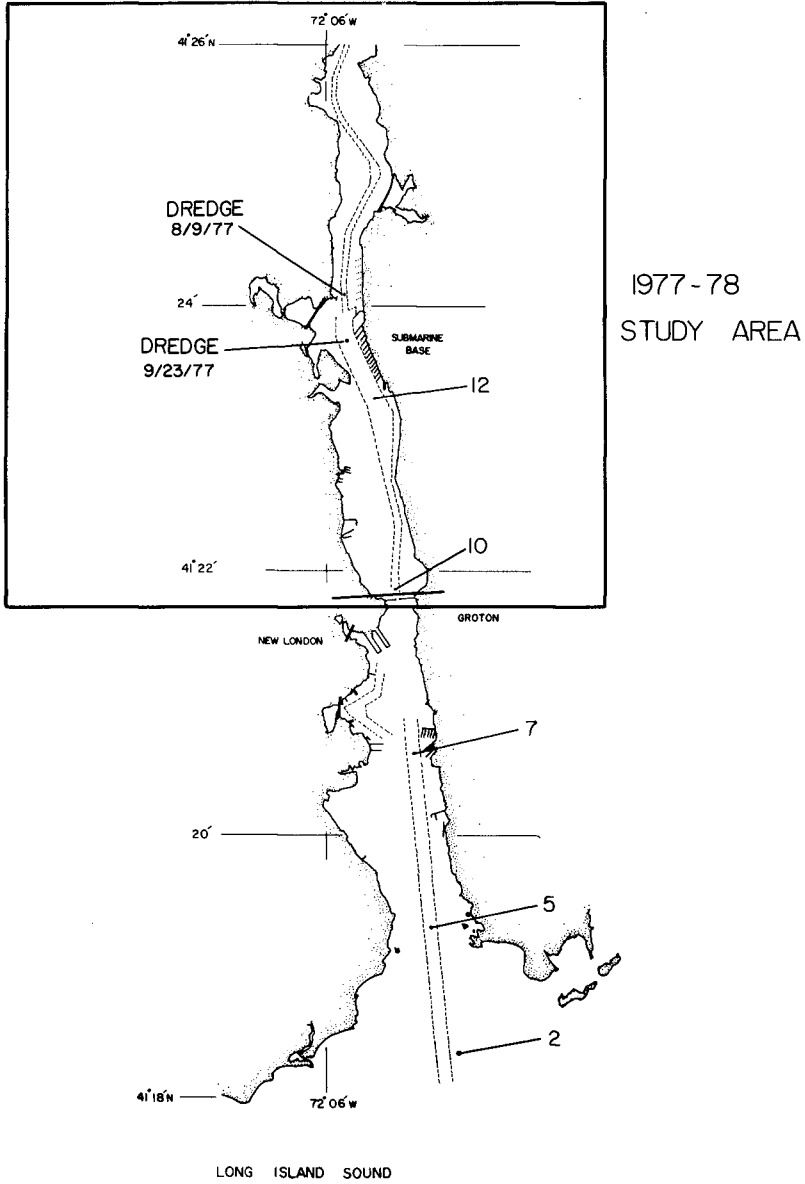


Fig. 2. Lower Thames River Estuary showing dredge locations during August and September, 1977 surveys. From (Bohlen et. al., 1978).

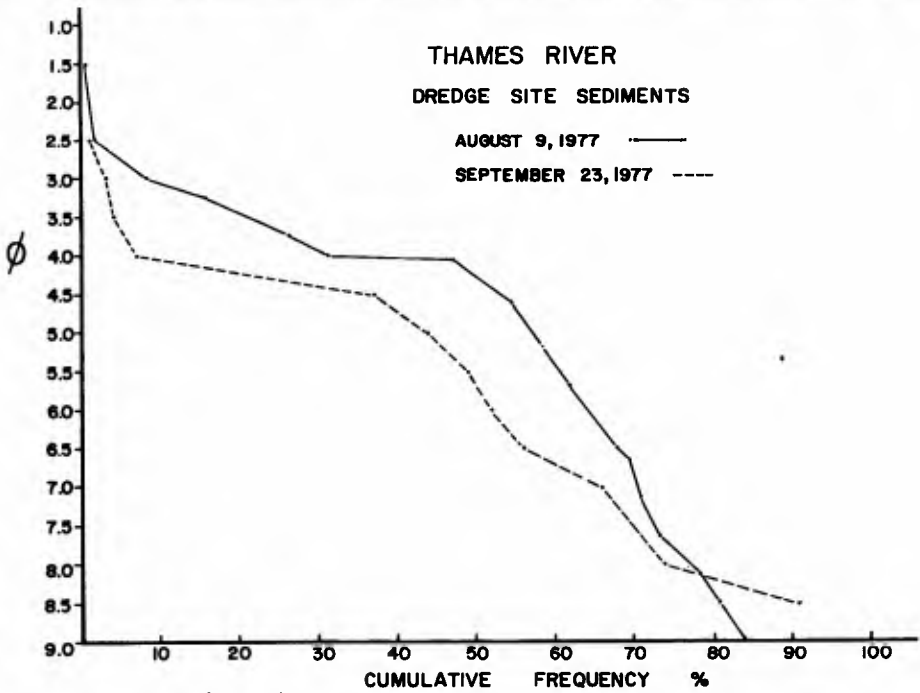
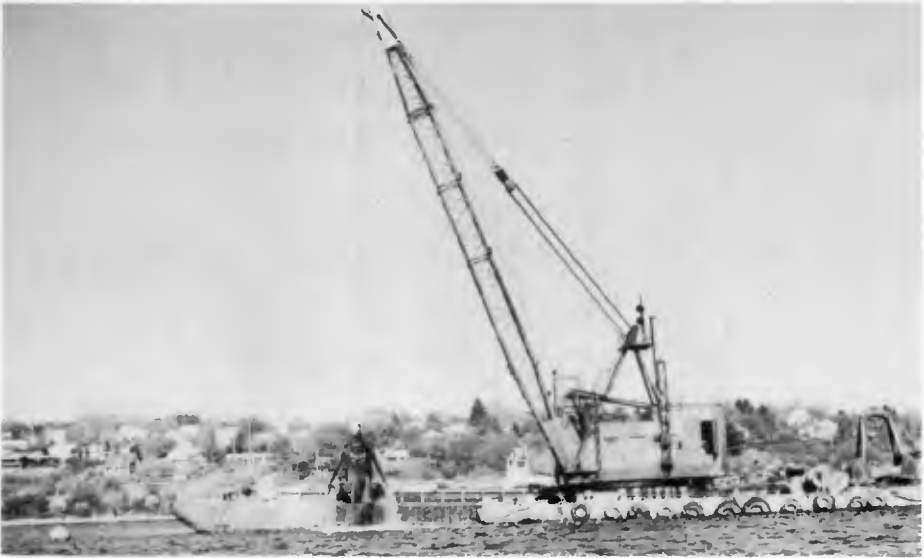


Fig. 3a (lower) Grain size characteristics of sediments being dredged in Thames River.

Fig. 3b (upper) Operating dredge and barge.



THAMES RIVER

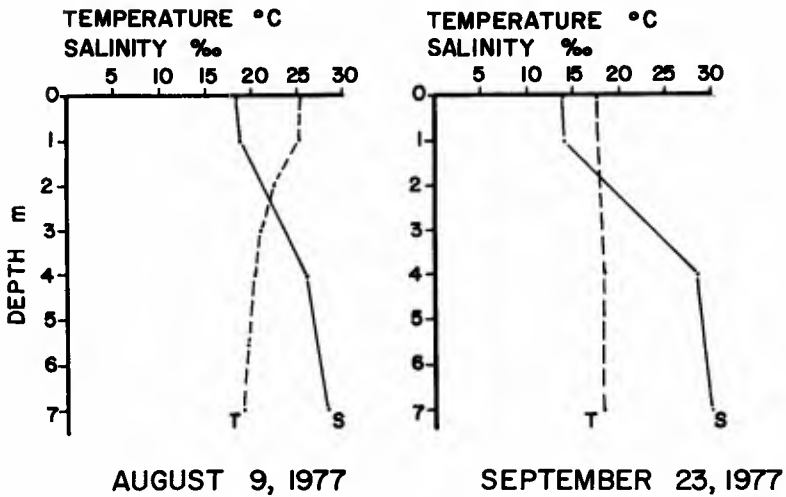


Fig. 4a (upper) Sediment washover from ascending bucket
 Fig. 4b (lower) Reference temperature and salinity distributions during August & September surveys.

shown in Figs. 5 and 6. Qualitatively, these distributions are quite similar. As expected maxima occur in the area adjacent to the dredge with concentrations averaging between 200 and 400 mg/l. These values exceed the ambient or background levels measured at an upstream station clear of dredge influence by factors ranging from 4 to 10. Proceeding downstream concentrations decay rapidly and in both cases return to background within approximately 700 m.

The observed suspended material distributions are similar in character to those displayed by a variety of dispersing materials and/or particles (see Sayre and Chang, 1968 e.g.). As such they can reasonably be considered to consist of three principal areas or zones.

a. An initial mixing zone - immediately adjacent to the dredge where bucket induced suspensions and mixing combine to produce the initial suspended material concentrations.

b. A secondary zone - analogous to the convection dominated region in classical dispersion theory (Fischer, 1967). Material concentrations in this area are expected to vary primarily in response to advection and gravitational settling. And,

c. A final zone - extending downstream from the limit of the secondary zone to the point where material concentrations again approach background levels. The field observations provide some useful insights into the factors governing the suspended material distributions in each of these zones.

1. The initial mixing zone. - This area is clearly bucket dominated. During each dredging sequence, bottom impact and washover serve to introduce sediments which are subsequently mixed through the water column by the mechanical agitation produced by the vertical ascent and descent of the bucket. The resultant vertical column of materials, representing the initial source or concentration immediately proceeds to move downstream at a rate governed by the local mean velocity. Following approximately 1 min. another column of materials is introduced by the next pass of the bucket. This delay results in an intermittent source favoring a high degree of spatial variability in the vicinity of the dredge (see Fig. 7). The displacement in peak concentrations observed during the September, 1977 survey (Fig. 6) is evidence of this spatial inhomogeneity.

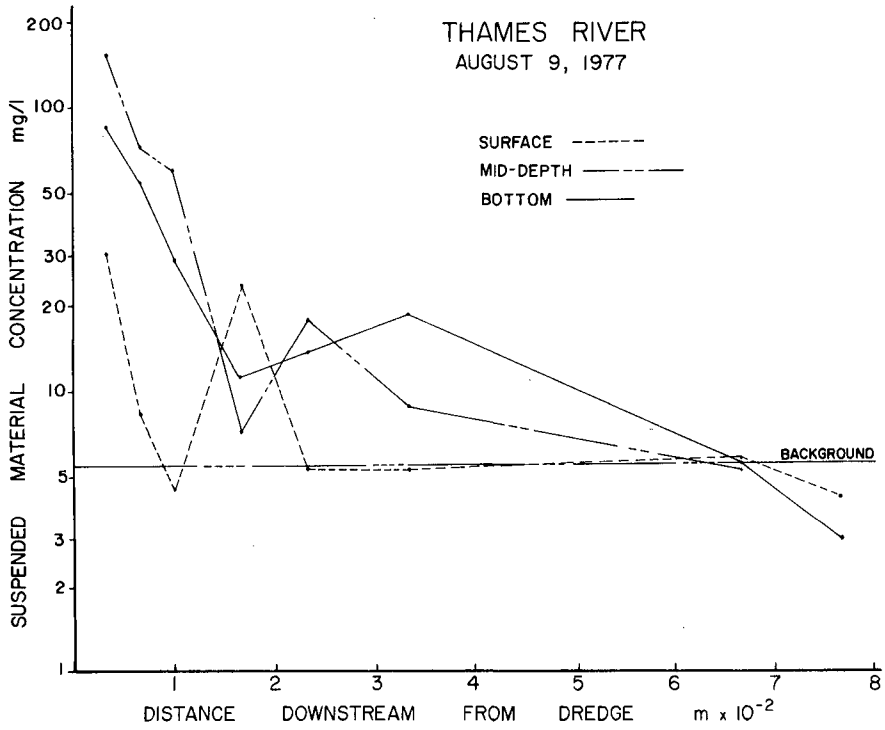


Fig. 5. Suspended material concentrations along the centerline of the plume downstream of the operating dredge. August 9, 1977. (from Bohlen, et. al., 1978).

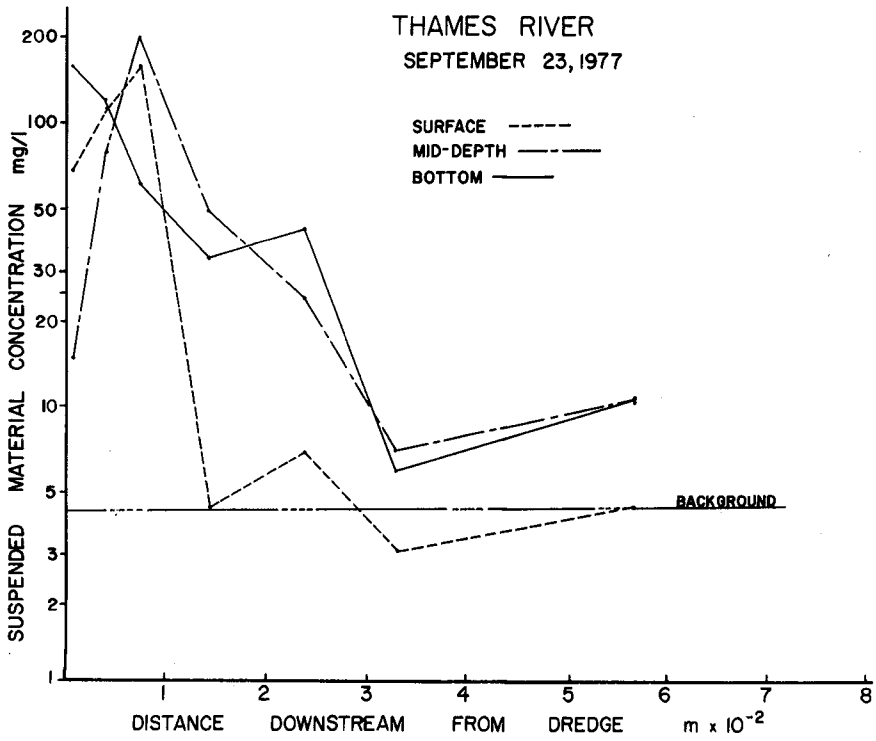


Fig. 6. Suspended material concentrations along the centerline of the plume downstream of the operating dredge, September 23, 1977. (from Bohlen et. al., 1978).

The initial dimensions of the vertical source columns are a function of the water depth and the horizontal area influenced by bucket induced mixing. The observations indicate that this latter area is several times larger than the cross-section of the bucket and has dimensions that appear to be simply proportional to the wake of the closed bucket. Examination of a typical dredging sequence (Fig. 7) shows the ascending bucket producing a very nearly circular wake having a diameter of approximately 16 m. The resultant mixing area of 201m² is substantially larger than the 12 m² cross-section of the bucket.

Given the above characteristics it appears possible to develop reasonable estimates of the horizontal mixing area using classical wake theory (Schlichting, 1968). If a simple equivalence is assumed between drag on the bucket and fluid momentum it can be shown that,

$$b \sim (\beta C_D A_f d)^{1/3} \quad (1)$$

where

b = half width of the wake

$\beta = \lambda/b = \text{Const}$ with λ defined as the characteristic mixing length within the wake

C_D = drag coefficient of the bucket

A_f = frontal area of the bucket

d = water depth

Observations of the residual wake (Fig.7) indicate characteristic eddy scales or mixing lengths within the wake of approximately 1 m yielding β values between 0.1 and 0.2. These values in combination with the observed wake dimensions, a bucket frontal area of 12 m², and water depths averaging 10 m suggest drag coefficients ranging between 20 and 40. At present the accuracy and general applicability of these numbers cannot be specified because of generally insufficient data. As a result, although the wake method appears internally consistent in terms of the limited observations provided in this study, its utility as a general means to predict the horizontal area of bucket induced mixing must remain speculative.

The mass of sediment suspended within the initial mixing zone is a function of the efficiency of the dredging process. Given the observed dimensions and suspended material concentrations ranging between 200 and 400 mg/ λ , an assumed specific gravity of 1.5 and negligible porosity indicates that approximately 2 to 4% of the mass of each bucket load is introduced into the water column. These numbers are similar to those observed in previous studies (Bohlen and Tramontano, 1977; Gordon, 1973) and appear to be representative of the general class of

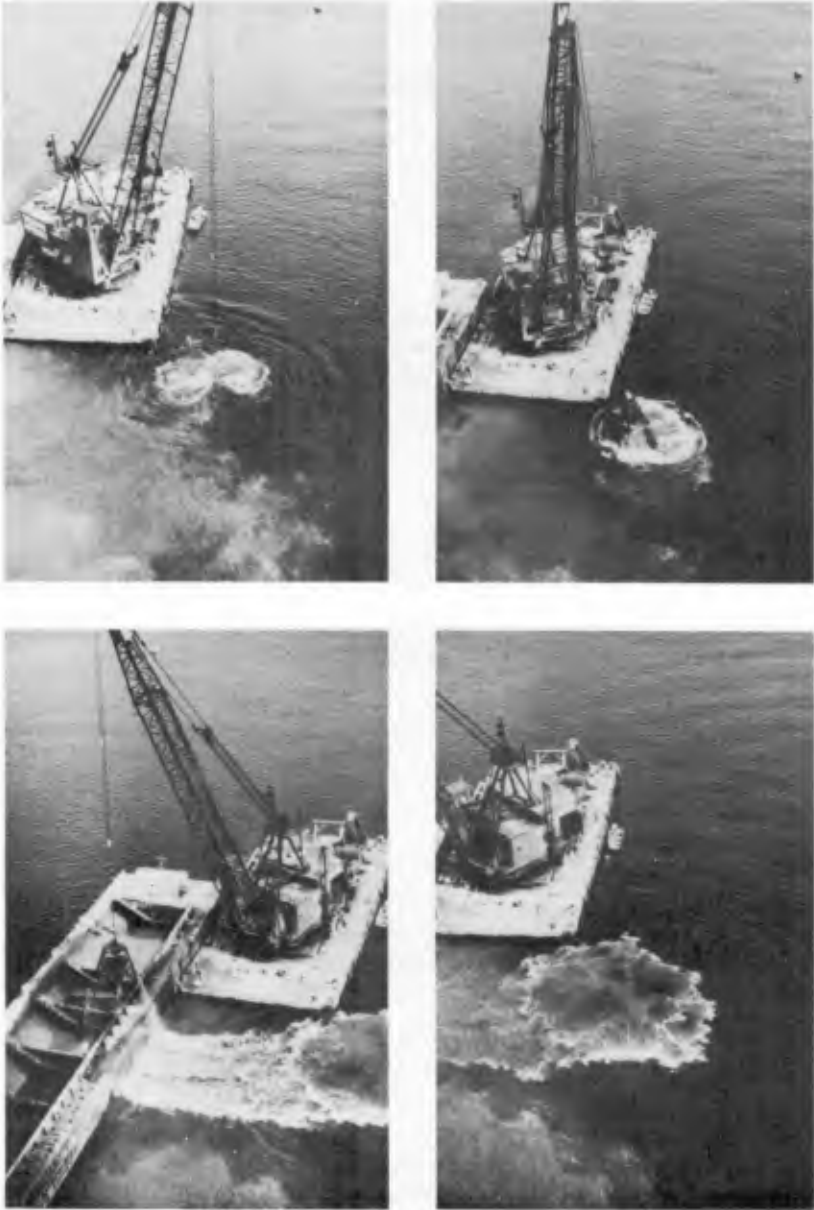


Fig. 7. A typical dredging sequence - beginning ascent upper left - residual wake - lower right. Thames River 1977 - 1978.

clam-shell bucket operations conducted in relatively cohesive, fine-grained sediments. If future work proves the value of the above wake method as a means of predicting mixing volumes, these values should permit reasonable estimates of the initial concentration levels adjacent to the dredge.

2. The Secondary Zone - Proceeding downstream from the initial mixing zone the cloud of suspended materials begins to disperse due to the combined effects of advection, turbulent diffusion, and gravitational settling. Concentrations decrease rapidly with values during the August survey falling by more than a factor of 10 within the first 100 m (Fig. 5). Such rapid rates of decay suggest that gravitational settling dominates the concentration variations in this area since the observed width of the plume is insufficient to provide the required dilutions. An estimate of the settling velocities required to affect the observed reductions can be developed using the methods described by Sumer (1977). He showed that the settling length L required to produce a given percent removal of materials suspended in typical channel flows could be evaluated using

$$L = \frac{-6 (\bar{U}) d}{k \lambda} \ln (1-r) \quad (2)$$

where \bar{U} = the average cross-sectional velocity

u_* = the shear velocity = $\bar{U} \sqrt{f/8}$

f = Darcy - Weisbach friction factor, assumed = 0.02

d = water depth

k = von Karman's constant = 0.42

λ = mean rate at which particles settle out of suspension

r = percentage of sediments removed

Solving for the case of the August survey where $\bar{U} = 30\text{cm/sec}$ and $r = 0.9$ at $L = 100\text{ m}$ yields a $\lambda = 40$ corresponding to an average assemblage settling velocity of 4.78cm/sec . This value is equivalent to the settling velocity of an individual quartz sphere having a mean diameter of 0.35 mm and is substantially higher than values computed using the average grain size characteristics of the dredged materials (Fig. 3a) in combination with standard graphical techniques (Vanoni, 1975). The cause of these differences is not immediately apparent. Some bias is undoubtedly introduced due to the neglect of diffusion. Given the spatial scales however, the magnitude of this error should be small. More likely, the differences result from the character of the settling process in this area. Within these high concentration zones particle-by-particle settling can be limited by processes tending to favor agglomeration of particles and the formation

of particle assemblages having settling velocities substantially higher than the individual member particles. Additional work remains before the details of these processes can be quantitatively specified. For the moment the field data are best taken as an indication of the effectiveness of these processes and the possible hazards inherent in the application of single particle settling velocities within models of suspended material plumes.

As rapid gravitational settling acts to remove the coarser grained materials from the water column, the initial distribution of suspended sediment concurrently spreads laterally under the effects of local turbulent mixing. The former process tends to reduce the average grain size of the materials in suspension while the latter reduces the influence of convective processes as the spatial scales of the plume approach those characterizing the local turbulence field. In time this combination produces conditions in which the distribution of suspended material behaves in a manner similar to that displayed by a neutrally buoyant dispersant. By definition, this occurs at the downstream limit of the secondary mixing zone. An estimate of the distance required for this transition to occur can be developed if the assumption is made that subsequent downstream distributions will be diffusion dominated. Applying a simple Fickian construct, the resultant distributions will have centerline concentrations varying exponentially with a form:

$$C(x) \approx C_0 e^{-\frac{\bar{U}_x}{2k}} \quad (3)$$

where x = longstream dimension

C_0 = an initial suspended material concentration

k = a dispersion coefficient $\sim u_* d$

Using the August survey data to test the "goodness of fit" of this expression (Fig. 8) indicates that slightly more than 100 m is required before the exponential reasonably conforms to the observed distribution. This is one indication of the downstream extent of the secondary mixing zone.

Another measure of the extent of the secondary mixing zone can be developed by considering the lateral spreading characteristics of the plume as it progresses downstream. The typical time t required for this cross-sectional mixing can be estimated using:

$$t = \frac{\ell^2}{K_z} \quad (4)$$

where ℓ = characteristic cross-stream length scale

K_z = lateral diffusion coefficient = $0.2 u_* d$

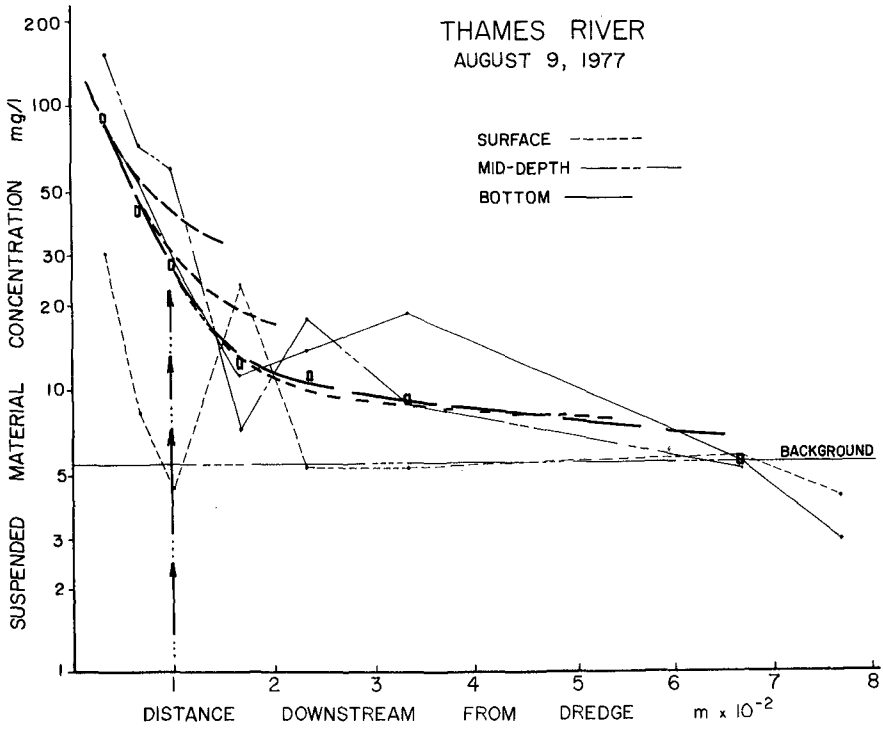


Fig. 8. Tests of the suitability of an exponential distribution function

- ——— □ Vertical average suspended material concentration
- - - - Exponentials beginning at various longstream locations
- ... → Inferred downstream limit of secondary mixing zone.

Fischer (1973) showed that this expression provides a useful means for evaluating the extent of the convection dominated zone. Since downstream of this zone the distributions of a neutrally buoyant dispersant can be predicted using one dimensional diffusion equations with solutions similar in form to (3), use of (4) should provide estimates similar to those given by the above curve fitting routine with the added advantage that these predictions require a minimum of data.

Evaluation of (4) for the Thames River study area using the August survey data indicates that

$$t \cong 300 \text{ sec}$$

Applying Fischer's (1973) criteria the concurrent convective time scales can be expected to range between 150 and 300 sec. At the observed average velocities these convective times imply that materials suspended by the dredge will have moved downstream distances of 50 to 100 m before the distributions become primarily diffusion dominated. The similarity between these values and those provided by the above curve fitting suggests that this method may provide the best means of predicting the longstream extent of the secondary mixing zone and encourages further investigation.

3, The final Mixing Zone - Downstream of the secondary zone, concentrations continue to progressively decay but at rates significantly lower than those observed nearer the dredge. The distributions in this, the final mixing zone are diffusion dominated although gravitational settling continues to act. The vertical average suspended material concentrations are essentially exponential in character (Fig. 8). Dispersion coefficients for this area were estimated using the guidelines provided by Fischer (1973). Constants of proportionality of 5-25 for the longitudinal coefficient and 0.15 to 0.25 for the lateral coefficient provided reasonable agreement with the field data. Despite this agreement however, additional work is required in this area with particular emphasis on the character and magnitude of dispersion and time and space variant interactions produced due to gravitational settling.

Summary

The field observations show that the suspended material plume induced by an operating, clam-shell bucket dredge is essentially a small scale feature. Under typical estuarine conditions the observed plumes had average longstream dimensions of approximately 700 m. The resultant distributions can be divided into three primary zones:

- An initial mixing zone - immediately adjacent to the dredge, where bucket operations tend to suspend and mix materials over a well defined vertical column.

- A secondary zone - extending downstream a distance of approximately 100 m in which material distributions vary primarily in response to gravitational settling.

-final mixing zone - where concentrations continue to decrease progressively approaching pre-project or background levels with variations governed primarily by turbulent diffusion.

Each of these areas appears amenable to reasonably straightforward modeling schemes sufficient to permit quantitative prediction of the suspended material distributions.

A variety of work however, remains to be done. In particular additional information on the adequacy of the wake method as a means of estimating mixing area is required. In addition more detailed observations of dredge efficiency should be obtained so that the functional relationships between sediment type, bucket size, character and operational techniques and the mass of sediment introduced into the water column can be established. Finally a comprehensive in situ investigation of sediment settling velocities is required. Each of the above studies would provide information essential within future efforts to quantify suspended sediment dispersion in the vicinity of coastal dredging operations.

Acknowledgments. This research has been supported by the U.S. Navy through contract N00140-77-C-6536. Donald F. Cundy, Raymond Sosnowski and Jack Tramontano assisted in the field work and laboratory analyses. The author gratefully acknowledges this support and assistance.

References

- Barnard, William D., 1978. Prediction and control of dredged material dispersion around dredging and open water pipeline disposal operations. U.S. Army Corps of Engineers, Waterways Experiment Station. Synthesis Report No. D 78, Vicksburg, Miss. 122 pps + App.
- Bohlen, W.F., Cundy, D.F., and J.M. Tramontano, 1978. Suspended material distributions in the wake of estuarine channel dredging operations. Estuarine and Coastal Marine Science (in press).
- Bohlen, W.F., and Tramontano, 1977. An investigation of the impact of dredging operations on suspended material transport in the lower Thames River estuary. Prepared for National Oceanic and Atmospheric Admin., Middle Atlantic Coastal Fisheries Center, Highlands, New Jersey. 54 pps + Apps.
- Fischer, H.B., 1973. Longitudinal dispersion and turbulent mixing in open channel flow. Ann. Rev. of Fluid Mechanics, Vol. 5; 59-78.
- Fischer, H.B., 1967. The mechanics of dispersion in natural streams. Proc. Amer. Soc. Civ. Eng.. J of Hyd. Div. Vol 93, Hy 6: 187-216.
- Gordon, R.B., 1973. Turbidity and siltation caused by dredging in coastal waters. (Unpublished manuscript). Prepared for United Illuminating Co. by Yale Univ., Dept. of Geology and Geophys., New Haven, Conn. 8pps + Figs.
- Huston, J. and Huston, W., 1976. Techniques for reducing turbidity with present dredging procedures and operation. Contract No. DACW 39-75-C-0073. U.S. Army Corps of Engineers, Waterways Experiment Station, Vicksburg, Miss.
- Morton, J.W., 1976. Ecological impacts of dredging and dredge spoils disposal: A literature review. Unpubl. MS. Thesis, Graduate School, Cornell Univ., 112 pps.
- Sayre, W.W. and F.M. Chang, 1968. A laboratory investigation of open channel dispersion processes for dissolved, suspended, and floating dispersants. U.S. Geological Survey Professional Pap. 433-E; 71 pps.
- Schlichting, H., 1968. Boundary Layer Theory. McGraw-Hill, New York, N.Y. 747 pps.

- Sumer, B.M., 1977. Settlement of solid particles in open-channel flow. Proc. Amer. Soc. Civ. Eng.. J. of Hyd. Div., Vol. 103, No. Hy 11: 1323-1337.
- Vanoni, V.A., 1975. Sedimentation engineering. Amer. Soc. of Civ. Eng. Manuals and Reports of Engineering Practice, No. 54, ASCE, New York, N.Y., 745 pps.
- Yagi, T., Koiwa, T., and Miyazami, S., 1977. Turbidity caused by dredging. Proc. of WODCON VII: Dredging. Environmental Effects and Technology: 1079-1109.

CHAPTER 122

MOVABLE BED MODEL TESTS ON DUNE EROSION

by

P. Vellinga*

1 Introduction

The primary sea defence system of the Netherlands consists for a large part of sandy beaches and dunes. The row of dunes, however, is rather narrow in some places, due to long-term erosion, and reinforcement has become necessary (Figure 1 and 2). In this connection a special governmental committee requested the co-operation of the Delft Hydraulics Laboratory to develop a design criterion for a dune sea defence system that could withstand a storm surge with a frequency of occurrence of once in 10,000 years (Figure 3). For that purpose all available field observations on dune erosion were analysed and a provisional, empirical, guide-line was developed in 1972 [1], but because of the limited amount of field data and the complexity of a theoretical approach it was decided to check the validity of this guide-line by means of a model investigation.

As no adequate scaling relationships are available for movable bed models with waves, the tests were set up in the form of a scale series. A large number of two-dimensional tests with various geometric scales using two types of sand ($D_{50} = 225 \mu\text{m}$ and $D_{50} = 150 \mu\text{m}$) was carried out in 1975. Simple relations were assumed for the model distortion n_l/n_d (length scale over depth scale) and for the morphological time scale n_t , namely:

$$n_l/n_d = n_d^\alpha; n_t = n_d^\beta,$$

in which α and β are constants, while n represents prototype value over model value. The values of α and β were determined by a correlation analysis and the following relations were found for $n_D = 1$: $n_l/n_d = n_d^{0,28}$; $n_t = 1$. Consequently the scale of the dune erosion quantity per unit length of coast is

$$n_A = n_l n_d = (n_d)^{2,28}.$$

On the assumption that these relations are also valid outside the scale range used, a prototype value for the dune erosion was found [1]. The model tests, however, produced a number of scale effects especially as prototype sands were used leading to profiles that were steeper than in the field. Although these scale effects have been implied by the scaling relations, the prototype result was very sensitive to minor changes in the empirically determined distortion relation. Therefore additional tests were carried out with finer sands to reduce the distortion of the model and consequently to increase the reliability of the prototype result. It is the results of these tests which are described in this paper.

* Project Engineer, Harbours and Coasts Branch, Delft Hydraulics Laboratory, Laboratory De Voorst, The Netherlands.

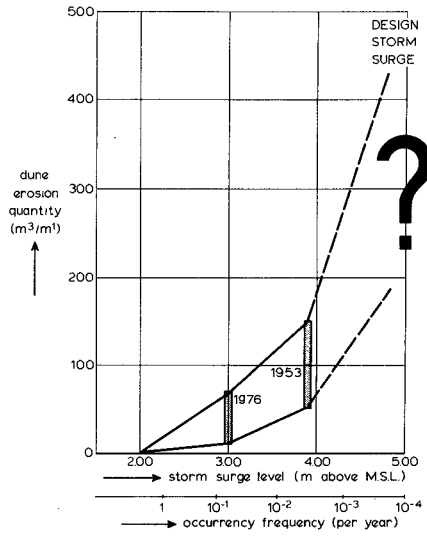
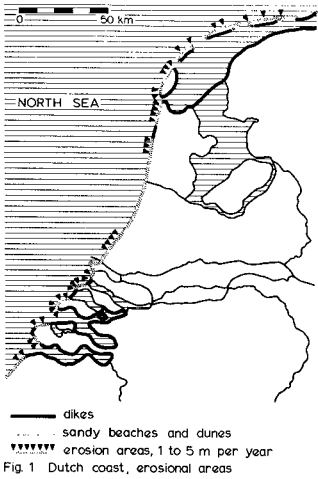


Fig 3 field measurements of dune erosion
 how much erosion will occur under design storm surge conditions ?

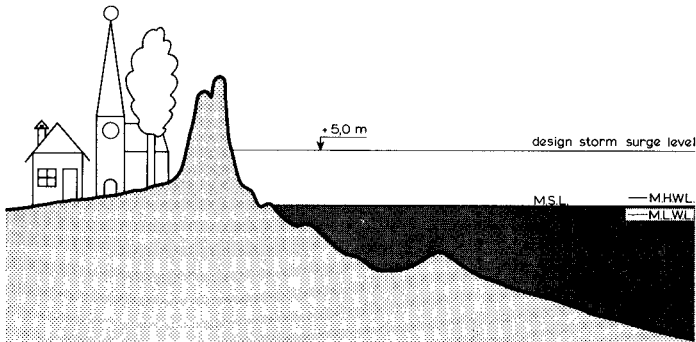


Fig 2 typical Dutch coastal profile

2 Scaling relations

The problems of scale effects in beach process modelling are not new, and especially geometric similarity in beach profile development has been given much attention. Kemp [2] suggested a distortion relation of the form $n_1/n_d = (n_d)^\alpha$ with $0.45 < \alpha < 0.65$, while Noda [3] found from his experiments with various materials: $n_1/n_d = (n_d)^{0.32} (n_\gamma)^{-0.386}$ in combination with $n_p(n_\gamma)^{1.85} = (n_d)^{0.55}$; (γ is the specific weight of sediment and D is the sediment size D_{50}). Saville [4], Saville and Watts [5], Kohler and Galvin [6] and Dean [7] stress the importance of the dimensionless fall velocity parameter H/Tw for the description of beach profile development, while theoretical and practical considerations lead Dalrymple and Thompson [8] to recommend $n(H/Tw) = 1$ as most promising scaling relation for the modelling of beach processes.

(H = wave height, T = wave period, w = fall velocity of sediment particles).

From the earlier tests on dune erosion with two types of sand Van de Graaff found indeed that the results from different sands compared very well using the H/Tw concept. Therefore the present tests have been carried out with the finer sands, assuming that equal H/Tw values imply geometrically similar profile development.

In fact, the condition $n(H/Tw) = 1$ could not be entirely satisfied for the design storm surge in view of the grainsize of the available fine sand and the possible model scales. Consequently a distortion of the model could not be prevented, the value of which can in the first instance be deduced from the requirement of kinematical similarity $n_1/n_d = n_u/n_w$ [9] (u = horizontal orbital velocity). Since the waves are reproduced according to Froude's Law, this relation can be written as $n_1/n_d = (n_d/n_w^2)^{0.5}$. In case $n_w = 1$ the relation $n_1/n_d = n_d^{0.5}$ follows, which agrees again with Kemp [2]. However, from the previous series it was found that $n_1/n_d = n_d^{0.28}$ is more realistic. Thus for different types of sand the relation $n_1/n_d = (n_d/n_w^2)^\alpha$ with $\alpha = 0.28$ would follow. The empirical exponent α incorporates any scale effect in sediment entrainment, wave breaking, wave run-up, etc.

3 Model tests

To check the suggested scaling relations for the finer sands a total of 24 tests was made, covering four types of sand and three different depth scales. The tests were carried out in the wind-wave flume of the Laboratory De Voorst (see Figures 4 and 5). Hydraulic prototype conditions as shown in Figure 6 were reproduced in all tests. The Pierson Moscovitch spectrum was used for the description of the wave field. The water level was kept constant at the maximum storm surge level because the time-scale of the morphological process is not fully understood. For each depth scale and each type of sand two tests were run with different initial profile steepness (see Table 1).

4 Test Results

During the tests the erosion profile was recorded at various times, and the results are shown in Figures 7 to 30, for the part of the profile that shows major changes and for the length of time with heaviest erosion. As can be seen from these plots, the profile-changes at a water depth greater than $\frac{1}{2} H_{0s}$ are relatively small; bars and troughs are formed at a later stage. An important phenomenon to be noticed from these recordings is that for tests with equal sand and depth scale, the form of the eroded coastal profile is independent of the initial profile. The erosion quantity above storm

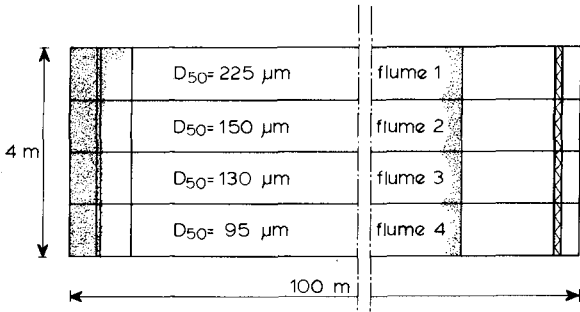


Fig. 4 plan view of model

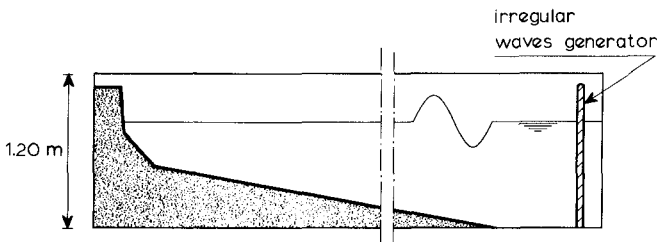


Fig. 5 cross-section of model

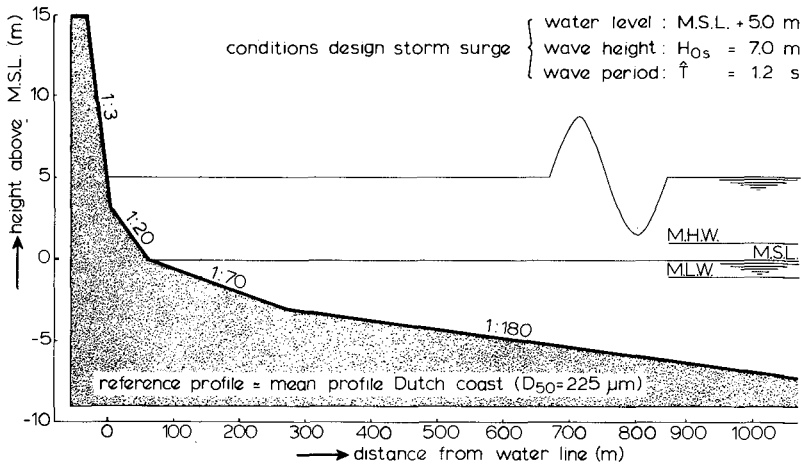


Fig. 6 reference profile and design storm surge conditions

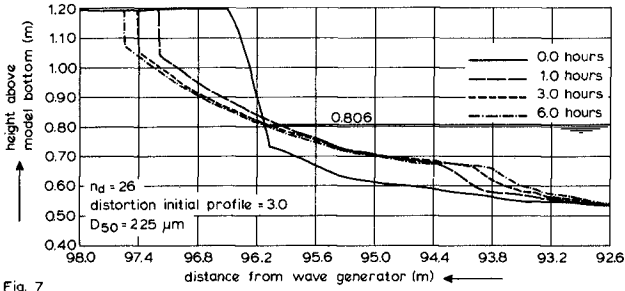


Fig. 7

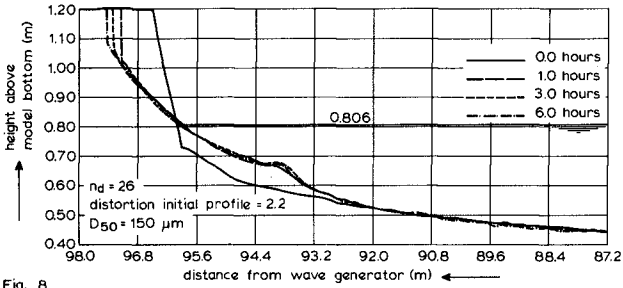


Fig. 8

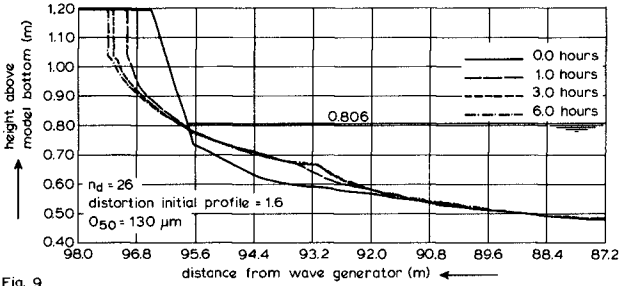


Fig. 9

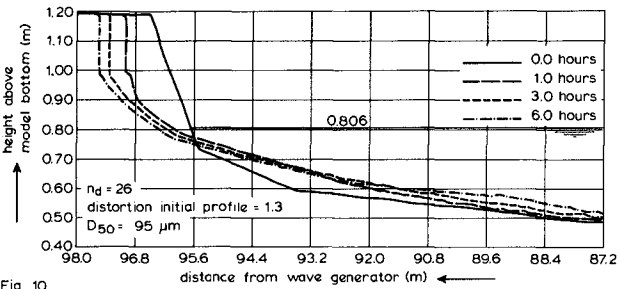


Fig. 10

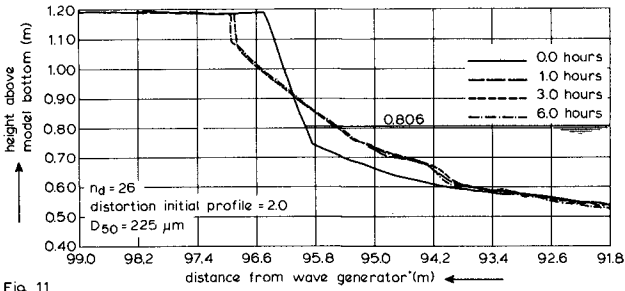


Fig. 11

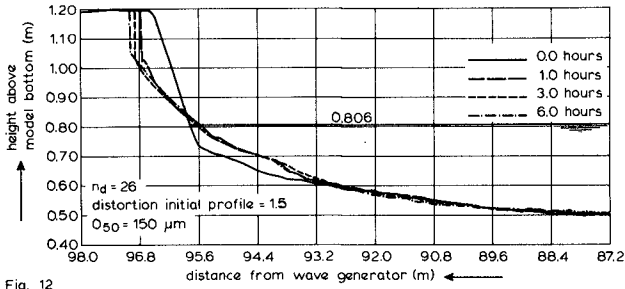


Fig. 12

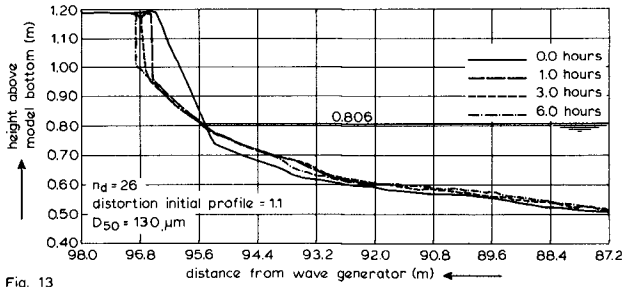


Fig. 13

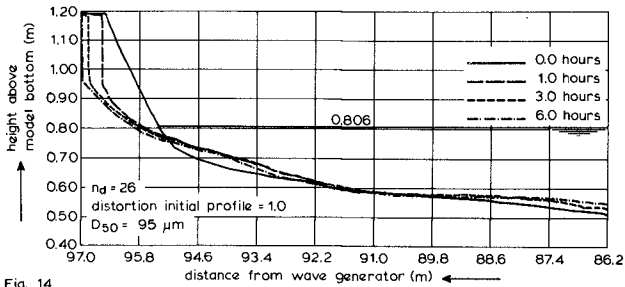


Fig. 14

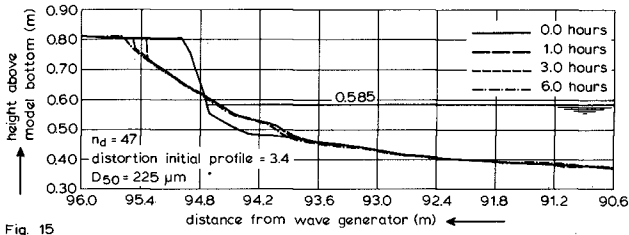


Fig. 15

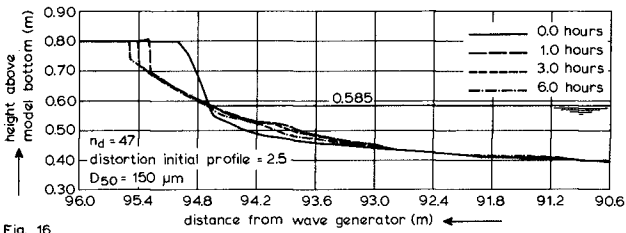


Fig. 16

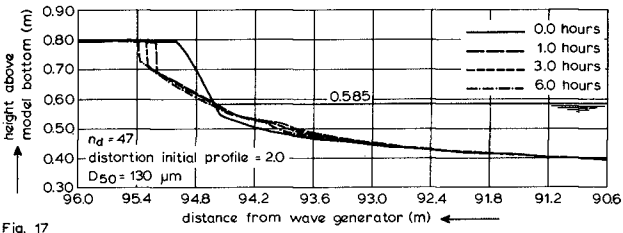


Fig. 17

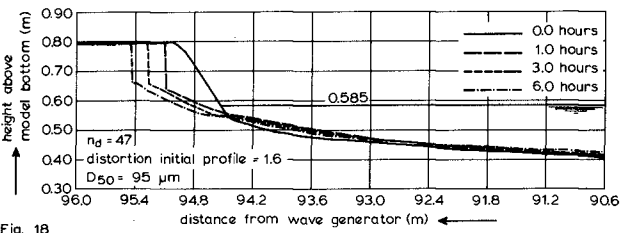
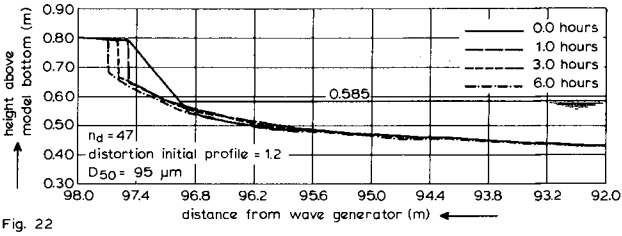
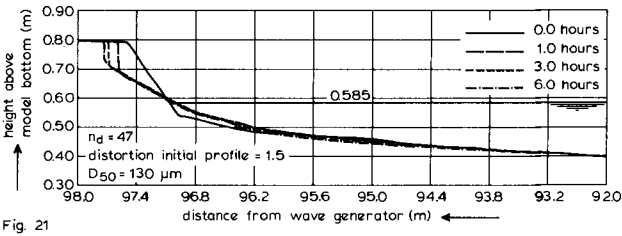
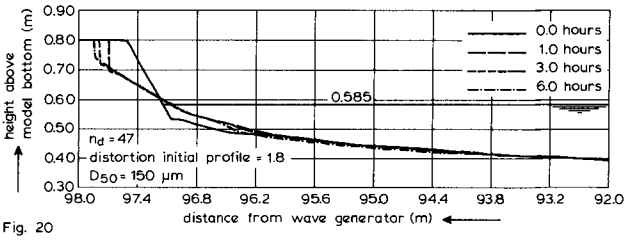
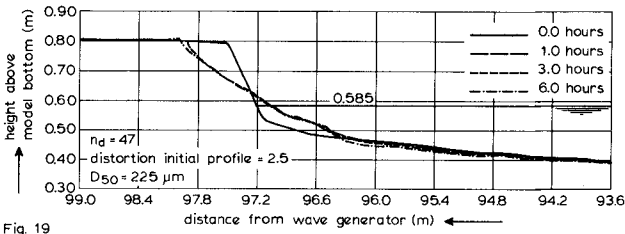


Fig. 18



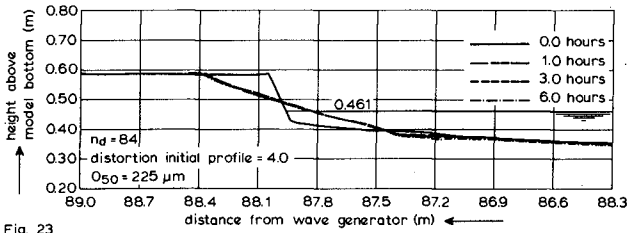


Fig. 23

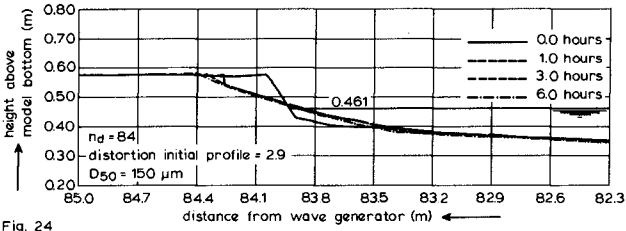


Fig. 24

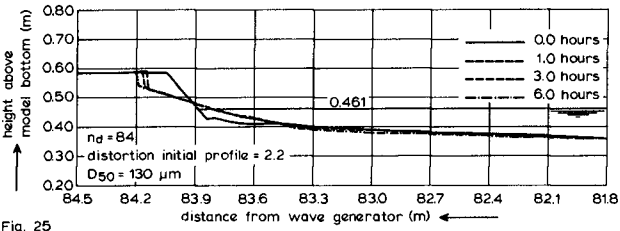


Fig. 25

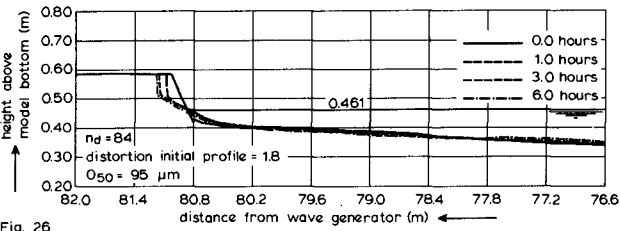


Fig. 26

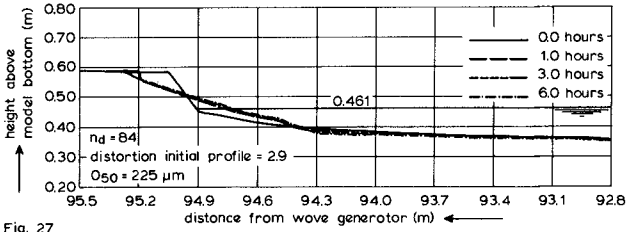


Fig. 27

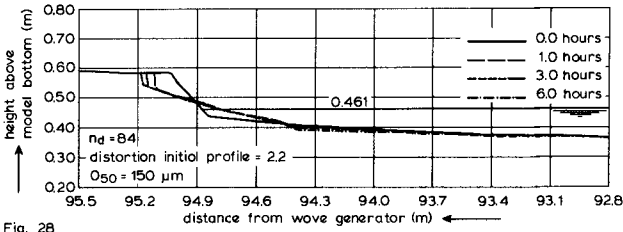


Fig. 28

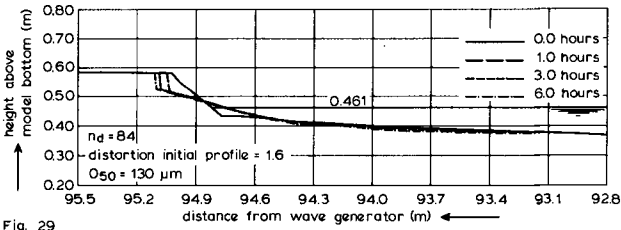


Fig. 29

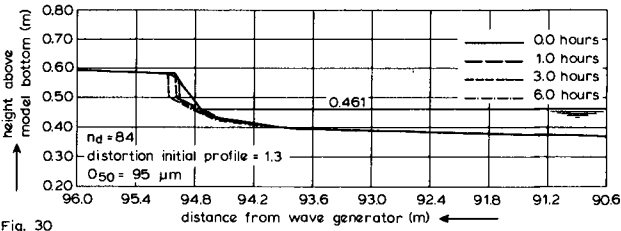


Fig. 30

surge level has been computed from these recordings, and the cumulative result is shown in Table 1. As from the first recording it was found that the initial profile was not in all cases reproduced as desired, a corrected steepness factor has been introduced (see Table 1). Other phenomena have also been recorded, like wave height, grainsize, ripples and water temperature.

From the wave height recordings it appears that close to the wave generator the significant wave height shows some scatter but is generally reasonably in accordance with scale; further down the flume, however, the wave height decreases considerably and is no longer exactly to scale (see Tables 1 and 2).

The bottom sediment, sampled at $t = 40$ hrs, was found to be the coarsest just seaward of the still water line.

The ripples were measured at $t = 6$ hrs (see Table 3); but a clear variation pattern could not be determined.

The water temperature was $12 \pm 3^\circ$ C for all tests.

5 Conversion of model results to prototype

The scaling relations established in the earlier scale series, combined with the dimensionless fall velocity parameter, are:

$$n_t = 1 \text{ and } n_1/n_d = (n_d/n_w^2)^{0.28}.$$

A reasonable agreement among the erosion quantities was found when all test results were converted to prototype with these scaling relations. A closer look, however, revealed that the erosion quantities, as well as the profile forms, from the tests with finer sands showed a clear dependency with the depth scale. This indicated that the α -value for the finer sands may not equal 0.28. Therefore a correlation analysis to find the optimal combination of time scale and distortion relationship, as described in [1], was carried out for each individual type of sand.

6 Correlation analysis of test results

The erosion quantities above storm surge level were taken as a basis to determine the "best" value of the empirical exponents in the relations $n_1/n_d = (n_d)^\alpha$ and $n_t = n_d^\beta$. For a certain β -value each α -value gives a correlation coefficient for the conformity of the erosion quantities of the tests with the different depth scale factors. The analysis was carried out for discrete model time-steps that, taking the time scale into account, fell within the relevant time period for dune erosion in the field (2 to 10 hours).

Each time step provided a "best" α -value and a corresponding maximum correlation coefficient. To find the "best" combination the average of the maximum correlation coefficients for the relevant time period has been plotted as a function of the value of β . In Figures 31 to 34 this graph is shown for the present tests, while in Figures 35 and 36 the results are shown for the combination of the present tests and the previous ones with coarser sands. The "best" combination of α and β can be seen to vary with the type of sand. An important trend to be noticed is that for the finer sands the best morphological time scale approaches the hydrodynamical time scale. Regarding the coarser sands, it was found that the differences in correlation coefficient are hardly significant when the hydrodynamical time scale is compared with the formerly found time scale $n_t = 1$. Therefore the time scale with more physical background $n_t = (n_d)^{0.5}$ was chosen for further elaboration of all tests results.

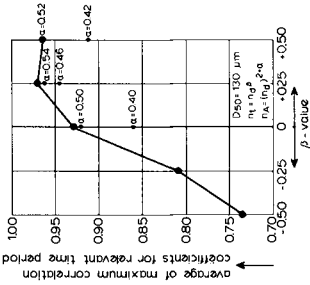


Fig. 31

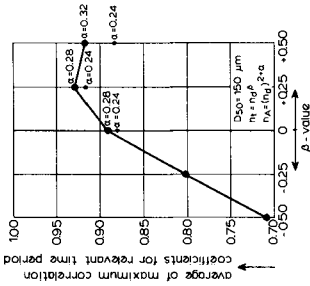


Fig. 32

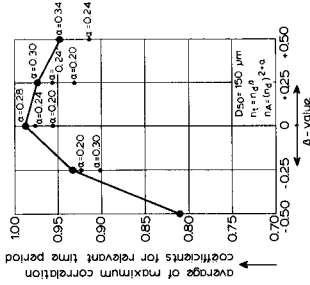


Fig. 33

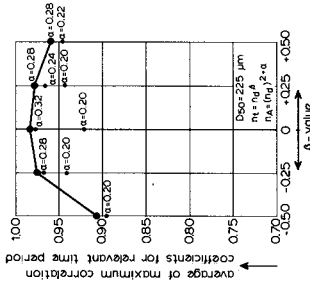


Fig. 34

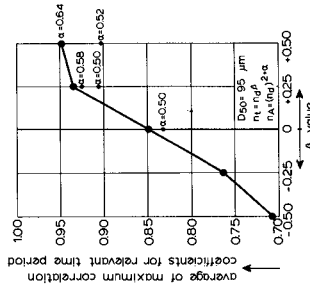


Fig. 35

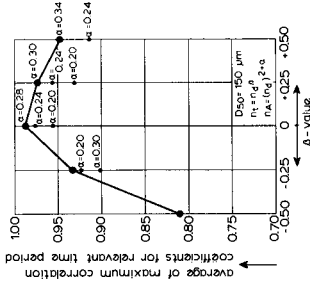


Fig. 36

Fig. 31 ... 36 Results of correlation analysis

The "best" α -values found for this time scale are shown in the mentioned graphs. It appears that α increases with decreasing particle diameter and that the "theoretical" value of 0.5 is approached for the finer sands. This seems logical, because the suspended transport with finer sands is more predominant than with coarser sands and thus the theoretical distortion relation based on kinematical similarity for a suspended particle should be more valid.

7 Discussion of the results

From the fact that the α -value was found to be a function of the absolute fall velocity of the sand particles it may be concluded that the dimensionless fall velocity parameter does not apply for the comparison of the test results. The higher α -values, however, may have purely physical reasons and perhaps the substitution of the significant deep water wave height H_{0s} and the spectrum top period \hat{T} and the fall velocity in stagnant water w in the H/Tw parameter is too simple. A better parameter may be something like H_*/Tw or H/Tw_* in which H_* is some function of H in the breaker zone and w_* is an adjusted fall velocity under breaking waves. However, the limited number of tests prohibited the determination of such adjusted parameters for the conversion of the model results to prototype values.

Another cause of the varying α -values may be the fact that the wave height recorded just outside the breaker zone was not exactly to scale due to wave height attenuation along the flume. This attenuation has been greater for tests with greater depth scale factors and finer sands, and so this phenomenon may have led to an overestimation of the α -value. Therefore, renewed analysis based on a H_{br}/Tw parameter in which H_{br} is determined from the actual wave recordings may well be more successful. Especially because this will lead to lower values of α for the finer sands there is a chance that a unique value for α will be found covering all types of sand. To carry out this analysis a large number of corrections has to be carried out because the scales of wave height, wave period and initial profile do not correspond. Consequently any prototype result found after such a correction would have a limited reliability.

For practical reasons, therefore, a simple approach has been made. Given a prototype situation that is to be reproduced to scale. It is assumed that the best tests to be performed are those with a H/Tw value equal to that in prototype. Unfortunately such tests could not be performed in the available model facility due to wave height and grain size limitations. Therefore a series of tests were carried out with various types of sand on various depth scales covering a range of smaller H/Tw values. Subsequently the results of these tests were extrapolated, for each type of sand separately, to imaginary tests having the required H/Tw value. The results obtained that way were converted to prototype by means of linear scaling ($n_1 = n_d$) as follows from the H/Tw concept.

The elaboration of the test results as indicated above can be summarized by means of the scaling relation $n_1/n_d = (n_d/n_w^2)^\alpha$ in which α is dependent on the type of sand and has values as already found from the correlation analysis.

8 Conversion to prototype with renewed scaling relations

The result of the conversion to prototype with the tentative scaling relations is rather good. Only the results from the tests with the second

finest sand ($D_{50} = 130 \mu\text{m}$) fall a little apart. The reliability of the α -value applied for this type of sand is relatively low due to the small number of tests. Therefore a correction based on the extrapolation of the α -values for the coarser sands with reference to the finest sand seems acceptable.

The ultimate α -values to be applied now are shown below, together with the corresponding grain sizes and fall velocities (from the Shore Protection Manual for 10°C [6]):

D_{50}	μm	225	150	130	95
fall velocity	m/s	0.0250	0.0130	0.0100	0.0060
α -value	-	0.28	0.34	0.40	0.64

The prototype results show greater conformity now; the erosion quantities are shown in Figure 37. On the horizontal axis the value 1 refers to model tests with an initial profile related to the prototype reference profile with the scaling relation $n_1/n_d = (n_d/n_w^2)^\alpha$. And thus the corresponding erosion refers to the average profile along the Dutch coast. Automatically the tests with initial profiles a factor S steeper than required correspond to prototype profiles a factor S steeper than the reference profile.

Also the erosion profiles have been converted to prototype, as shown in Figure 38. The water line has been chosen as a reference. Above this line the conformity is rather poor, but below it the erosion profiles agree very well. It should be borne in mind that comparison is only valid for the part of the profile that has really changed, thus to a depth of about $\frac{1}{2} H_{0s}$ (see Figures 7 to 30).

9 Evaluation

The conformity among the erosion quantities and the erosion profiles for prototype conditions gives support to the applied scaling relations. Regarding the actual prototype erosion quantities to be expected, it should be stated that a correction for the actual wave height in the model as suggested before will lead to lower α -values and consequently to smaller prototype erosion quantities.

The consequences for the prototype erosion caused by the uncertainty in the derived α exponent is shown in Figure 39. In this graph the prototype erosion quantity for the reference profile, derived from the tests with depth scale factor $n_d = 26$, is shown as a function of the α -value. The difference in prototype erosion for α -values between of 0.5 and 0.3 is only 20% for the finest sand.

From the model tests with prototype sand the corresponding difference is found to be 400%, and so it must be concluded that the reliability of the model tests has been greatly increased by the additional tests with very fine sands.

10 Reproduction of storm surge 1953

To verify the H/Tw parameter in a different manner, a final test was carried out. The 1953 storm surge, of which some prototype observations were available, was reproduced in the model. For this test α -values were not of any

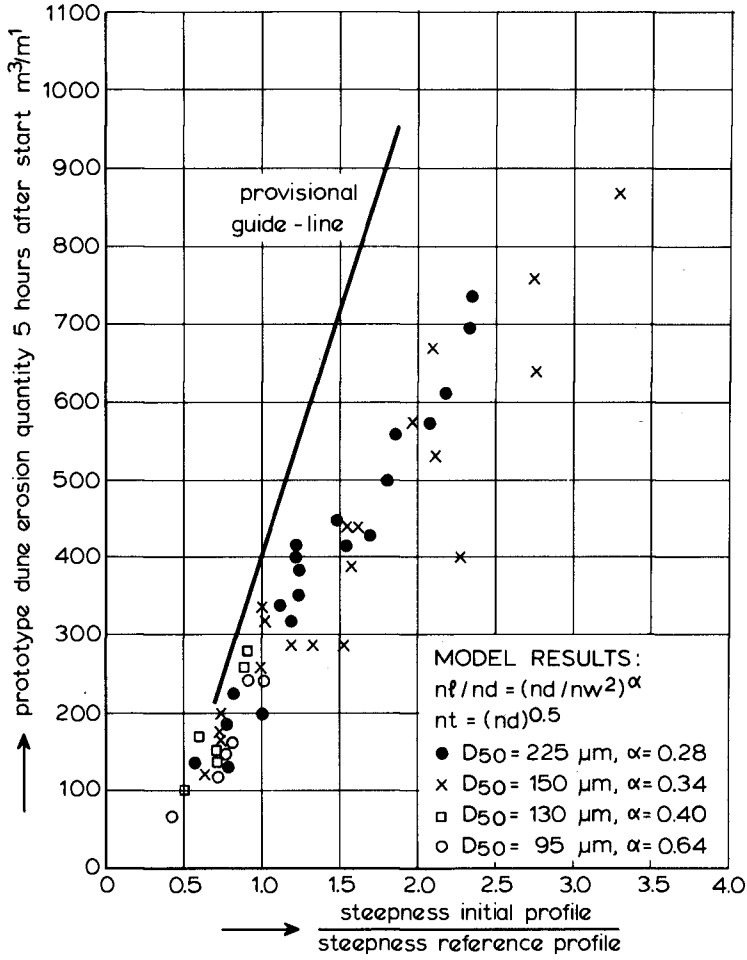


Fig. 37 prototype erosion quantity, model result compared with empirical guide-line

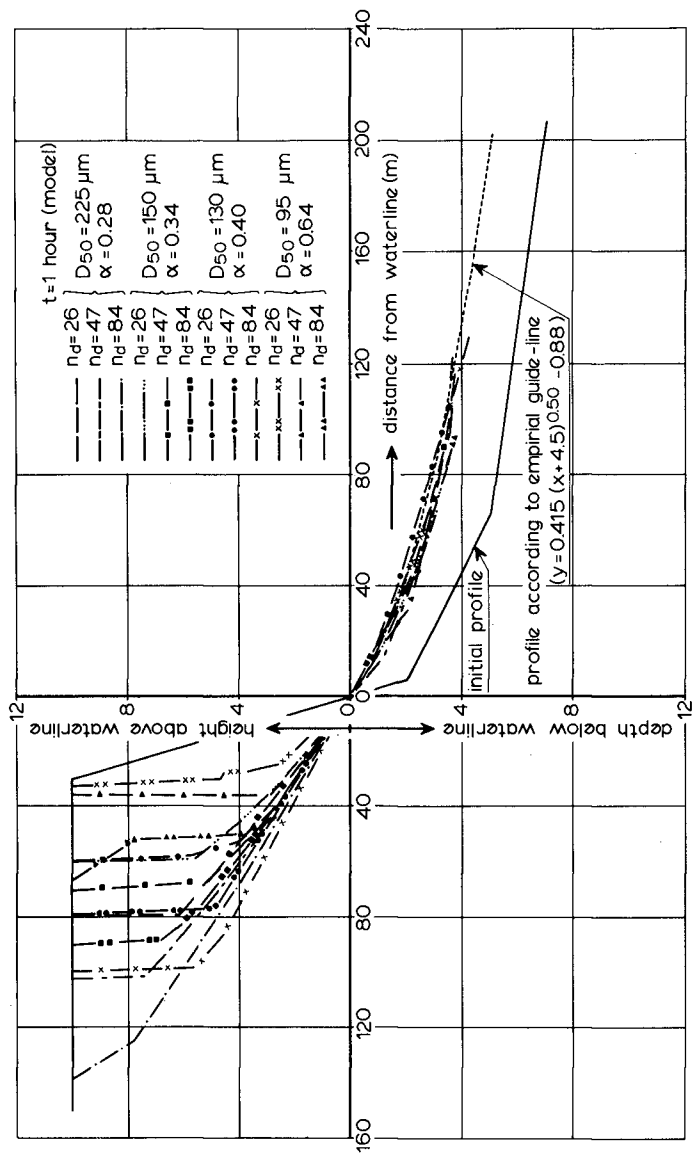


Fig. 38 prototype erosion profile

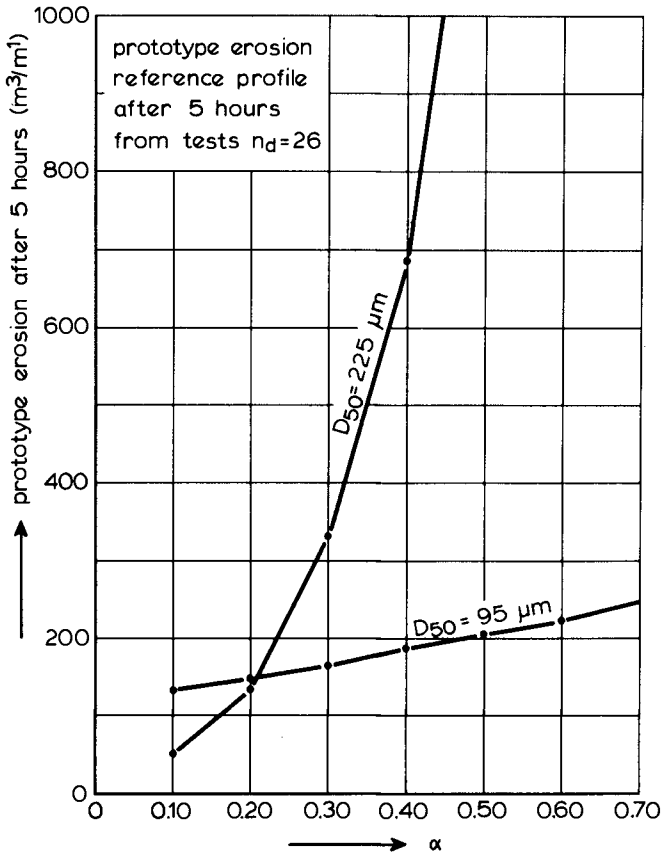


Fig. 39 prototype erosion as a function of α

importance because the H/Tw -value of the field conditions could be obtained in the model and consequently a profile distortion was not necessary. The field conditions showing a maximum storm surge level of 3.9 m above M.S.L., a wave height $H_{0s} = 5.0$ m, and a beach sand with $w = 0.025$ m/s have been reproduced with depth scale factor $n_d = 17$, thus $n_d = n_l = n_T^2 = n_w^2 = n_u^2 = 17$. Unfortunately the varying wave and water level conditions were reproduced on the formerly established time scale $n_t = 1$, because the time scale $n_t = n_d^{0.5}$ was not yet recognized at this stage of the model investigations. The final erosion quantity found from this test, and also the deliberately corrected quantity for $n_t = (n_d)^{0.5}$, fell within the range of quantities measured in the field, with the corrected value fitting best. Also the erosion profile agreed rather well with the field measurements, and therefore it must be concluded that this test supports the validity of the dimensionless fall velocity parameter H/Tw for small-scale modelling of beach processes.

11 Conclusions

- Results of model tests on dune erosion with very fine sand support the validity of the dimensionless fall velocity parameter H/Tw for small-scale modelling of beach processes.
- If the requirement $n(H/Tw) = 1$ cannot be satisfied in the model, a profile distortion based on kinematical similarity $n_l/n_d = n_u/n_w = (n_d/n_w^2)^\alpha$ with $\alpha = 0.5$, gives good results for the finer sands. For coarser sands ($D_{50} = 130 - 225 \mu\text{m}$) values of α ranging from 0.5 to 0.3 are found.
- A morphological time-scale equal to the hydrodynamical time scale $n_t = n_d^{0.5}$ is most plausible in view of the scaling of the fall velocity. This is supported by the model results of tests with very fine sand ($D_{50} \approx 100 \mu\text{m}$) and irregular waves.
- For the gentle beach profiles along the Dutch coast the model results support the earlier-developed and presently-used "provisional guide-line for dune erosion". For the steeper profiles, the model results fall below this guide-line.

REFERENCES

- 1 GRAAFF, J. van de., Dune erosion during a storm surge; Coastal Engineering (Journal), Volume 1, No. 2 August 1977.
- 2 KEMP, P.H. and PLINSTON, D.T., Beaches produced by waves of low phase difference; Proceedings American Society of Civil Engineers, Journal of the Hydraulics Division, September 1968.
- 3 NODA, K.E., Equilibrium beach profile scale-model relationship; Proceedings of the American Society of Civil Engineers, Journal of the Waterways, Harbours and Coastal Engineering Division, November 1972.
- 4 SAVILLE, T.Jr., Model studies of sand transport along an infinitely straight beach; Transactions Geophysical Union, 31, No. 4, 1950.
- 5 SAVILLE, T.Jr. and WATTS, G.M., Paper on subject No. 4, Coastal regime; XXIInd International Navigation Congress, Paris, 1969.
- 6 U.S. Army, Coastal Engineering Research Center, Shore Protection Manual, 1973.
- 7 DEAN, R.G., Heuristic models of sand transport in the surf zone; Proceedings of the Conference on Engineering Dynamics in the Coastal Zone, Sydney, May 1973.
- 8 DALRYMPLE, R.A. and THOMPSON, W.W., Study of equilibrium beach profile; Proceedings of the 12th Coastal Engineering Conference, Honolulu, 1976.
- 9 Le MEHAUTE, B., A comparison of fluvial and coastal similitude; Proceedings of the 12th Coastal Engineering Conference, Washington D.C. 1970.

test number	sand size D ₅₀ in μm	fall velocity at 10° C in m/s	depth scale factor %d	distortion initial profile (S)		water depth (m)	wave characteristics		time of sounding after start of test (hours)										
				desired	actual		H _{0a} (m)	T̄ (sec)	cumulative dune erosion quantity above storm surge level 10 ⁻¹¹ m ³ /m ²										
									erosion	0.1	0.3	1.0	3.0	6.0	10.5	16.5	25.5	40.0	
111	225	0.0250	84	4.0	3.90	0.461	0.091	1.31	erosion	124	132	148	158	150	174	206	248	334	
115	225	0.0250	84	2.9	2.71	0.461	0.091	1.31	erosion	51	52	59	51	37	32	36	49	87	
112	150	0.0130	84	2.9	2.93	0.461	0.091	1.31	erosion	77	104	162	176	176	249	313	411	542	
116	150	0.0130	84	2.2	1.89	0.461	0.091	1.31	erosion	37	56	66	72	95	117	145	199	282	
113	130	0.0100	84	2.2	2.09	0.461	0.091	1.31	erosion	44	56	91	95	116	170	193	229	306	
117	130	0.0100	84	1.6	1.44	0.461	0.091	1.31	erosion	46	47	55	76	101	145	191	256	310	
114	95	0.0060	84	1.8	2.00	0.461	0.091	1.31	erosion	21	49	85	145	191	320	389	484	584	
118	95	0.0060	84	1.3	1.18	0.461	0.091	1.31	erosion	21	25	58	95	165	242	312	443	496	
101	225	0.0250	47	3.4	3.50	0.585	0.163	1.76	erosion	383	449	510	600	651	760	872	1034	1303	
105	225	0.0250	47	2.5	2.45	0.585	0.163	1.76	erosion	308	331	366	395	419	468	523		838	
102	150	0.0130	47	2.5	2.44	0.585	0.163	1.76	erosion	465	571	636	776	865	975	1153	1381	1843	
106	150	0.0130	47	1.8	1.79	0.585	0.163	1.76	erosion	253	320	415	478	529	603	753	936	1225	
103	130	0.0100	47	2.0	2.02	0.585	0.163	1.76	erosion	377	469	540	634	734	903	1093	1337	1682	
107	130	0.0100	47	1.5	1.62	0.585	0.163	1.76	erosion	216	261	336	396	448	547	703	910	1157	
104	95	0.0060	47	1.6	1.73	0.585	0.163	1.76	erosion	318	473	646	956	1300	1648	2151	2662	2979	
108	95	0.0060	47	1.2	1.40	0.585	0.163	1.76	erosion	244	266	411	552	739	995	1314	1774	2271	
121	225	0.0250	26	3.0	3.08	0.806	0.292	2.35	erosion	1425	1838	2250	2914	3230	3623	3916	4141	3832	
125	225	0.0250	26	2.0	1.95	0.806	0.292	2.35	erosion	870	1052	1107	1265	1230	1260	1328	1349	1611	
122	150	0.0130	26	2.2	2.30	0.806	0.292	2.35	erosion	1327	1751	2207	2670	2734	2688	2747	2743	3027	
126	150	0.0130	26	1.5	1.48	0.806	0.292	2.35	erosion	493	1015	1293	1634	1690	1677	1729	1813	1946	
123	130	0.0100	26	1.6	1.62	0.806	0.292	2.35	erosion	978	1543	2345	3129	3464	3624	3836	4079	4077	
127	130	0.0100	26	1.1	1.10	0.806	0.292	2.35	erosion	520	779	1435	1964	2253	2300	2470	2606	3099	
124	95	0.0060	26	1.3	1.32	0.806	0.292	2.35	erosion	911	1610	2781	3891	4644	5183	5369	5323	5439	
128	95	0.0060	26	1.0	1.04	0.806	0.292	2.35	erosion	585	1175	1898	2673	3108	3943	4538	4729	4775	

Table 1 Test conditions and resulting erosion quantities

t	X	test number			
		111	112	113	114
		H _s	H _s	H _s	H _s
hours	m	m	m	m	
3.25	24	0.087	0.083	0.084	0.080
3.50	40	0.085	0.080	0.079	0.079
4.00	76	0.073	0.072	0.067	0.056
4.25	71	0.074	0.075	0.068	0.060
4.50	66	0.077	0.076	0.069	0.064
4.75	61	0.076	0.074	0.070	0.067
5.00	56	0.074	0.073	0.071	0.067
5.25	51	0.076	0.073	0.073	0.068

t	X	test number			
		115	116	117	118
		H _s	H _s	H _s	H _s
hours	m	m	m	m	
0.50	24	0.096	0.093	0.094	0.089
0.75	40	0.087	0.084	0.083	0.082
1.25	89.50	0.073	0.068	0.064	0.052
1.50	86.50	0.077	0.072	0.068	0.054
1.75	83.50	0.076	0.072	0.066	0.055
2.00	80.50	0.076	0.071	0.066	0.058
2.25	77.50	0.080	0.077	0.071	0.062
2.50	74.50	0.084	0.076	0.073	0.067
2.75	71.50	0.079	0.075	0.071	0.064

t	X	test number			
		101	102	103	104
		H _s	H _s	H _s	H _s
hours	m	m	m	m	
0.40	24	0.154	0.148	0.147	0.139
0.70	45	0.148	0.142	0.139	0.134
1.25	80	0.134	0.128	0.130	0.118
1.50	83	0.141	0.139	0.129	0.119
1.75	86	0.133	0.125	0.122	0.107
2.00	89	0.133	0.129	0.115	0.109
2.25	92	0.116	0.106	0.101	0.094
3.25	80	0.127	0.125	0.123	0.113
3.50	75	0.139	0.131	0.131	0.123
3.75	70	0.131	0.126	0.127	0.120
4.00	65	0.138	0.135	0.136	0.128
4.25	60	0.139	0.133	0.130	0.127

t	X	test number			
		105	106	107	108
		H _s	H _s	H _s	H _s
hours	m	m	m	m	
0.75	45.00	0.164	0.159	0.159	0.146
1.25	94.50	0.120	0.110	0.105	0.079
1.50	91.50	0.130	0.118	0.112	0.097
1.75	88.50	0.134	0.125	0.116	0.109
2.00	85.50	0.140	0.132	0.125	0.119
2.25	82.50	0.144	0.138	0.130	0.114
2.50	45.00	0.164	0.156	0.160	0.147
2.75	24.00	0.161	0.154	0.152	0.145
4.00	73.50	0.147	0.141	0.137	0.124
4.25	68.50	0.154	0.146	0.143	0.127
4.50	63.50	0.158	0.151	0.147	0.134
4.75	58.50	0.146	0.140	0.136	0.128
5.00	53.50	0.155	0.147	0.145	0.135

t	X	test number			
		121	122	123	124
		H _s	H _s	H _s	H _s
hours	m	m	m	m	
0.24	20.00	0.298	0.298	0.295	0.288
0.42	65.00	0.276	0.290	0.262	0.235
1.30	70.00	0.282	0.276	0.260	0.231
1.45	75.00	0.250	0.245	0.228	0.218
2.00	80.00	0.262	0.250	0.223	0.199
2.15	85.00	0.250	0.227	0.216	0.184
2.30	90.00	0.220	0.199	0.187	0.175
3.15	65.00	0.277	0.280	0.263	0.236
3.30	60.00	0.283	0.282	0.277	0.243
3.45	55.00	0.262	0.267	0.264	0.253
4.00	50.00	0.279	0.284	0.281	0.272
4.15	45.00	0.278	0.290	0.286	0.283
4.30	40.00	0.287	0.292	0.291	0.283
4.45	35.00	0.278	0.276	0.280	0.271
5.00	20.00	0.302	0.305	0.307	0.295

t	X	test number			
		125	126	127	128
		H _s	H _s	H _s	H _s
hours	m	m	m	m	
2.00	70.00	0.295	0.291	0.298	0.298
2.15	45.00	0.285	0.282	0.262	0.260
2.30	70.00	0.243	0.235	0.215	0.212
4.15	50.00	0.280	0.278	0.256	0.253
4.30	55.00	0.284	0.266	0.254	0.242
4.45	60.00	0.265	0.257	0.232	0.225
5.00	65.00	0.267	0.252	0.228	0.217
5.15	70.00	0.250	0.243	0.217	0.211
5.30	75.00	0.250	0.234	0.192	0.191
6.15	93.50	0.185	0.159	0.126	0.129
6.30	90.50	0.204	0.175	0.165	0.135
6.45	87.50	0.200	0.189	0.181	0.164
7.00	84.50	0.214	0.203	0.182	0.185
7.15	81.50	0.232	0.208	0.188	0.184
7.30	78.50	0.247	0.219	0.197	0.194
7.45	75.50	0.244	0.229	0.203	0.189

Table 2 Wave height recordings

t is time after start, X is distance from wave generator, H_s is significant wave height

test number	depth scale factor	distortion initial profile	average ripple height (cm) H _r	standard deviation σ _H (cm)	average ripple length (cm) L _r	standard deviation σ _{L_r} (cm)	L _r /H _r
D ₅₀ = 225 μm							
111	84	3.90	1.25	0.097	6.78	0.931	0.184
115	84	2.71	1.25	0.161	6.69	0.836	0.187
101	47	3.50	1.58	0.137	9.65	0.827	0.164
105	47	2.45	1.54	0.113	9.37	0.636	0.164
121	26	3.08	1.31	0.299	10.30	0.852	0.127
125	26	1.95	1.50	0.197	10.67	0.948	0.141
D ₅₀ = 150 μm							
112	84	2.93	0.99	0.159	5.94	0.331	0.167
116	84	1.89	1.02	0.054	5.65	0.319	0.181
102	47	2.44	1.11	0.025	7.15	0.405	0.155
106	47	7.79	1.09	0.081	7.12	0.244	0.153
122	26	2.30	0.94	0.098	7.32	0.920	0.128
126	26	1.48	1.07	0.101	7.41	0.526	0.144
D ₅₀ = 130 μm							
113	84	2.09	0.96	0.067	5.47	0.318	0.176
117	84	1.44	0.90	0.107	5.41	0.354	0.166
103	47	2.02	0.99	0.032	6.59	0.500	0.151
107	47	1.62	1.01	0.082	6.49	0.503	0.156
123	26	1.62	0.84	0.078	6.67	0.418	0.126
127	26	1.10	0.91	0.088	6.59	0.440	0.138
D ₅₀ = 95 μm							
114	84	2.00	0.75	0.084	4.50	0.381	0.167
118	84	1.18	0.77	0.103	4.51	0.488	0.171
104	47	1.73	0.77	0.105	5.30	0.421	0.145
108	47	1.40	0.78	0.036	5.30	0.247	0.147
124	26	1.32	0.68	0.181	6.21	0.713	0.110
128	26	1.04	0.84	0.120	6.22	0.378	0.135

Table 3 Recordings of ripples

CHAPTER 123

USING FENCES TO CREATE AND STABILISE SAND DUNES

Brian B. Willetts¹ and Christopher J. Phillips²

Introduction

Coastal sand dunes act as a barrier to wind and sea, as a reservoir of sand available to supply areas of eroding coast, and as a trap for mobile sand which would otherwise be blown inland and become a nuisance. Breaches of the dune system and areas bare of vegetation should be avoided or repaired in order to protect the stability of the dunes and so enable these useful functions to be sustained.

The agents of initial damage to the dunes are water, which undermines them, and animals (including man) which damage the protective vegetation by grazing or trampling. Of these, man has recently assumed predominant local importance because of the popularity of sea-side holidays and of the land-falls of certain marine engineering works such as oil and gas pipelines and sewage outfalls. The need is therefore increasing for active dune management programmes to ensure that under these accentuated pressures, the coast retain an equilibrium comparable with that delicately balanced equilibrium which obtains naturally at a particular location.

Such management programmes are already established in many countries. They tend, however, to be empirical and based on local experience (often of a very small number of people) because the difficulties of generalisation render transfer of information and technique meagre. Accounts of management techniques can be found in the literature (e.g. ref 1) but in most of such papers great emphasis is placed on vegetative restoration. Whilst this is the best way of re-introducing a lasting stability, it is often not a practical way of beginning the restoration of a deteriorating situation. The sand movement or the season may be such that planting alone is unlikely to be successful. It is the authors' opinion that, of the techniques at present available, the placement of porous fences provides the most effective means in relation to cost of creating and stabilising sand dunes (and should normally be supplemented by plantings).

The object of this paper is to present a simple numerical model of dune formation at a fence. The model is based on what is known of the physics of air and grain movements near the fence, and the purpose of approaching the problem at such a basic level is to seek sufficient understanding to enable information and prediction methods to be transferred from person to person and applied at different sites. This requires that the processes which take place at the fence be better understood than at present.

1. *Senior lecturer in engineering, University of Aberdeen, Scotland*
2. *Reservoir engineer, B.P. Petroleum Development Ltd., Aberdeen*

Previous work on sand movement and stabilisation has been reviewed at some length by the authors and a shortened bibliography provided (ref 2). The principal deduction of practical significance about sand fences which can be drawn from a study of the literature is that for best results a fence of approximately 40% porosity should be placed with its plane normal to the flow. Some uncorroborated recommendations can be found about multiple fence placings. Since natural winds vary in direction at a given site and since artificial deposits of greater height than a single fence are normally required, it is clear that this deduction from the literature is not an adequate background to practical dune management, but that more information is needed. We do not provide all this additional information and some remaining obscurities will be discussed at the end of the paper.

Uniform sand flow

As wind increases over a dry sand surface, a threshold is reached at which individual grains are dislodged by the wind and jerk forward or perform feeble saltations. At wind speeds only slightly greater than the threshold value, the population of saltating grains becomes dense enough to extract a substantial amount of momentum from the air layer adjacent to the sand surface, so screening the surface from wind strong enough to dislodge grains and changing the mechanism of dislodgement to one of intergranular collision. This mechanism is more effective than direct "plucking" by the wind, and if the wind speed is slightly reduced, the threshold at which grain motion stops is significantly lower than that at which it began in the rising wind.

A plot of point velocity against the logarithm of the distance of that point from the ground illustrates this point clearly. Fig 1 is an idealised form of such a diagram. The velocity profile corresponding to each mean "wind strength" can be characterised by the shear velocity, V_* , defined by

$$V_* = \sqrt{\frac{\tau_0}{\rho}} \quad (1)$$

where τ_0 is the surface shear stress and ρ is the fluid density.

The velocity at height z in the flow may be expressed as:

$$V_z = 5.75 V_* \log_{10} \frac{z}{k'} + V_t \quad (2)$$

As illustrated in fig 1, k' and V_t are the coordinates of the focus of velocity profiles which converge very nearly at a point, V_t being the threshold velocity. As the wind strengthens above the threshold, the velocity at any fixed height which is less than k' does not increase, and so the direct action of the wind remains insufficient to mobilise sand. It is also interesting to note that the effective origin of the logarithmic velocity profiles rises with wind strength, as the population of saltating grains becomes more dense.

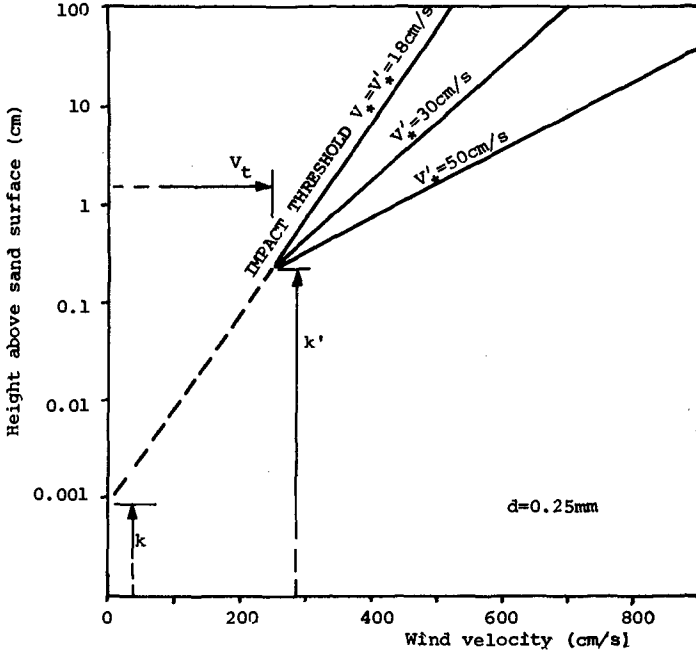


Fig 1 Velocity distributions of wind blowing over moving sand at three strengths, the lowest one corresponding to the threshold of motion.

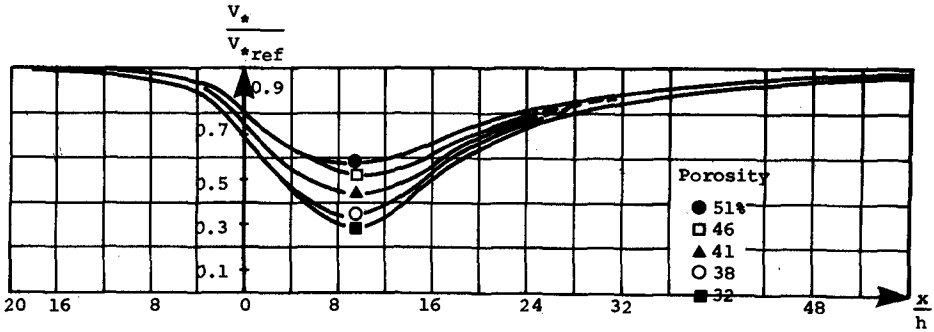


Fig 2 Shear velocity distribution with distance from the fence (of height h) for five fence porosities. (v_{*ref} is a value of shear velocity beyond the influence of the fence).

Of several formulae for calculating the uniform rate of sand transport, the best known is the early one of Bagnold (ref 3), viz:

$$q = C \left(\frac{d}{D} \right)^{0.5} \frac{\rho}{g} v_*^3 \quad (3)$$

in which d is the grain diameter,

D is the diameter of a "reference grain",

ρ is air density,

C is a coefficient which takes account of population grading and which is determined by experiment.

The range of values quoted for C is 1.5 - 2.8 so that big differences in predicted transport rate occur for different grain populations each having the same mean grain size. Consequently it is only with reluctance that one would choose a value of C by rule-of-thumb, and usually an experiment is needed to re-cast equation (3) in a form suitable for prediction. The sand used in all experiments reported here was a local dune sand having $d_{50} = 0.25$ mm and in measurements of uniform transport rate proved to obey the relationship

$$q = 4.02 \times 10^{-6} v_*^3 \quad (4)$$

This formula has been used throughout the reported work.

Non-uniformity and unsteadiness

Any change of condition, either spatial or temporal, whether of the sand or of the driving wind, initiates adjustments of the saltating cloud and the near-surface wind structure. Because the momentum exchanges inherent in these adjustments cannot, by the nature of the mechanisms involved, be made instantaneously, the influence of conditions before the change persist somewhat after it has taken place.

The introduction of a porous fence into a steady air-stream produces a local distortion of the near-surface flow which leads to deposition of sand. We have measured shear stress changes in the vicinity of a fence by means of Preston-tubes (surface Pitot-tubes) and have used the shear velocity pattern derived from these stress measurements to indicate the magnitude of the flow distortion. Calculations of sand deposition have been based on the graphs of shear velocity distribution (fig 2).

Unfortunately, because the velocity profile is distorted near the fence (particularly close to the ground), shear velocity alone no longer characterises the flow field at a particular location. As fig 3 shows, the velocity gradient at ground level (and hence shear stress and shear velocity) is not consistently related to the velocity at an arbitrarily chosen distance from the surface.

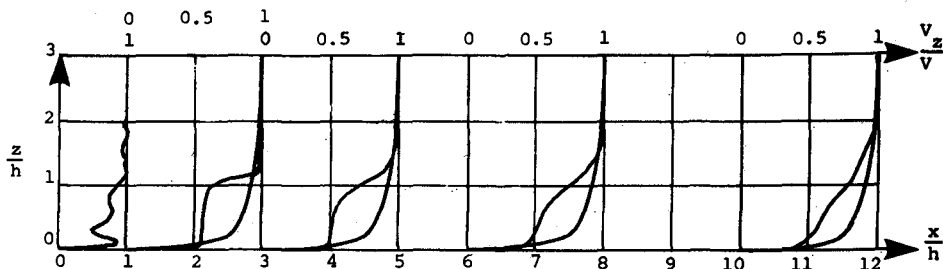


Fig 3 Distortion of velocity profile near the fence.

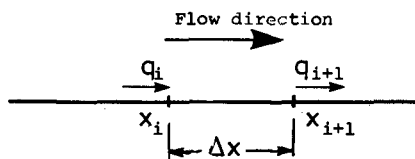


Fig 4 Control sector used in calculation method 1.

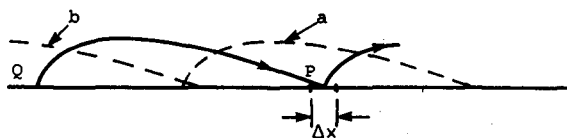


Fig 5 Scheme of calculation - method 2
 Removal rate of material at P calculated from local shear velocity and saltation a.
 Deposition rate at P calculated from shear velocity at Q and saltation b.

Since saltating grains experience the influence of the wind at considerable distances from the ground, it would be more rigorous to describe each velocity profile fully and to use the full description in calculating the behaviour of grains in the flow field. However, as a first approximation, shear velocity has been used as independent variable in this numerical work. The complications of a full description of the time-averaged flow field are such that use of the simplistic description has great advantages and, should it provide acceptable accuracy in calculation of deposits, could well be retained despite its crudity.

Calculation methods

Two methods have been used for calculating the deposition at a fence, both are more fully reported elsewhere (ref 4). Briefly the two schemes of calculation are as follows. Both are two dimensional and it is convenient to consider unit horizontal depth of field parallel to the fence.

Method 1 (Fig 4)

For the extent of the influence of the fence, space is divided into sectors Δx in the wind direction (normal to the fence). For the sector between locations x_i and x_{i+1} it is argued that the mean rise of surface level in time Δt is equal to the difference between the weight of sand entering the sector and leaving it in that time divided by the superficial area and the bulk density of the deposit. The rate at which material enters and leaves the sector is calculated by means of equation (4) from the local values of shear velocity at x_i and x_{i+1} respectively. Shear velocity values are obtained from fig 2. The calculation proceeds in the direction of increasing x for the extent of the fence's influence for each time increment. After each pass the fence height is adjusted to the extent it has been buried by the accumulating sand.

Method 2 (Fig 5)

Again, the ground is divided into stream-wise sectors of length Δx . In this method, however, the book-keeping is done in terms of erosion rates per unit area rather in terms of transport rates per unit width. For each sector, the change of surface level in Δt is made equal to the difference between the deposit rate of grains landing on it and the erosion rate of grains removed from it divided by the bulk density of the deposit. It is assumed that the erosion rate at a particular position can be calculated from the local value of boundary shear stress and that the deposition rate should be calculated from the value of shear stress at one saltation length upstream. In both cases the rates by area are obtained by dividing the transport rate per unit width by a saltation length. The appropriate saltation length is that of the saltation relative to which the unit of area is central.

Experimental evidence

Most of the evidence which is useful for direct checks on the calculation method derives from wind-tunnel experiments. Field checks require that changes of wind strength and direction are monitored continuously and there is little data available from experiments in which this has been done.

Wind tunnel measurements using 5 cm and 7.5 cm high fences of various porosities between 32% and 51% corroborate calculations by either method in respect of the size and shape of the deposit. However, the position of the deposit calculated from the shear stress profile by either method is misplaced upstream by a significant amount (the crest of the deposit is predicted to be upstream of the fence, whereas it is observed to be downstream of the fence both in the wind-tunnel and in the field). This error of position is approximately proportional to fence height and is corrected by introducing a numerical routine to represent; the jetting of flow between fence members. The routine raises the shear stress on the sand by a factor equal to the reciprocal of the porosity and operates with that enhanced shear stress on the net bed width. As fig 6 shows, the resulting prediction accords reasonably well with observation at miniature fences. (The figure shows an arbitrarily chosen porosity and flow condition, but comparisons are successful to approximately the same extent for other wind strengths, porosities and experiment durations).

Near its leading edge the deposit is considerably deeper in the numerical prediction than it is observed to be when measured in the wind-tunnel. A heavier deposit is predicted as soon as the boundary shear stress begins to fall than actually occurs. There are two obvious omissions from the calculation method which might be held responsible for this error of detail. The first is neglect of the velocity profile distortion in favour of dependence on boundary shear stress alone, the second is omission of the enhancement of boundary shear stress to be expected on the convex surface formed by the developing dune. Rough and ready checks have been run on both these influences. The incorporation in the calculation of pitot-static measurements of velocity made upstream of the fence at a distance above the bed equal to approximately three-quarters the maximum saltation height effects a small improvement in the prediction of the upstream portion of the deposit as compared with Preston tube measurements of shear stress at bed-level. Also, the introduction of empirical hill-effect shear stress enhancement reduces the thickness of this early deposit without substantially

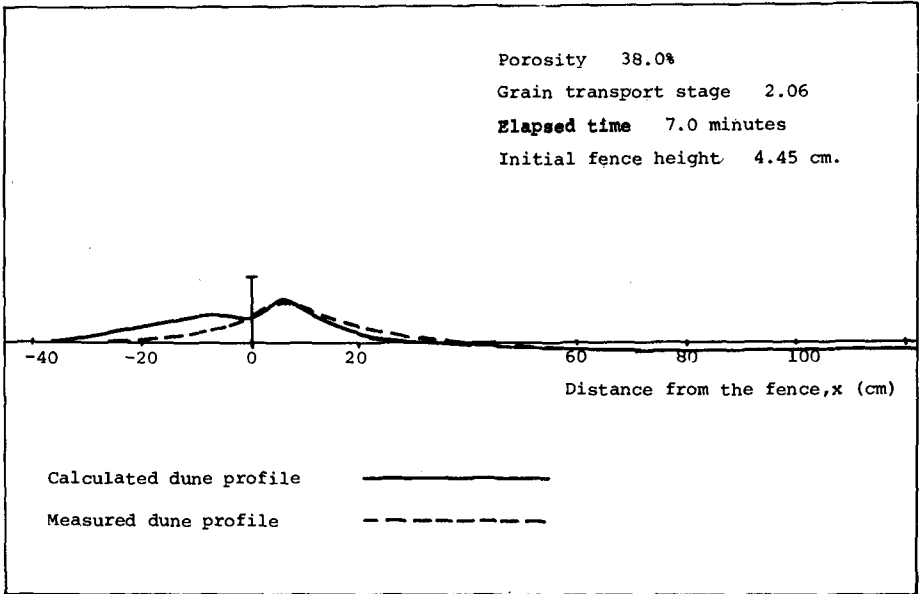


Fig.6 Comparison of measured dune profile with profile calculated for corresponding conditions and elapsed time, incorporating jetting.

changing the faithful down-wind modelling. However, the influence on transport rate of changes of surface gradient is not confined to that associated with changed shear stress; the angle and velocity at which moving grains attack the bed is also changed, and this has a significant effect on transport rate. The transport rate perturbation due to the hill effect is incapable of resolution at present, and its effect is confined to the zone upstream of the fence until the fence becomes submerged in sand. For these reasons the effect has been omitted from calculations so far, and the discrepancy at the leading edge of the deposit tolerated.

Scope for practical use of calculations

The calculation methods which have been reported have been applied only to the simplest possible circumstance, namely a fence on an initially flat sand surface with wind normal to the fence plane. Obviously practical applications would involve much more complicated geometry, and one is bound to ask whether the calculation method could be extended and modified successfully enough to become useful in real situations. The answer involves a closer look at the coastal dune system and particularly at the symptoms which show when major damage is impending (for the stable dunes require no predictive calculation).

Mature coastal dune areas consist of non-cohesive soil in undulating features usually covered almost completely in marram grass with smaller colonies of other plants tolerant of sand and salt. Such a system will survive quite high rates of deposition of incoming sand and is retentive of deposited sand because of the protection from wind given to the surface by vegetation. It is therefore quite stable, and before sand blowing can impair the stability of the dunes, there is usually preceding mechanical damage to vegetation, the removal of which exposes the bare sand to the wind. The agents of such damage may be waves, fresh-water streams, engineering works, grazing animals, vehicle or pedestrian access, and they often result in two particular types of erosion feature. The first, resulting from water attack, consists of exposure of a near-vertical sand face of considerable length, such as can often be seen when waves have reached the fore-dune. Wind processes are often important in the subsequent development of a feature initiated in this way but the present calculation method is not useful in this case. It fails because gravity, drying processes and secondary air flows dominate the situation. The second type of feature is even more important and is often called a "blow-out". It consists of a U-shaped trough often intersecting a dune ridge and growing in size by means of two processes. Sand is blown along the trough and out of it down-wind, thus increasing the depth of the feature and the steepness of its sides. At some point the vegetation securing these sides at more than the natural angle of repose is torn away, and sand and grass tussocks fall into the base of the blow-out. Wet or calm weather at this stage may enable the grass to re-establish itself and stabilise the

feature in the new geometry, but often the fallen debris is itself blown out of the trough so that the blow-out becomes both wider and deeper. Such blow-out development is a response to winds which blow along the axis of the feature (its base is protected from transverse winds) and it is reasonable to model the sand transport two-dimensionally as is done in the present calculation method rather than three dimensionally.

A common method of reversing the blow-out process is to place sand fences across the base of the blow-out to accumulate sand which is blown along its axis and so to reduce its depth. As this procedure improves the geometry of the feature, marram plantings are made to stabilise the new surfaces. The accumulation of sand at the fence in this case conforms closely to the assumptions of the reported numerical model; the sand is bare, the winds which propel the sand are virtually normal to the fence plane and initial longitudinal curvature of the sand surface is small. A useful indication of the growth of the sand deposit can be expected from calculation methods such as those described.

Caution is needed, however, in interpreting the results of such calculations. One difficulty, which is unavoidable, is that the rate of accumulation of sand depends on quite detailed features of the weather pattern (because the sand transport rate depends on dryness as well as wind strength and direction). It is common to base design predictions on an extreme event chosen statistically but not on the more difficult statistics of pattern occurrence. A second problem of interpretation concerns the imperfections of the present calculation methods, and is capable of reduction by improvement of those methods. There are several possible improvements, the important ones involving the effects of the dune shape on the boundary shear stress, and the influence of grain size distribution and characteristic grain shape on the uniform sand transport rate. Both of these matters merit further research.

It is also evident that the method of calculation of topographical changes from shear stress patterns can be applied to problems other than sand fence ones. Provided, in some other class of problem, it is possible to predict or measure the shear stress pattern, then consequent changes of topography will be calculable. The success of such calculations will be linked to the steepness of gradient of the shear stress change, but should be comparable with that of the fence calculations.

Conclusions

The deposition of sand at porous fences can be predicted with some success using uniform transport rate equations for the non-uniform conditions near the fence. It is necessary to incorporate the effect on sand of the locally high velocities of air between fence members.

The calculation is dependent on empirical descriptions of the flow field near the fence expressed, for the purpose of substitution in sand transport formulae, in terms of boundary shear stress. The pattern of boundary shear stress for a given porosity is scaled by fence height and therefore can be evaluated for any particular fence in terms of a dimensionless plot of data for a reference fence of the same porosity.

Scope for useful application of the calculation method is limited by ignorance of the mechanisms by which dune systems deteriorate, a topic which merits further work.

Acknowledgements

The junior author was supported in this work by the Science Research Council, finance for equipment and assistance was provided by the Natural Environment Research Council, and the work was housed and encouraged by the Head of the Engineering Department, University of Aberdeen.

References

1. Adriani, M.J. and Terwindt, J.H.J., "Sand Stabilisation and dune building". Rijkwaterstaat Communications No. 19.
2. Phillips, C.J. and Willetts, B.B., "A review of selected literature on sand stabilisation". Coastal Engineering (In press).
3. Bagnold, R.A., "The Physics of blown sand and desert dunes", Methuen, London (1941) Reprinted Chapman & Hall, London (1973).
4. Phillips, C.J. and Willetts, B.B., "Predicting sand deposition at porous fences". Jnl. Waterway, Port, Coastal and Ocean Div., A.S.C.E. (In press).

CHAPTER 124

BEACH GROUND-WATER OSCILLATIONS

Andrzej LEWANDOWSKI *

Ryszard B. ZEIDLER **

ABSTRACT

Oscillations of ground-water table were measured in perforated piezometers distributed across the Baltic beach at the coastal research station of Lubiatowo. From spectral and correlation analysis it appears that the most pronounced wind-wave oscillations having a period of about 6 seconds have not been detected in the beach, while longwave oscillations, dominant in the beach spectrum, correlate well with nearshore long waves. Among the longwave oscillations, it is only those having periods about or slightly longer than 100 seconds that obey the Boussinesq law. However, some longer waves may also be generated by the interaction of shorter waves. Oscillations with periods from 50 to 100 s are very coherent throughout the beach. In the absence of stochastic noise and variety of inputs, low values of coherence for other periods indicate presence of nonlinear effects. More light should be shed on the origin of this nonlinearity and theoretical tools should be tried to complement the Boussinesq model.

* Polish Academy of Sciences' Institute of Hydro-Engineering, Gdansk, Poland, Sen.Asst.

** ibidem, Asst.Prof.

INTRODUCTION

During the past decade, extensive measurements of hydro- and lithodynamical factors were continued in the Polish Academy of Sciences' coastal research station at Lubiatowo, stretching along a rectilinear coastline section some 100 km northwesterly of Gdańsk.

A set of nine measuring posts (Fig. 1), reaching a depth of 6 m at a distance of 700 m from shore line, permits investigations of waves, currents, turbulent diffusion, sediment transport etc.

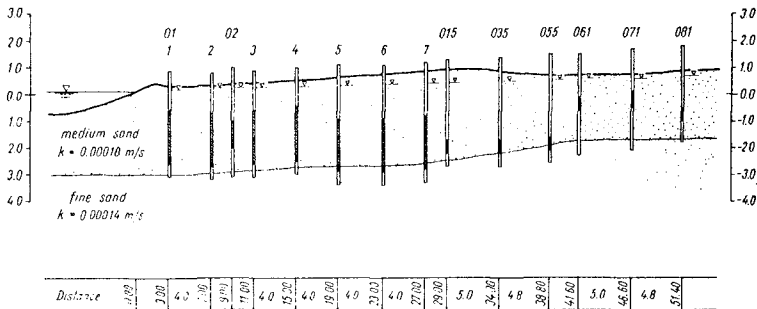


Fig.1 - Coastal Research Station at Lubiatowo

The data collected in two international expeditions of 1974 and 1976, together with relevant scientific results, can be found in References 1 and 2.

About five years ago the motion of ground water was added to the phenomena studied at Lubiatowo. Oscillations of ground-water table (GWT) were measured in the network of

piezometers shown in Fig.2 .



Measurements in piezometers No 01, 02, 015, 035, 055, 061, 071, 081 were carried out in 1974
 Measurements in piezometers No 1, 2, 3, 4, 5, 6, 7 were carried out in 1978

Fig.2 - Layout of Piezometers at Lubiatowo

All piezometers were made of 4-inch steel pipes, with filters as perforated sections lined with a filter gauze. The diameter of the gravel layer around the filter sections was 8 inches. The instrumentation for measurements of oscillations consisted of three resistance wave probes, electronic system HAG-1 (designed at the Institute) and recorder. Calibration of the piezometers in a wave flume has indicated that free surface oscillations having periods of 1 second and longer are undistorted.

Changes in the sea water level, both slow and fast, bring about oscillations of ground water in the beach, which can be felt far away from shore line, e.g. in case of strong storm surges. Recognition of long oscillations has economic bearings because of floods, agriculture of hindlands, water sources etc. Shortwave oscillations are also important, as they determine the dynamics and stability of coastline, penetration of water

and beach consolidation etc. Studies of these oscillations can elucidate hydro- and lithodynamical processes about civil engineering structures, e.g. distribution of pressures, dynamics of dikes and so forth.

A general description of the dynamics of beach ground water, using hydrochemical and hydrophysical indicators, has been given in the doctor's thesis of the junior author. This paper presents only the results concerning the ground-water oscillations. The measurements carried out under the thesis program have been revised and supplemented by this year's findings. The available experimental material is limited to longshore homogeneity, stationary conditions at the land boundary far off shore, and lack of atmospheric precipitation.

BASIC CHARACTERISTICS

Even a cursory glance at the records of ground-water oscillations exposes the effect of sea level oscillations on GWT. Under conditions of heavy storms (wave height H about 2 m some 350 m from shore line) this effect is pronounced as far as 50 m landwards (piezometers 051 - 055). Haphazard measurements in piezometer 061 have not detected shortwave GWT oscillations. The effect of lower sea waves ($H = 1$ m) can be distinguished by 30 m from shore line.

Since GWT oscillations are random, the theory of random processes has been harnessed in their analysis. Nevertheless, the stochastic findings have been combined with theoretical considerations for non-random ground-water filtration. - Fig.3 shows spectra of waves measured at stations D2 and D5 (150 and 350 m off shore) and GWT oscillations in piezometer P.01, located about 2 m from shore line. Note different ordinate scales. It can be seen that the frequency band of maximum energy (sea versus beach) do not overlap. In general, the spectral peak of wind waves and swell at Lubiatowo occurs at the linear frequency f about $0.16s^{-1}$, which corresponds to

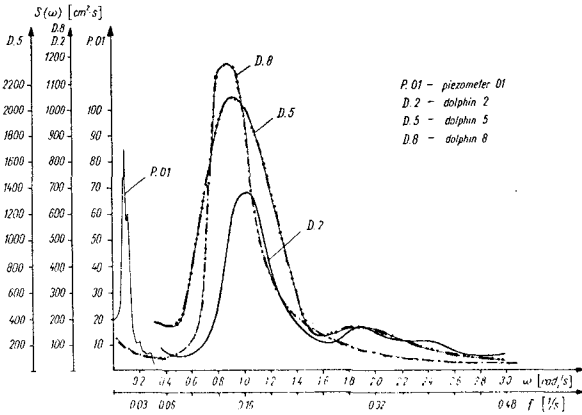


Fig.3 - Spectra of Sea Surface and GWT Oscillations

a period T of 6 s. These oscillations do not penetrate too far into land: the spectrum of P.01 does not contain significant 6-second components. On the other hand, because of technical shortcomings, the initial measurements of 1974 did not point to the presence of long sea waves, corresponding to those detected in the beach. It was only in this year's measurements, including recordings of sea surface displacements over hours, that it was possible not only to expose the longwave oscillations of water level in the nearshore zone but also to look at their correlation with the GWT oscillations.

The correlation and spectral analysis of GWT oscillations provides basic characteristics of the behavior of ground water in the beach. Fig.4 presents spectral densities measured in piezometers 01, 02 and 015. One can note characteristic confinement and displacement of the spectral band with distance, increasing from shore. The further landwards the given spectrum, the narrower its band and the more it is shifted towards lower frequencies. As they travel across the beach, shortwave oscillations become gradually filtered out, by the mechanism of damping. - Similar conclusions can be drawn from

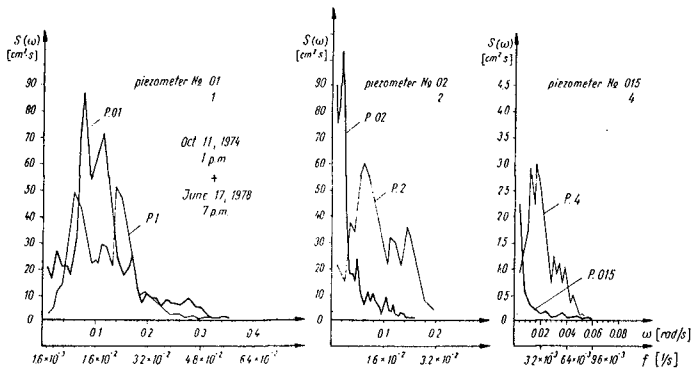


Fig.4 - GWT Oscillation Spectra

review of autocorrelation functions. The typical form of the latter (sinusoid(s) plus exponential attenuation) suggests the existence of a narrow-band random process with one (or two) sinusoidal signals. Principal parameters of these signals, determined from the spectral density peaks and clear-cut sinusoids in the autocorrelation functions, are given in Table 1.

The spectral density functions shown in Figures 5 and 6, normalized with regard to variances, expose some common features of the measured random functions. It appears that $S(\omega) \sim S(f)$ are decreasing power functions with an exponent about 3, which also falls with distance from shore line (3.1 at P.02 versus 2.7 at P.01). Attention should be called to the maxima of $S(f)$ (for f about 0.01 s^{-1}), especially in Fig. 5 for P.01. They might indicate the inflow of energy from outside (from the sea), conveyed by oscillations having periods $T = \frac{1}{f}$ about 100 seconds. The band of maxima in Fig.6, for P.02, is more smeared, which seems to point to the generation of longer GWT oscillations in the beach, which in turn could receive energy from shorter waves. This observation is

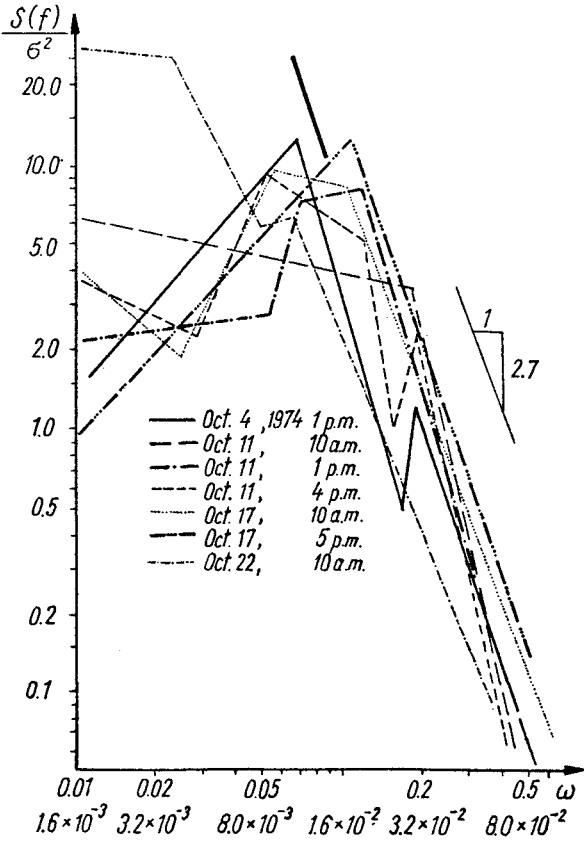


Fig.5 - Normalized GWT Spectra of P.01

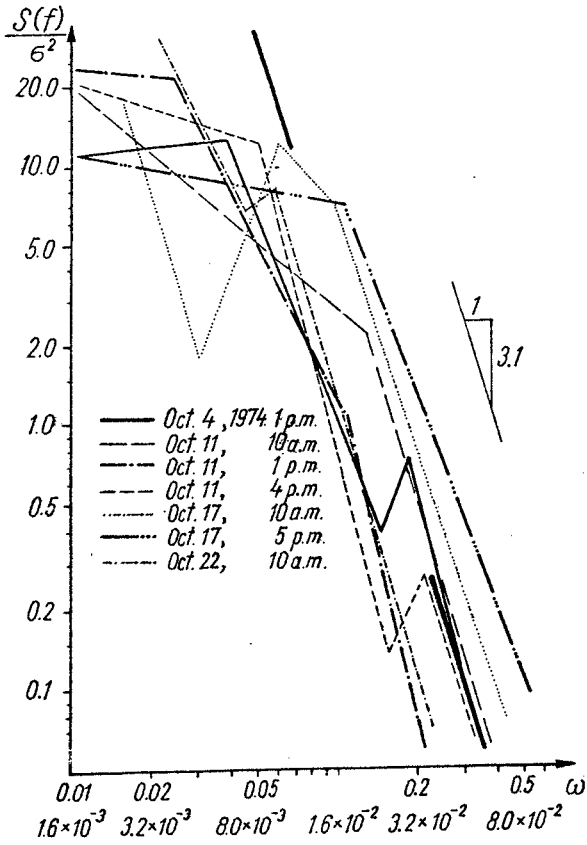


Fig.6 - Normalized GWT Spectra of P.02

Table 1 - Characteristics of Most Pronounced Situations with Wind Waves and GWT Oscillations

	Station D.2.8		Piezometer No. P.01		Piezometer No. P.02		Piezometer No. P.03		Piezometer No. P.04		
	h	T	h	f	h	f	h	f	h	f	
	cm	s	cm	Hz	cm	Hz	cm	Hz	cm	Hz	
4.10.1974,	16.00	75	4.1	0.24	3.9	0.014	3.8	137	0.007		
6.10.1974,	7.00	52	4.5	0.22			3.7	227	0.004		
9.10.1974,	19.00	53	4.3	0.23	10.6	0.019	1.5	110	0.009		
11.10.1974,	10.00	67	3.7	0.27	11.0	0.022	3.8	63	0.016	0.0011	
11.10.1974,	13.00	50	2.7	0.37	7.2	0.014	4.3	162	0.006	0.0015	0.017
11.10.1974,	16.00	72	3.8	0.26	7.6	0.017	5.1	151	0.0076		
11.10.1974,	19.00				5.5	0.016	4.0	128	0.0078		
17.10.1974,	10.00	70	3.4	0.29	6.3	0.019	2.5	116	0.0086		
17.10.1974,	17.00	64	4.1	0.24			1.5	104	0.010		
22.10.1974,	10.00				3.6	0.028	2.0	360	0.0028		
22.10.1974,	19.00				6.0	0.010	3.0	243	0.0041		
23.10.1974,	10.00				5.2	0.018	3.7	90	0.011	0.0010	
11.06.1978,	10.00	70	5.00	0.20	6.8	0.014				0.6	480
13.06.1978,	19.00	56	4.03	0.25	7.8	0.024				0.8	430
17.06.1978,	19.00	71	4.42	0.22	9.8	0.023	5.6	79	0.043	1.4	480

supported by the results for some autocorrelation functions, with the periods of sinusoidal signals growing longer, or even doubling, over a short distance between piezometers. Some secondary long waves, superimposed on primary oscillations close to the shore line and becoming uncreasingly distinct at greater distances, are shown in Table 1 for piezometer P.02.

Thus, tentative analysis of GWT oscillations (their simple stochastic characteristics) indicates that the waves having periods about 100 seconds are somehow critical: they travel across the beach without strong attenuation, so characteristic for shorter periods. On the other hand, longer waves can come from secondary sources (can be generated by interaction mechanisms). Deeper insight into the physical structure of GWT oscillations can be provided by a bit more sophisticated considerations presented below.

UNSTEADY FILTRATION AND SUPPLEMENTARY STOCHASTIC CHARACTERISTICS

Two-dimensional unsteady filtration of free-surface ground water in soil having inhomogeneous hydraulic properties is described by the Boussinesq equation

$$\frac{\partial \zeta}{\partial t} = \frac{\partial}{\partial x} \left[\frac{k}{\mu} (\zeta - h_s) \frac{\partial \zeta}{\partial x} \right] + \frac{\partial}{\partial y} \left[\frac{k}{\mu} (\zeta - h_s) \frac{\partial \zeta}{\partial y} \right] + \frac{w}{\mu} \quad \dots 1$$

in which

- $\zeta = \zeta(x, y, t)$ = elevation of ground-water table
- $h_s = h_s(x, y, t)$ = ordinate of floor of aquiferous stratum
- $k = k(x, y)$ = coefficient of permeability
- $\mu = \mu(x, y)$ = coefficient of yield
- $w = w(x, y, t)$ = source function

Equation (1) can be substituted by an explicit finite difference scheme with time as a parameter. The equivalent

equation was solved in ALGOL on an ODRA 1204 computer. For 160 by 220 m section of the Lubiatowo beach the boundary conditions were taken as constant water level far away from the sea, a sinusoidal variation of sea level at shore line and impermeability along the two remaining sides of the rectangle. The source function was taken as inhomogenous atmospheric precipitation measured in situ. All the boundary conditions have resulted from two-year investigations, the data of which was used for verification of the computations. The verification (comparison of computations with yearlong field measurements) has shown that the Boussinesq equation describes well the behavior of long waves having periods of several hours, or even longer. Moreover, it turned out that the filtration processes in the Lubiatowo beach are almost unidirectional, i.e. do not vary considerably along the beach over distances of hundreds of meters. Thus, they can be described fairly by the Boussinesq one-dimensional equation with constant coefficients:

$$\frac{\partial \zeta}{\partial t} = \frac{k}{\mu} h_s \frac{\partial^2 \zeta}{\partial x^2} \quad \dots 2$$

For the boundary conditions

$$\begin{array}{lll} \zeta = \zeta_0 \sin \omega t & \text{at} & x = 0 \\ \zeta = 0 & \text{at} & x \rightarrow \infty \\ \zeta = 0 & \text{at} & t = 0 \end{array}$$

a solution of Eq.2 for sufficiently long t assumes the form

$$\zeta = \zeta_0 \exp(-bx) \sin(\omega t - bx) \quad \dots 3$$

in which

$$b = \left(\frac{\omega \cdot \mu}{2k \cdot h_s} \right)^{1/2}$$

The Fourier transform of Eq.2 in the time domain is

$$\frac{k \cdot h_s}{\mu} \cdot \frac{\partial^2 S(f, x)}{\partial x^2} - j f S(f, x) = 0 \quad \dots 4$$

From its solution with respective boundary conditions (or through the Fourier transformation of the response function included in Eq.3) one obtains the following spectral density of GWT oscillations

$$S(f, x) = S_0(f) \exp\left(-\sqrt{\frac{f}{k \cdot h_s}} x\right) \quad \dots 5$$

in which $S_0(f)$ determines the spectrum of sea surface oscillations at the input to the area of ground-water motion ($x = 0$).

From solution (5) it follows that the spectrum of GWT oscillations should curve down to the abscissae axis: in the bilogarithmic system of Figures 5 and 6, because of the exponential factor in Eq.5, the straight lines $S(f)$ should become curvilinear with increasing f . Similarly, for higher x the curves $S(f)$ must be steeper.

Although the second tendency is fairly distinct (compare slopes of the curves for piezometers P.01 and P.02), the former trend is difficult to expose. From this fact it can be inferred that the Boussinesq equation is inadequate for the description of shortwave oscillations in the beach. At least three additional factors point to inadequacy. Firstly, the shortwave oscillations ($f \sim 0.01 \text{ s}^{-1}$) measured at Lubiatowo are attenuated much more strongly than it is given by the attenuation factor b in formula (5).

Secondly, the experimental data shows that the frequency modulation predicted by the Boussinesq $\sin(\omega t - bx)$ is unrealistic. The factor b computed for the known beach characteristics is much greater than that encountered in the

piezometers. Finally, the Boussinesq model does not shed light on the origin of very long oscillations (having however periods shorter than the diurnal oscillations mentioned with reference to Eq.1) ; these oscillations seem to be generated by interactions of shorter waves.

Further information about the ground-water motion is borne by such statistical characteristics as coherence and transfer functions. The coherence functions γ_{xy} computed for two different piezometers indicate that it is only GWT oscillations with periods about 100 seconds that come from the same source (read: from the sea, as sea surface oscillations) . This is illustrated by examples given in Fig.7.

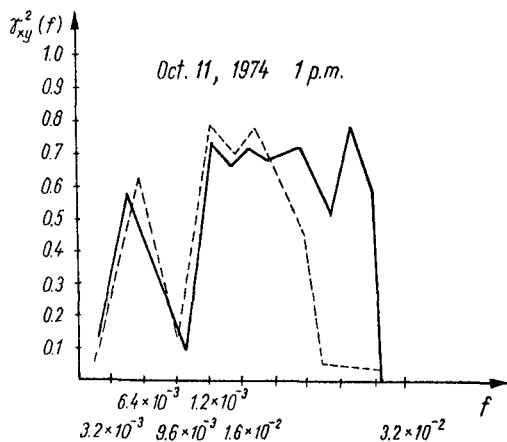


Fig.7 - Coherence Functions

The filtered data was obtained by the well-known filtering technique with a cosine kernel. - It can be seen that high values of coherence occur only in a narrow frequency band. Oscillations with other frequencies have coherences between 0 and 1.

For the ideal case of a linear constant-parameter dynamic system with single, strictly defined, input and output (a "deterministic" system), the coherence function is equal

to one. If γ_{xy} lies between 0 and 1, at least one of the three following cases is possible:

- a) results of measurements are subject to errors due to external noise
- b) the system which couples the input and output signals, $x(t)$ and $y(t)$ is nonlinear
- c) the output signal $y(t)$ is a resultant of a few input signals, instead of a single $x(t)$.

Analysis of the physical processes and experimental techniques inherent in this study of GWT oscillations makes it possible to exclude the cases (a) and (c), as irrelevant under the Lubiatowo conditions. Thus, the only acceptable explanation of the low coherence of most GWT oscillations is confined to nonlinear effects. The values of γ_{xy} measured in various situations indicate that the nonlinear effects are strong both in the band of "short" waves having periods T below 50s, in which GWT oscillations cannot be treated analytically by the Boussinesq equation, and in long waves, with T above 100 s, which might obey the Boussinesq approach but are subject to interaction effects.

The finding that the period T about 100s is somehow critical is also supported by the measured values of the amplification factor.

$$|H(f)| = H(f) \cdot \exp[i\theta(f)] \quad \dots 6$$

From the examples presented in Fig.8, with $|H(f)|$ computed for original GWT level series prior to and after filtering, it can be seen that attenuation of waves is smallest (high $H(f)$) for $f \approx 0.01s^{-1}$.

Analysis of the phase angle $\theta(f)$ shows that the waves passing across the beach (piezometers P.01 ... P.02 etc.) travel toward the dunes, and not along the shore (as should be in case of the edge wave type interaction waves). The phase velocities of these waves vary from 50 to 100 cm per s,

in good agreement with the values of ω/b for waves with periods longer than 100 seconds, another indication of the critical character of these oscillations.

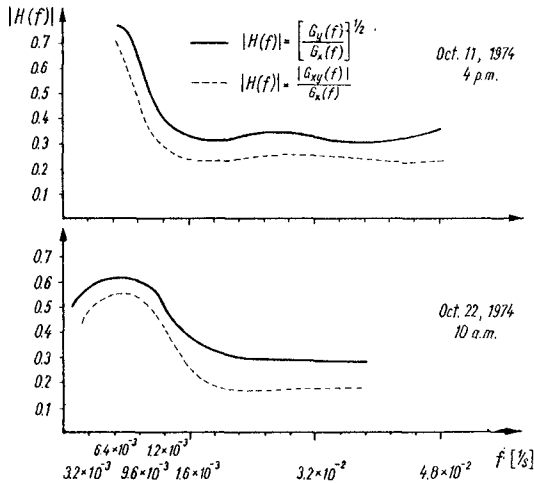


Fig.8 - Amplification Factor

ACKNOWLEDGEMENTS

This study was financially supported by the Polish Academy of Sciences under MR I.15.3.1 program. Dr. T. Piwecki of the Gdańsk Technical University is gratefully acknowledged for his computer routine, which permitted analysis of unsteady filtration.

REFERENCES

- 1 "Properties and Transformation of Hydrodynamical Processes in Coastal Zone of Nontidal Sea", Results of the international project LUBIATOWO 1974 in the coastal zone of the Baltic Sea, Raporty seria R, Nr 2a, Morski Instytut Rybacki; Gdynia 1976.
- 2 "Coastal Processes of Nontidal Sea", Results of the international expedition LUBIATOWO 1976, PRACE Inst. Bud. Wodnego PAN, No. 5a, Gdańsk 1978.

PROCEEDINGS
OF THE

Sixteenth Coastal Engineering Conference

August 27 to September 3, 1978
Hamburg, Germany

Volume III

Sponsored by
ASCE Coastal Engineering Research Council
ASCE Waterway, Port, Coastal and Ocean Division
Ministry for Research and Technology
of the Federal Republic of Germany
Free and Hanseatic City of Hamburg,
Association for Port and Coastal Engineering
and
International Association of the
Physical Sciences of the Oceans



Published by the American Society of Civil Engineers
345 East 47th Street, New York, N.Y. 10017
Net Price: \$50.00

ACKNOWLEDGMENTS

The following engineers served as the Organizing Committee for the Sixteenth International Conference on Coastal Engineering:

KARL-EDUARD NAUMANN, Chairman
Association for Port and Coastal Engineering (Hamburg)

HANS-WERNER PARTENSCKY, Co-Chairman
Technical University of Hannover

WINFRIED SIEFERT, Secretary
Port and River Authority, Cuxhaven

ALFRED FÜHRBÖTER
Technical University of Braunschweig

HARALD GÖHREN
Port and River Authority, Hamburg

JOHANN KRAMER
Board of Maritime Works, Aurich

HANS ROHDE
Federal Institute for Waterways Engineering, Hamburg

JOSEF SINDERN
Waterways and Navigation Board North, Kiel

HANS VOLLMERS
University of Federal German Armed Forces, München

The use of photographs by U. Muuss, N. Rüpke, and H. Engler for use on the Parts title pages is gratefully acknowledged.

**PART III
COASTAL STRUCTURES AND RELATED PROBLEMS**

Chapter 125 COASTAL STRUCTURES' EFFECTS ON SHORELINES Ronald M. Noble	2069
Chapter 126 ROSSLYN BAY BREAKWATER, QUEENSLAND, AUSTRALIA D. N. Foster, B. L. McGrath and W. Bremner	2086
Chapter 127 COASTAL STUDY OF ESPÍRITO SANTO, BRAZIL Paulo Augusto Vivacqua, Hildebrando de Araujo Góes Filho and Otávio de Sampaio Ferraz Jardim Sayão	2104
Chapter 128 PROBLEMS OF DESIGN AND CONSTRUCTION OF AN OFFSHORE SEAWATER INTAKE D. W. Standish-White and J. A. Zwamborn	2125
Chapter 129 WAVE TRANSMISSION THROUGH TRAPEZOIDAL BREAKWATERS Ole Secher Madsen, Paisal Shusang and Sue Ann Hanson	2140
Chapter 130 PERFORMANCE CHARACTERISTICS OF SUBMERGED BREAKWATERS J. Dattatri, H. Raman and N. Jothi Shankar	2153
Chapter 131 COMBINATION EFFECT OF PNEUMATIC BREAKWATER AND OTHER TYPE BREAKWATER ON WAVE DAMPING Yuichi Iwagaki, Toshiyuki Asano and Tsutomu Honda	2172
Chapter 132 SCRAP TYRE BREAKWATERS IN COASTAL ENGINEERING Robert Charles McGregor and Neil Sinclair Miller	2191
Chapter 133 NON-CONSERVATIVE WAVE INTERACTION WITH FIXED SEMI-IMMERSED RECTANGULAR STRUCTURES Robert B. Steimer and Charles K. Sollitt	2209

Chapter 134	
EFFECTS OF WAVE GROUPING ON BREAKWATER STABILITY	
R. R. Johnson, E. P. D. Mansard and J. Ploeg	2228
Chapter 135	
LOADINGS ON RUBBLE-MOUND BREAKWATERS DUE TO EARTHQUAKES	
H. Wang, C. Y. Yang, C. Lamison and S. S. Chen	2244
Chapter 136	
DOLOS-ARMORED BREAKWATERS: SPECIAL CONSIDERATIONS	
Robert D. Carver and D. Donald Davidson	2263
Chapter 137	
DOLOS PACKING DENSITY AND EFFECT OF RELATIVE BLOCK DENSITY	
J. A. Zwamborn	2285
Chapter 138	
PERFORMANCE OF DOLOS BLOCKS IN AN OPEN CHANNEL SITUATION	
Arthur Brebner	2305
Chapter 139	
A MODEL LAW FOR WAVE IMPACTS ON COASTAL STRUCTURES	
C. Ramkema	2308
Chapter 140	
LOAD ANALYSIS FROM WAVE GROUPS	
A. I. Kuznetsov and G. D. Khaskhatchikh	2328
Chapter 141	
IMPACT WAVE FORCES ON VERTICAL AND HORIZONTAL PLATE	
S. R. Massel, M. Oleszkiewicz and W. Trapp	2340
Chapter 142	
WAVE PRESSURES ON SLIT-TYPE BREAKWATERS	
Shoshichiro Nagai and Shohachi Kakuno	2360
Chapter 143	
DYNAMIC BEHAVIOR OF VERTICAL CYLINDER DUE TO WAVE FORCE	
Toru Sawaragi and Takayuki Nakamura	2378
Chapter 144	
WAVE FORCES INDUCED BY IRREGULAR WAVES ON A VERTICAL CIRCULAR CYLINDER	
Hajime Ishida and Yuichi Iwagaki	2397
Chapter 145	
LOADING AND RESPONSE OF CYLINDERS IN WAVES	
G. N. Bullock, P. K. Stansby and J. G. Warren	2415

Chapter 146	
WAVE FORCES ON A ROW OF CYLINDRICAL PILES OF LARGE DIAMETER	
J. C. W. Berkhoff and J. v. d. Weide	2433
Chapter 147	
WAVE LOADS ON HORIZONTAL CYLINDERS	
P. Holmes and J. R. Chaplin	2449
Chapter 148	
NON-BREAKING AND BREAKING WAVE LOADS ON A COOLING WATER	
OUTFALL	
G. R. Mogridge and W. W. Jamieson	2461
Chapter 149	
TRIPOD CONCEPT FOR PILE STRUCTURES IN FAST CURRENT	
J. Khanna and J. S. Wood	2481
Chapter 150	
NEW DIKE DESIGN CRITERIA BASING ON WAVE SPECTRA	
Hans Kaldenhoff and Suhan M. Gökcesu	2500
Chapter 151	
BLANKET THEORY AND LOWCOST REVETMENTS	
C. T. Brown	2510
Chapter 152	
EFFECTIVENESS OF SEADIKES WITH ROUGH SLOPES	
Osamu Toyoshima	2528
Chapter 153	
SCOURING AT THE TOE OF A SEAWALL DUE TO TSUNAMIS	
Hitoshi Nishimura, Akira Watanabe and Kiyoshi Horikawa	2540
PART IV	
COASTAL, ESTUARINE, AND ENVIRONMENTAL PROBLEMS	
Chapter 154	
SIMULATION OF WAVE/WIND FORCED HARBOR OSCILLATION	
S. K. Liu, H. S. Hou and C. C. Chang	2551
Chapter 155	
MIXING OF HEATED WATER DISCHARGED IN THE SURF ZONE	
Kiyoshi Horikawa, Ming-Chung Lin and Tamio O. Sasaki	2563
Chapter 156	
OUTFALL DIFFUSION MODELS FOR THE COASTAL ZONE	
D. C. L. Lam and C. R. Murthy	2584

Chapter 157	
LARGE SCALE TURBULENCE IN TIDAL CURRENTS	
John B. Hinwod	2598
Chapter 158	
3-D CURRENT MODEL WITH DEPTH VARYING EDDY VISCOSITY	
Bryan R. Pearce, Cortis Cooper and Susan Nelson	2602
Chapter 159	
MIXED LAYER MODELS FOR COASTAL WATERS	
Wm. J. Wiseman, Jr., L. J. Rouse, Jr. and O. K. Huh	2619
Chapter 160	
SOME DESIGN CRITERIA FOR OTEC INSTALLATIONS FOR KEAHOLE POINT, HAWAII	
Frederick C. Munchmeyer and Charles L. Bretschneider	2633
Chapter 161	
EXPERIMENTAL STUDY ON SCALE EFFECT OF TIDAL MODEL	
Haruo Higuchi, Hideichi Yasuda and Norio Hayakawa	2646
Chapter 162	
A TIDAL SURVEY FOR A MODEL OF AN OFFSHORE AREA	
W. J. van de Ree, J. Voogt and J. J. Leendertse	2656
Chapter 163	
THREE-DIMENSIONAL MODELLING OF THE IRISH SEA	
Norman Stuart Heaps	2671
Chapter 164	
THREE-DIMENSIONAL SGS ENERGY MODEL OF EASTERN BERING SEA	
S. K. Liu and J. J. Leendertse	2687
Chapter 165	
THE WIND-DRIVEN CIRCULATION IN THE NORTHERN ARABIAN SEA	
Khawaja Zafar Elahi and Jürgen Sündermann	2708
Chapter 166	
SHELF AND COASTAL BOUNDARY LAYER CURRENTS, MISKITO BANK OF NICARAGUA	
Richard L. Crout and Stephen P. Murray	2715
Chapter 167	
CHARACTERISTICS OF CIRCULATION IN BAY WATERS DUE TO WIND ACTION	
Akira Wada and Yoshihito Miyaike	2730

Chapter 168	
BEHAVIORS OF THE SALT WEDGE AND THE SALINITY DISTRIBUTION AT ESTUARIES	
Isao Yakuwa, Susumu Takahashi and Morimasa Ohtani	2746
Chapter 169	
LONGITUDINAL DISPERSION IN SHALLOW WELL-MIXED ESTUARIES	
J. Dronkers	2761
Chapter 170	
INTERFACIAL FRICTION COEFFICIENTS IN A TWO-LAYERED STRATIFIED FLOW	
Emmanuel Partheniades and Vassilios Dermisis	2778
Chapter 171	
STABILITY STUDY OF AN ARTIFICIAL SALT INTRUSION IN ESTUARIES	
C. Marche	2798
Chapter 172	
EFFECT OF HARBOURS ON SALT INTRUSION IN ESTUARIES	
A. Roelfzema and A. G. van Os	2810
Chapter 173	
TIDAL HYDRAULICS AND SALT BALANCE OF LAKE WORTH, FLORIDA	
J. van de Kreeke and J. D. Wang	2827
Chapter 174	
NUMERICAL TIDAL-SALINITY MODELS OF THE EMS ESTUARY	
Karsten Fischer	2840
Chapter 175	
A HYBRID MODEL OF THE ST. LAWRENCE RIVER ESTUARY	
E. R. Funke and N. L. Crookshank	2855
Chapter 176	
FIELD DATA ANALYSIS FOR CHESAPEAKE BAY MODEL VERIFICATION	
Ronald E. Nece and Norman W. Scheffner	2870
Chapter 177	
NUMERICAL STUDY OF DISTORTION IN A FROUDE MODEL	
T. A. McClimans and S. A. Gjerp	2887
Chapter 178	
IMPROVEMENTS ON TIDAL ESTUARIES AND THE EFFECTS ON TIDAL CURRENTS	
Hermann Harten	2905

Chapter 179	
INFLUENCE ON TEMPERATURE INCREASES IN TIDAL RIVERS CAUSED BY WASTE HEAT INJECTIONS WITH RESPECT TO TIDAL CYCLES AND STORM SURGES	
Horst Schwarze and Wilfried Falldorf	2915
Chapter 180	
OUTFLOW DYNAMICS AT A RIVER MOUTH	
Masakazu Kashiwamura and Shizuo Yoshida	2925
Chapter 181	
THERMAL AND BIOLOGICAL IMPACT OF LNG VAPORIZER DISCHARGE	
Peter A. Mangarella and Gordon A. Robilliard	2945
Chapter 182	
PREVENTION OF FREEZING IN FJORDS	
Sveinung Saegrov	2958
SUBJECT INDEX	2979
AUTHOR INDEX	3053



Eider Barrage and Lock

PART III

COASTAL STRUCTURES AND RELATED PROBLEMS

Light House, Weser Estuary



COASTAL STRUCTURES' EFFECTS ON SHORELINES

by Ronald M. Noble*

ABSTRACT

Coastal structures have caused significant impacts to adjacent shorelines, especially when these shorelines are composed of sand. Many times, these shoreline impacts have not been expected due to improper planning prior to the design and construction of these structures. Consequently, excessive erosion and/or deposition of sediment as a result of these structures has necessitated costly, and in some cases, continuous maintenance operations.

This paper reviews the expected shoreline effects for an offshore pier-trestle and breakwater system for an LNG marine terminal. Coastal structures originally proposed for the LNG marine terminal consisted of a 4,600-foot-long pile supported "T" head pier/trestle system and a 1,000-foot-long detached rubble-mound breakwater. This investigation involved field and historical aerial photographic examination of 30 structures in the Southern California Bight and a literature review of similar structures in other environments. Also, a review of theoretical and physical model studies applicable to structures within the coastal marine environment was conducted.

The results of this investigation of existing structures, in conjunction with theory and model studies, indicate that within the study region, pile-supported piers have no appreciable impact of the adjacent shoreline. This investigation also indicates that detached breakwaters produce only minimal impact when the offshore distance of the structure is greater than six times the breakwater length. Of course, consideration was also given to the structure's position relative to the littoral zone, to the depth of water at the shoreward face of the structure, and to the wave climate approaching the structure.

This study included a review of such factors as the local topography, nearshore bathymetry, beach processes, shoreline configuration, beach materials, range of water levels, and local wave climate. The controlling parameters identified in this study are discussed, and the final recommendations presented. This paper illustrates the importance of proper advance shoreline planning before the final design and construction of shoreline facilities.

*Associate, Dames & Moore, Los Angeles, California

INTRODUCTION

The construction of, or the nonconstruction of, coastal structures have resulted in significant impacts along our shorelines. It works both ways; structures built for inlet stabilization or for providing protection such as jetties and breakwaters, and for shoreline stabilization such as groins, bulkheads, revetments, etc. which have not properly considered the existing wave climate and shore processes taking place have resulted in costly maintenance operations; whereas, shoreline developments at other locations have not considered the potential erosion of shorelines from coastal processes and therefore, have not provided adequate coastal structures in the form of shoreline protection or the proper setback and floor elevation for development.

This paper discusses the assessment of the potential impact of a proposed marine terminal on the longshore movement of sand. This study was a preliminary assessment performed in a short time frame in order to ascertain whether the proposed marine terminal posed a significant impact to the adjacent shoreline and if more detailed studies were required.

Included in this study was a review of the site baseline conditions, the effects existing similar structures have had on adjacent shorelines, and theoretical and model studies pertaining to the effects of coastal structures on the littoral environment.

COASTAL STRUCTURES

A liquefied natural gas (LNG) facility has been proposed for construction at Point Conception, California (Figure 1) by Western LNG Terminal Associates. The original¹ proposed coastal structures for the LNG marine terminal consisted of a 4,600-foot-long pile supported "T" head pier/trestle system for LNG carrier offloading and a 1,000-foot-long detached rubble-mound breakwater for support boat and barge mooring.

The 4,600-foot main trestle and the 1/2-mile "T" head pier were to be supported by 60-inch-diameter piles placed four to a bent across the 50-foot pier/trestle width with bents placed approximately 130 feet on centers. The water depth at the pier head would be to approximately -60 feet mean lower low water (MLLW). The proposed rubble-mound breakwater would be located adjacent to the main trestle

¹The design specifications for the proposed coastal structures have been subsequently modified.

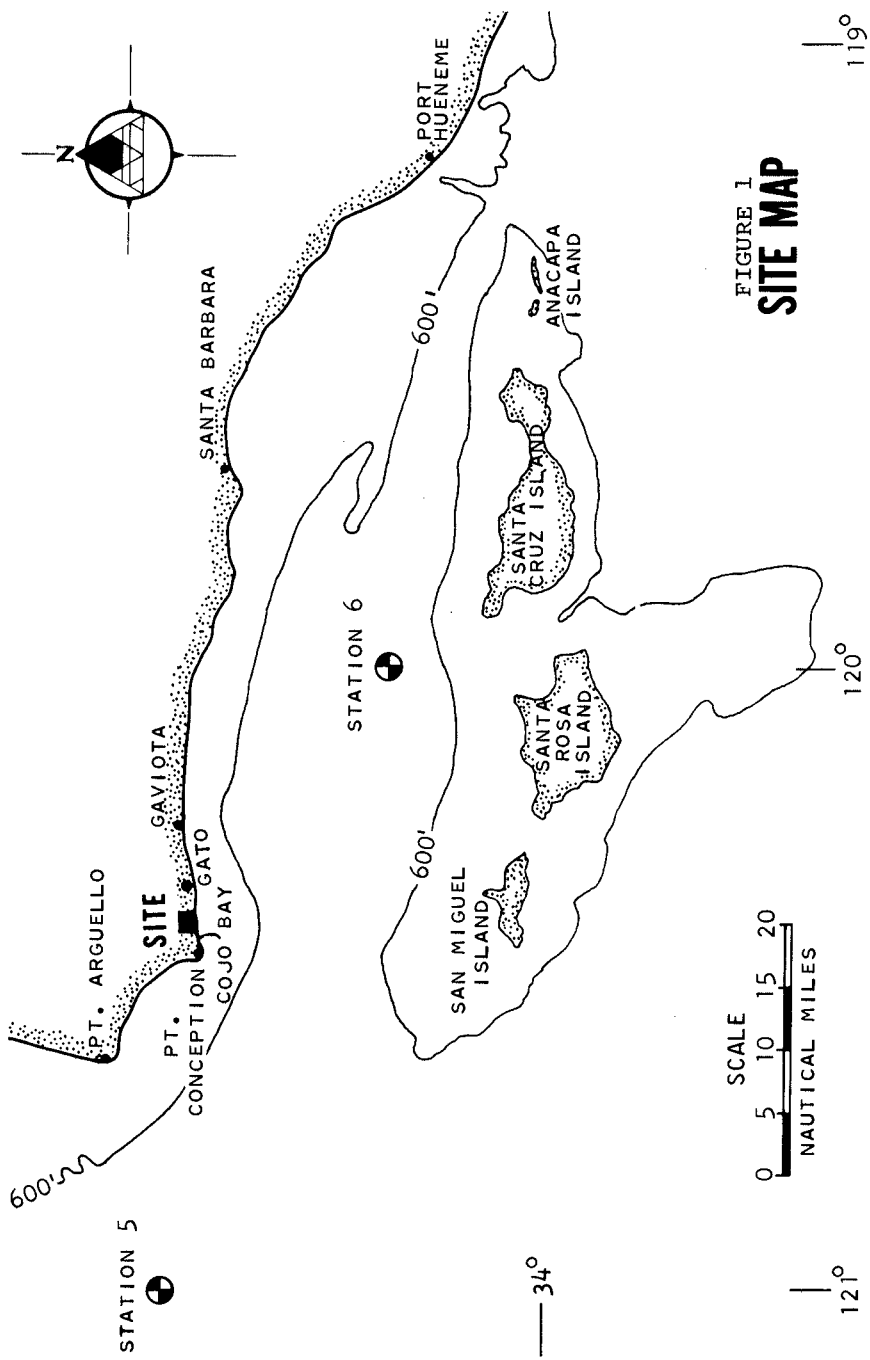


FIGURE 1
SITE MAP

on the trestle's east side and extend 1,000 feet from the trestle aligned approximately parallel to the shoreline along the -20-foot MLLW water depth contour.

The potential effect these proposed structures could have on the adjacent shoreline was assessed by considering the following:

- o Limited site field investigation
- o Review of existing similar structures
- o Review of literature on theoretical and model studies

In review of the above, a good understanding of the shore processes taking place in the site area is required, especially concerning wave climate, sediment transport volumes and sediment transport directions of movement.

EXISTING CONDITIONS

Longshore sediment transport is dependent on such physical conditions as wave climate, beach profile, shoreline configuration, sediment budget, currents, offshore bathymetry, and existing shoreline structures. Waves are the primary driving force controlling the longshore movement of sediment. Therefore, these physical conditions were investigated for the site area.

The proposed site is located at the west end of the Santa Barbara Channel in Santa Barbara County (see Figure 1). This location is approximately 2 miles east of Governement Point within what is known as the Southern California Bight. Due to the abrupt change in orientation of the coastline in the Point Conception area, the coastline within the Southern California Bight is sheltered from wave approach out of the northwest. Additionally, eight offshore islands within this region intercept a portion of the incoming open ocean wave energy from the west, southwest, and south. Consequently, this portion of the coastline may be thought of as a "semiprotected" open ocean coast.

The proposed LNG terminal site is exposed to wave activity from directions southeasterly clockwise through westerly. It is directly exposed to deepwater ocean wave conditions from directions southerly clockwise through westerly directions. Deepwater waves approaching from directions northwesterly through northerly will be refracted toward the east up the Santa Barbara Channel. Due to significant refraction effects and the natural protection

provided to the site by Government Point, these waves do not significantly affect the site. Deepwater ocean waves approaching the site from directions southeasterly clockwise through southerly directions will undergo the effects of diffraction and refraction around the Santa Barbara Islands before reaching the site area. Waves generated within the Santa Barbara Channel can also reach the site from these directions. Several wave hindcast and refraction studies performed in the vicinity of Point Conception were used to verify these findings.

Stations 5 and 6 from National Marine Consultants (1960) deepwater hindcast wave statistics are located in the Point Conception area as shown on Figure 1. There also presently exists wave gages both offshore and in the site area.

The coastline in the vicinity of the proposed site trends in a westward direction and turns northward upcoast from Point Arguello. Sedimentological studies conducted in this area have established the direction of net longshore sediment movement as west to east or downcoast and have also verified the fact that some sediment does move southward around the rocky promontories of Point Arguello and Point Conception. Additionally, investigations by Bowen and Inman (1966) and the U.S. Army Corps of Engineers (1965) have attempted to quantify the sediment transport rate along this portion of California coast. At present, estimates range between 50,000 and 100,000 cubic yards annually. Field and literature investigations suggest that most of this volume of sediment moves downcoast inside of the surf zone. Field studies conducted during the present investigation indicate that the effective boundary of the littoral zone at the site may be approximated by the -20-foot MLLW contour. Seasonal onshore/offshore migration of sand deposits and the redistribution of deposits during a storm event may move the position of the boundary seaward.

SHORELINE PIERS

To effectively assess the potential impact of the proposed pier on the longshore movement of sediment in the site area, case histories of existing piers were investigated and a review of the theory and model studies applicable to pile-supported structures was performed. In all, 20 piers were involved in this study, all situated within the Southern California Bight. The pier locations investigated are shown on Figure 2. The wave climate south of Point Conception, as previously mentioned, is strongly

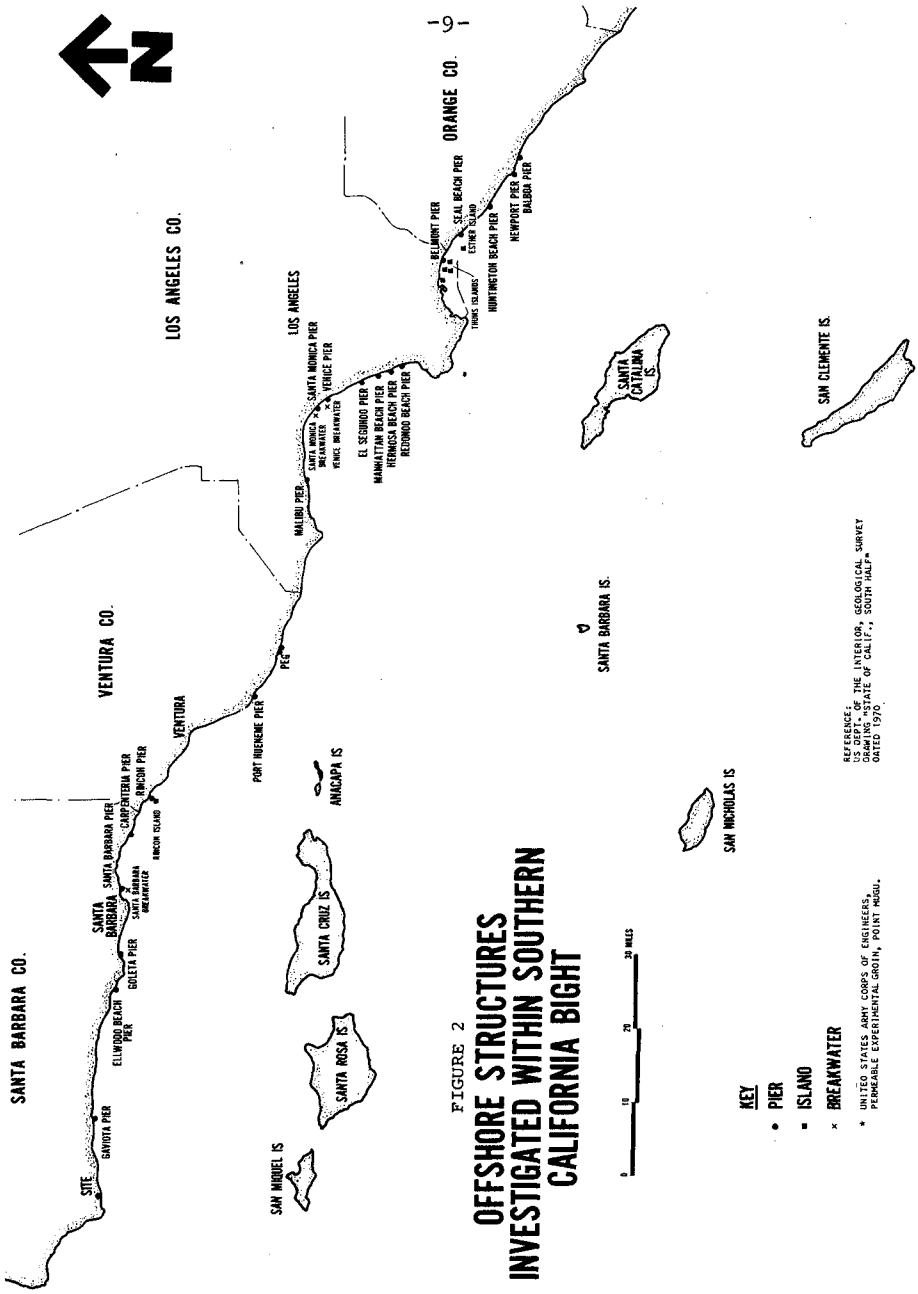


FIGURE 2
**OFFSHORE STRUCTURES
 INVESTIGATED WITHIN SOUTHERN
 CALIFORNIA BIGHT**



influenced by the change in orientation of the coastline and the presence of the offshore islands. Similarities between each of the pier environments are afforded by this regional physiography.

Factors reviewed for each pier structure are shown in Table I and were as follows:

o Environment

- Location of structure
- Wave exposure
- Physiographic setting
- Configuration of pier
- Net longshore transport

o Structural Characteristics

- Pile diameter
- Number piles per bent and pile spacing
- Bent spacing
- Length of structure
- Width of structure


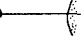
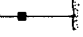
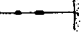

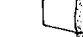








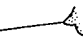

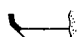
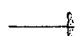
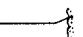
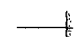

o Effects on Adjacent Shoreline

The piers in this study were all pile-supported structures with evenly spaced pile bents. The foot of each pier was located shoreward of the mean high water level, and the pile-supported structures extended seaward through the nearshore zone. Pile diameters were uniform over the length of each pier as were the bent spacings, and with few exceptions, the number of piles per bent was consistent over the length of the piers.

Although similarities existed between the various piers, the observed ranges in dimensions and configurations were large. The piers ranged in length from 625 to 2,500 feet and in width from 15 to 300 feet. Designs varied from straight "finger-type" piers to complex "U-shaped" or "Dog Leg" piers. Pile diameters ranged from 12 to 30 inches and exhibited a transverse, on center spacing of 4 to 28 feet. The 20 piers also exhibited a minimum bent spacing of 15 feet and a maximum of 60 feet.

Field inspections and historical aerial photographs provided the necessary information for evaluation of the impact on littoral sand transport for each of the structures. Field observations and review of the aerial photographs indicated that these piers have had a negligible effect on the adjacent shoreline. In two cases, where

TABLE I
PIERS INVESTIGATED WITHIN THE
SOUTHERN CALIFORNIA BIGHT

NAME OF STRUCTURE	LOCATION OF STRUCTURE	ENVIRONMENT				NET LONGSHORE TRANSPORT (cubic yds/year)
		WAVE ¹ EXPOSURE	PHYSIOGRAPHIC SETTING	CONFIGURATION OF PIERS		
Balboa Pier	Newport/Balboa Peninsula, Orange County	Open	Long continuous beach		> 200,000	
Newport Pier (McFadden Wharf)	Newport/Balboa Peninsula, Orange County	Open	Long continuous beach		> 200,000	
Huntington Beach Pier	Huntington Beach, Orange County	Open	Long continuous beach		> 200,000	
Seal Beach Pier	Seal Beach, Orange County	Semi Restricted	Long continuous beach		Not determined	
Belmont Pier	Long Beach, Los Angeles County	Restricted	Long continuous beach		Little or no	
Redondo Pier	Redondo Beach, Los Angeles County	Semi Restricted	Long continuous beach		Not determined	
Manhattan Fishing Pier	Manhattan Beach, Los Angeles County	Open	Long continuous beach		> 100,000 and < 270,000	
Hermosa Beach Pier	Hermosa Beach, Los Angeles County	Open	Long continuous beach		> 100,000 and < 270,000	
El Segundo Pier	El Segundo, Los Angeles County	Open	Long continuous beach		> 100,000 and < 270,000	
Venice Pier	Venice Beach, Los Angeles County	Open	Long continuous beach		270,000	
Santa Monica Pier	Santa Monica Beach, Los Angeles County	Semi Restricted	Long continuous beach		270,000	
Malibu Pier	Malibu Beach, Los Angeles County	Semi Restricted	Long continuous beach		> 200,000	
USACE PEG ² Point Mugu	Point Mugu, Ventura County	Open	Long continuous beach		> 500,000	
Port Hueneme Pier	Port Hueneme, Ventura County	Open	Long continuous beach		> 1,000,000	
Ventura Pier	Ventura Beach, Ventura County	Semi Restricted	Long continuous beach		> 500,000	
Rincon Pier	Rincon Point, Ventura County	Open	Headland		270,000	
Carpenteria Pier	Carpenteria Beach, Santa Barbara County	Open	Pocket beach		270,000	
Santa Barbara Pier	Santa Barbara, Santa Barbara County	Restricted	Long continuous beach		> 100,000	
Goleta Pier	Goleta, Santa Barbara County	Semi Restricted	Long continuous beach		> 200,000	
Ellwood Pier	Ellwood Pier, Santa Barbara County	Open	Long continuous beach		> 200,000	
Caviota Pier	Gaviota Beach, Santa Barbara County	Open	Pocket beach		> 200,000	

¹Initially most of the Southern California coastline is partially protected from the offshore islands.

²U.S. Army of Engineering, Permeable Experimental Groin, Point Mugu.

TABLE I (Continued)
PIERS INVESTIGATED WITHIN THE
SOUTHERN CALIFORNIA BIGHT

NAME OF STRUCTURE	STRUCTURAL CHARACTERISTICS					EFFECTS ON ADJACENT SHORELINE
	PILE ³ DIAMETER (inches)	NUMBER ³ PILES PER BENT AND PILE SPACING (feet on center)	BENT ³ SPACING (feet on center)	LENGTH OF STRUCTURE (feet)	WIDTH OF ³ STRUCTURE (feet)	
Balboa Pier	16 to 18	4 piles/bent 7 foot spacing	20 foot spacing	925	30	None
Newport Pier (McFadden Wharf)	16	4 piles/bent 6 foot spacing	20 foot spacing	1,025	24	None
Huntington Beach Pier	24	3 piles/bent 8 foot spacing	22 foot spacing	1,950	25	Minor scour at foot of structure
Seal Beach Pier	18	4 piles/bent 6 foot spacing	20 foot spacing	1,650	24	Minor upcoast erosion. Minor down-coast accretion
Belmont Pier	20	4 piles/bent 8 foot spacing	60 foot spacing	1,350	32	None
Redondo Pier	15	4-5 piles/bent 10 foot spacing	15 foot spacing	500	40-50	None
Manhattan Fishing Pier	30	2 piles/bent 14.5 foot spacing	25 foot spacing	660	20	None
Hermosa Beach Pier	18	3 piles/bent 7.5 foot spacing	32 foot spacing	875	20	None
El Segundo Pier	22	3 piles/bent 5.5 foot spacing	18 foot spacing	700	16.5	None
Venice Pier	22	1 pile/bent	16 foot spacing	935	30	None
Santa Monica Pier	15	30 piles/bent 6-8 foot spacing	18.5 foot spacing	875	300	Minor accretion at foot of pier
Malibu Pier	12 to 14	5 piles/bent 2-8 foot spacing	15 foot spacing	815	30	None
USACE PEC ² Point Mugu	14 inch square	Variable	Variable	700	15	None
Port Huenaena Pier	14	4 piles/bent 4-10 foot spacing	18 foot spacing	850	20	None
Ventura Pier	12 to 16	5 piles/bent 6 foot spacing	15 foot spacing	1,750	30	None
Rincon Pier	16	1-2 piles/bent 12 foot spacing	40 foot spacing	3,500	14	None
Carpenteria Pier	30	2 piles/bent 28 foot spacing	30 foot spacing	600	28	None
Santa Barbara Pier	12	7 piles/bent 4 foot spacing	8 foot spacing	2,200	30	None
Goleta Pier	12 to 16	3 piles/bent 6 foot spacing	15 foot spacing	650	15	None
Ellwood Pier	12	3 piles/bent 6 foot spacing	16 foot spacing	2,000	20	None
Gaviota Pier	16 to 18	4 piles/bent 7 foot spacing	16 foot spacing	625	22	None

²U.S. Army of Engineering, Permeable Experimental Groin, Point Mugu.

³Characteristic pertaining to the inshore portion of pier.

substantial accretion effects were observed, it was apparent that the presence of structures other than the pile-supported piers had been the cause.

The results of these "similar structure" observations for piers are supported by the result of two previously conducted studies, one by J.W. Johnson in 1973 and another by C.H. Evert and A.E. DeWall in 1975. Johnson inspected approximately 34 piers along the California coast and found no discernible effects on the adjacent shorelines as a result of pier installation. Everts and DeWall, in a beach survey conducted in North Carolina, likewise found that out of five fishing piers inspected, none had a significant effect on accretion or erosion along adjacent shorelines.

Theoretical/analytical studies have been conducted to determine the effects of pile-supported structures on the transmission of wave energy. Most of the studies have attempted to identify the factors which control or greatly influence the transmission losses as waves pass through pile structures. The purpose of these particular studies has been to evaluate the use of closely spaced piles as a breakwater (Wiegel, 1961; Macknight and Thomas, 1973) and to predict wave transmission losses through pile arrays (Costello, 1952, van Weele and Herbich, 1972). In these studies single rows and multiple rows of piles were considered. Both longitudinal and transverse pile spacings were varied along with diameter and total number of piles. Considerations were given to incident wave height and steepness and diffraction effects as the wave passed through the pile arrays. Results of these studies indicate that within a range of incident wave steepness, when pile spacing is greater than four times pile diameter, reflection and eddy losses are of minor importance and the ratio of transmitted wave height to incident wave height should approach unity. This holds true for both transverse and longitudinal pile spacings.

Predominant swell conditions within the Southern California Bight fall well within the wave steepness boundaries established in these investigations. In the case of the surveyed piers, both the longitudinal and the transverse pile spacing were beyond the "four-diameter" range. It would be expected from theory that transmissibility should be very close to unity for all of the structures examined; consequently, as wave energy losses are negligible, there should be a minimal impact on the littoral environment.

OFFSHORE STRUCTURES

To effectively assess the potential impact of the proposed breakwater on the longshore movement of sediment in the site area, case histories of nine existing offshore structures were investigated and a review of the theory applicable to these structures was performed. The structures examined included three detached breakwaters and six artificial islands, all located within the Southern California Bight. The offshore structure locations investigated are shown on Figure 2.







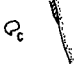
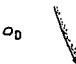

Factors reviewed for each offshore structure are shown in Table II and were as follows:

- o Environment
 - Location of structure
 - Wave exposure
 - Physiographic setting
 - Configuration of structure and adjacent shoreline
 - Net longshore transport
- o Structural Characteristics
 - Structure type
 - Depth at shoreward face of structure
 - Offshore distance to structure
 - Length of structure
 - Ratio: $\frac{\text{distance offshore}}{\text{length of structure}}$
- o Effect on Adjacent Shoreline

Like the piers, the detached structures may be defined by a set of measurable parameters. For the breakwaters, these parameters included the longshore length, the distance from the shoreline, and the depth of water at the shoreward face of the breakwater. Similarly, the measurable parameters for the artificial islands included the distance from shore (measured parallel to the predominant wave approach direction), the structural length (measured perpendicular to the predominant wave approach direction), and the depth of water at the shoreward face of the structure.

The detached breakwaters ranged in length from 600 to 2,800 feet, in distance from the shoreline from 600 to 1,850 feet, and in water depth at the shoreward face from 6

TABLE II
DETACHED BREAKWATERS AND ARTIFICIAL ISLANDS
INVESTIGATED WITHIN THE
SOUTHERN CALIFORNIA BIGHT

NAME OF STRUCTURE	LOCATION OF STRUCTURE	ENVIRONMENT			
		WAVE ¹ EXPOSURE	PHYSIOGRAPHIC SETTING	CONFIGURATION OF STRUCTURE AND ADJACENT SHORELINE ² (not to scale)	NET LONGSHORE TRANSPORT (cu. yds/year)
Venice Breakwater	Venice Beach, Los Angeles County	Open	Long continuous beach		270,000
Santa Monica Breakwater	Santa Monica Beach, Los Angeles County	Open	Long continuous beach		270,000
Santa Barbara Breakwater	Santa Barbara Harbor, Santa Barbara County	Open	Headland		270,000
Island Esther	Long Beach, Los Angeles County	Semi Restricted	Long continuous beach		Little or no longshore movement of sediment
Thums Islands Island "A"	Long Beach, Los Angeles County	Semi Restricted	Long continuous beach		Little or no net longshore movement of sediment
Thums Islands Island "B"	Long Beach, Los Angeles County	Restricted	Long continuous beach		Little or no net longshore movement of sediment
Thums Islands Island "C"	Long Beach, Los Angeles County	Semi Restricted	Long continuous beach		Little or no net longshore movement of sediment
Thums Islands Island "D"	Long Beach, Los Angeles County	Restricted	Long continuous beach		Little or no net longshore movement of sediment
Rincon Island	Long Beach, Los Angeles County	Open	Headland		270,000

¹Initially most of the Southern California coastline is partially protected from the offshore islands.


² Areas of accretion.

TABLE II (Continued)
 DETACHED BREAKWATERS AND ARTIFICIAL ISLANDS
 INVESTIGATED WITHIN THE
 SOUTHERN CALIFORNIA BIGHT

NAME OF STRUCTURE	STRUCTURAL CHARACTERISTICS					EFFECTS ON ADJACENT SHORELINE
	STRUCTURE TYPE	ORIGINAL DEPTH MLLW AT SEaward FACE OF STRUCTURE (feet)	ORIGINAL OFFSHORE DISTANCE ³ (D) TO 0' MLLW (feet)	LENGTH OF STRUCTURE (d) (feet)	RATIO D/d DISTANCE OFFSHORE/ LENGTH OF STRUCTURE (dimensionless ratio)	
Venice Breakwater	Rubble Mound	16-18	1,000	600	.60	Pronounced shoreline accretion (formation of tombolo)
Santa Monica Breakwater	Rubble Mound	23-25	1,850	1,800	1.02	Pronounced shoreline accretion (formation of tombolo)
Santa Barbara Breakwater	Rubble Mound	6-8	600	2,800	.21	Pronounced shoreline accretion
Island Esther	Sand filled core with armor rock perimeter	41-43	8,400	380	22.11	No discernable effect
Thuma Islands Island "A"	Sand filled core with armor rock perimeter	26-28	1,547	1,172	1.32	Shoreline accretion (May be due to an adjacent fill project - see text)
Thuma Islands Island "B"	Sand filled core with armor rock perimeter	26-28	2,604	1,085	2.40	No discernable effect
Thuma Islands Island "C"	Sand filled core with armor rock perimeter	26-28	5,555	1,085	5.12	Shoreline accretion
Thuma Islands Island "D"	Sand filled core with armor rock perimeter	39-41	6,614	868	7.62	No discernable effect
Rincon Island	Sand filled core with armor rock perimeter	41-44	5,500	535	10.28	No discernable effect

³Distance to shore parallel to predominant wave approach direction.

to 25 feet. The artificial islands ranged in length from 380 to 1,172 feet, in distance from the shoreline from 1,547 to 8,400 feet, and in water depth at the shoreward face from 26 to 44 feet.

Comparison of historical aerial photographs provided most of the information needed to assess the impact of the breakwater and artificial island structures on the littoral environment. These photographs indicated appreciable sediment buildup in the lee of each breakwater. Aerial photography of the artificial islands, before and after construction, showed that some of these structures also may have produced accretionary effects along the adjacent shorelines.

Previous case studies and field investigations have been conducted to evaluate the impact of offshore structures on the littoral zones. Most of these studies have acknowledged one or more of the following parameters as being important in performing this evaluation:

- o The length of the structure relative to its offshore distance
- o The incident wave length relative to the offshore distance of the structure
- o The depth of water at the shoreward face of the structure
- o The incident sector of wave approach at the structure and the resultant wave shadow in the lee of the structure
- o The position of the structure relative to this active littoral zone

Inman and Frautschy (1965) observed that along the southern California coast, pronounced accretion occurs if a detached breakwater is located offshore a distance of less than three to six times the length of the breakwater. Dames & Moore (1974) investigated the effects of artificial islands along the southern California coast on the inshore littoral processes. Through aerial photographic analysis they attempted to document what, if any, effects had occurred on the adjacent shoreline since the time of island construction. This study generally confirms the basic guideline put forth by Inman and Frautschy.

Theoretical and model studies conducted by Harms and others (1973) along with the investigations by Savage de

Saint Marc and Vincent (1968) indicate that a region of reduced wave energy will develop in the lee of an offshore structure. Further, the study by Savage de Saint Marc and Vincent indicates that the effect of an offshore structure on a given shore is dependent mainly on the length of the structure relative to its distance from the shoreline.

The detached structure case studies established distance to shore/length of structure relationship as being the controlling parameter in evaluating the impact of an offshore structure on the adjacent shoreline. Model study investigations supported this finding.

RESULTS

The proposed LNG terminal pier, like all of the piers investigated, is a pile-supported structure. Although the proposed pile diameter is larger than the pile diameters measured for existing piers, the pile density (pile area/total pier area) for the proposed structure is at the low end of pile densities for the surveyed piers. The longitudinal spacing is 20D (20 pile diameters) and the transverse spacing is 4D (4 pile diameters).

Potential impacts associated with the proposed pier are a function of pile density, pile spacing, and incident wave steepness. Pile densities for the piers investigated along the southern California coast produced no discernible impacts on the net longshore movement of sediment. These piers exist in an environment similar to that found at the proposed site, both in terms of wave exposure and longshore sediment transport rates. Because the pile density of the proposed LNG pier is lower than 90 percent of all the piers investigated, it is expected that this pier would have a negligible impact on the longshore movement of sand. Consideration of incident wave steepness and pile spacing from theoretical and model studies also supports the conclusion that the proposed pier would not significantly affect the longshore transport of sand.

Potential impacts associated with the proposed breakwater were found both in the similar structure/similar environment and the model studies to be primarily a function of the distance to shore/length of structure ratio. Of course, consideration was also given to the structure's position relative to the littoral zone and the wave climate approaching the structure. The proposed breakwater's distance to shore/length of structure ratio was approximately two, and its location was in the proximity of the effective littoral boundary. This could cause a substantial reduction in wave energy reaching the littoral zone

in the lee of the breakwater and, therefore, diminish the sediment transporting capacity of waves and currents in this area with a resultant deposition of sediment.

According to the findings of both the case studies and the model studies, at the proposed site, the distance offshore at which the breakwater would be expected to have no discernible impact on the adjacent shoreline would be 6,000 feet (6:1 ratio).

It was felt that the shoreline impact associated with the proposed breakwater would be significantly reduced, for a particular distance offshore, if the structure's length was shortened. In this manner, the ratio of 6:1 offshore distance/length of structure, established in both the similar structure/similar environment investigations and supported by the findings of model studies, could be maintained. However, it would still be important to verify if there would be any wave energy reduction in the effective littoral zone due to wave shadow effects caused by the breakwater.

REFERENCES

- Blume & Associates, 1974, Engineering and ecological evaluation of artificial island design, Rincon Island, Punta Gorda, California. U.S. Army Coastal Engineering Research Center, Technical Memorandum No. 43, 76 pp.
- Bowen, A.J., and Inman, D.L., 1966, Budget of littoral sands in the vicinity of Point Arguello, California. U.S. Army Coastal Engineering Research Center, Technical Memorandum No. 19, 44 pp.
- Costello, R.D., 1952, Damping of water waves by vertical circular cylinders. Trans. Amer. Geophys. Union, Vol. 33, No. 4.
- Dames & Moore, 1974, A study of the performance of certain artificial islands on the Pacific coast of the United States, 42 pp., tables and plates.
- Everts, C.H., and DeWall, A.E., 1975, Coastal sandlevel changes in North Carolina. Draft report, Coastal Engineering Research Center, U.S. Army Corps of Engineers.

- Harms, V.K., Sun, H.T., Wiegel, R.L., and Kian, M.A., 1973, Effects of large nearshore structures on wave motion in the vicinity of the structure and adjacent coast. University of California, Hydraulic Engineering Laboratory, HEL 1-22, 40 pp., figures and tables.
- Inman, D.L., and Frautschy, J.D., 1965, Littoral processes and the development of shorelines. Coastal Engineering, Santa Barbara Specialty Conference.
- Johnson, J.W., 1973, Proposal preparation for Department of Navigation and Ocean Development. Unpublished information.
- Macknight, A., and Thomas, R.B., 1973, Transmission coefficients through various types and arrangements of partial breakwaters. Proceedings, First Australian Conference on Coastal Engineering, Engineering Dynamics of the Coastal Zone, Sydney, The Institution of Engineers, Australia, May 14-17, 1973.
- National Marine Consultants, 1960, Wave statistics for seven deepwater stations along the California coast. Prepared for U.S. Army Engineer Districts, Los Angeles and San Francisco.
- Simison, E.J., Leslie, K.C., and Noble, R.M., 1978, Potential shoreline impacts from proposed structures at Point Conception, California. Coastal zone '78, San Francisco, California.
- Savage de Saint Marc, G., and Vincent, G., 1968, Transport littoral formation de Fleches et de Tombolos. University of California, Hydraulic Engineering Laboratory, HEL-2-17, 39 pp.
- U.S. Army Corps of Engineers, 1965, Report of the District Engineer on survey report for navigation, Cojo Anchorage, Point Conception, California. Unofficial report by the Los Angeles District, U.S. Army Corps of Engineers.
- van Weele, B.J., and Herbich, J.B., 1972, Wave reflection and transmission for pile arrays. Proceeding of the 13th Coastal Engineering Conference, Vancouver, B.C., Canada.
- Wiegel, R.L., 1961, Closely spaced piles as a breakwater. University of California, Institute of Engineering Research, IER, 140-6, 4 pp.

Rosslyn Bay Breakwater, Queensland, Australia

by

D.N. Foster⁽¹⁾, B.L. McGrath⁽²⁾, W. Bremner⁽³⁾

Introduction

The Queensland Harbours and Marine Department is charged with the responsibility of providing small craft facilities throughout the State. In 1964, the Department engaged a firm of consulting engineers, Blain, Bremner and Williams Pty. Ltd. to prepare a preliminary report on possible boat harbour sites between Yeppoon and Port Alma on the Central Queensland Coast.

Five sites were evaluated according to the following criteria:-

- (i) Degree of protection afforded
- (ii) Tidal access
- (iii) Degree of maintenance dredging anticipated
- (iv) Capital cost necessary to establish the harbour and the ability to construct the harbour in stages
- (v) Availability of foreshore area for development
- (vi) Accessibility by road transport and to established amenities
- (vii) Availability of suitable quarry material

The recommendation that the most suitable site would be at Rosslyn Bay (Figures 1 & 2) was accepted and approval to commence construction was obtained. A 105m rubble mound rock breakwater was constructed in 1968. The breakwater was extended to 210m in 1970 and was further extended to 300m in 1972.

In 1976 tropical cyclone 'David' extensively damaged the breakwater and harbour facilities. Subsequently the breakwater has been re-designed following model studies and reconstruction was completed in May 1978.

This paper discusses damage to the breakwater from wave and surge action, model studies and repair of the breakwater.

Original Design

The area on the Central Queensland Coast between Port Alma and

-
- (1) Associate Professor, University of New South Wales
 - (2) Senior Engineer, Smallcraft Facilities, Dept. Harbours & Marine, Queensland.
 - (3) Consulting Engineer, Blain, Bremner & Williams Pty. Ltd.

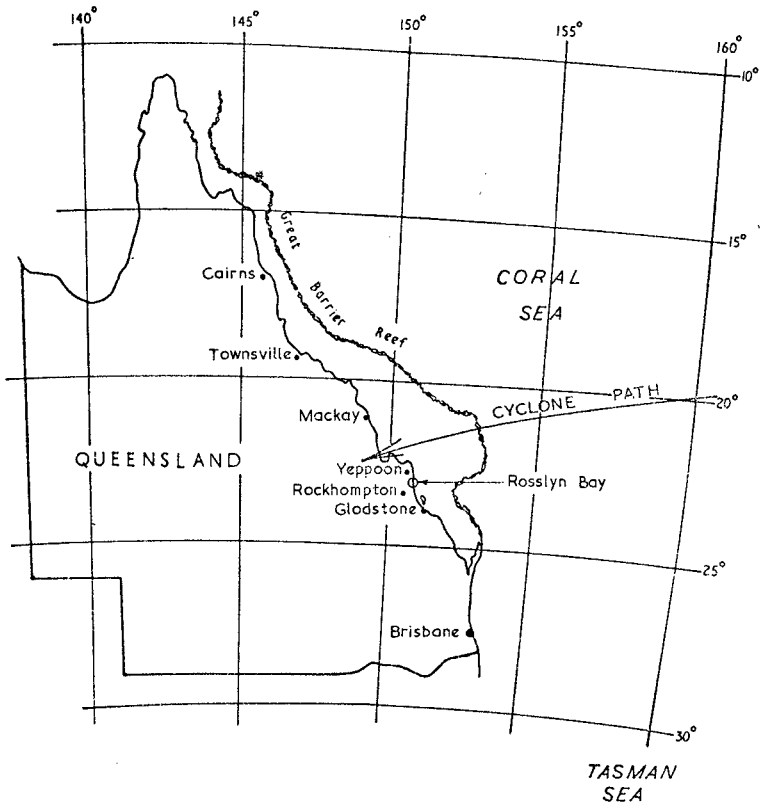


FIGURE 1: LOCALITY SKETCH
AND PATH OF CYCLONE DAVID.

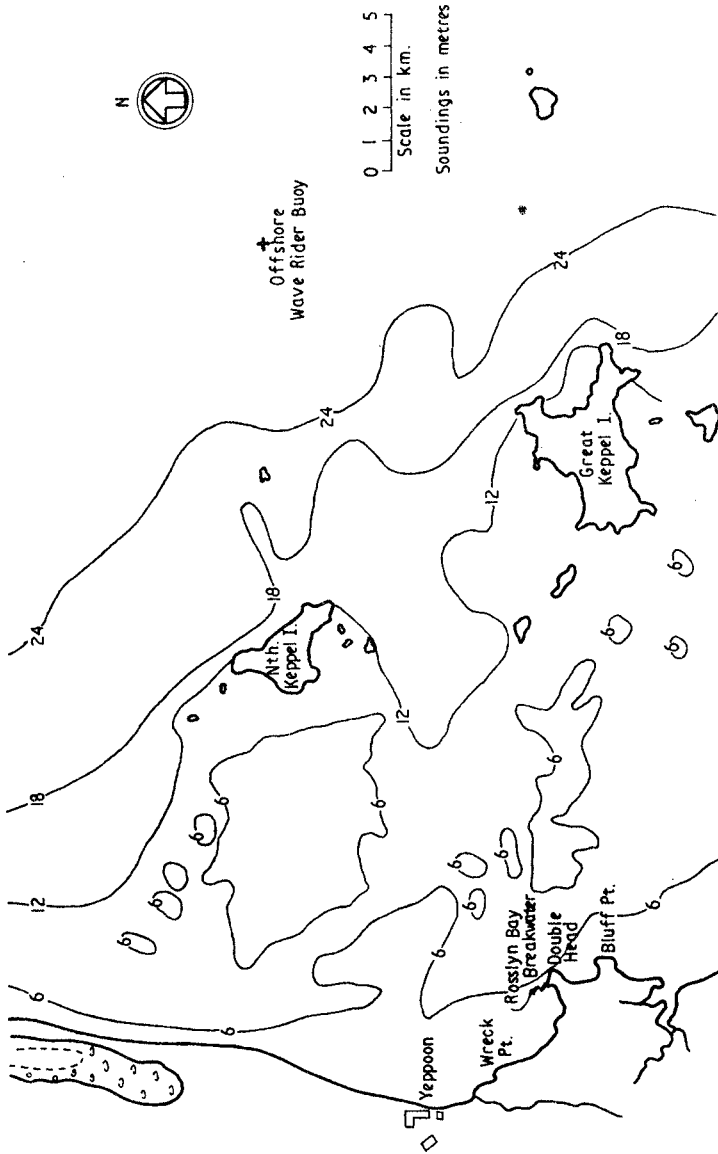


FIGURE 2: OFFSHORE TOPOGRAPHY AND LOCATION OF WAVE RIDER BUOY

Yeppoon, although sheltered from deep ocean swell by the Great Barrier Reef, has no natural boat havens (except for tidal estuaries) and is subject to cyclonic storms. The fetch length from the Great Barrier Reef to the coast is approximately 80 km. As any structure is subjected to large wave forces, construction of small craft harbours in the region is relatively costly. Tidal estuaries in the area (indeed on the whole of the eastern coast of Queensland) are generally avoided for boat harbour development because of the high frequency of major floods with accompanying high water levels and flow velocities, debris and siltation problems. However, they are used by small craft as shelter during cyclones.

Due to the limitation of available funds, economic considerations were a major factor in fixing the design of the harbour.

Double Head (Figure 2) provides a degree of natural shelter against the prevailing south-easterly winds. To provide protection against north-easterly weather and south-easterly waves diffracted around Double Head, a breakwater was constructed running parallel to the natural contours in a north-westerly direction. In order to reduce costs, the breakwater was designed to the minimum standards necessary to provide shelter against the majority of anticipated weather conditions. To construct a breakwater designed to provide protection during severe cyclonic conditions proved too costly for the available funds. This factor, together with the availability close by, of effective cyclone shelter to small craft in mangrove lined estuaries led to the decision to accept a higher than normal degree of risk of severe storm damage to the breakwater.

The following design criteria were adopted for the breakwater design:

High tidal level	4.27m above L.W.D.
Storm surge	1.22m
Wave height	2.13m
Crest level	7.32m above L.W.D.

A typical section through the breakwater and armour specification is shown in Figure 3. The seaward face was armoured with a nominal 3 ton rock. The crest was armoured with nominal $\frac{1}{2}$ ton rock blinded with fine material to provide an access road and was not designed to resist overtopping.

As there were no wave records for the area, the design storm surge and wave heights were estimated by hindcasting using available wind records. In Jan. 1967 the Consulting Engineer estimated from the available cyclone records that damage to the breakwater may occur once in every 10 years and such damage was likely to be severe. As it happened, the breakwater was severely damaged by overtopping some 8 years after construction of its first section.

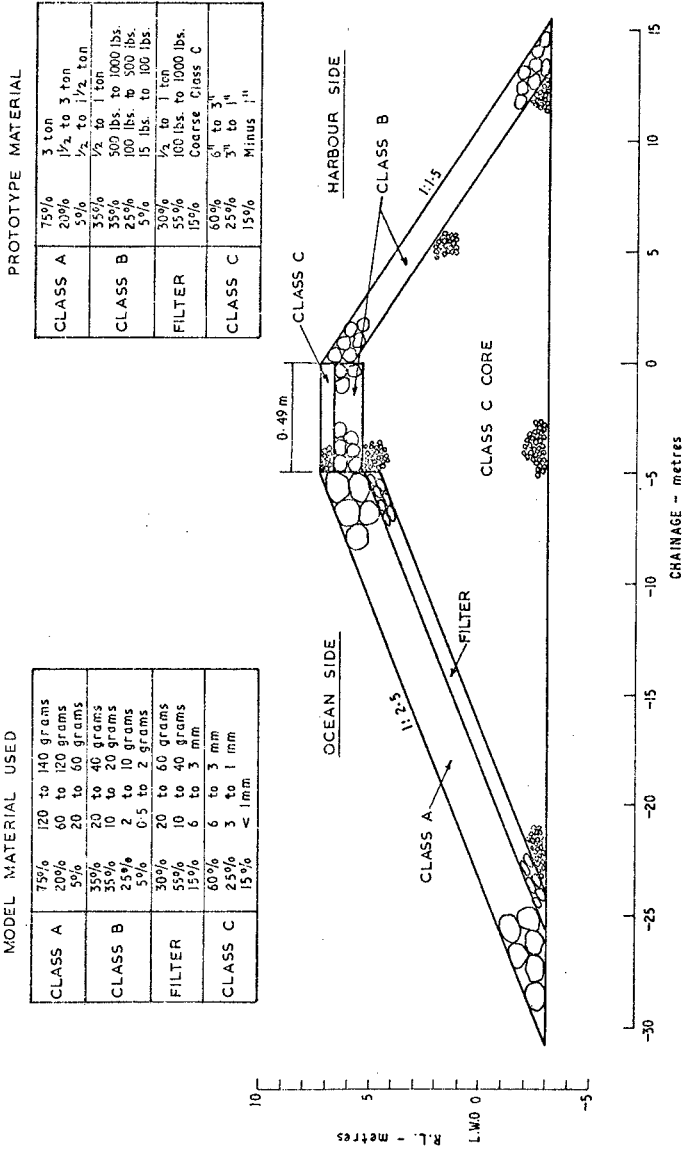


FIGURE 3: TYPICAL CROSS SECTION OF BREAKWATER

Cyclone "David"

Cyclone "David" originated in the Coral Sea on 15.1.76, moving first in a south-south-westerly direction and then west to cross the coast approximately 50 km north of the harbour at a speed of 28 km/hr. The path of the cyclone is shown in Figure 1. Central pressure as it crossed the coast was 961 mb and the radius to maximum wind was estimated by the Bureau of Meteorology to be 35 km using radar interpretation methods.

Associated with the cyclone, there was an intense high pressure system (central pressure 1010 to 1024 mb) located in the Tasman Sea some 1500 km to the south-south-east. The consequential steep pressure gradient resulted in a general strengthening of the south-east winds which had persisted since 15th January. This climatic situation is assessed as having had a significant influence on the abnormally long duration of the storm surge which accompanied the cyclone.

Deep water wave conditions during the cyclone were recorded at 12 hr. intervals on wave rider buoys at Double Island Point, 390 km to the south, Mackay 270 km to the north and Yeppoon immediately offshore of the harbour. Recorded wave conditions are given in Table 1.

Water levels during the cyclone were recorded on a network of tide gauges along the Queensland coastline. Storm tide levels at Rosslyn Bay and Gladstone are given in Table 2. Unfortunately the tide gauge at Rosslyn Bay was inoperative over part of the storm but a close estimate of water levels can be obtained from the Gladstone records.

A feature of the storm was the long duration of the surge which reached a maximum of 1.1m during the p.m. tide on 19.1.76. The peak water level of 5.3m occurred during the a.m. tide on 19.1.76.

Wave and storm tide conditions during the cyclone are summarised in Figure 4. Wave conditions at the breakwater are complicated by partial protection provided by two offshore islands approximately 15 km to the east and north-east of the harbour and refraction over a rather complex bed topography (see Figure 2).

From energy considerations wave heights at the breakwater have been estimated to be between 0.8 and 0.9 of the deepwater conditions. In-shore visual observations by two independent observers, one by Bremner and one by COPE,* during the peak of the storm estimated wave heights of 2.5 and 3.3m against a measured deep water significant height of 3.8m.

Wave conditions following the cyclone and prior to a detailed survey of

*COPE Coastal Observation Programme **Engineering** - A Beach Protection Authority, Department of Harbours and Marine, Visual Data Acquisition Programme

X

Table 1: Wave Data 'Cyclone David'

Date	Time	Double Is. Point			Yeppoon			Mackay		
		H. sig.	Tz.	Tp.	H. sig.	Tz.	Tp.	H. sig.	Tz.	Tp.
16	0300	0.90	7.0	-	0.50	4.75	-	0.52	2.80	-
	1500	1.75	4.65	-	1.29	4.60	-	1.23	3.50	-
17	0300	4.00	6.90	-	2.63	6.18	-	2.15	5.18	-
	1500	4.19	7.03	9.10	3.00	6.60	-	2.20	4.57	-
18	0300	4.60	7.60	9.90	3.15	6.56	-	1.90	4.87	-
	1500	5.80	8.32	10.70	3.56	7.25	-	1.87	5.10	-
19	0300	5.76	8.46	11.40	3.79	7.59	-	2.50	5.60	-
	1500	5.36	7.80	10.70	3.79	6.61	8.70	2.88	6.02	11.90
20	0300	4.82	8.24	10.60	3.84	7.74	9.60	2.41	5.32	6.40
	1500	3.14	7.19	9.80	2.03	5.67	7.60	1.66	4.57	5.60
21	0300	2.52	6.17	8.60	1.25	6.10	-	1.12	4.00	4.30
	1500	2.45	6.00	9.10	1.09	5.63	-	0.70	4.18	9.40
22	0300	2.11	5.69	8.50	1.38	5.39	-	0.80	3.90	9.50
	1500	2.15	5.69	8.00	1.90	5.27	-	-	-	-

H-sig - Significant wave height in metres = $H/3$
 Tz. - Zero crossing period in seconds
 Tp. - Peak energy period in seconds (where available)

Jan. 1976

Table 2: Tide Records during Cyclone 'David'

Station			Rosslyn Bay			Gladstone		
Date	Time	Tide	Ht.	Pre- dicted	Resid- ual	Ht.	Pre- dicted	Resid- ual
16.1.76	a.m.	L				0.7	0.8	-0.1
	a.m.	H				4.4	4.4	0.0
	p.m.	L				0.9	0.8	+0.1
	p.m.	H				3.8	3.7	+0.1
17.1.76	a.m.	L				0.9	1.2	+0.3
	a.m.	H				4.6	4.5	+0.1
	p.m.	L				0.9	0.7	+0.2
	p.m.	H				3.9	3.6	+0.3
18.1.76	a.m.	L				0.9	0.5	+0.4
	a.m.	H				4.7	4.5	+0.2
	p.m.	L				1.0	0.5	+0.5
	p.m.	H				4.1	3.8	+0.3
19.1.76	a.m.	L				1.1	0.6	+0.5
	a.m.	H				5.1	4.5	+0.6
	p.m.	L	1.5	0.5	+1.0	1.7	0.6	+1.1
	p.m.	H	4.9	3.9	+1.0	4.6	3.6	+1.0
20.1.76	a.m.	L	1.0	0.6	+0.4	1.3	0.7	+0.6
	a.m.	H	4.9	4.6	+0.3	4.7	4.3	+0.4
	p.m.	L	0.8	0.6	+0.2	0.9	0.9	0.0
	p.m.	H	3.9	3.9	0.0	4.0	3.8	+0.2

Notes:

1. Tide levels at Rosslyn Bay are based on Low Water Datum
2. Tide levels at Gladstone are based on Chart Datum
3. All units expressed in metres

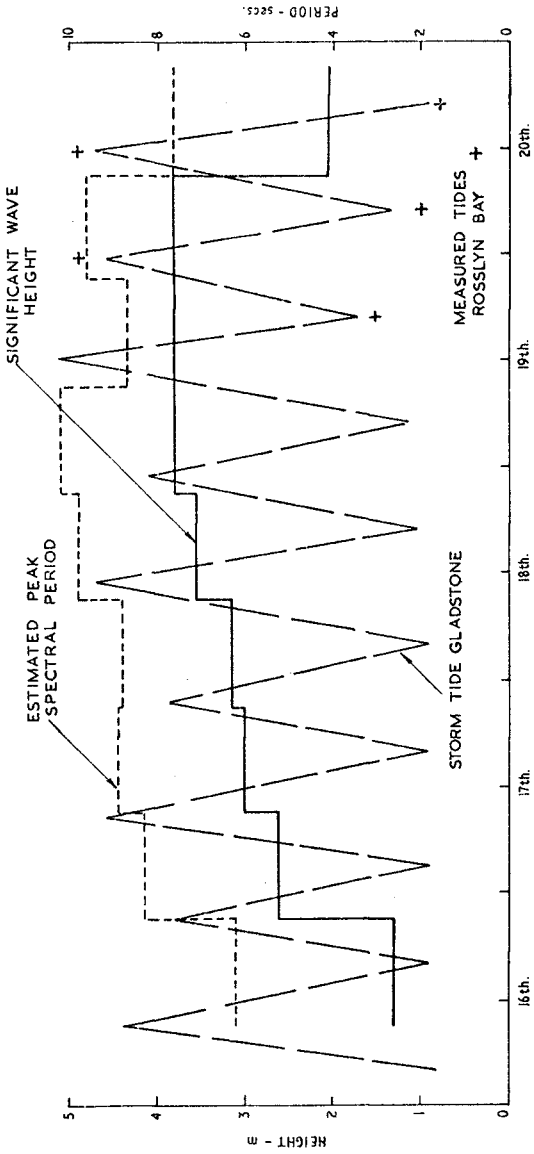


FIGURE 4: WAVE AND STORM TIDE CONDITIONS

the damage were mild with significant wave heights of less than 2m and zero crossing period of between 4.0 and 5.0 seconds.

Breakwater Damage

Inspection of Figure 4 shows that the breakwater was subjected to wave and surge conditions approaching or exceeding the design conditions from 17th to 20th January. Overtopping of the breakwater occurred at high tide with very heavy overtopping being observed during 19th and 20th. The observed history of damage is given in Table 3.

Table 3: History of Damage

Day Jan. 1976	Time (hours)	Damage
16th	2230	No observable damage
17th	0900	No observable damage
17th	2100	No observable damage
18th	0950	Slight damage
18th	1630	Slight damage
19th	1130	Heavy overtopping - slight damage
19th	2400	Heavy overtopping - minor damage
20th	Early hours	Major failure

Major damage to the breakwater occurred at or soon after the evening high tide on 19th. At this time the breakwater failed catastrophically with the crest being destroyed and lowered within a few hours by some 4m over most of its length. The majority of the rock was displaced landwards coming to rest immediately on the harbour side. There was little damage to the seaward face.

A survey of damage to the breakwater was undertaken 20 days following the failure as shown in Figure 5.

Some comments on the damage are worthy of note. The damage resulted from wave overtopping, the majority of the rock being displaced landwards. When damage occurred it was catastrophic, taking place over a few hours. Despite high combinations of wave and storm tide levels and heavy overtopping little damage was noted prior to final collapse. It is difficult to believe that the class C or B material at the crest (Figure 3) would withstand any significant overtopping as was observed to be the case (see section on model simulation of failure). It is possible that as a result of compaction under road traffic the crest acted as an impervious scour blanket giving protection until incipient failure occurred, after which total failure followed quickly. Damage was very uniform over the entire length of the breakwater except at one section where a wharf abutment on the harbour side acted as a buttress. At this location damage was slight. Little damage occurred to the seaward face for deep water wave heights of up to

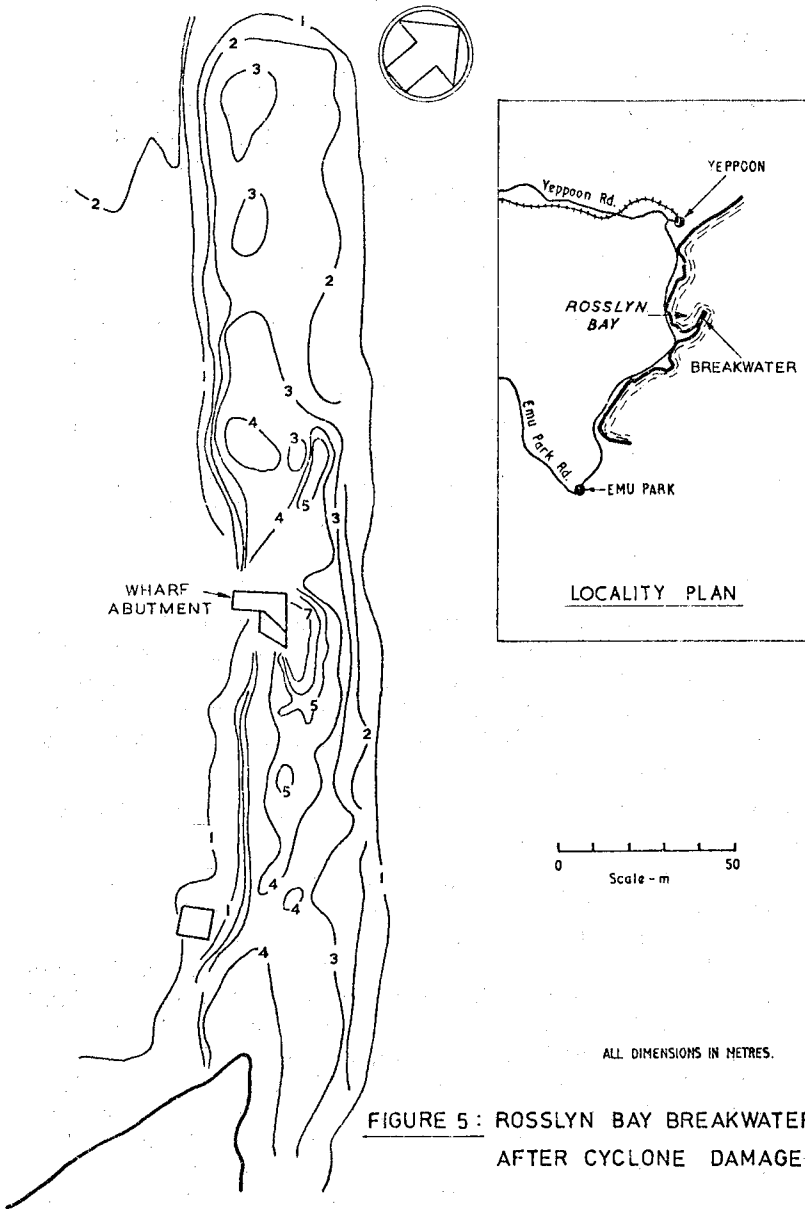


FIGURE 5 : ROSSLYN BAY BREAKWATER AFTER CYCLONE DAMAGE .

3.8m and estimated wave heights at the structure of between 3.0 and 3.4m. Equivalent damage coefficients in Hudson's equation are approximately 2.7 to 3.9 and wave conditions varied between breaking at low tide and non-breaking at high tide.

After failure the structure continued to give substantial protection by acting as a partially submerged breakwater, significantly reducing damage to the harbour infrastructure during the storm and enabling the harbour to be used for its design function under the more common weather conditions that followed. The action of prudent yachtsmen in removing their vessels from the harbour to nearby natural shelter at the onset of the cyclone resulted in the damage to moored vessels being not too severe.

Model Simulation of Failure

As part of the model studies to investigate methods of repairing the breakwater, tests were undertaken to simulate the failure. The test layout for the model is shown in Figure 6. The studies were carried out in a monochromatic wave flume using Froudian scaling. The model scale was 1:27.6. Test conditions reproduced were, offshore significant wave height (approximately H_{10} at the structure), peak spectral period and storm tide assuming a linear variation between high and low water. Typical test results are shown in Figure 7.

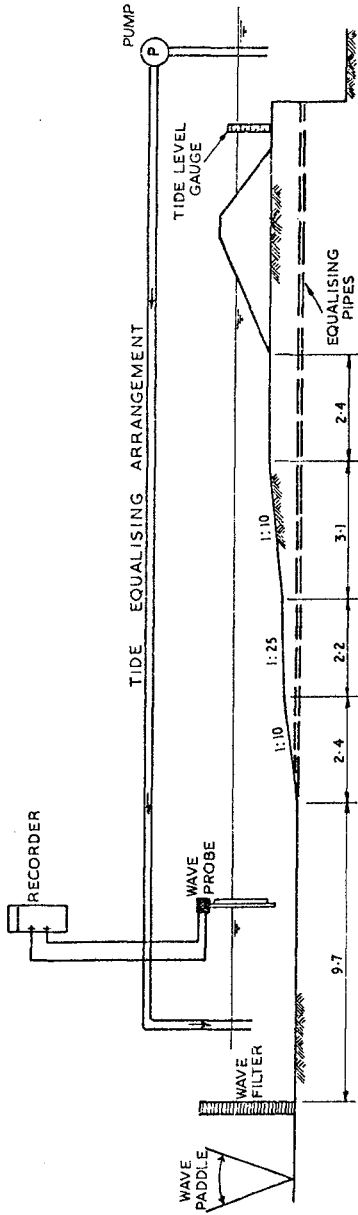
The test began at 2230 hours on 16th (low tide) and was continued until 0700 hours on 20th (low tide). Initial damage to the breakwater occurred at 0900 hours on 17th when the crest was destroyed in a landward direction.

Damage continued during each period of high tide when the crest was overtopped. The main damage was the result of overtopping and only a small proportion of the armour was displaced seaward.

At the completion of the test series the structure was subjected to continuous wave attack under stationary conditions corresponding to a wave height of 3.8m, wave period of 1.8s and a storm tide level of 5.1m. Little additional damage occurred indicating that near equilibrium conditions had been reached.

Repeating the test gave almost identical results both as to incidence of damage and the final profile.

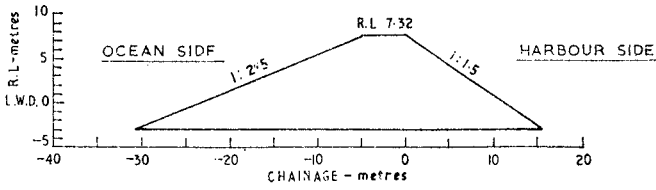
The mechanics of damage in the model and prototype were the same with the majority of damage resulting from rock being displaced from the crest and settling on the immediate harbour side. No significant damage occurred to the seaward face. However, the model differed from the prototype in that initial failure happened much earlier. As soon as the structure was significantly overtopped class C and B material was removed and the crest destroyed. (See comment on prototype damage). Damage in the model continued over five high tide



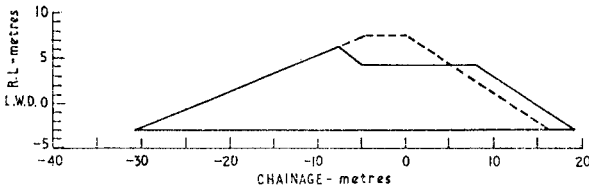
NOTE: ALL DIMENSIONS IN METRES

NOT TO SCALE

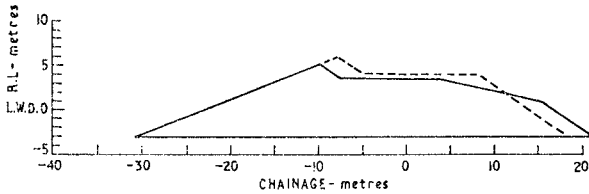
FIGURE 6: MODEL DETAILS



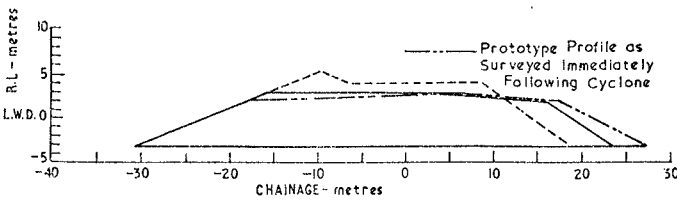
(1a) BREAKWATER AS CONSTRUCTED
2230 hr. 16th. Jan.



(1b) BREAKWATER PROFILE
0900 hr. 17th. Jan.



(1c) BREAKWATER PROFILE
1030 hr. 18th. Jan.



(1d) BREAKWATER PROFILE
2300 hr. 19th. Jan.

FIGURE 7: MODEL SIMULATION OF FAILURE

periods whilst the prototype damage occurred predominantly under one tide. The rate of damage (Froudeian scaling) was somewhat slower than the prototype. This was somewhat surprising (especially as the H_{10} height was used in the tests) as comparison between random and monochromatic wave tests on non-overtopped structures tend to indicate a faster rate of damage under monochromatic waves. It is possible that the higher waves in the spectra and wave period play a more significant role in the stability of overtopped structures.

The final profile reached in the model showed close agreement with the prototype. However, it is not known whether further damage to the prototype would have occurred if the storm had continued, whilst the final model profile was in equilibrium with the wave and surge conditions.

Modified Design

A section through the modified design is shown in Figure 8. The repair made as much use of the failed breakwater as possible. The design wave height was increased to 4.6m and the maximum storm tide level to 8.5m. The seaward face was flattened to 1 on 4 and the landward face to 1 on 2. Armour mass was increased to 5 tonne nominal and was carried over the crest and down the landward face to allow for overtopping.

Model tests indicated that the proposed design would be satisfactory although some damage could be expected, particularly at the crest under critical combination of wave period and storm tide conditions. A typical set of test results is shown in Figure 9. The tests were undertaken in a monochromatic wave flume using the design offshore significant wave height. Storm tide levels were increased in steps of 1m from RL 3m up to the maximum design value of 8.5m and then decreased in a similar manner. At each water level the structure was subjected to waves for an equivalent prototype duration of 82 minutes. The test was repeated over a range of wave periods of between 9 and 16 seconds. Rock displaced was counted as damage and expressed in terms of a percentage of the total number of armour rock. It will be noted that the rate of damage (particularly to the crest) is dependent upon both wave period and storm tide level. Maximum damage to the seaward face occurred for a wave period of 12 seconds and to the crest for a wave period of 14 seconds. At very high surge levels the crest is submerged and wave forces are reduced by a water cushion between the wave and the armour and damage is reduced. For the same reason it may be that a steeper landward face may have been more stable than the 1 in 2 slope used. However, this was not investigated in detail. Test results shown in Figure 9 are for random placed stone. By careful placement of the crest rock a substantial increase in stability could be obtained.

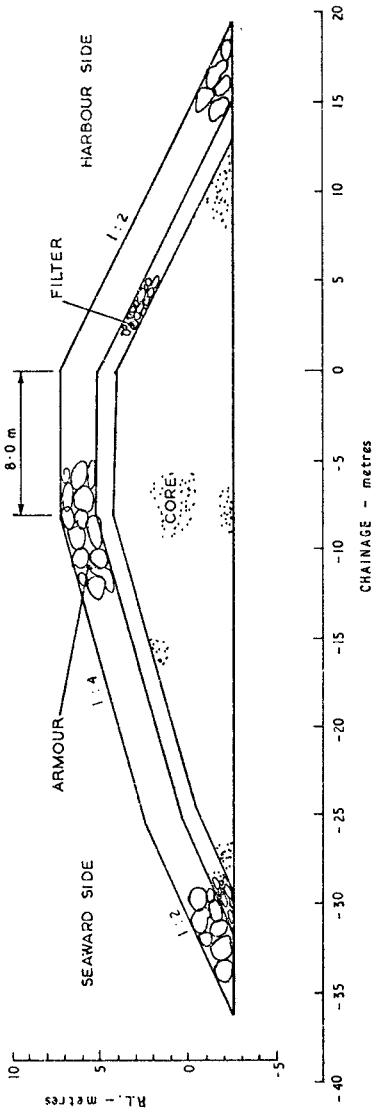


FIGURE 8: REPAIRED SECTION AS MODELLED

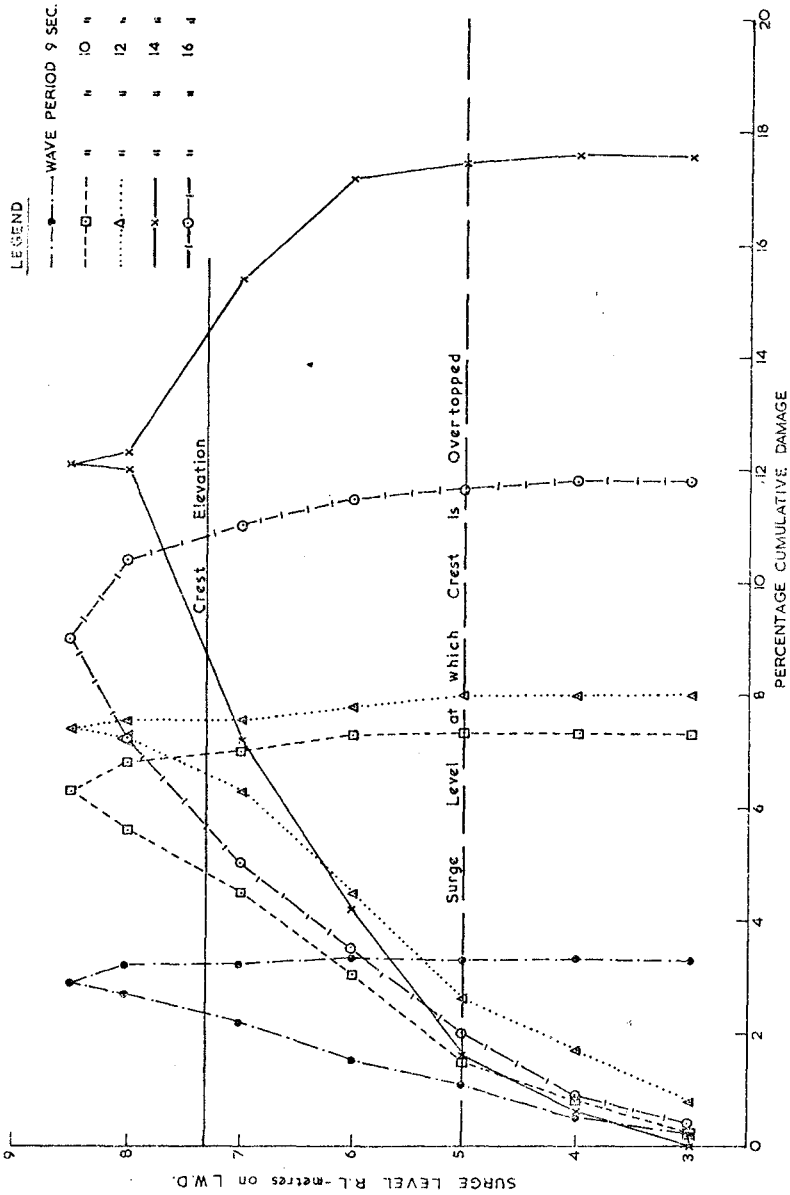


FIGURE 9 : DAMAGE AS A FUNCTION OF SURGE LEVEL FOR WAVE PERIODS FROM 9 - 16 SECONDS

Breakwater as Constructed

After the quarry was opened up the yield of 5 tonne rock was less than anticipated. For this reason the crest was actually armoured with 3.2 tonne modified cubes and the front and back slopes with a random mixture of 5 tonne rock and 3.2 tonne modified cubes on an approximately fifty-fifty basis. Repairs to the breakwater have been completed but as yet the structure has not been subjected to significant storm action.

Acknowledgement

The permission of the Director, Department of Harbours and Marine, Queensland, to publish this paper is gratefully acknowledged.

COASTAL STUDY OF ESPÍRITO SANTO/BRAZIL

by

Paulo Augusto Vivacqua (1), Hildebrando
de Araujo Góes Filho (2) and Otávio de
Sampaio Ferraz Jardim Sayão (3)

I - INTRODUCTION

The elimination of land transportation costs for raw materials and/or industrialized products has encouraged integration of industrial and port activities and, at many ports, facilities are being built for the installation of industrial complexes adjacent to the port areas.

This general trend has been clearly observed along the coast of the State of Espírito Santo, Brazil, north of Rio de Janeiro. Several new port terminals, associated with industrial plants, are under construction or were designed recently.

In fact, the State's port development began with its Commercial Port in Vitória, located at the mouth of the Santa Maria river. The following terminals connected with industries were built at a later date:

a) Tubarão Maritime Terminal, which was brought into operation in 1966, sited at the outer end of Espírito Santo Bay, 9 Km away from Vitória, for iron ore exports. This terminal belongs to the state-owned Companhia Vale do Rio Doce - CVRD. Iron ore exports reached more than 50 million ton per year during the last three years.

b) Ubu Maritime Terminal, inaugurated in 1977 and sited in the south of the State, was designed for exporting pelletized iron ore produced by a plant sited in the port area. This plant receives its raw material (ore fines) through a pipeline approximately 400 Km long. These facilities belong to privately-owned SAMARCO Mineração S.A., and will have a total export capacity of 7 million tons of pellets per year when it reaches its final expansion phase.

c) Barra do Riacho Port, which should start operation in 1978, built by PORTOCEL (owned jointly by PORTOBRÁS, Aracruz Celulose and CVRD) is intended to export wood chips and pulp produced at industrial facilities adjacent to the port.

In addition to these terminals, there are plans to build other ports which will handle goods to be produced by industries now moving into Espírito Santo.

-
- 1) Director of Amazônia Mineração S.A.; Professor of Hydraulics, Faculty of Engineering, Federal University of Espírito Santo, Rio de Janeiro, Brazil.
 - 2) Head of Port Department of Amazônia Mineração S.A.; Assistant Professor of Ports and Inland Waterways, Faculty of Engineering, Federal University of Rio de Janeiro, Brazil.
 - 3) Assistant Professor, Coastal Engineering Area, Federal University of Rio de Janeiro, (COPPE/UFRJ), Rio de Janeiro, Brazil.

The main already designed is Praia Mole Port, to be built just north of Tubarão in order to attend the steel mill of Companhia Siderúrgica de Tubarão - CST - being built in that area.

This terminal is planned mainly for export of steel products and for import of coal for steel production.

Several studies and surveys have been made for designing and constructing the above mentioned ports. These studies and surveys provide a rather reasonable sample of coastal conditions in Espírito Santo. This paper aims at analysing and consolidating the most pertinent Coastal Engineering data already collected, so as to serve as a possible guideline for future designers engaged in coastal studies in this area.

II - DESCRIPTION OF THE COAST AND ITS MAIN PORTS

The coast of the State of Espírito Santo, approximately 205 miles long (Fig. 1), may be divided into four well-defined areas:

a) For the first 84 miles, from the Lençóis Cape, at the extreme north, to the Doce River Mouth, the coast is almost entirely flat, low and sandy, covered with low vegetation, and uniformly shaped. The main feature in this area is the São Mateus river mouth, conspicuous for its long sand dunes.

b) For the next 46 miles, from the mouth of the Doce River to the Espírito Santo Bay, the coastal line rises against the background of the Aimorés mountains. The coast is again sandy, often interrupted by reddish cliffs and protected by occasional reefs that extend sometimes up to one mile into the sea.

c) The Espírito Santo Bay, approximately 2.5 miles long, is located between the Tubarão and Santa Luzia headlands. Here the Santa Maria River drains into the sea, its two main arms forming the Island of Espírito Santo, where the capital of the State is sited, with 300,000 inhabitants and forming the main commercial port of the area.

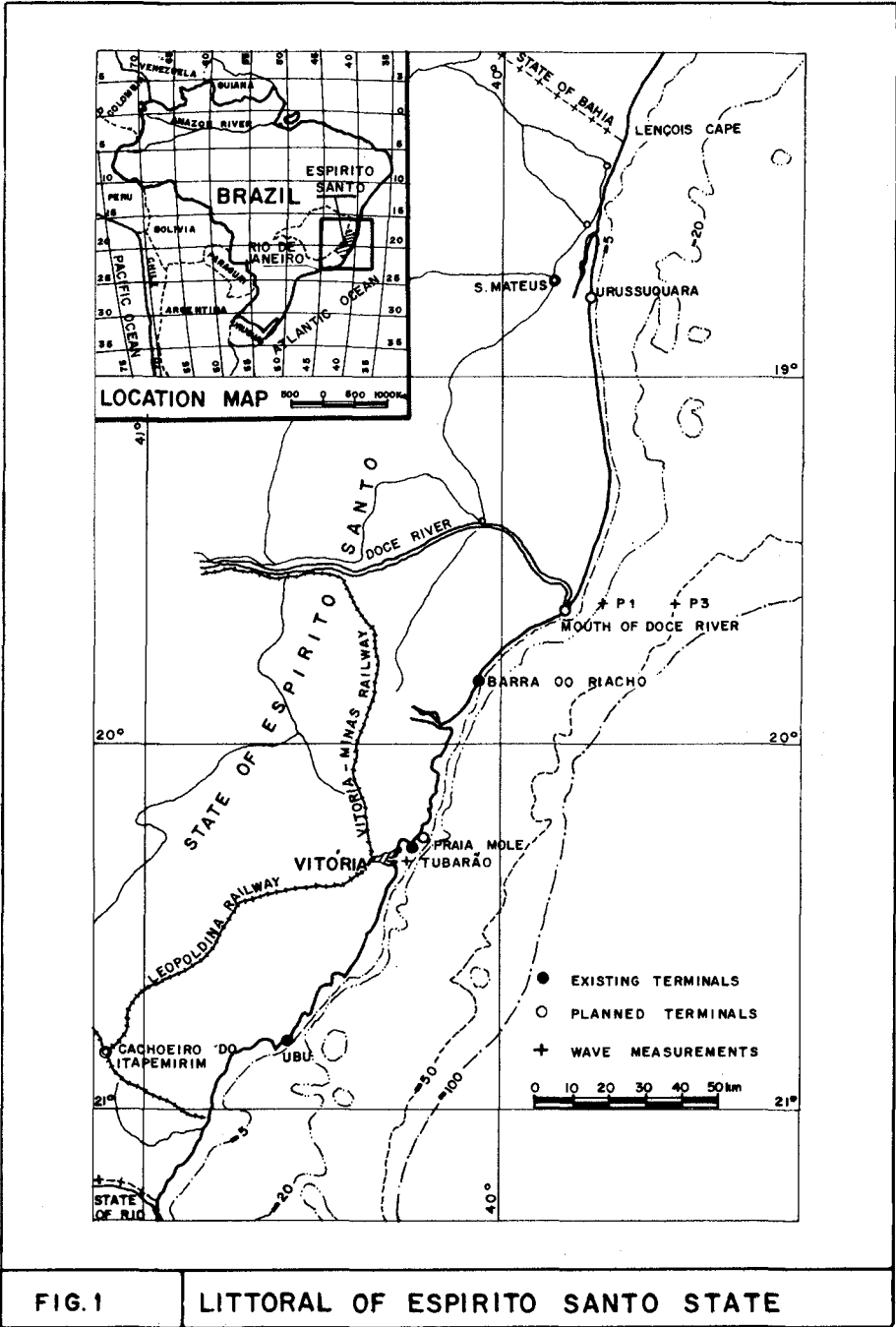
d) For the last 72 miles, from the Espírito Santo Bay to the Itabapoana River bar, the coastal aspect and shape are quite varied. The coastal plain becomes increasingly narrower in this area, as the Aimorés mountains reach closer and closer to the sea.

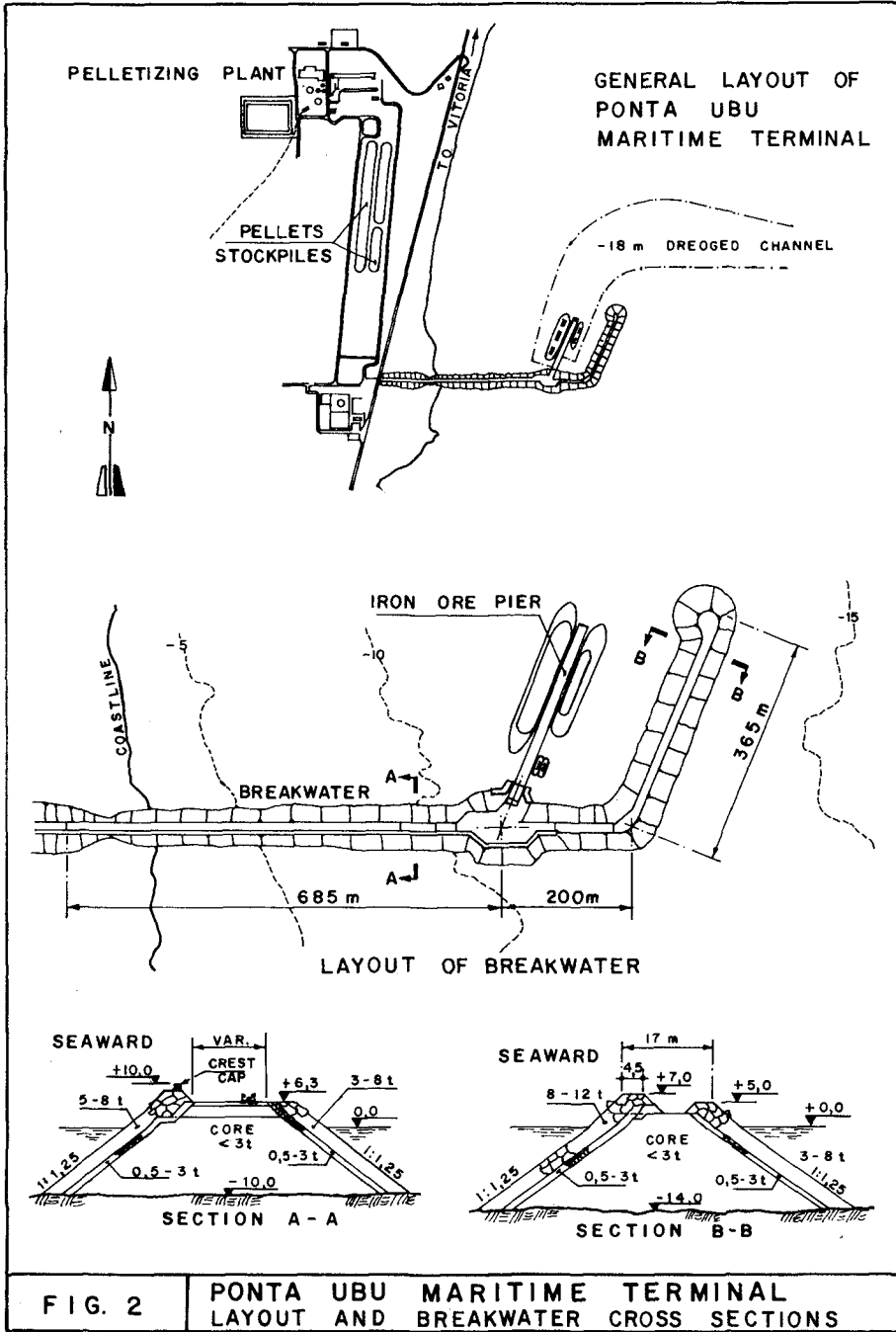
In these four areas some of the main specialized cargo terminals in Brazil are sited. Others are in design stage and should be built in the near future. A description of these ports is found below:

2.1 Existing Ports

2.1.1 Ubu Maritime Terminal

This maritime terminal, sited at the Ubu headland (Fig.2), was built for the export of 5 million tons of pelletized iron ore per year. The ore is mined in the State of Minas Gerais and is transferred through a pipeline, in the form of slurry, down to the port facilities, where it is pelletized and stockpiled for shipment. The harbor will take in ships up to 250,000 DWT after expansion (Ref. 1).





The marine terminal is formed by an "L" - shaped stone breakwater, 1,250 m long, and a 313 m long reinforced concrete pier. Ships reach the pier through a dredged channel, 18 m deep, which becomes wider near the pier so as to form a turning basin.

2.1.2 Tubarão Maritime Terminal

The Tubarão Maritime Terminal sited north of the city of Vitória, is designed for a yearly throughput of 60 million tons of iron ore. An additional ore handling berth was built between 1972 and 1973 to handle 270,000 DWT vessels (Pier nº 2), with a 2-mile approach channel dredged to a depth of - 23 m (Ref. 2). Fig. 3 shows the terminal's layout after expansion, including the originally built Pier nº 1, which can handle ships up to 100,000 DWT, as well as the protecting rubble mound breakwater.

2.1.3 Barra do Riacho

A specialized port complex at Barra do Riacho is under construction for the export of cellulose produced by local existing and future plants.

In their initial stage, the facilities will comprise a 200 m long berth capable of handling bleached pulp vessels of up to 35,600 DWT. This has involved the construction of protecting wharves and a docking pier, as well as dredging the approach channel and turning basin, as shown in Fig. 4.

In addition to the cellulose, the port complex will handle the raw materials required by the local plants, in the form of liquid or solid bulks. The largest vessels expected to call at this part of the port will be 30,000 DWT oil tankers.

2.2 Port Projects

In addition to these ports already in operation, the coast of the State of Espírito Santo is being considered for future facilities, for which hydrographic data have been gathered along the coast from north of the Doce River mouth to Espírito Santo Bay. (Refs. 3,4 and 5).

2.2.1 Praia Mole

A basic layout for the port facilities being planned for Praia Mole has been arrived at, the harbor being artificially protected by a 7 km long rubble mound breakwater, at an estimated dredging volume of 20 million cubic meters (Fig. 5).

The approach channel to the Praia Mole port will be dredged to a - 19 m depth, which will permit handling vessels up to 120,000 DWT. In addition to the general cargo and coal handling berths, which will service the steel plant, other specialized terminals are being contemplated within the basin of the port.

III - ANALYSIS OF EXISTING DATA

This section presents the main conclusions of the studies performed along the coast of Espírito Santo.

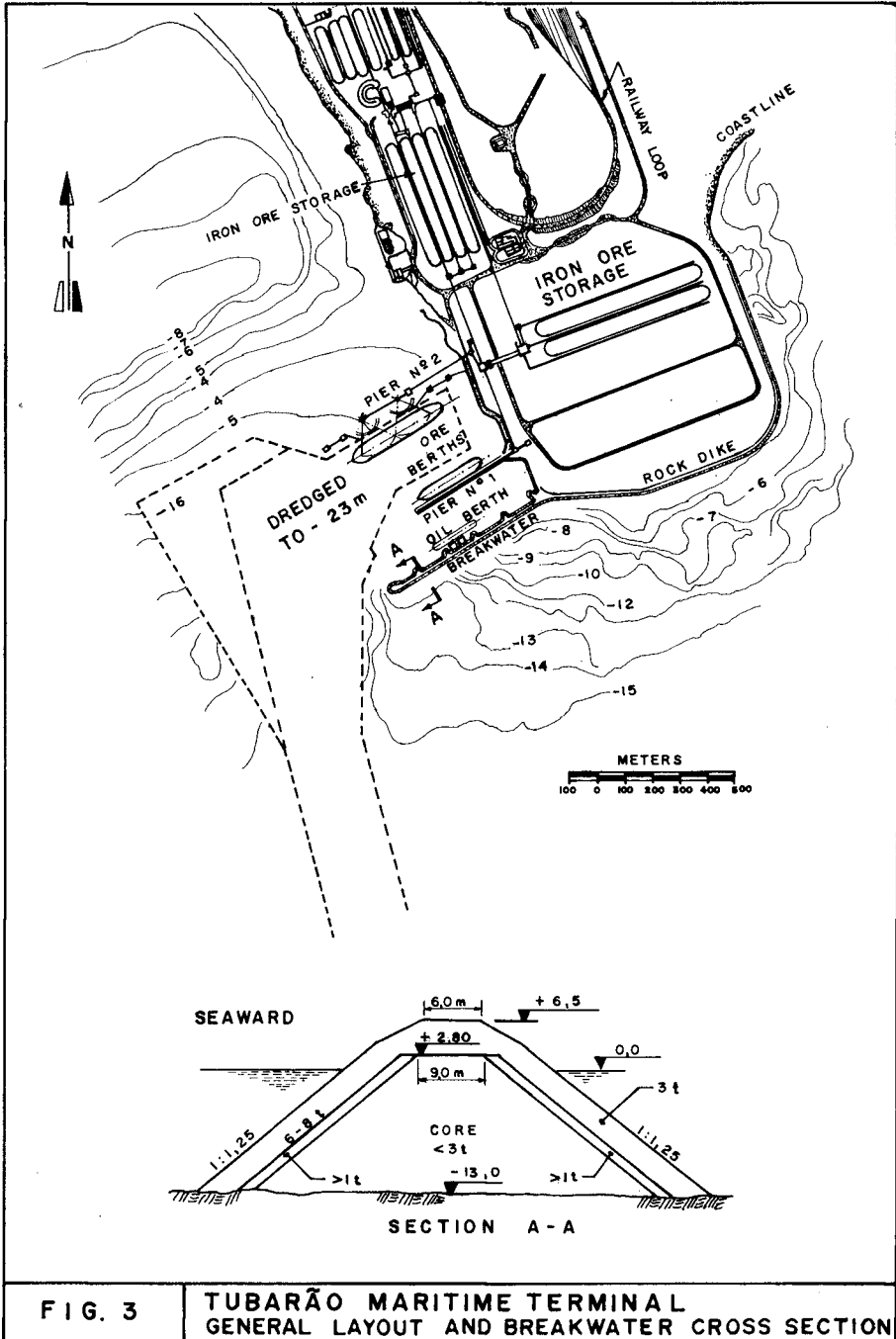


FIG. 3

TUBARÃO MARITIME TERMINAL
GENERAL LAYOUT AND BREAKWATER CROSS SECTION

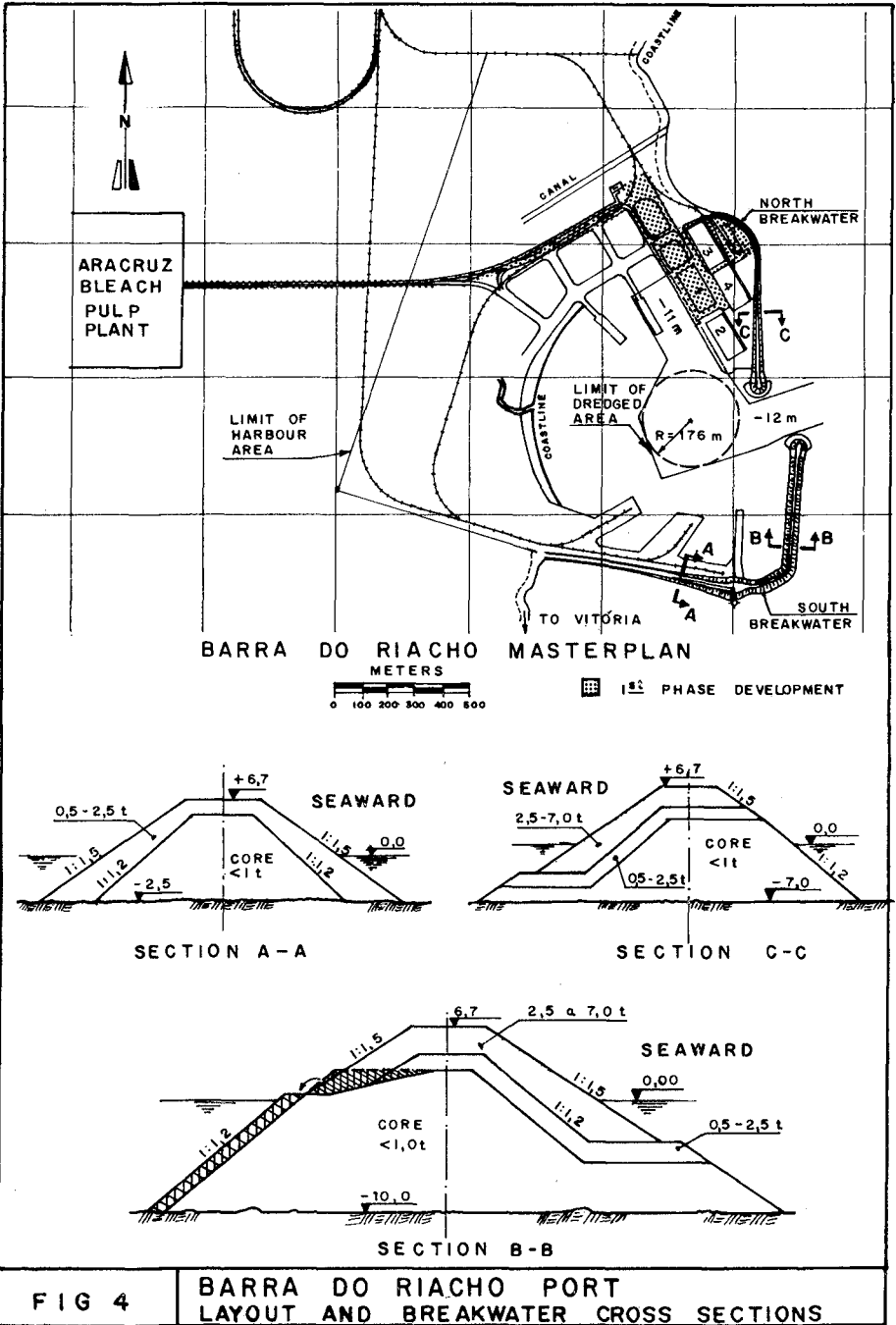
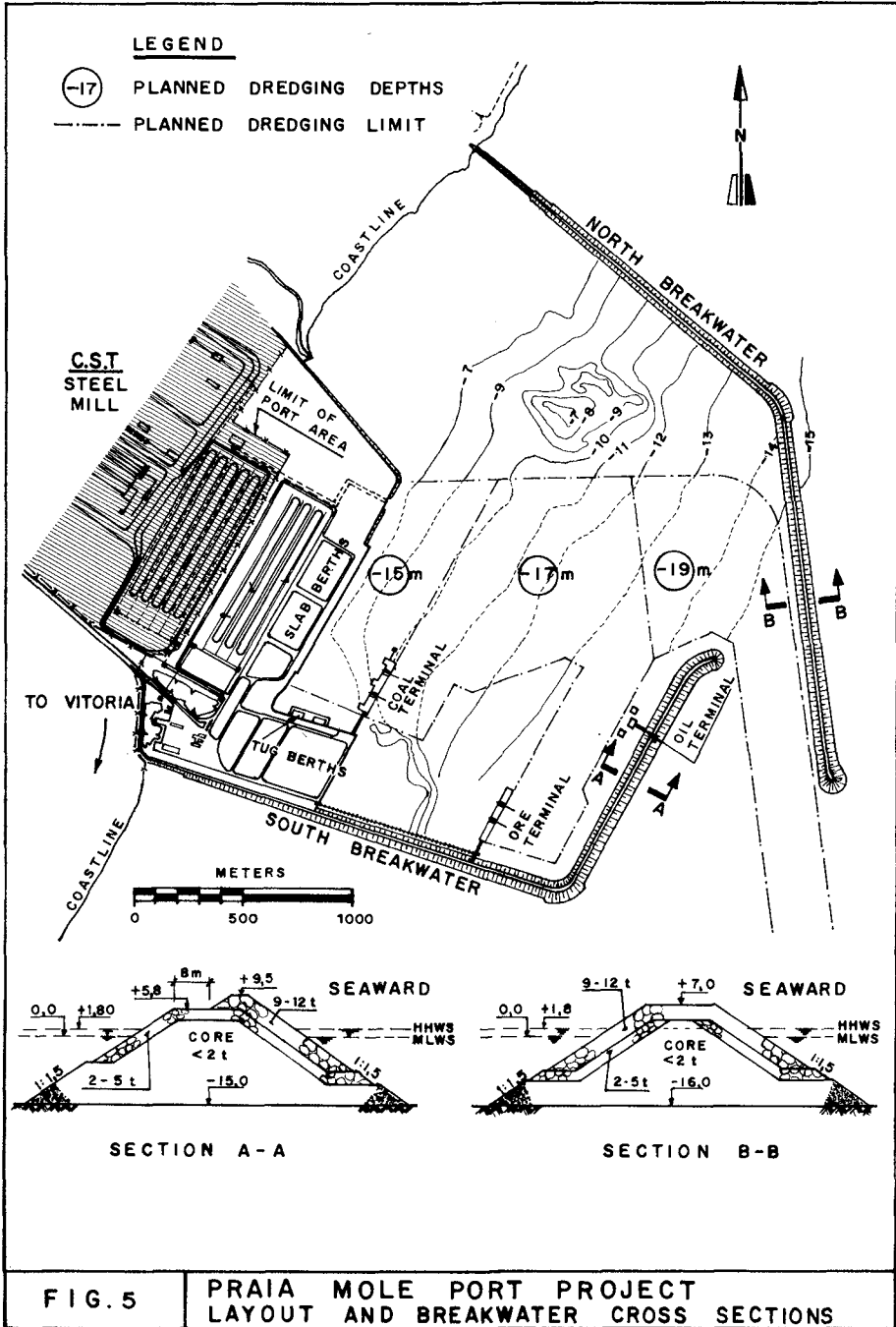


FIG 4

BARRA DO RIACHO PORT LAYOUT AND BREAKWATER CROSS SECTIONS



3.1 Wind Conditions

In general, the Brazilian east coast is considered to be a meteorologically very calm area, unaffected by violent tropical storms.

For the Barra do Riacho (PORTOCEL) project, the Danish Hydraulic Institute (DHI) performed anemographic measurements throughout the year of 1974 (Ref. 6). Such measurements are representative of the entire region, from Vitória to Doce River, and are presented in the wind rose of Fig. 6. Measurements made at Barra do Riacho have shown a maximum wind speed of 22 m/s, but only 0.3% of all measurements were in excess of 15 m/s.

The predominant wind directions are from NE-E and from S-SW, with the northeasterly winds dominating in strength. During more than 2.5% of the year, these winds exceed 10 m/s.

Daily maximum wind speeds at Barra do Riacho for the year of 1974 have been compared with measurements made at Vitória for the years 1971-73 (Ref.6). There was good agreement between data, which are shown in Fig. 6.

3.2 Wave Climate

The currently available information on wave conditions along the Espírito Santo coast stems from the wave observation sources listed below (items a and b) as well as from wave measurements mentioned in items c, d and e:

a) Ocean Wave Statistics, compiled from visual observations on ships by the National Physical Laboratory, London, covering a 9 year period. The Marsden Square areas that are of particular interest to this study are MS37 and MS40, set apart from each other by the 20° parallel, crossing slightly south of Barra de Santa Cruz. The Ubu, Tubarão and Praia Mole harbors belong to MS40, whereas Barra do Riacho and other planned harbors to be sited near mouth of Rio Doce River belong to MS37. Fig. 7 shows the deep-water roses for MS37 and MS40.

b) Atlas of Sea and Swell Charts-South Atlantic, compiled by the U.S. Navy Hydrographic Office also from visual observation in deep waters.

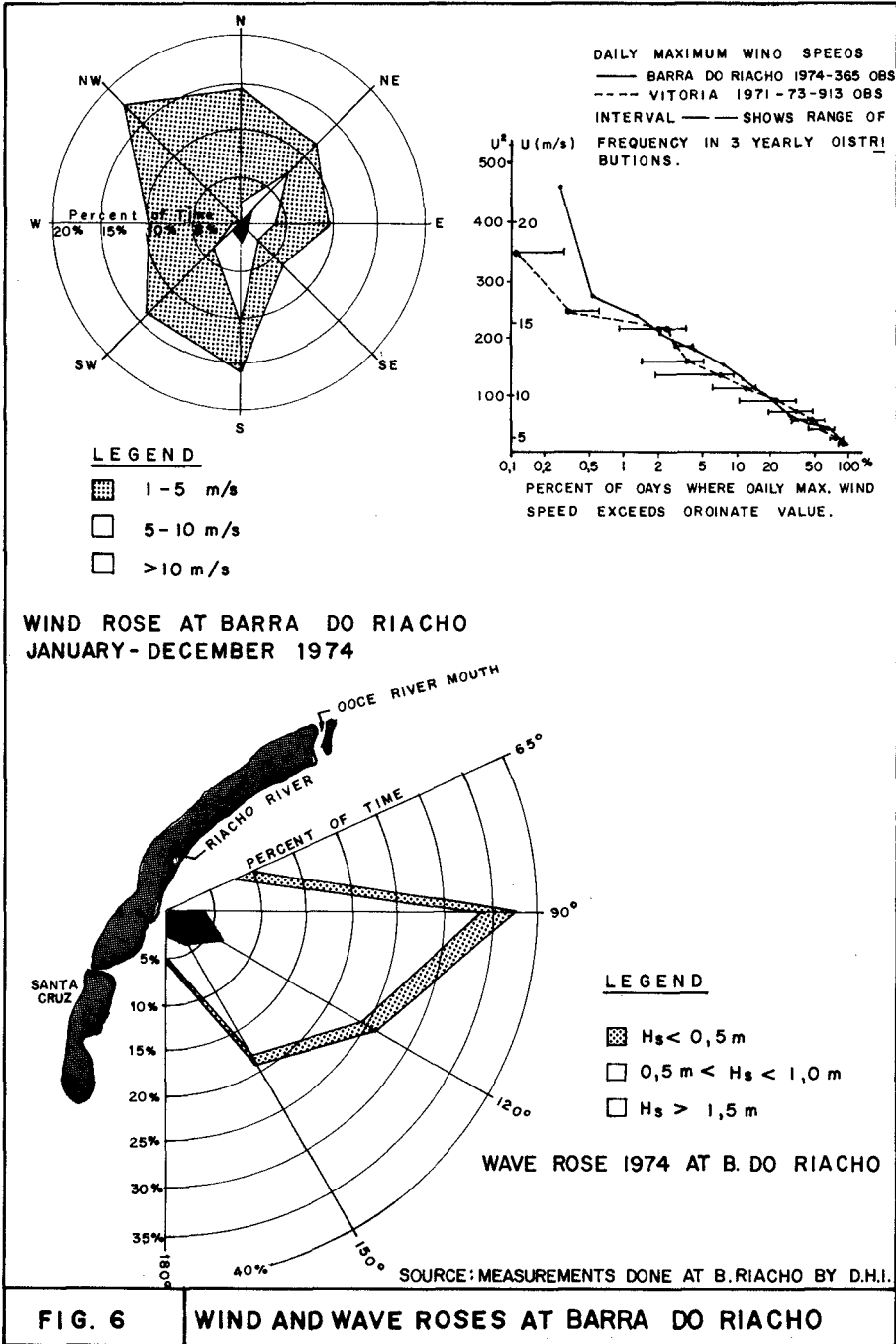
c) Measurements off Barra do Riacho, performed by DHI with the help of two wave recorders for a period of 15 months in 1973/74.

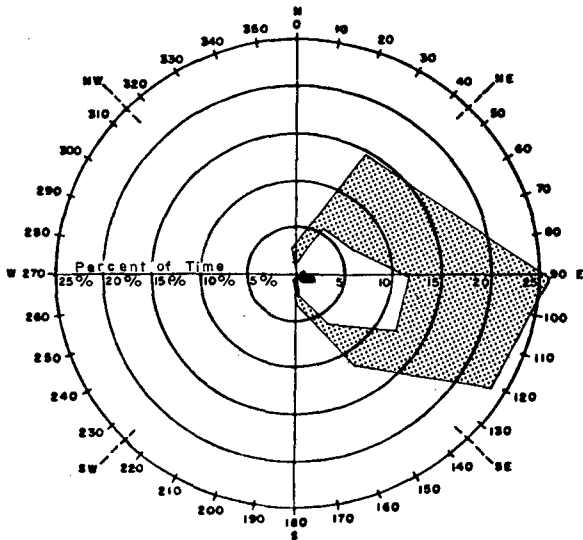
d) Wave measurements performed at Petrobrás Oil Rigs P1 and P2, for a period of 8 months, during 1972/73.

e) Wave measurements made at the Tubarão Iron Ore Terminal for a period of 9 months, during 1971/72.

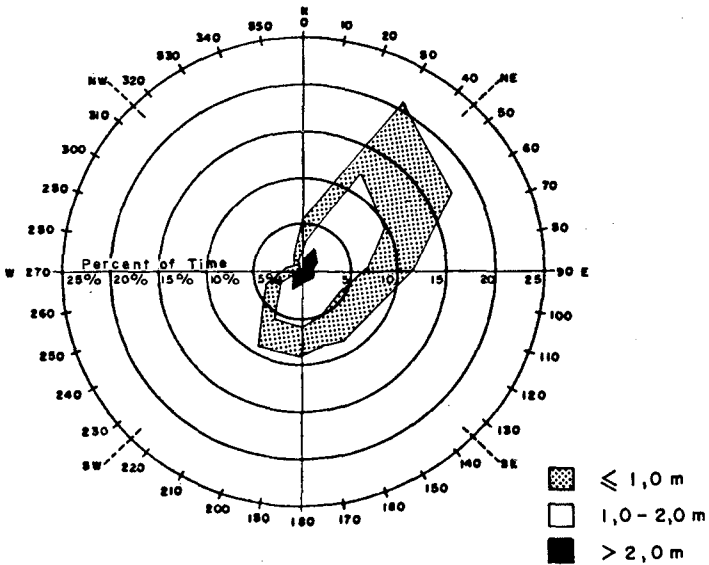
Table 1 below summarizes the data obtained from the various wave measurement campaigns up to 1974.

Due to the short duration of the measurement work performed by the Petrobrás P1 and P3 Oil Rigs and Tubarão Terminal, these data were not used for engineering purpose.





DEEP WATER WAVE ROSE MARSDEN SQUARE 37



DEEP WATER WAVE ROSE MARSDEN SQUARE 40

SOURCE : OCEAN WAVE STATISTICS

FIG. 7

DEEP WATER WAVE ROSES
MS 37 AND MS 40

TABLE I

WAVE CONDITIONS OBSERVED AT VARIOUS LOCATIONS
ON THE COAST OF THE ESPÍRITO SANTO STATE

LOCATION	Maritime Terminal of Tubarão (CVRD)	Petrobrás Oil Rigs P1 and P3	Barra do Riacho Port
OBSERVATION SITE	Seaward of Tubarão's breakwater	Off Doce River mouth	South of Riacho River mouth, off the Southern reef.
WATER DEPTH OF INSTRUMENT	9.0 m	P1: 22.0 m P3: 53.0 m	16.0 m
PERIOD OF MEASUREMENTS	June 1971 to April 1972	October 1972 to May 1973	September 1973 to December 1974
TYPE OF WAVE RECORDER	Pressure wave recorder (Hydro Products O.E.C. type WR 421)	Ultrasonic recorder (Neyrpic)	Waverider System (Datawell) and Pressure Wave recorder (OSPOS)
RECORDING PROGRAM	15 min. of continuous records, at 12 hours intervals	15 min. of continuous records, at 12 hours intervals	20 min. of continuous records each 3 hours (Datawell) and 15 min. each 3 hours (OSPOS)
AVERAGE WAVE PERIOD (\bar{T}_Z)	10 sec.	Between 7 and 8 sec.	8 sec.
HIGHEST OBSERVED SIGNIFICANT WAVE HEIGHT ($H_{S\max.}$)	4.25 m	2.7 m	2.2 m
MONTHS OF HIGHEST OBSERVED WAVES	June and September	March and May	June, July and September
MONTHS OF LOWEST OBSERVED WAVES	January and March	October and February	February, March and April
HIGHEST WAVE DIRECTIONS	S and SE	NE and S	S-SE
MOST FREQUENT WAVE DIRECTIONS	S and SE	E-NE and E	E and NE

The data obtained from wave recorders at Barra do Riacho are of good quality, and they supersede the ones originating from visual observations, which can be used only for comparison or on a preliminary basis.

DHI conclusions based on comparisons with the measured wave data are that wave heights calculated on the basis of deep water (observed) data will result in considerably higher waves, but with a direction distribution very similar to that obtained off Barra do Riacho during 1973/74.

Wave measurements made off Barra do Riacho by DHI in 1974 are shown in Fig. 6. Waves have been recorded by a Datawell Waverider together with an Ospos recorder. The Waverider was programmed to record a 20-minute time series every three hours, whereas the Ospos records were for 15 minutes every three hours. Observations of wave directions were performed by the local operator.

During the time interval covered by the observations the highest significant wave height was $H_s = 2.2$ m, corresponding to a maximum wave height of $H_{max} = 3.4$ m., at a depth of water of 16 m. The highest waves were measured in June, early July and September. Waves did not exceed $H_s = 1.5$ m from January through May, as well as during the greater part of July and October. The season with lowest waves was February to April. Mean wave periods between 5s and 15s were measured. The average mean period is 8s.

Along the Espírito Santo coast, from the Ubu Terminal up to the mouth of the Doce River the highest waves occur from S-SE, but most frequently wave directions are between E and NE. For the highest waves, the wave period varies between 8 and 12 s.

3.3 Water Levels and Currents

The water level variation caused by tide and storm surges has been reproduced by the Ospos wave recorder during the measurements performed by DHI. The discrete values of the water level obtained at Barra do Riacho were compared with the water level at the tide recorder at Vitória/Tubarão. The result was that the water level measured by the Ospos recorder at Barra do Riacho follows the tidal prediction for Vitória and Tubarão closely. From the predictions, the maximum yearly tidal range is found to be 1.8 m. In addition to the astronomical tide, the water level may be affected by rises resulting from storm surges.

On the grounds of DHI float tracking at Barra do Riacho (Ref. 6), it is estimated that a current velocity of 0.25 m/s will on the average be exceeded with a total duration of 75 days per year, and that a velocity of 0.6 m/s will be exceeded 24 hours per year.

3.4 Soil Characteristics

In the area between Tubarão and Barra do Riacho, the subsoil material is of a complex nature. In general, there occurs a predominantly sandy surface layer of average compactness. Underlying it, there is a stiff clayey layer of varying thickness, below which the soil again becomes sandy, though more compact than at the surface.

Sandstone reefs (limonitic "cangas") are commonly found in most of the Espírito Santo coastline. Reefs or "cangas" outcrop in certain areas, which makes dredging work difficult and reduces equipment productivity - a problem which occurred with major or lesser intensity while dredging at Tubarão, Ubu and Barra do Riacho was in process.

The analysis of bottom sediment samples indicates that the median diameter (D_{50}) of sandy material is of the order of 0.2 to 0.3 mm at Praia Molé, and it ranges between 0.4 and 0.6 mm at Barra do Riacho. Along the beach stretch south of the mouth of the Doce River (Fig. 8), the median diameter of sand varies from 0.15 to 0.6 mm when in water depths up to 10 m and from 0.15 to 0.9 mm at depths between 10 and 15 m.

3.5 Coastal Processes

The beach slopes which form the eastward boundary of the Espírito Santo coastal plain vary accordingly with the size of the sand material.

Both north and south of the Doce River mouth, these slopes are between 9° and 12°, but they may exceptionally be as steep as 15°. North of the Doce River, where finer sand is found, beach slopes may be as flat as 5°.

The large area of alluvial material which extends from Barra do Riacho, in the south, to Conceição da Barra, in the north, makes up a huge delta deposit formed by sediments brought down to the sea over geological times by the rivers in the area, particularly the Doce River (Ref. 7). Waves, tidal currents and wind action have shaped the seaward side of this delta to bring about the coastline configuration as it is today.

The Doce River delta formation process may be summarized as follows:

- The finer materials (silt and clay) are carried in suspension in the directions determined by currents. Waves stir up all sediments which may have been deposited in the sedimentary platform, where depths are small. Thus, the part of the delta formed by silt and clay has a tendency to migrate northwards along the coast, causing depths to decrease in this area as the submerged slopes gradually become less steep. This trend is confirmed by the shape of the alluvial fan of the river which expands little towards the south (see Fig. 8), while it becomes longer and wider towards the north, as indicated by bathymetric readings in the area. The result is an evident spread of the deltaic front towards the north.

- Coarser material (sand) is moved mainly by waves, being carried and deposited at each point in accordance with the local wave regime. Any sandy material not retained at the mouth, but flushed out to sea beyond the river bar, tends to be caught in areas relatively close to the mouth; there occurs a natural sorting of diameters, the less coarse material advancing further than the others.

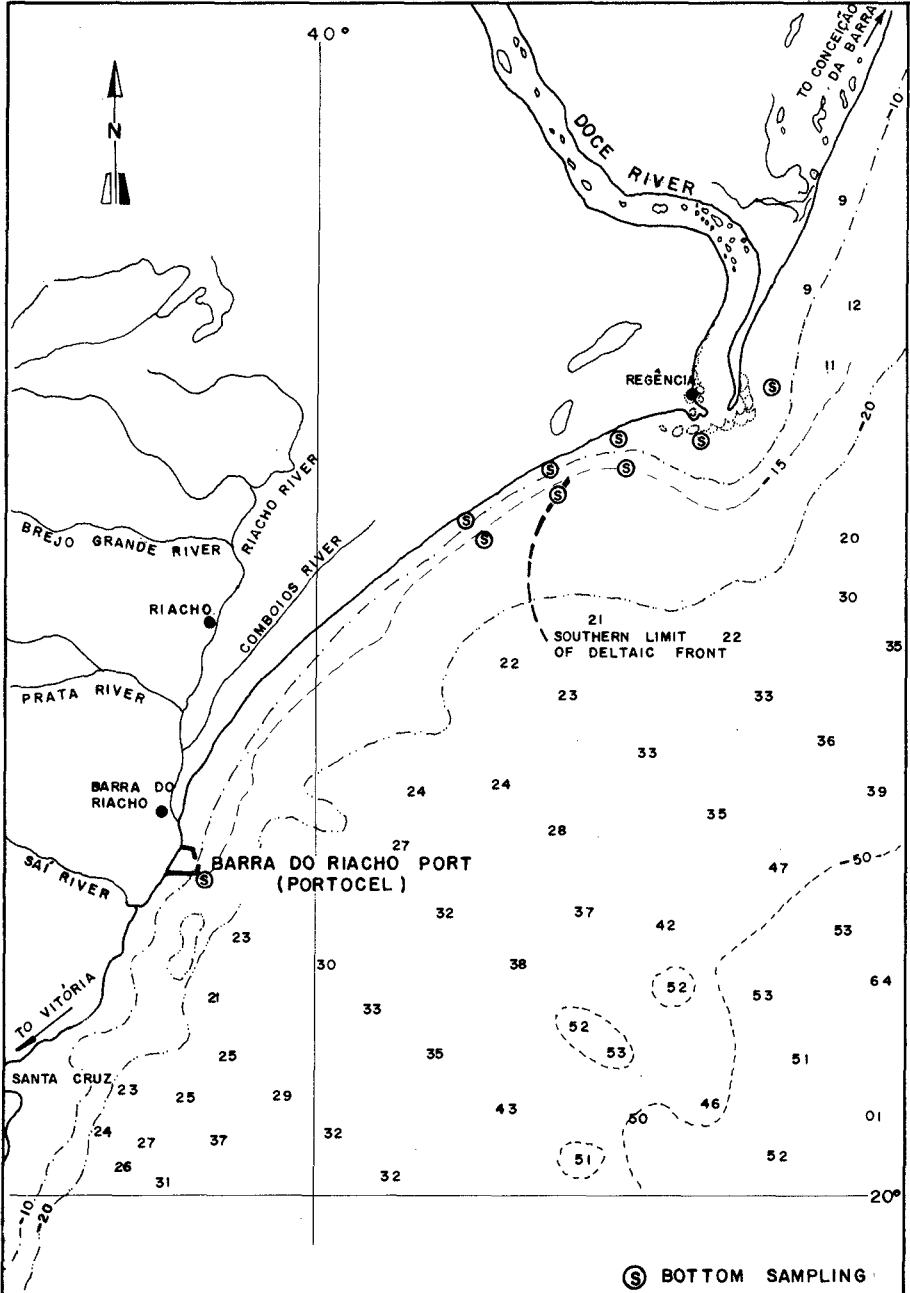


FIG. 8 MOUTH OF DOCE RIVER

The sand accumulates initially in the shallower zones of the alluvial fan itself. Waves are the determining factor for sand movement, due to the small depths and the gentle slope of the sedimentary platform which results in a wide surf zone.

The Doce River mouth constitutes an inflection point in the Espírito Santo coastline. South of it, the coastline heads SW, which gives it a smaller inclination with regard to the highest waves from SE and more protection against waves from NE. This coastal configuration has significant implications for sand movement along the coast.

Between Tubarão and Barra do Riacho the coastline is formed by a succession of pocket beaches between reef headlands. From Barra do Riacho to the south of the Doce River mouth, sand is moved either north or south, depending on the wave climate, but the net direction of the littoral drift is southward.

In the case of sand movement towards the north, sand is carried along the coast in this direction as long as waves from S and SE prevail; however, they will always tend to show an annual net movement towards the south, since this is the direction of the resulting littoral drift.

South of the Doce River mouth, the southward component of the littoral drift decrease as one moves down along the coast. It is estimated that, midway between Regência and Barra do Riacho (Ref. 5), the maximum annual littoral drift is about 500,000 m³/year while the net annual littoral drift is 150,000 m³/year, both southwards according to C.E.R.C.'s formula (Ref. 8) and Ocean Wave Statistics' deep water data. As one moves further south along the coast, the southward littoral drift decreases as the northward one increases; in the vicinity of Barra do Riacho, they practically cancel each other.

It has been gathered from examination of hydrographic charts, deep water wave data and aerial photographs, that the dominant direction of littoral drift north of the Doce River is northward. Typical signs of this are the shapes of bars, of beach stretches where natural sandstone spurs occur, and of tombolos formed in the lee side of the reefs.

A more accurate description or quantification of the littoral drift north of the Doce River can only be made after detailed knowledge of wave characteristics in the area has been obtained through wave measurement records and observation of directions for at least one whole year.

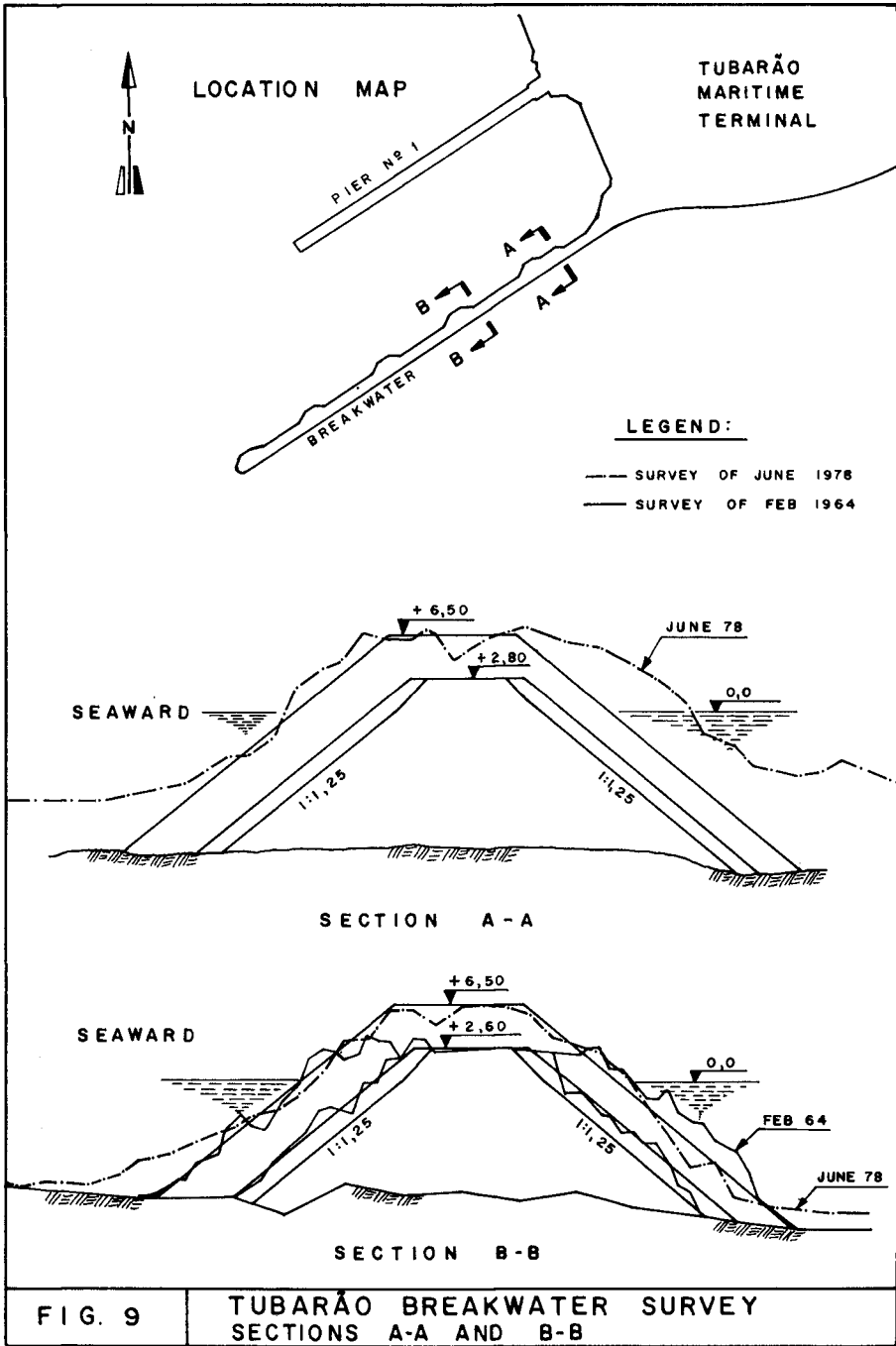
3.6 Breakwater Survey

Table 2 shows conditions for rubble mound breakwater designs for the artificial harbors along the Espírito Santo coast (Ubu, Tubarão and Barra do Riacho) and for the Praia Mole Harbor Project.

In June, 1978, CVRD performed a survey of the breakwater at the Tubarão Maritime Terminal, comprising the four cross-sections shown in Figs. 9 and 10.

TABLE 2
DESIGN CONDITIONS FOR RUBBLE MOUND BREAKWATERS

L O C A T I O N S I T E	WAVE CONDITIONS		WATER LEVEL	BREAKWATER CROSS SECTION CHARACTERISTICS				Crest Elevation (m)	Depth (m)
	Hs (m)	T (s)		HHWS (m)	Seaward slope (degrees)	Yr ³ (t/m ³)	K _D		
Ubu Breakwater Section A-A	4,2	8-14	+1,80	1,25	2,67	3,5	5-8	+10,0	10,0
Ubu Breakwater Section B-B	4,2	8-14	+1,80	1,25	2,67	3,5	8-12	+7,0	14,0
Tubarão Breakwater Section A-A	4,0	6-12	+1,80	1,25	2,6	3,5	6-8	+6,5	14,0
Praia Mole Project South Breakwater Section A-A	5,0	7-12	+1,80	1,5	2,7	4,0	9-12	+9,5	15,0
Praia Mole Project North Breakwater Section B-B	5,0	7-12	+1,80	1,5	2,7	4,0	9-12	+7,0	16,0
Barra do Riacho South Breakwater Section B-B	3,0	8-12	+1,80	1,5	2,64	3,3	2,5-7	+6,7	10,0
Barra do Riacho North Breakwater Section C-C	3,0	8-12	+1,80	1,5	2,64	3,3	2,5-7	+6,7	7,0



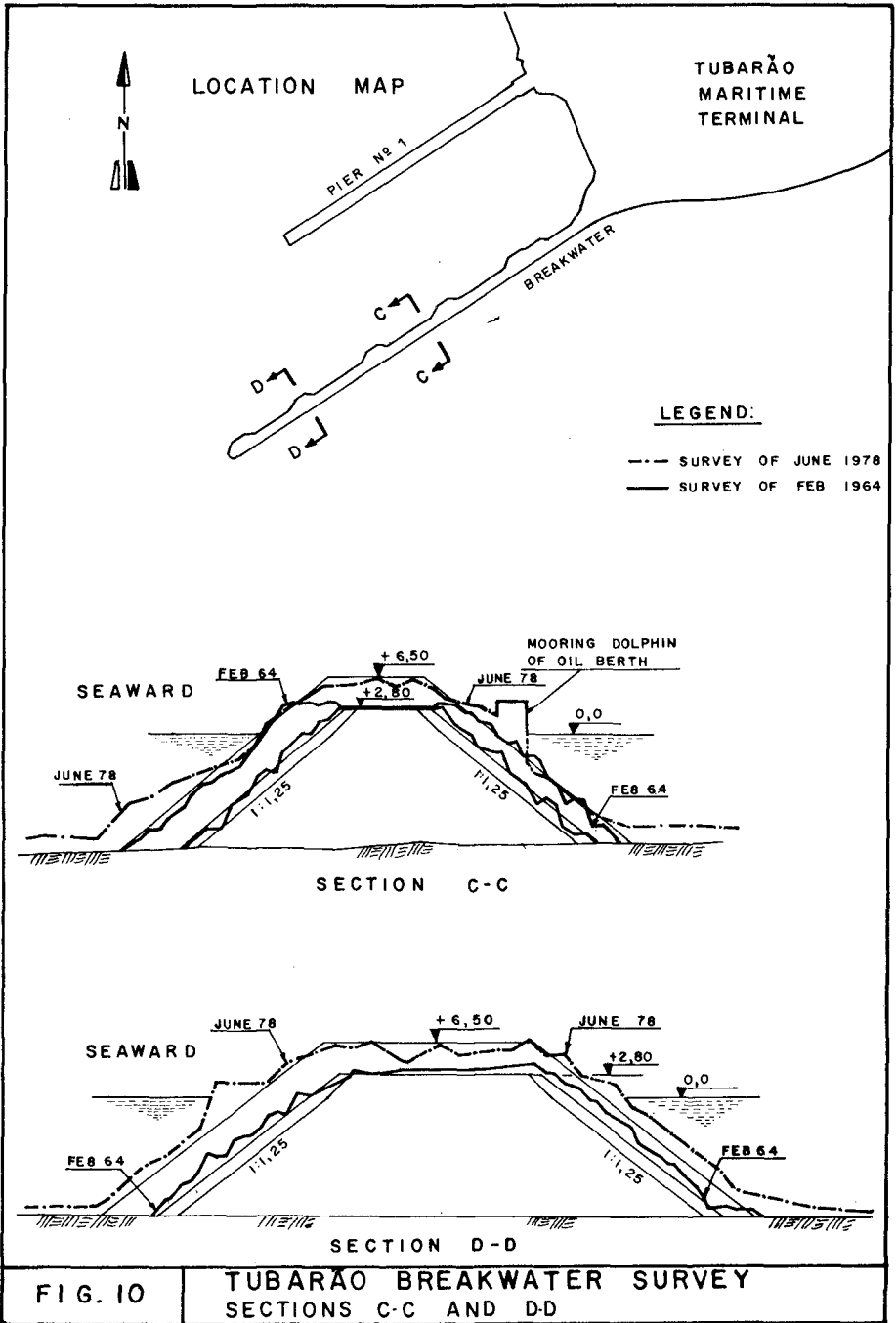


FIG. 10 TUBARÃO BREAKWATER SURVEY SECTIONS C-C AND D-D

The Tubarão breakwater extends in a straight line in the NE-SW direction, and provides protection for iron ore piers 1 and 2, in addition to the oil berth located at its lee side. It is directly exposed to wave action from the SE direction.

The survey shows an irregular cross-section. A certain amount of settlement of the breakwater crest was observed, probable due to loss of core material. The slope towards the sea is more regular from the shore end to the oil berth; from then on, it shows a decline of 1:1 at certain points above sea level which means that the armour stones were displaced by wave action and/or as a result of soil settlement. Below sea level the seaward slope has shown a flattening trend with time. No maintenance work has been done on the breakwater since it was built in 1963/64.

IV - CONCLUSIONS AND RECOMMENDATIONS

The port designs developed for the Espírito Santo coast have been based on different criteria. Due to the fact that wave climate measurements were made only for the harbor at Barra do Riacho, the various breakwaters were calculated with different design wave heights.

4.1 A comprehensive knowledge of wave characteristics is the basic requirement for Coastal Engineering designs. For the Espírito Santo coast, such characteristics will have to be determined by installing wave recorders at least at three points along the coastline: one north of the Doce River mouth, a second, south of the Doce River mouth, between Tubarão and Barra do Riacho (an OSPOS recorder is already being operated by INPH/PORTOBRÁS at Barra do Riacho); and a third, south of the Espírito Santo Bay, possibly near the Ubu Maritime Terminal. From the analysis of the data thus obtained, the distribution, of wave periods, wave heights at given depths, wave directions, as well as wave frequency and direction spectra can be obtained for each of these areas.

4.2 Additional studies are required to provide a better insight of coastal processes. In order to determine current direction and speed, it will be necessary to operate current meters for at least one year at certain points along the coast, preferably at those points where wave recording is carried out. To help quantify the littoral drift, the velocity of longshore currents may be measured and bottom sampling may be carried out at certain sites, from the shore to a depth of about 20 m, together with the analysis of such samples for determining mechanical and mineralogical characteristics. It is important to perform a mineralogical analysis of the materials carried by the Doce river, and to compare them with the heavy minerals found along the shoreline.

4.3 Systematic yearly surveys are also recommended for the cross-sections of the various breakwaters recently built on the Espírito Santo Coast, in order to evaluate the damage experienced in time.

V - ACKNOWLEDGEMENTS

The authors wish to thank the supporting material kindly provided by various companies, in particular CVRD for information on the Tubarão breakwater. The authors are also indebted to Prof. Victor Freire Motta of COPPE/UFRJ for helpful discussions and review of manuscript.

VI - REFERENCES

- Ref. 1 - Siegmann, E. F. and Jacobsen, L. "Projeto e Construção em Mar Aberto de um Terminal para Graneleiros de Grande Porte", Simpósio sobre Tendências Atuais no Projeto e Execução de Estruturas Marítimas, COPPE/UFRJ, Rio de Janeiro, abril de 1977.
- Ref. 2 - Soros, P. and Koman, B., "World's Largest Ore Port at Tubarão Brazil" - Ports and Harbors, November, 1974.
- Ref. 3 - Johnson, J. W., "New Port Development, North Coast of Estado do Espírito Santo", Report Submitted to CVRD, July 1970.
- Ref. 4 - Motta, V. F., "Relatório de Consultoria sobre Problemas de Engenharia de Costas, Associados à Construção de Porto na Costa Norte do Espírito Santo", agosto 1973.
- Ref. 5 - Sondotécnica S.A.- "Estudo do Porto de Regência - Barra do Riacho" - Relatório Final, outubro 1977.
- Ref. 6 - Danish Hydraulic Institute (DHI) - "Aracruz Harbour Terminal, Hydraulic Investigations" Rep. nº 4 submitted to Aracruz Celulose S.A., June 1975.
- Ref. 7 - Petrobrás S.A. (CENPES) - "Projeto Rio Doce (Relatório Final)", novembro 1975.
- Ref. 8 - U. S. Army C.E.R.C. - "Shore Protection Manual", 3rd Ed., 1977.

CHAPTER 128

PROBLEMS OF DESIGN AND CONSTRUCTION OF AN OFFSHORE SEAWATER INTAKE

by

D.W. STANDISH-WHITE^{*}

and

J.A. ZWAMBORN^{**}

ABSTRACT

A seawater intake had to be constructed for a diamond mine on the coast of Namibia just north of Oranjemund. The solution adopted consisted of a piled jetty with a dolos island on its seaward end protecting the pump chamber which was built of closely spaced concrete piles.

The paper briefly describes the various problems encountered during the construction of the intake, including :

- limited penetration of the piles leading to the failure of the first jetty,
- serious slump of the initial dolos island,
- breakages of dolosse due to excessive movements during storms,
- considerable wear of the vertical spindle pumps due to sand and surging.

Also described are the engineering solutions which had to be found at very short notice for immediate application.

INTRODUCTION

An assured supply of 2 200 m³ per hour (37 m³/min = 10⁴ U.S. gall/min) of sea water was required for a diamond recovery plant to be commissioned early in 1977 on the southern coast of Namibia (South-West Africa). This coastline consists of a particularly featureless beach of deep sand underlain by variable coarse boulder gravel beds covering saw-tooth profile schistose bed rock. Often pounded by high surf caused by heavy swells, a strong littoral drift transports large amounts of sea-bed material

* Consulting Civil Engineer, Anglo American Corporation of South Africa Limited, Johannesburg, South Africa.

** National Research Institute for Oceanology, CSIR, Stellenbosch, South Africa

northwards along the coast, depending on the prevailing weather conditions.

Various alternative solutions were considered for this sea water intake, including a submarine tunnel, an on-shore stilling basin, in-shore beach filtration ponds, radial interception caisson wells and finally a piled jetty with a vertical pump well formed of closely spaced piles at its seaward end situated in the centre of an artificial dolos island. All but the last alternative had already been tried before with varying degrees of success along the 200 km of arid coastline reserved exclusively for diamond mining.

Having no time to conduct extensive model studies but armed with offshore seabed profiles and various other regional marine data and experience, it was decided, because of the evident impracticability of the other solutions in this locality, and on the advice of the Specialist Marine Contractors, to opt for the offshore island approach.

ORIGINAL JETTY DESIGN

The design adopted was for a light precast concrete jetty carried on slim precast concrete piles, each with a stub rail toe to penetrate the heavy seabed gravels (see Fig. 1.a). This type of construction had been used successfully by the contractors in other situations along the same coast. Construction commenced late in 1974, but it soon became apparent that adequate penetration of the piles to the bedrock through the overlying layer of boulders and gravels was not being achieved and various means of grout stabilization of the toes were attempted in 1975. After 180m had been completed this jetty failed in a storm, partly through excessive pile settlements from the scouring action around some of the pile toes and partly because the whole structure was set too low, and this jetty was abandoned.

FINAL JETTY DESIGN

After full scale tests on shore, a redesigned special pile which would penetrate down to the bedrock and then allowed for subsequent axial drilling, rock anchoring and grouting was developed. The modified pile toe adopted consisted of a long, thick-walled steel tube with a specially hardened cutting edge (see Fig. 1.b). A new similar jetty 321 metres long (but 1.5m higher) was successfully constructed on this basis adjacent to the old one between September 1975 and February 1976 (see Figs. 2 and 3).

The old jetty was partially demolished to avoid any possible future interference with the stability of the new one due to its further collapse. Both the embedded and attached steelwork of the new structure were cathodically protected against corrosion using a constant impressed current and sacrificial anodes.

DAMAGE TO ORIGINAL DOLOS MOUND

The Contractor designed and constructed the first terminal island mainly of 6 ton dolosse below MSL, capped with 10 ton units above MSL, on a

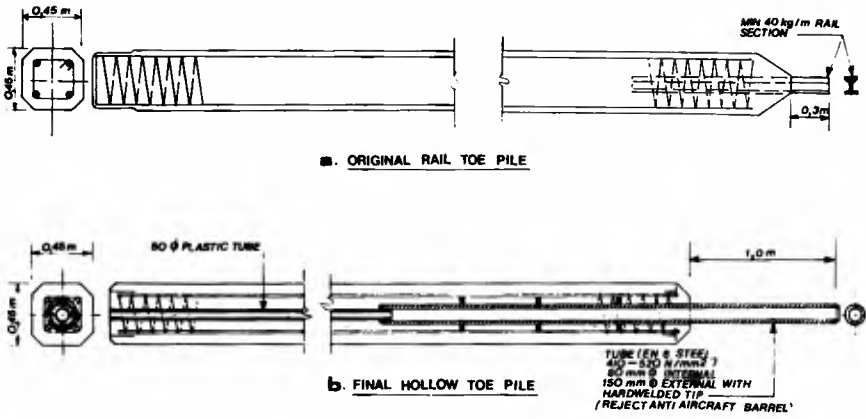


FIG. 1 SPECIAL PILE TOES



FIG. 2 NEW AND OLD JETTIES WITH DIAMOND RECOVERY PLANT IN THE BACKGROUND

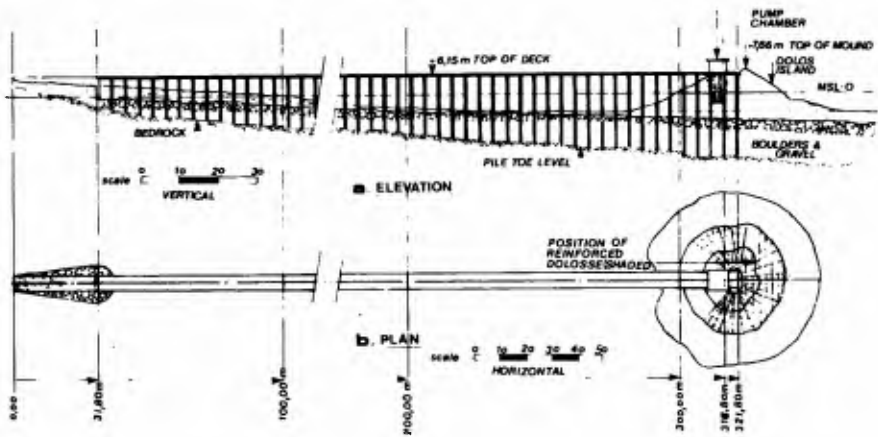


FIG. 3 FINAL JETTY LAY-OUT



FIG. 4 CLOSE-UP OF DAMAGED DOLOS MOUND

foundation of a carefully placed gravel mat. A total of 1100 6 ton and 120 10 ton dolosse were placed between April and June of 1976 but the mound settled considerably more than expected. At this stage, the National Research Institute for Oceanology was called in for advice and during an inspection in September 1976 it was noted that several 6 and 10 ton Dolosse had broken and the mound had slumped by about 3 to 4 m, exposing the pump chamber (see Fig. 4).

The apparent reasons for the damage to the dolos mound were :-

1. The dolos mass was too small, resulting in their removal from the mound.
2. Sea-bed changes of up to 4 to 5m have been recorded in the jetty area, and underscour of the mound itself could well have occurred, also resulting in larger waves.
3. Dolos breakage of up to 5 per cent occurred during placing and further breakages may have occurred due to excessive movements during heavy seas.
4. Possibly insufficient tensile strength of the original dolos concrete for the wave loads imposed.

REQUIRED DOLOS MASS

The structure was originally designed for a wave height of 6m, but a further study using more extensive wave data revealed that a 7,1m deep-sea wave could occur once in 25 years, which would increase (due to shoaling) to 7,7m at the seaward toe of the structure. The original foundation of the dolos mound was set at about -5m to mean sea level, but the water depth immediately seaward of the structure could well increase up to about 10m due to scour, and thus a 7,7m wave could reach the structure. A 7,7m wave height was therefore adopted for the re-design of the dolos mound.

Using a simple formula for a breakwater trunk¹, the following desirable dolos unit mass was deduced :-

$$W = (0,3H)^3 = (0,3 \times 7,7)^3 = 12,3t$$

Considering that the mound is effectively a 'double breakwater head', this mass should be further increased by 50 per cent to 18,5t as compared with the original 6 to 10t dolos design.²

Because no tower crane was readily available to handle such heavy units it was decided to try to increase the concrete density to 2,7t/m³ in an attempt to increase dolos stability. From all known stability formulae, the required block mass is inversely proportional to the relative density

to the third power³ and an 11,3t dolos should theoretically be as stable as an 18,5t dolos, if cast in the same moulds as the earlier 10t units, but with a nett density of 2,7t/m³. Moreover, the available tower crane could still handle these units. A re-design, using 11,3t dolosse of higher density to protect the pump well and an 8m wide toe protection of 6t normal density dolosse was therefore adopted as the best expedient in all the circumstances of the problem (see Fig. 5).

HYDRAULIC MODEL TESTS

Due to the exposed position of the structure - right in the breaker zone during heavy seas (see Fig. 6) - and because of its dissimilarity to usual breakwater structures, it was considered necessary to carry out confirmatory hydraulic model tests. Due to severe lack of time, only two simple tests using a 'half model' in a wave flume could be done, one test using normal density dolosse (2,31t/m³ in the model representing 2,37t/m³ prototype), and a second test with higher density dolosse (2,57t/m³ representing 2,63t/m³ prototype). The tests were done in a 1,5m wide and 0,7m deep regular wave flume with the model built on the available 1:20 slope (prototype slope was about 1:30). A water depth of -7,5m below mean sea level at the centre of the mound was used. The entire mound (half model) was built of 530 82 and 92 gr dolosse, representing 10,3 and 11,5t full scale units. Model wave heights were increased in small intervals up to the equivalent of 7 m high waves with a period of 11,5s. A model view is shown in Fig. 7.

With the *normal density* dolosse, the model showed the first damage for 5m high waves. The damage, particularly on the side of the mound, increased rapidly with the 7m waves causing a 2m slump thus exposing the pump sump to the direct wave forces. A marked improvement was obtained using the *high density* dolosse. With the 5m waves, very few dolosse were displaced (< 1%) while a total of only 17 model dolosse were displaced with the 7 m waves (about 4%).

HIGH DENSITY DOLOSSE

The tests thus confirmed the significantly greater stability for the higher density dolosse and a high density concrete mix was designed to produce the required 11,3t dolosse using the original 10t dolos moulds. Cost and time considerations ruled out importing a very suitable magnetite ore from inland with a relative density of 4,8t/m³ and any other densifying possibilities such as the use of cast steel Scrubber-Mill Balls. Some higher density aggregate was eventually obtained from the mine itself, being the lighter fraction (S.G. 2,89t/m³) from the heavy media separators of the diamond recovery process. A 2,7t/m³ concrete mix was achieved in the laboratory using this heavier aggregate, with a compressive strength of 40 MPa.

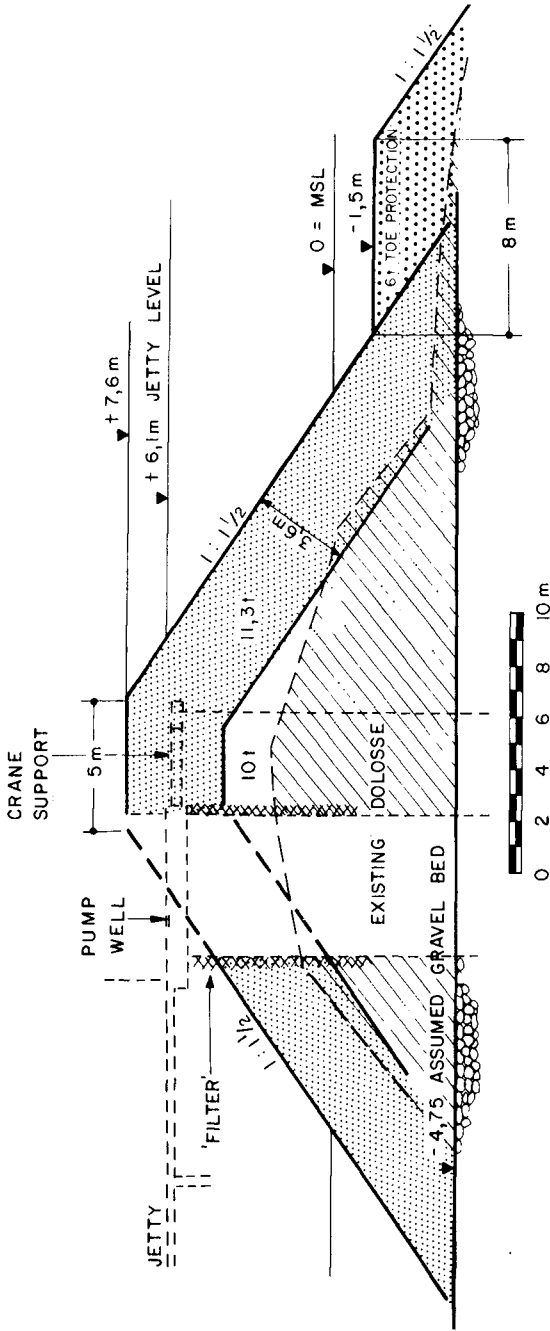


FIG. 5 RE-DESIGN OF DOLOS MOUND



FIG. 6 HEAVY SURF POUNDING THE STRUCTURE



FIG. 7 FLUME TEST ON 'HALF MODEL'
7 M BREAKING WAVES

Unfortunately it was later established that, because of high density aggregate supply problems from the mine, the concrete density actually obtained was only $2,55\text{t/m}^3$ and not the $2,7\text{t/m}^3$ required, thus making the dolosse still too light (maximum mass $10,7\text{t}$) for the accepted design wave height.

The physical dimensions of the dolosse were as follows : dolos height 3,00 m, waist to height ratio 0,313, circular fillets 0,033 of the dolos height and a volume of $4,2\text{m}^3$.

STORM DAMAGE DURING CONSTRUCTION OF THE REDESIGNED DOLOS MOUND

Placing the new heavier dolosse to the revised profiles began in the late summer (February 1977) and during the subsequent two months, half of the required additional 518 "ten ton" and 1 150 "six ton" dolosse had been placed. At this juncture the Contractor was on schedule to complete the mound before the winter storms, but the availability of the placing crane became less and less as the plant engineers used it while battling to keep the pumps operating at a rate sufficient to supply adequate water to the plant.

Early in May 1977 and before the island was complete, a heavy swell arose, coinciding with a near equinoxial high tide (2m variation). By then, 350 ten-ton capping units and 617 six-ton toe protection units had been placed.

Breakers of between 5 to 6m, corresponding to 4 to 5m incident waves with a projected occurrence of 7 and 1 day per year respectively, occurred continuously for three days. Over 100 dolosse were lost from the mound which represented about 10 per cent damage. The damage was especially heavy on the seaward side, where the mound slumped some 3m. The dolos breakages varied from a single fluke broken off to breaks through the shank. It was also obvious from the wear on the dolosse that the units had been thrown around during the storm.

The main reasons for the damage to the structure are as follows :

1. For an incident wave height of 5m, the model tests showed considerable damage for the $2,37\text{ t/m}^3$ but only 1% damage for the $2,63\text{ t/m}^3$ dolosse. For the $2,55\text{ t/m}^3$ dolosse, which were used on the island, several per cent damage, were therefore, to be expected.
2. It had been reported by the supervising staff that 5 per cent of the dolosse broke during placing which was probably caused by generally heavy surf conditions (see Fig. 6). This represents about 17 of the ten ton and 30 of the six ton units placed since February 1977. The broken dolosse were thrown around during the storm causing other units to break.
3. Because the crest of the mound was still several metres below its

final design height, the top layer of dolosse was relatively loose and exposed to the full overtopping breaker force, causing excessive dolos movement resulting in breakages.

4. The timing of the storm was also particularly destructive, because a freshly-built dolos structure usually requires an initial shakedown period for minor settlement caused by average waves.

FINAL COMPLETION OF THE DOLOS MOUND

Although attempts to produce high density dolosse have not been abandoned, the need to complete the dolos island, which forms the protection of the pump chamber, dictated an urgent 'engineering' solution. Accepting that the 10,7 ton dolosse were too light for the 7,1 m incident design wave height, it was decided to 'reinforce' them using sections of old 20 kg/m railway lines readily available on the mine. This rail reinforcement was tack-welded in a dolos shape to provide core reinforcement. Experience has since shown that this reinforcement holds the dolosse together well, even if the concrete cracks. Thus, although the steel may eventually corrode, it meanwhile contributes to the mound's stability by keeping the dolosse intact for a much longer period. A small beneficial increase in total mass also results from the steel inclusion but these 'reinforced' dolosse were made of normal density concrete (S.G. 2,4) and the mass of these units was therefore only about 10,0t.

It finally took a total of 2 414 six ton and 853 ten ton dolosse to complete the dolos mound in accordance with the profile shown in Fig. 8 (August 1977).

Settlement of approximately 1 metre has since occurred during its first winter season, but no heavy storms have been experienced so far. Considerable stability does now seem to have been achieved, together with calm pumping conditions. A close watch will be kept of the island's future performance and its behaviour will be correlated with wave heights recorded seaward of the jetty with a waverider buoy.

PUMP PROBLEMS

During the early commissioning of the large (175 kw) vertical spindle centrifugal pumps (Early 1977), it became apparent that surging and turbulence in the pump chamber was far greater than had been expected. A concrete baffle platform was then cast and lowered down the chamber and set at mean sea level, and the pumps were encased in stainless steel sleeves (see Figs. 9 and 10). These measures were highly successful in both supporting the pumps and in damping out the surges in the chamber. Completion of the final mound has also had a beneficial effect on surging and sand build-up in the sump.

The pump installation has necessarily been fully operational since July 1977, but was plagued with high wear rates due to the high

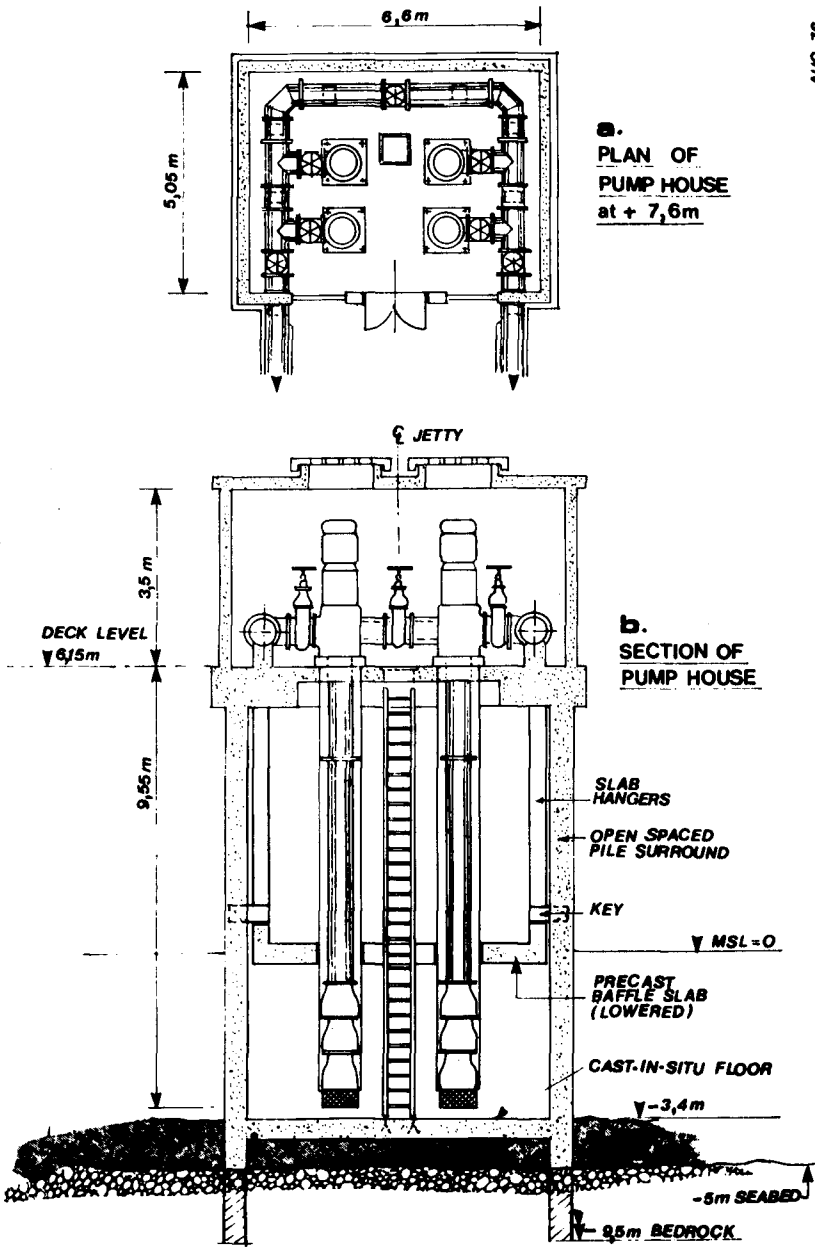
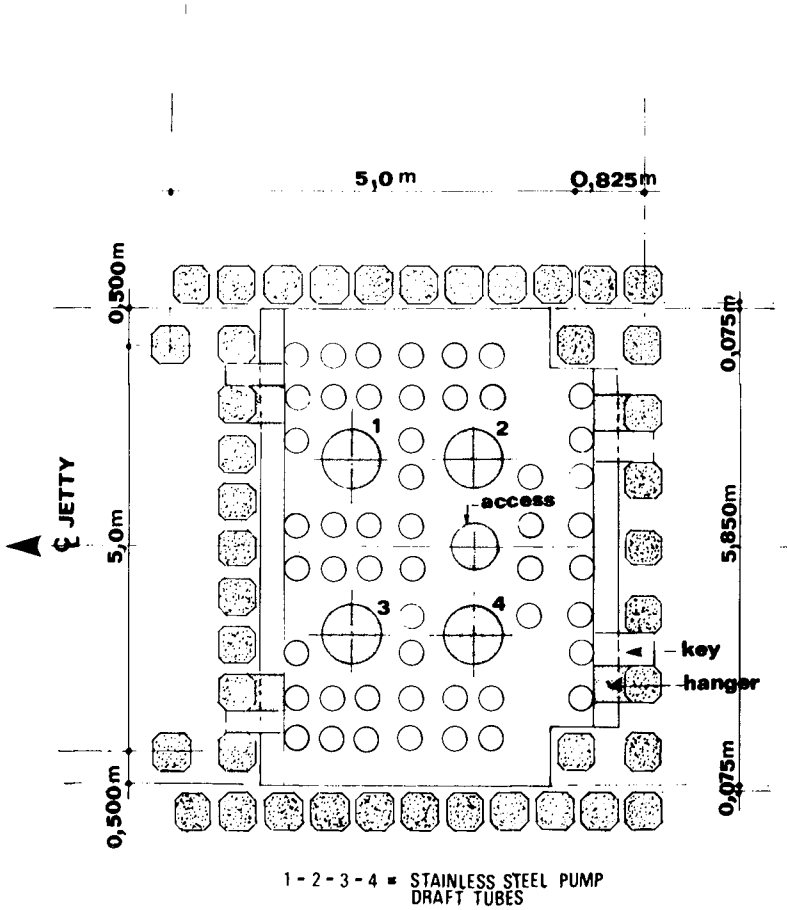


FIG. 9 PUMPHOUSE



SECTION AT MEAN SEA LEVEL

FIG. 10 PLAN OF BAFFLE SLAB IN PUMPING CHAMBER

percentage of sand suspended in the seawater inside the chamber. Each of the four pumps had an average initial life of only 30 days before lifting for replacement of the wearing components. A number of mechanical solutions were tried but no suitable vertical spindle pumps of this size and duty are on the market at present.

Very reluctantly, recourse had to be made to installing a pair of horizontal spindle, rubber-lined dredge pumps mounted on a platform underslung below the jetty in the immediate lee of the mound (see Fig. 8). This system has proved embarrassingly effective and reliable up to date. Two standby submersible pumps are installed in two of the draft tubes and an experimental vertical spindle pump with continuously grease-fed bearings is being operated in the third tube with good results over the past six months.

CONCLUSION

This paper is presented not as a technical success story but as an opportunity for fellow coastal engineers to assess and consider the many problems that presented themselves and perhaps to avoid them on a similar structure in the future.

Figs. 11 and 12 show the structure about one year after completion.

REFERENCES

1. Zwamborn, J.A. "Dolosse for Coastal Works". Proc. 5th S.A.I.C.F. Western Cape Convention, Stellenbosch, September 1976.
2. PIANC, "Final Report of the International Commission for the Study of Waves". Annex Bull. No. 25 Volume III, Brussel, 1976.

-----oO-----



FIG. 11 DREDGE PUMPS IN LEE OF DOLOS MOUND



FIG. 12 COMPLETED INSTALLATION, JULY 1978

CHAPTER 129

WAVE TRANSMISSION THROUGH TRAPEZOIDAL BREAKWATERS

by

Ole Secher Madsen⁽¹⁾, M.ASCE, Paisal Shusang⁽²⁾, and Sue Ann Hanson⁽³⁾

INTRODUCTION

In a previous paper Madsen and White (1977) developed an approximate method for the determination of reflection and transmission characteristics of multi-layered, porous rubble-mound breakwaters of trapezoidal cross-section. This approximate method was based on the assumption that the energy dissipation associated with the wave-structure interaction could be considered as two separate mechanisms: (1) an external, frictional dissipation on the seaward slope; (2) an internal dissipation within the porous structure. The external dissipation on the seaward slope was evaluated from the semi-theoretical analysis of energy dissipation on rough, impermeable slopes developed by Madsen and White (1975). The remaining wave energy was represented by an equivalent wave incident on a hydraulically equivalent porous breakwater of rectangular cross-section. The partitioning of the remaining wave energy among reflected, transmitted and internally dissipated energy was evaluated as described by Madsen (1974), leading to a determination of the reflection and transmission coefficients of the structure.

The advantage of this previous approximate method was its ease of use. Input data requirements were limited to quantities which would either be known (water depth, wave characteristics, breakwater geometry, and stone sizes) or could be estimated (porosity) by the design engineer. This feature was achieved by the employment of empirical relationships for the parameterization of the external and internal energy dissipation mechanisms. General solutions were presented in graphical form so that calculations could proceed using no more sophisticated equipment than a hand calculator (or a slide rule). This simple method gave estimates of transmission coefficients in excellent agreement with laboratory measurements whereas its ability to predict reflection coefficients left a lot to be desired.

Accepting the assumptions of the validity of linear long wave

-
- (1) Doherty Associate Professor in Ocean Utilization, R.M. Parsons Lab., Dept. of Civil Engineering, MIT, Cambridge, Mass.
 - (2) Engineer, Camp, Dresser and McKee, Consulting Engineering, Boston, Mass. (formerly Grad. Res. Assist., R.M. Parsons Lab., MIT).
 - (3) Graduate Student, Dept. of Civil Engineering, U. of California, Berkeley (formerly Undergrad. Assist. R.M. Parsons Lab., MIT).

theory, nonbreaking incident waves and the validity of the empirical relationships for the dissipative mechanisms the major assumption made in the previous approximate analysis is the separate treatment of external and internal dissipation. The present paper presents a more rigorous analysis of the wave-structure interaction in that external and internal dissipation are treated together rather than separately. Results obtained from this more elaborate analysis are compared and with results obtained from the previous simple procedure and with laboratory measurements of reflection and transmission characteristics of homogeneous, porous breakwaters of trapezoidal cross-section.

ANALYSIS

Governing Equations

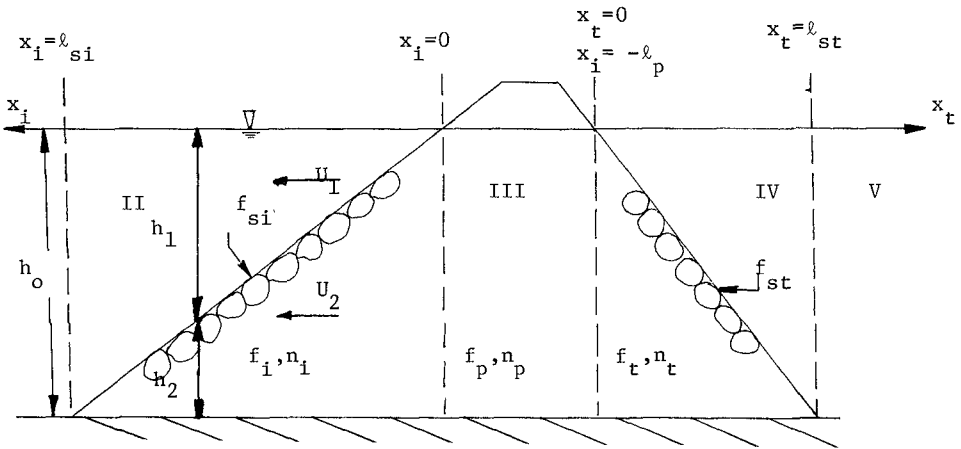


Figure 1: Definition Sketch

The analysis considers a homogeneous, trapezoidal breakwater subject to normally incident waves. The incident waves are assumed to be non-breaking and adequately described by linear long wave theory. Five different computational regions are identified in Figure 1. In regions I and V which are of constant depth, h_o , the general solutions for the wave motion is well known and consists of an incident and a reflected wave (Region I) and a transmitted wave (Region V). In Region III the general solution, after linearization of the flow resistance in the porous material, is given by Madsen (1974). Thus, we need only be concerned about the governing equations and the general solution for Regions II and IV, i.e., the slope regions.

For these regions the continuity equation reads

$$\frac{\partial \eta}{\partial t} + \frac{\partial (h_1 U_1)}{\partial x} + \frac{\partial (h_2 U_2)}{\partial x} = 0 \tag{1}$$

where h_1 , h_2 and U_1 , U_2 refer to the depths and discharge velocities in the water and porous wedges, respectively; and η is the free surface elevation.

The linearized momentum equation for the fluid wedge reads

$$\frac{\partial U_1}{\partial t} + g \frac{\partial \eta}{\partial x} + \frac{\tau_b}{\rho h_1} = 0 \quad (2)$$

in which g is gravity, ρ is fluid density, and τ_b , the bottom shear stress, is expressed in its nonlinear and linearized form as

$$\tau_b = \frac{1}{2} \rho f_w |U_1| U_1 = \rho f_s h_1 \omega U_1 \quad (3)$$

where f_w may be taken from the empirical expression developed by Madsen and White (1975), f_s is a linearized friction factor, and ω is the radian frequency of the incident waves. Substitution of (3) into (2) yields the linear momentum equation for the fluid wedge

$$\frac{\partial U_1}{\partial t} + g \frac{\partial \eta}{\partial x} + f_s \omega U_1 = 0 \quad (4)$$

The linearized momentum equation for the porous wedge is given by

$$\frac{1}{n} \frac{\partial U_2}{\partial t} + g \frac{\partial \eta}{\partial x} + f \frac{\omega}{n} U_2 = 0 \quad (5)$$

in which n is porosity and the flow resistance has been linearized by taking

$$\delta F = \rho(\alpha + \beta |U_2|) U_2 = \rho f \frac{\omega}{n} U_2 \quad (6)$$

Since the governing equations, (1), (4) and (5) are linear it is expedient to use complex variables. Thus, for a periodic motion of radian frequency ω we express the variables as the real part of the complex expressions given by

$$(\eta, U_1, U_2) = (\zeta(x), u_1(x), u_2(x)) e^{i\omega t} \quad (7)$$

with $i = \sqrt{-1}$.

Substituting (7) into (4) yields

$$u_1 = \frac{ig}{\omega} \frac{1}{1-if_s} \frac{d\zeta}{dx} \quad (8)$$

whereas (5) reduces to

$$u_2 = \frac{ig}{\omega} \frac{n}{1-if} \frac{d\zeta}{dx} \quad (9)$$

which expresses the fluid velocities in terms of the slope of the free surface.

With (7), (8) and (9), equation (1) may be written

$$\frac{\omega^2}{gh_0} (1-if_s)\zeta + \frac{d}{dx} \left[\frac{h_1}{h_0} \frac{d\zeta}{dx} \right] + \frac{n(1-if_s)}{1-if} \frac{d}{dx} \left[\frac{h_2}{h_0} \frac{d\zeta}{dx} \right] = 0 \quad (10)$$

Realizing that $h_1 + h_2 = h_0$ and therefore $h_1/h_0 = x/\ell_s$ and $h_2/h_0 = 1 - x/\ell_s$ for $0 < x \leq \ell_s$, and introducing the notation

$$\gamma = \frac{n(1-if_s)}{1-if} \quad (11)$$

we may write (10) in the form

$$\frac{\omega^2}{gh_0} (1-if_s)\zeta + \frac{d}{dx} \left[\left\{ \gamma + (1-\gamma) \frac{x}{\ell_s} \right\} \frac{d\zeta}{dx} \right] = 0 \quad (12)$$

Here $\omega^2/(gh_0) = k_0^2$ is the long wave dispersion relationship for waves in constant depth, h_0 . Introducing this notation and changing variable to

$$Z = \gamma + (1-\gamma) \frac{x}{\ell_s} \quad (13)$$

we finally obtain the simple governing equation for the surface wave amplitude

$$\frac{d}{dZ} \left[Z \frac{d\zeta}{dZ} \right] + \frac{(k_0 \ell_s)^2 (1-if_s)}{(1-\gamma)^2} \zeta = 0 \quad (14)$$

This equation reduces, as it should, to that of Madsen and White (1975) for the porosity $n \rightarrow 0$ or for the internal friction factor $f \rightarrow \infty$, both of which are limits resulting in an effectively impermeable slope.

General Solution

Equation (14) is of the Bessel type (Hildebrand, 1965) and its general solution may be expressed as

$$\zeta = A J_0(\text{Arg}) + B Y_0(\text{Arg}) \quad (15)$$

where Arg in the original variables is given by

$$\text{Arg} = \frac{2k_o \ell_s}{1-\gamma} \sqrt{1-if_s} \sqrt{\gamma + (1-\gamma)x/\ell_s} \quad (16)$$

From the property of Bessel Functions we further obtain the derivative

$$\frac{d\zeta}{dx} = - \frac{k_o \sqrt{1-if_s}}{\sqrt{\gamma + (1-\gamma)x/\ell_s}} [A J_1(\text{Arg}) + B Y_1(\text{Arg})] \quad (17)$$

where Arg again is given by (16).

The fluid velocities are obtained from (8) and (9) as

$$u_1 = -i \sqrt{\frac{g}{h_o}} \frac{1}{\sqrt{1-if_s}} \frac{1}{\sqrt{\gamma + (1-\gamma)x/\ell_s}} [A J_1(\text{Arg}) + B Y_1(\text{Arg})] \quad (18)$$

for the water wedge, and

$$u_2 = -i \sqrt{\frac{g}{h_o}} \frac{n \sqrt{1-if_s}}{1-if_s} \frac{1}{\sqrt{\gamma + (1-\gamma)x/\ell_s}} [A J_1(\text{Arg}) + B Y_1(\text{Arg})] \quad (19)$$

for the porous wedge.

From the general solutions presented above the solutions for the seaward and landward slopes are obtained by taking $x=x_1$ and $x=x_t$, respectively, and the appropriate ℓ_s , f_s , and n values (see Figure 1).

For Region III which is entirely porous the governing equations consist of the momentum equation which in its linearized form is identical to (5) and the continuity equation which reads

$$n \frac{\partial \eta}{\partial t} + h_o \frac{\partial U}{\partial x} = 0 \quad (20)$$

As previously mentioned the general solution to equations (5) and (20) was given by Madsen (1974) and in complex form it may be expressed as

$$\zeta_{III} = A_{pi} e^{ikx_i} + B_{pr} e^{-ik(x_i + \ell_p)} \quad (21)$$

where

$$k = \frac{\omega}{\sqrt{gh_o}} \sqrt{1-if_p} = k_o \sqrt{1-if_p} \quad (22)$$

and

$$u_{III} = -\sqrt{\frac{g}{h_0}} \frac{n_p}{\sqrt{1-if_p}} [A_{pi} e^{ikx_i} - a_{pr} e^{-ik(x_i + \ell_p)}] \quad (23)$$

Outside the structure the general solution is in Region I

$$\zeta_I = a_i e^{ik_0 x_i} + a_r e^{-ik_0 x_i} \quad (24)$$

$$u_I = -\sqrt{\frac{g}{h_0}} [a_i e^{ik_0 x_i} - a_r e^{-ik_0 x_i}] \quad (25)$$

where a_i is the incident wave amplitude and a_r is the complex amplitude of the reflected wave.

For Region V the motion consists of only the transmitted wave of complex amplitude a_t , i.e.,

$$\zeta_V = a_t e^{-ik_0 x_t} \quad (26)$$

$$u_V = \sqrt{\frac{g}{h_0}} a_t e^{-ik_0 x_t} \quad (27)$$

Matching Conditions

Assume for the moment that all linearized friction factors, porosities and incident wave characteristics are specified. The general solutions developed in the preceding section then contain 8 unknown constants of which the magnitudes of a_r , the reflected wave amplitude, and a_t , the transmitted wave amplitude, of course, are of primary interest in the present context. To determine the constants the general solutions for the surface elevation, ζ , and the horizontal discharge velocity, u , are matched at their common boundaries, i.e., at $x_i = \ell_{si}$, $0, -\ell$ ($x_t = 0$); and at $x_t = 0$ ($x_i = -\ell$) and ℓ_{st} . This yields 8 equations from which the 8 unknowns may be determined.

It is of special interest to note that the solution for the velocity in the water wedge, i.e., u_1 , is matched to the solution outside the structure at $x_i = \ell_{si}$ and $x_t = \ell_{st}$, whereas the velocity in the porous wedge, i.e., u_2 , is matched to the solution inside the structure, u , at x_i and $x_t = 0$. It is also noted that the value of the argument^p of the Bessel^t Functions in the general slope solution remain finite at $x = 0$ and $x = \ell_s$ since

$$\text{Arg} \quad \begin{array}{ll} 1 & \text{for } x = l_s \\ \sqrt{\gamma} & \text{for } x = 0 \end{array} \quad (28)$$

Evaluation of Linearized Friction Factors

Once the solution for given values of the linearized friction factors has been obtained Lorentz principle is invoked in order to obtain a new estimate for the friction factors. For the external dissipation Lorentz' principle takes the form of the integral

$$\frac{1}{T} \int_0^T dt \int_0^{l_s} \tau_b U_1 dx \quad (29)$$

being independent of whether τ_b is expressed by its nonlinear or linear form given by (3). Since f_w in (3) is taken from Madsen and White (1975) this leads to an equation for f_s . The integration is carried out on a high speed computer.

For the internal dissipation Lorentz' principle is expressed by the invariance of the integral

$$\frac{1}{T} \int_0^T dt \int_{\Psi} (\delta F) U_2 \delta \Psi \quad (30)$$

with frictional law used to express δF (equation 6). The integral in (30) is evaluated numerically over the appropriate volume, Ψ , by high speed computer. Since the nonlinear friction law in (6) contains two parameters, α and β , these must be specified before (3) yields a determination of the linearized friction factor f . The empirical expressions

$$\begin{aligned} \alpha &= \alpha_0 \frac{(1-n)^3}{n^2} \frac{v}{d^2} \\ \beta &= \beta_0 \frac{(1-n)}{n} \frac{1}{d} \end{aligned} \quad (31)$$

in which d is the stone diameter, v is the kinematic viscosity of the fluid. The constants α_0 and β_0 vary with the characteristics of the stones with a range of $800 < \alpha < 1500$ and $1.8 < \beta_0 < 3.6$. Since the stones used in the present experiments were highly angular (crushed quarry stones) values of $\alpha_0 = 1500$ and $\beta_0 = 3.6$ were used in (31).

With updated values for all friction factors the governing equations are again solved and renewed application of Lorentz' principle yield new values for the friction factors. From experience a final solution is obtained after 3 to 5 iterations.

COMPARISON WITH EXPERIMENTS

A set of 54 experiments on the reflection and transmission characteristics of homogeneous trapezoidal breakwaters were carried out in a 24 m long wave flume in the R.M. Parsons Lab. at MIT. The water depth was 30 cm and three wave periods (1.6, 1.8 and 2.0 sec.) were used. For each period 6 different values for the incident wave height were run on the structure having front slopes of 1 on 2.5, 2.0 and 1.5 with the rear slope remaining constant at 1 on 1.5. The stone material was crushed quarry stones with an equivalent diameter of $d = 1.5$ cm. Porosity was found to be 0.4.

The experiments were run continuously and incident reflected and transmitted wave amplitudes were determined by the accurate procedure developed and described by Madsen and White (1975). The structure was located approximately 12 m from the wave generator and reflection from the end of the wave flume was minimized by a 1 on 6 sloping absorber beach covered by horsehair.

Experimental results for reflection and transmission coefficients are shown in Figures 2a, b, c for a wave period of 2.0 sec. and front slopes of 1 on 1.5, 2 and 2.5, respectively. The experimental results are compared with predictions by the "new" method described in this paper (indicated by subscript N) as well as with predictions of the "old" method (indicated by subscript O) developed by Madsen and White (1977). From Figures 2a,b,c it is evident that the "new" as well as the "old" methods are quite successful in their prediction of transmission coefficients. It is, however, painfully obvious that both methods are quite weak in their ability to yield accurate predictions of the reflection coefficient. In fact, the "old" method yields high estimates of reflection coefficients whereas the "new" method yields low values. The discrepancy between the predicted and observed reflection coefficients is seen to increase with decreasing front slope.

A possible explanation for this discrepancy could be associated with an artificial discontinuity introduced in the analysis. Referring back to equation (1) it is seen that the storage term in the continuity equation is taken to be $\partial\eta/\partial t$ for the slope regions, i.e., storage is in the form of pure water on the slopes even in the areas where the water wedge pinches out. At the same time immediately inside the structure the storage term in the continuity equation, equation (20), indicates that storage takes place within the porous medium. This discontinuity was removed artificially by evaluating the slope solution at a value of $x = H/\tan\delta$, where δ is the slope, rather than at $x = 0$. It was found that this change had a relatively minor effect on the predicted transmission coefficients whereas the effect on predicted reflection coefficients was substantial. There was, however, no clear trend in the results obtained in this manner. Sometimes the reflection coefficient prediction improved, sometimes it got worse.

It is worthwhile to note that the experimental results for the

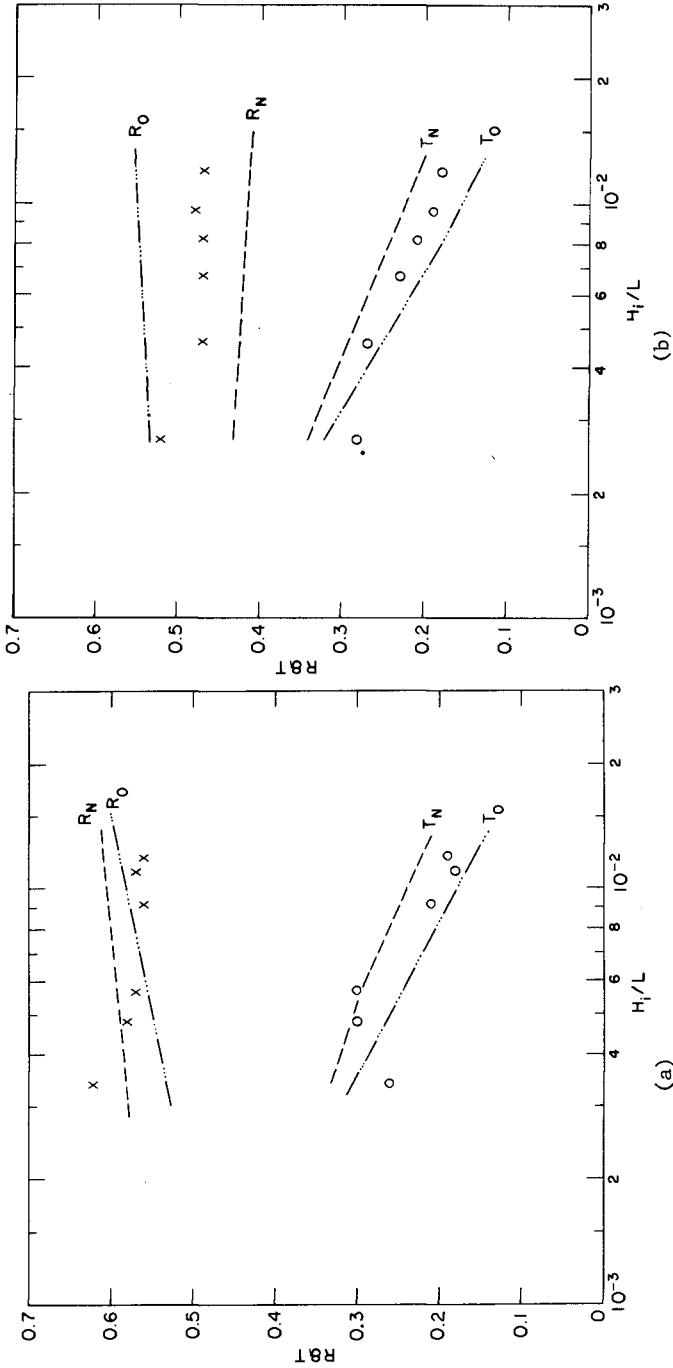


Figure 2: Comparison of Predicted and Observed Reflection (R) and Transmission Coefficients of Porous Trapezoidal Breakwaters. ——— Predictions by present method. - - - - - Predictions by previous method. Wave Period 2.0 sec., Water Depth 30.5 cm. Front slope 1 on 1.5(a), 1 on 2.0(b), 1 on 2.5(c).

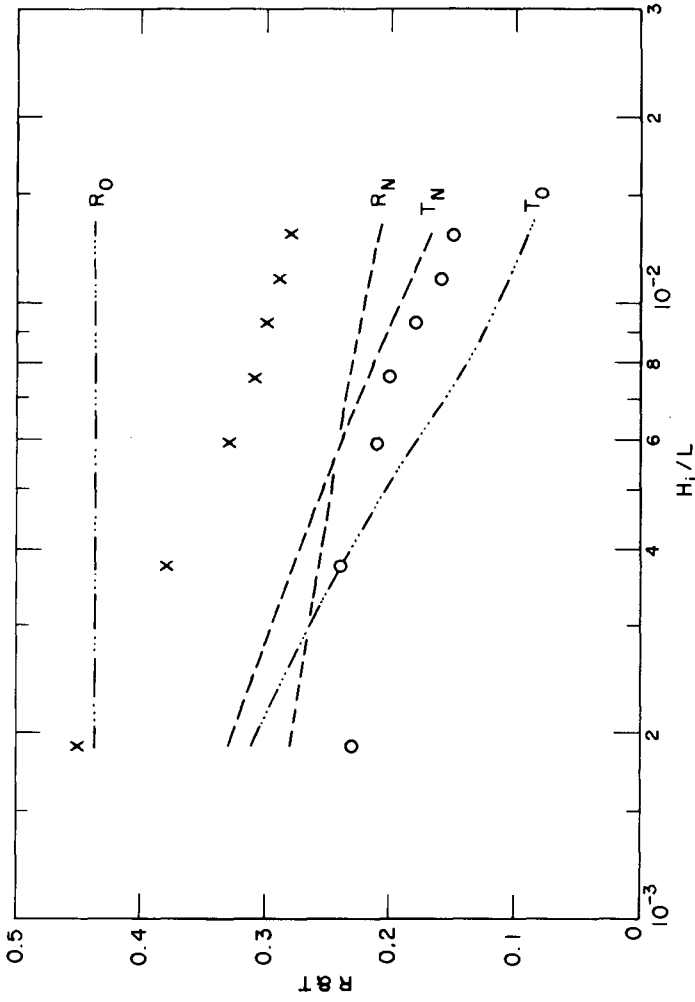


Figure 2(c): For legend see previous page.

reflection coefficients, which are believed to be quite accurately determined, on the gentler slope show a trend of decreasing reflection coefficient with increasing wave steepness (Figure 2). This feature, which cannot be reproduced by the "old" method appears to be represented by the results obtained from the present theory.

As a final test of the procedure developed in this paper predicted values of reflection and transmission coefficients are compared with the experimental results obtained by Sollitt and Cross (1972) for a multi-layered trapezoidal breakwater. To apply the present methodology the multi-layered breakwater is modeled as a homogeneous breakwater of the same geometry. The uniform stone size of the homogeneous breakwater is chosen so that the two breakwaters are hydraulically equivalent in the sense defined by Madsen and White (1977). The results are shown in Figure 3 (from Madsen and White, 1977) as dashed and dotted lines. Again the predicted transmission coefficients are in close agreement with measurements, whereas predicted reflection coefficients, although better than predictions afforded by the "old" method, still leave somewhat to be desired.

CONCLUSIONS

The present investigation was undertaken to improve on a previous simplified model for the determination of reflection and transmission characteristics of porous breakwaters of trapezoidal cross-section. The improvement consisted of a more rigorous analysis of the wave-structure interaction on the seaward and landward slopes of the breakwater thereby removing the somewhat artificial treatment in the previous model of external and internal dissipation as separate mechanisms.

The resulting theory retains the practicality of the previous theory in that only parameters which may be expected to be approximately known are needed to carry out the computations. However, the new theory is more elaborate and does require calculations to be carried out on a high speed computer.

From a comparison with experimental data it appears that the new as well as the old method are quite successful in their determination of transmission coefficients. Neither the new nor the old method is very successful in their prediction of reflection coefficients. For relatively gentle seaward slopes (1 on 2.0 to 2.5) the new method underpredicts whereas the old method overpredicts the reflection coefficient. For relatively steep seaward slopes both methods give reflection coefficients in reasonable agreement with observations. Slight changes in the assumed geometry of the breakwater have an insignificant effect on predictions of transmission coefficients by both the new and the old method. Whereas the old method is quite insensitive to breakwater geometry also for prediction of reflection coefficients, the new method is in this aspect very sensitive which suggests that a major renewed effort is needed if one wishes to obtain better predictions of reflection coefficients.

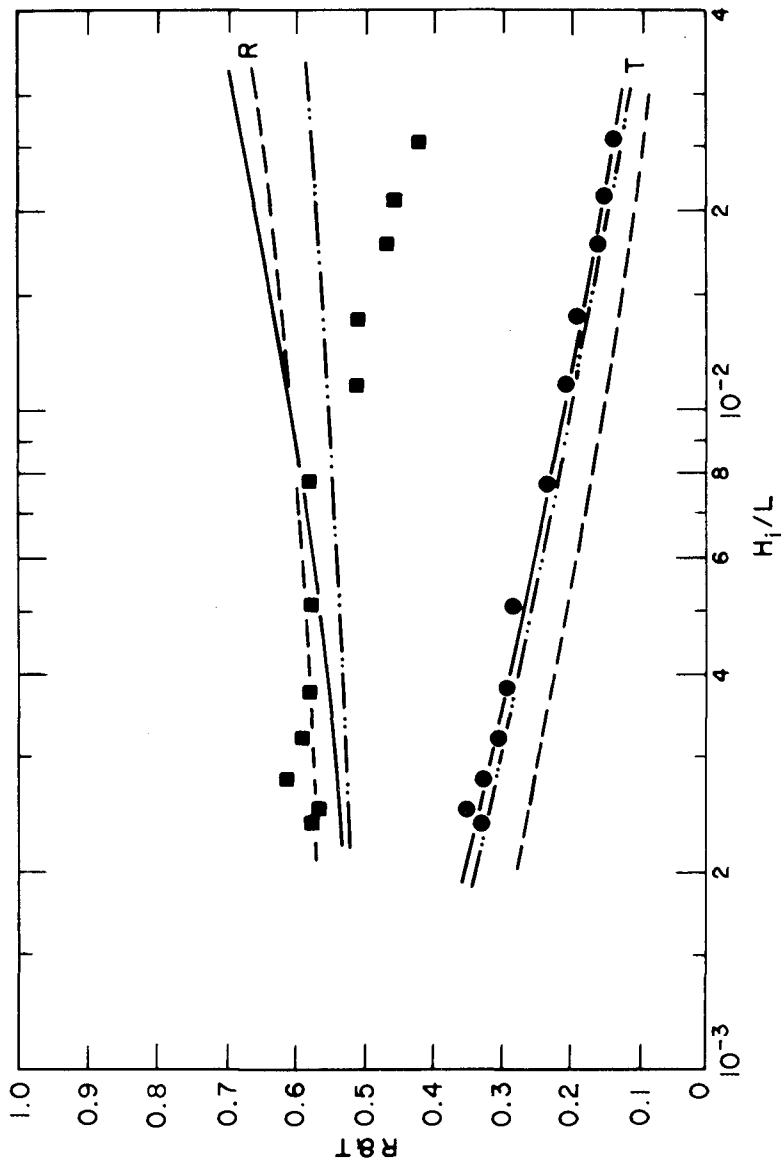


Figure 3: Comparison of predicted and observed reflection and transmission coefficients of trapezoidal, multi-layered breakwater tested by Sollitt and Cross (1972).
 - - - prediction by Madsen and White (1977); - · - · - prediction by present method.

ACKNOWLEDGMENTS

The research presented here was supported by the National Science Foundation, Water Resources, Urban and Environmental Engineering Program, under Grant No. ENG76-08982 A01. The junior author (Ms. Hanson) participated in the project as part of MIT's Undergraduate Research Opportunities Program (UROP) whose assistance is gratefully acknowledged.

REFERENCES

- Hildebrand, F.B., Advanced Calculus for Applications, Prentice Hall, New Jersey, 1965.
- Madsen, O.S., "Wave Transmission through Porous Structures," ASCE, Journal of the Waterways, Harbors and Coastal Engineering, Vol. 100, WW3, 1974, p. 169-188.
- Madsen, O.S. and S.M. White, "Reflection and Transmission Characteristics of Porous Rubble-Mound Breakwaters," Technical Report No. 207, R.M. Parsons Laboratory, Department of Civil Engineering, Massachusetts Institute of Technology, 1975.
- Madsen, O.S. and S.M. White, "Wave Transmission through Trapezoidal Breakwaters," Proceeding of the Fifteenth Coastal Engineering Conference, 1977, pp. 2662-2676.
- Sollitt, C.K. and R.H. Cross, "Wave Reflection and Transmission at Permeable Breakwaters," Technical Report No. 147, R.M. Parsons Laboratory, Department of Civil Engineering, Massachusetts Institute of Technology, 1972.

PERFORMANCE CHARACTERISTICS OF SUBMERGED BREAKWATERS

J. Dattatri¹, H. Raman², and N. Jothi Shankar³

INTRODUCTION

Submerged breakwater is a barrier with its crest at or slightly below the still water level. In situations where complete protection from waves is not required, submerged breakwaters offer a potentially economic solution. Submerged breakwaters have been effectively used to protect harbour entrances, to reduce siltation in entrance channels, against beach erosion, and for creation of artificial fishing grounds. However quantitative information available about the hydraulic behaviour of these submerged breakwaters is rather limited. Theoretical analysis of the problem has not proved satisfactory primarily because of the difficulties in quantifying the energy losses that always accompany these wave - structure interactions. Recourse has to be taken to laboratory studies to provide the necessary information regarding the performance characteristics of submerged breakwaters.

A comprehensive laboratory investigation to evaluate the performance characteristics of the submerged breakwaters of various types and shapes, permeable and impermeable was undertaken. The results of these investigations are presented in this paper.

¹Asst. Prof., Dept. of App. Mech. and Hydr., Karnataka Reg. Engrg. College, SURATHKAL (S.K) - 574157, India.

²Prof. and Head, Hydraulic Engineering Laboratory, Indian Institute of Technology, MADRAS - 600 036, India.

³Asst. Prof., Hydraulic Engineering Laboratory, Indian Institute of Technology, MADRAS - 600 036, India.

EXPERIMENTAL FACILITIES AND PROCEDURES

The experiments were conducted in a wave flume (25m x 0.9m x 0.9m) provided with a plunger type regular wave generator. The water surface time histories were recorded using a parallel - wire resistance probe in conjunction with a Kempf and Remmers three channel strip chart recorder.

The submerged breakwaters investigated were:

- 1) Horizontal fixed plate type,
- 2) Thin vertical wall type, Impermeable,
- 3) Triangular type, Impermeable,
- 4) Rectangular type, Permeable and Impermeable,
- 5) Trapezoidal type: Sea face sloping and beach face sloping, Permeable and Impermeable,
- 6) Trapezoidal type: Sea face sloping and beach face vertical, Impermeable.

The impermeable breakwater models were fabricated using mild steel and aluminium plates of 6mm thickness. For the sloping faces, a slope of 2 horizontal to 1 vertical was used. The details of all the breakwater models investigated is given in Fig.1. To study the influence of permeability, the breakwaters of the rectangular type (50 cm crest width) and the trapezoidal type (both faces sloping) were used. These breakwaters were formed using crushed stone aggregates, and the required cross-sections were maintained by confining the aggregates in wire mesh cages. Two types of aggregates, Type A and Type B were used. Type A aggregate had a median size of 16.5mm and a porosity of 0.41, while the Type B aggregate had a median size of 43.4 mm and a porosity of 0.42.

The water depth, d , was maintained constant at 50cm. The depth of crest submergence, d_s , of the breakwater was altered to any desired value by keeping the water depth constant but varying the crest level of the breakwater.

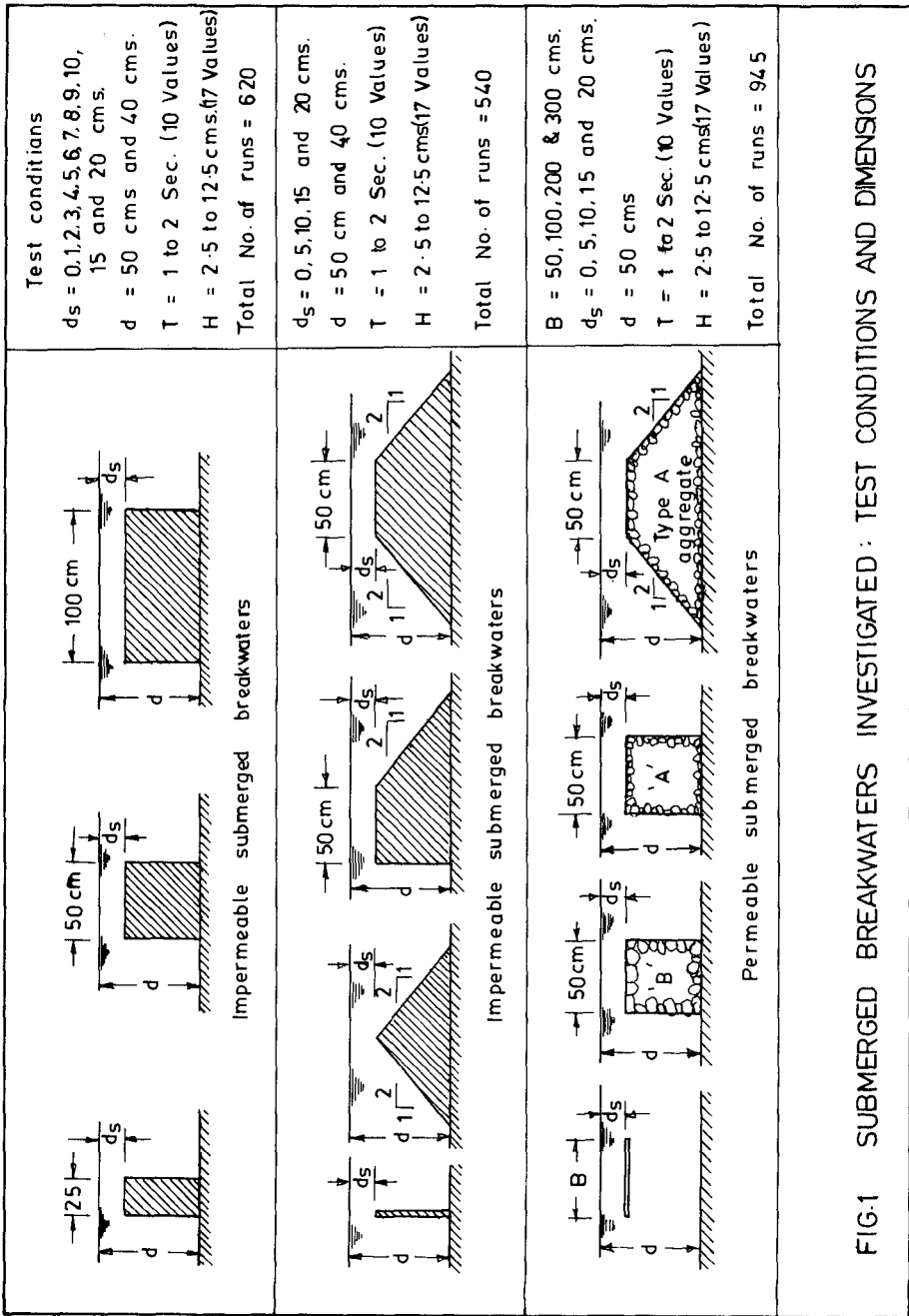


FIG-1 SUBMERGED BREAKWATERS INVESTIGATED : TEST CONDITIONS AND DIMENSIONS

Experiments were conducted covering a wide range of experimental conditions consistent with the available facility. The relative water depth, d/L was varied from 0.123 to 0.331, the incident wave steepness, H_1/L was varied from 0.007 to 0.083, while the relative depth of crest submergence d_s/d was varied from 0.0 to 0.4.

The incident wave characteristics, H_1 and L were measured in steady state runs without the breakwater in position. The transmitted wave was generally found to be irregular though periodic. To provide a basis for comparison of test results as free as possible from subjectivity, the equivalent wave height concept of Dick and Brebner (2) was used to evaluate the transmitted wave height, H_t . The reflected wave which results when the incident wave interacts with the structure, gives rise to a partial standing wave in front of the structure. The reflected wave height, H_r was evaluated by resolving the wave envelope of this partial standing wave. An equivalent wave height, H_l corresponding to the energy lost in the wave - structure interaction process was evaluated from energy balance considerations. The experimental data was processed using a IBM 370/155 digital computer facility.

PRESENTATION AND INTERPRETATION OF EXPERIMENTAL DATA

The data obtained from the experiments was analyzed using the method of dimensional analysis. The pertinent parameters influencing the phenomenon were obtained from dimensional considerations. The influence of the various parameters on the Transmission coefficient, $K_T (= H_t/H_1)$, the Reflection coefficient, $K_R (= H_r/H_1)$ and the loss coefficient, $K_L (= H_l/H_1)$ were analyzed. Restriction of space does not permit the presentation of all the results here. The important results regarding the study concerning the transmission coefficient only are presented here.

The complete details can be found in Reference 1.

The following dimensionless parameters can be considered to be important in the study of the transmission coefficient,

$$K_T = H_t/H_i = f(H_i/L, d/L, B/L, d_g/d, S, s, p)$$

in which H_t is the transmitted wave height, H_i is the incident wave height, L is the incident wave length, d is the depth of water, B is the crest width of the submerged breakwater, d_g is the depth of crest submergence below SWL, S is a parameter characterizing the shape of the breakwater, s is the slope of the breakwater faces, and p is the porosity of the breakwater. The dimensionless parameters H_i/L , d/L , B/L , and d_g/d represent the incident wave steepness, the relative depth of water, the relative crest width, and the relative depth of crest submergence respectively.

The shape has been represented by a variable, S only for mathematical definition. S will represent whether the breakwater is triangular, rectangular or trapezoidal. In the analysis that follows, the shape is not represented by assigning any specific value to S , but instead the shape will be specified. Similarly the slope, s was not varied but the distinction will be between a vertical face and a sloping face.

Influence of incident wave steepness, H_i/L on K_T

The incident wave steepness has an important influence on the wave breaking phenomenon. Waves near the critical steepness may be induced to break by the submerged breakwater, and since wave breaking process is always accompanied by energy losses, steeper waves are likely to be attenuated more than the flatter waves. Hence it can be logically concluded that the wave steepness is likely to be a significant parameter. In fig. 2. the transmission

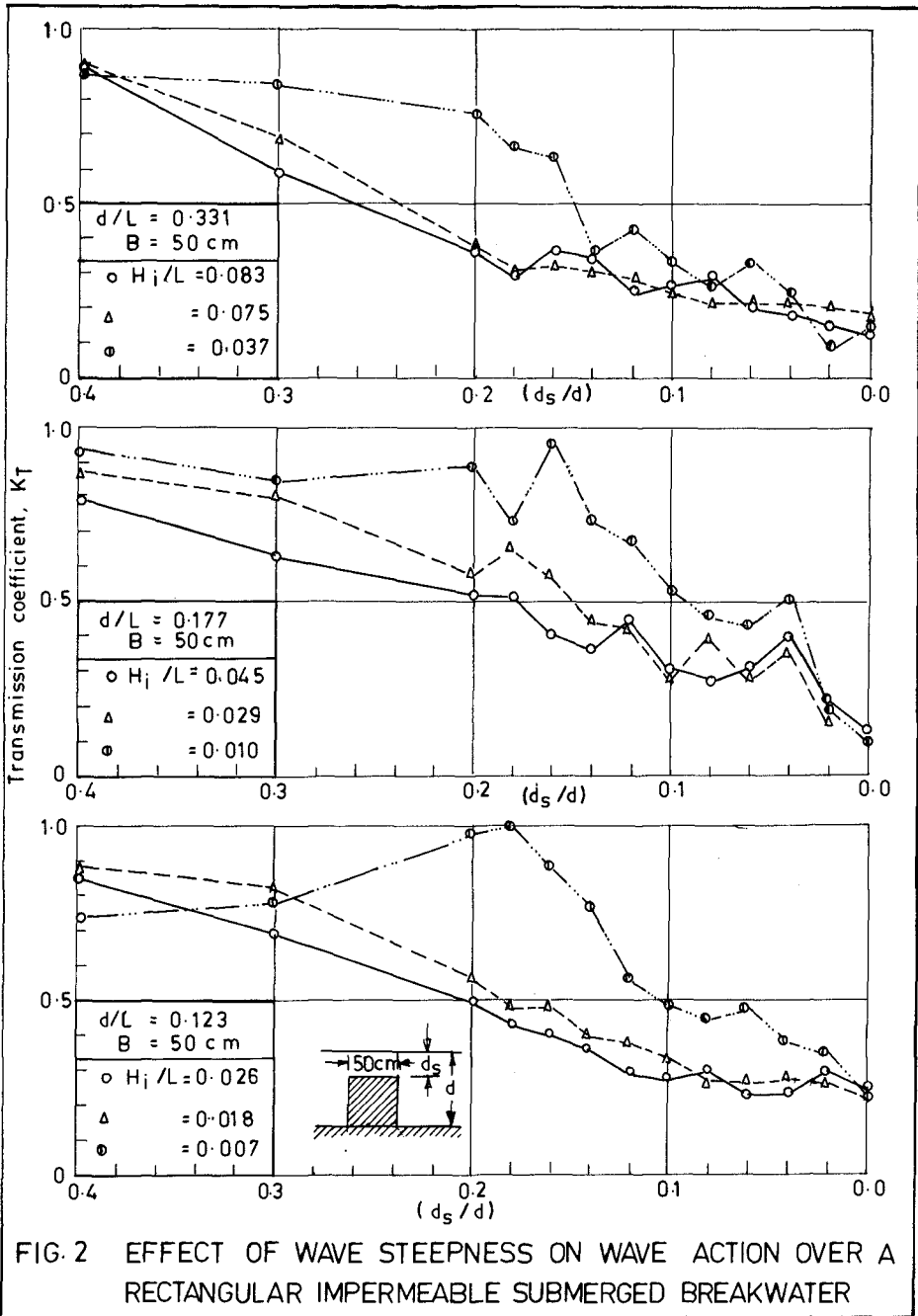


FIG. 2 EFFECT OF WAVE STEEPNESS ON WAVE ACTION OVER A RECTANGULAR IMPERMEABLE SUBMERGED BREAKWATER

coefficient, K_T is plotted against the relative depth of crest submergence, d_s/d , with the incident wave steepness, H_i/L as the third parameter. The curves for the higher steepness values appear to merge into one, indicating that in the range of higher wave steepnesses the influence of H_i/L on K_T is not significant. Similar tendencies were observed for data corresponding to other breakwaters also. Goda et al (3) and Johnson et al (4) have also arrived at similar conclusions.

Another important trend in Fig.2 is the influence of d_s/d on K_T . As d_s/d approaches zero, i.e., the crest of the breakwater approaches the SWL, there is a general decrease in K_T . For large values of d_s/d ($= 0.40$), the transmission is very high of the order of 75% to 95%. As such d_s/d values greater than 0.40, are not likely to be of any practical significance from the point of view of wave damping. In view of this, the maximum value of d_s/d used in the present investigation was restricted to 0.40.

Influence of relative water depth, d/L on K_T

The data to study the influence of the relative water depth, d/L on K_T is presented in Fig.3. To reduce the influence of other parameters, the incident wave steepness is maintained constant at 0.03. The data show very similar tendencies and in general it can be seen that the relative water depth does not have significant influence on K_T . In the range $d_s/d = 0.0$ to 0.2, the relative water depth did not have any influence, but in the range $d_s/d = 0.2$ to 0.4, larger values of d/L show a tendency towards slightly greater transmission. This is to be expected because larger values of d/L correspond to relatively deeper water waves, wherein more energy is concentrated near the surface. When d_s/d is also large, this energy concentrated near the surface is easily transmitted across the structure.

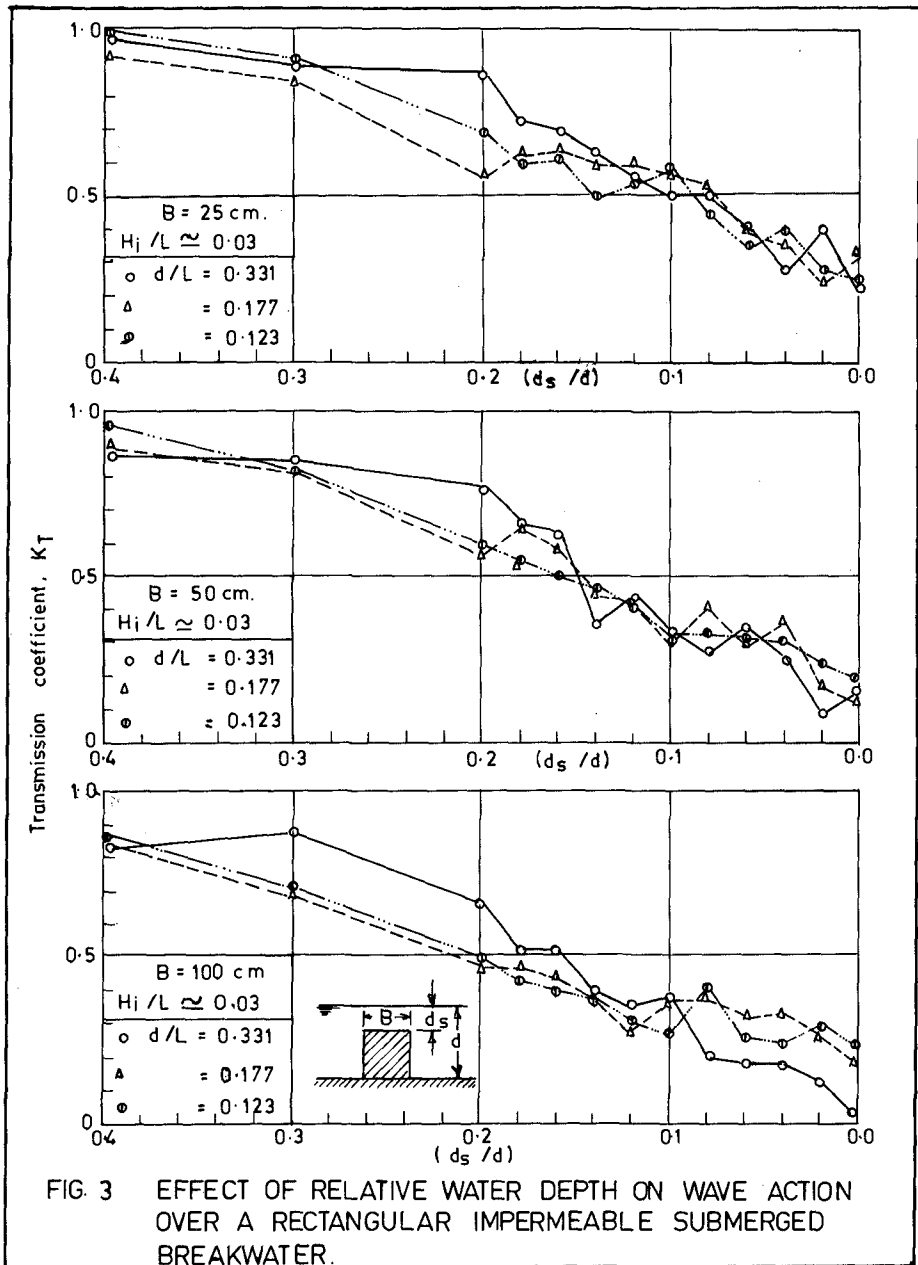


FIG. 3 EFFECT OF RELATIVE WATER DEPTH ON WAVE ACTION OVER A RECTANGULAR IMPERMEABLE SUBMERGED BREAKWATER.

Influence of relative crest width, B/L , and relative depth of crest submergence, d_s/d , on K_T .

In the case of impermeable submerged breakwaters, the energy transmission to the shoreward side must take place only above the crest of the breakwaters. The amount of energy transmitted across will naturally be more, if the depth of crest submergence is more. So it is logical to conclude that the relative depth of crest submergence, d_s/d is likely to be the most important parameter influencing the performance characteristics of the submerged breakwaters. This conclusion is in general also applicable to the permeable breakwaters also, since the energy transmitted through the structure is likely to be a small percentage of the energy transmitted over the crest.

The relative crest width, B/L influences the wave transformation over the breakwater. In the case of breakwaters with very small crest widths, it was observed that the incident wave steepens and reaches a condition when it is about to break. But before the wave can break, it enters the relatively deeper waters in the lee of the breakwater, which prevents the wave from breaking. In the case of breakwaters with sufficient crest width, the wave breaks resulting in a greater dissipation of energy and consequently lesser transmission. An increase in the crest width over the minimum necessary to trigger breaking, is unlikely to have any significant influence on the transmission characteristics.

The experimental data is in general agreement with these logical conclusions as can be clearly seen in Fig.4. The data for the rectangular impermeable breakwaters is plotted in Fig.4. in terms of K_T and B/L with d_s/d as the third parameter. The scatter of data is slightly large for small values of B/L . The data corresponding to the

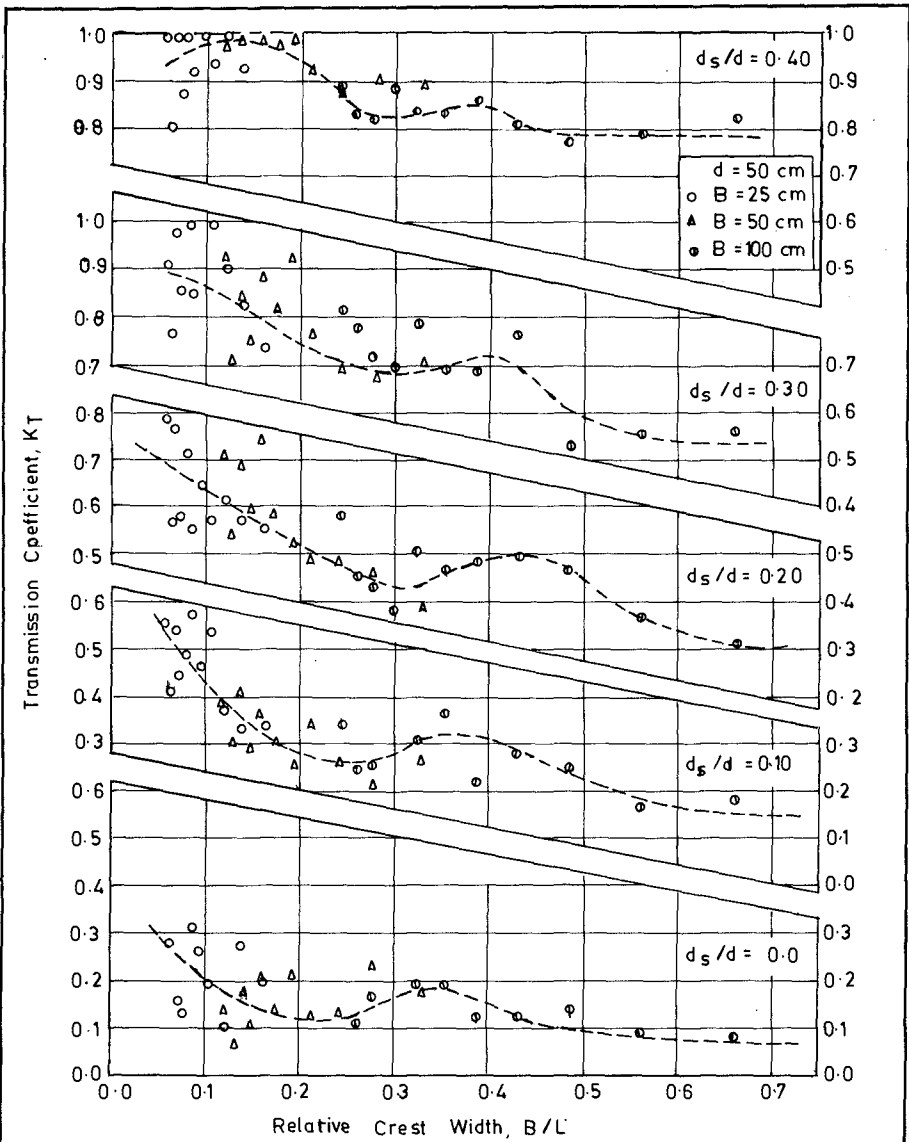


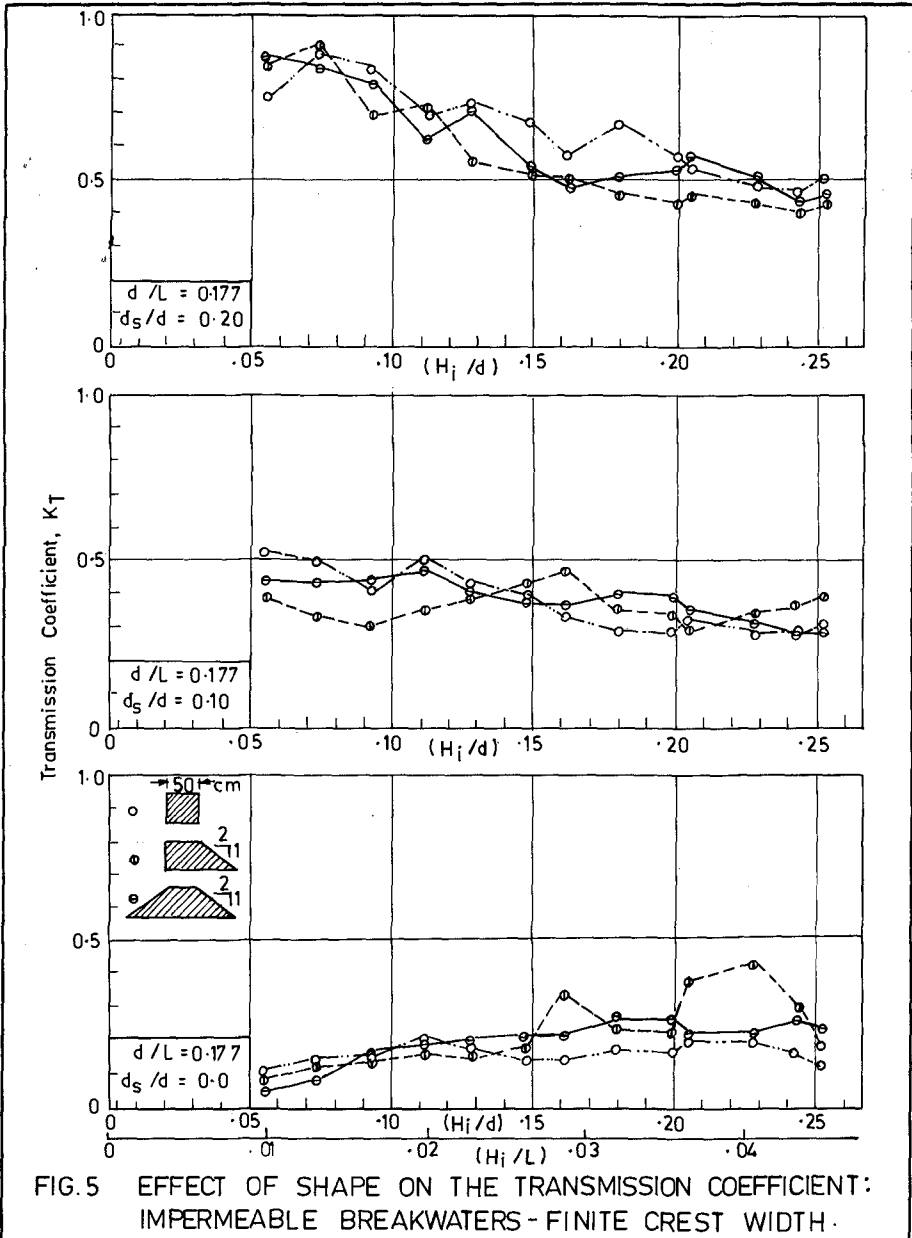
FIG. 4 TRANSMISSION COEFFICIENT VS RELATIVE CREST WIDTH:
RECTANGULAR IMPERMEABLE SUBMERGED BREAKWATER.

three crest widths (25, 50, and 100cm) overlap in this range and the scatter may be partly due to this. K_T decreases as B/L increases, until K_T reaches a minimum value. This occurs for B/L values between 0.2 and 0.3. The position of the minimum shifts gradually from 0.2 to 0.3, as d_s/d increases from 0.0 to 0.4. After the minimum is reached, K_T tends to increase slightly with further increase in B/L , before it becomes asymptotic. Increase of crest widths beyond $B/L = 0.3$, does not significantly add to the damping characteristics of these breakwaters. Fig.4 clearly points to the existence of an optimum crest width of the breakwater ($B/L = 0.2$ to 0.3). The K_T Vs B/L curves show some sort of a sinusoidal variation which cannot be satisfactorily explained.

The data in Fig.4 group themselves remarkably well for the different values of d_s/d , and the trend lines for constant values of d_s/d , show consistent tendencies. As is to be expected, larger values of crest submergence show greater transmission.

Influence of shape and slope

The transmission characteristics of the impermeable breakwaters of different shapes, but with finite crest width (50 cm) are shown in Fig.5. The transmission curves for the three shapes have very similar characteristics. In the case of the rectangular breakwaters, the reflections will be high, while for the trapezoidal breakwater, the reflection would be low but the losses are likely to be higher due to wave breaking. Thus in both cases, the transmission would be the same. Providing a slope on the beach face of the breakwater has not influenced the transmission characteristics in comparison with the trapezoidal breakwater with beach face vertical. Kabelac (5) has concluded that the magnitude of the wave attenuation depends not only



on the slope of the sea face of the breakwater, but also on its cross-sectional area. The cross-sectional areas of the three breakwaters whose results are presented in Fig.5, are 2500, 5000 and 7500 cm². But the transmission characteristics of all these three types are very nearly the same although the cross-sectional areas have a three fold variation.

It can be concluded that for the various shapes of the breakwaters tested in the present investigations, the transmission characteristics do not depend on the shape. Breakwaters with vertical faces on the sea side induce large reflections, creating partial standing waves. These create problems of scour and consequent undermining at the base of the breakwaters. Further, large reflections result in greater wave forces on the structure due to the formation of the standing wave. These considerations necessarily preclude the rectangular type of submerged breakwaters for practical use.

Submerged breakwaters with their sea faces sloping have the possible advantage that they allow for the free passage of sediment on its face compared to a vertical face. If the beach face of the breakwater is also sloping, the sediment trapping efficiency will be less. So the ideal one appears to be a breakwater with sea face sloping and beach face vertical. The prototype experience as reported by Kabelac (5) confirms the sediment trapping efficiency of these types of breakwaters, in addition to their efficient wave damping characteristics.

Influence of porosity

The experimental data to study the effect of porosity is presented in Fig.6. The data corresponding to the horizontal plate type is also included. This type can be considered as a rectangular breakwater with a porosity,

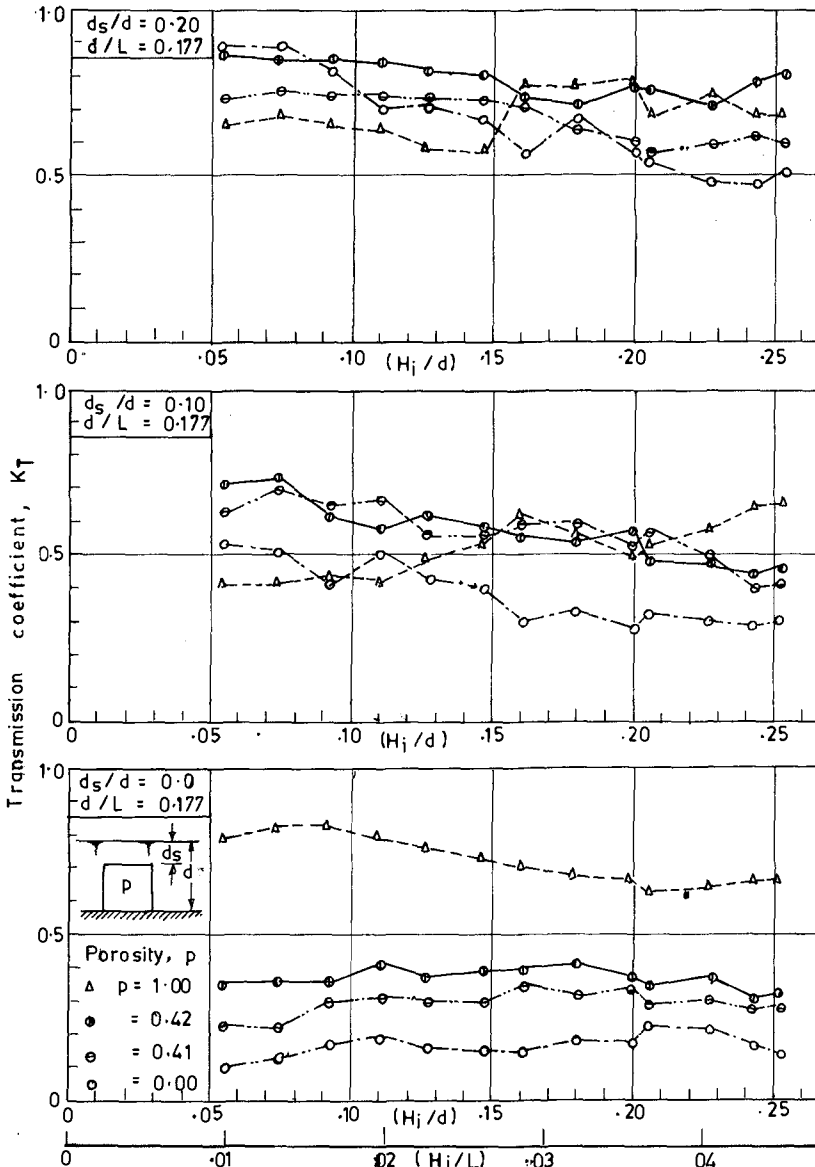


FIG. 6 EFFECT OF POROSITY ON THE TRANSMISSION COEFFICIENT: RECTANGULAR SUBMERGED BREAKWATER

$p = 1.0$, in comparison with the rectangular impermeable type which has a porosity, $p = 0.0$. In Fig.6, K_T is plotted against H_1/d (and H_1/L) with porosity, p as the third variable. The relative water depth, d/L was maintained constant. All the curves are nearly horizontal, which incidentally confirms the earlier conclusion that the wave steepness has no significant influence on K_T . Regarding the influence of porosity, a regular and a systematic trend is seen for the data corresponding to $d_s/d = 0.0$. The impermeable breakwater has the minimum transmission, and as the porosity increases, the transmission also increases. For $d_s/d = 0.10$, the impermeable breakwater has the minimum transmission for most of the range, but the data for other porosities cannot be distinguished from each other. For $d_s/d = 0.20$, the curves for the permeable and impermeable cases appear to merge. This is because for large depths of crest submergence, the energy transmitted through the breakwater will be a very small percentage of the energy transmitted on the top, and hence the porosity is unlikely to have any significant influence on K_T .

In general we find the behaviour of the permeable breakwaters to be very similar to the behaviour of the impermeable breakwaters. This is in contrast to the conclusion of Dick and Brebner (2) that permeable breakwaters behave differently from impermeable types. However it should be noted that the permeable breakwaters used by Dick and Brebner were of the nested tube type, while in the present case they were of crushed stones.

PERFORMANCE CHARACTERISTICS OF SUBMERGED BREAKWATERS

The investigations regarding the influence of the various parameters on the transmission coefficient, K_T as detailed above, indicate that the two parameters,

relative depth of crest submergence, d_s/d , and the relative crest width, B/L to be the most significant. The performance characteristics for each of the type of breakwater tested can be represented as K_T Vs B/L plots with d_s/d as the third parameter. Such a plot for the rectangular impermeable submerged breakwaters was presented in Fig.5. In Figs. 7 and 8, the performance characteristics of some of the other submerged breakwaters tested have been presented. An important feature of these plots is the considerable similarities and consistent tendencies.

TRANSMITTED WAVE CHARACTERISTICS

The waves formed shoreward of the submerged breakwaters were quite complex and showed the presence of several smaller waves. However periodicity was maintained and this period corresponds to the incident wave period. This indicates the generation of a system of harmonics with a fundamental frequency equal to that of the incident wave. To examine this aspect, some of the transmitted wave records were subjected to a spectral analysis and the results confirmed this. The generation of higher harmonics was found to be more pronounced when the crest of the breakwater is close to the still water level. However, in a majority of these cases, the energy contents of the higher harmonics were considerably less than that corresponding to the fundamental. Thus it can be concluded that the transmitted wave has the same fundamental frequency as the incident wave but part of the energy is shifted to the higher frequencies.

CONCLUSIONS

The results of the present investigations indicate that submerged breakwaters can effect substantial wave attenuation and can be successfully used in places where only partial protection from waves is required. The important parameters that influence the performance are the

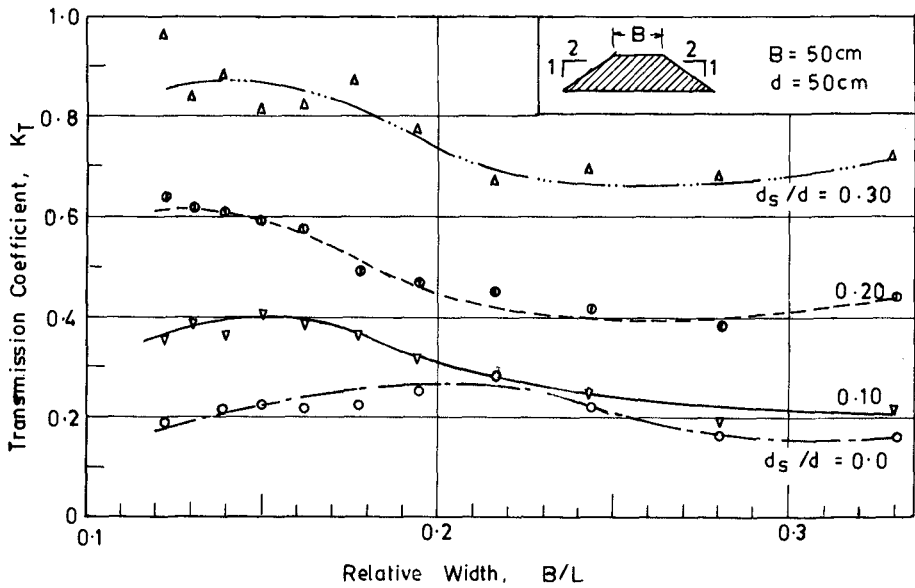
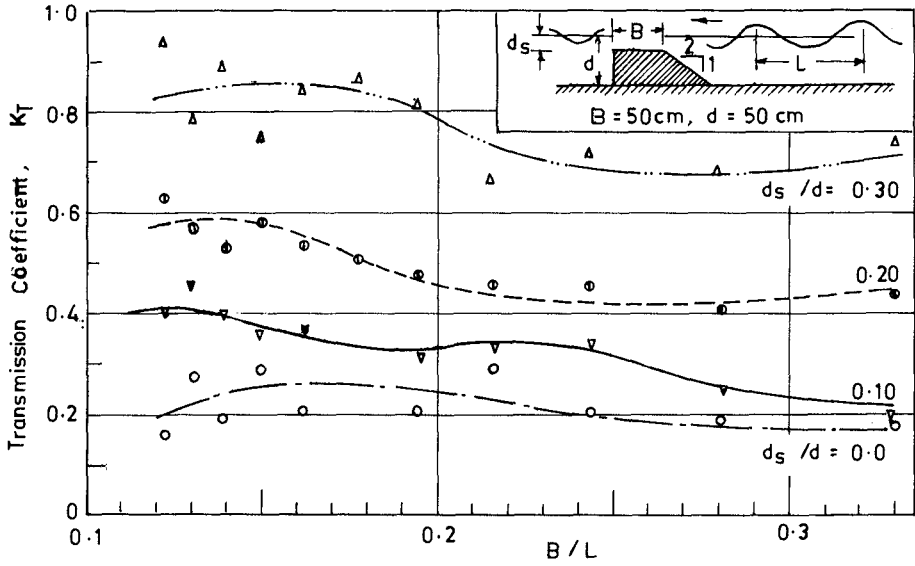


FIG. 7 PERFORMANCE CHARACTERISTICS OF TRAPEZOIDAL IMPERMEABLE SUBMERGED BREAKWATER.

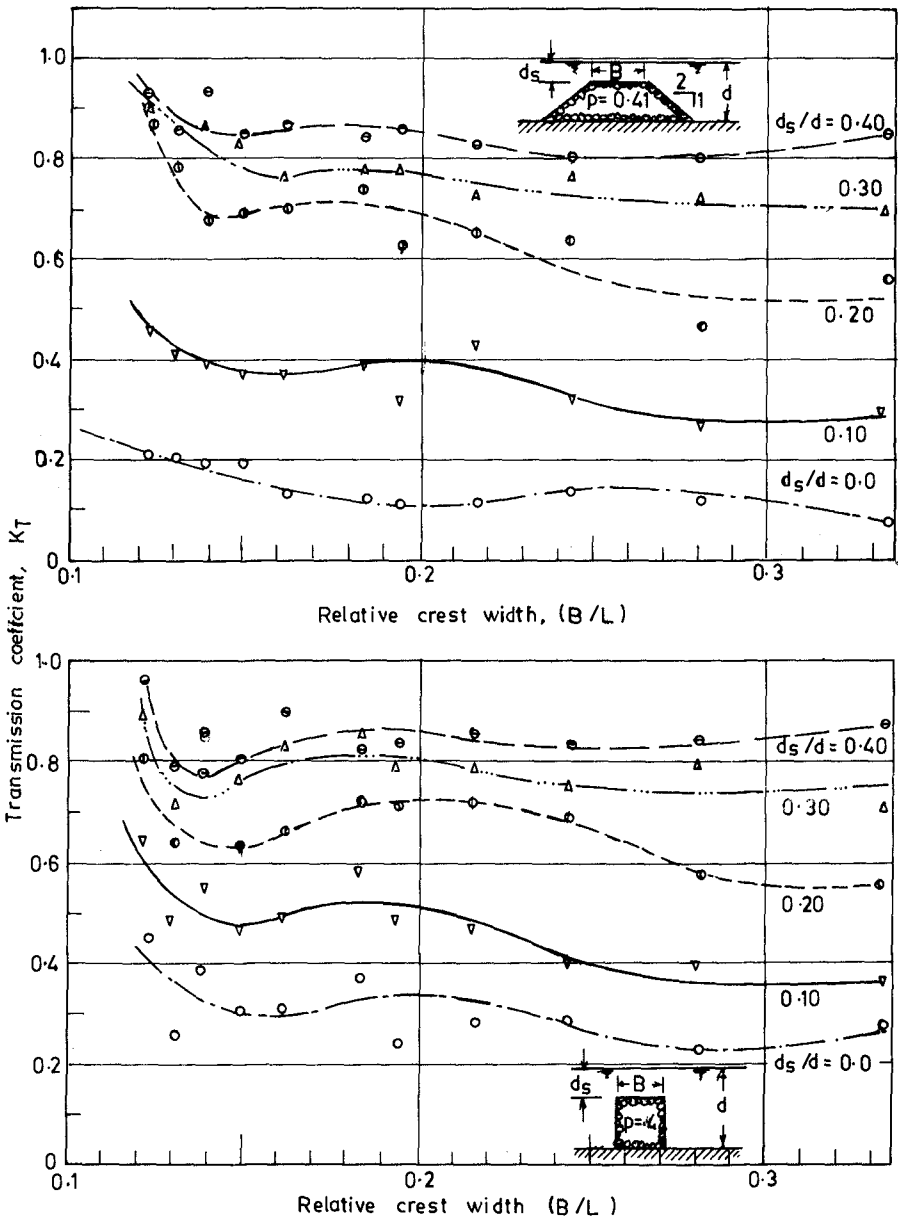


FIG. 8 PERFORMANCE CHARACTERISTICS OF PERMEABLE SUBMERGED BREAKWATERS.

crest width and the depth of crest submergence. Permeability does not have significant influence, particularly for large depths of crest submergence. The shape of the breakwater has significant influence on the reflection characteristics only. The ideal shape appears to be one with the sea face sloping and the beach face vertical. The transmitted wave has the same period as the incident wave, but for cases with the crest of the breakwater near the still water level, higher harmonics are generated.

The performance characteristics of the submerged breakwaters can be represented in the form of design charts with the relative crest width and the relative depth of crest submergence as the significant parameters. These curves show remarkable similarity for the different types studied.

REFERENCES

- 1) Dattatri, J., 'Analysis of Regular and Irregular Waves and Performance characteristics of Submerged Breakwaters', Ph.D. thesis, Hydraulic Engineering Laboratory, Indian Institute of Technology, Madras, India, Jan.1978.
- 2) Dick, T.M., and Brebner, A., 'Solid and Permeable Submerged Breakwaters', Proc. 11th Int. Coastal Eng. Con., 1968, pp. 1141-1158.
- 3) Goda, Y., Takeda, H., and Moriya, Y., 'Laboratory Investigations on Wave Transmission over Breakwaters', Report No.13, Port and Harbour Res. Inst., Yokosuka, Japan, 1967.
- 4) Johnson, J.W., Fuchs, R.A., and Morison, J.B., 'The Damping Action of Submerged Breakwaters', Trans. AGU, 32(5), 1951, pp. 704-718.
- 5) Kabelac, O.W., 'Model Tests of Coastal Protective structures in USSR', Jl. Waterways Div., ASCE, 89(1), 1963, pp.21-34.

COMBINATION EFFECT OF PNEUMATIC BREAKWATER AND OTHER TYPE BREAKWATER ON WAVE DAMPING

by

Yuichi Iwagaki,^{*} Toshiyuki Asano,^{**} Tsutomu Honda^{***}

ABSTRACT

This paper deals experimentally with combinations of the pneumatic breakwater and other type breakwaters in order to increase the effectiveness of wave damping.

Firstly, a submerged breakwater is picked up, and the wave damping effect of this combined type breakwater is examined. Results obtained in this experiment show that some improvements on the wave damping are found for low frequency waves that cannot be damped by the pneumatic breakwater only. The reason of appearance of the combination effect is explained that a part of energy of the transmitted waves over the submerged breakwater transfers to shorter period waves.

Secondly, a floating breakwater is combined with the pneumatic breakwater. Experiments show that the transmission factor for high frequency waves becomes smaller than that of the pneumatic breakwater only, while there is not so much wave damping effect for low frequency waves even when the floating breakwater is combined. In addition, a guide plate is set below the bottom of the floating breakwater in order to increase the horizontal flow velocity for a given air discharge. It is found that the velocity of horizontal surface flow by using the guide plate increases as much as about 1.3 times that in the case of the pneumatic breakwater only. As a result, a little improvement on the wave damping due to the guide plate is also found.

INTRODUCTION

The pneumatic breakwater is one of mobile breakwaters, so it has several specific characters of the mobile breakwater such as mobility, temporality, cheapness, etc. Besides these, it is pointed out as a special merit of the pneumatic breakwater from environmental point of view not to interrupt the exchange of water in harbors and facilities of air discharge are placed on the sea bottom.

However, existing studies on the pneumatic breakwater have clarified its defect that the effectiveness of wave damping suddenly disappears when the wave period becomes longer than a certain period. This property prevents it from practical use.

The horizontal flow velocity, which is strongly related to the wave damping, generated by the air bubble curtain, is proportional to $1/3$ power of the air discharge, so it is not expected to increase the horizontal flow velocity by increasing the air discharge.

In the present paper, in order to increase the damping effect, an attempt that other type breakwaters are combined with the pneumatic breakwater is carried out. The submerged breakwater and the floating breakwater are picked up as combined breakwaters.

^{*}Professor, ^{**}Research Assistant, Dept. of Civil Engineering, Faculty of Engineering, Kyoto University

^{***}Engineer, Kumagayagumi, Construction Co.

DAMPING CHARACTERISTICS OF PNEUMATIC BREAKWATER ONLY¹⁾Experimental apparatus and procedure

A wave tank used for the test was 27m long, 0.5m wide and 0.7m deep. The power of a compressor used was 5.5kW, and the maximum pressure was 7kg/cm². A pressure regulator was installed for reducing the pressure and keeping it constant. A pipe for discharging air set on the bottom was 47.5cm long and 1 inch in diameter. Nozzle holes of the pipe were 1mm in diameter and opened 6mm interval.

Experimental results

At first, characteristics of wave damping for monochromatic waves were examined. The result is shown in Fig.1. The transmission factor HT/HI (HT : transmitted wave height and HI : incident wave height) suddenly decreases with increase in the frequency of incident waves. A critical frequency, which is defined as the frequency of which waves are damped almost completely, shifts to lower frequency as the air discharge increases.

Secondly, experiments for random waves were carried out. The energy spectra of incident waves and transmitted waves are shown in Fig.2 as an example. As the air discharge increases, the power of the spectrum of transmitted waves decreases. This figure also shows that the powers of them increase reversely for the waves around 2Hz. This reason is considered that the air bubble curtain flow generates some disturbance of which frequency is around 2Hz on the water surface. The value of transmission factor for random waves shows close agreement with that for monochromatic waves, so it is concluded that the pneumatic breakwater has same characteristics for both waves.

COMBINATION WITH SUBMERGED BREAKWATER²⁾Experimental apparatus and procedure

A schematic view of experimental apparatuses is shown in Fig.3. The wave tank is the same as described previously. In the experiment, the following four models were provided as submerged breakwaters.

- 1) impermeable type and smooth surface
- 2) impermeable type and with roughness on the upper surface
- 3) permeable type and made of stellersheet
- 4) permeable type and made of ripraps

The impermeable type submerged breakwaters were made of vinyl chloride and anchors were put in it not to be swayed by the wave motion. The roughness were made of glass sticks of 10mm in diameter and placed on the upper surface at 30mm interval. The void ratio of stellersheet and ripraps, which were used as the materials of the permeable type submerged breakwater, were 98% and 45% respectively. The diameter of ripraps was about 30 ~ 60mm. The height of the submerged breakwater, Sh , was changed 30cm, 35cm, 40cm and 45cm for the impermeable type, 30cm, 35cm and 40cm for the permeable type. Only for the impermeable and 30cm high model, the width Sw was changed 20cm, 40cm and 60cm, and for others

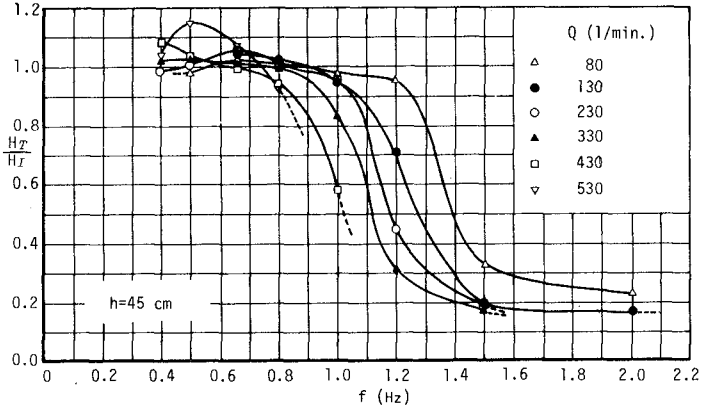


Fig.1 Relation between transmission factor of pneumatic breakwater and frequency of incident waves

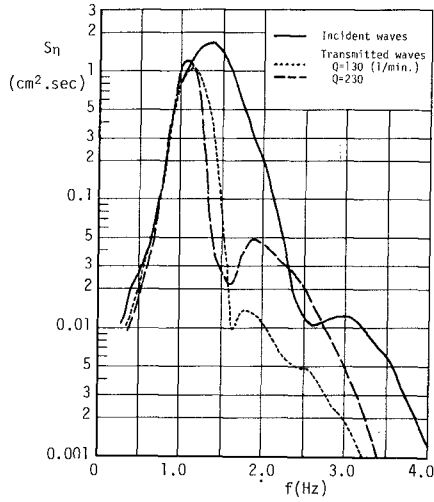


Fig.2 Damping effect of pneumatic breakwater for random waves

always $S_w=20\text{cm}$.

Experiments on the damping characteristics of the submerged breakwaters were carried out for monochromatic waves of $4\text{cm} \sim 6\text{cm}$ in height and $0.4\text{Hz} \sim 1.6\text{Hz}$ in frequency. The submerged breakwater was placed at the location where its front face was as far as 13m from the wave generator. Three wave gauges of electric resistance type were installed as shown in Fig.3. The first gauge was for incident waves, and other two were for transmitted waves. The reason why two gauges were installed was to examine the change of the transmission factor with measuring points.

Experiments of the submerged breakwater combined with the pneumatic breakwater were carried out for incident waves having the same characteristics as those used in the previous experiment. The air discharge was kept always constant 300 l/min , and this discharge corresponds to 7.09 l/sec.m under the condition of 0°C temperature and the atmospheric pressure.

Changing the distance between the air nozzle pipe and the submerged breakwater to $0\text{cm}, 45\text{cm}, 90\text{cm}, 135\text{cm}$ and 180cm onshore and offshore sides respectively, the most advantageous arrangement was investigated. The experiment on the wave damping was carried out under this arrangement.

Damping effect of submerged breakwater

The purpose of this study is to examine the combination effect, so the damping effect of the submerged breakwater is not concerned with this purpose directly. But the combination effect cannot be discussed unless the damping effect of an individual breakwater is clarified. The experimental results on the transmission factor of several kinds of submerged breakwaters are shown in Fig.4. The variation of the transmission factor H_T/H_I with the height of submerged breakwaters S_h , and with the kind of materials are presented herein. The transmission factor decreases with increase of the height for the same type submerged breakwater, and becomes smaller in the order of the impermeable type of smooth surface, the impermeable type of rough surface, the permeable type made of ripraps and the permeable type made of stellersheet.

However, the most effective submerged breakwater on the wave damping is not always the most effective one for the combination type breakwater. It is assumed that the combination effect is caused by the energy transfer to shorter period waves which can be damped by the pneumatic breakwater. If this assumption is right, a submerged breakwater which can transfer more part of energy of transmitted waves to shorter period waves is the most effective as the combination type breakwater. From this point of view, it becomes important to investigate the characteristics of transmitted waves over the submerged breakwater.

Fig.5 shows the comparison of the transmitted wave amplitude spectrum over the submerged breakwater with the incident wave amplitude spectrum. In this case, the wave frequency is 0.4Hz , and the submerged breakwater is impermeable, 40cm high and 20cm wide. It is found that the wave height at the fundamental peak frequency f_p , which corresponds to that of the incident monochromatic waves, decreases about 2cm , while the wave heights at the double and tripple frequencies of f_p increase conversely.

Fig.6 shows the amplitude spectra of incident and transmitted waves

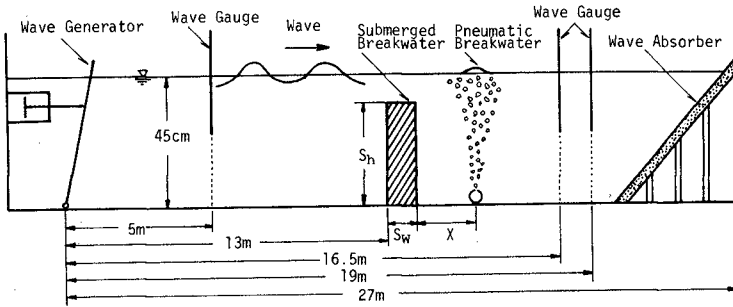


Fig.3 Experimental apparatus when submerged breakwater is combined with pneumatic breakwater

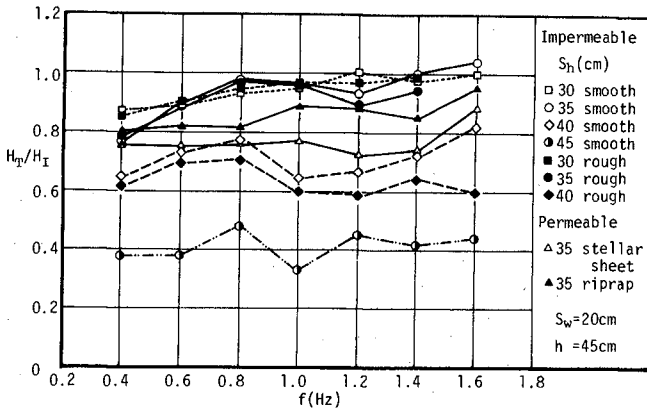


Fig.4 Relation between transmission factors of impermeable and permeable submerged breakwaters and frequency of incident waves

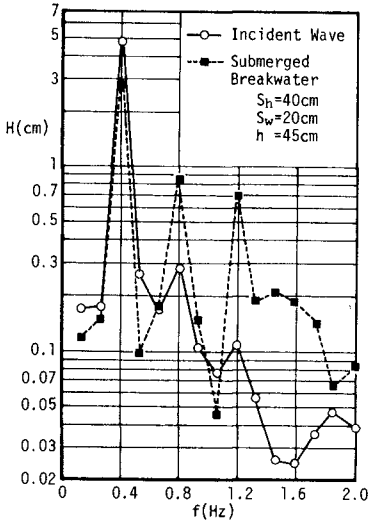


Fig.5 Comparison of amplitude spectra of transmitted waves over submerged breakwater and incident waves

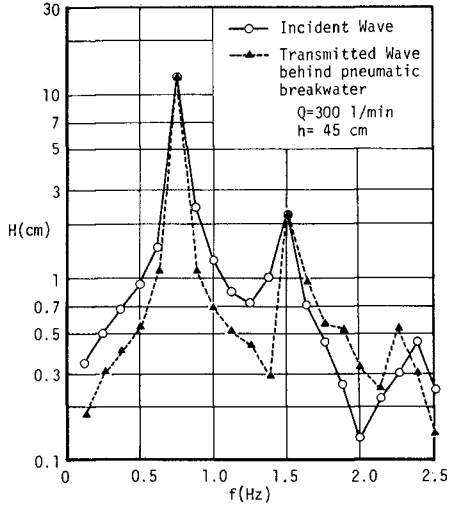


Fig.6 Comparison of amplitude spectra of transmitted waves through pneumatic breakwater and incident waves of finite amplitude with frequency of 0.77Hz

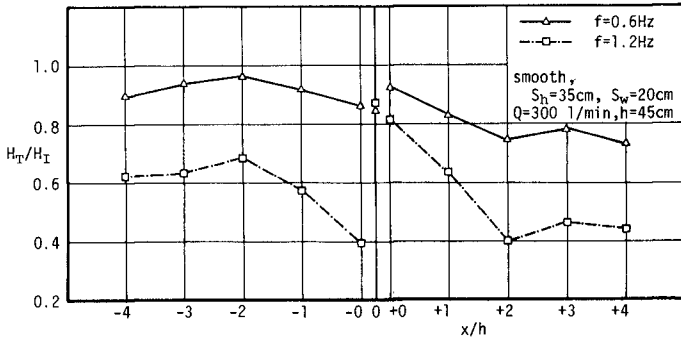


Fig.7 Variation of transmission factor with location of air nozzle pipe

through the pneumatic breakwater when incident waves are of finite amplitude and the frequency of 0.77Hz. It is found that the second harmonic component waves are not damped at all. That means that the pneumatic breakwater is not capable of damping bound waves of the second and third harmonics, even if their frequencies are in the region where the pneumatic breakwater is effective to wave damping. Therefore, it becomes important to clarify whether waves of the second and the third harmonics generated by passing over the submerged breakwater are free waves or bound waves.

A phase lag of component waves $\Delta\theta$ is obtained experimentally by calculating the phase spectrum from water surface variations measured at two points simultaneously. While a theoretical phase lag is calculated from the distance between recording points l and the wave length of component waves Lc , as follows

$$\Delta\theta = 2\pi l / Lc \quad (1)$$

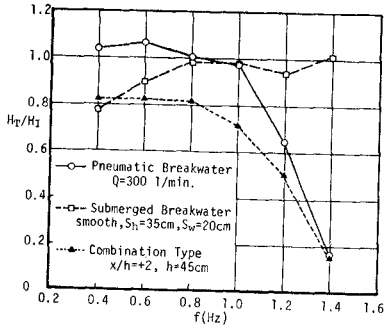
The comparison of the experimental phase lag with the theoretical one is shown in Table 1. Frequencies of waves used in this consideration are 0.586Hz and 0.781Hz. For free waves, the wave length Lc is calculated by the small amplitude wave theory, while for bound waves of the second harmonics Lc is assumed to be half of the wave length of fundamental component waves. The submerged breakwater used here is impermeable, smooth, 35cm and 40cm high and 20cm wide. The results of Cases 5, 7 and 8 show that experimental values of the phase lag of the second harmonic component waves agree well with theoretical results of free waves. Therefore, it is reasonable to conclude that these waves generated by passing over the submerged breakwater are free waves.

Advantageous arrangement of pneumatic breakwater and submerged breakwater

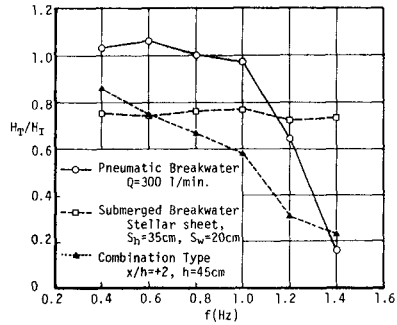
Fig. 7 shows the variation of the transmission factor with a location of the air nozzle pipe. The abscissa is the ratio of the distance between the air nozzle pipe and the submerged breakwater to the water depth, x/h , and the positive sign denotes the case when the air nozzle pipe is located onshore side. The submerged breakwater is in the section between $x/h = -0$, and $x/h = +0$. This figure shows the locations where the damping effect is remarkable are at $x/h \geq 2$ in the case when $f = 0.6\text{Hz}$, and at $x/h = -0$ and $x/h \geq 2$ in the case when $f = 1.2\text{Hz}$. From the results of two cases, the most advantageous arrangement is where the air nozzle pipe is located onshore side of the submerged breakwater apart more than twice the water depth. Accordingly, the location of the air nozzle pipe is determined to be at $x/h = 2$ in the following experiment.

Damping effect of pneumatic and submerged breakwater

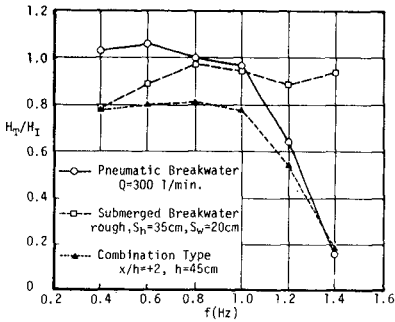
The wave damping effect of the combination type breakwater is examined by changing the size and material of the submerged breakwater. The results are shown in Fig. 8. The transmission factor of the combination type breakwater decreases compared with those of the pneumatic breakwater only and of the submerged breakwater only. That is, for low frequency waves which cannot be damped by the pneumatic breakwater only, it decreases to some extent. But from the results in Fig. 8, it is impossible to decide whether the combination effect exists or not. Therefore, the



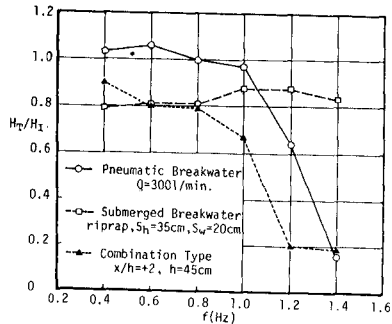
(1)



(3)



(2)



(4)

Fig.8 Transmission factors of pneumatic breakwater only, submerged breakwater only and combined breakwater

- (1) Impermeable type and smooth surface
- (2) Impermeable type and rough upper surface
- (3) Permeable type and made of stellarsheet
- (4) Permeable type and made of riprap

following equation is proposed as a quantitative expression of the combination effect:

$$ES = \left(\frac{HT}{HI}\right)_S \left(\frac{HT}{HI}\right)_P - \left(\frac{HT}{HI}\right)_{S+P} \quad (2)$$

in which $(HT/HI)_S$ and $(HT/HI)_P$ denote the transmission factors of submerged and pneumatic breakwaters only respectively. If the phenomenon is represented as a linear problem, the transmission factor of the combination type breakwater $(HT/HI)_{S+P}$ can be estimated as the product of each one. Consequently, the value of ES , which is the difference between the above mentioned product and the value of $(HT/HI)_{S+P}$, denotes the combination effect.

Fig.9 shows the transmission factors and the combination effects calculated by Eq.(2) for several kinds of combination type breakwaters. It is found from Figs.9 (a) and (b) that both the damping effect and the combination effect become remarkable as the height of the submerged breakwater increases. With regard to the width of the submerged breakwater, there is not so much difference of the damping effect as shown in Fig.9 (c). But in the case when $S_w=60\text{cm}$ the curve of combination effect has a clear peak at the frequency of 0.6Hz. This phenomenon may be concerned with the effect of the width of the submerged breakwater on wave energy transfer to higher frequency waves. Fig.9 (d) shows the comparison between the effects by the materials constructing the submerged breakwaters.

It is concluded that the permeable type breakwater, especially made of stellersheet, is more effective on the damping effect than the impermeable type breakwater, but with regard to the combination effect, the impermeable type is more predominant than that of the permeable type.

In each case, it is found that existance of the combination effect is limited in the region of the frequency from 0.5Hz to 1.4Hz. The reason why the combination effect does not appear in the region $f < 0.5\text{Hz}$ is that the double frequency 1.0Hz of incident waves is a critical frequency for wave damping of the pneumatic breakwater. On the other hand, when $f > 1.4\text{Hz}$, the combination effect also becomes negative because higher frequency waves are damped sufficiently by the pneumatic breakwater only.

COMBINATION WITH FLOATING BREAKWATER³⁾

Experimental apparatus and procedure

A schematic view of the experimental apparatus is shown in Fig.10. Floating bodies used as floating breakwaters were made of Lucite board, and 30 ~ 90cm long, 48cm wide and 10cm high. The floating body was supported by anchor ropes which were $\sqrt{3}$ times as long as the water depth. A guide plate was set below the bottom of the floating breakwater as shown in Fig.11 to guide the horizontal surface flow in the opposite direction to wave propagation. The figure shows two ways of setting the guide plate. In the following, the guide plate shown in Fig.11(a) is named a vertical guide plate, and the other plate shown in Fig.11 (b) is named an inclined guide plate. The vertical guide plate was placed at the position dividing the length of the floating body into the ratio of 7:3, and the length of the vertical plate was 9cm. The angle of inclination

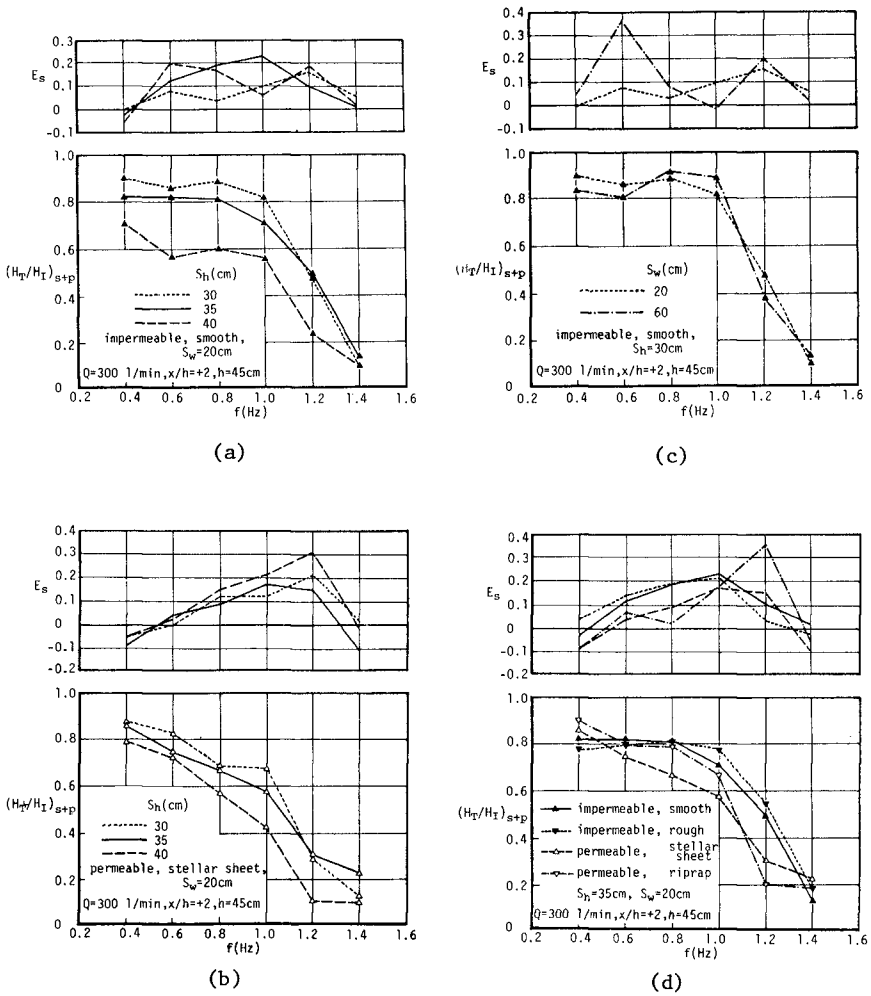


Fig.9 Combination effect and transmission factor of combination type breakwater

- (a) Effect of height of submerged breakwater
(Impermeable type, smooth surface)
- (b) Effect of height of submerged breakwater
(Permeable type, made of stellarsheet)
- (c) Effect of width of submerged breakwater
(Impermeable type, smooth surface)
- (d) Effect of materials constructing submerged breakwater

Table 1 Phase lag of component waves

Case	f(Hz)	Wave	Freq.Compo.	Sh (m)	Experimental $\Delta\theta$ (rad)	Theoretical $\Delta\theta$ (rad)	
						Free Waves	Bound Waves
1	0.586	Transmitted	fundamental	0.35	1.04	0.985	—
2	0.781	Incident	fundamental	—	1.46	1.44	—
3	0.781	Transmitted	fundamental	0.35	1.50	1.44	—
4	0.781	Transmitted	fundamental	0.40	1.43	1.44	—
5	1.17	Transmitted	double	0.35	2.94	2.83	1.97
6	1.56	Incident	double	—	2.94	4.89	2.87
7	1.56	Transmitted	double	0.35	4.91	4.89	2.87
8	1.56	Transmitted	double	0.40	4.78	4.89	2.87

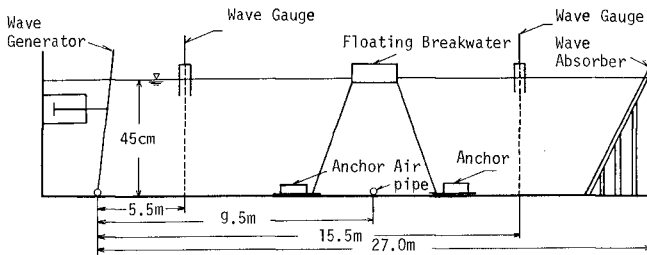


Fig.10 Experimental apparatus when floating breakwater is combined with pneumatic breakwater

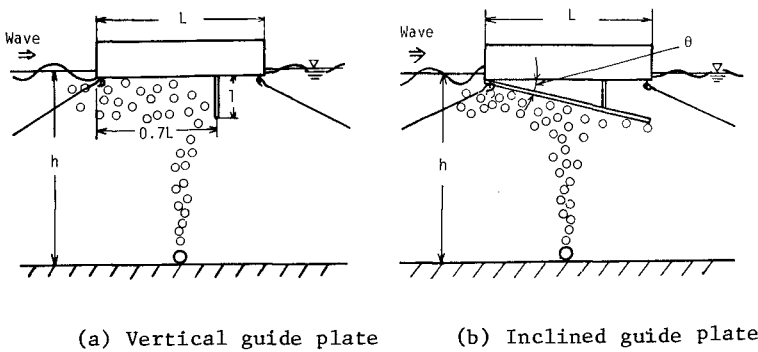


Fig.11 Setting ways of guide plate

of the inclined guide plate to the bottom of the floating body was kept constant 12° .

The water depth was 45cm, and the air discharge was 400 l/min throughout the experiments. This discharge corresponds to 15.15 l/sec.m under the condition of 0°C and the atmospheric pressure. Measurement of the horizontal flow velocity was carried out by a propeller type current meter of 18mm in diameter.

The draught depth of the floating body and the tension of anchor ropes are considered to affect significantly the transmission factor of the floating breakwater. Therefore, the draught depth was kept constant 2.5cm for the floating bodies which were 30cm, 45cm and 60cm long, and 2.0cm for ones which were 75cm and 90cm long. The tension was not measured, but the experiment was made to keep the tension nearly constant.

Characteristics of horizontal surface flow velocity

Experiments were carried out in the following four cases:

Case-1 The pneumatic breakwater was used only.

Case-2 The floating breakwater without a guide plate was combined with the pneumatic breakwater.

Case-3 The floating breakwater with a vertical guide plate was combined.

Case-4 The floating breakwater with an inclined guide plate was combined.

Some examples of the velocity profile of the horizontal surface flow are presented in Fig.12. In this case, the velocity was measured at the section horizontally from the air nozzle pipe the same distance as the water depth. The length of the floating breakwater was 45cm. It is found that the velocity of the horizontal surface flow in the case of combination with the floating breakwater, especially with the vertical guide plate, increases as much as about 1.3 times that in the case of the pneumatic breakwater only. Regarding the thickness of the horizontal surface flow, the results in Case-2 and Case-4 show a little decrease of the velocity compared with Case-1 of the pneumatic breakwater only.

Damping effect of pneumatic and floating breakwater

At first, in the case of combination with the floating breakwater without a guide plate, the damping effect was examined. Fig.13 shows transmission factors in cases of the pneumatic breakwater only, the floating breakwater only and the combination of both breakwaters. Both the pneumatic and floating breakwaters have similar characteristics to be effective for the waves of higher frequency than a certain frequency. This characteristics remains same when both breakwaters are combined, but for the waves of higher frequency than a certain frequency the transmission factor becomes smaller than that in the case of simple use.

Change of the transmission factor with the length of the floating body is shown in Fig.14. The transmission factor of the floating breakwater only decreases a little as its length becomes longer. While, this tendency is not clear when the floating breakwater is combined with the pneumatic breakwater. This phenomenon is explained from the observation as follows. Incident waves increase in their height due to the horizontal

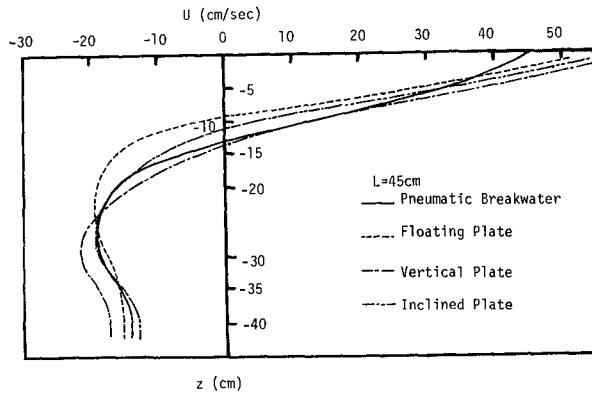


Fig.12 Velocity profiles of horizontal surface flow

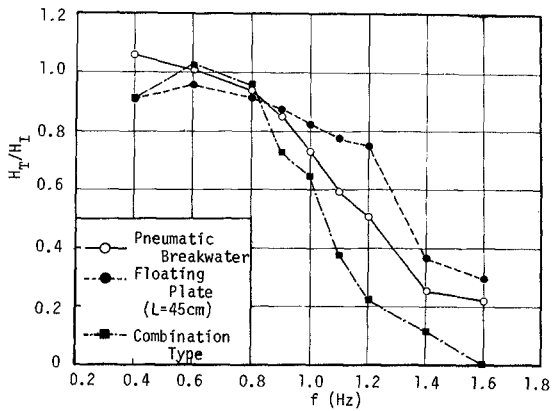
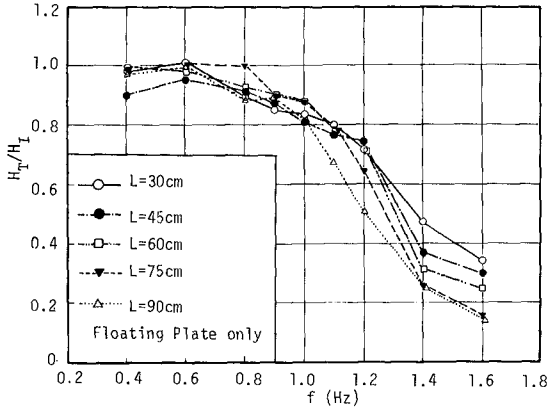
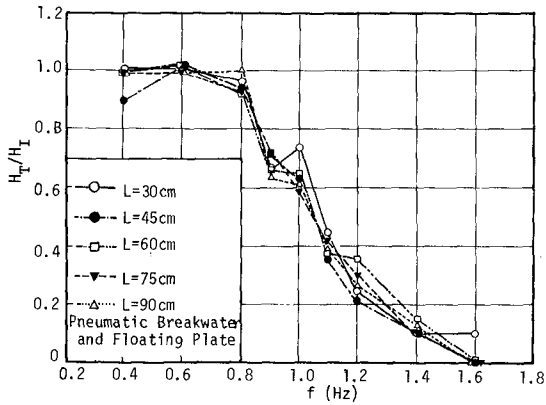


Fig.13 Transmission factors of pneumatic breakwater only, floating breakwater only and combined breakwater



(a)



(b)

Fig.14 Effect of length of floating body on transmission factor

- (a) Floating body only
- (b) Combination type breakwater

surface flow in the opposite direction, and wave energy is dissipated when waves clash in front of the floating breakwater. This result is rather convenient in practical use of the combination type breakwater, because it is not necessary to lengthen the floating breakwater.

Fig.15 shows the comparison of the transmission factors between the combination type breakwaters without the guide plate and with the guide plate, and between with the vertical guide plate and with the inclined guide plate. It is shown clearly that the transmission factor decreases when the guide plate is placed, but there is not so much difference between using the vertical guide plate and the inclined one.

The variation of the transmission factor with the method of supporting is examined by changing the anchor support into the fixed support. The length of the floating body used was changed 30cm, 60cm and 90cm. Fig.16 (a) is the case of the floating breakwater only and (b) is the case of the combination type breakwater. A considerable improvement on the wave damping effect is achieved by changing the anchor support into the fixed support. It is also shown that the waves of higher frequency than 1.2Hz are damped almost completely when the fixed support floating breakwater is combined.

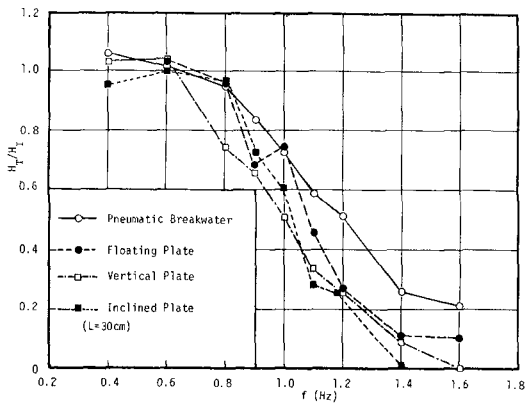
In the field, it is difficult to fix the floating breakwater, but it may be possible for the anchor support to make the damping effect strong as much as the fixed support by devising effective arrangement of the anchor ropes and making the spring constant of the anchor rope larger.

CONCLUSION

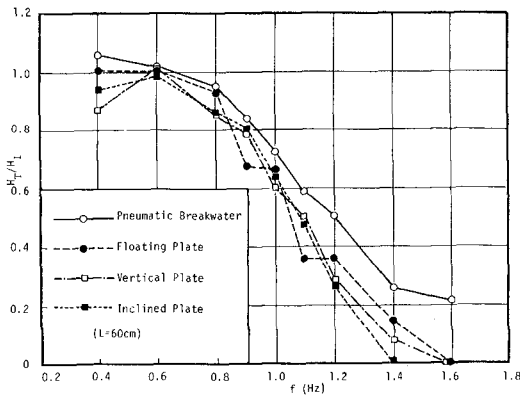
In the present paper, the improvement on the damping effect of waves by combining the submerged or the floating breakwater with the pneumatic breakwater has been investigated experimentally.

Main conclusions are as follows:

- 1) The combination type breakwater of the submerged and the pneumatic breakwaters is more effective on the wave damping than each breakwater only. The reason why the combination effect appears is explained as follows. When waves pass over the submerged breakwater, a part of the wave energy transfers to higher frequency waves which can be damped by the pneumatic breakwater. This phenomenon is confirmed by investigating the characteristics of waves passing over the submerged breakwater.
- 2) Four kinds of submerged breakwaters were provided for the tests. The permeable type submerged breakwater made of stellersheet is the most effective on the wave damping. However, concerning the combination effect, the impermeable type submerged breakwater is more effective than the permeable one.
- 3) The floating breakwater has similar characteristics to the pneumatic breakwater, so the weak point of the pneumatic breakwater is not improved at all for low frequency waves by combining the floating breakwater. But, for high frequency waves, the combination type breakwater is more effective than each breakwater only.



(a)

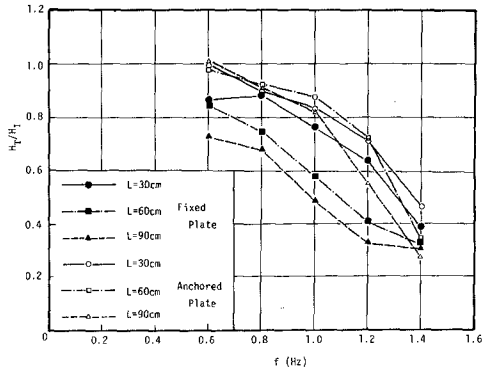


(b)

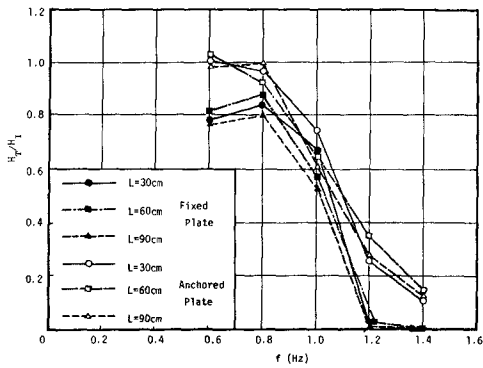
Fig.15 Comparison of transmission factors between combination type breakwaters with and without guide plates, and between with vertical and inclined guide plates (L: length of floating body)

(a) Case when $L=30\text{cm}$

(b) Case when $L=60\text{cm}$



(a)

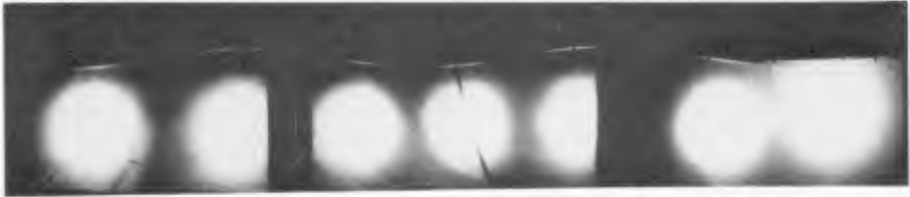


(b)

Fig.16 Effect of supporting method on transmission factor

(a) Floating breakwater only

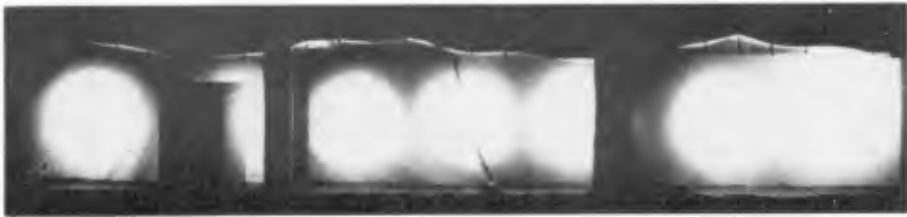
(b) Combination type breakwater



Incident Wave



Transmitted Wave behind Air Curtain



Transmitted Wave behind Submerged Breakwater



Transmitted Wave behind Combination Type Breakwater

Photo.1 Combination of submerged breakwater with pneumatic breakwater (impermeable type and smooth surface)

$f=1.2\text{Hz}$, $Q=300\text{ l/min}$, $h=45\text{cm}$, $Sh=35\text{cm}$, $Sw=20\text{cm}$

- 4) The guide plate was set below the bottom of the floating body to guide the horizontal surface flow in the opposite direction to wave propagation. It is found that the velocity of the horizontal surface flow increases by the guide plate. And the result on wave damping also shows the effectiveness of the guide plate.

ACKNOWLEDGEMENT

The authors would like to acknowledge the assistance of Mr.Y.Sudo and Mr.H.Mase in this experiment. A part of the present investigation was accomplished with the support of the Science Research Fund of the Ministry of Education for which the authors express their appreciation.

REFERENCES

- 1) Iwagaki, Y., and M.Yasui : A study on pneumatic breakwaters (1st report) — Fundamental properties of pneumatic breakwaters —, Proc., 22th Conf. on Coastal Eng. in Japan, pp.563-569, 1975 (in Japanese).
- 2) Iwagaki, Y., H.Ishida, T.Honda and Y.sudo : A study on pneumatic breakwaters (2nd report) — Combination with submerged breakwater —, Proc., 23th Conf. on Coastal Eng. in Japan, pp.158-163, 1976 (in Japanese)
- 3) Iwagaki, Y., T.Asano and H.Mase : A study on pneumatic breakwaters (3rd report) — Combination with floating breakwater —, Proc., 24th Conf. on Coastal Eng. in Japan, pp.290-294, 1977 (in Japanese)

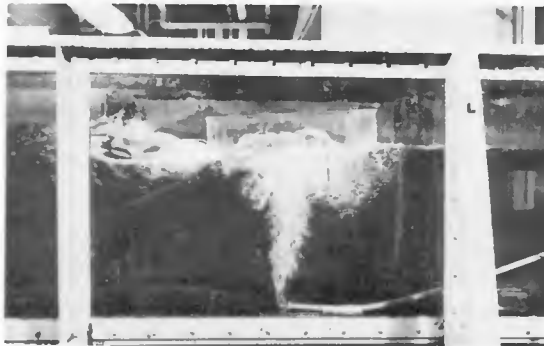


Photo.2 Combination of floating breakwater with vertical guide plate with pneumatic breakwater
 $f=1.2\text{Hz}$, $Q=400$ l/min, $L=45\text{cm}$

CHAPTER 132

SCRAP TYRE BREAKWATERS IN COASTAL ENGINEERING
by ROBERT CHARLES MCGREGOR and NEIL SINCLAIR MILLER*

1. INTRODUCTION

The problem of the protection of shorelines and coastal structures from wave action is one of long standing. More recently it has become necessary to examine the feasibility of providing the same sort of wave attenuation for locations further offshore. Where the need for protection is in shallow water, close to the shoreline, bed-based breakwaters are possible and floating breakwaters may only be desirable on the basis of one or more of the following grounds:

- a) cost,
- b) requirement for protection being of short duration,
- c) reduced interference with currents,
- d) adaptability to changing performance criteria,
- e) poor foundations.

As the water depth becomes larger, the costs of a fixed structure become prohibitive whereas only the anchoring fraction escalates for a floating breakwater.

There is an extensive literature extending from 1842 on the floating breakwater concept. Most of the references, however, are postwar following the wartime stimulation of interest in aid of assault landings. Recent sources of state-of-art information are Kowalski (1974) and Adey (1976). The use of scrap automobile tyres has been discussed by Candle (1974), Kowalski (1974, 1976), Noble (1976) and Harms (1978). Candle was proposing what may be called near rigid mats of tyres where neighbouring tyres move relatively little with respect to one another, whereas the Noble, Harms and Kowalski designs use the breakwater flexibility. In the Kowalski breakwater**, the tyres are formed into groups which are known as modules which allow the breakwater to "breathe" and so dissipate more energy by internal movement as well as making construction easier. Several breakwaters of a fairly simple form have been built using this concept. These have been operational in the U.S.A. for several years and have successfully protected at least one marina through hurricane conditions.

* Department of Naval Architecture and Ocean Engineering,
University of Glasgow, U.K.

** The design of breakwaters which make use of the innovations
of Professor Kowalski is proprietary.

The use of worn tyres in seawater is a safe way of reducing an increasingly important pollution problem. In Britain alone, about 25 million tyres are discarded annually and only a fraction of these are recycled at present. In many other countries, environmental regulations are more restrictive and old tyres become a liability and an eyesore. Tyres are completely non-toxic in seawater and do, in fact, attract marine life. (Tyres have been used as submerged reefs, where they are quickly covered by marine growth, and also as fishing islands, where anglers make use of the tyre's attractiveness to fish, by virtue of providing both a haven and a source of food.) The tyre's geometry is particularly convenient because while it can be constrained to float vertically it is bistable and will, if released, topple over in time and sink without causing any damage or becoming a hazard.

2. BACKGROUND

2.1 CONSTRUCTION

The construction of the Kowalski breakwater is in the form of modules (or groups) of tyres which may be tied together and used as prefabricated blocks in the on-site construction of the breakwater as a whole. The basic unit, which is shown in fig. 1 and 2, comprises of 18 tyres which are tied together so that they float with all tyres in a vertical plane. The air trapped in the crown of each car tyre which floats in this way gives a buoyancy force of about forty newtons (40N) giving a module sufficient buoyancy to support the weight of an average man. The heaving motion of the tyres during wave action is sufficient to allow the replenishment of air in the crowns but in some exceptional circumstances where the trapped air may be dissolved during prolonged calms urethane foam or other buoyancy material may be inserted in a fraction of the tyres. Buoyancy may also be reduced by air leaking from the crowns of lacerated tyres or by the growth of mussel spat or weeds.

The modules are fastened together using a minimum number of ties to permit tyres slight movement relative to each other. The choice of tying material depends on the application, environment and required life of the breakwater. It is possible to use nylon, dacron, polypropylene or stainless steel wire rope or chain, but each suffers from some disadvantage with respect to sea water corrosion or abrasion caused by the constant agitation of the tyres. Wire rope and chain have an additional disadvantage because of the weight involved. Since there is a need for structural integrity the use of reinforced rubber belting secured by nylon bolts is to be preferred for situations where durability over long periods is required.

In order to increase the attenuation of higher waves, a deeper module may be created from the basic one with the addition of six more tyres. The unit is three tyres deep.

Both sets of units may be connected into strings, and later mats, by the use of link tyres. This is shown in fig. 3 and, in the case of the basic modules, allows the breakwater great flexibility. This property is beneficial both in wave energy dissipation (the Cockerell raft wave energy device) and in the sharing of loads throughout the breakwater in heavy seas.

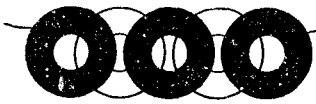


fig 1: Module - Side View

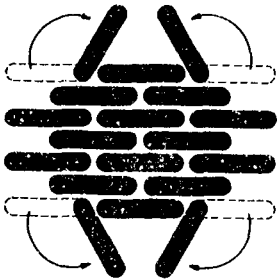


fig 2: Module - Plan View

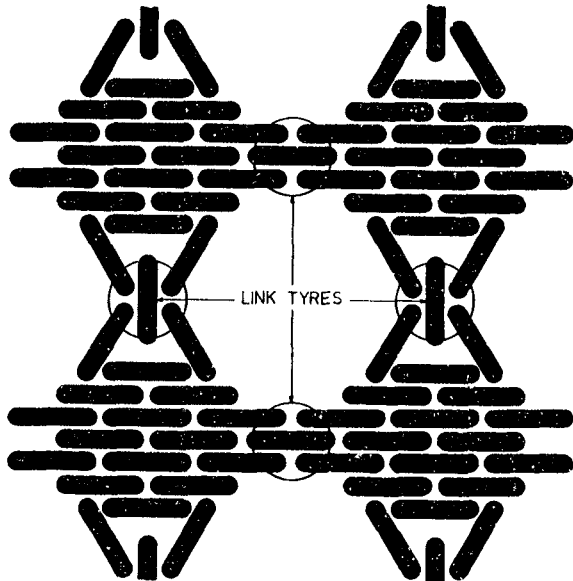


fig 3: Breakwater Mat

2.2 PERFORMANCE

A floating breakwater redistributes the waves energy approaching it in five ways. These are:

- 1) reflections from the forward face(s) of the breakwater,
- 2) dissipation of wave energy within the structure of the breakwater,
- 3) transmission of unsuppressed wave energy,
- 4) diffraction of the waves passing by the ends of the breakwater, into the protected region in the lee of the breakwater, and
- 5) generation of waves by the movement of the breakwater itself on the water behind the breakwater.

Different breakwater concepts give different relative importance to these effects. For example, a fixed concrete breakwater will have nearly total reflection, dissipate only a little as noise and spray, transmit a little by overtopping on occasions and generate none. On the other hand, a tyre breakwater reflects very little energy (depending to some degree on the modules which make up the leading edge), generates a little (depending on the trailing edge), leaving the balance to be shared, between dissipation through its flexibility, internal friction and fluid particle path interference and the unwanted transmission. All breakwaters which terminate at sea will diffract waves in some way and this is frequently an important design consideration since it means that the breakwater shadow zone is encroached on by waves travelling in new directions. These waves may interfere to the detriment of conditions in the protected area.

The measure of performance of a breakwater as a whole must be in terms of energy giving

$$\eta_E = 1 - \frac{\text{energy of waves to leeward}}{\text{energy of incoming waves to seaward}}$$

which is easily calculable in terms of the energy spectra in the two situations. Thus

$$\eta_E = 1 - \left(\frac{H_{SA}}{H_{SF}} \right)^2$$

It is desirable from the design point of view to know the transmission coefficient C_T which in the case of a regular wave train is simply

$$C_T = \frac{H_A}{H_F}$$

In the case of a mixed wave spectrum C_T is given by a ratio of Fourier components averaged from a sufficiently long stationary data record. The transmission coefficient is a function of wavelengths (or frequency since these are uniquely related for water of a given depth).

3. EXPERIMENT

3.1 ARRANGEMENT

The experiments were conducted using 1/4 scale car tyres in the Hydrodynamics Laboratory of the Department of Naval Architecture and Ocean Engineering at Glasgow University. This tank is 77m long, 4.6m wide and 2.4m deep and has a parabolic plunger wavemaker at one end which can be programmed to produce a pseudo-random sea made up nominally of 25 different frequency components with a return cycle of 100 time steps. Wave heights up to 0.4m can be produced.

Twenty-five breakwaters fabricated of basic and deep modules were constructed from the 1,300 tyres available and were tested for wave attenuation and mooring loads. The experimental layout is shown in fig. 4.

Previous breakwater tests (Kowalski 1976) had used several runs at discrete frequencies to analyse a particular breakwater, but on this occasion, because of the large amount of test work to be carried out, a broad spectrum was used and the results for a band of frequencies were analysed simultaneously, using F.F.T.'s. This approach is very efficient for a phenomenon of this type, provided adequate attention is paid to the amplitude errors and the coherence between the two wavetrains. In this experiment, the percentage error, which may be written as

$$\frac{100\%}{\sqrt{N_R N_F}}$$

where N_R is the number of runs and N_F is the number of frequencies averaged, was reduced to about 4%.

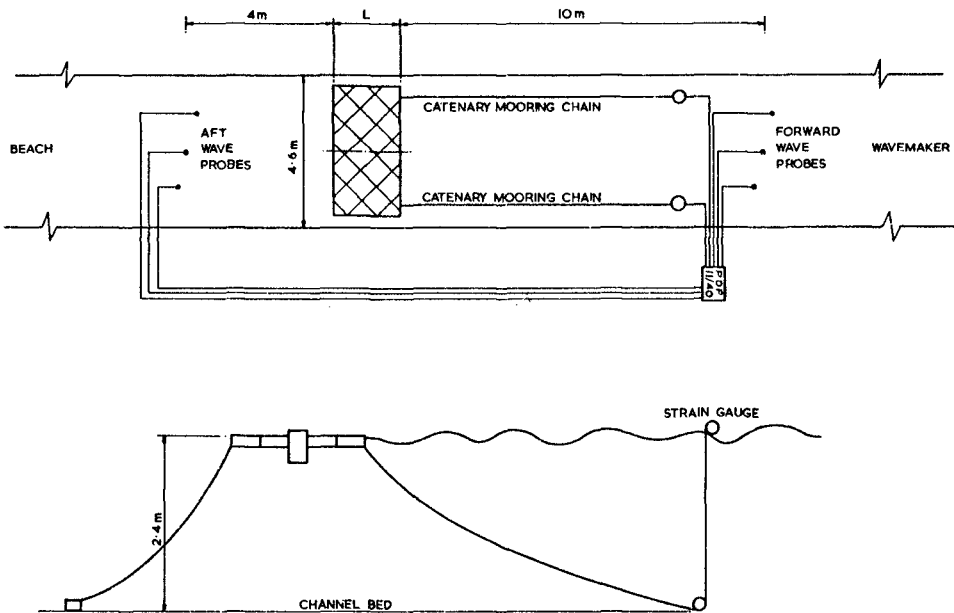


fig 4: Experimental Arrangement

3.2 WAVE PERFORMANCE

The analysis converts the digital record into an incoming wave spectrum $S_F(f)$, a transmitted wave spectrum $S_A(f)$ and a transmission coefficient $C_T(f)$. These are related by

$$[C_T(f)]^2 = \frac{S_A(f)}{S_F(f)}$$

An example of the computer output is shown in fig. 5 with some extra annotation to explain features.

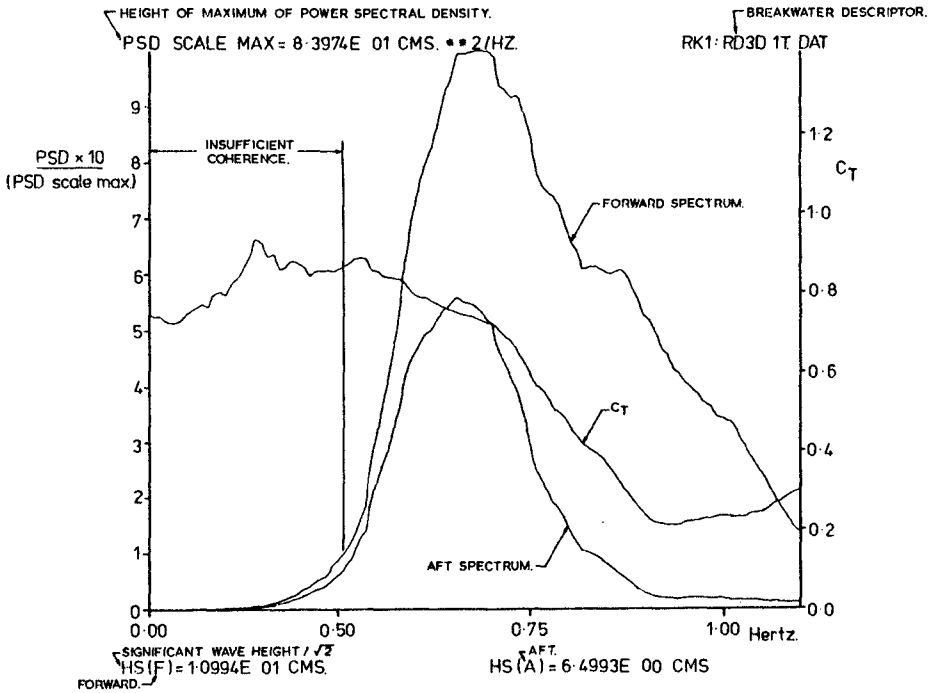


fig 5: Sample of presentation of experimental data as provided by PDP 11/40 Computer

To compare breakwaters it is necessary to use the frequency averaged transmission coefficient, given by

$$\overline{C_T} = \frac{H_{SA}}{H_{SF}} = \left[\frac{\int_0^\infty S_A(f) df}{\int_0^\infty S_F(f) df} \right]^{1/2}$$

plotted against a breakwater length which has been non-dimensionalised by a wavelength which is representative of the incoming wave spectrum $S_F(f)$.

When $\overline{C_T}$ was plotted against a breakwater length which was non-dimensionalised by a wavelength representative of the wave spectrum, then each of the breakwater 'families' (i.e. those made up of basic modules only, those with one row of deep modules, etc.) produced a discrete curve (McGregor (1978)). For the spectra used in the experiments, the curves for breakwater 'families' using single depth modules only was curved indicating that energy was passing under the breakwater whereas the curves for breakwaters incorporating the deeper modules were straight lines. If wave heights had been larger then these breakwaters would also have given curved lines but as it was, the depth of the breakwater was sufficient to impede the passage of the depth distributed energy. When the plot is made against a non-dimensional breakwater area (fig. 6) then the curves merge and a single straight line is an adequate representation. Although this suggests a law of dependence for scrap tyre breakwaters, such a conclusion would be premature in view of the non parallel trends discernable for individual 'families.'

3.3 MOORING LOADS

The mooring forces were analysed into histograms which were then compared with the Rayleigh probability distribution.

$$p(F) = \frac{2F}{E(F^2)} \exp\left[\frac{-F^2}{E(F^2)}\right]$$

where F is the force per cable and $E(F^2)$ is the expectation of F . For situations where the Rayleigh curve is a reasonable representation of the histogram the cumulative probability distribution

$$P(F > F_1) = \exp\left[\frac{-F_1^2}{E(F^2)}\right]$$

allows a predication of extreme forces to be made.

The closeness of the fit between the cable tensions and the Rayleigh distribution with the same expectation is illustrated in fig. 7. In each of the families the probability curve skews further towards the higher values for longer breakwaters. Close

comparison of data with the Rayleigh distribution indicated that the data is below the Rayleigh distribution in the tail. This discrepancy is sufficiently small to permit Rayleigh probability to be used for high force statistics at least in the first instance.

If the experimental spectrum were to persist on a breakwater for which the expectation was $300N^2$ then a total mooring load of 75N (approximately 5 times the mean) would be expected to occur once per year but the load could well exceed 64N daily. These are quite low loads on what would be one of the largest model breakwaters.

Further examination of the mooring indicates an apparent dependence on wetted surface area. This parameter often has significance in ship hydrodynamics and suggests the dominance of skin friction in producing drag forces. Further, it can be seen that the amount of energy dissipation is increased only at the expense of an increase in mooring loads. It is inevitable that some of the work done on the breakwater is transmitted to the moorings and it also demonstrates the value of internal friction in wave attenuation.

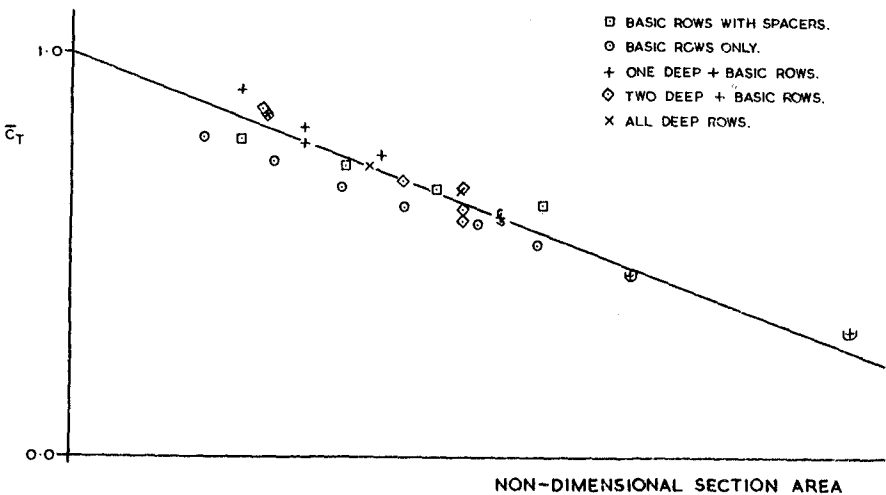


fig 6: Dependence of overall performance coefficient against a non-dimensional side section area (from McGregor 1978)

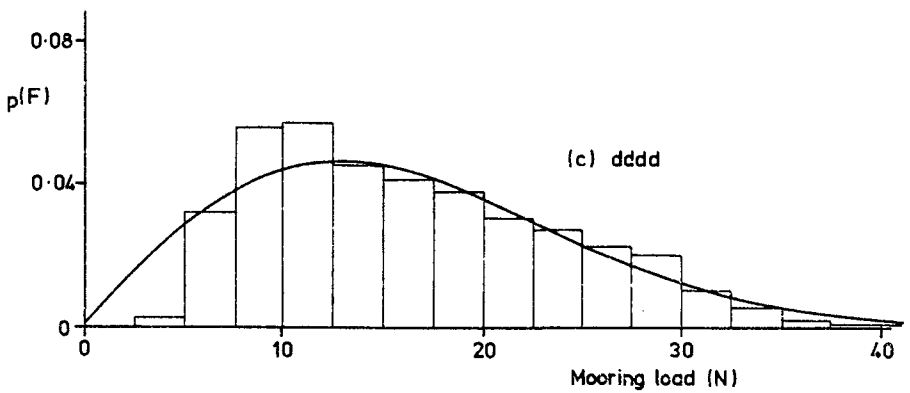
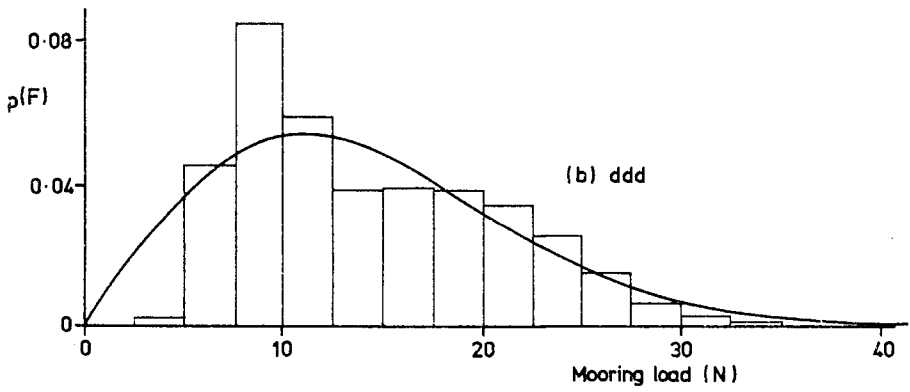
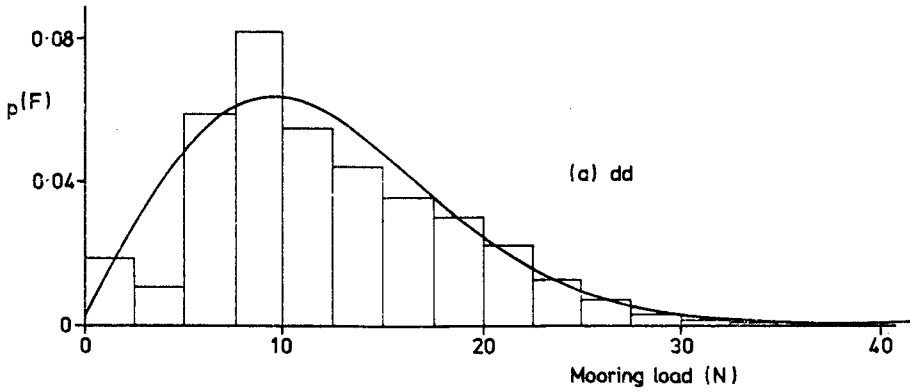


fig 7: Comparison of Mooring Load Histogram with Rayleigh Distribution

4. APPLICATIONS

4.1 RANGE

Tyre breakwaters can be used for a wide variety of applications namely

- a) inshore boat marinas,
- b) harbour entrances,
- c) creating safe natural anchorages,
- d) extending existing berths, quays or permanent breakwaters,
- e) temporary protection for work areas,
- f) fish farms,
- g) offshore operations, diving, pipelaying, pollution control,
- h) shoreline erosion.

Each of these requires that a breakwater should be adapted to the local situation using available information on fetch lengths, sea depths, prevalence of wind speeds and directions, tidal ranges, and currents and sea bed conditions. The application to fish farms is discussed in McGregor (1977). This paper will discuss design studies* relating to (c), (b) and (g).

4.2 CREATION OF SAFE ANCHORAGE ON ISLE OF GIGHA

The location of Gigha relative to other land masses is shown in fig. 8. The island lacks a natural anchorage which is secure from all directions. A site survey indicated that the anchorage which could most easily be rendered safe was a channel of about 60m width running from 10° to 190° on the south east of the island (fig. 9).

The northern end of the channel is dry at low tide and is sufficiently shallow to dissipate wave energy at high tide even if there were no bend to the east which has the effect of greatly reducing the fetch in the most vulnerable direction. The southern end of the channel is open to an arc around south. The fetch along the channel's axis is interrupted by Gigha Island (1000m away) and so the most vulnerable direction is due south. The distance to the nearest land along a line of sight is about 20 MM (Mull of Kintyre) but if the line is taken a few degrees to the west the fetch would double (Northern Ireland). The entrance to this anchorage is just deep enough but it is necessary to detour round a submerged rock which may be thought of as an extension to Sgeir Liath and also to avoid fouling with weed on the western side.

Since the most severe weather in this area is likely to be associated with westerly winds, the design condition was reduced to producing tolerable conditions in a sea corresponding to a wind speed of 23ms^{-1} (wind force 9). The waves, in this case, would have a significant wave height, H_s , of 2.2m (giving $H_{\text{max}} \sim 4\text{m}$)

**The breakwaters described have not been constructed at the time of writing.*

fig 8: Fetches to Gigha (km)

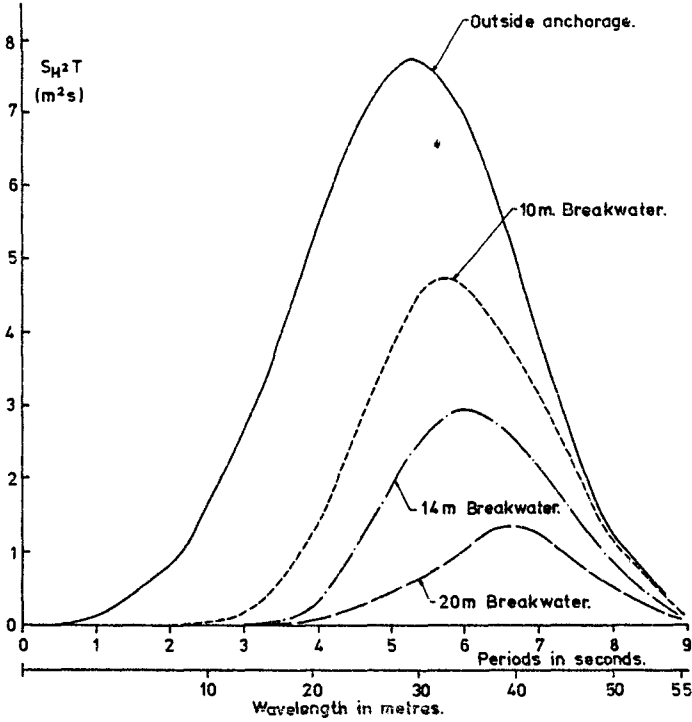
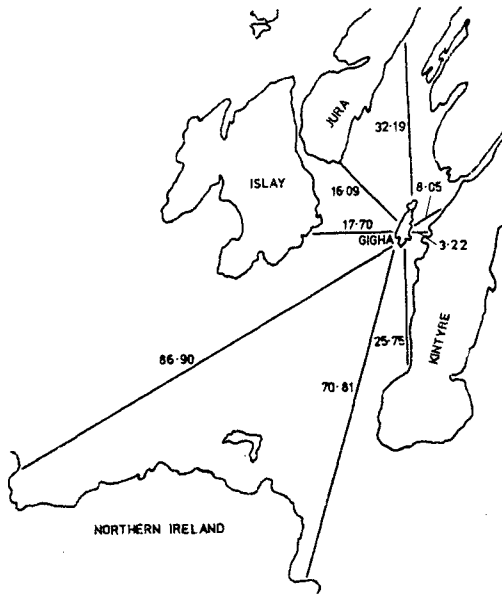


fig 10: Performances for three possible breakwaters at Gigha

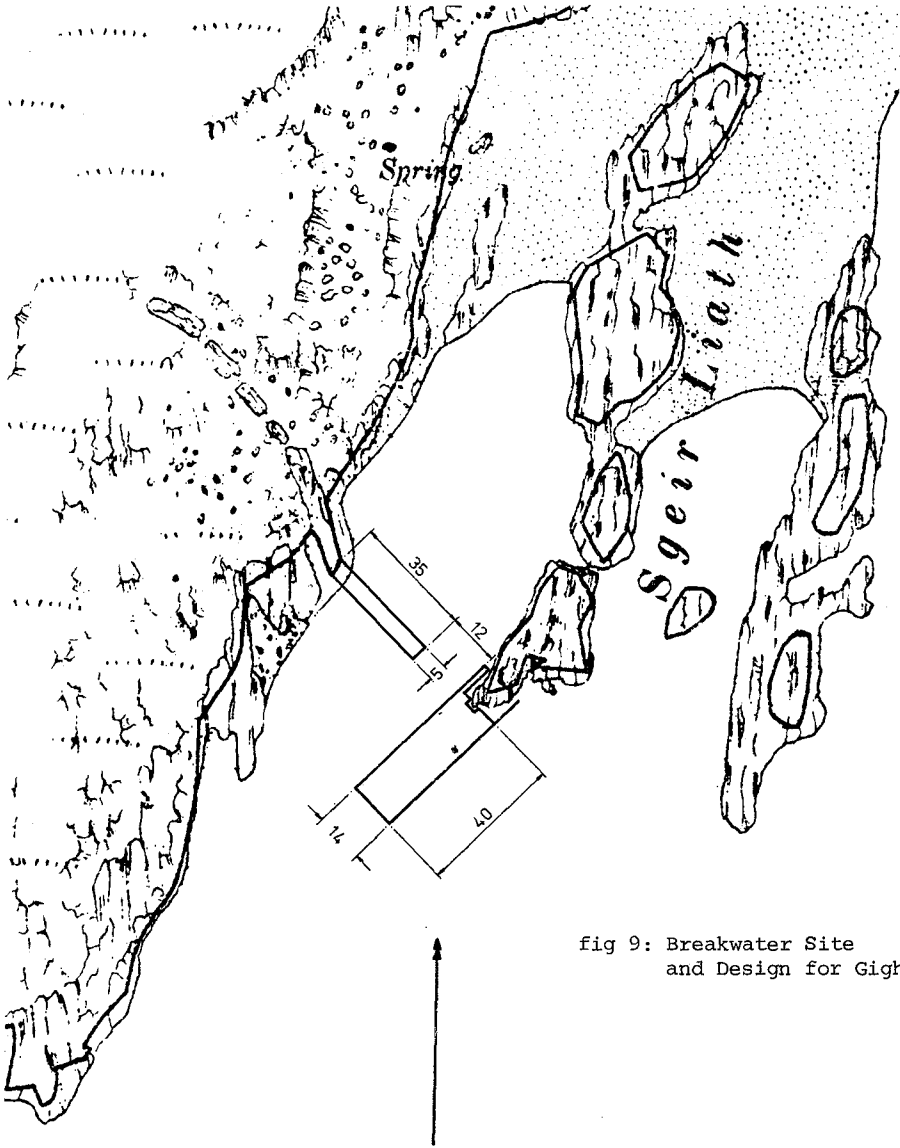
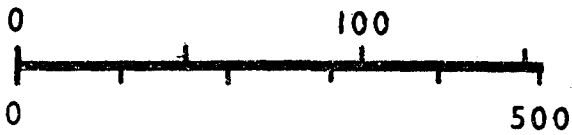


fig 9: Breakwater Site and Design for Gigha



and a significant period, T_s of 5.3s. However, since the channel is shallow and tides are small the wavelengths would be up to about 50m. The energy distribution curve is shown in fig. 10.

The requirement for access limits the breakwater length to about 40m and its width determines its efficiency (see fig. 10). The intermediate breakwater, which consisted of two rows of deep modules and nine rows of basic modules made from car tyres, was predicted to reduce H_s by 50% and would provide adequate protection. This breakwater and a smaller subsidiary one designed to inhibit diffracted and reflected waves are shown in fig. 9.

The maximum mooring load would be below 40 tonnes allowing manageable sizes of anchors to be used.

4.3 IMPROVEMENT OF HARBOUR ENTRANCE CONDITIONS AT WICK

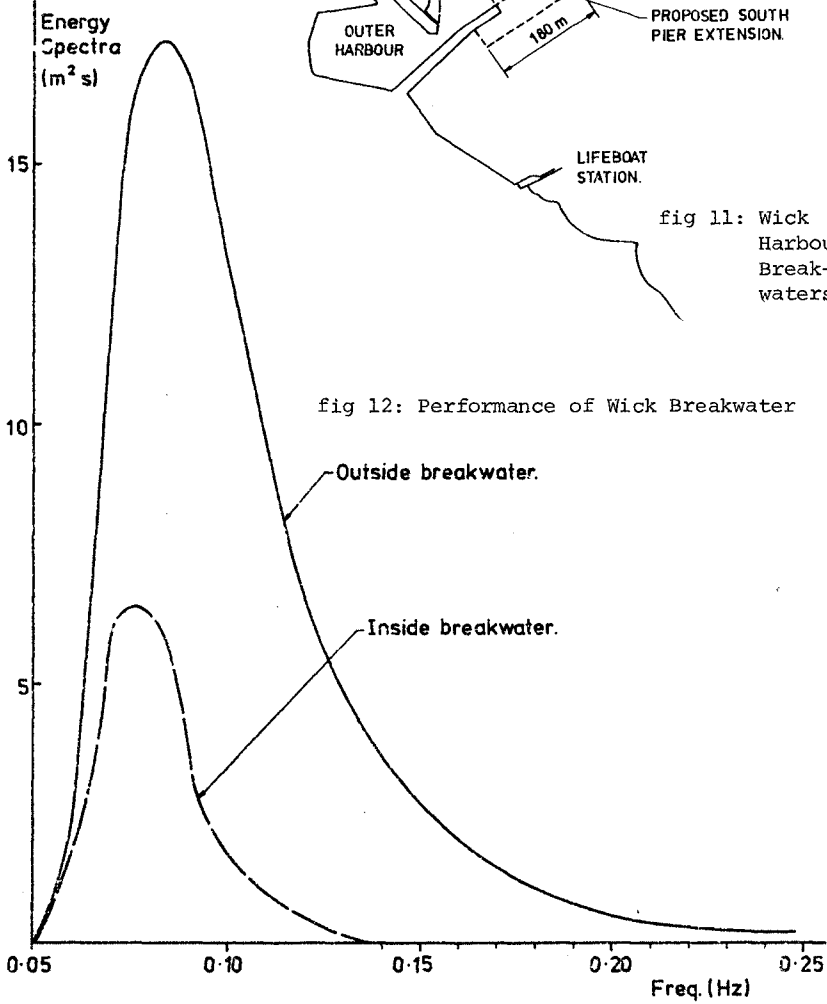
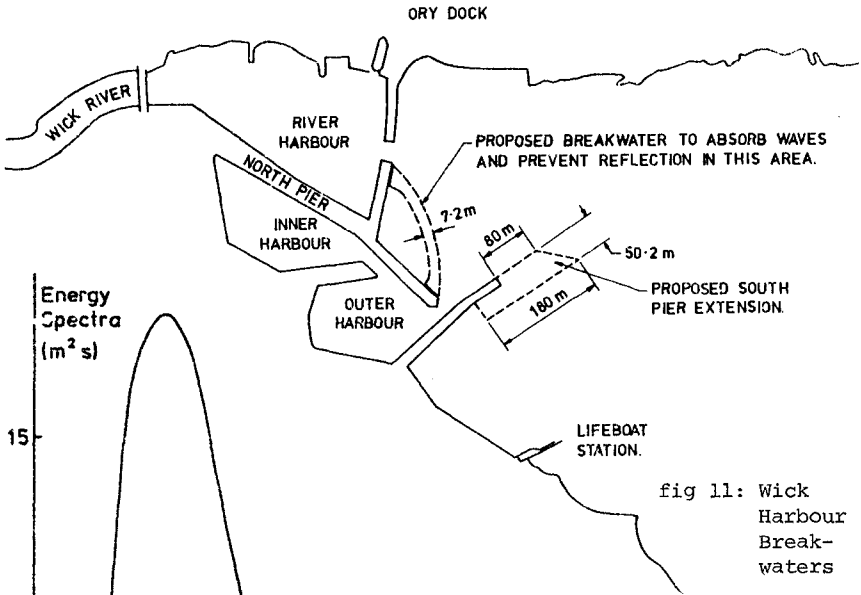
Wick Harbour has been the subject of several studies in recent years because of its location close to the oil fields and potential as a supply base. The 'topography' of the harbour is illustrated in fig. 11. There are two main engineering problems preventing these developments at present, namely

- 1) wave funelling within the bay coupled with reflexions from the river harbour and northern shore make the area close to the end of the south pier difficult to negotiate in easterly storms, and
- 2) sediment is carried into the area adjacent to the outer harbour.

These features inhibit reliability of supply and make harbour maintenance expensive. Solutions which have been proposed using conventional breakwaters, are very costly in an area where the sea is famed for its destruction of the Stevenson breakwater.

The scrap tyre breakwater designed for this situation (and shown in fig. 11) was based on one of the less ambitious proposals for a more normal breakwater. The south pier would be extended by about 80m by the floating breakwater which is also used to "armour" the south pier itself (to decrease overtopping). This breakwater, which would be 52m wide, would reduce H_s from 4m to 1.85m (fig. 12) and because of its relative transparency to the waves reflected from the river harbour it would not aggravate the production of standing wave conditions as a solid breakwater would. The extreme mooring loads would be less than 200 tonnes.

In conjunction with the major breakwater a smaller breakwater between the river and outer harbours would act as a spending beach by reducing the sediment carrying capacity of the waves behind it and stimulating the growth of a beach in this area. This breakwater would also ameliorate the standing wave situation close into the outer harbour entrance.



4.4 ASSISTANCE IN OIL CONTAINMENT

In the case of an oil field close to the shore, as in the Moray Firth, there is an increased danger that any spillage will cause widespread pollution along the coast. This danger may be reduced by an oil boom but these cease to be reliable for $H_s > 1.2\text{m}$ or so. These conditions are exceeded in the Moray Firth for roughly the equivalent of one day a week. This is too high a risk.

The reduction of the risk with a floating breakwater involves a rather different concept to that in either of the previous two examples, since it is now necessary to prevent waves exceeding a specified height from passing out across the perimeter of a large enclosed area.

From directional wind data (Plant 1968) cumulative probabilities of exceedence of wind speeds were drawn and curves of predicted wave heights against wind speed can be superimposed so allowing the probability of wave heights exceeding 1.2m from that direction to be deduced. The modification to this figure by the crescent breakwater required to give protection from this angle can be found by adding in the H_s v U curve when a breakwater is present. Samples of these curves are shown in fig. 13.

The total breakwater is created by taking the maximum of the crescent dimensions at each bearing. Two examples are shown in fig. 14. These reduce the risk of oil crossing the barrier to the equivalent of one day and 18 hours per month respectively. The percentage exceedences can be seen, inside and outside respectively, at the angle of the wave approach.

The total mooring load on such a breakwater would be of the order of 4000 tonnes. For mooring purposes the breakwater would be divided into sections to ensure that the loads were spread and facilitate any maintenance or replacement that may be necessary. A breakwater of this size would also afford a considerable measure of protection to the oil rig in stabilisation from passing ships being off course.

5. CONCLUSION

Scrap tyre floating breakwaters provide a practical, safe and economic option for many wave attenuation problems. There are also occasions when a floating breakwater is the only option.

CURVES OF CUMULATIVE PROBABILITY OF WIND SPEED

[Showing probability of significant wave heights with and without breakwater.]

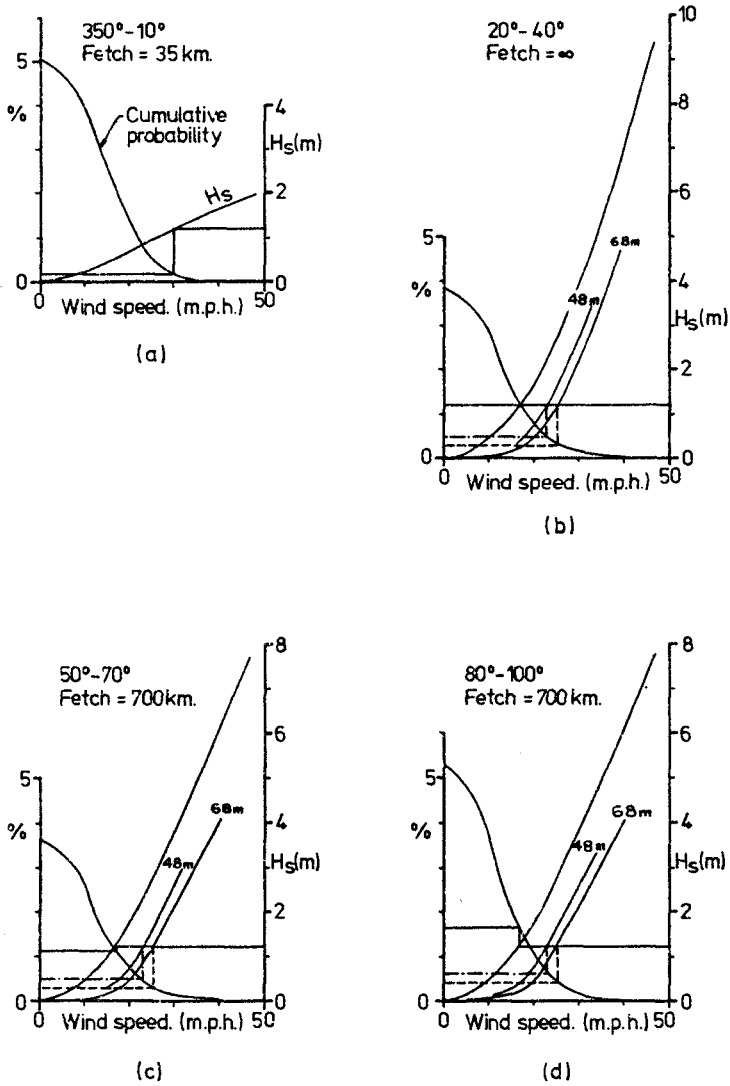


fig 13: Sample of Wind and Wave Probability Curves for Moray Firth with and without Breakwater

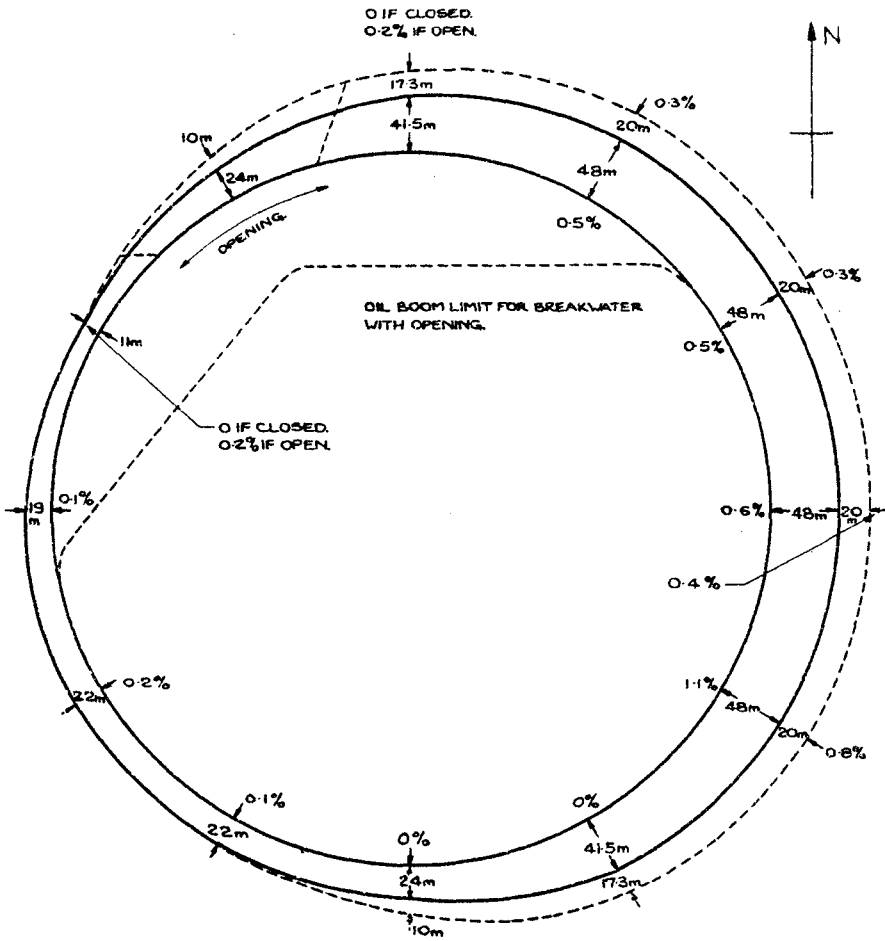


fig 14: Breakwaters for the Moray Firth showing risk of oil escape

REFERENCES

- Adee, B.H., 1976 "Review of developments and problems in using Floating Breakwaters". Proc. 1976 Offshore Tech. Conf. 2, 225-230
- Candle, R.D., 1974 "Goodyear Scrap Tire Floating Breakwater Concepts" Proc. 1974 Floating Breakwater Conf. 193-212
- Harms, V.W. and Bender, T.J., 1978 "Preliminary Report on the Application of Floating Tire Breakwater Design Data" Eng. Res. Rep. No. 78-1, Dept of Civ. Eng. SUNY, Buffalo
- Kowalski, T., 1974 Ed. Proc. 1974 Floating Breakwater Conf.
- Kowalski, T., 1976 "Scrap Tyre Floating Breakwaters for North Sea Operations". The Naval Architect, 6, 186-187
- McGregor, R.C., 1978 "Design of Scrap Tyre Floating Breakwaters with special reference to Fish Farms" Proc. Roy.Soc.Edinb., Vol 76B p115-133
- Noble, H.M., 1976 "Use of wave-maze flexible floating breakwater to protect offshore structures and landings", Proc. 1976 Offshore Tech. Conf. 215-224
- Plant, J.A., 1968 "Climate of the Coastal Region of the Moray Firth" Clim. Mem. No 62, Met. Office, England

CHAPTER 133

NON-CONSERVATIVE WAVE INTERACTION WITH FIXED SEMI-IMMERSED RECTANGULAR STRUCTURES

by

Lt. Robert B. Steimer¹
and
Dr. Charles K. Sollitt²

Introduction and Scope

Previous attempts to analytically describe wave reflection and transmission at surface penetrating structures have neglected losses due to flow expansion, contraction, and skin drag along the structure boundaries (Black and Mei, 1970; Ijima, et al., 1972). The model described in this study includes these effects and allows for the inclusion of a dissipative medium such as rubble or closely spaced piles in the region beneath the structure.

The problem of a fixed, two-dimensional structure in a train of monochromatic incident waves is modeled, as shown in Figure 1. The solution allows for 1) variable structure length and draft, 2) different depths in the regions fore, aft, and beneath the structure, 3) variable wave amplitude and period, and 4) turbulent and inertial damping in the region beneath the structure. An equivalent work technique is applied to linearize the damping beneath the structure, yielding a potential flow problem in all three regions. Amplitudes for the resulting series of eigenfunctions in each region are determined by matching pressure and horizontal mass flux at the region interfaces, orthogonalizing these expressions over the depth, and simultaneously solving the resulting equations to yield complex reflection and transmission coefficients. Complex horizontal and vertical force coefficients for the structure are also determined from the integrated Bernoulli equation.

The solution technique is computationally efficient. In general, five modes in the eigen series provide satisfactory convergence for the various hydrodynamic parameters. Approximately six-tenths of a computer system second are required to solve for a single wave-structure condition. The results compare favorably with variational methods used by others.

The effect of skin friction, expansion, and contraction losses tend to reduce both reflection and transmission coefficients by only a few percentage points over a wide range of wave frequencies. The addition

¹U.S. Navy Civil Engineering Laboratory, Construction Battalion Center, Port Hueneme, California, 93043.

²Civil Engineering Department, Oregon State University, Corvallis, Oregon, 97331.

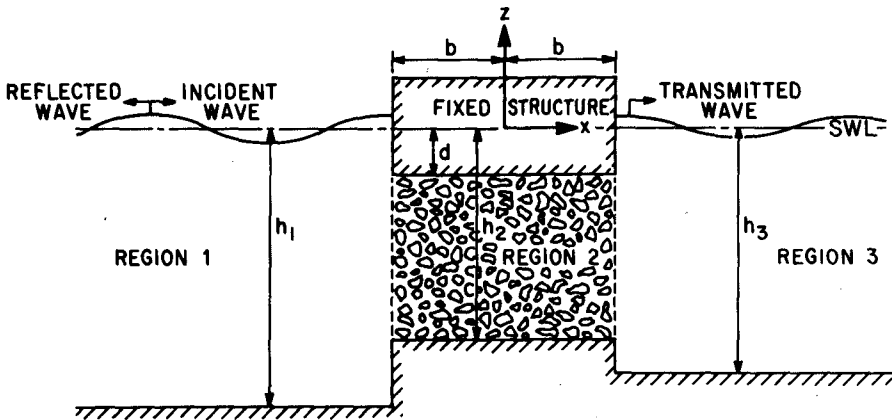


Figure 1. Definition Sketch

of a dissipative medium beneath the structure, however, causes considerable reduction in wave transmission at all wave frequencies while increasing reflection at low frequencies and reducing reflection at high frequencies. Increased inertial damping and decreased porosity in the medium below the structure uniformly decrease transmission and increase reflection.

Comparison with experimental data and other theories is made. New experimental data are presented. Design curves for various structure and wave parameters are presented and discussed.

Theory

Equations of Motion

Newton's Law states that the vector summation of forces acting on a fluid parcel is equal to the resultant vector acceleration of that parcel. The significant forces affecting free surface phenomena may be summarized as

$$\text{acceleration} = (\text{pressure} + \text{gravity} + \text{turbulent friction} + \text{laminar friction} + \text{inertial friction}) \text{ per unit mass}$$

In equation form this statement becomes

$$\frac{dq}{dt} = -\frac{1}{\rho} \nabla(p + \gamma z) - \beta_1 q|q| - \beta_2 q - \beta_3 \frac{\partial q}{\partial t} \quad (1)$$

where q = vector velocity
 ρ = mass density of fluid
 ∇ = gradient operator
 p = pressure
 γ = specific weight of fluid = ρg
 g = acceleration due to gravity
 $\beta_1, \beta_2, \beta_3$ = resistance coefficients

Convective accelerations may be ignored for small amplitude wave motions, thereby reducing the substantial acceleration to the local acceleration or

$$\frac{\partial q}{\partial t} = \frac{dq}{dt}$$

Combining the local acceleration with the inertial damping term in Eq. (1) yields

$$(1+\beta_3) \frac{\partial q}{\partial t} = -\frac{1}{\rho} \nabla(p + \gamma z) - \beta_1 q|q| - \beta_2 q \quad (2)$$

Now let

$$(1+\beta_3) = S \quad (3)$$

where S is an inertial coefficient which includes the effects of local accelerations and additional accelerations caused by local obstructions such as rubble, piles, abrupt corners on the structure, etc.

The laminar and turbulent friction terms are replaced by a single linear friction term which dissipates the same amount of energy over one wave period as the actual friction terms. This simplification permits an analytical solution to the problem without perturbing the equations of motion yet retains a non-linear dependence on wave amplitude. Then

$$-\beta_1 q|q| - \beta_2 q \text{ is replaced by } -f\omega q \quad (4)$$

where f = dimensionless friction coefficient
 ω = wave angular frequency (renders f dimensionless)

An additional condition is required to evaluate f since Eq. (4) is not satisfied by a simple equality. This condition is referred to as Lorentz's Condition of Equivalent Work, and it requires that both friction laws dissipate the same amount of energy over the region of interest during one wave cycle. In equation form this reads

$$f\omega \int_{\text{volume}} dV \int_{\text{period}} dt (q \cdot q) = \beta_1 \int_{\text{volume}} dV \int_{\text{period}} dt (q \cdot q|q|) + \beta_2 \int_{\text{volume}} dV \int_{\text{period}} dt (q \cdot q) \quad (5)$$

Then, on the average, the two friction laws are equivalent. Combining Eqs. (2), (3) and (4) yields

$$S \frac{\partial q}{\partial t} = -\frac{1}{\rho} \nabla(p + \gamma z) - f\omega q \quad (6)$$

A periodic fluid motion is sought for monochromatic waves, hence, the velocity time dependence becomes

$$q(x, z, t) = q(x, z) \exp(-i\omega t)$$

and

$$\frac{\partial q}{\partial t} = -i\omega q \quad (7)$$

Substituting Eq. (7) into Eq. (6) and combining terms

$$\omega(f-iS)q = -\frac{1}{\rho} \nabla(p + \gamma z) \quad (8)$$

The curl of the right hand side of Eq. (8) is identically equal to zero, therefore

$$\nabla \times q = 0$$

and since

$$\nabla \times (\nabla \text{ anything}) = 0$$

it is permissible to replace the vector velocity q with the scalar velocity potential, ϕ , according to

$$q = -\nabla\phi \quad (9)$$

Introducing Eq. (9) into Eq. (8) and combining terms

$$\nabla[-\omega(f-iS)\phi + \frac{1}{\rho}(p + \gamma z)] = 0 \quad (10)$$

The gradient of the bracketed term is equal to zero, therefore the term cannot be a function of spatial location. Requiring that the water surface displacement integrate to zero over one wave length further constrains the bracketed term, establishing that it must equal zero. Therefore, the gradient operator may be removed from Eq. (10), yielding the Bernoulli Equation, which may be solved for the pressure field.

$$\frac{p}{\rho} = -gz + \omega(f-iS)\phi \quad (11)$$

Note that Eq. (11) reduces to the linear wave theory Bernoulli Equation if no damping occurs ($f = 0$, $S = 1.0$).

Water is essentially incompressible in free surface flows. Consequently, conservation of mass reduces to the continuity equation which may be written as

$$\nabla \cdot q = 0 \quad (12)$$

Combining Eqs. (9) and (12) yields Laplace's Equation for irrotational, incompressible flow.

$$\nabla^2 \phi = 0 \quad (13)$$

Equations (11) and (13) are the appropriate equations of motion for the general problem of non-conservative, irrotational, incompressible flow. The velocity field is specified at all times, in all space by Eq. (13). Substitution of the solution to Eq. (13) into Eq. (11) prescribes the pressure field. In order to solve Eq. (11), however, boundary conditions are required to specify the integration constants.

Boundary Conditions

Laplace's Equation is a second order homogenous differential equation requiring two boundary conditions to specify the general solution. A third boundary condition is required to reference the pressure in Bernoulli's Equation. The three boundary conditions are determined by the physical restrictions imposed at the flow field boundaries.

Referring to Figure 1, the bottom boundary condition requires that the vertical velocity component vanish at an impermeable horizontal boundary. Thus

$$w = -\frac{\partial \phi}{\partial z} = 0 \text{ at } z = -h_1, -h_2 \text{ and } -h_3 \quad (14)$$

Similarly, under the bottom of the structure

$$w = -\frac{\partial \phi}{\partial z} = 0 \text{ at } z = -d \quad (15)$$

At the free surface, $z = \eta$, the pressure must be equal to zero. Hence,

$$p = 0 \text{ at } z = \eta \quad (16)$$

Also, the surface must rise and fall at a rate equal to the vertical velocity to maintain continuity at the free surface. Hence

$$\frac{d\eta}{dt} = w = -\frac{\partial \phi}{\partial z} \text{ at } z = \eta \quad (17)$$

Small amplitude wave motions produce negligible convective changes in η and permit an evaluation of w at the still water level to avoid transcendental functions of η . These simplifications reduce Eq. (17) to

$$\frac{\partial \eta}{\partial t} = -\frac{\partial \phi}{\partial z} \text{ at } z = 0 \quad (18)$$

Combining Eqs. (11), (16) and (18) yields the combined kinematic and dynamic free surface boundary condition.

$$\frac{\partial \phi}{\partial z} = -\frac{w}{g} (f - iS)\phi$$

In regions 1 and 3 of Figure 1, $f = 0$ and $S = 1.0$ so that

$$\frac{\partial \phi}{\partial z} = \frac{i\phi}{g} \text{ at } z = 0 \tag{19}$$

Boundary Value Problem

The boundary value problem for each of three regions fore, aft and beneath the structure is summarized in Figure 2. Each boundary value problem is prescribed by Laplace's Equation and the surface and bottom boundary conditions. Flow field boundaries are parallel to the coordinate axes, consequently, variable separation techniques may be used to solve Laplace's Equation. The boundary conditions are applied to evaluate the integration constants. The resulting solutions are presented in detail by Steimer (1977) and are summarized below. The incident wave is described by a single progressive wave in Eq. (20). The reflected and transmitted waves include a single progressive mode each and an infinite series of evanescent modes, as identified in Eqs. (21) and (22). Beneath the breakwater, the solution yields a single wave component corresponding to the progressive mode, Eq. (23), and two infinite series of evanescent modes, one decaying left to right, Eq. (24), and the other decaying right to left, Eq. (25).

$$\phi_i = \frac{ig}{\omega} A_i \exp i[k_{11}(x+b)-\omega t] \frac{\cosh K_{11}(z+h_1)}{\cosh K_{11}h_1} \tag{20}$$

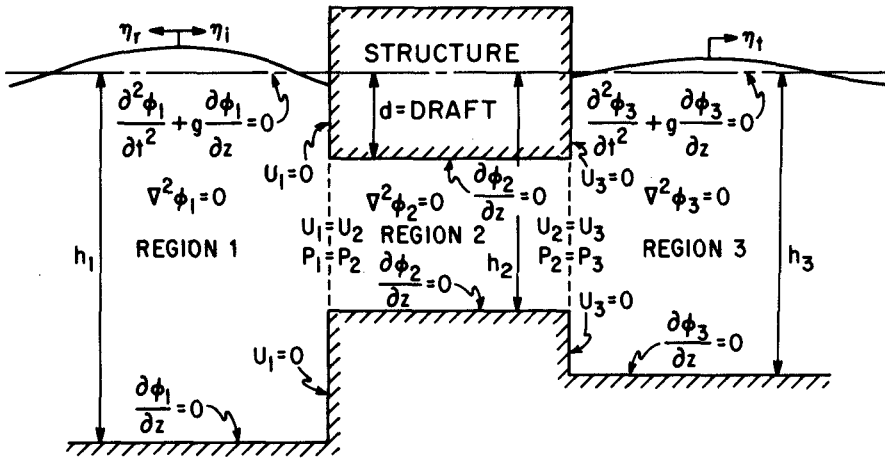


Figure 2. Boundary Value Problem

$$\phi_r = \sum_{N=1}^{\infty} \frac{ig}{\omega} A_{rN} \exp \left(-i[K_{1N}(x+b)+\omega t] \right) \frac{\cosh K_{1N}(z+h_1)}{\cosh K_{1N}h_1} \quad (21)$$

$$\phi_t = \sum_{N=1}^{\infty} \frac{ig}{\omega} A_{tN} \exp \left(i[K_{3N}(x-b)-\omega t] \right) \frac{\cosh K_{3N}(z+h_3)}{\cosh K_{3N}h_3} \quad (22)$$

$$\phi_o = \frac{ig}{\omega} (A_{a1} \frac{x}{b} + A_{b1}) \exp(-i\omega t) \quad (23)$$

$$\phi_a = \sum_{N=2}^{\infty} \frac{ig}{\omega(-1)^{N-1}} A_{aN} \exp[-K_{2N}(x+b)-i\omega t] \cos K_{2N}(z+h_2) \quad (24)$$

$$\phi_b = \sum_{N=2}^{\infty} \frac{ig}{\omega(-1)^{N-1}} A_{bN} \exp[K_{2N}(x-b)-i\omega t] \cos K_{2N}(z+h_2) \quad (25)$$

where: A_{ij} represent wave amplitudes in regions 1 and 3 and pressure head amplitudes in region 2; and K_{ij} represent separation constants or eigenvalue wave numbers in each region. The first subscript identifies the region, while the second subscript identifies the modal number.

The wave numbers are solved from dispersion equations in each region. The dispersion equations result from Eq. (19) in regions 1 and 3 and a combination of Eqs. (14) and (15) in region 2. The appropriate dispersion equation in regions 1 and 3 is

$$\omega^2 = g K_{ij} \tanh (K_{ij} h_i) \quad (26)$$

The K_{i1} wave numbers are the real roots of Eq. (26) and the K_{iN} wave numbers with $N \geq 2$ are the imaginary roots to Eq. (26). The appropriate dispersion equation in region 2 is

$$K_{2N} = \frac{(N-1)\pi}{(h_2-d)} \quad \text{for } N \geq 2 \quad (27)$$

Summarizing, the velocity potential in region 1 is

$$\phi_1 = \phi_i + \phi_r \quad (28)$$

The velocity potential in region 2 is

$$\phi_2 = \phi_o + \phi_a + \phi_b \quad (29)$$

The velocity potential in region 3 is

$$\phi_3 = \phi_t \quad (30)$$

Orthogonalized Interfacial Boundary Conditions

Only the incident wave amplitude in Eq. (20) is known. The remaining amplitudes are unknowns and must satisfy pressure and mass flux

continuity at the interfaces between regions. Pressure continuity requires that the pressure field solutions in each region provide identical results at common boundaries between regions. Thus

$$p_1 = p_2 \quad \text{at } x = -b \quad (31)$$

$$p_2 = p_3 \quad \text{at } x = +b \quad (32)$$

Referring to Eq. (11) and recognizing that $f = 0$, $S = 1.0$ in regions 1 and 3, Eqs. (31) and (32) become

$$\phi_1 = (S + if) \phi_2 \quad \text{at } x = -b \quad (33)$$

$$\phi_3 = (S + if) \phi_2 \quad \text{at } x = +b \quad (34)$$

Mass flux continuity requires that mass be conserved as flow proceeds from one region to another. Recognizing that region 2 may be occupied by a porous medium, the velocities within the pore spaces must increase inversely proportional to the porosity to maintain mass flux continuity at the interface. Thus, if ϵ is the porosity in region 2, the velocities normal to the interfaces will be related according to

$$\frac{\partial \phi_1}{\partial x} = \epsilon \frac{\partial \phi_2}{\partial x} \quad \text{at } x = -b \quad (35)$$

and

$$\frac{\partial \phi_3}{\partial x} = \epsilon \frac{\partial \phi_2}{\partial x} \quad \text{at } x = +b \quad (36)$$

Note that mass flux continuity reduces to velocity continuity if no porous medium exists.

Each interfacial boundary condition includes an infinite series of terms. The terms within the series may be separated to generate $4N$ equations to solve $4N$ unknown amplitudes by utilizing the orthogonal behavior of the z dependent separable functions. The boundary value problems in Figure 2 are all linear, homogenous, second order differential equations with linear, homogenous boundary conditions. Accordingly, they are properly posed Sturm-Liouville problems with orthogonal solutions having the useful property that products of two modal solutions, integrated between boundaries having homogenous boundary conditions, vanish unless the modes are identical (Hildebrand, 1965). Thus

$$\int_0^{-h_1} \phi_{iM} \phi_{iN} = 0 \quad \text{unless } M = N \quad (37)$$

Equation (37) applies equally well to derivatives of ϕ .

This behavior is utilized by multiplying Eqs. (33) and (34) by ϕ_2 and integrating from $z = -h_2$ to $z = -d$. Similarly, Eq. (35) is multiplied by $\frac{\partial \phi_1}{\partial x}$ and integrated from $z = -h_1$ to $z = 0$; and Eq. (36) is multiplied by $\frac{\partial \phi_3}{\partial x}$ and integrated from $z = -h_3$ to $z = 0$.

Note that $\frac{\partial \phi_1}{\partial x}$ and $\frac{\partial \phi_3}{\partial x}$ equal zero above $z = -d$ and below $z = -h_2$.

Evaluating these integrals provides the six equations listed below.

$$\sum_{N=1}^{\infty} C_{rN} \left[\frac{K_{11} \cosh K_{11} h_1}{K_{1N} \cosh K_{1N} h_1} \right] \left[\frac{\sinh K_{1N} (h_1-d) - \sinh K_{1N} (h_1-h_2)}{\sinh K_{11} (h_1-d) - \sinh K_{11} (h_1-h_2)} \right] + (C_{a1} - C_{b1}) \left[\frac{(S+if)(h_2-d) K_{11} \cosh K_{11} h_1}{\sinh K_{11} (h_1-d) - \sinh K_{11} (h_1-h_2)} \right] = -1 \quad (38)$$

$$\sum_{N=1}^{\infty} C_{rN} \left[\frac{\cosh K_{11} h_1}{\cosh K_{1N} h_1} \right] \frac{K_{1N}}{K_{11}} \left[\frac{(-1)^{(M-1)} \sinh K_{1N} (h_1-d) - \sinh K_{1N} (h_1-h_2)}{(-1)^{(M-1)} \sinh K_{11} (h_1-d) - \sinh K_{11} (h_1-h_2)} \right] \left[\frac{K_{11}^2 + K_{2M}^2}{K_{1N}^2 + K_{2M}^2} \right] - [C_{aM} + C_{bM} \exp(-2K_{2M}b)] \left[\frac{(h_2-d)(S+if)(\cosh K_{11} h_1)(K_{11}^2 + K_{2M}^2)}{2K_{11} [\sinh K_{11} (h_1-d) + (-1)^M \sinh K_{11} (h_1-h_2)]} \right] = -1$$

for $M \geq 2$ (39)

$$\sum_{N=1}^{\infty} C_{tN} \left[\frac{K_{11} \cosh K_{11} h_1}{K_{3N} \cosh K_{3N} h_3} \right] \left[\frac{\sinh K_{3N} (h_3-d) - \sinh K_{3N} (h_3-h_2)}{\sinh K_{11} (h_1-d) - \sinh K_{11} (h_1-h_2)} \right] - (C_{a1} + C_{b1}) \left[\frac{(S+if)(h_2-d)(K_{11} \cosh K_{11} h_1)}{\sinh K_{11} (h_1-d) - \sinh K_{11} (h_1-h_2)} \right] = 0 \quad (40)$$

$$\sum_{N=1}^{\infty} C_{tN} \left[\frac{\cosh K_{11} h_1}{\cosh K_{3N} h_3} \right] \frac{K_{3N}}{K_{11}} \left[\frac{(-1)^{(M-1)} \sinh K_{3N} (h_3-d) - \sinh K_{3N} (h_3-h_2)}{(-1)^{(M-1)} \sinh K_{11} (h_1-d) - \sinh K_{11} (h_1-h_2)} \right] \left[\frac{K_{11}^2 + K_{2M}^2}{K_{3N}^2 + K_{2M}^2} \right] - [C_{aM} \exp(-2K_{2M}b) + C_{bM}] \left[\frac{(h_2-d)(S+if)(\cosh K_{11} h_1)(K_{11}^2 + K_{2M}^2)}{2K_{11} (\sinh K_{11} (h_1-d) + (-1)^M \sinh K_{11} (h_1-h_2))} \right] = 0$$

for $M \geq 2$ (41)

$$C_{rM} \left[\frac{\cosh K_{11} h_1}{\cosh K_{1M} h_1} \right] \left[\frac{2K_{1M} h_1 + \sinh 2K_{1M} h_1}{2K_{11} h_1 + \sinh 2K_{11} h_1} \right] + C_{a1} \left[\frac{-4i\epsilon \cosh K_{11} h_1 [\sinh K_{1M} (h_1-d) - \sinh K_{1M} (h_1-h_2)]}{b K_{1M} (2K_{11} h_1 + \sinh 2K_{11} h_1)} \right] + \sum_{N=2}^{\infty} [-C_{aN} + C_{bN} \exp(-2K_{2N}b)] \left[\frac{K_{2N} K_{1M}}{K_{1M}^2 + K_{2N}^2} \right] \left[\frac{-4i\epsilon \cosh K_{11} h_1 [\sinh K_{1M} (h_1-d) + (-1)^N \sinh K_{1M} (h_1-h_2)]}{2K_{11} h_1 + \sinh 2K_{11} h_1} \right] = \delta_{M1} \quad (42)$$

$$\begin{aligned}
& -C_{tM} \left[\frac{\cosh K_{11} h_1}{\cosh K_{3M} h_3} \right] \left[\frac{2K_{3M} h_3 + \sinh 2K_{3M} h_3}{2K_{11} h_1 + \sinh 2K_{11} h_1} \right] \\
& + C_{a1} \left[\frac{-4i\epsilon \cosh K_{11} h_1 [\sinh K_{3M} (h_3-d) - \sinh K_{3M} (h_3-h_2)]}{b K_{3M} (2K_{11} h_1 + \sinh 2K_{11} h_1)} \right] \\
& + \sum_{N=2}^{\infty} [-C_{aN} \exp(-2K_{2N} b) + C_{bN}] \left[\frac{K_{2N} K_{3M}}{K_{3M}^2 + K_{2N}^2} \right] \\
& \left[\frac{-4i\epsilon \cosh K_{11} h_1 [\sinh K_{3M} (h_3-d) + (-1)^N \sinh K_{3M} (h_3-h_2)]}{2K_{11} h_1 + \sinh 2K_{11} h_1} \right] = 0 \quad (43)
\end{aligned}$$

Six equations result, rather than four, because orthogonalizing pressure continuity with respect to the inner modes generates two additional unique equations, one at each interface, for the propagating mode beneath the structure. Each equation is summed on N but is repeated for each M th eigenvalue. Equations (38) and (40) apply to the $M=1$ mode beneath the structure while Eqs. (39) and (41) complete the pressure continuity requirements for $M \geq 2$. Equations (42) and (43) are statements of mass flux continuity, orthogonalized with respect to the outer modes of regions 1 and 3, and apply to all $M \geq 1$. Thus $4M$ equations are produced to solve for $4M$ unknown amplitudes: M reflected waves, M transmitted, and M waves in both the $+x$ and $-x$ directions under the structure.

In Eqs. (38) through (43), the complex amplitudes A_{ij} have been rendered dimensionless by division with the incidental wave amplitude A_i and are denoted as C_{ij} . The Kronecker delta appears as δ_{M1} . The system of $4M$ equations becomes finite by establishing a finite upper limit for the N summation. The amplitude coefficients, C_{ij} , become smaller as j increases and experience with this set of equations, for most practical structural configurations, has demonstrated that summing on five modes is sufficient. Errors due to this finite summation are on the order of a few percent or less. Up to 20 modes have been utilized for unusual configurations such as thin plates.

The $4M$ system of linear algebraic, complex equations is solved via the IBM Scientific Subroutine SIMQ, modified to accept complex coefficients. Amplitudes and phases for each modal amplitude are determined by calculating the modulus and argument, respectively, of each C_{ij} . The reflection and transmission coefficients for the propagating modes are simply $|C_{r1}|$ and $|C_{t1}|$, respectively. Approximately six-tenths of a computer system second are required to solve for a single wave-structure condition described by a five mode series.

Theoretical Behavior

Predicted wave response, quantified as reflection and transmission coefficients, is presented for a hypothetical structure as a function of

dimensionless wave number in Fig. 3-a, b and c. The results show that shorter waves experience more reflection and less transmission at the structure. In addition, as the resistance beneath the structure is increased via an increase in the friction coefficient, f , inertial coefficient, S , or decrease in porosity, ϵ , reflection is increased, attenuation is increased and transmission is decreased. Figure 3-d demonstrates that increased frictional resistance beneath the structure leads to increased energy dissipation. However, an upper limit for energy dissipation is reached at 1/2 the available incident wave energy. Further increases in frictional resistance simply cause 50 percent of the wave energy to be reflected rather than completely absorbed and dissipated beneath the structure.

The results of the present analysis compare favorably with those predicted by other investigators utilizing alternative solution techniques. Sample comparisons are presented in Figs. 4 and 5. Reflection and transmission coefficients results are compared in Fig. 4-a, b, c and d for various structural configurations. The variational technique of Black (1970) in Figs. 4-a, c and d displays essentially identical results to the present theory with negligible resistance ($f=0, S=1.0, \epsilon=1.0$). John's shallow water dock theory (Ippen, 1966) also concurs. The matched asymptotic expansion theory of Tuck (1971) for a narrow slit in a thin, infinitely deep plate also agrees well with the present theory if finite values are used for the depth and plate thickness. Even the long wave behavior is reproduced well, contrasting the variational results in Fig. 4-b.

The horizontal and vertical forces induced by waves acting on the structure are evaluated by integrating the pressure distribution on vertical and horizontal structure surfaces, respectively. The vertical dynamic wave force component is

$$F_{VD} = \int_{-b}^{+b} p dx = \rho\omega(f-iS) \int_{-b}^{+b} \phi_2 dx$$

Substituting for ϕ_2 and evaluating the integral yields

$$F_{VD} = \gamma(S+if) \exp(-i\omega t) \left(2b A_{b1} + \sum_{N=2}^{\infty} \left[\frac{1-\exp(-2K_{2N}b)}{K_{2N}} \right] (A_{aN}+A_{bN}) \right) \tag{44}$$

The horizontal dynamic wave force component is the difference in forces on the two sides of the structure.

$$F_H = \int_0^{-d} p_1 dz - \int_0^{-d} p_3 dz = \int_0^{-d} \rho i \phi_1 (@x=-b) dz + \int_0^{-d} \rho i \phi_3 (@x=b) dz$$

Substituting for ϕ_1 and ϕ_3 and evaluating the integrals yields

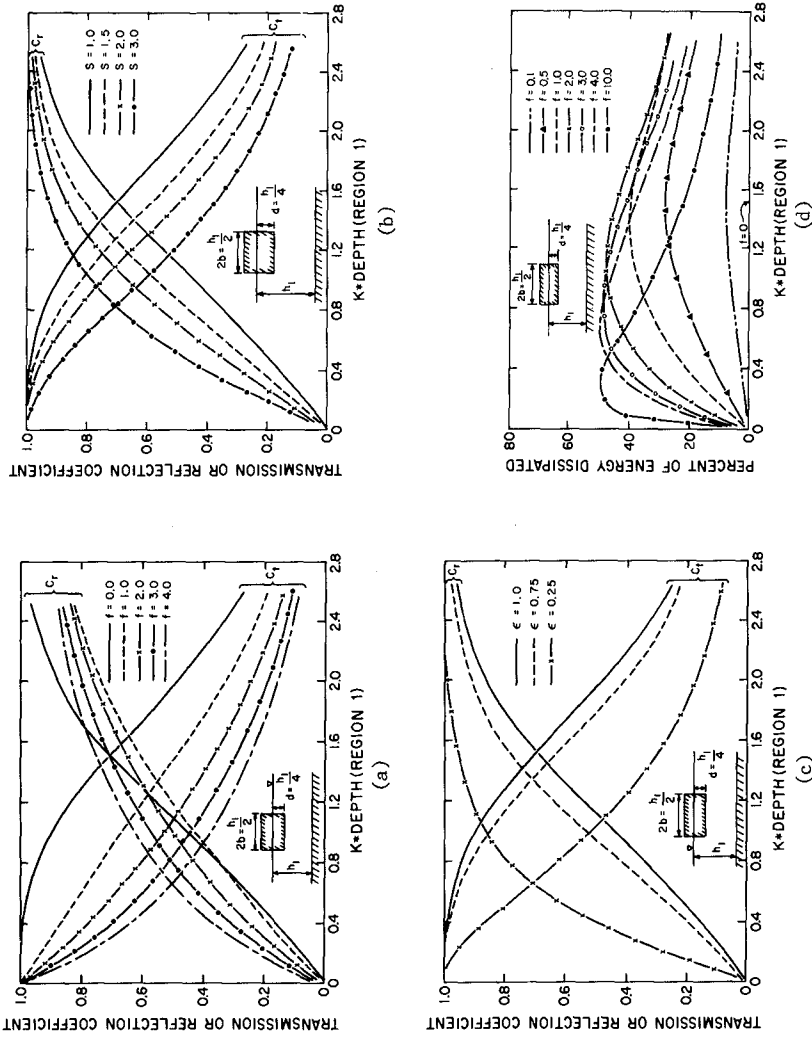


Figure 3. Theoretical Dependence of Wave Response on (a) Friction Coefficient, (b) Inertial Coefficient, (c) Porosity, (d) Friction Coefficient Related to Energy Dissipation

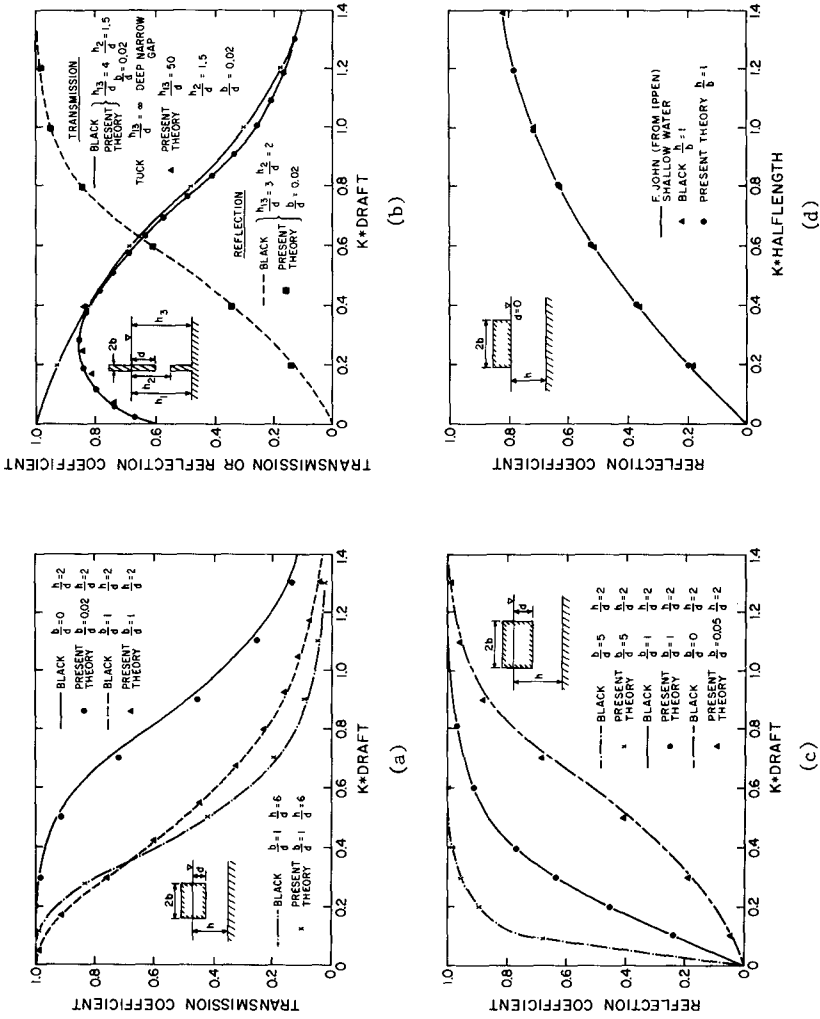
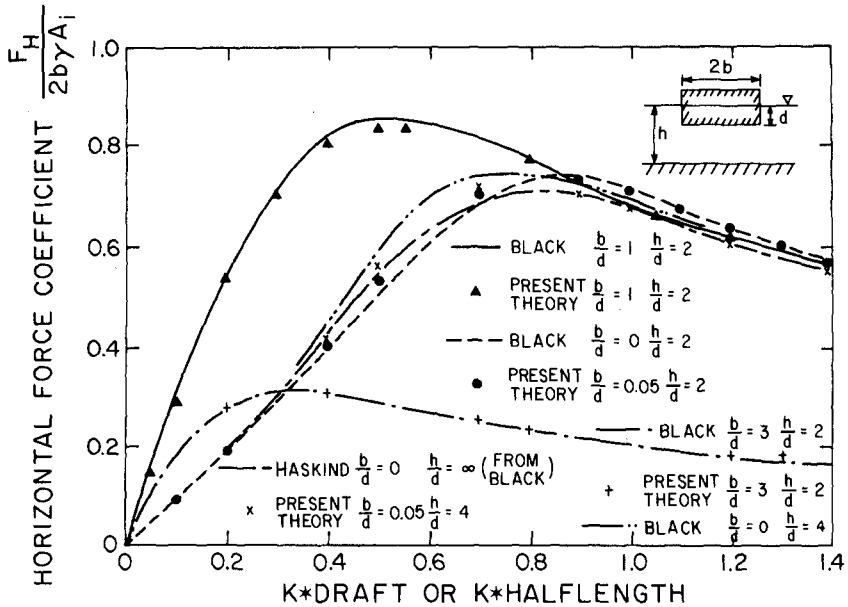


Figure 4. Predicted Wave Response Compared to Other Theories for Structures Characterized as (a) Finite Draft, (b) Thin Plate, (c) Finite Draft, (d) Zero Draft



(a)

(b)

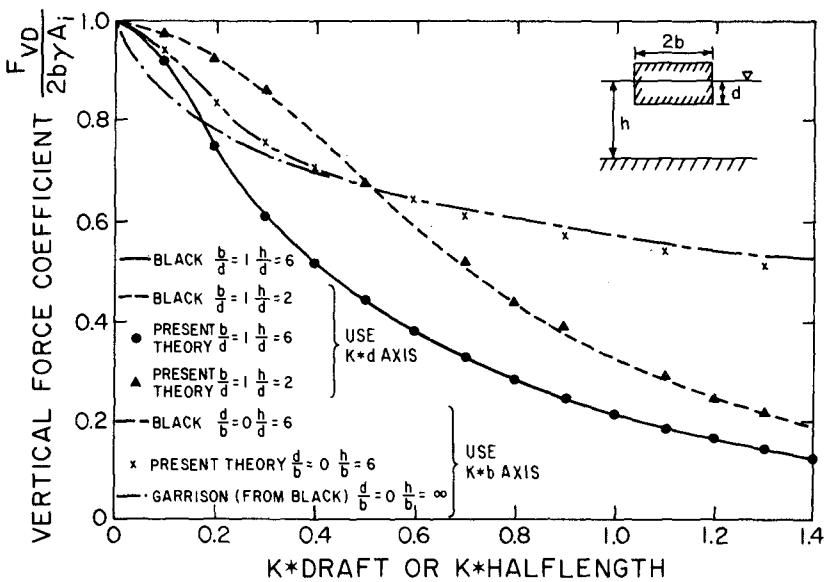


Figure 5. Predicted Wave Forces Compared to Other Theories (a) Horizontal Component, (b) Vertical Component

$$\begin{aligned}
 F_H = \gamma \exp(-i\omega t) & \left[\frac{A_1 [\sinh K_{11}(h_1-d) - \sinh K_{11}h_1]}{K_{11} \cosh K_{11}h_1} \right. \\
 & + \sum_{N=1}^{\infty} \frac{A_{rN} [\sinh K_{1N}(h_1-d) - \sinh K_{1N}h_1]}{K_{1N} \cosh K_{1N}h_1} \\
 & \left. - \sum_{N=1}^{\infty} \frac{A_{tN} [\sinh K_{3N}(h_3-d) - \sinh K_{3N}h_3]}{K_{3N} \cosh K_{3N}h_3} \right] \quad (45)
 \end{aligned}$$

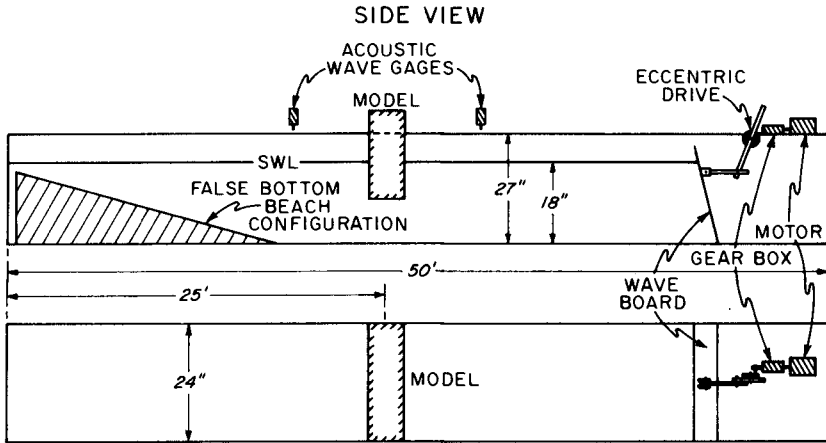
Dimensionless force components from Eqs. (44) and (45) have been graphed in Fig. 5-a and b. Results taken from Black (1970) include comparisons with the work of Garrison and Haskind. The comparisons are quite favorable, with only slight differences for very thin plates.

Experimental Results

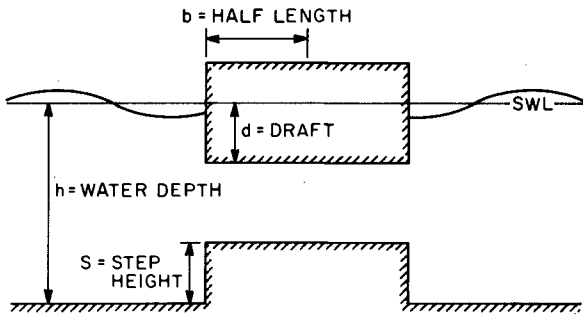
A small scale experimental program was conducted at Oregon State University to supplement the available data on wave reflection and transmission at rectangular structures. The experiment apparatus is described in Fig. 6-a and the geometric configurations tested are identified in Fig. 6-b. Each model was exposed to a variety of wave amplitudes and frequencies. Incident and reflected waves were resolved with a traversing wave gauge from measurements of the partial standing wave envelope. Transmitted wave measurements were acquired with a stationary wave gauge.

Transmission coefficient results are displayed in Fig. 7. Four combinations of draft, depth and step height are shown with results expressed relative to dimensionless wave numbers. Theoretical results are expressed for frictionless conditions. In general the agreement between experiment and theory is quite good. In Figs. 7-a, b and c, the theory tends to slightly overpredict the transmission coefficient. A non-zero value for the friction coefficient would tend to improve this correlation, indicating that real fluid effects may be modifying the experimental results. Figure 7-d shows the theory underpredicting transmission slightly for long waves. This model configuration has zero draft so that the long wave trough passes under the model without surface contact. The theory does not allow for the separation of the water and model surfaces, a condition which is unlikely to occur in the prototype.

Experimental and theoretical reflection coefficients are presented in Fig. 8-a and b. In general the theory tends to overpredict the measured reflection coefficients. Again, this correlation can be improved by utilizing a non-zero value for the friction coefficient, f , to account for real fluid effects. Small increases in f tend to decrease both the reflection and transmission coefficient as indicated in Figs. 3-a and 8-c. The frictional condition displayed in Fig. 8-c evaluates energy loss due to skin drag over the structure surface and expansion/contraction losses at the abrupt corners of the structure. The corrections indicated improve the correlation with the experimental data, however, larger losses need to be identified to further correct the predicted reflection



(a)



(b)

RUN #	b(in.)	S(in.)	h(in.)	d(in.)
1	4	0	18	8 1/8
2	4	0	18	6
3	4	0	18	2 3/4
4	4	8 1/4	18	2 3/4
5	4	8 1/4	18	5 1/2
6	4	8 1/4	18	0
7	4	0	18	0

Figure 6. Experimental Program (a) Apparatus, (b) Model Configurations

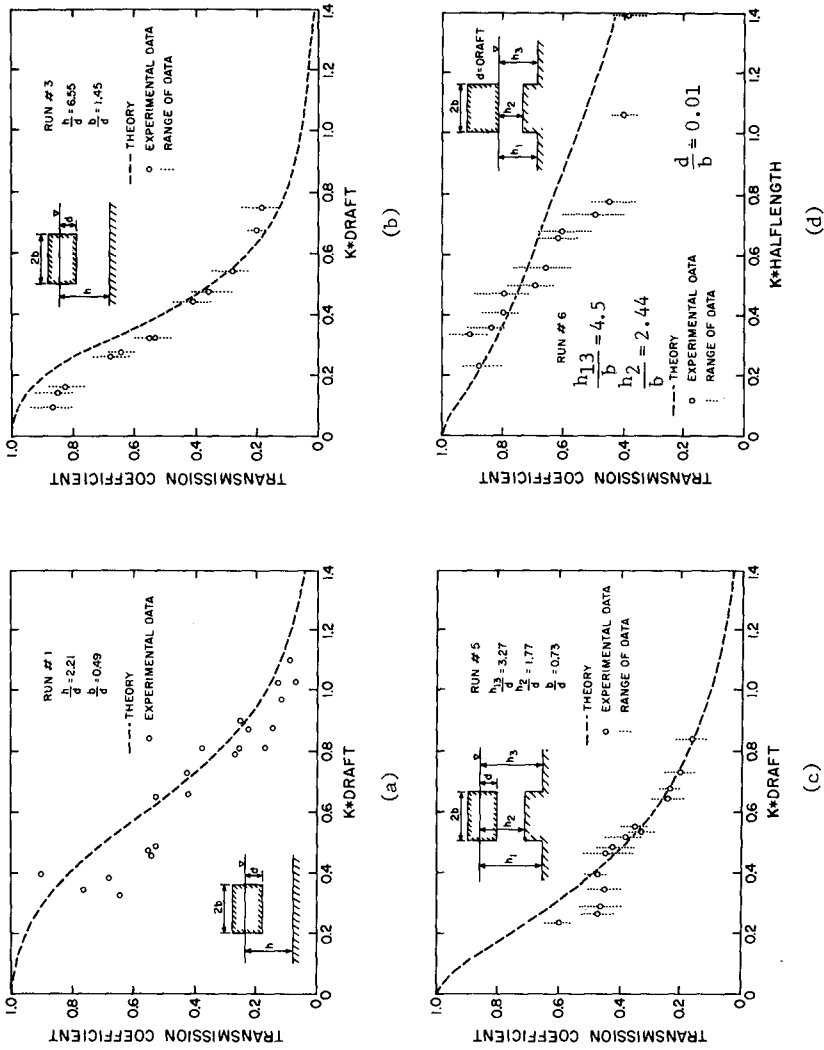


Figure 7. Comparison of Theoretical and Experimental Transmission Coefficients (a) Run #1, (b) Run #3, (c) Run #5, (d) Run #6

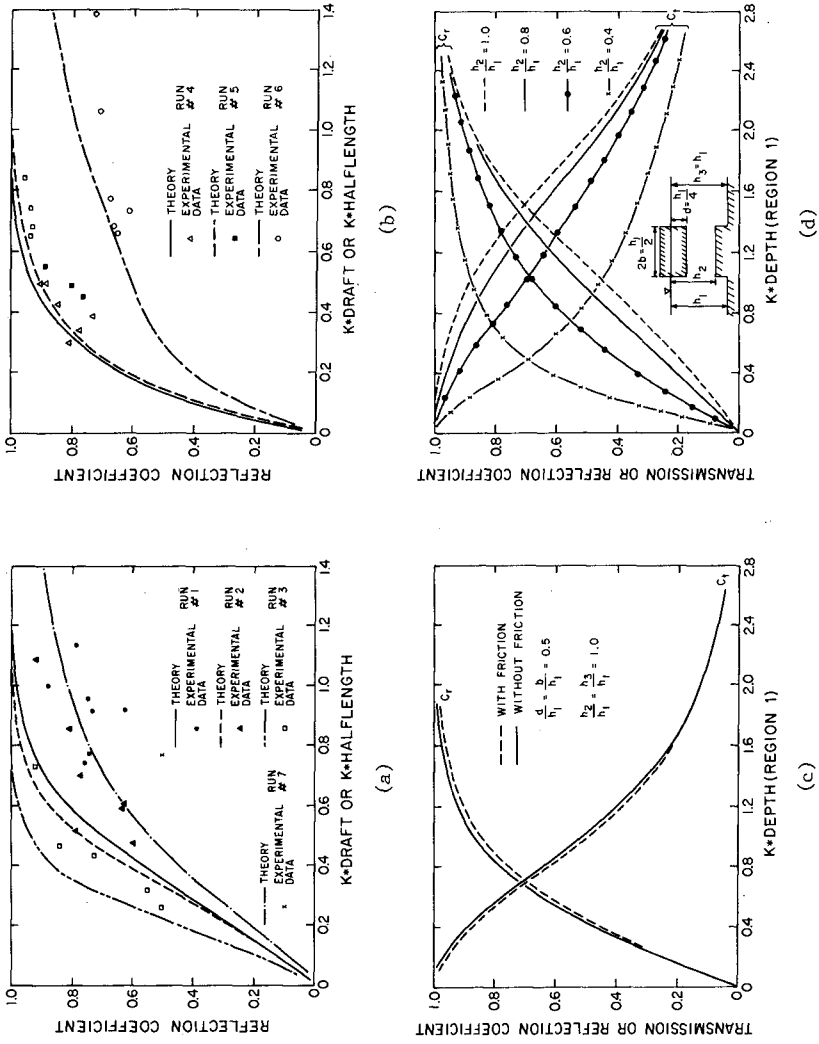


Figure 8. Comparison of Theoretical and Experimental Reflection Coefficients (a) Run #1, 2, 3, (b) Run #4, 5, 6, (c) Predicted Wave Response With and Without Friction, (d) Predicted Design Curves

coefficients. Evidently the steady flow relationships for skin friction and expansion/contraction losses are not adequate for addressing the same condition instantaneously in unsteady flows. A more complete discussion of friction coefficient evaluation is presented by Steimer (1977).

Design curves for various drafts and step heights have been prepared for the frictionless condition. A sample curve is presented in Fig. 8-d.

Conclusions

The theoretical analyses presented in this study correlates well with other rigorous analytical procedures and with available experimental data. The theory can accommodate a variety of rectangular structural configurations and it provides a rational method for incorporating real fluid losses. The solution technique is numerically efficient in providing reflection, transmission and force coefficients. Additional experimental work is required to validate force predictions and to suggest alternative friction laws to evaluate real fluid effects.

Acknowledgments

This work is a result of research sponsored in part by the Oregon State University Sea Grant College Program, U.S. Department of Commerce, under Grant No. 04-7-158-44085. The U.S. Government is authorized to produce and distribute reprints for governmental purposes notwithstanding any copyright notation that may appear hereon.

References

1. Black, J.L., and Mei, C.C., "Scattering and Radiation of Water Waves," Massachusetts Institute of Technology Water Resources and Hydrodynamics Laboratory Report No. 121, April, 1970.
2. Hildebrand, F.B., Advanced Calculus for Applications, Prentice Hall, Inc., N.J., 1965.
3. Ijima, T., et al., "Scattering of Surface Waves and the Motions of a Rectangular Body by Waves in Finite Depth," Proceedings, Japanese Society of Civil Engineering, No. 202, June 1972, pp. 33-48.
4. Ippen, A.T., ed., Estuary and Coastline Hydrodynamics, First ed., McGraw-Hill Book Company, Inc., New York, N.Y., 1966.
5. Steimer, R.B., "An Eigenvalue Wave Analysis of Fixed Semi-Immersed Rectangular Structures," Thesis for Master of Ocean Engineering Degree, Oregon State University, Corvallis, OR, 1977.
6. Tuck, E.O., "Transmission of Water Waves Through Small Apertures," Journal of Fluid Mechanics, Vol. 49, part 1, 1971, pp. 65-74.

CHAPTER 133

NON-CONSERVATIVE WAVE INTERACTION WITH FIXED SEMI-IMMERSED RECTANGULAR STRUCTURES

by

Lt. Robert B. Steimer¹
and
Dr. Charles K. Sollitt²

Introduction and Scope

Previous attempts to analytically describe wave reflection and transmission at surface penetrating structures have neglected losses due to flow expansion, contraction, and skin drag along the structure boundaries (Black and Mei, 1970; Ijima, et al., 1972). The model described in this study includes these effects and allows for the inclusion of a dissipative medium such as rubble or closely spaced piles in the region beneath the structure.

The problem of a fixed, two-dimensional structure in a train of monochromatic incident waves is modeled, as shown in Figure 1. The solution allows for 1) variable structure length and draft, 2) different depths in the regions fore, aft, and beneath the structure, 3) variable wave amplitude and period, and 4) turbulent and inertial damping in the region beneath the structure. An equivalent work technique is applied to linearize the damping beneath the structure, yielding a potential flow problem in all three regions. Amplitudes for the resulting series of eigenfunctions in each region are determined by matching pressure and horizontal mass flux at the region interfaces, orthogonalizing these expressions over the depth, and simultaneously solving the resulting equations to yield complex reflection and transmission coefficients. Complex horizontal and vertical force coefficients for the structure are also determined from the integrated Bernoulli equation.

The solution technique is computationally efficient. In general, five modes in the eigen series provide satisfactory convergence for the various hydrodynamic parameters. Approximately six-tenths of a computer system second are required to solve for a single wave-structure condition. The results compare favorably with variational methods used by others.

The effect of skin friction, expansion, and contraction losses tend to reduce both reflection and transmission coefficients by only a few percentage points over a wide range of wave frequencies. The addition

¹U.S. Navy Civil Engineering Laboratory, Construction Battalion Center, Port Hueneme, California, 93043.

²Civil Engineering Department, Oregon State University, Corvallis, Oregon, 97331.

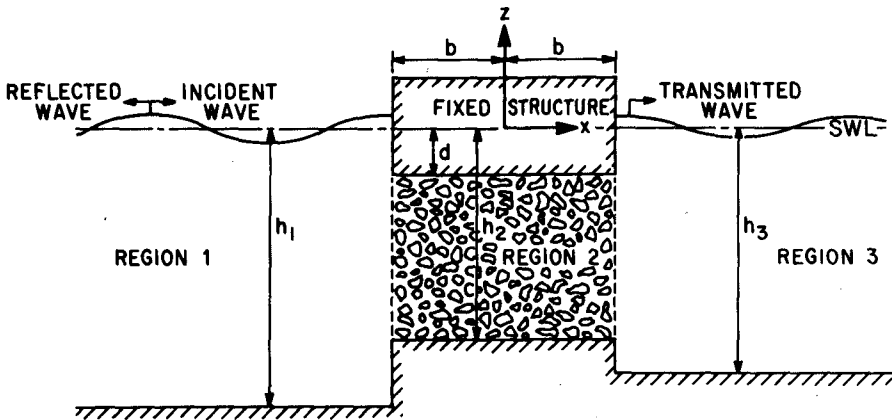


Figure 1. Definition Sketch

of a dissipative medium beneath the structure, however, causes considerable reduction in wave transmission at all wave frequencies while increasing reflection at low frequencies and reducing reflection at high frequencies. Increased inertial damping and decreased porosity in the medium below the structure uniformly decrease transmission and increase reflection.

Comparison with experimental data and other theories is made. New experimental data are presented. Design curves for various structure and wave parameters are presented and discussed.

Theory

Equations of Motion

Newton's Law states that the vector summation of forces acting on a fluid parcel is equal to the resultant vector acceleration of that parcel. The significant forces affecting free surface phenomena may be summarized as

$$\text{acceleration} = (\text{pressure} + \text{gravity} + \text{turbulent friction} + \text{laminar friction} + \text{inertial friction}) \text{ per unit mass}$$

In equation form this statement becomes

$$\frac{dq}{dt} = -\frac{1}{\rho} \nabla(p + \gamma z) - \beta_1 q|q| - \beta_2 q - \beta_3 \frac{\partial q}{\partial t} \quad (1)$$

where q = vector velocity
 ρ = mass density of fluid
 ∇ = gradient operator
 p = pressure
 γ = specific weight of fluid = ρg
 g = acceleration due to gravity
 $\beta_1, \beta_2, \beta_3$ = resistance coefficients

Convective accelerations may be ignored for small amplitude wave motions, thereby reducing the substantial acceleration to the local acceleration or

$$\frac{\partial q}{\partial t} = \frac{dq}{dt}$$

Combining the local acceleration with the inertial damping term in Eq. (1) yields

$$(1+\beta_3) \frac{\partial q}{\partial t} = -\frac{1}{\rho} \nabla(p + \gamma z) - \beta_1 q|q| - \beta_2 q \quad (2)$$

Now let

$$(1+\beta_3) = S \quad (3)$$

where S is an inertial coefficient which includes the effects of local accelerations and additional accelerations caused by local obstructions such as rubble, piles, abrupt corners on the structure, etc.

The laminar and turbulent friction terms are replaced by a single linear friction term which dissipates the same amount of energy over one wave period as the actual friction terms. This simplification permits an analytical solution to the problem without perturbing the equations of motion yet retains a non-linear dependence on wave amplitude. Then

$$-\beta_1 q|q| - \beta_2 q \text{ is replaced by } -f\omega q \quad (4)$$

where f = dimensionless friction coefficient
 ω = wave angular frequency (renders f dimensionless)

An additional condition is required to evaluate f since Eq. (4) is not satisfied by a simple equality. This condition is referred to as Lorentz's Condition of Equivalent Work, and it requires that both friction laws dissipate the same amount of energy over the region of interest during one wave cycle. In equation form this reads

$$f\omega \int_{\text{volume}} dV \int_{\text{period}} dt (q \cdot q) = \beta_1 \int_{\text{volume}} dV \int_{\text{period}} dt (q \cdot q|q|) + \beta_2 \int_{\text{volume}} dV \int_{\text{period}} dt (q \cdot q) \quad (5)$$

Then, on the average, the two friction laws are equivalent. Combining Eqs. (2), (3) and (4) yields

$$S \frac{\partial q}{\partial t} = -\frac{1}{\rho} \nabla(p + \gamma z) - f\omega q \quad (6)$$

A periodic fluid motion is sought for monochromatic waves, hence, the velocity time dependence becomes

$$q(x, z, t) = q(x, z) \exp(-i\omega t)$$

and

$$\frac{\partial q}{\partial t} = -i\omega q \quad (7)$$

Substituting Eq. (7) into Eq. (6) and combining terms

$$\omega(f-iS)q = -\frac{1}{\rho} \nabla(p + \gamma z) \quad (8)$$

The curl of the right hand side of Eq. (8) is identically equal to zero, therefore

$$\nabla \times q = 0$$

and since

$$\nabla \times (\nabla \text{ anything}) = 0$$

it is permissible to replace the vector velocity q with the scalar velocity potential, ϕ , according to

$$q = -\nabla\phi \quad (9)$$

Introducing Eq. (9) into Eq. (8) and combining terms

$$\nabla[-\omega(f-iS)\phi + \frac{1}{\rho}(p + \gamma z)] = 0 \quad (10)$$

The gradient of the bracketed term is equal to zero, therefore the term cannot be a function of spatial location. Requiring that the water surface displacement integrate to zero over one wave length further constrains the bracketed term, establishing that it must equal zero. Therefore, the gradient operator may be removed from Eq. (10), yielding the Bernoulli Equation, which may be solved for the pressure field.

$$\frac{p}{\rho} = -gz + \omega(f-iS)\phi \quad (11)$$

Note that Eq. (11) reduces to the linear wave theory Bernoulli Equation if no damping occurs ($f = 0$, $S = 1.0$).

Water is essentially incompressible in free surface flows. Consequently, conservation of mass reduces to the continuity equation which may be written as

$$\nabla \cdot q = 0 \quad (12)$$

Combining Eqs. (9) and (12) yields Laplace's Equation for irrotational, incompressible flow.

$$\nabla^2 \phi = 0 \quad (13)$$

Equations (11) and (13) are the appropriate equations of motion for the general problem of non-conservative, irrotational, incompressible flow. The velocity field is specified at all times, in all space by Eq. (13). Substitution of the solution to Eq. (13) into Eq. (11) prescribes the pressure field. In order to solve Eq. (11), however, boundary conditions are required to specify the integration constants.

Boundary Conditions

Laplace's Equation is a second order homogenous differential equation requiring two boundary conditions to specify the general solution. A third boundary condition is required to reference the pressure in Bernoulli's Equation. The three boundary conditions are determined by the physical restrictions imposed at the flow field boundaries.

Referring to Figure 1, the bottom boundary condition requires that the vertical velocity component vanish at an impermeable horizontal boundary. Thus

$$w = -\frac{\partial \phi}{\partial z} = 0 \text{ at } z = -h_1, -h_2 \text{ and } -h_3 \quad (14)$$

Similarly, under the bottom of the structure

$$w = -\frac{\partial \phi}{\partial z} = 0 \text{ at } z = -d \quad (15)$$

At the free surface, $z = \eta$, the pressure must be equal to zero. Hence,

$$p = 0 \text{ at } z = \eta \quad (16)$$

Also, the surface must rise and fall at a rate equal to the vertical velocity to maintain continuity at the free surface. Hence

$$\frac{d\eta}{dt} = w = -\frac{\partial \phi}{\partial z} \text{ at } z = \eta \quad (17)$$

Small amplitude wave motions produce negligible convective changes in η and permit an evaluation of w at the still water level to avoid transcendental functions of η . These simplifications reduce Eq. (17) to

$$\frac{\partial \eta}{\partial t} = -\frac{\partial \phi}{\partial z} \text{ at } z = 0 \quad (18)$$

Combining Eqs. (11), (16) and (18) yields the combined kinematic and dynamic free surface boundary condition.

$$\frac{\partial \phi}{\partial z} = -\frac{w}{g} (f - iS)\phi$$

In regions 1 and 3 of Figure 1, $f = 0$ and $S = 1.0$ so that

$$\frac{\partial \phi}{\partial z} = \frac{i\phi}{g} \text{ at } z = 0 \tag{19}$$

Boundary Value Problem

The boundary value problem for each of three regions fore, aft and beneath the structure is summarized in Figure 2. Each boundary value problem is prescribed by Laplace's Equation and the surface and bottom boundary conditions. Flow field boundaries are parallel to the coordinate axes, consequently, variable separation techniques may be used to solve Laplace's Equation. The boundary conditions are applied to evaluate the integration constants. The resulting solutions are presented in detail by Steimer (1977) and are summarized below. The incident wave is described by a single progressive wave in Eq. (20). The reflected and transmitted waves include a single progressive mode each and an infinite series of evanescent modes, as identified in Eqs. (21) and (22). Beneath the breakwater, the solution yields a single wave component corresponding to the progressive mode, Eq. (23), and two infinite series of evanescent modes, one decaying left to right, Eq. (24), and the other decaying right to left, Eq. (25).

$$\phi_i = \frac{ig}{\omega} A_i \exp i[k_{11}(x+b)-\omega t] \frac{\cosh K_{11}(z+h_1)}{\cosh K_{11}h_1} \tag{20}$$

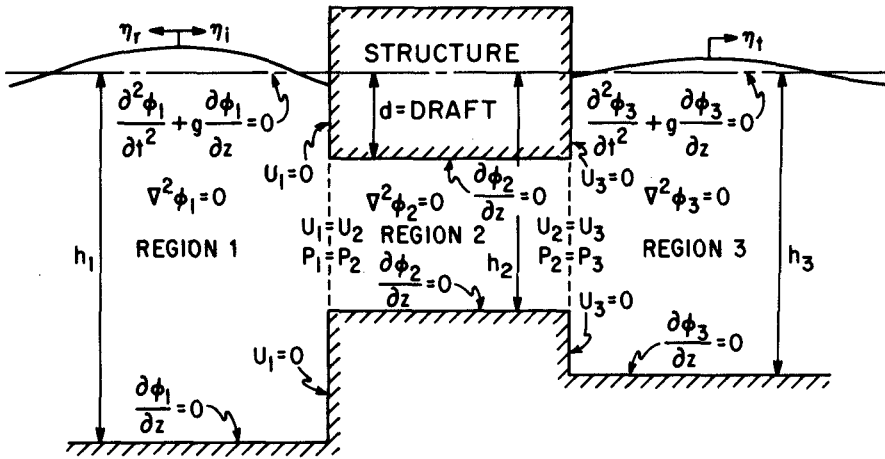


Figure 2. Boundary Value Problem

$$\phi_r = \sum_{N=1}^{\infty} \frac{ig}{\omega} A_{rN} \exp \left(-i[K_{1N}(x+b)+\omega t] \right) \frac{\cosh K_{1N}(z+h_1)}{\cosh K_{1N}h_1} \quad (21)$$

$$\phi_t = \sum_{N=1}^{\infty} \frac{ig}{\omega} A_{tN} \exp \left(i[K_{3N}(x-b)-\omega t] \right) \frac{\cosh K_{3N}(z+h_3)}{\cosh K_{3N}h_3} \quad (22)$$

$$\phi_o = \frac{ig}{\omega} (A_{a1} \frac{x}{b} + A_{b1}) \exp(-i\omega t) \quad (23)$$

$$\phi_a = \sum_{N=2}^{\infty} \frac{ig}{\omega(-1)^{N-1}} A_{aN} \exp[-K_{2N}(x+b)-i\omega t] \cos K_{2N}(z+h_2) \quad (24)$$

$$\phi_b = \sum_{N=2}^{\infty} \frac{ig}{\omega(-1)^{N-1}} A_{bN} \exp[K_{2N}(x-b)-i\omega t] \cos K_{2N}(z+h_2) \quad (25)$$

where: A_{ij} represent wave amplitudes in regions 1 and 3 and pressure head amplitudes in region 2; and K_{ij} represent separation constants or eigenvalue wave numbers in each region. The first subscript identifies the region, while the second subscript identifies the modal number.

The wave numbers are solved from dispersion equations in each region. The dispersion equations result from Eq. (19) in regions 1 and 3 and a combination of Eqs. (14) and (15) in region 2. The appropriate dispersion equation in regions 1 and 3 is

$$\omega^2 = g K_{ij} \tanh (K_{ij} h_i) \quad (26)$$

The K_{i1} wave numbers are the real roots of Eq. (26) and the K_{iN} wave numbers with $N \geq 2$ are the imaginary roots to Eq. (26). The appropriate dispersion equation in region 2 is

$$K_{2N} = \frac{(N-1)\pi}{(h_2-d)} \quad \text{for } N \geq 2 \quad (27)$$

Summarizing, the velocity potential in region 1 is

$$\phi_1 = \phi_i + \phi_r \quad (28)$$

The velocity potential in region 2 is

$$\phi_2 = \phi_o + \phi_a + \phi_b \quad (29)$$

The velocity potential in region 3 is

$$\phi_3 = \phi_t \quad (30)$$

Orthogonalized Interfacial Boundary Conditions

Only the incident wave amplitude in Eq. (20) is known. The remaining amplitudes are unknowns and must satisfy pressure and mass flux

continuity at the interfaces between regions. Pressure continuity requires that the pressure field solutions in each region provide identical results at common boundaries between regions. Thus

$$p_1 = p_2 \quad \text{at } x = -b \quad (31)$$

$$p_2 = p_3 \quad \text{at } x = +b \quad (32)$$

Referring to Eq. (11) and recognizing that $f = 0$, $S = 1.0$ in regions 1 and 3, Eqs. (31) and (32) become

$$\phi_1 = (S + if) \phi_2 \quad \text{at } x = -b \quad (33)$$

$$\phi_3 = (S + if) \phi_2 \quad \text{at } x = +b \quad (34)$$

Mass flux continuity requires that mass be conserved as flow proceeds from one region to another. Recognizing that region 2 may be occupied by a porous medium, the velocities within the pore spaces must increase inversely proportional to the porosity to maintain mass flux continuity at the interface. Thus, if ϵ is the porosity in region 2, the velocities normal to the interfaces will be related according to

$$\frac{\partial \phi_1}{\partial x} = \epsilon \frac{\partial \phi_2}{\partial x} \quad \text{at } x = -b \quad (35)$$

and

$$\frac{\partial \phi_3}{\partial x} = \epsilon \frac{\partial \phi_2}{\partial x} \quad \text{at } x = +b \quad (36)$$

Note that mass flux continuity reduces to velocity continuity if no porous medium exists.

Each interfacial boundary condition includes an infinite series of terms. The terms within the series may be separated to generate $4N$ equations to solve $4N$ unknown amplitudes by utilizing the orthogonal behavior of the z dependent separable functions. The boundary value problems in Figure 2 are all linear, homogenous, second order differential equations with linear, homogenous boundary conditions. Accordingly, they are properly posed Sturm-Liouville problems with orthogonal solutions having the useful property that products of two modal solutions, integrated between boundaries having homogenous boundary conditions, vanish unless the modes are identical (Hildebrand, 1965). Thus

$$\int_0^{-h_1} \phi_{iM} \phi_{iN} = 0 \quad \text{unless } M = N \quad (37)$$

Equation (37) applies equally well to derivatives of ϕ .

This behavior is utilized by multiplying Eqs. (33) and (34) by ϕ_2 and integrating from $z = -h_2$ to $z = -d$. Similarly, Eq. (35) is multiplied by $\frac{\partial \phi_1}{\partial x}$ and integrated from $z = -h_1$ to $z = 0$; and Eq. (36) is multiplied by $\frac{\partial \phi_3}{\partial x}$ and integrated from $z = -h_3$ to $z = 0$.

Note that $\frac{\partial \phi_1}{\partial x}$ and $\frac{\partial \phi_3}{\partial x}$ equal zero above $z = -d$ and below $z = -h_2$.

Evaluating these integrals provides the six equations listed below.

$$\sum_{N=1}^{\infty} C_{rN} \left[\frac{K_{11} \cosh K_{11} h_1}{K_{1N} \cosh K_{1N} h_1} \right] \left[\frac{\sinh K_{1N} (h_1-d) - \sinh K_{1N} (h_1-h_2)}{\sinh K_{11} (h_1-d) - \sinh K_{11} (h_1-h_2)} \right] + (C_{a1} - C_{b1}) \left[\frac{(S+if)(h_2-d) K_{11} \cosh K_{11} h_1}{\sinh K_{11} (h_1-d) - \sinh K_{11} (h_1-h_2)} \right] = -1 \quad (38)$$

$$\sum_{N=1}^{\infty} C_{rN} \left[\frac{\cosh K_{11} h_1}{\cosh K_{1N} h_1} \right] \frac{K_{1N}}{K_{11}} \left[\frac{(-1)^{(M-1)} \sinh K_{1N} (h_1-d) - \sinh K_{1N} (h_1-h_2)}{(-1)^{(M-1)} \sinh K_{11} (h_1-d) - \sinh K_{11} (h_1-h_2)} \right] \left[\frac{K_{11}^2 + K_{2M}^2}{K_{1N}^2 + K_{2M}^2} \right] - [C_{aM} + C_{bM} \exp(-2K_{2M}b)] \left[\frac{(h_2-d)(S+if)(\cosh K_{11} h_1)(K_{11}^2 + K_{2M}^2)}{2K_{11} [\sinh K_{11} (h_1-d) + (-1)^M \sinh K_{11} (h_1-h_2)]} \right] = -1$$

for $M \geq 2$ (39)

$$\sum_{N=1}^{\infty} C_{tN} \left[\frac{K_{11} \cosh K_{11} h_1}{K_{3N} \cosh K_{3N} h_3} \right] \left[\frac{\sinh K_{3N} (h_3-d) - \sinh K_{3N} (h_3-h_2)}{\sinh K_{11} (h_1-d) - \sinh K_{11} (h_1-h_2)} \right] - (C_{a1} + C_{b1}) \left[\frac{(S+if)(h_2-d)(K_{11} \cosh K_{11} h_1)}{\sinh K_{11} (h_1-d) - \sinh K_{11} (h_1-h_2)} \right] = 0 \quad (40)$$

$$\sum_{N=1}^{\infty} C_{tN} \left[\frac{\cosh K_{11} h_1}{\cosh K_{3N} h_3} \right] \frac{K_{3N}}{K_{11}} \left[\frac{(-1)^{(M-1)} \sinh K_{3N} (h_3-d) - \sinh K_{3N} (h_3-h_2)}{(-1)^{(M-1)} \sinh K_{11} (h_1-d) - \sinh K_{11} (h_1-h_2)} \right] \left[\frac{K_{11}^2 + K_{2M}^2}{K_{3N}^2 + K_{2M}^2} \right] - [C_{aM} \exp(-2K_{2M}b) + C_{bM}] \left[\frac{(h_2-d)(S+if)(\cosh K_{11} h_1)(K_{11}^2 + K_{2M}^2)}{2K_{11} (\sinh K_{11} (h_1-d) + (-1)^M \sinh K_{11} (h_1-h_2))} \right] = 0$$

for $M \geq 2$ (41)

$$C_{rM} \left[\frac{\cosh K_{11} h_1}{\cosh K_{1M} h_1} \right] \left[\frac{2K_{1M} h_1 + \sinh 2K_{1M} h_1}{2K_{11} h_1 + \sinh 2K_{11} h_1} \right] + C_{a1} \left[\frac{-4i\epsilon \cosh K_{11} h_1 [\sinh K_{1M} (h_1-d) - \sinh K_{1M} (h_1-h_2)]}{b K_{1M} (2K_{11} h_1 + \sinh 2K_{11} h_1)} \right] + \sum_{N=2}^{\infty} [-C_{aN} + C_{bN} \exp(-2K_{2N}b)] \left[\frac{K_{2N} K_{1M}}{K_{1M}^2 + K_{2N}^2} \right] \left[\frac{-4i\epsilon \cosh K_{11} h_1 [\sinh K_{1M} (h_1-d) + (-1)^N \sinh K_{1M} (h_1-h_2)]}{2K_{11} h_1 + \sinh 2K_{11} h_1} \right] = \delta_{M1} \quad (42)$$

$$\begin{aligned}
& -C_{tM} \left[\frac{\cosh K_{11} h_1}{\cosh K_{3M} h_3} \right] \left[\frac{2K_{3M} h_3 + \sinh 2K_{3M} h_3}{2K_{11} h_1 + \sinh 2K_{11} h_1} \right] \\
& + C_{a1} \left[\frac{-4i\epsilon \cosh K_{11} h_1 [\sinh K_{3M} (h_3 - d) - \sinh K_{3M} (h_3 - h_2)]}{b K_{3M} (2K_{11} h_1 + \sinh 2K_{11} h_1)} \right] \\
& + \sum_{N=2}^{\infty} [-C_{aN} \exp(-2K_{2N} b) + C_{bN}] \left[\frac{K_{2N} K_{3M}}{K_{3M}^2 + K_{2N}^2} \right] \\
& \left[\frac{-4i\epsilon \cosh K_{11} h_1 [\sinh K_{3M} (h_3 - d) + (-1)^N \sinh K_{3M} (h_3 - h_2)]}{2K_{11} h_1 + \sinh 2K_{11} h_1} \right] = 0 \quad (43)
\end{aligned}$$

Six equations result, rather than four, because orthogonalizing pressure continuity with respect to the inner modes generates two additional unique equations, one at each interface, for the propagating mode beneath the structure. Each equation is summed on N but is repeated for each M th eigenvalue. Equations (38) and (40) apply to the $M=1$ mode beneath the structure while Eqs. (39) and (41) complete the pressure continuity requirements for $M \geq 2$. Equations (42) and (43) are statements of mass flux continuity, orthogonalized with respect to the outer modes of regions 1 and 3, and apply to all $M \geq 1$. Thus $4M$ equations are produced to solve for $4M$ unknown amplitudes: M reflected waves, M transmitted, and M waves in both the $+x$ and $-x$ directions under the structure.

In Eqs. (38) through (43), the complex amplitudes A_{ij} have been rendered dimensionless by division with the incidental wave amplitude A_i and are denoted as C_{ij} . The Kronecker delta appears as δ_{M1} . The system of $4M$ equations becomes finite by establishing a finite upper limit for the N summation. The amplitude coefficients, C_{ij} , become smaller as j increases and experience with this set of equations, for most practical structural configurations, has demonstrated that summing on five modes is sufficient. Errors due to this finite summation are on the order of a few percent or less. Up to 20 modes have been utilized for unusual configurations such as thin plates.

The $4M$ system of linear algebraic, complex equations is solved via the IBM Scientific Subroutine SIMQ, modified to accept complex coefficients. Amplitudes and phases for each modal amplitude are determined by calculating the modulus and argument, respectively, of each C_{ij} . The reflection and transmission coefficients for the propagating modes are simply $|C_{r1}|$ and $|C_{t1}|$, respectively. Approximately six-tenths of a computer system second are required to solve for a single wave-structure condition described by a five mode series.

Theoretical Behavior

Predicted wave response, quantified as reflection and transmission coefficients, is presented for a hypothetical structure as a function of

dimensionless wave number in Fig. 3-a, b and c. The results show that shorter waves experience more reflection and less transmission at the structure. In addition, as the resistance beneath the structure is increased via an increase in the friction coefficient, f , inertial coefficient, S , or decrease in porosity, ϵ , reflection is increased, attenuation is increased and transmission is decreased. Figure 3-d demonstrates that increased frictional resistance beneath the structure leads to increased energy dissipation. However, an upper limit for energy dissipation is reached at 1/2 the available incident wave energy. Further increases in frictional resistance simply cause 50 percent of the wave energy to be reflected rather than completely absorbed and dissipated beneath the structure.

The results of the present analysis compare favorably with those predicted by other investigators utilizing alternative solution techniques. Sample comparisons are presented in Figs. 4 and 5. Reflection and transmission coefficients results are compared in Fig. 4-a, b, c and d for various structural configurations. The variational technique of Black (1970) in Figs. 4-a, c and d displays essentially identical results to the present theory with negligible resistance ($f=0, S=1.0, \epsilon=1.0$). John's shallow water dock theory (Ippen, 1966) also concurs. The matched asymptotic expansion theory of Tuck (1971) for a narrow slit in a thin, infinitely deep plate also agrees well with the present theory if finite values are used for the depth and plate thickness. Even the long wave behavior is reproduced well, contrasting the variational results in Fig. 4-b.

The horizontal and vertical forces induced by waves acting on the structure are evaluated by integrating the pressure distribution on vertical and horizontal structure surfaces, respectively. The vertical dynamic wave force component is

$$F_{VD} = \int_{-b}^{+b} p dx = \rho\omega(f-iS) \int_{-b}^{+b} \phi_2 dx$$

Substituting for ϕ_2 and evaluating the integral yields

$$F_{VD} = \gamma(S+if) \exp(-i\omega t) \left(2b A_{b1} + \sum_{N=2}^{\infty} \left[\frac{1-\exp(-2K_{2N}b)}{K_{2N}} \right] (A_{aN}+A_{bN}) \right) \tag{44}$$

The horizontal dynamic wave force component is the difference in forces on the two sides of the structure.

$$F_H = \int_0^{-d} p_1 dz - \int_0^{-d} p_3 dz = \int_0^{-d} \rho i \phi_1 (@x=-b) dz + \int_0^{-d} \rho i \phi_3 (@x=b) dz$$

Substituting for ϕ_1 and ϕ_3 and evaluating the integrals yields

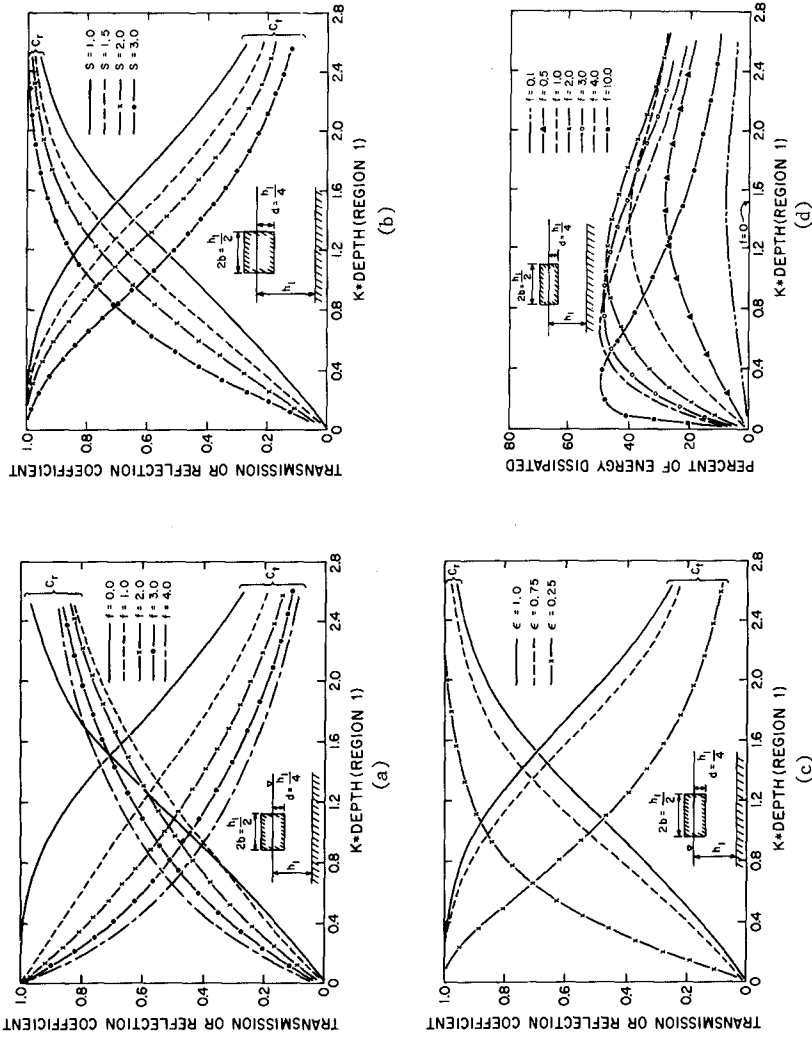


Figure 3. Theoretical Dependence of Wave Response on (a) Friction Coefficient, (b) Inertial Coefficient, (c) Porosity, (d) Friction Coefficient Related to Energy Dissipation

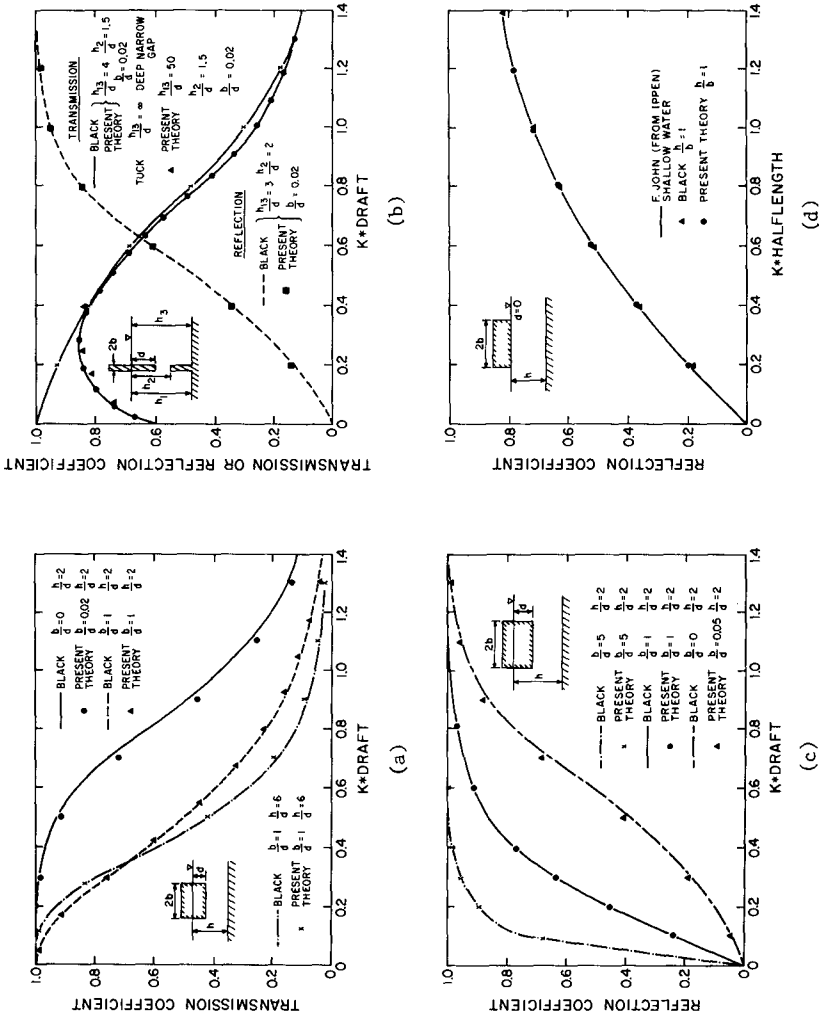
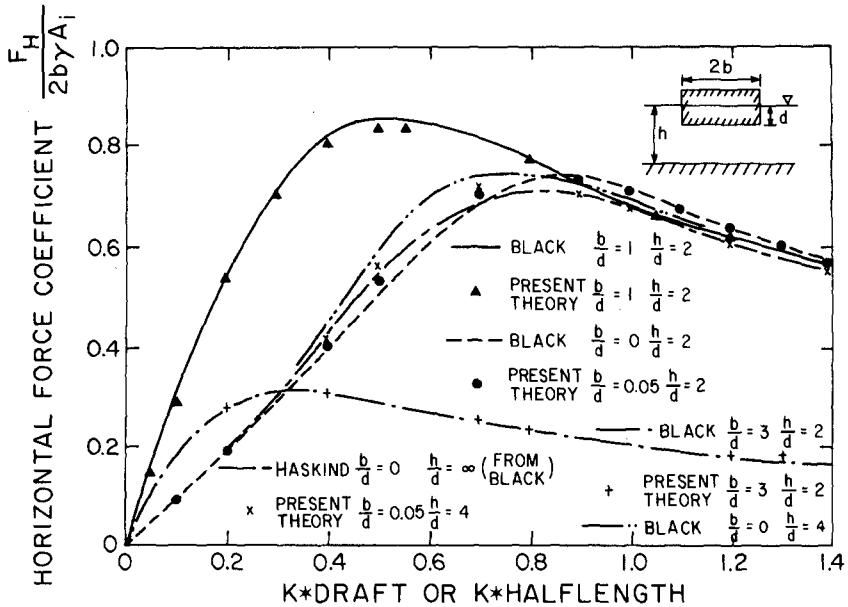


Figure 4. Predicted Wave Response Compared to Other Theories for Structures Characterized as (a) Finite Draft, (b) Thin Plate, (c) Finite Draft, (d) Zero Draft



(a)

(b)

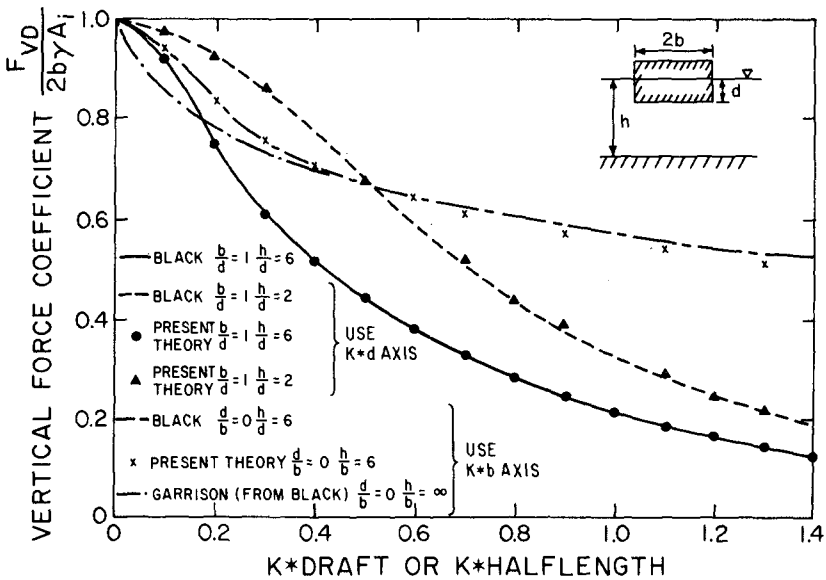


Figure 5. Predicted Wave Forces Compared to Other Theories (a) Horizontal Component, (b) Vertical Component

$$\begin{aligned}
 F_H = \gamma \exp(-i\omega t) & \left[\frac{A_1 [\sinh K_{11}(h_1-d) - \sinh K_{11}h_1]}{K_{11} \cosh K_{11}h_1} \right. \\
 & + \sum_{N=1}^{\infty} \frac{A_{rN} [\sinh K_{1N}(h_1-d) - \sinh K_{1N}h_1]}{K_{1N} \cosh K_{1N}h_1} \\
 & \left. - \sum_{N=1}^{\infty} \frac{A_{tN} [\sinh K_{3N}(h_3-d) - \sinh K_{3N}h_3]}{K_{3N} \cosh K_{3N}h_3} \right] \quad (45)
 \end{aligned}$$

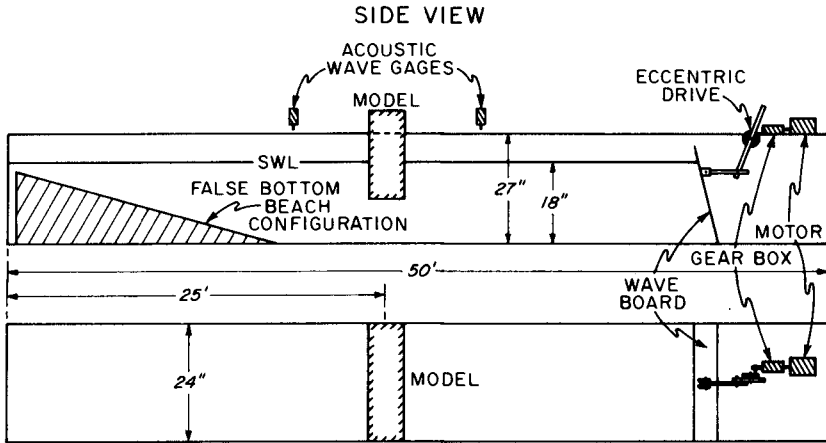
Dimensionless force components from Eqs. (44) and (45) have been graphed in Fig. 5-a and b. Results taken from Black (1970) include comparisons with the work of Garrison and Haskind. The comparisons are quite favorable, with only slight differences for very thin plates.

Experimental Results

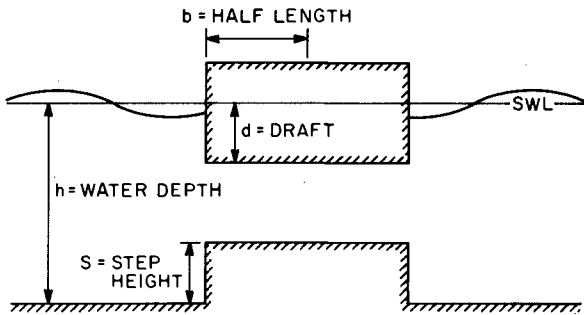
A small scale experimental program was conducted at Oregon State University to supplement the available data on wave reflection and transmission at rectangular structures. The experiment apparatus is described in Fig. 6-a and the geometric configurations tested are identified in Fig. 6-b. Each model was exposed to a variety of wave amplitudes and frequencies. Incident and reflected waves were resolved with a traversing wave gauge from measurements of the partial standing wave envelope. Transmitted wave measurements were acquired with a stationary wave gauge.

Transmission coefficient results are displayed in Fig. 7. Four combinations of draft, depth and step height are shown with results expressed relative to dimensionless wave numbers. Theoretical results are expressed for frictionless conditions. In general the agreement between experiment and theory is quite good. In Figs. 7-a, b and c, the theory tends to slightly overpredict the transmission coefficient. A non-zero value for the friction coefficient would tend to improve this correlation, indicating that real fluid effects may be modifying the experimental results. Figure 7-d shows the theory underpredicting transmission slightly for long waves. This model configuration has zero draft so that the long wave trough passes under the model without surface contact. The theory does not allow for the separation of the water and model surfaces, a condition which is unlikely to occur in the prototype.

Experimental and theoretical reflection coefficients are presented in Fig. 8-a and b. In general the theory tends to overpredict the measured reflection coefficients. Again, this correlation can be improved by utilizing a non-zero value for the friction coefficient, f , to account for real fluid effects. Small increases in f tend to decrease both the reflection and transmission coefficient as indicated in Figs. 3-a and 8-c. The frictional condition displayed in Fig. 8-c evaluates energy loss due to skin drag over the structure surface and expansion/contraction losses at the abrupt corners of the structure. The corrections indicated improve the correlation with the experimental data, however, larger losses need to be identified to further correct the predicted reflection



(a)



(b)

RUN #	b(in.)	S(in.)	h(in.)	d(in.)
1	4	0	18	8 1/8
2	4	0	18	6
3	4	0	18	2 3/4
4	4	8 1/4	18	2 3/4
5	4	8 1/4	18	5 1/2
6	4	8 1/4	18	0
7	4	0	18	0

Figure 6. Experimental Program (a) Apparatus, (b) Model Configurations

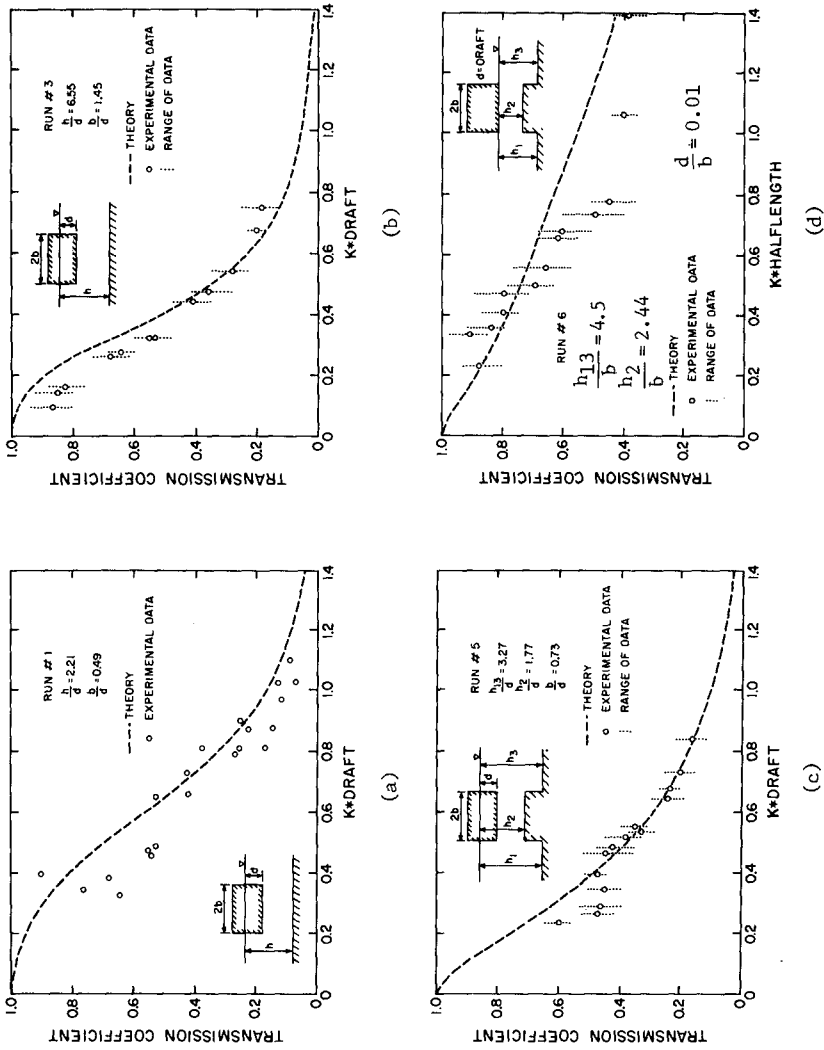


Figure 7. Comparison of Theoretical and Experimental Transmission Coefficients (a) Run #1, (b) Run #3, (c) Run #5, (d) Run #6

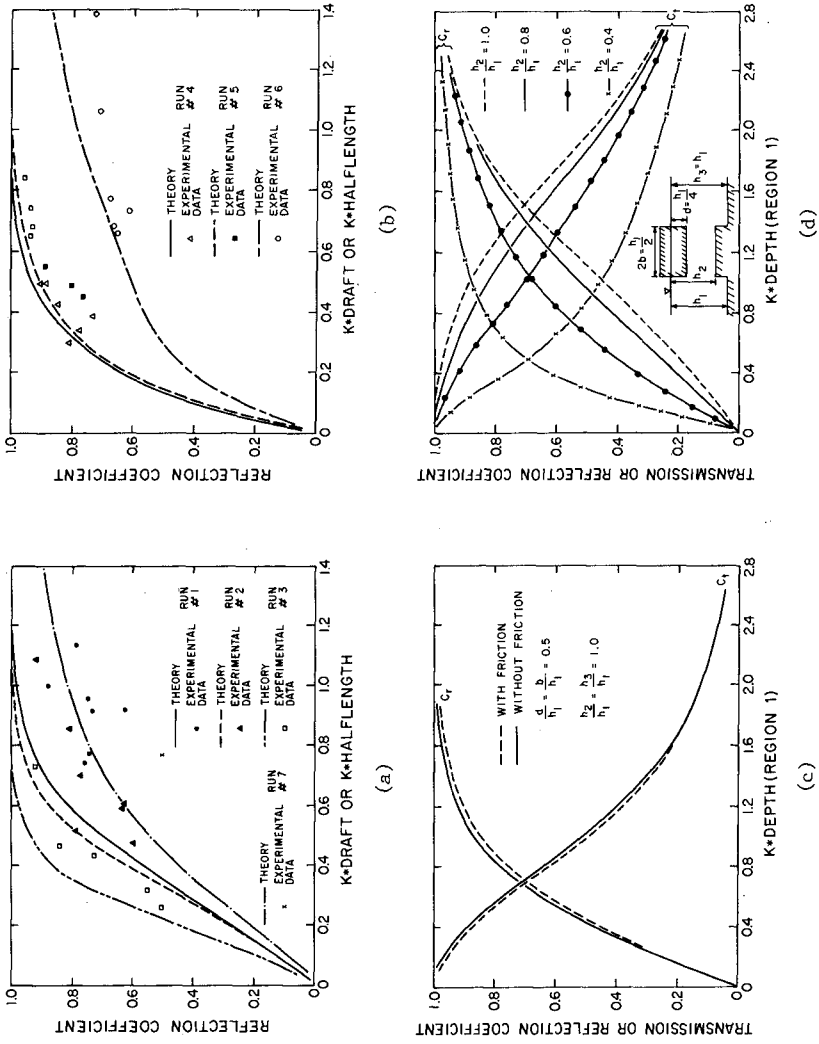


Figure 8. Comparison of Theoretical and Experimental Reflection Coefficients (a) Run #1, 2, 3, (b) Run #4, 5, 6, (c) Predicted Wave Response With and Without Friction, (d) Predicted Design Curves

coefficients. Evidently the steady flow relationships for skin friction and expansion/contraction losses are not adequate for addressing the same condition instantaneously in unsteady flows. A more complete discussion of friction coefficient evaluation is presented by Steimer (1977).

Design curves for various drafts and step heights have been prepared for the frictionless condition. A sample curve is presented in Fig. 8-d.

Conclusions

The theoretical analyses presented in this study correlates well with other rigorous analytical procedures and with available experimental data. The theory can accommodate a variety of rectangular structural configurations and it provides a rational method for incorporating real fluid losses. The solution technique is numerically efficient in providing reflection, transmission and force coefficients. Additional experimental work is required to validate force predictions and to suggest alternative friction laws to evaluate real fluid effects.

Acknowledgments

This work is a result of research sponsored in part by the Oregon State University Sea Grant College Program, U.S. Department of Commerce, under Grant No. 04-7-158-44085. The U.S. Government is authorized to produce and distribute reprints for governmental purposes notwithstanding any copyright notation that may appear hereon.

References

1. Black, J.L., and Mei, C.C., "Scattering and Radiation of Water Waves," Massachusetts Institute of Technology Water Resources and Hydrodynamics Laboratory Report No. 121, April, 1970.
2. Hildebrand, F.B., Advanced Calculus for Applications, Prentice Hall, Inc., N.J., 1965.
3. Ijima, T., et al., "Scattering of Surface Waves and the Motions of a Rectangular Body by Waves in Finite Depth," Proceedings, Japanese Society of Civil Engineering, No. 202, June 1972, pp. 33-48.
4. Ippen, A.T., ed., Estuary and Coastline Hydrodynamics, First ed., McGraw-Hill Book Company, Inc., New York, N.Y., 1966.
5. Steimer, R.B., "An Eigenvalue Wave Analysis of Fixed Semi-Immersed Rectangular Structures," Thesis for Master of Ocean Engineering Degree, Oregon State University, Corvallis, OR, 1977.
6. Tuck, E.O., "Transmission of Water Waves Through Small Apertures," Journal of Fluid Mechanics, Vol. 49, part 1, 1971, pp. 65-74.

CHAPTER 134

Effects of Wave Grouping on Breakwater Stability

by

R.R. Johnson*, E.P.D. Mansard** and J. Ploeg***

ABSTRACT

It has been found that certain sequences of waves, such as occurring within well defined wave groups, can cause greater damage to rubble mound structures, than equally high individual waves dispersed throughout a wave train. It has therefore been necessary to develop a new wave synthesizing technique, which allows control of the phasing of the wave frequencies, so that a similar degree of wave grouping can be produced in the laboratory as is expected to occur at a particular location in the prototype.

Also, during the course of this investigation, an attempt was made to simulate the strength of concrete armour units to the correct model scale. The breaking of armour units, due to their rocking or being displaced, resulted in a much higher percentage of damage, than would have been possible to predict from tests with commonly used model armour units.

INTRODUCTION

Rubble mound breakwaters undoubtedly belong to the oldest type of coastal structures, and therefore their design procedures have a long history. Simple empirical design criteria were originally based on full scale experiences with these structures. In the more recent past, extensive model testing in hydraulics laboratories throughout the world has modified the criteria considerably, mostly by including more parameters, but still making use of a number of empirical coefficients. This stems mostly from the difficulty of being able to define accurately the physical process of waves breaking on a structure.

Magoon and Baird (1) list some nine parameters affecting the stability of a rubble mound structure, while Bruun

*Assistant Professor, University of Tennessee at Chattanooga, Tennessee, U.S.A.

**Research Associate, Hydraulics Laboratory, National Research Council of Canada, Ottawa, Ontario K1A 0R6 Canada

***Head, Hydraulics Laboratory, National Research Council of Canada, Ottawa, Ontario K1A 0R6 Canada

and Gunbak (2) list a total of twelve parameters, which include most of the nine of the previous authors. Gravesen and Sorensen (3) have attempted to include some of the suggested parameters in their proposed design criteria and have further pointed out the importance of the occurrence of wave grouping, similar to a previous paper by Johnson and Ploeg (4) on this subject. As early as 1966, Carstens et al (5) show damage versus wave height curves for regular and irregular wave trains, with the latter differing in the amount of wave grouping due to different spectral shapes. The curves indicate clearly that the grouped wave train causes greater damage than the non-grouped for the same significant wave heights.

Most of the recently proposed breakwater design formulae are based on laboratory experiments using irregular wave generating equipment. Typically one sees in the literature comparisons between power spectral density functions of naturally occurring sea states and those obtained in wave flumes. Of course the shape of this amplitude spectrum is indeed an essential element in the definition of wave conditions, but if breakwater stability criteria do include a wave period parameter, as well as resonance phenomena as stated by Bruun and Johannesson (6), then the amplitude portion of the power spectral density function alone will not be sufficient to define the sea state. Perhaps somewhat too readily have oceanographers and coastal engineers in the early sixties assumed that a sea state is a continuous random process. Therefore, when a Fourier transform was performed on a recorded wave train, only the amplitude portion of the spectrum was kept and the phase spectrum was ignored as containing no relevant information when dealing with a random process.

It is well known that second order wave forces exerted on floating structures depend heavily on the occurrence of wave grouping. The stability of rubble mound breakwaters appears to be significantly affected by the actual sequence of certain waves in a particular wave train, which tend to occur in wave groups. To test the sensitivity of rubble mound breakwaters to wave grouping, an irregular wave generation technique was developed by Mansard and Funke (7) to allow independent control over the spectrum and the "groupiness" of a wave train, using the information contained in the phase spectrum to control groupiness. With this technique it is then possible to investigate the different modes of failure or stability criteria while maintaining the same energy spectrum, but varying the amount of groupiness. Tests show that different wave trains with similar power spectral density functions and therefore similar RMS values and peak frequencies, and similar wave height statistics, but different wave grouping, do result in rather different stability criteria.

In tests reported previously by Johnson and Ploeg (4), the importance of wave grouping was demonstrated by comparing the effects of a series of artificially constructed wave groups and a non-grouped wave train with the same amplitude spectrum, but randomly assigned phases. These two wave conditions are shown in Fig. 1, and the test results were for a 1:2 slope dolos armoured breakwater, where both wave trains exhibited a significant wave height of 7.6 m, a peak period of 11 s, and a maximum wave height of 11 m. For the non-grouped wave train, some of the dolosse were seen to "rock" in place, but not to the point of being displaced from their locations. However, the sequence of large waves in the artificially grouped wave train (containing no larger wave heights than those encountered in the non-grouped wave train, but consecutively following one another) produced continual displacement of 5 to 7 armour units and severe rocking of most of the armour with each wave group. Since the artificial groups appeared rather unrealistic, the tests

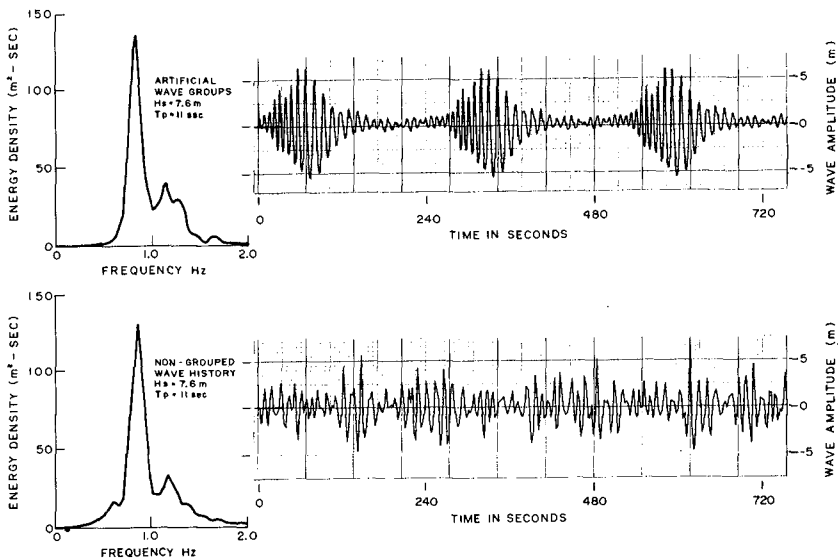


FIG.1 WAVE ENERGY DENSITY SPECTRA
AND GROUPED AND NON-GROUPED WAVE TRAINS

reported in this paper will show a comparison between the effects of a wave train synthesized to have the same degree of groupiness as an actual prototype wave record from a station on the east coast of Canada, and a wave train with the same spectral shape and wave statistics, but randomly assigned phases as commonly used in irregular wave generation.

Of the various types of armour units currently being used for breakwater protection, dolosse seem to be particularly sensitive to certain sequences of waves in a wave train because of the possibility of the units being broken when rocked by wave impact. Visual observations indicate that it appears to be the first wave in a group that loosens the unit, but the second and third waves which produce the damaging motion.

Recently tests have been carried out on a model of the Sines breakwater in Portugal by Ploeg and Mansard (8), where the tensile strength of the concrete in the shank of the dolosse was simulated to the correct model scale, thus allowing a more realistic view of the importance of the breaking of armour units during storm conditions. The tests indicated that for large dolosse, breakage is a key factor in determining a suitable stability criterion and therefore this effect must be taken into consideration when carrying out model tests of rubble mound breakwaters.

FLUME FACILITIES

The wave group effect tests were carried out in a flume described in Fig. 2. A 1:1.5 slope rubble mound breakwater, with dolosse for armour was placed 50 m from the wave board in a 75 m long flume. The 2 m wide flume was divided into a centre channel of 1 m and two side channels each of 0.5 m width. The breakwater was built in the middle channel only. The channel dividers extended from 30 m in front of the breakwater back to the end of a 1:20 slope beach behind the breakwater. The dividers reduced the influence of reflections from the breakwater back to the wave board, and for that reason they were perforated over part of their length. Experiments performed before and after construction of the breakwater showed the arrangement to be quite satisfactory. The hydraulically driven wave machine was computer controlled to generate any specified wave train. Wave height sampling was done with capacitance probes located 2.5 m from the wave board and 3 m in front of the breakwater as shown in Fig. 2. Glass panels in the flume at the location of the breakwater allowed for visual observations and photographic records to be made of the breakwater under wave action. Fig. 3 shows the cross section of the model breakwater, used for these experiments.

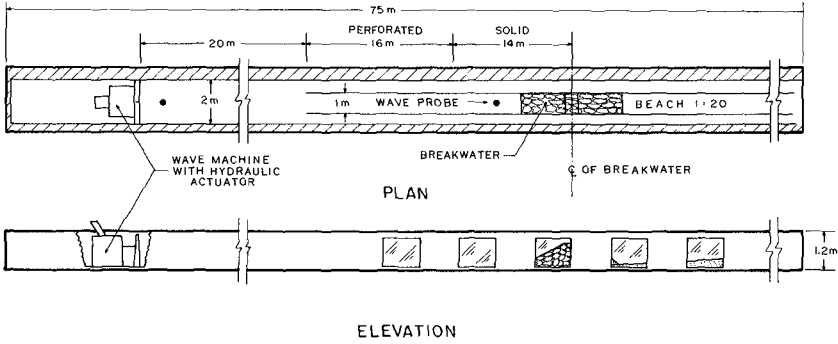


FIG. 2 WAVE FLUME-EXPERIMENTAL SET-UP

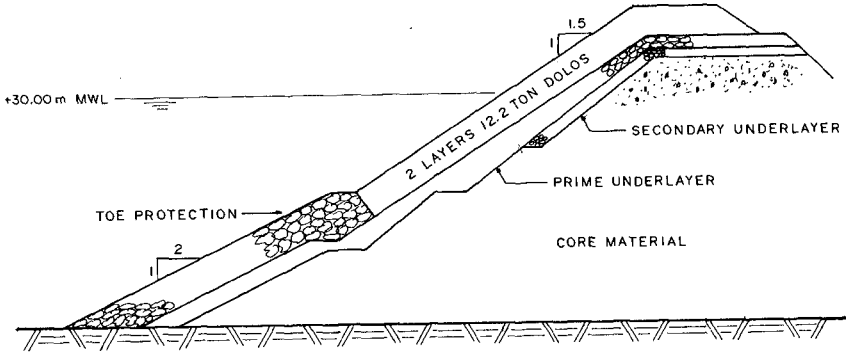


FIG. 3 CROSS-SECTION OF THE MODEL BREAKWATER

WAVE GENERATION

An essential part of this study has been the capability to generate at the test section in the wave flume a desired wave train. This has been achieved by means of a phase and amplitude compensated technique described by Mansard and Funke (9). It has also been necessary to use the synthesis technique, referred to earlier (7) which allows control over the phasing of the frequencies and therefore the groupiness of the wave conditions in the flume. The phase spectrum of a wave train has proven to be an important factor and if reproduced can lead to a predetermined amount of wave groupiness in any wave record.

Any periodic time record can be described as a Fourier series with the linear combination of all those cosine and sine functions which have the same period, say as

$$f(t) = a_0/2 + \sum_{n=1}^{\infty} a_n \cos \frac{2\pi n t}{T} + \sum_{n=1}^{\infty} b_n \sin \frac{2\pi n t}{T}$$

where:

$a_0/2$ - mean value

a_n, b_n - Fourier coefficients for the frequency component of the order 'n'

From these Fourier coefficients, the values of the amplitudes A_n , and the phase angles ϕ_n , associated with each frequency component can be derived as follows:

$$A_n = \sqrt{a_n^2 + b_n^2} \quad \text{and} \quad \phi_n = \tan^{-1} \frac{b_n}{a_n} \quad \text{for } n=1,2,3,\dots\infty$$

The variation of these amplitudes over the frequency is referred to as the "Amplitude Spectrum" and that of the phase angles over the frequency as the "Phase Spectrum". Hence any periodic time record can be represented by its Amplitude and Phase spectrum in the frequency domain.

In a laboratory simulation of sea states, very often, importance is attributed to the amplitude spectrum alone, thereby reproducing only the amplitude associated with each frequency component and disregarding the importance of its phase spectrum. One of the main reasons is that the phases appear to be randomly varying within $-\pi$ to π , and are assumed to contain no useful information.

It has been found that the phases can be important and that the use of the amplitude spectrum alone does not give a unique description of the wave record associated with it. A combination of the same amplitude spectrum with different phase spectra can result in entirely different wave trains (grouped or ungrouped). Hence if it is required to reproduce a particular wave record, say as found in the prototype, it is necessary to reproduce the phase spectrum associated with it and it is not sufficient to use randomly selected phases as most of the presently available synthesis techniques do.

In order to illustrate that identical amplitude spectra (Fig. 4a) can lead to different time functions depending on the particular choice of a phase spectrum, the following

two, perhaps somewhat extreme, cases are presented. In the first case, the phase spectrum is defined by means of a random selection via a noise generator with uniform distribution of numbers from $-\pi$ to $+\pi$ and in the second case, the phase is made to vary linearly over a limited range as illustrated in Fig. 4b. The time functions derived from these two identical amplitude spectra, but different phase spectra are, as shown in Fig. 4c, quite different. Further considerations of the relevance of the phase spectra are given in Funke and Mansard (10).

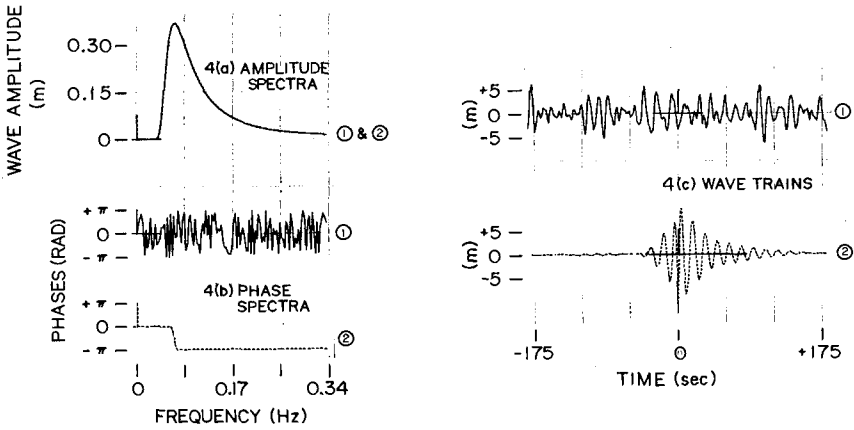


FIG. 4 EFFECT OF THE PHASE SPECTRA ON WAVE TRAINS

A measure of wave groupiness can perhaps be obtained by plotting the "instantaneous wave energy history" (IWEH) of a wave record. This function represents the square of the instantaneous water surface elevations, smoothed by taking a running average over a time interval equal to the period associated with the peak frequency of the energy density spectrum.

There are several steps involved in synthesizing a wave history with the same amount of grouping as observed in a prototype wave record. Sinusoidal waves of a frequency equal to the desired peak spectral frequency are modulated by the prototype IWEH. This modulation will produce a time series similar in grouping to that of the original wave record and may be analysed for the phase spectrum by Fourier analysis. The phase spectrum is then used with the desired amplitude spectrum in an inverse Fourier transform to produce a wave record with the proper wave height statistics

and with the frequencies phased to also give the specified wave grouping. This technique is described in full detail in the earlier referred to report of Funke and Mansard (7).

Three wave generation techniques were applied in the tests reported here. The first followed the technique briefly described above where a wave train was synthesized to have the same degree of wave grouping as a prototype wave record, but with a JONSWAP amplitude spectrum. The result is a well grouped wave history, shown in Fig. 5 with its IWEH, and which realistically simulates a prototype situation. The actual prototype wave record, with the corresponding IWEH is also shown in the same figure. For convenience, this synthesized wave train will be referred to as "grouped".

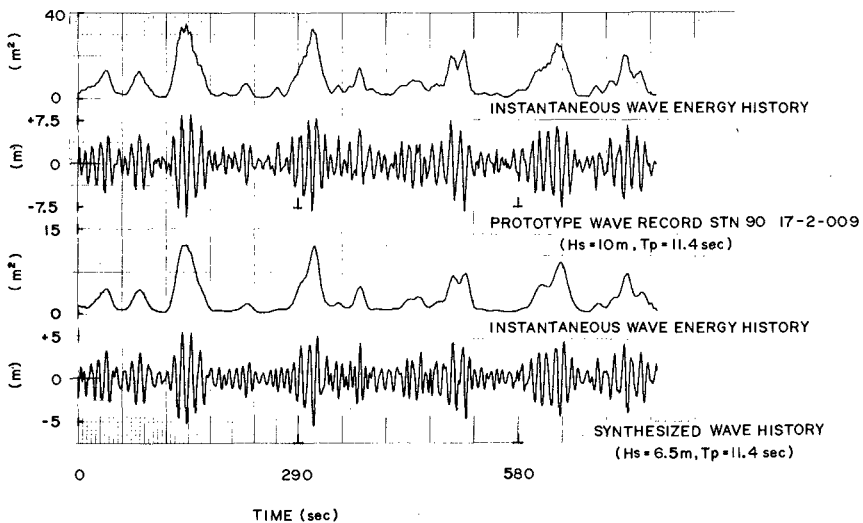


FIG.5 SYNTHESIS OF WAVE GROUPING FROM A PROTOTYPE WAVE RECORD

The second and more common technique, combined a randomly assigned phase spectrum with the same JONSWAP spectrum in an inverse Fourier transform to obtain a wave history of undetermined wave grouping. In this particular case the result is a wave train with little apparent grouping (Fig. 6), and will for convenience be referred to as "non-grouped". Again the IWEH of this non-grouped wave train has been calculated and is also shown in the figure. Fig. 7 presents a comprehensive comparison of the two wave trains

and their corresponding energy density spectra. It can clearly be seen, that whereas the two amplitude spectra are nearly identical, the wave trains are very different, as far as the degree of wave grouping is concerned. It is important to emphasize that using a randomly assigned phase spectrum can produce wave trains with either more or less grouping than a particular prototype record.

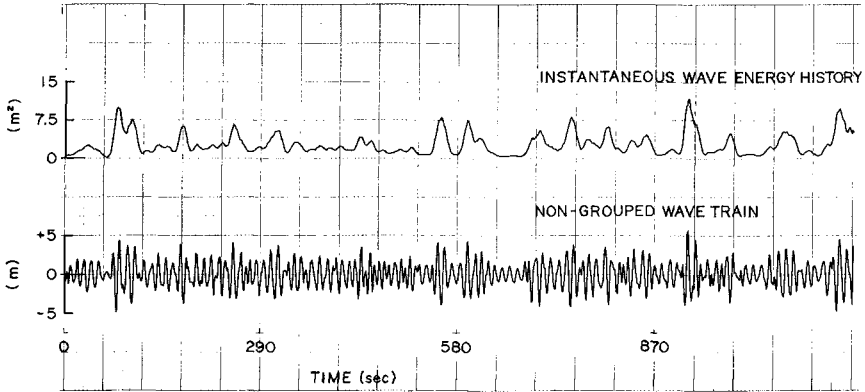


FIG. 6 NON-GROUPED WAVE TRAIN AND ITS INSTANTANEOUS WAVE ENERGY HISTORY

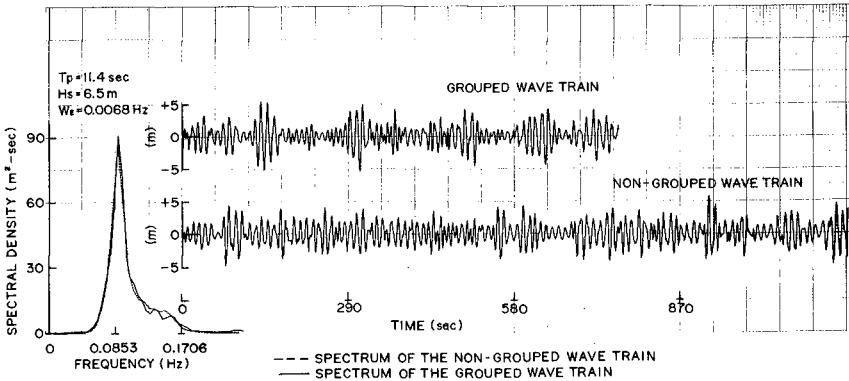


FIG. 7 COMPARISON OF THE GROUPED AND NON-GROUPED WAVE TRAINS

The third technique as presented in the earlier paper by Johnson and Ploeg (4) generated an accentuated and rather artificially grouped wave train, synthesized by an algorithm described by Funke (11) which phases consecutive waves in such a manner that they all focus at a predetermined distance from the wave maker. For convenience, this wave train was referred to as "artificially grouped" and is shown in Fig. 1.

TEST RESULTS AND DISCUSSION

The two examples of the grouped (synthesized to correspond to an observed wave record containing wave grouping) and the non-grouped (generated using a randomly assigned phase spectrum) wave trains, as recorded in deep water conditions, have been shown in Figs. 5, 6 and 7. Both wave trains have a peak period of 11.4 secs and a significant wave height of 6.5 m. To attempt to define the degree of wave groupiness, the RMS value of the instantaneous wave energy history (IWEH) is being proposed. The RMS value of the IWEH of the grouped wave train (Fig. 5) is 0.7 m, while for the non-grouped wave train this value is 0.57 m. The investigation indicates that the breakwater response to the two wave trains is quite different, with the grouped wave train causing severe rocking of the armour and several units to be completely displaced with every wave group (failure mode of 4), but the non-grouped wave train producing only some minor rocking and no displacements (failure mode of 2). A description of modes of failure is given by Baird and Paul (12).

Because the somewhat subjective nature of defining modes of failure, it is difficult to record the results of rubble mound breakwater stability tests precisely, and usable for later reference. The most comprehensive documentation of the results is probably a 16 mm film, made during this study. An edited version of this film was shown at the conference, clearly indicating the differences in the response of the breakwater to the non-grouped and the grouped wave trains.

As mentioned earlier, there does appear to be a mechanism by which the first wave in a group loosens up a unit, the second causes it to be pulled (or pushed) a little out from the armour layer, while the third wave rolls the unit up and down the face of the structure. The non-grouped wave train does not have the same sequence of waves and is therefore not as damaging. It may be possible to relate this partially to the build-up of pressure in the filter layers, and perhaps even the breakwater core, and the resultant stronger down rush.

In Fig. 8 damage factors have been plotted for two types of wave trains, versus the significant wave heights

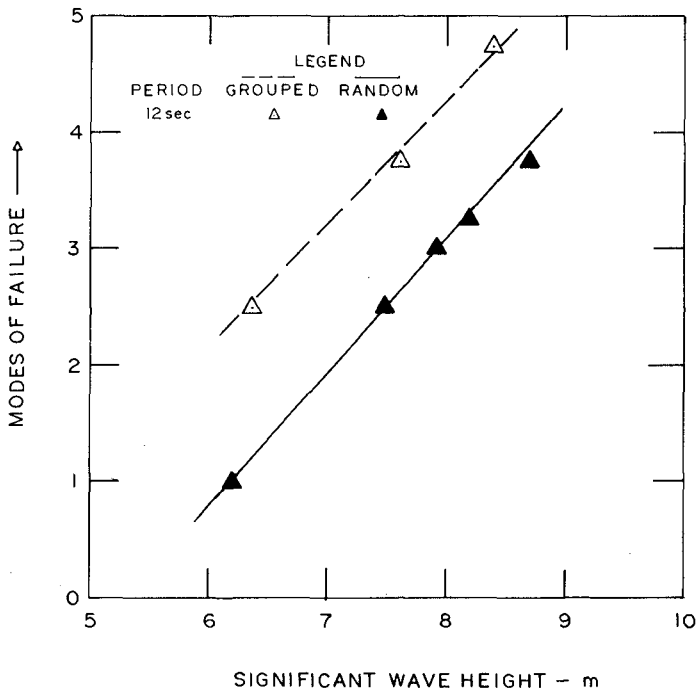


FIG. 8 DAMAGE CURVES FOR GROUPED AND NON-GROUPED WAVE TRAINS VERSUS SIGNIFICANT WAVE HEIGHTS

for the case of a peak period of 12 s. The dolos weight is 12.2 t (metric) modelled to a scale of 1:34.3 on a slope of 1:1.5 (Fig. 3). For equal damage factors the non-grouped wave train clearly permits a considerably higher design wave condition than the grouped.

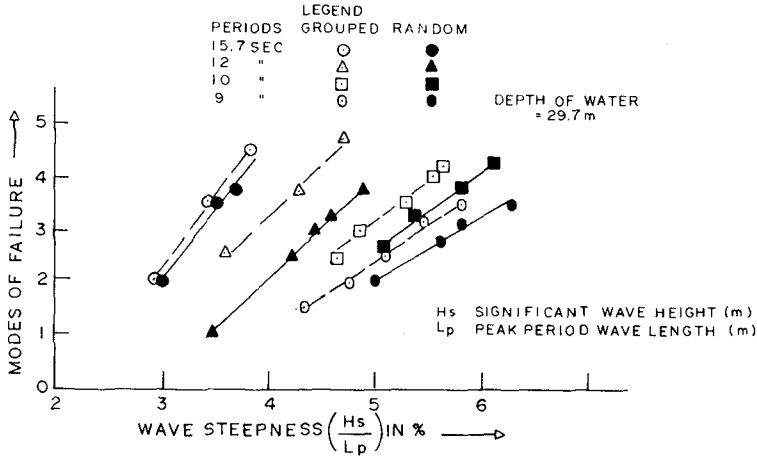


FIG.9 DAMAGE CURVES FOR GROUPED AND NON-GROUPED WAVE TRAINS VERSUS WAVE SLOPES

More extensive tests for different peak periods, dolos weights, water depths and model scales have been carried out and the results are consistently showing a marked difference between the response of grouped and non-grouped wave trains. Fig. 9 is a typical plot of damage factor against wave condition, expressed here as a wave slope parameter in order to include effects related to wave period and water depth. At the time these experiments were performed, however, the method for synthesizing wave grouping was not yet available and the tests were run directly with digitized prototype records, similar to the practice of the Danish Hydraulics Institute (Ref. 13). This means that the peak period variations were achieved by either stretching or compressing the wave history somewhat unrealistically, thus leaving the tests at long and short periods difficult to interpret.

The classification of grouped and non-grouped wave trains is at the present time not clearly defined. It relies mostly on interpretation only. An actual measure of the degree of wave groupiness would ideally come from a

spectral analysis of the IWEH thereby identifying the groups by amplitude, length and frequency of occurrence (and therefore for a given peak frequency, also an indication of the number of waves per group). However, the length of commonly available wave records is usually too short to give an adequate spectral distribution.

With the synthesis technique it is possible to construct wave histories of equal grouping regardless of the width of the power spectral density function, thus showing that spectral width alone cannot be a unique way of determining wave grouping. However, there does seem to be a relationship between the width of the spectrum and the way the amount of groupiness changes with propagation. Further tests are presently under way to consider this aspect.

The tests reported here are all for a dolos armour layer, but the conclusions apply in varying degrees to other types of armour also. The experiments with dolosse did, however, highlight an aspect which applies specifically to this type of unit.

Observing the severe rocking and indeed displacement of dolos units in the model, especially when exposed to the grouped wave trains, leads to the obvious question, how such units will perform when not only the hydraulic parameters are scaled, but also the structural ones. No material has unfortunately been found so far, which has all the correct physical properties to simulate unreinforced concrete (density, elasticity, tensile and compressive strength, friction, etc.) to the correct model scales. Prototype failures of dolos units occur most often through the shank; if it is assumed that this type of failure is mainly caused by exceeding the tensile bending strength of concrete, the model dolos units can be cut and a thin wafer of a material with the correct tensile strength can be inserted. The recent tests on the Sines breakwater (8) were run with a scale of 1:52. To simulate a concrete tensile strength in bending of 35 kg/cm^2 and using the Froude scaling law, a material needed to be used with a tensile strength of about 0.7 kg/cm^2 . A synthetic material, consisting of a mixture of stearic acid and polypropylene, used for artificially modelling the behaviour of ice in the laboratory, has approximately a strength of 0.75 kg/cm^2 . An extensive series of simple and cantilever beam tests was performed to establish the adequacy of inserting a thin wafer of this synthetic material within a much stronger material, to simulate the desired tensile bending strength correctly. Using this simulation technique with the dolos units, the Sines breakwater tests led to an extremely good comparison between prototype and model performance. The results of similar tests, but with commonly used model units, i.e. without scaling any of the strength parameters, were much more difficult to interpret. The actual breaking of the model units

caused immediately the breakage of many other dolosse and a very rapid, general deterioration of the structure. It became quite apparent, that the accepted philosophy of allowing a certain percentage of damage to a rubble mound breakwater as a design condition, can not be relied on when large artificial armour units are used. A 16 mm film of the behaviour of the two types of model units illustrates the differences very clearly. A photograph of the final profile (Fig. 10) shows in the foreground, the completely failed section where dolos units were used which simulated the tensile strength of concrete, but the apparently less damaged section in the background, where the commonly used units were placed.



FIG.10 PHOTOGRAPH OF DAMAGE TO MODEL BREAKWATER
USING MODIFIED DOLOS UNITS

CONCLUSIONS

Firstly, wave grouping has been shown to be an essential parameter in the correct model testing of rubble mound breakwater stability. Since both wave trains considered here had similar spectra and wave statistics, it is evident that one must define the degree of wave grouping as actually observed in nature or as may be expected to occur at a particular location. The typical wave parameters used so far, including a spectral width parameter, are not deemed to give sufficiently accurate description of a particular sea state to allow adequate reproduction in a laboratory wave flume. It is expected that a "groupiness" factor will have to be multi-dimensional, not only taking account of the presence of such groups, but also of the periodicity of their occurrence and their widths.

Secondly, without correctly scaling the strength of concrete of the armour units in model tests of rubble mound breakwaters, it is extremely difficult to determine accurately the percentage of damage. It is not possible to interpret correctly the motions of the armour units, without being able to establish when they will break. As soon as breakage begins to occur, the response of the structure changes drastically, leading very quickly to failure conditions.

REFERENCES

1. Magoon, O. and Baird, W.F., "Breakage of Breakwater Armour Units", Symposium on Design of Rubble Mound Breakwaters, April 1977, Isle of Wight.
2. Bruun, P. and Gunbak, A.R., "Risk Criteria in Design of Sloping Structure in Relation to $\zeta = \tan\alpha\sqrt{H/L_0}$ ", Symposium on Design of Rubble Mound Breakwaters, April 1977, Isle of Wight.
3. Gravesen, H. and Sorensen, T., "Stability of Rubble Mound Breakwaters", Proceedings 23rd PIANC Conference, Leningrad, September 1977.
4. Johnson, R.R. and Ploeg, J., "The Problem of Defining Design Wave Conditions", Ports '77, March 1977, ASCE Specialty Conference.
5. Carstens, T., Torum, A. and Traetteberg, A., "The Stability of Rubble Mound Breakwaters Against Irregular Waves", Proc. 10th Coastal Engineering Conference, September 1966, Tokyo.
6. Bruun, P. and Johannesson, P., "A Critical Review of Hydraulics of Rubble Mound Structures", Institute Report R3-1974, University of Trondheim, Div. of Port and Ocean Engineering.
7. Funke, E.R. and Mansard, E.P.D., "Synthesis of Realistic Sea States in a Laboratory Flume", Hydraulics Laboratory

- Report LTR-HY-66, December 1978, National Research Council of Canada, Ottawa.
8. Mansard, E.P.D. and Ploeg, J., "Model Tests of Sines Breakwater", Hydraulics Laboratory Report LTR-HY-67, October 1978, National Research Council of Canada, Ottawa.
 9. Funke, E.R. and Mansard, E.P.D., "Reproduction of Prototype Random Wave Trains in a Laboratory Flume", Hydraulics Laboratory Report LTR-HY-64, National Research Council of Canada, Ottawa.
 10. Funke, E.R. and Mansard, E.P.D., "On the Meaning of Phase Spectra in the Fourier Transform of Random Wave Trains", Hydraulics Laboratory Report LTR-HY-68, National Research Council, Ottawa.
 11. Funke, E.R., "SPLASH - Program for Synthesis of Episodic Waves in a Laboratory Flume", Hydraulics Laboratory Report LTR-HY-65, National Research Council, Ottawa.
 12. Paul, M.W. and Baird, W.F., "Discussion on Breakwater Units", Proc. of 1st International Conference on Port and Ocean Engineering Under Arctic Conditions, August 1971.
 13. Gravesen, H., Frederiksen, E. and Kirkegaard, J., "Model Tests with Directly Reproduced Nature Wave Trains", Proceedings 14th Coastal Engineering Conference, June 1974, Copenhagen.

LOADINGS ON RUBBLE-MOUND BREAKWATERS DUE TO EARTHQUAKES

by

H. Wang¹, C. Y. Yang², C. Lamison³ and S. S. Chen⁴Introduction

It might reasonably be asked, why study the reaction of a rubble-mound breakwater to earthquake loadings? After all, it is essentially a pile of rubble before an earthquake and is probably only a lower or otherwise deformed pile of rubble afterwards. Repairs are simply a matter of adding more stones. Even if damage occurred, the breakwater might still offer partial protection. This is precisely why, to date, breakwaters are mainly designed for wave loadings. There is practically no documented literature⁽¹⁾ concerning breakwater design for earthquake loading!

However, the oceans are now being tapped as possible locations for industrial installations such as offshore deep water ports, refineries, and power plants. Such facilities must be adequately protected since failures might result in heavy financial losses and cause severe environmental repercussions. Therefore, breakwaters which might be used for this protection can no longer be treated as structures whose failure would only be of secondary consequence. It is thus reasonable to ask whether breakwaters to serve these purposes should also be designed against earthquake loading, since even partial failures might not be acceptable. If they should, then what type of design problems can one expect to encounter and how should one handle them? The present work is aimed at exploring these problems through laboratory experiments.

At present, there is no existing breakwater⁽¹⁾ that has been designed on the basis of earthquake loading. Likewise, observations of breakwaters after continuous earthquakes are also scarce. Okamoto⁽²⁾ reports crumbling of riprap, uneven settlement and loosening or tilting of the upper parts of Japanese breakwaters that have undergone earthquakes. After the large Kanto earthquake of 1927, for instance, breakwaters at the ports of Yokosuka and Yokohama approximately 50 kilometers from the epicenter developed irregularities over their entire lengths. In no cases, however, did any of the breakwaters topple or overturn. During the great Alaska earthquake of 1964, breakwaters at Kodiak City and Seldovia, Kenai Peninsula were badly damaged. The damage to the Kodiak City breakwaters was well documented⁽³⁾ with photographs and surveys taken after the earthquake. The damage was attributed to both earthquake motion and the tsunamis which swept the area. Unfortunately, the

¹Professor, University of Delaware, Department of Civil Engineering, Newark, Delaware 19711, U.S.A.

²Professor, University of Delaware, Department of Civil Engineering, Newark, Delaware 19711, U.S.A.

³Engineer, Brown and Root Co., Houston, Texas, U.S.A.

⁴Graduate Student, University of California, Berkeley, California, U.S.A.

proportion of damage due to each cause could not be determined.

The present work represents an initial attempt to model the breakwater under earthquake loading, to identify failure modes, to determine the trends and degrees of relative importance of various factors and to estimate pressure distributions on the surface. It is an acknowledged fact that the armor layers are the main protection for a breakwater and the current practice in breakwater design is almost exclusively concentrated in the design of armor layer stability against wave force. One of the primary interests of the present tests is, thus, to examine the stability of these armor units against earthquake loading. The dolos was selected for the test program because it is gaining popularity in breakwater construction due to its superior stability against wave attack⁽⁴⁾.

Scaling Laws and Model Design

Breakwater Simulation. It is a well-known fact that proper modeling requires preservation of both geometrical and dynamical similarities. Since a rubble-mound breakwater is not monolithic, but an ensemble of discrete elements, the geometrical similitude requires that both the structural shape and individual elements maintain the same scale ratio.

The model scale is dictated by the model dolosse available for testing, which have dimensions shown in Figure 1. They weigh 210 g. each with specific weight equal to 2.34 g/cm^3 . The overall structure is modeled in accordance with a typical "three-layer breakwater in breaking wave environments" as recommended in the Shore Protection Manual⁽⁵⁾. The cross section of the model is shown in Figure 2. The crushed stones available for sublayer and core constructions have an average specific weight of 1.39 g/cm^3 as measured in air, while in actual breakwaters, heavier stones of approximate unit weight 1.68 g/cm^3 , are usually used. Table 1 provides the weight composition of crushed stones for the sublayer and the core in the model.

TABLE 1. WEIGHT DISTRIBUTIONS OF CRUSHED STONE FOR SUBLAYER AND CORE

<u>Sublayer</u>		
<u>Average Weight (g)</u>	<u>Percent</u>	<u>Retained on Sieve Size (cm)</u>
108/stone	22	3.80
42.5/stone	59	2.67
18.4/stone	17	1.59
4.8/stone	2	PAN
<u>Core</u>		
<u>Average Weight (g)</u>	<u>Percent</u>	<u>Retained on Sieve Size (cm)</u>
0.187/stone	27	0.942
0.074/stone	49	0.635
0.028/stone	18	0.475
0.012/stone	6	PAN

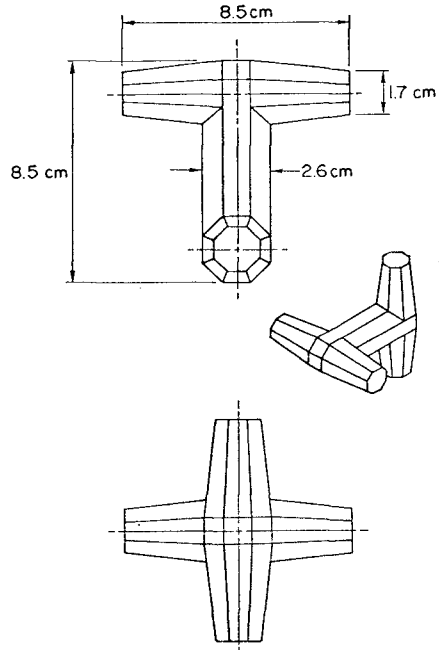


Figure 1. Dimensions of Armor Unit Used in the Experiment.

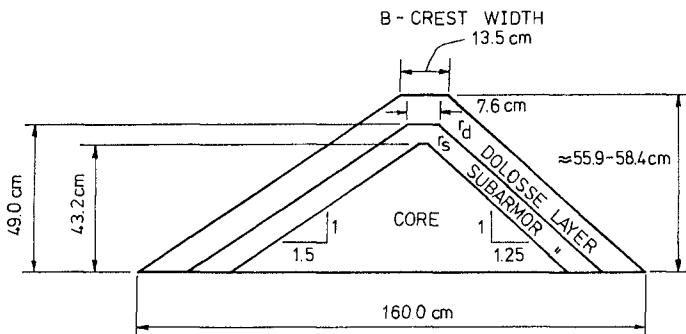


Figure 2. Model Breakwater Cross-Section.

The dynamic effect of an earthquake is mainly an inertia one. The similarity is preserved by the following criterion:

$$\left(\frac{U}{\sqrt{L(1 + C_a \Omega) a_e}} \right)_m = \left(\frac{U}{\sqrt{L(1 + C_a \Omega) a_e}} \right)_p \quad (1)$$

where U = characteristic velocity; L = characteristic length; C_a = added mass coefficient; Ω = density ratio of the fluid to that of the breakwater material and a_e = earthquake acceleration. The subscripts m and p refer to model and prototype, respectively.

If the model and the prototype are geometrically similar and have the same Ω ratio as the present case, the above equation reduces to a modified Froude number provided

$$\left(a_e \right)_m = \left(a_e \right)_p \quad (2)$$

To preserve the similarity of the body force, the Froude criterion should be observed, that is:

$$\left(\frac{U}{\sqrt{gL}} \right)_m = \left(\frac{U}{\sqrt{gL}} \right)_p \quad (3)$$

where g = acceleration of gravity. It is evident that this criterion is automatically satisfied if (1) and (2) are satisfied.

In order to simulate the frictional force of the system, one should first examine the contributing factors. The breakwater is now being looked upon as constructed of solid-fluid structural elements. The frictional force arises from both solid-to-solid contact and fluid-to-solid contact. These two types of frictional forces play opposite roles in breakwater stability. The frictional force due to the relative motion of fluid to solid is an upsetting force, whereas the force due to friction among solids offers the resistance. To model the former force properly, one requires the Reynolds criterion to be preserved:

$$\left(\frac{\rho UL}{\mu} \right)_m = \left(\frac{\rho UL}{\mu} \right)_p \quad (4)$$

where ρ = the density of the fluids and μ = the dynamic viscosity of the fluids.

This criterion is not compatible with the modeling conditions stated above. However, for a structure as bulky as a breakwater, appreciable error will not be introduced by not exactly modeling this force.

The frictional force developed among solid elements, if properly modeled, should follow the criterion below:

$$\left(\frac{ma}{\mu_s W} \right)_m = \left(\frac{ma}{\mu_s W} \right)_p \quad (5)$$

where μ_s = frictional coefficient between solids; m = element mass; and w = element weight. Based on Equation (1), this criterion reduces to

$$(\mu_s)_m = (\mu_s)_p \quad (6)$$

This means that the coefficients of friction in both model and prototype should be the same. The simplest and probably most accurate choice is to build the model with the same materials that one expects to be used in the prototype. In the armor layer, the interlocking behavior may play a dominant role in resisting deformation. Since interlocking among armor units is mainly a function of geometrical shape, there remains little choice but to preserve the shape of the armor units.

As to the elastic restoring force when the structure is subjected to earthquake loading, the apparent shear modulus of elasticity is probably the most pertinent parameter that should be properly modeled. To properly preserve this elastic behavior, the model has to be built with materials of considerably smaller modulus of elasticity than that of the prototype (of the order of the length ratio). Such materials, which at the same time have to satisfy the other modeling criteria as outlined above, are difficult, if not impossible, to find.

In general, the apparent modulus of elasticity affects the amount of energy that can be absorbed before failure. It also affects the natural period of the structure which in turn dictates the frequency at which failure is most likely to occur under vibrating loading. Since a breakwater, being a porous structure of no less than 30% porosity and constructed of discrete particles interacting through friction and interlocking, is a highly damped system the aspect of not being able to match the natural period between model and prototype is not a critical one. In the model the corresponding scaled shear modulus is considerably higher than required. This higher than required model shear modulus was deemed conservative from the point of view of energy absorption.

Earthquake Scaling and Selection. An earthquake can be considered as a vibratory ground motion with components in three orthogonal directions and the random characteristics of "white" noise. Only the horizontal motion was modeled. The principal direction of motion was chosen to be perpendicular to the face of the breakwater. A one-pulse earthquake was selected which corresponds to a prototype frequency of 1.61 Hz with varying amplitude from 0.2 g to greater than 1 g. The frequency was so selected as to provide a time history of motion that envelopes a typical earthquake spectrum similar to that of the El Centro earthquake as given by Newmark and Rosenblueth⁽⁶⁾.

Experiments

Setup. Testing of the model breakwater was done in a tank measuring 1.5 m (depth) by 2.3 m (width) by 37 m (length). A shake table was situated in the center of the tank at an elevation which both minimized the eccentricity of the applied load and allowed a wide range of water levels to be tested. The shake table was designed to support models up to one

ton and to impart horizontal acceleration motions up to 1.6 g. It was actuated by a 20 kip Gilmore hydraulic actuator with a Moog 72-102, 40 gallon per minute Servo valve, controlled by a Gilmore, Model 431B Servo Controller and a Model 112 Wavetek. A variety of wave forms can be generated with capability of all frequencies ranging from 1 to 100 Hz and double amplitudes of from 0.25 to 25 cm. The electronic hookup is shown schematically in Figure 3.

Stability Tests. A total of eight complete breakwaters was built and tested along with one case consisting of the breakwater core only. In general, each breakwater underwent at least four successive shakes. It was intended that each pulse be larger than the one preceding it and this was most often the case. Table 2 summarizes the cases tested.

TABLE 2. SUMMARY OF CASES TESTED

<u>Case</u>	<u>Breakwater Designation</u>	<u>Water Level As a Fraction of Breakwater Height</u>
Core*	Core	0**
455 Colosse	I	0**
455 Dolosse	II	0**
455 Dolosse	III	0**
455 Dolosse	IV	1/3
455 Dolosse	V	2/3
455 Dolosse	VI	1/2
505 Dolosse	VII	0**
505 Dolosse	VIII	1/3

*No Armor or Dolosse

**No Water

In each test case, the dolosse were placed randomly to an even calculated density as in a real breakwater. An exception was made at the toe of each face where the dolosse were placed in a regular fashion for maximum stability against the flat bottom. Detailed test procedures for this part can be found in Ref. (7).

Pressure Distribution Tests. The experiments in this test were divided into two groups. In the first group, a model breakwater with a vertical front face was tested to measure the pressure change on the front face at different elevations. In the second group, a model with a 30° inclined front face was tested. The model with the inclined faces was basically the same as the stability tests with slight front face angle adjustment.

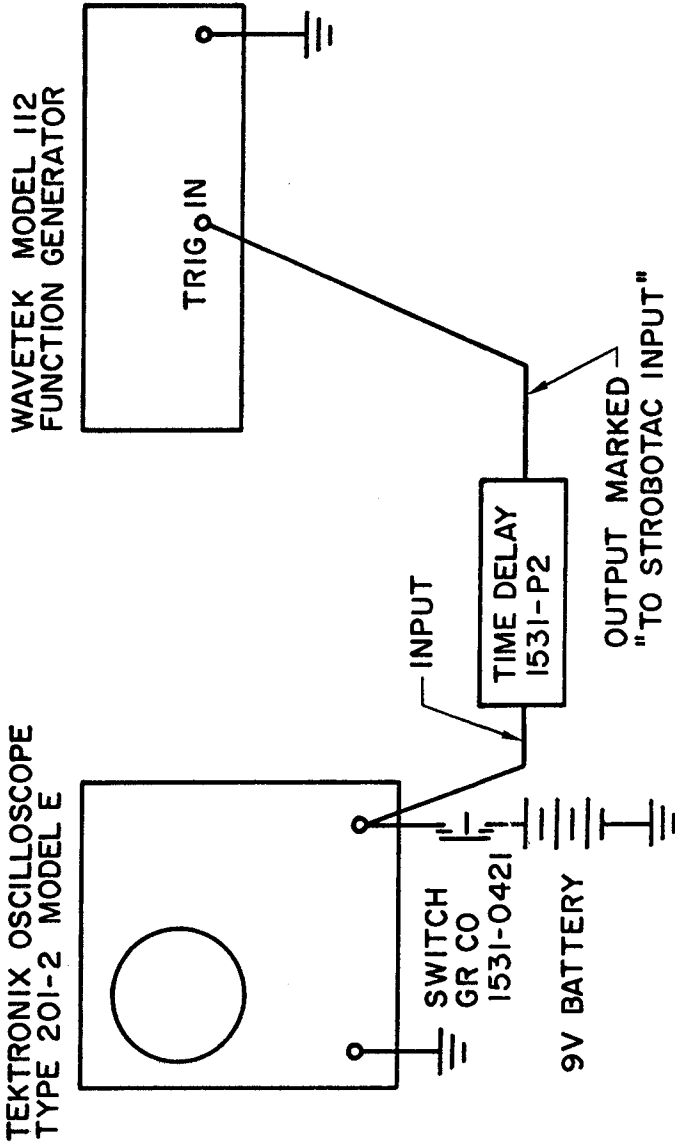


FIGURE 3. Electronic Hookups

For both models, pressure change on the surface of the breakwater at four different elevations were measured by Statham Model P131 and Viatran Model 103 pressure transducers. The water level in all tests was kept at 45 cm. The detailed test program is documented in Ref. (8).

Test Results

Stability. Post test surveys clearly indicated that the dominant mode of damage was settlement. None of the breakwaters tested showed any indications of a catastrophic sliding type failure. It was also apparent that the breakwater crest as opposed to the sides, was most sensitive to the shaking. The crest rounded and settled in much the same way as that of a rock-fill dam under similar conditions⁽⁹⁾. The observed effect of adding more dolosse (Cases VII and VIII) was an increased tendency for some to roll down the face of the breakwater. Possible cracking might have occurred at the crest during a test but none were observed afterwards. Bulging was also noted on the lower and middle parts of some breakwaters. Figure 4 illustrates the breakwater profile changes due to successive shaking.

As one would expect, the steeper slopes were slightly more sensitive to earthquake loading than the milder slopes. In the case tested, more dolos movement was observed on the rear slope (1.25:1) than the front slope (1.5:1) which resulted in, generally, greater outward displacement of the rear toe than the front toe (Figure 4). However, the dolos mat remained intact on both faces under all conditions. Some densification of the dolos layer occurred on the sloping parts of the breakwater at the expense of thinning the crest (less dolosse per unit area than originally).

The thinning in the dolos armor layer would develop into a rift as testing proceeded. On either side of the rift a single sparse layer of dolosse would remain, but this rapidly densified on the breakwater faces. In some cases, the crest became slanted toward the rear. While the crest sometimes remained level it never slanted appreciably towards the front or milder slope.

After examining the physical damages of the breakwater, it became clear that the change in crest elevation is the primary damage indicator. This change in elevation, expressed in terms of the percentage of height prior to the shake, has been plotted in Figure 5 as a function of horizontal acceleration.

As expected, the settlement increases with the acceleration as a trend, but a wide data scattering exists. This wide data scattering is at least partially attributed to the accuracy of the measurement which is about 1% of the total height. If an envelope is drawn around the points on this graph, the intersection of the acceleration lower bound and the zero damage line occurs around 0.4 g. This would indicate that a breakwater of the rubble-mound type is highly resistant to earthquake damage. Clough and Pirtz⁽⁹⁾ reached similar conclusions for rock-fill dams as they found no significant changes in profile until earthquakes produced accelerations of about .4 g. They attribute the relatively high degree of resistance to the flexibility resulting from the discrete nature of a rock-fill dam. Under cyclic loading at

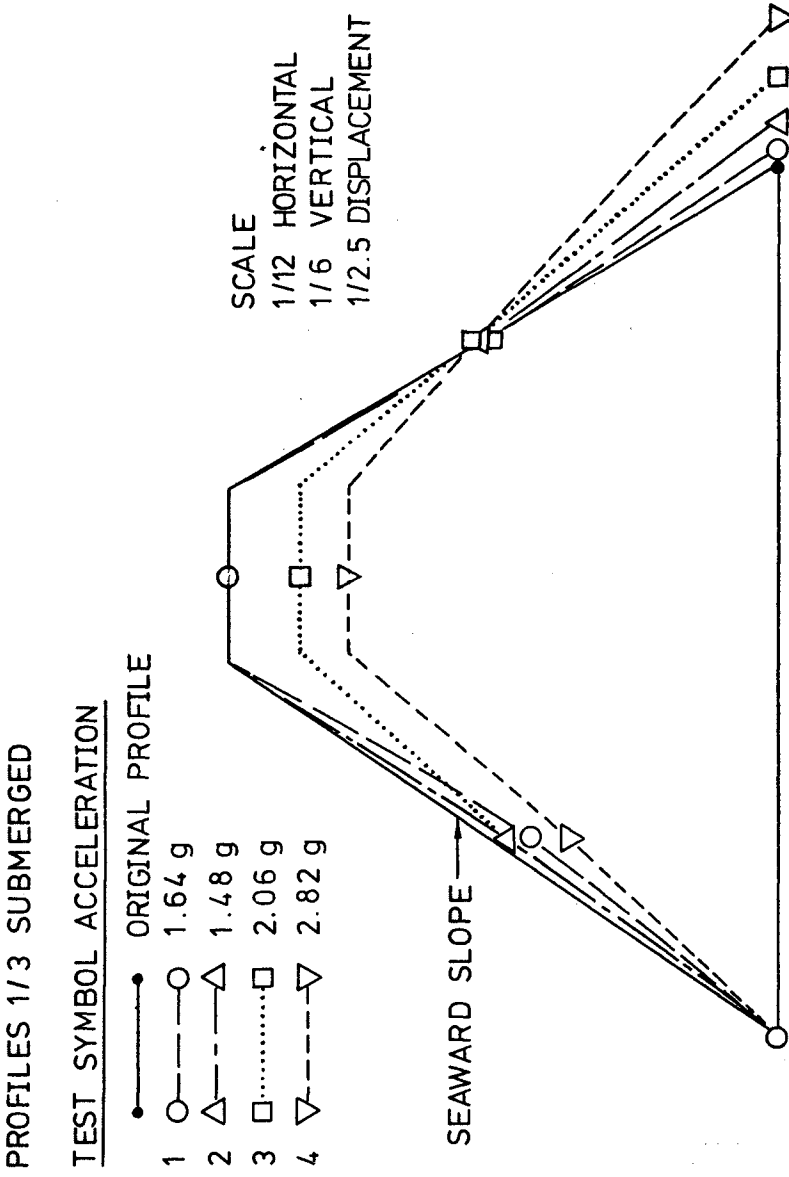
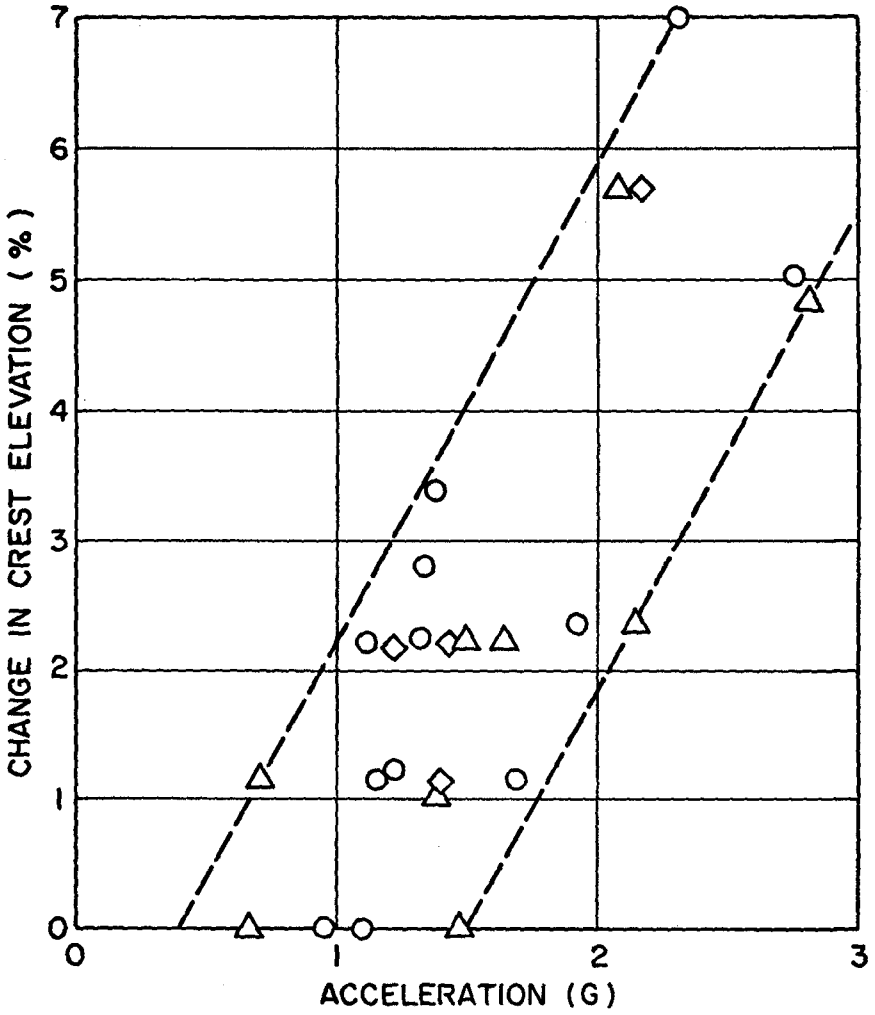


Figure 4. Breakwater Profile Changes Due to Earthquake



○ BREAKWATER DRY
 △ BREAKWATER 1/3 SUBMERGED
 ◇ BREAKWATER 1/2-2/3 SUBMERGED

FIGURE 5. Crest Elevation Change Versus Earthquake Acceleration

earthquake frequencies, the dam would tend to commence shearing in one direction only to find the force reversed and the next shearing displacement cancelling the first. Permanent deformation was mainly produced by shake down; a secondary effect. Further indications of this strength can also be seen in that, for all the earthquakes under about 1.5 g, the settlement is of the order that might be expected from normal shake down over a long period of time. Since settlement is the major mode of damage, one should expect that presettlement prior to the earthquake should also play an important role in addition to the earthquake magnitude. In other words,

$$\text{Settlement} = f(\text{presettlement, acceleration})$$

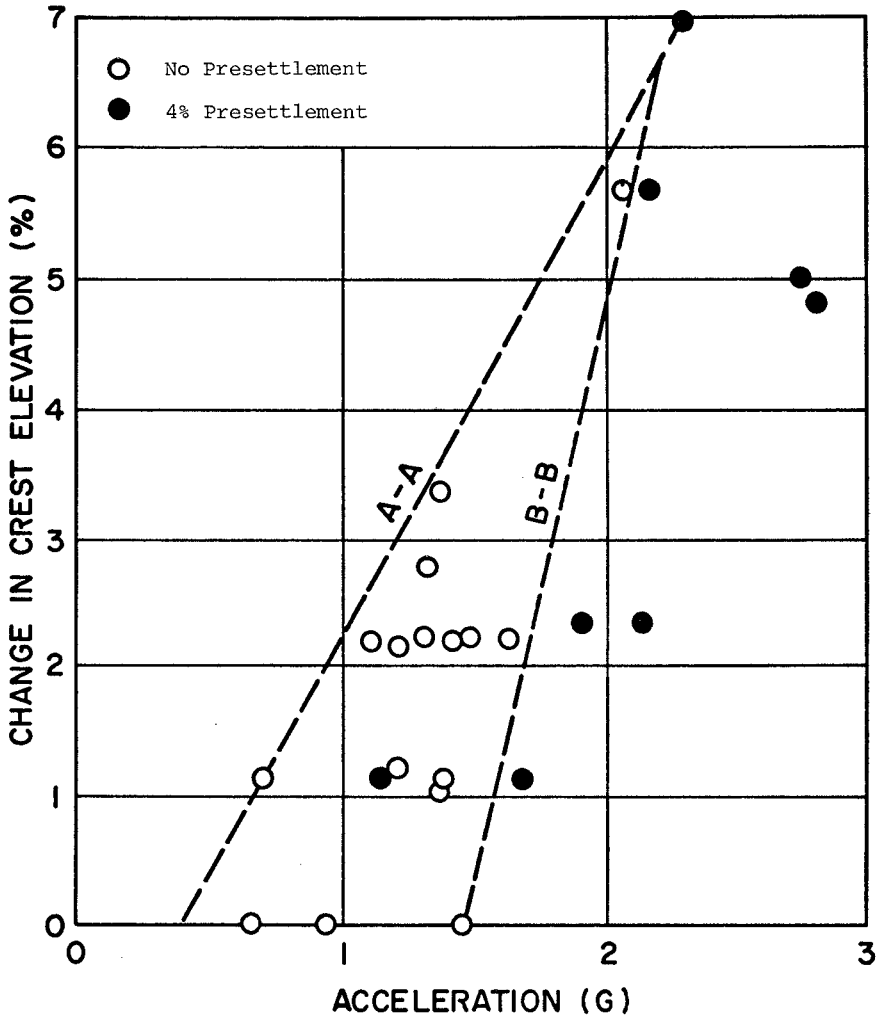
In the experiments, the best indicator of presettlement is probably the cumulative crest settlement prior to any specific test (defined as the total settlement sustained due to previous shakes, measured from a freshly-built model, prior to the specific test run). If this factor is taken into consideration, the data in Figure 5 can be replotted as shown in Figure 6. It is evident from this plot that a new breakwater is more susceptible to damage than an older one. The presettlement becomes less important for larger ground accelerations. In other words, for a large earthquake, the breakwater will settle the same amount irrespective of the degree of presettlement. This is because, for moderate shocks, the settlement is mainly due to internal densification which is certainly closely related to the initial density, whereas for strong shocks, the crest settlement is caused by change of structural shape and modification of side slopes as were observed during tests. For new breakwaters with little or no initial shake down, Line A-A provides a conservative design criterion; for cases of older breakwaters with more than 4% presettlement, Line B-B is a more reasonable criterion.

The small effect of water level on breakwater response was unexpected. An increased water level would reduce the intergranular effective stresses, here directly proportional to the frictional resistance of the breakwater to deformation. Thus, increased displacement might be expected at high water levels. While the very high water levels did display a tendency in this direction they were interspersed with data from all the lower water levels as well. The tests showing the least settlement for the applied loads were about equally divided between the 0 and 1/3 submerged breakwaters.

It is possible that the reduction in frictional resistance is too small to be apparent. It is also possible that the very nature of the settlement may be fairly independent of the intergranular friction as compared with the resistance due to the armor unit interlocking, which is clearly independent of submergence.

Pressure Distributions

(a) Theoretical Considerations. Westergaard⁽¹⁰⁾ was the first one who in 1933 solved the two-dimensional case of horizontal vibrations of a rigid dam with vertical upstream face placed at one end of an infinitely long reservoir of uniform depth. In the same year, Von Kármán⁽¹¹⁾ developed an approximate but very simple method for the same case. Wang et al.⁽¹²⁾ extended the Von Kármán theory to an inclined surface. The essential results of the latter are summarized here.



A-A DESIGN CURVE
B-B DESIGN CURVE

Figure 6. Effect of Presettlement on Breakwater Damage Due To Earthquakes.

Consider a unit slice of a breakwater with an inclined front face as shown in Figure 7. The following sets of equations can be established:

Continuity Equation

$$y a_x = b a_y \quad (7)$$

Equations of Motion in the x- and y-Directions

$$p = \rho b a_{xf} \quad (8)$$

$$p \cot \theta - p \frac{db}{dy} - b \frac{dp}{dy} = \rho b a_y \quad (9)$$

with the symbols as identified in Figure 8, and the subscript f refers to fluid.

The required boundary conditions are, at the water surface:

$$p = 0 \text{ at } y = h \quad (10)$$

and at the inclined front surface:

$$a_{xf} = a_x \sin^2 \theta \text{ for ideal fluid} \quad (11)$$

or

$$a_{xf} = a_x - a_y \cot \theta \text{ for non-slip boundary} \quad (12)$$

The close form solution for the ideal fluid case is

$$\ln \frac{k}{b} = \frac{1}{2} \ln \left| 2 \left(\frac{y}{b} \right)^2 - \frac{y}{b} \sin 2\theta + \sin^2 \theta \right| - \frac{\cos \theta}{\sqrt{8 - \cos^2 \theta}} \tan^{-1} \frac{4 \left(\frac{y}{b} \right) - \sin 2\theta}{2 \sin \theta \sqrt{8 - \cos^2 \theta}} \quad (13)$$

where k, the integration constant, is:

$$k = \sqrt{2} h \exp \left(- \frac{\pi \cos \theta}{2 \sqrt{8 - \cos^2 \theta}} \right) \quad (14)$$

Once the value of b is determined the pressure can be obtained from Equation (8).

(b) Comparison of Experiment With Theory. In Figure 9, the experimental results of the vertical wall case were compared with the extended Von Kármán theory and the experimental results of Zangar⁽¹³⁾.

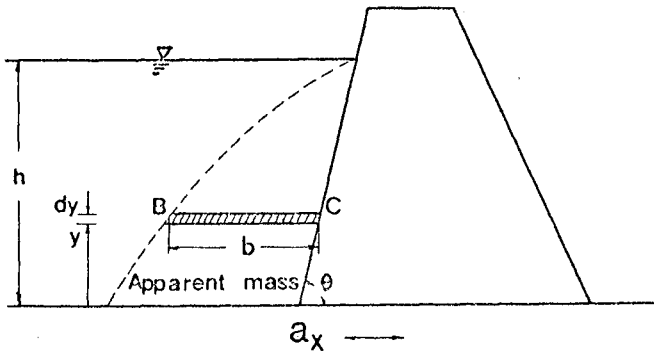


Figure 7. A Breakwater With An Inclined Front Face.

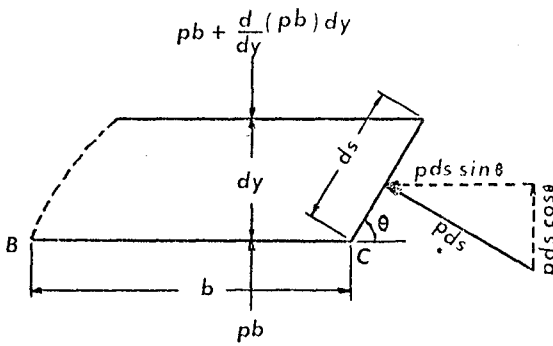


Figure 8. Equilibrium of Forces on a Fluid Element.

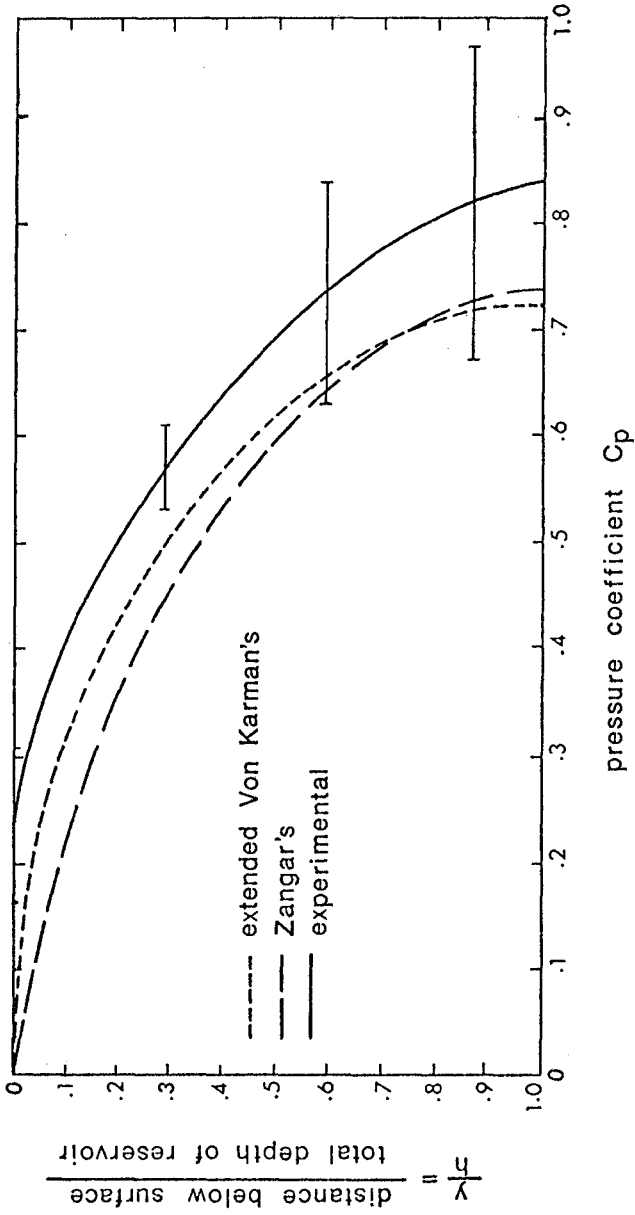


FIGURE 9. Comparison of Pressure Coefficients at Different Elevations on the Breakwater with a Vertical Front Face

The pressure coefficient, C_p , which appeared in the abscissa, is defined as

$$C_p = \frac{P}{\alpha \gamma h} \quad (15)$$

where γ is the specific weight of water and α is the ratio of horizontal earthquake acceleration to the gravitational acceleration, i.e.

$\alpha = \frac{a_x}{g}$. The experimental results for the inclined-surface case were shown in Figure 10, together with that of Sangar's and the theoretical curve.

It can be seen that for the vertical wall case, the comparisons were reasonably good with the exception that the pressure obtained in the experiment was non-zero at the free surface. This was caused by the surface waves induced by the breakwater motion. This effect was neglected in the theory. The surface-wave induced pressure became larger as the horizontal acceleration increased.

For the breakwater with a 30° inclined surface, the three curves were separated apart with the actually measured pressure significantly larger than that predicted by theory. The effect of surface wave, on the other hand, was not as pronounced as the vertical wall case.

Conclusions

Based on experimental evidence, rubble-mound breakwaters on a rigid foundation are found to be highly earthquake resistant. Extrapolating an envelope on the test result predicts that earthquakes of less than $1/2$ g would not affect a breakwater to any significant extent. Possible failure due to foundation is not included in the consideration.

The fundamental damage mode is clearly the settlement of the crest, coupled with slight slope deformation. Slope steepness has much the influence that might be expected; the crest settled more on the side adjoining the steeper slope, and the horizontal displacement at the toe was also larger on the steeper side. The armor layers, two layers of dolosse in this case, remained largely intact. No hole greater than three clustered units (a commonly-used measure to indicate the extent of core exposure) was observed for all the tests performed, which includes tests with a horizontal acceleration as high as 2.8 g. Under severe or repeated shocks, the dolosse mat tended to settle as a whole down the face of each side, causing thinning or rifting at the breakwater crest. Since settlement is the major mode of damage, presettlement becomes an important factor, which strengthens the resistance against earthquake loading.

Water level does not appear to be an important factor affecting the damage. One may tentatively conclude that the interlocking behavior of armor units plays an important role in earthquake resistance in addition to the internal friction of core material.

The approximate solution of Von Kármán agrees with experiments for the breakwater with a vertical face. For the breakwater having a face

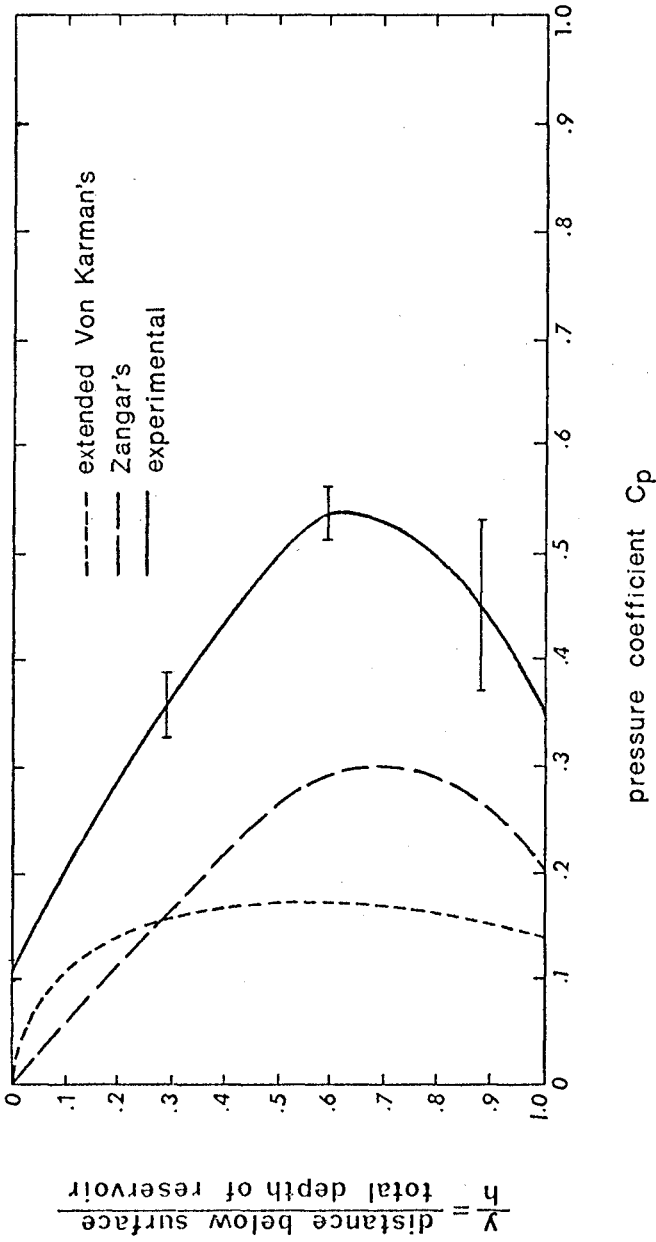


FIGURE 10. Comparison of Pressure Coefficients at Different Elevations on the Breakwater with a 30° Inclined Face

of large inclined angle, an approximate solution from the extended Von Kármán's theory deviates considerably from the experimental result. The maximum pressure is found to be at some distance above the bottom of the breakwater with 30° inclined face but at the base of the breakwater with a vertical face. The magnitude of maximum pressure as induced by earthquakes is not excessive as would result in structural damage. The total force, however, might contribute to the general instability.

In conclusion, rubble-mound breakwaters alone (without foundation consideration) are earthquake resistant in the structural sense. However, this conclusion should not be interpreted as suggesting that earthquake effects can be neglected in design. On the contrary, since crest elevation is an important factor in the functional and structural integrity of breakwaters against wave attack, the degree of possible settlement due to the design earthquake must be established and properly allowed for.

Acknowledgments

The work was partially supported by the U. S. Nuclear Regulatory Commission under Contract No. E(11-1)-2707.

References

1. Wang, H., "Synthesis of Breakwater Design and Review Procedures," Ocean Engineering Technical Report No. 3, Department of Civil Engineering, University of Delaware, Newark, Delaware, 1974.
2. Okamoto, S., Introduction to Earthquake Engineering, New York, N. Y., John Wiley & Sons, Inc., 1973.
3. National Academy of Sciences, The Great Alaska Earthquake of 1964: Oceanography and Coastal Engineering, "Effects of the Tsunamis: An Engineering Study," by Basil W. Wilson and Alf Torum, pp. 361-523, 1972.
4. Wang, H., "Guidelines for the Review and Evaluation of Breakwaters," Ocean Engineering Technical Report No. 15, Department of Civil Engineering, University of Delaware, Newark, Delaware, 1977.
5. U. S. Army Coastal Engineering Research Center, Shore Protection Manual, Washington, D. C.: U. S. Government Printing Office, 1973.
6. Newmark, N. M. and Rosenblueth, E., Fundamentals of Earthquake Engineering, 3rd ed., Englewood Cliffs, New Jersey: Prentice-Hall, 1971.
7. Lamison, C., "Response of the Rubble-Mound Breakwater to Earthquake Loads", M. S. Thesis, Department of Civil Engineering, University of Delaware, Newark, Delaware, 1976.
8. Chen, S. S., "Theoretical and Experimental Studies of the Response of Rubble-Mound Breakwaters Due to Earthquakes", M. S. Thesis, Department of Civil Engineering, University of Delaware, Newark, Delaware, 1977.

9. Clough, R. W. and Pirtz, D., "Earthquake Resistance of Rock-Fill Dams," Trans. ASCE, Vol. 123, pp. 792-810, 1958.
10. Westergaard, H. M., "Water Pressures on Dams During Earthquakes," Trans. ASCE, Vol. 98, 1933.
11. Von Kármán, T., "Discussion of 'Water Pressures on Dams During Earthquakes'", Trans. ASCE, Vol. 98, 1933.
12. Wang, H., Chen, S. S., and Yang, C. Y., "Water Pressures on Rubble-Mound Breakwater Due to Earthquakes", Abstract published in Proc. of Specialty Conf. on Mechanics of Engineering, ASCE-EMD, Univ. of Waterloo, Canada, May, 1976.
13. Zangar, C. N., "Hydrodynamic Pressure on Dams Due to Horizontal Earthquakes", Proc. Soc. Exp. Stress Analysis, Vol. 10, No. 2, 1953.

CHAPTER 136

DOLOS-ARMORED BREAKWATERS: SPECIAL CONSIDERATIONS

By

Robert D. Carver¹ and D. Donald Davidson²

INTRODUCTION

Rubble-mound breakwaters are used extensively throughout the world to provide protection from the destructive forces of storm waves for harbor and port facilities. In some locations, a proposed rubble-mound breakwater may be subject to attack by waves of such magnitude that quarrystone of adequate size to provide economic construction of a stable breakwater is not available. Under these circumstances, it is required that the protective cover layer consist of specially shaped concrete armor units.

In 1966, Merrifield and Zwamborn (1) introduced a new shape of armor unit, the dolos (Figure 1) which was acclaimed to have much higher stability characteristics than any existing armor unit. Site-specific model tests conducted at the U. S. Army Engineer Waterways Experiment Station (WES) by Davidson (2); Carver (3); Bottin, Chatham, and Carver (4); and Carver and Davidson (5) have shown dolos to exhibit an excellent stability response when exposed to breaking wave conditions.

Comprehensive stability tests of dolos also have been conducted at WES by Carver and Davidson (6) for a wide range of nonbreaking wave conditions. These tests used randomly placed dolosse with a first underlayer stone weight of $W_r/5$ and a density of units per given area (N/A) equal to $0.83 V^{-2/3}$, i.e., $n=2$, $k_\Delta=0.94$, and $P=56$ percent. It was concluded from this study that the stability response of dolos can be adequately predicted by the Hudson Stability Equation for the range of wave conditions investigated. Their data indicated an average stability coefficient (K) of 33 for dolosse use in a nonbreaking nonovertopping wave environment. Based on the lower limit scatter of their data, a K of 31 was approved for design.

OBJECTIVE

The objective of this paper is to investigate the effects on stability of (1) varying the first underlayer stone weight from $1/5$ to $1/20$ of the armor weight (W_r); (2) placing the dolosse in selected geometric patterns; and (3) reducing the number of dolosse used in the cover layer. As a basis for comparison, $K=33$ will be used.

¹Research Hydraulic Engineer, U. S. Army Engineer Waterways Experiment Station, Vicksburg, Miss. 39180.

²Chief, Wave Research Branch, U. S. Army Engineer Waterways Experiment Station, Vicksburg, Miss. 39180.

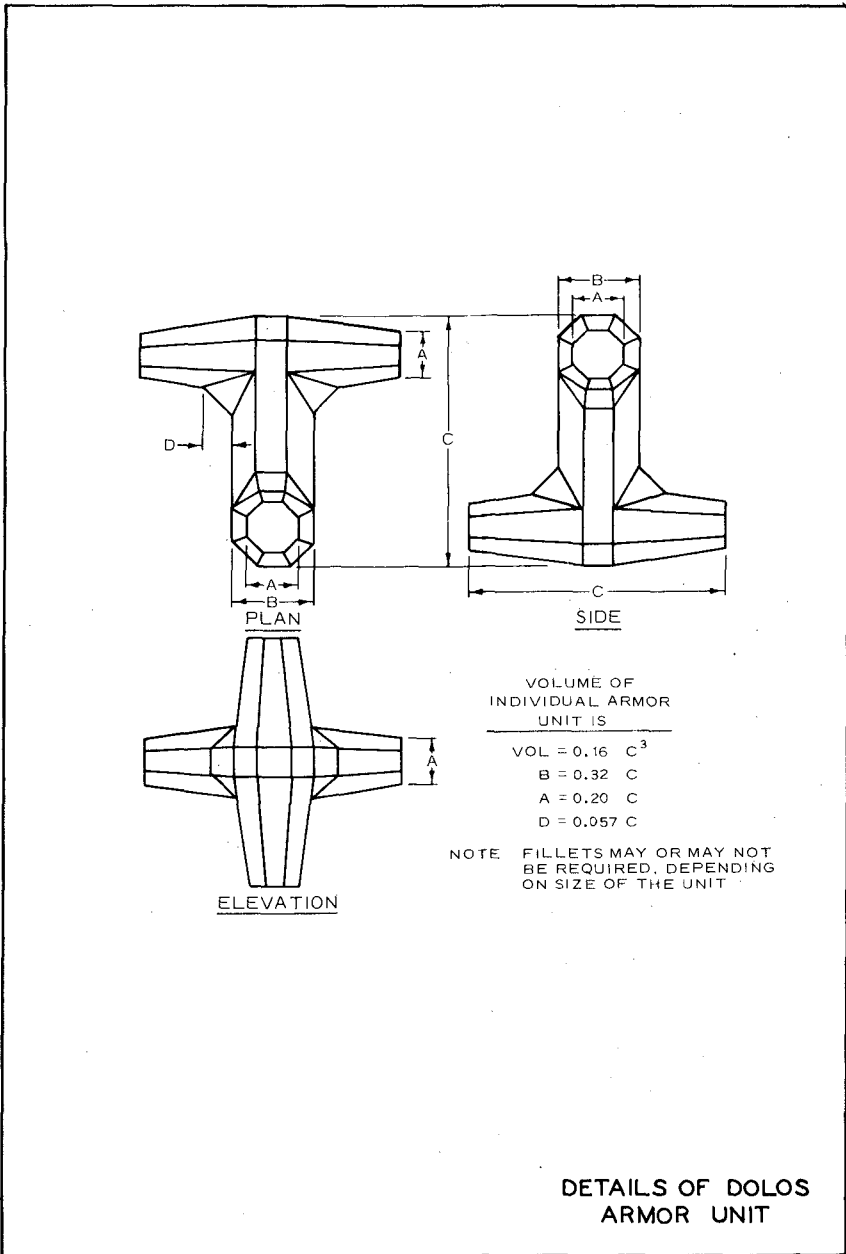


FIGURE 1

TEST EQUIPMENT AND MATERIALS

All wave action tests were conducted in a flat-bottomed, 1.5-m-wide, 1.2-m-deep, and 36-m-long concrete wave flume with test sections installed in the flume about 27 m from a vertical displacement wave generator. The generator is capable of producing sinusoidal waves of various periods and heights. Test waves of the required characteristics were generated by varying the frequency and amplitude of the plunger motion. Changes in water surface elevation as a function of time were measured by electrical wave-height gages in the vicinity where the toe of the test sections was to be placed and recorded on chart paper by an electrically operated oscillograph. The electrical output of the wave gages was directly proportional to their submergence depth.

The dolos armor units weighed 138 g and had a specific weight of 2.26 g/cm³. Sieve-sized limestone ($\gamma = 2.64$ g/cm³) of angular shape was used for the underlayers (W_1 and W_2) and the core (W_4). Rough granite armor stone (W_3) having an average length of approximately two times its width and an average weight of 172 g was used to armor those areas of the structures not protected by dolosse.

SCALE EFFECT CONSIDERATIONS

Hudson (7) has presented a detailed discussion of the design requirements necessary to ensure the preclusion of stability scale effects in small-scale breakwater models (critical $R_N = 3 \times 10^4$). For all tests reported herein the sizes of model armor units and wave dimensions were selected such that scale effects were insignificant (i.e., R_N was greater than 3×10^4).

METHOD OF CONSTRUCTING TEST SECTIONS

All model breakwater sections were constructed to simulate as nearly as possible prototype breakwater characteristics obtained by usual prototype methods of construction. Typical sections of the breakwater tested (Figure 2) were built as follows. The core material, dampened as it was dumped by bucket or shovel into the flume, was compacted with hand trowels to simulate natural consolidation resulting from wave action during construction of the prototype structure. Once the core material was in place, it was sprayed with a low-velocity water hose to ensure adequate compaction of the material. The underlayer stone was then added by shovel and smoothed to grade by hand or with trowels. No excessive pressure or compaction was applied during placement of the underlayer stone. Armor units used in the cover layers were placed in a random manner, i.e., laid down in such a way that no intentional interlocking of the units was obtained (except for the pattern-placement tests). After each test, the dolosse were removed from the breakwater, all of the underlayer stones and the stones in the cover layer below that portion of the cover layer comprised of dolosse were replaced to the grade of the original test section, and the dolosse were replaced.

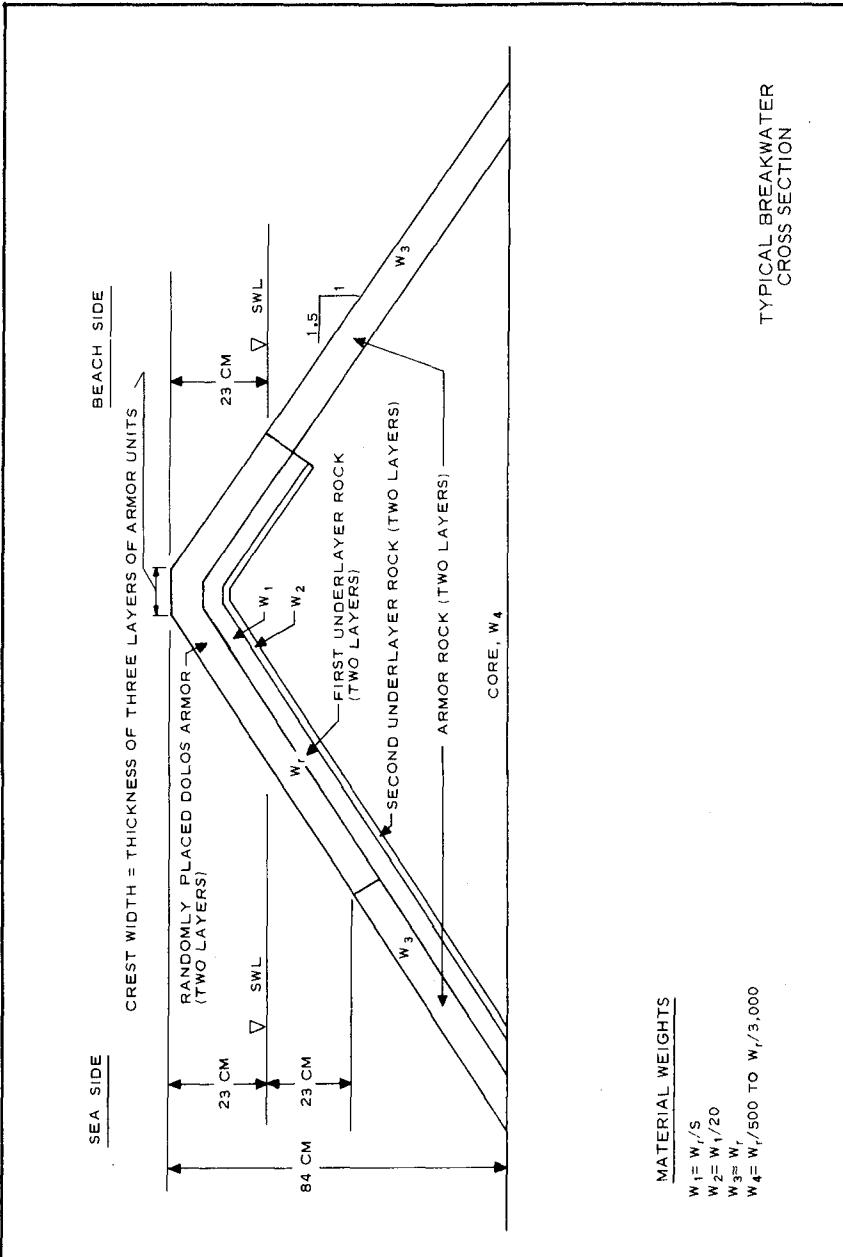


FIGURE 2

METHOD OF DETERMINING DAMAGE

In order to evaluate and compare breakwater stability test results, it is necessary to quantify the changes that have taken place in a given structure during attack by waves of specified characteristics. The WES damage-measurement technique requires that the cross-sectional area occupied by armor units be determined for each stability test section. Armor unit area is computed from elevations (soundings) taken at pre-determined locations over the seaward face of the structure before the armor is placed on the underlayer, after the armor has been placed but before the section has been subjected to wave attack, and finally after wave attack. Elevations are obtained with a sounding rod equipped with a circular spirit level for plumbing, a scale graduated in thousandths of a foot, and a ball-and-socket foot for adjustment to the irregular surface of the breakwater slope.

Sounding data for each test section were obtained as follows: after the first underlayer was in place, soundings were taken on the sea-side slope of the structure along rows beginning at and parallel to the longitudinal center line of the structure and extending in 7.5-cm horizontal increments to the junction with the secondary cover layer of armor stone. On each parallel row, 13 sounding points, spaced at 7.5-cm increments, were measured. This distance represented the middle 90 cm of a 152-cm-wide test section; the 31 cm of structure next to each wall was not considered because of the possibility of discontinuity effects between the armor units and the flume walls. Soundings were taken at the same points once the armor was in place and again after the structure had been subjected to wave attack.

Sounding data from each stability test were reduced in the following manner. The individual sounding points obtained on each parallel row were averaged to yield an average elevation at the bottom of the armor layer before the dolosse were placed and then at the top of the armor layer before and after testing. From these values, the cross-sectional armor area before testing and the area from which armor units were displaced (either downslope or off the section) were calculated. Damage was then determined from the following relation:

$$\text{Percent damage} = \frac{A_2}{A_1} (100)$$

where

A_1 = area before testing, cm^2

A_2 = area from which units have been displaced, cm^2

The percentage given by the WES sounding technique is, therefore, a measurement of an end area which converts to an average volume of armor material that has been moved from its original location (either downslope or off the structure). This particular method of measuring damage does not consider the rocking of individual armor units as exercised by some researchers. However, WES visual definition of no-damage from which the less than 5 percent displaced volume criterion determined by the sounding technique was developed is defined such that no significant movement of individual units is allowed after the initial movement of unnested

armor units (which are generally present on any newly constructed structure, but whose displacement does not significantly affect the composite cover layer) occurs, thus the rocking criterion does not play as important a part in our evaluation as those of other researchers.

SELECTION OF DESIGN WAVE HEIGHTS

Design wave heights for the no-damage criterion were determined by subjecting the test sections to monochromatic waves successively larger in height in 0.5-cm increments, until the maximum wave height was found that would produce no more than 5 percent damage. Each test wave was allowed to attack the breakwater for a cumulative period of 30 minutes, then the test sections were rebuilt prior to attack by the next added increment wave. This 30-minute interval allowed sufficient time for the test sections to stabilize, i.e., time for all significant movement of armor material to abate. During the tests, the wave generator was stopped as soon as reflected waves from the breakwater reached it, and the waves were allowed to decay to zero height before restarting the generator in order to prevent the test section from being exposed to uncontrolled wave groups and/or an undefined wave spectrum.

CORRELATION OF TEST RESULTS

Hudson (8) has presented the results of stability tests for the no-damage and no-overtopping criteria on rubble-mound breakwaters in which that part of the breakwater subjected to the most intense wave action was protected by smooth, randomly placed quarry-stone armor units. Based on those data, dimensional analysis and other analytical considerations, the following empirical stability equation (Hudson formula) was derived:

$$W_r = \frac{\gamma_r H^3}{K(S_r - 1)^3 \cot \alpha}$$

This equation is used to correlate the stability test data presented herein.

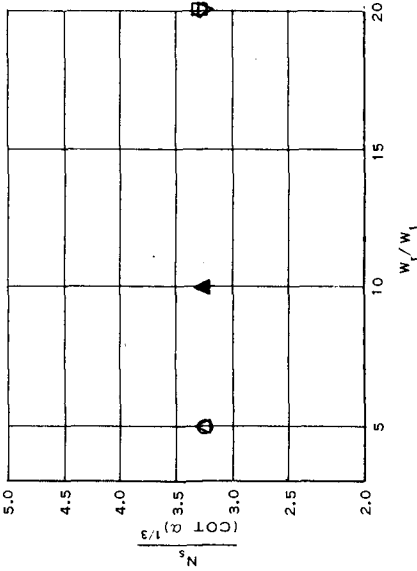
UNDERLAYER WEIGHT EFFECT TESTS

Underlayer weight effect tests were conducted with randomly placed armor and slopes of 1:2 and 1:3. The number of dolos units per given surface area, A , was $N = 0.83V^{-2/3}$ ($n=2$, $k_\Delta=0.94$, $P=56$ percent). Initially, the structure was built with a 1:2 slope and $W_1 = W_r/5$, and the design wave height for $T = 1.52$ sec was determined to be $H = 20.5$ cm. The breakwater was then reconstructed on the same 1:2 slope and tested for the same wave condition with $W_1 = W_r/10$ and $W_1 = W_r/20$. The stability response of the structure was almost identical in all 3 cases. The structure was then rebuilt at a 1:3 slope with $W_1 = W_r/5$ and the design wave height for $T = 1.52$ sec was determined to be $H = 22.5$ cm. The structure was then rebuilt and tested for the same wave condition with $W_1 = W_r/20$. Test results for the 1:3 slope were almost identical. Figure 3_r shows a plot of relative first-underlayer weight (W_r/W_1) versus the primary coverlayer stability number normalized for slope effects $N_s/(\cot \alpha)^{1/3}$. Thus, considering these

LEGEND

W_r = WEIGHT OF INDIVIDUAL DOLOSSE, G
 W_1 = WEIGHT OF 1ST UNDERLAYER STONE, G
 γ_r = SPECIFIC WEIGHT OF ARMOR UNIT, G/CM³
 H = HEIGHT OF DESIGN WAVE, CM
 K = EXPERIMENTAL COEFFICIENT
 S_r = SPECIFIC GRAVITY OF ARMOR UNIT, RELATIVE TO WATER IN WHICH PLACED (γ_r/γ_w)
 α = ANGLE OF BREAKWATER SLOPE, MEASURED FROM HORIZONTAL, DEG
 N_s = STABILITY NUMBER = $\frac{\gamma_r^{1/3} H}{W_r^{1/3} (S_r - 1)} = K (\cot \alpha)^{1/3}$

W_r/W_1	COT α
○	2
▲	2
▽	2
△	3
□	3



EFFECT OF FIRST UNDERLAYER STONE WEIGHT ON PRIMARY ARMOR STABILITY

$N_s / (\cot \alpha)^{1/3}$ VS W_r/W_1

FIGURE 3

two structure slopes, it is concluded that if first underlayer weights in the range of $W_u/5$ to $W_u/20$ have an effect on stability, it is minimal. These data are not presented to recommend changes in the existing underlayer sizing but they are of particular importance when quarry yield is not satisfactory for normal design requirements.

PATTERN-PLACEMENT TESTS

Tests also were conducted to determine if the stability of the dolosse could be increased by placing them in a geometric pattern. It is reasonable to assume that pattern placement will increase prototype placement costs to some extent; however, it was not thought inconceivable that some pattern could be found that would increase stability (reduce the armor weight required for a given design wave height) to the extent that the increased placement costs would be more than compensated for in material savings.

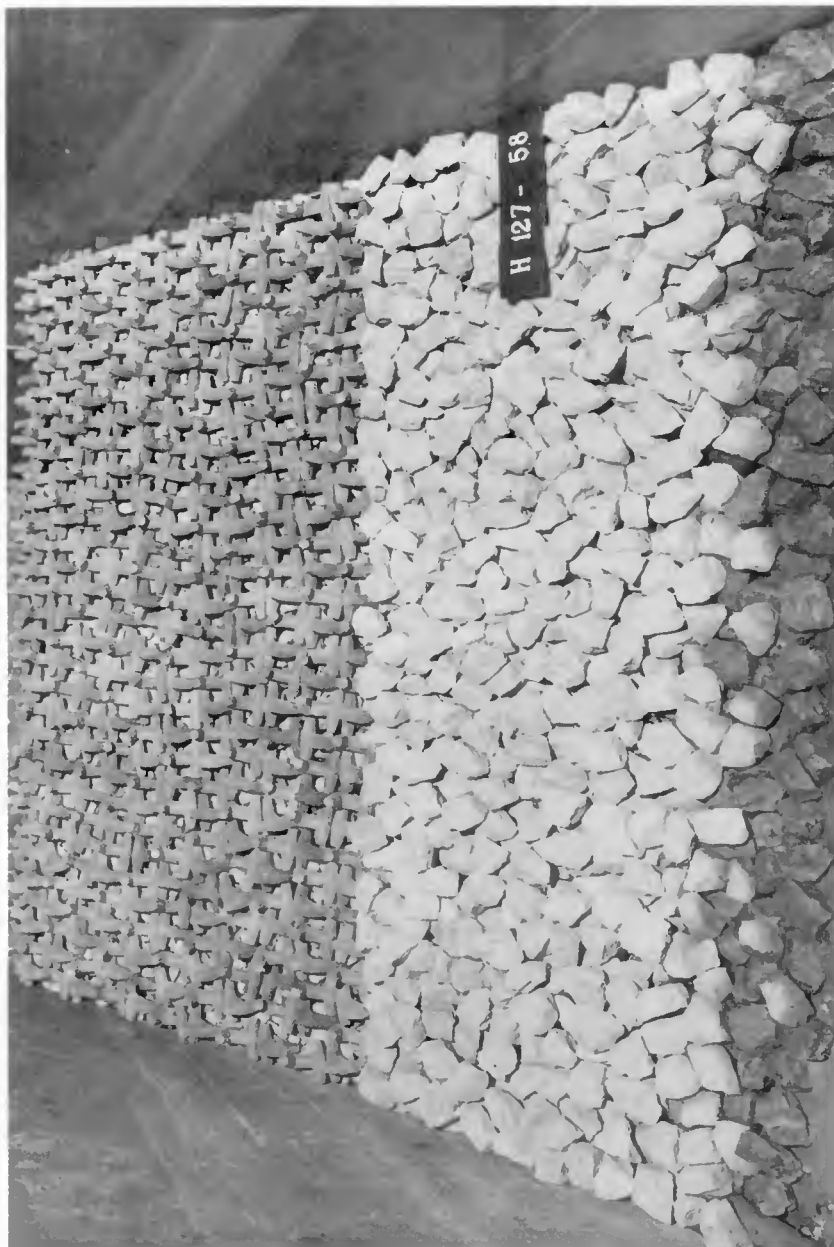
Three patterns were investigated at a 1:1.5 slope. Initially, the structure was built with randomly placed units and the design wave height for wave periods of 1.31 and 2.65 secs was determined to be $H = 18.5$ cm. Patterns were then tested with the design wave height determined for randomly placed units and their stability responses were classed: better, the same, or worse than the stability response of randomly placed units. Details of the patterns tested and general results were as follows:

a. Pattern 1 had the first layer of units placed with the shanks parallel to the slope and the vertical legs alternately upslope and downslope (Photograph 1). The second layer was placed in the horizontal plane of the slope with the shanks perpendicular to those of the first layer (Photograph 2). Attack of 2.65-sec, 18.5-cm, waves produced extensive damage (Photograph 3) with the first underlayer being exposed near the crown. Pattern 1 was less stable than random placement.

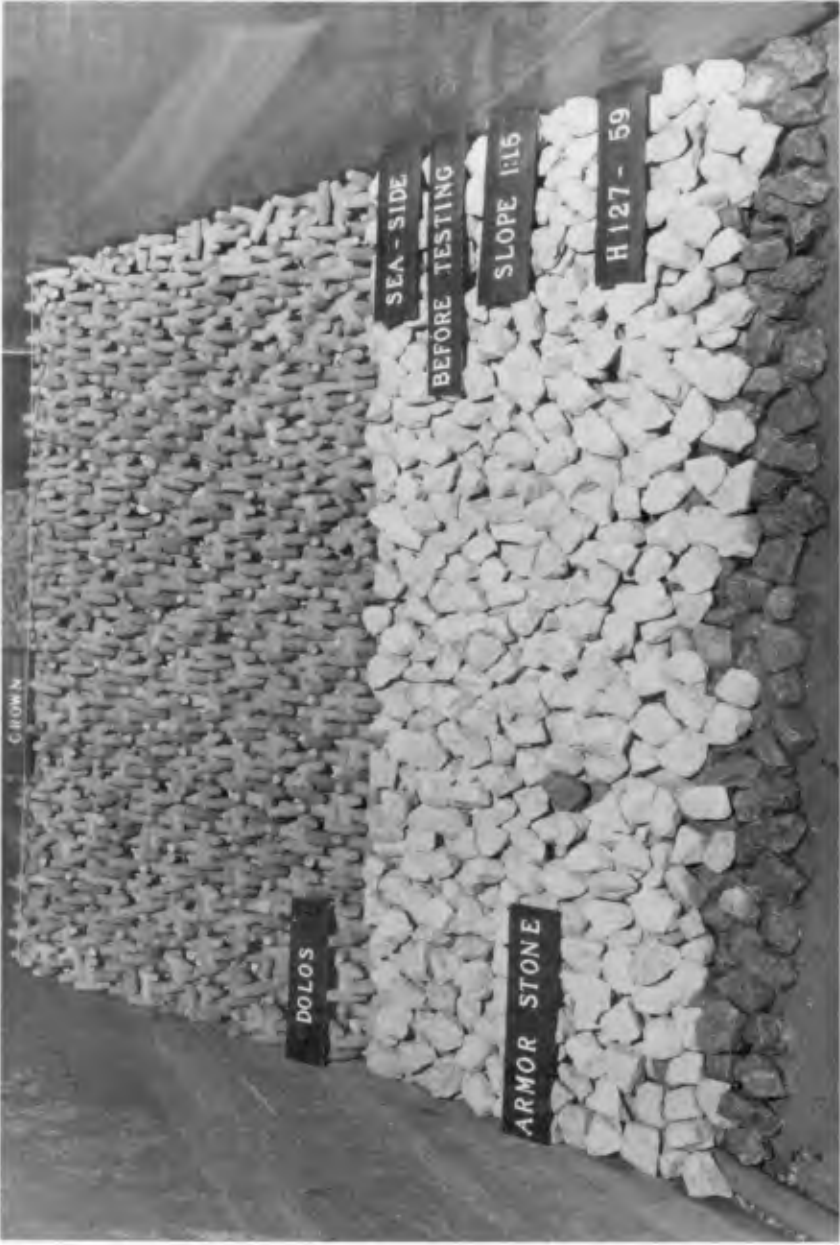
b. Pattern 2 was constructed with the shanks of all units parallel to the slope and the vertical leg downslope. Photograph 4 shows one layer of units in place while Photograph 5 shows the completed structure. Extensive damage was produced by 1.31-sec, 18.5-cm waves (Photograph 6). Pattern 2 was less stable than random placement.

c. Pattern 3 had the first layer of units placed with the shanks parallel to the slope and the vertical legs all upslope or downslope on alternating upslope rows (Photograph 7). The second layer of units was placed in the same manner to yield the complete structure (Photograph 8). Attack of 2.65-sec, 18.5-cm waves produced no damage (Photograph 9). Pattern 3 was more stable than random placement.

The pattern tests described above proved enlightening in that they showed that of the three geometric patterns selected for testing, two proved to be less stable than random placement. Based on these results, designers and construction supervisors are cautioned not to assume that any geometric pattern will increase stability.



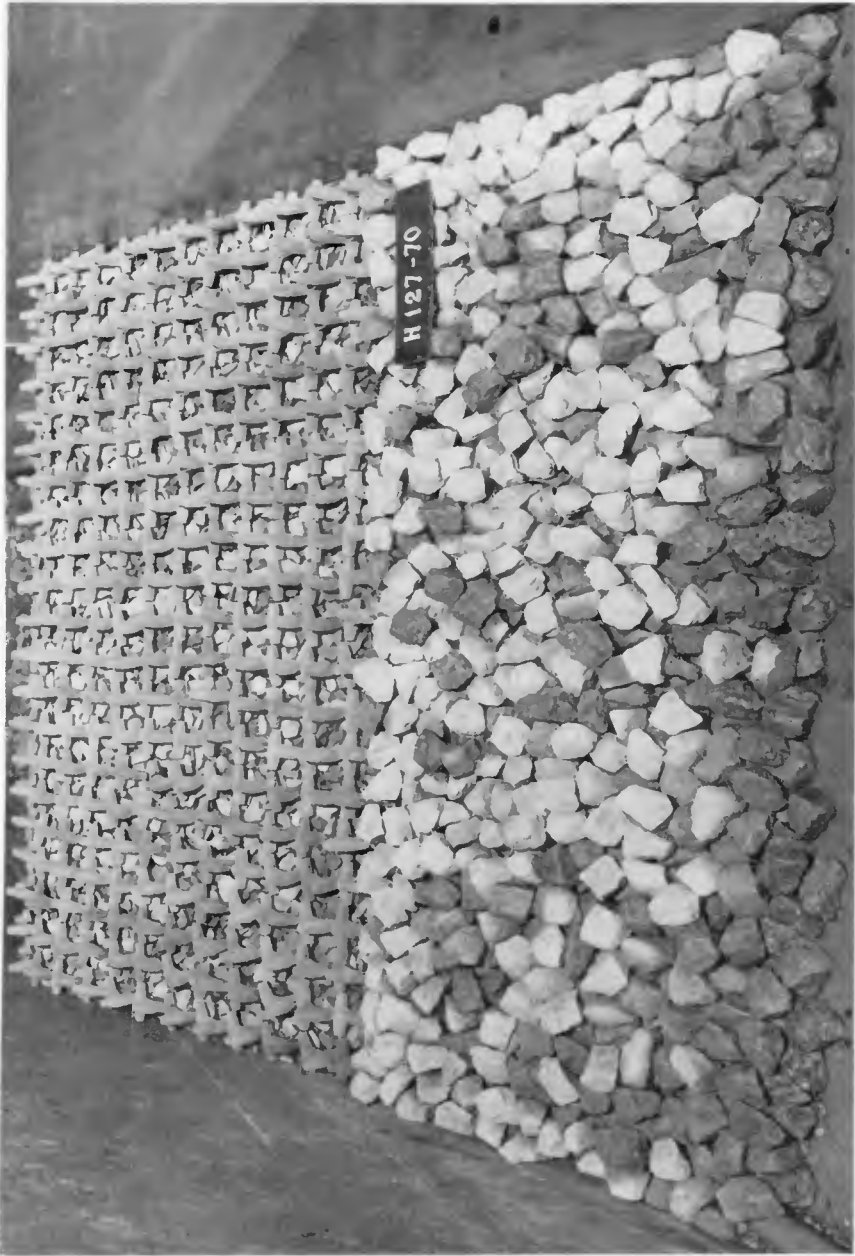
Photograph 1. Pattern 1 with one layer of armor units in place



Photograph 2. Pattern 1 with two layers of armor units in place



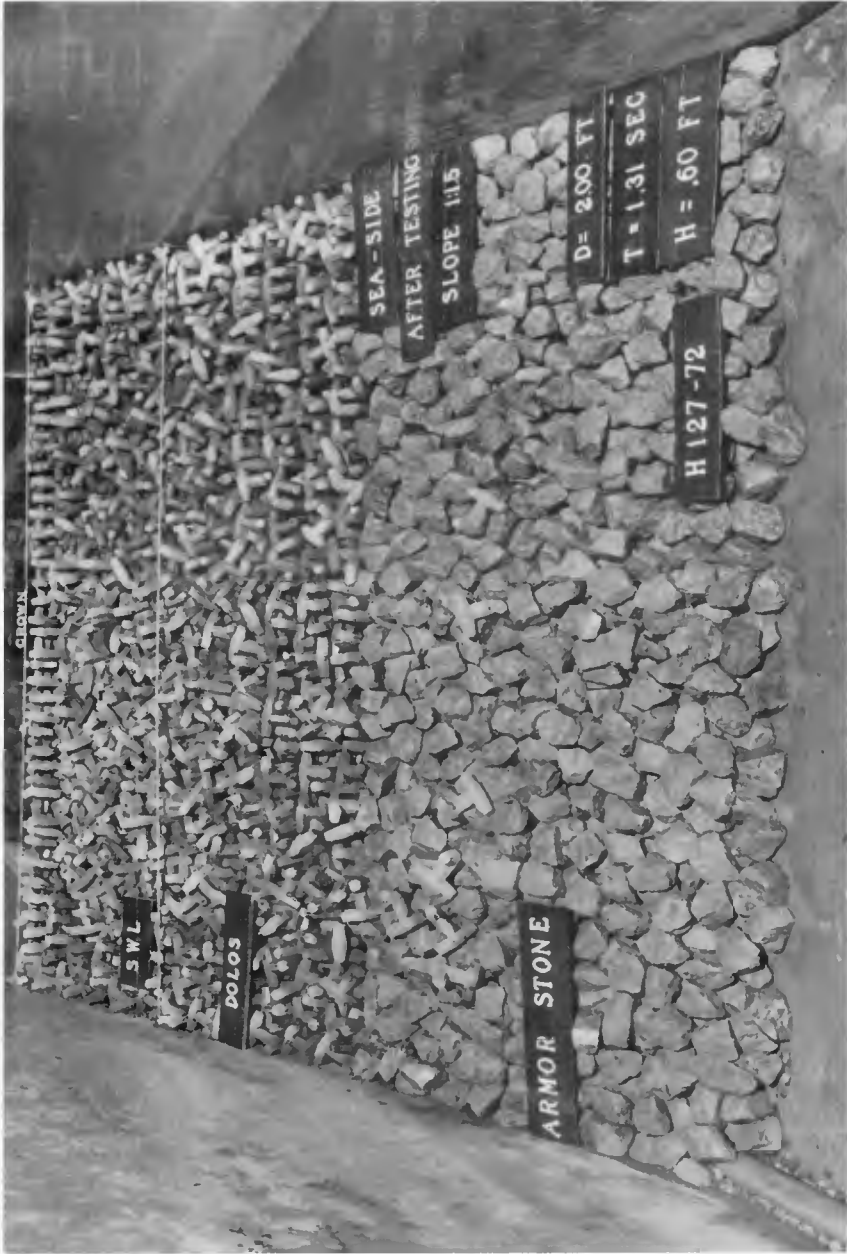
Photograph 3. Pattern 1 after attack of 2.65-sec, 18.5-cm waves



Photograph 4. Pattern 2 with one layer of armor units in place



Photograph 5. Pattern 2 with two layers of armor units in place



Photograph 6. Pattern 2 after attack of 1.31-sec, 18.5-cm waves



Photograph 7. Pattern 3 with one layer of armor units in place



Photograph 8. Pattern 3 with two layers of armor units in place



Photograph 9. Pattern 3 after attack of 2.65-sec, 18.5-cm waves

Subsequent stability tests showed Pattern 3 to meet the no-damage criterion for wave heights up to 20 cm at the 1:1.5 slope. This was a substantial enough increase over random placement that it was decided to test Pattern 3 at slopes of 1:2 and 1:3. Results of these tests are summarized as follows:

Sea-Side Slope	$H_{D=0}$, cm	K
1:1.5	20.0	42
1:2.0	22.0	43
1:3.0	25.0	44

Recalling that Carver and Davidson's (6) earlier tests yielded an average stability coefficient of 33 for random placed dolosse, the values of K presented above are quite impressive. Considering Pattern 3 as a two-layer system, values of k_A and P were determined to be 0.92 and 50 percent, respectively, or $N/A = 0.92 V^{-2/3}$.

THE EFFECT THE NUMBER OF DOLOS UNITS IN THE COVERLAYER HAS ON STABILITY

Limited tests were conducted using a 1:1.5 slope to determine the effect on stability of using a decreased number of armor units in the cover layers. For these tests, the structures were built using the random placement technique with approximately 25 percent fewer armor units than were used by Carver and Davidson (6) in the stability tests that yielded an average stability coefficient of 33. This armor unit coverage was sparse but could still be considered a two-layer system. Values of k_A and P were 0.62 and 50 percent, or $N/A = 0.62 V^{-2/3}$. These tests yielded a design wave height of 15 cm and thus a stability coefficient of 17, showing that reducing the number of armor units by approximately 25 percent reduced the stability coefficient by approximately 50 percent.

Similar results were found by Vonk (9) for dolos tests where model units representing 4.7 metric ton dolosse were reduced from 0.70 units per square meter ($N/A = 1.07 V^{-2/3}$) to 0.56 units per square meter ($N/A = 0.86 V^{-2/3}$). His data show that for 9-18 sec period waves, the stability coefficient at 2 percent damage dropped approximately 58 and 31 percent for breakwater slopes of 1:1.5 and 1:2, respectively. All these data illustrate the important role the number of armor units play in determining the stability coefficients that are being used today and emphasize the fact that prototype designs should never use less dolosse per given area than recommended by the particular data upon which the stability coefficient is based.

Although the data is limited and it is difficult to relate equivalent stability from different laboratories, Figure 4 indicates the general increase in K as the packing density coefficient (C) increase for dolosse. The data presented in Figure 4 are taken from Carver and Davidson (6), Shore Protection Manual (10); Merrifield and Zwamborn (1), and personal correspondence between Davidson and Zwamborn (11). Reference (6) and (10), K factors are based on the no-damage criteria of less than 5 percent damage by the sounding method previously described, whereas data in

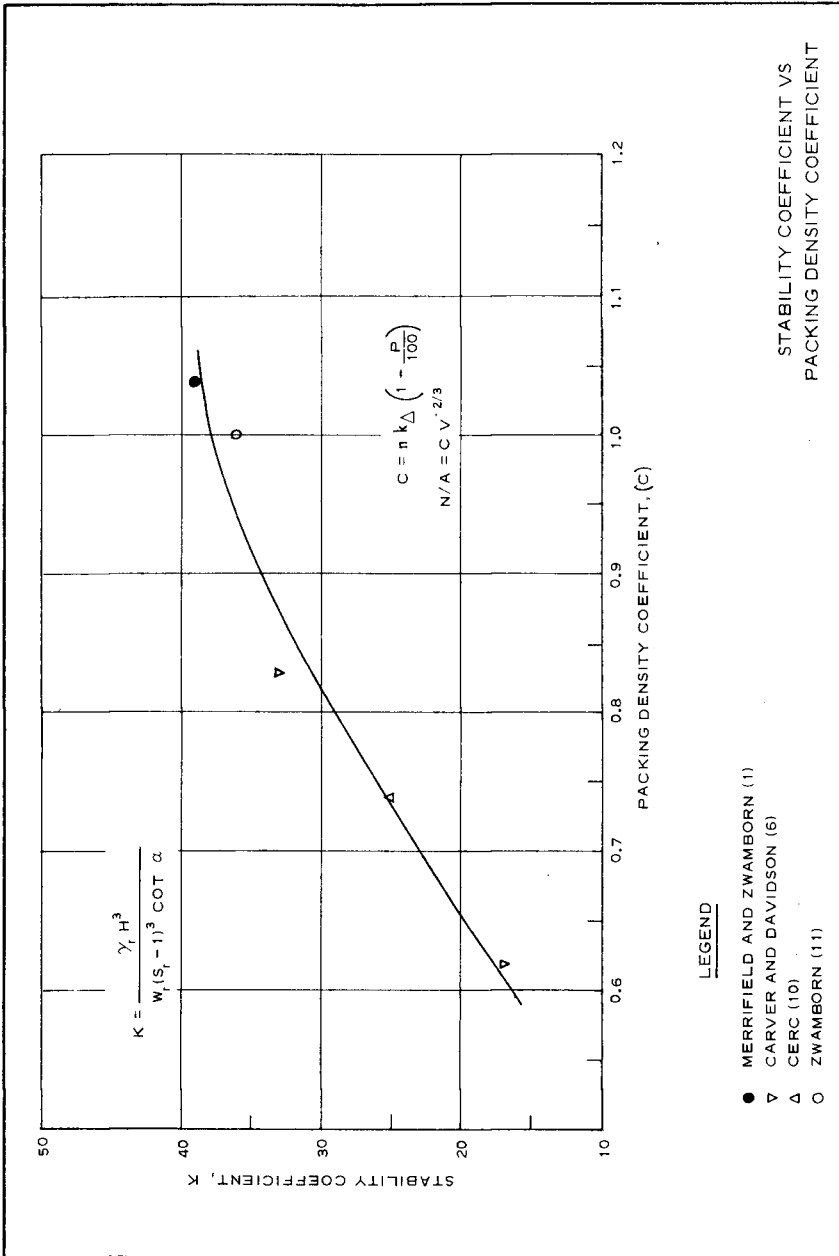


FIGURE 4

References (1) and (11) are based on 2 percent damage by number of displaced units. These data do not necessarily recommend an optimum number of dolosse to use per given area because the safety and economics of each prototype project should be considered on its own merits. They do show, however, that the number of dolosse used per given area is critical to the selection of the stability coefficient and should be considered accordingly.

CONCLUSIONS

Based on the tests and results described herein, in which dolos armor is used on nonovertopping breakwater trunks and subjected to non-breaking waves with a direction of approach of 90° , it is concluded that:

a. For sea-side slopes in the range of 1:2 to 1:3, variations in first-underlayer weights (W_1) from $W_r/5$ to $W_r/20$ do not have a significant effect on stability.

b. Placement of dolosse in geometric patterns may or may not increase stability over that obtained by random placement, depending on the selected pattern; thus caution should be taken not to assume that every geometric pattern will increase stability.

c. The number of dolosse in the cover layer definitely affects the stability coefficient; thus a designer should take precaution to assure that a given stability coefficient is commensurate with the number of dolos units per given area upon which that stability coefficient was developed.

ACKNOWLEDGEMENTS

The data presented in this paper were extracted from part of the model tests described in the Waterways Experiment Station (WES), Technical Report H-77-19, entitled, "Dolos Armor Units Used on Rubble-Mound Breakwater Trunks Subject to Nonbreaking Waves with No Overtopping," which was published for public release in November 1977. The comprehensive study was conducted at WES for the office, Chief of Engineers under the Corps of Engineers Civil Works Research and Development Program. The tests were conducted in the Wave Dynamics Division (Dr. Robert W. Whalin, Chief) of the Hydraulics Laboratory (Mr. H. B. Simmons, Chief); by Mr. R. D. Carver, Research Hydraulics Engineer; and Mr. W. G. Dubose, Engineering Technician, under the immediate supervision of Mr. D. D. Davidson, Chief of the Wave Research Branch.

Grateful acknowledgement is extended to the Office, Chief of Engineers for granting permission to publish this paper.

NOTATION

Variables

A	Surface area, m^2
C	Packing density coefficient, $C = nk_{\Delta} (1 - \frac{P}{100})$
D	Damage parameter
g	Acceleration due to gravity, m/sec
H	Wave height, cm
k_{Δ}	Coefficient of layer thickness
K	Stability coefficient, Hudson formula
l	Characteristic linear dimension of armor unit, cm
n	number of armor layers
N	Number of armor units
P	Porosity of breakwater material, percent
R_N	Reynolds stability number = $\frac{g^{1/2} H^{1/2} l}{\nu}$
S_r	Specific gravity ($S_r = \gamma_r / \gamma_w$)
T	Wave period, sec
V	Volume of an individual dolos, cm^3
W	Weight, gm
α	Angle of breakwater slope, measured from horizontal, degree
$\cot \alpha$	Reciprocal of breakwater slope
γ	Specific weight, g/cm^3
ν	kinematic viscosity

Subscripts

D	Refers to damage
r	Refers to armor unit
Δ	Refers to shape factor

REFERENCES

1. Merrifield E. M. and Zwamborn, J. A., "The Economic Value of a New Breakwater Armor Unit 'Dolos,'" Proceedings of the 10th Coastal Engineering Conference, Tokyo, Japan, Sep 1966.
2. Davidson, D. D., "Proposed Jetty-Head Repair Sections, Humbolt Bay California; Hydraulic Model Investigation," Technical Report H-71-8, U. S. Army Engineer Waterways Experiment Station, Vicksburg, Miss. 1971.
3. Carver, R. D., "Stability of Rubble-Mound Breakwater Laharia Harbor, Hawaii; Hydraulic Model Investigation," Miscellaneous Paper H-76-8, U. S. Army Engineer Waterways Experiment Station, Vicksburg, MS, 1976.

4. Bottin, R. R., Jr., Chatham, C. E., Jr., and Carver, R. D., "Waianae Small-Boat Harbor, Oahu, Hawaii, Design for Wave Protection; Hydraulic Model Investigation," Technical Report H-76-8, U. S. Army Engineer Waterways Experiment Station, Vicksburg, Miss., 1976.
5. Carver, R. D. and Davidson, D. D., "Stability of Rubble-Mound Breakwater Jubail Harbor, Saudi Arabia; Hydraulic Model Investigation," Technical Report H-76-20, U. S. Army Engineer Waterways Experiment Station, Vicksburg, Miss., 1976.
6. Carver, R. D. and Davidson, D. D., "Dolos Armor Units Used on Rubble-Mound Breakwater Trunks Subjected to Nonbreaking Waves with no Over-topping," Technical Report H-77-19, U. S. Army Engineer Waterways Experiment Station, Vicksburg, Miss., 1977.
7. Hudson, R. Y., "Reliability of Rubble-Mound Breakwater Stability Models; Hydraulic Model Investigation," Miscellaneous Paper H-75-5, U. S. Army Engineer Waterways Experiment Station, Vicksburg, Miss., 1975.
8. Hudson, R. Y., "Design of Quarystone Cover Layers for Rubble-Mound Breakwaters," Research Report No. 2-2, U. S. Army Engineer Waterways Experiment Station, Vicksburg, Miss., 1958.
9. Vonk, APM, "Breakwater Armor Units-Influence of Packing Density and Porosity on Stability," Report No. 321-4, Fisheries Development Corporation of S. A. LTD., Cape Town, South Africa, 1976.
10. U. S. Army Coastal Engineering Research Center, Shore Protection Manual, Vol. II, Washington, D. C., 1973.
11. Personal Correspondence, Letter from J. A. Zwamborn to D. D. Davidson, dated 4 April 1978, Subject, "Tests on Dolosse."

CHAPTER 137

DOLOS PACKING DENSITY AND EFFECT OF RELATIVE BLOCK DENSITY

by
J.A. ZWAMBORN*

ABSTRACT

Accuracy and compatibility of measuring and testing techniques are discussed briefly and a *plea* is made for *standardisation* to avoid, as far as possible, deviations in test results of different laboratories. One of the main causes of these differences is inconsistency in Dolos *packing densities* and corresponding layer thicknesses or shape factors. In an attempt to alleviate this problem three placing densities, namely 'light', 'mean' and 'dense' have been defined and their physical properties determined. Flume tests with regular waves, and Dolos armour units at these packing densities, showed very little difference in stability and, considering practical limitations during construction, it is suggested that the 'mean' packing density be used for a 'first design', followed by proper model tests. The results of tests with model Dolosse using three different *unit densities* were inconclusive and further tests using a wider range of densities are underway.

INTRODUCTION

The 'Dolos' breakwater armour unit is now used widely for harbour and shore protection works in various parts of the world.²⁰ Model tests on the stability of Dolosse have been carried out at several laboratories but differences in *definitions* and *test techniques* often preclude a direct comparison of the results.

There is, for example, considerable difference of opinion about the *number of Dolosse* required to form a so-called 'double layer' of armouring blocks^{20,11,3,7} and, because the number of Dolosse per unit area affects the economy as well as the stability of a structure, an attempt is made to define more clearly various packing densities. Some tests have also been done to determine the effect of the packing density on the stability of a Dolos armouring, as well as its possible influence on wave run-up.

According to all the known stability formulae, the armour block mass is inversely proportional to the *relative block density* to the third power¹⁴ and it is, therefore, attractive and, in certain cases imperative¹⁶, to use a higher than normal block density. Some doubt has been expressed, however, about the validity of this proportionality in the case of Dolosse¹⁹ and some tests with regular non-breaking waves were, therefore, done to determine the effect of relative block density on the stability of Dolosse.

ACCURACY AND COMPATIBILITY OF MEASURING TECHNIQUES

Definitions and test methods should be completely compatible if comparisons

* National Research Institute for Oceanology, CSIR, Stellenbosch, Republic of South Africa

are to be made between the results of tests on models done in different laboratories and when test data are to be compared with prototype data. This is of particular importance in the case of porosity of the armouring, the block shape factor or the layer thickness, and the damage recorded after wave action.

The *porosity* can be determined in two different ways, firstly, by placing, say, 5 to 10 layers of Dolosse in a container of known dimensions and filling the voids with water ('real' porosity) and, secondly, by determining the percentage voids in the container or of the model slope, from the difference of the 'total volume' and the volume of the Dolosse ('fictitious' porosity). A representative water level, in the case of the container tests, or the thickness of the armour, in the case of a model slope, can be judged by eye (to achieve a reasonable accuracy, 5 to 10 layers are used) or can be determined with the more reliable sounding technique.^{3, 5}

Both methods are used to determine porosity^{11, 18} and a comparison of the values obtained by these methods showed a consistent difference of 3,5 per cent, which is caused by the protrusion above the water surface of parts of the Dolosse. It is thus important to define the basis or method of measurement when values for porosity are given.

The U.S. Army Engineer Waterways Experiment Station (WES) developed a standard *sounding technique* in the early 1950's to measure the extent of damage to stone dumped randomly on a breakwater slope. The size of the original sounding disc was increased for Dolosse to $1,14 V^{1/3}$ with a grid spacing of $1,5 V^{1/3}$, (V is the block volume) to obtain an armour layer thickness "which visually appeared to represent an acceptable two-layer thickness."³ This technique was found to be very useful in determining the average armour thickness; repeat packing and sounding tests in a container showed a maximum variation of ± 3 per cent but repeat soundings of the same packing on Dolos slopes showed a variation of only $\pm 1\frac{1}{2}$ per cent). The *shape factor* $C = t/n V^{-1/3}$ (t being the measured thickness of n layers) follows directly from the armour layer thickness and the block volume and its value is therefore of the same accuracy.

A further check was made of the influence of the grid size and the disc diameter on the measured armour thickness. Container tests showed that for a *grid size* of up to double that specified, that is $3 V^{1/3}$, the thickness is hardly affected, the difference being less than 1 per cent. The layer thickness, however, is reduced slightly, almost linearly, for smaller *disc sizes*, i.e. a disc of one third of the size causes a reduction of just under 10 per cent. The latter should be taken into account when doing *prototype soundings* because normally, a relatively small plate or ball is used which would make the Dolos layer *appear* to be say, 10 per cent, thinner.

A comparison was also made between the *damage* measured according to the WES sounding technique and the damage derived from records of individual blocks which had been displaced. Repeat soundings showed that a 'damage' of 4 per cent (sum of the negative differences) could be obtained even before there had been any wave action. Thus the sounding technique cannot be expected to provide damage figures to an accuracy better than about 4 per cent which is considered a serious drawback, particularly as regards

localised damage. Compared with this, measurement of the movement of individual Dolosse provides a much more detailed and accurate record of damage because the movement of each Dolos can be recorded; with say 500 Dolosse in the test section, damage increments of 0,2 per cent can be differentiated.

In the past, blocks which were seen to be *rocking* continuously were sometimes also included in the measurement of damage because these blocks were assumed to have broken. Compared with the blocks which moved out of position (displaced units) the number of rocking blocks observed was quite small and, since the visual observations were rather subjective, the rocking was often neglected. Observations through glass-sided flumes have indicated, however, that considerable rocking movements do take place and a quantitative measuring technique was therefore developed to record these movements. The technique consists of *time-lapse cine pictures* of the Dolos slope, taken at the time when the wave trough has reached its lowest point on the slope. Subsequent projection of the film clearly shows the change in Dolos positions, representing Dolos movements between successive waves, on the entire exposed slope. The results are analysed by marking and counting the blocks separately which shows

- *continuous rocking or full roll-over* (no displacement)
- *intermittent rocking* (about two-thirds of the time)
- *occasional rocking* (about one-third of the time)

Present knowledge of the Dolos strength is insufficient to define acceptable degrees of rocking and it is *suggested* that, for the time being, all the above modes of movement be recorded separately, together with the number of displaced units, as discussed above. A more detailed description of the measuring techniques is given elsewhere²².

DIFFERENT PACKING DENSITIES

Definitions

The definition of the packing density of breakwater armour blocks is the *number of units* (e.g. Dolosse), N , per unit area of slope. The packing density may be expressed as follows :

$$N_n = \phi_n V^{-2/3}$$

with ϕ_n is the packing density parameter being related to the number of layers (n), the shape factor (C_n) and the 'fictitious' porosity (P_f) as follows : $\phi_n = n C_n (1 - P_f/100)$.

The layer thickness can be expressed as follows :

$$t_n = \tau_n V^{1/3}$$

where τ_n is the layer thickness parameter also related to the number of layers (n) and the shape factor (C_n), i.e. $\tau_n = n C_n$.

Differences of up to 35 per cent in the value of $\phi_{n=2}$ (double layer) are quoted in the literature.^{11,17} Because the number of armour units per unit area, and thus the value of ϕ , has a direct bearing on the economy of the structure and is also expected to influence both the stability as well as the safety of the breakwater, it was decided that a clear and

unambiguous *definition* for the packing density of a *single randomly placed layer* of Dolosse was needed urgently. The following definitions are therefore proposed (see Fig. 1) :

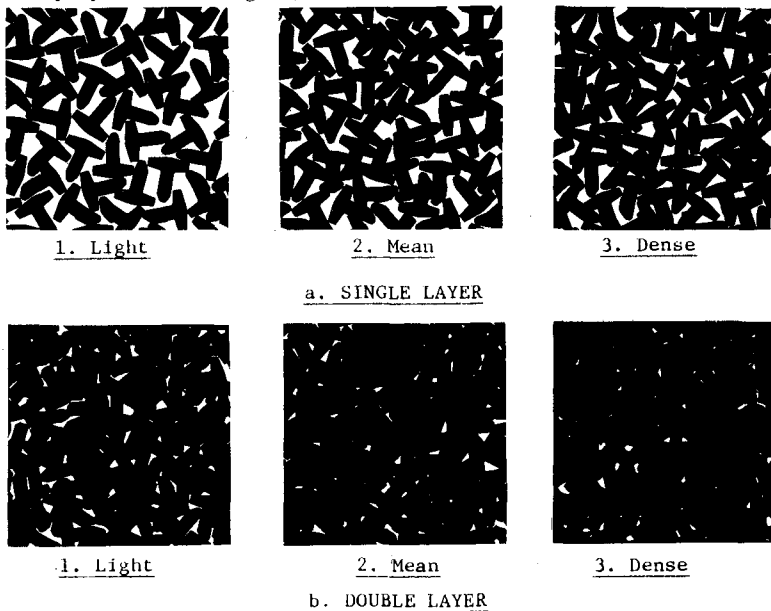


FIG. 1 PACKING DENSITIES

- light packing* - all Dolosse rest on the underlayer with two points (Fig. 1.a.1)
- mean packing* - average packing density judged to provide a proper first layer cover (Fig. 1.a.2)
- dense packing* - every Dolos touches the underlayer with at least one point (Fig. 1.a.3)

Packing tests

To determine the ϕ values for the above packing densities, a total of 65 packing tests were done by 8 different persons using a 0,5m by 0,5m area ($A = 0,25 \text{ m}^2$) and Dolosse with a height $h = 60 \text{ mm}$ ($V = 35,6 \times 10^{-6} \text{ m}^3$).

The following results were obtained :

Packing	Tests	Mean no. Dolosse ($N_{n=1}A$)	Variation max./min.	$\phi_{n=2} = \frac{2N}{n=1} V^{2/3}$
light	23	96	+ 5	0,83
mean	20	115	+ 8	1,00
dense	22	133	+ 8	1,15

As was to be expected, there is a reasonably large variation between the individual packing tests but, on average, the results were found to be very

consistent even with the large number of people involved in the tests. It is thus concluded that, given the above definitions, the three packing densities are reproducible to an acceptable degree of accuracy.

For a breakwater armouring, a 'double layer' of Dolosse is required, that is, $2N_{n=1}$. The corresponding $\phi_{n=2}$ values are included in the last column of the above table.

Placing technique

The packing densities, N , discussed above refer only to the number of units per unit area and *not* to the possible differences in *placing density*, i.e. differences in the number of units per unit of volume. Although it was found in the laboratory to be possible to achieve different placing densities,¹⁸ this is quite impractical in the prototype; the placing density will depend on the placing technique and conditions during placing and can, therefore, not be prescribed.

Since it is not considered possible to achieve a specific placing density in the prototype, a *standard technique* is used in the model whereby the Dolosse are held by the shank and dropped in position from a height of between h to $2h$. This is considered reasonably representative of prototype placing techniques.

On the model slopes, the Dolosse were always placed in *one operation* (full layer thickness) from the bottom upwards. A better interlocking is achieved in this way.

Porosity and layer thickness

The *physical properties*, namely, 'real' (P_r) and 'fictitious' (P_f) porosities, layer thickness (τ) and shape factor (C), were determined for the light, mean and dense packing densities using the results of 12 container tests and 10 tests each for the light and dense packing and 34 tests for the mean packing on a 1 in 1,5 model slope. The average physical properties of Dolosse at different packing densities were found to be as follows :

Packing density	ϕ (n=2)	Porosity in per cent				Relative armour layer thickness			
		Container tests (n=5)		Model slope (n=2)	Container tests (n=1 to 5)		Model slope (n=2)		
		P_r	P_f	P_f	$\tau_{n=2}$	$\tau_{n>2}$	$\tau_{n=2}$	$C_{n=2}$	
light	0,83	55,0	52,8	51,8	1,79	0,85	1,72	0,86	
mean	1,00	55,0	50,9	51,5	2,06	0,94	2,04	1,02	
dense	1,15	55,0	51,4	52,3	2,41	1,14	2,42	1,21	

The 'real' porosity is seen to be independent of packing density which is to be expected. Variations in the fictitious porosity are small and follow no particular trend so that the average value of 51,5 per cent, which applies to both the container and model slope tests, can safely be accepted for all three packing densities.

In the container tests, every layer was sounded from $n = 1$ to $n = 5$. The results showed that the *first layer* was always significantly *thicker* than the following layers because the first layer is packed onto underlayer stone in which the cavities are much smaller than they are in a Dolos layer. Thus $\tau_{n=2}$ is seen to be greater (about 7%) than $2\tau_1$

where t_i refers to the thickness of one layer in a multi-layer packing ($n > 2$). The same applies to the shape factor, C , which is found simply by dividing t_n by n . This should be borne in mind when the armouring in the above table, consists of *more than two layers* ($n > 2$). The model slope double-layer thickness and corresponding shape factor values are seen to agree closely with the container values.

The above physical properties apply strictly only to Dolosse with $r = 0,33$ but it was found that there is no significant difference in porosity or layer thickness for Dolosse with waist ratios varying from 0,30 to 0,35 and they can therefore *safely be used* for all Dolosse with *waist ratios* within this range.

For a normal *double layer*, the number of Dolosse per unit area follows from $N_{n=2} = \phi_{n=2} V^{-2/3}$ but for a large *mound* of Dolosse, consisting of many layers, the packing density per unit of volume (N') becomes :

$$N' = N/t = (1 - P_r/100)V^{-1} = 0,45/V$$

because $P_r = 55,0$ for all three packing densities.

For a structure of *irregular shape* (e.g. breakwater head) in which a *double layer* of Dolosse is used, the number of units per unit of volume may be useful :

$$N'_{n=2} = N_{n=2}/t_{n=2} = 0,485/V$$

which is also independent of packing density accepting $P_f = 51,5$.

Comparison with previous data

Previously reported data on required *number of Dolosse* and corresponding *layer thicknesses* are compared in the following table :

Source	Year	$\phi_{n=2}$	$\tau_{n=2}$
(a) Merrifield and Zwamborn ¹¹	1966	1,04	2,6
(b) CERC, SPM ¹⁷	1973	0,74	2,0
(c) Silva and Foster ¹⁵	1974	0,73	2,00
(d) Davidson ⁵	1976	0,67	1,60
(e) Vonk ¹⁸	1976	1,15	2,36
(f) Vonk ¹⁸	1976	1,08	2,12
(g) Vonk ¹⁸	1976	0,86	2,00
(h) Zwamborn ²⁰	1976	1,0	2,2
(i) Carver and Davidson ³	1977	0,83	1,88
(j) Carver and Davidson ³	1977	0,62	1,24
(k) Present paper : <i>light</i>	1978	0,83	1,72
(l) (based on soundings) <i>mean</i>	1978	1,00	2,04
(m) <i>dense</i>	1978	1,15	2,42

It is clear from the above that smaller layer thicknesses generally go with lower packing densities which is to be expected because $\phi = (1 - P_f/100)\tau$ with P being constant (thus intermediate values for ϕ and τ can be interpolated linearly. Most of the data compare reasonably well, except (a), (b) and (c) for which the τ values are relatively too high. In the tests described in (a) very roughly cast cement Dolosse were used for the original tests. Subsequent tests (h), (k), (l) and (m) were all done with smooth P.V.C. models.

All the Dolos applications in South Africa (involving a total of some 120 000 Dolosse) and several large schemes elsewhere (e.g. High Island Water scheme⁹ and Sines Harbour¹²) were built in accordance with a value $\phi = 1$ whereas in the U.S.A. and Australia values as low as $\phi = 0,67$ and, more recently, $\phi = 0,83$ are used, the latter being the same as the 'light' packing density defined in this paper.

Optimum packing density

Three packing densities have been defined above and the corresponding physical properties determined. The question now is, which density should be used for a particular harbour design?

Obviously, a low packing density reduces the initial cost. On the other hand, some test results indicate that stability of the armour is improved when the number of Dolosse is increased^{3,18}. There are also practical aspects to be taken into account; when a low packing density is used, placing accuracy and control must be very good, otherwise there is a possibility that the armour will have weak spots in it right from the beginning. It is interesting to note that in several instances, *during construction*, the armour was judged to be incomplete or too irregular after the theoretical number of Dolosse had been placed. This occurred, inter alia, at the Cape Town harbour extensions where some 10 per cent cent more Dolosse were used ($\phi \approx 1,13$), for the Port Elizabeth shore protection²⁰ where 2 per cent more Dolosse were used ($\phi = 1,06$) and for the Sines breakwater²¹ where the number of units was increased from $0,16/m^2$ ($\phi = 1,04$) to $0,18/m^2$ ($\phi = 1,17$), that is about 13 per cent more than the theoretical number.

A decision on the packing density to be used should be reached by carefully *weighing up* the initial capital cost, maintenance cost, practical considerations (construction methods and constraints) and the economic effects (interruption in port operation) of a part or complete failure of the structure. In order to be able to perform this type of economic analysis, it will be necessary to know the effect on the stability of different packing densities. Because of the complete lack of comparable data, it was decided to carry out some tests using the three packing densities discussed above.

MODEL TESTS ON EFFECT OF PACKING DENSITY ON STABILITY

Although, as discussed in the previous section, researchers have used various packing densities in stability tests it is virtually impossible, because of the differences in test conditions and the interpretation of damage, to compare directly the results of tests done by different laboratories.

Some *comparative tests* were done, however, by Vonk¹⁸, both with a 1 in 1,5 and a 1 in 2 slope. He found a significant *improvement* in the stability of a Dolos armour by increasing the packing density about 25 per cent from $\phi_{n=2} = 0,86$ to $\phi_{n=2} = 1,08$, particularly for the 1 in 1,5 slope. Carver and Davidson³ also report on some tests carried out with Dolosse on a 1 in 1,5 slope using different packing densities. They report a decrease of about 50 per cent in the stability factor, K_D , for a decrease of 25 per cent in the number of Dolosse (from $\phi = 0,83$ to $\phi = 0,62$) and an increase of 27 per cent in K_D for an increase of 11 per cent in N (from $\phi = 0,83$ to $\phi = 0,92$)^{*}. Silva and Foster¹⁵ found little difference in

* Carver and Davidson³ ascribe this improvement to the fact that the Dolosse were packed in a *pattern* but, considering the improvement in K_D for $\phi = 0,62$ to $\phi = 0,83$, the further increase in K_D could also be ascribed to the increased number of Dolosse.

the initiation of motion of the units but, at higher damage levels, there was a significant increase found with a higher packing density.

Thus, it appears that an *increase in the number of Dolosse per unit area improves stability*. Test data, however, are very sketchy and comparative tests were, therefore, done in the wave flume in Stellenbosch.

In the above, the stability factor is defined by Hudson's formula¹⁷, namely,

$$K_D = \frac{\gamma_s H_D^3}{W \Delta^3 \cot \alpha}$$

where γ_s is mass density, H_D is design wave height, W is block mass, Δ is relative block density i.e. $\gamma_s/\gamma-1$, γ is mass density of water and α is breakwater side slope.

Test facilities

The tests were done in the 160 m long (effective length), 3 m wide and 1,1 m deep wind-wave flume in Stellenbosch. Only *regular waves* were used for this test series which were produced by the translatory wave board. Waves were recorded with temperature compensated probes and wave height meters connected to standard chart recorders. During the wave calibration stage, the waves were measured where the model slope was to be



FIG. 2 MODEL VIEW

positioned in the stability tests (that is, near the intersection of the still water line and the top of the model slope) and a quarter wave length in front. During the actual tests, the waves were recorded from a trolley moving at an approximately constant speed over a distance of two wave lengths in front of the model.

Model lay-out and design

The flume was divided into *three* 0,75 m wide *test sections* leaving two narrow dummy channels of about half that width on either side (see Fig. 2). The core was built of clean 6mm (about 4 g) stone, the model slope

was 1 in 1,5 and the water depth 0,8m.

The particulars of the *model Dolosse* were as follows (based on accurate measurements of a representative sample of 170 Dolosse) :

Model Dolosse	W(g)	V(10 ⁻⁶ m ³)	γ_s	h(mm)	r
Mean	81,2	35,0	2,32	59,2	0,33
Max.deviation(%)	\pm 3,3	\pm 3,0	\pm 2,6	\pm 0,4	\pm 5,3

The 'test areas' were 750 x 750 mm² and 436, 526 and 605 Dolosse were placed in these areas representing a *double layer* of 'light', 'mean' and 'dense' packing respectively. They were placed in six 125 mm (about 2h) wide bands of different colour, three above and three below still water

level, i.e. from 208 mm below to 208 mm above water. Taking $K_D = 25$ ('first design' value²⁰), the design wave height for the model Dolosse follows from Hudson's formula, viz. $H_D = 144,5$ mm and the *area considered for damage* thus extended from $1,44 H_D$ above to $1,44 H_D$ below still water level. Above and below the 'test area', additional 81,2 g Dolosse were placed, but these were not considered for damage.

The underlayer stone mass used was $W = 81,2/5 = 16,2$ g. Sorted stone with a mean mass of 16,5 g was used.^u The thickness of the underlayer follows from $t_u = nCV^{1/3} = 43$ mm, using $n = 2$, $C = 1,15$ and $\gamma_s = 2,64^{20,17}$.

Test conditions and procedures

After the stone had been smoothed out the underlayer was profiled using the standard sounding technique on a 50 mm grid (see Fig. 12.a). The Dolosse were then placed in one operation, working from the bottom upwards, and were sounded on the same grid. The mean difference between the two soundings provided the *average layer thickness*, and the 'fictitious' porosity. The entire Dolos cover was replaced after each test series.

A test series consisted of 24 'bursts' of $2\frac{1}{2}$ min. or a total of 60 min. of wave action for each wave height increment, viz. 83, 100, 117, 134,5, 152, 168,5, 185, 203 and 221. The wave period for the entire series was constant at 1,75 s (the Ursell parameter, $U = HL^2/2d^3$ where L is wave length and d is waterdepth, varied between 1,33 and 4,05; the Iribarren number, $\xi = \tan\alpha/\sqrt{H/L_0}$ where L_0 is the deepwater wave length, varied from 5,06 to 2,90 while for $H_D = 144,5$ mm, $\xi_D = 3,83$ which represents the least stable condition according to Bruun and Günbak²).

Displacement of any units was recorded after each $2\frac{1}{2}$ min 'burst'. Small movements and *rocking* were recorded continuously by the cine technique, except during wave 'bursts' numbers 8 and 16 when the cine camera was used to record the maximum wave *run-up*.

Test results on stability of different packing densities

Because of the inherent variation in tests of this nature, 10 virtually identical *repeat runs* were made using the above-mentioned wave heights. Although a few tests were carried on until complete destruction, most of the test series were stopped when between 20 and 30 per cent damage had been reached, to reduce the time required for reconstruction of the slopes.

The *test results* are shown in Fig. 3 where the percentages of displaced Dolosse are plotted against wave height for each test. The results show considerable differences, particularly for the 'mean' packing density. The more consistent result for the 'light' packing could be ascribed to an, on average, somewhat better interlock between the Dolosse but the 'dense' packing results are equally consistent so that this explanation does not appear to hold.

The *average results* for the three packing densities are shown in Fig. 4. This figure shows the somewhat surprising result that all three packing densities display about the *same stability* and, on the basis of the present tests, stability does not appear to increase with the number of Dolosse, as was expected. There is, however, a difference in the type of collapse of the armour, i.e. the 'light' and 'mean' packing densities collapse more suddenly than the 'mean' and 'dense' packings respectively.

These differences, however, show up only for damage well exceeding 15 per cent.

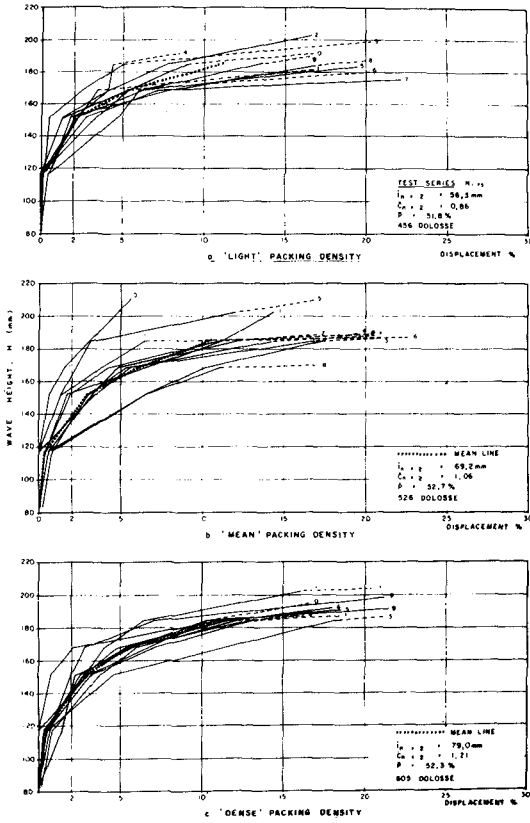


FIG. 3 PACKING DENSITY TESTS, DOLOS DISPLACEMENT VERSUS WAVE HEIGHT

FIG. 4 COMPARISON OF MEAN TEST RESULTS FOR 'LIGHT', 'MEAN', AND 'DENSE' PACKING DENSITIES

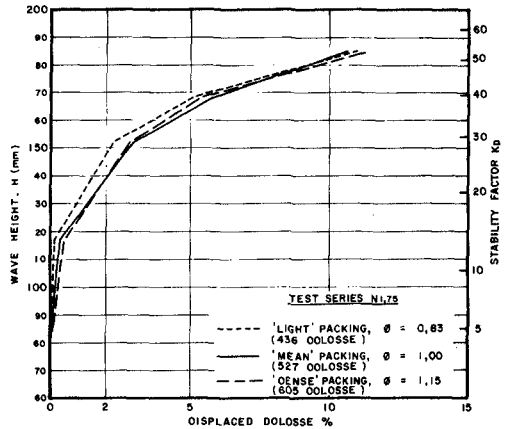


Figure 5 gives the percentages of displaced units as well as the *continuously* and *intermittently rocking* Dolosse. These results were derived from the time-lapse cine measurements. The percentages are not too much greater for the higher damage values but, at the 2 per cent displacement level, the increase due to continuous rocking is seen to be about 50 per cent while continuously plus intermittently rocking units add about 100 per cent to the damage caused by displacement. Although the percentage increase is somewhat smaller for the 'dense' packing, this is not considered to be very significant (see Fig. 5).

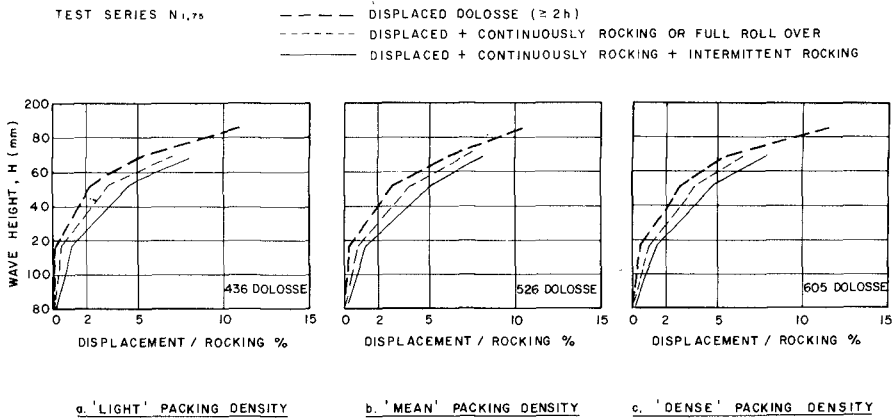


FIG. 5 PACKING DENSITY TESTS, MEAN DISPLACEMENT AND ROCKING VERSUS WAVE HEIGHT

The stability factors, K_D given in the following table, also show the lack of increased stability for higher packing densities :

Packing density	'Light', $\phi=0,83$			'Mean', $\phi=1,00$			'Dense', $\phi=1,15$		
	2	5	10	2*	5	10	2	5	10
K_D (displ.)	26,9	39,3	(50)	22,2	36,5	50,3	22,2	37,9	49,9
K_D (displ.+rock.)	16,6	30,2	-	15,4	28,5	-	15,2	29,7	-

The K_D factors, based on displacement, compare with the lowest values reported by Merrifield and Zwamborn¹¹ and are in reasonably good agreement with Carver and Davidson's more recent results³ ($K_D = 33$ for 5% damage, $\phi = 0,83$, best-fit line). The K_D values based on displacement plus continuous and intermittent rocking are seen to be considerably smaller, particularly for the small percentages damage.

As indicated before, the results are somewhat surprising in that there is *no obvious improvement* in stability for the higher packing densities.

The question thus arises whether it is worthwhile to use these higher densities. There are several reasons, however, against using the 'light' packing density, $\phi = 0,83$, namely :

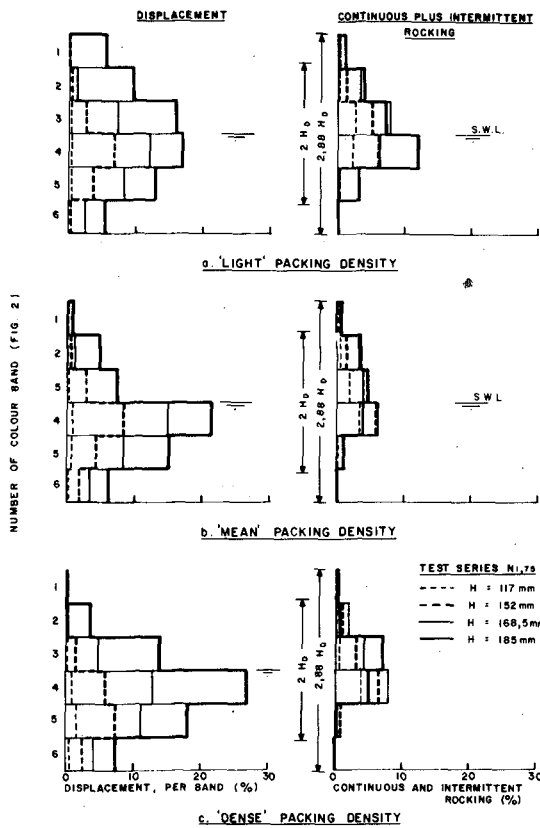
- a large portion of the armour lies underwater so that it is difficult to ensure the 'ideal' packing necessary with the 'light' packing density;
- breakage of more than three Dolosse in a cluster will cause loss of stability with the 'light' packing⁴;
- there is little reserve in the structure, particularly in the case of possible breakage of units;
- the wave run-up is about 5 per cent larger than that for 'mean' packing density (refer following section).

Considering the anchor shape of the Dolos, it would appear that the *optimum*

layer thickness could be $t_{n=2} = h$. In this case, maximum interlocking could be achieved if a certain percentage of the Dolosse came to rest with their shanks about perpendicular to the breakwater slope, acting as anchors. Based on the average measured layer thicknesses, the corresponding packing density would be $N = 0,9 V^{-2/3}$ ($\phi = 0,87 \approx 0,9$). Even so, depending on the type of structure, the method of placing and the quality of the control, it would be prudent to allow for about 10 per cent extra units to ensure an even packing density in practice, increasing the above packing density to $N = 1,0 V^{-2/3}$, that is, 'mean' packing density.

Areal distribution of damage

The average damage per Dolos colour band, for 10 repeat tests, is shown in Fig. 6. This figure shows the percentages damage due to displaced Dolosse as well as for the continuously plus intermittently rocking units.



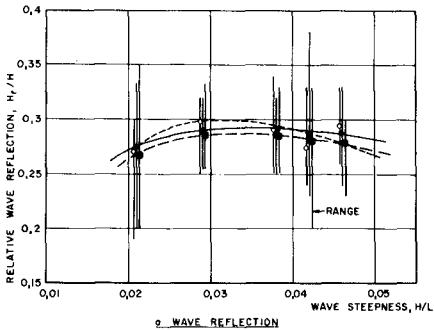
The results show that the main damage areas are located at and just below the still water line but the 'dense' packing shows maximum damage in band 5 for the waves up to 152 mm. This is thought to be due to the increase in the quantity of run-down water caused by the thicker cover layer. As the wave height increases, the damage becomes more widespread, both below and above water. On average, the 'dense' packing sustained more concentrated damage near the water line whereas the 'light' packing showed the widest distribution of damage. The complete absence of rocking units in band 6 is not necessarily correct because this band remains normally submerged and is therefore excluded from the cine recording.

FIG. 6 PACKING DENSITY TESTS - MEAN AREAL DISTRIBUTION OF DAMAGE

It is clear from the above that significant damage occurs outside the $2 H_D$ area normally considered and it is therefore *recommended* that damage be based on the area of the breakwater slope lying between $1,5 H_D$ above to $1,5 H_D$ below still water level.

Wave reflection and run-up

Some 100 wave reflection measurements for each of the three packing densities were used to compile Fig. 7a. There is seen to be very little variation in the average H_r/H values, that is, 0,27 to 0,30 and there is only a very small increase of reflection from the 'dense' to 'light' packing density.



Wave run-up values measured by the time-lapse cine technique are shown in Fig. 7b. About 70 records for each packing density collected during 7 tests were used to plot this figure. The results show a *significant increase* in wave run-up for increase in wave steepness and for smaller packing densities.

The results for the 'mean' packing density compare well with those obtained previously by Zwamborn and Beute¹⁹ and for the 'light' packing density with the results of Carver and Davidson³.

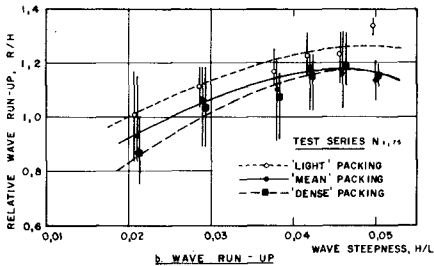


FIG. 7 WAVE REFLECTION AND RUN-UP VERSUS WAVE STEEPNESS FOR DIFFERENT PACKING DENSITIES

MODEL TESTS ON EFFECT OF BLOCK DENSITY ON STABILITY

All available formulae to determine the mass of armour units include the third power of the relative block density in the denominator, which would indicate that the block mass can be *reduced considerably* if a high relative density is used. This has obvious advantages and, in particular cases, circumstances may *dictate* the use of high-density concrete¹⁶.

A recent study of high-density concrete indicates that *high-strength* concrete can be produced using heavy aggregates, such as magnetite,

goethite, hematite and ilmenite⁶. However, since higher density would result in increased tensile stresses in the armour units, a *thorough strength analysis* should precede the use of such high densities, particularly for large units.

Doubt has also been expressed about the validity of the third power relationship in the case of Dolosse because their stability is, at least, partly the result of the *interlocking* of the units and an evaluation of available test results indicated a power of the relative density below three¹⁹. It was therefore felt that a further investigation of the effect on stability of relative block density, was essential.

Basic stability equation

Castro and Iribarren (1938)¹⁰ developed the first stability equation for rock armouring by equating the *drag force*, caused by the waves, with the resistance force, which depends on the *submerged mass* of the stone and the slope of the armouring. The basic form of their equation is :

$$\frac{V}{H^3} f(\alpha) = \frac{1}{K} \left(\frac{\gamma_s}{\gamma} - 1 \right)^x = \frac{\Delta^x}{K}$$

where $f(\alpha) = (\cos\alpha - \sin\alpha)^3$, K is a constant and $x = -3$. Many researchers have published variations to Iribarren's formula¹⁴, but they all use the same basic form, except for the replacement of H^3 by H^2T in some of the formulae. The main difference between the various formulae is the different forms of $f(\alpha)$. The well-known Hudson formula¹⁷ is obtained by setting $x = -3$, $f(\alpha) = \cot\alpha$ and $V = W/\gamma_s$.

The *inertial forces* on the armour units and *interlocking forces*, applicable to Dolosse, are not taken into account in the above formulae. The inertial force, which depends on the wave period, is estimated to be of the same order of magnitude as the drag force but the effect of interlocking is very difficult to quantify. Armour units are also not necessarily fully submerged when the combination of drag and inertial forces reaches a maximum, which would affect the right-hand term in the above equation.

Previous test results on the effect of unit density

Brandtzaeg has reported on *extensive tests* carried out by Kydland and Sodefjed using stone of different densities (1,725 to 4,72 t/m³), fluids with different densities (1,0 to 1,13 t/m³) and various breakwater slopes (1 in 1,25, 1 in 1,5 and 1 in 2)¹. He plotted relative wave height versus relative unit density for various percentages damage, arriving at a linear relationship of the form $H/V^{1/3} = \xi(\gamma_s/\gamma - \Psi)$, where ξ and Ψ are constants. Although the test results fit in quite well with this equation, the equation has no physical basis and it yields wave heights greater than zero for $\gamma_s = \gamma$, which, of course, is impossible.

The Kydland test results were, therefore, plotted in Fig. 8.a in accordance with the above equation with $f(\alpha) = \cot\alpha$ for 1 and 4 per cent damage. Mean lines have been drawn through the test points which show a *remarkably good fit* for $x = -2,00$, $K = 5,3$ and $x = -2,08$, $K = 9,5$. Hudson ascribes the disagreement with his own formula ($x = -3$) to *scale effects*, because the stability number should be independent of the density. This conclusion, however, appears to be *incorrect* in view of the results shown in Fig. 8.a.

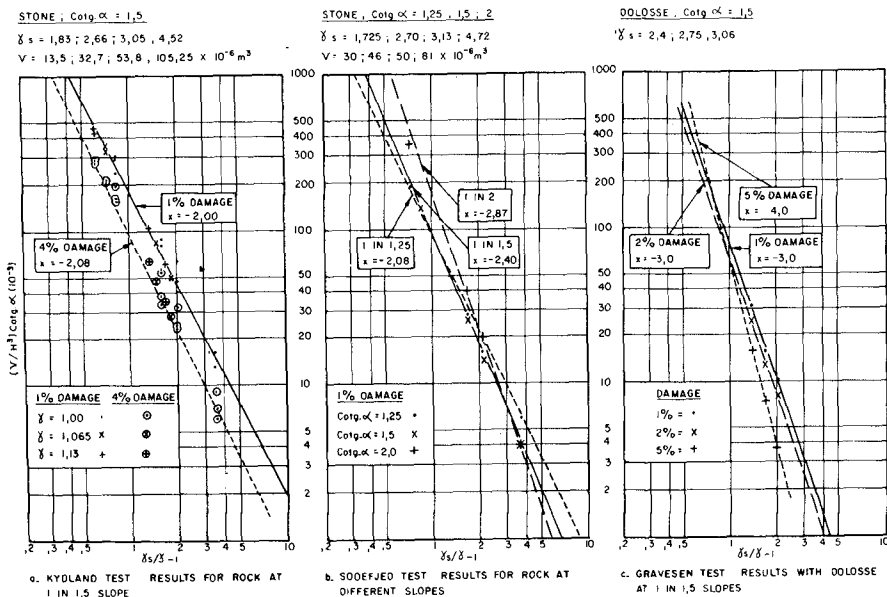


FIG. 8 RELATIVE UNIT VOLUME VERSUS RELATIVE UNIT DENSITY

Sodefjed's test results are plotted similarly in Fig. 8.b for 1 per cent damage. This figure shows different values of x, varying from - 2,08 to - 2,87, for the different breakwater slopes. Thus although it is again found that $x > - 3$, the x values do not agree with Kydland's data. Moreover, the variation of x with slope indicates that $f(\alpha) = \cot \alpha$ does not fully represent the slope effect (replacing $\cot \alpha$ by $(\cos \alpha)^3$ did not reduce the spread of the lines while $(\cos \alpha - \sin \alpha)^3$ made the spread distinctly worse¹⁴).

Some test results with Dolosse of different densities were reported by Gravesen and Sørensen⁹. These are plotted in Fig. 8.c indicating values of $x = - 3,0, - 3,0$ and $- 4,0$ for 1, 2 and 5 per cent damage, respectively. The data, however, are very limited and the drawing of general conclusions should be reserved until more test results become available.

Test facilities, model lay-out and design

The tests were done in the same facilities described before and the models were built in the same position in the flume (see Fig. 2). Three models were again tested side by side, namely Dolosse with specific densities of 2,31, 2,41 and 2,57. The model slopes were 1 in $1\frac{1}{2}$ and the water depth was again 0,8 m.

Details of the model Dolosse, based on representative samples of 50 Dolosse for each density, are given in the following table :

Model Dolosse	W(ρ)	V($10^{-6}m^3$)	γ_s	h(mm)	r
Mean	81,4	35,3	2,31	59,2	0,33
Max. deviation(%)	$\pm 2,1$	$\pm 3,0$	$\pm 1,9$	$\pm 2,4$	$\pm 5,2$
Mean	84,8	35,2	2,41	59,4	0,33
Max. deviation(%)	$\pm 2,3$	$\pm 2,8$	$\pm 2,1$	$\pm 2,5$	$\pm 4,8$
Mean	92,0	35,8	2,57	59,5	0,33
Max. deviation(%)	$\pm 2,5$	$\pm 2,0$	$\pm 2,1$	$\pm 2,1$	$\pm 3,7$

The slope area considered for damage was $750 \times 750 \text{ mm}^2$ on which 513 Dolosse were placed ('mean' packing, $\phi = 1,00$). The 'test area' extended from 255 mm below to 161 mm above still water level ($1,76 H_D$ to $1,11 H_D$ respectively). Below and above the 'test area', 120 g Dolosse were used while the underlayer was 43 mm thick, consisting of 11,4 g stone.

Test conditions and procedures

The same basic test procedures were followed as for the packing density tests. The tests were all done with regular waves of 1,75 s period using $2\frac{1}{2}$ min wave 'bursts' up to a total of 1 hour per wave height.

Tests No's D1 to D 3 and D 8 and D 9 were run with gradually increased wave heights whereas a sudden increase in wave height was used for Tests No's D 4 to D 7²².

Test results on Dolosse with different densities

A total of nine tests were done and the *test results* are shown in Fig. 9 which also shows the mean results for the six *progressive* tests. Considerable variations in the results of individual tests are again evident but the variations are seen to be less for the higher unit density. The 'suddenly' increased wave height tests show, on average, less stability for the $2,31 \text{ t/m}^3$ unit density (Fig. 9.a) but for the other two densities, the results of these tests *agree very well* with the mean of the 'progressive' increase tests (Figs. 9.b and c).

The comparison of the *mean lines* in Fig. 10 show an improvement in Dolos stability for increased unit density, which was expected. Although damage was below 2 per cent, the results compare very well with the results of the different packing density (N) series, for greater percentages damage the D series show greater stability (compare Figs. 4 and 10), which is thought to be mainly due to a shorter test time, i.e. larger wave height steps.^{13,22}

To check on the correctness of the *basic stability equation* the relative Dolos volumes were plotted, versus the relative submerged block density, similar to the plots in Fig. 8, and mean lines were drawn for the 1, 2, 5 and 10 per cent damage cases (displaced Dolosse). The *variation* in individual test results, however, was found to be much greater than for the Kydland and Sodefjed test data (based on stone) and no definite conclusion could be drawn from these test results with regard to the correct value for x . The large variation is probably *typical for Dolosse* because of the inherent differences in packing and subsequent interlocking, which does not apply to the same extent to stone.

It was therefore *concluded* that although increased unit density does increase Dolos stability, further tests with a greater range of unit densities are necessary to determine the correct relationship between stability and unit density. These tests are under way at present.²²

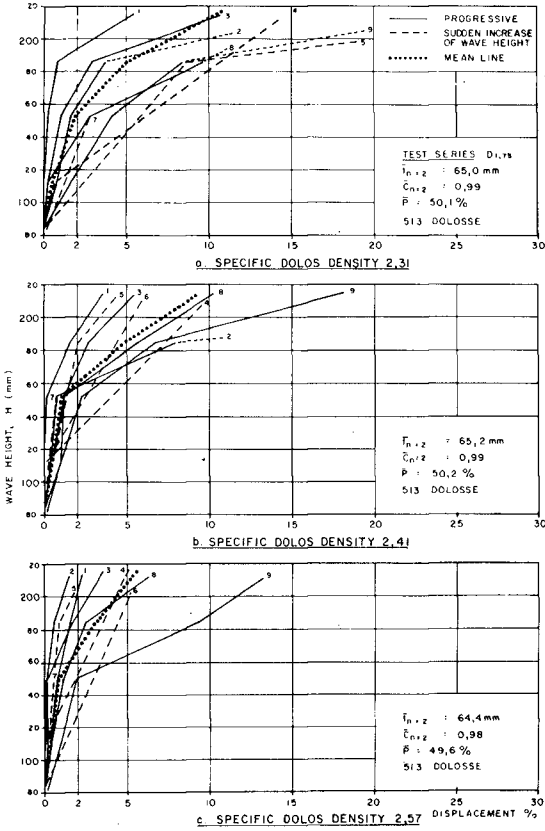


FIG. 9 DOLOS DENSITY TESTS, DOLOS DISPLACEMENT VERSUS WAVE HEIGHT

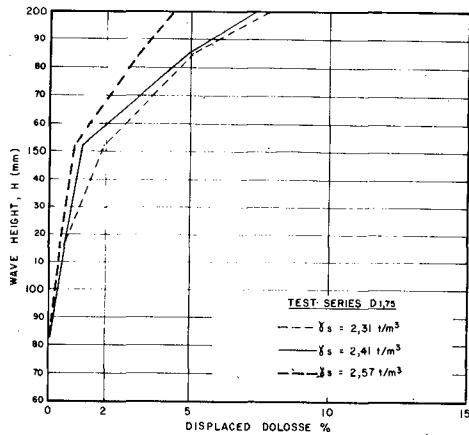


FIG. 10 COMPARISON OF MEAN TEST RESULTS FOR 2,31 ; 2,41 AND 2,57 SPECIFIC DOLOS DENSITIES

MEANS OF PROGRESSIVE TESTS

CONCLUSIONS AND RECOMMENDATIONS

It is absolutely essential to *standardize measuring and testing techniques* to make test results on Dolos stability compatible. Detailed proposals for standardization are made elsewhere²² but the main problem areas were found to be inconsistency in definitions and measurements of packing density, porosity, layer thickness (shape factor) and damage criteria which have led to unavoidable differences in reported test results from different laboratories.

Three *packing densities*, namely 'light' ($\emptyset = 0,83$), 'mean' ($\emptyset = 1,00$) and 'dense' ($\emptyset = 1,15$) have been defined in this paper and the corresponding layer thicknesses were found to be 1,72, 2,04 and 2,42 $V^{1/3}$, respectively, with a porosity of 51,5 per cent, independent of packing density.

Stability tests with a wave period of 1,75 s using these three *packing densities* showed little difference in damage, both based on displaced and displaced plus moving (rocking) units, the stability factor, K_D , being, on average, 24 and 16, respectively, for 2 per cent 'damage'. Wave reflection was found to be between 27 and 30 per cent, independent of placing density, but a difference of between 10 and 20 per cent was found between the wave run-up of the 'light' and 'dense' packing, depending on the wave steepness.

Taking also practical considerations into account, it is *recommended* that the 'mean' packing density be adopted for the 'first design' of a Dolos structure which should be checked by hydraulic model tests, preferably three-dimensional tests. Realistic wave conditions (e.g. irregular waves) should be reproduced in these tests and both displaced and rocking units should be carefully monitored. Tests should preferably include total destruction to determine the inherent safety of the structure.

Tests with model Dolosse having *different unit densities* (2,31, 2,41 and 2,57) showed greater stability for the higher densities but further tests with a greater unit density range are necessary to determine the relationship between stability and unit density.

REFERENCES

1. BRANDTZAEG, A. "The effect of unit weights of rock and fluid on the stability of rubble mound breakwaters". Proc. Xth Coast. Eng. Conf., Tokyo, September 1966.
2. BRUUN, P. and A. GUNBAK. "Stability of sloping structures in relation to $\xi = \tan\alpha/H/L_0$ risk criteria in design". Coastal Engineering, Vol. 1, 1977, Amsterdam.
3. CARVER, R.D. and D.D. DAVIDSON. "Dolos Armour Units used on rubble-mound breakwater trunks subjected to non-breaking waves with no overtopping". Report H-77-19, WES, Vicksburg, November 1977.
4. DAVIDSON, D.D. and D.G. MARKLE. "Effect of broken Dolosse on breakwater stability". Proc. XVth Coast. Eng. Conf., Hawaii, July 1976.
5. DAVIDSON, D.D. "Model tests on Dolosse". Private Communication, WES, Vicksburg, August 1976.
6. FERNANDEZ, R.M. "Technical and economical feasibility of using heavyweight aggregates in concrete breakwater blocks." Techn. Report No. 3, University of California, Berkeley, April 1977.
7. FOSTER, D.N. "Dolos as an armour unit with breaking waves". Abstracts, XVth Coast. Eng. Conf., Hawaii, July 1976.

REFERENCES (Continued)

8. CRAVESEN, H. and T. SØRENSEN. "Stability of rubble mound breakwaters". Proc. 24th Int. Nav. Congress, PIANC, Leningrad, 1977.
9. Hydraulics Research Station. "High Island Water Scheme - Hong Kong". HRU Report Ex 532, Wallingford, October 1970.
10. IRIBARREN CAVANILLES, R. "A formula for the calculation of rock-fill dikes". Techn. Report HE-116-295, University of California, Berkely, 1948 (translated).
11. MERRIFIELD, E.M. and J.A. ZWAMBORN. "The economic value of a new breakwater armour unit 'Dolos'". Proc. Xth Coast. Eng. Conf., Tokyo, September, 1966.
12. METTAM, J.D. "Design of main breakwater at Sines harbour". Proc. XVth Coast. Eng. Conf., Hawaii, July 1976.
13. MORAIS, C.C. "Irregular wave attack on a Dolos breakwater". Proc. XIVth Coast. Eng. Conf., Copenhagen, June 1974.
14. PIANC. "Final Report of the International Commission for the study of waves". Annex to Bull. No. 25, Vol. III, Brussel, 1976.
15. SILVA, E.J. and D.N. FOSTER. "Dolos as an armour unit in breakwater construction". Proc. Vth Aust. Conf. on Hydr. and Fluid Mech., Christchurch, December 1974.
16. STANDISH-WHITE, D.W. and J.A. ZWAMBORN. "Problems of design and construction of an offshore seawater intake". Proc. XIth Coast. Eng. Conf. Hamburg, July 1978.
17. U.S. ARMY, CERC. "Shore Protection Manual". Dept. of the Army, Corps of Engineers, 1973.
18. VONK, A.P.M. "Breakwater armour units - Influence of packing density and porosity on stability". Proc. Marine/Fresh water Conference, S.122, Port Elizabeth, July 1976.
19. ZWAMBORN, J.A. and J. BEUTE. "Stability of Dolos Armour Units". ECOR Symposium S71, Stellenbosch, November 1972.
20. ZWAMBORN, J.A. "Dolosse for Coastal Works". Proc. 5th SAICE Western Cape Convention, Stellenbosch, September 1976.
21. ZWAMBORN, J.A. "Analysis of causes of damage to Sines breakwater". Proc. Coastal Structures 79, CERC, Washington, March 1979.
22. ZWAMBORN, J.A. "Measuring techniques, Dolos packing density and effect of relative block density". NRIO Report, Stellenbosch, 1979.

NOMENCLATURE

A = area	t = armour layer thickness
C = block shape factor	U = $HL^2/2d^3$ = Ursell parameter
d = water depth	T = wave period
h = Dolos height	V = Dolos volume
H = wave height	W = Dolos mass
K_D or K = stability factor	x = exponent of relative density function, Δ
L = wave length	
n = number of armour layers	α = breakwater slope angle
N = packing density or number of blocks per unit area	ψ = constant
N' = number of blocks per unit volume	ϕ = $NV^{2/3}$ = packing density parameter
P_f = $(At - NV)/At$ = 'fictitious' porosity	γ = specific density of water
P_r = voids volume/ At = 'real' porosity	γ_s = specific density of Dolosse
r = Dolos waist to height ratio	τ = $\tau V^{-1/3}$ = layer thickness parameter
	ξ = $\tan\alpha/\sqrt{HL_0}$ = Iribarren number; also constant
	Δ = $\gamma_s/\gamma - 1$ = relative block density.

Subscripts -

D indicates design value
i indicates single layer
n is the number of layers
o means deep sea value
u relates to underlayer

CHAPTER 138

PERFORMANCE OF DOLOS BLOCKS IN AN OPEN CHANNEL SITUATION

ARTHUR BREBNER*

ABSTRACT

Tests on 100 gm model dolos units on the bed of an open-channel under steady state turbulent flow reveal that the dolos unit has no inherent interlocking property that would make it preferable to ordinary armour stone of the same weight in resisting movement. However interlocking can occur when dolos units are placed on a slope since the natural angle of repose of dolos units is much greater than that of ordinary armour stone, thus accounting for the enhanced K_D of dolosse in a breakwater situation.

INTRODUCTION

Model tests were conducted to compare the stability of dolos blocks, trunk width 0.35 times the overall height and mass 100 gm (0.23 lb) with rock armour of the same density and having an identical mass of 100 gm, in a steady flow of water in an open channel. Such tests could be thought of as tests preliminary to the construction of a barrier across a tidal inlet or as tests to compare the efficiency of dolosse with that of quarystone as protection against scour in a dam situation.

Most coastal laboratories have conducted extensive testing of both rock armour and dolos units for breakwater construction and it is generally agreed, for the same wave-height (approaching normally) and period, the same density of material and breakwater slope, that the weight of armour required for the stable-damage criteria is inversely proportional to K_D , the "hydraulic damage coefficient", which is directly related to the "shape" of the armour unit. Taking K_D as 4 for rock armour and 16 for the dolos block indicates that the latter unit can withstand a wave height

$$\sqrt[3]{\frac{16}{4}} = 1.58 \text{ times that for rock. Conversely a dolos unit of } 0.25$$

times the rock weight could withstand the same height of wave attack. It is assumed here that, for practical purposes, stability equations for rock are applicable to the dolos unit with its interlocking properties and its claimed high drag to weight coefficient and that "structural damage" is absent.

* Professor of Civil Engineering,
Coastal Engineering Laboratory,
Queen's University at Kingston, Canada.

RESULTS

With the superior behaviour of the dolos unit in an uprush and downrush wave situation one might reasonably expect that, in a free non-oscillatory current, this interlocking property could play a significant role in making the dolos unit more effective in resisting movement than an equal weight of quarrystone unit. However, a solitary unit would not behave much differently unless the drag coefficient was markedly different.

To determine whether the drag coefficients were markedly different many tests were carried out on individual dolosse and rocks in a wind tunnel and in a free stream of water. It was found experimentally that $C_D \times A$ or $C_L \times A$ where A is the projected area normal to the flow were essentially the same for a single dolos or a single rock. On the basis of these tests the effectiveness of the dolos unit is apparently entirely due to its interlocking properties.

Tests were now carried out in a tilting flume with a bed of rocks and a bed of dolosse of identical mass. With a constant flow rate the slope of the flume was gently increased so decreasing the depth over the bed and increasing the velocity.

The "wipe-out" velocity was essentially the same for both the quarrystone bed and the dolos bed. So much for interlocking in this situation! To have put in a dolos bed of 25% of the weight of a quarrystone bed - as one might have deduced from wave tests - would have meant that 25 gm dolos units would have 'wiped-out' at the same velocity as 25 gm rocks, namely, by Froude scaling, at a velocity of 0.8 times the "wipe-out" velocity for the 100 gm rock.

In an effort to discover why the dolos unit is effective as breakwater protection on a slope - usually 1:2 - but not on a horizontal bed, tests were carried out on the natural angle of repose of the rocks and the dolosse, both in air and water.

A box measuring 1 m x 0.5 m x 5 or 6 units thick was filled with either rocks or dolosse and gently vibrated on a concrete vibrating table. The box was then gradually tipped about the bottom edge. The packing angle for both rocks and dolosse was essentially the same, namely 40°. The failure angle of the rock was about 50° whereas the dolosse had an angle of repose of at least 80° - and in one remarkable test 91° (see Figure 1).

CONCLUSIONS

Thus, it may be concluded that the effectiveness of the dolos unit is not materially affected by the drag to weight ratio (which is similar to that of rock), but to its high natural angle of repose. However, this phenomenon can only be brought into play on a relatively steep slope and not on the horizontal. This would explain why dolos units are not as effective when the wave attack is

oblique (see H.R.S. Report IT159, April 1977 by A.F. Whillock" "Stability of Dolos Blocks Under Oblique Wave Attack"), and no more effective for scour protection in a horizontal situation than an equal weight of quarrystone. One can also suggest that the steeper the breakwater slope of dolosse when attacked by normal waves the better the dolos unit appears to be. Further one can also suggest that K_D for dolosse must be a function of breakwater slope.



Figure 1 - Totally Stable up to 91°
80% of Dolos Units Stable at 93°

A MODEL LAW FOR WAVE IMPACTS ON COASTAL STRUCTURES

by

C. Ramkema^{*}ABSTRACT

For the design of the storm surge barrier in the Eastern Scheldt, a study has been carried out on wave impacts against coastal and marine structures. First a review was made of relevant literature, including both wave impacts on coastal structures and slamming of sea-going vessels. From this, the so-called Bagnolds piston model emerged as most appropriate to describe the wave impacts caused by standing waves against protruding elements. This model was then further elaborated to include both adiabatic and isothermal compression of the air cushion and to allow for the compression of the water. Moreover, a model was developed to determine the spatial pressure distribution. Finally, experiments were performed, the results of which were in satisfactory agreement with the mathematical models. Based upon the results of these studies, a scaling law is presented here, from which the pressure magnitude and the time history of the impact in nature may be determined.

1 Scope of the Study

As part of the preliminary investigation for the development of the storm surge barrier in the Eastern Scheldt (Figure 1) tests were carried out to study the wave impacts on the sluice gates in this barrier. As a possible solution caissons placed on a rubble foundation were examined (Figure 2). Wave impacts induced by breaking waves were not observed here because of the relatively large foreshore depth; however, wave impacts might occur locally if the standing wave in front of the gate is impeded by protruding structural elements. Due to the specific shape of the structure, a volume of air is trapped between the protrusion and the rising water level which acts as a spring, resulting in a typical oscillating pattern of the impact pressure history. A literature study was made to find a suitable mathematical model which, after experimental verification, could be used for the conversion of these impacts to an impact in nature.

2 Review of Literature

The first effort to measure wave impacts on maritime structures was made by Stevenson [53] in Scerryvore Rocks 150 years ago. Until 1935 the measurements were performed with instruments unsuitable for these fast phenomena. The first excellent measurements with a high frequency range were executed in Dieppe by Rouville et al [49] and in a laboratory by Bagnold [5]. The development of mathematical wave impact and slamming models started with von Karman's model [31]. Because of the resemblance between the slamming phenomenon and the wave impact a historical review of investigations of both subjects is presented here, showing the relations between the various models (Figure 7).

The various mathematical models for wave impacts and slamming can be com-

* Project Engineer, Delft Hydraulics Laboratory, The Netherlands

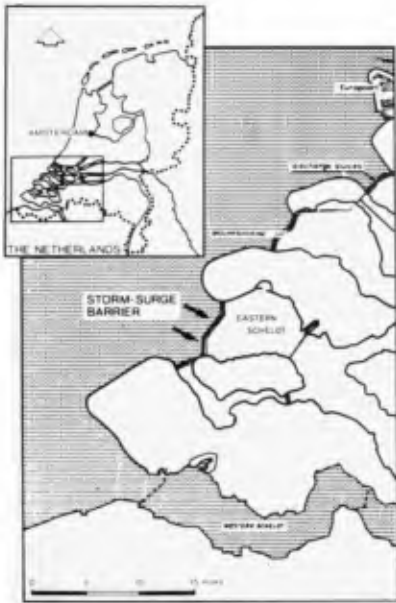


Fig. 1 Situation of the storm-surge barrier in the Eastern Scheldt

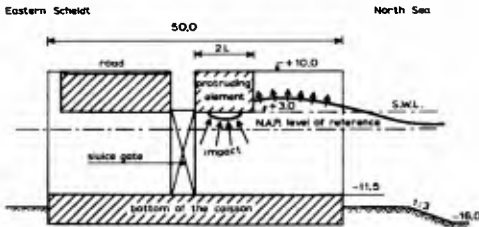


Fig. 2 Typical caisson-section for the storm-surge barrier (design 1975)

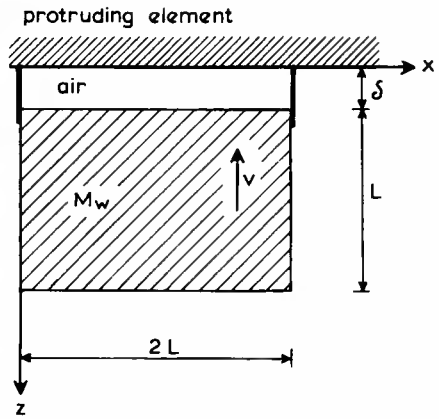


Fig. 4 The piston model of Bagnold

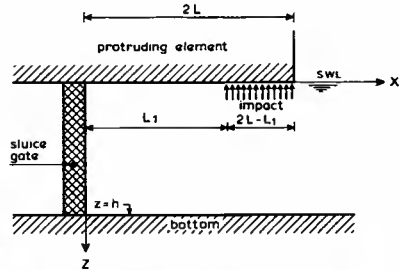


Fig. 5 Impact against the tip of the protrusion

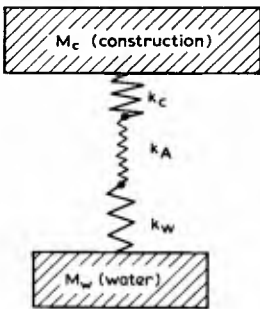


Fig. 3 The proces schematized as a mass-spring system



Fig. 6 Impression of the instrumental equipment for the test

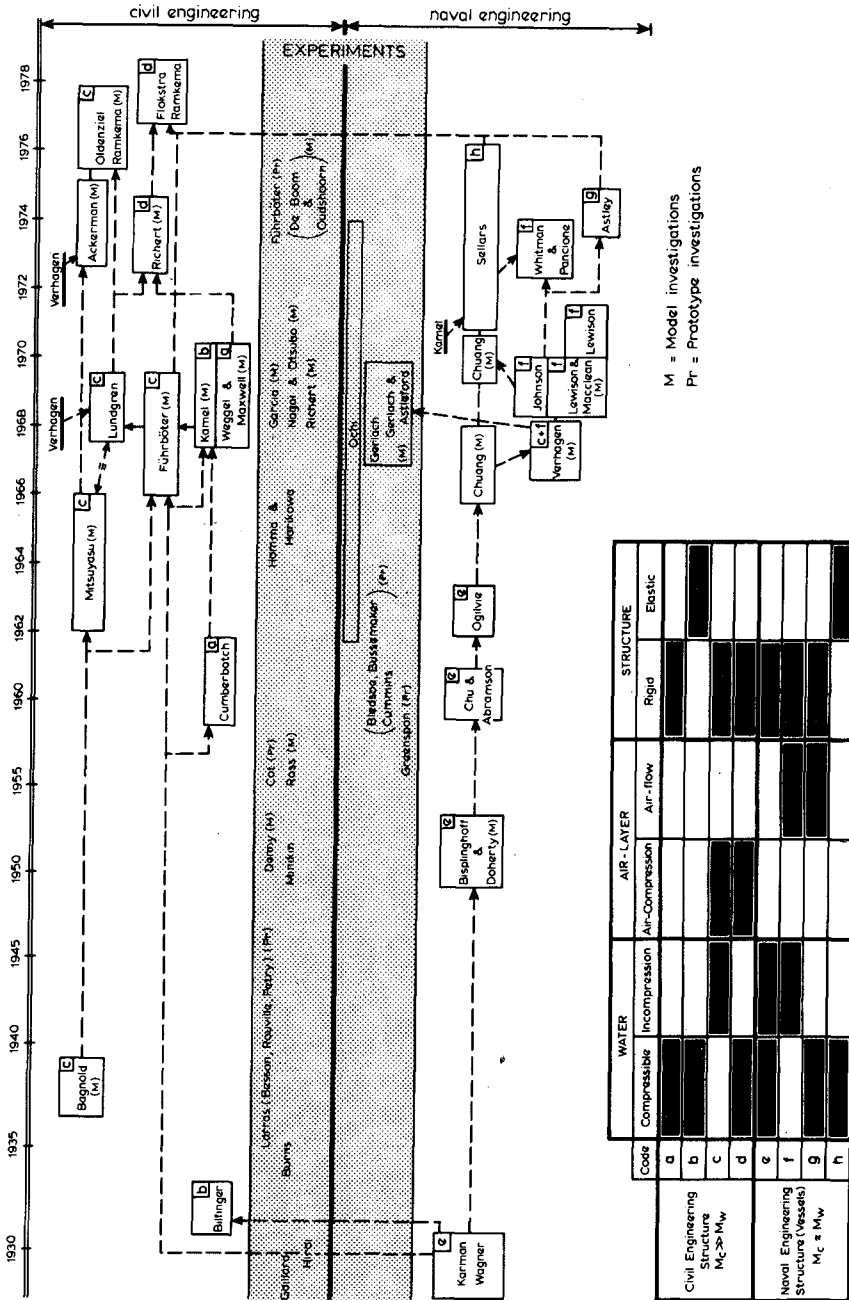


Fig. 7 Historical review of investigations on wave impact and slamming

bined into one general model (Figure 3), in which M_C is the mass of the construction; M_w is the equivalent hydraulic mass; and k_w , k_A and k_C are the spring constant of water, air and the construction respectively. For civil engineering constructions M_C is mostly much larger than M_w , whereas for ships and gates M_C and M_w are about equal.

The mathematical models in civil engineering can be divided into the way they take into account the importance of the compressed air layer with regard to the elasticity of the structure and the compressibility of water. Bagnolds model apparently is most appropriate to describe the impact against the protrusion, due to the specific air layer between the structure and the equivalent hydraulic mass.

The need for models in naval engineering first became apparent with the evident high pressures on V-shaped seaplane floats during landing. Later on, when the number of seaplanes decreased, impact pressures on high-speed ships stimulated research, as the calculated pressures on V-shaped wedges with the model developed by von Karman [31] were too conservative for these ships. Sellars [50,51] tried to explain the difference by accounting for the elasticity of the ship structure, whereas Verhagen [55] explains the difference by the elasticity of the air layer; the thickness of which is calculated by air flow between ship and water until the velocity of sound (C_A) is reached. For the subsequent stage he uses a Bagnold type piston model, with an air flow determined air layer thickness, for the determination of the impact pressure in which is accounted for the finite structure mass. However, the observed air layer between the caisson's protrusion and the water mass is mostly due to the specific shape of the protrusion and the water surface, so only the last part of Verhagen's model is appropriate for the description of our problem. Verhagen as well as Bagnold are supposing an adiabatic compression of the air layer.

Many experiments have been performed on civil and naval engineering structures, the results of which are generally expressed in the stagnation pressure: $\frac{1}{2} \rho v^2$, where ρ is the density of the water and v is the impact velocity. This is not further considered here, as in the impact process compressibility and air are certainly more important than the gravitational acceleration. Specially worth mentioning are the excellent experiments of Gerlach [21,22,23] in which the influence of liquid and gas properties and model shape on impact pressures of blunt rigid bodies is investigated. A more detailed literature description is in preparation by the author [44].

3 Theory

The observed air layer between the protruding element and the water mass gave evidence for the choice of Bagnold's piston model (in the tests $M_C \gg M_w$). Whether the compression of the air layer is adiabatic, isothermal or somewhere between depends upon such different factors as characteristic time of the phenomenon, the pressure magnitude, the air-water surface with regard to the air layer or bubble layer volume (the heat exchange by evaporation is much more important than by conductivity), the acceleration of the air-water surface and the irreversibility of the process. The significance of this question for model pressure conversion is evaluated in Paragraph 6.

Bagnold's model

The shape of the caisson and the protrusion is such that the phenomenon may be schematized as shown in Figure 4. A two-dimensional mass of water (M_w) with width $2L$ is travelling upward with a velocity v . For $z = \delta$ the

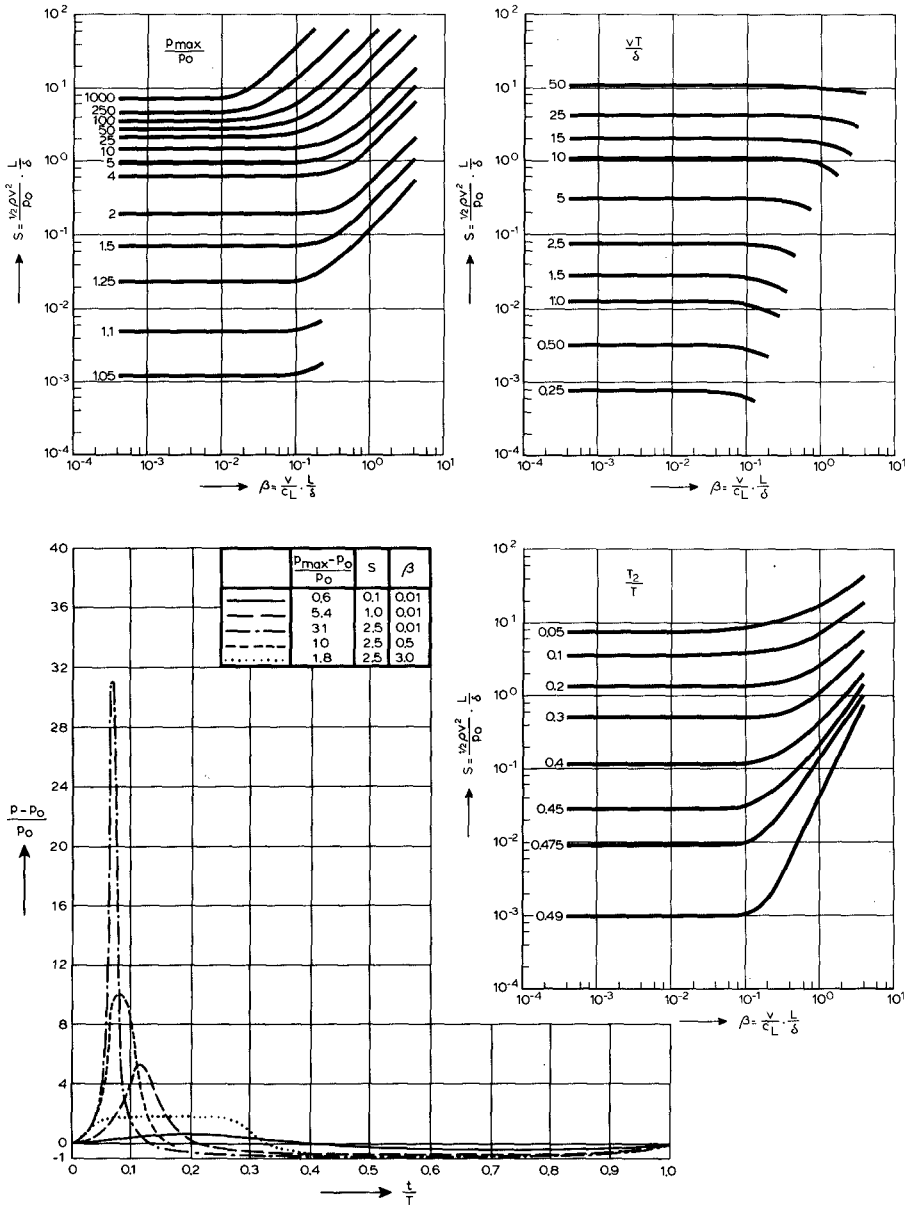


Fig. 8 Piston model with isothermal compression and compressible water: p_{max}/p_0 , $v T/\delta$ and T_2/T as a function of S and β

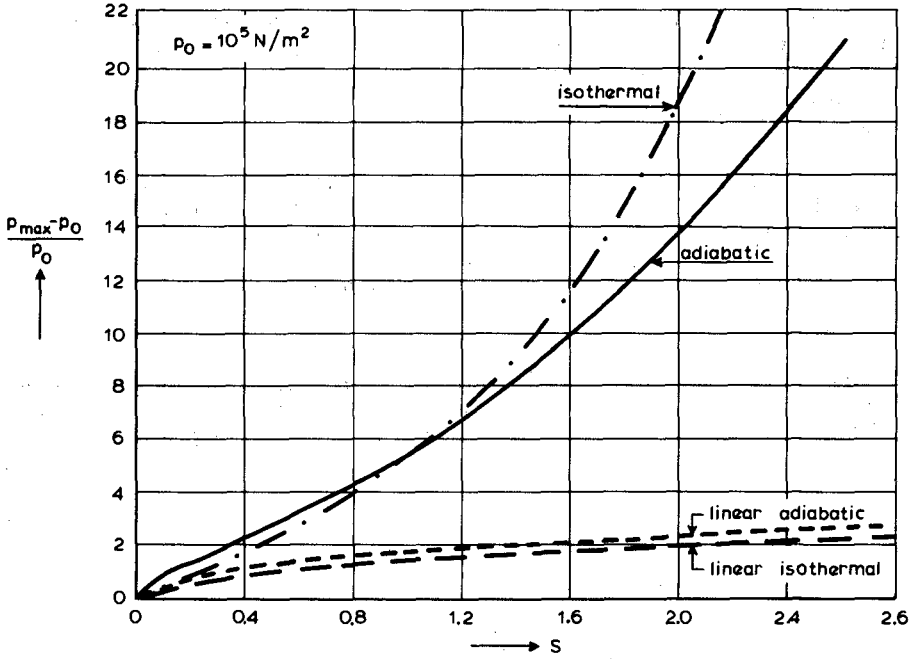


Fig. 9 Dimensionless peak pressure $(p_{max} - p_0)/p_0$ versus the impact number S for different compression models

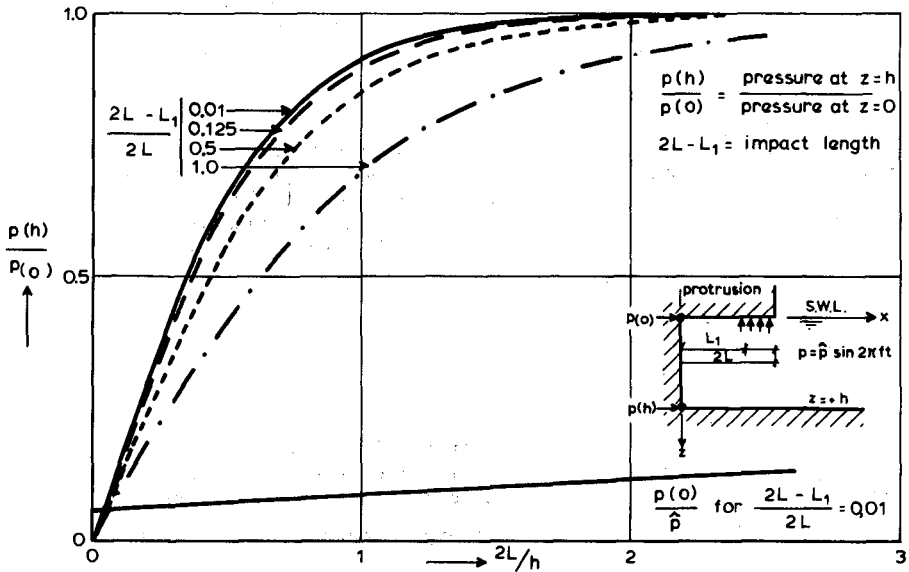


Fig. 10 Spatial distribution of the impact-pressure

air layer is blocked from the atmospheric pressure p_0 ; if the hydraulic mass of water per unit length is approximated by ρL^2 [58] the equation of motion can be written as:

$$M_w \frac{d^2 z}{dt^2} = p_2 L - p_0 L. \quad (1)$$

Here, forces due to the acceleration of gravity are neglected because in the time intervals under consideration the weight of the water mass will be small in general compared with the impact load. Moreover, the weight is compensated by the hydrostatic pressure.

The air compression is assumed to vary between adiabatic and isothermal, so:

$$p = p_0 \left(\frac{\delta}{z}\right)^\gamma, \quad (2)$$

where γ is the ratio between the specific heat at constant pressure and that at constant volume. For a linear compression, $|1 - z/\delta| \ll 1$, and with the initial conditions $z = \delta$ and $z = -v$, the following expressions can be derived for the maximum pressure:

$$p_{\max} = p_0 \left[1 + \sqrt{2 \gamma \frac{\frac{1}{2} \rho v^2 L}{p_0 \delta}} \right] = p_0 \left[1 + \sqrt{2 \gamma S} \right]. \quad (3)$$

The frequency of the oscillation is:

$$f = \frac{1}{2\pi} \sqrt{\frac{\gamma p_0}{\delta \rho L}}, \quad (4)$$

where S is defined as the impact number. The general solution for the dimensionless peak pressure $p_{\max} - p_0$, which satisfies Equations (1) and (2) with the mentioned initial conditions, is shown as a function of S in Figure 9. The graph for adiabatic compression is equivalent to Mitsuyasu's [38] and Lundgren's graph [36]. For a more detailed description of this derivation, see Ramkema et al [43].

Bagnold's model with compressible water

One of the basic criticisms of Bagnold's piston model is that for high impact numbers the pressure exceeds $\rho v c_w$ (where c_w is the velocity of sound in water). The one-dimensional mathematical model given below takes into account the compressibility of water. The impulse equation formulated in Lagrange coordinates with the centre on the air-water surface is:

$$\frac{\partial^2 z}{\partial t^2} \cdot \frac{\partial z}{\partial a} + \frac{1}{\rho} \frac{\partial p_w}{\partial a} = 0, \quad (5)$$

and the continuity equation is:

$$\rho \frac{\partial z}{\partial a} = \rho_0, \quad (6)$$

where a is the position of the water particles at $t=0$, ρ_0 is the local density of water at $t=0$, ρ is the local density of water, and p_w is the pressure distribution in the water column. After some rearrangements and the supposition that $\rho^2 \frac{\partial p_w}{\partial \rho}$ can be approximated with $\rho_0^2 c_w^2$, the equations can be written as:

$$\frac{\partial^2 z}{\partial t^2} - c_w^2 \frac{\partial^2 z}{\partial a^2} = 0, \quad (7)$$

with the initial conditions $z = a$ and $\frac{\partial z}{\partial t} = v$ for $-L < a < 0$ and the boundary conditions $p = p_0$ for $a = -L$ and $p_w = p$ (pressure in the air layer) for $a = 0$. The results of this piston model with compressible water are shown in Figure 8. The dimensionless maximum impact pressure p_{max}/p_0 , the dimensionless impact period $v T/\delta$, and the shape parameter T_2/T are given as a function of the impact number S and the compressibility number $\beta = v L/\delta c_w$; the ratio of the characteristic time interval for the impact pressure δ/v and the characteristic time interval for the compression wave L/c_w . For $\beta < 0.1$ and $S < 2$, compressibility of water can be neglected as can be seen from Figure 8. More detailed information is given in Ramkema et al [44].

Spatial pressure distribution

By supposing an homogeneous pressure field in the direction perpendicular to the draft (Figure 6), it is evident that for a wave impact against the whole length of the protruding structural element ($2L$) the pressure distribution over the gate will be almost uniform for large $2L/h$ values. For a small ratio $2L/h$, however, the pressure distribution over the gate will decrease exponentially with increasing z . To quantify this supposition, a mathematical model was used to describe the phenomenon [43]. Supposing a two-dimensional pressure field, zero viscosity, an irrotational motion and an incompressible fluid, this problem is solved by determining the following velocity potential ϕ which satisfies Laplace's equation and the boundary conditions:

$$\frac{\partial \phi}{\partial z} = 0 \text{ at } z = h, x > 0 \text{ and at } z = 0, 0 < x < L_1$$

$$\frac{\partial \phi}{\partial x} = 0 \text{ at } 0 < z < h, x = 0$$

$$p = p_m \cos 2\pi ft \text{ at } z = 0, L_1 < x < 2L.$$

The condition on the free surface ($z = 0$) is generally:

$$g \frac{\partial \phi}{\partial z} + \frac{\partial^2 \phi}{\partial t^2} = -\frac{1}{\rho} \frac{\partial \rho}{\partial t}, \quad (8)$$

where g is the gravitational acceleration. For high frequencies, $g \frac{\partial \phi}{\partial z}$ can be neglected with regard to $\frac{\partial^2 \phi}{\partial t^2}$. The ratio of the pressure amplitude at $z = h$ and at $z = 0$ is shown in Figure 10 as a function of $2L/h$ for different $(2L - L_1)/2L$ values.

4 Experimental Set-up

To verify the frequency behaviour of Bagnold's piston model and the spatial pressure distribution over the gate, a variety of tests has been made. The tests were performed with random waves in a $95 \times 0.90 \times 1.0 \text{ m}^3$ wind wave flume (Figure 11) provided with a flap-type wave generator. A scale model (1:50) was constructed from stainless steel (thickness 20 mm), representing a vertical face fronted by a rectangular protrusion with different lengths (figures 12 and 13). In this model wave impacts were measured at four locations to determine the frequency behaviour, and at six locations for the spatial pressure distribution. The unused holes were filled up with screw bolts flush with the front face of the wall. The wave impacts were measured with Statham PM 131TC pressure cells. The overall accuracy of the amplitude response of the total measuring system was about 90% for a frequency range of 0-2400 Hz. A general impression

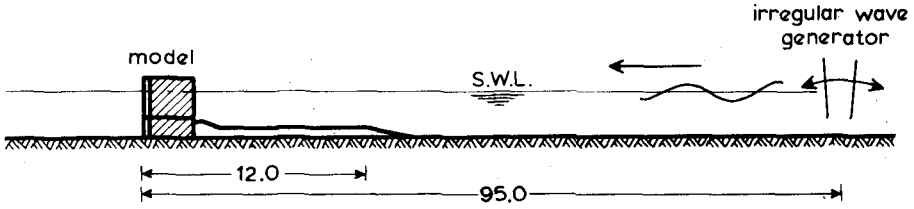


Fig. 11 Cross-section through wave channel

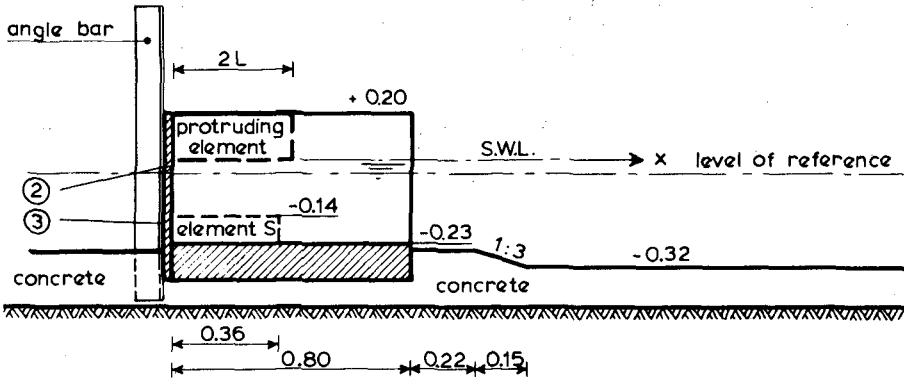


Fig. 12 Detail of test section

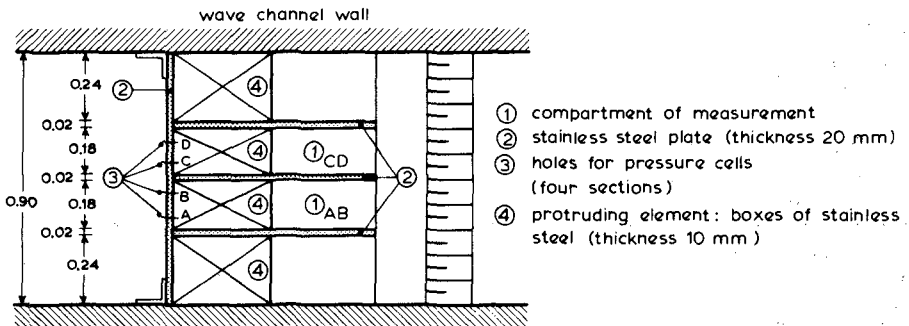


Fig. 13 Top view of test section

of the instrumental equipment for the tests is shown in Figure 6. The duration of each test was about 1000 zero crossing waves. However, the sensibility for wave impacts fluctuates strongly with the length of the protrusion and the water level with regard to the level of the protrusion. That is why the number of analysed impacts per test is not equal. Besides, only impacts $> 2000 \text{ N/m}^2$ were analysed. The tests for the spatial pressure distribution were limited to about 30 analysed wave impacts.

5 Experimental Results

In the investigation over 100 tests were made, a few of which had a geometry which could be used (see Tables 1 and 2) to test the given mathematical model. However, some general remarks based upon all the tests can be made:

- 1 The time history of the wave impact pressure can generally be described as a damped harmonic vibration. The impact frequency (f) is the reciprocal of the characteristic time of the vibration (Figure 14).
- 2 The impacts in the separated compartments AB and CD are uncorrelated for the frequency and the magnitude of the impact. However, the probability density functions for frequency and magnitude in the separated compartments are equal.
- 3 The pressure distribution in y-direction is about homogeneous in a compartment, with only a slight increase (about 10%) in the angles.
- 4 In general, the exceedance distribution for the impact pressure can be approximated, by a straight line, on logarithmic-linear paper. However, impacts smaller than 2000 N/m^2 are not taken into account (Figure 16).

To predict a maximum impact pressure it is necessary to know the maximum impact velocity, the minimum air layer thickness and the minimum protrusion length involved, but as a result of the mutual interactions this is extremely difficult. It is easier to predict the theoretical minimum impact frequency, which is a function of the maximum protrusion length involved and the maximum air layer thickness.

The impact frequency behaviour has been tested with four different lengths of the protruding element (Table 1). The analysed impacts did not exceed an impact pressure of $10,000 \text{ N/m}^2$ in model and the maximum air layer thickness could be visually estimated during the tests, being $1/10$ of the length of the protrusion. From each impact registration the impact pressure magnitude and the impact frequency were measured (Figure 15); the minimum and maximum value of the impact frequency are shown in the Table 1. With the visually estimated maximum air layer thickness and the length of the protrusion the theoretical minimum impact frequency can be calculated with Equation (4) for adiabatic ($\gamma = 1.4$) and isothermal compression ($\gamma = 1.0$). The linear approximation will be acceptable for impact pressures smaller than $10,000 \text{ N/m}^2$. The results of the comparison between the theoretical and the measured minimum impact frequency values is shown in Figure 18. It is evident that Bagnold's piston model is satisfactory for the prediction of the minimum impacts frequency, but whether the compression is adiabatic or isothermal cannot be concluded from this result.

The theory for the spatial pressure distribution over the gate was tested with the results of 7 tests carried out with 6 pressure cells, several of which were located in the protrusion. Depending upon the length $2L$, about 30 impacts of each test were analysed (as an example see Table 3 and Figure 17), and the coefficients, whose range is given in Table 2, were determined. The result of the comparison between the theoretical and the experimental maximum ratio p_B/p_{BB} is shown in Figure 19. As the theoretic-

test	protruding element		still water level (m)	wave conditions			positions of the pressure cells				frequency analysis			remarks
	length (m)	level (m)		reflection (%)	peak period (s)	significant wave height (m)	A (m)	B (m)	C (m)	D (m)	number of analysed impacts	minimum value of the frequency (s ⁻¹)	maximum value of the frequency (s ⁻¹)	
T 16	0.40	+ 0.06	+ 0.11	58	1.35	0.094	0	+ 0.04	- 0.02	+ 0.02	68	25	1050	compartment A, B compartment C, D wind velocity 4 m/s wind velocity 4 m/s
T 17	0.40	+ 0.06	+ 0.06	33	1.75	0.062	0	+ 0.04	- 0.02	+ 0.02	223	17	1550	
T 31	0.06	+ 0.06	+ 0.11	71	1.40	0.092	0	+ 0.04	- 0.02	+ 0.02	157	170	1250	
T 32	0.06	+ 0.06	+ 0.06	57	1.24	0.066	0	+ 0.04	- 0.02	+ 0.02	385 468	130 130	1650 1550	
T 39	0.06	+ 0.06	+ 0.11	73	1.39	0.084	0	+ 0.04	- 0.02	+ 0.02	46	130	1050	
T 40	0.06	+ 0.06	+ 0.06	57	1.23	0.068	0	+ 0.04	- 0.02	+ 0.02	278	120	1750	
T 49	0.18	+ 0.06	+ 0.11	67	1.40	0.096	0	+ 0.04	- 0.02	+ 0.02	170	38	400	
T 50	0.18	+ 0.06	+ 0.06	51	1.21	0.066	0	+ 0.04	- 0.02	+ 0.02	97	70	1750	
T 52	0.02	+ 0.06	+ 0.11	67	1.43	0.096	0	+ 0.04	- 0.02	+ 0.02	9	410	1600	
T 53	0.02	+ 0.06	+ 0.06	63	1.27	0.064	0	+ 0.04	- 0.02	+ 0.02	46	550	1800	

Table 1 Tests for frequency behaviour as a function of the length of the protruding element

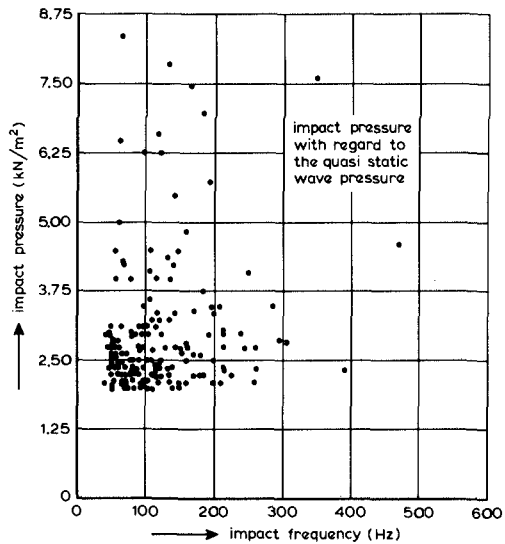


Fig. 15
Correlation between amplitude and frequency for impacts in compartment CD

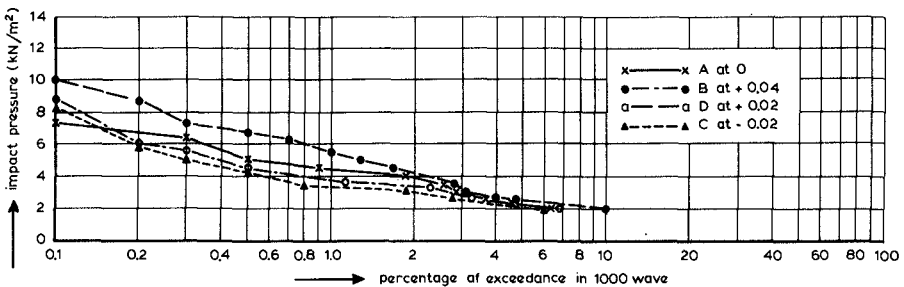
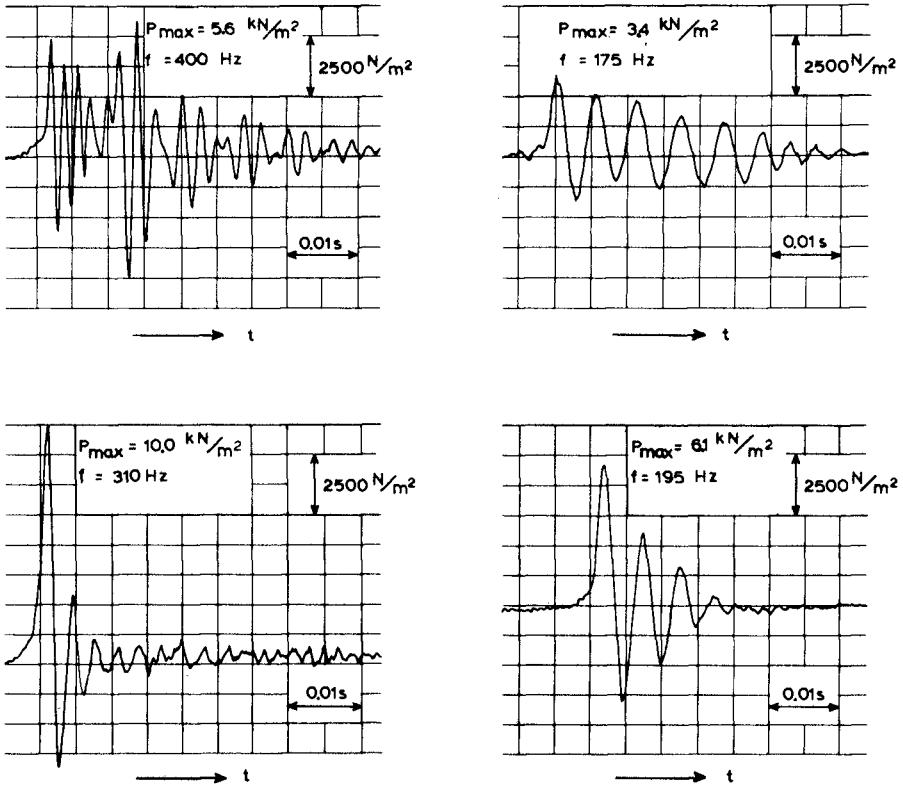


Fig. 16 T49: Exceedance distribution for wave impacts on the pressure cells: A, B, C and D



P_{\max} : impact pressure with regard to the quasi static wave pressure

Fig. 14 T32: Typical impact-pressure recorded at 0.04 m above reference level (section B)

test	protruding element		special element S	still water level (m)	wave conditions			position of the pressure cells in compartment A 8						coefficient analysis			
	length (m)	level (m)			reflection (%)	peak period (s)	significant wave height (m)	compartment A 8						number of analysed impacts	2 L/h	minimum value of the coefficient	maximum value of the coefficient
								1	2	3	4	5	6				
T 91	0.70	+ 0.06		+ 0.06	51	1.20	0.082	+ 0.04	- 0.08	- 0.20	+ 0.06 (x = 0.05)	+ 0.05 (x = 0.25)	+ 0.06 (x = 0.65)	38	2.42	0.08	0.80
T 92	0.40	+ 0.06		+ 0.06	33	1.22	0.062	+ 0.04	- 0.08	- 0.20	+ 0.06 (x = 0.04)	+ 0.06 (x = 0.20)	+ 0.06 (x = 0.36)	40	1.38	0.07	0.80
T 93	0.18	+ 0.06		+ 0.06	51	1.27	0.070	+ 0.04	- 0.04	- 0.12	+ 0.06 (x = 0.06)	+ 0.06 (x = 0.14)	20	0.62	0.08	0.77	
T 94	0.04	+ 0.06		+ 0.06	57	1.22	0.072	+ 0.04	0	- 0.04	- 0.12 (x = 0.03)	+ 0.06 (x = 0.03)	35	0.207	0.05	0.35	
T 95	0.02	+ 0.06		+ 0.06	83	1.24	0.066	+ 0.04	0	- 0.04	- 0.08	- 0.12 (x = 0.03)	25	0.069	0.03	0.18	
T 96	0.06	+ 0.06	x	+ 0.06	53	1.20	0.062	+ 0.04	0	- 0.04	- 0.08	- 0.12 (x = 0.03)	26	0.30	0.11	0.42	
T 97	0.06	+ 0.02	x	+ 0.06	49	1.03	0.040	0	- 0.04	- 0.08	- 0.12 (x = 0.03)	32	0.375	0.10	0.56		

Table 2 Tests for spatial distribution behaviour as a function of 2L/h

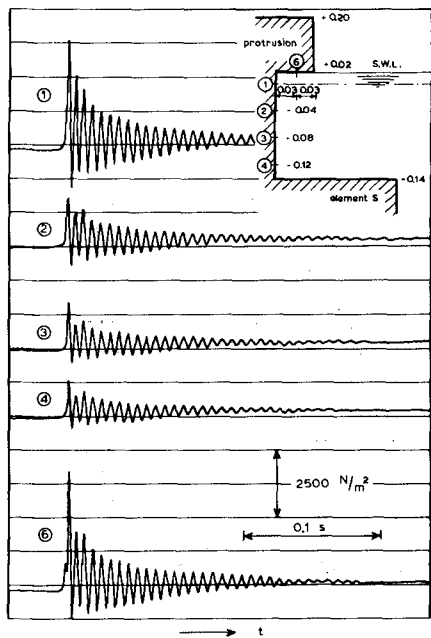


Fig. 17 T97: Typical simultaneous pressure recordings. Impact no. 21

impact no.	pressure on the pressure cells (mm)						frequency (s ⁻¹)	coefficient
	1	2	3	4	5	6		
1	20.5	10.5	8.0	7.0	24.5	150	0.34	
2	27.0	12.5	9.0	7.5	29.0	150	0.38	
3	33.0	14.5	14.5	11.5	47.5	200	0.35	
4	18.5	8.5	6.0	5.5	9.0	260	0.30	
5	14.5	9.0	7.0	6.0	17.0	160	0.41	
6	8.0	6.5	5.5	4.5	11.5	250	0.56	
7	29.0	14.0	10.0	8.5	36.0	150	0.29	
8	17.0	12.5	9.5	9.0	15.0	175	0.53	
9	25.0	14.0	11.0	9.5	31.0	180	0.38	
10	14.5	4.0	4.0	3.0	7.0	240	0.21	
11	10.0	3.0	3.0	2.0	7.0	220	0.20	
12	17.5	10.0	7.0	6.0	19.5	140	0.34	
13	12.0	5.5	4.0	4.0	16.5	200	0.33	
14	17.0	4.0	2.5	2.0	11.5	400	0.12	
15	22.5	12.0	9.0	7.5	26.0	140	0.33	
16	22.5	12.5	10.0	8.5	26.0	260	0.38	
17	19.5	4.5	3.0	2.0	6.0	1000	0.10	
18	21.0	11.5	8.0	7.0	23.0	130	0.33	
19	8.0	6.0	5.0	4.5	12.5	400	0.56	
20	22.5	10.0	7.5	6.0	17.0	160	0.27	
21	32.0	14.5	13.5	10.5	36.0	280	0.29	
22	12.5	9.0	7.0	6.5	14.5	640	0.52	
23	18.5	10.5	7.5	7.0	20.5	130	0.38	
24	14.5	6.5	4.5	3.5	20.5	180	0.24	
25	12.0	4.5	3.5	2.5	7.0	215	0.21	
26	18.5	8.0	6.5	5.0	14.5	190	0.27	
27	14.5	7.5	5.5	4.5	12.5	180	0.31	
28	39.0	24.0	18.5	16.0	46.5	150	0.41	
29	25.5	16.0	12.0	10.0	28.5	130	0.39	
30	24.0	12.0	8.5	8.0	28.0	130	0.33	
31	14.0	8.0	6.5	5.5	16.5	260	0.39	
32	8.5	4.5	3.0	2.0	12.0	240	0.24	

1 mm ≅ 125 N/m² with regard to the quasi static wave pressure

$$\text{coefficient} = \frac{\text{pressure on cell 4}}{\text{pressure on cell 1}}$$

Table 3 T97: Spatial pressure distribution of wave impacts

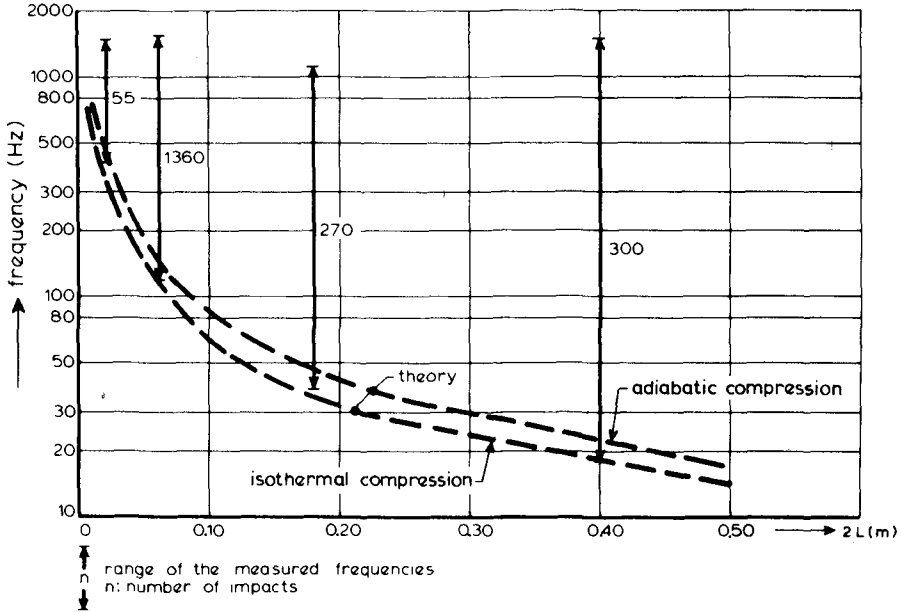


Fig. 18 Minimum frequencies as a function of the length of the protrusion ($2L$)

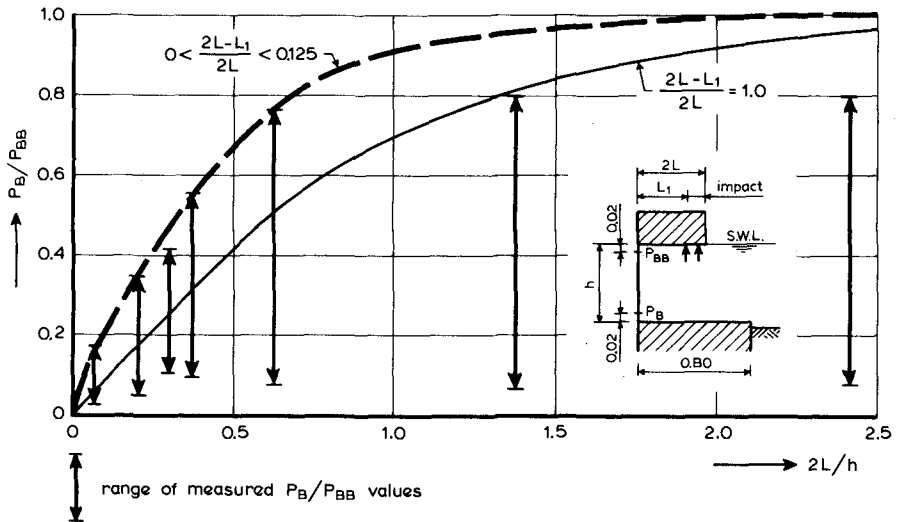


Fig. 19 Extreme spatial pressure distribution for $x = 0$, as a function of $2L/h$

cal curve hardly changes for $0 < \frac{2L - L_1}{2L} < 0.125$, only one curve has been drawn for these values. The second curve in this figure describes the situation in which the whole protrusion is struck by the standing wave, but this situation does not give the maximum coefficients. Due to the limited dimensions of the pressure cell, the mentioned ratio will be slightly larger than the theoretical $p(h)/p(o)$ ratio, but the comparison is still very satisfactory. However, for $2L/h > 1$, the experimental values are substantial smaller than the theoretical values. This was confirmed by the observations, where two impacts could be distinguished: one in front of the gate and a second at the end of the protrusion. The pressure on the gate as a result of this second impact was negligible and difficult to separate from the first. The results presented are spatial pressure distributions for impacts in front of the gate which, consequently, do not confirm the theoretical model.

6 Model Law

Although the agreement between the model experiments and the linear piston model was satisfactory, non-linear effects cannot be neglected for full-scale processes. Therefore the non-linear adiabatic and isothermal compression models have been elaborated (Paragraph 3). In order to use these mathematical models for the conversion of model-to-nature impact characteristics, the type of thermo-dynamic process, the influence of compressibility and the scaling factor of the impact-number S have to be determined. Because the shape of caisson and water surface is determinant for the air layer thickness and the hydraulic mass involved, the scaling factor for δ and L is linear ($n_\delta = n_L$; $n_v = n_l$). The external water movement obeys Froude's law, so $n_v = \sqrt{n_l}$ where the atmospheric pressure is equal in model and nature ($n_{p_0} = 1$). This results in a linear scale for the impact number S , or $n_S = n_l$. The thermodynamic similarity is difficult to evaluate. Due to the larger air volume and the higher pressure, the process in nature will be more adiabatic, whereas as a result of the larger air-water surface, the longer characteristic period and the state of the water surface the process in nature will be more isothermal than in model tests. However, in general the non-linear isothermal conversion is a little (10% for $p_{max} < 10 p_0$) more conservative, so this model was chosen. The influence of the compressibility can be evaluated with the compressibility number ($\beta = vL/\delta c_w$). For the model investigation $v < 1$ m/s, $2L < 0.40$ m and $c_w = 1540$ m/s; the minimum air layer thickness will be estimated with Verhagen's [55] first approximation for one-sided outflow $\delta = v \cdot 2L/c_A$, where c_A is the velocity of sound in air (≈ 340 m/s). So the compressibility number in model (1:50) has a maximum value of 0.11 and a minimum value, for $\delta = 1/10.2 L$, or 0.007. In nature this value will vary between 0.11 and 0.05. As can be seen from Figure 8, the influence of compressibility can be neglected, for $\beta < 0.1$ and $p_{max}/p_0 < 10$. The isothermal compression model law is presented in Figure 20 for $\beta < 0.1$ and $p_{max}/p_0 < 10$. If a similar time history of the impact in model and nature is supposed, the time scale can be related to the pressure scale if the total momentum obeys Froude's law. However, in general the full-scale time history is not similar to that in model due to the effect of the atmospheric pressure p_0 , which is equal in model and nature. Pressure amplitudes in model will generally be small with respect to the atmospheric pressure whereas in nature minimum values may approach zero pressure. Therefore the shape of the pressure fluctuation in full-scale may show sharp crests and flat troughs contrary to the sinusoidal fluctuation in model. Elaboration of the dimensionless fluctuation period vT/δ with Figure 21 shows that

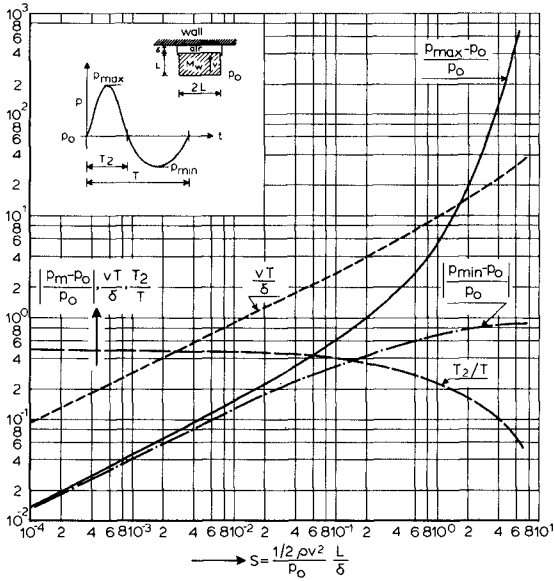


Fig. 20 Model-law for isothermal compression

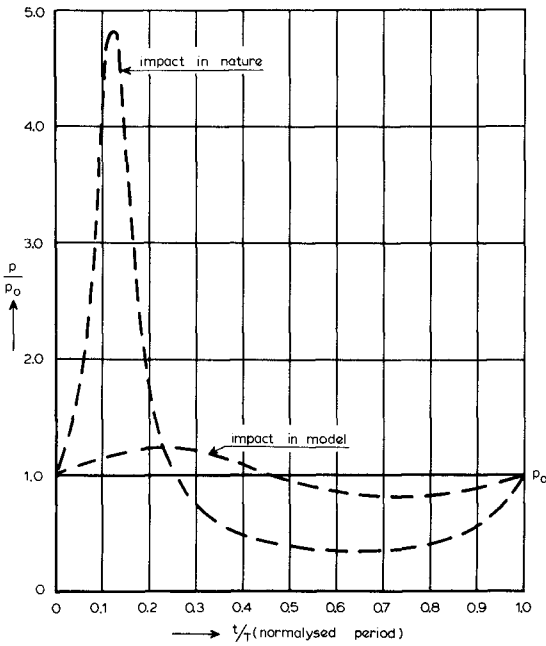


Fig. 21 Example of impact conversion

Example: impact conversion for a scalefactor 50

Model impact : $p_{max} - p_0 = 20 \text{ kN/m}^2$
 $f_{model} = 400 \text{ Hz}$

$S_{model} = 0.015$

length scalefactor: 50

$S_{nature} = 0.75$

Nature impact : $p_{max} - p_0 = 380 \text{ kN/m}^2$
 $p_{min} - p_0 = 65 \text{ kN/m}^2$
 $f = 8 \text{ Hz}$
 $T_2/T = 0.26$

$n_{yT}/\delta = n_S^{1/2}$ for practical impact pressures ($p_{\max} < 10 p_0$).

With the help of Figure 20, p_{\max} , p_{\min} , T_2/T and T of the given model impact pressure can be converted to an impact in nature. See as an example Figure 21 for $n_S = 50$.

The spatial pressure distribution over the gate in nature will be geometrically similar to the impact in model.

7 Discussion and Comments

As a result of the fact that the minimum impact frequency can well be predicted with Bagnold's linear piston model a non-linear isothermal compression model law is presented. The conversion of model impact pressures can easily be done with the help of Figure 20. However, it is questionable whether the described model law for an impinging standing wave against the protrusion is comparable, for example, with a breaking wave against a composite breakwater.

A striking feature of the described impact pressures was the damped oscillation, but this phenomenon was also seen by Bagnold [5], Mitsuyasu [38] Rouville et al [49], Ross [48], Gerlach [21], Chuang [12] and many others. The observed combination of an air layer and a maximum impact pressure at the same location was also observed in investigations from Richert [45], Ross [48], Gerlach [21], etc. However, the observed damping of impact pressures by breaking waves against breakwaters is much larger, which can be explained by the larger pressure radiation for flat structures like a breakwater front compared with the "hollow" structure used for the present tests. The conversion of a wave impact of breaking waves against a breakwater is dominated by the question: which part of the wave height (H) is involved in the process in nature compared with that in model? Supposing the breaking wave in a scale model ($M_C \gg M_w$) has all the features (geometrical and kinematic) of the wave in nature, then the wave height involved is on a linear scale and so is the thickness of the air layer resulting from the concave part of the breaking wave front. At the limit (but hardly imaginable) the thickness of the air layer is determined by the air flow (see Verhagen [55]). The flatness of the water surface (parallel to the breakwater front) required for this air flow process, however, has a very low probability of occurrence, especially in breaking wave fronts and has therefore been neglected. So the scale factor for the impact number S is n_1 , under the supposition of a linear scale for the involved wave height and the air layer thickness. The measured impact on the breakwater model can now be converted to an impact in nature as far as peak pressure, characteristic time and shape of the impact are concerned. With the help of Weggels' or Richert's mathematical model, or with the model presented here with modified boundary conditions, the spatial pressure distribution can be calculated. The response function of the structure will finally determine the response to this impact force.

Acknowledgements

The Author wishes to thank the Hoofdafdeling Waterloopkunde of the Delta-dienst of the Rijkswaterstaat for permission to publish the results of the investigation.

NOTATION

a	positions of the water particles at $t = 0$	p	pressure in the air layer
c_A	velocity of sound in air	p_0	atmospheric pressure (100,000 N/m ²)
c_w	velocity of sound in water	p_m	extreme pressure in the air layer
f	frequency of the pressure oscillation (1/T)	p_w	pressure in the water column
g	gravitational acceleration	S	impact number $\frac{1}{2} \frac{\rho v^2}{p_0} \cdot \frac{L}{\delta}$
h	distance between the protruding element and the bottom	t	time
k_A	"spring constant" of air	T	period of the impact pressure oscillation
k_C	"spring constant" of the construction	T_2	peak time of the impact pressure oscillation
k_w	"spring constant" of water	v	velocity of the water mass
L	length of the water column	z,x	vertical and horizontal coordinate
L_1	part of the protruding element (Figure 19)	β	water compressibility number $\frac{v}{c_w} \cdot \frac{L}{\delta}$
2 L	length of the protruding element	γ	ratio between the specific heat at constant pressure and that at constant volume
M_C	mass of the structure	δ	thickness of the air layer
M_w	equivalent hydraulic mass	ρ	density of water
n_i	scale factor of parameter i	ϕ	velocity potential
n_l	scale factor of length		

REFERENCES

- 1 AARTSEN, M.A. and VENIS, W.A., Model investigations on Wave Attack on Structures, IAHR 8th Congress, Montreal, Aug. 24-29, Vol. 1, 1959
- 2 ACKERMAN, N.L., Impact pressures produced by breaking waves, Procs. Coastal Engineering Conference, Copenhagen, Chap. 104, 1974
- 3 ASTLEY, R.J., An idealised model for flat-bottomed ship slamming, Procs. Fifth Australian Conference on Hydraulics and Fluid Mechanics, Vol. II, 1974
- 4 BAKER, W.E., WESTINE, P.S., GARZA, L.R., and HUNTER, P.A., Water Impact Studies of Model Apollo Command Module, Appendix A, Impact Simulation, Final Report, Southwest Research Institute, Project No. O2-1541, Aug. 1965
- 5 BAGNOLD, R.A., Interim report on wave pressure research, Journal of the Institution of Civil Engineers, London, Vol. 12, June 1939
- 6 BILFINGER, W., Molenbau und Wellenwirkung, Thesis presented to the Technischen Hochschule München, 1934
- 7 BISPLINGHOFF, R.L., and DOHERTY, C.S., Some Studies of the Impact of Vee Wedges on a Water Surface, Journal of the Franklin Institute, Vol. 153, 1952
- 8 BOOM, J. de en OUDSHOORN, B., Onderzoek naar de invloed van de dichtheid en de compressibiliteit van lucht op golfklappen, Afstudeerverslag Technische Hogeschool Delft, 1976
- 9 BRUNS, E. (1951), Berechnung des Wellenstosses auf Molen und Wellenbrecher, Jahrbuch der Hafenbautechnischen Gesellschaft, 9. Band, 1941-1949, Berlin, 1951
- 10 CHU, WEN-WHA and ABRAMSON, H.N., Hydrodynamic Theories of Ship Slamming - Review and Extension, Journal of Ship Research, Vol. 4, No. 4, Marz 1961
- 11 CHUANG, S.L., Investigation of Impact of Rigid and Elastic Bodies with water, Naval ship Research and Development Center, Report 3248, Febr. 1970
- 12 CHUANG, S.L., Experiments on slamming of Wedge-Shaped Bodies, Journal of Ship Research, Sept. 1967

- 13 COT, P.D., Le Laboratoire du Havre pour la mesure des efforts dus aux lames, Procs. Coastal Engineering Conference, Chap. 40, 1954
- 14 CUMBERBATCH, E., The Impact of a Water Wedge on a Wall, Journal of Fluid Mechanics, Vol. 7, Part 3, 1960
- 15 DENNY, D.F., Further Experiments on Wave Pressure, Journal of the Institution of Civil Engineers, Vol. 35, June 1951
- 16 FUHRBOTER, A. (1966), Der Druckschlag durch Brecher auf Deichböschungen, Mitteilungen des Franzius-Instituts für Grund- und Wasserbau der Technischen Hochschule Hannover, Heft 28, 1966
- 17 FUHRBOTER, A., Laboratory investigations of impact forces, Procs. Research on wave action, Vol. II, Delft, 1969
- 18 FUHRBOTER, A., Zufalls Prozesse bei der Belastung durch brechende Wellen, Technischen Universität: Jahresbericht des Sonderforschungsbereichs 79: 4, Hannover, 1973; Teilprojekt C. Deutscher Forschungsgemeinschaft, 1974
- 19 GAILLARD, D.D., Wave action in relation to engineering structures, The Engineer School, U.S. Army Corps of Engineers, Ft. Belvoir, 1935
- 20 GARCIA, W.J., An experimental study of breaking-wave pressures, U.S. Army Engineer Waterways Experiment Station, Research report H-68-1, Sept. 1968
- 21 GERLACH, C.R., Investigation of Water Impact of Blunt Rigid Bodies - Real Fluid Effects, Technical Report No. 1, Southwest Research Institute Project No. 02-2036, Dec. 1967
- 22 GERLACH, C.R., Investigation of Water Impact of Blunt Rigid Bodies - Size Scale Effects, Technical Report No. 2, Southwest Research Institute Project No. 02-2036, Nov. 1968
- 23 GERLACH, C.R., and ASTLEFORD, W.J., Investigation of Water Impact of Blunt Bodies, Final Report, Southwest Research Institute Project No. 02-2036, Dec. 1970
- 24 GREENSPON, J.F., Sea Tests of the U.S.C.G.C. Unimak Part 3 - Pressures, Strains, and Deflections of the Bottom Plating Incident to Slamming, NSRDC Report 978, Marz 1956
- 25 HAYASHI, T., and HATTORI, M., Pressure of the Breaker Against a Vertical Wall, Coastal Engineering in Japan, Vol. 1, Tokyo, 1958
- 26 HIROI, I., The Force and Power of Waves, The Engineer, Vol. 130, Aug. 1920
- 27 HOM-MA, M., and HORIKAWA, K., Wave Forces Against Sea Wall, Proc. Ninth Conference on Coastal Engineering, Lisbon, June 1964
- 28 HOM-MA, M., and HORIKAWA, K., Experimental Study on Total Wave Forces Against Sea Wall, Coastal Engineering in Japan, Vol. 8, Tokyo, 1965
- 29 JOHNSON, R.S., The effect of air compressibility in a first approximation to the ship slamming problem, Journal of Ship Research, Vol. 12, No. 1, Marz 1968
- 30 KAMEL, A.M., Shock Pressure on Coastal Structures, ASCE Journal of the Waterways, Harbors and Coastal Engineering Div., Vol. 96, No. WW3, Aug. 1970
- 31 Von KARMAN, T., The Impact on Seaplane Floats During Landing, National Advisory Committee for Aeronautics, TN 321, Washington D.C., 1929
- 32 LARRAS, J., Le Déferlement des lames sur les jetées verticales, Annales Ponts et Chaussées, 1937
- 33 LEWISON, G., and MacLEAN, W.M., On the Cushioning of Water Impact by Entrapped Air, Journal of Ship Research, Vol. 12, no. 2, June 1968
- 34 LEWISON, G., Slamming, Ship Division Report 138, National Physical Laboratory, Marz 1970
- 35 LEWISON, G., On the Reduction of Slamming Pressures, Transactions, RINA, Vol. 112, 1970

- 36 LUNDRGREN, H., (1969), Wave Shock Forces: An Analysis of Deformations and Forces in the Wave and in the Foundation, Procs. Research on Wave Action, Vol. II, Delft, 1969
- 37 MINIKIN, R.R., Winds, Waves and Maritime Structures, London, 1950
- 38 MITSUYASU, H., (1966), Shock Pressure of Breaking Wave, Procs. Coastal Engineering Conference, Vol. 1, Tokyo, Sept. 1966
- 39 MITSUYASU, H., Shock pressure of breaking waves, Coastal Engineering in Japan, Vol. 9, Tokyo, 1966
- 40 NAGAI, S. en OTSUBO, T., Pressures by breaking waves on composite-type breakwaters, Procs. Coastal Engineering Conference, London, Sept. 1968
- 41 OCHI, M.K. and MOTTER, L.E., Prediction of Slamming Characteristics and Hull Responses for Ship Design, The Society of naval architects and marine Engineers, Transactions, Vol. 81, 1973
- 42 OGILVIE, T.F., Compressibility effects in ship slamming, Schiffstechnik, Band 10, Heft 53, 1963
- 43 RAMKEMA, C., FLOKSTRA, C., and OLDENZIEL, D.M., and WATERLOOPKUNDIG LABORATORIUM, Golfklappen op de schuif in de Oosterschelde-Caisson, Verslag M 1335 deel I, band 1, April 1977
- 44 RAMKEMA, C., and FLOKSTRA, C., and WATERLOOPKUNDIG LABORATORIUM, Golfklappen; Een literatuuroverzicht en de invloed van de samendrukbaarheid van het water, verslag M 1335 deel II, (in preparation)
- 45 RICHERT, G., Experimental Investigation of Shock Pressures Against Breakwaters, Procs. Coastal Engineering Conference, Vol. II, London, Sept. 1968
- 46 RIGHERT, G., Model Law for shock pressures against breakwaters, Paper 55, Coastal Engineering Conference, London, Sept. 1968
- 47 RIGHERT, G., Shock pressures of breaking waves, Hydraulics Laboratory, Royal Institute of Technology, Stockholm, Bulletin No. 84, 1974
- 48 ROSS, C.W., Laboratory Study of Shock Pressures of Breaking Waves, Beach Erosion Board, Dept. of the Army, Corps of Engineers, Tech. Memo, No. 59, Washington, Feb. 1955
- 49 ROUVILLE, L.M.A. de, BESSON, P. et PETRY, P., Etat actuel des études internationales sur les efforts dus aux lames, Annales des Ponts et Chaussées, VII, Paris, 1938
- 50 SELLARS, F., Slamming Impact Pressure, MPR Associates Report MPR-282, June 1971
- 51 SELLARS, F., Water impact loads, Marine Technology, Vol. 13, No. 1, Jan. 1976
- 52 SKLADNEV, M.F. en POPOV, I.Y., Studies of wave loads on concrete slope protections of earth dams, Procs. Research on wave action, Vol. II, Delft, 1969
- 53 STEVENSON, T., The Design and Construction of Harbours, Edinburgh, 1874
- 54 VENIS, W.A. (1960), Determination of the Wave Attack Anticipated Upon a Structure from Laboratory and Field Observations, Procs. Coastal Engineering Conference, Vol. 2, The Hague, Aug. 1960
- 55 VERHAGEN, J.H.G., The Impact of a Flat Plate on a Water Surface, Journal of Ship Research, Vol. 11, No. 4, Dec. 1967
- 56 WAGNER, H., Über die Ladung von Seeflugzeugen, Zeitschrift für Flugtechnik und Motorluftschiffahrt, Band 22, 1931
- 57 WEGGEL, J.R., and MAXWELL, W.H.C. (1970), Numerical Model for Wave Pressure Distributions, ASCE Journal of the Waterways, Harbors and Coastal Engineering Division, Vol. 96, No. WW3, Aug. 1970
- 58 WESTERGAARD, H.M., Water Pressures on Dams During Earthquakes, Transactions of the ASCE, Vol. 98, Paper No. 1835, 1933
- 60 WHITMAN, A.M., and PANCIONE, M.C., A Similitude Relation for Flat-Plate Hydrodynamic Impact, Journal of Ship Research, Vol. 17, No. 1, Marz 1973

CHAPTER 140

LOAD ANALYSIS FROM WAVE GROUPS

A.I.Kuznetsov^x

G.D.Khaskhatchikh^{xx}

At the present time sea wave is described by means of two theoretical models, the first is based on regular waves, components of which do not change in time and space, and the second model is based on irregular waves, components of which are randomly changed. The latter coincides to the greater extent with the rolling sea, but even this model does not characterize it to the full. Taking sea wave for a random process, the model of irregular waves does not take into account the sequence of their alternation. From the point of view of probability, on which the model of irregular waves is based, the maximum wave may be followed by the minimum wave, and the greater period may be followed by the smallest one. The real sea wave, especially in shore zone, where the main engineering constructions are placed, is characterized by clearly expressed group structure, which includes alternation of a number of great and small waves and the maximum wave is always followed by the wave having almost the same parameters. Moving through the pointed measuring section, and also depending on the wave generating condi-

^x Doctor of technical sciences, Head of maritime structures laboratory, All-Union Research Institute for Transport Construction, Moscow, USSR.

^{xx} Candidate of technical sciences. Vice-Director of All-Union Research Institute for Transport, Construction, Moscow, USSR.

tions, the number of waves in the group is changed.

There is a tale about "the 9-th bar" - the greatest wave in the group consisting of nine waves, which coincides to a certain extent to the observations in situ. According to the linear potential theory, simple wave group may be obtained by means of addition of two sinusoidal waves with different but almost the same wave numbers and frequencies. In nature it is much more complex, but the nature of wave group structure is the same and is based on the existence of the several systems of quasi - regular waves in the field of the wind irregular waves which are characterized by their own frequencies, that the main energy of this system is concentrated on. These systems, interacting with each other, form groups of waves, and the spectrum of such wavering, when the peaks of the energy maxima of wave systems are widely distributed in their frequencies, is multimodal.

The main energy maximum of the spectrum has the least angular frequency (rad/sec), and the rest are placed in order of energy level decreasing according to increasing frequencies. The energy of spectrum components with the frequencies greater than the frequency of the third maximum, as a rule, is very small in general energy balance. The example of such energy spectrum of waves in the area Sheskhari (the Black sea) is shown in fig.1 (the angular frequency in rad/sec is presented on the X-axis and the spectrum density, normalized on the dispersion - sec, is on the Y-axis).^x

^x The existence in the wind wave field several systems of waves, characterized by their own wave length (phase speed) is mentioned in the works by L.F.Titov, Newman, Physical explanation of such wave field structure is presented in paper [1].

In this area the wave properties and also pressures on the breakwater of vertical type were measured. Waves near the vertical wall were characterized by narrow spectrum of directions and thus, data on pressure measured in situ should be referred to the wave interaction when they frontally approached the wall. The waves parameters were measured outside of the interference zone and also just near the wall. The pressure was registered on seven subsurface levels. The number of waves in one oscillogram was about one hundred. The storms with maximum wave height from 1,0 to 2,5 m were registered. The loads acting on the wall were defined according to the pressure values. The object was to compare the values measured in situ with the values calculated by theoretical formula. With this aim the maximum wave from one hundred registered waves (1% provision in the wave system) was chosen in the oscillogram. The calculations were made by the following formula:

$$\frac{p}{\gamma} = Z - \eta(t) - h r \sin \delta t [ch \varphi - ch a (H-Z)] + \quad (1)^x$$

$$+ a h^2 m [ch 2 \varphi - ch 2 a (H-Z)]$$

where $\frac{p}{\gamma}$ - pressure in the point defined by the coordinate Z ;
 h - the incident wave height;
 $\eta(t)$ - position of the free water surface at the wall in respect to the calm water level;
 $\delta = \frac{2\pi}{T}$ - angular frequency;
 $a = \frac{2\pi}{\lambda}$ - wave number;
 T - wave period;
 λ - wave length;
 H - water depth near the wall.

^x The results of calculation according to the formula (1) coincide with the calculations made with the help of charts, given in the Construction Codes of the USSR (SNiP 11-57-75).

$$\alpha = a h$$

$$\beta = a H$$

t - time

$$\varphi = a (H - \eta)$$

$$n = \frac{1 + 2\alpha \sin \beta t}{ch \beta \cdot \ell^{(\varphi - \beta)}} \quad ; \quad m = \frac{\cos^2 \beta t}{2 \operatorname{sh} 2\beta \cdot \ell^{(\varphi - \beta)}}$$

The intercepting point of the coordinates is situated on the calm water level and the axis O-Z is directed downward.

The formula (1) was preliminarily checked in the laboratory conditions on the regular wave and provided the coincidence with the experimental data within 10%.

Comparison of calculations made with the help of formula (1) with the data obtained in situ showed that the calculated load values were 30% greater than measured values (in some cases - 50%). In connection with that the assumption was made that there is some influence of group wave structure on pressure values and the mathematical model of wavering process near the vertical wall was as:

$$\eta(t) = \sum_K^k h_i \sin \delta_{i0} [1 + f(t)] t \quad (2)$$

where K - the number of wave systems (within 3)

which is defined according to the number of characteristic energy maxima of frequency spectrum;

δ_{i0} - the main frequency of system;

h_i - equivalent wave height of the system.

Wave heights h_i were derived from the assumption that maximum wave height according to the given realization (h_{max}) is the result of addition of equivalent system wave heights and also according to the fact that the energy is proportional to the square wave height. For the three wave systems the equations of connection will be following:

$$h_{max} = h_1 + h_2 + h_3 \quad (3)$$

$$\frac{h_1}{h_2} = \sqrt{\frac{S(\beta_{1,0})}{S(\beta_{2,0})}}; \quad \frac{h_1}{h_3} = \sqrt{\frac{S(\beta_{1,0})}{S(\beta_{3,0})}}; \quad \frac{h_2}{h_3} = \sqrt{\frac{S(\beta_{2,0})}{S(\beta_{3,0})}} \quad (4)$$

$S(\beta_{1,0})$, $S(\beta_{2,0})$, $S(\beta_{3,0})$ - the values of spectrum density maxima at frequencies $\beta_{1,0}$, $\beta_{2,0}$, $\beta_{3,0}$ (fig. 1).

With the help of the in situ occillograms it was shown, that it is possible to select a periodical function:

$$f_i(t) = A \cos Bt \quad (5)$$

with which on definite t (the interval of order 100 waves), the function $\eta(t)$, computer calculated according to (2), has a group structure, and its statistical and spectral characteristics are close to the natural irregular process. In the expression (5) B - the frequency of wave groups appearance - rad/sec (under suggestion of A. I. Kuznetsov).

Euler's equation was used to determine the pressure (on axis OZ).

$$\frac{\partial V_z}{\partial t} + \frac{\partial V_z}{\partial z} V_z = g - \frac{1}{\rho} \frac{\partial P}{\partial z} \quad (6)$$

In the course of its integration the value of vertical speed component according to the linear wave theory was written down as follows:

$$V_z = -\sum_1^3 \frac{\beta_i h_i \operatorname{sh} \beta_i (H-z)}{\operatorname{sh} \beta_i} \cos \beta_i t \quad (7)$$

As a result of integration (6) the formula for pressure value in the point of ordinate Z (with 3 components of wave field) was obtained:

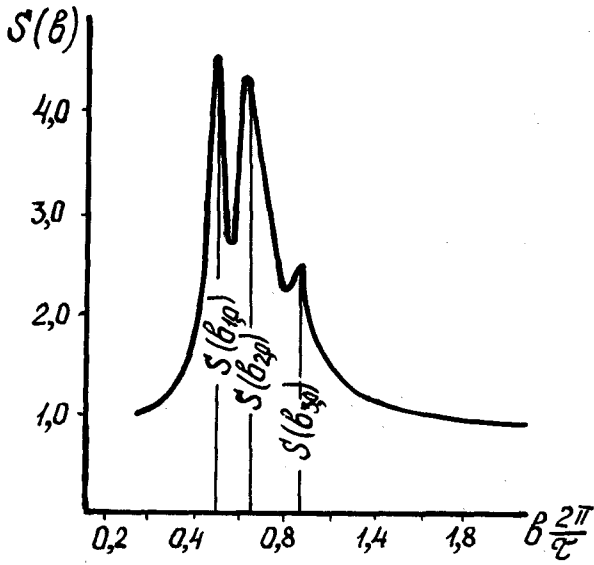


Fig.1. Example of wave oscillations spectrum in the area of Sheskhari

$$\begin{aligned}
 \frac{P}{\gamma} = & Z + \eta(t) - \sum_1^3 h_i \cdot m_i \cdot \sin b_i t [ch \varphi_i - ch a_i (H-Z)] + \\
 & + \sum_1^3 a_i h_i^2 m_i [ch 2\varphi_i - ch 2a_i (H-Z)] - \\
 & - 2h_1 h_2 \sqrt{\frac{a_1 \cdot a_2}{sh 2\beta_1 \cdot sh 2\beta_2}} [sh \varphi_1 \cdot sh \varphi_2 - sh a_1 (H-Z) \cdot sh a_2 (H-Z)] \cdot \cos b_1 t \cdot \cos b_2 t \\
 & - 2h_1 h_3 \sqrt{\frac{a_1 \cdot a_3}{sh 2\beta_1 \cdot sh 2\beta_3}} [sh \varphi_1 \cdot sh \varphi_3 - sh a_1 (H-Z) \cdot sh a_3 (H-Z)] \cdot \cos b_1 t \cdot \cos b_3 t \\
 & - 2h_2 h_3 \sqrt{\frac{a_2 \cdot a_3}{sh 2\beta_2 \cdot sh 2\beta_3}} [sh \varphi_2 \cdot sh \varphi_3 - sh a_2 (H-Z) \cdot sh a_3 (H-Z)] \cdot \cos b_2 t \cdot \cos b_3 t
 \end{aligned}$$

Notations in (8) are similar to those of (1).

By means of integrating (8) in the limits from $\eta(t)$ to H the load on the wall was determined.

All calculations were performed with the help of a computer.

As could be seen from the formula (8), besides members, which characterize each wave system separately, the pressure value is influenced also by cross members, which reflect the interaction of wave field components (the last three members of formula (8)). This expresses the influence of the group wave structure on the value of wave pressure. When $h_2 = h_3 = 0$ and $A = 0$ we have a system of regular waves and formula (8) is transformed into (1). The influence of the group wave structure on the pressure and loads values was checked according to the data obtained in situ in the course of several storms. Here are the results for the case of the greatest deviation of in situ data from calculated with the help of formula (1) at the maximum wave of 1% provision. Wave actions were characterized

by the average wave height $h = 0,75$ m, and the wave height of 1% provision $h_{1\%} = 1,8$ m. The spectral density function of the wavering had three sufficiently spaced maxima (fig. 2-a), from which those situated at high frequencies, were smoothed at the load spectrum, and especially at the wave pressure spectrum near the bottom at point with coordinate 11,2 m (fig. 2-b, 2-c). The mathematical model of the process was described by means of three wave systems with equivalent heights $h_1 = 0,78$, $h_2 = 0,54$, $h_3 = 0,48$ m and with frequencies respectively $b_{1,0} = 0,65$, $b_{2,0} = 1,10$, $b_{3,0} = 1,47$, parameter $A = 0,03$ and group frequency $B = 0,1$. Fig. 3 shows one of the most characteristic areas of in situ oscillogram of wave and wave pressures. The model of this recording together with the chronogram of the loads calculated by means of a computer according to formula (8) are presented at fig. 3-b and 3-c.

It could be seen from the comparison that the recording model somewhat lacks high frequency oscillations, but the group structure character in model and in situ are similar. In the course of comparison it should be kept in mind that the scale factors for models and for experiments performed in situ are quite different. The functions of spectrum density obtained by means of calculations illustrate the coincidence of energy distribution in accordance with frequencies in situ and in model (see fig.2 - dashed line). Finally, for the given example there is a comparison of wave pressure diagrams from the wave of 1% provision obtained in situ and also calculated considering (formula 8) and without consideration (formula 1) of the group wave structure, fig. 4. This comparison shows that pressure and load calculations without considering the group structure according to the theory of regular waves provide sufficient and sometimes excessive margin. Consideration of group structure of waves in the analytical description of the process makes it possible to draw closer in situ and computed data. But formula (8) could not be considered as a formula for

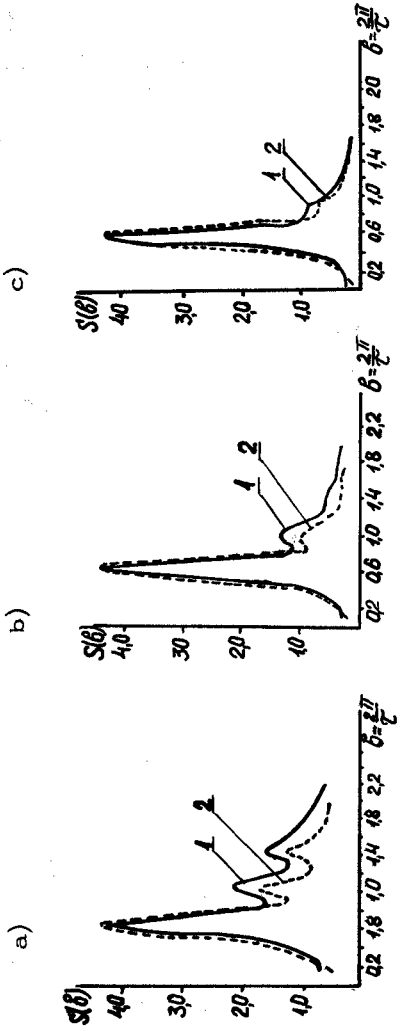


Fig. 2 In situ and calculated spectra:

- a) wave oscillations;
 - b) total loads;
 - c) pressures (near the bottom at point 11,2 m)
- 1 - in situ spectrum
2 - calculated spectrum

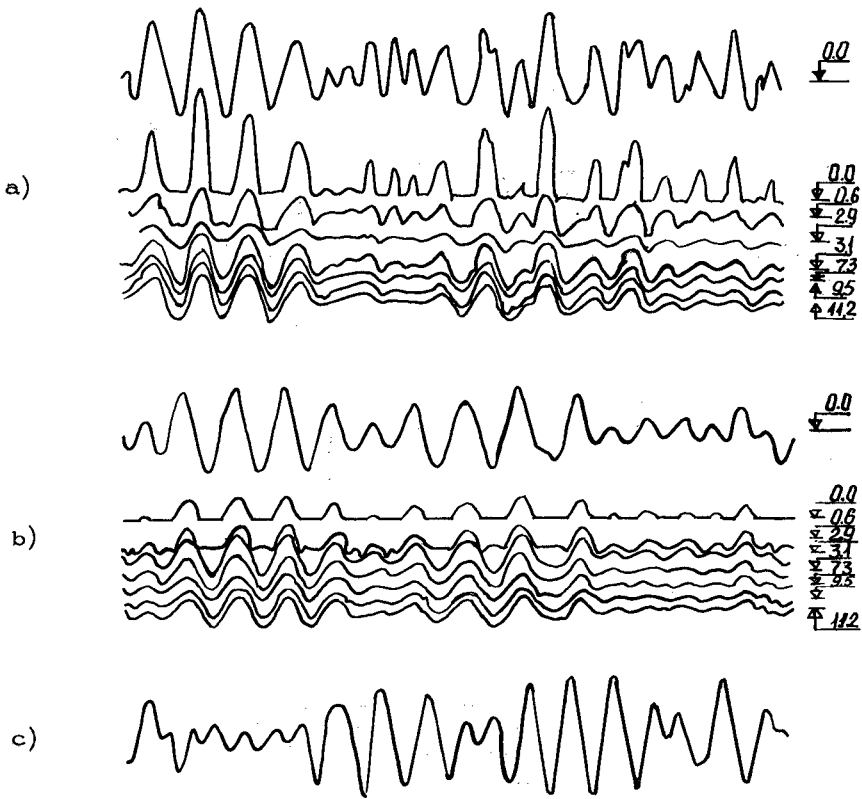


Fig. 3. Comparison between in situ and calculated realizations:

- a) oscillographic recording in situ;
- b) realization of wave oscillations and pressures obtained by means of calculation according to formula (8);
- c) calculated load chronograph trace.

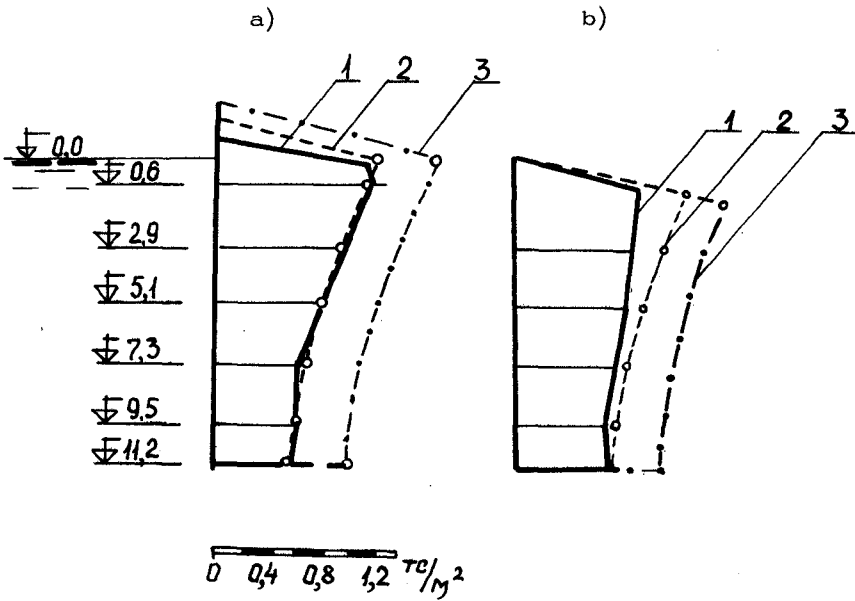


Fig. 4. Wave pressures epures:
 a) in the phase of wave crest;
 b) in the phase of wave trough.
 1 - measurements done in situ;
 2 - calculation according to formula (8);
 3 - calculation according to formula (1).

calculations, but only as a proof of the influence of wave group structure on the pressure and load values.

At present time according to the results of modelling wave actions on the constructions in wave tank with irregular waves, there is some information that hydrodynamic pressure and reactions in the elements of constructions (for pile structures) under the action of waves with group structure according to the intensity of action, depending on the number of waves in the group, take the intermediate position between regular and purely random waves.

The regular waves produce maximum pressure and reaction values and the irregular-minimum [2]. Above mentioned consideration of group structure draws the calculations quite close to the data obtained in situ that is why modeling of wave action on the constructions with regard to actions of only irregular waves without considering their group structure, could lead to the too low results.

Consideration of group structure in the course of wave loads calculation and wave modelling needs further investigation.

REFERENCES

- 1 Krylov U.M., Strekalov S.S., Tsyplouknin V.F. "Wind waves and their effects on structures", L., Hydrometeoisdat, 1976.
- 2 Halphin I.H., Pleshakov A.V. "On some peculiarities of group wave actions on the model of a drilling rig.". Scientific and technical collection of abstracts" Oil-field construction", no.7, Moscow, 1978.

IMPACT WAVE FORCES
ON VERTICAL AND HORIZONTAL PLATE

by

S.R. Massel ¹, M. Oleszkiewicz ², W. Trapp ³

INTRODUCTION

The hydrodynamic impact problem is a very difficult problem because the physics of what actually happens during the instant of impact are not understood. Despite of fact that a large number of references exist on the subject, many questions are left unanswered.

The object of this research is to investigate the problems of hydrodynamic impact associated with the water waves impacting on the vertical and horizontal plates. Of particular interest are the impact forces, their relation to the incident wave parameters and scale effect problems.

VERTICAL WALL BREAKWATER

Consider first the case of the vertical plate which can simulates easily the breakwater wall. The prediction of shock-pressures exerted by breaking waves is the most important thing to be known for the design of breakwaters. However due to great difficulties in the experiments, very little information is available in regard to the practical data of the shock pressures on the prototype objects. On the other hand, during the recent decades a large number of model investigations of shock pressures have been undertaken. They indicate that the configurations of breaking waves at breakwaters vary in a wide range depending upon the type of breakwaters, the characteristics of breakwaters, the characteristics of incident waves, the ratio of the depth of water in the front of the breakwater to the height of the incident wave.

In the previous research undertaken for example, by Nagai [7], Mitsuyasu [6], Hayasi [3], Rundgren [9], Richeart [8], Loginov [5] and others, the shock pressures at particular points of the vertical wall were considered. The results of these investigations give a very ambiguous picture of the problem; often they are contradictory and have been presented in a different way. Thus, it is extremely difficult to compare the results by different authors. The value of pressure depends very strongly on the position of the air cushion. Moreover, the considered wave is usually disturbed by the preceding wave, so it

¹ Assist. Prof., ² Res. Eng., ³ Sen. Res. Ass.
Institute of Hydroengineering of the Polish Academy
of Sciences, Gdańsk, Poland.

loses part of its energy before it reaches the wall. These factors are, to some extent, a random factors.

In order to predict the effective forces on the vertical wall and to avoid the influence of the air cushion configuration on the impact forces, in the present study, the total force on the breakwater wall will be considered. The vertical plate with two degrees of freedom (horizontal displacement and rotation around the horizontal axis) simulates the breakwater wall (Fig.1). The wave breaking is forced by the composite-type bottom on which the test wall is situated. The displacements of the two points are measured simultaneously by the Phillips' capacitive sensors. The deflection of the supporting rings is in the elastic range, therefore the forces at the two measuring points are related to the displacements by Hooke's law.

Numerous experiments indicate that, if for certain wave height, the breaking wave front is approximately plane and if it creates a very thin air cushion, the pressure peak reaches a maximum value. If the wave height is only slightly smaller, the wave front will be sloping backwards. On the other hand, if the wave height is larger, the air cushion will be thicker and the wave breaks further from the wall. Therefore, for a given wave period and a given depths h_1 and h_2 , it is only one wave height that is associated with the max. force.

The first series of experiments were carried out in the wave tank being 10 m long and 25 cm width for three various wave periods. For each period, the wave height corresponding max. force was chosen.

As was mentioned above, the max. impact forces may be treated as a random variables. In order to obtain a set of data which is sufficient for statistical analysis, the experiments were repeated many times.

Since the extension of model shock pressure into prototype scale is of particular interest for engineers, various model scales were also considered. Taken as a prototype was the breakwater on 6 m water depth subjected to the wave dimensions being 2,5 m height and 5-6 s period. Laboratory tests were conducted in the five scales $1/20$, $1/30$, $1/40$ and $1/50$. It means, that considering the scale $1/20$ as a reference scale, we obtain a set of experiments in the scales $1/1$, $1/1.5$, $1/2$ and $1/2.5$.

In the various scales, the corresponding wave parameters and water depths were calculated in accordance with the Froude's law. At the same time, the mechanical device for the impact force measurement has not been changed.

From the numerous laboratory tests we found that

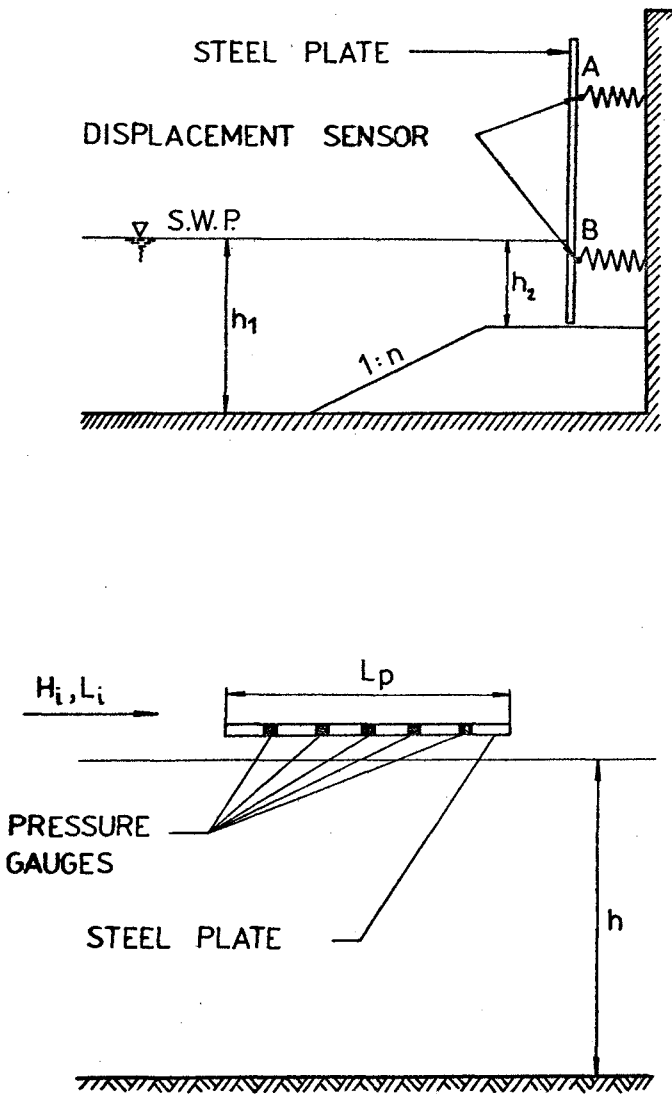


Fig.1 Vertical and horizontal plates.

probability density functions $f\left(\frac{R_1}{\bar{R}}\right)$ and $f\left(\frac{R_2}{\bar{R}}\right)$ (\bar{R} - mean value of the impact force R) are of the Weibull type

$$\left. \begin{aligned} f(x) &= ab \cdot x^{b-1} \exp(-ax^b) & \text{for } x > 0 \\ f(x) &= 0 & \text{for } x \leq 0 \end{aligned} \right\} \quad (1)$$

$$\text{where: } x = \frac{R_1}{\bar{R}_1} \quad \text{or} \quad x = \frac{R_2}{\bar{R}_2}$$

From Eq.1, it immediately follows that the probability distribution function $F(x)$ takes the form

$$F(x) = 1 - \exp(-ax^b) \quad (2)$$

Taking the derivative of Eq.2 gives

$$Y = \ln a + bX \quad (3)$$

$$\text{where: } Y = \ln \{-\ln [1 - F(x)]\}, \quad X = \ln\{x\} \quad (4)$$

Thus, the representation of the Eq.3 in the logarithmic scale is the straight line. In the Fig.2 the theoretical formula (3) is checked against the experimental data for the impact force R and various model scales. The agreement is quite satisfactory. However, for various scales the distribution parameters a and b takes a different values. When the parameters a and b are found from the Fig.2, the corresponding probability density functions can be easily calculated (see Fig.3).

The wave forces were measured in two points of the vertical plate. One supporting ring was approximately situated at the SWL (for wave force R_1 - point B), the other was above SWL (for wave force R_2 - point A). Fig.4 shows the example of the correlation between the force R_1 and R_2 . In each calculated cases the correlation coefficient was greater than 0.8.

As the mechanical measuring device was not scaled, it is difficult to say how much wave momentum is associated with the pulse and how much is dissipated by the mechanical and hydrodynamic dumping.

In order to give the answer on that question we considered the very simple model. In the first place, by way of experimental verification we found that the horizontal motion of the plate predominates over the rotation motion; in the record it is only one frequency that is visible. So we can state that the two degrees of freedom system is approximately equal to the two systems having one degree of freedom (Fig.5). The unknown characteristics of the measuring systems are defined by the special calibration tests.

The equation of motion of any single-degree-of-freedom system can be reduced to the equation of motion of a simple spring-mass system with damping

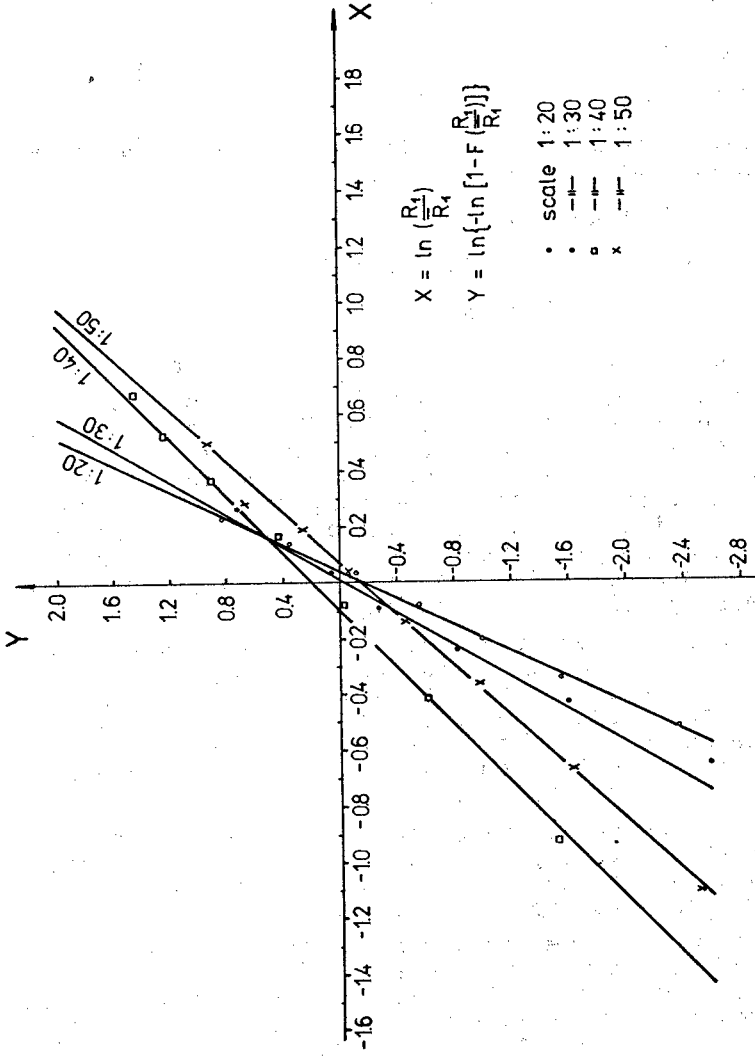


Fig.2 Probability distribution for max. forces in the logarithmic scales.

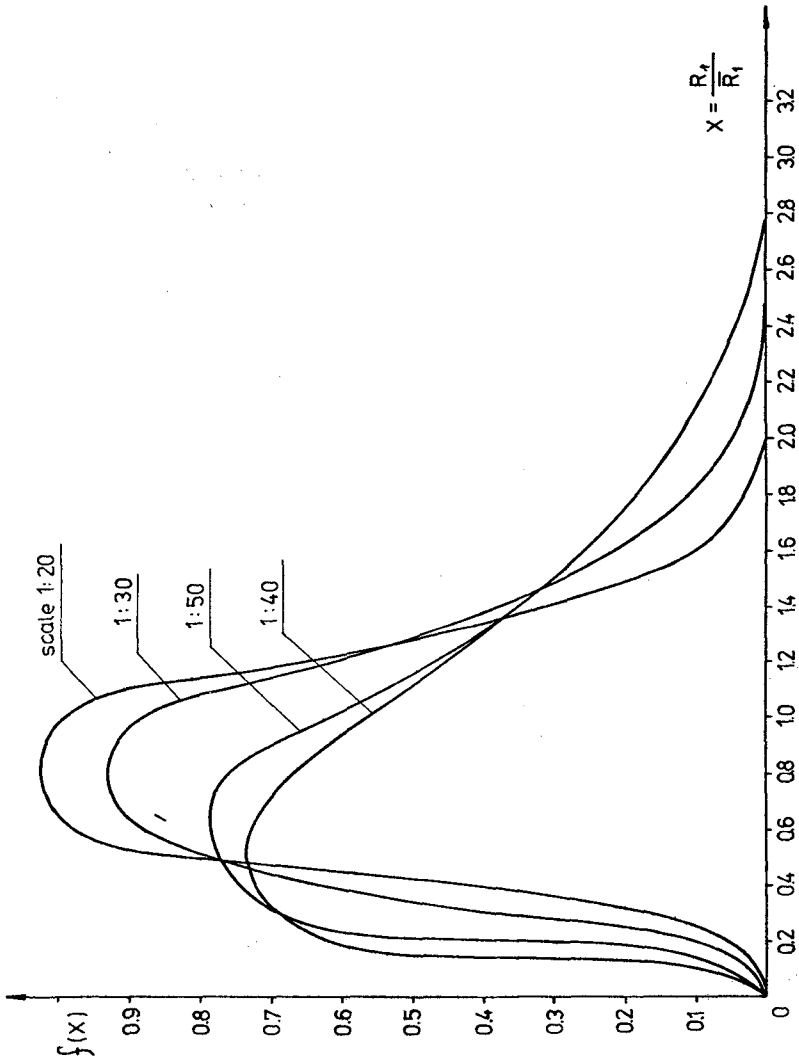


Fig.3 Probability density functions for max. forces.

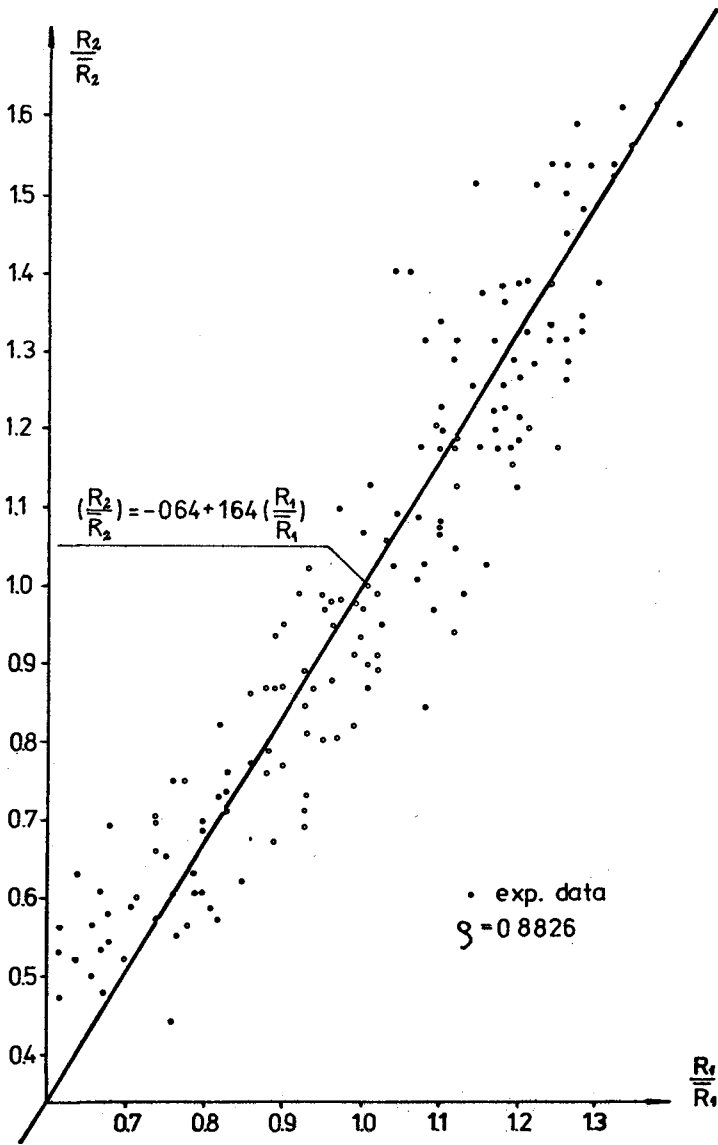


Fig.4 Correlation between forces.

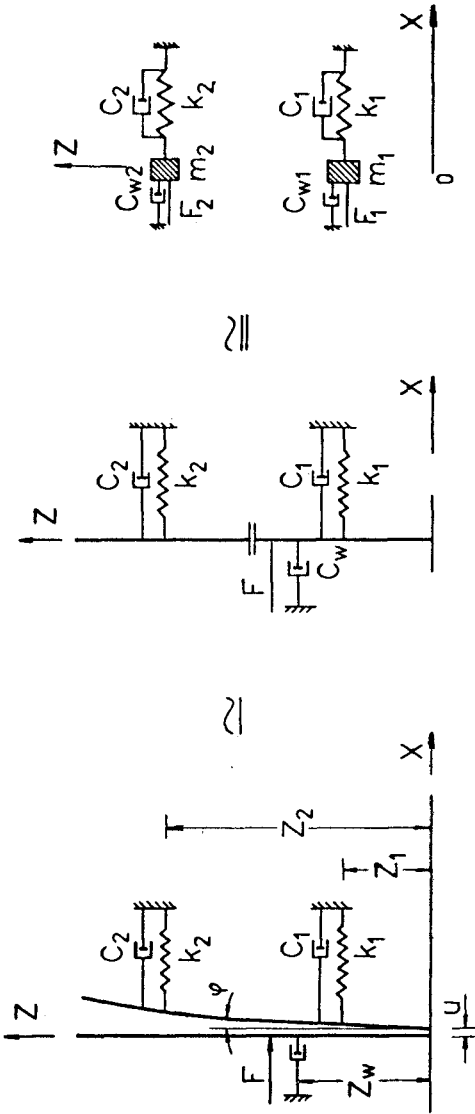


Fig.5 Equivalence of the measuring systems.

$$(m + m_a) \frac{d^2 u}{dt^2} + (C + C_a) \frac{du}{dt} + k \cdot u = P(t) \quad (5)$$

in which: u - displacement of the plate,
 m - mass of the vibrating part of system,
 m_a - added mass of the water participating
in vibration,
 C - mechanical dumping,
 C_a - hydrodynamic dumping,
 k - stiffness of the system,
 P - impact force.

As we know displacement u , the impact force $P(t)$ is given by the Volterra type integral equation

$$u(t) = \frac{1}{(m + m_a)\omega} \int_0^t P(\tau) \cdot e^{-h(t-\tau)} \sin \omega(t-\tau) d\tau \quad (6)$$

From numerical solution of the Eq. 6 follows that, the rise time of the impact force is less than or equal to $1/4$ of the natural period of the measuring system $T_n \approx 0.003 \div 0.005$ s. Moreover, only $\sim 40\%$ of the wave momentum is associated with the plate displacement; almost 60% of the momentum is dissipated due to mechanical and hydrodynamic dumping and added mass generation. It means, that the real maximum impact force is about 2.5 times greater than the force calculated simply from the displacement u by Hooke's law.

We consider now the problem of the force scaling. Usually, for the gravity wave phenomena, we use the Froude law of similarity. Thus for the mean wave force we have

$$\frac{\bar{R}_p}{\bar{R}_\lambda} = \lambda^3 \quad (7)$$

in which: \bar{R}_p - mean wave force for prototype,
 \bar{R}_λ - mean wave force in the scale $1:\lambda$.

At present we assume that in model experiments (scale $1:\lambda$) we obtain the wave force which is equal to \bar{R}_M . When no scale effect, the following relation becomes

$$\bar{R}_M = \bar{R}_\lambda \quad (8)$$

When it is not that case, we define the scale effect coefficient in the form

$$\eta_\lambda = \frac{\bar{R}_\lambda}{\bar{R}_M} \quad (9)$$

thus

$$\bar{R}_p = \bar{R}_\lambda \cdot \lambda^3 = \bar{R}_M \cdot \lambda^3 \cdot \eta_\lambda \quad (10)$$

Applying the above definition of the scale effect coefficient to the mean maximum forces we obtain the distribution of the η value as shown in Fig. 6. It should be noted that the experiments in the scale $1:20$ serve as a reference experiments. If we reduce model scale twice (from $1:1$

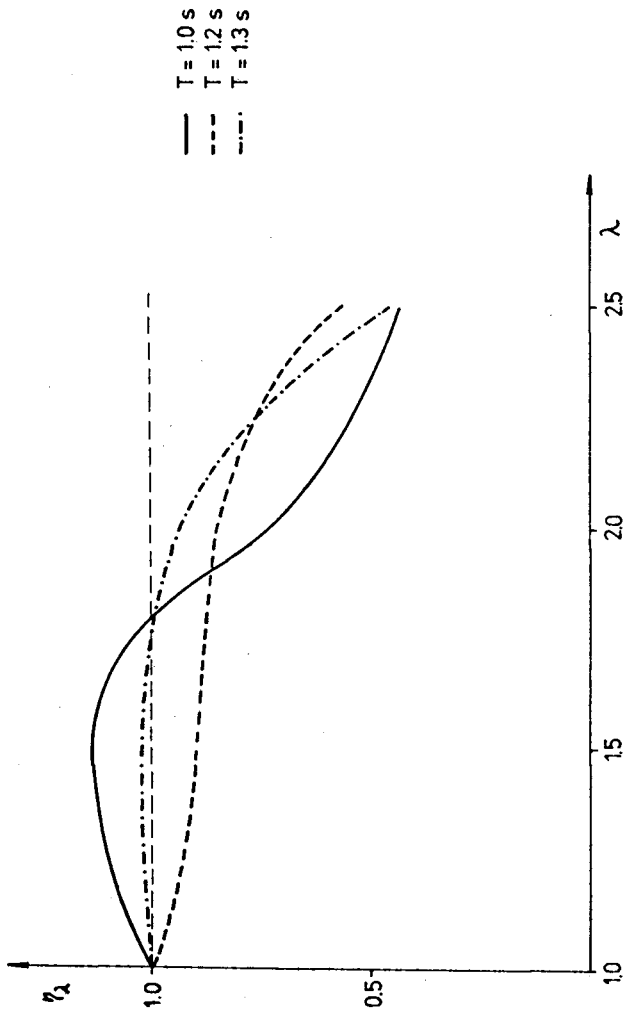


Fig.6 Scale effects coefficient for mean max. impact force.

to 1:2), the mean impact force at the model decreases less than it follows from Froude law for period $T=1s$. It means that $\bar{R}_M > \bar{R}_\lambda = \frac{1}{8} \bar{R}_P$ or $\bar{R}_M / \bar{R}_P > \sqrt[1]{2^3} = \frac{1}{8}$

Therefore, the prediction of the prototype forces basing on the model test (in this case) overestimates the real force. Thus, the scale effect coefficient $\eta_\lambda < 1$ has to be included (see Fig.6).

The scale effect concept can be extended to the maximum impact force with arbitrary probability of occurrence. From the calculations (not indicated here) follows that the relatively high scale effects may be expected for very low and very high probabilities.

The work reported in this part of paper is the first phase of a project intended to develop insight into breaking wave forces acting on breakwaters and the more efforts are needed towards better understanding of these sophisticated phenomena. First of all, the amount of the air content in the breaking wave is still not good defined. However, the air in the water influences strongly on the added mass vibrated with the plate.

HORIZONTAL PLATE IN THE SPLASH ZONE

An important class of forces for which there is not a large extensive history of study are the impact forces that act on horizontal members in so called "splash zone" [1,2,4,10]. The splash zone is a region wherein the particular horizontal members of the maritime structure are not usually considered to have continuous contact with the waves, but which are located at a height relative to the mean water surface, so that only occasional contact with the water will occur. The nature of the forces that occur during such contacts is essentially impulsive.

In order to provide some knowledge of the pressure distribution on the underside of horizontal members a laboratory study was made. The particular problem considered here is treated by the impact force measurements for a horizontal rigid plate, assuming that the wave system propagates in a direction of longitudinal axis of the plate. A illustration of the situation being analyzed is shown in Fig.7 for the progressive wave and in Fig.8 for the standing wave; the height of the plate (1 m length) above the mean water level is equal to S , H is the incident wave height and h is the water depth. The six electro-kinetic type pressure gauges are installed along the plate axis. The working frequency band for the pressure gauges is equal to $10^{-2} - 10^4$ Hz.

The records taken from the experiments illustrate the impulsive character of pressure. Sometimes due to disturbances underneath the platform, the peak pressure

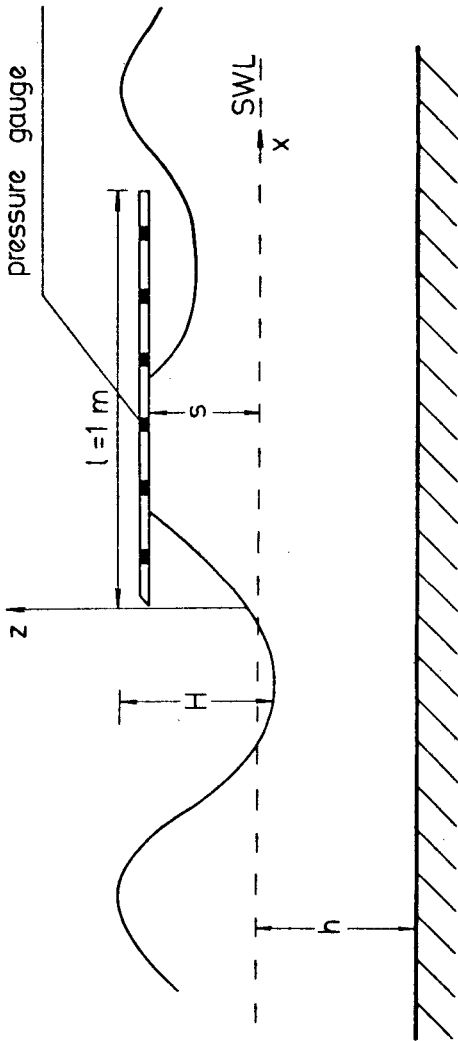


Fig.7 Definition scetch for progressive waves.

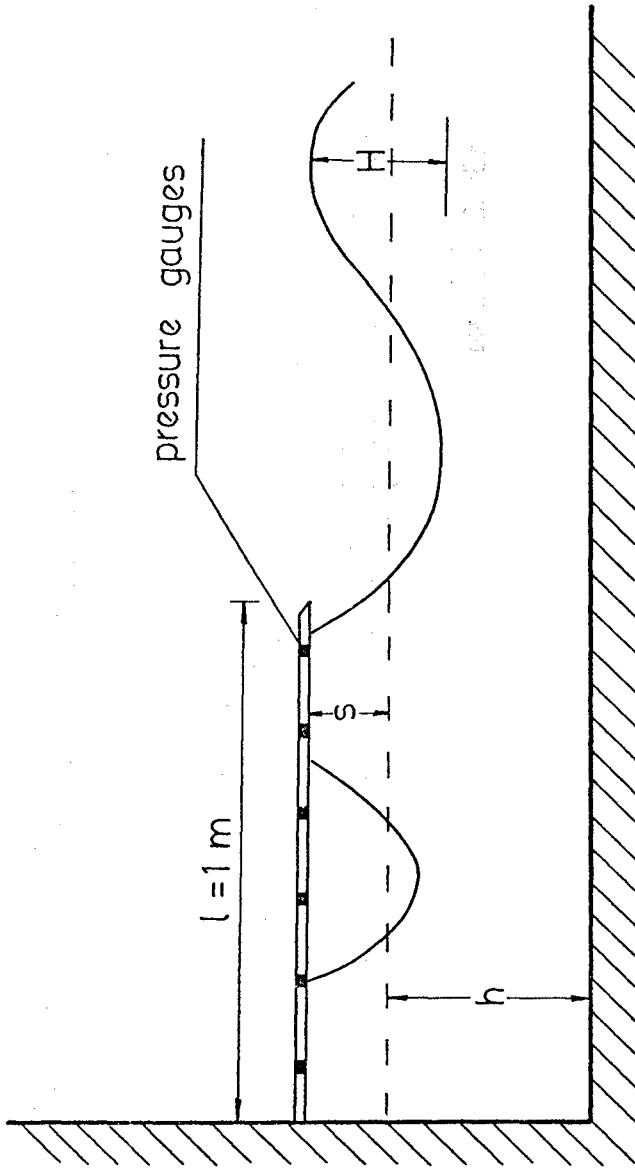


Fig. 8 Definition sketch for standing waves.

PROGRESSIVE WAVE

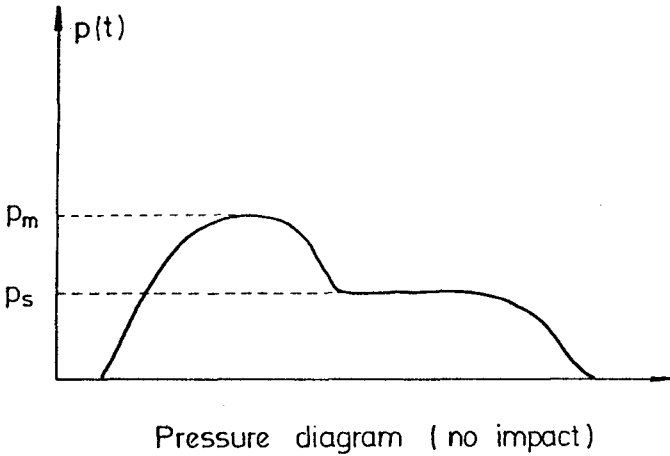
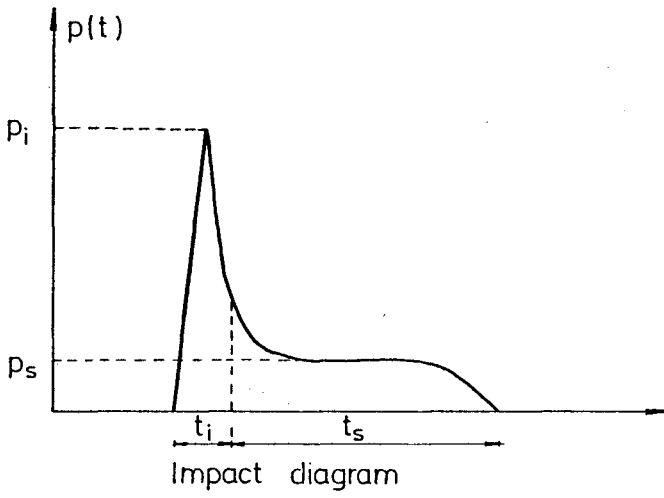


Fig.9 Notations for the impact pressures progressive waves

PROGRESSIVE WAVE

- slowly-varying pressure (p_s)
- ▼ peak pressure (p_i)
- max pressure when no impact (p_m)

$$\frac{x}{L} = 0.1$$

$$\frac{s}{H} = 0$$

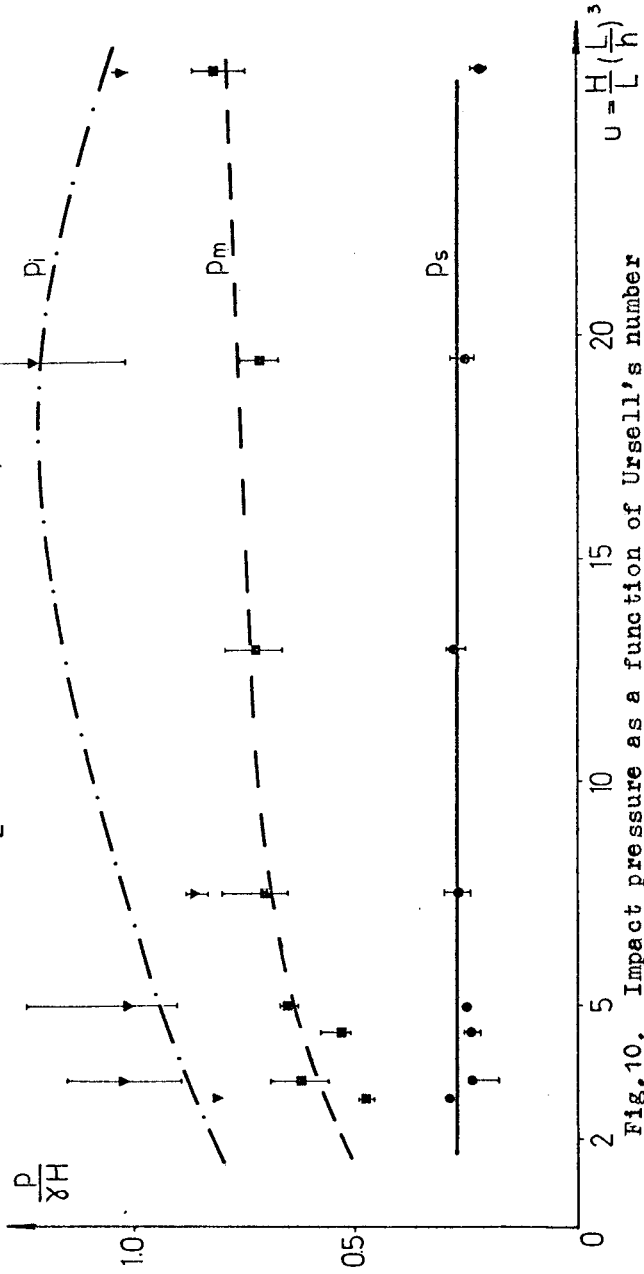


Fig.10. Impact pressure as a function of Ursell's number

PROGRESSIVE WAVE

$$\frac{s}{H} = \frac{2}{3}$$

$$\frac{x}{l} = 0.1$$

- slowly-varying pressure (p_s)
- ▼ peak pressure (p_i)
- max pressure when no impact (p_m)

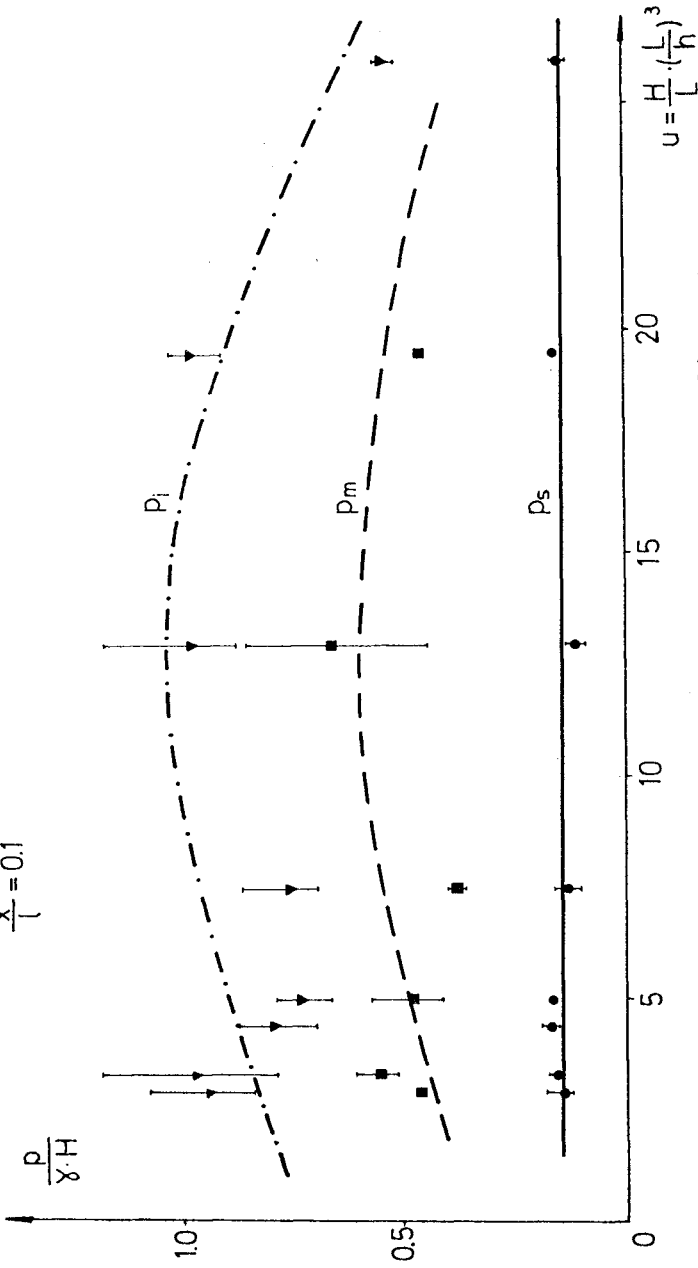


Fig. 11 Impact pressure as a function of Ursell's number

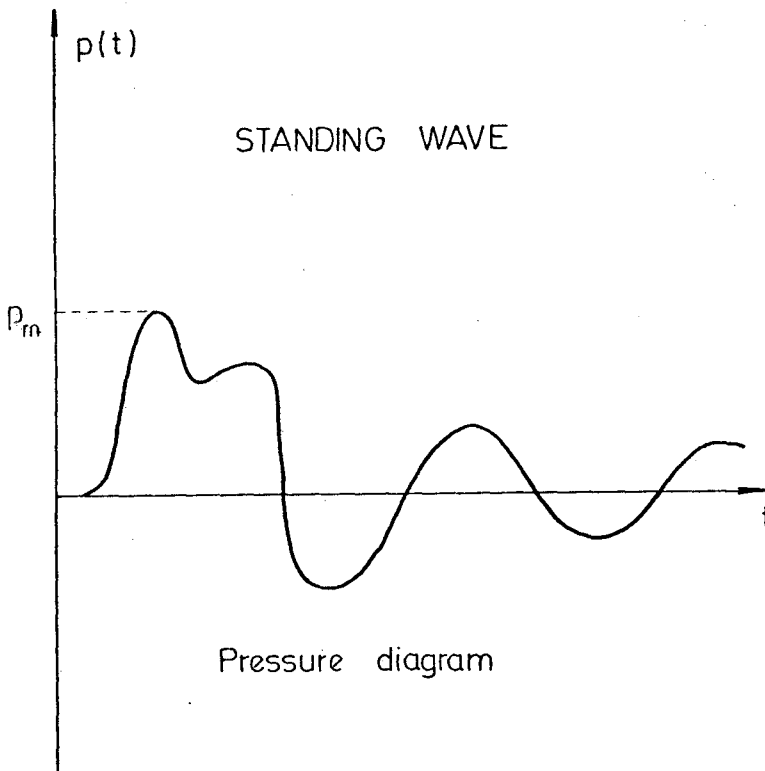


Fig.12 Notation for the impact pressures standing waves .

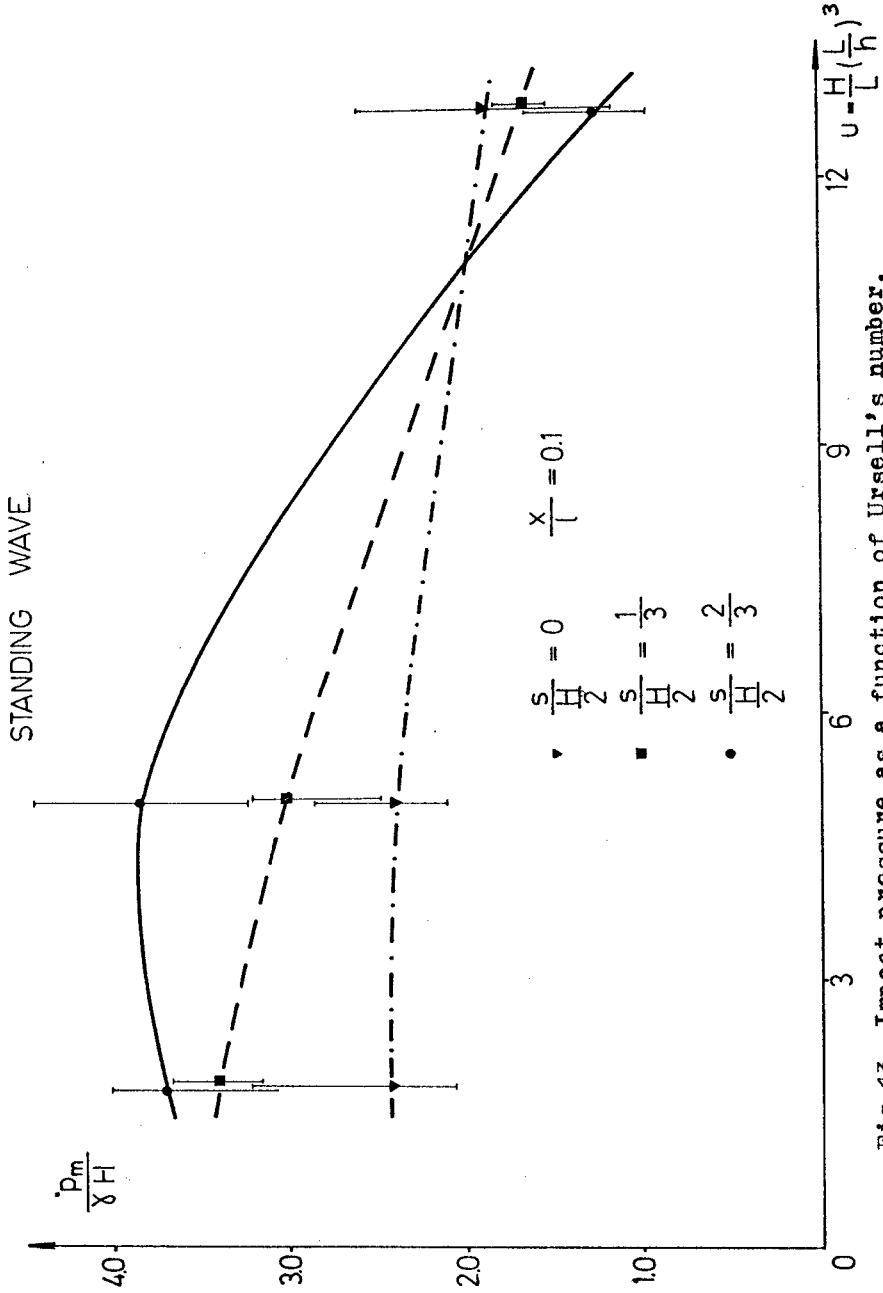


Fig. 13 Impact pressure as a function of Ursell's number.

is not so clearly pronounced. In order to classify the impacts induced by the progressive waves we use the notations given in Fig.9, in which p_i - peak pressure, p_s - slowly varying pressure and p_m - maximum pressure when no impact occurs.

The incident wave were Stokes' waves $2 \leq \frac{L}{h} \leq 8$ (L - wave length, h - water depth).

In Figs.10 and 11 the normalized wave induced pressure is plotted against the Ursell's number

$U = \frac{H}{L} \left(\frac{L}{h} \right)^3$ for nondimensional clearance $\frac{S}{\frac{H}{2}} = 0, \frac{1}{3}, \frac{2}{3}$
(S - clearance between the bottom of the horizontal plate and the still water level).

The data points are the results of the averaging of numerous experiments. Moreover, the standard deviation from the mean value is also indicated. The slowly-varying pressure p_s is almost constant in the considered range of Ursell's number. The highest value p_s is obtain when the plate is at the still water level ($S=0$).

The maximum pressure p_m (when no impact) is slowly-varying function of Ursell's number with max. value at $U \sim 10-15$. The same tendency for the peak pressure p_i is observed. In Figs.10 and 11 the best fittings of the experimental data are indicated by the solid and dashed lines.

When the standing waves are considered, it is hardly to distinguish the various types of pressure.

According to Fig.12 the analysis of the experimental data is restricted to the maximum pressure value p_m . The example of the result is given in Fig.13. The pressure p_m is also the slowly varying function of the Ursell's number.

CONCLUSIONS

With respect to measurement of the impact forces at the vertical wall due to breaking wave it was found that the maximum force can be treated as a random variable with the probability distribution of the Weibull type. The amount of the air entrapped into breaking wave produce some inconsistency with Froude scaling law. Thus, the statistical concept of the scale effects was introduced.

The preliminary study of the wave impact on the horizontal plate suggests that the peak pressure and the slowly-varying part of pressure are functions of the Ursell's number.

It should be pointed out that the more efforts are needed to better describing of these complicated phenomena.

REFERENCES

1. Dalton Ch., Nash J.M., Wave slam on horizontal members of an offshore platform. Proc. Offshore Techn. Conf., Paper 2500, Houston, 1976.
2. French J.A., Wave uplift pressures on horizontal platforms. Cal. Inst. of Techn., Rep. No.KH-R-19, 1969.
3. Hayasi T., Hattori M., Thrusts Exerted Upon Composite Type Breakwaters by the Action of Breaking Waves. Coastal Eng. in Japan, Vol.VII, Tokyo, 1964.
4. Kaplan P., Silbert M.N., Impact forces on platform horizontal members in the splash zone. Proc. Offshore Techn. Conf., Paper 2498, Houston, 1976.
5. Loginov V.N., Determination of Shock Impulse Caused by Waves Breaking Against a Vertical Wall. Trudy SNIIMF, No.26, 1960 in Russian .
6. Mitsuyasu H., Shock Pressure of Breaking Wave. Proc. 10th Conf. on Coastal Eng., ASCE, Vol.1, Tokyo, 1966.
7. Nagai S., Shock pressures exerted by breaking waves on breakwaters. Jour. of the Waterways and Harbors Div., ASCE, Vol.86, No.WW2, June, 1960.
8. Richert G., Shock Pressures of Breaking Waves. Bull. No.84, Hydr. Lab., Royal Inst. of Techn., Stockholm, 1974.
9. Rundgren L., Wave Forces. Bull. No.54, Div. of Hydraulics, Royal Inst. of Tech., Stockholm, 1958.
10. Wang H., Estimating wave pressures on a horizontal pier. Naval Civil Eng. Lab., Tech. Rep. R 546, Port Hueneme, California, 1967.

CHAPTER 142

WAVE PRESSURES ON SLIT-TYPE BREAKWATERS

by

Shoshichiro Nagai¹, F.ASCE and Shohachi Kakuno²

ABSTRACT

For severe storm waves with periods of 7.0 sec to 14.0 sec and heights of 6.3 m to 9.0 m, it was proved that the resultants of the maximum simultaneous pressures exerted by breaking waves on the slit-type breakwaters with the optimum relative chamber width of $l/L = 0.05$ to 0.07 were in most cases less than 70 per cent of those exerted on the conventional composite-type breakwaters.

INTRODUCTION

The experimental results in the previous study (2) showed that the resultants of the maximum simultaneous pressures exerted on the slit-type breakwaters by breaking waves with periods of 6.0 sec and 7.0 sec and heights of 3.3 m to 4.3 m were less than about 60 per cent of those exerted on the conventional composite-type breakwaters, while the resultants of the maximum simultaneous pressures exerted on the slit-type breakwaters by non-breaking or standing waves were a little less than or approximately equal to those on the conventional composite-type breakwaters.

For more severe storm waves with periods of 7.0 sec to 14.0 sec and heights of 6.3 m to 9.0 m, the resultants of the maximum simultaneous pressures exerted on the slit-type breakwaters located at a water depth of 16.0 m by breaking and non-breaking waves are presented herein, compared with those on the conventional composite-type breakwaters. Finally the optimum relative chamber width, l/L , for the slit-type breakwater is shown.

¹ Professor Emeritus, Director of Harbor and Coastal Engineering Laboratory, Osaka City University, Osaka, Japan

² Research Associate of Hydraulic Engineering, Faculty of Engineering, Osaka City University, Osaka, Japan

EXPERIMENTAL EQUIPMENT AND PROCEDURES

The experiments were carried out at a scale of 1/25 in a 100 m-long wave channel of 2 m-height and 1.2 m-width with a wind blower at the Harbor and Coastal Engineering Laboratory of Osaka City University.

Cross-Sections of Breakwater Model. — As the basic cross-section of the breakwater models used in the experiments, the south breakwater in the Port of Kashima (1) was selected, as shown in Fig. 1. The breakwater, 2,900 m in overall length, was constructed in 1969 at water depths from about 9 m to 20 m below the Datum Line (D.L.), and was severely hit by storm waves in January of 1970, the characteristics of which were hindcast to be $H_{1/10} = 10$ m and $T_{1/10} = 10$ sec to 12 sec. The vertical walls of reinforced concrete caisson were slid toward harbor-side by 0.24 m to 1.81 m. The experiments (1), which were conducted at a scale of 1/25 at the same wave channel as used at this experiment, showed that the maximum resultant pressure of $P_e = 193$ t/m was exerted by a wave with $H = 9.6$ m and $T = 8$ sec, and the value was confirmed by the maximum resultant pressure of $P_{cal} = 202$ t/m which was obtained by the wave-pressure formula (1).

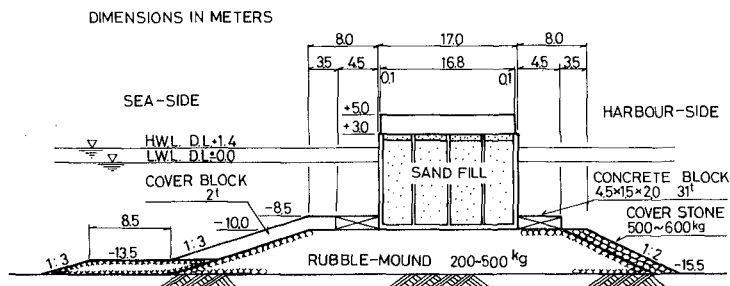


FIG. 1.- Cross-Section of Kashima South Breakwater

The five cross-sections of breakwater model were used in the experiments, as shown in Figs. 2 to 6 and Table 1. As known from Figs. 2 to 6 and Table 1, the width of wave chamber, l , was changed to be 6 m and 10 m. Fig. 7 shows the profile of the model sea bed and the position of a wave recorder for offshore waves.

Void Ratios of the Slit-Type Box Wave Absorber. — The void ratios of the slotted vertical front-wall and slotted horizontal bottom-wall of the wave absorber were constant $\lambda = 0.24$ and $\lambda' = 0.15$, respectively (2).

Conventional Composite-Type Breakwater. — The cross-sections of conventional composite-type breakwater were made by attaching a iron plate to the sea-side of the vertical front-wall of the slit-type breakwater from the top to the bottom.

TABLE 1.- Cross-Sections of Slit-Type Break-water used in the Experiments

Cross-Section (1)	Width of wave chamber 1 in meters (2)	Top width of rubble-mound B in meters (3)	Berm (4)	Top of rubble-mound in meters (5)	Sea bottom in meters (6)	Crown of caisson in meters (7)
I	10.0	8.0	With	D.L. - 8.5	D.L. - 16.0	D.L. + 5.0
II	6.0	7.0	With	D.L. - 8.5	D.L. - 16.0	D.L. + 5.0
III	6.0	8.0	Without	D.L. - 8.5	D.L. - 16.0	D.L. + 5.0
IV	6.0	12.0	Without	D.L. - 8.5	D.L. - 16.0	D.L. + 5.0
V	6.0	6.0	Without	D.L. - 8.5	D.L. - 16.0	D.L. + 5.0

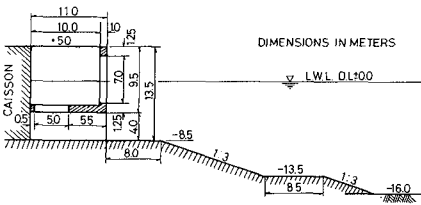


FIG. 2.- Cross-Section I

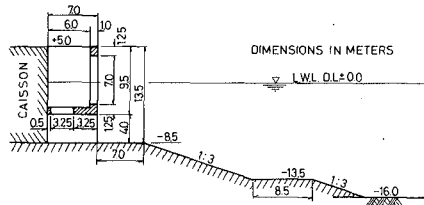


FIG. 3.- Cross-Section II

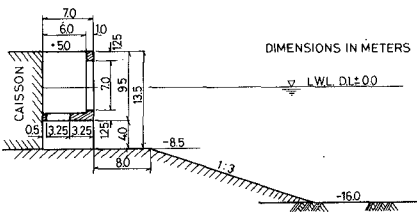


FIG. 4.- Cross-Section III

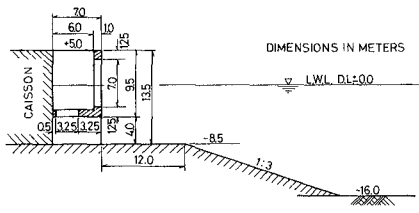


FIG. 5.- Cross-Section IV

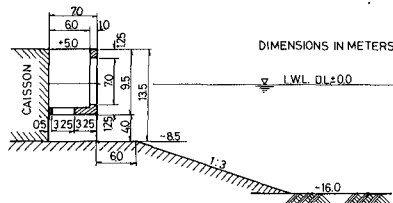


FIG. 6.- Cross-Section V

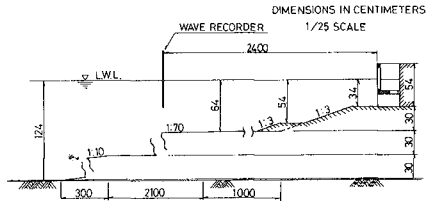


FIG. 7.- Profile of the Model

Figs. 8 and 9 show the positions of wave pressure gauges installed in the breakwater.

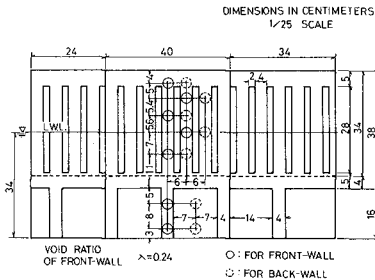


FIG. 8.- Positions of Pressure Gauges

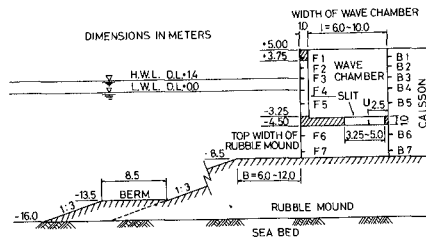


FIG. 9.- Positions of Pressure Gauges

Characteristics of Waves used in the Experiments. — The heights and periods of the waves used in the experiments were $H = 6.3$ m to 9.0 m and $T = 7.0$ sec to 14.0 sec. The wind velocity was constant 38 m/sec through the experiments. Table 2 summarizes all the conditions tested.

TABLE 2.- Conditions tested in the Experiments

Tidal level in meters (1)	Wind velocity in meters per second (2)	Incident wave		Steepness H/L (5)	Cross-Section used in experiment (6)	
		Period in seconds (3)	Wave height in meters (4)			
D.L. ± 0.00 (L.W.L.)	38	7.0	6.8	0.099	II	
			6.3	0.076	IV	
		8.0	7.0	0.084	II	
			8.0	0.096	I ~ V	
		10.0	6.9	0.062	IV	
			8.7	0.078	I ~ V	
		12.0	7.0	0.050	IV	
		9.0	0.065	III, IV		
		14.0	7.0	0.042	IV	
			8.7	0.053	I ~ V	
		0	8.0	7.8	0.094	I, II
			10.0	8.6	0.077	I, II
D.L. + 0.75	38	8.0	8.0	0.094	IV	
		10.0	8.7	0.077	IV	
		12.0	9.0	0.064	IV	
		14.0	8.7	0.051	IV	

EXPERIMENTAL RESULTS AND ANALYSIS

Maximum Simultaneous Wave Pressure and Maximum Wave Pressure Intensity for Breaking Waves. ——— Wave pressures exerted on five points of the slotted vertical front-wall (shown by F1 to F7 in Fig. 9) and on five points of the vertical solid back-wall (caisson) (shown by B1 to B7 in Fig. 9) were simultaneously measured. The maximum simultaneous wave pressures exerted on the slotted vertical front-wall and those on the solid back-wall do not simultaneously occur, and the former always occurred earlier than the latter. However, when the intensity of the wave pressure was small, the change of the maximum simultaneous pressures in a short time was so little that both maximum simultaneous pressures may be approximately considered to simultaneously occur. Therefore, for such cases the sum of both maximum simultaneous pressures was taken as the maximum simultaneous pressure exerted on the slit-type breakwater, as denoted by $P_{e \max}(\text{slit})$ (2).

When wave pressures are so strong as in the cases of this experiment, however, the maximum simultaneous pressures change rapidly even in a short minute. The experiment showed that the resultant of the maximum simultaneous pressures exerted on the slit-type breakwater, $P_{e \max}(\text{slit})$, was the sum of the resultant of the maximum simultaneous pressures exerted on the solid back-wall (caisson) and the resultant of the pressures simultaneously exerted with those of the back-wall on the slotted front-wall. Figs. 10 to 14 show the vertical distributions of the maximum simultaneous pressures exerted by strong breaking waves on the slit-type breakwaters with the cross-sections of I to V and those on the conventional composite-type breakwaters with the same cross-sections as I to V for comparison, respectively.

The resultants of the maximum simultaneous pressures on the slit-type breakwaters, $P_{e \max}(\text{slit})$, and those on the conventional composite-type breakwaters, $P_{e \max}(\text{compos.})$ are summarized in Tables 3 to 7 for the breakwaters with the cross-sections of I to V, respectively. These tables also show the resultants of the maximum simultaneous pressures obtained by the wave pressure formulas for conventional composite-type breakwaters, $P_{c \max}(\text{compos.})$ (3). The wave pressure formulas used for breaking waves were those for composite-type breakwaters with low rubble-mounds such as $0.40 \leq h_1/h_2 < 0.75$, and the resultants of the maximum simultaneous pressures for standing waves were calculated by use of P_A' and P_A (4).

Figs. 15 and 16 summarize the ratios of $P_{e \max}(\text{slit})$ over $P_{e \max}(\text{compos.})$ and $P_{e \max}(\text{slit})$ over $P_{c \max}(\text{compos.})$ for breaking waves. It may be stated from these figures that the ratios of $P_{e \max}(\text{slit})/P_{e \max}(\text{compos.})$ for breaking waves are within 0.48 to 0.81 in Fig. 15 and the ratios of $P_{e \max}(\text{slit})/P_{c \max}(\text{compos.})$ are 0.44 to 0.77 in Fig. 16, and in most of the cases of breaking waves both the ratios are less than 0.70.

According to Figs. 10 to 14, the maximum wave pressure intensities on the slotted front-walls and the solid back-walls of the slit-type breakwaters reduce to less than 60 % of those on the conventional solid caissons of composite-type breakwaters, and the reduction of the

pressure-intensity becomes larger as the intensity of shock pressure exerted on the caisson of composite-type breakwater becomes higher.

Effect of the Width of Wave Chamber. — Comparison among the values of $P_{e \max}(\text{slit})$ in Tables 3 (for cross-section I with $l = 10$ m), 4 (for cross-section II with $l = 6$ m) and 5 (for cross-section III with $l = 6$ m) shows that the width of the wave chamber, l , has no definite and noticeable effect on the resultant of the maximum simultaneous pressures of the slit-type breakwater. Figs. 10 and 12 also show that the width of the wave chamber has a slight effect on the vertical distribution of the maximum simultaneous pressures of the slit-type breakwater.

Effect of the Top-Width of Base-Rubble-Mound. — Effect of the top-width of the base-rubble-mound of the slit-type breakwater, B , on the wave pressures was tested by changing $B = 6.0$ m (section V), $B = 8.0$ m (section III) and $B = 12.0$ m (section IV). The experimental results are listed in Tables 7, 5 and 6, respectively. According to Tables 5 to 7, it may be stated that the top-width, B , has little effect on wave pressure for the slit-type breakwater, while the effect is remarkable for the conventional composite-type breakwater.

Maximum Simultaneous Wave Pressure for Standing Waves. — The maximum simultaneous wave pressures exerted on the slit-type breakwaters by standing waves and partial standing waves were almost same as or a little less than those for conventional composite-type breakwaters, when the heights of the top of vertical wall of composite-type breakwater from the still water level, H_c , were 2.5 m to 5.6 m which were comparable to the heights of incident waves, $H = 3.3$ m to 4.3 m (2). However, in the cases where the heights of incident waves were so large as $H = 7.0$ m to 9.0 m, compared with $H_c = 5.0$ m (constant), there was caused a large quantity of wave-overtopping over the vertical walls of the composite-type breakwaters, which resulted in reduction of the resultant of the maximum simultaneous pressures, $P_{e \max}(\text{compos.})$. Therefore the values of $P_{e \max}(\text{compos.})$ measured in these cases were less than $P_{c \max}(\text{compos.})$ calculated by the wave pressure formulas of P_A' and P_A (4). Since the heights of composite waves generated at the sea-side of the slit-type breakwaters were smaller than those generated at the sea-side of the conventional composite-type breakwaters, the quantity of wave-overtopping over the slit-type breakwaters was smaller than that in the composite-type breakwaters. This fact results in some cases where $P_{e \max}(\text{slit})$ were a little larger than $P_{e \max}(\text{compos.})$ and nearly same as or slightly smaller than $P_{c \max}(\text{compos.})$ calculated by the formulas of P_A' and P_A , as shown in Tables 3 to 7.

Upward Pressure on the Slotted Bottom-Wall. — The upward pressures exerted on the slotted horizontal bottom-wall by the waves transmitted underneath the wave absorber were as large as $p_u = 4.0$ t/m² to 8.0 t/m² which were nearly same as the intensities of the horizontal wave pressures exerted at the same level as the slotted bottom-wall on the solid back-wall. However, when the trough of a receding wave came considerably down below the bottom-wall, the wave severely hit upward on the bottom-wall at the time of upward moving, and the intensities of the upward pressures reached up to $p_u = 9.3$ t/m² to 13.4 t/m² which were much larger than the intensities of horizontal wave pressures

exerted at the same level on the solid back-wall. However, when the slotted bottom-wall was installed so as to be located a little lower than the lowest trough of the design wave, the intensities of the upward pressures reduced to $p_u = 8.5 \text{ t/m}^2$ to 7.2 t/m^2 , respectively. These experimental results are shown in Table 8.

OPTIMUM CHAMBER WIDTH FOR WAVE PRESSURE

As has already been mentioned, it was proved that the change of the width of wave chamber from $l = 6.0 \text{ m}$ to 10.0 m had no definite and noticeable effect on the intensities and their vertical distributions of the maximum simultaneous wave pressures exerted on the slit-type breakwaters by breaking waves and non-breaking waves.

As known in Tables 3 to 7, all of the largest breaking wave pressures for the slit-type breakwaters with cross-sections I to V were exerted by breaking waves with periods of 8.0 sec to 10.0 sec , which had wave-lengths of $L = 83 \text{ m}$ to 112 m . Therefore, for the width of wave chamber $l = 6.0 \text{ m}$, the ratios of l/L , which was designated as relative wave chamber width, were 0.07 to 0.05 . In the previous experiments (2), largest breaking wave pressures were exerted by breaking waves with a period of 7.0 sec , which had wave lengths of $L = 61 \text{ m}$ to 66 m . Since there were no noticeable differences between the maximum simultaneous pressures exerted on the slit-type breakwaters with different widths of wave chamber, $l = 3.75 \text{ m}$ and 5.50 m , the wave chamber width was decided $l = 3.70 \text{ m}$ for the slit-type breakwater in the Port of Osaka, which has been under construction since 1977. As the period of the design wave is 7.0 sec , and its wave lengths are $L = 61 \text{ m}$ to 66 m , the ratio of l and L is about 0.06 .

Therefore it may be stated that the optimum relative wave chamber width, $(l/L)_{\text{opt}}$, is 0.05 to 0.07 , on an average 0.06 , for slit-type breakwaters. More definitely and clearly speaking for the purpose of practical design, the optimum wave chamber width, l , would be 3.70 m or so for moderate waves with heights equal to or less than about 5.0 m and periods equal to or less than about 7.0 sec , and $l = 6.0 \text{ m}$ or so for larger waves with heights larger than 5.0 m till about 10.0 m and periods larger than 7.0 sec till about 15.0 sec .

REFLECTION COEFFICIENT OF SLIT-TYPE BREAKWATER

The heights, H_C , of the composite waves, generated at one to two wave lengths offshore of the slit-type breakwaters and composite-type breakwaters, were measured by visual observation through the glass wall of the wave channel in all the experiments. The coefficients of reflection of both the breakwaters, K_R , obtained from H_C , are shown in Tables 3 to 7. The values of K_R in the slit-type breakwaters are about 0.10 to 0.30 for breaking waves, and about 0.50 to 0.70 for non-breaking waves, while K_R in the composite-type breakwaters are about 0.50 to 0.60 for breaking waves and about 0.70 to 0.80 for non-breaking waves.

Fig. 17 shows relationships between K_R and T as well as K_R and l/L for the cross-section V of breakwater ($l = 6.0$ m) when the incident waves are $H_I = 8.0$ m to 9.0 m. The theoretical curve shown in Fig. 17 was obtained so as to $K_R = 0.20$ at $l/L = 0.15$.

CONCLUSIONS

It may be stated that the most outstanding characteristics of the slit-type breakwater, which denotes a special composite-type breakwater attached a slotted box-type wave absorber to the sea-side vertical wall of the caisson near the still water level, is to be able to reduce the resultants $P_{e \max}(\text{slit})$ of the maximum simultaneous shock pressures exerted by breaking waves to less than 70 % of those exerted on the conventional composite-type breakwaters, $P_{e \max}(\text{compos.})$, or $P_{c \max}(\text{compos.})$ which denotes the resultant of the maximum simultaneous pressures calculated by the wave pressure formulas for breaking waves (3). The point of action of these resultant pressures should be taken at the still water surface. The effect of width, l , of the wave chamber of the box-type wave absorber on the wave pressures is not so sensible as the effect on reflection coefficient, and the optimum relative chamber width, l/L , would be 0.05 to 0.07, on an average 0.06. It may be stated, therefore, for practical design that the optimum chamber width, l , would be 3.70 or so for moderate design waves with heights equal to or less than about 5.0 m and periods equal to or less than 7.0 sec, and $l = 6.0$ m or so for larger waves with heights larger than 5.0 m till about 10.0 m and periods larger than 7.0 sec till about 15.0 sec.

For non-breaking waves the $P_{e \max}(\text{slit})$ could be obtained from $P_{c \max}(\text{compos.})$, which denotes the resultant of the maximum simultaneous pressures calculated by the wave pressure formulas for non-breaking or standing waves (3) (4).

The top of the slotted vertical front-wall of the slit-type breakwater should be taken at the same level as the crown of the solid caisson wall for ordinary cases, and the slotted horizontal bottom-wall be installed at such a level as a little lower than the lowest trough of the design wave at the slit-type breakwater to avoid high upward pressures exerted from underneath the bottom-wall.

The void ratio of the slotted vertical front-wall should be $\lambda = 0.24$ or so and that of the slotted horizontal bottom-wall be $\lambda' = 0.15$ or so.

The coefficients of reflection, K_R , of the slit-type breakwaters which have the optimum chamber width, l , as described here, and the void ratios of $\lambda = 0.24$ and $\lambda' = 0.15$ are about 0.10 to 0.30 for breaking waves and about 0.50 to 0.70 for non-breaking waves. These values of K_R are smaller than about 0.50 to 0.60 for breaking waves and about 0.70 to 0.80 for non-breaking waves in the conventional composite-type breakwaters.

TABLE 3.- Comparison of the Maximum Simultaneous Pressures on a Slit-Type and a Composite-Type Breakwater (Cross-Section I)

Chamber width l=10.0 m, Top of base rubble-mound, D.L.-8.5 m, Top width of base rubble-mound, B=8.0 m, $w_0=1.03 \text{ t/m}^3$, With berm

tidal level in meters (1)	Wind velocity in meters per second (2)	Incident wave			H/L (6)	Height of composite wave in meters (7) (8)		Coefficient of reflection KR (9) (10)	Max. result. wave pressures in tons per meter (11) (12)		Slit-type $P_{e \text{ max}}(\text{slit})$ in tons per meter (13)	Ratios of wave pressure $P_e \text{ max}(\text{slit}) / P_{e \text{ max}} / P_{c \text{ max}}$ (14) (15)		Upward pressure P_u in tons per square meter (16)
		Wave height H in meters (4)	Wave length L in meters (5)	HC		Solid Slit	$P_{c \text{ max}}$ in tons per meter		$P_{e \text{ max}}$ in tons per meter	$P_e \text{ max}(\text{slit})$		$P_e \text{ max}(\text{slit}) / P_{e \text{ max}}$	$P_{c \text{ max}} / P_{e \text{ max}}$	
D.L.+0 (L.W.L.)		8.0	83.4	0.096	12.6	8.8	0.58	0.10	124.4*	133.6**	84.4	0.68	0.63	4.6 ~ 6.0
	38	8.7	111.8	0.078	14.8	11.3	0.70	0.30	170.0*	162.8**	89.7	0.53	0.55	5.8 ~ 7.0
		14.0	8.7	165.7	0.053	15.2	12.1	0.75	0.39	101.3	132.9 (A')	133.7	1.32	1.01
		8.0	83.4	0.094	12.6	8.6	0.62	0.10	101.5*	130.3**	73.4	0.72	0.56	4.0 ~ 4.9
	0	8.6	111.8	0.077	14.8	10.9	0.72	0.27	140.3*	161.0**	83.8	0.60	0.52	5.6 ~ 7.3
		14.0	8.6	0.052	15.1	12.0	0.76	0.40	93.7	131.3 (A')	106.7	1.14	0.81	6.1 ~ 7.6

* : denotes breaking wave pressure measured

** : denotes breaking wave pressure calculated

(A') : denotes the resultant of the max. simultaneous pressures calculated by the formula P_A'

TABLE 4.- Comparison of the Maximum Simultaneous Pressures on a Slit-Type and a Composite-Type Breakwater (Cross-Section II)

Chamber width l=6.0 m, Top of base rubble-mound,D.L.-8.5 m, Top width of base rubble-mound,B=7.0 m, $w_0=1.03 \text{ t/m}^3$, With berm

Tidal level in meters (1)	Wind velocity in meters per second (2)		Incident wave		H/L (6)	Height of composite wave in meters (7)		Coefficient of reflection KR (9)		Max.result.wave pressures (11)			Ratios of wave pressure (14)		Upward pressure Pu in tons per square meter (16)		
	Period T in seconds (3)	Wave height H in meters (4)	Wave length L in meters (5)	Pc in meters (8)		Solid Slit (9)	Fe max in tons per meter (11)	Pc max in tons per meter (12)	Pe max (slit) in tons per meter (13)	Pe max (slit) / Pe max (14)	Pc max / Pc max (15)						
				7.0	6.8	68.7	0.099	10.2	8.1	0.50	0.19	96.5*	91.3**	70.4	0.73	0.77	-
			8.0	7.0	83.4	83.4	0.084	11.8	8.6	0.69	0.23	117.8*	99.8**	72.5	0.62	0.73	-
	38		8.0	8.0	83.4	83.4	0.096	12.8	10.3	0.60	0.29	142.8*	128.2**	78.7	0.55	0.61	5.5
D.L.± 0 (L.W.L.)			10.0	8.7	111.8	111.8	0.078	14.6	13.3	0.68	0.53	134.2*	152.0**	109.1	0.81	0.72	7.5
			14.0	8.7	165.7	165.7	0.053	15.5	14.6	0.78	0.68	113.5	132.9 (A')	137.6	1.21	1.04	8.1
			8.0	7.8	83.4	83.4	0.094	11.9	10.3	0.53	0.32	160.6*	125.0**	76.6	0.48	0.61	4.7
	0		10.0	8.6	111.8	111.8	0.077	14.6	13.7	0.70	0.59	147.4*	150.3**	96.4	0.65	0.64	6.1
			14.0	8.6	165.7	165.7	0.052	15.4	14.3	0.79	0.66	106.0	131.3 (A')	133.6	1.26	1.02	8.0

* : denotes breaking wave pressure measured

** : denotes breaking wave pressure calculated

(A') : denotes the resultant of the max. simultaneous pressures calculated by the formula P_A'

TABLE 5.— Comparison of the Maximum Simultaneous Pressures on a Slit-Type and a Composite-Type Breakwater (Cross-Section III)

Chamber width l=6.0 m, Top of base rubble-mound, D.L.-8.5 m, Top width of base rubble-mound, B=8.0 m, $w_0=1.03 \text{ t/m}^3$, Without berm

Tidal level in meters (1)	Wind velocity in meters per second (2)	Incident wave		H/L (6)	Height of composite wave Hc in meters (7)		Coefficient of reflection KR		Max. result. wave pressures			Ratios of wave pressure		Upward pressure Pu in tons per square meter (16)	
		Period T in seconds (3)	Wave height H in meters (4)		Wave length L in meters (5)	Solid	Slit	Pe max in tons per meter (11)	Pc max in tons per meter (12)	Pe max (slit) in tons per meter (13)	Pe max (slit) / Pe max (14)	/Pc max (15)			
		8.0	8.0	83.4	0.096	12.4	10.1	0.55	0.26	148.5*	133.6**	102.5	0.69	0.77	5.8
D.L. † 0 (L.W.L.)	38	10.0	8.7	111.8	0.078	14.2	13.2	0.63	0.52	156.1*	162.8**	102.1	0.65	0.63	—
		12.0	9.0	139.1	0.065	14.1	13.4	0.57	0.49	131.4 (A')	136.0	122.0	0.93	0.90	—
		14.0	8.7	165.7	0.053	15.5	14.6	0.78	0.68	106.2 (A')	132.9	130.3	1.23	0.98	8.1

* : denotes breaking wave pressure measured

** : denotes breaking wave pressure calculated

(A') : denotes the resultant of the max. simultaneous pressures calculated by the formula P_A'

TABLE 6.- Comparison of the Maximum Simultaneous Pressures on a Slit-Type and a Composite-Type Breakwater (Cross-Section IV)

Chamber width l=6.0 m, Top of base rubble-mound, D.L.-8.5 m, Top width of base rubble-mound, B=12.0 m, $w_0=1.03 \text{ t/m}^3$, Without berm

Tidal level in meters (1)	Wind velocity in meters per second (2)	Incident wave			H/L (6)	Height of composite wave H_c in meters		Coefficient of reflection K_R		Max. result. wave pressures				Ratios of wave pressure		Upward pressure P_u in tons per square meter (16)
		Period T in seconds (3)	Wave height H in meters (4)	Wave length L in meters (5)		Solid Slit (7)	Slit (8)	Solid (9)	Slit (10)	Pe max in tons per meter (11)	Pc max in tons per meter (12)	Pe max (slit) in tons per meter (13)	$P_e \text{ max} / P_c \text{ max}$ (14)	$P_e \text{ max} / P_c \text{ max}$ (15)		
		8.0	6.3	83.4	0.076	10.0	7.8	0.59	0.24	91.2*	108.6**	47.6	0.52	0.44	4.0	
		8.0	8.0	83.4	0.096	12.8	10.0	0.60	0.25	166.9*	163.9**	99.3	0.60	0.61	4.9	
		10.0	6.9	111.8	0.062	11.1	9.5	0.61	0.34	111.6*	127.5**	75.6	0.67	0.59	4.9	
D.L. ± 0 (L.W.L.)	38	10.0	8.7	111.8	0.078	14.2	12.5	0.63	0.43	199.0*	186.2**	122.5	0.62	0.66	7.0	
		12.0	7.0	139.1	0.050	11.7	10.6	0.67	0.51	67.4	106.0 (A')	74.7	1.11	0.70	5.7	
		12.0	9.0	139.1	0.065	14.5	13.4	0.61	0.49	184.2*	194.8**	118.2	0.64	0.61	7.2	
		14.0	7.0	165.7	0.042	11.4	10.8	0.63	0.54	76.6	107.5 (A')	86.4	1.13	0.80	6.1	
		14.0	8.7	165.7	0.053	15.0	14.0	0.72	0.61	104.1	132.9 (A')	107.0	1.03	0.81	8.5	

* : denotes breaking wave pressure measured

** : denotes breaking wave pressure calculated

(A') : denotes the resultant of the max. simultaneous pressures calculated by the formula P_A'

TABLE 7.- Comparison of the Maximum Simultaneous Pressures on a Slit-Type and a Composite-Type Breakwater (Cross-Section V)

Chamber width l=6.0 m, Top of base rubble-mound, D.L.-8.5 m, Top width of base rubble-mound, B=6.0 m, $w_0=1.03 \text{ t/m}^3$, Without berm

Tidal level in meters (1)	Wind velocity in meters per second (2)	Incident wave		H/L (6)	Height of composite wave in meters		Coefficient of reflection K_R	Max. result. wave pressures				Ratios of wave pressure		Upward pressure P_u in tons per square meter (16)	
		Period T in seconds (3)	Wave height H in meters (4)		Wave length L in meters (5)	Hc		Solid Slit (7)	Silt (8)	Pe max in tons per meter (11)	Fc max in tons per meter (12)	Pe max (slit) in tons per meter (13)	Pe max (slit) / Pe max (14)		/Fc max (15)
		8.0	8.0	83.4	0.096	12.9	10.5	0.61	0.31	119.5*	128.2**	86.5	0.72	0.67	5.5
		10.0	8.7	111.8	0.078	15.2	13.0	0.75	0.49	97.6	97.6 (A)	102.0	1.05	1.05	-
		12.0	9.0	139.1	0.065	16.3	13.9	0.81	0.54	98.8	136.0 (A')	110.8	1.12	0.82	-
		14.0	8.7	165.7	0.053	15.3	13.7	0.76	0.57	93.8	132.9 (A')	130.9	1.40	0.99	7.9
D.L.+0 (U.W.L.)	38														

* : denotes breaking wave pressure measured

** : denotes breaking wave pressure calculated

(A) : denotes the resultant of the max. simultaneous pressures calculated by the formula P_A

(A') : denotes the resultant of the max. simultaneous pressures calculated by the formula P_A'

TABLE 8.- Up-Lift Pressures on the Bottom-Wall of Slit-Type Breakwater (Cross-Section IV)

Chamber width l=6.0m, Top of base rubble-mound,D.L.=8.5m, Top width of base rubble-mound,B=12.0m, $w_0=1.03t/m^3$, Without berm

Tidal level in meters (1)	Wind velocity in meters per second (2)	Incident wave		H/L (6)	Maximum resultant wave pressures			Upward pressure Pu in tons per square meter (10)
		Period T in seconds (3)	Wave height H in meters (4)		Wave length L in meters (5)	Solid wall		
					Pe max in tons per meter (7)	Pc max in tons per meter (8)	Pe max (slit) in tons per meter (9)	
D.L. ± 0.00 (L.W.L.)	38	8.0	8.0	0.096	166.9*	163.9**	99.3	4.9
D.L. + 0.75				0.094	-	157.1**	-	4.9
D.L. ± 0.00 (L.W.L.)	38	10.0	8.7	0.078	199.0*	186.2**	122.5	7.5
D.L. + 0.75				0.077	-	179.9**	-	7.0
D.L. ± 0.00 (L.W.L.)	38	12.0	9.0	0.065	184.2*	194.8**	118.2	13.4
D.L. + 0.75				0.064	-	191.6**	-	7.2
D.L. ± 0.00 (L.W.L.)	38	14.0	8.7	0.053	104.1	132.9	107.0	9.3
D.L. + 0.75				0.051	-	138.8	-	8.5

* : denotes breaking wave pressure measured

** : denotes breaking wave pressure calculated

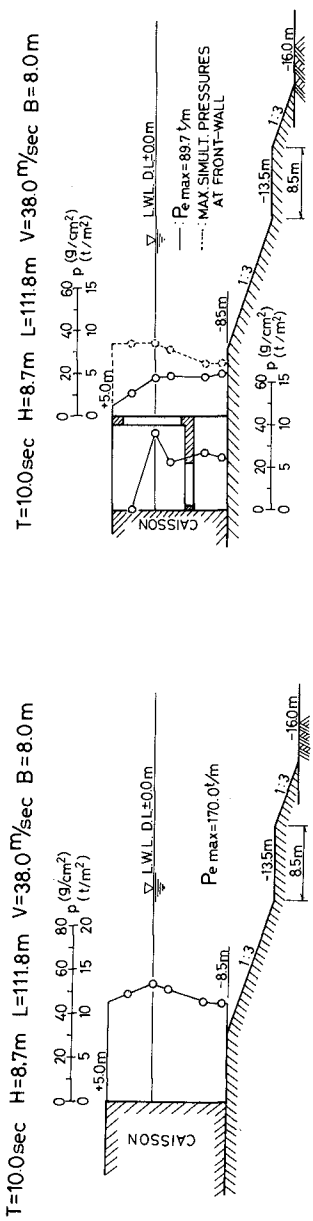


FIG. 10.- Comparison of the Maximum Simultaneous Pressures on a Slit-Type and a Composite-Type Breakwater (Cross-Section I)

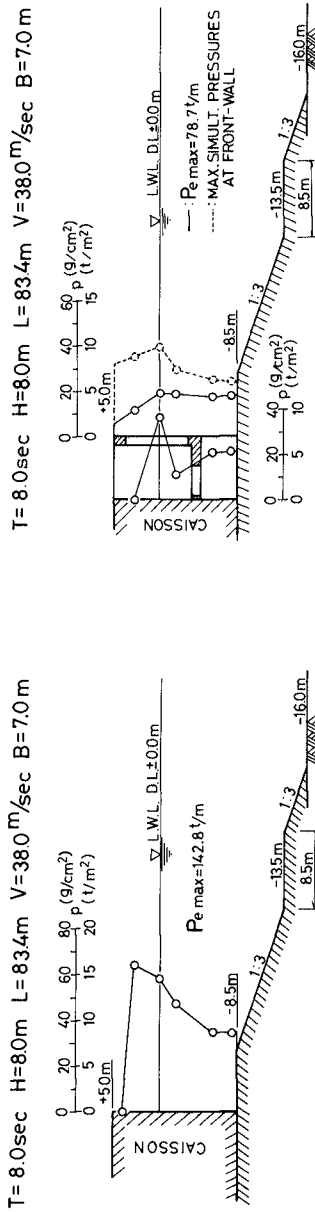
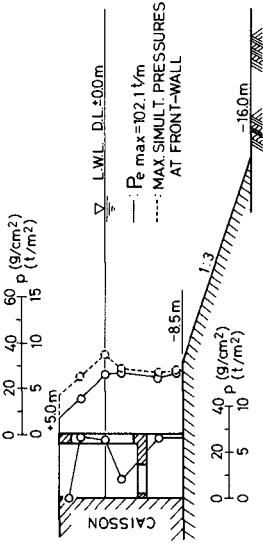


FIG. 11.- Comparison of the Maximum Simultaneous Pressures on a Slit-Type and a Composite-Type Breakwater (Cross-Section II)

T=10.0sec H=8.7m L=111.8m V=38.0^m/sec B=8.0m



T=10.0sec H=8.7m L=111.8m V=38.0^m/sec B=8.0m

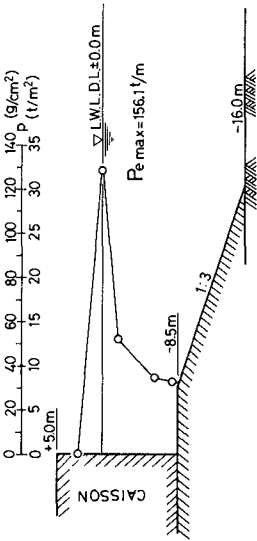
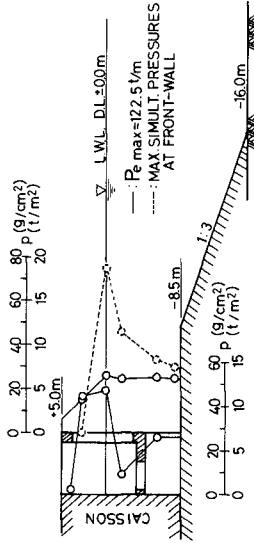


FIG. 12.- Comparison of the Maximum Simultaneous Pressures on a Slit-Type and a Composite-Type Breaker (Cross-Section III)

T=10.0sec H=8.7m L=111.8m V=38.0^m/sec B=12.0m



T=10.0sec H=8.7m L=111.8m V=38.0^m/sec B=12.0m

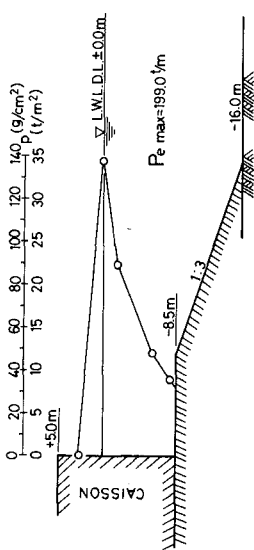


FIG. 13.- Comparison of the Maximum Simultaneous Pressures on a Slit-Type and a Composite-Type Breaker (Cross-Section IV)

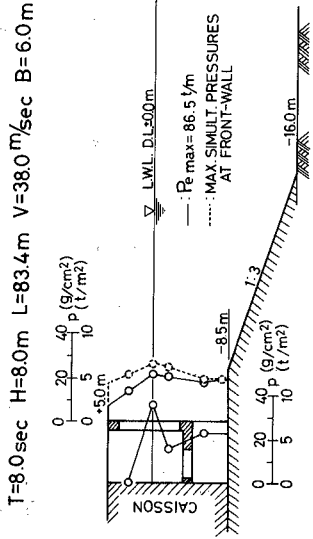
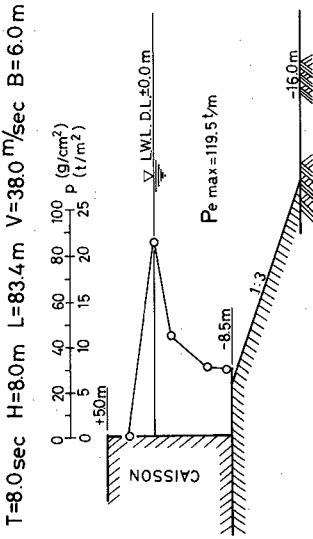


FIG. 14.- Comparison of the Maximum Simultaneous Pressures on a Slit-Type and a Composite-Type Breakwater (Cross-Section V)

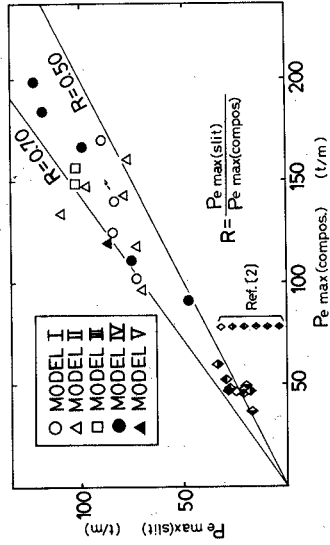


FIG. 15.- Ratio of $P_e \text{ max (slit)}$ and $P_e \text{ max (compos.)}$ (for Breaking Waves)

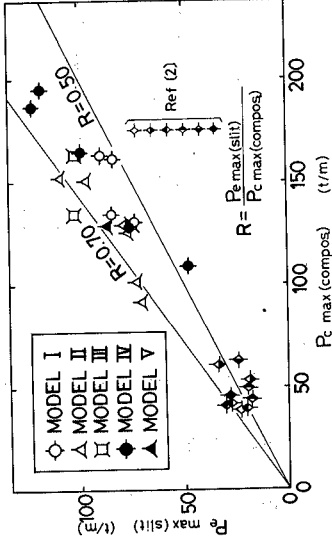


FIG. 16.- Ratio of $P_c \text{ max (slit)}$ and $P_c \text{ max (compos.)}$ (for Breaking Waves)

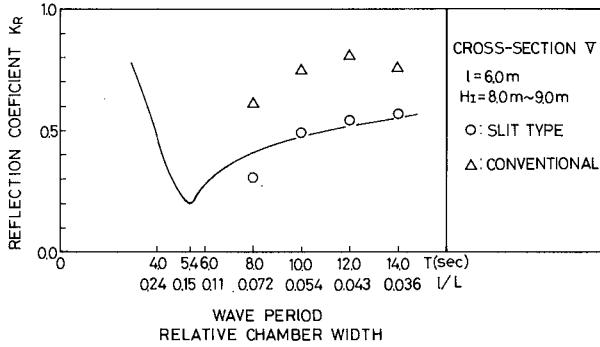


FIG. 17.- Relationships Between K_R and T (1/L)

APPENDIX - REFERENCES

1. Nagai, S., and Kurata, K., "Investigations of Wave-Pressure Formulas due to Damages of Breakwaters", Proc. of the 14th Coastal Eng. Conf., Copenhagen, June, 1974, pp. 1721 - 1740.
2. Nagai, S., and Kakuno, S., "Slit-Type Breakwater : Box-Type Wave Absorber", Proc. of the 15th Coastal Eng. Conf., Honolulu, July, 1976, pp. 2697 - 2716.
3. Nagai, S., and Otsubo, T., "Pressures by Breaking Waves on Composite-Type Breakwaters", Proc. of the 11th Coastal Eng. Conf., 1968, London.
4. Nagai, S., "Pressures of Partial Standing Waves", Journal of Waterways and Harbors Div., Proc. of ASCE., WW3, Aug., 1968.

CHAPTER 143

DYNAMIC BEHAVIOR OF VERTICAL CYLINDER DUE TO WAVE FORCE

Toru Sawaragi* and Takayuki Nakamura**

ABSTRACT

This paper describes the dynamic behavior of a fixed cylindrical pile due to both the in-line or longitudinal force and lift or transverse force in regular waves. Resonant response of the pile due to the lift force in the direction normal to the wave propagation direction is discovered at the period ratios of $T_w/T_n=2,3,4,5$ and 6 (T_w : the wave period, T_n : the natural period of the pile). Furthermore, the resonant responses in the wave propagation direction due to the in-line force also appear at the same period ratios, in addition to the well known resonance point of $T_w/T_n=1$. Moreover, dynamic displacements of the pile in the direction normal to the wave propagation direction are longer than those in the wave propagation direction when the period ratio is longer than 1.6 and Keulegan-Carpenter number is larger than 6.

Next, for the purpose of the ocean structural design, the methods of estimating the dynamic displacements in both directions and of estimating the dynamic displacements considering both are derived by using Morison's equation and lift force equation formulated by the authors. The displacements calculated are compared exactly with the experimental results to investigate the validity of the proposed method.

INTRODUCTION

In recent studies of wave force on a cylindrical pile, it has been discovered that a lift force acts on the pile in the direction normal to the wave propagation direction, in addition to a in-line force acting on the pile, as described by Morison's equation, in the wave propagation direction.

It was pointed out by Bidde¹⁾, Sarpkaya²⁾ and the authors³⁾ that the lift force has a magnitude as large as the in-line force, and that the frequency of the lift force is higher than that of the wave and the in-line force. On the other hand, considering the fact that the natural frequency (f_n) is generally higher than the wave frequency (f_w), the lift force may be important when the resonance response of a fixed off-shore structure in waves is examined. In fact, Wiegel et al⁴⁾ reported that 2-foot pile vibrates largely with the vibration period of 2.5 seconds in the direction normal to the wave propagation direction due to the alternate breaking of the large vortices under the large wave condition with the wave period being about 13 seconds. And they also reported that the test pile was broken by the lateral vibration described above.

With the above-described background, first, in this paper, the influence of lift force on the dynamic response of a cylindrical pile of cantilever type was investigated by experiments, and the effects of a period ratio (T_w/T_n) or a frequency ratio (f_w/f_n) and Keulegan-Carpenter number for the dynamic response are discussed. (T_w : the wave period and

*Professor, Department of Civil Engineering, Suita, Osaka, 565, Japan

**Assistant Professor, Department of Ocean Engineering, Ehime, Japan

equal to $1/f_w$, T_n ; the natural period of the pile and equal to $1/f_n$).

Secondly, in order to estimate the dynamic response in the in-line and normal direction, equations on dynamic displacements in two directions are derived by using the Morison's equation on the in-line force and the lift force equation formulated by the authors. Furthermore, the combined dynamic displacement is calculated, and these calculated results are compared with the experimental results.

EXPERIMENT

The wave tank used in this experiment was a 0.7m wide, 0.95m deep and 30m long wave channel at the Hydraulics Laboratory of Civil Engineering, Osaka University. A flap type wave generator was located at one end of the wave tank and a pebble beach was installed at the other end of the wave tank to absorb the wave energy.

Model cylinders used in this experiment were two kinds of cantilever type structure with a concentrated mass at its top as shown schematically in Fig. 1(A) and (B). Each model pile consisted of three parts, i.e., a concentrated mass, a circular cylinder and a spring bar. The mass was made of steel and had the same diameter as that of the cylinder. The spring bar was also made of steel and had a circular cross section with diameter of 5.5mm for the model pile of Fig. 1(A) and 5.9mm for that of Fig. 1(B). The model pile of Fig. 1(A) was fixed on the shelf in the square box made of steel with the same height as that of the horizontal flat bed. In this case, a 2.5cm cylinder made of acrylicresin was used for a circular cylinder and the water depth was kept constant at 35cm above the horizontal bed. On the other hand, the model pile of Fig. 1(B) was fixed on the channel-shaped steel having a height of 5cm that was rigidly connected to the bottom of the wave tank. In this case, a 3cm cylinder was used and the depth of the water was kept constant at 65cm above the bottom of the wave tank. The model pile of Fig. 1(A) was used only for the purpose of measuring the dynamic response in the comparatively small ranges of T_w/T_n and the one of Fig. 1(B) was used for that of T_w/T_n being large.

In this experiment, five kinds

of concentrated mass were mounted on these model piles, considering the efficiency of the wave generator and values of period ratio(T_w/T_n). The values of these masses are tabulated in Table 1(A) and (B) for the model pile of Fig. 1(A) and (B) respectively. In this table, the natural period T_n and the natural frequency f_n of the pile measured from the experiment of free vibration in water, and the logarithmic decrement δ measured from the experiment of free vibration in air are also tabulated for each mass.

In order to clarify the effects of Keulegan-Carpenter number and the period or frequency ratio on the dynamic response of the model pile, the region

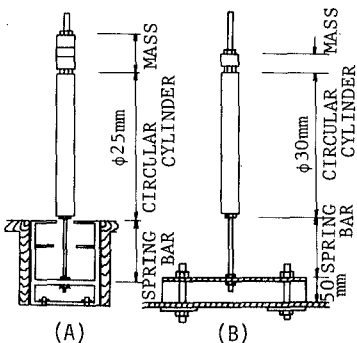


Fig. 1 Structural model of experimental cylinders

of the model ratio (T_w/T_n) wave fixed between 0.8 and 7.5, and the range of rmsK-C number (rms K-C), which is the root mean square value of Keulegan-Carpenter number at each vertical elevation of the cylinder, was from 2 to 20. The range of rms Reynolds number (rmsRe), which is the root mean square value of Reynolds number at each vertical elevation of the cylinder, was from about 2000 to 8000.

The wave condition used in this study was as follows, the wave height was fixed between 2cm and 16cm, and that of the wave period was 0.6sec to 2.3sec.

In this experiment, a 16-mm cine-camera was located right above the pile to measure the dynamic displacement at the top of it. Also the strain gages were mounted near the fixed end of the cantilever to measure the dynamic overturning moment in both directions. The wave gage used was a parallel-wire resistance type and was installed at the side of the model pile. Furthermore, in order to synchronize the 16mm-movie record with records of water surface elevation and dynamic moment, pulse signals of 10 Hz were utilized. The movie records were analyzed with an electronic graph-pen system, and then locus of the top of the model pile was reproduced with a graphic display system.

EXP. CYL.	mass (g)	T_n (sec)	f_n (Hz)	δ
(A)	0.276	0.504	1.984	0.040
	0.599	0.740	1.351	0.043
	0.914	0.930	1.075	0.045
(B)	0	0.298	3.356	0.993
	0.142	0.386	2.591	0.053

Table 1 Dynamic characteristic of the model pile

DYNAMIC BEHAVIOR OF THE MODEL PILE

1) DYNAMIC LOCUS OF THE MODEL PILE

Typical loci of the top of the model pile during one wave cycle of the incident wave (except (B-1)) are shown schematically in Fig. 2 with the frequency ratio as a parameter. In Fig. 2, the X-axis is the direction of the wave propagation direction and Y-axis is the direction normal to the wave propagation direction. From this figure, the following results are appeared. (A) : In the range of frequency ratio (f_w/f_n) larger than 0.9 (Fig. 2 (A-1) ~ (A-3)), the displacement of the top of the pile in the X direction is predominant in comparison with that in the Y direction and the locus shows a nearly straight line in the X direction. Because of the well-known resonance at $f_w/f_n=1$ due to the in-line force, the pile vibrates largely in the X direction. In this case, the frequencies of the displacements in both directions possess the wave frequency as shown in Fig. 3 (A). Here, Fig. 3 shows the time histories of the displacements in both directions and corresponds to the locus shown in Fig. 2, respectively. (B) : In the range of frequency ratio ranging from 0.6 to 0.9, the locus looks like a letter of infinity sign (∞), as shown in Fig. 2 (B-1) and (B-2). In this case, the Y-displacement has the second harmonic frequency, as shown in Fig. 3 (B), but the X-displacement has only the wave frequency. (C) ; When the frequency ratio ranges from 0.4 to 0.6, the locus is nearly a double ellipse as shown in Fig. 2 (C-1) and (C-2). In this case, the Y-displacement is much greater than the X displacement,

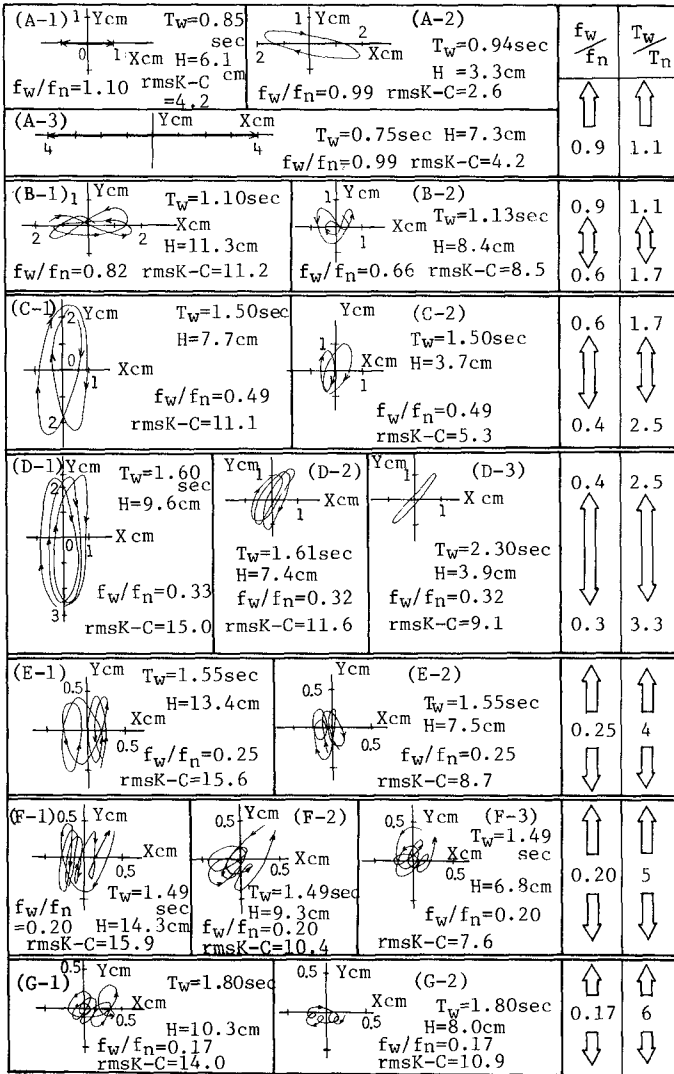


Fig.2 Loci of dynamic displacements at the top of the cylinder

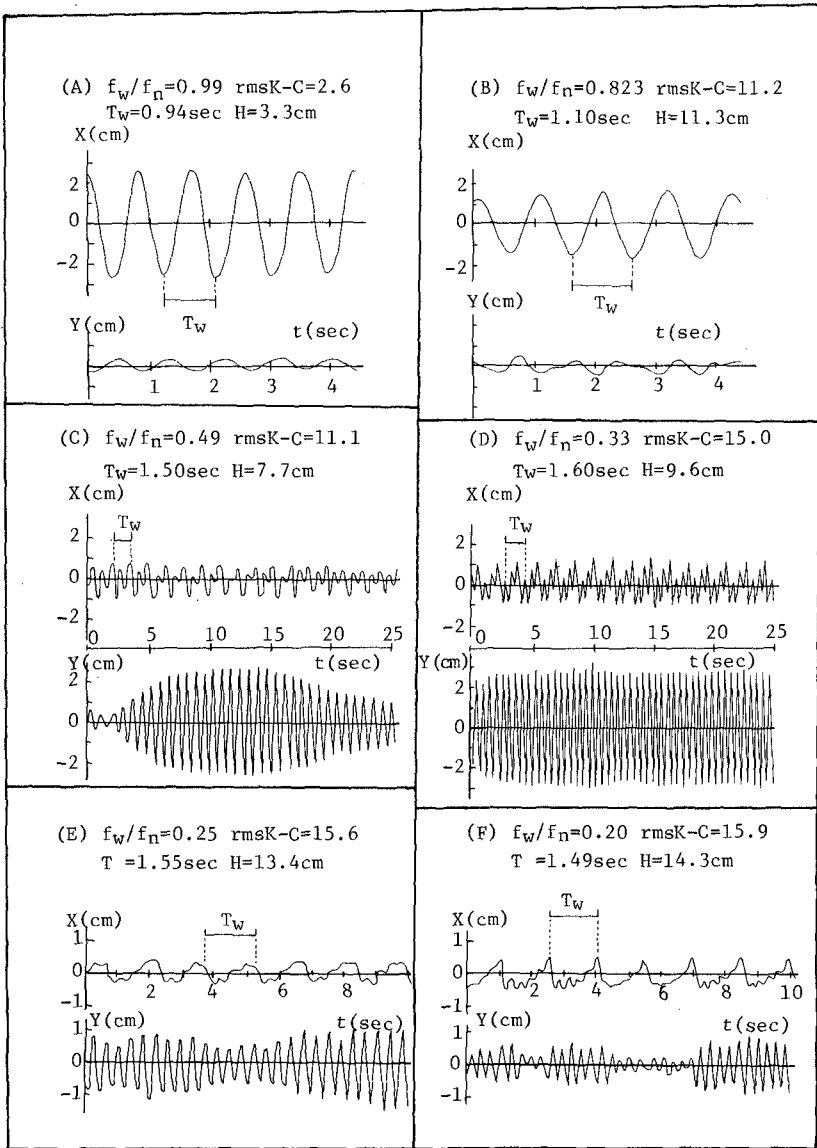


Fig. 3 Time history of the X and Y displacement

because the pile is resonated by the lift force component with the frequency two times as large as the wave frequency. Consequently, the Y displacement vibrates largely with the second harmonic frequency of the wave as shown in Fig. 3 (C). On the other hand, the X displacement has both the wave frequency and the second harmonic frequency of the wave. Since the characteristics of the lift force frequency will be given later, readers may want to refer to Fig. 6. (D) : With a frequency ratio ranging from 0.3 to 0.4 the locus shows a long ellipse and a triple ellipse as shown in Fig. 2 (D-1), (D-2) and (D-3). In this case, the pile is resonated at $f_w/f_n=1/3$ by the lift force component which corresponds to the third harmonic frequency of the wave. Therefore, the Y displacement vibrates largely with the frequency as shown in Fig. 3 (D). From this figure, it can be seen that the X displacement has also the third harmonic frequency of the wave in addition to the wave frequency, and like the case of (C), the Y displacement is larger than the X displacement. (E) : When the frequency ratio is nearly equal to 0.25, the locus is similar to the figure of a tetra ellipse and the Y-displacement has also the more significant magnitude compared with the X displacement (see Fig. 3(E)). Furthermore, the smaller the value of the frequency ratio, as shown in Fig. 2 (F-1), (F-2), (F-3), (G-1) and (G-2), the more complicated the dynamic locus becomes owing to the appearance of higher harmonic frequency components in both displacements, and in the range of frequency ratio nearly equal to $1/5$ and $1/6$, it can be seen that the Y displacement cannot be neglected in comparison with the X displacement. Here, the effect of rmsK-C on the locus is not clearly distinguishable, but the following features may be pointed out: when the frequency ratio nearly equals 1, the Y displacement appears only at comparatively small values of rmsK-C, and in the range of frequency ratio smaller than 0.9, the Y displacement decreases with decreasing values of rmsK-C and the Y displacement is equal to or smaller than the X displacement when the value of rmsK-C is comparatively small.

The reason for the higher harmonic frequency of the wave of the X displacement will be presented later.

2) RESONANT CHARACTERISTICS OF THE PILE

In order to examine the resonant characteristics of the pile due to the in-line and lift forces, the resonant curves in both directions were obtained. Fig. 4 and Fig. 5 show the resonant curves in the X and Y directions respectively with rmsK-C as a parameter. In these figures, the abscissa is the period ratio ($1/(f_w/f_n)$) and the ordinate is the so-called amplification ratio, i.e. the ratio of the dynamic displacement to the static displacement due to the wave forces. Here, the static displacements, X_s and Y_s , are calculated by means of the structural model shown in Fig. 9, and by using the Morison's equation on the in-line force and the lift force equation (Eq. 7) derived by the authors on the lift force. The linear wave theory is also used. The wave force is integrated from the bottom of the circular cylinder to the elevating water surface as a sinusoidal wave. In these figures, $X_{p/10}$ and $Y_{p/10}$ are measured one-tenth maximum dynamic displacements of X and Y respectively, since the Y displacement was irregular in regular waves as shown in Fig. 3.

From Fig. 4, it is clear that the resonant response due to a in-line

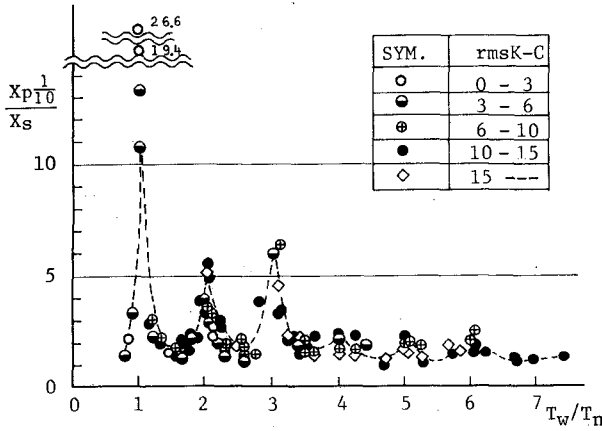


Fig. 4 amplification ratio in X-direction

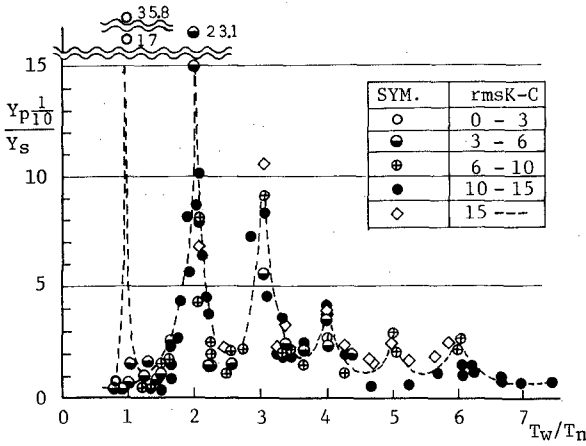


Fig. 5 Amplification ratio in Y-direction

lar cylinder in waves during one wave cycle. Here F_x and M_x are calculated by using the Morison's equation and the linear wave theory. Table 2 (I) is the result of the consideration of the effect of the finite amplitude nature, the wave force still being considered as a sinusoidal wave, i.e. the integral region of the wave force is from the bottom of the circular cylinder to the elevating water surface. On the other hand, Table 2 (II) indicates the result of neglecting the above-described effect. It is seen that F_x and M_x have higher harmonics than the wave frequency as shown in Table 2 (I) and (II). Moreover, it is clear that these components with the second harmonic frequency of the wave differ significantly between (I) and (II), but this significant difference between (I) and (II) cannot be seen when $n=3$. The non-linearity of the

force appears at the period ratios $T_w/T_n = 1, 2, 3, 4, 5$ and 6 , but there is no response at the period ratio $T_w/T_n = 7$. Among these resonances, the well-known resonance at $T_w/T_n=1$ is the most predominant, but the resonance at the period ratio $T_w/T_n = 2$ and 3 are also comparatively large.

The reason for the appearance of the response at $T_w/T_n=2$ and 3 may be due to the fact that the in-line force (F_x) and the over-turning moment (M_x) caused by the in-line force have higher frequency components than the wave based on the non-linearity of the drag force and the finite amplitude nature of the water wave. A good example illustrating this fact is presented in Table 2. This table shows the result of a harmonic analysis of F_x and M_x acting on a vertical circu-

	nf_w	(I)	(II)
F_x	n=1	18.46×10^{-3} (Kg)	18.38×10^{-3} (Kg)
	2	1.63	0.10
	3	2.13	2.08
	4	0.06	0.10
	5	0.31	0.31
	6	0.08	0.10
M_x	n=1	353.63×10^{-3} (Kg cm)	348.25×10^{-3} (Kg cm)
	2	56.03	1.89
	3	43.96	40.98
	4	3.76	1.89
	5	5.84	6.15
	6	1.29	1.89
T=1.5sec H=8cm rmsK-C=11.53 D=2.5cm			

Table 2 Harmonic analysis of F_x and M_x at $T_w/T_n=2$ and 3 are the most predominant in case of rmsK-C being larger than 3. It may be considered that these facts have a close relation with the frequency characteristics of a lift force and the magnitude as shown in Fig. 6 and 7. Fig. 6 shows the variation of the predominant non-dimensional lift energy ($S_L(nf_w)\Delta f/\sigma_L^2$, n=1-4) for each harmonic component of the wave frequency with rmsK-C. This figure was obtained by using the experimental result of the wave force on a rigidly supported vertical circular cylinder and was presented in Ref.(3), too. Here, $S_L(nf_w)\Delta f$ is the lift energy for the n-th harmonic of the wave frequency, and σ_L^2 is the variance of the lift force. From this figure, it can be seen that the predominant lift frequency equals the wave frequency in the range where rmsK-C is smaller than 3 approximately, corresponds to the second harmonic frequency of the wave in the rmsK-C range of 6 to 12, and equals the third harmonic frequency of the wave in the range of rmsK-C larger than 13, and the rest is the transition region from f_w to $2f_w$ and from $2f_w$ to $3f_w$. Fig. 7 shows the ratio of the one-tenth maximum lift force ($F_{L1/10}$) to the mean value of the maximum in-line forces (F_{Tm}) with rmsK-C as a parameter, and this figure was obtained by using the same experimental results described above. Furthermore, the experimental results of Sarpkaya⁵⁾, using the U-shaped water-tunnel, are given by the dotted line in Fig. 7. From this figure, the magnitude of the lift force increases rapidly as compared with the in-line force as rmsK-C increases (from 5 to 10) and it reaches the maximum value of 1.1 times the in-line force at rmsK-C=10.

Therefore, from the characteristics of the lift force described above, it can be considered that the resonance at $T_w/T_n=1$ in the Y-direction appears only when rmsK-C is lower than 3, due to the predominant lift force component having the waver frequency (see Fig. 6). However, this resonance can be neglected as shown later, because the magnitude of the lift force is comparatively smaller than that of the in-line force when

drag force and the effect of the finite amplitude nature of the water wave on the dynamics of the pile will be described later on in detail.

From Fig. 5, it is evident that the resonant response due to the lift force appears at the same period ratios as those in the X direction. In this case, however, the resonant condition depends on rmsK-C, i.e. the resonance at $T_w/T_n=1$ is predominant for values of rmsK-C smaller than 3, and the resonances

rmsK-C is smaller than 3 as shown in Fig. 7, and the dynamic displacement in the Y-direction is very small compared with that in the X-direction at this period ratio. Furthermore, at $T_w/T_n=2$, the resonant response appears only when rmsK-C is larger than 3, due to the predominant second harmonic frequency shown in Fig. 6. From the investigation described above, it can be concluded that the resonant characteristics of the pile due to both the in-line and the lift force have a close relation to the characteristics of the wave forces, including the frequency and magnitude of the wave force.

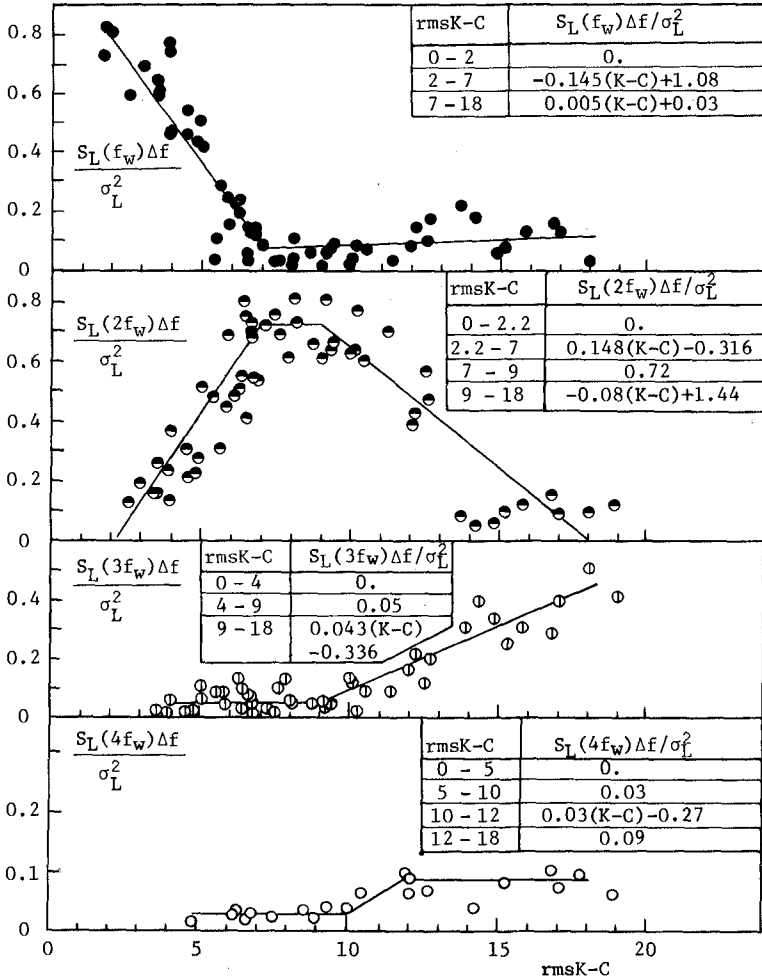


Fig. 6 Predominant lift energy versus rmsK-C

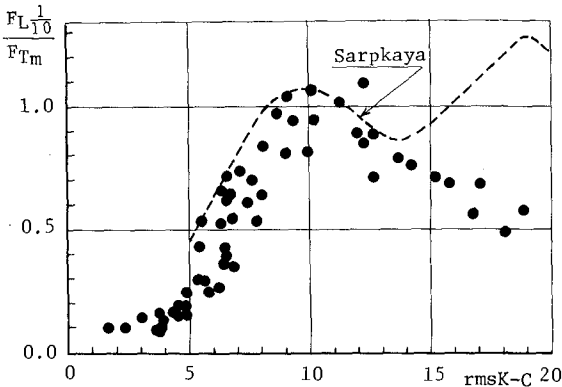


Fig. 7 Ratio of maximum one-tenth lift force to in-line force versus rmsK-C

X-displacement is predominant when the period ratio is smaller than 1.5 approximately. On the other hand, the Y-displacement is predominant in the range where the period ratio is larger than 1.5 and especially the predominance of the Y-displacement is conspicuous near the resonance points described above except at $T_w/T_n=1$, when rmsK-C is larger than 6. This reason can be given by the characteristics of the lift force as shown in Fig. 6 and Fig. 7.

Therefore, from the above-mentioned experimental results, it can be pointed out that rather than a in-line force, a lift force is the more significant force when the natural period of the structure is lower than the wave period and rmsK-C is higher than 6.

ESTIMATION OF DYNAMIC RESPONSE

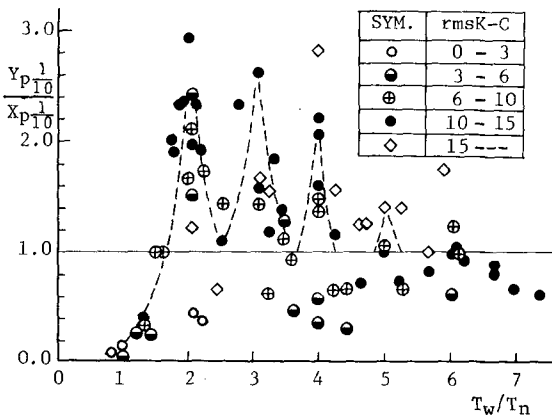


Fig. 8 Ratio of Y-displacement to X-displacement versus period ratio

3) MAGNITUDE OF THE Y-DISPLACEMENT

From the practical point of view, it may be important to know the magnitude of the Y-displacement in relation to the X-displacement. Fig. 8 shows the variation of the ratio of the Y-displacement to the X-displacement in terms of T_w/T_n . Here, the one-tenth maximum displacements in both directions are used. From this figure, it is clear that the

1) FORMULATION OF THE LIFT FORCE EQUATION

As mentioned above, the computation of a lift force is necessary in order to estimate the dynamic response of a structure due to it. However, it is difficult to formulate the lift force equation which can express the time variation of the lift force, because the lift force is generated by the alternate breaking of the eddies and it is irregular even in regular waves. Therefore,

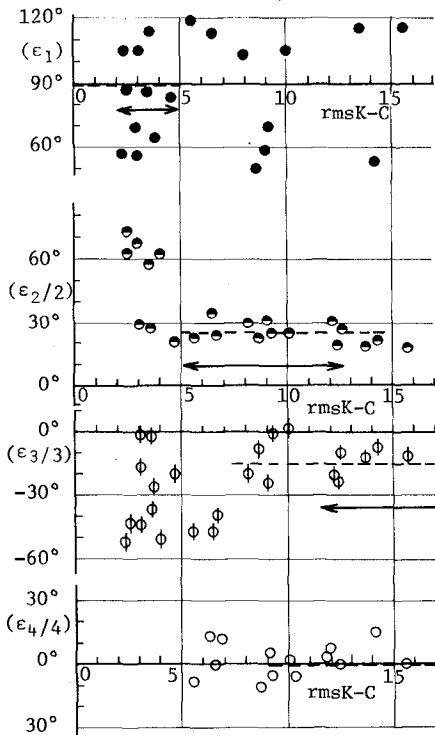


Fig. 9 Phase angle of the n-th harmonic lift force

the formulation of the lift force is performed empirically based on the experimental result of wave forces on a rigidly supported vertical circular cylinder.

It may be assumed that the formula is expressed by the superposition of each predominant frequency component of the lift force as shown in Fig. 6, given by Eq.(1).

$$f_L(t) = \sigma_L \sum_{n=1}^4 \frac{\sqrt{2S_L(nf_w)\Delta F}}{\sigma_L^n} \times \cos(2n\pi f_w t - \epsilon_n) \quad (1)$$

Here, $f_L(t)$: the lift force per unit length; $S_L(nf_w)$: the variance of the lift force; and ϵ_n : the phase angle between the n-th harmonic lift force component and the incident wave. The spectral energy of the n-th harmonic lift force may be given by the experimental result of Fig. 6. In this study, the non-dimensional n-th harmonic lift force energy is given by the empirical formula which is specified at the right side of Fig. 6, and it is shown by the solid line in this figure. Further, the phase angle was obtained by using the result of harmonic analysis of both the measured lift force and wave records. The change of phase angle with rms K-C is shown in Fig.9, in which

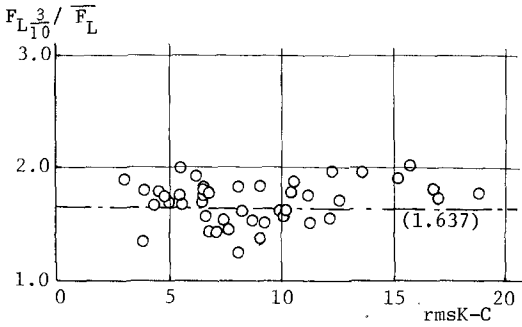
the predominant region of the n-th harmonic lift force is also shown by an arrow mark. The scattering of the experimental results is relatively large, but if attention is focussed on each predominant region ϵ_n may be considered as a constant value, i.e. $\epsilon_2/2 = 25^\circ$, $\epsilon_3/3 = -15^\circ$ and $\epsilon_4/4 = 0^\circ$. However, as ϵ_1 is scattered from 60° to 120° in the predominant region of f_w frequency, it seems to be quite all right to consider that the average value of ϵ_1 is 90° , because the magnitude of the lift force is quite small in comparison with the in-line force in the region where rmsK-C is smaller than 5, as shown in Fig. 7.

On the other hand, Chakrabalti et al⁶⁾ have presented the lift force as shown in Eq. 2.

$$f_L(t) = -\frac{1}{2} \rho D U_m^2 \sum_{n=1}^4 C_{L_n} \sin(2n\pi f_w t - \sigma_n) \quad (2)$$

Here, U_m : the maximum horizontal water particle velocity; C_{L_n} : the lift coefficient for the n-th harmonic lift force; D : the diameter of a circular cylinder; and ρ : the density of water.

Since the lift force in regular waves is irregular, $f_L(t)$ is considered as a random function of time. With the exception of C_{L_n} , the terms on the right hand side of Eq. (2) are the regular functions or constants.



Therefore, C_{Ln} must be a random variable. On the other hand, the distribution of the peak lift force is similar to the Rayleigh distribution from the authors' experiments³⁾. Fig.10 shows an example of the relation between the ratio of the significant value of the lift force and its mean value and rmsK-C. The theoretical value of this ratio based on the Rayleigh distribution is 1.637, and it is shown by a

Fig. 10 Ratio of significant lift force to mean lift force versus rmsK-C

straight line in Fig.10. As seen in this figure, the experimental values are scattered around the theoretical value independent of rmsK-C.

Moreover, the lift force spectra in the predominant region of each harmonic lift force component can be considered to be a narrow-band spectra^{3), 6)}. From the above investigations, the lift force can be assumed to be a random variable of the narrow-band Gaussian random process.

Thus, the variance of the lift force can be given by Eq. (3)⁷⁾,

$$\sigma_L^2 = E[f_L^2(t)] = \left(\frac{1}{2} \rho DU_m\right)^2 \frac{1}{2} E[C_L^2] \quad (3)$$

Here, C_L is the lift coefficient of the peak lift force and is a random variable of Rayleigh distribution. Therefore, using the following relation,

$$(C_L)_{rms} = \sqrt{E[C_L^2]} = C_{L1/10} / 1.8$$

σ_L is given by Eq. (4) from Eq. (3).

$$\sigma_L = \frac{1}{2} \rho DU_m^2 \left(\frac{C_{L1/10}}{1.8\sqrt{2}}\right) \quad (4)$$

The validity of Eq.(4) is examined by investigating Eq.(5) deduced from Eq.(4).

$$\sigma_L / \left(\frac{1}{2} \rho DU_m^2\right) = C_{L1/10} / (1.8\sqrt{2}) \quad (5)$$

Here, we express the value of the left-hand side of Eq.(5) as ξ , and that of the right-hand side of this equation as ξ' . The value of ξ can be calculated by the standard deviation of the lift force obtained from the measured lift force records. On the other hand, the value of ξ' can also be calculated by using the one-tenth maximum lift coefficient obtained semi-empirically by the authors³⁾ and is given by Eq. (6) :

$$C_{L1/10} = \begin{cases} 0.245[\text{rmsK-C}] + 0.245 & , 0 < \text{rmsK-C} < 9 \\ -0.155[\text{rmsK-C}] + 3.85 & , 9 < \text{rmsK-C} < 18 \end{cases} \quad (6)$$

If Eq.(4) is valid, ξ and ξ' have to agree with each other. This agreement of ξ and ξ' is shown in Fig. 11, from which it can be seen that ξ and ξ' agree well regardless of rmsK-C. Therefore, the lift force equation can be expressed as Eq.(7) from Eq.(2) and Eq.(4),

$$f_L(t) = \frac{1}{3.6} CL_{1/10} \rho DU_m^2 \sum_{n=1}^k \frac{S_L(nf_w)\Delta f}{\sigma_L^2} \cos(2n\pi f_w - \theta_n) \quad (7)$$

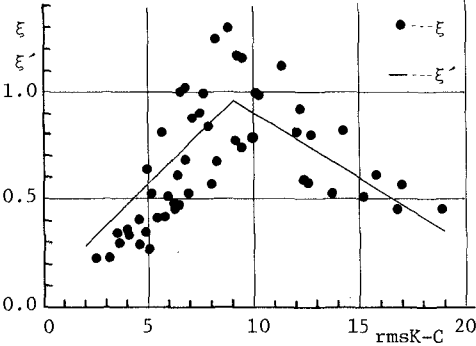
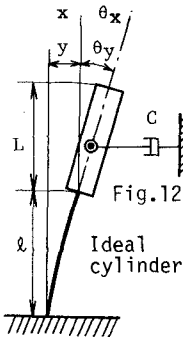


Fig.11 Comparison ξ and ξ' versus rmsK-C

placements of the top of pile, X and Y (X and Y are for the X and Y directions respectively), are given by the horizontal displacements at the bottom of the circular cylinder, x and y, and the rotation angles of the circular cylinder, θ_x and θ_y respectively. Furthermore, assuming $\sin\theta \approx \theta$, X and Y are given by Eq. (8).

$$\begin{aligned} X &= x + L \theta_x \\ Y &= y + L \theta_y \end{aligned} \quad (8)$$

Here, L : the distance from the bottom of the cylinder to the top of the pile.



In this study, the mass of the spring bar and the wave force on this bar are assumed to be negligible, because these values are very small. On these assumptions, the equation of motion of the pile in the X direction due to the in-line force may be given by Eq. (9) and Eq. (10). On the other hand, that in the Y direction may be given by Eq. (11) and Eq. (12). In these equations, it was assumed that the mutual influence between the vibrations of X and Y can be neglected.

$$\begin{aligned} (m+m_V) \frac{d^2x}{dt^2} + (m+m_V) G \frac{d^2\theta_x}{dt^2} + X \frac{dx}{dt} + G_A C \frac{d\theta_x}{dt} \\ + \frac{6EI}{l^3} (2x - l\theta_x) \end{aligned}$$

2) EQUATION OF MOTION OF THE PILE

In order to estimate the dynamic response of a single pile structure (see Fig. 1), the pile was idealized by a two-degree of freedom equivalent spring-mass system with a viscous damper as shown in Fig. 12. The idealization is based on the assumption that the rigidity of the cylinder section on Fig. 1 is much larger than that of the spring bar section, allowing to assume the circular cylinder and the concentrated mass to be a rigid body. In this case, the dis-

$$= \frac{1}{2} C_D \rho D \int_{z_L}^{h+\eta} (u - \frac{dx}{dt} - z^* \frac{d\theta_x}{dt}) | u - \frac{dx}{dt} - z^* \frac{d\theta_x}{dt} | dz + \int_{z_L}^{h+\eta} C_M \rho \frac{\pi D^2}{4} \frac{\partial u}{\partial t} dz \tag{9}$$

$$\begin{aligned} & (m + m_v) G \frac{d^2 x}{dt^2} + [I_G + I_{Gv} + (m + m_v) G^2] \frac{d^2 \theta_x}{dt^2} + G_{AC}^2 \frac{d\theta_x}{dt} + \frac{2EI}{\ell^3} (2\ell \theta_x - 3x) \\ & = \int_{z_L}^{h+\eta} z^* [\frac{1}{2} C_D \rho D (u - \frac{dx}{dt} - z^* \frac{d\theta_x}{dt}) | u - \frac{dx}{dt} - \frac{d\theta_x}{dt} | \\ & \qquad \qquad \qquad + C_M \rho \frac{\pi D^2}{4} \frac{\partial u}{\partial t}] dz \\ & + [mgG_A - \frac{\rho g \pi D^2 (h + \eta - z_L)^2}{8}] \theta_x \tag{10} \end{aligned}$$

$$\begin{aligned} & (m + m_v) \frac{d^2 y}{dt^2} + (m + m_v) G \frac{d^2 \theta_y}{dt^2} + C \frac{dy}{dt} + G_{AC} \frac{d\theta_y}{dt} + F_D \\ & \qquad \qquad \qquad + \frac{6EI}{\ell^3} (2y - \theta_y) = \int_{z_L}^{h+\eta} f_L(z) dz \tag{11} \end{aligned}$$

$$\begin{aligned} & (m + m_v) G \frac{d^2 y}{dt^2} + [I_G + I_{Gv} + (m + m_v) G^2] \frac{d^2 \theta_y}{dt^2} + G_{AC} \frac{d\theta_y}{dt} \\ & \qquad \qquad \qquad + G_{AC}^2 \frac{d\theta_y}{dt} + M_D + \frac{2EI}{\ell^3} (2\ell \theta_y - 3y) \\ & = \int_{z_L}^{h+\eta} z^* f_L(z) dz + [mgG_A - \frac{\rho g \pi D^2 (h + \eta - z_L)^2}{8}] \theta_y \tag{12} \end{aligned}$$

Here, G : distance from the lower end of the cylinder to the center of gravity including the added mass of the cylinder ; G_A : distance from the lower end of the cylinder to the center of gravity minus the added mass of the cylinder ; EI : flexible rigidity of the spring bar ; C : structural damping coefficient ; ℓ : length of the spring bar ; h : still water depth ; η : water surface elevation ; I_G : moment of inertia about the center of gravity due to the total mass minus the added mass of the cylinder ; I_{Gv} : moment of inertia about the center of gravity due to the added mass of cylinder ; C_D : drag coefficient ; C_M : mass coefficient ; u : horizontal water particle velocity ; m : total effective mass minus the added mass ; m_v : added mass of the cylinder given by Eq.(13).

$$m_v = C_v \pi \rho D (h + \eta - z_L) / 4 \quad (13)$$

In Eq.(13), C_v is the coefficient of added mass ($C_v = C_M - 1$); z_L : distance from the bottom of the water to the lower end of the cylinder; z^* : $z - z_L$; F_D and M_D are the fluid damping force and moment in the Y direction respectively, and these are given by Eq. (14) and (15).

$$F_D = \int_{z_L}^{h+\eta} \frac{1}{2} C_D \rho D \left(\frac{dy}{dt} + z^* \frac{d\theta_y}{dt} \right) \left| \frac{dy}{dt} + z^* \frac{d\theta_y}{dt} \right| dz \quad (14)$$

$$M_D = \int_{z_L}^{h+\eta} \frac{1}{2} C_D \rho D z^* \left(\frac{dy}{dt} + z^* \frac{d\theta_y}{dt} \right) \left| \frac{dy}{dt} + z^* \frac{d\theta_y}{dt} \right| dz \quad (15)$$

In this analysis, it is assumed that the lift force can be calculated by Eq.(7), and the values of drag and mass coefficients, C_D and C_M , assumes the following values, i.e. $C_D=1.5$ and $C_M=2.2$, based on the experimental results of the authors³⁷.

Since the equations of motion described above are nonlinear differential equations, no exact solution can be obtained. Hence, only approximate solutions can be obtained by using the numerical techniques. In this calculation, Newmark β -method⁸⁾ is used to solve the equation of motion. The value of β is selected as 1/6, which is equivalent to a linear acceleration method. The time interval, Δt , is taken as 0.005 sec, because the natural frequency of the second mode of the vibration model ranged from 31 to 35.5Hz for the five kinds of masses shown in Table 1. Taking a stationary response condition into account, the calculation time was as 15 seconds for each case.

3) CALCULATION RESULT

At first, the dynamic displacement in the X direction was computed to investigate the estimation described above (refer to Table 2). Fig. 13 shows a few examples of computation results in the X direction due to the in-line force for values of period ratio about 2 or 3. In this figure, the solid line indicates the calculated result by the method (I), which considers the effect of the finite amplitude nature of the wave, the latter being considered as a sinusoidal wave, on the in-line force, and the dotted line indicates the calculated result by the method (II), which neglects the above-mentioned effect on the in-line force. In other words the integral region of the wave force on the pile is from the lower end of the cylinder to the still water level; η in Eqs.(9) and (10) is assumed to be 0. The measured results are also shown in this figure by small circles.

From this figure, it can be seen that the calculated results by means of method (I) agree well with the measured results. On the other hand, there is much discrepancy in the frequency and magnitude of the displacement between the calculated results by method (II) and the measured results at the period ratio $T_w/T_n=2$, as shown in Fig. 13 (A) and (B). However, there is little difference between the results of methods (I) and (II) at $T_w/T_n=3$, as shown in Fig. 13 (C). From this fact, it can be considered that the resonance in the X direction at $T_w/T_n=2$ is caused by the finite amplitude nature of waves and that at $T_w/T_n=3$ is caused by the non-linearity of the drag force. Moreover, the dynamic displacement in

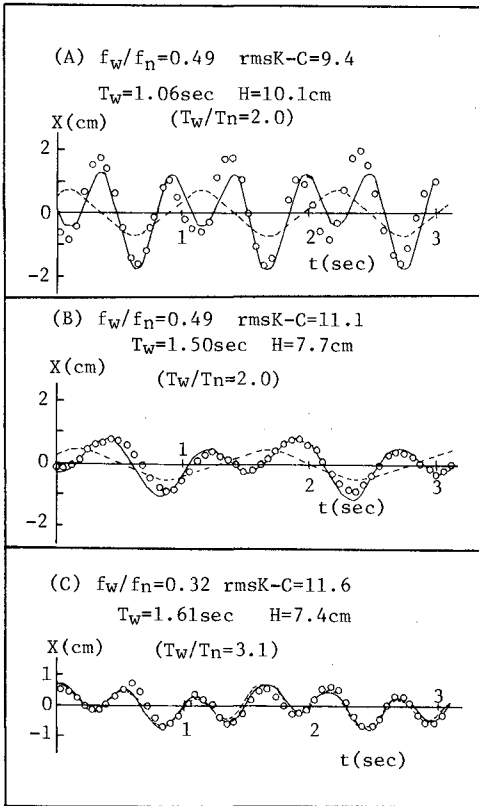


Fig. 13 Calculation results of cylinder displacement in the X direction

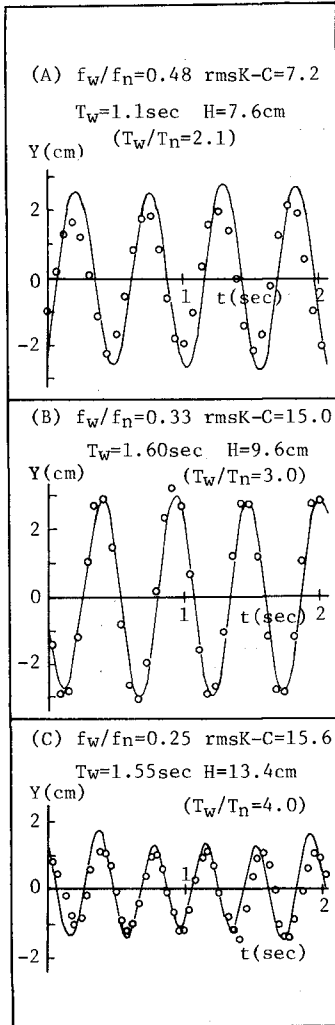


Fig. 14 Calculation results of cylinder displacement in the Y direction

the X direction for other ranges of the period ratio were computed by method (I). As a result, it was confirmed that the dynamic response in the X direction can be calculated by Eqs. (9) and (10) based on method (I) in the range where the period ratio is smaller than 6.5.

Next, the dynamic displacements in the Y direction due to the lift force were also computed by Eqs. (11) and (12) based on method (I) described above. Some examples at the resonance points in the Y direction are shown in Fig. 14. The solid line shows the calculated result and small circles denote the measured result. In this case, as the Y displacement is not regular, the displacement nearly equal to the maximum value is plotted for both the experimental and calculated results.

This figure indicates that the calculated results agree well with the measured results for each resonance point including the properties of the frequency and magnitude of the Y displacements. Therefore, it is concluded that the dynamic response in the Y direction due to the lift force can be calculated by Eqs. (7), (11) and (12).

Finally, the combined dynamic displacements of the pile were computed by composing the calculated displacements in two directions, because the maximum dynamic displacement considering both displacements is desired for an engineering design. Furthermore, comparison between the computed and measured combined dynamic responses gives the whole judgement for the validity of the estimation method of the dynamic responses in both directions. Fig. 15 shows this comparison, and the right-hand side of this figure is the calculated result while the left-hand side indicates the measured result. As in Fig. 2, the X-axis is the direction of the wave propagation direction and the Y-axis is the direction normal to the wave propagation direction. Because of the irregularity of the Y displacement, the combined dynamic displacements during one wave cycle in which the maximum combined displacement appears are plotted in Fig. 15. It is apparent that the period ratio gradually increases from (A) of $T_w/T_n \approx 1$ ($f_w/f_n \approx 1$) to (G) of $T_w/T_n \approx 5$ ($f_w/f_n \approx 1/5$). A little difference between the measured and calculated locus is observed in the case of (G), in Fig. 15. However, taking into consideration the irregularity of the Y displacement, the calculated results can safely be said to have good agreements with the experimental results. It is concluded that the combined dynamic displacement can be calculated by Eqs. (7), (9), (10), (11) and (12).

CONCLUSION

The dynamic behavior of a fixed circular pile due to the in-line and the lift forces is investigated from the theoretical and experimental stand point of view. It enabled us to arrive at the following conclusions.

First, the resonant responses of a single circular pile due to the lift force in the direction normal to the wave propagation direction are found to take place at the period ratios of $T_w/T_n = 2, 3, 4, 5$ and 6, when $rmsK-C$ is larger than 3. Furthermore, the resonant responses in the wave propagation direction due to the in-line force also appear at the same period ratios as the former case, in addition to the well known resonance at $T_w/T_n = 1$. Moreover, dynamic displacements of the cylinder due to the lift force in the direction normal to the wave propagation direction are larger than those in the wave propagation direction due to the in-line force at the above-mentioned resonance points except at $T_w/T_n = 1$, when $rmsK-C$ is

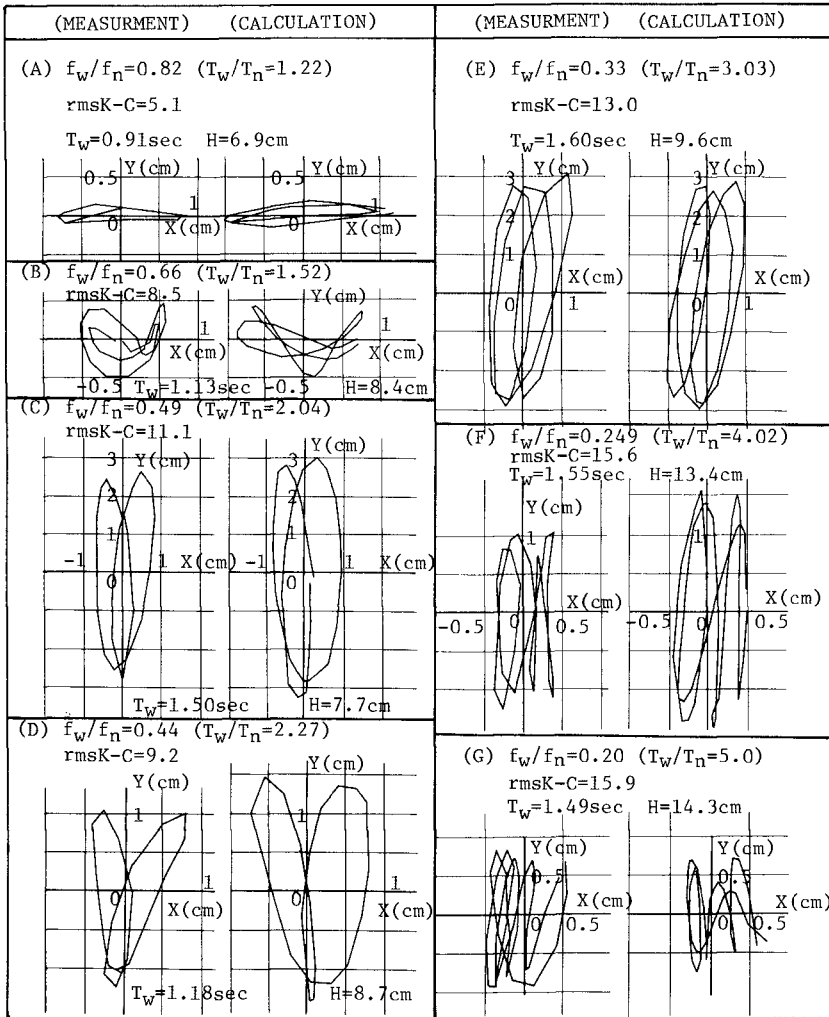


Fig. 15 Calculation results of dynamic loci

larger than 6. Therefore, the lift force is more significant than the in-line force when the natural period of the structure is smaller than the wave period and $rmsK-C$ is comparatively large.

Secondly, the dynamic displacements in both directions and the combined dynamic displacement can be calculated by applying the Morison's formula and the lift force equation to the equation of motion in each direction.

REFERENCES

- 1) Bidde, D.D.: Laboratory study of lift forces on circular piles, Journal of the Waterways, Harbors and Coastal Engineering Division, ASCE, Vol. 97, No. WW4, 1971, pp. 595-614.
- 2) Sarpkaya, T.: Forces on rough-walled circular cylinders in harmonic flow, Proc. 15th Conf. on Coastal Engineering, 1976, pp.2301-2330.
- 3) Sawaragi, T., Nakamura, T. and Kita, H. : Characteristics of lift forces on a circular pile in waves, Coastal Engineering in Japan, vol. 19, 1976, pp.59-71.
- 4) Wiegel, R.L., Beebe, K.F. and Moon, J. : Ocean wave forces on circular cylindrical piles, Journal of the Hydraulics Division, ASCE, Vol. 83, No. HY2, 1957, pp.1199-1~36.
- 5) Sarpkaya, T. : Forces on cylinders and spheres in a sinusoidally oscillating fluid, Journal of Applied Mechanics, ASME, Vol. 42, No. 1, 1975, pp.32-37.
- 6) Chakrabarti, S.K, Wolbelt, A.L. and Tom, W.A. : Wave forces on vertical circular cylinder, Journal of Waterways, Harbors and Coastal Engineering Division, ASCE, Vol. 102, No. WW2, 1976, pp.203-221.
- 7) Davenport, W.B. Jr and Root, W.L.: An introduction to the theory of random signals and noise, McGraw-Hill Inc., 1958, pp.145-175.
- 8) Biggs, J.M.: Introduction to structural dynamics, McGraw-Hill, Inc., 1964, pp.1-33.

CHAPTER 144

WAVE FORCES INDUCED BY IRREGULAR WAVES ON A VERTICAL CIRCULAR CYLINDER

Hajime Ishida

Lecturer, Department of Civil Engineering,
Kanazawa University, Kanazawa, Japan

and

Yuichi Iwagaki

Professor, Department of Civil Engineering,
Kyoto University, Kyoto, Japan

ABSTRACT

In order to examine the irregular wave forces on a small diameter cylinder, laboratory experiments have been conducted on water particle velocities and wave forces with various kinds of irregular waves. As the results, it is indicated that the time variation and the spectral distribution of wave forces can be calculated adequately from the water level variations by using the methods proposed by Reid¹⁾ and Borgman²⁾ respectively.

Moreover, with respect to the irregular wave forces on a large diameter cylinder, a new calculation method was shown by means of applying Reid's linear filters¹⁾ to MacCamy and Fuchs's diffraction theory³⁾.

INTRODUCTION

A number of studies have been done with respect to wave forces induced by periodic waves on marine structures, especially on a circular cylinder. Considering the irregularity of waves in the fields, however, it is very important to investigate the irregular wave forces systematically. In the case of periodic waves, Morison's equation and MacCamy and Fuchs's diffraction theory have been employed to estimate the wave forces respectively on a small and on a large diameter cylinder. Therefore, in the case of irregular waves, it is reasonable to investigate the wave forces by using these two methods in the same way.

Formerly, Reid has studied of the correlation of water level variations with wave forces on a circular cylinder for nonperiodic waves from the viewpoint of their time variations and indicated a method of calculation for the drag and inertia coefficients in Morison's equation. On the other hand, Borgman has shown a method of calculation for the wave force spectrum from the water level spectrum. These methods, however, have

been supported by experiments not sufficiently. As for the irregular wave forces on a large diameter cylinder, few studies have been presented till now.

Therefore, the authors have studied firstly the water particle velocities⁴⁾ in irregular waves, which play an important role in Morison's equation, and secondary the wave forces on a small diameter cylinder from the standpoints of the time variation and the power spectral distribution. Finally we show the method of calculation for irregular wave forces on a large diameter cylinder.

VELOCITIES AND ACCELERATIONS IN IRREGULAR WAVES

1-(1). Experiments

In order to investigate the water particle velocities and accelerations in irregular waves, laboratory experiments were carried out at the Department of Civil Engineering, Kyoto University.

The sketch of this experimental apparatus are shown in Fig.1. The dimension of the wave tank is 50cm wide, 70cm high and 27m long. The generator of irregular waves is installed at the end of the tank. A probe of the ultrasonic current meter shown in Photo.1 and a wave gauge were set 8m apart from the wave plate. At another end of the tank, the wave absorber was installed. The generator of irregular waves has fifteen band-pass filters which divide the frequency range $0.2 \sim 5.0$ Hz every $1/3$ oct., and therefore, irregular waves having various kinds of spectral distributions can be generated by regulating the output of each filter.

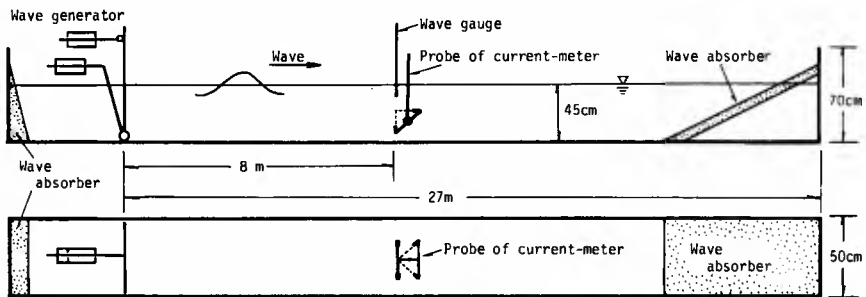


Fig.1 Schematic of experimental apparatus in the case of water particle velocity.

Photo.1 Probe of ultrasonic current meter.



1-(2). Analysis

Let the position of a wave gauge across the still water surface be taken as the origin of the coordinates, the direction of wave propagation as X-axis, and the vertical direction upward as Z-axis, respectively. If the water surface elevation of irregular waves at the position of a wave gauge is represented as

$$\eta(t) = \int_0^\infty M(\omega) \cos(\omega t - \theta(\omega)) d\omega, \dots\dots\dots (1)$$

the horizontal velocity u and vertical velocity w of a water particle, and the horizontal and vertical acceleration, \dot{u} and \dot{w} , are represented as follows¹⁾ by using the small amplitude wave theory:

$$u(t) = \int_0^\infty R_u(\omega) M(\omega) \cos(\omega t - \theta(\omega)) d\omega, \dots\dots\dots (2)$$

$$w(t) = - \int_0^\infty R_w(\omega) M(\omega) \sin(\omega t - \theta(\omega)) d\omega, \dots\dots\dots (3)$$

$$\dot{u}(t) = - \int_0^\infty \omega R_u(\omega) M(\omega) \sin(\omega t - \theta(\omega)) d\omega, \dots\dots\dots (4)$$

$$\dot{w}(t) = - \int_0^\infty \omega R_w(\omega) M(\omega) \cos(\omega t - \theta(\omega)) d\omega, \dots\dots\dots (5)$$

in which ω is the angular frequency, θ is the initial phase, $M(\omega)$ corresponds to the amplitude spectrum, and $R_u(\omega)$ and $R_w(\omega)$ are given by

$$R_u(\omega) = \frac{\omega \cosh k(h+z)}{\sinh kh}, \dots\dots\dots (6)$$

$$R_w(\omega) = \frac{\omega \sinh k(h+z)}{\sinh kh}, \dots\dots\dots (7)$$

$$\omega^2 = gk \tanh kh, \dots\dots\dots (8)$$

in which h is the water depth and k is the wave number.

Eqs. (6) and (7) give the theoretical frequency response functions of u and w to η , while experimental values of them are calculated from

$$R_u = \sqrt{\frac{S_u(\omega)}{S_\eta(\omega)}}, \dots\dots\dots (9)$$

$$R_w = \sqrt{\frac{S_w(\omega)}{S_\eta(\omega)}}, \dots\dots\dots (10)$$

in which $S_\eta(\omega)$, $S_u(\omega)$ and $S_w(\omega)$ are the power spectra of η , u and w respectively.

In order to calculate the time variations of u and \dot{u} from η , Reid proposed the following symmetrical and asymmetrical linear filters¹⁾:

$$G_s[y(t)] = a_0 y(t) + \sum_{n=1}^N a_n [y(t+n\tau) + y(t-n\tau)], \dots\dots\dots (11)$$

$$G_a[y(t)] = \sum_{n=1}^N b_n [y(t+n\tau) - y(t-n\tau)], \dots\dots\dots (12)$$

in which a_n and b_n are Fourier coefficients of their frequency response functions. Substituting $\eta(t)$ of Eq.(1) into $y(t)$ in Eqs.(11) and (12), they are deduced as follows:

$$G_s[\eta(t)] = \int_0^\infty [a_0 + 2 \sum_{n=1}^N a_n \cos n\omega\tau] M(\omega) \cos(\omega t - \theta(\omega)) d\omega, \dots\dots\dots(13)$$

$$G_a[\eta(t)] = - \int_0^\infty [2 \sum_{n=1}^N b_n \sin n\omega\tau] M(\omega) \sin(\omega t - \theta(\omega)) d\omega \dots\dots\dots(14)$$

Comparing Eq.(1) with Eqs.(13) and (14), it is found that G_s produces no phase change and has the frequency response function $[a_0 + 2 \sum_{n=1}^N a_n \cos n\omega\tau]$, and that G_a changes the phase by $\pi/2$ and has $[2 \sum_{n=1}^N b_n \sin n\omega\tau]$ as the frequency response function. It is also seen by comparing Eqs.(2) to (5) with Eqs.(13) and (14) that the time variations of required variables can be calculated from the water level variation $\eta(t)$ by selecting one of the frequency response functions and filters as shown in Table 2. In the calculation, $\tau=0.08$ sec and $N=25$ were adopted.

As the acceleration can not be measured directly, \dot{U} and \dot{W} are estimated by differentiating measured U and W with respect to time t . However, since the direct differentiation may enlarge errors due to noises more or less contained in measured U and W , they are differentiated after being passed through the following low-pass filter:

$$F_c(\omega) = \begin{cases} 1: \omega \leq 2\pi f_c \\ 0: \omega > 2\pi f_c \end{cases} \dots\dots\dots(15)$$

In actual calculations, this operation was carried out by using the filter G_s which has the frequency response function $\omega F_c(\omega)$. In the calculation, $f_c=4.0$ Hz, $\tau=0.08$ sec and $N=40$ were used.

Table 2 Correspondence of input, frequency response function and linear filter to output.

Input	Frequency response function	Linear filter	Output
Measured $\eta(t)$	$R_u(\omega)$	$G_s[\eta(t)]$	$u(t)$
	$\dot{R}_w(\omega)$	$G_a[\eta(t)]$	$w(t)$
	$\omega R_u(\omega)$	$G_s[\eta(t)]$	$\dot{u}(t)$
	$-\omega R_w(\omega)$	$G_s[\eta(t)]$	$\dot{w}(t)$
Measured $u(t)$	$\omega F_c(\omega)$	$G_a[u(t)]$	$\dot{u}(t)$
Measured $w(t)$		$G_a[w(t)]$	$\dot{w}(t)$

1-(3). Results and discussions

As an example, the results of Case I-10 are shown in Figs.2 through 9. In Fig.2, the power spectral densities S_η , S_u and S_w of η , u and w respectively are compared. In the frequency range for the large value of S_η , three power spectra resemble each other in shape. However, in the high frequency range (>1.5 Hz), the values of S_w become larger than those of S_u . This trend is seen in all cases. In the range of higher frequency than 2 Hz, the accuracy of the current meter becomes poor, so that the noise of the current meter can not be separated from the power of U and W .

Therefore, more detailed discussion on the characteristics of the high frequency components of u and w has no meaning.

In Figs. 3 and 4, experimental values of the frequency response functions calculated from Eqs. (9) and (10) are compared with the theoretical values by Eqs. (6) and (7) based on the small amplitude wave theory. In the low frequency range (<1.5 Hz), the experimental values agree well with the theoretical curves, but in the high frequency range (>1.5 Hz), the former becomes larger than the latter.

Fig. 5 shows an example of the time variation of measured η of irregular waves. Calculated values of u , w , \dot{u} and \dot{w} obtained by using measured η as an input to each linear filter (in Table 2) are plotted in Figs. 6 through 9. Fig. 6 shows the comparison between time variations of the measured u and the simultaneously calculated one. Both are in good agreement, but the measured value is slightly larger than the calculated one near the crest and trough. In Fig. 7, the time variation of measured w is compared with that of the simultaneously calculated one. In the vicinity of the trough the measured value is larger than the calculated one. Also the level of noise of the current meter in w is higher than that in u .

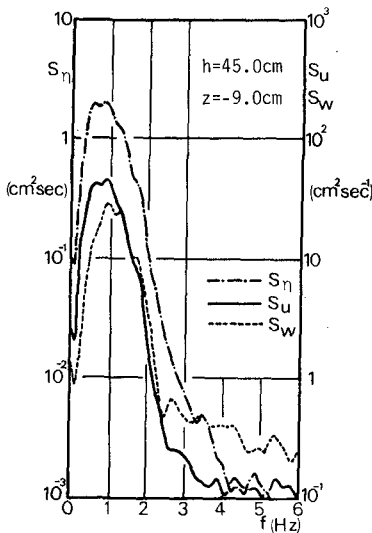


Fig. 2 Power spectral density distribution of η , u and w of irregular waves.

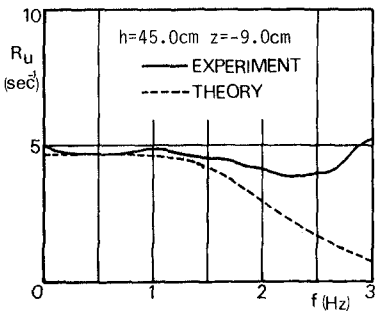


Fig. 3 Frequency response function of u to η under irregular waves.

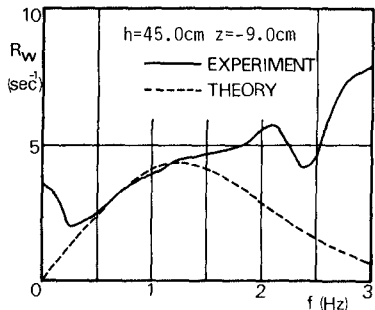


Fig. 4 Frequency response function of w to η under irregular waves.

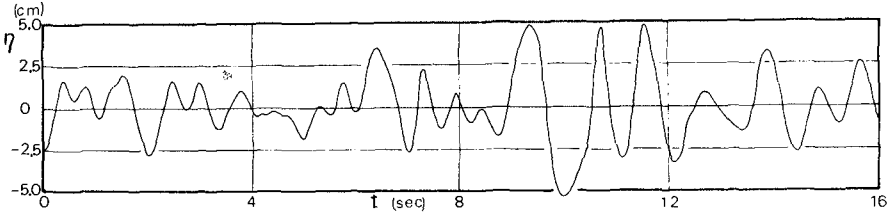


Fig. 5 Time variation of η of irregular wave.

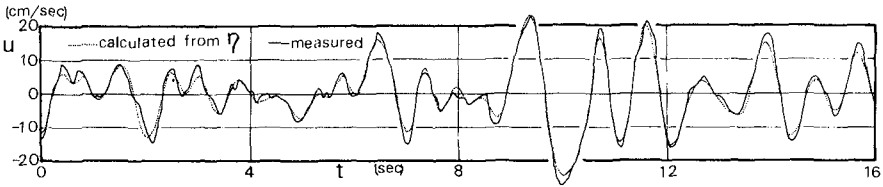


Fig. 6 Time variation of u in irregular wave.

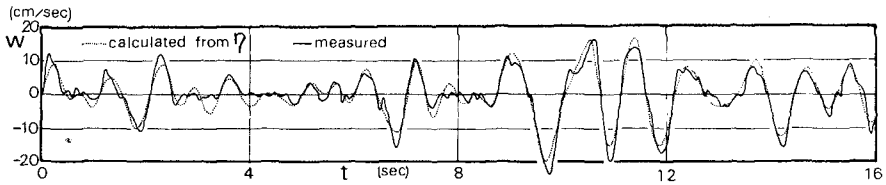


Fig. 7 Time variation of w in irregular wave.

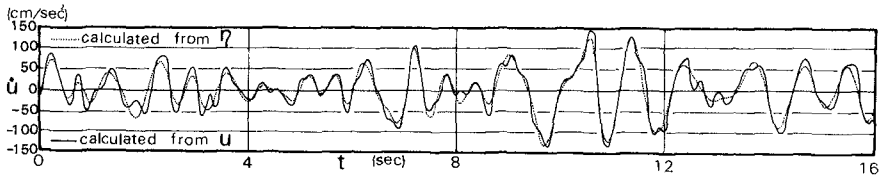


Fig. 8 Time variation of \dot{u} in irregular wave.

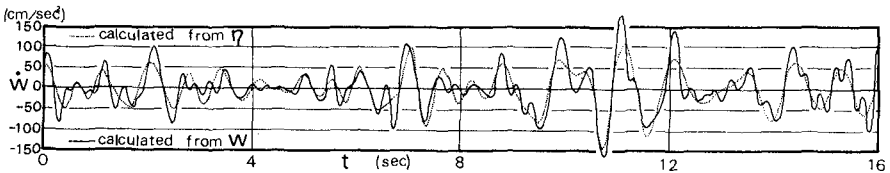


Fig. 9 Time variation of \dot{w} in irregular wave.

Fig.8 shows the comparison of the time variation of \dot{U} between that calculated from the time variation of η and that calculated from the measured U by passing it through the filter which has the frequency response function $\omega F_C(\omega)$ shown in Table 2. Both are in fairly good agreement, and however, since the measured U contains some noises, high frequency disturbances are seen in the curve of \dot{U} calculated from the measured U , even though it is passed through the low-pass filter $F_C(\omega)$. Fig.9 also shows the comparison of the time variation of \dot{W} between calculated from the measured η and calculated from the measured W . Higher level noises are contained in this case than in the case of U , so that the high frequency vibration in \dot{W} calculated from W is larger than that in \dot{U} calculated from U .

The discussion mentioned above is only for Case I-10. Now considering all cases of the irregular waves shown in Table 1, the following facts are obtained:

Regardless of the shape of power spectrum of water level variation, the measured value of frequency response function for the water particle velocity agrees well with the theoretical value based on the small amplitude wave theory in the low frequency range where the value of S_η is large. On the other hand, in the high frequency range, the measured value of the frequency response function becomes larger than the theoretical value. This trend is remarkable for W . This may explain the experimental fact that absolute values of measured time variations of U and W near the wave crest and trough, where the effect of high frequency components will appear, become larger than those calculated by the linear filters.

In the water particle accelerations, \dot{U} and \dot{W} , calculated from the measured U and W , there are bigger high frequency disturbances than in the case of \dot{U} and \dot{W} obtained from η . This is due to noises originally contained in measured U and W . However, relatively low noise level in U makes the difference between \dot{U} calculated by the two methods small, while the difference is big in the case of \dot{W} because of higher noise level.

The cut-off frequency of the low-pass filter, f_C , was 4.0 Hz in the calculation of Eq.(15). If we select a smaller f_C , noises are expected to be reduced. However, since the cause of the noise is a defect of the current meter itself, only the improvement of the current meter in future can solve this problem.

IRREGULAR WAVE FORCES ON A SMALL DIAMETER CYLINDER

2-(1). Experiments

In order to estimate irregular wave forces on a small diameter cylinder by using Morison's equation, laboratory experiments were carried out for 22 kinds of irregular waves in the same wave tank as mentioned in 1-(1).

The disposition of the experimental apparatus are also shown in Fig. 10. A wave gauge, the current meter and a circular cylinder were set 6m apart from the wave plate. The cylinder is 6cm in diameter and constructed of three parts, the upper and the lower cylinder and the segment with length of 4cm, as shown in Fig.11.

The data on wave forces on the segment are obtained by using the two strain gauges attached to the plate spring which suspends the segment from the upper cylinder. The natural frequency of this system in the still

water was 19.2 Hz. This frequency was so high as to avoid the experimental error caused by interactions of the segment to the waves.

In the experiment, the water depth was 45cm, and the depth of measuring point of wave forces were 10cm, 15cm and 20cm below the still water level. All of experimental data were recorded by the analog data recorder with 0.08 sec and 0.02 sec time interval.

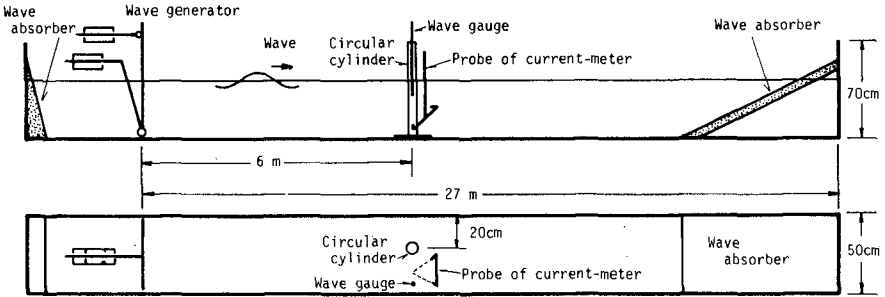


Fig.10 Schematic of experimental apparatus in the case of wave force.

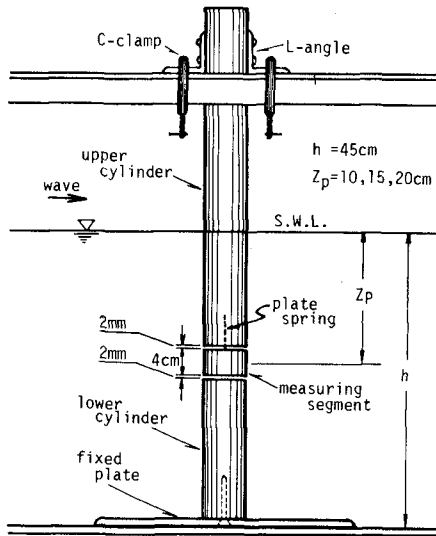


Fig.11 Schematic of circular cylinder.

2-(2). Analysis

The method of calculation for the time variation of irregular wave forces has been also shown by Reid as described below¹⁾:

Irregular wave forces as well as periodic ones can be expressed by the following Morison's equation:

$$F(t) = C_D \cdot \frac{\rho}{2} D u(t) |u(t)| + C_M \cdot \rho \frac{\pi D^2}{4} \dot{u}(t) \quad , \quad \dots\dots\dots(16)$$

in which ρ is the density, D is the diameter of cylinder, C_D and C_M are the drag and inertia coefficients respectively, and $u(t)$ and $\dot{u}(t)$ can be calculated from the following Eqs.(17) and (18):

$$C_D = \overline{F^*(t) \cdot F_1(t)} / \overline{F_1(t)^2} \quad , \quad \dots\dots\dots(17)$$

$$C_M = \overline{F^*(t) \cdot F_2(t)} / \overline{F_2(t)^2} \quad , \quad \dots\dots\dots(18)$$

These equations have been obtained by using the condition that the value of the variance between the measured wave force $F^*(t)$ and $F(t)$ of Eq.(16) is made least, in which $F_1(t)$ and $F_2(t)$ are respectively the drag and the inertia wave force in Eq.(16), and $\overline{\quad}$ indicates to take the average with respect to time t . The degree of differences between $F^*(t)$ and $F(t)$ can be known from their correlation coefficient r shown by the following equation:

$$r = \sqrt{1 - [\overline{\{F(t) - F^*(t)\}^2} / \overline{F^*(t)^2}]} \quad . \quad \dots\dots\dots(19)$$

This Reid's method was applied to all of experimental cases to obtain the values of C_D and C_M , and moreover, these values were employed to Eq.(16) to compare with $F^*(t)$ from the viewpoint of time variation. In the calculation, $\tau=0.02$ sec and $N=40$ were used.

On the other hand, the spectral distribution of wave forces, $S_F(f)$, can be calculated from the spectrum of water level variation, $S_\eta(f)$, by using the following equations obtained by Borgman²⁾:

$$S_{F1}(f) = \frac{8 d^2 \sigma^2}{\pi} S_u(f) + m'^2 S_{\dot{u}}(f) \quad , \quad \dots\dots\dots(20)$$

$$S_{F2}(f) = \frac{d^2 \sigma^2}{\pi} \left[\frac{8}{\sigma^2} S_u(f) + \frac{4}{3 \sigma^6} [S_u(f)]^{*3} \right] + m'^2 S_{\dot{u}}(f) \quad , \quad \dots\dots\dots(21)$$

$$\left. \begin{aligned} d &= C_D \cdot \frac{1}{2} \rho D \quad , \quad m' = C_M \cdot \frac{1}{4} \rho \pi D^2 \quad , \quad \sigma^2 = 2 \int_0^\infty S_u(f) df \quad , \\ [S_u(f)]^{*3} &= \int_{-\infty}^\infty [S_u(g)]^{*2} S_u(f-g) dg \quad , \\ [S_u(f)]^{*2} &= \int_{-\infty}^\infty S_u(g) S_u(f-g) dg \quad , \end{aligned} \right\} \dots\dots\dots(22)$$

in which f is the frequency, and $S_{F1}(f)$ and $S_{F2}(f)$ are respectively the first and the second approximation of wave force spectrum.

These equations were also applied to all of experimental cases and compared with the spectra, $S_{F*}(f)$, obtained from the measured wave force F^* . In the calculation of S_{F1} and S_{F2} , it is necessary to give the values of C_D and C_M , and therefore, the values obtained from Eqs.(17) and (18) were employed. As for the calculation of S_{η} and S_{F*} , the data with time interval 0.08 sec were used.

2-(3). Results and discussions

Table 3 shows the experimental cases of irregular wave forces, in which Z_p is the depth of the measuring point, (Wave freq.(Hz)) is the frequency range of band pass-filters employed to generate the waves, and C_D , C_M and r are respectively the drag, the inertia and the correlation coefficients calculated from Eqs.(17), (18) and (19) respectively. The values of C_D and C_M are respectively from 5.60 to 1.45 and from 2.30 to 1.51, and seem to become larger in both cases that Z_p is closer to the water surface and that the generated waves shown by (Wave freq.(Hz)) contain higher frequency component waves more powerfully. In irregular waves, as the measuring point become closer to the water surface, high frequency components of water particle velocities increase even if the frequency components of surface waves are not changed. Therefore, this trend may be generalized by the statement that the values of C_D and C_M increase according to increase in high frequency components of water particle velocities.

Table 3 Values of C_D , C_M and r in each experimental Case.

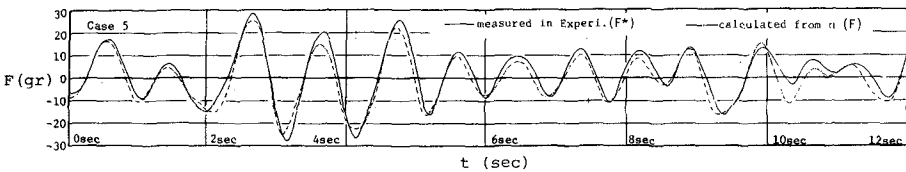
$h = 45 \text{ cm}$					
Case	z_p (cm)	Wave freq. (Hz)	C_D	C_M	r
1	-10	(0.5)	1.74	1.98	0.948
2		(0.8)	2.74	2.15	0.965
3		(1.0)	3.94	2.15	0.971
4		(1.25)	4.85	2.27	0.977
5		(0.2~1.0)	2.33	2.03	0.960
6		(0.8~1.25)	4.10	2.13	0.956
7		(0.5~1.6)	4.21	2.30	0.947
8		(0.4~2.5)	5.60	2.29	0.955
9		(0.2~5.0)	2.66	2.08	0.945
10	-15	(0.8)	2.70	1.92	0.971
11		(1.0)	2.74	1.94	0.980
12		(0.2~1.0)	2.19	1.95	0.966
13		(0.8~1.25)	2.60	2.04	0.975
14		(0.5~1.6)	2.56	2.02	0.961
15		(0.4~2.5)	2.26	1.88	0.962
16		(0.2~5.0)	2.62	1.99	0.967
17		(0.8)	1.46	1.57	0.958
18	(0.2~1.0)	1.85	1.53	0.959	
19	-20	(0.8~1.25)	2.06	1.64	0.966
20		(0.5~1.6)	2.38	1.63	0.962
21		(0.4~2.5)	1.71	1.51	0.958
22		(0.2~5.0)	1.45	1.57	0.956

The reasons why such tendencies appear are not necessarily clear now, but some discussions can be made as follows⁵⁾:

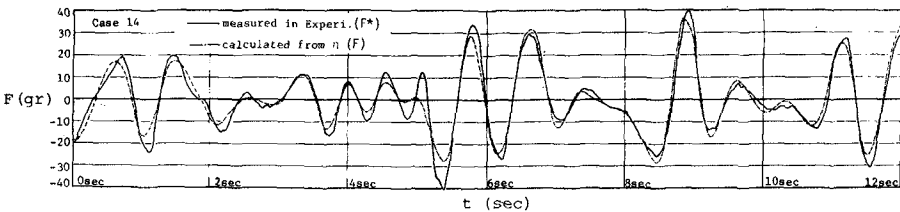
When the water particle velocities increase in high frequency components, each wave in one series of irregular waves tends to decrease the value of Keulegan-Carpenter's number⁶⁾ because smaller period of each wave is more possible. In such a case, the values of C_M become relatively larger because the reduction of the inertia force by wake vortices become smaller. Under such fluid conditions, the drag force may not become so large as to matter in practical application even if the values of C_D become large.

On the other hand, when the increase in high frequency components of velocities is caused by the increase in any nonlinearity not to be expressed by the superposition of small amplitude waves, the velocities and accelerations calculated from η by Reid's method may become a little smaller than actual ones, which may involve some risk of providing larger values of C_D and C_M . Therefore, the characteristics of C_D and C_M in irregular waves are still to be investigated.

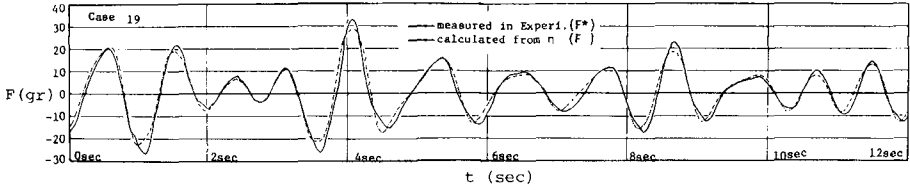
As examples of the time variation of irregular wave forces, the results of Cases 5, 14 and 19 (in Table 3) are respectively shown in Fig.12 (a), (b) and (c). The calculated wave forces F shown in chain lines agree fairly well with the measured values F^* shown in solid lines, which is also recognized from the fact that almost values of r in Table 3 are close to 1. Strictly speaking, however, F^* is slightly larger than F near the crest and trough as well as the velocity and acceleration. The difference of F from F^* is caused by not only the differences of calculated u and \dot{u} from their measured ones but also the method of calculation such that C_D and C_M are fixed to certain values over one series of irregular waves.



(a) Case 5



(b) Case 14



(c) Csaе 19

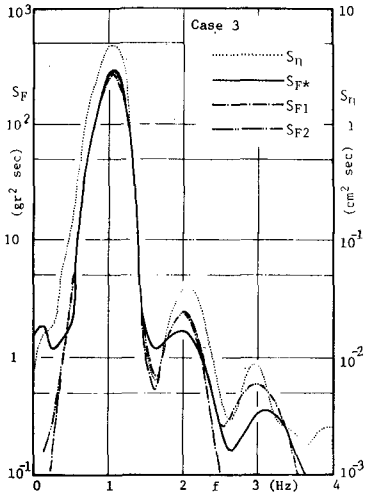
Fig.12 Time variation of wave forces, F^* and F , on small cylinder.

As examples of power spectral density distributions of wave forces, the results of Cases 3, 7, 14 and 19 (in Table 3) are shown in Fig.13(a), (b), (c) and (d) respectively. In each figure, the spectrum of the measured wave force, S_{F^*} , are shown in solid line, and the first and second approximations of theoretical spectrum, S_{F_1} and S_{F_2} , calculated from S_η by using Eqs.(20) and (21) respectively are shown in dotted lines.

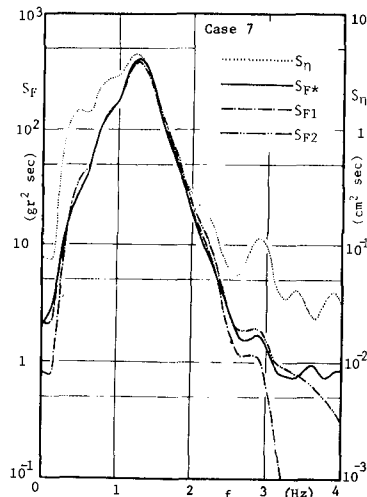
S_{F_2} contains the effect of nonlinear interactions of component waves with each other, but S_{F_1} and S_{F_2} are not so different from each other, and agree well with S_{F^*} .

Then, considering the results of all experimental cases shown in Table 3, the following facts are obtained:

The time variations of wave forces calculated from Reid's method are in fairly good agreement with the measured wave forces, and the spectral distributions of forces calculated from Borgman's method also agree well with ones obtained from the measured wave forces.



(a) Case 3



(b) Case 7

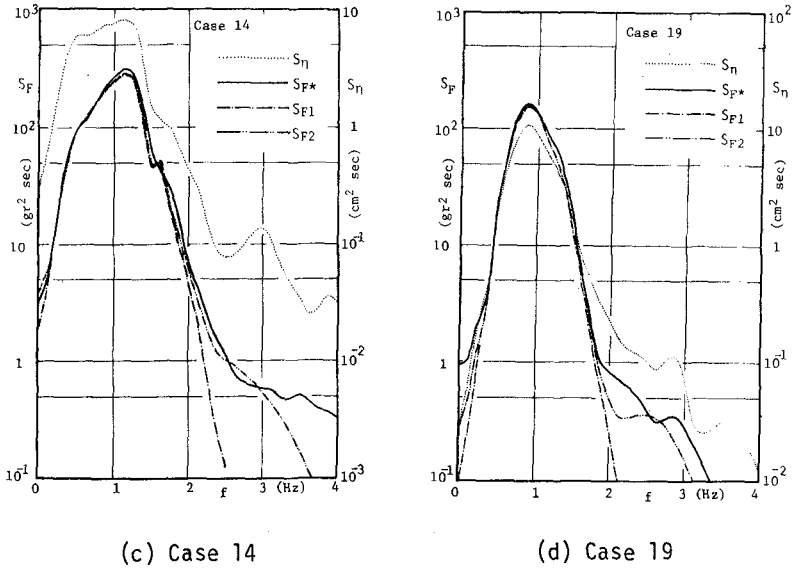


Fig.13 Power spectral density distributions, S_{F^*} , S_{F_1} , S_{F_2} and S_{η} .

IRREGULAR WAVE FORCES ON A LARGE DIAMETER CYLINDER

3-(1). Theory

The coordinate system is taken in the same way as mentioned in 1-(2), and moreover, the center axis of a cylinder is at $X=0$.

When the water level variation at $X=0$ is monochromatic as shown in Eq.(23), the induced wave force is represented as shown in Eq.(24) by MacCamy and Fuchs's diffraction theory³⁾:

$$\eta(t) = a \cos(\omega t - \delta) \quad , \quad \dots \dots \dots (23)$$

$$\begin{aligned}
 F(t) &= \text{Re} \left\{ 4 \rho g \frac{\cosh k(h+z)}{k \cosh kh} \frac{1}{H_1^{(W)}(kR)} a e^{-i(\omega t - \delta)} \right\} \\
 &= 4 \rho g \cdot C_1(\omega) \cdot a \cos(\omega t - \delta) \\
 &\quad - 4 \rho g \cdot C_2(\omega) \cdot a \sin(\omega t - \delta) \quad , \quad \dots \dots \dots (24)
 \end{aligned}$$

in which a is the amplitude, δ is the initial phase, g is the acceleration of gravity, $H_1^{(1)'}$ is the derivative of Hankel function of first kind of order 1, and C_1 and C_2 can be deduced as Eqs.(25) and (26) respectively, which become frequency response functions of wave forces to water level variations:

$$C_1(\omega) = \frac{\cosh k(h+z)}{k \cosh kh} \frac{J_1'(kR)}{J_1'^2(kR) + Y_1'^2(kR)} , \dots\dots\dots (25)$$

$$C_2(\omega) = \frac{\cosh k(h+z)}{k \cosh kh} \frac{Y_1'(kR)}{J_1'^2(kR) + Y_1'^2(kR)} , \dots\dots\dots (26)$$

in which R is the radius of the cylinder and J_1' and Y_1' denote the derivatives respectively of Bessel function of order 1 and of Neuman function of order 1.

In the next place, when the water level variation is irregular as shown in Eq.(27), the induced wave force is represented as Eq.(28) within the range of small amplitude wave theory:

$$\eta(t) = \int_0^\infty M(\omega) \cos(\omega t - \delta(\omega)) d\omega , \dots\dots\dots (27)$$

$$F(t) = 4\rho g \int_0^\infty C_1(\omega) \cdot M(\omega) \cos(\omega t - \delta(\omega)) d\omega - 4\rho g \int_0^\infty C_2(\omega) \cdot M(\omega) \sin(\omega t - \delta(\omega)) d\omega . \dots\dots\dots (28)$$

The first term in the right hand side of Eq.(28) has the same phase as Eq.(27) and the second term has the changed phase by $\pi/2$ from Eq.(27). Therefore, the time variation of wave forces can be calculated from the simultaneous water level variation by using both the symmetrical linear filter G_S which has the frequency response function $C_1(\omega)$ and the asymmetrical one G_a which has $C_2(\omega)$, as follows:

$$F(t) = 4\rho g G_S[\eta(t)] + 4\rho g G_a[\eta(t)] . \dots\dots\dots (29)$$

The validity of this calculation method were discussed by using the wave force data obtained in the experiment with the small diameter cylinder shown in 2-(1).

3-(2). Results and discussions

Figs.14 and 15 show the results obtained by applying the method shown in 3-(1) to Cases 3 and 7 shown in Table 3 respectively, in which, (a) shows the water level variation η used as the input data, and (b) shows the comparison between the measured wave force F^* and the calculated one F obtained as the output data. It is recognized from Fig.14(b) that the calculated wave force shown in chain line agrees well with the

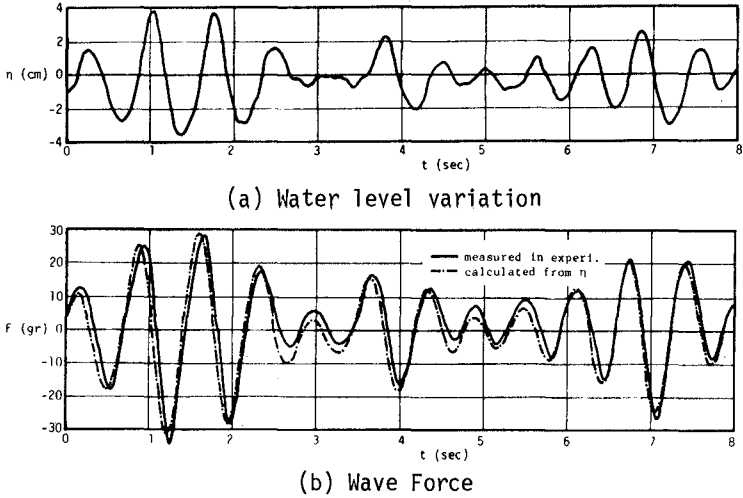


Fig.14 Time variation of wave forces on large cylinder (Case 3)

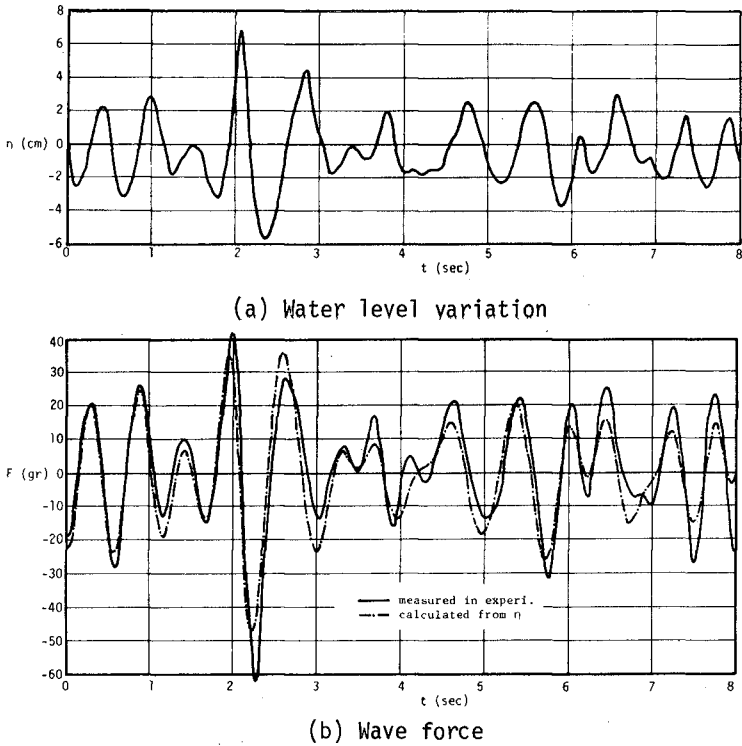


Fig.15 Time variation of wave forces on large cylinder (Case 7)

experimental one shown in solid line. This reason is considered that since the waves of Case 3 have the narrow band spectrum of which predominant frequency is relatively high value 1.0 Hz as shown in Fig.13(a), the drag force can be ignored. In another words, the difference between these two curves shows the drag force because the wave force calculated from the diffraction theory expresses only the inertia force.

On the other hand, Fig.15(b) indicates that the calculated wave force is fairl different from the experimental one because of the larger drag force. The reason of the increase in drag force may be understood from its wave spectra shown in Fig.13(b).

Now, considering the results of not only Cases 3 and 7 but also another cases, the following fact is obtained:

When the cylinder is so large in diameter that the inertia wave force is predominant to the drag one, the irregular wave forces can be estimated from only the water level variation by using this method.

CONCLUSION

The time variation of the horizontal and vertical velocities and accelerations of water particles can be predicted fairly well from the water level variation by using Reid's linear filters based on the small amplitude wave theory. Consequently, the time variation of the irregular wave forces can be adequately calculated from the water level variation by using Morison's equation in the case when the values of drag and inertia coefficients can be estimated. In such a case, also the spectral density distribution of wave forces can be calculated adequately from the spectrum of water level variation by using Borgman's method. In order to put these methods into practical application, however, the characteristics of the values of drag and inertia coefficients should be investigated from the standpoint, for example, of comparing with the results already obtained under periodic waves.

On the other hand, in such a case that each wave steepness in irregular waves becomes so large that the nonlinear characteristics can not be ignored, the linear filters may provide a little smaller values of the velocities and accelerations than the actual ones, which involve some risk of providing larger values of drag and inertia coefficients. Therefore, a certain nonlinear filters should be investigated in futuer.

Moreover, when the inertia wave force is predominant to the drag one, irregular wave forces on a cylinder can be calculated from only the water level variation by the method of applying Reid's linear filters to MacCamy and Fuchs's diffraction theory as presented in this paper.

ACKNOWLEDGEMENT

The authors wish to express their gratitude to Mr. Tetsuo Sakai, Mr. Tetsuo Senda and Mr. Yoshiteru Dobashi for their assistance through the experiments and data analysis. This work was partly supported by Scientific Research Funds from the Ministry of Education, Japan.

REFERENCES

- 1) Reid, R.O., "Correlation of water level variations with wave forces on a vertical pile for nonperiodic waves", Proc. 6th Conf. Coastal Eng., pp.749-786, 1957.
- 2) Borgman, L.E., "The spectral density for ocean wave forces", Proc. Special Conf. Coastal Eng., pp.147-182, 1965.
- 3) MacCamy, R.C. and Fuchs, R.A., "Wave forces on piles: Diffraction theory", Tech. Memo, No.69, B.E.B., pp.1-17, 1954.
- 4) Iwagaki, Y., Sakai, T. and Ishida, H., "Correlation of water particle velocity with water level variation for irregular waves", Coastal Eng. in Japan, Vol.16, pp.19-28, 1973.
- 5) Iwagaki, Y. and Ishida, H., "Flow separation, wake vortices and pressure distribution around a circular cylinder under oscillatory waves", Proc. 15th Conf. on Coastal Eng., pp.2341-2356, 1976.
- 6) Keulegan, G.H. and Carpenter, L.H., "Forces on cylinders and plates in an oscillating fluid", Jour. Res. Nat. Bur. Stand., Vol.60, No.5, pp.423-440, 1958.

CHAPTER 145

LOADING AND RESPONSE OF CYLINDERS IN WAVES

by G N Bullock¹, P K Stansby¹ and J G Warren²

1. Introduction

The nature of the wave-induced flow around a circular cylinder is to a large extent determined by the ratio of water-particle orbit size to cylinder diameter, characterized in regular waves by the Keulegan-Carpenter number KC (see Appendix II for definitions). When $D/L > 0.2$ wave scattering effects are negligible and it is conventional to describe the fluid loading in terms of drag and inertia forces in-line with the direction of wave propagation plus a transverse 'lift' force.

The idealised two-dimensional situation of a cylinder normal to planar sinusoidal flow has been investigated in U-tubes by Sarpkaya (10, 11). As KC advances above 2 vorticity starts to be shed and produces forces in addition to the inertia force which would result from the undisturbed fluid acceleration. The vortex-induced forces become more important as KC increases. Defining the drag force as the component of the in-line force in phase with the fluid velocity and the inertia force as the component in phase with the acceleration, it is found that the drag, inertia and lift can have comparable magnitudes when KC is between 8 and 25. This paper is concerned with the corresponding regime in waves.

In the idealised situation vortex shedding is almost perfectly correlated along the length of the cylinder but generally this will not be the case in waves. Here the degree of vortex coherence will influence the vortex-induced forces particularly the lift which is strongly dependent on history effects. Although the forces on fixed vertical cylinders have been measured, little is known about the loading on cylinders in general orientation in either unidirectional waves or planar flows. Real seas are further complicated by being random and multidirectional with the possibility of superimposed currents. The interaction of cylinder vibration with vortex shedding can be highly non-linear in currents, e.g see (12), but again little is known about what happens in waves.

Although scale influences the magnitude of forces when vortex shedding is important, small-scale experiments can qualitatively represent full-scale flows. Thus, the interrelation between the various parameters which influence wave loading may be studied in the relatively controlled environment of a laboratory channel. Furthermore, analysis techniques which have been justified on the model scale can then be applied with greater confidence to full-scale situations.

1. Civil Engineering Department, University of Salford, England
2. Taylor Woodrow Construction Ltd. London, England.

In this paper we consider the loading and response of small-diameter flexible cylinders with natural frequencies of vibration in excess of the dominant wave frequency. The way in which vortex shedding generates loading is illustrated by results from a mathematical model (13) and a brief review of experimental studies using fixed cylinders. This is followed by a description of an investigation in which flexible cylinders were mounted as vertical cantilevers in a laboratory wave channel. Both regular and 'random' waves were generated while structural frequencies were tuned through a range of values. Methods of predicting the in-line response are tested and the cross-flow response is evaluated.

With the test cylinder in regular waves, in-line and transverse displacements at still water level, x_0 and y_0 , depend upon

$$f_w, D, \rho, \mu, f_n, S_n, \bar{m}, \delta, t, k, d$$

Dimensional analysis gives

$$\frac{x_0}{D}, \frac{y_0}{D} = f\left(KC, Re, kd, \frac{S_n}{d}, \frac{t}{T}, \delta, \frac{\bar{m}}{\rho D^2}, Fr\right)$$

where the Reynolds number (Re) is effectively a scale parameter. In planar oscillatory flows the parameter kd , which indicates the degree of particle motion attenuation with depth, and S_n/d , which indicates the degree of wave non-linearity, both disappear.

2. Vortex Shedding in Planar Oscillatory Flows

A mathematical model of two-dimensional vortex shedding from the circular cylinder has been developed (13). Principles of potential flow are used and the separating shear layers are represented by discrete vortices. Fixing separation on the line through the cylinder centre normal to the incident velocity gives forces which are in reasonable agreement with experiment (11) at very high Reynolds numbers for $KC > 12$ (approx.). Fig. 1 shows the variation of non-dimensional in-line and lift force, $C_x(t)$ and $C_L(t)$, with time for $U = U_0 \cos(2\pi t/T)$ and $KC = 12.5$ and 18.4 . The in-line force is closely predicted by Morison's formula, $\frac{1}{2}\rho DU|U|C_D + \frac{1}{2}\rho\pi D^2 \dot{U}C_M$ with $C_D = 0.7$ and $C_M = 1.4$, even though there are complex asymmetric vortex motions which cause lift fluctuations at higher frequencies than the incident flow frequency. These vorticity patterns are sketched in Fig. 2 for $2.25 < t/T < 2.75$. The vorticity is concentrated in areas rather than at points.

The lift variations are not repetitive for the examples shown although nearly periodic forms have been observed in certain cases. This is in keeping with experimental studies at low Reynolds numbers (8). Fig. 2 shows that for $KC = 12.5$ the strong positive vortex shed in the previous half cycle moves towards the cylinder generating positive lift at $t/T = 2.25$ and 2.35 . At $t/T = 2.45$ positive vorticity rolling

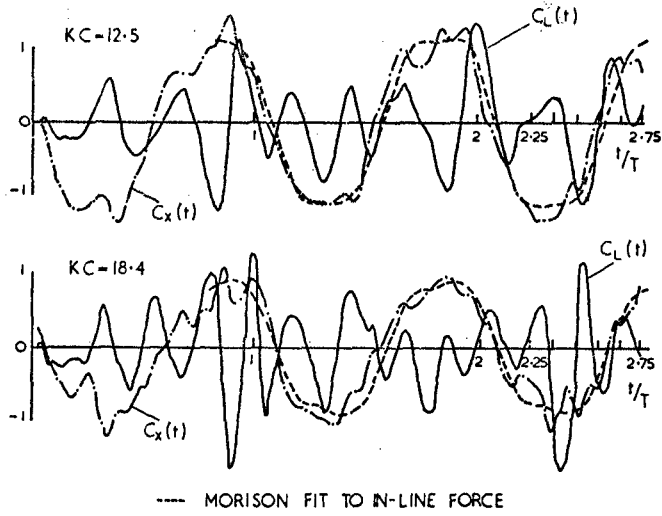


Fig. 1. Time histories of $C_x(t)$ and $C_L(t)$ from mathematical model

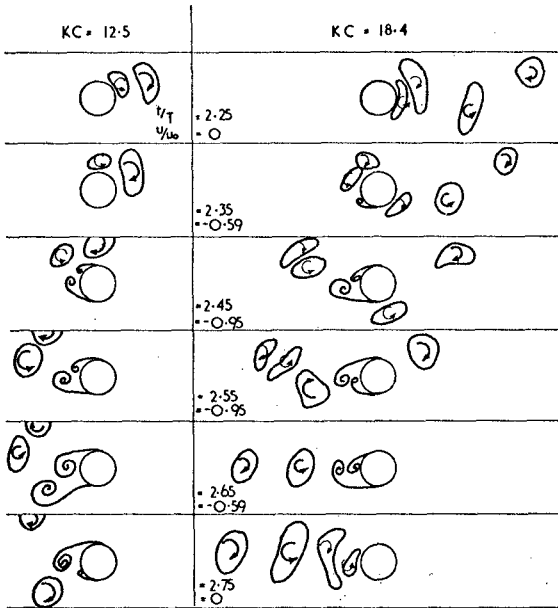


Fig. 2. Sketches of vortex movement to demonstrate generation of forces.

up close to the cylinder generates negative lift. At $t/T = 2.55$ and 2.65 negative vorticity rolling up close to the cylinder generates positive lift. By $t/T = 2.75$ two lumps of vorticity have been shed corresponding to those at $t/T = 2.25$. For $KC = 18.4$ the situation is similar, the four vortices shed causes four peaks in lift with an initial peak from the returning vorticity of the previous half cycle. The vorticity from earlier half cycles appears to have little effect. The rule that the ratio of lift frequency to flow frequency is $N + 1$ where N is the number of vortices shed per half cycle is thus demonstrated. However the rule does not always apply, particularly when N is large and the shed vortices vary considerably in strength.

3. Fixed Vertical Cylinder in Waves

Various investigators have measured wave forces on fixed vertical cylinders in laboratory wave channels. C_D and C_M have been calculated (using horizontal water-particle motions from third order wave theory) for a section close to the surface (9) and C_D values were found to be slightly greater than for planar oscillatory flows (10) with $10 < KC < 25$. Other tests (14) indicate that the use of C_D and C_M from U-tube experiments will give a good representation of local in-line forces.

Local lift forces have also been measured (2) and their Fourier components were found to be dependent on spanwise position. A non-uniform velocity distribution has been investigated in detail for a steady flow approaching a circular cylinder (7). The linear spanwise velocity variation caused vortex shedding, and hence lift frequencies to be roughly proportional to local velocity although these frequencies would be unchanged for several diameters as vortices were shed as distinct 'cells'. Thus vortex lines were not continuous throughout the depth. Such incident flows contain vorticity normal to the cylinder axis while waves are essentially irrotational. But a uniform, and hence irrotational flow incident on a tapered cylinder also produced cells of different frequency (4). It seems likely that incoherent cell structure will also occur in waves, at least when several vortices are shed per half cycle.

Lift fluctuating mainly at the wave frequency has been measured for $KC < 5$ (2) and this has not been observed in planar or other wave flows (to the writers' knowledge). This could however be due to wave non-linearity effects as vortex patterns due to the passage of a wave crest can be very different from those due to the passage of a trough (16). Local C_D and C_M values were also calculated in (2) and the high degree of scatter could in part be due to the use of linear wave theory. For $6 < KC < 14$ lift at almost entirely twice the wave frequency is in agreement with Isaacson and Maull (5) who measured the total force on the cylinder. However differences in magnitude may again be due to different non-linearity effects. For $KC > 16$ the rms lift has decreased (5) and contains several Fourier components of similar magnitude.

4. Flexible Vertical Cylinder in Waves

The present investigation was conducted in a 1.25m wide x 0.8m deep x 40m long laboratory channel with a computer-controlled, piston-type paddle at one end and a gently sloping, 10m long, 'beach' at the other (Plate 1). The beach was estimated to have a reflection coefficient that varied from 2.8% up to 5.0% over the range of wave frequencies considered. The temporal variation in water surface elevation was measured by capacitance-type wave gauges linked to the computer which was used for data collection and some analysis.

When regular waves were required the computer was programmed to adjust a sinusoidal paddle motion until waves with a specified frequency and standard deviation of water surface elevation were generated at the test section. A system was developed whereby data of the type presented in Fig. 3 could be automatically collected for up to 48 different wave conditions. 'Random' waves were generated by the use of an algorithm (3) in which pseudo-random noise is produced by feedback in a shift register and passed through a digital filter to give the paddle motion for the desired wave spectrum. Because this technique produces a deterministic time series it is possible to conduct a series of tests in nominally identical wave conditions.

Four 0.8m long cylinders with diameters ranging from 21mm to 54mm were used in the investigation (see Table 1). When a particular cylinder was under test it was mounted on the bottom of the channel in a 0.6m depth of water to form a vertical surface-piercing cantilever. The required degree of flexibility was achieved by fabricating each cylinder from Polypropylene tube (Young's Modulus of 700 MN/m^2) and the resonant frequency was controlled by use of a variable tip mass. Vibration was measured by means of two pairs of strain gauges positioned 25mm above the base and displacements were estimated on the basis of the first mode shape. Negligible motion was detected at frequencies associated with any higher mode.

The logarithmic decrements of structural damping were determined in free vibration tests to be between 0.18 and 0.22. The mass of each structure was generalised by use of an equivalent mass (\bar{m}) defined in the way that has become standard for estuarial structures. Thus \bar{m} is the mass/unit length of a uniform cylinder extending to mean water surface level which vibrates with the same energy, resonant frequency and mode shape as the original structure. Values of f_n were determined in still water tests. A particular test structure was then defined by means of the dimensionless parameters Fr , δ and $\bar{m}/\rho D^2$.

Regular Wave Tests

These tests were carried out with intermediate depth waves ($0.5 < kd < 3.0$) at surface Re between 4.6×10^3 and 17×10^3 and KC up to 28, all values calculated using linear theory.



Plate 1. General view of experimental equipment.

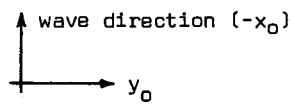
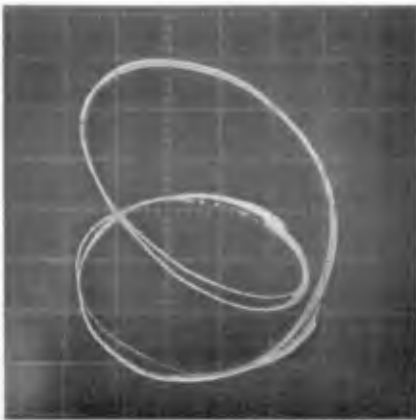


Plate 2. Oscilloscope traces of the temporal variation in x_0 and y_0 during series A test with $Fr = 2.0$ and $KC = 17$.

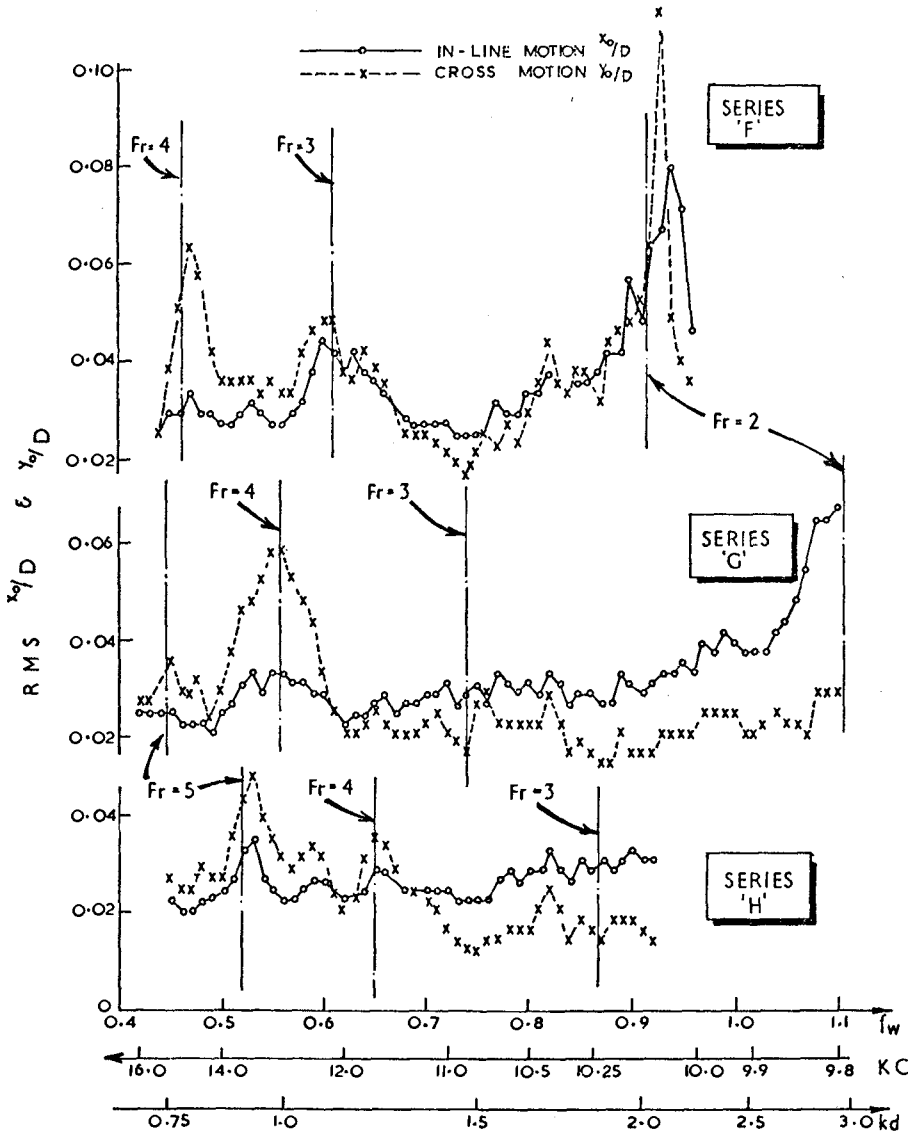


Fig. 3. Typical results for the variation in root-mean-square x_0/D and y_0/D against various parameters for regular waves.

Fig. 3 shows three typical sets of results for the variation in rms x_0/D and y_0/D against Fr , KC and kd . Additional parameters for these and other similar tests are given in Table 1. Because cross-flow response was often quite different from one wave cycle to the next, each point in Fig. 3 is based on 19,600 readings taken at 0.06 sec intervals (350 to 1300 wave cycles) to give sensible statistical estimates. For the range of parameters considered the cross-flow response can be much greater than the in-line response and both motions tend to increase as Fr approaches an integer value. The wave height for the runs in Fig. 3 was unchanged at 113mm. (The low level of reflection is considered to have little influence on the results).

The in-line response followed a very similar pattern in each wave cycle of a particular test but the form of the pattern depended upon the prevailing test parameters. Several attempts were made to predict the observed behaviour. In these the cylinder was divided into segments and the horizontal water-particle motion at the centre of each segment was calculated from simple theory. Local KC values were used in conjunction with data from U-tube experiments (10) to assign values to C_D and C_M in the Morison equation and hence to estimate the bending moment at the cylinder base. Wave-induced motion was predicted by assuming that the cylinder formed part of a linear, single-degree-of-freedom system and feeding a time series of base bending moments into a finite difference scheme based on the appropriate equation of motion. The best results were obtained when the Morison equation was extended to include relative motion terms, when some account was taken of the variation in water-surface elevation and when second order rather than first order wave theory was used. Fig. 4 shows a comparison of measured and predicted time-histories for base strain while Fig. 5 shows a more general comparison of rms x_0/D values. The predictions were good except when $Fr \approx 2$ and the experimental cylinder was subjected to strong transverse bending moments that varied at twice the wave frequency. In these circumstances, which occurred when the surface KC was around 13, the observed in-line motion was seriously underestimated.

The general success of the extended Morison equation when used with coefficients obtained with stationary cylinders suggests that the vorticity shed in a wave cycle is mainly dependent on the relative in-line fluid motion. However, in these experiments the cylinder motion was always small in comparison with the fluid motion. If we assume that the vorticity shed was largely independent of response, because vorticity was mainly responsible for in-line motion and entirely responsible for cross motion, it is reasonable to expect rms $y_0/rms x_0$ to be sensibly constant for situations with the same Fr , KC and kd . Further specification by $\bar{m}/\rho D^2$ and δ is conveniently avoided as they affect only the magnitude of the responses and S_n/d was the same in most tests. In the present case KC was a more important parameter than kd , so ratios of rms $y_0/rms x_0$ were calculated from the experimental results and plotted against Fr and KC . This produced a chart similar to Fig. 6 in which each dot indicates the location of a

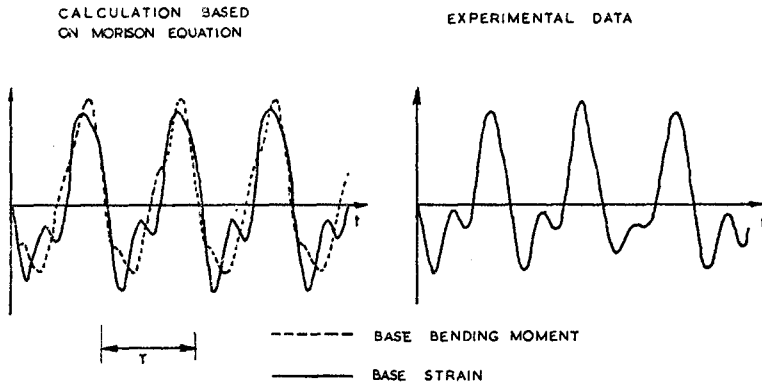


Fig. 4. Time histories of base bending moment and strain
 $Fr = 2.4$ $KC = 13.9$ $kd = 1.54$

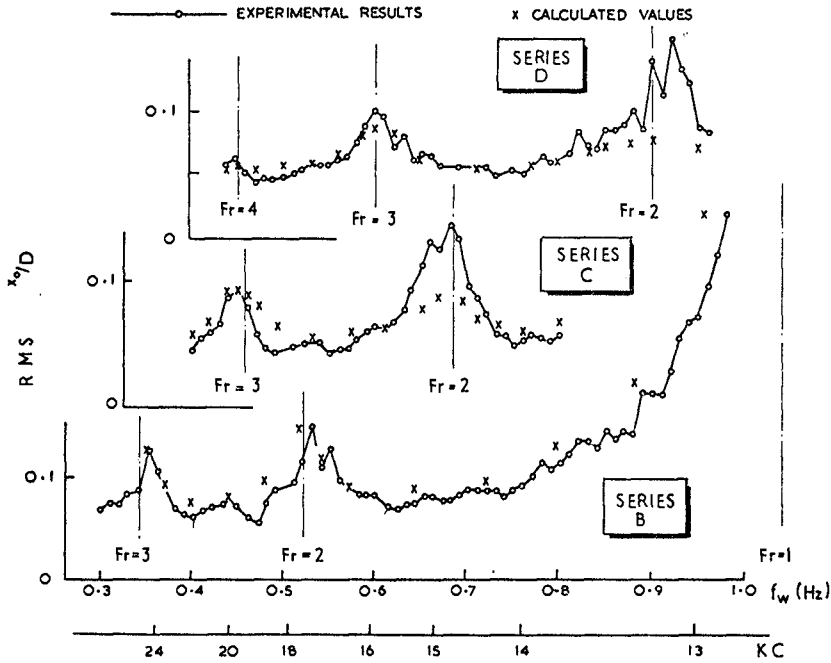


Fig. 5. Comparison of experimental and calculated values for root-mean-square x_0/D .

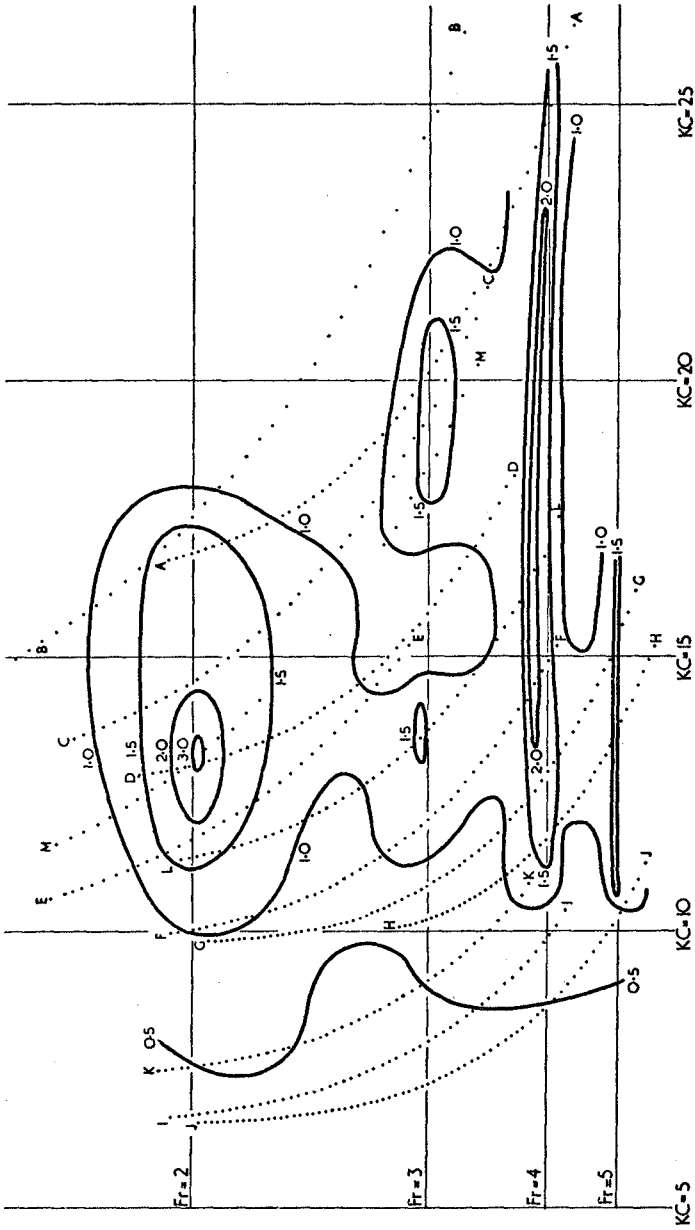


Fig. 6. Contours of $\text{rms } y_0/\text{rms } x_0$ against Fr and KC. Each dot indicates the location of a result from the series of tests A to M detailed in Table 1.

result from the series of tests A to M detailed in Table 1. (In each test k_d decreased from about 2.5 to 0.75 with increasing KC). The scatter in the values of $\text{rms } y_0 / \text{rms } x_0$ found within a given region of the chart was small enough (15) to justify the sketching of contours as shown. Values in excess of 3 were obtained only in the sensitive area around $Fr = 2$ and $KC = 13$ where the vorticity shed in a wave cycle was probably markedly dependent on response (see § 5).

Unlike the in-line motion, the transverse response tended to be very erratic with intermittent bursts of activity that varied in both magnitude and duration. However, during tests in which f_n was close to the frequency of a major component in the transverse bending moment, y_0 would occasionally follow repetitive patterns which could persist for many wave cycles. The most stable responses were generally associated with the sensitive area around $Fr = 2$ and $KC = 13$. When these broke down either the same pattern or its mirror image in the in-line plane was quickly re-established (Plate 2).

Some characteristics of the different types of motion are illustrated by the probability density histograms shown in Fig. 7, the right hand pair being for the conditions of Plate 2. The in-line histograms are asymmetric, mainly due to the different loading produced by the passage of wave crests as opposed to troughs, whereas the transverse histograms are symmetric. Because the cross motion varies from the very erratic to the near sinusoidal oscillations associated with a repetitive pattern, the corresponding probability density histograms are a combination of the 'bell-shaped' Gaussian and two-peaked, sine-wave density functions. The relative magnitudes of these forms within a particular histogram give an indication of the periods over which the different conditions were prevalent. Spectral analyses of both the in-line and transverse response show the variance to be mainly at harmonics of f_w , significant dynamic magnification occurring whenever f_n was close to a wave harmonic. A fair proportion of the in-line response always occurred at f_w but this was not true of the transverse motion.

Time-histories of in-line and transverse base bending moments were calculated from strain data for 82 seconds of selected tests. As would be expected spectral analyses reveal that most of the variance in the in-line moment occurred at f_w whereas the largest harmonic in the transverse moment depended upon the prevailing test parameters. An indication of the regions over which various harmonics predominate is shown in Fig. 8 which suggests that the boundary between adjacent regions moves towards higher KC as k_d increases. This is doubtless due to the increasingly non-uniform velocity distribution as one moves towards a condition of 'deep-water' waves. In these circumstances the local value of KC reduces with depth and it is quite possible for the dominant harmonic in the transverse loading near the surface to have higher frequency than that of the dominant harmonic in the loading further down (2).

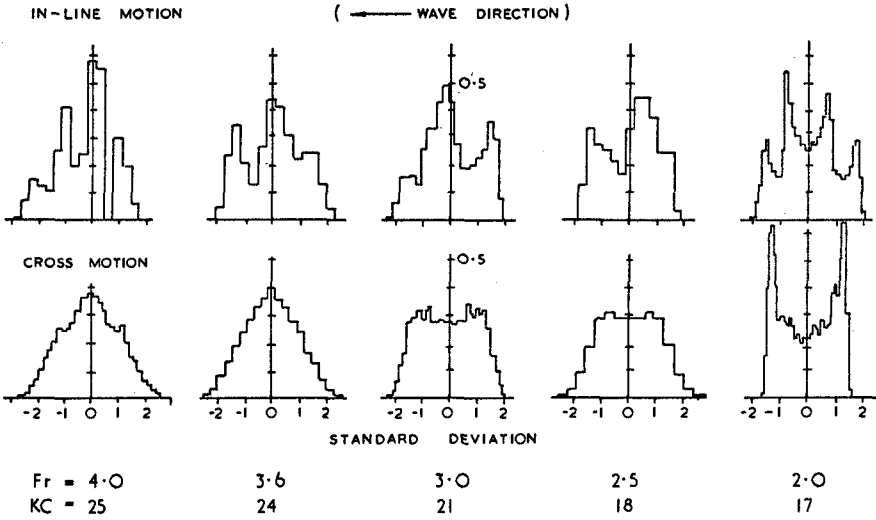


Fig. 7. Probability density histograms for structural motion in selected series A tests.

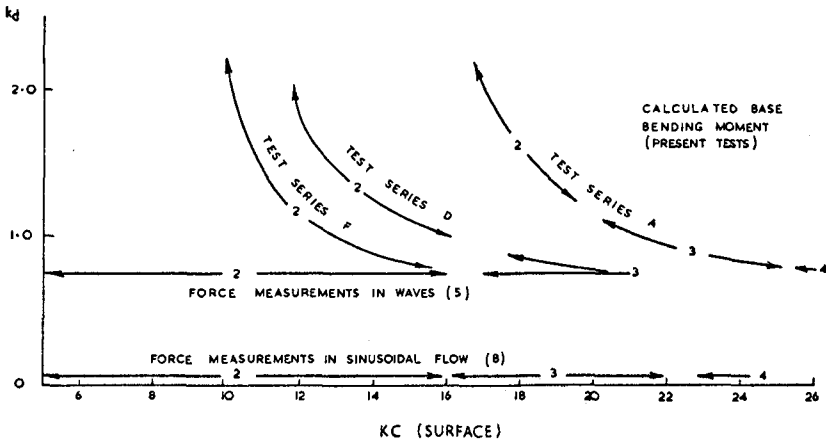


Fig. 8. Predominant harmonic in transverse moment or force

Random Wave Tests

During these tests the waves had a Pierson-Moskowitz spectrum with $S_{\eta} = 32\text{mm}$ and the variation in water-surface elevation was approximately Gaussian. Spectra for in-line and transverse response of the 28mm diameter cylinder when tuned to various f_n above the frequency of the wave spectral peak are shown in Fig. 9.

In most tests the in-line motion was dominated by vibration at the natural frequency although there was always significant response at frequencies associated with the peak of the wave spectrum. The spectral peak at f_n rapidly diminished as f_n was increased.

Predictions of in-line response were made in the frequency domain by applying transfer functions to the measured wave spectrum. The effects of structural movement were ignored so that base bending moment spectra could be calculated by use of linear wave theory and a linearised drag term in the Morison equation as proposed by Borgman (1). Guidance in the choice of values for the Morison coefficients was sought by calculating surface KC values for a regular wave with the same S_{η} as the wave spectrum and a frequency equal to that of the spectral peak. For the situation of Fig. 8 this gave $KC = 14$. U-tube experiments (10) indicate that around this value $C_D \approx 2$ and $C_M \approx 1$ and for simplicity these values were assumed to apply throughout the water depth. The response spectra obtained from the bending moment spectra by use of appropriate dynamic admittance terms were in remarkably close agreement with the experimental results (e.g Fig. 9). This is perhaps surprising as the calculations were drag-dominated and suggests that the errors inherent in the assumptions must at least partially cancel each other out. Refinement of the present calculations was not justified and new tests will be carried out to investigate this matter further.

The transverse response was of comparable magnitude to the in-line response but occurred only at frequencies near f_n . It was highly irregular and tended to be dominated by short bursts of above average motion which appeared to be either caused by the passage of a single wave or built up by a sequence of waves. Short bursts of high response at f_n also occurred in the in-line direction but did not necessarily coincide with those in the cross mode. Examination of the limited number of spectra obtained for the transverse response indicated that the variance did not always decline when f_n was increased. Instead there was a suggestion that the response increased when f_n was near an integer multiple of the dominant wave frequency in a manner reminiscent of the regular wave tests. It is interesting to note that the situation with $KC = 11$ and $Fr = 3.8$ occurred in both regular and random waves and the rms y_0 values were very similar (KC and Fr for random waves were calculated on the basis of a sine wave as previously described).

5. Analysis

The experiments were primarily concerned with the evaluation of response

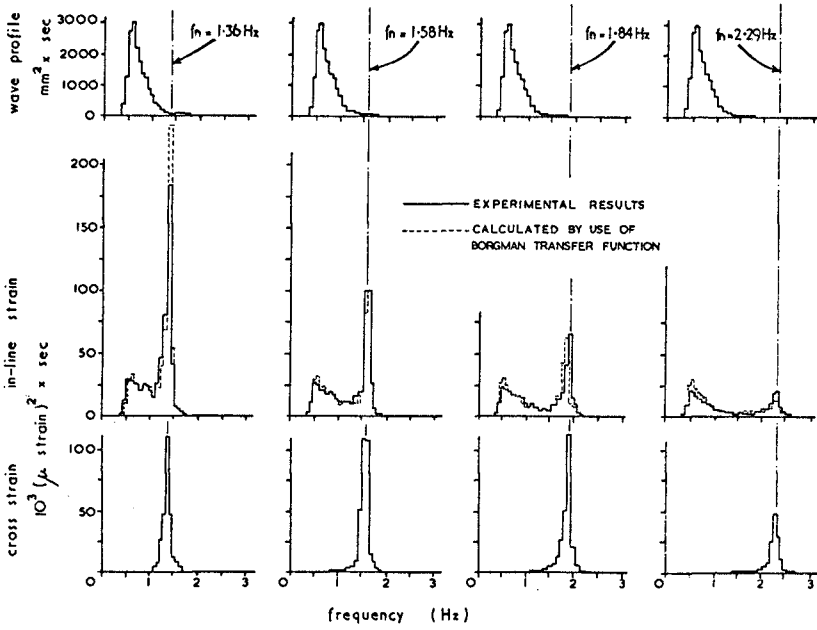


Fig. 9. Response of 28mm diameter cylinder in random waves.

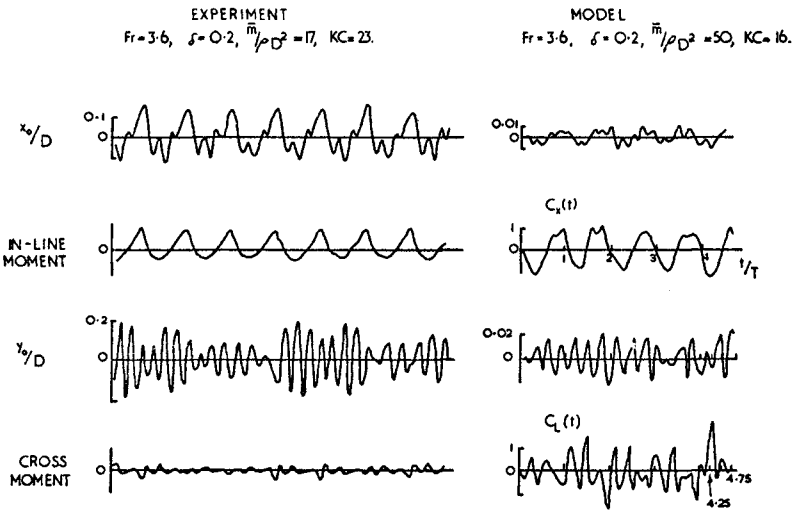


Fig. 10. Comparison of experimental results with results from the two-dimensional mathematical model

due to vortex shedding in waves. In regular waves definition of water-particle motions in an accepted manner together with the use of Morison's equation with relative motion terms and coefficients for fixed cylinders usually gave a good prediction of in-line response. This prediction was not disrupted by cross response which was often greater than the in-line response. An equivalent prediction method does not exist for cross motion and $\text{rms } y_0/D$ should ideally be defined by all the stated non-dimensional groups. To avoid this an approximate argument, which assumes that vorticity shed in a wave cycle is independent of the response which it generates, allows $\text{rms } y_0/\text{rms } x_0$ to be defined in terms of Fr , KC and kd . The contour plot of Fig. 6 is itself a justification for its method of presentation. The influence of kd is however omitted and Fig. 9 shows its effect on the dominant frequency of lift moment. This will affect the dependence of cross response on KC . It may be possible to weight KC through kd to overcome this.

The in-line response is underestimated by the above prediction for parameters approximately given by $1.8 < Fr < 2.2$ and $10 < KC < 17$. The area acceptably fits the contour plot and $\text{rms } y_0/\text{rms } x_0$ attains a maximum of 3. Lift moment is predominantly at twice the wave frequency and cross response and moment are at their most repetitive. Because drag and lift are vortex-induced it seems likely that the strength of the one vortex shed per half cycle is usually magnified by the response. This is analogous to the situation in currents where cross motion increases the vortex-induced forces which then increase the response in a feedback loop until equilibrium is reached, e.g see (12). The lift also 'locks-on' to the cylinder motion. However in waves, outside the sensitive area, cross response appears to have little influence on the vortex-induced forces in a permanent or long-term sense. Experiments with a linear mode response (6), which covered a range of δ , support this although the sensitive area was not found.

Cross response never defines the lift moment frequency and without this stabilising influence apparently stable patterns will always break down. In general cross response and moment are irregular and their fine structure is obviously interactive. Such patterns are shown in Fig. 10 and compared with the two-dimensional mathematical model. The potential-flow calculation accommodates cylinder velocities but only very small responses are considered because of the assumption of fixed separation. The KC of the high Reynolds number simulation is adjusted to give the same lift frequencies as the surface KC in waves. The different $\bar{m}/\rho D^2$ cause the model response to be roughly 1/10 of the experimental response but the interaction is similar for both. Lift acting against the motion reduces response while lift acting with the motion increases it. For the mathematical model the peak lift was greater than on the fixed cylinder but rms values were similar. It is important to note that in the experiment the small lift moment causes a greater response than the much larger in-line moment. The peaks in lift moment are considerably smaller than would be obtained by dividing the span into segments and summing the influence of lift maxima obtained from U-tube experiments through the associated KC values.

Extension of these results to other situations requires an interpretation of the physical processes involved. Magnification of vortex-induced forces by response is most likely when forces and response are nearly sinusoidal and at the same frequency (the situation of locking-on in steady currents). When the force is complex with spectral analysis indicating several harmonics of similar magnitude, feedback through a response at around the natural frequency would have to have a remarkable form to magnify the force in a permanent way.

Random waves will further reduce the possibility of permanent magnification and rms cross response can be as large in random waves as it is in regular waves for the same S_n and KC . The prediction of in-line response in the frequency domain by making several assumptions was remarkably good. However the validity of each assumption should be checked in isolation.

APPENDIX I - References

1. Borgman, L E "The Spectral Density of Ocean Wave Forces". Coastal Engineering, ASCE Specialty Conference, Santa Barbara, October 1965, pp 147-182.
2. Chakrabarti, S K, Wolbert, A L, and Tam, W A "Wave Forces on Vertical Circular Cylinders", Journal of Waterways, Harbours and Coastal Engineering Division, ASCE, Vol 102, No WW 2, Proc Paper 12140, May, 1976, pp 203-221.
3. Fryer, D K, Gilbert, G, and Wilkie, M J, "Wave Spectrum Synthesizers", Tech Memo 1/1972, Electrical and Mechanical Engineering Section, Hydraulics Research Station, Wallingford, UK, June, 1972.
4. Gaster, M "Vortex Shedding from Slender Cones at low Reynolds Numbers", Journal of Fluid Mechanics, Vol 38, 1971, pp 565-577.
5. Isaacson, M de St Q and Maull, D J, "Transverse Forces on Vertical Cylinders in Waves", Journal of Waterways, Harbour and Coastal Engineering Division, ASCE, Vol 102, No WW1, Proc Paper 11934, February, 1976, pp 49-60.
6. King, R, Prosser, M J, and Verley, R L P "The Suppression of Structural Vibrations Induced by Currents and Waves", Proc BDSS Conf, Trondheim, 1976, pp 263-283.
7. Mair, W A and Stansby, P K "Vortex Wakes of Bluff Cylinders in Shear Flow" Proc of the Int Symp on Modern Developments in Fluid Dynamics, SIAM, 1977, pp 129-150.

8. Maull, D J and Milliner, M G "Sinusoidal Flow Past a Circular Cylinder" to appear in Coastal Engineering.
9. Miller, B L and Matten, R B "A Technique for the Analysis of Wave Loading Data Obtained from Model Tests", NPL Report Mar Sci R 136, London, June, 1976.
10. Sarpkaya, T and Tuter, O "Periodic Flow About Bluff Bodies - Pt 1: Forces on Cylinders and Spheres in a Sinusoidally Oscillating Fluid", Report No NPS-59SL74091, Naval Postgraduate School, Monterey, California, 1974.
11. Sarpkaya, T "Vortex Shedding and Resistance in Harmonic Flow About Smooth and Rough Circular Cylinders at High Reynolds Numbers", Report No NPS-59SL76021, Naval Postgraduate School, Monterey, 1976.
12. Stansby, P K "Base Pressure of Oscillating Circular Cylinders", Journal of Engineering Mechanics Division, ASCE, Vol 102, No EM4 Proc Paper 12311, August, 1976, pp 591-600.
13. Stansby, P K "An Inviscid Model of Vortex Shedding from a Circular Cylinder in Steady and Oscillatory Far Flows", Proc Institution of Civil Engineers, London, Vol 63, Pt 2, Paper 8065, December, 1977, pp 865-880.
14. Susbielles, G G, "Wave Forces on Pile Sections due to Irregular and Regular Waves", Proc 7th Offshore Technology Conference, Paper No 1006, Houston, 1971.
15. Warren, J G "The Development and Use of a Wave Facility to Investigate the Dynamic Response of Circular Cylinders to Wave Action", PhD Thesis, University of Salford, 1977.
16. Zdravkovich, M M and Namork, S E "Formation and Reversal of Vortices around Circular Cylinders Subjected to Water Waves", Journal of Waterway, Port, Coastal and Ocean Division, ASCE, Vol 103, No WW 3, Proc Paper 13102, August, 1977, pp 378-383.

APPENDIX II - Notation

C_D = drag coefficient in Morison equation

C_M = inertia coefficient in Morison equation

$C_L(t) = Y / \frac{1}{2} \rho U_o^2 D$ = non-dimensional lift force

$C_X(t) = X / \frac{1}{2} \rho U_o^2 D$ = non-dimensional in-line force

D = cylinder diameter

d = water depth

f_n = structural frequency

- f_w = wave frequency
 Fr = structural frequency/wave frequency
 $k=2\pi/L$ = wave number
 $KC=U_0T/D$ = Keulegan-Carpenter number (at surface)
 L = wavelength
 \bar{m} = equivalent mass/unit length
 $Re=\rho U_0D/\mu$ = Reynolds number (at surface)
 $S\eta$ = standard deviation at water surface elevation
 T = wave period
 U_0 = amplitude of horizontal water-particle velocity (linear theory)
 x_0 = in-line cylinder displacement
 y_0 = transverse cylinder displacement
 X = in-line force
 Y = lift force
 δ = logarithmic decrement of structural damping
 μ = viscosity of water
 ρ = density of water

Acknowledgements

This work was in part supported by the Research Department, Taylor Woodrow Construction Ltd and the Science Research Council, for which the authors express their appreciation. Thanks are also due to the staff of the Civil Engineering Department, University of Salford for their assistance both with the experiments and with the preparation of this paper.

Table 1. Parameter values for regular wave tests.

SERIES	A	B	C	D	E	F	G	H	I	J	K	L	M
D(mm)	21	28	28	28	36	36	36	36	54	54	36	36	28
S η (mm)	40	40	40	40	40	40	40	40	40	40	30	45	30
$\bar{m}/\rho D^2$	17	48	32	19	38	24	16	12	27	20	24	24	48
$\delta \approx 0.2$ for all cases													

CHAPTER 146

WAVE FORCES ON A ROW OF CYLINDRICAL PILES OF LARGE DIAMETER

by

J.C.W. Berkhoff* and J. v.d. Weide**

Abstract

In order to determine wave forces on a row of three cylindrical piles (Figure 2), a numerical computation procedure was applied using a solution of the Helmholtz equation, in which the scattered wave field is described as the result of a series of singular sources located along the circumference of the pile [Berkhoff, 1976, reference 1]. Results of the computations were verified by means of model experiments, using both regular and irregular waves.

It is shown that for the two pile geometries, included in the study, strong mutual interference will occur, resulting in transverse forces which are much higher than those found for single piles.

1 Introduction

In order to protect the low-lying hinterland of the lower Rhine delta against flooding, the Dutch have developed the Delta scheme, which involves the closure of a number of estuaries and the construction of three storm-surge barriers, the largest of which is currently being designed. This structure will be located in the Eastern Scheldt and will consist of a group of three sluices, each consisting of a number of gates with a span of approximately 40 m. Gates are suspended between piers founded at the seabed, which locally has a depth of 38 m below sealevel.

For the construction of the piers, cylindrical cofferdams were envisaged, due to time constraints three of these cofferdams had to be used simultaneously. Due to the large dimensions of these structures a strong mutual interference had to be expected which might adversely effect current and wave forces. Therefore, a study was performed to determine wave forces on a row of cylindrical piles. Results of this study are presented in this paper.

2 Theoretical considerations

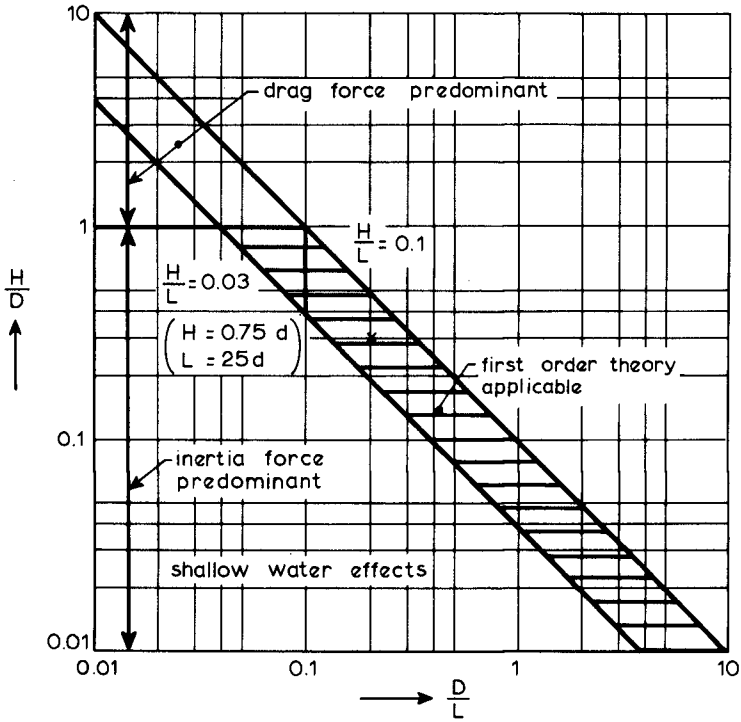
Wave forces have been the subject of many studies, resulting in a number of theories and computation techniques. Each of these has its own distinct field of application as may be demonstrated with the help of Figure 3.

For objects which are small with respect to the wave length ($D/L < 0.1$) it is assumed that the local flow field is only marginally affected by the presence of the object.

Consequently orbital velocities and accelerations within the fluid are computed for the undisturbed condition using conventional wave theories. Once local accelerations and velocities are known corresponding wave forces may be computed. In this respect two limiting conditions may be considered

* Head Mathematics Branch, De Voorst Laboratory,
Delft Hydraulics Laboratory

** Head Maritime Structures Branch, De Voorst Laboratory,
Delft Hydraulics Laboratory



H = wave height
 L = wave length
 D = characteristic length of object

FIG. 3 CHARACTERISTIC WAVE PARAMETERS

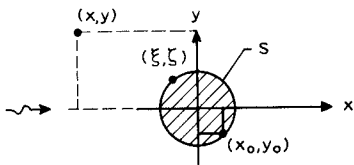


FIG.: 4 NOTATIONS

characterized by large and small values of the Keulegan Carpenter number

$$\frac{U_{\max} T}{D}$$

which, for deep water, is proportional to the ratio of wave height (H) over pile diameter (D).

For large value of H/D, drag forces are most important whereas for small values of H/D inertia forces predominate. In view of the dimensions of the cofferdam, the latter conditions applies for the present case. However, the ratio of the pile diameter over the wave length is such, that the effect of the structure on the local flow field can no longer be neglected. Resultant forces have to be derived, therefore, from a description of the local wave field which takes into account both the effect of the incident and the scattered waves.

Values of H/D and D/L are such that they fall within the hatched area bounded by the limiting wave steepness in deep water ($H/L = 0.1$) and the line $H/L = 0.03$, indicating roughly the limit beyond which shallow water effects strongly manifest themselves. In this area linear wave theory may be applied to describe the wave field. Mathematically the problem is then described as the solution of the Laplace equation

$$\frac{\partial^2 \phi}{\partial x^2} + \frac{\partial^2 \phi}{\partial y^2} + \frac{\partial^2 \phi}{\partial z^2} = 0 \quad (1)$$

which satisfies the following boundary conditions

$$\text{free surface: } \frac{\partial^2 \phi}{\partial t^2} + g \frac{\partial \phi}{\partial z} = 0 \quad (2)$$

$$\text{horizontal bottom } \frac{\partial \phi}{\partial z} = 0 \quad (3)$$

$$\text{surface of the pile } \frac{\partial \phi}{\partial n} = 0 \quad (4)$$

Furthermore the well known Sommerfeld condition should be fulfilled, stating that the scattered wave vanishes with increasing distance from the object.

In general, the solution of equation (1) is written as

$$\Phi = \phi_i + \phi_d \quad (6)$$

where

ϕ_i = potential of incident wave

ϕ_d = potential of scattered wave

The potential ϕ_i is expressed as

$$\phi_i = \frac{H g}{2 \omega} \frac{\cosh k(d+z)}{\cosh kd} e^{i(\omega t - mx)} \quad (7)$$

which satisfies condition 2 and 3, provided the dispersion relationship is valid, stating

$$\omega^2 = gk \tanh kd \quad (8)$$

The potential ϕ_d may be expressed as

$$\phi_d = \frac{H g}{2 \omega} \cdot \frac{\cosh k(d+z) \cdot F(x,y) \cdot e^{i\omega t}}{\cosh kd} \quad (9)$$

which also satisfies condition 2 and 3.

Substitution of (9) in (1) results in the well known Helmholtz equation

$$\frac{\partial^2 F(x,y)}{\partial x^2} + \frac{\partial^2 F(x,y)}{\partial y^2} + k^2 F(x,y) = 0 \quad (1')$$

The problem is defined now as a solution of equation (1'), which satisfies the boundary condition (5) and the Sommerfeld condition.

As early as 1954 McCamy and Fuchs [3] have solved this problem analytically for a single circular pile, by using a series of Bessel functions. Using the same procedure Spring and Monkmeyer [5] derived a solution for an array of two circular piles of arbitrary diameter and solved the problem for an infinite row of equally spaced equal cylinders exposed to perpendicular wave attack. The solution has been extended to waves from arbitrary direction of incidence by Massel [4], who presented an approximate solution. Recently, Chakrabarti [2], using the solution of Spring and Monkmeyer determined a solution for any arbitrary size at arbitrary angles to the incident wave. However, for an array of cylindrical piles of arbitrary cross-section no analytical solutions are available. Recourse had to be taken to a numerical technique, therefore, as described by Berkhoff. [1]

This was done by assuming that the scattered wave field may be considered as a result of a series of singular sources located along the circumference of the pile. Denoting the strength of the source distribution by $\alpha(\xi, \zeta)$ (see Figure 4) and the source potential function by $G(x, y, \xi, \zeta)$ the following expression is obtained for $F(x, y)$

$$F(x, y) = \int_S \alpha(\xi, \zeta) G(x, y, \xi, \zeta) ds$$

where

S = circumference of the piles

(ξ, ζ) = coordinate of the source point located at the object

A source potential function which is a solution of the Helmholtz equation (1') and which satisfies the Sommerfeld condition is found as

$$G(x, y, \xi, \zeta) = \frac{1}{2i} H_0'(k_0 r)$$

where

$$r = \sqrt{(x - \xi)^2 + (y - \zeta)^2}$$

and

H_0' = Hankel function of first kind and zero order.

The source strength $G(\xi, \zeta)$ is found from the boundary condition at the pile surface by putting

$$-\frac{\partial \phi_i}{\partial n} = \frac{\partial \phi_d}{\partial n}$$

which results in the integral equation

$$-\left[\frac{\partial e^{-imx}}{\partial n}\right]_{x_0, y_0} = \alpha(x_0, y_0) + \int_S \alpha(\xi, \zeta) \cdot \frac{\partial}{\partial n} \left[\frac{1}{2i} H_0^{(1)}(k_0 r) \right]_{x_0, y_0} ds$$

Where x_0, y_0 are the coordinates of an arbitrary point at the circumference of the object.

Once the wave potential is known, the pressures may be obtained from the Bernoulli equation

$$p = -\rho \frac{\partial \phi}{\partial t}$$

Integration of the pressures along the circumference of the pile yields the total wave force.

3 Results for circular piles

3.1 Introduction

In order to compare the results of the present theory with previous studies interaction effects were first studied for a row of 3 circular piles with a diameter of 18 metres, located 40 m apart. Results are given in a dimensionless form using the force coefficients

$$C_{F_x} = \frac{F_x}{\rho g H \operatorname{tgh} kd \cdot \frac{\pi D^2}{4}} \quad \text{and}$$

$$C_{F_y} = \frac{F_y}{\rho g H \operatorname{tgh} kd \cdot \frac{\pi D^2}{4}}$$

with

$F_{x,y}$ = maximum force in x or y direction respectively

ρ = density of water

g = acceleration of gravity

H = wave height

d = water depth

k = $2\pi/L$ with

L = wave length

D = pile diameter

Resultant forces were first computed by means of the theory described in section 2. In order to verify these results, model tests have been performed subsequently. These tests have been carried out in a model basin with dimensions 11 x 25 m², using a linear scale of 1 : 64. Both regular and irregular waves have been applied to determine the transfer function between wave heights and wave forces.

Finally, for a selected number of pile geometries, the effect of the distance between the piles has been studied experimentally.

3.2 Results of computations

Longitudinal and transverse force coefficients C_{F_x} and C_{F_y} are shown on Figures 5 and 6. Forces have been computed for each individual pile, using wave periods between 4 and 12 seconds and directions ranging from 0° to 30° . (0° corresponding to a direction perpendicular to the centerline of the pile array). It appears that results for a single pile are in good agreement with the analytical solution obtained by McCamy and Fuchs. Individual piles of a row of three piles may experience higher forces than single piles, due to mutual interference. These effects are most pronounced for transverse forces and are clearly shown for wave periods of 5 - 6 seconds.

3.3 Experimental verification

Results of computations have been verified experimentally, for the most critical position of the pile as shown on Figure 7. It appears that results for both regular and irregular waves are in good agreement with computed values.

Experiments have been repeated for various distances between the piles. As may be inferred from Figure 8 interference effects are most pronounced for l/D values in the order of 2. For higher values the effect of the mutual interference vanishes. Transverse forces for all tested arrangements were still higher than those for single piles, however.

4 Results for an array of cofferdams

4.1 Introduction

Forces on the array of cofferdams shown on Figure 2, have first been computed. It should be noted that the same dimensionless force coefficients have been used as for circular piles, which explains the high values of these coefficients in the graphs. Subsequently computed values were verified using the same experimental set up as described in section 3.1.

4.2 Results of computations

Longitudinal and transverse force coefficients C_{F_x} and C_{F_y} are shown on Figures 9 and 10. Forces have been computed for each individual pile, using wave periods between 4 and 12 seconds and directions ranging from 0° to 30° . It appears that for wave periods between 5..6 seconds, similar interference effects are observed as for circular piles. However, these effects are small compared to another strong interference, observed for a period of 10 seconds, which again is more pronounced for transverse forces. Plots of wave-heights around the piles show a strong amplification of wave-heights between the piles for this wave periods, as a result of interference between scattered and incident waves.

4.3 Experimental verification

Results of computations have been verified experimentally for the most critical position of the pile, as shown on Figure 11. Again computed results agree with experimental data, although transfer functions for C_{F_y} obtained by means of irregular wave show a less distinct amplification for 10 seconds, due to poor resolution of the spectral analysis in this range.

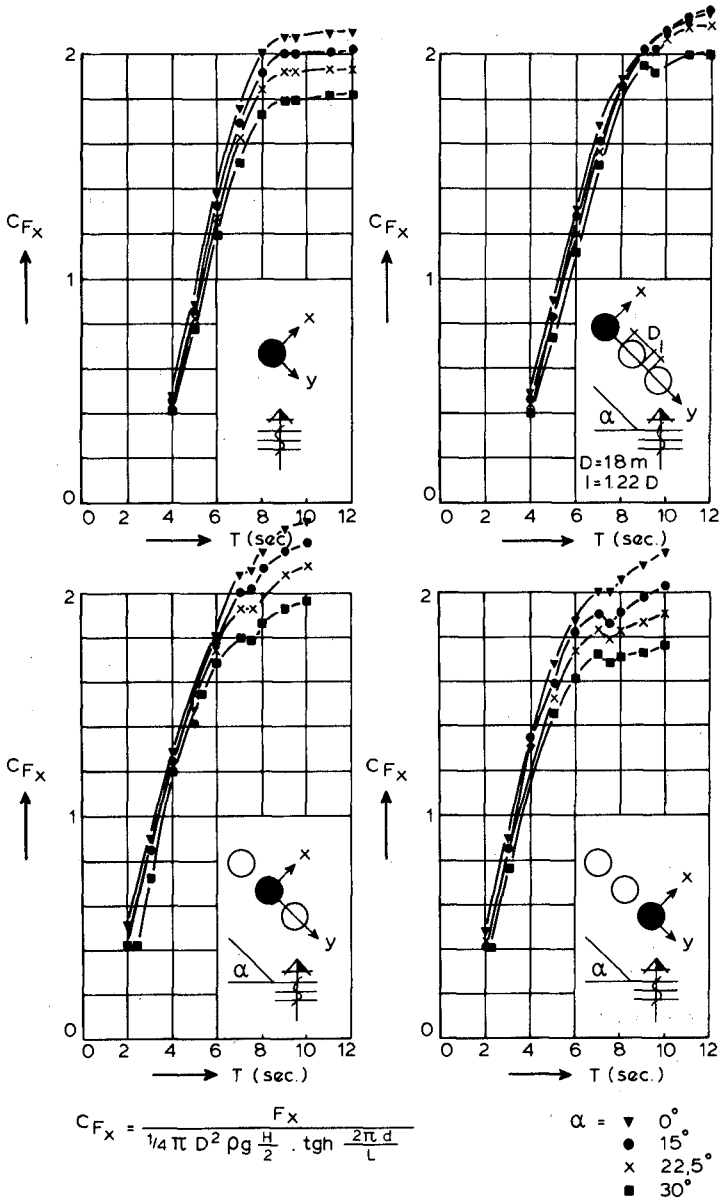


FIG. 5

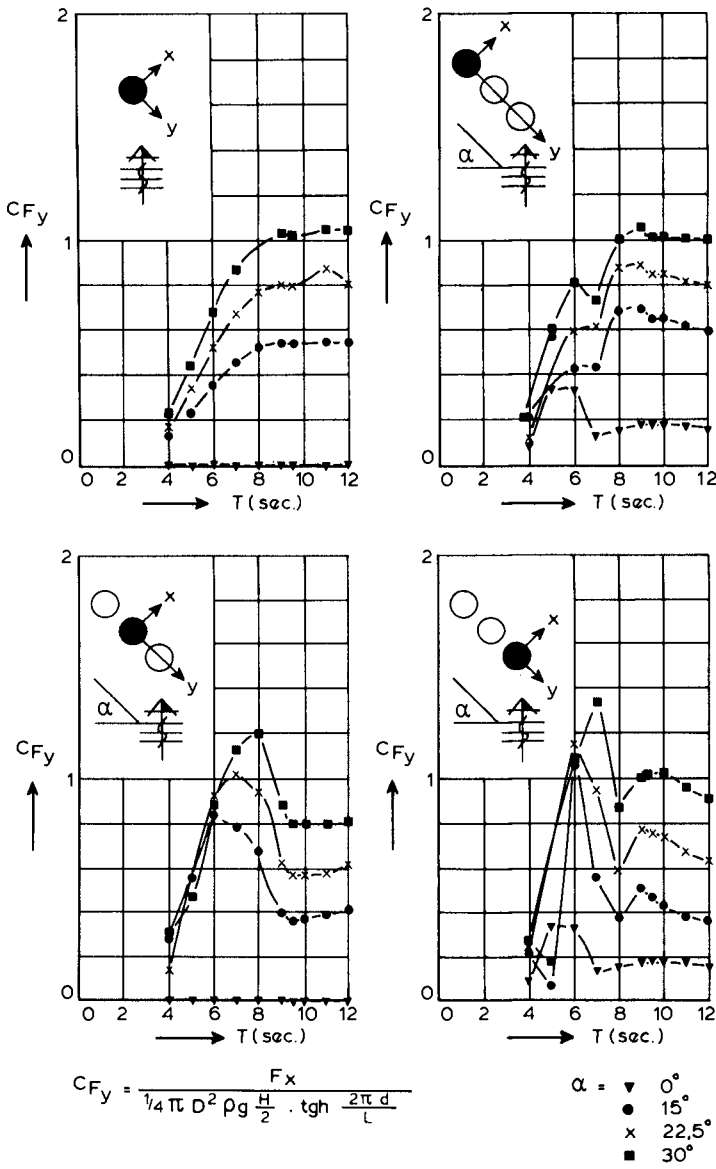


FIG. 6

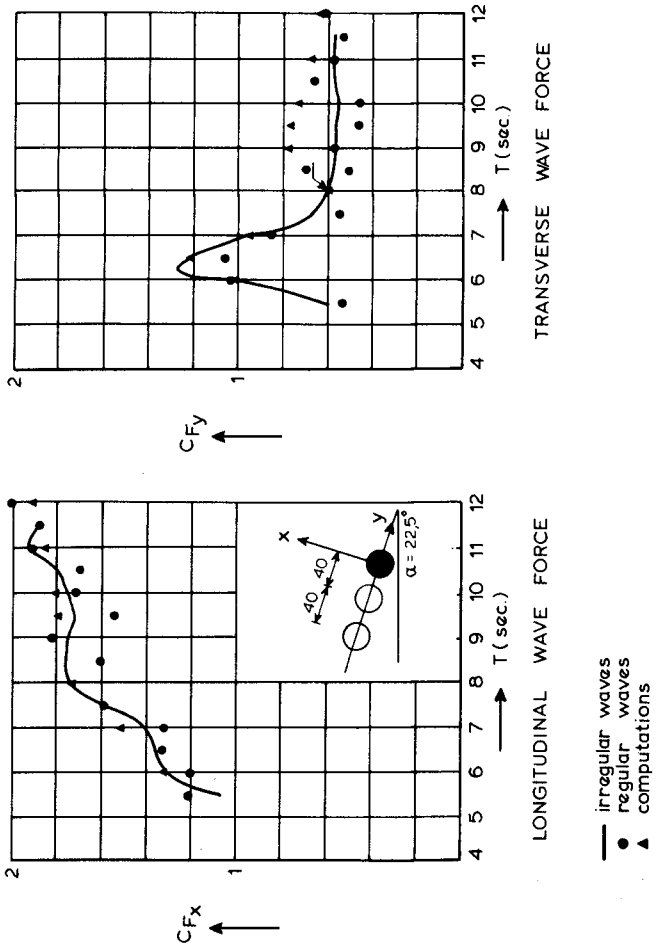


FIG. 7

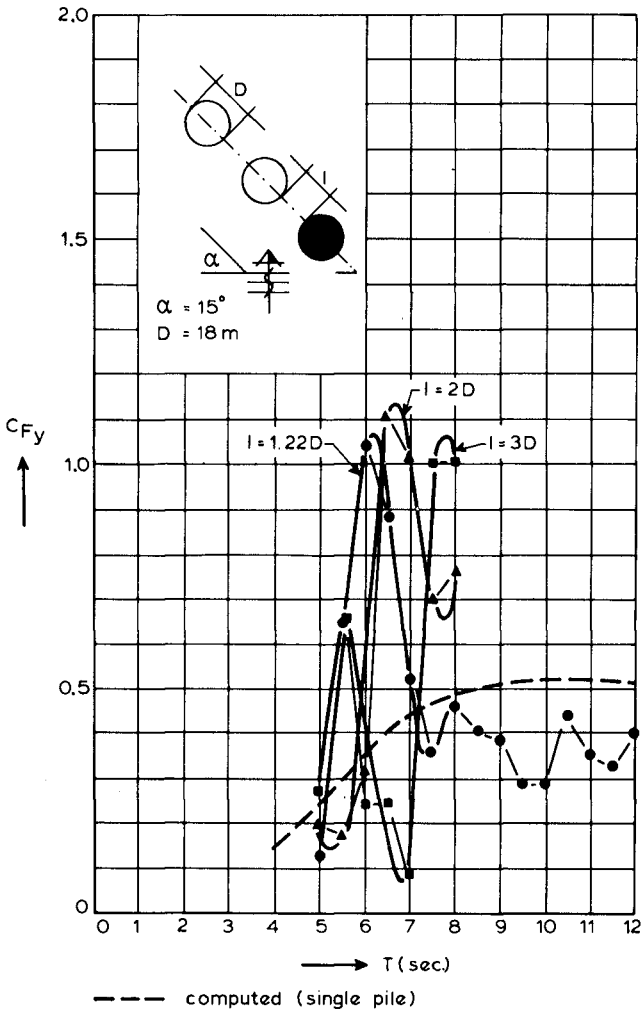


FIG. 8

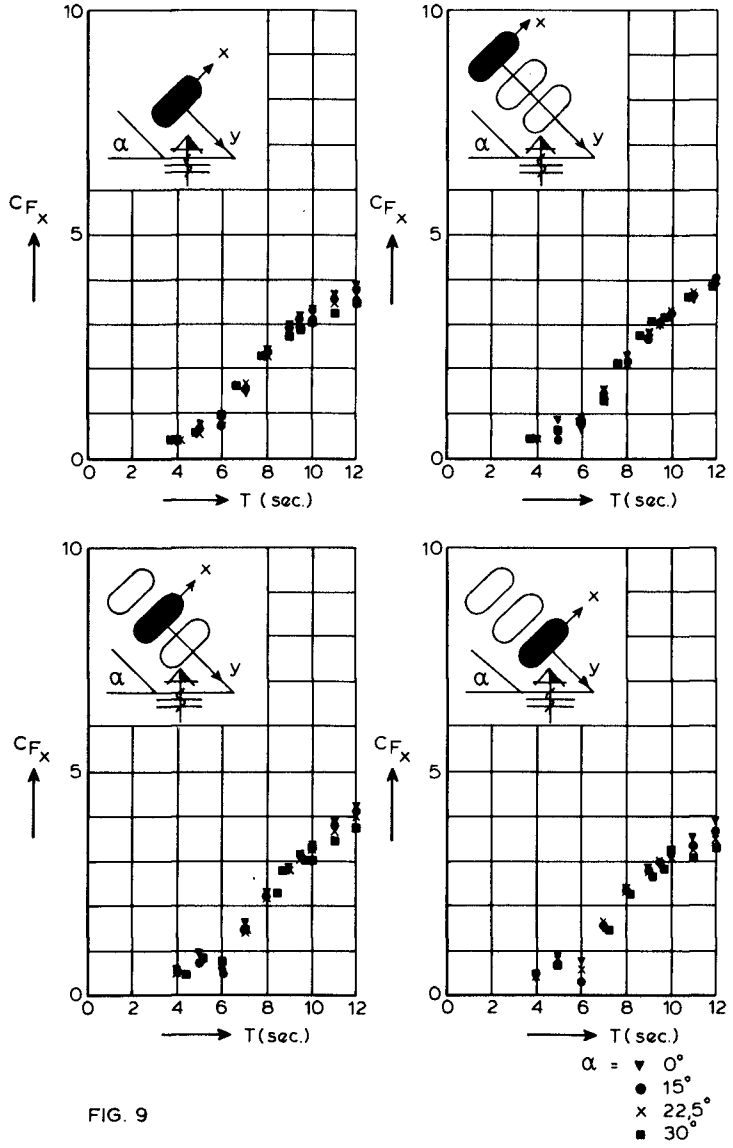


FIG. 9

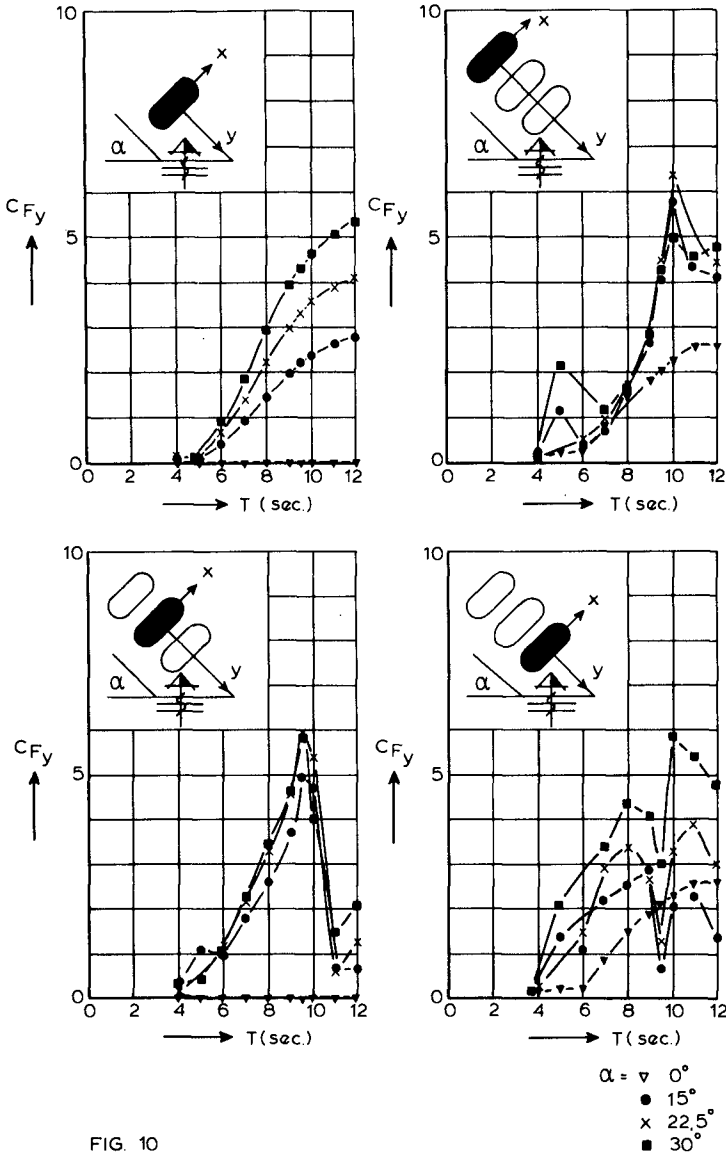


FIG. 10

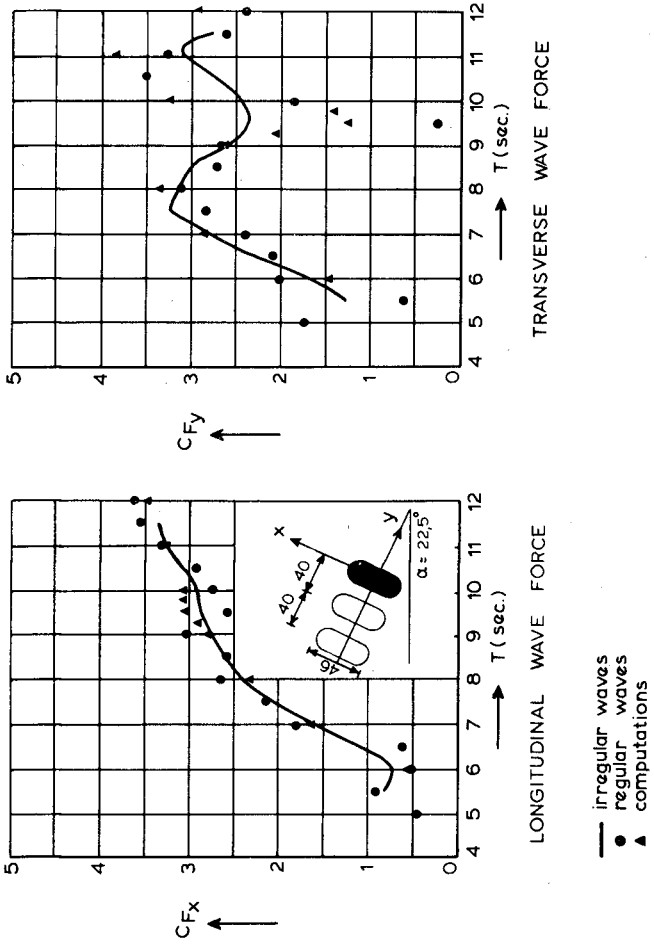


FIG. 11

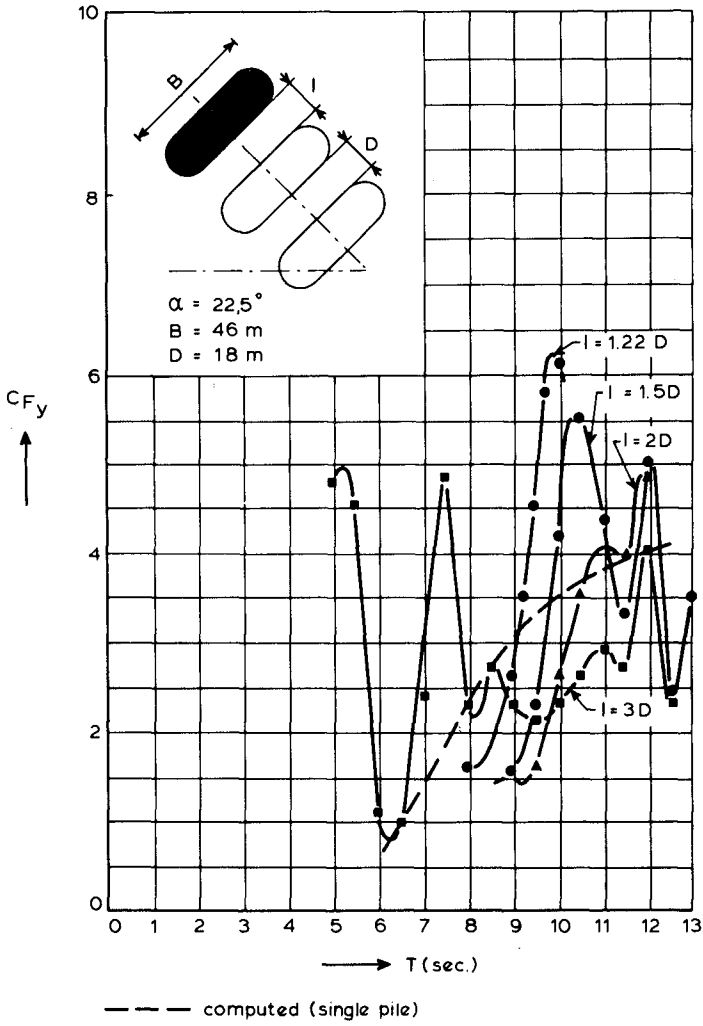


FIG. 12

Transverse forces measured for different distances between the piles (Figure 12), show highest amplification for closely spaced piles ($1/D=1.22$), values decrease with increasing distance between the piles. Obviously, critical wave periods causing maximum amplification are also shifted. Maximum forces for all configurations are, however much higher than those found for the individual piles.

REFERENCES

- 1 BERKHOFF, J.C.W., Mathematical models for Simple Harmonic Linear Water Waves. Wave Diffraction and Refraction. Thesis Delft Technological University, 1976.
- 2 CHAKRABARTI - SUBRATEA, K., Wave Forces on Multiple Vertical Cylinders A.S.C.E.-Journal of the Waterway, Port Coastal and Ocean Division WW2 - May 1978.
- 3 Mac CAMY, R.C. and FUCHS, R.A., Wave forces on Piles. A Diffraction theory Technical Memorandum No 69, Beach Erosion Board, Coastal Engineering Research Center U.S. Army, Washington DC, 1954.
- 4 MASSEL, S.R., Interaction of Water Waves With Cylinder Barrier A.S.C.E.-Journal of the Waterways, Harbours and Coastal Engineering Division Vol 102. No WW2, May 1976.
- 5 SPRING, B.H. and MONKMEYER, P.L., Interaction of plane waves with Vertical Cylinders. Proceedings of the 14th International Conference on Coastal Engineering, Copenhagen 1974.

WAVE LOADS ON HORIZONTAL CYLINDERS

by

P. Holmes¹ and J. R. Chaplin²INTRODUCTION

The problem of predicting wave induced loads on cylinders is an enormously complex one. It is clear from the scatter present in most experimental determinations of force coefficients that there are many individual factors which influence the mechanisms of flow induced loading. Among these are some, for instance Reynolds number, separation and periodic vortex shedding, which are inter-related and whose influences cannot be studied in isolation. Others, such as shear flow, irregular waves and free surface effects, can at least be eliminated in the laboratory, in order to approach an understanding of the more fundamental characteristics of the flow.

A vertical cylinder in uniform waves experiences an incident flow field which can be described in terms of rotating velocity and acceleration vectors, always in the same vertical plane, containing also the cylinder axis, whose magnitudes are functions of time and of position along the length of the cylinder. Some of the essential features of this flow can be studied under two-dimensional oscillatory conditions, in which either the cylinder or the fluid is oscillated relative to the other along a straight line (planar oscillatory flow). The incident velocity and acceleration vectors are then always concurrent, normal to the cylinder axis, and oscillating in magnitude with time.

According to Morison's equation (1), the total force per unit length on the cylinder in line with the velocity and acceleration vectors in this context, is the sum of the drag and inertia components:

$$F = F_d + F_i = C_d \frac{1}{2} \rho d U|U| + C_m \frac{\pi d^2}{4} \rho \frac{dU}{dt} \quad (1)$$

where C_d and C_m are the time-independent drag and inertia coefficients, U the instantaneous flow velocity, ρ the fluid density and d the cylinder diameter. From experiments in planar oscillatory flow around smooth cylinders, Sarpkaya (2, 3) found that C_d and C_m are functions of the Keulegan Carpenter number, $K_C = U_{\max} T/d$, where T is the period of oscillation, and of the Reynolds number, $Re = U_{\max} d/\nu$, when it is

1. Professor of Maritime Civil Engineering, University of Liverpool, U.K.
2. Lecturer in Civil Engineering, University of Liverpool, U.K.

greater than about 2×10^4 . Sarpkaya derived C_d and C_m from force records by a Fourier-averaging procedure.

Very much less attention has been given to wave loads on horizontal cylinders, although many characteristics of the flow are qualitatively different from those relating to vertical cylinders. Most of the investigations on horizontal cylinders have concentrated on the effects of proximity of the ocean bottom (4, 5, 6), so that particle orbits in the region of the cylinder were fairly flat ellipses. In some cases the flow is assumed to be planar oscillatory as described above. Mauli and Norman (7) measured wave forces on horizontal cylinders where particle orbits were almost circular and analysed the results in terms of horizontal and vertical load components. It is more instructive, however, to study the load components which are in line with the velocity and acceleration vectors respectively, since the drag and inertial contributions are then more readily distinguished. In the particular case when particle orbits in the region of the cylinder are circular, the incident flow around the cylinder is represented approximately by uniform flow described by a rotating velocity vector of constant magnitude. The actual flow deviates from this uniform condition as a result of the phase differences in the direction of wave propagation between particle motion on adjacent orbits, and because of the exponential decay of particle velocities with depth. However, providing the diameter of the cylinder is small compared with the wavelength the assumption of uniform ambient flow is a reasonable one. The undisturbed flow conditions around the cylinder can then be specified very simply. As in the case of the idealisation of flow around vertical cylinders in waves by planar oscillatory flow, some of the essential features of horizontal cylinders in waves can be represented in isolation. The ambient flow consists of a body of water moving without distortion or rotation around a circular orbit at the centre of which is the axis of the cylinder. The incident velocity and acceleration vectors are now of constant magnitude, rotating with constant angular velocity once in every wave period, with the latter leading the former by 90° . In this context the components of Morison's equation for force per unit length may be written:

$$F_d = \rho C_d \frac{1}{2} \rho d \Omega^2 R^2 \quad (2)$$

$$\text{and } F_i = C_m \frac{\pi d^2}{4} \rho \Omega^2 R \quad (3)$$

where F_d and F_i are respectively drag and inertia load per unit length, Ω is the wave angular frequency and R the radius of the particle orbit. The components F_d and F_i act in the directions of the velocity and acceleration vectors respectively and are thus now orthogonal. It is worth noting that viewed from a frame of reference centred on the axis of the cylinder and rotating with the wave frequency, the ambient flow, but for the re-cycling of the previously generated wake, is steady. Moreover, fluctuations with time in F_d and F_i can be caused only by this disturbed incident flow resulting from the previously generated wake, and by vortex shedding.

Like planar oscillatory flow, this simplified model of circular irrotational ambient flow around a cylinder can be used in the laboratory to reproduce some features of wave loading, in the absence of others which normally add to the complexity of interpreting experimental data. It is perhaps closer to the widely studied case of steady uni-directional flow around cylinders since the interference of the wake on the incident flow is less pronounced, and the magnitude of the velocity is steady. The analytical methods used to investigate separated flow around cylinders, such as the finite difference solution for the time-dependent Navier-Stokes equations (8), or the discrete vortex model (9), may be used also in this context without fundamental changes. However, they remain restricted or incomplete, and require experimental data for verification.

The purpose of this paper is to describe an experiment in which circular irrotational ambient flow around a cylinder was modelled by moving a cylinder without rotation around a circular orbit in initially still water. Allowing for the changed frame of reference, the motion of the fluid is identical in the two cases. However, forces experienced by the cylinder differ due to the presence of a pressure gradient in the fluid on the one hand and to the inertia of the cylinder itself on the other. The difference may easily be calculated, as shown below. Forces experienced by the cylinder were monitored continuously with time for Reynolds numbers in the range 0.4×10^5 to 2.4×10^5 and for Keulegan Carpenter numbers of 12.8, 24.0 and 35.7.

APPARATUS

The tests were carried out in a tank about 5m. square in plan, in a water depth of 90cm. The cylinder was supported with its axis vertical from an arm which rotated above the water surface about a central pivot. The apparatus is shown in Fig. 1. A one horsepower variable speed motor provided the drive to the central shaft and was mounted on the side of the tank to minimise vibrations in the cylinder support. In order that the cylinder should pass around its orbit without rotation, a secondary drive belt was provided between its axial support and a fixed central pulley. A number of alternative interchangeable belts facilitated different orbital radii. The use of toothed rubber timing belts throughout ensured perfectly synchronous rotation between the motor, the central drive shaft and the cylinder itself. A simple potentiometer with its end stops removed was connected to the motor and acted as an angular displacement transducer, from the output of which also the angular velocity of the arm could be derived.

The cylinder was mounted axially on a 5cm. diameter hollow alloy tube, cantilevered vertically downwards from the rotating arm, instrumented near its upper end with orthogonal pairs of strain gauges. Since the cylinder and its support did not undergo rotation the cable to the gauges was not subject to any overall twisting and could be connected directly to the conditioning instruments. The cylinder was made out of 15cm. diameter perspex tube of 10mm. wall thickness, and was airtight to minimise its mass. Its natural frequencies in air and water were respectively 14 Hz. and 9 Hz. End discs of diameter 25cm. were mounted on the cylinder as shown in Fig. 1. At its upper end a larger disc of diameter 60cm. was mounted on the fixed cylinder to minimise free surface interference on the instrumented cylinder.

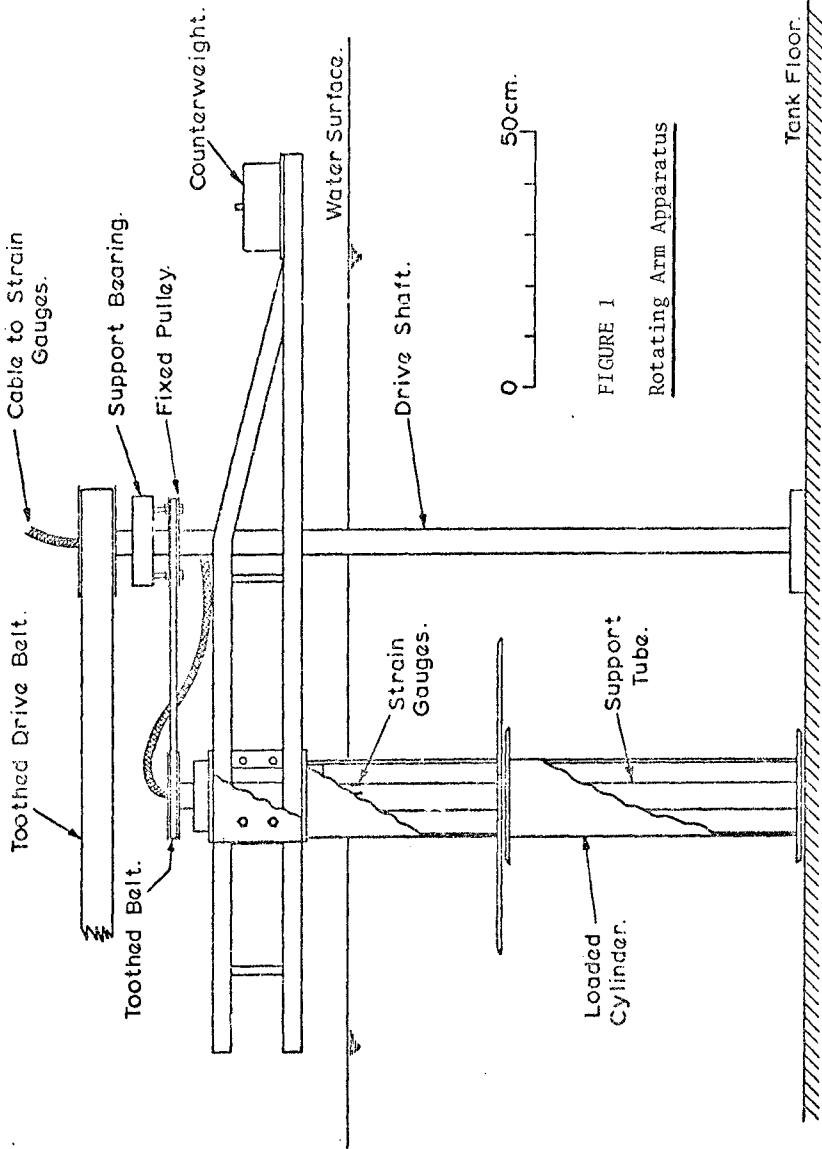


FIGURE 1
Rotating Arm Apparatus

Experiments were run on-line to a Data General Nova Computer which sampled the unfiltered outputs of the strain gauge amplifiers and angular displacement transducer at a frequency of 100 Hz. With the available core, maximum run time was about 40 seconds. The data was processed immediately after each test to provide radial and tangential load components (since the orientation of the gauges rotated with respect to the radial direction during each rotation) and velocities. Besides further digital processing the data was then available for conversion back to analogue form for plotting at a reduced speed on a pen recorder.

Initial strain gauge calibrations were carried out by loading the cylinder at its centre from weights hung over a pulley at the side of the tank. From subsequent tests in air, the effective mass of the cylinder and its support was determined from the outputs of the gauges responding to centrifugal forces. A more rapid method of calibration was then possible, since during each revolution of the apparatus in air, the strains in the cylinder support tube oscillated about zero. A sinusoid was fitted by least squares to the output of each pair of gauges from which their sensitivities and absolute orientations were derived. This method of calibration was applied before and after each series of tests, and in every case the stability of the gauges and instruments was found to be satisfactory. The effective mass of the cylinder and support was 5.47 kg.

RESULTS AND DISCUSSION

According to Morison's equation, the forces per unit length experienced by a cylinder passing around a circular orbit in otherwise still water are:

$$F_d = C_d \frac{1}{2} \rho d \Omega^2 R^2 \quad (4)$$

$$\text{and } F_i = C_a \frac{\pi d^2}{4} \rho \Omega^2 R + M \Omega^2 R \quad (5)$$

where R is the orbit radius, M the mass per unit length of the cylinder. The added mass coefficient C_a is given by $C_a = C_m - 1$. The primary object of the experiments described here was to investigate C_d and C_a as functions of the Reynolds number R_e and the Keulegan Carpenter number K_c . The components F_d and F_i correspond to the mean tangential and radially outward forces respectively measured on the cylinder. The derived values for C_d and C_a are time averaged; it is worth noting that since F_d and F_i are orthogonal, C_d and C_a can be derived independently.

In an ideal fluid $C_a = 1$. Although this result is normally derived in the context of concurrent velocity and acceleration vectors, it applies to all cases, whatever their relative orientations.

Tests were carried out with the 15cm. diameter cylinder located at three different radii on the rotating arm: 0.306m, 0.572m. and 0.852m. Since the Keulegan Carpenter number is given by:

$$K_c = \frac{2\pi R}{d} \quad (6)$$

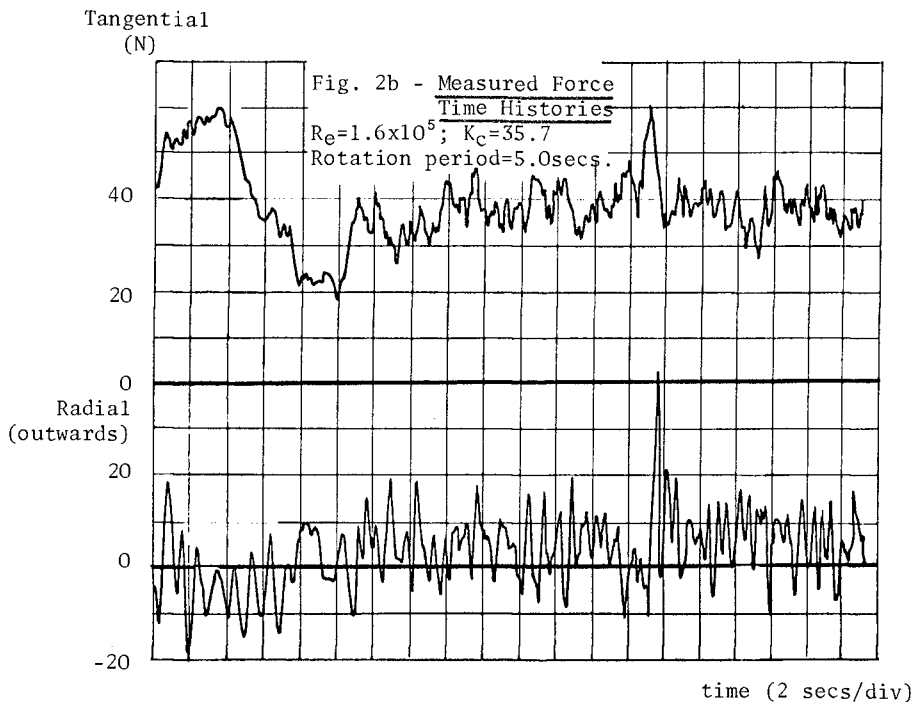
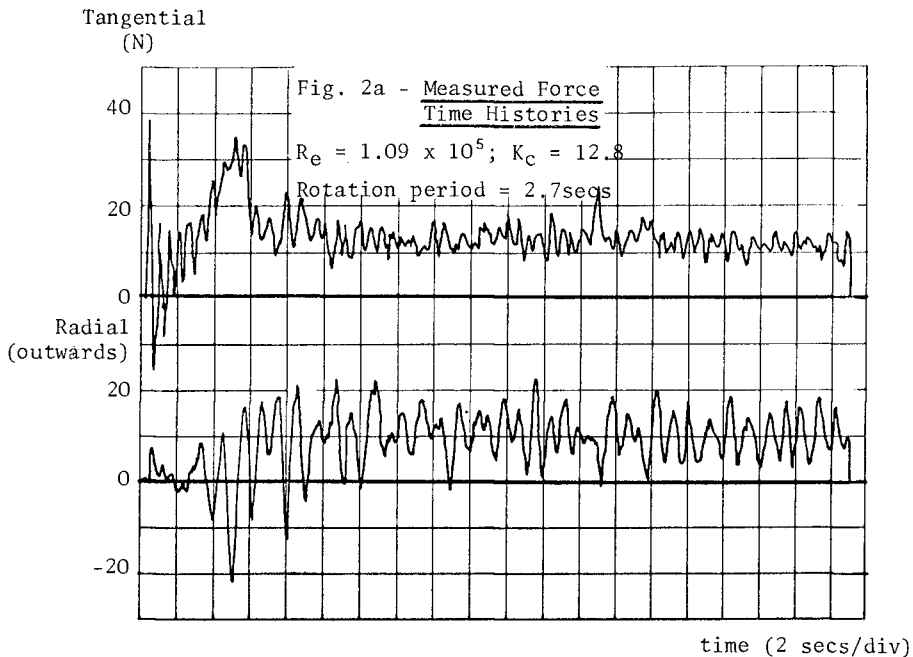
its value is independent of the speed of rotation, by which the Reynolds number is determined:

$$R_e = \frac{\Omega R d}{\nu} \quad (7)$$

The three radii used in the tests correspond to K_c values of 12.8, 24.0 and 35.7, respectively. The appearance of K_c and R_e directly as the independent parameters of the experiment is an advantage, since the flow-induced loads are expected to be functions of them only for rigid smooth cylinders.

Fig. 2 presents typical records of tangential and radial loads derived from the strain gauge outputs. In both cases the cylinder was accelerated from rest at the beginning of the record to a constant angular velocity. The first revolution of the cylinder around its orbit is characterized by abnormally high drag and oscillating lift associated with strong vortex shedding. Subsequently the cylinder passes into its own wake and the disturbances present result in a reduction in drag and oscillating lift. After two or three revolutions the mean drag and inertial loads stabilise and show very little variation with time. It is worth noting that the motion of the cylinder resulted in little overall rotation of the water in the tank, which would have caused a progressive reduction in flow-induced forces owing to reducing relative incident velocities. It is reasonable to assume that the cylinder does not stir the tank appreciably for the following reasons. Firstly, its dimensions are small compared with those of the tank itself. Secondly, the cylinder does not rotate; disregarding preferential decay of vorticity of one sense of rotation there is therefore no net addition of vorticity to the water in the tank from the motion of the cylinder.

Radial force records show fluctuations of irregular magnitudes at a frequency corresponding to a Strouhal number of about 0.2. Drag and added mass coefficients are presented in Fig. 3 as functions of R_e and K_c . Each point is derived from the mean radial and tangential force components recorded over a period of about 40 seconds. In each case three or four revolutions were completed before the recording was begun. Fig. 3 clearly shows that with increasing R_e , there is a reduction in C_d and an increase in C_a , depending also on K_c . Although it is clear that the reduction in C_d follows the expected behaviour close to transitional R_e , it is not easy to account for the equally dramatic change in C_a . In contrast to uniform or planar oscillatory flow around a cylinder, in the present case the orbital motion must result in asymmetry of the time-averaged characteristics of the wake. Although the rates at which vorticity is shed in the two shear layers are equal, the outer shear layer must be weaker since its separation point is moving away through the fluid more rapidly than that of the inner shear layer. This causes the vortex shedding to be an asymmetrical process, with unequal proportions of the shed vorticity finding its way into the major



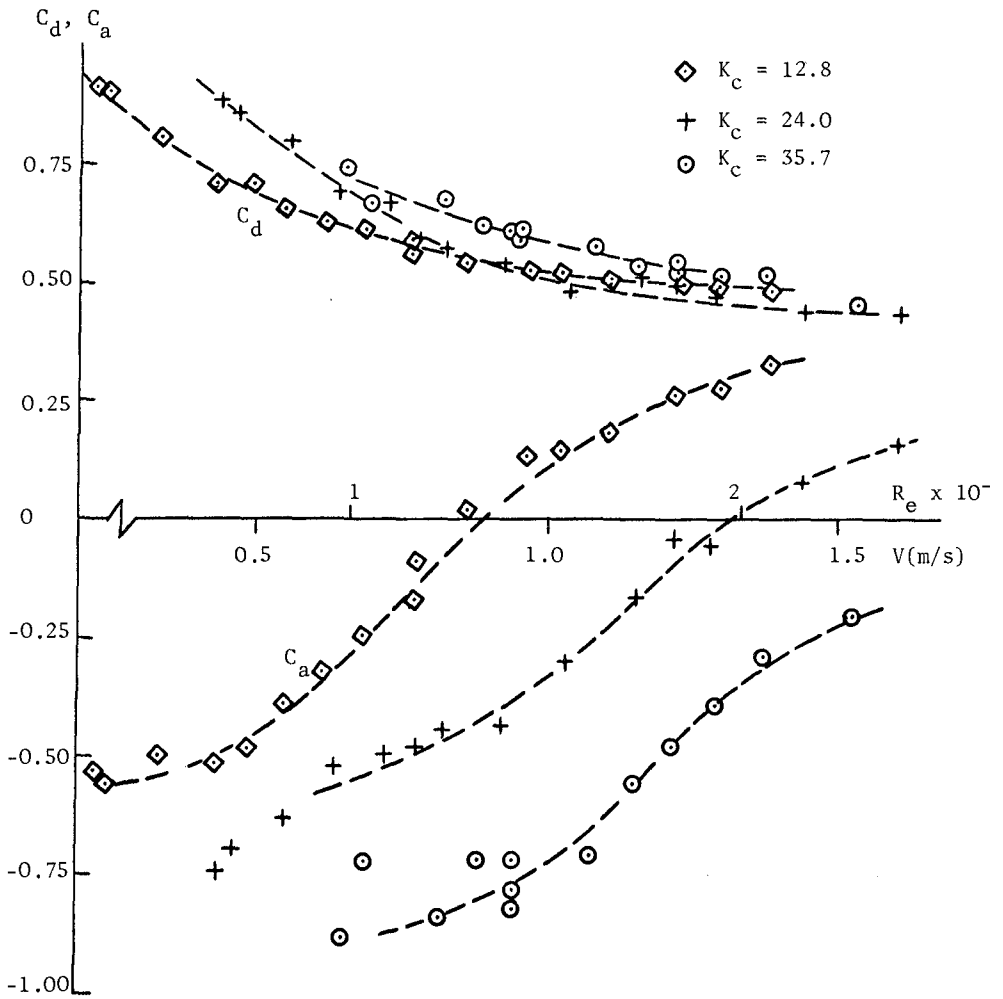


FIGURE 3

Drag Coefficient and Added Mass Coefficient as Functions of Reynolds Number at Keulegan Carpenter Numbers

vortices of alternate senses of rotation. Possibly modification of this mechanism at transitional Reynolds numbers causes the observed changes in C_a .

However, despite the obvious differences in flow conditions, it is interesting to compare the present results with those obtained by Sarpkaya (3) for planar oscillatory flow around a cylinder. Lines fitted to the data have been re-plotted with Sarpkaya's results in Figs. 4 and 5, where it is shown that there exists at least some qualitative agreement between the two sets of data. Agreement between inertia coefficients would suggest that the added mass of the cylinders were independent of the relative orientations of the velocity and acceleration vectors. As mentioned previously, this would be the case in an ideal fluid, but in a real fluid it is reasonable to expect that the effects of viscosity and the history of the flow would make contributions to the added mass. Qualitative agreement between the two sets of data would also suggest that a conceptual explanation of the observed changes at transitional Reynolds numbers must be sought in terms of the features common to both cases.

CONCLUSIONS

Circular orbital flow around a cylinder has been modelled experimentally by moving a cylinder around a circular path in otherwise still water. The nature of the resulting flow warrants further investigation since it displays many of the essential features present in wave-induced flow around cylinders, and yet is specified very simply.

With increasing Reynolds number over the range 0.4×10^5 to 2.4×10^5 the drag coefficient was found to fall from about 0.9 to 0.4, depending also on Keulegan Carpenter number. Simultaneously the added mass coefficient increased, becoming positive only for higher Reynolds numbers. In both respects the present results are in qualitative agreement with those of Sarpkaya (3) for planar oscillatory flow.

REFERENCES

1. Morison, J. R., O'Brien, M. P., Johnson, J. W. and Schaaf, S. A. 'The force exerted by surface waves on piles', Petroleum transactions, AIME, Vol. 189, 1950, p.149.
2. Sarpkaya, T. 'Forces on cylinders and spheres in a sinusoidally oscillating fluid', Journal of Applied Mechanics, ASME, March 1975, p.32.
3. Sarpkaya, T. 'Vortex shedding and resistance in harmonic flow about smooth and rough circular cylinders', Proc of First Int. Conf. on Behaviour of Offshore Structures, Trondheim, 1976, p.220.
4. Yamamoto, T. and Nath, J. H. 'High Reynolds number oscillating flow by cylinders', Proc. of 15th Int. Conf. on Coastal Engineering, Hawaii, 1976, p.2321.

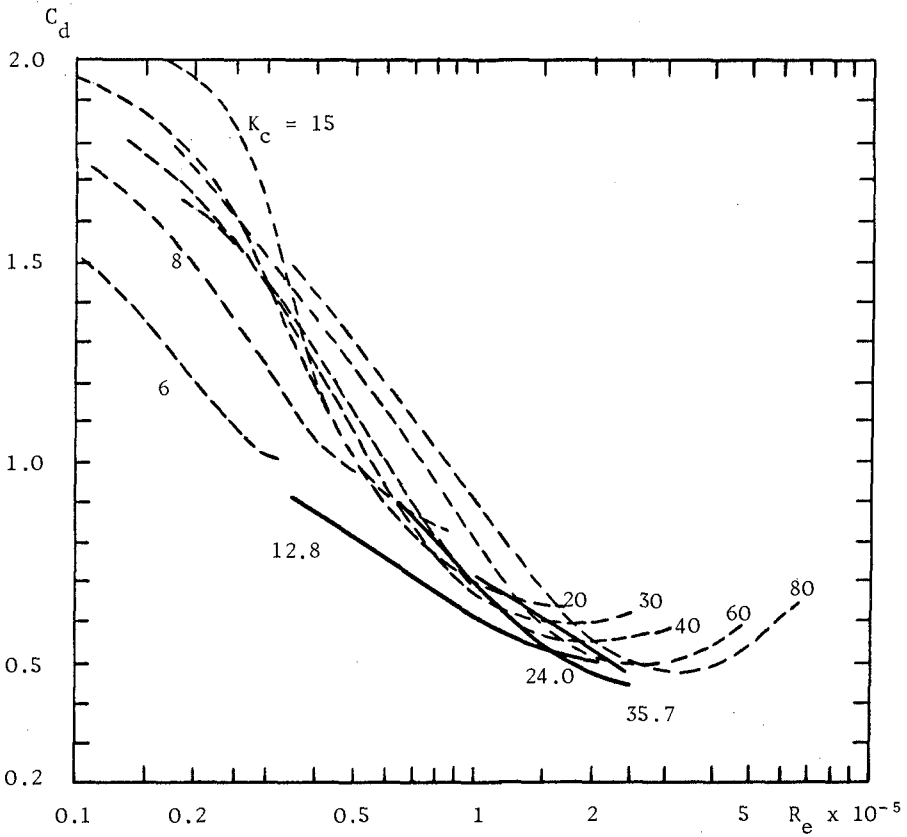


FIGURE 4

Drag Coefficient as A Function of Reynolds Number and Keulegan Carpenter Number

Dashed lines - Sarpkaya (Ref. 3); Solid lines - present results

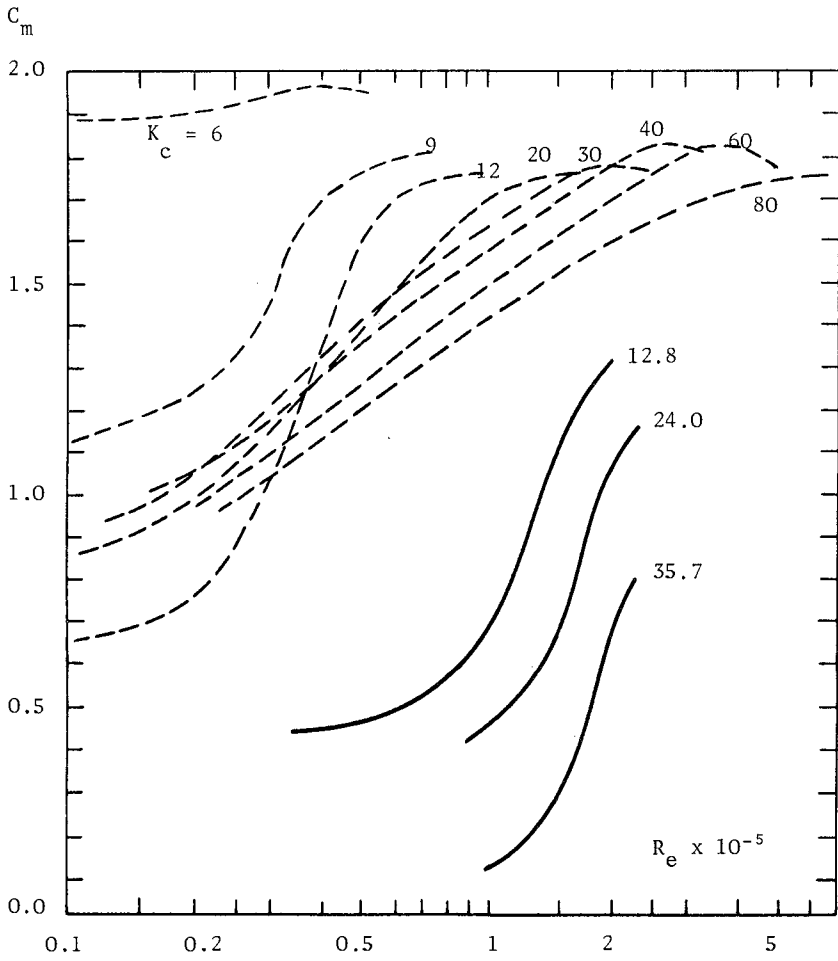


FIGURE 5

Inertia Coefficient as a Function of Reynolds Number and Keulegan Carpenter Number

Dashed Lines - Sarpkaya (Ref. 3); Solid lines - present results.

5. Nath, J. H., Yamamoto, T. and Wright, J. C. 'Wave forces on pipes near the ocean bottom', Proc. of Offshore Technology Conference, Houston, May 1976, OTC 2496.
6. Sarpkaya, T. 'Forces on cylinders near a plane boundary in a sinusoidally oscillating fluid', Fluid Mechanics in the Petroleum Industry, ASME, Dec. 1975, p.43.
7. Maull, D. J. and Norman, S. G. 'A horizontal cylinder in waves', Proc. of Symposium on Mechanics of Wave-Induced Forces on Cylinders, Sept. 1978, Bristol, U.K.
8. Roache, P. J. 'Computational Fluid Dynamics', Hermosa, Albuquerque, 1972.
9. Stansby, P. K. 'An inviscid model of vortex shedding from a circular cylinder in steady and oscillatory far flows', Proc. Inst. Civ. Engrs. Vol. 63, Part 2, 1977, p.865.

CHAPTER 148

NON-BREAKING AND BREAKING WAVE LOADS ON A COOLING WATER OUTFALL

by

G.R. Mogridge* and W.W. Jamieson**

ABSTRACT

Cooling water from a power generating station in Eastern Canada is pumped to an outfall and distributed into the ocean through discharge ports in the sidewalls of a diffuser cap. The cap is essentially a shell-type structure consisting of a submerged circular cylinder 26.5 ft in diameter and 14 ft high. It is located in 25 ft of water at low water level and 54 ft at high water level. Horizontal forces, vertical forces and overturning moments exerted by waves on a 1:36 scale model of the diffuser cap were measured with and without cooling water discharging from the outfall. Tests were run with regular and irregular waves producing both non-breaking and breaking wave loads on the diffuser cap.

The overturning moments measured on the diffuser cap were up to 150 percent greater than those on a solid submerged cylinder sealed to the seabed. Unlike sealed cylinders, all of the wave loads measured on the relatively open structure reached maximum values at approximately the same time. The largest wave loads were measured on the diffuser structure when it was subjected to spilling breakers at low water level. For a given wave height, the spilling breakers caused wave loads up to 100 percent greater than those due to non-breaking waves.

INTRODUCTION

A power generating station, located on the east coast of Canada, disposes of cooling water through a 12 ft diameter tunnel a distance of approximately 300 ft offshore, where it rises vertically to a diffuser structure which distributes the water through a number of discharge ports into the Bay of Fundy. The large arrows, in the schematic representation of the cooling water outfall in Fig. 1(a), indicate the flow direction of the warm water through the tunnel, into the diffuser cap and out of the discharge ports. The diffuser cap is a shell-type structure consisting basically of a submerged concrete circular cylinder with a solid top, an open bottom and a number of 5.5 ft square openings in the sidewalls. It is 26.5 ft in diameter, 14 ft high and is held in place by rock anchors. The bottom of the cap does not make a perfect seal with the seabed because of numerous gaps between the bottom of the structure and the seabed around its circumference. The cooling water outfall is located in a water depth of 25 ft at low water level (LWL), 39 ft at mean water level (MWL) and 54 ft at high water level (HWL). Since waves up to 50 ft high are expected at this location, the structure is exposed to breaking waves. The five arrows radiating outward from the diffuser cap in Fig. 1(b) show the direction of cooling water discharge in

*Associate and **Assistant Research Officers, Hydraulics Laboratory, Division of Mechanical Engineering, National Research Council of Canada, Ottawa, Ontario, Canada, K1A 0R6.

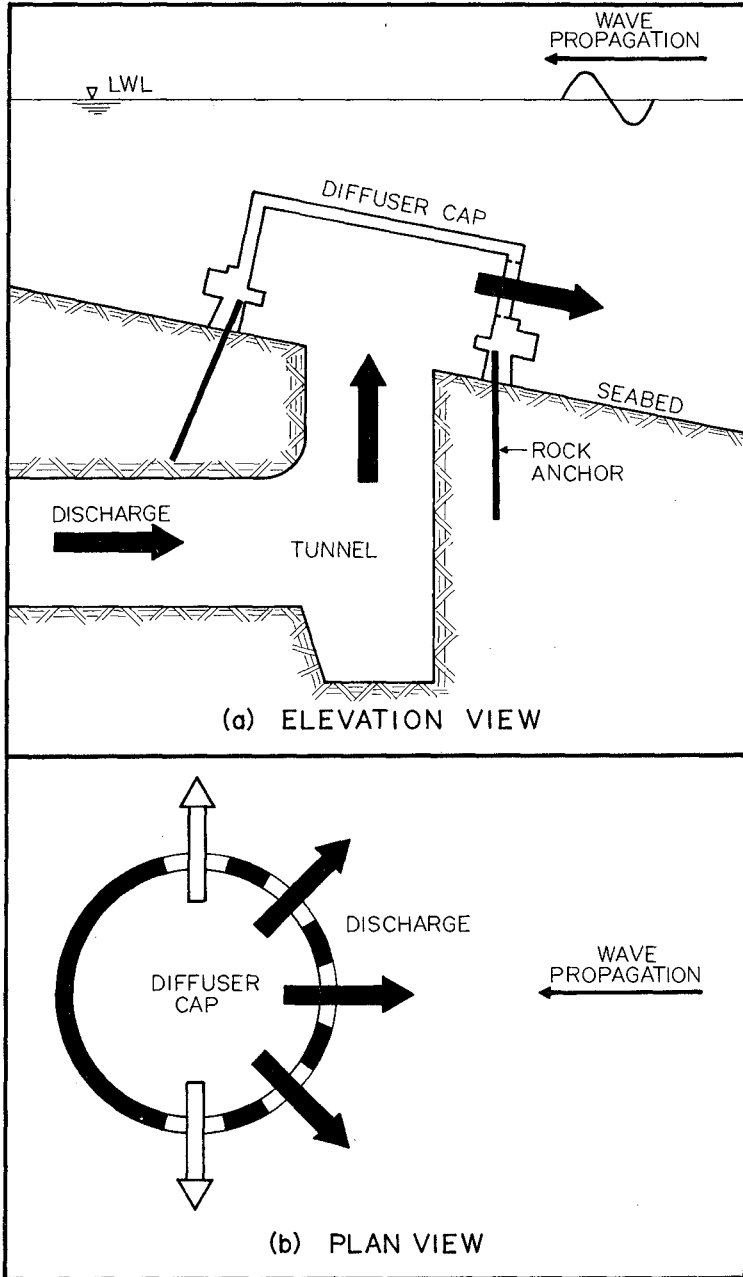


FIG.1 COOLING WATER OUTFALL

relation to the direction of wave propagation. The three shaded arrows indicate the present requirements of the power generating station, which call for 3 discharge ports ($N=3$) and a cooling water discharge Q of 300,000 gpm (US). In the near future, the cooling water outfall will be required to handle a discharge of 450,000 gpm (US) with five discharge ports ($N=5$) in operation as indicated by the five arrows in Fig. 1(b). After being damaged during a storm in February 1976, the anchoring system had to be redesigned to secure the diffuser cap to the seabed. The loads exerted by ocean waves and cooling water discharge were required to permit a safe design of the structure and its rock anchors.

Various methods, which use linear wave theory and neglect viscous effects, are available for predicting wave loads on large submerged structures resting on the seabed. For example, Garrison and Chow (6), and Hogben and Standing (10) have published linear numerical diffraction theories which use a source distribution over the immersed surface of a structure for the prediction of wave loads. For ease of computation, these methods have been simplified by Black (1), Garrison and Stacey (8), Fenton (4) and Isaacson (11). Gran (9) has presented an analytical method which does not satisfy all the boundary conditions but provides an approximate solution at minimum cost. Black, Mei and Bray (2) have presented a semi-analytical method using variational calculus while Yue, Chen and Mei (14) have proposed a method that they refer to as a hybrid element method which combines the use of variational principles and finite element techniques. All of these methods assume that structures, which sit on a flat bottom, are both solid and sealed to the seabed. For structures raised slightly above the seabed, both experimental and theoretical results have been presented by Gran (9) for cylinders, and by Chakrabarti and Naftzger (3) and Garrison and Snider (7) for hemispherical shells. To the authors' knowledge, no information is available in the literature concerning the calculation of wave loads on a relatively large shell-type structure such as the diffuser cap, which is not only raised above the seabed but has large openings in the side-walls. The prediction of the maximum design loads on the diffuser cap is further complicated by the existence of irregular waves, cooling water discharge and critically steep waves that result in spilling breakers in the vicinity of the outfall during storm conditions.

Since reliable theoretical methods were not available for predicting the wave loading on such a complex structure, it was necessary to perform model tests. The loading due to non-breaking and breaking waves in regular and irregular wave trains, and the effects of cooling water discharge were measured using a 1:36 Froude model. A digital computer was used for the acquisition, processing, plotting and storage of the experimental data.

EXPERIMENTAL METHOD

The photograph in Fig. 2 shows the 1:36 plexiglass scale model of the diffuser cap which was positioned in the centre of a 12 ft wide wave flume. A semiconductor strain gauge force dynamometer was used to measure the forces and overturning moments on the model. The sign convention (Fig.3) was chosen such that the horizontal force $F_x(t)$ is positive in the direction of wave propagation, the vertical force $F_z(t)$ is positive in the upward direction and the overturning moment $M_y(t)$ is positive in the counter-clockwise direction. The force dynamometer had an overall



FIG. 2 MODEL OF DIFFUSER CAP

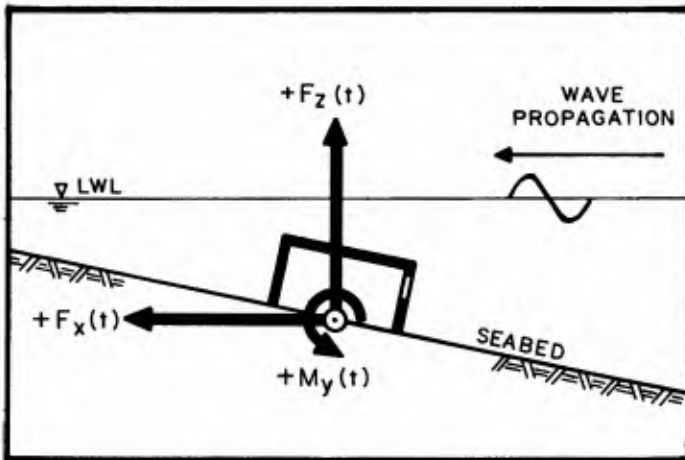


FIG. 3 SIGN CONVENTION

accuracy of within plus or minus three percent. It was mounted in a cavity in the floor of the wave flume below a steel base plate which was flush with the bottom. The diffuser cap was connected rigidly to the force dynamometer by four aluminum rods which passed freely through holes in the steel base plate. The discharge pipe, that was used in the model to simulate the prototype cooling water tunnel, did not touch or interfere with the operation of the force dynamometer. The exit of the model discharge pipe can be seen in Fig. 2 through the discharge port in the front of the diffuser cap. The natural frequency of vibration of the total measuring system with the model mounted was approximately 75 Hz when submerged in water, and therefore was sufficiently high to eliminate resonance problems.

In Fig. 4, the elevation and plan views of the wave flume show the experimental setup. Beach slopes, modelled from the prototype contours, were 1:50 offshore of the diffuser cap, 1:5 in the immediate vicinity of the cap and 1:8 onshore. Simulation of the cooling water discharge to the model was accomplished by a 300 gpm (US) pump and measured by a calibrated orifice meter. Water was pumped out of a reservoir at the end of the flume through a 2 in. diameter pipe to the diffuser cap and returned via two 3 in. diameter pipes under the floor of the flume from the area of the wave generator. Wave profiles were measured by two capacitance wave probes located as shown in Fig. 4.

Acquisition of data for forces, moments and wave profiles was accomplished using a digital computer. Force, moment and wave profile data were sampled at a rate of 100 data points per second for an interval of 8 sec. For irregular waves this rate was decreased to 20 data points per second to give total record lengths of 50 sec. The data was analysed and the results were automatically plotted and printed immediately following each test.

EXPERIMENTAL RESULTS

Non-Breaking Waves

To determine the effects of wave period T and water depth d on wave loading, the diffuser cap was subjected to regular non-breaking waves for various wave periods and wave heights at LWL, MWL and HWL. Fig. 5 shows typical test results for time series plots of wave loads and water surface elevations $\eta(t)$ measured at the diffuser cap and upwave of the cap. It may be observed that the phasing of the wave loads and water surface elevation are such that all the loads, $F_x(t)$, $F_z(t)$ and $M_y(t)$, reach maximum positive values near the time of still water level (SWL). Throughout the testing program, the experimental results indicated that the maximum positive magnitudes of the wave loads were always greater than the maximum negative values. Thus, only the magnitudes of the maximum positive loads will be considered in this paper. Fig. 6 shows the experimental measurements for the maximum values of horizontal force F_x , vertical force F_z and overturning moment M_y plotted against wave height H measured at the diffuser cap, for wave periods between 6 and 16 sec. There is only a small variation of wave loads with wave period, although the magnitudes of the wave loads tend to be largest at 10 and 12 sec. A larger variation in wave loading results for different depths of submergence of the diffuser cap as shown in Fig. 7. The largest forces and moments were measured on the diffuser cap when it was located in the shallowest water depth of 25 ft (LWL).

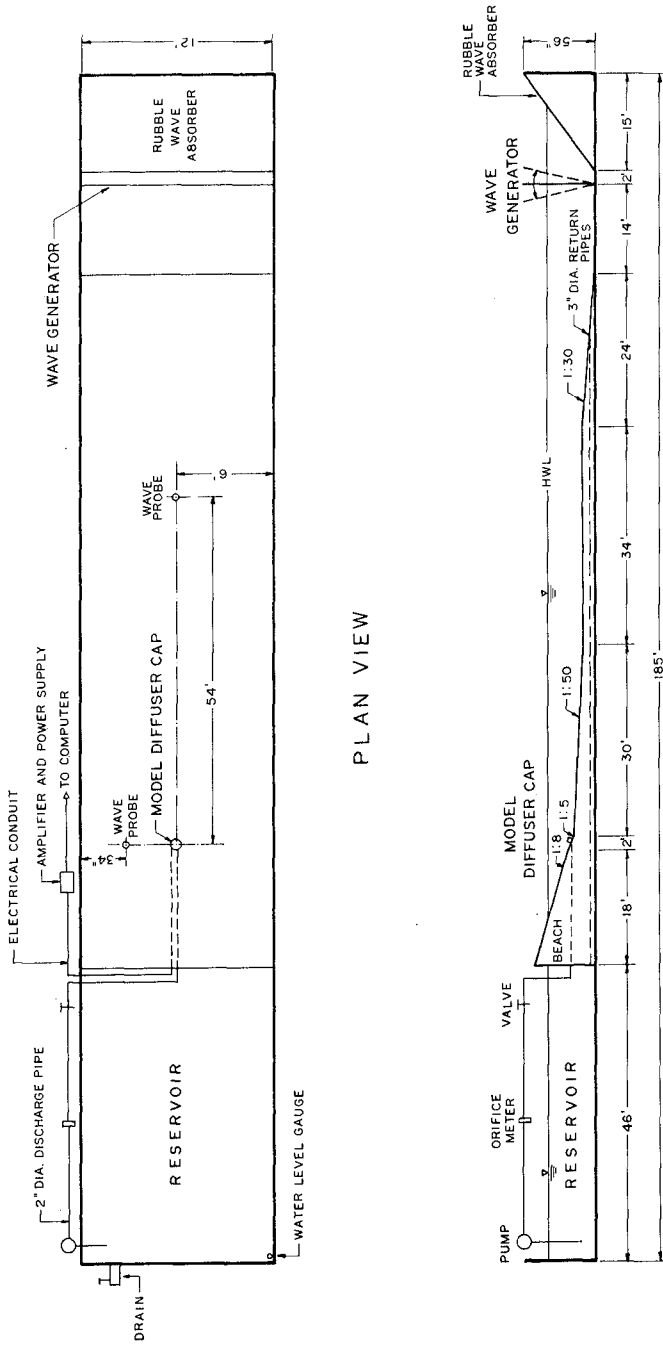
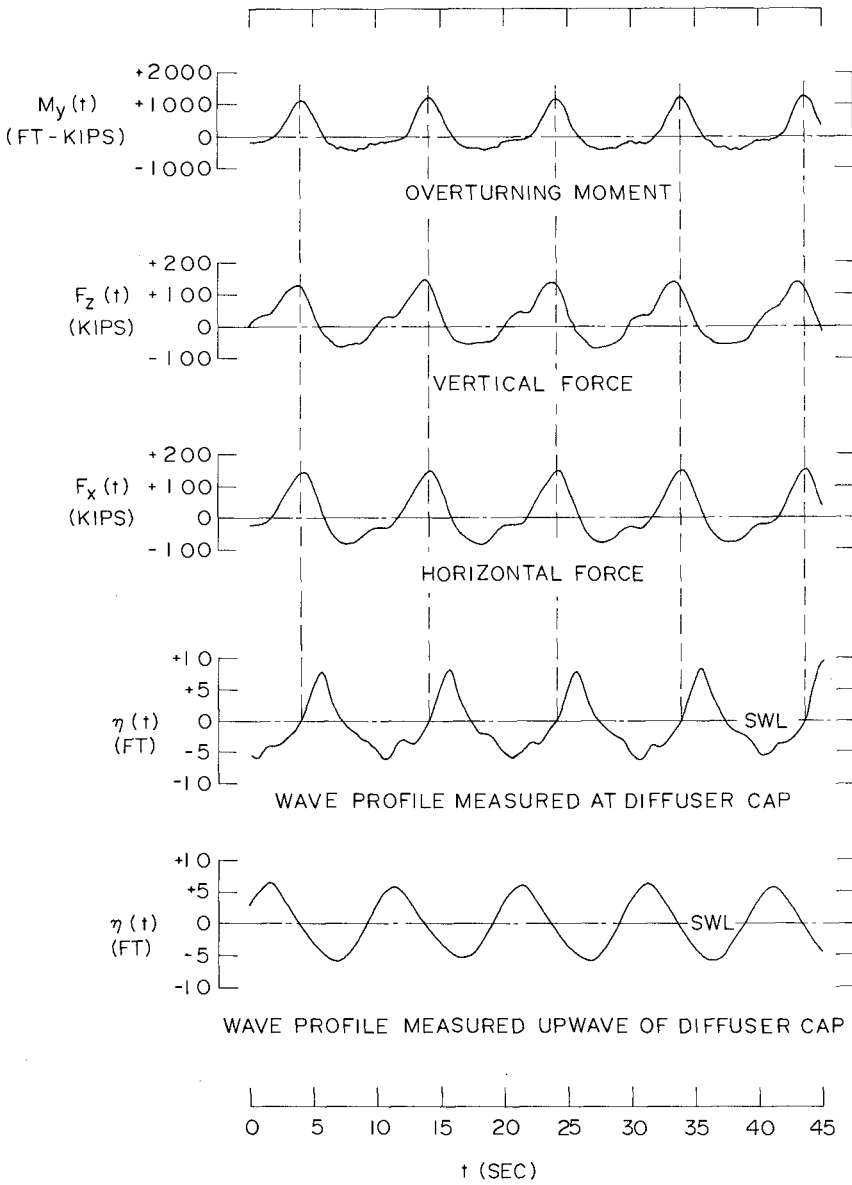


FIG. 4 ELEVATION AND PLAN VIEWS OF WAVE FLUME SHOWING EXPERIMENTAL SETUP

ELEVATION VIEW

PLAN VIEW



**FIG.5 TYPICAL TEST RESULTS
 NON-BREAKING REGULAR WAVES
 ($N=3, Q=0, d=25$ FT, $T=10$ SEC)**

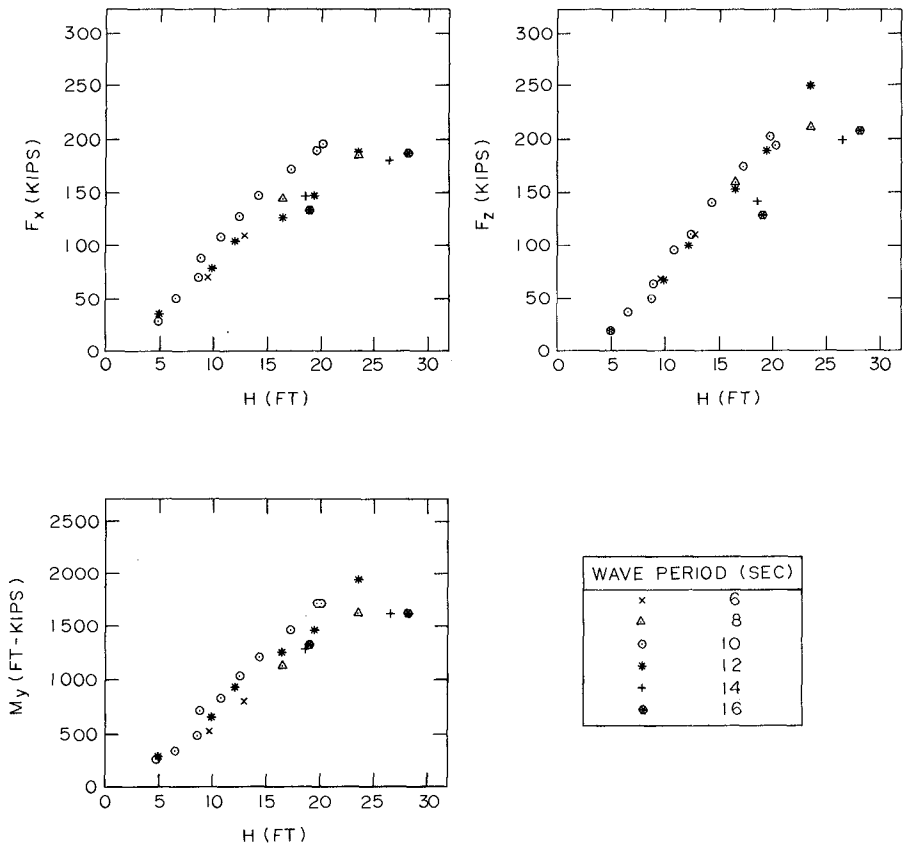


FIG. 6 VARIATION OF WAVE LOAD WITH WAVE PERIOD
 NON-BREAKING REGULAR WAVES
 (N=3, Q=0, d=25 FT)

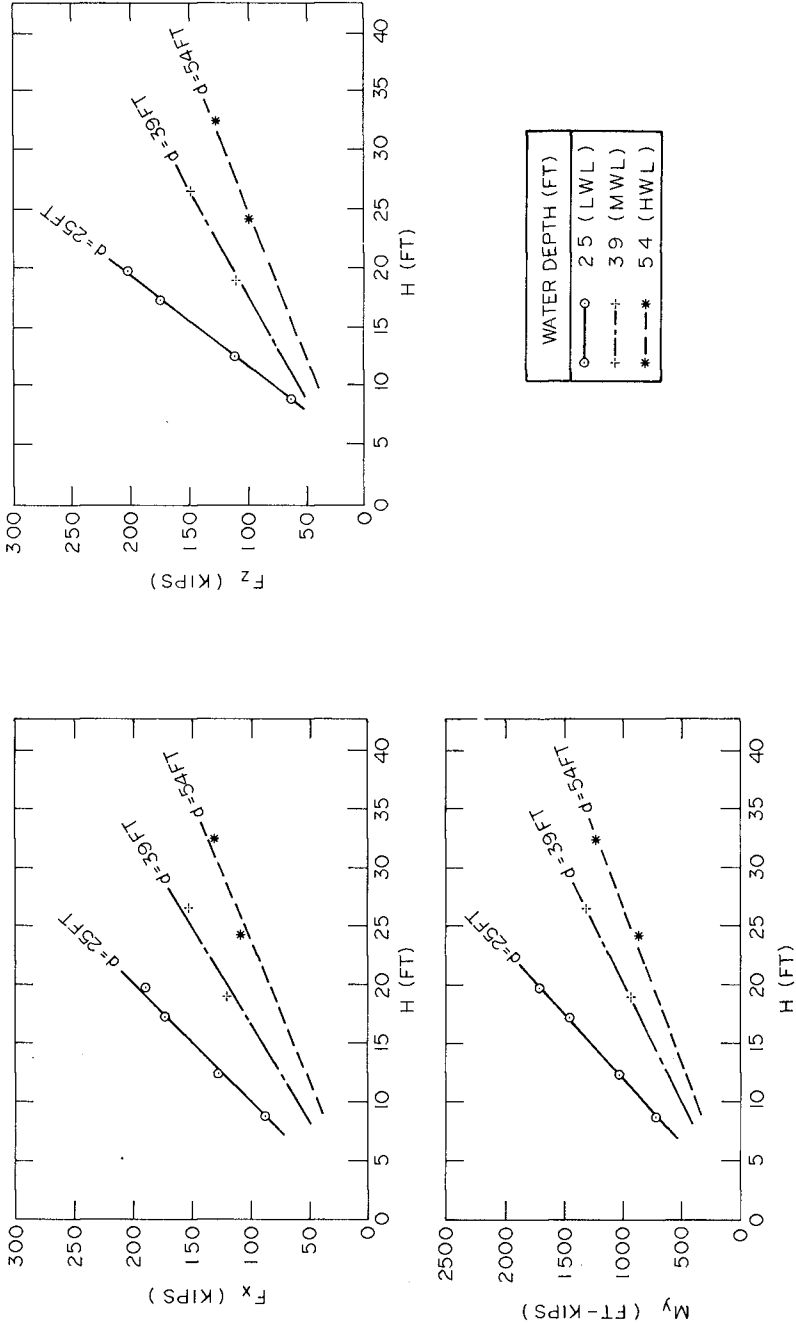


FIG. 7 VARIATION OF WAVE LOAD WITH WATER DEPTH
NON-BREAKING REGULAR WAVES
(N=3, Q=0, T=10 SEC)

A rigorous theoretical method for the prediction of non-breaking wave loads on a relatively open structure such as the diffuser cap does not presently exist. It may be of interest, however, to demonstrate some of the similarities and differences in wave loading between a ported submerged structure, such as the diffuser cap, and a solid submerged structure which is sealed to the seabed. Fig. 8 shows results for a wave period of 12 sec and a water depth of 25 ft for non-breaking regular waves. The wave loading shown for the sealed submerged cylinder, 26.5 ft in diameter and 14 ft high, was calculated using the linear numerical diffraction theory of Hogben and Standing (10).

The horizontal wave forces measured on the diffuser cap are quite similar in magnitude to those on the sealed submerged cylinder. However, it should be mentioned that for some tests, the horizontal forces on the diffuser cap vary as much as plus or minus 25 percent from those on the sealed cylinder. For both structures, F_x occurs approximately at the time of SWL which is indicative of inertial predominant horizontal forces.

The overturning moments on the diffuser cap are significantly larger than those on the sealed submerged cylinder calculated by the diffraction theory and are in fact up to 150 percent larger for some tests. For both the diffuser cap and the sealed cylinder, M_y occurs approximately at SWL.

The vertical forces measured on the diffuser cap are up to 75 percent smaller than those calculated for the sealed submerged cylinder (Fig. 8). The maximum vertical forces for the two cases not only vary significantly in magnitude, but also occur at different times with respect to the wave profile. The maximum uplift forces on the diffuser cap occur approximately at SWL, while those on the sealed cylinder occur near the wave trough. Similar phasing results were obtained experimentally by filling the diffuser cap with styrofoam, which caused the maximum vertical force to occur approximately at the trough; however, when the styrofoam was removed, the phasing reverted back to F_z occurring near the time of SWL. Thus, all the wave loads on the diffuser cap reach maximum values at the same time, resulting in a far more critical loading situation than for the sealed structure where F_z is out of phase with respect to F_x and M_y . The difference in phasing for the diffuser cap is due to the existence of the discharge ports in the offshore side of the cap. Calculations have indicated that if the same magnitude of pressure that exists on the offshore side of the sealed submerged cylinder is allowed to enter through the discharge ports into the diffuser cap, and contributions due to drag are included, a reasonable estimate of the total uplift force on the diffuser cap is possible and it is found to occur approximately at SWL as measured by experiment.

Gran (9) has shown that a gap underneath a solid cylinder causes similar variations in loading. That is, the gap tends to reduce the magnitude of F_z , increase M_y and have little effect on F_x . Garrison and Snider (7), and Chakrabarti and Naftzger (3) have also demonstrated that a substantial reduction in vertical force occurs when a hemispherical shell is held slightly above the ocean bottom, while the horizontal forces remain approximately the same. The analysis of Chakrabarti and Naftzger (3) shows that the pressure inside may be assumed to be uniform for small values of ka and can be approximated by the average pressure at the bottom of the corresponding sealed structure. The force on the raised structure can then be calculated by subtracting this pressure times the

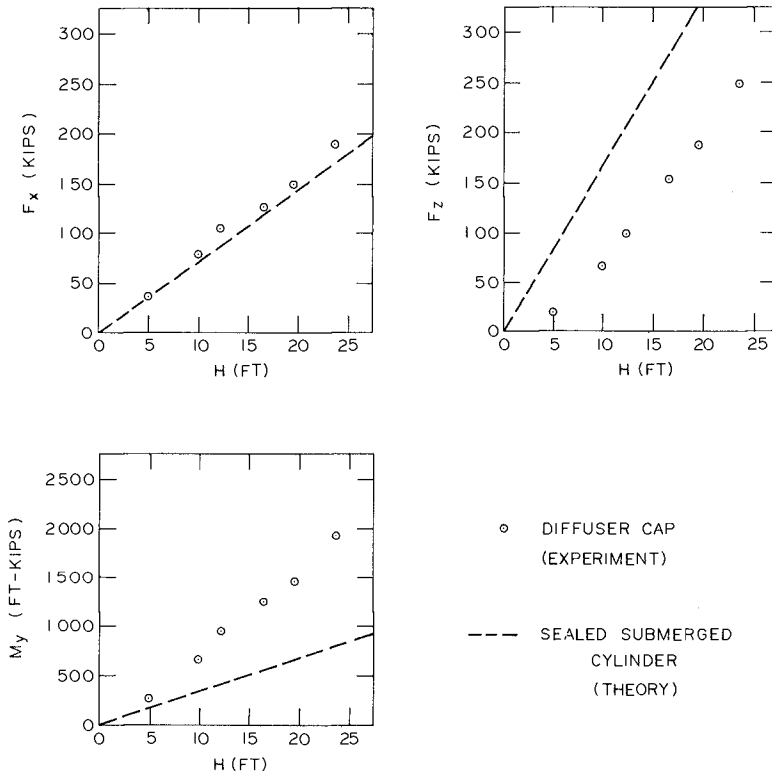


FIG.8 COMPARISON OF EXPERIMENTAL AND THEORETICAL RESULTS
 NON-BREAKING REGULAR WAVES
 ($N = 3, Q = 0, d = 25 \text{ FT}, T = 12 \text{ SEC}$)

area of the base from the force on the sealed structure. The same assumption of uniform pressure inside the structure cannot be made for the diffuser cap, since it has ports on one side causing an asymmetrical pressure distribution. The ports also cause the maximum vertical forces to occur approximately at SWL, whereas for the structures studied by the above authors, maximum values occurred near the trough.

For vertical circular cylinders projecting through the water surface, Mogridge and Jamieson (12) have indicated that there may be some viscous drag effects in the horizontal forces for ka less than 2.8, which for the diffuser cap diameter of 26.5 ft would be for periods greater than 10 sec. However, for the diffuser cap, the horizontal forces are almost entirely inertial, while the vertical forces appear to be due to the combined effects of inertia and drag. In order to substantiate this statement, the F_x and F_z data in Fig. 8 has been replotted in Fig. 9 on a logarithmic scale. Since inertial force is directly proportional to wave height, inertial force can be represented by a straight line with a slope of 1:1. In this plot, the solid line with a slope of 1:1 is fitted through the horizontal force data. A reasonably good fit confirms the existence of inertial predominant horizontal forces. The vertical force data in Fig. 9 lies on a slope greater than 1:1 and thus the force is not solely inertial but is due to the combined contributions of inertial force, drag force and possibly non-linear wave effects. The slope depends on the proportion of drag to inertial force and whether the drag coefficient is constant or a function of wave height.

Breaking Waves

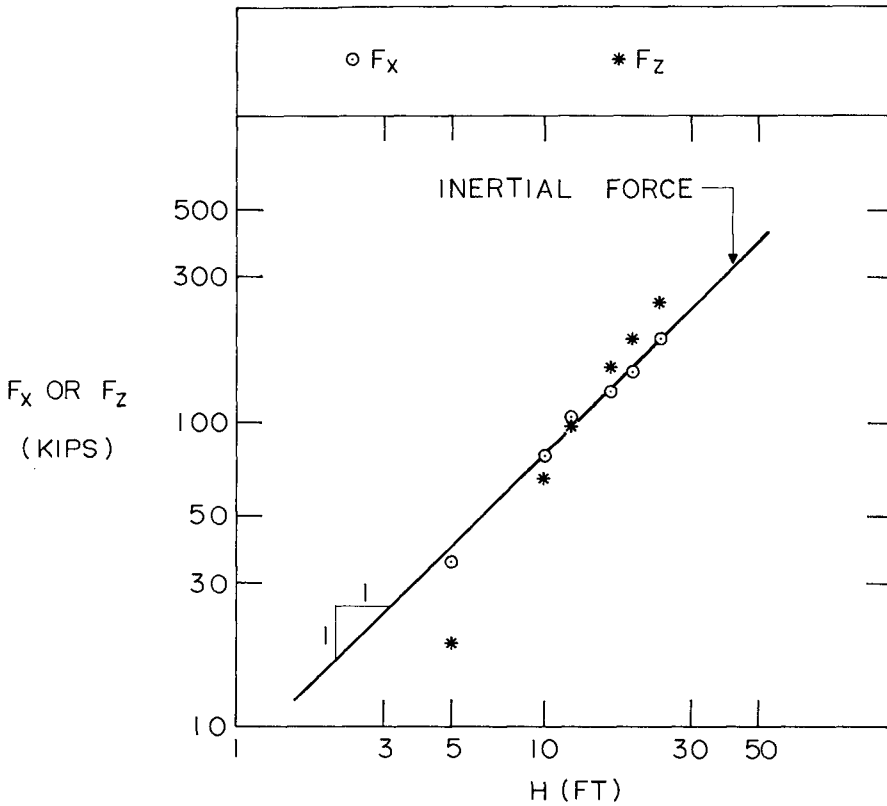
Breaking wave forces were also measured on the diffuser cap. The regular non-breaking wave heights were increased until relatively steep waves were generated at the wave board. The combination of these steep waves and the gentle bottom slope of 1:50 created spilling breakers in the vicinity of the diffuser cap. The magnitudes of the vertical forces due to spilling breakers were always maximum in the positive or upward direction. Occasionally, a plunging wave would break on the diffuser cap; however, this still did not cause the negative vertical forces to be larger than the positive values, possibly because even at LWL there was enough water above the diffuser cap to cushion the force of the breakers.

Non-breaking and breaking wave load data are plotted in Fig. 10 for $N=3$ and $N=5$. For a given wave height, spilling breakers often produce wave loads much larger than those caused by non-breaking waves. The data for the most extreme breaking wave conditions indicate wave loads as much as 100 percent greater than for non-breaking waves.

The breaking waves produce much more scatter in the wave load data than the non-breaking waves. The breaking mechanism apparently affects the period of the waves. Although the periods of the individual waves measured near the wave generator were all approximately 12 sec, at the diffuser cap a range of wave periods were measured. This variation in wave period at the structure probably accounts for some of the scatter of the data. However, most of the scatter is probably due to the variation in the degree of breaking at the structure. Spillage at the crest rapidly reduces the wave height, but does not significantly alter the fluid accelerations or pressures on the structure. Although not

— INERTIAL FORCE ➔ SLOPE = 1:1 ($F \propto H$)

INERTIAL FORCE + DRAG FORCE ➔ SLOPE > 1:1



**FIG.9 LOGARITHMIC PLOT OF F_x AND F_z
NON-BREAKING REGULAR WAVES
($N=3$, $Q=0$, $d=25$ FT, $T=12$ SEC)**

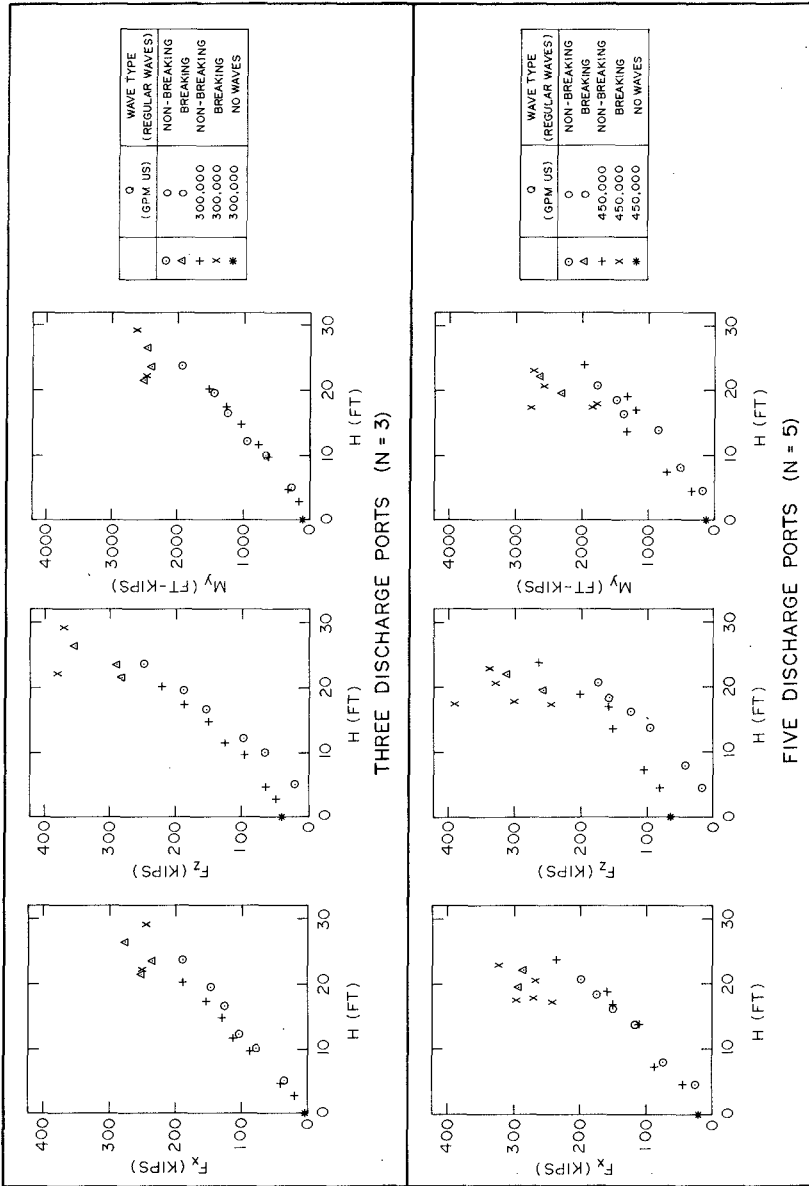


FIG. 10 WAVE FORCES AND OVERTURNING MOMENTS
($d = 25$ FT., $T = 12$ SEC)

shown here, wave loads can be plotted against instantaneous wave slope at the time of maximum loadings as in Mogridge and Jamieson (13) and correlations are somewhat better than plotting against wave height.

The maximum loads due to breaking waves generally occur near the time of SWL as for non-breaking waves, but there is enough of a phase shift in some tests to indicate that higher velocities cause significant increases in viscous drag forces.

Cooling Water Discharge

The effect of cooling water discharge on the wave loading is shown in Fig. 10. The upper plots show the results with a discharge of 300,000 gpm (US) while the lower plots are for 450,000 gpm(US). F_x and M_y show minimal differences in loading due to cooling water discharge for both non-breaking and breaking wave conditions. However, F_z does increase considerably due to discharge, particularly for low wave heights. For breaking waves, the increase in F_z due to discharge is not as well defined as for non-breaking waves because of the considerable scatter in the data caused by the spilling breakers.

Irregular Waves

The time series plot of the water surface elevation for the storm, which damaged the diffuser cap in February 1976, is shown in Fig. 11. This 20 minute prototype wave record, measured in relatively deep water, was reproduced directly in the wave flume at the wave board. That is, a Fourier analysis decomposed the wave record into sinusoidal components described by amplitude and phase angle for each frequency. Predetermined transfer functions, compensating for water depth and wave generator characteristics, were applied to each frequency component to give voltage amplitudes for generation of the required wave amplitudes at the wave board. Then, by means of an inverse Fourier transform, a voltage time series was obtained and used as input to the wave machine for the simulation of the prototype wave profile in the flume. Using this method of irregular wave generation, actual wave records can be reproduced with correct phasing between frequency components, which is important when grouping is present in the wave records. Further details are available in the report by Funke and Mansard (5).

A comparison of the prototype spectrum and the model spectrum measured 54 ft upwave of the diffuser cap at HWL, is shown in Fig. 12. The significant wave heights in the prototype and the model were 18.3 ft and 18.7 ft respectively, while the peak wave period was 13.4 sec in both spectra. This was one of the better fits between the model and prototype spectra because at HWL the water was sufficiently deep in the wave flume to minimize wave shoaling between the wave board and the wave probe.

The irregular waves, generated in the wave flume, produced non-breaking and breaking waves at the diffuser cap. As with regular waves, the wave loads reached maximum values at approximately the time of SWL and the largest wave loadings were measured at LWL. The analysis of the irregular wave data was treated on a wave-to-wave basis; that is, the largest wave loads and corresponding zero up-crossing wave heights were selected over the entire wave height range, disregarding wave period. Fig. 13 shows a comparison of the wave loading results due to the February 1976 storm, and the 10 and 12 sec regular waves. More scatter

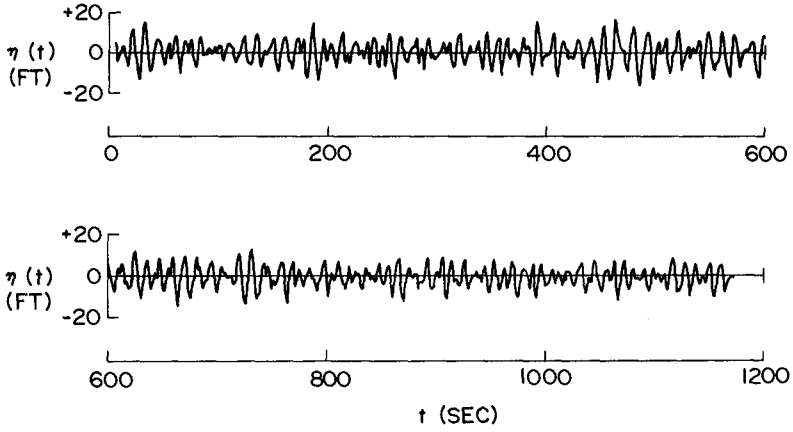


FIG.11 PROTOTYPE WAVE PROFILE
(FEBRUARY 2, 1976, 1500 HR)

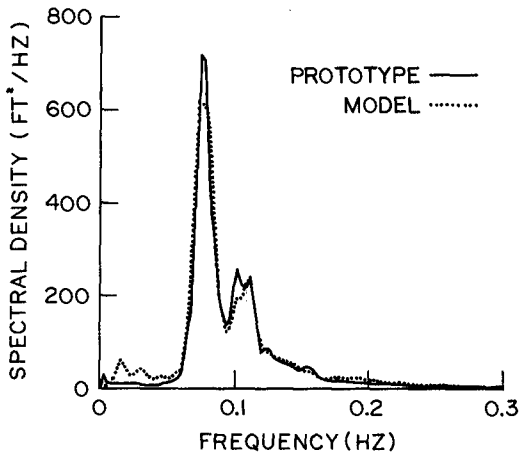


FIG.12 WAVE SPECTRA

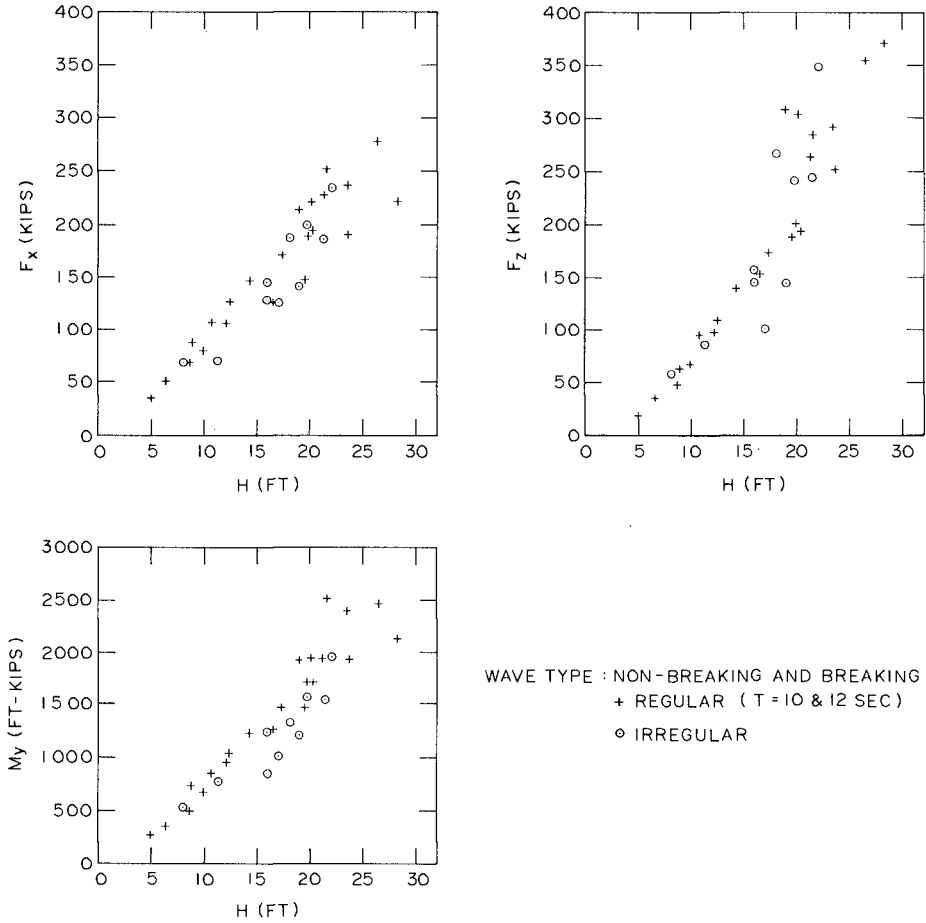


FIG.13 COMPARISON OF RESULTS FOR REGULAR AND IRREGULAR WAVES (N = 3 , Q = 0 , d = 25 FT)

results for the irregular waves because there is a much wider frequency range present than just 10 and 12 sec, and also because there is some breaking of the higher frequency waves even at low wave heights. Based on the limited number of tests analysed, using only one irregular wave record which consisted essentially of non-grouped waves, it appears that irregular wave loads are no more severe than regular wave loads. Negligible differences were also observed (13) between irregular and regular wave loadings when cooling water discharges of 300,000 gpm (US) and 450,000 gpm (US) were used. It should be emphasized that the irregular wave record used for these tests, produced the maximum possible wave heights and steepnesses at the diffuser cap because of the depth limitation. Therefore, it is most unlikely that any other irregular wave record would produce wave loads any higher. This does not mean that in general, wave load tests need not be conducted using irregular waves. On the contrary, it is possible that where wave heights are not limited by water depth, interaction of wave frequencies may produce groups of very high steep waves creating large structural loads. In addition, if it is anticipated that structural fatigue may be a problem, load distribution functions should be measured using irregular waves.

CONCLUSIONS

Horizontal forces, vertical forces and overturning moments on the diffuser cap of a cooling water outfall have been determined. Existing theoretical methods cannot be used to predict the loading on such an open submerged structure as the diffuser cap which is subjected not only to the combined loading of non-breaking waves and cooling water discharge, but also the extreme loadings imposed by breaking waves. A model testing program has resulted in the following conclusions:

1. A large variation in wave period causes only a small variation in wave loading. A larger variation in loading results for different depths of submergence of the diffuser cap. The largest forces and overturning moments, for a given wave height, occurred at low water level for 10 and 12 sec waves.
2. It cannot be assumed that the magnitude of the maximum wave loads on a shell-type structure raised above the bottom with ports in the sidewalls will be similar to those on a sealed structure. For example, the wave loads on the diffuser cap were such that, compared to a sealed submerged cylinder, the horizontal forces were generally within plus or minus 25 percent, the vertical forces were up to 75 percent smaller and the overturning moments were up to 150 percent larger.
3. All of the wave loads on a ported structure, similar to the diffuser cap, reach maximum values at about the same time. This results in a far more critical loading situation than for a sealed structure where the vertical force is approximately 90 degrees out of phase with respect to the horizontal force and overturning moment.
4. For a given wave height, spilling breakers on the diffuser cap caused loads up to 100 percent greater than those due to non-breaking waves. For both the non-breaking and breaking waves, the magnitude of the vertical force was always maximum in the upward direction.
5. Tests performed with simultaneous wave loading and cooling water discharge indicated that for low wave heights, the discharge through the diffuser structure could increase the uplift forces considerably;

however, for high waves and particularly for spilling breakers, the discharge did not significantly affect the magnitude of the wave loads.

6. Based on the limited number of tests using a non-grouped irregular wave train, the magnitudes of the maximum irregular wave loads on the diffuser cap were no more severe than the regular wave loads. This conclusion does not necessarily apply in general to other situations where such factors as wave grouping or fatigue stresses may be important.

ACKNOWLEDGEMENTS

This study was conducted for Eastern Designers and Company Limited, and New Brunswick Power Commission, both of Fredericton, New Brunswick, Canada.

REFERENCES

1. Black, J.L., "Wave Forces on Vertical Axisymmetric Bodies", Journal of Fluid Mechanics, Vol. 67, Part 2, 1975, pp. 369-376.
2. Black, J.L., C.C. Mei and M.C.G. Bray, "Radiation and Scattering of Water Waves by Rigid Bodies", Journal of Fluid Mechanics, Vol. 46, Part 1, 1971, pp. 151-164.
3. Chakrabarti, S.K. and R.A. Naftzger, "Wave Interaction with a Submerged Open-Bottom Structure", Eighth Annual Offshore Technology Conference, Houston, Paper No. OTC 2534, May, 1976, pp. 109-123.
4. Fenton, J.D., "Wave Forces on Vertical Bodies of Revolution", Journal of Fluid Mechanics, Vol. 85, Part 2, 1978, pp. 241-255.
5. Funke, E.R. and E.P.D. Mansard, "Reproduction of Prototype Random Wave Trains in a Laboratory Flume", Hydraulics Laboratory, National Research Council of Canada, Ottawa, Laboratory Technical Report No. LTR-HY-64, December, 1978.
6. Garrison, C.J. and P.Y. Chow, "Wave Forces on Submerged Bodies", Proc. ASCE, Vol. 98, No. WW3, August, 1972, pp. 375-392.
7. Garrison, C.J. and R.H. Snider, "Wave Forces on Large Submerged Tanks", Coastal and Ocean Engineering Division, Texas A&M University, Report No. 117-COE, January, 1970, 83 pp.
8. Garrison, C.J. and R. Stacey, "Wave Loads on North Sea Gravity Platforms: A Comparison of Theory and Experiment", Ninth Annual Offshore Technology Conference, Houston, Paper No. OTC 2794, May, 1977, pp. 513-524.
9. Gran, S., "Wave Forces on Submerged Cylinders", Fifth Annual Offshore Technology Conference, Houston, Paper No. OTC 1817, April-May, 1973, pp. 801-812.
10. Hogben, N. and R.G. Standing, "Wave Loads on Large Bodies", International Symposium on the Dynamics of Marine Vehicles and Structures in Waves, edited by R.E.D. Bishop and W.G. Price, Mechanical Engineering Publications Limited, London, 1975, pp. 258-277.
11. Isaacson, M. de St. Q., "Vertical Cylinders of Arbitrary Section in Waves", Proc. ASCE, Vol. 104, No. WW4, August, 1978, pp. 309-324.
12. Mogridge, G.R. and W.W. Jamieson, "Wave Loads on Large Circular Cylinders: A Design Method", Division of Mechanical Engineering, National Research Council of Canada, Ottawa, Mechanical Engineering

- Report No. MH-111, December, 1976, 40 pp.
13. Mogridge, G.R. and W.W. Jamieson, "Wave Loads on a Cooling Water Outfall, Coleson Cove, N.B.", Hydraulics Laboratory, National Research Council of Canada, Ottawa, Laboratory Technical Report No. LTR-HY-63, November, 1977, 101 pp.
 14. Yue, D.K.P., H.S. Chen and C.C. Mei, "A Hybrid Element Method for Diffraction of Water Waves by Three-Dimensional Bodies", International Journal for Numerical Methods in Engineering, Vol. 12, 1978, pp. 245-266.

NOTATION

a	Radius of hemisphere or cylinder
d	Water depth
$F_x(t)$	Horizontal force as a function of time
F_x	Maximum value of $F_x(t)$
$F_z(t)$	Vertical force as a function of time
F_z	Maximum value of $F_z(t)$
H	Wave height at diffuser cap
k	Wave number, $k = 2\pi/L$
L	Wave length
$M_y(t)$	Overturning moment as a function of time
M_y	Maximum value of $M_y(t)$
N	Number of discharge ports in diffuser cap
Q	Discharge through diffuser cap
T	Wave period
t	Time
$\eta(t)$	Water surface elevation as a function of time
π	3.141592...

CHAPTER 149

TRIPOD CONCEPT FOR PILE STRUCTURES IN FAST CURRENT

BY

J. Khanna M.ASCE * and J.S. Wood M.ASCE **

ABSTRACT

This paper describes a simple but elegant concept developed for the construction of offshore pile-supported structures in strong current. This tripod concept was developed during design studies for the Carajas Project which required an iron ore terminal at Ponta da Madeira, Sao Marcos Bay, in northern Brazil for mooring ships up to 300,000 DWT in up to 6 knot tidal currents. Experience during the construction of the Immingham oil terminal on the Humber River in England in 1968 had shown that cylindrical steel piles were susceptible to vortex-induced in-line and cross-flow vibrations. The cross-flow vibrations were particularly dangerous and occurred mainly during the construction phase when the individual piles could vibrate as cantilevers.

In the tripod concept all piles for the offshore structures, such as mooring and berthing dolphins, working platforms, approach trestle etc. are driven in groups of three from a working platform and immediately connected at the top to form a stable tripod module. The construction of the tripod module prevents the piles from vibrating in the dangerous cross-flow swaying mode. Some bow-string modes of vibration due to in-line and cross-flow excitations are still possible but these can be reduced by appropriate choice of pile diameter, pile slope and cap mass. If further attenuation of vortex-induced vibrations is necessary, then perforated shrouds over 20% of the pile-wetted length may be used.

This paper presents some results of the analysis, and hydro-elastic model testing carried out at the British Hydromechanics Research Association at Cranfield (U.K.) during 1975-76 which validated the efficacy of the tripod concept. Also presented are illustrations of the use of the concept, and design criteria for the design of tripod structures for locations where fast currents may be a problem.

* Chief Engineer - Civil, Swan Wooster Engineering Co. Ltd. Vancouver, Canada.

** Assistant Manager - Vancouver Office, Swan Wooster Engineering Co. Ltd. - Vancouver, Canada, formerly Deputy Project Manager, PROMON/HOWE-SWAN WOOSTER Consortium, for the Carajas Iron Ore Project, Rio de Janeiro, Brazil.

INTRODUCTION

During 1974-77, a consulting engineering consortium PROMON/HOWE - SWAN WOOSTER composed of PROMON ENGENHARIA, S.A. of Brazil, HOWE INTERNATIONAL LTD and SWAN WOOSTER ENGINEERING CO. LTD. of Canada was retained by AMAZONIA MINERACAO S.A. to carry out design studies and detailed design for the marine terminal for the Carajas Project. An iron ore shipping terminal was required at Ponta da Madeira in Sao Marcos Bay in northern Brazil for mooring ships up to 300,000 DWT. The site was protected from wind and waves, but was exposed to very strong tidal currents which for design purposes were estimated to be 6 knots.

The effect of these fast flowing currents created one of the most difficult design problems on the project. It was known that cylindrical steel piles in fast flowing current were susceptible to oscillations due to in-line and cross-flow excitations created by the shedding of vortices in the wake of the piles. This problem had surfaced acutely during the construction of the Immingham Oil Terminal on the Humber River in England in 1968, where ebb tidal currents reach a velocity of 5.5 knots. It was found (1)* that if any pile was left as a cantilever and allowed to oscillate across the flow, then the movements became so violent that 750 mm cylindrical steel piles, 12 mm wall thickness, would reach an amplitude at the top of + 1 m and snap off at the sea bed. Therefore each pile that was driven had to be instantly restrained by some temporary device such as wires and timbers to a stable part of the work. The restrained piles were, however, not immune to vibrations. These restrained piles and even completed structures were subject to in-line oscillations for several hours during the tidal flows. Extensive additional bracing was subsequently added to the Immingham terminal pile structures in order to ensure safety.

During the design studies at the Ponta da Madeira Terminal, a design concept evolved in which all the piles for the various structures would be driven in groups of three from a working platform and connected at the top to form stable tripods. At a later stage in the construction, the tripods would be capped to form the decks of the various terminal structures. Figure 1 shows the tripod concept during construction. The tripod concept for construction in fast flowing waters is not entirely original. We have recently become aware that native Indian fishermen in Yakima (Washington State) in U.S.A., use tripods in fast flowing streams to form platforms for fishing. (Figure 2).

*Figures in parentheses refer to References.

The construction of a tripod prevents the piles from vibrating in the dangerous cross-flow swaying mode. Some bow-string modes of vibration are still possible due to in-line excitations but these can be reduced by appropriate choice of pile diameter. If further attenuation of the vortex-induced vibrations is necessary, then spoilers in the form of lightweight fibreglass shrouds can be used. The tripod concept was verified by extensive hydroelastic model testing at the British Hydromechanics Research Association (BHRA) Laboratories at Cranfield (U.K.) during 1975-76.

This paper presents the theoretical basis for the tripod concept as well as some results of the hydroelastic model testing carried out at BHRA to validate the tripod concept. Also presented are illustrations of the use of the concept, and design criteria for the design of tripod structures for locations where fast currents may be a problem.



Figure 1 **Tripod concept during construction.**



Figure 2 Yakima fishermen on a platform built on tripods in fast current.

THEORETICAL BASIS

In fast flowing water, pairs of eddies or vortices are formed downstream of a circular section in a regular pattern known as the Karmen Vortex Street (Figure 3.). The eddy shedding causes hydraulic pressure differentials around the circular section resulting in the application of a periodic force to the pile. The frequency of shedding of vortex pairs is given by

$$F = \frac{SV}{D}$$

where F = frequency of shedding of vortex pairs
 S = Strouhal Number
 V = flow velocity
 D = pile diameter

The shedding of each pair of vortices is accompanied by a fluctuation in the lift force across the stream flow. When one of the pile natural frequencies is close to the vortex-pair shedding frequency, resonant amplification occurs leading to the possibility of structural failure. The shedding of each individual vortex creates a fluctuation in the in-line drag force. When one of the pile natural frequencies is close to the frequency of individual vortex-shedding (given by $2F$), the resonant amplification can occur in the in-line direction. The in-line excitation is an order of magnitude smaller than the cross-flow excitation so that in-line forces are not likely to cause swift structural failures due to overstressing but are likely to lead to fatigue failures.

Typical response of an individual pile to flowing water is shown in Figure 4, where, the reduced amplitude, y/D ,

where y = maximum displacement amplitude
 D = pile diameter

is plotted against, the reduced velocity, V/ND ,

where V = flow velocity
 N = pile natural frequency
 D = pile diameter.

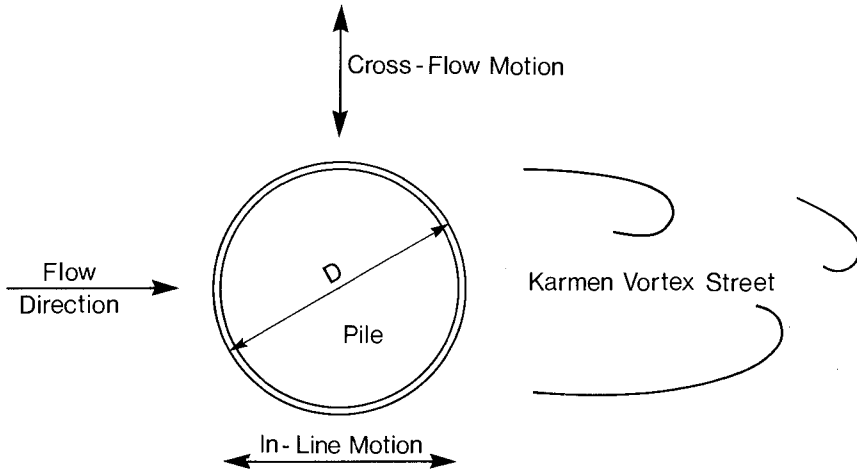


Figure 3 Flow around circular pile.

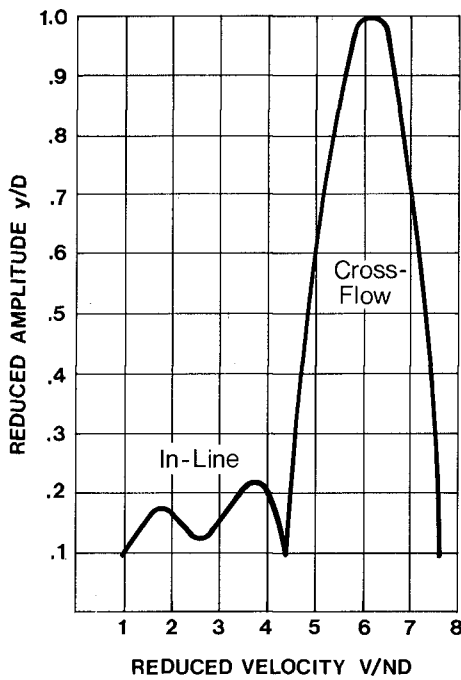


Figure 4 Response of cylindrical piles to flowing water.

In the range of Reduced Velocity from about 1 to 4, in-line vibrations can occur with a maximum displacement of about 20% of pile diameter. In the range of Reduced Velocity, from about 4 to 7, the more dangerous cross-flow vibrations can occur with a maximum response as much as the pile diameter.

The response of a cylindrical pile is also influenced by the damping present in the structural system and the water depth over which the vortex-induced excitation is transmitted to the pile. This influence is represented by King (3) as a stability parameter, K_s , where

$$K_s = \frac{2M_e \delta}{\rho D^2}$$

where

M_e = equivalent mass/unit length

δ = damping log. decrement

ρ = water mass density

For a pile with mass at the top

$$M_e = \frac{M_t Y_t^2 + \int_0^L m y^2 dx}{\int_0^h y^2 dx}$$

where M_t = top mass

Y_t = top displacement

m = pile mass including mass of entrained water and added mass

L = pile length

h = water depth

An example of the influence of stability parameter for the first normal in-line mode (3) is shown in Figure 5 where it is seen that as the stability parameter increases the vibration amplitude decreases. Based on the research on pile vibrations following the Immingham experience (3), King developed vibration limits for a single pile which was used as a basis for the development of design limits for the Ponta da Madeira terminal pile structures as shown in Figure 6.

This criteria, which was subsequently verified by testing at BHRA for completed structures, was used to design the individual tripod modules and the completed structures. In those instances where the structure Reduced Velocity and Stability Parameter were such as to allow in-line vibrations, (Reduced Velocity between 1.2 and 3.5, Stability Parameter less than 1) vortex spoilers in the form of shrouds were envisaged.

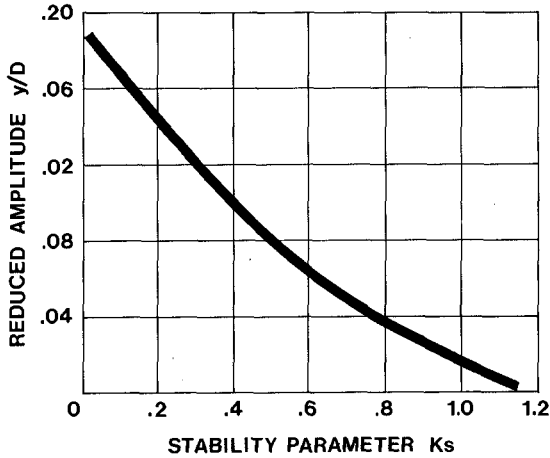


Figure 5 Stability parameter influence on in-line cylindrical pile response.

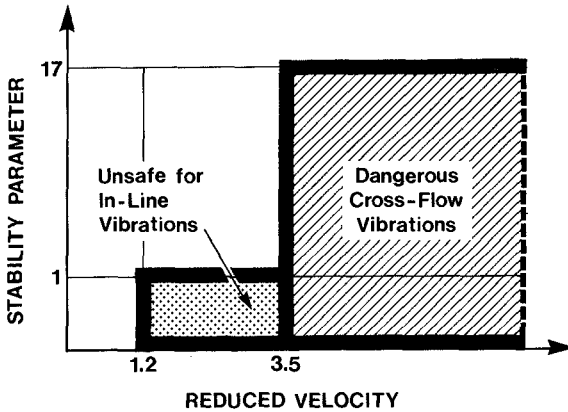


Figure 6 Design limits for single pile.

ANALYTICAL RESULTS

Various design options for the marine terminal structures which would satisfy the criteria given in Figure 6, were analysed. Some of the results of these analyses are shown in Figure 7. These results apply to pile structures in 40 m water depth subjected to a 6 knot current. It can be seen that a 1.5 m cantilever pile lies in the cross-flow maximum response range and would fail. In order to avoid failure, a cantilever pile requires a diameter of 3.5 m, which is an expensive pile to purchase and requires a large costly construction rig for installation. Furthermore, it can be seen that if 1.5 m piles were used as vertical piles to construct a terminal structure such as a mooring dolphin, then in spite of the connection at the top through a pile cap, the structure would still remain vulnerable to damaging cross-flow response at current velocity as low as 3 knots. However, if the same 1.5 m piles were installed as tripods then the dangerous cross-flow vibrations would be completely avoided. Some in-line vibrations might still occur because reduced velocity exceeds 1.2 (See Figure 6) but these could be checked using stability parameter for stress calculations and appropriate remedial steps, such as changing the pile diameter or using spoilers, taken. It can be seen, therefore, that tripods present an attractive solution for pile structures in fast current.

The tripod solution was compared with a conventional vertical pile solution for some of the terminal structures. The comparison for one of the mooring dolphins is shown in Figure 8, where it can be seen that two tripods comprising six 1.5 m piles can perform satisfactorily as a Mooring Dolphin structure, which for a conventional vertical pile design would require the use of four 3.5 m vertical piles, which represents a more expensive solution for the conditions at Ponta da Madeira.

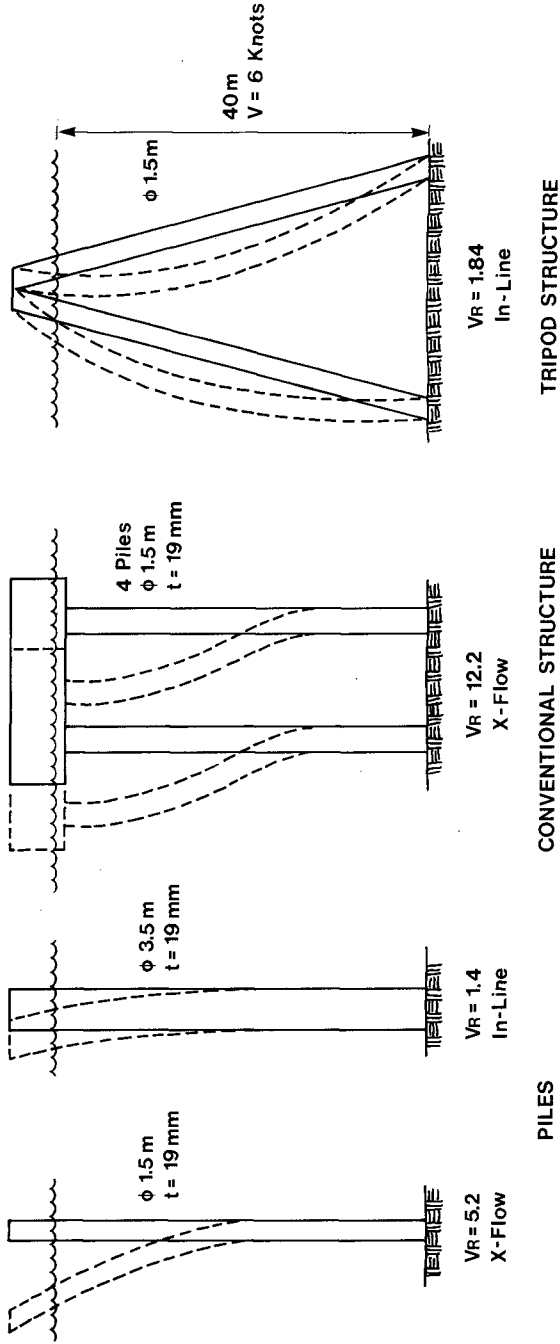
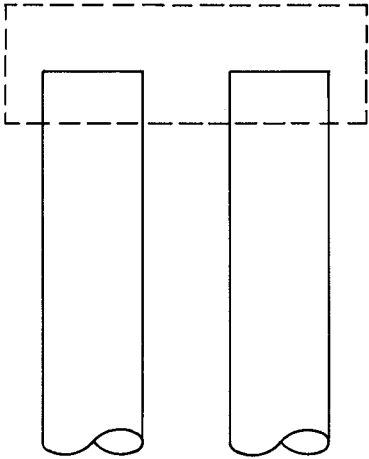
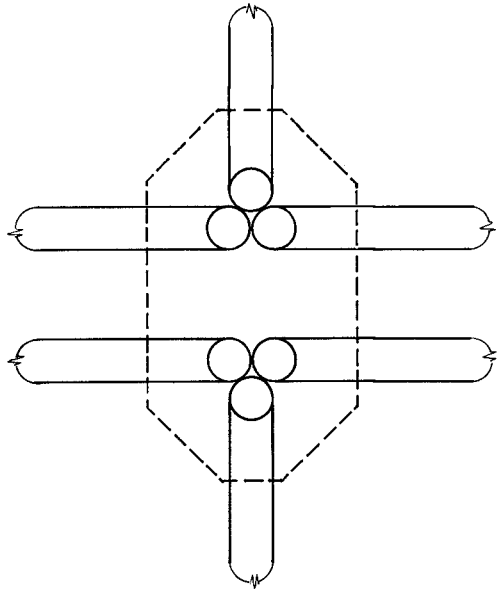
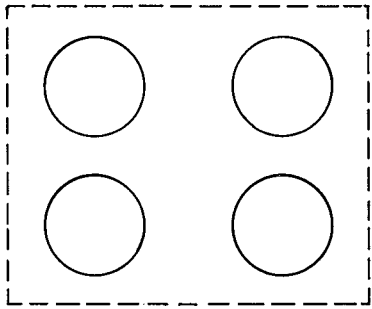
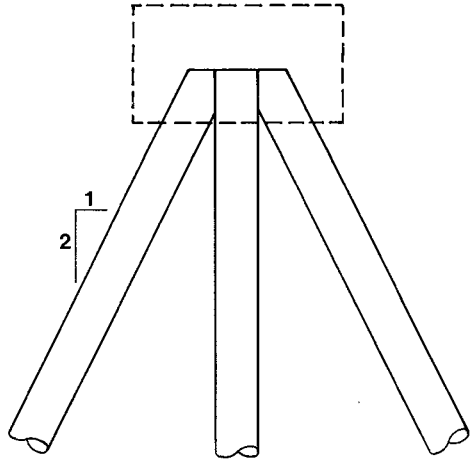


Figure 7 Flow response; Construction stage - Analytical Results.



4 piles - ϕ 3.5m

VERTICAL PILE ALTERNATE



6 piles - ϕ 1.5 m

TRIPOD SOLUTION

Figure 8 Mooring dolphin- Analytical results.

MODEL TEST RESULTS

The model tests were carried out at BHRA Cranfield. A scale of $1/39.4$ was used to construct hydroelastic models. Two individual tripod models were tested (Figure 9). Tripod 1 had 3 legs inclined at 1 in 2 batter. Tripod 2 had 2 legs inclined at 1 in 2, and 1 leg vertical. The tripods were tested to a scaled velocity of about 6.5 knots. Figure 10 shows tripod 1 in the test flume. The end conditions at the base were altered from pinned to fixed to simulate the construction stage and the completed stage. The end conditions at the top were altered to simulate various methods of holding the piles as tripods. It was found that there was little difference in the overall behaviour with various methods such as horizontal template, and side gusset plates to hold the top, because in each case a pinned condition was simulated at the top of the piles. However, gusset plates along the sides provided an efficient energy transmission path between individual piles making vibration suppression more difficult.

The two tripods essentially behaved as an assemblage of individual piles and structural oscillations recorded were predominantly in the bow-string mode although some coupled vibrations were also observed.

The majority of the tests were carried out with the Type 1 tripod because this was more flexible than tripod Type 2, It was concluded that the tripods could have significant oscillations during the construction stage.

Vortex spoilers in the form of perforated shrouds and radial fins were also tested. The perforated shrouds had a length of 20% of the pile wetted length. The shrouds had a diameter 20% greater than the pile diameter, and a 36% open area. The radial fins had a projection of 20% of the pile diameter and a length of 15% of the pile wetted length. Helical strakes were not tested due to the practical difficulty of installing them either before or after the pile driving.

Typical results for the individual tripod are shown in Figure 11. It can be seen that the tripod piles without any spoilers could develop vibration amplitude as much as 10% of the diameter. Radial fins reduced the amplitude of vibration to less than half the amount without spoilers but still left significant vibrations. However, perforated shrouds caused a reduction of the vibrations to negligible proportions. Some tests were performed with shrouds on a single leg or two legs. In some instance they effectively suppressed the vibrations but these were less effective if the shrouds were clamped on a pile in the wake of a leading pile.

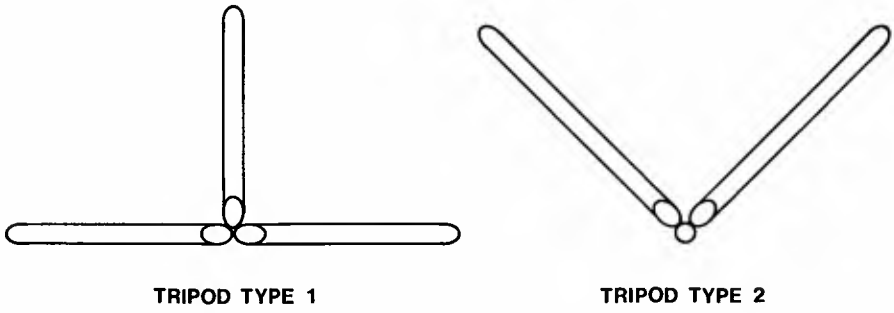


Figure 9 Model tripods tested.



Figure 10 Tripod 1 in test flume.

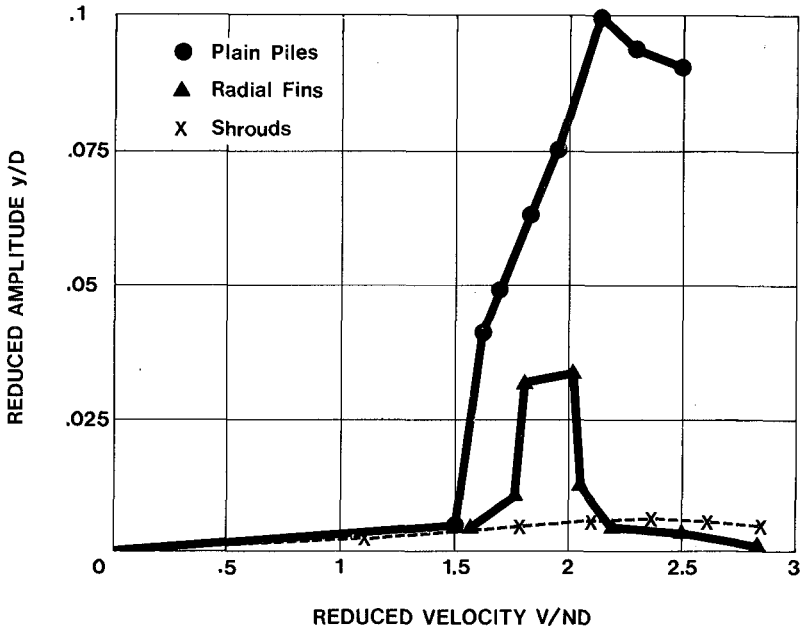


Figure 11 Tripod 1 test results.

The two tripods were then interconnected by a rigid wooden deck to which masses could be attached to simulate more closely a completed structure. The interconnected model tripods are shown in Figure 12. In this case the stability parameter was computed to about 3. The results of the tests are shown in Figure 13. It can be seen that no significant vibrations were observed. This provided a confirmation of the stability parameter concept.

The model tests verified that the criteria, shown in Figure 6, could be used for the design of the marine terminal structures. Further details of the test program and results are given in Reference 2.



Figure 12 Coupled tripods in flume.

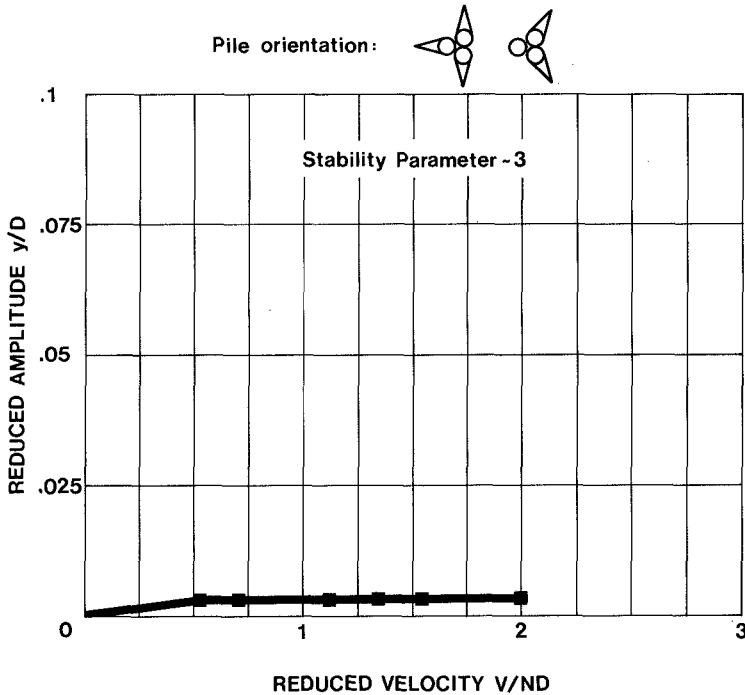


Figure 13 Coupled tripod test results.

CONCLUDING DISCUSSION

This paper has described the evolution and confirmation of the simple tripod concept for use in constructing marine terminal structures of piles in fast flowing current. An example of the final design of one of the berthing dolphins is shown in Figure 14. Based on these studies the following conclusions are drawn:

1. The modular tripod is an effective concept for construction of offshore pile-supported structures in fast current. For structures supporting mainly vertical loads, the pile slopes may be steep such as 1:3. For structures supporting mainly horizontal loads the pile slopes may be less steep such as 1:2.

2. The tripod modules and structures composed of them can be designed on the basis of criteria similar to those developed for individual piles (Ref.2). Using two design parameters, the reduced velocity V_R , and the stability parameter, K_S , where

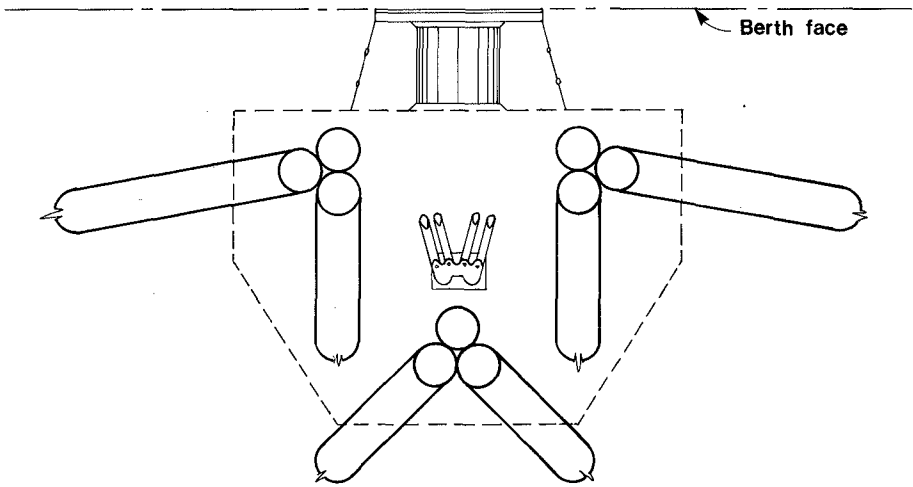
$$V_R = \frac{V}{ND} \quad V = \text{Velocity, } N = \text{pile nat. freq.} \\ D = \text{pile dia.}$$

$$K_S = \frac{2M_e \delta}{\rho D^2} \quad M_e = \text{equiva.mass/unit length,} \\ \delta = \text{log. dec. of damping,} \\ \rho = \text{mass density}$$

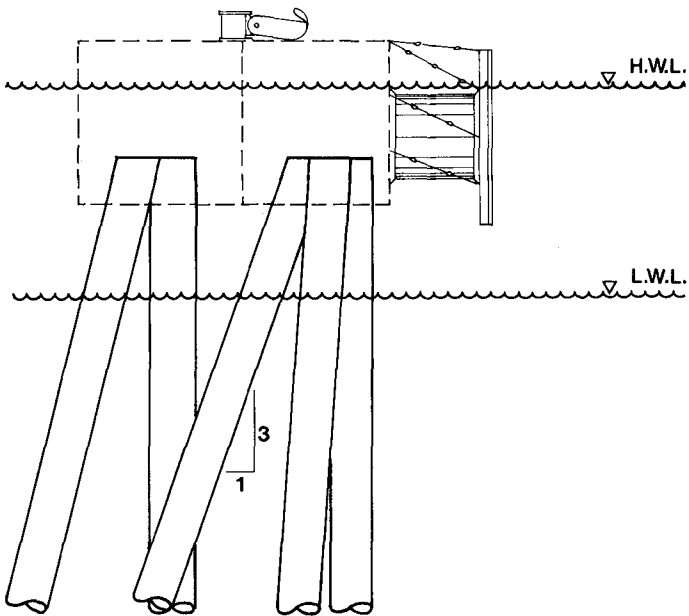
safety against vortex-induced vibrations is ensured if the following conditions are satisfied:

1. $V_R < 1.3, K_S$ any value (no significant vibration)
 2. $1.3 < V_R < 3.5, K_S > 1$ (no significant in-line vibration)
 3. $V_R > 3.5, K_S > 17$ (no significant cross-flow vibrations)
3. The design parameters V_R and K_S can be varied by changing pile diameter, R , pile slope and cap mass.
4. The tripods should be designed so as to definitely eliminate cross-flow bowstring vibrations. If in-line bowstring vibrations cannot be eliminated then the use of vortex-spoilers should be considered. Shrouds over 20% of the wetted lengths are adequate to control the vibrations and are omni-directional. Radial fins are not as effective as shrouds.

* * *



PLAN



ELEVATION

9 piles - ϕ 1.5 m

Figure 14 Berthing dolphin.

REFERENCES

1. Sainsbury, R.N. and King, D., "The Flow induced oscillations of marine structures", Proceedings, Institution of Civil Engineers, July, 1971.
2. Every, M.J., Prosser, M.J., and Khanna, J. "Hydroelastic Model Tests of Tripod Structures". I.A.H.R. Symp., Baden-Baden, 1977.
3. King R., "An Investigation of the Criteria for Controlling Sustained Self-Excited Oscillations of Cylinders in Flowing Water", Proc. 4th Biennial Symp. on Turbulence in Liquids, Univ. of Missouri-Rolla, U.S.A., Sept. 1975.

ACKNOWLEDGEMENTS

The tripod concept was developed during design studies for AMAZONIA MINERACAO S.A., BRAZIL by a consulting engineering consortium PROMON/HOWE-SWAN WOOSTER composed of PROMON ENGENHARIA S.A. of Brazil, HOWE-INTERNATIONAL LTD and SWAN WOOSTER ENGINEERING CO. LTD. of Canada. The hydroelastic model testing was carried out at B.H.R.A., Cranfield, (U.K.). The assistance of Mr. P.P.Barreto of PROMON, and of Mr. N. Allyn of SWAN WOOSTER, in the analytical assessment, is gratefully acknowledged. Acknowledgement is also due to Sisse Briemberg for the photograph of Yakima fishermen.

CHAPTER 150

New Dike Design Criteria Based on Wave Spectra

by

Dr.-Ing. Hans Kaldenhoff +

Dr.-Ing. Suhan M. Gökcesu ++

1. INTRODUCTION

The subject of this paper is the research upon the wave run up on even slopes under random wave conditions. This project was performed in order to get additional tools for dike designing questions.

Earlier works for this subject were performed under the basic idea that the sea can be represented by regular waves and a significant wave height. But the random sea is the result of the superposition of waves with different periods, lengths and amplitudes and they are even progressing in different directions. The values of all these parameters are random distributed. It seems questionable whether the results of former research using regular waves are sufficient especially for problems of wave and structure interactions. Severe damages on structures do force us to develop better design criteria.

2. PHYSICAL BACKGROUND

It is not possible to describe the complex properties of wind waves, the nonlinearity and irregularity of their variables by hydrodynamic laws. Thus it is necessary to use statistic laws and take the topography and the climatic conditions into consideration.

A well-known method is to regard the energy spectra of waves that is the energy density as a function of frequency. A second method describes the probability

+ Professor, Technical University of Berlin, Germany

++ Professor, University of Dar es Salaam, Tanzania

of wave amplitude and frequency with a distribution function and that allows to calculate directly the necessary wave parameters for any dimensioning procedure. That is one of the reasons why engineers favor this method as we did too. The Rayleigh-distribution is often used as it corresponds very well with normalized wave heights and normalized wave periods as well in deep as in shallow areas. This distribution function is steady and one-dimensional. It is used in the following form to describe the normalized wave height $\eta = H/\bar{H}$ and the normalized period $\tau = T/\bar{T}$.

$$F(\eta = \frac{H}{\bar{H}}) = 1 - \exp(-\frac{\pi}{4} \eta^2)$$

$$F(\tau = \frac{T}{\bar{T}}) = 1 - \exp(-\frac{\pi}{4} \tau^2)$$

These waves are progressing to the shore or other barricades. They become reflected and/or refracted, they even produce some kind of mass transport. This resulting motion on slopes is called run up and includes run up with breaking and without breaking. Depending on the wave and slope parameters different behavior of the run up and wash down is to be seen. Their terms are shown in figure 1.

R_{ZR} = height between the run up (upper turning point) and the following lowest wash down (lower turning point)

R_{ZA} = height between the wash down and the following run up

S_z = height between SWL and lower turning point (positive or negative referred to SWL)

The run up is the most important height, especially for designing purposes. Unfortunately there is no useful physical description of the run up and wash down depending on the producing waves. But it seems to be possible to refer the statistical behavior of the run up oscillation to the wave spectra.

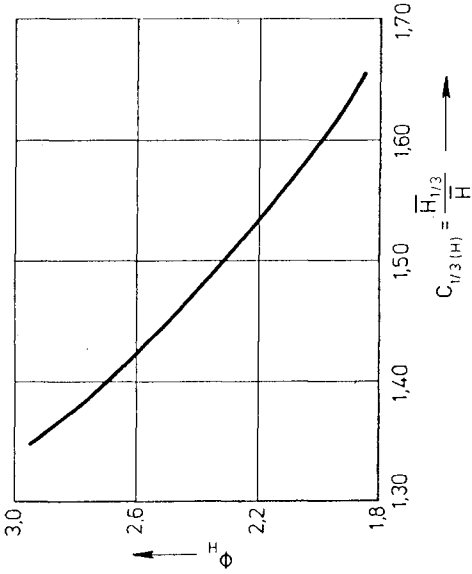


figure 2

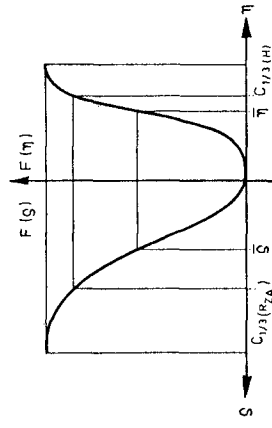


figure 4

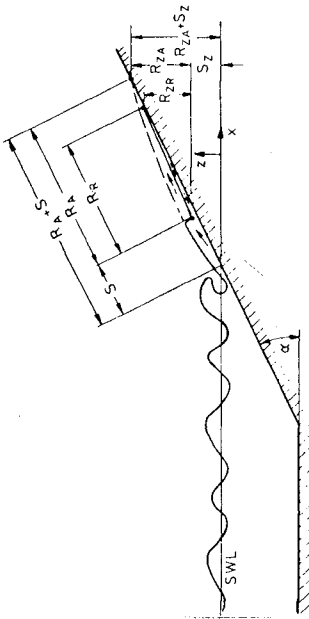


figure 1

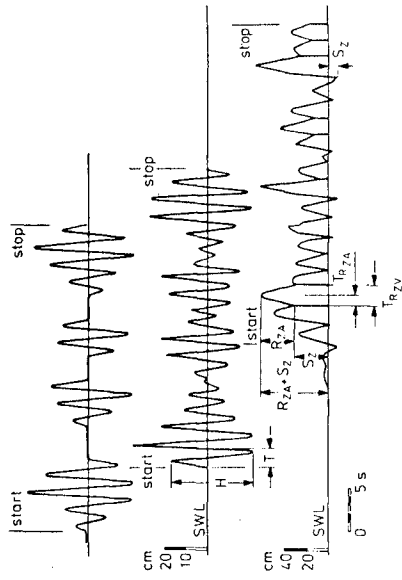


figure 3

As the random sea can be described by the statistical distribution of its parameters (in here the Rayleigh-distribution), we postulated the possibility to describe the run up oscillation parameters by the Rayleigh-distribution too.

3. MODEL TESTS AND RESULTS

To prove the postulate, physical model tests became necessary and the equipment of the laboratory allowed to produce any kind of a random sea in a free surface channel and to build any kind of slope in a large scale (1 : 10 to 1 : 5). The distribution function of the wave parameters are basically referred to the wave spectra of the German North Sea where measurements were being performed since 10 years by the research group Neuwark and their results are statistically analyzed in the above mentioned way. The exponents of the distribution functions of the wave heights are given in figure 2 as a function of the normalized significant height $C_{1/3}$.

The physical experiments were conducted by varying the following parameters:

- exponents of the distribution function of the normalized wave height, mean wave height and mean significant wave height
- water depth
- constant slope 1 : 3, 1 : 4, 1 : 6
- broken slope and berms

The whole program was coordinated that way, that the run up could be described by a one-dimensional distribution function for different parameters and it should be used as a designing tool.

The test channel is 90 m long, 4 m wide, 2 m deep and it is possible to generate 0.6 m high waves. The wave gauges are of the resistant type and their linearized signals were evaluated by a computer in on-line technics.

A special procedure was developed to generate the random sea. This procedure used different wave groups, the arrangements of which could be changed

to generate different wave trains. All of those trains had the same probability density function and their parameters agreed very well to the prototype conditions. Additionally the normalized wave height was varied. From all of those possible wave trains, which all fulfilled the prototype conditions, only six were chosen to run the tests with. For the tests three different water depths (1.0; 1.25; 1.50 m) were used.

Figure 3 gives an overall idea of the oscillation of the wave generator (upper curve), the water surface in front of the slope (middle curve) and the run up (lower curve). The parameters noticed in figure 3 were evaluated by the computer, directly using the following assumptions and equations.

- a. The normalized run up height ζ^* is Rayleigh-distributed if the normalized wave height follows the same distribution function.

$$F(\eta = \frac{H}{H}) = 1 - \exp(-\frac{\pi}{4} \eta^2)$$

$$F(\zeta^* = \frac{R_{ZA} + S_Z}{R_{ZA} + S_Z}) = 1 - \exp(-\frac{\pi}{4} \zeta^{*\phi_{(R_{ZA} + S_Z)}}$$

- b. According to the wave statistics it is assumed that the exponents of the run up distribution function are a function of their $C_{1/3}$ values.

$$\phi_{(R_{ZA} + S_Z)} = f(C_{1/3(R_{ZA} + S_Z)} = \frac{(R_{ZA} + S_Z)^{1/3}}{R_{ZA} + S_Z})$$

- c. All the distribution functions of the normalized run up and the wave parameters have each the same function value regarding their $C_{1/3}$ values, even if their exponents are different; see figure 4.

Assuming a. to c., it becomes possible to calculate the ϕ -exponent of the Rayleigh-equation for

the run up variables using the \emptyset -exponent of the Rayleigh-equation for the sea and their known $C_{1/3}$ values as well as the $C_{1/3}$ values of the run up tests.

$$\Phi_{(R_{\gamma_A}, S_{\gamma_A})} = \Phi_H \left(\frac{\ln C_{1/3(H)}}{\ln C_{1/3(R_{\gamma_A}, S_{\gamma_A})}} \right)$$

- d. We furthermore expected the mean values of the run up heights to be a function of the mean values of the wave heights and the structure parameters as well as the water depth.
- e. The assumption is made that it is possible to correlate the mean values of the wave heights and run up heights to the mean values of their $C_{1/3}$ values for constant water depths.

The above mentioned assumptions have been proved by using methods of the mathematical statistics such as the χ^2 - and Kolmogorov test with different significance levels to test the parent population or the correlation and regression analysis to find the function values. The probability of errors was better than 5%. This immense evaluation, test and calculation program could only be done by using computers. For the practical use, graphics were developed with dimensionless parameters.

The first results showed already that all the assumptions are right and useful. The relation between the dimensionless significant wave height and the dimensionless mean wave height is shown in figure 5. The correlation factor is 0.9729 which proves the linear correlation between those parameters for the chosen six parent populations. The regression curve goes through the origin and proves the physical background of this relation and the quotient of $\bar{H}_{1/3}/\bar{H} = 1.587$ differs only slightly from the theoretical value 1.598, calculated by Longuet - Higgins.

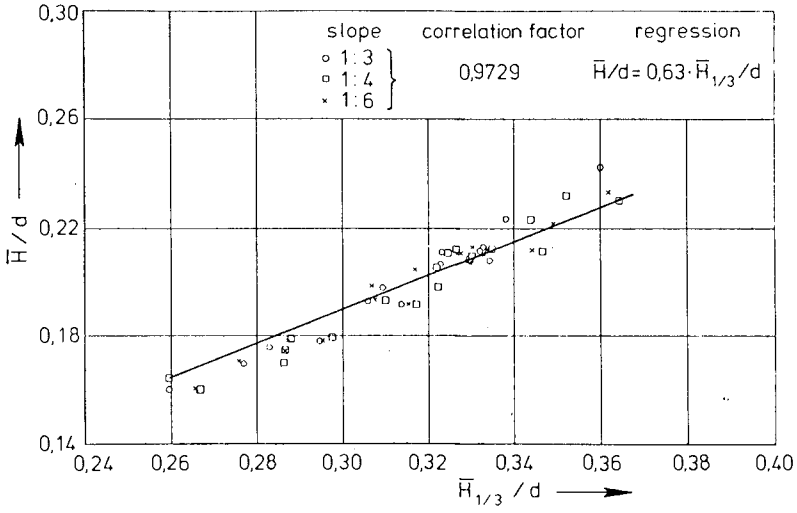


figure 5

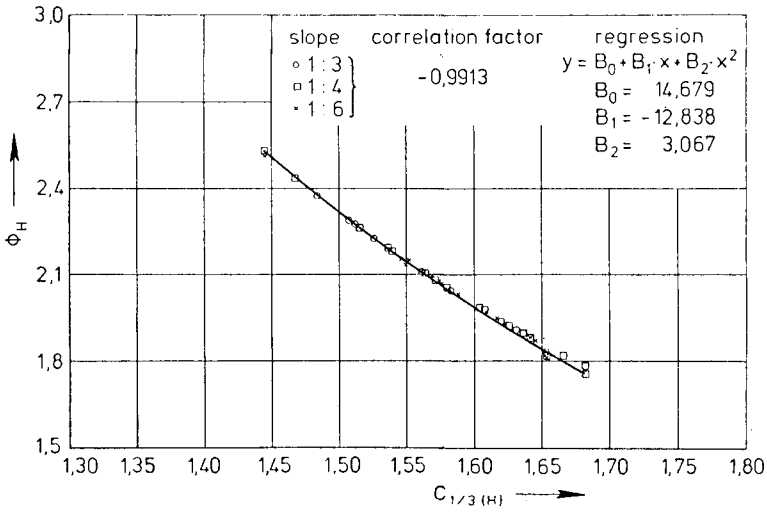


figure 6

Figure 6 shows the relation between the exponent of the wave height distribution function and the $C_{1/3}$ value of the six different wave trains. The correlation is not linear and the correlation factor of 0.9913 proves the excellent correlation of the exponents and underlines that the distribution exponent is a function of the $C_{1/3}$ value.

The relation between the mean dimensionless wave heights and their mean dimensionless run up heights is shown in figure 7. This result again proves the above mentioned assumption that the mean run up correlates to the mean wave heights depending on the slope. Moreover the diagram proves the tendency predicted by Webber and Bullock, but the actual results differ significantly. The linear relation between the run up and the significant run up is also to be seen from figure 7 and shows a correlation factor of 0.9715.

Finally the relation between the exponents of the distribution function and the run up and their $C_{1/3}$ values is drawn in figure 8. The measuring points show a parabolic curve with the high correlation factor of 0.9766.

Summarizing it should be stated that the basic assumption is proved and the relation between the wave heights and the run up could be found. Designing charts basing on this procedure with more parameters and broken slopes will be developed.

4. REFERENCES

1. Longuet - Higgins On the Statistical Distribution of the Heights of Sea Waves
J. Mar. Res., Vol.11, 3,
1952
2. Webber, N. B. A Model Study of the Distribution of Run-up of Wind-generated Waves on Sloping Sea Walls
Bullock, G. N. Proc. 11th Conf. Coast. Eng., London 1968

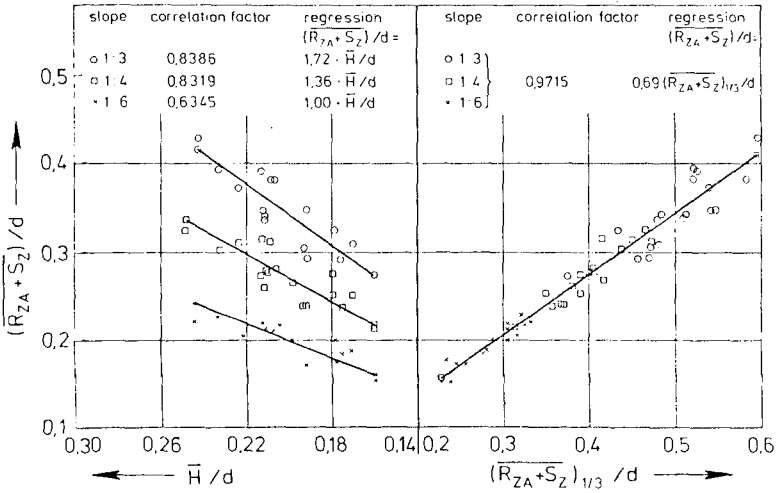


figure 7

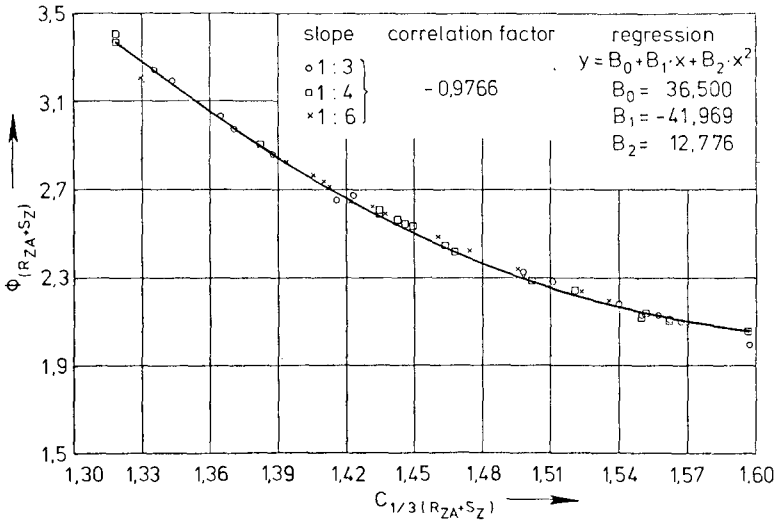


figure 8

3. Siefert, W. Analysis of Random Waves
Kaldenhoff, H. in Shallow Water and
 Laboratory Reproduction
 Proc. 16th Congr. IAHR,
 Sao Paulo, 1975

4. Gökcesu, S. Beitrag zum Auflaufvor-
 gang des natürlichen See-
 ganges im Flachwasserge-
 biet auf glatten Böschun-
 gen
 Inst. f. Wasserbau, TU
 Berlin, Mitteilung Nr. 87,
 Berlin 1976

CHAPTER 151

BLANKET THEORY & LOW COST REVETMENTS

BY C. T. BROWN*

Summary : This paper seeks to demonstrate that Hudson's equation for the stability of Rubble-mound armour- units is a particular solution of a more general theorem, for the particular case of discrete units of fixed geometric form. By re-developin the general theorem it is proposed that a linear relationship exists between the momentum of an incident wave and the slope-normal surcharge required for stability. From this concept, a new suite of armour units has been developed which discard the concept of minimum mass in favour of a minimum slope-normal dimension. In addition it is possible that the term in Hudson's equation, $\cot \alpha$, might be replaced by the term $\cos \alpha / \sin(\alpha + \beta)$, where β is the tangent to the breaker centreline.

Introduction

Contemporary breakwaters and revetments when suitable rock is economically unavailable use discrete armour units such as tribars, dolosse etc. which are generally characterised as being massive and of complex geometric form. Each armour unit is presently considered to be of fixed form, and hence there tends to be a unique relationship between the design conditions and the required unit size, larger units utilising more material than is required, smaller units having a sub-minimal factor of safety.

This fixed geometric relationship has operated against a flexible design approach, leading designers to specify a particular geometric form of specified mass for their design. It is questioned if this procedure allows contractors sufficient flexibility to optimise their construction methods to produce a low cost revetment. Examination of the current design formulae suggests that this rigidity is not necessary.

Theory

As any student of literature will report, there are any number of formulae for the design of rubble mound breakwaters. Accepting that at the most critical condition, there is a linear relationship between H and L, these equations are all of the form $W = K \gamma r \frac{H^3}{\phi(\alpha) \phi(\delta_s \delta_w)}$.

The most widely accepted of these formulae is that put forward by Hudson, namely $W = \frac{H^3 \gamma r}{K_D \cot \alpha (S_r - 1)^3}$.

* Consulting Engineer, Sydney, New South Wales, Australia.

(Note: It is always assumed that the mass density of the water in the slope is the same as that in the jet. For several reasons, it may be that the apparent density of the fluid is not that of water at rest. Thus, the relative density function might be better written in the form

$$\phi(\gamma) = \left(\frac{\gamma_r - \gamma_f}{\gamma_w} \right) \text{ where } \gamma_f \text{ is the density of the fluid in the revetment.}$$

For a properly designed armour layer, ultimate failure will entail the wholesale movement of the armour, then this relationship could be considered to apply to an overall, 'blanket', revetment.

$$\text{Putting } W = V \gamma_r = K_v \cdot l^3 \cdot \gamma_r$$

$$H = l \cdot (S_r - 1) \cdot (K_v K_D \text{Cot} \alpha)^{1/3}$$

i.e. armour stability is a linear relationship to material thickness and submerged density, for a given armour geometry described by $(K_v K_D)^{1/3}$.

This form of equation suggests that $K_v K_D$ is a constant. The corollary is that K_D can be designed by appropriate choices of K_v .

Returning now to the preliminary concepts, a number of mechanisms have been postulated for failure of rubble mound slopes - in particular slopes armoured with rock of oblate form.

There are two main classes of attack, the first with breaking, or broken, waves, the second where the wave has not broken.

In the first, the wave breaks on the slope, so destroying part of the energy, the wave running up the slope until the energy is either destroyed in the slope, reflected, or converted to potential energy, the flow then reversing and the potential energy, less losses, being returned seawards as a varying flow of water. In the non-breaking case, there is no energy loss due to breaker turbulence, so the potential energy (run-up) should be a greater proportion than before.

Imagining an armour layer which applies a slope normal surcharge and restrains the surface particles of the underlayer from motion, the hydrodynamic behaviour described above will result in a head loss across the structure.

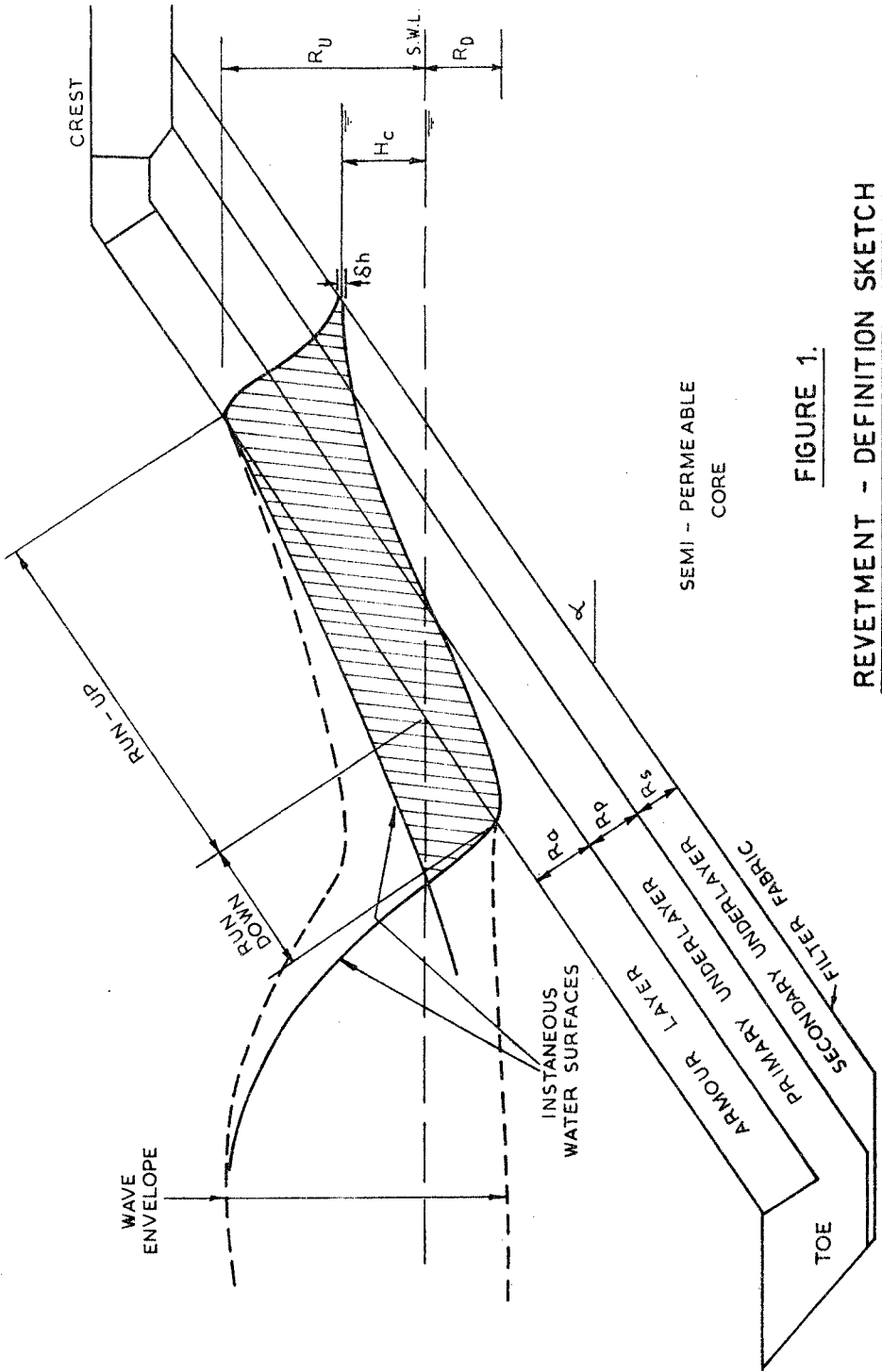
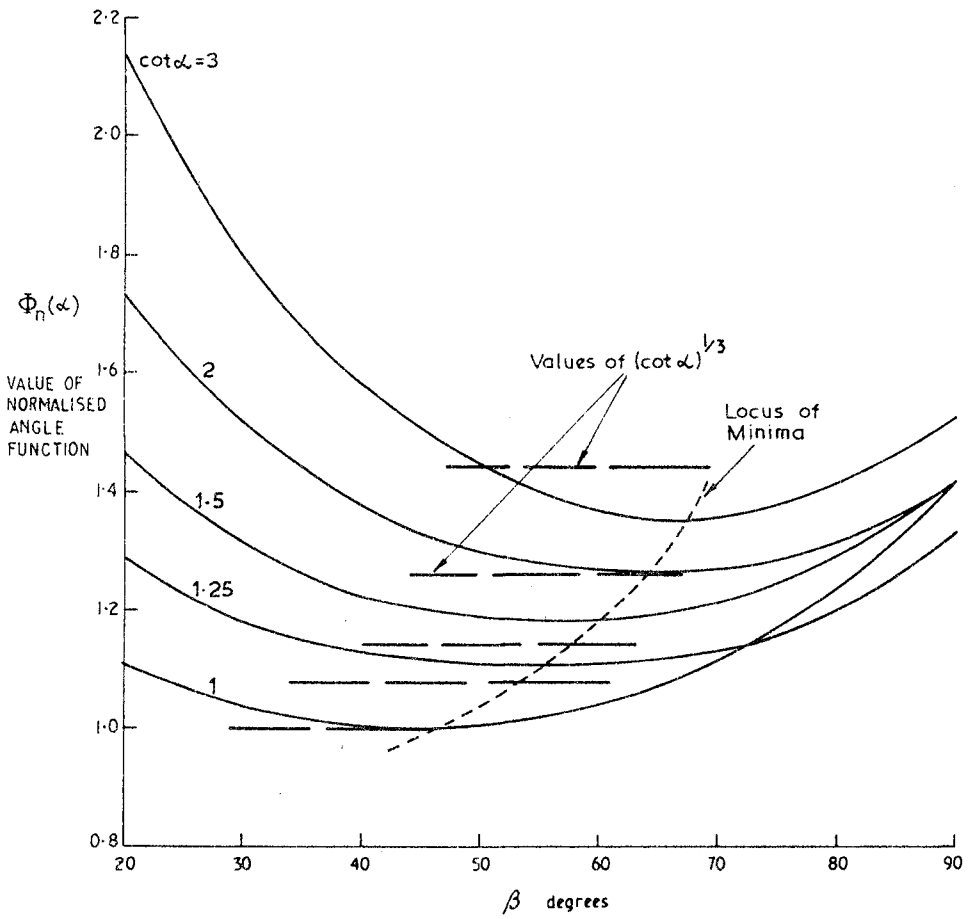


FIGURE 1.

REVETMENT - DEFINITION SKETCH



$$\Phi_n \alpha = \left(\frac{\cos \alpha}{s_i \alpha + \beta} \right) / \cos 46 \text{ vs } \beta$$

FIGURE 2a.

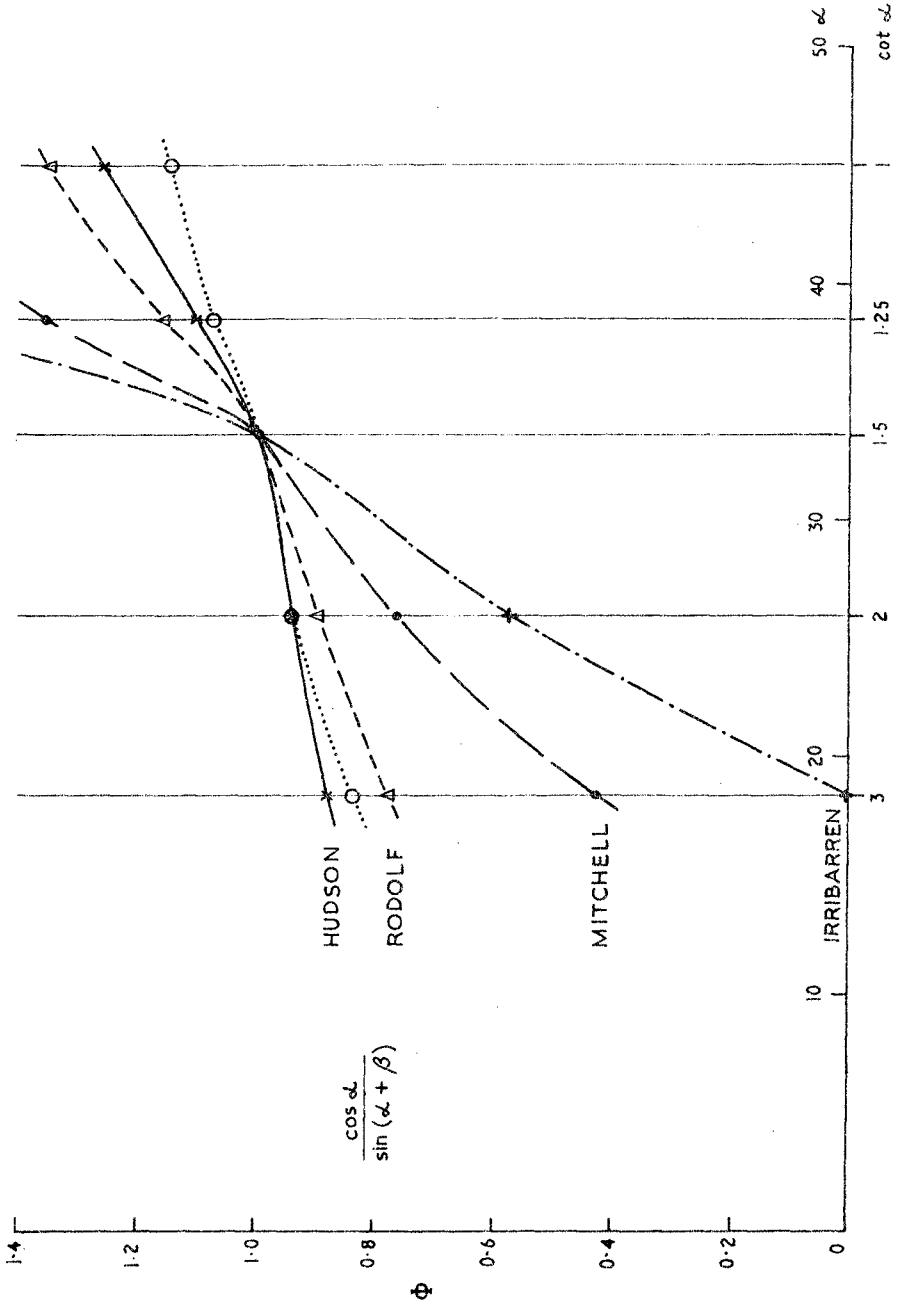


FIGURE 2b: RELATIVE VARIANCE OF WAVE FUNCTIONS

Allowing the surcharge to have a porosity p , consider the pressure sensed at a point on the under-layer. At 0 porosity no water will flow through the slope, and the static pressure will be that of the surcharge $(\frac{W \cos \alpha}{A})$. Under the

wave impact, a pressure $p = K_1 \rho g H_b$ will be induced. If the slope has a porosity of 100%, the underlayer some lower value, then the shock pressure will be some lesser value, occurring at the interface.

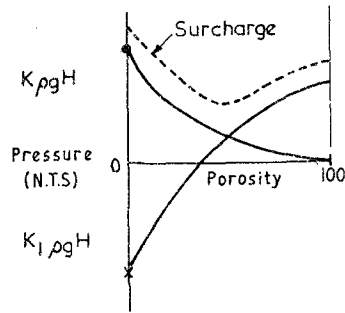


FIGURE 3.

On the drawdown, the position is reversed. For a 0% porosity cover, the head across the armour layer will maximise, and for 100% it will be zero. Efflux from the slope can be considered as a reverse jet.

The function of the armour layer is to surcharge the embankment at any level so that a positive interparticle reaction occurs, so keeping the slope stable. Thus a family of curves such as Fig. 3 could be drawn.

By inspection, it can be seen that an economic minimum can be expected for the slope-normal porosity. Examining the failure case, providing the unit area is not too large, it would appear that the safe unit has a porosity of less than optimum, so that loss of a single unit tends to the optimum condition by increasing the local porosity.

Apart from these structural performance effects, the porosity of the slope also affects both run-up and reflection. The effect on run-up is well known and documented in many standard works.

With regard to reflection, Sawaragi (1966), in his experiment on scour, demonstrated a relationship between reflection and slope-normal porosity of a permeable face. This effect seems mainly related to the damping due to the porous face, as the face appears to be thin compared to the three-dimensional porous core behind. Nevertheless, his experiment showed reflection as low as 20% for 20° slopes with surface porosity of 30%.

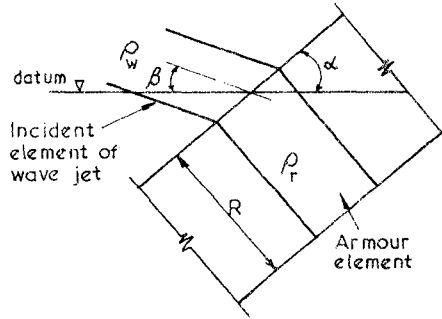


FIGURE 4.

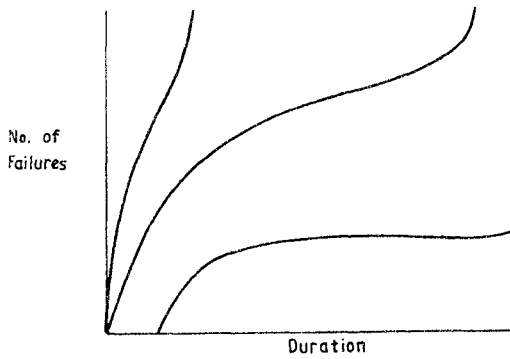


FIGURE 5a.

Referring to the definition sketch, it can be seen that, at maximum run-up, the wave can be typified by two domains, the part outside the slope, and the part within. Intuitively, it could be imagined that the first part will be reflected as if it were on a smooth impermeable slope. Ideally, the water within the slope would be released at a constant rate, i. e. a critically damped wave.

Thus maximising the internal voids and the adoption of the optimum slope face porosity should minimise both run-up and reflection.

By using an armour unit whose geometry may be altered along logical paths, it should therefore be possible to design a revetment for all three criteria, i. e. stability, run-up and reflection.

Using the concept of an armour layer 'veefaced' to the slope, a further examination of the forces is warranted.

Fig. 4 shows a water mass impinging upon the slope at an angle to the horizontal. The momentum flux of the jet normal to the surface is $F_i = \rho u^2 \sin(\alpha + \beta)$. At a depth L normal to the surface of the slope, a pressure P_L is induced, where $P_L = K_1 \rho_w u^2 \sin \theta$. Now

in shallow water $u^2 \simeq g d_b = K_2 \cdot g \cdot H_b$. Hence $p_i = K_1 \cdot K_2 \cdot \rho_w g H_b \sin \theta$

The resisting force due to the layer thickness L (ignoring for the moment any shear forces) is $F_a = (\rho_r - \rho_f) \cdot g \cdot L \cdot (1-p) \cdot \cos \alpha$.

Hence, at 'lift-off',

$$K_1 K_2 \rho_w \cdot g \cdot H_b \cdot \sin \theta = (\rho_r - \rho_f) \cdot g \cdot L (1-p) \cos \alpha$$

$$\text{or } L(1-p) = K \cdot \frac{H}{\left(\frac{\rho_r - \rho_f}{\rho_w}\right) \frac{\cos \alpha}{\sin(\alpha + \beta)}}$$

Plotting the function $\cos \alpha / \sin(\alpha + \beta)$ for values of α and β , a family of curves is obtained. The normalised values are shown in Figure 2a. It can be seen that the minimum values of the curves are close to the value for $(\cot \alpha)^{1/3}$, Hudson's empirical angle function.

The effects of wave steepness and reflection will be found in the values of K_2 and β .

Now the rise of water in the core voids is a time integral of the driving force above, it is a reasonable assumption that the outflow velocity is a scalar function of the inflow velocity. Hence the uplift pressure during downrush $\propto p_i$, and the above expression holds.

The component of force parallel to the slope may cause a sliding failure if too close to the crest or toe. For squat units, or poorly interlocked designs, the surface drag force can exercise an overturning moment, rotating the unit on the slope. This will often lead to positive feedback, and the element will become unstable and leave the slope.

Damage Behaviour

The literature contains a great deal of information concerning the behaviour of armour systems after damage.

In applying the damage criteria to any revetment, careful consideration must be given as to what is causing the damage. In coastal engineering, it is customary to present the damage history as shown in Fig. 5 a. A different perspective is shown by plotting instead the rate of damage as in Fig. 5 b, which is the typical way for production engineering.

Part A of the curve shows the initial rate of failure due to production faults etc. (i. e. poor placement), which rapidly falls too close to zero as the faulty items are discarded. A stable, near zero rate is then achieved, which represents the useful working life of the product. After this, wear, decay etc. begin to take their toll and the damage rate increases.

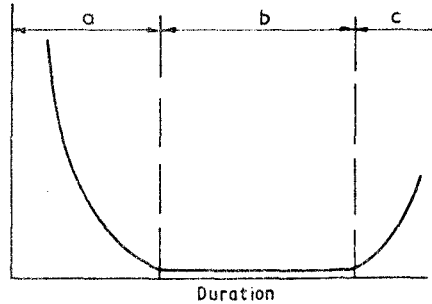


FIGURE 5b.

UTILITY OR DAMAGE CURVES

Now a product which can be produced to a high standard may have no apparent element 'A' to its utility curve.

Looking at revetment construction, if random placement is used, it must be expected that a statistical proportion of the units will be unstably placed and will be removed in the initial 'settling in' phase. It is important that the removal of these units does not cause any consequential damage, such as mechanical damage to adjacent units, other than that implied by the actual unit loss.

If a disciplined procedure for placement is adopted, utilising a unit deliberately designed to facilitate disciplined (pattern) placement, (such as a right prism), it can be anticipated that placement errors can be eliminated so that the utility curve is represented by sections B and C only.

The difference must be made here between disciplined (pattern) placement and uniform (undisciplined) placement. In uniform placement, units (e.g. Tribars) are placed randomly in a planar array. In pattern placement, randomness is almost non-existent, only being measurable in the tolerance measurements.

The advantages of pattern placement as against uniform or random placement are well shown in the case of Tribars.

Table 1 Stability Factor for Modes of Placement of Tribars

Placement	No. of Layers	k	Porosity %	Damage Criteria	K _D		Source
					K _D	K _D /n	
Pell-mell	2	1.0	54	1%	12	6	Hudson 9/60
Uniform	1	1.1	47	1%	25	25	Hudson 9/60
Uniform	1	1.0	-	-	15(25)	15	Jackson/68
Uniform	1	1.0	-	6%	12	12	Gordon/73
Uniform	1	1.0	-	-	25	25	Hudson/74
Pattern	1	1.0	-	2%	70	70	Gordon/73
Pattern	1	1.0	-	.1%	25	25	Gordon/73

Thus, pattern placement has reduced the unit mass by a factor of 4, the material usage by 37%, and damage rate reduced by a factor of ten.

In his observations, Gordon remarked that both pattern and uniform Tribars exhibited 'plateau' behaviour, such that finite amounts of damage occurred for short duration, followed by long periods of apparent stability. He did not observe the cause of the sudden instabilities, but I would venture that it was due to rearrangement of the underlayer, 'springing' the point or line contact between units, and so breaking the pattern. Use of planar contact faces prevents this catastrophic failure.

Practical Applications of Blanket Theory

Of the multitude of armour units and systems available for consideration, a reasonable number exist which can be assessed according to the 'linear' blanket theory outlined above. These systems include both free-standing armour units and interconnected systems.

The results of asterisked units have been reworked in accordance with the 'linear' theory outlined below, and used to demonstrate, where possible, the effect of porosity and/or interconnection.

Careful examination of the references indicates that the value of interconnections is only appreciable for very squat units, i. e. units where the eccentricity of disturbing motion can rotate the unit from the slope. This may be due either to high surface drag or to eccentric slope normal forces - probably the former. (This is a characteristic failure mode of random units. Indeed, some units, such as the dolosse, seem deliberately contrived to generate maximum drag at a maximum lever arm to the centre of gravity).

TABLE 2: CURRENT PATTERN UNITS

Armour Unit	Porosity	Type	Connection	Ref.
Svee Block	Internal (10-30%)	1D	Vee groove	18*
Cob	Internal (50%)	3D	Friction	19*
Revetment block	External(0-5	1D	Tongue & Groove	20*
do.	Nil		Shiplap	*
do.	Nil		V-G+ Shiplap	*
Tribar	External (50%)	3D	Point or line friction	12
Mod Cube	External (10%)	2D	Friction	13
Nami Ring	Both (64-80%)	1D	Line contact/ rods	22
Seabee	Internal (0-70%)	1D	Fullface friction	2*
Gabions	Internal (30-40%)	3D	Wire bound	21*
Gobimats	Both (30%)	2D	Attached to backing	4
Placed stone	-	2D	Friction, interference	7

Table 3 Comparison of Current 'Blanket' Units

Block (reference)	r	$\frac{s}{r-c}$ w	$\phi(\)$ (cot) ^{1/3}	p	$\frac{H_u}{R(1-p)}$	$C_B = \frac{H}{R(1-p)}$ $= \frac{1}{s \cdot \phi(\)}$
T+G()	2.3	1.3	1.26	0 - 2	4.26	2.6
T+G()	2.3	1.3	1.26	2 - 4	10.70	6.54
Shiplap()	2.3	1.3	1.26	0 -.5	8.8	5.37
Gobi	2.3	1.3	1.44	36	14	7.45
Naue	2.3	1.3				
Svee	2.3	1.3	1.078	16	10	7.15
	2.3	1.3	1.078	31	7.5	5.36
Cob	2.4	1.4	1.14	50	10	6.25
Seabee	2.69	1.69	1.14	24	12.5	6.5
			(1.14	35	14.5	7.5) ¹
			1.14	51	14	7.25
Gabions	2.67	1.67	1.26	35	9	4.3 *

¹ 15% of units removed from slope (face centre unit of each group of seven units) without inducing failure

* Failure in the case of gabions denotes pronounced departure from the as-built profile due to pumping. Due to multiplicity of redundant active bonds, structure fails by breakdown of

underlayers, or long term wear on wire cage.

The Seabee

The Seabee is an armour unit designed with the above arguments in mind, namely:-

1. Slope height is independent of area .
2. Porosity is variable.
3. Pattern is easily laid, and is unharmed by loss of any individual unit .
4. In plane forces are spread in a 120° form by face to face contact.
5. Each unit is in frictional contact with four adjacent units, and the units are thus in a zero, or compressive stress situation.
6. The major water paths are coaxial and disturbing forces thus have low moment generating capacity.

Because of its simple form, the Seabee allows for economical, rapid manufacture from a variety of materials and in any size. Due to the separation of water passages from contact faces, inter unit contact is maximised and drag force eccentricities minimised. By utilising high aspect ratios, the surface drag force due to uprush and downrush is of little consequence in armour element mechanics. By utilising the variable porosities available, the best combination of stability, reflection and run-up can be attained.

Plates 1 and 2 show views of an ocean front revetment at Wamberal, N.S.W. during and after construction.

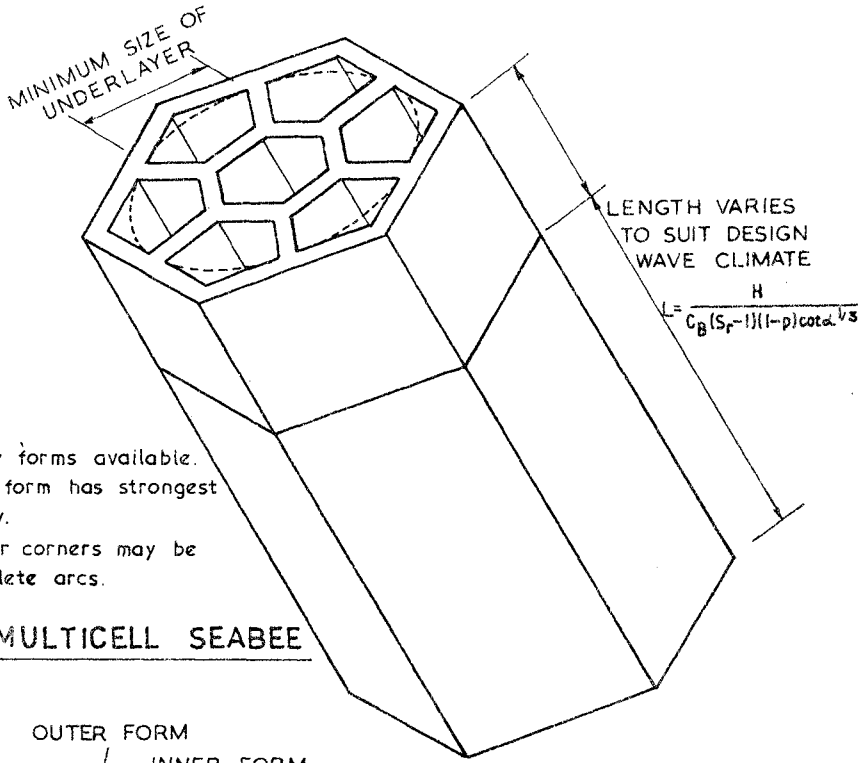
It should be noted that worldwide patents in respect of the Seabee system have been applied for and/or are pending.

Conclusions

A re-examination of Hudson's well known equation allows the proposition, that for a given material, $\frac{H}{L_0} = K \cdot \phi(\alpha)$ where K is a constant associated with the unit geometry[†]

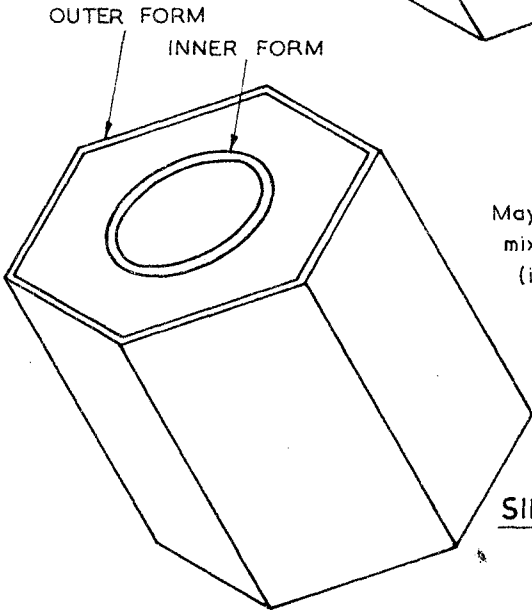
Many experiments have shown that Hudson's empirical angle function, $(\cot \alpha)^{1/3}$, describes to a reasonable degree the effect of the slope angle. Others have demonstrated the variability due to variations in H_0/L_0 . By considering the mechanics of the wave 'thrust' or jet, an alternate possible function is proposed:

$$\phi(\alpha) = \frac{\cos \alpha}{\sin(\alpha + \beta)}, \quad = \tan^{-1} \sqrt{\frac{d}{K H}}$$



Many forms available.
 This form has strongest
 array.
 Outer corners may be
 complete arcs.

MULTICELL SEABEE



May be all concrete, or
 mixed permanent forms
 (inner and outer) with
 insitu filling. Use of
 Multicell inner forms
 allows small underlay
 material to be used.

SINGLE CELL SEABEE

FIGURE 6: SEABEE EXAMPLE

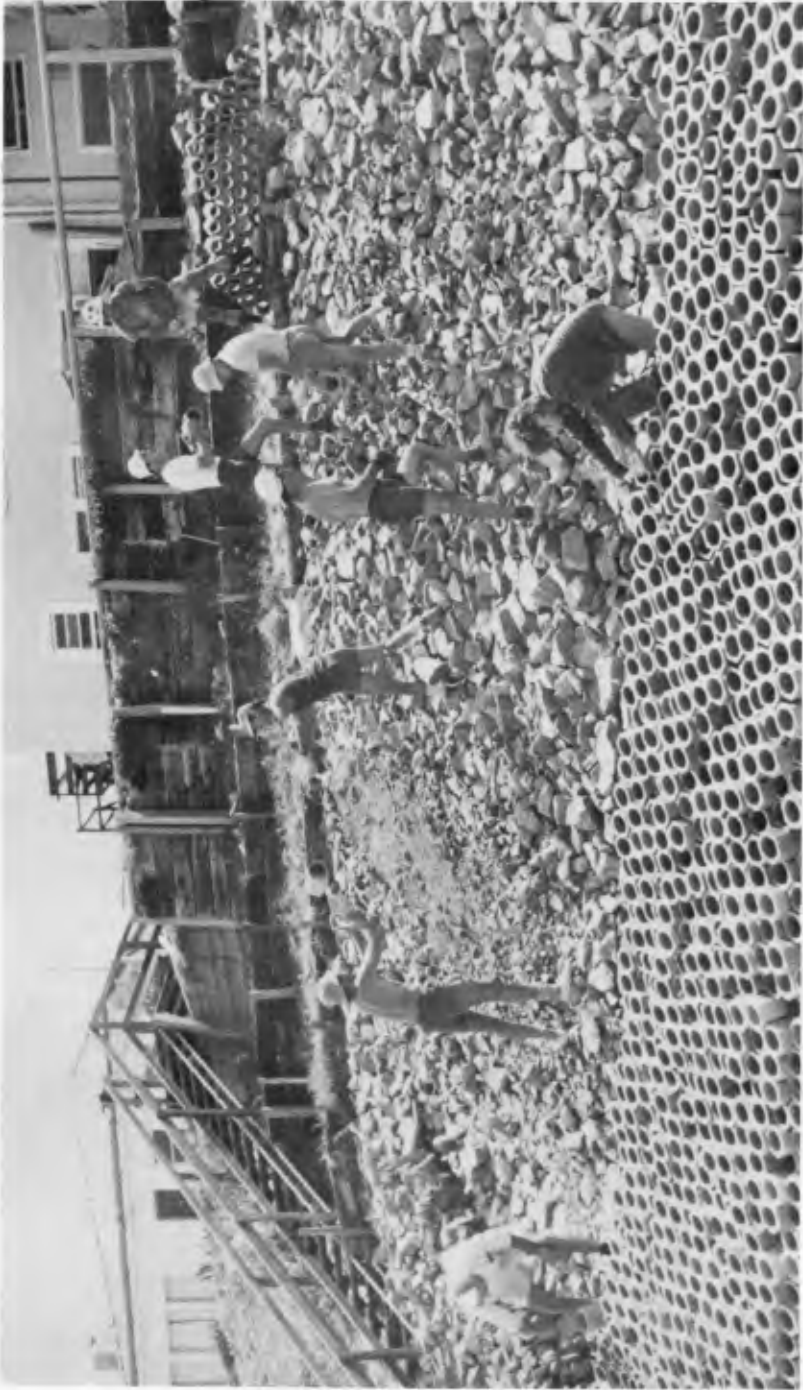


PLATE 1. CONSTRUCTION AT WAMBERAL BEACH NSW FEB. 78



PLATE 2 PRACTICAL COMPLETION AT WAMBERA BEACH
(TOTAL COST = \$110 PER FOOT RUN)

Variations in β give rise to a curve similar for that shown for waves of various steepness. A full justification has not been made for this new function, and it is proposed that this concept provides instead a justification for accepting Hudson's angle function as being a reasonable shorthand for the minimum stability case.

A corollary of this proposition is that the arbiter of both stability and economic worth is the value C_B and the ability of the form to maintain its properties through large changes in aspect ratio. Hudson's K_D is shown to be a relative stability factor only, applying only to fixed geometric forms.

Two basic routes apply, the first being the use of active mechanical bonding (e.g. reno mattresses, gobimats, rodded Nami rings). The second is to design the joint planes so that failure is only possible along the minimum force vector.

The Seabee is a unit designed in accordance with these principles. Laboratory units have been tested to K_D values of greater than 400, some units being too stable a size to determine their relative stability parameter. This unit allows full capability for post-design geometry changes, and highlights the need for alternative armour system specifications. Units of minimum mass or maximum weight may or may not be the most economic to construct.

Thus contracts might better be written about a number of alternate armour units or, in the case of suitable units, by specifying the required porosity and the minimum submerged surcharge, and prompting the tenderer to determine his own optimal unit size and type. This will not relieve the design engineer of his responsibilities but it should encourage a more aware approach by all parties.

Reference to the definition sketch shows that the volume of the wave (H, L) can be considered to be stored within the hysteresis loop of the water surface envelope. In permeable cores of suitable characteristics, this envelope passes through a single point at the surface of the (semi-)permeable core, where it is increasingly common to find a filter-cloth. For thinner underlayers, the envelope subtends a line at this surface, centred on the phreatic surface in the core, pumping the local filter-fabric/core formation. In such circumstances, cheap filter-cloths are a false economy. It might also be expected that the disturbing pressure drop across the armour layers could be related to the volume of the hysteresis loop and the elevation of the inner node. Before closing, it should be further noted that irregular or periodic wave trains cause the phreatic level to vary, so developing a secondary hysteresis effect.

Appendix: The value of β

the value of β can be approached as follows. Considering the wave

motion immediately prior to impact, the wave has a horizontal velocity

$$c = \frac{1}{2} \cdot \frac{L}{T} \sqrt{1 + \frac{4\pi d/L}{\sinh(4\pi d/L)}}$$

at impact, the vertical component of velocity is due to the loss in potential energy in falling from the wave crest to the point of impact, thus

$$w = \sqrt{g\Delta h}, \quad v = \sqrt{w^2 + c^2}$$

for shallow water

$$c \approx \sqrt{gd}, \quad v = \sqrt{g(d + \Delta h)} \approx \sqrt{K_2 g H}$$

Now

$$\begin{aligned} \beta &= \tan^{-1} c/w \\ &= \tan^{-1} \sqrt{d/\Delta h} \approx \tan^{-1} \sqrt{d/KH} \end{aligned}$$

Unfortunately there has not yet been time to check this relationship to see if it does indeed hold. But it is a concept that is easily grasped and gives values intriguingly close to those of both Hudson and Per Bruun.

References

- 1 Ahrens, J. P. The Influence of breaker type on rip-rap stability 12th Conference on Coastal Engineering, ASCE 1970 pp1557-66
- 2 Brown, C. T. Seabees-Variable Geometry Armour Units, Fourth Australian Conference on Coastal and Ocean Engineering, 1978 Preprints, pp 64-67
- 3 Brown, C. T. Gabions and Reno Mattresses for Coastal Revetments Water Research Laboratory of the University of NSW report, 1978 (in press)
- 4 Cox, A. L. Paving Block Study. Research report No 58, Louisiana Department of Highways, October 1971.
- 5 Danel, P. et al. Tetrapods and other precast blocks for Breakwaters. Proc. ASCE, Waterways and Harbours Division, Vol 86, No WW3, Sept. 1960
- 6 D'Angremond et al. Use of asphalt in breakwater construction. Proc. 12th Conference on Coastal Engineering, ASCE 1970 pp 1601-1628.
- 7 Debok, D.H. & Sollitt, C.K. A large-scale model study of Placed-Stone Breakwaters. Ocean Engineering, Oregon State University.
- 8 De-Carvalho, J. J. R & Vera-Cruz, D. On the Stability of Rubble-mound Breakwaters. Laboratorio Nacional de Engenharia Civil Tech Paper No. 200, Lisboa 1962
- 9 Font, J. B. Damage functions for a Rubble-mound Breakwater under the effect of swells. Proc. 12th Conference on Coastal Engineering, ASCE 1970, pp 1567-1586.

- 10 Gordon, A.D. The Stability of Armour Units against Breaking Waves. M.Eng.Sc. thesis University of NSW, March 1973.
- 11 Jachowski, R.A. Interlocking Precast Concrete Seawall. Proc. 9th Conference on Coastal Engineering, Lisbon, June 1964.
- 12 Hudson, R.Y. Laboratory Investigations of Rubble-mound Breakwaters. Proc. ASCE, Waterways & Harbours Division, Vol 85, No. WW3, Sept, 1959.
- 13 Hudson, R.Y. Concrete Armour Units., Misc. Paper H-74-2, WES., Vicksburg, January, 1974.
- 14 Manohar, M Seawalls & Breakwaters, Proc. I. C. E. (India) 1962 pp355-388
- 15 Per Bruun & Ali Riza Gunbak. Hydraulic and Friction Parameters affecting the stability of Rubble-mounds. PIANC Bulletin No 24 1976.
- 16 Popov, I. ya. & Ryabykh, V. M. Wave pressure on the slopes of Hydraulic Earth Structures. Izvestia VNIIG, 1971 vol 97, pp49-63
- 17 Sawarag, T. Scouring due to Wave action at the toe of Permeable Coastal Structure. Proc. 12th Conference on Coastal Engineering ASCE 1966 p1036+.
- 18 Svec, R. et al. The Stability properties of the Svec Block. Proc. 21st International Navigational Congress (PIANC) 1965, Section II-I, pp 133-162.
- 19 Anon. Tests of modified cob block. H. R. S. Wallingford, Report No Ex-622, April 1973.
- 20 Hall, J. V. Tests on machine made Interlocking Block. Proc. 12th Conference on coastal Engineering, ASCE 1966.
- 21 Palmer R.Q. U.S. Patent No 3990247, Nov. 1976.

CHAPTER 152

EFFECTIVENESS OF SEADIKES WITH ROUGH SLOPE

Osamu Toyoshima
Public Works Research Institute
Ministry Of Construction, Japan

ABSTRACT

The length of the coastline of Japan is very long, and it exceeds 31000 kilometers. In which, about 19000 kilometers are remained as natural coast, but 8000 kilometers are protected by the seadikes (inclusive of seawalls).

Before 1965, there were about 5900 kilometers of seadikes. Then, we have constructed more than 2100 kilometers of seadikes during the past ten years.

In Japan, sea and shore are all under the control of the Government, and 8000 kilometers of coastal structures have been constructed or improved as the Public Works. Before 1945, however, most of seadikes, though their length were not so long in that age, were constructed as reclamation works by private, and after the War, these private reclamation seadikes were changed to the government management and have been improved as the public works. These former seadikes were almost for the storm surge.

Since the early 1960's, beach erosion in Japan has become increasingly severe, and many seadikes have been constructed for measures against beach erosion. Because of customs of long standing and low cost, most of seadikes in that time were vertical type ones and made of concrete. Several years after construction, some of those seadikes were destroyed by the scouring at the toe of the seadikes due to the reflected waves. For the prevention of scouring, it is essential to dissipate wave energy and decrease the return flow on a dike face.

One of the measures is to make the face rough and permeable. Several inclined slope type seadikes with rough and permeable face were proposed by the author. Thirty or more experimental works of these new type seadikes have been carried out on every place where each conditions of wave and beach were respectively diverse. In parallel with constructions, numerous field investigations have been carried out under guidance of the author.

The effects were evaluated after the field investigations for more ten years, and most of these experimental works were effective.

TRANSITION OF SEADIKES STRUCTURE

Before 1940's, seadikes were constructed as the reclamation dikes under the private management and made of stone masonry as showed in Figure 1.

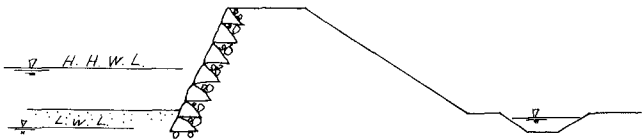


Fig.1 Former vertical type seadikes for storm surge

After the War the first improvement works were concrete facing of these masonry seadikes. In that time, the thickness of concrete facing was ordinary 30 cm.

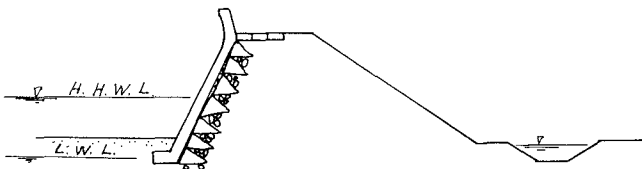


Fig.2 Concrete facing works after the War

On September 26, 1959 a extra-large typhoon attacked the Ise Bay. More than 5000 people died, and 680 kilometers of seadikes were destroyed. Damaged seadikes were restored as the concrete face inclined type seadikes as showed in Figure 3. The thickness of concrete were 50 cm in front and 20 - 25 cm in rear facing.

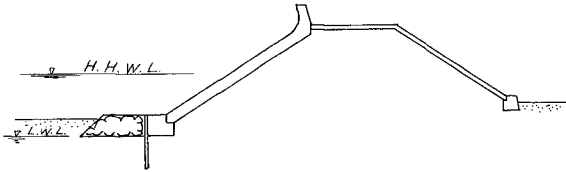


Fig.3 Typical seadikes after the "Ise Bay Typhoon"

After the "Ise Bay Typhoon", this inclined type seadikes had been used many coasts not only for storm surge but also as prevention works for beach erosion. Seadikes for storm surge had been constructed generally at the bottom of bays with very shallow water. Tidal ranges of these area are pretty large, and bed material are usually silt or fine sand. There have been almost no problems about the beach erosion and scouring at the toe of the seadikes.

Meanwhile, since the 1960's, beach erosion has become severe and many seadikes for beach erosion were constructed. Seadikes at that time were almost vertical type ones showed in Figure 4 or the inclined type ones such as shown in Figure 3.

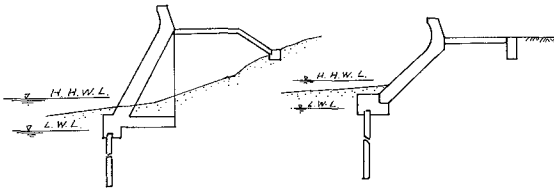


Fig.4 Vertical type seadikes in the 1960's

Different from the seadikes for storm surge, seadikes for beach erosion had been constructed on the sandy beach with pretty steep near shore. After the construction some of these seadikes have suffered considerably damage in every coasts.

From the first, the mechanism of beach erosion had not exactly been known yet in those days. In order to prevent the erosion of sand dunes and regression of shore line, seadikes had been constructed without considerable studies.

The incident waves were violently reflected on the steep front slope of seadikes. Forshore and the toe of seadikes were washed out with the reflected waves. Then, contrary to expectation, these seadikes encouraged the beach erosion.

EXAMPLES OF DAMAGED SEADIKES

Example (1)

The shore line had been receding gradually and the uprush had broken into the houses. Then, new seadikes were constructed.



Fig.5

However, the incident waves were violently reflected on the front slope foreshore and the toe of seadikes were washed out with reflected waves.

Contrary to expectation only one year after the construction, the seadike were destroyed and beach erosion has encouraged.



As the measure for wave overtopping and against scouring at the toe of the sea dikes, armour units had to be installed.

Lost beach have never reappeared.



Example (2)

This coast had been a stable bathing beach for long time.

On July 1970, a middling typhoon attacked the coast



Six monthes after, on January 1971, the shore-line greatly receded.

On July 1972, the beach have entirely vanished.



Example (3)

On March 1969, the shoreline was slowly receding, and gentle slope dune changed into the bluff



Seawalls had been built at the toe of the bluff until March 1972. However, on January 1973 the beach vanished.



Then we had to install armour units as the wave defence works.



PROPOSAL OF NEW TYPE SEADIKES

As the countermeasures against the foreshore erosion and the scouring at the toe of seadikes, the toe protection works, made of rip-rap or armour units, or underpinning works, made of cut-off wall or steel sheet pile, were constructed. Some of them were success, but another were ineffective.

Then, the author proposed the "Detached Breakwater System" at that time for these destructed coast. However, there had been many natural beaches needed some useful and effective seadikes. Then the author proposed some new type seadikes.

After many field experiences such as above-mentioned examples, the author thought that, points of attention and problems to be consider for the new seadikes were to be as follows:

- 1) Decrease the reflected waves from the front of seadikes as little as possible.
- 2) Make the front face more rough.
- 3) Make the front face permeable if possible.
- 4) Some partial collapses should be allowed, but never be destroyed the whole body of the seadikes.
- 5) Repair and reinforcement to be easy.
- 6) Structure to be simply and low cost.

The first new type seadikes the author proposed was a "Block faced seadike" covered the front slope with some artificial concrete blocks such as armour units.

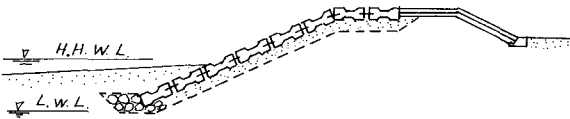


Fig.14 Block faced seadike

Fig.15 Hollow square block

The above shows a example of block faced seadikes used the "Hollow square block" which is used generally in Japan.

These block faced seadikes were constructed at more than ten sits in Japan, and most of them have been quite effective.



Fig.16 Block faced seadike

The above was constructed on 1966. The armour units are installed on the rip-rap.

Even now, they have been in existence without any accident.

In the same way, the next example is block faced seawall. This seawall has been constructed on 1977 as the restoration works of the former vertical type seawall.

A respectable wave attacked the coast on July 1978. Neighboring seawalls were destroyed about 100 meters in length, but this block faced seawall has been in existence without a change.



Fig.17 Block faced seawall



Fig.18 Cross section

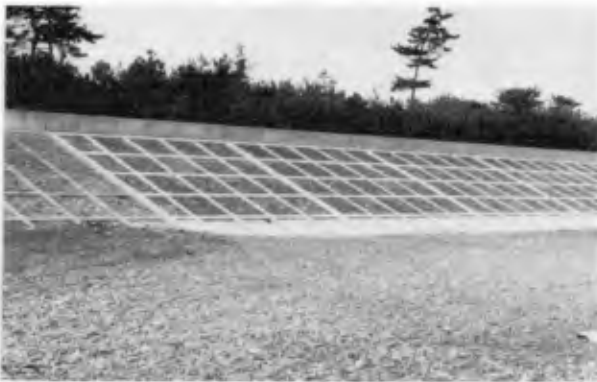
The second new type seadikes the author proposed was a "Lattice type seadikes".

It is covered the front slope with lattice works filled with rip-rap, cobbles, concrete blocks, armour units and soddings etc.

The first lattice type seadikes was constructed on 1967. The lattice has a 2 meters square and its member is made of concrete of a 40 by 50 cm section.

The compartment filled with rip-rap is showed in Figure 19, and filled with cobbles in Figure 20 and 21.

These were constructed on 1968 and 1976. The former has experienced several times violent waves during the past ten years. Fortunately,



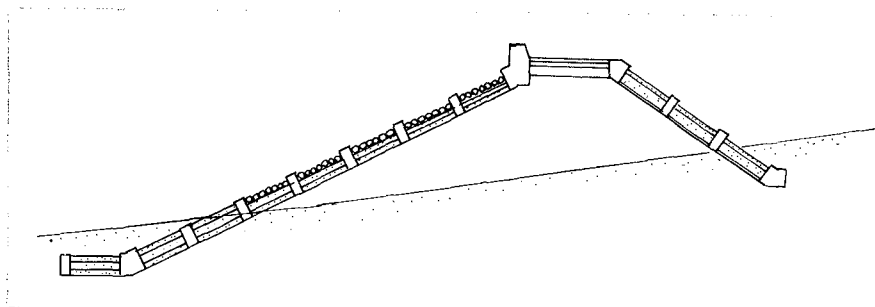


Fig.21 Cross section of the Lattice type seadikes

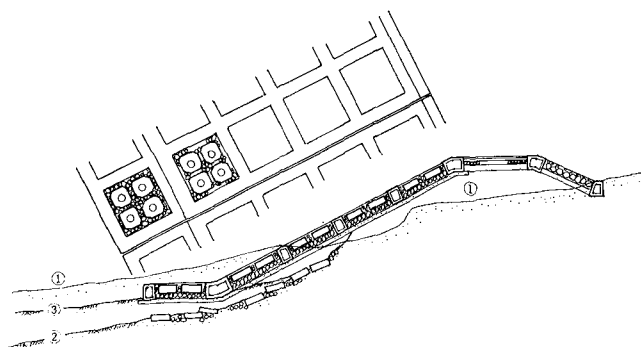


Fig.22 A example of partially collapsed seadike

The above seadike was partially collapsed at the low side compartments. However, the lattice were undamaged and the destruction did not amount to the whole body of the seadike.

If heavy storms attacked the front slope, the fills of the compartments will be collapsed. Then, the lattice should be designed strong enough to stand alone.

In the above, (1) is the section of before construction, (2) is just after the destruction, and (3) is several days after the destruction. Run off sand came back again of itself, and the beach was restored passably.

It is easy to repair this kind of seadikes collapses compared with reconstruct vertical type seadikes.

On the gentle and permeable slope, run up waves dissipate and percolate. Then, after the storms the quitted sand frequently come back to the fore shore, we can easily repair and restore the seadikes.

The next example also is the lattice type seadike. The compartment of the lattice is filled with concrete blocks, cobbles and grass. It was constructed on 1967 succeeding next to the existing vertical type seadike.

The change of the type of seadike was carried out according to the proposal of the author. Because, the fore shore in front of the existing vertical type seadike had begun to show a distinct tendency to the beach erosion.



Fig. 23 Lattice seadike

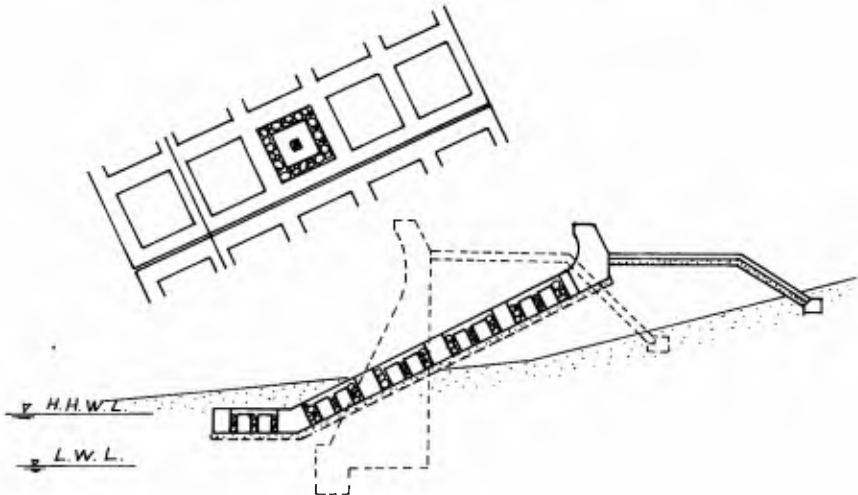


Fig.24 Cross section of the above seadike

Three years after the construction, the vegetables on the front slope have grown thick, as showed in Figure 25. And, these lattice type seadikes have been in existence without any damage.



Fig.25 Vegetables grew thick on the lattice slope

However, the fore shore in front of the vertical seadike has become narrow, and on 1975 the vertical seadike was partially destroyed by the middling waves. (Arrow mark in Fig.26)



Fig.26 Vertical seadike was partially destroyed

These proposed permeable and rough slope seadikes show that they are appropriate methods of the dune protection. The distinctive features of these new seadikes are not the non-destruction, but the easy restoration and don't encourage the beach erosion.

And, the proper countermeasures against beach erosion should depend on groins, detached breakwaters, nourishments and etc. (END)

CHAPTER 153

SCOURING AT THE TOE OF A SEAWALL DUE TO TSUNAMIS

by

Hitoshi Nishimura*

Akira Watanabe**

and

Kiyoshi Horikawa***

ABSTRACT

In this paper, the general features and mechanism of scouring at the toe of a seawall due to tsunami invasion are discussed based upon the results of two-dimensional experiments. The effects of the various slopes, bed material, water depth and wave conditions are separately investigated. After some consideration of the scouring mechanism, a critical condition for the occurrence of scouring is given in terms of two important parameters, namely, the rate of return flow from the land and water layer thickness in front of the seawall. These findings lend perspective towards the quantitative prediction of the total amount and pattern of scouring.

INTRODUCTION

Coastal structures on the Pacific coasts of Japan are continuously exposed to violent tsunamis and, as is well-known, damage to such structures is often caused by scouring at their toe. Although this is a serious problem in the field of coastal engineering, it is extremely difficult to analyze the whole process of tsunami deformation over a movable bed, which includes shoaling, breaking, reflection, overtopping, runup, and return flow. Furthermore, hydraulic phenomena have to be related to the amount of sand movement. And finally, for this phenomenon field data are lacking and difficult to obtain.

Herein, a series of two-dimensional experiments are described which were carried out under simplified conditions in order to clarify the scouring mechanism due to tsunamis.

* Assoc. Prof., Dept. of Civil Eng., Univ. of Tokyo, Tokyo, Japan.

** Assoc. Prof., Dept. of Civil Eng., Univ. of Tokyo, Tokyo, Japan.

*** Prof., Dept. of Civil Eng., Univ. of Tokyo, Japan.

DESCRIPTION OF EXPERIMENT

The model installed in a wave flume consists of a seawall with a sloping face, sloping sea bottom, and sloping land surface connected to the crown of the seawall as shown in Fig. 1. For each experimental run, a solitary wave simulating a tsunami wave was generated by allowing a mass of water from the head tank into the flume. The air valve is automatically operated to pump up the prescribed amount of water into the tank or to release it into the flume. Capacitance wave gages and a propeller current meter were used for the measurements. Deformation of the incident waves and bottom topography were recorded by a VTR system and a motor-driven camera.

Experimental conditions are given in Table 1, where underscoring indicates the standard conditions. Effects of each factor on the amount and the pattern of scouring were systematically investigated by shifting individual conditions from the standard condition.

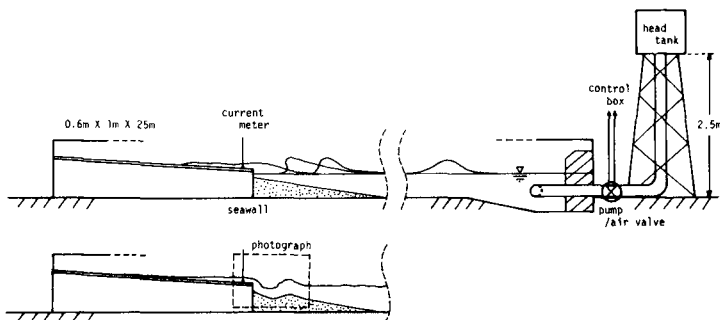


Fig. 1. Experimental installation.

Face slope of the seawall:	90°, 60°, 45°		
Land slope (fixed bed):	1/15, 1/30, 1/60, 1/120		
Bottom slope (movable bed):	1/5, 1/10, 1/15, 1/30		
Water depth at the toe:	15 cm, 10 cm, 5 cm, 0 cm		
Crown height of the seawall:	10 cm, 5 cm, 0 cm		
Incident wave height:	35 cm, 30 cm, 25 cm		
Bed material	<u>Mesalite</u>	Sand(A)	Sand(B)
Specific gravity:	1.65	2.65	2.65
Median grain size:	0.25	0.20	0.70

Table 1. EXPERIMENTAL CONDITIONS

EXPERIMENTAL RESULTS

A single incident solitary wave was caused to break on the slope, collide against the sea wall, overtop, and run up on the land slope as illustrated in Fig. 2. During these processes, only minor scouring if any takes place. Then the mass of water stored temporarily on land starts to flow back and this return flow is the significant contribution to scouring. Figure 3 is a brief description of general features of the present phenomena. The position and the amount of scouring at a given moment are controlled mainly by the instantaneous rate or velocity of the return flow and the thickness of the water layer receiving the flow. The influence of scouring is fed back to the water depth as well as to the wave behavior.

The effects of each factor on scouring found through the experiments are summarized as follows:

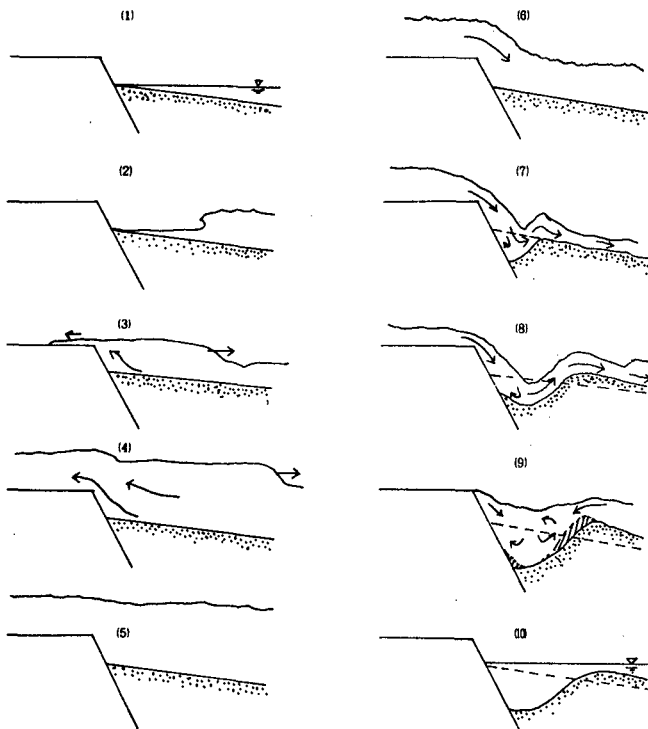


Fig. 2. Sketch of wave deformation and scouring processes.

- (1) A decrease of incident wave height or an increase of the crown height reduces the amount of the wave overtopping and scouring, but these factors are not necessarily advantageous for protection of the structure since the area of serious scouring approaches the toe in such cases.
- (2) When the face slope is mild, the amount of scouring is large and it occurs exactly at the toe.
- (3) The amount of scouring decreases considerably as the water depth in front of the seawall increases.
- (4) A milder land slope causes a larger amount of wave overtopping and a smaller return flow rate. The total amount of scouring depends on the instantaneous water depth when the return flow strikes the bottom.
- (5) The influence of the bottom slope is comparatively small.
- (6) The use of bed material with smaller specific gravity leads to much greater scouring, while the effect of grain size is not too significant (Fig. 4).
- (7) When waves are applied repeatedly, much less scouring is caused by each successive wave.

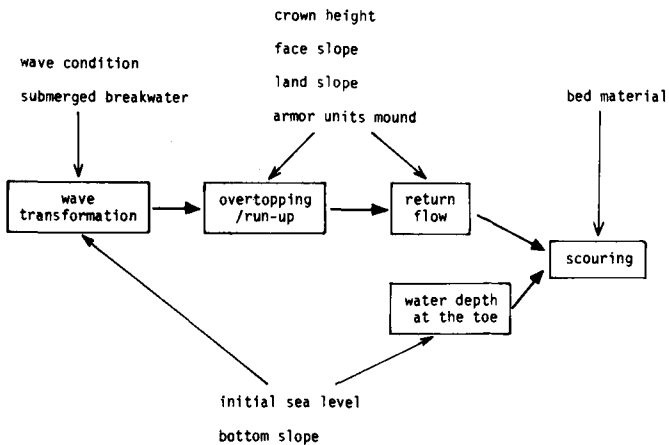


Fig. 3. Description of the wave deformation and scouring phenomena.

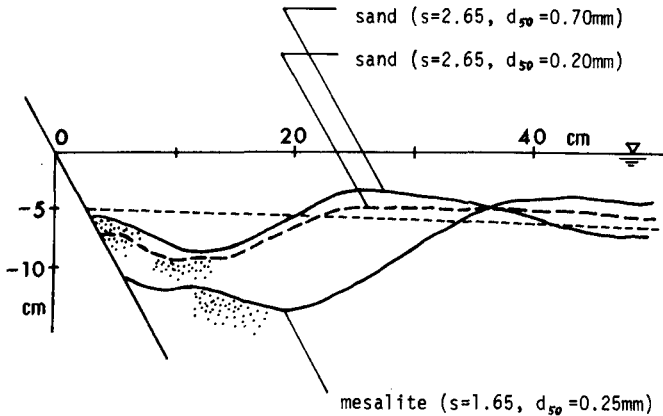


Fig. 4. Resultant scouring patterns.

DETAILED DISCUSSION OF SCOURING PHENOMENA

The amount of scouring cannot be simply related to the amount of wave overtopping or the maximum rate of return flow, since the water depth in front of the seawall is another important factor controlling the phenomena as was mentioned in the previous section. It effectively works as a buffer when the flow hits the sea bottom. For the discussion of this essential part of the total mechanism, some sets of experimental data with the vertical seawall and the sea bottom of standard sand (A) are selected here.

When the flow rate is large, the hydraulic phenomena near the seawall are extremely complicated and by no means easy to analyze. Therefore, it is more practical to define the water depth by taking the ambient sea level as the reference level. Assuming that there is no water in the flume and that the mass of water flows from the land slope to the sea bottom with the initial velocity measured at the crown, then the instantaneous shape of the nappe is easily calculated. Such a parabolic nappe actually appears when the sea level is lower than the crown. The outer end of the assumed nappe is almost always very close to the point of most intense scouring at that moment. As illustrated in Fig. 5, d_0 is the water depth measured from the reference sea level to the initial sea bottom at the end of assumed parabolic nappe. Now the value of d_0 is determined from the return flow velocity and the ambient sea level.

Figure 6 shows the measured variation of the return flow velocity v and the water depth d_0 for a particular case. As the scouring takes

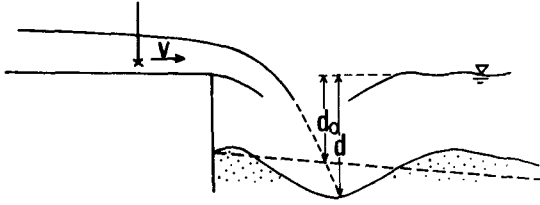


Fig. 5. Definition sketch.

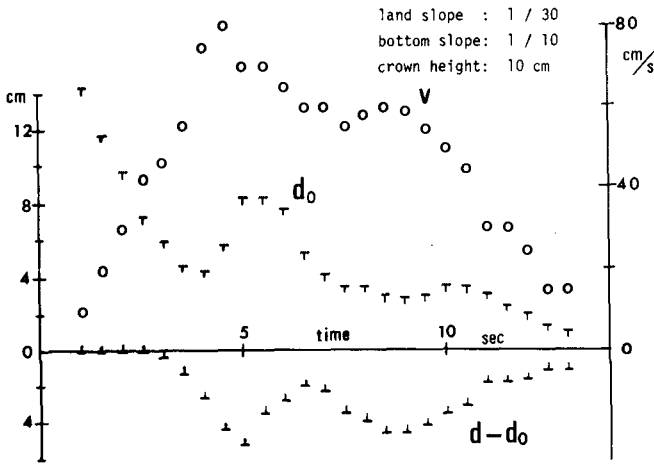


Fig. 6. Variation of the flow velocity and the reference water depth.

place, the bottom profile changes, adding some depth. The measured variation of the additional depth $d-d_0$ at the end of the nappe is also plotted in the same figure.

The flow velocity is replotted to the reference depth in Fig. 7. The dashed line shows the relationship between v and d_0 corresponding to the data in Fig. 6. The water depth is almost at its maximum when the return flow is initiated, and it decreases as the flow velocity increases. Then the water depth slightly increases because the end of the nappe is shifted by the increase of the velocity of the return flow. In this case, the water depth reaches its minimum value when the return flow terminates. The intense flow strikes the thin water layer and scouring results in the region of large flow velocity. Consequently, the process of the flow and depth variation is shifted in the figure in terms of the substantial water depth d as shown by the solid line.

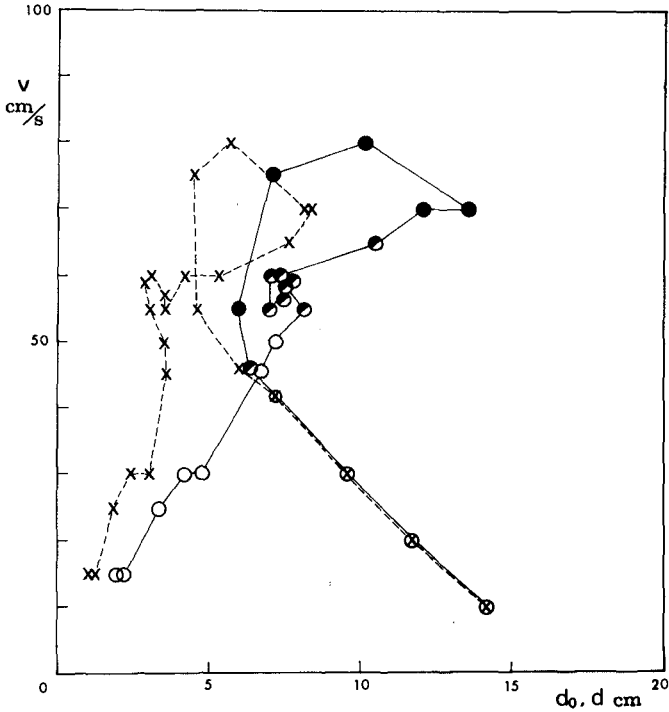


Fig. 7. Variation of the flow velocity to the reference water depth.

The solid circles on the line indicate the active motion of bed material and the half solid circles correspond to the less active motion of sand.

Similar plots are shown together in Fig. 8 for several cases for different conditions of land slope, bottom slope and initial sea level. It seems that there exists a critical condition for movement and non-movement of bed material. When the flow-depth variation is traced in the v - d plane, scouring begins immediately after crossing the dashed line and advances in such a way that the flow-depth combination follows the line. In principle, this curve can be used to predict the scouring pattern from a given variation of flow velocity and sea level. However, more careful investigation is necessary for the actual use of the curve. The circles connected by the solid line in Fig. 8 are the plot for the case of a steep land slope. Under such a conditions, the increase and decrease of the velocity of the return flow is comparatively rapid and the time duration of high velocity is not enough for completion of scouring. The space between the solid and dashed lines is to be filled by successive

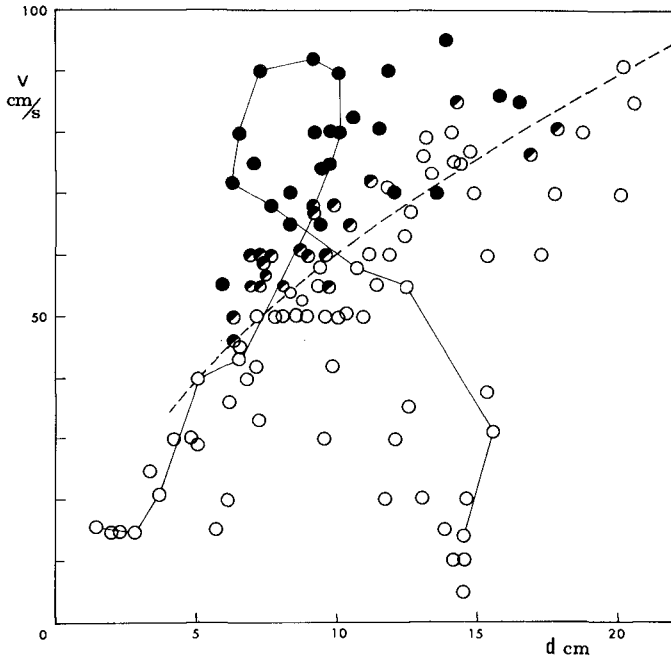


Fig. 8. Critical condition for sand movement.

waves. To conclude, the dashed line in Fig. 8 is considered to represent the ultimate profile under repeated action of tsunami waves.

Scouring phenomena due to tsunamis were investigated from various points of view in this study. It is noted, however, that further studies on similarity laws are indispensable for the quantitative prediction of scouring on actual coasts.



Port of Bremerhaven, Weser Estuary

PART IV

COASTAL, ESTUARINE, AND ENVIRONMENTAL PROBLEMS

Island Neuwerk, Elbe Estuary Tidal Flats



CHAPTER 154

SIMULATION OF WAVE/WIND FORCED HARBOR OSCILLATION

S. K. Liu,¹ H. S. Hou,² and C. C. Chang³

INTRODUCTION

This paper describes the methods used in an investigation of the response characteristics of a large man-made harbor under construction. In the investigation a three-dimensional finite difference model is applied in conjunction with physical models and field observations to assist in determining criteria for design and operation. In the modeling investigation, the dynamic response of the harbor system induced by tide, incoming short/long waves, wind stress and bottom dissipation are considered simultaneously. Particular emphasis of the study has been on the wave- and strong monsoon-induced oscillations that match the range of the resonant period of ships and mooring systems expected to operate in the harbor. The resolution required to handle short-period oscillation and wind stress precludes the possibility of using methods involving the inversion of extremely large matrices.

The results of the numerical simulation at important localities within the harbor system are later analyzed by spectral and cross-spectral methods. The same methods can then be used to study ships' responses at these localities with the predicted water level and three-dimensional current components.

THE HARBOR SYSTEM

Taichung Harbor (Fig. 1) is located on the west coast of Taiwan, facing Taiwan Strait, approximately 100 miles from the mainland. The harbor has been under construction for five years. At its completion, the harbor complex will be 9.5 kilometers long in the NNE-SSE direction. One of the major considerations in the design and planning process is the possible seiche motion induced by the persistent wind field in line with the main channel during the monsoon season usually lasting several months each year. Also of concern is the possible presence of short-period oscillations at facilities serving container ships, whose loading and unloading operations are sensitive to these oscillations, particularly when the oscillation period matches the natural frequency of the mooring system. To this end, it has been decided to develop a numerical model in conjunction with the physical model of the harbor system which will be capable of simulating tidal flow, wind-driven circulation and harbor oscillations.

¹ Senior Physical Scientist, The Rand Corporation, Santa Monica, California, U.S.A.

² Taichung Harbor Bureau. Present address: Director, Graduate Institute of Rivers and Oceanography, Taiwan Institute of Oceanography, Taiwan, Republic of China

³ Chief Engineer, Taichung Harbor Bureau, Taiwan, Republic of China

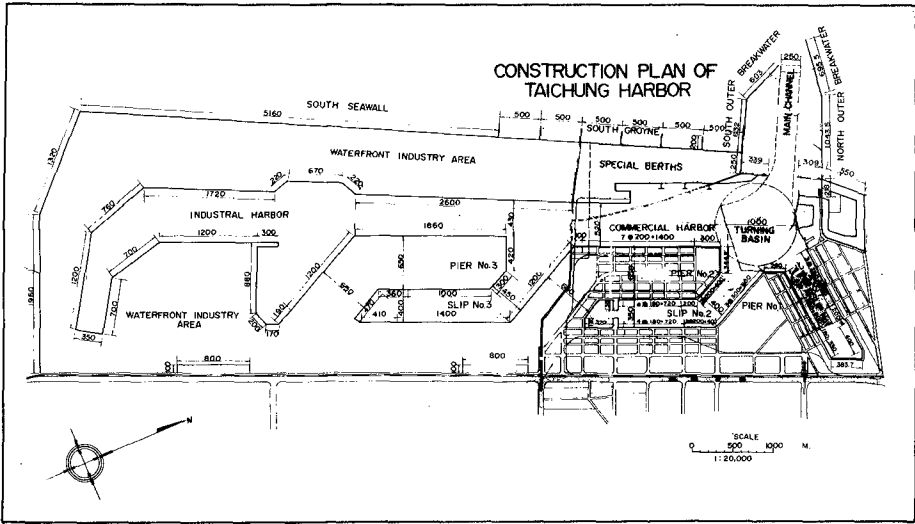


Figure 1

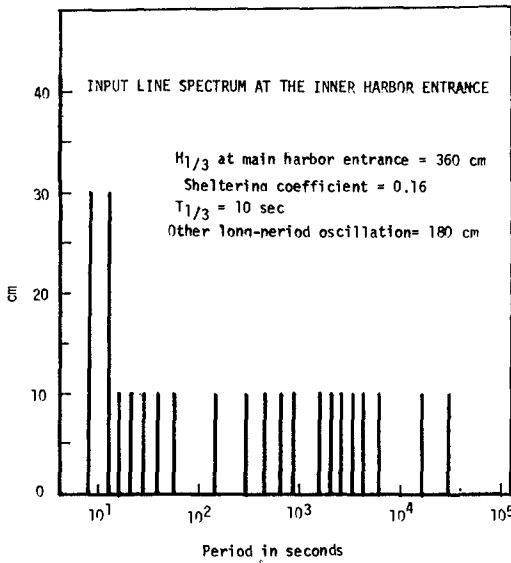


Figure 2

After evaluating existing numerical models in the public domain, the computational method described in Ref. 1 was adapted and simplified for this specific application. An explicit multilayer model was selected for the following reasons:

- (1) For harbor oscillation studies, due to the required temporal resolution for representing incoming waves with periods ranging from 9 seconds to 30 minutes, the size of the time integration is smaller than that required for maintaining the courant stability condition associated with the explicit solution method. Because of this requirement, the benefits associated with the implicit scheme cannot be realized yet for each integration step. Approximately twice as many numerical operations have to be performed as in an explicit scheme.
- (2) For studies involving wind drift and return currents, a multilayer model gives more accurate results than a vertically integrated model.
- (3) For investigating a harbor's dynamic behavior induced by wind stress, incoming waves, bottom stress, and the nonlinear advective acceleration, a model must include these essential terms in the computation.
- (4) In addition to the harbor's basic modes, higher modes generated by the aforementioned dynamic effects falling within the 20- to 40-second range are also of great importance to the operation of container ships. This condition precludes the possibility of using any method involving the inversion of extremely large matrices. Due to the size of the harbor system, in order to resolve oscillations within the range of interest, matrices of the size 450×450 would have to be inverted.
- (5) Velocity components in three directions as derived from a three-dimensional computation form a good basis for establishing a prediction method for responses of moored ships. This can be achieved by linking the computed water velocity components in three dimensions to the ship's response characteristics at a particular location according to experiments on ships' response in a physical model basin, which can be conducted separately.

From these considerations, a numerical model was established according to the basic scheme developed at the Rand Corporation to solve the following dynamic equations:

$$\frac{\partial u}{\partial t} + \frac{\partial(uu)}{\partial x} + \frac{\partial(uv)}{\partial y} + \frac{\partial(uw)}{\partial z} - fv + \frac{1}{\rho} \frac{\partial p}{\partial x} - \frac{1}{\rho} \left(\frac{\partial \tau_{xx}}{\partial x} + \frac{\partial \tau_{xy}}{\partial y} + \frac{\partial \tau_{xz}}{\partial z} \right) = 0 \quad (1)$$

$$\frac{\partial v}{\partial t} + \frac{\partial(vu)}{\partial x} + \frac{\partial(vv)}{\partial y} + \frac{\partial(vw)}{\partial z} + fu + \frac{1}{\rho} \frac{\partial p}{\partial y} - \frac{1}{\rho} \left(\frac{\partial \tau_{yx}}{\partial x} + \frac{\partial \tau_{yy}}{\partial y} + \frac{\partial \tau_{yz}}{\partial z} \right) = 0 \quad (2)$$

where x , y and z are Cartesian coordinates, positive eastward, northward and upward, respectively; u , v and w denote the respective components of velocity; f represents the Coriolis parameter; ρ is the density of water; τ_{xx} , τ_{xy} , τ_{xz} , etc. are components of stress tensor.

For the present study no correction has been made to account for the effect of vertical acceleration because the ranges of wave period in the investigation of hydrostatic pressure distribution are considered to be valid. For shorter wave studies in the future, Boussinesque terms of the form, if H and ζ denote depth and surface elevation, follow:

$$\frac{\partial^3 \zeta}{\partial t^2 \partial x} \left[\frac{(H + \zeta)^2 - \zeta^2}{2(H + \zeta)} \right] \quad \text{and} \quad \frac{\partial^3 \zeta}{\partial t^2 \partial y} \left[\frac{(H + \zeta)^2 - \zeta^2}{2(H + \zeta)} \right]$$

would have to be added to the momentum equations in the horizontal direction (Eqs. 1 and 2). In that case, a four-level time integration scheme has to be used instead of the three-level scheme employed presently. For waves of present concern, the hydrostatic principle applies:

$$\frac{\partial p}{\partial z} + \rho g = 0 \quad (3)$$

For incompressible fluids, the continuity equation is:

$$\frac{\partial u}{\partial x} + \frac{\partial v}{\partial y} + \frac{\partial w}{\partial z} = 0 \quad (4)$$

The basic numerical scheme for solving this set of equations and the treatments at open and closed boundary conditions can be found in Ref. 1.

BOUNDARY SPECIFICATIONS

In order to analyze the response of a harbor system under possible future conditions, wave energy with periods from 9 seconds to tidal frequencies were used to drive the system at the harbor's entrance. The spectral input was derived from long-term field data, including long-period oscillations induced by typhoons and reflected waves within Taiwan Strait originating from offshore areas.

The line spectrum for simulation input is shown in Fig. 2. This input line spectrum is applied for the majority of simulation runs. On several occasions, when the inner harbor entrance was used as the model's open boundary, for more efficient use of machine storage capacity, this input spectrum was multiplied by a set of wave sheltering coefficients obtained by physical model tests.

Because the length ratio between the harbor's boundaries and the entrance is approximately 100 to 1, the scheme of radiative open

boundary was not applied. The bottom stress coefficient used for computation was $55 \text{ m}^2/\text{sec}$. This value was derived from tests using the alluvial sediment which is homogeneously distributed in the construction area. The general composition of bed material is not expected to change in the near future.

The direction and speed of winter monsoons used for the simulation were derived from local weather statistics. The speeds have varied from 20 to 35 knots with run-in periods for different simulations. The time step size selected for different simulation tests ranged from 1.0 to 2.0 seconds for various temporal resolutions. The horizontal grid size ranged from 50m to 100m; the vertical layer thickness ranged from 3.0 to 14.0m, depending on different stages in the construction phase. A typical simulation period is 2.5 hours.

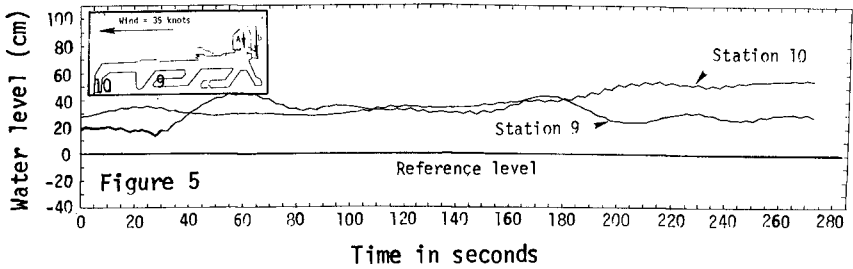
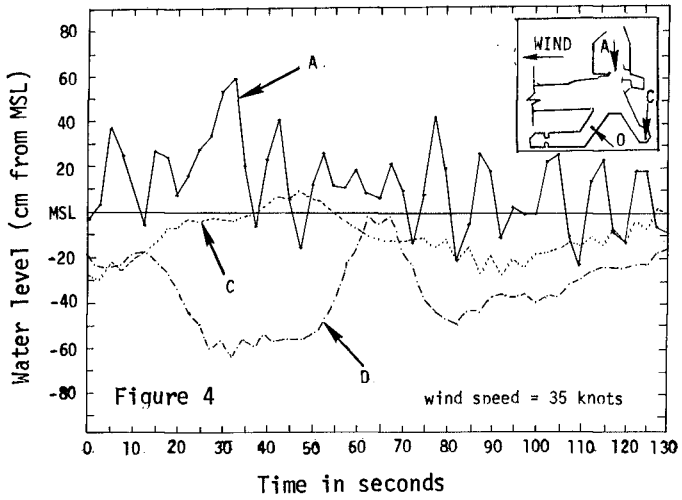
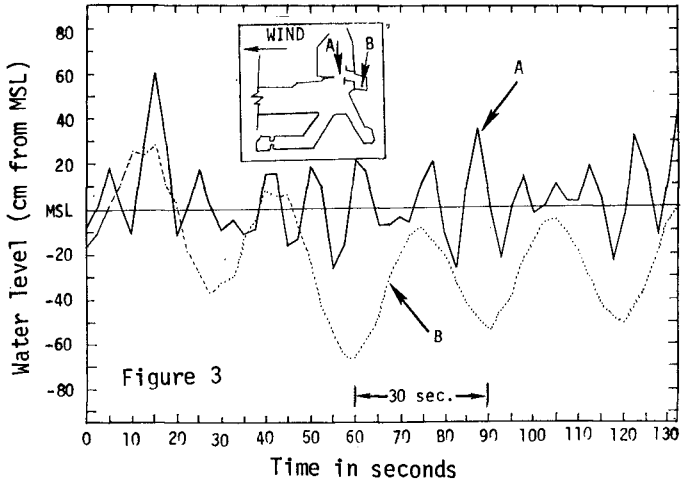
SIMULATION RESULTS

With the specified boundary and initial conditions a set of simulations was carried out for several system configurations representing different stages in the master construction plan. Results of the computation at important locations were recorded for further analysis and future restart. Figures 3 through 5 show the time histories of water level variation at several key locations.

The water level at the harbor's inner entrance, which contains the energy input at the open boundary, is shown in Fig. 3 as curve A. At this location, longer waves are not damped. On the other hand, within the fisherman's harbor (curve B of Fig. 3) shorter waves were damped. An oscillation of approximately 30 seconds is evident. As a consequence of wind stress, a negative setup of 25 cm occurred at this end of the harbor system. At locations in the main harbor system (Fig. 4), nonlinear effects become more pronounced. As shown by curves C and D in Fig. 4, water level variations contain waves of higher orders as the interaction between horizontal advective mechanisms and bottom and surface stress terms gives rise to a complicated pattern.

At the other end of the harbor system, patterns of oscillation become equally complicated, superimposed on the wind-induced setup of roughly 30 cm above the reference level. Because of its location, the water surface at station 9 contains more shorter-period oscillation than that found at station 10.

The spatial variation of water level elevation within the harbor system for the 10-year plan is illustrated in Fig. 6. Boundary effects on wave propagation are evident in this figure. To show the propagation and modifying process of longer period waves, the water levels at the entrance and at station 6 are plotted in Figs. 7 and 8 for a longer period of time. This section of 54 minutes was abstracted from the end portion of a 2.5-hour simulation. During this period, the water level at station 6 contains not only the basic mode of 12 minutes, but also modes induced by the nonlinear interactions.



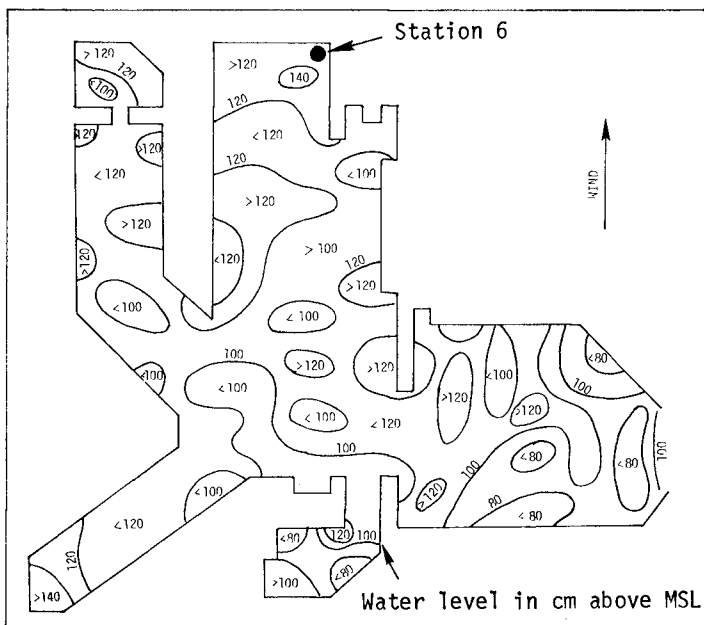


Figure 6

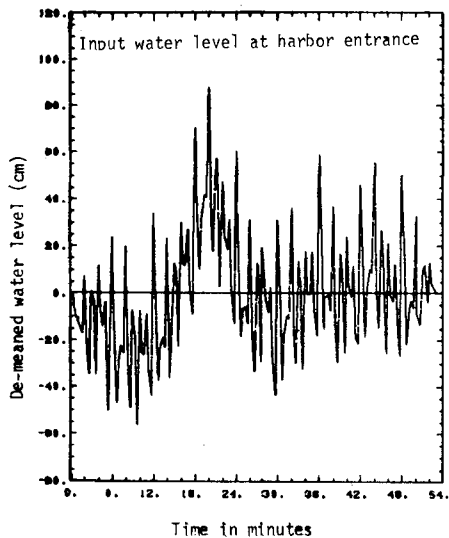


Figure 7

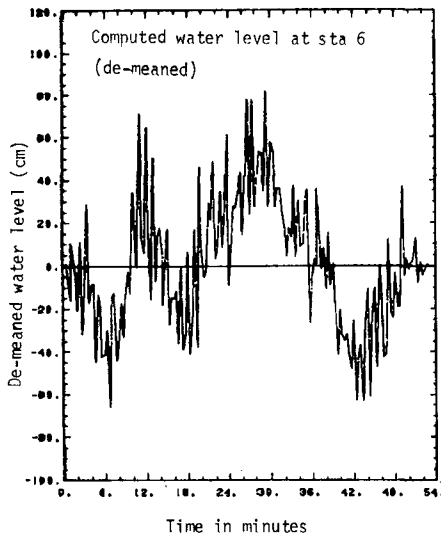


Figure 8

When the computed results are analyzed in the frequency domain (Figs. 9 and 10), the computed line spectra reveal distinct peaks at 52 seconds, 60 seconds, 120 seconds, and the basic mode at 12.5 minutes ($f = .08 \text{ min}^{-1}$). In the amplitude of the frequency response function (Fig. 11) which is the square of the amplitude ratio, it is shown that the 52-second oscillation is the most significant one. However, oscillations at other frequencies are also important, depending upon the type of ships operating in the vicinity. This graph also indicates that significant amplification would result if incoming waves contained periods from 50 seconds to 100 seconds: Phase differences from the harbor entrance to station 6 are presented in Fig. 12. Certain negative phase lags indicate that these oscillations are generated within the harbor system and are therefore not correlated with those entering from the harbor entrance.

Figure 13 is the amplitude ratio between the inner harbor entrance and the fishing harbor. A distinct peak at 30 seconds is the basic mode for that basin. For waves of shorter period, the ratio approaches 0.16, which agrees with the wave sheltering coefficient as obtained by means of wave tank tests.

The smallest basin in the harbor system is the workshop's basin situated next to the fisherman's harbor. The amplification factor in that basin is plotted in Fig. 14. The highest amplification factor is found at frequency 0.066 sec^{-1} , which corresponds to a period of 15 seconds.

The previous analyses in the frequency domain are computed using the direct Fourier transformation technique. If the computed results are compared with observed data, which unavoidably contains errors, spectral and cross-spectral density functions would have to be used.

Spectral density functions at station 6 are plotted in Fig. 15. The predictive impulse response function [2], as derived from spectral densities between the harbor's inner entrance and the fisherman's harbor, is presented in Fig. 16. The impulse response function has certain significance during time domain prediction if one wishes to compute water level oscillation within the harbor system from a future given wave climate at the harbor's entrance. This can be achieved by means of numerical convolution [2] without having to perform the simulation anew. It also has a definite advantage over its frequency domain equivalent, the frequency response function, because when a new data point is added to the input series, the output series can be readily obtained by the convolution scheme which involves only a limited number of computational operations. Unlike the frequency response function, in order to obtain the predicted new series, the new data series has to be transformed back and forth from time to frequency, then back to time domain. This would involve several orders more operations in the computation.

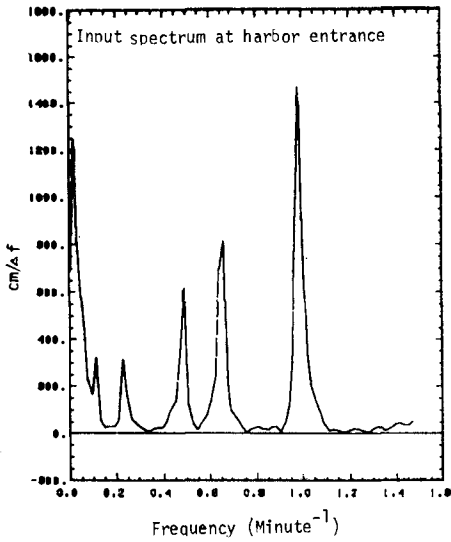


Figure 9

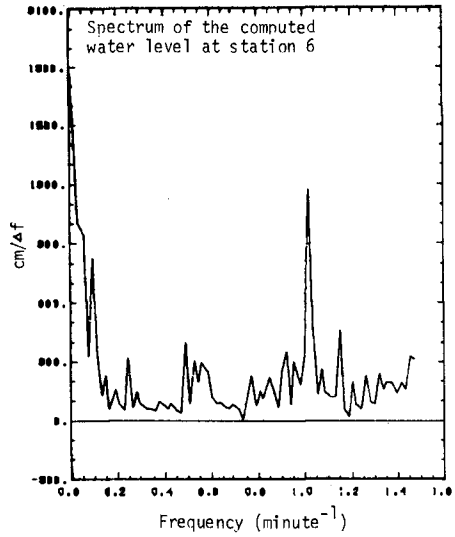


Figure 10

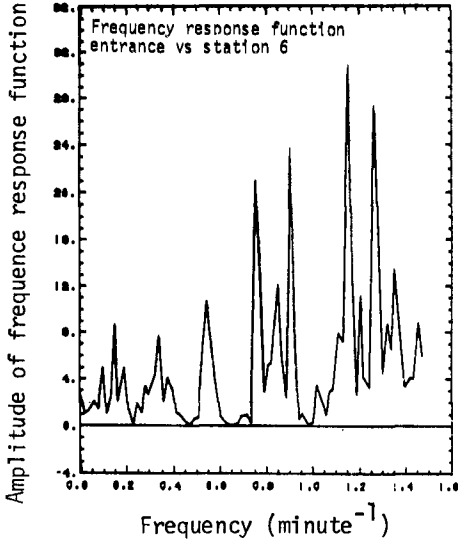


Figure 11

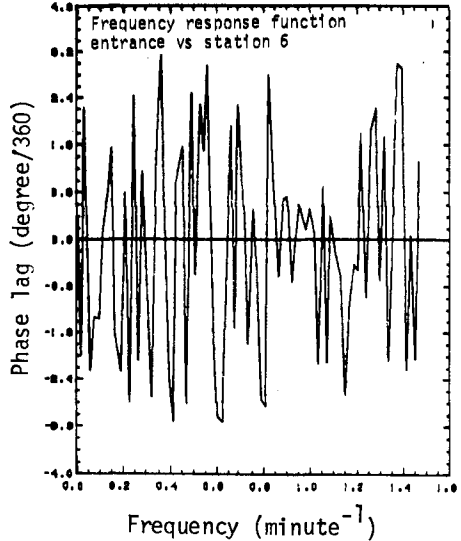


Figure 12

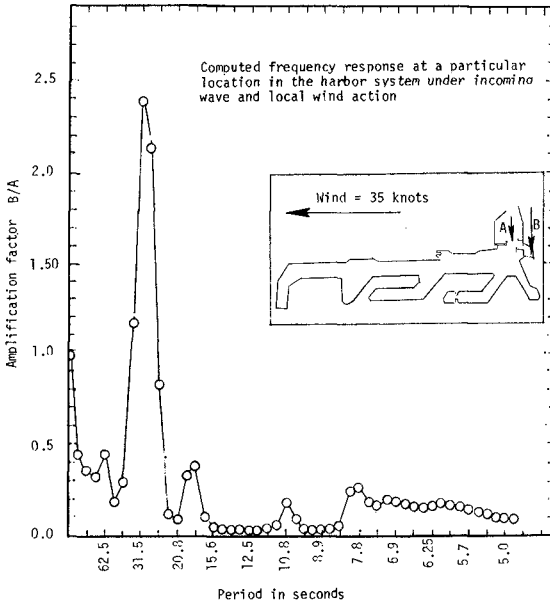


Figure 13

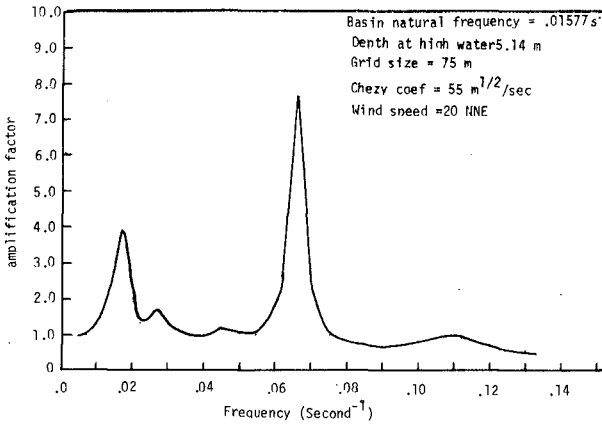


Figure 14

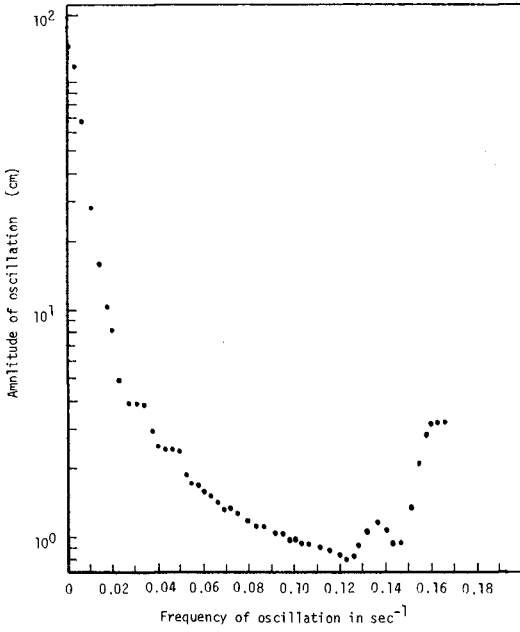


Figure 15

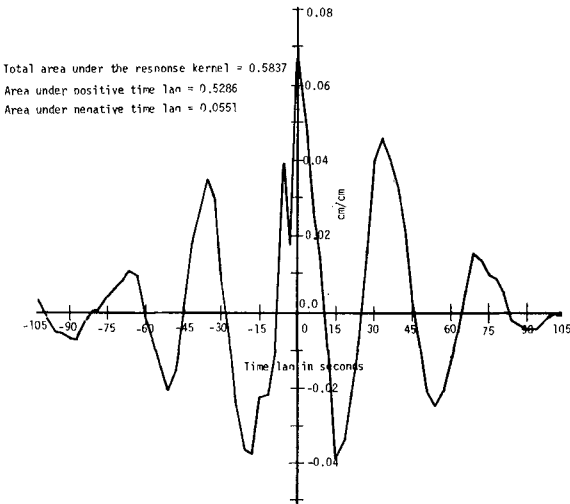


Figure 16

Acknowledgments

The authors wish to thank Messrs. C. T. Chung, C. Y. Hwang, and many other colleagues at the Taichung Harbor Bureau for their valuable assistance and discussions during the course of the study. Thanks also go to Prof. F. L. W. Tang and Dr. H. H. Hwang of the National Taiwan Cheng Kung University for valuable discussions. The authors wish to acknowledge the assistance of Mr. C. Luk of IBM Taiwan Corporation during the model's setup stage.

References

1. Leendertse, Jan J., and Shiao-Kung Liu, *A Three-Dimensional Model for Estuaries and Coastal Seas: Volume II, Aspects of Computation*, The Rand Corporation, R-1764-OWRT, June 1975.
2. Liu, Shiao-Kung, *Stochastic Analysis and Control of Urban Estuarine Water-Quality Systems: Vol. I - Estimation and Prediction*, The Rand Corporation, R-1622-NYC, December 1974.

CHAPTER 155

MIXING OF HEATED WATER DISCHARGED IN THE SURF ZONE

Kiyoshi Horikawa¹, Ming-Chung Lin² and Tamio O. Sasaki³

ABSTRACT

In this paper, a description is given on the mixing processes of heated water discharged into the surf zone, based on the field investigations.

In accordance with the flow characteristics observed, the flow region can be classified into three parts, namely the jet flow region, nearshore current region and coastal current region. In the jet flow region, the flow characteristics are expressed well by the two dimensional turbulent jet flow model and strongly influenced by the cusped bottom configuration formed under the interaction between the jet flow and nearshore currents. It is realized that the decay of plume centerline temperature is slower than the other cases owing to the influence of bottom slope, water depth and the direction of jet axis. By the dye tracer studies, in the nearshore current region the variance increases approximately with time at a power of 1.72 for longitudinal and of 1.95 for lateral respectively, while the diffusion coefficient increases with diffusion scale at a power of 1.43 for longitudinal and of 1.71 for lateral respectively. In the coastal current region, the representative isotherms are mainly in appearance either of the southerly alongshore or northerly stretch, possibly caused by some fairly long period waves.

The cloud of heated water was always confined within a certain strip of nearshore zone, likely in response to the existence of a turbulent boundary layer phenomena appeared in parallel to the coastline. Quantitative modelling of this resulting plume is then made. In addition, some pulsation patterns of isotherms were also observed. Finally, a graphical representation of the functional relationship between the relative temperature difference and the area within the specified isotherm is shown.

1. Professor, Department of Civil Engineering, University of Tokyo, Tokyo, Japan.
2. Postgraduate Student, Department of Civil Engineering, University of Tokyo, Tokyo, Japan.
3. Chief Research Engineer, Nearshore Environment Research Center, Tokyo, Japan.

INTRODUCTION

It was more than ten years ago when the heated water discharged from power stations was recognized as environmental pollutant. In accordance with the expansion of national economical activities in Japan, the facilities for electric power generation have been consolidated during the last twenty years by the extensive efforts of electric power industries. Figure.1 indicates the past growth tendency of electric power generated and supplied in Japan. From this diagram it is realized that the principal medium for electric power generation has changed drastically from hydraulic power to fossil-fuel power. The growth rates of hydraulic power and fossil-fuel power during the period of 1960 to 1975 were two and eight times respectively. Therefore the share of hydraulic power dropped from 60% to 22%, while that of fossil-fuel power increased from 40% to 72%. Another thing which should be mentioned is that the growth rate of nuclear power during the same period was surprisingly large, although its share was as small as 6% in 1975.

At any rate the thermal power, that is fossil plus nuclear fueled power plants, are playing a greater important role of electric energy supply to the Japanese society at present. It means that the operation of cooling water system consisting of intake and outlet structures is throwing into the society the various environmental problems which are still unsolved. It is generally said that the necessary amount of cooling water is 3 to 5 m³/sec per 100 MW of fossil-fuel power plant or 6 to 8 m³/sec per 100 MW of nuclear power plant. Therefore the amount of about 4000 m³/sec of cooling water is at present taken from bays as well as from open sea, and the same amount of heated water is discharged to the sea water region. Especially the nuclear power plants has normally been constructed in Japan on the coast facing the open sea.

As a typical setup for the cooling water system in Japan, the layout of the Fukushima Nuclear Power Plant No.1 of the Tokyo Electric Power Company will be shown in Fig.2. The cooling water is taken from the sheltered basins and the heated water is discharged into the surf zone on the open sea coast through the outlets installed at the roots of the breakwaters.

In order to predict the isotherm, say 1°C above the ambient water temperature, a simulation model established by Wada at the Central Research Institute for Electric Power Industries has been widely used in Japan [Wada, 1966]. In this model the existence of surf zone was completely eliminated. This assumption may hold good for heated plume discharged into a bay area where the short period wave action is negligibly small. On the other hand, in the case of heated water discharged into the surf zone, which is very common in Japan especially for nuclear power plants, the interaction between the discharged flow and the nearshore currents induced by breaking waves should be taken into consideration in the isotherm prediction. The senior author expressed the above opinion at a certain specified committee meeting in Japan about ten years ago.

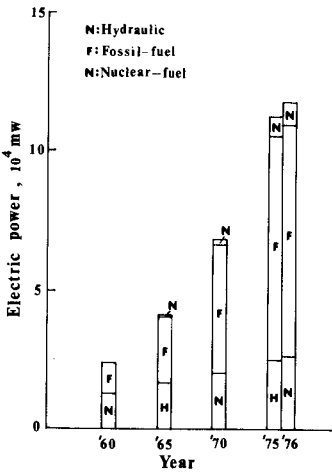


Fig.1 The tendency of electric power supply in Japan.

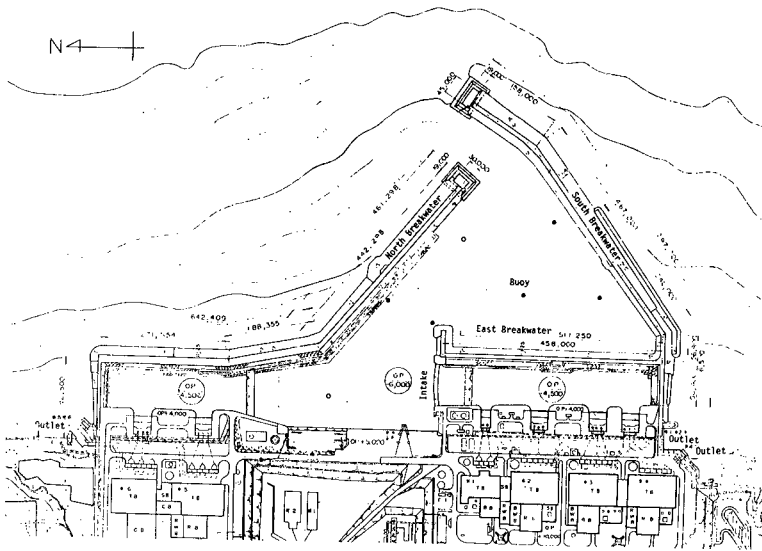


Fig.2 Configuration of Fukushima Nuclear Power Plant No.1.

During the last several years, we have had an opportunity to continue the field observations at the Fukushima Nuclear Power Station No.1, which is located at the northeastern Pacific coast of the Honshu Island in Japan. The first unit of 460 MW was installed and started to operate in 1971. The capacity of this plant increased gradually to 1244 MW in 1974, 2028 MW in 1976, and 2812 MW in 1978. According to the construction plan, the final total capacity of 4696 MW will be established in 1979. Following the above processes, the amount of heated water was 25 m³/sec initially, then increased to 69 m³/sec and is at present 159 m³/sec. After completing the construction works, the total discharge may reach to the amount more than 270 m³/sec.

SUBJECTS OF FIELD OBSERVATIONS

The subjects and measuring techniques of the present field observations are given in Table 1. The wave characteristics, current velocity and temperature in offshore region have been recorded continuously during the last several years by the efforts of the Tokyo Electric Power Company. Therefore we devoted our efforts mainly to grasp the relatively short term characteristics of flow pattern and temperature distribution induced by heated water discharge in the nearshore area.

In order to obtain the data of flow characteristics especially in the vicinity of outlets, dye and float tracing techniques were employed with the Balloon-borne Camera System. The dye used for the present tests was fluorescent sodium. On that occasion the Stereo Balloon-borne Camera System was applied to get any information on the complicated water surface configuration induced by the interaction between the incoming waves and jet flow.

For the latter subject, namely the water surface temperature distribution, the thermister or thermometer as well as the infrared photography were applied. Here we will explain the outline of the infrared photographic method. Figure 3 is the schematic diagram of the measuring instrument Fujitsu IRA-301, and Table 2 gives the main characteristics of the present instrument.

CLASSIFICATION OF FLOW REGION

Looking at the flow characteristics, the flow region seems to be classified into the following three parts as shown in Fig.4; namely the jet flow region, nearshore current region, and coastal current region. In the first region, the jet flow of heated water is predominant, while in the second region the interference between the discharged flow and nearshore currents must have an important role on the flow pattern as well as the temperature distribution. Beyond these two regions, the coastal current seems to play a primary role on the diffusion and dispersion processes.

Table 1. Subjects and Measuring Techniques Applied for Field Observation.

Subjects	Measures
Dye tracing } Jet flow characteristics	Balloon-borne Camera System (BACS)
Water surface configuration near outlet	Stereo BACS
Temperature distribution	{ Thermister and/or thermometer { Infrared photograph

Table 2. Performance of Fujitsu infrared scanner IRA-301.

Altitude	300 - 3300 m
Scanning cycle	100 cycle/sec
Field of view	92°
Instantaneous field of view	6.7 mrad
Sensitivity	0.1°C
Detector	Cd, Hg, Te photoconductive quantum type
Spectral range	8 - 14 μ , 2 - 14 μ
Record system	70 mm black and white film
Recording time	2.5 hours
Output record	70 mm film
Monitor system	Image monitor, signal monitor
Detect range	-10° — 80°C

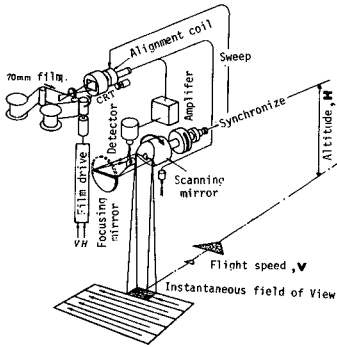


Fig.3 Schematic diagram of infrared scanner system.

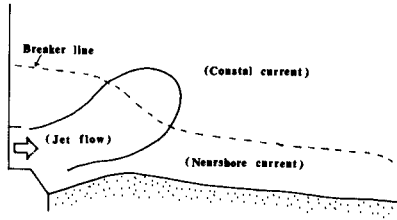


Fig.4 Three parts of flow region in the thermal plume.

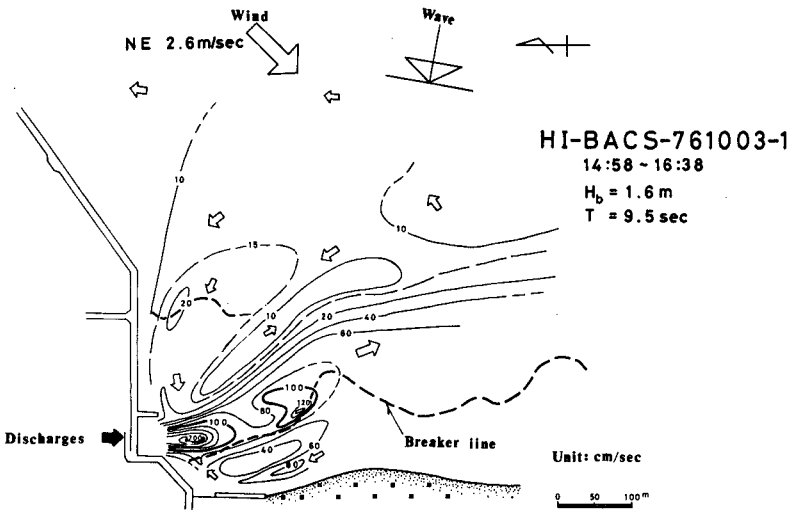


Fig.5 Typical example of surface current velocity distribution in the high tide.

CHARACTERISTICS IN EACH REGION

Jet Flow Region

Figures 5 and 6, obtained in the high tide and low tide respectively, illustrate two typical examples of surface current velocity distributions, from which the jet flow characteristics can be investigated.

Although the outlet flow was discharged in the alongshore direction, the axis of jet flow was shifted toward offshore. Through these investigations, we recognized that the shoreline configuration was deformed by the interaction between the jet flow and the nearshore currents especially the alongshore current. Figure 7 illustrates the situations stated above. That is to say, the nearshore bottom configuration seems to relate with the jet discharge and the longshore current velocity. Such cusped bottom configuration must have strong influence on the jet flow direction especially under the lower tide condition. When it is high tide, such influence will be diminished by the increase of water depth.

The above fact is also demonstrated in the alongshore temperature distribution patterns. Figure 8 gives some examples of the above patterns, from which it is realized that the alongshore decrease of water temperature is relatively small except in one case. The exceptional case was observed under the low tide condition. This result consists with the fact that the cusped pattern influences strongly on the jet flow direction when tide is low.

Now let us analyze the jet flow characteristics. By using the jet flow data obtained by the Balloon-borne Camera System, the axial variations of the maximum speed U_{max} and the width of jet flow b were read and plotted as shown in Figs. 9 and 10. The tendencies agree fairly well with those in the two-dimensional turbulent jet flow. Hence the eddy coefficient ϵ was evaluated by using the following equation based on the two-dimensional turbulent jet flow assumption (Schlichting, 1968) :

$$\epsilon = 0.037 b_{1/2} U_{max} \quad (1)$$

where $b_{1/2}$ is the half width of jet flow. The axial variation of ϵ was plotted as shown in Fig.11, where x is the distance measured along the jet axis from the outlet. From these results, it may be concluded that the actual jet flow can be simulated by the two-dimensional turbulent jet flow in spite of the complicated situations. The order of ϵ is of $10^4 \text{cm}^2/\text{sec}$.

Next the temperature distribution along the jet axis will be investigated. Figure 12 indicates the comparison of the present cases with other previous investigation data. From this comparison, it is realized that the temperature decrease seems to be smaller than the others owing to the influences of bottom slope, water depth and the direction of jet axis.

As a reference the water surface configuration in the vicinity of the outlet is demonstrated in Figs.13 and 14.

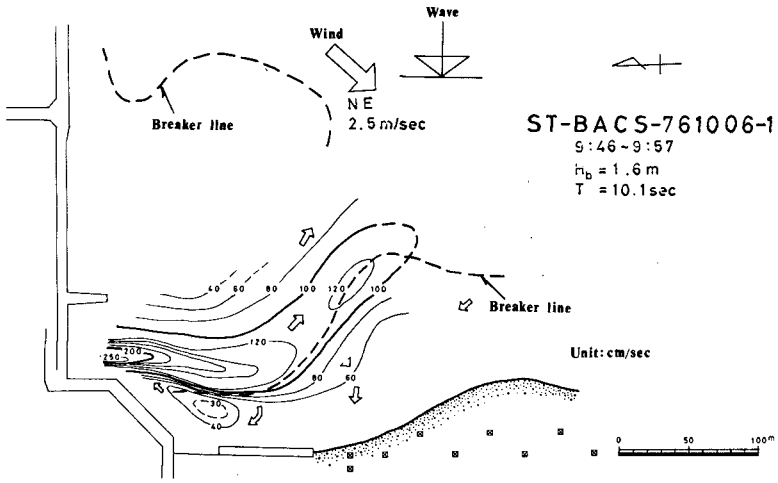


Fig.6 Typical example of surface current velocity distribution in the low tide.

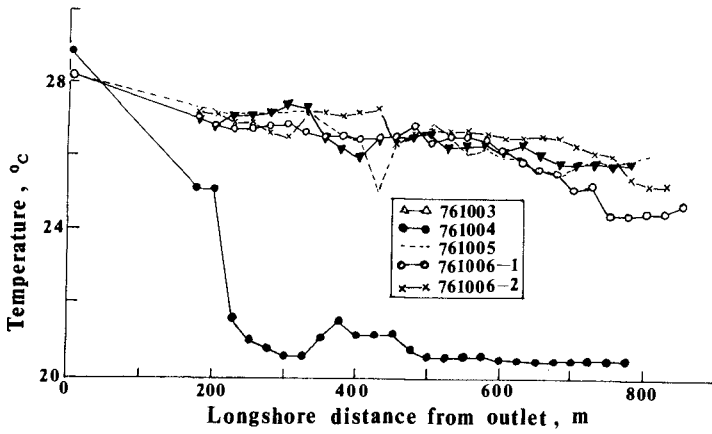


Fig.8 Alongshore temperature variations in the surf zone.

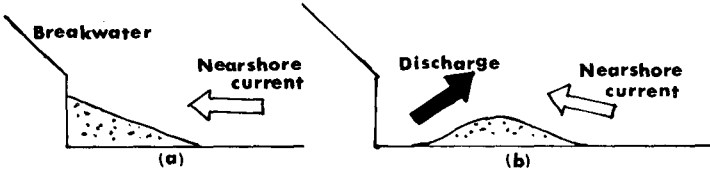


Fig.7 Schematic diagram for the formation of cusped shoreline. (a) without discharge, (b) with discharge.

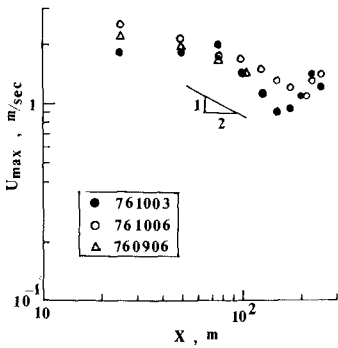


Fig.9 Variations of surface velocity along centerline of jet.

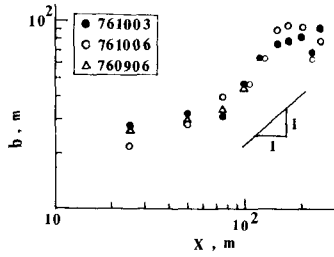


Fig.10 Variations of jet flow width.

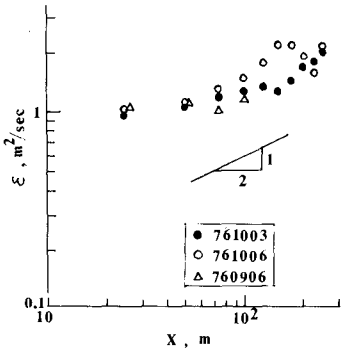
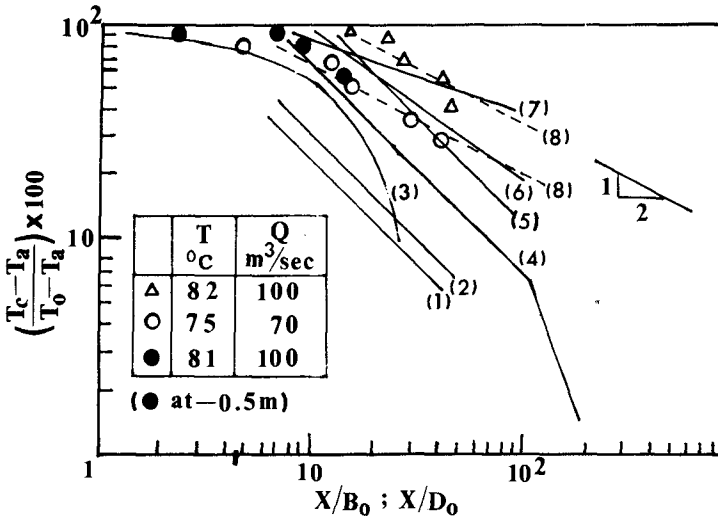


Fig.11 Variations of eddy coefficient of jet flow.



- (1),(2) ~ $(X/B_0)^{-1}$, 1 : 10, 1 : 4 rectangular nozzle respectively and deep water (Wiegel et al., 1966)
 - (3) Calculation by computer (Wada, 1966)
 - (4) Circular nozzle, deep water (Jen et al., 1966)
 - (5) ~ $(X/B_0)^{-1}$, 1:50 bottom slope
 - (6) ~ $(X/B_0)^{-0.7}$, 1:100 bottom slope
 - (7) ~ $(X/B_0)^{-1/4}$, 1:200 bottom slope
- (Wiegel et al., 1966)
- (8) ~ $(X/B_0)^{-1/2}$, the present study, 1:50 bottom slope, discharged parallel to the shoreline

Fig.12 Plume centerline temperature decay.
 B_0 = width of outlet,
 D_0 = diameter of nozzle.

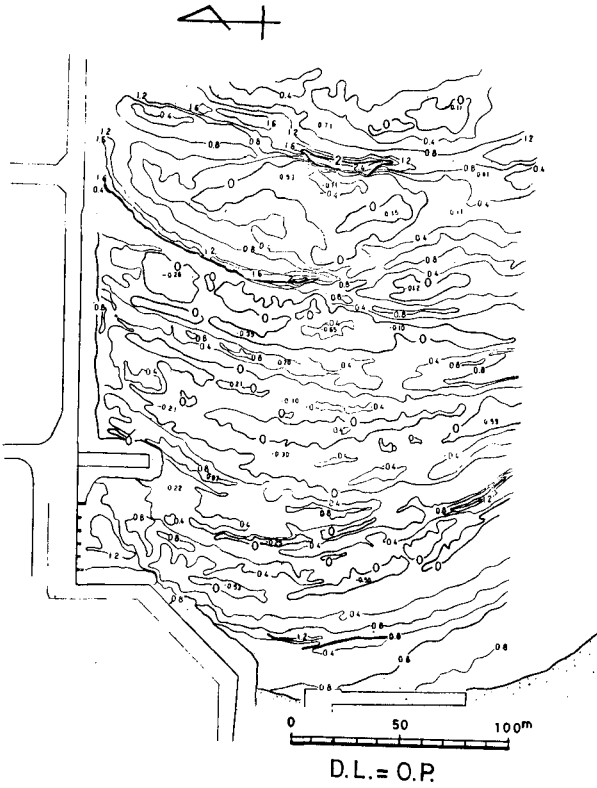


Fig.13 Contours of water level obtained by stereo camera photography.

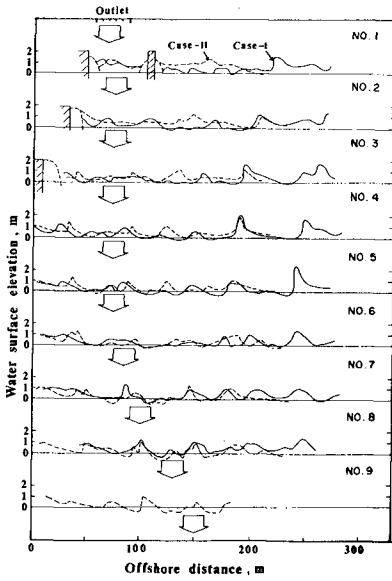


Fig.14 Water level changes in the transverse cross section. No.1 — No.9 denote the number of cross sections 25m separated parallel to the outlet.

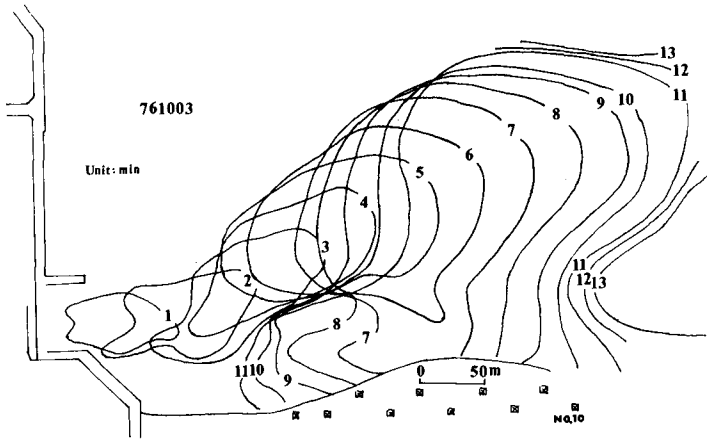


Fig.15 Typical example of dye tracer pattern.

Nearshore Current Region

In order to evaluate the global diffusion coefficient, we released dye at the outlet and took pictures of the dye cloud successively at a certain time interval from air by using the Balloon-borne Camera System. Figure 15 gives one example of the variations of dye diffusion pattern. Assuming that the dye concentration is expressed by the normal distribution, we evaluated the longitudinal and lateral variances of dye diffusion. Figure 16 shows the calculated results, in which the ordinate is the variance and the abscissa is the time elapsed since the dye was released. The exponents of t are 1.72 for longitudinal and 1.95 for lateral respectively. That is, the diffusion process of the present case is not expressed by the Fickian type, and is also different from the diffusion of inertial subrange in the isotropic turbulence. The order of the diffusion coefficient K is approximately equal to that of ϵ .

The relationship between the diffusion coefficient K and the scale of diffusion ℓ was investigated as shown in Fig.17. The exponents of ℓ are 1.43 for longitudinal diffusion and 1.71 for lateral diffusion respectively. At any rate the 4/3 power law may not be applicable to the present case. Okubo (1971) analyzed the numerous data of circular dye patch in the ocean and found that the variance σ^2 is proportional to $t^{2.34}$ as well as that the diffusion coefficient K is proportional to $\ell^{1.15}$. Comparing the Okubo results with the present ones, we can realize that the diffusion phenomena in the nearshore area is completely different from that in the ocean. This fact seems to be quite natural.

Coastal Current Region

Representative isotherms are illustrated in Fig.18. Type 1 is the southerly alongshore stretch of isotherms. Type 2 is the northerly stretch of isotherms along the breakwater. Finally, Type 3 is of intermediate between Types 1 and 2. The last type could be observed when the discharge of heated water was as small as 25 m³/sec, therefore at present Types 1 and 2 can only be seen due to the larger amount of heated water discharge.

It is quite interesting and important from the engineering view point to find out the real reason why such isotherm patterns as Types 1 and 2 are produced. At the present stage, we have not yet fully verified the following hypothetical explanation. According to the results of current measurement in the offshore region, we can observe clearly the alternating current in parallel to the coastline with the period of 1 to 2 days (Nakamura and Horikawa, 1977). The current amplitude is about 10 to 30 cm/sec and the current pattern is rather rectangular instead of sinusoidal. Such fairly long period waves may cause the alternating patterns of isotherms, that is from Type 1 to Type 2, and vice versa. At the present stage our collected data are still not enough to define the long period oscillations. The continental shelf wave may be one of the possible waves.

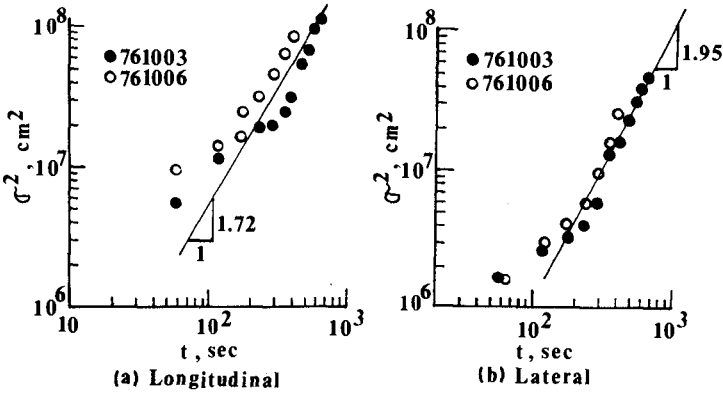


Fig.16 Variance versus diffusion time.

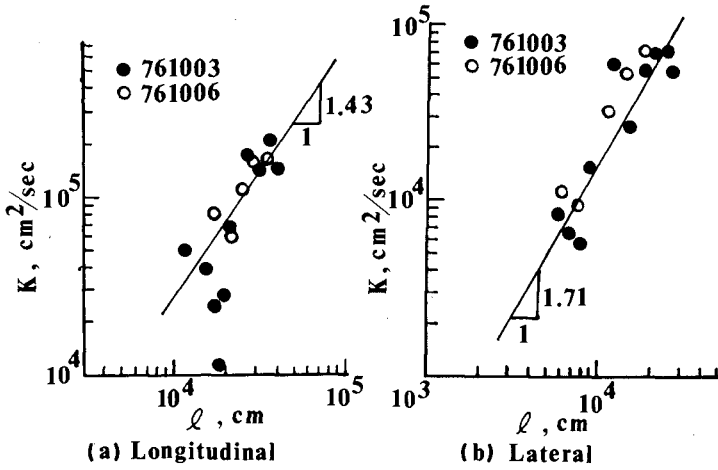


Fig.17 Dispersion coefficient versus scale of diffusion.

Fig. 18 Classification of three types of thermal plume at the Fukushima Nuclear Power Plant No. 1.

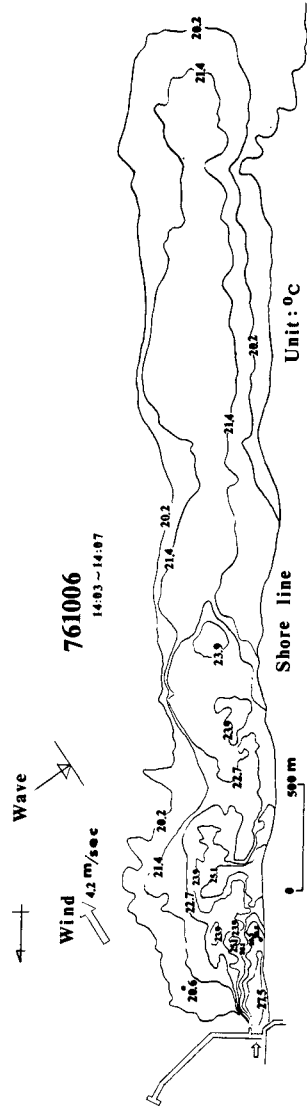
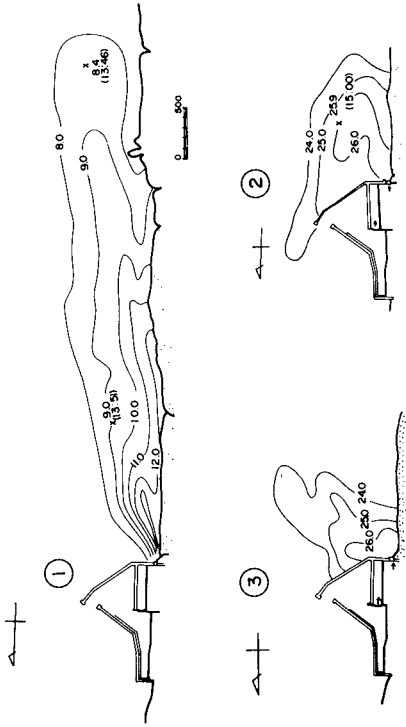


Fig. 19 Surface isotherms obtained by infrared scanner.

CHARACTERISTICS OF ISOTHERMS

The infrared photograph must be one of the most effective measures for surveying the surface water temperature distribution in a wide area. Figure 19 shows a part of results obtained by analyzing the infrared photographic image which was taken from the altitude of 1200 m above the sea level. The cloud of heated water extended southerly as far as 4.6 km from the outlet of the power station, and was confined within a certain strip of nearshore zone, whose width was about 600 m. The last fact is quite interesting and raises up a question why such a phenomenon was observed. One possible explanation is the existence of a turbulent boundary layer phenomena appeared in parallel to the coastline. Outside the boundary layer, that is in the offshore region, the diffusion is normally very weak, but inside the boundary layer the turbulent mixing is predominant. In order to clarify the above concept it is necessary to carry out the long-term simultaneous measurement of current velocities at various locations on a line perpendicular to the shoreline.

Let us look at the detailed structure of isotherms, from which pulsation patterns of isotherms are observed. To explain such phenomena, we may be able to point out the following factors. These are (1) the oscillation of water surface in the harbor basin, (2) the oscillatory pump regulation for supplying a constant amount of cooling water, (3) the undulatory internal jump formed just outside of the outlet, and (4) an alongshore long period oscillation in the nearshore area. The alongshore distance between two successive isotherm fronts at 22.7°C is evaluated as about 800 m. Here we will assume the front speed being 60 cm/sec which gives a rather moderate value. Then the period of pulsation is estimated to be about 22 min, which is approximately equal to the observed natural oscillation period of harbor basin.

In order to investigate more fine structure of temperature distribution, the closed up view of isotherms is shown in Fig.20. From this diagram we can see really complicated patterns caused by the interference between the jet flow and the nearshore currents, especially the rip currents.

By using these data, we drew in Fig.21 a diagram which shows the functional relationship between the relative temperature difference $(T - T_a) / (T_0 - T_a)$ and the area A covered by the isotherm of a specified temperature T . Here T_0 is the temperature at the outlet, and T_a at the ambient water. Table 3 illustrates the oceanographical and meteorological conditions under which these data were obtained. Figure 21 indicates that the area within the isotherms generally increases exponentially with decreasing relative temperature difference; that is

$$A = k_1 \exp(-k_2 T_r) \quad (2)$$

in which k_1 and k_2 are constants. In general the constants k_1 and k_2 must be a function of heated water discharge. The covered area for +1°C isotherm obtained by using the present relationship seems to be larger than that predicted by the Wada model. In order to get a more precise family of

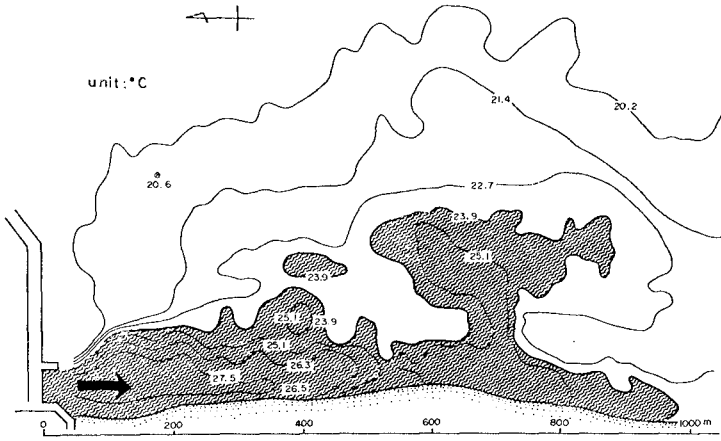


Fig.20 Surface isotherms in the vicinity of power plant showing the effects of nearshore current.

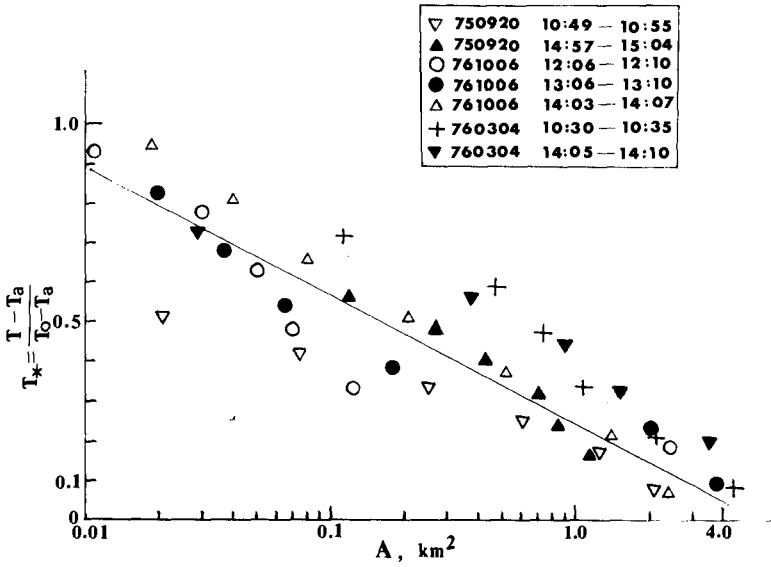


Fig. 21 Relationship between the area within isotherms and relative temperature difference.

Table 3. Oceanographical and meteorological conditions.

case	750920 10:49 —	750920 14:57 —	760304 10:30 —	760304 14:05 —	761006 12:06 —	761006 13:06 —	761006 14:03 —
term	10:55	15:04	10:35	14:10	12:10	13:10	14:07
Wave height, m	0.9 — 1.3	0.8 — 1.2	0.4 — 0.7	0.4 — 0.7			
Breaker height, m					2.0		
Wave period, sec					9.7		
Wave direction*	0	0	-22.5°	-22.5°	-12.0°		
Wind direction	E	SSE	NNW	NNE	NW		
Wind velocity, m/sec	8.0	6.0	4.8	4.8	4.2		
Tide	Ebb	Flood	Ebbing	Rising	Rising		
Discharge, m ³ /sec	56.4	56.4	111.3	111.3	86.8		
Outlet temperature, °C	28.9	29.2	15.1	15.3	27.8	27.8	27.9
Ambient water temperature, °C	23.0	23.0	7.0	7.0	19.7	19.6	19.7

* Measured clockwise from the east.

prediction curves, we have to accumulate more data under the various conditions of discharge. We evaluated the alongshore distance of the isotherm front under some appropriate assumptions by following the treatment of Csanady (1970) and obtained the value of 4 km which is fairly close to the actual distance of 4.6 km. The detail of the above computation will be given in Appendix of this paper.

CONCLUSION

Although the present investigations on heated water dispersion are only the preliminary ones, the observation data and the analyzed results seem to be quite valuable to get an insight into the real phenomena of heated water mixing in the nearshore area. The main conclusions are :

(1) The jet flow characteristics are expressed well by the two dimensional turbulent jet flow model.

(2) The jet flow direction and the alongshore temperature distribution are strongly influenced by the cusped configuration formed under the interference between the jet flow and nearshore currents.

(3) The eddy coefficient of jet flow was evaluated by using the jet flow characteristics. While the diffusion coefficient in the nearshore current region was evaluated by using the dye diffusion patterns.

(4) The detailed discussion on isotherm patterns was made from the various view points.

(5) A functional relationship between the relative temperature difference and the area covered by the specified isotherm was presented.

ACKNOWLEDGEMENTS

The present investigation was partly supported by the Scientific Research Fund of the Ministry of Education in Japan. The writers are deeply indebted to the personnel of the Coastal Engineering Laboratory, University of Tokyo, and of the Nearshore Environmental Research Center for accomplishing the field observations. The writers' thanks are also due to the people at the Tokyo Electric Power Company, who kindly forgave the writers' group to carry out the present investigations.

REFERENCES

- Csanady, G. T. (1970) : Dispersal of effluents in the great lakes, Water Res., Vol.4, pp.79-114.
- Jen, Y., R. L. Wiegel and I. Mobarek (1966) : Surface discharge of horizontal warm-water jet, J. of the power Div., Proc. of ASCE, Vol.92, No.P02, pp.1-30.
- Nakamura, Y. and K. Horikawa (1977) : Behavior of heated discharges from nuclear power plant in the surf zone, Proc. 24th Conf. on Coastal Eng. in Japan, pp.462-466 (in Japanese).

- Okubo, A. (1971) : Oceanic diffusion diagrams, Deep-Sea Res., Vol.18, pp. 789-802.
- Schlichting, H. (1968) : Boundary Layer Theory, McGraw-Hill Book Co., pp.696-698.
- Wada, A. (1967) : A study on phenomena of flow and thermal diffusion caused by outfall of cooling water, Proc. 10th Conf. on Coastal Eng., pp.1389-1411.
- Wiegel, R. L., I. Mobarek and Y.Jen (1966) : Discharge of warm water jet over sloping bottom, Modern Trends in Hydraulic Eng. Res., Golden Jubilee Symposia, Vol.2, Poona, India, pp.144-164.

< APPENDIX >

A COASTAL ENTRAPMENT MODEL OF HEATED WATER

In order to formulate the present phenomena, the following assumptions are made (see Fig.A) :

- (1) Steady state Phenomena,
- (2) Line source of heated water discharge,
- (3) Diffusion coefficient in y direction K_y being independent of y ,
- (4) Uniform water depth, and
- (5) Diffusion coefficient in x direction K_x being negligible,

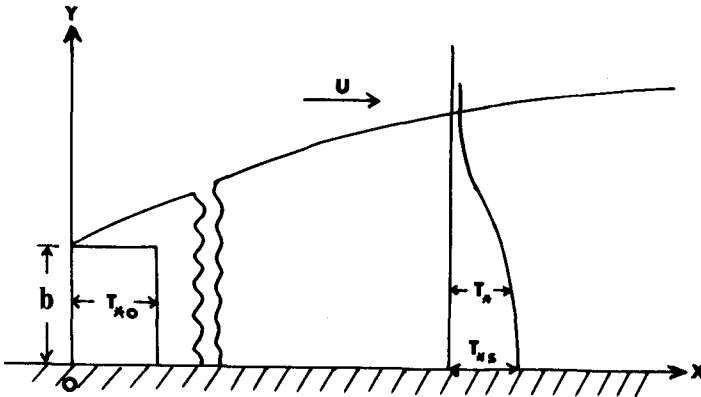


Fig. A Definition sketch.

Hence the basic equation is given by

$$U \frac{\partial T_{*}}{\partial x} = K_y \frac{\partial^2 T_{*}}{\partial y^2} \quad (1)$$

where $T_{*} = (T - T_a) / (T_0 - T_a)$, x and y are the axes taking along and perpendicular to the shoreline as shown in Fig.A, and U the uniform coastal current velocity. The boundary conditions are

$$T_{*} = \begin{cases} T_{*0}, & \text{at } x=0 \text{ and } b \geq y \geq -b \\ 0, & \text{at } x=0 \text{ and } |y| > b \end{cases} \quad (2)$$

Considering the condition of $x = Ut$, we can express the diffusion coefficient K_y by the next equation

$$K_y = \frac{1}{2} \frac{d\sigma_y^2}{dt} = \frac{U}{2} \frac{d\sigma_y^2}{dx} \quad (3)$$

where σ_y^2 is the variance in y direction. Then the solution of Eq.(1) is given by

$$\begin{aligned} T_{*}(x, y) &= \frac{T_{*0}}{\sqrt{2\pi} \sigma_y} \int_{-b}^b \exp\left\{-\frac{(y-y')^2}{2\sigma_y^2}\right\} dy' \\ &= \frac{T_{*0}}{2} \left[\operatorname{erf}\left(\frac{b-y}{\sqrt{2}\sigma_y}\right) + \operatorname{erf}\left(\frac{b+y}{\sqrt{2}\sigma_y}\right) \right] \end{aligned} \quad (4)$$

where T_{*0} is the initial temperature as shown in Fig.A.

On the basis of the two-dimensional jet flow, we assume

$$\sigma_y = p x \quad (5)$$

where p is an appropriate constant. Therefore Eq.(4) is rewritten as follows ;

$$T_{*}(x, y) = \frac{T_{*0}}{2} \left[\operatorname{erf}\left(\frac{b-y}{\sqrt{2} p x}\right) + \operatorname{erf}\left(\frac{b+y}{\sqrt{2} p x}\right) \right] \quad (6)$$

The relative temperature difference at the shoreline $y=0$, T_{*s} , is expressed by

$$\begin{aligned} T_{*s}(x) &= T_{*}(x, 0) = T_{*0} \operatorname{erf}\left(\frac{b}{\sqrt{2} p x}\right) \\ &\xrightarrow{x \rightarrow \infty} \frac{\sqrt{2}}{\pi} \frac{b}{p x} \end{aligned} \quad (7)$$

Given conditions for the present case are $b=30$, $T = 27.9^{\circ}\text{C}$, $T = 19.7^{\circ}\text{C}$, $T = 20.2^{\circ}\text{C}$, and the value of p is assumed to be 0.1 referring the value for lakes given by Csanady (1970). Therefore

$$T_{*s} = (20.2 - 19.7) / (27.9 - 19.7) = 0.06$$

$$x = \frac{\sqrt{2}}{\pi} \frac{b}{p} \frac{1}{T_{*s}} = \frac{\sqrt{2}}{3.14} \frac{30}{0.1 \times 0.06} \approx 4000 \text{ m} = 4 \text{ km}$$

The p value seems to vary depending on the discharge of heated water.

OUTFALL DIFFUSION MODELS FOR THE COASTAL ZONE

D. C. L. Lam and C. R. Murthy

Applied Research Division, National Water Research Institute,
Canada Centre for Inland Waters, Burlington, Ontario, Canada

Abstract Two approaches for developing outfall diffusion models for the coastal zone are discussed. The statistical model combines a simple Gaussian analysis with the time-series records of flow measurements to elucidate the dispersion patterns in a shore-parallel, a current-reversal, and stagnation flow regimes. The deterministic model explores the more complex characteristics of a plume in an advection-dominant situation. The cases of Fickian diffusion, shear diffusion, and inertial subrange hypothesis are studied. It is shown that a previously derived semi-empirical relationship produces an agreement at least as good as the optimized results of these theoretical models. These models are quite useful for site specific evaluation of potential continuous discharges of effluents into the coastal zone.

INTRODUCTION

The recent increase of industrial and energy development in the Great Lakes basins has created considerable concern in the capability of the coastal waters as intermediate buffer zones for receiving the waste effluents and subsequent mixing of the materials with offshore waters. The physical dynamics of the transport and dispersion mechanics in these zones are complex. At the present stage, the existing knowledge has largely been drawn from long term observational research programs conducted in the lake environment. The direct application of this information for site specific evaluation must require indepth interpolation and further tests for generality. One approach to explore the observational results is to develop deterministic and stochastic models, incorporating the empirical results.

The environmental data base has been established at our institute for the past ten years, and consists of statistical and climatological summaries of currents, temperature, diffusion parameters in several coastal sites of the Great Lakes. The flow regimes are fundamental in defining the types of dynamics encountered in this coastal area. The temperature data provide information about upwelling and downwelling episodes, internal wave characteristics and thermal plume structure near outfalls. The dye diffusion data have resulted in a series of eddy diffusion diagrams which relate the turbulent diffusion coefficients to the plume properties. This provides the background information to develop a package of computer programs designed to have a certain degree of predictive capability of the transport and dispersion characteristics for the nearfield and farfield zones. Recognizing the need for generality and flexibility in such a package, we have developed a number of models which can be applicable for different site situations and management problems. This paper describes two examples of these. While

both of them are designed for simulating the transport and dispersion of a conservative substance, they can be extended to include the simple decay or growth kinetics of nonconservative substances.

STATISTICAL MODEL

Strong shore-parallel currents within a few kilometres from the coast dominate organized flow patterns in the Great Lakes. These currents are of practical concern owing to their capability to transport pollutants introduced at the shoreline. Under conditions of steady shore-parallel currents, a continuous pollutant source located within the coastal zone would result in a quasi-steady state plume. Mean concentration distributions constructed from repeated instantaneous concentration profiles of a steady state plume approximates a Gaussian distribution (see Figure 1). For this reason, Gaussian diffusion models have been extensively used for quantitative modeling and dilution estimates of continuous effluent plumes.

Gross estimates of diffusion of effluent sources at a particular site can frequently be made by judicious application of coastal zone climatological data. These climatological data include statistical summaries of coastal currents and dispersal processes and are considered to be representative of the site in question.

In order to develop a statistical model, we have integrated the coastal zone climatology with a steady state Gaussian plume model following the approach of "air pollution" meteorology to estimate probable concentration of pollutants discharging from industrial stacks.

A depth integrated two dimensional cross-plume Gaussian distribution of concentration forms the basis of our calculations,

$$\bar{\chi}(x,y) = \frac{q}{2\sqrt{2\pi}\sigma_y hU} \text{Exp}\left(-\frac{y^2}{2\sigma_y^2}\right) \quad (1)$$

where

- x = direction of the mean current, U
- y = perpendicular to the mean current
- q = source strength
- σ_y = cross-plume standard deviation, related to eddy diffusivity $K_y = \sigma_y^2/2t$
- t = x/U
- h = depth of water

Introducing $q = \chi_s D$ (χ_s is source concentration and D is source discharge rate), a dilution factor $\eta = \frac{\bar{\chi}}{\chi_s}$ can be defined. From (1)

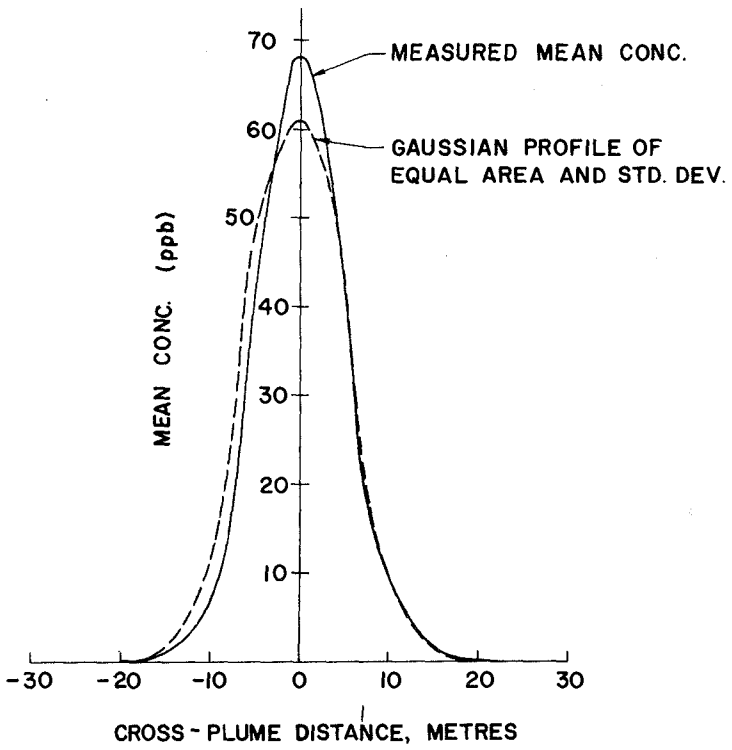


Figure 1: Gaussian Profile vs Observed Profile

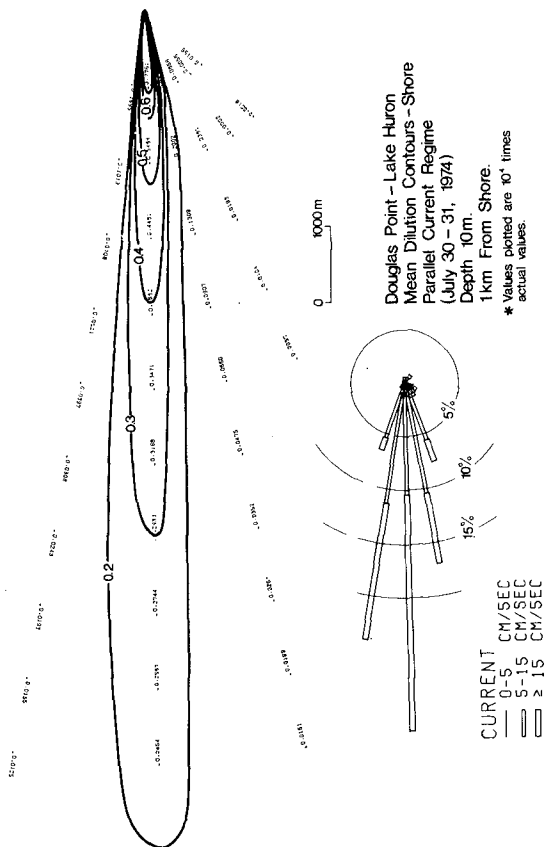


Figure 2: Simulated Results for a Shore-Parallel Current Regime

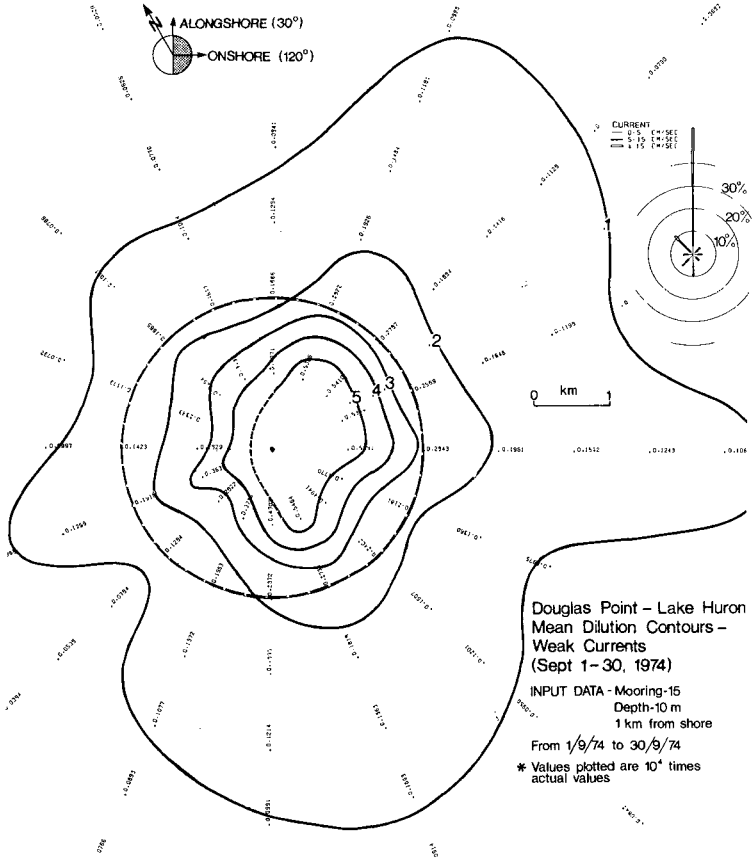


Figure 4: Simulated Results for a Weak Current Regime

we have

$$\eta = \frac{D}{2\sqrt{2}\pi\sigma_y hU} \text{Exp}\left(-\frac{y^2}{2\sigma_y^2}\right) \quad (2)$$

Under steady state conditions, the key parameters controlling the dilution ratio are (1) the mean current U and, (2) the eddy diffusivity K_y .

Over a period of time, the direction of the coastal current shifts. The current rose, which gives the joint current speed and direction frequency distribution, is a useful indicator of the flow characteristics. We will calculate the mean dilution over a period that is very long compared with that over which the mean current is computed.

To estimate cross-plume eddy diffusivity, we fall back on experimental data obtained from extensive dye plume diffusion experiments in the coastal zone of the Great Lakes (Murthy and Kenney, 1974).

An integrated computer program was developed incorporating the coastal current climatology data to the steady state Gaussian plume model given by Eq. (2).

Coastal climatological data on currents were divided into "episodes" describing the general characteristics of the flow such as (1) steady shore-parallel currents, (2) steady shore-parallel currents followed by frequent current reversals, etc. These "episodes" generally range from a few days to a month.

Using this model we have calculated mean dilution contours for two typical climatological "episodes" for the Douglas Point region in Lake Huron where a large nuclear power complex is currently under construction. Figure 2 shows a typical plot of mean dilution contours calculated for a shore-parallel current regime. Figure 3 on the other hand is for a case where the currents reversed quite frequently but essentially maintained a shore-parallel current regime (bimodal character). Figure 4 shows a case of weak currents interspersed between shore-parallel currents.

DETERMINISTIC MODELS

The simple Gaussian model as given by Eq. (1) represents a first order approximation of the cross-plume distribution of mean concentration. It corresponds to the simplest form of deterministic models namely the Fickian diffusion model, in which the eddy diffusivity is assumed to be a constant. While this simplification makes the statistical evaluation of the mean distribution quite practical, some of the more complex characteristics of a quasi-steady state plume cannot be simulated. There exists in the literature (e.g., Okubo, 1971) a number of turbulence models which relate the eddy diffusivity to the mean concentration itself, and are purported to include the effect of the

growth of the eddy size. In general, the cross-plume eddy diffusivity, K_y , in these models can be expressed in the following form,

$$K_y = c \sigma_y^n \tag{3}$$

$$\sigma_y = \left\{ \int_{-\infty}^{\infty} \bar{x}y^2 dy / \int_{-\infty}^{\infty} \bar{x} dy \right\}^{1/2} \tag{4}$$

where n and c are constants or parameters of the model, and σ_y is the cross-plume standard deviation. For certain choices of the constants n and c , the eddy diffusivity, K_y , as given by Eq. (3) has a specific meaning. Table 1 summarizes their theoretical significance.

n	c	Diffusion Law	Diffusion Parameters	Diffusion Model
0	$c \sim K_a$	$K_y = K_a$	K_a , Apparent Diffusivity	Fickian Diffusion
1	$c \sim q_s$	$K_y \sim q_s y$	q_s , Diffusion Velocity	Shear Diffusion
4/3	$c \sim \epsilon^{1/3}$	$K_y \sim \epsilon^{1/3} y^{4/3}$	ϵ , Energy Dissipation Parameter	Inertial Surbrange Diffusion

Table 1. Theoretical Significance of the Constants n and c

By means of statistical analysis of large volumes of ocean and lake dye diffusion data, Okubo (1971) and Murthy and Kenney (1974) have concluded that the actual environment does not always conform to any one of these theoretical models. For example, for the Great Lakes, the following semi-empirical seems to be more appropriate, (Murthy and Kenney (1974)).

$$K_y = .075 \sigma_y^{1.2} \tag{5}$$

During the period of 1972-1973, a new set of dye diffusion measurements were conducted in Lake Ontario. The information obtained from these measurements has not been included in the statistical analysis for estimating the diffusion law given in Eq. (5). Hence, this set of data serves the purpose as an independent check on the semi-empirical relationship as given in Eq. (5). In order to compare the effect of using the semi-empirical law and that of using the theoretical models in Table 1, a deterministic approach has been adopted. In this approach, as a contrast to the statistical analysis in Murthy and Kenney (1974), a numerical solution is sought for the steady state two-dimensional advection-diffusion equation,

$$U \frac{\partial \bar{X}}{\partial x} + V \frac{\partial \bar{X}}{\partial y} = \frac{\partial}{\partial x} (K_x \frac{\partial \bar{X}}{\partial x}) + \frac{\partial}{\partial y} (K_y \frac{\partial \bar{X}}{\partial y}) \tag{6}$$

where U and V are the mean flow velocities. To limit the scope of this analysis and to reduce the dimensionality, we have purposely selected one particular set of experiments in which the flow is predominantly shore-parallel and reasonably steady. This simplifies Eq. (6) to

$$U \frac{\partial \bar{\chi}}{\partial x} = \frac{\partial}{\partial y} (K_y \frac{\partial \bar{\chi}}{\partial y}) \quad (7)$$

because the mean flow can be aligned with the x coordinate (down-stream direction) so that the cross-plume velocity, V , and the diffusivity, K_x , can be omitted in the presence of the strong advection term in the x -direction on the left hand side of the equation.

To accommodate different models for K_y , and to avoid numerical dispersion (Lam, 1976), Eq. (6) is solved by an implicit finite difference scheme. In this scheme, the x -coordinate is identified as the marching direction, analogous to the time-coordinate in the simple heat conduction equation, so that the conventional Crank-Nicolson (central differencing) scheme can be used to update the cross-plume concentration for each increment of Δx in that direction. For the nonlinear forms of the eddy diffusivity in Eq. (3), i.e., for the cases in which $n \neq 0$, each update step will involve an internal iterative procedure. Specifically, for a fixed value of x , the standard deviation, σ_y , as defined in Eq. (4) is calculated numerically by using the known values of $\bar{\chi}$ along the y -direction. This value of σ_y will then prevail in the cross-plume direction at this value of x .

To proceed to the next interval at $x+\Delta x$, a new σ_y is needed, and is approximated by an appropriate guess. This guess will give rise to a solution of $\bar{\chi}$ at $x+\Delta x$ by the Crank-Nicolson procedure. Then, a new guess of σ_y is made by substituting this $\bar{\chi}$ into Eq. (4).

The process can be repeated iteratively, until some degree of consistence is reached between $\bar{\chi}$ and σ_y . It must be pointed out that under certain assumptions, such as constant flow velocity, it is possible to express σ_y in terms of the independent variable x or other length scales, so that the iteration procedure may not be necessary. However, Okubo (1976) has demonstrated the danger of applying such simplification, which may result in an eddy diffusion almost an order of magnitude too high.

Figure 5 shows the locations of the three measured profiles during an experiment conducted in Lake Ontario on June 16, 1972 (Murthy and Miners, 1977). Each of the profiles has been sampled several times in the cross-plume direction and at three different depths of 1m, 3m, and 6m beneath the water surface. To simplify the computation, these profiles have been averaged horizontally and also integrated vertically to provide the observational mean values, χ_0 , of concentration. In particular, the profile at the section ($x = 280$ m) close to the outfall is used as the initial condition for Eq. (7). The remaining two profiles are used to establish the least-square error, E , between the observed value χ_0 and the computed value $\bar{\chi}$,

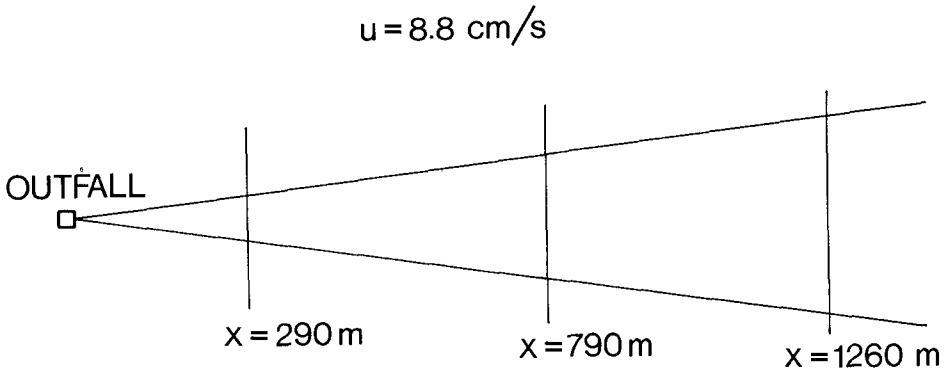


Figure 5: Locations of Measured Profiles

$$\text{i.e., } E = \sum_{x=790\text{m}} \{ \bar{\chi}_o(x,y) - \bar{\chi}(x,y) \}^2 + \sum_{x=1260\text{m}} \{ \bar{\chi}_o(x,y) - \bar{\chi}(x,y) \}^2 \quad (8)$$

For a given choice of n in Eq. (3), it is possible to choose an optimal value of c so that the least-square error is a minimum, i.e., $E = E_{\min}$. There are many computational techniques for solving this optimization problem. We have used the conjugate direction method (Powell, 1964) and the quasi-Newton method (Spath, 1967). Both of these methods gave practically the same results. Table 2 summarizes the results for the different cases of n . Instead of providing the optimized values of c in each case, we have calculated the corresponding diffusion parameters as explained in Table 1 by eliminating the proportionality constants in c (Okubo 1971) so that they can be compared directly to the measured range of these parameters. We have also included the least-square error associated with the computed results of the semi-empirical relationship, Eq. (5), in which case optimization is not necessary since both n and c are given.

From Table 2, based on the least-square errors, it can be seen that the semi-empirical model appears to produce the best fit to this particular set of data, and the constant diffusivity gives the worst case.

n	Diffusion Law	Diffusion Model	Optimized Diffusion Parameters	Observed Range (Ocean and Lake Data) (Okubo 1971, Sullivan 1971)	E or E_{min} (Errors as defined in Eq. (8))
0	$K_y = K_a$	Fickian Diffusion	Apparent Diffusivity $K_a = 5.9 \times 10^3 \text{ cm}^2/\text{s}$	$10^3 - 10^5 \text{ cm}^2/\text{s}$	1138 (E_{min})
1	$K_y \sim q_s \sigma_y$	Shear Diffusion	Diffusion Velocity $q_s = 0.32 \text{ cm/s}$.1 - .5 cm/s	995 (E_{min})
4/3	$K_y \propto \epsilon^{1/3} \sigma_y^{4/3}$	Inertial Subrange Diffusion	Energy Dissipation $\epsilon = 3. \times 10^{-3} \text{ cm}^2/\text{s}^3$	$2 \times 10^{-3} - 5 \times 10^{-3} \text{ cm}^2/\text{s}^3$	974 (E_{min})
1.2	$K_y = 1.2 \cdot .075 \sigma_y$	Semi-Empirical Model	-	-	958 (E)

Table 2: Comparison of Optimized Diffusion Parameters and their Observed Range

However, it must be emphasized that such comparison of E_{min} does not lead to a more definite conclusion, nor can it be used to discriminate models. Rather, the optimization procedures are merely used here as a tool to search for the best solution for each case of diffusion models. Indeed, the fact that the optimized diffusion parameters are within the range of the observed range shows that each of these theories can be applicable to the set of observations, provided that the values of c are chosen correctly. Since we have used equally successfully the semi-empirical relationship without any further adjustment of the value of c , we consider this quite a remarkable result in the verification of the semi-empirical law.

Figure 6 shows the computed profiles of using this law and other models as compared to the observed data. Figure 7 shows the centre line of the plume as computed by different models. The nonlinear models including that of Eq. (5) give practically the same kind of agreement with the data, whereas the constant diffusivity result, though quite acceptable, is not as accurate. This is consistent with the results in Table 2..

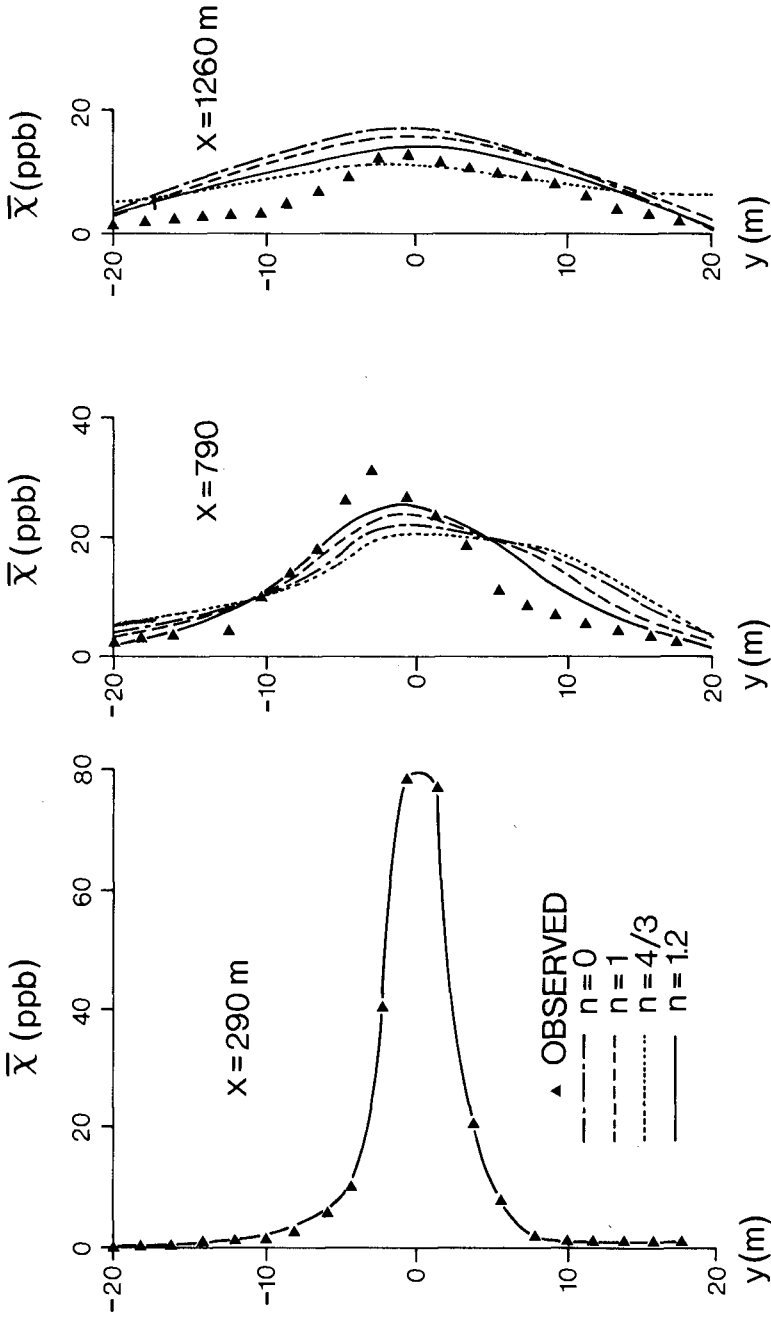


Figure 6: Computed and Observed Cross-Plume Profiles. The lines ($n = 0, 1, 4/3, 1.2$) represent computed results and the triangles represent the observed data.

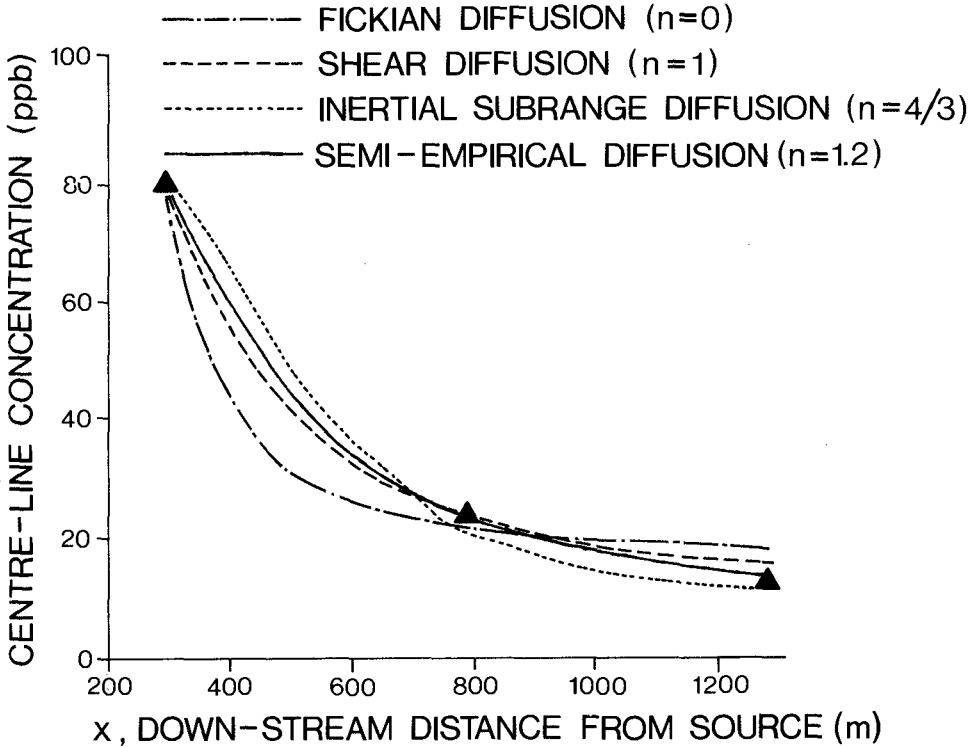


Figure 7: Computed and Observed Centre-Line Concentration
The symbols are the same as in Figure 6.

CONCLUSION

It has been demonstrated that it is possible to use a simple Gaussian statistical model for making first order estimates of the distribution of the mean concentration near an outfall in the far-field for different coastal flow regimes. A more rigorous examination of the second-order effects by means of numerical modeling and optimization methods reveals that the previously derived semi-empirical relationship produces at

least equally acceptable results as some of the well-tuned, nonlinear, theoretical models. Further analysis on a larger set of observed data and more general flow conditions is needed to establish the applicability and limitation of these models. This is being done at the National Water Research Institute, Canada, as part of an ongoing project to develop simulation models for the coastal zone systems.

Acknowledgements Karen Beal and Ken Miners provided the programming assistance.

REFERENCES

1. Lam, D.C.L., "Comparison of finite-element and finite-difference methods for nearshore advection-diffusion transport models." Finite element in Water Resources, Gray et al ed., Princeton University, N.J., p. 1. 115 - 1. 129, 1976.
2. Murthy, C.R. and B.C. Kenney, "Diffusion in coastal currents of large lakes." Rapp. P. - v. Reun. Const. int. Explor. Mer, 167, p. 111 - 120, 1974.
3. Murthy, C.R. and K.C. Miners, "Nearshore diffusion studies (IFYGL Project 89WM)." CCIW unpublished report, Dept. of Fisheries and Environment Canada.
4. Okubo, A., "Ocean diffusion diagrams." Deep Sea Research, 18, p. 789 - 802, 1971.
5. Okubo, A., "Remarks on the use of 'diffusion diagrams' in modeling scale-dependent diffusion." Deep-Sea Research, 23, p. 1213 - 1214, 1976.
6. Powell, J.J.D., "An efficient method for finding the minimum of a function of several variables without calculating derivatives." Computer J., 7, p. 155 - 162, 1964.
7. Spath, H., "Algorithm 315, The damped Taylor's Series Method for minimizing a sum of squares and for solving systems of nonlinear equations." Commun. of A.C.M., 10, p. 726 - 728, 1967.
8. Sullivan, P.J., "Some data on the distant-neighbour function for relative diffusion." J. Fluid Mech., 47, p. 601 - 607, 1971.

CHAPTER 157

LARGE SCALE TURBULENCE IN TIDAL CURRENTS

by John B. Hinwood¹

1. INTRODUCTION

Aerial photographs of tidal inlets sometimes show an orderly pattern of large eddies or cells aligned in long rows along the mean streamlines. The cells have only been observed where the velocity is high and have not been observed during strong winds. The observations of cells are described but their complete structure and origin are not yet known, however it has been established that density variations are not a factor.

2. OBSERVATIONS OF CELLS

Occurrence of Cells: The initial observation of the cells was made in Western Port, a large tidal inlet near Melbourne, Australia. Fig. 1 is taken from a colour transparency made by Pollock in 1973 and shows a 200 m × 300 m section of the channel in Western Port, completely occupied by cells. In this case the wind speed was less than 3 km/hr and was just sufficient to ruffle the water surface after a fetch of about 4 m. The cells are visible in the photograph because of the contrast between the unruffled water rising at the centre of the cells and the darker ruffled water descending at the edges of the cells. Individual cells could be followed for as long as 30 minutes.

Other tidal inlets where the same type of pattern has been found on aerial photographs are Delaware Bay, U.S.A. and Corner Inlet, Lakes Entrance, and Port Phillip, all near Melbourne.

In the last case the cells are visible because the rising columns of water entrain fine sand from the bed which settles out as this water flows outwards towards the descending edges of the cells.

At the location shown in Fig. 1, cells have been observed on about 10 occasions and have been shown not to be present on about the same number. In Port Phillip there have been 5 observations of cells in 20 sets of observations. The frequency of success in these observations was biased by making the later observations at supposedly favourable times. While the occurrence of cells cannot yet be predicted, they have only been observed around the times of peak ebb or flood current, usually near spring tide, and never in current velocities less than 0.8 m/s. They have not been observed under windy conditions.

¹ Senior Lecturer, Department of Mechanical Engineering,
Monash University, Melbourne, Australia

In the absence of natural indicators the presence of cells may be shown by dye traces, and this has been done in most of the observations described here. More importantly the dye traces reveal details of the flow field.

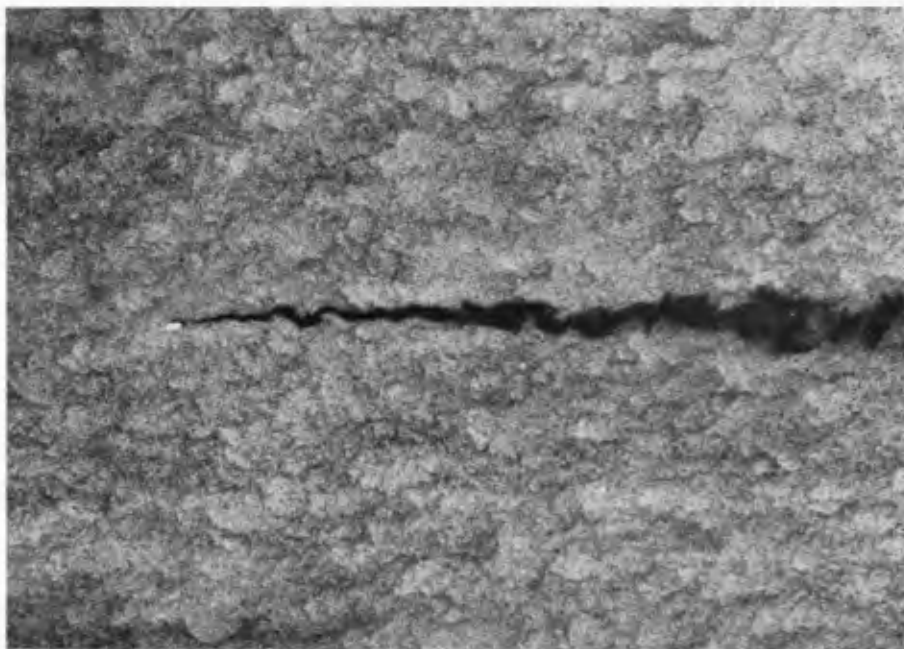


Fig. 1 Aerial Photograph of Cells and Dye Trace (black) in Western Port

Size of Cells: The cells observed in Western Port were in a region of the channel in North Arm, where the water depth ranges from 14 to 18 m and averages 16 m. The typical width of the largest cells measured on Fig. 1 was 20 m. The cell length was much less regular, and was about one to two times the cell width.

In Port Phillip the cells observed in the flow around the northern end of Swan Island were measured. The sea bed slopes smoothly up towards the island, and the flow was of uniform speed and was more or less parallel to the depth contours. The cell width increased from 3.5 m to 14 m as the depth increased from 4 m to 9 m.

3. ORIGIN OF THE CELLS

Density stratification has been eliminated as a possible mechanism as detailed measurement has shown no stratification in Western Port and Port Phillip near Swan Island. Vertical profiles of temperature and salinity were measured using a Hamon T/S meter reading to 0.1°C and 0.01‰. Additional surface readings were taken in a bucket which was carefully filled from the top centimeter of the water. Differences in temperature and salinity over the depth were less than the limit of reading.

The cells have not been observed in strong wind and have been observed in calm conditions. Furthermore the cells shown in Fig. 1 distorted rapidly when a light cross-wind sprang up, and lost their regular alignment in rows.

The possibility of wave/current interactions can also be eliminated. Cells forming on the ebb tide, inside the bays under calm conditions are not subject to either ocean waves or local wind chop. In several cases local wind chop appears on the photographs at an angle to the cells and with a much smaller wave length.

At bends in a canal or river, a secondary flow is produced, and may persist downstream as a helix with its axis parallel to the direction of flow.

The observations of cells near Swan Island were in curvilinear flow, but those in Western Port were in a long straight reach of channel. Nevertheless, the influence of a distant upstream bend might have persisted, and it is not possible to eliminate this mechanism as a possibility.

The interaction between the flow and the bed forms is another possible mechanism. There are 2 m dunes both upstream and downstream of the area shown in Fig. 1, although the area itself has a plane bed, and there are sand waves in Port Phillip. In the lee of a dune there is a flow separation which may become unstable producing weak vortices with axes aligned parallel to the flow. Nakagawa and Hinwood [1] discuss this mechanism further, but do not explain how the vortices transform into cells.

The analyses of flow over a wavy bed by Kennedy [2] and later workers have shown that a secondary flow is generated above a wavy bed. The three dimensional cellular flow would be the result of an array of dunes with crests parallel to the flow combined with an array perpendicular to the flow.

Side-Scan sonar traces were made of the sea bed in Western Port [3]. These traces did not show any marked variations in dune height in the transverse direction but did show dunes with crests perpendicular to the flow upstream of the zone of cellular flow. There must remain a possibility that these dunes are producing a secondary flow which gives rise to the cellular flow further downstream.

4. CONSEQUENCES OF CELLULAR FLOW

Over length scales smaller than a few cell dimensions, processes dependent upon turbulent transport will be affected by the discrete, and not continuous, nature of the turbulence. At greater length scales, the sum of effects of many discrete steps is indistinguishable from the effects of continuous processes.

In particular, the lateral mixing of a passive pollutant will approximate a binomial distribution after spreading over a few cell dimensions, but tends towards a normal distribution after spreading over many. At very small scales, the pollutant will be moved by the cellular eddies with very little mixing as shown in Fig. 1. Hence near the source higher peak pollutant concentrations are possible in a cellular flow.

For vertical transport of pollutant or momentum, the mixing length model of turbulence appears to be justified with a mixing length equal to the cell height — i.e. the total depth. Conditions very near the bed are likely to be dominated by the smaller inter-cellular scales and would require a different approach.

5. CONCLUSIONS

A highly ordered — "cellular" — structure of turbulence has been observed in strong tidal currents. The cell dimensions are in the order of the water depth and velocities about one-tenth those of the main current. The origin of the cells is not known, but cannot be attributed to density variations or to wind, and indeed wind disrupts the pattern.

The existence of the cells suggests that mixing could be described by a mixing length model using the typical cell dimensions. Near a source discharging into the flow, peak concentrations would be high, but far from the source the effects of action by many cells is likely to produce concentration patterns indistinguishable from those in other kinds of flow.

6. REFERENCES

1. Nakagawa, T. and Hinwood, J.B. (1978). A proposed model of large scale cellular motion in strong tidal flows. Proc. 4th Aust. Conf. Coastal Eng., Adelaide, Nov. 1978, pp 185-9 (to appear), Publ. Inst. Engrs. Aust.
2. Kennedy, J.F. (1963). The mechanics of dunes and antidunes in erodible-bed channels. J. Fluid Mech., 16: 521-544.
3. Slotta, L.S., Hinwood, J.B. and Tyshing, R.D. (1978). Side-scan sonar studies of sedimentation in harbors. Proc. 16th Int. Conf. Coastal Eng., Hamburg, Aug.-Sept. 1978, Paper No. 90, Publ. A.S.C.E.

CHAPTER 158

3-D CURRENT MODEL WITH DEPTH VARYING EDDY VISCOSITY

by

Bryan R. Pearce¹, Cortis Cooper², and Susan Nelson³

Introduction

The ability to quickly and accurately predict the three dimensional velocity field in a water body of variable lateral and vertical extent remains elusive. Yet the practical need for a predictive model has become more pressing due in part to increased public concern for the environment and the expanded search for offshore resources. For example, a 3-D⁴ velocity model could serve as the basis for predicting storm-induced current forces on offshore oil-production platforms.

Another application for 3-D circulation models is in the area of pollution control and in particular in predicting the trajectory of a surface pollutant such as oil. The state-of-the-art for predicting the advection of oil slicks is the "fixed wind factor" approach. The method consists of simply taking the center of mass movement to be a fixed percentage of the wind speed. When the factor is taken as 3%, as is commonly done, the procedure is known as the "3% rule". The Coriolis "force" is sometimes accounted for by deflecting the surface current a constant angle to the right of the wind velocity. This angle is the deflection angle.

Oil spill modelers usually justify the fixed wind factor approach by referencing a number of previous field and laboratory studies investigating the wind factor. Stolzenbach et al. (1977) compiled the results of the most often quoted experiments (Table 1). Note that the supposedly constant wind factor varies by a factor of five between investigators and that large variations occur even within an individual data set as shown by the standard deviations in Table 1.

¹Associate Professor of Civil Engineering, University of Maine, Orono, Maine 04473, U.S.A.

²New England Coastal Engineers, Penobscot Plaza, Bangor Maine 04401 U.S.A

³Research Assistant, Department of Civil Engineering, Massachusetts Institute of Technology, Cambridge, Massachusetts, U.S.A.

⁴A "three-dimensional model" is defined here as a model which yields the horizontal velocity variations both in the vertical direction as well as in the horizontal. Vertical velocity is neglected.

Table 1
 Summary of Various Experiments Investigating the Effect of Wind on Surface Drift

Name of Investigator	Nature of Experiment	mean wind factor (%)	stand. dev. (%)	deflection angle (degrees)	standard dev. (degrees)
Smith (1968)	hindcasting of observed oil slick	3.4	0.17	3.3 right	11.0
Tomczak (1964)	hindcasting of observed oil slick	4.3	N.A.	0.0	N.A.
"	field experiment with drift cards	4.2	"	"	"
Hughs (1956)	field experiment with drift cards	2.1	0.4	3.5 right	10.7
"	" " " "	2.2	0.4	0.3 left	8.6
Neumann (1966)	" " " "	4.2	N.A.	0.0	N.A.
Teeson et al. (1970)	field exper. with plastic sheets	2.8	1.1	13 right	7.0
Smith et al. (1974)	field exper. with drifting oil	0.8	0.7	none	none
Swartzberg (1971)	lab exper. with oil as drift med.	3.7	0.2	N.A.	N.A.
Keulegan (1951)	lab exper. (at high Reynolds #'s)	3.3	none	N.A.	N.A.
Van Dorn (1953)	field experiments in a small basin	3.3	none	N.A.	N.A.
Doebler (1966)	field exper. made off fixed platform using a drifting current pole	1.6	none	5.2 right	none
"	"	1.2	none	13.2 right	none
"	"	4.3	none	1.9 right	none
"	"	5.8	none	4.8 right	none
Wu (1968)	lab experiment	4.1	0.9	N.A.	N.A.

Ekman (1905) was one of the first to effectively address the problem of modeling the vertical structure of the horizontal velocities. One of his simplest models considers wind-induced drift only and is derived by simplifying the Navier-Stokes Equations to achieve a balance between the Coriolis "force" and the frictional force between water layers. The solution to the Ekman problem is:

$$u = V_0 e^{-(\pi/D)z} \cos\left(\frac{\pi}{4} - \left(\frac{\pi}{D}\right)z\right)$$

$$v = V_0 e^{-(\pi/D)z} \sin\left(\frac{\pi}{4} - \left(\frac{\pi}{D}\right)z\right) \quad (1)$$

$$D = \pi \sqrt{\frac{2N_v}{f}} \quad (2)$$

$$V_0 = \frac{\tau_{sy}}{\rho N_v a} \quad \text{and} \quad (3)$$

N_v = the vertical eddy viscosity coefficient

$$a = \sqrt{\frac{f}{N_v}}$$

and where z, u, v, τ_{sx} and τ_{sy} are defined in Figure 1

At $z = D$, the depth of frictional influence, it can be seen from Equations 1 that the velocity has been reduced to 1/23 of V_0 . The result of plotting Equations 1 is the classic Ekman "spiral". For infinitely deep water the surface current is aligned at 45° to the right of the wind.

For the case of finite depth Ekman carried out a similar analysis. In general, the "shallow water" solution will yield surface currents of both less magnitude and deflection than the infinitely deep case. However, for the case when the water depth is greater than 1/2 the frictional depth, the surface current no longer "feels" the effect of the bottom and behaves as if the water were "deep".

There are several characteristics of the Ekman approach which are unrealistic. For example, the Ekman-type solution predicts a deflection angle of 45° in deep water. Yet, as Madsen (1977) points out, surface drift experiments (Table 1) indicate the deflection angle to be much smaller (of the order 10°). Most of these experiments were performed in relatively shallow water and hence one might argue that the surface deflection would have been reduced due to the influence of the bottom. This does not appear to be the case. For example, consider the field experiment performed by Teeson et al. (1970). It is possible to establish the extent of bottom influence for these experiments if some value for the vertical eddy viscosity is specified. Since the value of N_v is not well known, it will be assumed that the 3% rule is roughly correct. This assumption allows an approximate evaluation of the vertical eddy viscosity using Equation 3. Plugging this value for N_v into Equation 2 yields a frictional depth for Teeson's experiments of

approximately 20 meters. Hence for the bottom to have significantly effected the surface current in Teeson's experiments, the water depth would have had to have been about 10m or less. In fact, Teeson's experiments were performed in water depths well above that -- in the range of 20 to 30 meters. Unsteady effects were also examined and rejected as the cause for the discrepancies (Cooper and Pearce(1977)). To understand why Ekman's Model apparently yields deflection angles which are too high, examine the assumption that the vertical eddy viscosity is constant in the vertical.

Ekman used the laminar analogy to write the interfacial frictional stresses as a function of the turbulent eddy viscosity coefficient, N_v , which in terms of the turbulent component of the velocities can be written as:

$$\begin{aligned}\tau_{xz} &= -\rho \overline{u'w'} = \rho N_v \frac{\partial u}{\partial z} \\ \tau_{yz} &= -\rho \overline{v'w'} = \rho N_v \frac{\partial v}{\partial z}\end{aligned}\quad (4)$$

where u' , v' , and w' are the turbulent components of the velocity in the x, y, and z direction respectively, (see Figure (1)).

It is clear that w' will be zero near a solid boundary and since $\partial u/\partial z$ (or $\partial v/\partial z$) will, in general, not be zero near a boundary, it follows from Equations 4 that N_v must be zero near that boundary. It is concluded that a realistic variation for N_v would be a shape with N_v near zero at the surface and the bottom and a maximum somewhere in between.

The above argument can be partially substantiated when one examines the effect of including a varying vertical eddy viscosity in the Ekman-type formulation. Madsen (1977) solved an unsteady form of the Ekman formulation. He assumed the vertical eddy viscosity to be zero at the surface and to increase linearly with depth. For steady state, his results indicate a deflection angle of approximately 10° at the surface-- a value consistent with the field observations in Table 1. Other aspects of Madsen's Model remain comparatively similar to Ekman's Model including the magnitude of the surface current and the total mass flux.

Another situation in which a vertical variation of the eddy viscosity results in more realistic flow patterns is for the case of flow in an infinitely long channel of finite depth with a wind blowing in the axial direction (i.e. 1-Dimensional flow). For this situation, an analytic solution assuming a constant vertical eddy viscosity yields a linear velocity profile. If instead, it is assumed that N_v varies parabolically (zero at the surface and the bottom) then the solution for the velocity is a logarithmic profile near the surface and the bottom. Intuitively this latter solution seems much more correct, since one would expect the velocity to exhibit a logarithmic profile near the surface and the bottom. This intuition is substantiated by laboratory experiments performed by Shemdin (1972).

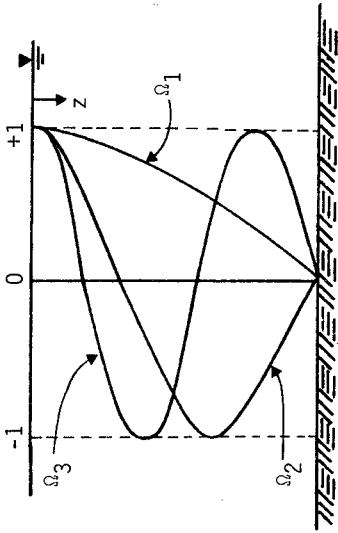


Figure 2: Plot of Prescribed Functions vs. Depth

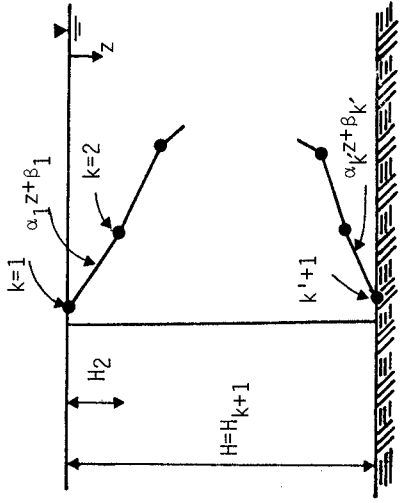


Figure 3: Functional Form for the Vertical Variation of N_v

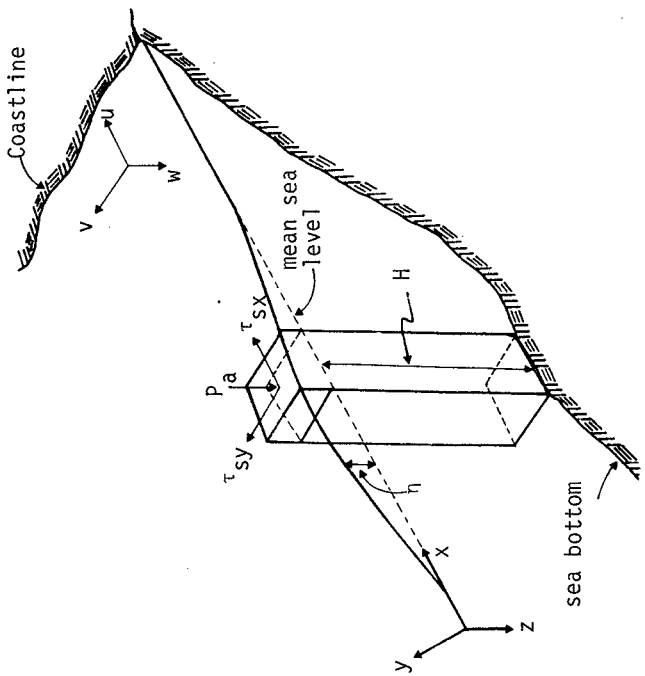


Figure 1: Definition of Variables Used in the Model

It is concluded that in order to realistically model the velocity profile, a vertical variation in the vertical eddy viscosity should be incorporated into a realistic 3-D model. Several modelers in the past, besides Madsen, have included a vertical variation in N_v .

Heaps (1972, 1974) has recently developed numerical models using a weighted residual technique. The outstanding features of these models include: (1) a relatively simple formulation, 2) reasonable computer-time requirements, and 3) a continuous functional form for the velocity profile.

Model Formulation

Thus, the modeling approach chosen by the authors has been to develop a 3-D model utilizing the Galerkin technique and incorporating a varying vertical eddy viscosity. The model is based upon the 3-D Momentum Equations with the following simplifying assumptions: i) vertical velocities are neglected and, ii) the laminar analogy is incorporated thus allowing the expression of the turbulent shear stresses in terms of the eddy coefficients. Thus the Momentum Equations become:

$$\begin{aligned} \frac{du}{dt} &= -g \frac{\partial \eta}{\partial x} + fv + \frac{\partial}{\partial x} (N_H \frac{\partial u}{\partial x}) + \frac{\partial}{\partial y} (N_H \frac{\partial u}{\partial y}) + \frac{\partial}{\partial z} (N_v \frac{\partial u}{\partial z}) \\ &\quad - \frac{1}{\rho} \frac{\partial P_a}{\partial x} - \frac{g}{\rho} \int_0^z \frac{\partial \rho}{\partial x} d\zeta \\ \frac{dv}{dt} &= -g \frac{\partial \eta}{\partial y} - fu + \frac{\partial}{\partial x} (N_H \frac{\partial v}{\partial x}) + \frac{\partial}{\partial y} (N_H \frac{\partial v}{\partial y}) + \frac{\partial}{\partial z} (N_v \frac{\partial v}{\partial z}) \\ &\quad - \frac{1}{\rho} \frac{\partial P_a}{\partial y} - \frac{g}{\rho} \int_0^z \frac{\partial \rho}{\partial y} d\zeta \end{aligned} \quad (5)$$

Conservation of mass yields an additional governing equation. The appropriate form of the continuity equation for an incompressible fluid is:

$$\frac{\partial \bar{U}}{\partial x} + \frac{\partial \bar{V}}{\partial y} = \frac{\partial \eta}{\partial t} \quad (6)$$

where \bar{U} and \bar{V} are the mass flux per unit length in the x and y directions respectively.

The surface boundary condition is:

$$\tau_{sx} = -\rho_s N_v \frac{\partial u}{\partial z} \quad \tau_{sy} = -\rho_s N_v \frac{\partial v}{\partial z} \quad @ \quad z = -\eta \quad (7)$$

where τ_{sx} and τ_{sy} are the surface shear stresses induced by the wind in the x and y direction, respectively and ρ_s is the density of water at the surface. Where τ_{sx} and τ_{sy} can be determined from the windspeed. A no-slip boundary condition at the bottom is assumed, or:

$$u = v = 0 \quad @ \quad z=H \quad (8)$$

The effect of bottom roughness can be included by varying the eddy viscosity near the bottom. For the case of an ideally smooth bottom, N_v will theoretically approach the value of the kinematic viscosity of water

near the bottom. As the bottom roughness increases, the value for N_V at the bottom can be expected to rise.

Thus, a set of governing differential Equations (5 and 6) and boundary conditions in the vertical (7 and 8) have been derived. The horizontal boundary conditions about the perimeter of the water body need not be introduced yet.

Application of a weighted residual technique begins by assuming a generalized functional relationship to approximate the true solution, or

$$\hat{u} = u_0 + \sum_{I=1}^{I'} c_I \Omega_I \quad \hat{v} = v_0 + \sum_{I=1}^{I''} d_I \Omega_I \quad (9)$$

where u and v are the "trial functions", c_I and d_I are the undetermined parameters, I' and I'' are the number of terms needed to reach the required degree of accuracy and Ω_I 's are prescribed functions. In theory, the only restriction in choosing the Ω_I 's is that they must satisfy the vertical boundary conditions when combined with the leading terms, u_0 and v_0 . In practice, however, they are chosen so as to approximate the true solution with as few terms as possible

The leading terms, u_0 and v_0 , are also somewhat arbitrary and may not have the same functional form as that assumed for the prescribed functions. These terms, however, when combined with the summation terms, must meet the necessary vertical boundary conditions. Using cosines, the trial functions can be written:

$$\hat{u} = u_0 + \sum_{I=1}^{I'} c_I \cos\left(\frac{a_I z}{H}\right) \quad \hat{v} = v_0 + \sum_{I=1}^{I''} d_I \cos\left(\frac{a_I z}{H}\right) \quad (10)$$

where a_I are prescribed constants.

To evaluate u_0 , v_0 , and the a_I 's the boundary conditions at the surface and bottom are utilized. It is found through trial and error that a sinusoidal function of the form.

$$u_0 = -\frac{H^T s_X}{\pi \rho N_V} \sin\left(\frac{\pi z}{H}\right) \quad v_0 = -\frac{H^T s_Y}{\pi \rho N_V} \sin\left(\frac{\pi z}{H}\right)$$

fits the required b.c. at the surface.

At the bottom boundary, u_0 and v_0 go to zero. Then, in order to meet the bottom b.c. (Equation 8) the a_I 's must be odd multiples of $\pi/2$ (i.e. $\pi/2, 3\pi/2, 5\pi/2, \dots$). Thus the trial functions can be written in final form:

$$\hat{u} = \frac{-H^T s_X}{\pi \rho N_V} \sin\left(\frac{\pi z}{H}\right) + \sum_{I=1}^{I'} c_I \cos\left(\frac{a_I z}{H}\right)$$

$$\hat{v} = \frac{-H^T s_Y}{\pi \rho N_V} \sin\left(\frac{\pi z}{H}\right) + \sum_{I=1}^{I''} d_I \cos\left(\frac{a_I z}{H}\right) \quad (11)$$

Figure 2 is a plot of the first three Ω_I terms.

Now that the trial functions have been specified, they can be substituted into the Momentum Equations (5). In general, there will be an error associated with this substitution, since the trial functions are not the exact solutions to the Momentum Equations. This error is commonly referred to as the "residual". Performing this substitution yields:

$$R = \frac{d\hat{u}}{dt} + g \frac{\partial \eta}{\partial x} - \frac{\partial}{\partial x} (N_H \frac{\partial \hat{u}}{\partial x}) - \frac{\partial}{\partial y} (N_H \frac{\partial \hat{u}}{\partial y}) - \frac{\partial}{\partial z} (N_V \frac{\partial \hat{u}}{\partial z}) - f\hat{v} + \frac{1}{\rho} \frac{\partial P_a}{\partial x} + g \frac{1}{\rho} \left(\int_0^z \frac{\partial \rho}{\partial x} dz \right) \neq 0 \quad (12)$$

For the sake of brevity, only the residual in the x direction is shown.

The error is minimized by specifying that the integral of the residual times a weighting function over a region be zero. For the case of interest, it is convenient to minimize the residual over a water column which yields:

$$\int_{-z}^H R W dz = 0 \quad (13)$$

W is specified as the prescribed function Ω_I (the Galerkin Method). Application of the Galerkin technique utilizes the orthogonality properties of Ω_I (i.e. $\cos(a_I z/H)$).

Taking $W = \Omega_I$ and substituting Equation 12 into Equation 13 yields:

$$\int_0^H R \Omega_J dz = \int_0^H \frac{d\hat{u}}{dt} \Omega_J dz + \int_0^H g \frac{\partial \eta}{\partial x} \Omega_J dz - \int_0^H \left(\frac{\partial}{\partial x} (N_H \frac{\partial \hat{u}}{\partial x}) + \frac{\partial}{\partial y} (N_H \frac{\partial \hat{u}}{\partial y}) \right) \Omega_J dz - \int_0^H \left(\frac{\partial N_V}{\partial z} \frac{\partial \hat{u}}{\partial z} \right) \Omega_J dz - \int_0^H N_V \frac{\partial^2 \hat{u}}{\partial z^2} \Omega_J dz - \int_0^H f \hat{v} \Omega_J dz + \int_0^H \frac{\partial P_a}{\partial x} \frac{\Omega_J}{\rho} dz + g \int_0^H \frac{1}{\rho} \left(\int_0^z \frac{\partial \rho}{\partial x} dz \right) \Omega_J dz \quad (14)$$

where J and I are both counters which are used interchangeably, and where the N_V term has been differentiated and conveniently separated into two terms. There is an equivalent Galerkin statement for the y direction.

Observe that the lower limit on the integration in Equation 14 has been moved from $z=-\eta$ to $z=0$. In order for this approximation to be valid, η must be much less than the still water depth, H . If this assumption was not made, then the integrals in Equation 14 would have to be continually reevaluated in time, since η is a function of time. This reevaluation would be computationally prohibitive.

In order to evaluate the integrals, a functional form for the vertical variation of the vertical eddy viscosity must be specified. This is done by approximating N_V with a series of linear segments as shown in

Figure 3. The slope (α_k), the intercept (β_k), and the number of segments (k') must be input by the model user. This linear approximation scheme has several obvious advantages. For instance, it is reasonably simple to integrate and it can approximate very complex forms.

Carrying out the integrations, yields:

$$0 = \frac{H}{2} \frac{\partial c_J}{\partial t} + HB_J \frac{\partial \eta}{\partial x} - \epsilon \frac{Hc_J}{2} + \tau'_x A_J - \sum_{I=1}^{I'} c_I \bar{\delta}\sigma_{IJ} + \tau'_y \frac{Hf}{\pi} \Gamma_J - f \frac{H}{2} d_J + \Delta P_{xJ} \tag{15}$$

where: $B_J, A_J, \bar{\delta}\sigma_{IJ}, \Gamma_J$ are constants which arise from the integration,

$$\tau'_x = \tau_{sx}/\rho ; \tau'_y = \tau_{sy}/\rho ;$$

ΔP_{xJ} is do to the surface pressure gradient and density gradients; ϵ is a parameter such that $\epsilon u = \partial/\partial x (N_H \partial u/\partial x) + \partial/\partial y (N_H \partial u/\partial y)$.

Equation 15 and its equivalent in the y-direction can be conveniently thought of as the governing Momentum Equations for a water column. All parameters are specified except the unknowns $c_J, d_J,$ and η . The Momentum Equations represent a set of $2I'$ equations with $2I' + 1$ unknowns. To solve for the unknowns, one more equation linking the c_J 's and d_J 's to η must be specified. This is accomplished using the Continuity Equation (6). With some manipulation, the mass fluxes, \bar{U}, \bar{V} , can be written in terms of the undetermined parameters.

Thus the original second order, nonlinear, Momentum Equations, along with the nonhomogeneous vertical boundary conditions have been reduced to a set of $2I'$ equations which are linear, first order PDE's. These $2I'$ equations coupled with the Continuity Equation and the boundary conditions about the horizontal perimeter of the water body, constitute a set of equations with a unique solution for the unknown variables $c_J, d_J,$ and η . Once the c_J 's and d_J 's are determined, then the velocities, u and v , can be found using Equation 11.

The governing differential equations can be solved using a variety of methods. It was decided to use the so called "split-time", finite difference scheme in the initial modeling. The method has been used with success by many numerical modelers in the past, such as Pearce (1972) and Reid et. al. (1968) and will not be described in detail here.

To apply the method, the water body is discretized in the manner shown in Figure 4. Note the subscripts ℓ and m , are spatial location counters which are associated with the x and y directions respectively. The time counter is n . There will be ℓ' grids in the x direction, m' grids in the y direction, and n' total time steps.

The next step is to apply the discretization to the governing differential equations, for example, Equation 15 yields.

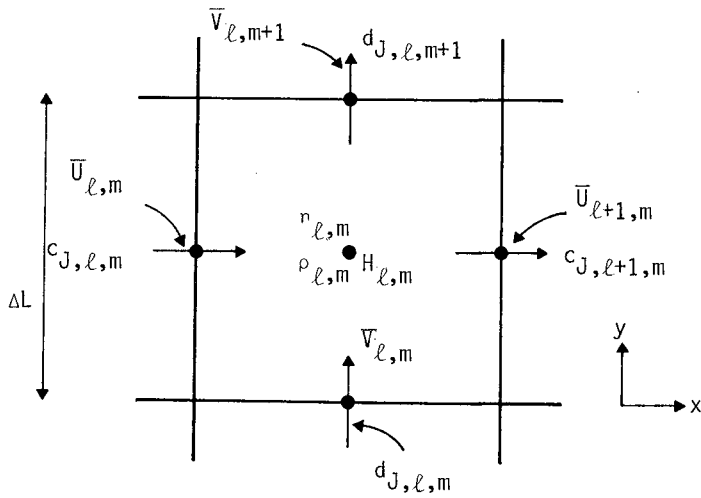
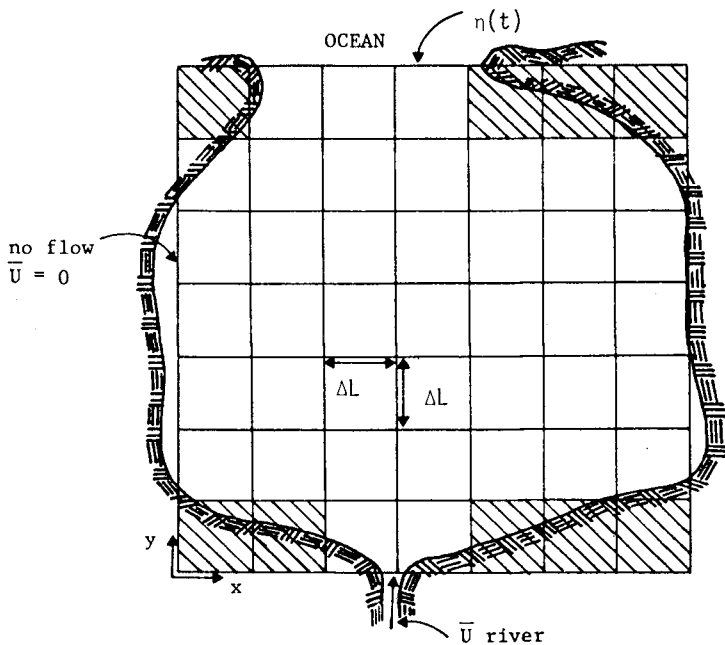


Figure 4: Finite Difference Discretization Scheme

$$c_j(\ell, m, n+1) = c_j(\ell, m, n) * \epsilon'(\ell, m, n) - B_j'(\ell, m, n) * \bar{\eta}_x - \bar{\tau}_{xj}(\ell, m, n) + C_3(\ell, m) *$$

$$\sum_{I=1}^{I'} c_I(\ell, m, n) * \bar{\delta}\sigma_{Ij}(\ell, m, n) + C_2 * d_j(\ell, m, n) - \Delta P_{xj}'(\ell, m, n) \quad (16)$$

where ϵ' is a constant associated with the horizontal eddy viscosity, C_2 is a constant associated with the Coriolis parameter, $\bar{\tau}_{xj}$ and $\Delta P_{xj}'$ are constants associated with the surface shear stress and pressure gradient, respectively and B_j' and C_3 are constants arising from the integrations.

$$\bar{\eta}_x = \eta(\ell, m, n + \frac{1}{2}) - \eta(\ell-1, m, n + \frac{1}{2})$$

Observe that Equation 16 explicitly expresses the "new" c_j 's at time $(n+1)$ in terms of the "old" c_j 's at time n . Also note that the "old" η 's are evaluated at time $n + 1/2$ instead of time n . This characteristic is the basis for the name "split-time". Similar manipulation yields the y equivalent to Equation 16.

Applying the discretization scheme to the Continuity Equation yields:

$$\eta(\ell, m, n + \frac{3}{2}) = \eta(\ell, m, n + \frac{1}{2}) + \frac{\Delta t}{\Delta L} (\bar{U}(\ell, m, n + 1) - \bar{U}(\ell+1, m, n + 1) + \bar{V}(\ell, m, n+1) - \bar{V}(\ell, m+1, n+1))$$

Verification

In order to check the convergence of the formulation as well as the program coding, the model was checked against several simple problems for which analytic solutions are available. The strategy was to start with the most simple case and then examine progressively more sophisticated cases.

The case of wind blowing along an infinitely long channel with a constant N_v was examined first. Figure 5 shows the various physical characteristics of the idealized channel which was used. The effect of the earth's rotation and the lateral shear stresses were neglected and the water density was assumed homogeneous.

The model was run to steady state which took approximately 8000 seconds to reach. Two cases were tried: one with $J' = 3$ and the other with $J' = 5$.

A comparison of the velocity profile from the model and the analytic solution is shown in Figure 6. The comparison is excellent for $J' = 3$ and $J' = 5$.

The model was next tested for a 1-D infinitely long channel

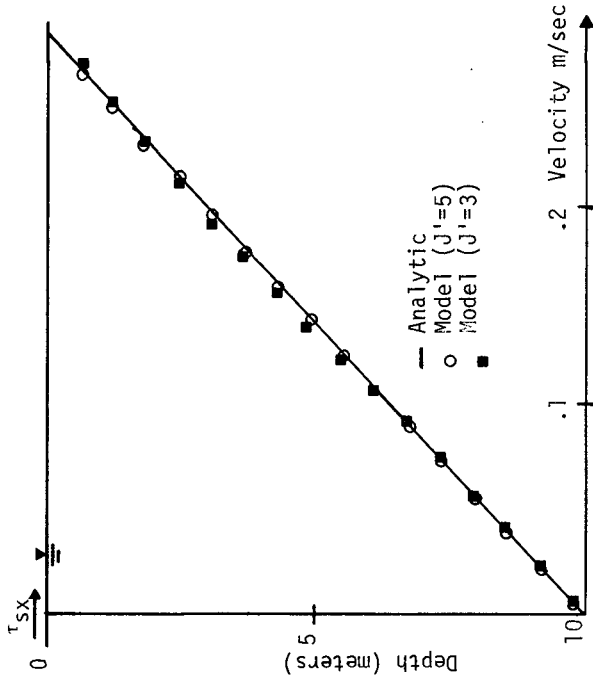


Figure 6: Comparison of Steady State Velocity Profile for the Case of a 1-D, Infinitely Long Channel with Constant N_v . ($N_v = 0.0465 \text{ m}^2/\text{sec}$)

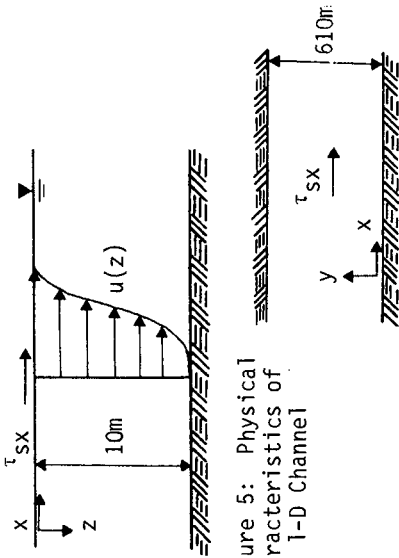


Figure 5: Physical Characteristics of the 1-D Channel

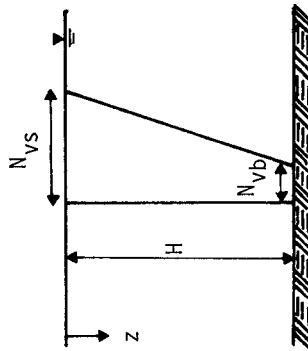


Figure 7: Linear Variation of N_v

identical to that described above except that N_v was no longer considered to be a constant but rather varied linearly as shown in Figure 7. The comparisons between the analytic and the model solutions shown in Figure 8 are poor. It was noted that the analytic solution displayed a very steep gradient near the bottom and it was suspected that more cosine terms were needed in order to approximate this steep gradient. Consequently, the number of terms was increased to eight. Though an improvement has been made by increasing the number of terms, that improvement is small when compared to the discrepancy which remains between the model and the analytic solution.

Spot checks of the computer results yielded no errors, nor did a thorough review of the model formulation. It was estimated that for reasonable values of N_v , the number of cosine terms needed in the model to achieve an acceptable approximation of a realistic velocity profile would be on the order of 20 terms. This poses problems for application of the model in its present form to real-world problems, since the computer time/storage requirements are unrealistic when more than 5 to 10 terms are required.

The future for a 3-D model using the Galerkin approach and a varying vertical eddy viscosity is, however, not as bleak as one might think. The problem with the formulation presented is simply that the trial function chosen, while very effective when dealing with the mild and unrealistic velocity gradients inherent to the constant N_v case, cannot cope effectively with the more realistic, logarithmic velocity profiles which can be created when N_v is allowed to vary with depth.

The poor convergence characteristics of the trial function used in the model can be traced to the choice of the u_0 component of the trial function (Equations 10 and 11). Recall that for the case of 1-D flow in an infinitely long channel with N_v small at the bottom, the u_0 term reaches a negative maximum near the bottom and has relatively sharp positive gradient between the maximum and the bottom (dashed line in Figure 8). Thus the function which must be simulated with a cosine series will have a steep negative gradient near the bottom. Such a function is very difficult to match using simple cosine functions which become zero at the bottom. A similar problem occurs when N_v becomes small near the surface.

Fortunately one can effectively eliminate this strong gradient near the surface by selecting an appropriate u_0 term. This means that the remaining portion to be simulated by the series of cosines will have a much milder slope and hence convergence will be much more rapid.

The choice of the functional form of u_0 depends a good bit upon which functional form one believes to most adequately represent the vertical variation of the vertical eddy viscosity. For the case of a linear variation one possible form of u_0 is.

$$u_0 = \frac{\tau_{sx} z^2 (z H)}{\rho H^2 N_{vb}} + \frac{\tau_{sx}}{\rho \alpha_1} \ln \left(\frac{N_{vb}}{N_{v1}} \right)$$

where: $N_{vb} = \alpha_1 H + \beta_1$ and $N_{v1} = \alpha_1 z + \beta_1$

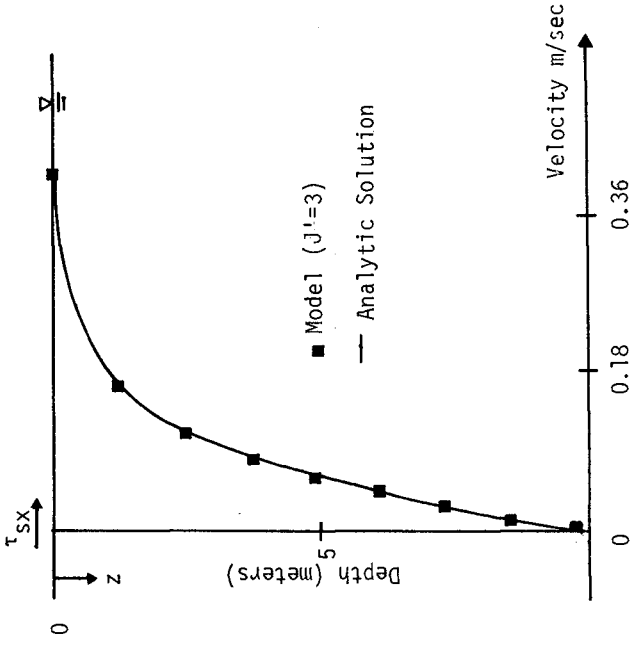


Figure 9: Comparison of Steady-State Velocity Profile from Revised Galerkin Model and Analytic Solution for 1-D Channel of Infinite Length with $C_b = \infty$

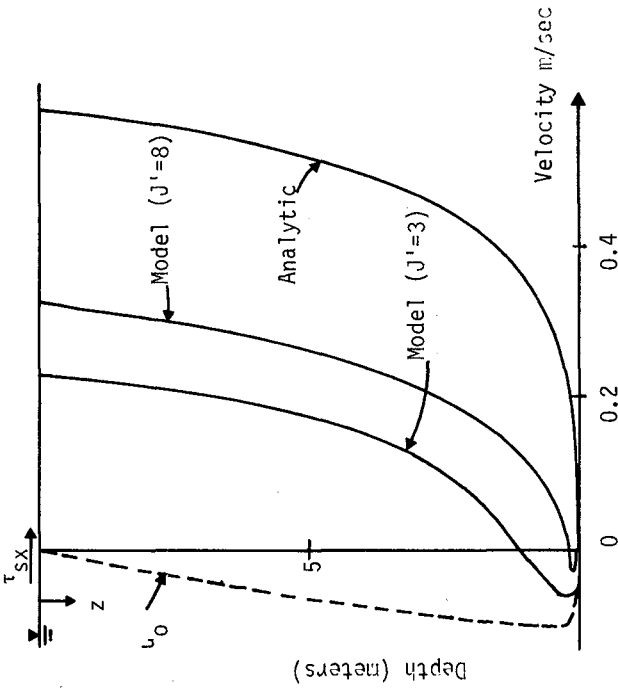


Figure 8: Comparison of Steady-State Velocity Profiles for 1-D Channel of Infinite Length. ($\alpha \bar{z} = 0.01414$ m/sec. and $\beta = 0.1417$ m²/sec)

Note that u_0 is composed of two parts. The second part is the analytic solution for a 1-D, infinitely long channel with a single, linear variation in N_V . This function will serve to moderate the velocity slope near the surface and thus hasten convergence. The first term of u_0 is needed to satisfy the boundary conditions and has a mild slope so as not to adversely affect convergence.

Steep gradients near the bottom are not so easily dealt with. This arises from the fact that one does not know the direction of flow near the bottom beforehand (unlike the situation at the surface). Hence it is seemingly impossible to pick a u_0 term which can help eliminate the sharp gradients near the bottom and thus hasten convergence. Our solution was to avoid these gradients by incorporating a slip velocity at the bottom similar to that used by Heaps (1972).

The Galerkin Model was then reformulated with the new u_0 and v_0 functions. Figure 9 compares the steady state analytic solution for a linearly varying eddy viscosity ($\alpha = .014$ m/sec, $\beta = .00093$ m²/sec) to that from the revised model. The 1-D channel was assumed very long and a no-slip bottom boundary condition was used by taking $C_b = \infty$. The figure indicates an excellent comparison using only three cosine terms.

The case with a slip velocity was examined next. Figure 9 indicates that the model compared very well with the analytic solution. Again this is not surprising, given the fact that the second part of u_0 nearly satisfies the analytic solution by itself.

Final verification is for a sea with an infinite lateral extent, with a linearly varying N_V and with a slip velocity at the bottom. The governing equations and the details of the analytic solution are shown in (Pearce, et al, 1978)

Figure 10 shows a comparison between the numerical, Galerkin Model and the analytic solution. The comparison between the analytic and numerical models is quite good.

Figure 11 shows a comparison for the case of constant eddy viscosity. The analytic model is the Ekman solution for a sea of infinite horizontal extent and finite depth. The comparison is not as good as in the previous figure. The reason for this is because in the case of constant N_V , the second term of the trial function (u_0) becomes linear, reaching a maximum at the surface and no longer aids the convergence.

The comparison for the constant N_V case can no doubt be improved by taking more cosine terms (only 3 cosine terms were used in the results shown in Figure 11). In any event, it must be remembered that the new formulation does fit the varying N_V case, which is more physically realistic than the constant N_V case. Future research will compare model results to prototype data.

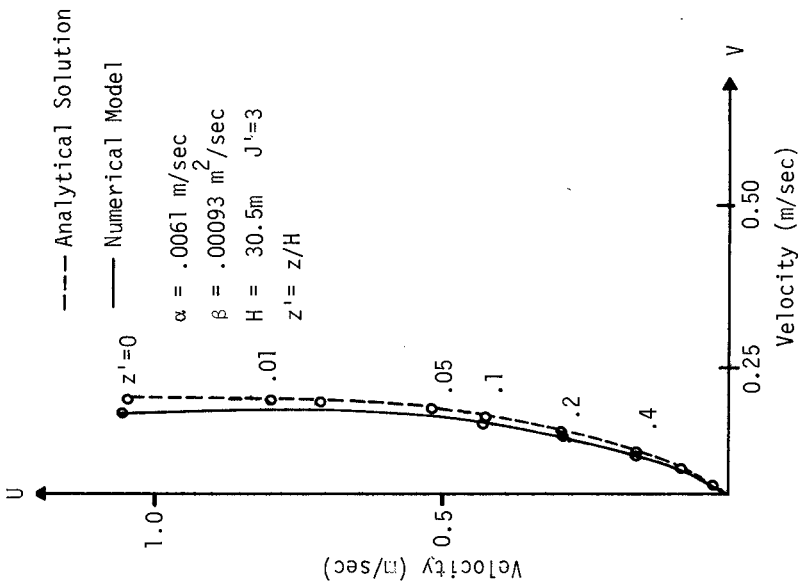


Figure 9: Comparison of 3-D Solution for Numerical and Analytical Models for Variable Eddy Viscosity

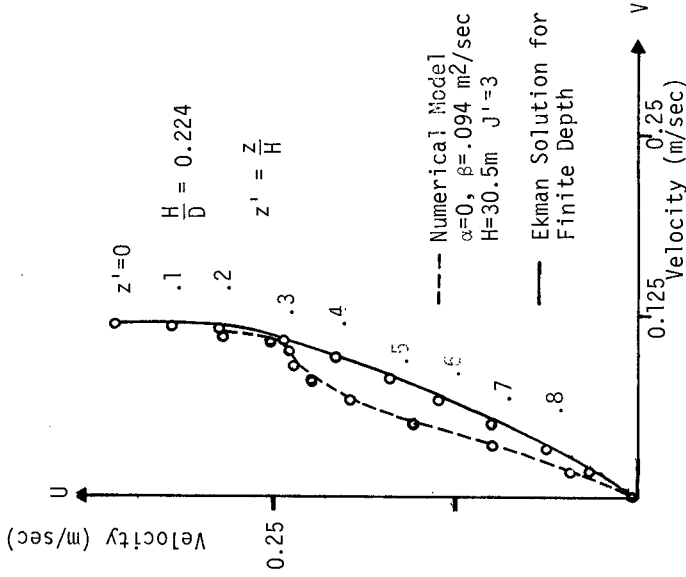


Figure 10: Comparison of 3-D Solution for Numerical and Analytical Models for Constant Eddy Viscosity

Acknowledgements

The research summarized in this paper was supported primarily by the National Weather Service of the National Oceanic and Atmospheric Administration. INTEVEP (Instituto Tecnológico del Petróleo Venezolano) is also acknowledged for its contribution to the research. Special thanks is extended to Dr. Celso Barrientos of the NWS and German Febres of INTEVEP.

References

Cooper, C.K., B.R. Pearce (1977), "A Three-Dimensional Numerical Model to Calculate Currents in Coastal Waters Utilizing a Depth Varying Vertical Eddy Viscosity," Ralph M. Parsons Lab. for Water Resources and Hydrodynamics, M.I.T., Technical Report No. 226.

Ekman, V.W. (1905), "On the Influence of the Earth's Rotation on Ocean Currents," *Ark. Mat. Astron. Fys.*, 2, 1-53.

Heaps, N.S. (1972), "On the Numerical Solution of the Three-Dimensional Hydrodynamic Equations for Tides and Storm Surges," *Mem. Soc. R. Sci. Liege*, 6 (2), 143-180.

Heaps, N.S. (1974), "Development of a Three-Dimensional Model of the Irish Sea," *Rapp. P.-V. Reun. Cons. Int. Explor. Mer.*, Dec. 1974, 147-162.

Madsen, O.S. (1977), "A Realistic Model of the Wind-Induced Ekman Boundary Layer," *Journal of Physical Oceanography*.

Pearce, B.R. (1972), "Numerical Calculation of the Response of Coastal Waters to Storm Systems", Coastal & Oceanographic Engineering Lab., U. of Florida, Technical Report No. 12.

Pearce, B.R., C. Cooper, and S. Nelson, (1978) "An Improved 3-Dimensional Numerical Model to Calculate Currents with a Depth Varying Vertical Eddy Viscosity" Technical Report, Department of Civil Engineering, University of Maine, Orono, in Press.

Reid, R.O., & B.R. Bodine (1968), "Numerical Model for Storm Surges in Galveston Bay", *Journal of the Waterways and Harbors Division, ASCE*, 94, WW1

Shemdin, O.H. (1972), "Wind Generated Current and Phase Speed of Wind Waves," *Journal of Physical Oceanography*, 2, 411-419.

Stolzenbach, K.D., O.S. Madsen, E.E. Adams, A.M. Pollack, and C.K. Cooper (1977), "A Review and Evaluation of Basic Techniques for Predicting the Behavior of Surface Oil Slicks," Ralph M. Parsons Lab. for Water Resources and Hydrodynamics, M.I.T., Technical Report No. 222.

Teeson, D., F.M. White and A. Schenck (1970), "Studies of the Simulation of Drifting Oil by Polyethylene Sheets," *Ocean Engineering*, 2, 1-11 Pergamon Press.

CHAPTER 159

MIXED LAYER MODELS FOR COASTAL WATERS

by

Wm. J. Wiseman, Jr., L. J. Rouse, Jr., and O. K. Huh

Coastal Studies Institute, Louisiana State University

Baton Rouge, Louisiana 70803

Abstract

The applicability of oceanic mixed-layer models to the case of wind mixing in a coastal region dominated by river runoff is explored. Two-dimensional effects and the propagation of internal-inertial waves out of the mixed layer are seen to be extremely important. Modification of the boundary conditions changes the appearance of the solutions as well. Further field work will be necessary to determine if additional terms, ignored in the oceanic models, might become important in the coastal region.

Introduction

The regions of strong haline stratification downdrift of the world's major river mouths account for only a small portion of the world's continental shelves, but they are extremely important because of the suspended sediment, nutrients, and pollutants these rivers carry. In order to properly manage such coastal zone areas, it is necessary to understand the mechanisms by which the freshwater, riverine effluent

mixes with the ambient shelf waters. Unfortunately, the space and time scales of the dynamics in these regions do not lend themselves to easy study by classical oceanographic methods. Cruises are not sufficiently synoptic to resolve the temporal scales of interest, and moorings generally are not sufficiently numerous to resolve the spatial scales.

For a number of years we have been investigating the applicability of remote sensing techniques to the study of coastal problems. In the case of mixing between fresh and salt water, a salinity sensor would seem optimal, but routinely available airborne or satellite-borne salinity sensors do not yet appear to have the necessary accuracy, e.g., Thomann (1973). We therefore have stressed the use of thermal sensors. Justifications for this are that over short time scales temperature may be considered as a quasi-conservative parameter, sensor technology is good, and, in the region of interest, temperature is relatively unimportant dynamically. For example, Figure 1 shows four traces of temperature and salinity versus depth from the same station. While the fresh-water inflow from the coast maintains a strong pycnocline all year, during summer the temperature structure reinforces the haline stratification and during winter tends to counteract it. The changeover occurs around April and November. In all cases, the basic density structure is two layered.

Following atmospheric cold-front passages, conditions are often excellent for thermal remote sensing. In Louisiana, such cold fronts occur with a 3- to 10-day recurrence interval from October through April when pulses of cold, dry polar continental air flow down the Mississippi River valley and out over the Gulf of Mexico (Fernandez-Partagas and Mooers, 1975;

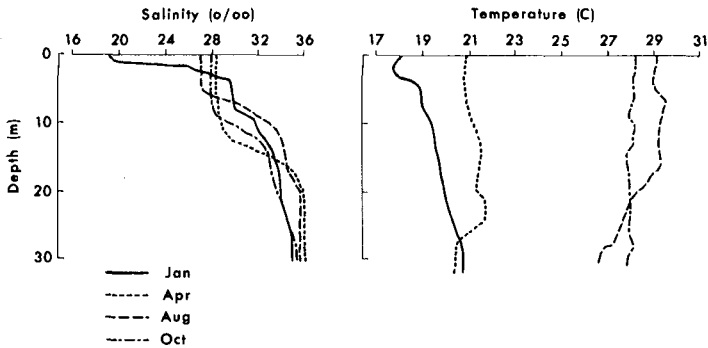


Figure 1. Temperature and salinity profiles from a station west of the Mississippi River delta.

Leipper, 1954; Huh et al., 1978). These cold-air outbreaks cool the surface waters of the coastal zone and form sea-surface temperature fronts (Huh et al., 1978), which are later distorted by mesoscale circulations on the shelf, e.g., Figure 2. It is images such as these that we hope eventually to couple with the output of a good oceanic mixed-layer model to hindcast the subsurface structure of coastal waters.

Oceanic Mixed-Layer Models

The influence of the oceanic mixed layer on weather has prompted numerous recent modeling efforts. An excellent model, which incorporates most of the successful aspects of previous models, has recently been published by Niiler (1975). The model assumes distributions observed in nature and then derives a set of equations consistent with these distributions. In the model, temperature is assumed to be the dominant density parameter and heat to be supplied by solar radiation at the sea surface. Mean temperature and mean horizontal momentum are assumed to be uniform throughout the

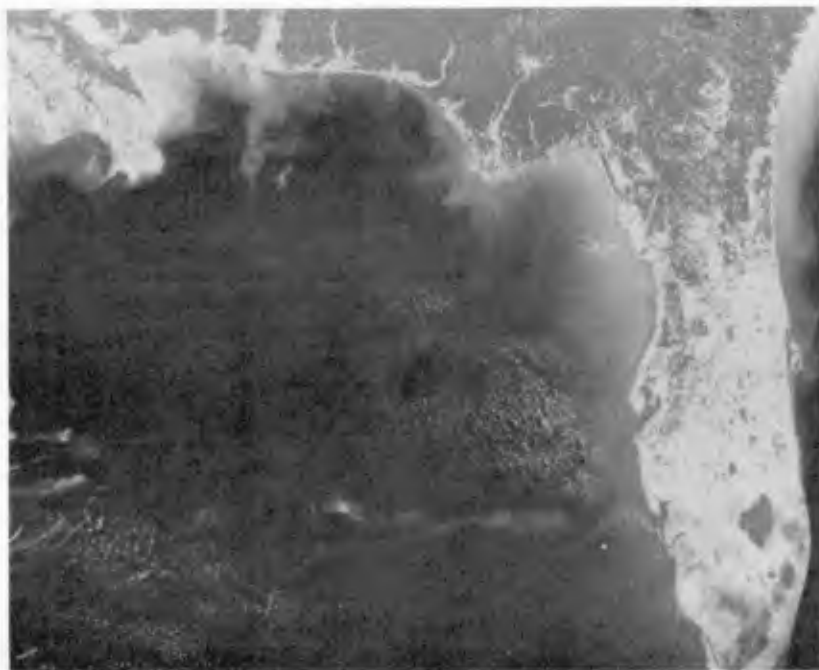


Figure 2. NOAA-5 thermal IR image of the northern Gulf of Mexico following a cold-front passage (26 January 1977). Colder waters are denoted by the lighter colors.

mixed layer except for two thin shear layers at the sea surface and at the bottom of the mixed layer. The surface layer is a wave-driven shear layer, while the lower shear layer separates the mixed layer from the quiescent fluid below. There exists a finite flux of heat and horizontal momentum into the top of this latter shear layer, but none out the bottom. These fluxes are used to bring fluid entrained from below up to the temperature and mean horizontal velocity of the mixed layer. The fluid is assumed to be incompressible, hydrostatic, and Boussinesq. At the scales of interest, both mean quantities and turbulent correlations are assumed to be horizontally homogeneous.

To determine the mean temperature, mean horizontal velocity and mixed layer depth, mean momentum, and heat are conserved, as well as turbulent kinetic energy. When there exists an excess input of energy from the wind, above and beyond that needed to mix the incoming heat through the mixed layer and to account for background dissipation, fluid is entrained from below. Other than this entrainment, though, the lower fluid is decoupled from the mixed layer. Dissipation of mean horizontal momentum in the mixed layer is accounted for by a quadratic friction law such as used by Pollard and Millard (1970). The model works extremely well in the situations for which it was designed and reproduces many of the observed features of the oceanic mixed layer.

Such a model may not, though, be useful for describing a strongly haline stratified coastal region, and it is therefore important to identify the necessary modifications to make it applicable to such a situation. Many of these will be points which Niiler has already identified as potential additions to his model. Whereas in the deep ocean, though, they may only be aesthetic improvements to an already good predictive model, in the coastal zone they contain the dominant physics.

It is apparent that, in the regions we are discussing, salinity must be included in the equation of state. As a very good first approximation we may even permit salinity to be the sole density parameter and consider temperature to be a dynamically passive contaminant. One consequence of this is that the dominant buoyancy flux is now no longer a distributed source at the sea surface but rather an isolated source at the lateral boundary of the study area. Niiler has also chosen to ignore evaporation minus precipitation as an important source

term and, to a first approximation, it is probably still negligible within the coastal zone. We estimate that the buoyancy flux across the sea surface (caused by sensible and latent heat loss and mass loss) due to a strong cold-front passage, e.g., Nowlin and Parker (1974), is only 20% to 25% of the buoyancy flux due to runoff during the same period and the two fluxes have opposite signs. One might argue that the time necessary for the freshwater input into the coastal boundary layer to mix across the region of interest is large compared to the time necessary for the buoyancy flux out of the sea surface due to a cold-front passage. If this be the case, then indeed it might be necessary to consider evaporation minus precipitation as important over short time scales at the offshore regions of interest.

The vertical distributions of mixed-layer properties for the coastal situation are similar to those for the open-ocean case. The surface shear layer, though, may need to be considered a bit more carefully since, if long waves are propagating into the area from the sea, then the wave-driven shear layer thickness may not be small compared to the mixed-layer thickness. In the coastal zone the mixed layer is only of the order of 10 meters thick rather than 100 meters, as in the oceanic case. Furthermore, the assumption of vertical homogeneity of mean horizontal momentum must be reconsidered. If the mean horizontal momentum is independent of depth, then over most of the mixed-layer depth generation of turbulent kinetic energy by the working of the Reynolds stresses against the mean shear may be ignored. In the oceanic case a mean horizontal velocity change of 10 cm/sec across the mixed layer is necessary for this term to become of the same order of

magnitude as the other retained terms in the turbulent kinetic energy equation (Niiler, 1975). In the case of the thinner coastal zone mixed layer, the mean horizontal velocity change must be only of the order of 1 cm/sec. Our measurements are not sufficiently accurate to resolve whether the mean horizontal velocity change is of this order of magnitude or not and therefore, in the interest of mathematical simplicity, we will initially ignore this term.

Niiler (1975) has also ignored the downward-propagation of internal-inertial wave momentum through the base of the mixed layer. In the conservation equation for mean momentum the loss of momentum by downward propagating internal-inertial waves is modeled by the frictional dissipation. If this momentum is transported to infinity, as it would be in an infinitely deep lower layer that is a good approximation to the deep ocean, then there is no further effect. If, however, the momentum is trapped in a shallow lower layer, it could significantly change the shear across the lower boundary of the mixed layer and thus affect the turbulent kinetic energy equation and the calculated mixed-layer depth. It is conceivable that such a situation could arise when the lower layer is extremely thin, as might be the case in a mixed layer lying over a broad, shallow shelf such as we find in the northern Gulf of Mexico.

Finally, the assumption of horizontal homogeneity must be relaxed. There will be horizontal density gradients imposed by the buoyancy flux at the coast. Coastal Ekman divergences will cause upwelling and downwelling. Also, one would assume that if lateral turbulent mixing is important, then the mixing length will become a function of the offshore distance as well.

As a first step to an understanding of the effects of cold-front passages on the mixed layer in the coastal zone, we have looked at the effects caused by the coastal boundary in an extremely simplified version of Niiler's model. The model has been extended to two dimensions; it is a two-layered model with offshore variation of the properties within the surface mixed layer. We have replaced the heat conservation equation with an equation for the conservation of salt so that our three equations are now

Conservation of mean horizontal momentum:

$$\frac{\partial \bar{u}}{\partial t} + \bar{k} \times \bar{u} = \frac{\bar{\tau}_o}{\rho_o} - \frac{C_D}{h^2} \bar{u} |\bar{u}| - gh \frac{\partial [(\rho_o - \rho) h / \rho_o]}{\partial x} \bar{i} \quad (1)$$

Conservation of salt:

$$h \frac{\partial s}{\partial t} + \bar{u} \frac{\partial s}{\partial x} = (s_o - s) \frac{\partial h_e}{\partial t} H \left(\frac{\partial h_e}{\partial t} \right) \quad (2)$$

Equation used to compute mixed layer depth:

$$\frac{\partial h}{\partial t} = \frac{2m_o \bar{\tau}_o / \rho_o^{3/2} h^2}{[gh^3 (\rho_o - \rho) / 2 - \bar{u} \cdot \bar{u}]} - w_E = \frac{\partial h_e}{\partial t} - w_E \quad (3)$$

where

$$\rho = 1 + bs \quad (4)$$

The variables in equations (1) - (4) have all been normalized. The symbol \bar{u} is mean horizontal transport, t is time, $\bar{\tau}_o$ is horizontal wind stress, ρ is density, ρ_o is a reference density, g is gravity, h is mixed-layer depth, x is the offshore coordinate in the direction of the unit vector \bar{i} , \bar{k} is the unit vector in the vertical direction, s is salinity, s_o is the reference salinity corresponding to ρ_o , h_e is the mixed-layer depth increment due to entrainment, $H(\cdot)$ is the Heaviside function, w_E is the vertical velocity at the base of

the mixed layer due to Ekman divergence (calculated from the continuity equation), and b is a constant. The term m_0 is a constant that determines the amount of energy available for entrainment, for which we have assumed Niiler's value. C_D , the friction coefficient used to model dissipation within the mixed layer, was taken from Daddio et al. (1978).

The mean horizontal momentum equation is linearized and driven by wind stress and a minor momentum source at the coast associated with the riverine influx. Crude, order of magnitude analyses suggest that lateral diffusion is less important than lateral advection of salt, and so the salt balance has no lateral diffusion term. It does, though, include an entrainment term. The equation for mixed-layer depth contains two terms; one is due to the Ekman divergence at the coast and the other is due to the entrainment prescribed by the conservation of turbulent kinetic energy. This latter allows entrainment when the bulk Richardson number

$$Ri = \frac{-g}{\rho_0} \frac{(\rho - \rho_0) h^3}{2 u^2} \quad (5)$$

is less than 1, but does not require the Richardson number to be equal to 1, as did Pollard et al. (1973) in an earlier model.

Initial conditions assumed for the model are an infinitely deep lower layer of 35 ‰ and a mixed layer with salinity of 25 ‰ at the coast, a linear gradient to 33.5 ‰ at 95 km offshore, and constant salinity thereafter. The initial mixed layer depth is 10 meters at 95 km from the coast and specified such that there does not exist a horizontal pressure gradient initially. The boundary conditions are a constant inflow of 25 ‰ water at the coast of a magnitude represent-

ing low river stage in the Mississippi River and a horizontally uniform time-varying, north-south wind stress (shown in Fig. 5).

Results

A plot of mixed-layer depth calculated by the model as a function of time and offshore distance is shown in Figure 3. The initial onshore wind stress tends to depress the pycnocline near the coast and entrain heavier fluid from below as the stress increases. When the stress shifts to an offshore direction, the pycnocline tends to rise to the surface. This tendency is initially overpowered by the entrainment due to the strength of the stress. As the wind decays, though, the Ekman divergence at the coast causes the pycnocline to rise. When the wind is turned off, an unbalanced pressure gradient exists at the coast. As this relaxes, internal-inertial waves propagate seaward.

Some inertial oscillations undoubtedly are also driven by the near-impulsive wind shift, but they seem to be less important. If a more realistic model of the vertical stratification were introduced, vertically propagating internal-inertial waves should result. Indeed, field data from the area during the period of frontal passages indicate the importance of these motions. The time series in Figure 4 shows such oscillations in the salinity structure and the speed time series. The slope of the isotachs suggests downward propagation in the lower layer. With the internal-inertial waves modeled properly, the shear across the base of the mixed layer would change and the entrainment probably would also be altered. The variations of pressure at the base of the mixed layer can be seen in Figure 5, where we have plotted only the

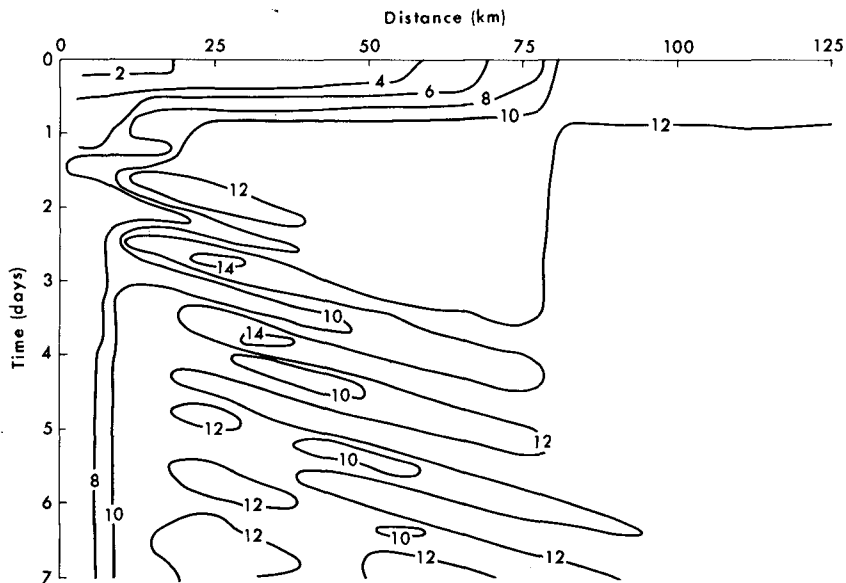


Figure 3. Contours of mixed-layer depth in meters as a function of time and offshore distance for the model conditions described in the text. The wind stress history is shown in Figure 5.

product of the normalized mixed-layer depth and the normalized salinity. This product is proportional to the desired pressure. It can be seen that, after the cessation of the wind stress, a strong onshore pressure gradient builds up in response to the continued input of fresh water at the coast, the only driving force for the model at this time. An alongshore geostrophic current develops to balance this pressure gradient in the model. Such a current does not, though, appear to develop to any great extent during the summer, when winds are light. It would appear that either horizontal mixing is important in practice or the full three-dimensional field of motion is necessary to describe the region, i.e., over the time scales with which we are dealing, the alongshore gradients of properties must also be considered or, most probably, frictional effects become extremely important (Crout and

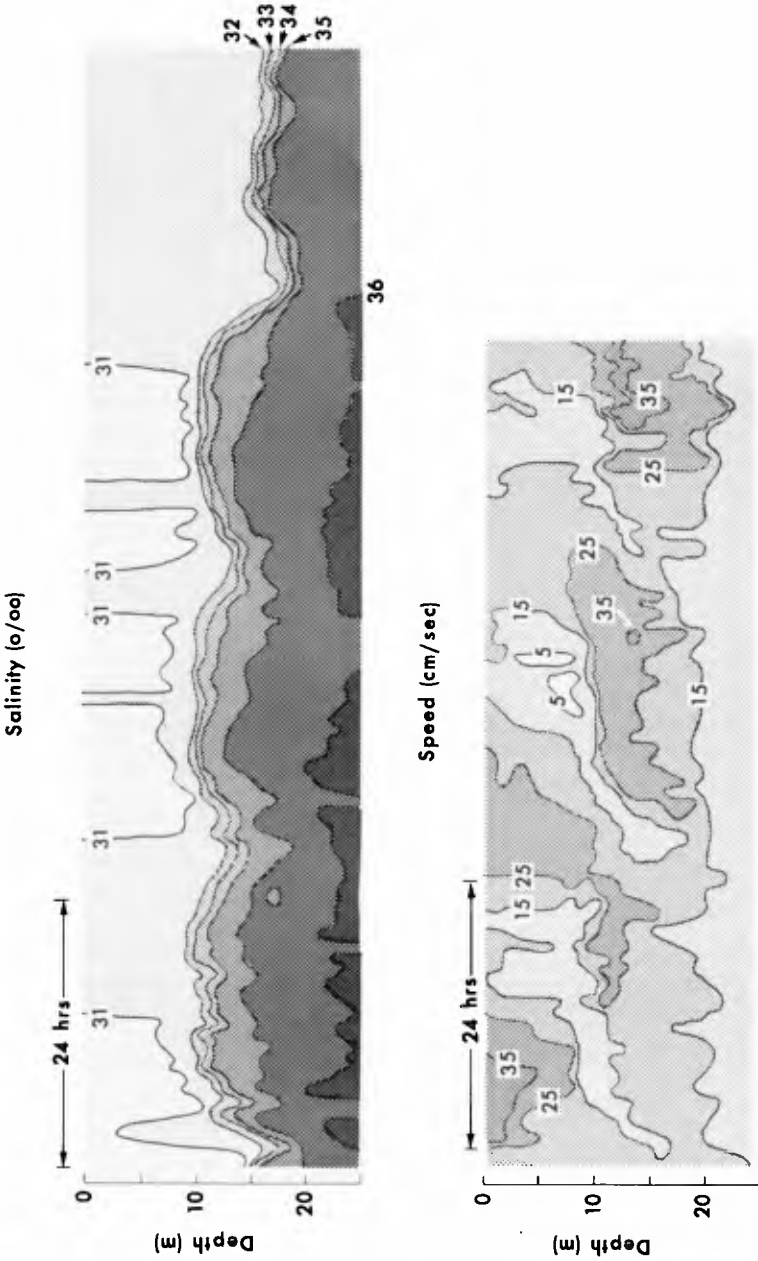


Figure 4. Contours of salinity (upper) and horizontal current speed (lower) as a function of time and depth for a station west of the Mississippi River delta. The data were collected in early October 1975, a period of moderate cold-front passages.

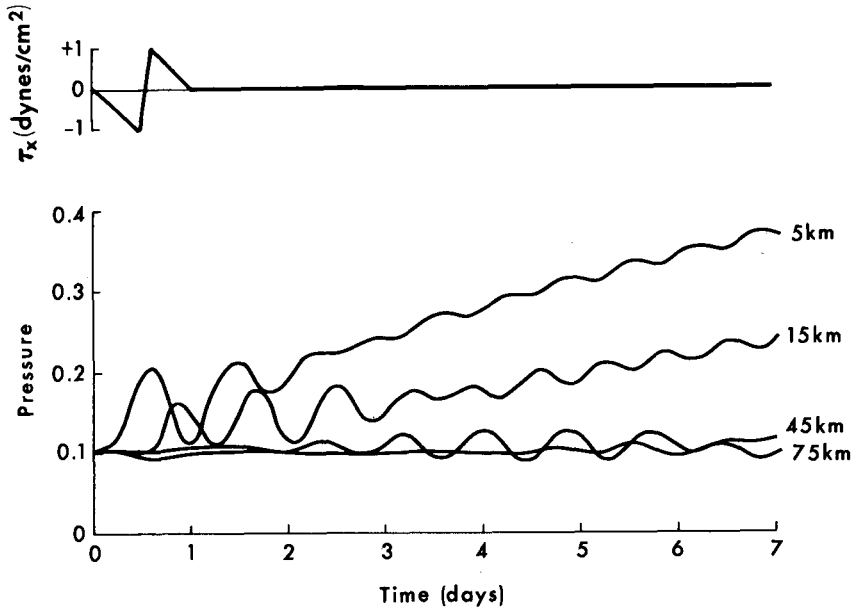


Figure 5. (Upper) Wind stress history for the model. (Lower) A pressure parameter (normalized mixed-layer depth x normalized salinity) at the base of the mixed layer, for selected offshore distances, as computed by the model.

Murray, 1979).

The next steps in the development of the model will be the incorporation of a more realistic wind stress, bottom topography, a realistic stratification in the lower layer and vertical propagation of internal waves, and, finally, addition of a conservation of heat equation. This will then permit interaction of the remote sensing and modeling capabilities.

Acknowledgments

This research was supported under a contract between the Geography Programs, Office of Naval Research, Arlington, Virginia 22217, and the Coastal Studies Institute, Louisiana State University. The support of the Arctic Program, Office of Naval Research, is also gratefully acknowledged.

References

- Crout, R. L., and S. P. Murray. 1979. Momentum transport in the brackish coastal boundary layer. Proc. 16th Internat. Conf. on Coastal Engr. (this volume).
- Daddio, E., Wm. J. Wiseman, Jr., and S. P. Murray. 1978. Inertial currents over the inner shelf at 30°N. J. Phys. Oceanogr. 8(4):728-733.
- Fernandez-Partegas, J., and C. N. K. Mooers. 1975. A subsynoptic study of winter cold fronts in Florida. Monthly Weather Review 103:742-744.
- Huh, O. K., Wm. J. Wiseman, Jr., and L. J. Rouse, Jr. 1978. Winter cycle of sea surface thermal patterns, northeastern Gulf of Mexico. J. Geophys. Res. 83(C9):4523-4529.
- Leipper, D. F. 1954. Marine meteorology of the Gulf of Mexico. Fishery Bull. 86, U.S. Fish and Wildlife Service.
- Niiler, P. P. 1975. Deepening of the wind-mixed layer. J. Mar. Res. 33(2):405-422.
- Nowlin, W. D., Jr., and C. A. Parker. 1974. Effects of a cold-air out-break on shelf waters of the Gulf of Mexico. J. Phys. Oceanogr. 4:467-486.
- Pollard, R. T., and R. C. Millard, Jr. 1970. Comparison between observed and simulated wind-generated inertial oscillations. Deep-Sea Res. 17:813-821.
- Pollard, R. T., P. B. Rhines, and R. O. R. Y. Thompson. 1973. The deepening of the wind-mixed layer. J. Geophys. Fluid Dynam. 3:381-404.
- Thomann, G. C. 1973. Remote measurement of salinity: repeated measurements over a single flight line near the Mississippi Sound. NASA/ERL Rept. 079, 14 pp.

CHAPTER 160

SOME DESIGN CRITERIA FOR OTEC INSTALLATIONS FOR KEAHOLE POINT, HAWAII

Frederick C. Munchmeyer¹ and Charles L. Bretschneider²

ABSTRACT

Ocean Thermal Energy Conversion, called OTEC, is presently getting much serious support for continued studies. Presently, there are potential OTEC sites off Punta Tuna, Puerto Rico; West Coast of Florida; New Orleans, Louisiana; and Keahole Point, Hawaii, the latter of which is the theme of this paper. The paper gives a summary of the early history of OTEC and its present status at Keahole Point, Hawaii, including design criteria. Any OTEC plant must operate throughout the normal environment, i.e. operational design sea state, including winds, waves and currents. The plant must be designed for the extreme environmental conditions, such as associated with hurricanes. The selection of an OTEC site depends on the availability of the resource, particularly associated with the temperature difference between the surface waters and the deep water. The change in the environmental parameters, and the consequences of any anticipated changes, are subjects of an environmental impact statement, the subject of which has been studied but is not reported here as part of this paper.

INTRODUCTION

The first successful OTEC plant was constructed by Georges Claude in Matanzas Bay, Cuba, in 1930. He was acutely aware of the design problems and made a number of qualitative statements concerning them (Claude, 1930). The second successful OTEC plant has not yet been built; however, early efforts to design such a plant face the same natural problems that Claude recognized and experienced. In Hawaii, where OTEC efforts have been active since 1972 and are accelerating, a number of OTEC design criteria have been studied at a site which is named Keahole Point. We present some of those data here, but before doing so it is instructive to review Claude's 1930 lecture.

He spoke to the American Society of Mechanical Engineers in New York on October 22, 1930, only a few weeks following his OTEC success in Cuba. Six months previously he had been awarded that Society's Fiftieth Anniversary Medal.

The editors of Mechanical Engineering remarked on his prior contributions "...especially the liquefaction of air and of oxygen and hydrogen, the production of nitrogen and ammonia [and]...the process in which

¹ Associate Professor, Department of Mechanical Engineering,
University of Hawaii

² Chairman and Professor, Department of Ocean Engineering,
University of Hawaii

acetylene is dissolved and stored under pressure in acetone..." This was the background of the man about whom the editors remarked further: "At the present time he is engaged in investigations relating to the industrial extraction of thermal energy from the sea..."

In his ASME lecture, Claude said that his "...dear master and friend, D'Arsonval, as far back as 1882..." observed that it is possible to utilize the difference in temperature between the surface of the tropical seas and the deep-sea water to generate power.

Italian and American inventors, between 1882 and 1930, had proposed closed cycle OTEC plants. Claude designed an open cycle plant because "...[the closed cycle] is burdened by...the necessity of transmitting enormous quantities of heat through the inevitably dirty walls of immense boilers with such a small difference in temperature."

He said that vocal critics of his ocean thermal energy ideas abounded, among them "Others [who] declared that it would be impossible to prevent the deep sea water from warming up too much during its ascent..."

In these extracts he also said: "It remained to be determined, however, whether the idea of procuring cold water from the bottom of the sea was chimerical or not.

"In a matter of this kind there is no precedent; all is unknown; theory no longer guides us, and we have to face that terrible adversary, the sea..."

"...a very large and expensive pipe would be needed to feed [the 60 kw] turbine...if the pipe had only the size required to feed the turbine, that is, not larger than 2 ft. in diameter, it would not be possible to insulate it sufficiently...For this reason it would be necessary to use a pipe 2 meters in diameter..."

"Various considerations, especially the proximity of deep water, led me to choose the island of Cuba...[however, bottom surveys] brought...disappointment...the existence of a high submarine cliff almost entirely around the island...The pipe, instead of lying all along its length...on the bottom of the sea...would have to drop down from the cliff into the abyss..."

"Anxious to avoid subjecting the tube to the pressure of the submarine current - much dreaded on those shores swept by the Gulf Stream, I was led to locate the plant in Matanzas Bay...However, the protection afforded here proved to be little or nothing...One day...[during his first efforts in August, 1929] these supposedly quiet waters got angry and sent to the bottom some hundred meters of [2 meter diameter steel] tubing."

Eventually, Claude assembled his mile long steel tube, in a river, and attempted to tow it to the ocean shore site. Bad weather and bad communications led to disaster; his first pipe sank in deep water.

"...I had gained in the [1929] struggle...a precious experience..."

In June 1930 his second tube also sank in deep waters when some of his crew proceeded against orders during the delicate maneuver of laying the pipe. On September 7, 1930 his third attempt to lay the mile long pipe succeeded. Pumping began as soon as all connections were made. The discharge water temperature "...finally...reacted 13 deg. cent. - a good result assuming that the temperature at the lower end of the tube was probably around 11 deg. cent." The system was completed and the turbine was started. "I got 12.5 kw. with warm water at 27.5 deg. cent. and cold water at 17 deg. cent., which increased to 22 kw. with temperatures of 27 deg. and 13 deg., respectively. These variations in the cold-water temperature were due partly to curious fluctuations of the Gulf Stream, and partly to a leak in the tube near the shore..."

Claude concluded his 1930 lecture by expressing "...most complete confidence in the future of this process..." and "certainty that... industries will never lack the precious energy that actuates them."

The data collection and analysis preceding the first OTEC plant at Keahole Point, Hawaii, follows closely Georges Claude's experiences. These efforts recognize more than one possible plant, one on shore as in Cuba and a few floating plants one mile seaward of the Point. We present data on five of Claude's subjects:

- "...the inevitably dirty walls of immense boilers,
- "the deep sea water...warming up...during its ascent,
- "...the pipe...lying all along its length...on the bottom of the sea...
- "...that terrible adversary, the sea, and
- "...the pressure of the submarine current."

Before reviewing these data, the Keahole site is described briefly.

KEAHOLE POINT

Keahole Point is on the west coast of the Island of Hawaii; latitude 19° 45' N, longitude 156° 05' W; see Figure 1. The land area was formed by a prominent lava flow. A 340 acre site has been dedicated to the Natural Energy Laboratory of Hawaii for development of OTEC and other energy concepts. A zone extending one mile into the sea, having a width of one-half mile has been reserved for research purposes. The data that follow pertain to this site.

BIOFOULING OF HEAT EXCHANGERS

The second successful OTEC plant will almost certainly be a closed cycle design, unlike Claude's open cycle. Thus it will utilize heat exchangers and be subject to "...the inevitable dirty walls." Figure 2

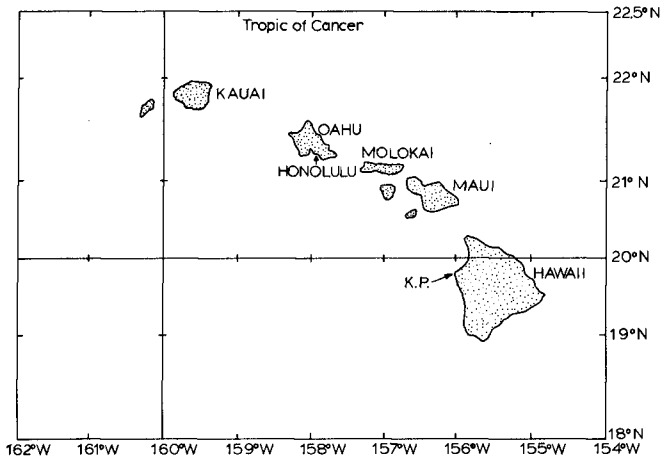


FIG. 1 LOCATION MAP OF HAWAIIAN ISLANDS

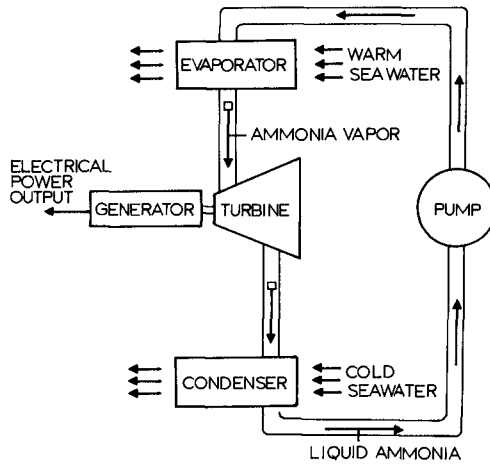


FIG. 2 OTEC CLOSED-CYCLE SYSTEM

describes the closed cycle system. In OTEC, the dirty walls are those exposed to sea water; the dirt is bacterial slime. The first field experiments probing this biofouling of heat exchangers were conducted at sea off Keahole. The primary results measure R_f , the resistance to heat transfer due to fouling, and also the effects of mechanical cleaning after fouling has reached significant levels.

Preliminary tests show that, after R_f has been allowed to grow 50 percent of clean tube resistance, moderate brushing will reduce R_f immediately to zero. After brushing, R_f grows back to the 50 percent level in approximately one month.

All recent experiments have been conducted *in situ*; small heat exchangers are positioned 300 m seaward of Keahole Point and 15 m below the surface. Tube materials and water flow velocities have been changed. No significant differences in the rate growth in R_f have been attributed to these two parameters. The experiments attempt to measure relatively small changes; the design maximum R_f may be in the order of 5 percent of clean tube resistance. A typical set of results is reported by Fetkovich, et al. (Fetkovich, 1977).

This problem will be common to OTEC plants ashore and afloat. A potential design is to control biofouling by brushing; the optimum brushing interval which will be measured in hours or days, cannot yet be predicted.

COLD WATER PIPE THERMAL DESIGN

An unpublished Master's thesis (Wong, 1978) shows that "the deep sea water...warming up...during its ascent" is not a problem for the floating plant at Keahole Point. For any reasonable floating plant pipe design and for power levels as low as 25 RW, the temperature rise of the deep sea water will be less than 1°F. This rise will decrease in magnitude at higher power levels.

The cold water ascending to an OTEC plant ashore may warm up by as much as 1°F. This would occur if the flow is slow or if the pipe diameter is small. Wong's study employed a characteristic temperature profile (Bathen, 1977) at Keahole Point, Figure 3, and the bottom profile (Noda, 1978), Figure 4. The normal current profile (after Merchant, 1975, and Bretschneider, 1978) is shown by curve A of Figures 5 and 6. Curves B and C include the Ekman wind driven current for wind speeds corresponding to Sea States 5 and 6 respectively. Curves D and E are design current profiles during hurricane conditions and are discussed later. The design current profiles were determined by Bretschneider (1978). He also showed that the annual variation in discharge temperature for a typical design would be less than 0.4°F. This estimate is due to changes in surface water temperatures; the inlet temperature is expected to remain more nearly constant.

A useful result of Wong's work is a relatively simple equation that predicts the rise in temperature with precision over a wide range of design variables. That equation is:

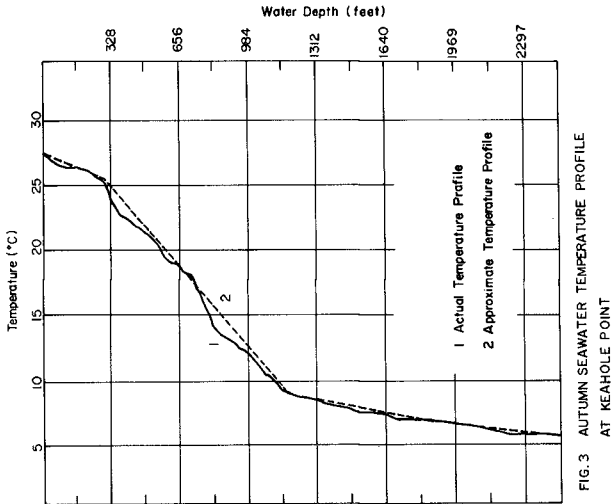


FIG. 3 AUTUMN SEAWATER TEMPERATURE PROFILE AT KEAHOLE POINT

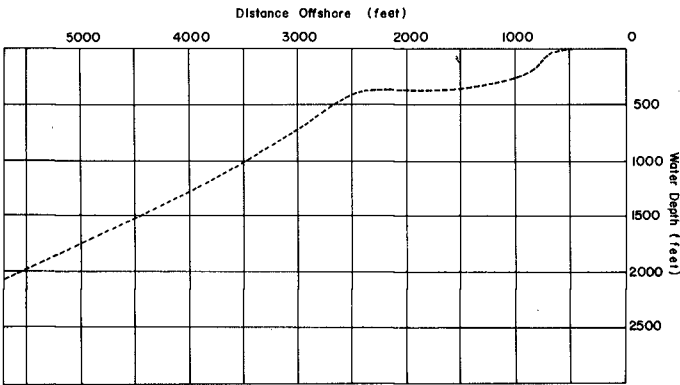
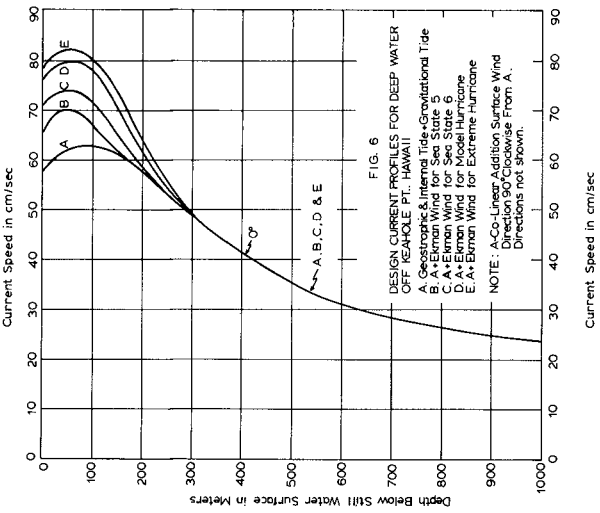
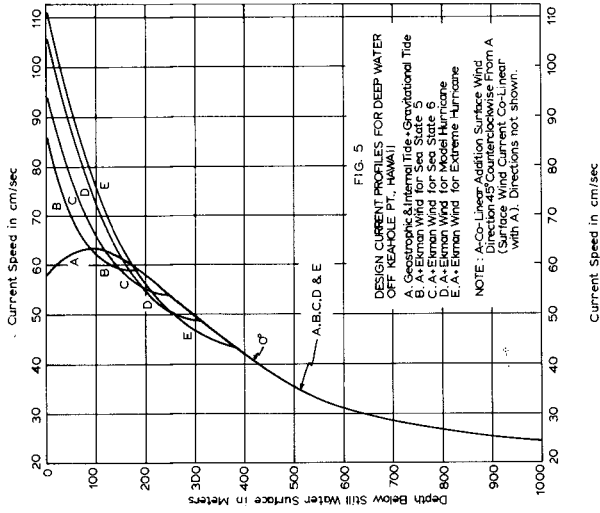


FIG. 4 BATHYMETRY PROFILE OFF KEAHOLE POINT IN A TRUE DIRECTION OF 175°



$$\Delta T = 3.57 \left[\frac{4}{\pi} \frac{\dot{Q} \ln (D_3/D_2)}{k} \right]^{-0.98}$$

In that equation:

- ΔT is temperature rise, °F;
- \dot{Q} is volumetric flow through the pipe, cubic feet per second;
- D_2, D_3 are inside and outside pipe diameters, feet;
- k is pipe wall conductivity, BTU/hour-foot-°F.

The equation holds for a bottom laid pipe extending one mile seaward of the point and for these ranges of the design variables:

- plastic and concrete pipes;
- nominal diameters from 1.0 to 8.0 feet;
- nominal flow velocities from 0.25 to 10.0 feet per second.

Wong's analysis shows a range of practical solutions to a specific design problem in which 3000 gallons per minute of deep sea water are required with a warming up during its ascent of 1°F or less.

THE BOTTOM PROFILE

"In matters of this kind there is no precedent...", said Claude. That statement still holds for many aspects of OTEC and particularly for the design of a large diameter pipe that reaches a mile to seaward and a half-mile down.

Claude wished for "the pipe lying all along its length on the bottom of the sea." Such a design could be attained at Keahole Point according to an unpublished survey (Noda, 1978). The slope on one possible pipe line path is shown in Figure 4.

This survey gives precise information about the bathymetry seaward of the point. It also gives the results of a visual survey by submarine along a probable pipeline path. The bottom is a smooth basalt slope, except for outcroppings at the 450 foot level, and channels through the outcrop.

EXTREME WAVE CONDITIONS FOR DESIGN

The design wave criteria can be obtained by a statistical analysis of recorded data, wave observation, or wave hindcasting. In a report, Rocheleau (1977) did a statistical analysis of U.S. Navy (SSMO data) Summary of Synoptic Meteorological Observations, and two sets of wave hindcasts of severe storms, one set of eleven storms from U.S. Army Corps

of Engineers (1968) and the other set of ten storms from Marine Advisors (1973). The statistical analysis of the hindcasts were based on four methods, and are discussed in another paper presented at the 1978 Coastal Engineering Conference by Bretschneider and Rocheleau (1978). Therefore, we will not go into the details.

Many potential OTEC plants will be located in the tropics, and where hurricanes occur, one will find that the design wave is of hurricane origin. Potential OTEC plants are considered for locations in the Gulf of Mexico, off Puerto Rico, and off Keahole Point, Hawaii, and in all cases are subjected to hurricanes. Figure 7 shows the paths of hurricanes and other tropical cyclones prior to 1925 (see Visher, 1925), and Figure 8 shows the paths of more recent hurricanes, all for the Hawaiian waters. The closest to Keahole Point seems to be Hurricane DOT, of August, 1959, the center of which was about 80 nautical miles to the southeast of the potential OTEC site. There is no reason to believe that some future hurricane will not come much closer to Keahole Point. Figure 9, from Bretschneider and Tamaye (1976), is based on the model hurricane of Bretschneider (1972a) using the hurricane parameters estimated from the hurricanes on record. This hurricane is estimated to be the one in one hundred year hurricane for the Keahole Point area. The design wave heights are also close to those obtained from the hindcast study of Rocheleau (1977) which includes two hurricanes.

It is believed that the model hurricane is an excellent means of obtaining the 100-year design hurricane waves. The model hurricane of Bretschneider (1972) was applied to all U.S. Weather Service standard project hurricanes for the Gulf of Mexico and the U.S. East Coast. The results of the maximum values of the significant waves were given in a report by Bretschneider (1972b). The model hurricane was applied to the parameters of Hurricane Camille, August 1969, as reported by Cardone, Pierson, and Ward (1976) three years after the model hurricane was published. It is of interest to note that the agreement between the measured wave heights and those of the model hurricane was quite good, particularly since the hurricane model was not calibrated by use of any hurricane data.

The parameters of Hurricane Camille, 1969, were: radius of maximum wind $R = 10$ nautical miles, forward speed $V_F = 10$ knots, central pressure from normal pressure $\Delta P = 3.1$ inches of mercury, and latitude $\phi = 29$ degrees. This corresponds to a medium size hurricane slightly greater than the standard project and slightly less than the probable maximum hurricane for the south coast of Louisiana, and the wave heights are comparable to those measured during Hurricane Camille. Thus the standard project and probable maximum hurricanes are also the basis of OTEC design criteria for the U.S. Gulf Coast and the U.S. East Coast. This then allows also a consistent method for comparing the Keahole Point OTEC hurricane design criteria with the other OTEC sites in the Gulf of Mexico and the east coast of U.S.A.

The design wind speed cannot be determined consistently from the statistical hindcasts of the waves, because the maximum wind is not

necessarily associated with the maximum significant wave height, which in general is also fetch dependent. However, the model hurricane does give the design wind speed in terms of the 10-minute 10-meter anemometer wind level. The design gust speed is taken as 1.45 times the 10-meter level. Thus the design hurricane wind speed occurs almost simultaneously with the design wave.

The 10-minute average wind speed was the basis for calculating the wind drift by use of the Ekman theory. However, the drag coefficient was modified by $\frac{1}{2}\sqrt{2}$ to take into account that the wind stress diagram through the maximum waves was considered to be represented by a triangular wind stress distribution.

There may be some criticism in determining the wind drift current in this manner, and perhaps the steady state Ekman transport equations do not really apply. Anyway, it will be difficult to measure the surface drift during a hurricane at the time of maximum wave generation.

It is interesting to note, however, that the Ekman wind drift current component in the direction of the design wave is very nearly equal to the wave mass transport velocity determined from the wave spectrum using Stokes second order theory for wave mass transport velocity. This is not true at all depths because the wave mass transport attenuates with depth somewhat more rapidly than the component of the Ekman wind drift in the direction of the wind.

The problem presently under investigation is to determine the proper resultant velocities, i.e. the coupling of the wave orbital velocities with the steady current profiles shown in Figures 5 and 6. The wave mass transport velocity is included in the Ekman wind drift by the very nature in which the wind stress and drag coefficients are determined. Therefore, one should subtract the wave spectrum mass transport velocity from the component of Ekman wind drift in the direction of the wind. If this is not done prior to coupling current and wave orbital velocities, too much wave mass transport in fact will be included. The wave mass transport velocity of the wave spectrum is less than that associated with the individual maximum design wave.

Along with the Keahole Point OTEC deep water facility, there will be shore-based facilities. In this case, the waves will break close to the coastline because the continental shelf is narrow and steep, as shown in Figure 4. The coastal facilities must be designed against the maximum breaking waves on the structure. There will be a slight increase in water depth near the coast due to storm surge and wave set-up, and these factors must be taken into account when selecting a particular shore-based facility. This includes the effect of wave refraction and the design depth should include the maximum tides.

Calculations were made by Rocheleau (1977) to obtain an estimate of the maximum run-up on the coast, and he found up to 16.5 feet above MLLW. This can only be preliminary design run-up until one determines the face and slope of the coastal protection for the shore-based facilities.

ACKNOWLEDGEMENTS

Some of the material and figures given in this paper were obtained from various reports prepared under U.S. Federal grants, including the Department of Energy (D.O.E.), the National Oceanographic and Atmospheric Administration (NOAA) Sea Grant Office, and the State of Hawaii.

REFERENCES

1. Bathen, K.H. (1977) "The Behavior of Nearshore Ocean Currents, Plankton Biology, Benthic Currents and Ocean Temperature to Depth of 2200 feet at a Potential OTEC Site off Keahole Point, Hawaii."
2. Bretschneider, C.L. (1972a) "A Non-Dimensional Stationary Hurricane Wave Model" Proc. Offshore Tech. Conf. Houston, OTC Paper No. 1517.
3. Bretschneider, C.L. (1972b) "Revisions to Hurricane Design Wave Practices" Proc. of the 13th Coastal Engineering Conf. Vancouver, Ch. 7, pp. 167-196, Pub. ASCE, N.Y.
4. Bretschneider, C.L. and E. Tamaye (1976) "Hurricane Wind and Wave Forecasting Technique" Proc. 15th Coastal Engineering Conf. Honolulu, Ch. 13, pp. 202-238, Pub. ASCE, N.Y.
5. Bretschneider, C.L. (1978) "Operational Sea State and Design Wave Criteria for Potential OTEC Sites" Proc. of an OTEC Workshop, Miami, Florida, U. of Miami (paper in press).
6. Bretschneider, C.L. and R. Rocheleau (1978) "An Evaluation of Extreme Wave Climate at Keahole Point, Hawaii" Proc. 1978 Conf. Coastal Engineering, Hamburg, Germany.
7. Cardone, V.J., W.J. Pierson and E.G. Ward (1975) "Hindcasting the Directional Spectra of Hurricane Generated Waves" Proc. Offshore Tech. Conf., Houston, OTC Paper No. 2332.
8. Claude, G. (1930) "Power from the Tropical Seas", Process Utilizing Difference Between Temperatures of Water at the Surface and at the Lower Depths--Expedients Employed in Locating and Submerging a Line of 6-Ft. Pipe a Mile and a Quarter in Length--Results with Experimental Plant--The Inventor's Predictions for the Future, Paris, France, December 1930.
9. Fetkovich, J.G., et al. (1977) "Studies of Biofouling in OTEC Plants" Proc. of the Second Ship Technology and Research Symposium, San Francisco, May 1977, the Society of Naval Architects and Marine Engineers, New York.
10. Merchant, R.J. (1975) "Application of Theoretical Techniques to Computation of Coastal Currents Effecting Proposed Ocean Thermal Energy Conversion Tests; Keahole Point, Hawaii, and Barbers Point, Oahu, Hawaii, Dept. of Ocean Engineering M.S. Plan B Paper, University of Hawaii (unpublished report).

11. Noda, E.K. (1977) "Site Selection Bathymetry Survey, Keahole Point, Hawaii," University of Hawaii Look Lab Report No. 78-43.
12. Rocheleau, R. (1977) "Evaluation of Extreme Wind and Wave Climate in Hawaii with Specific Applications to Keahole Point and the North Shore of Hawaii," University of Hawaii Look Lab Report No. 77-41.
13. Visher, S.S. (1925) TROPICAL CYCLONES OF THE PACIFIC, Bernice P. Bishop Museum Bull. No. 20, Kraus Reprint Co., New York (reprint 1971).
14. Wong, R.S. (1978) "A New Design Method to Determine the Total Temperature Change Between Suction and Discharge of a Fluid Flowing in a Pipeline." A Thesis submitted to the Graduate Division of the University of Hawaii in Partial Fulfillment of the Requirements for the Degree of Master Science in Mechanical Engineering, May 1978.

CHAPTER 161

EXPERIMENTAL STUDY ON SCALE EFFECT OF TIDAL MODEL

By

Haruo Higuchi*, Hideichi Yasuda** and Norio Hayakawa**

* Professor, Ehime University,
Matsuyama, Japan

** Research Engineer,
Chugoku Institute of Industrial Technology,
Kure, Japan

INTRODUCTION

The Seto Inland Sea is a national park of Japan whose complicated topography offers a much cherished scenic view. In recent years, however, it has been receiving increasing amount of both industrial and city sewage resulting in worsening of water pollution.

Investigation on the mass transport in near-shore region has been carried out by means of field observation, theoretical analyses, numerical analyses and hydraulic model studies by numerous researchers. One of the advantages of both numerical and hydraulic models is that the natural topography is modeled. Therefore simulations of diffusion have been made in various scales or under various parameters, and the mass transport mechanism have been studied. A hydraulic model reproduces the tidal level and volume transport on the basis of the Froudian law. The similarity of the velocity profile and diffusive phenomenon, however, is not guaranteed by this law on account, at least partly, of shortage of the field data. Among these phenomena tidal residual flow defined constant constituent in tidal current system is often observed in the hydraulic model, of which the existence is not so clear in the field, though it seems to play an important role on the large-scale diffusion.

In this paper, we present a comparative study of two hydraulic models of the Seto Inland Sea in order to better understand the effect of the scale effect of the hydraulic model. The larger model is built with scale ratio of 1 to 2000 and 1 to 159 in horizontal and vertical directions respectively (constructed by Chugoku Institute of Industrial Technology in 1974). The smaller model has scale ratio of 1 to 50000 and 1 to 500 in horizontal and vertical directions respectively (constructed by Disaster Prevention Research Institute, Kyoto University, in 1975). The experimental data of this comparative study are concerned with tides, tidal current and diffusions.

DESCRIPTION OF TWO MODELS

The both hydraulic models are mortared and the generating force of fluid motions is only tide propagated from the open ocean. In Fig. 1 is shown a plan view of the larger model which has three tide generators (Ref. 1). Fig. 2 shows a plan view of the smaller model which has only one tide generator producing the tide of Kii and Bungo channels. There is no tide generator at Kanmon strait in this model because the volume transport through this strait is very small compared with the

other two openings. Table 1 shows scale ratios of hydraulic factors in both models. The hydraulic factors except horizontal length and depth are based on the Froudian law. The hydraulic factors except horizontal length and depth are based on the Froudian law. The model tide we used was the semi-diurnal M_2 tide, which is a dominant constituent in the Seto Inland Sea. By the way, hydraulic values in this paper is expressed by prototype value.

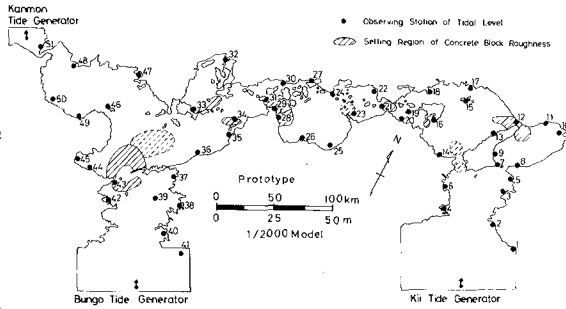


Fig. 1. Plan view of the larger model

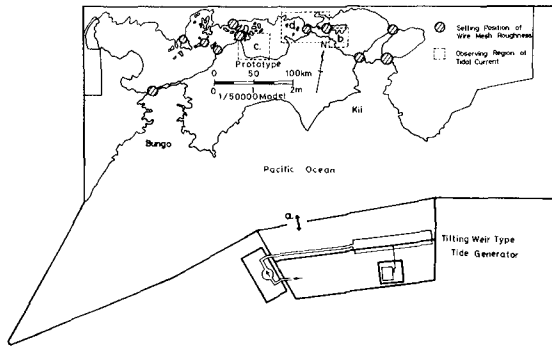


Fig. 2. Plan view of the smaller model

EXPERIMENTAL RESULTS

At first, adjustment of both models was done verifying amplitude and phase of tides at Kii and Bungo channels. Amplitude in the central region is twice as large as that in the open boundary in the prototype. Both models showed the tendency of producing greater tidal amplitude first. The difference has been corrected placing concrete blocks of various sizes in the larger model and wire mesh in the smaller model around the narrow straits.²⁾ Fig. 3 shows the distribution of the amplitude of M_2 constituent obtained by harmonic analyses. A solid line shows a distribution of prototype values. In this figure, filled circles and open circles show a distribution of the tidal ranges without roughness and with roughness respectively. Exaggerated roughness around narrow straits

Hydraulic factors	1/2000 model	1/50000 model	Ratio
Horizontal length	1/2000	1/50000	1/25
Depth	1/159	1/500	1/3.1
Period	1/159	1/2236	1/14.2
Horizontal velocity	1/12.6	1/22.4	1/1.8
Horizontal diffusivity	$1/2.5 \times 10^4$	$1/11.2 \times 10^5$	1/44.8
Discharge	$1/4 \times 10^6$	$1/1.56 \times 10^9$	1/140

Table 1. Hydraulic factors in both models

is so effective that it leads to the correct tidal range in the region away from the ocean as shown in this figure. M_2 -phase in the models agreed with that in the prototype which lags as much as 150 degrees in central region compared with the open boundary.

With the verified models, tidal current was measured. Floats on the sea surface were photographed and loci of their movement in the smaller model are shown in Fig. 4. From this figure the Seto Inland Sea can be classified into two areas. Area I is bays and sounds, which have a weak tidal current with a relatively strong residual component. And area II is narrows and straits, which is dominated by strong oscillatory current. In Fig 5 is shown distribution of the tidal residual circulation in both models so as to understand the outline of area I. The two patterns resemble each other but the smaller model has about twice stronger velocity of circulation than the larger one.

In order to investigate the tidal current in detail, we analyzed the tidal current distribution in the Eulerian manner at the b-region and the c-region in Fig. 2 which are representatives of area I and area II respectively. Values of tidal current were obtained at each fixed station by following numerous floats and the data was analyzed by harmonic method. Fig. 6 shows the amplitude of M_2 -component in the b-region. Direction of M_2 -current is about the same in both models, whereas larger amplitudes are recognized in the smaller model. Fig. 7 shows phase lag distribution of M_2 -component. Phase lag gradient in this region is steeper in the smaller model. In Fig. 8 is shown the Eulerian constant component called the tidal residual flow in tidal hydraulic model. In both models appear large circulations with the

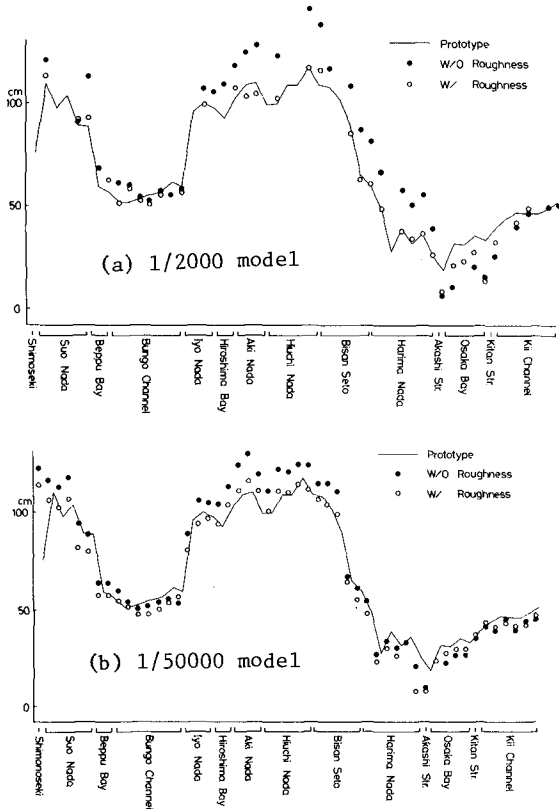


Fig. 3. Distribution of M_2 -amplitude of tidal range

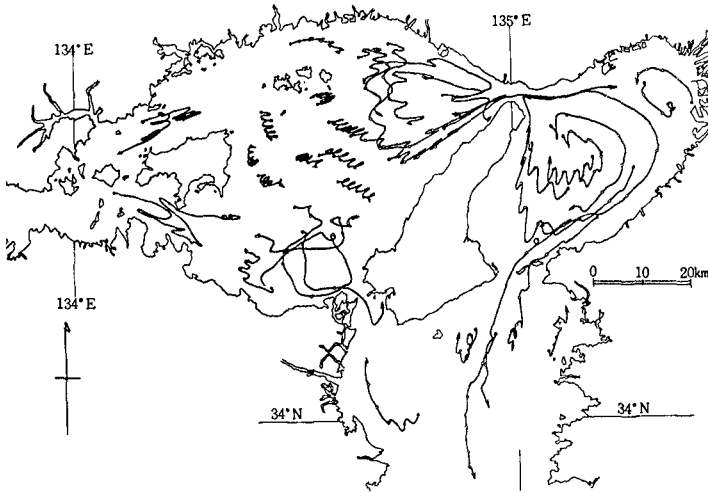
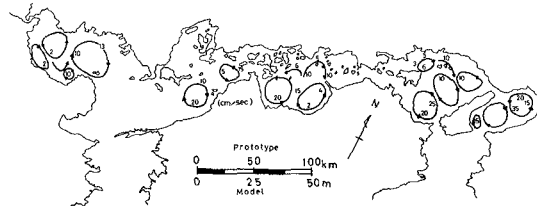
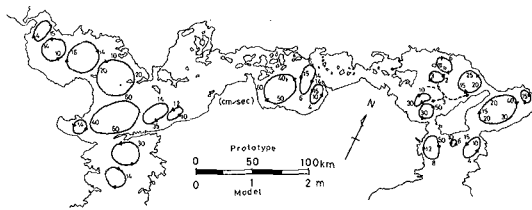


Fig. 4. Tidal loci for 5 cycles in the eastern part (1/50000 model)

same rotation; magnitude of the residual flow is about ten times larger in the small model. Though this measurement was done in the condition of verified tides in both models, M_2 -amplitude of tidal current is larger in the smaller model. This is considered that the stronger current was compensated by steepness of phase lag gradient and the volume transport agreed with each other. Steeper gradient of the phase lag and tidal residual circulation in the small model result in the stronger shear of flow. Fig. 9 shows time changes of the circulations calculated along that circuit. Circulation in this figure is divided by the area involved in the integral circuit; this is equivalent to the mean value of vorticity in the circuit. A circulation represents shear of flow and its peak and mean value is larger in the smaller model. In the c-region, the tidal residual circulation, which have not been clearly observed in prototype, can be found with the



(a) 1/2000 model



(b) 1/50000 model

Fig. 5. Distribution of tidal residual circulation

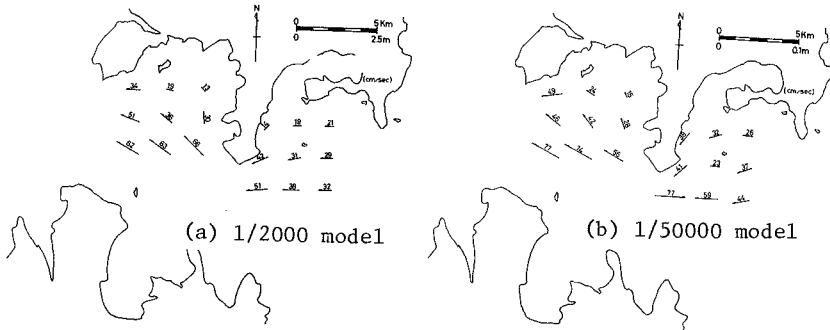


Fig. 6. M_2 -amplitude of tidal current

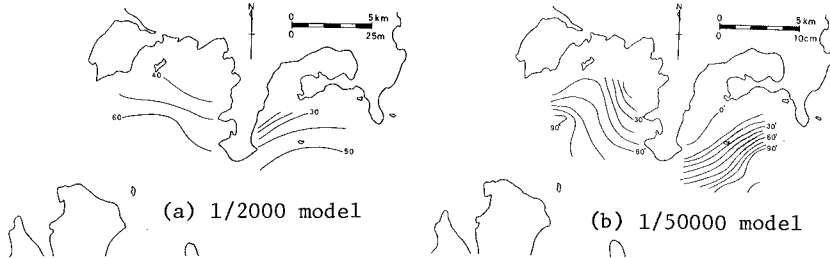


Fig. 7. M_2 -phase lag of tidal current

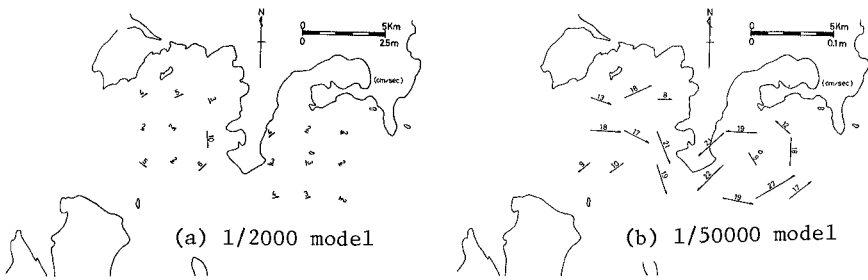


Fig. 8. Eulerian constant flow

strong and same rotation in both models. The tidal residual flows having a constant direction over long periods at each station have much effects on mass transport in the coastal region and strongly affect the diffusion experiment in hydraulic models. However, the similarity, that is, the generating mechanism of the flow have not been made clear yet. In this paper, since it is said that the tidal residual flow is generated by the non-linearity of the oscillatory component,³⁾ we have compared the tidal residual component and M_2 component between both models. Fig. 10 shows vectors of the tidal residual flow which forms the circulation with counter-clockwise rotation in both models. Nevertheless, the vectors and the diameter

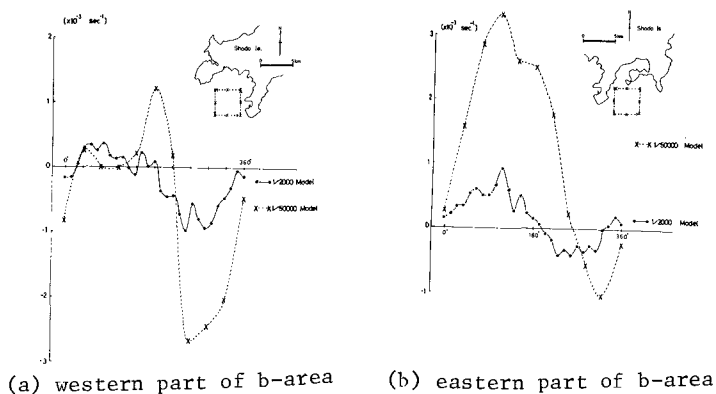


Fig. 9. Time change of circulation

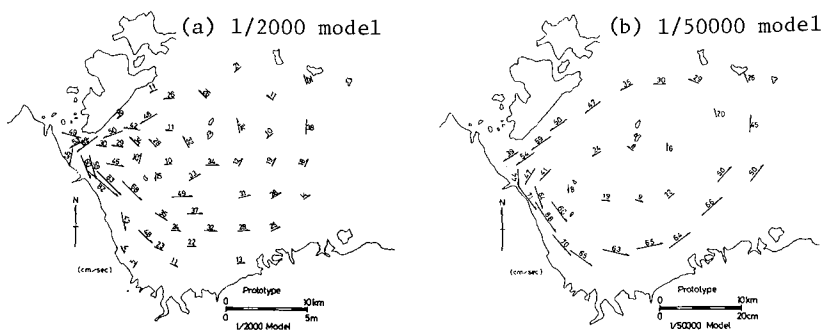
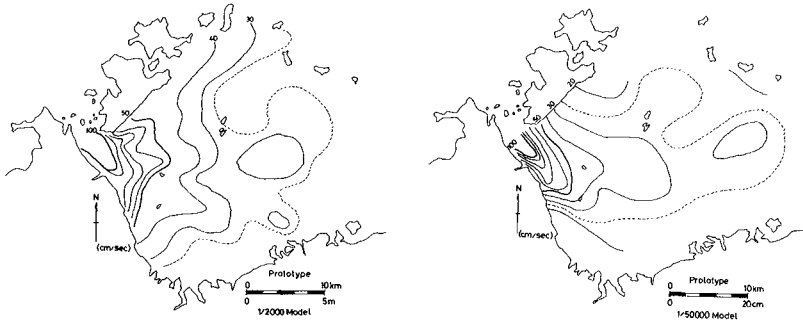


Fig. 10. Eulerian constant flow

of the circulation are larger in the smaller model. The distribution of M_2 -amplitude of major axis is shown in Fig. 11. Fig. 12 shows the distribution of the M_2 phase lag. Studying these figures, equi-amplitude line near the strait is biased more widely in the smaller model and equi-phase-lag lines run parallel to the tidal residual flow and the phase difference is larger in the smaller model. We can recognize that the biased equi-amplitude line and the phase difference substantiate the tidal residual flow.

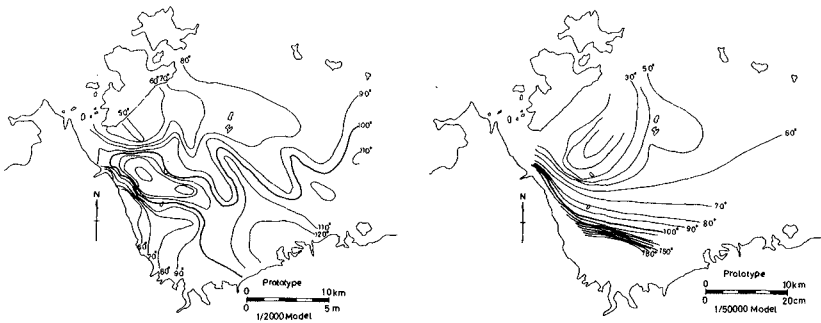
Diffusion experiment is conducted in the area-d of Fig. 2, where we can treat diffusion phenomenon as one-dimensional mass transport phenomenon. Fig. 13 shows distribution of dye concentration after ten cycles released instantaneously at Mizushima in the larger model. Solution of dye spreads diluting by degrees in the area-d called Bisan-Seto, where concentration is nearly homogeneous transversely and we can treat diffusion phenomenon as one-dimensional mass trans-



(a) 1/2000 model

(b) 1/50000 model

Fig. 11. Distribution of M_2 -amplitude of tidal current



(a) 1/2000 model

(b) 1/50000 model

Fig. 12. Distribution of M_2 -phase lag of tidal current

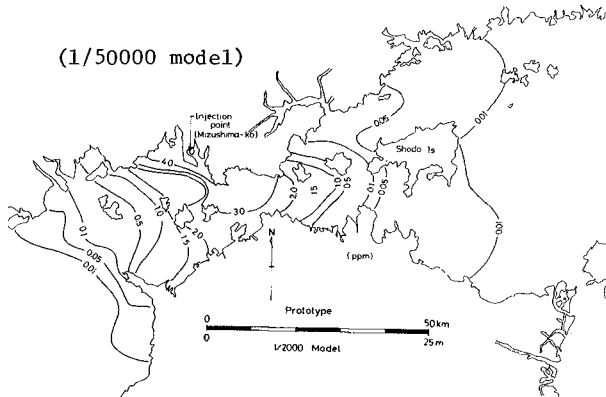


Fig. 13. Distribution of dye concentration after 10 cycles

port phenomenon. Comparative experiment of diffusion was carried out with use of many floats on water surface.

In Fig. 14 is shown time change of longitudinal variance of floats released instantaneously at the Mizushima sound in both models, where ●...● shows the case of floats in the smaller model, ○...○ floats in the larger model and △...△ dye in the larger one. Slope of these lines indicates the magnitude of diffusion and the coefficient of dispersion

are $0.75 \sim 1.3 \times 10^7 \text{ cm}^2/\text{sec}$, $1.3 \times 10^6 \text{ cm}^2/\text{sec}$ and $1.1 \sim 0.5 \times 10^6 \text{ cm}^2/\text{sec}$ in turn. From this figure, difference of the dispersion coefficient between floats and dye is not significant in the larger model. This suggests that dispersive power in this region is not given by vertical shear but by horizontal shear. Coefficient of one-dimensional diffusion in the smaller model is about ten times larger than that in the larger model. In order to study this difference, we obtained the diffusion-coefficient by means of following the motion of ten floats for one tidal cycle in area-b where we had measured Eulerian tidal flow. Tidal loci for one tidal cycle in this region are shown in Fig. 15. This shows that tidal vortex is stronger in the smaller model such as showing in Fig. 9. Table 2 indicates the process for diffusion coefficient with data of the initial variance and the variance after one tidal cycle. The variance σ_λ^2 was given as

$$\sigma_\lambda^2 = (\sigma_x^2 \sigma_y^2 - \sigma_{xy}^2)^{\frac{1}{2}}$$

where σ_y^2 corresponds to the value of latitude direction, σ_x^2 the value of longitude direction and σ_{xy}^2 is covariance. The scale of diffusion

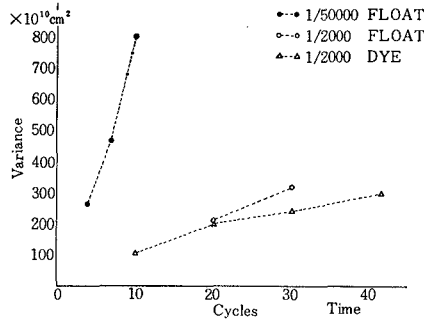


Fig. 14. Comparison of longitudinal variance between two models

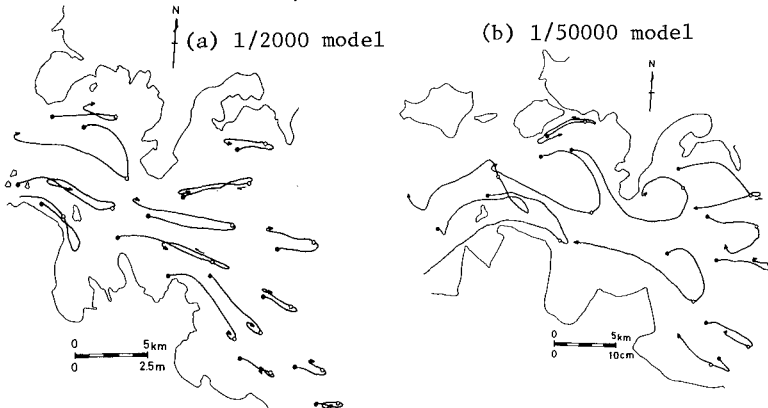


Fig. 15. Comparison of tidal loci between two models

	Initial Variance	Variance after one tidal cycle	Coefficient of Diffusion	Substantial Value of circulation
1/50000 Model	$1.75 \times 10^{10} \text{cm}^2$	$16.09 \times 10^{10} \text{cm}^2$	$32.1 \times 10^2 \text{cm}^2/\text{sec}$	$1.69 \times 10^{-3} \text{sec}^{-1}$
1/2000 Model	$2.36 \times 10^{10} \text{cm}^2$	$4.64 \times 10^{10} \text{cm}^2$	$5.15 \times 10^2 \text{cm}^2/\text{sec}$	$0.43 \times 10^{-3} \text{sec}^{-1}$

Table 2. Comparison of floats spreading speed between two models is the length of a tidal excursion or thereabouts. The last column shows averaged values of absolute circulations over one tidal cycle. This difference in both models corresponds to the diffusion coefficient's K_A that is obtained as follows,

$$K_A = \frac{1}{2} \cdot \frac{\sigma_{\lambda_2}^2 - \sigma_{\lambda_1}^2}{\Delta T}$$

where $\sigma_{\lambda_1}^2$ is the initial variance and $\sigma_{\lambda_2}^2$ is the variance after one tidal cycle; ΔT is the tidal period. This table suggest that horizontal shear of flow contributes to the diffusive effect of relatively large scale.

CONCLUSION

Without exaggerated roughness, both models showed the tendency of producing greater tidal ranges than the corresponding prototype values in the region away from the ocean. Exaggerated roughness around narrow straits has corrected wrong tidal ranges. From the results of comparative experiment with the verified models, we could recognize that the smaller model had following characteristics.

- (1) Oscillatory amplitude of tidal current and phase difference are larger.
- (2) Circulation (vorticity) is larger.
- (3) Constant flow (tidal residual flow) is larger.
- (4) Diffusion coefficient of large scale is larger.

Similarity of friction in hydraulic models has ever been considered only for bottom friction (Higuchi and Sugimoto,⁴ 1968 et al). But in the Seto Inland Sea having very complicated topography, effective friction may be due not only to bottom but to horizontal eddy viscosity which affects the form resistance. The larger the Reynolds number is, generally the smaller this form resistance is and the stronger the shear is. These explain that the separation of tidal flow is stronger in the smaller model and the smaller one has smaller horizontal viscosity due to turbulence, that is, the substantial turbulent Reynolds number affecting the flow pattern is relatively larger in it.

The smaller model is so small as showing Fig. 2 that we could not compare horizontally isotropic diffusion. Therefore we made the experiment of large scale diffusion called dispersion. Experimental result (2) and (4) shows that large scale diffusion is very influenced by horizontal local shear of tidal current velocity.

Though scale effect could not be induced as the numerical value,

it is suggested by those results that similarity of the tidal hydraulic model such as the Seto Inland Sea having complicated topography must be verified by not small scale phenomena hitherto done but large one covering a whole bay.

ACKNOWLEDGEMENTS

The authors wish to express their sincere thanks to Prof. C. Nakajima, Disaster Prevention Research Institute, Kyoto University, for his accommodations and encouragement. They also thank Mr. Y. Kitagawa, Disaster Prevention Research Institute, Kyoto University, and Mr. H. Takeoka, Ehime University, for their assistances in the experiment. Thanks are extended to Mr. Y. Takasugi, Chugoku Institute of Industrial Technology, for his assistances in the data analysis.

REFERENCES

- (1) N. Hayakawa, T. Higo, H. Tanabe, Y. Takasugi and M. Takarada; Multi-Phased Model Study of the Seto Inland Sea, Modelling 75, Symposium Proc., ASCE, 1975.
- (2) H. Higuchi, H. Yasuda and N. Hayakawa; Experimental Studies of Scale Effects on the Models of the Seto Inland Sea, Rept. Disaster Prevention Res. Inst., Vol. 19-B, 1976 (in Japanese).
- (3) H. Higuchi and T. Yanagi; Fundamental Study on the Tidal Residual Flow, Proc. of 22th Conf. on Coastal Eng. of JSCE, Nov. 1975 (in Japanese).
- (4) H. Higuchi and T. Sugimoto; Hydraulic Model Experiments on the diffusion due to tidal current (II), Rept. Disaster Prevention Res. Inst., Vol. 11-B, 1968 (in Japanese).

CHAPTER 162

A TIDAL SURVEY FOR A MODEL OF AN OFFSHORE AREA

W. J. van de Ree,¹ J. Voogt¹ and J. J. Leendertse²

INTRODUCTION

In support of engineering and environmental investigations for the construction of a storm surge barrier in the southwestern part of the Netherlands (Fig. 1), numerical models are being used. For one of these models, the so-called Randdelta II model, an extensive field survey was made of tides and currents to establish the boundary conditions and to adjust and verify the model. A description of this model and its adjustment procedures are presented elsewhere in these proceedings [1].

The survey was made in the period of August 25 to September 24, 1975. Since not all instruments could be installed and recovered simultaneously, the simultaneous observation period was effectively about 16 days.

A number of permanent water level recording stations are operated by the governments of the Netherlands and Belgium, and the data from these records could easily be obtained. In addition to these permanent stations, gauges were installed in many harbors and other suitable locations on the estuaries, and a total of 32 water level records of on-shore tide gauges was available for analysis. The reference levels of all these on-shore stations were determined by leveling to known benchmarks.

In addition to the on-shore stations, water level recorders were operational on instrument platforms constructed in preceding years in waters up to 10m in depth. These platforms or towers generally also contain instrumentation for wave and wind recording. The locations of these offshore stations are also shown in Fig. 1.

Along the location of the boundary of the model, bottom pressures were measured simultaneously with currents. The bottom pressures were recorded by a relatively simple instrument which punches a slowly-moving paper tape every half hour. The deviation of the mark on the tape from the ordinate on the tape is a measure of the bottom pressure. The accuracy of the readings from the tape is estimated at 2 or 3 cm water level variation.

In the model, the boundaries at the seaward side could best be described by water levels. Since the model covers, in addition to the Eastern and Western Scheldt, a section of the North Sea, the flow conditions in the major part of the model are predominately determined by the boundaries at the seaward sides of the model, and consequently the water levels

¹ Rijkswaterstaat, Delta Service, The Netherlands

² The Rand Corporation, Santa Monica, California, U.S.A.

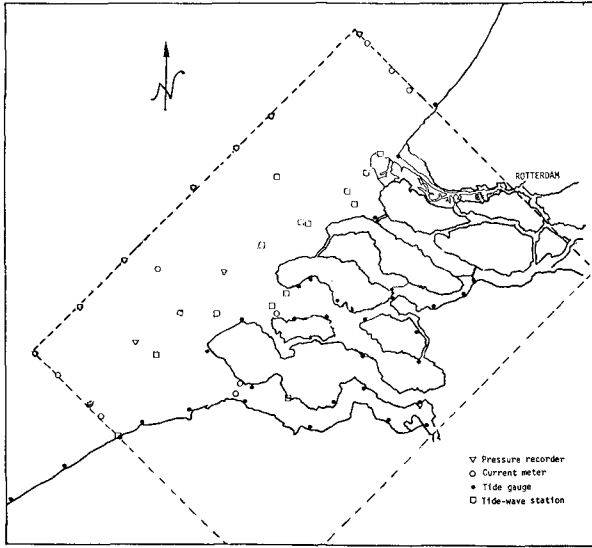


Fig. 1--Layout of models and locations of recording stations

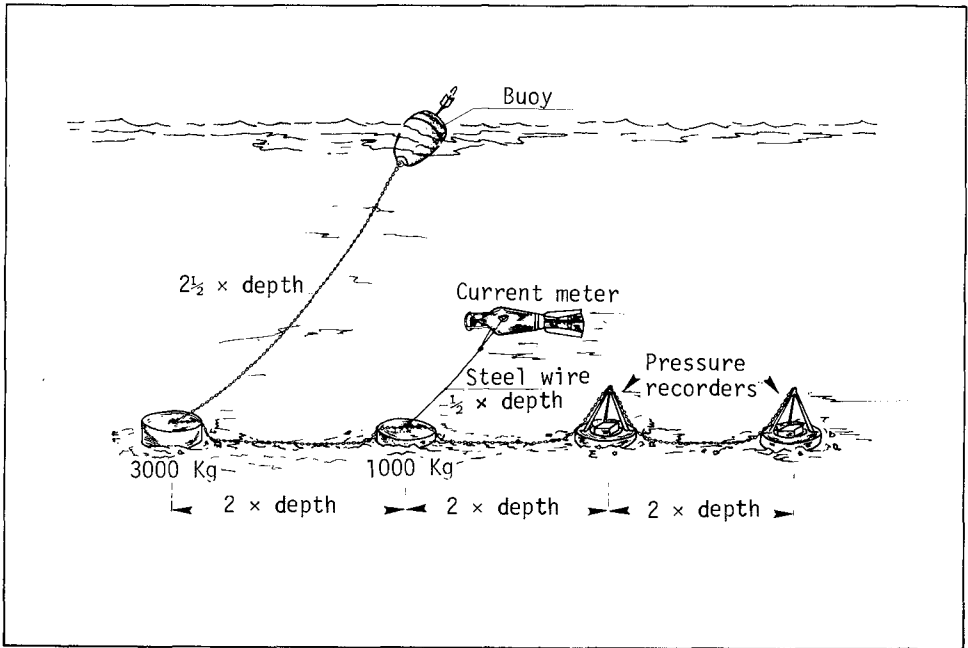


Fig. 2--Instrumentation for current and pressure recording

had to be determined with considerable accuracy and data had to be available at many points on the boundary.

In view of the importance of accurate water level data on the boundary, most stations on the boundary were equipped with two pressure recorders. A typical schematic of the instrumentation layout is shown in Fig. 2. In addition to the stations on the boundary, similar stations were situated inside the model area. Since most stations are located in waters where there is much fishing activity, heavy concrete blocks were used to retain the instruments in place. Even with these precautions, one of the interior stations was moved about a mile! The approaches to two of the largest ports in the world are in the survey area, consequently the location of the stations on the seaward boundaries was limited to areas outside the main fairways, and only a limited number of stations could be installed. Because of all the traffic and the fisheries in the survey area, all stations had to be marked by buoys.

Not all pressure recorders were working satisfactorily during the survey period, but at least one pressure recorder was working satisfactorily at each station.

Current data was recorded by a "Flachsee" current meter at a number of stations in the model area, as indicated in Fig. 1. Because of the large size of these instruments and the method of installation, the recordings were relatively free of noise and were indicative of the average velocity in a vertical water column.

To determine the total tidal flow into the estuaries, current surveys were also made in ranges across the inlets over periods of about 14 hours.

In view of the importance of the pressure data obtained at the boundary of the model area for the studies, much emphasis was given to the analysis of this data, and in the following sections of this paper a description will be given of this analysis.

ESTIMATION OF THE ACCURACY OF THE PRESSURE RECORDERS

The analysis of the bottom pressure recorders presented most of the problems, as the recorded data is pressure data, while water level data is required for the model. Consequently, the records had to be corrected for atmospheric pressure differences, temperature and salinity. In addition, it could be expected that the instruments would settle. To analyze the performance of these pressure recorders, a detailed analysis was made of the records of two recorders at a particular station near the middle of the long open boundary.

In Fig. 3 the water level histories for the two recorders for the period of September 2 through September 5, 1975 are plotted. In this figure the corrections for barometric pressure, temperature and salinity were made, thus the difference between the plotted points is indicative of

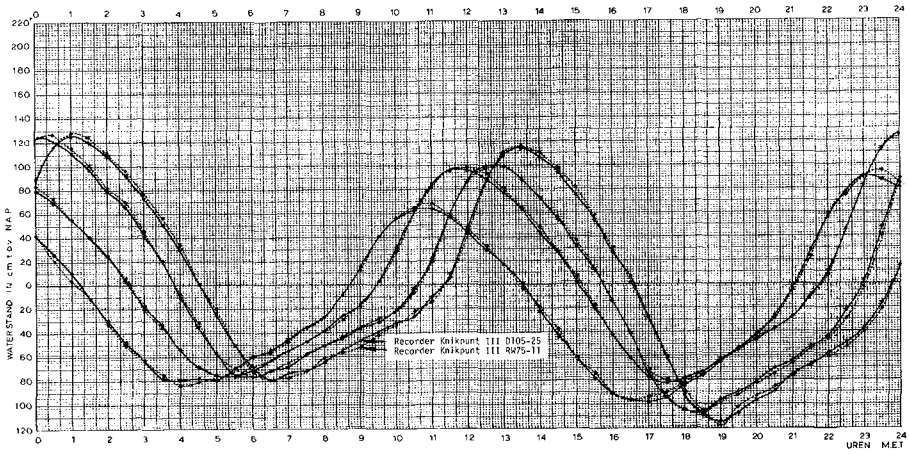


Fig. 3--Comparison of observed water levels obtained from two adjacent bottom pressure recorders for the period September 2-5, 1975

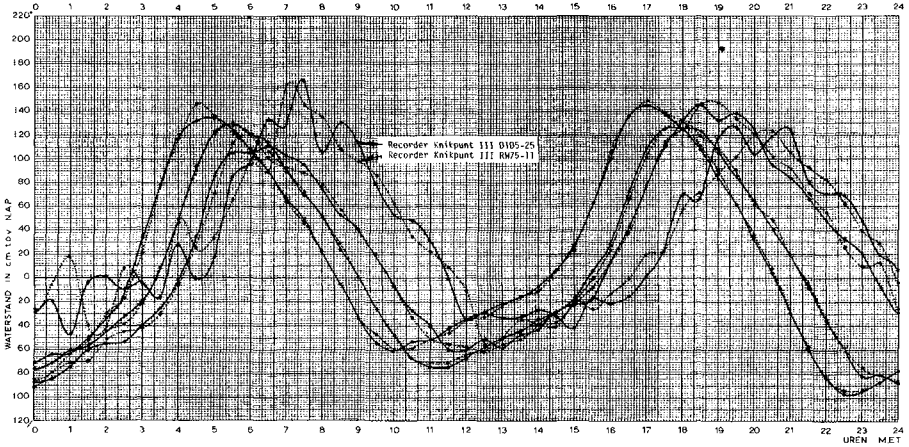


Fig. 4--Comparison of observed water levels obtained from two adjacent bottom pressure recorders for the period September 10-13, 1975, in which much wave action was present

the accuracy of the observations, the rate of settling and the influence of swell. The solid and dashed tide lines are smooth lines drawn through the points.

Figure 4 presents the same tide levels, but for a period with very heavy wave action. It will be noted that there are large differences between the two observations.

To gain more insight into the behavior of these two time series and their relative behavior, a cross-spectral analysis was made of the raw data for a 500-hour period. This period covered neap tides and a spring tide, as shown in the pressure record of one of the stations (Fig. 5). The computed spectra for one of the stations (Fig. 6) shows peaks for semi-diurnal tide and the overtides (M_4 , M_6 , M_8 , M_{10}). The coherency between the time series appears to be nearly one only for the diurnal and semi-diurnal tide components, as shown in the graph of the squared coherency in Fig. 7. The M_4 and M_6 tidal frequencies appear to be still strongly correlated, and the M_8 tidal frequency shows some coherency. Components with frequencies higher than 0.4 cycles per hour are essentially uncorrelated.

The amplitude of the frequency response (Fig. 8) appears to be approximately 0.92 in the low frequency range from zero to 0.2 cycles per hour. This value reflects the difference in the lower sensitivity of the second instrument, for which no correction was made as the raw data was processed. For higher frequencies the response function drops rapidly. The phase lag between the two time series is practically zero in the low frequencies (Fig. 9). In the higher frequencies an apparent lag is present.

Since the period of analysis contained a storm period in the latter part of the time series (Fig. 5), the same analysis was made for a period of 372 hours (15.5 days). In this analysis a high coherency was obtained over a larger range of frequencies, as can be seen by comparing Fig. 7 with Fig. 10. Even in the frequency band of the M_{10} tidal component the squared coherency is 0.8, and is thus quite well correlated.

The phase of the frequency response is near zero, as we would expect for two observations made close to each other (Fig. 11). The phase lag in the higher frequencies in the response function for the 500-hour records was apparently generated by swells and aliased into the frequency range of 0.5 to 1.0 cycles per hour (Fig. 9).

Since the response function obtained by cross-spectral analysis is an optimal estimate of the linear relationship between the two time series, the response function can be used for estimating the difference between them. This estimate is made by first deriving the impulse response function from the frequency response function and subsequent convolution of the first series, as described in Ref. 2. In contrast with the description in this reference, we used an impulse function with positive and negative time. The results of the convolution are shown, together

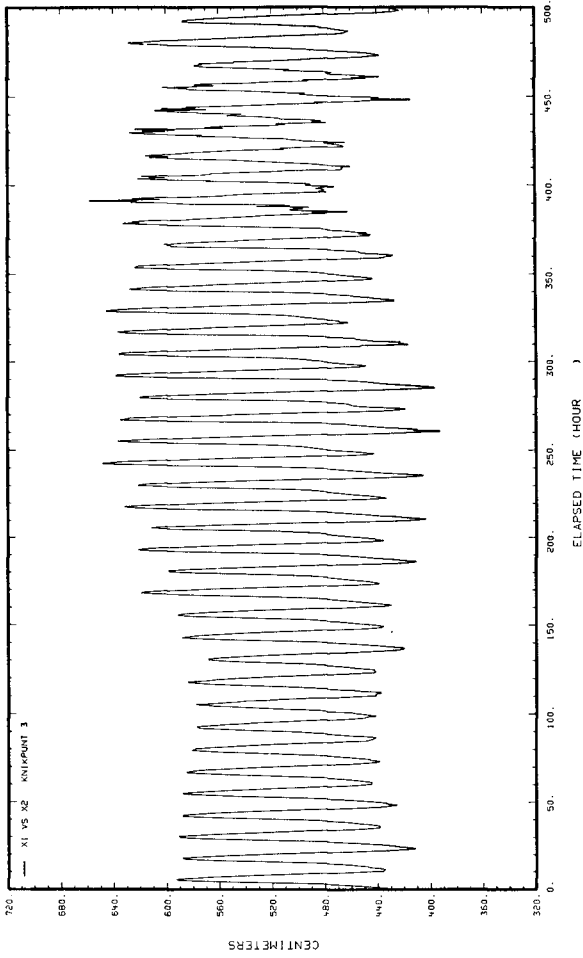


Fig. 5--Tide data from Knikpunt III used for cross-spectral analysis

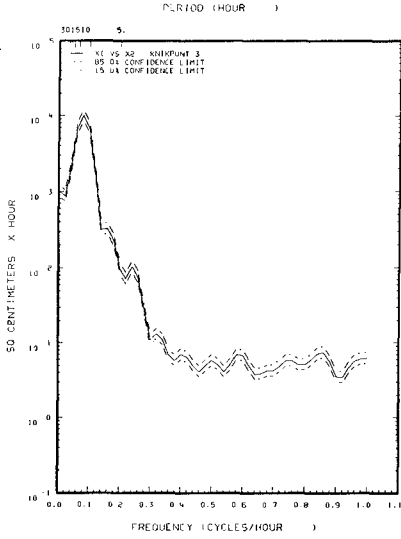


Fig. 6--Power spectrum of one of the pressure recorders at Knikpunt III

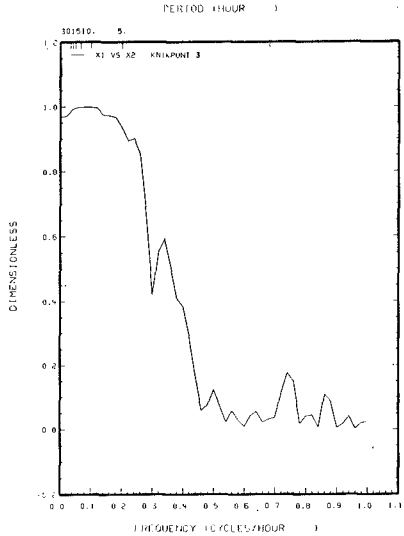


Fig. 7--Squared coherency between the pressure recorders at Knikpunt III

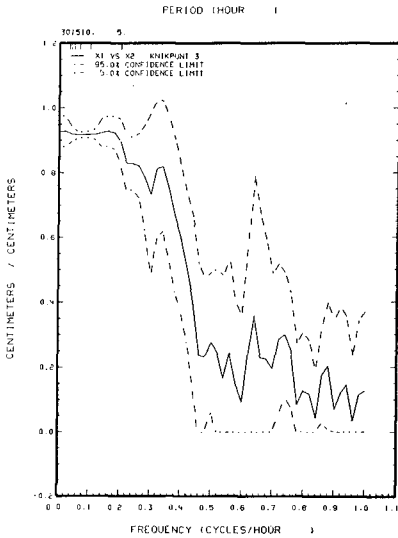


Fig. 8--Amplitude of the frequency response function between the pressure recorders at Knikpunt III, with confidence limits

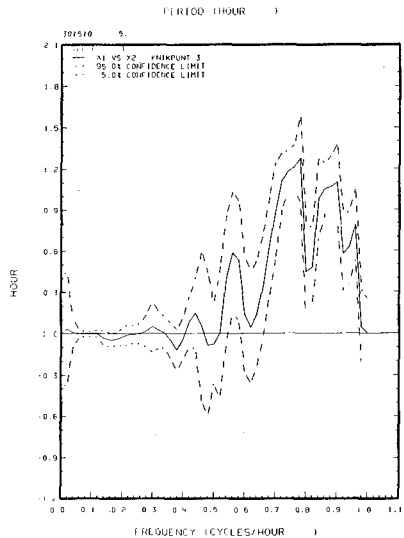


Fig. 9--Phase of the frequency response function between the pressure recorders at Knikpunt III with confidence limits

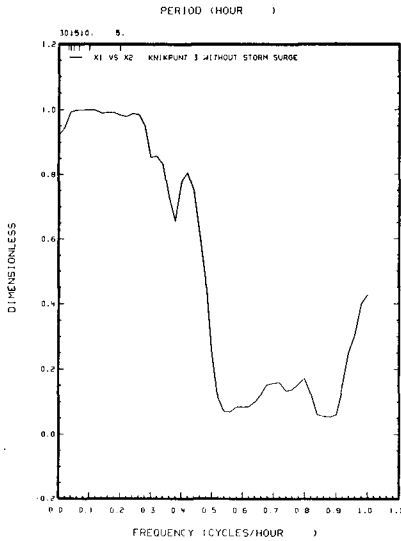


Fig. 10--Squared coherency between the pressure recorders at Knikpunt III for the recording period without the storm

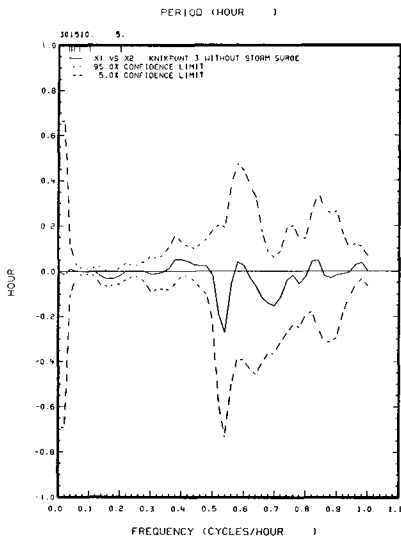


Fig. 11--Phase of the frequency response function between the pressure recorders at Knikpunt III with confidence limits for the recording period without the storm (15.5 days)

with the measured data, in Fig. 12. The differences are small and are plotted in Fig. 13. The standard deviation between the convolved series and the observed series appears to be 3.5 cm.

The difference between these series reflects reading errors, instrument errors and differentials in the rate of settling of the instruments. For the whole series of 500 hours, thus including the storm period, a similar analysis for the difference between the convolved and observed series appeared to be 5.8 cm. From this it was concluded that it would be most advantageous to use only the shorter series of 372 hours (15.5 days) in determining input conditions for the model.

ANALYSIS OF BOTTOM PRESSURE RECORDER DATA

After reading the data from the paper tapes of the instruments, a number of data processing steps were required to achieve water level estimates which could be used for the model study. Most of the processing could be done by computer.

In the first step, the recorded data was corrected for atmospheric pressure, salinity and temperature. Atmospheric pressure data was available from a nearby weather station, and for every half-hourly record the same air pressure correction was made in all records. Salinity and temperatures were measured regularly near the bottom pressure recording stations, and as this data was only very slowly varying, no large errors could be expected to originate from these density differences. The height of the salt water column at the gauge was computed from the readings on tape by:

$$Y_t = \left\{ 10.19(p_o - p_t) + a_o X_t + 35.3(T_t - T_o) \right\} / 1.024$$

where p_o = pressure at time of installation (millibars)

p_t = pressure at recording time t

a_o = instrument constant found by calibration

X_t = reading in 0.1 mm

T_t = sea water temperature at time of recording (Centigrade)

T_o = sea water temperature at time of installation

The constant 10.19 transfers millibars into mm of fresh water and the constant 1.024 represents the average density of sea water during the recording period.

Since the bottom pressure recorders were installed on the sea floor, settling could be expected. To investigate this settling, all data was filtered by taking running averages over a 24.5-hour period. This filter eliminates quite effectively the diurnal and semidiurnal tides without much loss of data at the end of the records. The filtered data for a number of recorders is shown in Fig. 14. By comparing these

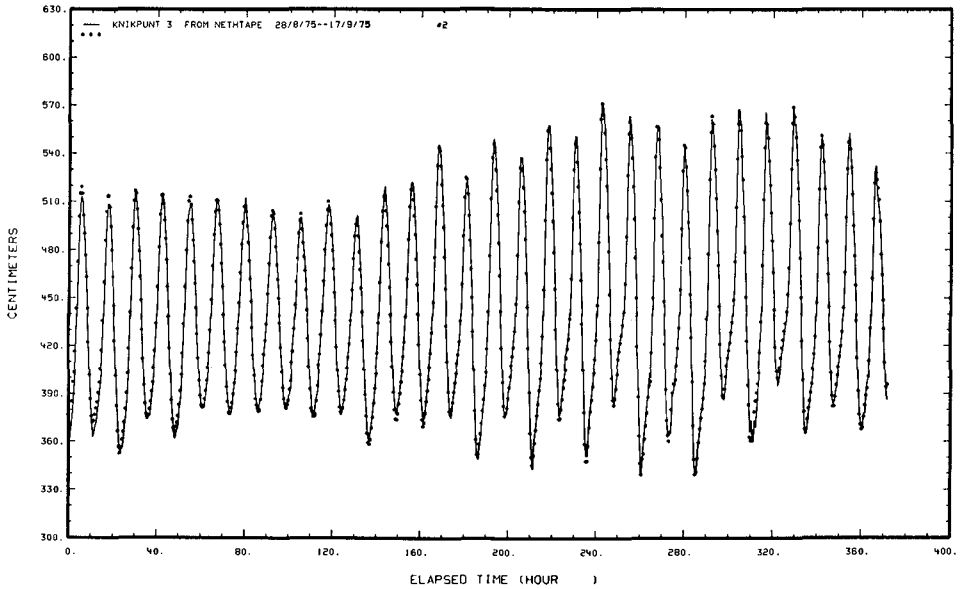


Fig. 12--Comparison between the observed time series and the convolved time series of bottom pressure from the other pressure recorder

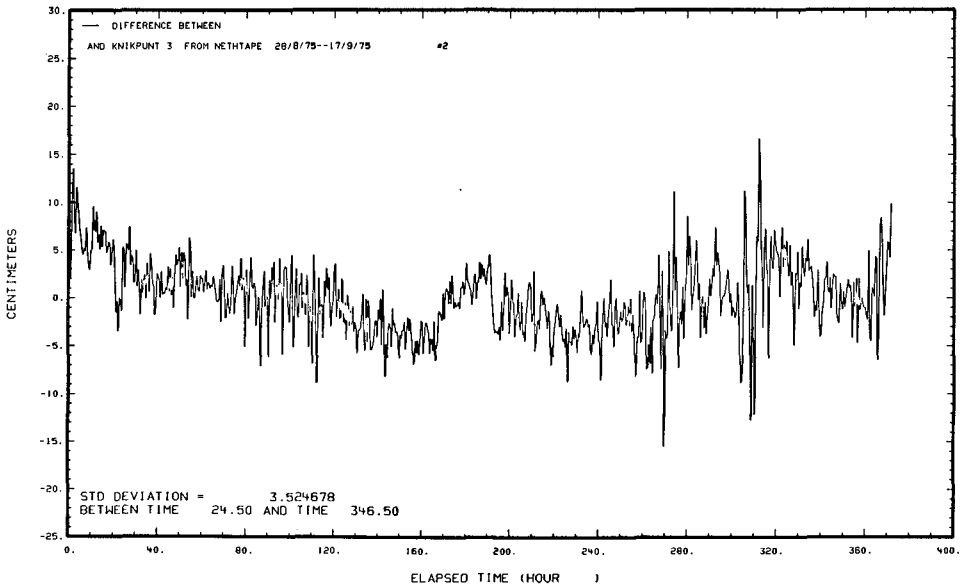


Fig. 13--Difference between the observed time series and the convolved time series

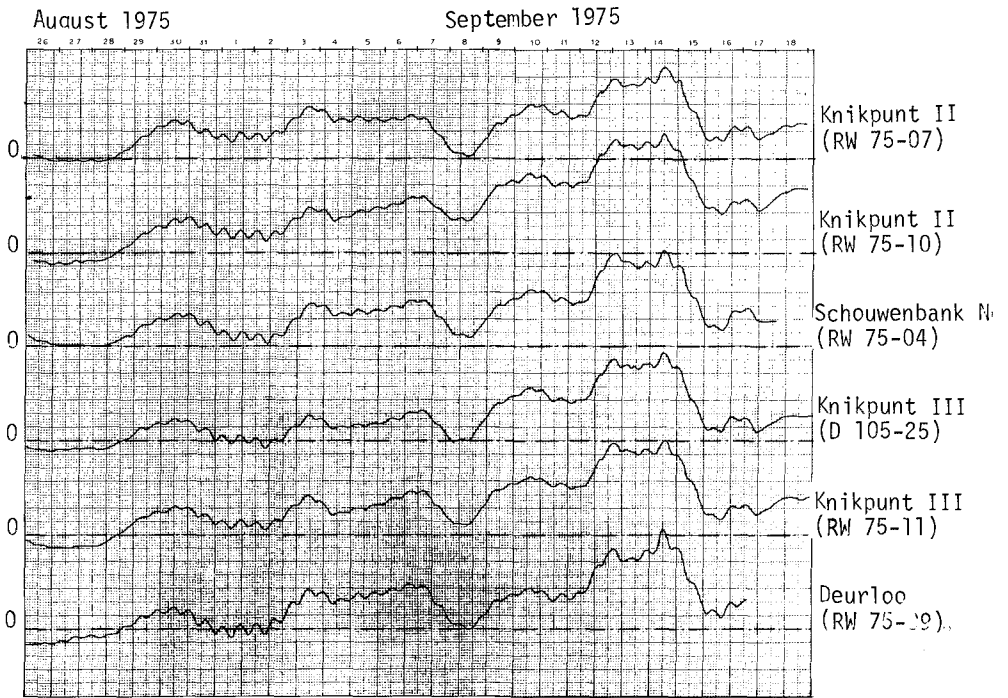


Fig. 14--Filtered tide data from a number of bottom pressure recorders

filtered records with similarly filtered water level records of adjacent fixed shore stations or instrument platforms, corrections for settling could be made rather easily.

From the filtered data of the fixed stations, which are all tied to the Dutch reference level N.A.P., it is apparent that the mean water levels have a slope along the coast. The mean levels are higher towards the northeast. The slope is approximately 1 cm per 20 km, and is apparently induced by the semidiurnal tidal wave which runs along the coast from southwest to northeast. The mechanism of this phenomenon is described by Van de Kreeke [3].

Not much is known about gradients of the mean water levels perpendicular to the coast. In computing the water levels at the bottom pressure recording stations from the shore stations and fixed offshore stations by use of the momentum equations and observed velocities from this survey and from a previous survey, no slope of the mean water levels could be found. Since the mean levels along the coast were known, the relation between the mean level of the bottom pressure recording station and the reference level could be determined. By this means the complete time histories of water levels at the boundary stations of the model could be determined for a period of about 16 days.

DATA PREPARATION FOR MODEL INPUT

Tide inputs have to be supplied at a number of stations at the open boundary of a two-dimensional model. The modeling system used for the Randdelta model can either make a linear interpolation of the water surface between these stations or interpolate amplitudes and phases of Fourier components between these stations.

The latter method is particularly appropriate here, as the long side of the Randdelta II model is in the direction of tidal wave propagation.

For the simulation period a 150-hour interval was selected. For this period Fourier components of all boundary stations were determined, and 75 of these components were used initially as input of the model. It appeared that the interpolation of amplitudes and phases along the boundary of the model perturbs the water levels by the errors in the observations. This is shown in Fig. 15, where water levels along the open boundary of the model are plotted at hourly intervals. The relatively short waves which are apparent would cause temporal inflow or outflow locally at the long open boundary during the simulation. This is naturally undesirable, and ways had to be found to reduce the errors at the boundary stations.

Again cross-spectral analysis was used. Each boundary station was correlated with three adjacent fixed stations, as shown in Fig. 16. With the impulse response function obtained from each of the relations, a convolution was made of the observed time history of the fixed station. Thus for each boundary station three convolved series were obtained. These three series were weighted according to the inverse

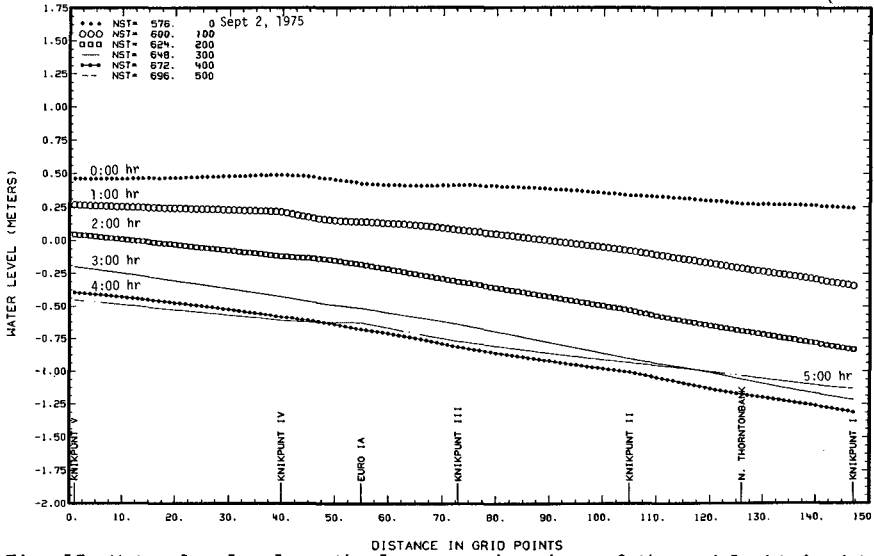


Fig. 15--Water levels along the long open boundary of the model obtained by linear interpolation of amplitudes and phases of the Fourier component of the observed data

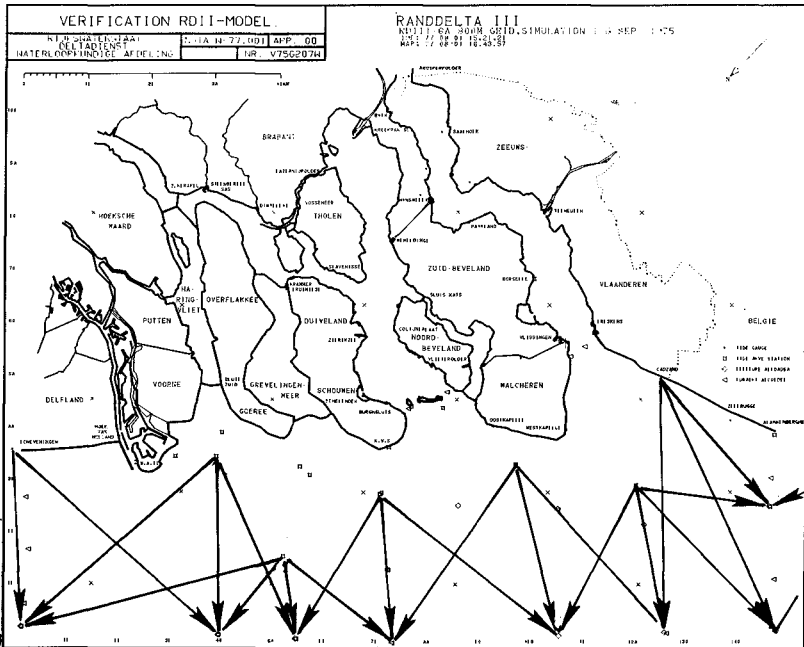


Fig. 16--Pattern of cross-correlation used for prediction of the boundary of the Randdelta II model.

square of the distance. As the accuracy of the fixed stations is relatively high and free of settling, the individual estimates obtained by convolution agreed well with the results of the observed data. Standard deviations were generally within three to five centimeters. Combining the three estimates, the standard deviations were about 3.5 cm.

From the convolved data, the Fourier components were determined again and the boundary was again determined by interpolation of amplitudes and phases. The water levels at the long open boundary, obtained by convolution and by direct observation, are shown at hourly intervals in Fig. 17. The water levels obtained by convolution are indicated by the arrows; it appears that they are essentially free of shorter waves.

The use of these boundary conditions obtained by convolution appeared satisfactory (Fig. 18). The flow fields near the boundary are now essentially unperturbed, as can be seen from the graphical outputs of the simulation for three of the boundary conditions shown in Fig. 17.

GENERAL APPLICATION OF BOUNDARY DETERMINATION TECHNIQUE

The rather extensive method of preparing the boundary conditions of this model with large open boundaries was originally developed to overcome very troublesome errors in the flow field during simulation. It is apparent that the work has very wide application. All fixed stations used in the cross-spectral analysis are permanent recording stations. The response functions appear to have high coherency in the important frequency ranges of the major tide components, thus it can be expected that they are generally applicable. This makes it possible to prepare model boundary conditions for any observed time period without making a new survey with about the same accuracy as is presently being used. The only exception would be storm periods, as these were excluded from our analysis.

References

1. Langerak, A., M. A. M. de Ras, and J. J. Leendertse, "Adjustment and Verification of the Randdelta II Model," *Proc. 16th Int. Conf. on Coastal Engineering*, Hamburg, 1978, (Chap. 61).
2. Jenkins, G. M., and D. G. Watts, *Spectral Analysis and Its Applications*, Holden-Day Publishing Co., San Francisco, 1969.
3. Van de Kreeke, J., *Tide-induced Mass Transport in Shallow Lagoons*, Dept. of Coastal and Ocean Engineering, University of Florida, Tech. Rept. No. 8, 1971.

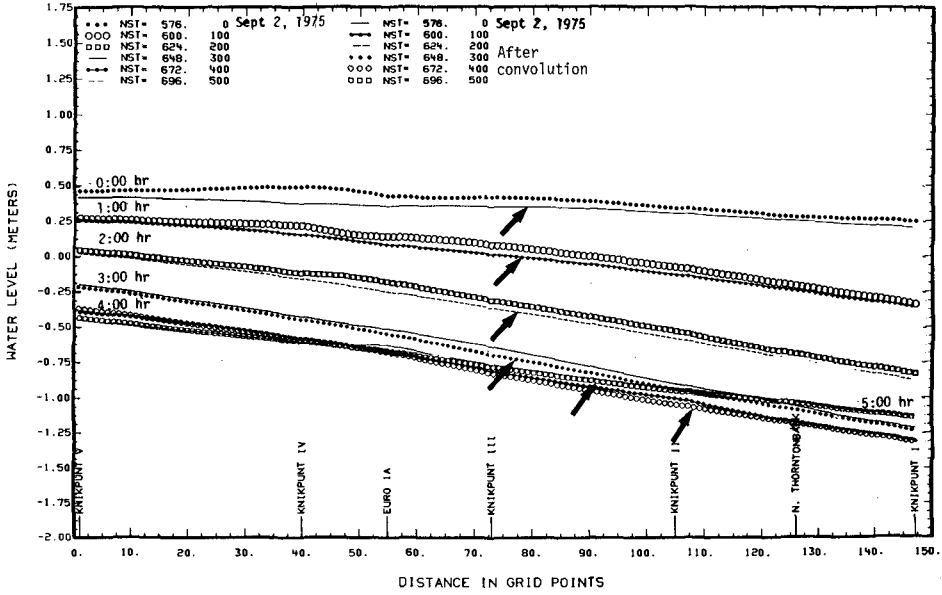


Fig. 17--Comparison of water levels along the long open boundary of the model obtained from the observed data and the convolved time series

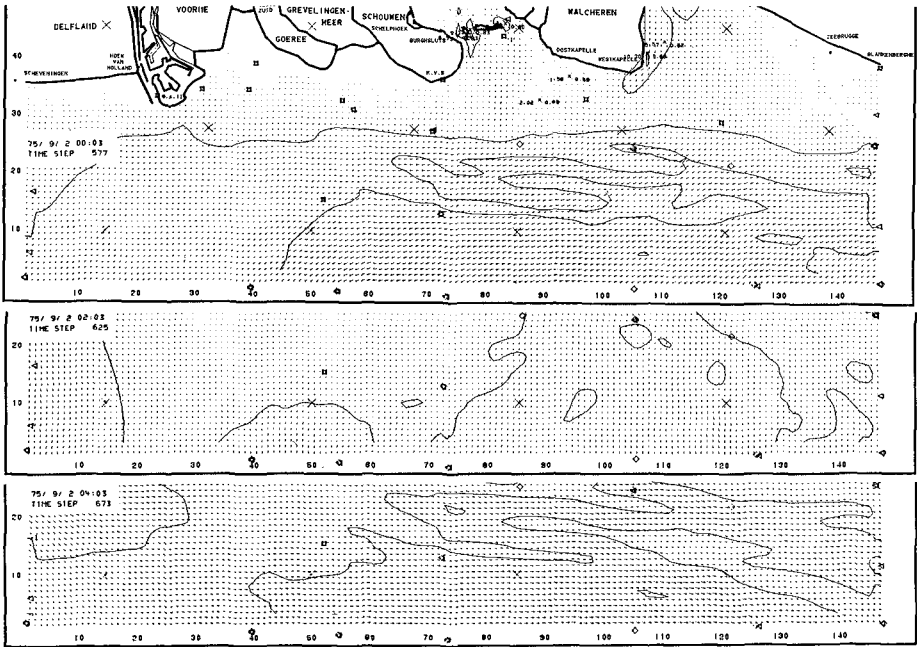


Fig. 18--Computed flow fields along the open boundary of the model for a few conditions shown in Fig. 16

CHAPTER 163

THREE-DIMENSIONAL MODELLING OF THE IRISH SEA

by

Norman Stuart Heaps *

ABSTRACT

Three-dimensional modelling of the Irish Sea has led to the determination of regimes of residual elevation and current due to wind, density and sea-surface gradient. These regimes are superimposed, along with tidal residuals from two-dimensional modelling, to yield first estimates of mean sea level distribution and long-term residual circulation.

INTRODUCTION

Earlier papers (Heaps 1974, Heaps and Jones 1977) have formulated a three-dimensional numerical model of the Irish Sea employing a new design in which the horizontal components of current are expanded in terms of a set of eigenfunctions through the depth. Coefficients of the expansion are determined in the horizontal and through time from a two-dimensional finite difference scheme based on the equations of motion and continuity transformed by vertical integration. In this way, the developing three-dimensional current structure is computed, also the changing pattern of sea-surface elevation.

The model has been used to determine the circulation in the Irish Sea produced by various uniform constant wind fields. Similarly, density currents have been computed, given horizontal density distributions obtained from observation. In most of this work a radiation condition has been employed on the open boundaries of the model.

More recently, estimates have been made of the residual circulation arising from nonlinear tidal effects in the Irish Sea. A two-dimensional vertically-integrated numerical model, on the same grid as the three-dimensional model, was used for this purpose. The tidal residuals have also been estimated using a two-dimensional model of finer mesh covering the same area but including the convective accelerations previously omitted from the equations of motion.

A situation has thus materialised where, after some years of work, we now have available, for the Irish Sea, a number of residual flow regimes due respectively to the effects of wind, density gradient and tide. The present paper represents a first attempt to superimpose these, along with a surface gradient flow, to yield the resultant long-term residual flow pattern in the Irish Sea. The results are tentative, even if only because it is assumed that a linear superposition of the various residual fields is permissible: neglected nonlinear interactions between the fields may be significant. Also, model parameters - particularly those defining friction - are not well known. Nevertheless, in spite of uncertainties and doubts, it is instructive at this stage to carry out a preliminary synthesis of residual currents in

* Senior Principal Scientific Officer, Institute of Oceanographic Sciences, Bidston Observatory, Birkenhead, Merseyside, England.

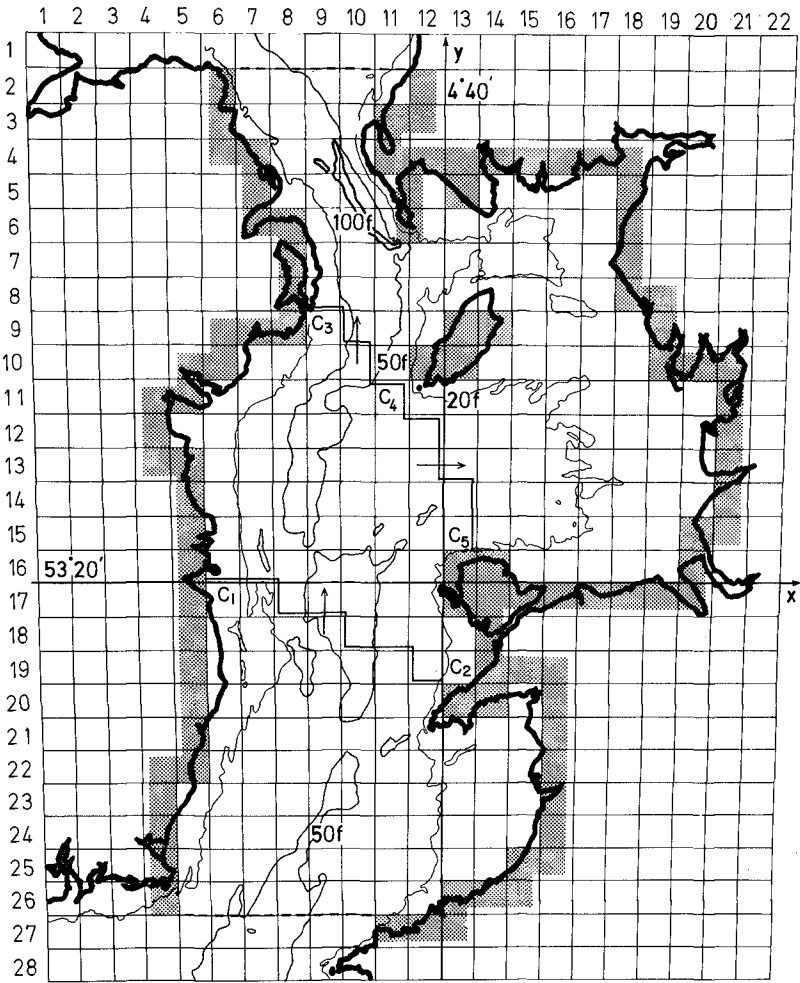


Figure 1. Finite-difference grid of the Irish Sea with a square mesh of side 7.5 nautical miles (13.9 km). Shaded areas delineate land boundaries of the numerical model. Dotted lines mark out the open boundaries. Contours are in fathoms. Flow sections C_1C_2 , C_3C_4 and C_4C_5 are indicated by double lines.

order to find out if the resulting distributions bear any relation to circulation patterns inferred from observations. Model results of this kind can sometimes suggest interesting areas for future measurements. Additionally, mean sea level distribution is a product of the superposition, yielding information on a relatively unexplored topic.

THEORY

The three-dimensional model of the Irish Sea was formulated on the grid network shown in figure 1. The grid has a square mesh of side 7.5 nautical miles and is constructed with reference to a central x -directed line along the parallel of latitude $53^{\circ}20'N$ and a central y -directed line along the meridian of longitude $4^{\circ}40'W$. The x coordinate increases to the east and the y coordinate to the north. Surface elevation ζ is evaluated at the central point of each elemental box, current u (in the x -direction) at the mid-point of each y -directed box side, and current v (in the y -direction) at the mid-point of each x -directed box side. Averaging u and v across an elemental box yields the current components at its centre. The model has open boundaries across the North Channel in the north and across St. George's Channel in the south.

The hydrodynamical equations of the model are

$$\frac{\partial \zeta}{\partial t} + \frac{\partial}{\partial x} \int_0^h u dz + \frac{\partial}{\partial y} \int_0^h v dz = 0, \quad (1)$$

$$\frac{\partial u}{\partial t} - \gamma v = -g \frac{\partial}{\partial x} (\zeta - \zeta') - g(\bar{z} + \zeta) \frac{1}{\rho} \frac{\partial \rho}{\partial x} + \frac{\partial}{\partial \bar{z}} \left(N \frac{\partial u}{\partial \bar{z}} \right), \quad (2)$$

$$\frac{\partial v}{\partial t} + \gamma u = -g \frac{\partial}{\partial y} (\zeta - \zeta') - g(\bar{z} + \zeta) \frac{1}{\rho} \frac{\partial \rho}{\partial y} + \frac{\partial}{\partial \bar{z}} \left(N \frac{\partial v}{\partial \bar{z}} \right), \quad (3)$$

where

$$\frac{\partial \zeta'}{\partial x} = \frac{\partial \bar{\zeta}}{\partial x} - \frac{1}{\rho g} \frac{\partial p_a}{\partial x}, \quad \frac{\partial \zeta'}{\partial y} = \frac{\partial \bar{\zeta}}{\partial y} - \frac{1}{\rho g} \frac{\partial p_a}{\partial y}. \quad (4)$$

Here t denotes time. Coordinates x, y are measured in the horizontal plane of the undisturbed sea surface and \bar{z} is depth below that surface. Also, h denotes the undisturbed depth of water, prescribed realistically over the grid at the mid-points of the box sides. Other symbols are $\bar{\zeta}$ the equilibrium tide, p_a atmospheric pressure on the sea surface, ρ the density of the water - in general a function of x and y , γ the geostrophic coefficient - regarded as a constant, g the acceleration of the Earth's gravity, and N a coefficient of vertical eddy viscosity - assumed to be independent of the depth coordinate \bar{z} and time t , and taken to vary with x and y so that N/h is a constant.

The equations are linear and are solved for ζ, u, v on the grid of figure 1 satisfying

$$-\rho N \left(\frac{\partial u}{\partial \bar{z}} \right) = F_s, \quad -\rho N \left(\frac{\partial v}{\partial \bar{z}} \right) = G_s \quad (5)$$

at the sea surface $\bar{z} = 0$ and

$$-\rho N(\partial u/\partial z) = k\rho u, \quad -\rho N(\partial v/\partial z) = k\rho v \quad (6)$$

at the sea bottom $z = h$, where F_s, G_s are the x, y components of wind stress and k is a constant coefficient of bottom friction. Solutions have been generated numerically through time from an initial state of no motion, prescribing zero normal flow on the land boundaries and a radiation condition on the open boundaries. In the limit as time advances, steady-state solutions have been obtained yielding motion under uniform constant wind stress (with $\partial p/\partial x = \partial p/\partial y = 0$) and also under fixed horizontal density gradients (with $F_s = G_s = 0$). Such solutions are described in this paper. They do not involve the tides but represent residual flows considered as perturbations on the predominant tidal motion - which essentially determines the frictional parameters N and k .

Concerning the method of solution, equations (1), (2), (3) are transformed by vertical integration to yield (with $\partial s/\partial x = \partial s/\partial y = 0$):

$$\frac{\partial s}{\partial t} = - \sum_{r=1}^M \left\{ \frac{\partial}{\partial x} (h a_r \phi_r u_r) + \frac{\partial}{\partial y} (h a_r \phi_r v_r) \right\}, \quad (7)$$

$$\frac{\partial u_r}{\partial t} = -\lambda_r u_r + \gamma v_r - g a_r \frac{\partial s}{\partial x} - \frac{g h b_r}{\rho} \frac{\partial p}{\partial x} + \frac{F_s}{\rho h}, \quad (8)$$

$$\frac{\partial v_r}{\partial t} = -\lambda_r v_r - \gamma u_r - g a_r \frac{\partial s}{\partial y} - \frac{g h b_r}{\rho} \frac{\partial p}{\partial y} + \frac{G_s}{\rho h}, \quad (9)$$

for $r = 1, 2, \dots, M$ where

$$u_r = \frac{1}{h} \int_0^h u \cos(\alpha_r z/h) dz, \quad v_r = \frac{1}{h} \int_0^h v \cos(\alpha_r z/h) dz. \quad (10)$$

Here, M is an integer chosen sufficiently large and

$$\left. \begin{aligned} \lambda_r &= N \alpha_r^2 / h^2, \quad a_r = \sin \alpha_r / \alpha_r, \\ \phi_r &= 2 / (1 + a_r \cos \alpha_r), \\ b_r &= [(1 + s/h) c \cos \alpha_r + \cos \alpha_r - 1] / \alpha_r^2, \end{aligned} \right\} \quad (11)$$

where α_r is the r th positive root, in ascending order, of

$$\alpha \tan \alpha = c, \quad (c = kh/N). \quad (12)$$

Finite difference solutions of the two-dimensional equations (7), (8), (9) determine the spatial fields of s, u_r, v_r ($r = 1, 2, \dots, M$) through time. The initial condition of no motion requires

$$s = u_r = v_r = 0 \quad \text{at} \quad t = 0 \quad (13)$$

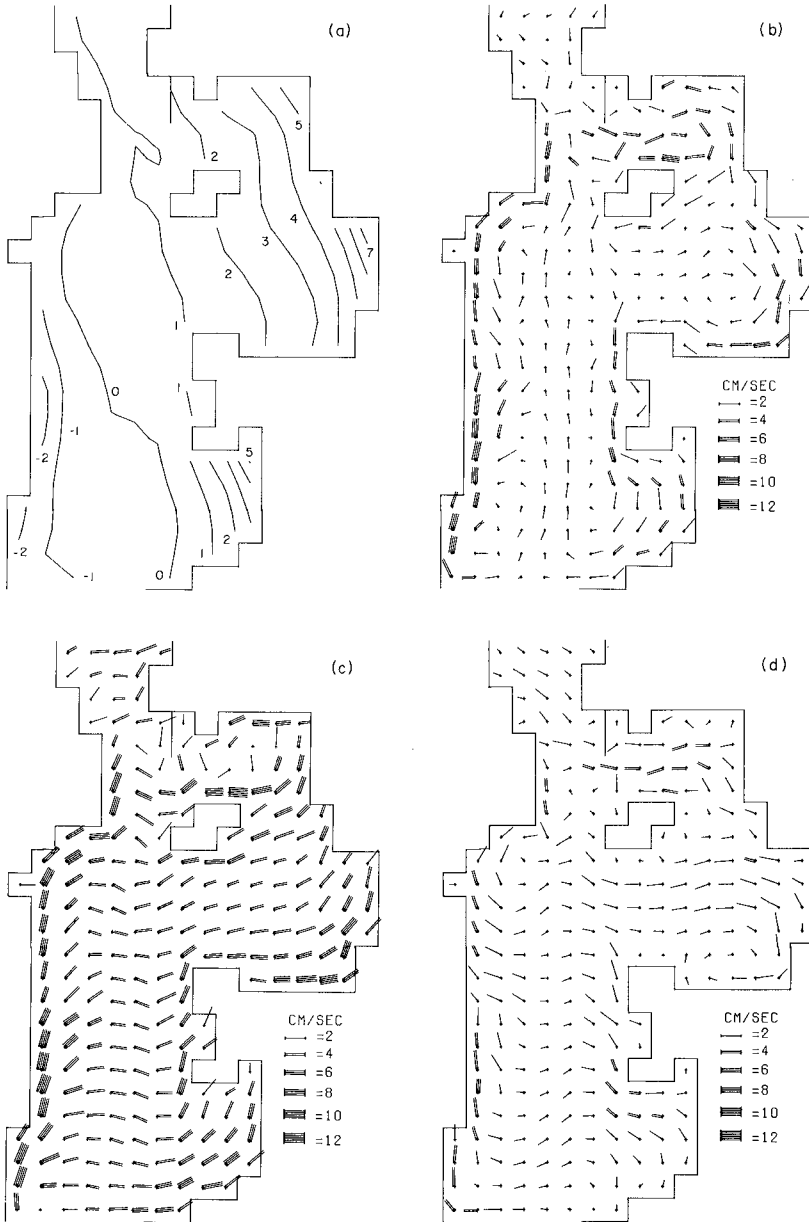


Figure 2. Wind-induced residuals W : (a) elevation contours in cm, (b) depth-mean currents, (c) surface currents, (d) bottom currents.

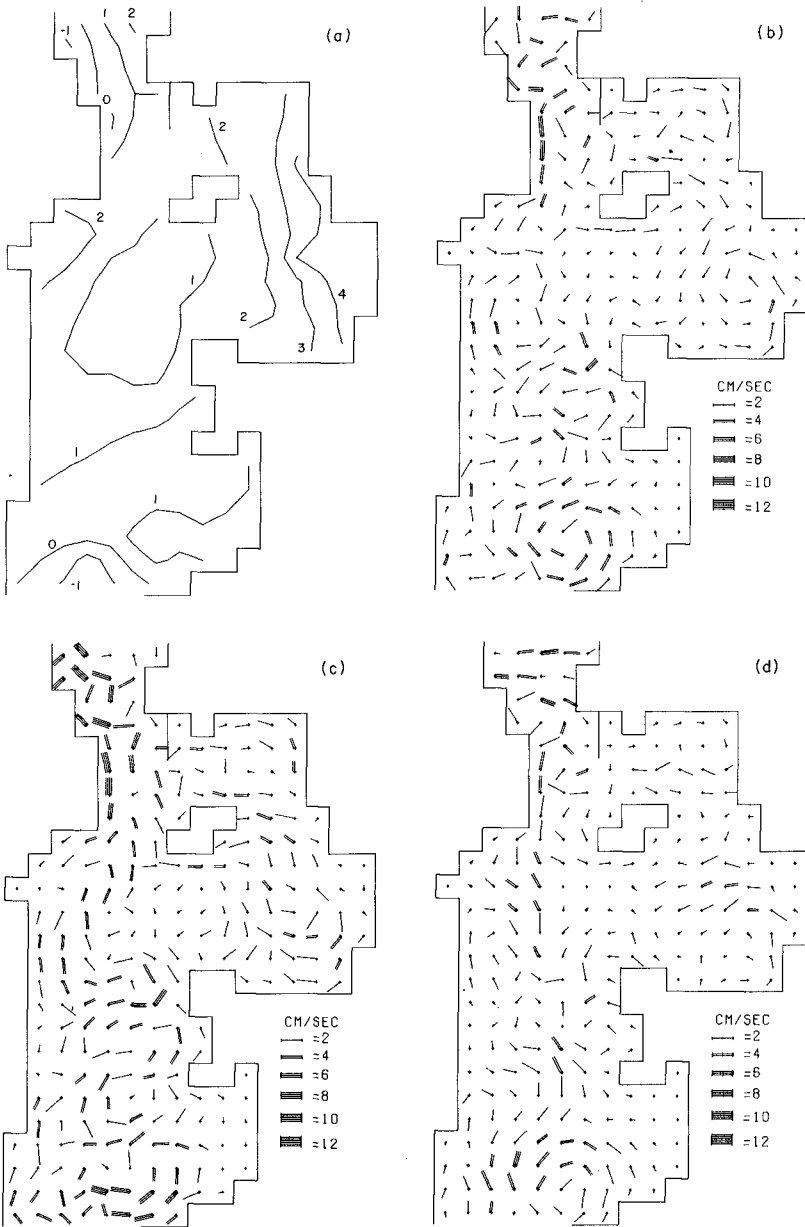


Figure 3. Density-induced residuals D_1 : (a) elevation contours in cm, (b) depth-mean currents, (c) surface currents, (d) bottom currents.

while on the land boundaries with zero normal flow :

$$u_r \cos \psi + v_r \sin \psi = 0 \quad (14)$$

and on the open boundaries with outward radiation like a simple progressive wave :

$$k \phi_r a_r (u_r \cos \psi + v_r \sin \psi) = (gh)^{1/2} \zeta, \\ u_r = v_r = 0, \quad r \geq 2; \quad (15)$$

ψ denotes the inclination of a boundary normal to the x -axis, directed out of the model area.

Having thus solved for u_r and v_r , the components of horizontal current at any depth are found from

$$u = \sum_{r=1}^M \phi_r u_r \cos(\alpha_r z/h), \quad v = \sum_{r=1}^M \phi_r v_r \cos(\alpha_r z/h) \quad (16)$$

yielding the three-dimensional current structure.

More detailed accounts of the theory and its application have been given by Heaps (1974) and Heaps and Jones (1977). As in the latter work, results given in the present paper correspond to the parametric values :

$$N/h = 0.1 \text{ cm/s}, \quad k = 0.2 \text{ cm/s}, \quad c = 2. \quad (17)$$

Also $M = 10$, which means that the expansions of current through the depth according to (16) are in terms of ten eigenfunctions or modes.

WIND-INDUCED RESIDUALS W

On the basis of data given by Hellerman (1967), annual mean wind stress conditions for the Irish Sea are taken as consisting of a uniform westerly stress of 1.0 dyn/cm^2 combined with a uniform southerly stress of 0.6 dyn/cm^2 . Corresponding residual elevations and currents derived from the three-dimensional model are shown in figure 2.

It is apparent from the figure that the winds produce a gradient of sea-surface elevation across the Irish Sea, elevation rising from -2 cm in the south-west to $+7 \text{ cm}$ in the north-east. Surface currents mostly between 3 and 8 cm/s are directed mainly to the east while bottom currents between 0 and about 3 cm/s are mainly west-going. The depth-mean currents show an anticlockwise circulation in Liverpool Bay, and in the north-south channel of the Irish Sea between Ireland and Wales these currents are north-going in the shallow coastal margins and south-going in the deeper central region.

Under the wind influence there is a net northward flow Q through the north-south channel across section C_1C_2 equal to $24.8 \times 10^3 \text{ m}^3/\text{s}$. This divides into a part Q_W passing to the west of the Isle of Man across section C_3C_4 equal to $8.9 \times 10^3 \text{ m}^3/\text{s}$, and a part Q_E passing to the east of the Isle of Man across section C_4C_5 equal to $15.9 \times 10^3 \text{ m}^3/\text{s}$. Figure 1 shows the flow sections C_1C_2 , C_3C_4 and C_4C_5 with

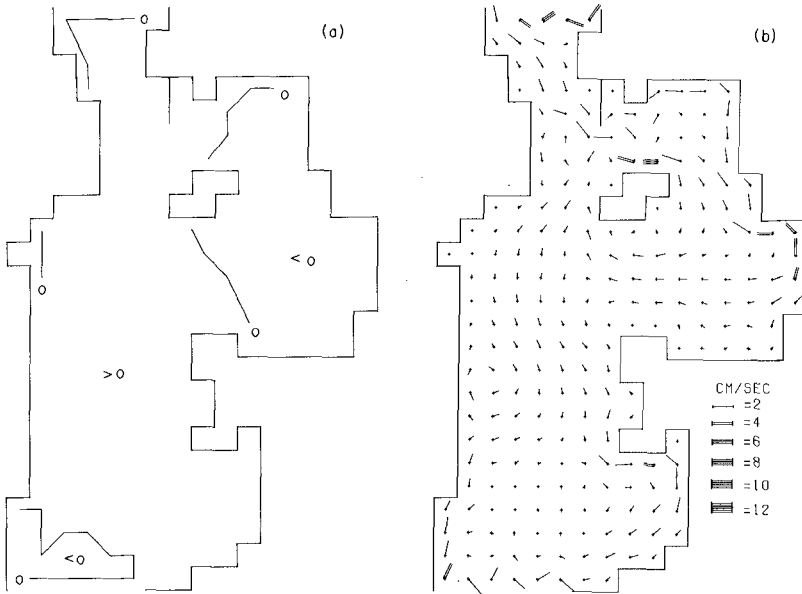


Figure 4. Tidal residuals T_1 : (a) elevation contours in cm, (b) depth-mean currents.

positive flow directions indicated. Table 1 sets out the corresponding flow values Q , Q_W and Q_E .

DENSITY-INDUCED RESIDUALS D_1

The residual elevations and currents of figure 3 are induced by a prescribed pattern of horizontal density gradients representative of the period 6-20 September 1971. The derivation of these results from the three-dimensional model has been fully described by Heaps and Jones (1977).

Manifestly, the elevation residuals build up to values exceeding 4 cm in the north-east from minimum values of around -1 cm near the northern and southern open boundaries. The current patterns are dominated by gyres of various scales, altogether forming a rather complex system of motion. In the Liverpool Bay region it is evident that water enters near the sea bottom moving eastwards and southwards towards the coast, leaving near the sea surface in directions between west and north. The vertically-integrated flow there constitutes a clockwise gyre. Generally, these density currents are smaller than the wind-induced currents of figure 2, particularly near the surface.

Table 1 shows that there is a density-induced flow northwards across C_1C_2 amounting to $17.9 \times 10^3 \text{ m}^3/\text{s}$. The greater part of this ($13.5 \times 10^3 \text{ m}^3/\text{s}$) passes to the west of the Isle of Man, in contrast to the behaviour of the wind-induced northwards flow of regime W (figure 2) most of which passes to the east of the Isle.

TABLE 1

Superposition of residual flows, with density currents D_1 and tidal residual T_1 ; *prescribed value.

Flow Regime	Q	Q_W	Q_E
	$10^3 \text{ m}^3/\text{s}$	$10^3 \text{ m}^3/\text{s}$	$10^3 \text{ m}^3/\text{s}$
Wind (W)	24.8	8.9	15.9
Density (D_1)	17.9	13.5	4.4
Tides (T_1)	43.4	16.8	26.6
$W + D_1 + T_1$	86.1	39.2	46.9
Surface gradient (G)	-39.4	-34.8	-4.6
$G_1 = 1.586G$	-62.5	-55.2	-7.3
$R_1 = W + D_1 + T_1 + G_1$	23.6*	-16.0	39.6

TIDAL RESIDUALS T_1

Employing the equations of motion and continuity in standard vertically-integrated form, including quadratic bottom friction but omitting the convective accelerations and the effects of drying banks, tides were generated on the grid of figure 1 in response to specified open boundary tides consisting of the principal harmonic constituent M_2 . The tidal simulation was carried out along the lines described by Flather and Heaps (1975). Fourier analysis of the results, for the constant term, yielded the elevation and depth-mean current residuals shown in figure 4.

The residual elevations are all less than 1 cm, being zero by design along each open boundary. Although the residual currents are small, mostly less than 1 cm/s, their uniformity conspires to produce a comparatively large northwards flow through the Irish Sea of $43.4 \times 10^3 \text{ m}^3/\text{s}$, over half of which passes to the east of the Isle of Man (table 1).

SURFACE-GRADIENT RESIDUALS G

Setting wind stress and density gradient to zero, the three-dimensional model was used to compute the system of residual elevations and currents in the Irish Sea maintained by an elevation of +1 cm along the northern open boundary with zero elevation along the southern open boundary. These residuals, denoted by G, were found to involve a net flow from north to south through the Irish Sea of $39.4 \times 10^3 \text{ m}^3/\text{s}$, most of this passing to the west of the Isle of Man (table 1).

SUPERPOSITION OF RESIDUAL FIELDS

It is assumed that the total (long-term) residuals in the Irish Sea, constituting a regime R_1 say, may be deduced by summing W, D_1 , T_1 and bG , where b is some as yet unknown multiplying factor. For consistency in the summation, T_1 is considered to have a three-

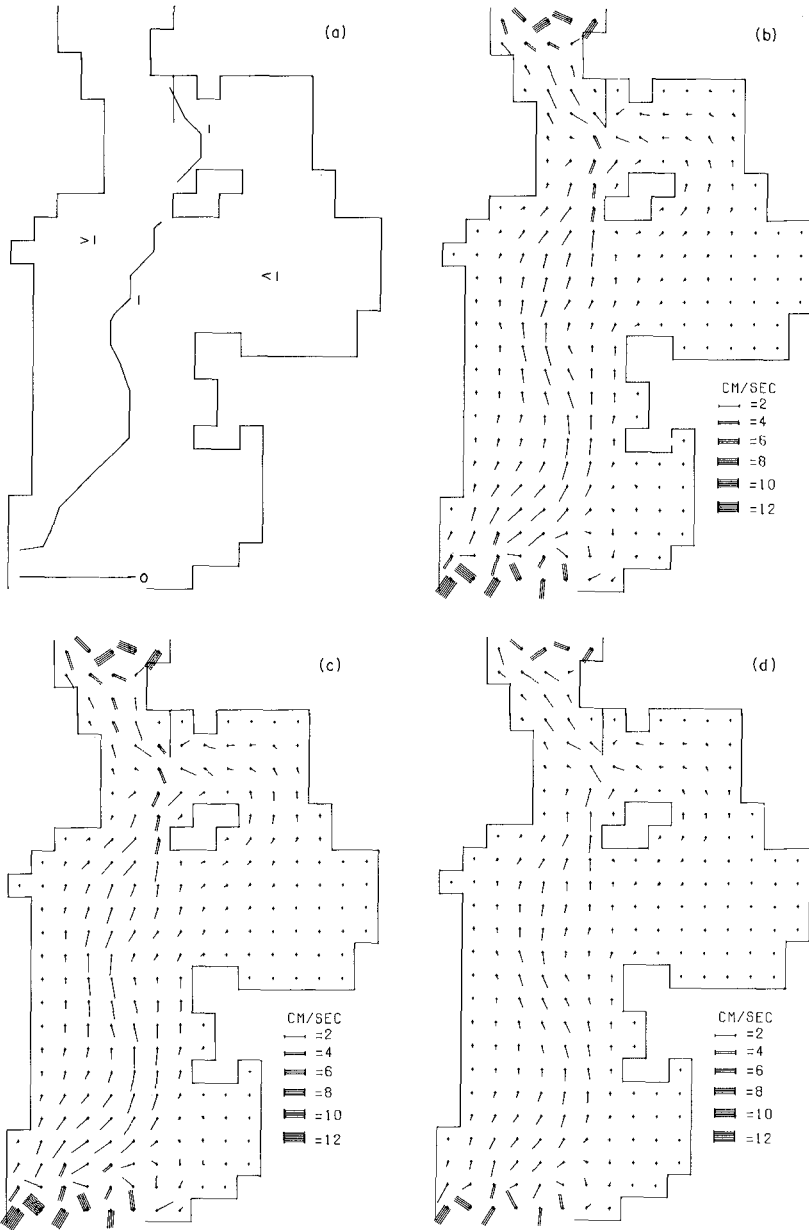


Figure 5. Surface-gradient residuals G_1 : (a) elevation contours in cm, (b) depth-mean currents, (c) surface currents, (d) bottom currents.

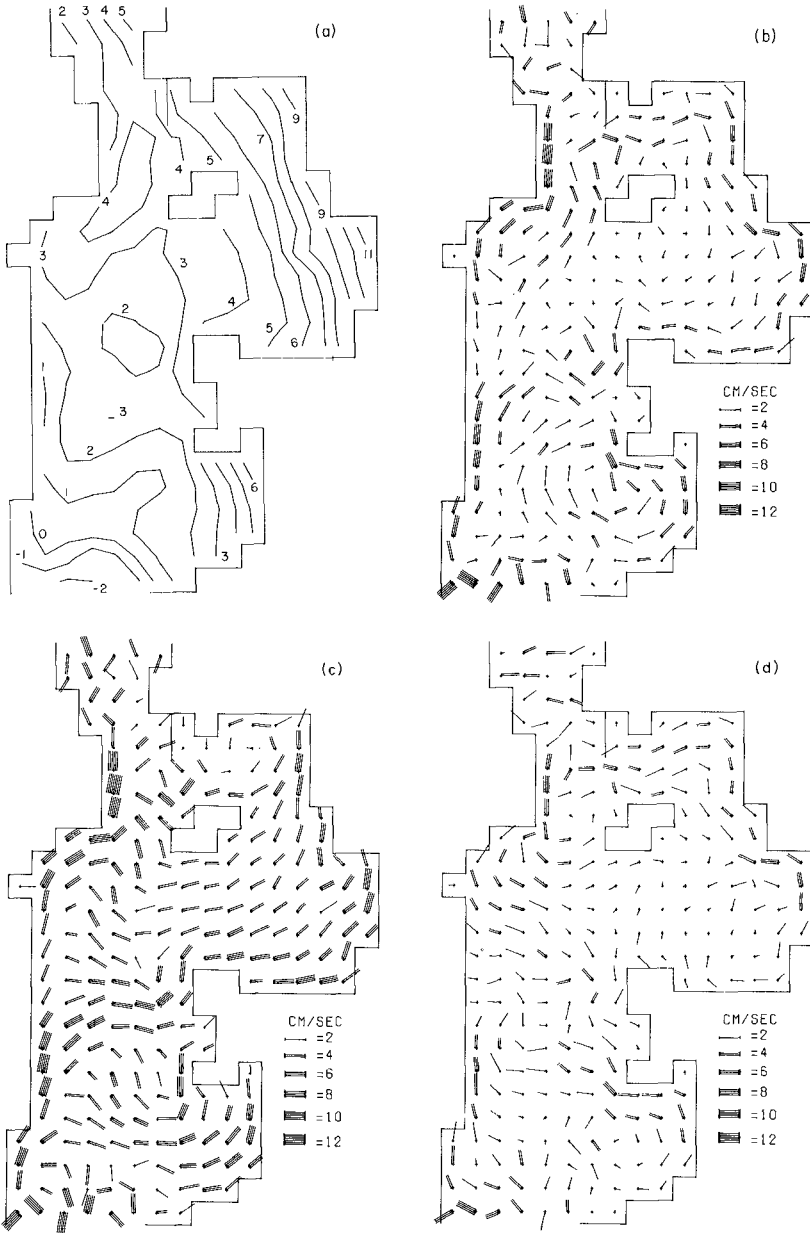


Figure 6. Total residuals R_1 : (a) elevation contours in cm, (b) depth-mean currents, (c) surface currents, (d) bottom currents.

TABLE 2

Superposition of residual flows, with density currents D_1 and tidal residuals T_2 ; *prescribed value.

Flow regime	Q	Q_W	Q_E
	$10^3 \text{ m}^3/\text{s}$	$10^3 \text{ m}^3/\text{s}$	$10^3 \text{ m}^3/\text{s}$
Wind (W)	24.8	8.9	15.9
Density (D_1)	17.9	13.5	4.4
Tides (T_2)	55.1	50.0	5.1
$W + D_1 + T_2$	97.8	72.4	25.4
Surface gradient (G)	-39.4	-34.8	-4.6
$G_2 = 1.883G$	-74.2	-65.5	-8.7
$R_2 = W + D_1 + T_2 + G_2$	23.6*	6.9	16.7

dimensional current structure, the current at any depth through a vertical being taken equal to the depth-mean current. The effects of barometric pressure are excluded, it being supposed that these influence surface level only - according to the statical law. Thus :

$$R_1 = W + D_1 + T_1 + G_1 \quad (18)$$

where

$$G_1 = bG. \quad (19)$$

The above procedure follows an approach due to Prandle (1978) in estimating residual elevations and flows in the Southern North Sea. Here, b is determined by requiring that R_1 should have a south to north flow across section C_1C_2 equal to $23.6 \times 10^3 \text{ m}^3/\text{s}$, in accordance with the long-term flow values determined by Wilson (1974) from measurements of the distribution of Caesium-137 in the Irish Sea. Thus, referring to table 1,

$$24.8 + 17.9 + 43.4 - 39.4b = 23.6 \quad (20)$$

so that

$$b = 1.586 \quad (21)$$

As subsequently evaluated, residuals G_1 are depicted in figure 5 and the total residuals R_1 in figure 6.

Figure 6 shows surface elevation rising to +11 cm in the north-eastern area of the Irish Sea from a minimum value of around -2 cm in the south. Between the open ends of the Sea there is evidently, at most, a 7 cm increase in elevation from south to north. Adding 2 cm to this in order to allow for a difference in mean barometric pressure of 2 mb between the open ends, a 9 cm increase in elevation from south to north is obtained, falling short of the 15 cm increase deduced from mean sea level studies (K. R. Thompson, private communication). The surface currents in R_1 are dominated by wind influence (compare figure 6 with figure 2). However, the bottom currents are

TABLE 3

Superposition of residual flows with density currents D_2 and tidal residuals T_2 ; *prescribed value.

Flow regime	Q $10^3 \text{ m}^3/\text{s}$	Q_W $10^3 \text{ m}^3/\text{s}$	Q_E $10^3 \text{ m}^3/\text{s}$
Wind (W)	24.8	8.9	15.9
Density (D_2)	23.6	20.7	2.9
Tides (T_2)	55.1	50.0	5.1
$W + D_2 + T_2$	103.5	79.6	23.9
Surface gradient (G)	-39.4	-34.8	-4.6
$G_3 = 2.028G$	-79.9	-70.6	-9.3
$R_3 = W + D_2 + T_2 + G_3$	23.6*	9.0	14.6

obviously influenced considerably both by the wind-induced and the density-driven residuals. In the Liverpool Bay area, the depth-mean currents indicate a movement of water eastwards and then northwards sensibly parallel to the coast; this pattern is reflected in the surface and the bottom current distributions.

REVISED TOTAL RESIDUALS

In recent work by R. Proctor at I.O.S. Bidston, the tides of the Irish Sea have been computed using a two-dimensional numerical model covering essentially the same area as that shown in figure 1 but having a mesh length smaller by one third. The convective accelerations and the effects of drying banks, previously omitted, have been included. It turns out that the associated tidal residuals, T_2 , are significantly different from the earlier residuals, T_1 . In particular, the residual currents of T_2 exhibit strong eddies not present in the residual currents of T_1 . Eddies of similar type, arising from the convective accelerations, have been computed by Tee (1976) for Minas Channel and Minas Basin at the head of the Bay of Fundy. Using T_2 instead of T_1 in the superposition of residual fields leads to a new system of total residuals, R_2 . Elevations and currents of this system are shown in figure 7 and the corresponding flows Q , Q_W and Q_E are given in table 2. Further, employing an alternative regime of density-induced residuals D_2 in the superposition leads to total residuals R_3 : see figure 8 and table 3. The residuals D_2 are representative of the period 17 September - 6 October 1972 and have been described by Heaps and Jones (1977).

The current distributions of R_2 and R_3 (which are similar) are manifestly complex, with scales of motion scarcely resolvable on the grid network of figure 1. Currents exceed 25 cm/s in places as indicated by the box vectors. There is a distinctive anticlockwise gyre in the Liverpool Bay area reminiscent of some observationally-based results presented by Ramster and Hill (1969). The complexity of the residual circulations is reflected in the associated residual

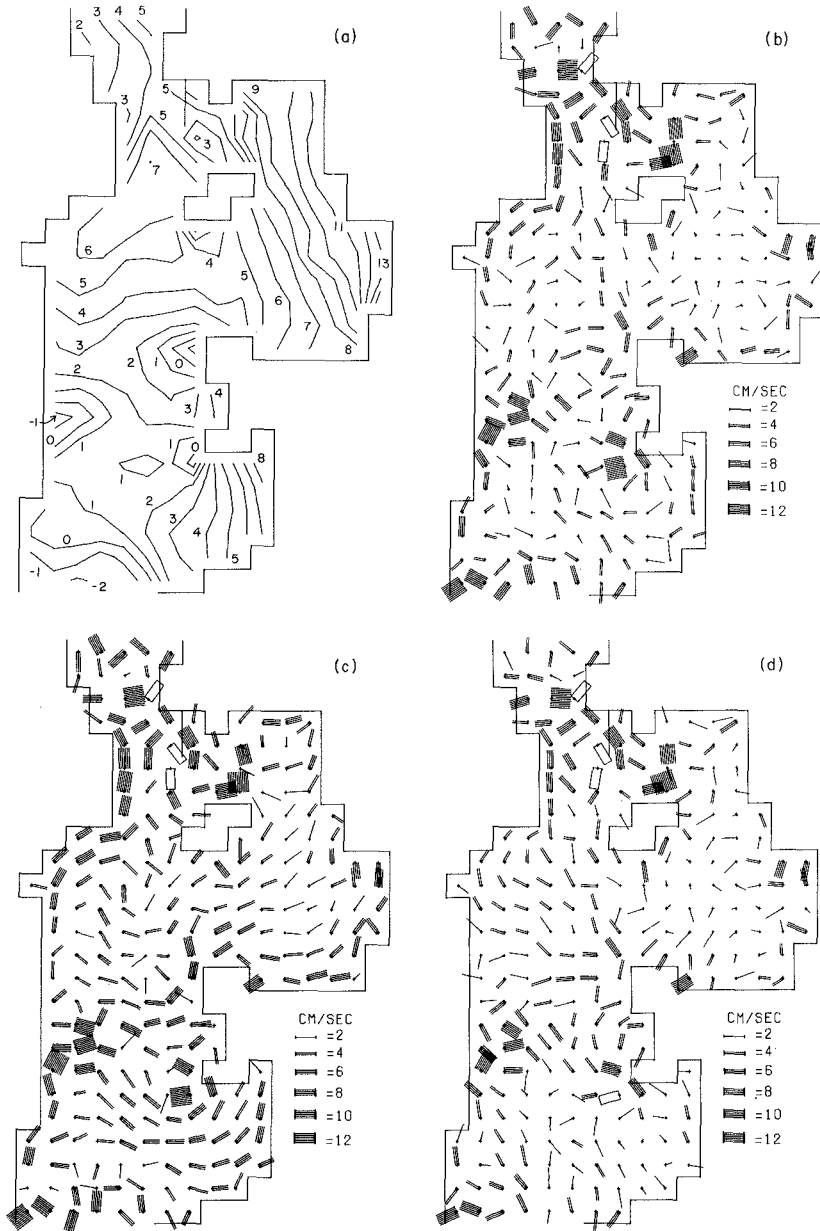


Figure 7. Total residuals R_2 : (a) elevation contours in cm, (b) depth-mean currents, (c) surface currents, (d) bottom currents.

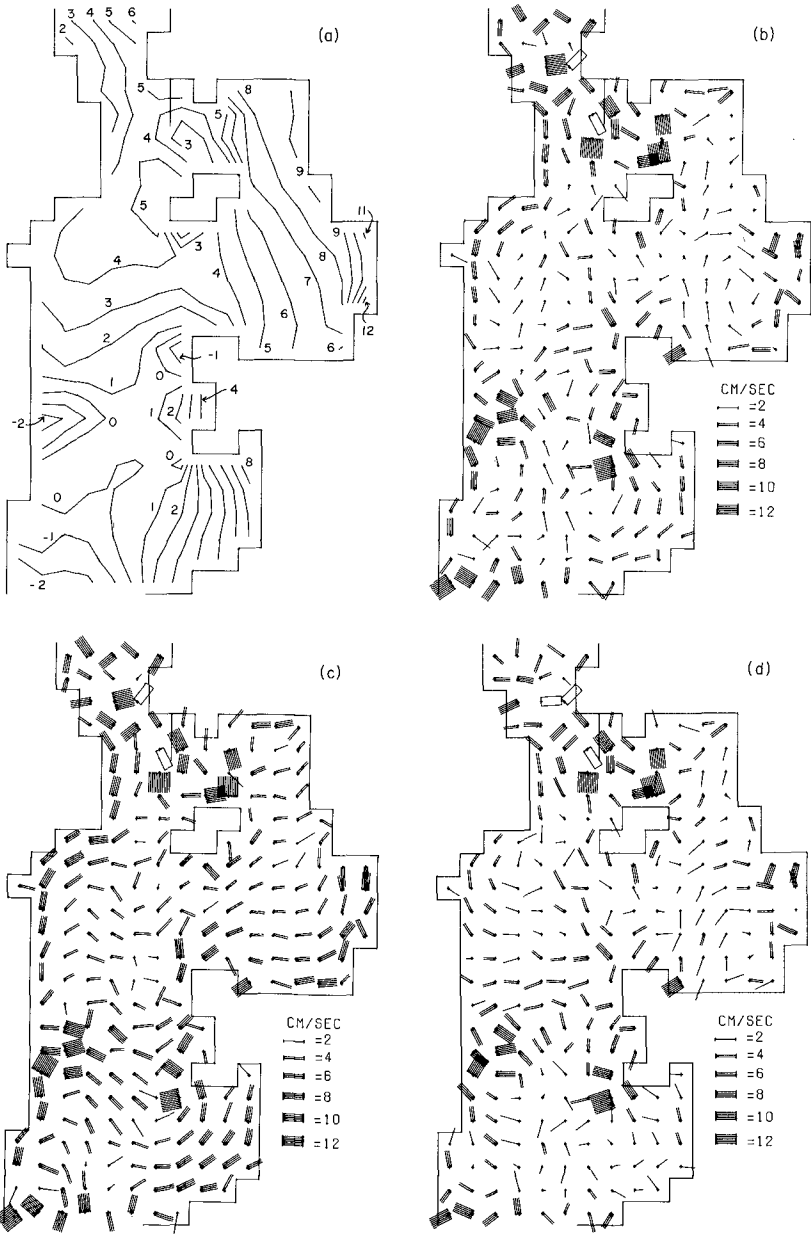


Figure 8. Total residuals R_3 : (a) elevation contours in cm, (b) depth-mean currents, (c) surface currents, (d) bottom currents.

elevations but, overall, these are similar to the residual elevations of R_1 . Tables 2 and 3 demonstrate that the north-going residual flows due to density gradients and tides tend to be balanced by the surface-gradient flows.

Our work on Irish Sea circulation is proceeding and a more comprehensive account of it will be prepared in due course.

ACKNOWLEDGEMENTS

I am indebted to Mr. J. E. Jones for much assistance in this investigation and am grateful to Mr. R. Proctor for permitting me to use some of the results of his work before their publication.

The work described in this paper was funded by a Consortium consisting of the Natural Environment Research Council, the Ministry of Agriculture, Fisheries and Food, and the Departments of Industry and Energy.

REFERENCES

- Flather, R.A. and Heaps, N.S. 1975. Tidal computations in Morecambe Bay. Geophys. J. R. astr. Soc., 42, 489-517.
- Heaps, N.S. 1974. Development of a three-dimensional numerical model of the Irish Sea. Rapp. P.-v. Réun. Con. int. Explor. Mer, 167, 147-162.
- Heaps, N.S. and Jones, J.E. 1977. Density currents in the Irish Sea. Geophys. J. R. astr. Soc., 51, 393-429.
- Hellerman, S. 1967. An updated estimate of the wind stress on the world ocean. Mon. Weath. Rev., 95, 607-626.
- Prandle, D. 1978. Residual flows and elevations in the Southern North Sea. Proc. R. Soc. Lond. A., 359, 189-228.
- Ramster, J.W. and Hill, H.W. 1969. Current system in the Northern Irish Sea. Nature, 224, 59-61.
- Tee, K.T. 1976. Tide-induced residual current, a 2D nonlinear numerical tidal model. J. mar. Res., 34, 603-628.
- Wilson, T.R.S. 1974. Caesium-137 as a water movement tracer in the St George's Channel. Nature, 248, 125-127.

CHAPTER 164

THREE-DIMENSIONAL SGS ENERGY MODEL OF EASTERN BERING SEA

S. K. Liu and J. J. Leendertse¹

This paper describes the development, adjustments and verification of a three-dimensional, nonhomogeneous model of Bristol Bay and the St. George Basin. The modeled area (Fig. 1) is situated on the continental shelf area at the southeastern corner of the Bering Sea, which has one of the largest shelf areas of the world's oceans. Because of this, the water mass movement in the modeled area is driven predominantly by wind and tide, whereas waters in the deeper basin to the west are part of the cyclonic Bering Sea slope current system flowing parallel to the continental shelf break. Annual cycles of surface heating and cooling and the duration, strength and phasing of these periods give a distinctive hydrodynamic behavior to the system. During autumn and winter, local negative buoyancy (vertically unstable) exists due to surface cooling and brine rejection during ice formation. In spring, positive buoyancy is added by fresh water runoff, ice melting and insulation. The hydrographic structure in the modeled area is further modified by the seasonal wind, with higher mean speed in autumn and winter.

I. DYNAMIC PROCESSES

In the modeling investigation reported here the physical process involved can essentially be described by a set of partial differential equations associated with the prototype hydrodynamic system. The equations of horizontal motion for an incompressible internally source-free fluid on a rotating earth in Cartesian coordinates with z-axis positive upward are:

$$\frac{\partial u}{\partial t} + \frac{\partial(uu)}{\partial x} + \frac{\partial(uv)}{\partial y} + \frac{\partial(uw)}{\partial z} - fv + \frac{1}{\rho} \frac{\partial p}{\partial x} - \frac{1}{\rho} \left(\frac{\partial \tau_{xx}}{\partial x} + \frac{\partial \tau_{xy}}{\partial y} + \frac{\partial \tau_{xz}}{\partial z} \right) = 0 \quad (1)$$

$$\frac{\partial v}{\partial t} + \frac{\partial(vu)}{\partial x} + \frac{\partial(vv)}{\partial y} + \frac{\partial(vw)}{\partial z} + fu + \frac{1}{\rho} \frac{\partial p}{\partial y} - \frac{1}{\rho} \left(\frac{\partial \tau_{yx}}{\partial x} + \frac{\partial \tau_{yy}}{\partial y} + \frac{\partial \tau_{yz}}{\partial z} \right) = 0 \quad (2)$$

where x, y and z are Cartesian coordinates, positive eastward, northward and upward, respectively; u, v and w denote the respective components of velocity; f represents the Coriolis parameter; ρ is the density of water; τ_{xx} , τ_{xy} , τ_{xz} , etc. are components of stress tensor.

The flow in the modeled area, the vertical acceleration of fluid motion associated with the predominant hydrodynamic process (i.e., tide- and wind-induced circulation) is approximately five orders of magnitude smaller in comparison with the gravitational acceleration. Therefore we can neglect the vertical acceleration and advection, and the equation of motion in the vertical direction becomes the hydrostatic equation

$$\frac{\partial p}{\partial z} + \rho g = 0 \quad (3)$$

The equation of continuity is

¹ The Rand Corporation, Santa Monica, California, U.S.A.

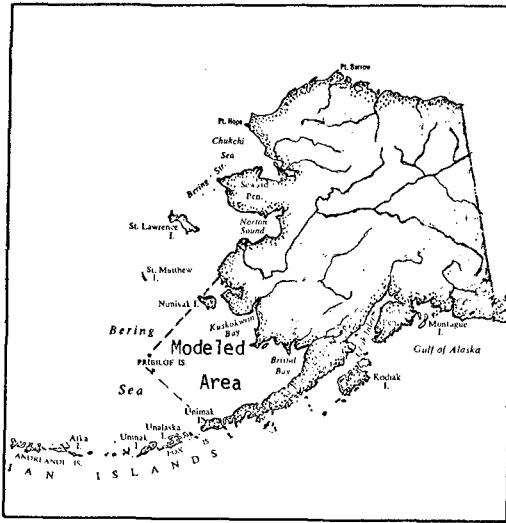


Fig. 1 Location map of Eastern Bering Sea and the approximate boundary of the modeled area

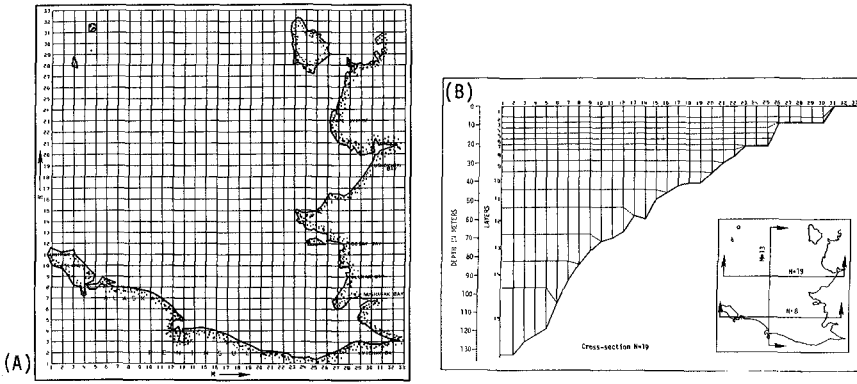


Fig. 2 Horizontal (A) and (B) distribution of grid dimensions of the modeled area

$$\frac{\partial u}{\partial x} + \frac{\partial v}{\partial y} + \frac{\partial w}{\partial z} = 0 \quad (4)$$

The equations of salt and heat balance are:

$$\frac{\partial s}{\partial t} + \frac{\partial(us)}{\partial x} + \frac{\partial(vs)}{\partial y} + \frac{\partial(ws)}{\partial z} - \frac{\partial[D_x(\partial s/\partial x)]}{\partial x} - \frac{\partial[D_y(\partial s/\partial y)]}{\partial y} - \frac{\partial[\kappa(\partial s/\partial z)]}{\partial z} = 0 \quad (5)$$

$$\begin{aligned} \frac{\partial T}{\partial t} + \frac{\partial(uT)}{\partial x} + \frac{\partial(vT)}{\partial y} + \frac{\partial(wT)}{\partial z} - \frac{\partial[D_x(\partial T/\partial x)]}{\partial x} \\ - \frac{\partial[D_y(\partial T/\partial y)]}{\partial y} - \frac{\partial[\kappa'(\partial T/\partial z)]}{\partial z} = 0 \end{aligned} \quad (6)$$

where s and T represent salinity and temperature; D_x and D_y are horizontal diffusion coefficients; κ and κ' are vertical exchange coefficients for salt and heat, respectively.

The relationship between density, salinity and temperature can be approximated by an equation of state in the form

$$\rho = \bar{\rho} + \rho'(s, T) \quad (7)$$

Similar equations can be written for subgridscale (SGS) turbulent energy densities and dissolved pollutant constituents:

$$\begin{aligned} \frac{\partial e}{\partial t} + \frac{\partial(ue)}{\partial x} + \frac{\partial(ve)}{\partial y} + \frac{\partial(we)}{\partial z} - \frac{\partial D_e(\partial e/\partial x)}{\partial x} \\ - \frac{\partial[D_y(\partial e/\partial y)]}{\partial y} - \frac{\partial[\kappa(\partial e/\partial z)]}{\partial z} + hD \pm S_e = 0 \end{aligned} \quad (8)$$

$$\begin{aligned} \frac{\partial p}{\partial t} + \frac{\partial(up)}{\partial x} + \frac{\partial(vp)}{\partial y} + \frac{\partial(wp)}{\partial z} - \frac{\partial D_p(\partial p/\partial x)}{\partial x} \\ - \frac{\partial[D_y(\partial p/\partial y)]}{\partial y} - \frac{\partial[\kappa(\partial p/\partial z)]}{\partial z} + hK_p \pm S_p = 0 \end{aligned} \quad (9)$$

where e is the subgridscale turbulent energy per unit mass; p denotes any pollutant concentration of concern; D_e is the dissipation rate for turbulent energy; κ' is the decay rate for the pollutant concentration; and S_e and S_p are the source and sink terms for turbulent energy and pollutant concentration, respectively.

The above set of partial differential equations describes the physical processes only in a limiting sense such that quasi-continuous spatial-temporal representation is required to describe the dynamic features of concern. In the process of finding the numerical solution to the differential equations of the mean flow, certain conceptual descriptions of the fine features of the dynamic behavior are being introduced. The way to describe these fine features becomes the product of an iterative learning process. The modeler's final formulation embodies not only the specific solution method associated with the PDE, but also the investigator's conceptual description of the prototype behavior that he or she learns through data and intermediate modeling results.

Because the prototype data system, the selected model and the modeling investigators are three components in a modeling investigation, an adaptive process takes place. At the beginning, a basic model is selected by the investigators so as to be representative of the basic environmental components of the prototype system according to the available general information about the system at that time. As the modeling effort proceeds, the investigators have an opportunity to look more closely at the involved dynamic processes through the analytic nature of the numerical model. A field sampling program can thus be designed more effectively to resolve the finer details of the system. From these data, new insight leads then to further refinement of the model, and so on.

During the course of our model development, changes in formulation often took place as a consequence of new insight into the dynamic features derived from reviewing the simulation results against updated prototype data. A finite difference model was selected for the study [1,2].

If we use the standard notation for summing, differencing and shifting as defined by

$$\begin{aligned} \bar{F}^x &= \frac{1}{2} [F(i + \frac{1}{2}) \Delta x, j \Delta y, k \Delta z, n \Delta t] + F[(i - \frac{1}{2}) \Delta x, j \Delta y, k \Delta z, n \Delta t] \\ \delta_x F &= \frac{1}{\Delta x} \left\{ F \left[\left(i + \frac{1}{2} \right) \Delta x, j \Delta y, k \Delta z, n \Delta t \right] - F \left[\left(i - \frac{1}{2} \right) \Delta x, j \Delta y, k \Delta z, n \Delta t \right] \right\} \\ F_+ &= F[i \Delta x, j \Delta y, k \Delta z, (n + 1) \Delta t] \\ F_- &= F[i \Delta x, j \Delta y, k \Delta z, (n - 1) \Delta t] \end{aligned}$$

where i, j, k, n denote the discrete representation in the x, y, z, t domain, the finite difference formulation finally adapted for the computation of the modeled area takes the following form [1]:

Equations (1) through (9) for level k with layer-average values, the continuity equation, the mass momentum, and SGS energy balance equations for the interior of the modeled system, and the equation of state are:

$$\bar{\delta}_t \zeta^z = - \sum_k [\delta_x (\bar{h}^x u) + \delta_y (\bar{h}^y v)] \quad \text{at } i, j, n \quad (10)$$

$$\begin{aligned} \bar{\delta}_t (\bar{h}^x u)^t &= - \delta_x (\bar{h}^x \bar{u}^x \bar{u}^x) - \delta_y (\bar{h}^y \bar{u}^x \bar{v}^y) - \bar{h}^x \delta_z (\bar{u}^z \bar{w}^x) + f \bar{h}^x \bar{v}^{xy} - \frac{1}{\rho^x} \bar{h}^x \delta_x p \\ &+ \frac{1}{\rho^x} [h \delta_z E_x \delta_z \bar{u}^{2t} + \delta_x (h A_x \delta_x u)_- + \delta_y \bar{h}^x \bar{A}_y^x \delta_y u_-] \quad \text{at } i + \frac{1}{2}, j, k, n \quad (11) \end{aligned}$$

where E_x is the vertical momentum exchange coefficient and A_x, A_y are horizontal exchange coefficients in x and y direction, respectively.

$$\begin{aligned} \bar{\delta}_t (\bar{h}^y v)^t &= - \delta_x (\bar{h}^x \bar{u}^y \bar{v}^x) - \delta_y (\bar{h}^y \bar{u}^y \bar{v}^y) - \bar{h}^y \delta_z (\bar{v}^z \bar{w}^y) - f \bar{h}^y \bar{u}^{xy} - \frac{1}{\rho^y} \bar{h}^y \delta_y p \\ &+ \frac{1}{\rho^y} \left[h \delta_z E_y \delta_z \bar{v}^{2t} + \delta_x \left(\bar{h}^x \bar{A}_x^y \delta_x v \right)_- + \delta_y (h A_y \delta_y v)_- \right] \quad (12) \\ &\text{at } i, j + \frac{1}{2}, k, n \end{aligned}$$

$$\begin{aligned} \bar{\delta}_t (\bar{h} s)^t &= - \delta_x (\bar{h}^x \bar{u} s^x) - \delta_y (\bar{h}^y \bar{v} s^y) - h \delta_z (w s^z) \\ &+ \delta_x (\bar{h}^x D_x \delta_x s)_- + \delta_y (\bar{h}^y D_y \delta_y s)_- - h \delta_z (\kappa \delta_z s^{2t}) \quad \text{at } i, j, k, n \quad (13) \end{aligned}$$

where D_x and D_y are the horizontal diffusion coefficients and k is the vertical mass exchange coefficient. For temperature we have,

$$\begin{aligned} \overline{\delta_t(\overline{hT})} &= -\delta_x(\overline{h^x u T^x}) - \delta_y(\overline{h^y v T^y}) - h \delta_z(\overline{w T^z}) \\ &+ \delta_x(\overline{h^x D_x} \delta_x T)_- + \delta_y(\overline{h^y D_y} \delta_y T)_- + h \delta_z(\kappa' \delta_z \overline{T^{2t}}) \end{aligned} \quad (14)$$

at i, j, k, n

where k' is the vertical thermodiffusion coefficient. For SGS energy density in the system,

$$\begin{aligned} \overline{\delta_t(\overline{he})} &= -\delta_x(\overline{h^x u e^x}) - \delta_y(\overline{h^y v e^y}) - h \delta_z(\overline{w e^z}) \\ &+ \delta_x(\overline{h^x D_x} \delta_x e)_- + \delta_y(\overline{h^y D_y} \delta_y e)_- + h \delta_z(E_e \delta_z \overline{e^{2t}}) \\ &+ S - Dh \quad \text{at } i, j, k, n \end{aligned} \quad (15)$$

where E_e is the vertical momentum exchange coefficient. For pollutant constituent concentration, we have

$$\begin{aligned} \overline{\delta_t(\overline{hP})} &= -\delta_x(\overline{h^x u P^x}) - \delta_y(\overline{h^y v P^y}) - h \delta_z(\overline{w P^z}) \\ &+ \delta_x(\overline{h^x D_x} \delta_x P)_- + \delta_y(\overline{h^y D_y} \delta_y P)_- + h \delta_z(\kappa \delta_z \overline{P^{2t}}) + S \end{aligned} \quad (16)$$

at i, j, k, n

The equation of state can be approximated by

$$\begin{aligned} \rho &= (5890 + 38T - 0.375T^2 + 3s) / [(1779.5 + 11.25T - 0.0745T^2) \\ &- (3.8 + 0.01T)s + 0.698(5890 + 38T - 0.375T^2 + 3s)] \end{aligned} \quad (17)$$

at $i, j, k, n + 1$

The continuity equation is used to compute the vertical velocity diagnostically:

$$\delta_z w = -\delta_x(\overline{h^x u}) - \delta_y(\overline{h^y v}) \quad \text{at } i, j, k, n+1$$

Similar equations for velocity components u and v can be written for the top and bottom layers, but now the effects of wind and bottom friction must be considered.

$$\begin{aligned} \overline{\delta_t(\overline{h^x u})} &= -\delta_x(\overline{h^x u} \overline{u^x}) - \delta_y(\overline{h^y v} \overline{u^y}) - \overline{h^x} \delta_z(\overline{u^x w^x}) + \overline{h^x} \tau^{xx} - \frac{1}{\overline{\rho^x}} \overline{h^x} \delta_x p \\ &+ \frac{1}{\overline{\rho^x}} \left[\phi \rho_a w_a^2 \sin \psi - (E_x \delta_z \overline{u^{2t}})_{k=3/2} + \delta_x(h A_x \delta_x u)_- \right. \\ &\left. + \delta_y(\overline{h^y A_y} \delta_y u)_- \right] \quad \text{at } i + \frac{1}{2}, j, 1, n \end{aligned} \quad (18)$$

$$\begin{aligned} \overline{\delta_t(\overline{h^y v})} &= -\delta_x(\overline{h^x u} \overline{v^x}) - \delta_y(\overline{h^y v} \overline{v^y}) - \overline{h^y} \delta_z(\overline{v^y w^y}) - \overline{h^y} \tau^{yy} - \frac{1}{\overline{\rho^y}} \overline{h^y} \delta_y p \\ &+ \frac{1}{\overline{\rho^y}} \left[\theta \rho_a w_a^2 \cos \psi - (E_y \delta_z \overline{v^{2t}})_{k=3/2} + \delta_x(\overline{h^x A_x} \delta_x v)_- \right. \\ &\left. + \delta_y(h A_y \delta_y v)_- \right] \quad \text{at } i, j + \frac{1}{2}, 1, n \end{aligned} \quad (19)$$

where ϕ represents the wind-stress coefficient, w_a is wind speed, and ρ_a represents the density of air. At the bottom layer, the momentum equation becomes

$$\begin{aligned} \overline{\delta_i(\overline{h^x u})} &= -\delta_x(\overline{h^x u^x}) - \delta_y(\overline{h^y v^x}) - \overline{h^x} \delta_z(\overline{w^x}) + f\overline{h^x v^{xy}} - \frac{1}{\overline{\rho^x}} \overline{h^x} \delta_x p \\ &+ \frac{1}{\overline{\rho^x}} [(E_x \delta_z \overline{u^{2i}})_{k=\kappa-1/2} - \overline{\rho^x} g u_- (u_-^2 + \overline{v^{xy}})^2]^{1/2} / (\overline{C^x})^2 \\ &+ \delta_x(h A_x \delta_x u)_- + \delta_y(\overline{h^x A_x^y} \delta_y u)_- \quad \text{at } i + \frac{1}{2}, j, K, n \end{aligned} \quad (20)$$

$$\begin{aligned} \overline{\delta_i(\overline{h^y v})} &= -\delta_x(\overline{h^x v^y}) - \delta_y(\overline{h^y v^y}) - \overline{h^y} \delta_z(\overline{w^y}) - f\overline{h^y u^{xy}} - \frac{1}{\overline{\rho^y}} \overline{h^y} \delta_y p \\ &+ \frac{1}{\overline{\rho^y}} [(E_y \delta_z \overline{v^{2i}})_{k=\kappa-1/2} - \overline{\rho^y} g v_- ((\overline{u^{xy}})^2 + v_-^2)]^{1/2} / (\overline{C^y})^2 \\ &+ \delta_x(\overline{h^y A_x^y} \delta_x v)_- + \delta_y(h A_y \delta_y v)_- \quad \text{at } i, j + \frac{1}{2}, K, n \end{aligned} \quad (21)$$

where C denotes the local Chezy's coefficient.

In the modeled area, each vertical motion of water mass has to work against buoyancy forces induced by the density gradient. If the available kinetic energy of the turbulent motion is insufficient to overcome this stabilizing effect, turbulence is inhibited and suppressed. As a consequence, the process of momentum and mass-heat exchange will be lower than the neutral stability condition. The criteria for the onset of this turbulence-suppressing process in the system can be obtained by the local density gradient and turbulent energy level. The exchange coefficient for stratified flow can thus be expressed as

$$E_x = \overline{\rho^{xz}} L \sqrt{e_-^{xz}} \exp \left[m \frac{g}{\overline{\rho^{xz}}} \frac{(\overline{L^z})^2 \delta_z(\overline{\rho^x})}{e_-^{xz}} \right] \quad (22)$$

$$E_y = \overline{\rho^{yz}} L \sqrt{e_-^{yz}} \exp \left[m \frac{g}{\overline{\rho^{yz}}} \frac{(\overline{L^z})^2 \delta_z(\overline{\rho^y})}{e_-^{yz}} \right] \quad (23)$$

$$\kappa = a_4 L \sqrt{e_-^{xz}} \exp \left[r \frac{g}{\overline{\rho^z}} (\overline{L^z})^2 \frac{\delta_z \rho}{e_-^z} \right] \quad (24)$$

$$E_e = a_1 L \sqrt{e_-^z} \exp \left[m \frac{g}{\overline{\rho^z}} (\overline{L^z}) \frac{\delta_z \rho}{e_-^z} \right] \quad (25)$$

where L is a length scale which is taken as a function of the distance from the bottom and surface boundaries as follows:

$$L = k' z (1 - z/d)^{1/2} \quad (26)$$

where k' is the von Karman constant, z represents the vertical distance from the bottom to the point considered, and d is the vertical distance from surface to bottom. In the computation, if the computed L is greater than half of the layer thickness, the latter is used as L. In the horizontal direction, the exchange coefficient is computed as a function of the local vorticity gradient.

$$A = \gamma |(\delta_x \overline{w^y} + \delta_y \overline{w^x})| (\Delta l)^3 \quad (27)$$

where Δl is the grid dimension. From A we obtain the horizontal exchange coefficient

$$D_x = \bar{A}^x \quad D_y = \bar{A}^y \quad (28)$$

In addition, the subgridscale horizontal mixing is estimated by the well-known four-third power law of the grid dimension.

In the interior, the generation of subgridscale energy is derived from

$$S = a_3 \overline{L \sqrt{e}}^2 [(\delta_z \bar{u}^x)^2 + (\delta_z \bar{v}^y)^2] \quad \text{at } i, j, k + 1/2. \quad (29)$$

In the bottom layer, energy which is taken out of the mean flow through the bottom stress immediately enters the subgridscale energy system as a source term.

$$R_x = \frac{1}{\bar{\rho}^x} (\tau^{xz})_{k+1/2} = gu[u^2 + (\bar{v}^{xy})^2]^{1/2} / (\bar{C}^x)^2 \quad \text{at } i + \frac{1}{2}, j, k, n \quad (30)$$

$$R_y = \frac{1}{\bar{\rho}^y} (\tau^{yz})_{k+1/2} = gv[u^2 + (\bar{v}^{xy})^2]^{1/2} / (\bar{C}^y)^2 \quad \text{at } i, j + \frac{1}{2}, k, n$$

$$S = \overline{u_- R_x^x} + \overline{v_- R_y^y} \quad \text{at } i, j, k, n \quad (31)$$

The rate of turbulent energy dissipation is determined from the concept that the dissipation rate depends on the transfer process from larger eddies to smaller eddies according to

$$D = a_2 e^{3/2} / L \quad (32)$$

In the model, the explicit integration scheme is used in the horizontal direction, whereas an implicit scheme is used in the vertical, thus removing the most stringent stability condition associated with the numerical solution method. Some modifications have also been made to handle arbitrary bathymetry in the computational scheme; they are described in [3].

II. MODEL SETUP AND ADJUSTMENT

Because of the nonhomogeneous hydrodynamic behavior, the vertical resolution is essential for good representation of the vertical fine structures in the modeled area. After a series of initial tests, a model of 15 layers was found to be necessary for resolving both the pycnocline and the bathymetric distribution using a vertical grid network with unequal distances. The horizontal and vertical schematization of the modeled area are illustrated in Fig. 2.

The initial conditions for model simulation were selected from a quasi-synoptic hydrographic survey conducted during early summer of 1976 by the National Oceanic and Atmospheric Administration involving 141 sampling stations. For the deeper portion of the bay, the mixed layer thickness was selected uniformly at 22m. CTD data in this area indicate some anomaly from this value, depending on the local wind condition. It is our opinion that this value (i.e., 22m) gives a good representative condition for that period. Any anomaly from this mean value induced by a transient wind field would be accounted for during the simulation.

The horizontal grid dimension of the model is 21.82 km, which is equal

in both directions. The vertical grid dimension (Fig. 2) was selected as such that it gives good resolution near the areas of density nonhomogeneity and at the same time provides accurate bathymetric representation of the system. The top layer is somewhat larger (6m) to accommodate the anticipated tidal range and wind setup near the coastal areas. The step size used for time integration was 3 min.

One of the most difficult and yet important tasks in the numerical simulation of coastal seas is the specification of open-boundary conditions. During the model's setup stage, only two major tidal components, namely, K1 and M2, were used in a series of test runs. The amplitude and phase of these two components were obtained from a set of two tidal charts compiled by NOAA using updated information up to that time. In the model's adjustment process, similar boundary conditions were applied, but now the computed amplitudes and phases at model interior points are compared to the reported values in the cotidal charts. During the course of adjustment, bottom stress coefficients were changed until amplitudes and phases of the main tidal components in the model agreed with the tidal charts.

Computed amplification and phase lag of tidal propagation between the model's boundaries and interior points have been used to adjust the bottom stress coefficients. A Chezy value of 700 (in cgs units) was found to be appropriate. Because of the relatively low tidal dissipation in the bay system, the dynamic field is not very sensitive to the selection of bottom stress coefficients as in many shallow tidal estuaries. On the other hand, the dynamic behavior near the pycnocline is sensitive to the selection of turbulent closure constants relating the vertical density gradient and the transport, generation, and decay of turbulence. After the adjustment process, the same values were used later for the model's verification run. These turbulent closure constants take the following values:

$$\begin{aligned}a_1 &= 1.0 \\a_2 &= .08 \\a_3 &= .08 \\a_4 &= .001\end{aligned}$$

During the initial stages of the study, a series of preliminary test runs was made for the adjustment of the model. During this period, only two tidal constituents were applied at the model's open boundary. As we have mentioned earlier, amplitude and phase of these two tidal components were derived from a set of two tidal charts compiled by NOAA, using updated information during that time.

For each of the simulation runs, the computed field of water level, velocity, temperature, salinity and turbulent energy densities were tabulated and graphed. Computed vertical profiles of salinity and temperature were compared against the observed profiles by which constants in the turbulent closure computations were determined.

III. MODEL VERIFICATION AND PREDICTION

After the model's adjustment phase, a particular period in 1976 was selected for verifying the predictability of the model and the establishment of a set of predictive parameters.

The beginning period from June 16 to June 19, 1976 was selected because during that period vertical pycnic structure was fully developed to represent the spring-summer conditions in the modeled area. In other words, once the model is verified, it can thus be considered useful for predictive purposes for the spring-summer period. Therefore, during the verification run, all the simulation parameters such as turbulent closure constants and bottom stress coefficients were kept the same as those used at the final stages of the model adjustment period.

For the model's verification run, the boundary conditions were obtained indirectly from field measurements. At several points along the boundary of the model, water level data were recorded over long periods of time. Unfortunately, the recording periods were not all simultaneous and did not coincide with the period of current observations in other parts of the modeled area. To make the most effective use of all data in our studies, we used predicted boundaries and simulated time periods for which current data were available for verification. The tide predictions were based upon tidal analysis by our co-workers at NOAA of pressure recordings at the boundary station. From this information, the tide was predicted at the stations which coincide with the field data stations. For the model boundaries between the locations where tide predictions were available, linear interpolation of tidal amplitudes and phases were used for each tidal constituent.

Basic input information used for the verification run were observed average wind condition over the area and the predicted tides at the model's open boundaries. By compiling ship's weather reports, an average SW wind of 15 knots for the verification period was derived. The speed and direction of the wind during that period did not change.

Cumulative effects of surface wind stress outside of the model's area are, of course, unknown unless measured water levels instead of the predicted water levels are used. However, because the model's open boundaries are located approximately halfway between the Kamchatka Peninsula, the USSR and Bristol Bay in the east/west direction, and also located halfway between the Chuktskiy Peninsula, the USSR, and the Alaskan Peninsula in the north/south direction, the model's open boundary is located approximately at the midpoint of the water surface due to wind setup for almost all wind directions. Due to this consideration, the predicted water level at open boundary requires no further wind adjustment for the purpose of our computation.

In this section, observed current at four locations is compared to the computed values, located nearest to those current meter deployments. The current meter locations in the field did not coincide with the grid system. Also, the local depth at the current meter locations is not

necessarily the same as in the model. Consequently, differences in computed and observed values can be expected for these reasons alone.

Figures 3 through 6 present the hourly observed current data and the computed current at locations near the current meter. Also presented in these graphs are the computed water level and the vertical velocity components.

Figure 3 contains four graphs. Graph A gives the water level at grid point (14,14) from dynamic computation. Graph B illustrates the computed east/west current components at four depths at this grid location plotted together with the hourly observed east/west current component at station BC-2 (see insert map), measured at a 20-meter depth. Graph C gives similar comparisons, but for the north/south velocity components. These computed values agree quite well with the reported average values. Some uncertainties still exist. These uncertainties include the true horizontal location of the station. Depth values in the model are schematized according to the published navigation chart, which may not represent the true local depth. Local depth of the mixed layer may also be slightly different from the modeled value. Finally, the predicted water level at the model's open boundary also contains certain random and systematic errors which would affect the computed results. Graph D contains six curves representing the computed vertical velocity components at six selected layers. The vertical velocity of these layers not only reveals tide-induced vertical displacements, but also contains instabilities induced by the vertical stratification. The dynamic behavior of each layer is closely related to the local vertical densimetric Froude number and the Brunt-Väisälä frequency. More detailed discussion on the vertical dynamic behavior will be given later. Figure 4 gives similar comparison graphs for station BC-5. In this figure, the currents are plotted as magnitudes and direction. The computed currents in the lower layers agree quite well with the observed values, whereas surface currents are in general higher than the computed magnitudes--particularly at their maximum range. The predicted current directions are excellent (Graph C). Some of the underestimates in the surface currents at this particular location may be traced to the low turbulent energy content. This is indicated by the dichotomic velocity distribution in the vertical (Graph D). Notice the lack of vertical velocity gradients in the bottom layers as compared to the similar graph in Fig. 3.

The next figure (5) represents the comparison at station BC-14, which is located very close to the Alaskan Peninsula. The computed currents agree well with the observed values, particularly for the east-west component. The vertical motions due to wind and tides increase the turbulence intensity close to the southern boundary and the salinity and temperature distributions are nearly homogeneous. Vertical displacements are very large, resulting in a vertically near-homogeneous structure.

Good agreement is also found at station BC-15 (Fig. 6). This station is shallower than the previous three stations. Vertical displacements of water columns show pronounced instabilities (Graph D), yet the magnitude is only about one-third of that at station BC-14.

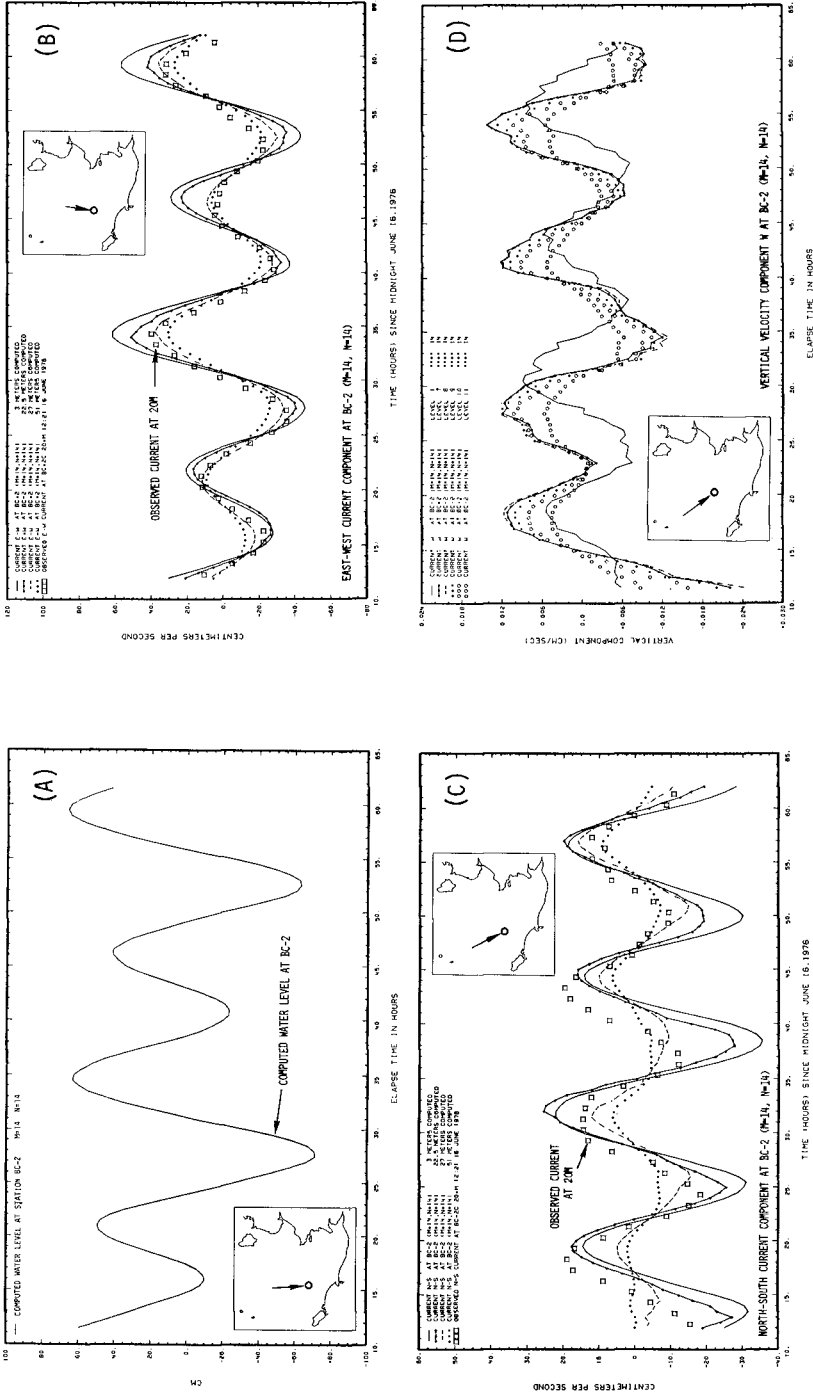


Fig. 3 --Comparison between the computed and the observed current component at a given location (B and C) together with the local water level (A) and vertical velocity component at six selected levels (D) during the period 0000 16 June through 1400 18 June 1976.

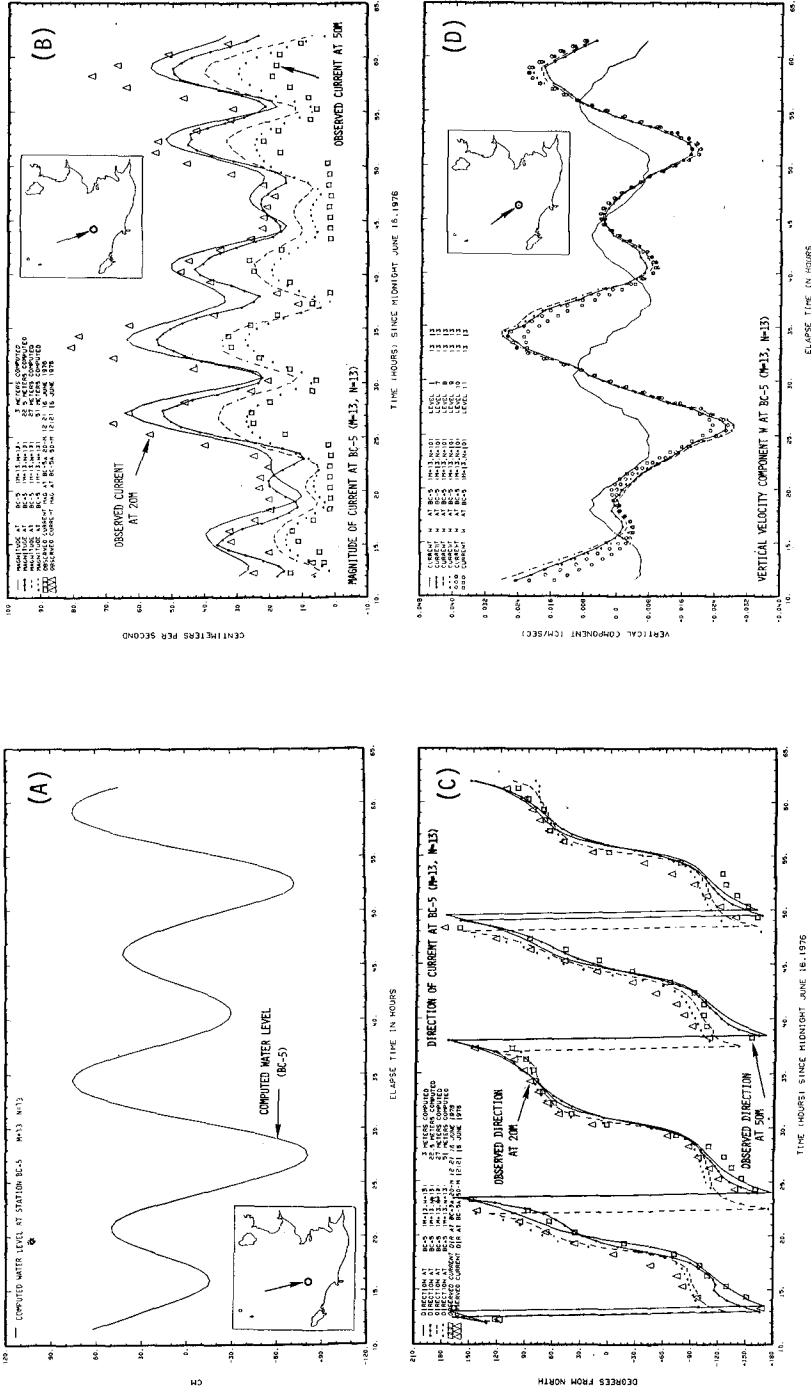


Fig. 4 --Comparison between the computed and the observed current speed and direction (B and C) together with the local water level (A) and vertical velocity component at six selected levels (D) during the period 0000 16 June through 1400 18 June 1976

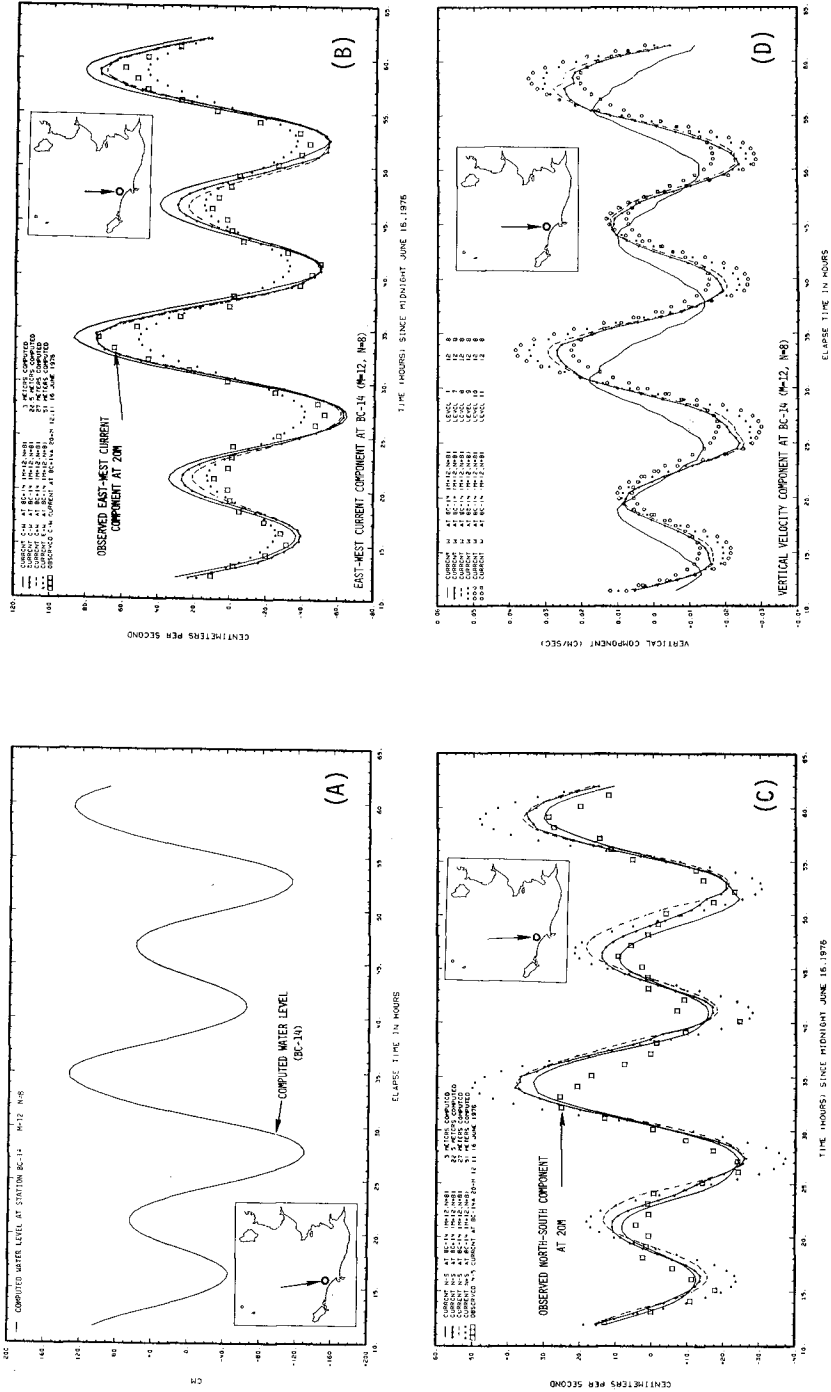


Fig. 5 -- Comparison between the computed and the observed current components at a given location (B and C) together with the local water level (A) and vertical velocity component at six selected levels (D) during the period 0000 hr 16 June through 1400 18 June 1976.

In the spring-summer period, stable stratifications are usually found in the waters with depth greater than 50 meters. This positive density gradient requires additional energy in the vertical turbulent exchange process. As a consequence, not only is upwelling being suppressed, but the bottom layers are also being insulated from the surface wind stress. Unlike the deeper layers where water is nearly neutrally stable, the upper layers tend to oscillate from their equilibrium position. This oscillation can often be characterized by the Brunt-Väisälä frequency which, in the upper layer, can be approximated by

$$N = \left\{ - \frac{g}{\rho_0} \frac{\partial \bar{\rho}}{\partial z} \right\}^{\frac{1}{2}}$$

where N is in radians per second, and ρ_0 is the reference density at the free surface.

From the observed data, the period of oscillation (i.e., $2\pi/N$) varies from a fraction of an hour in the thermocline to several hours in the deeper waters, although it is more difficult to measure in the lower layers. In the simulation the computed vertical velocity component also gives a convenient indication of the vertical displacements by means of frequency-domain analysis. To illustrate this dynamic behavior, we analyzed the vertical velocity component W for selected layers at several locations by the spectral method. For example, in the surface layer at station BC-14, the computed vertical velocity component contains not only tide-generated vertical displacements, but also oscillations induced by the stratification effect (Fig. 7). The shapes of these spectra all possess a similar slope; they fall approximately as f^{-2} at the lower frequencies and then flatten out to around f^{-1} above 0.5 cycles per hour. This characteristic shape agrees with the observed spectra of the first mode internal waves [4].

The computed coherency spectra are shown in Fig. 8. Higher coherencies are found generally in tidal frequencies. Coherency-associated vertical instabilities are between 0.5 and 0.6. This is in general agreement with the observations of Haurwitz, et al. [5].

A sequence of predicted results from the computations is presented in Fig. 9. Figure 9A shows the computed water level, velocity distribution in the surface layer and the rise and fall of the water surface at 1400 p.m., June 18, 1976. Computed velocity distribution in the 8th layer (depth = 27m) is presented in Fig. 9B. Figures 9C and 9D show the instantaneous distribution of salinity and temperature in the surface layer at 1400 p.m. June 18, 1976. At the same point in time, the vertical distribution of salinity, temperature and turbulent energy densities (in ergs per unit mass) through a cross-section are shown in Fig. 10.

The tidal propagation within the modeled area may be illustrated by a set of three-dimensional plots from the results of the hydrodynamic computation. A period of 12 hours of the verification period, from 0200 hour to 1400 hour June 18, 1976, is selected to demonstrate the

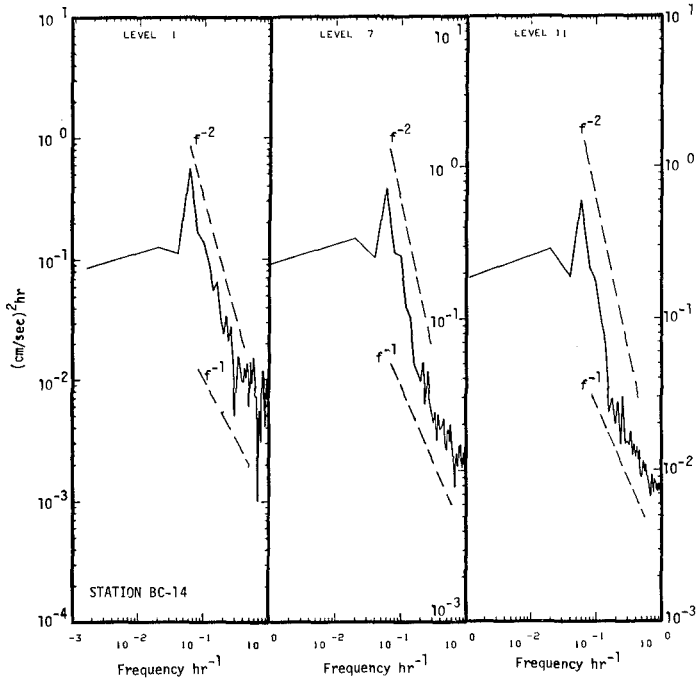


Fig. 7

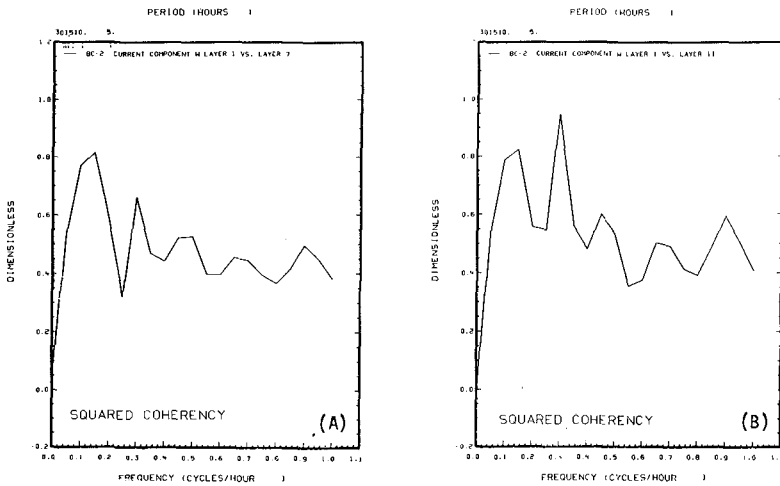


Fig. 8 Computed coherency spectra between the oscillation in the surface layer and layer 7 (A) and between the surface layer and layer 11 (B) near station BC-2

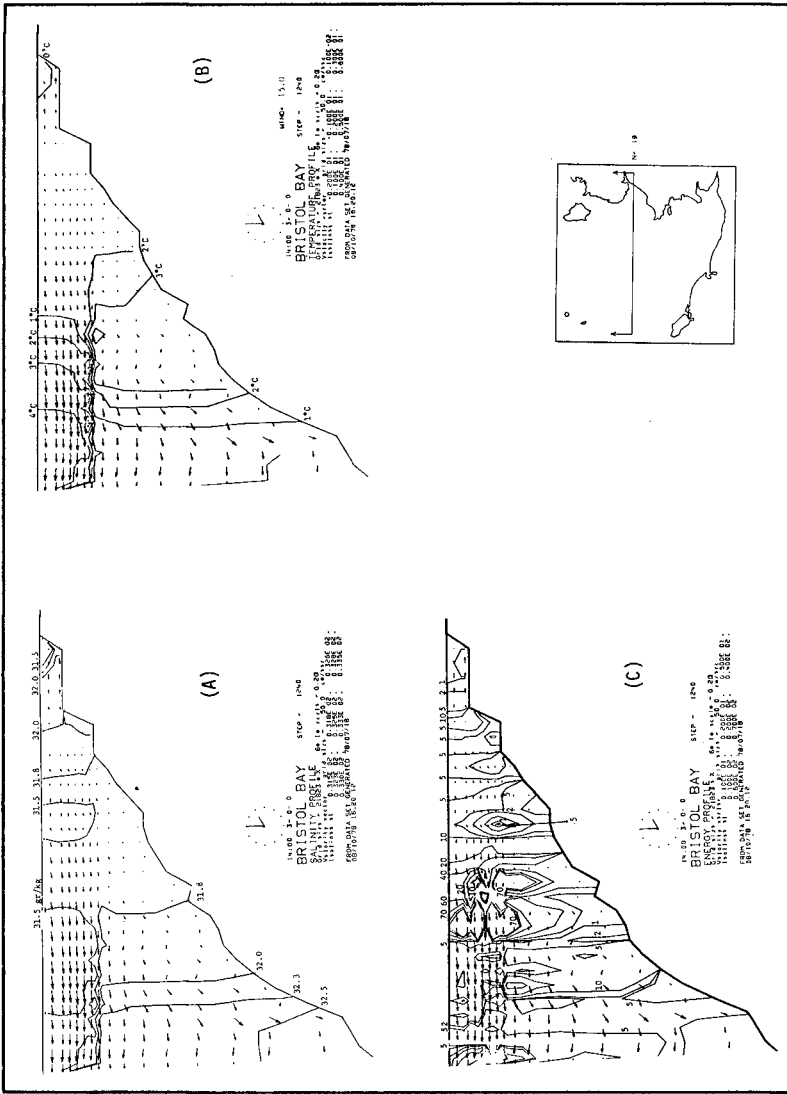


Fig. 10 Computed vertical distribution of salinity (A), temperature (B) and turbulent SGS energy (C) along a profile indicated in inset map at 1400 p.m. June 18, 1976. The vertical plotting scale for the vertical velocity component has been enlarged 727 times.

movement of the water surface in the modeled area. Figure 11 illustrates the rising and falling of the water surfaces in the modeled area at three-hour intervals as they would be seen by a spectator looking from the north toward the Alaska Peninsula. Higher tidal harmonics superimposed on the principal lunar and solar components are also evident. It should be pointed out that the result would be different if the computation were to be carried out assuming a homogeneous density structure. This is due primarily to the different vertical shear structures induced by the vertical density gradient and the modification of the horizontal pressure gradient caused by the variations in the horizontal density distribution.

The computed co-tidal charts for the diurnal and semi-diurnal components are presented in Figs. 12 and 13. These results are derived from 51 hours of computed results by means of 2-D Fourier transformation. They are compared to the observed charts for the K1 and M2 components derived from long-term data compiled by NOAA. Both the phase and the location of amphidromic points agree well with the observed chart. It seems our bottom friction coefficient is still somewhat on the high side.

Acknowledgment

This study was supported by the Bureau of Land Management through interagency agreement with the National Oceanic and Atmospheric Administration, under which a multi-year program responding to needs of petroleum development of the Alaskan continental shelf is managed by the Outer Continental Shelf Environmental Assessment Program (OCSEAP) Office.

References

1. Leendertse, Jan J., and Shiao-Kung Liu, *A Three-Dimensional Model for Estuaries and Coastal Seas: Volume IV, Turbulent Energy Computation*, The Rand Corporation, R-2187-OWRT, May 1977.
2. Liu, Shiao-Kung, and Alfred B. Nelson, *A Three-Dimensional Model for Estuaries and Coastal Seas: Volume V, Turbulent Energy Program*, The Rand Corporation, R-2188-OWRT, May 1977.
3. Liu, Shiao-Kung, and Jan J. Leendertse, *A Three-Dimensional Model for Estuaries and Coastal Seas: Volume VI, Bristol Bay Simulations*, (in preparation).
4. Gordon, R. L., "Internal Wave Climate Near the Coast of Northwest Africa during JOINT-1," *Deep-Sea Research*, Vol. 25, 1978, pp. 625-643.
5. Haurwitz, B., H. Stommel, and W. H. Munk, "On Thermal Unrest in the Ocean," *Rosby Memorial Volume*, Rockefeller Inst. Press, New York, 1959, pp. 74-94.

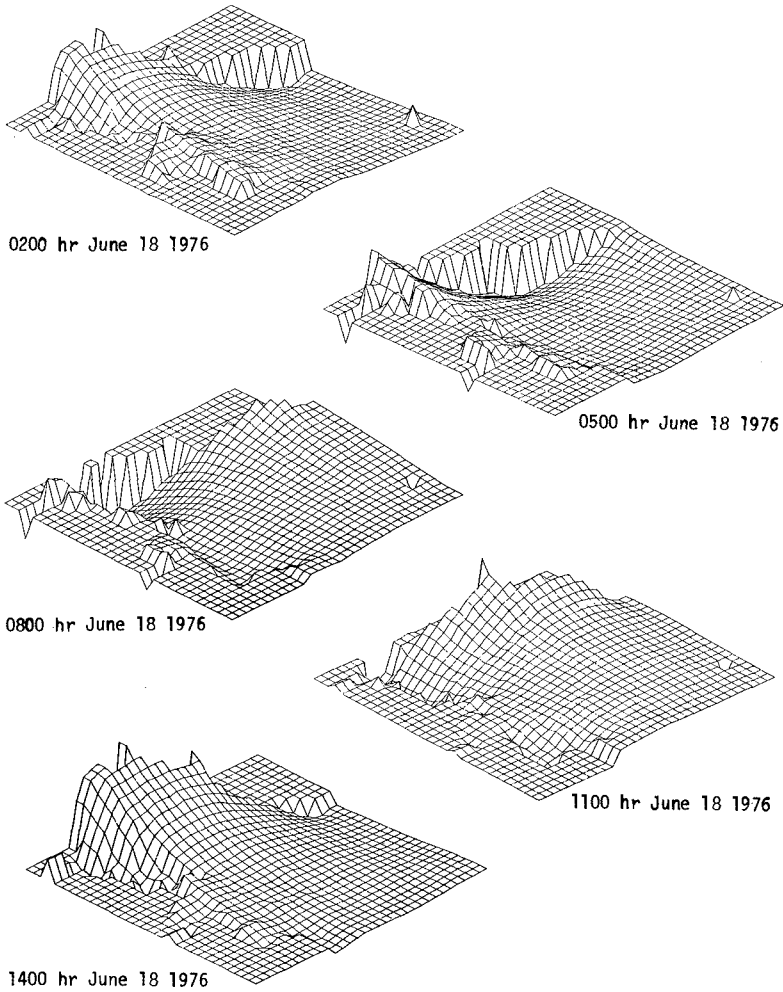


Fig. 11 Three-dimensional plots of the computed water surface movement in the modeled area during a 12-hour period in the verification run. Higher tidal harmonics superimposed on the principal lunar and solar components are evident.

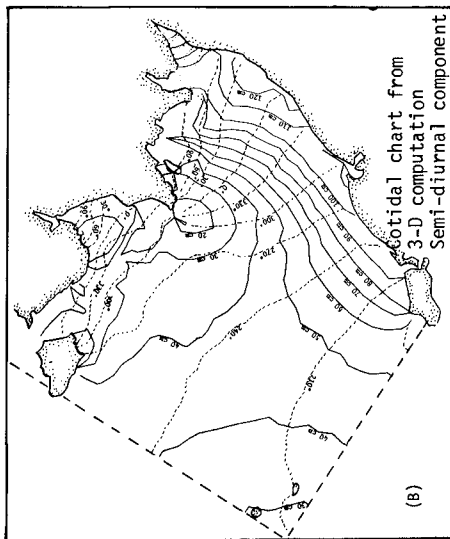
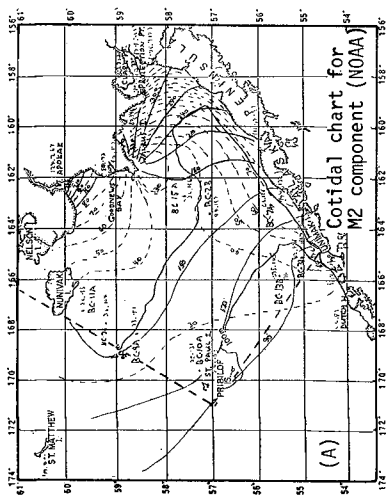


Fig. 13

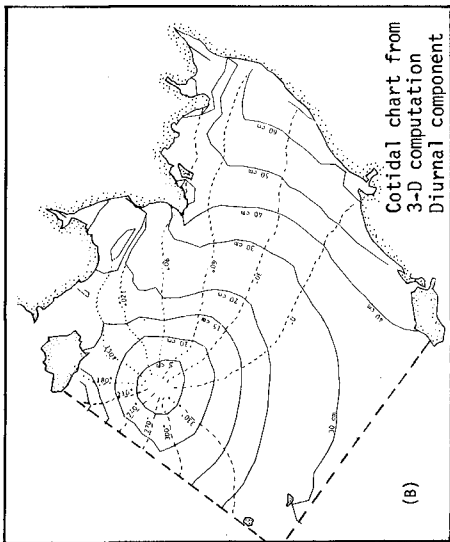
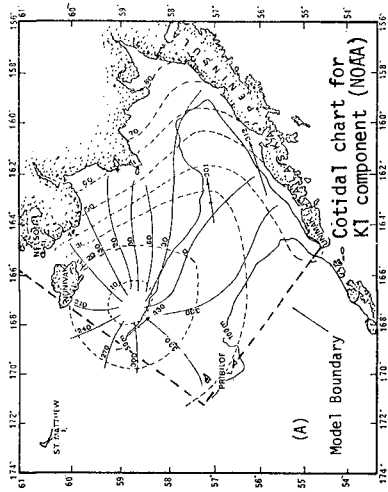


Fig. 12

CHAPTER 165

The Wind-Driven Circulation in the Northern Arabian Sea

Khawaja Zafar Elahi
Lecturer, Department of Mathematics
Quaid-I-Azam University, Islamabad, PAKISTAN

and

Jürgen Sündermann
Professor, Hamburg University, FED. REP. GERMANY

ABSTRACT

The circulation pattern in the northern Arabian Sea is presented for the well defined wind fields, which are classified as the South-West Monsoon and the North-East Monsoon. To check the reproduction ability of the model, first tidal waves are computed. The results shows a good agreement with the known values given in literature.

1. INTRODUCTION

The wind-driven circulation represents the major global systems of surface and subsurface currents found in the world ocean. These are caused by the wind, which blows in a steady direction during a reasonable time. It transmits momentum to watermasses through surface frictional stresses.

The Indian Ocean has many variable currents due to monsoon wind systems that blow across it, changing direction as the seasonal changes. Similar effects exist for the northern part of the Arabian Sea.

The well-developed wind fields are classified as:

South - West Monsoon and

North - East Monsoon.

The South - West monsoon lasts from May to September (summer monsoon). Wind direction during this time is from south-west wards over the North Indian Ocean.

The season of the North - East monsoon lasts from November to March and this is also known as the winter monsoon. Over the north Indian Ocean, i.e. the area of the Arabian Sea and Bay of Bengal, the winds blow from the NE-direction. These two wind-periods will be used to reproduce the wind-driven circulation patterns in the modelled area.

2. THE TWO-DIMENSIONAL HYDRODYNAMICAL-NUMERICAL MODEL

The computation of tides and wind driven circulations in the Northern Arabian Sea was based on the quasi-linear, vertically integrated hydrodynamical differential equations:

$$\begin{aligned} \frac{\partial u}{\partial t} - 2\omega \sin \phi v + \frac{r}{H} \sqrt{u^2+v^2} u - A \Delta u + \frac{g}{R \cos \phi} \frac{\partial \xi}{\partial \lambda} &= \frac{\mu}{H} \sqrt{u^2+v^2} u \\ \frac{\partial v}{\partial t} + 2\omega \sin \phi u + \frac{r}{H} \sqrt{u^2+v^2} v - A \Delta v + \frac{g}{R} \frac{\partial \xi}{\partial \phi} &= \frac{\mu}{H} \sqrt{u^2+v^2} v \\ \frac{\partial \xi}{\partial t} + \frac{1}{R \cos \phi} \left(\frac{\partial}{\partial \lambda} (Hu) + \frac{\partial}{\partial \phi} (Hv \cos \phi) \right) &= 0 \end{aligned}$$

The following notations have been used:

u, v	components of vertical averaged velocity in the x-, y-direction, resp.
ξ	water elevation
A_h	horizontal eddy coefficient
g	acceleration due to gravity
h	mean water depth
H	$h + \xi$ actual depth
r	bottom friction coefficient
R	radius of the Earth
t	time
U, V	components of the wind velocity
x, y	space coordinates in E- and N-direction, resp.
λ, ϕ	geographical longitude and latitude
μ	surface friction coefficient
ω	angular velocity of the Earth's rotation

In addition to these equations the following boundary conditions have been considered:

- On the closed boundaries normal and tangential components of velocity are taken to be zero.
- On the open boundaries, which are the supposed joining lines of the modelled part with the main ocean, water-levels as a function of time for 4 main tidal constituents are supposed to be known and are calculated by:

$$\zeta(t) = \sum_{i=1}^4 a_i \cos(\sigma_i t - \kappa_i)$$

where

A_i amplitude

σ_i frequency

κ_i phase of the incoming tide

Moreover, the velocity gradients in the normal direction are zero at an open boundary.

In the case of the circulation model, to avoid the domination of the tidal forces on the flow pattern, waterlevels are supposed to be equal to zero on the open boundaries.

The initial conditions are:

$u = v = 0$; $\zeta = 0$. The solution after a sufficient long time is independent of these conditions.

An explicit finite difference method is used to solve the governing equations, the method is given in detail in reference /1,2/. The sea area is covered with the computational grid shown in fig. 1.

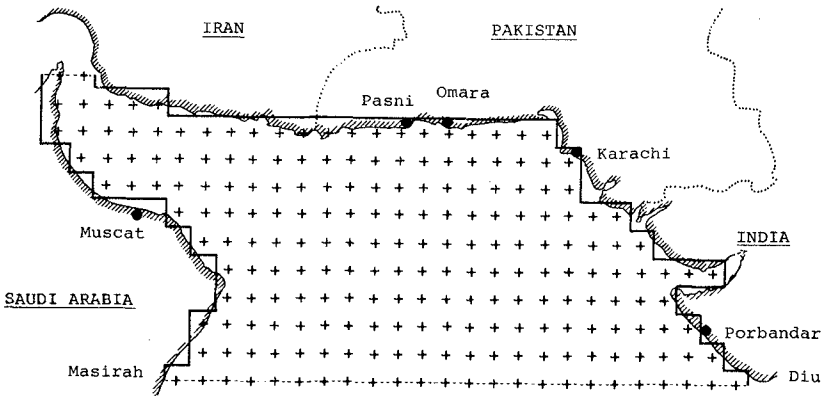


Fig. 1 Computational grid for the Northern Arabian Sea

The computational parameters used in model are as follow:

$\Delta\phi = \Delta\lambda = 0.5$ space step

$\Delta t = 1200$ s resp. 150 s time step

$A_h = 10^6$ cm²/s eddy coefficient

$r = 0.003$ bottom friction coefficient

$\mu = 3.2 \cdot 10^{-6}$ drag coefficient

$W = \sqrt{U^2 + V^2} \cdot \frac{1}{2} = 5$ m/s wind velocity

The larger time step is used for the circulation model, the smaller one for the tidal model.

In deep water areas instead of the real depth the EKMAN depth is used in the wind driven circulation model. As the system of equations is vertically integrated and the maximum depth in the area is 3500 m, wind is not effecting the whole depth, but only the upper layer, known as EKMAN depth. Under the special conditions of the Arabian Sea the value of this parameter is 72 m.

3. RESULTS

For the verification of the model at first the tidal waves in the area have been computed. The numerical results for principal semi-diurnal lunar tide M_2 are presented in fig.2 in the form of co-tide and co-range lines.

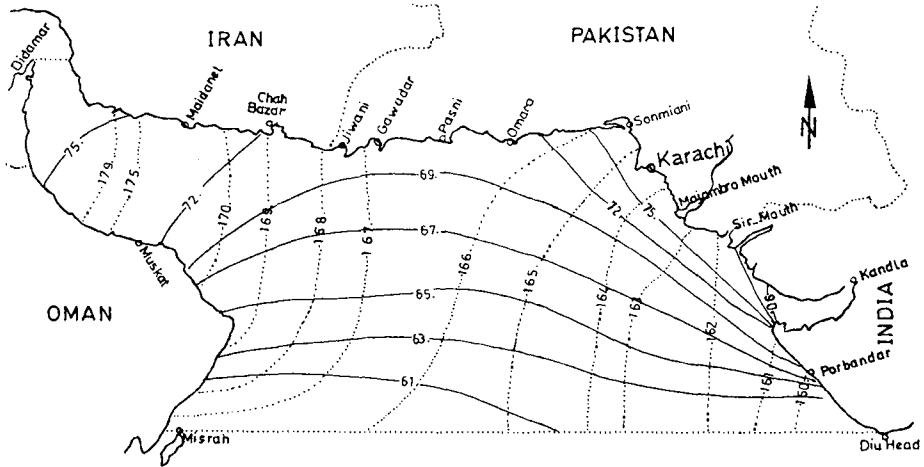


Fig. 2 M_2 -tide in the Northern Arabian Sea
 ——— isolines of amplitude in cm
 isolines of phase in degree related to Greenwich

The harmonic constants for the gauges Porbandar, Karachi, Ormara, Pasni and Muscat are used to compare the computed values. Results on the gauges Porbandar, Karachi and Pasni are in a very good agreement with the observed values, but is a little difference at the gauge Ormara. The observed value for this gauge is known only through the local tide table /3/ and as the results of the other two neighbouring

gauges are in good agreement, one can doubt about the observed value. The difference in values at gauge Muscat is due to cross influence of two open boundaries. The result for four major tidal harmonic constants are presented in table 1 in comparison with the observed values.

TIDAL CONSTITUENT		M_2		S_2		K_1		O_1	
SITE	a (cm)	c	o	c	o	c	o	c	o
	κ (deg.)								
Porbandar	a	67,92	65,0	27,57	24,0	45,17	46,0	24,11	24,0
	κ	161,43	157,0	191,51	220,0	345,89	336,0	342,10	342,0
Karachi	a	79,91	79,8	31,47	29,6	39,22	41,1	23,68	20,0
	κ	166,34	163,7	194,67	193,9	347,51	342,2	343,93	343,2
Omara	a	69,54	70,0	27,27	24,0	37,72	43,0	22,94	18,0
	κ	166,29	156,1	194,24	176,0	346,47	340,0	343,68	343,3
Pasni	a	68,98	69,0	27,07	26,0	37,38	31,0	22,91	24,0
	κ	166,37	165,0	194,48	192,0	346,42	346,0	343,79	346,3
Muscat	a	69,75	63,3	27,27	23,7	35,99	38,8	22,48	20,2
	κ	171,74	159,8	199,33	189,8	347,76	341,4	345,71	342,4

Tab. 1 Computed (c) and observed (o) amplitudes (a) and phases (κ) of the major tidal constituents

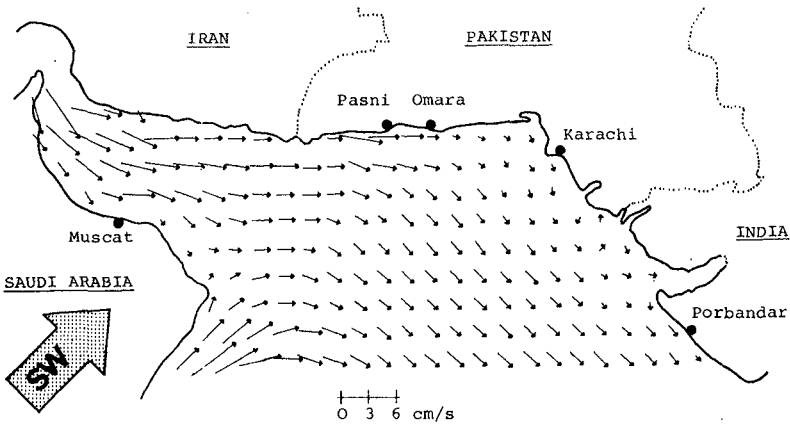


Fig. 3 Steady circulation in the Northern Arabian Sea during South-West Monsoon

The circulation pattern during the south-west monsoon is shown in fig. 3. The circulation field is characterized by a clockwise circulation superimposed by a tangential inflow from the Persian Gulf. The well known westward intensification caused by the latitudinal variation of the CORIOLIS force is seen along the Arabian coast. The circulation pattern is compared with the results of G. Schott, published in 1943 /4/ and presented in fig. 4. The computed results are in very good agreement with this circulation pattern.

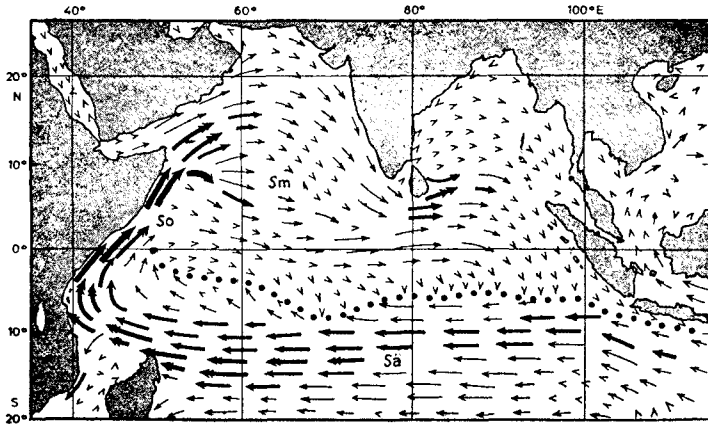


Fig. 4 Surface currents in the Indian Ocean in the Northern Summer (after G. Schott, 1943)

Effect of NE-monsoon is also studied and the result regarding the circulation pattern is shown in fig. 5.

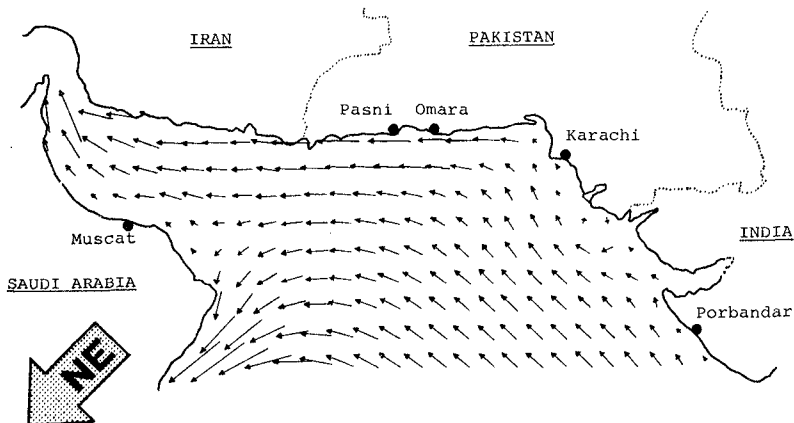


Fig. 5 Steady circulation in the Northern Arabian Sea during North-East Monsoon

REFERENCES

- /1/ Elahi, Kh. Z. Berechnung von lokalen Gezeitenphänomenen in einem Gebiet mit geringem Beobachtungsmaterial mit Anwendung auf die Somiani Bucht. Mitt. des Franzius-Inst. für Wasserbau und Küsteningenieurwesen der Techn. Univ. Hannover 48, 1978
- /2/ Hansen, W. Theorie zur Errechnung des Wasserstandes und der Strömungen in Randmeeren nebst Anwendungen Tellus 8, Nr. 3, p. 287 - 300, 1956
- /3/ Pakistan Tide Tables 1978 The Hydrographic Department, Pakistan Navy, Karachi
- /4/ Dietrich and Kalle, K. General Oceanography, John Wiley and Sons, New York, 1963

CHAPTER 166

SHELF AND COASTAL BOUNDARY LAYER CURRENTS, MISKITO BANK OF NICARAGUA

by

Richard L. Crout and Stephen P. Murray

Coastal Studies Institute, Louisiana State University

Baton Rouge, Louisiana 70803

Abstract

A 2-year study of the currents and salinity (density) fields has been conducted on the broad, shallow Miskito Bank of the eastern coast of Nicaragua.

Observations across the Bank show a southward-flowing low-salinity, seaward-thinning wedge of highly turbid water trapped against the coast within the first 25-40 km offshore. This so-called coastal boundary layer grades seaward into a northward-flowing shelf current of open-sea salinity that is essentially free of suspended sediment. Detailed transects across the coastal boundary layer show the salinity (density) structure to be closely coupled to the high-speed jet of south-flowing water.

Velocity and density measurements from the coastal boundary layer allow quantitative evaluation of each of the terms in the momentum balance equation and of the effect that each has on the circulation dynamics. The Coriolis force, the baroclinic and barotropic pressure gradient forces, and the internal friction force make important contributions to the on-offshore force balance. In the longshore balance, only the baroclinic pressure gradient force was found to be insignificant. A marked difference in this balance of forces was observed in the upper and lower layers of the water column in both the alongshore and on-offshore balances.

Introduction

Studies of continental shelf circulation have been varied in their scope. The middle and outer shelf has been studied primarily by physical oceanographers (Niiler 1975), while the innermost region, essentially the surf zone, has long been under intensive investigation by sedimentologists and engineers.

Much of the research has dealt with the circulation of the mid-shelf region on the United States East Coast, known as the Mid-Atlantic Bight. Stommel and Leetmaa (1972) and Csanady (1976) found that the circulation dynamics in the bight are the result of density differences, wind stress, and longshore surface elevations. On the shelf south of Long Island, observations show that longshore surface slope is balanced by the boundary frictional stresses (Scott and Csanady 1976).

In recent years the zone or prism of water extending out few tens of kilometers from the coast has come to be recognized as a distinct dynamical unit (Csanady 1977). The dominant role of wind stress on the shallow waters, the stratified water column arising from coastal runoff, and the blocking effect of the coast all combine to produce a flow field quite distinct from that on the shelf proper. This zone, commonly referred to as the coastal boundary layer (CBL), is of great practical importance since it is here that sewage and industrial wastes are dispersed offshore and alongshore, erosion of bottom sediment eventually affects beach behavior, and biological productivity reaches a maximum.

The CBL should be fully developed and approximately in a steady state along a shallow coast subject to large, constant, fresh-water runoff and strong persistent winds.

The objectives of this study were (a) to determine the circulation and salinity distributions on a shallow bank subject to a high freshwater input and strong, steady winds, (b) to identify the relationship between flow in the coastal boundary layer and that on the shallow shelf beyond the CBL, and (c) to measure or calculate the forces in the momentum balance of the CBL in order to understand the mechanics controlling its velocity and salinity fields. This experiment was part of a larger project undertaken to understand interrelationships between oceanographic, meteorologic, geologic, and morphologic processes on the Nicaraguan east coast (Owens and Roberts in press; Murray et al. in preparation; Hsu in press; Hsu in press).

Study Area

A suitable area for investigation of these points is found off the Caribbean coast of Nicaragua and Honduras, where the shallow platform of the Miskito Bank extends several hundred kilometers offshore. Figure 1 shows the southern half of this bank and the adjacent ocean area. Near the 100-m contour at the bank edge depths drop precipitously down to several thousand meters. The flat profile of this shallow-water bank is best illustrated by comparing it (Fig. 2) to a profile across the West Florida Shelf (Niiler 1976), considered to be an extremely low sloping continental shelf by North American standards.

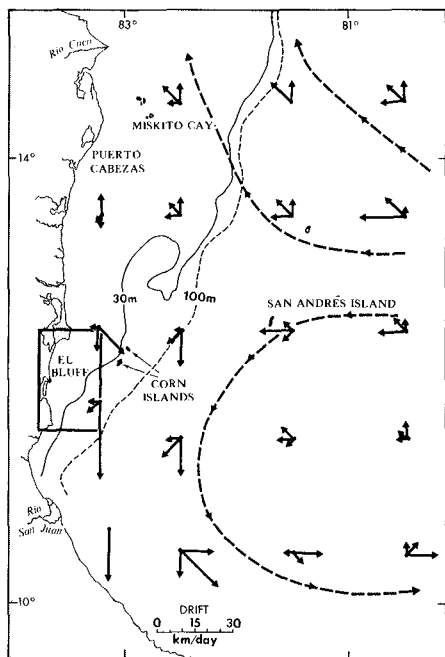


Figure 1. The southern half of the Miskito Bank, off Nicaragua. The outlined area along the coast was the site of a detailed study in 1977. Surface current vectors are plotted by 1° squares.

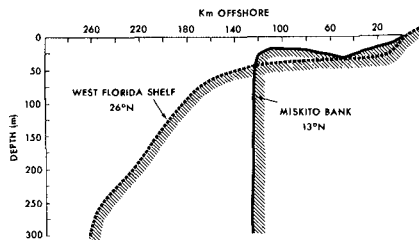


Figure 2. Comparative bathymetric cross-sections across the Miskito Bank and the West Florida shelf.

Winds across this bank are remarkably persistent in speed and direction, as shown by records from the U.S.-Colombian cooperative weather station on San Andres Island, located near the center of Figure 1. These data (Fig. 3) are a summary of the four times daily observations of surface wind velocity over the 3-year period 1970-72. Most of the year winds are 7-10 m/sec from the ENE, with steadiness factors above 90%. The steadiness factor is the ratio of the absolute value of the vector mean wind speed to the mean wind speed. There, high values, typical of the trade wind belt, indicate that winds are essentially steady and unidirectional over the duration of a month.

This stretch of the Nicaraguan coast is one of the truly rainy areas in the world. Rainfall increases from 3 m/yr in the north to 5 m/yr near the Costa Rican border. Values of 2-2.5 m/yr are considered typical for a tropical rain forest. Murray et al. (in preparation) have calculated that the eventual runoff from the coastal watersheds brings about $1.5 \times 10^{11} \text{ m}^3$ of fresh water each year to the Nicaraguan coast, three times more fresh water per unit length of coast than the Atlantic coast of the U.S.A. receives.

The Caribbean Current, moving westerly across the Caribbean as a well-defined stream of 0.5-1.0 m/sec speed, impacts the Miskito Bank just west of San Andres Island. On Figure 1 we have plotted by 1° squares the three surface current vectors that amount to at least 80% of the observations in the long-term averages for the period July-September available by octant from the

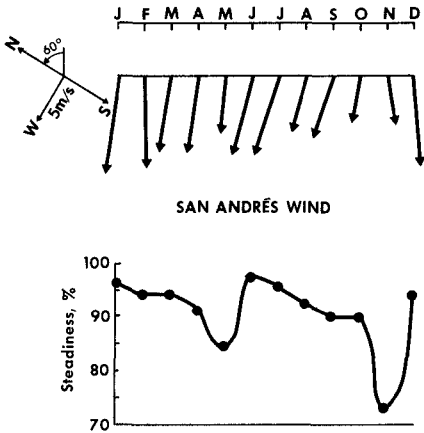


Figure 3. Monthly average wind velocities at San Andres Island (located on Figure 1). The steadiness factor is the ratio of the vectorially averaged wind speed to the average wind speed.

U.S. National Oceanographic Data Center (NODC). A bifurcation in the current on the Bank at about 13°N causes northerly flows north of this line and southerly flows south of it.

Initial Field Observations - August 1976

In August 1976 our research team, consisting of two physical oceanographers, a meteorologist, a geologist, and several technicians, conducted a general study of the currents, waves, boundary layer meteorology, and sedimentary processes across the bank (Murray et al. 1976). Figure 4 shows the cruise track and type of data collected from our research vessel, a 25-m fishing boat chartered out of El Bluff. One of the transects (25 August) of vertical profiles of salinity, temperature, and current velocities from El Bluff northeasterly out to mid-shelf delineated two main flow regimes on the shelf. Figure 5 shows a wedge of low-salinity (30-35 ppt) coastal boundary layer water within 25 km of the coast moving as a distinct unit at high speeds to the south. Salinity gradients along the track drop from 0.23 ppt/km inside to 0.03 ppt/km outside the CBL. Underneath and beyond the CBL there is a transition zone (10 km wide) of low to stagnant currents (0 ± 5 cm/sec), which gradually transform seaward to a distinct core of currents moving with moderate speed to the north. This outer shelf regime is typically well-mixed in the vertical.

A more detailed transect of salinity and current distribution across the coastal boundary layer, made on 26 August, is shown as Figure 6. The very low salinity effluent plume (10-14 ppt) from the Escondido River, which flows into Bluefields Bay behind El Bluff, is evident in the first 5 km offshore. Beyond the plume front salinities increase regularly seaward from 25 to 35 ppt, values considered as typical of the CBL waters. Figure 6 shows the density-salinity structure to be closely coupled to a high-speed jet of southerly flowing water with a maximum speed near the surface about 13 km offshore.

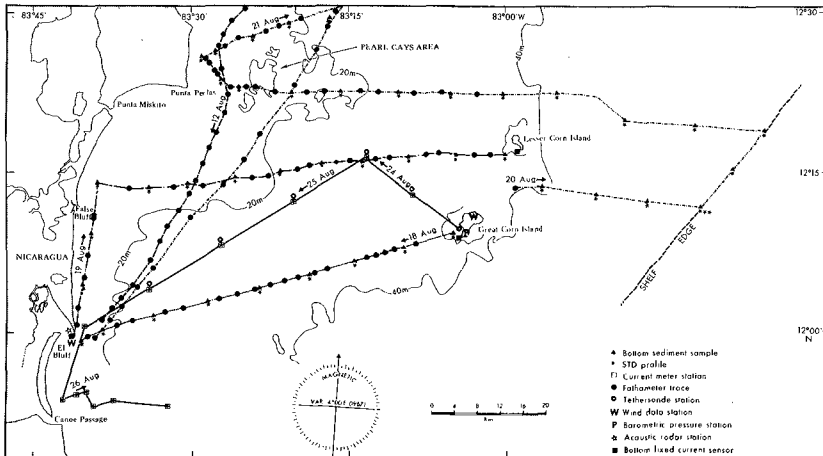


Figure 4. Type, time, and location of data collected during the August 1976 research cruise.

Overall there is good similarity between the salinity and velocity structure of the detailed CBL transect (Fig. 6) and the shelf transect (Fig. 5). A detailed comparison shows some differences, however. The CBL in Figure 5 has a nearshore speed maximum, penetrates no deeper than 10 m, and thins seaward to intercept the surface 30 km offshore. The section in Figure 6 shows that the CBL has a distinct offshore speed maximum, deepens seaward to at least an 18-m thickness, and probably extends as much as 40 km offshore. It is likely that the impact of the immense discharge of the Escondido River (which normally reaches 2,000 m³/sec in August) coming through the El Bluff and Canoe Passages downstream of the shelf transect, that enlarges the CBL and pushes the velocity maximum offshore. Note that the offshore jet is not accompanied by a shoreward rising of the density surfaces, as is usually observed in the Great Lakes (Csanady, 1977).

Coastal Boundary Layer Observations - 1977

Based on the previous year's results, a detailed field study conducted 18-21 September 1977 focused on the coastal boundary layer. Data were collected over the 4-day period along four transects taken perpendicular to the coast. Six stations were occupied along the first three transects and three along the final one, as shown in Figure 7. This detailed study area is outlined in Figure 1. A vertical profile of current observations was taken at each station utilizing a Marine Advisors Q-15 ducted current meter mounted with a pressure transducer for depth setting. Because the Plessey STD used to measure salinity and temperature malfunctioned, water samples were obtained simultaneously with the current readings and were analyzed later on a Guideline Autosal 8400 salinometer. The STD data prior to malfunction indicated that the CBL was relatively isothermal at 28°C (the same as the previous

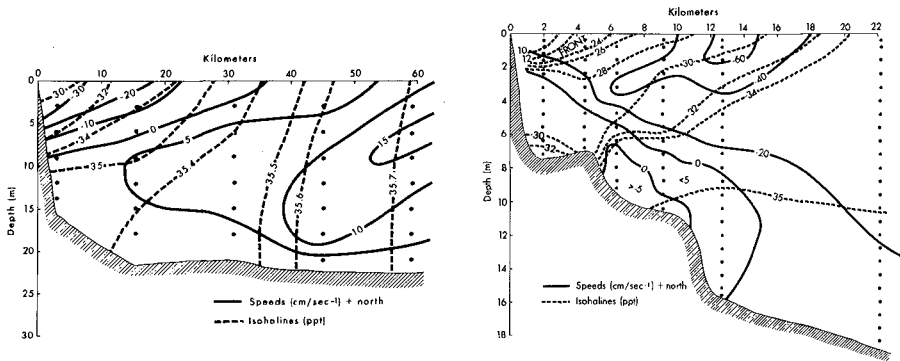


Figure 5. Cross section of Figure 6. Cross section of salinity and north-south current components across the shelf on a line northeast of El Bluff, 25 August 1976.

Cross section of salinity and north-south current components across the coastal boundary layer off Canoe Passage, 26 August 1976.

year), and this figure has been used in subsequent density calculations. Salinity and current observations were also taken in vertical profiles over a 25-hour period at the shelf edge in order to determine the importance of the tidal currents.

Circulation and salinity distribution. The horizontal salinity patterns at the 1.5 m depth level (Fig. 8) from Punta Perlas to Monkey Point provide insights into the spatial variability of the coastal boundary layer. Taking the 35-ppt isohaline as the seaward edge of the CBL, it can be seen that the coastal boundary layer varies from 15 to 25 km in width. A lens of fresher water resulting from discharge of the Rio Escondido is present off El Bluff. A tongue of 34 ppt seawater which intrudes northward into less saline water south of Punta Perlas indicates extreme flow curvature as the water passes the Point.

Salinity variations in the four cross sections are shown in Figure 9. The low-salinity baroclinic layer is wedge shaped in all four cases but does not extend fully to the bottom along line 4 off Monkey Point, where the offshore slope is quite steep. The situation appears much like that observed in estuaries; i.e., the deeper the water, the stronger the onshore intrusion of salt water and vice versa. For example, along the shallowest line (1) the 35.5 isohaline intercepts the bottom 25 km offshore, but along the steepest line (4) the same 35.5 isohaline hits the bottom about 3 km offshore. Thus for the same amount of fresh-water discharge we might expect considerably wider but vertically thinner CBLs off steeply sloping coasts than off shallow sloping coasts.

A comparison of current vectors at the 1.5-m depth in Figure 10 to the salinity patterns in Figure 8 indicates that velocities in the CBL are much higher than those in the outer well-mixed

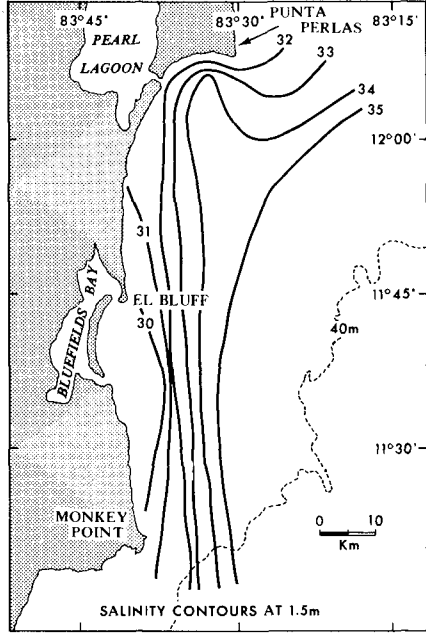
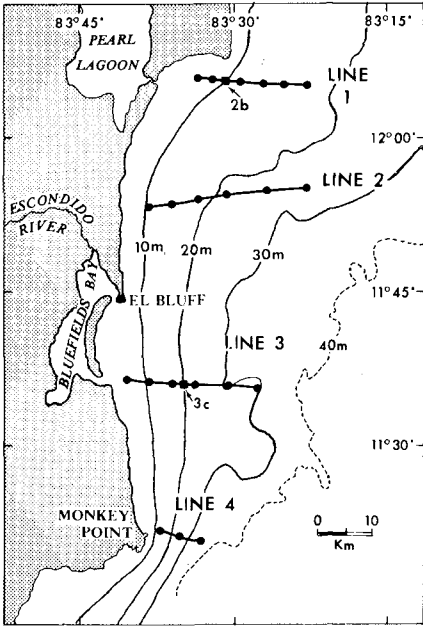


Figure 7. Detailed topography and location of stations for 18-21 September 1977 coastal boundary layer experiment. Computation of momentum balance at stations 3c and 2b are shown in Figures 12 and 13, respectively.

Figure 8. Near-surface salinity distribution, 18-21 September 1977.

region, which are slow and to the northwest. It is also apparent that maximum velocities occur in the core of the CBL and diminish toward each boundary. The flow has a strong tendency to be parallel to the bottom contours (shown in Figure 7), an effect which was studied in detail by Murray, 1975. Note that this topographic control is especially important to the current trajectories along line 2. The slow and variable velocities at the inner portion of line 1 are a result of the shallow depths in the region just south of Punta Perlas, where large mud banks were present. The CBL along this stretch of coast resembles a meandering jet, and we have sketched its probable inner and outer limits on Figure 10.

Figure 11 presents cross-sectional views of the north-south velocity components along the four lines. It is evident that a high-speed jet ($>70 \text{ cm s}^{-1}$) which reaches to the bottom has rounded Punta Perlas (Fig. 11). The seaward extent of the jet is not captured in the data of Line 1 and its outer boundary may lie 20 km

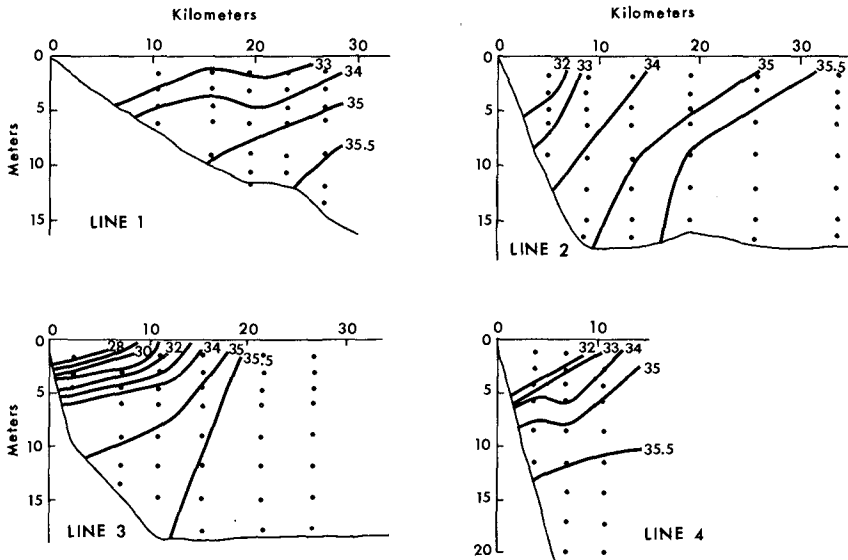


Figure 9. Cross sections of salinity at four time transects, 18-21 September 1977.

farther offshore. Velocities near the coast are negligible. Line 2 shows only weak, southerly flow as the axis of the current jet has turned nearly perpendicular into the coast in a westerly direction. In Line 3 the section is nearly perpendicular to the flow direction and shows a well-defined jet with a major core moving faster than 50 cm s^{-1} . Again the flow extends to the bottom, but is negligible against the coast. The bottom is much deeper in Line 4. As a consequence the flow does not reach below 13 m, but appears to have spread out laterally so that only about half of it is seen in our data. The steepened coast here reduces bottom friction, allowing both (a) higher speeds nearer the coast in the CBL and (b) slow-moving saltier water under the CBL to penetrate closer to the coast. Comparing the 0 cm/s isotachs in Figure 11 and the relative positions of the 35.5 ppt isohalines in Figure 9 shows that the most energetic portion of the coastal boundary layer is indeed confined to the brackish baroclinic layer inside the 35.5 ppt isohaline.

Momentum balance. The momentum equations, neglecting horizontal friction, and with x positive to the east, y positive to the north, and z positive down, can be written

$$\frac{du}{dt} = fv - \frac{1}{\rho} \frac{dp}{dx} - \frac{1}{\rho} \frac{\partial \tau_x}{\partial z} \quad (1a)$$

$$\frac{dv}{dt} = -fu - \frac{1}{\rho} \frac{dp}{dy} - \frac{1}{\rho} \frac{\partial \tau_y}{\partial z} \quad (1b)$$

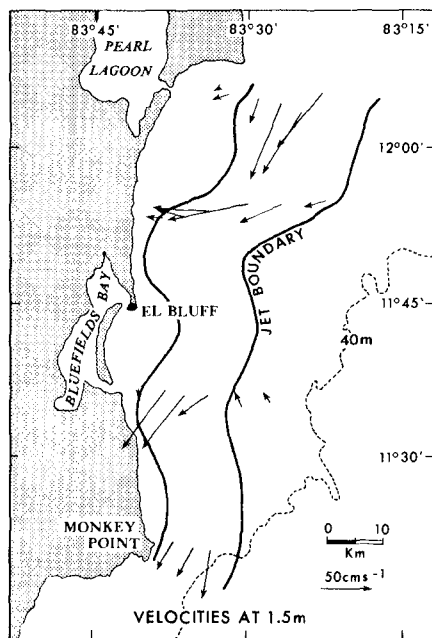


Figure 10. Near-surface velocity field and outline of coastal jet, 18-21 September 1977.

$$\frac{dw}{dt} = g - \frac{1}{\rho} \frac{dp}{dz} - \frac{1}{\rho} \frac{\partial \tau_z}{\partial z} \quad (1c)$$

where u , v , and w are the speeds in the x , y , and z directions, respectively, f is the Coriolis parameter, p is pressure, ρ is density, and τ is the Reynolds or eddy stress.

Due to steady wind and weather conditions over the 4-day observation interval, any temporal accelerations in the study area are most likely a result of tidal oscillations. Maximum accelerations, taken from time series of currents over a 24-hour period, were $2.8 \times 10^{-4} \text{ cm sec}^{-2}$ for $\partial u/\partial t$ and $3.0 \times 10^{-4} \text{ cm s}^{-2}$ for $\partial v/\partial t$. These values are an order of magnitude smaller than other terms in the momentum balance and are used to justify neglecting the temporal accelerations.

For motions on the time and space scales considered, (1c) reduces to the hydrostatic balance and can be used to transform (1a) and (1b) into

$$u \frac{\partial u}{\partial x} + v \frac{\partial u}{\partial y} = fv - \frac{g}{\rho} \int_0^z \frac{\partial \rho}{\partial x} dz - g \frac{\partial \eta}{\partial x} - \frac{1}{\rho} \frac{\partial \tau_x}{\partial z} \quad (2a)$$

$$u \frac{\partial v}{\partial x} + v \frac{\partial v}{\partial y} = -fu - \frac{g}{\rho} \int_0^z \frac{\partial \rho}{\partial y} dz - g \frac{\partial \eta}{\partial y} - \frac{1}{\rho} \frac{\partial \tau_y}{\partial z} \quad (2b)$$

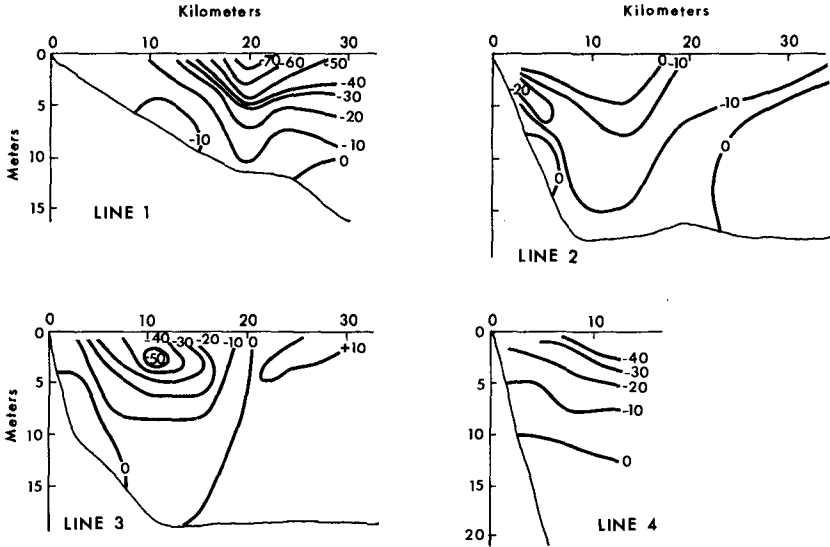


Figure 11. Cross sections of north-south (v) velocity components, 18-21 September 1977. The positive direction of v is north.

where η is the sea surface elevation, positive up, the second and third terms on the right-hand side are the baroclinic pressure gradient force and the barotropic pressure gradient force, respectively. At this junction all of the terms in the momentum equation may be calculated from the data collected during the field study except the barotropic pressure gradient and the internal friction terms. Integrating (2) over depth yields

$$\frac{1}{h} \int_0^h u \frac{\partial u}{\partial x} dz + \frac{1}{h} \int_0^h v \frac{\partial u}{\partial y} dz = f\bar{v} - \frac{g}{\rho h} \int_0^h \int_0^z \frac{\partial \rho}{\partial x} dz \cdot dz - g \frac{\partial \eta}{\partial x} - \frac{1}{\rho h} (\tau_{xb} - \tau_{xs}) \quad (3a)$$

$$\frac{1}{h} \int_0^h u \frac{\partial v}{\partial x} dz + \frac{1}{h} \int_0^h v \frac{\partial v}{\partial y} dz = -f\bar{u} - \frac{g}{\rho h} \int_0^h \int_0^z \frac{\partial \rho}{\partial y} dz \cdot dz - g \frac{\partial \eta}{\partial y} - \frac{1}{\rho h} (\tau_{yb} - \tau_{ys}) \quad (3b)$$

where h is the total water depth and τ_{xb} and τ_{yb} are bottom stresses in the x - and y -directions, respectively and are given by the expression

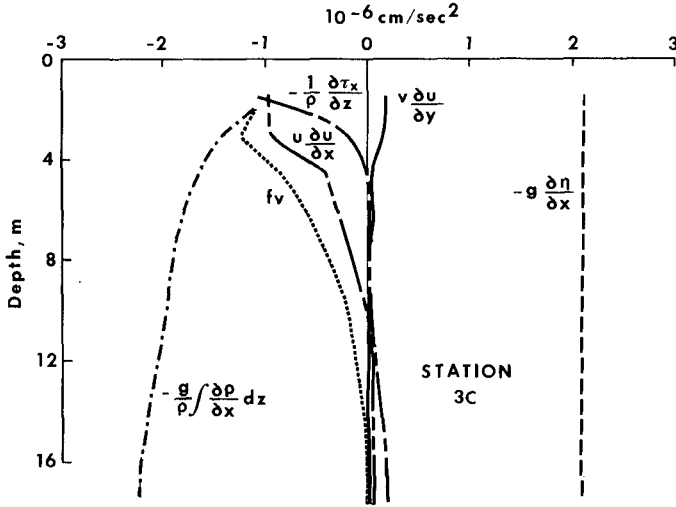


Figure 12. The vertical distribution of forces in the onshore-offshore (x) momentum equation at station 3c. A positive value of a force acts to the east, or offshore.

$$\tau_{xb} = \rho \kappa u_b |\vec{v}_b|, \quad \tau_{yb} = \rho \kappa v_b |\vec{v}_b| \tag{4}$$

where κ is a coefficient of bottom friction (2.5×10^{-3}), u_b and v_b are speed components 1 m above the bottom, and v_b is the corresponding velocity. Likewise, τ_{xs} and τ_{ys} are wind stress components given by the well-known expression

$$\tau_{xs} = \rho_a C_D u_w |\vec{w}|, \quad \tau_{ys} = \rho_a C_D v_w |\vec{w}| \tag{5}$$

where ρ_a is air density and C_D is the drag coefficient, given as 1.26×10^{-3} for the Miskito Bank study area (Hsu in press a). When these values are substituted into equations (3), they may be solved for the surface slopes, $\partial\eta/\partial x$, $\partial\eta/\partial y$. The values from equation (3) may then be substituted into equation (2) and the internal friction force term computed. Water density is easily computed from salinity and temperature by standard formulas. Thus all terms in the momentum equation (2) are now known either from observations or computations.

Stations 3c and 2b, located on Figure 7, give representative examples of the on-offshore and alongshore force balances in the CBL in Figures 12 and 13, respectively. For purposes of dis-

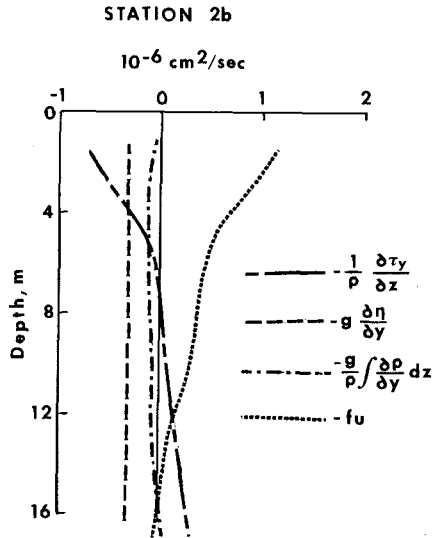


Figure 13. The vertical distribution of forces in the along-shore (y) momentum equation at station 2b. A positive value of a force acts to the north.

cussion the water column may conveniently be divided into two layers with respect to the force balance.

The baroclinic pressure gradient force is a direct result of the density field initiated by the large freshwater influx into the CBL. This force is directed toward the west or into the coast throughout the water column. In the surface layer this force is less than in the lower portion of the column. The lack of large density gradients parallel to shore results in an insignificant baroclinic pressure gradient force alongshore in the CBL.

The Coriolis force is a function of the current speed and is therefore large in the surface layers, where the speeds are large. As seen in Figure 12, this force is as important as the baroclinic pressure gradient force in the surface layer. The westward force generated by the Coriolis term diminishes below the surface layer as speeds lessen. Figure 13 shows that in the longshore direction this force is quite large and to the north. Again the Coriolis force is insignificant below the surface layer.

The barotropic pressure gradient terms play a large role in the on-offshore and longshore momentum equations, as shown in Figure 12 and 13. The magnitude of this force in the on-offshore direction is larger than any of the other forces; its direction is offshore, or to the east. Alongshore the contribution of the barotropic term is smaller than the on-offshore value, but the southward directed force remains important in the overall balance of forces. The on-offshore force is the result of the sea surface slope initiated by the wind stress, which piles water up against the coast, and the steric elevation of the nearshore water surface

due to the influx of fresh water with a high specific volume.

Figures 12 and 13 also give a representative idea of how the internal friction force behaves in the CBL. In the surface layer the components of the frictional force are directed to the south and east, while this force is in the opposite directions below this layer. As this term is calculated as a residual from the balance of the other terms, it will contain errors that could not be eliminated from the analysis. The largest errors should arise from the effects of the field accelerations, which could not be calculated at most stations due to sampling restrictions. Where these acceleration terms were computed, their contribution to the force balance was small and confined to the surface layer, as can be seen in Figure 12. Therefore, errors in the internal friction force term should have occurred only in the surface layer.

Summary

A 2-year study of the currents and salinity (density) fields has been conducted on the broad, shallow Miskito Bank of the eastern coast of Nicaragua. Tides are quite small on the bank, and the local trade winds are remarkably steady in both speed and direction, thus maximizing the likelihood of a steady-state current field. The adjacent coastal watersheds receive some of the highest rainfall rates in the world and consequently debouch large quantities of fresh water onto the shelf. The large-scale current field deduced from NODC ship drift data on a 1° square resolution show a major current stream (Caribbean Current) crossing the Caribbean from east to west, impacting and riding up onto the Miskito Bank and bifurcating into two arms, one flowing north and the other flowing south along the coast.

Observations across the Bank show a southward-flowing low-salinity, seaward-thinning wedge of highly turbid water trapped against the coast within the first 25-40 km offshore. This coastal boundary layer grades seaward into a northward-flowing shelf current of open sea salinity that is essentially free of suspended sediment. Detailed transects across the coastal boundary layer show the salinity (density) structure to be closely coupled to high-speed jet of south-flowing water.

The forces acting on the CBL in the on-offshore and the along-shore momentum balance were quantitatively evaluated from observations using finite-difference techniques. Each of the forces represented in the momentum balance is important to the circulation dynamics of the Miskito Bank coastal boundary layer, as can be seen in Figure 14, which is a schematic model of the balance of forces. The tremendous amount of rainfall that falls on the drainage basin of eastern Nicaragua creates strong density gradients in the CBL, which result in baroclinic pressure gradient forces that contribute significantly to the on-offshore momentum balance. This freshwater influx combines with setup against the coast caused by the trade winds and initiates a large barotropic pressure gradient force to the east which opposes the baroclinic pressure gradient force. High current speeds parallel to shore are acted on by the Coriolis force in the surface layer and produce another force that acts into the coast. The shallow depths ensure that frictional effects also come into play as forces in the water column. In the surface layer this force acts in concert

SUMMARY - BALANCE OF FORCES

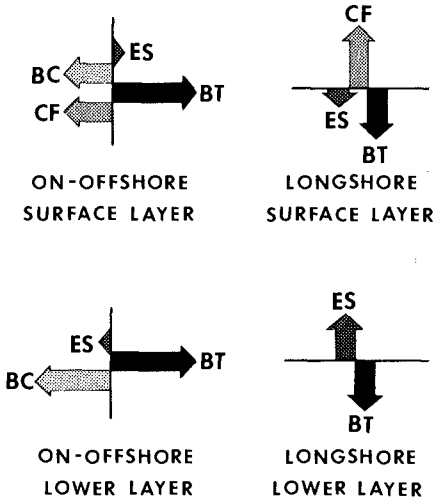


Figure 14. A diagrammatic summary of the balance of forces in the coastal boundary layer, 18-21 September 1977. BC represents baroclinic (density induced) pressure gradient force, BT barotropic or surface slope force, CF Coriolis force, ES eddy stress or internal friction force.

with the barotropic pressure gradient force toward the east but opposes it in the lower layers.

In the alongshore direction frictional forces behave in a similar fashion by acting in opposite directions in the two layers. Very small density gradients parallel to shore are not large enough to produce a significant baroclinic pressure gradient force. Coriolis terms act on velocity components in the surface layer and provides a force that acts toward the north. The remaining force, the barotropic pressure gradient force, is perhaps caused by the piling of water near the coast to the north by the Caribbean Current. The sea surface slope and the resulting barotropic force are directed toward the south.

Acknowledgements

This research was supported under a contract between the Geography Programs, Office of Naval Research, Arlington, Virginia 22217, and the Coastal Studies Institute, Louisiana State University. Mrs. Gerry Dunn drafted the illustrations.

References

- Csanady, G. T. 1976. Mean circulation in shallow seas. *J. Geophys. Res.* 81:5389-5399.
- Csanady, G. T. 1977. The coastal boundary layer. In *Estuaries, geophysics and the environment*, pp. 57-68. National Academy of Sciences, Washington, D.C., 127 pp.
- Hsu, S. A. In press a. Spatial and temporal variation of the momentum flux on the eastern Nicaraguan shelf. *Limnology and Oceanography*.
- Hsu, S. A. In press b. Rainfall variability affected by a broad, shallow shelf - east coast of Nicaragua. *Monthly Weather Review*.
- Murray, S. P. 1975. Trajectories and speeds of wind-driven currents near the coast. *J. Phys. Oceanog.* 5:347-360.
- Murray, S. P., Hsu, S. A., Roberts, H. H., Suhayda, J. N., and Coleman, J. M., 1976, Dynamics of a broad, shallow bank - the Miskito Bank Experiment. Unpublished trip report, Coastal Studies Inst., Louisiana State Univ., Baton Rouge, prepared for Geography Programs, Office of Naval Research, Arlington, VA, 22 pp.
- Murray, S. P., Hsu, S. A., Roberts, H. H., Owens, E. H., and Crout, R. L. In preparation. Dynamics and sedimentation on a broad, shallow bank. To be submitted to *J. Mar. Res.*
- Niiler, P. O. 1975. A report on the continental shelf circulation and coastal upwelling. *Review of Geophys. and Space Physics* 13:609-614.
- Niiler, P. P. 1976. Observations of low-frequency currents on the Western Florida continental shelf. In *Continental Shelf Dynamics*, 7th Liege Colloquium on Ocean Hydrodynamics (J. C. J. Nihoul, ed.), Univ. of Liege, 396 pp.
- Owens, E. H., and Roberts, H. H. In press. Variation of wave energy levels and coastal sedimentation, eastern Nicaragua. *Proc. 16th Internat. Conf. on Coastal Engr., Hamburg, Amer. Soc. of Civil Engr., N.Y.* (this volume).
- Scott, J. T., and Csanady, G. T. 1976. Nearshore current off Long Island. *J. Geophys. Res.* 81:5401-5409.
- Stommel, H., and Leetma, A. 1972. The circulation on the continental shelf. *Proc. Nat. Acad. Sci.* 69:3380-3384.

CHARACTERISTICS OF CIRCULATION
IN BAY WATERS DUE TO WIND ACTION

by Akira Wada* and Yoshihito Miyaike**

ABSTRACT

This report concerns with investigations into the three dimensional mechanism of flow motion in the sea water of Mikawa Bay for the purpose of elucidating the effect of wind, tidal current and topographical features on oceanic environmental fluctuations among factors related to the diffusion process in the bay.

On the assumption that dynamics of the bay water would be affected by the tidal currents and the flow caused by the wind, a numerical simulation analysis of the flow motion phenomenon in the bay water was conducted on the basis of the meteorological and oceanographical observation data collected at the points in the investigated sea region, so as to examine the circulation mechanism of the bay water caused by the above mentioned factors.

As the results of the simulation analysis by the numerical models, large-scale eddies caused by the tidal reciprocating current as well as the constant current as the tidal residual current can be seen in the bay. And also, in the winter time when the distribution of atmospheric pressure is stable, some circulation currents are formed in the bay by the wind-generating current.

Accordingly, it is considered that the formation of these currents has a considerable effect on the diffusion characteristics of substances in the bay.

I. INTRODUCTION

When the ocean is regarded as the environment, one of the research purposes in the nearshore oceanographical process is to determine the kinetic status of the ocean. The reason for it is that physical elementary processes such as flow motion and the density structure in the coastal ocean have their own fluctuations in time and space. Especially, as far as sea water mixing is concerned, it is necessary to grasp these problems in relation to the actual movement of the sea water and elucidate the ocean structure from the viewpoint of time and space scales in the motion. And moreover, it is quite essential to clarify the relation between the random process and the decisive process, so as to make sure how the combination of the above-mentioned two processes would affect the total sea water mixing phenomenon and the water mass formation.

As primary factors that dominate the diffusion phenomena of discharged water in the bay, the flow motion of seawater, dispersion process, topographical conditions, discharge conditions, etc. may be considered. These factors are complicately combined to form the diffusion phenomena of discharged water in the sea region. The reciprocating motion of a tidal current is not so important to a long-term fluctuation process such as water pollution, though it is important to the process of short time scale. Rather, a

* Central Research Institute of Electric Power Industry, Abiko City, Chiba Pref., JAPAN.

** Technical Laboratory, Chubu Electric Power Company, Nagoya City, Aichi Pref., JAPAN.

relatively slow flow motion, such as constant current component, is considered to dominate the diffusion of pollutants. Accordingly, to realize modelling of diffusion, it will be important to know how the constant current component is reproduced.

For this purpose, it is important to make clear the mutual relation between local flow motion in the bay and its whole sea region as well as the extent of contributions of each factor related to the diffusion process to variations in ocean environment. On the basis of these research developments, a reliable diffusion model system can be made in the coastal sea region which enables to make a very reliable prediction of ocean fluctuations in connection with the environmental assessment.

Quite recently the dynamic characteristics of the water in the bay have been elucidated by various analytical solutions and experiments as well as by the field surveys. It has become one of the important research objects in the investigation of the coastal sea region to grasp the dynamic mechanism of the bay water and elucidate the role of many elementary processes which affect the whole ecosystem in the bay.

In this paper, Mikawa Bay was selected as the sea regions for investigation. On the assumption that dynamics of the bay water would be affected by the tidal currents and the flow caused by the wind, a numerical simulation analysis of the flow motion phenomenon in the bay water was conducted on the basis of the meteorological and oceanographical observation data collected at the points in the investigated sea region, so as to examine the circulation mechanism of the bay water caused by the above-mentioned factors.

II. NATURAL ENVIRONMENT OF MIKAWA BAY

Mikawa Bay is, as shown in Fig. 1, the sea region surrounded by two peninsulas, Chita and Atsumi. This bay is connected to Ise Bay at the bay mouth where the Morosaki Channel and the Nakayama Channel meet. The sea bed at this point has terrace-like topography. The western part of Mikawa Bay is sometimes called Chita Bay and the eastern part Atsumi Bay. The water depth of the bay is approximately less than 15 meters and few ups and downs are recognized at the sea bottom. The

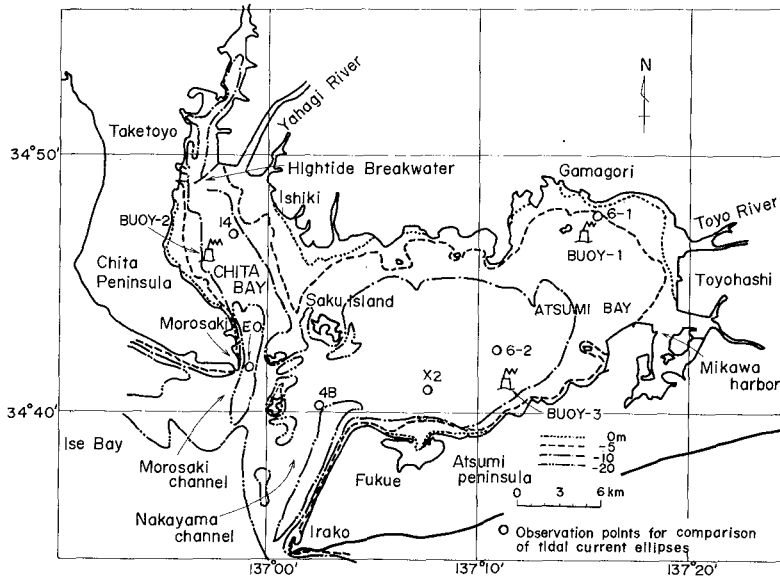


Fig. 1 Topography of Mikawa Bay

tongue shaped plateau with 2 or 3 m under the sea surface, stretching from Ishiki to Saku Island, divides the bay into two small bays, Chita and Atsumi. Both Morosaki and Nakayama Channels form a deep current moving path of 20 or 30 meters in depth, through which the sea water of this bay is exchanged with the water of Ise Bay.

The Yahagi River (average flow rate 24 m³/s) and the Toyo River (average flow rate 15 m³/s) are the main rivers flowing into Chita Bay and Atsumi Bay respectively.

As the topographical features around Mikawa Bay, it has a long stretch of hills less than 100 meters above the sea level in the Chita Peninsula, the Mikawa Plain, ruggy hills 300 meters or 400 meters above the sea level in the southern Mikawa and a long stretch of hills less than 250 meters above the sea level in the Atsumi Peninsula.

The sea water going into and out of Mikawa Bay is divided into two directions by the islands scattered at the bay mouth.

That is to say, one is the direction in which the sea water passes into Chita Bay through the Morosaki Channel and another is the direction in which the sea water passes into Atsumi Bay through the Nakayama Channel. In the center of the Nakayama Channel, the sea water turns in flow to Atsumi Bay 20 minutes earlier than the sea water in the Morosaki Channel. At both high tide and low tide, therefore, very complicated tidal currents are recognized at the mouth of Mikawa Bay. The flow velocity in these channels reaches approximately 1.0 m/s at average tide.

According to the tidal current constants obtained by 15 days-continuous observations at Mikawa Bay, the velocity ratio between the diurnal tide and the semidiurnal tide is 0.15 to 0.84, and the ratio between S₂ and M₂ is about 0.5. From the result of computation concerning energy spectrum for turbulent velocity as shown in Fig. 2, it is easily recognized that the semidiurnal tide is generally more predominant than the diurnal

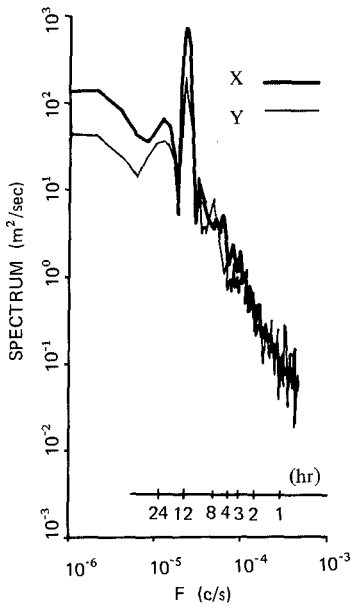


Fig. 2 Energy spectra for turbulent velocity

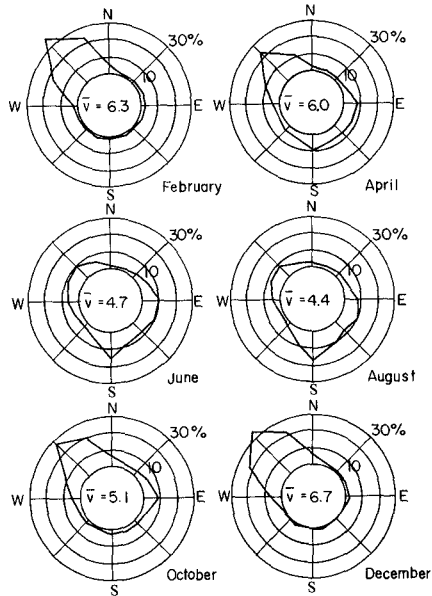


Fig. 3 Every two monthly wind blowing frequencies classified by wind directions and the average monthly wind velocities (1951~1960, Irako Meteorological Station)

tide, and especially, the branch component of M_2 tide is predominant.

The data on every two monthly wind blowing frequencies classified by wind directions and the average monthly wind velocities obtained for ten years from 1951 to 1960 at the Irako Meteorological Station in the Atsumi Peninsula are shown in Fig. 3. By observation data mean the average wind velocities measured for ten minutes every three hours. According to the data, spring, fall and winter have a high wind blowing frequency in WNW, NW and NNW directions. Especially in winter the frequency is very high, reaching as much as 90 %. On the other hand, in summer the wind blowing frequency in SW and SE directions is approximately 40 %, and these winds are seldom seen in other seasons. As for the frequencies throughout the year, the wind in NW direction accounts for about 60 %, the wind in S direction about 20 % and the one in other directions 20 %. As far as the wind velocity is concerned, the annual average velocity is 5.5 m/s. And, on the basis of the seasonal classification, the winter has the strongest season wind of 6.6 m/s and the summer has the weakest.

In the winter time, uniformity can be recognized in vertical distributions of water temperatures and salinities in Atsumi and Chita Bays. And there is no density stratification in these regions.

III. MODELLING OF THE SEASONAL WIND

3.1 Selection of the Seasonal Wind

The circulation of the sea water in Mikawa Bay caused by the wind generating current is supposed to be strongly affected by this seasonal wind in winter. The observation data of the wind were obtained at various points along the coast of Mikawa Bay in the winter time. The observation data collected covered three months from December, 1973 to February, 1974. Fifteen observation points were selected as shown in Fig. 4.

The most frequent wind directions and the average wind velocities at each observation point are shown in Fig. 4 along with stream line chart of wind.

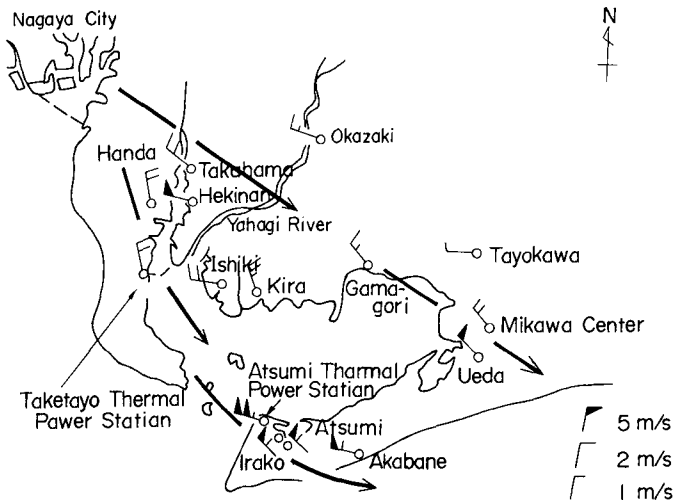


Fig. 4 Most frequent wind directions and the average wind velocities

Judging from the case when the distribution of atmospheric pressures of the winter type is stable and the seasonal wind is extremely predominant, it is concluded that the average distribution of seasonal winds at various spots along the coast of Mikawa Bay in the winter time can be expressed by the values of the most frequent wind direction and the average wind velocity to a great extent.

3.2 Stream Line Analysis of the Seasonal Wind

The wind called as the geostrophic wind exists in the higher layer of 1,000 to 2,000 m or more above the sea level.

In this case, the Coriolis' deflecting force and the pressure gradient force are balanced each other.

On the other hand, in the lower layer of several ten meters above the surface of earth, the effect of eddy viscosity caused by air turbulence and friction on the surface of earth are so great that the Coriolis' deflecting force can be ignored. But in the layers between the height of some 10 meters and the height of 1,000 to 2,000 meters, both the frictional force and the deflecting force must be taken into consideration.

The seasonal wind in winter time blows over Mikawa Bay through a wide flat earth like the Nobi plains and the sea region like Ise Bay. If the wind is regarded as being affected by the frictional effect of these surfaces, the effect caused by wind advectives is negligible. And, taking a steady state into consideration, the fundamental equations on the wind can be expressed as follows:

$$-fv = -\frac{1}{\rho} \frac{\partial p}{\partial x} + \frac{\partial}{\partial z} \left(K \frac{\partial u}{\partial z} \right), \quad fu = -\frac{1}{\rho} \frac{\partial p}{\partial y} + \frac{\partial}{\partial z} \left(K \frac{\partial v}{\partial z} \right), \quad \frac{\partial w}{\partial z} = 0 \quad (1)$$

where x, y : coordinates in the horizontal direction, z : coordinate in the vertical direction, u, v, w : wind velocity components in the x, y and z directions, f : parameter of Coriolis, p : pressure, K : coefficient of eddy viscosity, ρ : density.

The effect caused by the frictional force on and near the surface of earth is expressed by the second term of the right side. As for the equation (1), Prandtl obtained the solution as shown in the equation (3), assuming that the coefficient of the eddy viscosity can be expressed by

$$K = L^2 \left[\left(\frac{\partial u}{\partial z} \right)^2 + \left(\frac{\partial v}{\partial z} \right)^2 \right]^{1/2}, \quad L = [0.41(Z + Z_0)] / [1 + 0.178 \frac{Z}{u_g}], \quad (2)$$

$$\left. \begin{aligned} u' &= u_g (Z/H_R)^{1/n}, & v' &= u' (1 - Z/H_R) \frac{1}{n} \sqrt{2n + 1}, \\ n &= \log_{10} [H_R / \frac{Z_0}{Dz} + C_0/5.75] \end{aligned} \right\} \quad (3)$$

where Z : altitude from the earth (sea) surface. H_R (m): maximum altitude, in other words, the altitude at which the geostrophic wind is given. u_g : velocity at H_R , corresponding to the geostrophic wind. Z_0 : ground roughness, a constant determined by the status of the surface of earth. Dz : correction coefficient related to the mesh intervals in the z direction to be used for computation. C_0 : parameter which shows the stability

of the atmosphere, generally, following values are used, 5.0 during stable time, 7.0 during neutral time and 8.5 during unstable time. u' (m/s): velocity component in the same direction as the geostrophic wind at H_R . v' (m/s): velocity component in the left hand direction right angled to the leeward direction of the geostrophic wind at H_R .

The equation (3) shows the relations among the frictional force, the pressure gradient force and the geostrophic force. Accordingly, change in wind vector should be approximately expressed by equations concerning the rising and roundabout effects caused by topography and the escape of the wind from the topographical features at the minimum displacement.

In addition, the effect of frictional force on the surface of earth is so large that the geostrophic force can be ignored. And in the layer up to the altitude of some ten meters, the distribution of wind velocities in this layer can be expressed by the exponential law shown in the equation (4).

$$V/V_0 = (H/H_0)^{1/n} \quad (4)$$

where, V_0 : wind velocity at the reference altitude H_0 , V : wind velocity at the altitude H , n : constant obtained by the roughness of the surface of earth.

3.3 Results and Examination of Stream Line Analysis of the Seasonal Wind

Mikawa Bay is approximately some ten kilometers long in both length and width, and in comparison with this scale, the scale of the atmospheric pressure distribution of continental high pressures which are liable to cause seasonal wind in the winter time is extremely large. And also the topography along the coast of the bay is generally flat. Judging from these conditions, it can be regarded that the geostrophic wind is uniform at any point above Mikawa Bay when the winter seasonal wind exists. Since no observation data on the geostrophic wind at the height of H_R were obtained, this computation was made on the assumption of certain geostrophic wind. The atmospheric stability in this computation was set neutral, and the value of C_0 was therefore 7.0.

Judging from these computation results, it is concluded that no local difference is recognized in the velocity and direction of wind blowing over Mikawa Bay at the altitude of 100 meters. In other words, the wind blows at the speed of 5 ~ 6 m/s in the almost same direction.

On the other hand, the observation results show that the wind direction and velocity varies from point to point. This difference is attributable to various conditions such as the effects of topography near the place where the anemometer is installed and the effects of buildings and local winds peculiar to the spot, etc. Moreover, the computation results are based on such large scale model that these local effects cannot be reproduced.

IV. CHARACTERISTICS OF FLOW IN MIKAWA BAY

In Mikawa Bay, automatic sea condition observation buoys belonging to the Aichi Pref. Fisheries Experiment Station were set up at 3 points shown in Fig. 1, and the direction and velocity of flow in the layer 1 m below the water surface was observed every 1 hour.

In order to examine average flow characteristics in Mikawa Bay, seasonal average flow and occurrence frequency classified by directions of flow were obtained by the use of flow observation data obtained by means of these buoys.

Using each buoy, average flows (arithmetic average of data in each season) in winter (December, January and February), spring (April, May and June) and summer (August) were obtained as shown in Fig. 5. In Fig. 5, occurrence frequency in each direction during the observation period and longitudinal direction of M_2 component tide are shown.

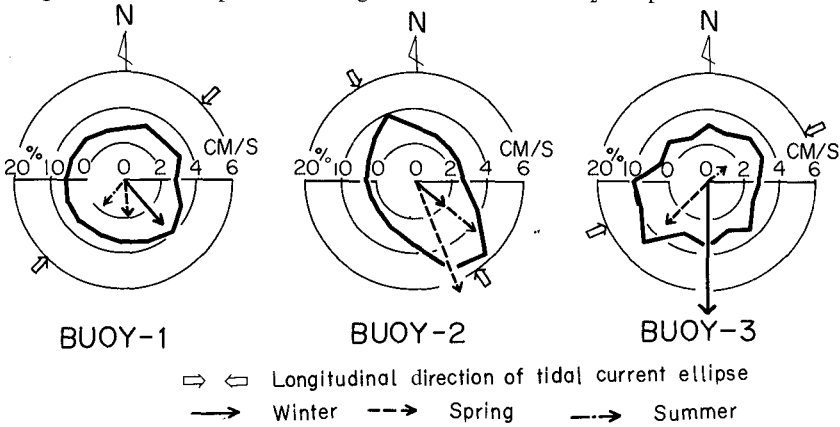


Fig. 5 Seasonal average flow and occurrence frequency classified by direction of flow

At Buoy 1 and Buoy 3, development of average flow in the direction which almost agrees with the blowing direction of a predominant winter seasonal wind was recognized in winter. At Buoy 2, on the other hand, development of average flow was recognized in spring and summer, though its direction was almost constant irrespective of seasons. Accordingly, at Buoy 2 and Buoy 3, higher occurrence frequency classified by flow directions is seen in the longitudinal direction of tide as well as in the direction which agrees with the direction of constant flow. At Buoy 1, however, almost uniform occurrence frequency is seen in either direction.

In order to examine the relation between wind blowing direction and flow direction at that time, the occurrence frequency classified by flow directions in each wind direction were obtained using data on the wind observed at the Irako Meteorological Station, as shown in Fig. 6.

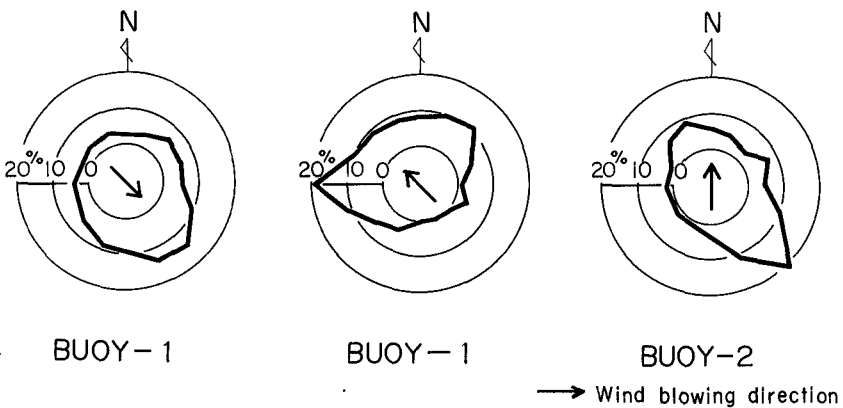


Fig. 6 Occurrence frequency classified by flow direction in each wind direction

That is, at Buoy 1, the distribution pattern of occurrence frequency classified by flow directions varies with each wind direction. In this case, regarding the northern wind (W-N-E), the occurrence frequency of flow heading in the direction which almost agrees with the wind blowing direction is high. As to the southern wind (ESE-S-WSW), on the other hand, the flow direction having high occurrence frequency does not agree with the wind blowing direction, considering that the direction of flow is easily affected by surrounding topography.

At Buoy 2 and Buoy 3, the occurrence frequency of flow heading in the direction which agree with the longitudinal direction of M_2 component tide is high irrespective of wind blowing directions. Especially, at Buoy 2, the occurrence frequency of flow heading in the direction which agrees with the direction of seasonal average flow shown in Fig. 5 is conspicuous. With 24 hours of moving average taken into account in the flow observation data, long-period fluctuation characteristics of flow more than one day were obtained. These characteristics are shown in the form of flow vector in Fig. 7.

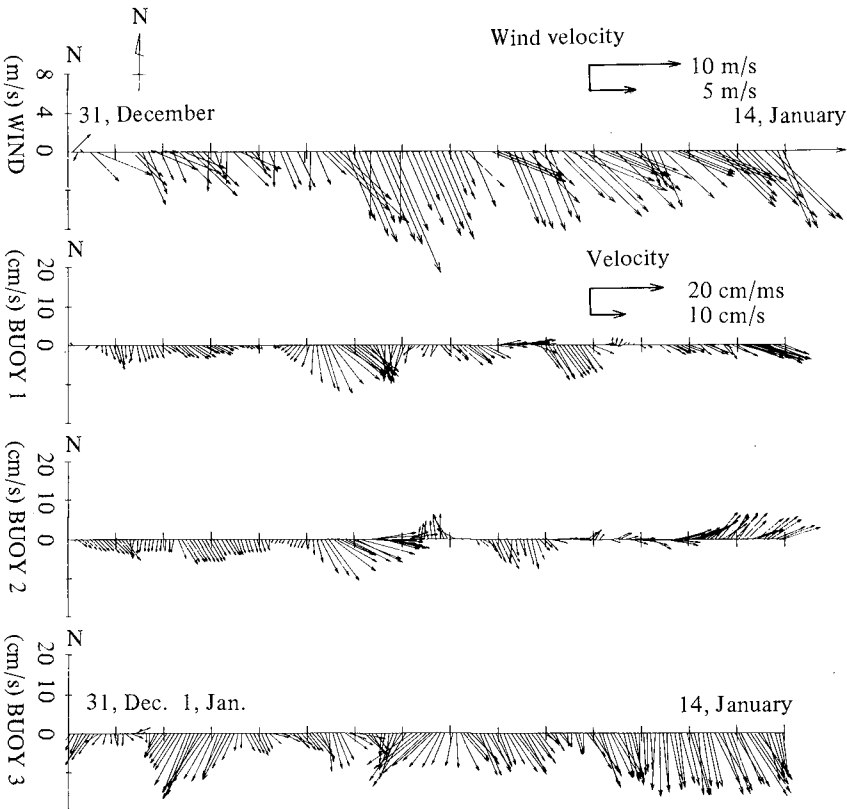


Fig. 7 Vectors of wind and flow in the sea

In order to study the effect of wind on long-period fluctuation of flow, the results of observations made on the wind at the Irako Meteorological station are shown in the form of vector which shows the wind blowing direction.

The flow vector suggests that the long-period fluctuation of flow exists in response to fluctuation of wind direction and wind velocity. The period of these fluctuations varies depending on seasons. In the wintertime, because of the existence of a predominant winter seasonal wind, there is possibility that the period of fluctuation extends over 10 days or more. In spring and summer, as the wind direction and wind velocity rapidly change with the weather which changes at a cycle of 2 or 4 days, the flow changes with a fluctuation cycle of 2 or 4 days. It is, therefore, presumed that the direction of flow vector does not always agree with the wind blowing direction, depending on wind directions, and the flow accompanied by the blowing of wind is sharply affected by surrounding topography.

Thus, considering fluctuation in flow velocity of annual scale in the bay, the existence of long-period phenomena of fluctuation in flow velocity owing to seasonal factors such as seasonal wind and density structure of sea water besides tidal residual flow can be conjectured.

V. ANALYSIS OF WIND GENERATING CURRENT AND TIDAL CURRENT

5.1 Numerical Model

In the sea water of Mikawa Bay in the winter time, there is an approximately uniform distribution of water temperatures and salinities from the sea surface to the bottom, and no density stratification is formed.

Based on this fact, as the first approximate solution, it was assumed that the flow motion of sea water in the bay caused by the wind generating current has a horizontal component. Also an analysis was made on the flow motion of sea water on the basis of the plane two dimensional model.

In order to investigate the mechanism of flow motion in the sea water of the bay caused by the wind-blowing action and the tidal action, a method based on the equations of motion and continuity for the fluid was employed to make analysis on the basis of the three dimensional models.

The fundamental technique for the calculation of dynamic behavior of sea water in the bay is an Eulerian finite-difference approximation to the Navier-Stokes equations.

$$\frac{\partial u}{\partial t} + \frac{\partial u^2}{\partial x} + \frac{\partial uv}{\partial y} + \frac{\partial uw}{\partial z} = -g \frac{\partial \zeta}{\partial x} + fv + \frac{\partial}{\partial z} (A_w \frac{\partial u}{\partial z}) + A_h \nabla^2 u \quad (5)$$

$$\frac{\partial v}{\partial t} + \frac{\partial uv}{\partial x} + \frac{\partial v^2}{\partial y} + \frac{\partial vw}{\partial z} = -g \frac{\partial \zeta}{\partial y} - fu + \frac{\partial}{\partial z} (A_w \frac{\partial v}{\partial z}) + A_h \nabla^2 v \quad (6)$$

$$\frac{\partial u}{\partial x} + \frac{\partial v}{\partial y} + \frac{\partial w}{\partial z} = 0 \quad (7)$$

where u , v and w are the velocity components along the x , y and z directions, ζ is the

elevation of water surface, f is Coriolis' parameter and A_h, A_w are the horizontal eddy viscosity, the vertical one, respectively.

The following equation was applied as the kinetic boundary condition on the water surface.

$$\frac{\partial \xi}{\partial t} + U_s \frac{\partial \xi}{\partial x} + V_s \frac{\partial \xi}{\partial y} - W_s = 0 \quad (8)$$

However, since the free surface doesn't agree with the cell surface, the marker was introduced in order to obtain a better approximate solution to the velocity of flow, and higher precision was confirmed by giving due consideration to the water surface.

The bay was divided into many cells of 1,000 m \times 1,000 m in the horizontal direction and 3.2 m in depth.

For the purpose of computing the flow motion mechanism of the wind generating current in the bay on the basis of the three dimensional model, the vector of wind on the sea obtained by the stream line analysis was applied to the sea surface as the frictional stress. The wind blowing over the sea at the altitude of 100 meters was converted into the wind at the altitude of 15 meters by adopting the exponential law. As the frictional coefficient of wind stress on the sea surface, $k = 3.2 \times 10^{-6}$ was adopted.

As the boundary conditions, the flow velocity is presumed to be zero at the fixed wall. And, in the equations (5) and (6), the frictional stresses at the surface and the bottom are given by the following equation:

$$\left. \begin{aligned} \tau_x &= k_{B1} U_w \sqrt{U_w^2 + V_w^2}, \\ \tau_y &= k_{B1} V_w \sqrt{U_w^2 + V_w^2} \end{aligned} \right\} \quad (9)$$

$$\left. \begin{aligned} \tau_{Bx} &= k_{B2} U \sqrt{U^2 + V^2}, \\ \tau_{By} &= k_{B2} V \sqrt{U^2 + V^2} \end{aligned} \right\} \quad (10)$$

where τ_x, τ_y : the wind frictional stress on the sea surface, τ_{Bx}, τ_{By} : the frictional stress on the sea bed, k_{B1} : frictional coefficient of wind stress on the sea surface, k_{B2} : frictional coefficient of wind stress on the sea bed, U_w, V_w : the wind velocities.

The boundary conditions on the line at the bay mouth between Irako and Toyohama were set as follows:

$$\xi = 0, \quad \partial^2 U / \partial S^2 = \partial^2 V / \partial S^2 = \partial^2 W / \partial S^2 = 0 \quad (11)$$

On the land, breakwaters and islands coasts as well as the sea bed, $u = v = w = 0$. Wind stress at the sea surface is expressed as follows:

$$A_w \frac{\partial u}{\partial z} = \tau_x, \quad A_w \frac{\partial v}{\partial z} = \tau_y. \quad (12)$$

On the other hand, the tidal level is determined on the boundary line between Irako and Morosaki. The tidal level and tidal hour are determined by the tidal constants in Mikawa Bay.

The branch tide M_2 (amplitude 53 cm, lag of the tide 183°) is set on the Irako side, and the branch tide at Morosaki M_2 (amplitude 55 cm, lag of the tide 183°) is set on the Toyohama side. On the boundary line between these two points, the values at both points must be interpolated on the boundary line.

The coefficients of the horizontal eddy viscosity and the vertical eddy viscosity are $10 \text{ m}^2/\text{s}$ and $0.01 \text{ m}^2/\text{s}$, respectively.

5.2 Analytical Results of Wind Generating Current and Tidal Current

In order to examine the circulation currents formed in the bay, the horizontal flow motions at various representative depths are shown in Fig. 8. These figures show that the analytical results obtained on the basis of the three-dimensional models are different from those based on the two dimensional plane models. That is, the formation of horizontal circulation currents can only be seen in the middle layer or the bottom layer and more predominant vertical circulation currents are seen in the wind blowing direction.

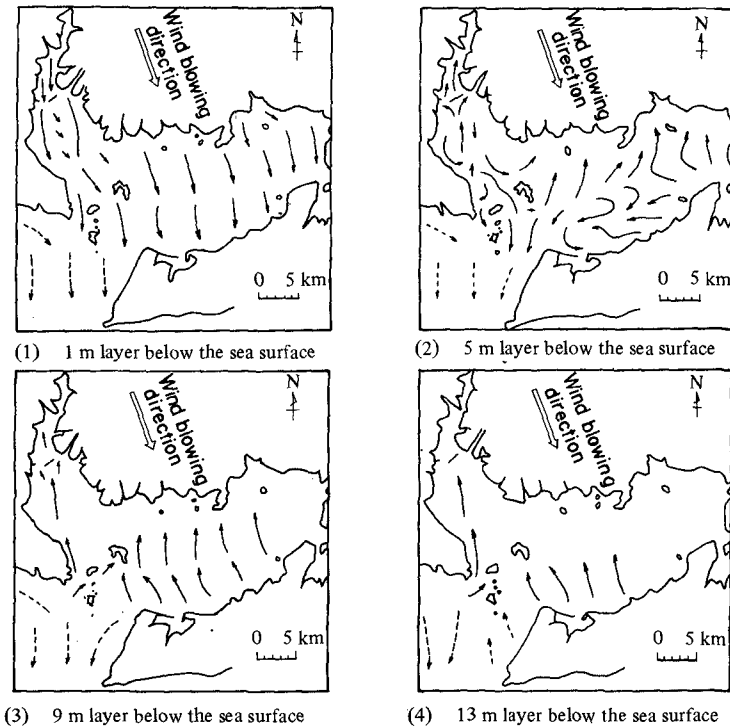


Fig. 8 Horizontal flow motions at various representative depth due to wind action

This type of circulation currents tends to be affected delicately by the topography of sea regions, especially by changes of sea bed configuration.

The existence of large scale vertical circulation currents are recognized in Chita Bay. And these currents flow toward the bay mouth in the surface layer, and run toward the innermost of the bay in the deep layer.

On the other hand, in the whole area of Mikawa Bay, such a large circulation current as to cover the total sea region is not recognized. In the surface layer, however, the flow in the wind blowing direction is predominant. In the middle layer, some small-scale horizontal circulation currents are recognized in the southern sea region and in the innermost of Mikawa Bay. In the deep layer, the vertical circulation current is considered to be formed as a compensation current for the current in the surface layer.

In order to examine if the results of numerical experiments on the tidal current agree with the measured results, comparisons were made between the analytical results and the measured results on the ellipses of the tidal currents. Figure 9 shows the points where the comparisons were made and some ellipses of the tidal currents of the M_2 component. (See Fig. 1)

Judging from these results, it is concluded that the results of the numerical experiments satisfactorily reproduce the tidal currents in Mikawa Bay.

The results obtained based on the three dimensional models are similar with those based on the two dimensional models.

5.3 Results of Computation and Consideration on Tidal Residual Current

From the results of numerical simulation on tidal current, the average value of tidal current in four tide cycles was obtained and with this as tidal residual current, its characteristics were examined. In Fig. 10 (1) through (3), the results of computation on tidal residual current are shown in plane flow vector in a typical water depth.

In this figure, only the steady current observed during a cold weather, season from October to April when no density layer is formed and the outflow of river water is relatively small was extracted, and its current direction and size are shown.

The generation of small-scale circulation currents are seen in the Morosaki Channel, in the neighborhood of the mouth of the storm tide protection breakwater in Chita Bay, and in the coastal region of Atsumi Bay.

The steady current measured in a cold weather season, especially in the sea region where a remarkable plane circulation current is recognized, is showing a current direction which well agrees with the flow pattern based on numerical simulation, thus backing up its existence, as shown in Fig. 10. In the meantime, the vertical circulation current based on tidal residual current is not recognized.

Although the circulation current has a very slow velocity, it is considered that the existence of this current plays a very important role in the long-term dispersion process of substances in the sea region along the coast of the bay.

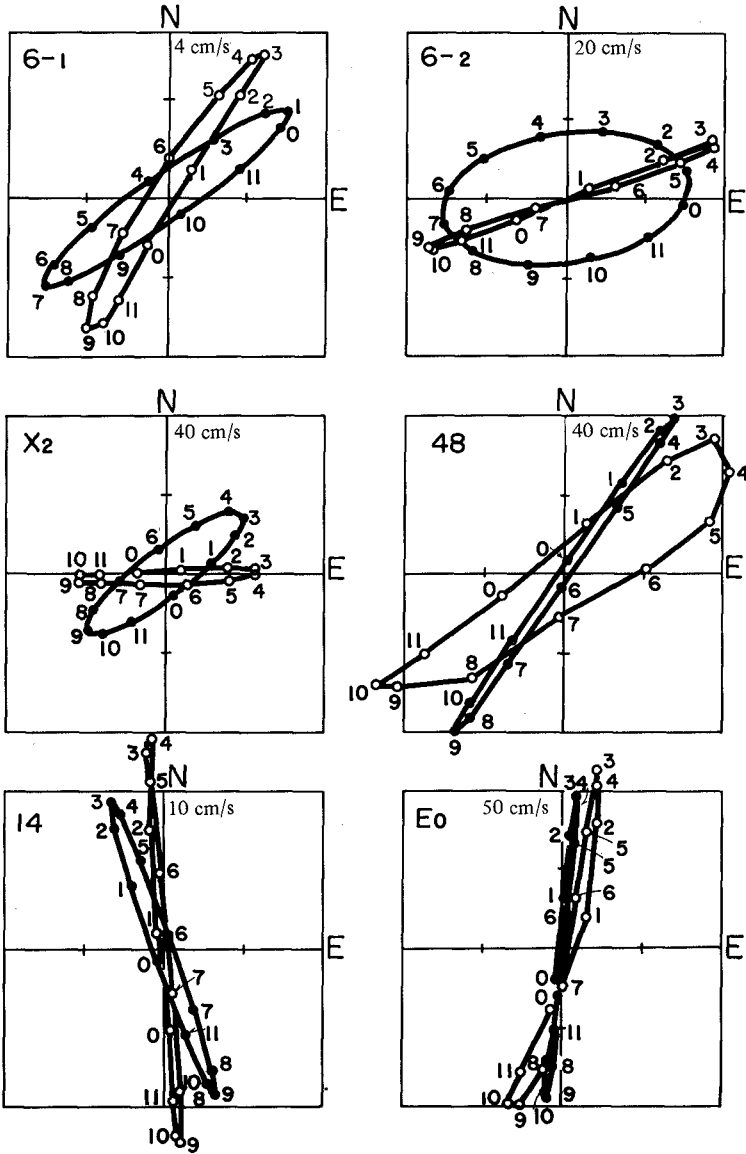


Fig. 9 Comparison between analytical results and results obtained by harmonic analysis of measured values for tidal current ellipses (—●—●— measured results, -○-○- analytical results)

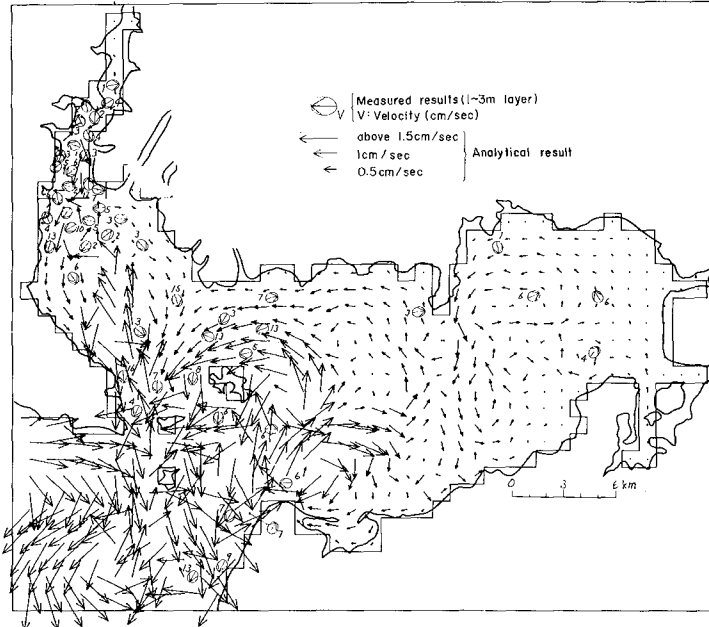


Fig. 10 (1) Tidal residual current (1.6 m layer below the sea surface)

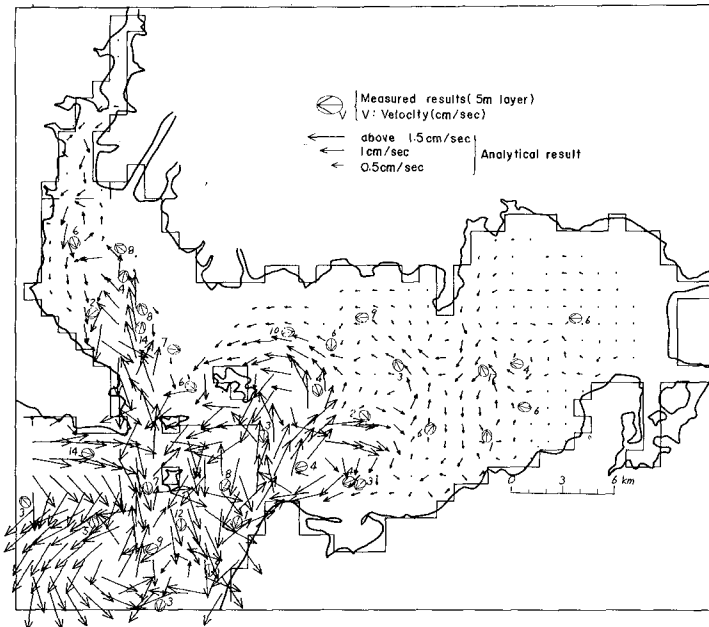


Fig. 10 (2) Tidal residual current (4.8 m layer below the sea surface)

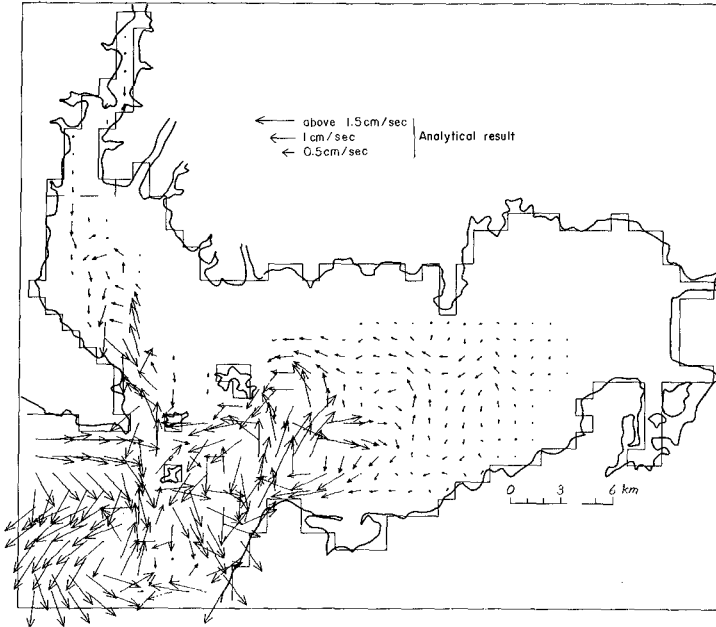


Fig. 10 (3) Tidal residual current (8 m layer below the sea surface)

VI. CONCLUSION

As the results of the simulation analysis conducted on the basis of the numerical models in Atsumi Bay and Chita Bay, large-scale eddies caused by the tidal reciprocating current as well as the constant current as the tidal residual current can be seen in the bays. And also, in the winter time when the distribution of atmospheric pressure is stable, several circulation currents are formed in the bay by the wind-generating current.

Accordingly, it is considered that the formation of these currents has a considerable effect on the diffusion characteristics of substances in the bays.

After comparative examinations between actual measurement and predicted analytical results based on the numerical model developed here, it was confirmed that this analytical method was effective to elucidate the three dimensional motion in real sea region.

ACKNOWLEDGEMENT

Some field data in this paper were offered by the Aichi Pref. Fisheries Experiment Station and the Hydrographical Office of the Maritime Safety Agency.

The authors would like to express their sincere thanks to the members of the Station and the Agency.

REFERENCES

- 1) Wada, A. & Miyaike, Y.: Characteristics of circulation in bay waters due to wind action, Coastal Engineering in Japan, Vol. 20, Japan Society of Civil Engineers, 1977.
- 2) Liggett, J. A.: Cell method for computing lake circulation, J. ASCE, HY3, 1970.
- 3) Sündermann, J.: Die hydrodynamisch-numerische Berechnung der Vertikalstruktur von Bewegungsvorgängen in Kanälen und Becken, Mitteilungen des Instituts für Meereskunde der Universität Hamburg, Nr. XIX, 1971.

CHAPTER 168

BEHAVIORS OF THE SALT WEDGE AND THE SALINITY DISTRIBUTION AT ESTUARIES

by

Isao Yakuwa,^{*} Susumu Takahashi,^{**} and Morimasa Ohtani^{***}

Abstract

The salt wedge has been observed by ultrasonic method at estuaries of the Ishikari, Shiribetsu and Rumoi River in Hokkaido, Japan. According to the records of the longitudinal profile of the salt wedge, behavior of the interface of salt and fresh water is strongly influenced by configurations of the water course and the river bed. Therefore, in this paper, a distance from the front of the salt wedge to the river mouth is divided into two or three sections in accordance with behavior of the interface, and the salinity distribution in the upper layer is estimated in each section.

By solving the differential equation of two dimensional salinity diffusion, the distribution is represented by terms of flow velocity, diffusion coefficients, depth of the upper layer and salinity at the boundary. Where, diffusion coefficients are determined by comparing evaluated longitudinal distribution of surface salinity with observed one.

By estimating the rate of salinity entrainment into the upper layer, the entrainment coefficient E at the interface is evaluated as $E = 0.4 \times 10^{-5} \sim 0.8 \times 10^{-3}$ at three estuaries.

* Professor, Department of Engineering Science, Hokkaido University, Sapporo, Japan.

** Associate Professor, Department of Engineering Science, Hokkaido University.

*** Research Assistant, Department of Engineering Science, Hokkaido University.

1. Introduction

Authors have observed¹⁾ many salt wedges at estuaries of the Ishikari, Shiribetsu and Rumoi River which flow through the west part of Hokkaido, Japan and pour into the Japan Sea (Fig. 1). Because the Japan Sea has only a small tidal range of about 30cm at its maximum throughout the year, the behavior of the salt wedge at every river mouth is controlled mainly by the river discharge.

While the Ishikari River, a length of about 300 km, is the longest river in Hokkaido, the Shiribetsu and the Rumoi River, lengths of about 130 and 35 km, are examples of middle and short rivers in Japan. Figure 2 shows estuaries of the three rivers. The critical discharges at which salt wedges begin to penetrate into river mouths are obtained as 550, 150 and 5.2 m³/s at estuaries of the Ishikari, Shiribetsu and Rumoi River respectively.

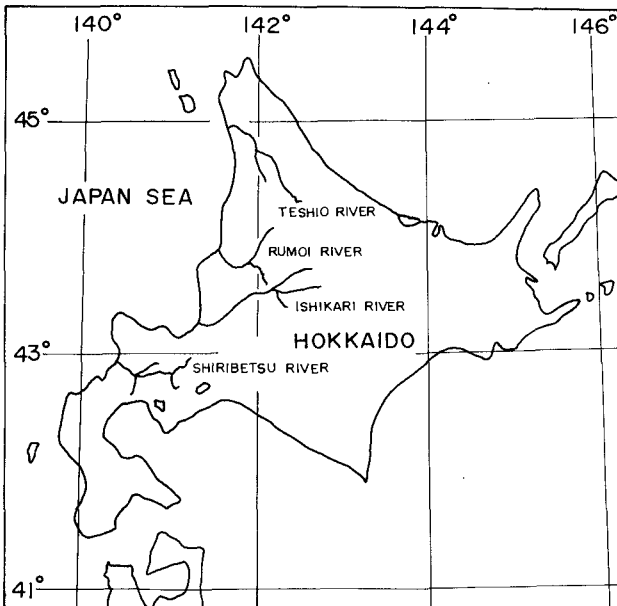
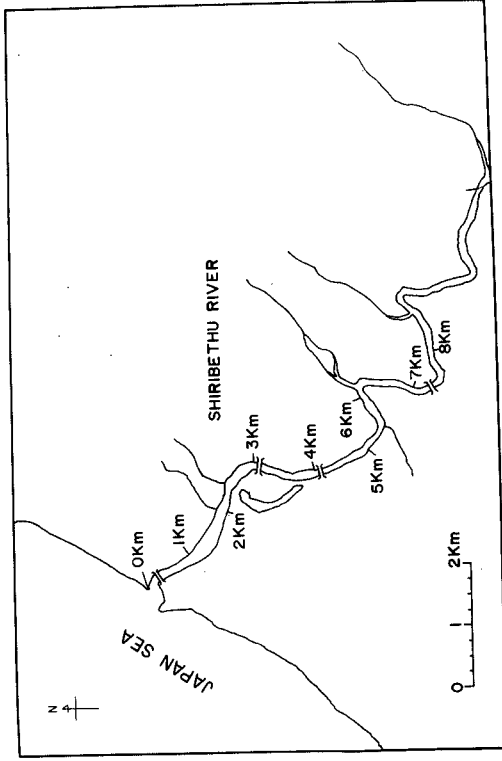
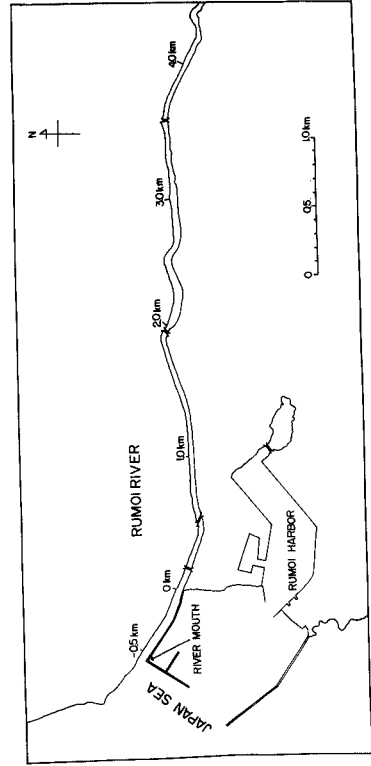


Fig. 1 Hokkaido District



(b) the Shiribetsu River



(c) the Rumoi River

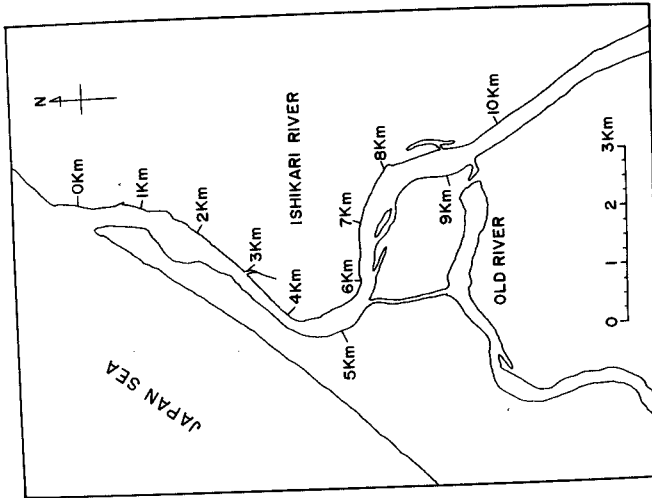


Fig. 2 Estuaries of the three rivers.
(a) the Ishikari River

The ultrasonic method has been used to observe longitudinal profiles of salt wedges. During each sail to record the salt wedge by means of echo-sounding, about 300 cc of the surface water was also sampled an interval of 30 ~ 60 seconds and its chlorinity was measured by chemical analysis to get the longitudinal distribution of surface salinity. At several stations along the salt wedge the boat was anchored and vertical distributions of flow velocity and chlorinity have also been measured.

Generally speaking, the interface of salt and fresh water is stable when the front of the salt wedge is penetrating into the river mouth or the salt wedge is in steady state. When the river discharge increases, however, a mixing of salt and fresh water through the interface grows intense and the front of the salt wedge begins to retrograde downstream.

But, according to records, behaviors of the salt wedge are strongly influenced by configurations of the water course and the river bed. At the location where the water course abruptly curves or there is a big projection on the river bed, a stronger mixing of salt and fresh water was found as compared with all other points, and sometimes a big projection prevented the front of the salt wedge from intrusion. In these cases, the profile of the salt wedge was different from the ideal case of straight water course and flat bed, and the rate at which the salt water entrained into the fresh water layer varied with locations even along one salt wedge in an estuary.

2. Diffusion of salinity in the fresh water layer

Taking x in the downstream direction along the river surface and y in the vertically downward direction, the differential equation of salinity diffusion in the fresh water layer is given by

$$U \frac{\partial S}{\partial x} = D_x \frac{\partial^2 S}{\partial x^2} + D_y \frac{\partial^2 S}{\partial y^2} \dots\dots\dots (1)$$

- where S : Cl concentration of the water
- U : mean velocity of the fresh water layer
- D_x : diffusion coefficient of x direction
- D_y : diffusion coefficient of y direction.

The boundary conditions are expressed by

$$\begin{aligned} \frac{\partial S}{\partial y} &= 0 & \text{at } y &= 0 \\ S &= S_0 & \text{at } y &= h_0 \\ S &= f(y) & \text{at } x &= 0 \end{aligned}$$

where h_0 is the depth of the fresh water layer. The transition layer is excluded from the definition of the fresh water layer in the present case. Under these conditions, the equation (1) can be solved²⁾ as

$$S = S_0 - \sum_{n=0}^{\infty} \left\{ \frac{(-1)^n 4S_0}{(2n+1)\pi} - \frac{2}{h_0} \int_0^{h_0} f(\lambda) \cos \frac{(2n+1)\pi\lambda}{2h_0} d\lambda \right\} \\ \times \cos \frac{(2n+1)\pi y}{2h_0} \cdot \exp \left\{ \frac{U}{2D_x} - \sqrt{\left(\frac{U}{2D_x}\right)^2 + \frac{(2n+1)^2 \pi^2 D_y}{4h_0^2 D_x}} \right\} x \dots \dots (2)$$

And chlorinity of the surface water is given by

$$(S)_{y=0} = S_0 - \sum_{n=0}^{\infty} \left\{ \frac{(-1)^n 4S_0}{(2n+1)\pi} - \frac{2}{h_0} \int_0^{h_0} f(\lambda) \cos \frac{(2n+1)\pi\lambda}{2h_0} d\lambda \right\} \\ \times \exp \left\{ \frac{U}{2D_x} - \sqrt{\left(\frac{U}{2D_x}\right)^2 + \frac{(2n+1)^2 \pi^2 D_y}{4h_0^2 D_x}} \right\} x \dots \dots \dots (3)$$

When the point of the front of the salt wedge is taken as $x = 0$, equations (2) and (3) are simplified by putting $f(y) = 0$.

By the use of observed values for U , h_0 and S_0 in equation (3), the longitudinal distributions of surface salinity can be calculated with various values of D_x and D_y . When one of the calculated distributions agreed fairly well with the observed distribution, these values of D_x and D_y were determined as diffusion coefficients of x and y direction.

Otsubo and Fukushima evaluated³⁾ entrainment coefficient E in stratified flow by solving equations of mass and volume conservation

$$\left. \begin{aligned} \frac{d(A_1 \rho_1 U)}{dx} &= B \rho_2 V \\ \frac{d(A_1 U)}{dx} &= BV \end{aligned} \right\} \dots \dots \dots (4)$$

- where A_1 : sectional area of upper layer
- B : width of upper layer
- ρ_1, ρ_2 : density of upper and lower layer
- U : velocity of upper layer
- V : entrainment velocity ($V = EU$),

and the velocity of lower layer was assumed to be zero. By transforming Eq. (4) into an equation of salinity, they led

$$\frac{S_2 - S_1}{S_{20} - S_{10}} = \exp \left(- \int_0^x \frac{E}{h} dx \right) \dots\dots\dots (5)$$

where h : depth of upper layer
 S_1, S_2 : mean values of salinity concentration in the upper and lower layer at point x
 S_{10}, S_{20} : values of S_1 and S_2 at point $x = 0$.

On the basis of observational results at the mouth of the Ishikari River, they obtained as the mean value of entrainment coefficient $E = 1.7 \times 10^{-5}$.

By assuming that values of $S_2, E, h (= h_0)$ are constant at interval from $x = 0$ to $x = x$, equation (5) leads to

$$S_1 = S_2 - (S_2 - S_{10}) \exp \left(- \frac{E}{h_0} x \right).$$

Therefore, when mean value of salinity concentration in the above equation is calculated by

$$S_1 = \frac{1}{h_0} \int_0^{h_0} S dy$$

with S in equation (2), entrainment coefficient E can be represented as

$$E = \frac{S_0}{S_2 - S_{10}} \sum_{n=0}^{\infty} \left\{ \frac{4}{(2n+1)^2 \pi^2} - \frac{(-1)^n 2}{h_0 S_0 (2n+1) \pi} \int_0^{h_0} f(\lambda) \cos \left(\frac{(2n+1)\pi \lambda}{2h_0} \right) d\lambda \right\} \\ \times \left\{ \sqrt{\left(\frac{h_0 U}{D_x} \right)^2 + \frac{D}{D_x} (2n+1)^2 \pi^2} - \frac{h_0 U}{D_x} \right\} \dots\dots\dots (6)$$

where $S_{10} = \frac{1}{h_0} \int_0^{h_0} f(y) dy$.

When $f(y) = 0$, E is given by

$$E = \frac{S_0}{S_2} \sum_{n=0}^{\infty} \frac{4}{(2n+1)^2 \pi^2} \left\{ \sqrt{\left(\frac{h_0 U}{D_x} \right)^2 + \frac{D_y}{D_x} (2n+1)^2 \pi^2} - \frac{h_0 U}{D_x} \right\}.$$

3. Observational results

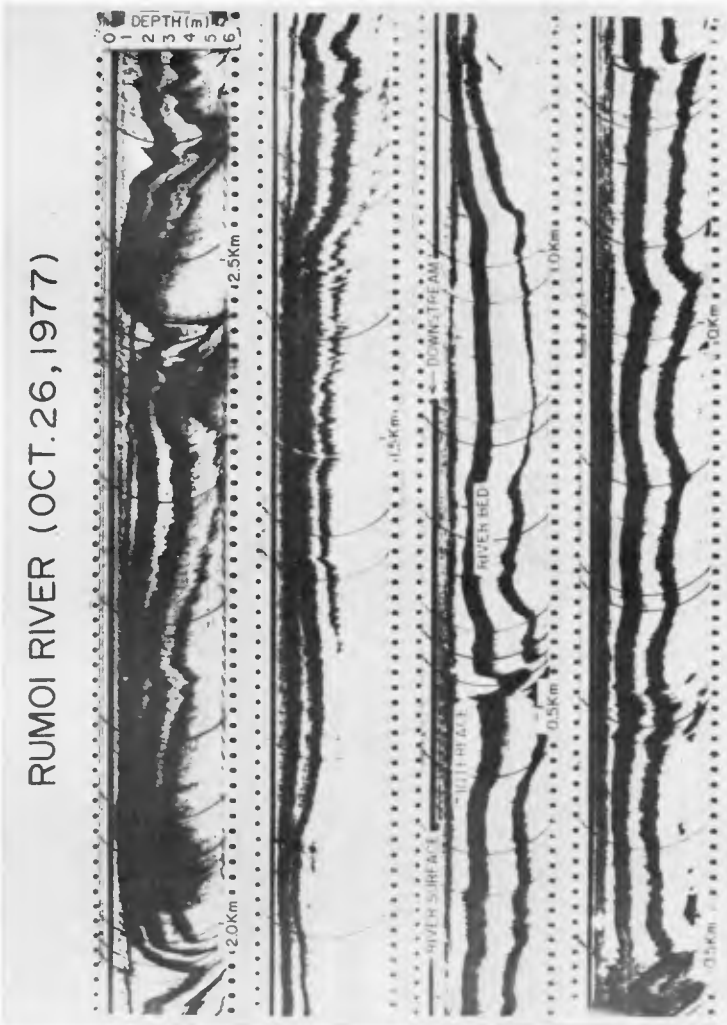
Figures 3 and 4 show longitudinal profiles of salt wedge and river bed recorded at mouthes of the Ishikari River on July 27, 1967, Shiribetsu River on July 23, 1977 and Rumoi River on October 26, 1977. Salt wedges had penetrated 8.4, 3.5 and 2.5 km upstream from the mouthes because river discharges (260, 27-29 and 1.7 m³/s respectively) had decreased then below critical discharges.

As shown in Fig. 4(a), there was a big projection on the river bed at a point 3.7 km from the mouth of the Ishikari River and the mixing of salt and fresh water abruptly increased there. At the mouth of the Shiribetsu River (Fig. 4(b)), the interface of salt and fresh water was disturbed and the mixing grew stronger near a projection of the bed about 2.0 km upstream. And at the Rumoi River (Fig. 4(c)), interface was separated into three sections of 0 (river mouth) ~ 1.0 km, 1.6 ~ 2.0 km and 2.1 ~ 2.5 km according to the profile of the river bed.

Figures 5(a), (b) and (c) show the longitudinal distributions of chlorinity of the surface water observed at the Ishikari, Shiribetsu and Rumoi River. According to figures, chlorinity increases rapidly near the points where the mixing is intense. Therefore, the distribution may be calculated from Eq. (3) by dividing a distance from the river mouth to the front of the salt wedge into two or three sections and using for each section constant values of U , h_0 , S_0 and S_2 . A range of sections at each estuary and observed values of U , h_0 , S_0 and S_2 in each section are indicated in Table 1 with boundary condition $f(y)$.

As shown in Fig. 5, the calculated distributions agree fairly well with the observed ones when the values of diffusion coefficients D_x and D_y are taken as given in Table 2.

Value of entrainment coefficient E in each section can be obtained from equation (6) using actual values of U , h_0 , S_0 , S_2 , D_x , D_y and $f(y)$ shown in Table 1 and 2. In Table 2, these values of E are also compared with ones calculated from equation (5) by use of observed values of S_1 , S_2 and h . A good coincidence between values calculated from equations (6) and (5) can be seen, though a distance of each section is very long.



(b) the Rumoi River (Oct. 26, 1977)

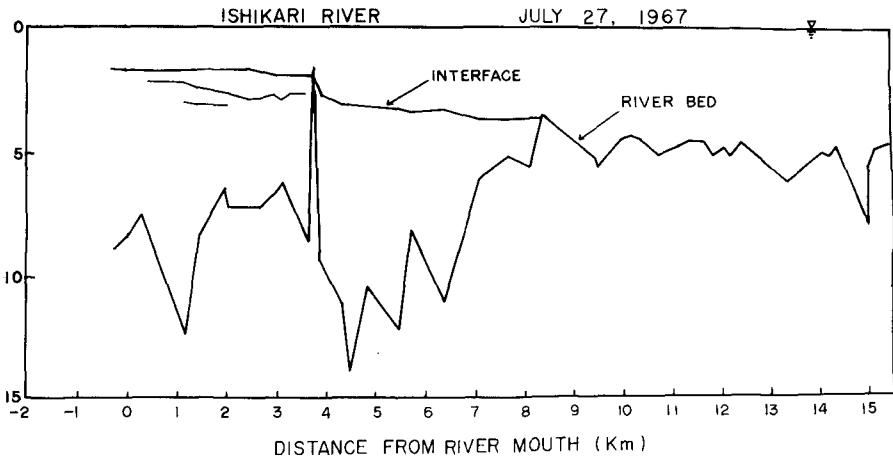
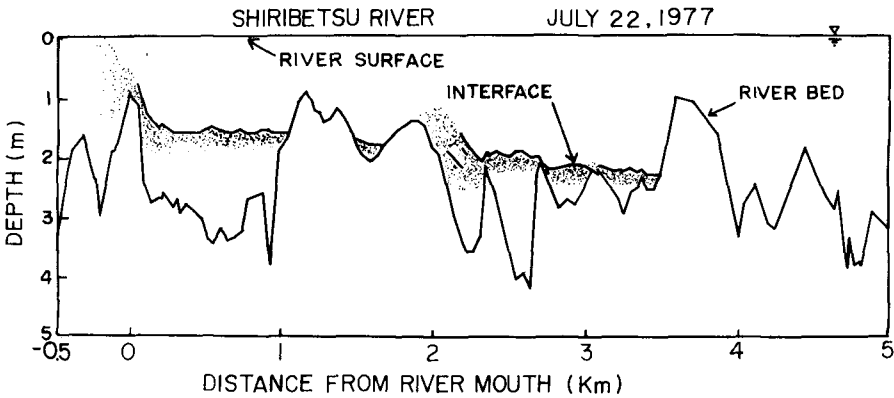
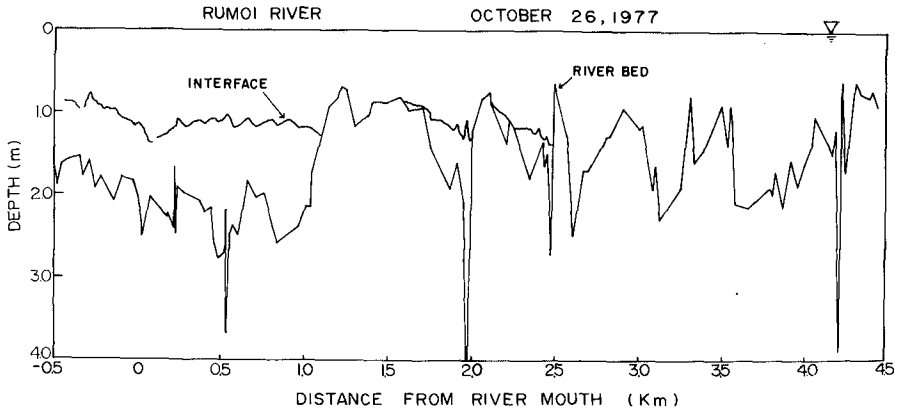


Fig. 4 Longitudinal profiles of the salt wedge at the river mouth
(a) the Ishikari River (July 27, 1967)



(b) the Shiribetsu River (July 23, 1977)



(c) the Rumoi River (Oct. 26, 1977)

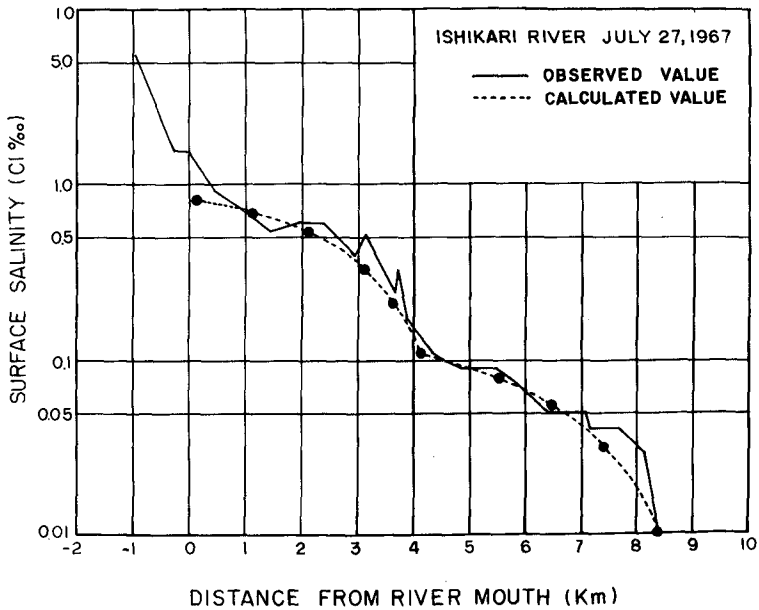
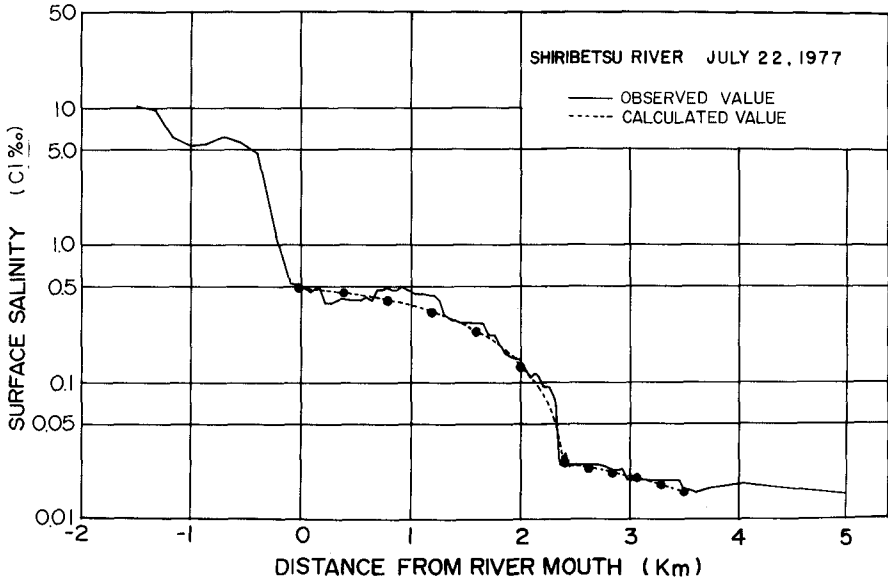
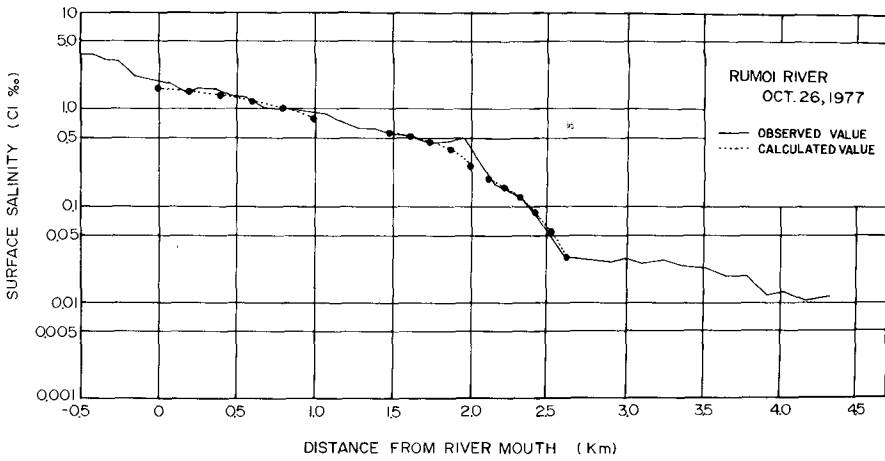


Fig. 5 Longitudinal distributions of surface chlorinity
(a) the Ishikari River (July 27, 1967)



(b) the Shiribetsu River (July 23, 1977)



(c) the Rumoi River (Oct. 26, 1977)

Table 1

Estuary	Discharge (m^3/s)	Section	Distance from the river mouth (km)	U (cm/s)	h_0 (cm)	S_0 (c1%)	S_2 (c1%)	$f(y)$ $a+by+cy^2$
Ishikari River (July 27, 1967)	260	I	Front 8.4 ~ 3.7	41.3	250	0.52	16.49	0
		II	3.7 ~ 0	76.5	100	1.12	15.47	$\begin{cases} a=0.319 \\ b=-4.61 \times 10^{-3} \\ c=1.26 \times 10^{-4} \end{cases}$
Shiribetsu River (July 23, 1977)	27 ~ 29	I	Front 3.5 ~ 2.4	15.0	150	0.074	15.99	0
		II	2.4 ~ 0	12.0	100	0.62	17.53	$\begin{cases} a=0.121 \\ b=-3.31 \times 10^{-3} \\ c=8.30 \times 10^{-5} \end{cases}$
Rumoi River (Oct. 26, 1977)	1.7	I	Front 2.5 ~ 2.1	6.3	100	0.46	4.25	0
		II	2.0 ~ 1.6	4.5	100	0.85	7.03	$\begin{cases} a=0.248 \\ b=4.04 \times 10^{-3} \\ c=1.96 \times 10^{-5} \end{cases}$
		III	1.0 ~ 0	4.2	100	2.02	12.80	$\begin{cases} a=0.770 \\ b=-8.95 \times 10^{-3} \\ c=2.14 \times 10^{-4} \end{cases}$

Table 2

Estuary	Section	D _x (C.G.S.)	D _y (C.G.S.)	E	
				Cal. from Eq. (6)	Cal. from Eq. (5)
Ishikari River (July 27, 1967)	I	3.0×10^8	13	0.22×10^{-4}	0.82×10^{-5}
	II	4.0×10^8	21	0.15×10^{-4}	0.21×10^{-4}
Shiribetsu River (July 23, 1977)	I	5.0×10^7	2.3	0.55×10^{-5}	0.44×10^{-5}
	II	5.0×10^7	12	0.18×10^{-4}	0.17×10^{-4}
Rumoi River (Oct. 26, 1977)	I	1.4×10^5	0.3	0.76×10^{-3}	0.14×10^{-3}
	II	4.1×10^5	0.4	0.56×10^{-4}	0.65×10^{-4}
	III	4.1×10^5	0.5	0.12×10^{-3}	0.59×10^{-4}

References

- 1) Fukushima, H., I. Yakuwa and S. Takahashi: Salinity diffusion at the interface of stratified flow in an estuary, Proc. 13th Congress IAHR, Vol. 3, pp. 191-197, 1969.
- 2) Yakuwa, I. and M. Ohtani: Longitudinal distribution of surface salinity in an estuary, Bull. Faculty of Eng. Hokkaido Univ., No. 54, pp. 135-141, 1969.
- 3) Otsubo, K. and H. Fukushima: Density currents in a river mouth with a small tidal range, Proc. 8th Congress IAHR, Vol. 4c, pp. 1-25, 1959.

CHAPTER 169

LONGITUDINAL DISPERSION IN SHALLOW WELL-MIXED ESTUARIES

J. Dronkers

Hydraulic Department of Deltaworks,
The Hague, Netherlands

- I. Introduction.
- II. Description of the model.
- III. The effect of mixing in the stagnant area.
- IV. The effect of non-tidal exchanges between the channel and the stagnant area.
- V. The effect of a phase-shift between tide and velocity.
- VI. Generalisation for other geometries.
- VII. Summary and conclusions.

I. Introduction.

In estuaries may be distinguished between several phenomena which are responsible for the dispersion of dissolved constituents. In this paper theoretical expressions are obtained for dispersion processes of a particular type, which appear mainly as a consequence of the tidal motion and the geometry. The results may be applied to estuaries with strong tidal mixing (tidal prism of the same order of magnitude as the average volume of the estuary) and a small fresh water discharge.

The cross-sections in the estuary are divided in two parts: a deep part, representing the channel, in which the longitudinal motion takes place, and a shallow part without longitudinal motion, representing a tidal flat, which is filled and emptied by the tide. The interaction between these two parts generates longitudinal dispersion related with the following three phenomena:

- mixing on the tidal flat caused by an irregular topography and by bottom friction,
- exchange of water between the channel and the tidal flat caused by eddies or density currents,
- the occurrence of a phase-shift between the tidal elevation and the tidal velocity.

An analytical expression for the contribution of these effects to the dispersion coefficient is obtained by considering the resulting transport of constituent through a fixed plane. The application of the model to general geometries is discussed, providing an approximate expression for the dispersion coefficient in natural situations. This expression shows the explicit dependency of the dispersion coefficient on geometrical and tidal parameters.

II. Description of the model

Longitudinal dispersion in estuaries related to the "trapping" of water outside the flow region has been studied by Schijf and Schönfeld [1] and by Okubo [2] for different types of geometry.

Okubo assumed that the exchange process between the channel and the traps is mainly due to some diffusion type process, neglecting the influence of the tidal elevation.

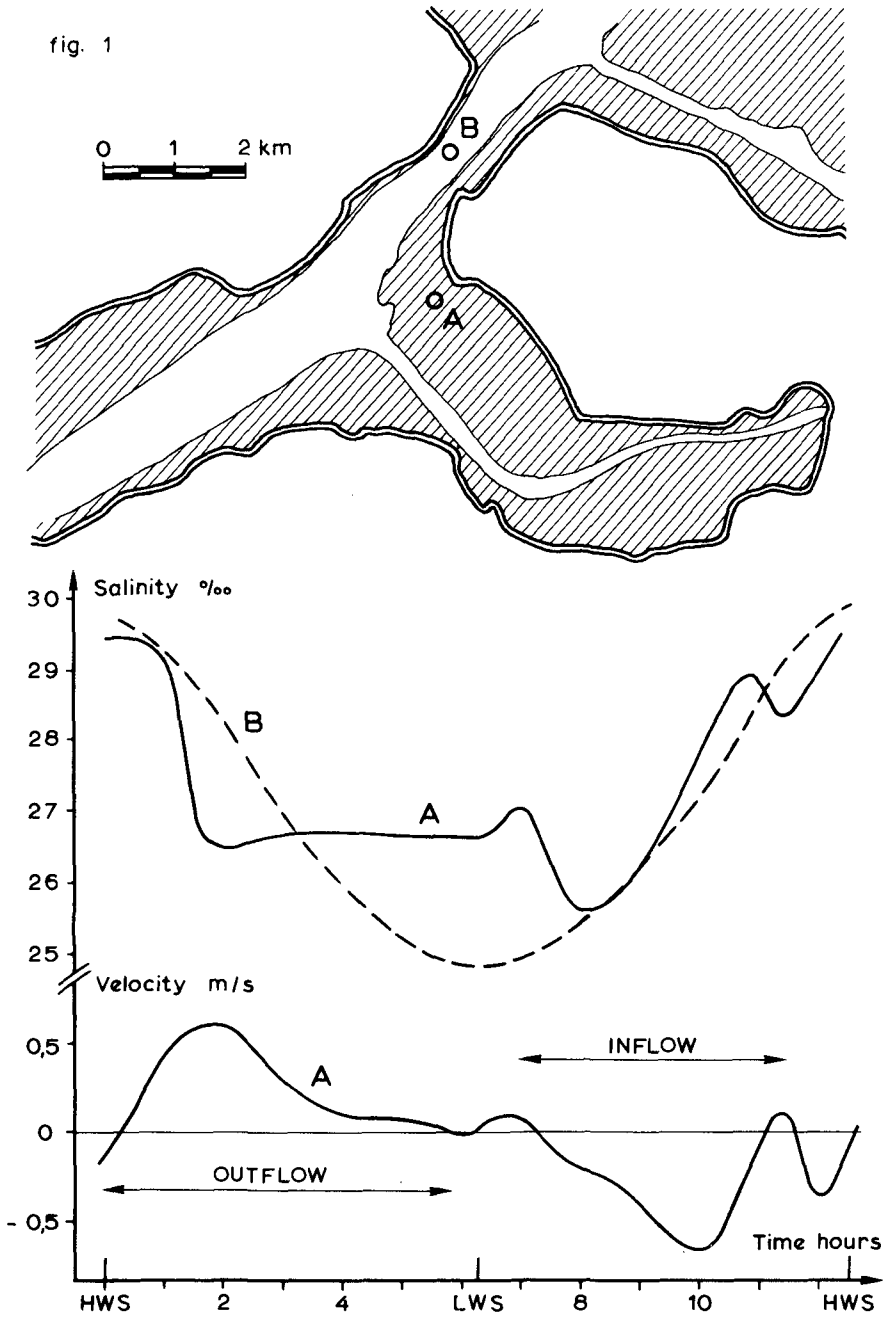
In this paper we consider the trapping of water on tidal flats, as was done by Schijf and Schönfeld. These authors suppose that the longitudinal dispersion arises from the fact that the filling and emptying of the tidal flats does not coincide in general with respectively flood and ebb.

Here it will be shown that often a larger contribution to the longitudinal dispersion is caused by the fact that strong mixing may occur on the tidal flats.

Salinity measurements in the estuary Oosterschelde in Holland provide evidence for mixing on the tidal flats. In fig. 1 a part of this estuary is shown; the shaded regions are tidal flats. Point A lies on the border of a tidal flat, point B lies in the channel.

The salinity of the water flowing onto the tidal flat during the flood period varies as a function of time in a similar way as the salinity in the channel. During the ebb period, when the water flows out of the tidal flat, the salinities on the tidal flat and in the channel behave very differently. The salinity measured in point A is nearly constant, which is precisely a consequence of the mixing which has taken place on the tidal flat.

fig. 1



The following two mechanisms are probably responsible for the mixing of the water on the tidal flat:

- a) The water entering the stagnant area at the end of the flood period has a higher salt concentration, and therefore a higher density than the water entering at the beginning of the flood period. The water with higher density will tend to spread out over the bottom (density currents). At the same time vertical mixing is caused by bottom and surface shear stresses (wind influence). This process ends up with complete mixing in the stagnant area.
- b) Tidal flats in many estuaries have an irregular bottom topography: there are many paths a fluid particle may follow to reach a particular point on a tidal flat. For the same reason fluid particles coming from different parts of the tidal flat can meet during the ebb-period.

A mathematical description of the longitudinal dispersion caused by the presence of tidal flats along a channel is developed in the sections III, IV and V. Successively are introduced the effect of mixing on the tidal flat, the effect of non-tidal exchanges (eddies, density currents) between the channel and the tidal flats, and the effect of a phase-shift between the tide and the tidal velocity.

The description is based on the calculation of the quantity Z , which represents the total amount of constituent which passes through a cross-section of the estuary between two successive periods of low-water slack (LWS).

The quantity Z is related to the LWS dispersion coefficient, D_{LWS} by the general equation

$$Z = T Q_0 c_{LWS} - T D_{LWS} A_{LWS} \frac{d}{dx} c_{LWS} \quad (1)$$

We call T the tidal period, A the channel cross-section, c the concentration and u the velocity; the subscript LWS refers to low-water slack. Further we have

$$Q_0 = \frac{1}{T} \int_{LWS}^{LWS+T} dt \int_A u dA \quad , \quad Z = \int_{LWS}^{LWS+T} dt \int_A u c dA \quad .$$

For the computations we will consider a particular tidal cycle for which $Q_0 = 0$. This simplification has negligible consequences for the results as long as $Q_0 T / A_0 \ll L$,

where A_0 is the average cross-section and L represents the tidal excursion (if u is independent of x):

$$L = \int_{LWS}^{LWS+T} dt \frac{1}{A} \int_A u dA$$

A few other simplifications will also be made:

- the velocity and concentration distribution are homogeneous in each cross-section of the channel,
- the longitudinal gradients of the velocity and the concentration are small. In particular:

$$\left| L^2 \frac{d^2 c}{dx^2} \right| \ll \left| L \frac{dc}{dx} \right|$$

- the fluid particles on the tidal flat have a zero longitudinal velocity component. Therefore, the tidal flat will also be called "stagnant area".

Instead of equation (1) another method to obtain the dispersion coefficient for a trap-channel system has been used by Okubo [2]. This method consists of solving the differential equations governing the system for an instantaneous injection. It is not possible to obtain analytical solutions for these equations in all the cases considered in this paper. The dispersion coefficient defined by Okubo is not identical with D_{LWS} defined here. The main difference is a factor A_{LWS} / A_0 .

III. The effect of mixing in the stagnant area

The influence of mixing in the stagnant area on the longitudinal dispersion in the estuary will first be examined in the following particular situation (see fig. 2): The stagnant area is represented by a narrow branch (width Δx) at the side of the channel, situated at $x = x_0$.

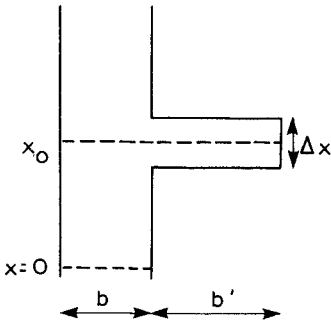


fig. 2 horizontal view

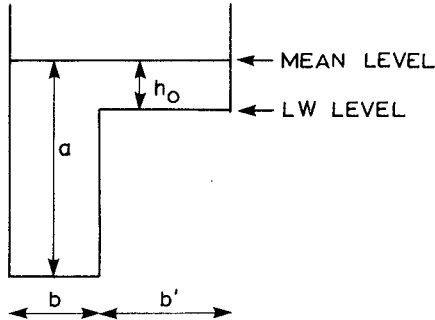


fig. 3 cross-section at $x = x_0$

The resulting amount of constituent ΔZ passing through a fixed plane at $x=0$ due to the mixing in the stagnant area is equal to the difference of the following two quantities:

- the amount of constituent which passes at flood through the plane $x=0$ and which is stored in the stagnant area.
- the amount of constituent flowing out of the stagnant area into the channel at a moment such that it passes the plane at $x=0$ during the ebb.

We suppose that low-water slack coincides with low water (LW) which is chosen as the time origin. Consider now a fluid particle which at time $t=0$ is at $x=0$. We call t_0 the time that this fluid particle reaches $x=x_0$. All the particles which pass by the plane $x=x_0$ in the time interval $t_0 < t < T-t_0$ also pass by the plane $x=0$ in the same tidal cycle. The resulting amount of constituent ΔZ passing the plane $x=0$ is therefore given by

$$\Delta Z = \int_{t_0}^{\frac{1}{2}T} dt \frac{dV'}{dt} c(x_0, t) + \int_{\frac{1}{2}T}^{T-t_0} dt \frac{dV'}{dt} c'(x_0, t) \quad (2)$$

Here $V'(t)$ is the volume of the stagnant area and $c'(x_0, t)$ the concentration in the stagnant area, which for $\frac{1}{2}T < t < T$ is constant and equal to

$$c'(x_0, \frac{1}{2}T) = \left[V'(0)c'(x_0, 0) + \int_0^{\frac{1}{2}T} dt \frac{dV'}{dt} c(x_0, t) \right] / V'(\frac{1}{2}T) \quad (3)$$

In order to obtain explicit expressions for ΔZ we have to specify the shape of the cross-section of the stagnant area. Here the depth with respect to mean level is taken constant and equal to the tidal amplitude h_0 (see fig. 3). Further we assume a sinusoidal tide, so that

$$V'(t) = h_0 b' \Delta x \left(1 - \cos \frac{2\pi t}{T} \right) \quad (4)$$

Neglecting the longitudinal gradient of the velocity, one can write for the path $X(t)$ of a fluid particle which at $t=0$ is at $x=0$:

$$X(t) = \frac{1}{2} L \left(1 - \cos \frac{2\pi t}{T} \right) \quad (5)$$

From this expression one can find t_0 as a function of x_0 . The concentration in the channel can be approximated by

$$c(x, t) = c(X(t), t) + \left[x - X(t) \right] \frac{\partial c}{\partial x} \Big|_{X(t), t} \quad (6)$$

During the flood period the concentration is constant along the path of a fluid particle (diffusion in the channel is neglected), so that

$$c(X(t), t) = c_{LWS}(x=0) \quad (7)$$

As a final approximation, which is discussed in the appendix, we set

$$\left. \frac{\partial c}{\partial x} \right|_{X(t), t} \approx \left. \frac{d}{dx} c_{LWS} \right|_{x=0} \quad (8)$$

Substitution of equations (3-8) in expression (2) yields the result

$$\Delta Z = h_0 b' \Delta x \frac{dc_{LWS}}{dx} x_0 \left(1 - \frac{x_0}{L}\right), \quad 0 \leq x_0 \leq L; \quad (9)$$

$$\Delta Z = 0 \quad \text{elsewhere.} \quad (9)$$

From this expression it appears that mixing in a local stagnant area only produces longitudinal dispersion over a distance which does not exceed the tidal excursion. For this particular transport mechanism the contribution of a second storage area can simply be added to the contribution of the first one. Integration therefore yields the longitudinal dispersion caused by a long stagnant area adjacent to the channel as shown in fig. 4. The result is

$$D_{LWS} = \frac{1}{6} \frac{h_0 b'}{A_{LWS}} \frac{L^2}{T} \quad (10)$$

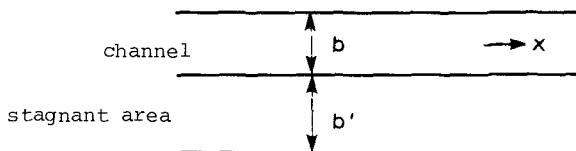


fig. 4 horizontal view

IV. The effect of non-tidal exchanges between the channel and the stagnant area.

In the preceding section it is assumed that the exchange of water between the channel and the stagnant area is only caused by the tide. In practice also exchanges caused by other mechanisms are present, like (turbulent) eddies and density currents, which take place without a net transfer of water. In this section the influence of these non-tidal exchanges, together with the assumption of complete mixing in the stagnant area will be studied.

We consider again the situation of fig. 2: a narrow trap located at $x = x_0$. The quantity of water which is exchanged per

unit time will be called Q_e . The total quantity of water flowing into the trap per unit time, Q_{in} , now equals:

$$Q_{in} = \frac{dV'}{dt} + Q_e, \quad 0 < t < \frac{1}{2}T; \quad Q_{in} = Q_e, \quad \frac{1}{2}T < t < T, \quad (11)$$

and the total quantity of water leaving per unit time,

$$Q_{out} = Q_e, \quad 0 < t < \frac{1}{2}T; \quad Q_{out} = -\frac{dV'}{dt} + Q_e, \quad \frac{1}{2}T < t < T. \quad (12)$$

The resulting amount of constituent ΔZ passing the plane $x = 0$ in a tidal period is given by a formula very similar to (2):

$$\Delta Z = \int_{t_0}^{T-t_0} dt [Q_{in}(t)c(x_0, t) - Q_{out}(t)c'(x_0, t)] \quad (13)$$

The concentration $c'(t) \equiv c'(x_0, t)$ can now be calculated from the mass-balance equation for the stagnant area:

$$\frac{d}{dt} [V'(t)c'(t)] = Q_{in}(t)c(x_0, t) - Q_{out}(t)c'(t)$$

The solution is

$$V'(t)c'(t) = V'(LWS)c'(LWS) \exp \left[-\int_{LWS}^t dt' \frac{Q_{out}(t')}{V'(t')} \right] + \int_{LWS}^t dt' Q_{in}(t')c(x_0, t') \exp \left[-\int_{t'}^t \frac{Q_{out}(t'')}{V'(t'')} \right] \quad (14)$$

In order to compute the formulas (13) and (14) one has to specify the exchange Q_e . Here the following assumptions are made:

- Q_e is proportional to the water depth in the stagnant area,
- exchange by eddies dominates exchange by density currents.

This assumption is plausible if the tidal velocity in the channel is important, and if the fresh water discharge and the depth of the stagnant area are small (these are all characteristics of the type of estuaries considered in this work). Then Q_e is minimum when the velocity is zero and maximum when the velocity is maximum.

From this follows the parametrisation

$$Q_e = \frac{\pi}{T} f_e V'(t) \left| \sin \frac{2\pi t}{T} \right| \quad (15)$$

The parameter f_e is defined as the fraction of the volume of the stagnant area which is exchanged with the channel during the flood period:

$$f_e = \int_0^{1/2 T} dt \frac{Q_e(t)}{V'(t)} \quad (16)$$

The dispersion coefficient D_{LWS} can now be calculated from the formulas (13) and (14) after substitution of the approximations (4-8). The result is

$$D_{LWS} = 2 \frac{h_0 b'}{A_{LWS}} \frac{L}{T} \Delta x \left\{ \frac{2}{f_e} \xi (1 - e^{-f_e(1-\xi)}) + \frac{1}{f_e^2} \left[-1 + e^{-f_e \xi} + \xi e^{f_e \xi} (e^{-2f_e} - e^{-4f_e}) \right] \right\} \quad (17)$$

for $\xi = x_0/L$ ranging from 0 to 1, and $D_{LWS} = 0$ elsewhere. In order to obtain the dispersion coefficient for a storage area with constant width extending along the channel one should consider the fact that a fluid particle can enter and leave the storage area several times during a tidal period. If it is assumed however that it is improbable that a fluid particle enters the stagnant area more than once, ($f_e \ll 1$), then the effect of several stagnant areas is the sum of the individual effects. The dispersion coefficient for a storage area extending along the channel is therefore obtained by integration of (17), with the result:

$$D_{LWS} = 2 \frac{h_0 b'}{A_{LWS}} \frac{L^2}{T} \left\{ \frac{1}{f_e} - \frac{3}{f_e^2} + \frac{4}{f_e^3} (1 - e^{-f_e}) - \frac{1}{f_e^4} (1 - e^{-f_e})^2 \right\} \quad (18)$$

Expanding this formula as a power series in f_e one finds

$$D_{LWS} = \frac{1}{6} \frac{h_0 b'}{A_{LWS}} \frac{L^2}{T} \left\{ 1 + f_e - \frac{19}{30} f_e^2 + \frac{7}{30} f_e^3 + \dots \right\} \quad (19)$$

Comparing with formula (10) it appears that the non-tidal exchanges between the channel and the stagnant area may amplify the effect of mixing in a stagnant area on the longitudinal dispersion in an estuary. For small values of f_e the result can be interpreted as a virtual increase of the volume of the storage area with a fraction equal to f_e . For very large values of f_e the fluid particles stored into the stagnant area will remain there only a very short time, so that the longitudinal dispersion decreases. Although equation (18) has been derived for small values of f_e , the result is also valid for large values of f_e . Indeed, the dispersion coefficient is proportional to the average square displacement of fluid particles with respect to the main motion times the number of fluid particles being displaced. The average square displacement of a fluid particle is proportional to the number of times n ($n \gg 1$) that it enters and leaves the stagnant area. On the contrary, the number of fluid particles

displaced is inverse proportional to the average number of times $\langle n \rangle$ that the same fluid particle enters and leaves the stagnant area.

V. Effect of a phase-shift between tide and velocity

Mainly due to bottom friction the tidal motion in an estuary differs from a standing wave. This implies that flood and ebb do not coincide with respectively rising and falling tide. It has been shown by Schijf and Schönfeld that this effect generates dispersion in the presence of tidal flats.

Due to the phase-shift between tide and velocity, the water in the stagnant area is submitted to an effective relative motion with respect to the water in the channel, during a tidal cycle. Therefore, assuming the average discharge Q_0 equal to zero, a fluid particle, which is not stored during the tidal cycle, will not return to its initial position; it will undergo a net displacement δ in the upstream direction. A fluid particle which remains in the stagnant area during some part of the tidal cycle will undergo a net displacement in the downstream direction.

Consider the path $X(t)$ of a fluid particle, which at time $t = LWS + T$ is at $x = 0$ (the time origin is chosen at LW). At $t = 0$ this fluid particle is at $x = -\delta$; it passes by the plane $x = x_0$ at times $t = t_0 < HWS$ and $t = t'_0 > HWS$.

The formulas of the preceding section can now be easily extended to this case; for a single trap at $x = x_0$ one obtains:

$$\Delta Z = \int_{t_0}^{t'_0} dt [Q_{in}(t)c(x_0, t) - Q_{out}(t)c'(x_0, t)] + I$$

for $0 \leq x_0 \leq L$, and

$$\Delta Z = -V'(t_0)c'(x_0, t_0) + V'(LWS)c'(x_0, LWS) + I$$

for $-\delta \leq x_0 < 0$, where

$$I = \int_{-\delta}^0 dx A_{LWS}(x) c_{LWS}(x)$$

(20)

In order to obtain a simpler expression we neglect non-tidal exchanges ($f_e = 0$) and integrate in the variable x_0 . For a stagnant area extending along the channel one then finds

$$Z = \int_{-\delta}^0 dx A_{LWS}(x) c_{LWS}(x) + \int_{LWS}^{1/2T} dt \int_0^{X(t)} dx c(x, t) \frac{\partial A'(x, t)}{\partial t}$$

$$\int_{1/2T}^T dt \int_0^{X(t)} dx c'(x,t) \frac{\partial A'(x,t)}{\partial t} + \int_T^{LWS+T} dt \int_0^{X(t)} dx c(x,t) \frac{\partial A'(x,t)}{\partial t} \quad (21)$$

Here $A'(x,t)$ represents the cross-section of the stagnant area.

The expression (21) is evaluated for the cross-section shown in fig. 3 and assuming a sinusoidal tide.

The net displacement δ can be found from equation (21), by putting $Z=0$ when $c(x,t) = c'(x,t) = \text{constant}$.

The result is

$$\delta = \frac{1}{2} \pi h_0 b' L \sin \varphi / (A_{LWS} - h_0 b' \cos \varphi) \quad (22)$$

with $\varphi = 2\pi LWS/T$ (the time origin is chosen at LW).

In the case of a phase-shift between tide and velocity longitudinal dispersion is generated even when no mixing takes place on the tidal flats. No mixing implies

$$c'(x,t) = c'(x, T-t) \quad (23)$$

Substitution in (21) yields:

$$D_{LWS} = \frac{2}{3} \frac{h_0 b'}{A_{LWS}} \frac{L^2}{T} \sin^2 \varphi \quad (24)$$

When complete mixing on the tidal flats is assumed one may substitute for $c'(x,t)$ the expression (3). The result is

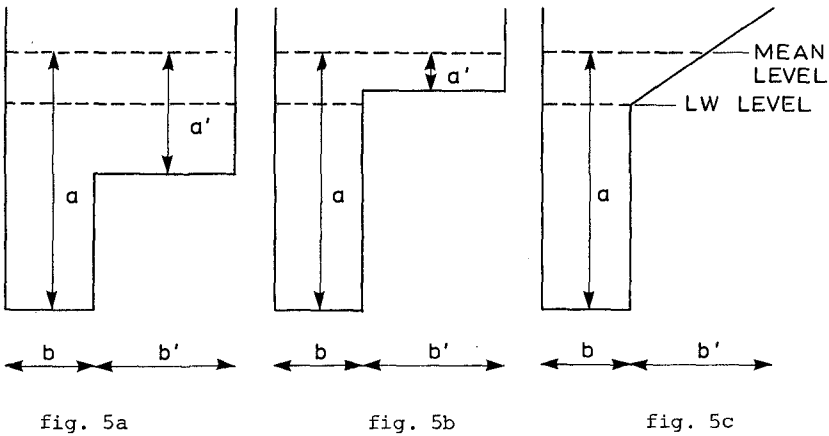
$$D_{LWS} = \frac{1}{6} \frac{h_0 b'}{A_{LWS}} \frac{L^2}{T} \left[1 + \left(1 + \frac{3\pi^2}{16} \right) \sin^2 \varphi \right] \quad (25)$$

In both the formulas (24) and (25) higher order terms in $h_0 b' / A_{LWS}$ have been omitted.

VI. Generalisation for real estuaries.

In the preceding sections a particular cross-section is considered, which may be very different from the type of cross-sections which occur in natural estuaries. In order to present results which can be applied for real estuaries, we will consider here some other types of cross-sections and derive from this more general expressions for the longitudinal dispersion coefficient.

The three particular cross-sections studied in this section are shown in fig. 5a - c.



- a) The depth of the stagnant area is greater than h_0 (fig. 5a). When the depth of the stagnant area becomes large the non-tidal exchanges between the channel and the stagnant area will play a more important role. We consider now the limit that the tidal elevation can be neglected with respect to the depth a' of the stagnant area, as was done by Okubo [2]. The exchange discharge Q_e is assumed to be constant. Computation of equation (13) yields the result

$$D_{LWS} = \frac{\pi^2}{4} \frac{a' b'}{A_{LWS}} \frac{L^2}{T} \frac{1}{f_e} \left(1 + \frac{\pi^2}{f_e^2}\right)^{-1} \left[1 - \frac{1 - e^{-2f_e}}{f_e(1 + \frac{\pi^2}{f_e^2})}\right] \quad (26)$$

With the approximations $f_e \ll 1$ and $a' b' \ll A_{LWS}$ this expression is identical to the one found by Okubo. The results also agree in the limit $f_e \gg 1$; the reason for this has been given previously.

In reality one may expect an important contribution of density currents to the non-tidal exchanges when the stagnant area is deep. The assumption of a constant Q_e should therefore be modified, as well as equation (26). This problem will not be treated here any further.

b) The depth of the stagnant area is smaller than h_0 (fig. 5b).

Instead of a' we write $h_0 \cos \vartheta$, where ϑ is a parameter ranging from 0 to π . The tidal volume per unit length of the stagnant area A'_t is equal to $A'_t = 2\eta h_0 b'$, with $\eta = \cos^2 \frac{1}{2} \vartheta$. In the case of complete mixing equation (13) yields

$$f_e(\eta) = \eta f_e(\eta = 1) \text{ and } D(\eta) = \eta^3 D(\eta = 1) \quad (27)$$

For the interpretation of this result one should consider the fact that the transport of water towards and from the stagnant area only takes place in a limited time interval during which the distance λ travelled by the fluid particles in the channel equals $\lambda = \eta L$. As shown in section III, the mixing in the stagnant area generates an effective transfer of fluid particles over distances smaller than or equal to λ : the distance λ is the maximum mixing length. The result (27) suggests that the dispersion coefficient depends on λ rather than on L .

Considering the effect of the phase-shift φ and no mixing in the stagnant area the result is

$$D_{LWS} = \frac{2}{3} \frac{h_0 b'}{A_{LWS}} \frac{L^2}{T} \sin^2 \varphi \cos^2 \frac{1}{2} \vartheta \left[1 + \cos \vartheta \sin^2 \frac{1}{2} \vartheta \right] \quad (28)$$

In this case the distance over which the mixing takes place at different times is given by the expression $X(t) - X(T-t) = L \sin \varphi \sin \frac{2\pi t}{T}$, which is independent of ϑ . Therefore to a good approximation the dispersion coefficient is equal to the square of $L \sin \varphi$ and to the tidal volume of the stagnant area, except for high tidal flats ($\vartheta > \frac{1}{2} \pi$).

c) The depth of the stagnant area varies linearly (fig. 5c).

The tidal volume of the stagnant area equals $A'_t = h_0 b'$; the dispersion coefficient is obtained from equation (2) by substituting

$$\frac{dA'}{dt} = \frac{1}{2} b' \left(1 - \cos \frac{2\pi t}{T} \right) \frac{dh}{dt}$$

For the case of complete mixing and $\varphi = f_e = 0$ one finds

$$D_{LWS} = \frac{1}{18} \frac{h_0 b'}{A_{LWS}} \frac{L^2}{T} \quad (29)$$

According to the discussion of formula (27) it appears that the dispersion coefficient is not just proportional to the tidal volume of the stagnant area, but that it also depends on the shape of the cross-section. The triangular shape brings about an extra factor $2/3$, with respect to the rectangular shape.

For the case with $\varphi \neq 0$ and no mixing one finds

$$D_{LWS} = \frac{1}{3} \frac{h_0 b'}{A_{LWS}} \frac{L^2}{T} \sin^2 \varphi \quad (30)$$

For this case the dispersion coefficient appears to be proportional to the tidal volume of the stagnant area; the result is independent of the shape of the cross-section.

The preceding considerations lead to the following generalisations:

- longitudinal dispersion caused by mixing on the tidal flats:

$$D_{LWS} = k \frac{A'_t}{A_{LWS}} \frac{\lambda^2}{T} \quad (31)$$

where k is a parameter depending on the shape of the cross-section of the tidal flat: $k = 1/12$ for a rectangular shape, $k = 1/18$ for a triangular shape. The distance $\lambda = L \cos^2 \frac{1}{2} \vartheta$

is the maximum mixing length.

- the increase of longitudinal dispersion caused by non-tidal exchanges between the channel and the tidal flats:

$$\begin{aligned} D(f_e) &= 12 \left\{ \frac{1}{f_e} - \frac{3}{f_e^2} + \frac{4}{f_e^3} (1 - e^{-f_e}) - \frac{1}{f_e^4} (1 - e^{-f_e})^2 \right\} D(f_e = 0) \\ &= \left\{ 1 + f_e - \frac{19}{30} f_e^2 + \frac{7}{30} f_e^3 + \dots \right\} D(f_e = 0) \quad (32) \end{aligned}$$

where f_e is defined in equation (16) as the fraction of the water volume on the tidal flat which is exchanged during the flood period.

- the increase of longitudinal dispersion caused by a phase-shift $\varphi = 2\pi(LWS - LW)/T$ between the tidal elevation and the tidal velocity depends in a rather complicated way on the shape of the cross-section of the tidal flat. When the phase-shift is large ($\sin \varphi \approx 1$) the mixing on the tidal flat only plays a minor role.
- longitudinal dispersion caused by the phase-shift φ , without mixing on the tidal flat, is to a good approximation independent of the shape of the cross-section except when the major part of the tidal flat is above mean level. Otherwise

$$D_{LWS} = \frac{1}{3} \frac{A'_t}{A_{LWS}} \frac{L^2}{T} \sin^2 \varphi \quad (33)$$

In spite of these generalisations it remains difficult to obtain from these formulas accurate estimates for the dispersion coefficients in real estuaries.

Specially the following problems should be mentioned:

- the specification of the part of the estuary cross-section which may be considered as "stagnant area",
- the definition of the maximum mixing length when the velocity distribution is inhomogeneous,
- the determination of the degree of mixing in the stagnant area,
- the estimation of exchange coefficient f_e .

The last two problems are also related to the occurrence of density effects, which therefore contribute implicitly in the formulas (31-33).

In Holland the estuaries Westerschelde, Oosterschelde and Eems belong to the class of shallow well mixed estuaries studied in this paper. In these estuaries the geometrical factor

A'_t / A'_{Lws} ranges between 0.3 and 0.45 and the maximum mixing length λ between 12 and 15 kilometers. Estimating the exchange coefficient f_e between 0.1 and 0.5, one finds values for the dispersion coefficient in the interval 88-273 m²/s. The measured dispersion coefficient is found in the interval 150-450 m²/s. The phase-shift φ is small and therefore contributes little. A small increase of the dispersion coefficient with increasing discharge, which has been observed experimentally, could be related to the influence of density effects on the mixing and exchange processes on the tidal flats.

VII. Summary and conclusions

Experimental evidence is shown for the occurrence of strong mixing on tidal flats. In estuaries with an important tidal motion and large tidal flats the mixing of water on the tidal flats produces longitudinal dispersion, which is enhanced by two other phenomena: the exchange of water between the channel and the stagnant area by other mechanisms than the tide (eddies, density currents) and the occurrence of a phase-shift between the tidal elevation and the tidal velocity due to the damping of the tidal wave in the estuary. Explicit expressions are given for the contribution of these phenomena to the longitudinal dispersion.

It is shown that the dispersion coefficient depends linearly on the tidal volume of the stagnant area and that it is proportional to the square of the maximum mixing length, which is the distance covered by a water particle in the channel during the period that the stagnant area is being flooded by the tide.

From the formulas it is possible to obtain for real estuaries an estimate of the dispersion caused by mixing and exchange processes on the tidal flats. For several estuaries in Holland

with an important tidal motion and large tidal flats, the results are compared to experimental values for the dispersion coefficient. It appears that the tidal flats account for about 50% of the longitudinal dispersion.

APPENDIX.

A. The sensitivity of the results for the approximation

$$\left. \frac{\partial c}{\partial x} \right|_{X(t),t} \approx \left. \frac{dc_{LWS}}{\partial x} \right|_{x=0} \quad (8)$$

In order to evaluate the first order correction term, we consider a small section in the channel of variable length $l(t)$, moving in such a way that no transport takes place through the front or the back. The difference between the concentrations in the front and in the back is constant, and equals Δc . When $l(t)$ is taken small enough, then

$$\Delta c = l(t) \left. \frac{\partial c}{\partial x} \right|_{X(t),t} \quad (34)$$

The function $l(t)$ can be obtained from the continuity equation

$$\frac{d}{dt} [A(t)l(t)] + l(t) \frac{dA'}{dt} = 0$$

which is solved for the model estuary (see fig. 3) and a sinusoidal tide, with the approximation

$$\gamma = h_0(b + b') / A_0 \ll 1$$

The result is

$$l(0) / l(t) = (1 - \gamma \cos \frac{2\pi t}{T}) / (1 - \gamma) \quad (35)$$

From this, and from the equations (8) and (37) follows

$$\left. \frac{\partial c}{\partial x} \right|_{X(t),t} = \left. \frac{dc_{LWS}}{\partial x} \right|_{x=0} \frac{1 - \gamma \cos \frac{2\pi t}{T}}{1 - \gamma} \quad (36)$$

Substitution in equation (21) introduces in the formulas (24) and (25) a factor $1 / (1 - \gamma)$ and some correction terms.

Assuming complete mixing in the stagnant area, the correction to the dispersion coefficient (25) has a relative magnitude of order $\gamma \sin 2\phi$

Assuming no mixing in the stagnant area, the dispersion coefficient (24) contains correction terms with a relative magnitude of order γ^2

REFERENCES

- [1] J.B. Schijf, J.C. Schönfeld, Theoretical considerations on the motion of salt and fresh water, Procc. Minn. Int. Hydraul. Conv., Minneapolis (1953) 321.
- [2] A. Okubo, Effect of shoreline irregularities on stream-wise dispersion in estuaries and other embayments, Neth. J. of Sea Res. 6 (1973) 213.

INTERFACIAL FRICTION COEFFICIENTS IN
A TWO-LAYERED STRATIFIED FLOW

By

Emmanuel Partheniades¹ and Vassilios Dermassis²

ABSTRACT

The friction factors at the interface in a two-layered stratified flow have been studied experimentally in a closed rectangular duct with freshwater flowing over a quasi-stagnant salt water. The analysis of the flow was based on the application of the one-dimensional mass and energy equations for each layer. It was found that the interfacial friction coefficient, \bar{f}_i , is best correlated with the dimensionless number ReF^2 , where Re and F are some non-densimetric Reynolds and Froude numbers of the flow, and with the relative density difference of the two layers $\Delta\rho/\rho$. Good agreement has been obtained with results of previous laboratory investigations and field data.

INTRODUCTION

The hydrodynamics of arrested saline wedges plays a dominant role in a variety of engineering problems related to estuarine hydraulics and, in general, to the management of stratified or nearly stratified estuaries. Among the most important parameters which appear in the pertinent equations are the shear stresses at the interface and at the bed as well as the related shear stress coefficients. Indeed equations are available which give the length of intrusion, L_i , and the shape of the salinity wedge in terms of the densimetric Froude number, F'_0 , and an average interfacial shear stress coefficient, \bar{f}_i , over the length of intrusion. These equations, developed by Schijf and Schoenfeld (15)*, are based on the energy balance in the upper and lower layer respectively, on negligible rates of salt water entrainment through the interface and on zero average velocity through any cross section of the salinity wedge. They have the following form:

¹Prof. of Hydraulic Structures, School of Engrg., Aristoteles University of Thessaloniki, Greece; and Prof. of Engrg. Sci., University of Florida, Gainesville, Florida, U.S.A.

²Instructor, Chair of Hydraulic Structures, School of Engrg., Aristoteles University of Thessaloniki, Greece. Currently Res. Assist., Dept. of Engrg. Sci., University of Florida, Gainesville, Florida, U.S.A.

*Numbers in parenthesis indicate references at the end of the paper.

$$\frac{\bar{f}_i}{8} \frac{x}{h_o} = \frac{h_1}{h_o} \left[\frac{1}{5(F'_o)^2} \left(\frac{h_1}{h_o}\right)^4 - \frac{1}{4(F'_o)^2} \left(\frac{h_1}{h_o}\right)^3 - \frac{1}{2} \left(\frac{h_1}{h_o}\right) + 1 \right] + 3(F'_o)^{2/3} \left[\frac{1}{10}(F'_o)^{2/3} - \frac{1}{4} \right] \tag{1}$$

and

$$L_i = \frac{2h_o}{\bar{f}_i} \left[\frac{1}{5(F'_o)^2} - 2 + 3(F'_o)^{2/3} - \frac{6}{5}(F'_o)^{4/3} \right] \tag{2}$$

where, referring to Fig. 1, h_o = the total depth of flow at the end of the salinity intrusion, h_1 = the fresh water depth, x = the distance from the ocean end of the channel and F'_o = the densimetric Froude number, defined by the Eq.:

$$F'_o = \frac{V_o}{\sqrt{g \frac{\Delta\rho}{\rho} h_o}} \tag{3}$$

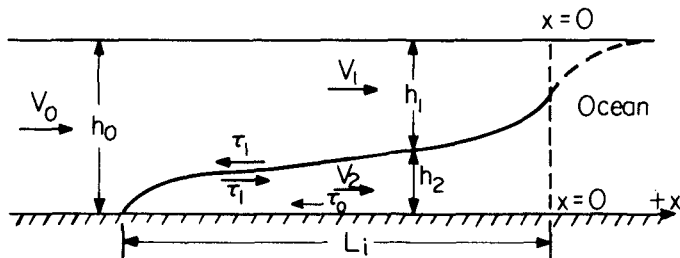


Fig. 1 Definition sketch of an arrested saline wedge

where V_o = the fresh water velocity upstream of the end of salinity intrusion, ρ = the fresh water density, $\Delta\rho$ = the density difference between the fresh water and salt water and g = the acceleration of gravity. With F'_o normally known the length of salinity intrusion, L_i , can be obtained from Eq. 2 if \bar{f}_i can be estimated. Likewise, knowing \bar{f}_i the shape of the arrested salinity wedge could be determined either from Eq. 1 or from an equation developed elsewhere (12).

The importance of the interfacial shear stress coefficient motivated numerous investigations for the purpose of linking f_i to some readily determinable gross flow and salinity parameters. The basic assumptions, however, and the methodology of approach varied widely among the various investigations, as expected. As a result, the graphical and analytical expressions obtained give, if applied to the same physical system, values of the f_i differing widely, sometimes by orders of magnitude. The flow within the interfacial zone

has often been assumed to be laminar. This is by no means the general case. On the contrary, experimental evidence suggests that the velocity may considerably exceed its critical value for salt water entrainment and mixing (10, 12) with the flow maintaining its stratified appearance with a sharp interface. Thus sufficient exchange of fresh and salt water may take place through the interface for Reynolds stresses to develop, while the rate of entrainment and mixing remains negligible in comparison to the fresh water flow rate.

The objective of this study has been the derivation of generalized relationships between the interfacial friction coefficient, \bar{f}_i , and the pertinent parameters which fully describe the flow and salinity conditions. The to-date results are herein reported*.

PARTIAL REVIEW OF EARLIER INVESTIGATIONS

Keulegan (9, 10) derived the following analytical expression for \bar{f}_i on the assumption of laminar flow conditions in the neighborhood of the interface:

$$\bar{f}_i = \frac{8T_i}{\rho V_0^2} = \frac{A_1}{R_0} \quad (4)$$

where T_i = average interfacial shear stress over the length of salinity intrusion, $R_0 = V_0 h_0 / \nu$, A_1 = a dimensionless constant equal to 152 for $h_{sc} = 0.5 (h_0)$ and h_{sc} = the value of h_s at the ocean entrance given by the equation:

$$h_{sc} = h_0 \left[1 - (F'_0)^{2/3} \right] \quad (5)$$

An experimental expression similar to Eq. 4 was derived by Bata and Knezevich for laminar density underflows (2) but with a value of $A_1 = 180$ and $R_e = 4Vh_0/\nu$. For turbulent underflows the same investigators found $\bar{f} = 0.010$ for smooth bottom and $\bar{f} = 0.020$ for rough bottom. It should be noted though, that \bar{f} is an average friction factor incorporating the frictional effects of bottom, interface and sidewall.

Shi-igai (14) calculated the energy dissipation, ϵ , per unit surface of fluid caused by the internal waves and defining $\tau_i = \epsilon/V_1$, where V_1 = the uniform velocity of the moving fresh water layer, derived the following Eq.:

$$f_i = \frac{2\tau_i}{\rho V_1^2} = 8\pi^2 \left(\frac{a}{\lambda} \right)^2 \frac{1}{R_e (F'_1)^2} \quad (6)$$

where $R_e = V_1 h_1 / \nu$, $F'_1 = V_1 / \sqrt{g \frac{\Delta\rho}{\rho} h_1}$, h_1 = thickness of the

upper layer, a = the amplitude and λ = the length of internal waves. On the basis of limited experimental data at that time the factor $8\pi^2(a/\lambda)^2$ was tentatively estimated to be about 12.

For a laminar density underflow under uniform conditions Ippen and Harleman (6) derived the following equation for the average friction coefficient \bar{f} , which incorporates, like in Bata and Knezevich experiments, the frictional resistance of both the bed and the interface:

$$\bar{f} = \frac{228}{R_e} \tag{7}$$

where $R_e = 4h_2V_2/\nu$, h_2 = the uniform depth of the underflow and V_2 = the average velocity of the latter.

Abraham and Eysink (1) reanalyzed some of the test data of Keulegan and Barr for values of $R_e = VR_1/\nu$ up to 1.5×10^4 . For $F'_0 \approx 0.8$ they found a smooth curve relating f_i to R_e in a log-log plot. The curve becomes flatter as the Reynolds number increases, something which is indicative of turbulent shear stresses within the interfacial zone.

Georgiev studied the case of a uniform underflow in a two-layered system and determined the Reynolds stresses at the interface by direct measurements with hot film. His experimental data satisfy the relationship:

$$f_i = \frac{0.275}{R_e^{0.276}} \tag{8}$$

where $R_e = V_2R_{h_2}/\nu$ ranged from 10^3 to 10^4 and where R_{h_2} = the hydraulic radius of the underflow. It is noteworthy that this last relationship is quite close to Blasius formula:

$$f = \frac{0.316}{R_e^{0.25}} \tag{9}$$

for smooth pipe flow (16). The scattering of Georgiev's points is relatively small; however, the unique dependence of f_i only on Reynolds number in a turbulent two-layered stratified flow and the narrow range of the latter raises doubts as to its universal validity.

More recently Harleman and Stolzenbach (7), using data of other investigators, arrived at the following experimental equation for f_i :

$$\frac{1}{\sqrt{f_i}} = 2 \log Re\sqrt{f_i} - 0.8 \tag{10}$$

where $R_e = 4VR_h/\nu$.

The scattering of the data points, however, which exceeds an order of magnitude, and the fact that f_i is given again as a function of only the Reynolds number for values of the latter as high as 6×10^6 raises, as in the previous case, serious questions.

Lofquist (11) conducted extensive experimental research on a two-layered system in which the lower layer was moving with uniform depth and velocity, while the upper one was quasi-stagnant. His results were given graphically with dependent variable the ratio β of the turbulent shear stresses to the corresponding laminar ones and independent variables the Reynolds number and the densimetric Froude number. For laminar flow at the interface Lofquist's relationship approaches quite closely that of Keulegan (9, 10).

At this point it would be interesting to compare the results obtained by various formulas for the South Pass of the Mississippi River (12). The given data are: $Q = 100,000$ cfs, $b = 1500$ ft, $h = 45$ ft, $V_0 = 1.48$ ft/sec, $\Delta\rho/\rho = 0.02$, $\nu = 1.09 \times 10^{-5}$ ft²/sec, $F'_0 = 0.275$ and a length of salinity intrusion, $L_i = 14$ miles. It is first observed that the critical velocity for the initiation of entrainment is (8, 10):

$$V_{1m} = 7.3 \left(\nu g \frac{\Delta\rho}{\rho} \right)^{1/3} \quad (11)$$

which for the given data gives $V_{1m} = 0.14$ ft/sec. This is much smaller than the fresh water velocity. Therefore, there is entrainment through the interface and the flow around it is turbulent. The following results can then be obtained:

- (a) Schijf and Schoenfeld Eq. 2 gives $\bar{f}_i = 0.00185$.
- (b) Keulegan's Eq. 4 gives $\bar{f}_i = 2.5 \times 10^{-5}$.
- (c) Bata and Knezevich's equation for $R_e = 244.4 \times 10^5$ gives $\bar{f} = 0.74 \times 10^{-5}$.
- (d) Shi-igai's Eq. 6, after properly converting R_e and F' to mean flow conditions over the wedge through Eqs. 1, 2, and 5, gives $f_i = 0.96 \times 10^{-5}$.
- (e) Harleman and Stolzenbach's Eq. 10 gives $\bar{f}_i = 0.0071$.
- (f) If a smooth boundary replaces the interface then for the values of $h_1 = 34.2$ ft, i.e. the mean fresh water depth, and $V_1 = 1.95$ ft/sec, i.e. the mean fresh water velocity, we obtain $\bar{f}_i = 0.0075$ which is quite close to the former.

The above example shows first that the actual value of \bar{f}_i

based on field measurement in real estuaries may exceed the values given by formulas based on the assumption of laminar flow around the interface by two to three orders of magnitude; second, that Shi-igai's theory seems to be valid rather for laminar flow near the interface and finally that Harleman and Stolzenbach's Eq. 12 gives too high values of \bar{f}_i bordering those corresponding to a smooth solid wall.

The results of the most important up to 1974 investigations have been reviewed and summarized by the Hydraulic Laboratory in Delft, Netherlands (3). Fig. 2 represents an attempt to find a relationship between \bar{f}_i and the Reynolds number $Re_1 = V_1 h_1 / \nu$ for the cases where the upper layer is moving and the lower one is quasi-stationary. It is readily seen that Ippen and Harleman's line, valid for laminar underflow and for $Re_1 \leq 1000$, crosses two groups of points by Rid-del; nevertheless, each group could very well correspond to a different line particularly since the flow for $Re_1 > 1000$ is turbulent. Lanzoni's line covers too narrow a range of Re_1 while Averkiev and Kinds data fall in a line almost parallel to that of Ippen and Harleman but exceeding it by a factor of about 5. Zanotti's data are too limited and too scattered and finally the only two field data cannot be meaningfully connected with the laboratory test data. It seems rather doubtful whether \bar{f}_i is indeed a function of the Reynolds number only. This conclusion is further strengthened by Fig. 3, which summarizes results of underflows with the lower layer only moving and where the spread of the experimental points approaches one order of magnitude. Clearly \bar{f}_i must depend on other factors besides Re_e . In fact \bar{f}_i seems to be very weakly correlated to Re_e with an average value of about 0.0208 for the group of points of low Re_e and 0.0144 for the group of points of high Re_e . The corresponding ranges are 0.008 to 0.08 for the first group and 0.008 to 0.0456 for the second. All these values are much higher than the $\bar{f}_i = 0.00185$ for the South Pass of the Mississippi River as estimated earlier. A trend similar to that of Fig. 3 has been observed in cases where both the upper and lower layers are moving in opposite directions.

Fig. 4 shows an attempt to correlate $\bar{f}_i/8$ with the product $Re_e (F')^2$ while using at the same time F' as a parameter. The correlation seems to be rather poor. The average value of \bar{f}_i is around 0.0160, that is quite close to the value of the previous figure. Fig. 5 (13) shows a summary of several test data where $\theta =$ the Keulegan number defined as:

$$\theta = \frac{1}{V} \left(v g \frac{\Delta \rho}{\rho} \right)^{1/3} \quad (12)$$

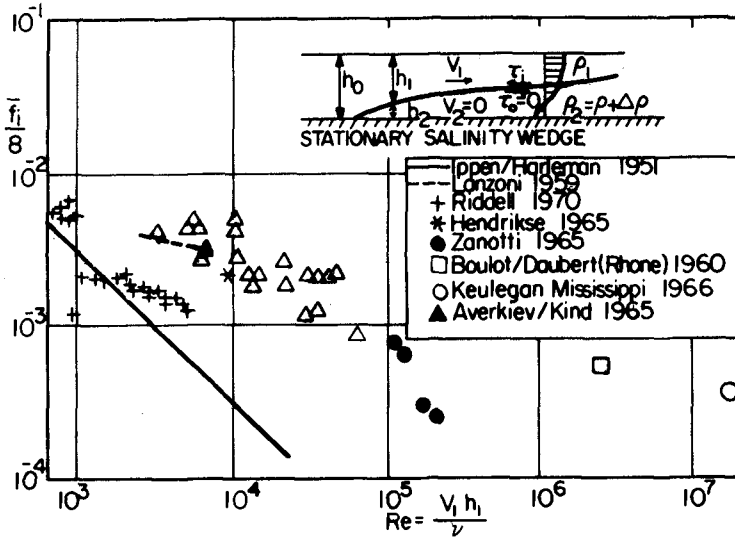


Fig. 2 Variation of \bar{f}_i with Re for flow in upper layer (3)

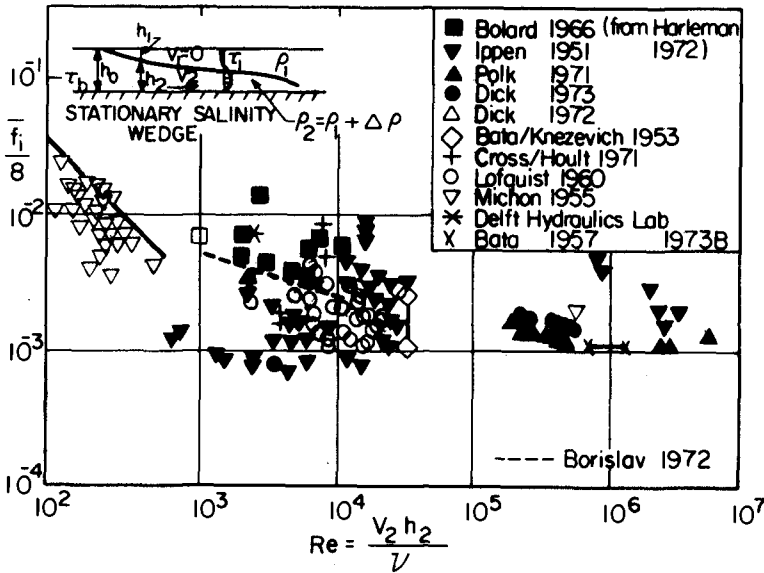


Fig. 3 Variation of \bar{f}_i with Re for flow in lower layer (3)

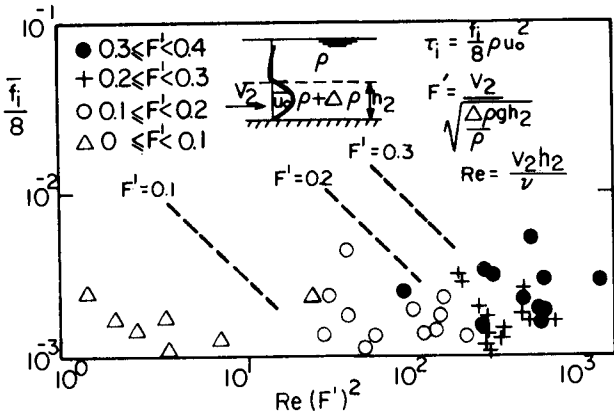


Fig. 4 Variation of \bar{f}_i with $Re(F')^2$ and F' according to Lofquist's experiments^(3, 11)

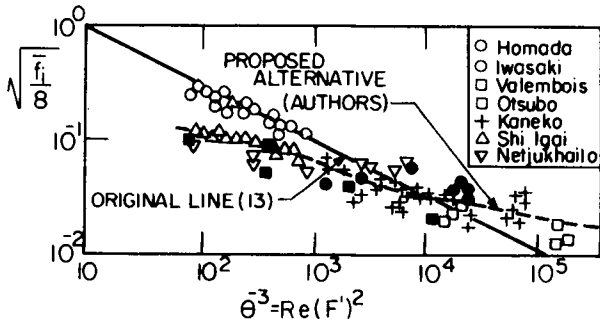


Fig. 5 Variation of \bar{f}_i with Keulegan's number θ

It is obvious that $\theta^{-3} = Re(F')^2$. It is observed that the results of Iwasaki fall on a straight line with little scattering; however, all other points fall on a distinctly different line whose mean slope with respect to the θ^{-3} axis is considerably smaller than that of the first line.

This limited review leads to two major observations: (a) None of the presented correlations seems to be of universal validity and, (b) in several plots the scattering of data points is too wide for reliable conclusions. Both observations suggest that either the correlation parameter or parameters were not properly selected, or additional flow and salinity parameters should be taken into consideration in a way that each one of them should have the maximum possible

weight on \bar{f}_1 . This is the objective of the experimental work to be presented.

EQUIPMENT AND PROCEDURE

Theoretical Analysis

The experimental studies were conducted in a 15 m long closed rectangular duct whose lower part was occupied by a quasi-stagnant salt water layer over which fresh water was flowing at predetermined rates (4). Application of the energy balance to each layer of a two-layered stratified flow (Fig. 6) gives:

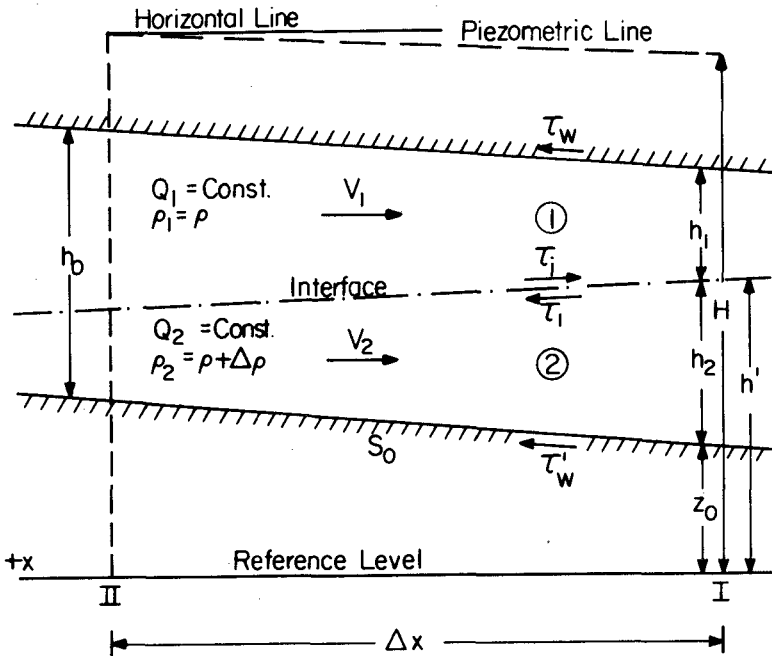


Fig. 6 Definition sketch for stratified two-layered flow in a closed duct

$$\frac{dH}{dx} + \frac{V_1}{g} \frac{dV_1}{dx} - S_{e1} = 0 \tag{13}$$

for the upper layer, where H = the elevation of piezometric line and S_{e1} = the slope of the energy grade line and

$$\left(1 - \frac{\Delta\rho}{\rho}\right) \frac{dH}{dx} + \frac{\Delta\rho}{\rho} \cdot \frac{dh'}{dx} + \frac{V_2}{g} \frac{dV_2}{dx} - S_{e2} = 0 \tag{14}$$

for the lower layer, where h' = the elevation of the interface and S_{e2} = the slope of the energy grade line. Considering that $h' = z_0 + h_2$, $h_1+h_2=h_0$ =depth of the duct=constant and $dz_0/dx = S_0$ = slope of the duct (Fig. 6) it follows that:

$$\left(1 - \frac{\Delta\rho}{\rho}\right) \frac{dH}{dx} + \frac{\Delta\rho}{\rho} S_0 - \frac{\Delta\rho}{\rho} \frac{dh_1}{dx} + \frac{V_2}{g} \frac{dV_2}{dx} - S_{e2} = 0 \tag{15}$$

For negligible rate of entrainment and mixing through the interface the continuity equation gives $h_1V_1 = \text{const.}$ and $h_2V_2 = \text{const.}$ Considering that $V_2 = 0$ for the lower layer, Eqs. 13 and 15 take the forms:

$$\frac{dH}{dx} - \frac{V_1^2}{gh_1} \cdot \frac{dh_1}{dx} - S_{e1} = 0 \tag{16}$$

and

$$\left(1 - \frac{\Delta\rho}{\rho}\right) \frac{dH}{dx} + \frac{\Delta\rho}{\rho} S_0 - \frac{\Delta\rho}{\rho} \frac{dh_1}{dx} - S_{e2} = 0 \tag{17}$$

For uniform boundary roughness S_e is given by:

$$S_e = \frac{\tau_b}{\gamma R_h} \tag{18}$$

where τ_b = the average boundary shear stress. In the present case, however, of a closed duct of finite width, b , and with composite roughness, i.e. with a Darcy-Weisbach friction coefficients f_i at the interface and f_w at the wall, Eq. 18 has to be modified. Considering the force balance of a small element of the duct it can readily be shown that:

$$(2h_1 + b)\tau_w + b\tau_i = bh_1\rho S_{e1} \tag{19}$$

Assuming now $\tau = \frac{f}{8} \rho V^2$ for both τ_w and τ_i it follows that:

$$S_{e1} = \frac{V_1^2}{gh_1} \left(\frac{f_w + f_i}{8} + \frac{h_1}{4b} f_w \right) \tag{20}$$

The same procedure for the lower layer gives:

$$S_{e2} = - \frac{V_1^2 f_i}{8g(h_0 - h_1)} \tag{21}$$

Then from Eqs. 16 and 17 it is finally obtained:

$$\frac{dh}{dx} = \frac{\frac{dh_1}{dx} \left[\frac{V_1^2}{g} + (h_o - h_1) \frac{\Delta\rho}{\rho} \right] + \frac{V_1^2 f_w}{8g} \left(1 + \frac{2h_1}{b} \right) - \frac{\Delta\rho}{\rho} (h_o - h_1) S_o}{(h_o - h_1) \left(1 - \frac{\Delta\rho}{\rho} \right) + h_1} \quad (22)$$

and

$$f_i = \frac{8 \left[\left(\frac{gh_1}{V_1^2} - \frac{\rho}{\Delta\rho} + 1 \right) \frac{dH}{dx} - S_o \right] - f_w \left(1 + \frac{2h_1}{b} \right)}{1 + \frac{V_1^2}{\frac{\Delta\rho}{\rho} g (h_o - h_1)}} \quad (23)$$

Eqs. 22 and 23 will serve as a basis for the analysis of the experimental data.

Basic Research Equipment

The basic research equipment, constructed at the Laboratory of Hydraulics and Hydraulic Structures of the School of Engineering of the University of Thessaloniki, Greece, is outlined in Fig. 7. (4) It consists of a rectangular plexiglass duct 15 m long, 50 cm wide and 20 cm high.

The duct is equipped with six tanks, T_1 to T_6 , necessary for the preparation, storage, supply and regulation of the flows of salt and fresh water. The entire duct-tank system has a length of 20 m. Tank T_1 is the main fresh water supply tank. It is located right below the downstream end of the duct and is 3 m long, 1 m wide and 1.20 m deep. The tank is divided by a 45° sharp crested weir into two chambers A and B of which A serves as a stilling basin and B as an equalization reservoir.

From chamber B of tank T_1 the fresh water is pumped through an axial flow pump to head tank, T_2 , where its kinetic energy is dissipated while the remaining large scale eddies are being reduced to a minimum by passage through two walls of perforated bricks. The tank is 1.5 m long, 0.90 m wide and 0.50 m deep and it is equipped with an adjustable overflow system so that the excess water returns to chamber B of the previous tank. Tank T_3 serves for the storage and supply of salt water, it is supported on a separate frame and it has a length of 2 m, a width of 1 m and a depth of 0.50 m. Tank T_4 is 2 m

long, 0.50 m wide and 0.40 m deep and it is essentially an extension of the main duct also constructed of plexiglass. It was used to control the slope of the piezometric line in the main duct through a gate, to collect the entrained salt water, which settles to the bottom and to discharge it. Provisions were made for the proper supply of fresh water in Tank T₁ so that the water levels in chambers A and B and, therefore, the flow discharge, remained practically constant.

Tank T₅ is just an accessory to Tank T₄, and, Tank T₆ is a sort of a booster tank to provide additional water for experiments with high discharge.

The salt water layer was formed by placing two variable

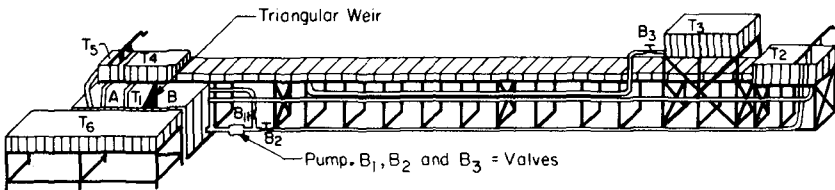
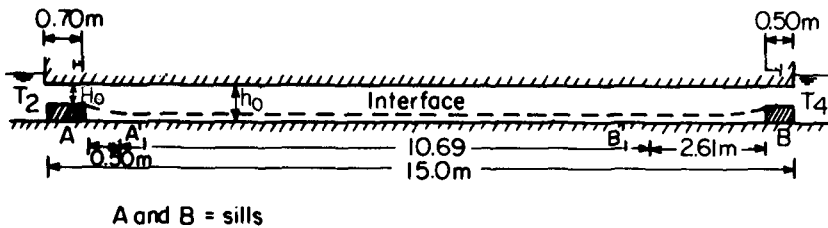


Fig. 7 Outline of experimental closed duct.



A and B = sills

Fig. 8 Location of sills.

height sills at points A and B of the duct 15 m apart, as shown in Fig. 8. The sill crest elevation was controlled by adding and subtracting 2.2 cm thick plexiglass blocks.

Procedure

Each experiment started by filling the between the sills space with salt water at predetermined salinity. Next, the fresh water was introduced initially at very low rates to avoid any mixing with salt water. Once the entire system was filled the experiments started at the selected flow rates. Upon the beginning of the fresh water flow, shear stresses at the interface developed as a result of which the level of the interface increased downstream and salt water was entrained over the sill to Tank T₄. The measurements were then taken over a time interval of 2 to 4 minutes for which the flow parameters were not changed measurably. The following variables were measured: The mean depth of the upper layer, \bar{h}_1 , the fresh water discharge, the average slope of the interface, the water temperature and the salinity distribution. At every section the interface was defined as the point at which the salinity was about the average of the salinities of the two layers. Since some water entrainment was unavoidable the salinity of recirculating fresh water was checked at regular time intervals and as soon as its density increased by one tenth of the original density difference, $\Delta\rho$, the tanks were emptied and refilled with fresh water.

In order to be able to observe the interfacial zone and its changes, fluorescent dye was added in the salt water.

ANALYSIS OF EXPERIMENTAL DATA

A total of 217 experiments were conducted for their analysis. Eqs. 22 and 23 had to be slightly transformed to the following forms in terms of average values of the variables over the measurement section:

$$\frac{d\bar{H}}{dx} = \frac{\frac{d\bar{h}_1}{dx} \left[\frac{\bar{v}_1^2}{g} + (h_o - \bar{h}_1) \frac{\Delta\rho}{\rho} \right] + \frac{\bar{v}_1^2 f_w}{8g} \left(1 + \frac{2\bar{h}_1}{b} \right) - \frac{\Delta\rho}{\rho} (h_o - \bar{h}_1) S_o}{(h_o - \bar{h}_1) \left(1 - \frac{\Delta\rho}{\rho} \right) + \bar{h}_1} \quad (24)$$

and

$$\bar{f}_1 = \frac{8 \left[\left(\frac{g\bar{h}_1}{\bar{v}_1^2} - \frac{\rho}{\Delta\rho} + 1 \right) \frac{d\bar{H}}{dx} - S_o \right] - f_w \left(1 - \frac{2\bar{h}_1}{b} \right)}{1 + \frac{\bar{v}_1^2}{g \frac{\Delta\rho}{\rho} (h_o - \bar{h}_1)}} \quad (25)$$

where the bar indicates average values over the effective channel length. $d\bar{H}/dx$ was first estimated from Eq. 24 and

its value was subsequently introduced in Eq. 25 for the evaluation of \bar{f}_i .

In each run the density profile was determined through a number of samples. Fig. 9 shows an example of such profiles for $H_0/h_0 = 0.45$ where H_0 and h_0 are defined in Fig. 8. The mean width of the interfacial zone, i.e. the zone where the density changes from ρ to $\rho + \Delta\rho$, was about 2 cm with a maximum deviation of 30%. The density variation within that zone was very nearly linear with the exception of the upper and lower 10% range of $\Delta\rho/\rho$.

The experiments have been grouped in 8 distinct groups on the basis of the following 8 values of the relative density difference, $\Delta\rho/\rho$: 3‰, 10‰, 15‰, 20‰, 25‰, 30‰, 35‰, and 40‰. Each group was then divided into four sub-groups on the basis of the initial fresh water depth, H_0 , i.e. the distance from the top of the sills to the top of the channel. The following values of H_0 were used: 0.156 m, 0.134 m, 0.112 m and 0.09 m.

It was first attempted to correlate \bar{f}_i with the Reynolds number:

$$R_e = \frac{4\bar{V}_1 \bar{R}_{h1}}{v} \quad \text{where} \quad \bar{R}_{h1} = \frac{b\bar{h}_1}{2(b+\bar{h}_1)} \quad (26)$$

and with the relative density difference, $\Delta\rho/\rho$, for various average fresh water depths, \bar{h}_1 . It was found that for each value of $\Delta\rho/\rho$ the log-log plot of \bar{f}_i vs R_e gave reasonably straight lines albeit with rather wide scattering sometimes by a factor of 2. However, the superposition of these curves did not reveal any consistent variation of \bar{f}_i - R_e lines with $\Delta\rho/\rho$ while at the same time the plot of all points for all values of $\Delta\rho/\rho$ indicated a wide spread with no specific trend.

Subsequent attempts to correlate \bar{f}_i with (a) $F'_1 = \bar{V}_1/\sqrt{\Delta\rho/\rho g \bar{R}_{h1}}$ as an independent variable and $\Delta\rho/\rho$ and \bar{h}_1 as

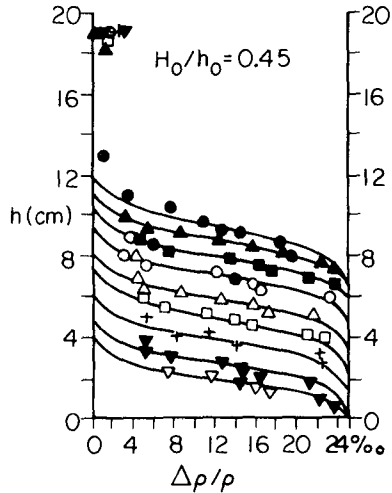


Fig. 9 Density profile in interfacial zone

parameters, (b) R_e as an independent variable and $\Delta\rho/\rho$ and F_1' as parameters (c) F_1' as independent variable and only R_e as a parameter and finally (d) $R_e(F_1')^2$ with F_1' as a parameter did not succeed either in discovering consistent trends of variation. This was indicative that the variables entering into the problems so far were not properly separated for the effect of each one to be clearly displayed.

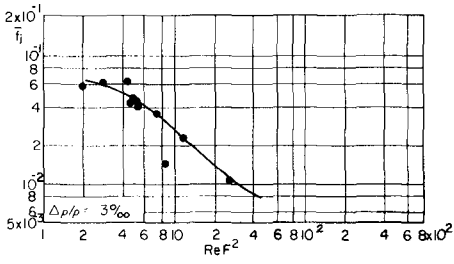
The first sign of success appeared when \bar{f}_i was plotted against $R_e F^2$, where F = the regular Froude number of the entire layer given by:

$$F = \frac{\bar{V}_1}{\sqrt{gR_{h0}}} \quad (27)$$

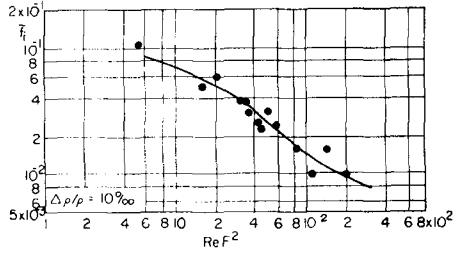
and where R_{h0} = the hydraulic radius of the entire cross section of the duct, while $\Delta\rho/\rho$ was treated as an independent parameter. That is the gravity forces, which generate the principal flow and the density parameter, which determines the buoyant forces responsible for the stratification and secondary flow, have now been separated.

Fig. 10 shows the plots of \bar{f}_i vs $R_e F^2$ for the eight values of $\Delta\rho/\rho$. The points give well defined mean lines with quite small scattering in comparison to the previous plots.

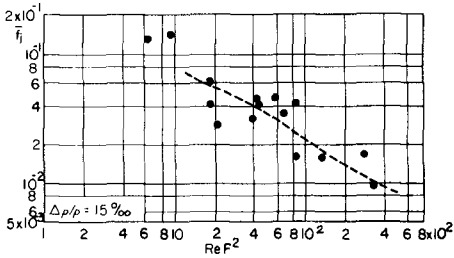
The eight average lines have been redrawn together in Fig. 11. It is observed that this family of curves follows a distinct and consistent pattern, with \bar{f}_i increasing with $\Delta\rho/\rho$ for the same $R_e F^2$. In Fig. 12 the line of the previous figure corresponding to $\Delta\rho/\rho = 20\text{‰}$ has been reproduced and the reanalyzed data of Abraham and Eysink (1) obtained for a quite different type of flow have been plotted. Those data fall very closely on the 20‰ curve and on its immediate extrapolation. Finally, the point corresponding to one single set of data from the South Pass of the Mississippi River (10, 12) has been plotted. In spite of the wide gap of the parameter $R_e F^2$ between the laboratory data and the Mississippi estuary data, the latter falls on a smooth extrapolation of the 20‰ line of the present study and is, moreover, consistent with the laboratory data of Abraham and Eysink. This is indicative that the correlation parameters have been properly selected and that an extrapolation of the family of curves of Fig. 11 to field conditions seems now quite possible if and when field data from several stratified estuaries become available. Fig. 12 shows a quantitative extrapolation of the curves to field conditions. This extrapolation, however, should be considered only tentative, since only one field data point was used.



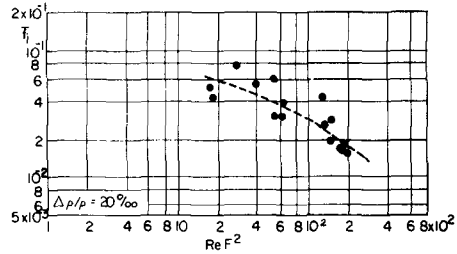
a. $\Delta \rho / \rho = 3\%$



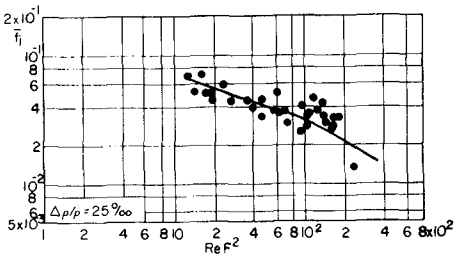
b. $\Delta \rho / \rho = 10\%$



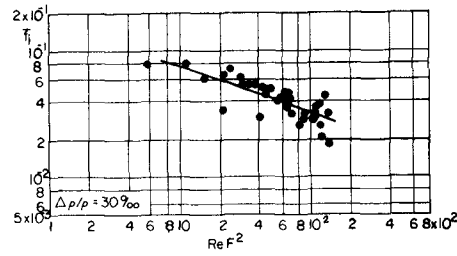
c. $\Delta \rho / \rho = 15\%$



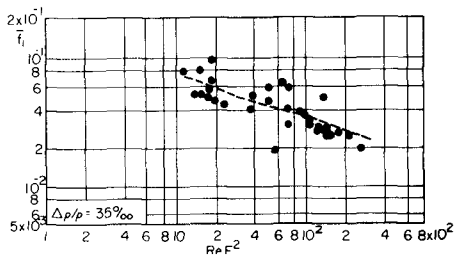
d. $\Delta \rho / \rho = 20\%$



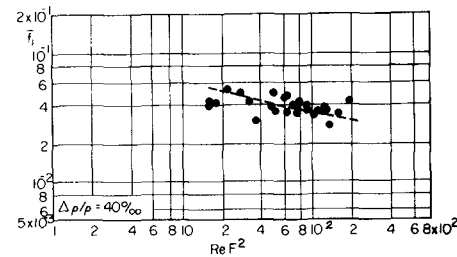
e. $\Delta \rho / \rho = 25\%$



f. $\Delta \rho / \rho = 30\%$



g. $\Delta \rho / \rho = 35\%$



h. $\Delta \rho / \rho = 40\%$

Fig. 10. Variation of \bar{f}_1 with $Re F^2$ for different values of $\Delta \rho / \rho$.

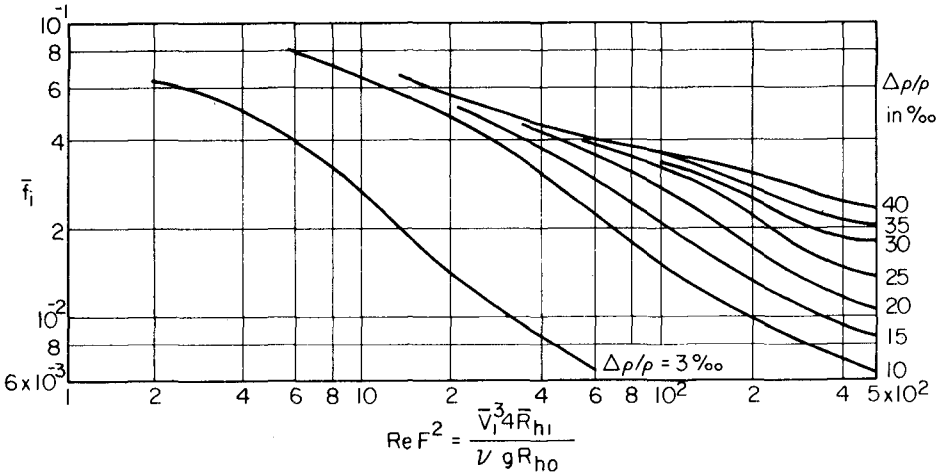


Fig. 11 Variation of \bar{f}_i with $Re F^2$ and $\Delta\rho/\rho$ (summary of lines of Fig. 10).

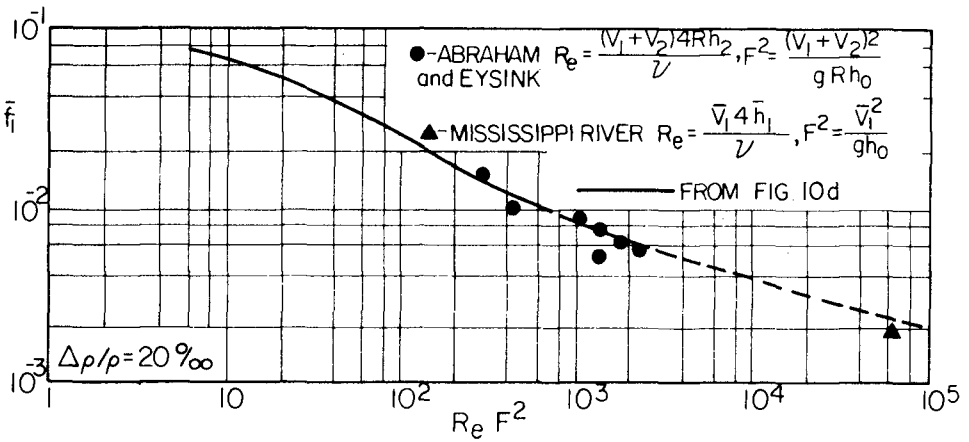


Fig. 12 Extrapolation and comparison of the 20‰ line (Fig. 10d) with earlier laboratory and field data.

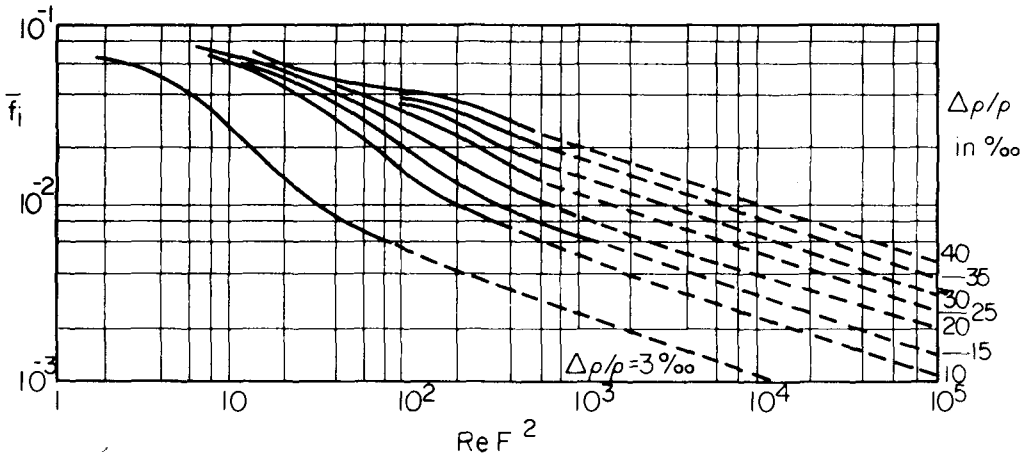


Fig. 13 Tentative extrapolation of curves of Fig. 11

SUMMARY AND CONCLUSIONS

The results of an experimental research on the interfacial friction coefficient in a two-layered stratified flow have been presented. The experiments were conducted in a closed rectangular duct with the salt water forming a quasi-stagnant pool over which fresh water was flowing.

A review of some of the most well-known research results prior to this study revealed a wide discrepancy between results obtained by various experimental and semitheoretical laws and sometimes a very wide scattering of experimental points within the same study. This was attributed to the restricted range of validity of certain assumptions and to the lack of introduction of the proper flow and salinity parameters.

The average interfacial friction coefficient, \bar{f}_i , over the measurement section of the duct was evaluated from the measured quantities on the basis of a one-dimensional flow analysis along the general lines of Schijf and Schoenfeld's approach for open channels. After several attempts it was found that \bar{f}_i can be best correlated with the number, $Re F^2 = 4\bar{V}^3 R_{h1} / \nu g R_{h0}$ and with the relative density difference, $\Delta\rho/\rho$. The results are given as a family of curves with $Re F^2$ as an abscissa and $\Delta\rho/\rho$ as an independent parameter. This correlation is further strengthened by the close agreement of reanalyzed laboratory data of earlier studies and of field data from the Mississippi River. On the basis of the latter, the derived family of curves has been tentatively extrapolated to field values of $Re F^2$, i.e. to values of the order of 10^5 .

ACKNOWLEDGEMENTS

The experimental work presented in this paper has been conducted at the Laboratory of Hydraulics and Hydraulic Structures of the University of Thessaloniki in Greece. This paper has been prepared at the Department of Engineering Sciences of the University of Florida as part of continuing research work by the authors on the dynamics of a two-layered stratified flow currently supported by the National Science Foundation under Grant No. ENG 76-11537. This support is gratefully acknowledged.

REFERENCES

1. Abraham, G., and Eysink, W. L. "Magnitude of Interfacial Shear in Exchange Flow" Journal of Hydraulic Research, I.A.H.R., Vol. 9, No.2, 1971.
2. Bata, G. L. and Knezevich, B. "Some Observations on Density Currents in the Laboratory and in the Field" Proc., Minn. Intern. Hydr. Conv., Sept., 1953, pp. 387 - 400.
3. Delft Hydraulics Laboratory, "Momentum and Mass Transfer in Stratified Flows" Report on Literature Study, R 880, Delft, Netherlands, Dec., 1974.
4. Dermisis, V. "A Study of the Interfacial Friction Coefficient in a System of two Fluids" Dissertation submitted to the School of Engineering of the Aristoteles University of Thessaloniki, Greece in fulfillment of the requirements for the the degree of Doctor in Civil Engineering (in Greek).
5. Georgiev, B. V. "Some Experimental Investigation on Turbulent Characteristics of Stratified Flows," Proceedings Intern. Symp. on Stratified Flows, Novosibirsk, USSR, Sept., 1972.
6. Harleman, D.R.F. "Stratified Flow" Ch. 26, Handbook of Fluid Dynamics Edited by V. Streeter, McGraw-Hill, 1961.
7. Harleman, D.R.F. and Stolzenbach, K.D. "Fluid Mechanics of Heat Disposal from Power Generation" Annual Review of Fluid Mech., Vol. 4, 1972, pp. 7-32.
8. Keulegan, G.H. "Interfacial Stability and Mixing in Stratified Flows" Research paper 2040, U.S. National Bureau of Standards, Vol. 43, 1949.
9. Keulegan, G.H. "Eighth Progress Report for Density Currents—Significant Stresses of Arrested Saline Wedges" Rept. No. 4267, National Bureau of Standards, Aug. 1955.

10. Keulegan, G.H. "The Mechanics of an Arrested Saline Wedge" Ch. 11, Estuary and Coastline Hydrodynamics, Edited by A.T. Ippen, McGraw-Hill, 1966.
11. Lofquist, K., "Flow and Stress near an Interface between Stratified Liquids" Physics of Fluids, Vol. 3, 1960, pp. 158-175.
12. Partheniades, E., Dermassis, V., and Mehta, A.J. "On the Shape and Interfacial Resistance of Arrested Saline Wedges" Proc., 16th Congress of the International Association for Hydraulic Research, San Paulo, Brazil, July 28-Aug. 2, 1975, Vol. I. Paper A-19, pp. 157-164.
13. Plate, E. and Friedrich, R. "The Stability of an Interface on Stratified Channel Flow" Proceedings, 15th Congress of Int. Assoc. for Hydr. Res. Vol. 3, San Paulo, Brazil, July, 1975, pp. 9-21.
14. Shi-igai, H. "On the Resistance Coefficient at the Interface between Salt and Fresh Water" Transactions, Japan Society of Civil Engineers, No. 123, Nov. 1960.
15. Schijf, J.B. and Shoenfeld, J.C. "Theoretical Considerations on the Motion of Salt and Fresh Water" Proceedings, Minnesota International Hydraulics Convention, Sept. 1953, pp. 321-333.
16. Schlichting, H., "Boundary Layer Theory" McGraw-Hill, 1960.

CHAPTER 171

STABILITY STUDY OF AN ARTIFICIAL SALT INTRUSION IN ESTUARIES

by

Dr. C. Marche, Eng.
Associate Professor, Civil Engineering Department
Ecole Polytechnique

A B S T R A C T

The stratification and salinity structure of the water mass in the lower portions of tidal estuaries are important factors of the general circulation and local water quality. In natural conditions an equilibrium can be observed in each estuary and depends on the geometry of the estuary, the motion of tides inside the estuary and the freshwater discharge.

Extensive studies of the salinity structure in the estuaries of the La Grande and Grande Baleine rivers have shown that water of high salinity content will be expected along the total length of the estuary, for the discharge expected during the fill up period.

Sand-bars being present in several transverse sections in these estuaries, it is of the greatest importance to verify if the saltwater introduced upstream of these bars by a provisionnal modification in the freshwater discharge would not be definitely present.

This paper presents the relevant parameters, the theoretical formulation and the results obtained for the above mentioned estuaries.

INTRODUCTION

The stratification and salinity structure of the water mass in the lower portions of tidal estuaries are important factors of the general circulation and local water quality. In natural conditions, an equilibrium can be observed in each estuary and depends on the geometry of the estuary, the motion of tides inside the estuary and the freshwater discharge. Any change in the range of variation of these factors affects this equilibrium and specially the salt intrusion length for all the stratified estuaries.

This problem is of the greatest interest in the northern region of Quebec where engineers are called upon to modify the natural flow regime of some estuaries; hydroelectric developments are planned upstream, two such cases in point being La Grande and Grande Baleine Rivers.

In these cases, the discharges will be modified in two phases, in the first phase, the discharge will decrease greatly downstream of the dam, in conjunction with the reservoir fill-up. In the second one, a discharge, often increased by the partial drainage of other basins, and therefore higher than the natural one must be considered as a definite change.

The studies of the salinity structure in the estuaries of La Grande and Grande Baleine rivers have shown that saltwater will be observed along the total length of the estuary for the discharge expected during the fill up period. However, the water mass will remain highly stratified in all parts of these estuaries.

Sand-bars being present in several transverse sections in these estuaries, it is of the greatest importance to verify if the saltwater introduced upstream these sand-bars by a provisionnal modification in the freshwater discharge, would not be definitely present.

The study presented here describes a method to calculate the minimal discharge ensuring the saltwater flushing downstream all bars in an estuary. Some results illustrate an application to the La Grande and Grande Baleine estuaries (Figures 1 and 2).

HYDRAULIC FORMULATION

The one dimensional equations of motion for the steady non-uniform flow of a two layered system given by Schijf and Schönfeld (1), have been used. Neglecting the vertical accelerations in the fluids, and considering only the mean velocities in the layers, the equations, in accordance with the notation of Figure 3, are:

- For the upper layer

$$\frac{dh}{dx} + \frac{dh'}{dx} + \frac{U}{g} \frac{dU}{dx} + S_{1e} - \tan \beta = 0 \quad (1)$$

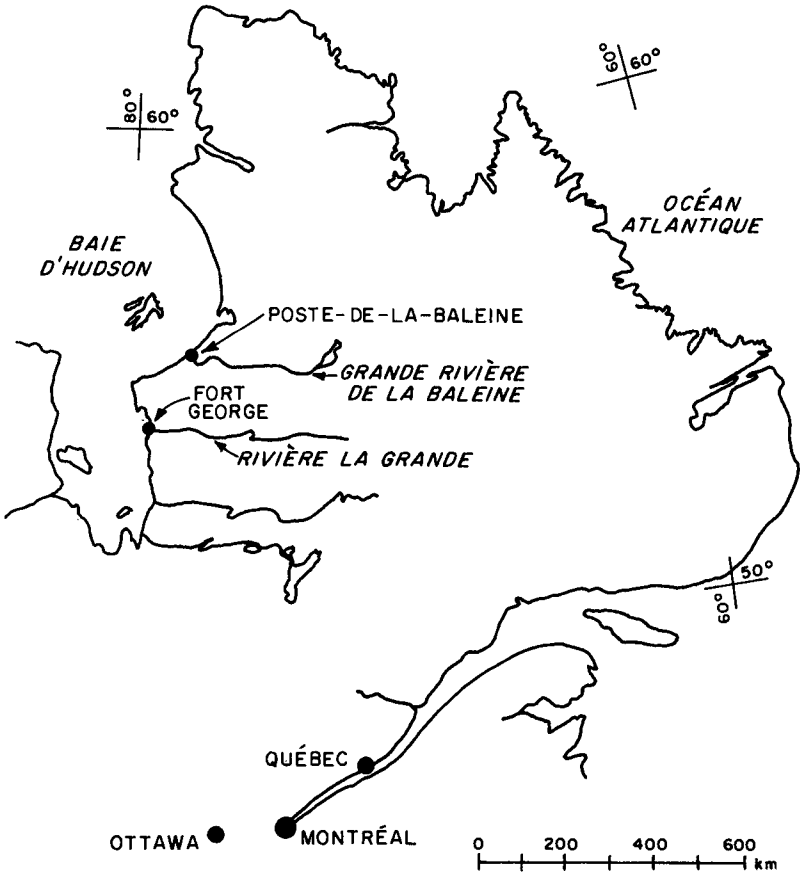


FIG. 1 LOCATION MAP

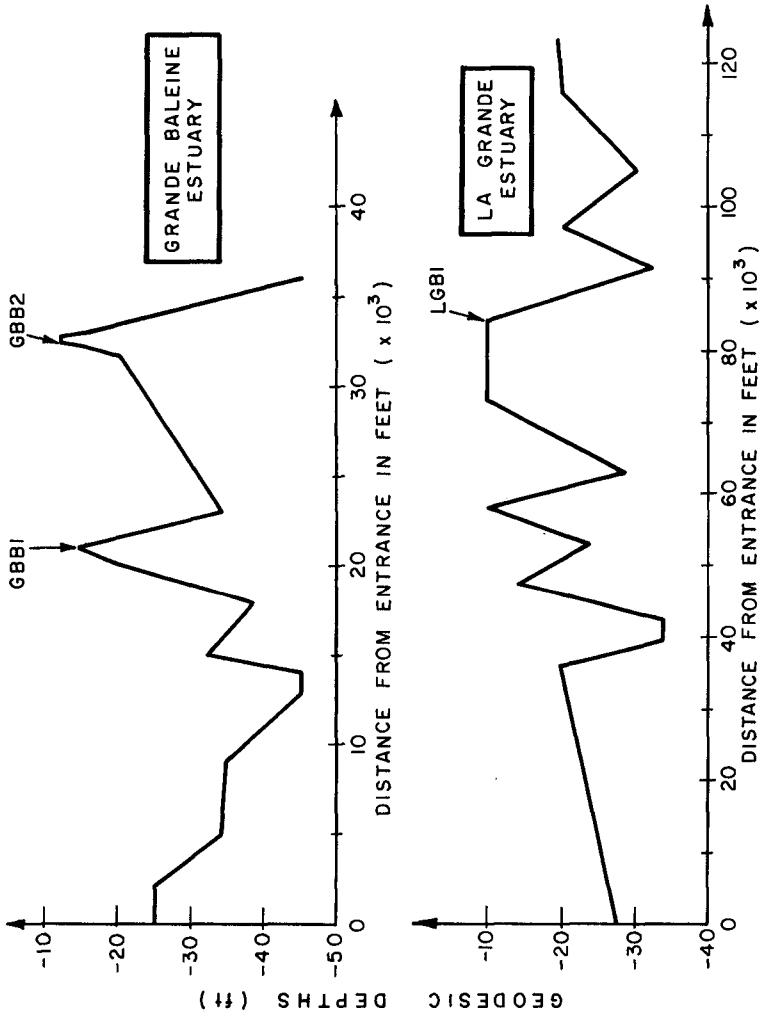


FIG. 2 THALWEG PROFILES

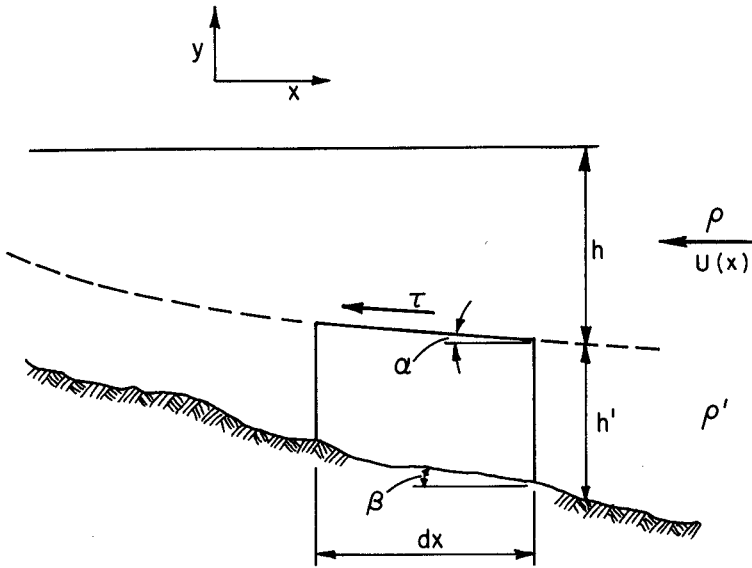


FIG. 3 DEFINITION SKETCH

and for the lower layer, considered as stationary one:

$$\left(1 - \frac{\Delta\rho}{\rho}\right) \frac{dh}{dx} + \frac{dh'}{dx} + S_{2e} - \tan\beta = 0 \quad (2)$$

The energy gradients S_{1e} and S_{2e} are defined by

$$S_{1e} = \frac{\tau_i}{\rho gh} \quad (3)$$

$$S_{2e} = \frac{\tau_o - \tau_i}{\rho gh'} = - \frac{\tau_i}{\rho gh'} \quad (4)$$

The shear stresses τ_o at the bottom, and τ_i at the interface are respectively

$$\tau_o = 0 \quad (5)$$

$$\tau_i = \rho f_i |U|U/8 \quad (6)$$

and expressions (3) and (4) become

$$S_{1e} = f_i |U|U/8gh \quad (7)$$

$$S_{2e} = -f_i |U|U/8gh' \quad (8)$$

in which f_i is the interfacial friction factor.

The continuity equation for the upper layer is

$$\frac{dh}{dx} = -\frac{h}{U} \frac{dU}{dx} \quad (9)$$

Equations (1) and (2) can be reformulated as

$$R = \frac{U}{g} \frac{dU}{dx} - f_i \frac{U^2}{8gh} \quad (10)$$

$$R = \frac{\Delta\rho}{\rho} \frac{dh}{dx} - f_i \frac{U^2}{8gh'} \quad (11)$$

in which

$$R = \frac{dH}{dx} - \tan\beta \quad (12)$$

can be practically neglected.

Substituting the continuity equation we obtain successively

$$\frac{dU}{dx} = -f_i \frac{U}{8h} \quad (13)$$

$$\frac{dh}{dx} = f_i \frac{U^2}{8g'h'} \quad (14)$$

Equations (9), (13) and (14) are used to find the general solution

$$F(h', x, Q) = 0 \quad (15)$$

and the freshwater discharge insuring the saltwater evacuation is found in a second step by solving

$$F(0, x, Q) = 0 \quad (16)$$

We must note that the function $h'(x, Q)$ obtained in consideration of a stationary lower layer, represents the different equilibrium positions taken by a saltwater intrusion upstream of a sand-bar for various freshwater discharges in the upper layer.

The solution of the simultaneous equations (9), (13) and (14) is obtained in three steps; first, replacing f_i by the average interfacial friction factor \bar{f}_i , the freshwater depth is given by

$$h = \bar{f}_i \frac{x}{8} + h_0 \quad (17)$$

and the saltwater depth by

$$h' = \frac{Q^2}{g'B^2} \frac{1}{\left(\bar{f}_i \frac{x}{8} + h_0\right)^2} \quad (18)$$

The constant h_0 is found at $x = 0$, by using the total water depth over the bar H_0 , and the relation

$$H_0 = h_0 + h'_0 \quad (19)$$

Hence

$$h_0^3 - H_0 h_0^2 + \frac{Q^2}{g'B^2} = 0 \quad (20)$$

In a second step the average interfacial friction factor \bar{f}_i can be computed by writing

$$\frac{dH}{dx} = \frac{dh}{dx} + \frac{dh'}{dx} \quad (21)$$

and finally

$$\frac{(\bar{f}_1 - \beta)}{8} \left(\frac{\bar{f}_1 x}{8} + h_0 \right)^3 = \frac{Q^2 \bar{f}_1}{4g'B^2} \quad (22)$$

In the third step the saltwater depth $h'(x, Q)$ is computed by use of Equation (18), and the relation between the minimum discharge ensuring the saltwater evacuation and the intrusion length is found by solving

$$h'(L_2, Q_2) = 0 \quad (23)$$

in each case.

Assuming the presence of salt upstream of sand-bar no 1 in the Grande Baleine estuary (GBB1), Figure 4 shows the successive interfaces computed for several freshwater discharges.

RESULTS

Based on recent studies of the salinity structure in the above mentioned estuaries (2) and (3), the relations between the salt intrusion length L_1 and the fluvial discharge Q_1 are available in each case (Figures 5 and 6). We have summarized on the same graph the flushing condition (L_2, Q_2) computed by solving equation (23) in each case. Figure 5 applies to the La Grande estuary, summaries the relevant data sets and gives in each case the minimal discharge ensuring the saltwater evacuation.

So, taking into account the 1315 cfs discharge anticipated during the reservoir fill up and the occurrence of spring tides, a salt intrusion length of 107000 ft is anticipated. Salt will be removed by any discharge of 34000 cfs or more. This result being under the normal operation discharge (118000 cfs), saltwater upstream LGB1 will be only a provisionnal modification of the salinity structure of the estuary.

Figure 6 applies to the Grande Baleine estuary. Using the same procedure and a minimal discharge of 1000 cfs, the intrusion length is found to be in the range of about 34000 ft. In this case, a freshwater discharge higher than 38000 cfs is able to remove saltwater downstream GBB2. The freshwater discharge must be higher than 22800 cfs to ensure that saltwater would not be definitely present upstream GBB1.

However, when a large intrusion length is considered as in the case of GBB1 in the prevision example, some of the assumptions (constant width, average interfacial friction factor on each segment) could affect the validity of the solution and it would be preferable to make use of a numerical technique of integration to solve the simultaneous equations (9), (13) and (14).

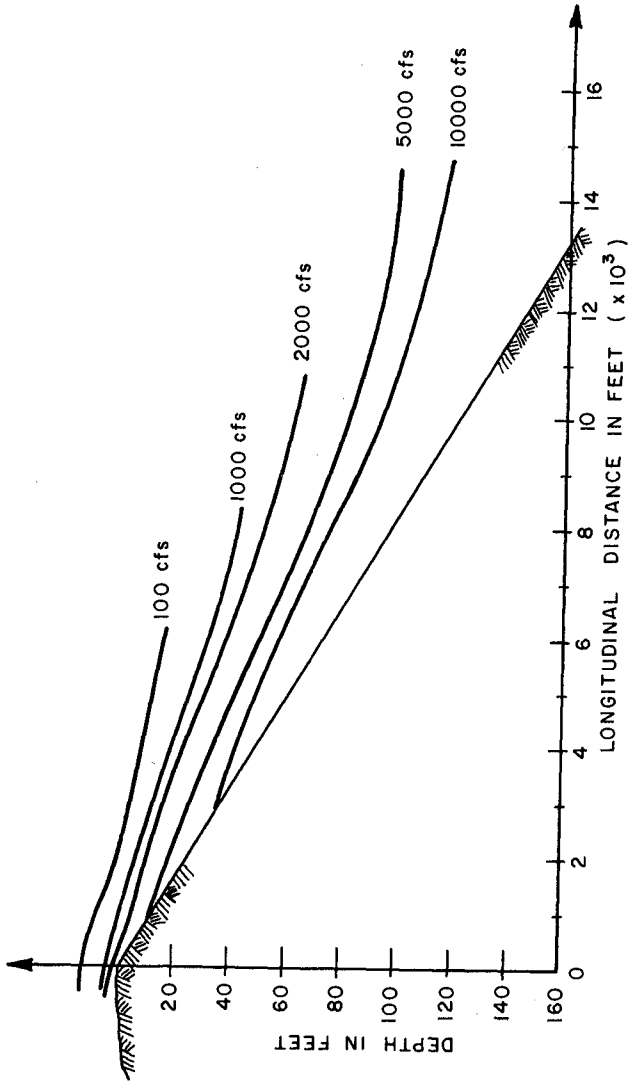


FIG. 4 COMPUTED INTERFACES FOR DIFFERENT DISCHARGES

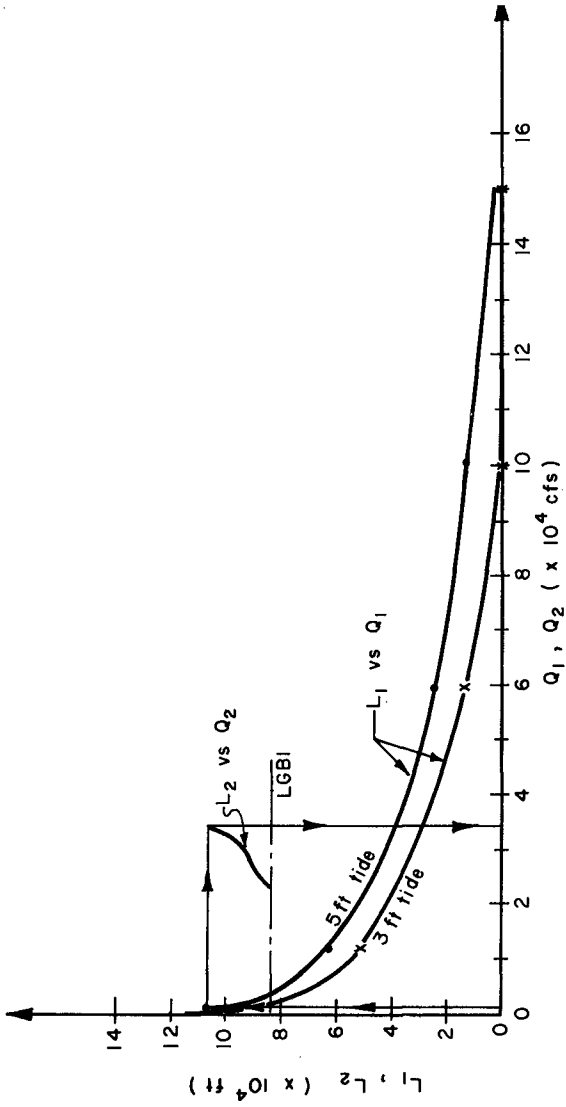


FIG. 5 SALT INTRUSION LENGTH AND FLUSHING CONDITIONS, LA GRANDE ESTUARY

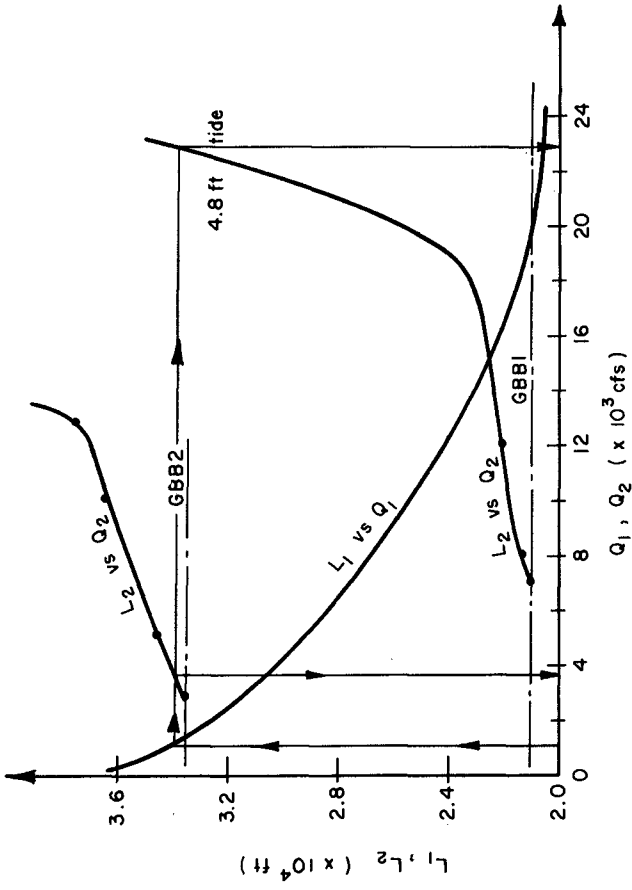


FIG. 6 SALT INTRUSION LENGTH AND FLUSHING CONDITIONS, GRANDE BALEINE ESTUARY

BIBLIOGRAPHIE

- (1) Schijf, J.B. and J.C. Schönfeld: Theoretical Considerations on the Motion of Saline Water from Locks, Proc. Minn. Intern. Hydr. Conv. Sept. 1953.
- (2) Marche, C. and T.T. Quach: Etude et contrôle de l'aménagement hydro-électrique d'une rivière sur l'équilibre salin dans son estuaire, Int. Ass. Hydr. Res. 17th International Congress, août 1977.
- (3) Boivin, R. Estuaire de la Grande Rivière de la Baleine. Etude sur modèle réduit LHL 696, juillet 1977.

ACKNOWLEDGMENTS

Acknowledgments are gratefully made to the Division Etudes Spéciales et Recherches, Hydro-Québec, for access and permission to use this study material.

CHAPTER 172

EFFECT OF HARBOURS ON SALT INTRUSION IN ESTUARIES

A. Roelfzema^{*}) and A.G. van Os^{**}), Delft Hydraulics Laboratory

^{*}) Research Engineer, ^{**}) Head Density Currents and Transport Phenomena Branch

ABSTRACT

A harbour, connected to a tidal river, will affect the salt intrusion in the river. To study the interaction between harbour and river a systematic investigation has been carried out in the tidal salinity flume of the Delft Hydraulics Laboratory (Fig. 1a). The investigation included measurements of the density distribution in harbour and river and measurements of the exchange phenomena in the harbour entrance. The study was executed as part of a long-term basic research program on salt intrusion in tidal rivers, commissioned to the Delft Hydraulics Laboratory by the Rijkswaterstaat (Dutch Government Public Works Department).

1 INTRODUCTION

Generally spoken, the salt distribution in a tidal river is mainly determined by its boundary conditions and by its geometry. This study deals with the effect of a harbour, being one of the geometry parameters of an estuary. A harbour considered in this way has in principle the same effects as a shoreline irregularity. Because of its fundamental character, the investigation has been carried out under strongly schematized circumstances with regard to the geometry of river and harbour. Under these circumstances the following parameters were varied systematically:

- the location X_1 of the harbour along the river, in relation to the salt intrusion length without a harbour, Li_0 (Fig. 1a)
- the surface area A_b of the harbour basin (Fig. 1c)
- the cross-section A_d of the harbour entrance (variation in depth and width) (Fig. 1c)
- the shape (rounded or sharp-edged) and orientation α of the entrance with respect to the river axis (Fig. 1c)
- the presence of an air bubble screen in the entrance, and
- the location of the harbour with respect to the location of its entrance (Fig. 1c).

Studying the interaction between harbour and river, stratification can be an important parameter. Therefore three different degrees of stratification were studied. These degrees were obtained by varying the tidal elevation a_0 of the sea and the fresh water discharge Q_f .

2 SET-UP OF THE MODEL

The perspex tidal salinity flume has a rectangular cross-section, 0.672 m wide and 0.50 m high. Its total length is about 100 m (Fig. 1a). The downstream end of the flume is formed by a schematized seabasin. By means of a control gate any periodic tidal movement of the waterlevel of this basin can be generated. The density of the seawater is kept constant by means of salt water injection. At the upstream end of the flume a constant and a periodically variable discharge of fresh water can be supplied separately. So, the theoretical length of the tidal river, simulated in the flume is not confined to the actual length of the flume. The possibility of varying this theoretical length implies variations in the applied periodic up-

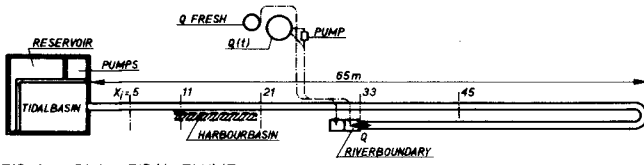


FIG 1a PLAN TIDAL FLUME

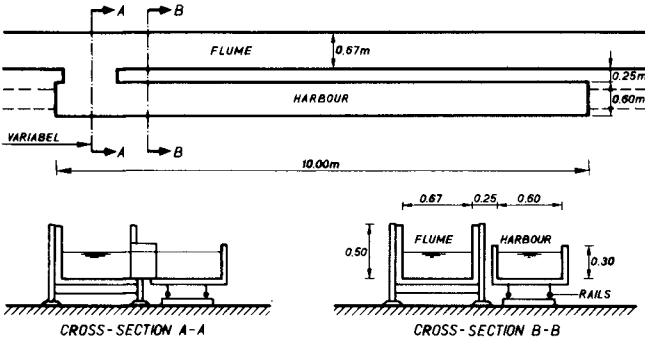


FIG 1b

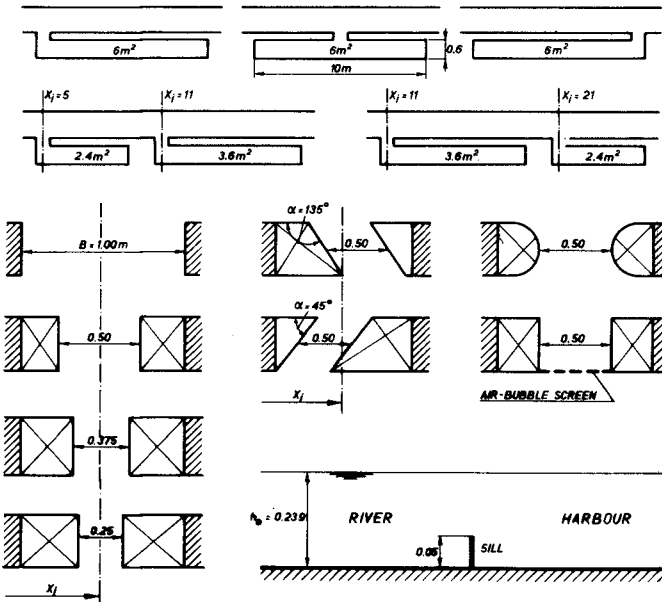


FIG 1c

SET-UP OF THE MODEL, HARBOUR PARAMETERS

stream discharge. A detailed description of the flume is given by Van Rees and Rigter (1969). For this investigation the flume has been extended with a perspex harbour construction (Figs. 1a and 1b).

Figure 1c shows the several variations of the geometry of harbour and harbour entrance. Figure 2 shows the sampling system of flume and harbour (entrance).

3 ANALYSIS OF SALT INTRUSION

Rigter (1973) analysed the salt intrusion in estuaries by means of dimensional analysis. He found:

$$\frac{L_{i \min}}{h_o} \frac{g}{C^2} = f\left(\frac{\hat{q}_{ebb}}{h_o \sqrt{\epsilon g h_o}}, \frac{q_f}{h_o \sqrt{\epsilon g h_o}}\right) \quad (1)$$

where: $L_{i \min}$ - minimum salt intrusion length
 h_o - mean waterdepth
 g - acceleration due to gravity
 C - roughness coefficient according to Chézy
 \hat{q}_{ebb} - maximum ebb discharge at the downstream boundary ($x = 0$) per unit of width
 q_f - fresh water discharge per unit of width
 ϵ - $\frac{\Delta \rho}{\rho}$, relative density difference

This means that different combinations of the parameters \hat{q}_{ebb} , q_f and h_o can give the same salt intrusion length. However, these different combinations will give a different degree of stratification. According to Simmons (1955) the stratification can be characterized by the flood number

$$\alpha = \frac{Q_f T}{P_t} \quad (2)$$

where: Q_f = total fresh water discharge
 T = tidal period
 P_t = flood volume: the volume of seawater entering the river during flood

Because of the mutual dependency of the tidal elevation a_o and the maximum ebb- and flood velocities, expression (2) can be written as

$$\alpha :: \frac{q_f}{\hat{q}_{ebb}} \quad (3)$$

Experimentally the following was found by the Waterways Experiment Station (1955):

$\alpha \leq 0.1$ well-mixed situation
 $0.2 < \alpha < 0.5$ partly mixed situation
 $\alpha \geq 1.0$ stratified situation

So, by varying \hat{q}_{ebb} and q_f it was possible to execute tests with nearly equal minimum salt intrusion length and different degrees of stratification. By doing so, the effect of the stratification on the harbour influences has been studied. Table 1 shows the parameters used in this research.

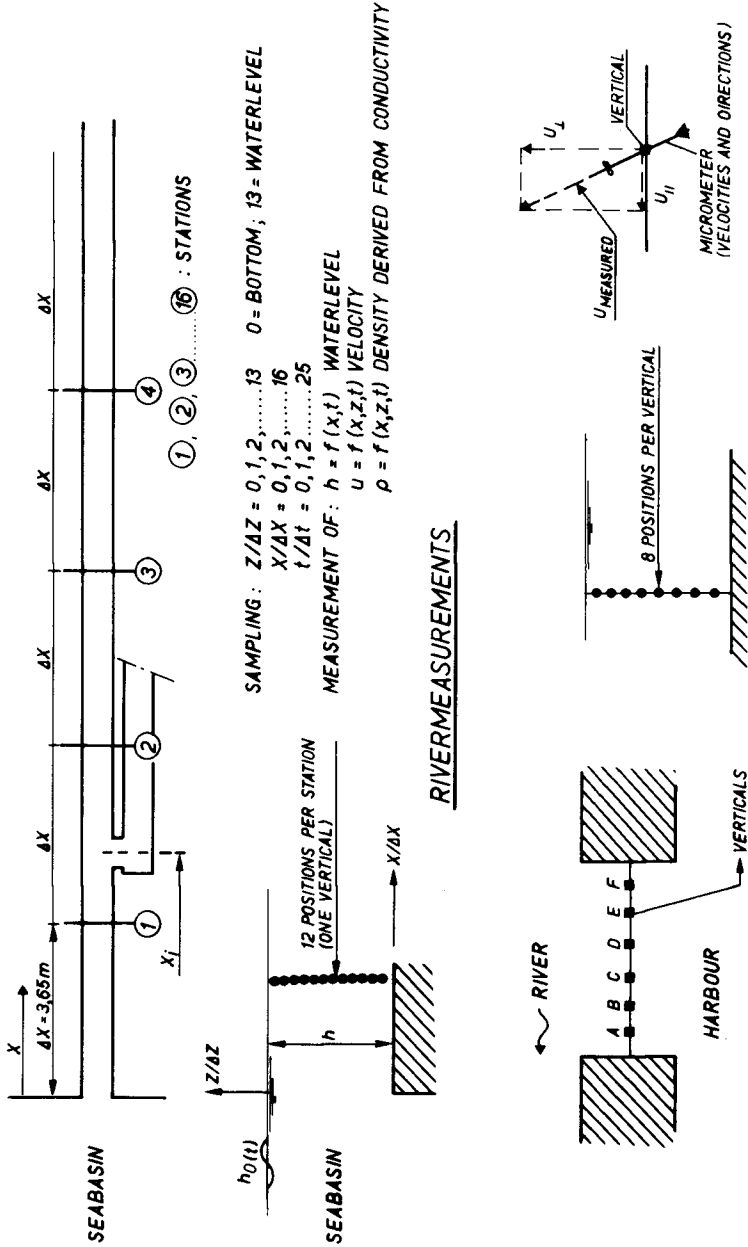


FIG. 2 SAMPLING SYSTEM

	C ($\text{m}^{\frac{1}{2}}/\text{s}$)	h_o (m)	$\Delta\rho$ (kg/m^3)	a_o (m)	\hat{q}_{ebb} (m^2/s)	q_f (m^2/s)	Li_{min} (m) <small>(experimental results)</small>	Li_{max} (m)	α
well-mixed	19	0.239	21.5	0.03125	0.0543	0.0026	20.50	54.00	0.165
partly mixed	19	0.239	21.5	0.0125	0.0347	0.0043	21.50	42.40	0.474
stratified	19	0.239	21.5	0.01	0.0324	0.0075	18.50	33.30	0.983

Table 1 Initial river conditions

Expression (1) indicates changes in Li_{min} when \hat{q}_{ebb} is changed. The connection of a harbour to the river will change \hat{q}_{ebb} , the actual value being dependent on the location and surface area of the harbour along the river. This effect can be calculated with a one-dimensional tidal computation. The results are given in Figure 3a as the relative change of the first Fourier component Q_1 ($\sim \hat{q}_{ebb}$) of the amplitude of the tidal discharge at the rivermouth as a function of the location of the standard harbour along the river ($X_1 = 0$ (no harbour), 5, 11, 21, 33, 45 and 60 m). The parameters of the standard harbour are those of the reference test T 406, see table 2. For these reference circumstances figure 3a shows a maximum change in Q_1 of approximately 3%, leading to an increase of salt intrusion length. From field observations Hensen (1953) found the same tendencies. A more theoretical consideration, again only by taking the tidal movements into account, has been given by Schijf and Schönfeld (1953). In their view a harbour affects the salt distribution in the river by the mixing interaction between river and harbour over the tidal period. More recently Okubo (1973) and Hamrick (1975) discussed the role of traps along a tidal river. Their studies, based on one-dimensional analytical expressions, indicate that the interaction between river and trap may play an important role in longitudinal dispersion in estuaries.

From these investigations it can be concluded that a harbour connected to a river will affect the salt intrusion by:

- changing the tidal discharges of the estuary
- generating exchange processes between harbour and river due to tidal storage and density differences

With respect to the effect of the location of the harbour along the river on the salt intrusion, the area of interest has therefore been subdivided into three parts:

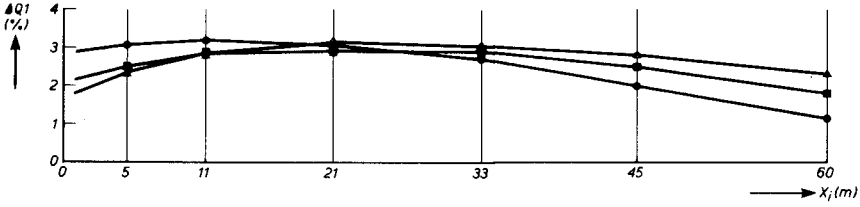
- part ①, between sea and minimum salt intrusion length, (Li_{min}).

Due to the combined effect of the increase of tidal discharges and of the exchange phenomena, a harbour connected in this part increases the salt intrusion.

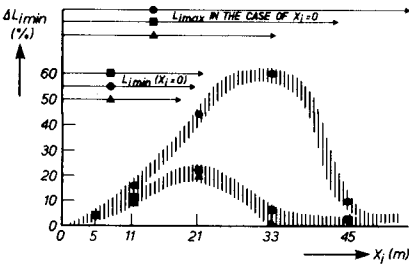
Because of the considerations that the density-induced contribution in the exchange phenomena at a location near the seabasin will be small compared with the contribution at a more upstream location, the tendency of the increase of salt intrusion length will be a positive one.

- part ②, between minimum and maximum salt intrusion length, (Li_{max}).

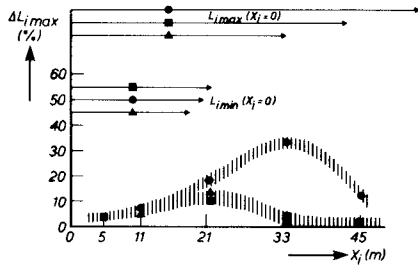
For the same reasons as mentioned for a harbour connected in part ①, a harbour connected in part ② will increase the salt intrusion. However, changing the harbour location from Li_{min} to Li_{max} , the density induced contribution in the exchange phenomena will diminish due to the



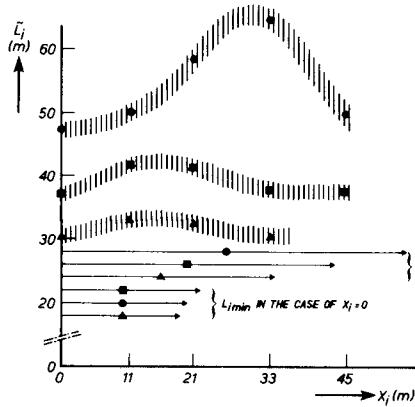
a) RELATIVE CHANGE OF THE AMPLITUDE OF THE TIDAL DISCHARGES NEAR THE SEABASIN



b) RELATIVE INCREASE OF MINIMUM INTRUSION LENGTH



c) RELATIVE INCREASE OF MAXIMUM INTRUSION LENGTH



d) TOTAL MEAN INTRUSION LENGTH

	$L_{i \min}$	$L_{i \max}$
T 401 ●	20,50	54,00
T 402 ■	21,50	42,40
T 403 ▲	18,50	33,30

NO HARBOUR ($x_j = 0$)

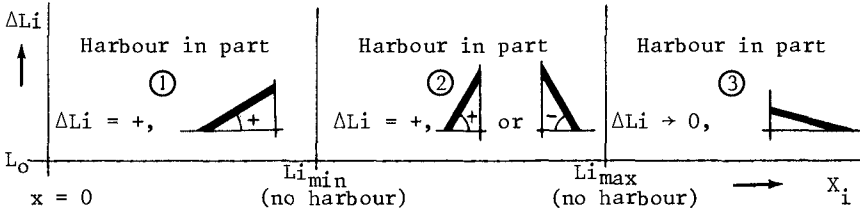
- WELL - MIXED
- PARTLY - MIXED
- ▲ STRATIFIED

FIG. 3

decreasing density differences between harbour and river. Therefore the positive tendency of the increase in part ①, will change into a negative one in part ②.

- part ③, upstream of $L_{i\max}$. A harbour connected in this part causes an increase of tidal discharges. The exchange phenomena only consist of the tidal effect and of the flow-induced effect. According to Rigger (1973) the increase of the tidal discharges due to the harbour location tends to zero, and therefore the increase of intrusion length too, will tend to zero.

This qualitative indication of the influence of the location of the harbour on the salt intrusion has been summarized below.



ΔL_i = increase of salt intrusion with respect to L_0
(L_0 = salt intrusion in case of no harbour)

X_i = location of the harbour

4 RESULTS SALT INTRUSION

Test results with respect to variation of the location of the standard harbour along the river are shown in Figure 3b (minimum intrusion length at about LWS) and in Figure 3c (maximum intrusion length at about HWS). They show a considerable increase of the salt intrusion in the river, with respect to the situation without a harbour. The tendencies of the analysis in Chapter 3 can be recognized clearly. The increase of about 60% for the well-mixed situation is striking. Figure 3d shows the tidal mean salt intrusion \bar{L}_i , with the same tendencies as the figure for minimum and maximum intrusion length.

In Figure 4 the longitudinal salt distribution is shown at LWS and HWS in the cases of no harbour ($X_i = 0$) and of a harbour located at $X_i = 11$ m. The effect of exchange currents between harbour and river is obvious. Table 2 gathers the results of the influence of "harbour parameters" on salt intrusion (partly mixed conditions, $X_i = 11$ m).

With respect to the salt intrusion in the river, it can be concluded that the magnitude of its increase depends largely on the location of the harbour along the river (Figs. 3). Compared to this, the influence of the so-called "harbour parameters" at $X_i = 11$ m (Table 2) is of secondary importance:

- reduction of the surface area of the harbour from 6 m^2 up to 3.6 m^2 reduces the maximum salt intrusion length with 0.80 m, while the reduction in the case of no harbour amounts to 2.20 m.
- doubling or reducing by half the width of 0.50 m of the harbour entrance, gives an increase of maximum intrusion length with 0.40 m and a decrease with 1.30 m respectively, these values again to be compared with the reduction of 2.20 m in the case of no harbour.
- variations in shape and orientation of the harbour entrance, show small differences in intrusion length with respect to the influence of the location of the harbour.

These conclusions are supported by the results of $\Delta L_{i\min}$ and $\Delta L_{i\max}$ of test T432, where the total surface area, being 6 m^2 , had been divided

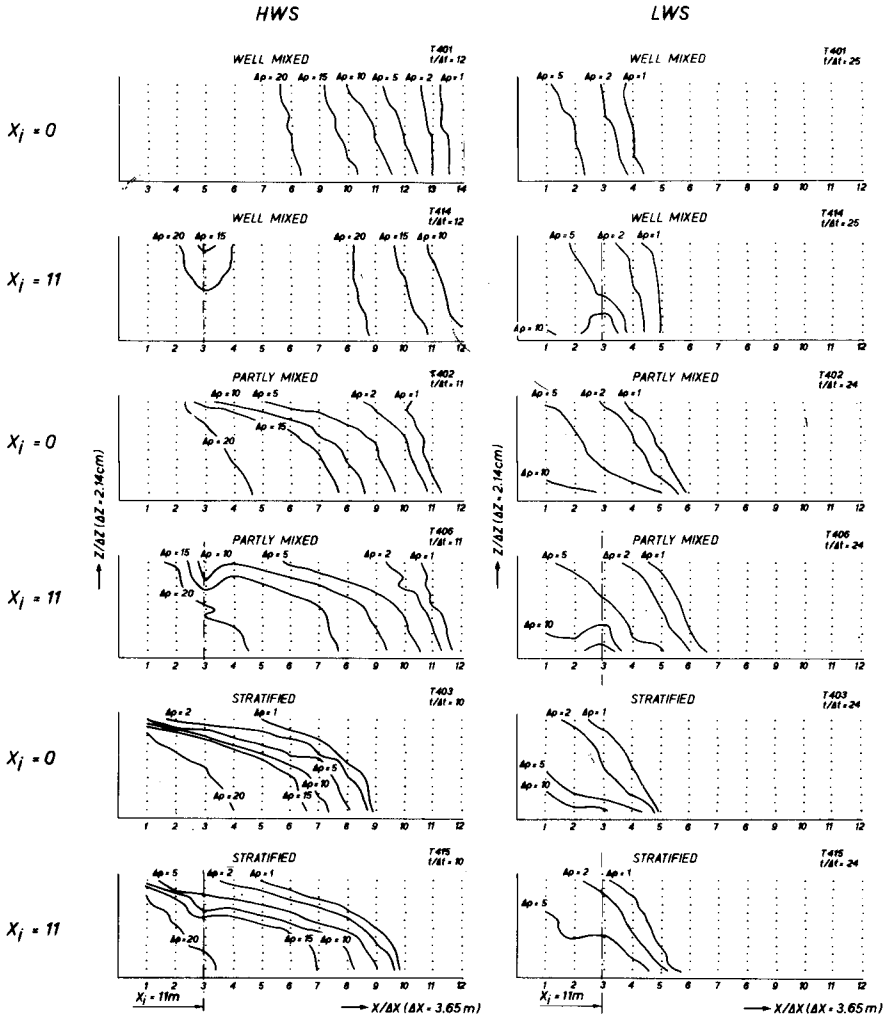


FIG. 4

into 3.6 m² connected to the river at $X_i = 11$ m and into 2.4 m² connected at $X_i = 21$ m (Table 2).

a)	Initial conditions		TEST	Li_{min} (m)	Li_{max} (m)	With respect to T402		
						ΔLi_{min}	ΔLi_{max}	%
	Without harbour		T402 ($X_i=0$)	21.50	42.40			
	With harbour at $X_i = 11$ m		T406 ($X_i=11$)	23.90	44.60	+2.40	+2.20	11.2 5.2
b)	Parameter (at $X_i = 11$ m)	reference test T406	test	Li_{min} (m)	Li_{max} (m)	With respect to T406		
						ΔLi_{min}	ΔLi_{max}	%
	surface area	6 m ²	T408 3.6 m ²	23.50	43.80	-0.40	-0.80	1.7 1.8
	width of the harbour entrance	0.5 m	T404 1 m	24.60	45.00	+0.70	+0.40	2.9 0.9
			T409 0.375 m	23.05	44.10	-0.85	-0.50	3.6 1.1
			T410 0.25 m	21.90	43.30	-2.00	-1.30	8.4 2.9
	orientation of the entrance	90°	T407 135°	23.20	44.20	-0.70	-0.40	2.9 0.9
			T428 45°	23.00	44.15	-0.90	-0.45	3.8 1.0
	shape of the entrance		T412	23.90	44.85	-	+0.25	- 0.6
	sill in the entrance	h (no sill)	T413 h-0.05	22.55	44.75	-1.35	-0.85	5.6 1.9
	location of the entrance with respect to the surface area		T 430	23.75	44.25	-0.15	-0.35	0.6 0.8
			T 427	23.15	44.20	-0.75	-0.40	3.1 0.9
	two connections		T431 $X_i=5, 11$	24.10	45.15	+0.20	+0.55	0.8 1.2
			T432 $X_i=11, 21$	22.60	47.05	-1.30	+2.45	5.4 5.5
	air bubble screen in entrance	no screen	T411	22.40	43.80	-1.50	-0.80	6.3 1.8

Table 2 Effect of harbour parameters on salt intrusion in the river

5. ANALYSIS EXCHANGE CURRENTS

In tidal circumstances exchange currents between harbour and river are composed of three components: the tidal effect T (the tidal filling and emptying of the harbour), the flow induced current effect C (eddies with vertical axis) and the density difference effect D. The principle of the corresponding flow phenomena of these components is drawn below (Table 3).

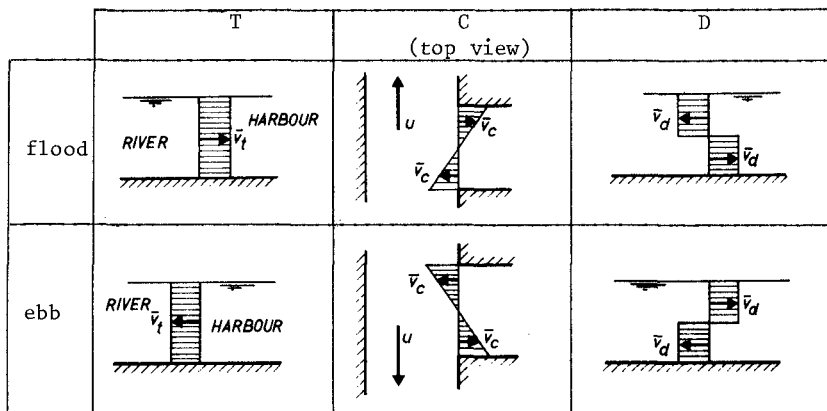


Table 3 Principle of the three exchange phenomena

It may be expected that the three components are not completely independent. However to understand the principle of each phenomenon it can be assumed that they are independent, so the velocities of the three components in the harbour entrance are proportional to respectively:

$$v_t :: \frac{dh}{dt} \quad (\text{tidal effect}) \quad (4)$$

$$v_c :: f(u) \quad (\text{current effect}) \quad (5)$$

$$v_d :: (\Delta\rho)^{\frac{1}{2}} \quad (\text{density effect}) \quad (6)$$

where u is the instantaneous velocity in the river at the harbour entrance, and $\Delta\rho$ is the instantaneous density difference between river and harbour water, so $v_d :: |\rho_{\text{river}} - \rho_{\text{harbour}}|^{\frac{1}{2}}$. By measuring horizontal velocities perpendicular to the cross-section in the harbour entrance one obtains a velocity representing the combined effect of the three components, flowing into the harbour or out of the harbour. Integration over the cross-section gives the total exchange discharge Q_e between harbour and river:

$$Q_e = \int \int \int_B^h v_{(x,z)} dh dB \quad (7)$$

So, the instantaneous exchange discharge in the tidal period is given by:

$$Q_e = T + C + D \quad (8)$$

Over a tidal period the total tidal mean exchange discharge is given by:

$$\tilde{Q}_e = \frac{1}{T} \int_0^T |Q_e(t)| dt \quad (9)$$

Literature indicates the important contribution of the density effect D in the total exchange, see for instance Allen and Price (1959), Abraham (1975/1976) and Vollmers (1976).

In homogeneous fresh tidal circumstances the total exchange in the harbour entrance is given by:

$$Q_{e.f} = T + C \quad (10)$$

The tidal effect ($:: \frac{dh}{dt}$) will be equal in homogeneous fresh circumstances and in salt-fresh circumstances. Assuming no interaction between the density effect and the flow-induced effect, expression (8) minus expression (10) results in

$$Q_e - Q_{e.f} = D \quad (11)$$

6 RESULTS EXCHANGE CURRENTS

As an example, test results of Q_e are given in Figure 5a for a harbour location $X_i = 11$ m. This figure gives the results of the mixed-, partly mixed-, stratified- and homogeneous fresh circumstances. Compared to the partly mixed circumstances the only difference with the homogeneous test is that $\rho_{\text{sea}} = \rho_{\text{fresh}} \approx 1000 \text{ kg/m}^3$. Tidal mean exchange discharges Q_e as a function of X_i are shown in Figure 5b.

The results show the strong dependency of the exchange discharges on the harbour location X_i . Besides the important contribution of the density component D is clear; up to 75% (under partly mixed circumstances), depending on the location X_i . The tests showed also that in salt-fresh

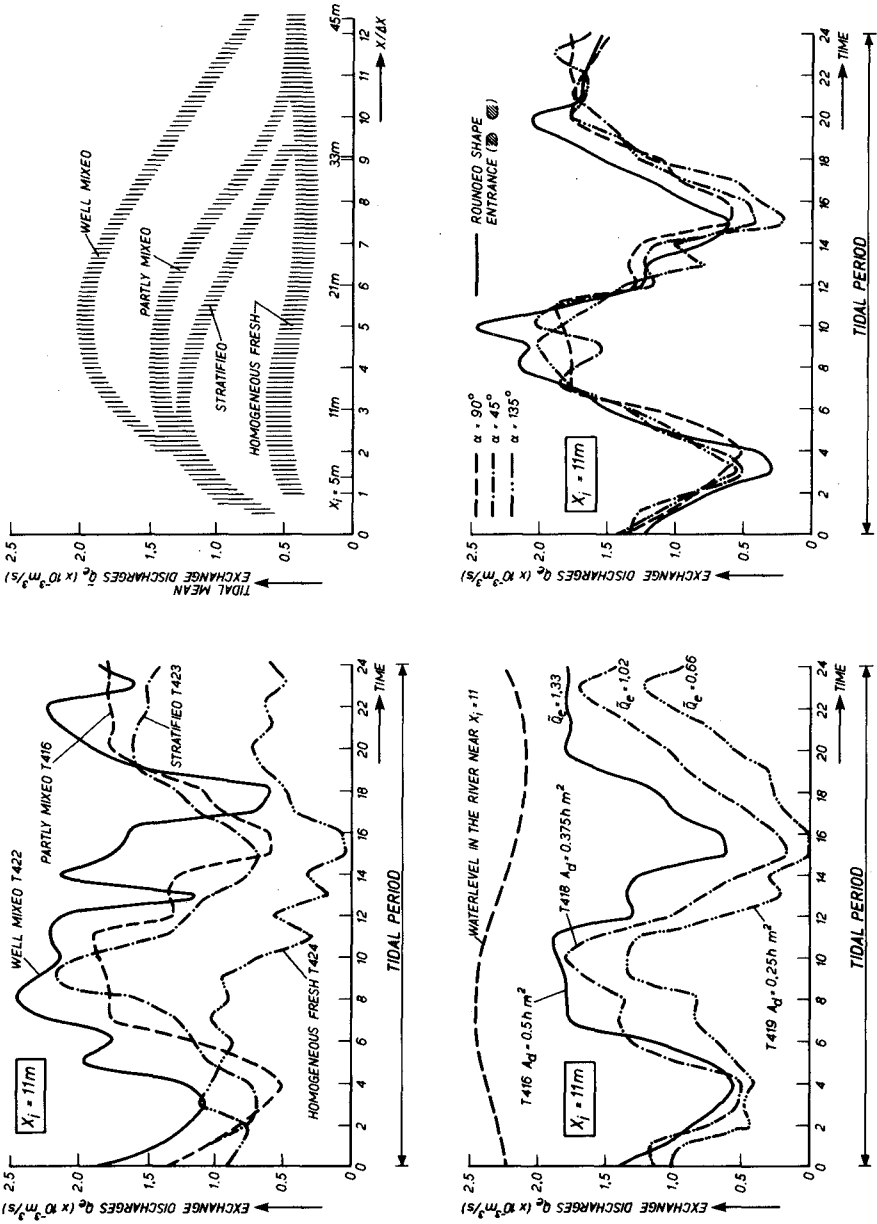


FIG. 5

circumstances maximum exchange discharges occur at HW and LW (density effect dominating). In homogeneous fresh circumstances the maxima appear in another phase of the tidal period, viz. when dh/dt (the tidal effect) and u (the flow-induced effect) have maximum values. Figure 5c shows the direct proportionality of exchange discharges to the width of the harbour entrance. According to Figure 5d orientation and shape (rounded- or sharp-edged) of the harbour entrance do not seem of much importance with respect to exchange discharges in salt-fresh circumstances. These results are similar to those with respect to the influence on the salt intrusion, indicating a direct relation between exchange discharges and increase in salt intrusion.

7 DISCUSSION

In Figure 6 tidal mean values for the exchange discharges $|\tilde{Q}_e|$ are plotted along with the increase of the tidal mean salt intrusion as a function of the harbour location. The results show a similar character. Analysis of tidal propagation and velocities of the various tests showed that dh/dt and the tidal velocity u did not vary much with respect to the harbour location along the area of interest (up to about 50 m from the sea). So, $T (=f(dh/dt))$ and $C (=f(u))$, too must have rather constant values along this area. With this respect, however, the homogeneous fresh test results of Figure 5b show at $X_1 = 11$ m a different behaviour. It is plausible that this behaviour should be attributed to the limitations of the velocity measuring instruments. The low velocities (some centimeters per second), present in the harbour entrance give rise to a relatively high rate of inaccuracy.

According to the above mentioned analysis the considerable variation of Q_e must be attributed mainly to the density component D . The driving force for D is the density difference $\Delta\rho$ between harbour density (hardly fluctuating) and river density (strongly fluctuating), (Figs. 7a, 7b and 7c). So, even in more mixed situations, exchange currents will occur, due to the periodically varying density of the river. Between harbour and river the transport of salt S can then be given by the proportionality:

$$S :: (T + C + D)\Delta\rho \quad (12)$$

A harbour behaves as a source and sink of salt to the estuary. Therefore increase of salt intrusion ΔLi is a function of S , so

$$\Delta Li = f(S) \quad (13)$$

The precise expression (13) will be subject of further research.

8 CONCLUSIONS

From the results of this research the following conclusions can be drawn:

- A harbour connected to a tidal river will increase the salt intrusion in that river as compared to the situation without a harbour (Fig. 3).
- The location of the harbour along the river with respect to the minimum and maximum salt intrusion length without harbour is an important parameter for the influence on the salt intrusion. Maximum influence is found with a harbour located in the vicinity of minimum salt intrusion length in the area between minimum and maximum intrusion length (Fig. 3).
- Increasing the cross-section of the harbour entrance or the surface area of the harbour also has an increasing effect on the salt intru-

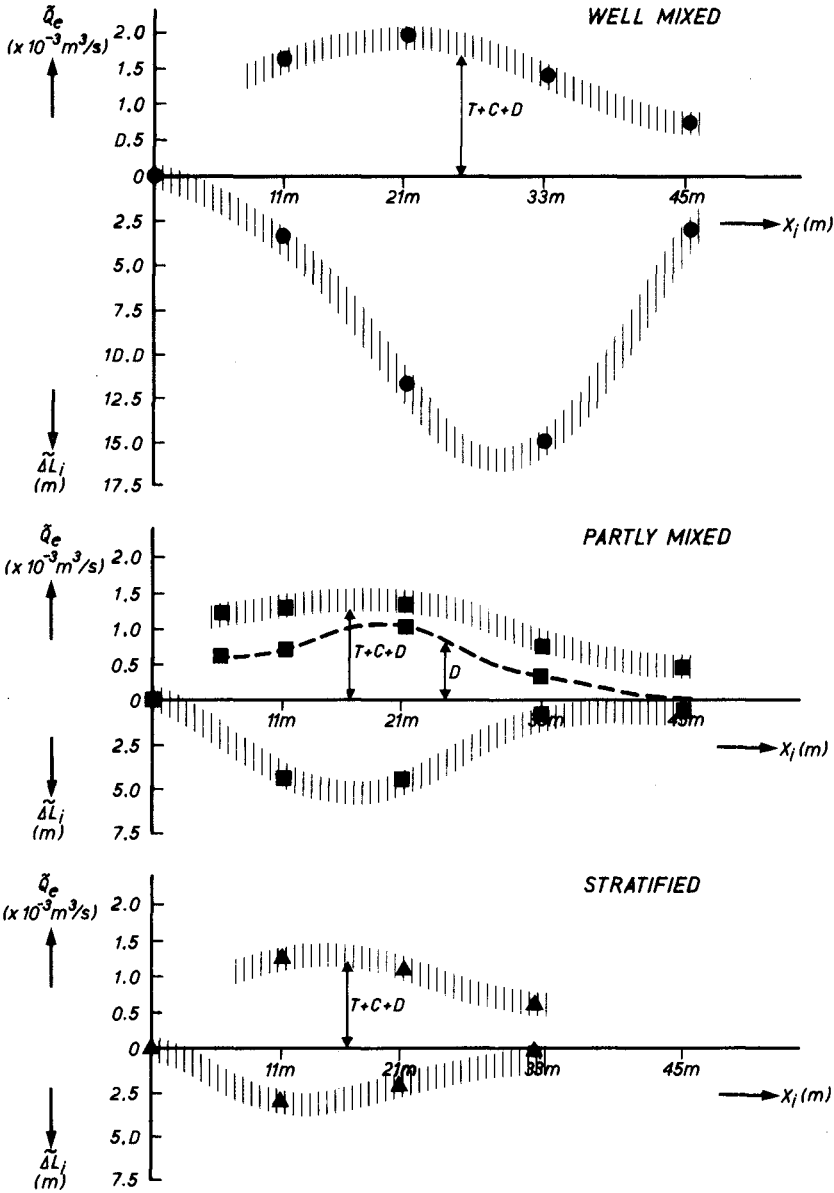


FIG. 6 TIDAL MEAN EXCHANGE DISCHARGES AND TIDAL MEAN INTRUSION LENGTHS AS A FUNCTION OF THE HARBOUR LOCATION X_j

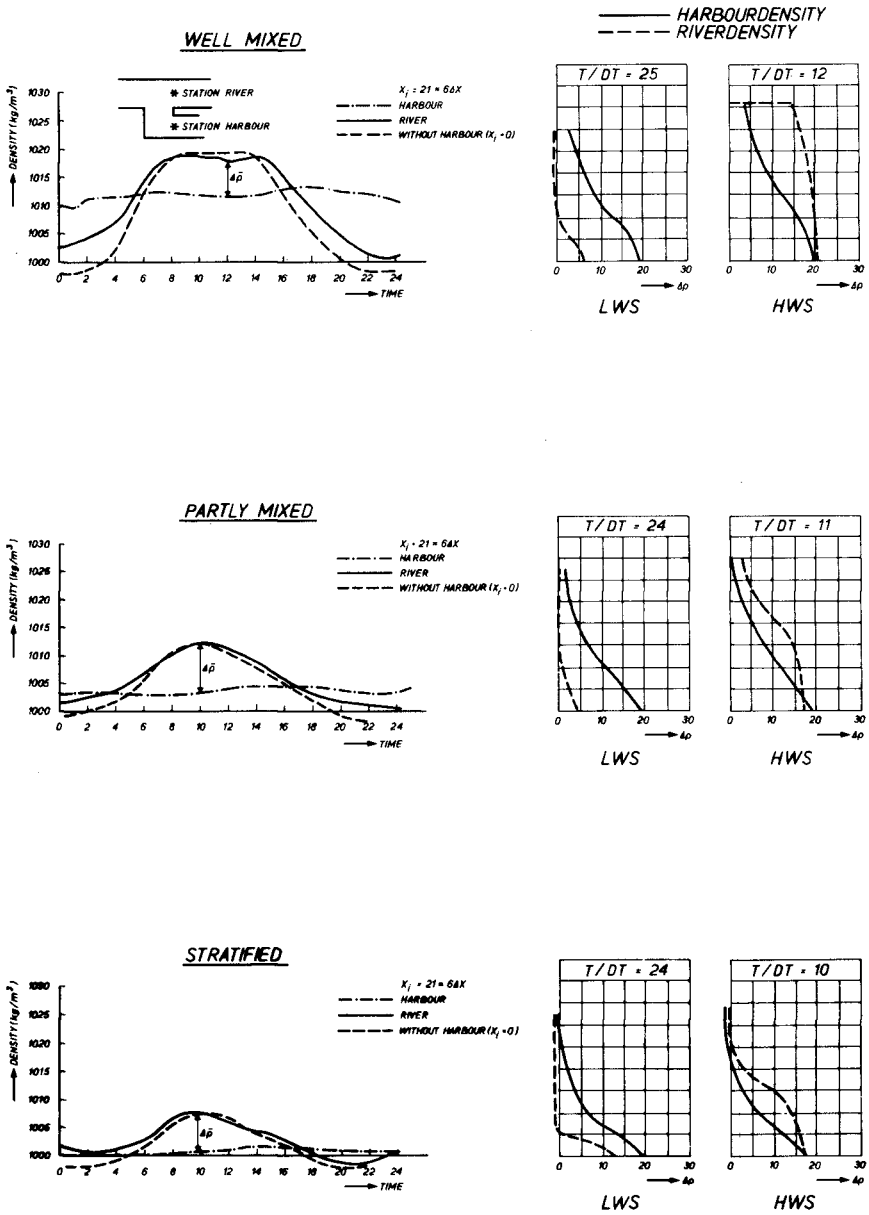


FIG. 7

sion. However, these "geometrical" effects are of minor importance when compared to the effect of the location of the harbour along the river (Table 2).

- The shape and orientation of the entrance with respect to the river hardly have significant effects on the salt intrusion length (Table 2).
- The exchange flows between harbour and river can be subdivided into three components: a tidal effect, a flow-induced effect and an effect due to the density differences between harbour and river (Fig. 7). The density effect is dominating in the situation where the harbour is located within the range where salt intrusion is present ($X_i < L_{i\max}$), (Figs. 5a, 5b and 6b).
- The similarity in the relationship between increase in salt intrusion and harbour location and between exchange flows and harbour location respectively proves that a direct relationship between increase in salt intrusion and exchange flows exists (Fig. 6).
- The results of this study can give a rough estimate of the influence of a planned harbour (re)construction along a tidal river. The detailed physical information resulting from this investigation also can be used for the development of mathematical models, describing salt intrusion affected by harbours or other shoreline irregularities.

REFERENCES

- 1 ABRAHAM, G., 1975-1976, "Reference notes on density currents", International Course in Hydraulic Engineering, Delft.
- 2 ALLEN, F.H. and PRICE, W.A., 1959, "Density currents and siltation in docks and tidal basins", Dock and Harbour Authority, 40, pp 72-76.
- 3 HAMRICK, J.M., 1975, "Salinity intrusion mechanics in estuaries", PROCs. Civil Engin. in the Oceans/III, Univ. Delaware, Newark, Vol. 2, pp. 1382-1399.
- 4 HENSEN, W., 1953, "Das Eindringen von Salzwasser in die Gezeitenflüsse und ihre Nebenflüsse, in Seekanäle und in Hafen", Mitteilungen der Hannoverschen Versuchsanstalt für Grundbau und Wasserbau, Franzius Institut der T.H. Hannover, Heft 3.
- 5 OKUBO, A., 1973, "Effect of shoreline irregularities on streamwise dispersion in estuaries and other embayments", Netherlands Journal of Sea Research 6 (1-2), 213-224.
- 6 REES, A.J. van and RIGTER, B.P., 1969, "Flume study on salinity intrusion in estuaries", XIIIth IAHR Congress, paper C33.
- 7 RIGTER, B.P., 1973, "Minimum length of salt intrusion in estuaries", PROC. ASCE 99, HY9: 1475-1496.
- 8 SCHIJF, J.B. and SCHÖNFELD, J.C., 1953, "Theoretical considerations on the motion of fresh and salt water", PROC. Minnesota, IAHR, Minneapolis pp. 321-333.
- 9 SIMMONS, H.P., 1955, "Some effects of upland discharge on estuarine hydraulics", PROC. ASCE, 81, paper 792.
- 10 VOLLMERS, H.J., 1976, "Harbour inlets on tidal estuaries", XVth International Conference on Coastal Engineering, PROC. Vol. II, Hawaii pp. 1854-1867.
- 11 WATERWAYS EXPERIMENT STATION, 1955, "Investigation of salinity intrusion and related phenomena, Interim report on results of flume control tests", Vicksburg, Mississippi.

NOTATION

a_0	tidal amplitude at $x = 0$	m
b	width of the flume	m
g	acceleration due to gravity	m/s^2
h	waterdepth	m
h_0	mean waterdepth	m
\hat{Q}_{ebb}	maximum ebb discharge at $x = 0$ per unit of width	m^2/s
q_f	fresh water river discharge per unit of width	m^2/s
t	time	s
u	velocity in x-direction on the river	m/s
$v_{t,c,d}$	exchange velocity in harbour entrance due to tide effect, current effect and density effect respectively	m/s
x	longitudinal direction	m
z	vertical direction	m
A_b	surface area of the harbour basin	m^2
A_d	cross-section of the harbour entrance	m^2
B	width of the harbour entrance	m
C	De Chézy coefficient for the river roughness	$m^{1/2}/s$
C	contribution from the current effect in the total exchange	m^3/s
D	contribution from the density effect in the total exchange	m^3/s
HW	high water	
HWS	high water slack	
Li_{min}	minimum salt intrusion length	m
Li_{max}	maximum salt intrusion length	m
\tilde{Li}	tidal mean salt intrusion length	m
Li_0	salt intrusion length without a harbour	m
LW	low water	
LWS	low water slack	
P_t	flood volume	m^3
Q_f	fresh river water discharge	m^3/s
$Q_{e,e.f}$	exchange discharges, salt/fresh and fresh respectively	m^3/s
S	salt transport through harbour entrance, due to exchange flows	kg/s
T	contribution from the tide effect in the total exchange	m^3/s
T_t	tidal period	s
X_i	location of the harbour along the river	m

NOTATION (continuation)

α	flood number	-
ϵ	relative density difference, $\Delta\rho/\rho$	-
$\Delta\rho$	density difference	kg/m ³
ρ	density	kg/m ³

CHAPTER 173

TIDAL HYDRAULICS AND SALT BALANCE OF LAKE WORTH, FLORIDA

J. van de Kreeke* and J. D. Wang*

Formulation of the Problem

In the central and southern part of Florida, groundwater levels are maintained via an intricate system of canals. During the rainy season large quantities of freshwater are discharged through the canals into the estuaries surrounding the Florida coast, resulting in a considerable lowering of the salinities. This in turn has an effect on the biota and in particular tends to reduce the species diversity.

A typical example is the Lake Worth lagoon, where salinities in the interior part can be as low as 10 ppt during the wet season and as high as 35 ppt at the end of the dry season. Based on the results of a biological study, it was concluded that maintaining salinities of 30 ppt or higher in the interior of the lagoon would permit the further expansion of the rich species assemblage presently existing in the more saline water near North Lake Worth Inlet, van de Kreeke, et al. [1977]. From the onset it was clear that this would require that large quantities of freshwater be diverted elsewhere. As part of the overall problem to arrive at a rational decision with respect to the amount of freshwater diversion the following specific problems are addressed in this paper:

- identification and quantification of freshwater sources.
- determination of freshwater/saltwater transport mechanisms and the resulting salinity distribution.
- the effect of reducing the freshwater inflow on the flushing time.

For this purpose a series of field measurements was carried out and mathematical models describing the hydrodynamics and salinity distribution were developed.

General Features

The Lake Worth lagoon, Fig. 1, is approximately 100,000 ft long and 1,500 ft wide. Depths vary from 7 ft in the interior to 30 ft near the Port of Palm Beach. The lagoon is connected to the ocean by two inlets, North Lake Worth Inlet with a cross-sectional area of 25,000 ft² and South Lake Worth Inlet with a cross-sectional area of approximately

* Division of Ocean Engineering, Rosenstiel School of Marine and Atmospheric Science, University of Miami

2,500 ft². The lagoon consists of a conveying channel intermittently bordered by shallow storage regions. The highly irregular bottom topography of Lake Worth, a result of dredge and fill operations, is indicated in Fig. 2.

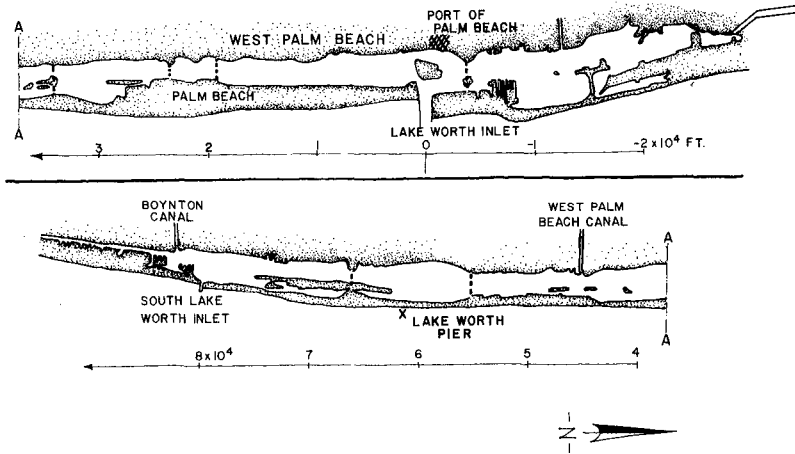


FIGURE 1—LAKE WORTH LAGOON; PLAN VIEW

Tides in the ocean off Lake Worth are semi-diurnal with an average amplitude of 1.4 ft. Starting at North Lake Worth Inlet and going north, tidal amplitudes and phase lags slightly increase, Fig. 3. South of the inlet tidal amplitudes increase, reaching a maximum at about $x = 16,000$ ft. A sharp decrease in tidal amplitude is found between $x = 16,000$ ft and $x = 23,000$ ft. For values of $x > 23,000$ ft the tidal amplitude gradually decreases to a value of 86% of the ocean tide at the southern extreme of the lagoon. Phase lags south of North Lake Worth show a somewhat similar pattern. Over the first 20,000 ft phase lags slightly decrease then show a sharp increase between $x = 20,000$ ft and $x = 23,000$ ft. For values of $x > 23,000$ ft, phase lags gradually increase to a maximum of 2 hours at the southern end of the lagoon. The sharp changes in tidal amplitude and phase at $x \approx 20,000$ ft can be contributed to a strong decrease in cross-sectional area and average depth in this region.

Cross-sectionally averaged tidal velocities are about 1 ft/sec in the northern part of the lagoon and 0.5 ft/sec in the southern part. Typical velocities in North Lake Worth Inlet and South Lake Worth Inlet are respectively 3 ft/sec and 6 ft/sec.

Readily identifiable sources of freshwater are the West Palm Beach Canal and the Boynton Canal of the South Florida Water Management District, see Fig. 1. A typical hydrograph for the West Palm Beach Canal is shown in Fig. 4. The hydrograph shows a seasonal pattern similar to the rainfall i.e. the bulk of the freshwater is discharged during the rainy season, May through September. Discharges of the Boynton Canal show a similar trend but are in general much smaller than those of the West Palm Beach Canal. Also because of its proximity to South Lake Worth Inlet the effect of the Boynton Canal discharges on the lagoon are less profound.

Field Measurements

To obtain insight in the salinity variations, and salt transport mechanisms and to aid in the development, calibration and verification of the mathematical models a series of field measurements were carried out consisting of:

- a time series of weekly salinity measurements at $x = 33,500$ ft covering a period of one year.
- a number of quasi-synoptic salinity profiles along the longitudinal axis of the lagoon during periods of High and Low Water
- simultaneous salinity - velocity measurements at $x = 15,000$ ft, $x = 40,000$ ft and $x = 68,000$ ft covering a full tidal cycle.

The results of the weekly salinity measurements are presented in Fig. 4. The gross features of the salinity variations correspond closely to the variations in freshwater inflow as characterized by the discharge of the West Palm Beach Canal. Lowest and highest salinities are respectively 15 ppt and 35 ppt. Attention is drawn to the relatively low steady state salinity of 34 ppt during the month of April when there was hardly any inflow from the West Palm Beach Canal and the Boynton Canal and offshore salinities were about 36 ppt. It is postulated that this is the result of groundwater seepage as will be discussed in the section Sources of freshwater inflow, flushing time. Fig. 4 also shows that the biologically preferred conditions of 30 ppt or higher in the interior region limit the discharge of the West Palm Beach Canal to between 100 - 200 cfs; at present highest discharges are on the order of 2000 cfs.

An example of the longitudinal salinity distribution is presented in Fig. 5. Minimum salinities are found near the discharge point of the West Palm Beach Canal and gradually increase going towards both inlets. North of the West Palm Beach Canal, tidal time variations in salinity are closely related to the tidal excursion. This is much less the case south of the West Palm Beach Canal, where the tides

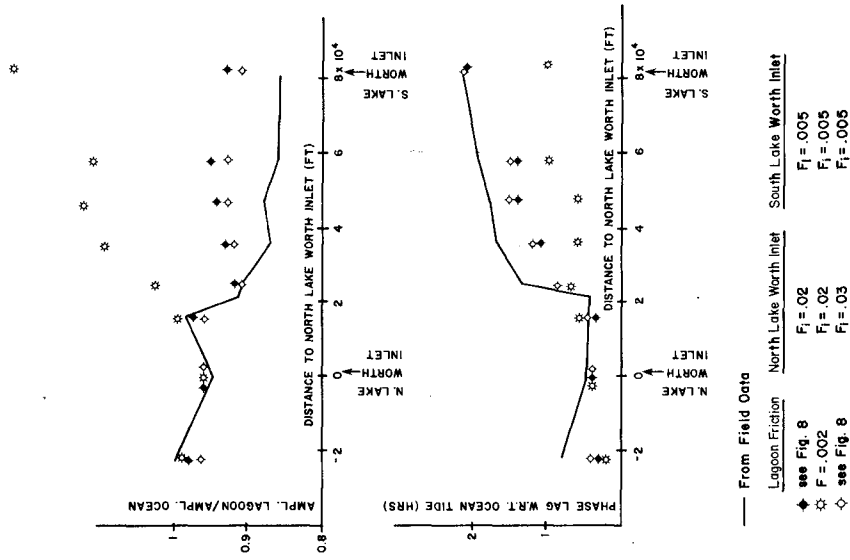


FIG. 2 BATHYMETRY OF LAKE WORTH

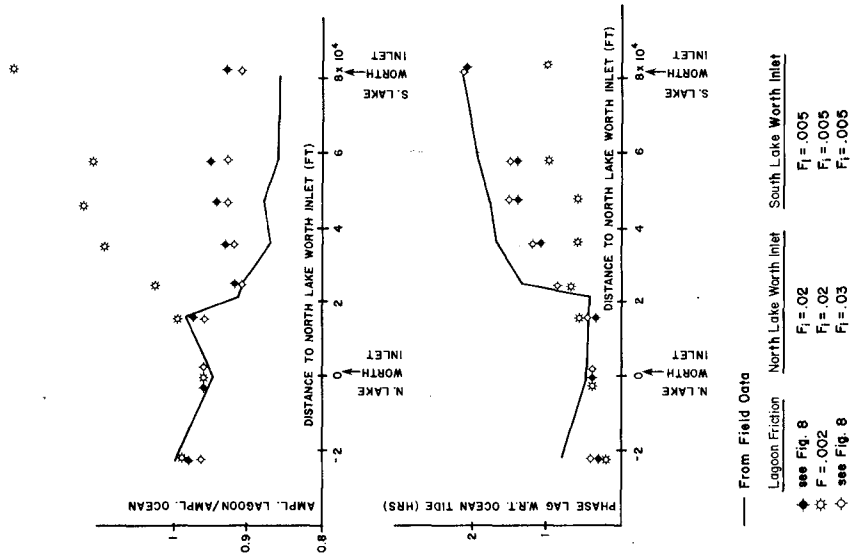


FIG. 3 TIDAL AMPLITUDES AND PHASE LAGS

entering North Lake Worth Inlet and South Lake Worth Inlet meet resulting in low tidal velocities.

Depending on the freshwater inflow, vertical stratification can be very strong especially in the southern part of the lagoon, Fig. 6. The stratification parameter used in this figure is the ratio of the mean vertical salinity over the surface salinity. Except close to the West Palm Beach Canal and the Boynton Canal lateral variations in salinities were less than 1 ppt.

Examples of measured water levels and discharges at $x = 40,000$ ft are presented in Fig. 7. In the same figure, as an indicator of the prevailing wind stress, the square of the wind velocity component parallel to the longitudinal axis of the lagoon is presented. The results are based on hourly values of wind speed and direction measured at the Palm Beach International Airport.

Data on tides and velocities indicated that on the average, high and low tides precede the times of slack water. A typical value is 30 min, however this can vary strongly depending on freshwater inflow, wind, type of tide and location. Times of maximum and minimum values of salinity correspond approximately to high and low tide.

Sources of Freshwater Inflow, Flushing Time

As mentioned earlier besides the West Palm Beach Canal and the Boynton Canal, groundwater seepage is expected to be an important source of freshwater. A conservative estimate of the magnitude of the groundwater seepage was made using the known steady-state salinity distributions for the first two weeks of September 1974 and September 1975. Except for the discharge of the West Palm Beach Canal, contributions of other sources were the same for both periods.

	<u>Sept. 1974</u>	<u>Sept. 1975</u>
Boynton Canal	0 cfs	0 cfs
Evaporation	63	63
Rainfall	0	0
West Palm Beach Canal	500	180
Groundwater seepage	Same for both periods based on observed groundwater levels	

Assuming the overall flushing time T_f to be the same for both periods, yields for the groundwater seepage a value of 300 cfs. The corresponding flushing time is 5 days. Note that for steady state conditions $T_f = V_r/Q_f$ in which V_r = freshwater content of the lagoon and Q_f = the sum of all freshwater sources and sinks. Values of V_r obtained from the measured salinity distribution in the lagoon were $V_r = 3.01 \times 10^8$ cuf for September 1974 and $V_r = 1.67 \times 10^8$ cuf for September 1975.

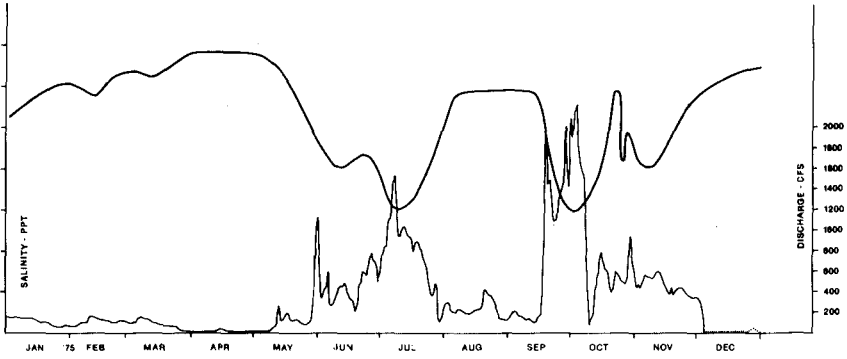


FIG. 4 TIDALLY AVERAGED SALINITY AT X = 33,500 FT. AND DISCHARGE OF W. PALM BEACH CANAL

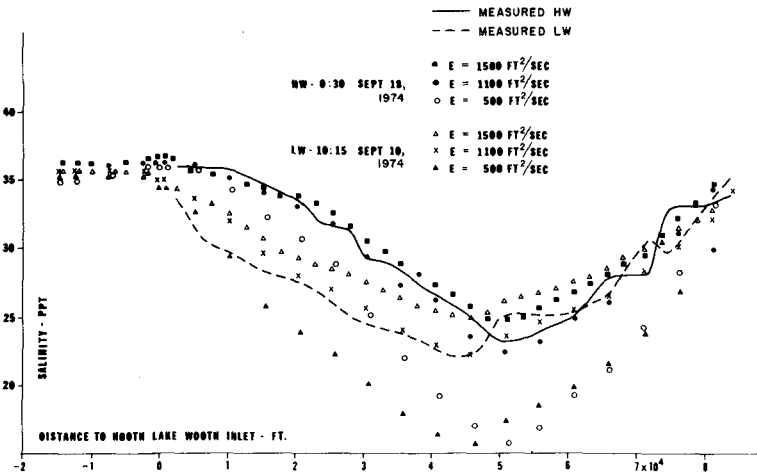


FIG. 5 COMPUTED AND MEASURED LONGITUDINAL SALINITY DISTRIBUTION

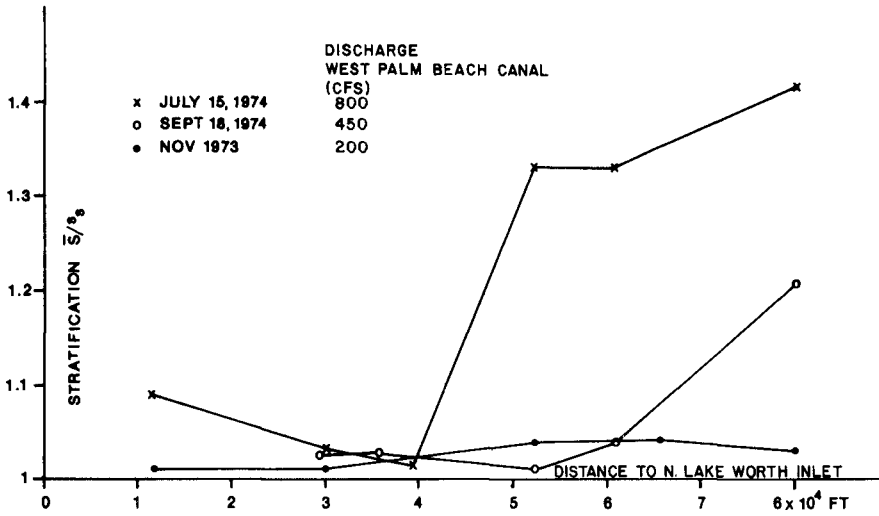


FIG. 6 SALINITY STRATIFICATION

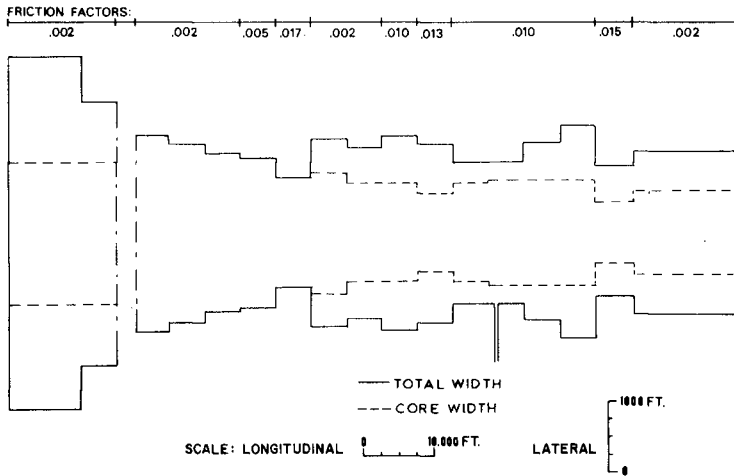
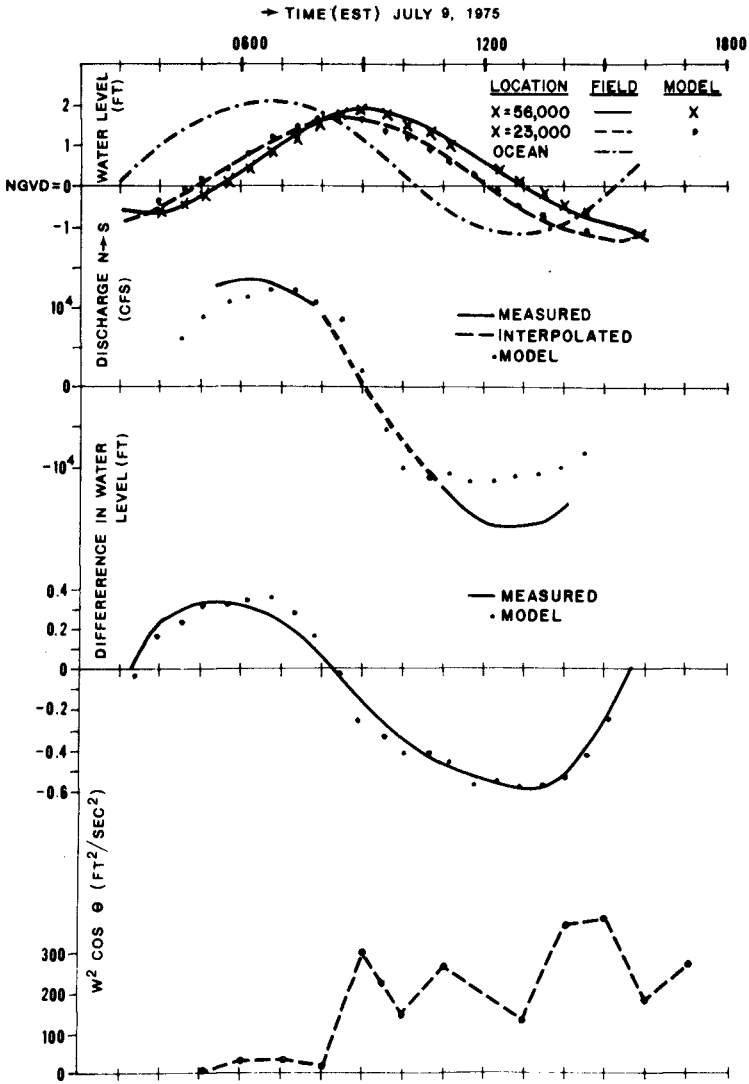


FIG. 8 SCHEMATIZATION OF LAKE WORTH



Discharges Measured At X = 40,000 Ft.

Difference in Waterlevels is Between Data at 23,000Ft. and 56,000Ft.

FIG. 7 WATER LEVELS AND DISCHARGES FOR JULY 9, 1975

Because of the increased density currents one could argue that instead of being the same, the flushing time decreases with increasing freshwater inflow (i.e. flushing time is shorter for September 1974). With this assumption the values for the groundwater seepage would be even larger and therefore the 300 cfs can be considered to be a conservative estimate.

Comparing with the contributions of the Boynton Canal and West Palm Beach Canal it follows that groundwater seepage is a source which needs to be accounted for when computing the salinity distribution in the Lake Worth lagoon.

Salt Transport Mechanisms

Tidally Averaged Transport

Transport mechanisms can be divided in advective and dispersive mechanisms. For Lake Worth the advection of salt is associated with the tidally averaged discharge. The tidally averaged discharge in addition to the freshwater inflow is determined by a tide-induced residual circulation between the two inlets. Unfortunately the discharge measurements carried out in the lagoon were not accurate enough to determine the value of the tide-induced residual circulation. An estimate of 200 cfs to the south was arrived at using an analytical model, van de Kreeke [1976]. A numerical model for the hydromechanics of the lagoon to be discussed in the next section yielded values of 150 cfs and 50 cfs to the south respectively without and with the presence of the baroclinic term in the dynamic equation. The dispersive mode of transport is associated with gravitational circulation, shear flow and trapping. Trapping is attributed to particles residing part of the tidal period in the storage regions (tidal flats) before returning to the conveying channel.

Based on field data an estimate of the advective salt transport and the salt transport by trapping at $x = 30,000$ ft is made for September 18, 1974. The data base was not sufficient to estimate the dispersive transport resulting from gravitational circulation and shear flow. At $x = 30,000$ ft the average cross-sectional area $A_0 = 15,000$ ft² and the tidal variation in cross-sectional area $A_2 = 2,000 \sin(\sigma t + 15^\circ)$. The tidally averaged salinity $\langle s \rangle = 27$ ppt, see Fig. 5 and the corresponding salt concentration $\langle c \rangle = 1.68$ lb/cuf. The tidal variation in salt $c_2 = 0.15 \sin(\sigma t + 15^\circ)$ lb/cuf, the tidal velocity $u_2 = -1 \cos \sigma t$ ft/sec. The phase angle of 15° corresponds with the earlier observed 30 min lag between slack water and high and low tide. Computer simulation for the flow on September 18 yielded a value of the tidally averaged discharge $\langle Q \rangle = 250$ cfs to the north. The corresponding advective salt transport $\langle Q \rangle \langle c \rangle = 420$ lbs/sec to

the north. An estimate of the trapping effect $A_0 \langle u_2 c_2 \rangle = 283$ lbs/sec to the south*. This shows trapping to be an important salt transport mechanism, but at the same time does not exclude the gravitational and shear flow as major contributors to the salt transport. In fact, as suggested by the relatively large vertical and lateral variations in salinity, gravitational circulation is probably the major dispersion mechanism close to the discharge point of the West Palm Beach Canal.

Tidal Time Variations

Tidal time variations in salinity are mainly a result of tidal advection as demonstrated by the oscillation of the salinity distribution over approximately the length of the tidal excursion see also Fig. 5.

Transport by Wind

In addition to the advective salt transport resulting from the tide-induced net circulation and the freshwater inflow, the effect of wind-induced currents should be mentioned. During the summer when freshwater inflow is largest, winds are predominantly from the south-east, resulting in a south - north current. The magnitude of the wind-induced currents cannot easily be computed in the 1-D model to be discussed in the next section. Attempts to determine the wind-induced circulation from long term current measurements failed because of fouling of the current meter by floating debris.

Salinity Model

To model the salinity distribution a real-time finite difference model was selected. The model is based on the one-dimensional advection-dispersion equation. In view of the multitude of transport mechanisms, it is realized that such a simplified model cannot correctly represent the physical processes. The best one can hope for is that after extensive calibration for a large set of freshwater discharges, the model will be of some use in comparing the effect on the salinity distributions of different freshwater diversion schemes.

The discharges in the advection-dispersion equation are derived from a model simulating the hydromechanics of the lagoon. This model uses the one-dimensional long wave equations including the convective

*It is usually assumed that trapping is the major contributor to the value of the covariance of u_2 and c_2 . To the authors knowledge this has never been proven.

term for the interior part of the lagoon. The flow in the inlet is described by an equation of the form

$$\Delta\eta = F_i \frac{L}{h} \frac{u^2}{g}$$

in which $\Delta\eta$ = head differences across the inlet, L = length of inlet, F_i = inlet coefficient, h = average depth, u = cross-sectionally averaged velocity, g = gravity acceleration. The equations constituting the hydromechanics model are solved by means of an explicit finite difference technique. Separate algorithms, based on the inlet equations are used to treat the connections between the lagoon and the ocean, van de Kreeke [1972]. The schematization of the lagoon as used in the computations is presented in Fig. 8.

To calibrate the hydromechanics model, inlet coefficients and friction factors F (= 1/8 of the Darcy Weisbach friction factor) for the interior of the lagoon had to be determined. The tide at Port of Palm Beach appeared to depend mainly on the characteristics of North Lake Worth Inlet and the surface area of the lagoon and to be rather insensitive to the inlet coefficient of South Lake Worth Inlet and the friction values in the interior of the lagoon. A relatively narrow range of values for the inlet coefficient $F_i = .02 - .03$ for North Lake Worth Inlet could therefore be determined by matching measured and computed tides at Port of Palm Beach. These relatively high values are a result of the actual flood and ebb currents not using the full cross-sectional area of the inlet. Based on simultaneous water level and discharge measurements a value of the inlet coefficient $F_i = 0.005$ was found for South Lake Worth Inlet. Friction factors in the lagoon were determined by matching computed and measured water levels in the stations $x = 15,000$ ft, $x = 40,000$ ft and $x = 68,000$ ft. Lastly the friction factor for North Lake Worth Inlet was adjusted to an ultimate value of $F_i = .02$ in order to yield an overall best fit of discharges in the lagoon. The final configuration of the friction factors is presented in Fig. 8. A value often cited in the literature is $F = 2 \times 10^{-3}$, which is considerably lower than the values for the Lake Worth lagoon. This should be attributed to energy losses associated with constrictions and variations in the bottom topography which are of the same order as the average depth, see Fig. 2. A similar trend for the values of the friction factors was found in Chincoteage Bay, Harleman and Lee [1969], with values of F ranging from 0.02 to 0.06. To illustrate the importance of the friction, tidal amplitudes and phases in the lagoon computed for different values of the friction factor are presented in Fig. 3.

An example of computed tides and discharges at $x = 40,000$ ft is presented in Fig. 7 using the values of the friction factors in Fig. 8. The agreement is reasonable with the ebb discharge (S to N) being slightly underestimated. This could be caused by wind which increased

during the ebb period. Although wind forcing was included in the model, an accurate representation of wind driven currents could not be achieved because of the one-dimensional treatment of the lagoon.

The numerical grid used for solving the advection-dispersion equation was the same as that for the hydrodynamic equations. To solve the equation an implicit finite difference scheme was used, van de Kreeke, et al. [1977]. Examples of computed salinity distributions for three values of the dispersion coefficient are presented in Fig. 5. The inflow of the West Palm Beach Canal and the Boynton Canal are respectively 500 cfs and 0 cfs. The distributed inflow (groundwater seepage, evaporation) is 218 cfs. A value of about $1100 \text{ ft}^2/\text{sec}$ seems to best describe the salinity distribution.

Conclusions

- In addition to the discharge of the flood control canals, groundwater seepage is an important source of freshwater for the Lake Worth lagoon.

- The overall flushing time for the Lake Worth lagoon is on the order of one week.

- For steady-state conditions the advective salt transport resulting from the tidally averaged discharge is in the near field balanced by a dispersive mode of transport associated with density currents and is in the far field balanced primarily by trapping. The tidally averaged discharge results from the freshwater inflow and a tide-induced residual circulation between the two inlets. Because of the lack of long term current measurements the effect of wind on the advective transport could not be discerned.

- Calibration of an earlier developed model simulating the hydro-mechanics of the lagoon yielded values of friction factors considerably higher than those cited in the literature. The reason for this is the irregular bathymetry, in particular the constrictions, leading to a three-dimensional flow pattern and increased dissipation. The associated stresses are not properly accounted for in the one-dimensional model which in turn is reflected in the friction coefficient.

- To describe the tidal time variations in the salinity distribution a numerical solution was developed for the advection - dispersion equation. A constant value of the longitudinal dispersion coefficient was assumed. Matching measured and computed salinity distributions for the early part of September 1974 yielded a value of the dispersion coefficient $E = 1100 \text{ ft}^2/\text{sec}$. It is emphasized that this value does not necessarily apply to periods with significantly

different freshwater inflow. Limited knowledge of the dependence of the dispersion coefficient on the freshwater inflow restricts the usefulness of the advection-dispersion model without further calibration.

Acknowledgement

This study was sponsored by the office of Water Research and Technology, Department of Interior, under Grant No. 14-31-0001-9038.

References

1. Harleman, D.R.F., C. H. Lee, "The Computation of Tides and Currents in Estuaries and Canals", Tech. Bull. No. 16. Committee of Tidal Hydraulics, Corps. of Engineers, September 1969.
2. van de Kreeke, J., "A Numerical Model for the Hydromechanics of Lagoons", Proceedings of the 13th Conference on Coastal Engineering Vancouver, Canada, pp 2253-2263, 1972.
3. van de Kreeke, J., "Increasing the Mean Current in Coastal Channels", Journal of the Waterways, Harbors and Coastal Engineering Division, ASCE, Vol. 102, No. WW2, pp 223-234, May 1976.
4. van de Kreeke, J., J. D. Wang, R. G. Rehner and M. A. Roessler, "Freshwater Inflow and its Effect on the Salinity and Biota of Shallow Lagoons". University of Miami, RSMAS, TR77-4, 1977.

NUMERICAL TIDAL-SALINITY MODELS OF THE EMS ESTUARY

Karsten Fischer

Lehrstuhl für Strömungsmechanik

Technische Universität Hannover

West Germany

1. Introduction

As a consequence of the increased usage of estuarine resources and capacities, the need of estuary models for research and prediction purposes has led to strong developments in this field and high levels of modelling art today. Depending on the specific problems to be investigated by the engineers, the complexity of the models and the cost of running them can vary drastically, and it is not always a priori clear which effects must be treated carefully, and which simplifications can be made, in order to get a model working accurately as well as economically.

Tidal and salinity models are used to obtain information on the salinity intrusion and the sediment transport in estuaries. They can be used as a starting point for more ecological models [1].

Two major problems are observed when constructing salinity intrusion models: First, the numerical errors of the simpler solution algorithms for the advection equation are too large to be negligible; and second, the use of vertically averaged models is questionable because the driving forces for the salinity intrusion process are varying strongly with the water depth.

However, solving the equations of motion and advection-diffusion by very elaborate algorithms on three-dimensional grids with reasonably fine grid spacings can hardly be done by the fastest computers that are commonly available today. As a consequence, two essential questions arise for numerical tidal and salinity models:

- a) what measure of numerical effort must be applied to obtain what measure of accuracy in the results, and
- b) what simplifications (by neglecting and averaging etc.) can be made within a given range of accuracy to restrict the model to the essential physical interactions?

The first question is very difficult to answer and has never

been investigated, in the author's opinion, in a more general way.

Assuming that the second question can be treated independently of the first, it is studied in this paper by application of various models of the Ems estuary, situated on the North Sea coast between the Netherlands and Germany.

2. Description of Numerical Models

High complexity of the geometry and the physical conditions usually encountered in estuaries was the reason for the development of a family of computer programs for calculating tidal and salinity motions. Information on the members of this program family is given below. The individual programs are based on an explicit finite difference simulation of the relevant partial differential equations, using a staggered grid formulation with mass-conservative and transportive (upstream) finite-difference expressions. The models are similar to those developed by Hansen [2], Leendertse [3], Sündermann [4], and Simons [5]. They can be run as self-standing modules or as subroutines, and they are easily applied for purposes of coupling and nesting of sub-models. The present paper gives an example for the coupling of two submodels. Applications are facilitated by a full dynamic storage assignment. As it is a program family for research purposes, all routines are highly modularized in order to allow for quick exchange and replacement of sub-units. No effort was undertaken to develop a comfortable user-oriented input-output structure (e.g. a problem-oriented language), because it was felt that such a structure is only useful if the model structure is not expected to change in the future; however, such a state of modelling art has, after the author's opinion, not yet been achieved for tidal-salinity estuary models.

2.1 One-dimensional Model

Equation of motion:

$$u_t + uu_x + \frac{r}{h}|u|u - \frac{\lambda}{h}|w|w - Au_{xx} + \frac{1}{\rho}p_x = 0 \quad (1)$$

Here, and in the following, differentiation is indicated by subscripts. t is the time coordinate, u the velocity along x , h the water depth, ρ the density, \bar{p} the average hydrostatic pressure, W the wind speed, r the bottom friction coefficient, λ the wind stress coefficient, and A the horizontal turbulent stress coefficient.

Equation of hydrostatic pressure:

$$p(z) = g \int_z^h \rho(z) dz \quad (2)$$

where z is the vertical coordinate, g the gravitational acceleration.

Equation of continuity:

$$b \zeta_t + (Fu)_x = 0 \quad (3)$$

where ζ is the tidal fluctuation part of h , b the surface width, and F the cross-sectional area.

Transport equation:

$$F \rho_t + (uF\rho)_x = (BF\rho_x)_x \quad (4)$$

where B is the dispersion coefficient.

2.2 Two-dimensional Horizontal Model

Equations of motion:

$$\begin{aligned} u_t + uu_x + vu_y - fv - A(u_{xx} + u_{yy}) + \frac{1}{\rho} \bar{p}_x \\ + \frac{r}{h} |u|u - \frac{\lambda}{h} |x_W| x_W = 0 \end{aligned} \quad (5)$$

$$\begin{aligned} v_t + uv_x + vv_y + fu - A(v_{xx} + v_{yy}) + \frac{1}{\rho} \bar{p}_y \\ + \frac{r}{h} |v|v - \frac{\lambda}{h} |y_W| y_W = 0 \end{aligned} \quad (6)$$

where u and v are the velocity components along the horizontal space coordinates x and y , respectively, x_W and y_W the wind speed components, f the Coriolis acceleration.

Equation of continuity:

$$\zeta_t + (uh)_x + (vh)_y = 0 \quad (7)$$

Transport equation:

$$h\rho_t + (u\rho h)_x + (v\rho h)_y = (Bh\rho_x)_x + (Bh\rho_y)_y \quad (8)$$

2.3 Two - Dimensional Vertical Model

Equation of motion:

$$u_t + uu_x - Au_{xx} - z_A u_{zz} + \frac{1}{\rho} P_x = 0 \quad (9)$$

where z_A is the vertical eddy viscosity coefficient.

Equation of continuity:

$$({}^X_F u)_x + ({}^Z_F w)_z = 0 \quad (10)$$

where w is the vertical velocity, X_F and Z_F the cross-sectional areas of the control volume, taken perpendicular to the x - and z -axes, respectively.

Transport equation:

$$b\rho_t + (ub\rho)_x + b(w\rho)_z = (bB\rho_x)_x + b({}^Z_B \rho_z)_z \quad (11)$$

where Z_B is the vertical eddy diffusivity coefficient.2.4 Three - dimensional Model

Equations of motion:

$$u_t + uu_x + vu_y - fv - A(u_{xx} + u_{yy}) - z_A u_{zz} + \frac{1}{\rho} p_x = 0 \quad (12)$$

$$v_t + uv_x + vv_y + fu - A(v_{xx} + v_{yy}) - z_A v_{zz} + \frac{1}{\rho} p_y = 0 \quad (13)$$

Continuity equation:

$$({}^X_F u)_x + ({}^Y_F v)_y + ({}^Z_F w)_z = 0 \quad (14)$$

Transport equation:

$$\rho_t + (u\rho)_x + (v\rho)_y + (w\rho)_z = (B\rho_x)_x + (B\rho_y)_y + ({}^Z_B \rho_z)_z \quad (15)$$

2.5 Boundary Conditions

In the vertically discretized models 2.3 and 2.4 the transport equations for the top and bottom layers are somewhat more complicated than eqs. (11) or (15) due to the variable layer thicknesses, but these formulae were omitted for

shortness. Wind and bottom stress are imposed as boundary conditions for the top and bottom layers, and the corresponding turbulence coefficients take account of the decay of eddy viscosity near these boundaries. The vertical eddy viscosity and diffusivity terms are treated by implicit finite differences in order to remove some general stability constraints. Surface, bottom, and lateral closed boundaries are simulated by non-slip velocities and vanishing normal density gradients. At open lateral boundaries, water levels, or normal velocities, densities, and normal gradients of the velocity are required; in most cases the normal gradients can be set zero.

3. Model Applications

Various models were applied to the Ems estuary, situated on the North Sea coast between the Netherlands and Germany. Fig. 1 shows the model area and the boundaries.

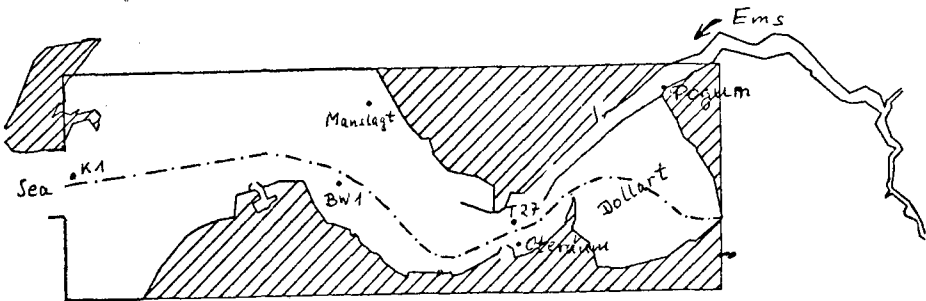


Fig. 1: The Ems estuary

Parts of the open sea boundaries were replaced by closed boundaries, as indicated in Fig. 1, but this artificial closed boundary was situated in regions of very shallow water and low flow velocities. The estuary was represented by a horizontal two-dimensional grid of 1.5 km spacing, supplemented by a horizontal one-dimensional appendix of 1.0 km spacing; the time step was 90 sec, due to a maximum water depth of about 16 m.

Because of the limited amount of available measured data, several assumptions had to be made. For the tidal motion, a near-normal measured tidal cycle of 12 h 25 m was used as periodic excitation of the boundary water level. A set of mean constant discharge values was taken to supply fresh water at three different locations. A set of salinity records, taken under appropriate discharge conditions, and

averaged over several measurement events, was applied to give the boundary condition at K 1 and used for comparison with calculated data at BW 1 and T 27 (see fig. 1).

3.1 Hydrodynamical Vertically Averaged Model

The first step in the model development was the construction of a vertically averaged model for the tidal hydrodynamics. This model was used to get information about the bottom friction and to verify the topographic data. Later on it was supplemented by the salinity transport module and run for comparisons with the vertically discretized model.

3.2 Baroclinic Vertically Discretized Model

This model and six layers of 2 - 3 m thickness in the horizontal two- and one-dimensional parts. The coupling of the model parts was done under conservation of water and salinity mass. The following parameters were found to give a satisfactory agreement between measured and calculated data:

bottom friction	$r = 0.006$
eddy viscosities	$Z_A = 0.0019 \text{ m}^2/\text{s}$
	$A = 0$
eddy diffusivities	$Z_B = 0.00023 \text{ m}^2/\text{s}$
	$B = 0$

Some of the model results are illustrated in fig. 2.

Here the values for velocity and salinity are vertically averaged data from the results of the three-dimensional model. Large areas of tidal flats can be observed in fig. 2 b; the drying- and wetting-mechanism was incorporated in the upper model layer. The relative stagnation of the salinity in shallow regions is evident in fig. 2 a; this is one of the most important mechanisms for dispersion. The irregularity of the velocities near the open boundary is of computational nature and does not affect the interior of the solution, because it is only effective on the tangential velocities at the boundary.

It can be seen in the figure that the representation of the Dollart area near the river inflow is represented only very schematically in the model, and this is indeed the region where the biggest deviations from the measured data occur.

Though the amount of information contained in a three-dimensional model is very large, only one further detail shall be illustrated because of space restrictions. Fig. 3 shows the time variation of the vertical profiles of

- a) the west-east component of the velocity, and
- b) the salinity at point BW 1.

2 a

2 b

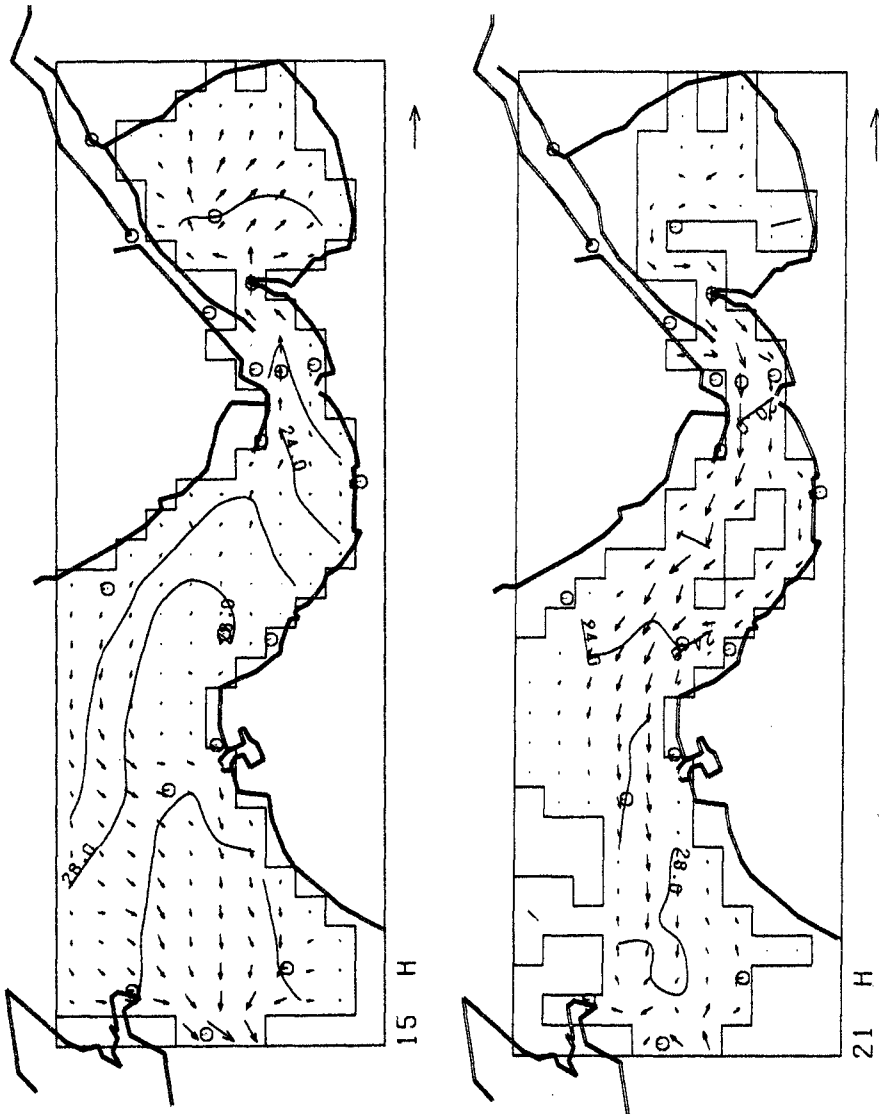
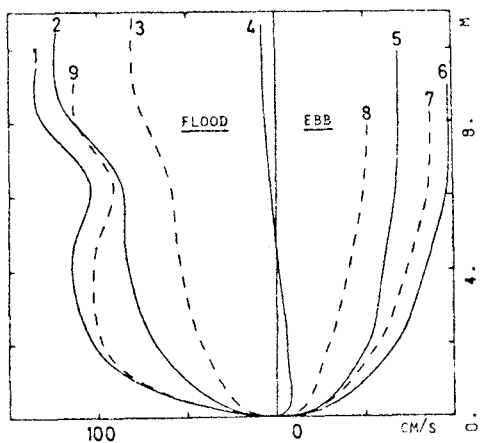
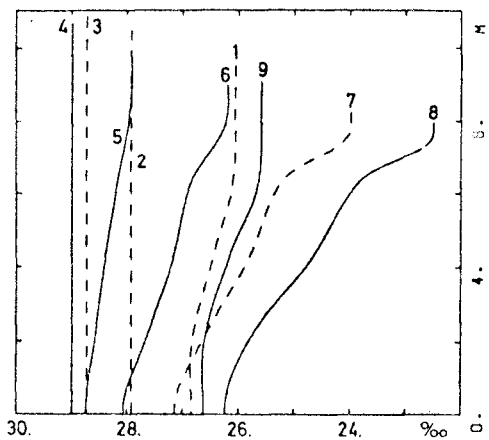


Fig. 2: Flow velocity and salinity near
 a) high water
 b) low water slack
 Reference arrows: 1 m/s
 Salinity values in ppt.



3 a



3 b

Fig. 3: a) Vertical velocity profiles at point BW 1
 b) Vertical salinity profiles at point BW 1
 Numbers at the curves indicate the sequence in time

The typical deviations of the vertical velocity profiles due to the baroclinic forces cannot be observed in Fig. 3 a, because these deviations are two orders of magnitude smaller than the tidal velocities shown in the figure. However, these deviations are most essential for the salinity intrusion process. The anomalies in the curves during flood tide are caused by the Coriolis force and geometrical effects.

The associated salinity profiles in Fig. 3 b show a certain degree of stratification during the ebb tide which is vanishing during flood tide. This effect is caused by the quicker motion of the upperlayers; during flood tide an unstable stratification can be reached which is followed by a rapid vertical mixing.

A test calculation without baroclinic forces showed no significant short-time changes in the vertical profiles of Fig. 3.

4. Model Calibration and Verification

Test runs with the vertically averaged model showed that a satisfactory representation of the tidal motions could be achieved with a constant bottom friction parameter everywhere, except in the region of the Dollart basin. Due to the fact that only a limited set of measurement data was present for comparison purposes, and that this work was a first study to investigate the model properties, it was decided to restrict the calibration to only global parameters that were constant in space and time. This restriction is of no practical interest because the work necessary for calibration is minimal and a three-dimensional model is usually difficult to be calibrated because of computer requirements.

As a first step, the tidal dynamics were calibrated by adjusting bottom friction and vertical eddy viscosity. The salinity transport module was not used in this phase. As a second step, the salinity transport was calibrated by adjusting the vertical eddy viscosity; then, the bottom friction had to be corrected in order to match the water level data. The second step had to be iterated in order to find an optimum solution for both parameters. For each salinity transport calibration, six tidal cycles were calculated, starting from the previously calculated model state. Finally, the stratification was fitted by tuning the vertical eddy diffusivity; this process could be done separately from the other calibration steps. Test calculations showed that the parameters of horizontal exchange A and B could be set zero.

Fig. 4 shows the results for the water level calculations at three points in the estuary. The deviations of the calculated values from the measured data are mainly caused by the over-schematization of the Dollart basin, and show up in the curves for Oterdum (near the river inflow) and Pogum (upstream in the river). The schematization of the

open-sea boundary by a closed boundary in the shallow parts does not lead to severe errors in the simulation.

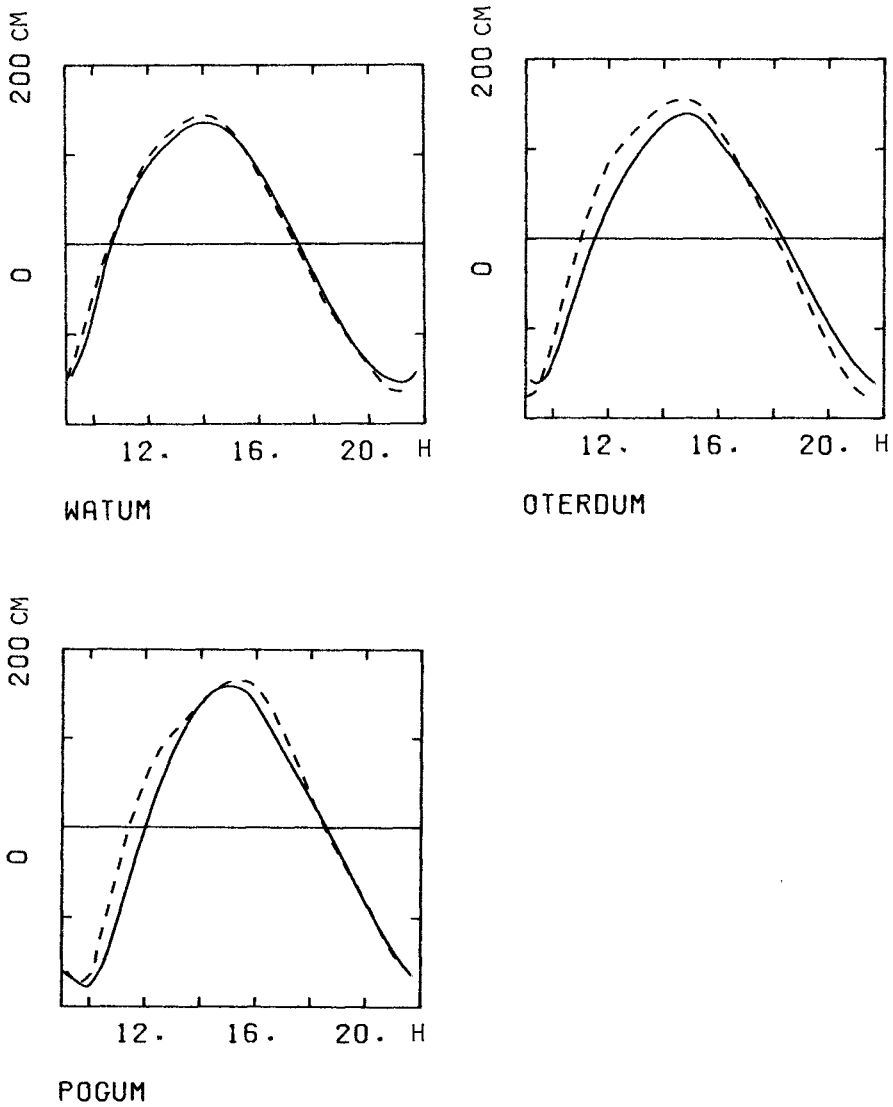


Fig. 4: Calculated (———) and measured (- - - - -) water levels vs. time

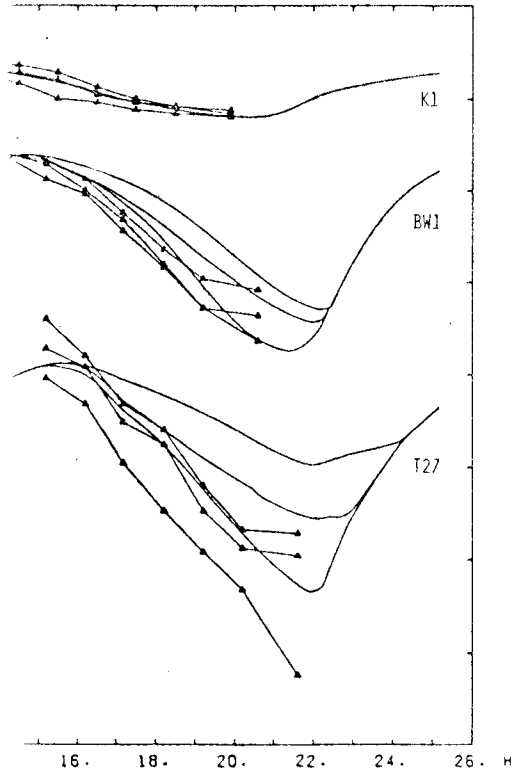


Fig. 5: Calculated (smooth lines) and "measured" (polygon-shaped lines) salinity vs. time. Each triple of curves represents salinity at bottom, center, and top of water column.

Fig. 5 shows salinity curves for three points in the estuary. The upper curves (K1) represent the "measured" and prescribed boundary data; for the model a fully mixed condition was taken. The salinity in the model is systematically too high, due to the large amount of numerical diffusion of the upstream differences scheme. However, as the "measured" data are averages taken from several measurement periods under different tidal conditions ⁶, they are associated with considerable intervals of scatter, and a comparison to the calculated prototype tide should not be too close. Tidal phase and range, average salinity, and degree of stratification appear to be acceptable from a practical point of view. The vanishing of the stratification during the flood period is

evident in the figure, and it is at least indicated in the measurement curves.

Salinity at the open boundary K 1 was varied in order to study the effect of this boundary condition in the interior. Taking a constant value of 30 ppt instead of the time variation shown in Fig. 5, the results in the interior of the model were changed only insignificantly. This result indicates that the average value of the boundary salinity is important, but slight variations in time do not affect the results strongly. As a consequence, it is not necessary to define the open model boundary so far outside in the sea that practically no tidal variations of the salinity can be observed; in the present example, the constant salinity condition was fully sufficient. No discrimination between inflow and outflow boundary condition had to be made because of the use of upstream differences.

A final verification of the model is given in Fig. 6.

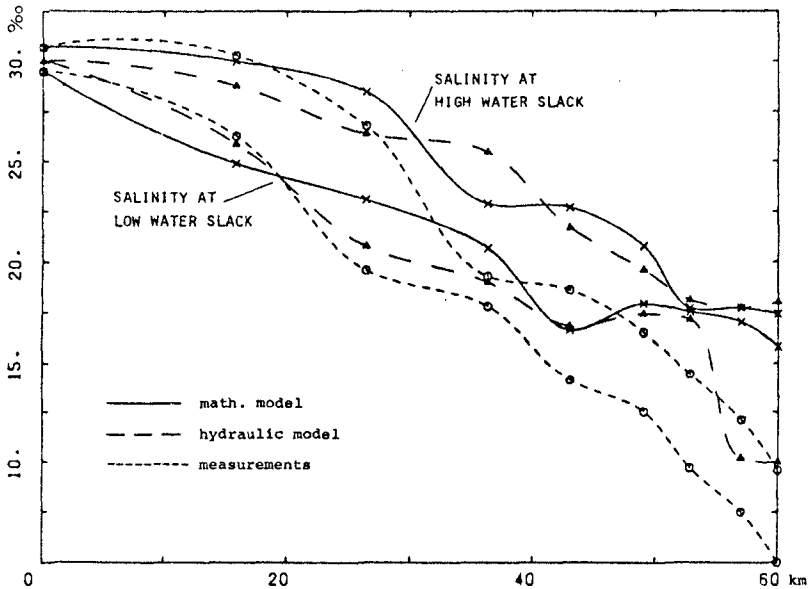


Fig. 6: Comparison of external salinity values along the estuary axis, obtained from mathematical model (———), hydraulic model (- - - - -), and measurements (······).

Here the extremal values of the salinity variation during the tidal cycle, taken along the estuary axis (dash-dot-line in Fig. 1), are shown for the present model calculation, a hydraulic model investigation performed by the Bundesanstalt für Wasserbau [7], and an average data set evaluated from several measurements. Due to the fact that the various curves have been obtained under different tidal (and possibly discharge) conditions, no perfect agreement can be expected. The largest deviations occur in the area of the Dollart basin, both for the mathematical and the hydraulic model. The figure shows that the approximation of the measurement data by both models is of comparable quality.

Another simulation of the salinity intrusion was tried with the vertically averaged model. It was impossible by fitting bottom friction and one global horizontal diffusion parameter to get acceptable results for the salinity distribution, as is demonstrated in another report [8]. Experiments with time- and space-variable diffusion parameters were not undertaken, but it is assumed that good results can be obtained when the model's number of degrees of freedom is high enough.

5. Conclusions

A satisfactory salinity intrusion simulation of a mixed estuary has been obtained by application of a spatially three-dimensional finite difference model with three adjustable parameters. The results of the mathematical model were of a quality comparable to the results of a hydraulic model. The salinity intrusion was found to be mainly influenced by the combined action of vertical eddy viscosity and bottom friction. The vertical eddy diffusivity parameter could be adjusted separately and had only influence on the vertical stratification. The accuracy of the simulation was limited by the grid coarseness and artificial diffusion effects of the numerical method. An analogous simulation by means of a vertically averaged model with constant horizontal diffusion parameter gave no acceptable results.

Given a certain range of desired accuracy in the results (mainly defined by the accuracy of the available measurement data), the following model restrictions were possible to obtain satisfactory results:

- a) constant vertical eddy viscosity,
- b) constant bottom friction,
- c) constant vertical eddy diffusivity,
- d) constant salinity at the open boundary,
- e) a coarse grid in the horizontal plane,
- f) only six vertical grid points.

These restrictions made a simulation of the vertical and lateral dispersive fluxes possible in the framework of a model consuming computer-time to a still moderate extent.

For practical purposes the following classification of models and their applications can be made. Vertically averaged models are useful for calculating the tidal dynamics, and this problem can be solved under neglect of baroclinic forces. A discretization in the lateral direction is necessary if the lateral depth variations are strong. For the salinity intrusion of a mixed estuary, a vertically discretized model should be used; lateral discretization is necessary when lateral depth variations are strong. For the salinity intrusion of a stratified estuary, the same conditions are met; however, in this case a stratification-dependent vertical eddy viscosity is probably necessary to be applied.

6. Acknowledgments

The present work was done with the help of funds of the Deutsche Forschungsgemeinschaft, Sonderforschungsbereich 79. The author is indebted to D. Steen of the Wasser- und Schifffahrtsamt Emden, for most of the measured data, to P. Ströhmoer of the Bundesanstalt für Gewässerkunde Koblenz, for an internal report on salinity measurements in the Ems estuary, and to the Bundesanstalt für Wasserbau, Hamburg, for the hydraulic model data.

7. References

1. O. Krogh, K. J. Dahl-Madsen, E. Gargas, H. Schrøder, "A Numerical Model of Oxygen Conditions in a Two-Layered Marine Environment", Proc. Int. Conf. on Water Resources Engineering, Bangkok 1978, p. 3 - 26.
2. W. Hansen, "Hydrodynamical Methods Applied to Oceanographic Problems", Mitt. Inst. Meereskunde, Univ. Hamburg 7, 1967.
3. J. J. Leendertse, "Aspects of the Computational Model for Long-Period Water Waves Propagation", Rand Memorandum 5294, 1967.
4. J. Sündermann, "Die Hydrodynamisch-Numerische Berechnung der Vertikalstruktur von Bewegungsvorgängen in Kanälen und Becken", Mitt. Inst. Meereskunde Univ. Hamburg 19, 1971.
5. T. J. Simons, "Development of Threedimensional Numerical Models of Great Lakes", Canada Center for Inland Waters, Scientific Series 12, Burlington 1973.
6. Ströhmer, Wander, "Untersuchungen über den chemischen und biologischen Zustand über das Selbstreinigungsvermögen und über die Belastbarkeit des Ems-Ästuars", Bundesanstalt für Gewässerkunde, Koblenz 1976.
7. Vollmers, Ohlmeyer, "Modellversuche für die Umleitung der Ems", Teil 3 Salzgehaltsverteilung, Bundesanstalt für Wasserbau, Hamburg 1976.
8. K. Fischer, "Numerical Salinity Intrusion Models", Proc. Int. Conf. on Water Resources Engineering, Bangkok 1978, p. 209 - 218.

CHAPTER 175

A HYBRID MODEL OF THE ST. LAWRENCE RIVER ESTUARY

by

E.R. Funke* AND N.L. Crookshank**

INTRODUCTION

A hydraulic model of the St. Lawrence River Estuary described by Ploeg (1) had to be partially dismantled because of space requirements in the laboratory. In order to re-establish an upstream boundary for the simulation outside the zone of influence of proposed navigational improvements to the lower estuary, a numerical model of the dis-banded upstream river section was dynamically coupled to the remaining hydraulic model. This combination of a numerical and physical model running simultaneously and interactively is referred to as a hybrid model and operates similar to the one described by Holz (2). The implementation of this hybrid configuration was undertaken in part to re-activate the St. Lawrence model as well as to study the feasibility of this novel approach in preparation for more ambitious model studies.

HYBRID MODEL

The hybrid modelling concept described in this paper is illustrated in Fig. 1. Here, a physical and a numerical model are running simultaneously and interactively by exchanging information at their interface with the numerical model operating in the time domain of the physical model.

The physical or scale model of the river system is controlled at two boundaries by a computer. At each control-interval the downstream boundary is controlled on a known tidal elevation, while the upstream boundary is controlled on a calculated discharge supplied by the numerical model. The simulation is therefore extended upstream from the limit of the physical model to the upstream limit of the numerical model whose downstream boundary is in turn supplied from a measured tidal elevation in the physical model.

The exchange of information at the interface is synchronized by having the numerical model operate in the time domain of the physical model. This implies that the numerical model is the slave of the master physical model, waiting to supply and to receive information.

*Senior Research Officer and **Engineer, Hydraulics Laboratory, National Research Council of Canada, Ottawa, Canada, K1A 0R6.

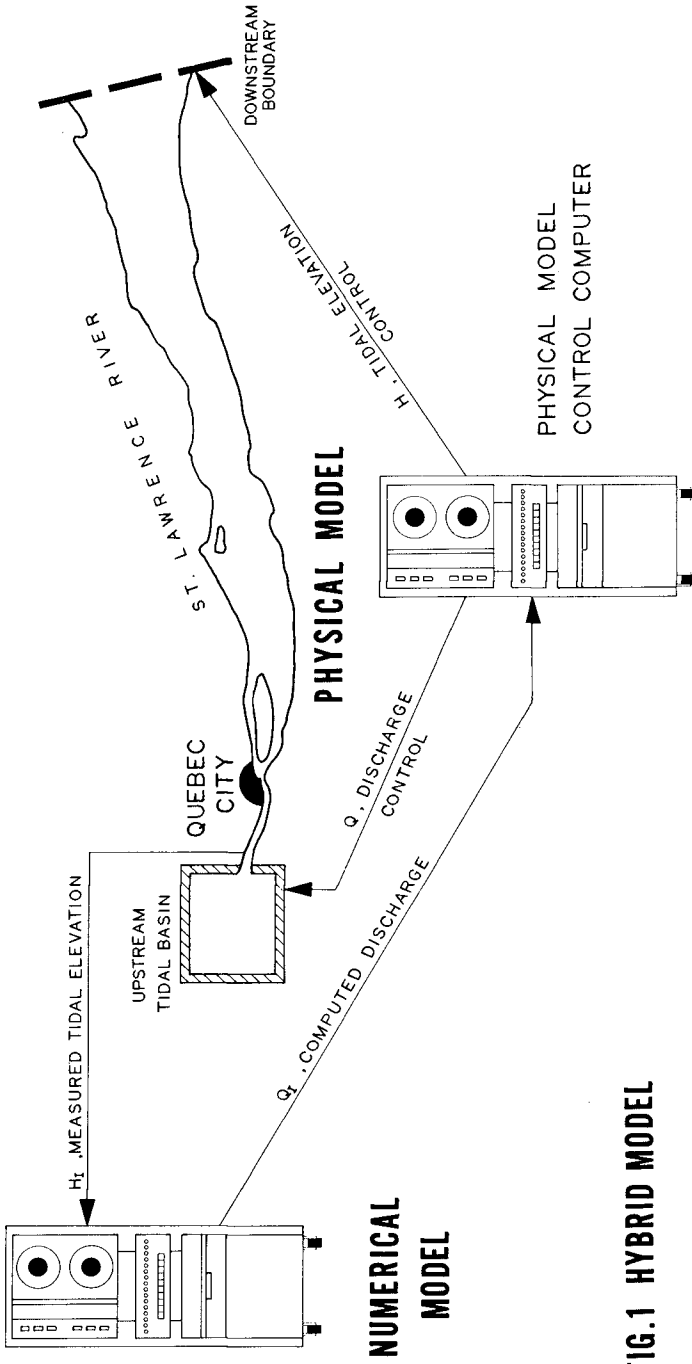


FIG.1 HYBRID MODEL

ST. LAWRENCE RIVER HYBRID MODEL

The original hydraulic model of the St. Lawrence River Estuary that had to be partially dismantled extended from Father Point in the lower estuary of the St. Lawrence River upstream to Montreal (Fig. 2). The section removed encompasses the stretch of river from Neuville to Montreal. In order to re-establish an independent upstream boundary for the simulation, a numerical model was formulated of this upstream portion of the river and was dynamically coupled to the remaining hydraulic model, Neuville to Father Point. The complete hybrid model therefore reproduces the tidal motion in the St. Lawrence River from Father Point to Montreal, a distance of 550 kilometers, leaving 330 kilometers simulated by the physical model, and 220 kilometers simulated by the numerical model.

At the downstream end of the hybrid model, the river itself is 47 kilometers wide with a depth of up to 300 meters. At Neuville, the coupling point of the two models, the width of the river is approximately 3 kilometers with a depth averaging 15 to 20 meters.

The tide entering the system at Father Point ranges from 1.5 to 4.5 meters in elevation with a maximum discharge of 2,000,000 cu m/sec. Propagating upstream, the tidal range peaks just downstream of Quebec City with ranges varying between 3.5 and 6.0 meters. This region also marks the limit of salt water penetration into the system. After Quebec City, the tide is attenuated rapidly by a narrow channel and increasing bed steepness. At Neuville, the coupling point, the tidal range is approximately 3 to 5 meters with the maximum discharge reaching 28,000 cu m/sec. At Montreal, no diurnal or semi-diurnal tidal components remain, leaving only a fresh water discharge averaging 7,000 cu m/sec.

PHYSICAL MODEL

The physical model, 165 meters in length, has a horizontal scale of 1:2000, and a vertical scale of 1:120. The downstream boundary is 23.5 meters wide and is connected to a bidirectional variable pitch impeller pump with a capacity of 1 cu m/sec. Computer control at this point follows a known vertical tide. The upstream boundary is discharge controlled by means of a fixed inflow into a 4 x 4 meter tidal basin and a variable outflow from this basin over a sharp edged 3 meter horizontal weir operating under computer control. The difference between basin inflow and outflow is the model discharge which is bidirectional and of the order of 0.02 cubic meter per second.

The data acquisition and control software is an advanced version of that described by Funke (3). The diur-

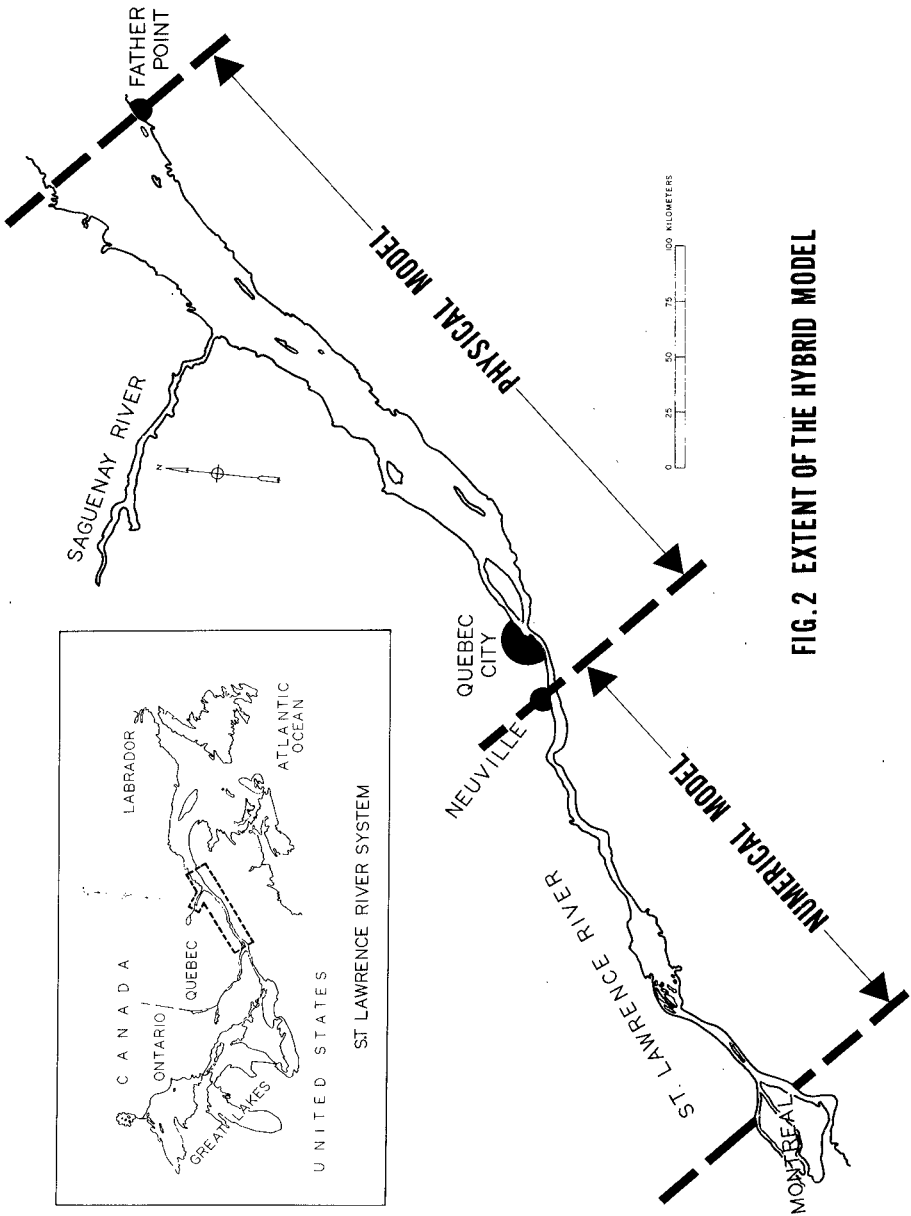


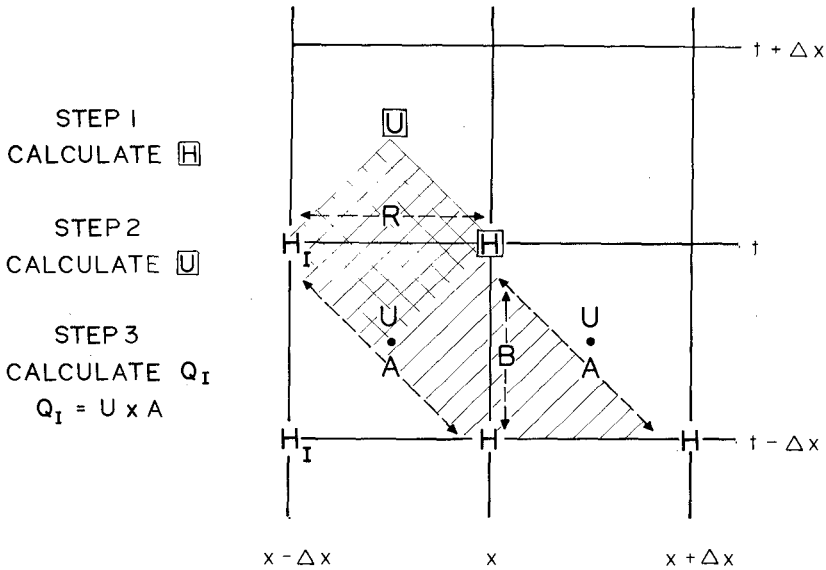
FIG. 2 EXTENT OF THE HYBRID MODEL

nal vertical tide and the pump control curve at the lower boundary are now harmonic recompositions of the Fourier coefficients for the specified tide and the control curve. This feature now makes it possible to generate 14 day tidal cycles including the injection of wind set-ups. The "controller", a computer subprogram dedicated to the generation of control signals to the actuators on the basis of measured differences between desired and actual values, is now implemented by means of a new error trajectory control algorithm which has proved more stable than the previously used three term controller. The sample interval is 1 second and a diurnal tide has a 490 second repetition period.

The on-line computer system and other hardware used for control and data acquisition on the physical model is also described by Funke (3). In addition, a second computer, an EAI Facer 1000 with 64 Kbytes of memory was added. This machine is similar to the control computer but slightly faster (1 second memory cycle time) and is dedicated to the numerical model. It therefore must run in parallel with the data acquisition and control computer. Both computers have access to several common peripherals including a serial data acquisition system. This analog to digital subsystem is a recently developed serial data link which carries the measurement data from distributed converter and transmitter stations along the model over a single wire loop to the computer centre, Ref. 4.

NUMERICAL MODEL

The numerical model, based on a one-dimensional explicit finite-difference solution of the shallow water wave equations, represents 220 kilometers of river by 58 sections of 3.2 and 4.8 kilometers. Inputs to this portion of the simulation are: upstream a constant discharge at Montreal and downstream a variable water elevation at Neuville as provided by a water level gauge on the hydraulic model. The numerical model in turn supplies an instantaneous discharge at Neuville which is returned to the control computer for the discharge control of the upper boundary. Since the hydraulic model dictates the time domain of the hybrid simulation, the solution time of the numerical model has to be synchronized to the hydraulic model. In order to reduce the time delay between the discharge computation and the discharge control, advantage is taken of the nature of the explicit solution which yields computed results after each finite distance step. A shore calculation is therefore performed to obtain the required discharge value at the lower boundary before proceeding upstream with the remainder of the calculations. This calculation is illustrated in Fig. 3.



Δx = DISTANCE INCREMENT

Δt = TIME INCREMENT

H = WATER ELEVATION

U = VELOCITY

H_I = WATER ELEVATION SUPPLIED BY PHYSICAL MODEL

Q_I = DISCHARGE SUPPLIED TO PHYSICAL MODEL

A = CROSS-SECTIONAL AREA

B = SURFACE BREADTH

R = HYDRAULIC RADIUS

**FIG. 3 CALCULATION OF Q_I
EXPLICIT FINITE-DIFFERENCE SCHEME**

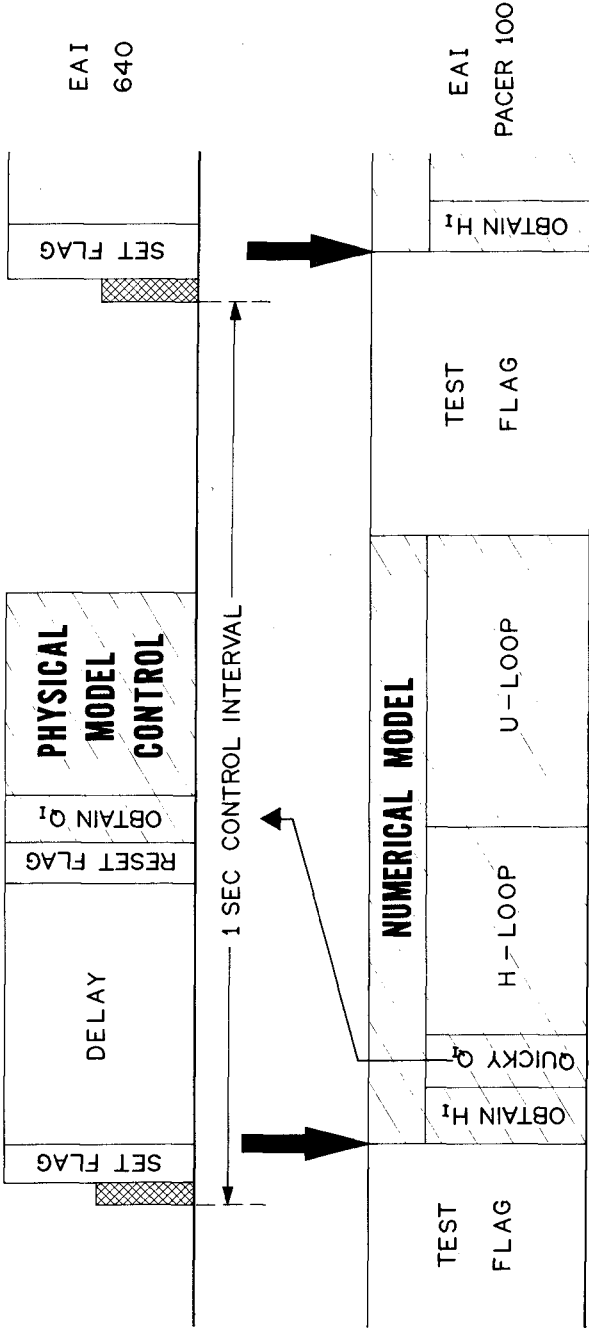
- Step (1): The water elevation immediately upstream from the boundary is calculated using the water elevation supplied from the physical model and previous numerical results. In a purely numerical model this H calculation would be repeated for each section of the river. However, in this case, before proceeding, steps (2) and (3) are executed.
- Step (2): The velocity at the interface is calculated using the just calculated water level and previous numerical results.
- Step (3): The required discharge (Q_I) is calculated, which can now be passed to the physical model.

The numerical model then continues by finishing up with the suspended water level calculations followed by the remainder of the velocity calculations.

DYNAMIC LINK

The computer to computer interface, which is used at this time, is not ideal because of the unavailability of the necessary bidirectional digital data link. Each of the two computers now relies upon the reading of analog signals to complete the data exchange between the models. A "handshake" arrangement is provided between the control computer and its slave, the dedicated numerical model processor. This is illustrated in Fig. 4.

At the start of each control interval, the control computer signals to its slave that the measured water elevation at Neuville is available. The slave is assumed to be in a standby position testing a flag at this time. On recognizing the signal, the slave samples the serial data acquisition system to obtain H_I , the interface water elevation and then computes Q_I , the discharge at the interface required for the physical model. The discharge is returned via the analog link to the control computer which was in a fixed delay state to allow for the data transfer. The control computer then proceeds with the generation of the two physical model control signals while the slave computer finishes the numerical model calculations and returns to its standby state.



H₁ = PHYSICAL MODEL WATER ELEVATION AT UPSTREAM BOUNDARY (HYBRID INTERFACE)
Q₁ = NUMERICAL MODEL DISCHARGE AT DOWNSTREAM BOUNDARY (HYBRID INTERFACE)

FIG.4 DYNAMIC LINK

PHYSICAL MODEL RESPONSE

In Fig. 5, the response of downstream boundary to the control signals is shown. At the downstream end of the model the boundary condition is provided by the known tidal elevation at Father Point, in this particular case the diurnal tide of June 22, 1967. The model was run by repeating this diurnal cycle and updating the control curve for the pump. For the first portion of the figure, without updating, there is considerable error between the actual and the desired tide as indicated by the error curve. However, once updating is initialized, the response of the model soon becomes quite satisfactory.

The upstream response of the physical model to the discharge curve provided by the numerical model for the same diurnal tide is shown in Fig. 6. The difference here is that no updating was necessary to obtain a satisfactory response. This can be explained from the fact that discharge control using weirs is inherently more stable than elevation control using pumps.

ANALYSIS OF RESULTS

A comparison of water elevations against recorded prototype values for two locations in the physical model immediately downstream of the coupling point is shown in Figs. 7 and 8. These stations are located in the area of prime interest during past investigations on the physical model.

Fig. 7 contains a comparison of results for St. Francois located 50 kilometers from the coupling point. The square points represent the actual prototype recorded values while the solid line shows the results from the physical model operated prior to dismantling the upper portion. The dashed line represents results from a numerical model run from Father Point to Montreal and finally the dotted line shows the output obtained from the hybrid model. Fig. 8 contains the results for Lauzon located 25 kilometers downstream of the coupling point.

From these two stations it is evident that the hybrid model results show an improvement on the numerical model while not showing the same degree of accuracy as obtained from the stand alone physical model. How can this be explained? It should be noted that:

- 1) the original physical model was very carefully calibrated and verified;
- 2) the numerical model used for coupling was not calibrated or verified to anywhere near the same degree of accuracy;

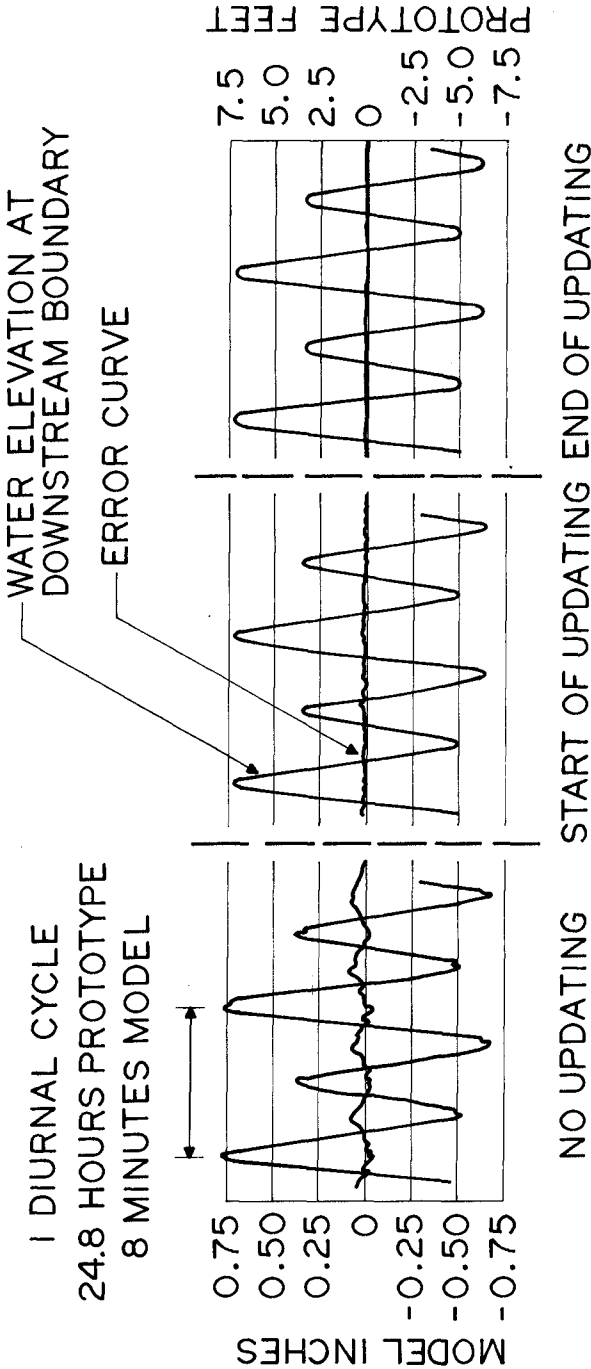
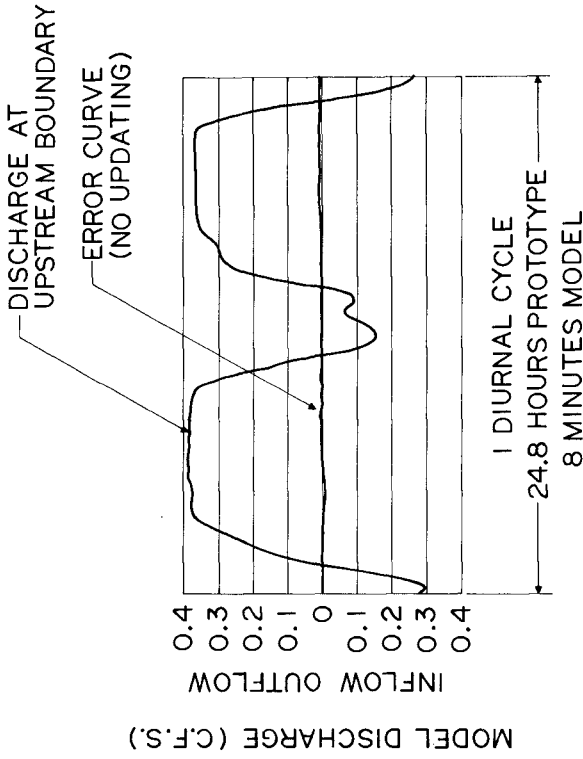


FIG.5 DOWNSTREAM PHYSICAL MODEL RESPONSE
TO CALIBRATION TIDE (22 JUNE, 1967)



TOTAL MODEL DISCHARGE = $4.18 \cdot 10^{10}$ CU.FT. (PROTOTYPE) OUTFLOW

TOTAL PROTOTYPE DISCHARGE = $4.29 \cdot 10^{10}$ CU.FT. (PROTOTYPE) OUTFLOW

FIG.6 UPSTREAM PHYSICAL MODEL RESPONSE TO DISCHARGE CURVE FROM NUMERICAL MODEL

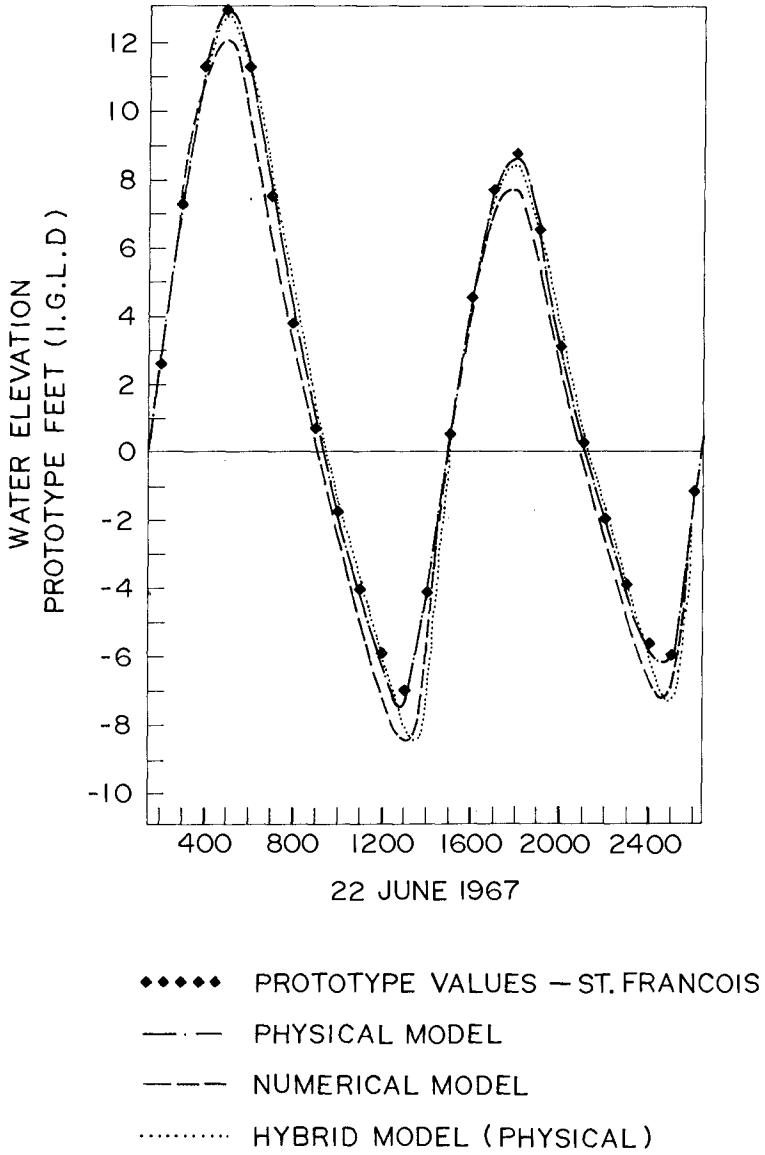
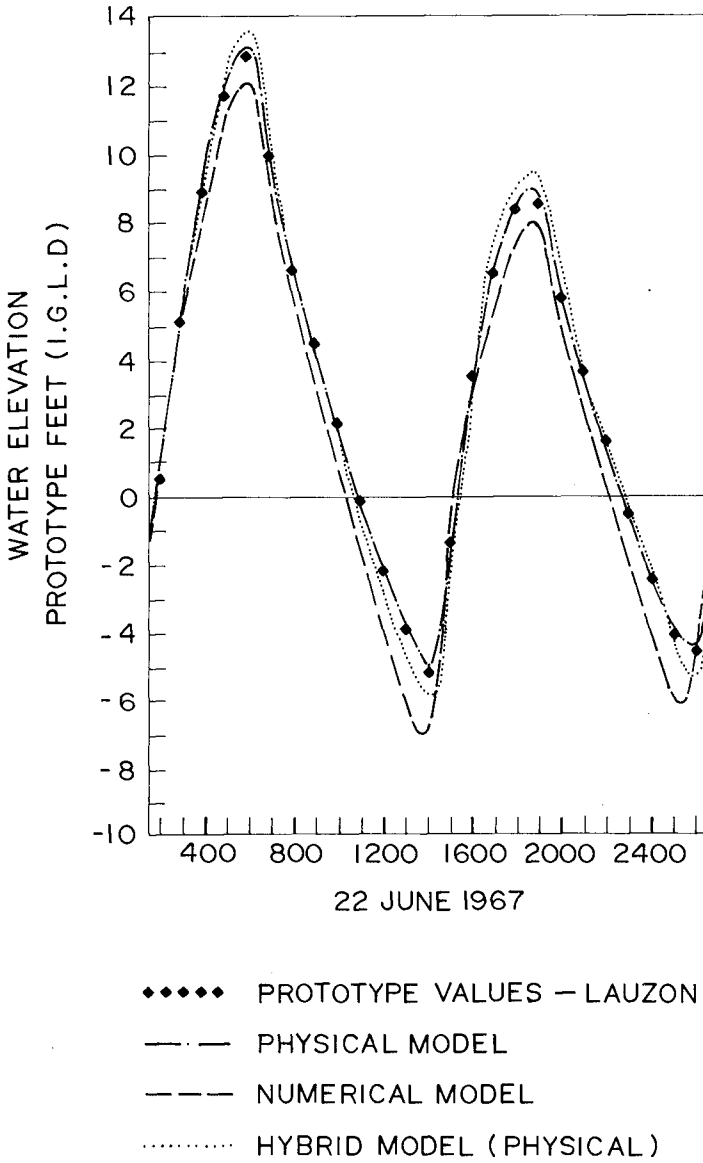


FIG. 7

**FIG.8**

- 3) the physical model has been inoperative for several years;
- 4) no attempt was made to calibrate the combined hybrid model.

Taking these points into consideration, the results are acceptable at this stage in the development of the hybrid model. With additional effort put into a new calibration it could be expected to obtain the same degree of accuracy as the previous physical model.

CONCLUSIONS

The following conclusions have been reached:

- 1) hybrid models are both technically and economically practical, providing a new way to extend the boundaries of a physical model to regions uninfluenced by proposed changes in the model. This would in many cases allow a larger scale to be used for the construction of the model, further exploiting the advantages of a physical model in investigating three-dimensionally complex flow patterns.
- 2) for other applications where more extensive numerical modelling would be required, time constraints would require considerably more computing power. This especially would be true if two-dimensional numerical models were necessary. The one-dimensional model used for the St. Lawrence, fully loaded existing facilities.
- 3) improved discharge control machinery would be necessary to operate two-dimensional hybrid interface control.

With these points taken into consideration, the following developments are under way in the laboratory:

- 1) to increase existing computing capacity for hybrid modelling, an HP 1000 computing system with 256 Kbytes of memory as well as a Floating Point Systems AP120B array processor have been purchased.
- 2) to achieve better control between physical and numerical models, development is under way of improved control machinery for multi-directional flow control which may be used to provide multi-point boundary control for two-dimensional models.

REFERENCES

- 1) Ploeg, J., "Comprehensive Tidal Study of the St. Lawrence River", 11th International Coastal Engineering Conference, September 1968, London, U.K.
- 2) Holz, K.P., "Analysis of Time Conditions for Hybrid Tidal Models", 15th Coastal Engineering Conference, July 1976, Honolulu, Hawaii.
- 3) Funke, E.R., "Computer Control of a Tidal Model", National Research Council DME Report MH-110, December 1972.
- 4) Wiegert, A.W. and Funke, E.R., "A Distributed Bidirectional Serial Data Acquisition System", National Research Council, Hydraulics Laboratory Report, LTR-HY-66.
- 5) Prandle, D.L. and Crookshank, N.L., "Numerical Model Studies of the St. Lawrence River", National Research Council DME Report MH-109, July 1972.

CHAPTER 176

FIELD DATA ANALYSIS FOR CHESAPEAKE BAY MODEL VERIFICATION

by

Ronald E. Nece¹ and Norman W. Scheffner²

INTRODUCTION

Chesapeake Bay is located on the eastern coastline of the United States. The bay and its tributaries form a large estuarine system having a surface area of about 11,400 sq km and reaching approximately 320 km northward from its mouth at the Atlantic Ocean to the mouth of the Susquehanna River, its primary inflow. The bay is a major shipping artery, with major ports at Norfolk-Hampton Roads and Baltimore; it also supports an extensive seafood industry, and serves as a tourist and recreation area for the 8 million-plus population in adjoining states. The need for addressing the complexities apparent in present and future management of the water resources of Chesapeake Bay was reflected in Section 312 of the River and Harbor Act of 1965 which directed the Corps of Engineers to undertake a complete investigation of water use and control of the Chesapeake Bay basin. A physical hydraulic model of the bay was specified as a major part of the study.

The maximum width of the bay is approximately 50 km, the mean depth of the bay proper is less than 8.5 m, and the maximum local depth is 53 m. Currents and salinities in the generally shallow, partially mixed estuary are strongly influenced by winds in addition to tides and to time-variable freshwater inflows from the drainage basin of approximately 166,000 sq km. The large size of the actual estuary ruled out the possibility of obtaining synoptic prototype data of sufficiently fine-grained detail against which to verify the recently constructed Chesapeake Bay model. This paper presents the procedures used in an initial treatment of the prototype data.

Consideration is given to two objectives in the treatment of the field data for purposes of model verification. First, the proper quasi-steady tide-freshwater inflow-boundary salinity combination for the bay was sought so that the long-term average salinity distribution could be obtained to provide a basis of comparison for no-wind verification tests

-
1. Professor of Civil Engineering, University of Washington, Seattle, Washington, U.S.A.
 2. Chief, Data Analysis Section, U.S. Army Engineer Waterways Experiment Station, Chesapeake Bay Model Project, Stevensville, Maryland, U.S.A.

on the physical model and which would be compatible with the management tool purposes of the model. The proper combination of inflow hydrographs and tides was necessary in order to obtain representative seasonal salinity distributions. In particular, procedures used to eliminate effects of low-frequency, non-astronomical energy associated with wind fields over the bay are discussed.

The limits of the area modeled are delineated in Figure 1. The distorted fixed-bed model has horizontal and vertical scale ratios of 1:1000 and 1:100, respectively. Tidal boundary conditions are provided at the Atlantic Ocean and at the Chesapeake and Delaware (C & D) Canal, a sea-level connection to Delaware Bay.

FIELD DATA PROGRAM

Prototype tidal height data collection was accomplished primarily by the United States National Ocean Survey (NOS). Tide gages covering the main bay and its tributaries were located at 75 stations indicated in Figure 2. Sampling began in 1970 and continued into 1974, with the majority of the data collected in 1971 and 1972. The time span for which data were obtained at each station is shown in Figure 3. The scale of the figure here precludes station identification and precise times of data collection; significant is the obvious shortage of synoptic tidal height data. The data were reduced by NOS and transferred to magnetic tape; tidal heights were given to the nearest 0.01 - ft and recorded in time increments of 30 minutes. In addition to the raw field data, NOS also provided harmonic analyses of tidal records at a number of stations. A 365-day analysis was performed at 49 stations where adequate records were available, and four 29-day analyses were performed at 16 other stations where the data sampled represented the seasonal variations of the tidal constituents; 37-constituent analyses were performed for the 365-day analyses.

Current velocity and salinity data were obtained through a joint effort of the Chesapeake Bay Institute (CBI, of Johns Hopkins University), the Chesapeake Biological Laboratory (University of Maryland) and the Virginia Institute of Marine Science (VIMS). The current and salinity data were generally taken concurrently. Velocity data were taken at a total of 770 sampling locations distributed over 205 stations; the number of depths at which data were taken varied from one for shallow areas to a maximum of 12 for deep-water stations. Three reports each were issued by VIMS and CBI concerning the data collection procedures; details on sampling in the main bay are given in representative References 1 and 2. Velocity-salinity ranges having more than one station are shown in Figure 4, where the number of stations is shown for each of these ranges. There were 8 main bay ranges, with range CB-00 (9 stations) at the mouth to range CB-07 (5 stations) north of Baltimore. Ranges (composed of one or more stations) or individual stations were established on 34 separate rivers or sub-bays, with the emphasis on the larger rivers entering Chesapeake Bay on its western shore. In order proceeding up the bay, the number of ranges or single stations on these rivers were: James, 8; York, 7; Rappahannock, 10; Potomac, 13; Patuxent, 7. Sampling times on

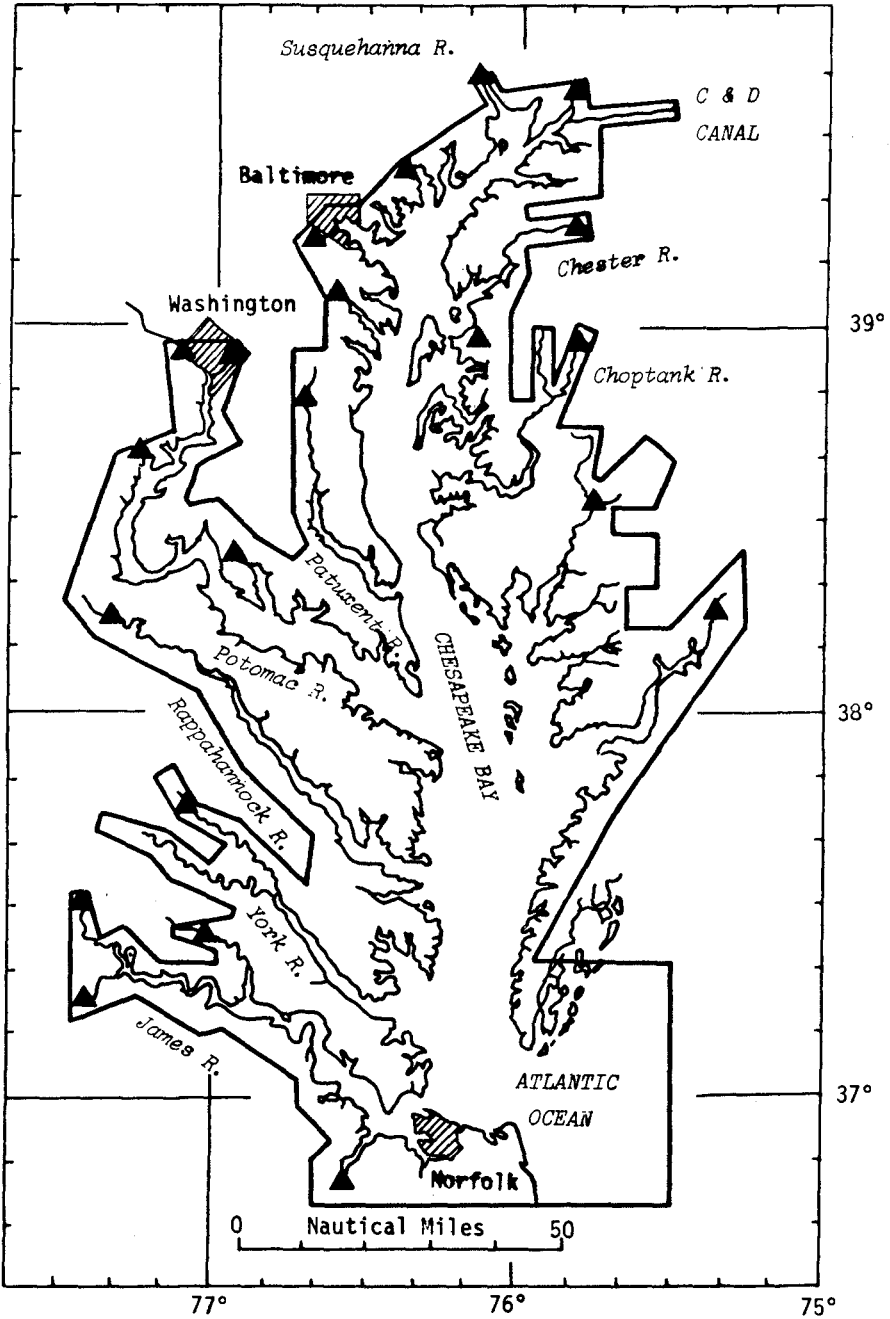


Figure 1. Model limits and freshwater inflow points.

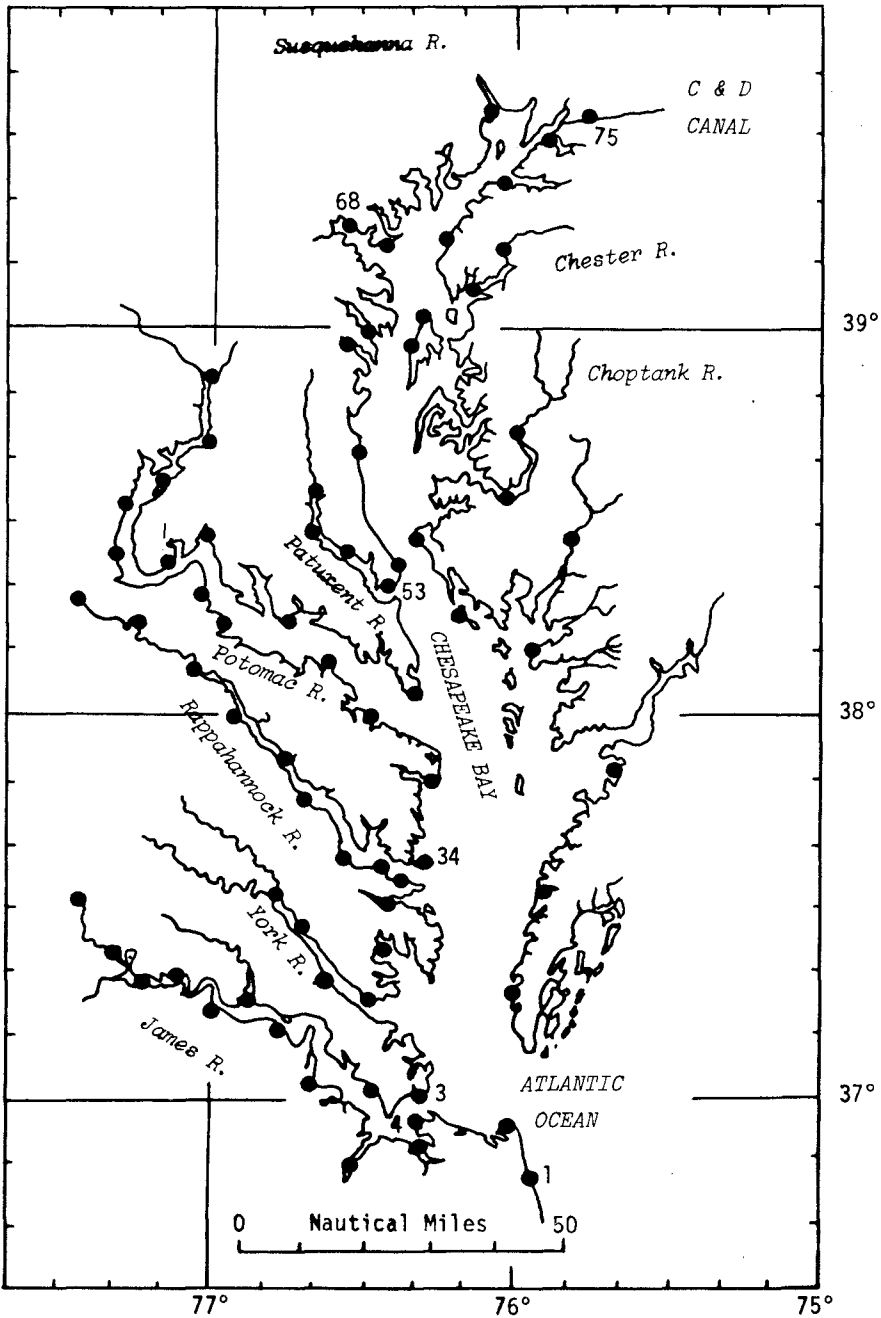


Figure 2. Prototype tide station locations.

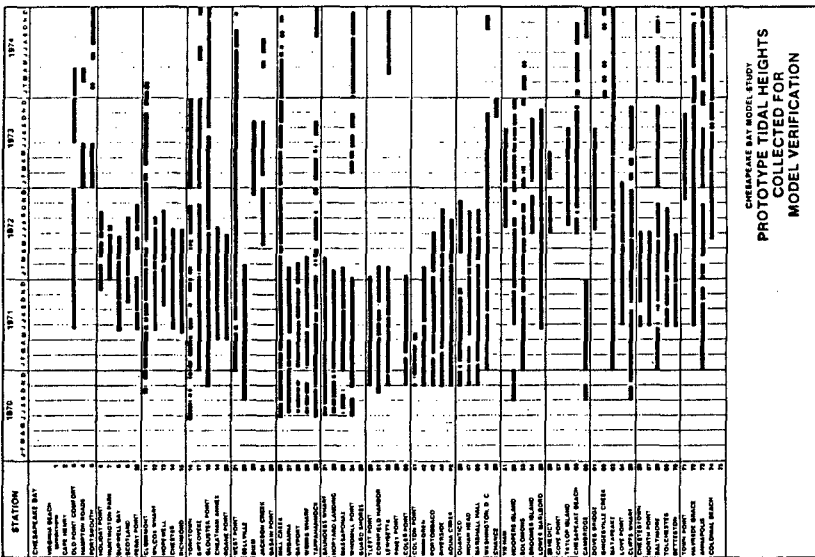
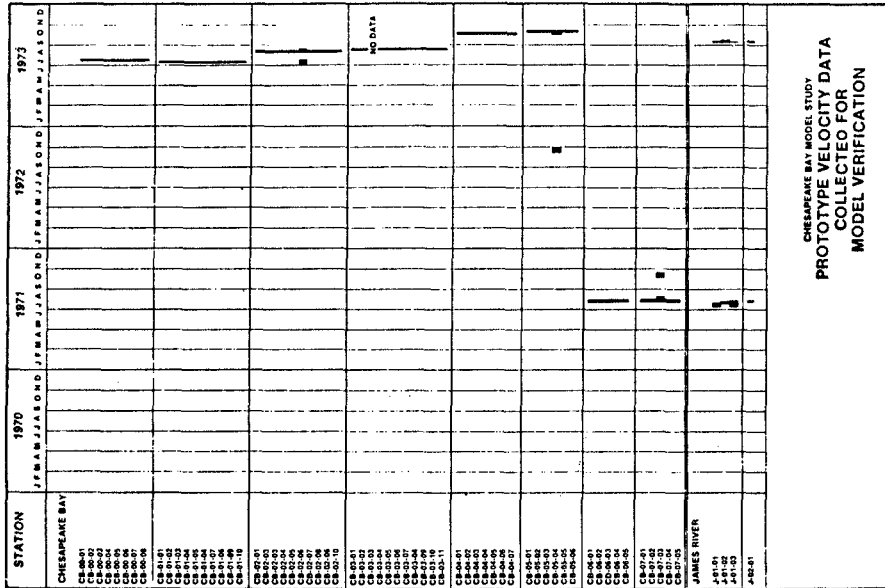


Figure 3. Periods of prototype tide records, and representative velocity sampling periods.

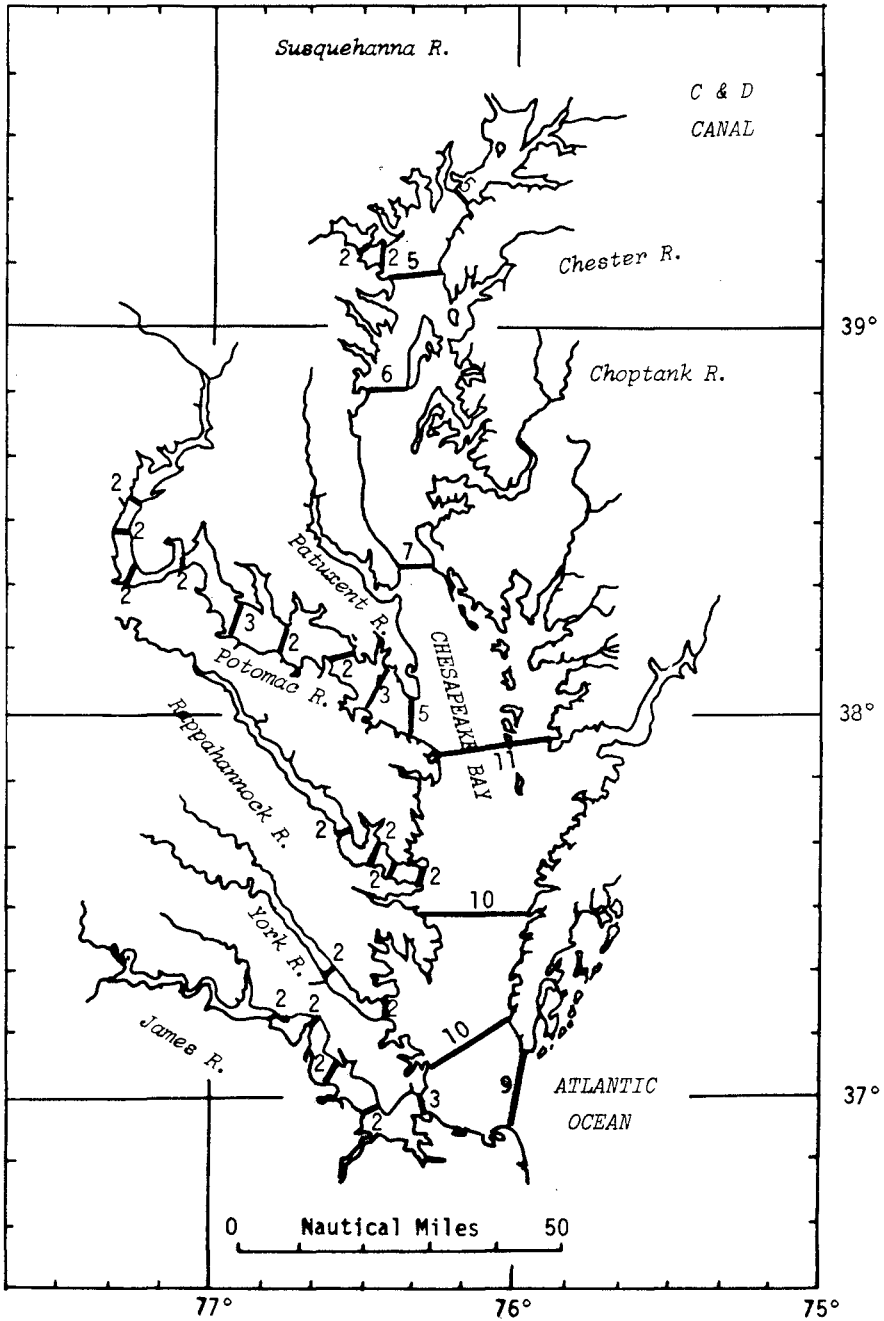


Figure 4. Prototype velocity - salinity ranges.

the main bay ranges are given in Figure 3.

Data were taken in 3-day or, more commonly, 5-day periods of record. Velocity magnitudes and directions were obtained using recording current meters. Velocity data were generally taken continuously at 10-, 20-, or 30-minute intervals. Salinity measurements were obtained with various in situ conductivity-temperature probes and also by laboratory analyses of water samples. All results were transferred to magnetic tapes for analysis. Sampling for salinities was done during 13-hour ('daylight') periods during the deployments at the respective stations. In addition, some slack salinity runs were conducted each month from January 1971 through December 1972 along the main channel of the bay to the upper limit of intrusion of sea-derived salinity (1).

Wind data were provided at 21 different stations located in various parts of the bay; 3 stations, distributed along the main axis of the bay, had daily observations for the complete period 1970-1973.

Relationships between freshwater inflows were based upon analyses performed by the Baltimore District, Corps of Engineers, on records for 70 U.S. Geological Survey stream gages during the water years 1969, 1970, 1971, and 1973. (The 1972 water year covered the effects of run-off from tropical storm Agnes, June 1972). Run-off from 126 drainage areas was consolidated for model purposes into the 21 discrete inflow points, shown on Figure 1. The average flow of the Susquehanna River (approximately $1,100 \text{ m}^3/\text{s}$) accounts for about one-half of the total run-off into the Chesapeake Bay.

TIDES

Various studies of Chesapeake Bay have revealed the existence of significant amounts of tidal energy associated with non-astronomical periods. Early spectral analysis performed at the U.S. Army Engineer Waterways Experiment Station (WES) on the field data taken for the Chesapeake Bay model project indicated a significant amount of tidal energy having a period of approximately 100 hours. Another more recent study of this non-tidal variability in Chesapeake Bay has been reported by Wang and Elliott (3). Their study revealed that non-tidal sea level fluctuations in the bay occurred at three dominant periods: 20, 5, and 2.5 days. The 20-day fluctuations originated from changes of sea level at the Atlantic coast (mouth of the bay) which had been generated by alongshore winds. The 5-day fluctuations were the result of non-local forcing due to the coastal sea level changes and local forcing due to lateral winds (Ekman effect) over the bay. The 2.5-day fluctuations were seiche oscillations forced by longitudinal winds over the bay; these fluctuations did not respond to the sea level changes at the coast.

Wind data studied in connection with the model project indicated that wind fields causing the above fluctuations tend to be fairly uniform over the area of the bay.

Because of the problems associated with this low frequency non-astronomical tide energy, it was decided that one of the approaches to

model verification would be to use only the M_2 tidal component. This method of M_2 verification, which eliminates low frequency wind effects as well as other long term effects, has been tested at WES in several physical models of estuaries and has been found to be satisfactory for initial verification. A number of reasons supporting this approach in the Chesapeake Bay study are listed below.

Tides in the Chesapeake Bay are more regular and semi-diurnal than they are mixed (4). Further, the double amplitude of the M_2 constituent as determined from the NOS harmonic analyses of prototype data for the model was, for almost all tide stations used, equal to more than 0.9 of the mean tide range for each respective station.

Most of the energy in the "semi-diurnal" tidal constituent frequencies is contained in the M_2 frequency. Table 1 lists the amplitudes of the 12 "semi-diurnal" constituents at three stations identified on Figure 2; the values are taken from the NOS 365-day harmonic analyses. Also shown are the mean ranges at the respective stations (4); the ratio of M_2 double amplitude to mean range at Station 68 (Baltimore) is the lowest of any station along the main bay.

Table 1

Amplitudes of "Semi-Diurnal" Tide Constituents at Selected Stations in Chesapeake Bay

Constituent	Angular Vel. Degrees/Hour	Amplitude, Feet		
		Sta. 3	Sta. 34	Sta. 68
M_2	28.9841	1.188	0.552	0.486
N_2	28.4397	0.230	0.119	0.104
S_2	30.0000	0.265	0.105	0.082
v_2	28.5126	0.051	0.028	0.023
L_2	29.5285	0.033	0.019	0.027
K_2	30.0821	0.059	0.032	0.031
μ_2	27.9682	0.041	0.015	0.006
$(2N)_2$	27.8954	0.032	0.013	0.012
λ_2	29.4556	0.023	0.003	0.013
T_2	29.9589	0.011	0.011	0.008
R_2	30.0411	0.003	0.001	0.008
$(2SM)_2$	31.0159	0.009	0.003	0.003
Mean Range		2.5	1.1	1.1

A pragmatic reason for using the procedure was that the ocean station providing source tide data was not available during the prototype data collection period; station 1 (Figure 2) was damaged by storms, and produced no data during the 1970-1974 period (Figure 3). Station 3 was then selected for source tide control in the initial verification tests.

As noted tidal data series were collected at non-concurrent times. However, the 365-day harmonic analysis at each of 49 stations provided an M_2 tidal amplitude and epoch which could be used to construct an M_2 tide for verification.

$$h_t = H_o + a \cos \left(\frac{2\pi\omega t}{360} - \frac{2\pi\epsilon}{360} \right) \quad (1)$$

where: h_t = M_2 tide height at any time t
 H_o = mean height above reference datum
 a = M_2 amplitude
 ω = M_2 constituent angular velocity ($^\circ$ /hr)
 ϵ = phase angle in degrees measured from equilibrium tide passing Greenwich at 0 hr GMT(epoch)
 t = time.

This procedure then provided tidal height data and phase relationships (times of arrival) for use in model verification without having to rely on the raw prototype data contaminated by wind effects which could not be reproduced in the model.

CURRENT VELOCITIES

The determination of an M_2 velocity from raw prototype data to be used in verification was not as straight forward as that of tidal heights. The difficulty was in eliminating wind contamination effects and extracting an M_2 velocity constituent from the non-synoptic current measurement series which were of 3-day or (usually) 5-day duration. The major problem was posed by the short length of the data series.

An initial effort was to apply a 144 point symmetric, non-recursive digital filter to the raw velocity data; the band pass filter was designed to retain only that semidiurnal portion of the signal having a period of between 11 and 14 hours. The time increment used corresponded to that of the data for each station. The set of 144 Fourier expansion coefficients so obtained were applied to the raw data series to obtain a filtered velocity as a function of time over the entire 3-day or 5-day sampling interval. A typical comparison of the filtered velocity so derived and the original raw data is shown in the top set of curves on the Figure 5; the data station is the most southerly on the velocity/salinity range at the bay mouth. The filtered velocity magnitudes are seen to be too large. Although this filtering process worked well with the smoother, longer tidal height data, the field velocity data were too choppy and the data series too short for good analysis. Because this procedure was not carried out further, details are not presented here.

A three-constituent harmonic analysis was performed on the

Velocities at CB-00-01, Depth = 3 Ft.

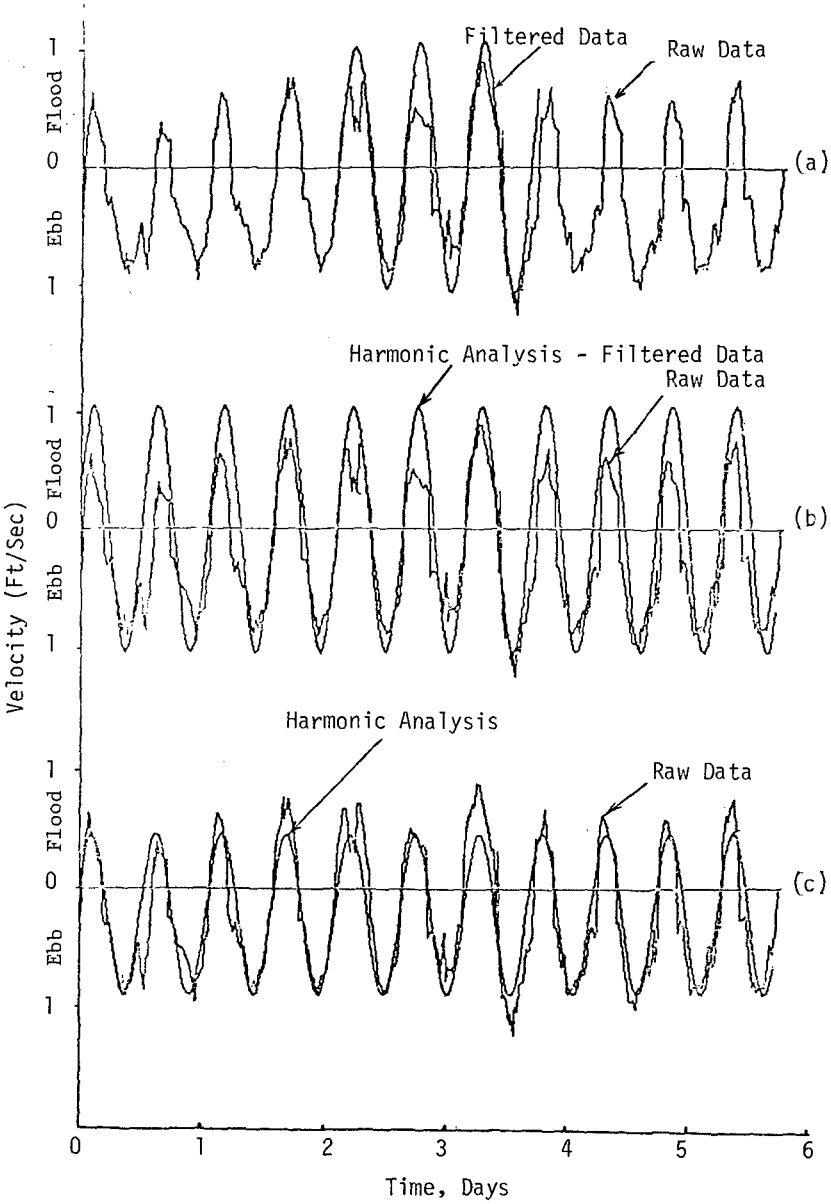


Figure 5. Sample prototype velocity data vs. results obtained by various analysis procedures (see text for details).

filtered, semi-diurnal velocity data to attempt the separation of the M_2 , N_2 and S_2 constituents. This was unsuccessful because the least squares solution to the harmonic analysis becomes unstable when the attempt is made to separate three constituents of nearly the same period from a short data record. Therefore, a one-constituent harmonic analysis (M_2 only) was applied to the filtered velocity data. This technique yields an M_2 amplitude which contains both the N_2 and the S_2 constituents, and retains the large amplitudes of the filtered data. The middle diagram on Figure 5 shows that the calculated velocity amplitudes are considerably larger than the raw data velocity amplitudes.

A single-constituent (M_2) harmonic analysis was then applied directly to the raw velocity data. The results of this least squares cosine curve fit, shown in the bottom diagram of Figure 5, produce a velocity curve which comes closer in amplitude to fitting the raw data than does the filtering processes described above. Since the curve resulting from the one-constituent harmonic analysis comes close to following the raw data, it evidently reflects many other astronomical constituents than just the M_2 . Therefore, a slightly different approach was used to separate the M_2 velocity amplitude from the results of the harmonic analysis. All of the approaches described above gave essentially the same M_2 phase angle value; therefore, the phase angle value resulting from the one-constituent analysis of the raw data was considered to be the valid M_2 constituent phase angle for velocity in the M_2 verification process.

Two factors led to the choice of procedure described below. Tide and current data at nearby stations were not synoptic, and gaps in the records prevented complete dependence on field data only. Consequently, an harmonic analysis using 12 major diurnal and semi-diurnal constituents (including the first six constituents listed in Table 1) was applied to a 2-month record of tidal data obtained at centrally located Station 53 (Figure 2) beginning June 1, 1971. The resulting individual constituent amplitudes and epochs were then used to synthesize a tidal record at Station 53 for approximately 2 1/2 years based on the relationship:

$$h_t = \sum_{n=1}^{12} a_n \cos \left(\frac{2\pi\omega_n t}{360} - \frac{2\pi\epsilon_n}{360} \right) \quad (2)$$

where: h_t = synthesized tidal height at time t
 a_n = nth constituent amplitude
 ω_n = nth constituent angular velocity ($^\circ$ /hr)
 ϵ_n = nth constituent epoch
 t = time

A 5-day one-constituent (M_2) harmonic analysis was then used on the synthesized series of data beginning on June 1, 1971, and leap-frogged every 12 hours. For example, at 0.5-hour intervals, there are 240 data points in 5 days, and harmonic analyses were run using points 1-240, 25-264, 49-288, etc., until the 2 1/2 year period was spanned. This resulted in a least squares cosine curve best fit yielding an M_2 tidal amplitude and phase angle for each 5-day data series beginning at time zero and then at each successive 12-hour time increment.

The common long wave assumption was then made that tidal amplitudes are proportional to the amplitudes of resulting tidal currents. (As a side comment, Hicks (5) has shown that Chesapeake Bay is long enough to contain just more than one complete tidal wave, and that the tide behavior in the lower and part of the middle bay is that of a long wave of translation).

The following relation was then used to relate the long term velocity and tidal height amplitudes to the corresponding velocity and tidal height amplitudes associated with the short 3-5 day period of record.

$$\frac{H}{h} = \frac{V}{v}$$

where: H = long-term M_2 component tidal amplitude.
 h = short-term M_2 tidal amplitude, derived from one constituent harmonic analysis (least squares best fit) of 5-day segment of the 2 1/2 year synthesized tide.
 V = long-term M_2 component velocity amplitude (to be used in verification)
 v = short-term M_2 component velocity amplitude derived from one constituent harmonic analysis of the 3-5 day raw data series.

In the above, H is the M_2 tidal amplitude obtained from the NOS 365-day harmonic analysis; h will not equal H because of the short period (5-day) portion of the synthesized tide from which the former was obtained. In this procedure, both h and v are obtained from comparable, short data series by least squares best fits of cosine curves, yielding phase angles, as well as amplitudes; the phase relationships for M_2 velocities V are thus established.

Results of this procedure are demonstrated in Figure 6. The upper diagram illustrates the variation of the multiplier H/h (by which v must be multiplied to obtain V for a 5-day period beginning on the date and time given in 12-hour increments on the abscissa) with time at Station 53. The curve designated as "Synthesized" was obtained as outlined above; the curve marked as "Prototype Data" was obtained using the actual prototype tidal height series instead of the 2 1/2-year synthesized tidal series at the station. The comparison indicates the general validity of the procedure.

The lower diagram in Figure 6 indicates how the H/h multiplier derived for the synthesized tide at Station 53 compared with the multiplier obtained from analysis of the raw prototype data at Station 34 for comparable times. The diagram provides an indirect indication that different sections of the bay respond in a comparable way to wind fields over the bay. Similar results were obtained for other locations in the bay, with good agreement between the multipliers based on the Station 53 synthesized tide and prototype tide data at the respective stations. Therefore, it was concluded that the H/h multiplier based on the synthesized tide at Station 53 could be used to obtain the M_2 velocity amplitude at the various stations and times corresponding to velocity data collection

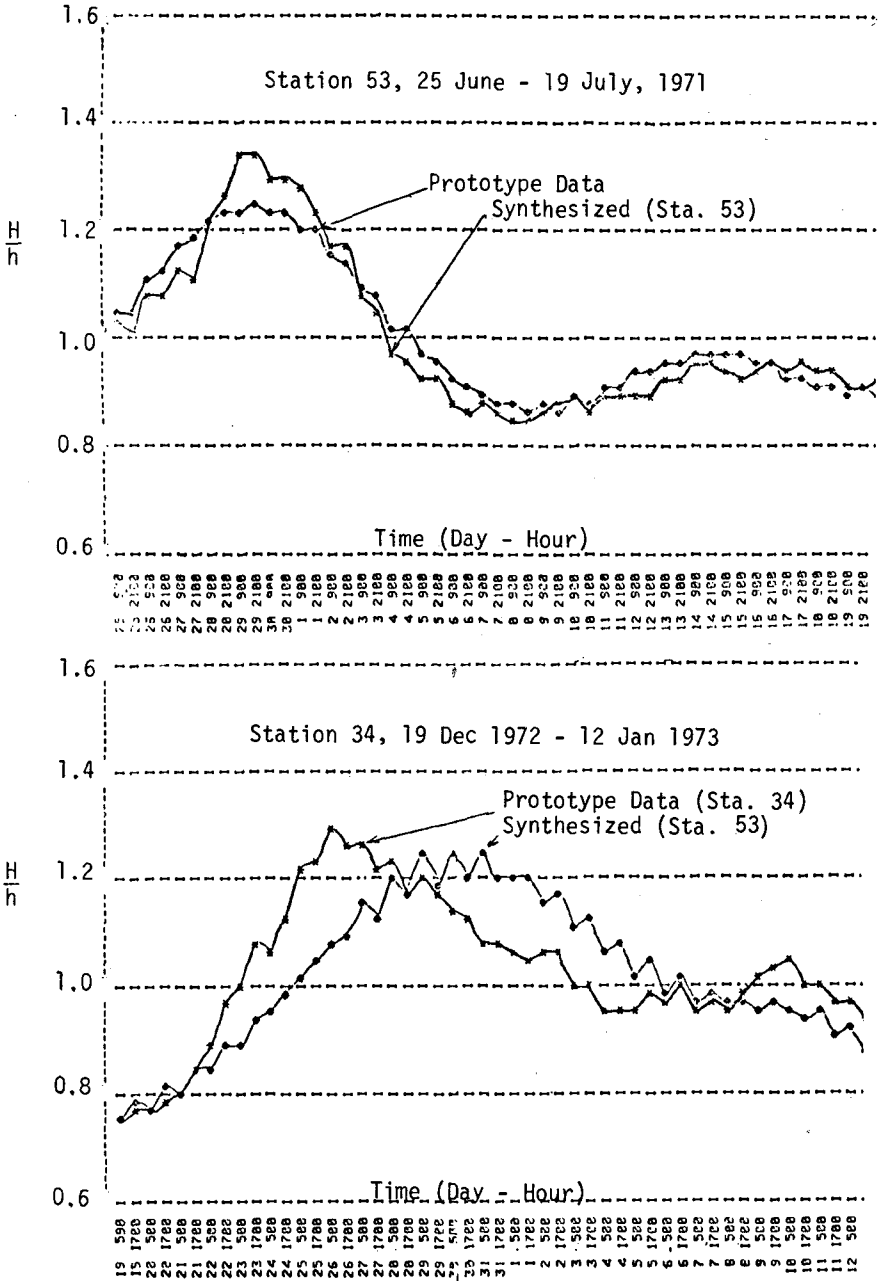


Figure 6. Prototype H/h values vs. H/h values derived from synthesized tide, Station 53.

periods at all stations.

SALINITY

Salinity data obtained as part of the prototype velocity-salinity program were too fragmentary to be of use for model verification. The same-slack salinity data taken at 12 stations along the longitudinal axis of the bay during the 2-year period 1971-1972 were of more value, although they were limited to the main bay only and because the only stations occupied were along the bay axis the transverse variations in salinity associated with the combination of Coriolis effects and predominate freshwater inflows from the western shore were not incorporated. A further problem related to the use of these data was that tropical storm Agnes occurred in June, 1972, and the "normal" summer salinity structure in the bay was not reestablished until approximately 100 days after the storm (6). Average salinity values based on the 1971-1972 same slack data were lower than long-term average values.

Salinity values selected for verification purposes were based upon results obtained by CBI over the period 1949-1961 (7). These data, taken on a total of 27 cruises during the stated period, are summarized in graphical presentations of four seasonal average salinity and temperature distributions over the Chesapeake Bay system. Specifically, charts of seasonal isohalines were presented for discrete depths. Figure 7 shows the seasonal average surface salinities for spring and autumn; these two sample plots show the range in seasonal salinities in the bay.

The long-term CBI salinity data (7) were reduced for model study use by the following process. At each prototype-model salinity station, values of the salinity were estimated by visual interpolation between isohalines on the CBI plots containing values for 6 different depths for each of 4 seasons. Salinity values obtained at each depth for each station for the 4 seasons were averaged, and the high and low values were recorded. The average values provide the basis of comparison for long-term model tests and for quasi-steady state tests using constant freshwater inflows and repetitive M_2 source tides. The lower drawing in Figure 8 shows the average salinity profile along the bay axis transect indicated in the upper drawing.

The spring and autumn salinities provided the limits anticipated when the model would be operated with seasonally varying freshwater inflows. The hydrograph employed was a two-year 'average' hydrograph; model tides at both the Atlantic Ocean and the C & D Canal were synthesized 16-constituent tides with repetitive 28-day cycles.

CONCLUSIONS

The methods employed in utilizing prototype data for verification of the Chesapeake Bay Model generally were not new individually, but were employed in the aggregate in order to best adapt the extensive, costly, and highly non-synoptic data over a large geographic area to a physical model incapable of reproducing the complicated physics of the prototype.

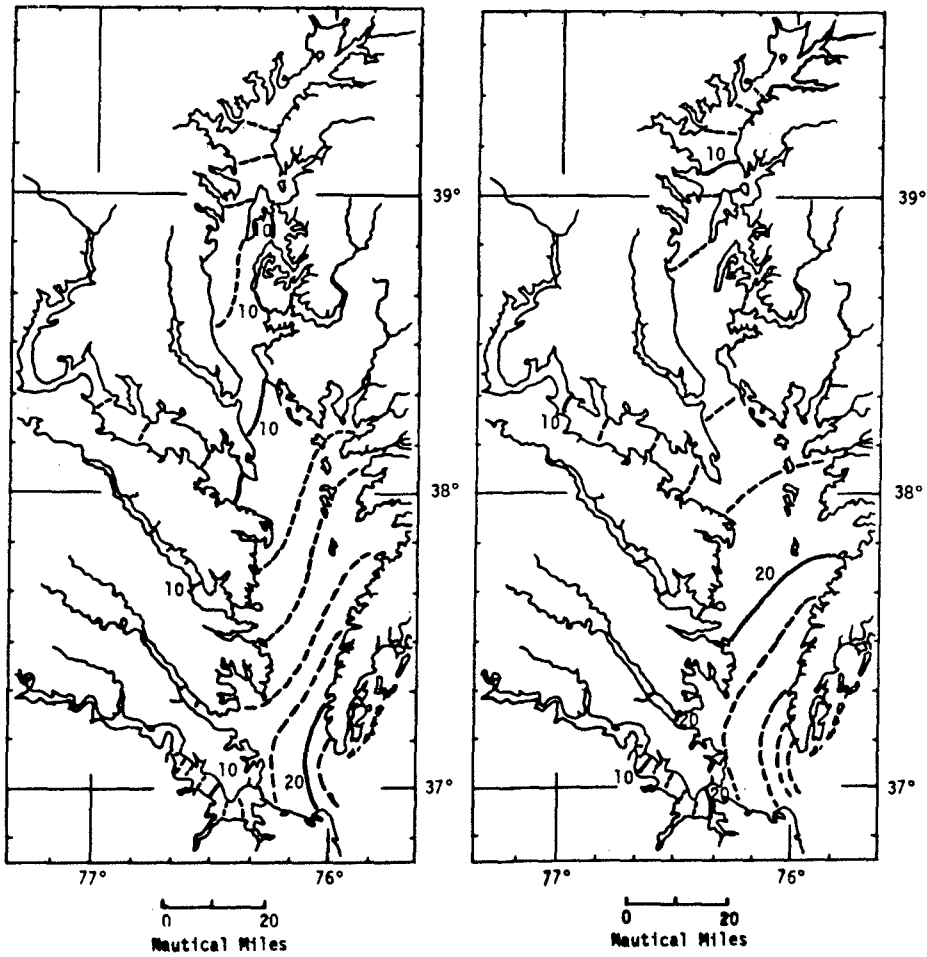


Figure 7. Long-term seasonal average surface salinities in Chesapeake Bay: left, spring; right, autumn.

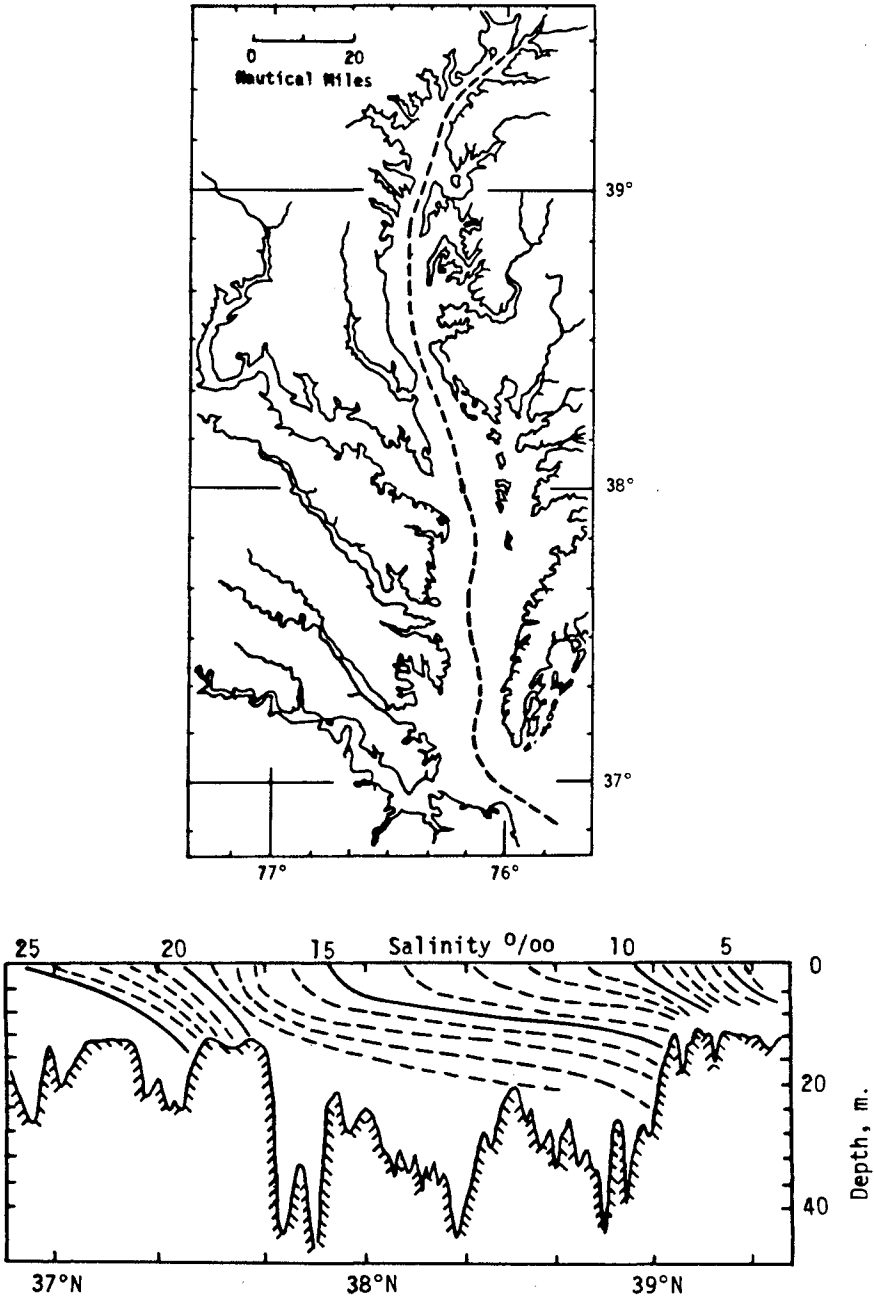


Figure 8. Long-term average salinity profile, Chesapeake Bay (lower) along bay axis (upper drawing).

The feasibility of verifying a physical hydraulic model by using tidal constituents, for example, has been demonstrated previously by Whalin et.al. (8). One of the recommendations (8) was that field experiments on the prototype should be designed to define the principal tidal constituents and their overtides for both the tidal elevation stations and the tidal velocity stations, with one month of record required as a minimum. Such a program is indeed possible for a prototype which is much smaller and simpler than Chesapeake Bay.

The questions to be asked of a model must be considered in the design of a field program mounted to provide prototype data for purposes of model verification. The fact that the salinity data taken specifically for this purpose could not be used points up the necessity for careful planning of field programs when these programs must, of necessity, be wide ranging and extensive. In addition, existing data must always be examined for possible use.

REFERENCES

1. Klepper, J.C., "A Report on the Prototype Current Velocity and Salinity Data Collected in the Upper Chesapeake Bay for the Chesapeake Bay Model Study", Chesapeake Bay Institute Special Report 27, Reference 72-12, December 1972.
2. Michael, J.A., "A Report on the Prototype Current Velocity and Salinity Data Collected in the Middle and Lower Chesapeake Bay for the Chesapeake Bay Model Study", Chesapeake Bay Institute Special Report 41, Reference 75-2, January 1975.
3. Wang, D.P. and A.J. Elliott, "Non-Tidal Variability in the Chesapeake Bay and Potomac River: Evidence for Non-Local Forcing", submitted to Journal of Physical Oceanography, March 1977.
4. "Tide Tables, East Coast of North and South America", United States Department of Commerce, National Oceanographic and Atmospheric Administration, National Ocean Survey, 1975.
5. Hicks, S.D., "Tidal Wave Characteristics of Chesapeake Bay", Chesapeake Science, 5, No. 3, pp. 103-113, Fall, 1964.
6. Hargis, W.J., "Studies of Certain Impacts of Tropical Storm Agnes on the Chesapeake Bay and its Tributaries", Virginia Institute of Marine Science report to National Oceanographic and Atmospheric Administration, August 1974.
7. Stroup, E.D. and R.J. Lynn, "Atlas of Salinity and Temperature Distribution in Chesapeake Bay 1952-1961 and Seasonal Averages 1941-1961", Chesapeake Bay Institute Graphical Summary Report 2, Reference 63-1, February 1963.
8. Whalin, R.W., F.C. Perry and D.L. Durham, "Model Verification for Tidal Constituents", Proceedings of The Fifteenth Coastal Engineering Conference (ASCE), Honolulu, Hawaii, pp. 3377-3395, July 1976.

CHAPTER 177

NUMERICAL STUDY OF DISTORTION IN A FROUDE MODEL

T. A. McClimans and S. A. Gjerp

River and Harbour Laboratory
Norwegian Institute of Technology
Trondheim, Norway

ABSTRACT

A numerical model utilizing a fully time-centered implicit (ADI) computational algorithm is used to investigate the effects of distortion of the laboratory model of the Tromsø sound where advective accelerations are important. The numerical model is used to study the individual effects of bottom and side resistance in order to obtain a better understanding of the dynamics and energetics of the tidal flow. Bottom friction is modeled by Chezy's formula. Correspondingly, a lateral viscosity proportional to the local velocity is used to obtain a realistic representation of turbulent lateral momentum exchange. Deviations between the results of the models and field observations are found to be within the natural variability from one tidal cycle to the next, indicating that the laboratory simulation is not seriously affected by distortion.

DISTORTED FROUDE MODELS

It is well known that laboratory simulations of geophysical systems require a geometrical exaggeration of the depth scale in order to produce a sufficiently turbulent flow with a reasonable horizontal dimension. This exaggeration is called model distortion. In an earlier paper (Audunson, et al., 1975) a comparison was made between numerical and laboratory models of dispersion in the Tromsø area. Current velocity patterns in the models compared favorably with field measurements; however, it was indicated that distortion may have caused a discrepancy regarding the simulation of dispersion.

Dispersion is an exceedingly difficult process to model because it depends on a wide spectrum of motions from the general circulation patterns, to the energy containing eddies and farther down the ladder to small scale turbulence. In general, however, the energy containing eddies will determine how much activity is present in the smaller eddies. The limitation of similitude will be the eddy size for which the quasi-two-dimensional turbulence transfers energy to the vertical turbulence. In a distorted model, vertical disper-

sion must be modeled independently of horizontal dispersion. This is perhaps the crucial point for most laboratory models, and it depends on the distortion.

For numerical models the extent of the turbulence spectrum modeled depends on the grid size. Thus to be of comparable resolution, a numerical model has to have a grid size on the order of the depth of the distorted model. The fine scale turbulence, which is not properly simulated in the distorted laboratory model can be calibrated in the numerical model by a variety of coefficients. In the laboratory model it is usually done by means of bottom roughness elements and strips extending into the main flow. Clearly, such calibrations represent an art which goes beyond the theoretical framework of Froude modeling.

Table 1 gives a summary of some dispersion studies in distorted Froude models. In general the models give less dispersion than that observed in nature (the prototype), but the agreement is remarkably good considering that only the tidal currents are simulated. The last entry in the table is the distortion study for Brouwershavense Gat, for which Abraham (1975) claimed good agreement with field measurements. From the table there does not appear to be any correlation between the quality of the simulation and the distortion. This is partly due to the fact that the type of flows vary considerably and roughness elements have been used in some cases. The larger dispersion in nature is probably due to wind effects (except perhaps for San Diego Bay). Sugimoto (1974), in reviewing other Froude model studies of dispersion, shows essentially the same result.

Table 1. Some dispersion tests in distorted Froude models.

<u>SOURCE</u>	<u>BASIN</u>	<u>DISTORTION</u>	<u>ARTIFICIAL ROUGHNESS</u>	<u>($\frac{\text{MODEL DISP.}}{\text{PROTOTYPE DISP.}}$)</u>
Bailey, et.al. (1966)	San Francisco Bay	10	Yes	> 0.5
Simmons & Hermann (1970)	San Diego Bay	5	Yes	0.75
McClimans (1973)	Borgenfjorden	25	No	0.55
Higuchi & Sugimoto (1974)	Seto Inland Sea	12	No	> 0.5
Abraham (1975)	Brouwershavense Gat	3 37½	Yes Yes	Less than 10% difference

Using the one dimensional dispersion equation for a fully developed turbulent channel flow, Fischer & Holly (1971) concluded that distorted Froude models are unlikely to be useful for pollutant dispersion studies. Abraham (1975) showed, however, that distortion is not a serious problem for wide, shallow estuaries for which dispersion is primarily due to horizontal eddies. Fischer (1976) concurs that dispersion studies in distorted laboratory models are feasible when the tidal advective processes of "pumping and chopping" dominate, and are adequately modeled. For wide, shallow estuaries, for which the tidal driving force is in near equilibrium with bottom friction, artificial roughness is necessary to model these processes adequately in a distorted model. Tidal straits, however, exhibit a different balance of forces and the dynamics of these regions warrant a new look at the problem.

ENERGETICS OF TIDAL STRAITS

An understanding of the energetics of the flow is the key to understanding the conditions for which distortion and bottom roughness must or may not be used. Of the energy supplied to the flow by the surface slope, how much dissipation occurs locally and how much downstream?

McClimans (1978) found that the most important resistance force for short tidal narrows is the advective acceleration which forms a jet that mixes with its surroundings downstream. The acceleration term scales to the Froude model law and is independent of distortion. The mixing, however, is affected by distortion if it is not strictly two dimensional.

Local friction was found to dominate when the ratio of the length of the sound to the hydraulic radius is greater than ca. 100. Both vertical and horizontal velocity shears provide friction. This becomes physically apparent through the development of viscous boundary layers, the thicknesses of which are important for diagnostics.

If the flow resistance is a form drag due to an irregular shoreline, the dynamics are essentially two dimensional and distortion has no limitation. This, however, applies only to the dynamics. It is also important to know to what degree the turbulence is two dimensional, for example, the degree to which the energy is transferred from the driving force to the backwaters. This is a measure of dispersion similitude and is a very difficult process to model.

THE TROMSØ SOUND

The currents in the Tromsø sound have been reported by Mosby (1943), Sætre (1972), McClimans (1974, 1977) and Audunson, et.al. (1975). A bathymetric map of the area is given in Fig. 1. The sill region has an average depth of ca. 7 m at low spring tide. The width at the sill is ca. 450 m.

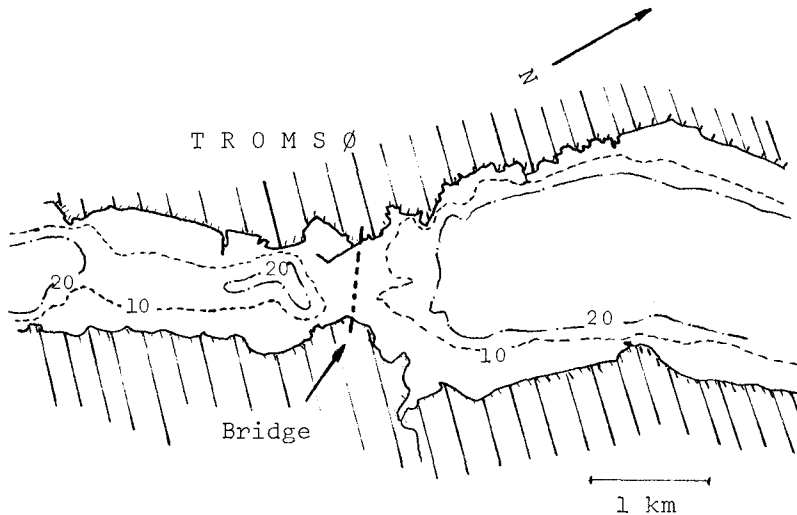


Fig. 1. Bathymetry of the Tromsø sound. Isobaths in meters. (Adapted from sea chart 451.)

Observations of water level and current speed north* are shown in Fig. 2. The two have opposite phases indicating a progressive wave propagating southwards through the sound. Due to the large velocities at the sill and the modest supply of fresh water to the area, the fluid may be considered homogeneous.

A vertical profile of the current speed at the sill (Fig. 3) shows that there is a thin boundary layer at the bottom, typical for accelerating flows. Thus we expect that a large portion of the dissipation of tidal energy occurs in a jet region downstream. The momentum exchange may thus be lateral as well as vertical. Due to the asymmetry of the topography in the sill region it is likely that the type of

* For simplicity we refer to the NE direction as north and the SW direction as south.

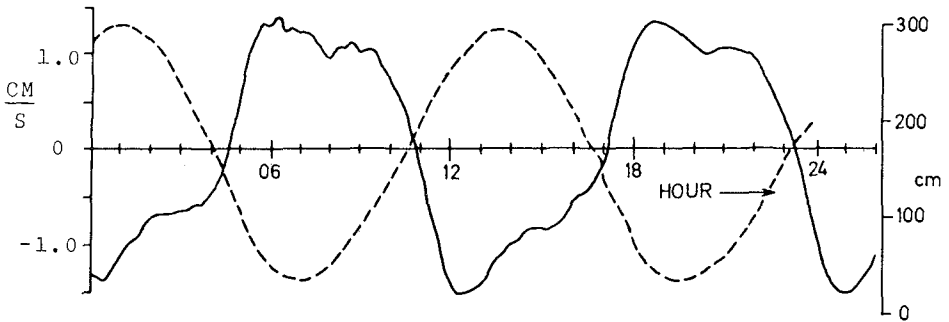


Fig. 2. Current speed north (—) and water level (---) in the Tromsø sound at the sill.

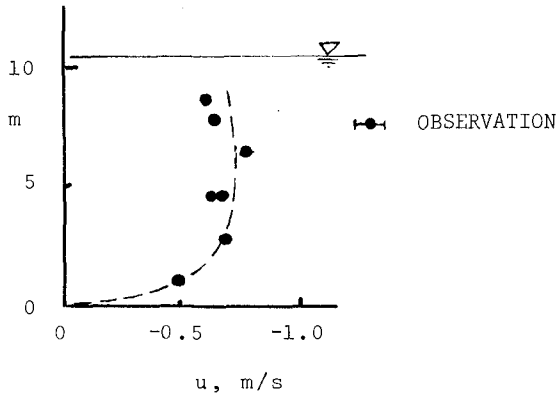


Fig. 3. Vertical velocity distribution in the middle of the sound ca. 1 h after high tide. ($\Delta H = 204$ cm)

momentum exchange is different for northern currents than for southern currents.

Audunson, et.al. (1975) compared laboratory and field measurements with a numerical model using bottom resistance alone. In the present work an improved version of the numerical model is used to investigate the individual effects of bottom and side resistance. This is done to obtain a better understanding of the dynamics and energetics of the process and determine which effects, if any, may be ascribed to geometrical distortion of a laboratory model.

THE LABORATORY MODEL

The laboratory model of the Tromsø sound (Næser, et.al., 1974) is a distorted Froude model. The length scale is 1:2000 (model to prototype) and the depth scale is 1:200, giving a distortion of 10. No roughness elements were necessary to calibrate the observed velocities in the sound to given tidal waves, implying that the macro-roughness of the topography is the important wall effect.

The particular challenge with this model was that the region has three open boundaries to the sea. Two of the three, however, are quite narrow. Here the advective accelerations dominate the momentum balance and influence the boundary conditions of the inner region. Jet currents from these narrows drive large circulations to the north and south of the Tromsø sound, and are a major factor in the long term dispersion properties of the area.

THE NUMERICAL MODEL

Basic equations for the dynamic model.

The numerical model is an improved version of a model introduced by Leendertse (1967). The model utilizes the vertically integrated equations of motion and continuity for an incompressible fluid. The horizontal velocity components u and v in the x and y directions, respectively, are integrated vertically from the bottom (at depth $-h(x,y)$) to the free surface (at height $\zeta(x,y,t)$, varying with time (t)), giving

$$U = \frac{1}{h + \zeta} \int_{-h}^{\zeta} u dz \quad (1)$$

$$V = \frac{1}{h + \zeta} \int_{-h}^{\zeta} v dz \quad (2)$$

The long wave approximation is used. The vertical accelerations and velocities are thus neglected, and the pressure is hydrostatic

$$p(z) = \rho g (\zeta - z) + p_0 \quad (3)$$

Here p_0 is the atmospheric pressure, ρ is the density, g is the acceleration of gravity and z is the vertical coordinate, positive upwards. The bottom stress vector is expressed as

$$\tau_v = \rho g C^{-2} \mathbf{v} |\mathbf{v}| \quad (4)$$

where $|\mathbf{v}|$ is the velocity amplitude and C is the so-called Chezy coefficient.

Vertical integration of the horizontal equation of motion over the region $z = -h(x,y)$ to $z = \zeta(x,y,t)$ employing (1) to (4) gives

$$\frac{\partial U}{\partial t} + U \frac{\partial U}{\partial x} + V \frac{\partial U}{\partial y} - fV + g \frac{\partial \zeta}{\partial x} + gU \frac{(U^2 + V^2)^{\frac{1}{2}}}{C^2(h + \zeta)} - \nabla \cdot \nu \nabla U = 0 \quad (5)$$

$$\frac{\partial V}{\partial t} + U \frac{\partial V}{\partial x} + V \frac{\partial V}{\partial y} + fU + g \frac{\partial \zeta}{\partial y} + gV \frac{(U^2 + V^2)^{\frac{1}{2}}}{C^2(h + \zeta)} - \nabla \cdot \nu \nabla V = 0 \quad (6)$$

where f is the Coriolis parameter, ν is the horizontal eddy viscosity, t is time and ∇ is a two-dimensional vector operator. In these equations the effects of the tide generating forces and derivatives introduced by vertical integration are neglected. The wind stress and barometric pressure are also neglected. The only driving force is thus the surface elevation $\zeta(t)$ at the open boundaries.

Using the kinematic boundary condition at the free surface and at the bottom, the vertically integrated equation of continuity is

$$\frac{\partial \zeta}{\partial t} + \frac{\partial}{\partial x} [(h + \zeta)U] + \frac{\partial}{\partial y} [(h + \zeta)V] = 0 \quad (7)$$

Numerical solution of the dynamic equations.

A space staggered scheme is used for the solution of (5) to (7). The spatial grid arrangement for the dependent variables, at any time step, is shown in Fig. 4. The solution technique is multioperational, consisting of an implicit x - sweep for calculation of $(U, \zeta)^{n+\frac{1}{2}}$, an explicit calculation of $(V)^{n+\frac{1}{2}}$, an implicit y - sweep for $(V, \zeta)^{n+1}$ and an explicit step for $(U)^{n+1}$ when integrating from time step n to $n+1$. Details of the solution technique are given by Leendertse (1967) and Hodgins (1977).

Using a fully time-centered scheme, first proposed by Leendertse, his (1967) difference scheme has been improved such that it is consistent with the differential equations, analytically stable (by the Fourier series method) and numerically stable and accurate (Hodgins, 1977). The improved version differs from Leendertse's original version only in the non-linear convective inertia terms, using what

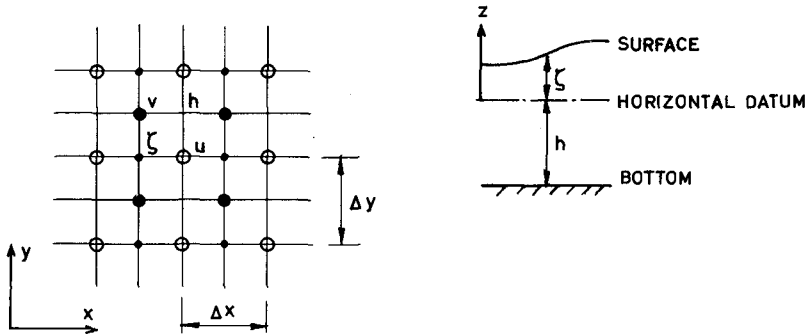


Fig. 4. Space grid for the dependent variables at any time step.

Leendertse described as the "preferred" expressions. The form of these non-linear terms are shown in Table 2.

Table 2. Comparison of the expressions for the non-linear terms in the Leendertse schemes. L-3 is the original Leendertse scheme and L-4 is the improved scheme. The double overbar denotes a symmetrical four-point space average.

DIFFERENTIAL TERM	DIFFERENCE METHOD	DIFFERENCE FORM L-3	DIFFERENCE FORM L-4
$U \frac{\partial U}{\partial x} + v \frac{\partial U}{\partial y}$	Implicit	$U^{n+\frac{1}{2}} \frac{\partial U^n}{\partial x} + \bar{v}^n \frac{\partial U^n}{\partial y}$	$U^{n+\frac{1}{2}} \frac{\partial U^{n+\frac{1}{2}}}{\partial x} + \bar{v}^n \frac{\partial U^n}{\partial y}$
$U \frac{\partial V}{\partial x} + v \frac{\partial V}{\partial y}$	Explicit	$\bar{U}^{n+\frac{1}{2}} \frac{\partial V^n}{\partial x} + v^{n+\frac{1}{2}} \frac{\partial V^n}{\partial y}$	$\bar{U}^{n+\frac{1}{2}} \frac{\partial V^{n+\frac{1}{2}}}{\partial x} + v^n \frac{\partial V^n}{\partial y}$
$U \frac{\partial U}{\partial x} + v \frac{\partial U}{\partial y}$	Explicit	$U^{n+\frac{1}{2}} \frac{\partial U^{n+\frac{1}{2}}}{\partial x} + \bar{v}^{n+1} \frac{\partial U^{n+\frac{1}{2}}}{\partial y}$	$U^{n+\frac{1}{2}} \frac{\partial U^{n+\frac{1}{2}}}{\partial x} + \bar{v}^{n+1} \frac{\partial U^{n+1}}{\partial y}$
$U \frac{\partial V}{\partial x} + v \frac{\partial V}{\partial y}$	Implicit	$\bar{U}^{n+\frac{1}{2}} \frac{\partial V^{n+\frac{1}{2}}}{\partial x} + v^{n+1} \frac{\partial V^{n+\frac{1}{2}}}{\partial y}$	$\bar{U}^{n+\frac{1}{2}} \frac{\partial V^{n+\frac{1}{2}}}{\partial x} + v^{n+1} \frac{\partial V^{n+1}}{\partial y}$

There are several ways of solving the implicit steps. Following Hodgins (1977), $[\zeta_{j-\frac{1}{2}}, U_j, \zeta_{j+\frac{1}{2}}]^{n+\frac{1}{2}}$ are used as the dependent variables of the momentum equation. The resulting tri-banded coefficient matrix then contains $(\partial U / \partial x)^{n+\frac{1}{2}}$. Using $(\partial U / \partial x)^n$ as the initial approximation, all solutions

are iterated to convergence in the ζ field. In all tests with the improved scheme, one adjustment in the approximation of $(\partial U/\partial x)^{n+\frac{1}{2}}$ (i.e. two calculations) is sufficient. An analogous separation of variables in the y - sweep momentum equations is used and the same iteration procedure is performed.

Solving the implicit sweeps in this way removes the restriction of the size of the time step Δt (Courant-Friedrich-Levy condition), but it doubles the time (and cost) of advancing from n to $n+1$ because of the iteration.

The improved scheme causes a further complication in the explicit steps. In the y momentum equation, for example, $(V_j)^{n+\frac{1}{2}}$ is a function of $(V_{j-1}, V_{j+1})^{n+\frac{1}{2}}$, resulting in a set of simultaneous linear equations. The calculation step is therefore not strictly "explicit". The solution of the set of equations can be achieved only with additional boundary conditions. In the present work the solution is iterated by successive approximations of $(V_{j-1}, V_{j+1})^{n+\frac{1}{2}}$. For smooth hydraulic problems, one adjustment is adequate. Further details are given in Hodgins (1977).

Boundary conditions.

At the open boundaries the water level ζ varies sinusoidally as

$$\zeta = A \sin(2\pi(t - \omega)/\tau) + \zeta_0 \quad (8)$$

where A is the tidal amplitude, τ is the tidal period, ζ_0 is the mean sea level and ω is the phase of the tidal wave relative to that in the southern part of the sound.

Along closed U-boundaries in the y -direction, a procedure is followed in which the effect of the side friction can be isolated to the viscous terms. A zero wall velocity is used in the viscous terms, while a slip condition is used in all other terms. A similar condition is used along closed V-boundaries in the x -direction.

To assure that no instabilities in the form of short waves can be introduced at the open boundaries, the equations are linearized over three points along these boundaries.

NUMERICAL TESTS

Numerical tests were made using the NORD-10 minicomputer at the River and Harbour Laboratory. The grid net was 16 x 56 points, giving sufficient details of jet currents and backwaters to discriminate the effects of bottom friction

and side friction. The calculations were performed with a grid length $\Delta x = \Delta y = 167$ m, a time step $\Delta t = 120$ s and a Courant number

$$\frac{\Delta t}{\Delta x} (8gd_{\max})^{\frac{1}{2}} = 43 \quad (9)$$

where d_{\max} is the maximum depth.

The dynamical equations were solved for bottom friction alone (Chezy model), for side friction alone (v -model) and a combination in which half of the flow resistance at the sill was accounted by each term (v -Chezy model). The Chezy friction coefficient was obtained from the earlier model (Audunson, et.al., 1975) with viscous damping. The results of the new scheme, without viscosity, were essentially the same as the earlier one.

A constant horizontal eddy viscosity is an oversimplification of the lateral turbulent momentum exchange and gives a very viscous flow with a weak development of backwaters. This was verified in an early test. The eddy viscosity is a function of the flow properties, the simplest one being a *linear* function of the flow speed. *This* gives a resistance force proportional to the square of the velocity, as in the Chezy friction law. Thus the v -model is based on an eddy viscosity

$$v = v_0 + C_1(U^2 + V^2)^{\frac{1}{2}} \quad (10)$$

in which v_0 is the molecular viscosity of water ($= 10^{-6}$ m²/s) and C_1 is a constant to be calibrated to the flow. For the Tromsø sound tests were run with $C = 29$ m²/s or $C_1 = 60$ m.

RESULTS AND COMPARISONS

Some of the results are compared with field and laboratory measurements in Figs. 5-7. Fig. 5 shows the current patterns, at high and low tide. Fig. 6 shows the lateral distribution of current speed at the sill for low and high tide and Fig. 7 shows the current speed at the sill through $1\frac{1}{2}$ tidal cycles.

The field measurements in Fig. 5 (Mosby, 1943) were averaged over ca. three hours of northern/southern currents, whereas the models give instantaneous pictures. The laboratory tests (Næser, et.al., 1974) showed that the circulation patterns farther to the north develop long after high and low tides.

In Fig. 7, the laboratory results show a high frequency

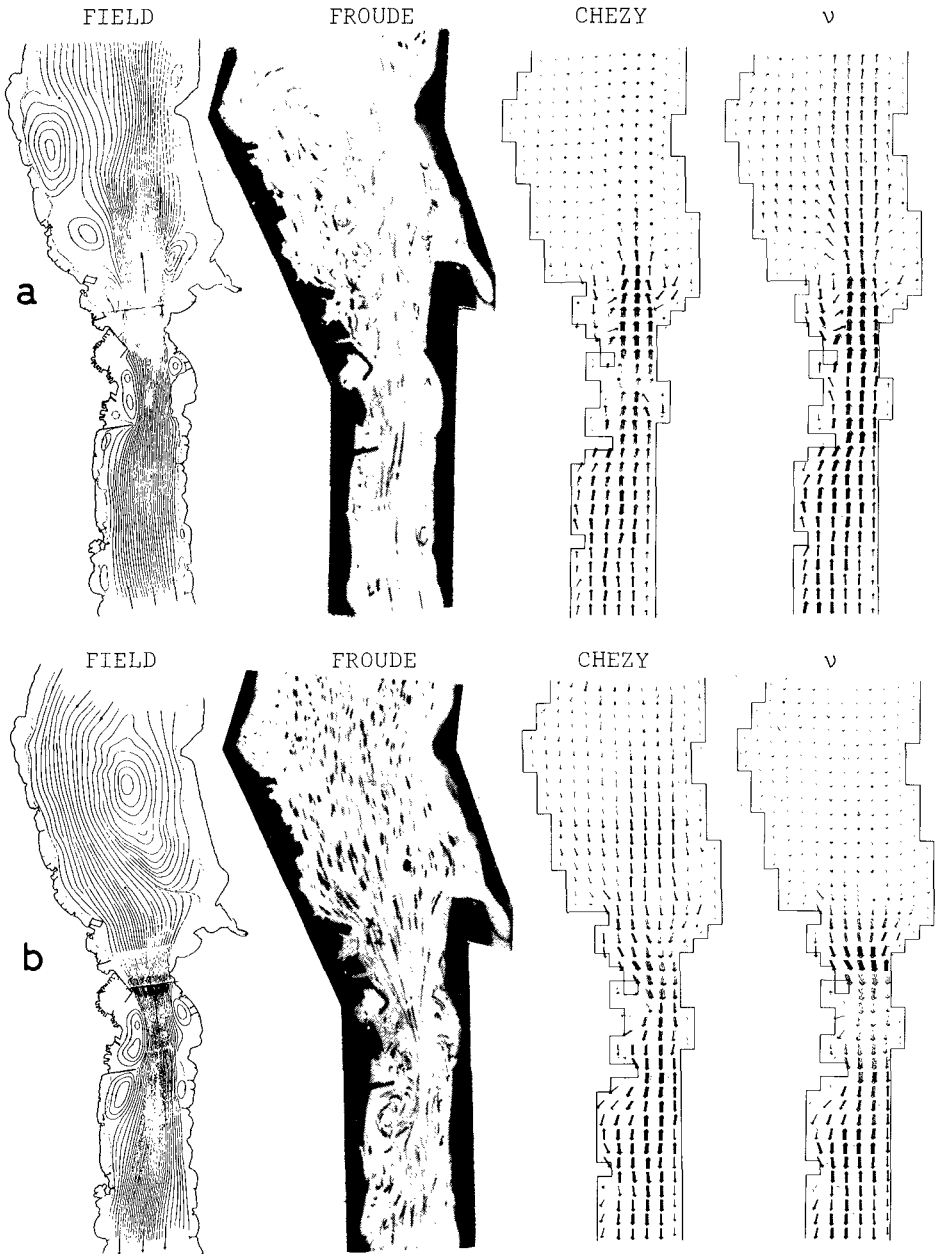


Fig. 5. Comparison of three models with nature at (a) low tide and (b) high tide.

fluctuation. This is the result of the regulation system controlling the tidal levels at the three seaward connections.

Qualitatively, all models give good results for the flow near the sill. It is possible to test the models quantitatively by three means; a) the lateral distribution of current speed at the sill (Fig. 6), b) the time history of current speed at the sill (Fig. 7) and c) the maximum reverse velocity in the backwaters on each side of the sill. The results for the last test are given in Table 3.

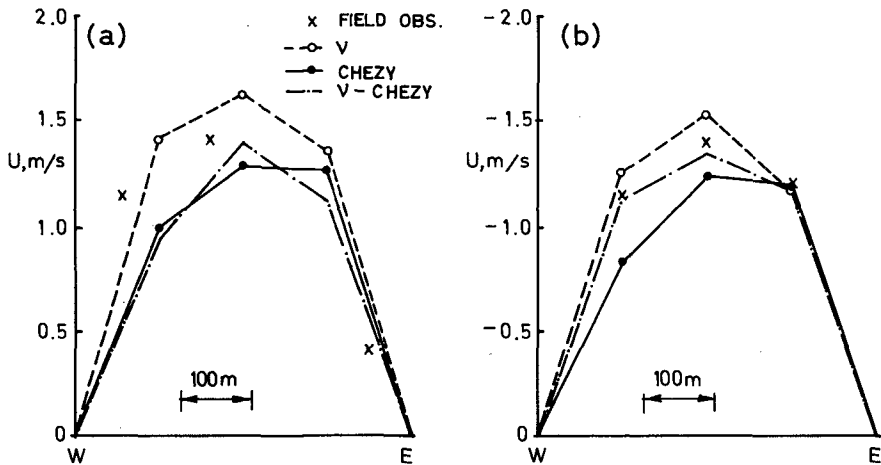


Fig. 6. Lateral distribution of current speed $u(y)$ at (a) low tide and (b) high tide.

Results of test a)

The available measurements from the laboratory model are not sufficiently detailed to subject it to this test. Of the numerical models, the v -model gives the best results for northern currents while a combined lateral/vertical friction (v -Chezy) model gives better results for southern currents.

Results of test b)

The laboratory model gives the best results. Of the numerical models, the v -Chezy model is best. (For southern currents, the Chezy model shows a better profile.)

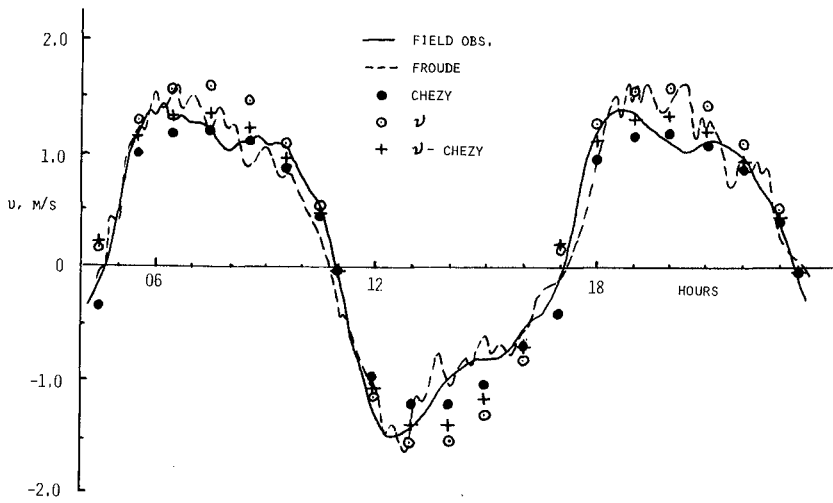
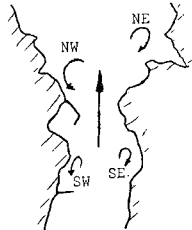


Fig. 7. A comparison of field measurements of current speed in the Tromsø sound with four models.

Table 3. Maximum reverse currents in the backwaters near the sill in the Tromsø sound. Values are given in cm/s in the reverse direction of the flow. The backwaters are identified on the map.

TIDAL PHASE		LOW TIDE = NORTHERN FLOW				HIGH TIDE = SOUTHERN FLOW			
BACKWATER		NW	NE	SW	SE	NW	NE	SW	SE
METHOD	FIELD OBS.	?	22	25	20	-	-	25	25
	FROUDE	40	16	18	8	-	-	17	20
	CHEZY	59	21	7	21	-	-	17	-
	v	41	14	8	0	-	-	18	-
	v-CHEZY	56	14	7	7	-	-	15	-



Results of test c)

Only the laboratory model gives backwaters in the same detail as those observed in the field. This must be a result of poor resolution, since there are so few grid points in the backwaters south of the sill. For northern flow, the Chezy model is about as good as the Froude model, whereas the v -model shows generally less energy in the eddies.

To sum up, the distorted Froude model gives a better simulation than the combined numerical efforts. A combination of side friction and bottom friction gives the best combined quantitative result. The differences between the various models, however, are not large and in many cases they are within the variability of the system.

In the above comparisons it should be noted that the magnitude of the velocities would be more accurately modeled with larger values of C and C_1 . This, however, does not affect the conclusions and has not been further pursued.

DISCUSSION OF TURBULENCE, FRICTION AND DISTORTION

The goal of the present study is to use the improved Leendertse scheme implemented by Hodgins (1977), to test hypotheses on the dynamics and energetics of the Tromsø sound in order to diagnose the possible effects incurred by distortion of the Froude model of the area. Since the Froude model gives a better simulation and shows more detail than the numerical models, we have to consider the hypothetical, limiting case of large distortion.

Infinite distortion will, in effect, eliminate bottom friction from the model, leading to the result of the v -model. The degree to which the v -model simulates lateral dispersion is thus the limit of the error which can be incurred by model distortion. Although the v -model gives good results locally (Fig. 6), it is inadequate for the backwaters, implying that the energetics cannot be explained in terms of side friction alone. Thus we can conclude that unlimited distortion is not dynamically correct and will lead to an error in dispersion similitude. In narrow passages, however, and perhaps also immediately downstream in a jet, lateral momentum and energy exchange must be included in a numerical simulation.

Bottom friction is also an essential factor in the Tromsø sound. This conclusion is not unexpected. The length to depth ratio of the Tromsø sound is greater than 100, which, according to McClimans (1978) means that local friction is a significant factor in the energetics of the flow. In spite of the thin boundary layer at the sill, the entire sill region exerts a significant friction force on the flow. This force is presumably partly bottom drag from the irregular

bottom and partly the effects of drag from the irregular shoreline.

The *local* flow resistance is a combination of the advective acceleration ($U\partial U/\partial x$) and the friction. A comparison of the numerical results shows that, at the sill, the advective acceleration is 4 times as large as the friction (corresponding to the location where the data in Fig. 3 was obtained), while over a length of three grid points the two terms are roughly equal (length to depth ≈ 50). For the entire length of the sill, the role of the advective acceleration is to transport the momentum to regions of weaker surface slopes where the local friction dominates over the advective acceleration. This process is taken into account in the different models in different ways: The Chezy model imparts the force to the bottom while the v -model imparts it to the neighboring regions and eventually to the shores and/or bottom.

The ocean circulation was simulated by Stommel (1948) using bottom friction and by Munk (1950) using side friction. Their models used resistance laws with coefficients that are independent of the flow velocity (i.e. Guldberg-Mohn friction and constant lateral viscosity). Their results also gave the large scale features, which depend mostly on the distribution of wind stress and the rotation of the earth. Thus, when other terms (e.g. accelerations) dominate the dynamics, the particular law of friction matters little. Friction provides an energy sink for the forcing function to avoid an accumulation of energy.

The present results show that lateral friction plays a significant role **for** the lateral velocity shear which is an important factor for dispersion studies. A constant lateral viscosity does not model the flow very well in a tidal strait. A viscosity proportional to the local velocity, corresponding to a Chezy friction law, models the flow quite well, especially near the sill. It appears that this viscosity law (10) is a good expression of the turbulence.

Eddy viscosity is proportional to the turbulent velocity times the integral length scale of the energy containing eddies. If the turbulent velocities are on the order of a tenth of the current velocities, then, from (10), $C_1 = 60$ m leads to a turbulent length scale on the order of 500 m. This is the order of the width at the sill as well as the width of the jet issuing from the sill. This seems reasonable and implies that the turbulent energy is contained in the large-scale horizontal eddies in tidal straits.

The build-up time for large eddies in the Tromsø sound is on the order of half a tidal cycle. The decay time appears to be longer, leaving a significant residual kinetic energy at current reversals. This leads to a time-smoothing of the

dissipation.

All models appear to give a reasonable estimate of the flow, within the variability of the field measurements from one tidal cycle to another. In view of this it seems unlikely that model distortion caused any large inaccuracies in the simulation of the flow. This may be due to the fact that the bottom resistance is in the form of macro-roughness (i.e. bottom topography) which is also exaggerated. It is also possible that the roughness of the model (smooth cement) was appropriate for the thin viscous boundary layers (Fig. 3). The skin friction coefficient is larger for the model Reynolds numbers than for the prototype Reynolds numbers. Distortion remedies this to some extent.

Calibration of the flow in a tidal channel with roughness elements is truly an art, since the energetics depends also on flow direction. Such a calibration of a distorted Froude model, when necessary, has the same effect as calibrating coefficients to the numerical models. The type of modeling used by Svensson (1978), in which the sources and sinks for the turbulent energy are taken into account in a realistic manner is perhaps a better way to obtain the proper energetics and dispersion characteristics of tidal flows in straits.

ACKNOWLEDGEMENTS

This work has been supported in part by Konesjonsavgiftsfondet (Fund of license fees) administered by the Norwegian Water Resource and Electricity Board, Department for the State Power Systems. We wish to thank J.P. Mathisen and J. Moe for valuable comments on the numerical schemes and for reviewing the manuscript.

REFERENCES

- Abraham, G., 1975. Hydraulic far-field modeling. Ch. 10B, European course on heat disposal from power generation in the water environment. Delft Hydraulics Laboratory.
- Audunson, T., Mathisen, J.P., Naser, H. and McClimans, T.A., 1975. A comparison between physical and mathematical modelling of a tidal fjord system in Northern Norway. Symposium on modelling techniques, 2nd Annual Symposium of the Waterways, Harbours and Coastal Engineering Division of ASCE, San Francisco (pp 1291-1310).
- Bailey, T.E., McCullough, C.A. and Gunnerson, C.G., 1966: Mixing and dispersion studies in San Francisco Bay. Sanitary Eng. Div. ASCE. Paper 4936. SA5 pp 23-45.
- Fischer, H.B., 1976. Mixing and dispersion in estuaries. Annual review of fluid mechanics. 8:107-133.
- Fischer, H.B. and Holley, E.R., 1971. Analysis of the use of distorted hydraulic models for dispersion studies. Water Resources Res. 7:46-51.
- Higuchi, H. and Sugimoto, T., 1974. Experimental study of horizontal diffusion due to the tidal current. Rapp. P-v. Réun. Cons. Int. Explor. Mer. 167: 177-184.
- Hodgins, S., 1977. An improved computational method for the shallow water wave equations based on the Leendertse (1967) finite difference scheme. River and Harbour Laboratory. Report STF60A 77058. 72 pp.
- Leendertse, J.J., 1967. Aspects of a computational model for long-period water-wave propagation. Memo. RM-5294-PR. The RAND Corporation. Santa Monica, 165 pp.
- McClimans, T.A., 1973. Physical oceanography of Borgefjorden. K. Norske Vidensk. Selsk. Skr. 2:1-43.
- McClimans, T.A., 1974. Resipientundersøkelser ved Tromsø. Delrapport nr. 2: Hydrofysiske målinger fra Tromsø-området, oktober-november 1973. River and Harbour Laboratory Report STF60 F74072. 12 pp. (In Norwegian.)
- McClimans, T.A., 1977. Measurements of swift tidal currents in the Tromsø area. Bulletins of the River and Harbour Laboratory 16E:47-68.

- McClimans, T.A., 1978. On the energetics of tidal inlets to landlocked fjords. *Mar. Science Comm.*, 4:121-137.
- Mosby, H., 1943. Strømmålinger i Tromsøundet 1940/41. Unpublished report. 71 pp. (In Norwegian.)
- Munk, W., 1950. On the wind-driven ocean circulation. *J. of Met.*, 7:79-93.
- Næser, H., Audunson, T. and McClimans, T.A., 1974. Resipientundersøkelser ved Tromsø. Spredning og fortykning av avløpsvann i området. Resultater fra modellforsøk. River and Harbour Laboratory, Report STF60 F75042. 93 pp. (In Norwegian.)
- Simmons, H.B. and Hermann, F.A., 1970. Effects of proposed second entrance on the flushing characteristics of San Diego Bay, California. Marine pollution of sea life fishing. News books Ltd., London. pp. 460-64.
- Stommel, H., 1948. The westward intensification of wind-driven ocean currents. *Trans. AGU.* 29:202-206.
- Sugimoto, T., 1974. Similitude of the hydraulic model experiment for tidal mixing. *J. Oceanogr. Soc. Jap.* 30:260-270.
- Svensson, U., 1978. A mathematical model of the seasonal thermocline. Dept. of Water Resources Engineering, Univ. of Lund. Report No. 1002. 187 pp.
- Sætre, H.J., 1972. Strømmålinger i Tromsøundet og Sandnesundet, Februar 1972. River and Harbour Laboratory Report, Proj. No. 600836, 20 pp. (In Norwegian.)

CHAPTER 178

IMPROVEMENTS ON TIDAL ESTUARIES AND THE EFFECTS ON TIDAL CURRENT

by
Hermann Harten*

ABSTRACT

With the enlargement of industrialization in the 19th century and the growth of world trade the sea navigation increased considerably. The sea routes had to be improved. This development continued very fast in the last 30 years. The capability of extension in the particular estuary (for example: Elbe, Weser, Jade, Ems) is limited. The improvements include not only the deepening of navigational channels, but also groins, training-walls, fixation of bars, partial or total damming up from by-channels, new localization of main navigational channel lines, new ports etc. The tidal low water is falling and the tidal high water rises, the tidal lift and the tidal volume increase and the flood-as well as the ebbcurrent is floating more powerfully through the tidal estuary. This shows the effect of constructions.

GENERAL

The tides come from the Atlantic Ocean and through the English Channel into the North Sea. The tide from the north is running along the British coast, converges with the tide coming from the Channel and transformed into a rotary tide the so-called amphidrome.

Fig. 1 shows the German Bight with the tidal rivers Elbe, Weser, Ems and the Ocean Bay of the Jade.

* Dipl.-Ing., Bundesanstalt für Wasserbau (BAW)
Hamburg, Fed. Rep. of Germany

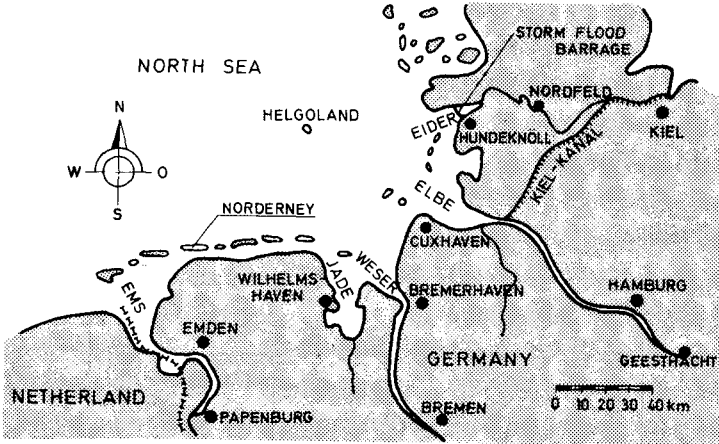


FIG. 1 - MAP OF THE GERMAN BIGHT

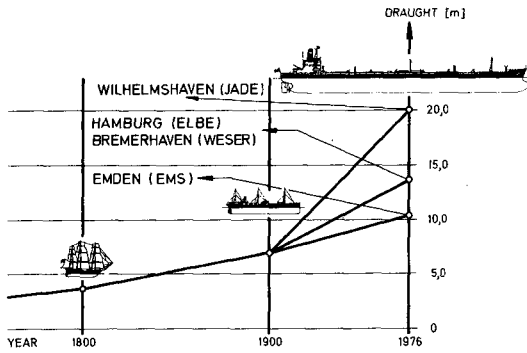


FIG. 2 - LINES OF SHIP-DRAUGHTS

These estuaries of the German coast may have been transport ways since prehistoric times. The draught of boats used at that time was unimportant and the natural depth of water was sufficient.

The marshland was small populated, and no dikes protected it against stormtides. The water masses could easily and extensively intrude. About the year 1000 A.D. first dikes were built. By and by due to the increase of population the entire coast had been diked [1], and stormtides ran upwards the river-beds only as the normal tides do.

Until the beginning of the 19th century the largest ships draught had reached 3.5 m only. With the expanding of industry during the 19th century and the growth of world trade the sea navigation increased considerably.

The ships were enlarged for economic reasons, and their development progressed from the sailing boat to the combined sailing-steamship, to the simple steamer, the present day large tankers and containerships. For that reason it was necessary to improve the sea-routes. Nowadays the possible ship-draught amounts to 20 m at the sea route Wilhelmshaven, 14 m to the harbours Bremerhaven and Hamburg, and 10 m to Emden (Fig. 2).

These improvements include not only the deepening of the navigational channels, but also groins, training walls, fixation of sand bars, partial or total damming up of whole estuaries or tributaries, relocations of main navigational channel lines, new ports etc.

Here the deepening of a navigational channel will be considered first theoretically.

The simple formula $v = \frac{Q}{F}$ being completed with the flood or ebb duration, shows an important dependance.

$$v_{im} = \frac{v_{Ti}}{D_i \cdot F_{im}}$$

- v_{im} [m/s] = mean flood or ebb velocity
 V_{Ti} [m³] = tidal volume (flood or ebb tide)
 D_i [s] = flood or ebb duration
 F_{im} [m²] = mean discharge cross section
 (flood or ebb tide)

If a discharge cross section is in natural balance to the discharge, presuming sandy bottom material, it is easy to realize that v_{im} is in relation with the bed material. In case of extending the discharge plane the flow velocity will be diminished, that means, assuming that the tidal volume as well as the flood and ebb duration are unchanged, sedimentation will occur on account of the lower velocity. This phase will last so long as a natural balance condition will be reached again. Therefore the dredging material, achieved by deepening of navigational channels, should be deposited lateral in the same cross section.

Thereby it is possible to give the river-system theoretical a perfect funnel-shape.

The formula of Manning-Strickler is:

$$v = K \cdot R^{2/3} \cdot I^{1/2}$$

Dividing the discharge cross section in many parts (Fig. 3) the formula can be written as follows:

$$v = K \cdot I^{1/2} \cdot \frac{1}{n} \sum_{i=1}^n t_i^{2/3}$$

where v is the velocity and K the friction factor, while I is the slope and t the water depth.

It is easy to understand that with rising water depth t_i in the simple section the velocity v rises, that means, in the deepened channel area there will be a concentration of stream.

While in the areas beside, the dredging goods deposited, by falling depth the velocity decreases. As generally, however, a hydraulic more favourable discharge cross section is re-

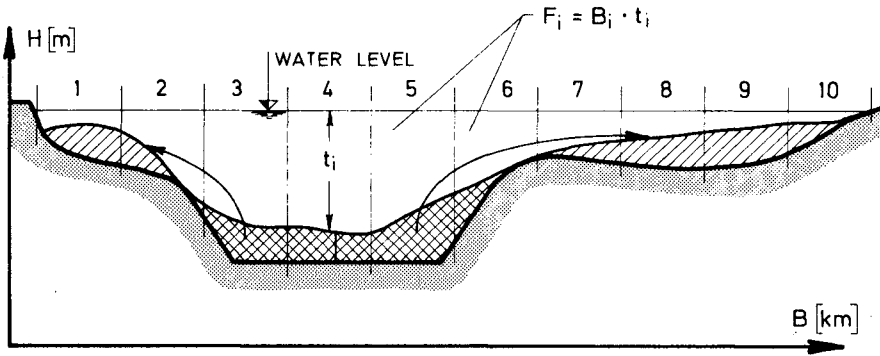


FIG. 3 - DISCHARGE CROSS SECTION

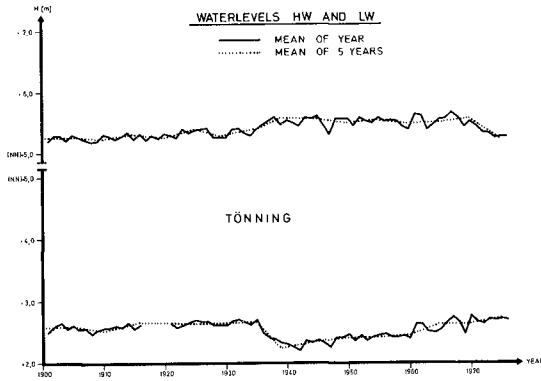


FIG. 4 - WATERLEVELS HW AND LW AT THE GAUGE TÖNNING

sulting from the deepening, the tide is also turning more unimpeded in the estuary. The tidal range is causing a tidal lift and tidal volume increase. Model investigations with an idealistic discharge profile give the following result: The increase of tidal lift goes to one quarter in the rise of high water (HW) and to three quarters in the fall of low water (LW). Moreover, time of progress is shortened and the flow velocities rise in the area of the improved main channel. But these effects are different for each estuary. Of course, the result depends on percentage of enlargement related for example to the normal mean water cross section and to other improvements. Except the total damming up, the tide can intrude better to the estuary because of less reflexion and less decrease of energy.

The following gives a description about changing of mean HW and LW levels resulting from improvement and in addition some information about stormtides.

River Eider

The graph (Fig. 4) shows the yearly mean tidal high and low water levels at the gauge Tönning from 1900 up to now. The row of dots marks the mean values over a period of five years. By the total damming up at Nordfeld in the year 1936 the HW rises 18 cm and the LW falls about 44 cm.

After such a drastic change in the flow conditions the river needs a long time (10 or even 30 years) to come back into the natural balance between flow and morphology.

In the year 1973 the storm flood barrage (line Hundeknöll/Vollerwiek) was completed. Result of model tests: The mean tide will not be influenced by the barrage. However, higher tides will be changed by this construction which will be closed during stormtides. Therefore a clear fall of the mean HW is effected.

River Elbe

The mean water level line of the gauge Cuxhaven shows a

small increase only, while the tidal lift in Hamburg-St.Pauli increases - rise of HW, fall of LW - because of the deepening of the Elbe up to Hamburg from 10 m to 13.5 m below chart datum and other improvements (Fig. 5); model values show the same tendency. The draught of inland navigation and the falling LW dictated the construction of the weir Geesthacht.

The stormtides from 1825 and 1962 are looking very similarly at the gauges Cuxhaven and Hamburg-St. Pauli. Also the tide from 1825 is lying in Cuxhaven as well as in Hamburg nearly 50 cm below the HW 1962, though there are very different morphological conditions.

A map of the river Elbe from 1816 (Beautempes-Beaupré) gives a good survey.

In the year 1865 (map by Schuback) the depth in the Hamburg region, especially near Blankenese, was 3.0 m, and in maximum 4.0 m below normal tidal LW.

Obviously the storm tide course depends not much on the deep channel parts of a cross section but more on the large storm flood section lying above.

River Weser

The registered water levels at the gauge Bremerhaven indicate few changes in water level only since any changes can be balanced rapidly in the vast area of the Outer Weser. The gauge Bremen, however, shows a clear decrease of LW level due to the deepening of the Inner and Outer Weser, and the relocation of the navigational channel into the, by nature already favoured, Fedderwarder Arm, from 1921 until 1928 (Fig. 6). Surely other measures also influence this decrease.

Stormtides show an accumulation about the years 1915 and 1975. Upon comparing the two tables of values (Fig. 6) one can recognize that not every stormtide from Bremerhaven appears in Bremen and vice versa.

Tidal Bay Jade

Both water gauges Wilhelmshaven and Norderney are situated in

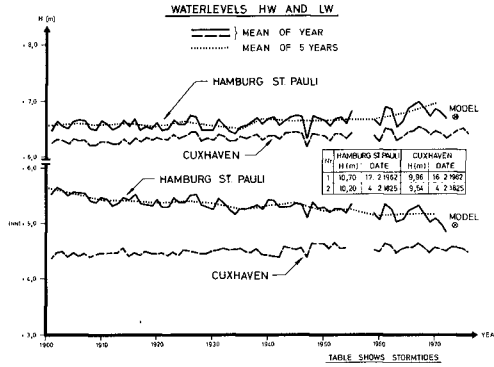


FIG. 5 - WATERLEVELS HW AND LW AT THE GAUGES CUXHAVEN AND HAMBURG- ST. PAULI

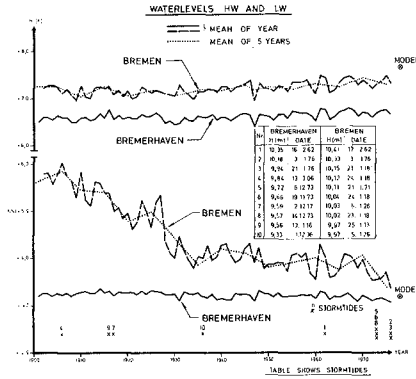


FIG. 6 - WATERLEVELS HW AND LW AT THE GAUGES BREMERHAVEN AND BREMEN

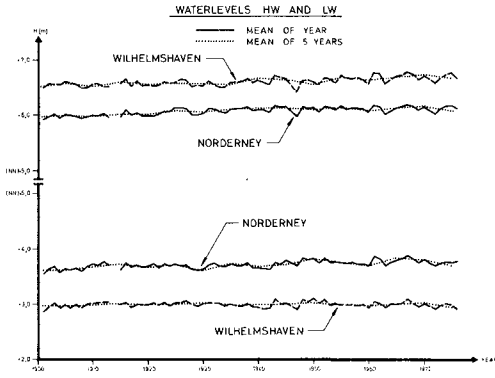


FIG. 7 - WATERLEVELS HW AND LW AT THE GAUGES WILHELMSHAVEN AND NORDERNEY

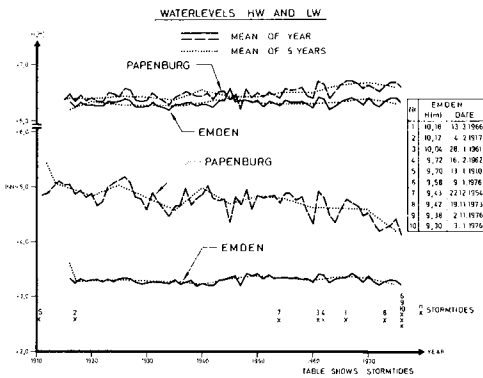


FIG. 8 - WATERLEVELS HW AND LW AT THE GAUGES EMDEN AND PAPENBURG

areas with adjoining large waterplanes, therefore the gauge Wilhelmshaven does not registrate any effect due to the Jade improvement from 10.0 m to 18.5 m below chart datum. The mean value of the gauge Wilhelmshaven rises a little in HW only. Within the increase of water levels at the gauge Norderney there is the rise of water level due to the settling of land in reach of the German Coast (Fig. 7).

River Ems

The gauge Emden is located in the mouth of the river Ems. More changes are shown at the gauge Papenburg (Fig. 8). Although no larger improvements were made in this region, it is possible that the fall of the water level (LW) results from improvements in the Outer Ems. By and by the river found back to a natural balance and the effect of improvement work reaches the upstream region. Stormtides were concentrated about the years 1910 and 1970.

With the knowledge of historical evolution, field measurements and the result of model tests navigational channels may be optimally improved.

REFERENCES

- [1] Rohde, H.: The History of the German Coastal Area, Harten, H.; Vollmers, H.: The Estuaries of the German North Sea Coast, Die Küste, Heft 32, 1978.
- [2] Harten, H.: Abdämmung der Eider, Modellversuche im Tidemodell, Mitteilungen der Bundesanstalt für Wasserbau, 1970, Nr. 40.
- [3] Harten, H.; Knieß, H.G.: Eiderdamm, Natur-und Modellmessungen, Wasserwirtschaft, Heft 12, 1976.
- [4] Hensen, W.; Wegener: Ausbau der seewärtigen Zufahrten zu den deutschen Nordseehäfen; Hansa, Hamburg 1971, Nr. 15.
- [5] Hovers, G.: Einfluß von Strombauwerken auf die morphologische Entwicklung eines Tideflusses; Mitteilungsblatt der Bundesanstalt für Wasserbau, 1973, Nr. 34.

CHAPTER 179

INFLUENCE ON TEMPERATURE INCREASES IN TIDAL RIVERS CAUSED BY WASTE HEAT INJECTIONS WITH RESPECT TO TIDAL CYCLES AND STORM SURGES

by

Horst Schwarze¹⁾ and Wilfried Falldorf²⁾

1) Dr.-Ing., Chief Engineer, Franzius-Institut of the
University of Hannover, Germany

2) Dipl.-Ing. Scientific Assistent, Franzius-Institut
of the University of Hannover, Germany

ABSTRACT

The influence of tidal cycles with neap and spring tides or of storm surge events on the distribution of temperature increases caused by heat injection in an estuary was investigated in a thermal-hydraulic model. The results of the model tests have shown, that under natural tidal conditions as of the Elbe River during tidal cycles as well as storm surge events in the far field region no higher temperature increases occurred than under mean tidal conditions.

INTRODUCTION

Far-field investigations on temperature increases in tidal rivers, caused by waste heat input, are carried out in hydraulic models as well as in mathematical models in general under consideration of mean tides. Natural hydrological conditions of a tidal river, however, are described unsufficiently by this means. The influence of a tidal cycle with neap and spring tides or storm surge events on the spreading of injected waste heat and on the corresponding temperature increases in a tidal river can probably be of importance for the judgement of a waste heat injection. Therefore, thermal hydraulic investigations were carried out in the FRANZIUS-INSTITUT in order to show the dependence of temperature increases with respect to natural tidal conditions.

PARAMETERS OF INFLUENCE

Temperature increases in the far field region of a tidal river in general depend on the spreading and mixing of the injected heated cooling water in the tidal river as well as on the heat exchange between the water surface and the atmosphere. The distribution of the cooling water in the tidal river is influenced

1. by the initial mixing in the near field region with a vertical and a horizontal spreading,
2. by the multiple load of a waterbody with heated cooling water in consequence of the tidal movement and
3. by the removal of waste heat out of the influential reach of the cooling water injection by the freshwater discharge as well as in the brackish water zone of a tidal river by the exchange of fresh water and salt water.

According to the difference between flood- and ebbways of the tides following one another a waterbody will more or less often pass the cooling water outlet moving downstream saw-likely. So it will not reach the outlet again with the flood-stream after several tides. Flood- and ebbways are determined by the portion of the fresh water discharge of the tidal river on the ebb discharge and by the different flood- and ebb tide volumes with respect to the semidiurnal and semimonthly inequality of the tide as well as beyond that by wind set-up effects (storm surges).

In every tide of a natural tidal cycle otherwise as in a sequence of equal mean tides different current and discharge distributions will occur according to different periods of flood- and ebbstream as well as different tidal falls and tidal rises. The phases of slackwater after ebb or flood current are of special influence on the horizontal spreading of the injected heated cooling water.

INVESTIGATIONS IN A THERMAL HYDRAULIC TIDE MODEL

1. Hydraulic tide model

In a thermal hydraulic tide model of the Elbe River in the FRANZIUS-INSTITUT especially the influences of tidal cycles and storm surges, not being considered in most of all thermal hydraulic investigations, on the temperature increases in the far field region of a tidal river were investigated. In this model 60 km of the Elbe River from the sea half-way to Hamburg were simulated in a scale of 1:300 for the lengths and 1:100 for the depths. Fig. 1 shows a part of the model region of about 30 km with the

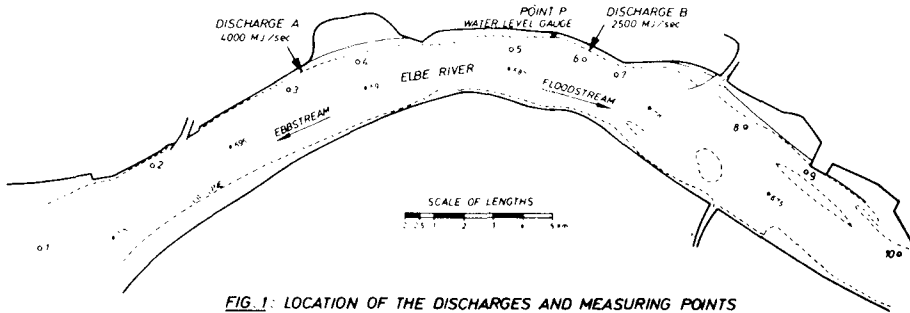


FIG. 1: LOCATION OF THE DISCHARGES AND MEASURING POINTS

outlets A and B for cooling water discharges of $Q_C = 92 \text{ m}^3/\text{s}$ and $Q_C = 60 \text{ m}^3/\text{s}$ respectively both heated up by $\Delta T_C = 10 \text{ K}$ (about 4,000 MJ/sec and about 2,500 MJ/sec). In model the cooling water discharge was constant during the total time of the tests.

The temperature measuring points 1 through 10, plotted in Fig. 1, only show a part of the actually used about 100 measuring points with temperature sensors in three water depths each, in order to be able to give a three-dimensional description of the tide dependent temperature increases in the far field region. All tidal curves shown in the following figures are measured at the tide gauge point P.

The control of the tide model as well as data collection and evaluation was carried out by a computer.

Before starting the model tests with tidal cycles and storm surges more than 20 mean tides had been controlled into the model. This number of tides under mean tide and mean fresh water discharge conditions is necessary so that a waterbody loaded with heated cooling water for the first time at the turn of the ebb current can move downstream so far that it will not reach the outlet with the flood current again.

2. Tests with a tidal cycle

2.1 Hydrological conditions

Fig. 2 shows schematically the difference between spring tides and neap tides in the model region of the Elbe River. The mean spring tidal range amounts to 295 cm and the mean neap tidal range amounts to 235 cm.

A typical tidal cycle of 18 days shown in Fig. 3 was chosen as model tide. In the neap time tides have tidal ranges about 16 % smaller than the mean tidal range of the 18 days period. Spring tidal ranges are about 14 % larger than mean tidal ranges.

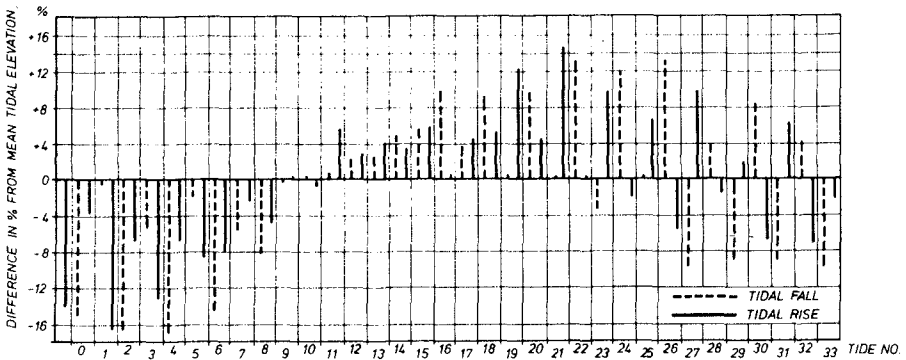
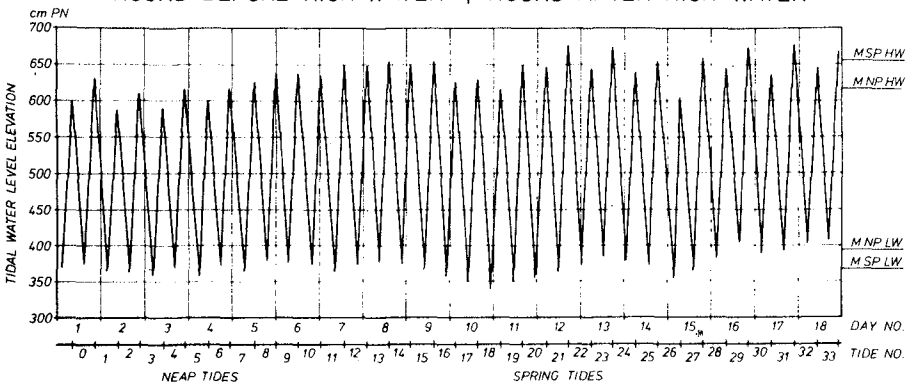
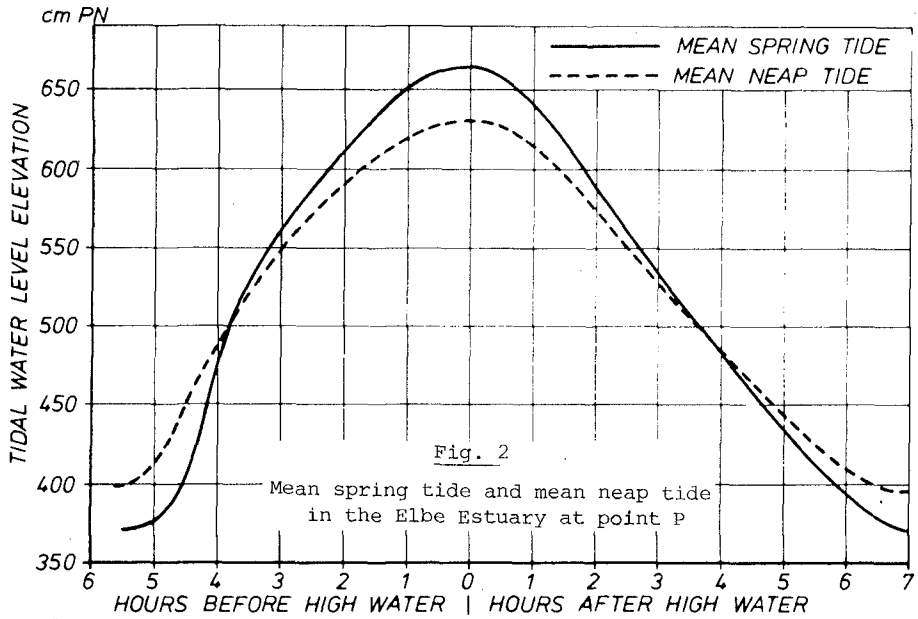


FIG. 3: TYPICAL TIDAL CYCLE OF 18 DAYS IN THE ELBE ESTUARY AT POINT P

2.2 Results of the model tests

Selected results of the model tests are plotted in Fig.4 as time dependent temperature increases of a neap tide (tide No 6) and of a spring tide (tide No 22) for the measuring points 2 (downstream of the cooling water outlets), 3 (near outlet A), 5 (near outlet B) and 8 (upstream of the outlets).

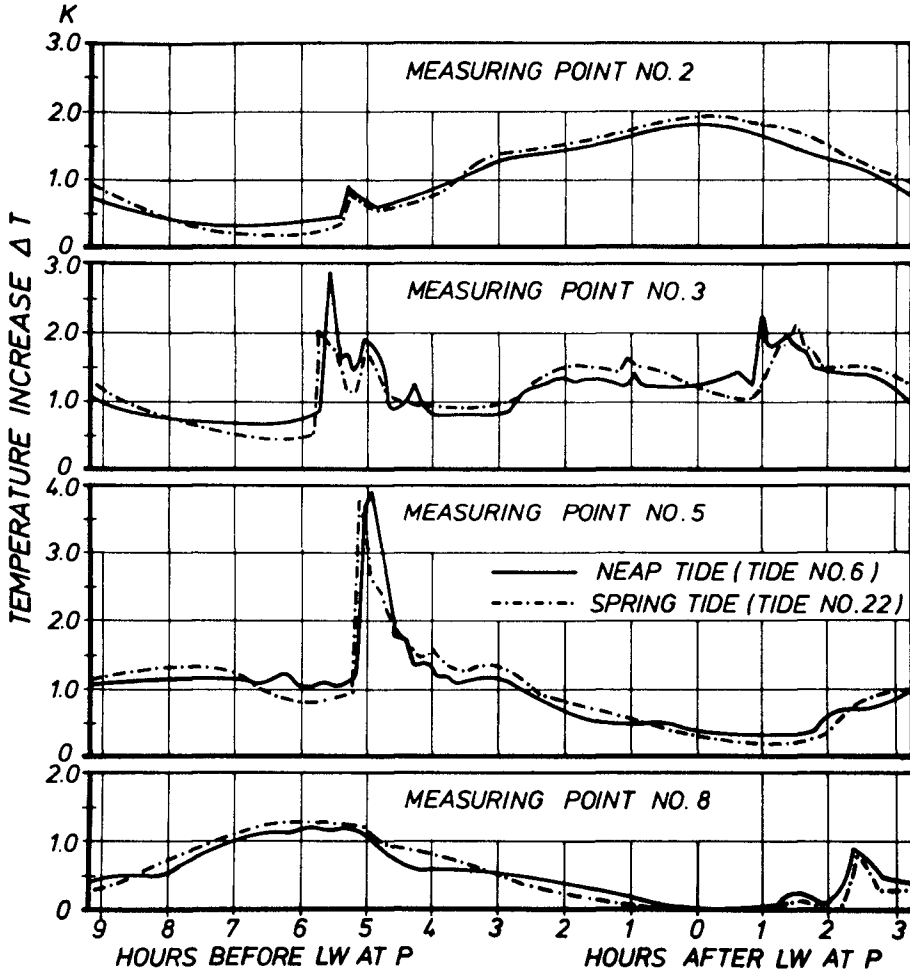


FIG.4: TEMPERATURE INCREASE DURING A NEAP TIDE AND A SPRING TIDE

The plots show that differences between the temperature increases only come to about 0.1 K in spite of the different tidal ranges of spring and neap tides. Mean

temperature increases of one tide are nearly equal for spring and neap tides.

The reasons for these results are, that temperature increases in the far field region depending mostly on the waste heat injected during previous tides react on different tidal conditions in the course of a tidal cycle only insignificantly.

3. Tests with storm surges

3.1 Hydrological conditions

For the investigations two in principle different storm surges were simulated in the model. Fig. 5 shows the model storm surges I and II. Both storm surges had the same maximum highest water levels, but different wind set-up behaviour. The wind set-up is defined as the water level difference between the predicted astronomical tide and the storm surge actually obtained in the prototype.

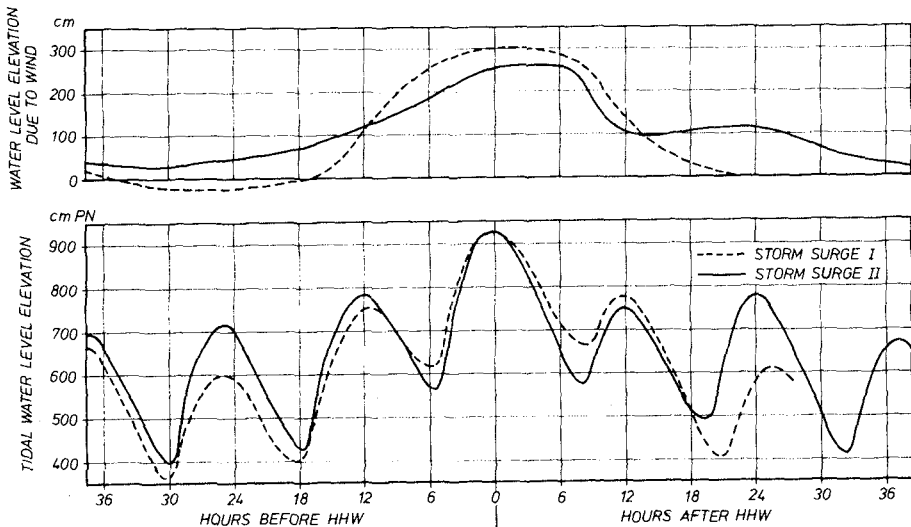


FIG. 5: COMPARISON OF THE TWO DIFFERENT STORM SURGES

In storm surge I the wind set-up rises after the first tide in about 1 1/2 tides from 0 up to 3 m and falls in about 1 tide to 0 again. In storm surge II, however, the wind set-up increases with the start of the first tide in about 3 tides to about 2.8 m and decreases in about 1 1/2 tide to 1 m and remains constantly on 1 m for 1 1/2 tide.

In Fig. 6 and Fig.7 a comparison of the tidal falls and tidal rises of the storm surges with those of mean tidal conditions is shown. The differences partly amount to more than 50 % in storm surge I and up to 40 % in storm surge II.

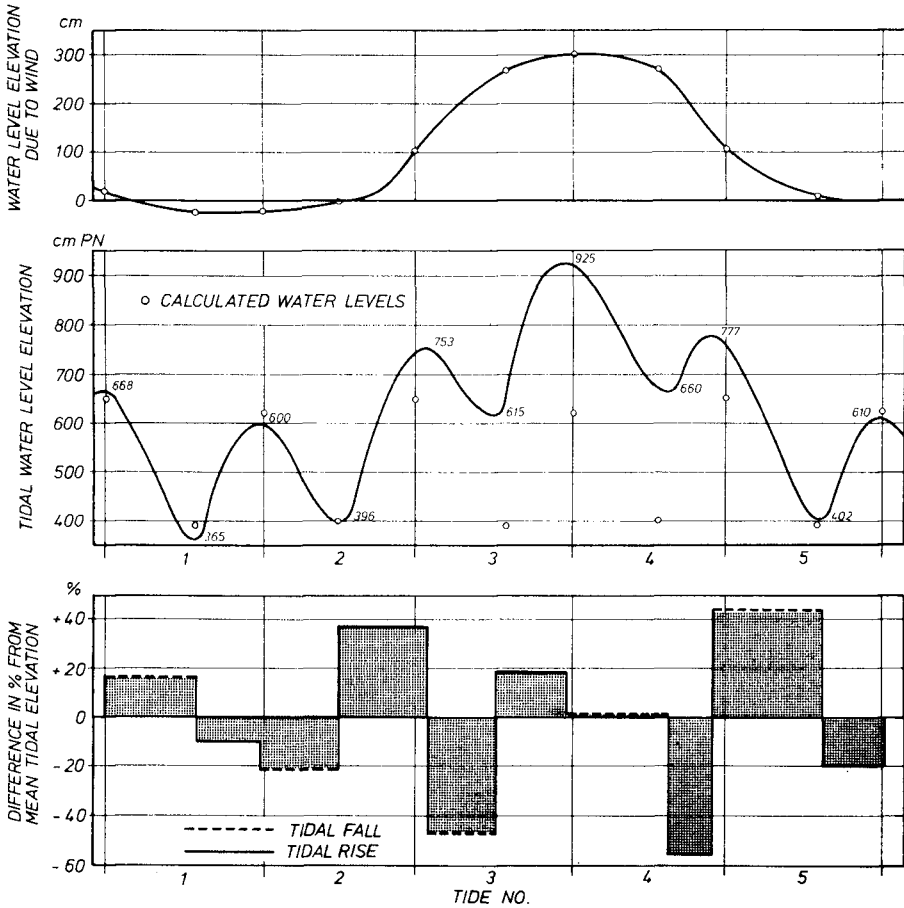


FIG. 6 : TIDAL WATER LEVEL ELEVATION DURING STORM SURGE I

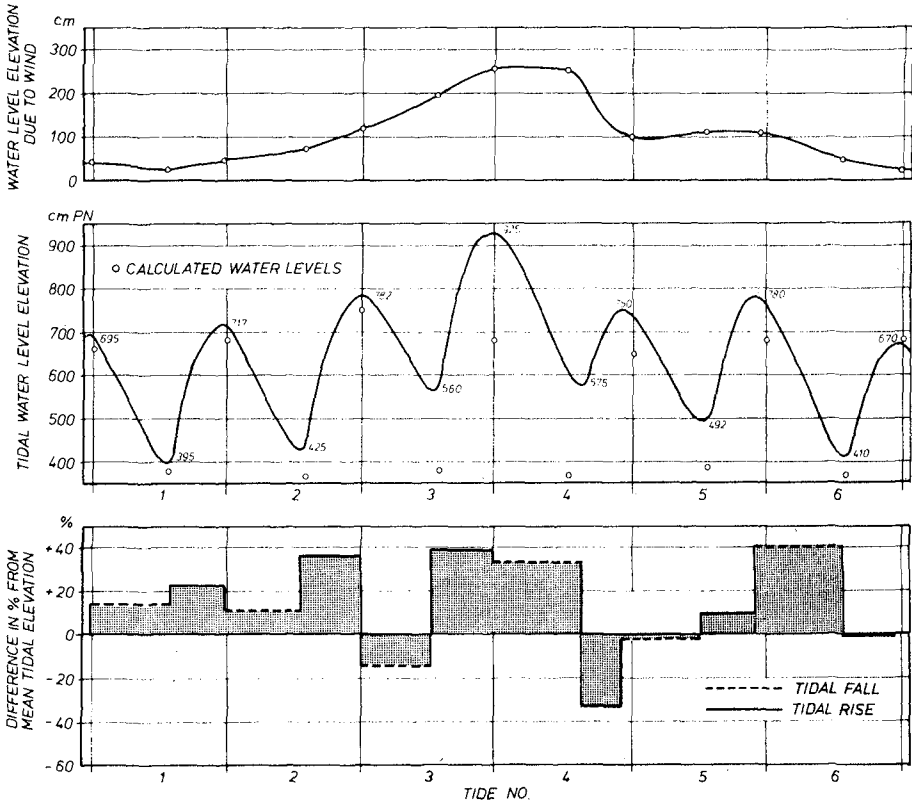


FIG. 7: TIDAL WATER LEVEL ELEVATION DURING STORM SURGE II

3.2 Results of the model tests

In Fig. 8 temperature increases averaged over one tide are plotted for the first, the second and the third tide respectively, i.e. the tides before HHW, along the measuring points No 1 through 10 (vid. Fig. 1) in a longitudinal section of the river region influenced by the injected waste heat.

Fig 8. shows, that mean temperature increases for storm surge I as well as for storm surge II because of the dominant currents in flood stream direction from tide to tide decrease downstream and increase upstream of the cooling water outlets.

It is obvious that the rapid rise of the wind set-up of storm surge I causes more remarkable decreases of the

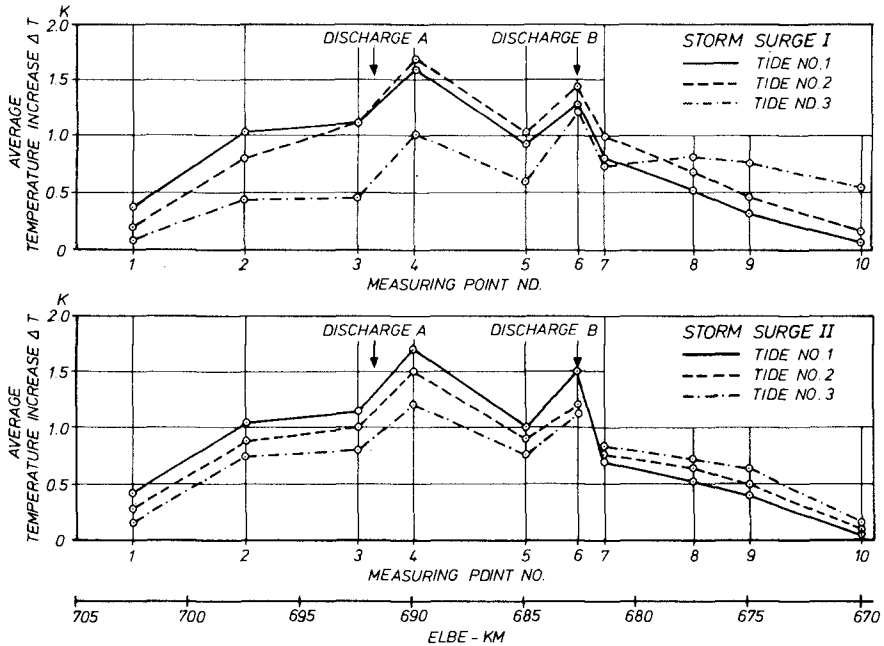


FIG. 8: AVERAGE TEMPERATURE INCREASE DURING THE STORM SURGES

average temperatures downstream and increases upstream respectively, than the slow rise of the wind set-up lasting over a longer time. The waste heat transported in the region upstream of the cooling water outlets by storm floods produces no higher temperature increases in the tidal river during the fall of the storm surge than obtained during the rise of the storm surge. The maximum temperature increases measured in the tidal river under mean tidal conditions were not exceeded during the investigated storm surge events. This is to trace back first of all to the bigger water volume available for the dilution of the injected cooling water.

CONCLUSION

In a thermal hydraulic tide model of the Elbe Estuary II in the FRANZIUS-INSTITUT the influences of tidal cycles and storm surges on the temperature increases in the far field region were investigated.

With the chosen hydrological boundary conditions, which correspond to natural tidal conditions of the Elbe River, no higher maximum temperature increases than for mean tides were obtained for tidal cycles or storm surges. Therefore for corresponding tidal conditions investigations with mean

tides can be admitted as representative for the judgement of thermal loads of tidal rivers.

Under other tidal conditions as for instance tides with remarkably higher semidiurnal or semimonthly inequalities or essentially more unfavorable ratios of fresh water discharge or cooling water discharge respectively and tidal discharges, i.e. a less number of passages of a waterbody at the outlets or a relatively higher admission of the tidal river with cooling water, investigations only with mean tides are not determining for the judgement of thermal loads of tidal rivers.

Storm surge events do not yield to higher temperature increases than mean tides in the lower regions of a tidal estuary first of all according to the bigger water volume available for mixing. But beyond that it must be noticed that a certain shifting of the admitted region upstream occurs. In that region no higher temperature increases than in the region influenced by waste heat injection under mean tidal conditions were measured.

Further basic investigations on the influence of different tidal conditions on temperature increases in a tidal river are projected.

OUTFLOW DYNAMICS AT A RIVER MOUTH

by

Masakazu Kashiwamura*

and

Shizuo Yoshida**

ABSTRACT

It has been extensively recognized from many past studies, that the interfacial Froude number must be unity at a river mouth, under the condition of a salt wedge existing inside the river. However, there seems no study having paid efforts to clarify how its numerical values distribute horizontally, inside or outside the river mouth. This problem has come to mind very important for the present authors, in order to obtain better understandings on the dynamical structure of the density current.

The river mouth has been thought to be an extremely singular place, from many field observations and laboratory experiments, because it forms a boundary between two quite different phases in flow pattern, inside and outside. For example, abrupt changes in velocity, thickness and mixing occur for the fresh water, at the river mouth. In order to solve its essential behavior, the transient motion of the fresh water, when it passes through the river mouth, was analysed based on some ideal conditions.

As a result, the flow of the fresh water was revealed to be identical in its property with the transonic flow in aerodynamics, where the interfacial Froude number plays a dominant part in place of the Mach number. If a salt wedge lies along the river bed, numerical values of the interfacial Froude number are known to be less than unity inside the river mouth. In such a case, the flow of the fresh water corresponds to the subsonic flow. On the other hand, once the fresh water passes through the river mouth, it changes into that of the supersonic flow, because the interfacial Froude number exceeds unity there. From those view points, horizontal distributions of the interfacial Froude number were investigated by rearranging past field data, and as a result, the wide area was occupied by the fresh water which was equivalent to the supersonic flow, and was stretching far offshore from the river mouth.

Next, the mechanism of mixing between the fresh water and the sea water was examined from both field measurements and laboratory experiments. As a result, different mechanisms were found to prevail inside the river mouth and outside, respectively. The outside mechanism is believed to belong to breaking of the interface due to the Kelvin-Helmholtz instability, but the inside is caused in a

* Professor, ** Instructor, Department of Engineering Science, Hokkaido university, Sapporo, Japan.

different manner that the interference of the interfacial wave to the roughness with a cusped shape which occurs along the interface in a certain condition, gradually breaks the interface, although the intensity of mixing is much less in the latter case.

Besides those two, if the tidal effect is remarkable, there is another type, in which vortices induced by a strong tidal current behind each of bed irregularities, attack the interface and destroy it.

INTRODUCTION

The present authors have continued a series of observational studies on the density current, for past twenty years, mainly in the neighborhood of the mouth of the Ishikari River, which is the second largest river in Japan and is the largest in Hokkaido. The location is shown in Fig. 1 and the enlarged map is shown in Fig. 2.

As the Japan Sea, to which the Ishikari River opens, has small tidal ranges, a typical salt wedge can be detected inside the Ishikari River, for the distance of several kilometers, in usual river discharges. Main studies performed so far, are as follows; the relationships between the river discharge and the length of the salt wedge, the interfacial friction, the transient flow of the fresh water passing through the river mouth, changes in velocity, thickness and density for the fresh water, mixing of the fresh water and the sea water, etc. Phenomena thus obtained in field observations are reproduced in laboratory experiments, and their properties are investigated in detail with changing the condition variously. Those results are finally analysed theoretically. Such a process is a conventional way for the authors.

Studies on dynamics of the outflow of the river water and the mechanism of mixing between the fresh water and the salt water are very important problems in near-shore regions including river mouths, but also for better understandings on the thermal discharge issued from nuclear or thermal power plants.

Several phenomena showing singularities of river mouths, which have been experienced in field observations and mathematical treatments will be presented in the followings. The other important problem on mixing will be described in the last paragraph.

2. REVIEW ON RESULTS OF THE PAST MEASUREMENTS

An example of vertical distributions in velocity, observed longitudinally along the Ishikari River, is shown in Fig. 3¹⁾, in which the river mouth is taken as the origin and the seaward direction is positive. Salinity distributions were observed at the same time but are not presented in the figure. However, it can easily be seen that the sea water flows upstream along the bed, and the fresh water flows down over the sea water and spreads out over the sea surface. It must be carefully observed, that the fresh water gains its maximum value in velocity, around the river mouth. In other words, the fresh water is temporarily accelerated at the river mouth, and decays again with the offshore distance. This fact has frequently been examined at any other observations.

Fig. 4 is another illustration of three kinds of observation made

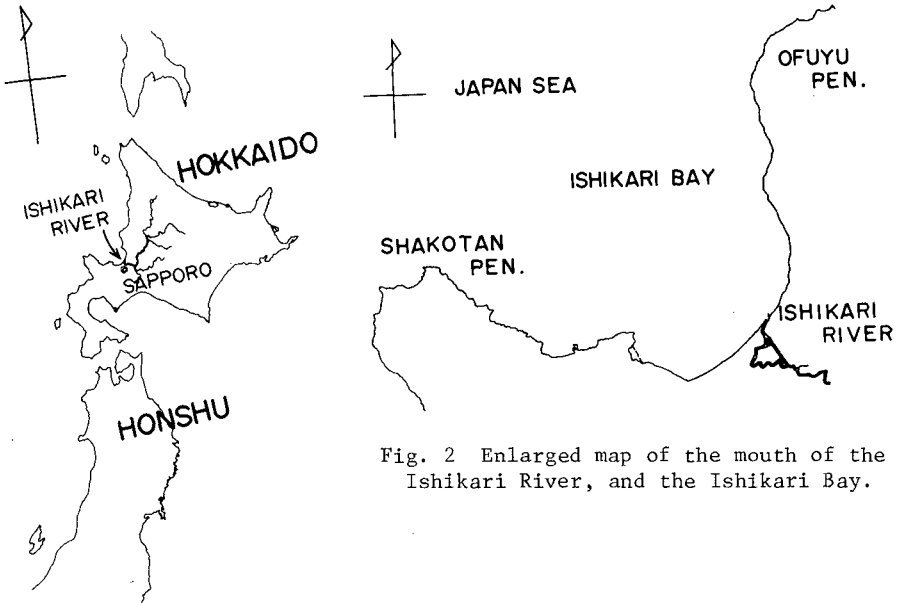


Fig. 2 Enlarged map of the mouth of the Ishikari River, and the Ishikari Bay.

Fig. 1 Location of Hokkaido and the Ishikari River.

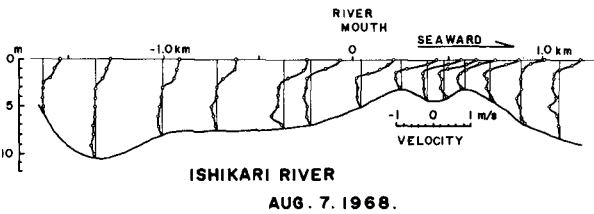
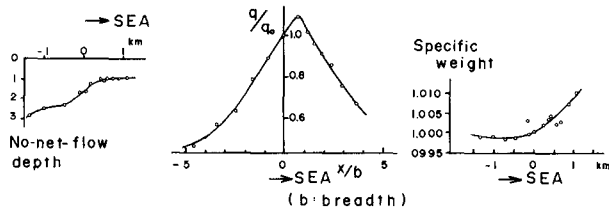


Fig. 3 Longitudinal distribution of the velocity along the Ishikari River around its mouth.

Fig. 4 Three kinds of quantity changing through the river mouth.



AUG. 7. 1968.

on the same day.^{1),2)} The left is the longitudinal change in no-net-flow depth, which means a depth where no velocity, upstream or downstream, is found. The depth is usually levelled at a little length below the density interface. The no-net-flow depth becomes suddenly shallower at the river mouth and the internal jump is formed. The central figure shows how the fresh water changes in velocity as mentioned before. The maximum is found at a short distance off the river mouth, where q denotes the velocity, q_0 is its value at the mouth, and b is the breadth of the river mouth. The right shows a longitudinal change in specific weight for the fresh water. Abrupt growth of mixing can be inferred between the fresh water and the salt water, outside the river mouth. From those three examples, the inside and the outside can be understood to be governed by different dynamical conditions.³⁾

Next, the flow patterns of the fresh water are reexamined.³⁾ Fig. 5 shows a plane map of stream lines for the fresh water, which was made from a great number of measurements on the velocity and its direction. The measurements needed many hours, but the result was not disturbed by the tide, because it is negligible in this sea area, as stated before. The growing rate of the spacing between two stream lines is shown against the distance in the lower figure, in which the width of the two stream lines at the distance of 400 m inside the mouth is taken as the standard, l_0 . The distance is measured along the line connecting every point with the highest velocity across any section of the surface flow. It can be understood that the spacing grows exponentially with the distance, viz., $l = l_0 \exp(kx)$.

Such a result is always detectable, under the condition of the salt wedge existing inside the river mouth. In the far offshore region, the same trend may not be considered to remain any more, by the effect of the sea current, wind and waves. Therefore, the exponential growth of the spacing should be considered as a transitional phenomenon, in the near shore region around the river mouth. When the river discharge increases, the numerical value of k also increases, and in an extreme case, k seems to become variable with the distance x . If the discharge decreases, the area where the value of k keeps constant becomes smaller within a limited scale. Then, it may be reasonable that k is, in general, taken as a function of x and Q which is the river discharge.

Fig. 6 shows all kinds of flow pattern, which were found experimentally in the past.^{3),4)} The top figure A is an extreme type which is obtainable in a very small river discharge, and the stream lines stretch radially in all directions from the river mouth. The bottom figure E is the other extreme type which occurs, if the river discharge reaches a great amount beyond a certain value, and the flow is that of a turbulent jet with the stream lines undistinguishable, but the border lines with both sided sea areas stretches initially parabolically with the distance, and finally becomes parallel in the offshore direction. There are several types, B, C and D, which are transitional between those two extremes.

The state of a salt wedge varies with the flow pattern, as shown in Fig. 7. The salt wedge develops extremely upstream in the case of A, and retreats conversely seawards in the case of E. Judging from the observational result of the salt wedge, the flow pattern in Fig. 5 seems to correspond to the case of B or C. The classification of the flow pattern, thus obtained, was made in laboratory experiments, in

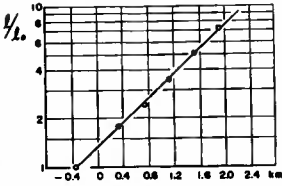
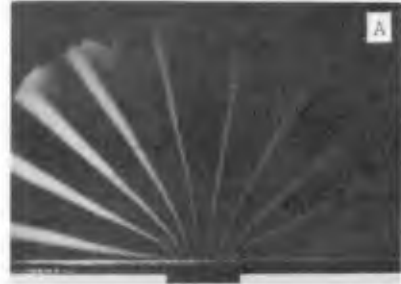
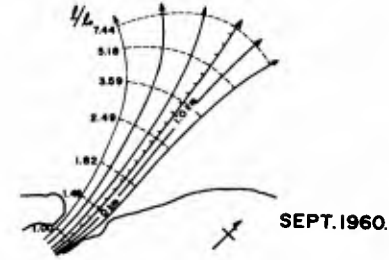


Fig. 5 Stream lines of the fresh water issued from the mouth of the Ishikari River.



Fig. 6 Various patterns of the fresh water issued from the outlet of an open channel.

which the transient acceleration of the fresh water was also found without exception in each case.

Fig. 8 (a), (b) and (c) show the acceleration areas in different conditions, with contour lines of identical values of velocity.²⁾ Other groups of lines with arrows are stream lines. The condition of (a) is close to that of A in Fig. 6, and the characteristic of potential flow is stressed at both corners, where the acceleration zones are remarkable, but along the center line, the acceleration is slightly detectable at the small distance off the mouth. The figure (b) seems to correspond to the flow of B or C in Fig. 6. The acceleration becomes remarkably stronger on the center line, and at the same time, at both corners. The figure (c) may belong to the type of C or D in Fig. 6. The acceleration at the corners goes down, while that on the center line grows up.

Such a kind of growth in transient acceleration on the center line is peculiar to the two-layered flow around the outlet or the river mouth. As for the type of E in Fig. 6, the investigation is still insufficient, by the reason of the limited condition in experiments.

It is understandable that the river mouth is a dynamically singular place, and it implies that different equations dominate the inside of the mouth, and the outside, respectively.

3. A THEORETICAL APPROACH WITH ENTRAINMENT TAKEN INTO CONSIDERATION

In order to analyse those interesting problems, the senior author, first, attempted a theoretical approach with the entrainment phenomenon taken into consideration. A simple model of the flow is shown in Fig. 9, where q denotes velocity, h the depth of the fresh water, and ρ the density of the fresh water. Those three are all variable with x . It is assumed that the density ρ_0 of the lower sea water is constant, and the entrained velocity V across the interface, into the fresh water, is proportional to the velocity q of the fresh water, viz. $V = Eq$, where E is the entrainment coefficient. In addition, the spacing l of stream lines is taken into account.

The problems are, thereby, arranged into the following one-dimensional equations.

$$\frac{d(qhl)}{dx} = Vl = Eq l \quad (1)$$

$$\frac{d(\rho qhl)}{dx} = \rho_0 V l = \rho_0 E q l \quad (2)$$

$$\frac{d(\rho q^2 h l)}{dx} = -(\rho_0 - \rho) g h l \frac{dh}{dx} \quad (3)$$

Eqs.(1), (2) and (3) are those of conservation of volume, mass and momentum, respectively. Besides, the empirical equation, that $l = l_0 \exp(kx)$, is employed in the differential form,

$$\frac{dl}{l} = K dx \quad (4)$$

where the coefficient k may, in general, be variable with x , as explained in the preceding paragraph. The following parameters, that $\epsilon = 1 - (\rho/\rho_0)$, $Re = hq/\nu$, $F_1^2 = q^2/\epsilon gh$ and $\psi = F_1^2 Re$, are also introduced,

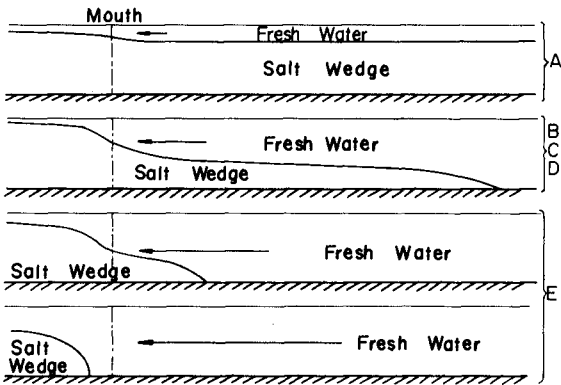


Fig. 7

Correspondence of the state of the salt wedge to the type of outflow pattern.

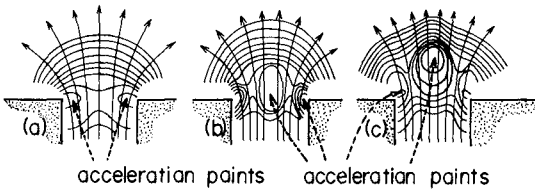


Fig. 8

Velocity distribution of the outflow illustrated with contour lines.

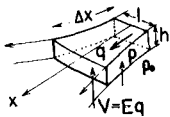


Fig. 9

Illustration of the model for the outflow of the fresh water.

where R_e is the Reynolds number, F_i is the interfacial Froude number and ψ is the third root of the inverse of the Keulegan number, respectively.

By rearranging those four equations, the followings are successively derived.

$$\frac{d\epsilon}{\epsilon} = -\frac{E}{h} dx \quad (5) \quad \frac{dq}{q} = \frac{\frac{E}{h}(1+F_i^2) - K}{1-F_i^2} dx \quad (6)$$

$$\frac{dh}{h} = -\frac{(2\frac{E}{h} - K)F_i^2}{1-F_i^2} dx \quad \frac{dF_i^2}{F_i^2} = \frac{3\frac{E}{h}(1+F_i^2) - K(2+F_i^2)}{1-F_i^2} dx \quad (7) \quad (8)$$

$$\frac{dR_e}{R_e} = (\frac{E}{h} - K) dx \quad (9) \quad \frac{d\psi}{\psi} = -\frac{2\frac{E}{h}(2+F_i^2) - 3K}{1-F_i^2} dx \quad (10)$$

It is, at the present, impossible to obtain a solution of each parameter against x , from those, because the characteristics of E and k have still been unsolved. However, there are a few equations which are convenient for calculating numerical values of some parameter from field observational data. For example, Eq. (5) is such one, which is useful for obtaining a distribution of the entrainment coefficient E , along the stream.

Table 1 shows various kinds of parameter varying with the distance x along the center line of the fresh-water flow at the Ishikari River. The right-end column gives the longitudinal change of E , which was obtained by using Eq. (5). If Eqs. (5) and (9) are combined, the value of k ought to be derived from the values of ϵ and R_e , which are obtainable from observations, but the validity of calculated values on k is still uncertain for lack of sufficient field data.

Distance ^m	ϵ	q ^{m³/s}	h ^m	F_i^2	R_i	R_e	ψ	E	
- 2 00	$\times 10^{-2}$ 2301	0.79	3.72	0.744	1.344	$\times 10^6$ 2.938	$\times 10^2$ 2.186	$\times 10^{-4}$ 3.233	
- 1 00	2299	0.99	3.63	1.198	0.835	3595	4.307	3.158	
river mouth	0	2297	1.07	3.65	1.433	0.698	3.798	5.442	22.41
1 00	2270	1.07	3.35	1.536	0.651	3585	5.507	4.427	
2 00	2237	1.06	3.05	1.680	0.595	3234	5.433	4.024	
3 00	2211	1.03	2.87	1.706	0.586	2956	5.043	27.26	
4 00	2195	1.01	2.75	1.724	0.580	2.778	4.790	17.54	
5 00	2183	0.99	2.66	1.722	0.581	2.634	4.536	14.01	
6 00	2172	0.97	2.55	1.733	0.577	2.474	4.288	12.91	

ISHIKARI RIVER AUG. 4. 1970.

Table 1

As for other parameters, they are also difficult to determine their numerical values particularly in the neighborhood of the river mouth, because the denominators included in right sides in Eqs. (6), (7), (8) and (10), are all $1 - F_i^2$, which becomes zero or very small at the mouth and then, has a great possibility to produce extended errors on estimating the values of parameters.

But, if we accept the general recognition, that $F_i = 1$ at the river mouth, when the salt wedge exists inside, all the numerators in Eqs. (6), (7), (8) and (10) must be also zero simultaneously. This fact leads to a single result, viz., $\frac{E}{kh} = 1/2$ at the river mouth. It can be concluded that three different parameters E , k and h must be

unified just at the river mouth, in a form of the above equation, although its validity is also uncertain at the present.

However, from many facts, thus described, it is inferable that the river mouth is expected, also in a mathematical sense, a very singular place. Then, it seemed important for the senior author to re-examine the essentials lying within a transient process given by the fresh water, when it passes through the river mouth. This will be described in the following paragraph.

4. SIMILARITY BETWEEN FRESH-WATER FLOW AND TRANSONIC FLOW

Idealizing the fresh-water flow to be inviscid, immiscible with the sea water, and also irrotational, a transient behavior of the fresh water, when it passes through the river mouth, is treated. To neglect mixing has the same meaning with the sea water stagnant, and it results no change in density for the fresh water, viz., ϵ can be put as a constant. The equations describing the motion of the fresh water are given as follows.

$$u \frac{\partial u}{\partial x} + v \frac{\partial u}{\partial y} + \epsilon g \frac{\partial h}{\partial x} = 0 \quad (11)$$

$$u \frac{\partial v}{\partial x} + v \frac{\partial v}{\partial y} + \epsilon g \frac{\partial h}{\partial y} = 0 \quad (12)$$

$$\frac{\partial}{\partial x} (h u) + \frac{\partial}{\partial y} (h v) = 0 \quad (13)$$

Eqs. (11) and (12) are equations of motion, and Eq. (13) is that of continuity. The axis x is taken in the offshore direction and y is parallel to the sea shore. The symbols u and v are components of velocity in the x and y axes, respectively.

First, transformation of Fig. (13) leads to,

$$\frac{\partial u}{\partial x} + \frac{\partial v}{\partial y} = -\frac{1}{h} (u \frac{\partial h}{\partial x} + v \frac{\partial h}{\partial y}) \quad (14)$$

Eqs. (11) and (12) can be transformed into

$$\left. \begin{aligned} \frac{1}{\epsilon g h} (u \frac{\partial u}{\partial x} + v \frac{\partial u}{\partial y}) &= -\frac{1}{h} \frac{\partial h}{\partial x} \\ \frac{1}{\epsilon g h} (u \frac{\partial v}{\partial x} + v \frac{\partial v}{\partial y}) &= -\frac{1}{h} \frac{\partial h}{\partial y} \end{aligned} \right\} (15)$$

The two right-handed sides in Eq. (15) are substituted into the right side in Eq. (14). Thus, the following is derived immediately.

$$\frac{\partial u}{\partial x} + \frac{\partial v}{\partial y} = \frac{1}{\epsilon g h} (u^2 \frac{\partial u}{\partial x} + u v \frac{\partial u}{\partial y} + u v \frac{\partial v}{\partial x} + v^2 \frac{\partial v}{\partial y})$$

Since the flow is irrotational, then

$$\frac{\partial u}{\partial y} = \frac{\partial v}{\partial x}, \quad u = \frac{\partial \phi}{\partial x}, \quad v = \frac{\partial \phi}{\partial y}$$

where ϕ is the velocity potential.

The above equation can be arranged into the form,

$$\left(1 - \frac{u^2}{\epsilon gh}\right) \frac{\partial^2 \phi}{\partial x^2} - 2 \frac{uv}{\epsilon gh} \frac{\partial^2 \phi}{\partial x \partial y} + \left(1 - \frac{v^2}{\epsilon gh}\right) \frac{\partial^2 \phi}{\partial y^2} = 0 \quad (16)$$

This expression is surprisingly the same in form with the well-known equation of the two-dimensional air flow, viz.

$$\left(1 - \frac{u^2}{a^2}\right) \frac{\partial^2 \phi}{\partial x^2} - 2 \frac{uv}{a^2} \frac{\partial^2 \phi}{\partial x \partial y} + \left(1 - \frac{v^2}{a^2}\right) \frac{\partial^2 \phi}{\partial y^2} = 0$$

where a is the local sound velocity. If we put $\sqrt{\epsilon gh}$ in place of a , the above becomes Eq. (16).

As is well known, the discriminant D of the above equation is written as,

$$D = \left(\frac{uv}{a^2}\right)^2 - \left(1 - \frac{u^2}{a^2}\right)\left(1 - \frac{v^2}{a^2}\right) = \frac{q^2}{a^2} - 1 = M^2 - 1$$

where $q = \sqrt{u^2 + v^2}$, and M is the local Mach number, that is, $M = q/a$.

Two-dimensional linear partial differential equations, in general, have three quite different types, elliptic for $D < 0$, parabolic for $D = 0$, and hyperbolic for $D > 0$. Therefore, properties of the air flow are classified as follows.

	Equation	Flow Characteristic
$M < 1$	elliptic	subsonic flow
$M = 1$	parabolic	sonic flow
$M > 1$	hyperbolic	supersonic flow

If a body is placed in a comparatively high subsonic flow, three different zones, for $M < 1$, $M = 1$ and $M > 1$, are frequently formed around the body, where the flow is subsonic,

sonic, and supersonic, respectively. The flow thus combined, is called a "transonic flow". All described here are well-known facts in aerodynamics.

As easily understandable from those mentioned so far, attention must be centered on that the fresh-water flow lies under a mathematically and dynamically identical condition with the air flow.

The discriminant of Eq. (16) is as follows.

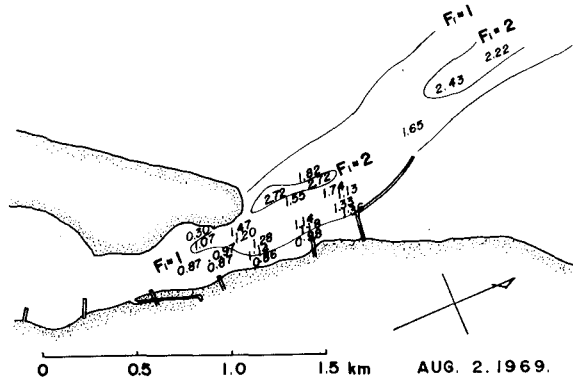
$$D = \frac{q^2}{\epsilon gh} - 1 = F_1^2 - 1 \quad (17)$$

The interfacial Froude number F_1 plays, undoubtedly, a dominant part on the fresh-water flow, as well as the Mach number M does on the air flow. Corresponding to, that $F_1 < 1$, $F_1 = 1$ and $F_1 > 1$, the mathematical condition varies as, elliptic, parabolic and hyperbolic, respectively.

In a case of the salt wedge existing inside the river, it is already known that $F_1 < 1$ for the inside, $F_1 = 1$ at the river mouth and $F_1 > 1$ for the outside.⁵⁾ This case corresponds to the transonic flow, where the inside is subsonic, the flow at the mouth is sonic, and the outside is supersonic. The reason, why various kinds of flow pattern occur as shown in Fig. 6, seems to depend deeply on the interfacial Froude number F_1 , whose value is determined at the distance far upstream from the mouth or at the front of the salt wedge.

Considering from those evidences described so far, there seems to be a possibility that the entire region including the outside has no

Fig. 12
Another example of
the distribution of
 F_1 , on 2 August,
1969.



5. ON THE MECHANISM OF MIXING BETWEEN TWO LAYERS

Descriptions in preceding paragraphs are those of hydraulic aspect on the dynamical behavior of the fresh water. In this paragraph, from more physical view points, the mechanism of mixing of the fresh water and the salt water, is examined in detail, by the junior author.

A great number of studies have been made on mixing by many researchers until now, but a decisive explanation on the entire phases in mixing, inside and outside the river mouth, has not been achieved yet. This paragraph is no exception, but some new mechanisms, which seem very important, have been discovered by the author, and then, a new opinion on mixing, inside and outside, will be presented.

As a conclusion, there are three mechanisms. One is that due to breaking of the interface between the fresh water and the salt water, based on the Kelvin-Helmholtz instability. Another is due to the interference of the interfacial gravity wave to the interfacial cusped roughness which arises in a certain condition. The last one is due to vortices generated behind bed irregularities by a strong tidal current.

5-1. Experimental Apparatus and Methods

Fig. 13 shows a general view of the experimental apparatus, which consists of a wide and shallow vessel, $3\text{ m} \times 2\text{ m} \times 0.5\text{ m}$ and a long channel with a rectangular cross-section, $6\text{ m} \times 0.08\text{ m} \times 0.15\text{ m}$. The former corresponds to the sea, and the latter to the river, respectively. The wide vessel is separated, upper and lower, with a vinyl film in order to generate a tide, in the manner that the upper salt water is moved, up and down, by taking in and out another water, from below, under the vinyl film. The surface level can be controlled to follow any tidal change. The controller is illustrated in a block diagram, as shown in Fig. 14.

Experiments were made in two cases, with the bed smooth, and rough with square wooden pieces. The flow, the surface level and the interface level were detected with a light beam illuminated through a very narrow slit, into the direction at a right angle with the channel, and with the aid of a solution of fluorescein sodium as a tracer, as shown

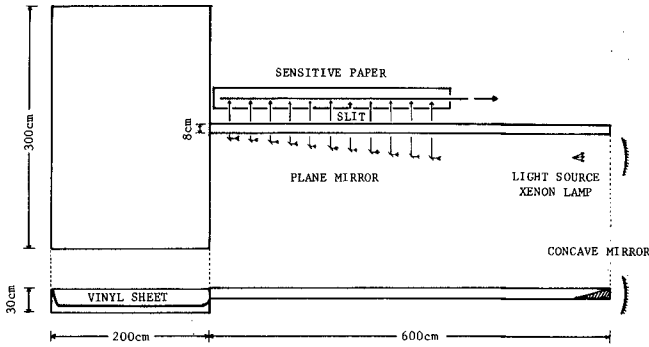


Fig. 13
General view of
the apparatus.

Fig. 14
Block diagram of
tide-generator
and controller.

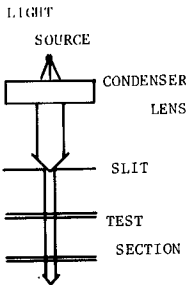
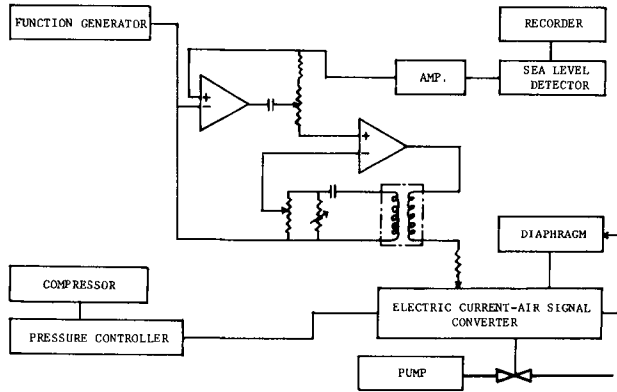


Fig. 15
Measurement device with
a light beam.

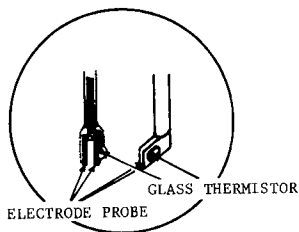


Fig. 16
Salinity detecting device
with an electrode and a
thermistor.

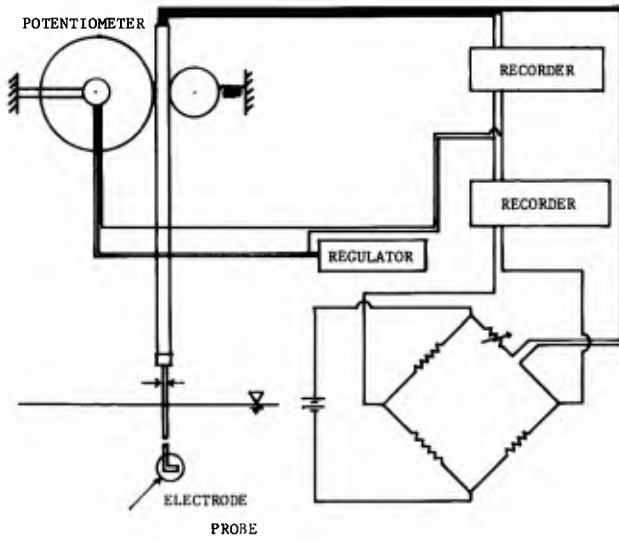


Fig. 17

Illustration for the mechanism of density measuring device, which contains a potentiometer for control of the level of an electrode probe.

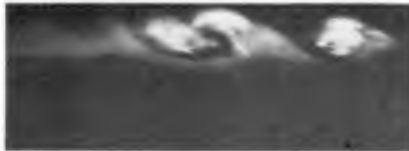


Photo.1

Unstable interfacial waves are breaking, with drawing spiral curves. They are caused by the Kelvin-Helmholtz instability.

in Fig. 15. This equipment can detect a motion of the tracer at an arbitrarily selected cross-section. Density was measured, through conversion, with an electrode, and a device specially designed to move the electrode, up and down, as shown in Figs. (16) and (17). The level of the electrode can be determined with a potentiometer, which is set in the device.

5-2. The Mechanism of Mixing in a Steady Two-Layered Flow

a) In a case of the outside of the river mouth

If a velocity of the fresh water is small enough, the interface, between the fresh water and the salt water, maintains itself very clearly, even at the distance far from the mouth. In such a case, the horizontal distribution of the fresh-water velocity was already shown in Fig. 8 (a). Once the velocity increases, this figure gradually approaches Fig. 8 (c). As mentioned before, acceleration area appear at both corners of the mouth and on the center line of the flow. In those special areas, the Keulegan number θ^7), which is denoted by $(\epsilon g \nu)^{1/3} / U$, where U is the velocity of the moving layer and ν is a coefficient of kinematic viscosity, is smaller than that of surrounding areas. Unstable interfacial waves appear in those areas, at first, at both corners where the condition that $\theta \leq 0.06-0.07$ is satisfied prior to other places.

Increase of the river discharge brings this condition also into the area on the center line of the flow off the mouth, and unstable waves develop there. Photo 1 shows such unstable interfacial waves, whose growing processes are very smooth with drawing spiral curves. This kind of waves is similar to that Thorpe discovered in an experiment of exchange flow⁸). The generating condition of this wave, which Thorpe determined, was that $\theta \leq 0.06$ and it is very close to that the author discovered. Therefore, it is inferable that the interfacial waves, which were observed by the author on the center line, are based on the mechanism of the Kelvin-Helmholtz instability. Those waves are detectable in laboratory experiments and also in field observations, where an ultrasonic echo-sounder is preferable. When such unstable waves occur at the interface, lumps of clear sea water buoy up intermittently on the surface, which is covered by the muddy fresh water.

b) In a case of the inside of the river mouth

In a steady flow, the upstream velocity within the salt wedge is so weak that no mixing appears, due to vortices which are produced by the interference with bed roughness. Then, the results will be described in a case with a smooth bed, in experiments. Keulegan discovered, in 1949, that the interface was destroyed by breaking of cusps of interfacial gravity waves, in experiments.⁷) The criterion of the limit of such cusped breaking was given by him, with three kinds of channel whose cross-sections were 2 cm \times 4 cm, 4 cm \times 8 cm and 11.3 cm \times 28.5 cm, respectively, as shown in the followings.

$$\theta = 0.178 \quad \text{for } R_e < 450 \quad (18)$$

$$\theta = 0.127 \quad \text{for } R_e > 450 \quad (19)$$

where $R_e = RU/\nu$, R is the hydraulic radius and U is the mean velocity of a moving layer.

Many researchers have accepted that this kind of cusped breaking

is the main cause of mixing in a steady flow. However, the investigation on its detailed mechanism and the theoretical treatments are still unsuccessful, in spite of many efforts paid through a series of studies on the instability of shear flows.

The junior author has discovered a noticeable fact, after a long-termed investigation, that the cusped breaking is induced little by the amplification of wave heights but is produced, in almost all cases, by a superposition of the interfacial gravity waves and a certain kind of waves which have not been detected by anyone yet. Those waves, thus newly found, are cycloidal in shape, as shown in Photo. 2, and differ from any kinds ever known, for example, at a point of their extremely slow motions. They are never believed to be identical to capillary waves at the interface, by comparison of numerical orders of their velocities. They seem to be rather interfacial roughness, than waves.

The breaking of interfacial waves takes place, in fact, in the manner that when any interfacial wave goes over one top of the cycloidal-shaped interfacial roughness, the wave deforms itself due to instability, into a shape of cusp, which grows gradually into a spiral, composed of the fresh water and the sea water, and this mechanism brings mutual entrainment between the two layers.

As shown in Photo. 3, the interfacial cycloidal roughness is caused only by a vortex formed in a spiral-shape, within the salt-water layer between the interface and the no-net-flow layer below. Thus, the spiral vortex plays a leading role over the entire mechanism of this kind of mixing. This vortex is induced by the instability due to the shear flow of the salt water, just below the density interface. Theoretical consideration has already been made, on this mechanism, and published by the junior author.⁹⁾

As mentioned thus far, the cusped breaking was revealed to have a local fine mechanism. Throughout those experiments, the overall condition of the cusped breaking was that $\theta \leq 0.13$, where θ is the Keulegan number. This value is consistent with that proposed by Keulegan, as shown in Eq. 19. It should be stressed that the dimension of the apparatus employed by the author is of the same order with that by Keulegan. Therefore, it is inferable that both the breakings observed by Keulegan and the author, are quite identical. But it must be noticed that the difference of apparatus in scale seems to result a different condition of the cusped breaking. Table 2 shows those different conditions. Limit values of the breaking are shown with θ and R_1 which is the Reynolds number with a representative length taken as a thickness of the moving layer. Although R_1 changes little with a scale of the apparatus, the limit value of θ increases with a growth in scale for the apparatus. There is no any more information yet outside those scales, but it seems certain that the cusped breaking occurs without exception in any scale, if $\theta \leq 0.13$.

It is believed that there must be such a type of mixing inside the actual river mouth, but it is difficult technically to detect it, because the phenomenon is too delicate to catch the entire process, and moreover, the mixing degree is much smaller than that experienced outside, in the type of the Kelvin-Helmholtz instability. Studies in this direction, therefore, should be made with more efforts, in future.

5-3. The Mechanism of Mixing due to Tide

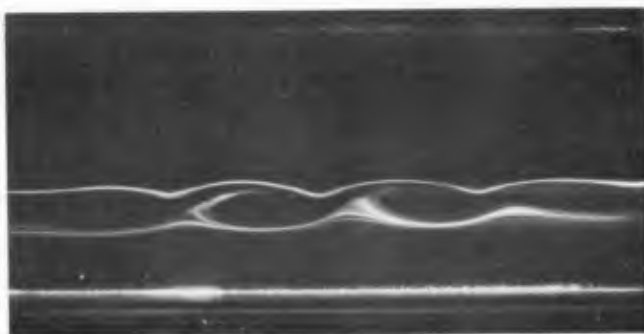


Photo. 2

The cycloidal shaped roughness formed at the density interface, and vortices generated below it. Those are newly found types of mixing.



Photo. 3

Breaking of the interfacial waves by the interference with the roughness formed along the density interface.

Table 2

Cross-section of moving layer	width height 30cm×30cm	width height 8cm×45cm	width height 8cm×15cm
The value of θ , at the limit of cusped breaking	0.215	0.177	0.13
The value of R_1 , at the limit of cusped breaking	1200-1300	1200-1500	1500-3000

It is well known that there can be three types of density current, inside the river mouth, viz., of negligible, of moderate, and of intense mixing. The two-layered flow belongs to the negligible mixing type and the salt wedge develops. This type is, in general, found at a river, which opens its mouth to the sea with a small tidal range. Contrary to this, the intense-mixing type is found in a case with a great tidal range. But, however great it is, the intense-mixing type cannot be reproducible in laboratory experiments, if the channel bed is smooth.

Many opinions agree with each other, about the reason for arising of the intense-mixing type, as that it is the tidal current induced inside the river. But, for the detailed mechanism, opinions are divided, such that, it is the increase of instability of the interface due to shear, breaking of the interface by internal waves, etc.

The junior author has arrived a conclusion that the bed roughness is the most dominant cause for it. In his experiments, even for the strongest tidal current, the interface was always stable, although it oscillated with a large amplitude. The shear flow near the interface, the interfacial wave itself, and the growth of the boundary layer at the bed can never be a destroyer of the interface. The further experiment brought to him a fact that only a single small obstacle at the bed could be a destroyer.

Photo. 4 shows such an example, in which the interface breaks at some distance behind a rectangular wooden piece, 0.6 cm \times 0.6 cm in cross-section, placed on the bed, under the tide of 1 cm in vertical range and of 333 sec. in period. This detailed mechanism is shown very clearly in Photo. 5, in which spiral vortices separate from the piece, next, grow along the border line of the wake behind the piece, and finally attack the interface and destroy it into mixing. But, it is noticeable that if the bed has a single obstacle, the interface, once broken, recovers its form again far downstream, accompanied by the decay of vortices.

Then, the establishment of the intense-mixing type needs a series of successively placed pieces, with suitable spacings. If the spacing is too small, vortices disappear, opposite to expectation, and the interface keeps its identity. According to the experiments, the intense-mixing type develops most effectively, in a condition of the spacing of 10-15 times as long as the height of the piece.

Spiral vortices produced behind the piece are probably caused by the instability of the free boundary layer which is formed downstream from the piece. The experimental results are compared with those obtained through theoretical studies by Lessen¹⁰⁾, and Tatum and Gotoh¹¹⁾, as shown in Fig. 19. The structure of flow at the distance of 2.1 cm behind the rectangular piece is illustrated in Fig. 18, where the uniform velocity U_∞ is 4.0 cm which was measured at a point of onset of unstable waves.

With those values and other data on the wave number κ and the distance x of onset of instability together, the dimensionless wave number $\kappa_* (= \delta \kappa)$ and the Reynolds number $R (= \delta U_o / \nu)$ were obtained as shown in Fig. 19, where $\delta = 0.439 \sqrt{\nu x / U}$ and $U_o = U_\infty / 2$. The calculated values are all within the unstable region, and therefore, the vortices are undoubtedly caused by the instability of the free boundary layer developed behind the rectangular piece.

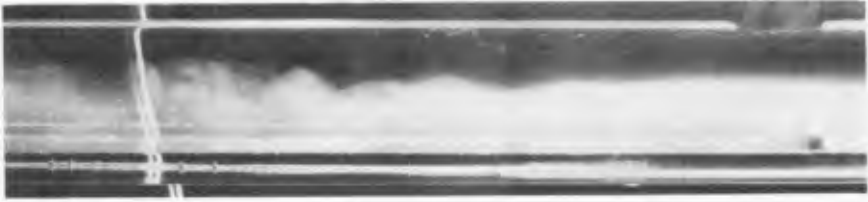


Photo. 4 The interface breaks at some distance behind a small piece placed on the bed, at the right hand. Vortices induced by a strong tidal current, plays a leading role on the breaking.

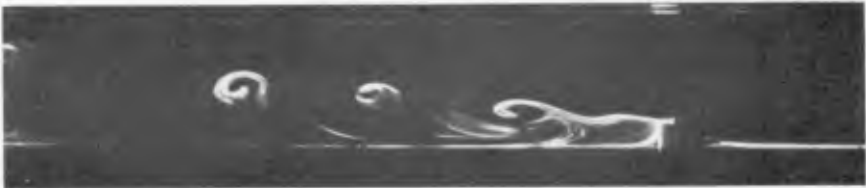


Photo. 5 Vortices induced by the tidal current behind a rectangular piece. They are formed through the instability of the free boundary layer behind the piece.

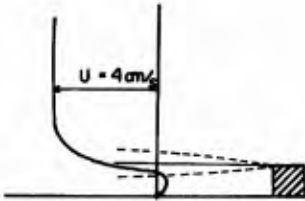


Fig. 18 velocity distribution behind the piece.

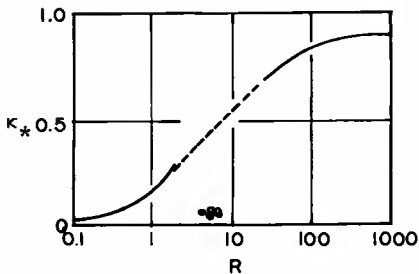


Fig. 19 Calculated points are all within the unstable zone. From this, Those vortices are proved to be formed by the instability of the free boundary layer.

CONCLUSION

This paper consists of two main parts, one of which is on the transient behavior of the fresh water, when it passes through a river mouth, and the other is on the mechanism of mixing of two layers inside and outside the river mouth.

In the former, the fresh-water flow is concluded to be dynamically identical with the transonic flow in aerodynamics. In the latter, three types of mixing are described. One is that of the Kelvin-Helmholtz instability, found outside the mouth. Another is a new type due to the interference of the interfacial waves and the roughness at the interface. This type is expected to occur inside the mouth. The last one is that induced by the tidal current.

The former part was made by the senior author and the latter was by the junior author. The authors are deeply indebted to the members of the laboratory, for their helpful collaboration, in field measurements, laboratory experiments and other works for preparing this paper.

REFERENCES

- 1) Kashiwamura, M. and Yoshida, S.: Transient acceleration of surface flow at a river mouth, Coastal Engineering in Japan, Vol. 14, 1971.
- 2) Kashiwamura, M. and Yoshida, S.: Flow pattern at a river mouth, International Symposium on Stratified Flows, NOVOSIBIRSK, IAHR, 1972, published by ASCE, 1973.
- 3) Kashiwamura, M. and Yoshida, S.: Outflow pattern of fresh water issued from a river mouth, Coast. Eng. in Japan, Vol. 10, 1967.
- 4) Yoshida, S. and Kashiwamura, M.: Tidal response of two-layer flow at a river mouth, Proceedings, 15th Coastal Engineering Conference, HONOLULU, 1976.
- 5) Kashiwamura, M.: Spread of river water over the sea, Hydraulic Series, 75-B-7, JSCE, 1975 (in Japanese).
- 6) Sears, W. F.: Transonic potential flow of a compressible fluid, J. Appl. Phys., Vol. 21, 1950.
- 7) Keulegan, G. H.: Interfacial instability and mixing in stratified flows, J. Res. Nat. Bur. Stand., Vol. 43, 1949
- 8) Thorpe, S. A.: A method of producing a shear flow in a stratified fluid, J. Fluid Mech., Vol. 32, 1968.
- 9) Yoshida, S.: On a mechanism for breaking of interfacial waves, Coast. Eng. in Japan, Vol. 20, 1977.
- 10) Lessen, M.: On stability of free laminar boundary layer between parallel streams, NASA, Rep. 979, 1950.
- 11) Tatum, T. and Gotoh, K.: The stability of free boundary layers between two-uniform streams, J. Fluid Mech., Vol. 7, 1960.

CHAPTER 181

THERMAL AND BIOLOGICAL IMPACT OF LNG VAPORIZER DISCHARGE

BY

PETER A. MANGARELLA AND GORDON A. ROBILLIARD*

ABSTRACT

A simplified steady state multilayered (horizontally homogeneous) thermal model is described and applied to assess the effects of the cold water discharge created by a proposed liquid natural gas (LNG) regasification facility. The model, similar to ones developed for predicting average cooling pond performance, accounts for advection and diffusion between layers, atmospheric and solid boundary heat exchange, and heat exchange due to tidal and density currents. For the configuration in which both the intake and discharge were located in a dredged turning and docking basin, recirculation created thermal deficits from -8°C to -17°C . Adverse environmental effects on migrating species (particularly various life stages of shrimp) and the benthic community and costs associated with auxiliary seawater heating suggested that other alternatives (such as a separate intake basin or an offshore diffuser) would be more appropriate.

*Senior Project Engineer and Senior Aquatic Biologist, Environmental Systems Division, Woodward-Clyde Consultants, 3 Embarcadero Center, San Francisco, California U.S.A.

INTRODUCTION

The importation of LNG requires the construction and operation of regasification facilities. In the process of vaporizing the LNG energy is required. In the case considered* the energy source was the water in a nearby bay. The vaporization process utilized a once-through system in which seawater drawn from the bay passed through the vaporizers, was cooled and then discharged back into the bay.

The bay, created by a barrier island, has a relatively uniform depth of around 3.5 m. The principal navigational channel in the bay is dredged to 11 m and is located approximately 1000 m offshore of the site. To accommodate the LNG carriers a turning and docking basin and approach channel dredged to 12.5 m was required. A typical cross section of the turning basin for a nearshore location is shown in Figure 1. The surface area of the turning and docking basin was about 1 square kilometer.

Since the bay is an estuarine system, the salinity varies spatially and temporally in response to freshwater inflow and tidal exchange with the Gulf of Mexico. Maximum salinity (~30 ppt) occurs near the tidal passes. The shallowness of the bay coupled with wind and tidal induced mixing promote vertically well-mixed conditions. However, in the deeper navigational channels Holmes (1977) indicates that strong longitudinal and vertical stratification may occur. The tides are classified as mixed and have a maximum astronomical range of about 0.5 m.

The proposed average production of natural gas was approximately 26 million cubic meters per day requiring a seawater flowrate of $92 \text{ m}^3 \text{ sec}^{-1}$. The temperature drop through the vaporizers (Figure 2) for average plant output varied from about -4.5°C to -5°C . For intake temperatures below 9°C auxiliary heating of the intake water was required to safeguard against ice formation in the vaporizers.

The original design called for discharging the colder water from the vaporizers into the bottom of the turning basin and withdrawing the water from near the surface of the same basin. The horizontal distance between the intake and discharge was about 950 meters.

It was reasoned that the continuous discharge of cold water into the bottom of the turning basin would tend to create a stratified thermal regime analogous to that found in a cooling pond. The discharge would create density currents which will spread out from the discharge point and create a cold layer of water extending over much of the bottom of the turning basin.

*This paper reports the findings of special studies associated with the environmental impact assessment of a proposed LNG regasification facility located on the Gulf Coast.

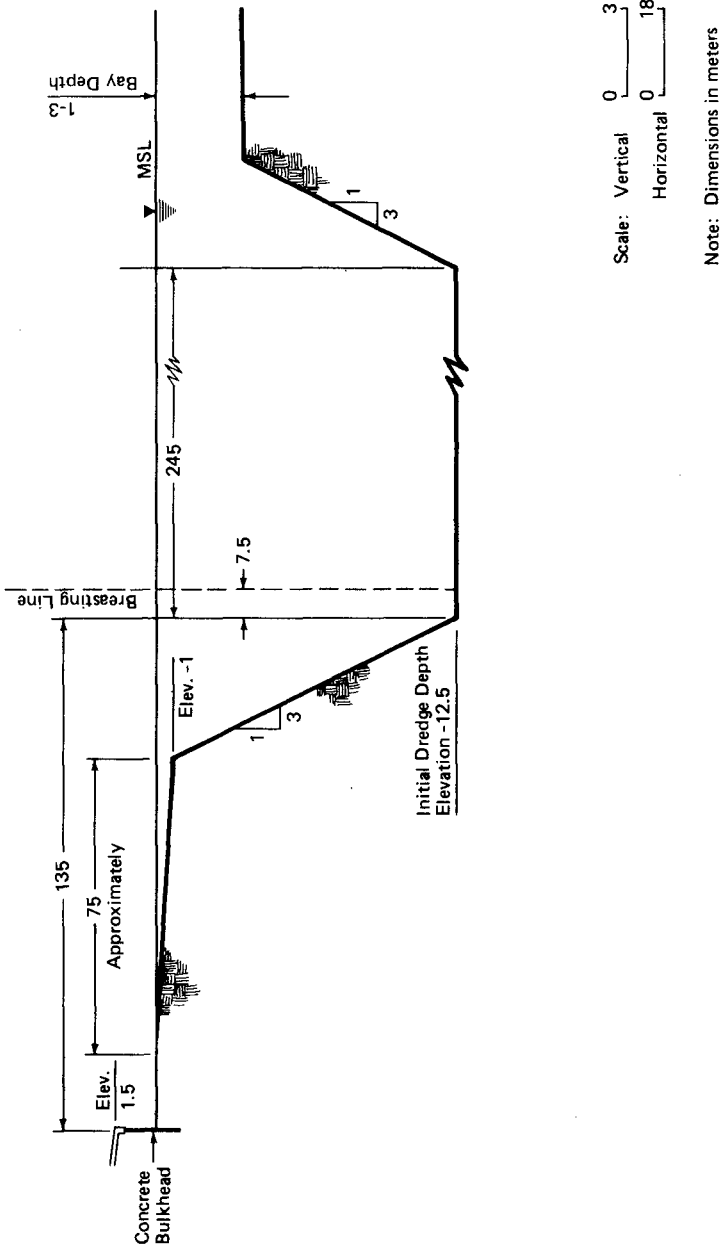


Figure 1. TYPICAL SECTION OF TURNING BASIN

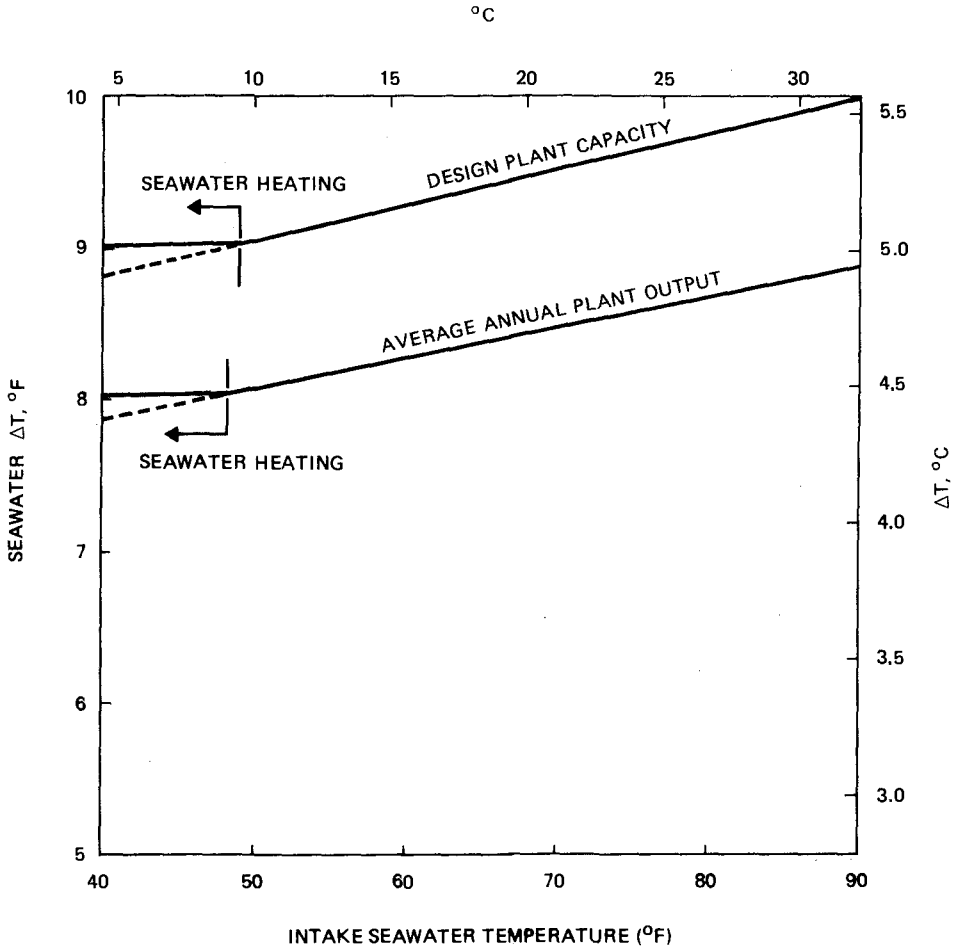


Figure 2. TEMPERATURE DROP ACROSS THE VAPORIZERS VERSUS INTAKE SEAWATER TEMPERATURE

On the other hand wind and tidal-induced mixing would tend to destratify the basin. Vertical and longitudinal mixing would also be created by interaction of tidal and density influenced flow between the approach channel and the turning and docking basin. It was concluded that, in spite of vertical mixing which might create local vertical well-mixed conditions for short time periods of the order of several days to a week, the monthly average condition would be adequately described by assuming a stably stratified system.

THERMAL MODEL

The conceptual model of a three-layered, stratified system and of the principal flow and heat exchange mechanisms governing the thermal balance in the basin is shown in Figures 3 and 4 using standard notation. The conservation equations for flow and energy applied to each layer form the basis of the model. Other elements of the model are: empirical surface and bottom heat exchange relations, estimates of mass and energy flux associated with tidal and density-induced currents, and the vaporizer temperature differential relationship already discussed.

The relationship for atmospheric heat exchange used the simplified rate equation relating heat flux to temperature differential via a heat exchange coefficient which is a function of wind speed and water temperature (Ryan and Stolzenbach, 1972). The values of the heat exchange coefficient and equilibrium temperature were computed from average monthly meteorological data. The bottom heat exchange was calculated using a similar formulation.

The mass and energy flux associated with density currents in the approach channel was based on a simplified counterflow model (Schijf and Schonfeld, 1953). The model assumed that the cold bottom layer of water in the turning basin would create a density flow out of the basin along the approach channel. Typical values of the calculated density current flowrate were $2.1 \text{ m}^3 \text{ sec}^{-1}$ for July and $1.4 \text{ m}^3 \text{ sec}^{-1}$ for January. The average tidal flowrate (over a half tidal cycle) in the approach channel was estimated at $3.5 \text{ m}^3 \text{ sec}^{-1}$ based on an estimate of the tidal prism.

The surface currents in the bay were quite strong because of the proximity of the site to major tidal passes. Given the strong surface currents it was assumed that the temperature of the surface layer of the turning basin (when located at either of two offshore sites) equalled the ambient surface temperature of the bay.

Diffusive flux between the surface and intermediate layers was calculated using the eddy diffusivity formulation given by Kullenberg (1971). The eddy diffusivity, a function of wind speed, stratification, and the vertical current shear, was of the order of 10^{-1} to $10^{-2} \text{ cm}^2 \text{ sec}^{-1}$ depending on the month and the intake discharge configuration.

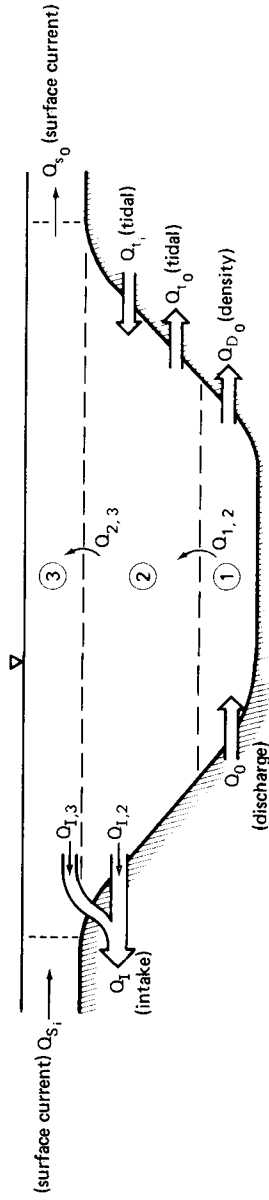


Figure 3. CONCEPTUAL MODEL OF FLOW WITHIN THE TURNING BASIN

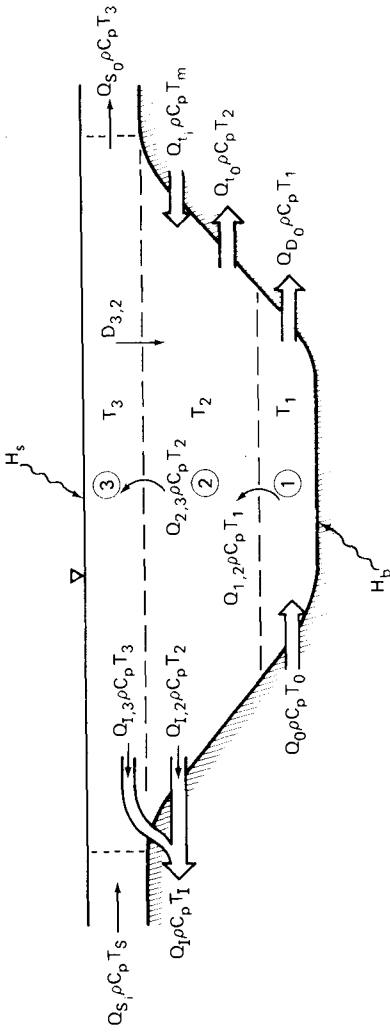


Figure 4. CONCEPTUAL MODEL OF HEAT EXCHANGE MECHANISMS WITHIN THE TURNING BASIN

The accuracy of the model is limited more by the deficiencies and assumptions used in conceptualizing the model than by the accuracy of the input data. The accuracy of similar cooling pond models (which do not involve many of the exchange processes considered here) has been examined by Ryan (1972). In general, Ryan found that comparisons of field data with model predictions were satisfactory after a suitable calibration. In this case no data were available for calibration and the results must therefore be considered preliminary. In spite of suspected deficiencies in the absolute accuracy of the model, results were of practical value in comparing the relative merits and deficiencies of alternative intake discharge configurations.

MODEL RESULTS

The model was applied to a series of intake-discharge configurations in which both the configuration and offshore location of the basin were varied (Table 1). As discussed earlier, these alternatives were considered after significant recirculation problems were discovered for the initial configuration (C1). Note that an offshore diffuser was also considered (C4).

Typical model predictions for the temperature of the bottom layer of the basin are given in Figures 5 and 6. Recirculation was predicted for all cases in which both the intake and discharge are in the same basin and the intake withdraws from the intermediate layer. During the winter (November through March) auxiliary heating was required for these cases. An estimate of the magnitude of the heating requirements is given in Table 2. Recirculation caused the temperature deficits to be a maximum in the summer as the surface layer warms and diffusive heat exchange between the surface and intermediate layer was limited by the stratification. For other cases the temperature deficit is relatively constant throughout the year.

ENVIRONMENTAL IMPACT OF INTAKE DISCHARGE CONFIGURATIONS

The major environmental impacts associated with the intake and discharge of seawater are (1) entrainment and impingement of organisms as a result of seawater intake, (2) cold shock to migratory organisms due to discharge of cooled seawater, (3) development of a cold water benthic community in the turning basin.

Among the cases analyzed (Table 1) the basin located at the 1-m isobath is less desirable than at the 2-m or 3-m isobaths because it is closer to the nearshore, shallow-water migration routes of shrimp and fish, and entrainment/impingement impacts are expected to be greater. There is relatively little difference between the impacts at the 2-m and 3-m isobaths: However, in cases A2 and B2, withdrawing water from

Table 1. TURNING BASIN LOCATIONS AND INTAKE-DISCHARGE CONFIGURATIONS CONSIDERED

Offshore Location of the Turning Basin	Intake & Discharge in the Turning Basin		Separate Intake Basin	Offshore Diffuser
	(1)*	(2)**	(3)	(4)
3-m isobath (A)	A1	A2	A3	
2-m isobath (B)	B1	B2	B3	
1-m isobath (C)	C1	N/A	C3	C4

*Intake withdraws from intermediate layer of basin in cases A1, B1, and surface layer in case C1.

**Intake withdraws 1/4 of total intake flowrate from surface layer and 3/4 from intermediate layer.

LEGEND FOR BASIN LOCATION
 A: 3-meter isobath
 B: 2-meter isobath
 C: 1-meter isobath

LEGEND FOR INTAKE-DISCHARGE CONFIGURATION
 1: intake and discharge in turning basin; intake withdraws from intermediate layer
 2: intake and discharge in turning basin; intake withdraws from surface and intermediate layers
 3: separate intake basin
 4: offshore diffuser

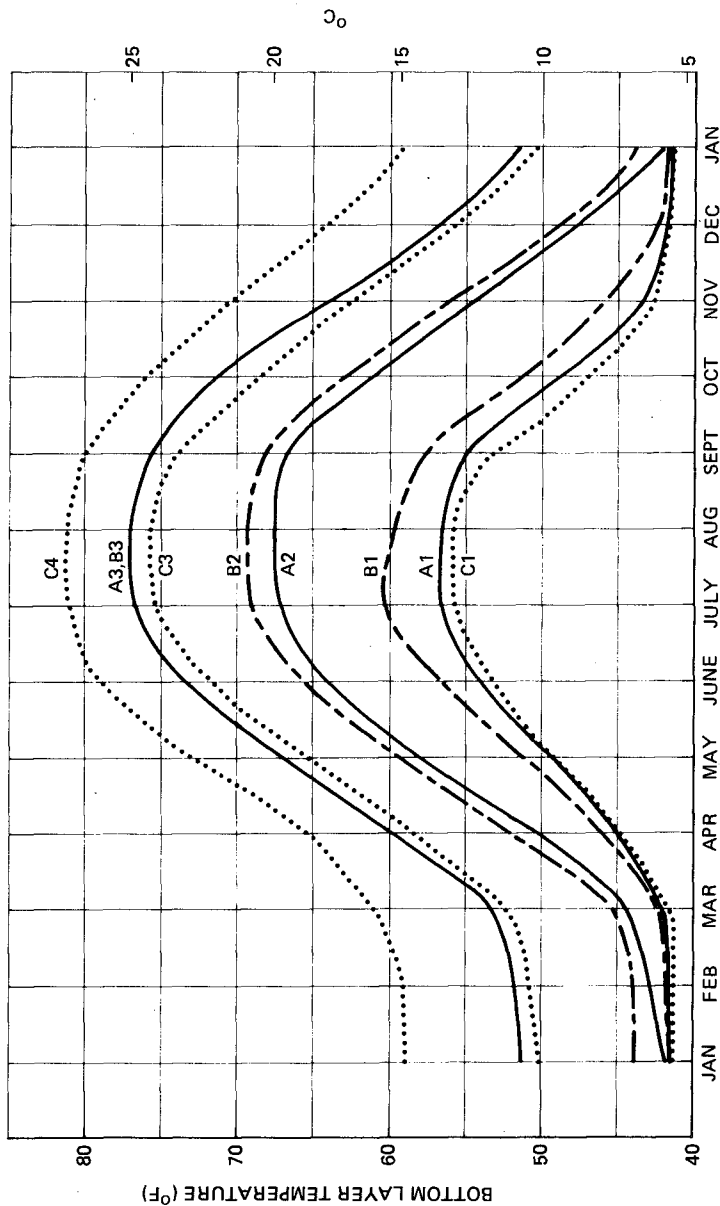


Figure 5. SUMMARY OF TEMPERATURE OF THE BOTTOM LAYER OF THE TURNING BASIN

LEGEND FOR BASIN LOCATION
 A: 3-meter isobath
 B: 2-meter isobath
 C: 1-meter isobath

LEGEND FOR INTAKE-DISCHARGE CONFIGURATION
 1: intake and discharge in turning basin; intake withdraws from intermediate layer
 2: intake and discharge in turning basin; intake withdraws from surface and intermediate layers
 3: separate intake basin
 4: offshore diffuser

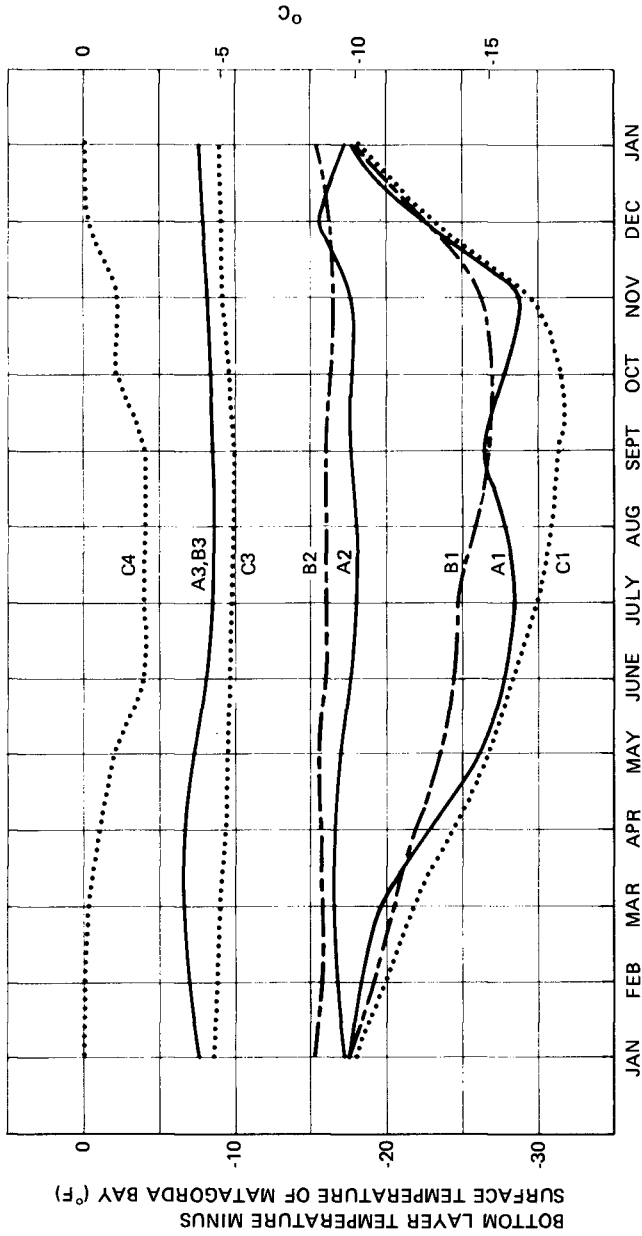


Figure 6. SUMMARY OF THE TEMPERATURE OF THE BOTTOM LAYER OF THE TURNING BASIN RELATIVE TO SURFACE TEMPERATURE OF MATAGORDA BAY

Table 2. SEAWATER HEATING REQUIREMENTS DUE TO RECIRCULATION
(Degrees Celsius - Months)

Offshore Location of Basin	Intake-Discharge Configuration			Offshore Diffuser (4)
	Intake and Discharge in Basin (1)*	(2)**	Separate Intake Basin (3)	
3-m isobath (A)	4.5	0	0	0
2-m isobath (B)	4	0	0	0
1-m isobath (C)	3	N/A	0	0

*Intake withdraws from intermediate layer of basin in A1, B1, and surface layer in C1.

**Intake withdraws 1/4 of total intake flowrate from surface layer, 3/4 from intermediate layer.

the surface layer would have potentially greater entrainment and impingement impacts because there tend to be more planktonic larval forms in the surface water layers.

Only in cases A1, B1 and C1, where the intake and discharge are both in the turning basin, and the intake withdraws water wholly from the turning basin, is there a potential ecologically significant difference in thermal regimes among turning basin locations. The 1-m location (case C1) is expected to result in a greater maximum cold shock impact than the 2-m or 3-m locations (cases B1 or A1).

Based on the assessment of thermal impact alone, the four intake-discharge configurations can be compared as follows. Discharge offshore (case C4) and intake in a separate basin (cases A3, B3 and C3) are expected to have the least impact; but one does not appear to be distinctly better than the other. Cases A2 and B2 are expected to have an intermediate level of impact. The greatest impacts are expected in cases A1, B1, and C1, primarily due to the accumulation of cold water in the bottom of the basin.

SUMMARY

A simplified steady state thermal model assuming horizontally homogeneous thermal conditions was useful in comparing the relative thermal impact created by several intake discharge configuration for an LNG regasification facility. Recirculation appeared to be a serious problem when both the intake and discharge were in the basin and the intake withdrew from below the surface of the upper mixed layer.

REFERENCES

- Holmes, C.W., 1977, "Effects of Dredged Channels on Trace-Metal Migration in an Estuary," Jour. Research U.S. Geol. Survey, Vol. 5, No. 2, p. 243-251.
- Jirka, G.H., Abraham G., and Harleman, D.R.F. (1975). An Assessment of Techniques for Hydrothermal Prediction. Prepared for the Nuclear Regulatory Commission, PB-250 509.
- Kullenberg, Gunnar, 1971. Vertical Diffusion in Shallow Waters. *Tellus XXIII*, 2, pp. 129-135.
- Ryan, P.J., 1972. Temperature Prediction and Design of Cooling Ponds, In Engineering Aspects of Heat Disposal from Power Generation, D.R.F. Harleman, ed., Massachusetts Institute of Technology, Department of Civil Engineering, R.M. Parsons Laboratory for Water Resources and Hydrodynamics.
- Ryan, P.J., and Stolzenbach, K.D., 1972. Environmental Heat Transfer. In Engineering Aspects of Heat Disposal from Power Generation, D.R.F. Harleman, ed., Massachusetts Institute of Technology, Department of Civil Engineering, R.M. Parsons Laboratory for Water Resources and Hydrodynamics.
- Schiff, J.B., and Schonfeld, J.C., 1953. Theoretical Considerations on the Motion of Salt and Fresh Water. Proceedings of the Minnesota International Hydraulic Convention, IAHR and Hydrodynamics Division, American Society of Civil Engineers.

CHAPTER 182

PREVENTION OF FREEZING IN FJORDS

by

SVEINUNG SÆGROV[†]

ABSTRACT

Criteria for the design of outlet arrangements from hydro-electric power stations, necessary to prevent ice formation in fjords in the winter months, are presented. The initial entrainment of seawater to the fresh water discharge has been investigated by means of laboratory models. A numerical model of the fjord dynamics, as well as a simplified analytic model, is used to study the estuarine circulation and entrainment in the fjord. Heat loss to the atmosphere is parametrized using small modifications of well known empirical formulas.

INTRODUCTION

As a result of power development, the fresh water supply to several Norwegian fjords is or will be increased during the winter months. This may lead to more severe ice conditions in cold periods. There are two reasons to avoid this: first, necessary ship traffic in the fjords will be obstructed; and second, there is a possibility of climate changes, due to an ice-covered fjord, that may be disastrous for fruit harvests.

[†] Address: River and Harbour Laboratory
Klaebuveien 153, N 7034 Trondheim, Norway.

By mixing the fresh water from the power station with warmer, more saline water in the fjord, the risk of freezing may be reduced. One way of doing this, is to discharge the fresh water below the pycnocline with a considerable velocity. The principle may be compared with the dilution of a submerged sewage outlet. In our case, however, the fresh water discharge is much greater and will influence the currents in the whole fjord.

The purpose of our investigations is to find the necessary mixing of fresh water with saline water to prevent freezing, and the discharge velocity and depth which will give this mixing.

FJORD DYNAMICS AND INITIAL MIXING

A typical Norwegian fjord shows large variations in the width, and usually one or more narrows are to be passed before the fresh water reaches the sea. Figure 1 shows the most important hydraulic conditions of a typical fjord. The fresh water discharge mixes with the fjord water and forms a brackish layer. If the fjord is deep, and the tidal and wind effects are of minor importance, it can be shown that the velocity and the depth of the brackish layer passing through the entrance of the fjord correspond to a densimetric Froude number for the brackish layer (F_d^1) equal to 1. This is called a hydraulic control. The densimetric Froude number is defined in this way:

$$F_d^1 = \frac{u}{\sqrt{g \cdot \frac{\Delta\rho}{\rho} \cdot h}} \quad (1)$$

where

u is the velocity of the brackish layer, h is the depth, ρ is the density, $\Delta\rho$ is the density difference between the layers and g is the acceleration of gravity.

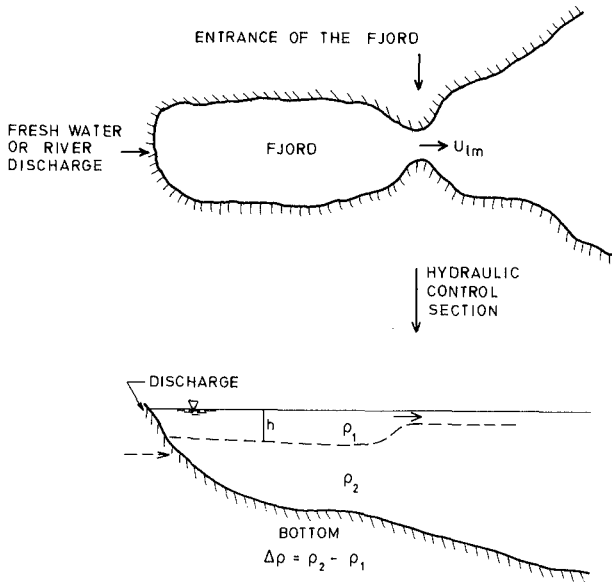


Figure 1. Some characteristics of fjord dynamics. u_{lm} is the velocity of the brackish water at the mouth, h is the thickness of the brackish water, ρ_1 is the density of the brackish water and ρ_2 is that of the fjord water.

The control condition also determines the depth of the brackish layer inside the fjord mouth. For further discussion of this see BINNEY (1972).

In many cases the fjord is narrow and the effects of the Earth's rotation can be neglected.

The details of the initial mixing process, which occurs at the fresh water outlet, are shown in Figure 2.

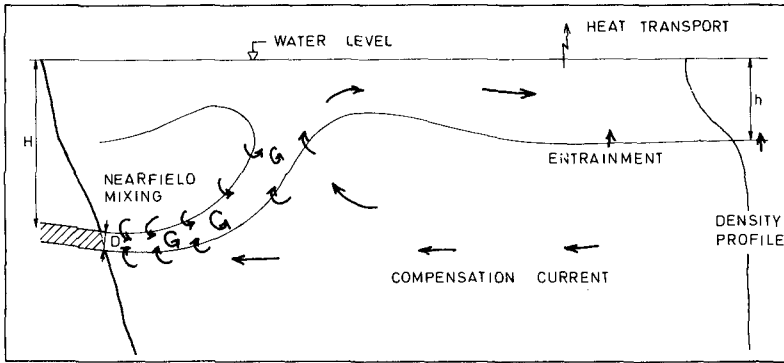


Figure 2. Mixing of fresh water and salt fjord water near the outlet. H is the outlet depth, D is the diameter and h is the thickness of the brackish layer in the fjord.

The discharge water enters the recipient with a considerable velocity (2-5 m/s). In the area near the outlet, the velocity leads to an intense mixing with the saline fjord water. The jet rises to the surface, and forms a brackish water current towards the fjord mouth. The influence of wind tends to maintain the turbulence in the upper brackish layer, and leads to entrainment to the brackish layer from below.

A typical density profile of the fjord is also shown in the figure. The brackish layer is rarely fully mixed and has therefore a density gradient.

LABORATORY EXPERIMENTS

The near field mixing is investigated quantitatively in a laboratory model. The experimental setup is shown in Figure 3.

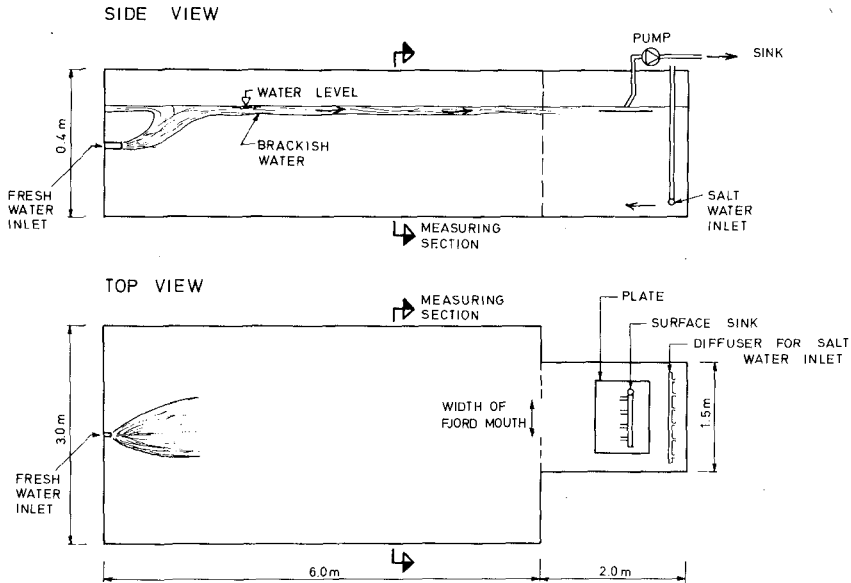


Figure 3. Arrangement for the laboratory experiments.

Fresh water is discharged into the salt water reservoir through tubes of various diameters and at various depths.

The width of the fjord mouth must be correctly scaled in the reservoir to simulate the hydraulic control (STIGEBRANDT 1975).

The brackish water is sucked from the surface by an arrangement which consists of a plate to prevent suction from the lower layer, and 4 pipes placed at an angle to the surface. In this way, the suction has no effects on the reservoir currents.

To maintain stationarity, salt water is supplied to the reservoir by means of a diffuser. This has a considerable outlet area to avoid turbulence. To avoid dynamic effects of the flow, a rough estimate of necessary salt water discharge has

to be made for each test.

During the experiments, horizontal and vertical profiles of salt and velocity are measured at the section shown in Figure 3.

The laboratory experiments are scaled geometrically according to the Froude scaling, that is that the Froude number F_d is the same in model and prototype (reality) (ABRAHAM, 1975). The definition of F_d for this purpose is:

$$F_d = \frac{u_o}{\sqrt{g \cdot \frac{\Delta\rho}{\rho} \cdot D}} \quad (2)$$

where

- u_o = discharge velocity,
- D = outlet diameter,
- $\Delta\rho$ = density difference fjord water-fresh water,
- ρ = density of fresh water,
- g = gravity acceleration

This gives the following scaling ratios, where the index m represents the model scale, p the prototype scale and r the ratio between the two.

Length scale	$L_r = L_m/L_p$
Volume scale	L_r^3
Time scale	$L_r^{0.5}$
Velocity scale	$L_r^{0.5}$
Discharge scale	$L_r^{2.5}$

In our tests we have used $L_r = 1:300$ for scaling ratios.

The experiments are carried out under the assumption that the topography has no prohibitive effect on the initial mixing process.

The results from the laboratory experiments are shown in Figures 4 and 5. Figure 4 shows how the mixing ratio P , defined as the brackish water flux through the measuring section relative to the fresh water discharge, depends on the densimetric Froude number F_d and the relative outlet depth of the jet H/D . Increased F_d or relative depth leads to increased mixing.

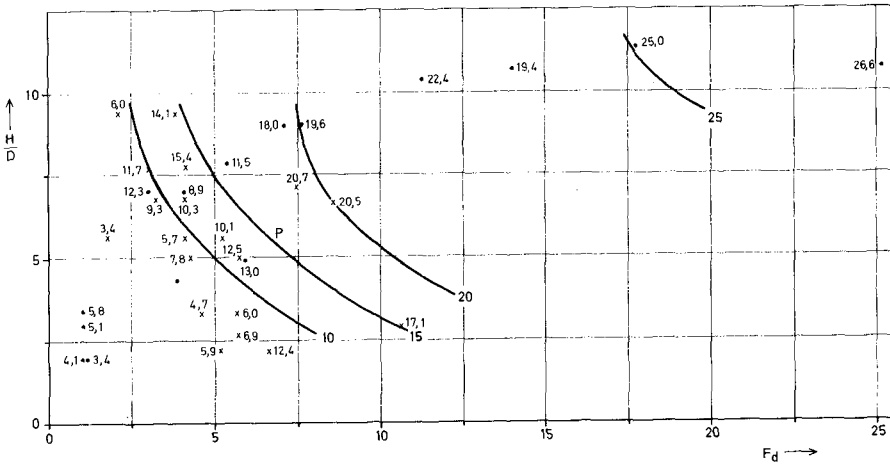


Figure 4. Mixing due to outlets below the brackish layer. P is the mixing ratio, F_d is the densimetric Froude number, H the outlet depth and D the outlet diameter.

As shown earlier, the densimetric Froude number depends on discharge velocity, diameter and density difference between

the fresh water and the fjord water.

A larger velocity gives a more intense mixing. In addition, the jet passes a longer distance before it reaches the surface. A smaller diameter, for example by using two outlet openings, leads to a larger contact area between the fresh water jet and the surrounding fjord water. All these effects lead to greater mixing, in accordance with the figure.

When the outlet depth is increased, the jet has a longer ascent through the fjord water. Increased depth also leads to a more vertical path for the jet. Experiments show that this leads to a greater mixing and a more homogeneous brackish layer.

When the outlet is near the surface, one has to take into account the thickness of the brackish water layer. Figure 5 shows some test results for outlets in or near the brackish layer. The figure shows how the mixing ratio P depends on the densimetric Froude number F_d and the thickness of the brackish layer compared to the outlet depth.

The figure clearly shows that for a given F_d , the mixing ratio will decrease if the thickness of the brackish layer increases or the outlet depth becomes smaller. One reason for this effect may be reentrainment of brackish water. This makes the mixing between fresh water and fjord water less efficient.

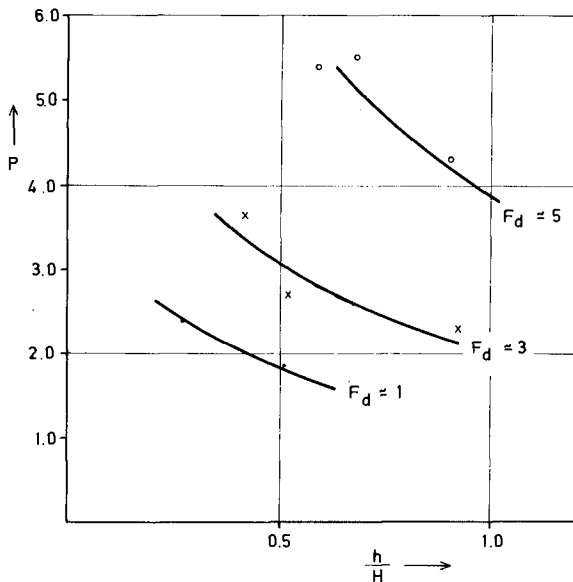


Figure 5. Mixing of fresh water outlets near the surface. P is the mixing rate, F_d is the densimetric Froude number, h the thickness of the brackish layer and H the outlet depth.

In Figure 6, the laboratory results are combined in a different way. The figure shows how the mixing ratio depends on the energy loss and the relative outlet depth. The energy loss at the outlet is defined as

$$h_f = \frac{u_o^2}{2g} + \frac{\Delta\rho}{\rho} \cdot H \quad (3)$$

The symbols are defined in eq. 2.

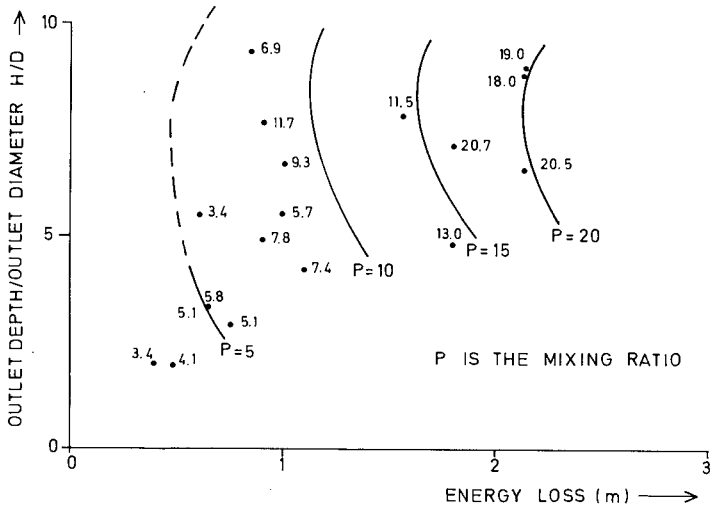


Figure 6. Mixing rate in the near field. Dependence of energy loss.

According to the results, there is an optimal outlet depth which is ca. 8 times the outlet diameter.

The laboratory experiments also show that there may arise a considerable stratification in the brackish water layer. The stratification is important because it prevents some of the heat content in the brackish layer from reaching the water surface. A criterion which we have applied is that we can use the entire brackish water as a heat magazin, provided the salinity difference within the brackish layer is less than 2 ppt. This limit is based on experience, and depends on wind homogenizing and convection due to cooling of saline surface water.

There is obviously a connection between the stratification and the mixing ratio. The higher the mixing ratio, the more complete is the mixing between the fresh water and fjord water.

HEAT TRANSPORT

The heat transport through the surface is governed by many meteorological processes. The main contributions in our cases are short and long wave radiation, evaporation, condensation and conduction. For the heat exchange between water and atmosphere, the following empirical equations are used:

Short wave radiation

$$H_s = (0.93 - C^2) H_{sc} \cdot (1-f) \quad (4)$$

C = cloud cover,

H_{sc} = sun radiation (W/m^2),

f = albedo of the surface, depends on latitude and time of day.

Only a fraction of the short wave radiation is absorbed by the water masses, the other part is reflected back to the atmosphere. The contribution from short wave radiation is not significant during the winter season.

Long wave radiation

$$H_l = 0.97 \cdot \sigma (T_a^4 (1 - 0.26 \exp(0.000888 T_a^2)) - T_s^4) \quad (5)$$

σ = Stefan Boltzmann constant = $5.67 \cdot 10^{-8} W/(\text{°K}^4 m^2)$

T_a = air temperature (°K)

T_s = surface temperature. (°K)

The long wave radiation is important for the heat budget. The sea surface radiates almost as a black body, and the outgoing energy from the long wave radiation is proportional to the fourth power of the absolute temperature. This is also a considerable amount of incoming energy due to long wave radiation.

Evaporation, condensation and conduction

$$H_e + H_c = - f(W) [(e_s - e_a) + C_1(T_s - T_a)] \quad (6)$$

e_s = saturation pressure at temp. T_s (mb)

e_a = vapour pressure at 2 m level (mb)

C = 61.3 Pa/°K

$f(W)$ = wind function.

Evaporation, condensation and conduction processes at the surface of the water depend on relative humidity and the temperature difference between air and water surface.

They also depend on the wind. This dependence is given by a wind function $f(W)$, which accounts for the forced convection of heat from the water surface due to shear generated motions in the air.

Wind function

$$f(W) = 0.027 (T_{sv} - T_{av})^{1/3} + 0.031 W \quad (7)$$

W = wind velocity (m/s)

$T_{sv} = T_s / (1 - 0.378 \frac{e_s}{p})$

$T_{av} = T_a / (1 - 0.378 \frac{e_a}{p})$

p = atmospheric pressure (10^2 Pa)

The total amount of heat exchange between water and atmosphere can be written as

$$H_n = H_s + H_l + H_e + H_c \quad (8)$$

Further details are given in RYAN et al. (1975).

MODEL OF THE ESTUARINE CIRCULATION

To account for the effect of mixing and cooling in the fjord, a numerical model of the fjord circulation has been developed.

The model describes the fjord circulation as a two layer system, in accordance with Figure 1. The upper layer of brackish water moves towards the fjord mouth, and a weak compensation current below the brackish water current supplies the brackish water to the mixing regions.

The equations for the brackish layer are developed from a work by STOMMEL and FARMER (1952) and presented in AUDUNSON et.al. (1976).

The equations are:

Conservation of volume

$$\frac{d(u h b)}{dx} = w_e b \quad (9)$$

Conservation of salinity

$$\frac{d(u h b S_1)}{dx} = w_e S_2 b \quad (10)$$

Conservation of momentum

$$\frac{d}{dx} (u^2 h b) - u w_e b = - g h b \frac{d\zeta}{dx} - \frac{1}{2} g h^2 \frac{b}{\rho_1} \frac{d\rho_1}{dx} + \left(\frac{\tau_\zeta}{\rho_1} - \frac{\tau_h}{\rho_1} \right) b \quad (11)$$

where w_e is the entrainment velocity, u the velocity of the brackish layer, h the thickness of the brackish layer, b the width of the fjord, S_1 the salinity of the brackish layer, S_2 the salinity of the fjord water, ζ the surface level, ρ_1 the density of the brackish layer, τ_ζ the friction force at the surface and τ_h the friction force at the boundary layer.

Further, a shear stress between the two layers, proportional to the square of the velocity, is included. (LONG, 1975). The lower layer is assumed to be in hydrostatic equilibrium

The boundary conditions are the volume flux, temperature and salinity of the mixing near the outlet of fresh water. In addition, the air temperature and the wind distribution within the fjord area are important input data. To simulate correct control condition, the width of the narrows is an important boundary condition. The density of the water is assumed to be independent of temperature.

The model contains the equations (4) - (8) for heat exchange with the atmosphere.

The equations are solved by means of the Runge Kutta integration method. From these equations and boundary conditions, the model gives values of temperature, salinity, velocity and thickness of the brackish layer step by step along the fjord.

The necessary initial mixing to keep the water temperature at the mouth of the fjord over the freezing point is estimated from the model by trial and error.

More details of the model are given in Norwegian by AUDUNSON et.al (1976).

SIMPLE SOLUTION FOR NECESSARY MIXING RATE

For small fjords, a simple solution gives the necessary mixing rate with sufficient accuracy.

To keep the fjord free from ice, the heat loss from the surface must be balanced by the heat supply from the initial mixing and heat supply from entrainment to the more turbulent upper layer.

In many cases, the heat supply from wind entrainment is negligible compared to initial entrainment. The heat supply of the fresh water **discharge** is also usually negligible. The equations for heat loss and heat supply can therefore be written as follows:

$$\text{Heat loss: } A \cdot H_n \quad (12)$$

$$\text{Heat supply: } (P-1)q_f \cdot \rho_2 \cdot C_p \cdot (T_b - T_s) \quad (13)$$

H_n = heat transport through the surface

A = surface area

P = mixing ratio

q_f = fresh water discharge

ρ_2 = density of fjord water

C_p = heat capacity

T_D = fjord temperature at the outlet depth

T_S = surface temperature.

The necessary mixing ratio P to prevent freezing in the fjord is thus

$$P = 1 + \frac{A \cdot H_n}{q_f \cdot \rho_2 \cdot C_p \cdot (T_D - T_S)} \quad (14)$$

In this simple analytic calculation, mean values of wind, air temperature, fjord temperature and salinity over the whole fjord basin are used. Comparisons between this calculation and the numerical model show little difference. With the above calculation, the necessary mixing ratio is overestimated by less than 10%.

APPLICATIONS

The above methods have been used to recommend design depths and diameters of the discharge tunnels from several planned power stations. In one case it has been prescribed how to regulate the fresh water discharge and the discharge velocity for various meteorological conditions (MATHISEN and SÆGROV 1977).

Figure 7 is a scheme of how the discharge should be varied to avoid freezing in the Aurland fjord with different air temperatures. The outlet consists of two tunnels, denoted R1 and R2. The one (R1) has a diameter of 3.1 m and the other one has a diameter of 3.6 m.

The depth of both is about 20 m. With two outlet tunnels one obtains a flexible arrangement to take care of variable fresh water discharges.

WIND (m/s)	SEATEMP. (°C)	OUTLET TUNNEL	AIRTEMPERATURE (°C)		
			-1 - -2	-2 - -5	-5 - -10
< 4 m/s	< 10 °C	R1	25 - 31	27 - 33	30 - 37
		R2	31 - 45	33 - 47	37 - 52
		R1 + R2	45 - 75	47 - 75	52 - 75
	> 10 °C	R1	22 - 26	24 - 28	27 - 31
		R2	26 - 37	27 - 41	31 - 46
		R1 + R2	37 - 75	41 - 75	46 - 75

Figure 7. The figure shows a plan to avoid ice formation during light winds with various air temperatures in the Aurland fjord. Due to variations of sea temperature and air temperature, the outlet opening and the fresh water discharge are to be varied according to the scheme. Numbers refer to the necessary discharge in m^3/s .

The scheme applies for a wind force less than 4 m/s. There are alternative schemes for sea temperature at the outlet depth less than $10^\circ C$ and higher than $10^\circ C$, and for various air temperatures.

Example: The sea temperature is less than $10^\circ C$, wind is less than 4 m/s, air temperature $-4^\circ C$ and the fresh water discharge is restricted to $40 m^3/s$. Then, according to Figure 7, the discharge of fresh water through the R2 tunnel will prevent ice formation. The energy cost amounts to a 1.3 m pressure height loss.

The energy cost of the method is estimated to 1-2 m pressure height loss for the conditions included in Figure 7.

The method presented here will be used at two Norwegian power

stations which are now under construction.

DISCUSSION

Several mathematical models are available for computing the dilution of buoyant discharges in stratified recipients. These models are useful for sewerage outlets. The fresh water supply from a hydro power plant, however, is an order of magnitude larger. This makes use of common mathematical models for the initial mixing doubtful. For example, due to the large amount of fresh water discharge, there is a considerable amount of kinetic energy left when the jet reaches the surface. The mathematical models do not take account of the mixing effect of this energy. Further, the width of the fjord mouth will control the stratification and thereby the residence time of the brackish water in the fjord. It is not possible to include this effect in the mathematical models for the initial dilution. To investigate the fresh water discharge from hydro power plants to fjords, laboratory studies are therefore necessary at the present state of the art.

The general laboratory studies which are discussed in this paper do not cover all of the hydraulic conditions one may expect in an arbitrary fjord. The width of the fjord mouth should be correct to ensure a correct stratification. The topography near the outlet may be of great importance. This has to be investigated for each case. The results presented here may be used as a first estimate for the design of an outlet arrangement to keep the fjord ice-free.

To develop the present method, a number of difficulties had to be overcome. The result gives a somewhat rough picture of one method for solving ice problems. The simple analytical calculation for the necessary initial

mixing uses average values of temperatures and wind over the whole fjord. The numerical model uses some simplifications for the circulation patterns of the fjord. The equations for heat exchange with the atmosphere are based on a large amount of data. However, the scatter is considerable. The wind function is based on data measured at rather high temperatures (25-30°C) and is subjected to some uncertainty for low temperatures. The laboratory results also show some scatter. Therefore, a great deal of work remains to be done to improve the method.

In 1981 the first power plant employing this method to prevent freezing will commence. This will give an opportunity to check the results at full scale.

Another device to obtain the necessary initial mixing, is a bubble curtain placed across the mouth of a river or a channel. This has also been studied at the River and Harbour Laboratory. A bubble curtain has been successfully used at the mouth of the Rana river for more than a decade (CARSTENS 1971).

ACKNOWLEDGEMENTS

The work that is presented here is a result of the efforts of a number of scientists at the River and Harbour Laboratory. In particular, research work conducted by T. Audunson, J.P. Mathisen, T. McClimans and A. Stigebrandt should be mentioned. The author wishes to thank T. McClimans and H. Rye for valuable advice and encouragement during this work.

The work has been supported by Konesesjonsavgiftsfondet, (Found of license fees) administered by the Norwegian Water Resources and Electricity Board.

REFERENCES

1. ABRAHAM, G. 1975: Hydraulic Near Field Modelling. European Course on Heat Disposal for Power Generation in the water Environment. Delft 1975.
2. AUDUNSON, T., MATHISEN, J.P., SCHEI, I. and STIGEBRANDT A. 1976: Forced entrainment of sea water into discharged water from the Loen power station, Nordfjord. River and Harbour Laboratory, Trondheim. Report no. STF60 F76096 (in Norwegian).
3. BINNEY, A.M. 1972: Research Note: Hugoniot's method applied to stratified flow through a constriction. J. Mech. Eng. Sci., 14:72-73.
4. CARSTENS, T. 1971: Prevention of ice formation by forced mixing. Proc. 1. Int Conf of Port and Ocean eng. under arctic conditions, Volume 1 pp 140-151 1971.
5. MATHISEN, J.P. and SÆGROV, S. 1977: Forced entrainment of sea water into discharged water from the Vangen power station, Aurland. River and Harbour Laboratory, Trondheim. Report no. STF60 F77061 (in Norwegian).
6. LONG, R.R. 1975: Circulations and Density Distributions in a deep, strongly stratified, two-layer Estuary. J. Fluid Mech., 79:753-768, 1975.
7. RYAN, P.L., JIRKA, H.I., STOLZENBACH, K.D. 1975: "Basic Physical Processes in Heat Transport" European Course on Heat Disposal from Power Generation in the Water Environment, Delft 1975.
8. STIGEBRANDT, A. 1975: Stationary Two-layer Flow in Estuaries. River and Harbour Laboratory, Trondheim. Report no. STF60 A75120 (in Swedish).
9. STOMMEL, H. and FARMER, H.G. 1952 : On the nature of estuarine circulation, part I, Technical Report, Ref. no. 5288 Woods Hole Oceanogr. inst.

Subject Index

- Acceleration; Bed roughness; Distortion; Friction coefficient (hydraulic); Laboratory tests; Mathematical models; Numerical analysis; Tidal effects**
Numerical Study of Distortion in a Froude Model, T. A. McClimans and S. A. Gjerp, 2887
- Acceleration; Damage; Earthquake loads; Earthquake resistant structures; Loading; Rubble-mound breakwaters; Seismic design; Settlement (structural); Slope stability**
Loadings on Rubble-Mound Breakwaters due to Earthquakes, H. Wang, C. Y. Yang, C. Lamison and S. S. Chen, 2244
- Accretion (geomorphology); Beach erosion; Beaches; Dynamic models; Geomorphology; Three-dimensional; Water depth; Wave energy; Wave height; Wave spectra**
Wave Power and Beach Stages: A Global Model, Andrew D. Short, 1145
- Accretion (geomorphology); Beach nourishment; Erosion; Groins (structures); Mathematical models; Rip currents; Shore-line cover; Wave diffraction; Wave refraction; Wind loads**
Mathematical Modeling of Shoreline Evolution, Bernard Le Mehaute and Mills Soldate, 1163
- Accretion (geomorphology); California; Dredging; Estuaries; Harbor facilities; Harbors; Littoral current; Littoral drift; Littoral materials; Sediment deposits; Sediments; Shoaling**
Maintenance of Santa Cruz Harbor, California, U.S.A., Orville T. Magoon and Don C. Baer, 1276
- Accuracy; Beach erosion; Field tests; Laboratory tests; Measurement; Sediments; Water depth; Wave height; Wave period**
Uses for a Calculated Limit Depth to Beach Erosion, Robert J. Hallermeier, 1493
- Acoustic measuring instruments; Currents (water); Ocean bottom; Surface waves; Water depth; Wave energy; Wave measurement**
Near-Bottom Current Measured by Acoustic Sensors, K. A. Selanger and T. Carstens, 878
- Aerial photography; Bathymetry; Color photography; Images; Remote sensing; Shallow water; Water depth**
Visible-Region Photographic Remote Sensing of Nearshore Waters, Tsuguo Sunamura and Kiyoshi Horikawa, 1439
- Aerial photography; Currents (water); Density; Eddies; Eddy currents; Mixing; Tidal currents; Turbulence; Velocity; Water depth; Wind loads**
Large Scale Turbulence in Tidal Currents, John B. Hinwood, 2598
- Airspeed; Beach erosion; Dunes; Erosion control; Fences; Sands; Sediment deposits; Soil stabilization; Wind forces; Wind pressure**
Using Fences to Create and Stabilise Sand Dunes, Brian B. Willetts and Christopher J. Phillips, 2040
- Air water interactions; Air-water interfaces; Forecasting; Shallow water; Storm surges; Temperature; Water depth; Water levels**
Storm Surge Forecasting Methods in Enclosed Seas, P. F. Hamblin, 998
- Air-water interfaces; Forecasting; Shallow water; Storm surges; Temperature; Water depth; Water levels; Air water interactions**
Storm Surge Forecasting Methods in Enclosed Seas, P. F. Hamblin, 998
- Amplitude; Buoys; Drifting (aquatic); Floating bodies; Mass transfer; Wave height; Wave period; Waves**
Drift Speed of Buoys in Waves, John H. Nath, 859
- Approximation method; Finite element method; Harbors; Integral equations; Oscillations; Tides; Water waves; Wave diffraction; Wave refraction**
A Combined FE-BIE Method for Water Waves, A. Hauguel, 715
- Aquifers; Ground water; Groundwater elevation; Littoral current; Oscillations; Piezometers; Wave height; Wave period; Wave spectrum**
Beach Ground-Water Oscillations, Andrzej Lewandowski and Ryszard B. Zeidler, 2051
- Armoring (streambed); Breakwaters; Coastal plains; Damage; Estuaries; History; Hydraulic models**
Models — Can We Learn from the Past? Some Thoughts on the Design of Breakwaters, W. A. Price, 25
- Armoring (streambed); Breakwaters; Density; Flumes; Slope stability; Stability; Standardization; Test reproducibility; Tests**
Dolos Packing Density and Effect of Relative Block Density, J. A. Zwamborn, 2285
- Armoring (streambed); Breakwaters; Rubble-mound breakwaters; Slope stability; Stability; Wave energy; Wave height**
Dolos-Armored Breakwaters: Special Consideration, Robert D. Carver and D. Donald Davidson, 2263
- Armoring (streambed); Costs; Revetments; Rubble-mound breakwaters; Slope stability; Stability; Wave energy; Wave pressure**
Blanket Theory and Low Cost Revetments, C. T. Brown, 2510
- Armoring (streambed); Open channel flow; Performance; Standardization; Test reproducibility; Tests; Turbulent flow; Wave period; Wave refraction**
Performance of Dolos Blocks in an Open Channel Situation, Arthur Brebner, 2305
- Australia; Breakwaters; Maintenance; Site selection; Storm surges; Tidal effects; Tidal waters; Wave height; Wave period**
Rosslyn Bay Breakwater, Queensland, Australia, D. N. Foster, B. L. McGrath and W. Bremner, 2086

- Australia; Cyclones; Frequencies; Mathematical models; Probability distribution functions; Tropical cyclones; Wave equations; Wave recorders (water waves); Wind forces; Wind pressure**
Wind Wave Frequencies in a Tropical Cyclone Region, Rodney J. Sobey, 76
- Barriers; Beach erosion; Coastal morphology; Delaware; Inlets (waterways); Littoral drift; Marshes; Morphology; Sedimentation; Tidal hydraulics**
Morphology of Coastal Barriers, Delaware, U.S.A., John C. Kraft, Chacko J. John and Evelyn M. Maurmeyer, 1232
- Barriers; Beaches; Breakwaters; Coastal plains; Diffraction; Groins (structures); Jetties; Littoral drift; Numerical analysis; Predictions; Refraction; Sediment transport**
Prediction of Beach PlanForms with Littoral Controls, Marc Perlin and Robert G. Dean, 1818
- Barriers; Boundary conditions; Netherlands; Responses; Storms; Storm surges; Surveys (data collection); Tidal hydraulics; Water levels**
A Tidal Survey for a Model of an Offshore Area, W. J. van de Ree, J. Voogt and J. J. Leendertse, 2656
- Barriers; Breakwaters; India; Performance; Shape; Silting; Underwater structures; Wave attenuation**
Performance Characteristics of Submerged Breakwaters, J. Dattatri, H. Raman and N. Jothi Shankar, 2153
- Barriers; Friction coefficient (hydraulic); Littoral current; Shores; Stresses; Surf; Water circulation; Wave energy; Wave propagation; Waves**
Longshore Currents Due to Surf Zone Barrier, P. Bettess, C. A. Fleming, J. C. Heinrich, O. C. Zienkiewicz and D. I. Austin, 776
- Barriers; Impact; Marine structures; Mathematical models; Pressure distribution; Scale effect; Standing waves; Storm surges; Wave energy; Wave pressure**
A Model Law for Wave Impacts on Coastal Structures, C. Ramkema, 2308
- Barriers; Islands (landforms); Littoral current; Littoral deposits; Littoral drift; Littoral materials; Sediment transport; Tracers; Wave height**
Littoral Drift along Bayshore of a Barrier Island, Yu-Hwa Hwang and T. H. Chang, 1614
- Bars (riverine); Beach erosion; Lakes; Nile River Valley; Oceans; Sediment deposits; Sediment load; Sediment transport; Storms; Water depth; Wave equations; Wave period**
Undulated Bottom Profiles and Onshore-Offshore Transport, Madhav Manohar, 1454
- Bathymetry; Bays (topographic features); Beach erosion; Beaches; Breakwaters; Diffraction; Sediment transport; Wave diffraction; Wave height; Wave phases**
Diffraction Calculation of Shoreline PlanForms, Robert G. Dean, 1903
- Bathymetry; Beach erosion; Beach nourishment; Morphology; Sands; Shore protection; Water depth**
Morphologic Effects of Westerland Beach Nourishment 1972, Dieter Wenzel, 1859
- Bathymetry; Bores (wave); Field tests; Littoral current; Model tests; Storms; Surf; Water circulation; Water levels; Wave height; Waves; Wind**
Comparison of Model and Observed Nearshore Circulation, James H. Allender, John D. Ditmars, Wyman Harrison and Robert A. Paddock, 810
- Bathymetry; Color photography; Images; Remote sensing; Shallow water; Water depth; Aerial photography**
Visible-Region Photographic Remote Sensing of Nearshore Waters, Tsuguo Sunamura and Kiyoshi Horikawa, 1439
- Bathymetry; Correlation analysis; Deep water; Frequencies; Intensity; Wave energy; Wave propagation; Waves; Wave spectra**
Deepwater Direction from an Intensity Array, Alan L. Higgins and Richard J. Seymour, 305
- Bays (topographic features); Beach erosion; Beaches; Breakwaters; Diffraction; Sediment transport; Wave diffraction; Wave height; Wave phases; Bathymetry**
Diffraction Calculation of Shoreline PlanForms, Robert G. Dean, 1903
- Bays (topographic features); Currents (water); Diffusion; Eddies; Environmental factors; Simulation; Tidal hydraulics; Water circulation; Wind loads**
Characteristics of Circulation in Bay Waters due to Wind Action, Akira Wada and Ioshihito Miyaike, 2730
- Bays (topographic features); Friction coefficient (hydraulic); Inlets (waterways); Mathematical models; Numerical analysis; Sediment transport; Storm surges; Tidal effects; Wave height**
Numerical Model Investigation of Selected Tidal Inlet-Bay System Characteristics, William N. Seelig and Robert M. Sorensen, 1319
- Beach erosion; Beaches; Beach sands; Edge effect; Littoral current; Littoral drift; Wave action; Wavelengths; Wave velocity**
Beach Cusps and Edge Waves, David A. Huntley and A. J. Bowen, 1378
- Beach erosion; Beaches; Breakwaters; Diffraction; Sediment transport; Wave diffraction; Wave height; Wave phases; Bathymetry; Bays (topographic features)**
Diffraction Calculation of Shoreline PlanForms, Robert G. Dean, 1903
- Beach erosion; Beaches; Dynamic models; Geomorphology; Three-dimensional; Water depth; Wave energy; Wave height; Wave spectra; Accretion (geomorphology)**
Wave Power and Beach Stages: A Global Model, Andrew D. Short, 1145
- Beach erosion; Beach nourishment; Dredging; Groins (structures); Sea walls; Shore protection; Spoil; Spoil banks**
Some Facts and Fancies about Beach Erosion, Richard Sylvester, 1888
- Beach erosion; Beach nourishment; Morphology; Sands; Shore protection; Water depth; Bathymetry**
Morphologic Effects of Westerland Beach Nourishment 1972, Dieter Wenzel, 1859

- Beach erosion; Breakwaters; Coastal structures; Erosion control; Littoral zone; Marine terminals; Piers; Rubble-mound breakwaters; Sands; Shoreline cover**
Coastal Structures' Effects on Shorelines, Ronald M. Noble, 2069
- Beach erosion; Coastal morphology; Delaware; Inlets (waterways); Littoral drift; Marshes; Morphology; Sedimentation; Tidal hydraulics; Barriers**
Morphology of Coastal Barriers, Delaware, U.S.A., John C. Kraft, Chacko J. John and Evelyn M. Maurmeyer, 1232
- Beach erosion; Coastal structures; Dikes; Erosion control; Japan; Land reclamation; Scouring; Sea walls; Shore protection; Wave energy; Wave reflection**
Effectiveness of Seadikes with Rough Slope, Osamu Toyoshima, 2528
- Beach erosion; Delaware; Hydraulic models; Inlets (waterways); Jetties; Sedimentation; Sheet piles; Tidal effects; Trends**
Case Studies of Delaware's Tidal Inlets: Roosevelt and Indian River Inlets, W. A. Dennie, G. A. Lanan and Robert A. Dalrymple, 1282
- Beach erosion; Dunes; Erosion; Movable bed models; Ripple marks; Sands; Scale effect; Shore protection; Storm surges**
Movable Bed Model Tests on Dune Erosion, P. Vellinga, 2020
- Beach erosion; Dunes; Erosion control; Fences; Sands; Sediment deposits; Soil stabilization; Wind forces; Wind pressure; Airspeed**
Using Fences to Create and Stabilize Sand Dunes, Brian B. Willetts and Christopher J. Phillips, 2040
- Beach erosion; Field tests; Laboratory tests; Measurement; Sediments; Water depth; Wave height; Wave period; Accuracy**
Uses for a Calculated Limit Depth to Beach Erosion, Robert J. Hallermeier, 1493
- Beach erosion; Lakes; Nile River Valley; Oceans; Sediment deposits; Sediment load; Sediment transport; Storms; Water depth; Wave equations; Wave period; Bars (riverine)**
Undulated Bottom Profiles and Onshore-Offshore Transport, Madhav Manohar, 1454
- Beach erosion; Littoral current; Littoral deposits; Littoral drift; Shallow water; Water depth; Wave energy**
Vocoidal Theory for All Non-Breaking Waves, D. H. Swart and C. C. Loubser, 467
- Beaches; Beach sands; Edge effect; Littoral current; Littoral drift; Wave action; Wavelengths; Wave velocity; Beach erosion**
Beach Cusps and Edge Waves, David A. Huntley and A. J. Bowen, 1378
- Beaches; Breaking energy; Coring; Histograms; Sediment deposits; Surf; Tidal effects; Tracers; Wave action; Wave height**
Depth of Disturbance of Sand in Surf Zones, Michael K. Gaughan, 1513
- Beaches; Breaking energy; Deep water; Particle trajectories; Slope; Velocity; Waves; Wave velocity**
Estimation of Water Particle Velocity of Breaking Wave, Tetsuo Sakai and Yuichi Iwagaki, 551
- Beaches; Breakwaters; Coastal plains; Diffraction; Groins (structures); Jetties; Littoral drift; Numerical analysis; Predictions; Refraction; Sediment transport; Barriers**
Prediction of Beach PlanForms with Littoral Controls, Marc Perlin and Robert G. Dean, 1818
- Beaches; Breakwaters; Diffraction; Sediment transport; Wave diffraction; Wave height; Wave phases; Bathymetry; Bays (topographic features); Beach erosion**
Diffraction Calculation of Shoreline PlanForms, Robert G. Dean, 1903
- Beaches; Breakwaters; Dredging; Hydraulic models; Inlets (waterways); Jetties; North Carolina; Sediment deposits; Simulation; Spoil banks**
Coastal Processes at Oregon Inlet, North Carolina, James T. Jarrett, 1257
- Beaches; Coastal engineering; Laboratory tests; Movable bed models; Scale effect; Sediments; Sediment transport; Wave height; Wave period**
Scale Relations for Equilibrium Beach Profiles, Hideaki Noda, 1531
- Beaches; Coastal plains; Littoral current; Littoral deposits; Models; Ocean bottom; Sediments; Sediment transport; Surf; Wave dispersion; Wave energy**
A Model Study of Alongshore Sediment Transport Rate, J. W. Kamphuis and J. S. Readshaw, 1656
- Beaches; Coastal plains; Probability; Probability distribution functions; Sea level; Statistical analysis; Storm surges; Tides**
Extreme Sea Levels from Tide and Surge Probability, D. T. Pugh and J. M. Vassie, 911
- Beaches; Dispersion; Environmental factors; Georgia; Inlets (waterways); Morphology; Sediment deposits; Tidal currents; Tidal effects; Wave energy; West Germany**
Process-Response Models for Depositional Shorelines: The German and the Georgia Bights, Dag Nummedal and Ian A. Fischer, 1215
- Beaches; Dynamic models; Geomorphology; Three-dimensional; Water depth; Wave energy; Wave height; Wave spectra; Accretion (geomorphology); Beach erosion**
Wave Power and Beach Stages: A Global Model, Andrew D. Short, 1145
- Beaches; Edge effect; Excitation; Interactions; Standing waves; Water depth; Waves; Wave tanks**
Excitation of Low Frequency Trapped Waves, Robert King and Ronald Smith, 449
- Beaches; Edge effect; Littoral current; Morphology; Resonance; Surf; Wave reflection; Waves; Wave spectra**
Surf Zone Resonance and Coupled Morphology, John Chappell and Lynn Donelson Wright, 1359
- Beaches; Field tests; Gravel; Littoral current; Littoral deposits; Littoral drift; Sediment transport; Storm surges; Tracers; Wave energy**
Field Experiment on Beach Gravel Transport, Masataro Hattori and Takasuke Suzuki, 1688

- Beaches; Littoral current; Littoral deposits; Littoral drift; Surf; Turbulence; Wave dispersion; Wave energy; Wave height; Wave reflection**
Morphodynamic Variability of High-Energy Beaches, Lynn Donelson Wright, B. G. Thom and John Chappell, 1180
- Beaches; Littoral current; Measurement; Surf; Suspended sediments; Water sampling; Wave height; Wave period; Waves; Wind velocity**
Surf Zone Measurements of Suspended Sediment, Timothy W. Kana, 1725
- Beaches; Littoral current; Models; Sediment concentration; Sediment load; Sediment transport; Two-dimensional; Wave period**
Onshore-Offshore Sediment Movement on a Beach, P. Nielsen, I. A. Svendsen and C. Staub, 1475
- Beaches; Littoral drift; Metal detectors; Monitoring; Sediment transport; Shingles (beach); Tracers**
Shingle Tracing by a New Technique, Peter Wright, J. S. Cross and N. B. Webber, 1705
- Beaches; Random processes; Slopes; Water depth; Wave height; Wavelength; Wave period; Waves; Wave tanks; Wave velocity**
Wave Length, Wave Velocity and Shoaling Characteristics of Random Waves, Akira Kimura and Yuichi Iwagaki, 320
- Beach nourishment; Bottom sediments; Dredges; Dredging; Models; Sediments; Spoil; Spoil banks**
Importance of Handling Losses to Beach Fill Design, R. D. Hobson and W. R. James, 1873
- Beach nourishment; Dredging; Groins (structures); Sea walls; Shore protection; Spoil; Spoil banks; Beach erosion**
Some Facts and Fancies about Beach Erosion, Richard Sylvester, 1888
- Beach nourishment; Erosion; Groins (structures); Mathematical models; Rip currents; Shore-line cover; Wave diffraction; Wave refraction; Wind loads; Accretion (geomorphology)**
Mathematical Modeling of Shoreline Evolution, Bernard Le Mehaute and Mills Soldate, 1163
- Beach nourishment; Morphology; Sands; Shore protection; Water depth; Bathymetry; Beach erosion**
Morphologic Effects of Westerland Beach Nourishment 1972, Dieter Wenzel, 1859
- Beach sands; Edge effect; Littoral current; Littoral drift; Wave action; Wavelengths; Wave velocity; Beach erosion; Beaches**
Beach Cusps and Edge Waves, David A. Huntley and A. J. Bowen, 1378
- Bed forms; Discharge (water); Dunes; Flow rates; Sediment deposits; Time dependence; Unsteady flow; Water depth**
Time Lag of Dunes for Unsteady Flow Conditions, Horst Nasner, 1801
- Bed forms; Friction coefficient (hydraulic); Hydrodynamic pressure; Hydrodynamics; Numerical analysis; Ocean bottom; Ripple marks; Tidal effects**
The Influence of Dune and Flow Parameters on the Friction Factor, Jurgen Sundermann, H. Vollmers and W. Puls, 1787
- Bed roughness; Distortion; Friction coefficient (hydraulic); Laboratory tests; Mathematical models; Numerical analysis; Tidal effects; Acceleration**
Numerical Study of Distortion in a Froude Model, T. A. McClimans and S. A. Gjerp, 2887
- Bed roughness; Estuaries; Mixing; Rivers; Saline water-freshwater interfaces; Salinity; Stream flow; Velocity distribution; Vortices; Wave energy**
Outflow Dynamics at a River Mouth, Masakazu Kashiwamura and Shizuo Yoshida, 2925
- Biological properties; Density currents; Discharge (water); Heat exchangers; Liquid natural gas; Model studies; Thermal pollution; Tidal currents; Vaporizers**
Thermal and Biological Impact of LNG Vaporizer Discharge, Peter A. Mangarella and Gordon A. Robilliard, 2945
- Bores (wave); Breaking energy; Energy dissipation; Energy losses; Predictions; Random processes; Shallow water; Wave height**
Energy Loss and Set-Up Due to Breaking of Random Waves, J. A. Battjes and J. P.F.M. Janssen, 569
- Bores (wave); Breaking energy; Hydraulic jump; Water depth; Wave height; Wave propagation; Waves; Wave velocity**
Spilling Breakers, Bores and Hydraulic Jumps, D. H. Peregrine and I. A. Svendsen, 540
- Bores (wave); Field tests; Littoral current; Model tests; Storms; Surf; Water circulation; Water levels; Wave height; Waves; Wind; Bathymetry**
Comparison of Model and Observed Nearshore Circulation, James H. Allender, John D. Ditmars, Wyman Harrison and Robert A. Paddock, 810
- Bottom sediments; Dredges; Dredging; Models; Sediments; Spoil; Spoil banks; Beach nourishment**
Importance of Handling Losses to Beach Fill Design, R. D. Hobson and W. R. James, 1873
- Boundary conditions; Coastal plains; Mixing; Ocean engineering; Ocean waves; Rivers; Runoff; Suspended sediments; Two-dimensional; Wave propagation; Wind loads**
Mixed Layer Models for Coastal Waters, W. J. Wiseman, Jr., L. J. Rouse, Jr. and O. K. Huh, 2619
- Boundary conditions; Forecasting; Morphology; Stability analysis; Tidal currents; Tidal flats; Tides; Two-dimensional; Water depth**
Two-Dimension Stability Analysis of Tidal Basins and Tidal Flats of Larger Extent, Eberhard Renger, 1971
- Boundary conditions; Mathematical models; Sand; Shear stress; Turbulent flow; Velocity distribution; Wave propagation; Wave velocity**
Near-Bottom Velocities in Waves with a Current, W. T. Bakker and Th. van Doorn, 1394
- Boundary conditions; Netherlands; Responses; Storms; Storm surges; Surveys (data collection); Tidal hydraulics; Water levels; Barriers**
A Tidal Survey for a Model of an Offshore Area, W. J. van de Ree, J. Voogt and J. J. Leendertse, 2656

- Boundary layer flow; Continental shelf; Currents (water); Littoral current; Nicaragua; Pressure gradients; Salinity; Suspended sediments**
Shelf and Coastal Boundary Layer Currents, Miskito Bank of Nicaragua, Richard L. Crout and Stephen P. Murray, 2715
- Brazil; Current meters; Harbor facilities; Littoral current; Littoral drift; Water depth; Wave height; Wave period; Wave recorders (water waves); Wave spectrum**
Coastal Study of Espirito Santo Brazil, Paulo Augusto Vivacqua, Hildebrando de Araujo Goes Filho and Octavio de Sampaio Ferraz Jardim Sayao, 2104
- Brazil; Meteorology; Ocean waves; Wave action; Wave energy; Wave height; Wave period; Wave recorders (water waves)**
Wave Climate in Some Zones off the Brazilian Coast, Alberto Homsí, 114
- Breaking energy; Classification; Field tests; Photographic analysis; Predictions; Water depth; Wave height; Wavelength; Waves**
Field Study of Breaking Wave Characteristics, Lee L. Weishar and Robert J. Byrne, 487
- Breaking energy; Coring; Histograms; Sediment deposits; Surf; Tidal effects; Tracers; Wave action; Wave height; Beaches**
Depth of Disturbance of Sand in Surf Zones, Michael K. Gaughan, 1513
- Breaking energy; Deep water; Particle trajectories; Slope; Velocity; Waves; Wave velocity; Beaches**
Estimation of Water Particle Velocity of Breaking Wave, Tetsuo Sakai and Yuichi Iwagaki, 551
- Breaking energy; Energy dissipation; Energy losses; Predictions; Random processes; Shallow water; Wave height; Bores (wave)**
Energy Loss and Set-Up Due to Breaking of Random Waves, J. A. Battjes and J. P.F.M. Janssen, 569
- Breaking energy; Hydraulic jump; Water depth; Wave height; Wave propagation; Waves; Wave velocity; Bores (wave)**
Spilling Breakers, Bores and Hydraulic Jumps, D. H. Peregrine and I. A. Svendsen, 540
- Breaking energy; Ocean waves; Probability density functions; Probability theory; Secondary waves; Surf; Wave height; Wave period; Waves; Wave spectra**
Probability Density Functions of Breaking Waves, Edward B. Thornton and George Schaeffer, 507
- Breakwaters; Coastal engineering; Coastal structures; Floating bodies; Oil spills; Tires; Wave action; Wave attenuation**
Scrap Tyre Breakwaters in Coastal Engineering, Robert Charles McGregor and Neil Sinclair Miller, 2191
- Breakwaters; Coastal plains; Damage; Estuaries; History; Hydraulic models; Armoring (streambed) Models — Can We Learn from the Past? Some Thoughts on the Design of Breakwaters, W. A. Price, 25**
- Breakwaters; Coastal plains; Diffraction; Groins (structures); Jetties; Littoral drift; Numerical analysis; Predictions; Refraction; Sediment transport; Barriers; Beaches**
Prediction of Beach PlanForms with Littoral Controls, Marc Perlin and Robert G. Dean, 1818
- Breakwaters; Coastal structures; Erosion control; Littoral zone; Marine terminals; Piers; Rubble-mound breakwaters; Sands; Shore-line cover; Beach erosion**
Coastal Structures' Effects on Shorelines, Ronald M. Noble, 2069
- Breakwaters; Computer programs; Harbors; Hydraulic models; Numerical analysis; Wave diffraction; Wave height; Wave reflection**
A Numerical Approach for the Determination of the Wave Height Distribution in a Harbour, Soren Kohlhase, Karl-Friedrich Daemrich, U. Berger, E. Tautenhain and O. Burkhardt, 664
- Breakwaters; Damage; Hydraulic models; Rubble-mound breakwaters; Stability; Wave energy; Wave height; Wave spectra; Wave tanks**
Effects of Wave Grouping on Breakwater Stability, R. R. Johnson, E. P.D. Mansard and J. Ploeg, 2228
- Breakwaters; Density; Flumes; Slope stability; Stability; Standardization; Test reproducibility; Tests; Armoring (streambed)**
Dolos Packing Density and Effect of Relative Block Density, J. A. Zwiaborn, 2285
- Breakwaters; Diffraction; Ocean waves; Random processes; Wave diffraction; Wave height; Wave reflection; Wave spectra**
Diffraction Diagrams for Directional Random Waves, Yoshimi Goda, Tomotsuka Takayama and Yasumasa Suzuki, 628
- Breakwaters; Diffraction; Sediment transport; Wave diffraction; Wave height; Wave phases; Bathymetry; Bays (topographic features); Beach erosion; Beaches**
Diffraction Calculation of Shoreline PlanForms, Robert G. Dean, 1903
- Breakwaters; Dredging; Hydraulic models; Inlets (waterways); Jetties; North Carolina; Sediment deposits; Simulation; Spoil banks; Beaches**
Coastal Processes at Oregon Inlet, North Carolina, James T. Jarrett, 1257
- Breakwaters; Experimentation; Friction coefficient (hydraulic); Ocean waves; Predictions; Wave dispersion; Wave height; Wave reflection**
Wave Transmission through Trapezoidal Breakwaters, Ole Secher Madsen, Paisal Shusang and Sue Ann Hanson, 2140
- Breakwaters; Field tests; Harbors; Laboratory tests; Models; Prototypes; Wave recorders (water waves); Waves**
A Comparison Between Model and Prototype Waves in Harbours, Sverre Bjordal and Alf Torum, 677
- Breakwaters; India; Performance; Shape; Silting; Underwater structures; Wave attenuation; Barriers**
Performance Characteristics of Submerged Breakwaters, J. Dattatri, H. Raman and N. Jothi Shankar, 2153

- Breakwaters; Japan; Land reclamation; Littoral current; Littoral drift; Movable bed models; Ocean bottom; Sediment transport; Waves**
Estimation Using a Movable Bed Model of Shoreline Change Caused by a Reclamation Projected into the Sea, Shoji Sato and Hiroaki Ozasa, 1839
- Breakwaters; Laboratory tests; Wave diffraction; Wave energy; Wave generation; Wave recorders (water waves); Wave spectra; Wind forces; Wind pressure**
Wind-Generated Wave Diffraction by Breakwater Gap, Hooshang Raissi and R. L. Wigle, 609
- Breakwaters; Maintenance; Site selection; Storm surges; Tidal effects; Tidal waters; Wave height; Wave period; Australia**
Rosslyn Bay Breakwater, Queensland, Australia, D. N. Foster, B. L. McGrath and W. Bremner, 2086
- Breakwaters; Model tests; Reflection; Refraction; Walls; Wave action; Wave diffraction; Wave reflection**
Influence of Breakwater-Reflection on Diffraction, Karl-Friedrich Daemrich and Soren Kohlhasse, 651
- Breakwaters; Ocean waves; Pneumatic systems; Underwater structures; Wave damping; Wave energy; Wave period; Waves**
Combination Effect of Pneumatic Breakwater and Other Type Breakwater on Wave Damping, Yuichi Iwagaki, Toshiyuki Asano and Tsutomu Honda, 2172
- Breakwaters; Permeability; Shallow water; Standing waves; Tests; Wave diffraction; Wave energy; Wave height; Wavelength; Wave tanks**
Wave Height Distribution Around Permeable Breakwaters, Shintaro Hotta, 695
- Breakwaters; Rubble-mound breakwaters; Slope stability; Stability; Wave energy; Wave height; Armoring (streambed)**
Dolos-Armored Breakwaters: Special Consideration, Robert D. Carver and D. Donald Davidson, 2263
- Breakwaters; Slots; Standing waves; Storms; Storm surges; Wave height; Wave period; Wave pressure; Wave reflection**
Wave Pressures on Split-Type Breakwaters, Shoshichiro Nagai and Shohachi Kakuno, 2360
- Buoys; Design criteria; Offshore platforms; Offshore structures; Surveys (data collection); Wave energy; Wave height; Wave recorders (water waves)**
Comparison of Shipborne Wave Recorder and Waverider Buoy Data Used to Generate Design and Operational Planning Criteria, C. G. Graham, G. Verboom and C. J. Shaw, 97
- Buoys; Drifting (aquatic); Floating bodies; Mass transfer; Wave height; Wave period; Waves; Amplitude**
Drift Speed of Buoys in Waves, John H. Nath, 859
- Buoys; Hurricanes; Measurement; Monitoring; Offshore platforms; Radar operation; Wave height; Waves; Wind; Wind speed**
HF Skywave Radar Measurement of Hurricane Winds and Waves, Joseph W. Maresca, Jr. and Christopher T. Carlson, 190
- Calculations; Fourier transformation; Interactions; Nonlinear systems; Sampling; Spectral analysis; Wave spectra**
Higher Order Wave Spectra, Paul C. Liu and Albert W. Green, 360
- Calibration; California; Instrumentation; Performance; Profile measurement; Sand; Sediment transport; Vehicles; Wave action**
Tracked Vehicle for Continuous Nearshore Profiles, Richard J. Seymour, Alan L. Higgins and David P. Bothman, 1542
- California; Dredging; Estuaries; Harbor facilities; Harbors; Littoral current; Littoral drift; Littoral materials; Sediment deposits; Sediments; Shoaling; Accretion (geomorphology)**
Maintenance of Santa Cruz Harbor, California, U.S.A., Orville T. Magoon and Don C. Baer, 1276
- California; Instrumentation; Performance; Profile measurement; Sand; Sediment transport; Vehicles; Wave action; Calibration**
Tracked Vehicle for Continuous Nearshore Profiles, Richard J. Seymour, Alan L. Higgins and David P. Bothman, 1542
- Canada; Dredging; Harbors; Models; Salinity; Sedimentation; Sediment transport; Silting; Suspended sediments; Temperature; Tidal effects; Turbidity**
Tidal Sedimentation in Gros-Cacouna Harbor, Georges Drapeau and Guy Fortin, 1986
- Canada; Field tests; Gravity waves; Hurricanes; Sediments; Sediment transport; Storms; Storm surges; Wave energy; Wave period; Wave velocity**
Infragravity Waves in Storm Conditions, R. A. Holman, David A. Huntley and A. J. Bowen, 268
- Centrifugal pumps; Concrete piles; Dredging; Failure; Intake structures; Jetties; Offshore structures**
Problems of Design and Construction of an Offshore Sea-Water Intake, D. W. Standish-White and J. A. Zwamborn, 2125
- Channel beds; Clays; Entrainment; Experimentation; Finite element method; Sediment concentration; Suspended sediments; Time dependence**
Concentration of Suspended Clay in Periodic Flow, Akira Watanabe, P. Thimakorn and A. Das Gupta, 1918
- Classification; Field tests; Photographic analysis; Predictions; Water depth; Wave height; Wavelength; Waves; Breaking energy**
Field Study of Breaking Wave Characteristics, Lee L. Weishar and Robert J. Byrne, 487
- Clays; Entrainment; Experimentation; Finite element method; Sediment concentration; Suspended sediments; Time dependence; Channel beds**
Concentration of Suspended Clay in Periodic Flow, Akira Watanabe, P. Thimakorn and A. Das Gupta, 1918
- Coastal engineering; Coastal structures; Floating hodies; Oil spills; Tires; Wave action; Wave attenuation; Breakwaters**
Scrap Tyre Breakwaters in Coastal Engineering, Robert Charles McGregor and Neil Sinclair Miller, 2191

- Coastal engineering; Flooding; Frequencies; Probability; Storm surges; West Germany; Wind forces; Wind pressure; Wind velocity**
Frequencies and Probabilities of Extreme Storm Surges (On the Time-Dependent Changes of the Probability of Extreme Storm Floods at the German North Sea Coast), Alfred Fohrboter, 949
- Coastal engineering; Laboratory tests; Movable bed models; Scale effect; Sediments; Sediment transport; Wave height; Wave period; Beaches**
Scale Relations for Equilibrium Beach Profiles, Hideaki Noda, 1531
- Coastal engineering; Mathematical models; Mathematics; Mixing; Physics; Sediments; Structures; Tidal currents; Wave energy; Waves**
Struggle of Physics and Mathematics in Coastal Engineering, H. Lundgren, 13
- Coastal morphology; Delaware; Inlets (waterways); Littoral drift; Marshes; Morphology; Sedimentation; Tidal hydraulics; Barriers; Beach erosion**
Morphology of Coastal Barriers, Delaware, U.S.A., John C. Kraft, Chacko J. John and Evelyn M. Maurmeyer, 1232
- Coastal plains; Confidence level; Ocean waves; Probability distribution functions; Shore protection; Statistical analysis; Wave height; Wave period**
On Long-Term Statistics for Ocean and Coastal Waves, Michel K. Ochi, 59
- Coastal plains; Cost effectiveness; Floods; Hurricanes; Numerical analysis; Predictions; Simulation; Storm surges; Texas; Tidal effects; Tsunamis; Water levels**
Coastal Flood Simulation in Stretched Coordinates, H. Lee Butler, 1030
- Coastal plains; Currents (water); Ripple marks; Sediment transport; Shear stress; Three-dimensional; Wave height; Waves; Wave tanks**
Sediment Transport and Ripples Due to Waves and Currents, Zbigniew Pruszk and Ryszard B. Zeidler, 1638
- Coastal plains; Damage; Estuaries; History; Hydraulic models; Armoring (streambed); Breakwaters**
Models — Can We Learn from the Past? Some Thoughts on the Design of Breakwaters, W. A. Price, 25
- Coastal plains; Damage; Ocean waves; Recreational facilities; Storm surges; West Germany**
Welcoming Address — IV, Hans-Werner Partensky, 10
- Coastal plains; Diffraction; Groins (structures); Jetties; Littoral drift; Numerical analysis; Predictions; Refraction; Sediment transport; Barriers; Beaches; Breakwaters**
Prediction of Beach PlanForms with Littoral Controls, Marc Perlin and Robert G. Dean, 1818
- Coastal plains; Diffusion; Dispersion; Mathematical models; Outfall sewers; Sewage effluents; Statistical analysis; Time series analysis; Waste disposal**
Outfall Diffusion Models for the Coastal Zone, D. C.L. Lam and C. R. Murthy, 2584
- Coastal plains; Dredging; Gravel; Great Britain; Licensing; Littoral drift; Sand; Shore protection; Tidal currents; Wave action; Wave energy; Wave refraction**
The Effect of Offshore Dredging on Coastlines, W. A. Price, J. M. Motyka and L. J. Jaffrey, 1347
- Coastal plains; Dynamic loads; Shore protection; Storm surges; Surf; Water levels; Wave energy; Wave recorders (water waves); Wave runoff**
Wave Set-Up in the Surf Zone, Uwe A. Hansen, 1071
- Coastal plains; Eigenvalues; Mass; Momentum; Offshore structures; Rip currents; Spacing; Surf; Wave action; Waves; Wave velocity**
Rip Current Spacing as an Eigenvalue, Noriyuki Iwata, 828
- Coastal plains; Evaluation; Geological maps; Littoral deposits; Littoral materials; Sedimentation; Sediment transport; Surveys (data collection)**
A New Method for the Representation of Sedimentary Sequences in Coastal Regions, Hansjorg Streif, 1245
- Coastal plains; History; Shore protection; Storm surges; West Germany**
Welcoming Address — I, Karl-Edward Naumann, 1
- Coastal plains; Littoral current; Littoral deposits; Models; Ocean bottom; Sediments; Sediment transport; Surf; Wave dispersion; Wave energy; Beaches**
A Model Study of Alongshore Sediment Transport Rate, J. W. Kamphuis and J. S. Readshaw, 1656
- Coastal plains; Littoral deposits; Littoral drift; Littoral zone; Samples; Sediment concentration; Suspended sediments; Wave height**
Sled System for Profiling Suspended Littoral Drift, J. P. Coakley, J. A. Savile, M. Pedrosa and M. Laroque, 1764
- Coastal plains; Mixing; Ocean engineering; Ocean waves; Rivers; Runoff; Suspended sediments; Two-dimensional; Wave propagation; Wind loads; Boundary conditions**
Mixed Layer Models for Coastal Waters, W. J. Wiseman, Jr., L. J. Rouse, Jr. and O. K. Huh, 2619
- Coastal plains; Probability; Probability distribution functions; Sea level; Statistical analysis; Storm surges; Tides; Beaches**
Extreme Sea Levels from Tide and Surge Probability, D. T. Pugh and J. M. Vassie, 911
- Coastal structures; Currents (water); Jetties; Numerical analysis; Ocean bottom; Scouring; Sediment transport; Time factors**
A Numerical Model for Sediment Transport, J. P. Lepetit and A. Hauguel, 1715
- Coastal structures; Dikes; Erosion control; Japan; Land reclamation; Scouring; Sea walls; Shore protection; Wave energy; Wave reflection; Beach erosion**
Effectiveness of Seadikes with Rough Slope, Osamu Toyoshima, 2528

- Coastal structures; Erosion control; Littoral zone; Marine terminals; Piers; Rubble-mound breakwaters; Sands; Shore-line cover; Beach erosion; Breakwaters**
Coastal Structures' Effects on Shorelines, Ronald M. Noble, 2069
- Coastal structures; Floating bodies; Oil spills; Tires; Wave action; Wave attenuation; Breakwaters; Coastal engineering**
Scrap Tyre Breakwaters in Coastal Engineering, Robert Charles McGregor and Neil Sinclair Miller, 2191
- Color photography; Images; Remote sensing; Shallow water; Water depth; Aerial photography; Bathymetry**
Visible-Region Photographic Remote Sensing of Nearshore Waters, Tsuguo Sunamura and Kiyoshi Horikawa, 1439
- Computation; Cylindrical bodies; Experimentation; Model tests; Numerical analysis; Piles; Transverse waves; Wave energy; Wave height; Wave interference**
Wave Forces on a Row of Cylindrical Piles of Large Diameter, J. C.W. Berkhoff and J. V.D. Weide, 2433
- Computation; Damping; Spectrum analysis; Tidal effects; Tides; Two-dimensional; Wave damping; Waves**
A New Approach for Tidal Computations, C. Le Provost, 1104
- Computer programs; Harbors; Hydraulic models; Numerical analysis; Wave diffraction; Wave height; Wave reflection; Breakwaters**
A Numerical Approach for the Determination of the Wave Height Distribution in a Harbour, Soren Kohlhase, Karl-Friedrich Daemrich, U. Berger, E. Tautenhain and O. Burkhardt, 664
- Concrete piles; Dredging; Failure; Intake structures; Jetties; Offshore structures; Centrifugal pumps**
Problems of Design and Construction of an Offshore Sea Water Intake, D. W. Standish-White and J. A. Zwamborn, 2125
- Confidence level; Ocean waves; Probability distribution functions; Shore protection; Statistical analysis; Wave height; Wave period; Coastal plains**
On Long-Term Statistics for Ocean and Coastal Waves, Michel K. Ochi, 59
- Continental shelf; Currents (water); Littoral current; Nicaragua; Pressure gradients; Salinity; Suspended sediments; Boundary layer flow**
Shelf and Coastal Boundary Layer Currents, Miskito Bank of Nicaragua, Richard L. Crout and Stephen P. Murray, 2715
- Cooling water; Discharge (water); Model studies; Rivers; Storm surges; Temperature effects; Thermal pollution; Tidal effects; Tidal hydraulics**
Influence on Temperature Increases in Tidal Rivers Caused by Waste Heat Injections with Respect to Tidal Cycles and Storm Surges, Horst Schwarze and Wilfried Falldorf, 2915
- Cooling water; Loads (forces); Outfall sewers; Scale effect; Tests; Thermal pollution; Wave energy; Wave height; Wave pressure**
Non-Breaking and Breaking Wave Loads on a Cooling Water Outfall, G. R. Mogridge and W. W. Jamieson, 2461
- Coral reefs and islands; Energy; Probability density functions; Spectral analysis; Surf; Wave action; Wave height; Wave period; Waves**
The Energy Spectra of Surf Waves on a Coral Reef, Theodore T. Lee and Kerry P. Black, 588
- Coring; Histograms; Sediment deposits; Surf; Tidal effects; Tracers; Wave action; Wave height; Beaches; Breaking energy**
Depth of Disturbance of Sand in Surf Zones, Michael K. Gaughan, 1513
- Correlation analysis; Deep water; Frequencies; Intensity; Wave energy; Wave propagation; Waves; Wave spectra; Bathymetry**
Deepwater Direction from an Intensity Array, Alan L. Higgins and Richard J. Seymour, 305
- Correlation techniques; Ocean waves; Offshore structures; Shore protection; Wave height; Wave period; Wave spectra**
The Observed Joint Distribution of Periods and Heights of Sea Waves, Yoshimi Goda, 227
- Cost effectiveness; Floods; Hurricanes; Numerical analysis; Predictions; Simulation; Storm surges; Texas; Tidal effects; Tsunamis; Water levels; Coastal plains**
Coastal Flood Simulation in Stretched Coordinates, H. Lee Butler, 1030
- Costs; Revetments; Rubble-mound breakwaters; Slope stability; Stability; Wave energy; Wave pressure; Armoring (streambed)**
Blanket Theory and Low Cost Revetments, C. T. Brown, 2510
- Cross sections; Estuaries; Inlets (waterways); Tidal currents; Tidal effects; Tidal flats; Two-dimensional; Wave tanks**
Periodic Flows from Tidal Inlets, D. L. Wilkinson, 1336
- Current meters; Harbor facilities; Littoral current; Littoral drift; Water depth; Wave height; Wave period; Wave recorders (water waves); Wave spectrum; Brazil**
Coastal Study of Espirito Santo Brazil, Paulo Augusto Vivacqua, Hildebrando de Araujo Goes Filho and Octavio de Sampaio Ferraz Jardim Sayao, 2104
- Currents (water); Density; Eddies; Eddy currents; Mixing; Tidal currents; Turbulence; Velocity; Water depth; Wind loads; Aerial photography**
Large Scale Turbulence in Tidal Currents, John B. Hinwood, 2598
- Currents (water); Density; Friction coefficient (hydraulic); Model studies; Three-dimensional; Water circulation; Wind loads**
Three Dimensional Modelling of the Irish Sea, Norman Stuart Heaps, 2671
- Currents (water); Design criteria; Energy conversion; Environmental effects; Environmental impact statements; Hurricanes; Site selection; Thermal energy; Waves; Wind**
Some Design Criteria for OTEC Installations for Keahole Point, Hawaii, Frederick C. Munchmeyer and Charles L. Bretschneider, 2633

- Currents (water); Diffusion; Eddies; Environmental factors; Simulation; Tidal hydraulics; Water circulation; Wind loads; Bays (topographic features)**
 Characteristics of Circulation in Bay Waters due to Wind Action, Akira Wada and Ioshihito Miyaike, 2730
- Currents (water); Dolphins (structures); Marine structures; Offshore platforms; Offshore structures; Pile foundations; Underwater foundations; Vibration**
 Tripod Concept for Pile Structures in Fast Current, J. Khanna and J. S. Wood, 2481
- Currents (water); Eddies; Oil spills; Three-dimensional; Viscosity; Water depth; Water pollution; Wind loads**
 3-D Current Model with Depth Varying Eddy Viscosity, Bryan R. Pearce, Cortis Cooper and Susan Nelson, 2602
- Currents (water); Edge effect; Frequencies; Littoral current; Ocean waves; Wave energy; Waves; Wave spectra; Wave velocity**
 Observation of Nearshore Current and Edge Waves, Tamio O. Sasaki and Kiyoshi Horikawa, 791
- Currents (water); Experimentation; Fetch; Wave generation; Wave height; Waves; Wave spectra; Wave tanks; Wave velocity; Wind forces; Wind pressure**
 Experimental Study of Wind Waves Generated on Currents, Hajime Kato and Hiroichi Tsuruya, 742
- Currents (water); Field tests; Sands; Sediment transport; Suspended load; Suspended sediments; Tidal effects; Wave action; Wave energy; Wave period; Waves**
 Effect of Waves on Sand Transport by Currents, Michael W. Owen and Michael F.C. Thorn, 1675
- Currents (water); Heated water; Jet flow; Mixing; Plumes; Surf; Temperature effects; Thermal pollution; Tracers; Turbulent flow**
 Mixing of Heated Water Discharged in the Surf Zone, Kiyoshi Horikawa, Ming-Chung Lin and Tamio O. Sasaki, 2563
- Currents (water); Jetties; Numerical analysis; Ocean bottom; Scouring; Sediment transport; Time factors; Coastal structures**
 A Numerical Model for Sediment Transport, J. P. Lepetit and A. Hauguel, 1715
- Currents (water); Littoral current; Nicaragua; Pressure gradients; Salinity; Suspended sediments; Boundary layer flow; Continental shelf**
 Shelf and Coastal Boundary Layer Currents, Miskito Bank of Nicaragua, Richard L. Crout and Stephen P. Murray, 2715
- Currents (water); Ocean bottom; Surface waves; Water depth; Wave energy; Wave measurement; Acoustic measuring instruments**
 Near-Bottom Current Measured by Acoustic Sensors, K. A. Selanger and T. Carstens, 878
- Currents (water); Ripple marks; Sediment transport; Shear stress; Three-dimensional; Wave height; Waves; Wave tanks; Coastal plains**
 Sediment Transport and Ripples Due to Waves and Currents, Zbigniew Pruszk and Ryszard B. Zeidler, 1638
- Currents (water); Sediment load; Sediments; Sediment transport; Wave action; Wave energy; Waves**
 Sediment Load under Waves and Currents, D. H. Willis, 1626
- Cyclones; Frequencies; Mathematical models; Probability distribution functions; Tropical cyclones; Wave equations; Wave recorders (water waves); Wind forces; Wind pressure; Australia**
 Wind Wave Frequencies in a Tropical Cyclone Region, Rodney J. Sobey, 76
- Cylindrical bodies; Diffraction; Particle trajectories; Spectral energy distribution; Time dependence; Water levels; Wave diffraction; Wave energy**
 Wave Forces Induced by Irregular Waves on a Vertical Circular Cylinder, Hajime Ishida and Yuichi Iwagaki, 2397
- Cylindrical bodies; Displacement; Dynamic characteristics; Dynamic response; Experimentation; Piles; Wave period; Wave propagation**
 Dynamic Behavior of Vertical Cylinder due to Wave Force, Toru Sawaragi and Takayuki Nakamura, 2378
- Cylindrical bodies; Drag; Experimentation; Loads (forces); Predictions; Reynolds number; Water flow; Wave energy; Wave pressure**
 Wave Loads on Horizontal Cylinders, P. Holmes and J. R. Chaplin, 2449
- Cylindrical bodies; Dynamic response; Loading; Mathematical models; Ocean waves; Responses; Water waves; Waves**
 Loading and Response of Cylinders in Waves, G. N. Bullock, P. K. Stansby and J. G. Warren, 2415
- Cylindrical bodies; Experimentation; Model tests; Numerical analysis; Piles; Transverse waves; Wave energy; Wave height; Wave interference; Computation**
 Wave Forces on a Row of Cylindrical Piles of Large Diameter, J. C.W. Berkhoff and J. V.D. Weide, 2433
- Damage; Dikes; Hydrodynamics; Statistical analysis; Wave height; Wave period; Wave runoff; Wave spectra**
 New Dike Design Criteria Based on Wave Spectra, Hans Kaldenhoff and Suhan M. Gokcesu, 2500
- Damage; Earthquake loads; Earthquake resistant structures; Loading; Rubble-mound breakwaters; Seismic design; Settlement (structural); Slope stability; Acceleration**
 Loadings on Rubble-Mound Breakwaters due to Earthquakes, H. Wang, C. Y. Yang, C. Lamison and S. S. Chen, 2244
- Damage; Estuaries; History; Hydraulic models; Armoring (streambed); Breakwaters; Coastal plains**
 Models — Can We Learn from the Past? Some Thoughts on the Design of Breakwaters, W. A. Price, 25
- Damage; Hydraulic models; Rubble-mound breakwaters; Stability; Wave energy; Wave height; Wave spectra; Wave tanks; Breakwaters**
 Effects of Wave Grouping on Breakwater Stability, R. R. Johnson, E. P.D. Mansard and J. Ploeg, 2228

- Damage; Ocean waves; Recreational facilities; Storm surges; West Germany; Coastal plains**
Welcoming Address — IV, Hans-Werner Partensky, 10
- Damping; Spectrum analysis; Tidal effects; Tides; Two-dimensional; Wave damping; Waves; Computation**
A New Approach for Tidal Computations, C. Le Provost, 1104
- Damping; Tidal currents; Tidal energy; Wave damping; Wave dispersion; Wave energy; Wave height; Wave runup; Waves; Wind speed**
Wave Climate Study in the Region of the East Frisian Islands and Coast, Hanz Dieter Niemyer, 134
- Deep water; Frequencies; Intensity; Wave energy; Wave propagation; Waves; Wave spectra; Bathymetry; Correlation analysis**
Deepwater Direction from an Intensity Array, Alan L. Higgins and Richard J. Seymour, 305
- Deep water; Particle trajectories; Slope; Velocity; Waves; Wave velocity; Beaches; Breaking energy**
Estimation of Water Particle Velocity of Breaking Wave, Tetsuo Sakai and Yuichi Iwagaki, 551
- Delaware; Hydraulic models; Inlets (waterways); Jetties; Sedimentation; Sheet piles; Tidal effects; Trends; Beach erosion**
Case Studies of Delaware's Tidal Inlets: Roosevelt and Indian River Inlets, W. A. Dennie, G. A. Lanan and Robert A. Dalrymple, 1282
- Delaware; Inlets (waterways); Littoral drift; Marshes; Morphology; Sedimentation; Tidal hydraulics; Barriers; Beach erosion; Coastal morphology**
Morphology of Coastal Barriers, Delaware, U.S.A., John C. Kraft, Chacko J. John and Evelyn M. Maurmeyer, 1232
- Density; Eddies; Eddy currents; Mixing; Tidal currents; Turbulence; Velocity; Water depth; Wind loads; Aerial photography; Currents (water)**
Large Scale Turbulence in Tidal Currents, John B. Hinwood, 2598
- Density; Estuaries; Flumes; Harbors; Mathematical models; Netherlands; Rivers; Saline water intrusion; Salinity**
Effect of Harbours on Salt Intrusion in Estuaries, A. Roelfzema and A. G. van Os, 2810
- Density; Flumes; Slope stability; Stability; Standardization; Test reproducibility; Tests; Armoring (streambed); Breakwaters**
Dolos Packing Density and Effect of Relative Block Density, J. A. Zwamborn, 2285
- Density; Friction coefficient (hydraulic); Model studies; Three-dimensional; Water circulation; Wind loads; Currents (water)**
Three Dimensional Modelling of the Irish Sea, Norman Stuart Heaps, 2671
- Density; Friction coefficient (hydraulic); Open channel flow; Saline water-freshwater interfaces; Salinity; Stratified flow; Two phase flow; Water flow**
Interfacial Friction Coefficients in a Two-Layered Stratified Flow, Emmanuel Partheniades and Vassilios Dermisiss, 2778
- Density currents; Discharge (water); Heat exchangers; Liquid natural gas; Model studies; Thermal pollution; Tidal currents; Vaporizers; Biological properties**
Thermal and Biological Impact of LNG Vaporizer Discharge, Peter A. Mangarella and Gordon A. Robilliard, 2945
- Design criteria; Energy conversion; Environmental effects; Environmental impact statements; Hurricanes; Site selection; Thermal energy; Waves; Wind; Currents (water)**
Some Design Criteria for OTEC Installations for Keahole Point, Hawaii, Frederick C. Munchmeyer and Charles L. Bretschneider, 2633
- Design criteria; Offshore platforms; Offshore structures; Surveys (data collection); Wave energy; Wave height; Wave recorders (water waves); Buoys**
Comparison of Shipborne Wave Recorder and Waverider Buoy Data Used to Generate Design and Operational Planning Criteria, C. G. Graham, G. Verboom and C. J. Shaw, 97
- Diffraction; Groins (structures); Jetties; Littoral drift; Numerical analysis; Predictions; Refraction; Sediment transport; Barriers; Beaches; Breakwaters; Coastal plains**
Prediction of Beach PlanForms with Littoral Controls, Marc Perlin and Robert G. Dean, 1818
- Diffraction; Ocean waves; Random processes; Wave diffraction; Wave height; Wave reflection; Wave spectra; Breakwaters**
Diffraction Diagrams for Directional Random Waves, Yoshimi Goda, Tomotsuka Takayama and Yasumasa Suzuki, 628
- Diffraction; Particle trajectories; Spectral energy distribution; Time dependence; Water levels; Wave diffraction; Wave energy; Cylindrical bodies**
Wave Forces Induced by Irregular Waves on a Vertical Circular Cylinder, Hajime Ishida and Yuichi Iwagaki, 2397
- Diffraction; Sediment transport; Wave diffraction; Wave height; Wave phases; Bathymetry; Bays (topographic features); Beach erosion; Beaches; Breakwaters**
Diffraction Calculation of Shoreline PlanForms, Robert G. Dean, 1903
- Diffusion; Dispersion; Mathematical models; Outfall sewers; Sewage effluents; Statistical analysis; Time series analysis; Waste disposal; Coastal plains**
Outfall Diffusion Models for the Coastal Zone, D. C.L. Lam and C. R. Murthy, 2584
- Diffusion; Dredges; Dredging; Estuaries; Models; Plumes; Sediment concentration; Spoil; Spoil banks; Suspended sediments**
Factors Governing the Distribution of Dredge-Resuspended Sediments, W. Frank Bohlen, 2001
- Diffusion; Eddies; Environmental factors; Simulation; Tidal hydraulics; Water circulation; Wind loads; Bays (topographic features); Currents (water)**
Characteristics of Circulation in Bay Waters due to Wind Action, Akira Wada and Ioshihito Miyaike, 2730

- Diffusion coefficient; Entrainment; Estuaries; Japan; Saline water-freshwater interfaces; Salinity; Ultrasonic tests**
Behaviors of the Salt Wedge and the Salinity Distribution at Estuaries, Isao Yakuwa, Susumu Takahashi and Morimasa Ohtani, 2746
- Diffusion coefficient; Experimentation; Hydraulic models; Japan; Scale effect; Tidal currents; Tidal hydraulics; Water circulation**
Experimental Study on Scale Effect of Tidal Model, Haruo Higuchi, Hideichi Yasuda and Norio Hayakawa, 2646
- Dikes; Erosion control; Japan; Land reclamation; Scouring; Sea walls; Shore protection; Wave energy; Wave reflection; Beach erosion; Coastal structures**
Effectiveness of Seadikes with Rough Slope, Osamu Toyoshima, 2528
- Dikes; Estuaries; Ports; Shipping; Shore protection; Storms; Tidal currents; West Germany**
Welcoming Address — II, Helga Elstner, 4
- Dikes; Hydrodynamics; Statistical analysis; Wave height; Wave period; Wave runup; Wave spectra; Damage**
New Dike Design Criteria Based on Wave Spectra, Hans Kaldenhoff and Suhan M. Gokcesu, 2500
- Discharge (water); Dunes; Flow rates; Sediment deposits; Time dependence; Unsteady flow; Water depth; Bed forms**
Time Lag of Dunes for Unsteady Flow Conditions, Horst Nasner, 1801
- Discharge (water); Estuaries; Hydraulic models; Model studies; Numerical analysis; Responses; Water levels; Water waves; Wave height**
A Hybrid Model of the St. Lawrence River Estuary, E. R. Funke and N. L. Crookshank, 2855
- Discharge (water); Heat exchangers; Liquid natural gas; Model studies; Thermal pollution; Tidal currents; Vaporizers; Biological properties; Density currents**
Thermal and Biological Impact of LNG Vaporizer Discharge, Peter A. Mangarella and Gordon A. Robilliard, 2945
- Discharge (water); Hydrodynamics; Meteorology; Rainfall; Salt marshes; Sediment transport; South Carolina; Suspended load; Tidal currents; Tidal effects; Tidal waters; Wind**
Hydrodynamics and Sediment Transport in a Salt Marsh Tidal Channel, Larry G. Ward, 1953
- Discharge (water); Model studies; Rivers; Storm surges; Temperature effects; Thermal pollution; Tidal effects; Tidal hydraulics; Cooling water**
Influence on Temperature Increases in Tidal Rivers Caused by Waste Heat Injections with Respect to Tidal Cycles and Storm Surges, Horst Schwarze and Wilfried Falldorf, 2915
- Dispersion; Environmental factors; Georgia; Inlets (waterways); Morphology; Sediment deposits; Tidal currents; Tidal effects; Wave energy; West Germany; Beaches**
Process-Response Models for Depositional Shorelines: The German and the Georgia Bights, Dag Nummedal and Ian A. Fischer, 1215
- Dispersion; Estuaries; Mixing; Model studies; Saline water-freshwater interfaces; Shallow water; Standing waves; Tidal flats; Tidal hydraulics**
Longitudinal Dispersion in Shallow Well-Mixed Estuaries, J. Dronkers, 2761
- Dispersion; Mathematical models; Outfall sewers; Sewage effluents; Statistical analysis; Time series analysis; Waste disposal; Coastal plains; Diffusion**
Outfall Diffusion Models for the Coastal Zone, D. C.L. Lam and C. R. Murthy, 2584
- Displacement; Dynamic characteristics; Dynamic response; Experimentation; Piles; Wave period; Wave propagation; Cylindrical bodies**
Dynamic Behavior of Vertical Cylinder due to Wave Force, Toru Sawaragi and Takayuki Nakamura, 2378
- Dissipation; Friction coefficient (hydraulic); Ocean bottom; Water depth; Water waves; Wave dispersion; Wave energy; Wave propagation; Wave spectra**
Bottom Dissipation in Finite-Depth Water Waves, S. V. Hsiao and O. H. Shemdin, 434
- Distortion; Friction coefficient (hydraulic); Laboratory tests; Mathematical models; Numerical analysis; Tidal effects; Acceleration; Bed roughness**
Numerical Study of Distortion in a Froude Model, T. A. McClimans and S. A. Gjerp, 2887
- Distribution functions; Predictions; Rainfall; Samples; Sampling; Wave energy; Wave height; Wave spectra; Wind velocity**
Extremal Prediction of Significant Wave Height, Enrique Copeiro, 285
- Dolphins (structures); Marine structures; Offshore platforms; Offshore structures; Pile foundations; Underwater foundations; Vibration; Currents (water)**
Tripod Concept for Pile Structures in Fast Current, J. Khanna and J. S. Wood, 2481
- Drag; Experimentation; Friction coefficient (hydraulic); Friction studies; Wave action; Wave energy; Wave reflection**
Non-Conservative Wave Interaction with Fixed Semi-Immersed Rectangular Structures, Robert B. Steimer and Charles K. Sollitt, 2209
- Drag; Experimentation; Loads (forces); Predictions; Reynolds number; Water flow; Wave energy; Wave pressure; Cylindrical bodies**
Wave Loads on Horizontal Cylinders, P. Holmes and J. R. Chaplin, 2449
- Dredges; Dredging; Estuaries; Models; Plumes; Sediment concentration; Spoil; Spoil banks; Suspended sediments; Diffusion**
Factors Governing the Distribution of Dredge-Resuspended Sediments, W. Frank Bohlen, 2001
- Dredges; Dredging; Models; Sediments; Spoil; Spoil banks; Beach nourishment; Bottom sediments**
Importance of Handling Losses to Beach Fill Design, R. D. Hobson and W. R. James, 1873
- Dredging; Estuaries; Harbor facilities; Harbors; Littoral current; Littoral drift; Littoral materials; Sediment deposits; Sediments; Shoaling; Accretion (geomorphology); California**
Maintenance of Santa Cruz Harbor, California, U.S.A., Orville T. Magoon and Don C. Baer, 1276

- Dredging; Estuaries; Models; Plumes; Sediment concentration; Spoil; Spoil banks; Suspended sediments; Diffusion; Dredges**
Factors Governing the Distribution of Dredge-Resuspended Sediments, W. Frank Bohlen, 2001
- Dredging; Failure; Intake structures; Jetties; Offshore structures; Centrifugal pumps; Concrete piles**
Problems of Design and Construction of an Offshore Sea Water Intake, D. W. Standish-White and J. A. Zwamborn, 2125
- Dredging; Gravel; Great Britain; Licensing; Littoral drift; Sand; Shore protection; Tidal currents; Wave action; Wave energy; Wave refraction; Coastal plains**
The Effect of Offshore Dredging on Coastlines, W. A. Price, J. M. Motyka and L. J. Jaffrey, 1347
- Dredging; Groins (structures); Sea walls; Shore protection; Spoil; Spoil banks; Beach erosion; Beach nourishment**
Some Facts and Fancies about Beach Erosion, Richard Sylvester, 1888
- Dredging; Harbors; Models; Salinity; Sedimentation; Sediment transport; Silting; Suspended sediments; Temperature; Tidal effects; Turbidity; Canada**
Tidal Sedimentation in Gros-Couana Harbor, Georges Drapeau and Guy Fortin, 1986
- Dredging; Hydraulic models; Inlets (waterways); Jetties; North Carolina; Sediment deposits; Simulation; Spoil banks; Beaches; Breakwaters**
Coastal Processes at Oregon Inlet, North Carolina, James T. Jarrett, 1257
- Dredging; Models; Sediments; Spoil; Spoil banks; Beach nourishment; Bottom sediments; Dredges**
Importance of Handling Losses to Beach Fill Design, R. D. Hobson and W. R. James, 1873
- Drifting (aquatic); Floating bodies; Mass transfer; Wave height; Wave period; Waves; Amplitude; Buoys**
Drift Speed of Buoys in Waves, John H. Nath, 859
- Drifting (aquatic); Water depth; Water surface; Wave tanks; Wind forces; Wind pressure; Wind velocity**
Wind-Induced Water Surface Set-Up and Drift Currents, Frederick L.W. Tang, Jin Wu, Charles C.C. Chang and Shan-Hwei Ou, 841
- Dunes; Erosion; Movable bed models; Ripple marks; Sands; Scale effect; Shore protection; Storm surges; Beach erosion**
Movable Bed Model Tests on Dune Erosion, P. Vellinga, 2020
- Dunes; Erosion control; Fences; Sands; Sediment deposits; Soil stabilization; Wind forces; Wind pressure; Airspeed; Beach erosion**
Using Fences to Create and Stabilise Sand Dunes, Brian B. Willetts and Christopher J. Phillips, 2040
- Dunes; Flow rates; Sediment deposits; Time dependence; Unsteady flow; Water depth; Bed forms; Discharge (water)**
Time Lag of Dunes for Unsteady Flow Conditions, Horst Nasner, 1801
- Dynamic characteristics; Dynamic response; Experimentation; Piles; Wave period; Wave propagation; Cylindrical bodies; Displacement**
Dynamic Behavior of Vertical Cylinder due to Wave Force, Toru Sawaragi and Takayuki Nakamura, 2378
- Dynamic loads; Shore protection; Storm surges; Surf; Water levels; Wave energy; Wave recorders (water waves); Wave runup; Coastal plains**
Wave Set-Up in the Surf Zone, Uwe A. Hansen, 1071
- Dynamic models; Geomorphology; Three-dimensional; Water depth; Wave energy; Wave height; Wave spectra; Accretion (geomorphology); Beach erosion; Beaches**
Wave Power and Beach Stages: A Global Model, Andrew D. Short, 1145
- Dynamic pressure; Frequencies; Hydrodynamic pressure; Responses; Stochastic processes; Wave generation; Wave spectra**
Analysis of Hinged Wavemakers for Random Waves, Robert T. Hudspeth, Douglas F. Jones and John H. Nath, 372
- Dynamic response; Experimentation; Piles; Wave period; Wave propagation; Cylindrical bodies; Displacement; Dynamic characteristics**
Dynamic Behavior of Vertical Cylinder due to Wave Force, Toru Sawaragi and Takayuki Nakamura, 2378
- Dynamic response; Loading; Mathematical models; Ocean waves; Responses; Water waves; Waves; Cylindrical bodies**
Loading and Response of Cylinders in Waves, G. N. Bullock, P. K. Stansby and J. G. Warren, 2415
- Dynamic response; Model studies; Temperature effects; Three-dimensional; Tidal effects; Water flow; Water levels; Wind loads**
Three-Dimensional SGS Energy Model of Eastern Bering Sea, S. K. Liu and J. J. Leendertse, 2687
- Dynamic response; Oscillation; Responses; Simulation; Wave damping; Wave energy; Wave period; Wave pressure; Wind loads; Wind pressure**
Simulation of Wave/Wind Forced Harbor Oscillation, S. K. Liu, H. S. Hou and Charles C.C. Chang, 2551
- Dynamics; Estuaries; Forecasting; Predictions; Storm surges; Tidal effects; Tidal energy; Tide gauges**
Storm Surge Prediction in Tidal Rivers: A New Conception, Winfried Siefert, 986
- Earthquake loads; Earthquake resistant structures; Loading; Rubble-mound breakwaters; Seismic design; Settlement (structural); Slope stability; Acceleration; Damage**
Loadings on Rubble-Mound Breakwaters due to Earthquakes, H. Wang, C. Y. Yang, C. Lamison and S. S. Chen, 2244
- Earthquake resistant structures; Loading; Rubble-mound breakwaters; Seismic design; Settlement (structural); Slope stability; Acceleration; Damage; Earthquake loads**
Loadings on Rubble-Mound Breakwaters due to Earthquakes, H. Wang, C. Y. Yang, C. Lamison and S. S. Chen, 2244

- Economic analysis; Environmental factors; Financing; Storms; Storm surges; Tidal waters; Water levels; Waterways (transportation); West Germany**
 Welcoming Address — III, Volker Hauff, 7
- Eddies; Eddy currents; Mixing; Tidal currents; Turbulence; Velocity; Water depth; Wind loads; Aerial photography; Currents (water); Density**
 Large Scale Turbulence in Tidal Currents, John B. Hinwood, 2598
- Eddies; Environmental factors; Simulation; Tidal hydraulics; Water circulation; Wind loads; Bays (topographic features); Currents (water); Diffusion**
 Characteristics of Circulation in Bay Waters due to Wind Action, Akira Wada and Ioshihito Miyaake, 2730
- Eddies; Oil spills; Three-dimensional; Viscosity; Water depth; Water pollution; Wind loads; Currents (water)**
 3-D Current Model with Depth Varying Eddy Viscosity, Bryan R. Pearce, Cortis Cooper and Susan Nelson, 2602
- Eddy currents; Mixing; Tidal currents; Turbulence; Velocity; Water depth; Wind loads; Aerial photography; Currents (water); Density; Eddies**
 Large Scale Turbulence in Tidal Currents, John B. Hinwood, 2598
- Edge effect; Excitation; Interactions; Standing waves; Water depth; Waves; Wave tanks; Beaches**
 Excitation of Low Frequency Trapped Waves, Robert King and Ronald Smith, 449
- Edge effect; Frequencies; Littoral current; Ocean waves; Wave energy; Waves; Wave spectra; Wave velocity; Currents (water)**
 Observation of Nearshore Current and Edge Waves, Tamio O. Sasaki and Kiyoshi Horikawa, 791
- Edge effect; Gravity waves; Littoral current; Rip currents; Surf; Temporal distribution; Variations; Wave spectra**
 Variability of Longshore Currents, R. T. Guza and Edward B. Thornton, 756
- Edge effect; Littoral current; Littoral drift; Wave action; Wavelengths; Wave velocity; Beach erosion; Beaches; Beach sands**
 Beach Cusps and Edge Waves, David A. Huntley and A. J. Bowen, 1378
- Edge effect; Littoral current; Morphology; Resonance; Surf; Wave reflection; Waves; Wave spectra; Beaches**
 Surf Zone Resonance and Coupled Morphology, John Chappell and Lynn Donelson Wright, 1359
- Eigenvalues; Mass; Momentum; Offshore structures; Rip currents; Spacing; Surf; Wave action; Waves; Wave velocity; Coastal plains**
 Rip Current Spacing as an Eigenvalue, Noriyuki Iwata, 828
- Energy; Probability density functions; Spectral analysis; Surf; Wave action; Wave height; Wave period; Waves; Coral reefs and islands**
 The Energy Spectra of Surf Waves on a Coral Reef, Theodore T. Lee and Kerry P. Black, 588
- Energy conversion; Environmental effects; Environmental impact statements; Hurricanes; Site selection; Thermal energy; Waves; Wind; Currents (water); Design criteria**
 Some Design Criteria for OTEC Installations for Keahole Point, Hawaii, Frederick C. Munchmeyer and Charles L. Bretschneider, 2633
- Energy dissipation; Energy losses; Predictions; Random processes; Shallow water; Wave height; Bores (wave); Breaking energy**
 Energy Loss and Set-Up Due to Breaking of Random Waves, J. A. Battjes and J. P.F.M. Janssen, 569
- Energy losses; Predictions; Random processes; Shallow water; Wave height; Bores (wave); Breaking energy; Energy dissipation**
 Energy Loss and Set-Up Due to Breaking of Random Waves, J. A. Battjes and J. P.F.M. Janssen, 569
- Entrainment; Estuaries; Japan; Saline water-freshwater interfaces; Salinity; Ultrasonic tests; Diffusion coefficient**
 Behaviors of the Salt Wedge and the Salinity Distribution at Estuaries, Isao Yakuwa, Susumu Takahashi and Morimasa Ohtani, 2746
- Entrainment; Experimentation; Finite element method; Sediment concentration; Suspended sediments; Time dependence; Channel beds; Clays**
 Concentration of Suspended Clay in Periodic Flow, Akira Watanabe, P. Thimakorn and A. Das Gupta, 1918
- Environmental effects; Environmental impact statements; Hurricanes; Site selection; Thermal energy; Waves; Wind; Currents (water); Design criteria; Energy conversion**
 Some Design Criteria for OTEC Installations for Keahole Point, Hawaii, Frederick C. Munchmeyer and Charles L. Bretschneider, 2633
- Environmental factors; Financing; Storms; Storm surges; Tidal waters; Water levels; Waterways (transportation); West Germany; Economic analysis**
 Welcoming Address — III, Volker Hauff, 7
- Environmental factors; Georgia; Inlets (waterways); Morphology; Sediment deposits; Tidal currents; Tidal effects; Wave energy; West Germany; Beaches; Dispersion**
 Process-Response Models for Depositional Shorelines: The German and the Georgia Bights, Dag Nummedal and Ian A. Fischer, 1215
- Environmental factors; Simulation; Tidal hydraulics; Water circulation; Wind loads; Bays (topographic features); Currents (water); Diffusion; Eddies**
 Characteristics of Circulation in Bay Waters due to Wind Action, Akira Wada and Ioshihito Miyaake, 2730
- Environmental impact statements; Hurricanes; Site selection; Thermal energy; Waves; Wind; Currents (water); Design criteria; Energy conversion; Environmental effects**
 Some Design Criteria for OTEC Installations for Keahole Point, Hawaii, Frederick C. Munchmeyer and Charles L. Bretschneider, 2633

- Erosion; Groins (structures); Mathematical models; Rip currents; Shore-line cover; Wave diffraction; Wave refraction; Wind loads; Accretion (geomorphology); Beach nourishment**
Mathematical Modeling of Shoreline Evolution, Bernard Le Mehaute and Mills Soldate, 1163
- Erosion; Movable bed models; Ripple marks; Sands; Scale effect; Shore protection; Storm surges; Beach erosion; Dunes**
Movable Bed Model Tests on Dune Erosion, P. Vellinga, 2020
- Erosion control; Fences; Sands; Sediment deposits; Soil stabilization; Wind forces; Wind pressure; Airstrip; Beach erosion; Dunes**
Using Fences to Create and Stabilise Sand Dunes, Brian B. Willetts and Christopher J. Phillips, 2040
- Erosion control; Japan; Land reclamation; Scouring; Sea walls; Shore protection; Wave energy; Wave reflection; Beach erosion; Coastal structures; Dikes**
Effectiveness of Seadikes with Rough Slope, Osamu Toyoshima, 2528
- Erosion control; Littoral zone; Marine terminals; Piers; Rubble-mound breakwaters; Sands; Shore-line cover; Beach erosion; Breakwaters; Coastal structures**
Coastal Structures' Effects on Shorelines, Ronald M. Noble, 2069
- Estuaries; Field data; Flood protection; Mathematical models; Numerical analysis; Surveys (data collection); Tidal effects; Water levels; Wave propagation; Wave velocity**
Adjustment and Verification of the RANDDELTA II Model, A. Langerak, M. A.M. deRas and J. J. Leendertse, 1049
- Estuaries; Flood routing; Hydraulic models; Hydrodynamics; Numerical analysis; Rivers; Shallow water; Tidal effects; Turbulence**
Hydrodynamic Modelling of the Southern North Sea, David Prandle, 1122
- Estuaries; Flumes; Harbors; Mathematical models; Netherlands; Rivers; Saline water intrusion; Salinity; Density**
Effect of Harbours on Salt Intrusion in Estuaries, A. Roelfzema and A. G. van Os, 2810
- Estuaries; Forecasting; Predictions; Storm surges; Tidal effects; Tidal energy; Tide gates; Dynamics**
Storm Surge Prediction in Tidal Rivers: A New Conception, Winfried Siefert, 986
- Estuaries; Groins (structures); Navigable canals; Stream flow; Stream gages; Tidal currents; Tidal effects; Water levels**
Improvements on Tidal Estuaries and the Effects on Tidal Current, Hermann Harten, 2905
- Estuaries; Harbor facilities; Harbors; Littoral current; Littoral drift; Littoral materials; Sediment deposits; Sediments; Shoaling; Accretion (geomorphology); California; Dredging**
Maintenance of Santa Cruz Harbor, California, U.S.A., Orville T. Magoon and Don C. Baer, 1276
- Estuaries; History; Hydraulic models; Armoring (streambed); Breakwaters; Coastal plains; Damage Models — Can We Learn from the Past? Some Thoughts on the Design of Breakwaters, W. A. Price, 25**
- Estuaries; Hydraulic models; Mathematical models; Model studies; Numerical analysis; Saline water intrusion; Salinity; Simulation; Tidal hydraulics**
Numerical Tidal-Salinity Models of the Ems Estuary, Karsten Fischer, 2840
- Estuaries; Hydraulic models; Model studies; Numerical analysis; Responses; Water levels; Water waves; Wave height; Discharge (water)**
A Hybrid Model of the St. Lawrence River Estuary, E. R. Funke and N. L. Crookshank, 2855
- Estuaries; Inlets (waterways); Tidal currents; Tidal effects; Tidal flats; Two-dimensional; Wave tanks; Cross sections**
Periodic Flows from Tidal Inlets, D. L. Wilkinson, 1336
- Estuaries; Japan; Saline water-freshwater interfaces; Salinity; Ultrasonic tests; Diffusion coefficient; Entrainment**
Behaviors of the Salt Wedge and the Salinity Distribution at Estuaries, Isao Yakuwa, Susumu Takahashi and Morimasa Ohtani, 2746
- Estuaries; Littoral deposits; Nicaragua; Rainfall; Sedimentation; Sediments; Sediment transport; Water circulation; Wave energy; Weathering**
Variations of Wave-Energy Levels and Coastal Sedimentation, Eastern Nicaragua, E. H. Owens and H. H. Roberts, 1195
- Estuaries; Mixing; Model studies; Saline water-freshwater interfaces; Shallow water; Standing waves; Tidal flats; Tidal hydraulics; Dispersion**
Longitudinal Dispersion in Shallow Well-Mixed Estuaries, J. Dronkers, 2761
- Estuaries; Mixing; Rivers; Saline water-freshwater interfaces; Salinity; Stream flow; Velocity distribution; Vortices; Wave energy; Bed roughness**
Outflow Dynamics at a River Mouth, Masakazu Kashiwamura and Shizuo Yoshida, 2925
- Estuaries; Models; Plumes; Sediment concentration; Spoil; Spoil banks; Suspended sediments; Diffusion; Dredges; Dredging**
Factors Governing the Distribution of Dredge-Resuspended Sediments, W. Frank Bohlen, 2001
- Estuaries; Ports; Shipping; Shore protection; Storms; Tidal currents; West Germany; Dikes**
Welcoming Address — II, Helga Elstner, 4
- Estuaries; Reefs; Storms; Tidal currents; Wave action; Wave height; Wave runoff; Waves; Wave spectra; Wind velocity**
Analysis of Storm Tide Waves, Volker Barthel, 1016
- Estuaries; Saline water-freshwater interfaces; Saline water intrusion; Salinity; Stratified flow; Tidal currents; Tidal hydraulics; Water quality**
Stability Study of an Artificial Salt Intrusion in Estuaries, C. Marche, 2798
- Evaluation; Geological maps; Littoral deposits; Littoral materials; Sedimentation; Sediment transport; Surveys (data collection); Coastal plains**
A New Method for the Representation of Sedimentary Sequences in Coastal Regions, Hansjorg Streif, 1245
- Excitation; Interactions; Standing waves; Water depth; Waves; Wave tanks; Beaches; Edge effect**
Excitation of Low Frequency Trapped Waves, Robert King and Ronald Smith, 449

- Experimental data; Flumes; Gravity waves; Interactions; Waveforms; Wave height; Wavelength**
Changes in Height of Short Waves on Long Waves, Michio Sato and Kazuo Nakamura, 400
- Experimentation; Fetch; Wave generation; Wave height; Waves; Wave spectra; Wave tanks; Wave velocity; Wind forces; Wind pressure; Currents (water)**
Experimental Study of Wind Waves Generated on Currents, Hajime Kato and Hiroichi Tsuruya, 742
- Experimentation; Finite element method; Sediment concentration; Suspended sediments; Time dependence; Channel beds; Clays; Entrainment**
Concentration of Suspended Clay in Periodic Flow, Akira Watanabe, P. Thimakorn and A. Das Gupta, 1918
- Experimentation; Friction coefficient (hydraulic); Friction studies; Wave action; Wave energy; Wave reflection; Drag**
Non-Conservative Wave Interaction with Fixed Semi-Immersed Rectangular Structures, Robert B. Steimer and Charles K. Sollitt, 2209
- Experimentation; Friction coefficient (hydraulic); Ocean waves; Predictions; Wave dispersion; Wave height; Wave reflection; Breakwaters**
Wave Transmission through Trapezoidal Breakwaters, Ole Secher Madsen, Paisal Shusang and Sue Ann Hanson, 2140
- Experimentation; Hydraulic models; Japan; Scale effect; Tidal currents; Tidal hydraulics; Water circulation; Diffusion coefficient**
Experimental Study on Scale Effect of Tidal Model, Haruo Higuchi, Hideichi Yasuda and Norio Hayakawa, 2646
- Experimentation; Littoral current; Littoral drift; Predictions; Sediments; Sediment transport; Siltation; Wave energy**
Longshore Sediment Transport Data: A Review, Matthew N. Greer and Ole Secher Madsen, 1563
- Experimentation; Loads (forces); Predictions; Reynolds number; Water flow; Wave energy; Wave pressure; Cylindrical bodies; Drag**
Wave Loads on Horizontal Cylinders, P. Holmes and J. R. Chaplin, 2449
- Experimentation; Model tests; Numerical analysis; Piles; Transverse waves; Wave energy; Wave height; Wave interference; Computation; Cylindrical bodies**
Wave Forces on a Row of Cylindrical Piles of Large Diameter, J. C.W. Berkhoff and J. V.D. Weide, 2433
- Experimentation; Piles; Wave period; Wave propagation; Cylindrical bodies; Displacement; Dynamic characteristics; Dynamic response**
Dynamic Behavior of Vertical Cylinder due to Wave Force, Toru Sawaragi and Takayuki Nakamura, 2378
- Failure; Intake structures; Jetties; Offshore structures; Centrifugal pumps; Concrete piles; Dredging**
Problems of Design and Construction of an Offshore SeaWater Intake, D. W. Standish-White and J. A. Zwamborn, 2125
- Fences; Sands; Sediment deposits; Soil stabilization; Wind forces; Wind pressure; Airspeed; Beach erosion; Dunes; Erosion control**
Using Fences to Create and Stabilise Sand Dunes, Brian B. Willetts and Christopher J. Phillips, 2040
- Fetch; Wave generation; Wave height; Waves; Wave spectra; Wave tanks; Wave velocity; Wind forces; Wind pressure; Currents (water); Experimentation**
Experimental Study of Wind Waves Generated on Currents, Hajime Kato and Hiroichi Tsuruya, 742
- Field data; Flood protection; Mathematical models; Numerical analysis; Surveys (data collection); Tidal effects; Water levels; Wave propagation; Wave velocity; Estuaries**
Adjustment and Verification of the RANDDELTA II Model, A. Langerak, M. A.M. deRas and J. J. Leendertse, 1049
- Field tests; Gravel; Littoral current; Littoral deposits; Littoral drift; Sediment transport; Storm surges; Tracers; Wave energy; Beaches**
Field Experiment on Beach Gravel Transport, Masataro Hattori and Takasuke Suzuki, 1688
- Field tests; Gravity waves; Hurricanes; Sediments; Sediment transport; Storms; Storm surges; Wave energy; Wave period; Wave velocity; Canada**
Infragravity Waves in Storm Conditions, R. A. Holman, David A. Huntley and A. J. Bowen, 268
- Field tests; Harbors; Laboratory tests; Models; Prototypes; Wave recorders (water waves); Waves; Breakwaters**
A Comparison Between Model and Prototype Waves in Harbours, Sverre Bjordal and Alf Torum, 677
- Field tests; Laboratory tests; Measurement; Sediments; Water depth; Wave height; Wave period; Accuracy; Beach erosion**
Uses for a Calculated Limit Depth to Beach Erosion, Robert J. Hallermeier, 1493
- Field tests; Laboratory tests; Ocean bottom; Oscillation; Ripple marks; Shallow water; Waves; Wind pressure**
On the Geometry of Ripples Due to Waves, M. S. Yalin and E. Karahan, 1776
- Field tests; Littoral current; Model tests; Storms; Surf; Water circulation; Water levels; Wave height; Waves; Wind; Bathymetry; Bores (wave)**
Comparison of Model and Observed Nearshore Circulation, James H. Allender, John D. Ditmars, Wyman Harrison and Robert A. Paddock, 810
- Field tests; Model studies; Saline water-freshwater interfaces; Saline water intrusion; Salinity; Sampling; Tidal hydraulics; Verification inspection**
Field Data Analysis for Chesapeake Bay Model Verification, Ronald E. Nece and Norman W. Scheffner, 2870
- Field tests; Photographic analysis; Predictions; Water depth; Wave height; Wavelength; Waves; Breaking energy; Classification**
Field Study of Breaking Wave Characteristics, Lee L. Weishar and Robert J. Byrne, 487

- Field tests; Sands; Sediment transport; Suspended load; Suspended sediments; Tidal effects; Wave action; Wave energy; Wave period; Waves; Currents (water)**
Effect of Waves on Sand Transport by Currents, Michael W. Owen and Michael F.C. Thorn, 1675
- Financing; Storms; Storm surges; Tidal waters; Water levels; Waterways (transportation); West Germany; Economic analysis; Environmental factors**
Welcoming Address — III, Volker-Hauff, 7
- Finite element method; Harbors; Integral equations; Oscillations; Tides; Water waves; Wave diffraction; Wave refraction; Approximation method**
A Combined FE-BIE Method for Water Waves, A. Hauguel, 715
- Finite element method; Sediment concentration; Suspended sediments; Time dependence; Channel beds; Clays; Entrainment; Experimentation**
Concentration of Suspended Clay in Periodic Flow, Akira Watanabe, P. Thimakorn and A. Das Gupta, 1918
- Fjords; Freezing; Heat loss; Hydroelectric powerplants; Ice control; Model studies; Numerical analysis; Outlet works; Saline water**
Prevention of Freezing in Fjords, Sveinung Saegrov, 2958
- Floating bodies; Mass transfer; Wave height; Wave period; Waves; Amplitude; Buoys; Drifting (aquatic)**
Drift Speed of Buoys in Waves, John H. Nath, 859
- Floating bodies; Oil spills; Tires; Wave action; Wave attenuation; Breakwaters; Coastal engineering; Coastal structures**
Scrap Tyre Breakwaters in Coastal Engineering, Robert Charles McGregor and Neil Sinclair Miller, 2191
- Flooding; Flowmeters; Inlets (waterways); Stress measurement; Tidal currents; Tidal flats; Velocity; Wave action; Wave velocity**
Velocity and Stress Measurements in a Tidal Inlet, David A. Huntley and Dag Nummedal, 1320
- Flooding; Frequencies; Probability; Storm surges; West Germany; Wind forces; Wind pressure; Wind velocity; Coastal engineering**
Frequencies and Probabilities of Extreme Storm Surges (On the Time-Dependent Changes of the Probability of Extreme Storm Floods at the German North Sea Coast), Alfred Fohrboter, 949
- Flood protection; Mathematical models; Numerical analysis; Surveys (data collection); Tidal effects; Water levels; Wave propagation; Wave velocity; Estuaries; Field data**
Adjustment and Verification of the RANDDELTA II Model, A. Langerak, M. A.M. deRas and J. J. Leendertse, 1049
- Flood routing; Hydraulic models; Hydrodynamics; Numerical analysis; Rivers; Shallow water; Tidal effects; Turbulence; Estuaries**
Hydrodynamic Modelling of the Southern North Sea, David Prandle, 1122
- Floods; Hurricanes; Numerical analysis; Predictions; Simulation; Storm surges; Texas; Tidal effects; Tsunamis; Water levels; Coastal plains; Cost effectiveness**
Coastal Flood Simulation in Stretched Coordinates, H. Lee Butler, 1030
- Florida; Friction coefficient (hydraulic); Model studies; Salinity; Salt balance; Salt water intrusion; Tidal hydraulics; Wind loads**
Tidal Hydraulics and Salt Balance of Lake Worth, Florida, J. van de Kreeke and J. D. Wang, 2827
- Flowmeters; Inlets (waterways); Stress measurement; Tidal currents; Tidal flats; Velocity; Wave action; Wave velocity; Flooding**
Velocity and Stress Measurements in a Tidal Inlet, David A. Huntley and Dag Nummedal, 1320
- Flow rates; Sediment deposits; Time dependence; Unsteady flow; Water depth; Bed forms; Discharge (water); Dunes**
Time Lag of Dunes for Unsteady Flow Conditions, Horst Nasner, 1801
- Flumes; Gravity waves; Interactions; Waveforms; Wave height; Wavelength; Experimental data**
Changes in Height of Short Waves on Long Waves, Michio Sato and Kazuo Nakamura, 400
- Flumes; Harbors; Mathematical models; Netherlands; Rivers; Saline water intrusion; Salinity; Density; Estuaries**
Effect of Harbours on Salt Intrusion in Estuaries, A. Roelfzema and A. G. van Os, 2810
- Flumes; Slope stability; Stability; Standardization; Test reproducibility; Tests; Armoring (streambed); Breakwaters; Density**
Dolos Packing Density and Effect of Relative Block Density, J. A. Zwamborn, 2285
- Forecasting; Hawaii; Meteorological data; Meteorology; Statistical analysis; Wave height; Wave recorders (water waves)**
An Evaluation of Extreme Wave Climate at Keahole Point, Hawaii, Charles L. Bretschneider and Richard E. Rocheleau, 152
- Forecasting; Mathematical models; Meteorological data; Meteorology; Numerical analysis; Predictions; Simulation; Storm surges; Water levels; Wind forces**
Numerical Storm Surge Forecasting, Manfred Engel, 975
- Forecasting; Morphology; Stability analysis; Tidal currents; Tidal flats; Tides; Two-dimensional; Water depth; Boundary conditions**
Two-Dimensional Stability Analysis of Tidal Basins and Tidal Flats of Larger Extent, Eberhard Renger, 1971
- Forecasting; Predictions; Storm surges; Tidal currents; Tidal effects; Tidal energy; Tide gages; Wind; Wind velocity**
Storm Surge Prediction by Combined Wind and Tide Data, Hermann Christiansen and Winfried Siefert, 965
- Forecasting; Predictions; Storm surges; Tidal effects; Tidal energy; Tide gages; Dynamics; Estuaries**
Storm Surge Prediction in Tidal Rivers: A New Conception, Winfried Siefert, 986

- Forecasting; Shallow water; Storm surges; Temperature; Water depth; Water levels; Air water interactions; Air-water interfaces**
Storm Surge Forecasting Methods in Enclosed Seas, P. F. Hamblin, 998
- Fourier transformation; Gravity waves; Storm surges; Surf; Water levels; Wave action; Wave dispersion; Wave period**
Anomalous Dispersion of Fourier Components of Surface Gravity Waves in the Near Shore Area, Fritz Busching, 247
- Fourier transformation; Interactions; Nonlinear systems; Sampling; Spectral analysis; Wave spectra; Calculations**
Higher Order Wave Spectra, Paul C. Liu and Albert W. Green, 360
- Freezing; Heat loss; Hydroelectric powerplants; Ice control; Model studies; Numerical analysis; Outlet works; Saline water; Fjords**
Prevention of Freezing in Fjords, Sveinung Saegrov, 2958
- Frequencies; Great Britain; Ports; Sampling; Sea level; Statistical analysis; Tidal waters; Water levels**
Analysis of Maximum Sea Level in Southern England, J. Graff and D. L. Blackman, 931
- Frequencies; Hydrodynamic pressure; Responses; Stochastic processes; Wave generation; Wave spectra; Dynamic pressure**
Analysis of Hinged Wavemakers for Random Waves, Robert T. Hudspeth, Douglas F. Jones and John H. Nath, 372
- Frequencies; Intensity; Wave energy; Wave propagation; Waves; Wave spectra; Bathymetry; Correlation analysis; Deep water**
Deepwater Direction from an Intensity Array, Alan L. Higgins and Richard J. Seymour, 305
- Frequencies; Littoral current; Ocean waves; Wave energy; Waves; Wave spectra; Wave velocity; Currents (water); Edge effect**
Observation of Nearshore Current and Edge Waves, Tamio O. Sasaki and Kiyoshi Horikawa, 791
- Frequencies; Mathematical models; Probability distribution functions; Tropical cyclones; Wave equations; Wave recorders (water waves); Wind forces; Wind pressure; Australia; Cyclones**
Wind Wave Frequencies in a Tropical Cyclone Region, Rodney J. Sobey, 76
- Frequencies; Probability; Storm surges; West Germany; Wind forces; Wind pressure; Wind velocity; Coastal engineering; Flooding**
Frequencies and Probabilities of Extreme Storm Surges (On the Time-Dependent Changes of the Probability of Extreme Storm Floods at the German North Sea Coast), Alfred Fohrboter, 949
- Friction coefficient (hydraulic); Friction studies; Wave action; Wave energy; Wave reflection; Drag; Experimentation**
Non-Conservative Wave Interaction with Fixed Semi-Immersed Rectangular Structures, Robert B. Steimer and Charles K. Sollitt, 2209
- Friction coefficient (hydraulic); Hydrodynamic pressure; Hydrodynamics; Numerical analysis; Ocean bottom; Ripple marks; Tidal effects; Bed forms**
The Influence of Dune and Flow Parameters on the Friction Factor, Jurgen Sundermann, H. Vollmers and W. Puls, 1787
- Friction coefficient (hydraulic); Inlets (waterways); Mathematical models; Numerical analysis; Sediment transport; Storm surges; Tidal effects; Wave height; Bays (topographic features)**
Numerical Model Investigation of Selected Tidal Inlet-Bay System Characteristics, William N. Seelig and Robert M. Sorensen, 1319
- Friction coefficient (hydraulic); Laboratory tests; Mathematical models; Numerical analysis; Tidal effects; Acceleration; Bed roughness; Distortion**
Numerical Study of Distortion in a Froude Model, T. A. McClimans and S. A. Gjerp, 2887
- Friction coefficient (hydraulic); Littoral current; Shores; Stresses; Surf; Water circulation; Wave energy; Wave propagation; Waves; Barriers**
Longshore Currents Due to Surf Zone Barrier, P. Bettess, C. A. Fleming, J. C. Heinrich, O. C. Zienkiewicz and D. I. Austin, 776
- Friction coefficient (hydraulic); Model studies; Salinity; Salt balance; Salt water intrusion; Tidal hydraulics; Wind loads; Florida**
Tidal Hydraulics and Salt Balance of Lake Worth, Florida, J. van de Kreeke and J. D. Wang, 2827
- Friction coefficient (hydraulic); Model studies; Three-dimensional; Water circulation; Wind loads; Currents (water); Density**
Three Dimensional Modelling of the Irish Sea, Norman Stuart Heaps, 2671
- Friction coefficient (hydraulic); Ocean bottom; Water depth; Water waves; Wave dispersion; Wave energy; Wave propagation; Wave spectra; Dissipation**
Bottom Dissipation in Finite-Depth Water Waves, S. V. Hsiao and O. H. Shemdin, 434
- Friction coefficient (hydraulic); Ocean waves; Predictions; Wave dispersion; Wave height; Wave reflection; Breakwaters; Experimentation**
Wave Transmission through Trapezoidal Breakwaters, Ole Secher Madsen, Paisal Shusang and Sue Ann Hanson, 2140
- Friction coefficient (hydraulic); Open channel flow; Saline water-freshwater interfaces; Salinity; Stratified flow; Two phase flow; Water flow; Density**
Interfacial Friction Coefficients in a Two-Layered Stratified Flow, Emmanuel Partheniades and Vassilios Dermissis, 2778
- Friction studies; Wave action; Wave energy; Wave reflection; Drag; Experimentation; Friction coefficient (hydraulic)**
Non-Conservative Wave Interaction with Fixed Semi-Immersed Rectangular Structures, Robert B. Steimer and Charles K. Sollitt, 2209
- Geological maps; Littoral deposits; Littoral materials; Sedimentation; Sediment transport; Surveys (data collection); Coastal plains; Evaluation**
A New Method for the Representation of Sedimentary Sequences in Coastal Regions, Hansjorg Streif, 1245

- Geomorphology; Three-dimensional; Water depth; Wave energy; Wave height; Wave spectra; Accretion (geomorphology); Beach erosion; Beaches; Dynamic models**
Wave Power and Beach Stages: A Global Model, Andrew D. Short, 1145
- Georgia; Inlets (waterways); Morphology; Sediment deposits; Tidal currents; Tidal effects; Wave energy; West Germany; Beaches; Dispersion; Environmental factors**
Process-Response Models for Depositional Shorelines: The German and the Georgia Bights, Dag Nummedal and Ian A. Fischer, 1215
- Gravel; Great Britain; Licensing; Littoral drift; Sand; Shore protection; Tidal currents; Wave action; Wave energy; Wave refraction; Coastal plains; Dredging**
The Effect of Offshore Dredging on Coastlines, W. A. Price, J. M. Motyka and L. J. Jaffrey, 1347
- Gravel; Littoral current; Littoral deposits; Littoral drift; Sediment transport; Storm surges; Tracers; Wave energy; Beaches; Field tests**
Field Experiment on Beach Gravel Transport, Masataro Hattori and Takasuke Suzuki, 1688
- Gravity waves; Hurricanes; Sediments; Sediment transport; Storms; Storm surges; Wave energy; Wave period; Wave velocity; Canada; Field tests**
Infragravity Waves in Storm Conditions, R. A. Holman, David A. Huntley and A. J. Bowen,
- Gravity waves; Interactions; Waveforms; Wave height; Wavelength; Experimental data; Flumes**
Changes in Height of Short Waves on Long Waves, Michio Sato and Kazuo Nakamura, 400
- Gravity waves; Littoral current; Rip currents; Surf; Temporal distribution; Variations; Wave spectra; Edge effect**
Variability of Longshore Currents, R. T. Guza and Edward B. Thornton, 756
- Gravity waves; Storm surges; Surf; Water levels; Wave action; Wave dispersion; Wave period; Fourier transformation**
Anomalous Dispersion of Fourier Components of Surface Gravity Waves in the Near Shore Area, Fritz Busching, 247
- Great Britain; Licensing; Littoral drift; Sand; Shore protection; Tidal currents; Wave action; Wave energy; Wave refraction; Coastal plains; Dredging; Gravel**
The Effect of Offshore Dredging on Coastlines, W. A. Price, J. M. Motyka and L. J. Jaffrey, 1347
- Great Britain; Ports; Sampling; Sea level; Statistical analysis; Tidal waters; Water levels; Frequencies**
Analysis of Maximum Sea Level in Southern England, J. Graff and D. L. Blackman, 931
- Groins (structures); Jetties; Littoral drift; Numerical analysis; Predictions; Refraction; Sediment transport; Barriers; Beaches; Breakwaters; Coastal plains; Diffraction**
Prediction of Beach PlanForms with Littoral Controls, Marc Perlin and Robert G. Dean, 1818
- Groins (structures); Mathematical models; Rip currents; Shore-line cover; Wave diffraction; Wave refraction; Wind loads; Accretion (geomorphology); Beach nourishment; Erosion**
Mathematical Modeling of Shoreline Evolution, Bernard Le Mehaute and Mills Soldate, 1163
- Groins (structures); Navigable canals; Stream flow; Stream gages; Tidal currents; Tidal effects; Water levels; Estuaries**
Improvements on Tidal Estuaries and the Effects on Tidal Current, Hermann Harten, 2905
- Groins (structures); Sea walls; Shore protection; Spoil; Spoil banks; Beach erosion; Beach nourishment; Dredging**
Some Facts and Fancies about Beach Erosion, Richard Sylvester, 1888
- Ground water; Groundwater elevation; Littoral current; Oscillations; Piezometers; Wave height; Wave period; Wave spectrum; Aquifers**
Beach Ground-Water Oscillations, Andrzej Lewandowski and Ryszard B. Zeidler, 2051
- Groundwater elevation; Littoral current; Oscillations; Piezometers; Wave height; Wave period; Wave spectrum; Aquifers; Ground water**
Beach Ground-Water Oscillations, Andrzej Lewandowski and Ryszard B. Zeidler, 2051
- Groups; Loading; Load transfer; Marine structures; Ocean waves; Wave action; Wave pressure; Wave tanks**
Suznetsov and G. D. Khaskhatchikh, 2328
Load Analysis from Wave Groups, A. I.
- Harbor facilities; Harbors; Littoral current; Littoral drift; Littoral materials; Sediment deposits; Sediments; Shoaling; Accretion (geomorphology); California; Dredging; Estuaries**
Maintenance of Santa Cruz Harbor, California, U.S.A., Orville T. Magoon and Don C. Baer, 1276
- Harbor facilities; Littoral current; Littoral drift; Water depth; Wave action; Wave period; Wave recorders (water waves); Wave spectrum; Brazil; Current meters**
Coastal Study of Espirito Santo Brazil, Paulo Augusto Vivaqua, Hildebrando de Araujo Goes Filho and Octavio de Sampaio Ferraz Jardim Sayao, 2104
- Harbors; Hydraulic models; Numerical analysis; Wave diffraction; Wave height; Wave reflection; Breakwaters; Computer programs**
A Numerical Approach for the Determination of the Wave Height Distribution in a Harbour, Soren Kohlhase, Karl-Friedrich Daemrich, U. Berger, E. Tautenhain and O. Burkhardt, 664
- Harbors; Integral equations; Oscillations; Tides; Water waves; Wave diffraction; Wave refraction; Approximation method; Finite element method**
A Combined FE-BIE Method for Water Waves, A. Hauguel, 715
- Harbors; Laboratory tests; Models; Prototypes; Wave recorders (water waves); Waves; Breakwaters; Field tests**
A Comparison Between Model and Prototype Waves in Harbours, Sverre Bjordal and Alf Torum, 677

- Harbors; Littoral current; Littoral drift; Littoral materials; Sediment deposits; Sediments; Shoaling; Accretion (geomorphology); California; Dredging; Estuaries; Harbor facilities**
Maintenance of Santa Cruz Harbor, California, U.S.A., Orville T. Magoon and Don C. Baer, 1276
- Harbors; Mathematical models; Netherlands; Rivers; Saline water intrusion; Salinity; Density; Estuaries; Flumes**
Effect of Harbours on Salt Intrusion in Estuaries, A. Roelfzema and A. G. van Os, 2810
- Harbors; Models; Salinity; Sedimentation; Sediment transport; Silting; Suspended sediments; Temperature; Tidal effects; Turbidity; Canada; Dredging**
Tidal Sedimentation in Gros-CaCouna Harbor, Georges Drapeau and Guy Fortin, 1986
- Hawaii; Meteorological data; Meteorology; Statistical analysis; Wave height; Wave recorders (water waves); Forecasting**
An Evaluation of Extreme Wave Climate at Keahole Point, Hawaii, Charles L. Bretschneider and Richard E. Rocheleau, 152
- Heated water; Jet flow; Mixing; Plumes; Surf; Temperature effects; Thermal pollution; Tracers; Turbulent flow; Currents (water)**
Mixing of Heated Water Discharged in the Surf Zone, Kiyoshi Horikawa, Ming-Chung Lin and Tamio O. Sasaki, 2563
- Heat exchangers; Liquid natural gas; Model studies; Thermal pollution; Tidal currents; Vaporizers; Biological properties; Density currents; Discharge (water)**
Thermal and Biological Impact of LNG Vaporizer Discharge, Peter A. Mangarella and Gordon A. Robilliard, 2945
- Heat loss; Hydroelectric powerplants; Ice control; Model studies; Numerical analysis; Outlet works; Saline water; Fjords; Freezing**
Prevention of Freezing in Fjords, Sveinung Saegrov, 2958
- Histograms; Sediment deposits; Surf; Tidal effects; Tracers; Wave action; Wave height; Beaches; Breaking energy; Coring**
Depth of Disturbance of Sand in Surf Zones, Michael K. Gaughan, 1513
- History; Hydraulic models; Armoring (streambed); Breakwaters; Coastal plains; Damage; Estuaries**
Models — Can We Learn from the Past? Some Thoughts on the Design of Breakwaters, W. A. Price, 25
- History; Shore protection; Storm surges; West Germany; Coastal plains**
Welcoming Address — I, Karl-Edward Naumann, 1
- Hurricanes; Mathematical models; Models; Numerical analysis; Radar operation; Storms; Wavelength; Wave propagation; Wind; Wind speed**
Radar Observations of Hurricane Wave Directions, B. D. King and O. H. Shemdin, 209
- Hurricanes; Measurement; Monitoring; Offshore platforms; Radar operation; Wave height; Waves; Wind; Wind speed; Buoys**
HF Skywave Radar Measurement of Hurricane Winds and Waves, Joseph W. Maresca, Jr. and Christopher T. Carlson, 190
- Hurricanes; Numerical analysis; Predictions; Simulation; Storm surges; Texas; Tidal effects; Tsunamis; Water levels; Coastal plains; Cost effectiveness; Floods**
Coastal Flood Simulation in Stretched Coordinates, H. Lee Butler, 1030
- Hurricanes; Sediments; Sediment transport; Storms; Storm surges; Wave energy; Wave period; Wave velocity; Canada; Field tests; Gravity waves**
Infragravity Waves in Storm Conditions, R. A. Holman, David A. Huntley and A. J. Bowen, 268
- Hurricanes; Site selection; Thermal energy; Waves; Wind; Currents (water); Design criteria; Energy conversion; Environmental effects; Environmental impact statements**
Some Design Criteria for OTEC Installations for Keahole Point, Hawaii, Frederick C. Munchmeyer and Charles L. Bretschneider, 2633
- Hydraulic jump; Water depth; Wave height; Wave propagation; Waves; Wave velocity; Bores (wave); Breaking energy**
Spilling Breakers, Bores and Hydraulic Jumps, D. H. Peregrine and I. A. Svendsen, 540
- Hydraulic models; Armoring (streambed); Breakwaters; Coastal plains; Damage; Estuaries; History**
Models — Can We Learn from the Past? Some Thoughts on the Design of Breakwaters, W. A. Price, 25
- Hydraulic models; Hydrodynamics; Numerical analysis; Rivers; Shallow water; Tidal effects; Turbulence; Estuaries; Flood routing**
Hydrodynamic Modelling of the Southern North Sea, David Prandle, 1122
- Hydraulic models; Inlets (waterways); Jetties; North Carolina; Sediment deposits; Simulation; Spoil banks; Beaches; Breakwaters; Dredging**
Coastal Processes at Oregon Inlet, North Carolina, James T. Jarrett, 1257
- Hydraulic models; Inlets (waterways); Jetties; Sedimentation; Sheet piles; Tidal effects; Trends; Beach erosion; Delaware**
Case Studies of Delaware's Tidal Inlets: Roosevelt and Indian River Inlets, W. A. Dennie, G. A. Lanan and Robert A. Dalrymple, 1282
- Hydraulic models; Japan; Scale effect; Tidal currents; Tidal hydraulics; Water circulation; Diffusion coefficient; Experimentation**
Experimental Study on Scale Effect of Tidal Model, Haruo Higuchi, Hideichi Yasuda and Norio Hayakawa, 2646
- Hydraulic models; Mathematical models; Model studies; Numerical analysis; Saline water intrusion; Salinity; Simulation; Tidal hydraulics; Estuaries**
Numerical Tidal-Salinity Models of the Ems Estuary, Karsten Fischer, 2840
- Hydraulic models; Model studies; Numerical analysis; Responses; Water levels; Wave waves; Wave height; Discharge (water); Estuaries**
A Hybrid Model of the St. Lawrence River Estuary, E. R. Funke and N. L. Crookshank, 2855

- Hydraulic models; Numerical analysis; Wave diffraction; Wave height; Wave reflection; Breakwaters; Computer programs; Harbors**
A Numerical Approach for the Determination of the Wave Height Distribution in a Harbour, Soren Kohlhasse, Karl-Friedrich Daemrich, U. Berger, E. Tautenhain and O. Burkhardt, 664
- Hydraulic models; Rubble-mound breakwaters; Stability; Wave energy; Wave height; Wave spectra; Wave tanks; Breakwaters; Damage**
Effects of Wave Grouping on Breakwater Stability, R. R. Johnson, E. P.D. Mansard and J. Ploeg, 2228
- Hydrodynamic pressure; Hydrodynamics; Numerical analysis; Ocean bottom; Ripple marks; Tidal effects; Bed forms; Friction coefficient (hydraulic)**
The Influence of Dune and Flow Parameters on the Friction Factor, Jurgen Sundermann, H. Vollmers and W. Puls, 1787
- Hydrodynamic pressure; Impact; Impact forces; Measurement; Scale effect; Water waves; Wave energy; Wave pressure; Wave spectra**
Impact Wave Forces on Vertical and Horizontal Plate, S. R. Massel, M. Oleszkiewicz and W. Trapp, 2340
- Hydrodynamic pressure; Numerical analysis; Stochastic processes; Wave generation; Wave height; Wavelength; Waves; Wave spectra; Wave tanks**
An Inclined-Plate Wave Generator, Fredric Raichlen and Jiin-Jen Lee, 388
- Hydrodynamic pressure; Responses; Stochastic processes; Wave generation; Wave spectra; Dynamic pressure; Frequencies**
Analysis of Hinged Wavemakers for Random Waves, Robert T. Hudspeth, Douglas F. Jones and John H. Nath, 372
- Hydrodynamics; Meteorology; Rainfall; Salt marshes; Sediment transport; South Carolina; Suspended load; Tidal currents; Tidal effects; Tidal waters; Wind; Discharge (water)**
Hydrodynamics and Sediment Transport in a Salt Marsh Tidal Channel, Larry G. Ward, 1953
- Hydrodynamics; Numerical analysis; Ocean bottom; Ripple marks; Tidal effects; Bed forms; Friction coefficient (hydraulic); Hydrodynamic pressure**
The Influence of Dune and Flow Parameters on the Friction Factor, Jurgen Sundermann, H. Vollmers and W. Puls, 1787
- Hydrodynamics; Numerical analysis; Rivers; Shallow water; Tidal effects; Turbulence; Estuaries; Flood routing; Hydraulic models**
Hydrodynamic Modelling of the Southern North Sea, David Prandle, 1122
- Hydrodynamics; Statistical analysis; Wave height; Wave period; Wave runoff; Wave spectra; Damage; Dikes**
New Dike Design Criteria Based on Wave Spectra, Hans Kaldenhoff and Suhan M. Gokcesu, 2500
- Hydroelectric powerplants; Ice control; Model studies; Numerical analysis; Outlet works; Saline water; Fjords; Freezing; Heat loss**
Prevention of Freezing in Fjords, Sveinung Saegrov, 2958
- Ice control; Model studies; Numerical analysis; Outlet works; Saline water; Fjords; Freezing; Heat loss; Hydroelectric powerplants**
Prevention of Freezing in Fjords, Sveinung Saegrov, 2958
- Images; Remote sensing; Shallow water; Water depth; Aerial photography; Bathymetry; Color photography**
Visible-Region Photographic Remote Sensing of Nearshore Waters, Tsuguo Sunamura and Kiyoshi Horikawa, 1439
- Imaging; Ocean waves; Radar; Radar photography; Surveys (data collection); Wave energy; Wave height; Wavelength**
The Use of Imaging Radar in Studying Ocean Waves, M. G. Mattie and D. Lee Harris, 174
- Impact; Impact forces; Measurement; Scale effect; Water waves; Wave energy; Wave pressure; Wave spectra; Hydrodynamic pressure**
Impact Wave Forces on Vertical and Horizontal Plate, S. R. Massel, M. Oleszkiewicz and W. Trapp, 2340
- Impact; Marine structures; Mathematical models; Pressure distribution; Scale effect; Standing waves; Storm surges; Wave energy; Wave pressure; Barriers**
A Model Law for Wave Impacts on Coastal Structures, C. Ramkema, 2308
- Impact forces; Measurement; Scale effect; Water waves; Wave energy; Wave pressure; Wave spectra; Hydrodynamic pressure; Impact**
Impact Wave Forces on Vertical and Horizontal Plate, S. R. Massel, M. Oleszkiewicz and W. Trapp, 2340
- India; Performance; Shape; Silting; Underwater structures; Wave attenuation; Barriers; Breakwaters**
Performance Characteristics of Submerged Breakwaters, J. Dattatri, H. Raman and N. Jothi Shankar, 2153
- Inlets (waterways); Jetties; North Carolina; Sediment deposits; Simulation; Spoil banks; Beaches; Breakwaters; Dredging; Hydraulic models**
Coastal Processes at Oregon Inlet, North Carolina, James T. Jarrett, 1257
- Inlets (waterways); Jetties; Sedimentation; Sheet piles; Tidal effects; Trends; Beach erosion; Delaware; Hydraulic models**
Case Studies of Delaware's Tidal Inlets: Roosevelt and Indian River Inlets, W. A. Dennie, G. A. Lanan and Robert A. Dalrymple, 1282
- Inlets (waterways); Littoral drift; Marshes; Morphology; Sedimentation; Tidal hydraulics; Barriers; Beach erosion; Coastal morphology; Delaware**
Morphology of Coastal Barriers, Delaware, U.S.A., John C. Kraft, Chacko J. John and Evelyn M. Maurmeyer, 1232
- Inlets (waterways); Mathematical models; Numerical analysis; Sediment transport; Storm surges; Tidal effects; Wave height; Bays (topographic features); Friction coefficient (hydraulic)**
Numerical Model Investigation of Selected Tidal Inlet-Bay System Characteristics, William N. Seelig and Robert M. Sorensen, 1319

- Inlets (waterways); Morphology; Sediment deposits; Tidal currents; Tidal effects; Wave energy; West Germany; Beaches; Dispersion; Environmental factors; Georgia**
 Process-Response Models for Depositional Shorelines: The German and the Georgia Bights, Dag Nummedal and Ian A. Fischer, 1215
- Inlets (waterways); Stress measurement; Tidal currents; Tidal flats; Velocity; Wave action; Wave velocity; Flooding; Flowmeters**
 Velocity and Stress Measurements in a Tidal Inlet, David A. Huntley and Dag Nummedal, 1320
- Inlets (waterways); Tidal currents; Tidal effects; Tidal flats; Two-dimensional; Wave tanks; Cross sections; Estuaries**
 Periodic Flows from Tidal Inlets, D. L. Wilkinson, 1336
- Instrumentation; Performance; Profile measurement; Sand; Sediment transport; Vehicles; Wave action; Calibration; California**
 Tracked Vehicle for Continuous Nearshore Profiles, Richard J. Seymour, Alan L. Higgins and David P. Bothman, 1542
- Intake structures; Jetties; Offshore structures; Centrifugal pumps; Concrete piles; Dredging; Failure**
 Problems of Design and Construction of an Offshore SeaWater Intake, D. W. Standish-White and J. A. Zwamborn, 2125
- Integral equations; Oscillations; Tides; Water waves; Wave diffraction; Wave refraction; Approximation method; Finite element method; Harbors**
 A Combined FE-BIE Method for Water Waves, A. Hauguel, 715
- Intensity; Wave energy; Wave propagation; Waves; Wave spectra; Bathymetry; Correlation analysis; Deep water; Frequencies**
 Deepwater Direction from an Intensity Array, Alan L. Higgins and Richard J. Seymour, 305
- Interactions; Nonlinear systems; Sampling; Spectral analysis; Wave spectra; Calculations; Fourier transformation**
 Higher Order Wave Spectra, Paul C. Liu and Albert W. Green, 360
- Interactions; Standing waves; Water depth; Waves; Wave tanks; Beaches; Edge effect; Excitation**
 Excitation of Low Frequency Trapped Waves, Robert King and Ronald Smith, 449
- Interactions; Waveforms; Wave height; Wavelength; Experimental data; Flumes; Gravity waves**
 Changes in Height of Short Waves on Long Waves, Michio Sato and Kazuo Nakamura, 400
- International compacts; Inventories; Questionnaires; Surveys (data collection); Wave height; Wave recorders (water waves)**
 A World Wave Data Centre, Laurence Draper, 51
- Inventories; Questionnaires; Surveys (data collection); Wave height; Wave recorders (water waves); International compacts**
 A World Wave Data Centre, Laurence Draper, 51
- Islands (landforms); Littoral current; Littoral deposits; Littoral drift; Littoral materials; Sediment transport; Tracers; Wave height; Barriers**
 Littoral Drift along Bayshore of a Barrier Island, Yu-Hwa Hwang and T. H. Chang, 1614
- Japan; Land reclamation; Littoral current; Littoral drift; Movable bed models; Ocean bottom; Sediment transport; Waves; Breakwaters**
 Estimation Using a Movable Bed Model of Shoreline Change Caused by a Reclamation Projected into the Sea, Shoji Sato and Hiroaki Ozasa, 1839
- Japan; Land reclamation; Scouring; Sea walls; Shore protection; Wave energy; Wave reflection; Beach erosion; Coastal structures; Dikes; Erosion control**
 Effectiveness of Seadikes with Rough Slope, Osamu Toyoshima, 2528
- Japan; Saline water-freshwater interfaces; Salinity; Ultrasonic tests; Diffusion coefficient; Entrainment; Estuaries**
 Behaviors of the Salt Wedge and the Salinity Distribution at Estuaries, Isao Yakuwa, Susumu Takahashi and Morimasa Ohtani, 2746
- Japan; Scale effect; Tidal currents; Tidal hydraulics; Water circulation; Diffusion coefficient; Experimentation; Hydraulic models**
 Experimental Study on Scale Effect of Tidal Model, Haruo Higuchi, Hideichi Yasuda and Norio Hayakawa, 2646
- Jet flow; Mixing; Plumes; Surf; Temperature effects; Thermal pollution; Tracers; Turbulent flow; Currents (water); Heated water**
 Mixing of Heated Water Discharged in the Surf Zone, Kiyoshi Horikawa, Ming-Chung Lin and Tamio O. Sasaki, 2563
- Jets; Laminar flow; Ocean bottom; Oscillation; Roughness (hydraulic); Velocity distribution; Vortex generators**
 Oscillatory Laminar Flow Above a Rough Bed, C. B. George and J. F.A. Sleath, 898
- Jetties; Littoral drift; Numerical analysis; Predictions; Refraction; Sediment transport; Barriers; Beaches; Breakwaters; Coastal plains; Diffraction; Groins (structures)**
 Prediction of Beach PlanForms with Littoral Controls, Marc Perlin and Robert G. Dean, 1818
- Jetties; North Carolina; Sediment deposits; Simulation; Spoil banks; Beaches; Breakwaters; Dredging; Hydraulic models; Inlets (waterways)**
 Coastal Processes at Oregon Inlet, North Carolina, James T. Jarrett, 1257
- Jetties; Numerical analysis; Ocean bottom; Scouring; Sediment transport; Time factors; Coastal structures; Currents (water)**
 A Numerical Model for Sediment Transport, J. P. Lepetit and A. Hauguel, 1715
- Jetties; Offshore structures; Centrifugal pumps; Concrete piles; Dredging; Failure; Intake structures**
 Problems of Design and Construction of an Offshore SeaWater Intake, D. W. Standish-White and J. A. Zwamborn, 2125

- Jetties; Sedimentation; Sheet piles; Tidal effects; Trends; Beach erosion; Delaware; Hydraulic models; Inlets (waterways)**
Case Studies of Delaware's Tidal Inlets: Roosevelt and Indian River Inlets, W. A. Dennie, G. A. Lanan and Robert A. Dalrymple, 1282
- Laboratory tests; Mathematical models; Numerical analysis; Tidal effects; Acceleration; Bed roughness; Distortion; Friction coefficient (hydraulic)**
Numerical Study of Distortion in a Froude Model, T. A. McClimans and S. A. Gjerp, 2887
- Laboratory tests; Measurement; Sediments; Water depth; Wave height; Wave period; Accuracy; Beach erosion; Field tests**
Uses for a Calculated Limit Depth to Beach Erosion, Robert J. Hallermeier, 1493
- Laboratory tests; Models; Prototypes; Wave recorders (water waves); Waves; Breakwaters; Field tests; Harbors**
A Comparison Between Model and Prototype Waves in Harbours, Sverre Bjordal and Alf Torum, 677
- Laboratory tests; Movable bed models; Scale effect; Sediments; Sediment transport; Wave height; Wave period; Beaches; Coastal engineering**
Scale Relations for Equilibrium Beach Profiles, Hideaki Noda, 1531
- Laboratory tests; Ocean bottom; Oscillation; Ripple marks; Shallow water; Waves; Wind pressure; Field tests**
On the Geometry of Ripples Due to Waves, M. S. Yalin and E. Karahan, 1776
- Laboratory tests; Wave diffraction; Wave energy; Wave generation; Wave recorders (water waves); Wave spectra; Wind forces; Wind pressure; Breakwaters**
Wind-Generated Wave Diffraction by Breakwater Gap, Hooshang Raissi and R. L. Wigle, 609
- Lakes; Nile River Valley; Oceans; Sediment deposits; Sediment load; Sediment transport; Storms; Water depth; Wave equations; Wave period; Bars (riverine); Beach erosion**
Undulated Bottom Profiles and Onshore-Offshore Transport, Madhav Manohar, 1454
- Laminar flow; Ocean bottom; Oscillation; Roughness (hydraulic); Velocity distribution; Vortex generators; Jets**
Oscillatory Laminar Flow Above a Rough Bed, C. B. George and J. F.A. Sleath, 898
- Land reclamation; Littoral current; Littoral drift; Movable bed models; Ocean bottom; Sediment transport; Waves; Breakwaters; Japan**
Estimation Using a Movable Bed Model of Shoreline Change Caused by a Reclamation Projected into the Sea, Shoji Sato and Hiroaki Ozasa, 1839
- Land reclamation; Scouring; Sea walls; Shore protection; Wave energy; Wave reflection; Beach erosion; Coastal structures; Dikes; Erosion control; Japan**
Effectiveness of Seadikes with Rough Slope, Osamu Toyoshima, 2528
- Licensing; Littoral drift; Sand; Shore protection; Tidal currents; Wave action; Wave energy; Wave refraction; Coastal plains; Dredging; Gravel; Great Britain**
The Effect of Offshore Dredging on Coastlines, W. A. Price, J. M. Motyka and L. J. Jaffrey, 1347
- Liquid natural gas; Model studies; Thermal pollution; Tidal currents; Vaporizers; Biological properties; Density currents; Discharge (water); Heat exchangers**
Thermal and Biological Impact of LNG Vaporizer Discharge, Peter A. Mangarella and Gordon A. Robilliard, 2945
- Littoral current; Littoral deposits; Littoral drift; Littoral materials; Sediment transport; Tracers; Wave height; Barriers; Islands (landforms)**
Littoral Drift along Bayshore of a Barrier Island, Yu-Hwa Hwang and T. H. Chang, 1614
- Littoral current; Littoral deposits; Littoral drift; Sediment transport; Storm surges; Tracers; Wave energy; Beaches; Field tests; Gravel**
Field Experiment on Beach Gravel Transport, Masataro Hattori and Takasuke Suzuki, 1688
- Littoral current; Littoral deposits; Littoral drift; Shallow water; Water depth; Wave energy; Beach erosion**
Vocoidal Theory for All Non-Breaking Waves, D. H. Swart and C. C. Loubser, 467
- Littoral current; Littoral deposits; Littoral drift; Surf; Turbulence; Wave dispersion; Wave energy; Wave height; Wave reflection; Beaches**
Morphodynamic Variability of High-Energy Beaches, Lynn Donelson Wright, B. G. Thom and John Chappell, 1180
- Littoral current; Littoral deposits; Models; Ocean bottom; Sediments; Sediment transport; Surf; Wave dispersion; Wave energy; Beaches; Coastal plains**
A Model Study of Alongshore Sediment Transport Rate, J. W. Kamphuis and J. S. Readshaw, 1656
- Littoral current; Littoral drift; Littoral materials; Sediment deposits; Sediments; Shoaling; Accretion (geomorphology); California; Dredging; Estuaries; Harbor facilities; Harbors**
Maintenance of Santa Cruz Harbor, California, U.S.A., Orville T. Magoon and Don C. Baer, 1276
- Littoral current; Littoral drift; Movable bed models; Ocean bottom; Sediment transport; Waves; Breakwaters; Japan; Land reclamation**
Estimation Using a Movable Bed Model of Shoreline Change Caused by a Reclamation Projected into the Sea, Shoji Sato and Hiroaki Ozasa, 1839
- Littoral current; Littoral drift; Predictions; Sediments; Sediment transport**
The Nearshore Sediment Transport Study, Richard J. Seymour and David B. Duane, 1555
- Littoral current; Littoral drift; Predictions; Sediments; Sediment transport; Silting; Wave energy; Experimentation**
Longshore Sediment Transport Data: A Review, Matthew N. Greer and Ole Secher Madsen, 1563

- Littoral current; Littoral drift; Water depth; Wave height; Wave period; Wave recorders (water waves); Wave spectrum; Brazil; Current meters; Harbor facilities**
Coastal Study of Espirito Santo Brazil, Paulo Augusto Vivacqua, Hildebrando de Araujo Goes Filho and Octavio de Sampaio Ferraz Jardim Sayao, 2104
- Littoral current; Littoral drift; Wave action; Wavelengths; Wave velocity; Beach erosion; Beaches; Beach sands; Edge effect**
Beach Cusps and Edge Waves, David A. Huntley and A. J. Bowen, 1378
- Littoral current; Measurement; Surf; Suspended sediments; Water sampling; Wave height; Wave period; Waves; Wind velocity; Beaches**
Surf Zone Measurements of Suspended Sediment, Timothy W. Kana, 1725
- Littoral current; Models; Sediment concentration; Sediment load; Sediment transport; Two-dimensional; Wave period; Beaches**
Onshore-Offshore Sediment Movement on a Beach, P. Nielsen, I. A. Svendsen and C. Staub, 1475
- Littoral current; Model tests; Storms; Surf; Water circulation; Water levels; Wave height; Waves; Wind; Bathymetry; Bores (wave); Field tests**
Comparison of Model and Observed Nearshore Circulation, James H. Allender, John D. Ditmars, Wyman Harrison and Robert A. Paddock, 810
- Littoral current; Morphology; Resonance; Surf; Wave reflection; Waves; Wave spectra; Beaches; Edge effect**
Surf Zone Resonance and Coupled Morphology, John Chappell and Lynn Donelson Wright, 1359
- Littoral current; Nicaragua; Pressure gradients; Salinity; Suspended sediments; Boundary layer flow; Continental shelf; Currents (water)**
Shelf and Coastal Boundary Layer Currents, Miskito Bank of Nicaragua, Richard L. Crout and Stephen P. Murray, 2715
- Littoral current; Ocean waves; Wave energy; Waves; Wave spectra; Wave velocity; Currents (water); Edge effect; Frequencies**
Observation of Nearshore Current and Edge Waves, Tamio O. Sasaki and Kiyoshi Horikawa, 791
- Littoral current; Oscillations; Piezometers; Wave height; Wave period; Wave spectrum; Aquifers; Ground water; Groundwater elevation**
Beach Ground-Water Oscillations, Andrzej Lewandowski and Ryszard B. Zeidler, 2051
- Littoral current; Predictions; Regression analysis; Statistical analysis; Stress; Surf; Wave spectra; Wave velocity; Wind velocity**
Wind-Generated Longshore Currents, Dag Nummedal and Robert J. Finley, 1428
- Littoral current; Rip currents; Surf; Temporal distribution; Variations; Wave spectra; Edge effect; Gravity waves**
Variability of Longshore Currents, R. T. Guza and Edward B. Thornton, 756
- Littoral current; Shores; Stresses; Surf; Water circulation; Wave energy; Wave propagation; Waves; Barriers; Friction coefficient (hydraulic)**
Longshore Currents Due to Surf Zone Barrier, P. Bettess, C. A. Fleming, J. C. Heinrich, O. C. Zienkiewicz and D. I. Austin, 776
- Littoral deposits; Littoral drift; Littoral materials; Ocean bottom; Sediments; Sediment transport; Shear stress; Surf; Water depth**
Distribution of Sand Transport Rate across a Surf Zone, Toru Sawaragi and Ichiro Deguchi, 1596
- Littoral deposits; Littoral drift; Littoral materials; Sediment transport; Tracers; Wave height; Barriers; Islands (landforms); Littoral current**
Littoral Drift along Bayshore of a Barrier Island, Yu-Hwa Hwang and T. H. Chang, 1614
- Littoral deposits; Littoral drift; Littoral zone; Samples; Sediment concentration; Suspended sediments; Wave height; Coastal plains**
Sled System for Profiling Suspended Littoral Drift, J. P. Coakley, J. A. Savile, M. Pedrosa and M. Laroque, 1764
- Littoral deposits; Littoral drift; Sediment transport; Storm surges; Tracers; Wave energy; Beaches; Field tests; Gravel; Littoral current**
Field Experiment on Beach Gravel Transport, Masataro Hattori and Takasuke Suzuki, 1688
- Littoral deposits; Littoral drift; Shallow water; Water depth; Wave energy; Beach erosion; Littoral current**
Vocoidal Theory for All Non-Breaking Waves, D. H. Swart and C. C. Loubser, 467
- Littoral deposits; Littoral drift; Surf; Turbulence; Wave dispersion; Wave energy; Wave height; Wave reflection; Beaches; Littoral current**
Morphodynamic Variability of High-Energy Beaches, Lynn Donelson Wright, B. G. Thom and John Chappell, 1180
- Littoral deposits; Littoral materials; Sedimentation; Sediment transport; Surveys (data collection); Coastal plains; Evaluation; Geological maps**
A New Method for the Representation of Sedimentary Sequences in Coastal Regions, Hansjorg Streif, 1245
- Littoral deposits; Models; Ocean bottom; Sediments; Sediment transport; Surf; Wave dispersion; Wave energy; Beaches; Coastal plains; Littoral current**
A Model Study of Alongshore Sediment Transport Rate, J. W. Kamphuis and J. S. Readshaw, 1656
- Littoral deposits; Nicaragua; Rainfall; Sedimentation; Sediments; Sediment transport; Water circulation; Wave energy; Weathering; Estuaries**
Variations of Wave-Energy Levels and Coastal Sedimentation, Eastern Nicaragua, E. H. Owens and H. H. Roberts, 1195
- Littoral deposits; Sediment concentration; Sediment transport; Sensors; Storms; Surf; Suspended sediments; Wave period**
Storm Induced Periodicities of Suspended Sand Movement, Jay E. Leonard and Benno M. Brenninkmeyer, 1744

- Littoral drift; Littoral materials; Ocean bottom; Sediments; Sediment transport; Shear stress; Surf; Water depth; Littoral deposits**
Distribution of Sand Transport Rate across a Surf Zone, Toru Sawaragi and Ichiro Deguchi, 1596
- Littoral drift; Littoral materials; Sediment deposits; Sediments; Shoaling; Accretion (geomorphology); California; Dredging; Estuaries; Harbor facilities; Harbors; Littoral current**
Maintenance of Santa Cruz Harbor, California, U.S.A., Orville T. Magoon and Don C. Baer, 1276
- Littoral drift; Littoral materials; Sediment transport; Tracers; Wave height; Barriers; Islands (landforms); Littoral current; Littoral deposits**
Littoral Drift along Bayshore of a Barrier Island, Yu-Hwa Hwang and T. H. Chang, 1614
- Littoral drift; Littoral zone; Samples; Sediment concentration; Suspended sediments; Wave height; Coastal plains; Littoral deposits**
Sled System for Profiling Suspended Littoral Drift, J. P. Coakley, J. A. Savile, M. Pedrosa and M. Larocque, 1764
- Littoral drift; Marshes; Morphology; Sedimentation; Tidal hydraulics; Barriers; Beach erosion; Coastal morphology; Delaware; Inlets (waterways)**
Morphology of Coastal Barriers, Delaware, U.S.A., John C. Kraft, Chacko J. John and Evelyn M. Maumeyer, 1232
- Littoral drift; Metal detectors; Monitoring; Sediment transport; Shingles (beach); Tracers; Beaches**
Shingle Tracing by a New Technique, Peter Wright, J. S. Cross and N. B. Webber, 1705
- Littoral drift; Movable bed models; Ocean bottom; Sediment transport; Waves; Breakwaters; Japan; Land reclamation; Littoral current**
Estimation Using a Movable Bed Model of Shoreline Change Caused by a Reclamation Projected into the Sea, Shoji Sato and Hiroaki Ozasa, 1839
- Littoral drift; Numerical analysis; Predictions; Refraction; Sediment transport; Barriers; Beaches; Breakwaters; Coastal plains; Diffraction; Groins (structures); Jetties**
Prediction of Beach PlanForms with Littoral Controls, Marc Perlín and Robert G. Dean, 1818
- Littoral drift; Predictions; Sediments; Sediment transport; Littoral current**
The Nearshore Sediment Transport Study, Richard J. Seymour and David B. Duane, 1555
- Littoral drift; Predictions; Sediments; Sediment transport; Silting; Wave energy; Experimentation; Littoral current**
Longshore Sediment Transport Data: A Review, Matthew N. Greer and Ole Secher Madsen, 1563
- Littoral drift; Sand; Shore protection; Tidal currents; Wave action; Wave energy; Wave refraction; Coastal plains; Dredging; Gravel; Great Britain; Licensing**
The Effect of Offshore Dredging on Coastlines, W. A. Price, J. M. Motyka and L. J. Jaffrey, 1347
- Littoral drift; Sediment transport; Storm surges; Tracers; Wave energy; Beaches; Field tests; Gravel; Littoral current; Littoral deposits**
Field Experiment on Beach Gravel Transport, Masataro Hattori and Takasuke Suzuki, 1688
- Littoral drift; Shallow water; Water depth; Wave energy; Beach erosion; Littoral current; Littoral deposits**
Vocoidal Theory for All Non-Breaking Waves, D. H. Swart and C. C. Loubser, 467
- Littoral drift; Surf; Turbulence; Wave dispersion; Wave energy; Wave height; Wave reflection; Beaches; Littoral current; Littoral deposits**
Morphodynamic Variability of High-Energy Beaches, Lynn Donelson Wright, B. G. Thom and John Chappell, 1180
- Littoral drift; Water depth; Wave height; Wave period; Wave recorders (water waves); Wave spectrum; Brazil; Current meters; Harbor facilities; Littoral current**
Coastal Study of Espirito Santo Brazil, Paulo Augusto Vivacqua, Hildebrando de Araujo Goes Filho and Octavio de Sampaio Ferraz Jardim Sayao, 2104
- Littoral drift; Wave action; Wavelengths; Wave velocity; Beach erosion; Beaches; Beach sands; Edge effect; Littoral current**
Beach Cusps and Edge Waves, David A. Huntley and A. J. Bowen, 1378
- Littoral materials; Ocean bottom; Sediments; Sediment transport; Shear stress; Surf; Water depth; Littoral deposits; Littoral drift**
Distribution of Sand Transport Rate across a Surf Zone, Toru Sawaragi and Ichiro Deguchi, 1596
- Littoral materials; Sedimentation; Sediment transport; Surveys (data collection); Coastal plains; Evaluation; Geological maps; Littoral deposits**
A New Method for the Representation of Sedimentary Sequences in Coastal Regions, Hansjorg Streif, 1245
- Littoral materials; Sediment deposits; Sediments; Shoaling; Accretion (geomorphology); California; Dredging; Estuaries; Harbor facilities; Harbors; Littoral current; Littoral drift**
Maintenance of Santa Cruz Harbor, California, U.S.A., Orville T. Magoon and Don C. Baer, 1276
- Littoral materials; Sediment transport; Tracers; Wave height; Barriers; Islands (landforms); Littoral current; Littoral deposits; Littoral drift**
Littoral Drift along Bayshore of a Barrier Island, Yu-Hwa Hwang and T. H. Chang, 1614
- Littoral zone; Marine terminals; Piers; Rubble-mound breakwaters; Sands; Shore-line cover; Beach erosion; Breakwaters; Coastal structures; Erosion control**
Coastal Structures' Effects on Shorelines, Ronald M. Noble, 2069
- Littoral zone; Samples; Sediment concentration; Suspended sediments; Wave height; Coastal plains; Littoral deposits; Littoral drift**
Sled System for Profiling Suspended Littoral Drift, J. P. Coakley, J. A. Savile, M. Pedrosa and M. Larocque, 1764

- Loading; Load transfer; Marine structures; Ocean waves; Wave action; Wave pressure; Wave tanks; Groups**
Load Analysis from Wave Groups, A. I. Kuznetsov and G. D. Khaskhatchikh, 2328
- Loading; Mathematical models; Ocean waves; Responses; Water waves; Waves; Cylindrical bodies; Dynamic response**
Loading and Response of Cylinders in Waves, G. N. Bullock, P. K. Stansby and J. G. Warren, 2415
- Loading; Rubble-mound breakwaters; Seismic design; Settlement (structural); Slope stability; Acceleration; Damage; Earthquake loads; Earthquake resistant structures**
Loadings on Rubble-Mound Breakwaters due to Earthquakes, H. Wang, C. Y. Yang, C. Lamison and S. S. Chen, 2244
- Loads (forces); Outfall sewers; Scale effect; Tests; Thermal pollution; Wave energy; Wave height; Wave pressure; Cooling water**
Non-Breaking and Breaking Wave Loads on a Cooling Water Outfall, G. R. Mogridge and W. W. Jamieson, 2461
- Loads (forces); Predictions; Reynolds number; Water flow; Wave energy; Wave pressure; Cylindrical bodies; Drag; Experimentation**
Wave Loads on Horizontal Cylinders, P. Holmes and J. R. Chaplin, 2449
- Load transfer; Marine structures; Ocean waves; Wave action; Wave pressure; Wave tanks; Groups; Loading**
Load Analysis from Wave Groups, A. I. Kuznetsov and G. D. Khaskhatchikh, 2328
- Maintenance; Site selection; Storm surges; Tidal effects; Tidal waters; Wave height; Wave period; Australia; Breakwaters**
Rosslyn Bay Breakwater, Queensland, Australia, D. N. Foster, B. L. McGrath and W. Bremner, 2086
- Marine structures; Mathematical models; Pressure distribution; Scale effect; Standing waves; Storm surges; Wave energy; Wave pressure; Barriers; Impact**
A Model Law for Wave Impacts on Coastal Structures, C. Ramkema, 2308
- Marine structures; Ocean waves; Wave action; Wave pressure; Wave tanks; Groups; Loading; Load transfer**
Load Analysis from Wave Groups, A. I. Kuznetsov and G. D. Khaskhatchikh, 2328
- Marine structures; Offshore platforms; Offshore structures; Pile foundations; Underwater foundations; Vibration; Currents (water); Dolphins (structures)**
Tripod Concept for Pile Structures in Fast Current, J. Khanna and J. S. Wood, 2481
- Marine terminals; Piers; Rubble-mound breakwaters; Sands; Shore-line cover; Beach erosion; Breakwaters; Coastal structures; Erosion control; Littoral zone**
Coastal Structures' Effects on Shorelines, Ronald M. Noble, 2069
- Marshes; Morphology; Sedimentation; Tidal hydraulics; Barriers; Beach erosion; Coastal morphology; Delaware; Inlets (waterways); Littoral drift**
Morphology of Coastal Barriers, Delaware, U.S.A., John C. Kraft, Chacko J. John and Evelyn M. Maurmeyer, 1232
- Mass; Momentum; Offshore structures; Rip currents; Spacing; Surf; Wave action; Waves; Wave velocity; Coastal plains; Eigenvalues**
Rip Current Spacing as an Eigenvalue, Noriyuki Iwata, 828
- Mass transfer; Wave height; Wave period; Waves; Amplitude; Buoys; Drifting (aquatic); Floating bodies**
Drift Speed of Buoys in Waves, John H. Nath, 859
- Mathematical models; Mathematics; Mixing; Physics; Sediments; Structures; Tidal currents; Wave energy; Waves; Coastal engineering**
Struggle of Physics and Mathematics in Coastal Engineering, H. Lundgren, 13
- Mathematical models; Meteorological data; Meteorology; Numerical analysis; Predictions; Simulation; Storm surges; Water levels; Wind forces; Forecasting**
Numerical Storm Surge Forecasting, Manfred Engel, 975
- Mathematical models; Models; Numerical analysis; Ocean engineering; Oceanography; Three-dimensional; Tidal currents; Tide gages; Two-dimensional; Water circulation**
Role of 2D and 3D Models in JONSDAP '76, A. M. Davies, 1085
- Mathematical models; Models; Numerical analysis; Radar operation; Storms; Wavelength; Wave propagation; Wind; Wind speed; Hurricanes**
Radar Observations of Hurricane Wave Directions, B. D. King and O. H. Shemdin, 209
- Mathematical models; Model studies; Numerical analysis; Saline water intrusion; Salinity; Simulation; Tidal hydraulics; Estuaries; Hydraulic models**
Numerical Tidal-Salinity Models of the Ems Estuary, Karsten Fischer, 2840
- Mathematical models; Netherlands; Rivers; Saline water intrusion; Salinity; Density; Estuaries; Flumes; Harbors**
Effect of Harbours on Salt Intrusion in Estuaries, A. Roelfzema and A. G. van Os, 2810
- Mathematical models; Numerical analysis; Ocean waves; Scale effect; Three-dimensional; Wave height; Wave propagation; Waves; Wave spectra**
Natural Wave Trains: Description and Reproduction, H. Lundgren and S. E. Sand, 312
- Mathematical models; Numerical analysis; Sediment transport; Storm surges; Tidal effects; Wave height; Bays (topographic features); Friction coefficient (hydraulic); Inlets (waterways)**
Numerical Model Investigation of Selected Tidal Inlet-Bay System Characteristics, William N. Seelig and Robert M. Sorensen, 1319

- Mathematical models; Numerical analysis; Surveys (data collection); Tidal effects; Water levels; Wave propagation; Wave velocity; Estuaries; Field data; Flood protection**
Adjustment and Verification of the RANDDELTA II Model, A. Langerak, M. A.M. deRas and J. J. Leendertse, 1049
- Mathematical models; Numerical analysis; Tidal effects; Acceleration; Bed roughness; Distortion; Friction coefficient (hydraulic); Laboratory tests**
Numerical Study of Distortion in a Froude Model, T. A. McClimans and S. A. Gjerp, 2887
- Mathematical models; Ocean waves; Responses; Water waves; Waves; Cylindrical bodies; Dynamic response; Loading**
Loading and Response of Cylinders in Waves, G. N. Bullock, P. K. Stansby and J. G. Warren, 2415
- Mathematical models; Outfall sewers; Sewage effluents; Statistical analysis; Time series analysis; Waste disposal; Coastal plains; Diffusion; Dispersion**
Outfall Diffusion Models for the Coastal Zone, D. C.L. Lam and C. R. Murthy, 2584
- Mathematical models; Pressure distribution; Scale effect; Standing waves; Storm surges; Wave energy; Wave pressure; Barriers; Impact; Marine structures**
A Model Law for Wave Impacts on Coastal Structures, C. Ramkema, 2308
- Mathematical models; Probability distribution functions; Tropical cyclones; Wave equations; Wave recorders (water waves); Wind forces; Wind pressure; Australia; Cyclones; Frequencies**
Wind Wave Frequencies in a Tropical Cyclone Region, Rodney J. Sobey, 76
- Mathematical models; Rip currents; Shore-line cover; Wave diffraction; Wave refraction; Wind loads; Accretion (geomorphology); Beach nourishment; Erosion; Groins (structures)**
Mathematical Modeling of Shoreline Evolution, Bernard Le Mehaute and Mills Soldate, 1163
- Mathematical models; Sand; Shear stress; Turbulent flow; Velocity distribution; Wave propagation; Wave velocity; Boundary conditions**
Near-Bottom Velocities in Waves with a Current, W. T. Bakker and Th. van Doorn, 1394
- Mathematical models; Shallow water; Water depth; Wave action; Wave diffraction; Wavelength; Wave propagation; Wave reflection; Wave refraction**
Computations of Short Waves in Shallow Water, M. B. Abbott, H. M. Petersen and Ove Skovgaard, 414
- Mathematics; Mixing; Physics; Sediments; Structures; Tidal currents; Wave energy; Waves; Coastal engineering; Mathematical models**
Struggle of Physics and Mathematics in Coastal Engineering, H. Lundgren, 13
- Measurement; Monitoring; Offshore platforms; Radar operation; Wave height; Waves; Wind; Wind speed; Buoys; Hurricanes**
HF Skywave Radar Measurement of Hurricane Winds and Waves, Joseph W. Maresca, Jr. and Christopher T. Carlson, 190
- Measurement; Scale effect; Water waves; Wave energy; Wave pressure; Wave spectra; Hydrodynamic pressure; Impact; Impact forces**
Impact Wave Forces on Vertical and Horizontal Plate, S. R. Massel, M. Oleszkiewicz and W. Trapp, 2340
- Measurement; Sediments; Water depth; Wave height; Wave period; Accuracy; Beach erosion; Field tests; Laboratory tests**
Uses for a Calculated Limit Depth to Beach Erosion, Robert J. Hallermeier, 1493
- Measurement; Surf; Suspended sediments; Water sampling; Wave height; Wave period; Waves; Wind velocity; Beaches; Littoral current**
Surf Zone Measurements of Suspended Sediment, Timothy W. Kana, 1725
- Metal detectors; Monitoring; Sediment transport; Shingles (beach); Tracers; Beaches; Littoral drift**
Shingle Tracing by a New Technique, Peter Wright, J. S. Cross and N. B. Webber, 1705
- Meteorological data; Meteorology; Numerical analysis; Predictions; Simulation; Storm surges; Water levels; Wind forces; Forecasting; Mathematical models**
Numerical Storm Surge Forecasting, Manfred Engel, 975
- Meteorological data; Meteorology; Statistical analysis; Wave height; Wave recorders (water waves); Forecasting; Hawaii**
An Evaluation of Extreme Wave Climate at Keahole Point, Hawaii, Charles L. Bretschneider and Richard E. Rocheleau, 152
- Meteorology; Numerical analysis; Predictions; Simulation; Storm surges; Water levels; Wind forces; Forecasting; Mathematical models; Meteorological data**
Numerical Storm Surge Forecasting, Manfred Engel, 975
- Meteorology; Ocean waves; Wave action; Wave energy; Wave height; Wave period; Wave recorders (water waves); Brazil**
Wave Climate in Some Zones off the Brazilian Coast, Alberto Homs, 114
- Meteorology; Rainfall; Salt marshes; Sediment transport; South Carolina; Suspended load; Tidal currents; Tidal effects; Tidal waters; Wind; Discharge (water); Hydrodynamics**
Hydrodynamics and Sediment Transport in a Salt Marsh Tidal Channel, Larry G. Ward, 1953
- Meteorology; Statistical analysis; Wave height; Wave recorders (water waves); Forecasting; Hawaii; Meteorological data**
An Evaluation of Extreme Wave Climate at Keahole Point, Hawaii, Charles L. Bretschneider and Richard E. Rocheleau, 152
- Mixing; Model studies; Saline water-freshwater interfaces; Shallow water; Standing waves; Tidal flats; Tidal hydraulics; Dispersion; Estuaries**
Longitudinal Dispersion in Shallow Well-Mixed Estuaries, J. Dronkers, 2761
- Mixing; Ocean engineering; Ocean waves; Rivers; Runoff; Suspended sediments; Two-dimensional; Wave propagation; Wind loads; Boundary conditions; Coastal plains**
Mixed Layer Models for Coastal Waters, W. J. Wiseman, Jr., L. J. Rouse, Jr. and O. K. Huh, 2619

- Mixing; Physics; Sediments; Structures; Tidal currents; Wave energy; Waves; Coastal engineering; Mathematical models; Mathematics**
Struggle of Physics and Mathematics in Coastal Engineering, H. Lundgren, 13
- Mixing; Plumes; Surf; Temperature effects; Thermal pollution; Tracers; Turbulent flow; Currents (water); Heated water; Jet flow**
Mixing of Heated Water Discharged in the Surf Zone, Kiyoshi Horikawa, Ming-Chung Lin and Tamio O. Sasaki, 2563
- Mixing; Rivers; Saline water-freshwater interfaces; Salinity; Stream flow; Velocity distribution; Vortices; Wave energy; Bed roughness; Estuaries**
Outflow Dynamics at a River Mouth, Masakazu Kashiwamura and Shizuo Yoshida, 2925
- Mixing; Tidal currents; Turbulence; Velocity; Water depth; Wind loads; Aerial photography; Currents (water); Density; Eddies; Eddy currents**
Large Scale Turbulence in Tidal Currents, John B. Hinwood, 2598
- Models; Numerical analysis; Ocean engineering; Oceanography; Three-dimensional; Tidal currents; Tide gages; Two-dimensional; Water circulation; Mathematical models**
Role of 2D and 3D Models in JONSDAP '76. A. M. Davies, 1085
- Models; Numerical analysis; Radar operation; Storms; Wavelength; Wave propagation; Wind; Wind speed; Hurricanes; Mathematical models**
Radar Observations of Hurricane Wave Directions, B. D. King and O. H. Shemdin, 209
- Models; Ocean bottom; Sediments; Sediment transport; Surf; Wave dispersion; Wave energy; Beaches; Coastal plains; Littoral current; Littoral deposits**
A Model Study of Alongshore Sediment Transport Rate, J. W. Kamphuis and J. S. Readshaw, 1656
- Models; Plumes; Sediment concentration; Spoil; Spoil banks; Suspended sediments; Diffusion; Dredges; Dredging; Estuaries**
Factors Governing the Distribution of Dredge-Resuspended Sediments, W. Frank Bohlen, 2001
- Models; Prototypes; Wave recorders (water waves); Waves; Breakwaters; Field tests; Harbors; Laboratory tests**
A Comparison Between Model and Prototype Waves in Harbours, Sverre Bjordal and Alf Torum, 677
- Models; Salinity; Sedimentation; Sediment transport; Silting; Suspended sediments; Temperature; Tidal effects; Turbidity; Canada; Dredging; Harbors**
Tidal Sedimentation in Gros-CaCouna Harbor, Georges Drapeau and Guy Fortin, 1986
- Models; Sediment concentration; Sediment load; Sediment transport; Two-dimensional; Wave period; Beaches; Littoral current**
Onshore-Offshore Sediment Movement on a Beach, P. Nielsen, I. A. Svendsen and C. Staub, 1475
- Models; Sediments; Spoil; Spoil banks; Beach nourishment; Bottom sediments; Dredges; Dredging**
Importance of Handling Losses to Beach Fill Design, R. D. Hobson and W. R. James, 1873
- Model studies; Monsoons; Tidal currents; Tidal hydraulics; Water circulation; Water levels; Waves; Wind loads**
The Wind-Driven Circulation in the Northern Arabian Sea, Khawaja Zafar Elahi and Jurgen Sundermann, 2708
- Model studies; Numerical analysis; Outlet works; Saline water; Fjords; Freezing; Heat loss; Hydroelectric powerplants; Ice control**
Prevention of Freezing in Fjords, Sveinung Saegrov, 2958
- Model studies; Numerical analysis; Responses; Water levels; Water waves; Wave height; Discharge (water); Estuaries; Hydraulic models**
A Hybrid Model of the St. Lawrence River Estuary, E. R. Funke and N. L. Crookshank, 2855
- Model studies; Numerical analysis; Saline water intrusion; Salinity; Simulation; Tidal hydraulics; Estuaries; Hydraulic models; Mathematical models**
Numerical Tidal-Salinity Models of the Ems Estuary, Karsten Fischer, 2840
- Model studies; Rivers; Storm surges; Temperature effects; Thermal pollution; Tidal effects; Tidal hydraulics; Cooling water; Discharge (water)**
Influence on Temperature Increases in Tidal Rivers Caused by Waste Heat Injections with Respect to Tidal Cycles and Storm Surges, Horst Schwarze and Wilfried Falldorf, 2915
- Model studies; Saline water-freshwater interfaces; Saline water intrusion; Salinity; Sampling; Tidal hydraulics; Verification inspection; Field tests**
Field Data Analysis for Chesapeake Bay Model Verification, Ronald E. Nece and Norman W. Scheffner, 2870
- Model studies; Saline water-freshwater interfaces; Shallow water; Standing waves; Tidal flats; Tidal hydraulics; Dispersion; Estuaries; Mixing**
Longitudinal Dispersion in Shallow Well-Mixed Estuaries, J. Dronkers, 2761
- Model studies; Salinity; Salt balance; Salt water intrusion; Tidal hydraulics; Wind loads; Florida; Friction coefficient (hydraulic)**
Tidal Hydraulics and Salt Balance of Lake Worth, Florida, J. van de Kreeke and J. D. Wang, 2827
- Model studies; Temperature effects; Three-dimensional; Tidal effects; Water flow; Water levels; Wind loads; Dynamic response**
Three-Dimensional SGS Energy Model of Eastern Bering Sea, S. K. Liu and J. J. Leendertse, 2687
- Model studies; Thermal pollution; Tidal currents; Vaporizers; Biological properties; Density currents; Discharge (water); Heat exchangers; Liquid natural gas**
Thermal and Biological Impact of LNG Vaporizer Discharge, Peter A. Mangarella and Gordon A. Robilliard, 2945
- Model studies; Three-dimensional; Water circulation; Wind loads; Currents (water); Density; Friction coefficient (hydraulic)**
Three Dimensional Modelling of the Irish Sea, Norman Stuart Heaps, 2671

Model tests; Numerical analysis; Piles; Transverse waves; Wave energy; Wave height; Wave interference; Computation; Cylindrical bodies; Experimentation

Wave Forces on a Row of Cylindrical Piles of Large Diameter, J. C.W. Berkhoff and J. V.D. Weide, 2433

Model tests; Reflection; Refraction; Walls; Wave action; Wave diffraction; Wave reflection; Breakwaters

Influence of Breakwater-Reflection on Diffraction, Karl-Friedrich Daemrich and Soren Kohlhasse, 651

Model tests; Storms; Surf; Water circulation; Water levels; Wave height; Waves; Wind; Bathymetry; Bores (wave); Field tests; Littoral current

Comparison of Model and Observed Nearshore Circulation, James H. Allender, John D. Ditmars, Wyman Harrison and Robert A. Paddock, 810

Momentum; Offshore structures; Rip currents; Spacing; Surf; Wave action; Waves; Wave velocity; Coastal plains; Eigenvalues; Mass

Rip Current Spacing as an Eigenvalue, Noriyuki Iwata, 828

Monitoring; Offshore platforms; Radar operation; Wave height; Waves; Wind; Wind speed; Buoys; Hurricanes; Measurement

HF Skywave Radar Measurement of Hurricane Winds and Waves, Joseph W. Maresca, Jr. and Christopher T. Carlson, 190

Monitoring; Sediment transport; Shingles (beach); Tracers; Beaches; Littoral drift; Metal detectors

Shingle Tracing by a New Technique, Peter Wright, J. S. Cross and N. B. Webber, 1705

Monsoons; Tidal currents; Tidal hydraulics; Water circulation; Water levels; Waves; Wind loads; Model studies

The Wind-Driven Circulation in the Northern Arabian Sea, Khawaja Zafar Elahi and Jurgen Sundermann, 2708

Morphology; Resonance; Surf; Wave reflection; Waves; Wave spectra; Beaches; Edge effect; Littoral current

Surf Zone Resonance and Coupled Morphology, John Chappell and Lynn Donelson Wright, 1359

Morphology; Sands; Shore protection; Water depth;

Bathymetry; Beach erosion; Beach nourishment
Morphologic Effects of Westerland Beach Nourishment 1972, Dieter Wenzel, 1859

Morphology; Sedimentation; Tidal hydraulics; Barriers; Beach erosion; Coastal morphology; Delaware; Inlets (waterways); Littoral drift; Marshes

Morphology of Coastal Barriers, Delaware, U.S.A., John C. Kraft, Chacko J. John and Evelyn M. Maurmeyer, 1232

Morphology; Sediment deposits; Tidal currents; Tidal effects; Wave energy; West Germany; Beaches; Dispersion; Environmental factors; Georgia; Inlets (waterways)

Process-Response Models for Depositional Shorelines: The German and the Georgia Bights, Dag Nummedal and Ian A. Fischer, 1215

Morphology; Stability analysis; Tidal currents; Tidal flats; Tides; Two-dimensional; Water depth; Boundary conditions; Forecasting

Two-Dimension Stability Analysis of Tidal Basins and Tidal Flats of Larger Extent, Eberhard Renger, 1971

Movable bed models; Ocean bottom; Sediment transport; Waves; Breakwaters; Japan; Land reclamation; Littoral current; Littoral drift

Estimation Using a Movable Bed Model of Shoreline Change Caused by a Reclamation Projected into the Sea, Shoji Sato and Hiroaki Ozasa, 1839

Movable bed models; Ripple marks; Sands; Scale effect; Shore protection; Storm surges; Beach erosion; Dunes; Erosion

Movable Bed Model Tests on Dune Erosion, P. Vellinga, 2020

Movable bed models; Scale effect; Sediments; Sediment transport; Wave height; Beaches; Coastal engineering; Laboratory tests

Scale Relations for Equilibrium Beach Profiles, Hideaki Noda, 1531

Mud; Mud systems; Sediment concentration;

Sediment transport; Shallow water; Suspended sediments; Tidal effects; Wave height; Waves; Wave spectrum

Suspension and Transportation of Fluid Mud by Solitary-Like Waves, John T. Wells, James M. Coleman and W. J. Wiseman, Jr., 1932

Mud systems; Sediment concentration; Sediment transport; Shallow water; Suspended sediments;

Tidal effects; Wave height; Waves; Wave spectrum; Mud

Suspension and Transportation of Fluid Mud by Solitary-Like Waves, John T. Wells, James M. Coleman and W. J. Wiseman, Jr., 1932

Navigable canals; Stream flow; Stream gages; Tidal currents; Tidal effects; Water levels; Estuaries; Groins (structures)

Improvements on Tidal Estuaries and the Effects on Tidal Current, Hermann Harten, 2905

Netherlands; Responses; Storms; Storm surges;

Surveys (data collection); Tidal hydraulics; Water levels; Barriers; Boundary conditions

A Tidal Survey for a Model of an Offshore Area, W. J. van de Ree, J. Voogt and J. J. Leendertse, 2656

Netherlands; Rivers; Saline water intrusion;

Salinity; Density; Estuaries; Flumes; Harbors; Mathematical models

Effect of Harbours on Salt Intrusion in Estuaries, A. Roelzfema and A. G. van Os, 2810

Nicaragua; Pressure gradients; Salinity; Suspended sediments; Boundary layer flow; Continental shelf; Currents (water); Littoral current

Shelf and Coastal Boundary Layer Currents, Miskito Bank of Nicaragua, Richard L. Crout and Stephen P. Murray, 2715

Nicaragua; Rainfall; Sedimentation; Sediments;

Sediment transport; Water circulation; Wave energy; Weathering; Estuaries; Littoral deposits

Variations of Wave-Energy Levels and Coastal Sedimentation, Eastern Nicaragua, E. H. Owens and H. H. Roberts, 1195

- Nile River Valley; Oceans; Sediment deposits; Sediment load; Sediment transport; Storms; Water depth; Wave equations; Wave period; Bars (riverine); Beach erosion; Lakes**
Undulated Bottom Profiles and Onshore-Offshore Transport, Madhav Manohar, 1454
- Nonlinear systems; Sampling; Spectral analysis; Wave spectra; Calculations; Fourier transformation; Interactions**
Higher Order Wave Spectra, Paul C. Liu and Albert W. Green, 360
- North Carolina; Sediment deposits; Simulation; Spoil banks; Beaches; Breakwaters; Dredging; Hydraulic models; Inlets (waterways); Jetties**
Coastal Processes at Oregon Inlet, North Carolina, James T. Jarrett, 1257
- Numerical analysis; Ocean bottom; Ripple marks; Tidal effects; Bed forms; Friction coefficient (hydraulic); Hydrodynamic pressure; Hydrodynamics**
The Influence of Dune and Flow Parameters on the Friction Factor, Jurgen Sundermann, H. Vollmers and W. Puls, 1787
- Numerical analysis; Ocean bottom; Scouring; Sediment transport; Time factors; Coastal structures; Currents (water); Jetties**
A Numerical Model for Sediment Transport, J. P. Lepetit and A. Hauguel, 1715
- Numerical analysis; Ocean engineering; Oceanography; Three-dimensional; Tidal currents; Tide gages; Two-dimensional; Water circulation; Mathematical models; Models**
Role of 2D and 3D Models in JONSDAP '76, A. M. Davies, 1085
- Numerical analysis; Ocean waves; Scale effect; Three-dimensional; Wave height; Wave propagation; Waves; Wave spectra; Mathematical models**
Natural Wave Trains: Description and Reproduction, H. Lundgren and S. E. Sand, 312
- Numerical analysis; Outlet works; Saline water; Fjords; Freezing; Heat loss; Hydroelectric powerplants; Ice control; Model studies**
Prevention of Freezing in Fjords, Sveinung Saegrov, 2958
- Numerical analysis; Piles; Transverse waves; Wave energy; Wave height; Wave interference; Computation; Cylindrical bodies; Experimentation; Model tests**
Wave Forces on a Row of Cylindrical Piles of Large Diameter, J. C.W. Berkhoff and J. V.D. Weide, 2433
- Numerical analysis; Predictions; Refraction; Sediment transport; Barriers; Beaches; Breakwaters; Coastal plains; Diffraction; Groins (structures); Jetties; Littoral drift**
Prediction of Beach PlanForms with Littoral Controls, Marc Perlin and Robert G. Dean, 1818
- Numerical analysis; Predictions; Simulation; Storm surges; Texas; Tidal effects; Tsunamis; Water levels; Coastal plains; Cost effectiveness; Floods; Hurricanes**
Coastal Flood Simulation in Stretched Coordinates, H. Lee Butler, 1030
- Numerical analysis; Predictions; Simulation; Storm surges; Water levels; Wind forces; Forecasting; Mathematical models; Meteorological data; Meteorology**
Numerical Storm Surge Forecasting, Manfred Engel, 975
- Numerical analysis; Radar operation; Storms; Wavelength; Wave propagation; Wind; Wind speed; Hurricanes; Mathematical models; Models**
Radar Observations of Hurricane Wave Directions, B. D. King and O. H. Shemdin, 209
- Numerical analysis; Responses; Water levels; Water waves; Wave height; Discharge (water); Estuaries; Hydraulic models; Model studies**
A Hybrid Model of the St. Lawrence River Estuary, E. R. Funke and N. L. Crookshank, 2855
- Numerical analysis; Rivers; Shallow water; Tidal effects; Turbulence; Estuaries; Flood routing; Hydraulic models; Hydrodynamics**
Hydrodynamic Modelling of the Southern North Sea, David Prandle, 1122
- Numerical analysis; Saline water intrusion; Salinity; Simulation; Tidal hydraulics; Estuaries; Hydraulic models; Mathematical models; Model studies**
Numerical Tidal-Salinity Models of the Ems Estuary, Karsten Fischer, 2840
- Numerical analysis; Sediment transport; Storm surges; Tidal effects; Wave height; Bays (topographic features); Friction coefficient (hydraulic); Inlets (waterways); Mathematical models**
Numerical Model Investigation of Selected Tidal Inlet-Bay System Characteristics, William N. Seelig and Robert M. Sorensen, 1319
- Numerical analysis; Stochastic processes; Wave generation; Wave height; Wavelength; Waves; Wave spectra; Wave tanks; Hydrodynamic pressure**
An Inclined-Plate Wave Generator, Fredric Raichlen and Jiin-Jen Lee, 388
- Numerical analysis; Surveys (data collection); Tidal effects; Water levels; Wave propagation; Wave velocity; Estuaries; Field data; Flood protection; Mathematical models**
Adjustment and Verification of the RANDELTA II Model, A. Langerak, M. A.M. deRas and J. J. Leendertse, 1049
- Numerical analysis; Tidal effects; Acceleration; Bed roughness; Distortion; Friction coefficient (hydraulic); Laboratory tests; Mathematical models**
Numerical Study of Distortion in a Froude Model, T. A. McClimans and S. A. Gjerp, 2887
- Numerical analysis; Wave diffraction; Wave height; Wave reflection; Breakwaters; Computer programs; Harbors; Hydraulic models**
A Numerical Approach for the Determination of the Wave Height Distribution in a Harbour, Soren Kohlhasse, Karl-Friedrich Daemrich, U. Berger, E. Tautenhain and O. Burkhardt, 664
- Ocean bottom; Ocean waves; Return flow; Sands; Scouring; Sea walls; Slopes; Tsunamis; Two-dimensional; Water depth; Wave energy; Waves**
Scouring at the Toe of a Seawall due to Tsunamis, Hitoshi Nishimura, Akira Watanabe and Kiyoshi Horikawa, 2540

- Ocean bottom; Oscillation; Ripple marks; Shallow water; Waves; Wind pressure; Field tests; Laboratory tests**
On the Geometry of Ripples Due to Waves, M. S. Yalin and E. Karahan, 1776
- Ocean bottom; Oscillation; Roughness (hydraulic); Velocity distribution; Vortex generators; Jets; Laminar flow**
Oscillatory Laminar Flow Above a Rough Bed, C. B. George and J. F.A. Sleath, 898
- Ocean bottom; Ripple marks; Tidal effects; Bed forms; Friction coefficient (hydraulic); Hydrodynamic pressure; Hydrodynamics; Numerical analysis**
The Influence of Dune and Flow Parameters on the Friction Factor, Jurgen Sundermann, H. Vollmers and W. Puls, 1787
- Ocean bottom; Sands; Sediments; Sediment transport; Surface waves; Velocity field; Water waves; Wave energy**
Sediment Motion Caused by Surface Water Waves, A. G. Davies and R. H. Wilkinson, 1577
- Ocean bottom; Scouring; Sediment transport; Time factors; Coastal structures; Currents (water); Jetties; Numerical analysis**
A Numerical Model for Sediment Transport, J. P. Lepetit and A. Hauguel, 1715
- Ocean bottom; Sediments; Sediment transport; Shear stress; Surf; Water depth; Littoral deposits; Littoral drift; Littoral materials**
Distribution of Sand Transport Rate across a Surf Zone, Toru Sawaragi and Ichiro Deguchi, 1596
- Ocean bottom; Sediments; Sediment transport; Surf; Wave dispersion; Wave energy; Beaches; Coastal plains; Littoral current; Littoral deposits; Models**
A Model Study of Alongshore Sediment Transport Rate, J. W. Kamphuis and J. S. Readshaw, 1656
- Ocean bottom; Sediment transport; Waves; Breakwaters; Japan; Land reclamation; Littoral current; Littoral drift; Movable bed models**
Estimation Using a Movable Bed Model of Shoreline Change Caused by a Reclamation Projected into the Sea, Shoji Sato and Hiroaki Ozasa, 1839
- Ocean bottom; Surface waves; Water depth; Wave energy; Wave measurement; Acoustic measuring instruments; Currents (water)**
Near-Bottom Current Measured by Acoustic Sensors, K. A. Selanger and T. Carstens, 878
- Ocean bottom; Water depth; Water waves; Wave dispersion; Wave energy; Wave propagation; Wave spectra; Dissipation; Friction coefficient (hydraulic)**
Bottom Dissipation in Finite-Depth Water Waves, S. V. Hsiao and O. H. Shemdin, 434
- Ocean engineering; Oceanography; Three-dimensional; Tidal currents; Tide gages; Two-dimensional; Water circulation; Mathematical models; Models; Numerical analysis**
Role of 2D and 3D Models in JONSDAP '76, A. M. Davies, 1085
- Ocean engineering; Ocean waves; Rivers; Runoff; Suspended sediments; Two-dimensional; Wave propagation; Wind loads; Boundary conditions; Coastal plains; Mixing**
Mixed Layer Models for Coastal Waters, W. J. Wiseman, Jr., L. J. Rouse, Jr. and O. K. Huh, 2619
- Oceanography; Three-dimensional; Tidal currents; Tide gages; Two-dimensional; Water circulation; Mathematical models; Models; Numerical analysis; Ocean engineering**
Role of 2D and 3D Models in JONSDAP '76, A. M. Davies, 1085
- Oceans; Sediment deposits; Sediment load; Sediment transport; Storms; Water depth; Wave equations; Wave period; Bars (riverine); Beach erosion; Lakes; Nile River Valley**
Undulated Bottom Profiles and Onshore-Offshore Transport, Madhav Manohar, 1454
- Ocean waves; Offshore structures; Predictions; Random processes; Vibration; Wave equations; Wave generation; Wave height; Waves; Wave tanks; Wave velocity**
Periodic Theory Velocity Prediction in Random Wave, John H. Nath and Koji Kobune, 340
- Ocean waves; Offshore structures; Shore protection; Wave height; Wave period; Wave spectra; Correlation techniques**
The Observed Joint Distribution of Periods and Heights of Sea Waves, Yoshimi Goda, 227
- Ocean waves; Pneumatic systems; Underwater structures; Wave damping; Wave energy; Wave period; Waves; Breakwaters**
Combination Effect of Pneumatic Breakwater and Other Type Breakwater on Wave Damping, Yuichi Iwagaki, Toshiyuki Asano and Tsutomu Honda, 2172
- Ocean waves; Predictions; Wave dispersion; Wave height; Wave reflection; Breakwaters; Experimentation; Friction coefficient (hydraulic)**
Wave Transmission through Trapezoidal Breakwaters, Ole Secher Madsen, Paisal Shusang and Sue Ann Hanson, 2140
- Ocean waves; Probability density functions; Probability theory; Secondary waves; Surf; Wave height; Wave period; Waves; Wave spectra; Breaking energy**
Probability Density Functions of Breaking Waves, Edward B. Thornton and George Schaeffer, 507
- Ocean waves; Probability distribution functions; Shore protection; Statistical analysis; Wave height; Wave period; Coastal plains; Confidence level**
On Long-Term Statistics for Ocean and Coastal Waves, Michel K. Ochi, 59
- Ocean waves; Radar; Radar photography; Surveys (data collection); Wave energy; Wave height; Wavelength; Imaging**
The Use of Imaging Radar in Studying Ocean Waves, M. G. Mattie and D. Lee Harris, 174
- Ocean waves; Random processes; Wave diffraction; Wave height; Wave reflection; Wave spectra; Breakwaters; Diffraction**
Diffraction Diagrams for Directional Random Waves, Yoshimi Goda, Tomotsuka Takayama and Yasumasa Suzuki, 628

- Ocean waves; Recreational facilities; Storm surges; West Germany; Coastal plains; Damage**
Welcoming Address — IV, Hans-Werner Partensky, 10
- Ocean waves; Responses; Water waves; Waves; Cylindrical bodies; Dynamic response; Loading; Mathematical models**
Loading and Response of Cylinders in Waves, G. N. Bullock, P. K. Stansby and J. G. Warren, 2415
- Ocean waves; Return flow; Sands; Scouring; Sea walls; Slopes; Tsunamis; Two-dimensional; Water depth; Wave energy; Waves; Ocean bottom**
Scouring at the Toe of a Seawall due to Tsunamis, Hitoshi Nishimura, Akira Watanabe and Kiyoshi Horikawa, 2540
- Ocean waves; Rivers; Runoff; Suspended sediments; Two-dimensional; Wave propagation; Wind loads; Boundary conditions; Coastal plains; Mixing; Ocean engineering**
Mixed Layer Models for Coastal Waters, W. J. Wiseman, Jr., L. J. Rouse, Jr. and O. K. Huh, 2619
- Ocean waves; Scale effect; Three-dimensional; Wave height; Wave propagation; Waves; Wave spectra; Mathematical models; Numerical analysis**
Natural Wave Trains: Description and Reproduction, H. Lundgren and S. E. Sand, 312
- Ocean waves; Wave action; Wave energy; Wave height; Wave period; Wave recorders (water waves); Brazil; Meteorology**
Wave Climate in Some Zones off the Brazilian Coast, Alberto Homsí, 114
- Ocean waves; Wave action; Wave pressure; Wave tanks; Groups; Loading; Load transfer; Marine structures**
Load Analysis from Wave Groups, A. I. Kuznetsov and G. D. Khaskhatchikh, 2328
- Ocean waves; Wave energy; Waves; Wave spectra; Wave velocity; Currents (water); Edge effect; Frequencies; Littoral current**
Observation of Nearshore Current and Edge Waves, Tamio O. Sasaki and Kiyoshi Horikawa, 791
- Offshore platforms; Offshore structures; Pile foundations; Underwater foundations; Vibration; Currents (water); Dolphins (structures); Marine structures**
Tripod Concept for Pile Structures in Fast Current, J. Khanna and J. S. Wood, 2481
- Offshore platforms; Offshore structures; Surveys (data collection); Wave energy; Wave height; Wave recorders (water waves); Buoys; Design criteria**
Comparison of Shipborne Wave Recorder and Waverider Buoy Data Used to Generate Design and Operational Planning Criteria, C. G. Graham, G. Verboom and C. J. Shaw, 97
- Offshore platforms; Radar operation; Wave height; Waves; Wind; Wind speed; Buoys; Hurricanes; Measurement; Monitoring**
HF Skywave Radar Measurement of Hurricane Winds and Waves, Joseph W. Maresca, Jr. and Christopher T. Carlson, 190
- Offshore structures; Centrifugal pumps; Concrete piles; Dredging; Failure; Intake structures; Jetties**
Problems of Design and Construction of an Offshore Sea Water Intake, D. W. Standish-White and J. A. Zwamborn, 2125
- Offshore structures; Pile foundations; Underwater foundations; Vibration; Currents (water); Dolphins (structures); Marine structures; Offshore platforms**
Tripod Concept for Pile Structures in Fast Current, J. Khanna and J. S. Wood, 2481
- Offshore structures; Predictions; Random processes; Vibration; Wave equations; Wave generation; Wave height; Waves; Wave tanks; Wave velocity; Ocean waves**
Periodic Theory Velocity Prediction in Random Wave, John H. Nath and Koji Kobune, 340
- Offshore structures; Rip currents; Spacing; Surf; Wave action; Waves; Wave velocity; Coastal plains; Eigenvalues; Mass; Momentum**
Rip Current Spacing as an Eigenvalue, Noriyuki Iwata, 828
- Offshore structures; Shore protection; Wave height; Wave period; Wave spectra; Correlation techniques; Ocean waves**
The Observed Joint Distribution of Periods and Heights of Sea Waves, Yoshimi Goda, 227
- Offshore structures; Surveys (data collection); Wave energy; Wave height; Wave recorders (water waves); Buoys; Design criteria; Offshore platforms**
Comparison of Shipborne Wave Recorder and Waverider Buoy Data Used to Generate Design and Operational Planning Criteria, C. G. Graham, G. Verboom and C. J. Shaw, 97
- Oil spills; Three-dimensional; Viscosity; Water depth; Water pollution; Wind loads; Currents (water); Eddies**
3-D Current Model with Depth Varying Eddy Viscosity, Bryan R. Pearce, Cortis Cooper and Susan Nelson, 2602
- Oil spills; Tires; Wave action; Wave attenuation; Breakwaters; Coastal engineering; Coastal structures; Floating bodies**
Scrap Tyre Breakwaters in Coastal Engineering, Robert Charles McGregor and Neil Sinclair Miller, 2191
- Open channel flow; Performance; Standardization; Test reproducibility; Tests; Turbulent flow; Wave period; Wave refraction; Armoring (streambed)**
Performance of Dolos Blocks in an Open Channel Situation, Arthur Brebner, 2305
- Open channel flow; Saline water-freshwater interfaces; Salinity; Stratified flow; Two phase flow; Water flow; Density; Friction coefficient (hydraulic)**
Interfacial Friction Coefficients in a Two-Layered Stratified Flow, Emmanouel Partheniades and Vassilios Dermisiss, 2778
- Oscillation; Responses; Simulation; Wave damping; Wave energy; Wave period; Wave pressure; Wind loads; Wind pressure; Dynamic response**
Simulation of Wave/Wind Forced Harbor Oscillation, S. K. Liu, H. S. Hou and Charles C.C. Chang, 2551

- Oscillation; Ripple marks; Shallow water; Waves; Wind pressure; Field tests; Laboratory tests; Ocean bottom**
On the Geometry of Ripples Due to Waves, M. S. Yalin and E. Karahan, 1776
- Oscillation; Roughness (hydraulic); Velocity distribution; Vortex generators; Jets; Laminar flow; Ocean bottom**
Oscillatory Laminar Flow Above a Rough Bed, C. B. George and J. F.A. Sleath, 898
- Oscillations; Piezometers; Wave height; Wave period; Wave spectrum; Aquifers; Ground water; Groundwater elevation; Littoral current**
Beach Ground-Water Oscillations, Andrzej Lewandowski and Ryszard B. Zeidler, 2051
- Oscillations; Tides; Water waves; Wave diffraction; Wave refraction; Approximation method; Finite element method; Harbors; Integral equations**
A Combined FE-BIE Method for Water Waves, A. Hauguel, 715
- Outfall sewers; Scale effect; Tests; Thermal pollution; Wave energy; Wave height; Wave pressure; Cooling water; Loads (forces)**
Non-Breaking and Breaking Wave Loads on a Cooling Water Outfall, G. R. Mogridge and W. W. Jamieson, 2461
- Outfall sewers; Sewage effluents; Statistical analysis; Time series analysis; Waste disposal; Coastal plains; Diffusion; Dispersion; Mathematical models**
Outfall Diffusion Models for the Coastal Zone, D. C.L. Lam and C. R. Murthy, 2584
- Outlet works; Saline water; Fjords; Freezing; Heat loss; Hydroelectric powerplants; Ice control; Model studies; Numerical analysis**
Prevention of Freezing in Fjords, Sveinung Saegrov, 2958
- Particle trajectories; Slope; Velocity; Waves; Wave velocity; Beaches; Breaking energy; Deep water**
Estimation of Water Particle Velocity of Breaking Wave, Tetsuo Sakai and Yuichi Iwagaki, 551
- Particle trajectories; Spectral energy distribution; Time dependence; Water levels; Wave diffraction; Wave energy; Cylindrical bodies; Diffraction**
Wave Forces Induced by Irregular Waves on a Vertical Circular Cylinder, Hajime Ishida and Yuichi Iwagaki, 2397
- Performance; Profile measurement; Sand; Sediment transport; Vehicles; Wave action; Calibration; California; Instrumentation**
Tracked Vehicle for Continuous Nearshore Profiles, Richard J. Seymour, Alan L. Higgins and David P. Bothman, 1542
- Performance; Shape; Silting; Underwater structures; Wave attenuation; Barriers; Breakwaters; India**
Performance Characteristics of Submerged Breakwaters, J. Dattatri, H. Raman and N. Jothi Shankar, 2153
- Performance; Standardization; Test reproducibility; Tests; Turbulent flow; Wave period; Wave refraction; Armoring (streambed); Open channel flow**
Performance of Dolos Blocks in an Open Channel Situation, Arthur Brebner, 2305
- Permeability; Shallow water; Standing waves; Tests; Wave diffraction; Wave energy; Wave height; Wavelength; Wave tanks; Breakwaters**
Wave Height Distribution Around Permeable Breakwaters, Shintaro Hotta, 695
- Photographic analysis; Predictions; Water depth; Wave height; Wavelength; Waves; Breaking energy; Classification; Field tests**
Field Study of Breaking Wave Characteristics, Lee L. Weishar and Robert J. Byrne, 487
- Physics; Sediments; Structures; Tidal currents; Wave energy; Waves; Coastal engineering; Mathematical models; Mathematics; Mixing**
Struggle of Physics and Mathematics in Coastal Engineering, H. Lundgren, 13
- Piers; Rubble-mound breakwaters; Sands; Shore-line cover; Beach erosion; Breakwaters; Coastal structures; Erosion control; Littoral zone; Marine terminals**
Coastal Structures' Effects on Shorelines, Ronald M. Noble, 2069
- Piezometers; Wave height; Wave period; Wave spectrum; Aquifers; Ground water; Groundwater elevation; Littoral current; Oscillations**
Beach Ground-Water Oscillations, Andrzej Lewandowski and Ryszard B. Zeidler, 2051
- Pile foundations; Underwater foundations; Vibration; Currents (water); Dolphins (structures); Marine structures; Offshore platforms; Offshore structures**
Tripod Concept for Pile Structures in Fast Current, J. Khanna and J. S. Wood, 2481
- Piles; Transverse waves; Wave energy; Wave height; Wave interference; Computation; Cylindrical bodies; Experimentation; Model tests; Numerical analysis**
Wave Forces on a Row of Cylindrical Piles of Large Diameter, J. C.W. Berkhoff and J. V.D. Weide, 2433
- Piles; Wave period; Wave propagation; Cylindrical bodies; Displacement; Dynamic characteristics; Dynamic response; Experimentation**
Dynamic Behavior of Vertical Cylinder due to Wave Force, Toru Sawaragi and Takayuki Nakamura, 2378
- Plumes; Sediment concentration; Spoil; Spoil banks; Suspended sediments; Diffusion; Dredges; Dredging; Estuaries; Models**
Factors Governing the Distribution of Dredge-Resuspended Sediments, W. Frank Bohlen, 2001
- Plumes; Surf; Temperature effects; Thermal pollution; Tracers; Turbulent flow; Currents (water); Heated water; Jet flow; Mixing**
Mixing of Heated Water Discharged in the Surf Zone, Kiyoshi Horikawa, Ming-Chung Lin and Tamio O. Sasaki, 2563
- Pneumatic systems; Underwater structures; Wave damping; Wave energy; Wave period; Waves; Breakwaters; Ocean waves**
Combination Effect of Pneumatic Breakwater and Other Type Breakwater on Wave Damping, Yuichi Iwagaki, Toshiyuki Asano and Tsutomu Honda, 2172
- Ports; Sampling; Sea level; Statistical analysis; Tidal waters; Water levels; Frequencies; Great Britain**
Analysis of Maximum Sea Level in Southern England, J. Graff and D. L. Blackman, 931

- Ports; Shipping; Shore protection; Storms; Tidal currents; West Germany; Dikes; Estuaries**
Welcoming Address — 11, Helga Elstner, 4
- Predictions; Rainfall; Samples; Sampling; Wave energy; Wave height; Wave spectra; Wind velocity; Distribution functions**
Extremal Prediction of Significant Wave Height, Enrique Copeiro, 285
- Predictions; Random processes; Shallow water; Wave height; Bores (wave); Breaking energy; Energy dissipation; Energy losses**
Energy Loss and Set-Up Due to Breaking of Random Waves, J. A. Battjes and J. P.F.M. Janssen, 569
- Predictions; Random processes; Vibration; Wave equations; Wave generation; Wave height; Waves; Wave tanks; Wave velocity; Ocean waves; Offshore structures**
Periodic Theory Velocity Prediction in Random Wave, John H. Nath and Koji Kobune, 340
- Predictions; Refraction; Sediment transport; Barriers; Beaches; Breakwaters; Coastal plains; Diffraction; Groins (structures); Jetties; Littoral drift; Numerical analysis**
Prediction of Beach PlanForms with Littoral Controls, Marc Perlin and Robert G. Dean, 1818
- Predictions; Regression analysis; Statistical analysis; Stress; Surf; Wave spectra; Wave velocity; Wind velocity; Littoral current**
Wind-Generated Longshore Currents, Dag Nummedal and Robert J. Finley, 1428
- Predictions; Reynolds number; Water flow; Wave energy; Wave pressure; Cylindrical bodies; Drag; Experimentation; Loads (forces)**
Wave Loads on Horizontal Cylinders, P. Holmes and J. R. Chaplin, 2449
- Predictions; Sediments; Sediment transport; Littoral current; Littoral drift**
The Nearshore Sediment Transport Study, Richard J. Seymour and David B. Duane, 1555
- Predictions; Sediments; Sediment transport; Silting; Wave energy; Experimentation; Littoral current; Littoral drift**
Longshore Sediment Transport Data: A Review, Matthew N. Greer and Ole Secher Madsen, 1563
- Predictions; Simulation; Storm surges; Texas; Tidal effects; Tsunamis; Water levels; Coastal plains; Cost effectiveness; Floods; Hurricanes; Numerical analysis**
Coastal Flood Simulation in Stretched Coordinates, H. Lee Butler, 1030
- Predictions; Simulation; Storm surges; Water levels; Wind forces; Forecasting; Mathematical models; Meteorological data; Meteorology; Numerical analysis**
Numerical Storm Surge Forecasting, Manfred Engel, 975
- Predictions; Storm surges; Tidal currents; Tidal effects; Tidal energy; Tide gages; Wind; Wind velocity; Forecasting**
Storm Surge Prediction by Combined Wind and Tide Data, Hermann Christiansen and Winfried Siefert, 965
- Predictions; Storm surges; Tidal effects; Tidal energy; Tide gages; Dynamics; Estuaries; Forecasting**
Storm Surge Prediction in Tidal Rivers: A New Conception, Winfried Siefert, 986
- Predictions; Water depth; Wave height; Wavelength; Waves; Breaking energy; Classification; Field tests; Photographic analysis**
Field Study of Breaking Wave Characteristics, Lee L. Weishar and Robert J. Byrne, 487
- Predictions; Wave dispersion; Wave height; Wave reflection; Breakwaters; Experimentation; Friction coefficient (hydraulic); Ocean waves**
Wave Transmission through Trapezoidal Breakwaters, Ole Secher Madsen, Paisal Shusang and Sue Ann Hanson, 2140
- Pressure distribution; Scale effect; Standing waves; Storm surges; Wave energy; Wave pressure; Barriers; Impact; Marine structures; Mathematical models**
A Model Law for Wave Impacts on Coastal Structures, C. Ramkema, 2308
- Pressure gradients; Salinity; Suspended sediments; Boundary layer flow; Continental shelf; Currents (water); Littoral current; Nicaragua**
Shelf and Coastal Boundary Layer Currents, Miskito Bank of Nicaragua, Richard L. Crout and Stephen P. Murray, 2715
- Probability; Probability distribution functions; Sea level; Statistical analysis; Storm surges; Tides; Beaches; Coastal plains**
Extreme Sea Levels from Tide and Surge Probability, D. T. Pugh and J. M. Vassie, 911
- Probability; Storm surges; West Germany; Wind forces; Wind pressure; Wind velocity; Coastal engineering; Flooding; Frequencies**
Frequencies and Probabilities of Extreme Storm Surges (On the Time-Dependent Changes of the Probability of Extreme Storm Floods at the German North Sea Coast), Alfred Fohrboter, 949
- Probability density functions; Probability theory; Secondary waves; Surf; Wave height; Wave period; Waves; Wave spectra; Breaking energy; Ocean waves**
Probability Density Functions of Breaking Waves, Edward B. Thornton and George Schaeffer, 507
- Probability density functions; Spectral analysis; Surf; Wave action; Wave height; Wave period; Waves; Coral reefs and islands; Energy**
The Energy Spectra of Surf Waves on a Coral Reef, Theodore T. Lee and Kerry P. Black, 588
- Probability distribution functions; Sea level; Statistical analysis; Storm surges; Tides; Beaches; Coastal plains; Probability**
Extreme Sea Levels from Tide and Surge Probability, D. T. Pugh and J. M. Vassie, 911
- Probability distribution functions; Shore protection; Statistical analysis; Wave height; Wave period; Coastal plains; Confidence level; Ocean waves**
On Long-Term Statistics for Ocean and Coastal Waves, Michel K. Ochi, 59

- Probability distribution functions; Tropical cyclones; Wave equations; Wave recorders (water waves); Wind forces; Wind pressure; Australia; Cyclones; Frequencies; Mathematical models**
Wind Wave Frequencies in a Tropical Cyclone Region, Rodney J. Sobey, 76
- Probability theory; Secondary waves; Surf; Wave height; Wave period; Waves; Wave spectra; Breaking energy; Ocean waves; Probability density functions**
Probability Density Functions of Breaking Waves, Edward B. Thornton and George Schaeffer, 507
- Profile measurement; Sand; Sediment transport; Vehicles; Wave action; Calibration; California; Instrumentation; Performance**
Tracked Vehicle for Continuous Nearshore Profiles, Richard J. Seymour, Alan L. Higgins and David P. Bothman, 1542
- Prototypes; Wave recorders (water waves); Waves; Breakwaters; Field tests; Harbors; Laboratory tests; Models**
A Comparison Between Model and Prototype Waves in Harbours, Sverre Bjordal and Alf Torum, 677
- Questionnaires; Surveys (data collection); Wave height; Wave recorders (water waves); International compacts; Inventories**
A World Wave Data Centre, Laurence Draper, 51
- Radar; Radar photography; Surveys (data collection); Wave energy; Wave height; Wavelength; Imaging; Ocean waves**
The Use of Imaging Radar in Studying Ocean Waves, M. G. Mattie and D. Lee Harris, 174
- Radar operation; Storms; Wavelength; Wave propagation; Wind; Wind speed; Hurricanes; Mathematical models; Models; Numerical analysis**
Radar Observations of Hurricane Wave Directions, B. D. King and O. H. Shemdin, 209
- Radar operation; Wave height; Waves; Wind; Wind speed; Buoys; Hurricanes; Measurement; Monitoring; Offshore platforms**
HF Skywave Radar Measurement of Hurricane Winds and Waves, Joseph W. Maresca, Jr. and Christopher T. Carlson, 190
- Radar photography; Surveys (data collection); Wave energy; Wave height; Wavelength; Imaging; Ocean waves; Radar**
The Use of Imaging Radar in Studying Ocean Waves, M. G. Mattie and D. Lee Harris, 174
- Rainfall; Salt marshes; Sediment transport; South Carolina; Suspended load; Tidal currents; Tidal effects; Tidal waters; Wind; Discharge (water); Hydrodynamics; Meteorology**
Hydrodynamics and Sediment Transport in a Salt Marsh Tidal Channel, Larry G. Ward, 1953
- Rainfall; Samples; Sampling; Wave energy; Wave height; Wave spectra; Wind velocity; Distribution functions; Predictions**
Extremal Prediction of Significant Wave Height, Enrique Copeiro, 285
- Rainfall; Sedimentation; Sediments; Sediment transport; Water circulation; Wave energy; Weathering; Estuaries; Littoral deposits; Nicaragua**
Variations of Wave-Energy Levels and Coastal Sedimentation, Eastern Nicaragua, E. H. Owens and H. H. Roberts, 1195
- Random processes; Shallow water; Wave height; Bores (wave); Breaking energy; Energy dissipation; Energy losses; Predictions**
Energy Loss and Set-Up Due to Breaking of Random Waves, J. A. Battjes and J. P.F.M. Janssen, 569
- Random processes; Slopes; Water depth; Wave height; Wavelength; Wave period; Waves; Wave tanks; Wave velocity; Beaches**
Wave Length, Wave Velocity and Shoaling Characteristics of Random Waves, Akira Kimura and Yuichi Iwagaki, 320
- Random processes; Vibration; Wave equations; Wave generation; Wave height; Waves; Wave tanks; Wave velocity; Ocean waves; Offshore structures; Predictions**
Periodic Theory Velocity Prediction in Random Wave, John H. Nath and Koji Kobune, 340
- Random processes; Wave diffraction; Wave height; Wave reflection; Wave spectra; Breakwaters; Diffraction; Ocean waves**
Diffraction Diagrams for Directional Random Waves, Yoshimi Goda, Tomotsuka Takayama and Yasumasa Suzuki, 628
- Recreational facilities; Storm surges; West Germany; Coastal plains; Damage; Ocean waves**
Welcoming Address — IV, Hans-Werner Partenscky, 10
- Reefs; Storms; Tidal currents; Wave action; Wave height; Wave runup; Waves; Wave spectra; Wind velocity; Estuaries**
Analysis of Storm Tide Waves, Volker Barthel, 1016
- Reflection; Refraction; Walls; Wave action; Wave diffraction; Wave reflection; Breakwaters; Model tests**
Influence of Breakwater-Reflection on Diffraction, Karl-Friedrich Daemrich and Soren Kohlhasse, 651
- Refraction; Sediment transport; Barriers; Beaches; Breakwaters; Coastal plains; Diffraction; Groins (structures); Jetties; Littoral drift; Numerical analysis; Predictions**
Prediction of Beach PlanForms with Littoral Controls, Marc Perlin and Robert G. Dean, 1818
- Refraction; Walls; Wave action; Wave diffraction; Wave reflection; Breakwaters; Model tests; Reflection**
Influence of Breakwater-Reflection on Diffraction, Karl-Friedrich Daemrich and Soren Kohlhasse, 651
- Refraction (water waves); Shear flow; Water depth; Wave action; Wave height; Wavelength; Wave period; Wave refraction**
Wave Refraction Across a Shearing Current, Ivar G. Jonsson and Ove Skovgaard, 722
- Regression analysis; Statistical analysis; Stress; Surf; Wave spectra; Wave velocity; Wind velocity; Littoral current; Predictions**
Wind-Generated Longshore Currents, Dag Nummedal and Robert J. Finley, 1428

- Remote sensing; Shallow water; Water depth; Aerial photography; Bathymetry; Color photography; Images**
Visible-Region Photographic Remote Sensing of Nearshore Waters, Tsuguo Sunamura and Kiyoshi Horikawa, 1439
- Resonance; Surf; Wave reflection; Waves; Wave spectra; Beaches; Edge effect; Littoral current; Morphology**
Surf Zone Resonance and Coupled Morphology, John Chappell and Lynn Donelson Wright, 1359
- Responses; Simulation; Wave damping; Wave energy; Wave period; Wave pressure; Wind loads; Wind pressure; Dynamic response; Oscillation**
Simulation of Wave/Wind Forced Harbor Oscillation, S. K. Liu, H. S. Hou and Charles C.C. Chang, 2551
- Responses; Stochastic processes; Wave generation; Wave spectra; Dynamic pressure; Frequencies; Hydrodynamic pressure**
Analysis of Hinged Wavemakers for Random Waves, Robert T. Hudspeth, Douglas F. Jones and John H. Nath, 372
- Responses; Storms; Storm surges; Surveys (data collection); Tidal hydraulics; Water levels; Barriers; Boundary conditions; Netherlands**
A Tidal Survey for a Model of an Offshore Area, W. J. van de Ree, J. Voogt and J. J. Leendertse, 2656
- Responses; Water levels; Water waves; Wave height; Discharge (water); Estuaries; Hydraulic models; Model studies; Numerical analysis**
A Hybrid Model of the St. Lawrence River Estuary, E. R. Funke and N. L. Crookshank, 2855
- Responses; Water waves; Waves; Cylindrical bodies; Dynamic response; Loading; Mathematical models; Ocean waves**
Loading and Response of Cylinders in Waves, G. N. Bullock, P. K. Stansby and J. G. Warren, 2415
- Return flow; Sands; Scouring; Sea walls; Slopes; Tsunamis; Two-dimensional; Water depth; Wave energy; Waves; Ocean bottom; Ocean waves**
Scouring at the Toe of a Seawall due to Tsunamis, Hitoshi Nishimura, Akira Watanabe and Kiyoshi Horikawa, 2540
- Revetments; Rubble-mound breakwaters; Slope stability; Stability; Wave energy; Wave pressure; Armoring (streambed); Costs**
Blanket Theory and Low Cost Revetments, C. T. Brown, 2510
- Reynolds number; Water flow; Wave energy; Wave pressure; Cylindrical bodies; Drag; Experimentation; Loads (forces); Predictions**
Wave Loads on Horizontal Cylinders, P. Holmes and J. R. Chaplin, 2449
- Rip currents; Sediment transport; Shoaling; Water waves; Wave diffraction; Wave height; Wave period; Wave refraction; Wave velocity**
Rip Currents and Their Causes, Robert A. Dalrymple, 1414
- Rip currents; Shore-line cover; Wave diffraction; Wave refraction; Wind loads; Accretion (geomorphology); Beach nourishment; Erosion; Groins (structures); Mathematical models**
Mathematical Modeling of Shoreline Evolution, Bernard Le Mehaute and Mills Soldate, 1163
- Rip currents; Spacing; Surf; Wave action; Waves; Wave velocity; Coastal plains; Eigenvalues; Mass; Momentum; Offshore structures**
Rip Current Spacing as an Eigenvalue, Noriyuki Iwata, 828
- Rip currents; Surf; Temporal distribution; Variations; Wave spectra; Edge effect; Gravity waves; Littoral current**
Variability of Longshore Currents, R. T. Guza and Edward B. Thornton, 756
- Ripple marks; Sands; Scale effect; Shore protection; Storm surges; Beach erosion; Dunes; Erosion; Movable bed models**
Movable Bed Model Tests on Dune Erosion, P. Vellinga, 2020
- Ripple marks; Sediment transport; Shear stress; Three-dimensional; Wave height; Waves; Wave tanks; Coastal plains; Currents (water)**
Sediment Transport and Ripples Due to Waves and Currents, Zbigniew Pruszk and Ryszard B. Zeidler, 1638
- Ripple marks; Shallow water; Waves; Wind pressure; Field tests; Laboratory tests; Ocean bottom; Oscillation**
On the Geometry of Ripples Due to Waves, M. S. Yalin and E. Karahan, 1776
- Ripple marks; Tidal effects; Bed forms; Friction coefficient (hydraulic); Hydrodynamic pressure; Hydrodynamics; Numerical analysis; Ocean bottom**
The Influence of Dune and Flow Parameters on the Friction Factor, Jurgen Sundermann, H. Vollmers and W. Puls, 1787
- Rivers; Runoff; Suspended sediments; Two-dimensional; Wave propagation; Wind loads; Boundary conditions; Coastal plains; Mixing; Ocean engineering; Ocean waves**
Mixed Layer Models for Coastal Waters, W. J. Wiseman, Jr., L. J. Rouse, Jr. and O. K. Huh, 2619
- Rivers; Saline water-freshwater interfaces; Salinity; Stream flow; Velocity distribution; Vortices; Wave energy; Bed roughness; Estuaries; Mixing**
Outflow Dynamics at a River Mouth, Masakazu Kashiwamura and Shizuo Yoshida, 2925
- Rivers; Saline water intrusion; Salinity; Density; Estuaries; Flumes; Harbors; Mathematical models; Netherlands**
Effect of Harbours on Salt Intrusion in Estuaries, A. Roelfzema and A. G. van Os, 2810
- Rivers; Shallow water; Tidal effects; Turbulence; Estuaries; Flood routing; Hydraulic models; Hydrodynamics; Numerical analysis**
Hydrodynamic Modelling of the Southern North Sea, David Prandle, 1122

- Rivers; Storm surges; Temperature effects; Thermal pollution; Tidal effects; Tidal hydraulics; Cooling water; Discharge (water); Model studies**
Influence on Temperature Increases in Tidal Rivers Caused by Waste Heat Injections with Respect to Tidal Cycles and Storm Surges, Horst Schwarze and Wilfried Falldorf, 2915
- Roughness (hydraulic); Velocity distribution; Vortex generators; Jets; Laminar flow; Ocean bottom; Oscillation**
Oscillatory Laminar Flow Above a Rough Bed, C. B. George and J. F. A. Sleath, 898
- Rubble-mound breakwaters; Sands; Shore-line cover; Beach erosion; Breakwaters; Coastal structures; Erosion control; Littoral zone; Marine terminals; Piers**
Coastal Structures' Effects on Shorelines, Ronald M. Noble, 2069
- Rubble-mound breakwaters; Seismic design; Settlement (structural); Slope stability; Acceleration; Damage; Earthquake loads; Earthquake resistant structures; Loading**
Loadings on Rubble-Mound Breakwaters due to Earthquakes, H. Wang, C. Y. Yang, C. Lamison and S. S. Chen, 2244
- Rubble-mound breakwaters; Slope stability; Stability; Wave energy; Wave height; Armoring (streambed); Breakwaters**
Dolos-Armored Breakwaters: Special Consideration, Robert D. Carver and D. Donald Davidson, 2263
- Rubble-mound breakwaters; Slope stability; Stability; Wave energy; Wave pressure; Armoring (streambed); Costs; Revetments**
Blanket Theory and Low Cost Revetments, C. T. Brown, 2510
- Rubble-mound breakwaters; Stability; Wave energy; Wave height; Wave spectra; Wave tanks; Breakwaters; Damage; Hydraulic models**
Effects of Wave Grouping on Breakwater Stability, R. R. Johnson, E. P. D. Mansard and J. Ploeg, 2228
- Runoff; Suspended sediments; Two-dimensional; Wave propagation; Wind loads; Boundary conditions; Coastal plains; Mixing; Ocean engineering; Ocean waves; Rivers**
Mixed Layer Models for Coastal Waters, W. J. Wiseman, Jr., L. J. Rouse, Jr. and O. K. Huh, 2619
- Saline water; Fjords; Freezing; Heat loss; Hydroelectric powerplants; Ice control; Model studies; Numerical analysis; Outlet works**
Prevention of Freezing in Fjords, Sveinung Saegrov, 2958
- Saline water-freshwater interfaces; Saline water intrusion; Salinity; Sampling; Tidal hydraulics; Verification inspection; Field tests; Model studies**
Field Data Analysis for Chesapeake Bay Model Verification, Ronald E. Nece and Norman W. Scheffner, 2870
- Saline water-freshwater interfaces; Saline water intrusion; Salinity; Stratified flow; Tidal currents; Tidal hydraulics; Water quality; Estuaries**
Stability Study of an Artificial Salt Intrusion in Estuaries, C. Marche, 2798
- Saline water-freshwater interfaces; Salinity; Stratified flow; Two phase flow; Water flow; Density; Friction coefficient (hydraulic); Open channel flow**
Interfacial Friction Coefficients in a Two-Layered Stratified Flow, Emmanuel Partheniades and Vassilios Dermisis, 2778
- Saline water-freshwater interfaces; Salinity; Stream flow; Velocity distribution; Vortices; Wave energy; Bed roughness; Estuaries; Mixing; Rivers**
Outflow Dynamics at a River Mouth, Masakazu Kashiwamura and Shizuo Yoshida, 2925
- Saline water-freshwater interfaces; Salinity; Ultrasonic tests; Diffusion coefficient; Entrainment; Estuaries; Japan**
Behaviors of the Salt Wedge and the Salinity Distribution at Estuaries, Isao Yakuwa, Susumu Takahashi and Morimasa Ohtani, 2746
- Saline water-freshwater interfaces; Shallow water; Standing waves; Tidal flats; Tidal hydraulics; Dispersion; Estuaries; Mixing; Model studies**
Longitudinal Dispersion in Shallow Well-Mixed Estuaries, J. Dronkers, 2761
- Saline water intrusion; Salinity; Density; Estuaries; Flumes; Harbors; Mathematical models; Netherlands; Rivers**
Effect of Harbours on Salt Intrusion in Estuaries, A. Roelfzema and A. G. van Os, 2810
- Saline water intrusion; Salinity; Sampling; Tidal hydraulics; Verification inspection; Field tests; Model studies; Saline water-freshwater interfaces**
Field Data Analysis for Chesapeake Bay Model Verification, Ronald E. Nece and Norman W. Scheffner, 2870
- Saline water intrusion; Salinity; Simulation; Tidal hydraulics; Estuaries; Hydraulic models; Mathematical models; Model studies; Numerical analysis**
Numerical Tidal-Salinity Models of the Ems Estuary, Karsten Fischer, 2840
- Saline water intrusion; Salinity; Stratified flow; Tidal currents; Tidal hydraulics; Water quality; Estuaries; Saline water-freshwater interfaces**
Stability Study of an Artificial Salt Intrusion in Estuaries, C. Marche, 2798
- Salinity; Density; Estuaries; Flumes; Harbors; Mathematical models; Netherlands; Rivers; Saline water intrusion**
Effect of Harbours on Salt Intrusion in Estuaries, A. Roelfzema and A. G. van Os, 2810
- Salinity; Salt balance; Salt water intrusion; Tidal hydraulics; Wind loads; Florida; Friction coefficient (hydraulic); Model studies**
Tidal Hydraulics and Salt Balance of Lake Worth, Florida, J. van de Kreeke and J. D. Wang, 2827
- Salinity; Sampling; Tidal hydraulics; Verification inspection; Field tests; Model studies; Saline water-freshwater interfaces; Saline water intrusion**
Field Data Analysis for Chesapeake Bay Model Verification, Ronald E. Nece and Norman W. Scheffner, 2870
- Salinity; Sedimentation; Sediment transport; Silting; Suspended sediments; Temperature; Tidal effects; Turbidity; Canada; Dredging; Harbors; Models**
Tidal Sedimentation in Gros-Couana Harbor, Georges Drapeau and Guy Fortin, 1986

- Salinity; Simulation; Tidal hydraulics; Estuaries; Hydraulic models; Mathematical models; Model studies; Numerical analysis; Saline water intrusion**
Numerical Tidal-Salinity Models of the Ems Estuary, Karsten Fischer, 2840
- Salinity; Stratified flow; Tidal currents; Tidal hydraulics; Water quality; Estuaries; Saline water-freshwater interfaces; Saline water intrusion**
Stability Study of an Artificial Salt Intrusion in Estuaries, C. Marche, 2798
- Salinity; Stratified flow; Two phase flow; Water flow; Density; Friction coefficient (hydraulic); Open channel flow; Saline water-freshwater interfaces**
Interfacial Friction Coefficients in a Two-Layered Stratified Flow, Emmanuel Partheniades and Vassilios Dermissis, 2778
- Salinity; Stream flow; Velocity distribution; Vortices; Wave energy; Bed roughness; Estuaries; Mixing; Rivers; Saline water-freshwater interfaces**
Outflow Dynamics at a River Mouth, Masakazu Kashiwamura and Shizuo Yoshida, 2925
- Salinity; Suspended sediments; Boundary layer flow; Continental shelf; Currents (water); Littoral current; Nicaragua; Pressure gradients**
Shelf and Coastal Boundary Layer Currents, Miskito Bank of Nicaragua, Richard L. Crout and Stephen P. Murray, 2715
- Salinity; Ultrasonic tests; Diffusion coefficient; Entrainment; Estuaries; Japan; Saline water-freshwater interfaces**
Behaviors of the Salt Wedge and the Salinity Distribution at Estuaries, Isao Yakuwa, Susumu Takahashi and Morimasa Ohtani, 2746
- Salt balance; Salt water intrusion; Tidal hydraulics; Wind loads; Florida; Friction coefficient (hydraulic); Model studies; Salinity**
Tidal Hydraulics and Salt Balance of Lake Worth, Florida, J. van de Kreeke and J. D. Wang, 2827
- Salt marshes; Sediment transport; South Carolina; Suspended load; Tidal currents; Tidal effects; Tidal waters; Wind; Discharge (water); Hydrodynamics; Meteorology; Rainfall**
Hydrodynamics and Sediment Transport in a Salt Marsh Tidal Channel, Larry G. Ward, 1953
- Salt water intrusion; Tidal hydraulics; Wind loads; Florida; Friction coefficient (hydraulic); Model studies; Salinity; Salt balance**
Tidal Hydraulics and Salt Balance of Lake Worth, Florida, J. van de Kreeke and J. D. Wang, 2827
- Samples; Sampling; Wave energy; Wave height; Wave spectra; Wind velocity; Distribution functions; Predictions; Rainfall**
Extremal Prediction of Significant Wave Height, Enrique Copeiro, 285
- Samples; Sediment concentration; Suspended sediments; Wave height; Coastal plains; Littoral deposits; Littoral drift; Littoral zone**
Sled System for Profiling Suspended Littoral Drift, J. P. Coakley, J. A. Savile, M. Pedrosa and M. Larocque, 1764
- Sampling; Sea level; Statistical analysis; Tidal waters; Water levels; Frequencies; Great Britain; Ports**
Analysis of Maximum Sea Level in Southern England, J. Graff and D. L. Blackman, 931
- Sampling; Spectral analysis; Wave spectra; Calculations; Fourier transformation; Interactions; Nonlinear systems**
Higher Order Wave Spectra, Paul C. Liu and Albert W. Green, 360
- Sampling; Tidal hydraulics; Verification inspection; Field tests; Model studies; Saline water-freshwater interfaces; Saline water intrusion; Salinity**
Field Data Analysis for Chesapeake Bay Model Verification, Ronald E. Nece and Norman W. Scheffner, 2870
- Sampling; Wave energy; Wave height; Wave spectra; Wind velocity; Distribution functions; Predictions; Rainfall; Samples**
Extremal Prediction of Significant Wave Height, Enrique Copeiro, 285
- Sand; Sediment transport; Vehicles; Wave action; Calibration; California; Instrumentation; Performance; Profile measurement**
Tracked Vehicle for Continuous Nearshore Profiles, Richard J. Seymour, Alan L. Higgins and David P. Bothman, 1542
- Sand; Shear stress; Turbulent flow; Velocity distribution; Wave propagation; Wave velocity; Boundary conditions; Mathematical models**
Near-Bottom Velocities in Waves with a Current, W. T. Bakker and Th. van Doorn, 1394
- Sand; Shore protection; Tidal currents; Wave action; Wave energy; Wave refraction; Coastal plains; Dredging; Gravel; Great Britain; Licensing; Littoral drift**
The Effect of Offshore Dredging on Coastlines, W. A. Price, J. M. Motyka and L. J. Jaffrey, 1347
- Sands; Scale effect; Shore protection; Storm surges; Beach erosion; Dunes; Erosion; Movable bed models; Ripple marks**
Movable Bed Model Tests on Dune Erosion, P. Vellinga, 2020
- Sands; Scouring; Sea walls; Slopes; Tsunamis; Two-dimensional; Water depth; Wave energy; Waves; Ocean bottom; Ocean waves; Return flow**
Scouring at the Toe of a Seawall due to Tsunamis, Hitoshi Nishimura, Akira Watanabe and Kiyoshi Horikawa, 2540
- Sands; Sediment deposits; Soil stabilization; Wind forces; Wind pressure; Airspeed; Beach erosion; Dunes; Erosion control; Fences**
Using Fences to Create and Stabilise Sand Dunes, Brian B. Willetts and Christopher J. Phillips, 2040
- Sands; Sediments; Sediment transport; Surface waves; Velocity field; Water waves; Wave energy; Ocean bottom**
Sediment Motion Caused by Surface Water Waves, A. G. Davies and R. H. Wilkinson, 1577
- Sands; Sediment transport; Suspended load; Suspended sediments; Tidal effects; Wave action; Wave energy; Wave period; Waves; Currents (water); Field tests**
Effect of Waves on Sand Transport by Currents, Michael W. Owen and Michael F.C. Thorn, 1675

- Sands; Shore-line cover; Beach erosion; Breakwaters; Coastal structures; Erosion control; Littoral zone; Marine terminals; Piers; Rubble-mound breakwaters**
Coastal Structures' Effects on Shorelines, Ronald M. Noble, 2069
- Sands; Shore protection; Water depth; Bathymetry; Beach erosion; Beach nourishment; Morphology**
Morphologic Effects of Westerland Beach Nourishment 1972, Dieter Wenzel, 1859
- Scale effect; Sediments; Sediment transport; Wave height; Wave period; Beaches; Coastal engineering; Laboratory tests; Movable bed models**
Scale Relations for Equilibrium Beach Profiles, Hideaki Noda, 1531
- Scale effect; Shore protection; Storm surges; Beach erosion; Dunes; Erosion; Movable bed models; Ripple marks; Sands**
Movable Bed Model Tests on Dune Erosion, P. Vellinga, 2020
- Scale effect; Standing waves; Storm surges; Wave energy; Wave pressure; Barriers; Impact; Marine structures; Mathematical models; Pressure distribution**
A Model Law for Wave Impacts on Coastal Structures, C. Ramkema, 2308
- Scale effect; Tests; Thermal pollution; Wave energy; Wave height; Wave pressure; Cooling water; Loads (forces); Outfall sewers**
Non-Breaking and Breaking Wave Loads on a Cooling Water Outfall, G. R. Mogridge and W. W. Jamieson, 2461
- Scale effect; Three-dimensional; Wave height; Wave propagation; Waves; Wave spectra; Mathematical models; Numerical analysis; Ocean waves**
Natural Wave Trains: Description and Reproduction, H. Lundgren and S. E. Sand, 312
- Scale effect; Tidal currents; Tidal hydraulics; Water circulation; Diffusion coefficient; Experimentation; Hydraulic models; Japan**
Experimental Study on Scale Effect of Tidal Model, Haruo Higuchi, Hideichi Yasuda and Norio Hayakawa, 2646
- Scale effect; Water waves; Wave energy; Wave pressure; Wave spectra; Hydrodynamic pressure; Impact; Impact forces; Measurement**
Impact Wave Forces on Vertical and Horizontal Plate, S. R. Massel, M. Oleszkiewicz and W. Trapp, 2340
- Scouring; Sea walls; Shore protection; Wave energy; Wave reflection; Beach erosion; Coastal structures; Dikes; Erosion control; Japan; Land reclamation**
Effectiveness of Seadikes with Rough Slope, Osamu Toyoshima, 2528
- Scouring; Sea walls; Slopes; Tsunamis; Two-dimensional; Water depth; Wave energy; Waves; Ocean bottom; Ocean waves; Return flow; Sands**
Scouring at the Toe of a Seawall due to Tsunamis, Hitoshi Nishimura, Akira Watanabe and Kiyoshi Horikawa, 2540
- Scouring; Sediment transport; Time factors; Coastal structures; Currents (water); Jetties; Numerical analysis; Ocean bottom**
A Numerical Model for Sediment Transport, J. P. Lepetit and A. Hauguel, 1715
- Sea level; Statistical analysis; Storm surges; Tides; Beaches; Coastal plains; Probability; Probability distribution functions**
Extreme Sea Levels from Tide and Surge Probability, D. T. Pugh and J. M. Vassie, 911
- Sea level; Statistical analysis; Tidal waters; Water levels; Frequencies; Great Britain; Ports; Sampling**
Analysis of Maximum Sea Level in Southern England, J. Graff and D. L. Blackman, 931
- Sea walls; Shore protection; Spoil; Spoil banks; Beach erosion; Beach nourishment; Dredging; Groins (structures)**
Some Facts and Fancies about Beach Erosion, Richard Sylvester, 1888
- Sea walls; Shore protection; Wave energy; Wave reflection; Beach erosion; Coastal structures; Dikes; Erosion control; Japan; Land reclamation; Scouring**
Effectiveness of Seadikes with Rough Slope, Osamu Toyoshima, 2528
- Sea walls; Slopes; Tsunamis; Two-dimensional; Water depth; Wave energy; Waves; Ocean bottom; Ocean waves; Return flow; Sands; Scouring**
Scouring at the Toe of a Seawall due to Tsunamis, Hitoshi Nishimura, Akira Watanabe and Kiyoshi Horikawa, 2540
- Secondary waves; Surf; Wave height; Wave period; Waves; Wave spectra; Breaking energy; Ocean waves; Probability density functions; Probability theory**
Probability Density Functions of Breaking Waves, Edward B. Thornton and George Schaeffer, 507
- Sedimentation; Sediments; Sediment transport; Water circulation; Wave energy; Weathering; Estuaries; Littoral deposits; Nicaragua; Rainfall**
Variations of Wave-Energy Levels and Coastal Sedimentation, Eastern Nicaragua, E. H. Owens and H. H. Roberts, 1195
- Sedimentation; Sediment transport; Silting; Suspended sediments; Temperature; Tidal effects; Turbidity; Canada; Dredging; Harbors; Models; Salinity**
Tidal Sedimentation in Gros-CaCouna Harbor, Georges Drapeau and Guy Fortin, 1986
- Sedimentation; Sediment transport; Surveys (data collection); Coastal plains; Evaluation; Geological maps; Littoral deposits; Littoral materials**
A New Method for the Representation of Sedimentary Sequences in Coastal Regions, Hansjorg Streif, 1245
- Sedimentation; Sheet piles; Tidal effects; Trends; Beach erosion; Delaware; Hydraulic models; Inlets (waterways); Jetties**
Case Studies of Delaware's Tidal Inlets: Roosevelt and Indian River Inlets, W. A. Dennie, G. A. Lanan and Robert A. Dalrymple, 1282
- Sedimentation; Tidal hydraulics; Barriers; Beach erosion; Coastal morphology; Delaware; Inlets (waterways); Littoral drift; Marshes; Morphology**
Morphology of Coastal Barriers, Delaware, U.S.A., John C. Kraft, Chacko J. John and Evelyn M. Maurmeyer, 1232

- Sediment concentration; Sediment load; Sediment transport; Two-dimensional; Wave period; Beaches; Littoral current; Models**
Onshore-Offshore Sediment Movement on a Beach, P. Nielsen, I. A. Svendsen and C. Staub, 1475
- Sediment concentration; Sediment transport; Sensors; Storms; Surf; Suspended sediments; Wave period; Littoral deposits**
Storm Induced Periodicities of Suspended Sand Movement, Jay E. Leonard and Benno M. Brenninkmeyer, 1744
- Sediment concentration; Sediment transport; Shallow water; Suspended sediments; Tidal effects; Wave height; Waves; Wave spectrum; Mud; Mud systems**
Suspension and Transportation of Fluid Mud by Solitary-Like Waves, John T. Wells, James M. Coleman and W. J. Wiseman, Jr., 1932
- Sediment concentration; Spoil; Spoil banks; Suspended sediments; Diffusion; Dredging; Dredging; Estuaries; Models; Plumes**
Factors Governing the Distribution of Dredge-Resuspended Sediments, W. Frank Bohlen, 2001
- Sediment concentration; Suspended sediments; Time dependence; Channel beds; Clays; Entrainment; Experimentation; Finite element method**
Concentration of Suspended Clay in Periodic Flow, Akira Watanabe, P. Thimakorn and A. Das Gupta, 1918
- Sediment concentration; Suspended sediments; Wave height; Coastal plains; Littoral deposits; Littoral drift; Littoral zone; Samples**
Sled System for Profiling Suspended Littoral Drift, J. P. Coakley, J. A. Saville, M. Pedrosa and M. Larocque, 1764
- Sediment deposits; Sediment load; Sediment transport; Storms; Water depth; Wave equations; Wave period; Bars (riverine); Beach erosion; Lakes; Nile River Valley; Oceans**
Undulated Bottom Profiles and Onshore-Offshore Transport, Madhav Manohar, 1454
- Sediment deposits; Sediments; Shoaling; Accretion (geomorphology); California; Dredging; Estuaries; Harbor facilities; Harbors; Littoral current; Littoral drift; Littoral materials**
Maintenance of Santa Cruz Harbor, California, U.S.A., Orville T. Magoon and Don C. Baer, 1276
- Sediment deposits; Simulation; Spoil banks; Beaches; Breakwaters; Dredging; Hydraulic models; Inlets (waterways); Jetties; North Carolina**
Coastal Processes at Oregon Inlet, North Carolina, James T. Jarrett, 1257
- Sediment deposits; Soil stabilization; Wind forces; Wind pressure; Airspeed; Beach erosion; Dunes; Erosion control; Fences; Sands**
Using Fences to Create and Stabilise Sand Dunes, Brian B. Willetts and Christopher J. Phillips, 2040
- Sediment deposits; Surf; Tidal effects; Tracers; Wave action; Wave height; Beaches; Breaking energy; Coring; Histograms**
Depth of Disturbance of Sand in Surf Zones, Michael K. Gaughan, 1513
- Sediment deposits; Tidal currents; Tidal effects; Wave energy; West Germany; Beaches; Dispersion; Environmental factors; Georgia; Inlets (waterways); Morphology**
Process-Response Models for Depositional Shorelines: The German and the Georgia Bights, Dag Nummedal and Ian A. Fischer, 1215
- Sediment deposits; Time dependence; Unsteady flow; Water depth; Bed forms; Discharge (water); Dunes; Flow rates**
Time Lag of Dunes for Unsteady Flow Conditions, Horst Nasner, 1801
- Sediment load; Sediments; Sediment transport; Wave action; Wave energy; Waves; Currents (water)**
Sediment Load under Waves and Currents, D. H. Willis, 1626
- Sediment load; Sediment transport; Storms; Water depth; Wave equations; Wave period; Bars (riverine); Beach erosion; Lakes; Nile River Valley; Oceans; Sediment deposits**
Undulated Bottom Profiles and Onshore-Offshore Transport, Madhav Manohar, 1454
- Sediment load; Sediment transport; Two-dimensional; Wave period; Beaches; Littoral current; Models; Sediment concentration**
Onshore-Offshore Sediment Movement on a Beach, P. Nielsen, I. A. Svendsen and C. Staub, 1475
- Sediments; Sediment transport; Littoral current; Littoral drift; Predictions**
The Nearshore Sediment Transport Study, Richard J. Seymour and David B. Duane, 1555
- Sediments; Sediment transport; Shear stress; Surf; Water depth; Littoral deposits; Littoral drift; Littoral materials; Ocean bottom**
Distribution of Sand Transport Rate across a Surf Zone, Toru Sawaragi and Ichiro Deguchi, 1596
- Sediments; Sediment transport; Silting; Wave energy; Experimentation; Littoral current; Littoral drift; Predictions**
Longshore Sediment Transport Data: A Review, Matthew N. Greer and Ole Secher Madsen, 1563
- Sediments; Sediment transport; Storms; Storm surges; Wave energy; Wave period; Wave velocity; Canada; Field tests; Gravity waves; Hurricanes**
Infragravity Waves in Storm Conditions, R. A. Holman, David A. Huntley and A. J. Bowen, 268
- Sediments; Sediment transport; Surf; Wave dispersion; Wave energy; Beaches; Coastal plains; Littoral current; Littoral deposits; Models; Ocean bottom**
A Model Study of Alongshore Sediment Transport Rate, J. W. Kamphuis and J. S. Readshaw, 1656
- Sediments; Sediment transport; Surface waves; Velocity field; Water waves; Wave energy; Ocean bottom; Sands**
Sediment Motion Caused by Surface Water Waves, A. G. Davies and R. H. Wilkinson, 1577

- Sediments; Sediment transport; Water circulation; Wave energy; Weathering; Estuaries; Littoral deposits; Nicaragua; Rainfall; Sedimentation**
Variations of Wave-Energy Levels and Coastal Sedimentation, Eastern Nicaragua, E. H. Owens and H. H. Roberts, 1195
- Sediments; Sediment transport; Wave action; Wave energy; Waves; Currents (water); Sediment load**
Sediment Load under Waves and Currents, D. H. Willis, 1626
- Sediments; Sediment transport; Wave height; Wave period; Beaches; Coastal engineering; Laboratory tests; Movable bed models; Scale effect**
Scale Relations for Equilibrium Beach Profiles, Hideaki Noda, 1531
- Sediments; Shoaling; Accretion (geomorphology); California; Dredging; Estuaries; Harbor facilities; Harbors; Littoral current; Littoral drift; Littoral materials; Sediment deposits**
Maintenance of Santa Cruz Harbor, California, U.S.A., Orville T. Magoon and Don C. Baer, 1276
- Sediments; Spoil; Spoil banks; Beach nourishment; Bottom sediments; Dredges; Dredging; Models**
Importance of Handling Losses to Beach Fill Design, R. D. Hobson and W. R. James, 1873
- Sediments; Structures; Tidal currents; Wave energy; Waves; Coastal engineering; Mathematical models; Mathematics; Mixing; Physics**
Struggle of Physics and Mathematics in Coastal Engineering, H. Lundgren, 13
- Sediments; Water depth; Wave height; Wave period; Accuracy; Beach erosion; Field tests; Laboratory tests; Measurement**
Uses for a Calculated Limit Depth to Beach Erosion, Robert J. Hallermeier, 1493
- Sediment transport; Barriers; Beaches; Breakwaters; Coastal plains; Diffraction; Groins (structures); Jetties; Littoral drift; Numerical analysis; Predictions; Refraction**
Prediction of Beach PlanForms with Littoral Controls, Marc Perlin and Robert G. Dean, 1818
- Sediment transport; Littoral current; Littoral drift; Predictions; Sediments**
The Nearshore Sediment Transport Study, Richard J. Seymour and David B. Duane, 1555
- Sediment transport; Sensors; Storms; Surf; Suspended sediments; Wave period; Littoral deposits; Sediment concentration**
Storm Induced Periodicities of Suspended Sand Movement, Jay E. Leonard and Benno M. Brenninkmeyer, 1744
- Sediment transport; Shallow water; Suspended sediments; Tidal effects; Wave height; Waves; Wave spectrum; Mud; Mud systems; Sediment concentration**
Suspension and Transportation of Fluid Mud by Solitary-Like Waves, John T. Wells, James M. Coleman and W. J. Wiseman, Jr., 1932
- Sediment transport; Shear stress; Surf; Water depth; Littoral deposits; Littoral drift; Littoral materials; Ocean bottom; Sediments**
Distribution of Sand Transport Rate across a Surf Zone, Toru Sawaragi and Ichiro Deguchi, 1596
- Sediment transport; Shear stress; Three-dimensional; Wave height; Waves; Wave tanks; Coastal plains; Currents (water); Ripple marks**
Sediment Transport and Ripples Due to Waves and Currents, Zbigniew Pruszk and Ryszard B. Zeidler, 1638
- Sediment transport; Shingles (beach); Tracers; Beaches; Littoral drift; Metal detectors; Monitoring**
Shingle Tracing by a New Technique, Peter Wright, J. S. Cross and N. B. Webber, 1705
- Sediment transport; Shoaling; Water waves; Wave diffraction; Wave height; Wave period; Wave refraction; Wave velocity; Rip currents**
Rip Currents and Their Causes, Robert A. Dalrymple, 1414
- Sediment transport; Silting; Suspended sediments; Temperature; Tidal effects; Turbidity; Canada; Dredging; Harbors; Models; Salinity; Sedimentation**
Tidal Sedimentation in Gros-CaCouna Harbor, Georges Drapeau and Guy Fortin, 1986
- Sediment transport; Silting; Wave energy; Experimentation; Littoral current; Littoral drift; Predictions; Sediments**
Longshore Sediment Transport Data: A Review, Matthew N. Greer and Ole Secher Madsen, 1563
- Sediment transport; South Carolina; Suspended load; Tidal currents; Tidal effects; Tidal waters; Wind; Discharge (water); Hydrodynamics; Meteorology; Rainfall; Salt marshes**
Hydrodynamics and Sediment Transport in a Salt Marsh Tidal Channel, Larry G. Ward, 1953
- Sediment transport; Storms; Storm surges; Wave energy; Wave period; Wave velocity; Canada; Field tests; Gravity waves; Hurricanes; Sediments**
Infragravity Waves in Storm Conditions, R. A. Holman, David A. Huntley and A. J. Bowen, 268
- Sediment transport; Storms; Water depth; Wave equations; Wave period; Bars (riverine); Beach erosion; Lakes; Nile River Valley; Oceans; Sediment deposits; Sediment load**
Undulated Bottom Profiles and Onshore-Offshore Transport, Madhav Manohar, 1454
- Sediment transport; Storm surges; Tidal effects; Wave height; Bays (topographic features); Friction coefficient (hydraulic); Inlets (waterways); Mathematical models; Numerical analysis**
Numerical Model Investigation of Selected Tidal Inlet-Bay System Characteristics, William N. Seelig and Robert M. Sorensen, 1319
- Sediment transport; Storm surges; Tracers; Wave energy; Beaches; Field tests; Gravel; Littoral current; Littoral deposits; Littoral drift**
Field Experiment on Beach Gravel Transport, Masataro Hattori and Takasuke Suzuki, 1688
- Sediment transport; Surf; Wave dispersion; Wave energy; Beaches; Coastal plains; Littoral current; Littoral deposits; Models; Ocean bottom; Sediments**
A Model Study of Alongshore Sediment Transport Rate, J. W. Kamphuis and J. S. Readshaw, 1656

- Sediment transport; Surface waves; Velocity field; Water waves; Wave energy; Ocean bottom; Sands; Sediments**
 Sediment Motion Caused by Surface Water Waves, A. G. Davies and R. H. Wilkinson, 1577
- Sediment transport; Surveys (data collection); Coastal plains; Evaluation; Geological maps; Littoral deposits; Littoral materials; Sedimentation**
 A New Method for the Representation of Sedimentary Sequences in Coastal Regions, Hansjorg Streif, 1245
- Sediment transport; Suspended load; Suspended sediments; Tidal effects; Wave action; Wave energy; Wave period; Waves; Currents (water); Field tests; Sands**
 Effect of Waves on Sand Transport by Currents, Michael W. Owen and Michael F.C. Thorn, 1675
- Sediment transport; Time factors; Coastal structures; Currents (water); Jetties; Numerical analysis; Ocean bottom; Scouring**
 A Numerical Model for Sediment Transport, J. P. Lepetit and A. Hauguel, 1715
- Sediment transport; Tracers; Wave height; Barriers; Islands (landforms); Littoral current; Littoral deposits; Littoral drift; Littoral materials**
 Littoral Drift along Bayshore of a Barrier Island, Yu-Hwa Hwang and T. H. Chang, 1614
- Sediment transport; Two-dimensional; Wave period; Beaches; Littoral current; Models; Sediment concentration; Sediment load**
 Onshore-Offshore Sediment Movement on a Beach, P. Nielsen, I. A. Svendsen and C. Staub, 1475
- Sediment transport; Vehicles; Wave action; Calibration; California; Instrumentation; Performance; Profile measurement; Sand**
 Tracked Vehicle for Continuous Nearshore Profiles, Richard J. Seymour, Alan L. Higgins and David P. Botham, 1542
- Sediment transport; Water circulation; Wave energy; Weathering; Estuaries; Littoral deposits; Nicaragua; Rainfall; Sedimentation; Sediments**
 Variations of Wave-Energy Levels and Coastal Sedimentation, Eastern Nicaragua, E. H. Owens and H. H. Roberts, 1195
- Sediment transport; Wave action; Wave energy; Waves; Currents (water); Sediment load; Sediments**
 Sediment Load under Waves and Currents, D. H. Willis, 1626
- Sediment transport; Wave diffraction; Wave height; Wave phases; Bathymetry; Bays (topographic features); Beach erosion; Beaches; Breakwaters; Diffraction**
 Diffraction Calculation of Shoreline PlanForms, Robert G. Dean, 1903
- Sediment transport; Wave height; Wave period; Beaches; Coastal engineering; Laboratory tests; Movable bed models; Scale effect; Sediments**
 Scale Relations for Equilibrium Beach Profiles, Hideaki Noda, 1531
- Sediment transport; Waves; Breakwaters; Japan; Land reclamation; Littoral current; Littoral drift; Movable bed models; Ocean bottom**
 Estimation Using a Movable Bed Model of Shoreline Change Caused by a Reclamation Projected into the Sea, Shoji Sato and Hiroaki Ozasa, 1839
- Seismic design; Settlement (structural); Slope stability; Acceleration; Damage; Earthquake loads; Earthquake resistant structures; Loading; Rubble-mound breakwaters**
 Loadings on Rubble-Mound Breakwaters due to Earthquakes, H. Wang, C. Y. Yang, C. Lamison and S. S. Chen, 2244
- Sensors; Storms; Surf; Suspended sediments; Wave period; Littoral deposits; Sediment concentration; Sediment transport**
 Storm Induced Periodicities of Suspended Sand Movement, Jay E. Leonard and Benno M. Brennknecher, 1744
- Settlement (structural); Slope stability; Acceleration; Damage; Earthquake loads; Earthquake resistant structures; Loading; Rubble-mound breakwaters; Seismic design**
 Loadings on Rubble-Mound Breakwaters due to Earthquakes, H. Wang, C. Y. Yang, C. Lamison and S. S. Chen, 2244
- Sewage effluents; Statistical analysis; Time series analysis; Waste disposal; Coastal plains; Diffusion; Dispersion; Mathematical models; Outfall sewers**
 Outfall Diffusion Models for the Coastal Zone, D. C.L. Lam and C. R. Murthy, 2584
- Shallow water; Standing waves; Tests; Wave diffraction; Wave energy; Wave height; Wavelength; Wave tanks; Breakwaters; Permeability**
 Wave Height Distribution Around Permeable Breakwaters, Shintaro Hotta, 695
- Shallow water; Standing waves; Tidal flats; Tidal hydraulics; Dispersion; Estuaries; Mixing; Model studies; Saline water-freshwater interfaces**
 Longitudinal Dispersion in Shallow Well-Mixed Estuaries, J. Dronkers, 2761
- Shallow water; Storm surges; Temperature; Water depth; Water levels; Air water interactions; Air-water interfaces; Forecasting**
 Storm Surge Forecasting Methods in Enclosed Seas, P. F. Hamblin, 998
- Shallow water; Suspended sediments; Tidal effects; Wave height; Waves; Wave spectrum; Mud; Mud systems; Sediment concentration; Sediment transport**
 Suspension and Transportation of Fluid Mud by Solitary-Like Waves, John T. Wells, James M. Coleman and W. J. Wiseman, Jr., 1932
- Shallow water; Tidal effects; Turbulence; Estuaries; Flood routing; Hydraulic models; Hydrodynamics; Numerical analysis; Rivers**
 Hydrodynamic Modelling of the Southern North Sea, David Prandle, 1122
- Shallow water; Water depth; Aerial photography; Bathymetry; Color photography; Images; Remote sensing**
 Visible-Region Photographic Remote Sensing of Nearshore Waters, Tsuguo Sunamura and Kiyoshi Horikawa, 1439

- Shallow water; Water depth; Wave action; Wave diffraction; Wavelength; Wave propagation; Wave reflection; Wave refraction; Mathematical models**
 Computations of Short Waves in Shallow Water, M. B. Abbott, H. M. Petersen and Ove Skovgaard, 414
- Shallow water; Water depth; Wave energy; Beach erosion; Littoral current; Littoral deposits; Littoral drift**
 Vocooidal Theory for All Non-Breaking Waves, D. H. Swart and C. C. Loubser, 467
- Shallow water; Wave height; Bores (wave); Breaking energy; Energy dissipation; Energy losses; Predictions; Random processes**
 Energy Loss and Set-Up Due to Breaking of Random Waves, J. A. Battjes and J. P.F.M. Janssen, 569
- Shallow water; Waves; Wind pressure; Field tests; Laboratory tests; Ocean bottom; Oscillation; Ripple marks**
 On the Geometry of Ripples Due to Waves, M. S. Yalin and E. Karahan, 1776
- Shape; Silting; Underwater structures; Wave attenuation; Barriers; Breakwaters; India; Performance**
 Performance Characteristics of Submerged Breakwaters, J. Dattatri, H. Raman and N. Jothi Shankar, 2153
- Shear flow; Water depth; Wave action; Wave height; Wavelength; Wave period; Wave refraction; Refraction (water waves)**
 Wave Refraction Across a Shearing Current, Ivar G. Jonsson and Ove Skovgaard, 722
- Shear stress; Surf; Water depth; Littoral deposits; Littoral drift; Littoral materials; Ocean bottom; Sediments; Sediment transport**
 Distribution of Sand Transport Rate across a Surf Zone, Toru Sawaragi and Ichiro Deguchi, 1596
- Shear stress; Three-dimensional; Wave height; Waves; Wave tanks; Coastal plains; Currents (water); Ripple marks; Sediment transport**
 Sediment Transport and Ripples Due to Waves and Currents, Zbigniew Pruszk and Ryszard B. Zeidler, 1638
- Shear stress; Turbulent flow; Velocity distribution; Wave propagation; Wave velocity; Boundary conditions; Mathematical models; Sand**
 Near-Bottom Velocities in Waves with a Current, W. T. Bakker and Th. van Doorn, 1394
- Sheet piles; Tidal effects; Trends; Beach erosion; Delaware; Hydraulic models; Inlets (waterways); Jetties; Sedimentation**
 Case Studies of Delaware's Tidal Inlets: Roosevelt and Indian River Inlets, W. A. Dennie, G. A. Lanan and Robert A. Dalrymple, 1282
- Shingles (beach); Tracers; Beaches; Littoral drift; Metal detectors; Monitoring; Sediment transport**
 Shingle Tracing by a New Technique, Peter Wright, J. S. Cross and N. B. Webber, 1705
- Shipping; Shore protection; Storms; Tidal currents; West Germany; Dikes; Estuaries; Ports**
 Welcoming Address — II, Helga Elstner, 4
- Shoaling; Accretion (geomorphology); California; Dredging; Estuaries; Harbor facilities; Harbors; Littoral current; Littoral drift; Littoral materials; Sediment deposits; Sediments**
 Maintenance of Santa Cruz Harbor, California, U.S.A., Orville T. Magoon and Don C. Baer, 1276
- Shoaling; Water waves; Wave diffraction; Wave height; Wave period; Wave refraction; Wave velocity; Rip currents; Sediment transport**
 Rip Currents and Their Causes, Robert A. Dalrymple, 1414
- Shore-line cover; Beach erosion; Breakwaters; Coastal structures; Erosion control; Littoral zone; Marine terminals; Piers; Rubble-mound breakwaters; Sands**
 Coastal Structures' Effects on Shorelines, Ronald M. Noble, 2069
- Shore-line cover; Wave diffraction; Wave refraction; Wind loads; Accretion (geomorphology); Beach nourishment; Erosion; Groins (structures); Mathematical models; Rip currents**
 Mathematical Modeling of Shoreline Evolution, Bernard Le Mehaute and Mills Soldate, 1163
- Shore protection; Spoil; Spoil banks; Beach erosion; Beach nourishment; Dredging; Groins (structures); Sea walls**
 Some Facts and Fancies about Beach Erosion, Richard Sylvester, 1888
- Shore protection; Statistical analysis; Wave height; Wave period; Coastal plains; Confidence level; Ocean waves; Probability distribution functions**
 On Long-Term Statistics for Ocean and Coastal Waves, Michel K. Ochi, 59
- Shore protection; Storms; Tidal currents; West Germany; Dikes; Estuaries; Ports; Shipping**
 Welcoming Address — II, Helga Elstner, 4
- Shore protection; Storm surges; Beach erosion; Dunes; Erosion; Movable bed models; Ripple marks; Sands; Scale effect**
 Movable Bed Model Tests on Dune Erosion, P. Vellinga, 2020
- Shore protection; Storm surges; Surf; Water levels; Wave energy; Wave recorders (water waves); Wave runup; Coastal plains; Dynamic loads**
 Wave Set-Up in the Surf Zone, Uwe A. Hansen, 1071
- Shore protection; Storm surges; West Germany; Coastal plains; History**
 Welcoming Address — I, Karl-Edward Naumann, 1
- Shore protection; Tidal currents; Wave action; Wave energy; Wave refraction; Coastal plains; Dredging; Gravel; Great Britain; Licensing; Littoral drift; Sand**
 The Effect of Offshore Dredging on Coastlines, W. A. Price, J. M. Motyka and L. J. Jeffrey, 1347
- Shore protection; Water depth; Bathymetry; Beach erosion; Beach nourishment; Morphology; Sands**
 Morphologic Effects of Westerland Beach Nourishment 1972, Dieter Wenzel, 1859

- Shore protection; Wave energy; Wave reflection; Beach erosion; Coastal structures; Dikes; Erosion control; Japan; Land reclamation; Scouring; Sea walls**
Effectiveness of Seadikes with Rough Slope, Osamu Toyoshima, 2528
- Shore protection; Wave height; Wave period; Wave spectra; Correlation techniques; Ocean waves; Offshore structures**
The Observed Joint Distribution of Periods and Heights of Sea Waves, Yoshimi Goda, 227
- Shores; Stresses; Surf; Water circulation; Wave energy; Wave propagation; Waves; Barriers; Friction coefficient (hydraulic); Littoral current**
Longshore Currents Due to Surf Zone Barrier, P. Bettess, C. A. Fleming, J. C. Heinrich, O. C. Zienkiewicz and D. I. Austin, 776
- Silting; Suspended sediments; Temperature; Tidal effects; Turbidity; Canada; Dredging; Harbors; Models; Salinity; Sedimentation; Sediment transport**
Tidal Sedimentation in Gros-CaCouna Harbor, Georges Drapeau and Guy Fortin, 1986
- Silting; Underwater structures; Wave attenuation; Barriers; Breakwaters; India; Performance; Shape**
Performance Characteristics of Submerged Breakwaters, J. Dattatari, H. Raman and N. Jothi Shankar, 2153
- Silting; Wave energy; Experimentation; Littoral current; Littoral drift; Predictions; Sediments; Sediment transport**
Longshore Sediment Transport Data: A Review, Matthew N. Greer and Ole Secher Madsen, 1563
- Simulation; Spoil banks; Beaches; Breakwaters; Dredging; Hydraulic models; Inlets (waterways); Jetties; North Carolina; Sediment deposits**
Coastal Processes at Oregon Inlet, North Carolina, James T. Jarrett, 1257
- Simulation; Storm surges; Texas; Tidal effects; Tsunamis; Water levels; Coastal plains; Cost effectiveness; Floods; Hurricanes; Numerical analysis; Predictions**
Coastal Flood Simulation in Stretched Coordinates, H. Lee Butler, 1030
- Simulation; Storm surges; Water levels; Wind forces; Forecasting; Mathematical models; Meteorological data; Meteorology; Numerical analysis; Predictions**
Numerical Storm Surge Forecasting, Manfred Engel, 975
- Simulation; Tidal hydraulics; Estuaries; Hydraulic models; Mathematical models; Model studies; Numerical analysis; Saline water intrusion; Salinity**
Numerical Tidal-Salinity Models of the Ems Estuary, Karsten Fischer, 2840
- Simulation; Tidal hydraulics; Water circulation; Wind loads; Bays (topographic features); Currents (water); Diffusion; Eddies; Environmental factors**
Characteristics of Circulation in Bay Waters due to Wind Action, Akira Wada and Ioshihito Miyaake, 2730
- Simulation; Wave damping; Wave energy; Wave period; Wave pressure; Wind loads; Wind pressure; Dynamic response; Oscillation; Responses**
Simulation of Wave/Wind Forced Harbor Oscillation, S. K. Liu, H. S. Hou and Charles C.C. Chang, 2551
- Site selection; Storm surges; Tidal effects; Tidal waters; Wave height; Wave period; Australia; Breakwaters; Maintenance**
Rosslyn Bay Breakwater, Queensland, Australia, D. N. Foster, B. L. McGrath and W. Bremner, 2086
- Site selection; Thermal energy; Waves; Wind; Currents (water); Design criteria; Energy conversion; Environmental effects; Environmental impact statements; Hurricanes**
Some Design Criteria for OTEC Installations for Keahole Point, Hawaii, Frederick C. Munchmeyer and Charles L. Bretschneider, 2633
- Slope; Velocity; Waves; Wave velocity; Beaches; Breaking energy; Deep water; Particle trajectories**
Estimation of Water Particle Velocity of Breaking Wave, Tetsuo Sakai and Yuichi Iwagaki, 551
- Slopes; Tsunamis; Two-dimensional; Water depth; Wave energy; Waves; Ocean bottom; Ocean waves; Return flow; Sands; Scouring; Sea walls**
Scouring at the Toe of a Seawall due to Tsunamis, Hitoshi Nishimura, Akira Watanabe and Kiyoshi Horikawa, 2540
- Slopes; Water depth; Wave height; Wavelength; Wave period; Waves; Wave tanks; Wave velocity; Beaches; Random processes**
Wave Length, Wave Velocity and Shoaling Characteristics of Random Waves, Akira Kimura and Yuichi Iwagaki, 320
- Slope stability; Acceleration; Damage; Earthquake loads; Earthquake resistant structures; Loading; Rubble-mound breakwaters; Seismic design; Settlement (structural)**
Loadings on Rubble-Mound Breakwaters due to Earthquakes, H. Wang, C. Y. Yang, C. Lamison and S. S. Chen, 2244
- Slope stability; Stability; Standardization; Test reproducibility; Tests; Armoring (streambed); Breakwaters; Density; Flumes**
Dolos Packing Density and Effect of Relative Block Density, J. A. Zwiarnborn, 2285
- Slope stability; Stability; Wave energy; Wave height; Armoring (streambed); Breakwaters; Rubble-mound breakwaters**
Dolos-Armored Breakwaters: Special Consideration, Robert D. Carver and D. Donald Davidson, 2263
- Slope stability; Stability; Wave energy; Wave pressure; Armoring (streambed); Costs; Revetments; Rubble-mound breakwaters**
Blanket Theory and Low Cost Revetments, C. T. Brown, 2510
- Slots; Standing waves; Storms; Storm surges; Wave height; Wave period; Wave pressure; Wave reflection; Breakwaters**
Wave Pressures on Split-Type Breakwaters, Shoshichiro Nagai and Shohachi Kakuno, 2360

- Soil stabilization; Wind forces; Wind pressure; Airspeed; Beach erosion; Dunes; Erosion control; Fences; Sands; Sediment deposits**
Using Fences to Create and Stabilise Sand Dunes, Brian B. Willetts and Christopher J. Phillips, 2040
- South Carolina; Suspended load; Tidal currents; Tidal effects; Tidal waters; Wind; Discharge (water); Hydrodynamics; Meteorology; Rainfall; Salt marshes; Sediment transport**
Hydrodynamics and Sediment Transport in a Salt Marsh Tidal Channel, Larry G. Ward, 1953
- Spacing; Surf; Wave action; Waves; Wave velocity; Coastal plains; Eigenvalues; Mass; Momentum; Offshore structures; Rip currents**
Rip Current Spacing as an Eigenvalue, Noriyuki Iwata, 828
- Spectral analysis; Surf; Wave action; Wave height; Wave period; Waves; Coral reefs and islands; Energy; Probability density functions**
The Energy Spectra of Surf Waves on a Coral Reef, Theodore T. Lee and Kerry P. Black, 588
- Spectral analysis; Wave spectra; Calculations; Fourier transformation; Interactions; Nonlinear systems; Sampling**
Higher Order Wave Spectra, Paul C. Liu and Albert W. Green, 360
- Spectral energy distribution; Time dependence; Water levels; Wave diffraction; Wave energy; Cylindrical bodies; Diffraction; Particle trajectories**
Wave Forces Induced by Irregular Waves on a Vertical Circular Cylinder, Hajime Ishida and Yuichi Iwagaki, 2397
- Spectrum analysis; Tidal effects; Tides; Two-dimensional; Wave damping; Waves; Computation; Damping**
A New Approach for Tidal Computations, C. Le Provost, 1104
- Spoil; Spoil banks; Beach erosion; Beach nourishment; Dredging; Groins (structures); Sea walls; Shore protection**
Some Facts and Fancies about Beach Erosion, Richard Sylvester, 1888
- Spoil; Spoil banks; Beach nourishment; Bottom sediments; Dredges; Dredging; Models; Sediments**
Importance of Handling Losses to Beach Fill Design, R. D. Hobson and W. R. James, 1873
- Spoil; Spoil banks; Suspended sediments; Diffusion; Dredges; Dredging; Estuaries; Models; Plumes; Sediment concentration**
Factors Governing the Distribution of Dredge-Resuspended Sediments, W. Frank Bohlen, 2001
- Spoil banks; Beach erosion; Beach nourishment; Dredging; Groins (structures); Sea walls; Shore protection; Spoil**
Some Facts and Fancies about Beach Erosion, Richard Sylvester, 1888
- Spoil banks; Beaches; Breakwaters; Dredging; Hydraulic models; Inlets (waterways); Jetties; North Carolina; Sediment deposits; Simulation**
Coastal Processes at Oregon Inlet, North Carolina, James T. Jarrett, 1257
- Spoil banks; Beach nourishment; Bottom sediments; Dredges; Dredging; Models; Sediments; Spoil**
Importance of Handling Losses to Beach Fill Design, R. D. Hobson and W. R. James, 1873
- Spoil banks; Suspended sediments; Diffusion; Dredges; Dredging; Estuaries; Models; Plumes; Sediment concentration; Spoil**
Factors Governing the Distribution of Dredge-Resuspended Sediments, W. Frank Bohlen, 2001
- Stability; Standardization; Test reproducibility; Tests; Armoring (streambed); Breakwaters; Density; Flumes; Slope stability**
Dolos Packing Density and Effect of Relative Block Density, J. A. Zwamborn, 2285
- Stability; Wave energy; Wave height; Armoring (streambed); Breakwaters; Rubble-mound breakwaters; Slope stability**
Dolos-Armored Breakwaters: Special Consideration, Robert D. Carver and D. Donald Davidson, 2263
- Stability; Wave energy; Wave height; Wave spectra; Wave tanks; Breakwaters; Damage; Hydraulic models; Rubble-mound breakwaters**
Effects of Wave Grouping on Breakwater Stability, R. R. Johnson, E. P.D. Mansard and J. Ploeg, 2228
- Stability; Wave energy; Wave pressure; Armoring (streambed); Costs; Revetments; Rubble-mound breakwaters; Slope stability**
Blanket Theory and Low Cost Revetments, C. T. Brown, 2510
- Stability analysis; Tidal currents; Tidal flats; Tides; Two-dimensional; Water depth; Boundary conditions; Forecasting; Morphology**
Two-Dimension Stability Analysis of Tidal Basins and Tidal Flats of Larger Extent, Eberhard Renger, 1971
- Standardization; Test reproducibility; Tests; Armoring (streambed); Breakwaters; Density; Flumes; Slope stability; Stability**
Dolos Packing Density and Effect of Relative Block Density, J. A. Zwamborn, 2285
- Standardization; Test reproducibility; Tests; Turbulent flow; Wave period; Wave refraction; Armoring (streambed); Open channel flow; Performance**
Performance of Dolos Blocks in an Open Channel Situation, Arthur Brebner, 2305
- Standing waves; Storms; Storm surges; Wave height; Wave period; Wave pressure; Wave reflection; Breakwaters; Slots**
Wave Pressures on Split-Type Breakwaters, Shoshichiro Nagai and Shohachi Kakuno, 2360
- Standing waves; Storm surges; Wave energy; Wave pressure; Barriers; Impact; Marine structures; Mathematical models; Pressure distribution; Scale effect**
A Model Law for Wave Impacts on Coastal Structures, C. Ramkema, 2308
- Standing waves; Tests; Wave diffraction; Wave energy; Wave height; Wavelength; Wave tanks; Breakwaters; Permeability; Shallow water**
Wave Height Distribution Around Permeable Breakwaters, Shintaro Hotta, 695

- Standing waves; Tidal flats; Tidal hydraulics; Dispersion; Estuaries; Mixing; Model studies; Saline water-freshwater interfaces; Shallow water**
Longitudinal Dispersion in Shallow Well-Mixed Estuaries, J. Dronkers, 2761
- Standing waves; Water depth; Waves; Wave tanks; Beaches; Edge effect; Excitation; Interactions**
Excitation of Low Frequency Trapped Waves, Robert King and Ronald Smith, 449
- Statistical analysis; Storm surges; Tides; Beaches; Coastal plains; Probability; Probability distribution functions; Sea level**
Extreme Sea Levels from Tide and Surge Probability, D. T. Pugh and J. M. Vassie, 911
- Statistical analysis; Stress; Surf; Wave spectra; Wave velocity; Wind velocity; Littoral current; Predictions; Regression analysis**
Wind-Generated Longshore Currents, Dag Nummedal and Robert J. Finley, 1428
- Statistical analysis; Tidal waters; Water levels; Frequencies; Great Britain; Ports; Sampling; Sea level**
Analysis of Maximum Sea Level in Southern England, J. Graff and D. L. Blackman, 931
- Statistical analysis; Time series analysis; Waste disposal; Coastal plains; Diffusion; Dispersion; Mathematical models; Outfall sewers; Sewage effluents**
Outfall Diffusion Models for the Coastal Zone, D. C.L. Lam and C. R. Murthy, 2584
- Statistical analysis; Wave height; Wave period; Coastal plains; Confidence level; Ocean waves; Probability distribution functions; Shore protection**
On Long-Term Statistics for Ocean and Coastal Waves, Michel K. Ochi, 59
- Statistical analysis; Wave height; Wave period; Wave runup; Wave spectra; Damage; Dikes; Hydrodynamics**
New Dike Design Criteria Based on Wave Spectra, Hans Kaldenhoff and Suhan M. Gokcesu, 2500
- Statistical analysis; Wave height; Wave recorders (water waves); Forecasting; Hawaii; Meteorological data; Meteorology**
An Evaluation of Extreme Wave Climate at Keahole Point, Hawaii, Charles L. Bretschneider and Richard E. Rocheleau, 152
- Stochastic processes; Wave generation; Wave height; Wavelength; Waves; Wave spectra; Wave tanks; Hydrodynamic pressure; Numerical analysis**
An Inclined-Plate Wave Generator, Fredric Raichlen and Jiin-Jen Lee, 388
- Stochastic processes; Wave generation; Wave spectra; Dynamic pressure; Frequencies; Hydrodynamic pressure; Responses**
Analysis of Hinged Wavemakers for Random Waves, Robert T. Hudspeth, Douglas F. Jones and John H. Nath, 372
- Storms; Storm surges; Surveys (data collection); Tidal hydraulics; Water levels; Barriers; Boundary conditions; Netherlands; Responses**
A Tidal Survey for a Model of an Offshore Area, W. J. van de Ree, J. Voogt and J. J. Leendertse, 2656
- Storms; Storm surges; Tidal waters; Water levels; Waterways (transportation); West Germany; Economic analysis; Environmental factors; Financing**
Welcoming Address — III, Volker Hauff, 7
- Storms; Storm surges; Wave energy; Wave period; Wave velocity; Canada; Field tests; Gravity waves; Hurricanes; Sediments; Sediment transport**
Infragravity Waves in Storm Conditions, R. A. Holman, David A. Huntley and A. J. Bowen, 268
- Storms; Storm surges; Wave height; Wave period; Wave pressure; Wave reflection; Breakwaters; Slots; Standing waves**
Wave Pressures on Split-Type Breakwaters, Shoshichiro Nagai and Shohachi Kakuno, 2360
- Storms; Surf; Suspended sediments; Wave period; Littoral deposits; Sediment concentration; Sediment transport; Sensors**
Storm Induced Periodicities of Suspended Sand Movement, Jay E. Leonard and Benno M. Brenninkmeyer, 1744
- Storms; Surf; Water circulation; Water levels; Wave height; Waves; Wind; Bathymetry; Bores (wave); Field tests; Littoral current; Model tests**
Comparison of Model and Observed Nearshore Circulation, James H. Allender, John D. Ditmars, Wyman Harrison and Robert A. Paddock, 810
- Storms; Tidal currents; Wave action; Wave height; Wave runup; Waves; Wave spectra; Wind velocity; Estuaries; Reefs**
Analysis of Storm Tide Waves, Volker Barthel, 1016
- Storms; Tidal currents; West Germany; Dikes; Estuaries; Ports; Shipping; Shore protection**
Welcoming Address — II, Helga Elstner, 4
- Storms; Water depth; Wave equations; Wave period; Bars (riverine); Beach erosion; Lakes; Nile River Valley; Oceans; Sediment deposits; Sediment load; Sediment transport**
Undulated Bottom Profiles and Onshore-Offshore Transport, Madhav Manohar, 1454
- Storms; Wavelength; Wave propagation; Wind; Wind speed; Hurricanes; Mathematical models; Models; Numerical analysis; Radar operation**
Radar Observations of Hurricane Wave Directions, B. D. King and O. H. Shemdin, 209
- Storm surges; Beach erosion; Dunes; Erosion; Movable bed models; Ripple marks; Sands; Scale effect; Shore protection**
Movable Bed Model Tests on Dune Erosion, P. Vellinga, 2020
- Storm surges; Surf; Water levels; Wave action; Wave dispersion; Wave period; Fourier transformation; Gravity waves**
Anomalous Dispersion of Fourier Components of Surface Gravity Waves in the Near Shore Area, Fritz Busching, 247
- Storm surges; Surf; Water levels; Wave energy; Wave recorders (water waves); Wave runup; Coastal plains; Dynamic loads; Shore protection**
Wave Set-Up in the Surf Zone, Uwe A. Hansen, 1071

- Storm surges; Surveys (data collection); Tidal hydraulics; Water levels; Barriers; Boundary conditions; Netherlands; Responses; Storms**
A Tidal Survey for a Model of an Offshore Area, W. J. van de Ree, J. Voogt and J. J. Leendertse, 2656
- Storm surges; Temperature; Water depth; Water levels; Air water interactions; Air-water interfaces; Forecasting; Shallow water**
Storm Surge Forecasting Methods in Enclosed Seas, P. F. Hamblin, 998
- Storm surges; Temperature effects; Thermal pollution; Tidal effects; Tidal hydraulics; Cooling water; Discharge (water); Model studies; Rivers**
Influence on Temperature Increases in Tidal Rivers Caused by Waste Heat Injections with Respect to Tidal Cycles and Storm Surges, Horst Schwarze and Wilfried Falldorf, 2915
- Storm surges; Texas; Tidal effects; Tsunamis; Water levels; Coastal plains; Cost effectiveness; Floods; Hurricanes; Numerical analysis; Predictions; Simulation**
Coastal Flood Simulation in Stretched Coordinates, H. Lee Butler, 1030
- Storm surges; Tidal currents; Tidal effects; Tidal energy; Tide gages; Wind; Wind velocity; Forecasting; Predictions**
Storm Surge Prediction by Combined Wind and Tide Data, Hermann Christiansen and Winfried Siefert, 965
- Storm surges; Tidal effects; Tidal energy; Tide gages; Dynamics; Estuaries; Forecasting; Predictions**
Storm Surge Prediction in Tidal Rivers: A New Conception, Winfried Siefert, 986
- Storm surges; Tidal effects; Tidal waters; Wave height; Wave period; Australia; Breakwaters; Maintenance; Site selection**
Rosslyn Bay Breakwater, Queensland, Australia, D. N. Foster, B. L. McGrath and W. Bremner, 2086
- Storm surges; Tidal effects; Wave height; Bays (topographic features); Friction coefficient (hydraulic); Inlets (waterways); Mathematical models; Numerical analysis; Sediment transport**
Numerical Model Investigation of Selected Tidal Inlet-Bay System Characteristics, William N. Seelig and Robert M. Sorensen, 1319
- Storm surges; Tidal waters; Water levels; Waterways (transportation); West Germany; Economic analysis; Environmental factors; Financing; Storms**
Welcoming Address — III, Volker Hauff, 7
- Storm surges; Tides; Beaches; Coastal plains; Probability; Probability distribution functions; Sea level; Statistical analysis**
Extreme Sea Levels from Tide and Surge Probability, D. T. Pugh and J. M. Vassie, 911
- Storm surges; Tracers; Wave energy; Beaches; Field tests; Gravel; Littoral current; Littoral deposits; Littoral drift; Sediment transport**
Field Experiment on Beach Gravel Transport, Masataro Hattori and Takasuke Suzuki, 1688
- Storm surges; Water levels; Wind forces; Forecasting; Mathematical models; Meteorological data; Meteorology; Numerical analysis; Predictions; Simulation**
Numerical Storm Surge Forecasting, Manfred Engel, 975
- Storm surges; Wave energy; Wave period; Wave velocity; Canada; Field tests; Gravity waves; Hurricanes; Sediments; Sediment transport; Storms**
Infragravity Waves in Storm Conditions, R. A. Holman, David A. Huntley and A. J. Bowen, 268
- Storm surges; Wave energy; Wave pressure; Barriers; Impact; Marine structures; Mathematical models; Pressure distribution; Scale effect; Standing waves**
A Model Law for Wave Impacts on Coastal Structures, C. Ramkema, 2308
- Storm surges; Wave height; Wave period; Wave pressure; Wave reflection; Breakwaters; Slots; Standing waves; Storms**
Wave Pressures on Split-Type Breakwaters, Shoshichiro Nagai and Shohachi Kakuno, 2360
- Storm surges; West Germany; Coastal plains; Damage; Ocean waves; Recreational facilities**
Welcoming Address — IV, Hans-Werner Partenscky, 10
- Storm surges; West Germany; Coastal plains; History; Shore protection**
Welcoming Address — I, Karl-Edward Naumann, 1
- Storm surges; West Germany; Wind forces; Wind pressure; Wind velocity; Coastal engineering; Flooding; Frequencies; Probability**
Frequencies and Probabilities of Extreme Storm Surges (On the Time-Dependent Changes of the Probability of Extreme Storm Floods at the German North Sea Coast), Alfred Fohrboter, 949
- Stratified flow; Tidal currents; Tidal hydraulics; Water quality; Estuaries; Saline water-freshwater interfaces; Saline water intrusion; Salinity**
Stability Study of an Artificial Salt Intrusion in Estuaries, C. Marche, 2798
- Stratified flow; Two phase flow; Water flow; Density; Friction coefficient (hydraulic); Open channel flow; Saline water-freshwater interfaces; Salinity**
Interfacial Friction Coefficients in a Two-Layered Stratified Flow, Emmanouel Partheniades and Vassilios Dermisiss, 2778
- Stream flow; Stream gages; Tidal currents; Tidal effects; Water levels; Estuaries; Groins (structures); Navigable canals**
Improvements on Tidal Estuaries and the Effects on Tidal Current, Hermann Harten, 2905
- Stream flow; Velocity distribution; Vortices; Wave energy; Bed roughness; Estuaries; Mixing; Rivers; Saline water-freshwater interfaces; Salinity**
Outflow Dynamics at a River Mouth, Masakazu Kashiwamura and Shizuo Yoshida, 2925
- Stream gages; Tidal currents; Tidal effects; Water levels; Estuaries; Groins (structures); Navigable canals; Stream flow**
Improvements on Tidal Estuaries and the Effects on Tidal Current, Hermann Harten, 2905
- Stress; Surf; Wave spectra; Wave velocity; Wind velocity; Littoral current; Predictions; Regression analysis; Statistical analysis**
Wind-Generated Longshore Currents, Dag Nummedal and Robert J. Finley, 1428

- Stresses; Surf; Water circulation; Wave energy; Wave propagation; Waves; Barriers; Friction coefficient (hydraulic); Littoral current; Shores**
 Longshore Currents Due to Surf Zone Barrier, P. Bettess, C. A. Fleming, J. C. Heinrich, O. C. Zienkiewicz and D. I. Austin, 776
- Stress measurement; Tidal currents; Tidal flats; Velocity; Wave action; Wave velocity; Flooding; Flowmeters; Inlets (waterways)**
 Velocity and Stress Measurements in a Tidal Inlet, David A. Huntley and Dag Nummedal, 1320
- Structures; Tidal currents; Wave energy; Waves; Coastal engineering; Mathematical models; Mathematics; Mixing; Physics; Sediments**
 Struggle of Physics and Mathematics in Coastal Engineering, H. Lundgren, 13
- Surf; Surface waves; Turbulence; Vibration; Wave action; Wave energy; Wave equations; Wave height; Wave propagation; Waves**
 Wave Characteristics in the Surf Zone, I. A. Svendsen, P. A. Madsen and J. Buhr Hansen, 520
- Surf; Suspended sediments; Water sampling; Wave height; Wave period; Waves; Wind velocity; Beaches; Littoral current; Measurement**
 Surf Zone Measurements of Suspended Sediment, Timothy W. Kana, 1725
- Surf; Suspended sediments; Wave period; Littoral deposits; Sediment concentration; Sediment transport; Sensors; Storms**
 Storm Induced Periodicities of Suspended Sand Movement, Jay E. Leonard and Benno M. Brenninkmeyer, 1744
- Surf; Temperature effects; Thermal pollution; Tracers; Turbulent flow; Currents (water); Heated water; Jet flow; Mixing; Plumes**
 Mixing of Heated Water Discharged in the Surf Zone, Kiyoshi Horikawa, Ming-Chung Lin and Tamio O. Sasaki, 2563
- Surf; Temporal distribution; Variations; Wave spectra; Edge effect; Gravity waves; Littoral current; Rip currents**
 Variability of Longshore Currents, R. T. Guza and Edward B. Thornton, 756
- Surf; Tidal effects; Tracers; Wave action; Wave height; Beaches; Breaking energy; Coring; Histograms; Sediment deposits**
 Depth of Disturbance of Sand in Surf Zones, Michael K. Gaughan, 1513
- Surf; Turbulence; Wave dispersion; Wave energy; Wave height; Wave reflection; Beaches; Littoral current; Littoral deposits; Littoral drift**
 Morphodynamic Variability of High-Energy Beaches, Lynn Donelson Wright, B. G. Thom and John Chappell, 1180
- Surf; Water circulation; Water levels; Wave height; Waves; Wind; Bathymetry; Bores (wave); Field tests; Littoral current; Model tests; Storms**
 Comparison of Model and Observed Nearshore Circulation, James H. Allender, John D. Ditmars, Wyman Harrison and Robert A. Paddock, 810
- Surf; Water circulation; Wave energy; Wave propagation; Waves; Barriers; Friction coefficient (hydraulic); Littoral current; Shores; Stresses**
 Longshore Currents Due to Surf Zone Barrier, P. Bettess, C. A. Fleming, J. C. Heinrich, O. C. Zienkiewicz and D. I. Austin, 776
- Surf; Water depth; Littoral deposits; Littoral drift; Littoral materials; Ocean bottom; Sediments; Sediment transport; Shear stress**
 Distribution of Sand Transport Rate across a Surf Zone, Toru Sawaragi and Ichiro Deguchi, 1596
- Surf; Water levels; Wave action; Wave dispersion; Wave period; Fourier transformation; Gravity waves; Storm surges**
 Anomalous Dispersion of Fourier Components of Surface Gravity Waves in the Near Shore Area, Fritz Busching, 247
- Surf; Water levels; Wave energy; Wave recorders (water waves); Wave runoff; Coastal plains; Dynamic loads; Shore protection; Storm surges**
 Wave Set-Up in the Surf Zone, Uwe A. Hansen, 1071
- Surf; Wave action; Wave height; Wave period; Waves; Coral reefs and islands; Energy; Probability density functions; Spectral analysis**
 The Energy Spectra of Surf Waves on a Coral Reef, Theodore T. Lee and Kerry P. Black, 588
- Surf; Wave action; Waves; Wave velocity; Coastal plains; Eigenvalues; Mass; Momentum; Offshore structures; Rip currents; Spacing**
 Rip Current Spacing as an Eigenvalue, Noriyuki Iwata, 828
- Surf; Wave dispersion; Wave energy; Beaches; Coastal plains; Littoral current; Littoral deposits; Models; Ocean bottom; Sediments; Sediment transport**
 A Model Study of Alongshore Sediment Transport Rate, J. W. Kamphuis and J. S. Readshaw, 1656
- Surf; Wave height; Wave period; Waves; Wave spectra; Breaking energy; Ocean waves; Probability density functions; Probability theory; Secondary waves**
 Probability Density Functions of Breaking Waves, Edward B. Thornton and George Schaeffer, 507
- Surf; Wave reflection; Waves; Wave spectra; Beaches; Edge effect; Littoral current; Morphology; Resonance**
 Surf Zone Resonance and Coupled Morphology, John Chappell and Lynn Donelson Wright, 1359
- Surf; Wave spectra; Wave velocity; Wind velocity; Littoral current; Predictions; Regression analysis; Statistical analysis; Stress**
 Wind-Generated Longshore Currents, Dag Nummedal and Robert J. Finley, 1428
- Surface waves; Turbulence; Vibration; Wave action; Wave energy; Wave equations; Wave height; Wave propagation; Waves; Surf**
 Wave Characteristics in the Surf Zone, I. A. Svendsen, P. A. Madsen and J. Buhr Hansen, 520

- Surface waves; Velocity field; Water waves; Wave energy; Ocean bottom; Sands; Sediments; Sediment transport**
Sediment Motion Caused by Surface Water Waves, A. G. Davies and R. H. Wilkinson, 1577
- Surface waves; Water depth; Wave energy; Wave measurement; Acoustic measuring instruments; Currents (water); Ocean bottom**
Near-Bottom Current Measured by Acoustic Sensors, K. A. Selanger and T. Carstens, 878
- Surveys (data collection); Coastal plains; Evaluation; Geological maps; Littoral deposits; Littoral materials; Sedimentation; Sediment transport**
A New Method for the Representation of Sedimentary Sequences in Coastal Regions, Hansjorg Streif, 1245
- Surveys (data collection); Tidal effects; Water levels; Wave propagation; Wave velocity; Estuaries; Field data; Flood protection; Mathematical models; Numerical analysis**
Adjustment and Verification of the RANDDELTA II Model, A. Langerak, M. A.M. deRas and J. J. Leendertse, 1049
- Surveys (data collection); Tidal hydraulics; Water levels; Barriers; Boundary conditions; Netherlands; Responses; Storms; Storm surges**
A Tidal Survey for a Model of an Offshore Area, W. J. van de Ree, J. Voogt and J. J. Leendertse, 2656
- Surveys (data collection); Wave energy; Wave height; Wavelength; Imaging; Ocean waves; Radar; Radar photography**
The Use of Imaging Radar in Studying Ocean Waves, M. G. Mattie and D. Lee Harris, 174
- Surveys (data collection); Wave energy; Wave height; Wave recorders (water waves); Buoys; Design criteria; Offshore platforms; Offshore structures**
Comparison of Shipborne Wave Recorder and Waverider Buoy Data Used to Generate Design and Operational Planning Criteria, C. G. Graham, G. Verboom and C. J. Shaw, 97
- Surveys (data collection); Wave height; Wave recorders (water waves); International compacts; Inventories; Questionnaires**
A World Wave Data Centre, Laurence Draper, 51
- Suspended load; Suspended sediments; Tidal effects; Wave action; Wave energy; Wave period; Waves; Currents (water); Field tests; Sands; Sediment transport**
Effect of Waves on Sand Transport by Currents, Michael W. Owen and Michael F.C. Thorn, 1675
- Suspended load; Tidal currents; Tidal effects; Tidal waters; Wind; Discharge (water); Hydrodynamics; Meteorology; Rainfall; Salt marshes; Sediment transport; South Carolina**
Hydrodynamics and Sediment Transport in a Salt Marsh Tidal Channel, Larry G. Ward, 1953
- Suspended sediments; Boundary layer flow; Continental shelf; Currents (water); Littoral current; Nicaragua; Pressure gradients; Salinity**
Shelf and Coastal Boundary Layer Currents, Miskito Bank of Nicaragua, Richard L. Croust and Stephen P. Murray, 2715
- Suspended sediments; Diffusion; Dredges; Dredging; Estuaries; Models; Plumes; Sediment concentration; Spoil; Spoil banks**
Factors Governing the Distribution of Dredge-Resuspended Sediments, W. Frank Bohlen, 2001
- Suspended sediments; Temperature; Tidal effects; Turbidity; Canada; Dredging; Harbors; Models; Salinity; Sedimentation; Sediment transport; Silting**
Tidal Sedimentation in Gros-CaCouna Harbor, Georges Drapeau and Guy Fortin, 1986
- Suspended sediments; Tidal effects; Wave action; Wave energy; Wave period; Waves; Currents (water); Field tests; Sands; Sediment transport; Suspended load**
Effect of Waves on Sand Transport by Currents, Michael W. Owen and Michael F.C. Thorn, 1675
- Suspended sediments; Tidal effects; Wave height; Waves; Wave spectrum; Mud; Mud systems; Sediment concentration; Sediment transport; Shallow water**
Suspension and Transportation of Fluid Mud by Solitary-Like Waves, John T. Wells, James M. Coleman and W. J. Wiseman, Jr., 1932
- Suspended sediments; Time dependence; Channel beds; Clays; Entrainment; Experimentation; Finite element method; Sediment concentration**
Concentration of Suspended Clay in Periodic Flow, Akira Watanabe, P. Thimakorn and A. Das Gupta, 1918
- Suspended sediments; Two-dimensional; Wave propagation; Wind loads; Boundary conditions; Coastal plains; Mixing; Ocean engineering; Ocean waves; Rivers; Runoff**
Mixed Layer Models for Coastal Waters, W. J. Wiseman, Jr., L. J. Rouse, Jr. and O. K. Huh, 2619
- Suspended sediments; Water sampling; Wave height; Wave period; Waves; Wind velocity; Beaches; Littoral current; Measurement; Surf**
Surf Zone Measurements of Suspended Sediment, Timothy W. Kana, 1725
- Suspended sediments; Wave height; Coastal plains; Littoral deposits; Littoral drift; Littoral zone; Samples; Sediment concentration**
Sled System for Profiling Suspended Littoral Drift, J. P. Coakley, J. A. Saville, M. Pedrosa and M. Larocque, 1764
- Suspended sediments; Wave period; Littoral deposits; Sediment concentration; Sediment transport; Sensors; Storms; Surf**
Storm Induced Periodicities of Suspended Sand Movement, Jay E. Leonard and Benno M. Brenninkmeyer, 1744
- Temperature; Tidal effects; Turbidity; Canada; Dredging; Harbors; Models; Salinity; Sedimentation; Sediment transport; Silting; Suspended sediments**
Tidal Sedimentation in Gros-CaCouna Harbor, Georges Drapeau and Guy Fortin, 1986
- Temperature; Water depth; Water levels; Air water interactions; Air-water interfaces; Forecasting; Shallow water; Storm surges**
Storm Surge Forecasting Methods in Enclosed Seas, P. F. Hamblin, 998

- Temperature effects; Thermal pollution; Tidal effects; Tidal hydraulics; Cooling water; Discharge (water); Model studies; Rivers; Storm surges**
Influence on Temperature Increases in Tidal Rivers Caused by Waste Heat Injections with Respect to Tidal Cycles and Storm Surges, Horst Schwarze and Wilfried Falldorf, 2915
- Temperature effects; Thermal pollution; Tracers; Turbulent flow; Currents (water); Heated water; Jet flow; Mixing; Plumes; Surf**
Mixing of Heated Water Discharged in the Surf Zone, Kiyoshi Horikawa, Ming-Chung Lin and Tamio O. Sasaki, 2563
- Temperature effects; Three-dimensional; Tidal effects; Water flow; Water levels; Wind loads; Dynamic response; Model studies**
Three-Dimensional SGS Energy Model of Eastern Bering Sea, S. K. Liu and J. J. Leendertse, 2687
- Temporal distribution; Variations; Wave spectra; Edge effect; Gravity waves; Littoral current; Rip currents; Surf**
Variability of Longshore Currents, R. T. Guza and Edward B. Thornton, 756
- Test reproducibility; Tests; Armoring (streambed); Breakwaters; Density; Plumes; Slope stability; Stability; Standardization**
Dolos Packing Density and Effect of Relative Block Density, J. A. Zwamborn, 2285
- Test reproducibility; Tests; Turbulent flow; Wave period; Wave refraction; Armoring (streambed); Open channel flow; Performance; Standardization**
Performance of Dolos Blocks in an Open Channel Situation, Arthur Brebner, 2305
- Tests; Armoring (streambed); Breakwaters; Density; Flumes; Slope stability; Stability; Standardization; Test reproducibility**
Dolos Packing Density and Effect of Relative Block Density, J. A. Zwamborn, 2285
- Tests; Thermal pollution; Wave energy; Wave height; Wave pressure; Cooling water; Loads (forces); Outfall sewers; Scale effect**
Non-Breaking and Breaking Wave Loads on a Cooling Water Outfall, G. R. Mogridge and W. W. Jamieson, 2461
- Tests; Turbulent flow; Wave period; Wave refraction; Armoring (streambed); Open channel flow; Performance; Standardization; Test reproducibility**
Performance of Dolos Blocks in an Open Channel Situation, Arthur Brebner, 2305
- Tests; Wave diffraction; Wave energy; Wave height; Wavelength; Wave tanks; Breakwaters; Permeability; Shallow water; Standing waves**
Wave Height Distribution Around Permeable Breakwaters, Shintaro Hotta, 695
- Texas; Tidal effects; Tsunamis; Water levels; Coastal plains; Cost effectiveness; Floods; Hurricanes; Numerical analysis; Predictions; Simulation; Storm surges**
Coastal Flood Simulation in Stretched Coordinates, H. Lee Butler, 1030
- Thermal energy; Waves; Wind; Currents (water); Design criteria; Energy conversion; Environmental effects; Environmental impact statements; Hurricanes; Site selection**
Some Design Criteria for OTEC Installations for Keahole Point, Hawaii, Frederick C. Munchmeyer and Charles L. Bretschneider, 2633
- Thermal pollution; Tidal currents; Vaporizers; Biological properties; Density currents; Discharge (water); Heat exchangers; Liquid natural gas; Model studies**
Thermal and Biological Impact of LNG Vaporizer Discharge, Peter A. Mangarella and Gordon A. Robilliard, 2945
- Thermal pollution; Tidal effects; Tidal hydraulics; Cooling water; Discharge (water); Model studies; Rivers; Storm surges; Temperature effects**
Influence on Temperature Increases in Tidal Rivers Caused by Waste Heat Injections with Respect to Tidal Cycles and Storm Surges, Horst Schwarze and Wilfried Falldorf, 2915
- Thermal pollution; Tracers; Turbulent flow; Currents (water); Heated water; Jet flow; Mixing; Plumes; Surf; Temperature effects**
Mixing of Heated Water Discharged in the Surf Zone, Kiyoshi Horikawa, Ming-Chung Lin and Tamio O. Sasaki, 2563
- Thermal pollution; Wave energy; Wave height; Wave pressure; Cooling water; Loads (forces); Outfall sewers; Scale effect; Tests**
Non-Breaking and Breaking Wave Loads on a Cooling Water Outfall, G. R. Mogridge and W. W. Jamieson, 2461
- Three-dimensional; Tidal currents; Tide gages; Two-dimensional; Water circulation; Mathematical models; Models; Numerical analysis; Ocean engineering; Oceanography**
Role of 2D and 3D Models in JONSDAP '76, A. M. Davies, 1085
- Three-dimensional; Tidal effects; Water flow; Water levels; Wind loads; Dynamic response; Model studies; Temperature effects**
Three-Dimensional SGS Energy Model of Eastern Bering Sea, S. K. Liu and J. J. Leendertse, 2687
- Three-dimensional; Viscosity; Water depth; Water pollution; Wind loads; Currents (water); Eddies; Oil spills**
3-D Current Model with Depth Varying Eddy Viscosity, Bryan R. Pearce, Cortis Cooper and Susan Nelson, 2602
- Three-dimensional; Water circulation; Wind loads; Currents (water); Density; Friction coefficient (hydraulic); Model studies**
Three Dimensional Modelling of the Irish Sea, Norman Stuart Heaps, 2671
- Three-dimensional; Water depth; Wave energy; Wave height; Wave spectra; Accretion (geomorphology); Beach erosion; Beaches; Dynamic models; Geomorphology**
Wave Power and Beach Stages: A Global Model, Andrew D. Short, 1145
- Three-dimensional; Wave height; Wave propagation; Waves; Wave spectra; Mathematical models; Numerical analysis; Ocean waves; Scale effect**
Natural Wave Trains: Description and Reproduction, H. Lundgren and S. E. Sand, 312

- Three-dimensional; Wave height; Waves; Wave tanks; Coastal plains; Currents (water); Ripple marks; Sediment transport; Shear stress**
Sediment Transport and Ripples Due to Waves and Currents, Zbigniew Pruszk and Ryszard B. Zeidler, 1638
- Tidal currents; Tidal effects; Tidal energy; Tide gages; Wind; Wind velocity; Forecasting; Predictions; Storm surges**
Storm Surge Prediction by Combined Wind and Tide Data, Hermann Christiansen and Winfried Siefert, 965
- Tidal currents; Tidal effects; Tidal flats; Two-dimensional; Wave tanks; Cross sections; Estuaries; Inlets (waterways)**
Periodic Flows from Tidal Inlets, D. L. Wilkinson, 1336
- Tidal currents; Tidal effects; Tidal waters; Wind; Discharge (water); Hydrodynamics; Meteorology; Rainfall; Salt marshes; Sediment transport; South Carolina; Suspended load**
Hydrodynamics and Sediment Transport in a Salt Marsh Tidal Channel, Larry G. Ward, 1953
- Tidal currents; Tidal effects; Water levels; Estuaries; Groins (structures); Navigable canals; Stream flow; Stream gages**
Improvements on Tidal Estuaries and the Effects on Tidal Current, Hermann Harten, 2905
- Tidal currents; Tidal effects; Wave energy; West Germany; Beaches; Dispersion; Environmental factors; Georgia; Inlets (waterways); Morphology; Sediment deposits**
Process-Response Models for Depositional Shorelines: The German and the Georgia Bights, Dag Nummedal and Ian A. Fischer, 1215
- Tidal currents; Tidal energy; Wave damping; Wave dispersion; Wave energy; Wave height; Wave runup; Waves; Wind speed; Damping**
Wave Climate Study in the Region of the East Frisian Islands and Coast, Hanz Dieter Niemyer, 134
- Tidal currents; Tidal flats; Tides; Two-dimensional; Water depth; Boundary conditions; Forecasting; Morphology; Stability analysis**
Two-Dimension Stability Analysis of Tidal Basins and Tidal Flats of Larger Extent, Eberhard Renger, 1971
- Tidal currents; Tidal flats; Velocity; Wave action; Wave velocity; Flooding; Flowmeters; Inlets (waterways); Stress measurement**
Velocity and Stress Measurements in a Tidal Inlet, David A. Huntley and Dag Nummedal, 1320
- Tidal currents; Tidal hydraulics; Water circulation; Diffusion coefficient; Experimentation; Hydraulic models; Japan; Scale effect**
Experimental Study on Scale Effect of Tidal Model, Haruo Higuchi, Hideichi Yasuda and Norio Hayakawa, 2646
- Tidal currents; Tidal hydraulics; Water circulation; Water levels; Waves; Wind loads; Model studies; Monsoons**
The Wind-Driven Circulation in the Northern Arabian Sea, Khawaja Zafar Elahi and Jurgen Sundermann, 2708
- Tidal currents; Tidal hydraulics; Water quality; Estuaries; Saline water-freshwater interfaces; Saline water intrusion; Salinity; Stratified flow**
Stability Study of an Artificial Salt Intrusion in Estuaries, C. Marche, 2798
- Tidal currents; Tide gages; Two-dimensional; Water circulation; Mathematical models; Models; Numerical analysis; Ocean engineering; Oceanography; Three-dimensional**
Role of 2D and 3D Models in JONSDAP '76, A. M. Davies, 1085
- Tidal currents; Turbulence; Velocity; Water depth; Wind loads; Aerial photography; Currents (water); Density; Eddies; Eddy currents; Mixing**
Large Scale Turbulence in Tidal Currents, John B. Hinwood, 2598
- Tidal currents; Vaporizers; Biological properties; Density currents; Discharge (water); Heat exchangers; Liquid natural gas; Model studies; Thermal pollution**
Thermal and Biological Impact of LNG Vaporizer Discharge, Peter A. Mangarella and Gordon A. Robilliard, 2945
- Tidal currents; Wave action; Wave energy; Wave refraction; Coastal plains; Dredging; Gravel; Great Britain; Licensing; Littoral drift; Sand; Shore protection**
The Effect of Offshore Dredging on Coastlines, W. A. Price, J. M. Motyka and L. J. Jaffrey, 1347
- Tidal currents; Wave action; Wave height; Wave runup; Waves; Wave spectra; Wind velocity; Estuaries; Reefs; Storms**
Analysis of Storm Tide Waves, Volker Barthel, 1016
- Tidal currents; Wave energy; Waves; Coastal engineering; Mathematical models; Mathematics; Mixing; Physics; Sediments; Structures**
Struggle of Physics and Mathematics in Coastal Engineering, H. Lundgren, 13
- Tidal currents; West Germany; Dikes; Estuaries; Ports; Shipping; Shore protection; Storms**
Welcoming Address — II, Helga Elstner, 4
- Tidal effects; Acceleration; Bed roughness; Distortion; Friction coefficient (hydraulic); Laboratory tests; Mathematical models; Numerical analysis**
Numerical Study of Distortion in a Froude Model, T. A. McClimans and S. A. Gjerp, 2887
- Tidal effects; Bed forms; Friction coefficient (hydraulic); Hydrodynamic pressure; Hydrodynamics; Numerical analysis; Ocean bottom; Ripple marks**
The Influence of Dune and Flow Parameters on the Friction Factor, Jurgen Sundermann, H. Vollmers and W. Puls, 1787
- Tidal effects; Tidal energy; Tide gages; Dynamics; Estuaries; Forecasting; Predictions; Storm surges**
Storm Surge Prediction in Tidal Rivers: A New Conception, Winfried Siefert, 986
- Tidal effects; Tidal energy; Tide gages; Wind; Wind velocity; Forecasting; Predictions; Storm surges; Tidal currents**
Storm Surge Prediction by Combined Wind and Tide Data, Hermann Christiansen and Winfried Siefert, 965

- Tidal effects; Tidal flats; Two-dimensional; Wave tanks; Cross sections; Estuaries; Inlets (waterways); Tidal currents**
 Periodic Flows from Tidal Inlets, D. L. Wilkinson, 1336
- Tidal effects; Tidal hydraulics; Cooling water; Discharge (water); Model studies; Rivers; Storm surges; Temperature effects; Thermal pollution**
 Influence on Temperature Increases in Tidal Rivers Caused by Waste Heat Injections with Respect to Tidal Cycles and Storm Surges, Horst Schwarze and Wilfried Falldorf, 2915
- Tidal effects; Tidal waters; Wave height; Wave period; Australia; Breakwaters; Maintenance; Site selection; Storm surges**
 Rosslyn Bay Breakwater, Queensland, Australia, D. N. Foster, B. L. McGrath and W. Bremner, 2086
- Tidal effects; Tidal waters; Wind; Discharge (water); Hydrodynamics; Meteorology; Rainfall; Salt marshes; Sediment transport; South Carolina; Suspended load; Tidal currents**
 Hydrodynamics and Sediment Transport in a Salt Marsh Tidal Channel, Larry G. Ward, 1953
- Tidal effects; Tides; Two-dimensional; Wave damping; Waves; Computation; Damping; Spectrum analysis**
 A New Approach for Tidal Computations, C. Le Provost, 1104
- Tidal effects; Tracers; Wave action; Wave height; Beaches; Breaking energy; Coring; Histograms; Sediment deposits; Surf**
 Depth of Disturbance of Sand in Surf Zones, Michael K. Gaughan, 1513
- Tidal effects; Trends; Beach erosion; Delaware; Hydraulic models; Inlets (waterways); Jetties; Sedimentation; Sheet piles**
 Case Studies of Delaware's Tidal Inlets: Roosevelt and Indian River Inlets, W. A. Dennie, G. A. Lanan and Robert A. Dalrymple, 1282
- Tidal effects; Tsunamis; Water levels; Coastal plains; Cost effectiveness; Floods; Hurricanes; Numerical analysis; Predictions; Simulation; Storm surges; Texas**
 Coastal Flood Simulation in Stretched Coordinates, H. Lee Butler, 1030
- Tidal effects; Turbidity; Canada; Dredging; Harbors; Models; Salinity; Sedimentation; Sediment transport; Silting; Suspended sediments; Temperature**
 Tidal Sedimentation in Gros-CaCouna Harbor, Georges Drapeau and Guy Fortin, 1986
- Tidal effects; Turbulence; Estuaries; Flood routing; Hydraulic models; Hydrodynamics; Numerical analysis; Rivers; Shallow water**
 Hydrodynamic Modelling of the Southern North Sea, David Prandle, 1122
- Tidal effects; Water flow; Water levels; Wind loads; Dynamic response; Model studies; Temperature effects; Three-dimensional**
 Three-Dimensional SGS Energy Model of Eastern Bering Sea, S. K. Liu and J. J. Leendertse, 2687
- Tidal effects; Water levels; Estuaries; Groins (structures); Navigable canals; Stream flow; Stream gages; Tidal currents**
 Improvements on Tidal Estuaries and the Effects on Tidal Current, Hermann Harten, 2905
- Tidal effects; Water levels; Wave propagation; Wave velocity; Estuaries; Field data; Flood protection; Mathematical models; Numerical analysis; Surveys (data collection)**
 Adjustment and Verification of the RANDDELTA II Model, A. Langerak, M. A.M. deRas and J. J. Leendertse, 1049
- Tidal effects; Wave action; Wave energy; Wave period; Waves; Currents (water); Field tests; Sands; Sediment transport; Suspended load; Suspended sediments**
 Effect of Waves on Sand Transport by Currents, Michael W. Owen and Michael F.C. Thorn, 1675
- Tidal effects; Wave energy; West Germany; Beaches; Dispersion; Environmental factors; Georgia; Inlets (waterways); Morphology; Sediment deposits; Tidal currents**
 Process-Response Models for Depositional Shorelines: The German and the Georgia Bights, Dag Nummedal and Ian A. Fischer, 1215
- Tidal effects; Wave height; Bays (topographic features); Friction coefficient (hydraulic); Inlets (waterways); Mathematical models; Numerical analysis; Sediment transport; Storm surges**
 Numerical Model Investigation of Selected Tidal Inlet-Bay System Characteristics, William N. Seelig and Robert M. Sorensen, 1319
- Tidal effects; Wave height; Waves; Wave spectrum; Mud; Mud systems; Sediment concentration; Sediment transport; Shallow water; Suspended sediments**
 Suspension and Transportation of Fluid Mud by Solitary-Like Waves, John T. Wells, James M. Coleman and W. J. Wiseman, Jr., 1932
- Tidal energy; Tide gages; Dynamics; Estuaries; Forecasting; Predictions; Storm surges; Tidal effects**
 Storm Surge Prediction in Tidal Rivers: A New Conception, Winfried Siefert, 986
- Tidal energy; Tide gages; Wind; Wind velocity; Forecasting; Predictions; Storm surges; Tidal currents; Tidal effects**
 Storm Surge Prediction by Combined Wind and Tide Data, Hermann Christiansen and Winfried Siefert, 965
- Tidal energy; Wave damping; Wave dispersion; Wave energy; Wave height; Wave runoff; Waves; Wind speed; Damping; Tidal currents**
 Wave Climate Study in the Region of the East Frisian Islands and Coast, Hanz Dieter Niemeyer, 134
- Tidal flats; Tidal hydraulics; Dispersion; Estuaries; Mixing; Model studies; Saline water-freshwater interfaces; Shallow water; Standing waves**
 Longitudinal Dispersion in Shallow Well-Mixed Estuaries, J. Dronkers, 2761
- Tidal flats; Tides; Two-dimensional; Water depth; Boundary conditions; Forecasting; Morphology; Stability analysis; Tidal currents**
 Two-Dimension Stability Analysis of Tidal Basins and Tidal Flats of Larger Extent, Eberhard Renger, 1971

- Tidal flats; Two-dimensional; Wave tanks; Cross sections; Estuaries; Inlets (waterways); Tidal currents; Tidal effects**
Periodic Flows from Tidal Inlets, D. L. Wilkinson, 1336
- Tidal flats; Velocity; Wave action; Wave velocity; Flooding; Flowmeters; Inlets (waterways); Stress measurement; Tidal currents**
Velocity and Stress Measurements in a Tidal Inlet, David A. Huntley and Dag Nummedal, 1320
- Tidal hydraulics; Barriers; Beach erosion; Coastal morphology; Delaware; Inlets (waterways); Littoral drift; Marshes; Morphology; Sedimentation**
Morphology of Coastal Barriers, Delaware, U.S.A., John C. Kraft, Chacko J. John and Evelyn M. Maurmeyer, 1232
- Tidal hydraulics; Cooling water; Discharge (water); Model studies; Rivers; Storm surges; Temperature effects; Thermal pollution; Tidal effects**
Influence on Temperature Increases in Tidal Rivers Caused by Waste Heat Injections with Respect to Tidal Cycles and Storm Surges, Horst Schwarze and Wilfried Falldorf, 2915
- Tidal hydraulics; Dispersion; Estuaries; Mixing; Model studies; Saline water-freshwater interfaces; Shallow water; Standing waves; Tidal flats**
Longitudinal Dispersion in Shallow Well-Mixed Estuaries, J. Dronkers, 2761
- Tidal hydraulics; Estuaries; Hydraulic models; Mathematical models; Model studies; Numerical analysis; Saline water intrusion; Salinity; Simulation**
Numerical Tidal-Salinity Models of the Ems Estuary, Karsten Fischer, 2840
- Tidal hydraulics; Verification inspection; Field tests; Model studies; Saline water-freshwater interfaces; Saline water intrusion; Salinity; Sampling**
Field Data Analysis for Chesapeake Bay Model Verification, Ronald E. Nece and Norman W. Scheffner, 2870
- Tidal hydraulics; Water circulation; Diffusion coefficient; Experimentation; Hydraulic models; Japan; Scale effect; Tidal currents**
Experimental Study on Scale Effect of Tidal Model, Haruo Higuchi, Hideichi Yasuda and Norio Hayakawa, 2646
- Tidal hydraulics; Water circulation; Water levels; Waves; Wind loads; Model studies; Monsoons; Tidal currents**
The Wind-Driven Circulation in the Northern Arabian Sea, Khawaja Zafar Elahi and Jurgen Sundermann, 2708
- Tidal hydraulics; Water circulation; Wind loads; Bays (topographic features); Currents (water); Diffusion; Eddies; Environmental factors; Simulation**
Characteristics of Circulation in Bay Waters due to Wind Action, Akira Wada and Ioshihito Miyaike, 2730
- Tidal hydraulics; Water levels; Barriers; Boundary conditions; Netherlands; Responses; Storms; Storm surges; Surveys (data collection)**
A Tidal Survey for a Model of an Offshore Area, W. J. van de Ree, J. Voogt and J. J. Leendertse, 2656
- Tidal hydraulics; Water quality; Estuaries; Saline water-freshwater interfaces; Saline water intrusion; Salinity; Stratified flow; Tidal currents**
Stability Study of an Artificial Salt Intrusion in Estuaries, C. Marche, 2798
- Tidal hydraulics; Wind loads; Florida; Friction coefficient (hydraulic); Model studies; Salinity; Salt balance; Salt water intrusion**
Tidal Hydraulics and Salt Balance of Lake Worth, Florida, J. van de Kreeke and J. D. Wang, 2827
- Tidal waters; Water levels; Frequencies; Great Britain; Ports; Sampling; Sea level; Statistical analysis**
Analysis of Maximum Sea Level in Southern England, J. Graff and D. L. Blackman, 931
- Tidal waters; Water levels; Waterways (transportation); West Germany; Economic analysis; Environmental factors; Financing; Storms; Storm surges**
Welcoming Address — III, Volker Hauff, 7
- Tidal waters; Wave height; Wave period; Australia; Breakwaters; Maintenance; Site selection; Storm surges; Tidal effects**
Rosslyn Bay Breakwater, Queensland, Australia, D. N. Foster, B. L. McGrath and W. Bremner, 2086
- Tidal waters; Wind; Discharge (water); Hydrodynamics; Meteorology; Rainfall; Salt marshes; Sediment transport; South Carolina; Suspended load; Tidal currents; Tidal effects**
Hydrodynamics and Sediment Transport in a Salt Marsh Tidal Channel, Larry G. Ward, 1953
- Tide gages; Dynamics; Estuaries; Forecasting; Predictions; Storm surges; Tidal effects; Tidal energy**
Storm Surge Prediction in Tidal Rivers: A New Conception, Winfried Siefert, 986
- Tide gages; Two-dimensional; Water circulation; Mathematical models; Models; Numerical analysis; Ocean engineering; Oceanography; Three-dimensional; Tidal currents**
Role of 2D and 3D Models in JONSDAP '76, A. M. Davies, 1085
- Tide gages; Wind; Wind velocity; Forecasting; Predictions; Storm surges; Tidal currents; Tidal effects; Tidal energy**
Storm Surge Prediction by Combined Wind and Tide Data, Hermann Christiansen and Winfried Siefert, 965
- Tides; Beaches; Coastal plains; Probability; Probability distribution functions; Sea level; Statistical analysis; Storm surges**
Extreme Sea Levels from Tide and Surge Probability, D. T. Pugh and J. M. Vassie, 911
- Tides; Two-dimensional; Water depth; Boundary conditions; Forecasting; Morphology; Stability analysis; Tidal currents; Tidal flats**
Two-Dimension Stability Analysis of Tidal Basins and Tidal Flats of Larger Extent, Eberhard Renger, 1971
- Tides; Two-dimensional; Wave damping; Waves; Computation; Damping; Spectrum analysis; Tidal effects**
A New Approach for Tidal Computations, C. Le Provost, 1104

- Tides; Water waves; Wave diffraction; Wave refraction; Approximation method; Finite element method; Harbors; Integral equations; Oscillations**
A Combined FE-BIE Method for Water Waves, A. Hauguel, 715
- Time dependence; Channel beds; Clays; Entrainment; Experimentation; Finite element method; Sediment concentration; Suspended sediments**
Concentration of Suspended Clay in Periodic Flow, Akira Watanabe, P. Thimakorn and A. Das Gupta, 1918
- Time dependence; Unsteady flow; Water depth; Bed forms; Discharge (water); Dunes; Flow rates; Sediment deposits**
Time Lag of Dunes for Unsteady Flow Conditions, Horst Nasner, 1801
- Time dependence; Water levels; Wave diffraction; Wave energy; Cylindrical bodies; Diffraction; Particle trajectories; Spectral energy distribution**
Wave Forces Induced by Irregular Waves on a Vertical Circular Cylinder, Hajime Ishida and Yuichi Iwagaki, 2397
- Time factors; Coastal structures; Currents (water); Jetties; Numerical analysis; Ocean bottom; Scouring; Sediment transport**
A Numerical Model for Sediment Transport, J. P. Lepetit and A. Hauguel, 1715
- Time series analysis; Waste disposal; Coastal plains; Diffusion; Dispersion; Mathematical models; Outfall sewers; Sewage effluents; Statistical analysis**
Outfall Diffusion Models for the Coastal Zone, D. C.L. Lam and C. R. Murthy, 2584
- Tires; Wave action; Wave attenuation; Breakwaters; Coastal engineering; Coastal structures; Floating bodies; Oil spills**
Scrap Tyre Breakwaters in Coastal Engineering, Robert Charles McGregor and Neil Sinclair Miller, 2191
- Tracers; Beaches; Littoral drift; Metal detectors; Monitoring; Sediment transport; Shingles (beach)**
Shingle Tracing by a New Technique, Peter Wright, J. S. Cross and N. B. Webber, 1705
- Tracers; Turbulent flow; Currents (water); Heated water; Jet flow; Mixing; Plumes; Surf; Temperature effects; Thermal pollution**
Mixing of Heated Water Discharged in the Surf Zone, Kiyoshi Horikawa, Ming-Chung Lin and Tamio O. Sasaki, 2563
- Tracers; Wave action; Wave height; Beaches; Breaking energy; Coring; Histograms; Sediment deposits; Surf; Tidal effects**
Depth of Disturbance of Sand in Surf Zones, Michael K. Gaughan, 1513
- Tracers; Wave energy; Beaches; Field tests; Gravel; Littoral current; Littoral deposits; Littoral drift; Littoral materials; Sediment transport**
Littoral Drift along Bayshore of a Barrier Island, Yu-Hwa Hwang and T. H. Chang, 1614
- Transverse waves; Wave energy; Wave height; Wave interference; Computation; Cylindrical bodies; Experimentation; Model tests; Numerical analysis; Piles**
Wave Forces on a Row of Cylindrical Piles of Large Diameter, J. C.W. Berkhoff and J. V.D. Weide, 2433
- Trends; Beach erosion; Delaware; Hydraulic models; Inlets (waterways); Jetties; Sedimentation; Sheet piles; Tidal effects**
Case Studies of Delaware's Tidal Inlets: Roosevelt and Indian River Inlets, W. A. Dennie, G. A. Lanan and Robert A. Dalrymple, 1282
- Tropical cyclones; Wave equations; Wave recorders (water waves); Wind forces; Wind pressure; Australia; Cyclones; Frequencies; Mathematical models; Probability distribution functions**
Wind Wave Frequencies in a Tropical Cyclone Region, Rodney J. Sobey, 76
- Tsunamis; Two-dimensional; Water depth; Wave energy; Waves; Ocean bottom; Ocean waves; Return flow; Sands; Scouring; Sea walls; Slopes**
Scouring at the Toe of a Seawall due to Tsunamis, Hitoshi Nishimura, Akira Watanabe and Kiyoshi Horikawa, 2540
- Tsunamis; Water levels; Coastal plains; Cost effectiveness; Floods; Hurricanes; Numerical analysis; Predictions; Simulation; Storm surges; Texas; Tidal effects**
Coastal Flood Simulation in Stretched Coordinates, H. Lee Butler, 1030
- Turbidity; Canada; Dredging; Harbors; Models; Salinity; Sedimentation; Sediment transport; Silting; Suspended sediments; Temperature; Tidal effects**
Tidal Sedimentation in Gros-CaCouna Harbor, Georges Drapeau and Guy Fortin, 1986
- Turbulence; Estuaries; Flood routing; Hydraulic models; Hydrodynamics; Numerical analysis; Rivers; Shallow water; Tidal effects**
Hydrodynamic Modelling of the Southern North Sea, David Prandle, 1122
- Turbulence; Velocity; Water depth; Wind loads; Aerial photography; Currents (water); Density; Eddies; Eddy currents; Mixing; Tidal currents**
Large Scale Turbulence in Tidal Currents, John B. Hinwood, 2598
- Turbulence; Vibration; Wave action; Wave energy; Wave equations; Wave height; Wave propagation; Waves; Surf; Surface waves**
Wave Characteristics in the Surf Zone, I. A. Svendsen, P. A. Madsen and J. Buhr Hansen, 520
- Turbulence; Wave dispersion; Wave energy; Wave height; Wave reflection; Beaches; Littoral current; Littoral deposits; Littoral drift; Surf**
Morphodynamic Variability of High-Energy Beaches, Lynn Donelson Wright, B. G. Thom and John Chappell, 1180
- Turbulent flow; Currents (water); Heated water; Jet flow; Mixing; Plumes; Surf; Temperature effects; Thermal pollution; Tracers**
Mixing of Heated Water Discharged in the Surf Zone, Kiyoshi Horikawa, Ming-Chung Lin and Tamio O. Sasaki, 2563

- Turbulent flow; Velocity distribution; Wave propagation; Wave velocity; Boundary conditions; Mathematical models; Sand; Shear stress**
Near-Bottom Velocities in Waves with a Current, W. T. Bakker and Th. van Doorn, 1394
- Turbulent flow; Wave period; Wave refraction; Armoring (streambed); Open channel flow; Performance; Standardization; Test reproducibility; Tests**
Performance of Dolos Blocks in an Open Channel Situation, Arthur Brebner, 2305
- Two-dimensional; Water circulation; Mathematical models; Models; Numerical analysis; Ocean engineering; Oceanography; Three-dimensional; Tidal currents; Tide gages**
Role of 2D and 3D Models in JONSDAP '76, A. M. Davies, 1085
- Two-dimensional; Water depth; Boundary conditions; Forecasting; Morphology; Stability analysis; Tidal currents; Tidal flats; Tides**
Two-Dimension Stability Analysis of Tidal Basins and Tidal Flats of Larger Extent, Eberhard Renger, 1971
- Two-dimensional; Water depth; Wave energy; Waves; Ocean bottom; Ocean waves; Return flow; Sands; Scouring; Sea walls; Slopes; Tsunamis**
Scouring at the Toe of a Seawall due to Tsunamis, Hitoshi Nishimura, Akira Watanabe and Kiyoshi Horikawa, 2540
- Two-dimensional; Wave damping; Waves; Computation; Damping; Spectrum analysis; Tidal effects; Tides**
A New Approach for Tidal Computations, C. Le Provost, 1104
- Two-dimensional; Wave period; Beaches; Littoral current; Models; Sediment concentration; Sediment load; Sediment transport**
Onshore-Offshore Sediment Movement on a Beach, P. Nielsen, I. A. Svendsen and C. Staub, 1475
- Two-dimensional; Wave propagation; Wind loads; Boundary conditions; Coastal plains; Mixing; Ocean engineering; Ocean waves; Rivers; Runoff; Suspended sediments**
Mixed Layer Models for Coastal Waters, W. J. Wiseman, Jr., L. J. Rouse, Jr. and O. K. Huh, 2619
- Two-dimensional; Wave tanks; Cross sections; Estuaries; Inlets (waterways); Tidal currents; Tidal effects; Tidal flats**
Periodic Flows from Tidal Inlets, D. L. Wilkinson, 1336
- Two phase flow; Water flow; Density; Friction coefficient (hydraulic); Open channel flow; Saline water-freshwater interfaces; Salinity; Stratified flow**
Interfacial Friction Coefficients in a Two-Layered Stratified Flow, Emmanuel Partheniades and Vassilios Dermisis, 2778
- Ultrasonic tests; Diffusion coefficient; Entrainment; Estuaries; Japan; Saline water-freshwater interfaces; Salinity**
Behaviors of the Salt Wedge and the Salinity Distribution at Estuaries, Isao Yakuwa, Susumu Takahashi and Morimasa Ohtani, 2746
- Underwater foundations; Vibration; Currents (water); Dolphins (structures); Marine structures; Offshore platforms; Offshore structures; Pile foundations**
Tripod Concept for Pile Structures in Fast Current, J. Khanna and J. S. Wood, 2481
- Underwater structures; Wave attenuation; Barriers; Breakwaters; India; Performance; Shape; Silting**
Performance Characteristics of Submerged Breakwaters, J. Dattatri, H. Raman and N. Jothi Shankar, 2153
- Underwater structures; Wave damping; Wave energy; Wave period; Waves; Breakwaters; Ocean waves; Pneumatic systems**
Combination Effect of Pneumatic Breakwater and Other Type Breakwater on Wave Damping, Yuichi Iwagaki, Toshiyuki Asano and Tsutomu Honda, 2172
- Unsteady flow; Water depth; Bed forms; Discharge (water); Dunes; Flow rates; Sediment deposits; Time dependence**
Time Lag of Dunes for Unsteady Flow Conditions, Horst Nasner, 1801
- Vaporizers; Biological properties; Density currents; Discharge (water); Heat exchangers; Liquid natural gas; Model studies; Thermal pollution; Tidal currents**
Thermal and Biological Impact of LNG Vaporizer Discharge, Peter A. Mangarella and Gordon A. Robilliard, 2945
- Variations; Wave spectra; Edge effect; Gravity waves; Littoral current; Rip currents; Surf; Temporal distribution**
Variability of Longshore Currents, R. T. Guza and Edward B. Thornton, 756
- Vehicles; Wave action; Calibration; California; Instrumentation; Performance; Profile measurement; Sand; Sediment transport**
Tracked Vehicle for Continuous Nearshore Profiles, Richard J. Seymour, Alan L. Higgins and David P. Bothman, 1542
- Velocity; Water depth; Wind loads; Aerial photography; Currents (water); Density; Eddies; Eddy currents; Mixing; Tidal currents; Turbulence**
Large Scale Turbulence in Tidal Currents, John B. Hinwood, 2598
- Velocity; Wave action; Wave velocity; Flooding; Flowmeters; Inlets (waterways); Stress measurement; Tidal currents; Tidal flats**
Velocity and Stress Measurements in a Tidal Inlet, David A. Huntley and Dag Nummedal, 1320
- Velocity; Waves; Wave velocity; Beaches; Breaking energy; Deep water; Particle trajectories; Slope**
Estimation of Water Particle Velocity of Breaking Wave, Tetsuo Sakai and Yuichi Iwagaki, 551
- Velocity distribution; Vortex generators; Jets; Laminar flow; Ocean bottom; Oscillation; Roughness (hydraulic)**
Oscillatory Laminar Flow Above a Rough Bed, C. B. George and J. F. A. Sleath, 898
- Velocity distribution; Vortices; Wave energy; Bed roughness; Estuaries; Mixing; Rivers; Saline water-freshwater interfaces; Salinity; Stream flow**
Outflow Dynamics at a River Mouth, Masakazu Kashiwamura and Shizuo Yoshida, 2925

- Velocity distribution; Wave propagation; Wave velocity; Boundary conditions; Mathematical models; Sand; Shear stress; Turbulent flow**
Near-Bottom Velocities in Waves with a Current, W. T. Bakker and Th. van Doorn, 1394
- Velocity field; Water waves; Wave energy; Ocean bottom; Sands; Sediments; Sediment transport; Surface waves**
Sediment Motion Caused by Surface Water Waves, A. G. Davies and R. H. Wilkinson, 1577
- Verification inspection; Field tests; Model studies; Saline water-freshwater interfaces; Saline water intrusion; Salinity; Sampling; Tidal hydraulics**
Field Data Analysis for Chesapeake Bay Model Verification, Ronald E. Nece and Norman W. Scheffner, 2870
- Vibration; Currents (water); Dolphins (structures); Marine structures; Offshore platforms; Offshore structures; Pile foundations; Underwater foundations**
Tripod Concept for Pile Structures in Fast Current, J. Khanna and J. S. Wood, 2481
- Vibration; Wave action; Wave energy; Wave equations; Wave height; Wave propagation; Waves; Surf; Surface waves; Turbulence**
Wave Characteristics in the Surf Zone, I. A. Svendsen, P. A. Madsen and J. Buhr Hansen, 520
- Vibration; Wave equations; Wave generation; Wave height; Waves; Wave tanks; Wave velocity; Ocean waves; Offshore structures; Predictions; Random processes**
Periodic Theory Velocity Prediction in Random Wave, John H. Nath and Koji Kobune, 340
- Viscosity; Water depth; Water pollution; Wind loads; Currents (water); Eddies; Oil spills; Three-dimensional**
3-D Current Model with Depth Varying Eddy Viscosity, Bryan R. Pearce, Cortis Cooper and Susan Nelson, 2602
- Vortex generators; Jets; Laminar flow; Ocean bottom; Oscillation; Roughness (hydraulic); Velocity distribution**
Oscillatory Laminar Flow Above a Rough Bed, C. B. George and J. F. A. Sleath, 898
- Vortices; Wave energy; Bed roughness; Estuaries; Mixing; Rivers; Saline water-freshwater interfaces; Salinity; Stream flow; Velocity distribution**
Outflow Dynamics at a River Mouth, Masakazu Kashiwamura and Shizuo Yoshida, 2925
- Walls; Wave action; Wave diffraction; Wave reflection; Breakwaters; Model tests; Reflection; Refraction**
Influence of Breakwater-Reflection on Diffraction, Karl-Friedrich Daemrich and Soren Kohlhase, 651
- Waste disposal; Coastal plains; Diffusion; Dispersion; Mathematical models; Outfall sewers; Sewage effluents; Statistical analysis; Time series analysis**
Outfall Diffusion Models for the Coastal Zone, D. C. L. Lam and C. R. Murthy, 2584
- Water circulation; Diffusion coefficient; Experimentation; Hydraulic models; Japan; Scale effect; Tidal currents; Tidal hydraulics**
Experimental Study on Scale Effect of Tidal Model, Haruo Higuchi, Hideichi Yasuda and Norio Hayakawa, 2646
- Water circulation; Mathematical models; Models; Numerical analysis; Ocean engineering; Oceanography; Three-dimensional; Tidal currents; Tide gages; Two-dimensional**
Role of 2D and 3D Models in JONSDAP '76, A. M. Davies, 1085
- Water circulation; Water levels; Wave height; Waves; Wind; Bathymetry; Bores (wave); Field tests; Littoral current; Model tests; Storms; Surf**
Comparison of Model and Observed Nearshore Circulation, James H. Allender, John D. Ditmars, Wyman Harrison and Robert A. Paddock, 810
- Water circulation; Water levels; Waves; Wind loads; Model studies; Monsoons; Tidal currents; Tidal hydraulics**
The Wind-Driven Circulation in the Northern Arabian Sea, Khawaja Zafar Elahi and Jurgen Sundermann, 2708
- Water circulation; Wave energy; Wave propagation; Waves; Barriers; Friction coefficient (hydraulic); Littoral current; Shores; Stresses; Surf**
Longshore Currents Due to Surf Zone Barrier, P. Bettess, C. A. Fleming, J. C. Heinrich, O. C. Zienkiewicz and D. I. Austin, 776
- Water circulation; Wave energy; Weathering; Estuaries; Littoral deposits; Nicaragua; Rainfall; Sedimentation; Sediments; Sediment transport**
Variations of Wave-Energy Levels and Coastal Sedimentation, Eastern Nicaragua, E. H. Owens and H. H. Roberts, 1195
- Water circulation; Wind loads; Bays (topographic features); Currents (water); Diffusion; Eddies; Environmental factors; Simulation; Tidal hydraulics**
Characteristics of Circulation in Bay Waters due to Wind Action, Akira Wada and Ioshihito Miyake, 2730
- Water circulation; Wind loads; Currents (water); Density; Friction coefficient (hydraulic); Model studies; Three-dimensional**
Three Dimensional Modelling of the Irish Sea, Norman Stuart Heaps, 2671
- Water depth; Aerial photography; Bathymetry; Color photography; Images; Remote sensing; Shallow water**
Visible-Region Photographic Remote Sensing of Nearshore Waters, Tsuguo Sunamura and Kiyoshi Horikawa, 1439
- Water depth; Bathymetry; Beach erosion; Beach nourishment; Morphology; Sands; Shore protection**
Morphologic Effects of Westerland Beach Nourishment 1972, Dieter Wenzel, 1859
- Water depth; Bed forms; Discharge (water); Dunes; Flow rates; Sediment deposits; Time dependence; Unsteady flow**
Time Lag of Dunes for Unsteady Flow Conditions, Horst Nasner, 1801

- Water depth; Boundary conditions; Forecasting; Morphology; Stability analysis; Tidal currents; Tidal flats; Tides; Two-dimensional**
Two-Dimension Stability Analysis of Tidal Basins and Tidal Flats of Larger Extent, Eberhard Renger, 1971
- Water depth; Littoral deposits; Littoral drift; Littoral materials; Ocean bottom; Sediments; Sediment transport; Shear stress; Surf**
Distribution of Sand Transport Rate across a Surf Zone, Toru Sawaragi and Ichiro Deguchi, 1596
- Water depth; Water levels; Air water interactions; Air-water interfaces; Forecasting; Shallow water; Storm surges; Temperature**
Storm Surge Forecasting Methods in Enclosed Seas, P. F. Hamblin, 998
- Water depth; Water pollution; Wind loads; Currents (water); Eddies; Oil spills; Three-dimensional; Viscosity**
3-D Current Model with Depth Varying Eddy Viscosity, Bryan R. Pearce, Cortis Cooper and Susan Nelson, 2602
- Water depth; Water surface; Wave tanks; Wind forces; Wind pressure; Wind velocity; Drifting (aquatic)**
Wind-Induced Water Surface Set-Up and Drift Currents, Frederick L.W. Tang, Jin Wu, Charles C.C. Chang and Shan-Hwei Ou, 841
- Water depth; Water waves; Wave dispersion; Wave energy; Wave propagation; Wave spectra; Dissipation; Friction coefficient (hydraulic); Ocean bottom**
Bottom Dissipation in Finite-Depth Water Waves, S. V. Hsiao and O. H. Shemdin, 434
- Water depth; Wave action; Wave diffraction; Wavelength; Wave propagation; Wave reflection; Wave refraction; Mathematical models; Shallow water**
Computations of Short Waves in Shallow Water, M. B. Abbott, H. M. Petersen and Ove Skovgaard, 414
- Water depth; Wave action; Wave height; Wavelength; Wave period; Wave refraction; Refraction (water waves); Shear flow**
Wave Refraction Across a Shearing Current, Ivar G. Jonsson and Ove Skovgaard, 722
- Water depth; Wave energy; Beach erosion; Littoral current; Littoral deposits; Littoral drift; Shallow water**
Vocoidal Theory for All Non-Breaking Waves, D. H. Swart and C. C. Loubser, 467
- Water depth; Wave energy; Wave height; Wave spectra; Accretion (geomorphology); Beach erosion; Beaches; Dynamic models; Geomorphology; Three-dimensional**
Wave Power and Beach Stages: A Global Model, Andrew D. Short, 1145
- Water depth; Wave energy; Wave measurement; Acoustic measuring instruments; Currents (water); Ocean bottom; Surface waves**
Near-Bottom Current Measured by Acoustic Sensors, K. A. Selanger and T. Carstens, 878
- Water depth; Wave energy; Waves; Ocean bottom; Ocean waves; Return flow; Sands; Scouring; Sea walls; Slopes; Tsunamis; Two-dimensional**
Scouring at the Toe of a Seawall due to Tsunamis, Hitoshi Nishimura, Akira Watanabe and Kiyoshi Horikawa, 2540
- Water depth; Wave equations; Wave period; Bars (riverine); Beach erosion; Lakes; Nile River Valley; Oceans; Sediment deposits; Sediment load; Sediment transport; Storms**
Undulated Bottom Profiles and Onshore-Offshore Transport, Madhav Manohar, 1454
- Water depth; Wave height; Wavelength; Wave period; Waves; Wave tanks; Wave velocity; Beaches; Random processes; Slopes**
Wave Length, Wave Velocity and Shoaling Characteristics of Random Waves, Akira Kimura and Yuichi Iwagaki, 320
- Water depth; Wave height; Wavelength; Waves; Breaking energy; Classification; Field tests; Photographic analysis; Predictions**
Field Study of Breaking Wave Characteristics, Lee L. Weishar and Robert J. Byrne, 487
- Water depth; Wave height; Wave period; Accuracy; Beach erosion; Field tests; Laboratory tests; Measurement; Sediments**
Uses for a Calculated Limit Depth to Beach Erosion, Robert J. Hallermeier, 1493
- Water depth; Wave height; Wave period; Wave recorders (water waves); Wave spectrum; Brazil; Current meters; Harbor facilities; Littoral current; Littoral drift**
Coastal Study of Espirito Santo Brazil, Paulo Augusto Vivacqua, Hildebrando de Araujo Goes Filho and Octavio de Sampaio Ferraz Jardim Sayao, 2104
- Water depth; Wave height; Wave propagation; Waves; Wave velocity; Bores (wave); Breaking energy; Hydraulic jump**
Spilling Breakers, Bores and Hydraulic Jumps, D. H. Peregrine and I. A. Svendsen, 540
- Water depth; Waves; Wave tanks; Beaches; Edge effect; Excitation; Interactions; Standing waves**
Excitation of Low Frequency Trapped Waves, Robert King and Ronald Smith, 449
- Water depth; Wind loads; Aerial photography; Currents (water); Density; Eddies; Eddy currents; Mixing; Tidal currents; Turbulence; Velocity**
Large Scale Turbulence in Tidal Currents, John B. Hinwood, 2598
- Water flow; Density; Friction coefficient (hydraulic); Open channel flow; Saline water-freshwater interfaces; Salinity; Stratified flow; Two phase flow**
Interfacial Friction Coefficients in a Two-Layered Stratified Flow, Emmanouel Partheniades and Vassilios Dermisis, 2778
- Water flow; Water levels; Wind loads; Dynamic response; Model studies; Temperature effects; Three-dimensional; Tidal effects**
Three-Dimensional SGS Energy Model of Eastern Bering Sea, S. K. Liu and J. J. Leendertse, 2687
- Water flow; Wave energy; Wave pressure; Cylindrical bodies; Drag; Experimentation; Loads (forces); Predictions; Reynolds number**
Wave Loads on Horizontal Cylinders, P. Holmes and J. R. Chaplin, 2449

- Water levels; Air water interactions; Air-water interfaces; Forecasting; Shallow water; Storm surges; Temperature; Water depth**
Storm Surge Forecasting Methods in Enclosed Seas, P. F. Hamblin, 998
- Water levels; Barriers; Boundary conditions; Netherlands; Responses; Storms; Storm surges; Surveys (data collection); Tidal hydraulics**
A Tidal Survey for a Model of an Offshore Area, W. J. van de Ree, J. Voogt and J. J. Leendertse, 2656
- Water levels; Coastal plains; Cost effectiveness; Floods; Hurricanes; Numerical analysis; Predictions; Simulation; Storm surges; Texas; Tidal effects; Tsunamis**
Coastal Flood Simulation in Stretched Coordinates, H. Lee Butler, 1030
- Water levels; Estuaries; Groins (structures); Navigable canals; Stream flow; Stream gages; Tidal currents; Tidal effects**
Improvements on Tidal Estuaries and the Effects on Tidal Current, Hermann Harten, 2905
- Water levels; Frequencies; Great Britain; Ports; Sampling; Sea level; Statistical analysis; Tidal waters**
Analysis of Maximum Sea Level in Southern England, J. Graff and D. L. Blackman, 931
- Water levels; Water waves; Wave height; Discharge (water); Estuaries; Hydraulic models; Model studies; Numerical analysis; Responses**
A Hybrid Model of the St. Lawrence River Estuary, E. R. Funke and N. L. Crookshank, 2855
- Water levels; Waterways (transportation); West Germany; Economic analysis; Environmental factors; Financing; Storms; Storm surges; Tidal waters**
Welcoming Address — III, Volker Hauff, 7
- Water levels; Wave action; Wave dispersion; Wave period; Fourier transformation; Gravity waves; Storm surges; Surf**
Anomalous Dispersion of Fourier Components of Surface Gravity Waves in the Near Shore Area, Fritz Busching, 247
- Water levels; Wave diffraction; Wave energy; Cylindrical bodies; Diffraction; Particle trajectories; Spectral energy distribution; Time dependence**
Wave Forces Induced by Irregular Waves on a Vertical Circular Cylinder, Hajime Ishida and Yuichi Iwagaki, 2397
- Water levels; Wave energy; Wave recorders (water waves); Wave runoff; Coastal plains; Dynamic loads; Shore protection; Storm surges; Surf**
Wave Set-Up in the Surf Zone, Uwe A. Hansen, 1071
- Water levels; Wave height; Waves; Wind; Bathymetry; Bores (wave); Field tests; Littoral current; Model tests; Storms; Surf; Water circulation**
Comparison of Model and Observed Nearshore Circulation, James H. Allender, John D. Ditmars, Wyman Harrison and Robert A. Paddock, 810
- Water levels; Wave propagation; Wave velocity; Estuaries; Field data; Flood protection; Mathematical models; Numerical analysis; Surveys (data collection); Tidal effects**
Adjustment and Verification of the RANDDELTA II Model, A. Langerak, M. A.M. deRas and J. J. Leendertse, 1049
- Water levels; Waves; Wind loads; Model studies; Monsoons; Tidal currents; Tidal hydraulics; Water circulation**
The Wind-Driven Circulation in the Northern Arabian Sea, Khawaja Zafar Elahi and Jurgen Sundermann, 2708
- Water levels; Wind forces; Forecasting; Mathematical models; Meteorological data; Meteorology; Numerical analysis; Predictions; Simulation; Storm surges**
Numerical Storm Surge Forecasting, Manfred Engel, 975
- Water levels; Wind loads; Dynamic response; Model studies; Temperature effects; Three-dimensional; Tidal effects; Water flow**
Three-Dimensional SGS Energy Model of Eastern Bering Sea, S. K. Liu and J. J. Leendertse, 2687
- Water pollution; Wind loads; Currents (water); Eddies; Oil spills; Three-dimensional; Viscosity; Water depth**
3-D Current Model with Depth Varying Eddy Viscosity, Bryan R. Pearce, Cortis Cooper and Susan Nelson, 2602
- Water quality; Estuaries; Saline water-freshwater interfaces; Saline water intrusion; Salinity; Stratified flow; Tidal currents; Tidal hydraulics**
Stability Study of an Artificial Salt Intrusion in Estuaries, C. Marche, 2798
- Water sampling; Wave height; Wave period; Waves; Wind velocity; Beaches; Littoral current; Measurement; Surf; Suspended sediments**
Surf Zone Measurements of Suspended Sediment, Timothy W. Kana, 1725
- Water surface; Wave tanks; Wind forces; Wind pressure; Wind velocity; Drifting (aquatic); Water depth**
Wind-Induced Water Surface Set-Up and Drift Currents, Frederick L.W. Tang, Jin Wu, Charles C.C. Chang and Shan-Hwei Ou, 841
- Water waves; Wave diffraction; Wave height; Wave period; Wave refraction; Wave velocity; Rip currents; Sediment transport; Shoaling**
Rip Currents and Their Causes, Robert A. Dalrymple, 1414
- Water waves; Wave diffraction; Wave refraction; Approximation method; Finite element method; Harbors; Integral equations; Oscillations; Tides**
A Combined FE-BIE Method for Water Waves, A. Hauguel, 715
- Water waves; Wave dispersion; Wave energy; Wave propagation; Wave spectra; Dissipation; Friction coefficient (hydraulic); Ocean bottom; Water depth**
Bottom Dissipation in Finite-Depth Water Waves, S. V. Hsiao and O. H. Shemdin, 434
- Water waves; Wave energy; Ocean bottom; Sands; Sediments; Sediment transport; Surface waves; Velocity field**
Sediment Motion Caused by Surface Water Waves, A. G. Davies and R. H. Wilkinson, 1577

- Water waves; Wave energy; Wave pressure; Wave spectra; Hydrodynamic pressure; Impact; Impact forces; Measurement; Scale effect**
Impact Wave Forces on Vertical and Horizontal Plate, S. R. Massel, M. Oleszkiewicz and W. Trapp, 2340
- Water waves; Wave height; Discharge (water); Estuaries; Hydraulic models; Model studies; Numerical analysis; Responses; Water levels**
A Hybrid Model of the St. Lawrence River Estuary, E. R. Funke and N. L. Crookshank, 2855
- Water waves; Waves; Cylindrical bodies; Dynamic response; Loading; Mathematical models; Ocean waves; Responses**
Loading and Response of Cylinders in Waves, G. N. Bullock, P. K. Stansby and J. G. Warren, 2415
- Waterways (transportation); West Germany; Economic analysis; Environmental factors; Financing; Storms; Storm surges; Tidal waters; Water levels**
Welcoming Address — III, Volker Hauff, 7
- Wave action; Calibration; California; Instrumentation; Performance; Profile measurement; Sand; Sediment transport; Vehicles**
Tracked Vehicle for Continuous Nearshore Profiles, Richard J. Seymour, Alan L. Higgins and David P. Bothman, 1542
- Wave action; Wave attenuation; Breakwaters; Coastal engineering; Coastal structures; Floating bodies; Oil spills; Tires**
Scrap Tyre Breakwaters in Coastal Engineering, Robert Charles McGregor and Neil Sinclair Miller, 2191
- Wave action; Wave diffraction; Wavelength; Wave propagation; Wave reflection; Wave refraction; Mathematical models; Shallow water; Water depth**
Computations of Short Waves in Shallow Water, M. B. Abbott, H. M. Petersen and Ove Skovgaard, 414
- Wave action; Wave diffraction; Wave reflection; Breakwaters; Model tests; Reflection; Refraction; Walls**
Influence of Breakwater-Reflection on Diffraction, Karl-Friedrich Daemrich and Soren Kohlhasse, 651
- Wave action; Wave dispersion; Wave period; Fourier transformation; Gravity waves; Storm surges; Surf; Water levels**
Anomalous Dispersion of Fourier Components of Surface Gravity Waves in the Near Shore Area, Fritz Busching, 247
- Wave action; Wave energy; Wave equations; Wave height; Wave propagation; Waves; Surf; Surface waves; Turbulence; Vibration**
Wave Characteristics in the Surf Zone, I. A. Svendsen, P. A. Madsen and J. Buhr Hansen, 520
- Wave action; Wave energy; Wave height; Wave period; Wave recorders (water waves); Brazil; Meteorology; Ocean waves**
Wave Climate in Some Zones off the Brazilian Coast, Alberto Homs, 114
- Wave action; Wave energy; Wave period; Waves; Currents (water); Field tests; Sands; Sediment transport; Suspended load; Suspended sediments; Tidal effects**
Effect of Waves on Sand Transport by Currents, Michael W. Owen and Michael F.C. Thorn, 1675
- Wave action; Wave energy; Wave reflection; Drag; Experimentation; Friction coefficient (hydraulic); Friction studies**
Non-Conservative Wave Interaction with Fixed Semi-Immersed Rectangular Structures, Robert B. Steimer and Charles K. Sollitt, 2209
- Wave action; Wave energy; Wave refraction; Coastal plains; Dredging; Gravel; Great Britain; Licensing; Littoral drift; Sand; Shore protection; Tidal currents**
The Effect of Offshore Dredging on Coastlines, W. A. Price, J. M. Motyka and L. J. Jaffrey, 1347
- Wave action; Wave energy; Waves; Currents (water); Sediment load; Sediments; Sediment transport**
Sediment Load under Waves and Currents, D. H. Willis, 1626
- Wave action; Wave height; Beaches; Breaking energy; Coring; Histograms; Sediment deposits; Surf; Tidal effects; Tracers**
Depth of Disturbance of Sand in Surf Zones, Michael K. Gaughan, 1513
- Wave action; Wave height; Wavelength; Wave period; Wave refraction; Refraction (water waves); Shear flow; Water depth**
Wave Refraction Across a Shearing Current, Ivar G. Jonsson and Ove Skovgaard, 722
- Wave action; Wave height; Wave period; Waves; Coral reefs and islands; Energy; Probability density functions; Spectral analysis; Surf**
The Energy Spectra of Surf Waves on a Coral Reef, Theodore T. Lee and Kerry P. Black, 588
- Wave action; Wave height; Wave runoff; Waves; Wave spectra; Wind velocity; Estuaries; Reefs; Storms; Tidal currents**
Analysis of Storm Tide Waves, Volker Barthel, 1016
- Wave action; Wavelengths; Wave velocity; Beach erosion; Beaches; Beach sands; Edge effect; Littoral current; Littoral drift**
Beach Cusps and Edge Waves, David A. Huntley and A. J. Bowen, 1378
- Wave action; Wave pressure; Wave tanks; Groups; Loading; Load transfer; Marine structures; Ocean waves**
Load Analysis from Wave Groups, A. I. Kuznetsov and G. D. Khaskhatchikh, 2328
- Wave action; Waves; Wave velocity; Coastal plains; Eigenvalues; Mass; Momentum; Offshore structures; Rip currents; Spacing; Surf**
Rip Current Spacing as an Eigenvalue, Noriyuki Iwata, 828
- Wave action; Wave velocity; Flooding; Flowmeters; Inlets (waterways); Stress measurement; Tidal currents; Tidal flats; Velocity**
Velocity and Stress Measurements in a Tidal Inlet, David A. Huntley and Dag Nummedal, 1320

- Wave attenuation; Barriers; Breakwaters; India; Performance; Shape; Siting; Underwater structures**
 Performance Characteristics of Submerged Breakwaters, J. Dattatri, H. Raman and N. Jothi Shankar, 2153
- Wave attenuation; Breakwaters; Coastal engineering; Coastal structures; Floating bodies; Oil spills; Tires; Wave action**
 Scrap Tyre Breakwaters in Coastal Engineering, Robert Charles McGregor and Neil Sinclair Miller, 2191
- Wave damping; Wave dispersion; Wave energy; Wave height; Wave runup; Waves; Wind speed; Damping; Tidal currents; Tidal energy**
 Wave Climate Study in the Region of the East Frisian Islands and Coast, Hanz Dieter Niemeyer, 134
- Wave damping; Wave energy; Wave period; Wave pressure; Wind loads; Wind pressure; Dynamic response; Oscillation; Responses; Simulation**
 Simulation of Wave/Wind Forced Harbor Oscillation, S. K. Liu, H. S. Hou and Charles C.C. Chang, 2551
- Wave damping; Wave energy; Wave period; Waves; Breakwaters; Ocean waves; Pneumatic systems; Underwater structures**
 Combination Effect of Pneumatic Breakwater and Other Type Breakwater on Wave Damping, Yuichi Iwagaki, Toshiyuki Asano and Tsutomu Honda, 2172
- Wave damping; Waves; Computation; Damping; Spectrum analysis; Tidal effects; Tides; Two-dimensional**
 A New Approach for Tidal Computations, C. Le Provost, 1104
- Wave diffraction; Wave energy; Cylindrical bodies; Diffraction; Particle trajectories; Spectral energy distribution; Time dependence; Water levels**
 Wave Forces Induced by Irregular Waves on a Vertical Circular Cylinder, Hajime Ishida and Yuichi Iwagaki, 2397
- Wave diffraction; Wave energy; Wave generation; Wave recorders (water waves); Wave spectra; Wind forces; Wind pressure; Breakwaters; Laboratory tests**
 Wind-Generated Wave Diffraction by Breakwater Gap, Hooshang Raissi and R. L. Wigle, 609
- Wave diffraction; Wave energy; Wave height; Wavelength; Wave tanks; Breakwaters; Permeability; Shallow water; Standing waves; Tests**
 Wave Height Distribution Around Permeable Breakwaters, Shintaro Hotta, 695
- Wave diffraction; Wave height; Wave period; Wave refraction; Wave velocity; Rip currents; Sediment transport; Shoaling; Water waves**
 Rip Currents and Their Causes, Robert A. Dalrymple, 1414
- Wave diffraction; Wave height; Wave phases; Bathymetry; Bays (topographic features); Beach erosion; Beaches; Breakwaters; Diffraction; Sediment transport**
 Diffraction Calculation of Shoreline PlanForms, Robert G. Dean, 1903
- Wave diffraction; Wave height; Wave reflection; Breakwaters; Computer programs; Harbors; Hydraulic models; Numerical analysis**
 A Numerical Approach for the Determination of the Wave Height Distribution in a Harbour, Soren Kohlhasse, Karl-Friedrich Daemrich, U. Berger, E. Tautenhain and O. Burkhardt, 664
- Wave diffraction; Wave height; Wave reflection; Wave spectra; Breakwaters; Diffraction; Ocean waves; Random processes**
 Diffraction Diagrams for Directional Random Waves, Yoshimi Goda, Tomotsuka Takayama and Yasumasa Suzuki, 628
- Wave diffraction; Wavelength; Wave propagation; Wave reflection; Wave refraction; Mathematical models; Shallow water; Water depth; Wave action**
 Computations of Short Waves in Shallow Water, M. B. Abbott, H. M. Petersen and Ove Skovgaard, 414
- Wave diffraction; Wave reflection; Breakwaters; Model tests; Reflection; Refraction; Walls; Wave action**
 Influence of Breakwater-Reflection on Diffraction, Karl-Friedrich Daemrich and Soren Kohlhasse, 651
- Wave diffraction; Wave refraction; Approximation method; Finite element method; Harbors; Integral equations; Oscillations; Tides; Water waves**
 A Combined FE-BIE Method for Water Waves, A. Hauguel, 715
- Wave diffraction; Wave refraction; Wind loads; Accretion (geomorphology); Beach nourishment; Erosion; Groins (structures); Mathematical models; Rip currents; Shore-line cover**
 Mathematical Modeling of Shoreline Evolution, Bernard Le Mehaute and Mills Soldate, 1163
- Wave dispersion; Wave energy; Beaches; Coastal plains; Littoral current; Littoral deposits; Models; Ocean bottom; Sediments; Sediment transport; Surf**
 A Model Study of Alongshore Sediment Transport Rate, J. W. Kamphuis and J. S. Readshaw, 1656
- Wave dispersion; Wave energy; Wave height; Wave reflection; Beaches; Littoral current; Littoral deposits; Littoral drift; Surf; Turbulence**
 Morphodynamic Variability of High-Energy Beaches, Lynn Donelson Wright, B. G. Thom and John Chappell, 1180
- Wave dispersion; Wave energy; Wave height; Wave runup; Waves; Wind speed; Damping; Tidal currents; Tidal energy; Wave damping**
 Wave Climate Study in the Region of the East Frisian Islands and Coast, Hanz Dieter Niemeyer, 134
- Wave dispersion; Wave energy; Wave propagation; Wave spectra; Dissipation; Friction coefficient (hydraulic); Ocean bottom; Water depth; Water waves**
 Bottom Dissipation in Finite-Depth Water Waves, S. V. Hsiao and O. H. Shemdin, 434
- Wave dispersion; Wave height; Wave reflection; Breakwaters; Experimentation; Friction coefficient (hydraulic); Ocean waves; Predictions**
 Wave Transmission through Trapezoidal Breakwaters, Ole Secher Madsen, Paisal Shusang and Sue Ann Hanson, 2140

- Wave dispersion; Wave period; Fourier transformation; Gravity waves; Storm surges; Surf; Water levels; Wave action**
Anomalous Dispersion of Fourier Components of Surface Gravity Waves in the Near Shore Area, Fritz Busching, 247
- Wave energy; Beach erosion; Littoral current; Littoral deposits; Littoral drift; Shallow water; Water depth**
Vocoidal Theory for All Non-Breaking Waves, D. H. Swart and C. C. Loubser, 467
- Wave energy; Beaches; Coastal plains; Littoral current; Littoral deposits; Models; Ocean bottom; Sediments; Sediment transport; Surf; Wave dispersion**
A Model Study of Alongshore Sediment Transport Rate, J. W. Kamphuis and J. S. Readshaw, 1656
- Wave energy; Beaches; Field tests; Gravel; Littoral current; Littoral deposits; Littoral drift; Sediment transport; Storm surges; Tracers**
Field Experiment on Beach Gravel Transport, Masataro Hattori and Takasuke Suzuki, 1688
- Wave energy; Bed roughness; Estuaries; Mixing; Rivers; Saline water-freshwater interfaces; Salinity; Stream flow; Velocity distribution; Vortices**
Outflow Dynamics at a River Mouth, Masakazu Kashiwamura and Shizuo Yoshida, 2925
- Wave energy; Cylindrical bodies; Diffraction; Particle trajectories; Spectral energy distribution; Time dependence; Water levels; Wave diffraction**
Wave Forces Induced by Irregular Waves on a Vertical Circular Cylinder, Hajime Ishida and Yuichi Iwagaki, 2397
- Wave energy; Experimentation; Littoral current; Littoral drift; Predictions; Sediments; Sediment transport; Silting**
Longshore Sediment Transport Data: A Review, Matthew N. Greer and Ole Secher Madsen, 1563
- Wave energy; Ocean bottom; Sands; Sediments; Sediment transport; Surface waves; Velocity field; Water waves**
Sediment Motion Caused by Surface Water Waves, A. G. Davies and R. H. Wilkinson, 1577
- Wave energy; Wave equations; Wave height; Wave propagation; Waves; Surf; Surface waves; Turbulence; Vibration; Wave action**
Wave Characteristics in the Surf Zone, I. A. Svendsen, P. A. Madsen and J. Buhr Hansen, 520
- Wave energy; Wave generation; Wave recorders (water waves); Wave spectra; Wind forces; Wind pressure; Breakwaters; Laboratory tests; Wave diffraction**
Wind-Generated Wave Diffraction by Breakwater Gap, Hooshang Raisi and R. L. Wigle, 609
- Wave energy; Wave height; Armoring (streambed); Breakwaters; Rubble-mound breakwaters; Slope stability; Stability**
Dolos-Armored Breakwaters: Special Consideration, Robert D. Carver and D. Donald Davidson, 2263
- Wave energy; Wave height; Wave interference; Computation; Cylindrical bodies; Experimentation; Model tests; Numerical analysis; Piles; Transverse waves**
Wave Forces on a Row of Cylindrical Piles of Large Diameter, J. C. W. Berkhoff and J. V.D. Weide, 2433
- Wave energy; Wave height; Wavelength; Imaging; Ocean waves; Radar; Radar photography; Surveys (data collection)**
The Use of Imaging Radar in Studying Ocean Waves, M. G. Mattie and D. Lee Harris, 174
- Wave energy; Wave height; Wavelength; Wave tanks; Breakwaters; Permeability; Shallow water; Standing waves; Tests; Wave diffraction**
Wave Height Distribution Around Permeable Breakwaters, Shintaro Hotta, 695
- Wave energy; Wave height; Wave period; Wave recorders (water waves); Brazil; Meteorology; Ocean waves; Wave action**
Wave Climate in Some Zones off the Brazilian Coast, Alberto Homs, 114
- Wave energy; Wave height; Wave pressure; Cooling water; Loads (forces); Outfall sewers; Scale effect; Tests; Thermal pollution**
Non-Breaking and Breaking Wave Loads on a Cooling Water Outfall, G. R. Mogridge and W. W. Jamieson, 2461
- Wave energy; Wave height; Wave recorders (water waves); Buoys; Design criteria; Offshore platforms; Offshore structures; Surveys (data collection)**
Comparison of Shipborne Wave Recorder and Waverider Buoy Data Used to Generate Design and Operational Planning Criteria, C. G. Graham, G. Verboom and C. J. Shaw, 97
- Wave energy; Wave height; Wave reflection; Beaches; Littoral current; Littoral deposits; Littoral drift; Surf; Turbulence; Wave dispersion**
Morphodynamic Variability of High-Energy Beaches, Lynn Donelson Wright, B. G. Thom and John Chappell, 1180
- Wave energy; Wave height; Wave runup; Waves; Wind speed; Damping; Tidal currents; Tidal energy; Wave damping; Wave dispersion**
Wave Climate Study in the Region of the East Frisian Islands and Coast, Hanz Dieter Niemyer, 134
- Wave energy; Wave height; Wave spectra; Accretion (geomorphology); Beach erosion; Beaches; Dynamic models; Geomorphology; Three-dimensional; Water depth**
Wave Power and Beach Stages: A Global Model, Andrew D. Short, 1145
- Wave energy; Wave height; Wave spectra; Wave tanks; Breakwaters; Damage; Hydraulic models; Rubble-mound breakwaters; Stability**
Effects of Wave Grouping on Breakwater Stability, R. R. Johnson, E. P. D. Mansard and J. Ploeg, 2228
- Wave energy; Wave height; Wave spectra; Wind velocity; Distribution functions; Predictions; Rainfall; Samples; Sampling**
Extremal Prediction of Significant Wave Height, Enrique Copeiro, 285

- Wave energy; Wave measurement; Acoustic measuring instruments; Currents (water); Ocean bottom; Surface waves; Water depth**
Near-Bottom Current Measured by Acoustic Sensors, K. A. Selanger and T. Carstens, 878
- Wave energy; Wave period; Wave pressure; Wind loads; Wind pressure; Dynamic response; Oscillation; Responses; Simulation; Wave damping**
Simulation of Wave/Wind Forced Harbor Oscillation, S. K. Liu, H. S. Hou and Charles C.C. Chang, 2551
- Wave energy; Wave period; Waves; Breakwaters; Ocean waves; Pneumatic systems; Underwater structures; Wave damping**
Combination Effect of Pneumatic Breakwater and Other Type Breakwater on Wave Damping, Yuichi Iwagaki, Toshiyuki Asano and Tsutomu Honda, 2172
- Wave energy; Wave period; Waves; Currents (water); Field tests; Sands; Sediment transport; Suspended load; Suspended sediments; Tidal effects; Wave action**
Effect of Waves on Sand Transport by Currents, Michael W. Owen and Michael F.C. Thorn, 1675
- Wave energy; Wave period; Wave velocity; Canada; Field tests; Gravity waves; Hurricanes; Sediments; Sediment transport; Storms; Storm surges**
Infragravity Waves in Storm Conditions, R. A. Holman, David A. Huntley and A. J. Bowen, 268
- Wave energy; Wave pressure; Armoring (streambed); Costs; Revetments; Rubble-mound breakwaters; Slope stability; Stability**
Blanket Theory and Low Cost Revetments, C. T. Brown, 2510
- Wave energy; Wave pressure; Barriers; Impact; Marine structures; Mathematical models; Pressure distribution; Scale effect; Standing waves; Storm surges**
A Model Law for Wave Impacts on Coastal Structures, C. Ramkema, 2308
- Wave energy; Wave pressure; Cylindrical bodies; Drag; Experimentation; Loads (forces); Predictions; Reynolds number; Water flow**
Wave Loads on Horizontal Cylinders, P. Holmes and J. R. Chaplin, 2449
- Wave energy; Wave pressure; Wave spectra; Hydrodynamic pressure; Impact; Impact forces; Measurement; Scale effect; Water waves**
Impact Wave Forces on Vertical and Horizontal Plate, S. R. Massel, M. Oleszkiewicz and W. Trapp, 2340
- Wave energy; Wave propagation; Waves; Barriers; Friction coefficient (hydraulic); Littoral current; Shores; Stresses; Surf; Water circulation**
Longshore Currents Due to Surf Zone Barrier, P. Bettess, C. A. Fleming, J. C. Heinrich, O. C. Zienkiewicz and D. I. Austin, 776
- Wave energy; Wave propagation; Waves; Wave spectra; Bathymetry; Correlation analysis; Deep water; Frequencies; Intensity**
Deepwater Direction from an Intensity Array, Alan L. Higgins and Richard J. Seymour, 305
- Wave energy; Wave propagation; Wave spectra; Dissipation; Friction coefficient (hydraulic); Ocean bottom; Water depth; Water waves; Wave dispersion**
Bottom Dissipation in Finite-Depth Water Waves, S. V. Hsiao and O. H. Shemdin, 434
- Wave energy; Wave recorders (water waves); Wave runoff; Coastal plains; Dynamic loads; Shore protection; Storm surges; Surf; Water levels**
Wave Set-Up in the Surf Zone, Uwe A. Hansen, 1071
- Wave energy; Wave reflection; Beach erosion; Coastal structures; Dikes; Erosion control; Japan; Land reclamation; Scouring; Sea walls; Shore protection**
Effectiveness of Seadikes with Rough Slope, Osamu Toyoshima, 2528
- Wave energy; Wave reflection; Drag; Experimentation; Friction coefficient (hydraulic); Friction studies; Wave action**
Non-Conservative Wave Interaction with Fixed Semi-Immersed Rectangular Structures, Robert B. Steimer and Charles K. Sollitt, 2209
- Wave energy; Wave refraction; Coastal plains; Dredging; Gravel; Great Britain; Licensing; Littoral drift; Sand; Shore protection; Tidal currents; Wave action**
The Effect of Offshore Dredging on Coastlines, W. A. Price, J. M. Motyka and L. J. Jaffrey, 1347
- Wave energy; Waves; Coastal engineering; Mathematical models; Mathematics; Mixing; Physics; Sediments; Structures; Tidal currents**
Struggle of Physics and Mathematics in Coastal Engineering, H. Lundgren, 13
- Wave energy; Waves; Currents (water); Sediment load; Sediments; Sediment transport; Wave action**
Sediment Load under Waves and Currents, D. H. Willis, 1626
- Wave energy; Waves; Ocean bottom; Ocean waves; Return flow; Sands; Scouring; Sea walls; Slopes; Tsunamis; Two-dimensional; Water depth**
Scouring at the Toe of a Seawall due to Tsunamis, Hitoshi Nishimura, Akira Watanabe and Kiyoshi Horikawa, 2540
- Wave energy; Waves; Wave spectra; Wave velocity; Currents (water); Edge effect; Frequencies; Littoral current; Ocean waves**
Observation of Nearshore Current and Edge Waves, Tamio O. Sasaki and Kiyoshi Horikawa, 791
- Wave energy; Weathering; Estuaries; Littoral deposits; Nicaragua; Rainfall; Sedimentation; Sediments; Sediment transport; Water circulation**
Variations of Wave-Energy Levels and Coastal Sedimentation, Eastern Nicaragua, E. H. Owens and H. H. Roberts, 1195
- Wave energy; West Germany; Beaches; Dispersion; Environmental factors; Georgia; Inlets (waterways); Morphology; Sediment deposits; Tidal currents; Tidal effects**
Process-Response Models for Depositional Shorelines: The German and the Georgia Bights, Dag Nummedal and Ian A. Fischer, 1215

- Wave equations; Wave generation; Wave height; Waves; Wave tanks; Wave velocity; Ocean waves; Offshore structures; Predictions; Random processes; Vibration**
 Periodic Theory Velocity Prediction in Random Wave, John H. Nath and Koji Kobune, 340
- Wave equations; Wave height; Wave propagation; Waves; Surf; Surface waves; Turbulence; Vibration; Wave action; Wave energy**
 Wave Characteristics in the Surf Zone, I. A. Svendsen, P. A. Madsen and J. Buhr Hansen, 520
- Wave equations; Wave period; Bars (riverine); Beach erosion; Lakes; Nile River Valley; Oceans; Sediment deposits; Sediment load; Sediment transport; Storms; Water depth**
 Undulated Bottom Profiles and Onshore-Offshore Transport, Madhav Manohar, 1454
- Wave equations; Wave recorders (water waves); Wind forces; Wind pressure; Australia; Cyclones; Frequencies; Mathematical models; Probability distribution functions; Tropical cyclones**
 Wind Wave Frequencies in a Tropical Cyclone Region, Rodney J. Sobey, 76
- Waveforms; Wave height; Wavelength; Experimental data; Flumes; Gravity waves; Interactions**
 Changes in Height of Short Waves on Long Waves, Michio Sato and Kazuo Nakamura, 400
- Wave generation; Wave height; Wavelength; Waves; Wave spectra; Wave tanks; Hydrodynamic pressure; Numerical analysis; Stochastic processes**
 An Inclined-Plate Wave Generator, Fredric Raichlen and Jiin-Jen Lee, 388
- Wave generation; Wave height; Waves; Wave spectra; Wave tanks; Wave velocity; Wind forces; Wind pressure; Currents (water); Experimentation; Fetch**
 Experimental Study of Wind Waves Generated on Currents, Hajime Kato and Hiroichi Tsuruya, 742
- Wave generation; Wave height; Waves; Wave tanks; Wave velocity; Ocean waves; Offshore structures; Predictions; Random processes; Vibration; Wave equations**
 Periodic Theory Velocity Prediction in Random Wave, John H. Nath and Koji Kobune, 340
- Wave generation; Wave recorders (water waves); Wave spectra; Wind forces; Wind pressure; Breakwaters; Laboratory tests; Wave diffraction; Wave energy**
 Wind-Generated Wave Diffraction by Breakwater Gap, Hooshang Raissi and R. L. Wigle, 609
- Wave generation; Wave spectra; Dynamic pressure; Frequencies; Hydrodynamic pressure; Responses; Stochastic processes**
 Analysis of Hinged Wavemakers for Random Waves, Robert T. Hudspeth, Douglas F. Jones and John H. Nath, 372
- Wave height; Armoring (streambed); Breakwaters; Rubble-mound breakwaters; Slope stability; Stability; Wave energy**
 Dolos-Armored Breakwaters: Special Consideration, Robert D. Carver and D. Donald Davidson, 2263
- Wave height; Barriers; Islands (landforms); Littoral current; Littoral deposits; Littoral drift; Littoral materials; Sediment transport; Tracers**
 Littoral Drift along Bayshore of a Barrier Island, Yu-Hwa Hwang and T. H. Chang, 1614
- Wave height; Bays (topographic features); Friction coefficient (hydraulic); Inlets (waterways); Mathematical models; Numerical analysis; Sediment transport; Storm surges; Tidal effects**
 Numerical Model Investigation of Selected Tidal Inlet-Bay System Characteristics, William N. Seelig and Robert M. Sorensen, 1319
- Wave height; Beaches; Breaking energy; Coring; Histograms; Sediment deposits; Surf; Tidal effects; Tracers; Wave action**
 Depth of Disturbance of Sand in Surf Zones, Michael K. Gaughan, 1513
- Wave height; Bores (wave); Breaking energy; Energy dissipation; Energy losses; Predictions; Random processes; Shallow water**
 Energy Loss and Set-Up Due to Breaking of Random Waves, J. A. Battjes and J. P.F.M. Janssen, 569
- Wave height; Coastal plains; Littoral deposits; Littoral drift; Littoral zone; Samples; Sediment concentration; Suspended sediments**
 Sled System for Profiling Suspended Littoral Drift, J. P. Coakley, J. A. Savile, M. Pedrosa and M. Larocque, 1764
- Wave height; Discharge (water); Estuaries; Hydraulic models; Model studies; Numerical analysis; Responses; Water levels; Water waves**
 A Hybrid Model of the St. Lawrence River Estuary, E. R. Funke and N. L. Crookshank, 2855
- Wave height; Wave interference; Computation; Cylindrical bodies; Experimentation; Model tests; Numerical analysis; Piles; Transverse waves; Wave energy**
 Wave Forces on a Row of Cylindrical Piles of Large Diameter, J. C.W. Berkhoff and J. V.D. Weide, 2433
- Wave height; Wavelength; Experimental data; Flumes; Gravity waves; Interactions; Waveforms**
 Changes in Height of Short Waves on Long Waves, Michio Sato and Kazuo Nakamura, 400
- Wave height; Wavelength; Imaging; Ocean waves; Radar; Radar photography; Surveys (data collection); Wave energy**
 The Use of Imaging Radar in Studying Ocean Waves, M. G. Mattie and D. Lee Harris, 174
- Wave height; Wavelength; Wave period; Wave refraction; Refraction (water waves); Shear flow; Water depth; Wave action**
 Wave Refraction Across a Shearing Current, Ivar G. Jonsson and Ove Skovgaard, 722
- Wave height; Wavelength; Wave period; Waves; Wave tanks; Wave velocity; Beaches; Random processes; Slopes; Water depth**
 Wave Length, Wave Velocity and Shoaling Characteristics of Random Waves, Akira Kimura and Yuichi Iwagaki, 320
- Wave height; Wavelength; Waves; Breaking energy; Classification; Field tests; Photographic analysis; Predictions; Water depth**
 Field Study of Breaking Wave Characteristics, Lee L. Weishar and Robert J. Byrne, 487

- Wave height; Wavelength; Waves; Wave spectra; Wave tanks; Hydrodynamic pressure; Numerical analysis; Stochastic processes; Wave generation**
An Inclined-Plate Wave Generator, Fredric Raichlen and Jiin-Jen Lee, 388
- Wave height; Wavelength; Wave tanks; Breakwaters; Permeability; Shallow water; Standing waves; Tests; Wave diffraction; Wave energy**
Wave Height Distribution Around Permeable Breakwaters, Shintaro Hotta, 695
- Wave height; Wave period; Accuracy; Beach erosion; Field tests; Laboratory tests; Measurement; Sediments; Water depth**
Uses for a Calculated Limit Depth to Beach Erosion, Robert J. Hallermeier, 1493
- Wave height; Wave period; Australia; Breakwaters; Maintenance; Site selection; Storm surges; Tidal effects; Tidal waters**
Rosslyn Bay Breakwater, Queensland, Australia, D. N. Foster, B. L. McGrath and W. Bremner, 2086
- Wave height; Wave period; Beaches; Coastal engineering; Laboratory tests; Movable bed models; Scale effect; Sediments; Sediment transport**
Scale Relations for Equilibrium Beach Profiles, Hideaki Noda, 1531
- Wave height; Wave period; Coastal plains; Confidence level; Ocean waves; Probability distribution functions; Shore protection; Statistical analysis**
On Long-Term Statistics for Ocean and Coastal Waves, Michel K. Ochi, 59
- Wave height; Wave period; Wave pressure; Wave reflection; Breakwaters; Slots; Standing waves; Storms; Storm surges**
Wave Pressures on Split-Type Breakwaters, Shoshichiro Nagai and Shohachi Kakuno, 2360
- Wave height; Wave period; Wave recorders (water waves); Brazil; Meteorology; Ocean waves; Wave action; Wave energy**
Wave Climate in Some Zones off the Brazilian Coast, Alberto Homsí, 114
- Wave height; Wave period; Wave recorders (water waves); Wave spectrum; Brazil; Current meters; Harbor facilities; Littoral current; Littoral drift; Water depth**
Coastal Study of Espirito Santo Brazil, Paulo Augusto Vivacqua, Hildebrando de Araujo Goes Filho and Octavio de Sampaio Ferraz Jardim Sayao, 2104
- Wave height; Wave period; Wave refraction; Wave velocity; Rip currents; Sediment transport; Shoaling; Water waves; Wave diffraction**
Rip Currents and Their Causes, Robert A. Dalrymple, 1414
- Wave height; Wave period; Wave runup; Wave spectra; Damage; Dikes; Hydrodynamics; Statistical analysis**
New Dike Design Criteria Based on Wave Spectra, Hans Kaldenhoff and Suhan M. Gokcesu, 2500
- Wave height; Wave period; Waves; Amplitude; Buoy; D-rafting (aquatic); Floating bodies; Mass transfer**
Drift Speed of Buoys in Waves, John H. Nath, 859
- Wave height; Wave period; Waves; Coral reefs and islands; Energy; Probability density functions; Spectral analysis; Surf; Wave action**
The Energy Spectra of Surf Waves on a Coral Reef, Theodore T. Lee and Kerry P. Black, 588
- Wave height; Wave period; Waves; Wave spectra; Breaking energy; Ocean waves; Probability density functions; Probability theory; Secondary waves; Surf**
Probability Density Functions of Breaking Waves, Edward B. Thornton and George Schaeffer, 507
- Wave height; Wave period; Waves; Wind velocity; Beaches; Littoral current; Measurement; Surf; Suspended sediments; Water sampling**
Surf Zone Measurements of Suspended Sediment, Timothy W. Kana, 1725
- Wave height; Wave period; Wave spectra; Correlation techniques; Ocean waves; Offshore structures; Shore protection**
The Observed Joint Distribution of Periods and Heights of Sea Waves, Yoshimi Goda, 227
- Wave height; Wave period; Wave spectrum; Aquifers; Ground water; Groundwater elevation; Littoral current; Oscillations; Piezometers**
Beach Ground-Water Oscillations, Andrzej Lewandowski and Ryszard B. Zeidler, 2051
- Wave height; Wave phases; Bathymetry; Bays (topographic features); Beach erosion; Beaches; Breakwaters; Diffraction; Sediment transport; Wave diffraction**
Diffraction Calculation of Shoreline PlanForms, Robert G. Dean, 1903
- Wave height; Wave pressure; Cooling water; Loads (forces); Outfall sewers; Scale effect; Tests; Thermal pollution; Wave energy**
Non-Breaking and Breaking Wave Loads on a Cooling Water Outfall, G. R. Mogridge and W. W. Jamieson, 2461
- Wave height; Wave propagation; Waves; Surf; Surface waves; Turbulence; Vibration; Wave action; Wave energy; Wave equations**
Wave Characteristics in the Surf Zone, I. A. Svendsen, P. A. Madsen and J. Buhr Hansen, 520
- Wave height; Wave propagation; Waves; Wave spectra; Mathematical models; Numerical analysis; Ocean waves; Scale effect; Three-dimensional**
Natural Wave Trains: Description and Reproduction, H. Lundgren and S. E. Sand, 312
- Wave height; Wave propagation; Waves; Wave velocity; Bores (wave); Breaking energy; Hydraulic jump; Water depth**
Spilling Breakers, Bores and Hydraulic Jumps, D. H. Peregrine and I. A. Svendsen, 540
- Wave height; Wave recorders (water waves); Buoys; Design criteria; Offshore platforms; Offshore structures; Surveys (data collection); Wave energy**
Comparison of Shipborne Wave Recorder and Waverider Buoy Data Used to Generate Design and Operational Planning Criteria, C. G. Graham, G. Verboom and C. J. Shaw, 97
- Wave height; Wave recorders (water waves); Forecasting; Hawaii; Meteorological data; Meteorology; Statistical analysis**
An Evaluation of Extreme Wave Climate at Keahole Point, Hawaii, Charles L. Bretschneider and Richard E. Rocheleau, 152

- Wave height; Wave recorders (water waves); International compacts; Inventories; Questionnaires; Surveys (data collection)**
A World Wave Data Centre, Laurence Draper, 51
- Wave height; Wave reflection; Beaches; Littoral current; Littoral deposits; Littoral drift; Surf; Turbulence; Wave dispersion; Wave energy**
Morphodynamic Variability of High-Energy Beaches, Lynn Donelson Wright, B. G. Thom and John Chappell, 1180
- Wave height; Wave reflection; Breakwaters; Computer programs; Harbors; Hydraulic models; Numerical analysis; Wave diffraction**
A Numerical Approach for the Determination of the Wave Height Distribution in a Harbour, Soren Kohlhase, Karl-Friedrich Daemrich, U. Berger, E. Tautenhain and O. Burkhardt, 664
- Wave height; Wave reflection; Breakwaters; Experimentation; Friction coefficient (hydraulic); Ocean waves; Predictions; Wave dispersion**
Wave Transmission through Trapezoidal Breakwaters, Ole Secher Madsen, Paisal Shusang and Sue Ann Hanson, 2140
- Wave height; Wave reflection; Wave spectra; Breakwaters; Diffraction; Ocean waves; Random processes; Wave diffraction**
Diffraction Diagrams for Directional Random Waves, Yoshimi Goda, Tomotsuka Takayama and Yasumasa Suzuki, 208
- Wave height; Wave runup; Waves; Wave spectra; Wind velocity; Estuaries; Reefs; Storms; Tidal currents; Wave action**
Analysis of Storm Tide Waves, Volker Barthel, 1016
- Wave height; Wave runup; Waves; Wind speed; Damping; Tidal currents; Tidal energy; Wave damping; Wave dispersion; Wave energy**
Wave Climate Study in the Region of the East Frisian Islands and Coast, Hanz Dieter Niemeyer, 134
- Wave height; Waves; Wave spectra; Wave tanks; Wave velocity; Wind forces; Wind pressure; Currents (water); Experimentation; Fetch; Wave generation**
Experimental Study of Wind Waves Generated on Currents, Hajime Kato and Hiroichi Tsuruya, 742
- Wave height; Waves; Wave spectrum; Mud; Mud systems; Sediment concentration; Sediment transport; Shallow water; Suspended sediments; Tidal effects**
Suspension and Transportation of Fluid Mud by Solitary-Like Waves, John T. Wells, James M. Coleman and W. J. Wiseman, Jr., 1932
- Wave height; Waves; Wave tanks; Coastal plains; Currents (water); Ripple marks; Sediment transport; Shear stress; Three-dimensional**
Sediment Transport and Ripples Due to Waves and Currents, Zbigniew Pruszk and Ryszard B. Zeidler, 1638
- Wave height; Waves; Wave tanks; Wave velocity; Ocean waves; Offshore structures; Predictions; Random processes; Vibration; Wave equations; Wave generation**
Periodic Theory Velocity Prediction in Random Wave, John H. Nath and Koji Kobune, 340
- Wave height; Waves; Wind; Bathymetry; Bores (wave); Field tests; Littoral current; Model tests; Storms; Surf; Water circulation; Water levels**
Comparison of Model and Observed Nearshore Circulation, James H. Allender, John D. Ditmars, Wyman Harrison and Robert A. Paddock, 810
- Wave height; Waves; Wind; Wind speed; Buoys; Hurricanes; Measurement; Monitoring; Offshore platforms; Radar operation**
HF Skywave Radar Measurement of Hurricane Winds and Waves, Joseph W. Maresca, Jr. and Christopher T. Carlson, 190
- Wave height; Wave spectra; Accretion (geomorphology); Beach erosion; Beaches; Dynamic models; Geomorphology; Three-dimensional; Water depth; Wave energy**
Wave Power and Beach Stages: A Global Model, Andrew D. Short, 1145
- Wave height; Wave spectra; Wave tanks; Breakwaters; Damage; Hydraulic models; Rubble-mound breakwaters; Stability; Wave energy**
Effects of Wave Grouping on Breakwater Stability, R. R. Johnson, E. P.D. Mansard and J. Ploeg, 2228
- Wave height; Wave spectra; Wind velocity; Distribution functions; Predictions; Rainfall; Samples; Sampling; Wave energy**
Extremal Prediction of Significant Wave Height, Enrique Copeiro, 285
- Wave interference; Computation; Cylindrical bodies; Experimentation; Model tests; Numerical analysis; Files; Transverse waves; Wave energy; Wave height**
Wave Forces on a Row of Cylindrical Piles of Large Diameter, J. C.W. Berkhoff and J. V.D. Weide, 2433
- Wavelength; Experimental data; Flumes; Gravity waves; Interactions; Waveforms; Wave height**
Changes in Height of Short Waves on Long Waves, Michio Sato and Kazuo Nakamura, 400
- Wavelength; Imaging; Ocean waves; Radar; Radar photography; Surveys (data collection); Wave energy; Wave height**
The Use of Imaging Radar in Studying Ocean Waves, M. G. Mattie and D. Lee Harris, 174
- Wavelength; Wave period; Wave refraction; Refraction (water waves); Shear flow; Water depth; Wave action; Wave height**
Wave Refraction Across a Shearing Current, Ivar G. Jonsson and Ove Skovgaard, 722
- Wavelength; Wave period; Waves; Wave tanks; Wave velocity; Beaches; Random processes; Slopes; Water depth; Wave height**
Wave Length, Wave Velocity and Shoaling Characteristics of Random Waves, Akira Kimura and Yuichi Iwagaki, 320
- Wavelength; Wave propagation; Wave reflection; Wave refraction; Mathematical models; Shallow water; Water depth; Wave action; Wave diffraction**
Computations of Short Waves in Shallow Water, M. B. Abbott, H. M. Petersen and Ove Skovgaard, 414

- Wavelength; Wave propagation; Wind; Wind speed; Hurricanes; Mathematical models; Models; Numerical analysis; Radar operation; Storms**
Radar Observations of Hurricane Wave Directions, B. D. King and O. H. Shemdin, 209
- Wavelength; Waves; Breaking energy; Classification; Field tests; Photographic analysis; Predictions; Water depth; Wave height**
Field Study of Breaking Wave Characteristics, Lee L. Weishar and Robert J. Byrne, 487
- Wavelength; Waves; Wave spectra; Wave tanks; Hydrodynamic pressure; Numerical analysis; Stochastic processes; Wave generation; Wave height**
An Inclined-Plate Wave Generator, Fredric Raichlen and Jiin-Jen Lee, 388
- Wavelength; Wave tanks; Breakwaters; Permeability; Shallow water; Standing waves; Tests; Wave diffraction; Wave energy; Wave height**
Wave Height Distribution Around Permeable Breakwaters, Shintaro Hotta, 695
- Wavelengths; Wave velocity; Beach erosion; Beaches; Beach sands; Edge effect; Littoral current; Littoral drift; Wave action**
Beach Cusps and Edge Waves, David A. Huntley and A. J. Bowen, 1378
- Wave measurement; Acoustic measuring instruments; Currents (water); Ocean bottom; Surface waves; Water depth; Wave energy**
Near-Bottom Current Measured by Acoustic Sensors, K. A. Selanger and T. Carstens, 878
- Wave period; Accuracy; Beach erosion; Field tests; Laboratory tests; Measurement; Sediments; Water depth; Wave height**
Uses for a Calculated Limit Depth to Beach Erosion, Robert J. Hallermeier, 1493
- Wave period; Australia; Breakwaters; Maintenance; Site selection; Storm surges; Tidal effects; Tidal waters; Wave height**
Rosslyn Bay Breakwater, Queensland, Australia, D. N. Foster, B. L. McGrath and W. Bremner, 2086
- Wave period; Bars (riverine); Beach erosion; Lakes; Nile River Valley; Oceans; Sediment deposits; Sediment load; Sediment transport; Storms; Water depth; Wave equations**
Undulated Bottom Profiles and Onshore-Offshore Transport, Madhav Manohar, 1454
- Wave period; Beaches; Coastal engineering; Laboratory tests; Movable bed models; Scale effect; Sediments; Sediment transport; Wave height**
Scale Relations for Equilibrium Beach Profiles, Hideaki Noda, 1531
- Wave period; Beaches; Littoral current; Models; Sediment concentration; Sediment load; Sediment transport; Two-dimensional**
Onshore-Offshore Sediment Movement on a Beach, P. Nielsen, I. A. Svendsen and C. Staub, 1475
- Wave period; Coastal plains; Confidence level; Ocean waves; Probability distribution functions; Shore protection; Statistical analysis; Wave height**
On Long-Term Statistics for Ocean and Coastal Waves, Michel K. Ochi, 59
- Wave period; Fourier transformation; Gravity waves; Storm surges; Surf; Water levels; Wave action; Wave dispersion**
Anomalous Dispersion of Fourier Components of Surface Gravity Waves in the Near Shore Area, Fritz Busching, 247
- Wave period; Littoral deposits; Sediment concentration; Sediment transport; Sensors; Storms; Surf; Suspended sediments**
Storm Induced Periodicities of Suspended Sand Movement, Jay E. Leonard and Benno M. Brennkmeier, 1744
- Wave period; Wave pressure; Wave reflection; Breakwaters; Slots; Standing waves; Storms; Storm surges; Wave height**
Wave Pressures on Split-Type Breakwaters, Shoshichiro Nagai and Shohachi Kakuno, 2360
- Wave period; Wave pressure; Wind loads; Wind pressure; Dynamic response; Oscillation; Responses; Simulation; Wave damping; Wave energy**
Simulation of Wave/Wind Forced Harbor Oscillation, S. K. Liu, H. S. Hou and Charles C. C. Chang, 2551
- Wave period; Wave propagation; Cylindrical bodies; Displacement; Dynamic characteristics; Dynamic response; Experimentation; Piles**
Dynamic Behavior of Vertical Cylinder due to Wave Force, Toru Sawaragi and Takayuki Nakamura, 2378
- Wave period; Wave recorders (water waves); Brazil; Meteorology; Ocean waves; Wave action; Wave energy; Wave height**
Wave Climate in Some Zones off the Brazilian Coast, Alberto Homsi, 114
- Wave period; Wave recorders (water waves); Wave spectrum; Brazil; Current meters; Harbor facilities; Littoral current; Littoral drift; Water depth; Wave height**
Coastal Study of Espirito Santo Brazil, Paulo Augusto Vivacqua, Hildebrando de Araujo Goes Filho and Octavio de Sampaio Ferraz Jardim Sayao, 2104
- Wave period; Wave refraction; Armoring (streambed); Open channel flow; Performance; Standardization; Test reproducibility; Tests; Turbulent flow**
Performance of Dolos Blocks in an Open Channel Situation, Arthur Brebner, 2305
- Wave period; Wave refraction; Refraction (water waves); Shear flow; Water depth; Wave action; Wave height; Wavelength**
Wave Refraction Across a Shearing Current, Ivar G. Jonsson and Ove Skovgaard, 722
- Wave period; Wave refraction; Wave velocity; Rip currents; Sediment transport; Shoaling; Water waves; Wave diffraction; Wave height**
Rip Currents and Their Causes, Robert A. Dalrymple, 1414
- Wave period; Wave runoff; Wave spectra; Damage; Dikes; Hydrodynamics; Statistical analysis; Wave height**
New Dike Design Criteria Based on Wave Spectra, Hans Kaldenhoff and Suhan M. Gokcesu, 2500

- Wave period; Waves; Amplitude; Buoys; Drifting (aquatic); Floating bodies; Mass transfer; Wave height**
Drift Speed of Buoys in Waves, John H. Nath, 859
- Wave period; Waves; Breakwaters; Ocean waves; Pneumatic systems; Underwater structures; Wave damping; Wave energy**
Combination Effect of Pneumatic Breakwater and Other Type Breakwater on Wave Damping, Yuichi Iwagaki, Toshiyuki Asano and Tsutomu Honda, 2172
- Wave period; Waves; Coral reefs and islands; Energy; Probability density functions; Spectral analysis; Surf; Wave action; Wave height**
The Energy Spectra of Surf Waves on a Coral Reef, Theodore T. Lee and Kerry P. Black, 588
- Wave period; Waves; Currents (water); Field tests; Sands; Sediment transport; Suspended load; Suspended sediments; Tidal effects; Wave action; Wave energy**
Effect of Waves on Sand Transport by Currents, Michael W. Owen and Michael F.C. Thorn, 1675
- Wave period; Waves; Wave spectra; Breaking energy; Ocean waves; Probability density functions; Probability theory; Secondary waves; Surf; Wave height**
Probability Density Functions of Breaking Waves, Edward B. Thornton and George Schaeffer, 507
- Wave period; Waves; Wave tanks; Wave velocity; Beaches; Random processes; Slopes; Water depth; Wave height; Wavelength**
Wave Length, Wave Velocity and Shoaling Characteristics of Random Waves, Akira Kimura and Yuichi Iwagaki, 320
- Wave period; Waves; Wind velocity; Beaches; Littoral current; Measurement; Surf; Suspended sediments; Water sampling; Wave height**
Surf Zone Measurements of Suspended Sediment, Timothy W. Kana, 1725
- Wave period; Wave spectra; Correlation techniques; Ocean waves; Offshore structures; Shore protection; Wave height**
The Observed Joint Distribution of Periods and Heights of Sea Waves, Yoshimi Goda, 227
- Wave period; Wave spectrum; Aquifers; Ground water; Groundwater elevation; Littoral current; Oscillations; Piezometers; Wave height**
Beach Ground-Water Oscillations, Andrzej Lewandowski and Ryszard B. Zeidler, 2051
- Wave period; Wave velocity; Canals; Field tests; Gravity waves; Hurricanes; Sediments; Sediment transport; Storms; Storm surges; Wave energy**
Infragravity Waves in Storm Conditions, R. A. Holman, David A. Huntley and A. J. Bowen, 268
- Wave phases; Bathymetry; Bays (topographic features); Beach erosion; Beaches; Breakwaters; Diffraction; Sediment transport; Wave diffraction; Wave height**
Diffraction Calculation of Shoreline PlanForms, Robert G. Dean, 1903
- Wave pressure; Armoring (streambed); Costs; Revetments; Rubble-mound breakwaters; Slope stability; Stability; Wave energy**
Blanket Theory and Low Cost Revetments, C. T. Brown, 2510
- Wave pressure; Barriers; Impact; Marine structures; Mathematical models; Pressure distribution; Scale effect; Standing waves; Storm surges; Wave energy**
A Model Law for Wave Impacts on Coastal Structures, C. Ramkema, 2308
- Wave pressure; Cooling water; Loads (forces); Outfall sewers; Scale effect; Tests; Thermal pollution; Wave energy; Wave height**
Non-Breaking and Breaking Wave Loads on a Cooling Water Outfall, G. R. Mogridge and W. W. Jamieson, 2461
- Wave pressure; Cylindrical bodies; Drag; Experimentation; Loads (forces); Predictions; Reynolds number; Water flow; Wave energy**
Wave Loads on Horizontal Cylinders, P. Holmes and J. R. Chaplin, 2449
- Wave pressure; Wave reflection; Breakwaters; Slots; Standing waves; Storms; Storm surges; Wave height; Wave period**
Wave Pressures on Split-Type Breakwaters, Shoshichiro Nagai and Shohachi Kakuno, 2360
- Wave pressure; Wave spectra; Hydrodynamic pressure; Impact; Impact forces; Measurement; Scale effect; Water waves; Wave energy**
Impact Wave Forces on Vertical and Horizontal Plate, S. R. Massel, M. Oleszkiewicz and W. Trapp, 2340
- Wave pressure; Wave tanks; Groups; Loading; Load transfer; Marine structures; Ocean waves; Wave action**
Load Analysis from Wave Groups, A. I. Kuznetsov and G. D. Khaskhatchikh, 2328
- Wave pressure; Wind loads; Wind pressure; Dynamic response; Oscillation; Responses; Simulation; Wave damping; Wave energy; Wave period**
Simulation of Wave/Wind Forced Harbor Oscillation, S. K. Liu, H. S. Hou and Charles C.C. Chang, 2551
- Wave propagation; Cylindrical bodies; Displacement; Dynamic characteristics; Dynamic response; Experimentation; Piles; Wave period**
Dynamic Behavior of Vertical Cylinder due to Wave Force, Toru Sawaragi and Takayuki Nakamura, 2378
- Wave propagation; Wave reflection; Wave refraction; Mathematical models; Shallow water; Water depth; Wave action; Wave diffraction; Wavelength**
Computations of Short Waves in Shallow Water, M. B. Abbott, H. M. Petersen and Ove Skovgaard, 414
- Wave propagation; Waves; Barriers; Friction coefficient (hydraulic); Littoral current; Shores; Stresses; Surf; Water circulation; Wave energy**
Longshore Currents Due to Surf Zone Barrier, P. Bettess, C. A. Fleming, J. C. Heinrich, O. C. Zienkiewicz and D. I. Austin, 776
- Wave propagation; Waves; Surf; Surface waves; Turbulence; Vibration; Wave action; Wave energy; Wave equations; Wave height**
Wave Characteristics in the Surf Zone, I. A. Svendsen, P. A. Madsen and J. Buhr Hansen, 520

- Wave propagation; Waves; Wave spectra; Bathymetry; Correlation analysis; Deep water; Frequencies; Intensity; Wave energy**
 Deepwater Direction from an Intensity Array, Alan L. Higgins and Richard J. Seymour, 305
- Wave propagation; Waves; Wave spectra; Mathematical models; Numerical analysis; Ocean waves; Scale effect; Three-dimensional; Wave height**
 Natural Wave Trains: Description and Reproduction, H. Lundgren and S. E. Sand, 312
- Wave propagation; Waves; Wave velocity; Bores (wave); Breaking energy; Hydraulic jump; Water depth; Wave height**
 Spilling Breakers, Bores and Hydraulic Jumps, D. H. Peregrine and I. A. Svendsen, 540
- Wave propagation; Wave spectra; Dissipation; Friction coefficient (hydraulic); Ocean bottom; Water depth; Water waves; Wave dispersion; Wave energy**
 Bottom Dissipation in Finite-Depth Water Waves, S. V. Hsiao and O. H. Shemdin, 434
- Wave propagation; Wave velocity; Boundary conditions; Mathematical models; Sand; Shear stress; Turbulent flow; Velocity distribution**
 Near-Bottom Velocities in Waves with a Current, W. T. Bakker and Th. van Doorn, 1394
- Wave propagation; Wave velocity; Estuaries; Field data; Flood protection; Mathematical models; Numerical analysis; Surveys (data collection); Tidal effects; Water levels**
 Adjustment and Verification of the RANDDELTA II Model, A. Langerak, M. A.M. deRas and J. J. Leendertse, 1049
- Wave propagation; Wind; Wind speed; Hurricanes; Mathematical models; Models; Numerical analysis; Radar operation; Storms; Wavelength**
 Radar Observations of Hurricane Wave Directions, B. D. King and O. H. Shemdin, 209
- Wave propagation; Wind loads; Boundary conditions; Coastal plains; Mixing; Ocean engineering; Ocean waves; Rivers; Runoff; Suspended sediments; Two-dimensional**
 Mixed Layer Models for Coastal Waters, W. J. Wiseman, Jr., L. J. Rouse, Jr. and O. K. Huh, 2619
- Wave recorders (water waves); Brazil; Meteorology; Ocean waves; Wave action; Wave energy; Wave height; Wave period**
 Wave Climate in Some Zones off the Brazilian Coast, Alberto Homs, 114
- Wave recorders (water waves); Buoys; Design criteria; Offshore platforms; Offshore structures; Surveys (data collection); Wave energy; Wave height**
 Comparison of Shipborne Wave Recorder and Waverider Buoy Data Used to Generate Design and Operational Planning Criteria, C. G. Graham, G. Verboom and C. J. Shaw, 97
- Wave recorders (water waves); Forecasting; Hawaii; Meteorological data; Meteorology; Statistical analysis; Wave height**
 An Evaluation of Extreme Wave Climate at Keahole Point, Hawaii, Charles L. Bretschneider and Richard E. Rocheleau, 152
- Wave recorders (water waves); International compacts; Inventories; Questionnaires; Surveys (data collection); Wave height**
 A World Wave Data Centre, Laurence Draper, 51
- Wave recorders (water waves); Wave runup; Coastal plains; Dynamic loads; Shore protection; Storm surges; Surf; Water levels; Wave energy**
 Wave Set-Up in the Surf Zone, Uwe A. Hansen, 1071
- Wave recorders (water waves); Waves; Breakwaters; Field tests; Harbors; Laboratory tests; Models; Prototypes**
 A Comparison Between Model and Prototype Waves in Harbours, Sverre Bjordal and Alf Torum, 677
- Wave recorders (water waves); Wave spectra; Wind forces; Wind pressure; Breakwaters; Laboratory tests; Wave diffraction; Wave energy; Wave generation**
 Wind-Generated Wave Diffraction by Breakwater Gap, Hooshang Raissi and R. L. Wigle, 609
- Wave recorders (water waves); Wave spectrum; Brazil; Current meters; Harbor facilities; Littoral current; Littoral drift; Water depth; Wave height; Wave period**
 Coastal Study of Espirito Santo Brazil, Paulo Augusto Vivacqua, Hildebrando de Araujo Goes Filho and Octavio de Sampaio Ferraz Jardim Sayao, 2104
- Wave recorders (water waves); Wind forces; Wind pressure; Australia; Cyclones; Frequencies; Mathematical models; Probability distribution functions; Tropical cyclones; Wave equations**
 Wind Wave Frequencies in a Tropical Cyclone Region, Rodney J. Sobey, 76
- Wave reflection; Beach erosion; Coastal structures; Dikes; Erosion control; Japan; Land reclamation; Scouring; Sea walls; Shore protection; Wave energy**
 Effectiveness of Seadikes with Rough Slope, Osamu Toyoshima, 2528
- Wave reflection; Beaches; Littoral current; Littoral deposits; Littoral drift; Surf; Turbulence; Wave dispersion; Wave energy; Wave height**
 Morphodynamic Variability of High-Energy Beaches, Lynn Donelson Wright, B. G. Thom and John Chappell, 1180
- Wave reflection; Breakwaters; Computer programs; Harbors; Hydraulic models; Numerical analysis; Wave diffraction; Wave height**
 A Numerical Approach for the Determination of the Wave Height Distribution in a Harbour, Soren Kohlhasse, Karl-Friedrich Daemrich, U. Berger, E. Tautenhain and O. Burkhardt, 664
- Wave reflection; Breakwaters; Experimentation; Friction coefficient (hydraulic); Ocean waves; Predictions; Wave dispersion; Wave height**
 Wave Transmission through Trapezoidal Breakwaters, Ole Secher Madsen, Paisal Shusang and Sue Ann Hanson, 2140
- Wave reflection; Breakwaters; Model tests; Reflection; Refraction; Walls; Wave action; Wave diffraction**
 Influence of Breakwater-Reflection on Diffraction, Karl-Friedrich Daemrich and Soren Kohlhasse, 651

- Wave reflection; Breakwaters; Slits; Standing waves; Storms; Storm surges; Wave height; Wave period; Wave pressure**
Wave Pressures on Split-Type Breakwaters, Shoshichiro Nagai and Shohachi Kakuno, 2360
- Wave reflection; Drag; Experimentation; Friction coefficient (hydraulic); Friction studies; Wave action; Wave energy**
Non-Conservative Wave Interaction with Fixed Semi-Immersed Rectangular Structures, Robert B. Steimer and Charles K. Sollitt, 2209
- Wave reflection; Wave refraction; Mathematical models; Shallow water; Water depth; Wave action; Wave diffraction; Wavelength; Wave propagation**
Computations of Short Waves in Shallow Water, M. B. Abbott, H. M. Petersen and Ove Skovgaard, 414
- Wave reflection; Waves; Wave spectra; Beaches; Edge effect; Littoral current; Morphology; Resonance; Surf**
Surf Zone Resonance and Coupled Morphology, John Chappell and Lynn Donelson Wright, 1359
- Wave reflection; Wave spectra; Breakwaters; Diffraction; Ocean waves; Random processes; Wave diffraction; Wave height**
Diffraction Diagrams for Directional Random Waves, Yoshimi Goda, Tomotsuka Takayama and Yasumasa Suzuki, 628
- Wave refraction; Approximation method; Finite element method; Harbors; Integral equations; Oscillations; Tides; Water waves; Wave diffraction**
A Combined FE-BIE Method for Water Waves, A. Hauguel, 715
- Wave refraction; Armoring (streambed); Open channel flow; Performance; Standardization; Test reproducibility; Tests; Turbulent flow; Wave period**
Performance of Dolos Blocks in an Open Channel Situation, Arthur Brebner, 2305
- Wave refraction; Coastal plains; Dredging; Gravel; Great Britain; Licensing; Littoral drift; Sand; Shore protection; Tidal currents; Wave action; Wave energy**
The Effect of Offshore Dredging on Coastlines, W. A. Price, J. M. Motyka and L. J. Jaffrey, 1347
- Wave refraction; Mathematical models; Shallow water; Water depth; Wave action; Wave diffraction; Wavelength; Wave propagation; Wave reflection**
Computations of Short Waves in Shallow Water, M. B. Abbott, H. M. Petersen and Ove Skovgaard, 414
- Wave refraction; Refraction (water waves); Shear flow; Water depth; Wave action; Wave height; Wavelength; Wave period**
Wave Refraction Across a Shearing Current, Ivar G. Jonsson and Ove Skovgaard, 722
- Wave refraction; Wave velocity; Rip currents; Sediment transport; Shoaling; Water waves; Wave diffraction; Wave height; Wave period**
Rip Currents and Their Causes, Robert A. Dalrymple, 1414
- Wave refraction; Wind loads; Accretion (geomorphology); Beach nourishment; Erosion; Groins (structures); Mathematical models; Rip currents; Shore-line cover; Wave diffraction**
Mathematical Modeling of Shoreline Evolution, Bernard Le Mchoute and Mills Soldate, 1163
- Wave runup; Coastal plains; Dynamic loads; Shore protection; Storm surges; Surf; Water levels; Wave energy; Wave recorders (water waves)**
Wave Set-Up in the Surf Zone, Uwe A. Hansen, 1071
- Wave runup; Waves; Wave spectra; Wind velocity; Estuaries; Reefs; Storms; Tidal currents; Wave action; Wave height**
Analysis of Storm Tide Waves, Volker Barthel, 1016
- Wave runup; Waves; Wind speed; Damping; Tidal currents; Tidal energy; Wave damping; Wave dispersion; Wave energy; Wave height**
Wave Climate Study in the Region of the East Frisian Islands and Coast, Hanz Dieter Niemeier, 134
- Wave runup; Wave spectra; Damage; Dikes; Hydrodynamics; Statistical analysis; Wave height; Wave period**
New Dike Design Criteria Based on Wave Spectra, Hans Kaldenhoff and Suhan M. Gokcesu, 2500
- Waves; Amplitude; Buoys; Drifting (aquatic); Floating bodies; Mass transfer; Wave height; Wave period**
Drift Speed of Buoys in Waves, John H. Nath, 859
- Waves; Barriers; Friction coefficient (hydraulic); Littoral current; Shores; Stresses; Surf; Water circulation; Wave energy; Wave propagation**
Longshore Currents Due to Surf Zone Barrier, P. Bettess, C. A. Fleming, J. C. Heinrich, O. C. Zienkiewicz and D. I. Austin, 776
- Waves; Breaking energy; Classification; Field tests; Photographic analysis; Predictions; Water depth; Wave height; Wavelength**
Field Study of Breaking Wave Characteristics, Lee L. Weishar and Robert J. Byrne, 487
- Waves; Breakwaters; Field tests; Harbors; Laboratory tests; Models; Prototypes; Wave recorders (water waves)**
A Comparison Between Model and Prototype Waves in Harbours, Sverre Bjordal and Alf Torum, 677
- Waves; Breakwaters; Japan; Land reclamation; Littoral current; Littoral drift; Movable bed models; Ocean bottom; Sediment transport**
Estimation Using a Movable Bed Model of Shoreline Change Caused by a Reclamation Projected into the Sea, Shoji Sato and Hiroaki Ozasa, 1839
- Waves; Breakwaters; Ocean waves; Pneumatic systems; Underwater structures; Wave damping; Wave energy; Wave period**
Combination Effect of Pneumatic Breakwater and Other Type Breakwater on Wave Damping, Yuichi Iwagaki, Toshiyuki Asano and Tsutomu Honda, 2172

- Waves; Coastal engineering; Mathematical models; Mathematics; Mixing; Physics; Sediments; Structures; Tidal currents; Wave energy**
Struggle of Physics and Mathematics in Coastal Engineering, H. Lundgren, 13
- Waves; Computation; Damping; Spectrum analysis; Tidal effects; Tides; Two-dimensional; Wave damping**
A New Approach for Tidal Computations, C. Le Provost, 1104
- Waves; Coral reefs and islands; Energy; Probability density functions; Spectral analysis; Surf; Wave action; Wave height; Wave period**
The Energy Spectra of Surf Waves on a Coral Reef, Theodore T. Lee and Kerry P. Black, 588
- Waves; Currents (water); Field tests; Sands; Sediment transport; Suspended load; Suspended sediments; Tidal effects; Wave action; Wave energy; Wave period**
Effect of Waves on Sand Transport by Currents, Michael W. Owen and Michael F.C. Thorn, 1675
- Waves; Currents (water); Sediment load; Sediments; Sediment transport; Wave action; Wave energy**
Sediment Load under Waves and Currents, D. H. Willis, 1626
- Waves; Cylindrical bodies; Dynamic response; Loading; Mathematical models; Ocean waves; Responses; Water waves**
Loading and Response of Cylinders in Waves, G. N. Bullock, P. K. Stansby and J. G. Warren, 2415
- Waves; Ocean bottom; Ocean waves; Return flow; Sands; Scouring; Sea walls; Slopes; Tsunamis; Two-dimensional; Water depth; Wave energy**
Scouring at the Toe of a Seawall due to Tsunamis, Hitoshi Nishimura, Akira Watanabe and Kiyoshi Horikawa, 2540
- Waves; Surf; Surface waves; Turbulence; Vibration; Wave action; Wave energy; Wave equations; Wave height; Wave propagation**
Wave Characteristics in the Surf Zone, I. A. Svendsen, P. A. Madsen and J. Buhr Hansen, 520
- Waves; Wave spectra; Bathymetry; Correlation analysis; Deep water; Frequencies; Intensity; Wave energy; Wave propagation**
Deepwater Direction from an Intensity Array, Alan L. Higgins and Richard J. Seymour, 305
- Waves; Wave spectra; Beaches; Edge effect; Littoral current; Morphology; Resonance; Surf; Wave reflection**
Surf Zone Resonance and Coupled Morphology, John Chappell and Lynn Donelson Wright, 1359
- Waves; Wave spectra; Breaking energy; Ocean waves; Probability density functions; Probability theory; Secondary waves; Surf; Wave height; Wave period**
Probability Density Functions of Breaking Waves, Edward B. Thornton and George Schaeffer, 507
- Waves; Wave spectra; Mathematical models; Numerical analysis; Ocean waves; Scale effect; Three-dimensional; Wave height; Wave propagation**
Natural Wave Trains: Description and Reproduction, H. Lundgren and S. E. Sand, 312
- Waves; Wave spectra; Wave tanks; Hydrodynamic pressure; Numerical analysis; Stochastic processes; Wave generation; Wave height; Wavelength**
An Inclined-Plate Wave Generator, Fredric Raichlen and Jjin-Jen Lee, 388
- Waves; Wave spectra; Wave tanks; Wave velocity; Wind forces; Wind pressure; Currents (water); Experimentation; Fetch; Wave generation; Wave height**
Experimental Study of Wind Waves Generated on Currents, Hajime Kato and Hiroichi Tsuruya, 742
- Waves; Wave spectra; Wave velocity; Currents (water); Edge effect; Frequencies; Littoral current; Ocean waves; Wave energy**
Observation of Nearshore Current and Edge Waves, Tamio O. Sasaki and Kiyoshi Horikawa, 791
- Waves; Wave spectra; Wind velocity; Estuaries; Reefs; Storms; Tidal currents; Wave action; Wave height; Wave runoff**
Analysis of Storm Tide Waves, Volker Barthel, 1016
- Waves; Wave spectrum; Mud; Mud systems; Sediment concentration; Sediment transport; Shallow water; Suspended sediments; Tidal effects; Wave height**
Suspension and Transportation of Fluid Mud by Solitary-Like Waves, John T. Wells, James M. Coleman and W. J. Wiseman, Jr., 1932
- Waves; Wave tanks; Beaches; Edge effect; Excitation; Interactions; Standing waves; Water depth**
Excitation of Low Frequency Trapped Waves, Robert King and Ronald Smith, 449
- Waves; Wave tanks; Coastal plains; Currents (water); Ripple marks; Sediment transport; Shear stress; Three-dimensional; Wave height**
Sediment Transport and Ripples Due to Waves and Currents, Zbigniew Pruszek and Ryszard B. Zeidler, 1638
- Waves; Wave tanks; Wave velocity; Beaches; Random processes; Slopes; Water depth; Wave height; Wavelength; Wave period**
Wave Length, Wave Velocity and Shoaling Characteristics of Random Waves, Akira Kimura and Yuichi Iwagaki, 320
- Waves; Wave tanks; Wave velocity; Ocean waves; Offshore structures; Predictions; Random processes; Vibration; Wave equations; Wave generation; Wave height**
Periodic Theory Velocity Prediction in Random Wave, John H. Nath and Koji Kobune, 340
- Waves; Wave velocity; Beaches; Breaking energy; Deep water; Particle trajectories; Slope; Velocity**
Estimation of Water Particle Velocity of Breaking Wave, Tetsuo Sakai and Yuichi Iwagaki, 551
- Waves; Wave velocity; Bores (wave); Breaking energy; Hydraulic jump; Water depth; Wave height; Wave propagation**
Spilling Breakers, Bores and Hydraulic Jumps, D. H. Peregrine and I. A. Svendsen, 540
- Waves; Wave velocity; Coastal plains; Eigenvalues; Mass; Momentum; Offshore structures; Rip currents; Spacing; Surf; Wave action**
Rip Current Spacing as an Eigenvalue, Noriyuki Iwata, 828

- Waves; Wind; Bathymetry; Bores (wave); Field tests; Littoral current; Model tests; Storms; Surf; Water circulation; Water levels; Wave height**
Comparison of Model and Observed Nearshore Circulation, James H. Allender, John D. Ditmars, Wyman Harrison and Robert A. Paddock, 810
- Waves; Wind; Currents (water); Design criteria; Energy conversion; Environmental effects; Environmental impact statements; Hurricanes; Site selection; Thermal energy**
Some Design Criteria for OTEC Installations for Keahole Point, Hawaii, Frederick C. Munchmeyer and Charles L. Bretschneider, 2633
- Waves; Wind; Wind speed; Buoys; Hurricanes; Measurement; Monitoring; Offshore platforms; Radar operation; Wave height**
HF Skywave Radar Measurement of Hurricane Winds and Waves, Joseph W. Maresca, Jr. and Christopher T. Carlson, 190
- Waves; Wind loads; Model studies; Monsoons; Tidal currents; Tidal hydraulics; Water circulation; Water levels**
The Wind-Driven Circulation in the Northern Arabian Sea, Khawaja Zafar Elahi and Jurgen Sundermann, 2708
- Waves; Wind pressure; Field tests; Laboratory tests; Ocean bottom; Oscillation; Ripple marks; Shallow water**
On the Geometry of Ripples Due to Waves, M. S. Yalin and E. Karahan, 1776
- Waves; Wind speed; Damping; Tidal currents; Tidal energy; Wave damping; Wave dispersion; Wave energy; Wave height; Wave runoff**
Wave Climate Study in the Region of the East Frisian Islands and Coast, Hanz Dieter Niemeyer, 134
- Waves; Wind velocity; Beaches; Littoral current; Measurement; Surf; Suspended sediments; Water sampling; Wave height; Wave period**
Surf Zone Measurements of Suspended Sediment, Timothy W. Kana, 1725
- Wave spectra; Accretion (geomorphology); Beach erosion; Beaches; Dynamic models; Geomorphology; Three-dimensional; Water depth; Wave energy; Wave height**
Wave Power and Beach Stages: A Global Model, Andrew D. Short, 1145
- Wave spectra; Bathymetry; Correlation analysis; Deep water; Frequencies; Intensity; Wave energy; Wave propagation; Waves**
Deepwater Direction from an Intensity Array, Alan L. Higgins and Richard J. Seymour, 305
- Wave spectra; Beaches; Edge effect; Littoral current; Morphology; Resonance; Surf; Wave reflection; Waves**
Surf Zone Resonance and Coupled Morphology, John Chappell and Lynn Donelson Wright, 1359
- Wave spectra; Breaking energy; Ocean waves; Probability density functions; Probability theory; Secondary waves; Surf; Wave height; Wave period; Waves**
Probability Density Functions of Breaking Waves, Edward B. Thornton and George Schaeffer, 507
- Wave spectra; Breakwaters; Diffraction; Ocean waves; Random processes; Wave diffraction; Wave height; Wave reflection**
Diffraction Diagrams for Directional Random Waves, Yoshimi Goda, Tomotsuka Takayama and Yasumasa Suzuki, 628
- Wave spectra; Calculations; Fourier transformation; Interactions; Nonlinear systems; Sampling; Spectral analysis**
Higher Order Wave Spectra, Paul C. Liu and Albert W. Green, 360
- Wave spectra; Correlation techniques; Ocean waves; Offshore structures; Shore protection; Wave height; Wave period**
The Observed Joint Distribution of Periods and Heights of Sea Waves, Yoshimi Goda, 227
- Wave spectra; Damage; Dikes; Hydrodynamics; Statistical analysis; Wave height; Wave period; Wave runoff**
New Dike Design Criteria Based on Wave Spectra, Hans Kaldenhoff and Suhan M. Gokcesu, 2500
- Wave spectra; Dissipation; Friction coefficient (hydraulic); Ocean bottom; Water depth; Water waves; Wave dispersion; Wave energy; Wave propagation**
Bottom Dissipation in Finite-Depth Water Waves, S. V. Hsiao and O. H. Shemdin, 434
- Wave spectra; Dynamic pressure; Frequencies; Hydrodynamic pressure; Responses; Stochastic processes; Wave generation**
Analysis of Hinged Wavemakers for Random Waves, Robert T. Hudspeth, Douglas F. Jones and John H. Nath, 372
- Wave spectra; Edge effect; Gravity waves; Littoral current; Rip currents; Surf; Temporal distribution; Variations**
Variability of Longshore Currents, R. T. Guza and Edward B. Thornton, 756
- Wave spectra; Hydrodynamic pressure; Impact; Impact forces; Measurement; Scale effect; Water waves; Wave energy; Wave pressure**
Impact Wave Forces on Vertical and Horizontal Plate, S. R. Massel, M. Oleszkiewicz and W. Trapp, 2340
- Wave spectra; Mathematical models; Numerical analysis; Ocean waves; Scale effect; Three-dimensional; Wave height; Wave propagation; Waves**
Natural Wave Trains: Description and Reproduction, H. Lundgren and S. E. Sand, 312
- Wave spectra; Wave tanks; Breakwaters; Damage; Hydraulic models; Rubble-mound breakwaters; Stability; Wave energy; Wave height**
Effects of Wave Grouping on Breakwater Stability, R. R. Johnson, E. P.D. Mansard and J. Ploeg, 2228
- Wave spectra; Wave tanks; Hydrodynamic pressure; Numerical analysis; Stochastic processes; Wave generation; Wave height; Wavelength; Waves**
An Inclined-Plate Wave Generator, Fredric Raichlen and Jiin-Jen Lee, 388

- Wave spectra; Wave tanks; Wave velocity; Wind forces; Wind pressure; Currents (water); Experimentation; Fetch; Wave generation; Wave height; Waves**
Experimental Study of Wind Waves Generated on Currents, Hajime Kato and Hiroichi Tsuruya, 742
- Wave spectra; Wave velocity; Currents (water); Edge effect; Frequencies; Littoral current; Ocean waves; Wave energy; Waves**
Observation of Nearshore Current and Edge Waves, Tamio O. Sasaki and Kiyoshi Horikawa, 791
- Wave spectra; Wave velocity; Wind velocity; Littoral current; Predictions; Regression analysis; Statistical analysis; Stress; Surf**
Wind-Generated Longshore Currents, Dag Nummedal and Robert J. Finley, 1428
- Wave spectra; Wind forces; Wind pressure; Breakwaters; Laboratory tests; Wave diffraction; Wave energy; Wave generation; Wave recorders (water waves)**
Wind-Generated Wave Diffraction by Breakwater Gap, Hooshang Raissi and R. L. Wigle, 609
- Wave spectra; Wind velocity; Distribution functions; Predictions; Rainfall; Samples; Sampling; Wave energy; Wave height**
Extremal Prediction of Significant Wave Height, Enrique Copeiro, 285
- Wave spectra; Wind velocity; Estuaries; Reefs; Storms; Tidal currents; Wave action; Wave height; Wave runoff; Waves**
Analysis of Storm Tide Waves, Volker Barthel, 1016
- Wave spectrum; Aquifers; Ground water; Groundwater elevation; Littoral current; Oscillations; Piezometers; Wave height; Wave period**
Beach Ground-Water Oscillations, Andrzej Lewandowski and Ryszard B. Zeidler, 2051
- Wave spectrum; Brazil; Current meters; Harbor facilities; Littoral current; Littoral drift; Water depth; Wave height; Wave period; Wave recorders (water waves)**
Coastal Study of Espirito Santo Brazil, Paulo Augusto Vivacqua, Hildebrando de Araujo Goes Filho and Octavio de Sampaio Ferraz Jardim Sayao, 2104
- Wave spectrum; Mud; Mud systems; Sediment concentration; Sediment transport; Shallow water; Suspended sediments; Tidal effects; Wave height; Waves**
Suspension and Transportation of Fluid Mud by Solitary-Like Waves, John T. Wells, James M. Coleman and W. J. Wiseman, Jr., 1932
- Wave tanks; Beaches; Edge effect; Excitation; Interactions; Standing waves; Water depth; Waves**
Excitation of Low Frequency Trapped Waves, Robert King and Ronald Smith, 449
- Wave tanks; Breakwaters; Damage; Hydraulic models; Rubble-mound breakwaters; Stability; Wave energy; Wave height; Wave spectra**
Effects of Wave Grouping on Breakwater Stability, R. R. Johnson, E. P.D. Mansard and J. Ploeg, 2228
- Wave tanks; Breakwaters; Permeability; Shallow water; Standing waves; Tests; Wave diffraction; Wave energy; Wave height; Wavelength**
Wave Height Distribution Around Permeable Breakwaters, Shintaro Hotta, 695
- Wave tanks; Coastal plains; Currents (water); Ripple marks; Sediment transport; Shear stress; Three-dimensional; Wave height; Waves**
Sediment Transport and Ripples Due to Waves and Currents, Zbigniew Pruszek and Ryszard B. Zeidler, 1638
- Wave tanks; Cross sections; Estuaries; Inlets (waterways); Tidal currents; Tidal effects; Tidal flats; Two-dimensional**
Periodic Flows from Tidal Inlets, D. L. Wilkinson, 1336
- Wave tanks; Groups; Loading; Load transfer; Marine structures; Ocean waves; Wave action; Wave pressure**
Load Analysis from Wave Groups, A. I. Kuznetsov and G. D. Khaskhatchikh, 2328
- Wave tanks; Hydrodynamic pressure; Numerical analysis; Stochastic processes; Wave generation; Wave height; Wavelength; Waves; Wave spectra**
An Inclined-Plate Wave Generator, Fredric Raichlen and Jiin-Jen Lee, 388
- Wave tanks; Wave velocity; Beaches; Random processes; Slopes; Water depth; Wave height; Wavelength; Wave period; Waves**
Wave Length, Wave Velocity and Shoaling Characteristics of Random Waves, Akira Kimura and Yuichi Iwagaki, 320
- Wave tanks; Wave velocity; Ocean waves; Offshore structures; Predictions; Random processes; Vibration; Wave equations; Wave generation; Wave height; Waves**
Periodic Theory Velocity Prediction in Random Wave, John H. Nath and Koji Kobune, 340
- Wave tanks; Wave velocity; Wind forces; Wind pressure; Currents (water); Experimentation; Fetch; Wave generation; Wave height; Waves; Wave spectra**
Experimental Study of Wind Waves Generated on Currents, Hajime Kato and Hiroichi Tsuruya, 742
- Wave tanks; Wind forces; Wind pressure; Wind velocity; Drifting (aquatic); Water depth; Water surface**
Wind-Induced Water Surface Set-Up and Drift Currents, Frederick L.W. Tang, Jin Wu, Charles C.C. Chang and Shan-Hwei Ou, 841
- Wave velocity; Beach erosion; Beaches; Beach sands; Edge effect; Littoral current; Littoral drift; Wave action; Wavelengths**
Beach Cusps and Edge Waves, David A. Huntley and A. J. Bowen, 1378
- Wave velocity; Beaches; Breaking energy; Deep water; Particle trajectories; Slope; Velocity; Waves**
Estimation of Water Particle Velocity of Breaking Wave, Tetsuo Sakai and Yuichi Iwagaki, 551
- Wave velocity; Beaches; Random processes; Slopes; Water depth; Wave height; Wavelength; Wave period; Waves; Wave tanks**
Wave Length, Wave Velocity and Shoaling Characteristics of Random Waves, Akira Kimura and Yuichi Iwagaki, 320

- Wave velocity; Bores (wave); Breaking energy; Hydraulic jump; Water depth; Wave height; Wave propagation; Waves**
Spilling Breakers, Bores and Hydraulic Jumps, D. H. Peregrine and I. A. Svendsen, 540
- Wave velocity; Boundary conditions; Mathematical models; Sand; Shear stress; Turbulent flow; Velocity distribution; Wave propagation**
Near-Bottom Velocities in Waves with a Current, W. T. Bakker and Th. van Doorn, 1394
- Wave velocity; Canada; Field tests; Gravity waves; Hurricanes; Sediments; Sediment transport; Storms; Storm surges; Wave energy; Wave period**
Infragravity Waves in Storm Conditions, R. A. Holman, David A. Huntley and A. J. Bowen, 268
- Wave velocity; Coastal plains; Eigenvalues; Mass; Momentum; Offshore structures; Rip currents; Spacing; Surf; Wave action; Waves**
Rip Current Spacing as an Eigenvalue, Noriyuki Iwata, 828
- Wave velocity; Currents (water); Edge effect; Frequencies; Littoral current; Ocean waves; Wave energy; Waves; Wave spectra**
Observation of Nearshore Current and Edge Waves, Tamio O. Sasaki and Kiyoshi Horikawa, 791
- Wave velocity; Estuaries; Field data; Flood protection; Mathematical models; Numerical analysis; Surveys (data collection); Tidal effects; Water levels; Wave propagation**
Adjustment and Verification of the RANDDELTA II Model, A. Langerak, M. A.M. deRas and J. J. Leendertse, 1049
- Wave velocity; Flooding; Flowmeters; Inlets (waterways); Stress measurement; Tidal currents; Tidal flats; Velocity; Wave action**
Velocity and Stress Measurements in a Tidal Inlet, David A. Huntley and Dag Nummedal, 1320
- Wave velocity; Ocean waves; Offshore structures; Predictions; Random processes; Vibration; Wave equations; Wave generation; Wave height; Waves; Wave tanks**
Periodic Theory Velocity Prediction in Random Wave, John H. Nath and Koji Kobune, 340
- Wave velocity; Rip currents; Sediment transport; Shoaling; Water waves; Wave diffraction; Wave height; Wave period; Wave refraction**
Rip Currents and Their Causes, Robert A. Dalrymple, 1414
- Wave velocity; Wind forces; Wind pressure; Currents (water); Experimentation; Fetch; Wave generation; Wave height; Waves; Wave spectra; Wave tanks**
Experimental Study of Wind Waves Generated on Currents, Hajime Kato and Hiroichi Tsuruya, 742
- Wave velocity; Wind velocity; Littoral current; Predictions; Regression analysis; Statistical analysis; Stress; Surf; Wave spectra**
Wind-Generated Longshore Currents, Dag Nummedal and Robert J. Finley, 1428
- Weathering; Estuaries; Littoral deposits; Nicaragua; Rainfall; Sedimentation; Sediments; Sediment transport; Water circulation; Wave energy**
Variations of Wave-Energy Levels and Coastal Sedimentation, Eastern Nicaragua, E. H. Owens and H. H. Roberts, 1195
- West Germany; Beaches; Dispersion; Environmental factors; Georgia; Inlets (waterways); Morphology; Sediment deposits; Tidal currents; Tidal effects; Wave energy**
Process-Response Models for Depositional Shorelines: The German and the Georgia Bights, Dag Nummedal and Ian A. Fischer, 1215
- West Germany; Coastal plains; Damage; Ocean waves; Recreational facilities; Storm surges**
Welcoming Address — IV, Hans-Werner Partenscky, 10
- West Germany; Coastal plains; History; Shore protection; Storm surges**
Welcoming Address — I, Karl-Edward Naumann, 1
- West Germany; Dikes; Estuaries; Ports; Shipping; Shore protection; Storms; Tidal currents**
Welcoming Address — II, Helga Elstner, 4
- West Germany; Economic analysis; Environmental factors; Financing; Storms; Storm surges; Tidal waters; Water levels; Waterways (transportation)**
Welcoming Address — III, Volker Hauff, 7
- West Germany; Wind forces; Wind pressure; Wind velocity; Coastal engineering; Flooding; Frequencies; Probability; Storm surges**
Frequencies and Probabilities of Extreme Storm Surges (On the Time-Dependent Changes of the Probability of Extreme Storm Floods at the German North Sea Coast), Alfred Fohrboter, 949
- Wind; Bathymetry; Bores (wave); Field tests; Littoral current; Model tests; Storms; Surf; Water circulation; Water levels; Wave height; Waves**
Comparison of Model and Observed Nearshore Circulation, James H. Allender, John D. Ditmars, Wyman Harrison and Robert A. Paddock, 810
- Wind; Currents (water); Design criteria; Energy conversion; Environmental effects; Environmental impact statements; Hurricanes; Site selection; Thermal energy; Waves**
Some Design Criteria for OTEC Installations for Keahole Point, Hawaii, Frederick C. Munchmeyer and Charles L. Bretschneider, 2633
- Wind; Discharge (water); Hydrodynamics; Meteorology; Rainfall; Salt marshes; Sediment transport; South Carolina; Suspended load; Tidal currents; Tidal effects; Tidal waters**
Hydrodynamics and Sediment Transport in a Salt Marsh Tidal Channel, Larry G. Ward, 1953
- Wind; Wind speed; Buoys; Hurricanes; Measurement; Monitoring; Offshore platforms; Radar operation; Wave height; Waves**
HF Skywave Radar Measurement of Hurricane Winds and Waves, Joseph W. Maresca, Jr. and Christopher T. Carlson, 190

- Wind; Wind speed; Hurricanes; Mathematical models; Models; Numerical analysis; Radar operation; Storms; Wavelength; Wave propagation**
Radar Observations of Hurricane Wave Directions, B. D. King and O. H. Shemdin, 209
- Wind; Wind velocity; Forecasting; Predictions; Storm surges; Tidal currents; Tidal effects; Tidal energy; Tide gages**
Storm Surge Prediction by Combined Wind and Tide Data, Hermann Christiansen and Winfried Siefert, 965
- Wind forces; Forecasting; Mathematical models; Meteorological data; Meteorology; Numerical analysis; Predictions; Simulation; Storm surges; Water levels**
Numerical Storm Surge Forecasting, Manfred Engel, 975
- Wind forces; Wind pressure; Airspeed; Beach erosion; Dunes; Erosion control; Fences; Sands; Sediment deposits; Soil stabilization**
Using Fences to Create and Stabilise Sand Dunes, Brian B. Willetts and Christopher J. Phillips, 2040
- Wind forces; Wind pressure; Australia; Cyclones; Frequencies; Mathematical models; Probability distribution functions; Tropical cyclones; Wave equations; Wave recorders (water waves)**
Wind-Wave Frequencies in a Tropical Cyclone Region, Rodney J. Sobey, 76
- Wind forces; Wind pressure; Breakwaters; Laboratory tests; Wave diffraction; Wave energy; Wave generation; Wave recorders (water waves); Wave spectra**
Wind-Generated Wave Diffraction by Breakwater Gap, Hooshang Raissi and R. L. Wigle, 609
- Wind forces; Wind pressure; Currents (water); Experimentation; Fetch; Wave generation; Wave height; Waves; Wave spectra; Wave tanks; Wave velocity**
Experimental Study of Wind Waves Generated on Currents, Hajime Kato and Hiroichi Tsuruya, 742
- Wind forces; Wind pressure; Wind velocity; Coastal engineering; Flooding; Frequencies; Probability; Storm surges; West Germany**
Frequencies and Probabilities of Extreme Storm Surges (On the Time-Dependent Changes of the Probability of Extreme Storm Floods at the German North Sea Coast), Alfred Fohrboter, 949
- Wind forces; Wind pressure; Wind velocity; Drifting (aquatic); Water depth; Water surface; Wave tanks**
Wind-Induced Water Surface Set-Up and Drift Currents, Frederick L.W. Tang, Jin Wu, Charles C.C. Chang and Shan-Hwei Ou, 841
- Wind loads; Accretion (geomorphology); Beach nourishment; Erosion; Groins (structures); Mathematical models; Rip currents; Shore-line cover; Wave diffraction; Wave refraction**
Mathematical Modeling of Shoreline Evolution, Bernard Le Mehaute and Mills Soldate, 1163
- Wind loads; Aerial photography; Currents (water); Density; Eddies; Eddy currents; Mixing; Tidal currents; Turbulence; Velocity; Water depth**
Large Scale Turbulence in Tidal Currents, John B. Hinwood, 2598
- Wind loads; Bays (topographic features); Currents (water); Diffusion; Eddies; Environmental factors; Simulation; Tidal hydraulics; Water circulation**
Characteristics of Circulation in Bay Waters due to Wind Action, Akira Wada and Ioshihito Miyaike, 2730
- Wind loads; Boundary conditions; Coastal plains; Mixing; Ocean engineering; Ocean waves; Rivers; Runoff; Suspended sediments; Two-dimensional; Wave propagation**
Mixed Layer Models for Coastal Waters, W. J. Wiseman, Jr., L. J. Rouse, Jr. and O. K. Huh, 2619
- Wind loads; Currents (water); Density; Friction coefficient (hydraulic); Model studies; Three-dimensional; Water circulation**
Three Dimensional Modelling of the Irish Sea, Norman Stuart Heaps, 2671
- Wind loads; Currents (water); Eddies; Oil spills; Three-dimensional; Viscosity; Water depth; Water pollution**
3-D Current Model with Depth Varying Eddy Viscosity, Bryan R. Pearce, Cortis Cooper and Susan Nelson, 2602
- Wind loads; Dynamic response; Model studies; Temperature effects; Three-dimensional; Tidal effects; Water flow; Water levels**
Three-Dimensional SGS Energy Model of Eastern Bering Sea, S. K. Liu and J. J. Leendertse, 2687
- Wind loads; Florida; Friction coefficient (hydraulic); Model studies; Salinity; Salt balance; Salt water intrusion; Tidal hydraulics**
Tidal Hydraulics and Salt Balance of Lake Worth, Florida, J. van de Kreeke and J. D. Wang, 2827
- Wind loads; Model studies; Monsoons; Tidal currents; Tidal hydraulics; Water circulation; Water levels; Waves**
The Wind-Driven Circulation in the Northern Arabian Sea, Khawaja Zafar Elahi and Jurgen Sundermann, 2708
- Wind loads; Wind pressure; Dynamic response; Oscillation; Responses; Simulation; Wave damping; Wave energy; Wave period; Wave pressure**
Simulation of Wave/Wind Forced Harbor Oscillation, S. K. Liu, H. S. Hou and Charles C.C. Chang, 2551
- Wind pressure; Airspeed; Beach erosion; Dunes; Erosion control; Fences; Sands; Sediment deposits; Soil stabilization; Wind forces**
Using Fences to Create and Stabilise Sand Dunes, Brian B. Willetts and Christopher J. Phillips, 2040
- Wind pressure; Australia; Cyclones; Frequencies; Mathematical models; Probability distribution functions; Tropical cyclones; Wave equations; Wave recorders (water waves); Wind forces**
Wind Wave Frequencies in a Tropical Cyclone Region, Rodney J. Sobey, 76
- Wind pressure; Breakwaters; Laboratory tests; Wave diffraction; Wave energy; Wave generation; Wave recorders (water waves); Wave spectra; Wind forces**
Wind-Generated Wave Diffraction by Breakwater Gap, Hooshang Raissi and R. L. Wigle, 609

- Wind pressure; Currents (water); Experimentation; Fetch; Wave generation; Wave height; Waves; Wave spectra; Wave tanks; Wave velocity; Wind forces**
Experimental Study of Wind Waves Generated on Currents, Hajime Kato and Hiroichi Tsuruya, 742
- Wind pressure; Dynamic response; Oscillation; Responses; Simulation; Wave damping; Wave energy; Wave period; Wave pressure; Wind loads**
Simulation of Wave/Wind Forced Harbor Oscillation, S. K. Liu, H. S. Hou and Charles C.C. Chang, 2551
- Wind pressure; Field tests; Laboratory tests; Ocean bottom; Oscillation; Ripple marks; Shallow water; Waves**
On the Geometry of Ripples Due to Waves, M. S. Yalin and E. Karahan, 1776
- Wind pressure; Wind velocity; Coastal engineering; Flooding; Frequencies; Probability; Storm surges; West Germany; Wind forces**
Frequencies and Probabilities of Extreme Storm Surges (On the Time-Dependent Changes of the Probability of Extreme Storm Floods at the German North Sea Coast), Alfred Fohrboter, 949
- Wind pressure; Wind velocity; Drifting (aquatic); Water depth; Water surface; Wave tanks; Wind forces**
Wind-Induced Water Surface Set-Up and Drift Currents, Frederick L.W. Tang, Jin Wu, Charles C.C. Chang and Shan-Hwei Ou, 841
- Wind speed; Buoys; Hurricanes; Measurement; Monitoring; Offshore platforms; Radar operation; Wave height; Waves; Wind**
HF Skywave Radar Measurement of Hurricane Winds and Waves, Joseph W. Maresca, Jr. and Christopher T. Carlson, 190
- Wind speed; Damping; Tidal currents; Tidal energy; Wave damping; Wave dispersion; Wave energy; Wave height; Wave runoff; Waves**
Wave Climate Study in the Region of the East Frisian Islands and Coast, Hanz Dieter Niemeyer, 134
- Wind speed; Hurricanes; Mathematical models; Models; Numerical analysis; Radar operation; Storms; Wavelength; Wave propagation; Wind**
Radar Observations of Hurricane Wave Directions, B. D. King and O. H. Shemdin, 209
- Wind velocity; Beaches; Littoral current; Measurement; Surf; Suspended sediments; Water sampling; Wave height; Wave period; Waves**
Surf Zone Measurements of Suspended Sediment, Timothy W. Kana, 1725
- Wind velocity; Coastal engineering; Flooding; Frequencies; Probability; Storm surges; West Germany; Wind forces; Wind pressure**
Frequencies and Probabilities of Extreme Storm Surges (On the Time-Dependent Changes of the Probability of Extreme Storm Floods at the German North Sea Coast), Alfred Fohrboter, 949
- Wind velocity; Distribution functions; Predictions; Rainfall; Samples; Sampling; Wave energy; Wave height; Wave spectra**
Extremal Prediction of Significant Wave Height, Enrique Copeiro, 285
- Wind velocity; Drifting (aquatic); Water depth; Water surface; Wave tanks; Wind forces; Wind pressure**
Wind-Induced Water Surface Set-Up and Drift Currents, Frederick L.W. Tang, Jin Wu, Charles C.C. Chang and Shan-Hwei Ou, 841
- Wind velocity; Estuaries; Reefs; Storms; Tidal currents; Wave action; Wave height; Wave runoff; Waves; Wave spectra**
Analysis of Storm Tide Waves, Volker Barthel, 1016
- Wind velocity; Forecasting; Predictions; Storm surges; Tidal currents; Tidal effects; Tidal energy; Tide gages; Wind**
Storm Surge Prediction by Combined Wind and Tide Data, Hermann Christiansen and Winfried Siefert, 965
- Wind velocity; Littoral current; Predictions; Regression analysis; Statistical analysis; Stress; Surf; Wave spectra; Wave velocity**
Wind-Generated Longshore Currents, Dag Nummedal and Robert J. Finley, 1428

Author Index

- Abbott, M. B.**
Computations of Short Waves in Shallow Water, with
H. M. Petersen and Ove Skovgaard, 414
- Allender, James H.**
Comparison of Model and Observed Nearshore
Circulation, with John D. Ditmars and Wyman
Harrison, 810
- Asano, Toshiyuki**
See Yuichi Iwagaki, 2172
- Baer, Don C.**
See Orville T. Magoon, 1276
- Bakker, W. T.**
Near-Bottom Velocities in Waves with a Current,
with Th. van Doorn, 1394
- Barthel, Volker**
Analysis of Storm Tide Waves, 1016
- Battjes, J. A.**
Energy Loss and Set-Up Due to Breaking of Random
Waves, with J. P.F.M. Janssen, 569
- Berger, U.**
See Soren Kohlhase, 664
- Berkhoff, J. C.W.**
Wave Forces on a Row of Cylindrical Piles of Large
Diameter, with J. V.D. Weide, 2433
- Bettess, P.**
Longshore Currents Due to Surf Zone Barrier, with
C. A. Fleming and J. C. Heinrich, 776
- Bjorndal, Sverre**
A Comparison Between Model and Prototype Waves
in Harbours, with Alf Torum, 677
- Black, Kerry P.**
See Theodore T. Lee, 588
- Blackman, D. L.**
See J. Graff, 931
- Bohlen, W. Frank**
Factors Governing the Distribution of Dredge-
Resuspended Sediments, 2001
- Bothman, David P.**
See Richard J. Seymour, 1542
- Bowen, A. J.**
See R. A. Holman, 268
See David A. Huntley, 1378
- Brebnar, Arthur**
Performance of Dolos Blocks in an Open Channel
Situation, 2305
- Bremner, W.**
See D. N. Foster, 2086
- Brenninkmeyer, Benno M.**
See Jay E. Leonard, 1744
- Bretschneider, Charles L.**
An Evaluation of Extreme Wave Climate at Keahole
Point, Hawaii, with Richard E. Rocheleau, 152
See Frederick C. Munchmeyer, 2633
- Brown, C. T.**
Blanket Theory and Low Cost Revetments, 2510
- Bullock, G. N.**
Loading and Response of Cylinders in Waves, with
P. K. Stansby and J. G. Warren, 2415
- Busching, Fritz**
Anomalous Dispersion of Fourier Components of
Surface Gravity Waves in the Near Shore Area,
247
- Butler, H. Lee**
Coastal Flood Simulation in Stretched Coordinates,
1030
- Byrne, Robert J.**
See Lee L. Weishar, 487
- Carlson, Christopher T.**
See Joseph W. Maresca, Jr., 190
- Carstens, T.**
See K. A. Selanger, 878
- Carver, Robert D.**
Dolos-Armored Breakwaters: Special Consideration,
with D. Donald Davidson, 2263
- Chang, Charles C.C.**
See Frederick L.W. Tang, 841
See S. K. Liu, 2551
- Chang, T. H.**
See Yu-Hwa Hwang, 1614
- Chaplin, J. R.**
See P. Holmes, 2449
- Chappell, John**
Surf Zone Resonance and Coupled Morphology, with
Lynn Donelson Wright, 1359
See Lynn Donelson Wright, 1180
- Christiansen, Hermann**
Storm Surge Prediction by Combined Wind and Tide
Data, with Winfried Siefert, 965
- Coakley, J. P.**
Sled System for Profiling Suspended Littoral Drift,
with J. A. Saville and M. Pedrosa, 1764
- Coleman, James M.**
See John T. Wells, 1932
- Cooper, Cortis**
See Bryan R. Pearce, 2602
- Copeiro, Enrique**
Extremal Prediction of Significant Wave Height, 285
- Crookshank, N. L.**
See E. R. Funke, 2855
- Cross, J. S.**
See Peter Wright, 1705
- Crout, Richard L.**
Shelf and Coastal Boundary Layer Currents, Miskito
Bank of Nicaragua, with Stephen P. Murray, 2715

- Daemrich, Karl-Friedrich**
Influence of Breakwater-Reflection on Diffraction,
with Soren Kohlhase, 651
See Soren Kohlhase, 664
- Dalrymple, Robert A.**
Rip Currents and Their Causes, 1414
See W. A. Dennie, 1282
- Das Gupta, A.**
See Akira Watanabe, 1918
- Dattatri, J.**
Performance Characteristics of Submerged
Breakwaters, with H. Raman and N. Jothi Shankar,
2153
- Davidson, D. Donald**
See Robert D. Carver, 2263
- Davies, A. G.**
Sediment Motion Caused by Surface Water Waves,
with R. H. Wilkinson, 1577
- Davies, A. M.**
Role of 2D and 3D Models in JONSDAP '76, 1085
- Dean, Robert G.**
Diffraction Calculation of Shoreline PlanForms, 1903
See Marc Perlin, 1818
- de Araujo Goes Filho, Hildebrando**
See Paulo Augusto Vivacqua, 2104
- Deguchi, Ichiro**
See Toru Sawaragi, 1596
- Dennie, W. A.**
Case Studies of Delaware's Tidal Inlets: Roosevelt
and Indian River Inlets, with G. A. Lanan and
Robert A. Dalrymple, 1282
- deRas, M. A.M.**
See A. Langerak, 1049
- Dermissis, Vassilios**
See Emmanuel Partheniades, 2778
- de Sampaio Ferraz Jardim Sayao, Octavio**
See Paulo Augusto Vivacqua, 2104
- Ditmars, John D.**
See James H. Allender, 810
- Drapeau, Georges**
Tidal Sedimentation in Gros-CaCouna Harbor, with
Guy Fortin, 1986
- Draper, Laurence**
A World Wave Data Centre, 51
- Dronkers, J.**
Longitudinal Dispersion in Shallow Well-Mixed
Estuaries, 2761
- Duane, David B.**
See Richard J. Seymour, 1555
- Elahi, Khawaja Zafar**
The Wind-Driven Circulation in the Northern
Arabian Sea, with Jurgen Sundermann, 2708
- Elstner, Helga**
Welcoming Address -- II, 4
- Engel, Manfred**
Numerical Storm Surge Forecasting, 975
- Falldorf, Wilfried**
See Horst Schwarze, 2915
- Finley, Robert J.**
See Dag Nummedal, 1428
- Fischer, Ian A.**
See Dag Nummedal, 1215
- Fischer, Karsten**
Numerical Tidal-Salinity Models of the Ems Estuary,
2840
- Fleming, C. A.**
See P. Bettess, 776
- Fohrboter, Alfred**
Frequencies and Probabilities of Extreme Storm
Surges (On the Time-Dependent Changes of the
Probability of Extreme Storm Floods at the
German North Sea Coast), 949
- Fortin, Guy**
See Georges Drapeau, 1986
- Foster, D. N.**
Rosslyn Bay Breakwater, Queensland, Australia, with
B. L. McGrath and W. Bremner, 2086
- Funke, E. R.**
A Hybrid Model of the St. Lawrence River Estuary,
with N. L. Crookshank, 2855
- Gaughan, Michael K.**
Depth of Disturbance of Sand in Surf Zones, 1513
- George, C. B.**
Oscillatory Laminar Flow Above a Rough Bed, with
J. F.A. Sleath, 898
- Gjerp, S. A.**
See T. A. McClimans, 2887
- Goda, Yoshimi**
Diffraction Diagrams for Directional Random Waves,
with Tomotsuka Takayama and Yasumasa Suzuki,
628
The Observed Joint Distribution of Periods and
Heights of Sea Waves, 227
- Gokcesu, Suhan M.**
See Hans Kaldenhoff, 2500
- Graff, J.**
Analysis of Maximum Sea Level in Southern
England, with D. L. Blackman, 931
- Graham, C. G.**
Comparison of Shipborne Wave Recorder and
Waverider Buoy Data Used to Generate Design
and Operational Planning Criteria, with G.
Verboom and C. J. Shaw, 97
- Green, Albert W.**
See Paul C. Liu, 360
- Greer, Matthew N.**
Longshore Sediment Transport Data: A Review, with
Ole Secher Madsen, 1563
- Guza, R. T.**
Variability of Longshore Currents, with Edward B.
Thornton, 756
- Hallermeier, Robert J.**
Uses for a Calculated Limit Depth to Beach Erosion,
1493

- Hamblin, P. F.**
Storm Surge Forecasting Methods in Enclosed Seas, 998
- Hansen, J. Buhr**
See I. A. Svendsen, 520
- Hansen, Uwe A.**
Wave Set-Up in the Surf Zone, 1071
- Hanson, Sue Ann**
See Ole Secher Madsen, 2140
- Harris, D. Lee**
See M. G. Mattie, 174
- Harrison, Wyman**
See James H. Allender, 810
- Harten, Hermann**
Improvements on Tidal Estuaries and the Effects on Tidal Current, 2905
- Hattori, Masataro**
Field Experiment on Beach Gravel Transport, with Takasuke Suzuki, 1688
- Hauff, Volker**
Welcoming Address — III, 7
- Hauguel, A.**
A Combined FE-BIE Method for Water Waves, 715
See J. P. Lepetit, 1715
- Hayakawa, Norio**
See Haruo Higuchi, 2646
- Heaps, Norman Stuart**
Three Dimensional Modelling of the Irish Sea, 2671
- Heinrich, J. C.**
See P. Bettess, 776
- Higgins, Alan L.**
Deepwater Direction from an Intensity Array, with Richard J. Seymour, 305
See Richard J. Seymour, 1542
- Higuchi, Haruo**
Experimental Study on Scale Effect of Tidal Model, with Hideichi Yasuda and Norio Hayakawa, 2646
- Hinwood, John B.**
Large Scale Turbulence in Tidal Currents, 2598
- Hobson, R. D.**
Importance of Handling Losses to Beach Fill Design, with W. R. James, 1873
- Holman, R. A.**
Infragravity Waves in Storm Conditions, with David A. Huntley and A. J. Bowen, 268
- Holmes, P.**
Wave Loads on Horizontal Cylinders, with J. R. Chaplin, 2449
- Homsí, Alberto**
Wave Climate in Some Zones off the Brazilian Coast, 114
- Honda, Tsutomu**
See Yuichi Iwagaki, 2172
- Horikawa, Kiyoshi**
Mixing of Heated Water Discharged in the Surf Zone, with Ming-Chung Lin and Tamio O. Sasaki, 2563
See Tamio O. Sasaki, 791
See Tsuguo Sunamura, 1439
See Hitoshi Nishimura, 2540
- Hotta, Shintaro**
Wave Height Distribution Around Permeable Breakwaters, 695
- Hou, H. S.**
See S. K. Liu, 2551
- Hsiao, S. V.**
Bottom Dissipation in Finite-Depth Water Waves, with O. H. Shemdin, 434
- Hudspeth, Robert T.**
Analysis of Hinged Wavemakers for Random Waves, with Douglas F. Jones and John H. Nath, 372
- Huh, O. K.**
See W. J. Wiseman, Jr., 2619
- Huntley, David A.**
Beach Cusps and Edge Waves, with A. J. Bowen, 1378
Velocity and Stress Measurements in a Tidal Inlet, with Dag Nummedal, 1320
See R. A. Holman, 268
- Hwang, Yu-Hwa**
Littoral Drift along Bayshore of a Barrier Island, with T. H. Chang, 1614
- Ishida, Hajime**
Wave Forces Induced by Irregular Waves on a Vertical Circular Cylinder, with Yuichi Iwagaki, 2397
- Iwagaki, Yuichi**
Combination Effect of Pneumatic Breakwater and Other Type Breakwater on Wave Damping, with Toshiyuki Asano and Tsutomu Honda, 2172
See Akira Kimura, 320
See Tetsuo Sakai, 551
See Hajime Ishida, 2397
- Iwata, Noriyuki**
Rip Current Spacing as an Eigenvalue, 828
- Jaffrey, L. J.**
See W. A. Price, 1347
- James, W. R.**
See R. D. Hobson, 1873
- Jamieson, W. W.**
See G. R. Mogridge, 2461
- Janssen, J. P.F.M.**
See J. A. Battjes, 569
- Jarrett, James T.**
Coastal Processes at Oregon Inlet, North Carolina, 1257
- John, Chacko J.**
See John C. Kraft, 1232
- Johnson, R. R.**
Effects of Wave Grouping on Breakwater Stability, with E. P.D. Mansard and J. Ploeg, 2228

- Jones, Douglas F.**
See Robert T. Hudspeth, 372
- Jonsson, Ivar G.**
Wave Refraction Across a Shearing Current, with Ove Skovgaard, 722
- Kakuno, Shohachi**
See Shoshichiro Nagai, 2360
- Kaldenhoff, Hans**
New Dike Design Criteria Based on Wave Spectra, with Suhan M. Gokcesu, 2500
- Kamphuis, J. W.**
A Model Study of Alongshore Sediment Transport Rate, with J. S. Readshaw, 1656
- Kana, Timothy W.**
Surf Zone Measurements of Suspended Sediment, 1725
- Karahan, E.**
See M. S. Yalin, 1776
- Kashiwamura, Masakazu**
Outflow Dynamics at a River Mouth, with Shizuo Yoshida, 2925
- Kato, Hajime**
Experimental Study of Wind Waves Generated on Currents, with Hiroichi Tsuruya, 742
- Khanna, J.**
Tripod Concept for Pile Structures in Fast Current, with J. S. Wood, 2481
- Khaskhatchikh, G. D.**
See A. I. Kuznetsov, 2328
- Kimura, Akira**
Wave Length, Wave Velocity and Shoaling Characteristics of Random Waves, with Yuichi Iwagaki, 320
- King, B. D.**
Radar Observations of Hurricane Wave Directions, with O. H. Shemdin, 209
- King, Robert**
Excitation of Low Frequency Trapped Waves, with Ronald Smith, 449
- Kobune, Koji**
See John H. Nath, 340
- Kohlhase, Soren**
A Numerical Approach for the Determination of the Wave Height Distribution in a Harbour, with Karl-Friedrich Daemrich and U. Berger, 664
See Karl-Friedrich Daemrich, 651
- Kraft, John C.**
Morphology of Coastal Barriers, Delaware, U.S.A., with Chacko J. John and Evelyn M. Maurmeyer, 1232
- Kuznetsov, A. I.**
Load Analysis from Wave Groups, with G. D. Khaskhatchikh, 2328
- Lam, D. C.L.**
Outfall Diffusion Models for the Coastal Zone, with C. R. Murthy, 2584
- Lamison, C.**
See H. Wang, 2244
- Lanan, G. A.**
See W. A. Dennie, 1282
- Langerak, A.**
Adjustment and Verification of the RANDELTA II Model, with M. A.M. deRas and J. J. Leendertse, 1049
- Lee, Jiin-Jen**
See Fredric Raichlen, 388
- Lee, Theodore T.**
The Energy Spectra of Surf Waves on a Coral Reef, with Kerry P. Black, 588
- Leendertse, J. J.**
See A. Langerak, 1049
See W. J. van de Ree, 2656
See S. K. Liu, 2687
- Le Mehaute, Bernard**
Mathematical Modeling of Shoreline Evolution, with Mills Soldate, 1163
- Leonard, Jay E.**
Storm Induced Periodicities of Suspended Sand Movement, with Benno M. Brenninkmeyer, 1744
- Lepetit, J. P.**
A Numerical Model for Sediment Transport, with A. Hauguel, 1715
- Le Provost, C.**
A New Approach for Tidal Computations, 1104
- Lewandowski, Andrzej**
Beach Ground-Water Oscillations, with Ryszard B. Zeidler, 2051
- Lin, Ming-Chung**
See Kiyoshi Horikawa, 2563
- Liu, Paul C.**
Higher Order Wave Spectra, with Albert W. Green, 360
- Liu, S. K.**
Simulation of Wave/Wind Forced Harbor Oscillation, with H. S. Hou and Charles C.C. Chang, 2551
Three-Dimensional SGS Energy Model of Eastern Bering Sea, with J. J. Leendertse, 2687
- Loubser, C. C.**
See D. H. Swart, 467
- Lundgren, H.**
Natural Wave Trains: Description and Reproduction, with S. E. Sand, 312
Struggle of Physics and Mathematics in Coastal Engineering, 13
- Madsen, Ole Secher**
Wave Transmission through Trapezoidal Breakwaters, with Paisal Shusang and Sue Ann Hanson, 2140
See Matthew N. Greer, 1563
- Madsen, P. A.**
See I. A. Svendsen, 520
- Magoon, Orville T.**
Maintenance of Santa Cruz Harbor, California, U.S.A., with Don C. Baer, 1276
- Mangarella, Peter A.**
Thermal and Biological Impact of LNG Vaporizer Discharge, with Gordon A. Robilliard, 2945

- Manohar, Madhav**
Undulated Bottom Profiles and Onshore-Offshore Transport, 1454
- Mansard, E. P. D.**
See R. R. Johnson, 2228
- Marche, C.**
Stability Study of an Artificial Salt Intrusion in Estuaries, 2798
- Maresca, Joseph W., Jr.**
HF Skywave Radar Measurement of Hurricane Winds and Waves, with Christopher T. Carlson, 190
- Massel, S. R.**
Impact Wave Forces on Vertical and Horizontal Plate, with M. Oleszkiewicz and W. Trapp, 2340
- Mattie, M. G.**
The Use of Imaging Radar in Studying Ocean Waves, with D. Lee Harris, 174
- Maurmeyer, Evelyn M.**
See John C. Kraft, 1232
- McClimans, T. A.**
Numerical Study of Distortion in a Froude Model, with S. A. Gjerp, 2887
- McGrath, B. L.**
See D. N. Foster, 2086
- McGregor, Robert Charles**
Scrap Tyre Breakwaters in Coastal Engineering, with Neil Sinclair Miller, 2191
- Miller, Neil Sinclair**
See Robert Charles McGregor, 2191
- Miyaike, Ioshihito**
See Akira Wada, 2730
- Mogridge, G. R.**
Non-Breaking and Breaking Wave Loads on a Cooling Water Outfall, with W. W. Jamieson, 2461
- Motyka, J. M.**
See W. A. Price, 1347
- Munchmeyer, Frederick C.**
Some Design Criteria for OTEC Installations for Keahole Point, Hawaii, with Charles L. Bretschneider, 2633
- Murray, Stephen P.**
See Richard L. Crout, 2715
- Murthy, C. R.**
See D. C.L. Lam, 2584
- Nagai, Shoshichiro**
Wave Pressures on Split-Type Breakwaters, with Shohachi Kakuno, 2360
- Nakamura, Kazuo**
See Michio Sato, 400
- Nakamura, Takayuki**
See Toru Sawaragi, 2378
- Nasner, Horst**
Time Lag of Dunes for Unsteady Flow Conditions, 1801
- Nath, John H.**
Drift Speed of Buoys in Waves, 859
Periodic Theory Velocity Prediction in Random Wave, with Koji Kobune, 340
See Robert T. Hudspeth, 372
- Naumann, Karl-Edward**
Welcoming Address — I, 1
- Nece, Ronald E.**
Field Data Analysis for Chesapeake Bay Model Verification, with Norman W. Scheffner, 2870
- Nelson, Susan**
See Bryan R. Pearce, 2602
- Nielsen, P.**
Onshore-Offshore Sediment Movement on a Beach, with I. A. Svendsen and C. Staub, 1475
- Niemeyer, Hanz Dieter**
Wave Climate Study in the Region of the East Frisian Islands and Coast, 134
- Nishimura, Hitoshi**
Scouring at the Toe of a Seawall due to Tsunamis, with Akira Watanabe and Kiyoshi Horikawa, 2540
- Noble, Ronald M.**
Coastal Structures' Effects on Shorelines, 2069
- Noda, Hideaki**
Scale Relations for Equilibrium Beach Profiles, 1531
- Nummedal, Dag**
Process-Response Models for Depositional Shorelines: The German and the Georgia Bights, with Ian A. Fischer, 1215
Wind-Generated Longshore Currents, with Robert J. Finley, 1428
See David A. Huntley, 1320
- Ochi, Michel K.**
On Long-Term Statistics for Ocean and Coastal Waves, 59
- Ohtani, Morimasa**
See Isao Yakuwa, 2746
- Oleszkiewicz, M.**
See S. R. Massel, 2340
- Owen, Michael W.**
Effect of Waves on Sand Transport by Currents, with Michael F.C. Thorn, 1675
- Owens, E. H.**
Variations of Wave-Energy Levels and Coastal Sedimentation, Eastern Nicaragua, with H. H. Roberts, 1195
- Ozasa, Hiroaki**
See Shoji Sato, 1839
- Partenscky, Hans-Werner**
Welcoming Address — IV, 10
- Partheniades, Emmanuel**
Interfacial Friction Coefficients in a Two-Layered Stratified Flow, with Vassilios Dermis, 2778
- Pearce, Bryan R.**
3-D Current Model with Depth Varying Eddy Viscosity, with Cortis Cooper and Susan Nelson, 2602

- Pedrosa, M.**
See J. P. Coakley, 1764
- Peregrine, D. H.**
Spilling Breakers, Bores and Hydraulic Jumps, with I. A. Svendsen, 540
- Perlin, Marc**
Prediction of Beach PlanForms with Littoral Controls, with Robert G. Dean, 1818
- Petersen, H. M.**
See M. B. Abbott, 414
- Phillips, Christopher J.**
See Brian B. Willetts, 2040
- Ploeg, J.**
See R. R. Johnson, 2228
- Prandle, David**
Hydrodynamic Modelling of the Southern North Sea, 1122
- Price, W. A.**
The Effect of Offshore Dredging on Coastlines, with J. M. Motyka and L. J. Jaffrey, 1347
Models — Can We Learn from the Past? Some Thoughts on the Design of Breakwaters, 25
- Pruszk, Zbigniew**
Sediment Transport and Ripples Due to Waves and Currents, with Ryszard B. Zeidler, 1638
- Pugh, D. T.**
Extreme Sea Levels from Tide and Surge Probability, with J. M. Vassie, 911
- Puls, W.**
See Jurgen Sundermann, 1787
- Raichlen, Fredric**
An Inclined-Plate Wave Generator, with Jiin-Jen Lee, 388
- Raissi, Hooshang**
Wind-Generated Wave Diffraction by Breakwater Gap, with R. L. Wigel, 609
- Raman, H.**
See J. Dattatri, 2153
- Ramkema, C.**
A Model Law for Wave Impacts on Coastal Structures, 2308
- Readshaw, J. S.**
See J. W. Kamphuis, 1656
- Renger, Eberhard**
Two-Dimension Stability Analysis of Tidal Basins and Tidal Flats of Larger Extent, 1971
- Roberts, H. H.**
See E. H. Owens, 1195
- Robilliard, Gordon A.**
See Peter A. Mangarella, 2945
- Rocheleau, Richard E.**
See Charles L. Bretschneider, 152
- Roelfzema, A.**
Effect of Harbours on Salt Intrusion in Estuaries, with A. G. van Os, 2810
- Rouse, L. J., Jr.**
See W. J. Wiseman, Jr., 2619
- Saegrov, Sveinung**
Prevention of Freezing in Fjords, 2958
- Sakai, Tetsuo**
Estimation of Water Particle Velocity of Breaking Wave, with Yuichi Iwagaki, 551
- Sand, S. E.**
See H. Lundgren, 312
- Sasaki, Tamio O.**
Observation of Nearshore Current and Edge Waves, with Kiyoshi Horikawa, 791
See Kiyoshi Horikawa, 2563
- Sato, Michio**
Changes in Height of Short Waves on Long Waves, with Kazuo Nakamura, 400
- Sato, Shoji**
Estimation Using a Movable Bed Model of Shoreline Change Caused by a Reclamation Projected into the Sea, with Hiroaki Ozasa, 1839
- Saville, J. A.**
See J. P. Coakley, 1764
- Sawaragi, Toru**
Distribution of Sand Transport Rate across a Surf Zone, with Ichiro Deguchi, 1596
Dynamic Behavior of Vertical Cylinder due to Wave Force, with Takayuki Nakamura, 2378
- Schaeffer, George**
See Edward B. Thornton, 507
- Scheffner, Norman W.**
See Ronald E. Nece, 2870
- Schwarze, Horst**
Influence on Temperature Increases in Tidal Rivers Caused by Waste Heat Injections with Respect to Tidal Cycles and Storm Surges, with Wilfried Falldorf, 2915
- Seelig, William N.**
Numerical Model Investigation of Selected Tidal Inlet-Bay System Characteristics, with Robert M. Sorensen, 1319
- Selanger, K. A.**
Near-Bottom Current Measured by Acoustic Sensors, with T. Carstens, 878
- Seymour, Richard J.**
The Nearshore Sediment Transport Study, with David B. Duane, 1555
Tracked Vehicle for Continuous Nearshore Profiles, with Alan L. Higgins and David P. Bothman, 1542
See Alan L. Higgins, 305
- Shankar, N. Jothi**
See J. Dattatri, 2153
- Shaw, C. J.**
See C. G. Graham, 97
- Shemdin, O. H.**
See B. D. King, 209
See S. V. Hsiao, 434
- Short, Andrew D.**
Wave Power and Beach Stages: A Global Model, 1145

- Shusang, Paisal**
See Ole Secher Madsen, 2140
- Siefert, Winfried**
Storm Surge Prediction in Tidal Rivers: A New Conception, 986
See Hermann Christiansen, 965
- Skovgaard, Ove**
See M. B. Abbott, 414
See Ivar G. Jonsson, 722
- Sleath, J. F.A.**
See C. B. George, 898
- Smith, Ronald**
See Robert King, 449
- Sobey, Rodney J.**
Wind Wave Frequencies in a Tropical Cyclone Region, 76
- Soldate, Mills**
See Bernard Le Mehaute, 1163
- Sollitt, Charles K.**
See Robert B. Steimer, 2209
- Sorensen, Robert M.**
See William N. Seelig, 1319
- Standish-White, D. W.**
Problems of Design and Construction of an Offshore SeaWater Intake, with J. A. Zwamborn, 2125
- Stansby, P. K.**
See G. N. Bullock, 2415
- Staub, C.**
See P. Nielsen, 1475
- Steimer, Robert B.**
Non-Conservative Wave Interaction with Fixed Semi-Immersed Rectangular Structures, with Charles K. Sollitt, 2209
- Streif, Hansjorg**
A New Method for the Representation of Sedimentary Sequences in Coastal Regions, 1245
- Sunamura, Tsuguo**
Visible-Region Photographic Remote Sensing of Nearshore Waters, with Kiyoshi Horikawa, 1439
- Sundermann, Jurgen**
The Influence of Dune and Flow Parameters on the Friction Factor, with H. Vollmers and W. Puls, 1787
See Khawaja Zafar Elahi, 2708
- Suzuki, Takasuke**
See Masataro Hattori, 1688
- Suzuki, Yasumasa**
See Yoshimi Goda, 628
- Svendsen, I. A.**
Wave Characteristics in the Surf Zone, with P. A. Madsen and J. Bühr Hansen, 520
See D. H. Peregrine, 540
See P. Nielsen, 1475
- Swart, D. H.**
Vocoidal Theory for All Non-Breaking Waves, with C. C. Loubser, 467
- Sylvester, Richard**
Some Facts and Fancies about Beach Erosion, 1888
- Takahashi, Susumu**
See Isao Yakuwa, 2746
- Takayama, Tomotsuka**
See Yoshimi Goda, 628
- Tang, Frederick L.W.**
Wind-Induced Water Surface Set-Up and Drift Currents, with Jin Wu and Charles C.C. Chang, 841
- Thimakorn, P.**
See Akira Watanabe, 1918
- Thom, B. G.**
See Lynn Donelson Wright, 1180
- Thorn, Michael F.C.**
See Michael W. Owen, 1675
- Thornton, Edward B.**
Probability Density Functions of Breaking Waves, with George Schaeffer, 507
See R. T. Guza, 756
- Torum, Alf**
See Sverre Bjordal, 677
- Toyoshima, Osamu**
Effectiveness of Seadikes with Rough Slope, 2528
- Trapp, W.**
See S. R. Massel, 2340
- Tsuruya, Hiroichi**
See Hajime Kato, 742
- van de Kreeke, J.**
Tidal Hydraulics and Salt Balance of Lake Worth, Florida, with J. D. Wang, 2827
- van de Ree, W. J.**
A Tidal Survey for a Model of an Offshore Area, with J. Voogt and J. J. Leendertse, 2656
- van Doorn, Th.**
See W. T. Bakker, 1394
- van Os, A. G.**
See A. Roelfzema, 2810
- Vassie, J. M.**
See D. T. Pugh, 911
- Vellinga, P.**
Movable Bed Model Tests on Dune Erosion, 2020
- Verboom, G.**
See C. G. Graham, 97
- Vivacqua, Paulo Augusto**
Coastal Study of Espirito Santo Brazil, with Hildebrando de Araujo Goes Filho and Octavio de Sampaio Ferraz Jardim Sayao, 2104
- Vollmers, H.**
See Jurgen Sundermann, 1787
- Voogt, J.**
See W. J. van de Ree, 2656
- Wada, Akira**
Characteristics of Circulation in Bay Waters due to Wind Action, with Ioshihito Miyaike, 2730

Wang, H.

Loadings on Rubble-Mound Breakwaters due to Earthquakes, with C. Y. Yang and C. Lamison, 2244

Wang, J. D.

See J. van de Kreeke, 2827

Ward, Larry G.

Hydrodynamics and Sediment Transport in a Salt Marsh Tidal Channel, 1953

Warren, J. G.

See G. N. Bullock, 2415

Watanabe, Akira

Concentration of Suspended Clay in Periodic Flow, with P. Thimakorn and A. Das Gupta, 1918
See Hitoshi Nishimura, 2540

Webber, N. B.

See Peter Wright, 1705

Weide, J. V. D.

See J. C. W. Berkhoff, 2433

Weishar, Lee L.

Field Study of Breaking Wave Characteristics, with Robert J. Byrne, 487

Wells, John T.

Suspension and Transportation of Fluid Mud by Solitary-Like Waves, with James M. Coleman and W. J. Wiseman, Jr., 1932

Wenzel, Dieter

Morphologic Effects of Westerland Beach Nourishment 1972, 1859

Wigel, R. L.

See Hooshang Raissi, 609

Wilkinson, D. L.

Periodic Flows from Tidal Inlets, 1336

Wilkinson, R. H.

See A. G. Davies, 1577

Willetts, Brian B.

Using Fences to Create and Stabilise Sand Dunes, with Christopher J. Phillips, 2040

Willis, D. H.

Sediment Load under Waves and Currents, 1626

Wiseman, W. J., Jr.

Mixed Layer Models for Coastal Waters, with L. J. Rouse, Jr. and O. K. Huh, 2619
See John T. Wells, 1932

Wood, J. S.

See J. Khanna, 2481

Wright, Lynn Donelson

Morphodynamic Variability of High-Energy Beaches, with B. G. Thom and John Chappell, 1180
See John Chappell, 1359

Wright, Peter

Shingle Tracing by a New Technique, with J. S. Cross and N. B. Webber, 1705

Wu, Jin

See Frederick L. W. Tang, 841

Yakuwa, Isao

Behaviors of the Salt Wedge and the Salinity Distribution at Estuaries, with Susumu Takahashi and Morimasa Ohtani, 2746

Yalin, M. S.

On the Geometry of Ripples Due to Waves, with E. Karahan, 1776

Yang, C. Y.

See H. Wang, 2244

Yasuda, Hideichi

See Haruo Higuchi, 2646

Yoshida, Shizuo

See Masakazu Kashiwamura, 2925

Zeidler, Ryszard B.

See Zbigniew Pruszk, 1638
See Andrzej Lewandowski, 2051

Zwamborn, J. A.

Dolos Packing Density and Effect of Relative Block Density, 2285
See D. W. Standish-White, 2125

—

